Global COE Program

International Urban Earthquake Engineering Center

for Mitigating Seismic Mega Risk

10CUEE CONFERENCE PROCEEDINGS

10th International Conference on Urban Earthquake Engineering (10CUEE)

Center for Urban Earthquake Engineering

Tokyo Institute of Technology

Tokyo Tech

CUEE

Executive and Program Committee

Kohji Tokimatsu (Chair)
Hideki Kaji
Kazuhiko Kasai
Suzumu Kono
Ryota Matsui
Saburoh Midorikawa
Hitoshi Morikawa
Shojiro Motoyui
Junichiro Niwa
Tatsuo Ohmachi
Ryuzo Ohno
Toshihiro Osaragi
Hiroyasu Sakata
Eiichi Sasaki
Hiroko Suzuki
Akihiro Takahashi
Jiro Takemura
Toru Takeuchi
Akira Wada
Satoshi Yamada
Hiroaki Yamanaka

Global COE program entitled **"International Urban Earthquake Engineering Center for Mitigating Seismic Mega Risk"**

Center for Urban Earthquake Engineering (CUEE), Tokyo Institute of Technology
CUEE O-okayama Office TEL/FAX: +81-(0) 3-5734-3200
CUEE Suzukakedai Office TEL/FAX: +81-(0) 45-924-5576/5199
URL: http://www.cuee.titech.ac.jp

Preface

It is a signal pleasure to extend an invitation to our 10th International Conference on Urban Earthquake Engineering (10CUEE) being held again this year, 2013, here in Tokyo on March 1st and 2nd. The conference has been convened each March since 2004, under two consecutive five-year Center-of-Excellence programs headquartered at the **Center for Urban Earthquake Engineering (CUEE)** at Tokyo Tech. As is widely known, our current *Global-COE program (August 2008—March 2013)* is entitled "International Urban Earthquake Engineering Center for Mitigating Seismic Mega Risk".

Over the past decade we have aimed not only to promote research to mitigate the seismic "mega"-risk confronting vast present-day metropolises in earthquake-prone regions throughout the world, but also to produce next-generation practitioners and researchers responsible for developing new strategies and practices for seismic risk reduction. We have sponsored the conference each year in the interest of fostering and stimulating intensive information dissemination and technology transfer, while looking to promote and extend an international network that with your help has been directed to the formation of younger researchers through a sustained and now, we believe, truly global collaborative effort.

The Conference this year features state-of-the-art technical presentations on divers topics relevant to Urban Earthquake Engineering, followed by a significant choice of theme-based parallel sessions. Once again there will be a large number of papers related to lessons learned from the catastrophic damage and loss of life occasioned by the *2011 Great East Japan Earthquake and Tsunami* of just two years ago. Having commenced with 66 papers and only 15 overseas participants in March 2004, our Conference this year comprises more than 270 presentations, attracting some 450 participants with nearly 200 overseas guests. As in previous years, 10CUEE is slated this year to include *Special Educational Sessions* and *Best Presentation Awards for Young Researchers*. This year in 2013 about 130 papers are targeted for these Educational Sessions, which, I am convinced, have over the past ten years opened up a new career space for a number of younger researchers. To facilitate participation of this younger cohort, Travel Grants have been awarded once more in 2013 to some forty individuals for participation at 10CUEE.

As 2013 marks the final year of our second five-year program, 10CUEE will be the last conference held under the auspices of this particular Global-COE program. We look forward to continuing to host similar gatherings in future— but on this occasion we shall endeavor to summarize and set in perspective the legacy of our current five-year program, while looking with optimism toward possible ramifications of what has so far been accomplished. We remain confident that the March 2013 event will once again stimulate intensive information dissemination and technology transfer, as well as promote and uphold the now well-established and robust international network of our community. Our hope is that this conference will offer an excellent opportunity for all of us dedicated to Urban Earthquake Engineering to take stock of developments in our joint field.

Kohji Tokimatsu

Global-COE Program Leader and Director of CUEE Tokyo Tech

Table of contents

Paper ID Page

Keynote Lectures

01-377 Exposure Data Development for the Global Earthquake Model: Inventory Data Capture Tools 1
R.T. Eguchi, J. Bevington, Z. Hu and C. Huyck

20-385 Evaluation of Tsunami Force acted on Bridges by Great East Japan Earthquake 7
Kyuichi Maruyama, Yasushi Tanaka, Kenji Kosa, Akira Hosoda, Norimi Mizutani and Tomoaki Nakamura

G-COE Resumé

08-067 Retrofit of Damaged Structures according to Response Control Concept 17
Toru Takeuchi

17-049 Predicting Spatiotemporal Distribution of People for Risk Assessment and Disaster Management 25
Toshihiro Osaragi and Takuya Oki

20-502 Ground-Motion-Induced Damage of Bridges during the 2011 Great East Japan Earthquake..... 31
Kazuhiko Kawashima

Engineering Seismology

01-378 Estimation of Dynamic Behavior of Historical Church in Armenia using Microtremor Survey 41
H. Morikawa, S. Sasano, S. Motoyui, Y. Fujita and A. Mutoh

01-220 Shallow Structure of Taipei Basin Using Receiver Function Technique 47
Che-Min Lin, Kuo-Liang Wen, Tao-Ming Chang and Chun-Hsiang Kuo

01-317 Empirical Site Correction for Ground Motion Simulation 53
K. L. Wen, J. Y. Huang and C. T. Chen

01-363 Use of Airborne Optical and Thermal Imagery for the Detection of Building Damage due to the 2012 61
Tsukuba Tornado, Fumio Yamazaki, Daiki Hanada and Kentaro Suzuki

01-328 Aleatory and Epictemic Uncertainties of Ground-Motion Models. Results from Recent European Projects 69
Fabrice Cotton, Adrian Rodriguez, Ralph Archuleta, Elise Delavaud, Céline Beauval and Mathieu Causse

01-380 Estimation of Mega-Earthquakes Source Models for Strong Motion Prediction: Application for Central Andes 73
Nelson Pulido

Paper ID Page

01-404 Synthesis of Ground Motions of 1999 Taiwan MeiShan Earthquake by Empirical Green's Function Method 79
Huei-Tsyr Chen and Shang-Hong Wei

01-330 Finite Difference Simulation of Long-Period Ground Motion based on Various Source Models of the Anticipated Nankai Trough Megathrust Earthquake 87
Takahiro Maeda, Nobuyuki Morikawa, Shin Aoi and Hiroyuki Fujiwara

01-046 Fundamental Property of Cross Terms of Ground Transfer Function 93
Hiroyuki Goto

20-291 Comparison of ground motion attributes from 2011 Tohoku-Oki mainshock and two subsequent events 99
Tadahiro Kishida, Jonathan P. Stewart, Robert W. Graves, Saburoh Midorikawa, Hiroyuki Miura, Yousef Bozorgnia and Kenneth W. Campbell

01-193 Site Response during Strong Shaking - Estimated from the 2011 Tohoku Earthquake- 107
Kenichi Tsuda

01-231 Preliminary Analysis of Attenuation Relationship for Response Spectra on Bedrock based on Strong Motion Records Including the 2011 Mw9.0 Tohoku Earthquake 113
Hongjun Si, Saburoh Midorikawa, Hideaki Tsutsumi, Changjiang Wu, Toshiyuki Masatsuki, and Akemi Noda

01-360 High Intensity Records Observed in the 2011 Tohoku Earthquake 119
Saburoh Midorikawa, Tomohiro Atsumi, and Hiroyuki Miura

01-410 Strong Motion Pulses Observed during the 2011 Tohoku Earthquake and Their Modeling 125
Atsushi Nozu

20-198 Local Site Effects Observed in Shinagawa and Odawara, Japan, during the 2011 off the Pacific Coast of Tohoku Earthquake 135
Seiji Tsuno, Hiroaki Yamanaka, Saburoh Midorikawa, Hiroyuki Miura, Shin'ichi Sakai, Naoshi Hirata, Hiroe Miyake, Minoru Sakaue and Kazuki Koketsu

01-252 Exploration of Site Characteristics by Microtremor Observations in the Central Area of Thailand 139
N. Poovarodom, A. Jirasakjamroonsri and N. Plalinyot

01-464 Estimation of Deep Subsurface Structures for Prediction of Long-period Ground Motion Characteristics around the Tachikawa Fault 145
Koichiro Saguchi and Hiroaki Yamanaka

01-018 Analysis of HVSR of Microtremor on Different Seismic Site Conditions 151
Chun-Hsiang Kuo, Kuo-Liang Wen, Che-Min Lin, Jyun-Yan Huang and Tao-Ming Chang

01-476 Surface-wave Phase Velocity Inversion using Markov Chain Monte Carlo Method for Estimation of Local Site Amplification 159
Hiroaki Yamanaka

Paper ID Page

01-487 An Evaluation of Subsurface Structure with Inclined Bedrock Using Microtremor Array Exploration 165
Kentaro Motoki, Tetsushi Watanabe, Kenichi Kato, Kojiro Takesue, Hiroaki Yamanaka, Masanori Iiba and Shin Koyama

01-495 Simulation of H/V Spectral Ratios of Microtremors with Directional Dependency 171
Shinichi Matsushima, Florent De Martin, Takanori Hirokawa, Hiroshi Kawase and Francisco J. S Sánchez- Sesma

01-014 Deaggregation of New National Seismic Hazard Maps for Indonesia 175
Achmad Fauzi and Usama Juniansyah Fauzi

01-194 Estimation of Urban Growth Using Time-Series Landsat Satellite Images in Lima, Peru..... 179
Hiroyuki Miura, Saburoh Midorikawa and Masashi Matsuoka

01-362 Web-based Quick Estimation System of Strong Ground Motion Maps Using Observation Records and Engineering Geomorphologic Classification Map..... 187
Masashi Matsuoka, Naotaka Yamamoto and Kazue Wakamatsu

01-401 A Basic Study on the Rapid Prediction of Seismic Ground Motions Using P-waves Observed in Deep Boreholes 195
H. Miyakoshi, S. Tsuno, S. Yamamoto and N. Iwata

20-173 Impact Analysis of the Great East Japan Earthquake by Running Spectrum Analysis of the Newspaper 203
Muneyoshi Numada and Kimiro Meguro

01-384 The Impact of the 2011 Tohoku Tsunami Disaster and Implications to Tsunami-resilient Community 211
Shunichi Koshimura, Satomi Hayashi and Hideomi Gokon

01-051 Comparison of Several Common Transfer Functions for Site Effect Study in Taipei Basin..... 215
Jyun-Yan Huang, Luo-Liang Wen, Chun-Te Chen, Shuen-Chiang Chang and Hsien-Jen Chiang

01-070 A Site-Specific Seismological Model within a Bayesian Updating Framework 223
Alin Radu and Mircea Grigoriu

01-079 Analysis and Study of Site Effect in Kaohsiung and Pingtung area in Taiwan 231
Chiang Hsien-Jen and Wen Kuo-Liang

01-091 Application of Waveform Inversion to Actual Seismic Refraction Data for Retrieving Shallow 2D S-wave Velocity Profile 237
Amrouche Mohamed and Hiroaki Yamanaka

01-204 Reliability of Dispersion Measurement from Microtremors with Seismic Interferometry 241
Kosuke Chimoto and Hiroaki Yamanaka

01-295 Study for Seismic Microzoning in Damascus City, Syria, from Strong Motion Simulation Considering Local Site Amplification 245
Hussam Eldein Zaineh, Hiroaki Yamanaka and Yadab Prasad Dhakal

Paper ID Page

01-318 Improved Method of Data Analysis for the Gravity and Magnetic Exploration System..... 251
Satoshi Tokue, Yumiko Ogura, Hitoshi Morikawa, Shigeo Matsuda, Masayuki Saeki, Takuya Suzuki and Eri Ohzawa

01-364 Estimation of Ground Structure Using Gravity Survey Method around Furukawa, Japan, where was severely damaged by 2011 Tohoku Earthquake 257
Sakkrawit Sripunyaphikhup, Hitoshi Morikawa, Hiroyuki Goto, Masayuki Inatani, Yumiko Ogura, Satoshi Tokure, Xinrui Zhang, Shohei Hamasaki, Masahiro Iwasaki, Masayuki Araki and Sumio Sawada

01-366 The Significance of the Ratio of Power Spectra between Two Sites in the Wavefield of Microtremor..... 261
Xinrui Zhang and Hitoshi Morikawa

01-097 Using Stochastic Finite-Fault Method to Simulate Ground Motion from 2010 Jiashian, Taiwan, Earthquake 267
Fu-Ming Wu, Kuo-Liang Wen, Jyun-Yan Huang and Chun-Te Chen

01-126 Simulation of Stochastic Ground Motion with Site Correction Using Equivalent-Linear Method at Taipei Basin Downhole Arrays..... 273
Saifuddin, Kuo-Liang Wen, Jyun-Yan Huang and Hsien-Jen Chiang

01-188 Long-Period Ground Motion Simulations in the Kanto Basin using Diverse Velocity Models for the Hypothetical Tokai Earthquake..... 281
Yadab P. Dhakal and Hiroaki Yamanaka

01-236 Fundamental Research for Enhancement of Estimation on Earthquake Ground Motion-Development of a Method for Crustal Deformation Analysis Using High-Fidelity Three-Demensional Crustal Structure Model-..... 287
Ryoichiro Agata, Tsuyoshi Ichimura, Mamoru Hyodo, Takane Hori, Kazuro Hirahara and Muneo Hori

01-403 Stochastic Modeling of Bhuj (2001) Earthquake and Synthesis of Seismic Scenarios for the Surat Region, India..... 291
T.P.Thaker and K.S.Rao

Geotechnical Engineering

02-243 Simulation of Liquefaction-Induced Void Redistribution in a Centrifuge Test..... 301
R. W. Boulanger, R. Kamai and K. Ziotopoulou

02-405 Liquefaction Potential Evaluation: Energy-based Method versus Stress-based Method 307
Takaji Kokusho

02-546 Number of Equivalent Cyclic Shear and Effective Duration for Soil Liquefaction in Tokyo Bay Area during the 2011 Great East Japan Earthquake..... 317
Hiroshi Arai

Paper ID Page

02-162 Effect of Grain Size Distributions on Liquefaction Resistance for a Large Number of Loading Cycles 325
Jun Izawa and Yoshitaka Murono

02-234 Comparison between Damage Distribution and Estimated Liquefaction Potential in Chiba City 331
Toru Sekiguchi and Shoichi Nakai

02-359 Dynamic Behavior of a Structure on Desaturated Sand under RElatively Long Shaking..... 335
Jiro Takemura

02-213 Development of Soil Pressures under Lateral Loading 343
Anne Lemnitzer and Albert Luu

02-321 Dynamic Centrifuge Model Test of Building with Embedded Footing on Semi-Rigidly Connected Pile Heads in Liquefiable Soil 353
Sadayuki Ishizaki, Kohji Tokimatsu and Toshiaki Nagao

02-354 Use of Pre-Shaking for Soil-Pile System Identification in Centrifuge Shaking Table Tests ... 359
C. J. Lee, W. Y. Hung, C.H Tsai, T. Chen, Y. C. Tu and M.H. Hsieh

02-103 A Case Study on Multiple Mechanism Model in Three Dimensional Soil-Structure Interaction Analyses 365
Ryo Ueda and Ariyoshi Yamada

02-116 Long-Term Settlement of Holocene Clay Ground after the 2011 Great East Japan Earthquake 371
Naohiro Nigorikawa and Yoshiharu Asaka

02-038 Estimation of Bearing Capacity and Pull-out Resistance of a Pile with or without a Wing Plate in Alternately Cyclic Loading based on Centrifugal Model Tests 379
Hiroko Suzuki , Kei Inamura, Kohji Tokimatsu, Masatoshi Wada and Hideyuki Mano

02-027 Applicability of Equivalent Linear Seismic Response Analysis under Large Earthquakes 385
Nozomu Yoshida

02-322 Effect of Input Motion Characteristics on Seismic Deformation of a River Levee..... 393
Ryosuke Uzuoka, Jorge Shimabukuro and Masumitsu Kuse

02-406 Measurements of Translational and Rotational Dynamic Stiffness for a Model Levee on Peat 399
Edward T. Reinert, Scott J. Brandenberg and Jonathan P. Stewart

02-480 Confining Effect of Bearing Plate and Helix on Sliding Resistance of Reinforced Slope using Steel Pipe Piles 405
Akihiro Takahashi and Yohei Nakamichi

02-365 A Study on the Characteristics of the Ground Surface Deformation Induced by the Reverse Fault Slip 409
Y.Y, Chang, C.J, Lee , W.C, Huang , W.J, Huang and W.Y, Hung

02-207 Methodology for Combining Microtremor Measurements and Simplified Ground Response Analysis 415
Atsushi Mikami

Paper ID Page

02-339 Implicit Stress-Update Algorithm for the Constitutive Model to Describe Cyclic Behavior Based on Finite Deformation Theory 423
Tomohide Takeyama and Shinya Tachibana

02-289 Seismic Earth Pressure and Sidewall Friction acting on Embedded Pile Cap and Pile's Stress..... 429
Shuji Tamura and Takenori Hida

03-163 Evaluation of Collapse and Non-Collapse of Parallel Bridges Affected by Liquefaction and Lateral Spreading..... 439
Benjamin Turner, Scott Brandenberg and Jonathan Stewart

02-064 Numerical Evaluation of Failure Mechanisms of Pile Foundation in Liquefiable Soils 445
Mohammad Reza Salami, Katsuichiro Goda and Subhamoy Bhattacharya

20-415 Liquefaction Induced Ground Deformation Observed at Gohno-ike Pond in Kamisu City during 2011 Great East Japan Earthquake 455
S. Kanemitsu, Y. Tsukamoto and S. Kawabe

02-223 Effects of Drainage and Dewatering on Differential Settlement of Wooden Houses Founded on Liquefiable Soils..... 459
Yasutsugu Suzuki, Kohji Tokimatsu, Takahiko Hidekawa and Naohito Adachi

02-275 Numerical Modeling Issues in Predicting Post-Liquefaction Reconsolidation Strains and Settlements 469
Katerina Ziotopoulou and Ross W. Boulanger

02-340 Modeling of Earthquake Induced Uplift of Tunnels in Liquefiable Soil..... 477
Siau Chen Chian and Kohji Tokimatsu

02-284 Effects of Non-homogeneity on Liquefaction in Stratified Soil Deposits 483
Manika Maharjan and Akihiro Takahashi

02-333 Centrifuge Model Study on the Effect of Shield Tunneling on Adjacent Pile Foundation..... 493
Ittichai Boonsiri, Jiro Takemura and Sakae Seki

02-203 Stress Reduction Effect of Structure due to Basemat Uplift and Soil Yielding..... 499
Takafumi Inoue and Atsushi Mikami

02-117 Evaluating One Dimensional Site Response Analysis using Borehole Arrays..... 505
Georgios Zalachoris and Ellen M. Rathje

02-348 Evaluation of Local Sites Effects in Lima City, Peru from Ground Motion Data..... 515
Selene Quispe, Hiroaki Yamanaka, Hernando Tavera, Fernando Lazares and Zenon Aguilar

02-040 Centrifugal Modeling of Undercut Slopes Subjected to Pseudo-static Loading 523
Mohammad Hossein Khosravi, Jiro Takemura and Thirapong Pipatpongsa

02-118 Pullout Resistance of Geocell Placed as Reinforcement in Gravelly Soil Backfill..... 533
Xinye Han, Takashi Kiyota and Fumio Tatsuoka

02-337 Centrifuge Model Tests on Failure Pattern of Cement Treated Ground 539
Yuki Yoshida, Tomohide Takeyama and Masaki Kitazume

Paper ID Page

50-536 Experimental Investigation on Dewatering and Drainage Methods to Mitigate Liquefaction Damage to Existing Houses 543
Kohji Tokimatsu, Kazushi Tohyama, Hiroko Suzuki and Yasutsugu Suzuki

02-219 Basic Physical Model Test on Seismic Performance of Fill Induced by Suffusion 549
Kazuki Horikoshi, Lin Ke and Akihiro Takahashi

02-249 Criteria for Determining Gmax in Laboratory Element Tests Using Disk Type Piezoelectric Transducers 555
Muhammad Irfan and Taro Uchimura

02-120 Comparison between CPT and SDS Data for Soil Classification in Christchurch 561
Seyed Yasin Mirjafari Miandeh, Rolando P. Orense and Naoaki Suemasa

02-327 Effects of Internal Erosion on Cyclic Resistance of Gap-Graded Cohesionless Soil 567
Lin Ke and Akihiro Takahashi

Lifeline Systems

03-191 Relationships between Damage to Railway Structures and Seismic Intensity in the 2004 Niigata-ken Chuetsu Earthquake and the 2007 Niigata-ken Chuetsu-Oki Earthquake 573
Shuichi Taya and Saburoh Midorikawa

03-132 Experimental Investigation of the Stresses in a Tank Shell Resulting from Uplift during Earthquakes 579
Miguel Ormeno-Godoy, Tam Larkin and Nawawi Chouw

03-054 Evaluation of Gas Distribution Pipelines Network Subjected to Seismic Wave Propagation in Greater Tehran Area, Iran 585
Danesh Nourzadeh, Khosrow Bargi and Shiro Takada

Structural Engineering-Concrete

04-408 Collapse Vulnerability Assessment of Existing Concrete Buildings 591
K.J. Elwood, M. Baradaran Shoraka and T.Y. Yang

04-361 Low Ductility Concrete Wall Test considering Perpendicular Wall Action 599
Carlos Zavala, Patricia Gibu, Luis Lavado, Jenny Taira, Lourdes Cardenas and Luis Ceferino

04-368 CFD Analysis of Wind Pressure on the Complex High-Rising Structure 603
Qiong Xing and Jiang Qian

50-503 Dynamic Analysis of Existing Non-Conforming Concrete Gymnasia with Steel Roof 611
T. Ohmura and S. Hayashi

04-375 FRP-Retrofitted T-Beam-Wide-Column Joints Under Cyclic Loading 619
Kiang Hwee Tan and Aziz Ahmed

04-382 Seismic Performance of Reinforced Concrete Buildings Incorporating Soil-Structure Interaction 625
Wanchai Yodsudjai, Sarawoot Charoensuttikul and Piya Chotickat

Paper ID Page

04-224 Residual Structural Capacity of RC Superstructure of Open-type Wharf Damaged by Earthquake Motion 633
Mitsuyasu Iwanami, Yuichiro Kawabata, Ema Kato and Takahiro Nishida

04-379 Study on Bond Property of Corroded Reinforcing Bar Under Cyclic Loading..... 641
Tomohiro Miki and Takuya Shiomi

04-349 Mechanical Behavior and Strengthening Methods of RC Beams Damaged by Corrosion in Anchorage Part of Rebars..... 647
Koji Matsumoto, Makoto Mori and Junichiro Niwa

04-402 Strategy for Seismic Upgrading of Public Schools 657
Hsiao, F. P.; Hwang, S. J.; Chung, L. L.; Yeh, Y. K.; Jean, W. Y.; Shen, W. C.; Chiou, T. C.; Chow, T. K.; Yang, Y. S. and Chao, Y. F.

04-131 Substructure Pseudo-Dynamic Tests of Reinforce Concrete Frames with Soft-First-Story 661
Hideto Kanno, Naofumi Teramoto, Tetsuya Nishida and Jun Kobayashi

04-013 Earthquake-Resistant Design of Lightly-Reinforced and Low-Rise Concrete Walls..... 667
Julian Carrillo

04-334 Experimental Study on Cracking Strength of Confined Masonry Walls subjected to Shear Force 677
K. Nishimura, Y. Goto and S. Murai

04-324 Calculation of Load-Capacity of RC Beams by Lattice Model Arranged by Experiment Results 685
Yuki Nakata, Ken Watanabe, Tadatomo Watanabe and Junichi Abe

04-045 Three-Dimensional Nonlinear Beam-Truss Model for Non-Planar Reinforced Concrete Walls..... 689
Yuan Lu and Marios Panagiotou

04-048 Influence of Post-Tensioned Ropes on the Dynamic Response of Innovative Mortar-Free Interlocking Structures 699
Majid Ali and Nawawi Chouw

04-094 Shear Behavior of Polypropylene Fiber Reinforced ECC Beams with Reduction of Shear Reinforcements..... 709
Rui Zhang, Koji Matsumoto and Junichiro Niwa

04-096 Shear Behavior of Steel and Synthetic Fiber Reinforced Concrete Beams 717
Pitcha Jongvivatsakul, Koji Matsumoto and Junichiro Niwa

04-119 Behavior of Prestressed Concrete Beams Having Ruptured Strands Strengthened in Flexure by Externally Bonded CFRP Sheets..... 725
Thi Thu Dung Nguyen, Koji Matsumoto, Yuji Sato, Asami Iwasaki and Junichiro Niwa

04-142 Evaluation of Shear Capacity of RC Beams using UFC Permanent Formwork with Different Shear Span to Effective Depth Ratio 731
Puvanai Wirojjanapirom, Koji Matsumoto, Katsuya Kono and Junichiro Niwa

Paper ID Page

04-154 Bond Strength and Bond-Slip Behavior of Steel Reinforcement in High-Performance Fiber-Reinforced Cementitious Composites 737
Matthew J. Bandelt and Sarah L. Billington

04-182 Large-Scale Testing and Analysis of Concrete-Encased Steel Coupling Beams Under Large Ductility Demands 743
Christopher J. Motter, John W. Wallace, David C. Fields, John D. Hooper and Ron Klemencic

04-237 Behavior of Reinforced Concrete Flab Slabs Systems Under Corner and Center Support Failure Scenarios 753
S. Prasad and T. C. Hutchinson

04-281 Seismic Performance and Modeling of Post-Tensioned, Precast Concrete Shear Walls 761
Ahmet Can Tanyeri, Jack P. Moehle and Takuya Nagae

12-033 Effect of Electro-Welded Wire Mesh on the Seismic Vulnerability of Thin RC Shear Walls in Lima, Peru 769
Luis G. Quiroz and Yoshihisa Maruyama

04-505 Shaking Table Test of a Large-scale Self-centering Reinforced Concrete Frame 775
Xilin Lu, Ye Cui, Jingjing Liu, Ying Zhou and Wensheng Lu

04-114 Experimental Investigation of Large Reinforced Concrete Special Moment Resisting Frame Beams 781
Tea Visnjic, Marios Panagiotou, Jack Moehle and Grigoris Antonellis

04-125 Nonlinear Response Assessment and Seismic Retrofit of Reinforced Concrete Buildings..... 791
Jason P. Palacio, Alem J. Pablo, Eric A. Tingatinga and William Mata

04-165 Experimental Evaluation of Out-of-Plane Wall-to-Beam Connections under Cyclic Loading 799
Saman Abdullah, David Naish and Nagi Abo-Shadi

04-228 Seismic Vulnerability Assessment Method of Low-Rise RC Buildings with Masonry Infill Walls 807
Hamood Alwashali and Masaki Maeda

04-233 Process of Collapse for RC Frame Including Shear Column 817
Kazuto Matsukawa, Xiu Liu and Masaki Maeda

04-240 Experimental Study on Reinforced Concrete Frames with Buckling Restrained Braces 825
Yusuke Maida, Zhe Qu, Shoichi Kishiki, Toshio Maegawa, Makoto Hamada, Hiroyasu Sakata and Akira Wada

04-302 Experimental Study on Influence of Bending Radius of Main Tensile Bars on Stress Transmission in Reinforced Cncrete Knee Joints with Prectical Detail 831
Tuvshin Batjarga and Hisato Hotta

10-299 A Study on Structural Performance of CES Shear Walls with Eccentrically Arranged Wall Panel 837
Suguru Suzuki, Hiroshi Kuramoto and Tomoya Matsui

Paper ID Page

04-176 Nonlinear Finite Element Analysis of Reinforced Concrete Structure Considering Multiple Cracking Failure 843
Fangtao Sun, Seizo Tanaka, Muneo Hori, Tsuyoshi Ichimura and Maddegedara Lalith

04-134 Assessment of Seismic Collapse Safety of Reinforced Concrete Frame Buildings Designed by Two Generations of Chinese Seismic Provisions 849
Wenwen Luo, Yingmin Li, Zhe Qu, Hiroyasu Sakata, Heping Zhong and Jun Han

04-197 Effect of Soil-Flexibility on Nonlinear Response of High-Rise Buildings during Collisions Under the El-Centro Earthquake 857
Ayman Abdelhamed and Sayed Mahmoud

Structural Engineering-Steel

05-543 Elastic Local Buckling Strength of Rectangular Hollow Section Column under Biaxial Bending Share 863
Kikuo Ikarashi , Kosuke Sato and Tao Wang

05-130 Method of Small-scale Shaking Table Test overcoming the Scaling Effect 869
Yuko Shimada, Kenta Takahashi and Satoshi Yamada

05-326 Numerical Analysis on Plastic Deformation Capacity of Steel Beam under Verious Loading Histories 875
Satoshi Yamada, Yu Jiao and Shoichi Kishiki

05-298 Effects of Core Plates Local Buckling for Cumulative Deformation Capacity of Buckling Restrained Braces 881
Ryota Matsui and Toru Takeuchi

05-107 Predictive Equations for Modeling Cyclic Buckling and Fracture of Steel Braces 889
Dimitrios Lignos and Emre Karamanci

05-400 Improvement in SSWS Design and Study on the Performance of Steel Frame-SSWS System 899
Yiyi Chen and Ke Ke

05-300 Experimental Study on Buckling-Restrained Steel Plate Shear Walls with Different Aspect Ratios 905
Y. Lu; G.Q. Li; H.J. Jin ; X.L. Liu and F.F. Sun

04-352 Static Test and Numerical Analysis of Composite Concrete Steel-Plate Shear Walls with Binding Bars 915
Deyuan Zhou, Limeng Zhu and Ying Zhou

05-099 Behavior of Steel Tube-Double Steel Plate-Concrete Composite Walls Subjected to Axial Force and Cyclic Loading 923
X. Ji, F. Jiang and J. Qian

Paper ID Page

05-345 Vibration Tests on Single Layer Lattice Domes Subjected to Horizontal Bi-directional Earthquake Motions 933
Tomohiko Kumagai, Takunori Ozawa, Toru Takeuchi and Toshiyuki Ogawa

05-484 Damage Detection for Steel Structures Using the Hilbert-Huang Transform Approach 939
Wen-Ko Hsu and Dung-Jiang Chiou

05-189 Member Damages of High-Rise Building Structures under Severe Earthquakes: Effect of Member Deterioration 945
Yongtao Bai, Akihiko Kawano and Shitaro Matsuo

05-108 Study on Column Behavior in a Full-Scale Steel Building Subjected to Strong Ground Motions on Shaking Table 953
Tran Tuan Nam and Kazuhiko Kasai

05-024 Cyclic Loading Test on RHS Columns under Bi-Directional Horizontal Forces 959
Takanori Ishida, Yuko Shimada and Satoshi Yamada

05-031 Test on Eccentric Beam-to-RHS Column Conecctions 967
Norihito Miki, Yu Jiao, Satoshi Yamada, Shoichi Kishiki and Takashi Hasegawa

05-342 Evaluation of the Composite Beam Stress Subjected to Bending and Axial Force 973
Yoriyuki Matsuda and Kazuhiko Kasai

05-102 Effect of Column Base Behavior on Seismic Performance of Multi-Story Steel Moment Resisting Frames 979
Yao Cui and Satoshi Yamada

05-008 Evaluation of the Response Modification Coefficient Including Collapse Assessment of SCBFs 985
Po-Chien Hsiao, Dawn E. Lehman and Charles W. Roeder

05-092 Seismic Test and Design of Buckling-Restrained Brace Connections Tenth International Conference on Urban Earthquake Engineering 995
Pao-Chun Lin, Keh-Chyuan Tsai, An-Chien Wu and Ming-Chieh Chuang

05-175 Cyclic Loading Tests of Single Angle Brace Focusing on Out-of-plane Stiffness of Gusset Plate 1005
Hayato Asada and Tsuyoshi Tanaka

05-209 Cyclic Loading Tests of Steel Slit-dampers with Various Shapes 1011
Yu Jiao, Yukako Katsuyama and Mamoru Kohno

Structural Engineering-Bridge

06-483 3-D Dynamic Analysis of Bridges in Ultimate States under Earthquakes 1017
Tzu-Ying Lee, Kun-Jun Chung and Yi-Wen Chen

06-288 Fiber Model Analyses of Steel Bridge Circular Columns Considering Local Buckling 1023
Koji Kinoshita

06-465 Development of an Anomalies Detection Method Based on Nonlinearity Expression 1029
Eiichi Sasaki and Nguyen Khac Thanh

Paper ID Page

06-179 Investigation of the Effects of Model Complexity on the Predicted Seismic Response of Bridge Pile Foundations 1033
Omrani R, Mobasher B, Zareian F and Taciroglu E

06-157 Analytical Investigation on the Effect of Number of Vehicles on the Seismic Response of a Horizontally Curved Bridge Model 1041
Hartanto Wibowo, Danielle M. Sanford, Ian G. Buckle and David H. Sanders

06-148 Investigation of the Resistance of Older Steel Bridge Bearings under Bidirectional Seismic Loading 1049
Xiaohu Fan and Jason McCormick

03-285 Precast Concrete Bridge Columns Made with Unbonded Pre-Tensioning and Hybrid Fiber Reinforced Concrete for Improved Seismic Resistance 1059
O.S. Haraldsson, G. Finnsson, P.M. Davis, M.O. Eberhard and J.F. Stanton

Structural Engineering-Timber

07-021 Performance-Based Seismic Retrofit of Soft-Story Light-Frame Wood Buildings 1067
John W. van de Lindt, Pouria Bahmani, Mikhail Gershfeld, Xiaoyun Shao, Weichiang Pang, Michael D. Symans and Gary Mochizuki

07-343 Performance-Based Seismic Design for Wood Houses using Equivalent Linearization Method 1073
Hiroshi Isoda and Shu Nagaoka

07-164 Collapsing Analysis of Shake Table Tests of Three Story Post-and-Beam Wood Houses 1081
Takafumi Nakagawa, Tatsuya Miyake, Hiroshi Isoda, Naohito Kawai and Takahiro Tsuchimoto

07-218 Ultimate Earthquake Resistance of Torsionally Coupled Structure Having Ductile Timber Shear Walls 1091
Yoshihiro Yamazaki, Hiroyasu Sakata and Kazuhiko Kasai

07-357 Seismic Response Analysis of Wooden Structure with Passive Control System Using Simplified Spring Model 1099
Kazuhiro Matsuda, Kazuhiko Kasai and Hiroyasu Sakata

07-323 Flexural Performance of Japanese Traditional Mortise - Tenon Joint with Split Wedge 1105
Hiroyasu Sakata, Yoshihiro Yamazaki, Takuya Noguchi and Yoshimitsu Ohashi

07-093 New Damage Avoidance Connection for Multi-Story Timber-Steel Hybrid Moment Frame Buildings 1115
Mamoon Jamil, Pierre Quenneville and Charles Clifton

07-251 Basic Study on Torsional Behaviour of Two-Story Timber Houses with Eccentricity 1121
Kento Suzuki, Hiroyasu Sakata and Yoshihiro Yamazaki

07-185 Experimental Study on Timber Framed Masonry Structures 1127
Andreea Dutu, Hiroyasu Sakata and Yoshihiro Yamazaki

Paper ID Page

Structural Engineering-Other

21-145 Post-Earthquake Investigation and Seismic Evaluation of a Damaged RC Building in Van, Turkey 1137
Viorel Popa, Radu Vacareanu and Faruk Karadogan

07-413 Performance of Sandwich Columns under Eccentric Cyclic Load 1147
H.-L. Hsu and C.-Y. Zhan

07-161 Urban Seismic Response Sensitivity of Adjacent Buildings 1153
H. B. Mason, W. S. White and M. H. Scott

07-222 Damage Assessment of Buildings. Case Study of an Educational Building 1159
Claudiu-Sorin Dragomi

07-056 Damping Characteristics of Steel Plate Concrete Wall Based on the Cyclic Load Test 1167
Sung Gook Cho, Dookie Kim, Gihwan So and Woong Ki Park

07-057 Lateral Force Resistance Characteristics of Steel Plate Concrete Wall Based on the Push-over Test 1175
Sung Gook Cho, Dookie Kim, Woong Ki Park and Gihwan So

07-113 Effect of RC Tie-Columns on Confined Brick Panels Subjected to In-Plane Alterned Loading 1181
A. Bourzam, T. Ikemoto, M. Miyajima and S. Fukada

21-006 Shear Design of Structural Walls 1187
JW Wallace, C. Segura and T. Tran

04-168 Static Loading Test of RC Shear Walls with Multi-Openings Failing in Flexural Mode 1195
Masato Sakurai, Hiroshi Kuramoto and Tomoya Matsui

07-065 Residual Seismic Performance of Scaled Three-Story Steel Frames Tested on a Shaking Table Using the Substitute Damping Model 1203
Miguel Diaz Figueroa, Koichi Kusunoki and Akira Tasai

07-166 Investigation of Dynamic Stability on Effect of Restoration for Aged Castle Masonry Wall 1211
Yasutaka Noma, Tsuyoshi Nishimura, Hiroyuki Yamamoto, Hiroyoshi Kasa, Tatsuaki Nishigata and Kazuhiko Nishida

07-187 Seismic Behavior of Ottoman Empire Classical Period Stone Masonry Walls 1217
Cem Demir, Emre Dogu, Medine Ispir and Alper Ilki

07-200 Stress Strain Characteristics of Polypropylene band (PP-band) and Fiber Reinforced Polymer (FRP) Composite Retrofitted Masonry Wall Systems 1225
Saleem Muhammad Umair, Muneyoshi Numada and Kimiro Meguro

07-202 An Experimental Study of Nonlinear Short-Period Structures with Uplift under Near-Fault Pulse Motions 1231
Yuanzhi Chen, Tam Larkin and Nawawi Chouw

07-270 Controlled Soft Story Mechanism as a Seismic Protection System 1239
Hossein Agha Beigi, Timothy Sullivan, Constantin Christopoulos and Gian Michele Calvi

Paper ID Page

07-303 Two Directional Seismic Response Evaluation of Buildings Which Do Not Have Well-regulated Plane Shapes 1247
Yoshina Takahashi and Hisato Hotta

07-332 3-Dimensional FEM Analysis of Shield Tunnel and its Application on Rebound Estimation 1253
Yang Shen, Kiwamu Tsuno, Takashi Nakayama and Sohichi Hirose

Advanced Technologies

08-341 Cyclic Testing of Aluminum Alloy Core Buckling Restrained Braces (BRBs) 1259
Cigdem Karatas and Oguz Cem Celik

08-267 Sensitivity Analyses of Variations on Seismic Response via Viscous Damper Placement in Planar Building Structures 1269
Ersin Aydin, Baki Ozturk and Deniz Guney

11-012 Generalized Optimal Locations of Viscous Dampers in Two-Way Asymmetrical Buildings 1279
Jui-Liang Lin, Manh-Tien Bui and Keh-Chyuan Tsai

04-351 Use of Three Kinds of Dampers for a Steel Tall Building Shaken by 2011 East Japan Earthquake--China-Japan Cooperation Program (Part 1) 1287
Xilin Lu, Kazuhiko Kasai, Ying Zhou, Dagen Weng, Kun Ding, Shunming Gong, Yue Jiang and Tetsuo Yamashita

08-506 Effective Retrofit Using Dampers for a Steel Tall Building Shaken by 2011 East Japan Earthquake -- China-Japan Cooperation Program (Part 2) 1295
Kazuhiko Kasai, Xilin Lu, Wuchuan Pu, Tetsuo Yamashita and Yousuke Arakawa and Ying Zhou

08-369 Blind Simulation of Full Scale Free Vibration Tests on a Three Story Base Isolated Building 1303
Giuseppe Oliveto, Anastasia Athanasiou and Mario Granata

08-112 Pounding in Three Dimensional Base Isolated Buildings 1317
Armin Masroor and Gilberto Mosqueda

08-153 Selection of Appropriate Viscous Damping Model for Nonlinear Time-History Analysis of Base-Isolated Reinforced Concrete Buildings 1325
Deepak R. Pant and Anil C. Wijeyewickrema

08-274 Simulation and Sensitivity of the Critical Load Behavior of Elastomeric Seismic Isolation Bearings 1333
Gordon P. Warn and Xing Han

08-152 Design for Uniform Risk to Standardized Nuclear Power Plants Using Seismic Isolation 1339
Troy A. Morgan and Brian M. McDonald

08-180 Identification of Mass Eccentricities from Seismic Response of Three Dimensional Buildings 1343
Roshanak Omrani, Ralph E. Hudson and Ertugrul Taciroglu

Paper ID Page
08-090 The Behavior of RC Rocking Wall-Frame Buildings under Pulse-Like Ground Motions 1349
H.A.D. Samith Buddika and Anil C. Wijeyewickrema
08-050 Modal Identification of Output-only Structures under Ambient Vibration 1357
Weixing Shi, Xi Chen and Jin Wang
05-347 Active Vibration Control Tests of Arch Structures Using Acceleration Feedback 1365
Ken'ichi Minowa, Tomohiko Kumagai and Toshiyuki Ogawa
08-205 Seismic Response and Performance of Fixed Base and Base Isolated Structures Considering Continued Functionality Damage State 1373
Sarun Chimamphant and Kazuhiko Kasai
08-069 An Inerter Vibration Isolation System for the Control of Seismically Excited Structures 1381
Irina F. Lazar, David J. Wagg and Simon A. Neild
08-151 Seismic Pounding of Base-Isolated Buildings under Bidirectional Excitation 1389
Deepak R. Pant and Anil C. Wijeyewickrema
08-294 Real-time Hybrid Testing of a Smart Base Isolation System Employing a Magnetorheological Damper 1399
Pei-Ching Chen, Keh-Chyuan Tsai and Pei-Yang Lin
08-241 Study on Implementation of Remote Building Damage Assessment System during Large Scale Earthquake Disaster 1409
Makoto Fujiu, Miho Ohara and Kimiro Meguro
08-214 A Preliminary Study on the Identification of Seismic Isolation Systems from Earthquake Records 1415
Anastasia Athanasiou, Giuseppe Oliveto, Mineo Takayama and Keiko Morita
05-025 Experimental Study on U-Shaped Steel Dampers under 2D Random Loading Histories 1425
Diana Ene, Yu Jiao, Shoichi Kishiki, Satoshi Yamada, Yoshinao Konishi, Norihisa Kawamura and Masao Terashima
08-255 Influence of Unbonding Material on Low-cycle Fatigue Perfomance of Buckling-Restrained Braces 1431
Chun-Lin Wang, Quan Chen, Tao Li and Shao-Ping Meng
08-257 A New Restraining System for Buckling-Restrained Braces 1437
Quan Chen, Tao Li, Chun-Lin Wang and Shao-Ping Meng
08-258 Behaviour and Design of an All-Steel Self-Centering Buckling-Restrained Brace 1443
Peng Zeng, Quan Chen, Chun-Lin Wang, Tsutomu Usami and Shao-Ping Meng
08-397 Development of Ring-Shaped Steel Plate Shear Walls that Resist Buckling for Improved Seismic Performance 1449
Matthew R. Eatherton, Natalia Egorova and Abhilasha Maurya
08-160 Seismic Response of Recentering Precast Composite Concrete-Dual-Shell-Steel Columns 1457
Gabriele Guerrini and Jose' I. Restrepo
08-171 Seismic Response of a Rocking, Post-Tensioned HyFRC Bridge Column 1465
William Trono, Gabriel Jen, Claudia Ostertag and Marios Panagiotou

Paper ID Page

08-263 Hybrid Testing of a Four-Span Curved Bridge 1475
Chia-Ming Chang, Thomas M. Frankie, Pedro F. Silva, David H. Sanders, Daniel A. Kuchma, and Billie F. Spencer, Jr.

Non-Structural Components and Contents

09-023 Numerical Seismic Fragility of Fire Sprinkler Piping Systems with Threaded Joints 1485
Siavash Soroushian, Manos Maragakis, Arash E. Zaghi, Alicia Echevarria, Yuan Tian and Andre Filiatrault

09-412 Ceiling Systems Design and Installation Lessons from the Canterbury Earthquakes 1495
Rajesh P Dhakal and Gregory MacRae

50-580 The Behavior of Ceiling with Steel Furring during Earthquakes 1505
Shojiro Motoyui and Yasuaki Satoh

09-020 Seismic Capacity Improvement of Lightweight-Mortar Infilled Stud Wall Systems 1513
George C. Yao, Wei-Chung Chen and Yi-Chiao Chen

09-184 Fundamental Study on Simple Evaluation Method for Seismic Resistance of Wall and Fixed Furniture 1521
Yutaka Yokoyama, Takeshi Yokoi and Yuki Kawamura

50-593 Behavior on Building Equipments under Seismic Excitations 1529
Kunio Mizutani, Haeyoung Kim, Takuya Nakai, Yasushi Kurokawa and Takao Kawashima

New Design Criteria and Methods

10-373 Influence of Ground Motion Spectral Shape and Duration on Seismic Collapse Risk 1533
Reagan Chandramohan, Ting Lin, Jack W. Baker and Gregory G. Deierlein

10-009 Low Damage Construction - Some Systems Issues 1541
Gregory MacRae

10-063 Seismic Retrofitting Design Method of Existing RC Buildings with Buckling Restrained Braces 1545
Fatih Sutcu, Toru Takeuchi and Ryota Matsui

10-084 Determination of Ground Surface Deformation Type Based on Field Data 1551
Naser Amirhesari and Kazuo Tani

04-350 Study on the Intensity Measure of Incremental Dynamic Analysis Considering High-Modes Effect for Tall Buildings 1561
Ying Zhou, Ningfen Su and Xilin Lu

10-297 Rocking Foundations with Different Shapes on Different Soils 1567
Manouchehr Hakhamaneshi, Bruce L. Kutter, Shuji Tamura, Andreas G. Gavras, Weian Liu and Lijun Deng

10-135 Estimation of the Maximum Response of Base Isolated Structures 1575
Parisara Thiravechyan and Kazuhiko Kasai

Paper ID Page

Earthquake Engineering Practice

11-286 Observed and Predicted Performance of Reinforced Concrete Buildings in the Canterbury Earthquake Sequence 1581
Dan Bech, Bill Tremayne,Lisa Oliver and Jenny Fisher

11-170 Global Experience: Seismic Risk Reduction and Disaster Reconstruction Programs 1589
H Kit Miyamoto and Amir SJ Gilani

11-053 Regional Predictions of Earthquake-Induced Landslides: A Study of the Niigata-ken Chuetsu Earthquake 1595
Yubing Wang and Ellen M. Rathje

Earthquake Loss Estimation

10-230 Seismic Safety and United States Design Practice for Steel-Concrete Composite Frame Structures 1603
Mark D. Denavit, Jerome F. Hajjar, Tiziano Perea and Roberto T. Leon

12-307 Evaluation of Seismic Vulnerable Areas in Lima City by Using Satellite Information 1613
Miguel Estrada, Masashi Matsuoka and Hiroyuki Miura

12-081 Development of Heuristic Seismic Vulnerability Curves of Key Building Types in the Philippines 1617
E.A. Tingatinga, B. Pacheco, J. Hernandez, U. Ignacio, F. Germar, R.E. Longalong, W. Mata, M.C. Pascua, R. Suiza and L.R. Tan

12-310 Transparent Global Earthquake Risk and Loss Estimation 1623
Nicole Keller and H. Kit Miyamoto, Ph.D

12-174 Methodology for Life Cycle Cost Assessment of Self-Centering Concentrically Braced Frame Systems 1629
David A. Roke, Akhilesh Chandra, Qindan Huang and Kallol Sett

12-066 Fragility Curves for Reinforced Concrete Buildings to Earthquake-Induced Slope Displacements 1635
Stavroula D. Fotopoulou and Kyriazis D. Pitilakis

12-129 Development of Fragility Curves of Mid-Rise Reinforced Concrete Moment-Resisting Frame Structures in the Greater Metro Manila Area, Philippines 1645
Raniel Suiza, Benito Pacheco, Jaime Hernandez, Jr., Eric A. Tingatinga, Liezl R. Tan, Marie C. Pascua, Romeo E. Longalong, William Mata, Ulpiano Ignacio, Jr., Fernando Germar and Mark A. Zarco

12-278 Earthquake Risk Analysis Method Applied to a Town in Hungary 1651
Orsolya Kegyes-Brassai and Richard P. Ray

12-141 Development of a Rapid Condition Assessment Tool for Reinforced Concrete Moment Frame Building in the Philippines 1657
Liezl Raissa E. Tan and Jaime Hernandez Jr.

Paper ID Page

Information and Computing Technology

14-034 Damping Performance Analysis and Verification of Heavy-Loading Hydraulic Damper..... 1667
Jing-Long Tong and Kuang-Yuh Huang

14-338 Transformation and Integration of Building Information Model Data for Vulnerability Assessment and Disaster Mitigation..... 1675
Chia-Ying Lin and Chien-Cheng Chou

14-106 Development of Simulation System for Estimation of Urban Earthquake Disasters Considering Local Soil Properties Using High Performance Computing 1681
Kohei Fujita, Tsuyoshi Ichimura, Muneo Hori, M. L. L. Wijerathne and Seizo Tanaka

14-346 2-D Wave Analyses for Fluid-Saturated Porous Solids Using Convolution Quadrature Boundary Element Method..... 1685
Akira Furukawa, Fumika Chikazawa, Takahiro Saitoh and Sohichi Hirose

Response Records

19-388 Building Monitoring Earthquake Response Network in Lima 1691
Patricia Gibu, Carlos Zavala, Luis Lavado, Ricardo Proaño and Lucio Estacio

19-186 Bridge and Adjacent Downhole Array Responses during Earthquakes at Eureka, California..... 1695
Ning Wang and Ahmed Elgamal

19-206 System Identification, Structural Health Monitoring and Damage Detection of a Steel Reinforced Concrete Structure of Urban Disaster Prevention Research Center in Tsukuba, Japan 1703
Goran Jekikj, Koichi Morita and Mihail Garevski

19-215 Seismic Response of an RC Building Strengthened with Pin-supported Walls during the 2011 Tohoku Earthquake 1713
Zhe Qu, Hiroyasu Sakata, Saburoh Midorikawa and Akira Wada

19-181 Study on the Rocking Effect of an Eight-story SRC Building 1721
Ligang Li, Toshihide Kashima, Akihiro Nakamura and Masaomi Teshigawara

Socio-Economic Issues

16-072 On Development of Seismic Resistant Design for Structural Steel Building in Indonesia 1731
Muslinang Moestopo

16-331 Telecommunication at the Time of Earthquake 1735
Takanobu Ito

16-123 Confirmation of Building Safety for Regional Contribution Activities of Companies in a Time of the Tokyo Inland Earthquake 1741
Hiroaki Maruya

14-376 Building a Decision and an Operations Support System using the Agent-Based Simulation Model..... 1749
Kenichi Ishibashi and Shinichi Tsuburaya

Paper ID Page

16-122 Disaster and Economic Structural Change: An Empirical Analysis using Input-Output Framework 1753
Yasuhide Okuyama

20-320 Verification of the National Reconstruction Agency as an Institutional Scheme for Reconstruction after Large-scale Disasters 1759
Hideki Kaji

16-086 Effects of Electric Power Failure on the Level-of-service of the Railway Transport in Tokyo Metropolitan Area 1765
Ryosuke Fujita, Daisuke Fukuda and Hideki Yaginuma

16-196 Analysis on Urban Land Use Control Systems in Tsunami Affected Areas by the 2011 Great East Japan Earthquake 1771
Shoichi Ando

16-358 Evacuation Situation of Futaba District Residents following the Fukushima Nuclear Accident 1779
Keiichi Sato

16-386 Development & Application of 'Ichi-Nichi-Mae Project' for Disaster Awareness; 'If We were Back the Day before the Disaster, How can We better Prepare?' 1785
Satoru Nishikawa, Tomohisa Sashida, Mikiko Ikegami, Hajime Kagiya, Noriko Suzuki and Kazuyuki Nakagawa

16-247 Seismic Vulnerability Evaluation of Non-Engineered Structures in Pakstan --A Statistical Approach Based on Cumulative Opinion of Professionals-- 1795
Zaheer Abbas Kazmi, Muhammad Irfan and Tauqir Ahmed

Human Behavior

16-029 The Use of Geospatial Technologies and Local Area Spatial Analysis to Understand Sub-Neighborhood Scale Impediments to Recovery after a Catastrophic Disaster 1803
Andrew Curtis

17-245 On the Enhancements of Agents' Navigation Skills of a Multi Agent Systems Based Mass Evacuation Analysis 1809
Maddegedara Lalith, Leoneland, A. Melgar and Muneo Hori

20-398 Foreigners' Experience and Behavior in the Great East Japan Disasters 2011 1817
Dr. Md. Faiz Shah and Dr. Osamu Murao

17-292 Patterns of Awareness of Crisis, Real Time Decision-Making and Action for Survival 1825
Fujii Haruyuki and Inoue Rimi

17-336 Method to Measure Circulation Space Using an Autocad Application 1829
Xue Ma and Ryuzo Ohno

17-238 Behavior Analysis of Stranded Person Using Mobile GPS Data 1835
Masashi Shiina, Makoto Fujiu and Kazuyuki Takada

Paper ID Page

17-454 Evacuation Behavior Model Considering Various Attributes of Residents and Transient Occupants 1839
Takuya Oki and Toshihiro Osaragi

17-239 Evaluation of Car Evacuation Method against Tsunami Using Micro Simulation..... 1847
Kohei Onomura, Makoto Fujiu and Kazuyuki Takada

17-335 Spatial Characteristics Transformation of Self-built and Donated Post Disaster Housing..... 1851
Rachma Marcillia Syam and Ryuzo Ohno

Tsunami

01-290 Evaluation of Building Damage Ratio in Asahi City, Chiba Prefecture after the 2011 off the Pacific Coast of Tohoku Earthquake and Tsunami 1859
Yoshihisa Maruyama, Ken Kitamura and Fumio Yamazaki

20-035 Building Damage Characteristics Based on Surveyed Data and Fragility Curves of the 2011 Great East Japan Tsunami..... 1865
Anawat Suppasri, Erick Mas, Ingrid Charvet, Rashmin Gunasekera, Kentaro Imai, Yo Fukutani, Yoshi Abe and Fumihiko Imamura

18-140 Evaluation of Tsunami Load Based on Damage Observations after Great East Japan Earthquake..... 1871
Akihiko Obata, Tetsuya Nishida, Naofumi Teramoto, Hideto Kanno and Jun Kobayashi

18-030 Punching Failure of Kamaishi Breakwater Caisson Foundation during the 2011 Great East Japan Tsunami 1875
Jeremy D. Bricker, Hiroshi Takagi and Jun MItsui

20-381 Probing on the Mechanism of the 2011 Great East Japan Earthquake and Tsunami..... 1883
Zhang Jiagui

18-311 Development of Tsunami Structural Design Provisions for the USA 1889
G. Chock

18-246 Dynamic and Static Approaches in Description of Tsunami Generation..... 1899
Kolesov S.V. and Nosov M.A.

18-044 Physical basis for specification of numerical grid in tsunami simulation 1903
M.A. Nosov

18-195 Simulation of Three Dimensional Tsunami Inundation into the Inside of a Building..... 1909
Shusaku Inoue and Yasunori Mizushima

18-208 Development of a Failure Analysis Method of Structure due to Tsunami Impact..... 1913
S. Tanaka, F. Sun, M. Hori, T. Ichimura and M. L. L. Wijerathne

18-133 Feasibility of Evacuation at the Pakarang Cape in Thailand Based on Tsunami Inundation Model and Human Evacuation Simulation..... 1917
Erick Mas, Anawat Suppasri, Patchanok Srivihok, Shunichi Koshimura and Fumihiko Imamura

Paper ID Page

18-177 Tsunami Inundation Mapping Using Remote Sensing Analysis and Numerical Modeling in Lima, Peru 1923
Bruno Adriano, Erick Mas, Shunichi Koshimura, Yushiro Fujii, Sheila Yauri, Cesar Jimenez and Hideaki Yanagisawa

18-190 A Study on Dynamic Response of Rein-Forced Building by Fluid-Structure Interaction Analysis 1929
Yasunori Mizushima and Shusaku Inoue

18-043 Potential and Vortex Residual Fields in the Ocean due to Tsunamigenic Earthquakes: a Fully Analytical Solution of the Axisymmetric Model Problem 1933
Gulnaz N. Nurislamova and Mikhail A. Nosov

18-068 Dynamic and Static Approaches in Simulation of Horizontal Motions of Water that Accompany Tsunami Formation and Propagation..... 1937
Anastasia V. Moshenceva, Mikhail A. Nosov and Sergey V. Kolesov

18-110 Tsunami Intensity and Its Relation to Source Parameters 1943
Anna V. Bolshakova and Mikhail A. Nosov

Lessonsd Learnt-from Recent Earthquake

20-210 Damage of RC Building with Coupled Shear Walls Caused by the 2011 Great East Japan Earthquake..... 1949
Atsushi Nagaya, Kazuyoshi Hotta, Yuko Kato, Susumu Takahashi, Masaki Maeda, Santiago Pujol and Toshikatsu Ichinose

20-212 Damage of Six-Story RC Building with Coupling Beams Having Aspect Ratios Larger than 2.0... 1959
Yuko Kato, Atsushi Nagaya, Kazuyoshi Hotta, Ying Wang, Susumu Takahashi, Masaki Maeda, Santiago Pujol and Toshikatsu Ichinose

20-253 Performance of the Building of the Faculty of Engineering at Tohoku University during the Great East Japan Earthquake of 2011 1967
Suzuki Kazuki,Hamood Alwashali, Maeda Masaki, Ying Wang, Pujol Santiago and Hnose Toshikatsu

20-037 Preparedness before Disaster in Tokyo Uraban Area 1977
Nam-Yi Yun and Masanori Hamada

21-312 Seismic Response of Non-Engineered Buildings in Nepal During September 18, 2011 Nepal-Sikkim Earthquake..... 1985
Kabir Shakya, Deepak Raj Pant, Manika Maharjan, Satish Bhagat, Anil C. Wijeyewickrema and Prem Nath Maskey

Other

22-172 Practical Study of The Earthquake Disaster Prevention Childcare for Infants with the Simulated Experience..... 1991
Nobuyuki Yamada

10CUEE CONFERENCE PROCEEDINGS
10th International Conference on Urban Earthquake Engineering
March 1-2, 2013, Tokyo Institute of Technology, Tokyo, Japan

EXPOSURE DATA DEVELOPMENT FOR THE GLOBAL EARTHQUAKE MODEL: INVENTORY DATA CAPTURE TOOLS

Ronald T. Eguchi[1)], John Bevington[2)], Zhenghui Hu[3)], and Charles K. Huyck[4)]

1) President and CEO, ImageCat, Inc., Long Beach, California, USA
2) Director, ImageCat Ltd., Guildford, UK
3) Senior Programmer, ImageCat, Inc., Long Beach, California, USA
4) Executive Vice President, ImageCat, Inc., Long Beach, California, USA
rte@imagecatinc.com, jb@imagecatinc.com, zh@imagecatinc.com, ckh@imagecatinc.com

Abstract: The Global Earthquake Model represents an open initiative to develop software and tools for assessment of global seismic risk. This paper describes an open-source software suite and protocols for populating a Global Exposure Database of structural information being developed by GEM's Inventory Data Capture Tools (IDCT) risk global component. Several data collection methods are used: remote sensing, direct field observations, and statistically-inferred mapping schemes. Data are collected on pre-earthquake inventory, as well as post-event damage: rudimentary building information from optical satellite or aerial sensors, including building footprints and heights. Field-based observations collected on digital and paper tools by survey teams allow expert users to generate detailed structural information, including structural type, year built, and occupancy. Mapping schemes allow the generation of exposure information for user-defined areas of homogenous urban land use, using sampled field observations. These methods converge to feed GEM's Global Exposure Database and the Earthquake Consequences Database.

1. INTRODUCTION

Over half a million people died in the last decade due to earthquakes, most of these in less-developed countries. However, recent earthquakes in Japan and New Zealand have reminded global populations that despite high levels of development and investment in mitigation strategies, seismic activities still account for major human and economic losses globally. A precursor to negating some of the risk to human life and economic risk, and potentially offsetting the latter through insurance, is having the ability to measure, understand and manage seismic risk. An understanding of physical vulnerability of structures in the built environment requires knowledge of the configuration and characteristics of urban building stock. These data offer valuable baseline information in responding to disasters and to estimate human and financial consequences resulting from the event. Insurance penetration in the most developed countries has led to the use of modeled probabilistic risk assessments to aid risk understanding. However, there are few risk models currently developed and operational in less-developed countries, partly due to a lack of insurance penetration in these regions. Recent years have also seen a trend towards developing open and transparent models to sit alongside the proprietary models widely used in the insurance industry. The latter models can be expensive to use and do not promote understanding of risk at the most fundamental grass-roots level of community risk assessment. Providing the tools for an open-source risk model promotes an understanding of risk in previously un-modeled or poorly-modeled regions, subsequently leading to mitigation and resilience-building activities such as an increased number of insurance products, promotion of building codes and retrofitting activities.

The public-private Global Earthquake Model (GEM) Foundation drives an international effort aimed at the development of state-of-the-art, widely accepted datasets, models and open-source tools/software. With the goal of collaboratively advancing seismic hazard and risk assessment worldwide, these will be made available through the web-based OpenQuake platform, which will be powered by a calculation engine (Silva et al., 2012 and Monelli et al., 2012). Development of a global model of seismic risk through an open, participatory process is at the core of the effort (Pinho, 2012) and international consortia are currently developing the global components of the model. Fig. 1 shows the inter-relationships between the risk global components, which will allow platform-users to generate new exposure data, access existing vulnerability functions and search historical damage surveys and consequences datasets. The hazard global components are aimed at developing methods, datasets and standards for assessing earthquake hazard, by combing data on historic seismic events, active faults, global instrumentation, and ground motion and strain predictions.

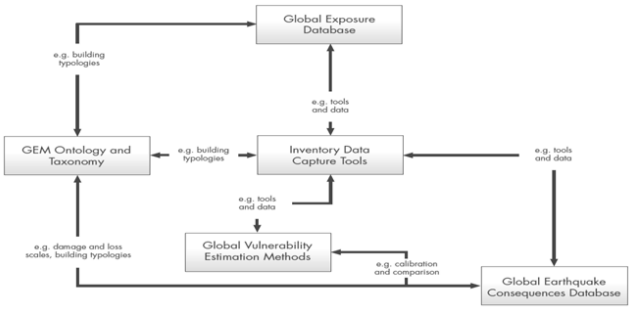


Figure 1 Inter-relationship between the GEM Risk Global Components (GEM, 2011)

The GEM Risk global component is tasked with providing standards for vulnerability estimation (damage, and human and social and economic losses), and also provides a database of physical and socio-economic consequences from past events globally - the Earthquake Consequences Database (ECD). Underpinning this is the Global Exposure Database (GED); a homogeneous database of global building stock that contains spatial, structural and occupancy-related information. The GED stores information on the global building stock using existing datasets and also using customized tools and protocols, whilst adhering to the standards of classification and relationships defined by the Ontology and Taxonomy consortium.

1.1 Inventory Data

A building inventory is a catalogue of the buildings and facilities in each class of a taxonomy, used in loss models to define the exposure to specific hazards, based on insurance exposure data (overview and details of insured properties for an area of interest). This underlying building characterization that serves as input data for which the losses are calculated, and typically requires building characteristics such as type, age, height, occupancy, building value and location (Born and Martin, 2006, Erdik et al., 2010). It is often the case that catastrophe loss models are limited in their ability to provide accurate estimations due to poor estimations of exposure information. This can have a significant impact on the modeled loss or consequences (Coburn and Spence, 1992, Jaiswal et al., 2008), which is apparent by the order of magnitude difference between modeled and actual losses sustained by the insurance industry in several recent natural catastrophes (Conway et al., 2008, Global Reinsurance, 2008)

GEM aims to generate global exposure data for its open-source model through the collection of building inventory information at several geographic scales, from level 0 (country) to level 3 (per-building, Table 1). The GED4GEM consortium is collating global datasets for inventory characterization at levels 0 and 1, including global housing and population data. IDCT is charged with developing the tools and user protocols for collection of inventory data at levels 2 and 3 (regional to per-building precision). A similar set of tools and protocols will also be developed for the collection of earthquake damage information at granularity levels 2 and 3. These data populate the GED and ECD databases, respectively. This paper presents the rationale and workflow of GEM's Inventory Data Capture Tools alongside a description of the tools and methods under development. The three major components of 1) remote sensing, 2) direct field observations, and 3) mapping schemes are presented in context with the wider aims of the GEM Risk global components as the tools underpin much of the analytical ambitions of the model. The method of each tool is described, alongside a status report at time of writing (end of 2012).

Table 1 Geographic Scales of Exposure Data in the GED. IDCT tools will populate levels 2 & 3

Precision level	Source	Grid/Vector	Statistical significance
Level 0	Global (LANDSCAN, PAGER, GRUMP)	30" (~ 1 km)	Country
Level 1	Sub-country database (UN-HABITAT, national census, GEM regional programmes), Urban density, RS (aggregated, < 1 km)	30" (~ 1 km)	Region/municipality
Level 2	Regional sub-country database (Mapping Schemes)	10/15", Vector	Region/municipality
Level 3	Per-building database (remote sensing, ground surveys)	Vector	Single building

2. THE INVENTORY DATA CAPTURE SUITE

Developing a building exposure model requires a combination of expert judgment, established classification typologies and geo-spatial technologies and tools. With this in mind, the IDCT consortium is developing a suite of tools and user protocols that follow a three-pronged workflow - see Fig.2. Firstly, remotely-sensed satellite imagery provides a data source for deriving individual building footprints and larger areas of homogenous urban land use. Second, field teams characterize building attributes using a series of data collection forms for both inventory and post-earthquake damage. Once these characteristics are input into a database, the third component, the Spatial Inventory and Damage Data (SIDD) tool, provides a workbench for the iterative generation of mapping schemes using the homogeneous areas of land use (derived from remote sensing) combined with sampled field data. This workflow produces regional (level 2) and per-building (level 3) inventory datasets. Data from the field tools can also be used to directly populate the Global Exposure Database at level 3. These workflows are described in detail in Fig. 2.

The types of data to be collected are fundamentally defined by the end-user depending on the use case. However, the GEM tools are pre-designed to collect all parameters required to generate new vulnerability functions or calculate risk information using existing vulnerability functions. Data are generated using one or all of the following methods: automatic and manual

remote sensing image interpretation (Section 2.1), direct field observations (Section 2.2), crowdsourced photo interpretation (Section 2.2.3). IDCT offers users a flexible framework allowing data collection missions to be tailored according to the availability of engineering expertise, analysts, hardware or software. All tools described in the user protocols supplied with the GEM tools are open-source, with directions to commonly used commercial software where performance may be greater.

of imagery, image pre-processing, analytical and GIS editing tools are all described in the protocols. All of these software tools and their supporting user guides will be made available as a single download from the OpenQuake site.

Remote sensing tools to extract seismic consequences data are also provided in the IDCT toolset. Analysis of pre- and post-event satellite or aerial imagery can be interpreted by expert users to identify buildings

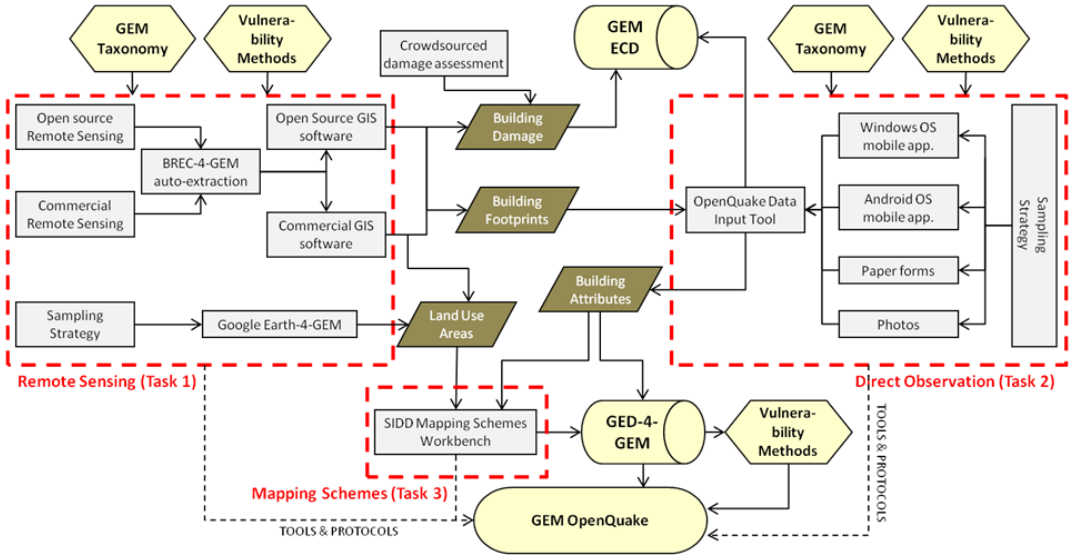


Figure 2 Detailed IDCT Workflow. Major tasks of remote sensing, direct observation and mapping schemes are shown in red. Main data developed are shown in green. Tools are in grey and GEM components external to IDCT are shown in yellow.

2.1 Task 1 – Remote Sensing

Images captured from satellite and aerial sensors have become a staple data source for risk managers in the past decade. The availability of internet tools such as Google Earth has increased the public awareness and general uptake of image processing to extract information on the makeup of urban areas.

IDCT provides a suite of software tools and user guides to enable the extraction of building outlines from imagery for level 3 exposure development, or derivation of areas of homogeneous land use for regional exposure (level 2). These GIS data captured from imagery provide vector location information by delineating in the image the outline of where the building intersects the ground (building "footprint"). Tools to derive height information based on the presence of shadows in imagery are also provided. The IDCT tools are primarily developed in the open-source GIS and Image Analysis package, Quantum GIS (QGIS). The GRASS GIS plug-in is also required, and BREC-4-GEM, a custom toolbar for automatic extraction of building footprints and height data (Gamba et al., 2009), has been developed as an extension to the software (Fig. 3). Two use-case scenarios provide the workflow for the user guides: 1) extraction of building footprints, and 2) delineation of urban land use. Sourcing

that have been collapsed or heavily damaged by earthquakes (e.g., Ghosh et al., 2011).

Automatic change detection techniques are provided to distinguish areas of significant change between these time periods. However, the web interface that facilitates manual identification of damaged buildings provides the main RS consequences toolkit. Based on an interface developed for the Global Earth Observation Catastrophe Assessment Network (GEO-CAN), the Tomnod Disaster Mapper (Barrington et al., 2011) provides pre-and post-event satellite images for assessment by expert image analysts and engineers. Data captured from the RS toolkit can be manually uploaded to GEM's OpenQuake platform and integrated in the GED and ECD.

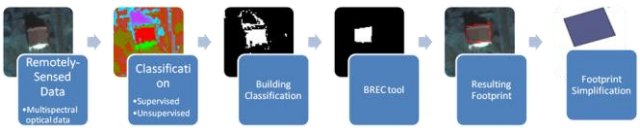


Figure 3 Workflow of BREC automatic footprint extraction tool

2.2 Task 2 – Direct Observation

Remote sensing, while useful for determining location, and potentially height of buildings, has large

uncertainties when manually assessing occupancy, structural type or year built. IDCT therefore fuses the image-based analytics with field observations (Task 2, Fig. 2). A suite of field tools is being developed by the consortium and includes both digital and paper forms for data collection, as well as protocols for collection of location information and field photographs. Digital tools are currently under development for laptop and tablet based hardware. The laptop tool is developed for Windows operating system (OS), while the tablet is being designed to run on the Android OS. The choice of which platform to support was made after extensive user consultation through a questionnaire sent to existing field reconnaissance teams.

The DO field tools are designed to directly incorporate the GEM taxonomy, allowing users to collect information using dropdown forms and pre-loaded options for all attributes to be collected. The tools will have tabbed-functionality to allow maximum ease of use, rather than prescribing a linear data collection process. The DO tools consist of several pre-loaded forms for collection of inventory and damage data. These reflect the GEM taxonomy:

1. Basic building inventory (parameters including, location, structural material type, occupancy, year of construction, lateral-load resisting system and height) – for use in GED
2. Detailed building inventory (to include additional secondary modifiers) - for use in GED
3. Post-event Damage (pre-loaded damage scales for building components) - for use in ECD
4. Interior survey (for when the survey team has access to the inside of the building. To include non-structural elements) - for use in GED and ECD.

The pre-loaded forms in the digital tools also include metadata on location, date, time, surveyor details and additional project information. In addition, templates for paper forms for collecting the same information as in the digital forms are being provided so that the DO capture tools do not discriminate between users based on hardware availability. The DO tools are currently under development in partnership with the UK Earthquake Engineering Field Investigation Team (EEFIT). Other global field reconnaissance teams are also being consulted through the iterative development and testing process, due for completion in early 2012.

2.2.1 Field Photographs

Alongside the digital and paper forms, the user will be provided with information on the types of hardware required to generate geo-tagged photographs. Photographs are an invaluable data source to be collected in field missions for many reasons, including: A photograph may be the best way to describe something (although it may need some accompanying text explaining what is shown in the photograph); if one is in a hurry and there is no time to write detailed notes, a photo can be used to record the moment and notes can be added later (see Data Input section 2.2.3). The protocols provide a 'common sense' approach, recording many parameters, including geo-location, look direction, data and time information, amongst others. It is hoped the protocol can provide best practice on the collection of field photos for both inventory and consequences data capture.

2.2.2 Sampling Strategy

Planning field deployments to collect information for statistical inferring any of the risk parameters relies on having statistically valid samples of observations. IDCT will provide users with a protocol for establishing a custom sampling strategy for each of their field deployments to identify those buildings to survey. The protocol details the following:

- A procedure that allows for variable levels of resources to carry out reconnaissance for a subset of the total population of structures
- A procedure for creating efficient, stratified samples of buildings. By "strata," what is meant here are consecutive ranges of some measurable building features such as building height, distance from population centers, or topographic slope.
- Procedures for extrapolating to the population.
- Procedures to elicit and employ local builder or building-department expertise, for inferring non-visible features from visible ones based on local knowledge.

2.2.3 Data Input (PRIZM)

IDCT provides users with a user-friendly online import tool, currently under development, to manage the collation of field information once teams have returned from their mission(s). This tool is integrated within the OpenQuake online system and will allow the input of photographs, digital forms and manual input of paper forms. A unique linkage system will allow linking of GPS photos to building footprints where users can establish links to photographs for each building surveyed. The photos are then analyzed by engineers and experts who can manually populate the database through visual interpretation of the field footage.

These tools will promote ultimate flexibility for field teams who have limited numbers of trained analysts or engineers, by assigning inexperienced analysts to field photograph collection while engineers can use crowdsourcing as a data input technique through visual interpretation of the field photographs in the online web interface. The system may also in the future allow the public to submit their own GPS photos or for engineers to share their findings or invite fellow scientists to validate their interpretations through the social networking

functionality of OpenQuake. This potential functionality is currently in the design phase.

2.3 Task 3 – Mapping Scheme Design

Mapping schemes are the IDCT tool for generation of regional exposure information (GED level 2), and serve as a way to harness the best-available data for inventory generation at a regional scale. These can often utilize inventory data extracted from individual country- or region-specific research studies (Jaiswal et al., 2008). In the IDCT suite of tools, mapping schemes are generated using the Spatial Inventory and Damage Data (SIDD) tool, a desktop-based workbench for loading, editing, testing and creating mapping schemes - statistical representations of inventory data that are applied to homogenous areas of land use or building type.

The main functions of SIDD are to: 1) receive data from the remote sensing and direct observation tasks; 2) develop mapping schemes or access a library of prebuilt mapping schemes; 3) apply mapping schemes; 4) format and export data to GEM OpenQuake. SIDD serves as a conduit between base data sets derived from both ground observations and remotely sensed sources and a GEM compliant file. Data are loaded into SIDD from the remote sensing module (Task 1, Fig. 2) and the field data collection tool (Task 2, Fig. 2) and processed into a GEM-suitable file. Data from task 1 and/or task 2 are loaded into a local data repository on the user's hard drive. In addition, the user has the option of loading land use data, or delineations of "homogenous land use zones". Zones that are homogenous (areas which are sufficiently similar in terms of attributes such as density and land use) will be characterized by a mapping scheme.

Once data are loaded into SIDD, mapping schemes are identified or created. Mapping schemes are tools for the statistical inference of structural parameters given data from a specific area. Data may be based on regional defaults, expert opinion, survey data, or a combination of these factors. After the mapping schemes are assembled, users apply the mapping scheme and the results output, either as exposure data or consequence data. For the development of inventories, the application of SIDD is likely to be an iterative process with users checking the results carefully and adjusting both geographic and statistical data to develop a final exposure data set that is valid according to the best available combination of field-based and remotely-sensed data. Preliminary testing of the method has revealed users may need to iteratively edit the mapping schemes and base layers before posting the final results (Bevington et al., 2012). The SIDD system is designed as a workbench of tools, rather than a linear process, to facilitate these types of adjustments. Additionally, the protocol will recommend statistical checks to validate the data set.

3. TESTBED SITES

Development of the IDCT tools is ongoing using a number of test sites that have been identified globally. There are four main testing phases: 1) Pilot Study 1 – Tool Development, completed May 2012; 2) Pilot Study 2 – Beta Testing; (inventory), completed July 2012; 3) Pilot Study 3 – Beta Testing (damage) completed July 2012; and 4) Pilot Study 4 – Demonstration, due in 2013.

The tools are currently under development and being demonstrated on imagery and field data collected in Pisco, Peru, Messina, Italy, Bishkek, Kyrgyzstan, Padang and Mataram, Indonesia and Pylos, Greece. Protocols have been updated during these tests, and the validity of the sampling strategy protocol is also tested. The recent earthquakes of Port-au-Prince, Haiti and Christchurch, New Zealand provide valuable imagery and ground-based validation data in which to test the remote sensing and crowdsourced damage assessment techniques. It is currently envisioned that the final demonstration of the full suite of IDCT tools in mid 2013 will focus on the city of Istanbul, Turkey.

4. CONCLUSIONS

One of the most poorly understood areas of disaster risk management is the building stock information that exists in a region. The IDCT component of the Global Earthquake Model is tasked with generating a set of open-source software tools and supplementary user-friendly guides to aid the understanding of seismic risk globally. These tools are aimed at being globally generalizable, with characterization of inventory stock at multiple geographic scales; from regional to per-building capture. Remote sensing plays a major role in the pre-event inventory capture, but also in post-earthquake damage assessment. Emerging methods (e.g. crowdsourcing) and field capture technologies (e.g. tablet-based tools for survey teams) will be used to facilitate a range of domain experience levels. Field tools provide the majority of the inventory characterization, but can be costly to develop for a full assessment of buildings over large areas. The development, application, and validation of mapping schemes are a primary function of the SIDD tool. These tools allow users to generate custom earthquake exposure databases and post-event consequences databases that can be made publically available through GED4GEM and GEMECD. The IDCT tools will be integrated with the GEM's OpenQuake web interface and will be released in 2013.

Acknowledgments:

The authors would like to thank the full IDCT team seismologists, engineers and geographers for their ongoing enthusiasm and commitment to this project. The support of the coordinators and staff at the Global Earthquake Model Foundation has been tremendous throughout. The authors would also like to recognize the support from the GEM Scientific Board and the IDCT internal advisory committee: Fumio

Yamazaki (Chair), Friedemann Wenzel, Hannes Taubenboeck, Ed Parsons and Rowan Douglas.

References:

Barrington, L., Ghosh, S., Greene, M., Har-Noy, S., Berger, J., Gill, S., Lin, A. and Huyck, C. (2011) Crowdsourcing earthquake damage assessment using remote sensing imagery. *Annals of Geophysics* **54:6**, 680-687.

Bevington, J., Eguchi, R., Ghosh, S., Graf, W., Hu, Z., Amyx, P., Huyck, C., Huyck, M., Eguchi, M. and Vicini, A. (2012) *Indonesia Building Exposure Development*. Report for GEM IDCT Deliverable 13, Pilot Study 1. v.1.0.

Born, P. & Martin, W. (2006) Catastrophe Modeling in the Classroom. *Risk Management and Insurance Review* **9**, 219-229.

Coburn, A. and Spence, R. (1992) Factors determining human casualty levels in earthquakes- Mortality prediction in building collapse: *Proceedings of the Tenth World Conference on Earthquake Engineering*, Madrid, Spain, 5989-5994.

Conway, T., Zarinejad, N. and Conway, T. (2008) Raising the bar on Catastrophe data. The Ernst & Young 2008 Catastrophe Exposure Data Quality Survey. Ernst & Young LLP.

Erdik, M., Sesetyan, K., Demircioglu, M.B., Hancilar, U., Zulfikar, C., Durukal, E., Kamer, Y., Yenidogan, C., Tuzun, C., Cagnan, Z., Harmandar, E., (2010), Rapid Earthquake Hazard and Loss Assessment for Euro-Mediterranean Region, *Acta Geophysica*, **58**:**5**, 855 -892.

Gamba, P. Dell'Acqua, F. Lisini, G. (2009) BREC: The Built-up area RECognition tool. 2009 *Joint Urban Remote Sensing Event*, Shanghai, China. 20-22 May 2009.

Ghosh, S., Huyck, C., Greene, M., Gill, S., Bevington, J., Svekla, W., DesRoches, R. and Eguchi, R., (2010). Crowd-Sourcing for Rapid Damage Assessment: The Global Earth Observation Catastrophe Assessment Network (GEO-CAN), *Earthquake Spectra* **27**, S179-S198.

Global Earthquake Model (2011) Global Earthquake Model 2009-2010 Report. Second edition.

Global Reinsurance (2008) Gustav/Ike losses significantly underestimated. *Global Reinsurance*. 9 October, 2008.

Grossi, P. (2004) Sources, nature, and impact of uncertainties on catastrophe modeling. *13th World Conference on Earthquake Engineering*. Vancouver, B.C., Canada.

Huyck, C., Hu, Z., Bevington, J., Ghosh, S. and Eguchi, R. (2011) Inference of Structural Characteristics for Regional Building Inventories Using Remotely Sensed Data and Ground Observations. *Ninth International Workshop on Remote Sensing for Disaster Response*, Stanford, CA. 15-16 September 2011.

Jaiswal, K. and Wald, D., 2008, Creating a global building inventory for earthquake loss assessment and risk management: *U.S. Geological Survey Open-File Report 2008-1160*.

Monelli, D., Pagani, M. and Weatherill, G. A. (2012). The hazard component of OpenQuake: the calculation engine of the Global Earthquake Model. *Proceedings of the 15th World Conference on Earthquake Engineering*. Lisbon, Portugal, paper n. 4180.

Pinho, R. (2012) GEM: a participatory framework for open, state-of-the-art models and tools for earthquake risk assessment worldwide. *Proceedings of the 15th World Conference on Earthquake Engineering*, Lisbon, Portugal, paper n. 4929.

Silva, V., Crowley, H., Pagani, M., Monelli, D., Pinho, R. (2012) Development and application of OpenQuake, an open source software for seismic risk assessment. *Proceedings of the 15th World Conference on Earthquake Engineering*, Lisbon, Portugal, paper n. 4917.

EVALUATION OF TSUNAMI FORCE ACTED ON BRIDGES BY GREAT EAST JAPAN EARTHQUAKE

Kyuichi Maruyama[1)], Yasushi Tanaka[2)], Kenji Kosa[3)]
Akira Hosoda [4)], Norimi Mizutani[5)], Tomoaki Nakamura[6)]

1) Professor, Dept. of Civil & Environmental Engineering, Nagaoka University of Technology, Japan
2) Assistant Professor, Dept. of Civil & Environmental Engineering, Nagaoka University of Technology, Japan
3) Professor, Department of Civil & architectural Engineering, Kyushu Institute of Technology, Japan
4) Associate Professor, Faculty of Urban Innovation, Yokohama National University, Japan
5) Professor, Graduate School of Engineering, Department of Civil Engineering, Nagoya University, Japan
6) Designated Lecturer, Institute for Advanced Research, Nagoya University, Japan
kmarui@vosnagaokaut.ac.jp, yasuxi@vosnagaokaut.ac.jp, kosa@civil.kyutech.ac.jp
concrete@ynusac.jp, mizutani@civil.nagoya-u.ac.jp, tnakamura@nagoya-u.ac.jp

Abstract: This paper deals with what tsunami force has acted on bridges by Great East Japan Earthquake broken out in March 11, 2011. Almost all data were collected on the bridges in the inundation area. Washed away bridges as well as survived ones were analyzed by the equation proposed by Kosa. Since the velocity of tsunami was a key factor in the equation, the simulation using hydraulic technology was developed and compared with the observed data.

1. INTRODUCTION

Great East Japan Earthquake in March 11, 2011 caused the greatest tsunami we have ever had in one thousand years in Japan. Comparing the damage by the earthquake itself, the damage by the tsunami was much serious for our modern life in the area of eastern Japan.

It was a shocking scene that a lot of bridges near the shore were washed away while very few bridges inland suffered from the earthquake. Since the Great Hanshin Earthquake in 1995, bridge engineers and researchers have been working hard on how to improve the seismic design of bridge structures. The damage of bridge by tsunami was completely out of our concerns because we have never had such damage since modern bridge technology has been introduced in one hundred years.

Right after the earthquake, JSCE has set up a research committee on the tsunami force acting to bridges, consisting of members from various fields such as bridge engineering, concrete engineering, structural engineering and coastal engineering. The authors have been involved in the committee as directive members. This paper is a kind of mid-term report on what we have studied in one and a half years.

2. DAMAGE OF BRIDGES BY TSUNAMI

At the first stage any data of bridges which located in the inundation area from Aomori prefecture in the north to Chiba prefecture in the south were collected by both internet media and on site survey. Fig.1 shows satellite images taken before and after the earthquake.



(a) Before Earthquake (25th June, 2010)



(b) After Earthquake (6th April, 2011)

Figure 1 Satellite Images

Field survey was conducted several times to confirm the details of bridges. Finally, the statistic data are summarized as shown in Table 1. The total number of bridges within the inundation area was 1,793 and the number of washed away bridges was 252, including 28 of railway bridges and 40 of major road bridges.

Table 1 Number of Bridges in the Area of Inundation

Pref.	Iwate	Miyagi	Fukushima	Ibaraki	Chiba	Total
Washed away or moved	78	102	68	2	2	252
Unclear	0	0	8	0	0	8
Survived	427	692	384	30	-	1533
Total	505	794	460	32	2	1793

In order to analyze the damage of bridges, the data of each bridge, such as type, dimension and structural details were collected from authorities who take care of bridges. Currently, the data of more than 400 bridges are collected and the database is now processed. Using the database, some trials have started to categorize bridges by their types and dimensions to see what a key is for resisting tsunami. Fig.2 shows the number of bridges with or without suffering from washed away in comparison with categorized items, such as type of bridge and bridge length. In the figure, only the survived bridges located near the washed away bridges are selected for comparison.

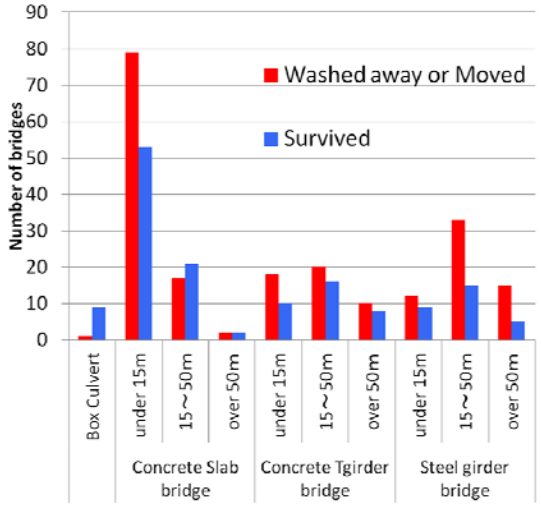


Figure 2 Damage Analysis of Bridge

Fig.2 may not give us a clear tendency on what influences the damage of bridge. This is because no consideration is taken for the velocity and the height of tsunami at the location of bridge.

3. EVALUATION OF BRIDGE RESISTANCE AGAINST TSUNAMI

Kosa (2010), one of the authors, has already started the investigation on the tsunami force acting on bridges after surveying the damage of bridges due to the tsunami of Sumatra Earthquake in 2004. The following discussions are based on his method.

Tsunami force acting to a bridge girder can be treated as a hydro dynamic force indicated by Eq.1, while the resistance of girder is mainly due to self weight computed by Eq.2 or Eq.3. The difference between Eq.2 and 3 lies in the existence of buoyancy judging from the comparison of girder height with tsunami height. Eq.2 should be used when a bridge girder is not submerged at the attack of tsunami, while Eq.3 is for the case of bride girder being submerged and having buoyancy at tsunami.

$$F = \frac{1}{2}\rho_w C_d v^2 A_h \tag{1}$$

$$C_d = \begin{cases} 2.1 - 0.1\cdot(B/D) & (1 < B/D < 8) \\ 1.3 & (8 \le B/D) \end{cases}$$

$$S = \mu W \tag{2}$$

$$S = \mu(W - U) \tag{3}$$

Where, ρ_w is density of water (1030kg/m^3); C_d is the drag coefficient with its value decided based on reference (Japan Road Association, 2002), B and D are width and depth of girder; v is tsunami velocity (6.0m/s is used based on surveys of the Tohoku area); A_h is the projected pressure area of the girder in the horizontal direction; μ is friction coefficient (0.6, based on research by Rabbat et al. (1985)); W is the girder's self weight (kN), and U is buoyancy (kN) as computed by Eq. 4.

$$U = \rho_w g V \tag{4}$$

Where, V is volume of the bridge girder inner the tsunami (m^3).

The ratio of girder resistance (S) to tsunami force (F) is an index to judge whether a bridge girder is washed away or not by tsunami. The indicator β is introduced in this paper as shown in Eq. 5.

$$\beta = \frac{S}{F} \tag{5}$$

When β is smaller than 1.0, a bridge girder has a great possibility of being washed away by a given magnitude of tsunami. Although the velocity of tsunami is most important in this study, observe records of velocity of tsunami are very few at the site of bridge. In this study, some recorded videos throughout the Tohoku area were used for determination of velocity. The average value of velocity is taken as 6.0m/s based on the research by Fu et al. (2012) and this value is used for analysis.

For evaluation of Eq.5 with comparison of the actual behavior of bridge girder, the observed condition of girder is defined as shown in Table 2. Three levels are introduced; Rank A (completely washed away) to Rank C (slightly damaged).

Fig.3 illustrates the computed β values for 37 different types of girders. When β is larger than 1.5, the girders had Rank C damage. When β is smaller than 0.6, the girders suffered the damage of Rank A.

Table 2 Definition of Damage of Bridge Girder

Damage level	Observed condition of superstructure
Rank A	Washed away
Rank B	Moved but not fallen from abutment
Rank C	Slightly damaged

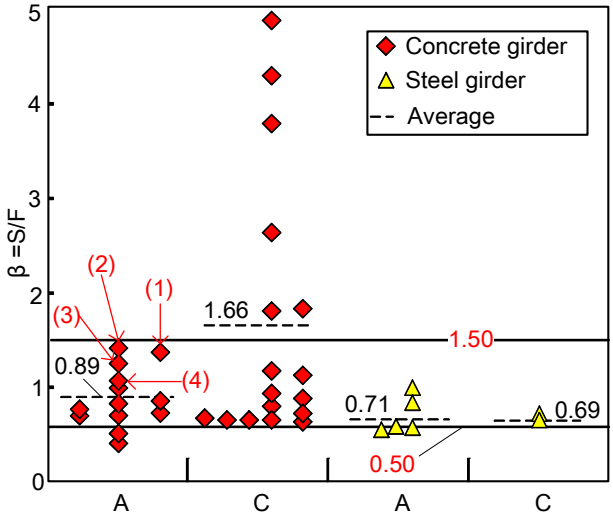


Figure 3 Computed β Values and Damage Level

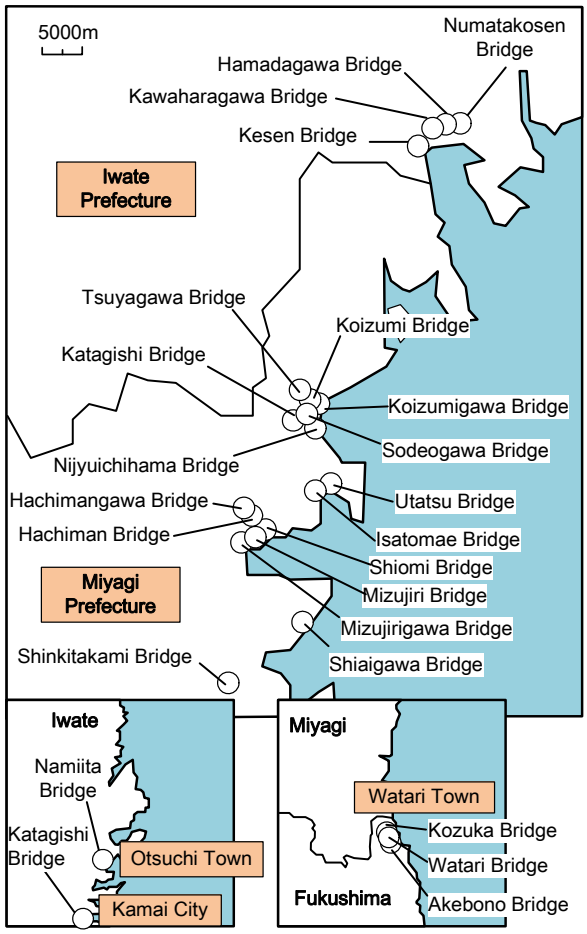


Figure 4 Bridges for Computation of β Value

There exists a gap of β value between Rank A and Rank C, but β could be effective to evaluate how safe a bridge girder is against tsunami. Fig.4 shows the location of bridge used for computation of β values in Fig. 3. For going into further discussion, the types of bridge girder are summarized in Figs.5 and 6. The types of girder shown in Fig.3 have β value of larger than 2.0. In fact, these girders have survived. On the other hand, girders in Fig. 6 having β value of smaller than 0.6 were all washed away by the tsunami on March 11, 2011.

In general, survived girders are made of prestressed concrete having a relatively low height and wider width of cross section. All girders in Fig.5 look flat in shape to compare with girders shown in Fig.6. In addition, the height of pier should play a important role because the velocity of tsunami is a function of tsunami height. The higher the tsunami height is, the faster the tsunami velocity.

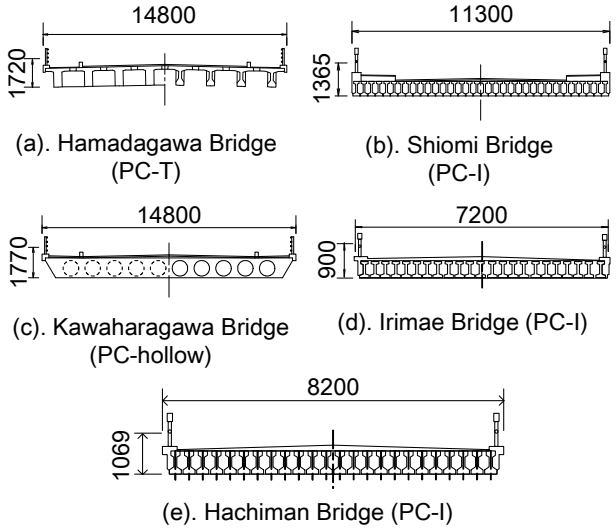


Figure 5 Types of Survived Girder

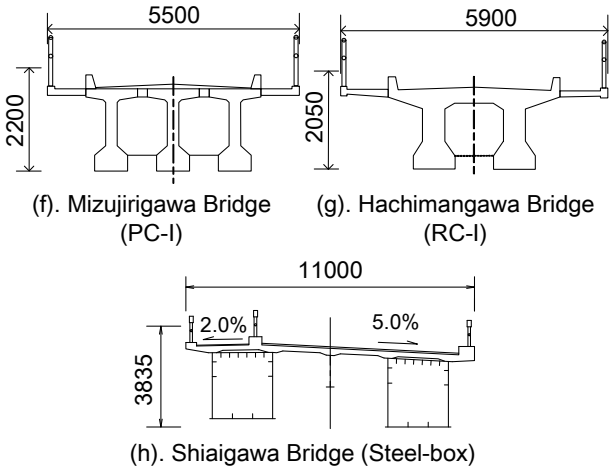


Figure 6 Types of Washed Away Girder

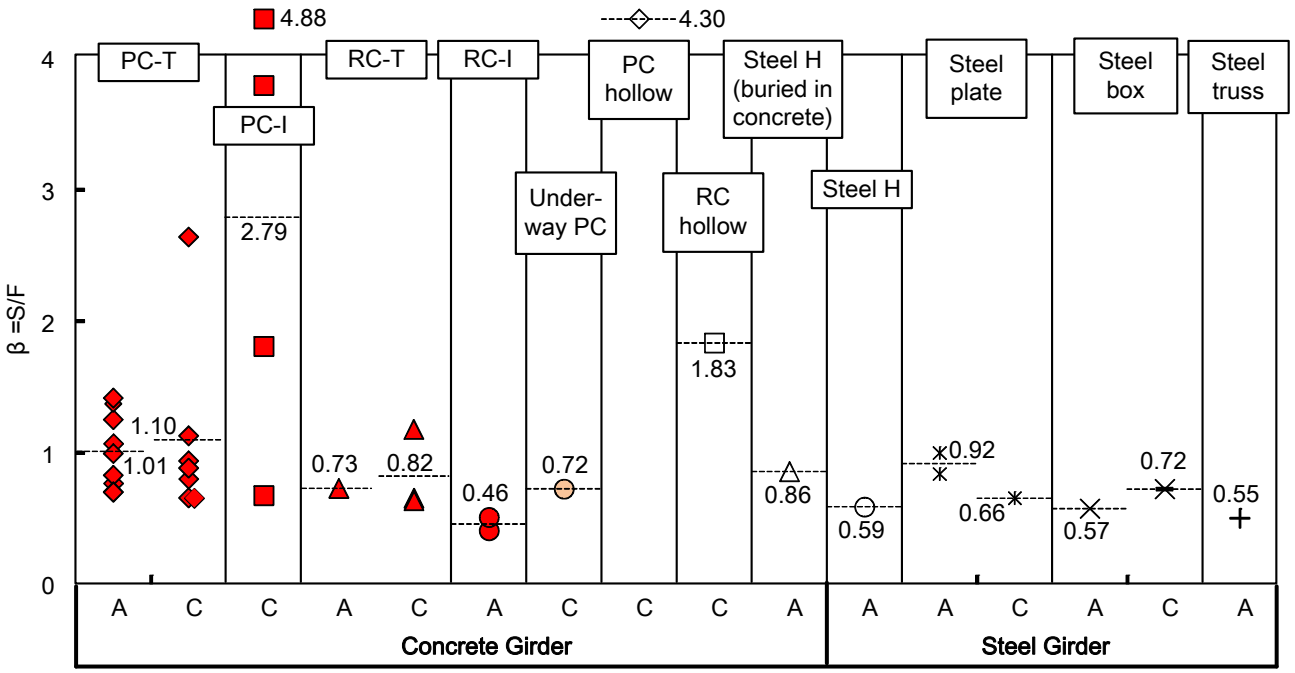


Figure 7 Classification of β by Girder Type

In the previous research works done by Kosa et al. (2010); Zheng et al. (2012), obvious differences are recognized in the value of β for Rank A and Rank C. But Fig.3 shows some discrepancy. As discussed previously the β value of Rank A girders (washed away girders) should be less than 1.0. In fact there observed some girders whose computed β values are larger than 1.0. Similarly some girders categorized in Rank C (slightly damaged girder) show β values being smaller than 1.0.

Bridge girders having β value of larger than 1.0 with actual damage being ranked as A are listed in Table 3. These four are all prestressed concrete girders with cross section of T shape. The relationship between β values and damaged ranks is re-examined by the type of girder as shown in Fig.7. Prestressed concrete T-girders might have undertaken larger tsunami force than that expected by β value.

In general, the reason for such discrepancy might be attributed to the assumption in which the tsunami velocity is constant as 6.0 m/s in this study.

Table 3 Rank A Concrete Bridges with β larger than 1.0

Rank A concrete bridges with β larger than 1.0			
No.	Name	β	Girder Type
(1)	Numatakosen	1.37	PC-T
(2)		1.41	PC-T
(3)	Shimoya	1.25	PC-T
(4)	Kozuka	1.07	PC-T

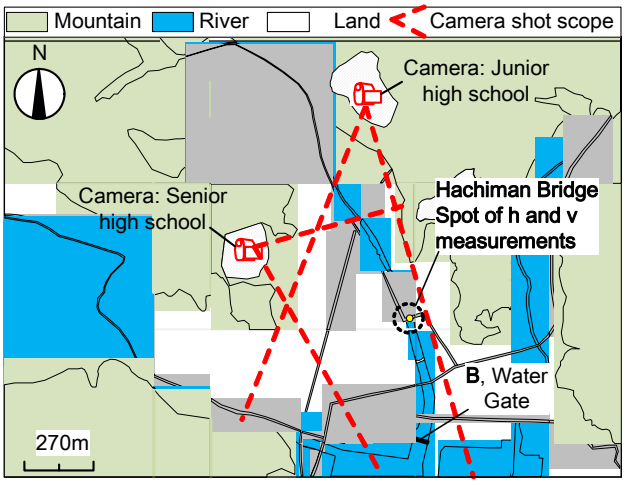


Figure 8 Location of Video Camera

4. CHARACTERISTICS OF TSUNAMI IN THE CITY (SHIZUGAWA)

Japan Meteorological Agent keeps observation of earthquakes and tsunamis constantly at certain points in Japan. The equipments to measure tsunami height and velocity, however, are set in the sea, not inland. The agent does not have any records of tsunami velocity in residential areas. Fortunately, some citizens have taken motion pictures of tsunami in the city by digital cameras.

Based on the motion pictures taken by citizens, the characteristics of tsunami in the city are able to be analyzed. Fig.8 shows the location of video camera in Shizugawa area in Minamisanriku-Chou, Miyagi prefecture. Both cameras were focused on the bridge named Hachiman Bridge. Fig.9 shows the side view of Hachiman Bridge with key reference dimensions. Figs.10 and 11 show static pictures cut out from the recorded motion pictures at 7.05 second and 7.53 second.

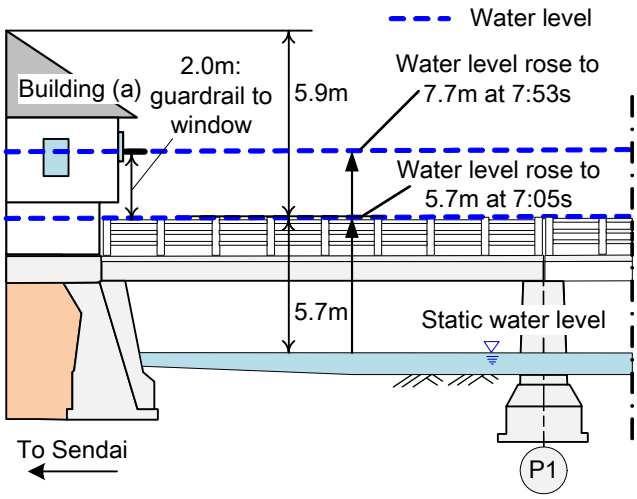


Figure 9 Side View of Hachiman Bridge

In advance of picture analysis, key reference height is estimated as follows;

a) The height from the top of guardrail to static water level: 5.7 m
b) The height from the top of building-(a) to the top of guardrail: 5.9 m
c) The height from the top of guardrail to the window of building-(a) : about 2.0 m

These are shown in Fig.9.

The analysis of tsunami is done in such a way that the surface of tsunami reached the top of guardrail at 7:05 second of motion picture, meaning that the tsunami height was 5.7 m. The surface of tsunami reached the window of a house at 7:53 second, meaning that the tsunami height was 7.7 m. Comparing these two set of data, the rising speed of tsunami can be determined. Motion picture analysis tells that the tsunami height rose with the speed of 3.19 m/min at a time of 4 minutes after the hit of tsunami on Hachiman bridge, and that the tsunami ran up to the maximum 14.8 m high at 7 min. after the hit, at a rising speed of 1.1 m/min. The average rising speed of tsunami height is estimated to be 2.24 m/min. It was relatively low speed, inferring that the wave shape was not the bore type.

There observed much debris flowing in the picture. These are good references to measure the velocity of tsunami. For example, take debris (1) and debris (2) in the motion picture and trace them with a certain time interval shown in the picture. Accurate distance of debris move can be confirmed by both an internet media (Google Earth; Fig 13) and on site survey.

By the above mentioned process, the wave height and velocity of tsunami can be estimated. Based on the analyzed results the relationship between tsunami height and tsunami velocity is obtained and shown in Fig.12. In the figure the assumption that the velocity should be 0 when the tsunami height is 0 is added. When the tsunami began to fall back, the velocity was treated as 0 as well. Before the tsunami reached about 2m, the tsunami velocity rose to about 6 m/s.

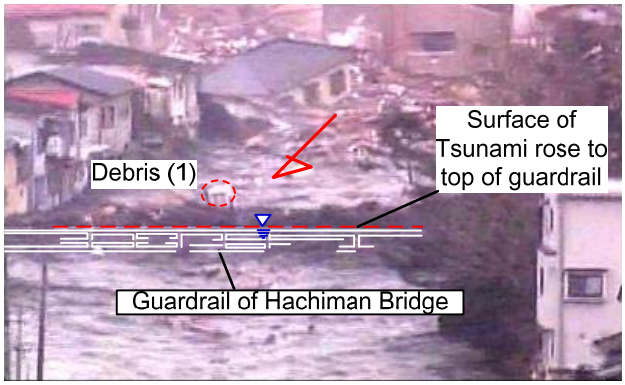


Figure 10 Shot of Tsunami Wave at 7:05s

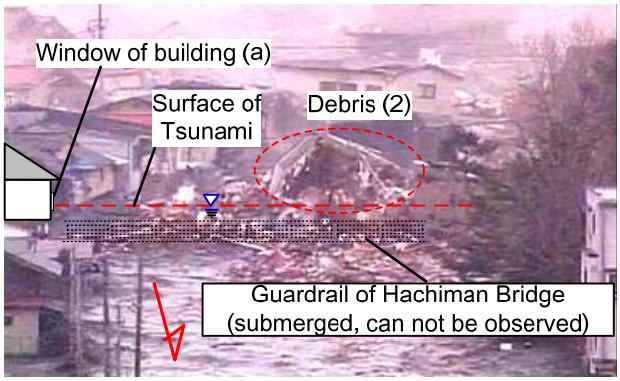


Figure 11 Shot of Tsunami Wave at 7:53s

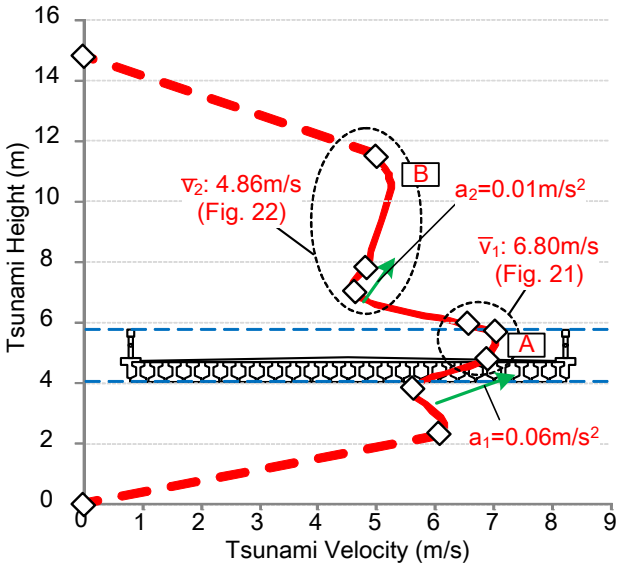


Figure 12 Time-depended Variation of Tsunami Height (Hachiman Bridge)

The velocity of tsunami increased continually before the tsunami hit the bridge girder. The maximum velocity is estimated as 7.02m/s just before the tsunami reached the

bridge girder. When the tsunami ran up to about 6m high, the bridge began to be inundated and the tsunami velocity got to decrease to about 4.86m/s (average of area B in Fig.12). After tsunami height reached about 12m, velocity decreased to 0 gradually.

Fig.12 tells two things. Firstly, the tsunami velocity continuously increases up to the maximum before the tsunami begins to overflow the bridge girder. Secondly, the tsunami velocity decreased suddenly when the bridge girder is inundated. In addition, Hachiman Bridge has a local geographical feature showing that the level of girder is the same as the level of embankment. When the tsunami height rises up to the level of girder, the tsunami would overflow to the land area and that results in the reduc of tsunami energy and velocity

5. RESISTANT MECHANISM OF HACHIMAN BRIDGE GIRDER

In the previous section, the characteristics of tsunami in the city were discussed in details. In particular, the height and the velocity of tsunami at the site of Hachiman Bridge are certainly evaluated. Although Hachiman Bridge has fortunately survived from the tsunami, it must be very important to establish a proper model which is able to explain why Hachiman Bridge was not washed away by the tsunami. As mentioned in section 2, the details of more than 400 bridges in inundation area are collected and arranged in the database. Not only the mechanism for washed away bridges but also that for survived ones is necessary for further discussions on existing bridges in other areas where a huge tsunami is expected to come near future.

Figs 14 and 15 show the possible mechanisms for resistance of Hachiman Bridge against tsunami. Fig.14 represents tsunami wave acts on the girder of bridge, whereas tsunami in Fig.15 acts on the girder like flood in the condition of the girder submerged deeply.

For discussions of these cases, Eq.1 is extended to Eq. 6 as below.

$$F = \frac{1}{2}\rho_w C_d A v^2 + C_m \rho_w AB\frac{dv}{dt} + (\rho_w g h_1 A_1 - \rho_w g h_2 A_2) \qquad (6)$$

Where, C_m is inertia coefficient, assumed to be 1.0; B is bridge width (m); dv/dt is acceleration of tsunami (m/s^2); h_1 and A_1 are the water depth (m) and pressure area (m^2) at the downstream side of girder; h_2 and A_2 are the water depth (m) and pressure area (m^2) at the upstream side of girder.

Eq.6 consists of both hydrodynamic force and hydrostatic force. The mechanism-1 requires both forces, but the mechanism-2 needs only hydrodynamic force because the water head between upstream and downstream of the girder becomes zero. For computation of resistance of the girder, Eq.2 should be used for the mechanism-1 and Eq.3 for the mechanism-2.

Computed results are shown in Fig.16. Either mechanism indicates the survival of girder against the tsunami, but the mechanism-1 gives lower safety.

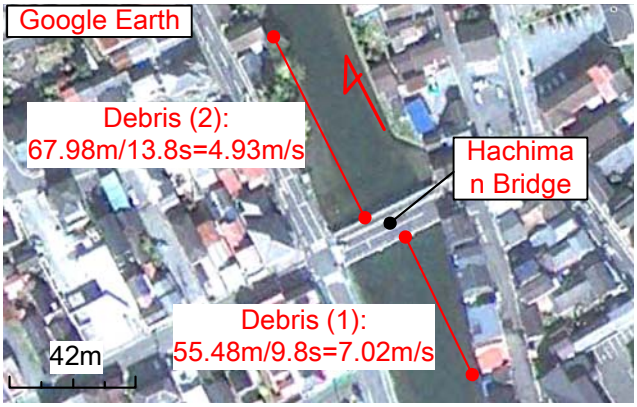


Figure 13 Estimation of Tsunami Velocity

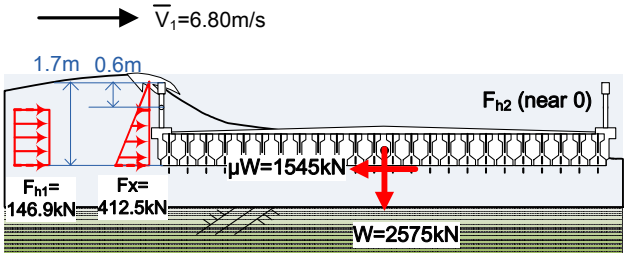


Figure 14 Possible Mechanism - 1

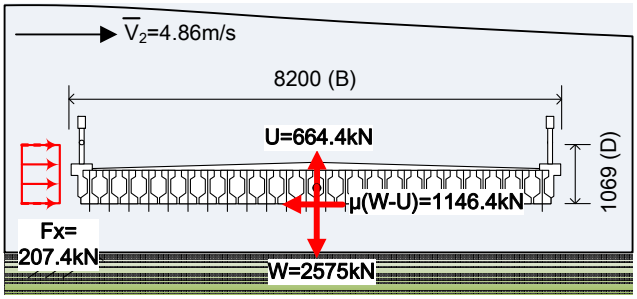


Figure 15 Possible Mechanism - 2

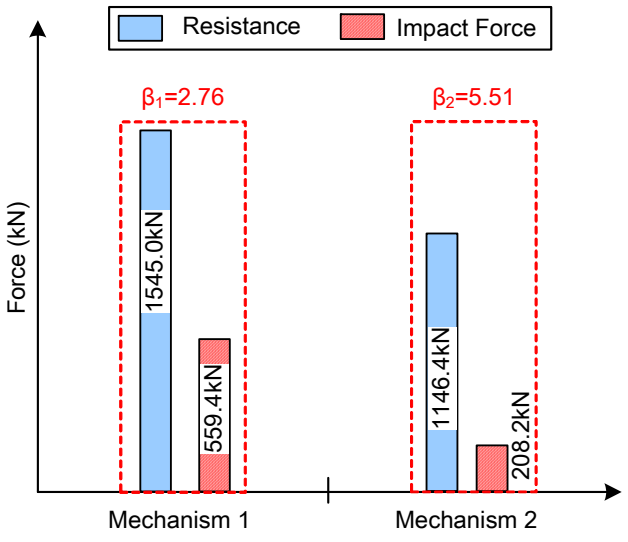


Figure 16 β- Values based on Possible Mechanisms

6. EXPERIMENTAL ANALYSIS

6.1 Experimental Setup and Conditions

A series of hydraulic experiments based on the Froude similarity with a length scale of 1/50 were conducted using a wave flume in the Department of Civil Engineering, Nagoya University, Japan (12.5 m × 2.22 m × 1.0 m). To generate long-period waves, a piston-type wave generator with a maximum stroke of 1.5 m was installed in the flume.

Figs. 17 and 18 show the experimental setup. Fig.19 shows the cross-section of a bridge model, which is made of acrylic plates. The cross-sectional dimensions of the bridge model are determined to simulate a superstructure of the Utatsu bridge, Japan, which was damaged in the 2011 Tohoku earthquake tsunami. The length of the bridge model is 0.3 m. The specific weight of the bridge model is lower than that of the prototype due to the limitation of the wave generator. As shown in Figs, 17 and 18, the flume is divided into three 0.31-m-wide sections, which are slightly wider than the length of the bridge model. In a section, a bridge model is put on 0.1-m-high piers to observe whether the bridge model moves or not. In another section, another bridge model is fixed at the same height as the movable bridge model to measure wave force and pressure acting on it. The wave force and pressure are measured using a load cell (Nissho: LMC-3520-50NWP) and pressure transducers (Kyowa: PS-05KCM3Z5P). The position of the pressure transducers is presented in Fig. 19. In the other section, no bridge model is set to measure water surface elevation and flow velocity in the absence of the bridge model. The water surface elevation and the flow velocity are measured using capacitance-type wave gauges (Kenek: CHT6-40) and a propeller-type velocimeter (Kenek: VOT2-100-05N). The cross-shore position of the velocimeter is the same as the seaward edge of the bridge model, and its vertical position is the same as the center of the bridge model.

A single long-period wave was generated toward the bridge models. The offshore still water depth h was set at 0.49 m. The time during which the wave paddle was displaced forward and backward, T, was set at 20.0 s.

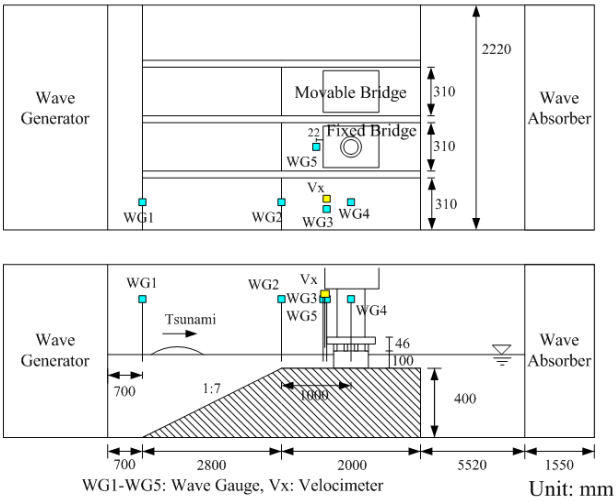


Figure 17 Schematic View of the Experimental Setup

The stroke of the wave paddle S was changed from 1.24 to 1.38 m. In total, five cases were conducted.



Figure 18 Bridge Models

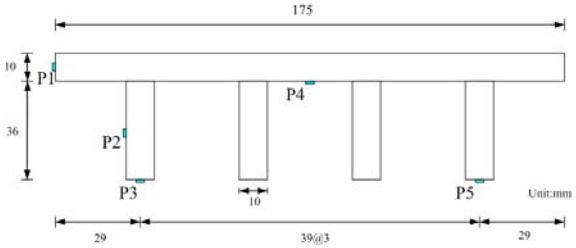


Figure 19 Cross-Section of Bridge Model

6.2 Experimental Results and Discussion

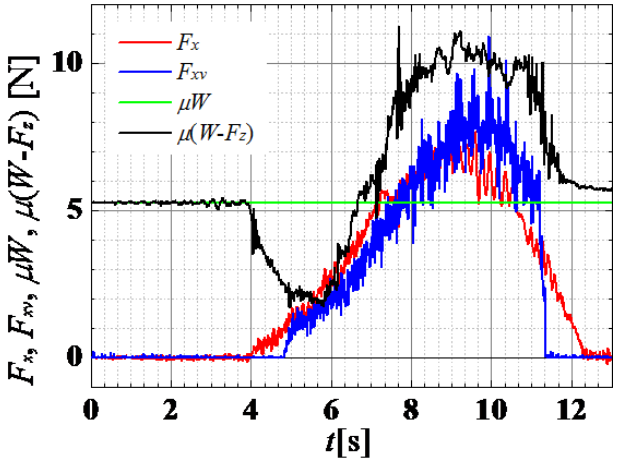
Fig. 20 shows the wave force acting on the fixed bridge model. In the figure, F_x is the horizontal wave force measured using the load cell, and F_{xv} is that estimated by Eq.1

As shown in Fig. 20, the value of F_x gradually increases after the tsunami impinges the bridge model, and reaches its maximum at around 5 s after the impingement. Figure 20 also indicates that although the maximum value of F_{vx} slightly overestimates that of F_x, the time series of F_x is in good agreement with that of F_{xv}. Consequently, the horizontal wave force acting on the bridge model can be evaluated from the flow velocity using Eq. 1.

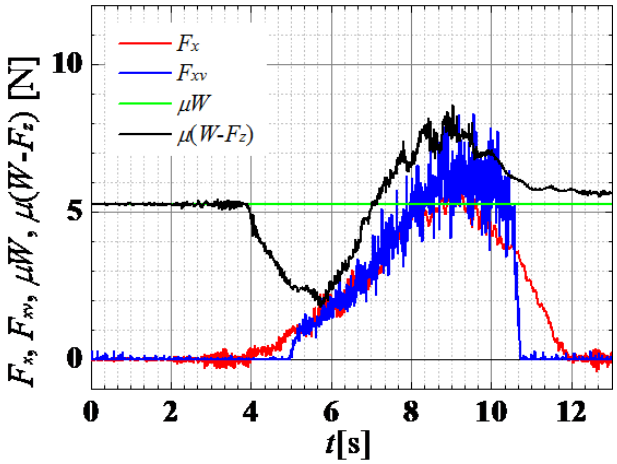
In Fig. 20, the friction force $\mu\,(W - F_z)$ and its initial value $\mu\,W$ are also presented. Here, W is the weight of the bridge model, F_z is the vertical wave force measured using the load cell, and μ is the static friction velocity, which was determined to be 0.45 by the trial-and-error method. Since a decrease in $\mu\,(W - F_z)$ is equivalent to an increase in F_z, Fig.20 shows that the value of F_z increases after the water surface impinges the bottom of the bridge model. Following that, the value of F_z conversely begins to decrease, and reaches its minimum at the almost same moment as the maximum value of F_x. Because of these changes in F_z, the value of $\mu\,(W - F_z)$ decreases and reaches its minimum shortly before $t = 6$ s. Conversely, it increases and reaches its maximum at around $t = 9$ s.

The bridge model is expected to start moving when the value of F_x exceeds that of $\mu\,(W - F_z)$. In the hydraulic

experiments, it was observed that the bridge model began to move at approximately 2 s after the tsunami impingement in the case of Fig. 20(a), while the bridge model did not move in the case of Fig. 20(b). Fig. 20(a) indicates that the value of F_x slightly exceeds that of $\mu(W - F_z)$ shortly before t = 6 s, suggesting that the bridge model begins to move at this moment. On the other hand, Fig. 20(b) shows that the value of F_x does not reach that of $\mu(W - F_z)$, suggesting no motion of the bridge model. These results are consistent to the observation. Furthermore, a comparison between F_x and μW shows that the value of F_x exceeds that of μW at about t = 8 s in both cases. However, as described earlier, the bridge model began to move at around 2 s after the tsunami impingement for Fig. 20(a), and did not move for Fig. 20(b). This suggests that it is essential to consider the vertical wave force F_z when calculating the static friction force. From these results, it is found that the motion of the bridge model can be assessed using the horizontal wave force F_x and the static friction force $\mu(W - F_z)$.



(a) S = 1.38 m (the bridge moved)



(b) S = 1.24 m (no bridge movement)

Figure 20 Wave Force and Static Friction Force Acting on Fixed Bridge Model

7. NUMERICAL ANALYSIS

To examine whether the motion of a bridge can be evaluated by numerical simulations or not, some numerical experiments were conducted using a three-dimensional coupled fluid-structure-sediment interaction model (Nakamura et al. 2011), which is based on a large-eddy simulation (LES) model that can be applied to tsunami-bridge interaction. Figure 21 shows a schematic view of the computational domain modeled from an experimental setup of Nakao et al. (2010). A bridge model with the dimensions of 80 mm × 200 mm × 20 mm is fixed at a height of 65 mm from the bottom in the hydraulic experiments. In this study, a movable bridge model with the same dimensions is adopted instead of the fixed bridge model. The density of the movable bridge model is changed as 1.0×10^3, 1.5×10^3, 2.0×10^3, and 2.5×10^3 kg/m^3. Toward the movable bridge model, a bore-like flow is generated by the dam break with an initial water height of 250 mm. Detailed explanation of the coupled model can be found in Nakamura et al. (2011).

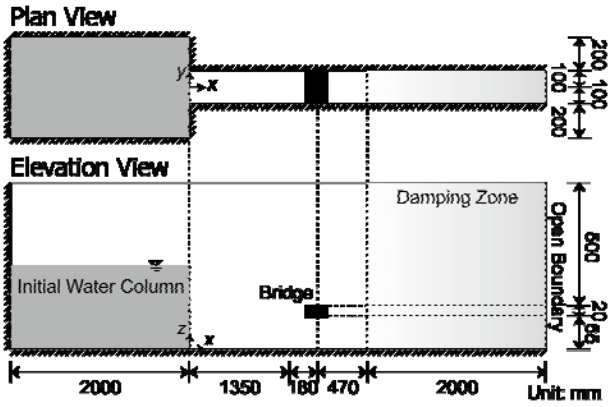


Figure 21 Computational Domain

Figs. 22 and 23 show the bridge motion and the surrounding water surface deformation for the density of the movable bridge model of 1.0×10^3 and 2.0×10^3 kg/m^3. For the light bridge model with the density of 1.0×10^3 kg/m^3, as indicated in Figure 22, the water mass splashes up in front of the bridge model at the impingement of the flow. At this moment, it is observed in Figure 24 that the pressure increases at the front surface of the bridge model. In contrast, the pressure conversely decreases around the bottom surface of the bridge model due to the formation of a vortex, suggesting that an increase in the maximum static friction force acting on it. Figure 22 also shows that no motion of the bridge model is observed until t = 2.2 s. However, although no figure is presented, the horizontal force acting on the bridge model exceeds the maximum static friction force shortly after t = 2.2 s. The bridge model accordingly begins to slide, and finally moves downstream. For the heavy bridge model with the density of 2.0×10^3 kg/m^3, Figure 23 shows that its motion is not observed after the flow is subsided. From these results, it is suggested that the coupled model has the computational capability to simulate the

motion of a bridge. However, a comparison with hydraulic experiments is not conducted in terms of the motion of a bridge. To address the issue, it is recommended that further studies be conducted to verify the validity of the coupled model and clarify the mechanism of the bridge motion.

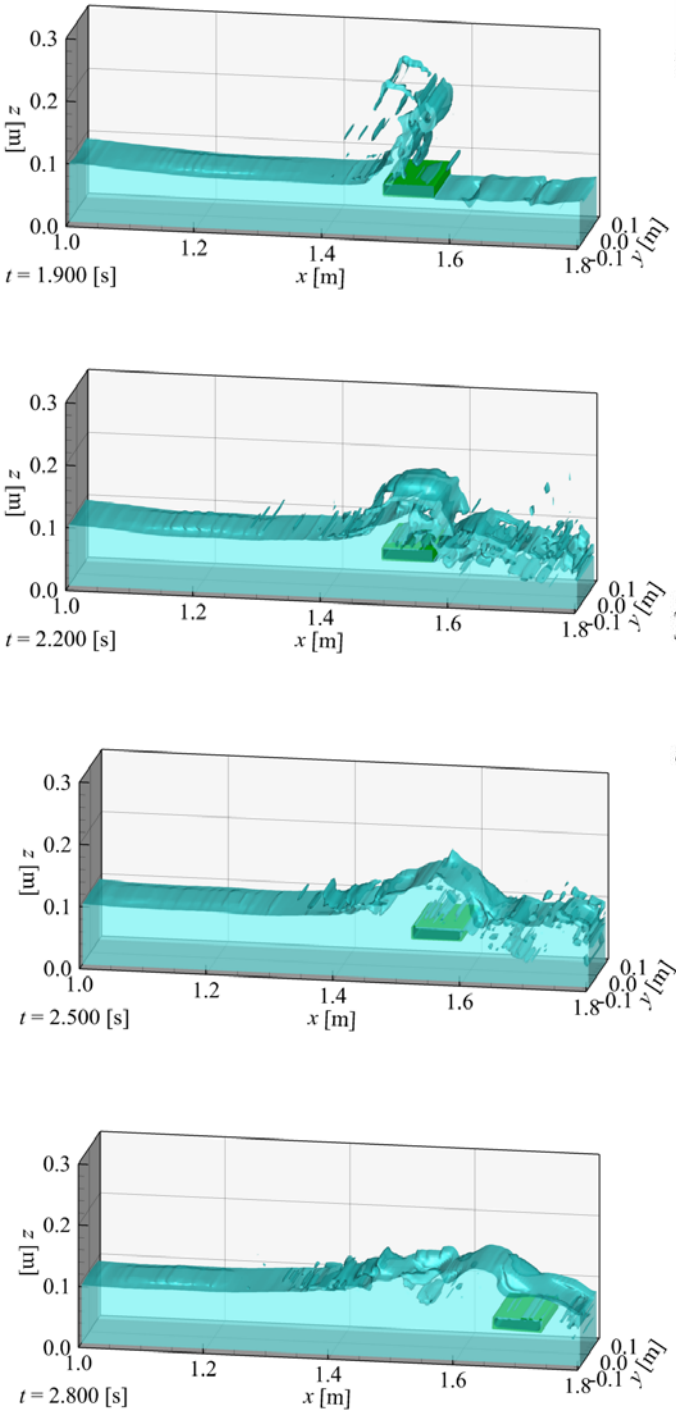


Figure 22 Water Surface Deformation around Bridge Model with Density of 1.0×10^3 kg/m^3

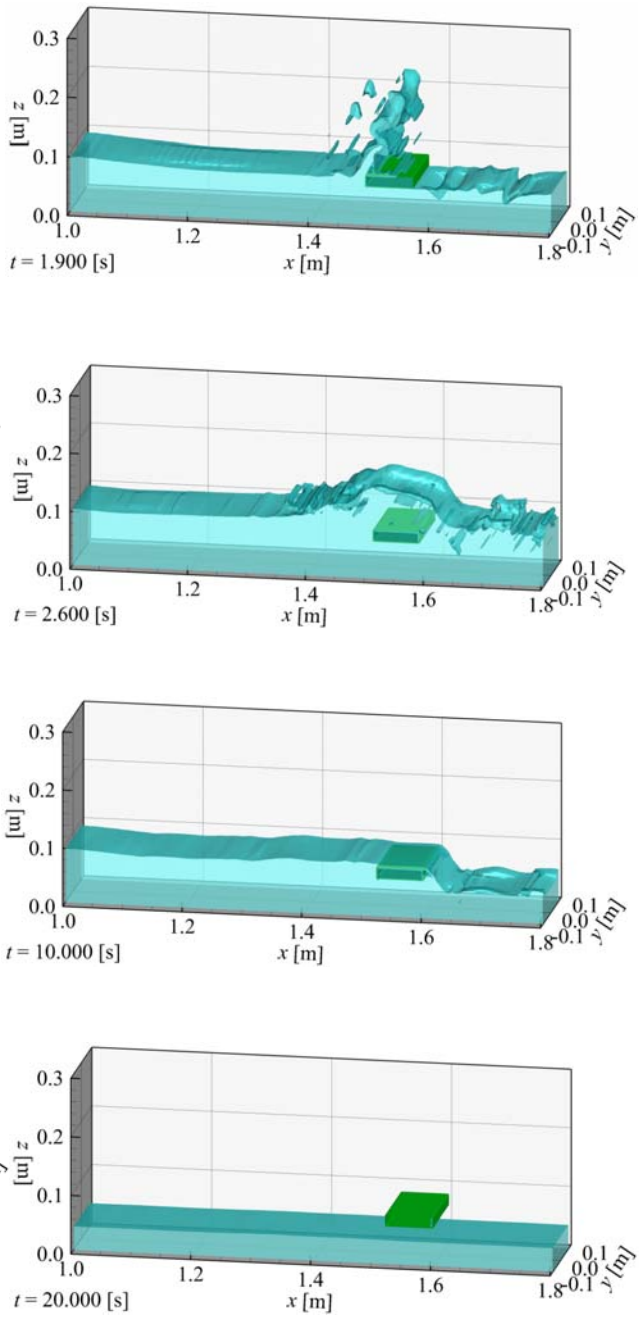


Figure 23 Water Surface Deformation around Bridge Model with Density of 2.0×10^3 kg/m^3

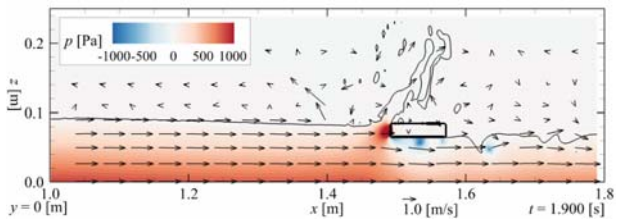


Figure 24 Pressure Distribution along $y = 0.0$ m Plane ($t = 1.9$ s for 1.0×10^3 kg/m^3)

8. CONCLUSIONS

The research work in the paper covers the field survey of damage of bridges by the tsunami on March 11, 2011, the damage analysis based on database, the characteristic of tsunami after coming up the land, and the hydraulic experiment with development of numerical simulation technique. The followings are concluded.

(1) Internet media is a powerful tool to survey the damage by tsunami in wide area.
(2) More than 200 out of 1793 bridges in the inundation area of east Japan (Tohoku region) were washed away by the tsunami. Comparing survived bridge girders with washed ones, girders with rather shallow cross sections are observed much resistive against tsunami.
(3) Water pressure acted on bridge girder may be evaluated by combination of hydrodynamic and hydrostatic pressures. The location of bridge and the height of pier might influence the condition of girder at the attack of tsunami, whether the girder is submerged or not.
(4) Some characteristics of tsunami coming up in the land are examined by observation of motion pictures taken by citizens. The velocity of tsunami in the land increases linearly as the height of tsunami increases. After the height of tsunami reaches to the girder, the velocity of tsunami around the girder may reduce while the height of tsunami still increases.
(5) Two mechanisms on how girders survive against tsunami could be considered depending upon the condition of girder, whether the girder is submerged or not.
(6) Experimental examination was conducted to see how a girder behaved at the attack of tsunami, and what water pressure acted on a girder. A numerical simulation technique has been developed. However, it needs some more time to establish a reliable simulation model.

Acknowledgements:
A part of this study was conducted by the support of JSPS Grant-in-Aid for Scientific Research (A) 24246079. The authors acknowledge the support very much. The authors' thanks are extended to the assistance of Mr. Takuya Shiraishi, a graduate student at Nagaoka University of Technology, and Mr. Yutaro Sawa, an undergraduate student at Nagoya University.

References:

Fu L., Kosa, K., Hedeki, S., and Zheng, Y., "Damage to Structures due to Tsunami and Evaluation of Tsunami Velocity in Shizugawa", Proc. of JCI. Vol.34, 2012, pp. 805-810

Graduate School of Resource Sciences of Department of Civil and Environmental Engineering of Akita University., "Survey of bridge structures of Miyagi Prefecture", Apr. 2011, (http://www.str.ce.akita-u.ac.jp/br/miyagi_str.html)

Japan Road Association, "Specifications for Highway Bridges Part I Common", 2002, pp. 52-57

Kosa, K., Nii, S., Shoji, G. and Miyahara, K., "Analysis of Damaged Bridge by Tsunami due to Sumatra Earthquake", Journal of Structural Engineering, JSCE, Vol. 55A, 2010, pp. 454-463 (in Japanese).

Komatsu, T., Ogushi, K., "Newly Organized Hydraulics, Rikotosho", Apr. 2011, pp. 9-12

Nakamura, T., Yim, S. C., and Mizutani, N. (2011). "Numerical simulation on local scouring around bottom-mounted movable short cylinder," *Proc., Coastal Structures 2011*, ASCE, C4-087, 12 pp.

Nakao, H., Izuno, K., and Kobayashi, H. (2010). "Study on relation of velocity and wave height to hydrodynamic force on bridges by tsunami," *J. Structural Eng.*, JSCE, Vol. 56A, pp. 564-575 (in Japanese).

Rabbat, B.G. and Russel, H.G., "Friction coefficient of steel on concrete or grout", Journal of Structural Engineering, ASCE, Vol. 111, No. 3, 1985, pp. 505-515

Zheng, Y., Kosa, K., Hideki, S., Fu, L., "Damage to Structures in Rikuzentakata Region Due to Tsunami," Proc. of JCI. Vol.34, 2012, pp. 811-816

RETROFIT OF DAMAGED STRUCTURES ACCORDING TO RESPONSE CONTROL CONCEPT

Toru Takeuchi[1)]

1) Professor, Department of Architecture and Building Engineering, Tokyo Institute of Technology, Japan
ttoru@arch.titech.ac.jp

Abstract: In the Great East Japan Earthquake of 2011, many truss-based structures such as school gymnasia and steel towers were damaged owing to the effect of not only Tsunami but the consequent earthquake shake. Typical failure patterns include buckling and fracture of axial members, and damage around the anchored joints of steel frames of reinforced concrete structures. Conventional retrofit methods that restore the original design pose the risk of an identical failure under similar circumstances. The latest response control techniques that involve avoiding damage to braces and bearings can be applied for overcoming this limitation. In this paper, we discuss a method for retrofitting damaged gymnasia using base-isolation bearings or buckling retrained braces and present examples of the method's real-world application.

1. INTRODUCTION

Many schools in the Iwate, Miyagi, and Ibaragi prefectures were damaged owing to seismic shakes resulting from the Great East Japan Earthquake of 2011 (referred to as the 2011 earthquake, hereinafter) and the Chuetsu-oki Earthquake in 2007. Furthermore, communications and truss towers in electric power plants were damaged. In this paper, we propose a retrofit strategy for these structures based on response control techniques and discuss some examples in depth.

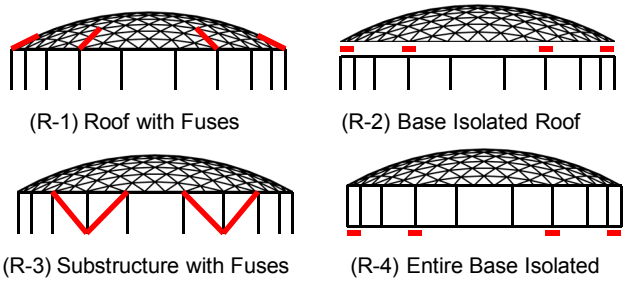


Figure 1 Response Control Concepts for Latticed Roofs

2. RETROFIT USING BASE-ISOLATION BEARINGS

Figure 1 shows a response-control-based method proposed by the Takeuchi et al. (2012.6)[1]. for retrofitting steel roof structures such as domes, latticed shells, and gymnasia. In (R-1), energy-dissipation fuses are installed for protection against the in-plane vibration of the roofs; these are effective in reducing horizontal responses. Here, we use the word "fuse" for elasto-plastic dampers with stable hysteresis, which work as structural elements until their yield strength. In (R-2), base-isolation bearings are installed at the roof's supporting points; these are effective in reducing both horizontal and vertical responses of the roof. Such a system has been installed in several newly constructed structures. (R-3) shows a structure in which energy-dissipating fuses are installed in the substructures and are expected to produce the same effect as that of (R-2). These types of structures are widely used in the construction of stadia and gymnasia. Buckling-restrained braces (BRBs), being in a same situation as those used for multistory buildings, are commonly used as energy-dissipation devices. (R-4) shows a base-isolation system for an entire structure; this structure has been used in the construction of multistory buildings such as airport terminals.

One of the most typical types of damage to school gymnasia due to the 2011 earthquake was failure at the points where steel roof bearings are anchored to concrete

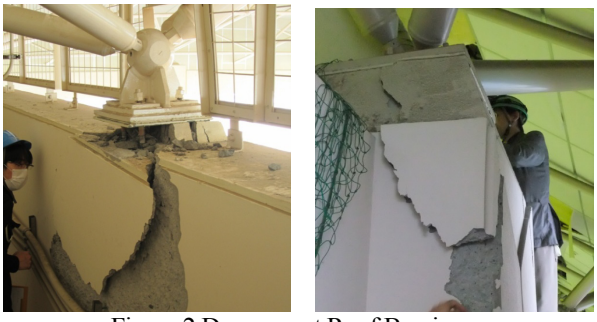


Figure 2 Damages at Roof Bearings

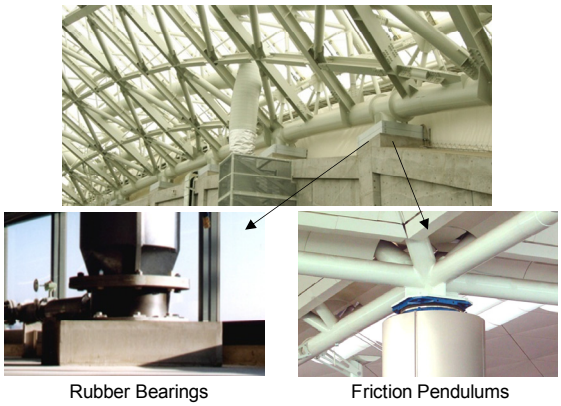


Figure 3 Base Isolation Bearings at Roof Supports

frames[2]. Figure 2 shows damages to gymnasia in the Ibaragi prefecture; in both cases, severe cracking occurred at the beam and column heads, i.e., the points where anchor bolts are fixed. It is assumed that these damages are caused by underestimation of anchor strength against side failure and by the difficulty in estimating the reaction forces on bearings governed by the complex response characteristics of raised shell roofs supported by cantilevered reinforced concrete (RC) walls.

The retrofitting of damaged anchored bearings is difficult. It usually involves covering damaged parts with steel plates, in-filling additional concrete, and fixing with bolts. However, retrofitting often warrants partial reconstruction of beams, columns, exterior walls, and interiors, and the strength and performance of the repaired bearings are usually in line with those of the original design. In cases where the bearings are designed as rollers, they are required to allow for up to 100 mm of displacement because of the cantilevered columns' deformation. Inserting rubber bearings or friction pendulums as base-isolation bearings into roof support points could be an effective, alternative method of retrofitting. Figure 3 shows the examples of cases where base-isolation bearings were inserted into the supporting points of reticulated roofs. Figure 4 shows that the insertion of base isolation bearings into the support points of a latticed roof causes a drastic decrease in the horizontal and vertical components of acceleration along the roof[3]. This result indicates the simplicity and cost-effectiveness of these retrofit methods.

3. RETROFIT USING ENERGY-DISSIPATION FUSES

An easier and more practical retrofit can be achieved by replacing the vertical braces with energy-dissipation members. This concept is shown in Figure 5. Elasto-plastic fuses or viscous dampers can be used as energy-dissipation members; the former are effective in reducing roof displacement, and the latter are effective in reducing roof acceleration. Figure 6 shows the effects of energy-dissipation members on horizontal and vertical accelerations[4]. Increasing the stiffness of the supporting structures increases the response accelerations of raised roofs in the vertical as well as the horizontal directions[5]. As shown in Figure 6 (b), conventional retrofits that involve strengthening the vertical braces can increase the response acceleration along the roof, thus also increasing the risk of damaging the ceiling and any suspended lights. In contrast, response-control retrofit using energy-dissipation fuses or viscous dampers can effectively reduce the roof's response accelerations, as shown in Figure 6 (c) and 6 (d).

In the 2011 earthquake, typical damage patterns such as vertical brace buckling and fractures were widely observed for steel gymnasia. Figure 7 (a) shows the interior of a two-story school gymnasium in Tsukuba, constructed in the early 70s. The first story was constructed using composite, and the second using steel. The roof comprises latticed L-section truss beams supported by steel columns and L-section braces. All vertical braces of this structure underwent severe buckling and fracture, as shown in Figure 7 (b), (c). The ultimate shear strength of the braces allowed for a load equivalent to only 9–14% of the roof's weight and this was inadequate for withstanding the seismic impact of the 2011 earthquake.

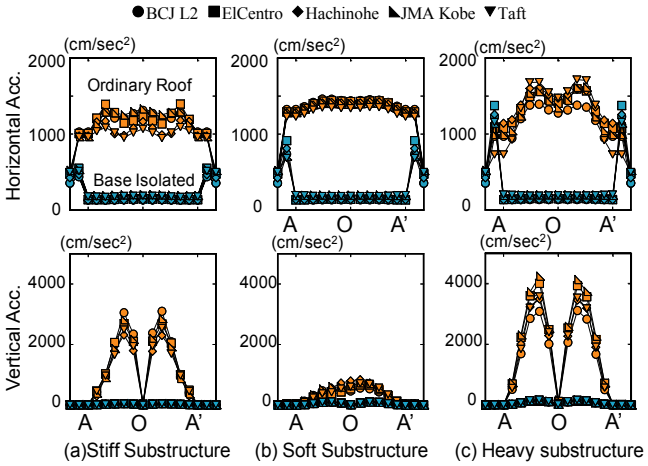


Figure 4 Reduction of Roof Response due to Use of Base-isolation Bearings

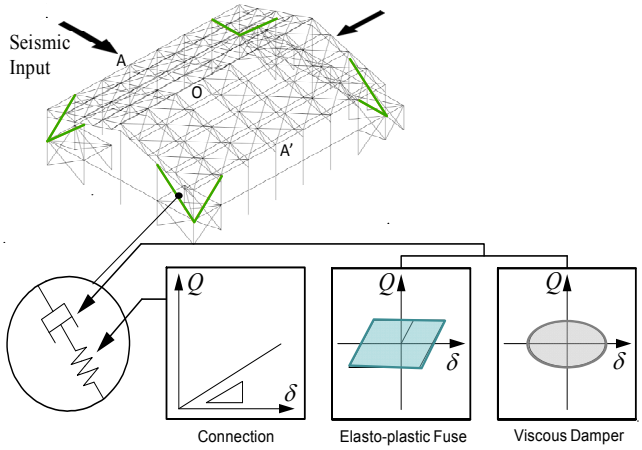


Figure 5 Retrofit of Gymnasia with Ebergy-dissipaton Fuses

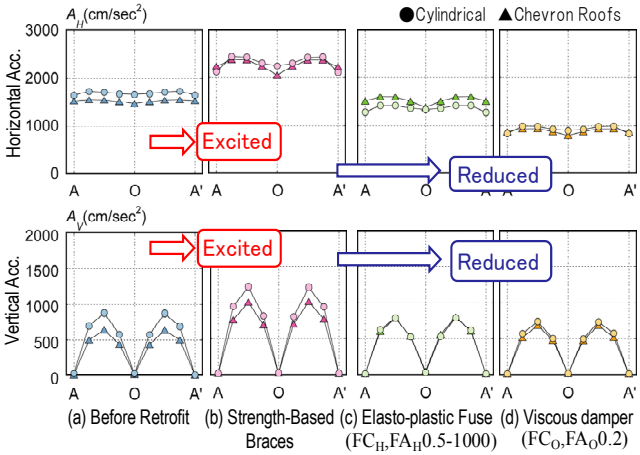


Figure 6 Reduction of Roof Response due to Energy-dissipation Fuses



(a) Interior View of Gymnasium



(b) Brace Buckling



(c) Brace Fracture

Figure 7 Damage to Gymnasium due to 2011 Earthquake (Tukuba O Junior High School)



(a) Attachement of BRB on the Existing Frame





(b) Site-welded connections for BRB

Figure 9 Construction of BRB Retrofit

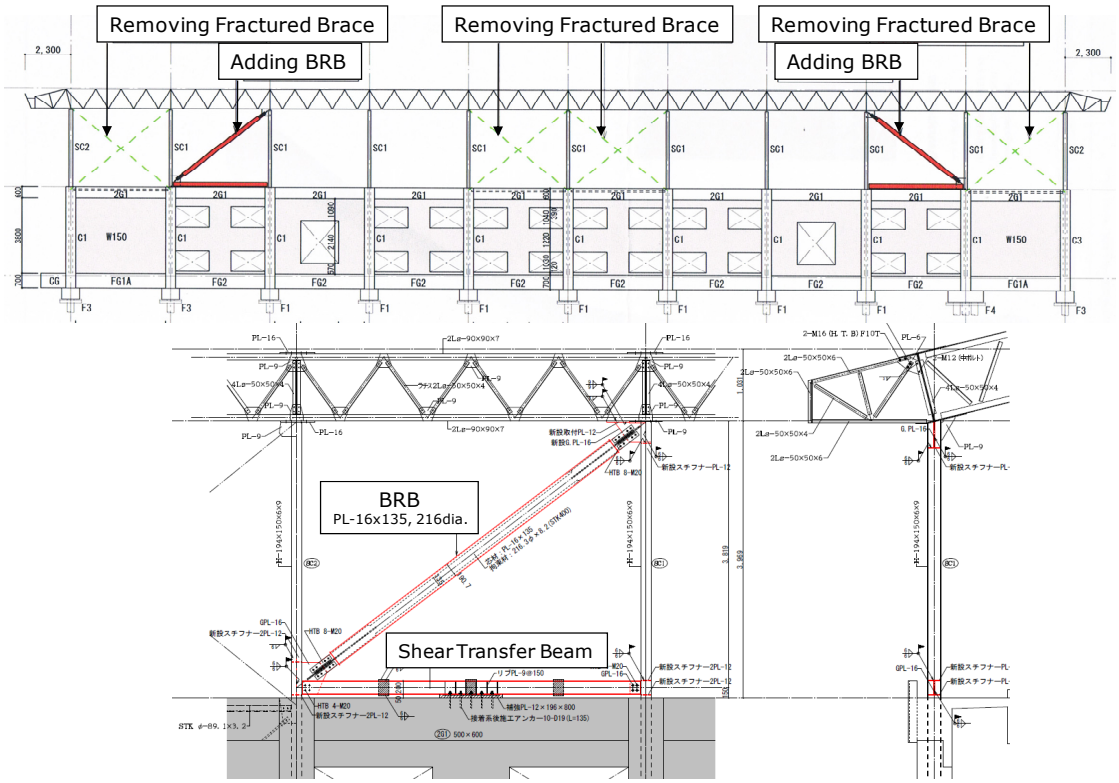


Figure 8 Retrofit of Damaged Gymnasium with BRB

Apart from the vertical braces, a few roof diagonals buckled as well, and many of lighting equipments suspended from the roof fell off. Conventional retrofitting involves the replacement of these braces with wider L-section braces; however, this way, the risk of further buckling due to larger aftershocks remains. To achieve a more robust and damage-tolerant retrofit, we used BRBs instead of L-section braces. Figure 8 shows the longitudinal layout of BRBs. The 24 original braces were replaced with 8 BRBs, which can withstand 557 kN of axial yield forces each and shear forces equivalent to 76–80% of the roof's weight in total. The BRBs are expected to dissipate the impact of seismic inputs larger than those of the 2011 earthquake and prevent severe damage to the roof and the braces themselves. Equivalent seismic indexes, obtained by multiplying the shear force ratio and brace material ductility, are around 211% of the roof's weight. As shown in Figure 8, BRBs were attached by welding gusset plates to the existing frames, and additional shear-force transfer beams were anchored to the RC floor beams.

The retrofit design work was carried out in May 2012, and construction took place between September and December 2012. Figure 9 shows details of the retrofit construction. Figure 9 (a) shows the overall view of the attached BRB, and Figure 9 (b) shows details of the lower and upper connections. The construction was carried out easily, with each BRB attachment taking one day, including site welding and fixture.

Such BRB retrofits are gaining popularity. Figure 10 (a) shows another gymnasium near the border between the Fukushima and Ibaragi prefectures. This gymnasium is a single-story steel construction with a cylindrical shell roof reinforced with vertical braces along the longitudinal



(a) Interior View



(b) BRB Attachement Details

Figure 10 BRB Retrofit in A Junior High School

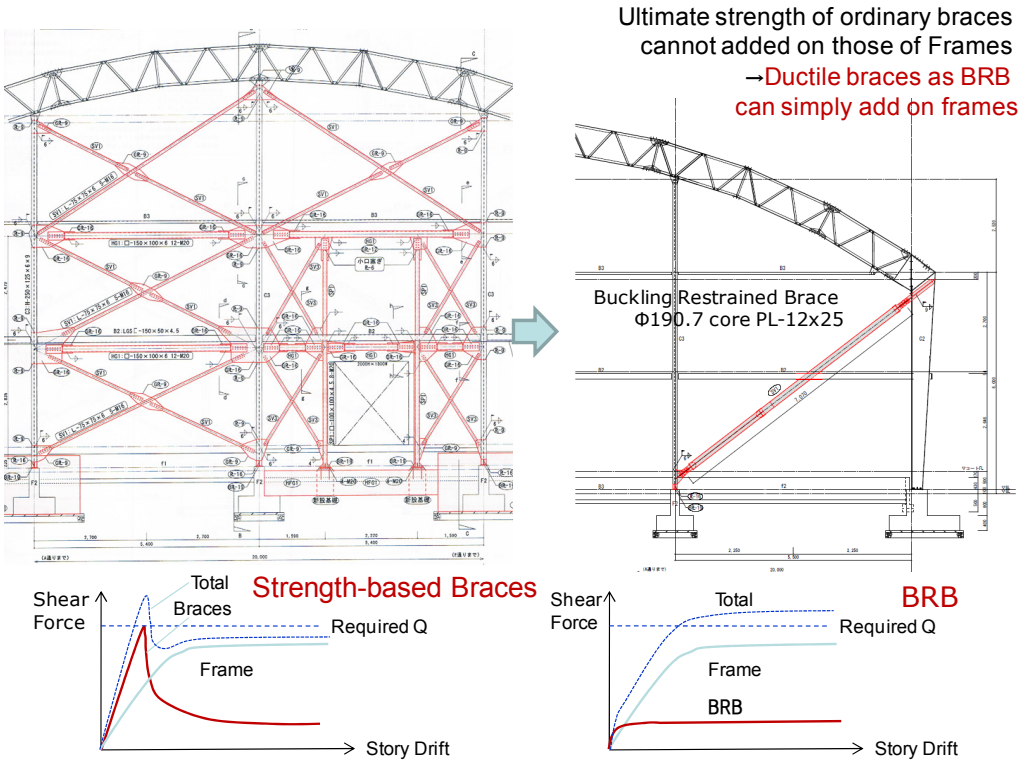


Figure 11 Strength-based Retrofit vs. BRB retrofit

direction. Although the 2011 earthquake did not damage this building, a seismic retrofit was planned because the shear strength of the original braces was equal to only 16% of the roof's weight, which is insufficient against expected future seismic impacts. It was found that the ultimate shear strength in the transverse direction equals 57% of the roof's weight, which is also less than the requirement of 70%. First, the addition of L-section braces was planned under the conventional approach. However, doing so warranted the use of a large number of braces for achieving the 70% shear strength requirement, because the story drift angle at the ultimate shear strength of the latticed frame was expected to be around 2%, and could not be achieved using the additional braces, which reached buckling strength at a 0.13% story drift angle (left part of Figure 11). We proposed, and eventually selected, BRB retrofit as the alternative, because their strength can be added to the original frames directly for maintaining stable hysteresis up to a 3% story drift angle (right part of Figure 11). Consequently, only four additional braces were required. The transverse strength of the BRB-reinforced structure is 91% of the roof's weight, and the expected seismic index, including energy-dissipation effects, touches 230%.

The construction sites are shown in Figure 10 (b). The designed BRBs have a yield strength of around 100 kN and a diameter of 190 mm at the restrainers. These braces are composed of series connections of shorter BRBs and circular section braces, which can pass through the wind-resisting latticed beams, as shown in Figure 9 (c). As in the previous example, gusset plates were welded to the existing frames, and BRBs were fixed using friction bolts.

4. RETROFIT OF TRUSS TOWERS USING BRBs

A similar response control concept with energy-dissipation members can be applied to retrofit various truss structures [1]. Figure 12 shows the layouts of the energy-dissipation members. In (T-1), the devices are installed parallel to the main frame, whereas in (T-2), each chord member is replaced with a corresponding device in each truss column. (T-3) shows another layout for replacing the diagonal members with energy-dissipation members. For arranging such devices in truss frames, the following steps may be followed in general design.

1) For low-stiffness truss structures, the energy-dissipation members should be installed such that they connect two points that are subjected to the largest relative displacement due to expected loads.
2) For high-stiffness truss structures, initially a pushover analysis should be conducted without evaluating buckling, and then, the yielded members should be replaced with energy-dissipation members.

Figure 13 shows the application of the above method to communication towers erected on RC buildings. These communication towers composed of tubular members are designed mainly to withstand wind forces. However, recent studies have indicated that there is a risk of damage to the

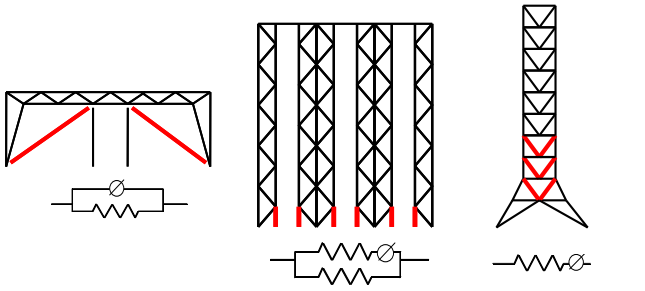


Figure 12 Response Control Concepts for Truss Structures

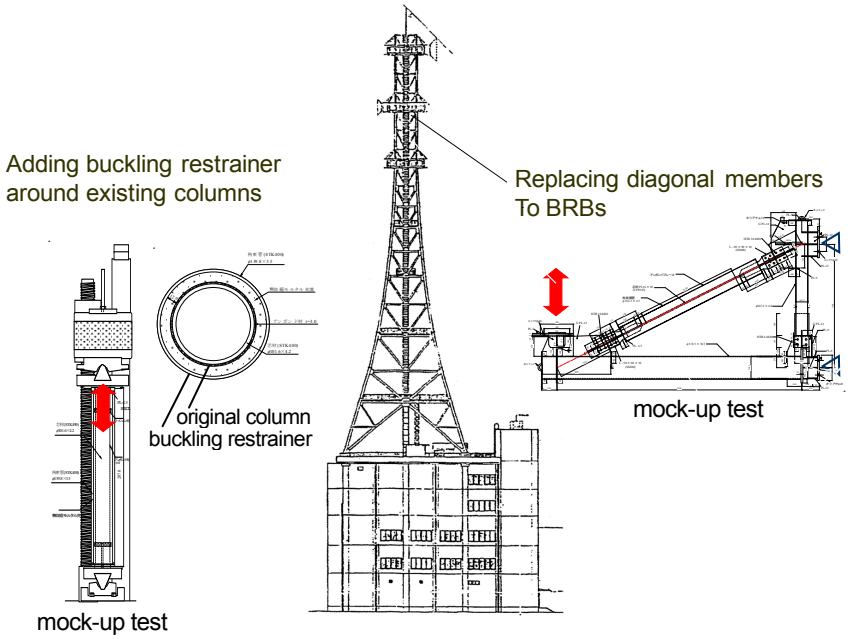
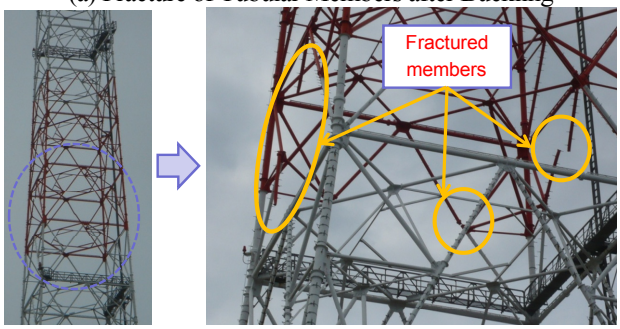


Figure 13 BRB Retrofit Concepts for Truss Towers



(a) Fracture of Tubular Members after Buckling



(b) Truss Tower Fractured by Chuetsu-oki Eatrhquake

Figure 14 Fractures of Tubular Members after Buckling

diagonal members and the leg columns owing to expected earthquakes in the Tokai region. The planned retrofit includes the replacement of diagonal members with BRBs and the addition of buckling restrainers around the existing column members. These actions are similar to those taken for (T-2) and (T-3), shown in Figure 12.

Before carrying out the retrofitting, we investigated cumulative deformation capacities of the tubular members post buckling by performing cyclic loading tests on 1:1 size mock scale models of the truss frames [6]. As shown in Figure 14 (a), tubular braces undergo local buckling in addition to and after the entire frame buckles, and fracture soon thereafter because of plastic strain concentration at the point of local buckling. In the 2007 Chuetsu-Oki Earthquake, diagonal tubular members of truss towers at nuclear power plants near the epicenter fractured after buckling, thereby validating the findings of the mock scale model experiment (Figure 14 (b)).

This fracture process can be evaluated using the idea of a strain concentration index α_c [7]. This idea assumes local strain amplitudes by multiplying normalized axial deflections (defined as the ratio of axial deformation to original length) and concentration indexes; fracture is considered to have occurred when the amplitude of the cumulative local strain reaches the low-cycle fatigue curves of the tube material (Figure 15). For evaluating the concentration index α_c,

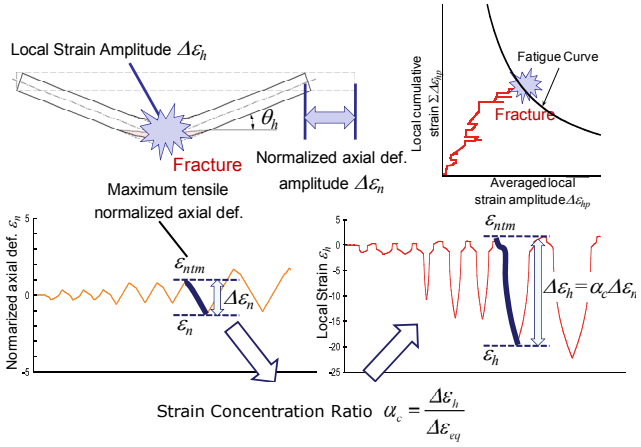
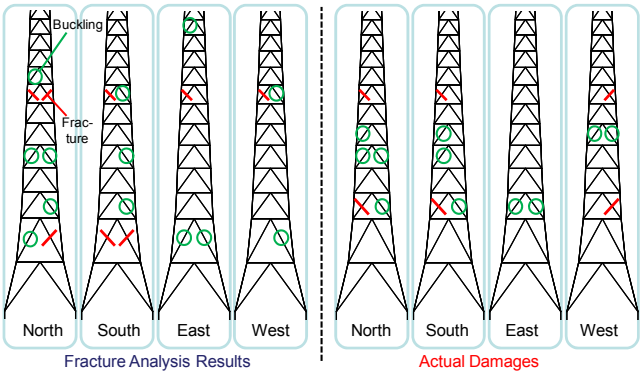


Figure 15 Fracture Prediction by Stress Concentration Index



(b) Fracture Analysis results (c) Actural Damage

Figure 16 Comparison of Fracture Analysis with Actual Damages



Figure 17 Retrofitted Communication Tower

simple equations for the pre-buckling, post overall buckling, and post local buckling phases have been proposed [7] and can be used for time-history analyses. We evaluated the fractured towers shown in Figure 14 and compared the results with the actual damages shown in Figure 16. The fracture analysis results generally agree with the actual failure pattern; therefore, the assumed fracture mechanisms are considered valid. Because such fractures are caused by partial stress concentration at critical members, an effective retrofit method is to replace these members with stable energy-dissipation members such as BRBs, in which the plastic strain is evenly distributed along the braces. The actual retrofitted communication tower is shown in Figure 17; it involved the use of BRBs.

Several retrofit options are compared in Figure 18 (a). One of these is the addition of buckling restrainers around members having insufficient increasing axial strength; the bucking restrainers prevent buckling, thus resulting in increased axial strength (center of Figure 18 (a)). This enhances the structure's seismic responses, and requires additional reinforcement around level 1. The other option is to replace the insufficiently strong members with BRBs (right side of Figure 18 (a)). The analyzed acceleration responses of each of the options are shown in Figure 18 (b). The option involving replacement with BRBs has the minimum response acceleration throughout the height, higher performance, and the lowest construction cost. Consequently, this option was selected and applied to around 50 towers in Tokai religion.

Figure 18 (c) shows the retrofit work for a communication tower in the Mie prefecture. Retrofitting of 20 BRB members could be completed in just six days with three workers, thus proving to be one of the most practical and cost-effective retrofit methods.

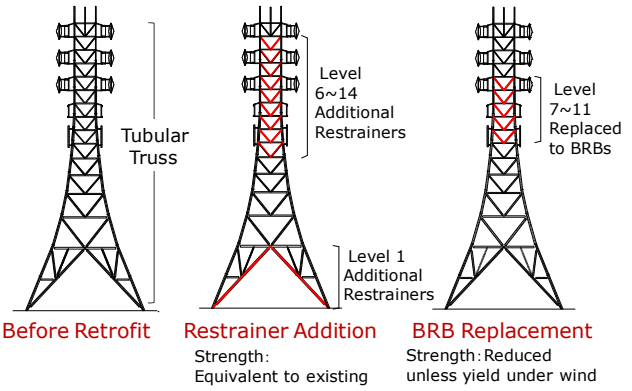
5. CONCLUSIVE REMARKS

We proposed the use of and applied the response control concept for the retrofitting of damaged gymnasia and towers with energy-dissipating members.

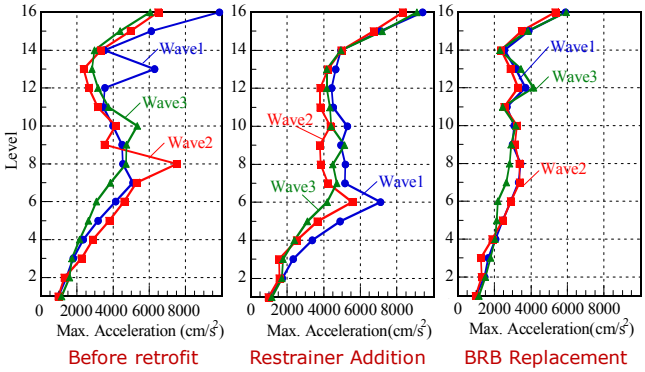
1) For retrofitting damaged bearings of steel roofs of gymnasia and improving performance, the use of base-isolation bearings is considered to be an effective solution.
2) Replacing the vertical braces of a gymnasia with energy-dissipation members, i.e., BRBs, is also a practical and effective retrofit solution for preventing further damage to braces and roof structures. This concept has already been implemented in several retrofits.
3) Similar concepts are applicable to the retrofitting of truss towers, and have been implemented in several structures.

Acknowledgement

This research was supported by the Ibaragi Building Center and its committee members, AIJ Committee for Shell and Spatial Structures, Tokyo Electric Power Co., Ltd., Chubu Electric Power Co., Ltd, and Nippon Steel Sumikin Engineering Co., Ltd.



(a) Retrofit Options



(b) Comparison of Retrofit Options



(c) Construction Site

Figure 18 Seismic Retrofit of Tower with BRB

References

[1] T. Takeuchi, S. D. Xue, S. Nakazawa, S. Kato: Recent Applications of Response Control Techniques to Metal Spatial Structures, *Journal of the International Association for Shell and Spatial Structures*, Vol.53 (2012), No.2, n.172, pp.99-110, 2012.6

[2] T. Takeuchi: Damages of School Facilities in the Great East Japan Earthquake, *9th International Conference on Urban Earthquake Engineering/4th Asia Conference on Earthquake Engineering*, 2012.3

[3] K. Takamatsu, T. Takeuchi, T. Kumagai, T. Ogawa: Response Evaluation of Seismically Isolated Lattice Domes using Amplification Factors, *International Conference Proceedings of IASS2009* (Valencia), pp.120-121, 2009.10

[4] T. Takeuchi, Y. Tsutsumi, T. Kumagai, T. Ogawa: Seismic Retrofit of Steel-structure School Gymnasia with Energy-dissipation Braces, *International Conference Proceedings of IASS2010* (Shanghai), 2010.11

[5] T. Takeuchi, T. Ogawa, T. Kumagai: Seismic Response Evaluation of Lattice Shell Roofs using Amplification Factors, *Journal of the International Association for Shell and Spatial Structures*, Vol.48 (2007), No.3, 2007.12

[6] Y. Ookouchi, T. Takeuchi, T. Uchiyama, K. Suzuki, T. Sugiyama, T. Ogawa, S. Kato: Experimental Studies of Tower Structures with Hysteretic Dampers, *Journal of the International Association for Shell and Spatial Structures*, Vol.47 (2006), No.3, p.229-236, 2006.12

[7] T. Takeuchi, R. Matsui: Cumulative Cyclic Deformation Capacity of Circular Tubular Braces under Local Buckling, *Journal of Structural Engineering, ASCE*, Vol.137, No.11, pp.1311-1318, 2011.11

10CUEE CONFERENCE PROCEEDINGS
10th International Conference on Urban Earthquake Engineering
March 1-2, 2013, Tokyo Institute of Technology, Tokyo, Japan

PREDICTING SPATIOTEMPORAL DISTRIBUTION OF PEOPLE FOR RISK ASSESSMENT AND DISASTER MANAGEMENT

Toshihiro Osaragi [1] and Takuya Oki [2]

1) Professor, Department of Mechanical and Environmental Informatics, Tokyo Institute of Technology, Japan
2) Graduate Student, Graduate School of Information Science and Engineering, Tokyo Institute of Technology, Japan
osaragi@mei.titech.ac.jp, oki@os.mei.titech.ac.jp

Abstract: In order to discuss in detail the environment and urban systems, it is necessary to consider not only static physical objects like buildings, but also the spatiotemporal aspects like the distribution of population. This paper aims to construct models that describe the spatiotemporal distribution of population in urban areas. The models are composed of parameters describing the number of persons per unit floor-area of buildings, which varies according to the time fluctuation factors and the location factors, and are calibrated using a person trip survey data and GIS data. We discuss the characteristics of the spatiotemporal distribution of population and the accuracy of the models, and demonstrate that the proposed models can benefit all phases of urban planning which include risk assessment and disaster management.

1. INTRODUCTION

Ordinal modeling techniques of environment and urban systems based only on static physical objects like buildings do not always describe a certain aspects of their realities. Due to human activities and mobility by rapid urban transportation systems, the distribution of population varies according to time (Osaragi, 2009). This is especially true in metropolitan areas. Thus, the next step in modeling of the urban environment is to take population and institutions into account (Aubrecht et al., 2009). In order to consider population in spatial models, it would be a possible means to use spatially referenced demographic data aggregated to census tracts. The problem with census tracts is that they are not regular in size making inter-comparisons very difficult (Aubrecht et al., 2009). Namely, we need a model which enables us to estimate spatiotemporal distribution of population for any places in various size and various shapes.

Accurately estimating population exposure is a key component of catastrophe loss modeling, one element of effective risk analysis and emergency management (Freire and Aubrecht, 2010). Recently, numerous studies have addressed planning for disasters from various approaches, with an emphasis on planning for serious earthquakes. Until now, estimates of human casualties have relied on the static distribution of population provided by the national census and other counts. Thus, the recent-approved studies are based on a seismic intensity map, and only consider resident population from the census data.

However, the actual spatial distribution of transient occupants in any busy metropolitan area changes by the hour, or even by the minute, so static estimates of the population distribution are of limited utility (Osaragi, 2009). Thus, more accurate estimation of population exposure and risk assessment requires moving beyond using simple residence-based census data (Freire and Aubrecht, 2010). An accurate and dynamic view of the population distribution would thus be extremely useful. For detailed analysis such as modeling of hazards and risk exposure there is a need for even more detailed population distribution (Aubrecht et al., 2009).

Concerning methods such as spatial disaggregation of population, the key is to combine such methods with earth observation data and remote sensing techniques in order to achieve fully integrated urban system models (Bracken and Martin, 1989; Sim, 2005; Steinnocher et al., 2006). With the increasingly available census data and remotely sensed data, to discuss their relationship is one of important issue in GIS data integration (Chen, 1998; Chen, 2002). Aubrecht et al. (2009) have demonstrated how disaggregated population data can improve estimation of exposure to earthquake hazard. Also, Freire and Aubrecht (2010) modeled and mapped nighttime and daytime population distribution patterns at high resolution in order to assess the spatiotemporal human exposure to earthquake risk in the Lisbon Metropolitan Area. They combined the population distribution maps with the seismic hazard intensity map to assess potential exposure and produced new daytime and nighttime overall seismic risk map.

In the present study, we construct models which describe the spatiotemporal distribution of transient occupants of the Tokyo Metropolitan area in terms of “When?” (time of day), “Where?” (location or facility), and “How many?” (population). These models employ data of a Person-Trip survey data (PT data) conducted in the Tokyo Metropolitan area in 1998, comprising transient population

data for periods of the day, municipal zones, and building types. Additional information is taken from GIS data about buildings (building type, floor area, spatial distribution), which have recently come to include a wealth of local information from national and local public organizations. These data sets are combined to create a model emulating the spatiotemporal distribution of population in any desired spatial unit of Tokyo. This paper describes our evaluation of the accuracy of the models and examines the spatial units in which they can be applied by searching for the smallest subdivisions of an area for urban planning using traditional Japanese address units (chō-chōme) and geometric cells, and offers basic information in an attempt to suggest new avenues for research.

2. MODEL FOR ESTIMATING SPATIO-TEMPORAL DISTRIBUTION OF POPULATION

2.1 Definition of "Transient Occupants"

"Transient occupants of the metropolitan area" are defined as the union of several sets of individuals: (1) Occupants of all types of buildings (housing, businesses, educational institutions, etc.); (2) occupants outside buildings (pedestrians, cyclists, etc.); and (3) passengers (occupants of trains, automobiles, and other transportation facilities). The spatiotemporal distribution of railroad passengers was discussed in Osaragi (2009), and automobile passengers in Osaragi and Shimada (2009). In this paper, occupants inside buildings and occupants outside buildings are collectively defined as "transient occupants".

2.2 Formulation of Spatiotemporal Distribution Model for Occupants Inside Buildings

First, we consider $y_{ij}(t)$, the number of transient occupants in building type j in zone i at time t. $N_i(t)$, the total number of occupants in zone i at time t, is obtained by summing $y_{ij}(t)$ over all building types j:

$$N_i(t) = \sum_j y_{ij}(t) \quad (1)$$

Next, we consider that $y_{ij}(t)$ is proportional to the scale of the building denoted by x_{ij} [m^2], the total floor area of building type j in zone i. The number of transient occupants $y_{ij}(t)$ can be obtained by multiplying x_{ij} by the density of transient occupants $\gamma_{ij}(t)$ [persons/m^2], which depends not only on the type of building j and time t, but is also highly dependent on the characteristics (advantages) of the location of zone i. Thus, $y_{ij}(t)$ is calculated as follows:

$$y_{ij}(t) = \gamma_{ij}(t)\, x_{ij} \quad (2)$$

Next, we consider $\gamma_{ij}(t)$ can be divided into two parts: the time fluctuation factor $\alpha_j(t)$, which is common to all zones, and the location factor β_{ij}, which is independent from time. Thus, $y_{ij}(t)$ can be expressed as follows:

$$y_{ij}(t) = \alpha_j(t)\, \beta_{ij} x_{ij} \quad (3)$$

Here, if $\alpha_j(t)$ is normalized to 1 as the mean for all times, the location factor β_{ij} can be considered a parameter expressing the mean density of transient occupant in whole day.

Next, we describe β_{ij} using either (i) unique parameter (dummy variable) for each zone i, or (ii) data describing the characteristics of location of zone i, such as the mean time to the nearest station, the number of buildings by scale and the floor area of buildings. A former model that attempts to use unknown but unique parameters b_{ij} of zone i is called a "*descriptive model*" and expressed as follows:

$$\beta_{ij} = b_{ij} \quad (4)$$

On the other hand, the latter model is called a "*predictive model*", in which β_{ij} is described using unknown parameters (b_{j0}, b_{jk}) and an explanatory variable z_{ik} (where k is the suffix of a variable), which includes the mean time to the nearest station in zone i and variables about buildings normalized by dividing by the geographical area of zone i. Hence, we describe the predictive model as follows:

$$\beta_{ij} = \sum_k b_{jk} z_{ik} + b_{j0} \quad (5)$$

The descriptive model is limited in its geographical scope since it is uniquely determined by its zone. However, within the zone itself, the user can "zoom in" to small portions of the zone for fine-scale estimates of the transient occupants there. In contrast, the predictive model can be used anywhere, as long as sufficient GIS data (explanatory variables) have been obtained. It also assists us to understand the degree of influence of explanatory variables on the number of transient occupants.

2.3 Modeling of Occupants outside Buildings

Occupants outside buildings are generally individuals transiting between buildings. This is especially true during the morning and evening rush hours, when most of the occupants outside buildings are transiting between railway stations and buildings. There are also large numbers of transient occupants in the vicinity of large buildings. As a first step toward describing the number of occupants outside buildings, the floor areas of all buildings and the numbers of boarding or disembarking passengers are considered. Specifically, we describe $y_{i*}(t)$, the number of occupants outside buildings in zone i at time t, using the terms of potential E_i for the number of boarding or disembarking passengers, the total floor area of buildings x_{ij}, and the unknown parameters $\gamma_{i*}(t)$ and $\gamma_{ij}(t)$:

$$y_{i^*}(t) = \gamma_{i^*}(t) E_i + \sum_j \gamma_{ij}(t) x_{ij} \quad (6)$$

where $\gamma_{i*}(t)$ is the ratio of transient occupants derived from boarding or disembarking passengers. $\gamma_{ij}(t)$ [persons/m^2] is the density of transient occupants, which depends not only on the type of building j and time t, but is also highly dependent on the characteristics (advantages) of the location of zone i. E_i expresses the decay in the number of passengers with distance from the station, given in the following equation. E_i is calculated by considering not only the stations within zone i, but also other stations close to the zone i.

$$E_i = \sum_l V_l \sum_{m=1}^{n_{il}} \exp[-2d_{iml}] \Big/ \sum_i \sum_{m=1}^{n_{il}} \exp[-2d_{iml}] \ , \quad (7)$$

where V_l is the number of boarding or disembarking passengers per day at station l (extracted from PT data), n_{il} is the number of locations from which station l is the nearest in zone i, d_{iml} is transit (walking) time from location m in zone i to station l.

Next, $\gamma_{i*}(t)$ and $\gamma_{ij}(t)$ are described as follows, using the product of the time fluctuation factor and the location factor:

$$y_{i*}(t) = \alpha_*(t)\beta_{i*}E_i + \sum_j \alpha_{j*}(t)\beta_{ij}x_{ij} \ . \quad (8)$$

$\alpha_*(t)$ can be considered a coefficient distributed in accordance with the number of railway passengers during various time periods throughout the day. The areas around urban stations are considerably more crowded just after the start of business hours, and the vicinities of the stations in outlying suburbs also become crowded at earlier periods corresponding to the respective commuting times into the city. Thus, one would expect time-based fluctuations of $\alpha_*(t)$ to vary greatly between the downtown region and the suburbs. Therefore, zones are classified into 3 areas based on accessibility to the city center using the dummy variable δ_i^p (defined as δ_i^1=1 ($T \le 2$), δ_i^2=1 ($2 < T \le 10$) and δ_i^3=1 ($10 < T$), $\delta_i^1+\delta_i^2+\delta_i^3$=1, using the time T (min) necessary to get from zone i to the Yamanote Line, a ring railway in central Tokyo):

$$y_{i*}(t) = \sum_p \delta_i^p \alpha_*^p(t)\beta_{i*}^p E_i + \sum_j \alpha_j(t)\beta_{ij}x_{ij} \ . \quad (9)$$

A descriptive model describing β_{i*}^p and β_{ij} are created using unknown parameters (b_{i*}^p, b_{ij}), which are unique to zone i.

$$\beta_{i*}^p = b_{i*}^p \ , \quad (10)$$

$$\beta_{ij} = b_{ij} \ . \quad (11)$$

A predictive model describing β_{i*}^p and β_{ij} is created using unknown parameters (b_{*k}^p, b_{*0}^p, b_{jk}, b_{j0}) and explanatory variable z_{ik}, which represents the mean time to the nearest station from buildings in zone i, variables about buildings normalized by dividing by the geographical area of zone i.

$$\beta_{i*}^p = \sum_k b_{*k}^p z_{ik} + b_{*o}^p \ , \quad (12)$$

$$\beta_{ij} = \sum_k b_{jk} z_{ik} + b_{jo} \ . \quad (13)$$

3. IMPLEMENTING THE MODEL

3.1 Pre-processing of Data

The PT data are in text form and not directly linked to the spatial data. Thus, they are address-matched in the GIS data, and the "*zones*", which are the spatial unit for aggregation in the PT data, are constructed in the GIS data. The source of the GIS data used here is *Tokyo City Planning Geographic Information System Data* conducted in the Tokyo Metropolitan area in 1996. The entirety of the Tokyo Metropolis is designated as the region for analysis. The transient occupants of the prefecture are extracted from the PT data for the total of 417 zones (see Figure 1) for each period of the day. Also, the floor area of buildings and number of buildings by size are extracted from the GIS data for each zone.

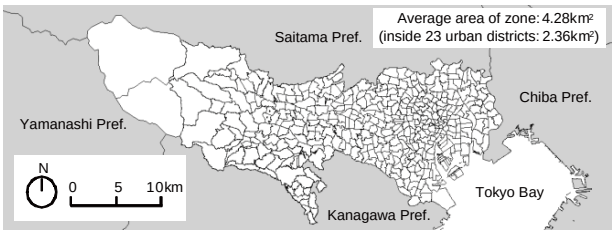


Figure 1 Study Area and Boundaries of Zones

3.2 Calibration of Descriptive Model

3.2.1 Method for estimating parameters of model

A descriptive model is estimated for each building type (14 types, including occupants outside buildings). Figure 2 shows the method for estimating parameters. Since the parameter $\gamma_{ij}(t)$ is divided into two parameters $\alpha_j(t)$ and b_{ij}, they are iteratively estimated by using multiple regression analysis as follows. First, (1) all the values of parameters $\alpha_j(t)$ and b_{ij} are set to 1. Next, (2) create an explanatory variable b_{ij} x_{ij}, and estimate the values of $a_j(t)$ by regression analysis so that the average value of $a_j(t)$ becomes 1. Next, (3) create an explanatory variable $a_j(t)$ x_{ij} using the estimated values of $a_j(t)$, and estimate the values of b_{ij} by regression analysis. Then, (4) check whether the estimated values of parameters $\alpha_j(t)$ and b_{ij} are converged. In case they are not enough converged, repeat the process from (2) to (4).

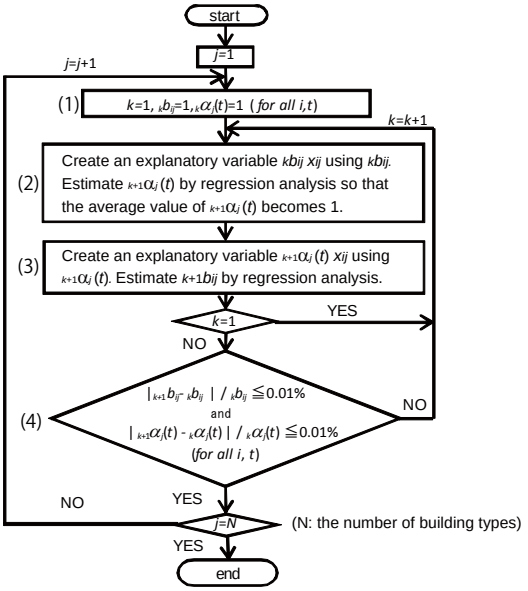


Figure 2 Method for estimating parameters

3.2.2 Model results and observations

Figure 3 shows the estimated values of time fluctuation factor $\alpha_j(t)$ for each building type (the temporal resolution is 1 hour). The fluctuations in $\alpha_j(t)$ vary according to the building types. For instance, the values of residences/ dormitories abruptly decrease between 7:00 and 9:00, and gradually increase from 18:00 to 24:00. I contrast, that of offices/companies/banks is vice versa. The values of other commercial facilities, which include restaurants, show a

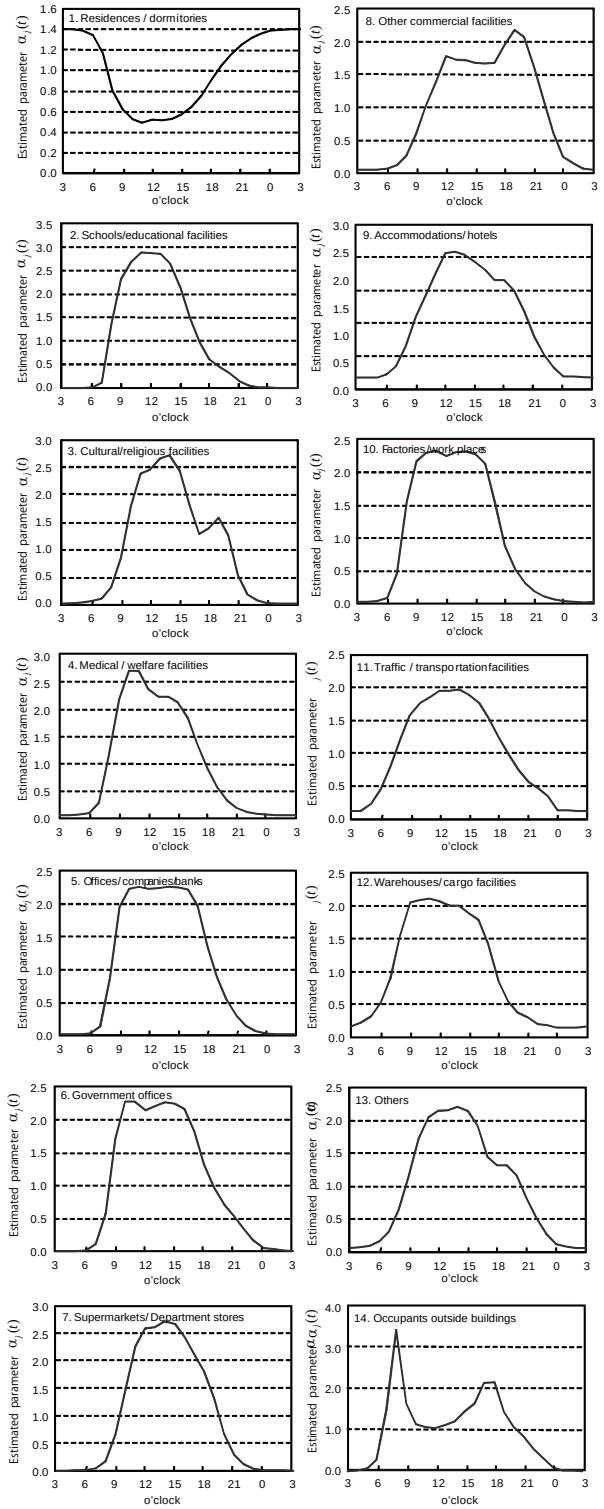


Figure 3 Estimated values of parameters *aj*(*t*)

peak around 19:00. The values of occupants outside buildings show two sharp peaks in the morning and evening, which indicate there are many commuters in the process of traveling to destinations. The values of accommodations/ hotels show only the number of employees and people using facilities (meeting rooms, restaurants, and so on). This is because PT data does not include the guests living outside the study area.

Figure 4 presents the spatiotemporal distributions of density of transient occupants, i.e., the value of $\gamma_{ij}(t)$ (= $\alpha_j(t)$ b_{ij}) for residences/dormitories and offices/companies/banks, which are typical buildings with large number of transient occupants. The time-dependent fluctuation of the transient occupants appears clearly. Some fluctuations of residences/dormitories are even greater in the environs. This indicates that the density of transient occupants is higher in the suburban area than in the city center. The number of individuals leaving these zones increases with time after the early morning, so the transient occupant density falls, as shown in the figure. Correspondingly, the figures for offices/companies/ banks show a low density at 8:00, with no marked difference between regions, but with the passage of time, the density of transient occupants becomes relatively high, especially in zones around Tokyo station. The results for residences/dormitories and for offices/companies/ banks show nearly opposite trends in their distributions, indicating movement between the two building types. The spatial movement between residences and offices is clearly visible here.

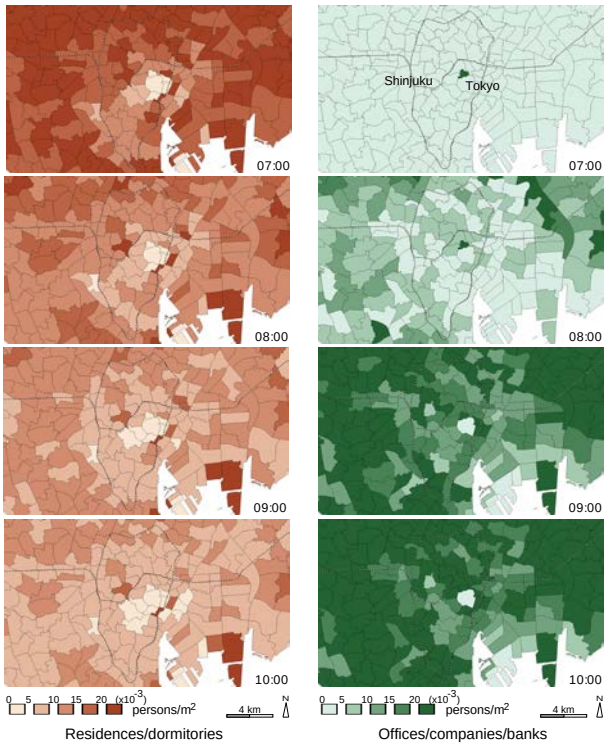


Figure 4 Spatiotemporal distribution of density of transient occupants

3.3 Calibration of Predictive Model

3.3.1 Method for estimating parameters of model

A predictive model is estimated for various types of buildings using building data (floor area, number of buildings of each scale) as explanatory variables describing location factors β_{ij}. However, a residual of the estimate is found along the railway lines, so variables expressing the

railroad service area of railway lines in each zone are incorporated to eliminate that influence.

The parameters are estimated using the method shown in Figure 2. The *t*-values of the parameters and the Akaike Information Criterion (AIC) are calculated in order to evaluate the balance among compatibility and conciseness of the model. The explanatory variables are extracted for every building type and examined to validate whether they are theoretically possible to be used. Table 1 presents the explanatory variables describing location factors, which are statistically significant; only the signs of the estimated parameters are given to simplify the presentation of their influences.

3.3.2 Model results and observations

Table 1 provides the explanatory variables for typical buildings with large numbers of transient occupants. For example, as for the model of residences/dormitories, the coefficient for the number of small-scale detached houses (-80m^2) is positive (+). This indicates that the greater the number of small-scale detached houses in a region, such as in a neighborhood of wooden houses, the greater the density of transient occupants.

Table 1. Variables used in predictive model and their estimated parameters

Objective variable (classification in PT data) The # of occupants	Explanatory variables (classification in GIS data)	
	Building floor area	Significant variables describing local factors and signs of the estimated parameters
Residences/ dormitories	Detached house/ flat/house with shop/house with factory	(+): Detached house(-80m^2), Access time to Yamanote Line, Mita-Tojo Line**, Keikyu-Tokaido Line**, Shinjuku-Ikebukuro Line**, Shinjuku Line** (-): Flat(5000m^2-), Shunjuku2-Sobu-Oshiage- Kameedo Line**, Hibiya-Ginza-Hanzomon Line**, Yamanote Line**
Schools/educational facilities	School	(+):School(400m^2-), Supermarket/Department store(320m^2-) (-): School(-70m^2)
Offices/ companies/banks	Office	(+):Hibiya Line**, Ginza Line** (-): Office(650m^2-), Government office(-80m^2), Time to the nearest station, Oedo Line**
Supermarkets/ Department stores	Supermarket / Department store	(+):Recreational facility*, Detached house(-80m^2) (-):Time to the nearest station
Occupants outside buildings	the # of Passengers	(+):House with shops*, Recreational facility(460m^2-) (-):
	Detached house/ flat/house with shop or factory	(+):Recreational facility(460m^2-), School(400m^2-) (-):
	Office	(+):Hospital(-65m^2) (-): Time to the nearest station

Note: [*] indicates building floor area, [**] indicates dummy variable of railway services area, and variable with the size of floor area indicates the number of buildings in each zone. The sign of the estimated parameter is shown by (+) or (-).

4. VALIDATION OF MODELS

Figures 5 and 6 provide the accuracies of some of the predictions (relationship between actual measurements and model-predicted transient occupants in each zone) of the descriptive model and the predictive model. The results of the descriptive models are markedly consistent with actual measurement (value of PT data). This fact indicates that once we can accurately describe the location factor of each zone, we can obtain extremely precise estimates of the dramatic time-based fluctuations in the number of transient occupants in a city, simply by knowing the floor area of buildings. The results of the predictive model are not as precise as those of the descriptive model. Still, this model shows good accuracy for a simple regressive model.

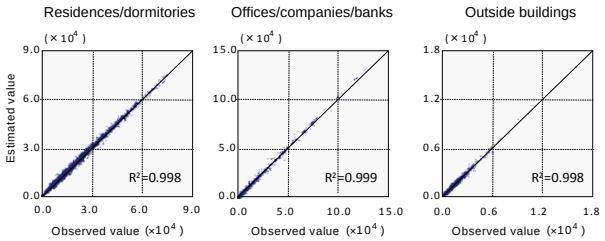


Figure 5 Compatibility of descriptive models

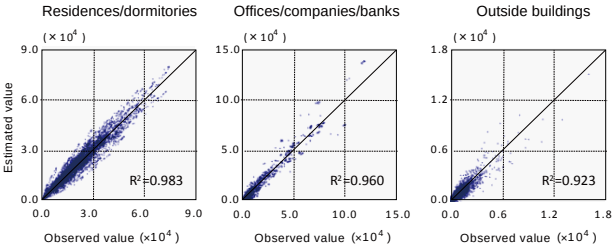


Figure 6 Compatibility of predictive models

Figure 7 shows some results of changes of the mean absolute error and error ratio of the predictive model over time for each building type. In building types prone to higher numbers of transient occupants, such as residences/ dormitories and offices/companies/banks, the mean absolute error is not small enough, but the error ratio is around 0.1. From the viewpoint of the error ratio to the total number of transient occupants, the results show good accuracy in whole day. Buildings with extremely low numbers of transient occupants from the middle of the night to the early morning hours (cultural facilities, etc.) show high error ratios, that is, inferior estimation accuracy. However, the zone totals, comprised of the occupancies of all building types, showed good accuracy in estimates of transient occupant population.

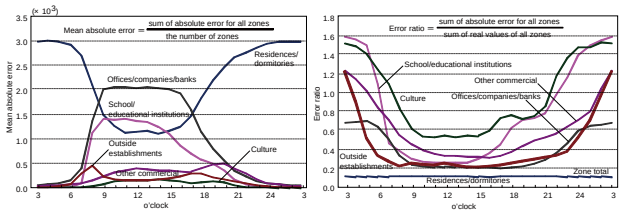


Figure 7 Estimation error of predictive model according to time

5. SUMMARY AND CONCLUSIONS

Models were constructed to estimate the spatiotemporal distribution of transient occupants of the Tokyo Metropolitan area, specific to each type of building in the region, based on information on the scale, type and location features available for buildings in digital maps that have recently become available. These models were successful in visualizing the spatiotemporal fluctuations in transient occupant population while selecting the size of spatial unit by evaluating the estimation error. Future studies by the present authors will examine applications of these models for simulating wide-area rescue activities following a devastating earthquake, behavior of commuters returning home from their offices/ schools on foot, and other topics (Osaragi and Tanaka, 2011).

In order to construct a simulation model for evacuation-efforts following a severe earthquake, we should consider not only the spatiotemporal distribution of occupants remaining in the city, but also of transient occupants, i.e., people who are walking or otherwise in the process of using transportation in the city (Osaragi, 2009; Osaragi and Shimada, 2009). The importance of these kinds of studies lies in its implications for quick emergency response and recovery. For instance, congested streets would impede people from arriving at medical centers or emergency activities, such as firefighting and rescue of persons. In addition, under extreme pedestrian congestion, they might be injured or even accidentally crushed. In the case of a secondary earthquake, the vicinities of large-scale stations already congested with pedestrians, could lead to serious confusion. Hence, we need to consider micro-scale pedestrian flow under such extreme scenarios by using the spatiotemporal database provided in the present study in order to establish emergency and evacuation planning.

The models proposed in the present study were created to offer basic data for a variety of analyses of urban areas, of which disaster mitigation planning is just one example. As Aubrecht et al. (2011) suggested, high-detail spatiotemporal distribution on human activities can be of great value in disaster risk management and simulation, but also in regional and environmental planning as well as geomarketing analysis.

Acknowledgements:

This research is part of an effort supported by a Grant-in-Aid (21310105) from the Japan Ministry of Education, Culture, Sports, Science and Technology Health (MEXT) and a Labor Sciences Research Grant, Scientific Research (B). This paper was originally presented at the AGILE conference (Osaragi and Hoshino 2012). The author would like to give his special thanks to Mr. Takeshi Hoshino for computer-based numerical calculations.

References:

Aubrecht C, Köstl M, Steinnocher K (2011) Population Exposure and Impact As-sesment: Benefits of Modeling Urban Land Use in Very High Spatial and Thematic Detail, Computational Vision and Medical Image Processing Com-putational Methods in Applied Sciences, Springer, 19, 75-89.

Aubrecht C, Steinnocher K, Hollaus M, Wagner W (2009) Integrating earth observation and GIScience for high resolution spatial and functional modeling of urban land use, Computers, Environment and Urban Systems 33:15-25.

Bracken, I., & Martin, D. (1989) The generation of spatial population distributions from census centroid data. Environment and Planning, A/21, 537–543.

Chen, K. (1998) Correlations between census dwelling data and remotely sensed data. In Proceedings: SIRC 98 – 10th annual colloquium of the spatial information research centre. Dunedin, New Zealand.

Chen, K. (2002) An approach to linking remotely sensed data and areal census data. International Journal of Remote Sensing, 23(1), 37–48.

Freire S, Aubrecht C (2010) Towards improved risk assessment: Mapping the spatio-temporal distribution of human exposure to earthquake hazard in the Lisbon metropolitan area, Gi4DM2010, Turin Italy.

Osaragi T (2009) Estimating spatio-temporal distribution of railroad users and its application to disaster prevention planning, Lecture Notes in Geoinformation and Cartography, Advances in GIScience, Eds. M.Sester et al., Springer, 233-250.

Osaragi T, Shimada R (2009) Spatio-temporal distribution of automobile for disaster prevention planning, Journal of Architectural Planning and Engineering, 641:1561-1568.

Osaragi T, Tanaka S (2011) Simulation model of individual decision making and behavior for returning home after a devastating earthquake, the 12th International Conference on Computers in Urban Planning and Urban Management.

Osaragi T, Hoshino T (2012) Predicting Spatiotemporal Distribution of Transient Occupants in Urban Areas, Lecture Notes in Geoinformation and Cartography, Bridging the Geographic Information Sciences, Eds. J. Gensel et al., Springer, 307-325, 2012.

Sim, S. (2005). A proposed method for disaggregating census data using object-oriented image classification and GIS. International Archives of Photogrammetry, Remote Sensing and Spatial Information Sciences, XXXVI (Part 8/W27).

Steinnocher, K., Weichselbaum, J., & Köstl, M. (2006) Linking remote sensing and demographic analysis in urbanised areas. In P. Hostert, A. Damm, & S. Schiefer (Eds.), Proceedings: First workshop of the EARSeL SIG on urban remote sensing. Berlin, Germany.

10CUEE CONFERENCE PROCEEDINGS
10th International Conference on Urban Earthquake Engineering
March 1-2, 2013, Tokyo Institute of Technology, Tokyo, Japan

GROUND-MOTION-INDUCED DAMAGE OF BRIDGES DURING THE 2011 GREAT EAST JAPAN EARTHQUAKE

Kazuhiko Kawashima

Professor, Department of Civil Engineering, Tokyo Institute of Technology, Japan
kawashima@kba.biglobe.ne.jp

Abstract: This paper presents damage of bridges during the 2011 Great East Japan earthquake. Effectiveness of recent development of seismic design and implementation of seismic retrofit is evaluated based on comparison of the damage during the 2011 Great East Japan earthquake and the 1978 Miyagi-ken-oki earthquake.

1. INTRODUCTION

The Great East Japan earthquake (M_w9.0) occurred on March 11, 2011 along the Japan Trough in the Pacific Ocean. This was the largest earthquake which ever historically occurred around Japan. The fault zone extended 450km and 200km in the north-south and west-east directions, respectively, as shown in Fig. 1. Extensive damage occurred in a wide region in the east Japan.

A number of strong motion accelerations were recorded in the damaged areas by the National Institute of Earth Science and Disaster Prevention (NIED) and Japan Meteorological Agency (JMA). Most accelerations were recorded at stiff sites as it was the purpose of NIED and JMA to record base-rock accelerations. Fig. 2 shows typical acceleration records along the Pacific Coast. Ground accelerations continued over 200s, and they had at least two wave groups reflecting the fault rupture process. The highest peak ground acceleration of 27.0 m/s^2 was recorded at Tsukidate City. However the high acceleration was resulted from a single pulse with 0.2 second period, therefore response acceleration at 1.0s was only 5.1m/s^2. Consequently damage of bridges and buildings was very minor in Tsukidate City. This clearly shows that only PGA cannot be a reliable index for seismic design.

At soft soil sites in the north Miyagi-ken and south Iwate-ken (refer to Fig. 1), ground accelerations included longer period components leading to higher response accelerations at 0.5-1.5s. For example, response acceleration was over 16 m/s^2 at 0.8 s in Osaki as shown in Fig. 3.

Seismic design code of bridges was extensively enhanced since 1990 (JRA 1990, 1995, 1996, 2002, 2012, Kawashima and Unjoh 1997, Kawashima 2006). Only a combination of the static elastic analysis assuming 0.2-0.3 seismic coefficient and the allowable stress design approach (seismic coefficient method) was used until 1990 (JRA 1964, 1971, 1980). The static elastic method is still in use today but a combination of the inelastic static analysis and the Type I and II design ground motions as shown in Fig. 4 has been the main stream approach in the post-1990 codes. Thus the seismic demand was much enhanced in the post-1990 design codes.

Type I design ground motion represents the ground motions which are induced by an M8 subduction earthquake while Type II design ground motion represents near-field ground motions which are induced by a M7 earthquake. Deterministic ground motions are used in Japan since probabilistic ground motions assuming Poisson's distribution underestimates ground motions when a target earthquake occurs. Zoning coefficient c_z is multiplied to get design ground motion. Zoning map (very high, high, and moderate seismic zones) depends on a probabilistic hazard map, however conservative values are assigned to moderate seismic zone (c_z=0.7) compared to very high seismic zone (c_z=1.0) since seismological information available now is incomplete. Conservative zoning coefficient ($c_Z \geq 0.7$) was very effective to avoid underestimation of design ground motions due to unknown faults in past earthquakes.

Elastic and inelastic dynamic response analyses have been conducted on routine basis for bridges with complex structural response since 1995. Seismic isolation has been implemented since the early 1990s (TRCNLD 1988, PWRI 1992, PWRI 2011, Unjoh et al 2010). This led to extensive implementation of elastomeric bearings, including lead rubber bearings and high damping rubber bearings.

Since the 1980s, over 30,000 reinforced concrete columns in existing bridges with mid-height cutoff of longitudinal steel and insufficient development length have been seismically retrofitted (JRA 1988, 2002).

It is important to note that a number of bridges in a part of the region affected by the 2011 Great East Japan Earthquake (north Miyagi-ken and south Iwate-ken, refer to Fig. 1) suffered extensive damage during the M7.4 1978 Miyagi-ken-oki earthquake (EERI 1978). The 1978 Miyagi-ken-oki earthquake occurred off Sendai. The epicenter was 38.2 N and 142.2 E, and the fault extended 30 km and 80 km in NS and EW directions as shown in Fig. 1. Fig. 5 compares 5% damped response accelerations of records near Kaihoku Bridge in Ishinomaki City during the 1978 Miyagi-ken-oki earthquake and the 2011 Great East Japan earthquake. Since the accelerations were recorded on the surface of shallow soil underlaid by soft rock, the acceleration responses are high at 0.2-0.5s with sharp decrease of response acceleration over

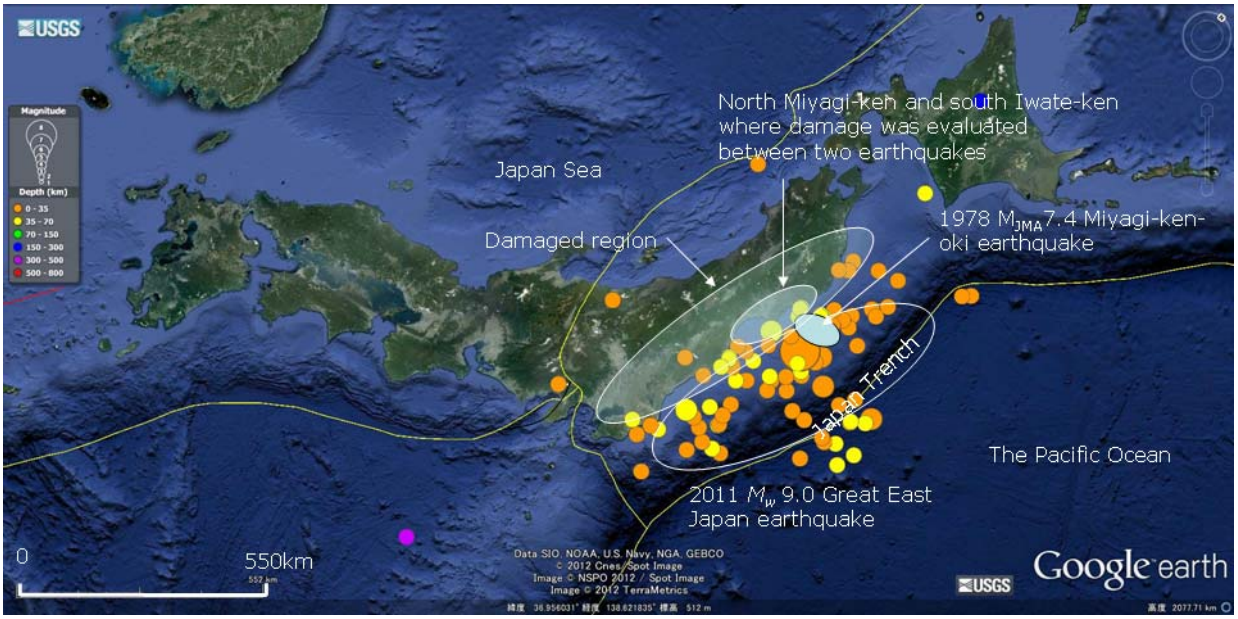


Figure 1 Fault zone of 2011 Great East Japan earthquake, damaged region, and north Miyagi-ken and south Iwate-ken where damage was compared with that from the 1978 Miyagi-ken-oki earthquake

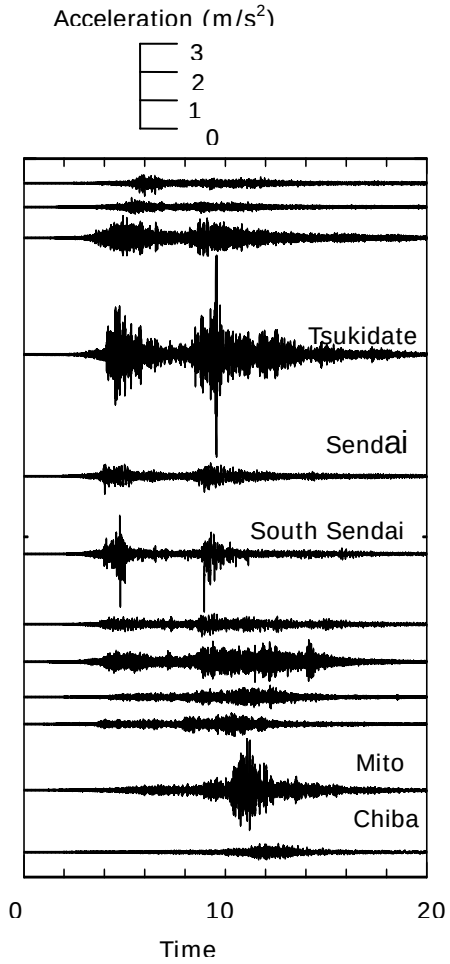
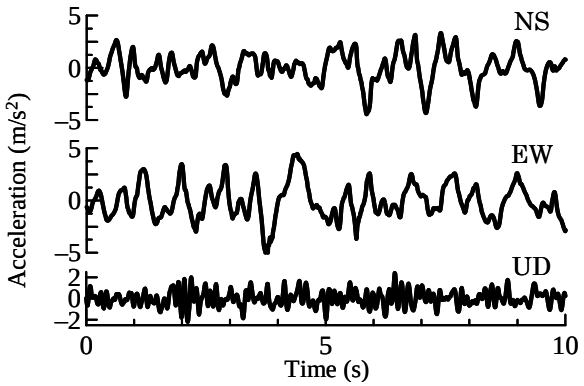
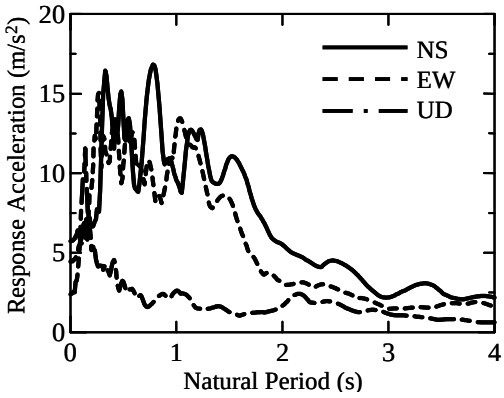


Figure 2 Acceleration records along the Pacific Coast



(a) Accelerations



(b) 5% damped response accelerations

Figure 3 Acceleration recorded at Fyrukawa, Osaki City

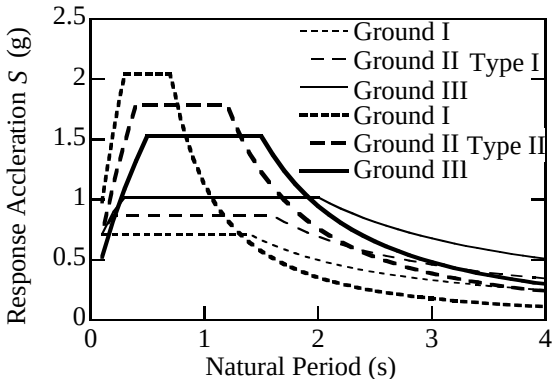
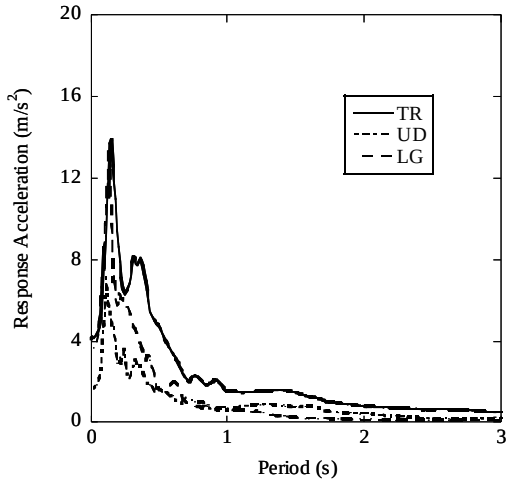
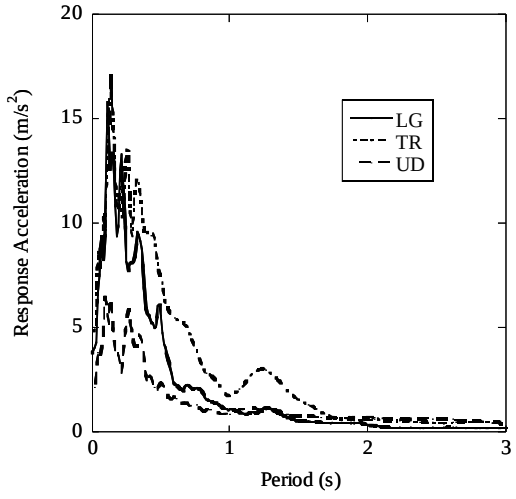


Figure 4 Type I and Type II design ground motions



(a) 1978 Miyagi-ken-oki earthquake



(b) 2011 Great East Japan earthquake

Figure 5 Comparison of 5% damped acceleration response near Kaihoku Bridge, (a) 1978 Miyagi-ken-oki earthquake, (b) 2011 Great East Japan earthquake

0.5s. Since the ground acceleration near Kaihoku Bridge was one of the few records during the 1978 Miyagi-ken-oki earthquake, the record has been widely used in dynamic response analyses as a typical strong ground acceleration. Thus comparison of records between the two earthquakes is shown here at this site. It is seen that intensity of ground accelerations in terms of response accelerations during the 2011 Great East Japan earthquake was slightly larger than or in the similar level with the one during the 1978 Miyagi-ken-oki earthquake. Note that response accelerations were much larger at 1-2s at soft soil sites than the value shown in Fig. 5. Response accelerations at high intensity areas during the 2011 Great East Japan earthquake were close to but smaller than the Type II design ground motions.

Thus, the 2011 earthquake was a valuable opportunity to evaluate the effectiveness of recent developments of the seismic design codes by comparing damage sustained in the two earthquakes. Comparison was made for damage at north Miyagi-ken and south Iwate-ken where extensive damage occurred during the 1978 Miyagi-ken-oki earthquake (refer to Fig. 1). Damage is described for three bridge categories: (1) bridges designed based on pre-1990 design codes (JRA 1964, 1971, 1980 codes), (2) the first category bridges which had been retrofitted based on post-1990 code (JRA 1990, 1995, 1996, 2002 codes) prior to the 2011 Great east Japan earthquake, and (3) bridges designed based on post-1990 design codes.

In addition to ground shaking induced damage, damage due to tsunami inundation occurred extensively (JSCE 2011, Kawashima et al 2011). However it is not presented in this paper.

2. DAMAGE STATISTICS

Table 1 shows number of national road bridges control by Tohoku Regional Bureau, Ministry of Land, Infrastructure, Transport and Tourism (JSCE 2012, NILIM & PWRI 2011). There were 1,909 bridges consisting of 1,157 bridges on main routes, 415 pedestrian bridges along main routes, and 337 bridges over main routes. Of the 1,909 bridges, 867 bridges (45%) were undamaged, 885 bridges (46%) were damaged by ground shaking, and 154 bridges (8%) were damaged by tsunami. Although it was easily identified that drag of spans, lean of handrails, erosion of abutment backfills and scouring of foundations were developed by tsunami, it was difficult to identify whether cracks of piers and abutments were developed by ground shaking or tsunami. Therefore damage of bridges which were submerged by tsunami at least deck level was counted as damage by tsunami. It should be noted that there was no bridges which collapsed due to ground shaking, while 12 bridges collapsed due to tsunami.

Table 2 classifies deterioration degree of structural performance and serviceability for traffic of 1,572 national road bridges (1,157 bridges on main routes and 415 pedestrian bridges) shown in Table 1. The damage degree and serviceability for traffic were evaluated in accordance with the standard procedure of Guide Specifications for Earthquake Countermeasures - Post Earthquake Countermeasures (JRA 1988, 2008). There were 12 bridges and 13 bridges which were evaluated as A_S rank (collapse or extensive deterioration) and A rank (major damage), respectively, and 29 bridges were completely interrupted for traffic.

Table 1 Number of national road bridges inspected and damaged (JSCE 2012)

Type of bridges	No. of bridges inspected	No. of bridges which could not be inspected	No. of bridges undamaged	No. of bridges damaged by ground shaking	No. of bridges submerged by tsunami
Main bridges	1,157	0	445	619	93
Side pedestrian bridges	415	0	167	190	58
Bridges over main routes	337	3	255	76	3
Total	1,909	3	867	885	154

Table 2: Degree of deterioration of structural damage and serviceability of 1,572 national road bridges (JSCE 2012)

(a) Structural deterioration degree

Damage degree	No. of bridges
A_S: Collapse or extensive deterioration	12 (0.7%)
A: Major damage	13 (0.8%)
B: moderate damage	32 (2.0%)
C: Minor damage	103 (6.6%)
D: No damage	1,412 (89.8%)
Total	1,572 (100%)

(b) Serviceability deterioration

Serviceability	No. of bridges
A: Interrupted	29 (1.8%)
B: Traffic is possible with care	433 (27.5%)
C: No effect	1,110 (70.%)
Total	1,572 (100%)

Table 3: Damage modes of 1,572 national road bridges (JSCE 2012)

Locations	Types of damage	No. of Damage Modes
Overall bridge	Collapse, Offset of superstructures	27 (1.6%)
Superstructures	Cracks and deformation of superstructures	88 (5.1%)
Pavements	Cracks	93 (5.4%)
Expansion joints	Cracks, opening and closure, settlement	173 (10.0%)
Handrail	Lean of handrails by tsunami	149 (8.7%)
Bearings	Failure of bearings and concrete seats	147 (8.6%)
Bearing support	Failure of cap beams under bearings	60 (3.5%)
Unseating prevention devices	Failure of anchor bars or connections	32 (1.9%)
Abutment wall and parapet walls	Cracks or spalling of cover concrete	126 (7.3%)
Side wall of abutments	Cracks or spalling of cover concrete	73 (4.3%)
Backfill of abutments	Settlement	659 (38.4%)
Piers and columns	Cracks or spalling of cover concrete	42 (2.4%)
Scouring of foundations	Scouring due to tsunami	46 (2.7%)
Total		1,715 (100.0%)

Table 3 shows damage modes of 1,572 national road bridges. As there were bridges which suffered more than one mode of damage, the total number of damage mode is over 1,572. Twenty seven bridges collapsed or their spans offset extensively. Common damage mode was settlement of abutment backfills, cracks and spalling of abutment concrete walls, damage of bearings and their supports, and opening and closure of expansion joints. Note that those damage modes are related to permanent tilting of abutments and piers. In particular, as abutments are subjected to dynamic earth pressure from backfill side to bridge side, it often tilts toward bridge side. Lean of handrails and scouring of foundations were developed by tsunami. However no bridges collapsed due to scouring.

3. PERFORMANCE OF BRIDGES CONSTRUCTED IN ACCORDANCE WITH PRE-1990 CODES

Extensive damage occurred at the bridges which were designed in accordance with pre-1990 design codes and the bridges which had not yet been retrofitted. For example, Fig. 6 shows flexural-shear failure of reinforced concrete piers at Fuji Bridge and Esaki Bridge. The damage was resulted from an overestimated shear capacity and an inadequate development of longitudinal bars at cut-off (Kawashima, Unjoh and Hoshikuma 1995). It was the mandate practice prior to the pre-1980 design codes. This mode of damage occurred extensively during the 1995 Kobe, Japan earthquake (Kawashima and Unjoh 1997). Extensive investigation



(a) Fuji Bridge



(b) Esaki Bridge

Figure 6 Flexure-shear failure of columns due to termination of longitudinal bars with insufficient development (NLIM & PWRI 2011)

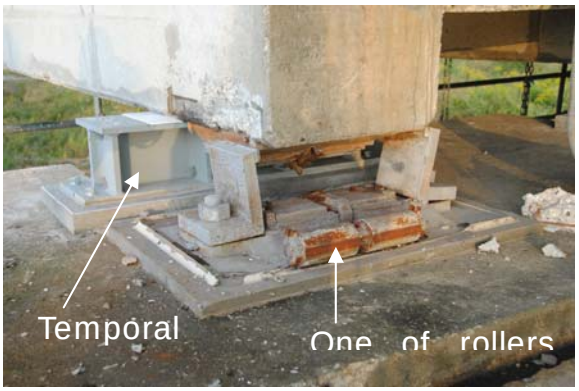
was directed to clarify the failure mechanism of such damage, including a series of large scale shake table experiments using E-Defense (Kawashima et al 2011). It should be noted that damage progresses shortly once shear cracks were initiated under this failure mechanism. Seismic retrofit was initiated in the 1980s (Akiyama, Nakajima and Kogure 1990), and it was accelerated after the 1995 Kobe earthquake. Consequently, during the 2011 Great East Japan earthquake, damage due to this mechanism did not occur at the bridges which had been retrofitted.



Figure 7 Yuriage Bridge



(a) 1978 Miyagi-ken-oki earthquake



(b) 2011 Great East Japan earthquake

Figure 8: Damage of steel roller and pin bearings, Yuriage Bridge

Yuriage Bridge (refer to Fig. 7) suffered extensive damage at reinforced concrete hollow and solid columns, an end of PC concrete girders, and steel pin and roller bearings during the 1978 Miyagi-ken-oki earthquake. Since the damaged columns were repaired and retrofitted by reinforced concrete jacketing, they did not suffer damage again. However steel pin and roller bearings suffered extensive damage again in the similar mode as shown in Fig. 8. It is obvious that steel pin and roller bearings are vulnerable to seismic action, because the stress builds up to failure at a pin bearing, and relative displacement accommodated by a roller bearing is generally only ± 100-200 mm which is much smaller than displacement demand under a strong excitation.

Furthermore, exactly the same end of a PC concrete girder which suffered damage during the 1978 Miyagi-ken-oki earthquake suffered again as shown in Fig. 9. It was a critical zone due to concentration of the seismic force, the dead load reaction and the PC anchor force.

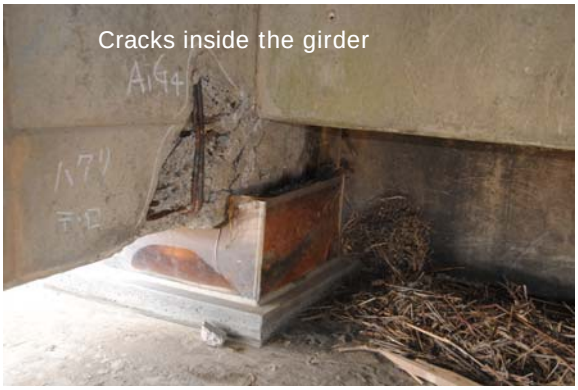
Tennoh Bridge (refer to Fig. 10) built in 1959 suffered extensive damage during the 1978 Miyagi-ken-oki earthquake, and the bridge suffered extensive damage again during the 2011 Great East Japan earthquake at the same members. Fig. 11 (a) an (b) shows failure of a fixed steel bearing and its support during the 1978 Miyagi-ken-oki earthquake. Since detection of the bearing failure under a span was difficult after the earthquake, there was a high risk that this bridge



(a) 1978 Miyagi-ken-oki earthquake



(b) 2011 Great East Japan earthquake



(c) Cracks inside the PC girder

Fig. 9 Damage of a PC girder at the end support, Yuriage Bridge

collapsed due to this damage if a strong aftershock had occurred. Extensive damage of steel bearings occurred again during the 2011 Great east Japan earthquake as shown in Fig. 11(c). Steel bearings are vulnerable because stress builds up to failure in a fixed bearing and relative displacement accommodated by a movable bearing is smaller than displacement demand.

Fig. 12(a) and (b) shows rupture and local buckling of upper and



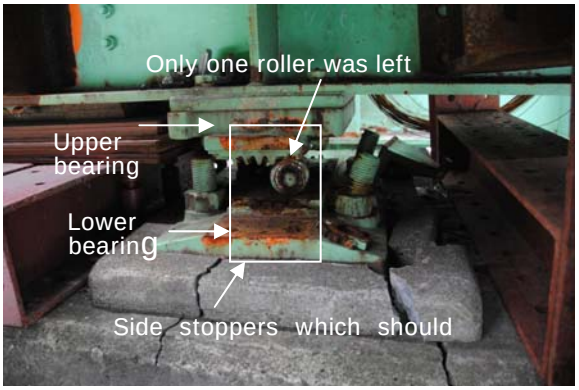
Figure 10 Tennoh Bridge



(a) Damage of bearing seat, 1978 Miyagi-ken-oki earthquake

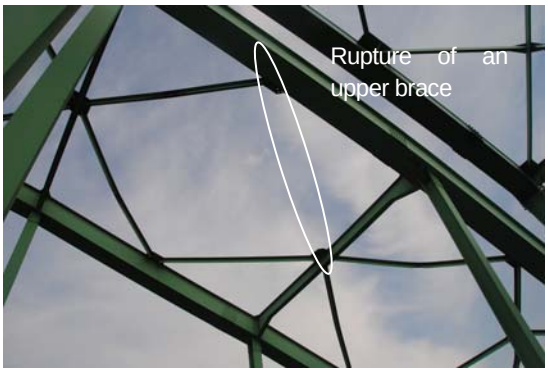


(b) Extensive failure of concrete seat, 1978 Miyagi-ken-oki earthquake

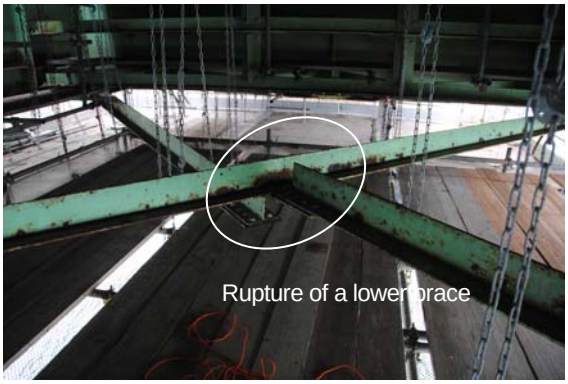


(c) Damage of a roller bearing, 2011 great East Japan earthquake

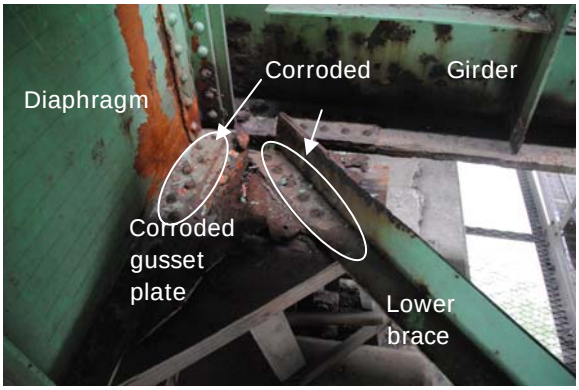
Figure 11 Damage of steel bearings, Tennoh Bridge



(a) Rupture and buckling of upper braces



(b) Rupture of a lower brace



(c) Disconnection of a lower brace to a girder web plate and a diaphragm

Figure 12 Rupture and buckling of braces during the 2011 Great East Japan Earthquake

lower braces. Connection of a lower brace to a girder web plate and a diaphragm by a gusset plates was deteriorated due to corrosion of rivets and a gusset plate as shown in Fig. 12(c). Since similar disconnection occurred at several lower braces, it is considered that a large torsion response of the truss bridge occurred due to deterioration of torsional rigidity, and this resulted in extensive rupture and buckling of upper braces. This truss bridge was about to collapse during the earthquake.



(a) Damage of a RC pier during the 1978 Miyagi-ken-oki earthquake



(b) Retrofitted pier did not suffer damage during the 2011 Great East Japan Earthquake

Figure 13 Effect of retrofit, Sendai Bridge

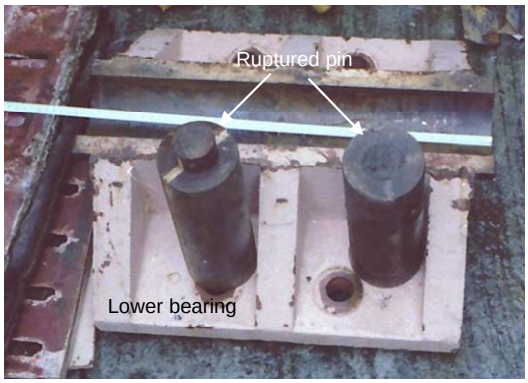
4. PERFORMANCE OF BRIDGES WHICH HAD BEEN RETROFITTED

Damage of bridges which had been retrofitted suffered virtually no damage during the 2011 Great East Japan earthquake. For example, Sendai Bridge which is an extremely important bridge in Sendai City suffered extensive damage at reinforced concrete piers during the 1978 Miyagi-ken-oki earthquake as shown in Fig. 13(a). After the earthquake, the piers were repaired by RC jacket and further retrofitted by fiber reinforced plastic sheet wrapping as shown in Fig. 13(b). Steel bearings were replaced with elastomeric bearings. Consequently the bridge suffered no damage during the 2011 Great East Japan earthquake.

Shin-Iino-Gawa Bridge (refer to Fig. 14) which carries National Road 45 over Kitakami River suffered extensive damage at steel pin and roller bearings as shown in Fig. 15(a) and (b) during the 1978 Miyagi-ken-oki earthquake. The bridge was retrofitted prior to the 2011 Great East Japan earthquake such that 1) several reinforced concrete piers were retrofitted by steel jacketing (refer to Fig. 14), 2) steel bearings were replaced with elastomeric beatings as shown in Fig. 15(c), and 3) nonlinear viscous dampers were installed between a superstructure and a substructure as shown in Fig. 16. As



Figure 14 Shin-Iino-Gawa Bridge



(a) Rupture of a pin during the 1978 Miyagi-ken-oki earthquake



(b) Pull out of anchor bars, 1978 Miyagi-ken-oki earthquake



(c) 2011 Great east Japan Earthquake

Figure 15 Effectiveness of replacement of steel bearings with elastomeric bearings

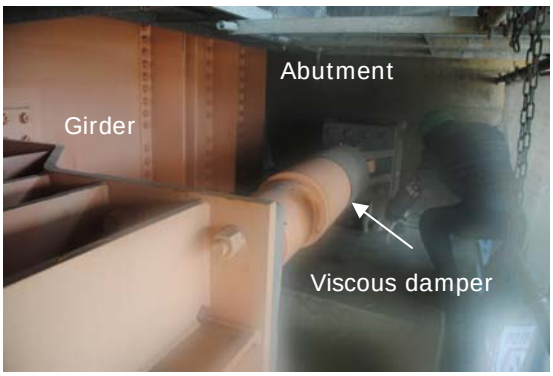


Figure 16 Viscous damper installed as a part of seismic retrofit

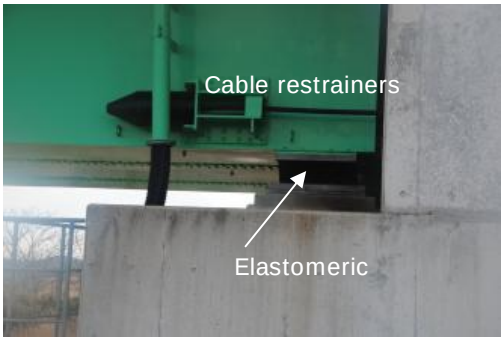
a result, the bridge suffered no damage during the 2011 Great East Japan earthquake.

5. PERFORMANCE OF BRIDGES CONSTRUCTED IN ACCORDANCE WITH THE POST-1990 CODES

Bridges which were designed in accordance with the post-1990 codes suffered essentially no damage during the Great East Japan earthquake. For example, Fig. 17 shows Shin-Tennoh Bridge. The bridge was constructed in 2002 at only 200 m upstream of Tennoh Bridge which suffered extensive damage during the Great East Japan earthquake (refer to Figs. 10-12). Elastomeric bearings and new cable restrainers which satisfy the requirements of the post-1990 design code were set. Shin-Tennoh Bridge suffered no damage.



(a) Spans and columns without damage

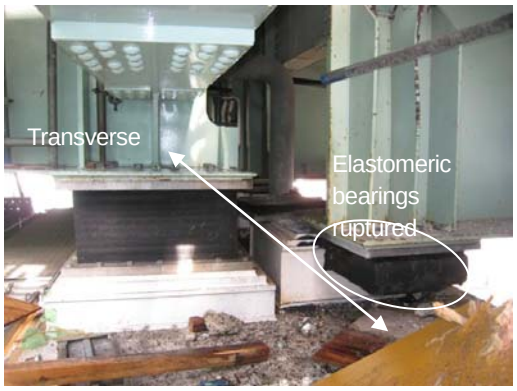


(b) Elastomeric bearings and cable restrainers

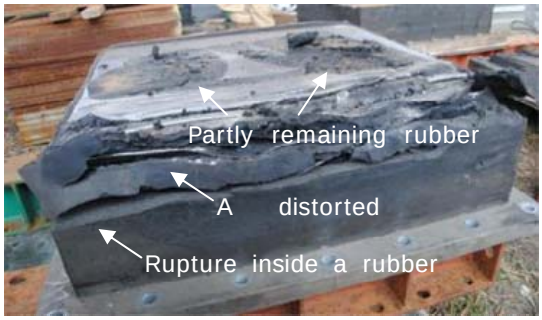
Figure 17 Shin-Tennoh Bridge



(a) Elastomeric bearings which supported the right span ruptured



(b) Rupture of elastomeric bearings



(c) Failure of an elastomeric bearing



(c) drift and settlement of deck

Figure 18 Damage of Sendai-Tobu Viaduct

Since elastomeric bearings are flexible allowing to absorb relative displacement between superstructures and substructures, elastomeric bearings generally performed quite well under the extreme ground motions during 2011 Great East Japan earthquake. However it should be noticed that even elastomeric bearings ruptured in some bridges. For example, elastomeric bearings ruptured at several locations in Sendai-Tobu Viaduct. For example, a deck offset by 0.5m in the transverse direction as shown in Fig. 18(a). Not only rupture occurred inside rubbers layers but also rubber layers were detached from steel shim plates as shown in Fig. 18(b). It is considered that deformation over capacity was developed in the damage bearings.

6. CONCLUSIONS

Ground-motion-induced damage of bridges during the 2011 Great East Japan earthquake was presented. Effectiveness of recent development of seismic design and implementation of seismic retrofit was evaluated based on comparison of the damage developed during the 1978 Miyagi-ken-oki earthquake. Based on the results presented herein, the following conclusions may be deduced:

1) Ground-motion-induced damage of bridges which were built in accordance with the post-1990 design code was very limited during the 2011 Great East Japan earthquake. It was extensively effective for mitigating damage of bridges during the 2011 Great East Japan earthquake to have enhanced the shear and flexural capacity as well as ductility capacity of piers and implemented elastomeric bearings and strengthened unseating prevention devices.

2) Bridges which were built in accordance with the pre-1990 codes and bridges which had not yet been retrofitted suffered extensive damage in a similar mode to the damage which was developed during the 1978 Miyagi-ken-oki earthquake. Prompt and appropriate seismic retrofit is required for those bridges.

Acknowledgements:

The author expresses sincere appreciation for a number of organizations and persons for support of the damage investigation. Kind support of the Ministry of Land, Infrastructure and Transportation is greatly appreciated. Special appreciation is extended to Drs. Kosa, K., Takahashi, Y., Akiyama, M., Nishioka, T., Watanabe, G., Koga, H., and Matsuzaki, H., members of the Reconnaissance Damage Investigation Team, Japan Society of Civil Engineers. Special appreciation is also extended to Dr. Yen, F., FHWA and Professor Buckle, I., University of Nevada, Reno, and members of National Institute of Land and Infrastructure and Public Works Research Institute including Drs. Tamura, K., Kuwabara, T., Unjoh, S. and Hoshikuma, J. for a joint investigation as a part of the UJNR Panel on Wind and Seismic Effect. Financial support based on J-RAPID by the Japan Science and Technology Agency is greatly acknowledged.

References:

Akimoto, T., Nakajima, H. and Kogure, F. (1990), "Seismic Strengthening of Reinforced Concrete Piers on Metropolitan Expressway", Proc. 1st US-Japan Workshop on Seismic Retrofit of Bridges, Tsukuba Science City, Japan, 280-298.

Earthquake Engineering Research Institute (1978),

"Reconnaissance Report on Miyagi-ken-oki, Japan Earthquake", CA, USA.

Japan Road Association (1964), "Design Specifications for Steel Bridges", Maruzen, Tokyo, Japan.

Japan Road Association (1971), "Guide Specifications of Seismic Design of Highway Bridges", Maruzen, Tokyo, Japan.

Japan Road Association (1980, 1990, 1996, 2002 2012), "Part V Seismic Design, Design Specifications of Highway Bridges", Maruzen, Tokyo, Japan.

Japan Road Association (1988, 2008), "Guide Specifications for Earthquake Countermeasures - Post Earthquake", Maruzen, Tokyo, Japan, 1988, 2008.

Japan Road Association (1988, 2002), "Guide Specifications for Earthquake Countermeasures - Pre Earthquake Countermeasures", Maruzen, Tokyo, Japan.

Japan Society of Civil Engineers (2011), "Report on Reconnaissance Damage Investigation to Civil Engineering Facilities Resulted from 2011 Great East Japan Earthquake", Earthquake Engineering Research Committee, Tokyo, Japan.

Japan Society of Civil Engineers (2012), "Damage of Bridges due to the 2011 Great East Japan Earthquake", Earthquake Engineering Committee, Tokyo, Japan.

Kawashima, K., Unjoh, S. and Hoshikuma, J. (1995), "A Seismic Evaluation Method of RC Bridge Piers with Inadequate Anchoring Length at Termination of Main Reinforcements", Journal of JSCE, 525 (33), 83-95.

Kawashima, K. and Unjoh, S. (1997), "The Damage of Highway Bridges in the 1995 Hyogo-ken-nanbu Earthquake and Its Impact of Japanese Seismic Design," Journal of Earthquake Engineering, 12(3), 505-541.

Kawashima, K. (2006), "Seismic Design of Bridges after 1995 Kobe Earthquake," Journal of Disaster Research, 1(2), 262-271.

Kawashima, K., Kosa, K., Takahashi, Y., Akiyama, M., Nishioka, T., Watanabe, G., Koga, H., and Matsuzaki, H. (2011), "Damage of Bridges during 2011 Great East Japan Earthquake", Proc. 43rd Joint Meeting, US-Japan Panel on Wind and Seismic Effects, UJNR, Tsukuba, Japan, 165-178.

National Institute for Land and Infrastructure Management and Public Works Research Institute (2011), "Quick Report on Damage to Infrastructures by the 2011 Off the Pacific Coast of Tohoku Earthquake", Technical Note of NILIM, No. 646, Technical Note of PWRI, No. 4204, Tsukuba, Japan

Public Works Research Institute (1992), "Manual for Seismic Isolation of Bridges", Tsukuba Science City, Japan.

Public Works Research Center (2011), "Manual for Seismic Isolation and Control of Bridges", Tokyo, Japan.

Technical Research Center for National Land Development (1988), "Guidelines for Seismic Isolation of Bridges", Tokyo, Japan.

Unjoh, S., Yabe, M., and Kawashima, K. (2010), "Implementation of Seismic Isolation for Bridges in Japan". Proc. 5th World Conference on Structural Control and Monitoring, 1-12 (CD-ROM), Tokyo, Japan.

10CUEE CONFERENCE PROCEEDINGS
10th International Conference on Urban Earthquake Engineering
March 1–2, 2013, Tokyo Institute of Technology, Tokyo, Japan

ESTIMATION OF DYNAMIC BEHAVIOR OF HISTORICAL CHURCH IN ARMENIA USING MICROTREMOR SURVEY

Hitoshi Morikawa[1)], Shiro Sasano[1)], Shojiro Motoyui[1)], Yasuhito Fujita[2)], and Atsushi Mutoh[3)]

1) Professor, Department of Built Environment, Tokyo Institute of Technology, Japan
2) Assistant Professor, Department of Built Environment, Tokyo Institute of Technology, Japan
3) Professor, Department of Architecture, Meijo University, Japan
morika@enveng.titech.ac.jp

Abstract: Historical Churches in Armenia may have many experiences of earthquake ground motion. Thus, some of them have been damaged partially or severely. We had carried out the microtremor survey at two historical churches, which are Hripsime Church constructed around 7th century and Cathedral at Etchimiadzin around 5th century, to identify the dynamic characteristic. Four sensors are used simultaneously for the observations and vibration modes are estimated from the Fourier amplitudes.

1. INTRODUCTION

Armenia is located at middle between Black Sea and Caspian Sea and in a high seismicity area. The Turkish Anatolian fault, which is a most active fault in the world, reaches to Armenia. Armenia, thus, have experienced often destructive damage by large earthquakes such as 1988 Spitak earthquake. On the other hand, many historical structures, whose ages are more than 1000 years, are still remaining in the country and they face the risk of collapse or severe damage by future earthquakes (eg., Strzygowski, 1918; Cuneo, 1988). It is important for us to forward such the historical structures to next generation without any damage.

For this propose, a "health diagnosis" of structure is required using a non-destructive technique. Our ultimate goal is to estimate its static and/or dynamic performance through detailed numerical analysis after modelling a target structure numerically. For this kind of approach, it is very important to construct an appropriate model of the structure. This means that dynamic characteristics have to be accurately determined for the structure on the basis of some measured data. To know the dynamic behavior of the structure, microtremor survey is one of useful techniques, because microtremors are generated by natural and/or artificial sources such as sea waves, human activities etc. From the properties of the microtremors, it can be treated as stationary processes though their amplitude is quite small. We have carried out simultaneous measurements of microtremors at some different points in the target structure.

The microtremor survey must be suitable for this situation, because we can measure anytime and anywhere and just put the sensors on the structure without any destruction. Furthermore, the dynamic behaviour of the structure can be obtained directly from the data (eg. Motoki and Seo, 2009). On the other hand, it is very difficult to estimate the non-linear characteristics of the structure because of too small amplitude of microtremors, though its dynamic characteristics may be expected during large earthquake ground motion. However, at least, we can obtain the linear characteristics as most basic parameters for dynamic behaviour.

Preliminary results are shown for the dynamic characteristics of two historical churches in Armenia.

2. OBSERVATIONS

Structures of our target are Hripsime Church and Cathedral at Etchimiadzin, whose main parts were constructed from 5th to 7th century, however, many parts may be reconstructed as needed until now. The detailed history of their reconstruction and renovations are not clear.

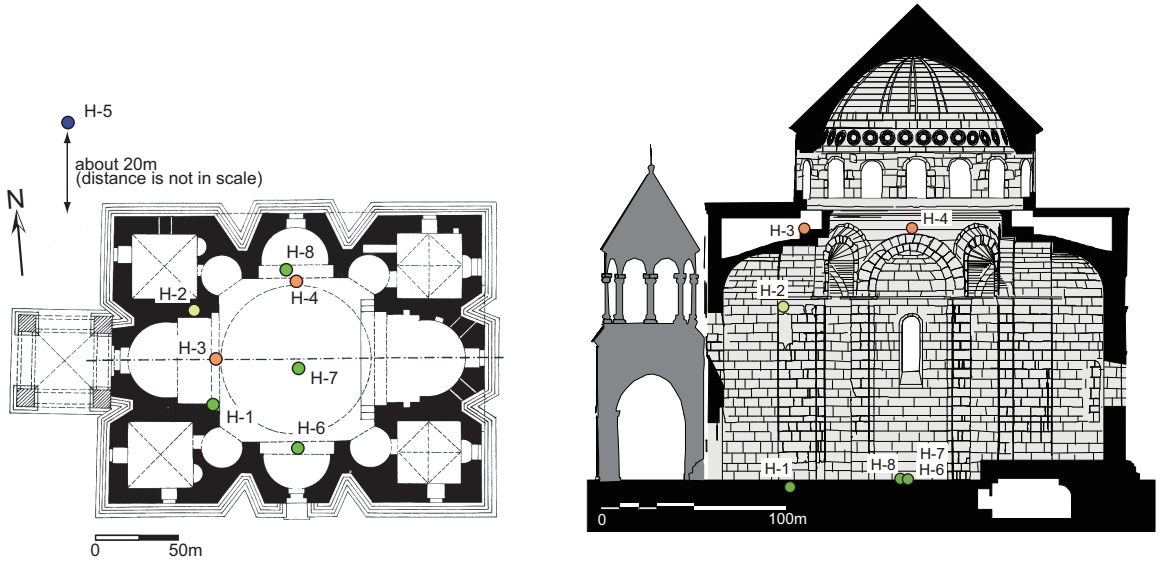
For the microtremor observations, we used moving-coil-type velocity sensors and digital data loggers.

The data logger includes amplifier with 256-time gain, anti-alias filter with about 35 Hz cut-off and a client software of NTP (network time protocol) to synchronize NTP server. The logger can digitize analog data with 200 samples per second and 24-bit resolutions. The digitized data are sent to local host computer via network and also stored in the SD card on the system board.

The error of time synchronization to NTP server is less than 3 ms when the system is activating more than one hour, and less than 500 μs when more than three hours. This logger can also record internal circuit noise simultaneously, thus the signal-to-noise ratio (S/N) can be ex-

Table 1 List of observations for Armenian historical structures

Obs. ID	Date [AMT (UTC+4)]	Time	Duration [min]	Site	Place	Data Observed
#1	Nov. 8,	18:45	60	Hripsime Church (inside)	H-1, H-2, H-3, H-4	microtremors
	2012	20:09	10	Hripsime Church (inside)	H-1, H-2, H-3, H-4	step response
		20:32	7	Hripsime Church (inside)	H-1, H-2, H-3, H-4	total noise
#2	Nov. 9,	10:56	10	Hripsime Church (outside)	H-5	step response
	2012	11:21	20	Hripsime Church (outside)	H-5	microtremors
#3	Nov. 9,	12:32	10	Hripsime Church (inside)	H-1, H-6, H-7, H-8	step response
	2012	12:46	20	Hripsime Church (inside)	H-1, H-6, H-7, H-8	microtremors
#4	Nov. 9,	17:06	11	Cathedral at Etchimiadzin	E-1, E-2, E-3, E-4	step response
	2012	18:23	10	Cathedral at Etchimiadzin	E-1, E-2, E-3, E-4	total noise
		18:36	36	Cathedral at Etchimiadzin	E-1, E-2, E-3, E-4	microtremors
#5	Nov. 9,	19:41	10	Cathedral at Etchimiadzin	E-1, E-2, E-3, E-5	step response
	2012	19:59	16	Cathedral at Etchimiadzin	E-1, E-2, E-3, E-5	microtremors



(a) Plan (b) E-W Section

Figure 1 Plan and section of Hripsime Church and sensor locations for the microtremor observation.

tended at least 6dB in frequency range lower than 1Hz.

Natural period of the velocity sensor is about 0.5 s and one chassis includes three components: two orthogonal horizontal and one vertical components.

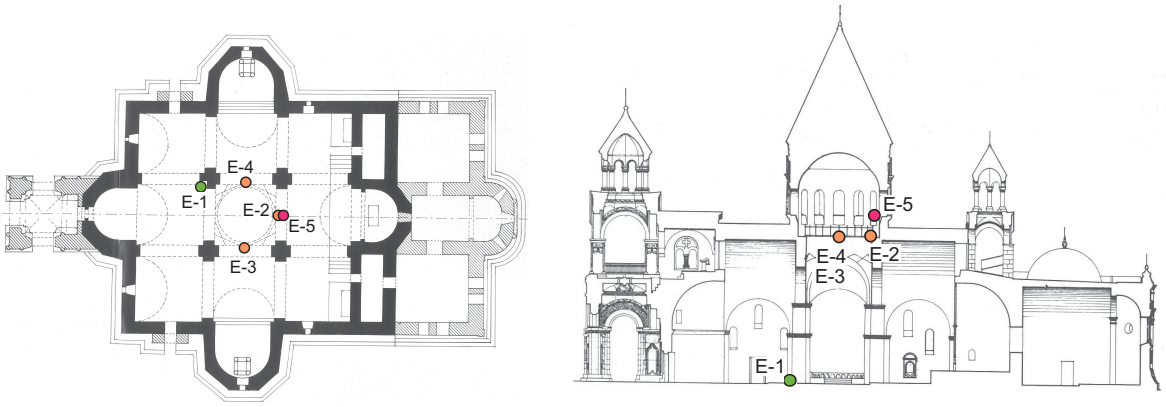
For the observation, four sets of one sensor and one logger are used simultaneously. A laptop computer is also used as a NTP server to deliver time information to four loggers, and NTP server is synchronized to PPS (pulse per second) signal from GPS (global positioning system) receiver. Before the observation of microtremors for structures, we have observed two signals: one is step responses of each sensor to determine the natural period and damping factor at the site, and the other is total noise of observation system using dummy resistance with same value as coil resistance of sensor, instead of sensor.

Observations were carried out as listed in Table 1 and locations of the sensors for each observation are shown in Figs.1 and 2. The observation systems and sensor settings for observation #1 are shown in Fig.3. Observation #2 was huddle test, which were carried out outside of the church, to compare the responses of sensors.

3. ANALYSIS AND PRELIMINARY RESULTS

3.1 Huddle Test

The instrumental correction are performed for all the data. For this, the record of step responses are used. The step responses are recorded at least 10 times at the site. Optimum values of natural period, T_0, and dumping factor, h, are searched for each observation and sensor, using theoretical shape of step response function for one-degree-



(a) Plan (b) Section

Figure 2 Plan and section of Cathedral at Etchimiadzin and sensor locations for the microtremor observation.



(a) Data loggers and laptop computers: one controls data loggers and other works as an NTP server synchronizing GPS signal.

(b) Sensor at H-1. The sensor is set the basement of column. A small box at left of sensor is dummy resistance for noise measurement.

(c) Sensor at H-3. The sensor is set on a corridor of the drum. Signal cable is connected to the dummy resistance.

Figure 3 Setting of the observation system at Hripsime Church (Observation #1).



(a) Site for huddle test (b) Systems

Figure 4 Observation #2 (huddle test).

of-freedom system. Specific T_0 and h for each observation are applied to the instrumental correction and the correction is carried out in the frequency range between 0.05 and 4 seconds.

For the analysis, we apply the Fourier transform to obtain the Fourier amplitudes. 81-second portions are picked up from the data and Fourier amplitudes are calculated, smoothed by Hanning window, and averaged over whole the portions.

To confirm differences of the sensor responses among sensors, we have carried out the huddle test, which is #2 of Table 1. The sensors, thus, are set closely each other as shown in Fig.4. From this test, it is confirmed that the differences among sensor responses can be negligible.

The site for huddle test is outside of Hripsime Church.

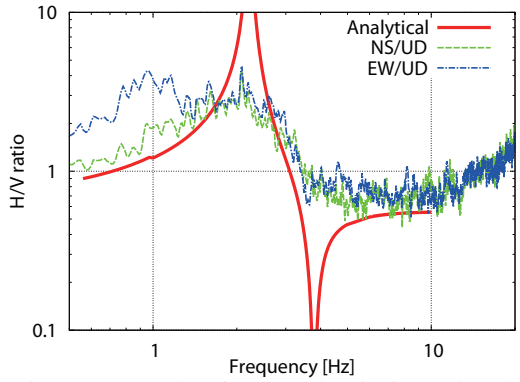
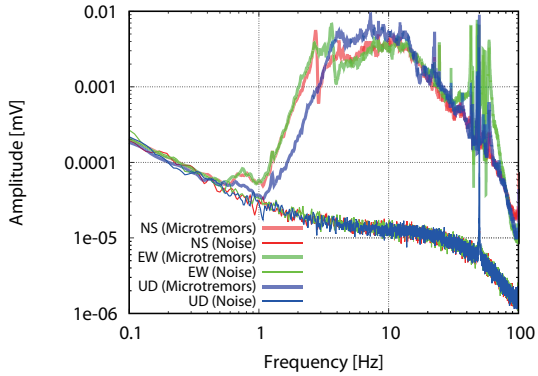


Figure 5 H/V spectral ratio around Hripsime Church and analytical elasticity of Rayleigh wave.

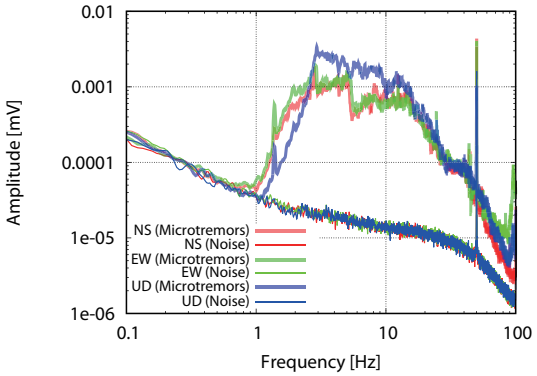
Table 2 An example of velocity structure

Thickness [m]	Density [t/m^3]	V_S [km/s]	V_P [km/s]
48	1.8	0.38	1.9
∞	2.1	1.3	2.5

Thus, we can calculate horizontal-to-vertical (H/V) spectral ratio to estimate the ground structure around Hripsime Church as shown in Fig.5. The shapes of NS/UD and EW/UD are slightly different around 1 Hz, though a peak



(a) Hripsime Church (H-1)



(b) Cathedral at Etchimiadzin (E-1)

Figure 6 Examples of signal and noise level during observation.

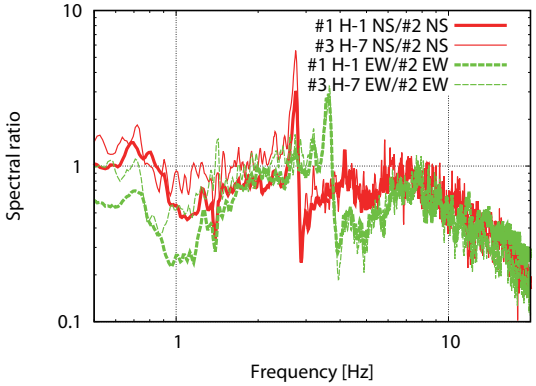


Figure 7 Spectral ratio between ground level (#1 and #3) of the church and outside (#2).

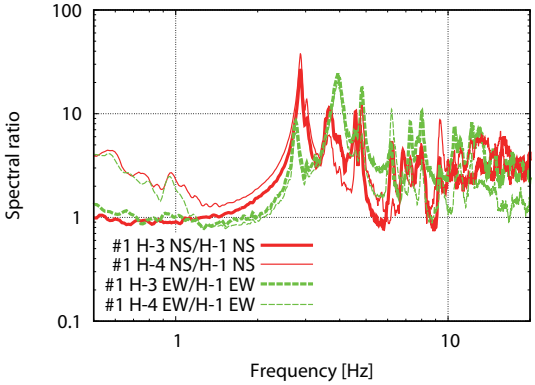


Figure 8 Spectral ratio between corridor of drum (H-3 and H-4) and ground level (H-1) from #1.

is found around 2 Hz. Since the phase velocity is not available because of no array observation, it is difficult to find appropriate velocity model. Table 2 is a very simple example of velocity structure with two layers to explain the observed H/V spectral ratio. We just consider the peak around 2 Hz to fit the analytical ellipticity of Rayleigh wave.

3.2 Signal and Noise Level

The power of microtremors are generally very small and the ground condition at the target site seems to be good. Thus, the noise level of observation system is very important. The data logger can observe simultaneously the circuit noise and remove it as post-processing. However, we had to use very long signal cables to connect between sensors and loggers because of the situation of the church. Furthermore, the moving-coil-type velocity sensor is very high impedance system. This means that the long signal cables can be a good antenna of noise and signal must be contaminated by noise.

To observe the signal and noise level, we record data using dummy resistance instead of sensor. The value of resistance is same as coil resistance of sensor. The dummy resistance can be found in Fig.3. Fig.6 shows the Fourier amplitudes of the signal and noise. The signal without any instrumental correction and noise are compared in observed voltage. Sharp peak is shown at 50 Hz, which is hum noise caused by electric power supply and noise less than 10 Hz shows a typical feature of 1/f noise.

Since the natural period of sensor is 0.5 second (2 Hz), the response sensitivity is decreased less than 2 Hz. In general, the microtremor level is very small around 1 Hz, thus, the signal level becomes lower than noise level. However, the frequency range higher than 1 Hz can recognize the signal. From this, we discuss the frequency range between 1 and 20 Hz and the instrumental correction is performed for the signal in this range.

3.3 Dynamic Behaviour of Hripsime Church

Fourier amplitudes show distinguishing shape on the ground floor of the church, which can be shown as the response for rocking-sway motion. In this observation, we did not carry out simultaneous observation outside and inside of church. The spectral ratios, however, are calculated using the data obtained through observation #1, #2, and #3. Fig.7 shows the spectral ratio for ground level of the church to outside. Although dates of observations of #1 and #3 are different, the shapes of spectral ratios are very similar mutually, especially, at 2.7 Hz for NS component and 3.6 Hz for EW component. Furthermore, the ratios between outside and other places on ground floor, that is, H-1, H-6, and H-8 are very similar. This suggests that the church vibrate rigidly and may include rocking-sway motion, whose natural frequencies depend on direction.

Fig.8 shows the spectral ratios of same directions between corridor of drum and ground level. These data are obtained simultaneously. The peaks for ratio of NS and EW components locate about 2.9 Hz and 3.7 Hz, respec-

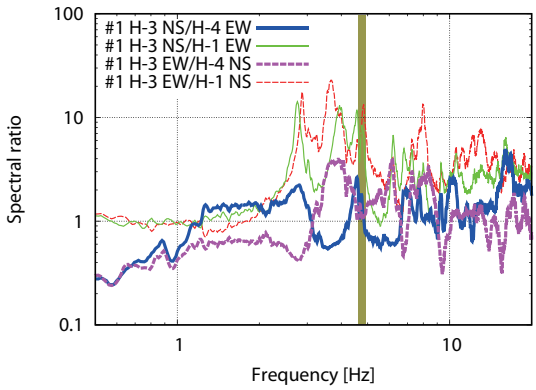


Figure 9 Spectral ratio between NS and EW at different and same level (#1).

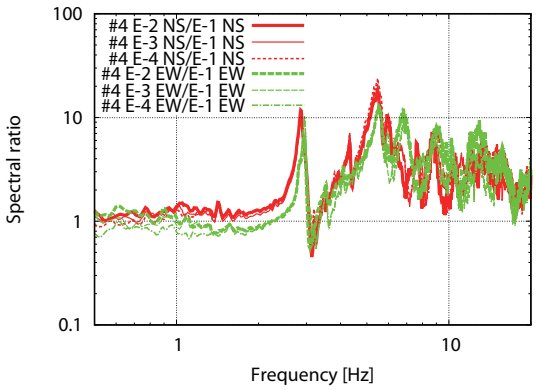


Figure 10 Spectral ratio between corridor of drum (H-2, H-3, and H-4) and ground level (H-1) from #4.

Table 3 Summary of vibration modes (Hripsime Church)

Mode	Frequency [Hz]	Note
1st	2.9	Translatory motion in NS
2nd	3.7	Translatory motion in EW
3rd	4.8	Torsional motion

tively. It is noted that the level of peaks at 2.9 Hz and 3.7 Hz are different. The peaks at 2.9 Hz predominate for NS component and 3.7 Hz for EW component. This means that the first and second mode of the vibrations are translatory motion to NS and EW directions, respectively. The structure is not perfect system, thus, the modes may leak to other modes. This may be a reason for the small peaks for EW component at 2.7 Hz and NS component at 3.6 Hz.

First and second modes of the vibration are clear to determine as shown in Fig.8, however, detection of third mode is slightly difficult. The third mode is assumed as torsional motion of drum and dome. If the torsional motion predominates, the ratios of NS/EW between drum level and ground level must show a peak with same level and the ratios of NS/EW at different sites on drum level must be almost one. Fig.9 shows the spectral ratios: the thin lines stands for the ratios between drum level and ground level, and thick lines for the ratios between NS and EW of different sites on drum level. Solid and dashed lines show the NS/EW and EW/NS, respectively.

To search the above described conditions, we can find the shaded area of Fig.9 around 4.8 Hz. In this area, the thick lines take almost one and peak levels of thin lines are not so different. This frequency corresponds to the third peak of Fig.8. From this, it is suggested that the torsional mode of church is about 4.8 Hz.

The first to third modes of Hripsime Church are summarized in Table 3.

3.4 Dynamic Behaviour of Cathedral at Etchimiadzin

Same analysis as Hripsime Church is applied to the data of Cathedral at Etchimiadzin. The spectral ratios between drum level and ground level in same direction are shown in Fig.10. It seems to be difficult from this figure to discuss the mode shape, because of less difference between different directions. Though large peaks appear at 2.9 Hz and 5.5 Hz for NS and EW components, differences are found at 4.3 Hz and 6.0 Hz for only NS component and at 6.8 Hz for only EW component.

First mode must be at 2.9 Hz and some other mode can be at 5.5 Hz, however, it is difficult to determine other mode at 4.3, 6.0, and 6.8 Hz in this time. Thus, discussion of phase must be necessary for appropriate detection of mode.

4. CONCLUSIONS

We have carried out microtremor observations at two historical structures in Armenia, which are Hripsime Church and Cathedral at Etchimiadzin, to determine their dynamic behaviours. The observation was performed at four sites simultaneously using velocity sensors with three component.

From the discussion of Fourier amplitudes, first three modes are detected for Hripsime Church: we found translatory motion in NS direction at 2.9 Hz, translatory motion in EW direction at 3.7 Hz, and torsional motion at 4.8 Hz. On the other hand, it is very difficult to determine the mode for Cathedral at Etchimiadzin. We can find just candidate of the mode at some frequencies such as 2.9 Hz and 5.5 Hz.

These properties are obtained from discussion of only the Fourier amplitudes. To confirm and improve the reliability of mode detections, we have to discuss phase in the future.

Acknowledgements: This research was partially supported by JSPS KAKENHI (21254004).

References:

Cuneo, P. (1988), *Architettura Armena*, Roma.

Motoki, K. and Seo, K. (2009), "A Study on the Dynamic Characteristics of Historical Monuments in Eastern Anatolia Using Microtremor Measurements," Historical Architecture of Eastern Anatolia in the Middle Age, under the Prospect on Interactive Building-Techniques, edited by Sasano, S., Yokohama.

Strzygowski, J. (1918), *Die Baukunst der Armenier und Europa*, Wien.

10CUEE CONFERENCE PROCEEDINGS
10th International Conference on Urban Earthquake Engineering
March 1-2, 2013, Tokyo Institute of Technology, Tokyo, Japan

SHALLOW STRUCTURE OF TAIPEI BASIN USING RECEIVER FUNCTION TECHNIQUE

Che-Min Lin[1], Kuo-Liang Wen[2, 3], Tao-Ming Chang[1] and Chun-Hsiang Kuo[1]

1) Associate Research Fellow, National Center for Research on Earthquake Engineering, NARL, Taiwan
2) Professor, Institute of Geophysics, National Central University, Taiwan
3) Division Manager, National Center for Research on Earthquake Engineering, NARL, Taiwan
cmlin@ncree.narl.org.tw, wenkl@ncree.narl.org.tw, tmchang@ncree.narl.org.tw, chkuo@ncree.narl.org.tw

Abstract: Receiver Function is a conventional technique for studying the structure of crust and upper mantle beneath the seismometer. In this study, we apply the Receiver Function technique on the high-frequency acceleration seismograms recorded by TSMIP stations of CWB to estimate the shallow S-wave velocity structure in Taipei Basin. The results show the feasibility of the high-frequency Receiver Function technique for estimating shallow structures.
The Taipei basin is a triangular alluvium basin with the complex Tertiary basement and the weak Quaternary alluvium. The site effects of the basin amplifying and extending the seismic waves result in the major seismic disasters in Taipei. From the variations of receiver function waveforms with respect to azimuth, the complex structure beneath the stations can be concluded, such as a dipping plane or large lateral velocity heterogeneity. The averaged Receiver Function of each station we calculated discreetly exhibit the converted waves reflected the main shallow interfaces. The waveforms and arrival times varied with the local sites of stations. After the forward modeling and inversions of receiver functions, the depths and shapes of the Tertiary basement and other main interfaces inside the Taipei basin were estimated and generally agree with that of previous studies.

1. INTRODUCTION

Taipei Basin, including the Taipei City, the capital of Taiwan, and the New Taipei City, located in the northern Taiwan is the metropolitan areas with the highest population density. The basin was filled with thick and soft Quaternary deposits which amplified the incident seismic waveforms (Wen and Peng, 1998). The site effects of the basin structure have caused several seismic disasters in the Taipei Basin. The building collapses caused by the 1999 Chi-Chi earthquake (M_L 7.3) and 2002/3/31 east coast earthquake (M_L 6.8) were the significant examples recently. According to widely distributed 30 drilling wells and 300 shallow reflection seismic lines, the Tertiary basement and the Quaternary strata above the basement were described (Teng et al., 2001; Wang et al., 2004). However, the structures of some major interfaces affecting the propagation of seismic wave in the basin are still unclear. For reducing the earthquake hazards in the future, the complete and detailed S-wave velocity structure under the Taipei Basin is essential to conduct site-effect estimations, theoretical simulations of strong motion, and seismic hazard assessments.

Teleseismic receiver function method has been developed to provide local information on S-wave velocity discontinuities beneath the recording station (Langston, 1979; Owen et al., 1984; Ammon et al., 1990; Ammon, 1991). The method is excellent at clearly showing the Ps converted phases used to estimate the depth of the discontinuities even if seismograms are contaminated by noise and scattering waves. The receiver functions of stations distributing over a region are efficient to estimate their three dimensional structures. Because the largest S-wave velocity discontinuity generally coincides with the Moho, the method was popularly used to study the structures from the lower crust to the upper mantle. However, if the site is filled by sediments, the sediment-bedrock interface becomes a major velocity discontinuity. The waveforms from these receiver functions are dominantly controlled by the sedimentary structures within the first few seconds after the direct P arrival. Information from the deeper structure may be masked by multiples from this large near-surface discontinuity (Zelt and Ellis, 1998). As a result, the sensitivity of the receiver functions to variations in both the velocity and thickness of the surface layer becomes dramatically increased. Julià et al. (2004) inverted the seismic velocities and densities for the sedimentary cover in the New Madrid Seismic Zone. The whole thicknesses of the Cenozoic and Cretaceous sediments within the depth of one kilometer are respectively estimated by performing an inversion of receiver functions computed at individual broadband station. Zheng et al. (2005) applied the receiver function method to image the sedimentary structure of the Bohai Bay Basin in Eastern China. The sedimentary cover with the depth about 2-12 km in the basin were well estimated. The aim of this study is to apply the receiver function technique on the high-frequency acceleration seismograms recorded by Taiwan Strong Motion Instrumentation Program (TSMIP) stations of Central

Weather Bureau (CWB) to estimate the shallow S-wave velocity structure in Taipei Basin.

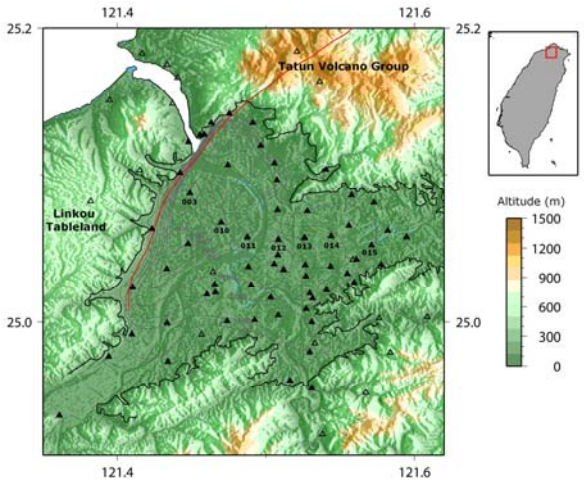


Figure 1 Topography of the Taipei Basin. The thick black lines are the boundaries of the Taipei Basin. The depth contours of the Tertiary basement in the basin are shown by the gray lines (Wang et al., 2004). The thick red line is the Sanchiao Fault indicated as an active fault. The TSMIP stations are shown as triangles in which the filled ones are the stations we used in the study. The stations we mentioned in the article are marked with a number which is the station name without the heading "TAP" below the station

2. GEOLOGIC BACKGROUND

Taipei Basin is a triangular basin with about 20 km length of the side (Fig. 1). The basin is bounded by the Pleistocene Tatun Volcano groups in the north, Western foothills in the southeast, and Linko tableland in the west. The elevation of topography around the basin varies between sea level and about 1100 m. Four young formations are found sitting flat above the basement which is at most 700 m deep (Teng et al. 2001). During the Pliocene and the Pleistocene age, gravels and conglomerates were widely deposited in the Linkou area which was a delta fan produced by reverse faulting activities. About 400 thousand years ago, the area became a tensile environment and resulted in that the Hsinchuang fault altered its sense of movement and became a normal fault, now rename as Sanchiao fault. The normal faulting activities of the Sanchiao fault caused the sinking of the Taipei basin and took shape the basin. Thus, the deepest part of the basin is along the NW border, where the Sanchiao fault is located.

Four newly deposited unconsolidated strata were overlying the basement because of the geohistory of the Taipei Basin. The top near-surface layer, called the Sungshan Formation, dominates the site effects because of its loose sand and silt content (Wen et al. 1995). The Chingmei Formation beneath the Sungshan Formation is mainly composed of gravels and overlies the sand-and-silt Wuku Formation. The fourth Quaternary stratum is the gravel-rich Banchiao Formation overlay on the Tertiary Basement. Based on the data of drilling wells and shallow reflection seismic lines, the two major discontinuities in the basin, the bottom of the Songshan Formation (Fig. 2) and the basement (Fig. 1), were respectively figured. The Songshan Formation is relatively thin (about 50 m) with very low S-wave-velocity. The deepest of the Tertiary Basement is about 700–1000 m along the western border of the Taipei Basin. Table 1 shows the P- and S-wave velocities and depths of the strata in the Taipei Basin (Wang et al., 2004).

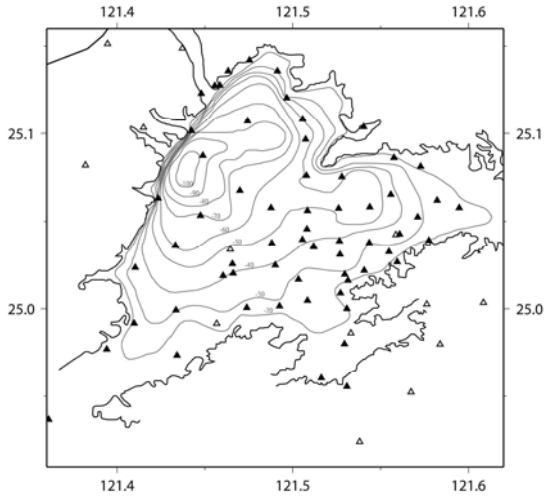


Figure 2 Depth contours of the Sungshan Formation which is the topmost strata of the Taipei Basin (Wang et al., 2004). The TSMIP stations are shown as triangles in which the filled ones are the stations we used in the study

Table 1 P- and S-wave velocities and depths of the strata in the Taipei Basin (Wang et al., 2004)

Stratum	Depth (m)		P-wave (km/sec)	S-wave (km/sec)
	NW	SE		
Sungshan Formation	0-20	0-15	450	170
	20-50	15-35	1500	230
	50-100	35-50	1600	340
Chingmei Formation	100-160	50-100	1800	450
Wuku Formation	160-320	100-200	2000	600?
Banchiao Formation	320-700?	200-300	2200	880?
Tertiary Basement	-	-	3000	1500?

3. ANALYSIS OF RECEIVER FUNCTION

In the Taipei Basin, the dense TSMIP stations provide a large number of excellent seismic data for our study. The instruments installed at the stations are all tri-axial accelerometer (Liu et al., 1999). Sixty-four TSMIP stations located in the Taipei Basin were chosen (Fig. 1). The period of the database is from 1992 to 2009. The earthquakes we used are all local ones occurred within or around the Taiwan Island. Each waveform was visually inspected to eliminate

recordings with low signal-to-noise ratios, anomalous glitches, and calibration issues. The pickings of the P- and S-wave arrivals were also reviewed. We commutated the receiver functions of the seismograms in acceleration rather than velocity used for teleseismic receiver function. In the commutation of receiver functions, the width a = 50 of the Gaussian low-pass filter and the water level c = 0.05 were applied. Figure 3a shows all receiver functions of the TAP010 in order of back-azimuth. Because most earthquakes located in the seismic zone of eastern Taiwan and Western Foothills, the back-azimuth just cover the range from 110° to 220°. Most receiver functions of TAP010 exhibits two apparent converted phases at 0.6 and 1.0 second. In the receiver functions, the systematic variation of converted phase waveforms versus ray back azimuth and the appearance of seismic energy on both the radial and transverse components both reflect the existence of the dipping velocity discontinuity.

After the selection the receiver functions with similar and reasonable waveform, the average receiver functions for each station were calculated. The average of seventeen receiver functions for TAP010 (Fig. 3) enhances the converted phases and reduce the inharmonic arrivals. The average receiver functions of seven TSMIP stations (marked in Fig. 1) located on an E-W direction line in the Taipei Basin are drawn in Fig. 4. The difference of receiver functions between stations is obvious, but the similar converted phase can be observed at most stations with different arrival times. The stations located on the western side where the basin is deeper show later arrival times, and the stations located on the eastern side where the basin is shallower show earlier arrival times. The converted phases with the arrival times less than 1.5 second should produced by the shallow velocity discontinuity within the basin. The variation of arrival times versus location proves the shape of basin affect the high-frequency receiver function. The receiver function technique is effective to analyze the strong motion data observed in the Taipei Basin.

In the study, Genetic Algorithms (GA) was applied to search for the S-wave velocity model with the best fitness between observed and synthetic receiver function. GA searching is a powerful global optimization method. The algorithm consists of selection, crossover, and mutation of individuals in a population; it can search both globally and locally for an optimal solution (Goldberg, 1989). According to the Table 1 (Wang et al., 2004), we assumed a model with six layers covering a half space for the GA searching. The P- and S- velocities of the layers were fixed to avoid the trade-off between the velocity and thickness of layers. We estimated the thickness of each stratum based on the assumption that all the strata in the basin are homogeneous. The searching range of S-wave velocity model was shown by the blue dash lines in Fig. 5a. The full GA process included conducting fifty GA searches. Each GA search was terminated at the 500th generation. The population size of each generation was fifty. Therefore, the total number of repetitions for forward modeling was 1,250,000.

Figure 5a shows the results of the GA searching for the station TAP010. The results of GA searching display the effective convergence of the wide searching ranges for thickness. The synthetic receiver function corresponding to the best model fit the observed one well (Fig. 5b). The phases converted at the four major interfaces under the Taipei Basin were identified. The inverted S-wave velocity model of TAP010 slightly overestimates the depth of the Tertiary Basement in previously study (Fig. 1). The high contrast of the basement produces the converted phase observed at 1 second. The biggest phase observed at 0.6 second converts at the bottom of the Wuku Formation with the depth of about 200 m. The bottom of the Sungshan and Chingmei Formation produced the small converted phases respectively at 0.3 and 0.4 second.

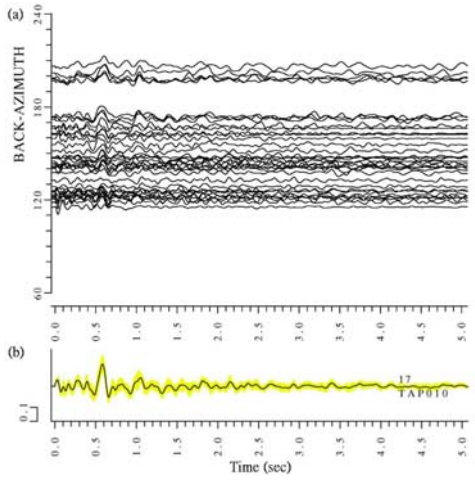


Figure 3 Receiver functions of TAP010. (a) shows the all receiver functions of earthquakes we used in order of back-azimuth. (b) is the average of the seventeen selected receiver function for TAP010. The yellow shadow shows the standard deviation

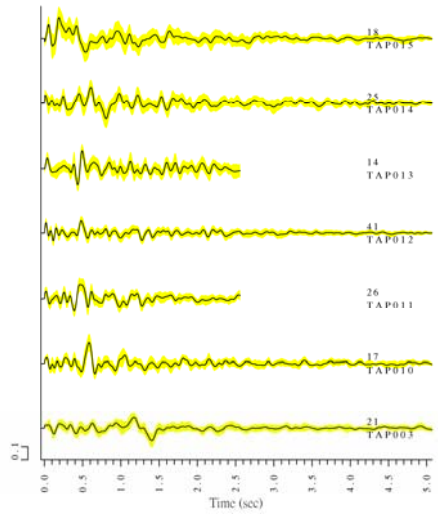


Figure 4 Average receiver functions of seven TSMIP stations located on an E-W direction line in the Taipei Basin and marked in Fig. 1. The yellow shadows show the standard deviations. The numbers of receiver functions we used to average for the stations are shown above the station names

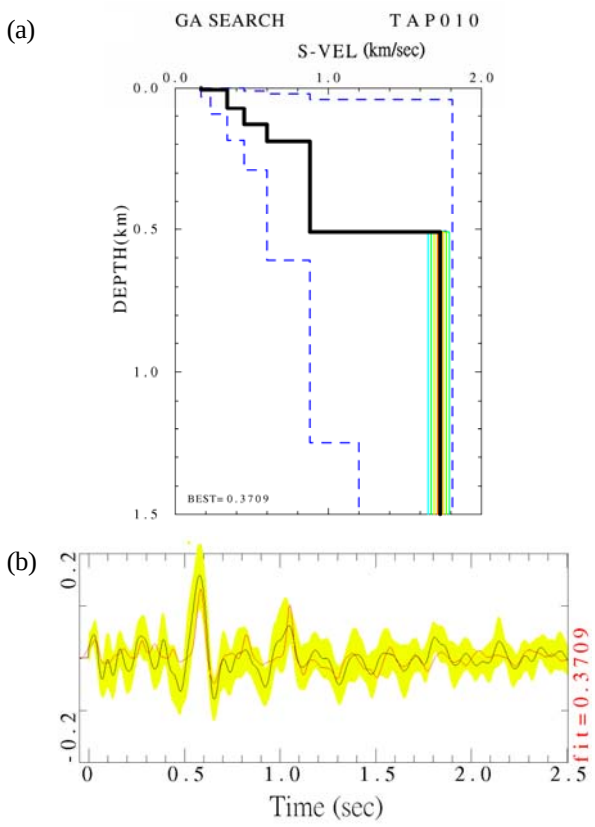


Figure 5 Best result of TAP010 searched by Genetic Algorithm. (a) is the S-wave velocity model of GA searching. The blue dash lines show the searching range of the S-wave velocity in the GA searching. The black bold line is the S-wave velocity model with the best fitness of the GA searching. The lines with various colors are the best twenty models. (b) is the comparison between the observed average receiver function (black line) and the synthetic one (red line) with the best fitness based on the GA searching

4. STRUCTURES OF TAIPEI BASIN

The above-mentioned analysis process of receiver function was applied to the sixty-four TSMIP stations in the Taipei Basin. The average receiver functions were calculated and modeled to estimate the 1D S-wave velocity models for the stations. Because the velocities of layers were fixed, the depths of the major interfaces were easily identified. We combined the 1D models of all the stations widely distributed in the basin to delineate the 3D structures of the strata. Figure 6 are the depth contour maps of the four major interfaces under the Taipei Basin delineated based on the synthetics of the receiver functions. The thickness of the topmost Sungshan Formation is between 80 m in southeast and 120 m in northwest. The distribution of the strata we estimated agrees with the result of the drilling and seismic surveys (Fig. 2), but there are two noticeable differences between Fig. 6a and Fig. 2. The deepest range we estimated in the northwest is larger than that of Fig. 2 (Wang et al., 2004). The bottom of the Sungshan Formation in Sungshan area in Fig. 2 is the deepest part of the eastern half with a shape of extended platform in the depth of about 50 m. Our result controlled by the receiver function of TAP014 in the same area exhibits much deeper depth. The deep-hole shape under TAP014 is abnormal and may result from the multiple and close phases (Fig. 4).

Although the TSMIP stations are not dense enough to figure out the deep shape of the Tertiary Basement along the northwestern border in the basin, several stations located in the area, including TAP003, TAP016 and TAP094, exhibit the depth of more than 600 m for the basement. The Tertiary Basement we delineated (Fig. 6d) shows similar trend with the Fig. 2 (Wang et al., 2004). The basement gradually dips from southeast to northwest. The deepest part along the northwest border form a sharp graben because the normal faulting activities. We also delineated the bottom of the Chingmei and Wuku Formations. The distributions for the two layers both agree with the estimation of Wang et al. (2004) (Table 1). According to the shapes of the four major interfaces, the gradual change of the sedimentary environment can be presumed.

5. CONCLUSIONS

The receiver function technique has applied on the high-frequency acceleration seismograms recorded by TSMIP stations of CWB to estimate the shallow S-wave velocity structure in the Taipei Basin. The averaged receiver function of each station exhibit apparent converted phases reflected the major shallow interfaces under the basin. After the forward modeling of GA searching, we delineated the brief 3D structures of the four Quaternary strata under the Taipei basin. The thicknesses and shapes of the interfaces we estimated are all comparable with that of the previous drilling and seismic survey. The results proved that the high-frequency receiver function is feasible to figure out the shallow discontinuity with high velocity contrast. The technique will provide another tool to study the shallow sedimentary structures which is essential to conduct site-effect estimations, theoretical simulations of strong motion, and seismic hazard assessments.

Because the shallow structures are usually more complex, the high-frequency receiver function is easy to be contaminated by not only the artificial noise but also the non-horizontal and inhomogeneous layers. Besides, the receiver function analysis theoretically requires near-vertical incidence plane waves to elucidate the structure directly beneath a seismic station. We suggest that the high-frequency receiver function should apply on the seismic station with a lot of data. The original seismic waveforms and receiver functions should be carefully inspected and selected for the waveform with real converted phases of velocity discontinuities. The sufficient data will help conclude the systemic receiver functions to estimate the structures we are interesting in.

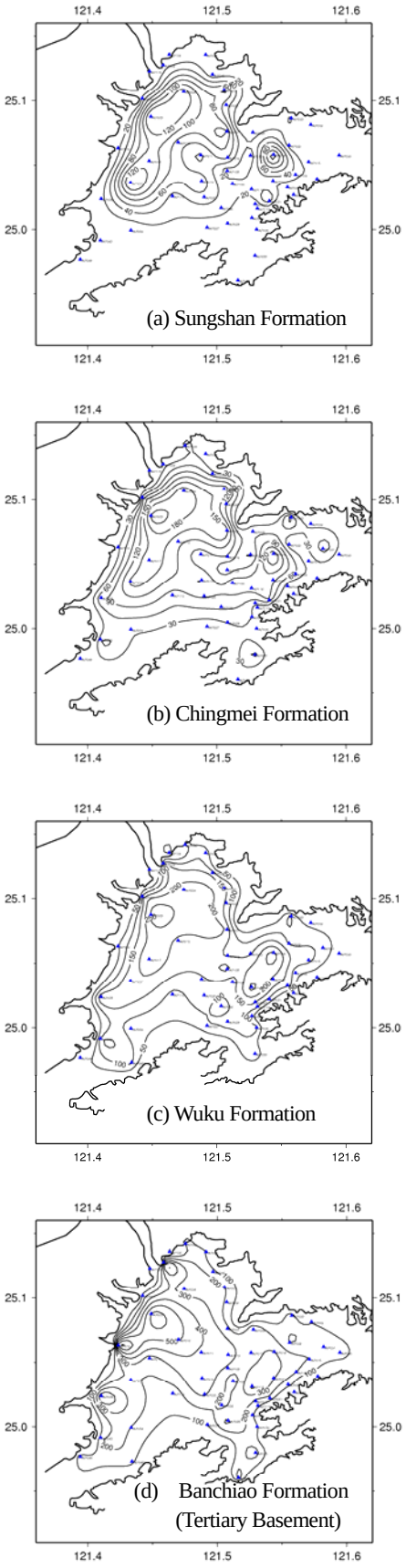


Figure 6 Depth contour (meter) maps of the four major interfaces under the Taipei Basin estimated based on the synthetics of the receiver functions for the TSMIP stations shown respectively by the triangles

References:

Ammon, C. J., Randall, G. E., and Zandt, G. (1990), "On the Non-uniqueness of Receiver Function Inversions," *J. Geophys. Res.*, **95**, 15303-15318.

Ammon, C. J. (1991), "The Isolation of Receiver Effects from Teleseismic P Waveforms," *Bull. Seism. Soc. Am.*, **81**, 2504-2510.

Goldberg, D. E. (1989), "Genetic algorithms in search, optimization, and machine learning," Addison-Wesley.

Julià, J., Herrmann, R. B., Ammon, C. J., and Akinci, A. (2004), "Evaluation of Deep Sediment Velocity Structure in the New Madrid Seismic Zone," *Bull. Seism. Soc. Am.*, **94**, 334-340.

Langston, C. A. (1979), "Structure under Mount Rainier, Washington, Inferred from Teleseismic Body Waves," *J. Geophys. Res.*, **84**, 4749-4762.

Lin, K. S., Shin, T. C., and Tsai, Y. B. (1999), "A Free-Field Strong Motion Network in Taiwan: TSMIP," *Terr. Atmos. Ocean.*, **10**, 377-396.

Owens, T. J., Zandt, G., and Taylor, S. R. (1984), "Seismic Evidence for an Ancient Rift Beneath the Cumberland Plateau, Tennessee: A Detailed Analysis of Broadband Teleseismic P Waveforms," *J. Geophys. Res.*, **89**, 7783-7795.

Teng, L. S., Lee, C. T., Peng, C. H., Chen, W. F., and Chu, C. J. (2001), " Origin and Geological Evolution of the Taipei Basin, Northern Taiwan," *Western. Pac. Earth Sci.*, **1**, 115–142.

Wang, C. Y., Lee, Y. H., Ger, M. L., and Chen, Y. L. (2004), "Investigating subsurface structures and P- and S-wave velocities in the Taipei basin," *Terr. Atmos. Ocean.*, **15**, 609–627.

Wen, K. L., Fei, L. Y., Pen, H. Y., and Liu, C. C. (1995), "Site Effect Analysis from the Records of the Wuku Downhole Array," *Terr. Atmos. Ocean.*, **6**, 285-298.

Wen, K. L., and Peng, H. Y. (1998), "Site Effect Analysis in the Taipei Basin: Results from TSMIP Network Data," *Terr. Atmos. Ocean. Sci.*, **9**, 691–704.

Zelt, B. C., and Ellis, R. M. (1998), "Receiver Function Studies in the Trans- Hudson Orogen, Saskatchewan," *Can. J. Earth Sci.*, **36**, 585–603.

10CUEE CONFERENCE PROCEEDINGS
10th International Conference on Urban Earthquake Engineering
March 1-2, 2013, Tokyo Institute of Technology, Tokyo, Japan

EMPIRICAL SITE CORRECTION FOR GROUND MOTION SIMULATION

Kuo-Liang Wen[1)], Jyun-Yan Huang[2)], and Chun-Te Chen[3)]

1) Professor, Department of Earth Sciences, National Central University, Taiwan
Division Head, National Center for Research on Earthquake Engineering, NARL, Taiwan
2) PhD Candidate, Department of Earth Sciences, National Central University, Taiwan
3) PhD Candidate, Department of Earth Sciences, National Central University, Taiwan
wenkl@earth.ncu.edu.tw, 986402005@cc.ncu.edu.tw, 956402004@cc.ncu.edu.tw

Abstract: The site response is not easy to consider for ground motion estimation especially in the basin area. Where 1D, 2D, or 3D basin response need to be considered in the simulation. In this study, we try to use empirical site correction term for the ground motion simulation in the Taipei basin. The method of the stochastic point-source modeling is used to simulate the rock site ground motion in the Taipei basin area. Empirical site corrections are calculated by the spectral ratios between observed earthquake record and stochastic point-source modeled for rock site. The empirical site correction model is then used to simulate four target earthquake ground motions on the soft soil sites within the Taipei basin. The 1999 Chi-Chi, Taiwan earthquake had surface rupture occurred and were simulated by finite-fault modeling. Residual between the observed and simulated ground motions are discussed in the time and frequency domains, and also compared with that from the ground motion prediction equation method which engineer application usually used.

1. INTRODUCTION

An earthquake record observed on a seismic station should include the effects from source, path, and local site. In many earthquakes, sit effect shown an important part of these three effects, for instance, 1985 Michoacan, Mexico earthquake and 1999 Chi-Chi, Taiwan earthquake. Anderson et al. (1996) indicated that the top soft alluvium layer will acted an important role for site effects. For this reason, study the site effects is critical on seismic hazard mitigation for the future earthquakes.

Recently, numerical simulation of strong ground motion is widely used in engineering analyses for the regions with less earthquake data (Beresnev and Atkinson 1998; Sokolov et al. 2001). For soft soil basin, many studies already worked on real basin by 3D ground motion simulation (Lee et al. 2008; Miksat et al. 2010). But, mostly, it still limited in lower frequency response which can not directly used for engineering and hazard mitigation problem.

The method of the stochastic point-source modeling is used in this study to simulate the rock site ground motion in the Taipei basin area. Empirical site corrections are calculated by the spectral ratios between observed earthquake records and stochastic point-source modeled for rock site. The empirical site correction model is then used to simulate the ground motions of other events, not used in the previous empirical site correction analysis, for the soil sites within the Taipei basin. Also, we try the same empirical site correction model for the 1999 Chi-Chi, Taiwan earthquake ground motion by finite-fault modeling for the larger earthquake magnitude than the events used for calculating the site correction function. Residuals between the observed and simulated ground motions are discussed in the time and frequency domains, and also compared with that from the ground motion prediction equation (GMPE) method which engineer usually used.

2. DATA AND METHOD

Stochastic method included both point source and finite-fault modeling for different magnitude events in this study. The point source model use the code SMSIM developed by Boore (2009), and the finite-fault method involves discretization of the fault plane into smaller sub-faults, each of which is assigned a ω-square spectrum. The stochastic finite-fault method was incorporated in the code EXSIM (Motazedian and Atkinson 2005; Assatourians and Atkinson 2007; Boore 2009).

The method consists of two steps. First, earthquakes with magnitude less than 6 and focal

depth less than 40 km are selected to do the stochastic point source modeling of the rock site response. Totally, 203 earthquakes recorded by the stations in the Taipei basin area from 1991 to 2009 are used to generate the site correction functions for the soft soil site within the Taipei basin (Figure 1). Compared the observation and simulation records for the class B stations outside the Taipei basin can generate the rock site correction function for the ground motion simulation of rock site. Table 1 lists parameters used for the rock site simulation by SMSIM code are followed D'Amico et al. (2012). The empirical site correction function for each soft soil station within the Taipei basin is calculated from the observation record to the rock site simulation for that soil site. Based on the many earthquakes results, the average site correction function can be used as final empirical site correction function for that station. The empirical site correction function also can be used to study the site effects of the Taipei basin.

Then, another 4 events (red stars in Figure 1), which are not used in the previous empirical site correction analysis, are used as a validation test for this ground motion simulation. It included 3 earthquakes with magnitude from 5.5 to 6.2 by stochastic point source modeling method and the 1999 Chi-Chi, Taiwan 7.6 earthquake by the finite-fault modeling method. Parameters used for the Chi-Chi earthquake simulation by EXSIM code that are referred to D'Amico et al. (2012) (Table 2). Source parameters following Chang et al. (2000) and slip distribution useing the result from Ma et al. (2001). The simulation and observation records are compared to see whether the empirical site correction model suitable or not. The biases in frequency and time domains are defined as the logarithm of the ratio of the observed to simulated Fourier spectra and peak ground accelerations over all sites shown in Eq. (1) and Eq. (2) as follow:.

$$\mathrm{DSDP} = \sum_{0.2}^{10}\left(\left|\log_{10}\left(\frac{\mathrm{FASo}}{\mathrm{FASs}}\right)\right| \times \mathrm{df}\right) \quad (1)$$

$$\sigma_{\mathrm{lnErr}} = \sqrt{\frac{1}{\mathrm{N}}\sum_{i=1}^{\mathrm{N}}(\mathrm{Residual}_i)^2} \quad (2)$$

$$\mathrm{Residual} = ln\mathrm{PGA_o} - ln\mathrm{PGAs} \quad (3)$$

where subscript represent observation data and *s* represent simulation data.

One of the main factors that affect the GMPE method is existence of the site effects. Therefore, it is necessary to take account of the site effects in applying the attenuation relationship for ground motion prediction. In this study, we used two-step method to predict the best results of PGA shake map.

First step, we got the PGA of each site by PGA attenuation relationship (Jean and Loh 2001; Jean et al. 2006), which follows the model proposed by Campbell (1981). The attenuation equation can be expressed as follow:

$$Y_{att}=0.00369e^{1.75377M}[R+0.12220e^{0.78315M}]^{-2.05644}$$
$$\sigma_{\mathrm{lnErr}} = 0.78 \quad (4)$$

where Y_{att} is predicted PGA value and R is the closest distance to the source.

Second step, the site correction of each station can be simplified by the following equation:

$$ln(PGA_{obs})_S = C_0 + C_1 \times ln(Y_{att})_S \quad (5)$$

where PGA_{obs} is the observed PGA value, and Y_{att} is the predicted PGA value obtained from the attenuation relationship law. In Eq. (5), the values of C_0 and C_1 are the site-dependent parameters for corrections on site effects

3. EMPIRICAL SITE EFFECTS

Due to the site effects in the Taipei basin are not easy to identify from theoretical analysis, maybe it needs to consider 2D or 3D basin responses. In this study, the empirical site effects are calculated from the spectra ratios of the observation with respect to the synthetic motions which did not consider the basin structure. For each station within the Taipei basin, we calculated the average spectral ratio to represent the site correction function for that station. Figure 2 shows the general transfer functions for stations within the Taipei basin with different site classifications. The site classification of the strong motion stations are referred from the Engineering Geological Database for TSMIP (EGDT, Kuo et al. 2012).

Figure 3 represents the contour of the dominant frequency in the Taipei basin from the empirical site correction functions. The distribution of the dominant frequencies shows that the areas near the basin edge have a higher dominant frequency, but within the basin have two low dominant frequency zones. The dominant frequency distribution correlated with the soil layer thickness, and the low dominant frequency zone occurs over the deepest part of the soil layer.

Previous survey (Wen and Peng 1998) indicated the top soft soil layer, the Sungshan

formation, within the Taipei basin react to the site effects at low frequency and it also shown the same result in the study. Figure 4 presents the contour of the empirical site functions at 0.5 and 2.0 Hz in the Taipei basin. It is very clearly to show that the high amplification hot spots occurred in two areas, the western and eastern part of the Taipei basin, for 0.5 Hz response. These areas are also the deepest parts of the Sungshan formation. This amplification should be due to the wave resonated within the soft soil layer. But the high amplification area for 2.0 Hz response change to basin edge areas except the western part of deep alluvium part.

4. SIMULATION OF THE TARGET EARTHQUAKES

The empirical site correction model is then used to simulate four target earthquake ground motions on the soft soil site within the Taipei basin. Residual between the observed and simulated ground motions are discussed in the time and frequency domains, and also compared with that from the attenuation equation (GMPE) method which engineer usually used.

4.1 Simulation of Moderate Events

Due to the empirical site correction function for each station was calculated from the earthquakes with magnitude less than 6.0 and focal depth less than 40 km. In the validation, we selected three moderate events with M_w 5.5, 5.6, and 6.2, but one with focal depth of 76 km. Figure 5 shows an example of the frequency and time domain results of the station TAP007 for the June 9, 2003 earthquake. In this figure, the black lines are observation data, blue lines are the simulations on rock site condition, and red lines are the simulation results after applied the site correction functions. The bias in the spectrum (DSPD) reduce from 3.7093 (rock site) to 2.1834 (after site correction). Compare the peak ground acceleration distribution of simulation and observation for the same event, he residual map (Figure 6) shows most area had a good PGA prediction, only the southern part has a little under estimate. One thing need to point out that the observed PGA in the residual calculation does not filter any frequency band in this study.

The same earthquake also predicted the PGA distribution based on the GMPE method. First, using the rock site attenuation equation calculated the PGA in Taipei basin based on the magnitude and distance; then done the site correction for each station following the two steps method (Jean et al. 2006; Wen et al. 2009). Figure 7 shows the PGA results from different methods include rock site condition and after site correction. Black closes are the observed PGA. Blue triangles are the stochastic point source results for rock site (not consider the soft basin) and red triangles are the results added empirical site correction function for each station. Residure (σ_{lnErr}) of the June 9, 2003 earthquake reduce from 0.979 to 0.389 after applied the empirical site correction function. Dash line indicated the GMPE of Jean et al. (2006), and σ_{lnErr} = 1.325; but it reduce to 0.336 after second step of the site correction shown in circles.

Another shallow earthquake of September 10, 2000 also shows the same characteristics. σ_{lnErr} reduce from 1.1 to 0.487 for stochastic simulation, and from 1.458 to 0.456 for GMPE method. The results for March 24, 1995 earthquake with focal depth 76 km still shown the σ_{lnErr} reduction effect, but the values are all greater than other two shallow events. The magnitude of this event is Mw5.6 that is around the same with other two events and in the database range for analysis empirical site correction function. So, the simulation results not so good as others should due to the different site responses for shallow and deep earthquakes found in Taipei basin (Sokolov et al. 2009). The bias in frequency domain (DSPD) for the deep event is 3.10 also greater than 1.83 and 2.12 of the two shallow events. GMPEs for shallow and deep earthquakes also found are different by many studies. This also can explain the larger bias for PGA of the 1995 deep event than those two shallow events for the GMPE results in the time domain.

4.2 Simulation of the 1999 Chi-Chi Earthquake

Due to the 1999 Chi-Chi, Taiwan earthquake, magnitude Mw=7.6, occurred along with a surface fault rupture. The stochastic ground motion simulation needs to use finite fault model (EXSIM). Figure 8 shows an example of the simulated results of station TAP003. From all the simulation time histories we can draw the PGA contour and compared with the observation. The residual map of the PGA simulation is displayed in Figure 9. We have a satisfactory prediction in the most area of basin but there has one underestimates occurred in western part and a large part overestimated in the eastern part of the basin. These mismatches may due to the large magnitude earthquake did not used in calculation of the empirical site correction function or the source spectrum did not exactly simulated by the finite fault model. So, DSPD (Figure 10) reach to 4.06 which is

greater than previous three moderate magnitude earthquakes. The PGA simulation seems had a good result compare to the results of three moderate events. σ_{lnErr} = 0.472 for EXSIM of rock site simulation and reduce to 0.304 after applied empirical site correction for each station. For GMPE simulation, σ_{lnErr} = 0.76 for rock site direct calculated from attenuation equation and reduce to 0.387 after site correction.

5. DISCUSIONS AND CONCLUSIONS

The stochastic point source model which has been calibrated on rock sites was used to obtain the site transfer function for each soil site within the Taipei basin. The empirical site correction function for each soil station was calculated from average the results of 203 magnitude less than 6.0 and depth less than 40 km earthquakes. Then, the ground motion simulation can be performed for moderate magnitude earthquakes by the stochastic point source simulation to rock basement and added the empirical site correction to get the final ground motion simulation. The biases of the stochastic simulation results compared with observation are around the same compared with the GMPE simulation.

For the 1999 Chi-Chi, Taiwan earthquake with surface rupture and large magnitude (Mw=7.6), the stochastic finite fault model was used and the empirical site correction function still used that from the previous analysis. Although the spectrum bias is larger than that of the moderate magnitude earthquake simulations, the PGA from EXSIM included the site correction function still show a good simulation with σ_{lnErr} = 0.304 which is even better than GMPE result of σ_{lnErr} = 0.387 after site correction. This shows the ground motion prediction already can go more high frequency from seismology method. The simulation results in the time domain will have around the same biases compared to the results from GMPE method which engineering usually used. Specially, the simulation results from this kind ground motion simulation method not only can predict the PGA as GMPE method done but also can have time history with the spectrum under limited bias or uncertainty.

The bias analysis in this study suggested more detail works need to be done. Hope it will reduce the uncertainty of the ground motion simulation for different magnitude earthquake. More accurate ground motion prediction can provide a good reference for the future seismic hazard mitigation. The empirical site transfer function was calculated from the ratio between observation and simulation earthquake records. Effects from the magnitude level for source effects, ground motion level for nonlinear site effects, and focal depth for propagation path or direction should be considered in the future study.

Acknowledgements:

The earthquake data were provided by the Seismological Center, Central Weather Bureau, Taiwan. The site classification information was from EGDT of National Center for Research on Earthquake Engineering, NARL, Taiwan. This study is supported by National Science Council, Taiwan, under the grant no. NSC 101-2116-M-008-021.

References:

Anderson, J.G., Lee, Y., Zeng, Y., and Day, S. (1996), "Control of Strong Motion by the Upper 30 Meters," *Bull. Seism. Soc. Am.*, **86**(6), 1749-1759.

Assatourians, K. and Atkinson, G.M. (2007), "Modeling Variable-stress Distribution with the Stochastic Finite-fault Technique," *Bull. Seism. Soc. Am.*, **97**, 1935-1949.

Atkinson, G.M. and Boore, D.M. (2006), "Earthquake Ground-motion Prediction Equations for Eastern North America," *Bull. Seism. Soc. Am.*, **96**, 2181-2205.

Beresnev, I.A. and Atkinson, G.M. (1998), "Stochastic Finite-fault Modeling of Ground Motions From the 1994 Northridge, California, Earthquake. I. Validation on Rock Sites," *Bull. Seism. Soc. Am.*, **88**, 1392-1401.

Boore, D.M. (2009), "Comparing Stochastic Point-source and Finite-source Ground-motion Simulations: SMSIM and EXSIM," *Bull. Seism. Soc. Am.*, **99**, 3202-3216.

Campbell, K.W. (1981), "Near-source Attenuation of Peak Horizontal Acceleration," *Bull. Seism. Soc. Am.*, **71**, 2039–2070.

Chang, G., Wu, Y.M., and Shin, T.C. (2000), "Relocating the 1999 Chi-Chi Earthquake, Taiwan," *Terr. Atmos. Ocean Sci.*, **11**, 581–590.

D'Amico S., Akinci, A., and Malagnini, L. (2012), "Predictions of High-frequency Ground-motion in Taiwan Based on Weak Motion Data," *Geophy. J. Int.*, **189**, 611-628.

Jean, W.Y. and Loh, C.H. (2001), "A Study on the Classification of Site Effects and Its Application to the Seismic Hazard and Microzonation," *10th International Conference on Soil Dynamics and Earthquake Engineering, SDEE'2001*, Volume of Extended Abstracts, 82.

Jean, W.Y., Chang, Y.W., Wen, K.L., and Loh, C.H. (2006), "Early Estimation of Seismic Hazard for Strong Earthquakes in Taiwan," *Natureal Hazards*, **37**, 39-53.

Kuo, C.H., Wen, K.L., Hsieh, H.H., Lin, C.M., Chang, T.M., and Kuo, K.W. (2012), "Site Classification and Vs30 Estimation of Free-field TSMIP Stations Using the Logging Data of EGDT, *Engineering Geology*, **129-130**, 68-75.

Lee, S.-J., Chen, H.-W., and Huang, B.-S. (2008), "Simulations of Strong Ground Motion and 3D Amplification Effect in the Taipei Basin by Using a Composite Grid Finite-difference Method," *Bull. Seism. Soc. Am.*, **98**(3), 1229–1242.

Ma, K.F., Mori, J., Lee, S.J., and Yu, S.B. (2001), "Spatial and Temporal Distribution of Slip for the 1999 Chi-Chi, Taiwan, Earthquake," *Bull. Seism. Soc. Am.*, **91**, 1069–1087.

Miksat, J., Wen, K.-L., Wenzel, F., Sokolov, V., and Chen, C.-T. (2010), "Numerical Modelling of Ground Motion in the Taipei Basin: Basin and Source Effects," *Geophys. J. Int.*, **183**, 1633–1647.

Motezedian, D. and Atkinson, G.M. (2005), "Stochastic Finite-fault Modeling Based on a Dynamic Corner Frequency," *Bull. Seism. Soc. Am.*, **95**, 995-1010.

Sokolov, V.Y., Loh, C.H., and Wen, K.L. (2001), "Empirical Models for Site-and Region-dependent Ground-motion Parameters in the Taipei Area: A Unified Approach," *Earthquake Spectra*, **17**, 313-331.

Sokolov, V.Y., Wen, K.-L., Miksat, J., Wenzel, F., and Chen, C.-T. (2009), "Analysis of Taipei Basin Response for Earthquakes of Various Depth and Location Using Empirical Data," *Terr. Atmos. Ocean Sci.*, **20**(5), 687-702.

Wen, K.L. and Peng, H.Y. (1998), "Site Effect Analysis in the Taipei Basin: Results from TSMIP Network Data," *Terr. Atmos. Ocean. Sci.*, **9**(4), 691-704.

Wen, K.L., Huang, M.W., Wu, T.H., Chang, C.L., Liu, S.Y., Kuo, M.C., and Chang, Y.W. (2009), "Probabilities and Shakemaps of the Potential Earthquakes in Taiwan," *Proc. 6th International Conference on Urban Earthquake Engineering, Tokyo Institute of Technology, Japan*, 107-113.

Table 1 Modeling Parameters for SMSIM (D'Amico et al. 2012)

Parameter
Stress (bar):
30 for Mw < 4.5; 50 for 4.5 ≤ Mw < 5.5;
70 for 5.5 ≤ Mw < 6.5
Radiation-strength factor: 1.0
Quality factor: $350 \bullet f^{0.32}$
Geometric spreading R^b: b
-1.2 for 1 < R < 10 km
-0.7 for 10 < R < 40 km
-1.0 for 40 ≤ R < 80 km
-0.5 for R ≥ 80 km
Kappa (sec): 0.05
Crustal amplification:
ENA-A (Atkinson and Boore 2006)
Crustal shear-wave velocity (km/sec): 3.2
Crustal density (gm/cm^3): 2.8

Table 2 Modeling Parameters of EXSIM for the 1999 Chi-Chi Earthquake ((D'Amico et al. 2012)

Parameters for Mainshock
Fault orientation (strike/dip)
5°/34° (Chang et al. 2000)
Fault dimensions along strike and dip (km)
110 by 40 (Ma et al. 2001)
Depth of the upper edge of the fault (km): 0
Magnitude(Mw): 7.6
Subfault dimensions (km): 5x5
Stress parameter (bar): 90
Rupture velocity (km/sec): 0.8xVs
Subfault source duration: $1/f_{osf}$
Pulsing percent: 50%
Parameters for Each Subfault
Shear-wave velocity (km/sec): 3.2
Density (gm/cm^3): 2.8
Quality factor: $350 \bullet f^{0.32}$
Geometric spreading
-1.2 for 1 < R < 10 km
-0.7 for 10 < R < 40 km
-1.0 for 40 ≤ R < 80 km
-0.5 for R ≥ 80 km
Kappa (sec): 0.05

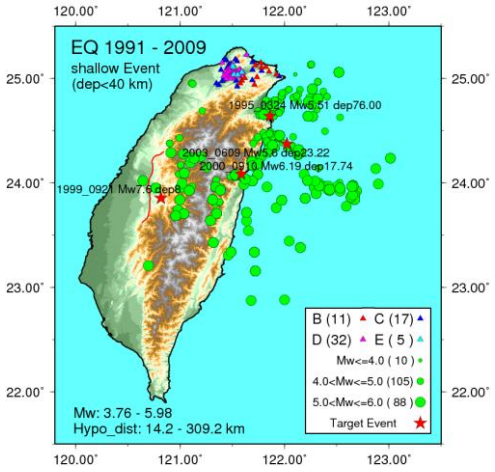


Figure 1 Epicenter Locations of 203 Earthquakes (green circles) and 4 Target Events (red stars). Triangles Show the Strong Motion Stations.

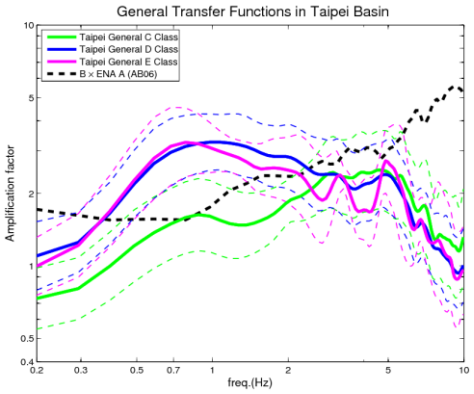


Figure 2 General Transfer Functions for Stations Within the Taipei Basin for Different Site Classifications.

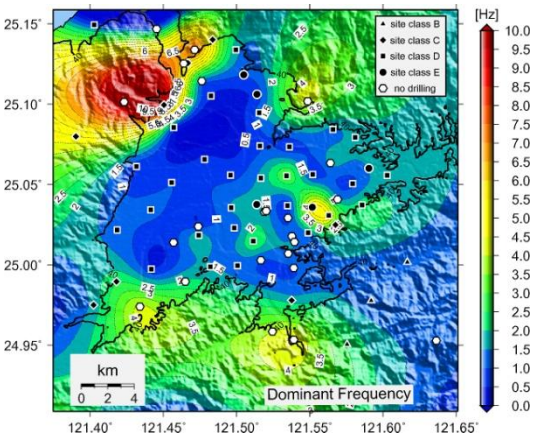


Figure 3 Contour of Dominant Frequency in the Taipei Basin from the Empirical Site Transfer Function of Each Station.

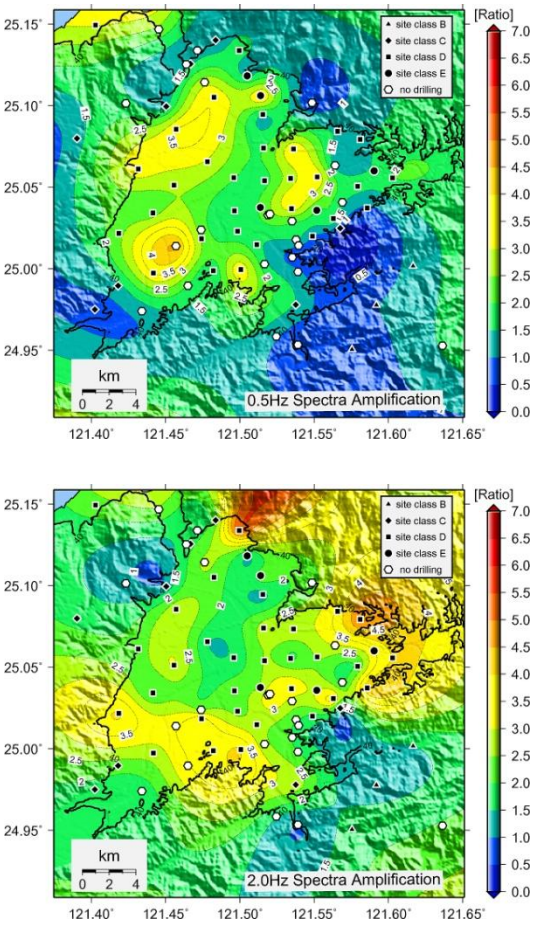


Figure 4 Contour of the Empirical Site Transfer Functions at 0.5 and 2.0 Hz in the Taipei Basin Area.

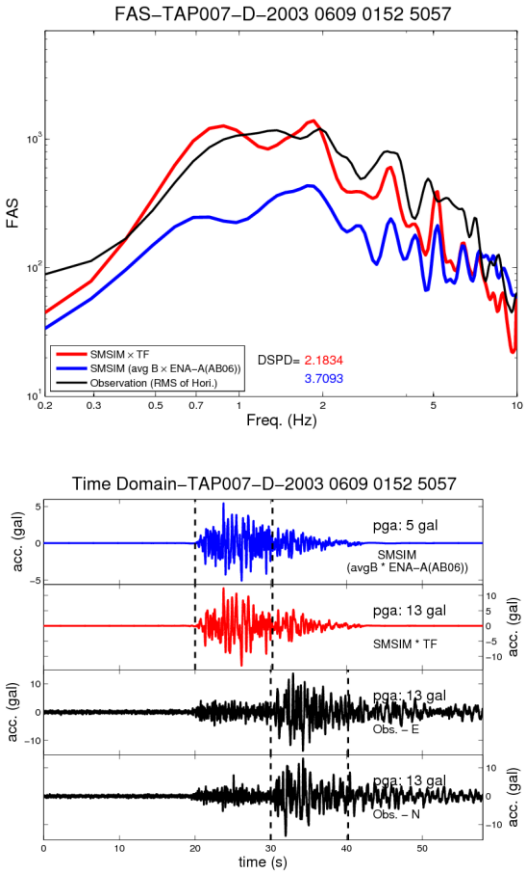


Figure 5 Frequency and Time Domain Results of the Station TAP007 for the June 9, 2003 Earthquake.

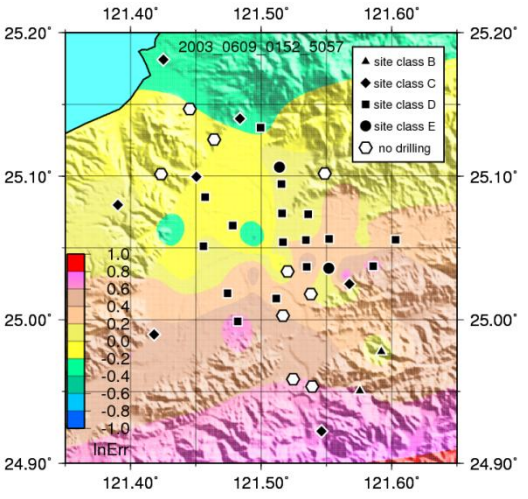


Figure 6 PGA Residual Map of the June 9, 2003 Earthquake.

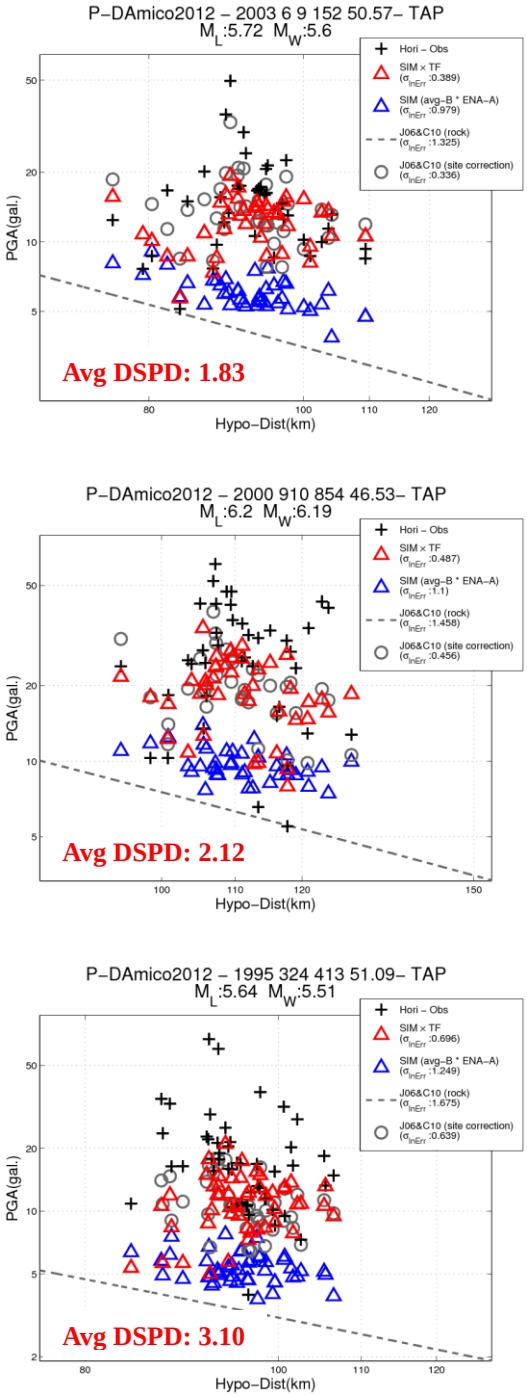
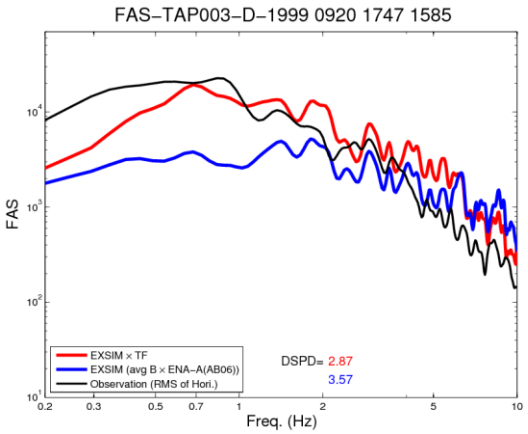


Figure 7 Comparisons of Observed and Simulated PGA for the Three Moderate Magnitude Earthquakes From Different Methods Include Rock Site Condition and After Site Correction.



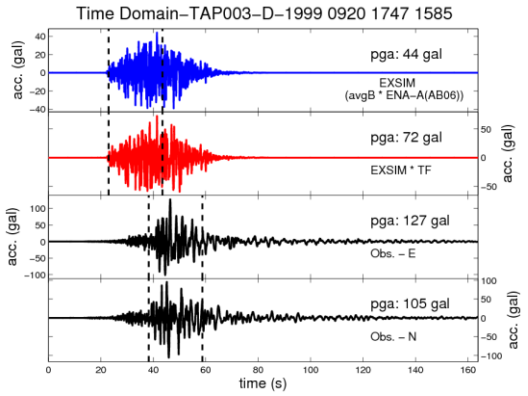


Figure 8 Simulated Time History and Amplitude Spectrum of 1999 Chi-Chi, Taiwan Earthquake at Station TAP003.

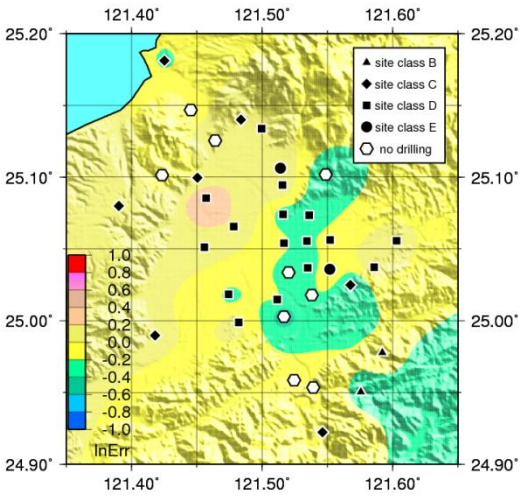


Figure 9 PGA Residual Map of the 1999 Chi-Chi, Taiwan Earthquake Simulated by EXSIM Code.

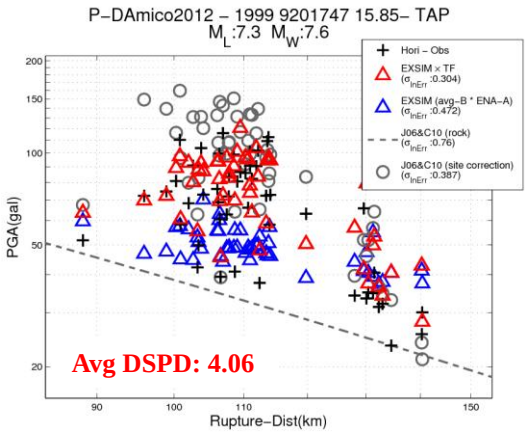


Figure 10 Comparisons of Observed and Simulated PGA for the 1999 Chi-Chi, Taiwan Earthquake From Different Methods Include Rock Site Condition and After Site Correction.

10CUEE CONFERENCE PROCEEDINGS
10th International Conference on Urban Earthquake Engineering
March 1-2, 2013, Tokyo Institute of Technology, Tokyo, Japan

USE OF AIRBORNE OPTICAL AND THERMAL IMAGERY FOR THE DETECTION OF BUILDING DAMAGE DUE TO THE 2012 TSUKUBA TORNADO

Fumio Yamazaki[1], Daiki Hanada[2] and Kentaro Suzuki[2]

1) Professor, Department of Urban Environment System, Chiba University, Japan
2) Graduate student, Department of Urban Environment System, Chiba University, Japan
fumio.yamazaki@faculty.chiba-u.jp, d.hanada@chiba-u.jp, z9t0222@students.chiba-u.jp

Abstract: On May 6, 2012, a strong tornado attacked Tsukuba City, Ibaraki Prefecture, Japan. It has caused heavy property losses in a concentrated area. An early detection of building damage is very important for quick response after an occurrence of natural disasters. Aerial visible images are widely used to detect building damage because they can cover a wide area quickly with very high spatial resolution. However, these images cannot be taken without sunlight, which could generate a "blank time" if a disaster occurs in the nighttime. On the other hand, aerial thermal-infrared images can be taken both in the daytime and nighttime without depending on sunlight although it has an inferior spatial resolution compared with aerial visible images. It is considered to be possible to detect building damage from the temperature distribution of an urban surface. In this study, detection of building damage and debris is carried out from aerial thermal-infrared images taken over Tsukuba City on May 8, 2012, both at daytime and nighttime. Spatial characteristics of temperature distribution, such as non-uniformity, are considered to grasp building damage and debris.

1. INTRODUCTION

On May 6, 2012, three powerful tornados were generated in Tochigi and Ibaraki Prefectures, Japan, almost at the same time. These tornados caused severe property losses and some casualties although in narrow areas, such as Tsukuba City. This event was considered to be a good case to test the capability of airborne remote sensing in damage detection, especially using visible and thermal infrared imagery (van Aardt *et al.*, 2011).

Remote sensing is widely used especially for the sites where the access from the ground is limited and the damage distribution covers wide areas (Rathje and Adams, 2008; Eguchi *et al.*, 2008; Dell' Acqua and Gamba, 2012). Various platforms and sensors have been developed recently for satellite remote sensing and its spatial resolution has been improved significantly (Joyce *et al.*, 2009), Airborne remote sensing, however, still has advantages over satellite remote sensing in spatial resolution, immediacy and applicability in cloudy conditions by flying under high-altitude clouds.

Damage detection using visible imagery is simple and common. However, visible imagery cannot be taken in the nighttime, and thus "blank time" may occur in emergency response after a disaster strikes. On the other hand, thermal infrared (TIR) imagery can be taken both in the daytime and nighttime without depending on sunlight. Yamazaki *et al.* (2009) confirmed that clear edges of buildings, roads, and vegetation can be extracted from aerial TIR images of urban areas. Hanada and Yamazaki (2012) recently used ASTER's TIR images for grasping flooded areas by tsunamis caused by the March 11, 2011 Tohoku, Japan earthquake. Satellite TIR imagery, however, has low spatial resolution, e.g. 90 m for ASTER and 60 m for Landsat-7. Hence, its application to small-scale damage is difficult. However, airborne TIR imagery has much higher spatial-resolution, say order of 2 to 3 m, and hence, it can be used for damage detection of individual buildings, especially at nighttime when visible sensors cannot be used.

In this study, we acquired visible and TIR images from a helicopter two days after the tornado in Tsukuba City. The TIR images taken at daytime and nighttime were compared with the visible image at daytime. Visual damage inspection was first carried out by the authors using the daytime visible image for a hard-hit area of the city. The TIR images were then compared with the result of the damage inspection. The temperature distribution from the TIR images was further investigated by employing building footprints from the visible image and GIS. The temperature distribution within a footprint was compared with the damage grade of the building and the capability of aerial TIR images in damage detection was studied.

2. THE MAY 6, 2012 TORNADO IN TSUKUBA

A strong tornado was generated in Joso City, Ibaraki Prefecture, on May 6, 2012 at 12:35. It caused significant damages along its path with 17 km in length and 500 m in width until its end at Tsukuba City (**Figure 1**). The moving speed of the tornado was about 60 km/h (passing 17 km in 18 min) based on the analysis of meteorological Radar by Japan Meteorological Agency (JMA, 2012). JMA judged the Fujita scale of the tornado as F2 (the average wind speed of 50-69 m/s in 7 s) based on their field survey after it passed

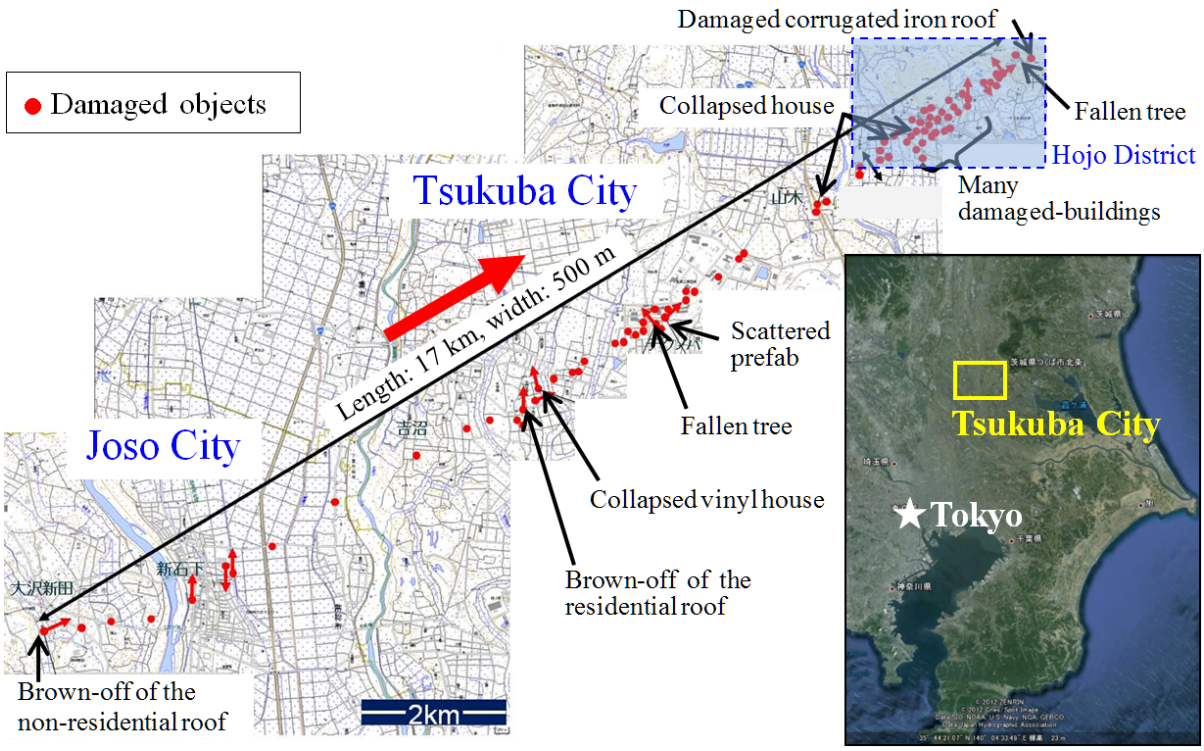


Figure 1 Detail map of the tornado's path and resultant damages, modified from JMA (2012).

by. However, it was changed to F3 (the average wind speed of 70-92 m/s in 5 s) in June 8, 2012 because the resultant damages were found to be so severe; for example, one wood-frame house was overturned upside-down with its concrete base.

This event is ranked as one of the strongest and most damaging tornados in Japan. By this tornado, one person was killed and 37 people were injured as of May 9, 2012, and 1093 buildings were damaged as of August 31, 2012 only in Tsukuba (Tsukuba City, 2012). In the recent years, the number of strong tornados is increasing in Japan, probably due to the climate change. Prediction of the occurrence time and location of a tornado is still very difficult because its time-span is short and its affecting area is small. However, enhancement of tornado prediction, its early warning and rapid response are strongly desired to reduce human casualties due to tornados.

We conducted a field survey of Hojo district, Tsukuba City, to obtain ground truth data from 14:00 to 16:00 on May 8, 2012, almost at the same time of our daytime's aerial image acquisition. Typical damages by the tornado were blown-off of building roofs, broken windows, and falling-down of trees and electric poles. Since these types of damages, other than the damage to building walls, can generally be observed from vertical imagery, we thought this is a good opportunity to test the capability of aerial TIR imagery for building damage assessment as well as that of optical imagery. We surveyed the hard-hit area and took ground photos of severely damaged buildings with their GPS location data.

The route of our field survey in Hojo district on May 8, 2012 was shown by the blue line in **Figure 2a**. We walked around the hard-hit area with digital cameras and hand-held GPSs. The weather condition of the day was cloudy with the maximum air temperature 24.8 ^{o}C, and minimum air temperature 13.4 ^{o}C.

Typical damage scenes are shown in **Figure 2** (**b-i**). Many buildings were collapsed or brown off their roofs, and these were covered by blue sheet (**b**). Trees were uprooted, and a wooden house was overturned upside-down with its concrete base (**e**). The Fujita scale was changed to F3 by this damage. Many objects were covered with mud because the tornado hit the area with rain (**f**). This might affect the surface temperature. Debris and mud on roads were mostly cleaned up already at the time of our field survey although some still remained. Recovery efforts were very fast because the tornado damage was localized. Restoration of electric poles and cables were going on with many trucks and workers (**i**).

3. VISIBLE AND TIR IMAGES USED AND ANALYSIS METHOD

In this study, the detection of building damage was carried out for the tornado that hit Tsukuba City. As a study area, Hojo district, a northern part of Tsukuba City, was selected where the most serious damage was observed by the tornado (**Figures 1** and **2**). Assessment of building damage was carried out using by TIR and visible images

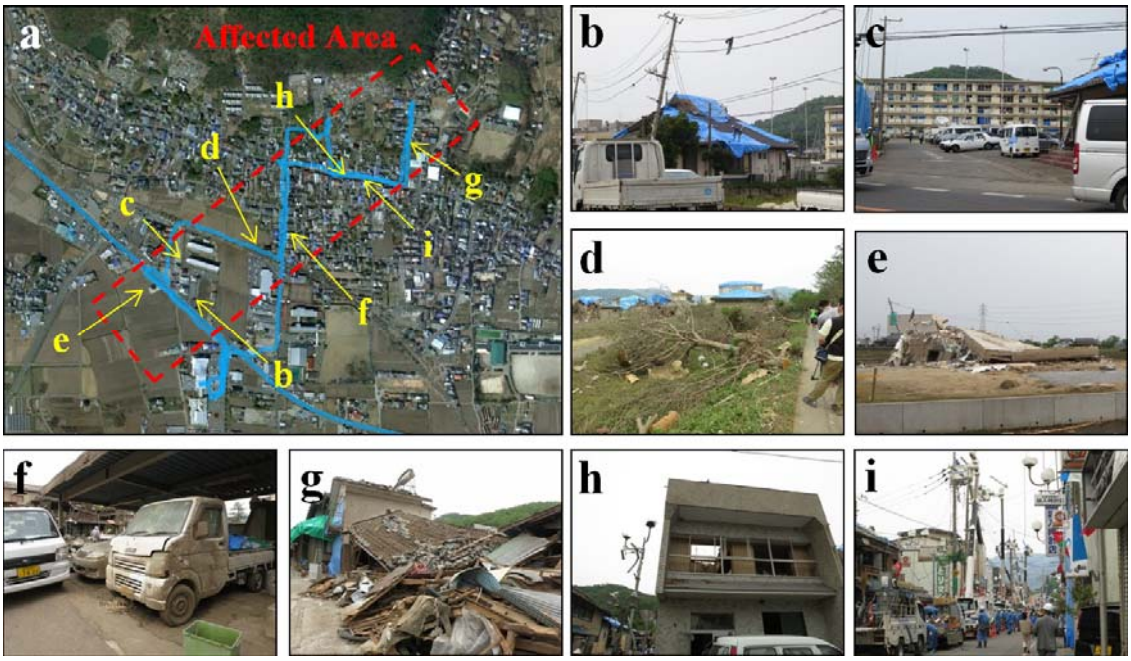


Figure 2 (a) The area of field survey in Hojo district, Tsukuba City and photo shooting locations, (b) Blue-sheet on the roof, (c) Damage on the side wall of an apartment building, (d) Fallen trees along street, (e) Overturned wooden house with its concrete base, (f) Cars stained with tornado's mud water, (g) Buildings that reduced to debris, (h) Brown-off of the roof (the sky is seen from the window), (i) Restoration work of electric poles and cables.

taken from a helicopter of SKYMAP co. by our request after the tornado. **Figure 3** (**a, c**) show a part of the post-event visible and TIR images taken at daytime (about 14:00) on May 8, 2012 while (**d**) shows a part of the TIR image taken at nighttime (about 19:30) on the day.

These images were taken from a small helicopter from the height of 460 m. The visible image with 0.25 m pixel size was created by mosaicing high-definition television (HDTV) scenes from a SONY handy video camera. The thermal-infrared (TIR) images with 1.54 m pixel size were mosaiced from ones taken by a TIR camera (NEC TS7302). Building footprints were created on a GIS system from the daytime aerial visible image by the present authors in order to use them in damage assessment for individual buildings.

The damage assessment was carried out in the following steps; Firstly building footprints were manually created from the daytime aerial visible image and an existing Zenrin digital map on ArcGIS software (**Figure 3b**). Then, damage status of each building was detected visually from the daytime aerial visible image based on the building damage classification shown in **Figure 4**. This classification was applied here, modified from the floor damage criteria by the Cabinet Office of Japan (2009), which is recommended to use when evaluating the monetary loss of residential structures for local governments. In the classification, the damage level of each wooden house is judged by 5 grades: such as no to slight (G0-G1), minor (G2), moderate (G3), major damage (G4) and collapse (G5). We employed the method based on the damaged percentage of a roof (*R*) since it is suitable to apply to vertical aerial images.

The damage level of each building was also estimated from the temperature distribution obtained from the daytime and nighttime TIR images. The average temperature and its slope angle within a building footprint were calculated and they were compared with the damage grade. The slope angle was calculated for a 3x3-pixels window (ArcGIS Resource Center, 2011). A large slope angle means a large difference in temperature between adjacent pixels while a small slope angle indicates a small difference. We considered that a severer building damage level might lead to higher variability in temperature distribution within a footprint. The average temperature within each footprint was also calculated for the daytime and nighttime TIR images using ArcGIS software. An open DXF file was generated by ArcGIS and a histogram of the average temperature for each building was made for each damage grade.

4. RESULTS OF DAMAGE EXTRACTION

4.1 Visual Damage Assessment from the Post-event Visible Image

Figure 4 shows the result of our visual damage inspection from the daytime aerial visible image. It is seen that the grades G3-G5 buildings were located along the path of the tornado. The path of the tornado was clearly seen from the visible image, and the center line was drawn as shown in **Figure 5**. The parallel lines were also drawn up to 200 m from the center line to the both sides in 20 m interval. The damage ratio for each distance class was calculated and shown also in **Figure 5**. It is observed that the collapsed

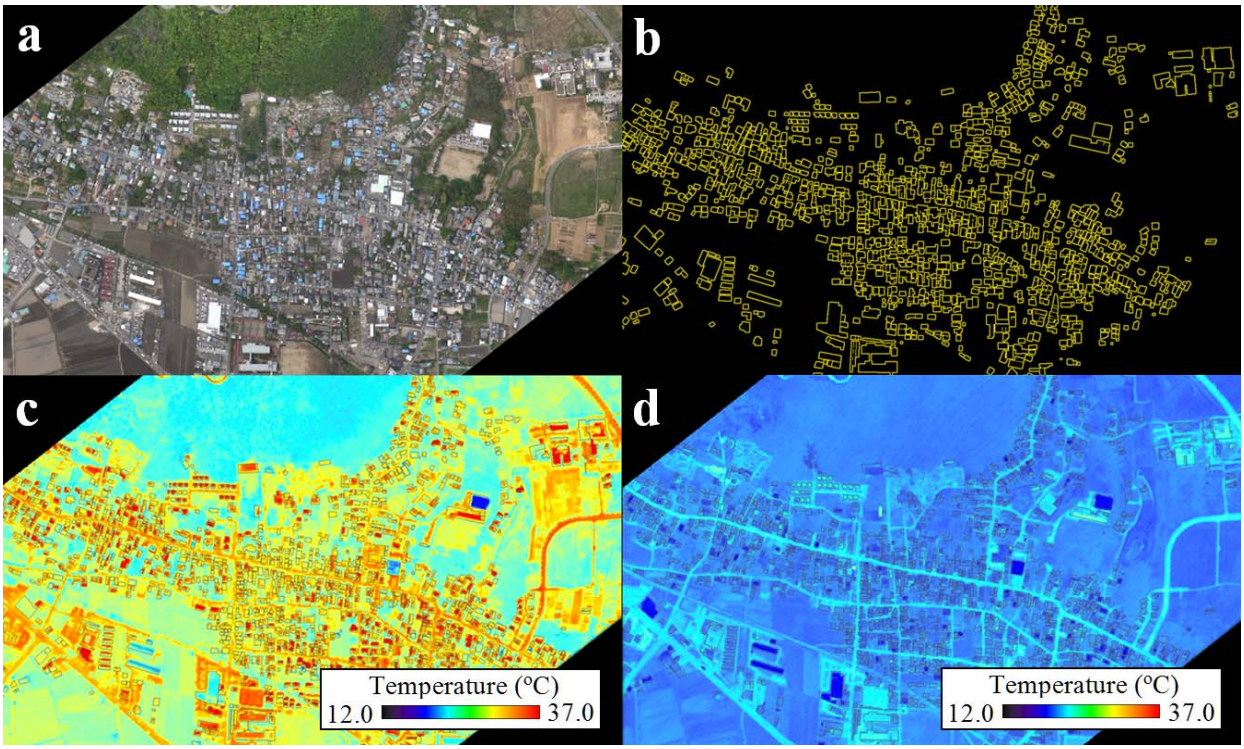
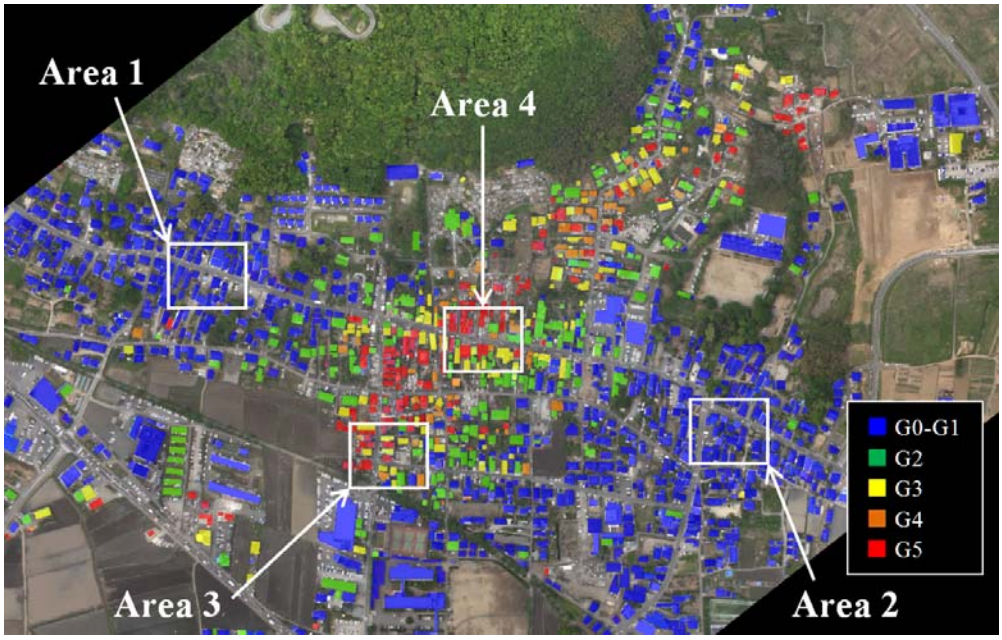


Figure 3 (**a**) Visible image of Hojo district in Tsukuba City at daytime, (**b**) building footprints created from (a), (**c**) TIR image at daytime, and (**d**) TIR image at nighttime on May 8, 2012 taken from helicopter.



Damage Level	G2	G3	G4	G5
Roof damage ratio $R = \frac{Damaged\ Roof}{Roof}$				
	0%<R≤20%	20%≤R<50%	50%≤R<70%	R≥70%

Figure 4 Damage classification result by our visual inspection for the daytime aerial visible image.

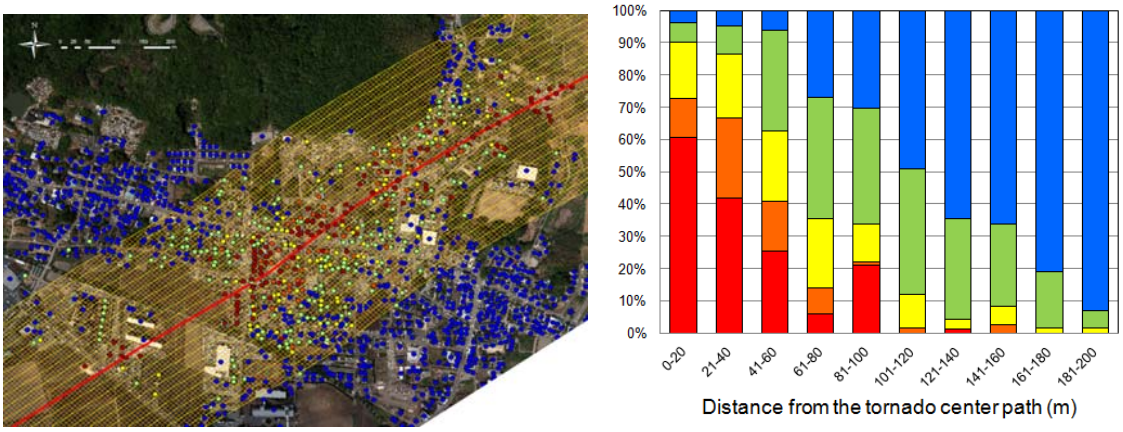


Figure 5 The center path of the tornado detected from our visual inspection and its parallel lines within 200 m (left) and the damage ratio of buildings for 20 m interval from the center path (right)

Table 2 Comparison of the result by our visual inspection on the daytime optical image and that from field observation by Tsukuba Fire Department for 730 buildings within 200 m from the tornado path in Hojo district

Visual Inspection \ Field Survey	G5	G4, G3	G2	G1, G0	User's Accuracy
G5	82	17	6	8	72.6%
G4, G3	27	56	40	22	38.6%
G2	9	34	100	39	54.9%
G1, G0	0	15	102	172	59.5%
Producer's Accuracy	69.5%	45.9%	40.3%	71.4%	Overall Acurracy 56.2%

buildings (G5) were located mostly within 60 m from the center path of the tornado. No collapsed building was found outside of the 100 m lines from the center path. Almost no damaged buildings were seen outside of the 200 m lines from the center path. The damage due to the tornado was concentrated in a narrow range although tornado paths are unpredictable.

In our visual damage inspection, some buildings were judged as no damage although some damages on their side surfaces were seen in our field survey, i.e. the apartment building in **Figure 2c**, because the damage was judged only from the roof condition of the vertical visible image. This might be the reason of the difference between our inspection result with the damage assessment result by Tsukuba Fire Department from the ground, as shown in **Table 2**. The damage assessment in their field survey was conducted by looking from outside, and thus damages to side walls and facade could mostly be seen. G3 and G4 were grouped as one class because their results did not distinguish these two.

It is seen from the table that the user's accuracy and producer's accuracy are almost the same level in this area, which indicates that both vertical photos and ground survey have weakness; the former sees only a top view while the latter mostly a side view of a building. In case of building damage due to tornados, damages to roofs prevail and hence vertical areal images are suitable to detect damages. On the contrary, damages due to earthquakes are more difficult to extract from vertical aerial images since damages to side walls are usually significant.

In this study, our visual inspection result was used as the reference data for the aerial TIR images since the both data were acquired from the same vertical view angle, where only the damage condition or the temperature of the roof was seen.

4.2 Temperature Characteristics of Non-damaged Areas from Daytime and Nighttime TIR Images

The characteristics of the TIR images at non-damaged areas were discussed first. **Figure 6** shows the locations of two target non-damaged areas in **Figure 4**. **Figure 7** shows the surface temperature within the building footprints from the daytime and nighttime TIR images, superimposed on the visible image. From the daytime roof temperature distributions in **Figure 7** (**a**, **c**), the roofs mostly show high temperature although some low temperature roofs exist. From the nighttime roof temperature distributions in **Figure 7** (**b**, **d**), the buildings showing high temperature at daytime are still in relatively higher temperature at nighttime. It is observed that the roof temperature within a footprint of a non-damaged building is mostly uniformly distributed but the effects of surrounding vegetation, shadow and footprint's inaccuracy can be observed around the outline.

Figure 8 shows the slope angle of the surface

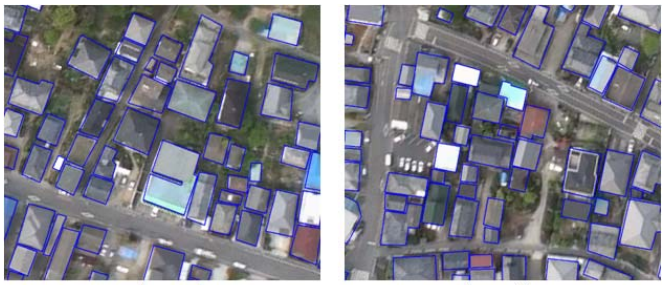


Figure 6 Target areas of non-damage in Figure 4

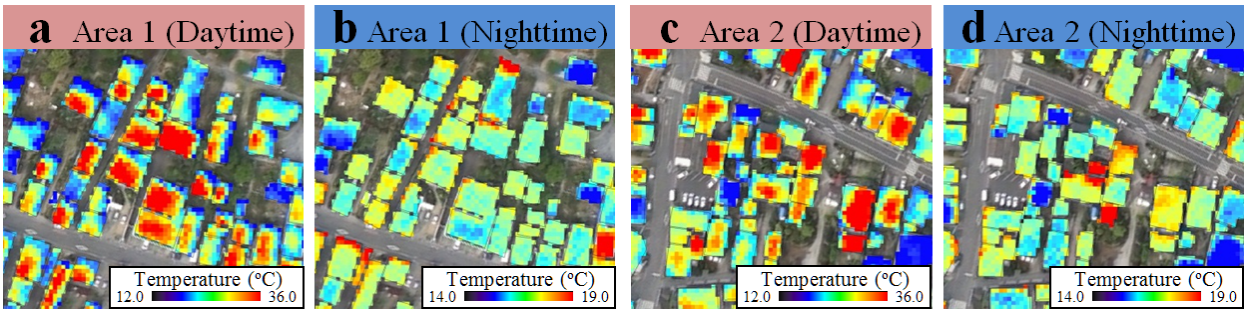


Figure 7 Temperature within building footprints for non-damage areas, **a**, **c**: Daytime, **b**, **d**: Nighttime

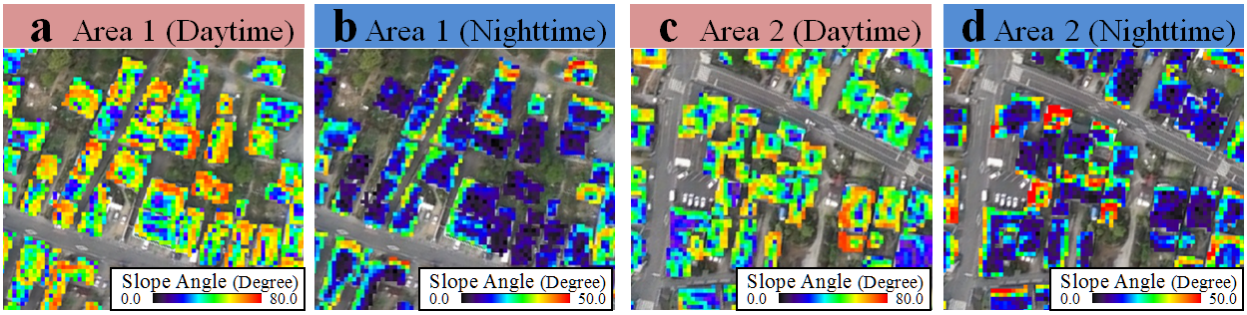


Figure 8 Slope angle of the temperature within building footprints in Figure 7, **a**, **c**: Daytime, **b**, **d**: Nighttime

temperature within the footprints. In calculation of the slope angle, the temperature of the adjacent pixels affected the result although the angle is shown only within the footprints. In the daytime slope angles in **Figures 8** (**a**, **c**), high temperature roofs show generally larger slope angles because the temperature difference with their surroundings is large due to the difference of surface materials. In the nighttime slope angles in **Figure 8** (**b**, **d**), the slope angles within some building outlines are displayed red color affected by surrounding road or vegetation. However most building roofs are in low temperature with uniform distribution, and thus their temperature changes within their outlines are small.

4.3 Temperature Characteristics of Heavily-damaged Areas from Daytime and Nighttime TIR Images

Next the characteristics of the TIR images at heavily-damaged areas were discussed. **Figure 9** show the locations of two target heavily-damaged areas in **Figure 4**. **Figure 10** shows the surface temperature within the building footprints from the daytime and nighttime TIR images, superimposed on the visible image. From the daytime roof temperature distributions in **Figure 9** (**a**, **c**), damaged roofs mostly show low temperature because they were covered by blue sheet or reduced to debris. The nighttime roof temperature distributions in **Figure 9** (**b**, **d**) also exhibit low values. The temperature distributions for heavily-damaged buildings are seen to be somewhat different from those of non-damaged ones both at daytime and nighttime, but this observation is highly affected by the material, color and orientation of the roof, shadow and surrounding conditions.

Figure 11 shows the slope angle of the surface temperature within the footprints. In the daytime slope angles in **Figure 11** (**a**, **c**), many buildings show small values as in purple to blue colors. It is also observed that the pixels with large angles are few probably because buildings were reduced debris and it spread in and outside of the original building footprints. Many materials were mixed up by building collapse and thus many objects became a

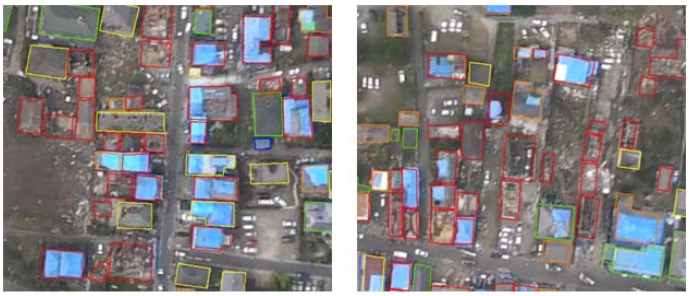


Figure 9 Target areas of heavy-damage in Figure 4

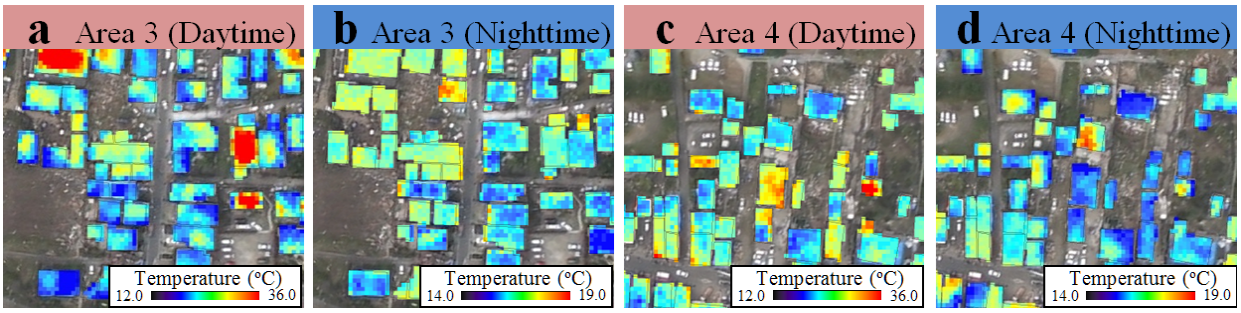


Figure 10 Temperature within building footprints for heavy-damage areas, **a**, **c**: Daytime, **b**, **d**: Nighttime

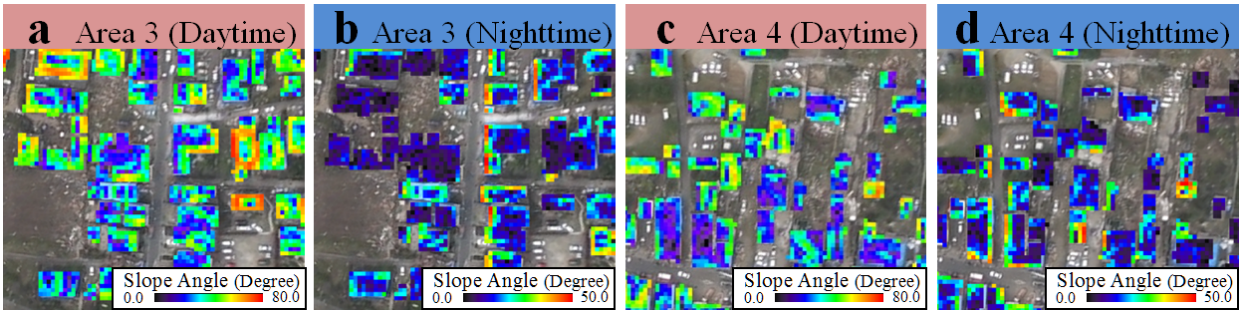


Figure 11 Slope angle of the temperature within building footprints in Figure 10, **a**, **c**: Daytime, **b**, **d**: Nighttime

mixed-pixel (mixel) condition for the low resolution TIR images (1.54 m). This characteristic is remarkable especially for the upper left building group in **Figure 11b**. Most footprint areas show small changes as in dark blue color. It can be seen in the visible image of Area 3 that the spread debris in the area became the similar condition as soil. This kind of debris spread was also observed in our field survey, and hence there is possibility to use this more uniform temperature distribution with the surroundings in early damage detection from TIR images.

4.4 Distribution of Average Temperature within Footprint for Each Damage Level

Figure 12 shows the cumulative distributions of the average temperature within building footprints for each damage level. Here, buildings other than in Hojo district were also counted. From the daytime graph, the average roof temperatures for non-damaged buildings are seen to be widely distributed in the range from 20 to 40 ^{o}C. On the contrary, those for damaged buildings are displayed in a narrower range from 24 to 35 ^{o}C and the range gets small as the damage level gets higher. For collapsed buildings (G5), the average temperature becomes in the range from 25 to 33 ^{o}C. This is because that the roofs were lost and the footprint areas were covered by the mixture of various materials like debris and mud. If we can use a much higher-resolution TIR image, a wider temperature distribution can be seen in more detail. But at this time, the resolution of our TIR images are 1.54 m, and thus most debris became in a mixel condition and the temperature distributions became flat. The histogram for damaged buildings at daytime tends to be in a narrow range and the average values were decreased for 2 or 3 ^{o}C.

From the nighttime graph, the average temperatures for most buildings are seen in narrower ranges, around 17 ^{o}C, compared with the daytime graph, as typically observed for collapsed buildings (G5). The cumulative distributions for damaged buildings at nighttime also tend to be in narrower ranges, the same as the daytime case. This kind of temperature characteristics in aerial TIR images may be used

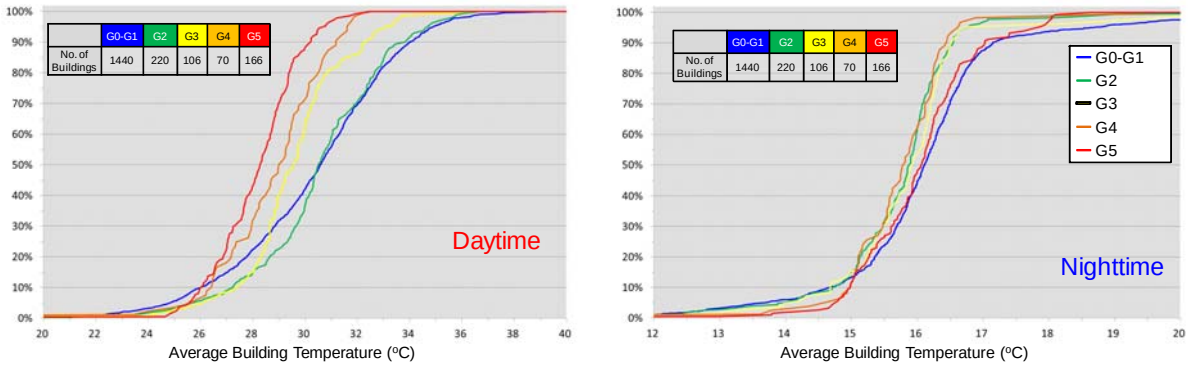


Figure 12 Cumulative distributions of average temperature within footprint for each damage level

in early damage detection in the future although more examples for various conditions should be tested.

5. CONCLUSIONS

In this study, aerial thermal infrared images were used to grasp building damages caused by the tornado that hit Tsukuba City on May 6, 2012. We acquired visible and TIR images over Hojo district of the city from a helicopter two days after the tornado struck. First building footprint data were created manually from the acquired visible image and the existing GIS map. Visual damage inspection was then carried out using the daytime visible image for the hard-hit area. The TIR images were then compared with the result of the damage inspection. The temperature distribution within the footprints was further investigated on a GIS.

From the average temperature distribution within non-damaged and damaged building footprints, non-damaged buildings showed higher temperatures with a larger range than those of damaged buildings. This observation may be explained by the fact that due to the collapse of roofs, the sunlight did not reach the roof locations and thus the temperature there was generally reduced. The change of temperature within each footprint was also evaluated using the slope angle of the temperature. But the slope angle was also strongly affected by the temperature itself, and hence a clear trend was not found.

From the distributions of the average temperature within building footprints for five damage levels, that for the collapsed level was distributed in a narrower range than that for non-damaged one's both at daytime and nighttime. The temperature distribution was seen to become flat as the damage level goes up. This is due to the mixed-pixel of debris and others around the original footprint, especially for the low spatial-resolution TIR images used in this study.

We tested the aerial TIR images after the tornado in this study because TIR imagery can be obtained even at nighttime and thus is possible to reduce "blank time" after a disaster strikes. However, due to the limitation of its spatial resolution, about 1.5 m in the current example, it was not so easy to detect small damage to individual buildings. Another important drawback of TIR imagery is that it is highly affected by the roof material, color and its orientation as well as the surrounding condition and the weather and air-temperature. Hence, more case studies are necessary in the future to utilize aerial TIR imagery for early damage detection after a disaster strike, especially at nighttime.

References:

ArcGIS resource center (2011), How Slope Works, http://help.arcgis.com/en/arcgisdesktop/10.0/help/index.html#/na/009z000000vz000000/

Cabinet Office of Japan (2009), Operational Guidelines of Damage Certification Criteria for Residences (in Japanese). URL: http://www.bousai.go.jp/hou/pdf/shishinall.pdf

Dell' Acqua, F. and Gamba, P. (2012) Remote Sensing and Earthquake Damage Assessment Experiences, Limits, and Perspectives, *Proceedings of the IEEE*, Vol. 100, No. 10, pp. 2876-2890.

Eguchi, R.T., Huyck, C., Ghosh, S., and Adams, B.J. (2008), The Application of Remote Sensing Technologies for Disaster Management, *the 14th World Conference on Earthquake Engineering*, CD-ROM.

Hanada, D., and Yamazaki, F. (2012), Detection of Flooded Areas by the Tohoku Earthquake/Tsunami Using ASTER Thermal Infrared Images, *9th International Conference on Urban Earthquake Engineering*, CD-ROM, 235-239.

Japan Meteorological Agency (2012), Report of the Tornado Occurred on May 6, 2012 (in Japanese). http://www.jma.go.jp/jma/press/1206/08b/toppu120608.html

Joyce, K.E., Belliss, S.E., Samsonov, S.V., McNeill, S.J., and Glassey, P.J. (2009), A Review of the Status of Satellite Remote Sensing and Image Processing Techniques for Mapping Natural Hazards and Disasters, *Progress in Physical Geography*, 33(2) , pp. 183–207.

Mitomi, H., Yamazaki, F., and Matsuoka, M. (2000), Automated Detection of Building Damage due to Recent Earthquakes using Aerial Television Images and Photographs, *Proc. of the 21st Asian Conference on Remote Sensing*, Vol. 1, 401-406.

Rathje, E, and Adams, B.J. (2008), The Role of Remote Sensing in Earthquake Science and Engineering, Opportunities and Challenges, *Earthquake Spectra*, 24(2), 471–492.

Tsukuba City (2012), Damage Situation by the Tornado Occurred on May 6, 2012 (in Japanese).

van Aardt, J., McKeown, D., Faulring, J., Raqueño, N., Casterline, M., Renschler, C., Eguchi, R. *et al.* (2011), Geospatial Disaster Response during the Haiti Earthquake: A Case Study Spanning Airborne Deployment, Data Collection, Transfer, Processing, and Dissemination, *Photogrammetric Engineering & Remote Sensing*, Vol. 77, No. 9, September 2011, pp. 943–952.

Yamazaki, F., Murakoshi, A., and Sekiya, N. (2009), Observation of Urban Heat Island using Airborne Thermal Sensors, *2009 Urban Remote Sensing Joint Event*, IEEE, Shanghai, China.

10CUEE CONFERENCE PROCEEDINGS
10th International Conference on Urban Earthquake Engineering
March 1-2, 2013, Tokyo Institute of Technology, Tokyo, Japan

ALEATORY AND EPICTEMIC UNCERTAINTIES OF GROUND-MOTION MODELS. RESULTS FROM RECENT EUROPEAN PROJECTS

Fabrice Cotton[(1)], Elise Delavaud[(1)], Adrian Rodriguez[(3)], Ralph Archuleta[(4)], Céline Beauval [(1)], Mathieu Causse[(1)] and Emeline Maufroy [(1)]

1) Institut des Sciences de la Terre, University Joseph Fourier, Grenoble, France
2) Disaster Prevention Research Institute, Kyoto University, Uji, Japan
3) Civil and Environmental Engineering Department, Virginia Tech, Pullman, USA
4) Department of Earth Science, University of California, Santa Barbara, California

Abstract: The goal of this presentation is to present work performed recently in Europe to better understand strong ground motions and evaluate epistemic and aleatory uncertainties of ground-motion models. The methodologies used to select and weight empirical ground motion models used to build the new European seismic-hazard map (Shared FP7 project Delavaud et al., 2012) will first be presented. This methodology aims to build a logic tree which capture the epistemic uncertainty related to the prediction of ground-motions in Europe. This analysis has taken into account experts opinions but we also the use of new data-driven selection methods (e.g. Beauval et al., 2012). The random ground-motion-prediction variability of the chosen empirical models strongly influences the seismic hazard curve computation, in particular for long return periods. One of the key challenges of seismology is to be able to calibrate and analyze the physical factors that control the ground-motion variability. In a second part, I then will present new strategies to better understand the controlling factors of this variability. The exponential growth of seismological near-field records provides the opportunity to separate the source, propagation, and site factors controlling the ground-motion variability (Al-Atik et al., 2010; Rodriguez et al., 2011, 2013). Our results suggest that moderate earthquakes are more 'variable' for a given magnitude than large ones. Our data analysis shows that some stations are also showing larger variability ground motion than others, and that ground motion might be more variable at short distances than at large distances. We suggest (Cotton et al., 2013) that the between-event ground-motion variability gives an upper boundary to the earthquake stress-drop variability. This quantification of stress-drop variability offers a new way to calibrate future earthquakes aground-motion simulations.

1. INTRODUCTION

For seismically active areas, the estimation of ground motions is conducted through statistical analyses of existing ground motion data, that is, the development of ground motion prediction equations (GMPE).

Given the large amount of existing ground-motion prediction equations (GMPEs), the selection of the appropriate set of GMPEs capable of reflecting the center, body, and range of observed ground motion in large regions is a major challenge and potential source for unintended differences in hazard estimates between regions. The methodologies used to select and weight empirical ground motion models used to build the new European seismic-hazard map (Shared FP7 project Delavaud et al., 2012) will then be presented. This methodology aims to build a logic tree which captures the epistemic uncertainty related to the prediction of ground-motions in Europe. This analysis has taken into account experts opinions but we also the use of new data-driven selection methods (e.g. Beauval et al., 2012).

The random ground-motion-prediction variability of the chosen empirical models strongly influences the seismic hazard curve computation, in particular for long return periods. In a second part, I then will present new strategies to better understand the controlling factors of this "aleatory" variability. New strong-motions databases provide the opportunity to separate the source, propagation, and site factors controlling the ground-motion variability (Al-Atik et al., 2010; Rodriguez et al., 2011, 2012). We also suggest (Cotton et al., 2012) that the observed between-event ground-motion variability may offer a new way to calibrate future earthquakes and ground-motion simulations.

2. GROUND-MOTION LOGIC TREE FOR PSHA IN EUROPE

A new pan-European compilation of well-calibrated strong- and weak-motion records has first been built. This new database incorporates well-calibrated waveforms from key earthquake databases from other region of the world (to complement the European data coverage in the near-field and high magnitude range).

The Seismic Hazard Harmonization in Europe (SHARE) project, which began in June 2009, aims at establishing new standards for probabilistic seismic hazard assessment in the Euro- Mediterranean region. In this context, a logic tree for ground-motion prediction in Europe has been constructed. Ground-motion prediction équations (GMPEs) and weights have been determined so that the logic tree captures epistemic uncertainty in ground-motion prediction for six different tectonic regimes in Europe. This strategy, described in Delavaud et al. (2012) has the

particularity of combining two complementary and independent approaches: expert judgment and data testing. A set of six experts was asked to weight pre-selected GMPEs while the ability of these GMPEs to predict available data was evaluated with the method of Scherbaum et al. (Bull Seismol Soc Am 99:3234–3247, 2009). Results of both approaches were taken into account to commonly select the smallest set of GMPEs to capture the uncertainty in ground-motion prediction in Europe. For stable continental regions, two models, both from eastern North America, have been selected for shields, and three GMPEs from active shallow crustal regions have been added for continental crust. For subduction zones, four models, all non-European, have been chosen. Finally, for active shallow crustal regions, we selected four models each of them from a different host region but only two of them were kept for long periods. In most cases, a common agreement has been also reached for the weights. In case of divergence, a sensitivity analysis of the weights on the seismic hazard has been conducted, showing that once the GMPEs have been selected, the associated set of weights has a smaller influence on the hazard.

Based on the results of both the expert judgment and the testing, a consensus set of GMPEs was determined for each tectonic regime. Models supported by the empirical data testing and the experts' choices (first category) were selected while the models that were not supported by the data testing and not chosen by the experts (fourth category) have been rejected. For the rest of the models (second and third categories), discussions were held between the experts and ground-motion modeling group to decide on their rejection or selection. Weights were also determined but different propositions were retained for sensitivity analyses.

This task involved roughly a dozen institutions with the goal, in a limited amount of time (18 months), to commonly define a logic tree that would capture the center, body, and range of ground motion.T he principal idea that guided our strategy was to gather as much knowledge as possible from independent sources and different methods. Based on the characteristics of the available GMPEs determined by Douglas (2011), we first identified the best candidates using the rejection criteria of Cotton et al. (2006) and Bommer et al. (2010). Afterward, expert judgment highlighted the sets of GMPEs that were, according to the experts, capable of capturing epistemic uncertainties, while testing using observational data showed GMPEs capable of closely predicting past ground motions.

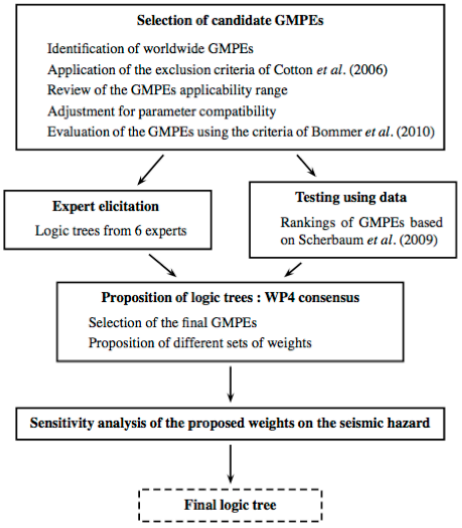


Figure 1. Methods used to capture epistemic uncertainties of GMPE's: expert elicitation and data-testing. Adapted from Delavaud et al. (2012)

From this experience, we have learnt lessons and identified weaknesses in our methodology. First, a great effort should be dedicated to the collection of data and meta-data in order to get as much information as possible from the GMPE testing. In our case, data were not sufficient to cover the center, body, and range of ground motions in Europe. Secondly, the procedure for the selection and weighting of GMPEs by experts should be clearly defined. Within the SHARE project, most experts required more guidance and information (e.g., What do weights represent? How will they be used afterward?). Selecting GMPEs and assigning weights is still not an obvious task, although Scherbaum and Kühn (2011) have recently proposed a method. To build a logic tree is not to give a quality measure to each candidate GMPE independently from the others but rather to identify the set of models that together, with a certain weighting, can capture the perceived epistemic uncertainty. In the context of the SHARE project that covers a large area, the set of GMPEs had to be the smallest one. The robustness of the proposed logic tree is a crucial property. For ASCR, the SHARE GMPE selection is in agreement with the data testing of Delavaud et al. (2012) who used an independent dataset to rank candidate GMPEs for Europe and Middle East. Regular updates of the logic tree should be planned to take new data and new GMPEs into account

2. TOWARD BETTER ESTIMATION OF GROUND-MOTION VARIBILITY (sigma).

2.1 Can sigma be reduced ?

With the aim of assessing the seismic hazard at a given site, one of the key steps includes the assessment of the ground motion expected from a future earthquake. For this, most seismic hazard studies make use of ground motion models (GMPEs), derived from existing seismic motion databases. In this framework, the random variability associated to the ground motion predictions ("sigma")

strongly influences the seismic hazard curve computation, in particular for long return periods.

Over the past 40 years, despite an increase in the number of available records, an improvement of processing tools and the increased complexity of the equations, the values of « sigma » have remained and the source, propagation, or site factors controlling sigma are still poorly understood. Since the GMPEs are derived using data recorded on multiple sites during earthquakes generated from different seismic sources, the difficulty lies on quantifying the influence of individual components on the overall uncertainty.

In traditional Probabilistic Seismic Hazard Assessment (PSHA), the underlying assumption is that the ground-motion uncertainty computed by a GMPE from a global data set (e.g., a dataset that includes various sites and various earthquakes from multiple sources) is the same as the variability at a single site. This is known as the "ergodic" assumption. For site-specific PSHA, additional information on site response can be used to improve the prediction of the GMPE at the site. In this case, the ergodic sigma must also be reduced to reflect this additional information. This reduction can only be accomplished with an adequate understanding of the factors that control ground motion variability.

Given the recent improvements in the number of available good quality ground motion recordings, and in particular the increased number of well recorded ground motions available at single sites from multiple occurrence of earthquakes in the same region, the possibility of removing (partially or fully) the ergodic assumption from the hazard assessment practice, and therefore of reducing the variability of ground motion, has become more and more concrete, at least in some areas of the world. Recently, much research has been devoted to the comparison between the "sigma" associated to ground motions from regional GMPEs based on regressions over large databases and either, the "sigma" associated to a given seismic station ("single station sigma") or the "sigma" associated to an individual seismic source ("single source sigma"). The main conclusion of these studies is that the sigma related to an individual seismic station is, for most stations, smaller than the one associated to the overall database. [e.g. Atkinson 2006, Rodriguez-Marek et al. 2011].

These results are highly motivating since they show that sigma values may be refined and that we now have the opportunity to understand the physical factors that control ground-motions variabilities. Ground-motion variability is usually divided into between-events variability and within-event variability. The presentation will describe and discuss some recent results and analysis performed on these two variability components.

2.2 Evaluation of the within-event (site-corrected) variability using data from various tectonic régions

The mean ground-motion residual at a station represents the site term. Quantification of site terms permits a more elaborate treatment of the ground motion uncertainty: the within-event component is split into a site-to-site and an event and site corrected (PhiSS) components.

In a recent study (Rodriguez-Marek et al., 2013) we estimate the PhiSS for five databases from different regions worldwide (California, Switzerland, Taiwan, Turkey, and Japan). We investigate the potential dependency of PhiSS on region, Vs30, distance and magnitude. The results show that the variability of PhiSS across the different regions is small when compared with the within-event standard deviation. In other words the variability in the ergodic among regions is significantly larger than the variability of among regions. This is one of the most striking results of this study: the value of single-station sigma (within appears to be largely region-independent. The average value of PhiSS is 0.45, with relatively small variation across spectral periods. The values of PhisSS show no specific trend with Vs30. Records at shorter distance show a higher PhiSS value; however, there is a potential that this is due to the scarcity of data at shorter distances. We observe (Rodriguez et al;, 2013) that PhiSS are larger for smaller magnitude earthquakes. This trend mimics the trend observed for the ergodic in various GMPEs. The larger values for small magnitudes can also be a reflection of a poorer constrain of metadata for these earthquakes, or can be due to the lack of data at larger magnitudes.

Estimates of single station sigma show considerable variability in the values of single-station sigma at different stations, and, in particular, that some stations are more variable then others. Investigation on the physical causes (e.g. geology, geophysics parameters) of such a large variability is actually carried out using simulations. Preliminary results (Maufroy et al., in preparation) show that topographic effects may play an important role to explain these larger values.

2.3. Between-event variability and sigma of stress-drop

Stress drop is a fundamental parameter in the description of earthquake source scaling properties. As we use ground-motion simulations to guide our understanding of earthquake hazard, it is imperative to know what standard deviation (sigma) should be used for the stress drop distribution. The ground-motion simulations should certainly not use a distribution with a sigma larger than is necessary.

The between-events residual represents average source effects (averaged over all azimuths) and reflects the influence of factors such as stress drop and variation of slip in space and time that are not captured by the inclusion of magnitude, style of faulting, and source depth.Two points confirm the link between stress-drop and between-event ground-motion variability. The between-events variability decreases when magnitude increases. This could be due to a higher stress drop variability of small earthquakes as suggested by Oth et al. (2010) or a reduced quality of the characterization (depth, distance, magnitude) of small earthquakes. Moreover the between-event variability is smaller for datasets that include earthquakes of a similar tectonic region, which also suggest a stress-drop control.

Using the theory of stationary Gaussian random functions and a simple source Brune's model we then have shown in a recent paper (Cotton et al., 2013) that there is proportionality between PGA and the stress-drop. According to this relation, the observed between-event PGA variability is a way to evaluate an upper bound of the stress-drop variability for a given region.

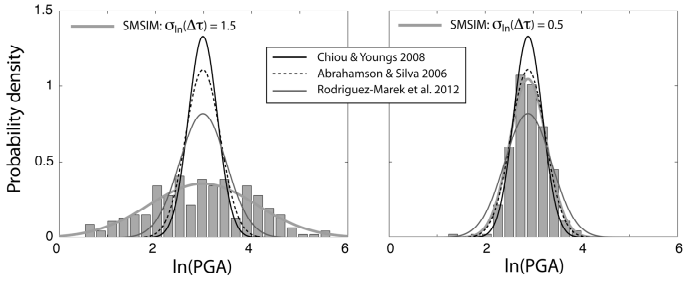


Figure 2. The result of computing PGA with two different values of variability on the natural log of stress drop. Histograms are from 200 runs with a lognormal distribution of stress drop with sigma of 1.5 (typical value from seismic results) and 0.5 (typical value inferred from GMPEs). As expected the GMPE's produce a good fit to the histogram because the inferred sigma (see text) was deduced from the GMPEs. Adapted from Cotton et al. (2013)

We show that stress-drop variability derived from the observed between-event ground-motion variability is much lower than those derived from source parameter studies, i,e., those based on corner frequency analysis. The variability of the stress drop analyzed trough source studies has always about a factor of 10-30 around the mean. We show that the standard deviation (sigma) of seismically determined stress drops is about 3-4 times larger than the sigma of the inferred stress drop based on ground motion prediction equations (GMPEs). This inconsistency does not make sense. Is the seismically derived variability real, or is it a consequence of the method for determining the stress drop? We suggest that stress-drop, determined by corner frequency, has greater uncertainty than that implied by the ground-motion data.

3. CONCLUSIONS

Recent improvements in the number of available good quality ground motion recordings allow to reduce the epistemic uncertainty of ground-motion models and refine the ground-motion aleatory variability.

To complement the expert opinions, testing of the candidate GMPEs against empirical data provides key informations to evaluate the applicability of candidate models by evaluating their probability to have generated the available data. Expert judgment and data testing are complementary and independent approaches that have been adopted to build the ground-motion logic tree used to define the new PSHA map of Europe (SHARE-GEM project).

The amazing quality of new networks and datasets (e.g. Knet and Kiknet networks in Japan) gives also the unique opportunity to identify the components of ground motion variability at a single site that are repeatable rather than purely random (e.g. the site response), so these can be removed from the aleatory variability and transferred to the quantification of epistemic uncertainty. Our results suggest that moderate earthquakes are more 'variable' for a given magnitude than large ones. Our data analysis shows that some stations are also showing larger variability ground motion than others, and that ground motion might be more variable at short distances than at large distances. We suggest (Cotton et al., 2013) that the between-event ground-motion variability gives an upper boundary to the earthquake stress-drop variability.

A better knowledge of ground-motion variability is then critical both for empirical ground-motions model developments (e.g. GMPE's) but also help to calibrate the variability of key simulations parameters (e.g. stress-drop).

Acknowledgements:

The authors acknowledge support from the Japan Ministry of Education, Culture, Sport, Science, and Technology (MEXT) for establishing the Center for Urban Earthquake Engineering (CUEE) in Tokyo Institute of Technology. This support makes possible the forthcoming international conference. The support of the Kyoto University makes possible the sabbatical research work of the main author in Japan. This work has been funded by EC-Research Framework programmes FP7, Seismic Hazard Harmonization in Europe, contract number 226967 and NERA (Network of European Research Infrastructures for Earthquake Risk Assessment and Mitigation) project, contract number 262330 and the Pegasos Refinement Project (Switzerland)

References:

Al Atik, L., N. Abrahamson, J. Bommer, F. Scherbaum, F. Cotton and N. Kuehn, 2010. The Variability of Ground-Motion Prediction Models and its Components, Seismological Research Letter, 81, 794 – 801, doi: 10.1785/gssrl.81.5.7

Beauval, C., H. Oksuz, A. Laurendeau, E. Delavaud, F. Cotton, Ph. Guéguen. On the use of small magnitude ground motions for the selection of ground-motion prediction equations in low-seismicity régions, 2012. Bulletin of the Seismological Society of America, 102, doi: 10.1785/0120110271

Cotton, F., Archuleta R. and M. Causse. 2013. What is sigma of stress drop ? Seismological Research Letter, in press

Delavaud, E., F. Cotton, S. Akkar, F. Scherbaum, L. Danciu, C. Beauval, S. Drouet, J. Douglas, R. Basili, A. Sandikkaya, M. Segou, E. Faccioli and N. Theodoulidis, 2012. Toward a Ground-Motion Logic Tree for Probabilistic Seismic Hazard Assessment in Europe. Journal of Seismology. DOI 10.1007/s10950-012-9281-z

Rodriguez-Marek, A., Montalva, G.A., Cotton, F. and F. Bonilla. Analysis of Single-Station Standard Deviation using the KiK-net data, 2011. Bulletin of the Seismological Society of America, 101, 1242–1258, doi: 10.1785/012010025

Rodriguez-Marek, A., F. Cotton, N.Abrahamson, S. Akkar,. L., Al-Atik, B.Edwards, G. Montalva and H.Mousad. A model for single-station standard deviation using data from various tectonic regions, submitted.

10CUEE CONFERENCE PROCEEDINGS
10th International Conference on Urban Earthquake Engineering
March 1-2, 2013, Tokyo Institute of Technology, Tokyo, Japan

ESTIMATION OF MEGA-EARTHQUAKES SOURCE MODELS FOR STRONG MOTION PREDICTION: APPLICATION FOR CENTRAL ANDES

Nelson Pulido

Senior Researcher, National Research Institute for Earth Science and Disaster Prevention, Japan. nelson@bosai.go.jp

Abstract: The recent 2011 Tohoku-oki earthquake occurred in a region where giant megathrust earthquakes were not expected. This earthquake proved the difficulty to assess seismic hazard mainly based on information from historical earthquakes. In this study we propose a methodology to estimate the slip distribution of megathrust earthquakes based on a model of interseismic coupling (ISC) distribution in subduction margins as well as information of historical earthquakes, and apply the method to the Central Andes region in Peru. The slip model obtained from geodetic data represents the large scale features of asperities within the megathrust, which is appropriate for simulation of long period waves and tsunami modelling. For the simulation of a broadband strong ground motion it becomes necessary to introduce small scale heterogeneities to the source slip to be able to simulate high frequency ground motions. To achieve this purpose we propose "broadband" source models constructed by adding the slip model inferred from the geodetic data, and short wavelength slip distributions obtained from a Von Karman PSD function with random phases. Using these slip models and assuming several hypocenter locations we calculate a set of strong ground motions within Lima and incorporate site effects obtained from microtremors array surveys.

1. INTRODUCTION

Recent mega-earthquakes in Sumatra (2004), Chile (2010) and Japan (2011) have highlighted the enormous hazard associated with these giant subduction events. In particular the 2011 Tohoku-oki earthquake proved the difficulty to assess seismic hazard mainly based on information from historical earthquakes. Due to the limited span of earthquake catalogues, other source of information such as geological or geodetic data might be considered for hazard assessment of future mega-earthquakes. In recent years the development of GPS and SAR interferometry is making possible to measure the strain build up associated with plate convergence in many earthquake prone regions around the world (Chlieh et al., 2008, and Perfettini et al. 2010). Recent studies have suggested that subducting plates are either locked or creeping aseismically, and that a patchwork of locked or coupled regions during the interseismic period may be related with asperities of earthquakes (Moreno et al. 2010). In this study we propose a methodology for seismic hazard estimation of megathrust earthquakes based on a model of interseismic coupling (ISC) distribution of subduction zones as well as information of historical earthquakes, and apply the method to the Central Andes region in Peru. Central Peru, North of the Nazca ridge, has been repeatedly affected by large earthquakes such as the 28 October 1746 which is reportedly the worst earthquake Lima has experienced since its foundation. Intensity reports as well as a tsunami record suggest a moment magnitude of ~8.8 for this earthquake (Dorbath et al. 1990). The 1746 earthquake was followed by a long period of quiescence until a sequence of magnitude 7-8 earthquakes in the 20th century starting with the 1940 earthquake up to the M8.1 Pisco earthquake in 2007 (Sladen et al., 2010) (Figure 1A). We use this information combined with an interseismic coupling model of Central Andes to elaborate a scenario for a megathrust earthquake that could likely affect the Lima metropolitan region.

2. SCENARIO EARTHQUAKES

2.1 Interseismic coupling (ISC and scenario earthquake

A model of interseismic coupling (ISC) for Central Andes (Chlieh et al 2011) indicates the existence of two strongly coupled regions, the first one off-shore Lima and the second one off-shore Pisco city (Figure 1B). Assuming an interseismic period of 265 years since the last megathrust earthquake that stroke Central Andes in 1746, up to 2010, we obtained a slip deficit equivalent to an earthquake with a moment magnitude of 8.9 (Figure 1C).

2.2 Broadband slip scenario earthquake

The geodetic slip model (GSM) obtained from the ISC, has a maximum slip of approximately 15 m, the source dimensions are approximately 500 km along strike and 160 km along dip, and the grid spacing is 20 km (Figure 2A). The moment magnitude, calculated using a rigidity of 39GPa is 8.9. The GSM is characterized by a smooth distribution of asperities (Figure 2A). This model is appropriate for the simulation of long period seismic waves

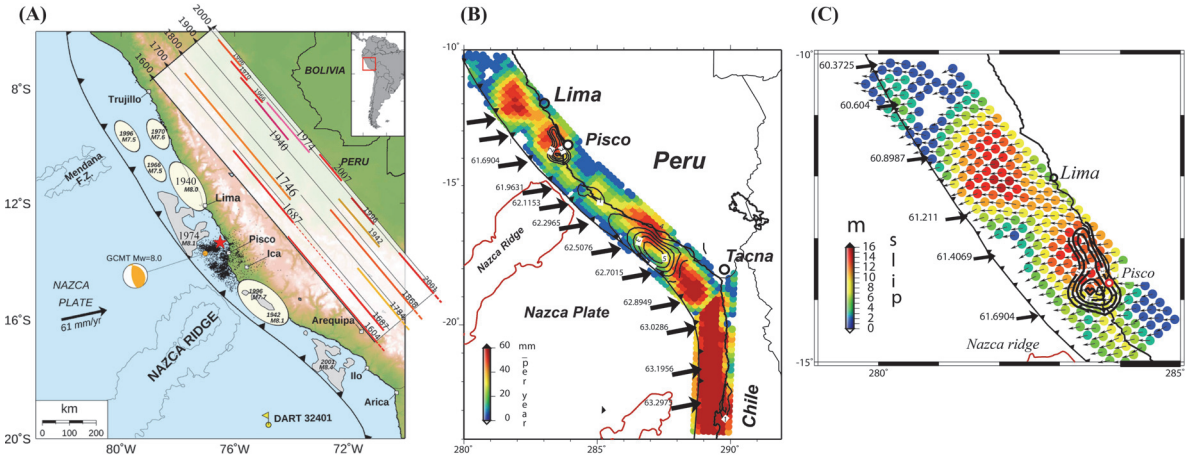


Figure 1. A) Historical earthquakes along the Nazca subduction zone in Peru (Sladen et al. 2010). B) Slip deficit rate model in Peru and northern Chile obtained from geodetic measurements (Chlieh et al. 2010). C) Slip distribution of a scenario earthquake for the subduction zone off-Lima, obtained by combining the slip deficit rate in (B) with an interseismic period of 265 years since the 1746 earthquake. The slip contours of the 2007 Pisco earthquake are shown in black

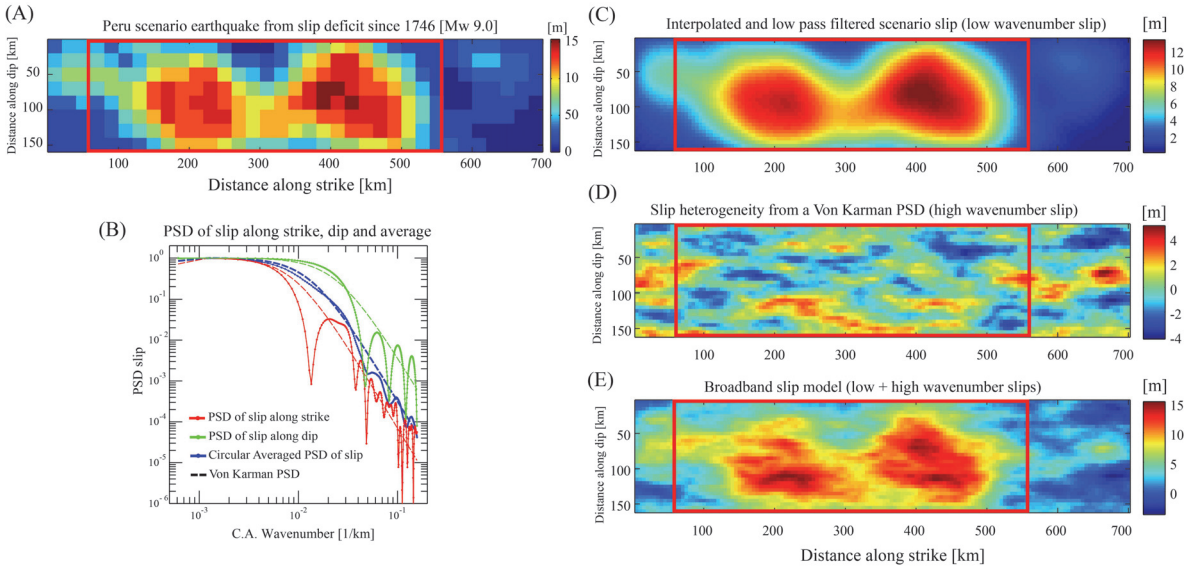


Figure 2 A) Slip distribution of the Central Andes scenario earthquake from ISC model. B) PSD of slip along strike (red), dip (green) and circular average (blue). Dashed lines correspond to the best fit Von Karman PSD function to the PSD of slip. C) Interpolated (to a 5 km grid spacing) and low-pass wavenumber filtered slip in A). D) Short wavelength slip obtained from the Von Karman PSD function of slip in B) and a random phase. E) Broadband slip obtained by adding low and high wave number slips in C and D. Red boxes indicate the assumed source area for the slip scenarios.

as well as for tsunami modelling. However for the simulation of a broadband strong ground motion it becomes necessary to introduce small scale complexities to the source slip to be able to simulate high frequency ground motions. To achieve this purpose we propose a "broadband" source model in which large scale features of the model are constructed from the GSM, and the short wavelength slip distribution is obtained from spatially correlated random noise. To obtain the parameters of this short wavelength slip we first calculate the power spectrum density (PSD) of our GSM, along the strike and dip directions (red and green lines in Figure 2B), as well as for a circular average (blue line in Figure 2B), and then fit a Von Karman PSD function to the observed spectra,

$$P(k_s, k_d) = \frac{k_s k_d}{\left[1 + a_s^2 k_s^2 + a_d^2 k_d^2\right]^{H+1}} \qquad (1)$$

where k_s and k_d are wavenumbers along strike and dip, a_s and a_d are the autocorrelation distances along strike and dip, and H is the Hurst exponent defining the spectral decay. Our fit to the PSD of the GSM yielded values of 110 km^{-1}, 40 km^{-1}, and 1 for a_s, a_d and H respectively (dashed lines in Figure 2B). To calculate a "broadband" slip we first interpolate the original GSM to a smaller grid interval, and apply a low-pass filter for wavenumbers smaller than a crossover wavenumber (k_{cross}) equal to 0.05, to get a long wavelength slip distribution (Figure 2C). Then we generate a correlated random slip model by using the aforementioned Von Karman PSD function (eq. No.1) using a random phase,

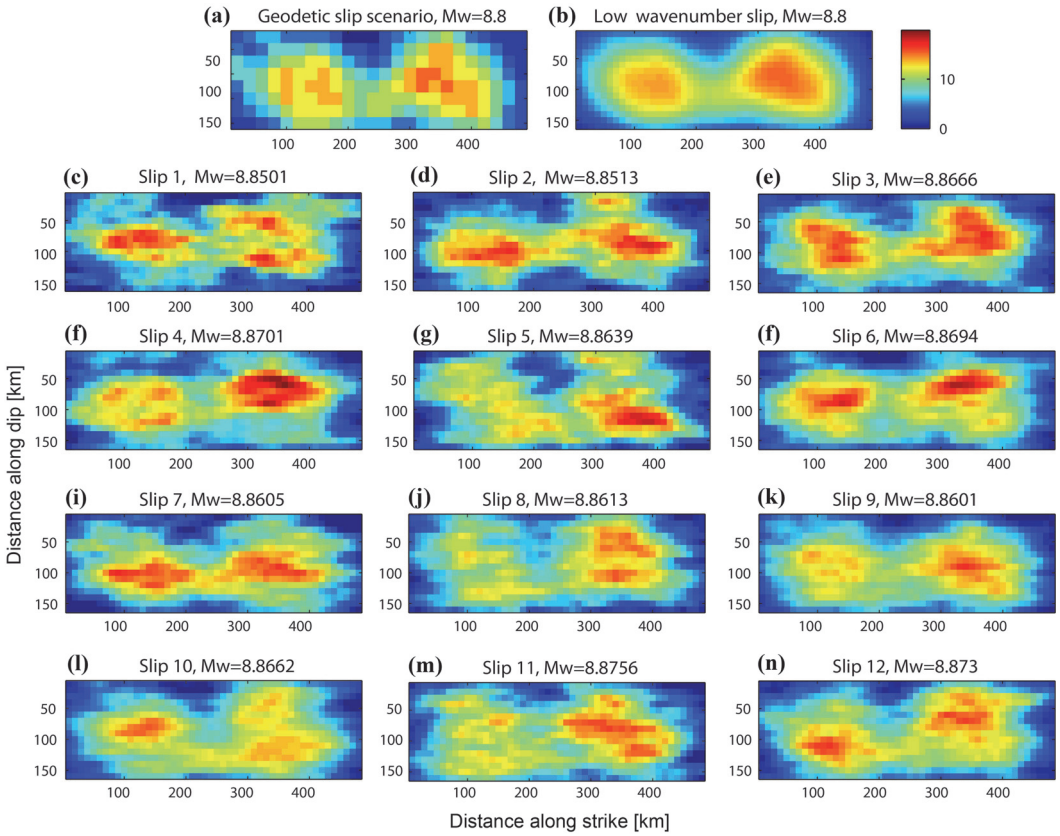


Figure 3 a) Slip scenario obtained from ISC model. b) Interpolated and low-pass wavenumber filtered slip model in a). c) to n) Broadband slip scenarios for 12 random realizations of short wavelength slip.

and apply a high-pass filter for wavenumbers above k_{cross} (Figure 2D). Finally we add the long and short wavelength slips to get a broadband wavelength slip (Figure 2E). The k_{cross} value was selected to approximately correspond to the size of the long wavelength asperity (125 km) (Figure 2C), which is about 5 times the corner wavenumber of GSM.

2.3 Broadband slip realizations

In order to obtain several broadband slips to be used for the strong motion simulations in Central Andes region, we compute a number of short wavelength slip models realizations. For this purpose we generate 12 sets of normally distributed random numbers with mean 0 and standard deviation 1 for the same source area used for the GSM, calculate their FFT in the wavenumber domain along strike and dip, multiply their spectral amplitude by the square root of the Von Karman PSD function of slip (eq. 1), and get them back to the spatial domain. We finally obtained 12 broadband slip realizations (Figures 3c to 3n). For the Central Andes strong motion simulations we have selected a subfault size of 10km.

3. STRONG MOTION SIMULATIONS

3.1 Strong motion simulation

To perform the strong motion simulations we follow the finite fault hybrid method of Pulido and Kubo (2004), and use the 12 broadband slip source models obtained previously. We assumed 9 different locations of starting points of the rupture (Figure 4A). Main parameters for the simulations are the stress drop, moment and rise time distributions across the fault plane, as well as the rupture velocity. We calculated the stress drop distributions for all the broadband slips following Ripperger and Mai. (2004). Rise times of subfaults are assumed to be proportional to the square root of slip. The rupture velocity is assumed to be 72% of the average S-wave velocity at the source, and we added a 5% fluctuation to enhance high frequency radiation. Maximum frequency f_{max} is set to 10Hz , and we use a Q value obtained for the Lima region ($Q=80f^{0.63}$) (Quispe, 2011). For the simulation of low frequency waveforms we used a 1D velocity model obtained for the Lima region (Dorbath et al. 1991). The simulation domain covers all Lima metropolitan region, spanning an area of 50 km by 55 km (white rectangle in Figure 4A), and a grid spacing of 5 km. We calculated the ew, ns and ud components of broadband frequency strong ground motions at every grid point (169 points) for a seismic bedrock condition (Vs=3454 m/s), for all slip models and assumed hypocenters. This yielded a total of 108 fault rupture scenarios and more than 50 thousand synthetic accelerograms. We added site amplifications up to the engineering bedrock (~400 m/s) by performing the convolution between the seismic bedrock waveforms with the soil transfer functions at every grid point. Site amplifications were obtained from 8 array microtremors surveys performed at representative geotechnical zones within Lima. (Calderón et al., 2012). In order to include soil amplifications for the shallowest soil we used an empirical

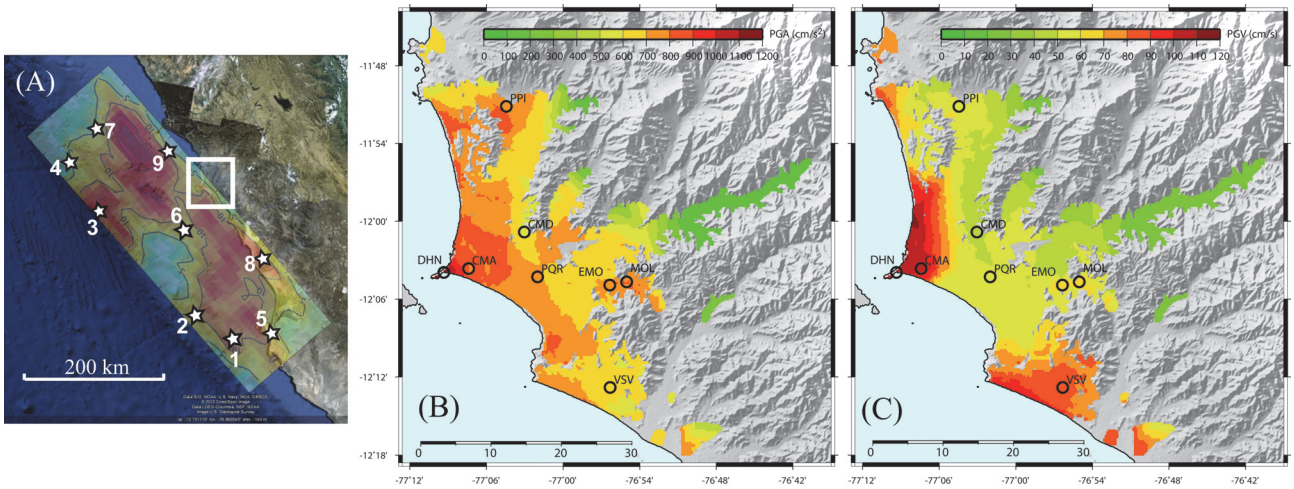


Figure 4 A) Scenario slip No.5 (Figure. 3g) and all assumed hypocenter locations for the rupture scenarios (stars). The simulation region in Lima is indicated by a white rectangle. B) Average of simulated PGA distributions in Lima for slip No.5 and all assumed hypocenters in A). These results include soil amplification. C) Same as A) but for the simulated PGV.

equation relating the soil amplification and the average S-wave velocity for the shallowest 10m of soil (Vs10) (Calderón, 2012). This information allowed us to calculate the PGA and PGV values at a grid spacing of approximately 250m.

3.3 Strong motion simulation results in Lima

In Figures 4B and 4C we can observe the PGA and PGV distributions for the slip model that yielded the largest ground motion amplitudes among the 12 broadband slip models considered (slip No.5, Figure 3g), averaged for all assumed rupture starting points scenarios. We can observe that the largest values of PGA are above 1000 cm/s^2 at Callao, La Punta (DHN). Large values of PGA were also obtained in Puente Piedra Province (800 cm/s^2) (PPI). These large values of PGA are closely related with the large amplifications for the shallower soil at these sites. The PGV distribution on the other hand displays the largest values for Callao (above 100 cm/s), followed by large PGV values in Villa El Salvador district (above 80 cm/s) (VSV). These large values of PGV are also closely related with the very large soil amplifications observed at Callao for periods around 1s, and at Villa El Salvador for periods around 0.8s to 1.5s (Calderon et al. 2012).

3.4 Comparison with records from the 1974 and 1966 earthquakes

The damaging earthquakes of 1966 (Mw8.0) and 1974 (Mw8.0) that occurred in the subduction zone off-shore Lima (Figure. 1a) were recorded by a strong motion station at Parque de la Reserva (PQR) in central Lima (Figure 4). At the same location we calculated broadband strong motions for all scenarios, by including site amplifications obtained from results of a microtremor array survey at this site (Calderon et al. 2012). In Figure 5A we may observe several simulated accelerograms at PQR in blue colors, and the observed strong motion records during the 1974 earthquake (red) and 1966 earthquake (orange) for the NS component. In dark blue we display the simulated accelerogram obtained from slip No. 5 and hypocenter No.1. This scenario generates a PGA at PQR similar to the average value of PGA for slip No. 5 (Figure 4B). The waveform in blue corresponds to slip No.7 and hypocenter No.1, which generates a PGA value comparable to the average PGA for all 108 rupture scenarios considered in this study. The waveform in light blue corresponds to the previous scenario but for a seismic bedrock outcrop condition. We can observe that the PGA amplitudes of the scenarios are about 2~3 times larger than the values observed at PQR during the 1966 and 1974 earthquakes. We can also observe that the simulated PGA values for a seismic bedrock outcrop condition (Figure 5A, 5B, light blue), are about 2~3 times smaller than the simulations that incorporate site amplifications (Figure 5A, 5B, blue). A similar observation can be made from the comparison of simulated and observed PGV amplitudes at PQR (Figure 5B).

In Figure 6A and 6B we can observe the acceleration and velocity response spectra for all the waveforms detailed in Figure 5. Here we can observe that the spectral amplitudes of the simulated waveforms are as large as 4 times the values observed during the 1974 and 1966 earthquakes at PQR. Another interesting feature is that all the simulated spectra for our scenarios at PQR have a large spectral peak at a period around 0.35s, which is also a clear feature of the observed acceleration and velocity spectra from the 1974 and 1966 earthquakes (Figure 6A and 6B). These results and the observation of a large amplification at this period in the transfer function at PQR (Calderon et al. 2012), strongly suggest that this large spectral peak is due to site effects. Other interesting feature can be observed at the velocity response spectra for periods longer than 5s. At this range the spectral amplitudes for all scenarios are similar, which may suggest that they might be largely influenced by the source characteristics, as the soil transfer function at PQR above 5s displays no amplification (Calderon et al. 2012)

3. CONCLUSIONS

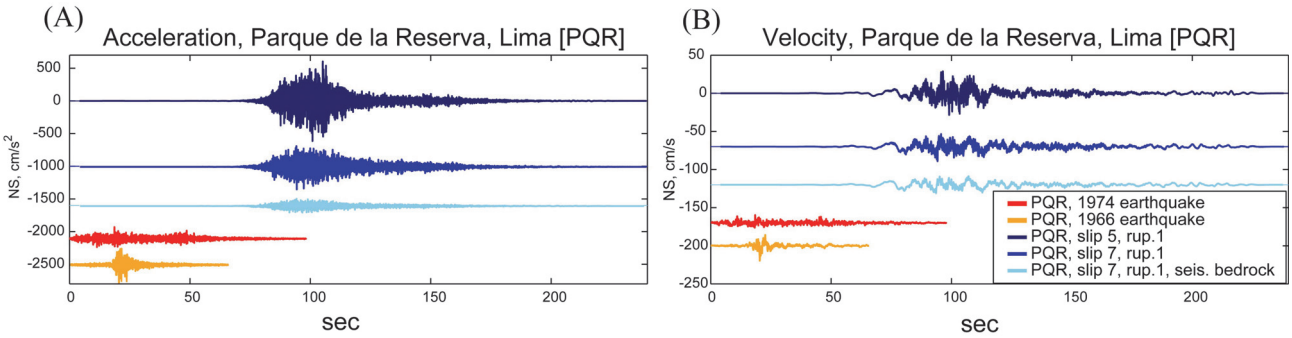


Figure 5 A) Simulated accelerograms at PQR, for slip No.5 and hypocenter No.1 (dark blue), slip No.7 and hypocenter No.1 (blue), and slip No.7 and hypocenter No.1 for a seismic bedrock soil condition (light blue). The accelerograms in red and orange correspond to records at PQR from the 1974 and 1966 Lima earthquakes. B) Same as in A) but for velocity.

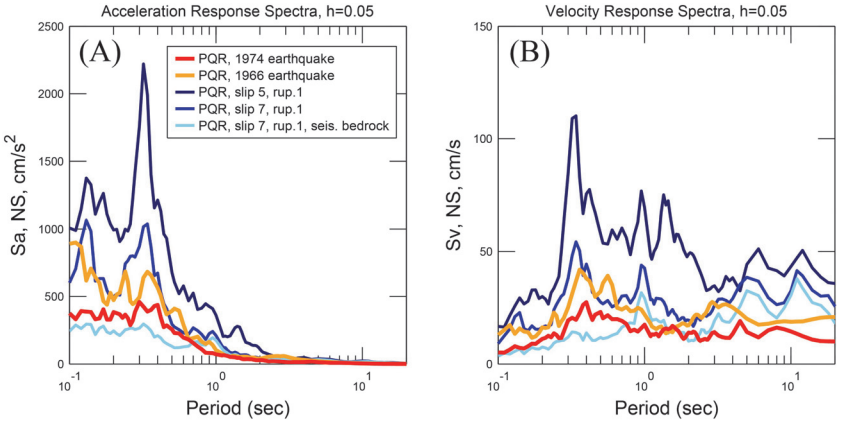


Figure. 6 A) Acceleration response spectra of the simulated NS accelerograms at PQR, for slip No.5 and hypocenter No.1 (dark blue), slip No.7 and hypocenter No.1 (blue), and slip No.7 and hypocenter No.1 for a seismic bedrock soil condition (light blue). The response spectra in red and orange correspond to records at PQR from the 1974 and 1966 Lima earthquakes. B) Same as in A) but for velocity response spectra.

We have developed a methodology for the estimation of slip scenarios for a future megathrust earthquake originated from the convergence between the Nazca plate and the South American plate. This methodology is based on estimations of interseismic coupling at the megathrust obtained from space geodesy measurements as well as information of historical earthquakes.

Our results show that the Central Andes region in Peru has the potential of generating an earthquake with moment magnitude of 8.9, a peak slip of 15 m and a source area of approximately 500 km along strike and 165 km along dip. We constructed 12 broadband slip source scenarios by adding this long wavelength slip model obtained from geodetic data, with 12 short wavelength slips obtained from a Von Karman PSD function of slip. We calculated the EW, NS and UD components of strong ground motions at Lima for the 12 scenario slips by including 9 possible hypocenter locations for each slip model. Our simulations incorporate site amplifications obtained by microtremors array surveys conducted at the representative geotechnical zones in metropolitan Lima as well as site amplifications based on the average of S-waves for the shallowest 10m of soil. Our simulation results display values of PGA and PGV above 1000 cm/s^2 and 80 cm/s in Lima, for the slip model producing the largest ground motions averaged for all hypocenters locations. Our results indicate that the simulated PGA and PGV in Lima are in average 2~3 times larger than the values observed in PQR, central Lima, during the 1974 and 1966 earthquakes. The observed records and our simulations at PQR indicate a large short period site amplification at 0.35s. Simulated spectral values at PQR at this period are as large as 4 times the values observed during the 1974 and 1966 earthquakes.

Acknowledgements:
I would like to thank Diana Calderon and Toru Sekiguchi for providing microtremor measurements results as well as geothecnical information of Lima city. Also thanks to Mohamed Chlieh for making available his interseismic coupling model of Central Andes, and to Hernando Tavera for providing strong motion recordings at PQR.

References:

Calderon, D., T. Sekiguchi, S. Nakai, Z. Aguilar, and F. Lazares, (2012), Study of soil amplification base don microtremor and seismic records in Lima Peru, *Jour. Japan Assoc. Earthq. Eng.*, **12**, (2), 1-20.

Calderon, D., Dynamic characteristics of the soils in Lima, Peru, by estimating shallow and deep shear-wave velocity profiles, Doctoral thesis in engineering, Graduate School of Engineering, Chiba University, 113 pages, 2012.

Chlieh, M., H. Perfettini, H. Tavera, J.-P. Avouac, D. Remy, J.-M.

Nocquet, F. Rolandone, F. Bondoux, G. Gabalda, and S. Bonvalot, 2011. Interseismic coupling and seismic potential along the Central Andes subduction zone, *J. Geophys. Res.*, **116**, B12405, doi:10.1029/2010JB008166.

Dorbath, L., et al. (1990), Assessment of the size of large and great historical earthquakes in Peru, *Bull. Seismol. Soc. Am.*, **80**(3), 551– 576.

Dorbath, L., C. Dorbath, E. Jimenez, and L. Rivera, (1991), Seismicity and tectonic deformation in the Eastern Cordillera and the sub-Andean zone of central Peru, *Journal of South American Earth Sciences*, **4**, No.1/2, 13-24.

Perfettini, H., et al. (2010), Aseismic and seismic slip on the Megathrust offshore southern Peru revealed by geodetic strain before and after the Mw8.0, 2007 Pisco earthquake., *Nature*, **465**, P. 78–81. doi:10.1038/nature09062.

Pulido, N., and T. Kubo, (2004), Near-Fault Strong Motion Complexity of the 2000 Tottori Earthquake (Japan) from a Broadband Source Asperity Model, *Tectonophysics*, **390**, 177-192.

Quispe G., (2010), Preliminary analysis for evaluation of local site effects in Lima city, Peru from strong ground motion data by the spectral method, Master Thesis, National Graduate Institute for Policy Studies, Building Research Institute, Japan, 32p.

Ripperger, J., and P. M., Mai, (2004), Fast computation of static stress changes on 2D faults from final slip distributions, *Geophys. Res. Lett.*, **31**, L18610, doi:10.1029/2004GL020594.

Sladen, A., et al. (2010), Source model of the 2007 Mw 8.0 Pisco, Peru earthquake: Implications for seismogenic behavior of subduction megathrusts, *J. Geophys. Res.*, **115**, B02405, doi:10.1029/2009JB006429.

10CUEE CONFERENCE PROCEEDINGS
10th International Conference on Urban Earthquake Engineering
March 1-2, 2013, Tokyo Institute of Technology, Tokyo, Japan

SYNTHESIS OF GROUND MOTIONS OF 1999 TAIWAN MEISHAN EARTHQUAKE BY EMPIRICAL GREEN'S FUNCTION METHOD

Huei-Tsyr Chen[1] and Shang-Hong Wei[2]

1) Professor, Department of Civil Engineering, National Central University, Taiwan
2) Graduate Student, Department of Civil Engineering, National Central University, Taiwan
chenht@ncu.edu.tw, redred90011@hotmail.com

Abstract: The probability for MeiShan fault in Taiwan to generate an earthquake of magnitude 7.1 is 9.75% within next 10 years as reported in 2010. Applying empirical Green's function (EGF) method, the forward analysis was adopted to synthesize the observed motion of target event and in this study, the target event that we synthesized is MeiShan earthquake (Mw= 5.85) which occurred on Oct. 22, 1999 using the small event (Mw= 4.05) of the main fault occurred on Oct.28 1999. The results show that EGF method can simulate the observed motions at the rock site (CHY41) very well, while the agreement is not so good for the alluvium site (CHY38 and others). For the nonlinear responses of a three-degree-of-freedom model considered, the synthesized motions render smaller responses than the observed motions and the spike in the ground motion seems to affect the displacement significantly.

1. INTRODUCTION

An accurate broadband scenario earthquake motions for a target city or region is of primary importance to develop effective countermeasures to reduce its future earthquake damages. Through years, the methods proposed can be classified into three categories: theoretical Green's function method, empirical Green's function method and empirical method basing on statistical information. Although the numerical computation of 3D theoretical Green's function using computer has been developed, the inability to obtain enough geophysical and geotechnical properties along the path of wave propagation from source to site makes the application of theoretical Green's function method difficult. On the other hand, the empirical Green's function (EGF) method proposed by Hartzell (1978) uses the small earthquakes as Green's function to synthesize large earthquakes. Revisions have been made by Irikura (1983,1986) and others. The advantages of EGF method are that the effects of propagation path and local site conditions are included and the broadband estimation of strong ground motions can be made as long as the small earthquake records from aftershocks exhibit the accurate broadband frequency range. As a result, the EGF method now becomes a popular approach for generating the scenario earthquakes.

In Taiwan, MeiShan fault is located in the Chiayi County and passes through the campus of National Chung-Cheng University. In 1906 this fault generated an earthquake of magnitude 7.1 which killed more than 1000 people. On January 21, 2010, The National Science Council of Taiwan announced that the probability for this fault to generate an earthquake of magnitude 7.1 is 9.75% within next 10 years and 44.92% within next 50 years. Thus, the generation of scenario earthquake motions over Chiayi area from MeiShan fault becomes a critical task. In this paper the EGF method obeying an ω^{-2} spectral scaling is adopted to simulate the main target event of MeiShan earthquake (Mw= 5.85) occurred on Oct. 22, 1999 using the aftershock (Mw= 4.05) records occurred on Oct.24 1999 as empirical Green's function. The comparisons of the observed and synthesized motions will also be made using the nonlinear responses of a three-story reinforced concrete building.

2. EMPIRICAL GREEN'S FUNCTION METHOD

For EGF method used this study we adopted the formulation by Irikura (1986) which is based on a scaling law of fault parameters for large and small events (Kanamori and Anderson, 1975) and the ω^{-2} source spectra (Aki, 1967). The fault of target event is divided into some subfaults first, and each subfault is deemed as a point source (Fig. 1). For EGF method the record of small event such as foreshock or aftershock which occurred in the area of the main fault is treated as the waveform for each subfault, known as empirical Green's function, and is then stacked to simulate the waveform generated by the main fault, as shown in Eq. (1).

$$U(t) = \sum_{i=1}^{N} \sum_{j=1}^{N} \frac{r}{r_{ij}} \{F(t) * (C \cdot u(t))\} \qquad (1)$$

where U(t) is the synthesized waveform for the large event, F(t) a filtering function to adjust a difference in slip time function between the large event and small event, u(t) the waveform of small earthquake, r is the hypocentral distance of the small earthquake and r_{ij} is the distance from each subfault to the site, C the ratio of stress drop between target and small events, N the source dimension of target event and small event and * the convolution. The values of C and N are obtained from Eqs. (2) and (3).

$$N = \sqrt{\frac{U_0}{u_0} \cdot \frac{a_0}{A_0}} \qquad (2)$$

$$C = \frac{1}{N}\frac{A_0}{a_0} \qquad (3)$$

where U_0 and u_0 are the constant levels of amplitude of the displacement spectra of large and small events, respectively, and A_0 and a_0 the constant levels of amplitude of the acceleration spectra of large and small events, respectively. Figure 2 is the illustration of spectral ratios of target and small events.

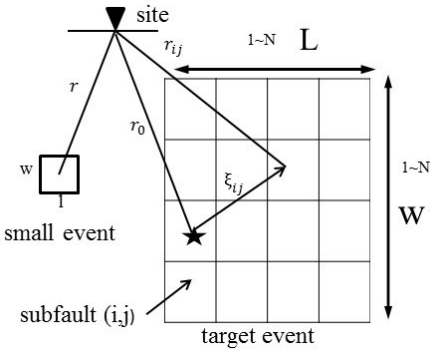


Figure 1 Geometric Relation between Fault and Observation Site

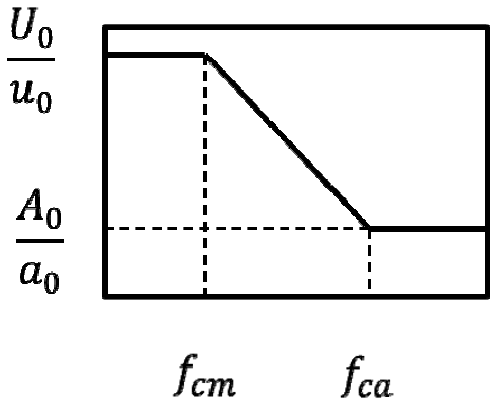


Figure 2 Illustration of Spectra Ratio of Target and Small Events

For F(t) we chose the form by Nakamura et al. given in the recipe issued by The Headquarters for Earthquake Research, Japan (2008), as shown in Fig. 3, and the interested readers can refer to that reference for the detailed formulation of this slip-velocity time function and the definition of the relevant parameters.

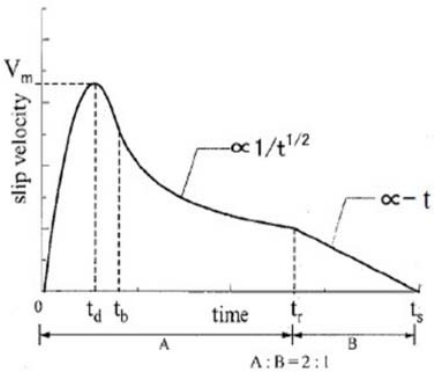


Figure 3 Slip-velocity time function (from recipe)

3. SYNTHESIS OF GROUND MOTIONS FOR 1999 MeiShan earthquake

In this study, the target event that we simulated is MeiShan earthquake (Mw= 5.85) which occurred on Oct. 22, 1999 and the small event (Mw= 4.05) of the main fault occurred on Oct.24 1999 was used as the empirical Green's function. In this study four stations labeled as CHY 09, CHY38, CHY39 and CHY 41 were selected where only CHY 41 can be classified as rock site and Fig. 4 shows the locations of these stations relative to the epicenter of the earthquake. In the syntheses of motions of main event, the forward analysis was conducted for the EW component of the records for a frequency range between 0.2Hz and 10Hz and the fault mechanism is the one which can render good agreement for the waveforms of all stations. The C and N values obtained using Eqs. (2) and (3) from the data set are 1.02 and 8, respectively. Additional parameters used for the synthesis are depicted in Table 1. In this paper the discussions will be given only for CHY38 and CHY41.



Figure 4 Locations of Stations Considered in Synthesizing the Main Events

Table 1 Parameters Used for the Synthesis

length:	9.6 km
width:	9.6 km
dip angle:	68.03°
rake angle:	71.16°
strike angle:	356.56°
Stress drop (average)	2.08E+06 Pa
Stress drop (background)	0.75E+06 Pa
Stress drop (asperity)	1.42E+07 Pa

Figure 5 and Figure 6 show the waveforms of small events for CHY 038 and CHY 041, respectively. Based on the several trials, the final fault model adopted is as shown in Fig. 7 where the black region is treated as inactive region which is based on the observation that most of the aftershocks occurred on the left side and the red star and colored region are the hypocenter and asperity. Shown in Figures 8 and 9 are the observed waveforms, synthesized waveforms and their Fourier amplitude spectra, respectively. From Figure 8, it can be seen that the agreement between the observed and synthesized motions at CHY41 are good. From Figure 9, the large spike in the observed motion at CHY38 can not be reproduced in the synthesized motion; however, if we neglect this, the waveforms of the observed and synthesized motions are basically similar and that maybe the reason why their Fourier amplitude spectra agree well.

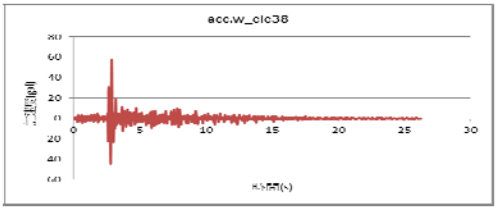


Figure 5 Waveform of Small Event at CHY38

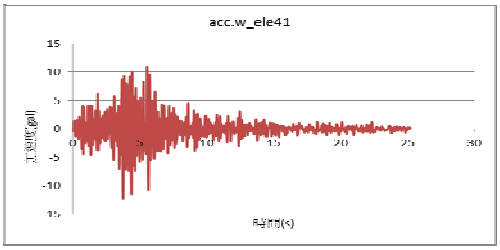


Figure 6 Waveform of Small Event at CHY41

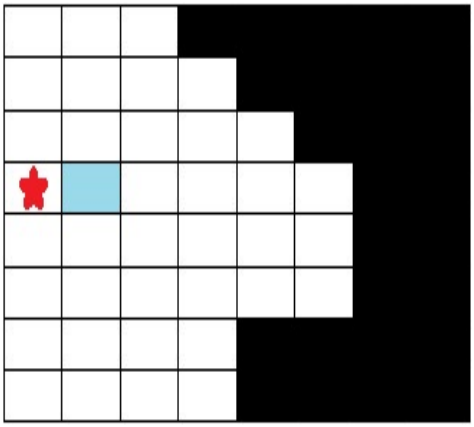
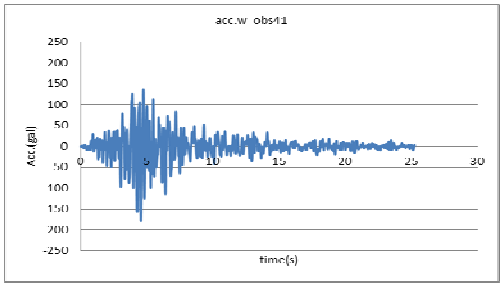
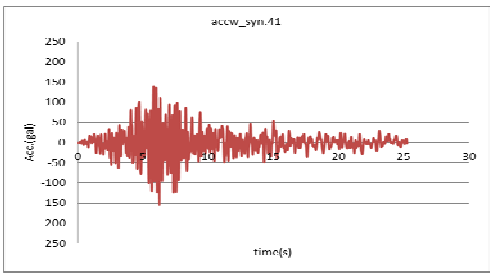


Figure 7 Fault Model for Synthesizing the Main Events





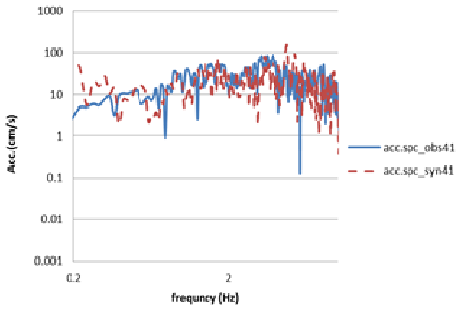


Figure 8 Observed Waveform, Synthesized Waveform and Fourier Spectra at CHY41

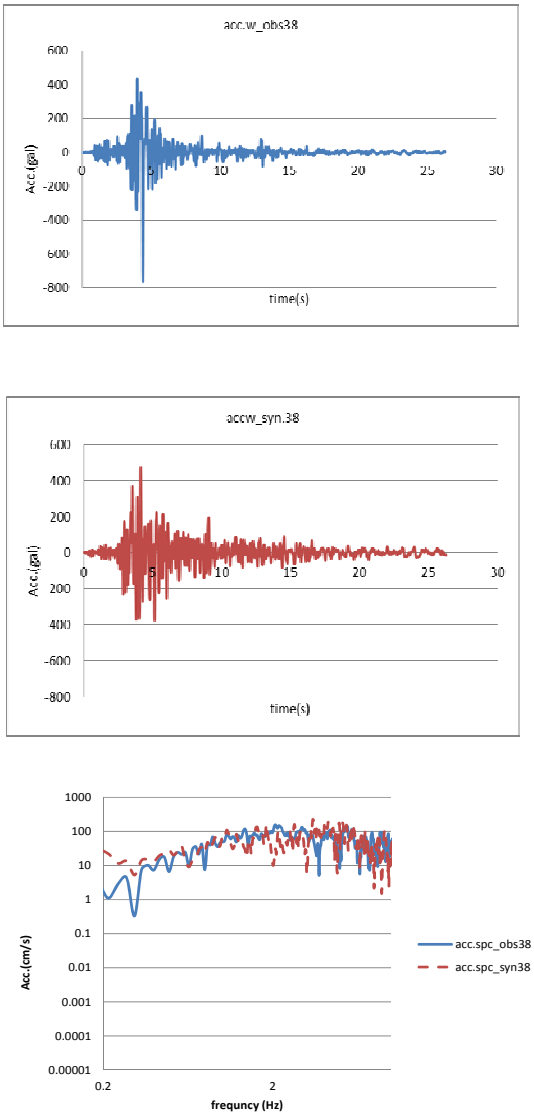


Figure 9 Observed Waveform, Synthesized Waveform and Fourier Spectra at CHY38

In order to further investigate the conformability of the observed and synthesized waveforms, a hypothetical three-story reinforced concrete building modeled as a three-degree-of-freedom lumped mass system, also known as stick model, was adopted. In this model, the masses are m_1= 1.69x10^4 kg, m_2= 1.581x10^4 kg and m_3= 1.412x10^4 kg and the stiffness of sticks of the stories is k_1= 1.512x10^7 N/m, , k_2= 2.012x10^7 N/m and k_3= 2.012x10^7 N/m. The nonlinear behavior of stick of each story assumes to follow the Takeda model (Takeda, 1970). The story drifts corresponding to crack for each stick are d_1= 6.3mm, d_2= 4.9mm and d_3= 4.2mm, and those corresponding to yielding are D_1= 21.8mm, D_2= 18.9mm and D_3= 17.2mm. Shown in Figure 10 are the time-history responses of acceleration, displacement and the story-shear and story-drift relation for each floor of the structure at CHY41. Generally the responses computed using synthesized waveform as input are smaller than those computed using observed waveform as input; however, the system under the action of both motions remains elastic. Figure 11 depicts the time-history responses of acceleration, displacement and the story-shear and story-drift relation for each floor of the structure at CHY38. Again, generally the responses subjected to synthesized motions are smaller those subjected to observed motions, especially for displacement responses. For the responses subjected to observed motion, the spike-like responses can be observed, while those are not shown for those subjected to synthesized motion. A point should be noted that for the observed motion it exhibits a spike which causes larger story drifts on all floors and forces the system to enter the plastic deformation significantly, leading to the more cycles in the hysteresis loop of the stick of first floor. However, if the structure at CHY38 is subjected to the synthesized motion, only slight plastic deformations can be seen on the first and second floor

4. CONCLUSIONS

In this study, the target event that we simulated is MeiShan earthquake (Mw= 5.85) which occurred on Oct. 22, 1999 using the small event (Mw= 4.05) of the main fault occurred on Oct.28 1999 as the empirical Green's function. Applying EGF method, the forward analysis was adopted to synthesize the observed motion The results show that EGF method can simulate the observed motions at the rock site (CHY41) very well, while the agreement is not so good for the alluvium site (CHY38 and others). The nonlinear responses of a three-degree-of-freedom lumped mass model were computed to further investigate the conformability of the observed and synthesized motions. For the model considered, the synthesized motions render smaller responses than the observed motions and the spike in the ground motion seems to affect the displacement significantly. Finally the hybrid approach will be adopted to generate scenario earthquakes in Chiayi area in the future.

Acknowledgements:
In the course of this study the valuable discussions and comments from Prof. Takao Kagawa of Tottori University are very much appreciated.

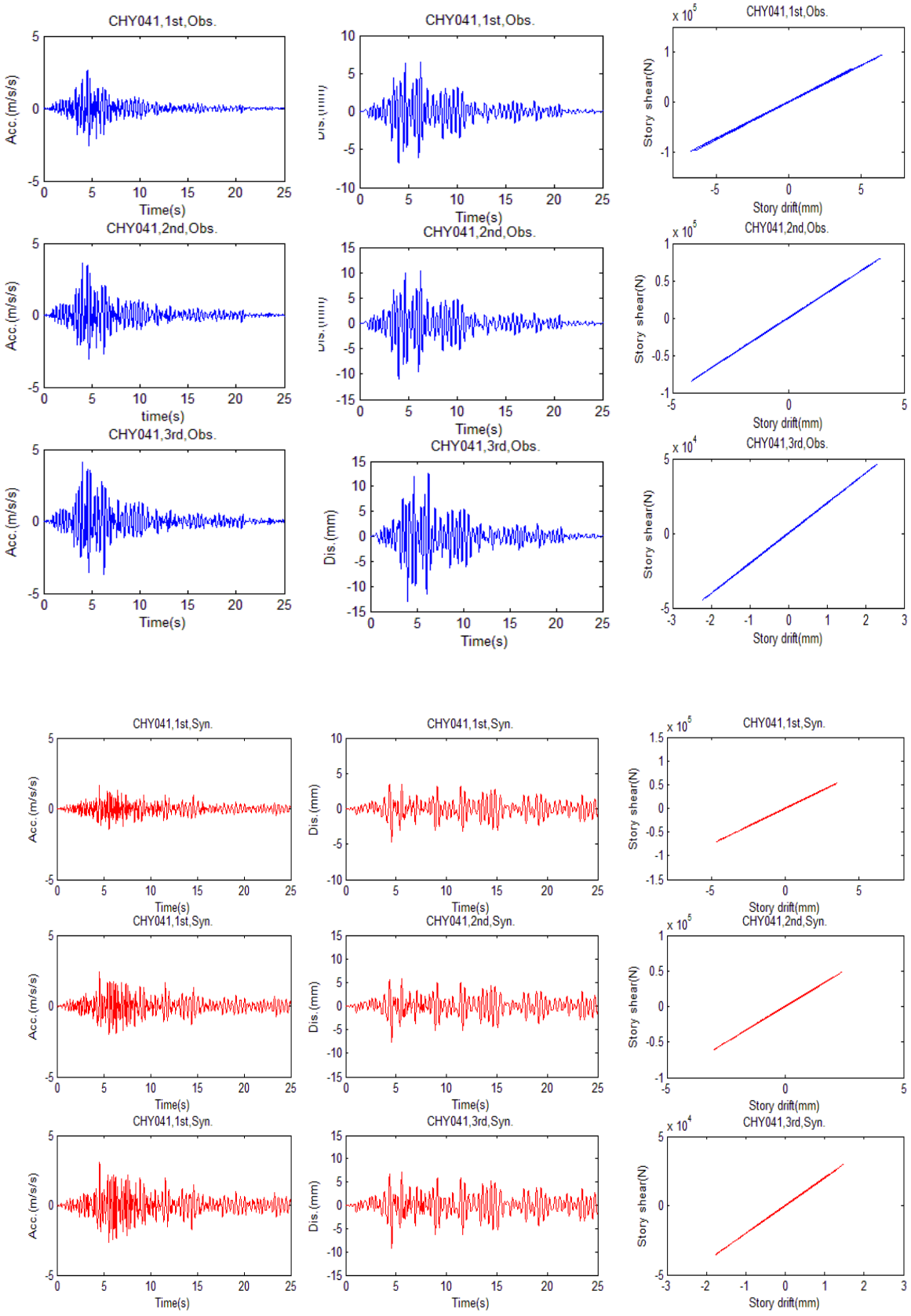


Figure 10 Time-History Responses of Acceleration, Displacement and the Story-Shear and Story-Drift Relation for Each Floor of the Structure at CHY41

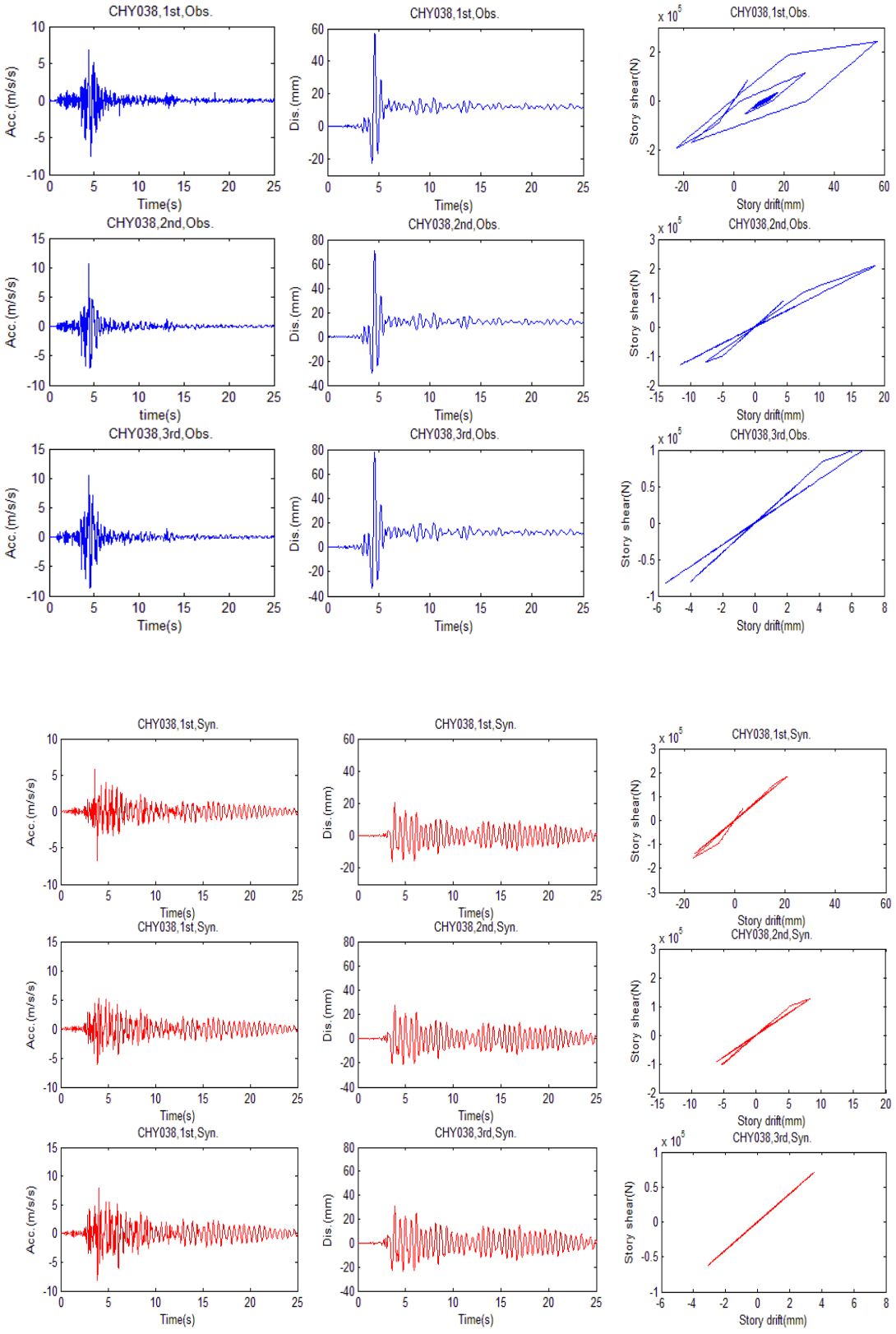


Figure 11 Time-History Responses of Acceleration, Displacement and the Story-Shear and Story-Drift Relation for Each Floor of the Structure at CHY38

References:

Aki, K. (1967), "Scaling Law for Seismic Spectrum," Journal of Geophysics Research, **72**, 1217-1231.

Kanamori, H. and Anderson, D.L. (1975), "Theoretical Basis of Some Empirical Relations in Seismology," Bulletin of Seismological Society of America, **65**, 1063-1095.

Irikura, K. (1983), "Semi-Empirical Estimation of Strong Ground Motions During Earthquakes," Bulletin of Disaster Prevention Research Institute, **33**, 63-104

Irikura, K. (1986), "Prediction of Strong Acceleration Motions Using Empirical Green's Function," Proceedings of 7th Japan Earthquake Engineering, 151-156.

Hartzell, S.H. (1978),"Earthquake Aftershocks as Green's Function," Geophysics Research Letter,**5**, 1-4

Takeda, T., Sozen, M.A. and Nielsen, N.N. (1970), "Reinforced Concrete Response to Simulated Earthquakes," Journal of the Structural Division,. **96**, (12), pp.2557-2673.

"Strong Ground Motion Prediction Method ("Recipe") for Earthquakes with Specified Source fault", (2008), The Headquarters of Earthquake Research Promotion, Japan, Appendix 12-13.

10CUEE CONFERENCE PROCEEDINGS
10th International Conference on Urban Earthquake Engineering
March 1-2, 2013, Tokyo Institute of Technology, Tokyo, Japan

FINITE DIFFERENCE SIMULATION OF LONG-PERIOD GROUND MOTION BASED ON VARIOUS SOURCE MODELS OF THE ANTICIPATED NANKAI TROUGH MEGATHRUST EARTHQUAKE

Takahiro Maeda[1], Nobuyuki Morikawa[2], Shin Aoi[3], and Hiroyuki Fujiwara[4]

1) Research Fellow, National Research Institute for Earth Science and Disaster Prevention, Japan
2) Senior Researcher, National Research Institute for Earth Science and Disaster Prevention, Japan
3) Senior Researcher, National Research Institute for Earth Science and Disaster Prevention, Japan
4) Director, National Research Institute for Earth Science and Disaster Prevention, Japan
tmaeda@bosai.go.jp, morikawa@bosai.go.jp, aoi@bosai.go.jp, fujiwara@bosai.go.jp

Abstract: Evaluation of long-period ground motions for many possible scenarios is important to understand a possible range of long-period ground motions. To understand a variation of long-period ground motion caused by uncertainty of source model, we performed a finite difference simulation using 55 source models of the anticipated Nankai Trough megathrust earthquake in southwest Japan. The source models were constructed by assuming various possible source parameters including rupture area, asperity location, and hypocenter. We also included the scenario which contains large slip area near the trough following the lesson we learned from the 2011 Tohoku-oki earthquake. Simulated velocity response spectra have large variation by a factor of a few hundred depending on different rupture area. Among the source models with same rupture area, simulated velocity waveforms vary greatly according to the hypocenter location. The simulated waveforms of the scenarios including large slip near the trough show significantly large amplitude and long duration at some sedimentary basins. T he amplitude and duration of these waveforms decrease by applying a boxcar-like slip velocity function to the large slip area near the trough instead of the Kostrov-like function.

1. INTRODUCTION

Megathrust earthquakes in the Nankai Trough in southwest Japan have been occurring with an interval of 100-200 years. Mainly, there are two patterns of Nankai Trough earthquake; one is the series of smaller earthquakes in short time period and second is the single larger event ruptured at once. The most recent example of the first case is the series of earthquake in 1944 Tonankai earthquake (M7.9) and in 1946 Nankai earthquake (M8.0). The most recent example of the second case is the 1707 Hoei earthquake (M8.4).

For improving seismic hazard assessment to prepare for the anticipated Nankai Trough earthquake, it is important to understand a possible range of ground motion caused by uncertainty of source model. In this study, we evaluate long-period ground motions of the Nankai Trough earthquake, which will cause damage to high-rise and large-scale structures, using many scenarios with various possible parameters including rupture area, asperity location, and hypocenter. In the possible parameters, we also include the scenario; the large slip near the trough following the lesson from the 2011 Tohoku-oki earthquake. The long-period ground motions are simulated by the finite difference method using characterized source model and recently developed three-dimensional velocity structure model of Japan.

2. SEISMIC SOURCE MODEL

We use a characterized source model in the long-period ground motion simulation. The characterized source model is defined by three kinds of parameters: outer, inner, and extra fault parameters. These parameters are determined based on a 'recipe' for predicting strong ground motion (Irikura and Miyake, 2001). Although the 'recipe' for the crustal earthquake has been validated using observed records of many earthquakes, that for the subduction-zone earthquake, especially for megathrust earthquakes, has been validated using insufficient data. We should note that the ground-motion simulation results may be modified after improving the 'recipe' for the subduction-zone earthquake.

The outer fault parameters define an overall character of the source model. At first we define source areas of the anticipated Nankai Trough earthquakes (Figure 1). An occurrence pattern of the Nankai Trough earthquakes is assumed that respective earthquakes occur independently or that multiple earthquakes occur in a correlated manner. As for the respective earthquakes, we define source areas of the Nankai earthquake (ANNKI), the Tonankai earthquake (ATNKI), and the hypothetical Tokai earthquake (ATOKI) based on the model reported by Earthquake Research Committee (2001). We also model the Hyuga-nada (AHGND) area as a source area, since Furumura et al. (2011) pointed out that a source area of the 1707 Hoei

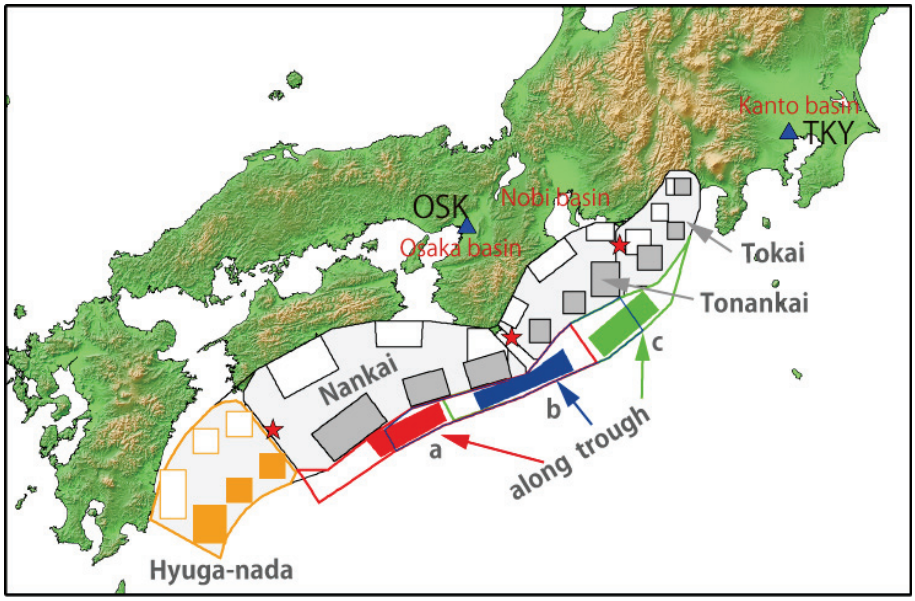


Figure 1 Characterized source models for the Nankai Trough earthquakes. Grey regions are the source area of the Nankai, Tonankai, and hypothetical Tokai earthquakes. Orange region is a source area of Hyuga-nada. Red, blue and green regions are source areas along the trough. Solid and open squares in the source area are asperities of shallower and deeper cases, respectively. Red stars are the hypocenters. Blue triangles are the sites for comparing simulation results.

earthquake extends to this area. In addition, we assume the large slip area along the trough following the lesson from the 2011 Tohoku-oki earthquake and model three source areas along the trough (Figure 1; ATRGHa-c). We model source areas for the case of correlated occurrence as a combination of the respective source area. These are the Nankai-Tonankai area (ANNI1), the Tonankai-hypothetical Tokai area (ANNI2), the Nankai -Tonankai-hypothetical Tokai area (ANNI3), the Nankai -Tonankai-hypothetical Tokai area with along the trough area (ANNI4a-c), and the Nankai-Tonankai-hypothetical Tokai area with the Hyuga-nada area (ANNI5). We estimate the rupture area S for each source area by taking into account geometry of plate interface and then calculate seismic moment M_0 and average slip D by assuming an average stress drop $\Delta\sigma$ of 3.0 MPa and rigidity of 40.4 GPa.

As for the inner fault parameters, combined area of asperities (a large slip areas) S_a and average slip of asperities D_a are derived by a scaling relationship to the seismic moment proposed by Murotani et al. (2008); S_a=0.2S and D_a=2.2D. The number of asperity for the ANNKI, ATNKI, ATOKI, and AHGND is three and their area ratio is 2:1:1, while the number of asperity for ATRGHa-c is one. We assume two kinds of asperity location; deeper and shallower cases. As for the case of correlated occurrence, we assume that the asperity area is similar to the respective earthquake and calculate average slip and seismic moment with respect to a total rupture area. Source parameters are shown in Table 1. We use a slip velocity time function approximated from dynamic rupture simulation proposed by Nakamura and Miyatake (2000).

The extra fault parameters define propagation pattern of rupture. We assume three hypocenters; west (boundary of the Nankai and Hyuga-nada areas), center (boundary of Nankai and Tonankai areas), and east (boundary of the Tonankai and Tokai areas). The rupture propagates radially from the hypocenter at a constant rupture velocity (2.7km/s). The rupture in each asperity starts from a point at the moment the rupture front reaches the point.

3. LONG-PERIOD GROUND MOTION SIMULATION

We simulate long-period ground motions using a three dimensional (3-D) finite difference (FD) method with discontinuous grids (Aoi and Fujiwara, 1999; Aoi et al., 2004). To accommodate details of 3-D subsurface structure into the FD model, we used discontinuous grids that consist of a fine grid spacing of 200 m in horizontal and of 100m in vertical for regions shallower than 8 km that contain low-velocity sedimentary layers, and a three times coarser grid spacing for deeper region (8 ~ 70 km). The total number of grid points is about 2 billion. The 3-D velocity structure model used in the FD simulation is the Japan integrated velocity structure model (Koketsu et al., 2008), which includes basin, crust, plate and oceanic structures. The lowest S-wave velocity is 500m/s in the structure model and thus the FD simulation is valid for period more than 2 second. However the characterized source model used in the FD simulation does not contain short period component, and thus we consider that the FD simulation is valid for period more than about 5 second. Inelastic attenuation is introduced in the same way as in Graves (1996) and we assume a reference period for Q-value of 5 second.

Table 1 Source Parameters Used in the FD Simulation

				ANNKI	ATNKI	ATOKI	ATRGH	AHGND	ANNI1	ANNI2	ANNI3	ANNI4	ANNI5
total			S (km^2)	35800	14500	9400	12500	19000	51200	23600	60300	72800	80500
			Mo (Nm)	8.3.E+21	2.2.E+21	1.1.E+21	1.7.E+21	3.2.E+21	1.4.E+22	4.5.E+21	1.8.E+22	2.4.E+22	2.8.E+22
			$\Delta\sigma$ (MPa)	3.0	3.0	3.0	3.0	3.0	3.0	3.0	3.0	3.0	3.0
			Mw	8.5	8.2	8.0	8.1	8.3	8.7	8.4	8.8	8.9	8.9
asperity	Nankai	1	S (km^2)	3580	-	-	-	-	3580	-	3580	3580	3580
			M_{0a} (Nm)	2.1.E+21	-	-	-	-	2.9.E+21	-	3.3.E+21	3.6.E+21	4.0.E+21
			$\Delta\sigma_a$(MPa)	15.0	-	-	-	-	15.3	-	15.2	15.1	15.3
		2, 3	S (km^2)	1790	-	-	-	-	1790	-	1790	1790	1790
			M_{0a} (Nm)	7.6.E+20	-	-	-	-	1.0.E+21	-	1.2.E+21	1.3.E+21	1.4.E+21
			$\Delta\sigma_a$(MPa)	15.0	-	-	-	-	15.3	-	15.2	15.1	15.3
	Tonankai	1	S (km^2)	-	1450	-	-	-	1450	1450	1450	1450	1450
			M_{0a} (Nm)	-	5.5.E+20	-	-	-	7.4.E+20	7.7.E+20	8.6.E+20	9.2.E+20	1.0.E+21
			$\Delta\sigma_a$(MPa)	-	15.0	-	-	-	15.3	14.8	15.2	15.1	15.3
		2, 3	S (km^2)	-	725	-	-	-	725	725	725	725	725
			M_{0a} (Nm)	-	2.0.E+20	-	-	-	2.6.E+20	2.7.E+20	3.0.E+20	3.2.E+20	3.6.E+20
			$\Delta\sigma_a$(MPa)	-	15.0	-	-	-	15.3	14.8	15.2	15.1	15.3
	Tokai	1	S (km^2)	-	-	940	-	-	-	940	940	940	940
			M_{0a} (Nm)	-	-	2.9.E+20	-	-	-	4.0.E+20	4.5.E+20	4.8.E+20	5.4.E+20
			$\Delta\sigma_a$(MPa)	-	-	15.0	-	-	-	14.8	15.2	15.1	15.3
		2, 3	S (km^2)	-	-	470	-	-	-	470	470	470	470
			M_{0a} (Nm)	-	-	1.0.E+20	-	-	-	1.4.E+20	1.6.E+20	1.7.E+20	1.0.E+01
			$\Delta\sigma_a$(MPa)	-	-	15.0	-	-	-	14.8	15.2	15.1	15.3
	along trough	a, b, c	S (km^2)	-	-	-	2500	-	-	-	-	2500	-
			M_{0a} (Nm)	-	-	-	7.6.E+20	-	-	-	-	2.1.E+21	-
			$\Delta\sigma_a$(MPa)	-	-	-	15.0	-	-	-	-	15.1	-
	Hyuganada	1	S (km^2)	-	-	-	-	1900	-	-	-	-	1900
			M_{0a} (Nm)	-	-	-	-	8.3.E+20	-	-	-	-	1.5.E+21
			$\Delta\sigma_a$(MPa)	-	-	-	-	15.0	-	-	-	-	15.3
		2, 3	S (km^2)	-	-	-	-	950	-	-	-	-	950
			M_{0a} (Nm)	-	-	-	-	2.9.E+20	-	-	-	-	5.4.E+20
			$\Delta\sigma_a$(MPa)	-	-	-	-	15.0	-	-	-	-	15.3
back ground			S (km^2)	28640	11600	7520	10000	15200	41140	18820	48360	58360	64760
			M_{0b} (Nm)	4.7.E+21	1.2.E+21	6.3.E+20	9.6.E+20	1.8.E+21	8.1.E+21	2.5.E+21	1.0.E+22	1.4.E+22	1.6.E+22
			$\Delta\sigma_b$(MPa)	1.8	1.8	1.8	3.0	1.8	1.4	1.3	1.2	1.1	1.0

4. RESULTS

We simulate long-period ground motions for 55 scenarios. Figures 2 compares the simulated ground velocity for scenarios ANNI3, ANNI4a-c, and ANNI5 with different hypocenter and asperity location at Osaka (OSK) and Shinjuku in Tokyo (TKY). Among these scenarios, the hypocenter has a greater impact on waveforms, followed by the asperity location, and then the rupture area. S waves from deeper asperities of the Nankai area and later phases from the along trough 'a' area have significant influence at OSK. Later phases from the along trough 'b' and 'c' areas elongate a duration of long-period ground motion at TKY.

Figure 3 compares the simulated velocity response spectra for all simulated scenarios. These spectra have large scattering by a factor of few hundred. The spectra of scenarios ANNI3, ANNI4a-c, and ANNI5 at OSK and TKY have scattering by a factor of 4-10 and 2-4, respectively. The scattering at TKY is small because TKY locates on the forward rupture direction of the hypothetical Tokai area in the scenarios. Because the difference of seismic moment between the scenarios ANNI3, ANNI4a-c, and ANNI5 is small by a factor of two (Table 1), the large scattering indicates the hypocenter and asperity location have greater effect on simulation results than the rupture area.

5. DISCUSSION AND CONCLUSIONS

Figure 4 shows histograms and cumulative frequency distribution of simulated peak ground velocity (PGV) and simulated velocity response spectra (Sv) at period of 5 and 10 seconds. The histograms show contribution of the rupture area. The scenarios with wider rupture areas (colored bars) have larger PGV and Sv than those with smaller rupture areas (grey bars). In particular, the scenarios ANNI4a generate significantly large PGV and Sv at OSK. The cumulative frequency distributions show contribution of hypocenter and asperity location. The scenarios with western hypocenter (red symbols) generate large PGV and Sv at OSK and TKY.

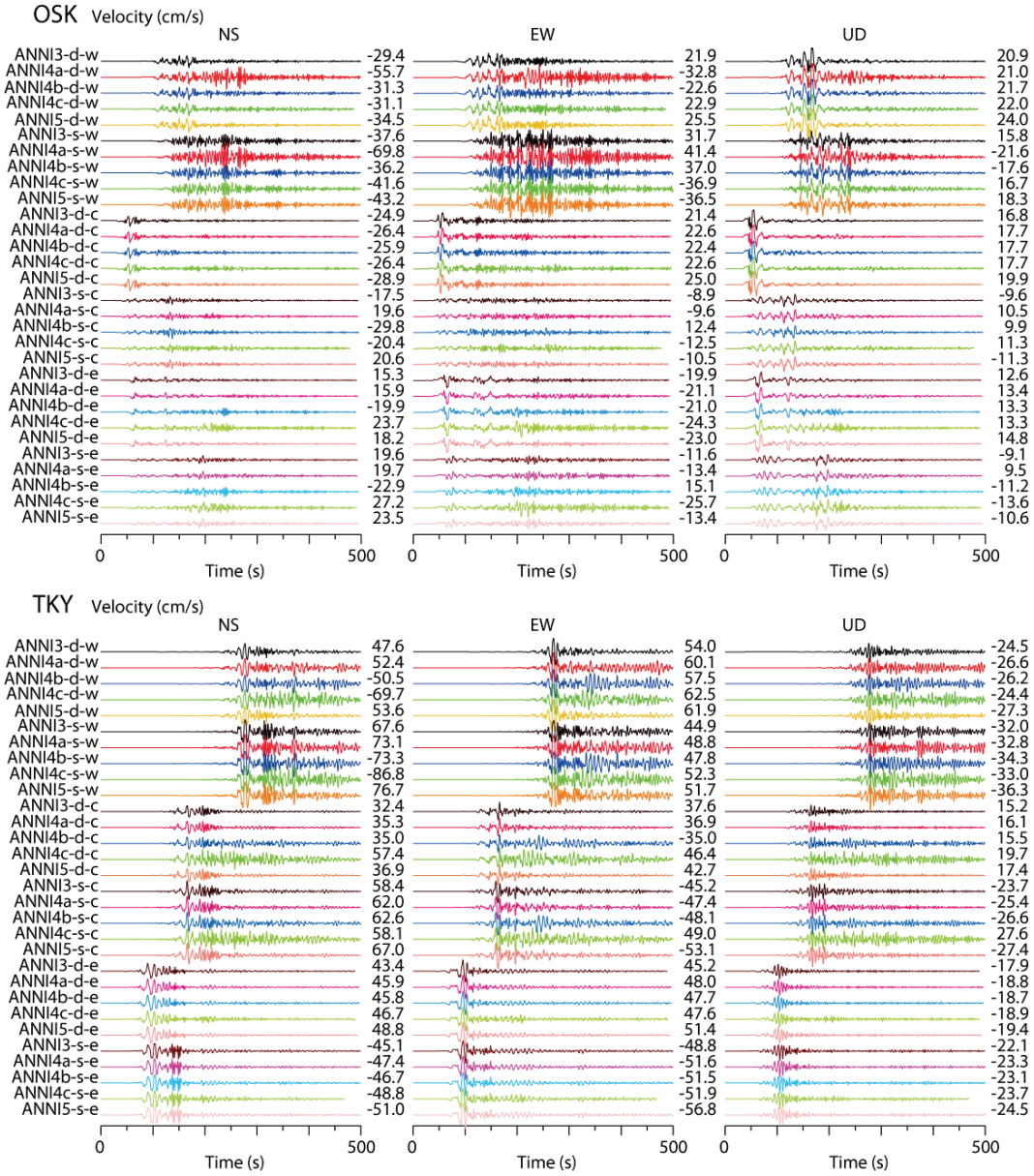


Figure 2 Results of the 3-D FD simulation for 30 scenarios at (a) OSK, (b) TKY. Scenario name shown in the left means [source area]-[asperity location (deep, shallow)]-[hypocenter (west, center, east)]. The numbers on the right indicate the peak amplitude in cm/s.

To assess a character of PGV and Sv distribution (Figure 4), we make PGV and Sv maps showing maximum, median (second quartile), interquartile range (iqr: the difference between the third and first quartiles), and maximum scenario using simulation results of 55 scenarios (Figure 5). These maps show a possible range of long-period ground motions from the anticipated Nankai Trough earthquakes. Large maximum and median values on accretionary prism suggest that the accretionary prism greatly contributes to the generation and propagation of long-period ground motions. The maximum scenario maps show that the scenarios ANNI5 with deep asperity contribute maximum values in the left half area in the map, especially in PGV and Sv 10s. These are the effect of long-period S wave from the Nankai area. In the maximum scenario maps of Sv 5s, the red and green areas distribute in land area wider than PGV and Sv 10s indicating greater effect of the along trough area on Sv 5s values.

In the maximum value maps, the Sv 5s values are larger than Sv 10s values at the Osaka and Nobi basins, while the Sv 10s values are larger than Sv 5s values at the Kanto basin. The Osaka and Nobi basins have large difference between the maximum and median values and have small iqr. This feature indicates that these basins are greatly influenced by a few specific scenarios as shown in Figure 4. However, the Kanto basin has relatively large median values and iqr. This indicates that the long-period ground motions in Kanto basin are generally large among the simulated scenarios.

In the FD simulation, we use a Kostrov-like slip velocity time function proposed by Nakamura and Miyatake (2000). However, applying this function to the interpolate

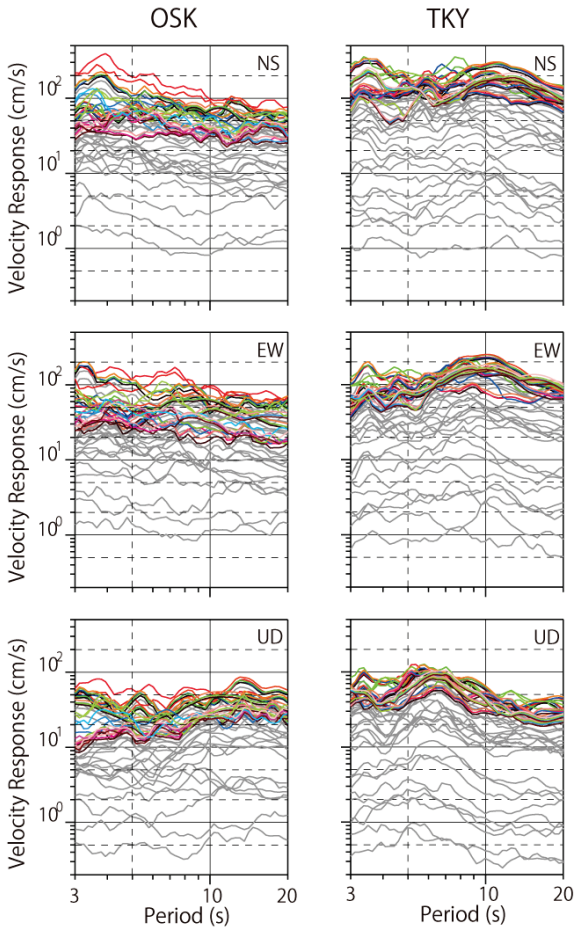


Figure 3 Velocity response spectra (h=0.05) of the 3-D FD simulation results for 55 scenarios at OSK and TKY. Color of the lines corresponds to scenarios shown in Figure 2. Grey lines correspond to other smaller scenarios.

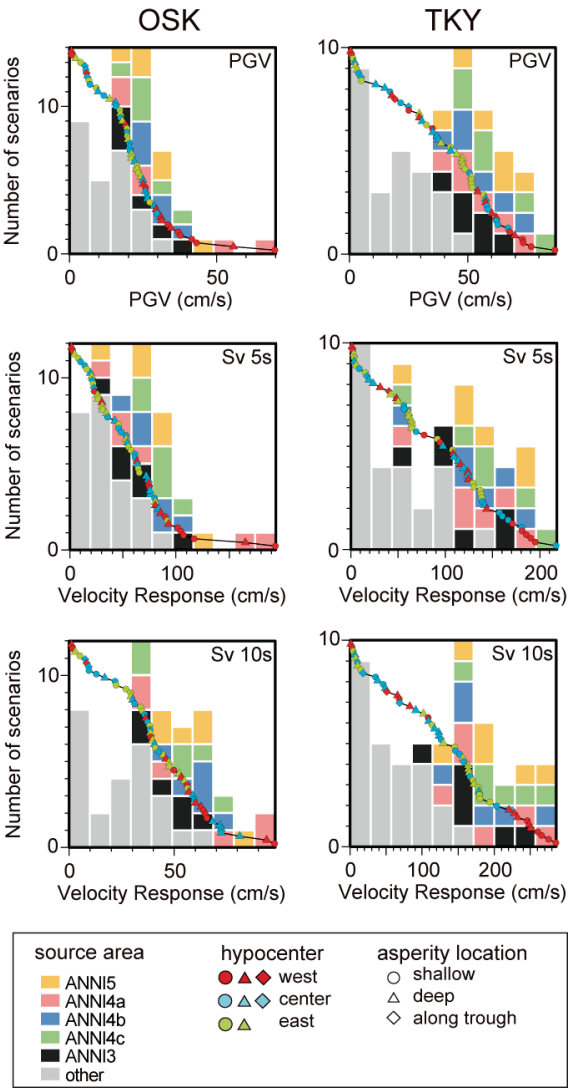


Figure 4 Histograms and cumulative frequency distribution of peak ground velocity (PGV) and velocity response spectra (Sv) at period of 5 and 10 seconds for 55 scenarios at OSK and TKY. Histograms are color-coded according to the source area. Cumulative curves are color-coded according to the hypocenter and depicted using different symbols according to the asperity location.

earthquakes is a contentious issue, especially in a shallow source area. To assess a contribution of source time function, we apply a boxcar like time function to the along trough area. The simulation result shows that PGV values decrease by a factor of two (Figure 6). This indicates that the significant large amplitudes at OSK as shown in Figure 4 are controlled by selection of the slip velocity function. Selection of appropriate source time function is important and it is a future task.

Acknowledgements:

Some of the figures in this paper were made using GMT (Wassel and Smith, 1995). This study is supported by the Support Program for Long-Period Ground Motion Hazard Maps of the Japan Ministry of Education, Culture, Sport, Science, and Technology (MEXT).

References:

Aoi, S. and Fujiwara, H. (1999), "3-D finite difference method using discontinuous grids," *Bulletin of the Seismological Society of America*. **89**, 918-930.

Aoi, S., Hayakawa, T. and Fujiwara, H. (2004), "Ground motion simulator: GMS," *Butsuri Tansa*. **57**, 651– 666 (in Japanese with English abstract).

Earthquake Research Committee (2001), "On the long-term evaluation of earthquakes in the Nankai trough," http://www.jishin.go.jp/main/chousa/01sep_nankai/index.htm.

Furumura, T., Imai, K. and Maeda, T. (2011), "A revised tsunami source model for the 1707 Hoei earthquake and simulation of tsunami inundation of Ryujin Lake, Kyushu, Japan," *Journal of Geophysical Research*. **116**, B02308, doi:10.1029/2010JB007918.

Graves, R. W. (1996), "Simulating seismic wave propagation in 3D elastic media using staggered grid finite differences," *Bulletin of the Seismological Society of America*. **86**, 1091–1106.

Irikura, K., and Miyake, H. (2001), "Prediction of strong ground motions for scenario earthquakes," *Journal of Geography*. **110,** 849-875 (in Japanese with English abstract).

Koketsu, K., Miyake, H., Fujiwara, H. and Hashimoto, T. (2008), "Progress towards a Japan integrated velocity structure model and long-period ground motion hazard map," *Proceedings of the 14th World Conference on Earthquake Engineering*. S10-038.

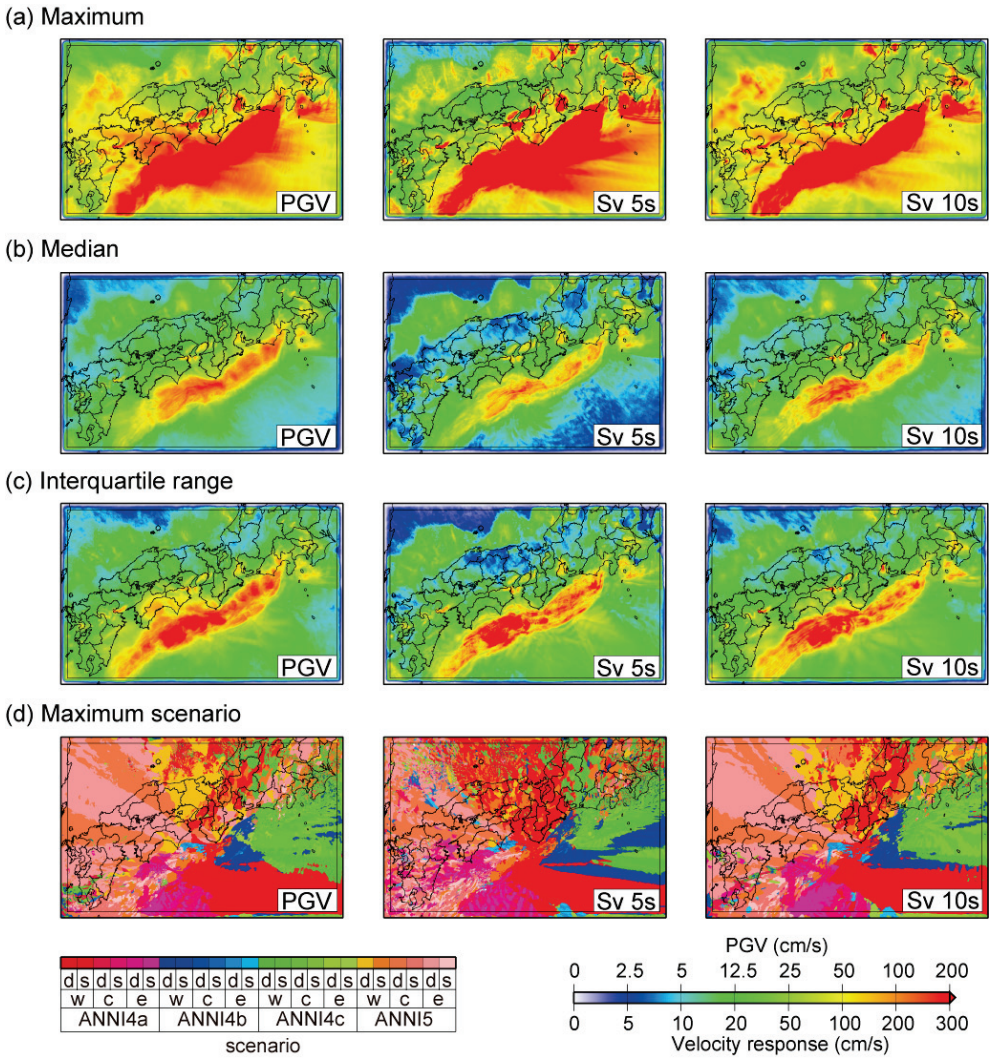


Figure 5 Peak ground velocity (PGV) and velocity response spectra (Sv) maps showing (a) maximum value, (b) median value, (c) interquartile range and (d) maximum scenario among 55 scenarios. Color scales for PGV and Sv are shown in bottom right, and that for the maximum scenario is shown in bottom left.

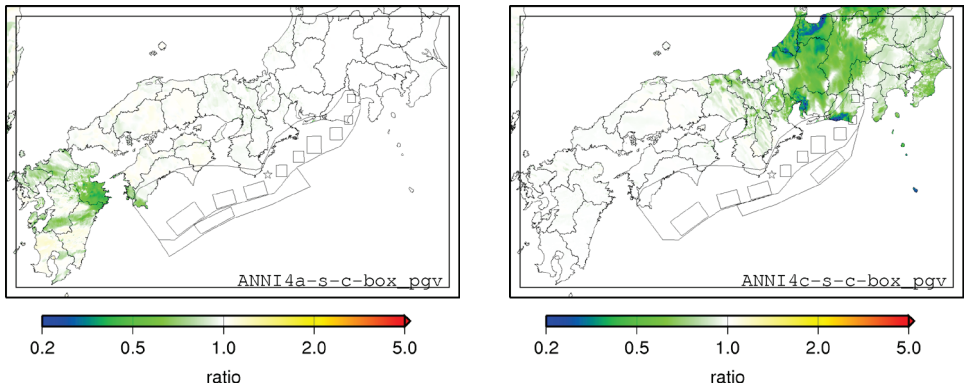


Figure 6 Map showing peak ground velocity ratio between scenarios using boxcar-like slip velocity time function and Kostrov-like slip velocity function. Left: ANNI4a and right: ANNI4c scenarios.

Murotani, S., Miyake, H. and Koketsu, K. (2008), "Scaling of characterized slip models for plate-boundary earthquakes," *Earth, Planets and Space*. **60**, 987-991.

Nakamura, H., and Miyatake, T. (2000), "An approximate expression of slip velocity time functions for simulation of near-field strong ground motion," *Zisin*. **53**, 1-9 (in Japanese with English abstract).

Wessel, P., and Smith, W. H. F. (1995), "New version of the Generic Mapping Tools released," *Eos Transactions, American Geophysical Union*. **76**, 329.

10CUEE CONFERENCE PROCEEDINGS
10th International Conference on Urban Earthquake Engineering
March 1-2, 2013, Tokyo Institute of Technology, Tokyo, Japan

FUNDAMENTAL PROPERTY OF CROSS TERMS OF GROUND TRANSFER FUNCTION

Hiroyuki Goto[1)]

1) Assistant Professor, Disaster Prevention Research Institute, Kyoto University, Japan
goto@catfish.dpri.kyoto-u.ac.jp

Abstract: Normalized energy density (NED) is one of the essential quantities for a ground transfer function of a 1D layered structure model. This quantity is regarded as a type of norm for the power of the ground transfer function. The cross term of the functions is defined as an extension of the NED. The cross term is physically defined as the correlation coefficient between the two ground transfer functions. The cross term detects the harmony of two transfer functions; a finite value is obtained only in the case where peak frequencies coincide. The properties of the cross term is analytically proved for a two-layered case and numerically shown for three- and four-layered cases.

1. INTRODUCTION

The elastic wave propagations inside an elastic material are a fundamental topic for understanding certain aspects of engineering and scientific issues. For example, in seismology, earthquake engineering, and exploration geophysics, seismic wave propagation through the crust structure is regarded as elastic wave propagation; this property has been discussed based on elastic wave theory (e.g., Aki and Richards, 2002; Kennett 2002).

As the seismic waves radiating from an earthquake source travel through the crust structure, they are amplified, attenuated and elongated the duration owing to reflection, refraction, and scattering. Then, the wave arrives at the ground surface layer. In earthquake engineering, the amplification of the seismic wave owing to the ground surface layer, which is a deposit of soil overlying the basement, is an important issue to be addressed for earthquake disaster mitigation, e.g., seismic microzonation (Borcherdt, 1970).

Because the material velocity generally decreases in the shallower part of the underground, the incident angle of the wave can be assumed to be vertical at the engineering basement that consists of about 400-700 m/s of S-wave velocity material. This process highlights the importance of determining how to quantify a ground transfer function, which is a frequency-dependent amplification factor of a seismic wave from the basement to the ground surface. The ground transfer function has been evaluated based on elastic wave theory. Numerous approaches incorporating an inelastic attenuation, nonlinear behavior of soil, etc., are available, e.g., the Haskell matrix method by Haskell (1960), SHAKE by Schnabel et al. (1972), and DYNEQ by Yoshida and Suetomi (1996). Several researchers have applied them to discuss the ground motion observations during actual earthquakes (e.g., Suetomi and Yoshida, 1998).

Recently, Goto et al. (2011a) suggested a conserved quantity named normalized energy density (NED) in the ground surface layer. The NED is an interesting property of the ground transfer function; the frequency average of the power only depends on the impedance ratio between the uppermost surface layer and the basement, but does not depend on the physical property between them. This provides a potential constrain to the parameter space in evaluating the ground transfer function; for instance, the NED allows a direct estimation of the total damping of the ground surface layer (Goto et al., 2011b).

From this definition, the NED is regarded as a type of norm of the ground transfer function. In this article, more general discussion similar to the NED is presented, focusing on the cross term of the different transfer functions.

2. NORMALIZED ENERGY DENSITY

Normalized energy density (NED) is a quantity defined in reference to a multilayered structure that consists of n horizontal layers (#1-n) over a half space basement #0, as shown in Figure 1. The S-wave velocity of Layer #k is β_k, the density is ρ_k, and the thickness is h_k. When 2D SH waves vertically propagate into the layers through the interface between layer #n and basement #0, the NED for layer #k is defined as follows (Goto et al., 2011a):

$$\mathrm{NED}_k = \lim_{\Omega\to\infty} \frac{1}{\Omega} \int_0^{\Omega} \rho_k \beta_k \left| \frac{A_k(\omega)}{A_0(\omega)} \right|^2 d\omega \qquad (1)$$

where A_0 is a Fourier amplitude of the upgoing wave through the basement #0 and A_k is a Fourier amplitude of the upgoing wave through the layer #k. ω is the angular

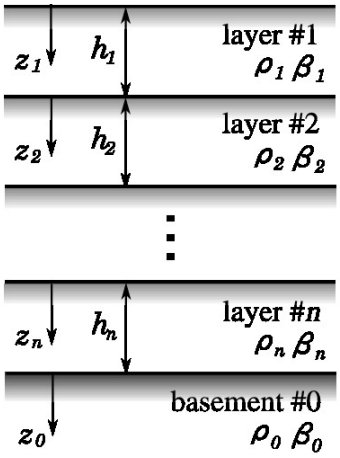


Figure 1 Model of multilayered structure in definition of NED.

frequency. The integration is only applied to a positive value of ω instead of the original definition (Goto et al., 2011a), wherein both the negative and positive sides are integrated. This is permitted because the integrand is an even function when $|A_k/A_0|$ is causal.

A ground transfer function of the structure is usually defined by $H=2A_1/A_0$. The NED for layer #1 can be represented by the transfer function as

$$\mathrm{NED}_1 = \lim_{\Omega\to\infty} \frac{1}{\Omega} \int_0^{\Omega} \frac{\rho_1\beta_1}{4} \left|H(\omega)\right|^2 d\omega \tag{2}$$

Because the amplitude ratio A_k/A_0 depends on only the physical parameters of each layer and basement, the NED is evaluated from the physical parameters independent of the property of the incident waves.

The NED is proven to be constant, $\mathrm{NED}=\rho_0\beta_0$, through the layer #1-n and basement #0, analytically for a two-layered case and numerically for the case of more than three layers (Goto et al., 2011a). This means that the NED is a conserved quantity through the layered structure and is evaluated without a detailed physical property when a transfer function and an impedance $\rho_1\beta_1$, in the uppermost layer are available.

To generalize the discussion, a particular model of the structure is represented by a complex function $a(\omega)$ incorporating the impedance ratio $R_a=\rho_1\beta_1/\rho_0\beta_0$, as

$$a(\omega) = \sqrt{R_a}\,\frac{A_1(\omega)}{A_0(\omega)} \tag{3}$$

a depends on a physical property of the structure, and satisfies the following relation,

$$\langle a^* a\rangle \equiv \lim_{\Omega\to\infty} \frac{1}{\Omega} \int_0^{\Omega} a^* a\, d\omega = 1 \tag{4}$$

where a^* denotes a complex conjugate of a. Equation (4) is equivalent to $\mathrm{NED}_1=\rho_0\beta_0$ that is the property of the NED.

3. CROSS TERMS OF TWO DIFFERENT TRANSFER FUNCTIONS

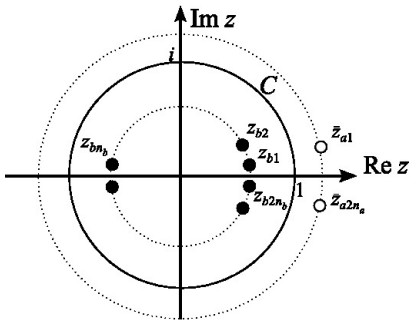


Figure 2 Unit circle C and poles $\bar{z}_{ak}$ and z_{bl} on a complex plane.

3.1 Two-layered case

Let a and b to be the functions representing the model of layered structures; both satisfy the principle defined by Eq.(4). Here, a cross term of a and b is defined as follows:

$$\langle a^* b\rangle \equiv \lim_{\Omega\to\infty} \frac{1}{\Omega} \int_0^{\Omega} a^* b\, d\omega \tag{5}$$

In the case of $a=b$, the cross term is equal to 1 by definition. For a two-layered case, a and b are explicitly evaluated as,

$$a = \frac{\sqrt{R_a}}{\cos(\omega h_a/\beta_a) + iR_a \sin(\omega h_a/\beta_a)} \tag{6}$$

$$b = \frac{\sqrt{R_b}}{\cos(\omega h_b/\beta_b) + iR_b \sin(\omega h_b/\beta_b)} \tag{7}$$

where R_a and R_b are the impedance ratios of the layer to the basement. h_a and h_b are the thicknesses of the layers, and β_a and β_b are the S-wave velocities of the layer. i denotes an imaginary unit.

Here, a complex value $z=\exp(i\omega h/\beta)$ with a unit absolute value is defined. If one supposes that h_a/β_a and h_b/β_b are represented by a product of h/β and some non-negative integer, n_a and n_b, then this assumption limits the ratio of h_a/β_a and h_b/β_b to being a rational number. In the case represented in this paper, the following representations are available:

$$\begin{cases} \cos(\omega h_a/\beta_a) = \frac{1}{2}(z^{n_a} + z^{-n_a}) \\ \sin(\omega h_a/\beta_a) = \frac{1}{2i}(z^{n_a} - z^{-n_a}) \end{cases} \tag{8}$$

$$\begin{cases} \cos(\omega h_b/\beta_b) = \frac{1}{2}(z^{n_b} + z^{-n_b}) \\ \sin(\omega h_b/\beta_b) = \frac{1}{2i}(z^{n_b} - z^{-n_b}) \end{cases} \tag{9}$$

and a and b are rewritten by z as follows:

$$a = \frac{\frac{2\sqrt{R_a}}{1+R_a} z^{n_a}}{z^{2n_a} + \frac{1-R_a}{1+R_a}}, \qquad b = \frac{\frac{2\sqrt{R_b}}{1+R_b} z^{n_b}}{z^{2n_b} + \frac{1-R_b}{1+R_b}}. \tag{10}$$

z is located on a unit circle on the complex plane and moves counterclockwise as ω increases. This means that z and a function of z are periodic with a period of $2\pi\beta/h$. In the case, the integration in Eq.(5) is modified into a complex integration along the unit circle C.

$$\langle a^* b\rangle \equiv \frac{1}{2\pi i} \oint_C a^* b z^{-1}\, d\omega \tag{11}$$

The representation is allowed to evaluate the integral based on the residue theorem. The integrand $a^* b z^{-1}$ is represented by

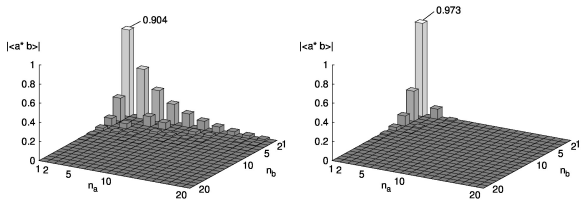


Figure 3 Absolute values of cross term $\langle a^* b \rangle$ with respect to n_a and n_b for case $\{R_a, R_b\}=\{0.5, 0.2\}$ (left) and case $\{R_a, R_b\}=\{0.5, 0.8\}$ (right).

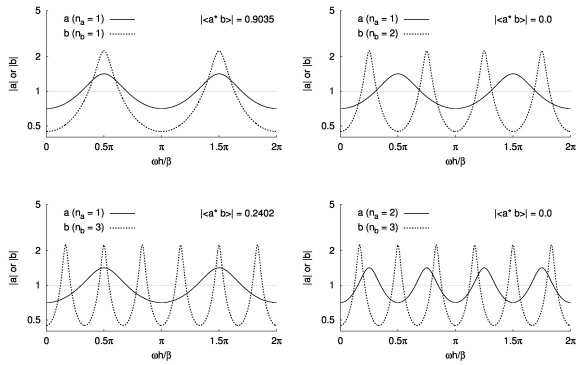


Figure 4 Absolute values of a and b associated with $\omega h/\beta$ for case $\{R_a, R_b\}=\{0.5, 0.2\}$. Each panel corresponds to $\{n_a, n_b\}=\{1, 1\}$ (top left), $\{1, 2\}$ (top right), $\{1, 3\}$ (bottom left), and $\{2, 3\}$ (bottom right).

$$a^* b z^{-1} = \frac{\frac{2\sqrt{R_a}}{1-R_a}\frac{2\sqrt{R_b}}{1+R_b} z^{n_a+n_b-1}}{\left[z^{2n_a}+\frac{1+R_a}{1-R_a}\right]\left[z^{2n_b}+\frac{1-R_b}{1+R_b}\right]}. \quad (12)$$

and the poles are located at

$$\bar{z}_{ak} = \left(\frac{1+R_a}{1-R_a}\right)^{1/2n_a} e^{(2k-1)\pi i/2n_a} \quad k\in\{1,\ldots,2n_a\} \quad (13)$$

$$z_{bl} = \left(\frac{1-R_b}{1+R_b}\right)^{1/2n_b} e^{(2l-1)\pi i/2n_b} \quad l\in\{1,\ldots,2n_b\} \quad (14)$$

Because R_a and R_b are the physical positive values, $\bar{z}_{ak}$ is located outside of the unit circle, as shown in Fig.2.

Based on the residue theorem, the cross term is evaluated from a sum of the residues corresponding to z_{bl}.

$$\langle a^* b \rangle = \sum_{l=1}^{2n_b} \underset{z=z_{bl}}{\mathrm{Res}} [a^* b z^{-1}] \quad (15)$$

where the residue is represented, as follows:

$$\underset{z=z_{bl}}{\mathrm{Res}} [a^* b z^{-1}] = \frac{-\frac{2\sqrt{R_a}}{1-R_a}\frac{\sqrt{R_b}}{2n_b(1+R_b)} z_{bl}^{n_a+n_b}}{z_{bl}^{2n_a}+\frac{1+R_a}{1-R_a}}. \quad (16)$$

From the definition, z_{bl+nb} for l=1,…,n_b is equal to $-z_{bl}$ (see Fig.2). This suggests that z_{bl}^{2na} is equal to z_{bl+nb}^{2na}. z_{bl+nb}^{na+nb} is also equal to $-z_{bl}^{na+nb}$ when n_a+n_b is an odd value. Thus, the cross term vanishes in cases where n_a+n_b=odd.

For high values of n_a and n_b, the limit to the value of the cross term $\langle a^* b \rangle$ becomes zero. A detailed description is in Goto (2013). If n_a and n_b are regarded to be infinite values when the ratio of h_a/β_a and h_b/β_b is not a rational number, the cross term is also vanished in this case. Only for a pair of low values of n_a and n_b, does the term provide a finite value.

Figure 3 shows the absolute values of the cross term $\langle a^* b \rangle$ with respect to a set of n_a and n_b values for cases of R_a=0.5, R_b=0.2, and R_a=0.5, R_b=0.8. Each value is calculated based on Eq.(15), whereas the value of a pair that n_a and n_b are not coprime are set as zero. For example, the pair of n_a=n_b=5 gives the same cross term with the pair of n_a=n_b=1, whereas the non-coprime pair is not essential in discussing the convergence for the large n_a and n_b. It should be referred to the corresponding value for n_a=n_b=1. In either case, the cross term becomes zero when n_a+n_b=odd as analytically proved, and the other values monotonically decrease depending on n_a and n_b. This also implies the cross terms are not zero for low values of n_a and n_b.

Figure 4 shows the absolute values of a and b associated with $\omega h/\beta$ for a case R_a=0.5 and R_b=0.2, and each panel corresponds to the pairs of $\{n_a, n_b\}=\{1, 1\}$, $\{1, 2\}$, $\{1, 3\}$, and $\{2, 3\}$. The cross terms $\left|\langle a^* b \rangle\right|$ are evaluated as 0.9035, 0.0, 0.2402, and 0.0, respectively. When n_a and n_b are odd, the peak values of both $|a|$ and $|b|$ appear at 0.5π and 1.5π. n_a+n_b=odd is equivalent to the case where n_a and n_b are odd when n_a and n_b are coprime. Thus, the condition n_a+n_b=odd has the clear physical meaning that peak values of $|a|$ and $|b|$ appear at the same angular frequency. This suggests that $\langle a^* b \rangle$ quantifies a harmony between two different layered structure.

3.2 Multilayered case

The cross term $\langle a^* b \rangle$ is also available for multilayered cases. However, the analytical approach introduced in the two-layered case is not easily applicable. Some of the numerical simulations are performed to discuss the properties of the cross term.

As discussed in the two-layered case, the cross term strongly depends on the values of n_a and n_b, which correspond to the harmony of peak frequencies. Because the variables are not defined for the general multilayered case, a hypothetical model for n_a and n_b is constructed from a particular model. Let h_{ak} and β_{ak} to be a thickness and the S-wave velocity of a kth layer in model a. A thickness h_{bk} for the hypothetical model b is calculated from a pair of n_a and n_b:

$$h_{bk} = h_{ak}\frac{\beta_{bk}}{\beta_{ak}}\frac{n_b}{n_a} \quad (17)$$

This is consistent with the definition of n_a and n_b in the two-layered case.

For the three- and four-layered cases, a Monte Carlo simulation is performed. First, fifty sets of layered models \$a\$ are generated from random numbers within the range 10-700m/s for S-wave velocity, 1000-2000kg/m^3 for the density of every layer, and 1000-2000kg/m^3 for the density of the basement. The S-wave velocity of the basement is set at an impedance ratio equal to 0.5. The total thickness of the layers is generated within the range of 1-50m and then divided into layers with a random thickness. Fifty additional sets of layered model candidates are also generated under the same condition as model a, except for the layer thickness. The S-wave velocity of the basement is set such that the impedance ratio is equal to 0.2. Then, the layer thickness of

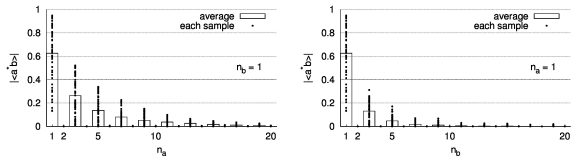


Figure 5 Absolute values of cross terms $\langle a^* b \rangle$ for three-layered case ($\{R_a, R_b\}=\{0.5, 0.2\}$) with respect to n_a (n_b=1) (left) and n_b (n_a=1) (right).

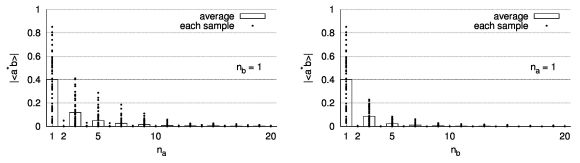


Figure 6 Absolute values of cross terms $\langle a^* b \rangle$ for four-layered case ($\{R_a, R_b\}=\{0.5, 0.2\}$) with respect to n_a (n_b=1) (left) and n_b (n_a=1) (right).

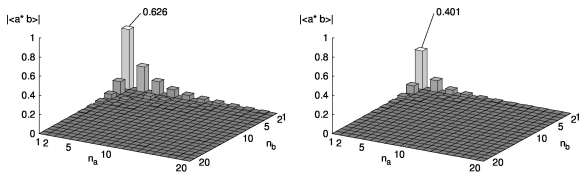


Figure 7 Average over absolute values of the cross term $\langle a^* b \rangle$ with respect to n_a and n_b for three-layered case (left), and four-layered case (right).

each of the fifty model candidates are scaled via the relation in Eq.(17) for a given pair of n_a and n_b, and construct the model *b*. The cross terms are calculated between the fifty pairs of *a* and *b* by varying n_a and n_b for each pair. The integrations are approximated by numerical integration every $0.1s^{-1}$$ up to $1.0\times6s^{-1}$.

Figures 5 and 6 show the absolute values of the cross term for the three- and four-layered cases, respectively. Each panel corresponds to the case n_b=1 and n_a=1. Fifty samples are indicated as the points, and the average over the samples is also plotted via a bar chart. The impedance ratio of the uppermost layer to the basement is constant, 0.5 in model *a* and 0.2 in model *b*, whereas the variation among the samples are observed. The variation decreases as n_a or n_b increases. Similar to the two-layered case, the cross term is significantly small when n_a+n_b is odd.

Figure 7 shows the averages over fifty samples of absolute values of the cross term for three- and four-layered cases, respectively. The results are similar to the results for the two-layered case (Fig.3); the values almost vanish when n_a+n_b is odd, and they monotonically decrease depending on n_a and n_b, although the values are the averages over all the samples.

4. DISCUSIONS AND CONCLUSIONS

Let the transfer functions for a model *a* and model *b* be denoted as H_a and H_b. The cross term of the transfer functions is proportional to $\langle a^* b \rangle$ as

$$\langle H_a{}^* H_b \rangle = \frac{4}{\sqrt{R_a R_b}} \langle a^* b \rangle \tag{18}$$

This indicates that the properties of the cross terms discussed in Sections 3 are transferrable to the properties of the cross terms between the transfer functions with a factor depending on the impedance ratios R_a and R_b. $H_a{}^* H_b$ is a cross spectrum between the observed signals on the ground surface when the incident wave contains a constant power in frequency, such as that of white noise (e.g., Zerva, 2009). This implies that the frequency average of the *normalized* cross spectrum must obey the property described in Sections 3.

When the values of the transfer function in each frequency are regarded as a set of samples, Pearson's correlation coefficient between the transfer functions can be defined as

$$C_{ab} \equiv \frac{\langle \left(H_a - \langle H_a \rangle\right)^* \left(H_b - \langle H_b \rangle\right) \rangle}{\sqrt{\langle \left|H_a - \langle H_a \rangle\right|^2 \rangle \langle \left|H_b - \langle H_b \rangle\right|^2 \rangle}} \tag{19}$$

Because the correlation coefficient is invariant, it gives the same value when it is defined by *a* and *b*.

$$C_{ab} = \frac{\langle \left(a - \langle a \rangle\right)^* \left(b - \langle b \rangle\right) \rangle}{\sqrt{\langle \left|a - \langle a \rangle\right|^2 \rangle \langle \left|b - \langle b \rangle\right|^2 \rangle}} \tag{20}$$

Using the property of the NED represented by Eq.(4), $\langle |a|^2 \rangle$ and $\langle |b|^2 \rangle$ are identically 1. When the average of *a* and *b* is supposed to be zero, as described in Goto (2013), the correlation coefficient C_{ab} is equal to the cross term of *a* and *b*.

$$C_{ab} = \langle a^* b \rangle \tag{21}$$

This provides a clear physical meaning of the cross term as being the correlation coefficient between the transfer functions.

The cross term of ground transfer functions is defined as an extension of the NED. The cross term gives a finite value only in cases where peak frequencies coincide. This finding suggests that the cross term detects the harmony of two transfer functions. The properties are analytically proved for a two-layered case, and numerically shown for three- and four-layered cases. The cross term physically implies the correlation coefficient between the two ground transfer functions.

Although the explicit application of the findings regarding the cross terms is not clear at this time, the essential property of the transfer function will provide some new insights for the transfer functions; for instance, the correlation coefficients are not equivalent to the average of the cross term within the finite frequency range, whereas they are deeply linked as the frequency range broaden.

References:

Aki, K. and P.G. Richards, "Quantitativ Seismology 2nd edn", University Science Books, California, 2002.

Kennett, B.L.N., "The Seismic Wavefield, Volume I: Introduction and Theoretical Development", Cambridge University Press, 2002.

Borcherdt, R.D., "Effects of local geology on ground motion near San Francisco bay", *Bull. Seism. Soc. Am.*, **60**, 29-61, 1970.

Haskell, N.A., "Crustal reflection of plane SH waves", *J. Geophys. Res.*, **45**, 4147-4151, 1960.

Schnabel, P.B., J. Lysmer and H.B. Seed, "SHAKE A computer program for earthquake response analysis of horizontally layered sites", *Report No.EERC72-12*, University of California, Berkeley, 1972.

Yoshida, N. and I. Suetomi, "DYNEQ: a computer program for dynamic analysis of level ground based on equivalent linear method", *Reports of Engineering Research Institute, Sato Kogyo CO., Ltd.*, 61-70, 1996.

Suetomi, I. and N. Yoshida, "Nonlinear behavior of surface deposit during the 1995 Hyogoken-Nambu earthquake", *Soils and Foundations, special issue on geotechnical aspects of the January 17, 1995 Hyogoken-Nambu earthquake*, 11-22, 1998.

Goto, H., S. Sawada and T. Hirai, "Conserved quantity of elastic waves in multi-layered media: 2D SH case -Normalized Energy Density-", *Wave Motion*, **48**, 602-612, 2011.

Goto, H., S. Sawada, Y. Kawamura, T. Hirai and T. Akazawa, "Definition of normalized energy density and its application to direct estimation of damping property", *The 4th International IASPEI/IAEE Symposium on the Effects of Surface Geology on Seismic Motion*, 2011.

Zerva, A., "Spatial variation of seismic ground motions: modeling and engineering applications", CRC Press, 2009.

10CUEE CONFERENCE PROCEEDINGS
10th International Conference on Urban Earthquake Engineering
March 1-2, 2013, Tokyo Institute of Technology, Tokyo, Japan

COMPARISON OF GROUND MOTION ATTRIBUTES FROM 2011 TOHOKU-OKI MAINSHOCK AND TWO SUBSEQUENT EVENTS

Tadahiro Kishida[1)], Jonathan P. Stewart[2)], Robert W. Graves[3)], Saburoh Midorikawa[4)], Hiroyuki Miura[5)], Yousef Bozorgnia[1)] , and Kenneth W. Campbell[6)]

1) Post-Doctoral Scholar (TK) and Executive Director (YB), Pacific Earthquake Engineering Research Center, Berkeley, CA, USA
2) Professor and Chair, Dept. of Civil & Environmental Engineering, Univ. of California, Los Angeles, CA, USA
3) Seismologist, US Geological Survey, Pasadena, CA, USA
4) Professor, Tokyo Institute of Technology, Japan
5) Associate Professor, Hiroshima University, Japan
6) Vice President, EQECAT Inc, Beaverton OR, USA

tkishida@berkeley.edu, jstewart@seas.ucla.edu, rwgraves@usgs.gov, ,
smidorik@enveng.titech.ac.jp, hmiura@hiroshima-u.ac.jp, yousef@berkeley.edu, kcampbell@eqecat.com

Abstract: The M_w 9.0 Tohoku-oki Japan earthquake and many of its subsequent aftershocks and triggered events were very well recorded, providing opportunity for detailed study of source, path, and site effects. In previous work, we utilized mainshock data to demonstrate faster attenuation with distance in backarc than in forearc regions, positive event terms for high frequency intensity measures for multiple ground motion prediction models, and minimal scaling of site amplification with V_{s30} at high frequencies. In this paper, we consider two subsequent events, one M_w 6.7 on the plate interface that ruptured in the mainshock and one M_w 6.3 inland from the volcanic front, to examine if similar ground motion features are apparent from these data sets. We continue to find evidence for the divergence in attenuation rate in forearc and backarc regions, despite the fact that the events are located on opposite sides of the volcanic front. The site response for these events does not appear to follow previously observed patterns for Japan, being relatively similar to V_{s30}-scaling in active crustal regions generally.

1. INTRODUCTION

The M_w 9.0 Tohoku-oki earthquake occurred on March 11 2011 along the plate boundary off the Pacific Coast of Japan. In prior work (Stewart et al., 2013), we reviewed the mainshock source solutions and selected a representative source model for engineering application; we described the uniform ground motion processing applied to approximately 2000 available triaxial accelerograms; and we described the results of data analysis to investigate source, path and site effects. For short period ground motion intensity measures, we found faster attenuation with distance in backarc than in forearc regions, positive event terms for multiple ground motion prediction models at short periods, and minimal scaling of site amplification with V_{s30}. Many of these effects disappeared at long periods.

Many of these observations are of substantial practical significance for ground motion prediction, and therefore there is interest in seeing if they are repeatable. This paper represents a first step in this direction. We select two well recorded events that occurred subsequent to the mainshock, one M_w 6.7 on the same plate interface that ruptured in the mainshock and one M_w 6.3 inland from the volcanic front. Identical data processing procedures are applied to these recordings as were used for the mainshock. Our objective is to see if similar ground motion features are apparent from these data sets as were found from the mainshock.

2. SELECTED EVENTS AND AVAILABLE DATA

We selected two events from the Japan Meteorological Assoc. (JMA) web site (http://www.seisvol.kishou.go.jp/eq/sourceprocess/). Attributes of the two events are given in Table 1. We refer to the 12 March 2011 event as 'crustal' and the 23 June 2011 event as 'interface.' As shown in Figure 1, the crustal event occurred in the backarc region. It had a reverse-slip mechanism and a shallow focal depth (8 km). The interface event occurred near the northwest corner of the mainshock fault plane (Fig. 1). It had a reverse-slip mechanism along a 17 deg. westward dipping fault plane and a focal depth of 36 km, which are consistent with rupture along the plate interface. In addition, this event is located close to the 03-11-2011 M_w 7.4 aftershock (Fig 1), which is also inferred to have rupture at the plate interface.

Table 1. Attributes of selected events

Date	M_w	Top-Ctr Lat, Long	Depth to top (km)	Length, width (km)	Strike / dip (°)
3/2011	6.3	37.051, 138.532	4.4	12, 12	26 / 32
6/2011	6.7	39.982, 142.588	36	18, 12	185/17

There are hundreds of well recorded events following the Tohoku mainshock. Our reasons for selecting these specific events were:

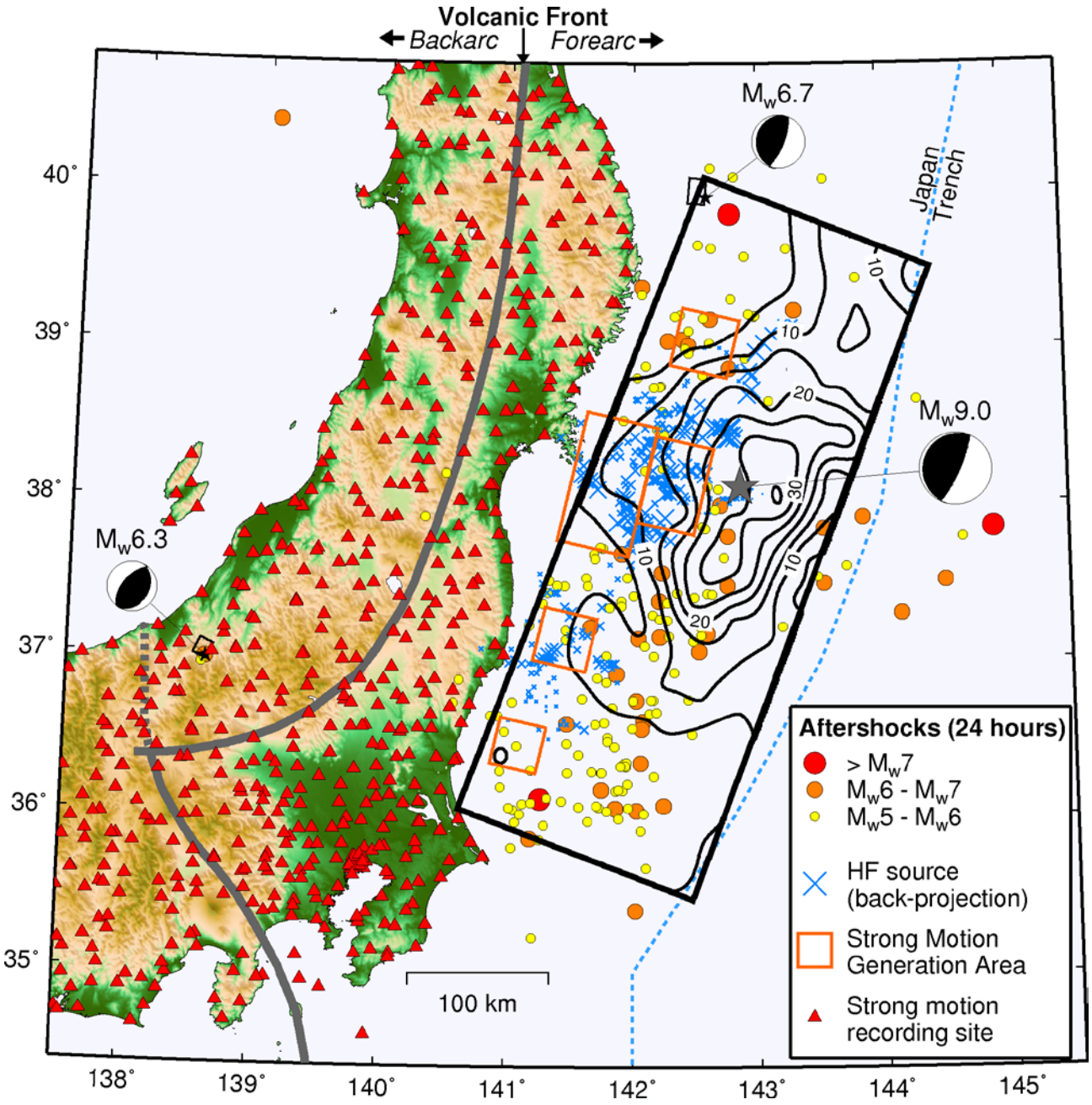


Figure 1. Map view showing surface projections of two selected triggered events for this study (Mw 6.3 crustal event and Mw 6.7 interface event) along with various attributes of mainshock fault model selected by Stewart et al. (2013), which is derived from Yokota et al. (2011). Mainshock fault attributes shown are the Strong Motion Generation Areas of Kurahashi and Irikura (2011) (orange rectangles) and the high-frequency back-projection source locations of Meng et al. (2011) (blue crosses). Contours indicate slip (m) for the Yokota et al. rupture model. Colored circles show aftershocks within the first 24 hours following the mainshock. Dashed blue line indicates location of Japan Trench and the gray star is the JMA epicenter of the mainshock. The red triangles denote the locations of some of the strong motion recording sites considered in our analysis (additional stations were considered beyond the limits of the map).

1. *Location relative to plate boundary.* We sought events on, and inboard from, the plate boundary. This was to see if the forearc/backarc path effects are similar for waves travelling principally in a forearc-to-backarc direction (source to instruments) or vice-versa. We are also interested in event-term trends for these earthquakes relative to the mainshock.
2. *Recordings*. We sought events with numerous uniformly processed recordings using standard Pacific Earthquake Engineering Research (PEER) procedures (Darragh et al., 2004; Chiou et al., 2008) as of 12/2012. The crustal & interface events produced 520 & 472 records.
3. *Magnitude*. We sought events with similar magnitudes.

For the crustal event, we took the fault plane solution of Nagumo (2012). We examined several other fault plane solutions for this event from the JMA web site (http://www.seisvol.kishou.go.jp/eq/sourceprocess/event/201103120359near.pdf, last accessed Dec 2012) and NIED web site (http://cais.gsi.go.jp/YOCHIREN/report/kaihou86/07_04.pdf, last accessed Dec 2012). The Nagumo model was selected because its fault plane solution is most clearly documented. For the interface event, we take the only available fault plane solution, which is from the JMA web site (http://www.seisvol.kishou.go.jp/eq/sourceprocess/ event/20110623near.pdf, last accessed Jan 2013). Both of the selected fault planes are shown in Figure 1.

For both events, we obtained available ground motion records from the Knet and Kik-net arrays at the NIED web site (http://www.kyoshin.bosai.go.jp/kyoshin/, last accessed Dec 2012). A total of 554 and 641 three-component uncorrected digital accelerograms were selected for the crustal and interface events, respectively. Sponsored by the PEER center, those motions were processed by Pacific Engineering and Analysis following PEER/NGA protocols (Darragh et al., 2004; Chiou et al., 2008), which include selection of record-specific corner frequencies to optimize the usable frequency range. For Kik-net sites, only data from the ground surface stations are considered.

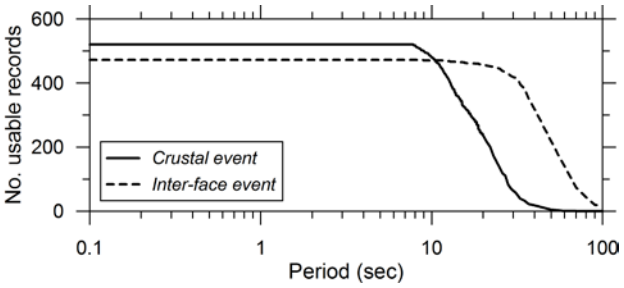


Figure 2. Number of usable two-component horizontal records as function of spectral period for the two data sets

The most important filter is the low-cut filter, which removes low frequency noise effects. We take the minimum usable frequency as $1.25 \times f_{HP}$, where f_{HP} is the high-pass (equivalent to low-cut) corner frequency used in the processing. Using the filtered records, we computed the intensity measures of peak acceleration (PGA), peak velocity (PGV), and pseudo-acceleration response spectra at a range of periods between 0.01 and 10.0 sec. Figure 2 presents the number of usable recordings as a function of period. A usable recording for period T is defined as having both horizontal components with $T < 1/(1.25\ f_{HP})$. The data set is seen to fall off for periods beyond about 10-30 sec.

3. DATA ANALYSIS

3.1 Analysis Procedures

The data analysis follows the same procedures described in Stewart et al. (2013), and hence is described here only briefly. Essentially, we compute total residuals (data minus model in natural log units) using an applicable ground motion prediction equation (GMPE). In this case, we use the Zhao et al. (2006) GMPE. Event terms are computed using the mean of total residuals for conditions where distance attenuation bias is judged to not significantly contaminate the results. Distance attenuation trends are evaluated from the trends of residuals with distance.

A second set of residuals is computed as the difference between data and the GMPE for rock conditions (described in Stewart et al., 2013). These residuals are used to evaluate the scaling of ground motions with the time averaged shear wave velocity in the upper 30 m of the site (V_{s30}).

3.2 Distance Attenuation

Figure 3 shows RotD50 values (i.e, median of single-azimuthal ground motions; Boore, 2010) for PGA, 0.1 s, 1.0 s, and 3.0 s pseudo-acceleration (PSA) at 5% damping versus rupture distance. Also shown in Figure 3a are medians (μ) and medians ± one intra-event standard deviation (ϕ_{ln}) for the ZEA (Zhao et al.) 2006 GMPE for the site category having $V_{s30} \approx 300$ m/s. Figure 4 shows total residuals versus rupture distance. Forearc and backarc sites are distinguished in both Figures 3 and 4.

Several significant trends are evident from Figure 3 and 4. The crustal event occurs in the backarc region and produced backarc recordings from nearly zero distance to large distance. Forearc recordings begin at about 80 km. As shown by the binned median residuals, the forearc recordings have an upward shift relative to the backarc, which is consistent with previously observed trends of faster distance attenuation in backarc than forearc regions (Ghofrani and Atkinson, 2011). This is generally consistent with what we saw with the Tohoku mainshock, but interestingly in this case, the waves are crossing the volcanic front in opposite directions.

The interface event has forearc recordings starting at around 60 km and backarc recordings beginning at about 120 km. Backarc residuals have a clear downward shift relative to the forearc, which is the same trend observed with the Tohoku mainshock data (Ghofrani and Atkinson, 2011; Skarlatoudis and Papazachos, 2012; Stewart et al 2013). Hence, the apparent differences in anelastic attenuation rate in forearc and backarc regions appear to be stable across events and source locations (relative to volcanic front).

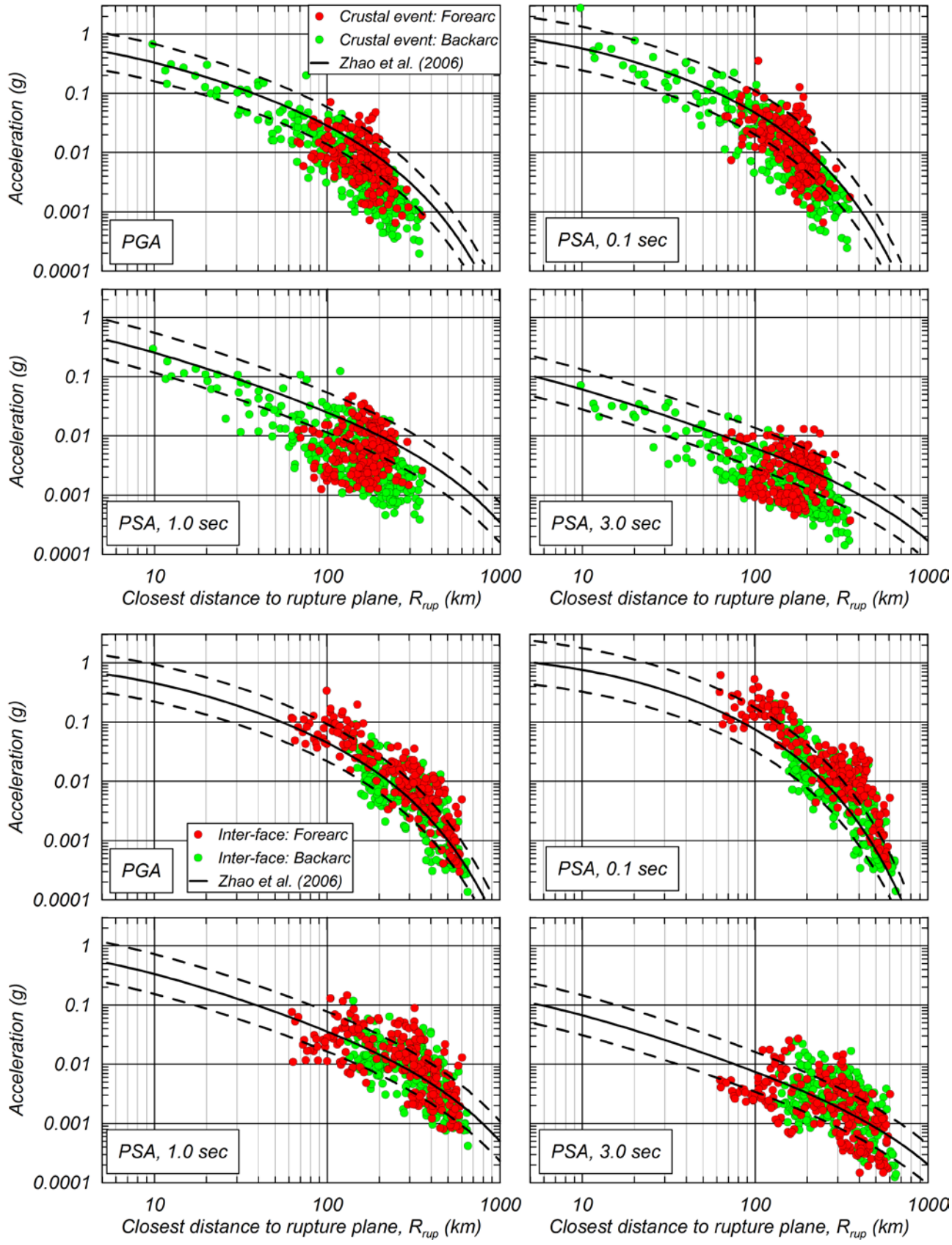


Figure 3. Ground motion intensity measures plotted against distance for crustal (top) and interface (bottom) triggered events. Backarc and forearc records shown with separate symbols. Zhao et al. 2006 GMPE shown for soil site condition.

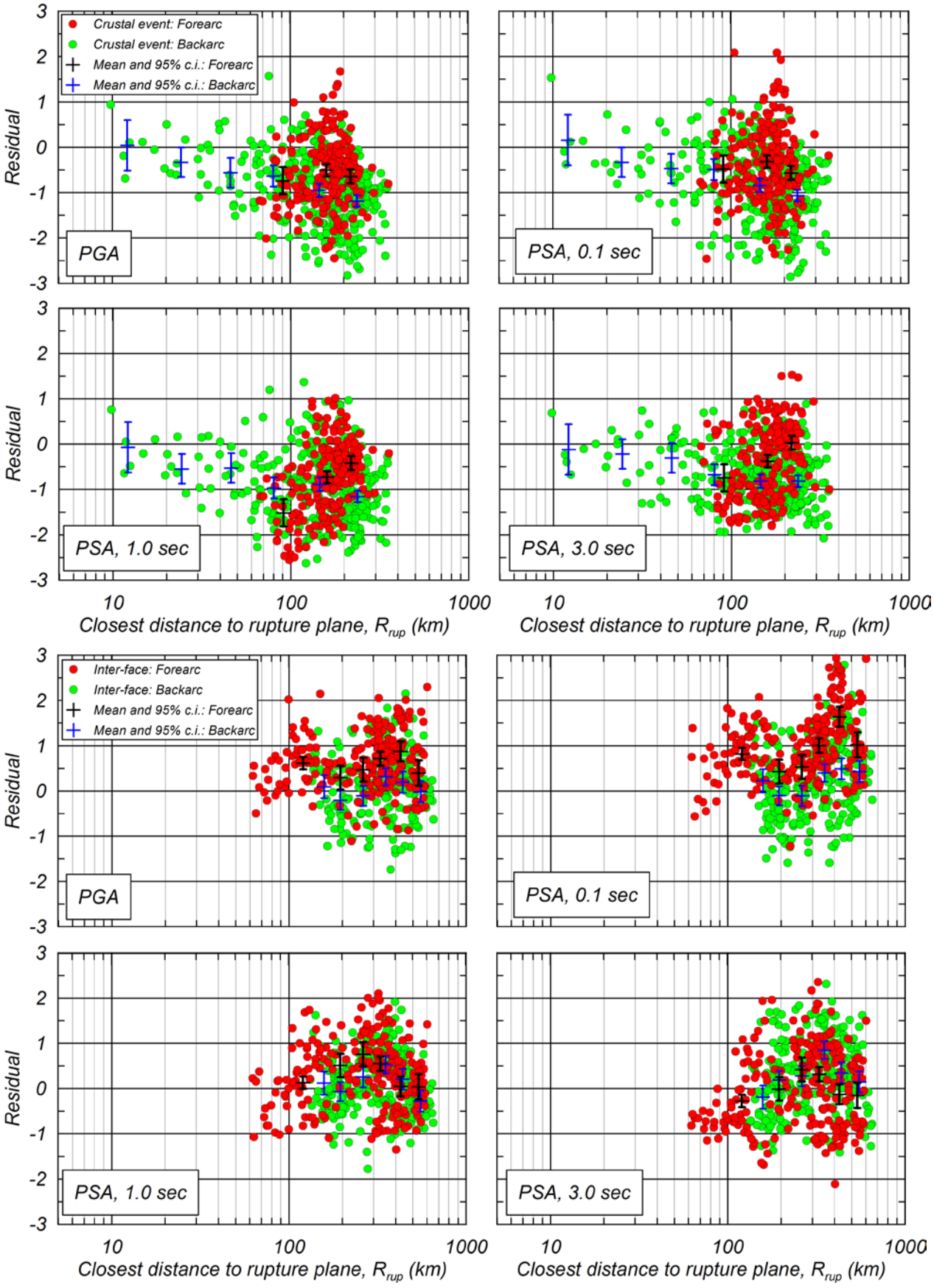


Figure 4. Distance-dependence of total residuals for crustal (top) and interface (bottom) events relative to ZEA 2006 GMPE.

3.3 Event Terms

As shown in Figure 4, in most cases the residuals are not centered at zero ordinate, indicating systematic misfits of the GMPE relative to the data. Since the events are well recorded, this bias is practically equivalent to an event term as would be calculated from a mixed-effects regression (e.g., Abrahamson and Youngs, 1992). Non-zero event terms (η) are typical; what is of interest is to see if the event terms are consistent with event-to-event scatter (represented by event term standard deviation τ) as observed from previous earthquakes. Figure 5 shows event terms, calculated using the following data for the two earthquakes:

1. For the crustal event, we use a combination of backarc recordings with closest distance (R_{rup}) < 70 km and forearc to R_{rup} < 250 km. We include the close-distance backarc records because the distance attenuation is dominated by geometric spreading in that region.
2. For the interface event, we use forearc recordings with R_{rup} < 250 km.

Event terms are taken as median residuals for the ZEA 2006 GMPE as a function of spectral period. Also shown in Figure 5 are the $\pm$ τ model (inter-event standard deviation) from ZEA 2006. We note that the mainshock and interface event terms have a similar trend with period, whereas the crustal event is different because of an increase at long period. One possible explanation for this is stronger surface waves excited by the shallow crustal event compared to the lack of surface waves for the relatively deep interface event. These surface waves would be more pronounced at the longer periods due to the higher attenuation of shorter periods in the shallow crust. Analyses of additional events are needed to determine whether these effects are accidental or systematic.

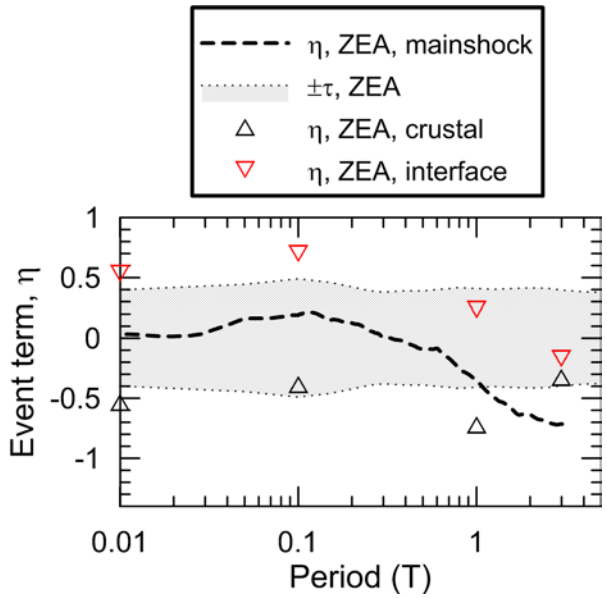


Fig. 5. Estimated event terms of Tohoku-oki mainshock and two triggered events relative to the ZEA 2006 GMPE. Also shown is the ZEA inter-event standard deviation (τ).

3.4 Site Response

A meaningful analysis of site effects from these data sets is complicated by the significant distance attenuation misfits identified in Section 3.2, which cause large non-zero residuals for reasons unrelated to site response. Accordingly, for the analysis of site effects, we use the subset of data used for event term computations (described in Section 3.3), for which distance attenuation trends are relatively well-matched by the ZEA GMPE. We use intra-event reference site residuals, which are total reference site residuals corrected to zero mean through subtraction of the event term (details in Stewart et al. 2013).

Figure 6 shows the trends of ZEA 2006 reference site residuals for the crustal event against V_{s30} for the intensity measures of PGA and PSA at 0.1, 1.0, and 3.0 sec. A log-linear regression is also shown.

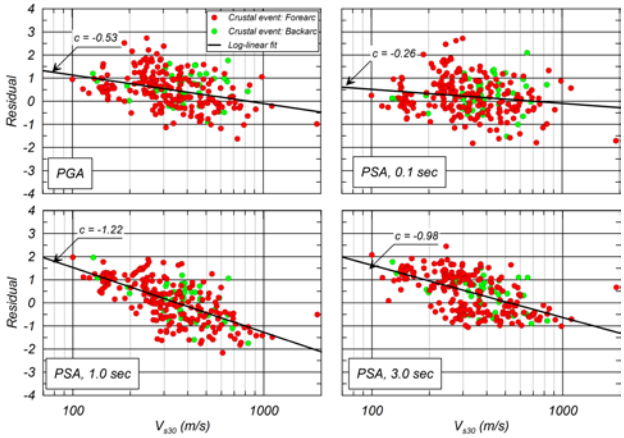


Fig. 6. Reference rock residuals of crustal event using ZEA 2006 GMPE for rock site conditions, showing scaling of site factors with V_{s30}.

Figure 7 shows the slopes of the fit lines (denoted as c) for both events against trends presented previously for the Tohoku mainshock and a representative model for active crustal regions (ACRs; Choi and Stewart, 2005). The slopes from these events differ from those for the mainshock at short periods, having stronger V_{s30} scaling. These differences may be influenced by nonlinearity.

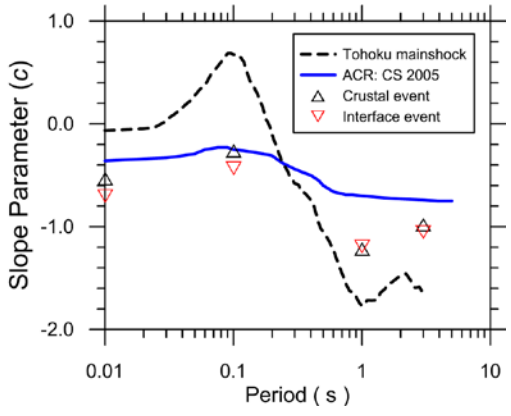


Fig. 7. V_{s30}-scaling of rock residuals (c parameter) from mainshock, subsequent events, and ACR model

4. CONCLUSIONS

In a separate paper investigating the attributes of the Tohoku-oki mainshock data (Stewart et al., 2013), we found important attributes of the ground motions that have substantial practical importance for seismic hazard analysis. Among those attributes were: (*i*) faster anelastic attenuation in the backarc region as compared to the forearc region; (*ii*) positive event terms at short periods that decrease as period increases; and (*iii*) scaling of site amplification with V_{s30} that is substantially reduced from that in active crustal regions at short periods but enhanced at long periods (weaker and stronger V_{s30}-scaling, respectively). We note here that the analysis of site effects from the Tohoku mainshock did not consider nonlinearities.

In this paper, we examine the repeatability of these effects using an admittedly small data set of two events subsequent to the mainshock – one a crustal event in the backarc region and one occurring at the plate interface on the mainshock fault plane. Both events are well recorded and the data was uniformly processed using standard PEER procedures in the same manner as the mainshock data.

We find the variable anelastic attenuation rates to be repeatable, even though one of the considered events occurred on the backarc side of the volcanic front. This is perhaps our most significant finding in this paper. The interface event terms follow a similar form to those from the mainshock, whereas the crustal event shows a different pattern at long periods, but we cannot draw statistically significant inferences from so few earthquakes. The V_{s30}-scaling from these events was much stronger at short periods than had been observed in the mainshock, but relatively consistent at long periods. The differences at short period may be a result of nonlinearity, but further study will be required to understand these differences.

Acknowledgements:

Partial supports for this work to PEER is provided by the USGS/NEHRP and FM Global, and which are gratefully acknowledged.

References:

Abrahamson, NA and RR Youngs (1992). A stable algorithm for regression analyses using the random effects model, *Bull. Seismol. Soc. Am.*, 82, 505–510.

Boore, DM (2010). Orientation-independent, nongeometric-mean measures of seismic intensity from two horizontal components of motion, *Bull. Seismol. Soc. Am.*, 100, 1830 – 1835.

Chiou, B, R Darragh, N Gregor, and WJ Silva (2008), NGA project strong-motion database. *Earthquake Spectra*, 24(1), 23–44.

Choi, Y. and Stewart, J.P. (2005). Nonlinear site amplification as function of 30 m shear wave velocity, *Earthquake Spectra*, 21 (1), 1-30.

Darragh, R, WJ Silva, and N Gregor (2004). Strong motion record processing for the PEER center, Proc. Workshop on Strong Motion Record Processing, Richmond, CA, May 26-27, 2004 (http://www.cosmos-eq.org/recordProcessingPapers.html).

Ghofrani, H and GM Atkinson (2011). Forearc versus backarc attenuation of earthquake ground motion, *Bull. Seismol. Soc. Am.*, 101, 3032–3045.

Kurahashi, S, and K Irikura (2011). Source model for generating strong ground motions during the 2011 off the Pacific coast of Tohoku Earthquake, *Earth Planets Space*, 63, 571-576.

Meng, LS, A Inbal, and JP Ampuero (2011). A window into the complexity of the dynamic rupture of the 2011 Mw 9 Tohoku-Oki earthquake, *Geophys. Res. Lett.*, 38, L00G07, doi:10.1029/2011GL048118.

Nagumo, H. (2012), Rupture process of northern Nagano Prefecture earthquake on March 12th, 2011 (Mj6.7), Annual Meeting of Japan Association for Earthquake Engineering, Japan Association for Earthquake Engineering.

Skarlatoudis, A and CB Papazachos (2012). Preliminary study of the strong ground motions of the Tohoku, Japan, earthquake of 11 March 2011: Assessing the influence of anelastic attenuation and rupture directivity, *Seismol. Research Lett.*, 83, 119-129.

Stewart, JP, S Midorikawa, RW Graves, K Khodaverdi, T Kishida, H Miura, Y Bozorgnia, and KW Campbell (2013). Implications of Mw 9.0 Tohoku-oki Japan earthquake for ground motion scaling with source, path, and site parameters, *Earthquake Spectra*. Accepted.

Yokota, Y, K Koketsu, Y Fujii, K Satake, S Sakai, M Shinohara, and T Kanazawa (2011). Joint inversion of strong motion, teleseismic, geodetic, and tsunami datasets for the rupture process of the 2011 Tohoku earthquake, *Geophys. Res. Lett.* 38, L00G21, doi:10.1029/2011GL050098.

Zhao, JX, J Zhang, A Asano, Y Ohno, T Oouchi, T Takahashi, H Ogawa, K Irikura, HK Thio, PG Somerville, Y Fukushima, and Y Fukushima (2006). Attenuation relations of strong ground motion in Japan using site classification based on predominant period, *Bull. Seismol. Soc. Am.*, 96, 898–913.

10CUEE CONFERENCE PROCEEDINGS
10th International Conference on Urban Earthquake Engineering
March 1-2, 2013, Tokyo Institute of Technology, Tokyo, Japan

SITE RESPONSE DURING STRONG SHAKING – ESTIMATED FROM THE 2011 TOHOKU EARTHQUAKE-

Kenichi Tsuda

1) Researcher, Institute of Technology, Shimizu Corporation, Japan
kenichi.tsuda@shimz.co.jp

Abstract: The 2011 Tohoku earthquake, largest earthquake recorded in Japan (Mw 9.0) produced large ground motions and brought severe damage on broad area. Kanto area, more than 300 km away from the hypocenter, experienced severe damage from large ground motions amplified by the deep sedimentary basin. Also these amplified ground motions produced nonlinear soil behavior causing the liquefaction.

In order to get better understandings for the nonlinear soil behavior, the precise comparison of site response between during strong shaking like the main event of this earthquake and during moderate or weak ground shaking. I have used the data from seismograph arrays densely deployed on the Kanto area. The arrays include K-NET, KiK-net and other strong motions arrays etc. I compared the site response by using moderate sized event (Tsuda *et al.*, 2010) and the site response computed from this earthquake incorporated the finite faults effects based on the source model obtained by Asano and Iwata (2012) with four strong motion generation areas (SMGA). The comparison of site response could lead to the better understandings of how site response has been changed dependent of level of ground motions.

1. INTRODUCTION

The observed ground motions are constituted by three different factors: seismic source (source effects), wave propagation through heterogeneous earth's interior (path effects), and local geological conditions (site effects). This relationship can be represented by the following equation;

$$O(t) = S(t) * P(t) * G(t) \qquad (1)$$

where * is the convolution operator, O(t) is the observed records, S(t) means the source effects of earthquake ruptures, P(t) means the path effects of wave propagation through the heterogeneous earth's interior, and G(t) means the site response close to the stations. This basic equation has been used to estimate site response based on the observed records.

The off-coast of Tohoku earthquake (Tohoku-Oki earthquake) with moment magnitude M_w 9 is one of the largest earthquakes in Japan that has been well recorded in the near vicinity of the source area (Aoi *et al*, 2012). The source area extends to almost 500 km along the latitude and 200km along dip (*e.g.*, Simons, *et al.*, 2011; Suzuki *et al.*, 2011). Figure 1 shows the observed waveforms along the coast line (Asano and Iwata, 2012). As seen, four distinct wave packets are recognized. The observed records of this event are also characterized by the longer duration of strong shaking. One site recorded a JMA intensity value of 7 (maximum value of this scale) and 28 sites recorded values of 6+. The observed PGA values from K-NET and KiK-net showed large accelerations for many sites (19 sites showed PGA larger than 1 g) and strong motion duration longer than 80 s (time interval between 5% and 95% of the Arias intensity).

Some records observed on the deep sediment sites showed different types of nonlinear soil behavior, going from traditional high frequency deamplification to liquefaction (Bonilla *et al.*, 2011). Some of these sites are located far fromw the faults area, such as the Chiba and Tokyo prefectures. For example, Fujikawa (2011) reported that boil sand or liquefaction could be seen for some sites around the eastern area of Tokyo located on soft soil.

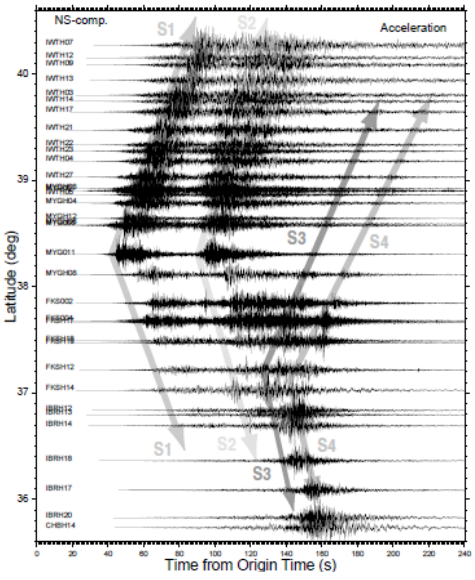


Figure 1 Record section of the NS component of acceleration according to the latitude. Each waveform is normalized by its maximum amplitude. Arrows indicate the distinctive wave packets seen on the records (Asano and Iwata, 2012)

Also the report compiled by the Shimizu corporation (2011) showed that the location with being seen the liquefaction during or after the mainshock of Tohoku-earthquake are very broad. Since then, many researchers have analyzed the observed data to understand the phenomena and tried to reproduce the records based on various kinds of assumption. However, observed records themselves already include the source and path effects. This means the separation of source and path effects are necessary to estimate site response during strong shaking.

In this study, we have tried to estimate the site response during strong shaking after separating source and path effects. The resultant site responses have been compared to those obtained by using the weak motion data i.e., linear case. This comparison indicates that how the site response changed during the strong shaking.

2. DATA

Among the sites with observed records showing nonlinear soil behavior, the K-NET station CHB024 is picked in this study as a target site. This site is located in the Chiba prefecture and faces Tokyo Bay. Even though this site located on the deep sedimentary basin is more than 300 km away from the hypocenter of this earthquake, the observed records showed the striking features of nonlinear soil behavior have been seen mentioned as Bonilla *et al.* (2011). The observed waveforms of the two horizontal components are shown in Figure 2 (a).

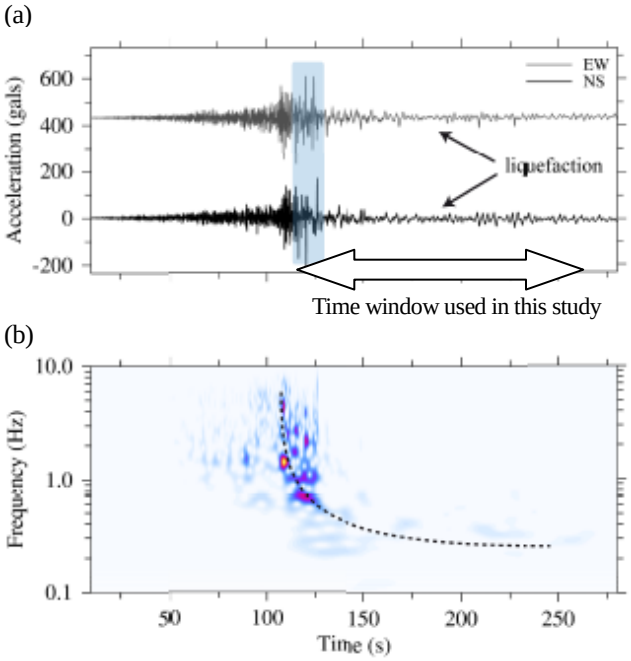


Figure 2 Observed records at the station of CHB024 (a) acceleration time histories of horizontal components (b) energy spectral density as a function of time (Bonilla *et al.*, 2011)

The shaded area shows strong cyclic mobility and looks start liquefaction after that phase. Bonilla *et al.* (2011) investigated the Stockwell transform to estimate how the frequency contents have been changed during strong shaking. Figure 2 (b) shows the results and apparent frequency shift to the lower side could be seen after the phase corresponding to the shaded area in Figure 2(a). In this study, the time window of 150sec showing Figure 2(a) that corresponds to the S-wave portion and includes the onset of nonlinear soil behavior is used to estimate site response for strong shaking. Two horizontal components are used and vectorial summed for each frequency after Fourier amplitude spectra are calculated. As for the estimation of site response for weak motion, the data obtained by the moderate sized events are used with the time window of 10 sec for S waves (Tsuda *et al*., 2010 and Hayakawa *et al.*, 2010).

3. METHOD OF ESTIMATING SITE RESPONSE

In order to estimate site response, we have to separate the source and path effects from observed records. However, separation of those effects is sometimes difficult. Usually the way to separation is based on the spectral inversion analysis (Iwata and Irikura, 1988; Yamanaka *et al.*, 1998), however, the site response is the relative values to the reference site and the selection of the reference is always the issues for this analysis. For this problem, Tsuda *et al.* (2006) proposed the method of spectral inversion method independent of the selection of reference site. Explaining the detail concept for this spectral inversion analysis applied in this study is beyond this study, we explain briefly how the site response is estimated for the weak motion (linear case) and strong motion (nonlinear case).

3.1 Site Response for the Weak Motion

In a frequency domain, the observed records representing the equation (1) can be rewritten as a multiplication:

$$|A(f)| = |S(f)|\,|Site(f)|\,R^{-1}\,e^{-\pi f R / Q(f)\beta} \qquad (2)$$

where f is frequency, $|A(f)|$ is the acceleration amplitude spectrum of the recorded ground motion, $|S(f)|$ is the source spectrum, $Q(f)$ is the quality factor, which is assumed to be frequency dependent, $|Site(f)|$ is the site response amplitude, R is the distance from source to site, and β is the average shear wave velocity of the medium (3.7 km/s, Yamanaka *et al.*, 1998). Following equation 3 uses Boatwright's (1978) representation of a source spectrum (Brune, 1970), in which the amplitude of the source spectrum has a nonlinear dependence on the corner frequency:

$$|S(f)| = C\,M_o(2\pi f)^2 \cdot f_c^2 / (f^4 + f_c^4)^{0.5} \qquad (3)$$

where

$$C = (G_0 \cdot F^{rad}) / (4\pi\rho V_S^3) \qquad (4)$$

C depends on the radiation parameter of the source: F^{rad} is

the effects of this radiation pattern coefficients on site response estimation will be discussed, the material parameters for source area (3200 [kg/m³] for density: ρ and 4.46 km/s for shear wave velocity: V_S, Fukuyama *et al.*, 1998) and the free surface effect G_o is included.

Tsuda *et al.* (2010) applied the idea of Tsuda *et al.* (2006) to estimate site response by using the data for moderate sized events surrounding the Kanto area. Hayakawa *et al.* (2010) updated those site responses especially for the longer period. They incorporated the effects of radiation pattern (focal mechanism) into the estimation of site response especially for the lower frequency range (< 0.5 Hz) based on the same data set by Tsuda *et al.* (2010). They assumed the theoretical radiation calculated by the focal mechanism determined by the National Research Institute for Earth Science and Disaster Prevention (Fukuyama *et al.*, 1998).

The site responses for the weak motion are combined the results of Hayawaka *et al.* (2010) for lower than 0.5 Hz and Tsuda *et al.* (2010) for higher than 0.5 Hz. The site response for weak motion at CHB024 site is shown in Figure 3.

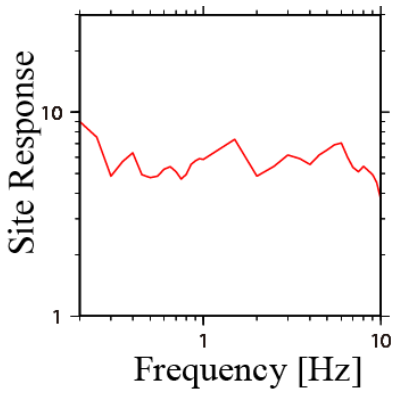


Figure 3 Estimated site responses for weak motion at CHB024 site.

3.2 Site Response for the Strong Motion

The idea of spectral inversion analysis is based on the point-source approximation *i.e.*, the fault finiteness is not incorporated. Tsuda and Steidl (2006) have tried to estimate site response during strong shaking for two large events, 2003 (Mw 7.0) and 2005 (Mw 7.2) Miyagi-Oki earthquakes. They incorporated the fault finiteness by incorporating the effects of radiation pattern for low frequency range. This study follows the similar procedures based on the source model for the Tohoku-Oki earthquake.

The number of source model for this earthquake has been already proposed based on the various kinds of data. Asano and Iwata also proposed the source model composed of four strong motion generation areas (SMGA) using the empirical Green's function method. The location of SMGA and the hypocenters of empirical Green's function and hypocenter of the main shock are shown in Figure 4.They used two moderate sized events as the empirical Green's functions with frequency range of 0.1 – 10.0 Hz. They estimated the source parameters, such as the spatial dimensions, stress drop, rise times, rupture starting points inside SMGA and velocity of rupture propagation for each SMGA.

Table 1 Source Parameters for each SMGA (Asano and Iwata, 2012)

	SMGA1	SMGA2	SMGA3	SMGA4
Strike [deg]	195	195	198	203
Dip [deg]	13	13	17	20
Area [km^2]	1296.0	1296.0	1225.0	1225.0
Seismic Moment [Nm]	4.57E+20	5.33E+20	3.07E+20	1.16E+20
Stress Drop [Mpa]	23.9	27.8	17.5	6.6
Average Slip [m]	5.2	6.1	3.7	1.4
Corner Frequency [Hz]	0.0815	0.0814	0.0838	0.0838

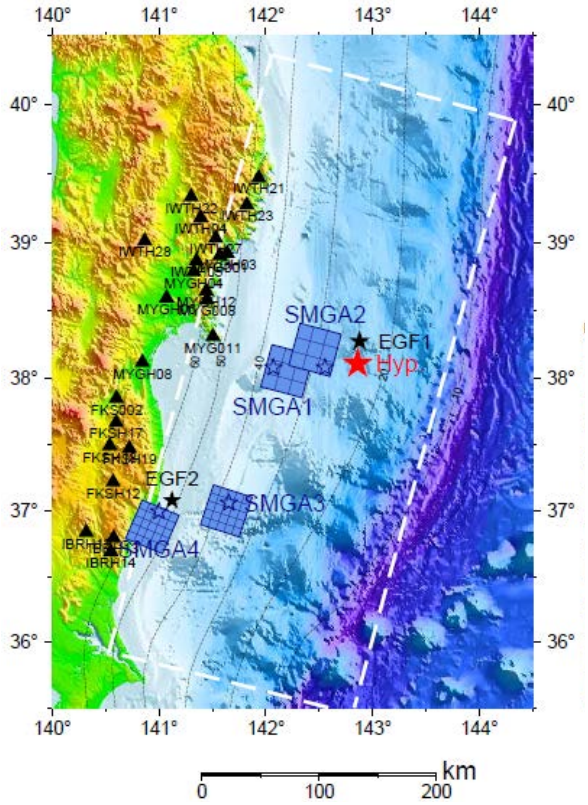


Figure 4 Source model by Asano and Iwata (2012) composed of four SMGAs. The blue open stars denote the rupture starting points of each SMGA. The broken rectangle indicates the fault plane of the 2011 Tohoku-Oki earthquake by Suzuki *et al.* (2011).

The source parameters determined by Asano and Iwata are listed on Table 1. The corner frequency is calculated based on the following relations (Brune, 1970)

$$f_c = 0.37\ Vs\ (16\ \Delta\sigma / 7\ M_o)^{(1/3)} \quad (5)$$

where $\Delta\sigma$ is the stress drop and M_o is the seismic moment for each SMGA, respectively. Each value is used on the Table 1. Vs is the shear wave velocity around the source area (4.46 km/s).

The source spectrum (Equation 3) is calculated for each SMGA. They summed to make the source spectrum for the whole mainshock. The observed waveform (Figure 2) of this site has only one wave packet unlike the sites close to the fault plane (Figure 1). This feature leads to the summation of source spectrum for each spectrum without any correction based on any features, such as the distance to the site, size of each SMGA, and seismic moment ratio etc. As for the radiation pattern coefficient, the theoretical values (Aki and Richards, 2002) are considered in the 0.1-0.5 Hz and the isotropic radiation (radiation pattern coefficient is 0.63, Boore and Boatwright, 1984) are used higher than 0.5 Hz. The focal mechanism for each SMGA to calculate the radiation pattern coefficient is listed on Table 1. The rake angle is set 90° because of its type of earthquake and assumed to be constant for whole area of SMGA .

The path effects represented by the quality factor Q(f) used the results by Tsuda *et al.* (2010) as a function of frequency:

$$Q(f) = 107f^{0.52} \quad (6)$$

The hypocentral distances in equation (2) assumed the distance between rupture starting points for each asperity (blue open stars in each SMGA of figure 5) and the site. After correction of source, path effects and geometrical spreading to the observed amplitude spectrum |A(f)|, the site responses are estimated as follows:

$$|Site(f)| = R|A(f)| / (|S(f)|\ e^{-\pi f R / Q(f)\beta}) \quad (7)$$

The source spectrum summed for four SMGA corresponds to the area of radiating for strong motion not from the entire area. On the contrary, the seismic waves observed at site include the waves look radiated from the entire area. This leads to the underestimation of source spectrum. Thus, the source spectrum in Equation 7 is corrected by the ratio of seismic moment based on the values determined by NIED (Fukuyama *et al.*, 1998) in this study.

4. Results

In Figure 5(a), the site response for the strong motion is shown. The site response for the weak motion is also plotted to compare it. The ratio of site response between strong motion/weak motion is shown in Figure 5(b). As seen on the figure, the site response for the strong motion showing apparent deamplification compare to the weak motion especially above 0.5 Hz. As for the lower frequency range, the data used to estimate site response for weak motion might be contaminated by the noise. On the contrary, the predominant frequencies around 1.5 Hz in weak motion looks shifting to lower than 1 Hz of site response for strong motion.

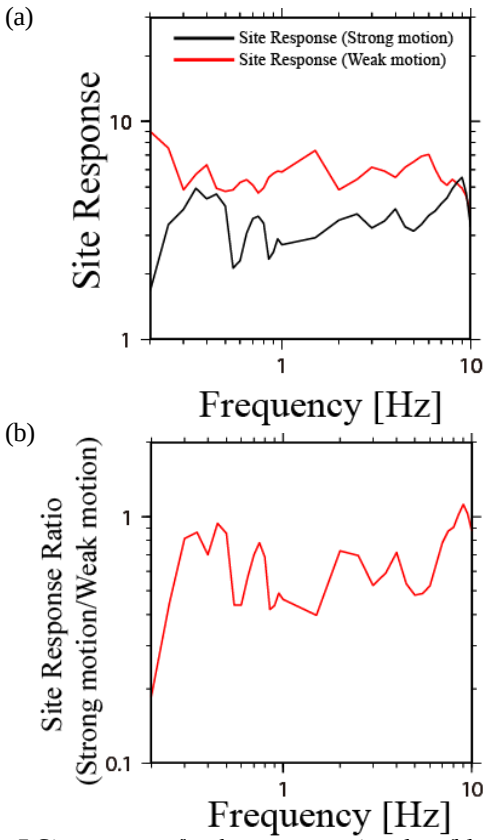


Figure 5 Site response for the strong motion data (black line) and weak motion data (red line) (a) and site response ratio between weak motion and strong motion (b).

5. Summary

The site responses for strong motions of the mainshock of the 2011 Tohoku earthquake have been compared to those for moderate sized events on the CHB024 site. The observed record for this site shows distinct nonlinear soil behavior during the mainshock. The source and path effects are corrected based on the previous studies including the focal mechanism and quality factors. The site responses for the weak motion include the effects of radiation pattern especially in lower frequency range.

The comparison of site response shows the clear deamplification and shift of lower frequency range of predominant frequencies of site response. The estimation of site response for strong motion are based on some assumptions such as how the rupture directivity are incorporated how source spectrum for each SMGA are summed, quality factor or total moment values for the main

shock etc. These assumptions should be validated for the better estimation of site response for strong motion and will be discussed in the future. The investigation of the conditions for how site responses have been changed as a function of soil conditions, ground motion parameters such as PGA, PGV or Arias Intensity etc is the next step. And the compilations of these conditions are very useful for the ground motion prediction for future large events on the sites of soft soil such as CHB024 site.

Acknowledgements:

The authors acknowledge support from the Japan Ministry of Education, Culture, Sport, Science, and Technology (MEXT) for establishing the Center for Urban Earthquake Engineering (CUEE) in Tokyo Institute of Technology. This support makes possible the forthcoming international conference, as well as international joint research projects and exchange programs with overseas universities. This research is supported by JST on J-RAPID "Quantitative assessment of nonlinear soil response during the great Tohoku earthquake" (P.I. Prof. Kawase, Kyoto University).

References:

Aki, K. and P. Richards. (2002). Quantitative Seismology, 2nd edition, University Science Books.

Aoi, S. T. Kunugi, W. Suzuki, N. Morikawa, H. Nakamura, S. Senna and H. Fujiwara (2012) Strong motion characteristics of the 2011 Tohoku-Oki Earthquake, *Zisin* **64**, 169-182 (in Japanese with English abstract).

Asano K., and I. Iwata (2012) Source model for strong ground motion generation in 0.1-10 Hz during the 2011 Tohoku earthquake, Earth Planets Space (Accepted for publication).

Boatwright, J. (1978). Detailed spectral analysis of two small New York State earthquakes, *Bull. Seism. Soc. Am.* **68,** 1117-1131.

Boore, D. M., and J. Boatwright. (1984). Average body-wave radiation coefficient, *Bull .Seism. Soc. Am.* **74**, 1615-1621.

Bonilla, L. F., K. Tsuda, N. Pulido, J. Regnier, and A. Laurendneau (2011) Nonlinear site response evidence of K-NET and KiK-net records from the 2011 off the Pacific coast of Tohoku Earthquake, Earth, Planets Space, **63**, 785-789.

Brune, J. N. (1970). Tectonic stress and the spectra of seismic shear waves from earthquakes, *J. Geophys. Res*, **75,** 4997-5009.

Fujikawa, S. Personal communication, 2011.

Fukuyama, E., M. Ishida, D. S. Dreger, and H. Kawai (1998). Automated seismic moment tensor determination by using on-line broadband seismic waveforms, *Zisin.* **51**, 149-156. (Japanese with English abstract)

Hayakawa, T, K. Tsuda, and K. Koketsu (2010) THE SITE RESPONSE IN THE PERIOD RANGE OF 2 TO 4 SEC IN THE KANTO BASIN, presented at 2010 Fall meeting, AGU, San Francisco, Calif., 132-17 Dec.

Iwata, T., and K. Irikura. (1988). Source parameters of the 1983 Japan Sea earthquake sequence, *J. Phys. Earth*. **36**, 155-184.

Shimizu Corporation (2011) Report on the Tohoku Area Pacific Off Shore Earthquake http://www.shimz.co.jp/english/theme/earthquake/outline.html

Simons, M., S. E. Minson, A. Sladen, F. Ortega, J. Jiang, S. E. Owen, L. Meng, J-P. Ampuero, S. Wei, R. Chu, D. V. Helmberger, H. Kanamori, E. Hetland, A. W. Moore, and F.H. Webb. The 2011 Magnitude 9.0 Tohoku-Oki Earthquake: Mosaicking the Megathrust from Seconds to Centuries,*Science*, 10.1126 science.1206731, 2011

Suzuki, W., S. Aoi, H. Sekiguchi, and T. Kunugi, (2011) Rupture process of the 2011 Tohoku-Oki mega-thrust earthquake (M9.0) inverted from strong-motion data, Geophys. Res. Lett., 38, L00G16, doi:10.1029/2011GL049136, 2011.

Tsuda, K. K. Koketsu, Y. Hisada., and T. Hayakawa (2010) Inversion Analysis of Site Responses in the Kanto Basin Using Data from a Dense Strong Motion Seismograph Array, *Bull. Seism. Soc. Am.* **100,** 1276-1287

Tsuda, K., Archuleta, R., and Koketsu, K. (2006). Quantifying spatial distribution of site response by use of the Yokohama High-Density Strong Motion Network, *Bull. Seism. Soc. Am.* **96,** 926-942.

Tsuda, K. and J. Steidl (2006) Nonlinear site response from the 2003 and 2005 Miyagi-Oki earthquakes, Earth Planets Space, **58**, 1593-1597.

Yamanaka, H., A. Nakamaru., K. Kurita., and K. Seo. (1998). Evaluation of site effects by an inversion of S-wave spectra with a constraint condition considering effects of shallow weathered layers, *Zisin* **51,**193-202 (in Japanese with English abstract).

10CUEE CONFERENCE PROCEEDINGS
10th International Conference on Urban Earthquake Engineering
March 1-2, 2013, Tokyo Institute of Technology, Tokyo, Japan

PRELIMINARY ANALYSIS OF ATTENUATION RELATIONSHIP FOR RESPONSE SPECTRA ON BEDROCK BASED ON STRONG MOTION RECORDS INCLUDING THE 2011 M_W9.0 TOHOKU EARTHQUAKE

Hongjun Si[1], Saburoh Midorikawa[2], Hideaki Tsutsumi[3], Changjiang Wu[4], Toshiyuki Masatsuki[5], and Akemi Noda[5]

1) Senior Researcher, Seismic Engineering Division, Kozo Keikaku Engineering Inc., Japan
2) Professor, Center for Urban Earthquake Engineering, Tokyo Institute of Technology, Japan
3) Director, Japan Nuclear Energy Safety Organization, Tokyo, Japan
4) Senior Researcher, Japan Nuclear Energy Safety Organization, Tokyo, Japan
5) Engineer, Seismic Engineering Division, Kozo Keikaku Engineering Inc., Japan
shj@kke.co.jp, smidorik@enveng.titech.ac.jp, tsutsumi-hideaki@jnes.go.jp, wu@jnes.go.jp, toshi-masatsuki@kke.co.jp, akemi-noda@kke.co.jp

Abstract: During the 2011 off the Pacific coast of Tohoku Earthquake (refer as the 2011 Tohoku earthquake), an abundant of strong ground motion records has been derived. This provides us opportunity to develop a GMPE to be applicable to a M9 class earthquake. In this study, we updated the database of strong ground motion on hard rock to include the records from the Tohoku earthquake and the main aftershocks and induced earthquakes. The new data are mainly derived from the observation stations of KiK-net and are estimated on hard rock with a shear-wave speed over 2 km/sec. Based on the new database, we updated the GMPE for response spectra on hard rock. The feature and the validity of the GMPE are discussed.

1. INTRODUCTION

During the 2011 M_w9.0 off the Pacific coast of Tohoku Earthquake (refer as the Tohoku earthquake hereafter), an abundant of strong ground motion records has been derived. This is the first time that the strong motion recordings from a M9 class earthquake have been derived at over thousands stations. Based on the analysis of the data, it is indicated that the attenuation characteristics of the peak ground motion for a M9 class earthquake may be different from those for a M8 or smaller earthquakes (e.g., Si et al., 2011a, b). This implies that for the prediction of strong ground motion for a M9 class earthquake, the data from the 2011 Tohoku earthquake should be included to the database used in the development of the ground motion prediction equation (GMPE).

On the other hand, so far, a database of strong ground motion on hard rock has been constructed, and preliminarily a GMPE has been developed based on the database (Si et al., 2011c). Since the largest earthquake included in the current database is M_w8.3, it is necessary to include the data from the Tohoku earthquake.

In this study, we updated the database to include the records from the Tohoku earthquake and its main aftershocks and induced earthquakes. Based on the database, we updated the GMPE for response spectra on hard rock. In this paper, the preliminary results of the updated database and GMPE will be presented.

2. DATA

2.1 Outline of the database

The strong ground motion records from 7 earthquakes including the 2011 Tohoku earthquake are collected and added to the database established by Si et al. (2011c). Among these earthquakes, there are 3 crustal earthquakes, 3 inter-plate earthquakes, and 1 intra-plate earthquake. Totally, there are 14 crustal earthquakes, 11 inter-plate earthquakes, and 9 intra-plate earthquakes in the database. Table 1 show the earthquakes used in this study. Figure 1 shows the histogram of the earthquake type and the plot of moment magnitude versus the focal depth.

In the database, the distance definitions are fault distance (FD) and the equivalent hypocentral distance (EHD), both measured from the fault plane for each earthquake. The moment magnitudes are adopted from the global CMT resolution. The range of M_w is from 5.5 to 9.1.

Figure 2 shows the distribution of M_w and FD of the records in the database. From the figure, it can be confirmed that the near-field data are also included in the database.

All the data added in this study are recorded at stations of KiK-net operated by National Research Institute for Earth Science and Disaster Prevention (NIED). Response spectrum is defined as GMRotI50 proposed by Boore et al. (2006) for horizontal components, and response spectra for vertical components. The updated database for response spectra on hard rock is consists of the records derived at

Table 1 Earthquakes used in this study

EQ. No.	EQ. NAME	Initial Date	Time	Mw	Depth	Fault Type	Number of Data
1	Nihon-kai Chubu	1983.05.26	11:59	7.8	6.0	Inter	3
2	Eastern Off Chiba	1987.12.17	11:08	6.7	30.0	Intra	10
3	Off Kushiro	1993.01.15	20:06	7.6	105.0	Intra	8
4	Off Noto-hanto	1993.02.07	22:27	6.3	15.0	Crustal	3
5	Hokkaido-Nansei-Oki	1993.07.12	22:17	7.7	10.0	Inter	4
6	Hokkaido-Toho-Oki	1994.10.04	22:22	8.3	35.0	Intra	5
7	Sanriku-Haruka-Oki	1994.12.28	21:19	7.7	35.0	Inter	11
8	Hyogo-ken Nanbu	1995.01.17	5:46	6.9	10.0	Crustal	34
9	North-Western Kagoshima	1997.03.26	17:31	6.1	6.0	Crustal	3
10	North-Western Kagoshima	1997.05.13	14:38	6.0	7.0	Crustal	3
11	Izu Hanto Toho-Oki	1998.05.03	11:09	5.6	3.0	Crustal	8
12	Western Tottori	2000.10.06	13:30	6.8	11.0	Crustal	50
13	Geiyo	2001.03.24	15:27	6.7	51.0	Intra	40
14	Miyagi-ken Oki	2002.11.03	12:37	6.4	46.0	Inter	21
15	Hyuganada	2002.11.04	13:36	5.6	35.0	Intra	9
16	Miyagi-ken Oki	2003.05.26	18:24	7.0	71.0	Intra	33
17	Northern Miyagi	2003.07.26	7:13	6.1	12.0	Crustal	9
18	Tokachi Oki	2003.09.26	4:50	8.3	35.0	Inter	16
19	Chuetsu	2004.10.23	17:56	6.6	10.0	Crustal	30
20	Kushiro-oki	2004.11.29	3:32	7.0	48.0	Inter	5
21	Western Fukuoka	2005:03:20	10:53	6.6	9.0	Crustal	25
22	Miyagi-ken Oki	2005.08.16	11:46	7.1	42.0	Inter	42
23	Chuetsu-oki	2007.07.16	10:13	6.6	10.0	Crustal	22
24	Ibaraki-oki	2008.05.08	1:45	6.8	51.0	Inter	11
25	Iwate-Miyagi Nairiku	2008.06.14	8:43	6.9	10.0	Crustal	30
26	Northern Iwate	2008.07.24	0:26	6.8	108.0	Intra	24
27	Surugawa	2009.08.11	5:07	6.2	23.0	intra	30
28	Tohoku	2011.03.11	14:46	9.1	25.0	Inter	34
29	Off-Iwate	2011.03.11	15:08	7.4	32.0	Inter	10
30	Off-Ibaraki	2011.03.11	15:15	7.9	38.0	Inter	20
31	Norther Nagano	2011.03.12	3:59	6.3	7.0	Crustal	15
32	Eastern Shizuoka	2011.03.15	22:31	6.0	10.0	Crustal	13
33	Off Miyagi	2011.04.07	23:32	7.1	59.0	Intra	35
34	Hama-dori	2011.04.11	17:16	6.7	10.0	Crustal	20

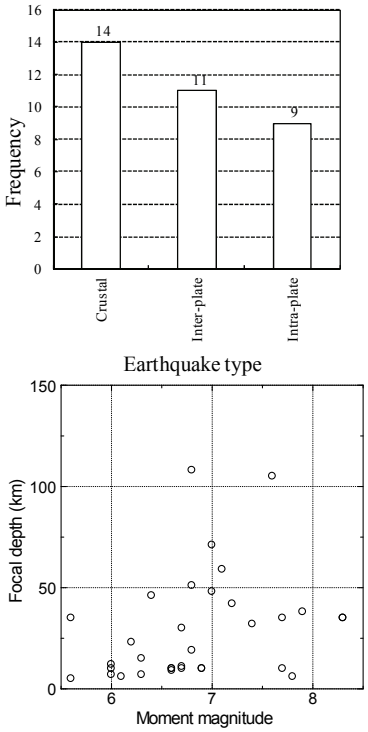


Figure 1 histogram of the earthquake type (upper) and the plot of moment magnitude vs. the focal depth (lower)

stations in KiK-net, and F-NET by NIED, RK-NET by Central Research Institute of Electric Power Industry (CRIEPI), and the dam observation stations by Japan Commission on Large Dams (JCOLD), National Institute for Land and Infrastructure Management (NILIM) and Miyagi prefecture.

2.2 Estimation of ground motion on hard rock

As the same as in Si et al. (2011c), the new data added to the database were selected to be recorded at stations where the underground seismograph is located on the hard rock with a Vs≧2km/s. The strong motion observation system of KiK-net is a vertical array in which the seismographs are installed both on the ground surface and on the bottom of the borehole. By taking the advantage of the vertical array, firstly the parameters of the soil profile in the borehole are identified by fitting the transfer function defined as the ratio of the Fourier spectra of the seismic wave recorded on ground surface and the bottom of the borehole, then the strong motions on bedrock are directly estimated based on the records on ground surface and the theoretic amplification factor calculated based on the identified soil profile. All the data from KiK-net are derived by using this method.

3. REGRESSION ANALYSIS

3.1 Regression analysis for distance dependency

We performed a two-step regression analysis. In the first step, the regression model shown in Eq.(1) fits to the data to remove the distance dependency by determining the regression coefficients, including the event term b (T).

$$\log SA(T) = b(T) + g(X) - kX + \varepsilon(T)$$
$$g(X) = \begin{cases} -\log(X + C); D \le 30km \\ 0.6\log(1.7D + C) - 1.6\log(X + C); D > 30km \ \& \ X \ge 1.7D \end{cases}$$
$$C = 0.0055 \cdot 10^{0.5M_w}, T < 0.3s$$
$$= 0.0028 \cdot 10^{0.5M_w}, T \ge 0.6s$$
$$k = 0.003, T < 0.3s$$
$$= 0.002, T \ge 0.6s \qquad (1)$$

Where, SA(T) shows GMTRotI50, an average response spectra proposed by Boore et al. (2006) for horizontal components, and response spectra for vertical components. X show fault distance (FD) or equivalent hypocentral distance (EHD). D shows the focal depth.

Function of g(X) shows modeling for different attenuation rates for shallow and deep earthquake originally proposed by Midorikawa and Ohtake (2002).

C shows the saturation of strong motion in short-distance when using fault distance, and k shows the coefficient for anelastic attenuation. Here, since no sufficient data to determine the coefficient of C and k based on regression method, we adopt the values of PGA and PGV in Si and Midorikawa (1999) for short- and long-period, respectively (See Eq. (1)). At the transition periods, interpolation between short- and long-period is used.

When fitting the data, following weighting schemes are used: 8 for distance ≤ 25km; 4 for ≤50km; 2 for ≤ 100km. Figure 3 shows examples of the fit of strong motion data and the regression model. The same operation is applied to all the dataset.

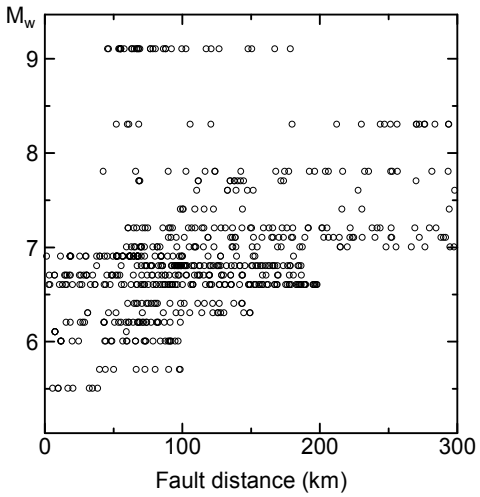


Figure 2 Distribution of Mw vs. fault distance

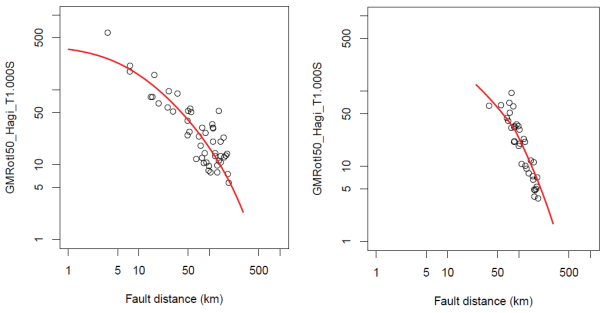


Figure 3 Example of fitting of the regression model and the observation data at period of 1.0 s. (No.12 (left) and 13 (right) earthquakes in Table 1)

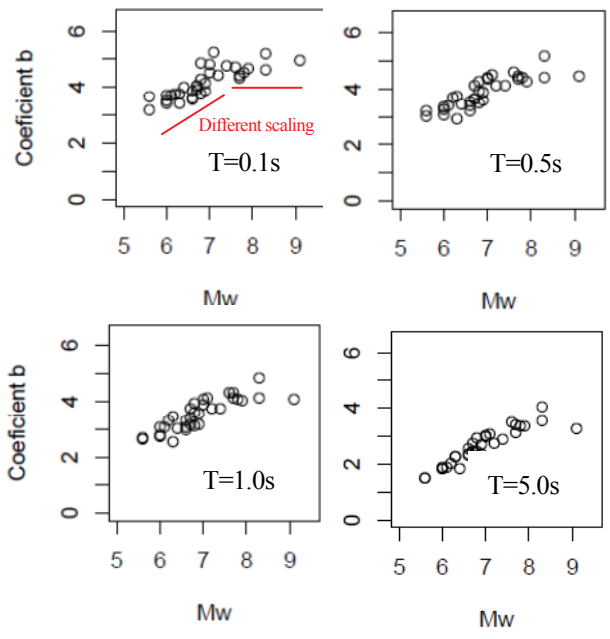


Figure 4 Plots of coefficient b (T) versus M_w

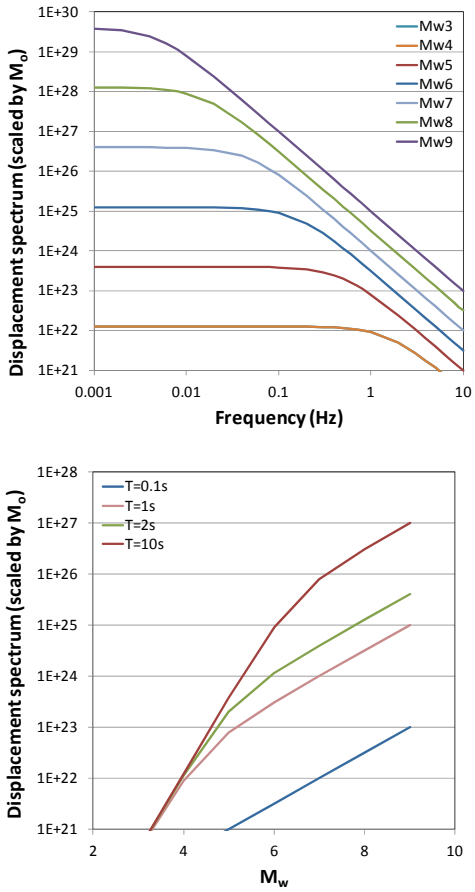


Figure 5 illustration of scaling law for source spectra. (upper: far-field displacement spectra; lower: amplitude of the displacement spectra at different periods versus M_w.)

3.2 Regression model for b (T)

The results for b (T) are plotted Versus M_w in Figure 4. From the Figure, it can be confirmed that b (T) are strongly correlated with M_w until M_w 7 or 8. For the earthquakes with larger M_w, the scaling becomes weak. This phenomenon has been interpreted by the saturation of ground motion (especially relatively short-period ground motion) with large M_w (cf., Si et al., 2011a, b). For long-period ground motion, in addition to the saturation for M_w, the difference in scaling of M_w inferred based on the seismic source spectra, as shown in Figure 5, should also be considered (e.g., Fukushima and Midorikawa, 1993). In Figure 5, for the case T=10s and $M_w \geqq 6$, the scaling of M_w can be represented by two straight lines with different slops.

In order to model the feature described above, regression model for b (T) adopted in this study is shown in Eq. (2). In the equation, $a_1(T)$ and $a_2(T)$ are the straight lines showing different scaling with M_w. M_w of the inflection point between the two straight lines is decided based on data and the results by Si et al. (2011a, b).

$$b(T) = \begin{cases} a_1(T)M_w + \sum d_i(T)S_i + h(T)D + \varepsilon_1(T) \\ M \leq 8.3 or M \leq 7.5 if T \geq 2s \\ a_2(T)M_w + \sum d_i(T)S_i + h(T)D + \varepsilon_2(T) \\ M > 8.3 or M > 7.5 if T \geq 2s \end{cases} \quad (2)$$

Where, D shows the focal depth. S_i is a category variable, showing the earthquake type defined as crustal, inter- and intra-plate earthquake, the same as that used in Si and Midorikawa (1999).

In the regression analysis, a weighted multi-variable least square method is used. The weighting schemes are as follows: 8 for earthquakes with No. of records ≥ 30; 4 for ≥ 20; 2 for ≥ 10. For the periods shorter than 5s, all data are used in the analysis. For the periods longer than 5s, only the earthquakes with M_w over 6 are used.

Since the focal depth maybe correlated with earthquake type, in this study, the coefficient for focal depth h (T) are firstly determined based on the data for inter- and intra-plate earthquake separately. Then, if both the results are derived successfully, the average values are used. Finally h (T) is simplified by a straight line in logx-y plane.

4. RESULTS

Figure 6 shows the coefficients derived in this study. From the figure, a_1 (T) increase with period T; a_2 (T) is zero for the case of FD, showing the saturation with M_w. For EHD, a_2 (T) are almost the same non-zero values for only long-period (T≧2s). The coefficients for earthquake type, d_i (T), generally decrease with T for intra-plate earthquakes. This seems to meet the consensus of the feature for an intra-plate earthquake. The coefficient of focal depth, h (T), varies in the range of 0.011 to -0.002, corresponding to the periods from 0.1s-10s. This also show reasonable tendency by comparing with the previous studies.

Figure 6 also shows the comparison of the coefficient of M_w, a_1 (T), derived in this study and those in the other recent studies. From the figure, the results in this study show similar tendency with the others, e.g., Uchiyama and Midorikawa (2006), Kanno et al. (2006). This implied that, the results in this study are reasonable.

Figure 7 shows the prediction by the GMPE derived in this study. Figure 8 shows the ratio of V/H based on the prediction. Figure 9 shows the standard deviation for the GMPE. The prediction for response spectra are calculated under the following condition: a crustal event, at a fault distance of 50km; M_w of the target earthquakes are 6, 7 and 8. From the results, it can be confirmed that, (1) the amplitudes increase with M_w; (2) amplitudes for intra-plate earthquake generally larger than those from crustal and inter-plate earthquake; (3) The ratios of V/H are generally consistent with the past study but show M_w dependency for longer periods; (4) the standard deviations are around 0.3 in ten-based logarithm.

In order to check the validity of the GMPE proposed in this study, the observation data on hard rock which not included in the database used in the development of GMPE are used in the comparison with the prediction. Figure 10 shows the results for the data from the 1999 M_w7.62 Chi-Chi earthquake. The data are adopted from NGA database (NGA flatfile, 2008). Vs30 of the station of ILA063 is about 1.0 km/s. From the figure, it can be confirmed that the observation is well consistent with the prediction.

5. CONCLUSIONS

In this study, we updated the database of response spectra on hard rock including the recording from the 2011 Tohoku earthquake. Based on the database, we derived a new GMPE for response spectra on bedrock. The standard deviation is relatively small. Comparison with the observation data in NGA database shows a good agreement. This implied that our model is reasonable.

Acknowledgements:

The authors acknowledge supported by the Research Found from an incorporated administrative agency, Japan Nuclear Energy Safety Organization. The strong motion data is provided by the KiK-net, K-NET and F-NET by NIED, RK-NET by CRIEPI, Dam records by JCOLD, NILIM, and the Miyagi prefecture. Figures are plotted by Plots and R. Part of the regression analysis is performed using the R language. The authors thank Professor Tatsuo Ohmachi, Dr. Yoshiaki Shiba, Dr. Shojiro Kataoka, Professor Kazuki Koketsu, and Dr. Hiroe Miyake for their fruitful suggestion. The thanks also go to Mr. Akihiro Sawaii, Mr. Toshio Kuriyama, and Dr. Reiko Tajima for their great help.

References:

Boore, D.M., Watson-Lamprey, J., and Abrahamson, N. A. (2006) "GMRotD and GMRotI: Orientation-independent measures of ground motion," *Bulletin of the Seismological Society of America*, **96**, 1502-1511.

NGA flatfile (2008): *http://peer.berkeley.edu/nga/flatfile.html* (last accessed: 16 Jan., 2013).

Kanno, T., Narita, A., Morikawa, N., Fujiwara, H., and Fukushima, Y. (2006) "A New Attenuation Relation for Strong Ground Motion in Japan Based on recorded data," *Bulletin of the Seismological Society of America*, **96**(3), 879-897.

Midorikawa, S., and Ohtake, Y. (2002), "Attenuation relationships of peak ground acceleration and velocity considering attenuation characteristics for shallow and deeper earthquakes," *Proceedings of 11th Japan Earthquake Engineering Symposium*, **1**, 609-614.

Sato, T. Okawa, I., Nishikawa, T., Sato, T., and Seki, M. (2010), "Prediction of waveforms of long-period ground motions for hypothetical earthquakes using empirical regression relations of response spectra and phase spectra," *J. Struct. Constr. Eng. AIJ*, **649**, 521-530 (in Japanese).

Si, H. and Midorikawa, S. (1999), "New attenuation relationship for peak ground acceleration and velocity considering effects of fault type and site condition," *J. Struct. Constr. Eng. AIJ*, **523**, 63-70 (in Japanese).

Si, H., Kuyuk, H. S., Koketsu, K. and Miyake, M. (2011a) "Attenuation characteristics of peak ground motion during the 2011 Tohoku, Japan, earthquake," *Seismol. Res. Lett.* **82**, 460.

Si, H., Koketsu, K. & Miyake, M, Midorikawa S. (2011b) "Attenuation Characteristics of Peak Ground Motions from Giant Earthquakes - The 2011 Tohoku Earthquake and Other Giant Earthquakes -," S51E-03 presented in *AGU Fall meeting*.

Si, H., Midorikawa, S., Tsutsumi, H., Noda, A., and Masatsuki, T. (2011c) "preliminary study of new attenuation relationship for response spectra on seismic bedrock including near source data," *Proceedings of the 8th International Conference on Urban Earthquake Engineering*, 75-78.

Uchiyama, Y. and Midorikawa, S. (2006), "Attenuation relationship for response spectra on engineering bedrock considering effects on focal depth," *J. Struct. Constr. Eng. AIJ*, **606**, 81-88.

Noda, S., Yashiro, K., Takahashi, K., Takemura, M., Ohno, S., Tohdo, M. and Watanabe, T. (2002) "response spectra for design purpose of stiff structures on rock sites," *OECD-NEA Workshop on the Relations between Seismological Data and Seismic Engineering Analysis.*

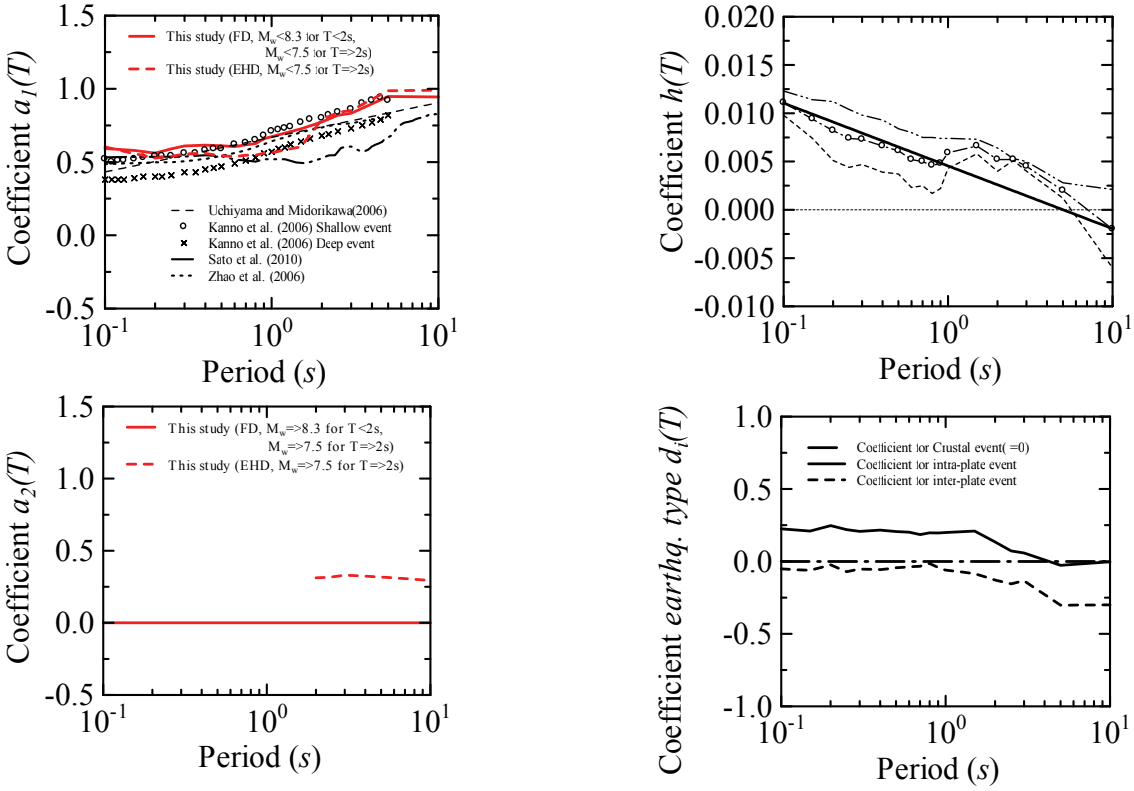


Figure 6 Coefficients $a_1(T)$, $a_2(T)$, h(T) and d(T), and the comparison of $a_1(T)$ with the recent previous studies.

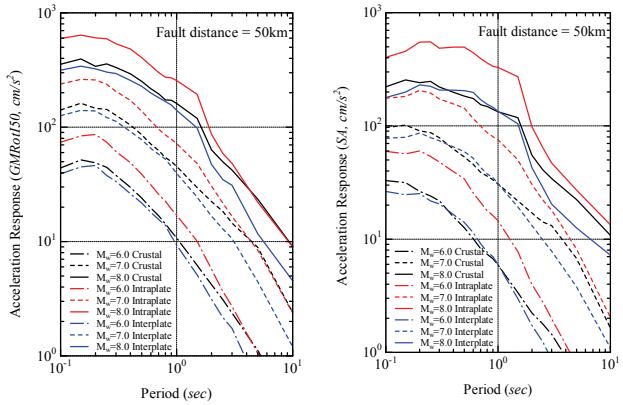


Figure 7 Predicted response spectra based on the results (Left: horizontal component; Right: vertical component)

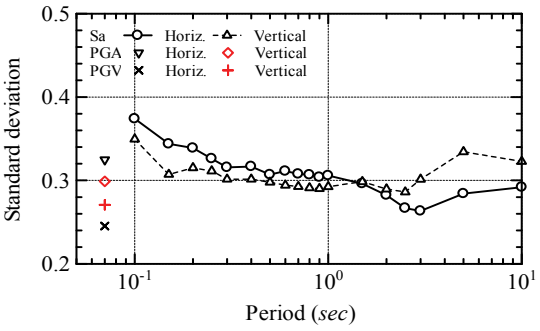


Figure 9 Standard deviation for the GMPE proposed in this study.

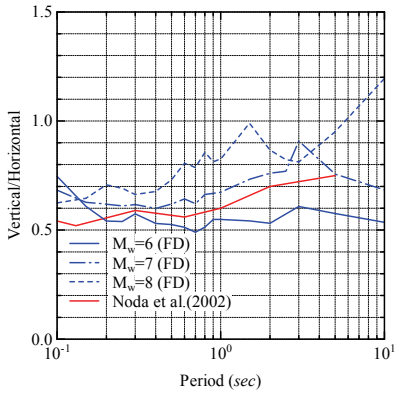


Figure 8 Ratio of vertical/horizontal (prediction by GMPE in this study. The red line show the results by Noda et al. (2002)

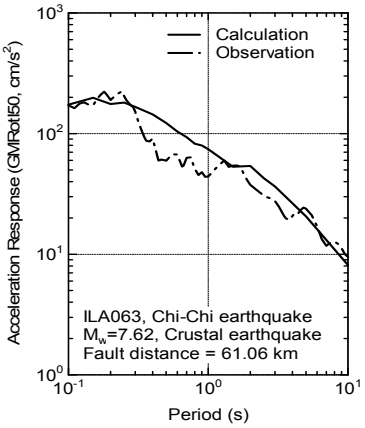


Figure 10 Comparison of prediction and observation of response spectra for records at ILA063 during the 1999 M_w 7.62 Chi-Chi earthquake

10CUEE CONFERENCE PROCEEDINGS
10th International Conference on Urban Earthquake Engineering
March 1-2, 2013, Tokyo Institute of Technology, Tokyo, Japan

HIGH INTENSITY RECORDS OBSERVED IN THE 2011 TOHOKU EARTHQUAKE

Saburoh Midorikawa[1], Tomohiro Atsumi[2], and Hiroyuki Miura[3]

1) Professor, Department of Built Environment, Tokyo Institute of Technology, Japan
2) Graduate Student, Department of Built Environment, Tokyo Institute of Technology, Japan
3) Associate Professor, Department of Architecture, Hiroshima University, Japan
smidorik@enveng.titech.ac.jp, atsumi.t.ab@m.titech.ac.jp, hmiura@hiroshima-u.ac.jp

Abstract: The Tohoku earthquake produced many strong motion records. Peak ground accelerations higher than 1 g are observed at 32 sites. Among the 32 records, spike-like wave forms are seen in 18 records, which may be due to cyclic mobility of sandy soils. Peak ground velocities higher than 70 cm/s are observed at 34 sites with softer site class. The records whose velocity response amplitude (h=0.05) is higher than 300 cm/s are observed at 34 sites. The spectra of the records are larger than high intensity records observed in the 1995 Kobe and 1994 Northridge earthquakes.

1. INTRODUCTION

The 2011 Off the Pacific Coast of Tohoku earthquake (hereafter Tohoku earthquake) of Mw 9.0 hit northeastern Japan. From the Tohoku earthquake, several thousands of strong motion records were obtained owing to dense strong motion observation networks in Japan. These records will provide valuable insight on ground motion characteristics of gigantic earthquakes. The characteristics of the observed records, however, have not fully examined because the number of the records are too large. Among the records, there are many intensive records such as those with peak acceleration of over 1g. In this paper, we select the high intensity records and introduce their features.

2. COLLECTION OF RECORDS

The Tohoku earthquake produced many strong motion records. In Japan, many nation-wide strong motion networks have been developed such as K-NET (about 1,000 sites) and KiK-net (about 700 sites) by National Research Institute for Earth Science and Disaster Prevention (NIED) , the JMA-net (about 600 sites) by Japan Meteorological Agency (JMA), the Prefectures-net (about 2,800 sites) by each prefectural office and the MLIT-net (about 700 sites) by Ministry of Land, Infrastructure and Transport (MLIT) (Midorikawa, 2005).

About 1,200 K-NET and KiK-net records were made available soon after the earthquake (NIED, 2011). JMA released about 400 records from their net together with about 500 records from the Prefectures-net (JMA, 2011; Japan Meteorological Business Support Center, 2012). Another 500 data from the Prefectures-net were made available from other sources such as SK-net (SK-net, 2011). MLIT released about 150 records from their net (MLIT, 2011). The Building Research Institute (BRI), the Port and Airport Research Institute (PARI) and Tohoku Institute of Technology also released their records (BRI, 2011; PARI, 2011, Kamiyama et al., 2012).

We collected and compiled the records on ground from these sources. Some of the data had errors or noises and abandoned. The total number of the compiled records is about 2,800. Figure 1 shows the peak groud accelerations and velocities of the compiled records.

For site classification, the average shear-wave velocity to 30m depth, V_{s30}, is calculated at K-NET, KiK-net and other sites where the PS logging data is available. As about half of the sites have no logging data, V_{s30} is estimated based on geomorphologic categories by using correlations developed to link geomorphologic units to V_{s30} by Matsuoka et al. (2006). The sites are classified into four NEHRP site classes; B, C, D and E which correspond to V_{s30} of 760 to 1500 m/s, 360 to 760 m/s, 180 to 360 m/s and less than 180 m/s, respectively.

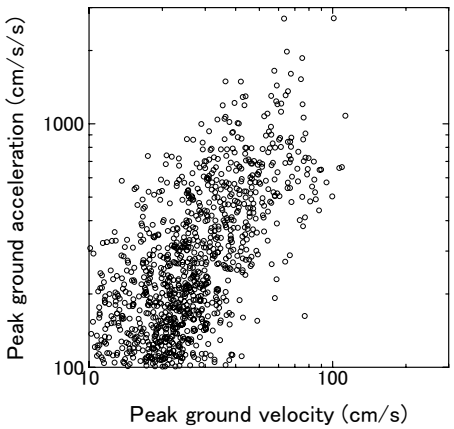
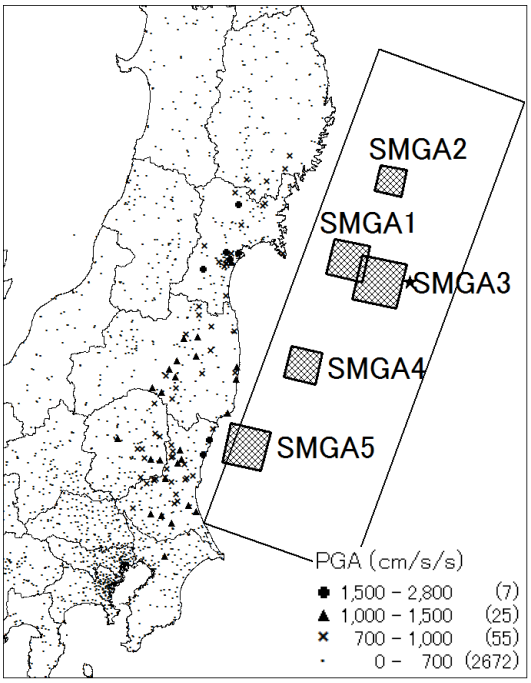


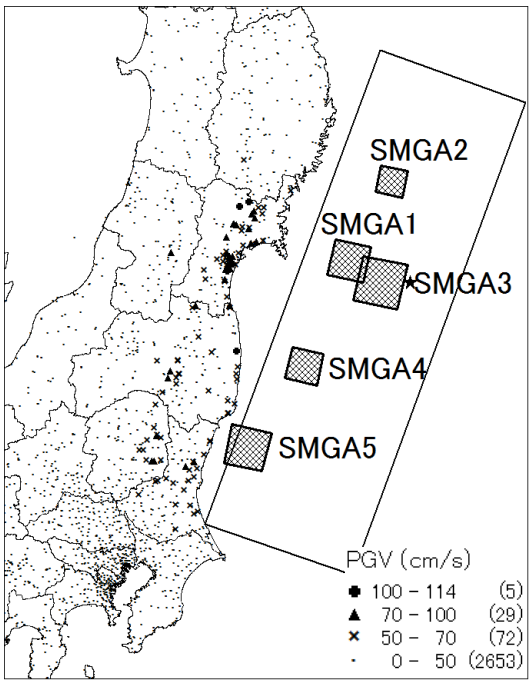
Figure 1 Peak Ground Accelerations and Velocities of Data

3. PEAK VALUES OF HIGH INTENSITY RECORDS

Among the records, peak ground accelerations higher than 2 g and 1 g are observed at 2 sites and 32 sites, respectively. Peak ground velocities higher than 100 cm/s and 70 cm/s are observed at 5 sites and 34 sites, respectively. Locations of the sites are shown in Figs. 2. The figures also show the fault plane of the earthquake derived from long period data by Koketsu et al. (2011) and strong motion generation areas derived from shorter period strong motions by Irikura and Kurahashi (2012).



(a) High Acceleration Data

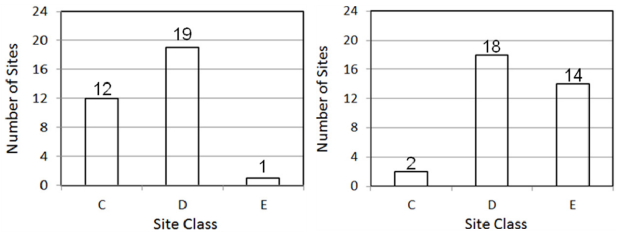


(b) High Velocity Data

Figures 2 Locations of High Intensity Records

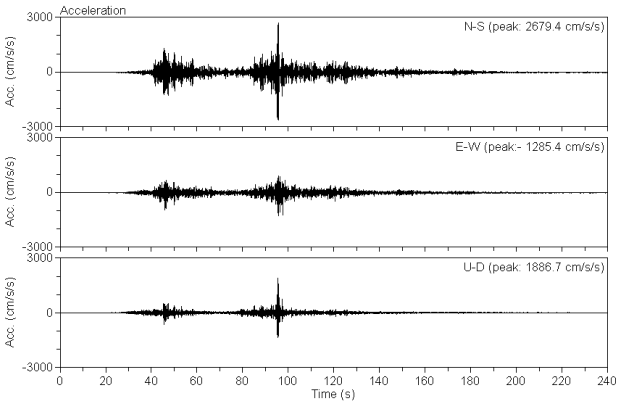
Higher accelerations and velocities are observed in Miyagi, Fukushima, Ibaragi and Tochigi prefectures, and the number of sites with higher velocities are larger in Miyagi prefecture and smaller in Ibaragi prefecture in comparison with that with higher acceleration. Figures 3 show the distributions of the site class of the sites where observed acceleration and velocity are higher than 1 g and 70cm/s, respectively. For higher acceleration records, the site class is distributes mostly at C (stiff site) or D (intermediate site), but in D or E (soft site) for higher velocity records.

The maximum peak acceleration observed is about 2.8 g at K-NET Tsukidate, Miyagi prefecture. The acceleration time history of the record is shown in Figs. 4. The waveform is composed of two distinct phases producing long duration of strong shaking. In the second phase, pulse-like high accelerations appear in the north-south and vertical components. Such high acceleration pulses are not observed at the surrounding sites.

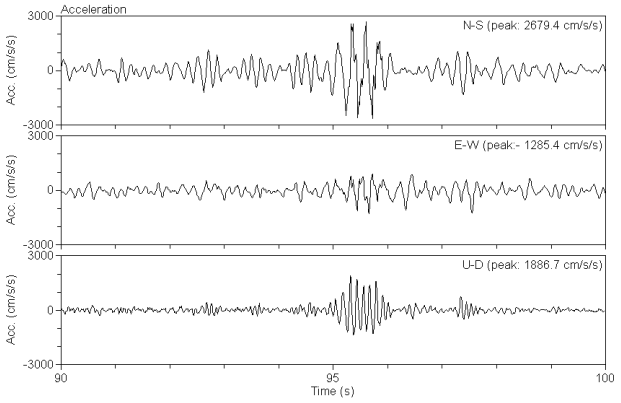


(a) High Acceleration Data (b) High Velocity Data

Figures 3 Distribution of Site Class



(a) Total View of Record



(b) Close-up of Main Part

Figures 4 Acceleration Time Histories at K-NET Tsukidate

Figure 5 shows the orbit of the high-pass-filtered displacement in the vertical (NS-UD) plane, showing an arc-like shape. This suggests that the foundation of the instrument caused combination of sway and rocking motions. The high acceleration at K-NET Tsukidate may be due to partial uplifting of the foundation of the instrument, as has been discussed by Motosaka and Tsamba (2011), and may not necessarily indicate actual ground acceleration.

The arc-like orbit results that the ratio of the period of the horizontal motion to that of the vertical motion is two. Therefore, if the wave forms of horizontal and vertical components are similar and the ratio of the periods is two, the record will be affected by partial uplifting of the foundation. Of the 32 records with over 1g acceleration, nine records have such features. In many cases, the horizontal periods are 0.2 to 0.4 sec.

Figures 6 show the acceleration time history of the record at Kawasaki town, Miyagi prefecture where the peak ground acceleration of 2.7 g is observed. The wave form is spike-like and suggests the effect of cyclic mobility of sandy soils. Of the 32 records with over 1g acceleration, 18 records have such spike-like feature. The boring data are available for 7 records of the 18 records. As shown in Fig. 7, sandy soils such as silt, sand or sandy gravel are found at the sites. Thus, among the 32 records with acceleration higher than 1 g, 27 records might be affected by partial uplifting of the foundation or cyclic mobility of sandy soils. The remaining five records have peak acceleration smaller than 1.3 g.

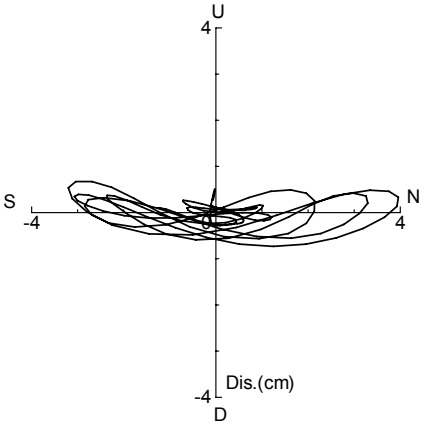


Figure 5 Displacement Orbit of K-NET Tsukidate Record

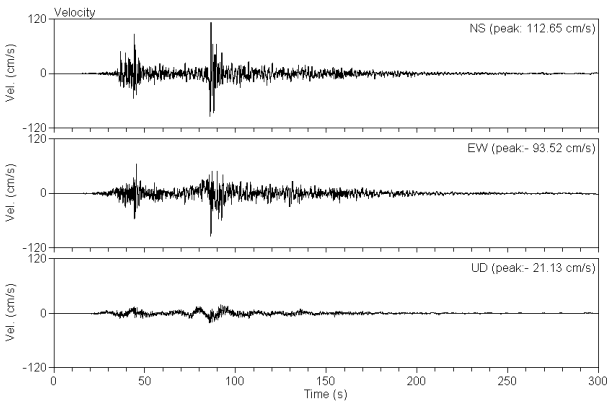
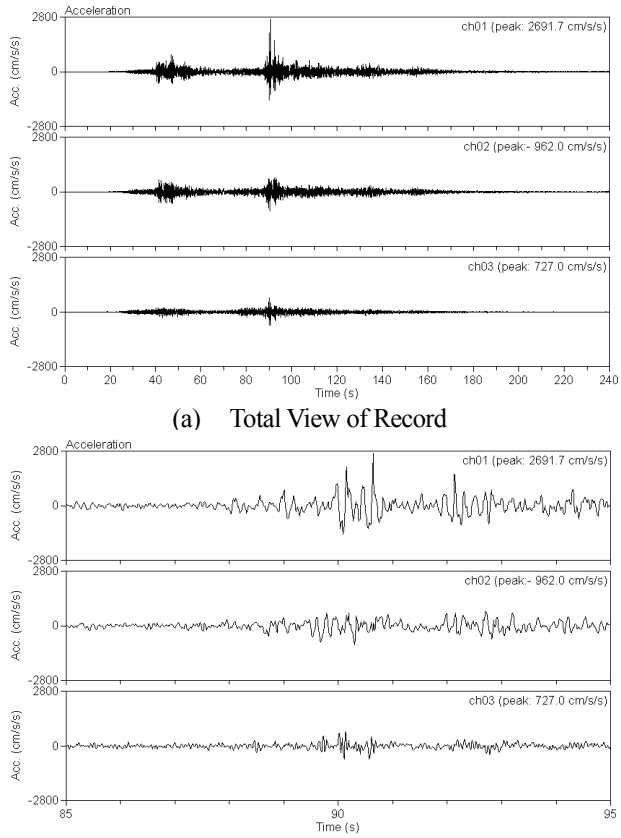


Figure 8 Velocity Time History at Shichigo J. H. School



(a) Total View of Record

(b) Close-up of Main Part

Figures 6 Acceleration Time Histories at Kawasaki Town

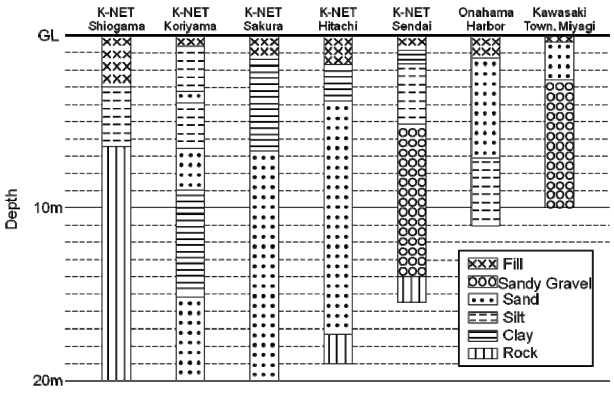


Figure 7 Boring Data at Strong Motion Sites

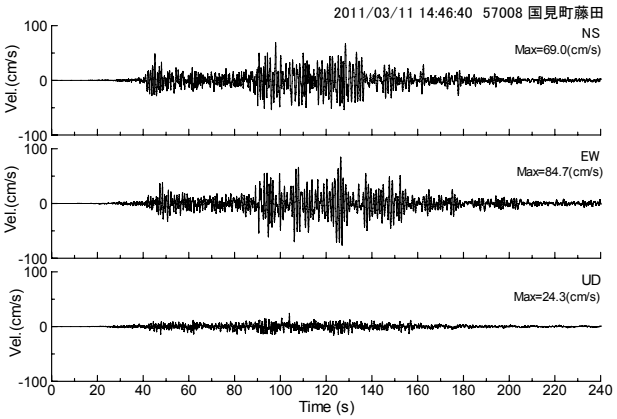
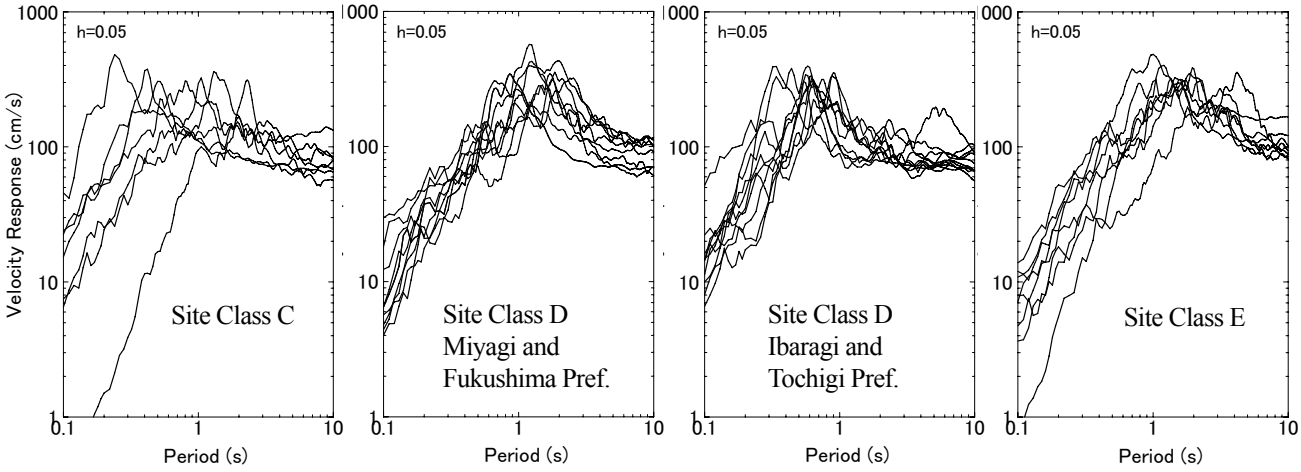


Figure 9 Velocity Time History at Kunimi Town



Figures 10 Two-dimensional Velocity Response Spectra (h=0.05) of High Intensity Records

The maximum peak velocity observed is about 110 cm/s at the Shichigo junior high school in Sendai city. The velocity time history of the record is shown in Fig. 8. The duration of strong shaking is short. On the other hand, the records with longer duration are also observed. Figure 9 show the velocity time history of the record at Kunimi town, Fukushima prefecture. The peak velocity is about 85 cm/s and the duration of strong shaking seems more than 1 minute. The long duration might be because that the site is close to several strong motion generation areas (SMGAs) as shown in Figs. 1 and strong shakings from different SMGAs continuously arrived at the site.

3. SPECTRA OF HIGH INTENSITY RECORDS

The records whose two-dimensional horizontal velocity response spectrum (h=0.05) has the amplitude higher than 300 cm/s are also selected. The number of the selected records is 34. Figures 10 show the two-dimensional velocity response spectra of the selected records for different site classes; C, D and E. No record is selected at site class B.

At site class C (stiff site), the spectra are rather constant with period, but show peaks at periods of 1 to 2 sec. at site class E (soft site). At site class D (intermediate site) where many records are available, the spectra observed at the northern area (Miyagi and Fukushima prefecture) and the southern area (Ibaragi and Tochigi prefectures) are separately shown in the figure. The spectra at the northern and southern areas tend to have peaks at periods of 1 to 2 sec. and at periods of 0.5 to 1 sec., respectively. This suggest that the SMAG at the northern part might generate longer period motion than that at the southern part.

The maximum velocity response amplitude observed is about 600 cm/s at Kunimi town. At the site, the Kunimi town office building with three storied RC structure was damaged and demolished. Figure 11 shows the two-dimensional velocity response spectrum (h=0.05) at Kunimi town. The spectrum has a sharp peak at period of 1.2 sec. with amplitude of 570 cm/s.

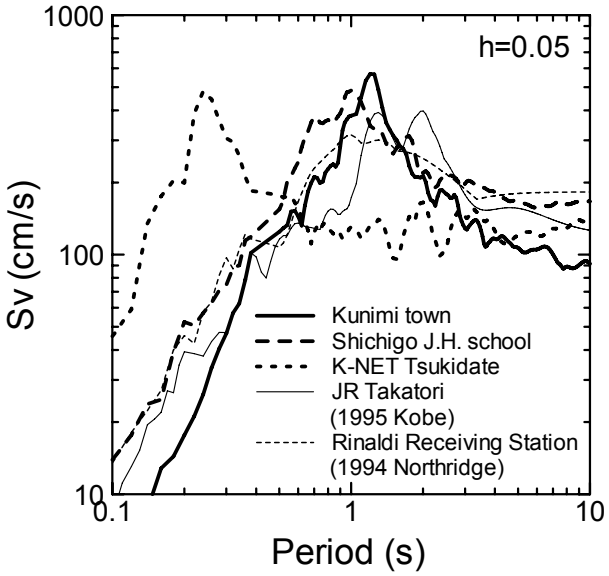


Figure 11 Comparison of Two-dimensional Velocity Response Spectra of High Intensity Records in the 2011 Tohoku, 1995 Kobe and 1994 Northridge Earthquakes

The figure also shows the spectra of the records with maximum peak acceleration and velocity; K-NET Tsukidate and Shichigo junior high school. The spectrum at Shichigo is similar with that at Kunimi but the spectrum at K-NET Tsukidate is much smaller at periods longer than 0.5 sec. The observed building damage around the sites was that some wooden houses were collapsed at Kunimi town (Itagaki et al., 2011) and building damage was very small at K-NET Tsukidate (Midorikawa and Miura, 2011). The observed damage seems to be consistent with the spectra.

For comparison, the spectra of high intensity records in past damage earthquakes such as the JR Takatori record in the 1995 Kobe earthquake and the Rinaldi Receiving Station in the 1994 Northridge earthquake are shown in the figure. The spectra at Kunimi town and Shichigo are larger than those at Takatori and Rinaldi. It is confirmed that very high intensity records have been obtained in the Tohoku earthquake.

4. CONCLUDING REMARKS

The Tohoku earthquake produced many strong motion records. Peak ground accelerations higher than 1 g are observed at 32 sites. Among the 32 records, spike-like wave forms are seen in 18 records, which may be due to cyclic mobility of sandy soils. Peak ground velocities higher than 70 cm/s are observed at 34 sites with softer site class. The records whose velocity response spectrum (h=0.05) has the amplitude higher than 300 cm/s are observed at 34 sites. The maximum velocity response amplitude is about 570 cm/s at Kunimi town. The spectra are larger than high intensity records observed in the 1995 Kobe and 1994 Northridge earthquakes.

Acknowledgements:

The strong motion data used in this study are provided by NIED, JMA, MLIT, PARI, BRI and Tohoku Institute of Terchnology. This study is partially supported by the Global COE Program "International Urban Earthquake Engineering Center for Mitigating Seismic Mega Risk" and the Grants-in-Aid for Scientific Research "Construction of Next Generation Ground Motion Prediction Equation (Project Number: 23241054, Principal Investigator: K. Koketsu)".

References:

BRI (2011), http://smo.kenken.go.jp/smdb

Irikura, K. and Kurahashi, S. (2012), "Simulation of strong ground motions from the 2011 Tohoku earthquake and a recipe of predicting strong ground motions," *Japan Geoscience Union Meeting 2012*, SSS26-017.

Itagaki, N. et al. (2011), "Damage to wooden building," *Preliminary Reconnaissance Report of the 2011 Tohoku-Chiho Taiheiyo-Oki Earthquake, AIJ*, 120-123 (in Japanese).

Japan Meteorological Business Support Center (2012), *Acceleration Time History Data 2011 DVD*

JMA (2011), http://www.seisvol.kishou.go.jp/eq/kyoshin/jishin/index.html

Kamiyama, M. et al. (2012), "Strong-Motion Records Obtained by an Array Observation System During the 2011 Great East Japan Earthquake," *Journal of Disaster Research,* **7**(6), 672-681.

Koketsu, K. et al. (2011), "A unified source model for the 2011 Tohoku earthquake," *Earth and Planetary Science Letters,* **310**(3-4), 480-487.

Matsuoka, M. et al. (2006), "Average Shear-wave Velocity Mapping Using Japan Engineering Geomorphologic Classification Map," *Journal of Structural Engineering and Earthquake Engineering, JSCE*, **23**(1), 57s-68s.

Midorikawa, S. (2005), "Strong Motion Networks in Japan – Progress after the 1995 Kobe earthquake –," *Proceedings of the International Symposium on Earthquake Engineering (ISEE Kobe 2005)*, **1**, A-91-A-96.

Midorikawa, S. and Miura, H. (2011), "K-NET Strong Motion Record and Nearby Damage during the 2011 Off the Pacific Coast of Tohoku Earthquake," *Summaries of Technical Papers of Annual Meeting, AIJ*, **B-2**, 37-38 (in Japanese).

MLIT (2011), http://www.nilim.go.jp/lab/rdg/index.htm

Motosaka, M. and Tsamba, T. (2011), "Investigation of High Acceleration Records at K-NET Tsukidate Station During the 2011 Off the Pacific Coast of Tohoku Earthquake," *Proceedings of the 8th Annual Meeting of Japan Association for Earthquake Engineering*, 24-25.

NIED (2011), http://www.kyoshin.bosai.go.jp/index_en.html

PARI (2011), http://www.mlit.go.jp/kowan/kyosin/eq.htm

SK-net (2011), http://www.sknet.eri.u-tokyo.ac.jp/

10CUEE CONFERENCE PROCEEDINGS
10th International Conference on Urban Earthquake Engineering
March 1-2, 2013, Tokyo Institute of Technology, Tokyo, Japan

STRONG MOTION PULSES OBSERVED DURING THE 2011 TOHOKU EARTHQUAKE AND THEIR MODELING

Atsushi Nozu[1)]

1) Head of Engineering Seismology Division, Port and Airport Research Institute, Japan
nozu@pari.go.jp

Abstract: The 2011 Tohoku, Japan, earthquake is obviously the first M9 earthquake which was recorded by dense strong motion networks such as K-NET, etc. From engineering point of view, the most striking feature of strong ground motions of the earthquake is the generation of strong-motion pulses in the frequency range from 0.2 to 1 Hz observed at many sites along the coast of Miyagi through Ibaraki Prefecture. It is significantly important to consider the generation of such pulses in the strong-motion prediction for mega earthquakes, especially when the prediction is aimed at seismic design of structures. To model strong motion pulses from the Tohoku earthquake, a source model including nine subevents with relatively small size (on the order of several kilometers) was developed for the earthquake. The sizes of the subevents were determined so that the width of the pulses can be reproduced appropriately. The agreement between the observed and calculated ground motions was quite satisfactory, especially for velocity waveforms. Strong ground motions from the same earthquake have been modeled using a source model with SMGAs with a size of tens of kilometers. However, the relatively small width of the observed pulses requires smaller subevents. The author redefines the small subevents as SPGAs.

1. INTRODUCTION

The 2011 Tohoku, Japan, earthquake is obviously the first M9 earthquake which was recorded by dense strong motion networks such as K-NET (Kinoshita, 1998) and KiK-net (Aoi et al., 2000), etc. From engineering point of view, the most striking feature of strong ground motions of the earthquake is the generation of strong-motion pulses in the frequency range from 0.2 to 1 Hz observed at many sites along the coast of Miyagi through Ibaraki Prefecture. It is significantly important to consider the generation of such pulses in the strong-motion prediction for mega earthquakes, especially when the prediction is aimed at seismic design of structures. In this study, to model strong motion pulses from the Tohoku earthquake, a source model including nine subevents with relatively small size (on the order of several kilometers) was developed for the earthquake. The sizes of the subevents were determined so that the width of the pulses can be reproduced appropriately. The agreement between the observed and calculated ground motions was quite satisfactory, especially for velocity waveforms.

The small subevents used in the present study is, in essence, equivalent to the "super asperities" proposed by Matsushima and Kawase (2006), because their source model is aimed at explaining strong motion pulses from the 1978 Miyagi-ken oki earthquake (M_w7.6). The author, however, redefines the subevents as SPGAs (Strong-motion Pulse Generation Areas), because the definition of "asperity" itself is currently somewhat ambiguous.

2. WHAT ARE STONG MOTION PULSES?

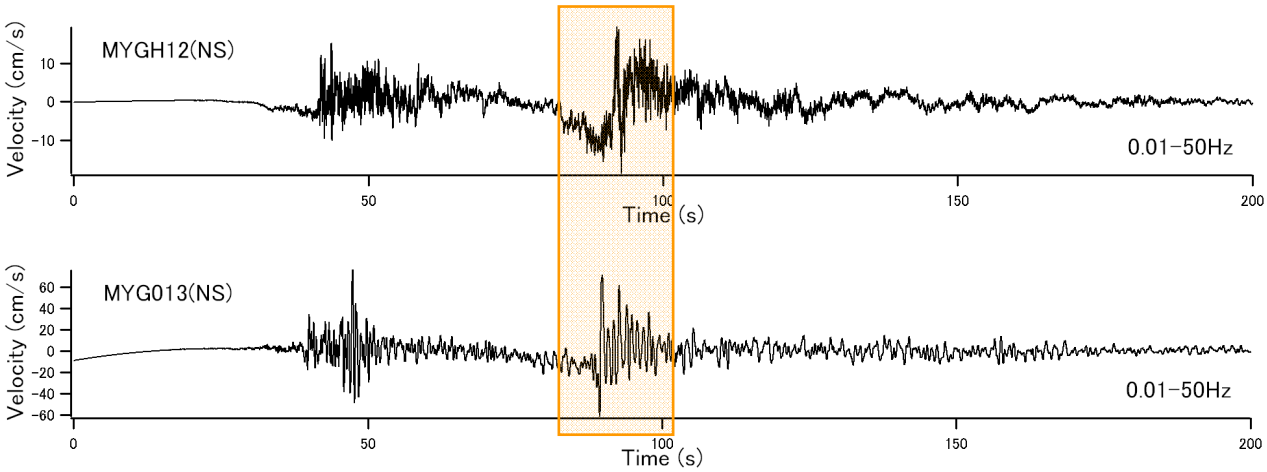
Figure 1 (top) shows the broadband (0.01-50 Hz) velocity waveforms observed at two strong motion stations located in Miyagi Prefecture during the 2011 Tohoku, Japan, earthquake. The broadband velocity waveforms can be regarded as the superposition of very low-frequency ground motion, which presumably came from the large slip area (e.g., Suzuki et al., 2011; Koketsu et al., 2011), plus the large-amplitude short-period pulses. The most typical short-period pulses are indicated by the hatches.

If we remove low-frequency components lower than 0.2 Hz, which are less important for the majority of engineered structures, from the broadband waveforms, the result is the velocity waveforms (0.2-50 Hz) shown in Figure 1 (middle). It can be seen that the short-period pulses dominate the waveforms in this frequency range.

Furthermore, if we remove high-frequency components higher than 1 Hz, which are again less important for many types of structures including port structures, the result is the velocity waveforms (0.2-1 Hz) shown in Figure 1 (bottom). It can be recognized that the velocity waveforms in this frequency range are dominated by distinctive, almost discrete pulses.

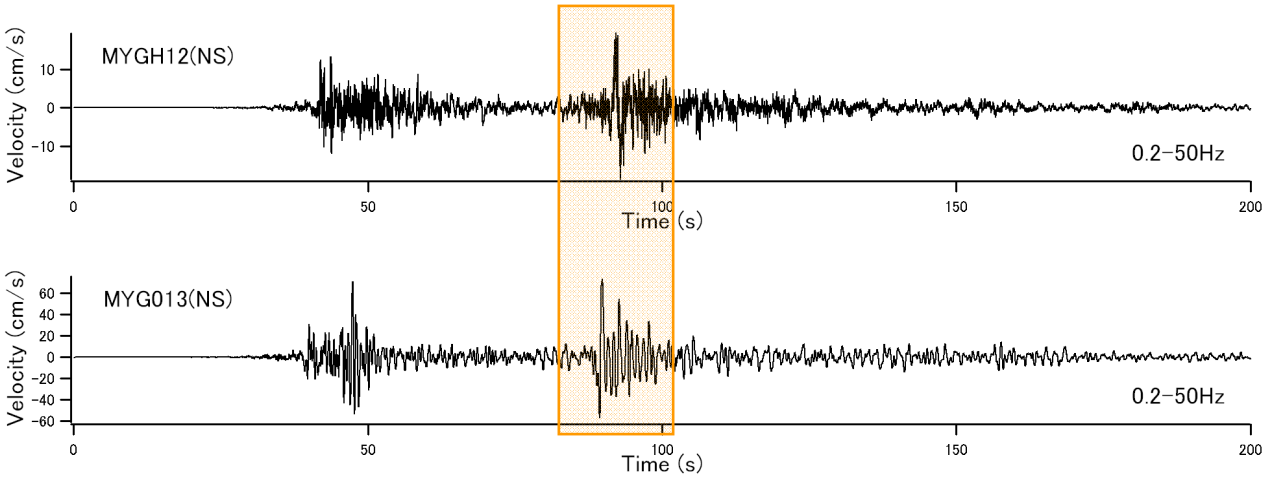
Strong ground motions in this frequency range have significant effects on a wide range of structures including port structures and tall buildings. In addition, the report of Sakai et al. (2002) indicates the importance of this frequency range even for general buildings. Therefore, when we try to

0.01-50 Hz (broadband)



↓ **remove low frequency components lower than 0.2Hz**

0.2-50 Hz



↓ **remove high frequency components higher than 1Hz**

0.2-1Hz

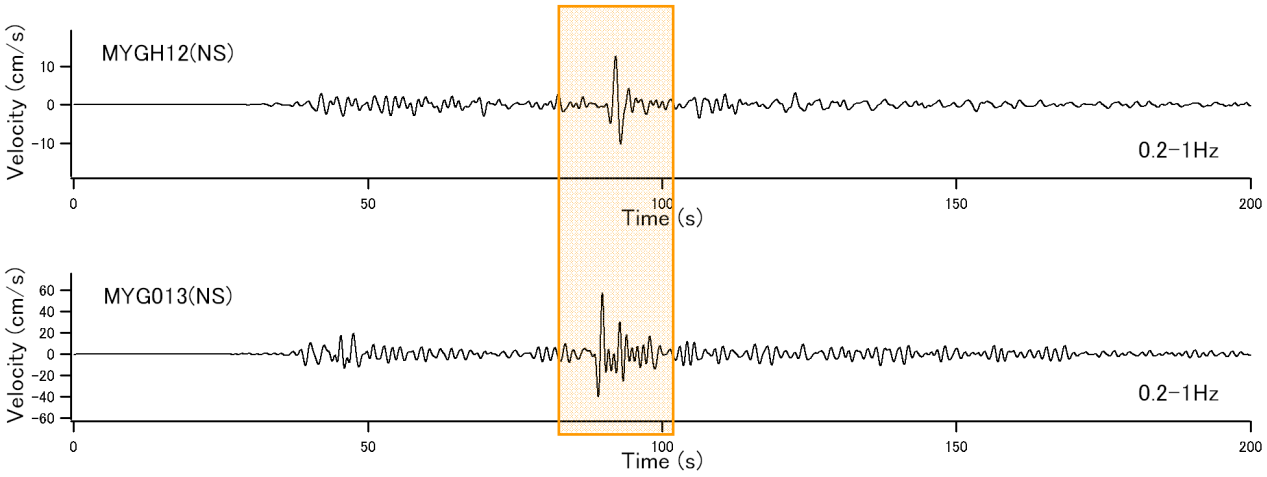


Figure 1 Examples of strong motion pulses observed during the 2011 Tohoku earthquake

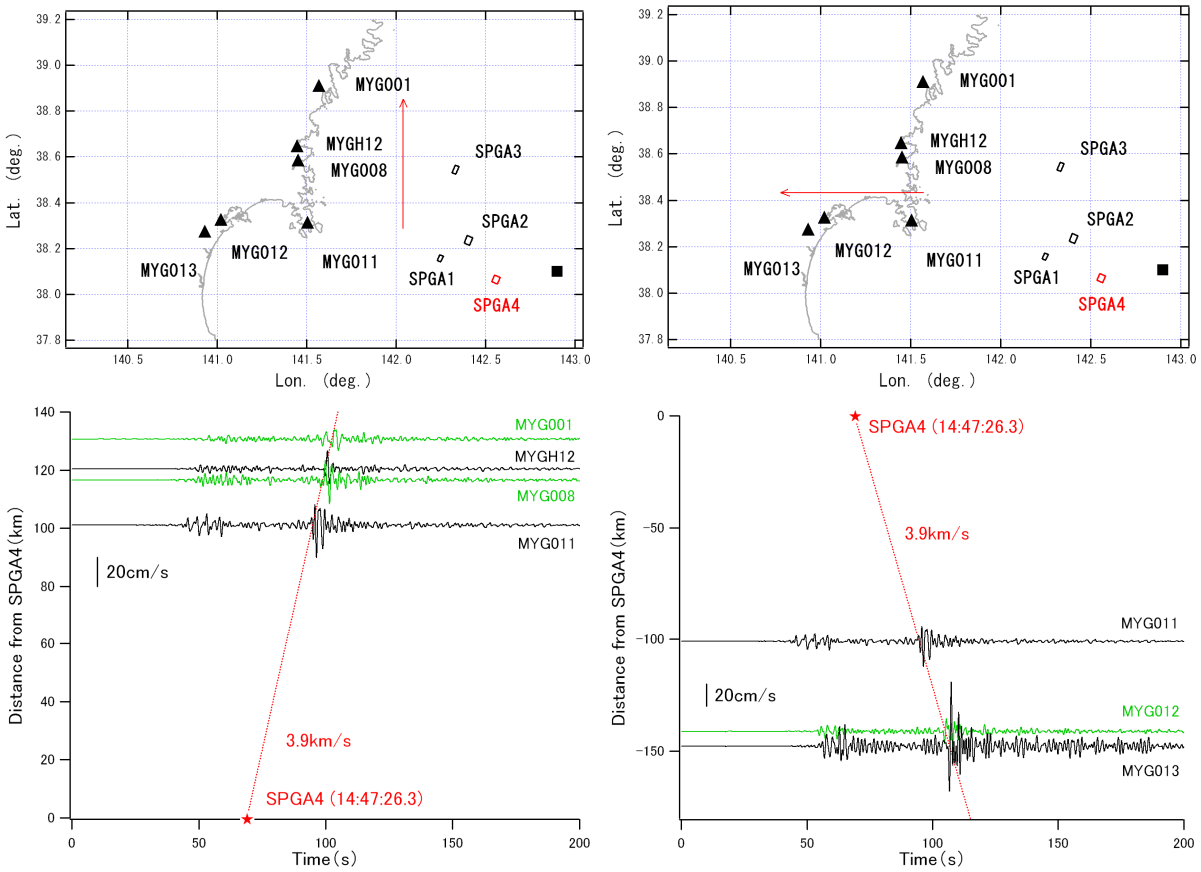


Figure 2 Propagation of strong motion pulses from south to north (left) and from east to west (right)

construct a source model for mega-thrust earthquakes, we should pay special attention to the characteristics of strong ground motions in this frequency range.

The importance of the pulses in Figure 1 (bottom) is that they appear in the frequency range relevant to structural damage. Thus, they are referred to as the "strong motion pulses" in this article.

Strong motion pulses were observed not only at these two stations but also at many other stations. They almost dominate velocity waveforms at Sendai City, Miyagi Prefecture (e.g., Figure 5 of Ohno et al., 2012). These pulses might also have been responsible for damage to bridges in the same region (e.g., Takahashi, 2012). Similar pulses were observed in other regions in Japan including Fukushima and Ibaraki Prefectures during the 2011 Tohoku earthquake. The author's primary intention in this study is to construct a source model which can explain such pulses.

3. PROPAGATION OF STRONG MOTION PULSES

If we paste up records from neighboring stations, we can clearly observe the propagation of strong motion pulses. For example, Figure 2 shows the propagation of the most significant strong motion pulse for this event, from south to north (left) and from east to west (right).

In the paste-ups, the bottom axis indicates the time from the initial rupture at the hypocenter. In the left panel, the pulse propagates from MYG011 to the north, which indicates that the source of the pulse is located at least south of MYG011. In the right panel, the pulse propagates from MYG011 to the west, towards Sendai City. At MYG013, the pulse is amplified due to the site effects (Nozu and Nagao, 2005).

In the paste-ups, the left axis indicates the distance from SPGA4, which is estimated to be a subevent which generated the pulse (see Chapter 4). The red dotted line indicates the theoretical arrival time for the assumed rupture time of SPGA4 at 14:47:26.3 and the assumed S-wave velocity of 3.9 km/s. These assumptions are found to be consistent with the arrival times of the pulse at these stations.

4. MODELING OF STRONG MOTION PULSES

4.1 Method Used to Calculate Strong Ground Motions

In this study, forward modeling approach was used to develop a source model that can explain strong motion pulses. For any candidate source model, strong ground motions were calculated based on site amplification and phase characteristics (Kowada et al., 1998; Nozu et al., 2006; Nozu and Sugano, 2008), which can take into

account the effect of sediments both on Fourier amplitude and Fourier phase of strong ground motions. Outline of the method can be described as follows.

The first step is to evaluate ground motions from a small event (Green's function). The Fourier amplitude of the Green's function is evaluated as a product of the source spectrum |S(f)|, the path effect |P(f)| and the site amplification factor |G(f)|. The source spectrum is assumed to follow the ω^{-2} model (Aki, 1967). As for the path effect, geometrical spreading and nonelastic attenuation are considered (Boore, 1983). As for the site amplification factor, the empirical site amplification factor is used. As for the Fourier phase of the Green's function, the Fourier phase of an actual record at the site of interest is used. Thus, we can obtain a time domain Green's function which incorporates the effects of sediments both on Fourier amplitude and Fourier phase. The Green's function in the frequency domain can be written as follows:

$$|S(f)|\ |P(f)|\ |G(f)|\ O_s(f)\ /\ |O_s(f)|_p, \qquad (1)$$

where $O_s(f)$ is the Fourier transform of an actual record at the site of interest and $|O_s(f)|_p$ is its Parzen-windowed amplitude (band width of 0.05 Hz is used). If several records are available at the site, it is recommended to choose an event which has a similar incident angle and a similar backazimuth with the target event. The second step is to superpose Green's functions to obtain strong ground motions from a large event (or a subevent of a large event) in the same way as the EGF method (e.g., Miyake et al., 2003). The resultant synthetic ground motions basically follow the ω^{-2} model.

For the particular application to the Tohoku earthquake, the Q value estimated for the region (Satoh and Tatsumi, 2002) and the site amplification factors estimated based on spectral inversion technique (e.g., Nozu and Nagao, 2005; Nozu et al., 2006) were used. Some of the small events used to determine the Fourier phase of the Green's functions are shown in Figure 3.

At two sites MYGH10 and FKS001, where the effect of soil nonlinearity was anticipated, the Green's functions were corrected for multiple nonlinear effects based on the simplified formula proposed by Nozu and Morikawa (2004) with nonlinear parameters (ν_1, ν_2)=(0.80, 0.008) for MYGH10 and (0.90, 0.005) for FKS001.

4.2 Off Miyagi Prefecture

The forward modeling was started with off Miyagi prefecture. Figure 4 shows the observed ground velocities at three strong motion stations MYG011, MYGH12 and MYGH06 located in Miyagi prefecture. As already pointed out by many researchers (e.g., Kurahashi and Irikura, 2011), strong ground motions in Miyagi prefecture include two distinctive wave packets, indicating contributions from at least two subevents. Then, as already done by other researchers (e.g., Asano and Iwata, 2011), the locations and the rupture times of the subevents were determined based on the arrival times of the S waves corresponding to different wave packets (indicated by vertical red bars in Figure 4). The estimated locations on the fault plane are indicated as SPGA1 and SPGA4 in Figures 3 and 5. The estimated location of SPGA1 was close to the hypocenter of the 1978 off Miyagi prefecture earthquake (M7.4).

Then, assuming rectangular SPGAs which involve the estimated locations as local rupture starting points, the parameters for the SPGAs were determined through forward modeling approach. The estimated parameters include the length, the width, the seismic moment of the SPGAs as well as the relative locations of the SPGAs with respect to the rupture starting points. In the forward modeling approach, the parameters were determined so that the velocity waveforms in the strong motion stations in the frequency range from 0.2-1 Hz are reproduced as accurately as possible. Throughout the study, the rupture velocity was fixed to 3.0 km/s and the rise time was fixed to the width of the SPGA divided by the rupture velocity and multiplied by 0.25.

The estimated parameters for SPGA1 and SPGA4 are listed in Table 1. The resultant waveforms, i.e., the synthetic waveforms with contributions from two SPGAs namely, SPGA1 and SPGA4 are compared with the observed waveforms in Figure 6. The agreement between the observed and synthetic waveforms is basically satisfactory. In particular, the amplitude and the width of S-wave pulses are reproduced very well, indicating that the estimated seismic moment and the size of the SPGAs are appropriate (although different assumption on the rupture velocity may lead to different estimation of the size). In Figure 6, however, some phases included in the observed waveforms are not included in the synthetic waveforms as indicated by crosses. To improve the results, two more SPGAs, namely, SPGA2 and SPGA3 were introduced (Figures 3 and 5). The synthetic waveforms with contributions from four SPGAs agree quite well with the observed waveforms as shown in Figure 7.

4.3 Off Fukushima Prefecture

At stations around the border of Miyagi and Fukushima Prefectures such as MYGH10 and FKS001, the contributions from four SPGAs off Miyagi prefecture can almost explain the observed waveforms as shown in Figure 8. At stations further south, however, the contributions from the SPGAs off Miyagi prefecture alone cannot explain the observed waveforms as shown in Figure 9. In particular, three distinctive pulses are present in the observed waveforms as indicated by crosses, which do not appear in the synthetics. The locations and the rupture times of three SPGAs corresponding to these pulses were estimated based on the arrival times of the S-waves. The estimated locations of the three SPGAs, namely, SPGA5, SPGA6 and

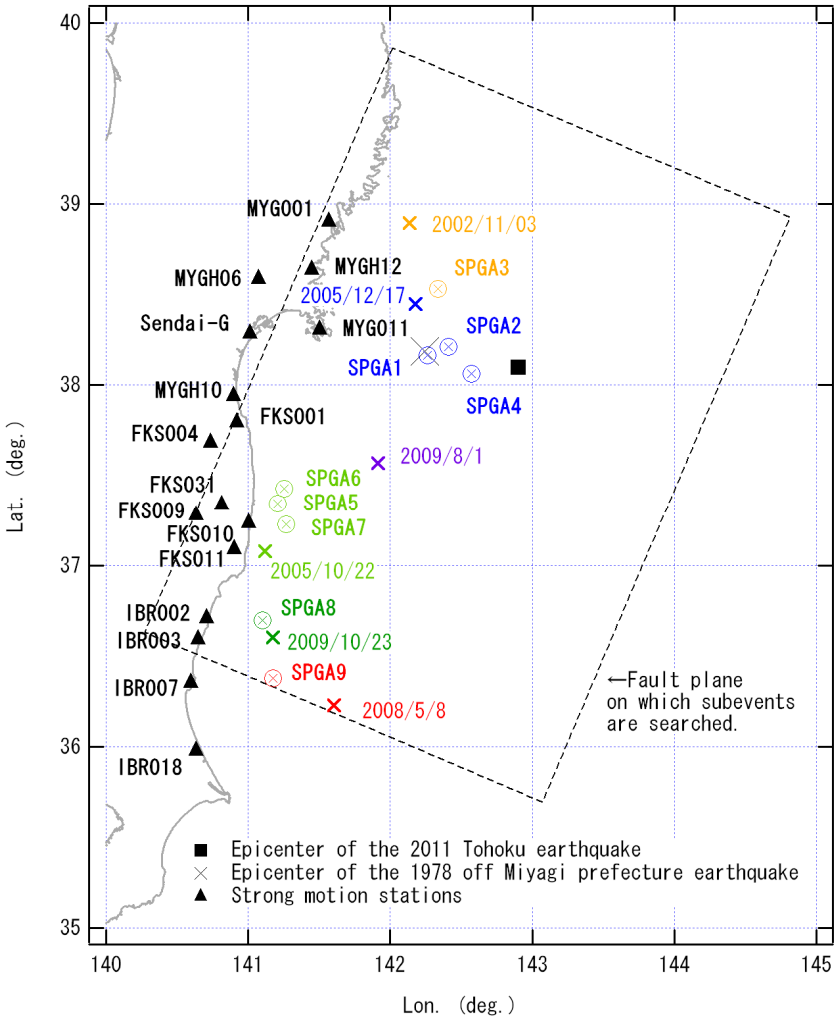


Figure 3 The proposed source model composed of nine SPGAs. The triangles indicate strong motion stations. The crosses indicate epicenters of small events used to determine phase characteristics.

Table 1 Parameters for the proposed SPGA model

	Rupture time (h:m:s)	Length (km)	Width (km)	Area (km^2)	M_0 (Nm)	Rise time (s)
SPGA1	14:46:43.5	3.0	2.0	6.0	8.00E+18	0.17
SPGA2	14:46:46.9	4.0	3.0	12.0	8.00E+18	0.25
SPGA3	14:47:33.4	4.0	2.0	8.0	4.00E+18	0.17
SPGA4	14:47:26.3	3.5	3.0	10.5	2.10E+19	0.25
SPGA5	14:47:57.1	3.0	4.0	12.0	3.00E+18	0.33
SPGA6	14:48:04.4	3.0	4.0	12.0	3.00E+18	0.33
SPGA7	14:48:15.0	6.0	2.0	12.0	5.00E+18	0.17
SPGA8	14:48:25.8	8.0	3.0	24.0	9.00E+18	0.25
SPGA9	14:48:30.9	7.0	7.0	49.0	2.00E+19	0.58

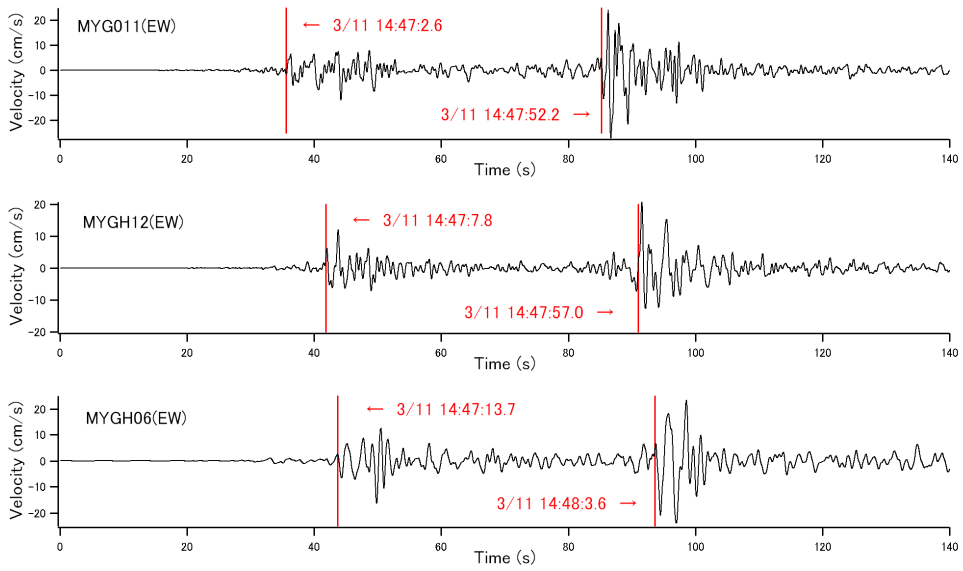


Figure 4 Observed ground velocities at MYG011, MYGH12 and MYGH06 (EW components; Borehole records are shown for MYGH12 and MYGH06)

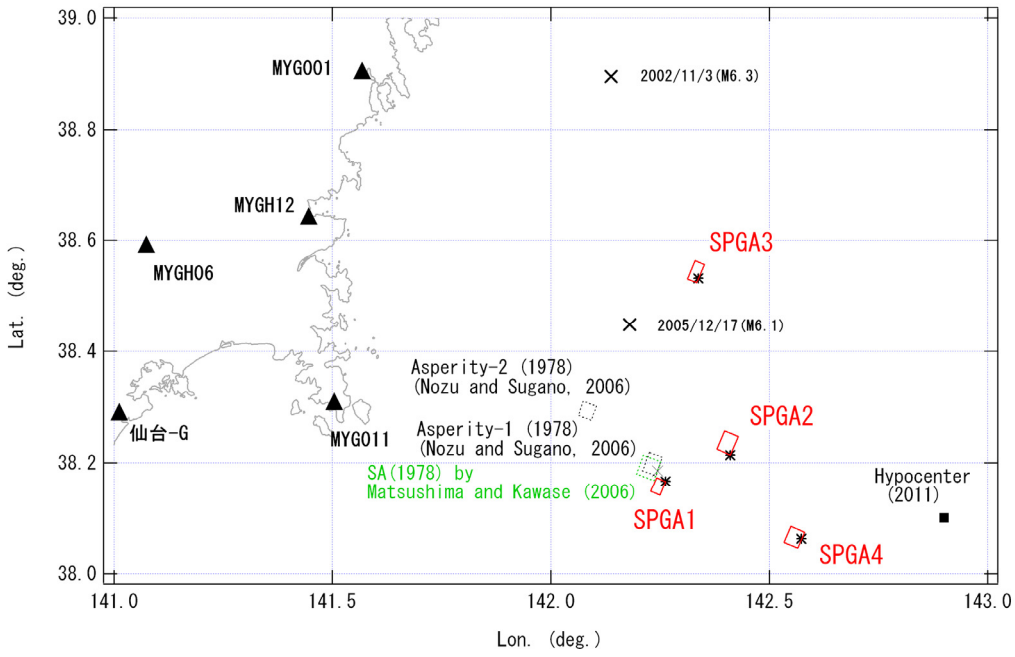


Figure 5 Detailed locations of four SPGAs off Miyagi Prefecture

SPGA7 were close to the coast of Fukushima Prefecture as shown in Figure 3 and Figure 10 (left). The parameters for the SPGAs were determined through forward modeling. The resultant parameters are given in Table 1. The synthetic waveforms with contributions from three SPGAs off Fukushima Prefecture are compared with the observed waveforms in Figure 11. The agreement between the observed and synthetic waveforms is satisfactory.

4.4 Off Ibaraki Prefecture

A similar analysis was conducted for strong motion stations in Ibaraki Prefecture and two more SPGAs, namely, SPGA8 and SPGA9 were identified as shown in Figure 10 (right) and Table 1.

5. DISCUSSION

One important character of the source model developed here is that the size of the subevent is significantly smaller than the “asperities” or “SMGAs” conventionally assumed for a mega-thrust earthquake. In fact, the dimension of the SPGAs used in our analysis was around several kilo meters, while other authors (e.g., Kurahashi and Irikura, 2011; Asano and Iwata, 2011) propose “SMGAs” with a dimension of several tens of

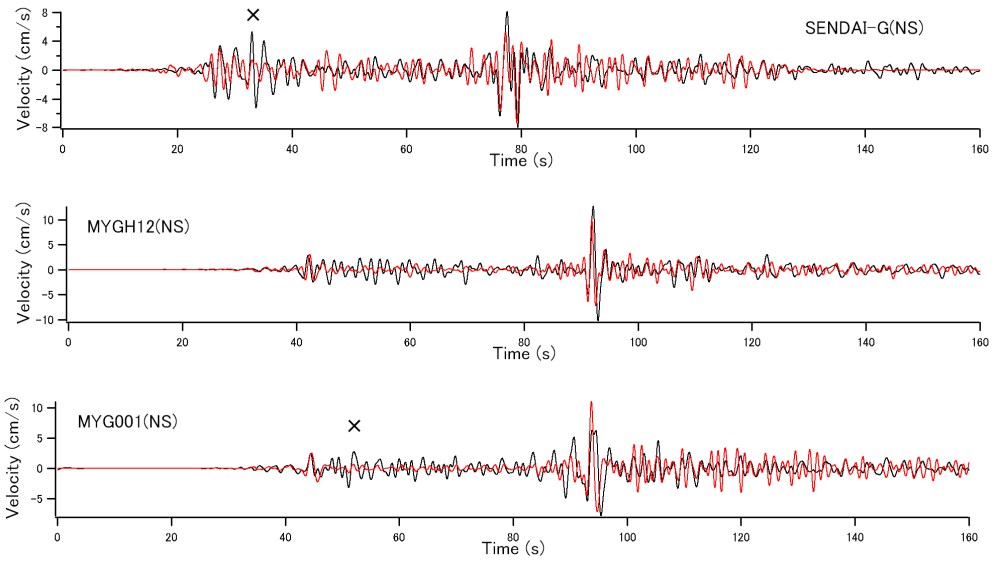


Figure 6 Observed (black) and synthetic (red) velocity waveforms (0.2-1 Hz). Contributions from SPGA1 and SPGA4 are considered in the synthetic waveforms.

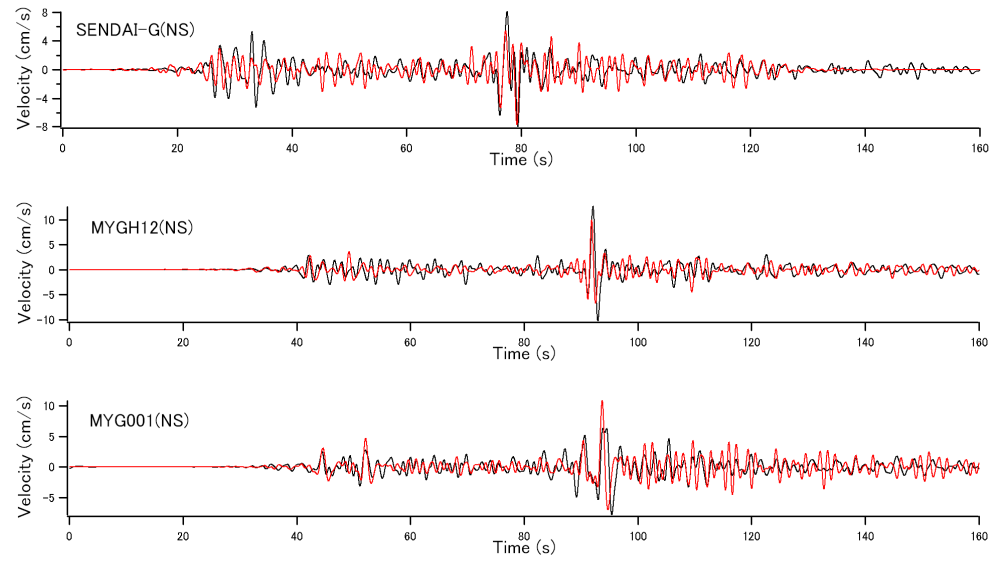


Figure 7 Observed (black) and synthetic (red) velocity waveforms (0.2-1 Hz). Contributions from four SPGAs off Miyagi Prefecture are considered in the synthetic waveforms

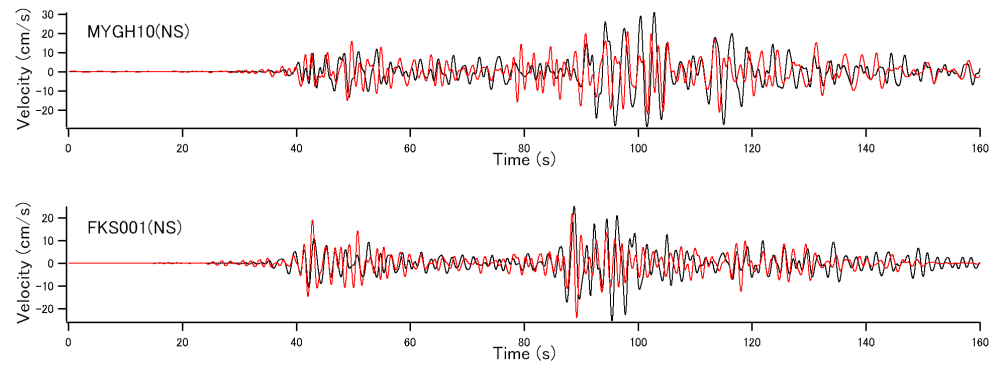


Figure 8 Observed (black) and synthetic (red) velocity waveforms (0.2-1 Hz). Contributions from four SPGAs off Miyagi prefecture are considered in the synthetic waveforms.

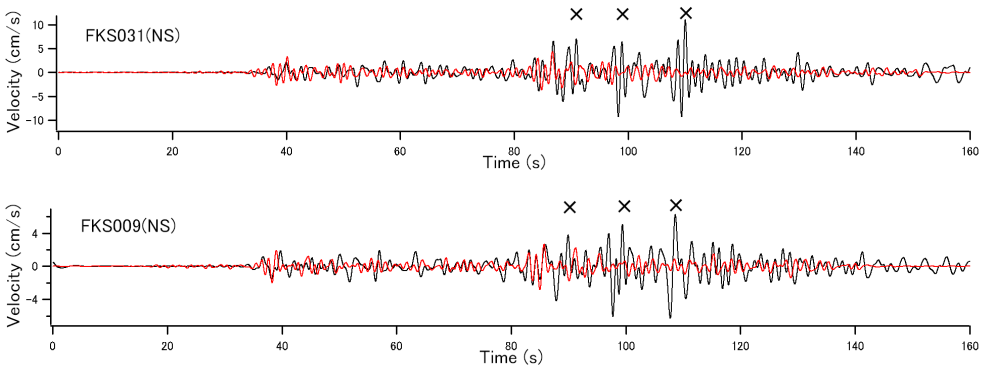


Figure 9 Observed (black) and synthetic (red) velocity waveforms (0.2-1 Hz). Contributions from four SPGAs off Miyagi prefecture are considered in the synthetic waveforms.

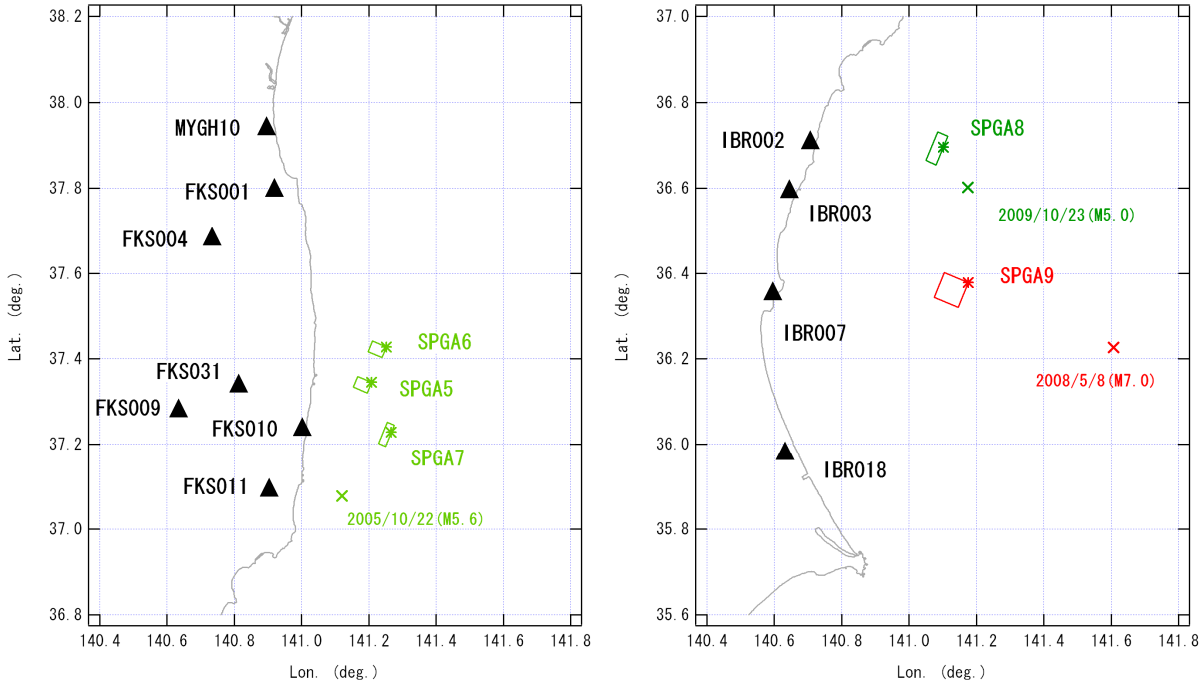


Figure 10 Detailed locations of SPGAs off Fukushima (left) and off Ibaraki (right) Prefectures.

kilo meters for the same event. It should be noted that the small size of the subevents used in this study is a natural reduction from the fact that, at many sites along the coast of Tohoku, strong motion pulses were observed and their pulse widths were around one to several seconds. As is well known, the duration of rupture of a subevent is related to the pulse width. If the dimension of a subevent is around several tens of kilo meters, then the pulse width will be more than 10 s and will not agree with the observed width. This is the reason why small subevents are needed to accurately reproduce strong ground motions in the frequency range from 0.2-1 Hz, which is of great importance from engineering point of view. Different assumptions on the rupture velocity may lead to different estimation of the size, but it will not significantly affect this conclusion.

Although the primary objective of the present source model is to explain strong ground motions in the frequency range from 0.2-1 Hz, it is basically applicable to higher frequencies. Figure 12 shows the comparison of the observed and synthetic Fourier spectra (0.2-10 Hz) at selected sites. Figure 13 shows the comparison of the observed and synthetic velocity envelopes (0.2-10 Hz) at the same sites. In these figures, the synthetic waveforms were calculated considering nine SPGAs. Basically, the agreement between the observed and synthetic Fourier spectra and velocity envelopes is satisfactory. Thus, the present model is basically applicable to high frequencies up to 10 Hz. In particular, the agreement in Fourier amplitude in Figure 12 indicates that strong ground motions from subevents of a mega-thrust earthquake follow the ω^{-2} model (Aki, 1967), because the simulation method used in this study is based on the ω^{-2} model.

6. CONCLUDING REMARKS

From engineering point of view, the most striking feature of strong ground motions of the 2011 Tohoku

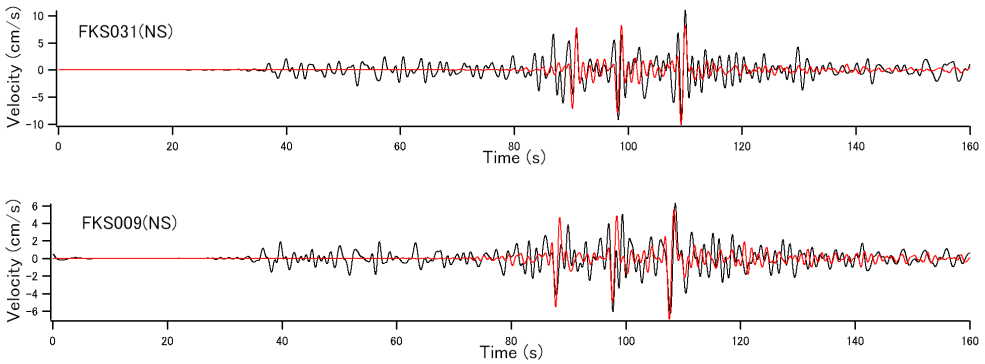


Figure 11 Observed (black) and synthetic (red) velocity waveforms (0.2-1 Hz). Contributions from three SPGAs off Fukushima Prefecture are considered in the synthetic waveforms.

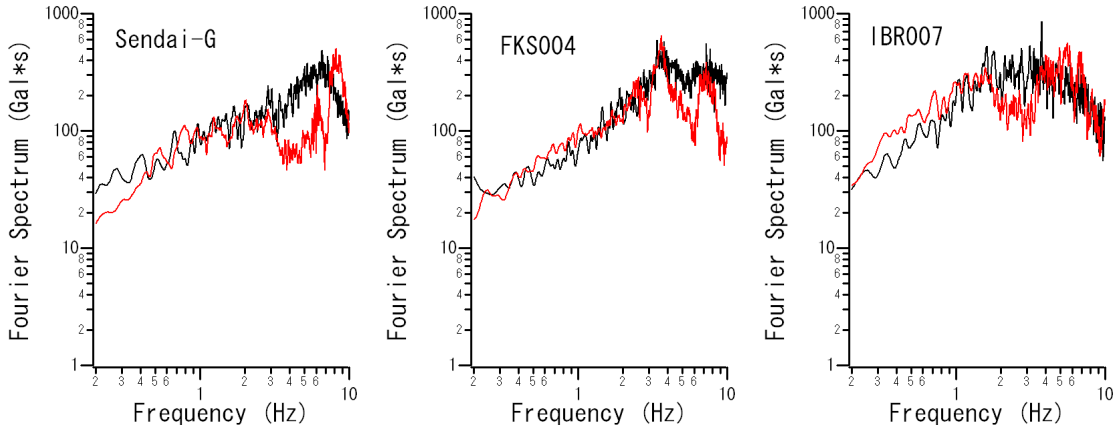


Figure 12 Observed (black) and synthetic (red) Fourier spectra (0.2-10 Hz). Contributions from nine SPGAs off Miyagi through off Ibaraki are considered in the synthetic spectra. The spectra are the composition of two horizontal components and smoothed with a Parzen window with a band width of 0.05 Hz.

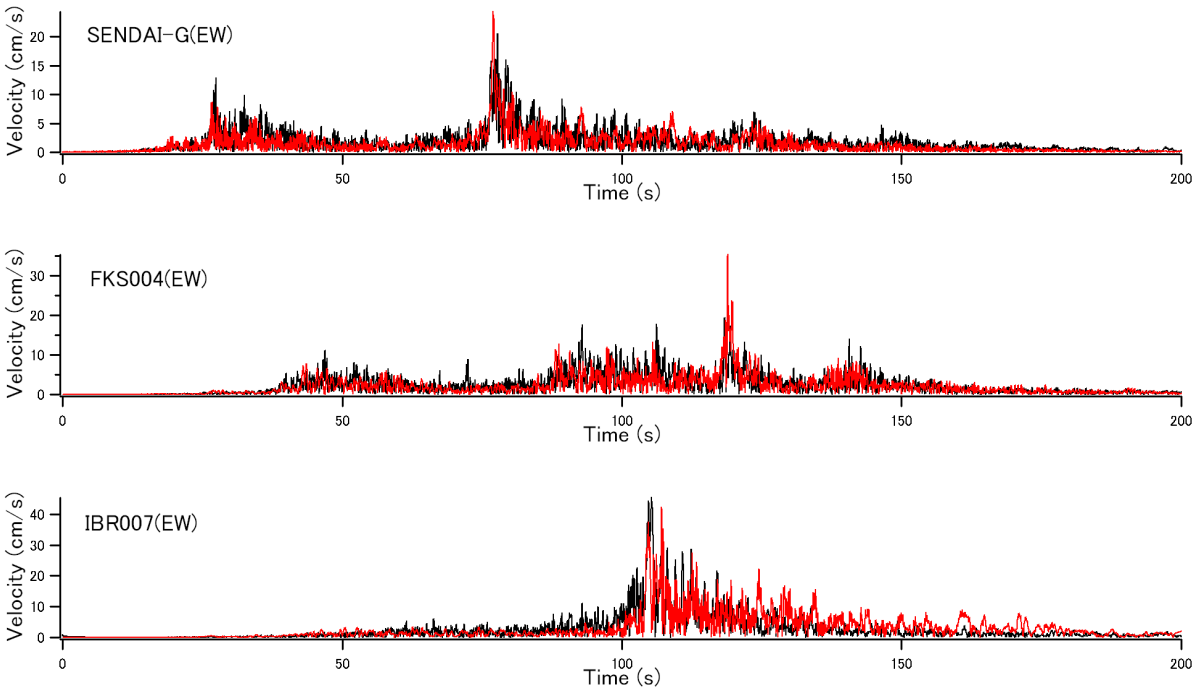


Figure 13 Observed (black) and synthetic (red) velocity envelopes (0.2-10 Hz). Contributions from nine SPGAs off Miyagi through off Ibaraki are considered in the synthetic envelopes.

earthquake is the generation of pulses in the frequency range from 0.2 to 1 Hz observed at many sites along the coast of Miyagi through Ibaraki Prefecture. It is significantly important to consider the generation of such pulses in the strong-motion prediction for mega earthquakes, especially when the prediction is aimed at seismic design of structures.

To model strong motion pulses from the Tohoku earthquake, a source model with rectangular subevents was developed for the earthquake. The locations of the subevents were determined from the arrival times. The sizes of the subevents were determined so that the width of the pulses can be reproduced appropriately.

The constructed source model involves 9 subevents with relatively small size (on the order of several kilometers), located off-the-coast of Miyagi through off-the-coast of Ibaraki. The strong ground motions from the source model were calculated based on site amplification and phase characteristics (Nozu et al., 2006). The agreement between the observed and calculated ground motions was quite satisfactory, especially for velocity waveforms (0.2-1.0 Hz) including near-source pulses.

Strong ground motions from the same earthquake have been modeled using a source model with SMGAs with a size of tens of kilometers (e.g., Kurahashi and Irikura, 2011; Asano and Iwata, 2011). However, the relatively small width of the observed pulses requires smaller subevents.

The small subevents used in the present study is, in essence, equivalent to the "super asperities" proposed by Matsushima and Kawase (2006), because their source model is aimed at explaining strong motion pulses from the 1978 Miyagi-ken oki earthquake (M_w7.6). The author, however, redefines the subevents as SPGAs (Strong-motion Pulse Generation Areas), because the definition of "asperity" itself is currently somewhat ambiguous.

The observed strong motion pulses require a very high moment rate within a small area. The future work should be aimed at revealing the dynamics of SPGAs.

Acknowledgements:

The author would like to thank the National Research Institute for Earth Science and Disaster Prevention (NIED) for providing important strong motion data. The digital data of the site amplification factors and the computer program used to generate synthetics in this article including FORTRAN source code are open to public (Nozu and Nagao, 2005; Nozu and Sugano, 2008).

References:

Aki, K. (1967), "Scaling law of seismic spectrum", *J. Geophys. Res*. **71**, 1217-1231.

Aoi, S., Obara, K., Hori, S., Kasahara, K. and Okada, Y. (2000), "New strong-motion observation network: KiK-net", *Eos Trans. Am. Geophys. Union* **81**, 329.

Asano, K. and Iwata, T. (2011), "Strong ground motion generation during the 2011 off the Pacific coast of Tohoku earthquake revealed by the broadband strong motion simulation", *The Seismological Society of Japan 2011 Fall Meeting,* A11-06 (in Japanese).

Boore, D.M. (1983), "Stochastic simulation of high-frequency ground motions based on seismological models of the radiated spectra", *Bull. Seism. Soc. of Am.* **73**, 1865-1894.

Kinoshita, S. (1998), "Kyoshin Net (K-net)", *Seim. Res. Lett.* **69**, 309-332.

Koketsu, K., Yokota, Y., Nishimura, N., Yagi, Y., Miyazaki, S., Satake, K., Fujii, Y., Miyake, H., Sakai, S., Yamanaka, Y. and Okada, T. (2011), "A unified source model for the 2011 Tohoku earthquake", *Earth Planet. Sci. Lett.*, **310**, 480-487.

Kowada, A., Tai, M., Iwasaki, Y. and Irikura, K. (1998), "Evaluation of horizontal and vertical strong ground motions using empirical site-specific amplification and phase characteristics", *J. Struct. Constr. Eng.,* AIJ **514**, 97-104 (in Japanese with English abstract).

Kurahashi, S. and Irikura, K. (2011), "Source model for generating strong ground motions during the 2011 off the Pacific coast of Tohoku Earthquake", *Earth Planets Space* **63**, 571-576.

Matsushima, S. and Kawase, H. (2006), "Source model of a subduction zone earthquake with super-asperity", *Chikyu Monthly* **S55**, 98-102 (in Japanese).

Miyake, H., Iwata, T. and Irikura, K. (2003), "Source characterization for broadband ground-motion simulation: kinematic heterogeneous source model and strong motion generation area", *Bull. Seism. Soc. Am.* **93**, 2531-2545.

Nozu, A. and Morikawa, H. (2004), "Assessment of soil nonlinearity using empirical Green's function method", *Proceedings of 13WCEE*, No.2368.

Nozu, A. and Nagao, T. (2005), "Site amplification factors for strong-motion sites in Japan based on spectral inversion technique", *Technical Note of the Port and Airport Research Institute,* No.1102 (in Japanese with English abstract).

Nozu, A., Nagao, T. and Yamada, M. (2006), "Simulation of strong ground motions based on site-specific amplification and phase characteristics", *Third International Symposium on the Effects of Surface Geology on Seismic Motion*, Grenoble, France.

Nozu, A. and Sugano, T. (2008), "Simulation of strong ground motions based on site-specific amplification and phase characteristics – accounting for causality and multiple nonlinear effects –", *Technical Note of the Port and Airport Research Institute,* No.1173 (in Japanese with English abstract).

Ohno, S., Mitsuya, E. and Motosaka, M. (2012), "Site amplification characteristics in Sendai City during the 2011 Tohoku Earthquake, Japan", *Journal of Japan Association for Earthquake Engineering*, **12**, 339-353 (in Japanese with English abstract).

Sakai, Y., Koketsu, K. and Kanno, T. (2002), "Proposal of the destructive power index of strong ground motion for prediction of building damage ratio", *J. Struct. Constr. Eng.*, AIJ **555**, 85-91 (in Japanese with English abstract).

Satoh, T. and Tatsumi, Y. (2002), "Source, path and site effects for crustal and subduction earthquakes inferred from strong motions records in Japan", *J. Struct. Constr. Eng.*, AIJ **556**, 15-24 (in Japanese with English abstract).

Suzuki, W., Aoi, S., Sekiguchi, H. and Kumagai, T. (2011), Rupture process of the 2011 Tohoku-oki mega-thrust earthquake (M_W9.0) inverted from strong motion data, *Geophys. Res. Lett.*, **38**, L00G16, doi:10.1029/2011GL049136.

Takahashi, Y. (2012), "Damage of rubber bearings and dampers of bridges in 2011 Great East Japan Earthquake", *Proc. of the International Symposium on Engineering Lessons Learned from the 2011 Great East Japan Earthquake*, 1333-1342.

10CUEE CONFERENCE PROCEEDINGS
10th International Conference on Urban Earthquake Engineering
March 1-2, 2013, Tokyo Institute of Technology, Tokyo, Japan

LOCAL SITE EFFECTS OBSERVED IN SHINAGAWA AND ODAWARA, JAPAN, DURING THE 2011 OFF THE PACIFIC COAST OF TOHOKU EARTHQUAKE

Seiji Tsuno[1], Hiroaki Yamanaka[2], Saburoh Midorikawa[3] , Hiroyuki Miura[4] , Shin'ichi Sakai[5] , Naoshi Hirata[6] , Hiroe Miyake[7] , Minoru Sakaue[8] , Kazuki Koketsu[9]

1) Assistant Senior Researcher, Disaster Prevention Technology Division, Railway Technical Research Institute, Japan
2) Professor, Interdisciplinary Graduate School of Science and Engineering, Tokyo Institute of Technology, Japan
3) Professor, Interdisciplinary Graduate School of Science and Engineering, Tokyo Institute of Technology, Japan
4) Associate Professor, Graduate School of Engineering, Hiroshima University, Japan
5) Associate Professor, Earthquake Research Institute, University of Tokyo, Japan
6) Professor, Earthquake Research Institute, University of Tokyo, Japan
7) Assistant Professor, Earthquake Research Institute, University of Tokyo, Japan
8) Technical Officer, Earthquake Research Institute, University of Tokyo, Japan
9) Professor, Earthquake Research Institute, University of Tokyo, Japan
stsuno@rtri.or.jp, yamanaka@depe.titech.ac.jp, smidorik@enveng.titech.ac.jp, hmiura@hiroshima-u.ac.jp, coco@eri.u-tokyo.ac.jp, hirata@eri.u-tokyo.ac.jp, hiroe@eri.u-tokyo.ac.jp, sakaue@eri.u-tokyo.ac.jp, koketsu@eri.u-tokyo.ac.jp

Abstract: Strong ground motions were locally observed in Shinagawa to Kawasaki and in Odawara, Japan, during the 2011 off the Pacific coast of Tohoku Earthquake (Mw 9.0). Velocity responses for periods of 2 and 3 seconds at the northern area of the Haneda airport, Shinagawa were larger than 100 cm/sec and those at the center of the Ashigara Valley, Odawara were larger than 200 cm/sec. To comprehend the wave packets in which earthquake ground motions for periods of 2 and 3 seconds were largely excited, we applied the time-frequency analysis to seismic records observed in these areas. The ground motions in Shinagawa were dominated for periods of 1.5 to 5 seconds in main phases. On the other hand, the ground motions in the Ashigara Valley were dominated for periods of 1.5 to 3.5 seconds in main phases. In the Ashigara Valley, seismic records in the bed rock are obtained. Also, a S-wave velocity structure in the valley is already estimated by the previous study. After the 1-D analysis of earthquake motions, we concluded that the large velocity responses were amplified by the local site effects due to the deep S-wave velocity structures in the Ashigara Valley.

1. INTRODUCTION

During the 2011 off the Pacific coast of Tohoku Earthquake (Mw 9.0), strong ground motions of more than 30 cm/sec were observed at plenty of sites in the Tokyo Metropolitan Area which is located around 150 km far from the seismic fault. Also, long-period ground motions for more than 2 seconds were observed throughout the Kanto Region (Tsuno et al., 2012). Seismic records for this giant earthquake were obtained at more than 1000 stations in the Kanto Region by several seismic observation networks, such as MeSO-net, K-NET, KiK-net, SK-net and so on. Especially, MeSO-net (Sakai and Hirata, 2009) installed with an interval distance of about 5 km has high densely covered the Tokyo Metropolitan Area with more than about 250 stations. In this paper, we focused on earthquake ground motions in Shinagawa and Odawara where the local site effects were clearly observed. We evaluated the earthquake ground motions observed in these specific areas, by the pseudo velocity response spectra (h=5%) and the time-frequency analyses.

2. GROUND MOTIONS OBSERVED IN THE KANTO REGION, DURING THE 2011 OFF THE PACIFIC COAST OF TOHOKU EARTHQUAKE

2.1 Data Used in this Study

In this study, we used seismic records in the Kanto Region obtained at about 1150 stations which are maintained by 21 institutes, as shown in Figure 1.

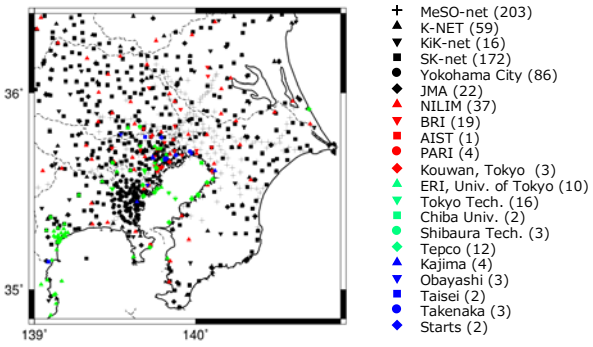


Figure 1 Locations of seismic stations used in this study. Legend shows institutions maintained stations and the number of stations.

2.2 Distributions of Pseudo Velocity Response for Periods of 2 and 3 Seconds in the Kanto Region

Distributions of pseudo velocity responses (h=5%) for periods of 2 and 3 seconds in the Kanto Region during the 2011 off the Pacific coast of Tohoku Earthquake (Mw 9.0) are shown in Figure 2 and Figure 3, respectively. Here, pseudo velocity response spectra were calculated by the geometric mean of those for NS and EW components. The complex distributions of earthquake ground motions in the Kanto Region were shown by velocity responses for periods of 2 and 3 seconds, using seismic records of the main shock observed at seismic stations of about 1150. In the Kanto Region, velocity responses for periods of 2 and 3 seconds were significantly large over 100 cm/sec in Shinagawa to Kawasaki and the Ashigara Valley, Odarawa, except in the southern area of Kasumigaura near the southern edge of the seismic fault. Especially, in the Ashigara Vellay despite of the long distance of about 200km far from the seismic fault, velocity responses for a period of 3 seconds exceeded 200 cm/sec at a certain site.

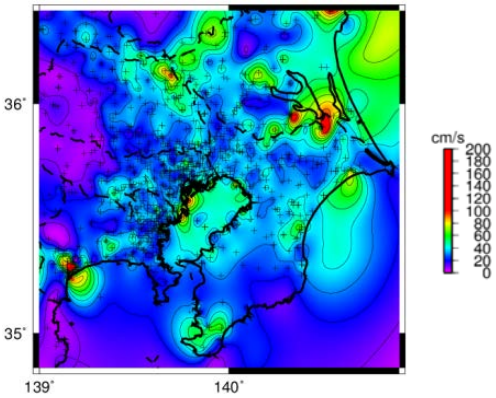


Figure 2 Distributions of pseudo velocity response (h=5%) for a period of 2 seconds observed in the Kanto Region.

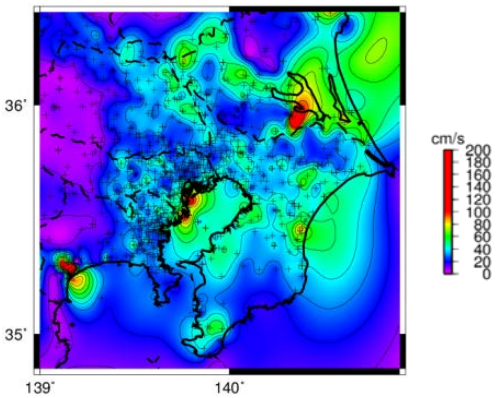


Figure 3 Distributions of pseudo velocity response (h=5%) for a period of 3 seconds observed in the Kanto Region.

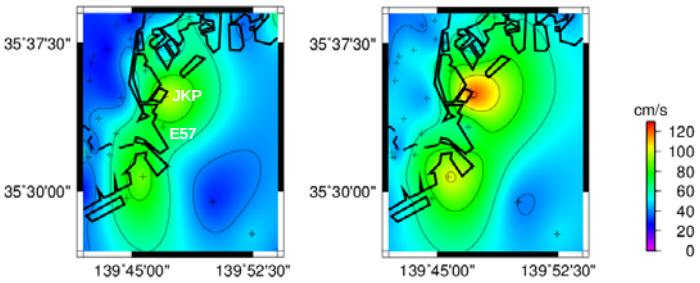
3. LOCAL SITE EFFECTS OBSERVED IN SHINAGAWA AND ODAWARA

3.1 Local Site Effect Observed in Shinagawa

Distributions of pseudo velocity responses (h=5%) for periods of 2 and 3 seconds observed in Shinagawa to Kawasaki are shown in Figure 4. Pseudo velocity responses for a period of 3 seconds at JKP, which is located at the northern area of Haneda airport, exceeded 100 cm/sec. Also, pseudo velocity responses for a period of 3 second at E57, which is located near Haneda airport, were larger than 50 cm/sec. On the other hand, pseudo velocity responses for periods of 2 and 3 seconds at the inland from the Tokyo Bay were less than 50 cm/sec. The significant difference of earthquake ground motions at the Tokyo Bay Area and the inland, in spite of the same distance from the seismic fault, indicated that the local site effects play an important role to evaluate strong ground motions.

Velocities processed by integration of accelerations and high pass filter with a cutoff period of 50 seconds for JKP and E57 are shown in Figure 5. Pseudo response velocity spectra (h=5%) for JKP and E57 are shown in Figure 6. Main phases of S-waves at JKP and E57 arrived at around 100 seconds after arrivals of P-waves. Ground motions of more than 2 cm/sec last for 400 seconds after arrivals of S-waves at JKP, which the continuous recording system has been installed. Large velocity responses were dominated for periods of 1.5 to 5 seconds, in spite of the long distance of about 150 km from the seismic fault. Especially, velocity responses exceeded 100 cm/sec for periods of 2 to 3.5 seconds. Note that velocity responses for NS component at both JKP and E57 were larger than those for EW component.

Also, we applied the time-frequency analysis by STFT (Short-Time Fourier Transform) to velocity waveforms for NS and EW components observed at JKP (Figure 7). We used a Gaussian time window of 20 seconds for STFT. Strong ground motions for periods of 1.5 to 5 seconds are lasting in main phases of S-waves for about 40 seconds.



(a) Period of 2 seconds (b) Period of 3 seconds

Figure 4 Distributions of pseudo velocity response (h=5%) for periods of 2 and 3 seconds observed in Shinagawa to Kawasaki.

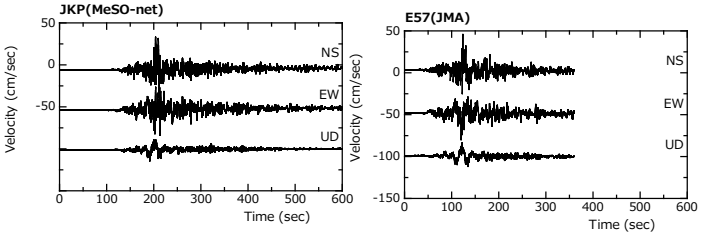


Figure 5 Velocities observed at JKP (left) and at E57 (right).

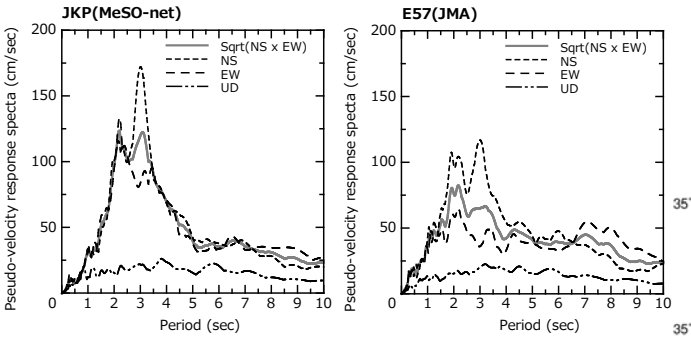


Figure 6 Pseudo velocity response spectra (h=5%) at JKP (left) and E57 (right).

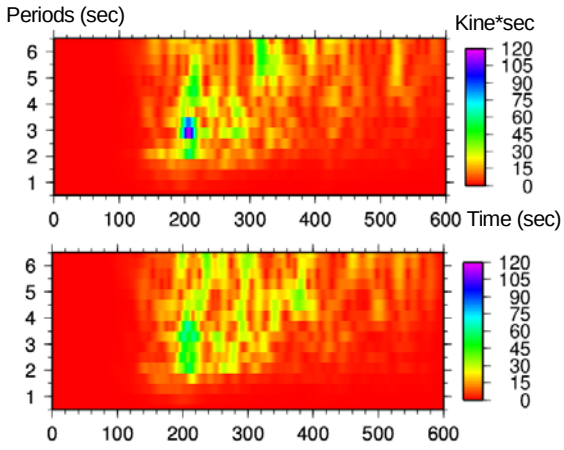


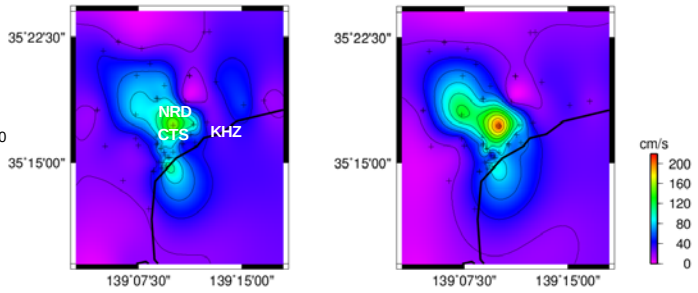
Figure 7 Time-frequency analysis by STFT for NS component (upper) and EW component (bottom) at JKP.

3.2 Local Site Effect Observed in Odawara

Distributions of pseudo velocity responses (h=5%) for periods of 2 and 3 seconds observed in the Ashigara Valley, Odawara are shown in Figure 8. Pseudo velocity responses for a period of 3 seconds at NRD, which is located at the center of the Ashigara Valley, exceeded 200 cm/sec. Also, pseudo velocity responses for a period of 3 seconds in the valley were larger than 75 cm/sec. On the other hand, pseudo velocity responses for periods of 2 and 3 seconds at KHZ, which is located at the rock site outside the valley, were less than 50 cm/sec. The strong ground motions observed in the Ashigara Valley might be amplified by the local site effects due to the soft-soil sedimentary deposits.

Velocities processed by integration of accelerations and high pass filter with a cutoff period of 50 seconds for NRD and CTS are shown in Figure 9. Pseudo response velocity spectra (h=5%) for NRD and CTS are shown in Figure 10. Main phases of S-waves at NRD and CTS arrived at around 100 seconds after arrivals of P-waves. Ground motions of more than 2 cm/sec last for 200 seconds after arrivals of S-waves at NRD. Large velocity responses were dominated for periods of 1.5 to 3.5 seconds, in spite of the long distance of about 200km from the seismic fault. Especially, velocity responses at NRD exceeded 200 cm/sec for periods of 2 to 3 seconds. Note that velocity responses for NS component at the both sites were larger than those for EW component.

Also, we applied the time-frequency analysis by STFT to velocity waveforms for NS and EW components observed at JKP (Figure 11). We used a Gaussian time window of 20 seconds for STFT. Strong ground motions for periods of 1.5 to 3.5 seconds are lasting in main phases of S-waves for about 40 seconds.



(a) Period of 2 seconds (b) Period of 3 seconds

Figure 8 Distributions of pseudo velocity response (h=5%) for periods of 2 and 3 seconds observed in the Ashigawa Valley, Odawara .

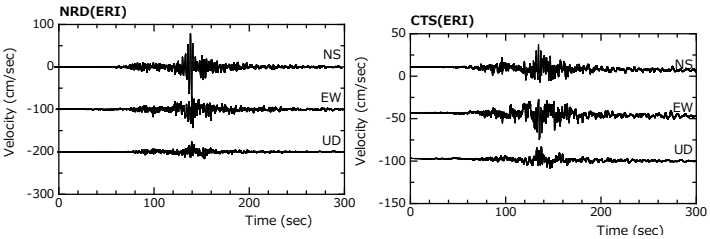


Figure 9 Velocities observed at NRD (left) and at CTS (right).

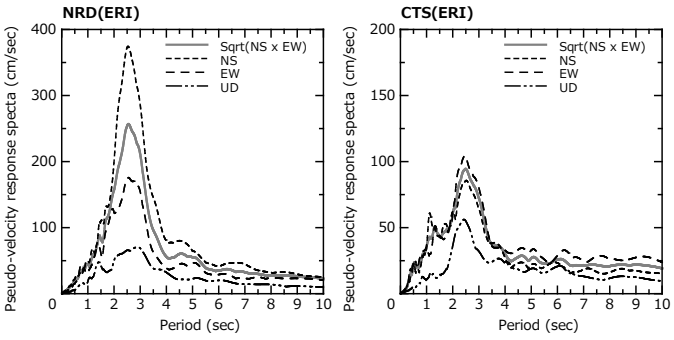


Figure 10 Pseudo velocity response spectra (h=5%) at NRD (left) and CTS (right).

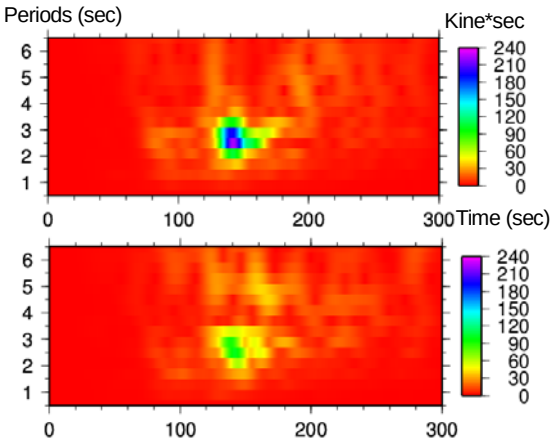


Figure 11 Time-frequency analysis by STFT for NS component (upper) and EW component (bottom) at NRD.

4. DISCUSSION

In the Ashigara Valley, large velocity responses for periods of 2 and 3 seconds observed at NRD might be amplified by the local site effects due to the deep velocity structures. To explain that, we removed site amplifications from earthquake ground motions observed at NRD by the multi-reflection theory assumed a vertical input of SH-waves and then, we compared the waveforms on the basement simulated at NRD to ground motions observed at the rock site of KHZ. When we removed the site amplifications from earthquake ground motions, we used the S-wave velocity structure at NRD (Kanno et al., 1999) estimated by the SPAC method, as shown in Figure 12. The earthquake motions simulated at NRD reproduced well those observed at KHZ (See Figure 13). The validity of the S-wave velocity structure proposed at NRD is demonstrated and also, the result indicates that the large velocity responses for periods of 2 and 3 seconds were amplified by the local site effects due to the deep S-wave velocity structures in the Ashigara Valley.

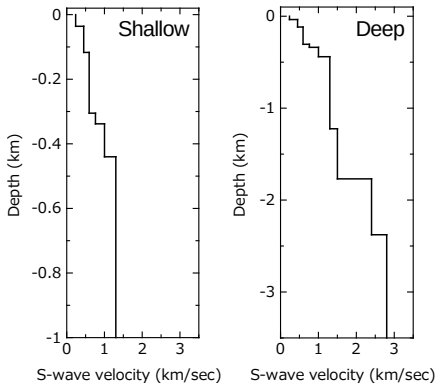


Figure 12 S-wave velocity structure at NRD proposed by Kanno et al., 1999.

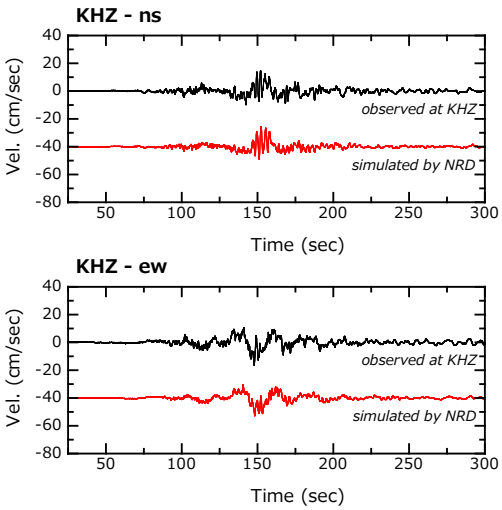


Figure 13 Comparisons of velocities on the basement simulated by the 1-D analysis to those observed at the rock site of KHZ. Results for NS and EW components are shown in the upper and the bottom, respectively.

5. CONCLUSIONS

In this study, we evaluated the strong ground motions for periods of 2 and 3 seconds locally observed in Shinagawa to Kawasaki along the Tokyo Bay and in the Ashigara Valley, Odawara, Japan, during the 2011 off the Pacific coast of Tohoku Earthquake (Mw 9.0). In Shinagawa to Kawasaki, velocity responses for a period of 3 seconds over 100 cm/sec were dominated in main phases for about 40 seconds. And also, in the center of the Ashigara Valley, velocity responses for a period of 3 seconds over 200 cm/sec were dominated in main phases for about 40 seconds. In the Ashigara Valley, earthquake motions simulated by the 1-D analysis at the sedimentary site were in good agreement with those observed at the rock site. Therefore, we concluded that the large velocity responses for periods of 2 and 3 seconds were amplified by the local site effects due to the deep S-wave velocity structures in the Ashigara Valley.

Acknowledgements:

We used seismic records by MeSO-net, K-NET, KiK-net, SK-net, Yokohama City, JMA, NILIM, BRI, AIST, PARI, Tokyo Metro. Govt., ERI Univ. of Tokyo, Tokyo Tech., Chiba Univ., Shibaura Tech., Tepco, Kajima, Obayashi, Taisei, Takenaka and Starts. We profoundly thank to these 21 institutes for providing us seismic records of the 2011 off the Pacific coast of Tohoku Earthquake. This work is one part of 'Special project for earthquake disaster mitigation in the Tokyo Metropolitan Area' supported by Ministry of Education Culture, Sports, Science and Technology, Japan.

References:

Kanno, T., Kudo, K., Takahashi, M., Sasatani, T., Ling, S., and Okada, H. (1999), "Estimation of Underground Structure using Array Observations of Microtremors in Ashigara Valley", *Proceeding of the SEGJ conference*, 342-346.

Sakai, S. and Hirata, N. (2009), "Distribution of the Metropolitan Seismic Observation Network ", *Bull. Earthq. Res. Inst. Univ. Tokyo*, **84**, 57-69.

Tsuno, S., Yamanaka, H., Midorikawa, S., Yamamoto, S., Miura, H., Sakai, S., Hirata, N., Kasahara, K., Kimura, H., and Aketagawa, T. (2012), "Characteristics of Long-Period Ground Motions in the Tokyo Metropolitan Area and its Vicinity, by Recording Data of the 2011 Off the Pacific Coast of Tohoku Earthquake (Mw 9.0) and the Aftershocks", *Journal of JAEE, **12**(5)*,102-116.

10CUEE CONFERENCE PROCEEDINGS
10th International Conference on Urban Earthquake Engineering
March 1-2, 2013, Tokyo Institute of Technology, Tokyo, Japan

EXPLORATION OF SITE CHARACTERISTICS BY MICROTREMOR OBSERVATIONS IN THE CENTRAL AREA OF THAILAND

Nakhorn Poovarodom[1], Amorntep Jirasakjamroonsri[2], and Nonthakorn Plalinyot[3]

1) Associate Professor, Faculty of Engineering, Thammasat University, Pathumthani 12120, Thailand
2) Graduate Student, Faculty of Engineering, Thammasat University, Pathumthani 12120, Thailand
3) Graduate Student, Faculty of Engineering, Thammasat University, Pathumthani 12120, Thailand
pnakhorn@engr.tu.ac.th, amorntep_aj@hotmail.com, nonthakorn_plalinyot@hotmail.com

Abstract: This paper presents results of extensive microtremor surveys in the central area of Thailand. The studied area is a large flat plain underlain by alluvial and deltaic sediments of the Chaophraya Basin. Field investigations were conducted for 126 sites distributed almost evenly in the studied area. The Horizontal-to-Vertical spectral ratio (H/V) method was used to estimate predominant period and the Spatial Autocorrelation (SPAC) method to determine shear wave velocity profile from phase velocity dispersion curve and inversion analysis. Site classifications based on the predominant period and the average shear wave velocity are presented and discussed. The area along the Gulf of Thailand and the south-east part exhibit very low average shear wave velocity from the surface to 30-m depth (V_{S30}) of 70 m/s and long predominant period (Tp) of 1.1 second, while high V_{S30} of 550 m/s and short Tp of 0.2 second are found in the north, west and east parts which are boundary of the plain. From a number of site characteristic data, relations among average shear wave velocity at different depth and predominant period are examined.

1. INTRODUCTION

Several observations from past earthquakes have revealed that seismic waves could be remarkably modified by local site conditions. Therefore, evaluation of site effects from site characteristics have been considered as a main issue to specify appropriate ground motions for earthquake resistant design of structures. Some common practices for site characterization given in design codes inferred from dynamic properties of a site include average shear wave velocity from the surface to 30-m depth (since NEHRP 1994) andS site predominant period (Japan Road Association, 1990).

Conventional seismic methods for surveying shear wave velocity have crucial disadvantages as they are costly, time consuming and difficult to conduct in urban areas. Alternatively, observations by microtremor have been proposed as an efficient tool to evaluate site effects from several advantages such as economical, environmentally friendly for urban areas and effective for low or moderate seismicity.

The central area of Thailand which covers the capital city, Bangkok, and the vicinity provinces is founded on deltaic sediments of main rivers of the country. The area, with a population of over ten million, is located about 120 to 300 km from low to moderate seismicity faults and over 400 km from the highly active Sumatra subduction zone. Site effects in this area have been regularly observed from distant earthquakes. Although the new seismic regulation for Thailand (DPT 2009) after the recent Probabilistic Seismic Hazard Assessment (PSHA) studies (Ornthammarath et. al. 2010, Palasri and Ruangrassamee 2010) have included the site effects into seismic consideration, there have been very few investigations of site classification in the country. From the current limited information, this study aims to quantitatively investigate site characteristics of subsoils using economical and practical technique of microtremor observations in order to provide sufficient data for site characterization in the central area of Thailand. The technique of single point observation with Horizontal-to-Vertical spectral ratio (H/V) method to estimate the predominant period and the technique of array observation with Spatial Autocorrelation (SPAC) technique for exploration of shear wave velocity profile down to about 90 m were conducted. Following the prior work (Poovarodom and Plalinyot 2013), this paper presents results of investigation for 126 sites in approximately 150 km (north-south) by 250 km (east-west) area. Discussions on relations among the obtained results such as the shear wave velocity at different depth and the predominant period are provided.

2. MICROTREMOR OBSERVATION TECHNIQUES

Microtremor observations have been raised up as an efficient tool for evaluating site effects. This technique has several advantages; economical, environment friendly for urban area and effective for low or moderate seismicity area.

In this study, the microtremor measurements, which can be readily conducted on the ground surface without making a borehole, are conducted for extensive surveys in the studied area to provide site characteristics useful for ground motion evaluation. Two techniques were employed, the Horizontal-to-Vertical spectral ratio (H/V) method to estimate the predominant period and the Spatial Autocorrelation (SPAC) technique for exploration of shear wave velocity profile.

2.1 Horizontal to Vertical Spectral Ratio Method (H/V spectral ratio)

Nakamura (1989) proposed this technique to interpret records of microtremors for the dominant period of subsoil sediments and also the estimated amplification level. In this method, the ratios of horizontal to vertical Fourier Spectra of microtremors are used to eliminate the source effect. This technique requires the horizontal and vertical component of microtremors measured at a single station only. The H/V spectrum plots are obtained by taking the ratio of the Fourier Spectra of the horizontal to the Fourier Spectra of the vertical component, as shown in equation 1.

$$\text{H/V spectrum} = \frac{\sqrt{F_{NS} \times F_{EW}}}{F_{UD}} \tag{1}$$

where F_{NS}, F_{EW} and F_{UD} are the Fourier amplitude spectra in the north-south, east-west and up-down directions, respectively. The peak of the H/V spectrum plot is interpreted as predominant period and amplification ratio. In spite of the wide popularity of the H/V spectral ratio method, there exists inconsistency of the assumption used in this method with theory. Nakamura's method assumes that microtremors are composed of body waves and thus is theoretically inconsistent with the results that show that microtremors are composed of surface waves. However, a number of researches have experienced that the H/V spectral ratio can be utilized to estimate the predominant period of a site, and it has broadly been applied to evaluate site effect and seismic microzonation.

2.2 Spatial Autocorrelation Method (SPAC method)

This technique was proposed by Aki (1957) based on the relationship between the temporal and spatial spectra of waves to obtain phase velocity dispersion curve. The basis of SPAC method is to simultaneously record the vertical component of microtremors for several positions to obtain Rayleigh wave samples propagating from a wide range of azimuthal angles. The coherency spectrum can then be computed for any pair of sensor in the array to evaluate the correlation among them to determine phase velocity characteristic which is dispersive. The coherencies for all measurement pairs having the same spatial distance are then azimuthally averaged to provide the spatial autocorrelation coefficients of inter-station distance r, $\rho(\omega, r)$. By assuming that, the wave energy propagates with only one velocity at each frequency, ω, it can be shown that the spatial autocorrelation coefficient for a circular array is given by (Aki, 1957, Okada, 2003):

$$\rho(\omega, r) = J_0\left(\frac{\omega r}{c(\omega)}\right) \tag{2}$$

where J_0 is the Bessel function of the first kind with the zero-th order and $c(\omega)$ is the (dispersive) phase velocity at frequency ω for the Rayleigh waves with the fundamental mode. From the dispersion relation of phase velocity and frequency, the results from field observations are then compared with those derived theoretically from a horizontally layered earth model by iteration procedure. The results of best-fit shear wave velocity–depth profile can be determined from the inversion analysis, in which this study applies the technique developed by Yokoi (2005) which employs the combination of Down Hill Simplex Method with Very Fast Simulated Annealing.

3. FIELD OBSERVATIONS AND DATA ANALYSIS

3.1 Area of Study

The investigated area is located within latitudes 13° 10' N to 14° 40' N and longitudes 99° 40' E to 101° 20' E, covering Bangkok and the vicinity provinces named Ratchaburi in the west, Phra Nakhorn Si Ayutthaya in the north, Samut Sakhon and Samut Prakan in the south, and Nakhon Nayok and Chachoengsao in the east. The area lies on a large alluvial plain of delta area where four main rivers, Chaopraya, Tha Chin, Mae Klong and Bang Pakong, empty into the Gulf of Thailand in the south. Figure 1 shows the investigated area where 126 observation sites are distributed almost evenly inside.



Figure 1 Area of Study

The plain consists of thick soft clay in which the thickness increases gradually from the north to the south, and more sharply near the edge of the basin in the west and east direction (AIT 1981). Generally, the thickness of soft clay with very low shear strength is 15 to 20 meters at the central area. The depth of bedrock is estimated to be in an order of 500 meters or deeper, but there is no sufficient information available.

3.2 Microtremor Observation

The vibration measuring system used in this work consists of a 24-bit seismic recorder and four units of tri-axial velocity sensor with a natural period of 2 seconds. The arrangement of sensors for SPAC observation was selected as equilateral triangular array where one unit is placed at the center of circular and the other three are on the perimeter allowing simultaneously record of six pairs of observation with two different radiuses, i.e. r and $\sqrt{3}r$. The array sizes consist of small radius of 10 m to large radius of 50 m. For each observation, data were collected for 20 minutes with sampling frequency of 200 Hz. The data of one station measurement were analyzed for H/V spectrum ratio and the data of array measurement were used for SPAC analysis. The maximum depth for inversion analysis was set to 90 m which is approximately equal to the maximum distance between the two sensors.

4. RSULTS AND DISCUSSIONS

4.1 Predominant Period

From H/V spectral plot, the identified period at the spectral peak is interpreted as the predominant period, T_P. It is noted that, due to limitation of the sensor, the peak for period longer than 2 second was not identified in this study. T_P values are found in a range of 0.2 to 1.1 second. Figure 2 presents a map of variation of T_P where solid line and number indicate contour line of area having approximately the same T_P. The sites with longest T_P are located in the south-east part which contains the deepest layer of soft soil. Area along the Gulf of Thailand and in Bangkok metropolitan also exhibit considerably long T_P, longer than 0.8 second. T_P decreases toward the north, east and a west direction as soil becomes stiffer around the edge of the basin.

4.2 Shear Wave Velocity

The results of shear wave velocity are presented as the average shear wave velocity from the surface to 30-m depth (V_{S30}) and they are shown as a contour map in Figure 3. V_{S30} varies considerably in the area, from 70 to 550 m/s. The sites with lowest V_{S30} are located in the south-east part which is the same area of longest T_P. Area along the Gulf of Thailand and central of Bangkok exhibits low V_{S30} which is also consistent with distribution of thick soft clay. As soil becomes stiffer toward the edge of the studied area, V_{S30} increased and the hardest soil sites in this study are located near the boundary of the plain.

Variations of shear wave velocity are illustrated as 2D cross-sectional profiles in Figure 4 and 5 for north-to-south and west-to-east directions, respectively. In these figures, color lines represent constant average shear wave velocity of 100, 150, 200, 250 and 300 m/s for different sites. The depth of the level for a specific average value is shown in the vertical axis. Shear wave velocity profile for each site is also shown in these figures. From Figure 4, depth of any specific value of the average shear wave velocity increases from the north to the south indicating that shear wave velocity at the same depth becomes lower toward the southern part. In Figure 5, high average shear wave velocities are found in shallow layers of the area near the edge, in Ratchaburi and Chachoensao. Profiles of shear wave velocities drop sharply after the boundary. Shallow shear wave velocities are almost invariant at the central area. Deep shear wave velocities tend to decrease in Samutprakarn where V_{S30} is minimum.

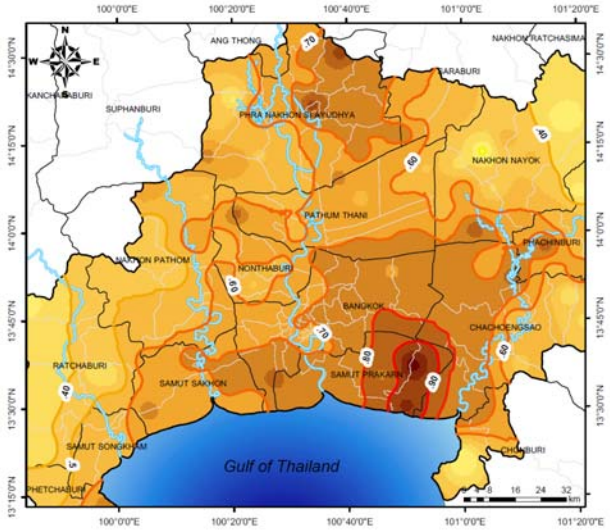


Figure 2 Contour Map of T_P

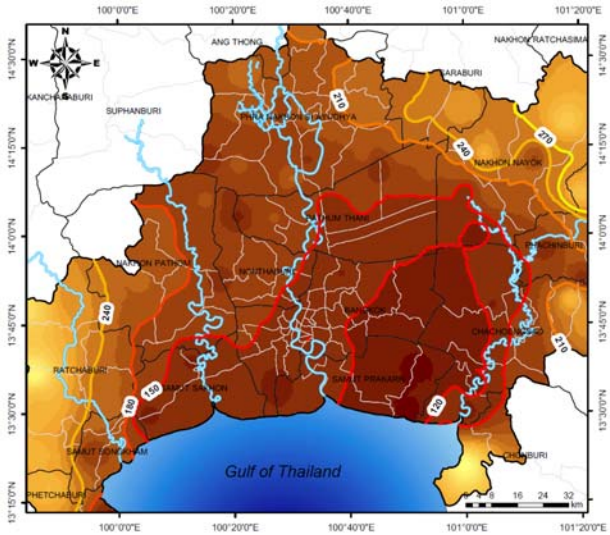


Figure 3 Contour Map of V_{S30}

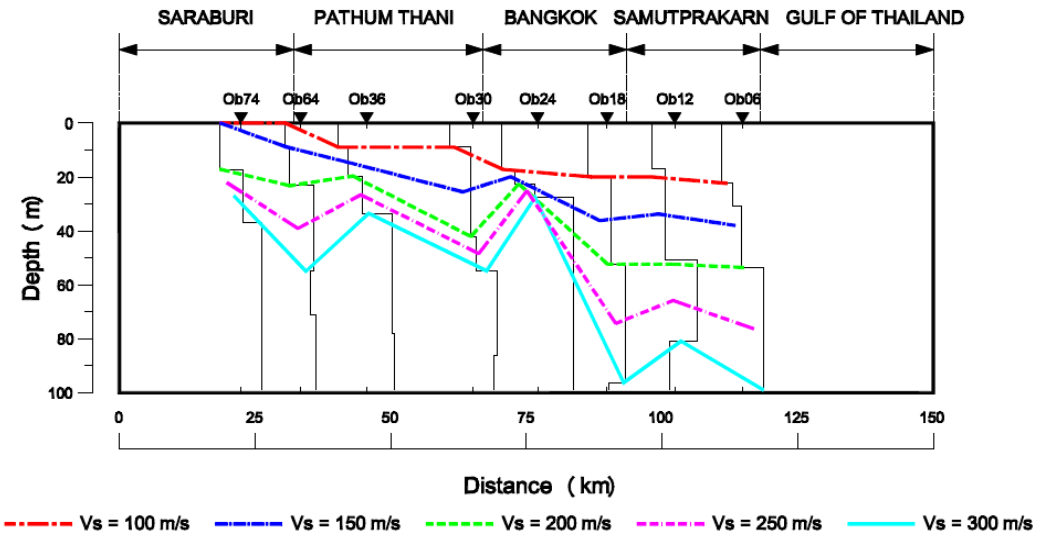


Figure 4 Cross-Sectional Profile of Shear Wave Velocity (North-to-South direction)

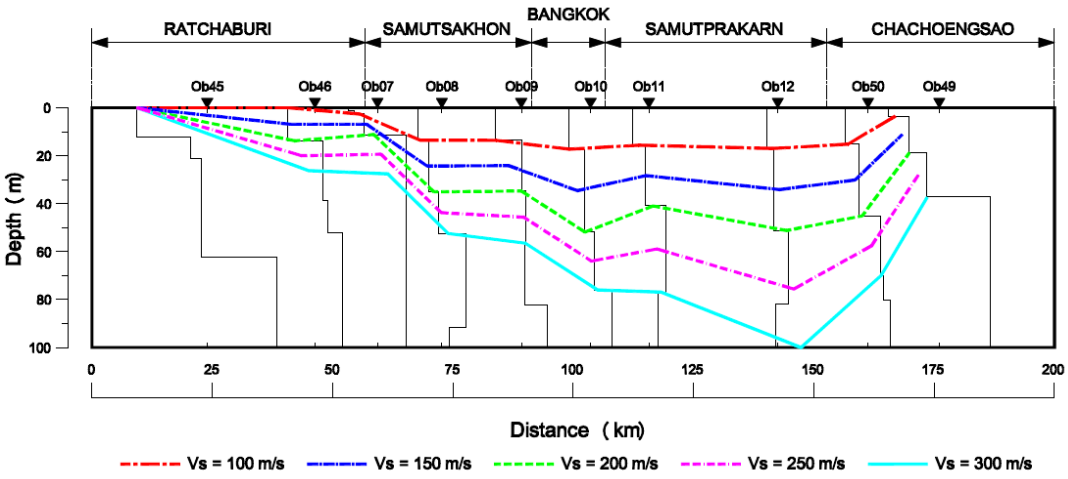


Figure 5 Cross-Sectional Profile of Shear Wave Velocity (West-to-East direction)

4.3 Relations among V_S and *Tp*

From a number of site characteristic data presented in the preceding sections, relations among average shear wave velocity at different depth V_{SD} and predominant period are discussed. In the following discussion, the statistical correlation among the average shear wave velocity from the surface to 10, 30, 60 and 90-m depth (V_{S10}, V_{S30}, V_{S60} and V_{S90}) together with *Tp* are examined by regression analysis. First, the consistency of V_{SD} is investigated by considering relations of V_{SD} with V_{S30}. The generalized relation among V_{SD} and V_{S30} is written as a form in Eq. (1).

$$V_{SD} = \alpha_1 (V_{S30})^{\beta_1} \tag{1}$$

Eq. (1) can be used for the regression analysis to determine the coefficient α_1 and β_1 by re-written in a form of linear relationship as:

$$y = a + \beta x \tag{2}$$

In which $y = \log(V_{SD})$, $a = \log(\alpha_1)$, $x = \log(V_{S30})$ and $\beta = \beta_1$. The plots of Eq. (2) can provide the interception a at $x = 0$ and slope β of the straight line by minimizing the standard error of estimate between the measured and the predicted values. Figure 6 presents the plot of $x = \log(V_{S30})$ and $y = \log(V_{SD})$, and the results of regression analyses are shown for α_1, β_1 and the coefficient of determination, R^2 in Table 1.

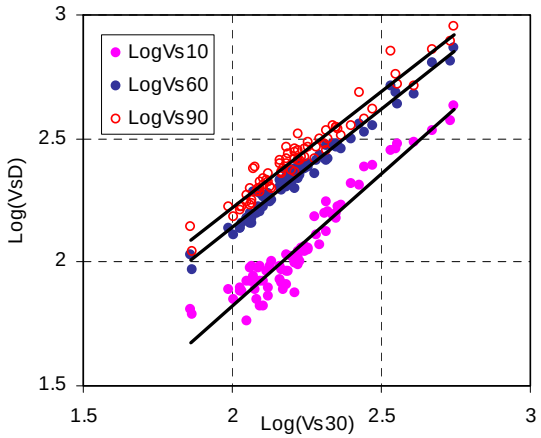


Figure 6 Relations among V_{S30} with V_{S10}, V_{S60} and V_{S90}

Table 1 Regression Analysis Results of V_{S10}, V_{S60} and V_{S90}

	α_1	β_1	R^2
V_{S10}	0.569	1.035	0.851
V_{S60}	1.635	0.961	0.971
V_{S90}	2.174	0.939	0.941

From the above regression results, the exponent of Eq. (1) is almost unity indicating that the relations between V_{S30} and V_{SD} are nearly in linear proportion. In addition, high correlations among V_{S30} with V_{S60} and V_{S90} are obtained from their considerably large R^2 while it is lower for correlations between V_{S30} and V_{S10}. This can be inferred that V_{S30} may represent deeper shear wave velocity profile for this area quite well. However shallow average shear wave velocity of V_{S10} may not appropriately represent deeper velocity structures in the case of thick deposits as in this area.

Similar regression analyses are conducted for determination of correlation among the average shear wave velocity at different depth and the predominant periods obtained in this study. The relations among V_{SD} and the predominant frequency (1/ Tp) can be written in Eq. (3). The results of regression analysis are presented in Figure 7 and Table 2.

$$V_{SD} = \alpha_2 (1/T_P)^{\beta_2} \qquad (3)$$

The relations between V_{SD} and (1/ Tp) are also close to linear function. Moreover their correlations are considerable, especially for deep V_{SD}. However, lower correlation with V_{S10} is observed. These observations address the applicability of H/V spectral ratio technique that the information of deep ground structure could be appropriately achieved but not that of the uppermost layers.

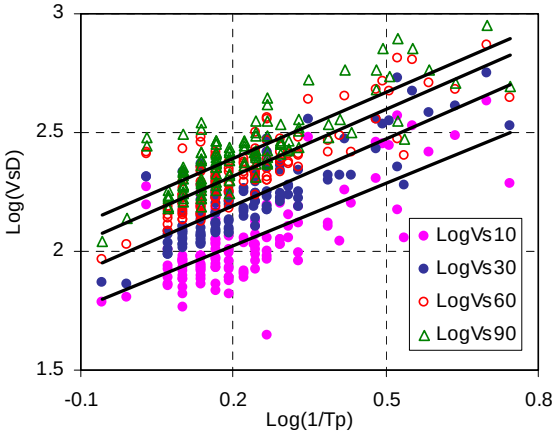


Figure 7 Relations among (1/ TP) with V_{S10}, V_{S30}, V_{S60} and V_{S90}

Table 2 Regression Analysis Results of (1/ Tp) and V_{S10}, V_{S30}, V_{S60}, V_{S90}

	α_2	β_2	R^2
V_{S10}	70.4	0.880	0.471
V_{S30}	100.7	0.934	0.658
V_{S60}	135.2	0.934	0.687
V_{S90}	160.6	0.930	0.689

5. CONCLUDING REMARKS

Site characterizations in the central area of Thailand by microtremor observation are reported in this paper. From 126 observation sites, shear wave velocities, by SPAC method, and predominant periods, by H/V spectral ratio method, are presented and discussed. The area along the Gulf of Thailand and the south-east part of the studied area exhibit very low V_{S30} of 70 m/s and long predominant period of 1.1 second while high V_{S30} of 550 m/s and short predominant period of 0.2 second are found near the boundary of the Chaophraya basin.

The relations among the average shear wave velocity at different depth, from 10 m to 90 m, and the predominant periods at site are examined. It was shown that shallow shear wave velocities to 10 m depth, influenced by the top layer of weathered soil, were not reasonably correlated with deep shear wave velocities. Higher correlations were observed among V_{S30} and deeper shear wave velocities. In addition, the predominant periods were found to be more correlated with deep average shear wave velocity by higher value of the coefficient of determination than average shear wave velocity at 10 m depth.

Acknowledgements:

The authors acknowledge support from the Thailand Research Fund, research number RDG5330026 and the 2011 research fund from the National Research Council of Thailand. The authors are grateful to Dr. Toshiaki Yokoi (Building Research Institute, Japan) for his valuable consultations on microtremor techniques.

References:

Aki K. (1957), "Space and Time Spectra of Stationary Stochastic Waves, with Special Reference to Microtremors", *Bulletin of the Earthquake Research Institute*, No. 22 , 415–456.

AIT (1981). Investigation of land subsidence caused by deep well pumping in the Bangkok area. Asian Institute of Technology, Thailand.

Building Seismic Safety Council (2004), NEHRP Recommended Provisions for Seismic Regulations for New Buildings and Other Structures, Part 1: Provisions (2003 Edition), FEMA 450, Federal Emergency Management Agency, Washington, D.C.

Department of Public Works and Town & Country Planning (DPT) (2009), "Standard for Earthquake Resistant Design of Buildings, DPT standard 1302" (in Thai).

Japan Road Association (1990) Specifications for Highway Bridges Part V, Seismic Design. Maruzen Co., LTD

Nakamura Y. (1989), "A Method for Dynamic Characteristics Estimation of Subsurface using Microtremor on the Ground Surface", *Q. Rep. Railw. Tech. Res. Inst.* 30, No. 1, 25–33.

Okada H. (2003), "The Microtremor Survey Method (translated by Koya Suto)", Geophysical Monograph Series, No.12, Society of Exploration Geophysicists.

Ornthammarath T., Warnitchai P., Worakanchana K., Zaman S., Sigbjörnsson R., and Lai C.G. (2010). Probabilistic seismic hazard assessment for Thailand, Bulletin of Earthquake Engineering, 9:2, 367-394.

Palasri C. and Ruangrassamee A. (2010). Probabilistic seismic hazard maps of Thailand, Journal of Earthquake and Tsunami, 4:4, 369-386.

Poovarodom N. and Plalinyot N. (2013), "Site Characterization in the Greater Bangkok Area by Microtremor Observations", Journal of Earthquake Engineering, DOI: 10.1080/13632469.2012.707346.

Yokoi T. (2005), "Combination of Down Hill Simplex Algorithm with Very Fast Simulated Annealing Method-an Effective Cooling Schedule for Inversion of Surface Wave's Dispersion Curve", *Proc. of the Fall Meeting of Seismological Society of Japan.* B049.

10CUEE CONFERENCE PROCEEDINGS
10th International Conference on Urban Earthquake Engineering
March 1-2, 2013, Tokyo Institute of Technology, Tokyo, Japan

ESTIMATION OF DEEP SUBSURFACE STRUCTURES FOR PREDICTION OF LONG-PERIOD GROUND MOTION CHARACTERISTICS AROUND THE TACHIKAWA FAULT

Koichiro Saguchi[1] and Hiroaki Yamanaka[2]

1) Postdoctoral Fellow, Department of Environmental Science and Technology, Tokyo Institute of Technology, Japan
2) Professor, Department of Environmental Science and Technology, Tokyo Institute of Technology, Japan
saguchi.k.aa@m.titech.ac.jp, yamanaka @depe.titech.ac.jp

Abstract: Tachikawa fault is one of the most activity faults in the Tokyo metropolitan area and when large earthquake will occur by this fault in the near future, it is expected that large economic and human loss will happen around this area. However, three dimensional subsurface structural model is not clear still enough for the estimation of the strong ground motions in this area. In this study, we estimated the three dimensional subsurface structural model using the receiver function method from the obtained records of the K-NET, KiK-NET and SK-net. We calculated the receiver functions from 20 to 50 seismic records obtained at the 60 stations, and we identified the subsurface structural model using inversion based on the simulated annealing method. We constructed the three-dimensional subsurface structural model in this area obtained from P-wave and S-wave velocity profiles of thick sediments at each station. Moreover, we calculated Radial/Vertical spectral ratios with this three dimensional model. The results indicate that the characteristics of the calculated predominant period display good agreement with the observed one during the 2011 off the Pacific coast of Tohoku Earthquake.

1. INTRODUCTION

Since the 2011 off the Pacific coast of Tohoku Earthquake, there have been increased seismic activities in the Tokyo metropolitan area. Tachikawa fault is one of the most activity faults in the Tokyo metropolitan area and when large earthquake will occur by this fault in the near future, it is expected that large economic and human loss will happen around this area. Therefore it is required to estimate the strong ground motions accurately in this area. However, three-dimensional subsurface structure including detailed fault geometry is not clear still enough for the prediction of the strong ground motions in this area.

In this study, we estimated the three-dimensional subsurface structural model using the receiver function method (Langston 1979, Kobayashi et al., 1998) from the obtained records of the K-NET and KiK-NET of National Research Institute for Earth Science and Disaster Prevention (NIED), and SK-net provided by the Tokyo metropolitan area comprehensive network. We calculated the receiver functions from 20 to 50 seismic records obtained at the 60 stations, and we identified the subsurface structural model using inversion based on the simulated annealing method. We constructed the three dimensional subsurface structural model in this area obtained from P-wave and S-wave velocity profiles of thick sediments at each station. Moreover, we calculated Radial/Vertical spectral ratios with this three dimensional model. Finally, we discuss the long-period ground motion characteristics during the 2011 off the Pacific coast of Tohoku Earthquake around the Tachikawa fault based on a constructed three-dimensional subsurface structural model.

2. SPATIAL DISTRIBUTION OF PS-P TIME BY THE RECEIVER FUNCTION METHOD

Tachikawa fault zone located about 20km western of Tokyo metropolitan, and a total length of this fault zone is about 33km consists with Naguri and Tachikawa fault as shown in Figure 1. Many seismic records was observed at seismic stations (K-NET, KiK-NET and S K-net) around those faults. Figure .1 also shows distribution of the depth up to the seismic basement based on "Long-period ground motion hazard maps" (Headquarters for Earthquake Research Promotion 2009). The seismic basement became deep gradually from west to east from this distribution, and it is not confirmed that the geometry of a subsurface structure are change drastically around the Tachikawa fault.

In this study, we calculated the receiver functions from the seismic records obtained at the 60 stations as shown in Figure 1. Seismic records was used at each station from 20 to 50 records in the 70 earthquakes (over Mj = 4.5) within 100km of the epicentral distance as shown in Figure 2. In the calculation of the receiver function at each station, we used the first 5 seconds from the onset of the P-wave in these records. A band-pass filter with a frequency range from 1.0 to 5.0Hz was applied during the calculations. An example of the resultant receiver function at TKYH02 (KiK-NET) is

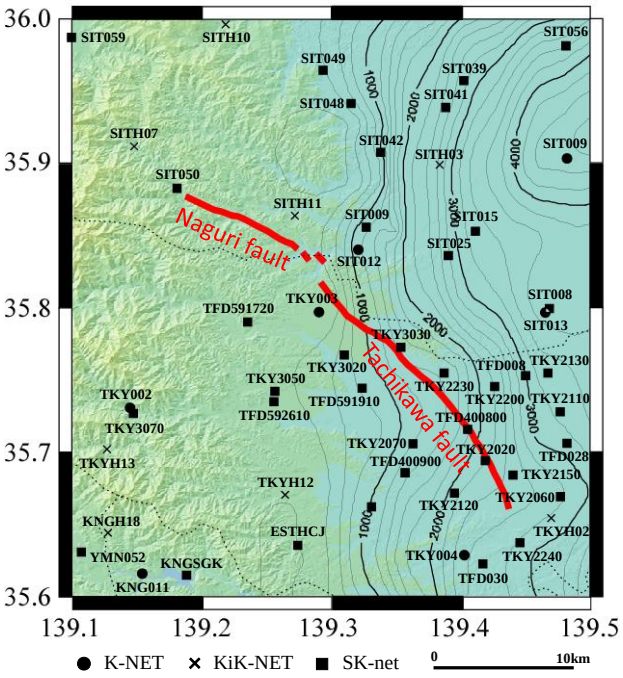


Figure 1 Seismic stations around the Tachikawa fault zone

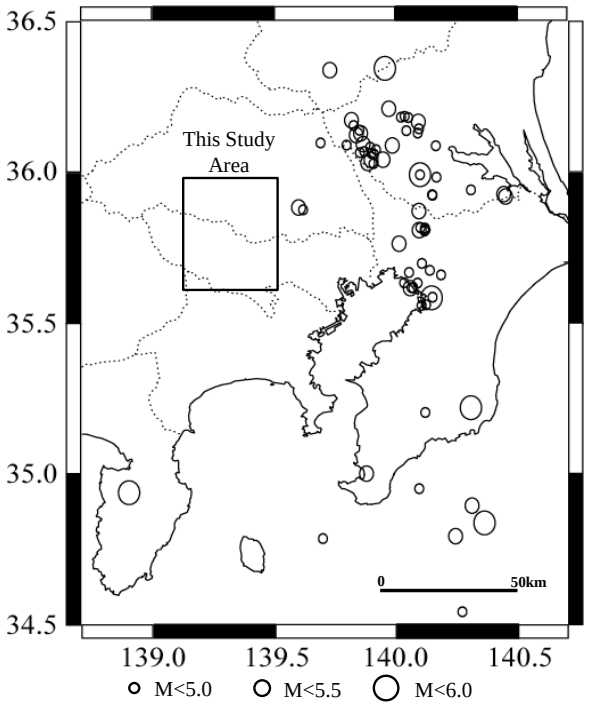


Figure 2 Epicenter of the earthquakes that was used for the receiver function method analysis

shown in Figure 3. PS-P time is indicating 1.3 seconds in the observed receiver functions as shown in Figure 3.

Figure 4 shows the distribution of PS-P time at all seismic observation stations obtained from the analysis of the receiver function method. We found that PS-P time is significantly different across the Tachikawa fault as shown in Figure 4. PS-P time has become longer in the eastern part of the Tachikawa fault although that has become shorter in the western part of the Tachikawa fault. Therefore, it will be assumed that there are thick sedimentary layers in the eastern part of the fault although there are not sedimentary layers in the western part of the fault.

Figure 5 shows the distribution of a difference between observation and theoretical PS-P time. A theoretical PS-P time obtained from the receiver functions calculated with the subsurface structural model base on "Long-period ground motion hazard maps", and the theoretical receiver functions are calculated by the method of Haskell (1962). It is almost the same as the theoretical and observed PS-P time at the stations on the eastern part of the Tachikawa fault (i.e. TKY2200, TFD400800) as shown in Figure 5. The observed PS-P time is shorter than the theoretical one at the station on the western part of the Tachikawa fault, especially TKY2070.

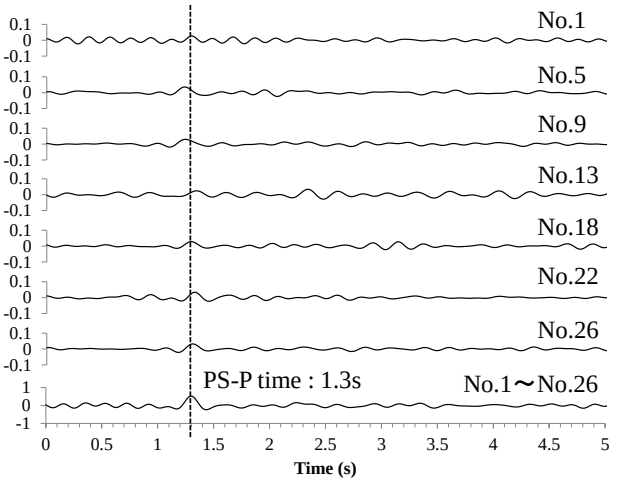


Figure 3 Receiver functions at TKYH02 (KiK-net)

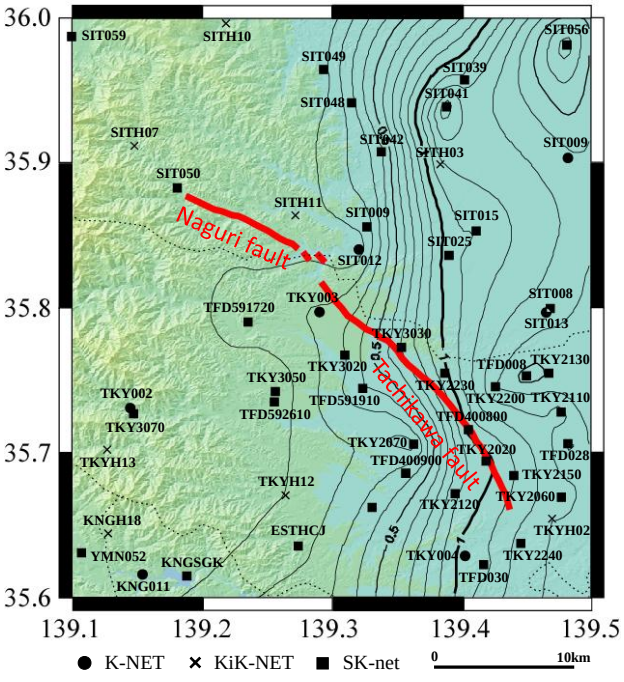


Figure 4 Distribution of the P-SP time obtained from the receiver function method analysis

Thus, it is considered that sedimentary layers are very thin than the subsurface structural model based on "Long-period seismic hazard map". Further, around the Naguri fault, it is possible that the sedimentary layers in the southern part are thicker than the northern part of the fault.

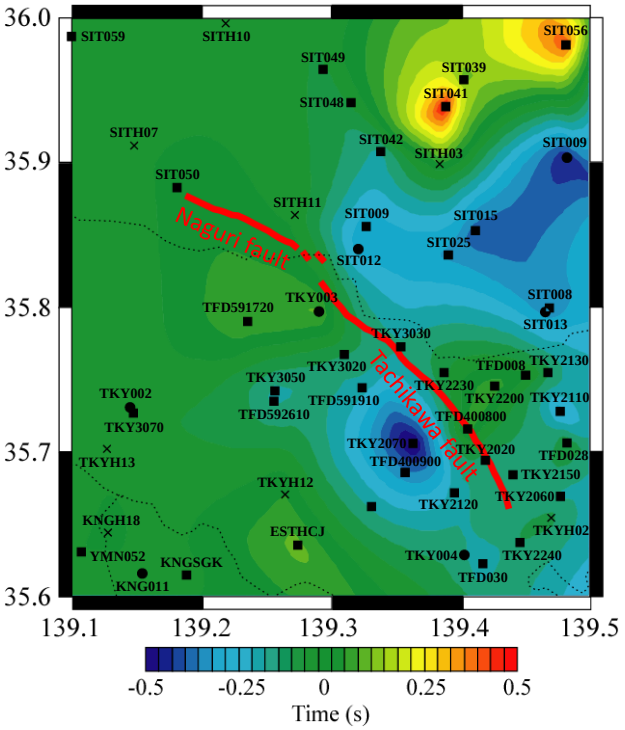


Figure 5 Distribution of the time difference between the observed P-SP time and the theoretical one based on "Long-period seismic hazard map"

3. IDENTIFICATION OF SUBSURFACE STRUCTURE BY SIMULATED ANNEALING

We identified the subsurface structural model at each seismic observation station from the receiver function calculated from the observed record using the simulated annealing method (Ingber 1989, Yamanaka 2001).

We identified the layer thickness (H) in the search range set of the 1-200% of the initial value because the trade-off occurs between the layer thickness and P and S-wave velocity. Initial subsurface structural model at each station based on "long-period seismic hazard map" was used in the inversion. Evaluation function in the identification of subsurface structure is defined as the following equation (Kurose and Yamanaka 2006).

$$E_m = \frac{1}{N}\sum_{n=1}^{N}\left|\frac{R.F.^{C}(t_n) - R.F.^{O}(t_n)}{\sigma(t_n)}\right| \qquad (1)$$

Where $R.F.^{C}(t_n)$ is the theoretical receiver function, $R.F.^{O}(t_n)$ is the observed receiver function, $\sigma(t_n)$ is the standard deviation of the observed receiver function $R.F.^{O}(t_n)$ at time t_n and N is the number of data, respectively.

Figure 6 shows a comparison between the receiver function (Obs.) observed at TKYH02 (KiK-NET) and the inverted receiver function (Inv.) as an example of the identified result. In addition, receiver function (Ini.) calculated with the underground structure model by "Long-Period Ground Motion Hazard Maps" as an initial model is also shown in Figure .6. The receiver function with identification results is good agreement with the observed receiver function, and it is indicated that the layer thickness of individual layers are inverted very well.

Figure 7 shows examples of the P and S-wave velocity profiles at TFD400800 and TKY2070 (SK-net) obtained from inversion. Velocity profiles are mainly approximated by 4 sedimentary layers and seismic basement with P-wave velocity of 5.5km/s and S-wave velocity of 3.2km/s around the Tachikawa fault zone. The thickness of the sedimentary layers at TKY2070 and TFD400800 which are located in the western part and eastern part of the Tachikawa fault was 0.3km and 2.1km, respectively. Therefore, it is indicated that a basement depth in those profiles at down-thrown side of the fault is larger than that at up-thrown side with a difference of about 1.8km. On the other hand, it is estimated that the seismic basement of the Naguri fault dropped toward to the southwest with a difference of about 0.3km according to inverted subsurface structures at SITH11 (KiK-NET) and TFD591720 (SK-net).

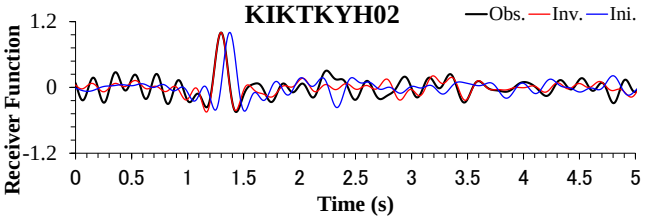


Figure 6 Identified receiver function obtained from the inversion using the simulated annealing method at TKYH02 (KiK-net)

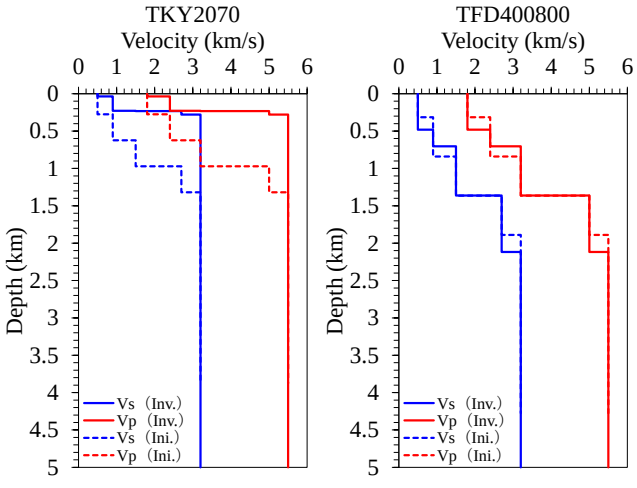


Figure 7 Identified subsurface structural models obtained from the inversion using the simulated annealing method (Left:TKY2070 (Sk-net), Right: TFD400800 (Sk-net))

4. THREE-DIMENSIONAL SUBSURFACE STRUCTURE NEAR THE TACHIKAWA FAULT ZONE AREA

We constructed the three-dimensional subsurface structural model near the Tachikawa fault zone obtained from P-wave and S-wave velocity profiles of thick sediments at each station. Figure 8 shows distribution of depth to the top of the seismic basement (Vp=5.5km/s, Vs=3.2km/s) in the three- dimensional subsurface structural model around the Tachikawa fault zone obtained from the inversion using the receiver functions. It is indicated that the seismic basement is steeply inclined around the Tachikawa fault as shown in Figure 8.

Figure 9 shows the ratio of the depth of the upper of the seismic basement between the inverted three-dimensional subsurface structural model to the "Long-period ground motion hazard maps" model shown in Figure 1. Near the Tachikawa fault, it is indicated that the seismic basement evaluated by this study has become shallow in the southwestern part of the fault as shown in Figure 9. In addition, around the Naguri fault, it is denoted that the seismic basement evaluated by this study has become deep in the southern part of the fault. The seismic basement obtained from inversion display good agreement with the "Long-period ground motion hazard maps" model in the western part of Tokyo metropolitan area and the southern part of Saitama prefecture as shown in this figure.

5. LONG-PERIOD GROUND MOTION CHARACTERISTICS AROUND THE TACHIKAWA FAULT DURING THE 2011 OFF THE PACIFIC COAST OF TOHOKU EARTHQUAKE

Tsuno et al. (2012) evaluated the characteristics of the long-period ground motions and site amplifications in the Kanto plain including Tokyo metropolitan area by the main shock and aftershocks of the 2011 off the Pacific coast of Tohoku Earthquake. Here, we discuss the corresponding with the sedimentary layers thickness of the inverted three-dimensional subsurface structural model and the predominant period of the Fourier spectrum which were observed during the main shock around the Tachikawa fault zone area.

Figure 10 shows the distribution of the predominant period of the Fourier spectrum with the horizontal component which synthetic two components around the Tachikawa fault zone. Figure 10 also shows distribution of the depth up to the seismic basement based on inverted three-dimensional subsurface structural model using receiver functions. It should be noted that our target period range is from 0.5 to 10 seconds. The distribution of predominant periods observed at the eastern part of the Tachikawa fault is about 3 to 4 seconds as shown in Figure 10. The distribution of predominant periods observed at the western part of the Tachikawa fault is around 1 second. It seems that the distribution of predominant period doesn't display good agreement with the depth of the upper seismic basement.

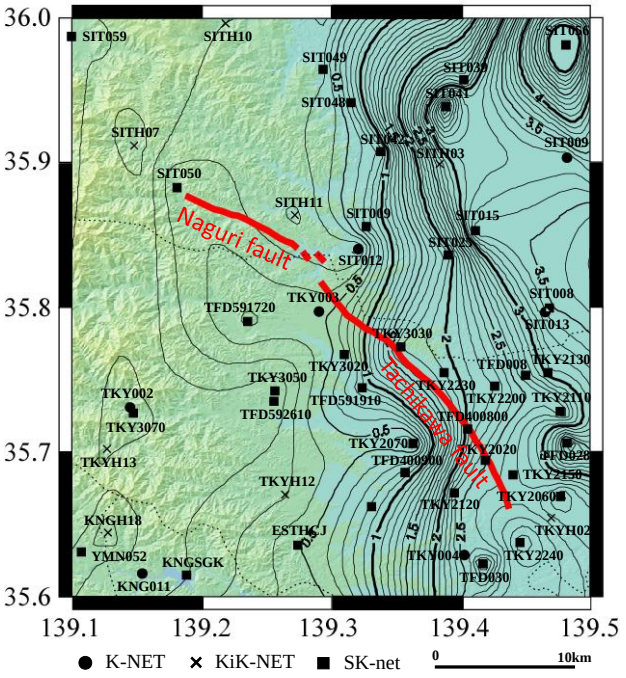


Figure 8 Distribution of depth to the top of the seismic basement (Vp=5.5km/s, Vs=3.2km/s) in the three- dimensional subsurface structural model

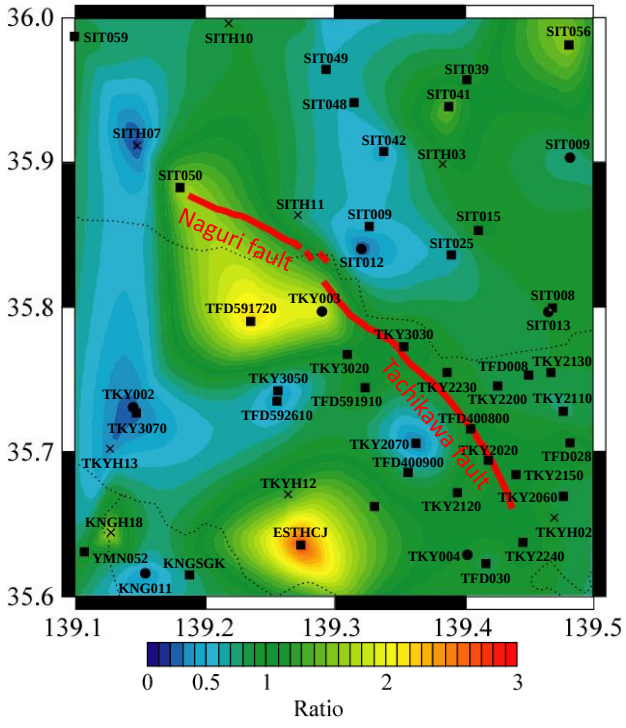


Figure 9 Distribution of the ratio of the depth of the upper seismic basement between the inverted three-dimensional subsurface structural model to the "Long-period ground motion hazard maps" model shown in Figure 1

Figure 11 shows the distribution of the predominant period of the Radial/Vertical spectral ratios around the Tachikawa fault zone. The distribution of predominant

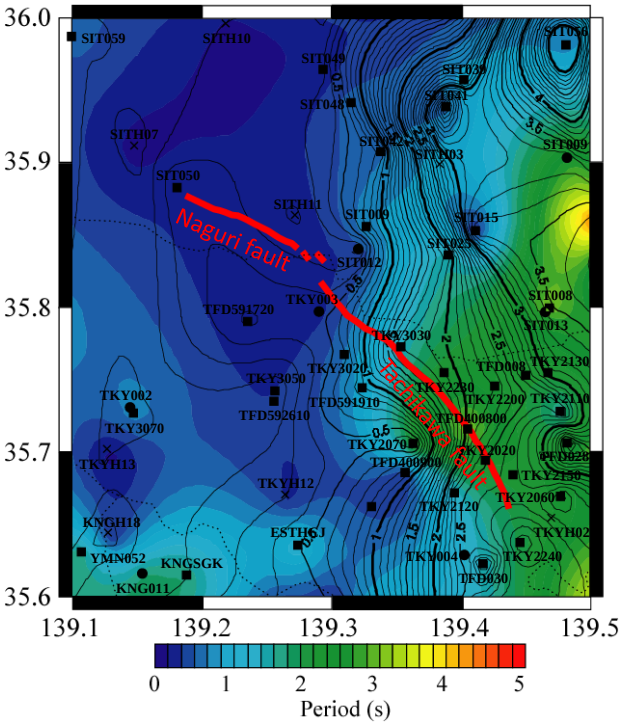


Figure 10 Distribution of the predominant periods of the Fourier spectrum with the horizontal component

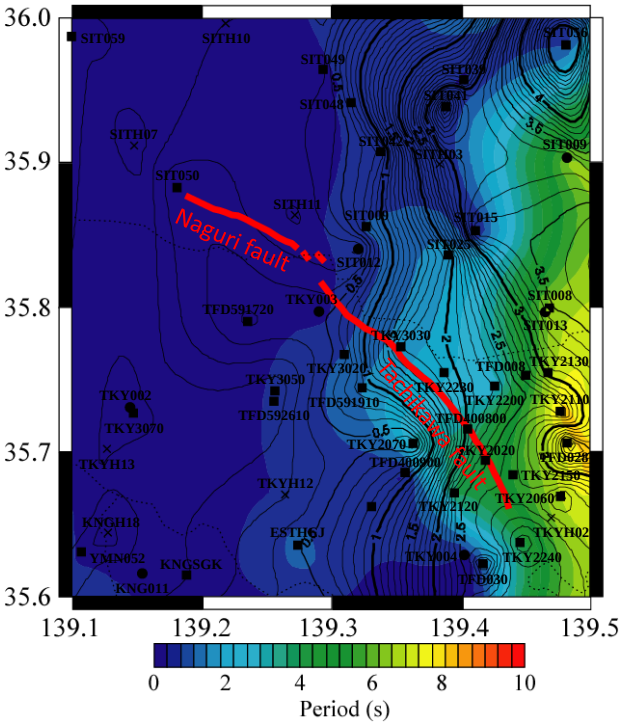


Figure 11 Distribution of the predominant periods of the Radial/Vertical spectral ratios

periods observed at the eastern part of the Tachikawa fault is about 5 to 8 seconds as shown in Figure 11. The distribution of predominant periods observed at the western part of the Tachikawa fault is about 2 second or less. Therefore, the difference has appeared clearly across the fault, it seems that the distribution of predominant period display good agreement with the depth of the upper seismic basement near the Tachikawa fault. In addition, it is corresponds that long period ground motions are remarkable at the region having thick sedimentary layers, especially northern part of the Yokohama city.

Moreover, we calculated the Radial/Vertical spectral ratios with inverted three-dimensional subsurface structural model as shown in Figure 12. The results indicate that the characteristics of the calculated predominant period of the Radial/Vertical spectral ratios near the Tachikawa fault display good agreement with the observed one during the main shock. However, the characteristics of the calculated predominant period of the Radial/Vertical spectral ratios in the northeastern part of this model don't display good agreement with the observed one. Therefore, It was suggested that the further investigation for the subsurface structures is required.

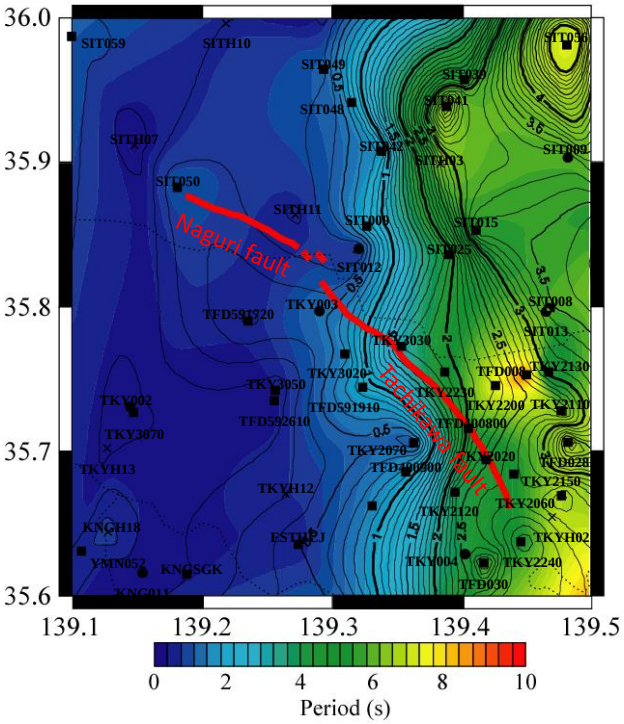


Figure 12 Distribution of the predominant periods of the the Radial/Vertical spectral ratios obtained from the inverted three-dimensional subsurface structural model

6. CONCLUSIONS

In this study, we estimated the three-dimensional subsurface structural model around the Tachikawa fault zone using the receiver function method. We identified the subsurface structural model using inversion based on the simulated annealing method, and we constructed the three-dimensional subsurface structural model in this area obtained from P-wave and S-wave velocity profiles of thick sediments at each station. Moreover, we calculated Radial/Vertical spectral ratios with this three dimensional model. The results indicate that the characteristics of the calculated predominant period display good agreement with

the observed one near the Tachikawa fault during the 2011 off the Pacific coast of Tohoku Earthquake.

Acknowledgements:

The authors acknowledge support from the Japan Ministry of Education, Culture, Sport, Science, and Technology (MEXT) for our research project. In this study, we used the seismic wave data provided by the K-NET and KiK-net of National Research Institute for Earth Science and Disaster Prevention (NIED). In addition, we used the SK-net seismic recording by the Tokyo metropolitan area comprehensive network. We acknowledge whom these data are concerned.

References:

Langston , C.A. (1979), "Structure under Mount Rainier, Washington, inferred from teleseimic bodywaves," *J. Geophys. Res*., 84, 4749-4762

Earthquake Research Committee.(2012), "Long-Period Ground Motion Hazard Maps (2012)", Headquarters for Earthquake Research Promotion, http://www.jishin.go.jp/ main/chousa/ 06mar_yosoku-e/index-e.htm.

Kobayashi, K., Uetake, T., Mashimo, M. and Kobayashi, H. (1998), "An Investigation on Detection Method Of P to S Converted Waves for Estimating Deep Underground Structures," *J. Struct. Constr. Eng.*, AIJ, No.505, 45-52. (in Japanese)

Haskell, N. A. (1962), "Crustal reflection of plane P and SV waves," *J. Geophys. Res.* 67, 4751-4767

Ingber, L. (1989), "Very fast simulated annealing," *Math. Comput. Modeling*, Vol.2, pp.967-973

Yamanaka, H. (2001), "Application of simulated annealing to inversion of surface wave phase velocity – Comparison of performances between SA and GA inversions -," *BUTSURI-TANSA*, Vol.54, No.4, pp.197-206. (in Japanese)

Kurose, T. and Yamanaka, H.(2006), "Joint inversion of receiver function and surface-wave phase velocity for estimation of shear-wave velocity of sedimentary layers," *Exploration Geophysics*, 37, 93-101

Tsuno, S., Yamanaka, H., Midorikawa, S., Yamamoto, S., Miura, H., Sakai, S., Hirata, N., Kasahara, K., Kimura, H. and Aketagawa, T. (2012), "Characteristics of long-period ground motions in the Tokyo Metropolitan Area and its vicinity, by recording data of the 2011 off the Pacific coast of Tohoku Earthquake (Mw 9.0) and the aftershocks," JAEE, Vol.12, No.5,102-116 .(in Japanese)

10CUEE CONFERENCE PROCEEDINGS
10th International Conference on Urban Earthquake Engineering
March 1-2, 2013, Tokyo Institute of Technology, Tokyo, Japan

ANALYSIS OF HVSR OF MICROTREMOR ON DIFFERENT SEISMIC SITE CONDITIONS

Chun-Hsiang Kuo[1], Kuo-Liang Wen[2], Che-Min Lin[3], Jyun-Yan Huang[4], and Tao-Ming Chang[5]

1) Associate Research Fellow, National Center for Research on Earthquake Engineering, Taiwan
2) Professor, Institute of Geophysics, National Central University, Taiwan
3) Associate Research Fellow, National Center for Research on Earthquake Engineering, Taiwan
4) Ph.D. Candidate, Institute of Geophysics, National Central University, Taiwan
5) Associate Research Fellow, National Center for Research on Earthquake Engineering, Taiwan
chkuo@ncree.narl.org.tw, wenkl@earth.ncu.edu.tw, cmlin@ncree.narl.org.tw, 986402005@cc.ncu.edu.tw, tmchang@ncree.narl.org.tw

Abstract: Single station of microtremor measurements were employed at stations of Taiwan Strong Motion Instrumentation Program (TSMIP) in the Taipei area (TAP) and thus the Horizontal to Vertical Spectral Ratio (HVSR) of microtremor can be derived after a standard data processing. In addition, the Engineering Geological Database for TSMIP (EGDT), including logging data such as P- and S-wave velocities, N values, specific gravity, and various soil parameters, is constructed and the Vs30-based seismic site conditions at those stations were assessed (Kuo et al., 2012). Since both of the microtremor measurements and S-wave velocity profiles are available at 60 TSMIP stations in the Taipei area, the properties of HVSR of microtremor on different seismic site conditions are studied as well as an experimental correlation of the sedimentary depths from boreholes, the dominate frequencies from microtremorôs HVSR, and the average S-wave velocities of deposits. Remarkable properties of microtremorôs HVSR including dominate frequency, falling frequency, and amplification are learned in this study to help us discriminate between different site conditions. A quick approach of the site classification according to the criteria of National Earthquake Hazard Reduction Program (NEHRP) is proposed via HVSR of microtremor.

1. INTRODUCTION

Seismic waves are usually amplified by local unconsolidated sediments at specific frequencies during strong motions, that is, the so called site effect, a significant issue in seismology, earthquake engineering, and seismic hazard assessment. The fact of different seismic site conditions can cause varied site effects, was recognized more than hundred years ago (Milne, 1898). It was noted that ñIt is an easy matter to select two stations within 1000 feet of each other where the average range of horizontal motion at the one station shall be five times, and even ten times, greater than it is at the otherò. This showed the site effect could be evident at two nearby stations.

Microtremors (also called microseism, ambient noise, or seismic noise) are caused by various natural and artificial signals, such as winds, tides, rains, traffics, and mechanical vibrations. Those signals always exist and thus the time of measurements is very short in comparison with that for earthquakes. After Nakamura (1989) proposed the single station HVSR method, microtremor became a popular tool to assess site response, i.e., resonance frequency and amplification factor at a specific site. Several studies (Delgado et al., 2000; Dinesh et al., 2010; García-Jerez et al, 2006; Parolai et al., 2002) developed relations between thickness of sedimental layers and resonant frequency of microtremor, which then can be used to estimate the thickness of sediments in whole study region; otherwise, S-wave velocity was estimated by a developed empirical relation with depth.

Prior to the present study of developing HVSR models on different seismic site conditions, a reliable site classification is the fundamental. The Engineering Geological Database for TSMIP is constructed by the National Center for Research on Earthquake Engineering (NCREE) and the Central Weather Bureau (CWB), including logging data at more than 400 stations, Vs30 and the site classification of the drilled stations also have been accomplished (Kuo et al., 2011; 2012) according to the criteria of NEHRP (BSSC, 2001). This study focused on the Taipei area due to the various site conditions and abundant related studies for developing HVSR models. The site classification and Vs30 at 11 stations of class B, 20 stations of class C, 32 stations of class D, and 5 stations of class E sites were available in TAP from the EGDT as shown in Figure 1 (Kuo et al., 2012). Microtremor measurements were employed at most of those stations for the development of the HVSR model on different seismic site conditions.

Since most of the velocity profiles of EGDT are less than 35 m, additional deeper velocity profiles were required to evaluate the empirical correlation between depth of sediments and dominate frequency of microtremorôs HVSR. The Strong Motion Downhole Array and the Broadband Downhole Seismic Network in the Taipei Basin were installed by the Central Geological Survey and the Institute of Earth Science of Academia Sinica from 1991 and 2005, respectively. Both S-wave velocity profiles and microtremor measurements were available at several stations of the downhole arrays and the depths are from 80 m to 292 m (Wen and Yeh, 1996, 1998; Wen et al., 1995; Huang et al., 2008).

HVSR of microtremor at different geological zones were usually grouped into different categories according to the shapes of HVSR (Tuladhar et al., 2004), and sometimes a representative velocity profile may be available in a zone (Rodríguez and Midorikawa, 2004). Since enough stations with seismic site conditions from EGDT are known and the HVSR are also available, we can therefore evaluate the correlations between HVSR of microtremor and seismic site conditions in the Taipei area.

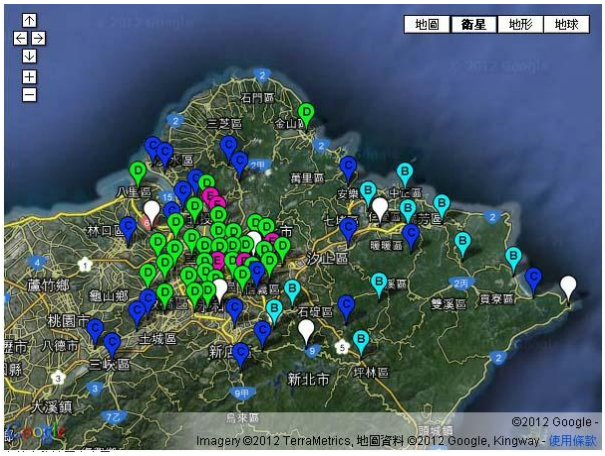


Figure 1 The site classification of EGDT (Kuo et al., 2012) in the Taipei area displayed in the Google Maps. The aqua marks with a letter B mean the class B sites; the blue marks with a letter C mean the class C sites; the green marks with a letter D mean the class D sites; the fuchsia marks with a letter E mean the class E sites; the white marks without any letter mean no borehole at the station.

2. LOCAL GEOLOGY AND DATA ACQUISITION

2.1 Geology in the Taipei Area

The Taipei area contains the triangular Taipei Basin with a region of about 20 km across, as well as the surrounding Tatun volcanic region (Pleistocene), Linkou area (Pleistocene), and Western Foothills (Miocene) in the North, the West, and the Southeastern, respectively.

Inside the Taipei Basin are four Quaternary sedimentary formations covering on the Tertiary bedrocks. Taipei City is the capital of Taiwan, located in the Taipei Basin, subject severe damages during large earthquakes, like Hualien earthquake in 1986, Chi-Chi earthquake in 1999, and Hualien earthquake in 2002, due to significant site effect (Wen et al., 1995; Wen and Peng, 1998). The relevant Sungshan Formation is the topmost layer composed mainly of soft silty clays and silty sands and believed the major cause of the seismic wave amplification. Below the Sungshan Formation are the Chingmei, Wuku, and Banchiao Formations in order. The thickness contours of the Sungshan Formation and the depth of Tertiary bedrocks were indicated by Wang et al. (2004), as well as the seismic velocities of the sedimentary layers. The average shear-wave velocity of Sungshan Formation throughout the whole basin is around 170-340 m/s. The largest depth of the bedrock is in the northwest of the basin and may be shallower than 50 m around the basin edge.

2.2 Microtremor Measurements and Data Processing

Two types of instruments were used in this study, SAMTAC-801B (recorder) and VSE311C (sensor) manufactured by Tokyo Sokushin, and the alternative K2 with an EpiSensor made by Kinemetrics. Sampling rate is 200 point per second and the recording period is 18 minutes. The appropriate location for our microtremor measurements was on the side of stations to ensure the geological conditions are identical to the stations and boreholes. The instrumental response was eliminated in the procedure of HVSR. Microtremor at a number of 60 stations was measured up to now and the distribution was shown in Figure 2 as triangles, including 10 of class B, 17 of class C, 28 of class D, and 5 of class E. Of cause, those stations have Vs30 and were classified as in Figure 1.

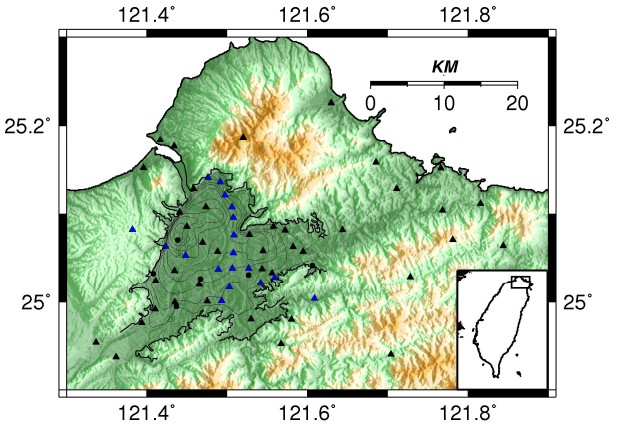


Figure 2 The distribution of the stations contain the microtremor measurements. The triangles are stations from EGDT; the circles are stations of downhole arrays with larger depths. S-wave velocity profiles are available in all of those stations displayed here. The blue stations indicate two profiles of HVSR in N-S and E-W directions across the Taipei Basin.

Multi-windows with 8192 points of each was used to cut the microtremor recordings, and 6% cosine taper was implemented at both ends of each window. The recordings

must be checked and the windows contaminated by unusual noise can be deleted in advance; however the number of selected windows should be more than 20. A geometric mean horizontal Fourier spectrum was calculated, smoothed 5 times using three points approach and then divided by the smoothed vertical Fourier spectrum. After averaging the HVSR of each window, the mean HVSR at one station was derived.

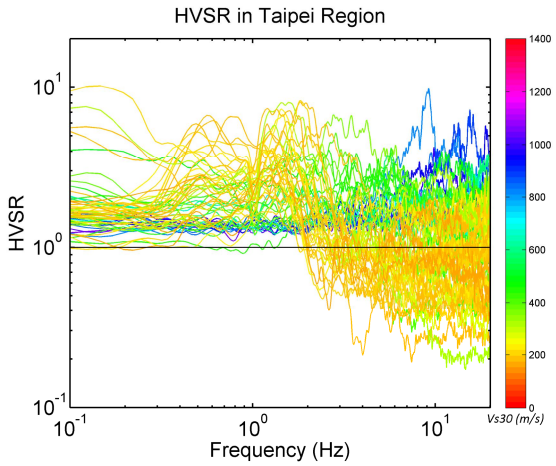


Figure 3 HVSR at the 60 strong motion stations of TAP from the EGDT with different Vs30. The resonance peaks with larger Vs30 seems at the higher frequency; on the other hand, the resonance peaks with smaller Vs30 were located at lower frequency.

3. HVSR OF DIFFERENT SITE CLASSES

The Taipei area was selected as the preliminary research area for the noteworthy site effects in the basin, varied site conditions in whole region, and sufficient reference materials. These advantages, particularly abundant velocity profiles from logging measurements are significant for the qualitative and quantitative analyses in developing the new models of HVSR and new technique on site assessment using microtremor.

HVSR at the 60 strong motion stations were derived (Figure 3) following the standard data processing introduced in the above section and plotted in different colors according to the Vs30 at each station. The dominate frequencies of HVSR increase as the Vs30 become higher. However, the amplification factors of HVSR of different Vs30 are very similar. The amplification factors of the dominate frequency lower than 2 Hz are almost equal to those of higher than 9 Hz, and the others between 2 and 9 Hz are smaller.

Moreover, we categorized these HVSR curves into classes of B, C, D, and E according to the site classification of Kuo et al. (2012) (Figure 4). Stations of class B, the Vs30 is between 760 and 1500 m/s, situated on hard rocks or sometimes covered with a thin regolith and therefore the dominant frequencies of HVSR are unremarkable or relatively higher with strong amplification. The stations of class C, which are situated on soft rocks or stiff soils, have more obvious amplification at comparatively lower resonant frequency than the class B. The HVSR curves of classes D and E are amplified at relatively lower dominant frequencies.

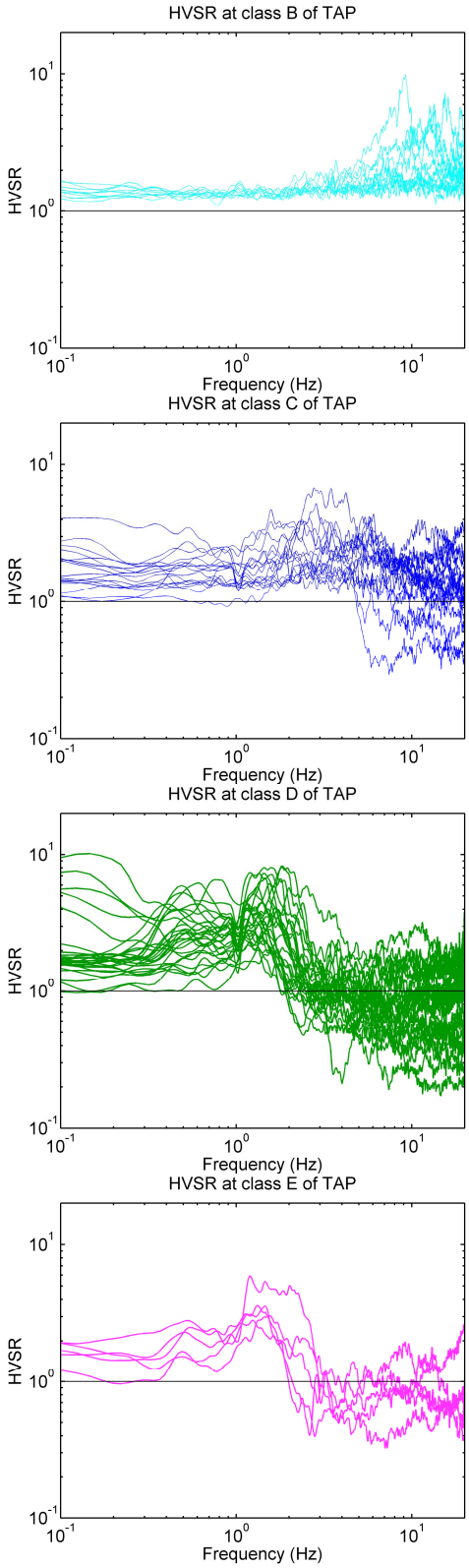


Figure 4 The categorized HVSR curves according to the site classification of Kuo et al. (2012). From top to bottom is class B, class C, class D, and class E.

Figure 5 shows the average HVSR of four classes, the difference of shape and dominant frequency are very clear. The dominant frequency increased with Vs30, except for class D and E. The HVSR in the two classes, in terms of shapes, the dominant frequencies, the double peaks, and the amplification factors are quite similar that it often difficult to group them into two specific classes. We speculated that the similarity is because the thickness of sediments at sites of D and E is mostly greater than 30 meters so Vs30 can not tell the differences from the HVSR. Since dominant frequency is related to the thickness of sediments rather than the variation of velocities, the distinction in two classes are not prominently seen. The other possible reason is the Vs30 of the 5 stations are close to the boundary of class D and E (180 m/s), so that the difference between the HVSR of the two classes is not notable.

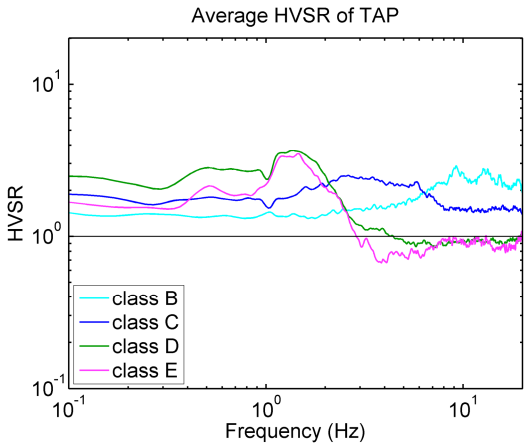


Figure 5 Averaged HVSR of class B, C, D, and E. Different dominant frequencies were very clear except for class D and E.

Additionally, Figure 4 shows a notable phenomenon, that is, deamplication, in the relative high frequencies. We therefore called the threshold of the deamplification as ñfalling frequencyò, at which the deamplication starts to occur. This could be found in all HVSR curves of class D, class E, and several of class C. The occurrence of ñfalling frequencyò is another important property of HVSR found in this study which could also be used to distinguish site classes. The falling frequency of microtremorôs HVSR always occurs at a site covered with soft sediments. The signal of microtremor tends to resonate within the covering sedimental layer and then Rayleigh waves are generated. The effect of Rayleigh waves in the vertical component become relatively larger and thus the spectral ratio of horizontal to vertical fall into values less than one on those frequencies, i.e. Rayleigh waves become dominant in microtremor on the higher frequency band. It can be found in all stations of class D and E, as well as several stations of class C. In contrast, the HVSR larger than one because of the lack of Rayleigh waves at hard rock sites. Consequently, the phenomenon of falling frequency is very clear in the average HVSR of D and E in Figure 5. Otherwise, the falling frequency of class E is lower than that of class D, possibly due to lower S-wave velocity of sediments. Maybe this criterion can be used as an index for distinguishing sites into classes D and E. This needs, however, further validation.

4. THE EMPIRICAL CORRELATION BETWEEN DOMINATE FREQUENCY AND THICKNESS OF SEDIMENTS

The well-known empirical correlation (Equation 1) of thickness of sediments (H), S-wave velocities (Vs), and dominant frequency (F) has been widely used in estimations of depths of bedrocks (e.g., Wooley and Street, 2002).

$$H = Vs / 4F \tag{1}$$

However, the empirical equation has some divergence owing to the difference in local geology. We used the drilling profiles of EGDT and refer to some other velocity profiles of deep boreholes in the Taipei Basin, estimating the relation between resonant frequency and the depth of bedrock by least-square method. The data (red circles) as well as the estimated result (blue curve) are shown in Figure 6. S-wave velocity is larger than 600 m/s and an obvious boundary exists above the indentified bedrock. The correlation coefficient (R) is as high as 0.92. The experimental correlation is $H = 64.02 \times F^{-0.92}$ as shown in Figure 6. The exponent of dominant frequency is -0.92, very near to the value of -1 in Equation (1). The coefficient 64.02 therefore can be seen as a quarter of the average Vs of a particular depth that causes the resonance peak and thus the average Vs of the sediments in the Taipei area is about 256 m/s, agree well with the average S-wave velocity of the first sedimentary layer, i.e. the Sungshan Formation.

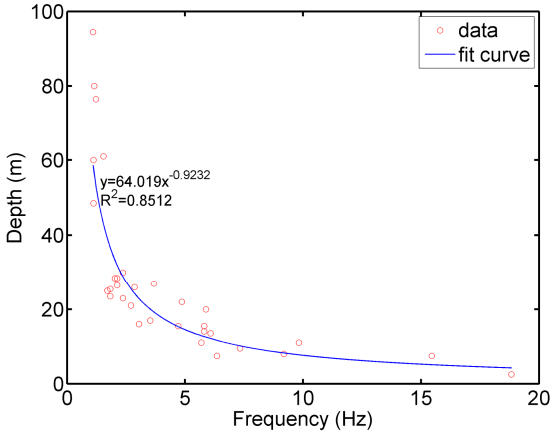


Figure 6 The open red circles are data points and blue curve is the result of regression using least-square method in the Taipei area. The correlation coefficient is 0.92.

As we can see in Figure 4 and 5, almost all of the HVSR at those stations of class D and E with two resonant peaks, which indicates two strong subsurface interfaces

(engineering and geological bedrocks) inside the Taipei Basin. The dominate frequency used for the regressed equation is the one at higher frequency of class D and E. For those stations of class B and C, only one or non-obvious peak can be found. We speculate the higher peak was caused by the interface between the first soft layer and the bedrock. The first soft layer is the Sungshan Formation inside the basin and a regolith in the surrounding mountain areas. Furthermore, the discrepancies between the empirical correlation and the result from borehole become larger and the depth usually underestimated at the lower frequency in Figure 6. This might because the average S-wave velocity increased with the extended sedimentary thickness.

5. DISCUSSIONS

Figure 7 shows the HVSR in the NS and EW profiles across the Taipei Basin. The stations were marked as blue triangles in Figure 2, ten stations contained in the N-S direction and nine in the W-E direction from top to bottom in Figure 7. TAP001 is the co-station of the profiles. We can see different fluctuations of the resonant peaks of those HVSR in the two profiles. In the N-S profile, the dominate frequencies of the 3rd to 8th stations are lower than the first two and last two stations. In the W-E profile, the dominate frequency of the 3rd station is the lowest. Roughly speaking, the fluctuation of HVSR in W-E is much larger than in the N-S direction. This means the variation of the depth of the Sungshan Formation in the W-E profile is larger than in the N-S profile. According to the depth contour of the Sungshan Formation drawn by Wang et al. (2004), the depth variation is about 30 m in the N-S profile; however, more than 50 m in the E-W profile. In the N-S profile, TAP094 is grouped into class C; TAP096, TAP005, and TAP001 are grouped into class E; the others are class D. As for the W-E profile, TAP052 and TAP089 are grouped into class C; TAP001 is grouped into class E; TAP071 is grouped into class B; the others are class D (Kuo et al., 2012).

In addition to logging (Kuo et al., 2011, 2012), surface geology (Lee et al., 2001), elevation (Chiou et al., 2008), and slope (Allen and Wald, 2009), H/V response spectral ratios of earthquakes were usually used by studies of site classification (Phung et al., 2006; Zhao et al., 2006; Ghasemi et al., 2009). Zhao et al. (2006) found the 5% damping average response spectral ratios of the horizontal to vertical components of earthquakes for all site classes were not strongly affected by magnitude, hypocentral distance, and focal depth, so that an site classification index (SI) from the empirical H/V response spectral ratios was designed for the site classification of K-net in Japan. Ghasemi et al. (2009) utilized an improved SI for the site classification of the strong motion stations in Iran because surface geology and Vs30 are not available at most of the stations. Actually, Phung et al. (2006) applied the 5% damping average response spectrum of the horizontal component normalized with respect to average PGA on stations without known site classification. Although the HVSR of response spectra were also tested in the study, it resulted in lower accuracy than the normalized horizontal response spectra. They developed the scheme based on the 87 station for which the site conditions are known by surface geology from Lee et al. (2001); however, it was indicated that many stations were misclassified in Lee et al.ôs (2001) result according to the measured velocity profiles of logging data (Kuo et al., 2011, 2012).

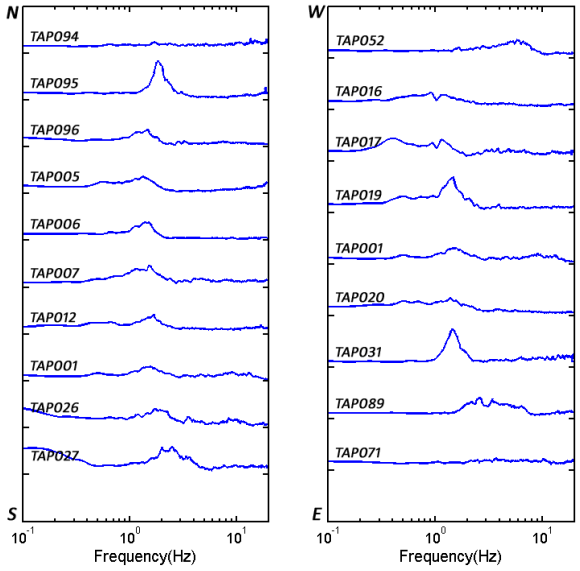


Figure 7 The HVSR in the NS (left) and EW (right) profiles across the Taipei Basin in Figure 2. Ten stations are contained in the N-S direction and nine stations are in the W-E direction. TAP001 is the co-station of the profiles.

Since the exact site classification is available at a large number of stations in the Taipei area, a reliable empirical horizontal to vertical spectral ratio method can be developed. Otherwise, an approach which can eliminate the effects of source, path, and soil nonlinearity to decrease the uncertainty is desirable. Therefore, we propose the technique recognizing features of microtremorôs HVSR of different site classes. The process of horizontal to vertical spectral ratio can eliminate source and path effects, and microtremor is not subject to soil nonlinearity.

Spearmanôs rank correlation coefficient was exploited to calculate SI for each site class at a particular site (Ghasemi et al., 2009). We therefore employed the absolute value of the same correlation coefficient in this study as in the following.

$$SI_k = \left| 1 - 6 \sum \frac{d_i^2}{n(n^2-1)} \right| \qquad (2)$$

Where subscript K means the Kth site class (i.e. B, C, D, and E in the present study), d_i is the difference between each rank of corresponding values of X_k and Y at a particular frequency of i. X_k is the average HVSR for the Kth site class,

Y is the mean HVSR shown in Figure 5 for the site of interest, and n is the number of frequencies. SI_k equals unity when the ranks of corresponding values of HVSR for a site of interest is identical to the mean HVSR of a particular site class, that is, a perfect positive correlation between X_k and Y, or it is less than one.

As described in the paragraphs above and shown in Figure 5, we are aware of the properties of dominate frequency, falling frequency, and amplification, and thus those indices were considered as weighting factors with given values between 0 and 1 afterwards. The geometric mean of SI_k multiplied by the other three weighting factor is the finial site classification index, which is also between zero and unity. After calculating each finial site classification index for a site of interest, the site class with the largest SI was assigned to the site of interest.

Table 1 The site classifications in the Taipei area by the logging data from EGDT (Kuo et al., 2012) and using HVSR method in this study.

HVSR \ EGDT	B	C	D	E	Total
B	9	0	0	0	9
C	1	15	0	0	16
D	0	2	28	3	33
E	0	0	0	2	2
Total	10	17	28	5	60

Table 2 The site classifications in the Taipei area by the logging data from EGDT (Kuo et al., 2012) and from other studies (Chiou et al., 2008; Lee et al., 2008; Allen and Wald, 2009).

Chiou \ EGDT	B	C	D	E	Total
B	2	0	0	0	2
C	4	8	4	0	16
D	0	5	15	4	24
E	0	0	0	0	0
Total	6	13	19	4	42

Lee \ EGDT	B	C	D	E	Total
B	10	8	1	0	19
C	1	12	4	1	18
D	0	0	19	2	21
E	0	0	8	2	10
Total	11	20	32	5	68

Wald \ EGDT	B	C	D	E	Total
B	0	2	0	0	2
C	9	13	7	2	31
D	2	5	25	3	35
E	0	0	0	0	0
Total	11	20	32	5	68

Using this approach a result of site classification was obtained, and is better than that only considering the similarity of shapes for HVSR. The percentage of classifying a site into the correct class is increased from 65% (considering only similarity of HVSR) to 90% (further considering the weighting factors of dominate frequency, falling frequency, and amplification) as shown in Table 1. Afterwards, the site classifications in the same area were acquired from the other studies (Chiou et al., 2008; Lee and Tsai, 2008; Allen and Wald, 2009) as listed in Table 2. In Table 1 and 2, the site classification of EGDT is according to the Vs30 calculated from measured S-wave velocity profiles of strong motion stations, and then categorized them into each class on the basis of NEHRPôs criteria. Actually, the other three studies in Table 2 also consulted parts of the EGDT, that is, some site conditions were known by them in advance of their studies. The percentages of correct site classifications in comparison with the EGDT are 59.5%, 63.2%, and 55.9% for Chiou et al. (2008), Lee and Tsai (2008), and Allen and Wald (2009), respectively. No site was classified into class E in the results of Chiou and Wald which used the evaluated correlations between Vs30 and elevation or slope. This might imply the use of only the surface parameters like elevation and slope can not tell sites of class E owing to almost identical surface geological conditions of class D and E. On the other hand, the developed HVSR method met the difficulty in telling the soft soil classes though, a certain level of the identification ability is owned since the subsurface information is brought by the microtremor we used.

6. CONCLUSIONS

The approach of using HVSR can eliminate the effects of source, path; otherwise, soil nonlinearity is no more a problem in the utilization of microtremor instead of earthquakes, and thus pure site effect is obtained theoretically. This study is evaluating the correlation between site classes and HVSR and then qualitative analysis of HVSR was also achieved. The S-wave velocity information of EGDT is a very important foundation and criterion for this study. Various site conditions of stations and enough microtremor measurements in the Taipei area are also essential.

Even though the previous studies consulted and directly use the Vs30 from parts stations of the EGDT, the accuracy of the classifications are still lower than only using the similarity of HVSR. Stations of class B are situated on hard rocks or sometimes covered with a thin regolith so that the dominant frequencies are unremarkable or relatively higher with strong amplification. The HVSR curves of classes D and E are amplified at relatively lower dominant frequencies with two resonant peaks. The HVSR with two peaks are all inside the Taipei Basin that we speculate they are caused by engineering and geological bedrocks. The higher velocity in the first layer than class D and E as well as lower subsurface velocity than class B may be the reason that the amplification factor of class C usually lower than the others.

The similarity of HVSR between class D and E makes the classification of a soft soil site into a suitable class of D or E more difficult than distinguishing a soft soil site from a hard rock site. However, the present result of this study is better than the others. From the fluctuation of the two profiles in Figure 7, we know the depth variation in the W-E profile is larger than in the N-S profile. The empirical

correction of sedimentary depth and dominate frequency will be adopted to calculate the depth of bedrock at each stations in the near future.

Acknowledgements:

The authors acknowledge velocity profiles of downhole arrays in the Taipei Basin provided by Dr. Win-Gee Huang of IES. The measurements of microtremor were greatly helped by many people in the Strong Ground Motion Laboratory of National Central University, Taiwan.

References:

Allen, T.I. and Wald, D.J. (2009), ñOn the Use of High-Resolution Topographic Data as a Proxy for Seismic Site Conditions (VS30),ò *Bulletin of the Seismological Society of America*, **99**(2A), 935-943.

Building Seismic Safety Council, BSSC (2001), ñNEHRP Recommended Provisions for Seismic Regulations for New Buildings and Other Structures,ò Washington, DC.

Chiou, B.S.J., Darragh, R., Gregor, N., Silvad, W. (2008), ñNGA Project Strong Motion Database,ò *Earthquake Spectra*, **24**(1), 23-44.

Delgado, J., López Casado, C., Estévez, A., Giner, J., Cuenca, A., and Molina, S. (2000), ñMapping Soft Soils in the Segura River Valley (SE Spain): A Case Study of Microtremor as An Exploration Tool,ò *Journal of Applied Geophysics*, **45**(1), 19-32.

Dinesh, B.V., Nair, G.J., Prasad A.G.V., Nakkeeran, P.V., and Radhakrishna, M.C. (2010), ñEstimation of Sedimentary Layer Shear Wave Velocity Using Micro-tremor H/V Ratio Measurements for Bangalore City,ò *Soil Dynamics and Earthquake Engineering*, **30**(11), 1377-1382.

García-Jerez, A., Luzón, F., Navarro, M., and Pérez-Ruiz, J.A. (2006), ñCharacterization of the Sedimentary Cover of the Zafarraya Basin, Southern Spain, by Means of Ambient Noise,ò *Bulletin of the Seismological Society of America*, **96**(3), 957-967.

Ghasemi, H., Zare, M., Fukushima, Y., and Sinaeian, F. (2009), ñApplying Empirical Methods in Site Classification, Using Response Spectral Ratio (H/V): A Case Study on Iranian Strong Motion Network (ISMN),ò *Soil Dynamics and Earthquake Engineering*, **29**(1), 121-132.

Huang, W.G., Huang, B.S., Chen, K.C., Liu, C.C., Lin, C.R., Tsao S.H., Hsieh, Y.C., and Chen, C.H. (2008), ñObservations Using the Taipei Basin Broadband Downhole Seismic Network: The 26 December 2006, Pingtung Earthquake Doublet, Taiwan,ò *Terrestrial, Atmospheric and Oceanic Sciences*, **19**(6), 761-766.

Kuo, C. H., Wen, K.L. Hsieh, H.H., Chang, T.M., Lin, C.M., and Chen, C.T. (2011), ñEvaluating Empirical Regression Equations for Vs and Estimating Vs30 in Northeastern Taiwan,ò *Soil Dynamics and Earthquake Engineering*, **31**(3), 431-439.

Kuo, C.H., Wen, K.L., Hsieh, H.H., Lin, C.M., Chang, T.M., and Kuo, K.W. (2012), ñSite Classification and Vs30 Estimation of Free-field TSMIP Stations Using the Logging Data of EGDT,ò *Engineering Geology*, **129-130**, 68-75.

Lee, C.T., Cheng, C.T., Liao, C.W., Tsai, Y.B. (2001), ñSite Classification of Taiwan free-field strong-motion stations,ò *Bulletin of the Seismological Society of America*, **91**(5), 1283-1297.

Lee and Tsai. (2008), ñMapping Vs30 in Taiwan,ò *Terrestrial, Atmospheric and Oceanic Sciences*, **19**(6), 671-682.

Milne, J. (1898), ñSeismology,ò London, K. Paul, Trench, Trubner & co., ltd.

Nakamura, Y. (1989), ñA Method for Dynamic Characteristics Estimation of Subsurface Using Microtremor on the Ground Surface,ò *Quarterly Report of Railway Technical Research Institute*, **30** (1), 25-33.

Parolai, S., Bormann, P., and Milkereit, C. (2002), ñNew Relationships Between Vs, Thickness of Sediments, and Resonance Frequency Calculated by the H/V Ratio of Seesmic Noise for the Cologne Area (Germany),ñ *Bulletin of the Seismological Society of America*, **92**(6), 2521-2527.

Phung, V., Atkinson, G.M., Lau, D.T. (2006), ñMethodology for Site Classification Estimation Using Strong Ground Motion Data from the Chi-Chi, Taiwan, Earthquake,ò *Earthquake Spectra*, **22**(2), 511-531.

Rodríguez, V.H.R. and Midorikawa, S. (2004), ñSite Classification Based on Spectral Amplification Patterns for Microtremor H/V Rations,ò *13th World Conference on Earthquake Engineering*, Paper No. 1770.

Tuladhar, R., Yamazaki, F., Warnitchai, P., and Saita, J. (2004), ñSeismic Microzonation of the Greater Bangkok Area Using Microtremor Observations,ò *Earthquake Engineering and Structure Dynamics*, **33**(2), 211-225.

Wang, C.Y., Lee, Y.H., Ger, M.L., and Chen, Y.L. (2004), ñInvestigating Subsurface Structures and P- and S-wave Velocities in the Taipei Basin,ò *Terrestrial, Atmospheric and Oceanic Sciences*, **15**(4), 609-627.

Wen, K.L., Fei, L.Y., Peng, H.Y., and Liu, C.C. (1995), ñSite Effect Analysis from the Records of the Wuku Downhole Array,ò *Terrestrial, Atmospheric and Oceanic Sciences*, **6**(2), 285-298.

Wen, K.L. and Yeh, Y.T. (1996), ñThe Comprehensive Investigation on the Subsurface Geology and Engineering Environment in the Taipei Basin in 1996 (I),ò *Report of Central Geological Survey, Ministry of Economic Affairs*. No. 85-006.

Wen, K.L. and Peng, H.Y. (1998), ñSite Effect Analysis in the Taipei Basin: Results from TSMIP Network Data,ò *Terrestrial, Atmospheric and Oceanic Sciences*, **9**(4), 691-704.

Wen, K.L. and Yeh, Y.T. (1998), ñThe Comprehensive Investigation on the Subsurface Geology and Engineering Environment in the Taipei Basin in 1998 (I),ò *Report of Central Geological Survey, Ministry of Economic Affairs*. No. 87-004.

Woolery, E.W. and Street, R. (2002), ñ3D Near-Surface Soil Response from H/V Ambient-Noise Ratios,ò *Soil Dynamics and Earthquake Engineering*, **22**(9-12), 865-876.

Zhao, J.X., Irikura, K., Zhang, J., Fukushima, Y., Somerville, P.G., Asano, A., Ohno, Y., Oouchi, T., Takahashi, T., and Ogawa, H. (2006), ñAn Empirical Site-Classification Method for Strong-Motion Stations in Japan Using H/V Response Spectral Ratio,ò *Bulletin of the Seismological Society of America*, **96**(3), 914-925.

10CUEE CONFERENCE PROCEEDINGS
10th International Conference on Urban Earthquake Engineering
March 1-2, 2013, Tokyo Institute of Technology, Tokyo, Japan

SURFACE-WAVE PHASE VELOCITY INVERSION USING MARKOV CHAIN MONTE CARLO METHOD FOR ESTIMATION OF LOCAL SITE AMPLIFICATION

Hiroaki Yamanaka

Professor, Dept. Environmental Science and Technology, Tokyo Institute of Technology, Japan
yamanaka@depe.titech.ac.jp

Abstract: In this study, an applicability of Markov Chain Monte Carlo method in surface-wave phase velocity inversion is examined. Numerical examinations were conducted using synthetic phase velocity of Rayleigh wave in a layered model of a deep sedimentary basin. The Metropolis-Hasting procedure was used to sample the model space, and final inverted model is derived from averaging S-wave velocity and thickness for the sampled models. The inverted model was similar to the true model with regardless of observed standard deviations of the phase velocity. We also estimated resolutions for the model parameters using their standard deviations of the sampled models, and shows that the resolution depends on the standard deviations of the synthetic phase velocity. We also evaluated variations of one-dimensional amplifications using the sampled models for the phase velocity with different standard deviations. The dominant periods and their amplitudes do not depend on the observed errors of the phase velocity, while amplification factors at high frequency are different from each other. We applied the method to actual phase velocity data obtained in a microtremor exploration in the Kanto basin. These numerical experiments and the actual application clearly indicate a high applicability of the method in the phase velocity inversion. The averaged amplification factors for the sampled models show a smoothed spectral shape without any peaks at periods less than one second, while the amplitudes at the predominant period are common for most of the sampled models.

1. INTRODUCTION

It is known that S-wave velocity distribution in depth is one of the crucial factors to estimate the effects of surface geology on seismic motion during an earthquake. Various kinds of geophysical exploration techniques have been developed to know S-wave velocity profile in shallow and deep soils. One of the most inexpensive explorations is the technique using microtremors. In particular microtremor array exploration is capable to provide a 1D S-wave velocity profile from records of microtremors in an array deployed on the surface. Because of the easy field operations, this technique is widely used in geophysical explorations for evaluation of the local site effects in various kinds of soil conditions (e.g., Okada, 2003).

The microtremor array technique is principally based on estimation of phase velocity of surface wave (mainly Rayleigh waves) and its inversion to a 1D S-wave velocity profile. Frequency–wave number spectral analysis and spatial autocorrelation method have been used in retrieving Rayleigh-wave phase velocity from array records of vertical microtremors (Okada, 2003). Least square approaches are traditionally used in phase velocity inversion in microtremor array exploration. It is well known that the least square methods have some difficulties in practical applications, such as numerical instability and trapping at local minimum models. In particular, the existence of local minimum solution leads to the dependence of final solution to initial model assumed in advance. This practical difficulty in the phase velocity inversions can be solved with an application of heuristic approaches. The heuristic approaches in the inversions are one of Monte Carlo methods, but models with small misfit are effectively searched using various kinds of the algorithms. One of the typical approaches is genetic algorithms and simulated annealing (e.g., Yamanaka, 2005). Since these methods do not use the derivatives of misfit function to be minimized, a chance for trapping of solution at local minimum models is smaller than those in the conventional least square methods. Therefore these methods have been widely applied in actual inversions of surface-wave phase velocity in actual microtremor exploration work (e.g., Yamanaka et al., 2000). One of the disadvantages of these heuristic inversions is difficulty in estimation of model resolution.

In this study Markov Chain Monte Carlo method is applied in surface wave phase velocity inversion for the microtremor exploration. I first explained the computational procedure of the method. Then, the applicability of the method is examined using synthetic phase velocity data of Rayleigh wave. I finally applied the method to actual

Rayleigh wave phase velocity data from the microtremor explorations in the Tokyo basin. I also discuss variation of amplification factors using sampled models to know the effects of model uncertainty.

2. MCMC METHOD

The Markov Chain Monte Carlo method is one of numerical statistic approaches where the probability density function for the target distribution is numerically estimated using random sampling of parameters. It is significantly difficult to sample randomly wide parameter spaces with conventional Monte Carlo methods. The MCMC method is however capable to sample a complex function having many unknown parameters with reasonable computational cost with an assumption of stationary Markov chain condition. The method is originally used for numerical estimation of probability density functions of arbitrary functions, and applied in various kinds of science and technologies (e.g., Gilk et al., 1996).

The MCMC methods reply on the Bayes theorem. According to the theorem, the probability density function p(**m/d**) of model parameters, m, with given data, **d**, is derived from

$$p(\mathbf{m}\,|\,\mathbf{d}) = p(\mathbf{d}\,|\,\mathbf{m})p(\mathbf{m})/\,p(\mathbf{d}) \qquad (1)$$

Here p(**m**) is a prior distribution of the model parameters, and p(**d**) is the distribution of the data. p(**d**|**m**) is a conditional probability density function of **d** for given **m**, and corresponds to a likelihood function. p(**m**|**d**) is called posterior distribution of the model parameters. Because we usually have the data before the inversions, the probability distribution of data p(**d**) is constant. Then equation (1) is written in the form,

$$p(\mathbf{m}\,|\,\mathbf{d}) \propto p(\mathbf{d}\,|\,\mathbf{m})p(\mathbf{m}) \qquad (2)$$

This equation shows how the distribution of the model parameters is modified after having the data. The likelihood function in our inversion of the surface-wave phase velocity can be expressed by

$$p(\mathbf{d}\,|\,\mathbf{m}) = L(\mathbf{m}) = \exp\left[-E(\mathbf{m})\right] \qquad (3)$$

where E(**m**) is a misfit function defined using the least-squared differences between the observed phase velocity, $C^o(T_i)$, and the calculated phase velocities, $C^c(T_i)$, as

$$E(\mathbf{m}) = \sum_i \left[\frac{C^o(T_i) - C^c(T_i)}{\sigma(T_i)}\right]^2 \qquad (4)$$

Here $\sigma(T_i)$ is a standard deviation of the observed phase velocity at a period of T_i. When we do not have a prior information on model parameters, p(**m**) is a uniform distribution. The equation (3) can be simplified as

$$p(\mathbf{m}\,|\,\mathbf{d}) \propto p(\mathbf{d}\,|\,\mathbf{m}) = \exp\left[-E(\mathbf{m})\right] \qquad (5)$$

The distribution of the model parameters can be estimated from this equation using the misfit function. It is noted that the inversion based on this approach does not provide the best model that fits the observed phase velocity with the minimum errors, but a distribution of the model parameters. Therefore we can estimate an accuracy of the model parameters together with the model parameters which can be the average of the models of the distribution. It is not usually an easy task to evaluate the distribution by drawing samples of model parameters.

One of the ways for this evaluation is through a Markov chain as its stationary distribution. Markov chain is known as sampling state where the sampling result only depends on the current model, and does not depend on history of the sampling. Assuming the Markov chain, the sampling results converge to the distribution of the parameters. We apply the numerical procedure based on Metropolis-Hasting algorithm (Hastings, 1970) to construct a Markov chain for estimation of the stationary distribution of the equation (5).

The sampling process with the MCMC method in a finite length of iterations more or less depends on initial model assumed. It is known that the MCMC algorithms can generate a stationary sampling after long-term iterations. Therefore some of the sampled data must be rejected before it reaches a stationary state of a Markov chain. The term for the rejection of the data sampled before the stationary sate is called burn-in period. In order to determine the burn-in period for extracting the stationary part of the sampled data, I used a convergence criteria by Geweke (1992). From the sampled data with enough many iterations, the average (g_1) and standard deviation (σ_1) for the first n data are calculated. I also calculated those (g_2 and σ_2) for the m data from the end of the iteration. Then Z-value is calculated as

$$Z = (g_1 - g_2)\big/\sqrt{\sigma_1 - \sigma_2} \qquad (6)$$

It is indicated that the sampling is convergent with a significant level of 5%, if the Z-value is less than 1.96 (Geweke, 1992). In this study, n and m are set to be 10% and 50 % of the number of the sampled data after deleting the data in the burn-in period

3. NUMERICAL TESTS

The inversion based on the MCMC method is examined using synthetic phase velocity for Rayleigh wave. In particular we focus on the phase velocity inversion for profiling an S-wave velocity profile of deep sedimentary layers of a large basin.

The S-wave velocity model shown in Figure 1 and Table 1 are used to generate synthetic phase velocity data for fundamental Rayleigh waves in the numerical test. This is one of typical S-wave velocity models of the deep sedimentary basin, such as Kanto basin in Japan (e.g., Yamanaka and Yamada, 2006). I calculated fundamental Rayleigh-wave phase velocity for the model at periods from 0.1 to 2Hz. Then the phase velocity is contaminated with random noises whose are generated by adding a uniform random value having amplitude of 5% of the phase velocity. The standard deviation for the synthetic phase velocity is also assumed to be 10 % of the assumed phase velocity. The resultant phase velocity is also displayed in Figure 1. The S-wave velocity and the thickness for each layer in the 4-layer model are optimized in the inversion of the phase velocity. P-wave velocity is given from S-wave velocity using an empirical relationship by Kitsunezaki et al (1996).

The density for each layer is given in advance.

An initial model is randomly generated within the search limits in Table 1. Then, the initial model is modified through the MCMC sampling. Figure 2 shows the variations of the S-wave velocity and thickness of each layer. The parameters for the initial 5000 models are different from the true values showing a dependency on the initial model assumed. Then, the parameters for the first and second layers seem to converge around the true values showing a stationary state of the Markov chain. The other parameters vary gradually to the true values, and converge after 70000 iterations.

The Z-values are calculated for different burn-in periods as can seen in Figure 3. The Z-values in the figure indicates the maximum value among the Z-values for all of the parameters. The Z-value rapidly decreases beyond the burn-in period of 70000 models, and it becomes less than 2.0 after 80000 models were removed as the burn-in period. Therefore, we can use the models beyond this burn-in period to evaluate the distribution of the model parameters.

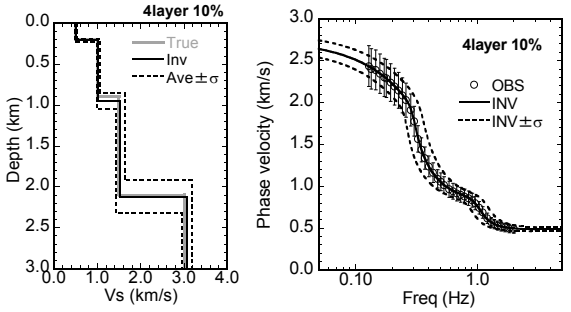


Figure 1. True and inverted S-wave velocity models (left) and synthetic Rayleigh wave phase velocity (right) for the true model with phase velocity for the inverted model.

Table 1 Model parameters and search limits for numerical test.

Vs (km/s)		Thickness (km)		Density (g/cm^3)
True	Search limits	true	Search limits	
0.5	0.2-1.6	0.2	0.02-1.4	1.8
1.0	0.4-1.8	0.7	0.05-1.6	1.9
1.5	0.6-2.5	1.2	0.1-2.	2.0
3.0	2.2-3.5	-	-	2.3

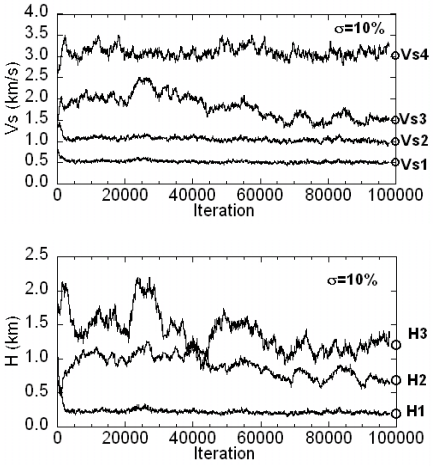


Figure 2. Variation of S-wave velocity and thickness from MCMC sampling for synthetic phase velocity in Fig.1.

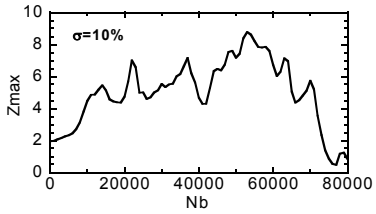


Figure 3. Relationship between Z-values and burn-in period.

The distributions of the S-wave velocities and the thicknesses are evaluated for the sampled models after the burn-in processing as shown in Figure 4. The average values and the standard deviations for the parameters are also shown in the figure. The distribution of the S-wave velocity and the thickness for the top layer are very narrow and sharp indicating a high resolution, while those for the deep part are wider distribution than those for the top layer. The relatively low resolution is due to the lack of the phase velocity at periods lower than 0.1 Hz. However, the distributions of all the parameters are enough to determine the final inverted model. The inverted model shown by a broken line in Figure 1 was derived from averaging the parameters of all the models sampled with the MCMC method. The two models are quite similar, though a slight differences of the depth to the interface at a depth of about 1km. Since we assumed the small standard deviation for the observed data, the standard deviation of the estimated parameters is also very small. The phase velocities for the inverted model are also compared with the observed data in Figure 1. The observed phase velocities at all the periods are well explained by the theoretical phase velocity.

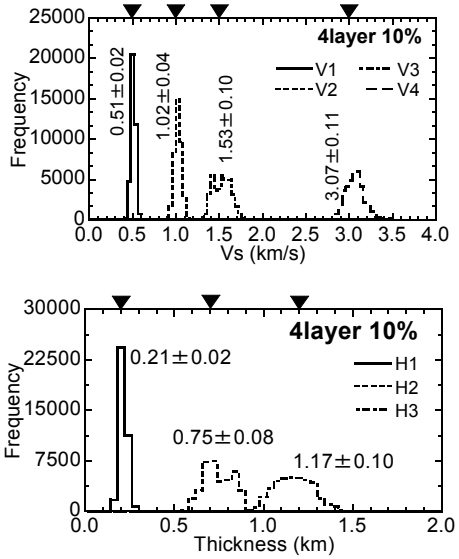


Figure 4. Distributions of S-wave velocity (left) and thickness (right) from sampled models.

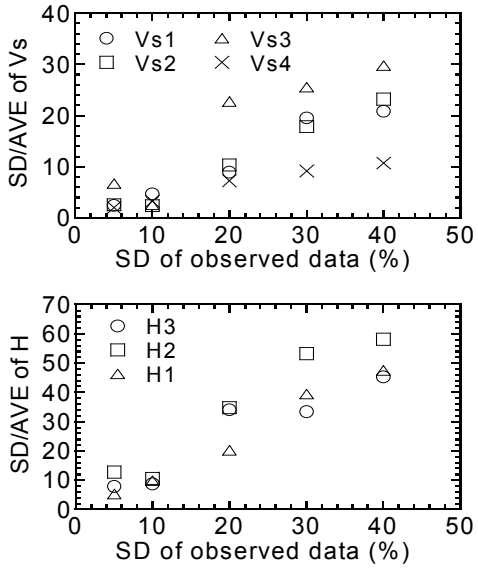


Figure 5. Relationship between standard deviations of observed phase velocity and coefficient of variations of S-wave velocity and thickness of the sampled data.

It is well known in the least-squares inversion theory that the errors in the observation determine the accuracy of the parameters. Here we investigate the effects of the observational errors assumed on the variations of the parameters. First we generated the synthetic Rayleigh waves with the different standard deviations from 5 to 40 % in the similar manner explained above. Then the similar samplings were conducted for each synthetic data. Figure 5 displays the relationships between the standard deviations for the observed phase velocity and parameters for the sampled models. It is noted that each value is normalized with its average to obtain variation coefficients. The coefficients for the parameters in the shallow part are more affected by the observational errors than the deep part. This figure also indicates that the observed phase velocity must be obtained with an accuracy of 30 % for an estimation of S-wave velocity in the top layers with an accuracy of 10 %. Similarly we can see that high accuracy phase velocity data are needed for estimating the thickness with the same accuracy. This numerical test clearly indicates the advantage of the inversion based on the MCMC method for estimation of not only an inverted profile but also its accuracy from a probability distribution of the model parameters.

4. VARIATIONS OF AMPLIFICATIONS

Once we estimated the variation of the parameters for the inverted S-wave profile, the variation of the amplification factors can be also obtained numerically. Here I calculated 1D amplification factors for the vertically propagating S-waves in the 1D models sampled in the MCMC method. Q-value is assumed to be Vs/10. Figure 6 shows averaged amplification factors with ±their standard deviation. The amplitudes and peak periods for the fundamental mode are very stable with small standard deviations. However, the variations at periods shorter than 1 second are large. The variations for the amplification factors at the predominant period are less influenced with the observational errors of the phase velocity than those for the high frequencies. This indicates that the amplification factors at the predominant periods are well constrained with the phase velocity from the microtremor explorations.

Similar calculations of the amplifications were conducted using the sampled models for the phase velocities with the different observational errors. Figure 7 shows the averaged amplification factors for the sampled models. The amplifications at the fundamental modes at a period of about 6 seconds are very similar to each others. This indicates again that the fundamental peak is well estimated from the phase velocity, although the observational errors for the phase velocity are large. On the other hands, the peaks of the amplification factors with large errors become small at periods shorter than 1 second. In particular the amplifications for the errors of 40 % have no dominant peaks at periods less than 1 second. Since the amplifications for the models from inversions of the phase velocity with large errors have peaks at different periods except for the fundamental modes, the averaged amplifications are smoothed in the averaging process at short period ranges. This suggests the difficulties for the estimation of accurate amplifications at short periods from long-period microtremor phase velocity.

The relationship between the standard deviation of the observed phase velocities and the coefficient of variations for the predominant peak period and the maximum amplitudes are shown in Figure 8. It can be seen that the peak period and the maximum amplitudes are insensitive to the observation errors. Since the maximum amplitude of the amplification factors is mainly controlled by the impedance contrast between the top layer and the basement, the low values of the variation coefficients are due to the high accuracy of S-wave velocity in the shallow part of the models.

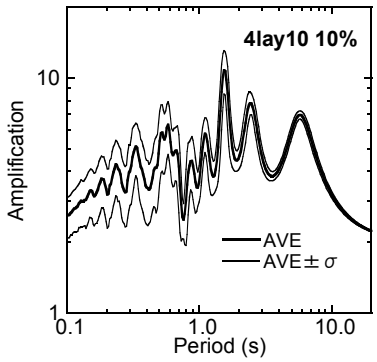


Figure 6. Average and average+-standard deviation for one-dimensional amplification factors calculated for the sampled models in inversion of phase velocity in Fig.1.

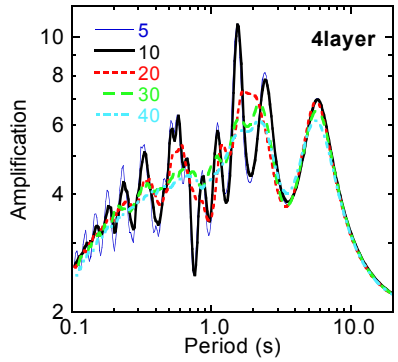


Figure 7. Average one-dimensional amplification factors calculated for sampled models in inversion of phase velocity with different standard deviations of phase velocity from 5 to 40% in Fig.1.

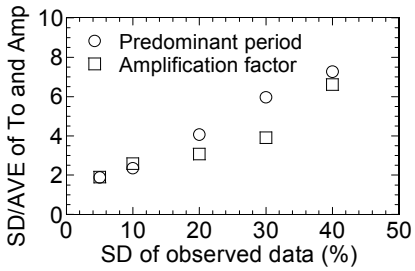


Figure 8. Relationship between standard deviations of observed phase velocity and coefficient of variations of predominant period and maximum amplitude of 1D amplification factors for the sampled data.

5. APPLICATION TO ACTUAL PHASE VELOCITY

I apply the MCMC inversion method to Rayleigh wave phase velocity from actual microtremor array exploration in the Kanto basin. Here, the phase velocity at ASO in Yamanaka et al. (2000) was used as shown in Figure 9. They inverted the observed phase velocity with a genetic algorithm to derive a 1D S-wave velocity profile that is also shown in Figure 9.

The MCMC inversion was conducted assuming a 4-layer model. The inverted S-wave velocity profile is derived from averaging the parameters for all the sampled models after the burn-in operation. The inverted profile is almost the same as that from the genetic inversion. The comparison between the observed and the theoretical phase velocities can be seen in Figure 9. The distributions of the S-wave velocities and the thicknesses for the sampled models are shown in Figure 10. The parameters for the top layer are well resolved with the narrow distributions. The S-wave velocity for the second layer is also inverted with a high accuracy, while the distribution of its thickness is broad showing a low resolution. Furthermore the parameters for the third layer and basements distribute in wide ranges. The lack of the phase velocity data at periods more than 4 seconds is the main reasons for the low resolutions of the parameters of the third layer.

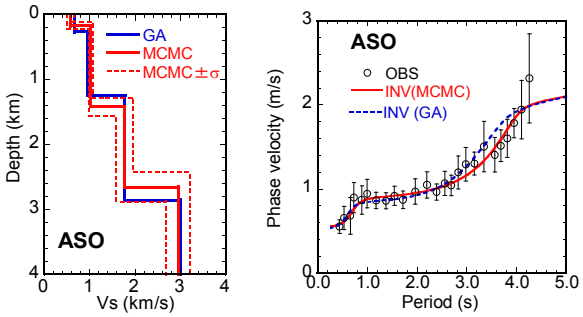


Figure 9.Comparison of inverted results from previous study and this study. Left is S-wave velocity profiles and right is phase velocities for the inverted models with observed ones.

The sampled models from the inversion of the phase velocity at ASO were used to know the variation of the amplification factors. Figure 11 shows the averaged amplification factor with standard deviation. Similar to the numerical experiments, the amplifications at the dominant period are very accurately estimated with a small standard deviation. However, short period amplifications show large variations. Because peaks for the higher mode are dominant at different periods for the sampled models, the amplification factors become smoothed without any trough and peaks. Figure 11 also shows the amplification factor for the best model from conventional inversion based on GA. The amplification factors at longer than 5 seconds including peak at the fundamental period for the model from the genetic inversion are very similar to those for the averaged one from the MCMC inversion. However, they are not the same at some periods shorter than 1 second. It is noted that the amplification is underestimated for the model from the GA due to its spectral trough.

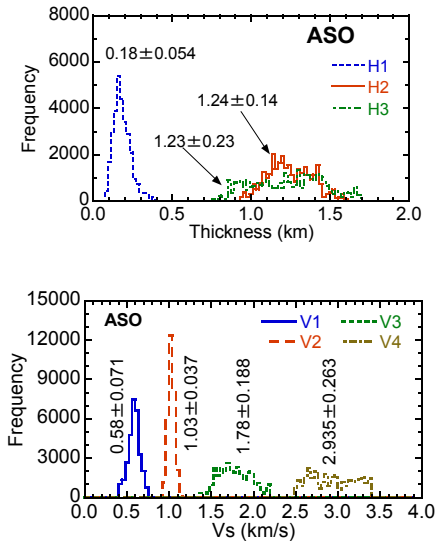


Figure 10. Distributions of S-wave velocity (left) and thickness (right) from sampled models by MCMC inversion of the observed phase velocity at ASO in Figure 9.

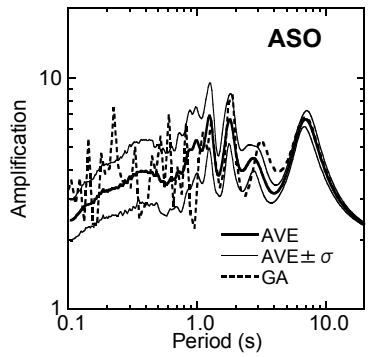


Figure 11. Average and average±standard deviation for one-dimensional amplification factors calculated for the sampled models in inversion of phase velocity at ASO in Fig.9, shown by thick and thin lines. Broken line shows amplification factors for the model derived with hybrid heuristic inversion of the observed phase velocity.

6. CONCLUSIONS

I applied the Markov Chain Monte Carlo method to surface wave phase velocity inversion. The numerical test of the method was conducted using the synthetic Rayleigh wave phase velocity data. The method can evaluate not only an inverted S-wave velocity profile, but also probabilistic distributions of the model parameters from which we can understand model resolutions. This can be addressed as one of the powerful advantages for the method. Since the MCMC inversion method requires only the calculation of the misfit function just like genetic algorithms and simulated annealing, this method is also very robust during computations. I also apply this method to the observed phase velocity data from actual microtremor explorations in the Kanto basin. The results of the inversion clearly indicated a high resolution of the S-wave velocity and the thickness for the shallow part and a low resolution for the deep part, because of the absence of phase velocity at long-periods. Using the sampled models the variations of the 1D amplification factors were estimated. The averaged amplification factors for the sampled models show a smoothed spectral shape without any peaks at periods less than one second, while the amplitudes at the predominant period are common for most of the sampled models.

Acknowledgements:

A part of this work was conducted in 'Special project for earthquake disaster mitigation in the Tokyo Metropolitan Area' supported by Ministry of Education Culture, Sports, Science and Technology, Japan, and with Grant-in-Aid for Scientific Research (No.22310108) by Japan Society for the Promotion of Science.

References:

Geweke, J. [1992] "Evaluating the accuracy of sampling-based approaches to the calculation of posterior moments", *Bayesian statistics*, **4**, 169-193.

Gilks, W.R., S. Richardson, D.J. Spiegelhalter [1996], "Markov Chain Monte Carlo in Practice", Chapman & Hall/CRC.

Hastings, W.K. [1970], "Monte Carlo sampling methods using Markov chains and their applications", *Biometrika*, **57**, 549-603.

Kitsunezaki C., N. Goto, Y. Kobayashi, T. Ikawa, M. Horike, T. Saito, T. Kurota, K. Yamane, and K. Okuzumi [1990], "Estimation of P- and S- wave velocity in deep soil deposits for evaluating ground vibrations in earthquake", *Jour. Japan Soc. Natural Disaster Science*, **9**, 1-17 (in Japanese).

Molnar, S., S.T. Dosso, and J. F. Cassidy [2010], "Bayesian inversion of microtremor array dispersion data in southwestern British Columbia", *Geophy. J. Int*., **183**, 923-940.

Okada, H. [2003], "The microtremor survey method", Soc. Exp. Geohy., Tulsa, OK.

Yamanaka, H. and N. Yamada [2006], "Modeling 3D S-wave Velocity Structure of Kanto Basin for Estimation of Earthquake Ground Motion", *Geophysical exploration (Butsuri-Tansa),* **59**, 6, 549-560 (in Japanese with English abstract).

Yamanaka, H [2005], "Comparison of performance of heuristic search methods for phase velocity inversion in shallow surface wave methods", *J. Env. and Eng. Geophys*., **10**, 163-173.

Yamanaka,H., et al.[2000], "Exploration of basin structure by microtremor array technique for estimation of long-period ground motion", *12th World Conf. Earthq. Eng*. CDROM, No.1484.

10CUEE CONFERENCE PROCEEDINGS
10th International Conference on Urban Earthquake Engineering
March 1-2, 2013, Tokyo Institute of Technology, Tokyo, Japan

AN EVALUATION OF SUBSURFACE STRUCTURE WITH INCLINED BEDROCK USING MICROTREMOR ARRAY EXPLORATION

Kentaro Motoki[1)], Tetsushi Watanabe[1)], Kenichi Kato[2)], Kojiro Takesue[3)], Hiroaki Yamanaka[4)], Masanori Iiba[5)], and Shin Koyama[6)]

1) Manager, Earthquake and Soil Dynamics Research Department, Kobori Research Complex INC., Japan
2) Senior General Manager, Earthquake and Soil Dynamics Research Department, Kobori Research Complex INC., Japan
3) Senior Research Engineer, Technical Research Institute, Kajima Corporation, Japan
4) Professor, Department of Civil Engineering, Tokyo Institute of Technology, Japan
5) Senior Research Fellow, Structural Department, Building Research Institute, Japan
6) Chief Research Engineer, Structural Department, Building Research Institute, Japan
kmoto@kobori-takken.co.jp, watanabe@kobori-takken.co.jp, katokenichi @kobori-takken.co.jp, k-takesue@kajima.com, yamanaka@depe.titech.ac.jp, iiba-m@kenken.go.jp, skoyama@kenken.go.jp

Abstract: In this study, we conducted microtremor array exploration at a site with inclined bedrock to deduce S-wave velocity in shallow soil. The S-wave velocity of the 1st layer and the depth to engineering bedrock evaluated from microtremor array exploration are consistent with the results of measurement-while-drilling, surface wave exploration method and H/V spectra of microtremors. In order to estimate the effect of bedrock inclination on the phase velocity, 2D model was constructed from aligning the 1D profiles. The difference between the phase velocities from FEM analysis with the 1D and 2D models can be recognized in the long period range.

1. INTRODUCTION

An amplification factor at an inclined bedrock site is significantly influenced by laterally propagating seismic waves (e.g. Watanabe, *et al.* 2011). The damage was concentrated in near Kego fault during the 2005 west off Fukuoka prefecture earthquake, and it was interpreted that the amplification was affected by irregular shallow subsurface structure (Motoki *et al.* 2006). Not only a subsurface structure at a site but also ones around a site are required for a precise estimation of amplification factor at an inclined bedrock site.

Microtremor array explorations have been made use of an estimation of amplification factor of subsurface geology for application to an earthquake resistant design (e.g. Fukumoto and Mimachi 2006) and to a damaged area during a disastrous earthquake (e.g. Asano *et al.* 2009). Microtremor array exploration can be regarded as one of the most useful methods to obtain a number of subsurface structures because of the high mobility and the high cost performance of it.

S-wave velocity profiles based on microtremor measurements are evaluated with a stratified media. In that analysis, microtremors are assumed to consist of Rayleigh wave, and 1D model is applied to an inversion (e.g. Yamanaka and Ishida 1995). Therefore, the point is applicability of Rayleigh wave for 1D model at a site with inclined bedrock.

As pointed out by previous studies on an applicability of 1D model for microtremor array exploration, body wave and higher mode Rayleigh wave are dominated around the points near highly irregular subsurface structure, and the phase velocities at these points cannot be reproduced only with 1D model, consequently (Nakagawa and Nakai 2010 Uebayashi *et al.* 2009, Sato *et al.* 2006). Although subsurface structures are inversed with 2D or 3D model ideally, it is too difficult to apply to a practical engineering. It can be considered that it is important to reveal applicability of 1D model through a field test.

In this study, we demonstrate applicability of 1D model in microtremor array exploration by comparing with the results of measurement-while-drilling, surface wave exploration and H/V spectra of microtremors at a site of irregular subsurface structure. We investigate the influence of the irregular subsurface structure on the phase velocities with numerical analysis.

2. TARGET SITE AND MEASUREMENTS

We selected the site where the the shape of the upper boundary of engineering bedrock by a sounding technique, measurement-while-drilling (hereafter MWD, Nishi *et al.*, 1997) was regarded as an irregular site. The MWD can produce a continuous soil resistance index, called Np value corresponding to N value by standard penetration test (hereafter SPT). This site was leveled in mountainous area and

the outside of a site is a slope face. Figure 1 shows the contour map of the depth to 25 of Np value and N value and microtremor measurement points.

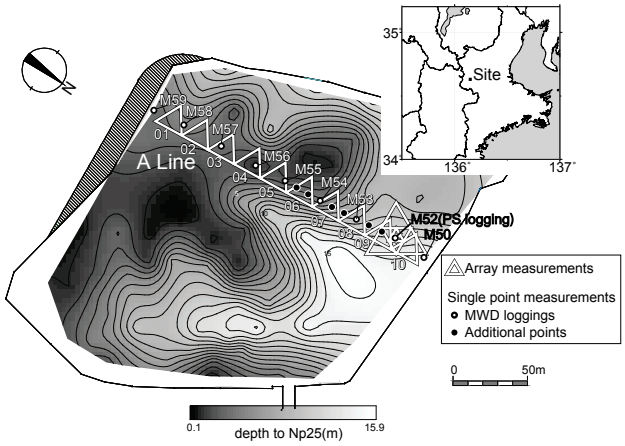


Figure 1 Contour Map of Np25 Estimated by MWD and the Arrangement of Microtremor Measurements

We deployed 10 sets of microtremor array measurements aligning along A line in Figure 1 where the soil deposits are thick in the northern part and thin in the southern part. We measured another one of microtremor array nearby the hole conducted PS logging, M52 in Figure 1. In addition to microtremor array measurements, we carried out microtremor measurements using a single three-component sensor at the MWD logging points and the additional points interpolating the steep area of the shape of the bedrock. The surface wave exploration using an artificial source (Hayashi *et al*., 2001) was also conducted along A line in Figure 1.

We installed 7 vertical accelerometers at the vertexes of 2 equilateral triangles with sides of 10m and 20m long and the center of them for a set of microtremor array measurement. In the aligning array, a vertex of adjacent arrays is located at the same point as a vertex and 10 sets consist of the continuous measurement. In the array at M52, we had 3 turns, which consisted of equilateral triangles with sides of 2.5m, 5m, 10m, 20m and 40m long.

The surface wave exploration consisted of recordings taken with 24 sensors with a sampling interval of 2m. A sinker of 20kg weight was used for an artificial source. The source was set at 5m, 10m and 15m far from the sensors to the north side.

The P- and S-wave velocities at the depths from GL-1m to GL-26m with an interval of 1m are evaluated by PS logging at M52 using the downhole method.

Figure 2 shows the results of PS logging, MWD and SPT at M52. The Np values by MWD are consistent with the N values by SPT. It can be found that the Np values quickly change at the depth where the Np values are 25 and 150, and those depths correspond to the geological boundary among the bank, the strongly weathering granite and the weathering granite. The S-wave velocity of the first layer is estimated 200m/s by PS logging. The engineering bedrock of which S-wave velocity is 460 m/s appears at the 17.5m depth, that corresponds to the depth to 150 of the Np value and the upper boundary of the weathering granite. The granite of which S-wave velocity is 2200m/s at the about 23.5m depth causes the high contrast surface with the weathering granite. The depths of granite were not estimated by MWD logging because of the strength of the percussion drill.

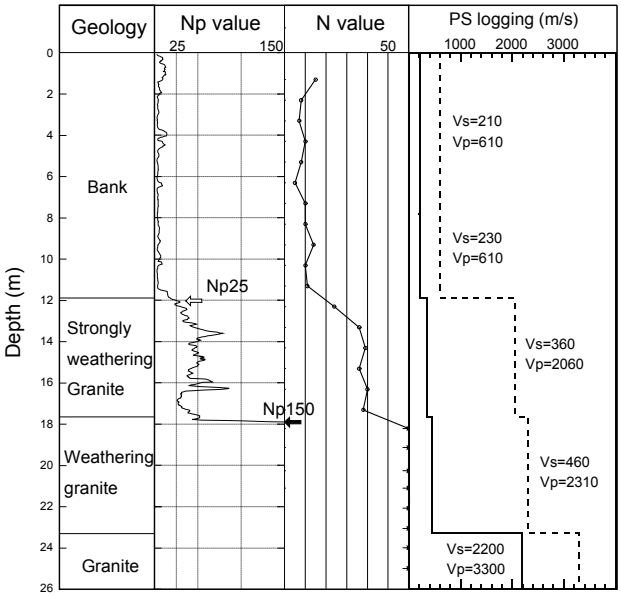


Figure 2 Comparison of the Results of the PS logging, the MWD and SPT at the Point M52 Shown in Figure 1

3. RESULTS OF MICROTREMOR MEASUREMENTS

3.1 Data Processing

More than 10 segments which had a 20.48 second each were picked up from the microtremor record as samples for Fourier analysis avoiding the noise inferred from the amplitude. SPAC method (Aki 1957) was adopted to evaluate the phase velocity. The logarithmic Parzen window suggested by Konno and Ohmachi (1995) was applied to smooth spectra. The normal dispersion part in the phase velocities were used for an inversion.

3.2 Phase velocity

Figure 3 shows comparison of the phase velocities between evaluated from microtremor records and theoretically calculated with the model shown in Figure 2. The evaluated phase velocity is consistent with the calculated one. Therefore, we use this model as a reference model in an inversion.

Figure 4 shows the phase velocity evaluated from the continuous array measurements from 01 to 10. The phase velocity at the point 04 is the fastest of all 10 points and the value of the phase velocity is gradually decreasing being distant from the point 04. This feature qualitatively approximates to the distribution of the thickness of the 1st layer shown in Figure 1 and it can be considered that the differ-

ence of the depth to the bedrock reflects the transition of the phase velocities.

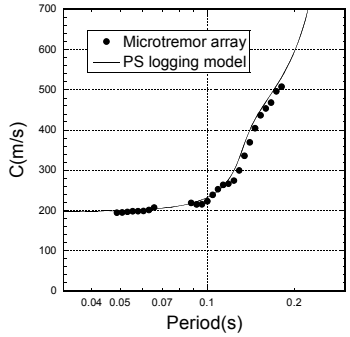


Figure 3 Comparison of Phase Velocities at M52 between Evaluated by Microtremor Array Measument and Calculated for Fundamentarl Mode Rayleigh Wave with the PS Logging Model Shown in Figure 2

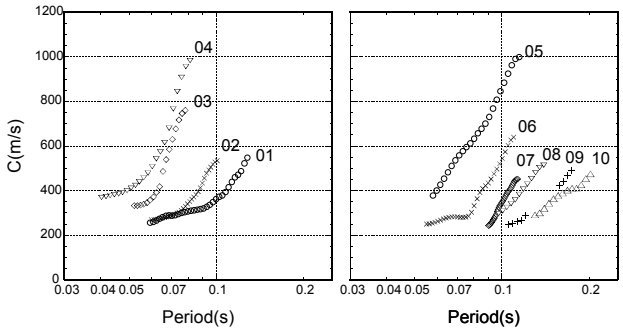


Figure 4 Transition of Phase Velocities Evaluated by Continuous Array Measurements

4. ESTIMATION OF SUBSURFACE STRUCTURE ON INCLINED BEDROCK

4.1 Subsurface Structure Inverted with 1D Model

In this chapter, S wave velocity profiles are deduced from the observed phase velocities. The phase velocities are averaged to divide logarithmically equal frequency axis. Since 1 turn of the measurement with a equilateral triangles with sides of 10m and 20m long was carried out and the phase velocity was picked up only from the part showing normal dispersion, .available frequency ranges are restricted. As Suzuki and Yamanaka (2010) pointed out, it is difficult to avoid trade-off relation between thickness and S-wave velocity of shallow layer in an inversion using only a phase velocity, especially for the restricted frequency range. This study focuses on the shape of the bedrock, and it is important to stabilize the thickness of shallow layer. Therefore, we apply a restricted inversion model that the 2 unknown parameters are the depth to the last layer and the S-wave velocity of the 1st layer. The reference model is referred to the result of the PS logging shown in Figure 2 and is set to 4 layer model that the 1st layer (Vs=210m/s) and 2nd layer (Vs=230 m/s) were arranged into 1 layer. In the inversion model, S-wave velocities of other layers are fixed to the reference model and thicknesses of shallow layers are changed proportionally. When the S-wave velocity of the 1st layer is faster than that of the 2nd layer, the S-wave velocity of 2nd layer is made equal to that of 1st layer. The P-wave velocity is calculated by the empirical relation reported by Kitsunezaki *et al*., (1990).

We adopt Genetic Algorithm as a heuristic search method, and objective function is following.

$$misfit = \sum \left| \frac{O(f) - C(f)}{O(f)} \right| \tag{1}$$

O(f) and C(f) are respectively observed phase velocity and calculated phase velocity assumed the fundamental mode of Rayleigh wave. Population, maximum generation and crossover rate are set to 15, 40 and 0.9, respectively. 20 times calculation with the different seed for random numbers, and the final result is averaged of the solutions within allowable error of 2 percents of the minimum misfit.

4.2 Comparison among the Result of Subsurface Structures Including Other Exploration Method

Figure 5 shows the result of the each exploration performed in this study. First, we focus on the comparison of the S-wave velocity of the 1st layer. Near the ground surface, the S-wave velocity evaluated by surface wave exploration can be considered more credible than other explorations because of the numbers of densely arranged sensors and the apparent active source. The velocities of the 1st layer were estimated more than 300 m/s at the point 04 and about 200 m/s in the northern part. The results of microtremor array exploration and surface wave exploration are consistent with each other.

Next, we focus on the depth of the engineering bedrock. The depth of the geological boundary by MWD can be considered the most credible, because the result of the other exploration include trade-off relation between thickness and S-wave velocity, and the percussion drill for MWD directly contacted to the material. The transitions of the Np value are indicated by thin line. The depths of the engineering bedrock correspond to the depth of Np 150 as shown in Figure 2 and are plotted in Figure 5(b).

The depths of 410 m/s in S-wave velocity by surface wave exploration are regarded as a depth of the engineering bedrock paying attention to the phase velocity that are equivalent to those calculated from 4 layer models by microtremors. The depths are drawn only shallower than 15m, because of low sensitivity in deeper than 15m due to the small artificial source.

The depths of the engineering bedrock by microtremors are deeper in the northern part than the center and the southern part, and this shape is similar to the depth by Np 150. Except for the both end of the measurement line, the depths of the bedrock by all explorations are consistent with each other. The depths estimated by microtremors are relatively deep in the norther part from 150m and the southern part to the 50m comparing with the results of other 3 explorations. The both outsides of the measurement site are steep slope face, and this irregularity has a possibility to affect to the

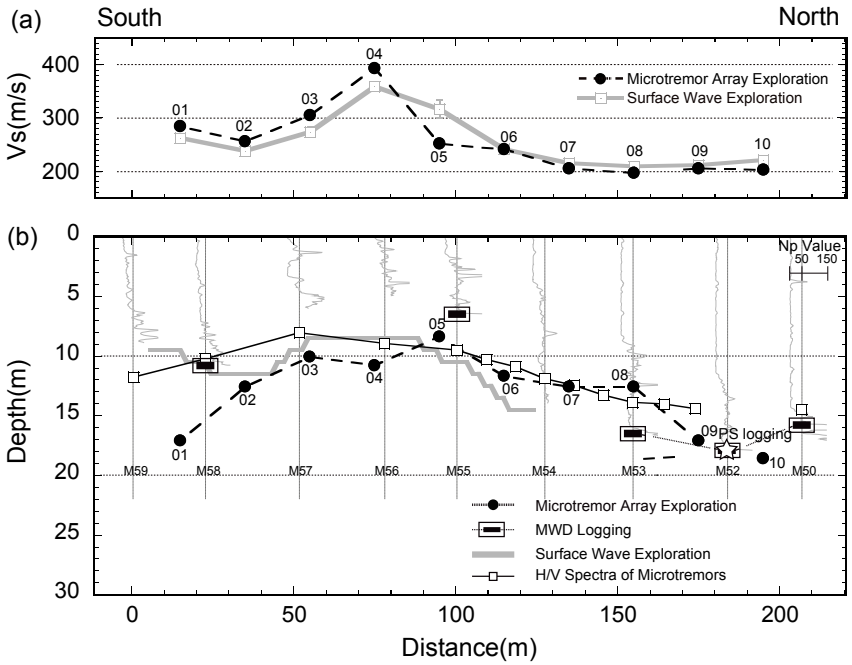


Figure 5 Comparison of the Results among Microtremor Array Exploration, Surface Wave Exploration, MWD Logging and H/V Spectra of Microtremors. (a) S-wave Velocity of 1st Layer, (b) Depth to Engineering Bedrock

phase velocity. Nakagawa and Nakai (2010) concluded that the contamination to the phase velocity due to the structural irregularity appeared near the steep slope. Uebayashi *et al*. (2009) pointed out that the deeper basement is estimated by microtremors comparing to the result of the borehole, because the complexity of the wavefield due to the irregular subsurface structure decrease the value of SPAC coefficient. The depth near the both end of the measurement line evaluated by microtremors can be overestimated, taking their expertise into account.

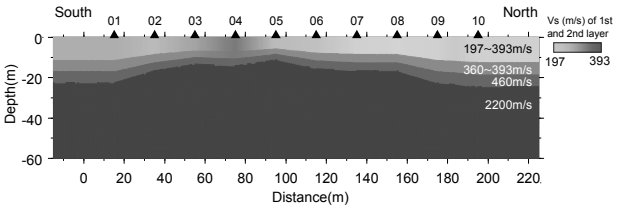


Figure 6 Constructed 2D Model with 1D Model Evaluated by Microtremor Array Exploration

5. INFLUENCE OF INCLINED BEDROCK TO PHASE VELOCITY

Even though the result of microtremor array exploration is consistent with the results of other explorations as shown in Figure 5, a problem of influence due to the irregularity of the subsurface structure is still remained. In order to consider this influence, we construct 2D model by interpolating 1D models of subsurface structure and examine the difference between the phase velocities through simulated with 1D and 2D models.

Figure 6 shows 2D model constructed interpolating the S-wave velocities of 1st and 2nd layers and the depth of the layer boundaries linearly. The outside of the model is set to strata, and the boundary conditions are set to viscous boundary at the bottom and energy transmitting boundary at the lateral ends. The damping rate is set to 0.02. The excitation is set to the fundamental mode Rayleigh wave into the both lateral ends. The phase velocities are derived from the average of the velocities calculated from coherence of vertical motions at 3m, 5m and 10m far from the center.

Figure 7 shows the phase velocities obtained with 1D and 2D model at the points of 01, 04 and 06. The phase velocities at the point 01 and 04 with incident into north end of 2D model and at the point 06 with incident into south end are similar to those with 1D model. On the contrary, the phase velocities with incident with opposite end to above case appear unstable and the obvious discrepancy from the result with 1D model in the long period range. This feature cannot be recognized in the short period range. Since the phase velocity in the short period range is affected by the S-wave velocity near the ground surface, it is confirmed that the S-wave velocity in shallow soil above the inclined bedrock can be estimated by the phase velocity. Furthermore, good agreement in Figure 5 (a) supports this conclusion.

Turbulence of the phase velocity in the long period range appears when the surface wave propagates from deeper area to shallower area in the depth of the bedrock boundary. This feature can be regarded as the turbulence due to the contamination by the body wave and higher mode Rayleigh wave (Nakagawa and Nakai, 2010).

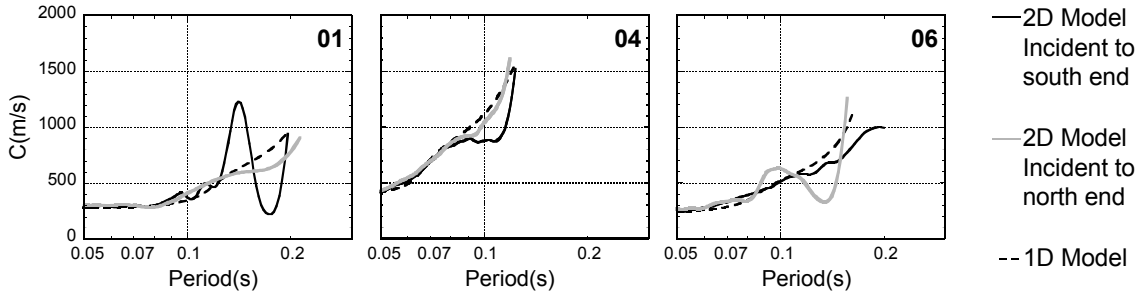


Figure 7 Comparison of the Phase Velocities Numerically Calculated with 2D model Shown in Figure 5 and 1D Model

In order to consider the influence of the irregularity of the subsurface geology on the turbulence in the phase velocity, we estimate the phase velocities with the cut models shown in Figure 8. Model I and II are set up for simulation extent to limit 30m and 15m far from point 01 to the north side, respectively. We simulated the case of the incidence from the south end of the model.

Figure 9 shows the phase velocities calculated with model I and II. The phase velocities in the shorter period range than 0.12 second are similar to each other. On the contrary, it can be recognized that the calculated phase velocity is approximated to the result of 1D model with the more limited model. This suggests that a spatial extent related with phase velocity depends on a period. Therefore, microtremor array exploration can be applied to deduction of the subsurface structure with 1D model even at an inclined bedrock site, paying attention to the period range for an inversion.

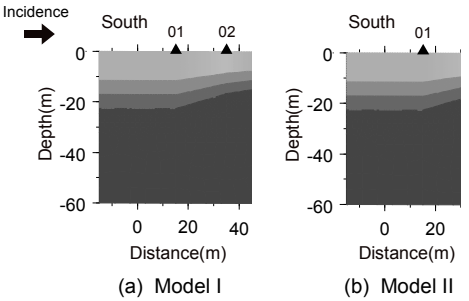


Figure 8 2D Model Limited Area for Numerical Simulation

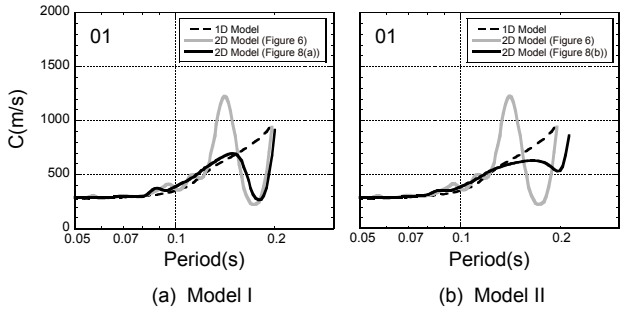


Figure 9 Phase Velocities Calculated with Limited Model

6. CONCLUSIONS

We conducted mictrotremor array exploration at an inclined bedrock site where had been leveled in mountainous area. The structure of the inclined bedrock was deduced by 10 subsurface structures evaluated with 1D model. The following features were found in this research.

1. The S-wave velocities near the ground surface evaulated by microtremor array are consistent with the result of the surface wave exploration.

2. The depths of the engineering bedrock evaluated by microtremor array are consistent with the result of the MWD, the H/V of microtremors and the surface wave exploration.

3. The phase velocity calculated by numerical analysis with 2D model is similar to the phase velocity calculated with 1D model in the short period range.

4. On the contrary, the difference of the numerical phase velocities between 1D model and 2D model can be recognized in the long period range. The turbulence of the phase velocity with 2D model is appeared in the case of the surface wave propagating from deep area to shallow area in the engineering bedrock.

5. It is required that we pay attention to the period range to apply an inversion, while a conventional inversion technique with 1D model is applied to an inclined bedrock site.

Acknowledgements:

This work made use of GMT software (Wessel and Smith, 1998). A part of this research was supported by the Japan Ministry of Land, Infrastructure, Transport and Tourism. The measurement site was provided from Fujimori Kogyo Co., LTD. Measurements were assisted by Dr. Seiji Tsuno, Dr. Shunichi Fukumoto, Mr. Takeshi Sugiyama and students who belong to Tokyo Institute of Technology. Constructive comments by the deceased Dr. Kenji Miura had made progress since commencing this research.

References:

Aki, K.(1957), Space and time spectra of stationary stochastic waves, with spacial reference to microtremors, Bull. Earth. Res. Inst. Univ. Tokyo, **35**(3) 415-457.

Asano, K., Iwata, T., Iwaki, A., Kuriyama, M. and Suzuki, W. (2009), Ground Motion Characteristics in Anamizu Town Obtained from Earthquake and Microtremor Observations, Zisin - J. Seism. Soc. Japan, 2nd Series, **62**, 121-135.

Fukumoto, S. and Mimachi, T. (2006), Application of Microtremor Array Explorations for Architectural Seismic Design, BUTURI-TANSA, **59**(2) 151-162.

Hayashi, K., Suzuki, H. and Saito H. (2001), Surface Wave Method Using Artificial Sources, Oyo Technical Report, **21**, 9-39.
Kitsunezaki, C. Goto, N., Kobayashi, Y., Ikawa, T., Horike, M., Saito, T., Kuroda, T., Yamane, K. and Okuzumi, K. (1990), Estimation of P- and S- Wave Velocities in Deep Soil Deposits for Evaluating Ground Vibrations in Earthquake, J. JSNDS, **9**(3), 1-17.
Konno, K. and Ohmachi, T. (1995), A Smoothing Fuction Suitable for Estimation of Amplification Factor of the Surface Ground from Microtremor and Its Application, J. Japan Soc. Civil Eng., **525**/I-33, 247-259.
Motoki, K., Yamanaka, H., Seo, K. and Kawase, H. (2006), An Estimation of Site Amplification by Irregular Subsurface Structure near Kego Fault from Aftershock Records of the 2005 West off Fukuoka Prefecture Earthquake, J. Struct. Constr. Eng., AIJ, **602**, 129-137.
Nakagawa, H. and Nakai, S. (2010), Effect of an Irregular Ground on Microtremor H/V Spectra and Dispersion Curve, J. Struct. Constr. Eng., AIJ, Vol.75, No. 656, 1827-1835.
Nishi, K., Sasao, H., Suzuki, Y., Takesue, K. and Sanematsu, T. (1997), A New Sounding Technique Using Rotary Percussion Drill, J. Technol. Des., AIJ, **5**, 69-73.
Sato, H., Sato, K., Higashi, S. and Shumuta, Y. (2006), Application of Microtremor Array Exploration for Seismic Retrofit Strategy Learnt from the Damages of the Electric Power Facilities during Recent Large Earthquakes, BUTURI-TANSA, **59**(2), 141-150.
Suzuki, H. and Yamanaka, H. (2010), Joint Inversion Using Earthquake Ground Motion Records and Microtremor Survey Data to S-Wave Profile of Deep Sedimentary Layers, BUTURI- TANSA, **63**(3), 215-227.
Uebayashi, H.,Kawabe, H., Kamae, K., Miyakoshi, K. and Horike, M. (2009), Robustness of Microtremor H/V Spectra in the Estimation of an Inclined Basin-Bedrock Interface and Improvement of the Basin Model in Southern Part in Osaka Plain, J. Struct. Constr. Eng., AIJ, **642**, 1453-1460.
Watanabe, T., Kato, K., Iiba, M. and Koshika, N. (2011), A Fundamental Study on Effects of Inclined Engineering Bedrock on Amplification Characteristics in Surface Layer, J. Technol. Des. AIJ, **36**, 455-458.
Wessel, P., and Smith, W.H.F. (1998), New improved version of Generic Mapping Tools released. EOS, Trans. AGU, **79**, 579.
Yamanaka, H. and Ishida, H. (1995), Phase Velocity Inversion Using Genetic Algorithms, J. Struct. Constr. Eng., AIJ, **468**, 9-17

10CUEE CONFERENCE PROCEEDINGS
10th International Conference on Urban Earthquake Engineering
March 1-2, 2013, Tokyo Institute of Technology, Tokyo, Japan

SIMULATION OF H/V SPECTRAL RATIOS OF MICROTREMORS WITH DIRECTIONAL DEPENDENCY

Shinichi Matsushima[1)], Florent De Martin[2)], Takanori Hirokawa[3)], Hiroshi Kawase[4)], and Francisco J. Sánchez-Sesma[5)]

1) Associate Professor, Disaster Prevention Research Institute, Kyoto University, Kyoto, Japan
2) Project Manager, Risks and Prevention Division, BRGM, Orléans France
3) Structural Engineer, Yamashita Sekkei Inc., Nihombashi, Tokyo, Japan
4) Professor, Disaster Prevention Research Institute, Kyoto University, Kyoto, Japan
5) Professor, Instituto de Ingeniería, Universidad Nacional Autónoma de México, C.U., Mexico
matsushima@zeisei.dpri.kyoto-u.ac.jp, F.DeMartin@brgm.fr, hirokawa-t@yamashitasekkei.co.jp, kawase@zeisei.dpri.kyoto-u.ac.jp, sesma@unam.mx

Abstract: The authors have proposed a new theory to calculate the Horizontal-to-Vertical (H/V) spectral ratio of microtremors assuming that the wave field is completely diffuse which is not limited to horizontally flat-layered 1D structures and have attempted to apply the theory to understand the observed microtremor data. For a sufficiently flat, horizontally layered structure, we can easily calculate the theoretical Green's function for that 1D model but for a laterally heterogeneous underground structure, such as the case of Uji campus where significant directional dependency of microtremor H/V spectral ratios were observed, a numerical approach is needed to interpret the H/V spectral ratios. We performed numerical analyses by Spectral Element Method using point source in both the 1D and 2D models to examine the effect of the 2D basin structure on the H/V spectral ratio of microtremors. As a result, we found that the 2D basin structure clearly changes the characteristics of the H/V spectral ratio in both perpendicular and parallel directions relative to the basin edge and we have succeeded to simulate qualitatively the difference between the two orthogonal horizontal components as a result of directional dependence as seen in the observed H/V spectral ratio of microtremors at Uji campus.

1. INTRODUCTION

The authors have proposed a new theory to calculate the Horizontal-to-Vertical (H/V) spectral ratio of microtremors assuming that the wave field is completely diffuse (Sánchez-Sesma *et al*., 2011), based on the diffuse field theory (Perton *et al*., 2009) and have attempted to apply the theory to understand the observed microtremor data. It is anticipated that this new theory can be applied to understand the subsurface velocity structure as well as the condition of lateral heterogeneity, since the new theory to calculate the H/V spectral ratio of mircrotremors is not limited to horizontally flat-layered 1D structures.

As observational evidence of non 1D microtremor H/V spectral ratios, we have discovered significant directional dependency at a site in Uji campus, Kyoto University, Japan, where the bedrock depth varies from east to west from 250m to 420m within the distance of 1km. This directional dependence can be considered to be the result of 2D subsurface structure (Hirokawa *et al*., 2011).

For a sufficiently flat, horizontally layered structure, we can easily calculate the theoretical Green's function for that 1D model but for a laterally heterogeneous underground structure, such as the case of Uji campus, a numerical approach is needed to interpret the H/V spectral ratios. We performed numerical analyses by Spectral Element Method (SEM) using point source in both 1D and 2D models to examine the effect of the 2D basin structure on the H/V spectral ratio of microtremors.

2. THE EFFECT OF 2D BASIN STRUCTURE

Microtremor measurements were made at four sites in Uji campus (Hirokawa *et al*., 2010) and the H/V spectral ratios showed significant directional depencency as shown in Figure 1. The H/V spectral ratios for each observed data for NS and EW components are computed separately without averaging the two horizontal components as done in conventional H/V spectral ratio studies. From these figures, we can see that for every site except for site A the amplitude of the peak ratio of NS/UD is about 4.0, larger than that of EW/UD, which is about 2.5 and that the peak frequency of NS/UD ratio is 0.5Hz, slightly smaller than that of EW/UD, which is about 0.6Hz (Hirokawa *et al*., 2011).

At Uji campus, previous surveys and research by

Koizumi *et al*. (2002) show that the bedrock is dipping east to west from the Obaku fault that runs in the north south direction several hundreds of meters east of the campus. In this study we assume a 2D structure which the bedrock depth varies from 250m to 420m within a distance of 1km and construct a 2D one-layered basin structure shown in Figure 2.

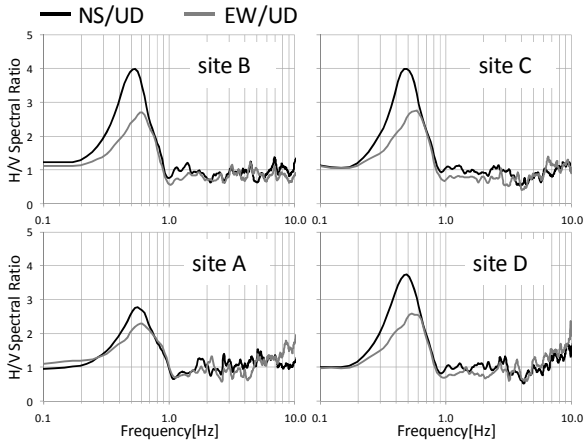


Figure 1 Average NS/UD and EW/UD spectral ratios of June 21st, 2010, observed at four sites in Uji campus of Kyoto University (Matsushima *et al*., 2012).



Figure 2 Top 500m of the section of the 2D basin structure (after Hirokawa *et al*., 2011)

3. THEORY

It has been recently derived that the H/V spectral ratios of microtremors corresponds to the square root of the ratio of the sum of the corresponding imaginary parts of horizontal displacements for horizontal unit harmonic loads and the imaginary part of vertical displacement for a vertically applied unit harmonic load (Sánchez-Sesma *et al*., 2011).

Theoretical energy density at a given point $\mathbf{x_A}$ can be written as Eq. (1) and since it is proportional to $\langle u_1^2 \rangle = \langle H_1^2 \rangle$, the H/V spectral ratio can be written as Eq. (2). From Eqs. (1) and (2), theoretical H/V spectral ratio can be derived as Eq. (3).

$$E(\mathbf{x_A}) = \rho\omega^2 \langle u_m(\mathbf{x_A}) u_m^*(\mathbf{x_A}) \rangle = -2\pi\mu E_S k^{-1} \times \mathrm{Im}[G_{mm}(\mathbf{x_A}, \mathbf{x_A})] \quad (1)$$

$$\frac{H(\omega)}{V(\omega)} = \sqrt{\frac{E_1(\mathbf{x},\omega) + E_2(\mathbf{x},\omega)}{E_3(\mathbf{x},\omega)}} \quad (2)$$

$$\frac{H(\omega)}{V(\omega)} = \sqrt{\frac{\mathrm{Im}[G_{11}(\mathbf{x},\mathbf{x};\omega)] + \mathrm{Im}[G_{22}(\mathbf{x},\mathbf{x};\omega)]}{\mathrm{Im}[G_{33}(\mathbf{x},\mathbf{x};\omega)]}} \quad (3)$$

In an equipartitioned field, it will be valid even if we take only one horizontal component of Eq. (3), so the directional H/V spectral ratio can be derived as Eq. (4).

$$\frac{H_m(\omega)}{V(\omega)} = \sqrt{\frac{\mathrm{Im}[G_{mm}(\mathbf{x},\mathbf{x};\omega)]}{\mathrm{Im}[G_{33}(\mathbf{x},\mathbf{x};\omega)]}} \left[m = 1,2\right] \quad (4)$$

This shows that with our new theory, we can calculate the H/V spectral ratio of mircrotremors in two orthogonal horizontal components separately meaning that it is not limited to horizontally flat-layered 1D structures.

4. SIMULATION OF H/V SPECTRAL RATIO

In order to take into account of the 2D or 3D subsurface structure, we need to incorporate a numerical approach for Green's function calculation. In this study we use the 3D Spectral Element Method (SEM) code ÉFISPEC3D (De Martin, 2011), to study cases of laterally heterogeneous elastic layers over a half-space.

4.1 Flat Layered Velocity Model

For calibration purposes, we first checked that numerical calculations by SEM give the same results as theoretical ones. We assume a flat-layered model with a single layer over half-space, equivalent to velocity model at site C. The characteristics of the 3D SEM calculation are listed in Table 1 and the velocity model for the flat-layered case is listed in Table 2. For simplicity, we used here a one layer model. Figure 3a displays the schematic image of the velocity model of the one layer 1D model. Figure 4a shows the mesh of the model for the one layer 1D model. It is a mesh composed by structured hexahedra designed to be accurate (i.e., without numerical dispersion) with seven Gauss–Lobatto–Legendre (GLL) nodes per wavelength at 5 Hz (we use polynomials of order 6 to sample the wave field; therefore, each hexahedron contains 7 x 7 x 7 = 343 GLL nodes). The bedrock is meshed with hexahedra of size 396m and the layer is meshed with hexahedra of size 132m. A mesh tripling is used inside the bedrock to refine the mesh just below the layer. We apply a unit load to the surface of the model at the target position and retrieve the imaginary part of the Green's function from the response at the same position. We note that the unit load is applied as a spatial Dirac positioned at a GLL node common to four hexahedra.

Figure 5 shows the comparison of theoretical and numerical results for the 1D velocity model shown in Table 2 and Figure 3a. Figure 5a is the imaginary part of Green's function for horizontal (dark gray) and vertical (light gray) components. The dotted and solid lines are results of the 3D SEM and 1D theory, respectively. The SEM results shows very good match to the theoretical ones. Figure 4b is the H/V spectral ratio derived from the imaginary part of Green's function shown in Figure 4a. Since the imaginary part of Green's function show good match, the H/V spectral ratio also shows very good match, naturally.

Table 1 Characteristics of the three-dimensional SEM calculation

Parameter	One layer 1D	One layer 2D basin
Model size	Length 40km Width 40km Depth 40km	Length 16km Width 16km Depth 10km
Minimum Element Size	132m	
Total Elements	1,693,366	289,069
Order of polynomial's shape function	6	
Maximum Frequency	5 Hz	
Minimal number of GLL nodes at 5 Hz	7	
Time Increment	0.0035 s	
Time Step	58000	
Total Duration	20.0 s	

Table 2 One layer one-dimensional velocity model equivalent of site C for testing SEM calculation

	Thickness [m]	P wave velocity [m/s]	S wave velocity [m/s]	Density [kg/m^3]	$Q_{s,p}$
1	390	1,985	661	1,930	9999
bedrock	-	5,083	2,348	2,600	9999

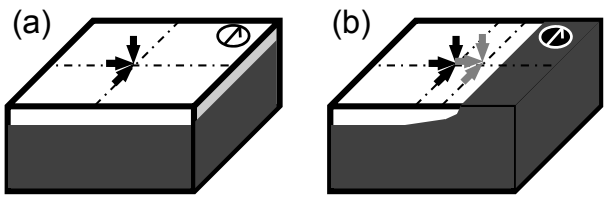


Figure 3 Schematic image of (a) one layer one-dimensional velocity model and (b) one layer two-dimensional basin model, used for three-dimensional SEM calculation. The arrows show the directions of the unit loads

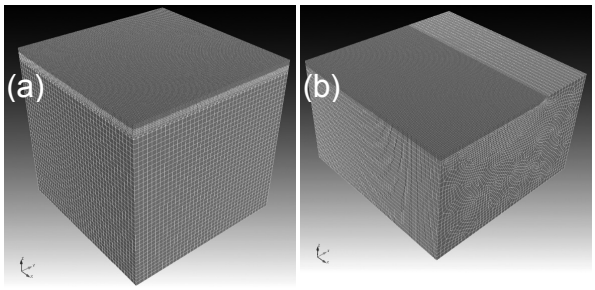


Figure 4 Mesh of the model for (a) one layer one-dimensional velocity model and (b) one layer two-dimensional basin model for three-dimensional SEM calculation

4.2 Layered 2D Velocity Model

Now we consider a laterally heterogeneous velocity structure. We use a 2D velocity model and calculate the 3D wave field. The 2D velocity model consists of one layer over half-space that gradually gets shallow from west to east and eventually pinches out as shown in Figure 3b. The maximum depth of the 2D basin in the model is 420m. The parameters of the model are listed in Table 3. The mesh used

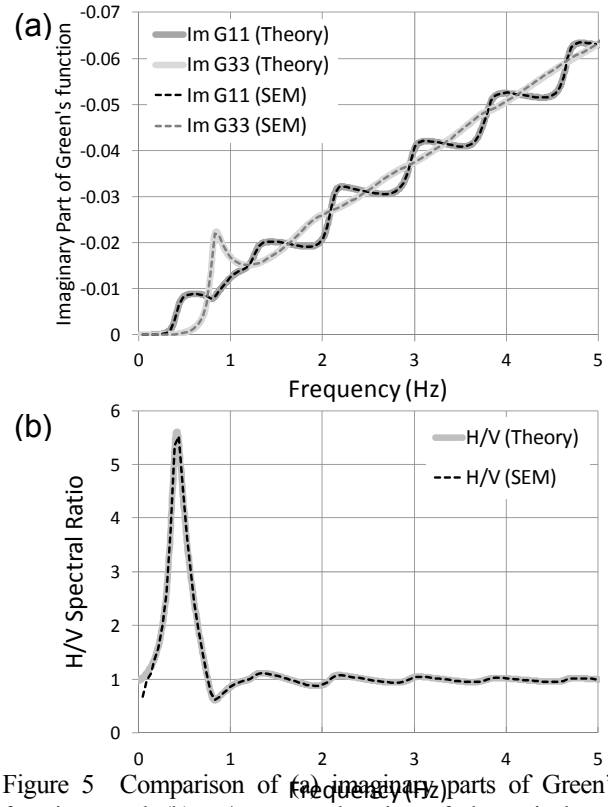


Figure 5 Comparison of (a) imaginary parts of Green's functions and (b) H/V spectral ratios of theoretical and numerical results for one layer one-dimensional velocity model in Table 3. The two calculations show very good match

by the SEM calculation is shown in Figure 4b. To honor the interface between the layer and the bedrock (especially at the basin edge), we use a mesh composed by unstructured hexahedra. As for the flat layered model, the mesh is also designed to be accurate with seven GLL nodes per wavelength at 5 Hz. For this model, we first calculate the H/V spectral ratio at a position of site C which is about 920m away from the basin edge and corresponds to the black arrows in Figure 3b. The H/V spectral ratio for this case is shown in Figure 6. The spectral ratios for NS/UD (black dotted line) and EW/UD (gray dotted line) show different characteristics with the amplitude larger for NS/UD ratio and peak frequency higher for EW/UD ratio. Although it is not as large as the observed, the difference between NS/UD and EW/UD ratios is well reproduced at least qualitatively. Another fact that we can point out is that the H/V spectral ratio is largely affected by the 2D basin structure and the amplitude of the spectral ratio for 2D basin model is much smaller than that of the 1D theory (solid black line). If we look at the wave propagation for unit loads on the surface of the model, we can clearly see the effect of the basin edge in the response at the same point as the load even in the direction parallel to the basin edge.

Next, we perform a second calculation for the target position at 260m from the basin edge, which is 660m to the east from site C, as shown by the gray arrows in Figure 3b. The depth of the bedrock at this point is about 270m. The H/V spectral ratios for this case are shown in Figure 7. We

can see that for this case the difference between NS/UD (black dotted line) and EW/UD (gray dotted line) ratios becomes larger and the peak amplitude of the spectral ratios become smaller compared to those at site C, although the amplitude of the H/V spectral ratio for a 1D theory (solid line) is similar to that at site C.

Table 3 One layer one-dimensional velocity model equivalent of site C for testing SEM calculation

	Thickness [m]	P wave velocity [m/s]	S wave velocity [m/s]	Density [kg/m^3]	$Q_{s,p}$
1	< 420	1,985	661	1,930	9999
bedrock	-	5,083	2,348	2,600	9999

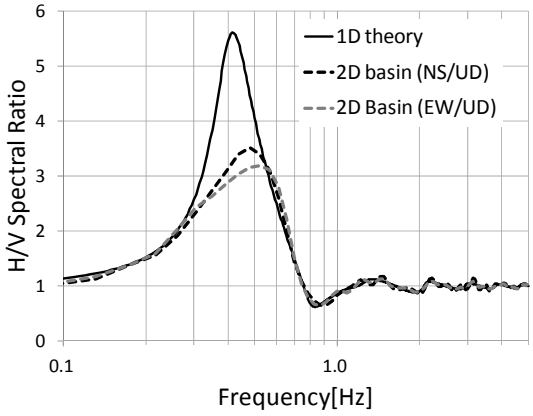


Figure 6 Spectral ratios of NS/UD and EW/UD (black and gray dotted line, respectively) at site C for the one layer two-dimensional basin model compared with the one layer one-dimensional theory (solid line)

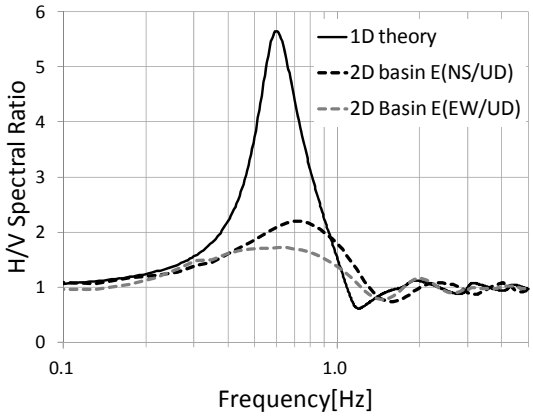


Figure 7 Spectral ratios of NS/UD and EW/UD (black and gray dotted line, respectively) at site 660m east of site C, 260m from the basin edge for the one layer two-dimensional basin model compared with the one layer one-dimensional theory (solid line)

5. CONCLUSIONS

In order to simulate the H/V spectral ratio for a site with lateral heterogeneity, we used a 3D SEM code to numerically calculate Green's functions to derive numerical H/V spectral ratios by the same procedure as the theoretical 1D H/V spectral ratios. From the comparison with theoretical and observational H/V spectral ratios, we confirmed the validity to use a SEM to calculate numerical H/V spectral ratios from the imaginary part of the Green's function for sites with lateral heterogeneity. We also confirmed that a SEM is adapted for solving such a difficult wave propagation problem that consists of modeling accurately the receiver located at the same location than a free surface point force. From the comparison of H/V spectral ratios for the 1D homogeneous model and the 2D basin model at two sites, we found that the 2D basin structure has significant effect on the H/V spectral ratios. They make the peak frequency slightly higher and the amplitude smaller and the frequency characteristics for NS/UD and EW/UD ratios are different. This indicates that when interpreting the H/V spectral ratio as an indicator for subsurface velocity structure, we need to first confirm that there is no strong influence from a lateral heterogeneity near the site, i.e. H/V spectral ratio for two orthogonal horizontal components are the same. If it is not the case, we need to take into account the fact that the H/V spectral ratio will be different from 1D theory.

Acknowledgements:

Partial support from MEXT Grant-in-Aid for Scientific Research (A) No.21241044, 2009-2012 (P.I. Hiroshi Kawase, DPRI, Kyoto Univ.) and (B) No.23310121, 2011-2015 (P.I. Tomotaka Iwata, DPRI, Kyoto Univ.) is greatly appreciated. A part of this work was carried while one of the authors (S.M.) was staying at BRGM (French Geological Survey) supported by JSPS-DPRI project "Strategic Young Researcher Overseas Visits Program for Accelerating Brain Circulation".

References:

De Martin, F. (2011), "Verification of a Spectral-Element Method Code for the Southern California Earthquake Center LOH.3 Viscoelastic Case", *Bulletin of the Seismological Society of America*, **101**(6), 2855-2865 (in Japanese with English abstract).

Hirokawa, T., Matsushima, S., Kawase, H. (2011), "Directional Dependency of Microtremor H/V Spectra with Special Reference to Lateral Heterogeneity of Bedrock Depth", *Summaries of Technical Papers of Annual Meeting 2011 Architectural Institute of Japan*, 151-152.

Koizumi, N., Tsukuda, E., Takahashi, M., Yokota, H., Iwata, T., Irikura, K., Uesuna, S., Takagi, K. and Hasegawa M. (2002), "Structural Profile of the Oubaku Fault", *Zisin 2*, **55**(2) 153-166 (in Japanese with English abstract).

Matsushima, S., Kawase, H., Hirokawa, T. and Sánchez-Sesma, F.J. (2011), "Directional Dependence of H/V Spectral Ratio of Microtremors Caused by Lateral Heterogeneity", *15th World Conference on Earthquake Engineering*, No. 1663.

Perton, M., Sánchez-Sesma, F.J., Rodríguez-Castellanos, A., Campillo, M. and Weaver, R.L. (2009), "Two Perspectives on Equipartition in Diffuse Elastic Fields in Three Dimensions", *Journal of Acoustical Society of America*, **126**(3), 1125-1130.

Sánchez-Sesma, F.J., Rodríguez, M., Iturrarán-Viveros, U., Luzón, F., Campillo, M., Margerin, L., García-Jerez, A., Suarez, M., Santoyo, M.A. and Rodríguez-Castellanos A. (2011), "A theory for microtremor H/V spectral ratio: Application for a layered medium", *Geophysical Journal International Express Letters,* **186**(1), 221-225, doi: 10.1111/j.1365-246X.2011.05064.x.

10CUEE CONFERENCE PROCEEDINGS
10th International Conference on Urban Earthquake Engineering
March 1-2, 2013, Tokyo Institute of Technology, Tokyo, Japan

DEAGGREGATION OF NEW NATIONAL SEISMIC HAZARD MAPS FOR INDONESIA

Achmad Fauzi[1)] and Usama Juniansyah Fauzi[3)]

1) Assoc. Professor, Faculty of Civil Engineering and Earth Resources, Universiti Malaysia Pahang, Malaysia
2) Former Master Student, Faculty of Civil and Environmental Engineering, Institut Teknologi Bandung, Indonesia
fauziwahab@ump.edu.my, usama@iis.u-tokyo.ac.jp

Abstract: The new Indonesia Seismic Hazard Maps for revising the previous map in SNI 03-1726-2002 was published in July 2010. These maps developed by Team for Revision of Seismic Hazard Maps of Indonesia were based on probabilistic approach for 2% probability of exceedance (PE) in 50 years and deterministic approach by using three-dimensional seismic source models and by considering latest geological and seismological data and fragility curve of buildings. Seismic sources were represented by subduction, fault, and background zones. The new maps were developed based on PSHA method. A principal advantage of the probabilistic method is combining all the possible earthquakes affecting the site. This paper presents deaggregation of Indonesia Seismic Hazard Map 2010. Deaggregation for peak ground acceleration, 0.2-sec and 1.0-sec pseudo spectral acceleration (SA) is performed for 2% PE in 50 years (2475 years mean return period). The maps of mean and modal of magnitude and distance presented here are intended to provide information about the distribution of probabilistic seismic sources and to provide suggestions for seismic sources to use in developing artificial ground motion.

1. INTRODUCTION

Indonesia is located in a tectonically very active area at the point of convergence of three major plates and nine smaller plates creating a complex network of plate boundaries (Bird, 2003). The existence of interactions between these plates puts Indonesia in an earthquake prone region (Milson et al., 1992). Several great earthquake occurrences in Indonesia in the last six years inquire revision of seismic hazard parameters. Some of the great earthquakes are the 2004 Aceh Earthquake (Mw9.0-9.3) which was followed by tsunami, the 2005 Nias Earthquake (Mw 8.7), the 2009 Tasik Earthquake (Mw 7.3), and the latest 2009 Padang Earthquake (Mw 7.6). These earthquakes have caused thousands of casualties, destruction and damage to thousands of infrastructure and buildings, as well as billions of US dollars required for reconstruction and rehabilitation.

The Team for Revision of Seismic Hazard Maps of Indonesia has produced several new seismic hazard maps for Indonesia. The final model and maps were issued in 2010 as Summary of Study Team for Revision of Seismic Hazard Maps of Indonesia. The method and results given in this summary are the basis for BSN (National Standardization Agency) recommended seismic design provisions for the next edition of the Indonesian Earthquake Resistant Building Code SNI 03-1726 which will be issued in this year. This summary presented seismic hazard maps computed for sites on bed rock (Vs = 760 m/s2) at the 10% PE in 50 year and 2% PE in 50 year.

The seismic source models used in this study are subduction sources, fault sources, and background sources. Seismic hazard parameters for subduction considered recurrence relationship that includes truncated exponential model and pure characteristic model. For fault sources, truncated exponential model and characteristic model with aleatory uncertainty in the magnitude using a normal distribution sigma of ± 0.12 were used. For background source, only truncated exponential model were used in the development of hazard maps. Several attenuation functions including NGA and logic-tree were used. The detail information on seismic source models and seismic parameters for development seismic hazard maps appear in Asrurifak, 2010 and Fauzi, 2011.

This paper, in conjunction with Team for Revision of Seismic Hazard Maps of Indonesia, intends to convey information about the distribution of probabilistic seismic sources with explain typical values of earthquake magnitude and distance that are making the largest contributions to the seismic hazard maps. Identifying the predominant sources of hazard will lead to better choices for the design earthquake's characteristics. Performing deaggregations at more than one period will help to determine if one source dominates at all periods and clarify the need for one, or more than one, design earthquake (Halchuck and Adams, 2004).

2. PROBABILISTIC SEISMIC HAZARD ANALYSIS

PSHA was developed by McGuire (1976) is based on the probability concept developed by Cornell (1968). It is assumed that the earthquake magnitude M and distance R as a continuous independent random variables. In general, form of total probability theorem can be expressed in the

following formula

$$H(a) = \sum v_i \iint P[A > a | m, r] \, fMi(m) \, fRi|Mi(r,m) dr dm \quad (1)$$

where v_i is annual rate of earthquakes (with magnitude higher than some threshold value of M_{oi}) in source I, and $fMi(m)$ and $fRi|Mi(r,m)$ are probability density functions on magnitude and distance, respectively. $P[A > a | m, r]$ is the probability that an earthquake of magnitude m at distance r produces a peak acceleration A at the site that is greater than a.

The seismic hazard analysis was performed using this following procedure: 1) conducting literature review on geology, geophysics and seismology to identify activity of seismic sources in and around Indonesian region, 2) collecting and processing recorded earthquake data for entire Indonesian region, 3) modeling seismic source zones based on the advance models appropriate with USGS software, 4) determining seismic parameters which include a-b values, maximum magnitudes, and slip-rates, 5) calculating spectral acceleration based on the total probability theorem, 6) mapping spectral hazard includes peak ground acceleration (PGA) and short period (0.2 s) and 1.0 s period spectra values.

Software for PSHA used in this study obtained from the USGS. A site spacing of 0.1 degrees in latitude and longitude and area between 94°E to 142°E longitudes and 12°S to 8°N latitude were used in the analysis. The ground motion parameters obtained from this study computed for sites on bed rock (Vs = 760 m/s2). The verification seismic models and parameters in this research with Team for Revision of Seismic Hazard Maps of Indonesia are shown in Fauzi, 2011.

The method of deaggregation of hazard is separates the contributions into a limited number of bins of (annular) distance, magnitude, and ground-motion uncertainty (McGuire, 1995). For this research the distance annular width, ΔR, is 5 km and the magnitude bins is 0.5. For subduction sources, the maximum considered source to site distance is 1000 km. For fault and background sources, the maximum considered source to site distance is 200 km. Using PSHA result, the relative contribution of sources to the overall hazard results at the given site are deaggregated in different types of bins to determine and understand. The integration of the PSHA is carried out and the final results are presented often in terms of 3D M-R-ε bins or even geographical deaggregation (4D) (Harmsen and Frankel, 2001).

The mean distance and mean magnitude presented here are the weighted mean values of R and M, respectively, for all sources that contribute to hazard at each grid location. The modal distance and modal magnitude are the (R, M) pair having the largest contribution in the hazard deaggregation at each grid location. The maps develop using the grid increment of 0.1 degrees in both latitude and longitude and in area between 94°E to 142°E longitudes and 12°S to 8°N latitude so that deaggregations seismic hazard are performed for more than 96,600 sites. Software for Deaggregation PSHA used in this study obtained from the USGS.

4. SEISMOSECTONIC MODEL

Seismic parameters used in this study were derived from published journals, proceedings, previous researches conducted by team members, and latest information obtained during this study. This study has then compiled and integrated previous and current studies. Earthquake source parameters were determined based on earthquake catalog, geological, and seismological information of active faults. The earthquake catalog covered earthquake period between 1900 to 2009, relocated catalog by the year 2005, and area between 90oE to 145oE longitudes and 15oS to 15oN latitudes.

Seismic sources were divided into subduction, fault, and background zones by considering recurrence relationship that includes truncated exponential model, pure characteristic model, and both models. Geometry of fault and subduction were represented by three-dimensional (3D) models based on the result of tomography and slip-rates of faults were determined by considering the results of GPS measurement. Background source zones were modeled using gridded seismicity based on spatially smoothed earthquake rates. The earthquake catalog was used for developing gridded seismicity starting from 1900 to 2009 and the updated Engdahl catalog up to 2009 was used for control geometry of subduction. Several well-known attenuation functions were selected in accordance with the mechanism of seismic source including the Next Generation Attenuation (NGA). Logic tree was also applied to account for epistemic uncertainty including recurrence model, maximum magnitude, and several attenuation functions.

3. RESULTS AND DISCUSSION

One purpose of deaggregation analysis is to find plausible (R,M) pairs from which to choose accelerograms, A(t), for input to seismic design programs for structural response (Harmsen, et. Al 2003). The maps of mean and modal magnitude and distance for 10% probability of exceedance (PE) in 50 yr are shown in Figure 1 to Figure 4. Maps of mean and modal magnitude and distance for 2% probability of exceedance (PE) in 50 yr are shown in Figure 5 to Figure 8.

The analysis result showed that the maps of modal results are associated the highest contribution, for the areas near the fault, magnitude and distance of fault control. In areas far from the fault, the magnitude and distance from the subduction control and for areas far from faults and subduction, gridded seismicity model control. The mean magnitude and distance associated with the average of contribution from multimodal / multi scenario earthquake. The mean and modal maps showed different values of pair magnitude and distance so that most sites receive contributions from a broad distribution of source magnitudes and distances.

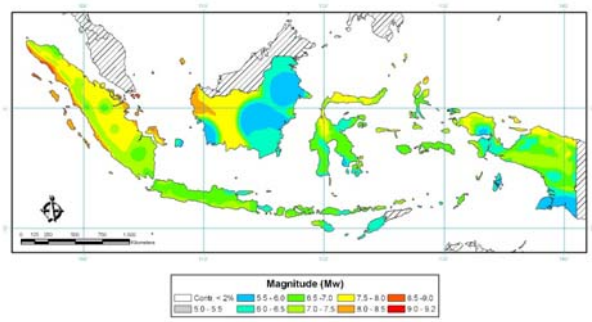


Figure 1 Mean magnitude map of 0.2 sec. spectral acceleration at bedrock for 2% probability of exceedance in 50 years

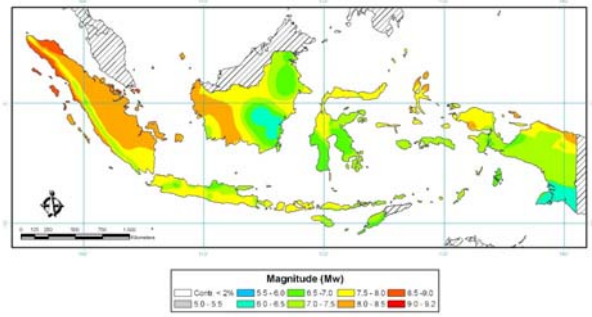


Figure 2 Mean magnitude map of 1.0 sec. spectral acceleration at bedrock for 2% probability of exceedance in 50 years

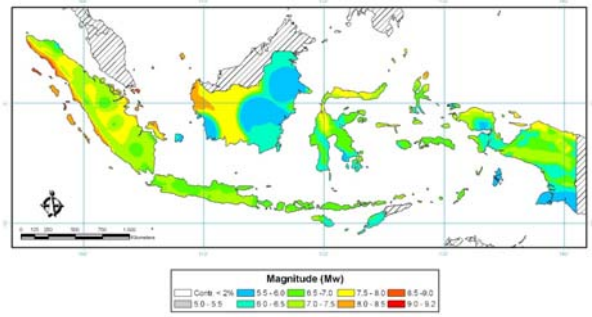


Figure 3 Mean magnitude map of peak ground acceleration at bedrock for 2% probability of exceedance in 50 years

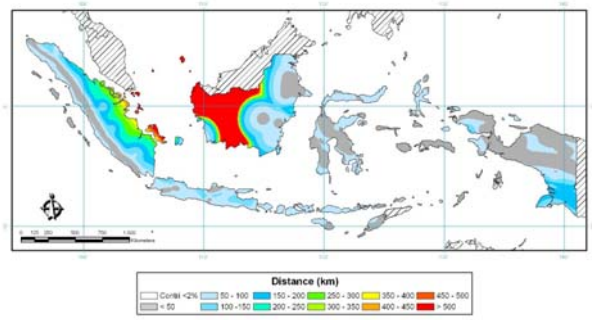


Figure 4 Mean distance map of 0.2 sec. spectral acceleration at bedrock for 2% probability of exceedance in 50 years

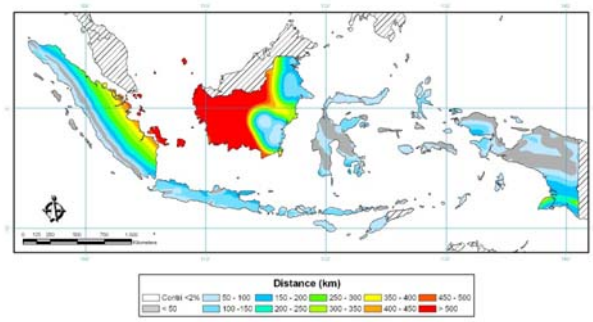


Figure 5 Mean distance map of 1.0 sec. spectral acceleration at bedrock for 2% probability of exceedance in 50 years

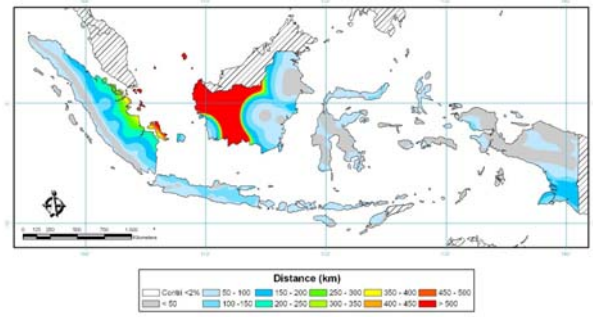


Figure 6 Mean distance map of peak ground acceleration at bedrock for 2% probability of exceedance in 50 years

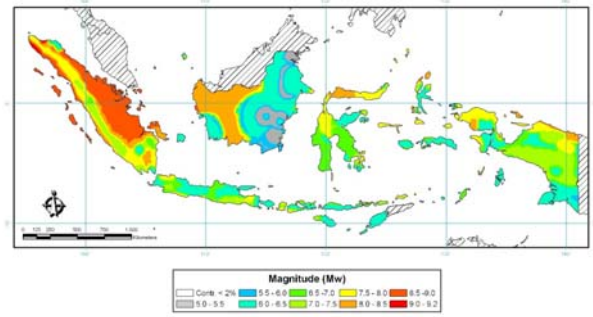


Figure 7 Modal magnitude map of 0.2 sec. spectral acceleration at bedrock for 2% probability of exceedance in 50 years

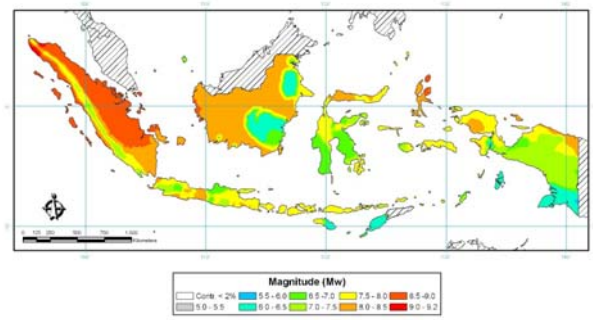


Figure 8 Modal magnitude map of 1.0 sec. spectral acceleration at bedrock for 2% probability of exceedance in 50 years

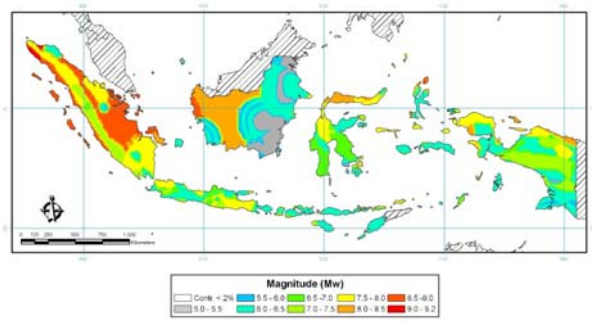


Figure 9 Modal magnitude map of peak ground acceleration at bedrock for 2% probability of exceedance in 50 years

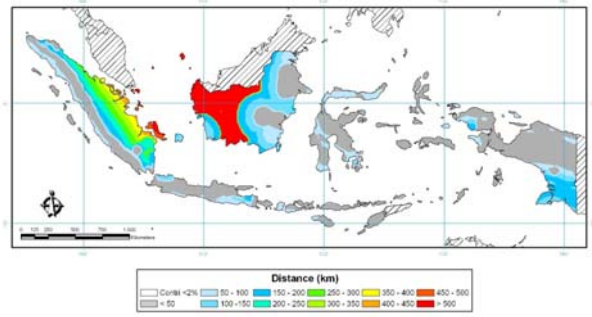


Figure 10 Modal distance map of 0.2 sec. spectral acceleration at bedrock for 2% probability of exceedance in 50 years

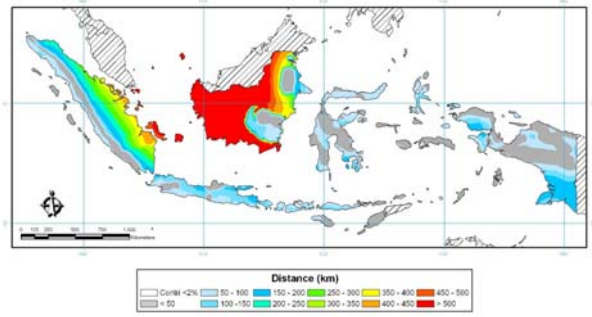


Figure 11 Modal distance map of 1.0 sec. spectral acceleration at bedrock for 2% probability of exceedance in 50 years

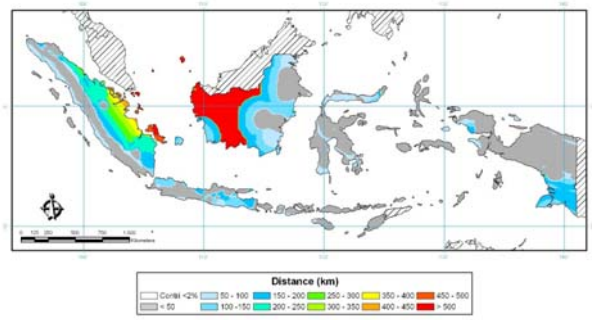


Figure 12 Modal distance map of peak ground acceleration at bedrock for 2% probability of exceedance in 50 years

3. CONCLUSIONS

For most locations, the deaggregation reveal that more than one design earthquake will be required for engineering purposes. The maps of mean and modal of magnitude and distance presented here are intended to convey information about the distribution of probabilistic seismic sources and to provide prescriptions or suggestions for seismic sources to use in building design or retrofit projects. The information of deaggregation analysis can and perhaps should be considered in a complex seismic-resistant design decision-making environment.

Acknowledgements:

The writers wish to his sincerest gratitude to Team for Revision of Seismic Hazard Maps of Indonesia, for allowing writers to incorporate the valuable data when the Team developed new Indonesia Seismic Hazard Maps. The writers are also deeply indebted to USGS (S. D. Harmsen and M. D. Petersen) for providing the writers with technical discussions and the software for PSHA and PSHA Deaggregation. Financial support for the research was provided by Universiti Malaysia Pahang and Institut Teknologi Bandung, Indonesia.

References:

Asrurifak, M (2010), Peta Respon Spektra Indonesia Untuk Perencanaan Struktur Bangunan Tahan Gempa Dengan Model Sumber Gempa Tiga Dimensi Dalam Analisis Probabilitas. Disertasi Doktor Teknik Sipil ITB, Indonesia.

Cornell, C.A., (1968), Engineering Seismic Risk Analysis, Bulletin of the Seismological Society of America, Vol. 58.

Fauzi, Usama Juniansyah. (2011). Peta Deagregasi Indonesia Berdasarkan Analisis Probabilitas Dengan Sumber Gempa Tiga Dimensi. Tesis Magister Teknik Sipil ITB, Indonesia.

Frankel, A.D., Petersen, M.D., Mueller, C.S., Haller, K.M., Wheeler, R.L., Leyendecker, E.V., Wesson, R.L., Harmsen, S.C., Cramer, C.H., Perkins, D.M., dan Rukstales, K.S., (2002), Documentation for the 2002 Update of the National Seismic Hazard Maps, U.S. Geological Survey Open-File Report 02-420.

Halchuk, A and Adams, J. (2004). Deaggregation of Seismic Hazard For Selected Canadian Cities. 13th World Conference on Earthquake Engineering. Vancouver, B.C., Canada. August 1-6, 2004. Paper No. 2470

Harmsen, S.C.; Frankel, A. D.; and Petersen, M. D. (2003). Deaggregation of U.S. Seismic Hazard Sources: The 2002 Update. Open File Report 2003-03-440. U.S. Geological Survey.

Harmsen, S.C. and Frankel, A. (2001). Geographic Deaggregation of Seismic Hazard in the United States. Bulletin of the Seismological Society of America, 91, 1, pp. 13–26, February 2001.

Irsyam, M., Asrurifak M., Hendriyawan, B Budiono, Triyoso W., dan Anita Firmanti, (2010), Development of Spectral Hazard Maps for Proposed Revision of Indonesia Seismic Building Code, Geomechanic and Geoengineering an International Journal, Vol. 5. No. 1, 35-47, DOI: 10.1080/17486020903452725.

Irsyam M., Asrurifak M., Hendriyawan, Budiono B., Triyoso W., dan Hutapea B., (2008), Usulan Revisi Peta Seismic Hazard Indonesia Dengan Menggunakan Metode Probabilitas Dan Model Sumber Gempa Tiga Dimensi, Prosiding Seminar HATTI, 18-19 Nopember 2008, ISBN 978-979-96668-6-4.

McGuire, R. K. (1995). Probabilistic seismic hazard analysis and design earthquakes: closing the loop. Bull. Seism. Soc. Am. 85, 1275–1284.

Tim Revisi Peta Gempa Indonesia. (2010). Ringkasan Hasil Studi Tim Revisi Peta Gempa Indonesia 2010, Bandung 1 Juli 2010. Laporan Studi

10CUEE CONFERENCE PROCEEDINGS
10th International Conference on Urban Earthquake Engineering
March 1-2, 2013, Tokyo Institute of Technology, Tokyo, Japan

ESTIMATION OF URBAN GROWTH USING TIME-SERIES LANDSAT SATELLITE IMAGES IN LIMA, PERU

Hiroyuki Miura[1)], Saburoh Midorikawa[2)], and Masashi Matsuoka[3)]

1) Associate Professor, Department of Architecture, Hiroshima University, Japan
2) Professor, Department of Built Environment, Tokyo Institute of Technology, Japan
3) Associate Professor, Department of Built Environment, Tokyo Institute of Technology, Japan
hmiura@hiroshima-u.ac.jp, smidorik@enveng.titech.ac.jp, matsuoka.m.ab@m.titech.ac.jp

Abstract: In order to develop building inventory data for building damage assessment in Lima, Peru, distribution of urban growth is estimated by time-series analysis of satellite Landsat images. Spectral indices calculated from the images are used to evaluate changed areas from vegetated and bare ground areas to built-up areas. Threshold analysis is performed to difference of the indices between the multi-temporal images to identify the spatial distribution of the expansion of the built-up areas. The result shows that the older built-up areas are widely distributed in the central part of Lima and the newer built-up areas are expanded to the northern, southern and eastern suburban areas.

1. INTRODUCTION

Due to the rapid urban growth in developing countries, built-up areas have been dramatically expanded to suburban areas with poor ground conditions such as steep slope areas. In order to discuss seismic vulnerability of such urban areas, it is important to identify spatial distribution and its temporal change of the built-up areas. The identification of the age of the built-up areas could be also useful to estimate construction age of the buildings and to evaluate seismic performance of the buildings.

In developing countries, however, detailed building inventory data that includes construction age information has been rarely developed. Remote sensing technology would be powerful tool to easily identify spatial distribution of the built-up areas. Peru is one of the developing countries located in a zone of high seismicity. Since Lima, the capital of Peru, is prone to be struck by a large earthquake in near future, disaster preparedness such as building damage assessment should be enhanced in the urban areas. In this study, to develop building inventory data for the damage assessment in Lima, spatial growth of the urbanized areas is evaluated by time-series analysis of satellite Landsat images.

2. DATA USED

Figure 1 shows the land use map in Lima with 1/25,000 scale developed in 2004. Orange and green blocks indicate built-up and vegetated areas, respectively. The land use map is digitized and geo-referenced in the geographical information system. Each pixel of the map image is classified into three categories; built-up area, vegetated area and other area (bare grounds and roads). Figure 2 shows the distribution of the land use with the resolution of 30 m. Pink, green and gray pixels indicate built-up, vegetated and other areas, respectively. The built-up areas in Fig. 2 represent the current distribution of the urbanized areas.

In this study, the time-series satellite Landsat-TM (Thematic Mapper) images are used for the estimation of urban growth because large number of images has been stored since 1970s. After searching the database of the Landsat images (USGS 2012), we found an oldest cloud free image in Lima observed in 1987. In order to capture the expansion of the built-up areas after decades, we also searched another images observed about ten and twenty years after the oldest image and found cloud free images observed in 1998 and 2006. These three Landsat images are used in this study. Figure 3 and Table 1 show the characteristics of the images. As shown in Fig. 3, the western coastal area in Lima is covered with cloud in the 2006 image. The Landsat image observed in 2002 is supplementary used in the cloud cover area. The Landsat-TM data consists of seven band images that cover visible, near infrared, mid infrared and thermal spectral range. The spatial resolution of the images is 30 m.

From the comparison between the time-series Landsat images in Fig. 3, many vegetated areas and bare ground areas in the older images are changed to built-up areas in the newer images. In this study, the age of the built-up areas are estimated by identifying the changed areas from the vegetated and bare ground areas to the built-up areas in the Landsat images.



Fig. 1 Landuse map in Lima (2004)

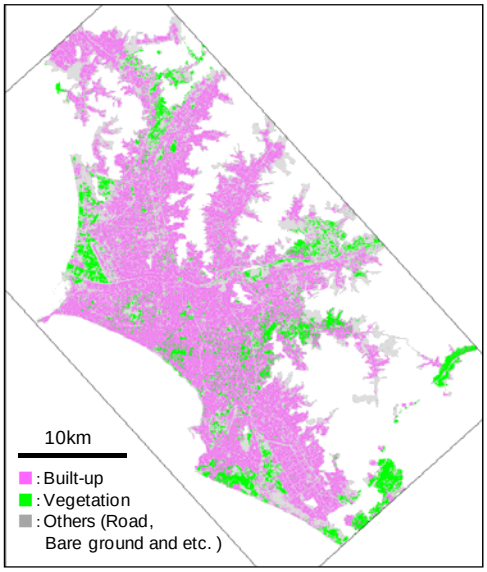
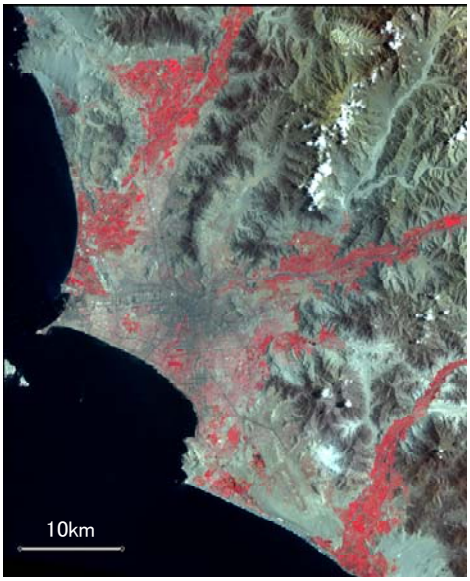
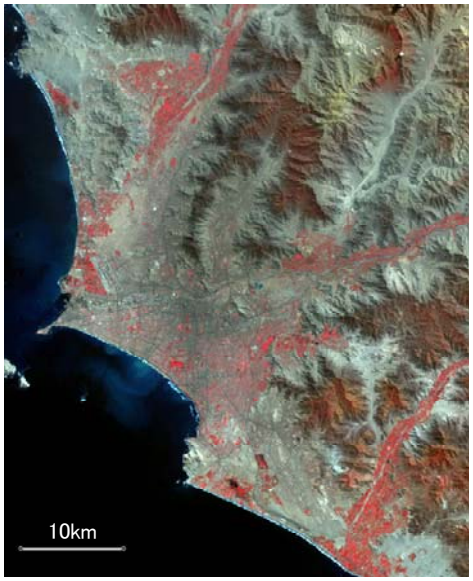


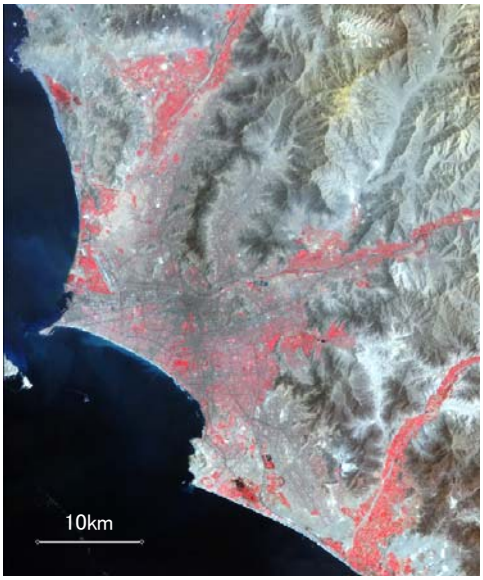
Fig. 2 Digitized landuse image



1987/3/5



1998/5/6



2002/01/17



2006/5/12

Fig. 3 Landsat images observed in 1987, 1998, 2002 and 2006 (False color composite)

Table 1 Characteristics of Landsat images used in this study

Satellite	Sensor	Date	Num. of Bands	Resolution
Landsat-5	Thematic Mapper (TM)	1987/3/5	7 bands	30 m
Landsat-5	Thematic Mapper (TM)	1998/5/6	7 bands	30 m
Landsat-5	Thematic Mapper (TM)	2002/1/17	7 bands	30 m
Landsat-5	Thematic Mapper (TM)	2006/5/12	7 bands	30 m

3. SPECTRAL INDEX CALCULATION

3.1 Evaluation of Vegetated Areas

Spectral indices calculated from combination of multi-band images have been widely used to evaluate vegetated and bare ground areas in remote sensing technology. NDVI (normalized difference vegetation index), one of the powerful indices to evaluate vegetated areas in satellite images, is calculated from the following equation.

$$NDVI = \frac{B4 - B3}{B4 + B3} \quad (-1 \le NDVI \le 1) \qquad (1)$$

Here, *B3* and *B4* indicate the digital number (DN) of the band 3 (red) and band 4 (near infrared) images, respectively. Higher NDVI values represent greater density of greenness. Figure 4 shows the distribution of NDVI calculated from the images. Figure 5 illustrates the close-up of the 2004 land use map and the 2006 NDVI image. As shown by arrows in the figure, the green areas in the land use map show high NDVI in the image, indicating that NDVI is useful to evaluate vegetated areas in the image.

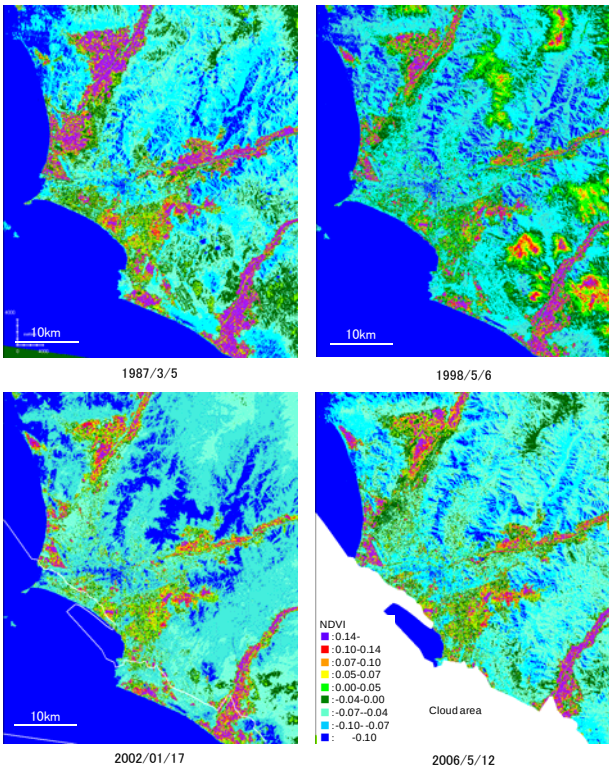


Fig. 4 NDVI images in 1987, 1998, 2002 and 2006

3.2 Evaluation of Bare Ground Areas

NDSI (normalized difference soil index) has been used as one of the spectral indices to evaluate bare ground areas from satellite images (Takeuchi and Yasuoka 2005). NDSI is also calculated from the combination of the multi-band images by the following equation.

$$NDSI = \frac{B5 - B4}{B5 + B4} \quad (-1 \le NDSI \le 1) \qquad (2)$$

Here, *B5* indicates the DN of the band 5 (mid infrared) image. Higher NDSI values would indicate greater possibility of bare ground in the image. Chen *et al.* (2010), however, pointed out that it is sometimes difficult to discriminate bare ground areas from built-up areas from only NDSI image because their spectral characteristics are similar each other in the near and mid infrared band images. In this study, other spectral indices are also calculated to evaluate bare ground areas.

$$NBI = \frac{B3 \times B5}{B4} \qquad (3)$$

$$NUI = \overline{B3} + \overline{B6} - \overline{B4} - \overline{B5} \qquad (4)$$

$$\overline{Bn} = \frac{Bn - Ave_{Bn}}{SD_{Bn}} \times 50 + 100 \quad (n = 3, 4, 5, 6)$$

NBI (new built-up index) proposed by Chen *et al.* (2010) is based on the characteristics that DNs of band 3 in bare ground areas are generally larger than those in built-up areas. Higher NBI values would indicate greater possibility of bare ground areas in the image. NUI (normalized urban index) proposed by Saito *et al.* (2002) is calculated based on the characteristics that DNs in built-up and bare ground area are higher in band 3 and 6 (thermal)

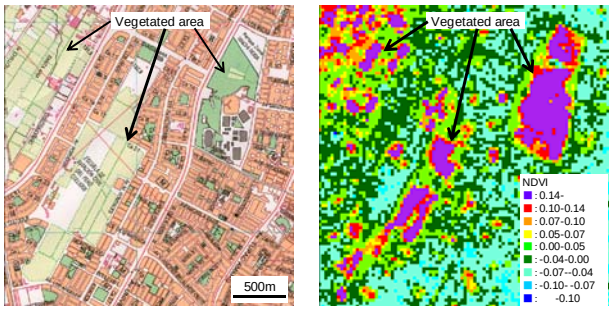


Fig. 5 Comparison of 2004 landuse map and 2006 NDVI image

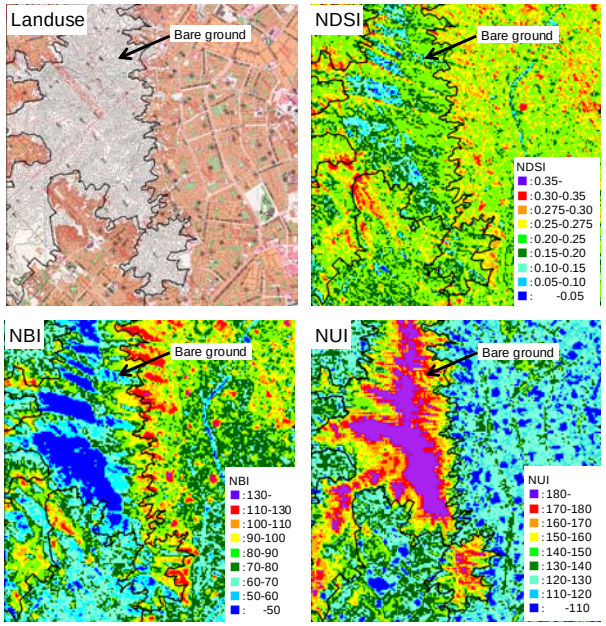


Fig. 6 Comparison of 2004 landuse map, NDSI, NBI and NUI images in 2006

than in band 4 and 5. NUI values in built-up and bare ground areas would be higher than in vegetated areas.

Figure 6 shows the distribution of the indices calculated from the 2006 Landsat image with the comparison of the 2004 land use map. Arrows in the figures indicate bare ground and mountain areas. The distribution of NDSI shows that NDSI in the bare ground areas is generally lower than that in the built- up areas. However, the boundary between the bare ground and the built-up areas could not be clearly identified in the NDSI image because many low NDSI pixels are distributed in the built-up areas. Also in the NBI image, it is difficult to identify the boundary between the bare ground and built-up areas because low NBI pixels are distributed not only in the bare ground areas but also in the built-up areas. On the contrary, in the NUI image, it is much easier to identify the boundary because NUI in the bare ground areas is much higher than that in the built-up areas. This may be because that the surface temperature in the bare ground is higher than that in the built-up areas and NUI is only the index based on the thermal band (band 6). In this study, the NUI image is used to evaluate bare ground areas. Figure 7 shows the distribution of NUI calculated from the Landsat images.

4. BUILT-UP AGE CLASSIFICATION

4.1 Methodology

The NDVI values are high in vegetated areas while they become lower in built-up areas changed from the vegetated areas. The NUI values are also high in bare ground areas while they become lower in newly developed built-up areas. Therefore, the differences of NDVI and NUI between the multi-temporal images are used to estimate the growth of the built-up areas.

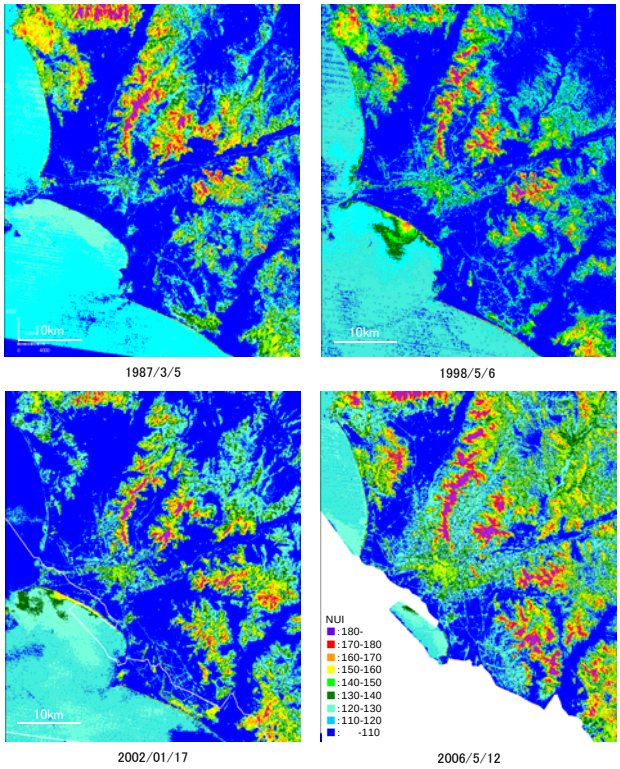


Fig. 7 NUI images in 1987, 1998, 2002 and 2006

In order to apply the method, validation data such as high-resolution images observed in the past and the present is necessary. Aerial photographs observed in 1984 are available in Lima. As shown solid line area in Fig. 8, the aerial photos are acquired in newly developed area located at the northern part of Lima. We assume that the 1984 aerial photos timely correspond to the 1987 Landsat image. The aerial photos are black-and-white images and the spatial resolution is approximately 20 cm. Recently, high-resolution satellite images are easily available. The satellite WorldView-2 (WV2) images observed in 2010 are used for the validation. The coverage of the 2010 WV2 images is shown in Fig. 8. We assume that the 2010 WV2 images timely correspond to the 2006 Landsat image. The spatial resolution is 50 cm.

Firstly, the built-up pixels are extracted from the 2004 land use map shown in Fig. 2 and only the built-up pixels are analyzed in the following procedure. The difference of NDVI and NUI between the 2006 and 1987 Landsat images is calculated for each pixel. Larger negative difference of the indices indicates greater possibility of the area where vegetation or bare ground is changed to built-up area.

Figure 9 shows the comparison of (a) the 1984 aerial photos, (b) the 2010 WV2 images and the distribution of the difference of (c) NDVI and (d) NUI. Purple and red color pixels in Fig. 9 (c) and (d) represent larger negative values of the difference of the indices. As shown in solid line polygons, training pixels are visually selected as changed areas. Green and orange line polygons represent the changed areas from the vegetated and bare ground areas to the built-up areas, respectively. Purple line polygons

represent the built-up areas in all the images, indicating the old built-up areas. The distribution of NDVI difference shows that many purple and red color pixels are concentrated in the green polygons. The distribution of NUI difference also shows that many purple and red pixels are concentrated in the orange polygons.

Histograms of the NDVI and NUI difference are illustrated in Fig. 10 (a) and (b) by extracting the training pixels of the polygons in Fig. 9. Red and blue lines in the histograms indicate the pixels of the changed areas from the vegetated and bare ground areas to the built-up areas, respectively. Black lines indicate the pixels of the old built-up areas in all the images.

From Fig. 10(a), the difference of NDVI in the old built-up areas shows almost larger than -0.1 while the difference of NDVI in the changed areas from the vegetated areas are widely distributed from -0.6 to 0.0. In this study, the threshold value for the difference of NDVI is selected at -0.1 to discriminate the changed areas from the unchanged areas.

From Fig. 10(b), the difference of NUI in the old built-up areas shows larger than 10 while the difference of NUI in the changed areas from the bare ground areas are distributed from -60 to 40. In this study, the threshold value for the difference of NUI is selected at 10 to discriminate the changed areas from the unchanged areas.

Table 2 shows the result of the classification accuracy based on the threshold analysis proposed above. The table shows the number of pixels in each land use, the percentages of correct classification and mis-classification. From the result of the thresholding using the difference of NDVI, about 75% of the changed pixels in the vegetated areas are correctly classified. Almost 100% of the bare ground and the old built-up areas are classified. From the result of the thresholding using the difference of NUI, about 80% of the changed pixels in the bare ground areas are correctly classified. Almost 100% of the vegetated and old built-up areas are classified.

4.2 Result of Built-up Age Classification

Based on the threshold values examined in the previous section, the built-up age classification is performed using the time-series Landsat images. Figure 11 shows the flowchart of the classification. First, the built-up pixels are extracted from the 2004 land use map. The difference of NDVI and NUI between the 2006 and 1998 Landsat images is calculated for the built-up pixels. The threshold analysis is performed based on the threshold values. The pixels whose difference values are lower than the thresholds are classified to the newer built-up areas developed after 1998. The pixels whose difference values are higher than the thresholds are classified to the older built-up areas and analyzed in the following steps. The difference of NDVI and NUI between the 1998 and 1987 Landsat images is calculated for the older built-up pixels.

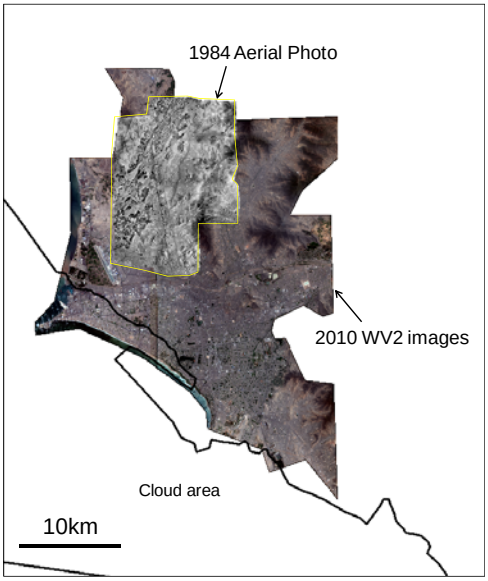


Fig. 8 Coverage of 1984 aerial photos and 2010 WV2 images

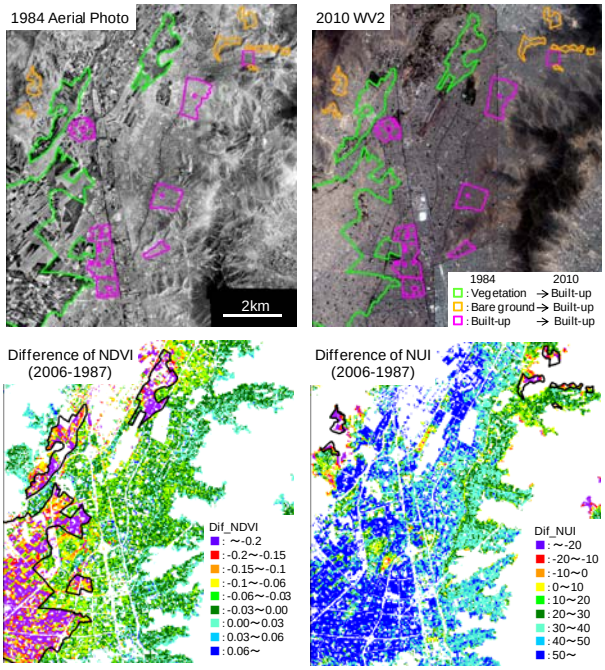


Fig. 9 Comparison of (a) 1984 aerial photo, (b) 2010 WV2 image, (c) difference of NDVI and (d) difference of NUI

The pixels whose difference values are lower than the thresholds are classified to the newer built-up areas developed between 1987 and 1998. The pixels whose difference values are higher than the thresholds are classified to the older built-up areas developed before 1987. In the cloud-cover areas of the 2006 image, same procedure is applied to the 2002 image instead of the 2006 image. Finally, the built-up age classification is estimated by combining the results.

Figure 12 shows the result of the built-up age classification. The pink, red and yellow pixels indicate the

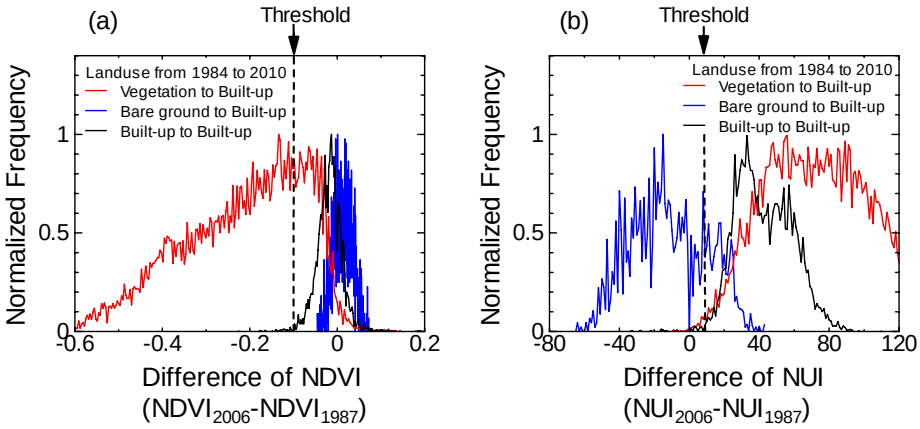


Fig. 10 Histograms of difference of NDVI and difference of NUI

Table 2 Classification accuracy of threshold by difference of NDVI and NUI

Landuse change from 1984 to 2010	Num. of Pixels	Threshold by Difference of NDVI			Threshold by Difference of NUI		
		Correctly classified (%)	Mis-classified (%)	Total (%)	Correctly classified (%)	Mis-classified (%)	Total (%)
Vegetation to Built-up	486,540	75.2	24.8	100.0	99.3	0.7	100.0
Bare ground to Built-up	30,105	100.0	0.0	100.0	80.5	19.5	100.0
Built-up to Built-up	149,859	99.5	0.5	100.0	99.3	0.7	100.0

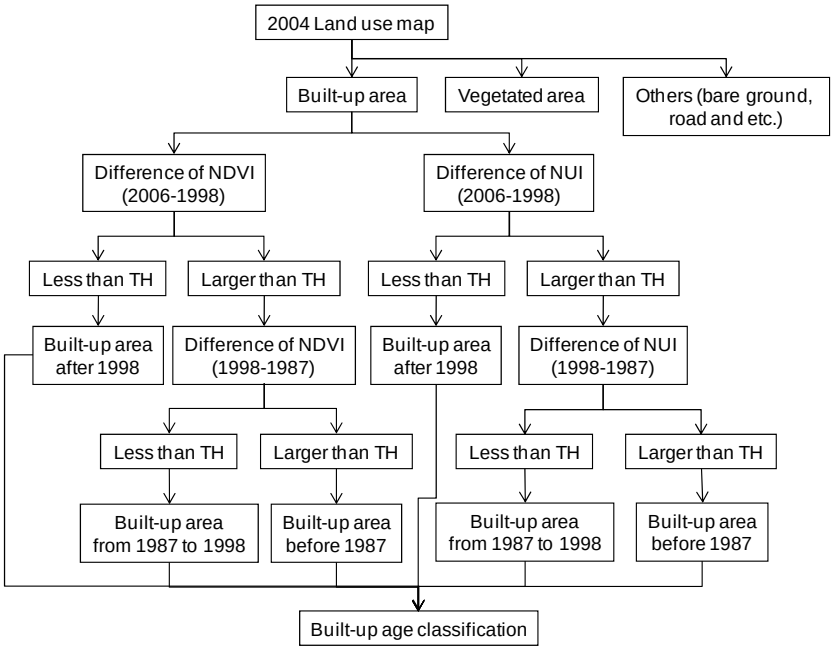


Fig. 11 Flowchart of built-up age classification using landuse map, NDVI and NUI images (TH: Threshold value)

built-up areas developed before 1987, between 1987 and 1998 and after 1998, respectively. Green and gray pixels represent vegetated areas and others, respectively. The result shows that most of the built-up areas in Lima had been developed before 1987. The newer built-up areas are expanded to the suburban areas in the northern, southern and eastern part of Lima.

Table 3 shows the number of pixels in each built-up area calculated from Fig. 12. The total area in each built-up area is also calculated from the mesh size of the Landsat images (30m x 30m). The total built-up area in Lima is about 1600 km2. About 70% of the total was developed before 1987. About 20% and 10% of the total were developed between 1987 and 1998, and after 1998, respectively.

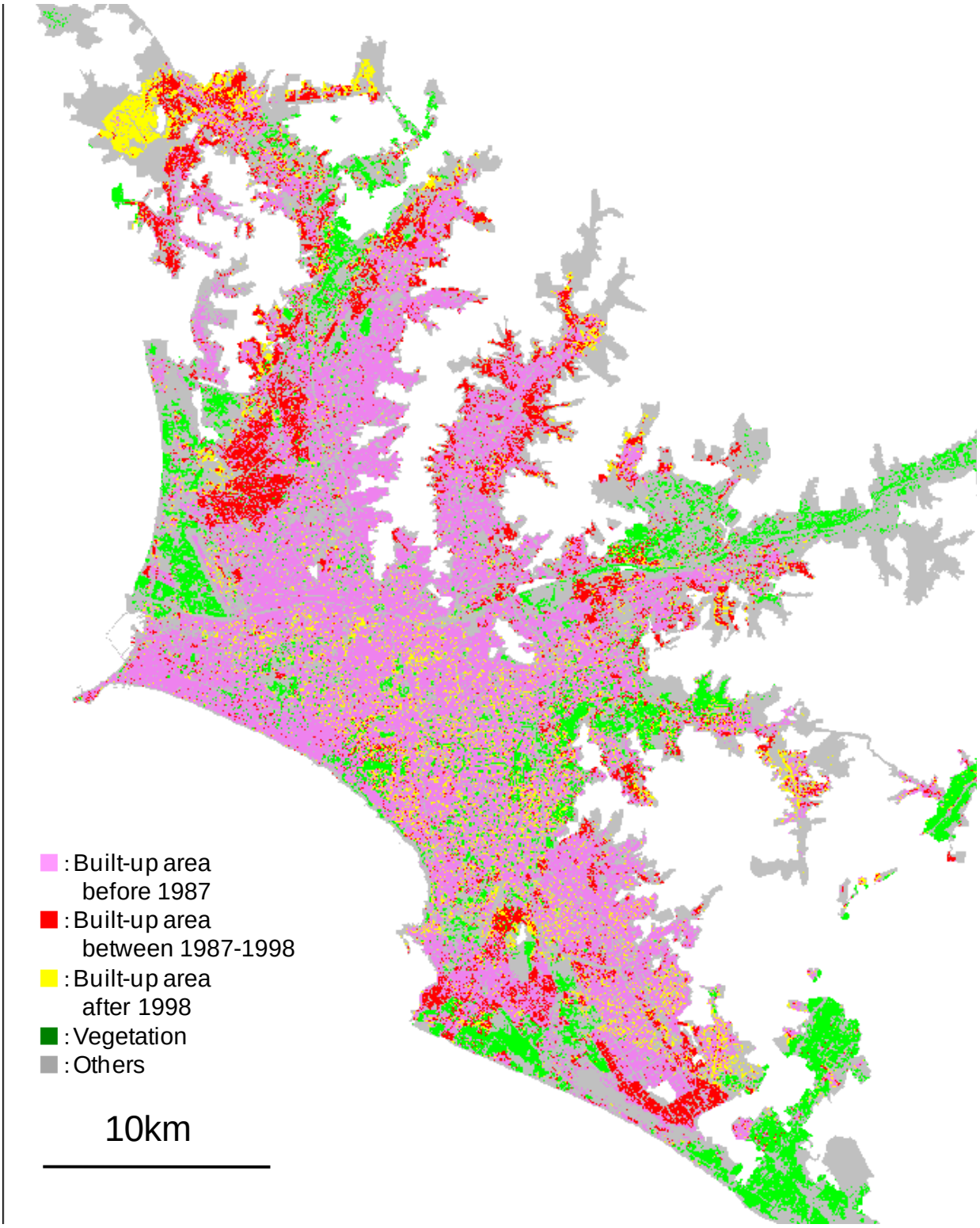


Fig. 12 Result of built-up age classification

Table 3 Number of pixels and area of each built-up area

Age	Num. of Pixels	Area (km^2)	Percent (%)
Built-up before 1987	1,192,567	1,073	68.1
Built-up between 1987-1998	314,830	283	18.0
Built-up after 1998	243,192	219	13.9
Total	1,750,589	1,576	100.0

5. CONCLUDING REMARKS

In order to develop the building inventory data in Lima, Peru, the distribution of the age of the built- up areas is estimated using the existing land use map and the time-series Landsat images. The changed areas from the vegetated and bare ground areas to the built-up areas are evaluated based on the spectral indices calculated from the images. The difference values of NDVI and NUI between the multi-temporal images are used to extract the changed areas. The threshold analysis is performed to estimate the spatial distribution of the built-up ages. The result shows that the older built-up areas before 1987 are widely distributed in Lima and the newer built–up areas are expanded to the suburban areas.

Acknowledgements:

This study was done as a part of SATREPS project "Enhancement of Earthquake and Tsunami Disaster Mitigation Technology in Peru" (Principal Investigator: Prof. Fumio Yamazaki, Chiba University) financially supported by JICA and JST.

References:

Chen, J., Manchun, L., Liu, Y., Shen C. (2010) "Extract Residential Areas Automatically by New Built-Up Index", *Proceedings of 18th International Conference on Geoinformatics*, 1-5.

Saito, I, Piao, M. and Ishihara, O. (2002) "Extraction of Land Covering Changes by Landsat TM Data", *Journal of Architecture, Planning and Environmental Engineering*, **561**, 79-85 (in Japanese).

Takeuchi, W. and Yasuoka, Y. (2005) "Development of Normalized Vegetation, Soil and Water Indices Derived from Satellite Remote Sensing Data", *Journal of the Japan Society Photogrammetry and Remote Sensing*, **43**(6), 7-19 (in Japanese).

USGS (2012), "Landsat Search and Download", http://landsat.usgs.gov/Landsat_Search_and_Download.php.

10CUEE CONFERENCE PROCEEDINGS
10th International Conference on Urban Earthquake Engineering
March 1-2, 2013, Tokyo Institute of Technology, Tokyo, Japan

WEB-BASED QUICK ESTIMATION SYSTEM OF STRONG GROUND MOTION MAPS USING OBSERVATION RECORDS AND ENGINEERING GEOMORPHOLOGIC CLASSIFICATION MAP

Masashi Matsuoka[1)], Naotaka Yamamoto[2)], and Kazue Wakamatsu[3)]

1) Associate Professor, Dept. of Built Environment, Tokyo Institute of Technology, Japan
2) Researcher, Geological Survey of Japan, National Institute of Advanced Industrial Science and Technology, Japan
3) Professor, Department of Civil and Environmental Engineering, Kanto Gakuin University, Japan
matsuoka.m.ab@m.titech.ac.jp, naotaka.yamamoto@aist.go.jp, wakamatu@kanto-gakuin.ac.jp

Abstract: QuiQuake (**Qui**ck estimation system for earth**Quake** maps triggered by observation records) is a seismic event triggered quick estimation system for the generation of earthquake maps using earthquake observation records. It is a system which provides extensive and detailed strong ground motion maps such as PGA, PGV, and seismic intensity right after a seismic event in and around Japan. QuiQuake also uses the combinations of amplification capability map and observed seismic records. The amplification capability is estimated from geomorphologic conditions, based on the Japan Engineering Geomorphologic Classification Map, with spatial resolution of 7.5 arc-second and 11.25 arc-second in latitude and longitude, respectively. The automatic calculation of spatial interpolation, including consideration of the attenuation characteristic from the seismic source, is started by harvesting the seismic data recorded at strong ground motion observation stations. The strong motion maps are published online using an Open Geospatial Consortium (OGC) standard web service interface..

1. INTRODUCTION

The GEO Grid (Global Earth Observation Grid) system (Sekiguchi et al., 2008) of the National Institute of Advanced Industrial Science and Technology, Japan (AIST) has developed a web service system for earthquake disaster response throughout Japan. The GEO Grid aims at providing integrated service using a wide array of geoscientific information such as geologic maps and other digital geographically referenced data, and assembles them into easy-to-use formats for potential stakeholders from several fields such as environmental conservation, resource exploration, hazard evaluation, and risk management. To provide these services, AIST set up web-based systems using Grid and Web service technologies in accordance with international standards. In order to take effective countermeasures against seismic disasters and implement business continuity plans (BCPs) for municipalities and private companies, the quick estimation of strong ground motions is very essential at the early stages of disaster response activities (e.g. Yamazaki et al., 1998; Ariki et al., 2004). QuiQuake (**Qui**ck estimation system for earth**Quake** maps triggered by observation records) is a seismic event triggered quick estimation system for the generation of earthquake maps using earthquake observation records. It is one of the geological hazard related applications on GEO Grid and the first system which estimates and illustrates the extensive and detailed ground motion maps such as peak ground acceleration (PGA), peak ground velocity (PGV), and JMA (Japan Meteorological Agency)-scale instrumental seismic intensity (I_{JMA}), right after an earthquake occurs. In this system, an amplification capability of ground motion and Vs30 average shear-wave velocity map, which is estimated from a 250-m grid cell map of the Japan Engineering Geomorphologic Classification Map (JEGM) (Wakamatsu and Matsuoka, 2011), are also used for the spatial interpolation calculation to generate strong motion maps. The interpolation also takes into account the characteristics of soil conditions. The strong ground motion maps are automatically calculated and published through an Open Geospatial Consortium (OGC) standard web service interface, right after the seismic observation data are released by the National Research Institute for Earth Science and Disaster Prevention (NIED). In this paper, we present the outline of QuiQuake, the data and algorithms used to generate strong ground motion maps.

2. QUIQUAKE OUTLINE AND CALCULATION PROCEDURE

Data flow and spatial interpolation procedure are shown in Fig. 1. The QuiQuake generates two kinds of strong ground motion maps with 250-m spatial resolution. The first one is QuakeMap which is calculated using the published seismic observation records at the portal site of the NIED. The second map is the QuickMap which is an output of

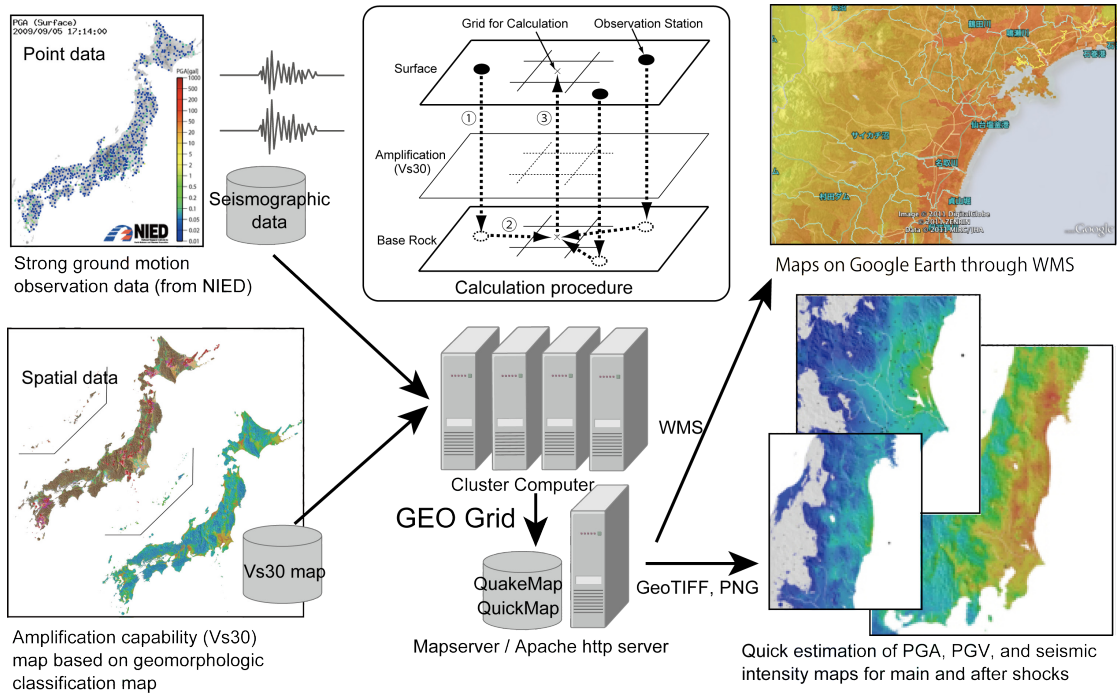


Figure 1 System overview and calculation procedure

quick estimation system. It is calculated using the near real-time information of strong ground motion parameters delivered by NIED right after an earthquake. Both maps are generated and published automatically using parallel computing techniques implemented by AIST's GEO Grid computer clusters.

The first phase of the generation of the ground motion maps is the processing of the near real-time observation data from K-NET (Kyoshin network). The ground motion parameters at the recording stations were assigned to the amplification capabilities estimated from the average shear-wave velocity of the ground in the upper 30 m (Vs30). The data are then converted to a base-rock level (Vs30 = 600 m/s) by using amplification factors. Since the earthquake motion on the ground surface is affected by the amplification characteristics of surface layers, the spatial interpolation by IDW (Inverse Distance Weighted) is carried out at the base-rock (outcrop) level. Finally, the spatial distributions of the ground motion parameters such as PGA, PGV, and I_{JMA} on the ground surface are obtained by multiplying the corresponding amplification factor for each grid cell. Following the aforementioned procedure, QuickMap could be generated.

When seismic waveform records at seismic stations from the K-NET and KiK-net (Kiban Kyoshin network) are published at the portal site, QuakeMap generation starts. The data are downloaded automatically and ground motion parameters, PGA, PGV, and I_{JMA} at the stations are calculated. Using the application factor, the parameters recorded on the surface are converted to values at the base rock level. For QuakeMap, one of the stochastic interpolation methods, called "Simple Kriging" with a prior trend component, is used to estimate the spatial distributions of ground motion parameters at the base rock level. The trend component is assigned for the attenuation relation obtained at the ground base level for each seismic event based on the location of the epicentre. PGA, PGV, and I_{JMA} maps on the ground surface are finally calculated by multiplying the amplification factors.

3. GROUND CONDITION AND AMPLIFICATION CAPABILITY MAPS

Local geologic and ground conditions play important roles in characterizing and estimating the site amplification capability of strong ground motion and geotechnical hazards. Accurate evaluation of site amplification characteristics requires detailed soil profile information such as the data on shear-wave velocity structures. However, high-density boring or PS-logging data throughout Japan are not available. It has been determined that approximate estimation of site amplification is possible using the average shear-wave velocity of ground in the upper 30 meters, also known as Vs30 (Borcherdt and Gibss, 1976; Joyner and Fumal, 1984; Midorikawa et al., 1994). Estimating Vs30s covering wider area could be done using surface geology and/or geomorphologic conditions, and digital elevation model. A product of Earthquake Hazard Program, SkakeMap, developed by the U.S. Geological Survey (USGS) uses Vs30 map for the key parameter to estimate site amplification characteristics (Wald et al., 2005). The QuiQuake also uses Vs30 as an amplification parameter and

Table 1 Description of geomorphologic map units in the 7.5-arc-second JEGM (Wakamatsu and Matsuoka, 2011)

Geomorphologic map unit	Definition and general characteristics	Subsurface soil condition	General depth of groundwater*
Mountain	Steeply to very steeply sloping topography with highest elevation and relative relief within a grid cell of more than approximately 200 m. Moderately to severely dissected.	Pre-Quaternary hard to soft rock.	Deep
Mountain footslope	Gently sloping topography adjoining mountains and composed of material sourced from the mountains such as colluvium, talus, landslide, and debris flow deposits.	Loose debris and soils consisting of colluvium, talus, landslide, and debris flow deposits.	Deep
Hill	Steeply to moderately sloping topography with higher elevation and relative relief within a grid cell of approximately 200 m or less. Moderately dissected.	Pre- Quaternary and Quaternary hard to soft rock.	Deep
Volcano	Steeply to moderately sloping topography with higher elevation and larger relative relief, composed of Quaternary volcanic rocks and deposits.	Quaternary hard to soft volcanic rock and/or deposits.	Deep
Volcanic footslope	Gently sloping topography located around skirt of volcano including pyroclastic-, mud- and lava-flow fields, and volcanic fan produced by dissection of volcanic body. Slightly dissected.	Quaternary loose to dense volcanic deposits consisting of ash, scoria, pumice, pyroclastic flow, lava, debris avalanche, etc.	Deep
Volcanic hill	Moderately sloping topography composed of pyroclastic flow deposits. Moderately to severely dissected.	Loose to moderately loose pyroclastic flow deposits such as ash, scoria, and pumice.	Deep
Rocky strath terrace	Fluvial or marine terrace with flat surface and step-like form, including limestone terrace of emerged coral reef. Thickness of subsurface soil deposits is less than 5 m.	Hard to soft rock.	Deep
Gravelly terrace	Fluvial or marine terrace with flat surface and step-like form. Covered with subsurface deposits (gravel or sandy soils) more than 5 m thick.	Dense gravelly soil.	Deep
Terrace covered with volcanic ash soil	Fluvial or marine terrace with flat surface and step-like form. Covered with cohesive volcanic ash soil to more than 5 m thick.	Stiff volcanic ash (cohesive soil).	Deep
Valley bottom lowland	Long and narrow lowland formed by river or stream between steep to extremely steep slopes of mountain, hill, volcano, and terrace.	Moderately dense to dense gravel or boulders in mountain, but loose sandy soil to very soft cohesive soil in plain.	Shallow
Alluvial fan	Semi-cone-like form composed of coarse materials, which is formed at the boundary between mountains and lowland. Slope gradient is more than 1/1000.	Dense gravel with boulders to moderately dense sandy gravel.	Deep in the central part of fan but shallow in the distal part of fan
Natural levee	Slightly elevated area formed along the riverbank caused by fluvial deposition during floods.	Loose sandy soil.	Shallow
Back marsh	Swampy lowland formed behind natural levees and lowlands surrounded by mountains, hills, and terraces.	Very soft cohesive soil containing peat or humus.	Very shallow
Abandoned river channels	Swampy shallow depression along former river course with elongated shape.	Very loose sandy soil occasionally covered with soft	Very shallow

		cohesive soil.	
Delta and coastal lowland	Delta: flat lowland formed at the river mouth by fluvial accumulation. Coastal lowland: flat lowland formed along shoreline by emergence of shallow submarine deposits, including discontinuous lowlands along sea- or lake- shore.	Loose fluvial sandy soil over-lying very soft cohesive soil.	Shallow
Marine sand and gravel bars	Slightly elevated topography formed along shoreline, composed of sand and gravel, which was washed ashore by ocean wave and/or current action.	Moderately dense to dense marine sand or gravel occasionally with boulder.	Shallow
Sand dune	Wavy topography usually formed along shoreline or river, comprised of fine to moderately aeolian sand; generally overlies sandy lowland.	Very loose to loose fine to medium sand.	Deep at crest of dune but shallow near base of dune
Lowland between coastal dunes and/or bars	Swampy lowland formed behind dunes or bars	Very soft cohesive soil containing peat or humus.	Very shallow
Reclaimed land	Former bottom flat of sea, lake, lagoon, or river that has been reclaimed as land by drainage.	Loose sand overlying very soft cohesive soil, sometimes covered with loose sandy fill.	Very shallow
Filled land	Former water body such as sea, lake, lagoon, or river reclaimed as land by filling.	Very loose to loose sandy fill, overlying very soft cohesive soil or loose sandy soils.	Very shallow to shallow
Rock shore, Rock reef	Irregular topography of rock or coral around beach zone.	Pre- Quaternary and Quaternary hard to soft rock	Near sea level
Dry riverbed	Nearly flat, irregular topography without water in normal time.	Loose sandy to gravelly alluvial soil, occasionally with boulders.	Very shallow
River bed	Nearly flat, irregular topography with varying water cover and having erosion and accumulation parts.	Loose sandy to gravelly alluvial soil, occasionally with boulders	
Lake	Inland water body.		
Nearshore waters	Nearshore water body.		

* Deep: deeper than 3 m below the ground surface, Shallow: within 3 m of the ground surface, Very shallow: within 1 m of the ground surface

Japan Engineering Geomorphologic Classification Map (JEGM) for the source of ground condition data.

3.1 7.5-arc-second JEGM

The map contains an attribute of geomorphologic land classification in grid cells that are 7.5 arc-seconds latitude × 11.25 arc-seconds longitude in size (approximately 250 × 250 m^2). A description of geomorphologic map units is presented in Table 1, together with the corresponding general ground conditions and general depth of groundwater. These criteria were based on the purpose of the mapping project, the identification and classification of subsurface ground conditions using standard geomorphologic classification. The geomorphologic factors presented in Table 1 are known to be correlated with subsurface ground and hydrologic conditions (e.g. Zuidam, 1986). Figure 2(a) shows a sample image of the 7.5-arc-second JEGM overlaid on the shade map created from the digital elevation model covering the entire country of Japan. The total number of cells of the map is approximately 6 million.

3.2 Average Shear-wave Velocity (Vs30) and Amplification Capabilities

The Vs30 values covering approximately 2,000 sites all over Japan were calculated from a previous study (Matsuoka et al., 2006). Geomorphologic units for all PS-logging data sites were interpreted. Then the correlation between geomorphologic units and geographical information derived from the JEGM and the Vs30 values were examined. It was found that the Vs30s showed some dependency on altitudes, slopes, and distances from mountains or hills formed during older periods (Pre-Tertiary or Tertiary). Based from this observation, a multiple linear regression formula for each geomorphologic unit was developed to estimate the Vs30 using elevation (*Ev*), slope (*Sp*), and distance (*Dm*) from a mountain or a hill as explanatory variables. The basic regression formula is

$$\log Vs30 = a + b\log Ev + c\log Sp + d\log Dm \pm \sigma \qquad (1)$$

where *a*, *b*, *c*, and *d* are regression coefficients, and σ as the standard deviation. The units of *Ev*, *Sp*, and *Dm* are meters, 1000 times tangent values, and kilometers, respectively. When the value of the explanatory variable is less than 1, we fixed the value as 1. Table 2 shows the regression coefficients and standard deviation of each geomorphologic unit obtained by regression analysis. The regression coefficients show that the higher is the elevation, the steeper is the slope. On the other hand, the shorter the distance from the mountain or hill the higher is the Vs30.

The Vs30 distribution with 250 m spatial resolution was computed using Eq.(1) and the attributes of the geomorphologic classification in the 7.5-arc-second JEGM, together with the geologic age, elevation, and slope values. Figure 2(b) shows the Vs30 map covering Japan. The Vs30 values are approximately 150 m/s on delta and coastal lowland, reclaimed land and back marsh. The areas covering valley bottom lowland also show a rather small Vs30

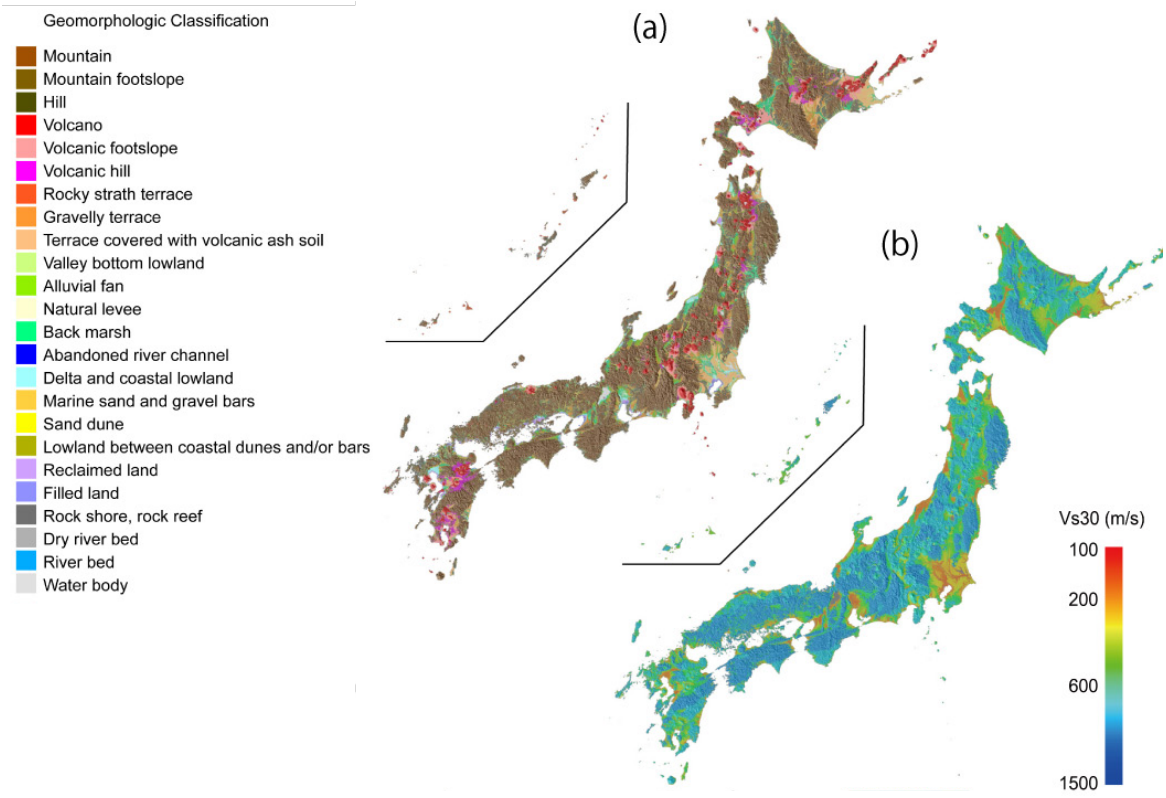


Figure 2 (a) 7.5-arc-second JEGM and (b) Vs30 map

Table 2 Regression coefficient of Eq.(1) (Matsuoka et al., 2006)

Geomorphologic map unit	*a*	*b*	*c*	*d*	s.d.
Mountain (Pre-Tertiary)	2.900	0	0	0	0.139
Mountain (Tertiary)	2.807	0	0	0	0.117
Mountain footslope	2.602	0	0	0	0.092
Hill	2.349	0	0.152	0	0.175
Volcano	2.708	0	0	0	0.162
Volcanic footslope	2.315	0	0.094	0	0.100
Volcanic hill	2.608	0	0	0	0.059
Rocky strath terrace	2.546	0	0	0	0.094
Gravelly terrace	2.493	0.072	0.027	-0.164	0.122
Terrace covered with volcanic ash soil	2.206	0.093	0.065	0	0.115
Valley bottom lowland	2.266	0.144	0.016	-0.113	0.158
Alluvial fan	2.350	0.085	0.015	0	0.116
Natural levee	2.204	0.100	0	0	0.124
Back marsh	2.190	0.038	0	-0.041	0.116
Abandoned river channel	2.264	0	0	0	0.091
Delta and coastal lowland	2.317	0	0	-0.103	0.107
Marine sand and gravel bars	2.415	0	0	0	0.114
Sand dune	2.289	0	0	0	0.123
Reclaimed land	2.373	0	0	-0.124	0.123
Filled land	2.404	0	0	-0.139	0.120

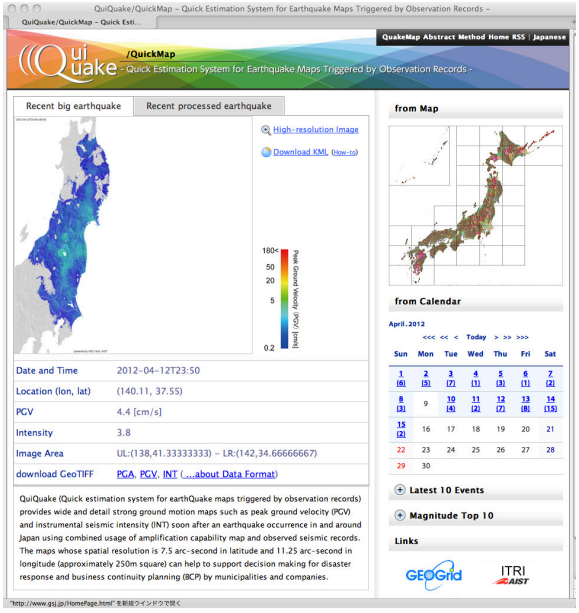


Figure 3 QuickMap portal site (http://qq.ghz.geogrid.org/QuickMap/index.en.html

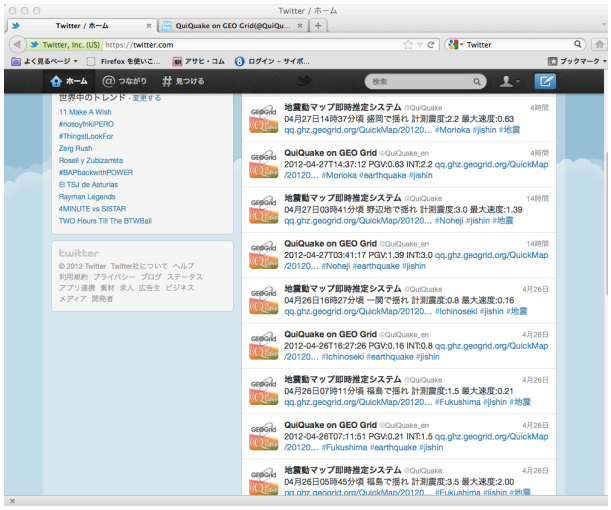


Figure 4 QuickMap twitter log (@QuiQuake)

ranging from 180 to 200 m/s. To draw amplification capability maps, Vs30 was converted into the amplification factors for PGA, PGV, and I_{JMA} with respect to stiff soil, which corresponds to grounds with Vs30 of 600 m/s, using the empirical relationships (Fujimoto and Midorikawa 2006; Midorikawa et al., 2008).

4. PUBLICATIONS AND VERIFICATION

4.1 Portal Site and OGC Standards Publishing

The QuickMap results are generally available within 5 minutes after the occurrence of a 7.0 magnitude earthquake on QuiQuake homepage (http://qq.ghz.geogrid.org/QuickMap/index.en.html). Figure 3 shows the QuickMap portal site.

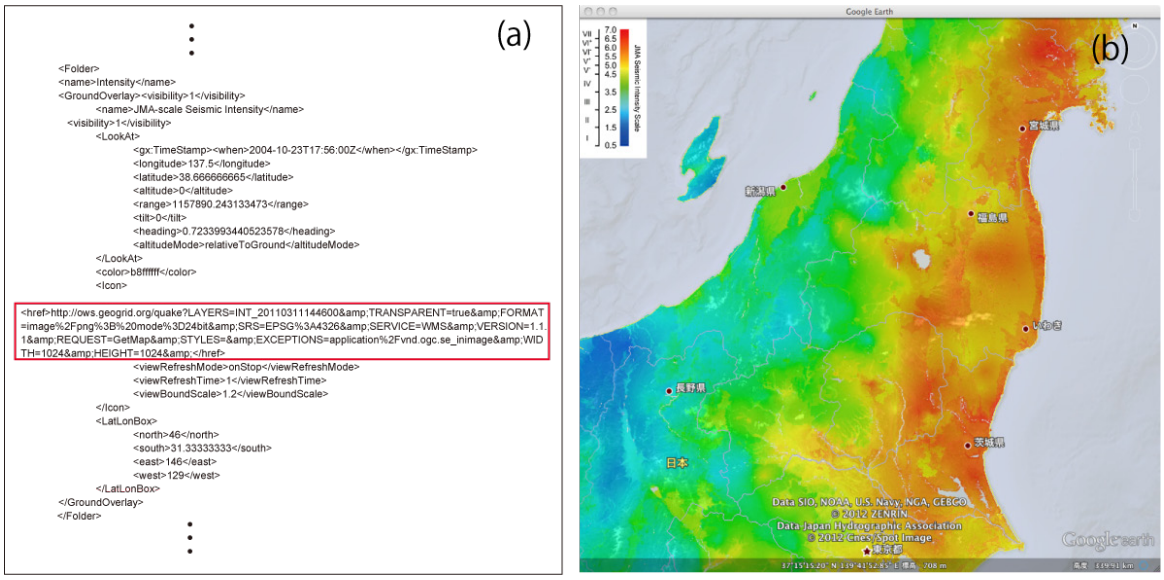


Figure 5 (a) Example of KML document containing the WMS URI of QuakeMap imagery. Red rectangle highlights the inserted WMS URI. (b) Spatial distribution of I_{JMA} of the 2011 Tohoku earthquake overlaid on Google Earth platform.

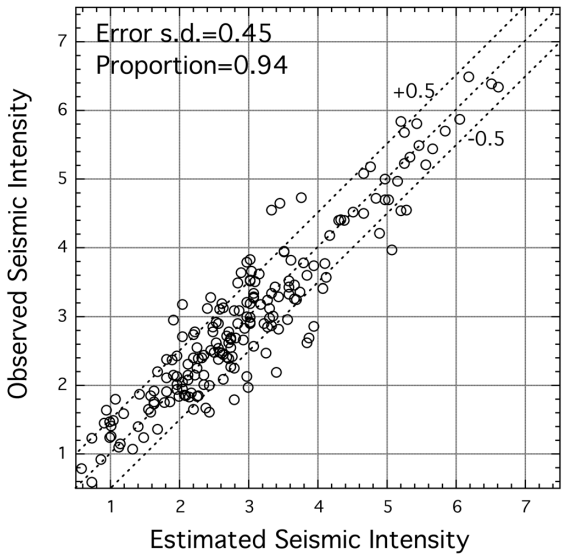


Figure 6 Comparison of the observed ground motion recorded by other organizations' seismic network stations and the estimated values at the stations estimated by Kriging using K-NET and KiK-net sites, and the amplification capability from Vs30 map for the 2004 Niigata-ken Chuetsu earthquake (Matsuoka et al., 2011)

The 8-bit unsigned integer GeoTiff file, which can be converted to the physical value of ground motion parameters, is downloadable from the site. Since calculation area is automatically determined to include the observation points where shaking occurred, the computation time is dependent on the magnitude of an earthquake. The automatic delivery of a message on Twitter (@QuiQuake) by "BOT" notifies that QuickMap is already available (see in Fig. 4). The QuakeMap, which take longer computation time than QuickMap, are also released on the homepage (http://qq.ghz.geogrid.org/QuakeMap/index.en.html). Furthermore, QuakeMap results for more than 8,600 major earthquakes after June 1996 have been computed and archived such that they chronologically represent the seismic motions over the last 16 years.

Earth observation data, such as strong motion observation records, shake maps, geological conditions, and remote sensing imagery are GIS based data that can be fully utilized through synergy with other GIS data available on the Internet. The most widely accepted standards are OGC (Open Geospatial Consortium) specifications such as the Web Map Service (WMS), Web Feature Service (WFS), and the Web Coverage Service (WCS). Since the QuickMap and QuakeMap contain information on each location-based grid-cell, it was decided to disseminate the maps using WMS/WCS. The example of KML document with WMS URI of QuakeMap imagery of the I_{JMA} distribution covering the 2011 Tohoku, Japan earthquake affected area is displayed on Google Earth as shown in Fig. 5.

4.2 Verification of QuakeMap Results

The accuracies of the estimated I_{JMA} in QuakeMap using strong motion observation records from other organizations' networks during the recent nine earthquakes; the 2000 Tottori-ken-seibu, the 2003 Miyagi-ken-oki, the 2003 Miyagi-ken-hokubu, the 2003 Tokachi-oki, the 2004 Niigata-ken Chuetsu, the 2005 Fukuoka-ken-seiho, the 2007 Noto-hanto-oki, the 2007 Niigata-ken Chuetsu-oki, and the 2008 Iwate-Miyagi-nairiku earthquakes were determined (Matsuoka et al., 2011). As in described in Section 2, ground motion values were estimated based on Simple Kriging of the K-NET and KiK-net data and the amplification capability estimated from the Vs30. The estimated I_{JMA} values were compared with observed I_{JMA} values recorded at

seismic stations owned by other organizations, such as the JMA, the Port and Airport Research Institute, the Central Research Institute of Electric Power Industry, the East Japan Railway Company, the NEXCO East, and the Committee of Earthquake Observation and Research in the Kansai Area. The standard deviation of estimation error (residual of the estimated and actual values) from the nine earthquakes is approximately 0.5 in I_{JMA}. Figure 6 shows the comparison for the 2004 Niigata-ken Chuetsu earthquakes. A relatively good agreement between the observed values and the estimated ones in QuakeMap is observed.

5. CONCLUSIONS

This paper outlines the components of the QuiQuake, which provides a 250-m resolution strong ground motion maps covering wide area, for quick disaster response right after an earthquake occurrence throughout Japan, is presented. In this system, an amplification capability map of ground motion (Vs30 map) based on Japan Engineering Geomorphologic Classification Map (JEGM) and seismic observation records from K-NET and KiK-net released by the National Research Institute for Earth Science and Disaster Prevention (NIED) are processed on a GEO Grid cluster computer of AIST. The use of the GEO Grid system in producing strong ground motion maps offers the following advantages: a) fully automatic, quick, and multi-task computing for mainshock and continued aftershocks, b) publication of the maps through Open Geospatial Consortium (OGC) compliant Web GIS server, and c) possibility to expand more stabilized and redundant operations by Virtual Machine in external servers and Cloud system.

Acknowledgements:

The QuiQuake system is supported by the National Research Institute for Earth Science and Disaster Prevention (NIED), the Japan Nuclear Energy Safety Organization (JNES), and ITOCHU Techno-Solutions Corporation (CTC). The system uses the data records of strong motion network (K-NET and KiK-net) administrated by NIED and the published program of Prof. Y. Hisada, Kogakuin University, to calculate instrumental seismic intensity. "RApid Shake Map simulator with Observed records (RASMO)" which was developed by Dr. I. Suetomi, Eight-Japan Engineering Consultants Inc. and Mr. M. Hashimoto, Kozo Keikaku Engineering Inc. and published by Kawasaki Laboratory, NIED is used for interpolation calculation. We optimized the software for fast calculation in the GEO Grid system. For validation of the system, we used the data from the JMA, the Port and Airport Research Institute, the Central Research Institute of Electric Power Industry, the East Japan Railway Company, the NEXCO East, and the Committee of Earthquake Observation and Research in the Kansai Area. To all of the aforementioned scientists and organizations, we would like to express our gratitude.

References:

Ariki, F., Shima, S. and Midorikawa, S. (2004), "Earthquake disaster prevention of Yokohama City," *Journal of Japan Association for Earthquake Engineering,* **4**(3), 148-153.

Borcherdt, R.D. and Gibss, J.F. (1976), "Effects of local geological conditions in the San Francisco bay region on ground motions and the intensities of the 1906 earthquake," *Bulletin of Seismological Society of America*, **66**(2), 467-500.

Fujimoto, K. and Midorikawa, S. (2006), "Relationship between average shear-wave velocity and site amplification inferred from strong motion records at nearby station pairs," *Journal of Japan Association for Earthquake Engineering,* **6**(1), 11-22 (in Japanese with English abstract).

Joyner, W.B. and Fumal, T.E. (1984), "Use of measured shear-wave velocity for predicting geologic and site effects on strong ground motion," *8th World Conference on Earthquake Engineering*, **2**, 777-783.

Matsuoka, M., Wakamatsu, K., Fujimoto K. and Midorikawa, S. (2006), "Average shear-wave velocity mapping using Japan Engineering Geomorphologic Classification Map," *Journal of Structural Engineering and Earthquake Engineering*, **23**(1), 57s-68s.

Matsuoka, M., Wakamatsu, K. and Hashimoto, M. (2011), "Liquefaction potential estimation based on the 7.5-arc-second Japan Engineering Geomorphologic Classification Map," *Journal of Japan Association for Earthquake Engineering*, **11**(2), 20-39 (in Japanese with English abstract).

Midorikawa, S., Matsuoka, M. and Sakugawa, K. (1994), "Site effects on strong-motion records observed during the 1987 Chiba-ken-toho-oki, Japan earthquake," *9th Japan Earthquake Engineering Symposium*, **3**, 85-90.

Midorikawa, S., Komazawa, M. and Miura, H. (2008), "Relationships between average shear-wave velocity and site amplification factors obtained by records from Yokohama dense strong-motion network," *Journal of Japan Association for Earthquake Engineering*, **8**(3), 19-30 (in Japanese with English abstract).

Open Geospatial Consortium (OGC). Available: http://www.opengeospatial.org/ (Access on 1 April, 2012)

Sekiguchi, S., Tanaka, Y., Kojima, I., Yamamoto, N., Yokoyama, S., Tanimura, Y., Nakamura, R., Iwao, K. and Tsuchida, S. (2008), "Design principles and IT overviews of the GEO Grid," *IEEE Systems Journal*, **2**(3), 374-389.

Wakamatsu, K. and Matsuoka, M. (2011), "Developing a 7.5-sec site-condition map for Japan based on geomorphologic classification," *Earthquake Resistant Engineering Structures VIII*, WIT Press, 101-112.

Wald, D.J., Worden, B.C., Quitoriano, V., and Pankow, K.L. (2005), *ShakeMap Manual: Technical Manual, User's Guide, and Software Guide*, U.S. Geological Survey, USA.

Yamazaki, F., Noda, S. and Meguro, K. (1998), "Developments of early earthquake damage assessment systems in Japan," *Structural Safety and Reliability,* ICOSSAR'97, 1573-1580.

Zuidam, R.A.van (1986), *Aerial Photo-interpretation in terrain analysis and geomorphologic mapping*, Smits Publishers, Hague.

10CUEE CONFERENCE PROCEEDINGS
10th International Conference on Urban Earthquake Engineering
March 1-2, 2013, Tokyo Institute of Technology, Tokyo, Japan

A BASIC STUDY ON THE RAPID PREDICTION OF SEISMIC GROUND MOTIONS USING P-WAVES OBSERVED IN DEEP BOREHOLES

Hiroyuki Miyakoshi[1)], Seiji Tsuno[2)], Shunroku Yamamoto[3)], and Naoyasu Iwata[4)]

1) Researcher, Railway Technical Research Institute, Japan
2) Assistant Senior Researcher, Railway Technical Research Institute, Dr. Eng., Japan
3) Laboratory Head, Railway Technical Research Institute, Dr. Eng., Japan
4) Assistant Senior Researcher, Railway Technical Research Institute, Japan
miyakoshi@rtri.or.jp, stsuno@rtri.or.jp, syama@rtri.or.jp, iwata@rtri.or.jp

Abstract: To predict ground motions of local earthquakes in real time, we proposed a new method to directly estimate amplitudes of S-waves on the surface using amplitudes of P-waves obtained by KiK-net in the Kanto region. After analyzing many seismic records observed on the surface and in the deep borehole, we concluded that it is effective for an EEW system to rapidly estimate S-waves on the surface by the empirical relationship between peak amplitudes of P-waves in the deep borehole and S-waves on the surface. Also, we confirmed that the estimation accuracy of S-waves on the surface are improved using the empirical relationship between peak amplitudes of S-waves in the deep borehole and on the surface.

1. INTRODUCTION

In the railway field of Japan, to ensure the safety of trains running in a certain area which strong shakings will attack during earthquakes, the earthquake early warning (EEW) system using estimated earthquake information about the hypocentral distance and the magnitude has been installed practically since 1990's (Nakamura, 1996 and Ashiya et al., 2007).

Since many railway business operators bring in the EEW system to safely stop trains during earthquakes, the rapidness and the reliability for the EEW system have been essential. Recently, to improve the EEW system and issue the EEW as soon as possible, investigations of lead times and amplitudes of seismic records obtained in the deep borehole are performed (Iwakiri et al., 2012).

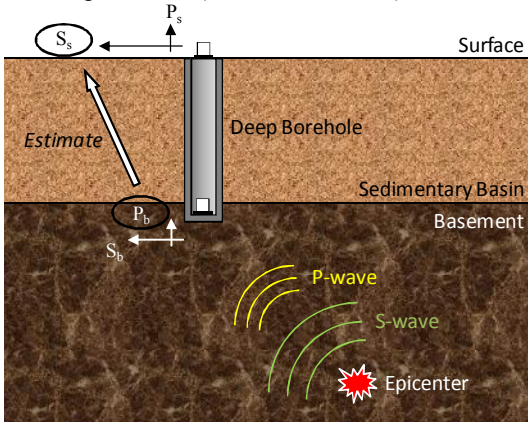


Fig.1 A Pattern Diagram of the New Method to Directly Predict Amplitudes of S-waves on the Surface (S_s) by Amplitudes of P-waves Observed in the Deep Borehole (P_b).

In the case of local earthquakes, the present system using P-waves on the surface may not work efficiently due to the shortness of P-S time delay. Therefore, we proposed the new method to directly predict amplitudes of S-waves on the surface by amplitudes of P-waves observed in the deep borehole, as shown in Fig.1. This method could make the lead time longer for propagation of seismic-waves through thick sedimentary basins. To apply this method to local earthquakes occurred beneath the Kanto region, at first, we performed a basic investigation for statistical relationships of P-waves/S-waves observed in the deep borehole and on the surface, using KiK-net data in the Tokyo Metropolitan Area and its vicinity.

2. SEISMIC STATIONS AND EARTHQUAKE DATA USED IN THIS STUDY

In this study, we used earthquake accelerograms recorded in the boreholes deeper than 2000m and on the surface at 6 seismic stations of KiK-net by NIED. Fig.2 shows locations of these seismic stations. Details of these seismic stations are described in Table 1. We selected local earthquakes whose epicenters are located from 34.5N to 37.0N and from 138.5E to 141.0E for the Kanto region, Japan.

We picked the on-set of P-waves and S-waves using a vertical (UD) component and horizontal (NS or EW) components, respectively. Data in which arrivals of P-waves and S-waves are not clear were excluded. PGAs of P-waves and S-waves were obtained using the UD component and the vector sum of NS and EW components, respectively. We processed accelerations and velocities by the band-pass filter using third-order Butterworth type with

the cutoff frequency of 0.1 and 20Hz.



Fig.2 Locations of Seismic Stations Used in this Study.

Table 1 Details of Seismic Stations Used in this Study.

No.	Code	Name	Latitude (N, °)	Longitude (E, °)	Depth of Borehole (m)	Remark
1	SITH01	IWATSUKI	35.9290	139.7349	3510	
2	CHBH04	SHIMOHSA	35.7966	140.0206	2300	
3	TKYH11	KOTO	35.6114	139.8125	3000	
4	SITH04	TOKOROZAWA	35.8028	139.5353	2000	Not on the basement (Suzuki 2002)
5	KNGH10	YOKOHAMA	35.4991	139.5195	2000	Not on the basement (Suzuki 2002)
6	TKYH02	FUCHU	35.6539	139.4704	2753	

The number of events and periods of earthquake data for each seismic station used in this study are shown in Table 2. The periods of earthquake data are largely different for each station. Distribution of epicenters and focal depths of earthquakes used in this study are shown in Fig.3. SITH01 (Iwatsuki) and CHBH04 (Shimohsa) tend to record earthquakes occurred beneath the northeast of the Kanto area. On the other hand, SITH04 (Tokorozawa), KNGH10 (Yokohama) and TKYH02 (Fuchu) tend to record earthquakes occurred beneath the southwest of the Kanto area. Locations of epicenters for TKYH11 (Koto) have more variety than those for other stations, because TKYH11 is located at the central Kanto area. Furthermore, at SITH01, earthquakes whose epicenters are located in the north of Ibaraki Pref. and Hama-dori of Fukushima Pref. are recorded, due to aplenty of many aftershocks of the 2011 Off the Pacific Coast of Tohoku Earthquake. Earthquakes which are occurred in the northwest of Chiba Pref. and the south of Ibaraki Pref. with focal depths of 40 to 80 kilometers are often recorded in all the stations. Frequency histograms of JMA magnitudes (Mj) of earthquakes for each station are shown in Fig.4. The dataset mainly consists of Mj 3.5 to 5.5 and the majority of the dataset is Mj 4.0 to 4.5 for all the stations.

Table 2 The Number of Events and Periods of Earthquake Data for Each Station Used in this Study.

No.	Code	Number	Period Selected
1	SITH01	154	2008.03.24～2012.03.17
2	CHBH04	204	2003.04.08～2008.12.31
3	TKYH11	157	2005.04.11～2012.03.27
4	SITH04	99	2002.12.23～2008.10.08
5	KNGH10	147	2003.03.13～2008.12.31
6	TKYH02	111	2008.04.04～2012.01.29

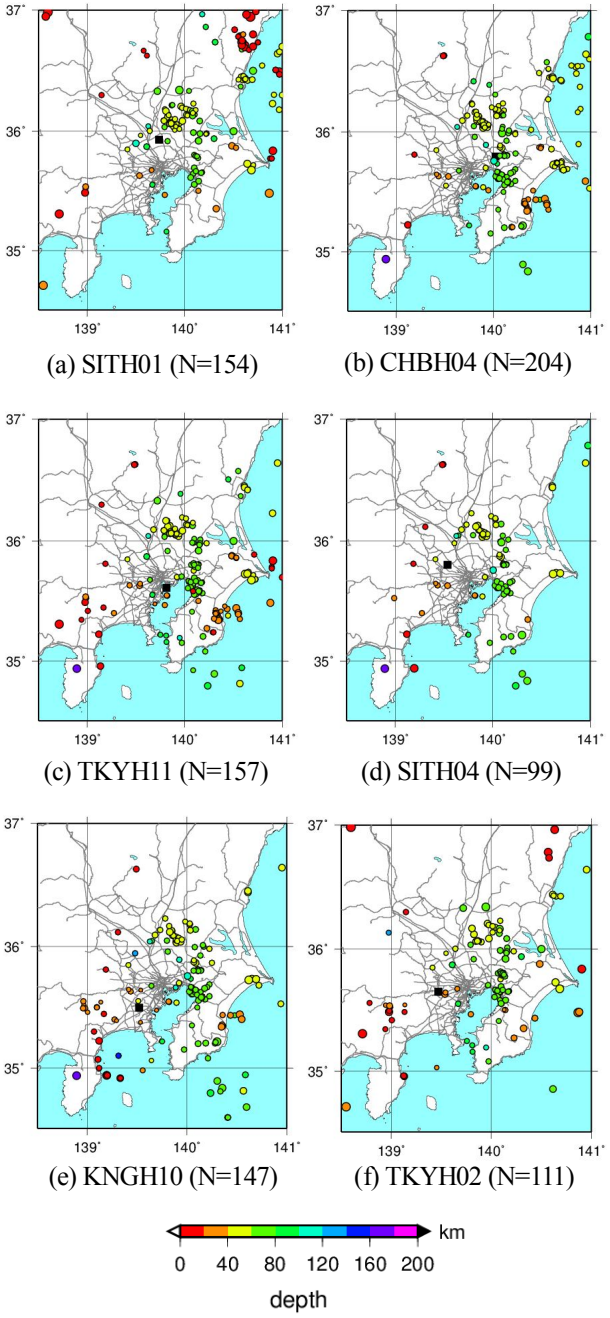
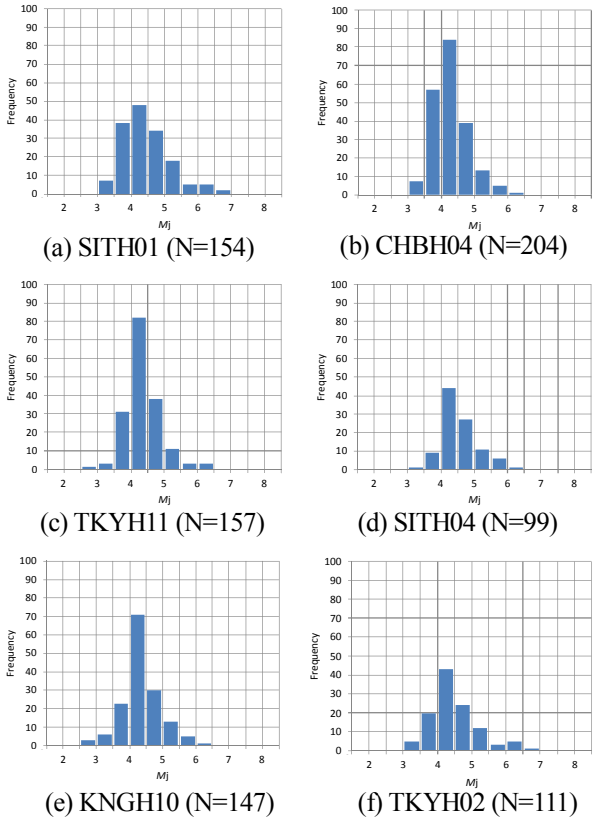


Fig.3 Distribution of Epicenters and Depths of Earthquakes for Each Station Used in this Study. Black Squares Show Locations of Seismic Stations. N Shows the Number of Data.



(a) SITH01 (N=154) (b) CHBH04 (N=204)

(c) TKYH11 (N=157) (d) SITH04 (N=99)

(e) KNGH10 (N=147) (f) TKYH02 (N=111)

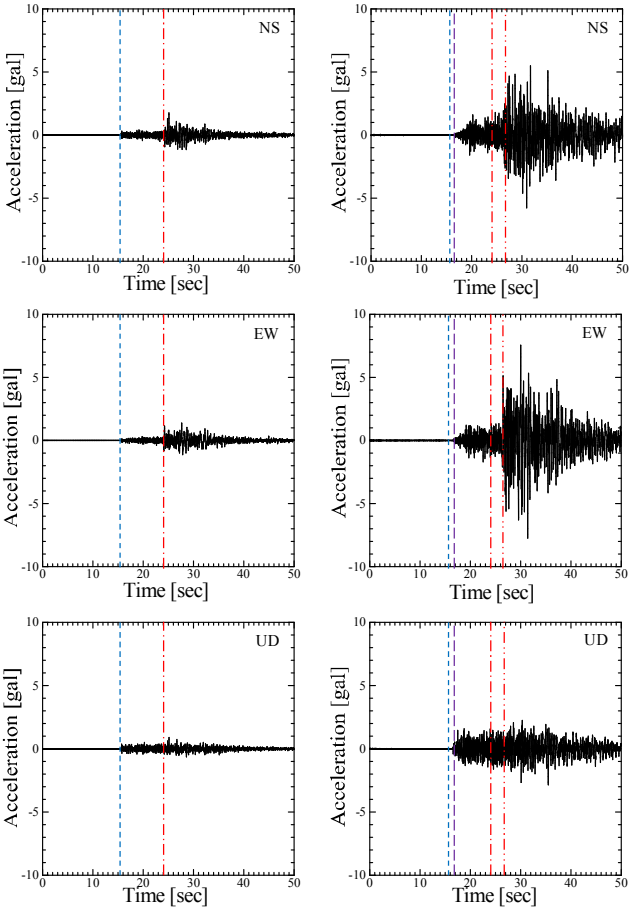
Fig.4 Frequency Histograms of JMA Magnitude of Earthquakes for Each Station Used in this Study. N Shows the Number of Data.

3. LEAD TIME UNTIL ARRIVALS OF S-WAVES ON THE SURFACE BY ARRIVALS OF P-WAVES IN THE DEEP BOREHOLE

An example of accelerations observed in the deep borehole and on the surface at TKYH02 is shown in Fig.5, respectively. The earthquake whose magnitude and depth of hypocenter are 5.0 and 50km is used. In this case, a time difference between the arrival of P-wave in the deep borehole and the arrival of S-wave on the surface is 10.7s. We count up time differences between arrivals of P-waves in the deep borehole and arrivals of S-waves on the surface for each station using all earthquake data. The result is shown in Fig.6. The lead time of 5s is ensured at least and the average of lead times is about 10s for all the stations. The time differenece depends on the hypocentral distance.

4. EXAMINATION ON PEAK AMPLITUDES OF P-WAVES AND S-WAVES IN THE DEEP BOREHOLE AND ON THE SURFACE

Here, we examine about relationships between S-waves in the deep borehole (S_b) and S-waves on the surface (S_s), P-waves in the deep borehole (P_b) and S-waves in the deep borehole (S_b), using the peak amplitudes of accelerations and velocities.



(a) Waveforms Observed in the Deep Borehole. (b) Waveforms Observed on the Surface.

Fig.5 An Example of Acceleration Waveforms at TKYH02. Short-dashed Line, Long-dashed Line, Chain Line and Chain Double-dashed Line Show the Arrival Time of P-wave in the Deep Borehole, that of P-wave on the Surface, that of S-wave in the Deep Borehole and that of S-wave on the Surface, respectively.

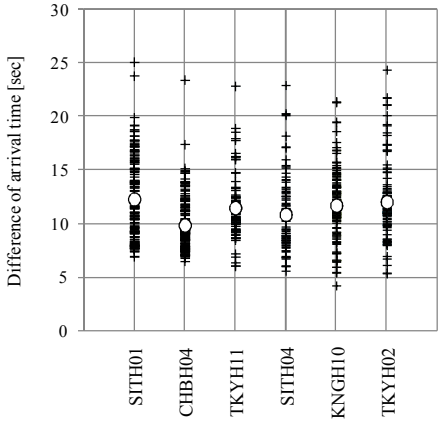
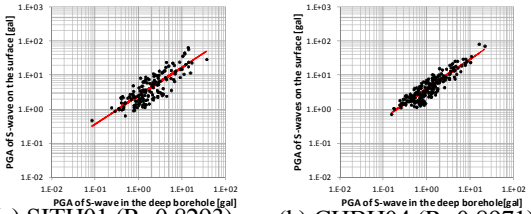


Fig.6 Time Differences between Arrivals of P-waves in the Deep Borehole and those of S-waves on the Surface. Open Circles Show Geometric Averages.

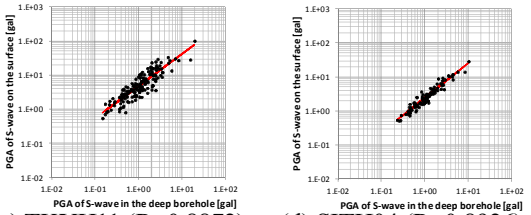
4.1 The Relationship between S_b and S_s

Relationships of PGA and PGV between S_b and S_s for each station are shown in Fig.7 and Fig.8, respectively.



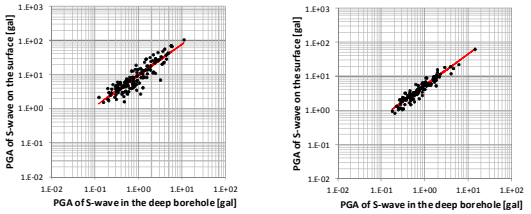
(a) SITH01 (R=0.8293)

(b) CHBH04 (R=0.8971)



(c) TKYH11 (R=0.8872)

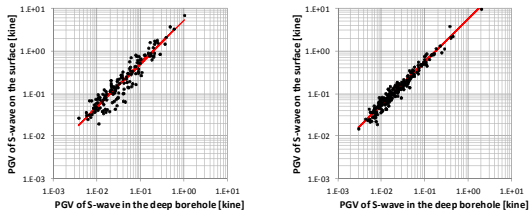
(d) SITH04 (R=0.8926)



(e) KNGH10 (R=0.8926)

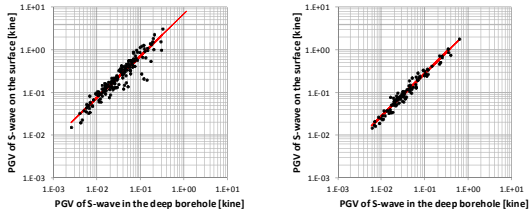
(f) TKYH02 (R=0.9460)

Fig.7 Relationships of PGA between S-waves in the Deep Borehole and S-waves on the Surface. Lines and R Show Linear Regression Lines and Correlation Coefficients, respectively.



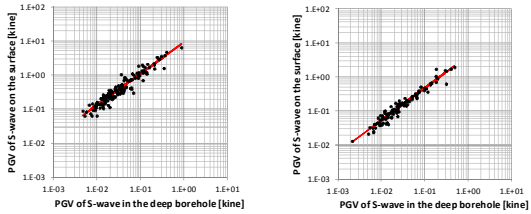
(a) SITH01 (R=0.9360)

(b) CHBH04 (R=0.9751)



(c) TKYH11 (R=0.9451)

(d) SITH04 (R=0.9804)



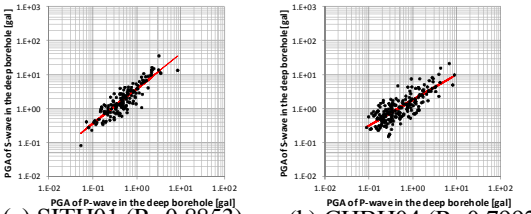
(e) KNGH10 (R=0.9562)

(f) TKYH02 (R=0.9740)

Fig.8 Relationships of PGV between S-waves in the Deep Borehole and S-waves on the Surface. Lines and R Show Linear Regression Lines and Correlation Coefficients, respectively.

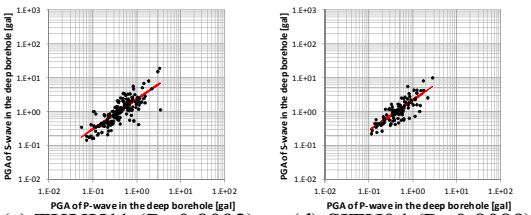
4.2 The Relationship between P_b and S_b

Relationships of PGA and PGV between P_b and S_b for each station are shown in Fig.9 and Fig.10, respectively.



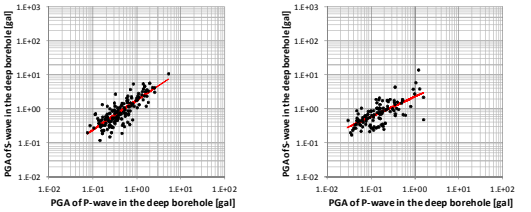
(a) SITH01 (R=0.8853)

(b) CHBH04 (R=0.7992)



(c) TKYH11 (R=0.8092)

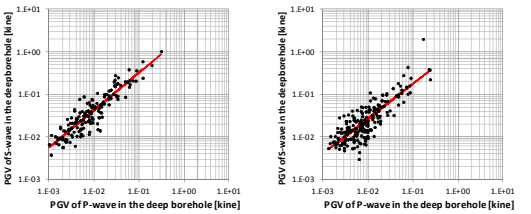
(d) SITH04 (R=0.8089)



(e) KNGH10 (R=0.7986)

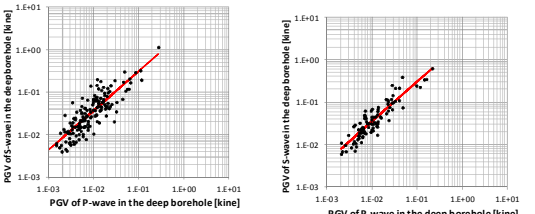
(f) TKYH02 (R=0.6795)

Fig.9 Relationships of PGA between P-waves in the Deep Borehole and P-waves at the Basement. Lines and R Show Linear Regression Lines and Correlation Coefficients, respectively.



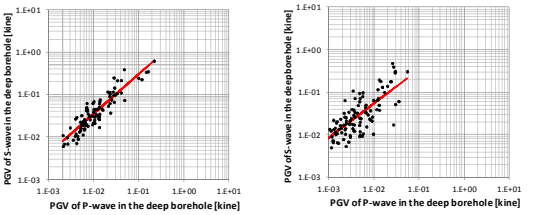
(a) SITH01 (R=0.9074)

(b) CHBH04 (R=0.8300)



(c) TKYH11 (R=0.8420)

(d) SITH04 (R=0.9056)



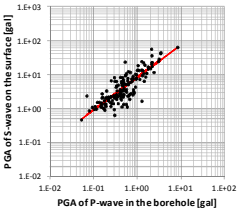
(e) KNGH10 (R=0.8568)

(f) TKYH02 (R=0.7603)

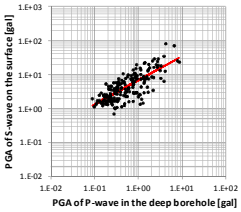
Fig.10 Relationships of PGV between P-waves in the Deep Borehole and S-waves at the Basement. Lines and R Show inear Regression Lines and Correlation Coefficients, respectively.

4.3 The Relationship between P_b and S_s

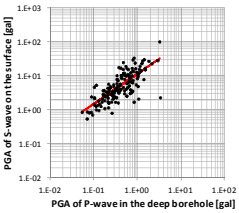
Relationships of PGA and PGV between P_b and S_s for each station are shown in Fig.11 and Fig.12.



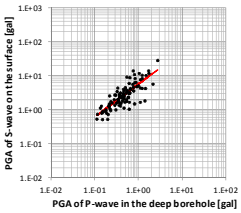
(a) SITH01 (R=0.8853)



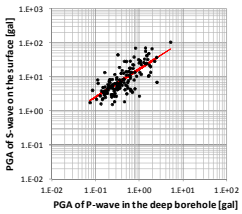
(b) CHBH04 (R=0.7992)



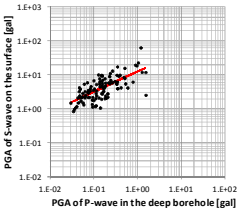
(c) TKYH11 (R=0.8092)



(d) SITH04 (R=0.8089)

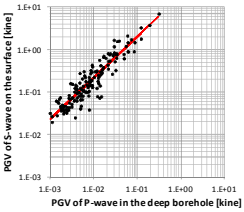


(e) KNGH10 (R=0.7986)

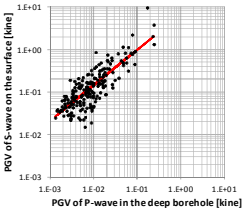


(f) TKYH02 (R=0.6795)

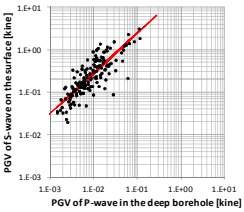
Fig.11 Relationships of PGA between P-waves in the Deep Borehole and S-waves on the Surface. Lines and R Show Linear Regression Lines and Correlation Coefficients, respectively.



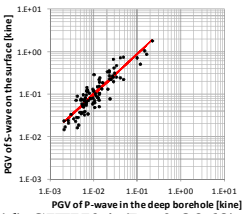
(a) SITH01 (R=0.9212)



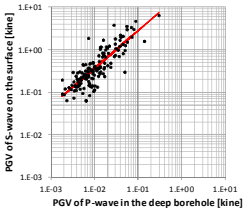
(b) CHBH04 (R=0.8151)



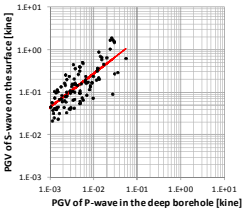
(c) TKYH11 (R=0.8376)



(d) SITH04 (R=0.8962)



(e) KNGH10 (R=0.8350)

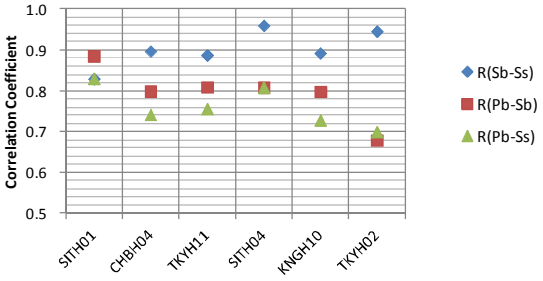


(f) TKYH02 (R=0.7637)

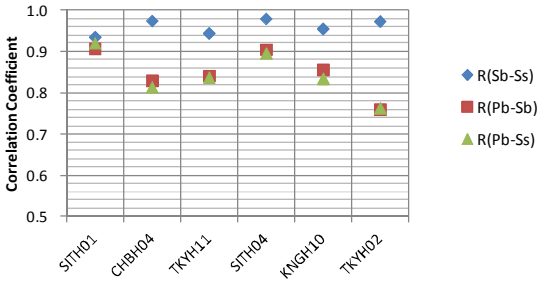
Fig.12 Relationships of PGV between P-waves in the Deep Borehole and S-waves on the Surface. Line and R Show Linear Regression Lines and Correlation Coefficients, respectively.

4.4 Discussion

Correlation coefficients between peak amplitudes, which are R in Fig.7-Fig.12 are shown in Fig.13. The correlation coefficients between peak amplitudes of S_b and S_s are the highest values in the range from 0.8 to 0.9. Those correlation coefficients between peak amplitudes of S_b and S_s may be affected mainly by the S-wave velocity structures beneath the seismic stations. On the other hand, correlation coefficients between peak amplitudes of P_b and S_b are relatively low values in the range from 0.7 to 0.8. Those correlation coefficients between peak amplitudes of P_b and S_b may be affected by radiation patterns of individual earthquakes. Therefore, correlation coefficients between peak amplitudes of P_b and S_s may be affected by both S-wave velocity structures beneath the seismic stations and radiation patterns of earthquakes. For data at 6 stations used in this study, correlation coefficients between PGV of S_b and S_s are higher than those between PGA of S_b and S_s.



(a) PGA



(b) PGV

Fig.13 Correlation Coefficients between Peak Amplitudes of PGA and PGV for Each Station Shown in Fig.7-12. In the Legend, 'S' and 'P' Mean S-waves and P-waves and Additional Characters 'b' and 's' Mean Borehole and Surface, respectively.

5. RAPID PREDICTIONS OF PEAK AMPLITUDES OF S-WAVES ON THE SURFACE USING THOSE OF P-WAVES OBSERVED IN THE DEEP BOREHOLE

For several earthquakes, we tried to estimate amplitudes of S-waves on the surface using the regression line calculated above. The regression equation is expressed as

$$\log y = a \log x + b \qquad (1)$$

where a and b are parameters determined by least-square method and described in Table 3. Two types of estimations for amplitudes of S_s, which are the two step method by S_b-S_s

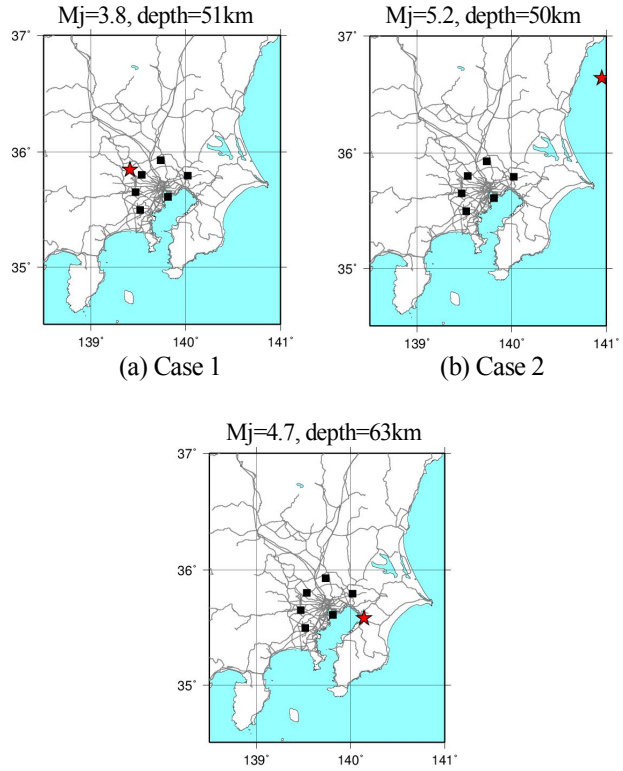
and P_b-S_b regression lines and the direct method by P_b-S_s regression line, are considered. Information of earthquakes used in this estimation is shown in Fig.14.

The estimation results of PGA and PGV on the surface are shown in Fig.15 and Fig.16, respectively. Estimation results by both methods are almost same. The misfits between the estimated values and the observed values correspond to the variations between the regression equation and observations (see Fig.7-Fig.12).

Table 3 List of Parameters of Regression Lines Calculated.

Station	PGA					
	$R(S_b\text{-}S_s)$		$R(P_b\text{-}S_b)$		$R(P_b\text{-}S_s)$	
	a	*b*	*a*	*b*	*a*	*b*
SITH01	0.8287361	0.3967097	1.0264770	0.5881789	0.9618229	0.9197746
CHBH04	0.8665275	0.5943393	0.7592371	0.2590747	0.7091455	0.8341433
TKYH11	0.9458339	0.6787651	0.8873777	0.3735656	0.8839586	1.0499890
SITH04	1.0278360	0.3831438	0.9012464	0.3435796	0.9649459	0.7494424
KNGH10	0.9171724	0.9830039	0.8734486	0.2565605	0.8190095	1.2250400
TKYH02	0.9299855	0.7295886	0.5916023	0.3582101	0.5987402	1.1031820

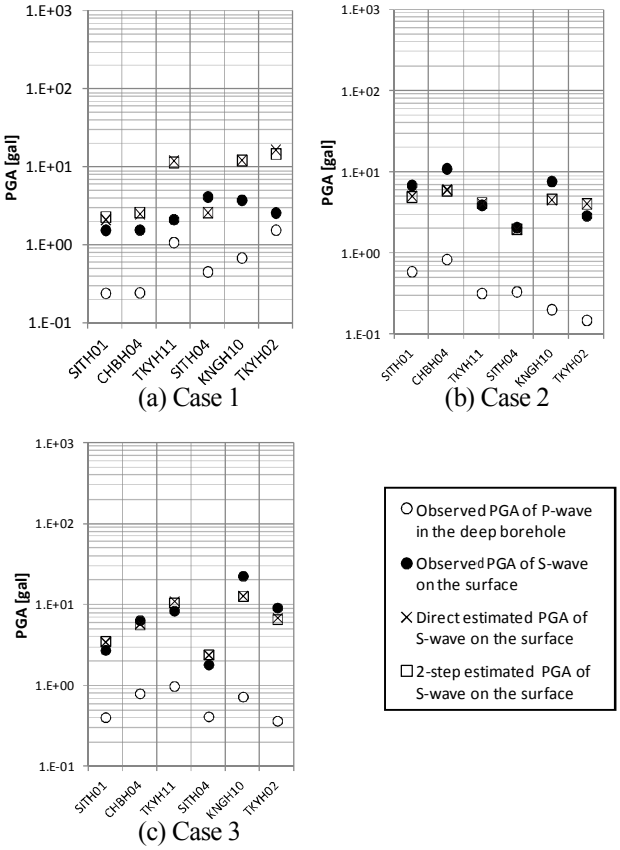
Station	PGV					
	$R(S_b\text{-}S_s)$		$R(P_b\text{-}S_b)$		$R(P_b\text{-}S_s)$	
	a	*b*	*a*	*b*	*a*	*b*
SITH01	1.0175450	0.7210087	0.8805891	0.3847807	0.9717966	1.2701620
CHBH04	1.0109380	0.7561994	0.8222326	0.0647053	0.8371322	0.8338489
TKYH11	0.9787581	0.8356404	0.9266900	0.4190697	0.9544852	1.3441980
SITH04	1.0068380	0.4537914	0.9409550	0.4285778	0.9563670	0.9029979
KNGH10	0.9169221	0.9552937	0.9512759	0.3813498	0.8889350	1.3379260
TKYH02	0.9502232	0.6252853	0.8049152	0.3484429	0.7887830	1.0134980



(a) Case 1 (b) Case 2

(c) Case 3

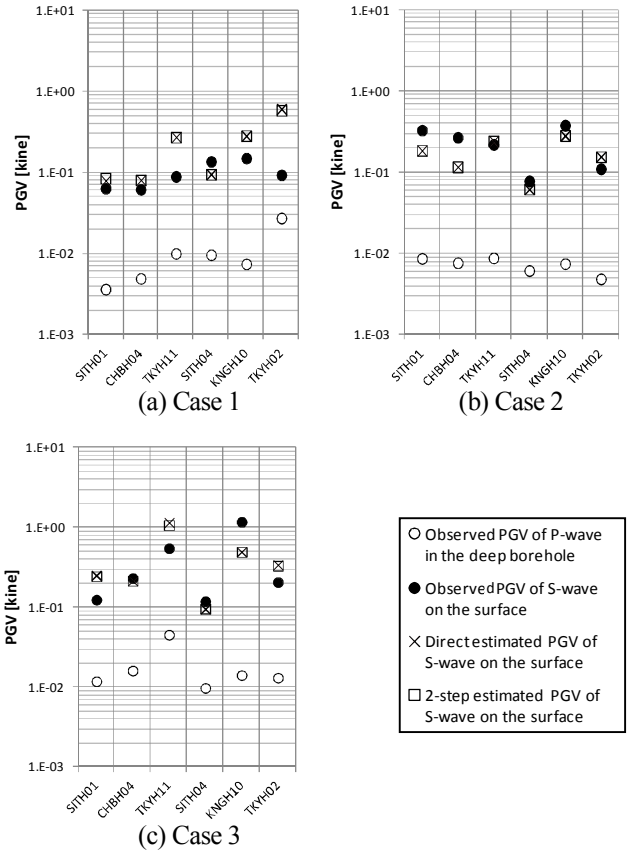
Fig.14 Locations of Earthquakes and Stations Used in this Estimation. Black Squares and Gray Stars Show Locations of Seismic Stations and Epicenters , respectively.



(a) Case 1 (b) Case 2

(c) Case 3

Fig.15 Comparisons of PGA Estimated to those Observed.



(a) Case 1 (b) Case 2

(c) Case 3

Fig.16 Comparisons of PGV Estimated to those Observed.

6. CONCLUSIONS

To predict the local earthquakes occurred beneath the Kanto region, we performed a basic investigation for the lead time and the accuracy of prediction of ground motions on the surface, using earthquakes recorded in the deep borehole. As a result, we obtain the following knowledges.

1) Time differences between arrivals of P-waves in the deep borehole and arrivals of S-wave on the surface ensure 5s at least and the average of lead time is about 10s.

2) It is effective to estimate S-waves on the surface using the empirical relationship between the peak amplitudes of P-waves in the deep borehole and those of S-waves on the surface.

3) The estimation accuracy of S-waves on the surface are improved using the empirical relationships between peak amplitudes of S-waves in the deep borehole and on the surface.

In the future, we investigate the relationships between the empirical relations obtained in this study and velocity structures / radiation patterns to improve the accuracy of this method.

Acknowledgements:

The authors thank NIED to provide us strong motion data by KiK-net. Figures are drawn using GMT.

References:

Nakamura, Y. (1996), "Research and Development of Intelligent Earthquake Disaster Prevention Systems UrEDAS and HERAS," *Journal of Structural Mechanics and Earthquake Engineering*, **531**(I-34), 1-33.

Ashiya, K., Sato, S., Iwata, N., Korenaga, M., Nakamura, H. (2007), "Application of earthquake early warning information to earthquake alarm systems in railways," *BUTSURI-TANSA*, **60**(5), 387-397.

Iwakiri, K., Hoshiba, M., Ohtake, K., Shimoyama, T. (2012), "Application of Strong Motion Data Observed in and around Southern Kanto to the Earthquake Early Warning System," *Quarterly Journal of Seismology*, **75**, 37-59.

Suzuki, H. (2002), "Underground Geological Structure beneath the Kanto Plain, Japan," *Report of National Research Institute for Earth Science and Disaster Prevention*, **63**, 526-532.

10CUEE CONFERENCE PROCEEDINGS
10th International Conference on Urban Earthquake Engineering
March 1-2, 2013, Tokyo Institute of Technology, Tokyo, Japan

IMPACT ANALYSIS OF THE GREAT EAST JAPAN EARTHQUAKE BY RUNNING SPECTRUM ANALYSIS OF THE NEWSPAPER

Muneyoshi Numada[1] and Kimiro Meguro[2]

1) Research Associate, International Center for Urban Safety Engineering (ICUS), the Institute of Industrial Science (IIS), the University of Tokyo, Japan
2) Professor/Director, International Center for Urban Safety Engineering (ICUS), the Institute of Industrial Science (IIS), the University of Tokyo, Japan
numa@iis.u-tokyo.ac.jp, meguro@iis.u-tokyo.ac.jp

Abstract: Huge amount of digital data of the Great East Japan Earthquake is provided by the highly-developed digital data delivery system and storage technology. But as of now, the method and/or technique for analysis is not yet satisfactory. This paper proposes a running spectrum technique of text data for the purpose of analyzing changes or trend along the disaster management cycle. For verification of this technique, news reported by the newspaper Fukushima Minpo has been used. The result shows the characteristics of data change in the time domain.

1. INTRODUCTION

Huge amount of digital information related to the Great East Japan Earthquake has been released or published by newspapers, wire agencies and TV stations. The volume of information, by far, exceeds that of past disasters because tools to send out information have dramatically changed: websites, Twitter, Facebook and other Internet-based platforms are now widely used as popular sources for news updates. The contents covered include many different kinds of events and problems that were caused simultaneously by the earthquake. Reports on regional damage induced by the earthquake and tsunami, economical problems in the Tokyo metropolitan area, the Fukushima nuclear power plant accident and much other information spread out at the same time.

By using the cloud computing technology, more and more digital contents can be produced and stored in the digital world. This new innovative environment, incorporating powerful delivery data system and storage capacity, enables us to use information more easily for different purposes. Yet, the quality of data analysis technique in the disaster management field is far from enough. We need efficient means to distinguish important events out of the vast amount of information, to get the grasp of movements within a certain time frame, to know the changes occurring in the disaster management phase and so on.

Some algorithms in document/ literature evaluation method suggest using association rules such as TF-IDF, Z-score and MMI. The association rules and TF-IDF are based on term co-occurrence frequencies, while Z-Score and Mutual Information Measure (MIM) are based on term co-occurrence probabilities [1]. The characteristics of disaster-related-information change or shift in accordance with each disaster management cycle phase, which are namely damage mitigation, preparedness, prediction and early warning, damage assessment, emergency disaster response, recovery, and reconstruction/restoration.

When handling this kind of information with characteristics that depend on time-changing/shifting, it is necessary to make analysis within a certain time span. Therefore, we propose a dynamic analysis technique of document/literature/text with considerations on time series to offer proper and appropriate responses. This paper shows the overview of proposed techniques. News from the newspaper Fukushima Minpo has been used for its verification. The proposed technique is a powerful tool to effectively analyze the huge amount of digital data, thereby responding to the upcoming society with growing volume of information.

2. RUNNING SPECTRUM ANALYSIS OF TEXT DATA

2.1 Running spectrum analysis

Running spectrum analysis is a method widely used in the seismic ground motion analysis for understanding the wave characteristics in time and frequency domain. It is an approach that shifts a time interval as the analysis point to conduct analysis within a certain time frame. In our research, the target is further expanded to the document/ literature/ text field. Moving-average method is used for dynamic analysis (see Figure 1).

2.2 Flow of text data running spectrum analysis

Figure 2 shows the flow of running spectrum analysis text data proposed in this research.

Firstly, Japanese Kanji letters, Katakana letters,

numbers and alphabets are extracted from the documents separately as keywords. For this purpose, we have developed an "extract-keyword-program (EKP)". The EKP can extract each keyword individually and accurately. For example, “hinan” (“evacuation” in English) and “hinansya” (“evacuee” in English) are identified as different keywords within the same document. The EKP can also count the frequency of appearance within one certain day or all the days during the specified period. Users can freely reset the period depending on purposes.

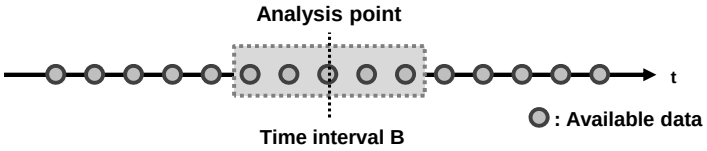


Figure 1 Time interval B of moving average method

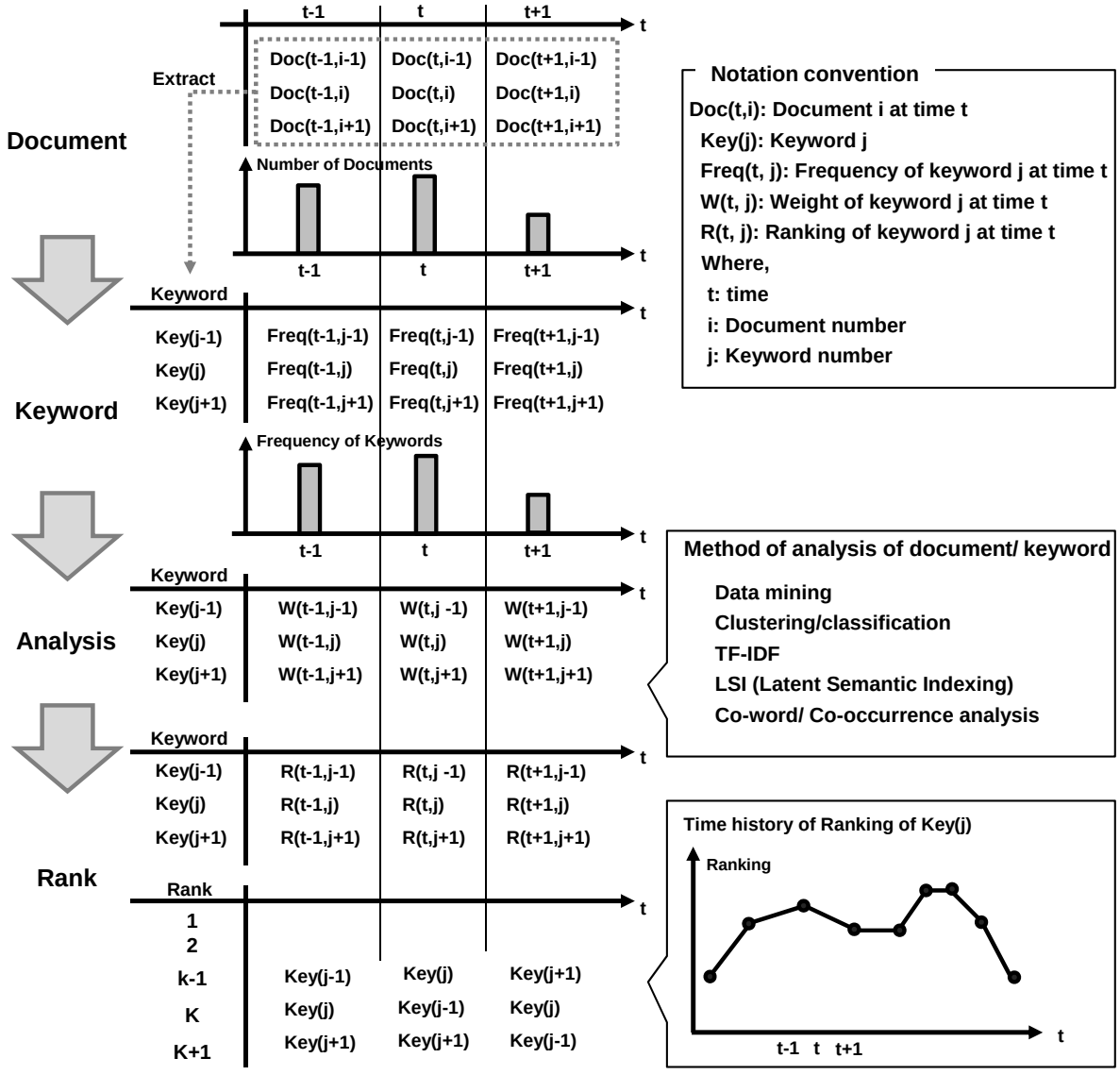


Figure 2 Flow of running spectrum technique

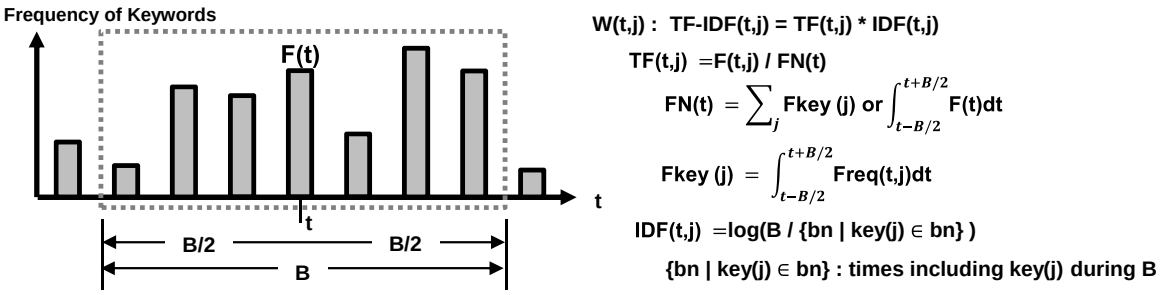


Figure 3 TF-IDF of running spectrum technique

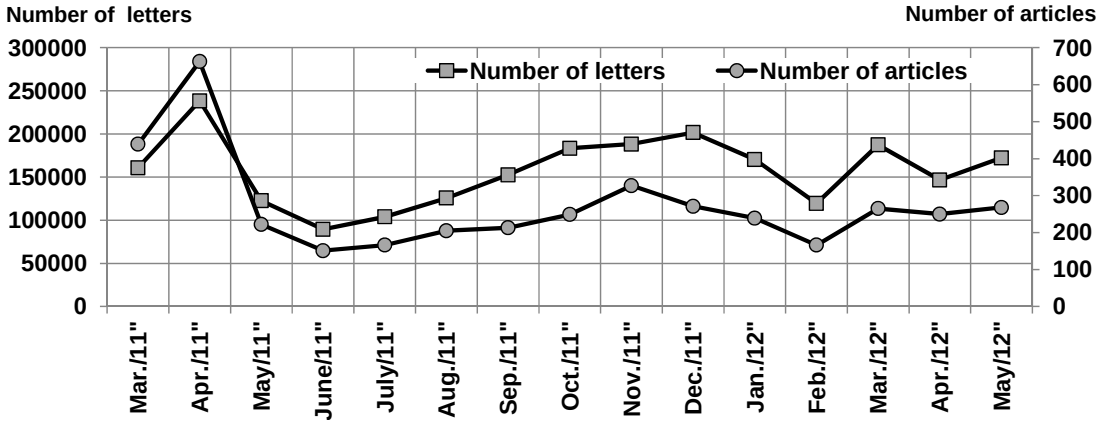


Figure 4 Archives of Fukushima Minpo newspaper

Secondly, keywords are reviewed and analyzed. The weights of all extracted keywords are calculated, respectively. Suggested algorithms for keyword analysis are: Clustering, TF-IDF, LSI, and Co-occurrence. Our proposed system can choose the most suitable weighing approach according to the purposes and requirements of each user. In this paper, we have used TF-IDF (Term Frequency-Inverse Term Frequency) in the time span B for verification as shown in Figure 3. TF-IDF is a statistical measurement method to evaluate the degree of importance of a specified keyword in a document among a collection of numerous documents. The importance level is determined by the frequency and distribution within the collection of all documents [1].

Thirdly, after the evaluation of the importance of each keyword in certain time span B, all keywords are ranked according to its weights.

3. CASE STUDY OF FUKUSHIMA MINPO NEWSPAPER

3.1 Newspaper data

Fukushima Minpo is a local newspaper, with circulation of 250 thousand copies per day, the largest in Fukushima Prefecture [2]. This paper repeatedly reports on nuclear power plant accidents as the company office is located near the site. Figure 4 shows news report archives from March 2011 to May 2012, analyzing articles by the running spectrum approach described above.

3.2 Extracting keywords

Figure 5 shows the number of keyword items and its frequency. A total of 67,881 different keywords have been extracted. Frequency is shown as “1” in 44,022 items (64.85% of the total), indicating that the keyword appears only one time. Most newspaper articles report the name, gender and age of those dead or injured, therefore the number of keywords with only one-time appearance equals the number of items.

Figure 6 represents keywords with high frequency. “Refuge” is listed as the most frequently used keyword with 1,696 appearances, followed by “residents” with 1,614 times over the period from March 2011 to May 2012. Keywords related to nuclear power accidents such as “decontamination”, “nuclear power plant accident”, “influence”, “radioactive material”, “children”, “dose of radiation” etc. are ranked high. In this case study, one-letter words have been omitted because the keyword alone often has no meaning by itself and therefore should be interpreted within idioms, phrases and contexts.

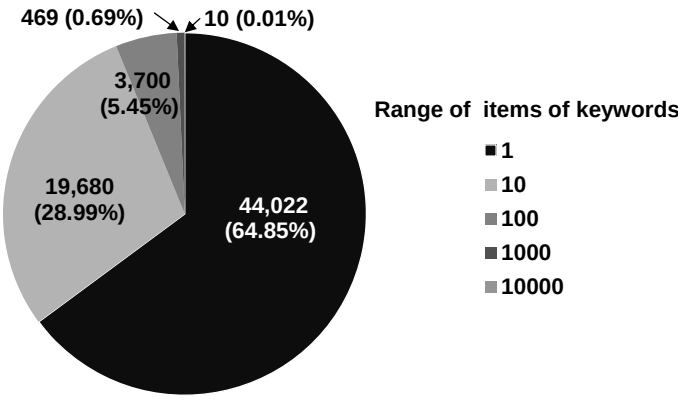


Figure 5 The number of keyword items and its appearance within a certain range

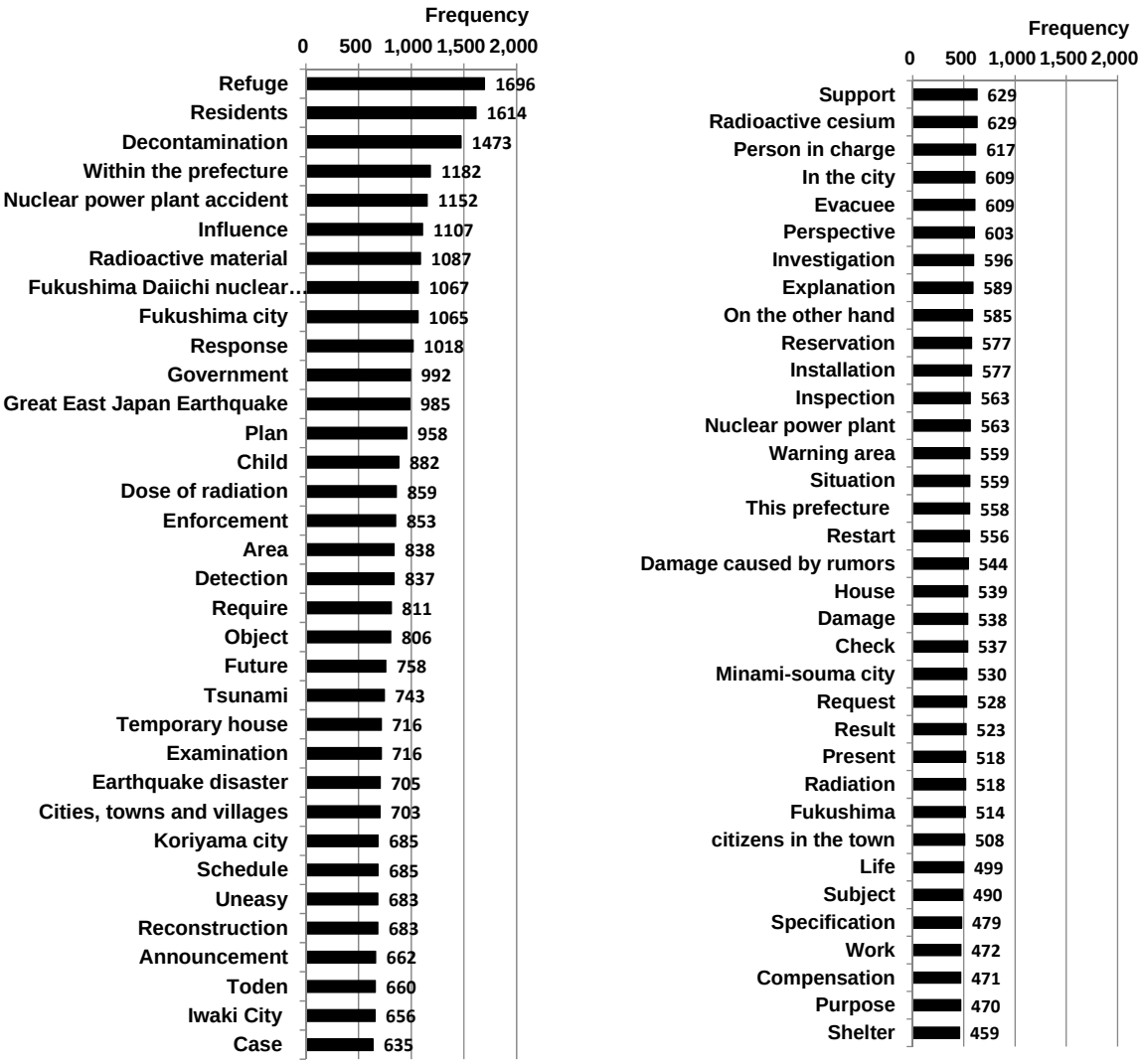


Figure 6 List of Keywords and its appearance frequency (high frequency part)

3.3 Results of running spectrum analysis

By using the proposed analysis technique, all keywords have been ranked respectively according to the results of a weighting algorithm on daily or monthly level, and have been listed in order of the ranks. We get to understand which keywords received attention at the time, also tracing down the hottest keywords changing with the circumstances of the moment.

1. *Time-chart of the top ranked keywords*: Table 1 shows the time chart of the top three ranked keywords in March 2011 as a sample period for B =3, 7 and 31 days respectively due to space limit of paper.

Table 1 Time chart of ranking of keywords: The number of each keyword shows the ranking in a day

		B=3			B=7			B=31		
		1	2	3	1	2	3	1	2	3
2011/3/11	Keyword	Fukushima city	Tsunami	Center	Tsunami	Evacuation	Disaster victim	Evacuation	Refgue	Response
	TF-IDF	0.015883551	0.015883551	0.015883551	0.018548882	0.017122045	0.014268371	0.011379498	0.008301542	0.00700664
2011/3/12	Keyword	Tsunami	Center	Evacuation	Koriyama city	Disaster victim	Evacuation	Evacuation	Refgue	Response
	TF-IDF	0.015694461	0.015694461	0.013078718	0.012867705	0.012432837	0.010567912	0.010424237	0.007525328	0.006362433
2011/3/13	Keyword	Center	Generating	Offer	Disaster victim	Koriyama city	Evacuation	Evacuation	Refgue	Acceptance
	TF-IDF	0.0078379	0.006531583	0.006531583	0.010186057	0.007477532	0.007099373	0.009608205	0.006706398	0.005774015
2011/3/14	Keyword	Koriyama city	Disaster victim	Suffering a calamity	Disaster victim	Evacuation	Koriyama city	Evacuation	Refgue	Acceptance
	TF-IDF	0.013906485	0.00812641	0.005794369	0.004954192	0.004816576	0.004577634	0.00848648	0.005924964	0.005415054
2011/3/15	Keyword	Koriyama city	Debris	Business	Debris	Acceptance	Activity	Evacuation	Refgue	Acceptance
	TF-IDF	0.004075026	0.003943332	0.003943332	0.003477323	0.003367127	0.003134146	0.007611582	0.005316452	0.005158004
2011/3/16	Keyword	Business	Work	Part	Pregrant	Debris	Niigata prefecture	Evacuation	Acceptance	Refgue
	TF-IDF	0.003505464	0.002804371	0.002804371	0.004234184	0.003024417	0.003024417	0.006875769	0.004735527	0.004667562
2011/3/17	Keyword	Directions	Woman	Blanket	Pregrant	Numerical value	Detection	Evacuation	NPPA	Acceptance
	TF-IDF	0.002985359	0.002985359	0.002985359	0.003365795	0.002512373	0.002476428	0.005917921	0.004134774	0.004134774
2011/3/18	Keyword	Pregrant	Citizen	Niigata prefecture	Last spring	Detection	Citizen	Evacuation	Acceptance	NPPA
	TF-IDF	0.004227755	0.003019825	0.003019825	0.002929957	0.002916061	0.002287094	0.005238582	0.003820034	0.003746572
2011/3/19	Keyword	Detection	Pregrant	Postponement	Last spring	Citizen	Detection	Evacuation	Acceptance	NPPA
	TF-IDF	0.003803307	0.003803307	0.003259977	0.002766884	0.002753761	0.002046127	0.00515258	0.00375732	0.003432535
2011/3/20	Keyword	Last spring	Goods	water supply	Citizen	Restart	Holding	Evacuation	Acceptance	NPPA
	TF-IDF	0.002856718	0.002711134	0.002448616	0.002561441	0.002291816	0.002167283	0.00449686	0.003282702	0.003125135
2011/3/21	Keyword	Student	Successful applicant	Citizen	Citizen	Postponement	Holding	Evacuation	NPPA	Acceptance
	TF-IDF	0.004139459	0.003725513	0.003311567	0.002102648	0.002102648	0.001895543	0.003872551	0.002961342	0.002884521
2011/3/22	Keyword	Difficulty	Aizuwakamatsu	Holding	Holding	Last spring	Postponement	Evacuation	Election	NPPA
	TF-IDF	0.002420517	0.002420517	0.002117953	0.001622171	0.001622171	0.00152268	0.003243887	0.002655386	0.002600224
2011/3/23	Keyword	Postponement	Holding	Life in refuge	Student	Holding	Last spring	Evacuation	Election	Acceptance
	TF-IDF	0.001975951	0.001873851	0.001606158	0.001690023	0.00159819	0.00159819	0.003220538	0.002636273	0.002519098
2011/3/24	Keyword	Holding	Large scale disaster	Life in refuge	Student	Holding	Last spring	Evacuation	Election	Acceptance
	TF-IDF	0.00155485	0.001332728	0.001332728	0.001740252	0.001645689	0.001645689	0.00319999	0.002619453	0.002503025
2011/3/25	Keyword	Restoration	Tokyo metropolitan	Large scale disaster	Student	Holding	Election	Evacuation	Election	Acceptance
	TF-IDF	0.0018989	0.001624766	0.001624766	0.001907318	0.001803677	0.001704338	0.00272265	0.002608714	0.002492764
2011/3/26	Keyword	Attendance	Tomioka	Tokyo metropolitan	Election	Reservation	Holding	Election	Acceptance	Detection
	TF-IDF	0.0031762	0.002117467	0.002117467	0.002433493	0.001899479	0.001778247	0.002572594	0.002458249	0.002356063
2011/3/27	Keyword	Radioactive material	Tomioka	Sea water	Election	Reservation	Acceptance	Election	Acceptance	Detection
	TF-IDF	0.004758472	0.003568854	0.003568854	0.002680526	0.002052694	0.001967165	0.002538725	0.002425886	0.002325045
2011/3/28	Keyword	Acceptance	Investigation	Residents	Attendance	Acceptance	Radioactive material	Election	Acceptance	Detection
	TF-IDF	0.006747479	0.003680443	0.003169465	0.002555711	0.002283299	0.001885678	0.00255324	0.002439756	0.002338339
2011/3/29	Keyword	Reservation	Fukushima	Accident	Hotel	Victim	Japanse style hotel	Election	Acceptance	Postponement
	TF-IDF	0.002895657	0.002895657	0.002778622	0.004084614	0.003681503	0.003155574	0.002503027	0.002391774	0.002221838
2011/3/30	Keyword	Temporary back-home	Inside Shelter	Accident	Victim	Hotel	Japanse style hotel	Election	Postponement	Acceptance
	TF-IDF	0.002825649	0.002825649	0.002711444	0.004174883	0.003578471	0.003227033	0.002442267	0.002418047	0.002333715
2011/3/31	Keyword	Victim	Hotel	Restart	Victim	Hotel	Japanse style hotel	Postponement	Election	Acceptance
	TF-IDF	0.005894993	0.005359084	0.003751359	0.004514461	0.003869538	0.003489515	0.002507653	0.002359851	0.002214332

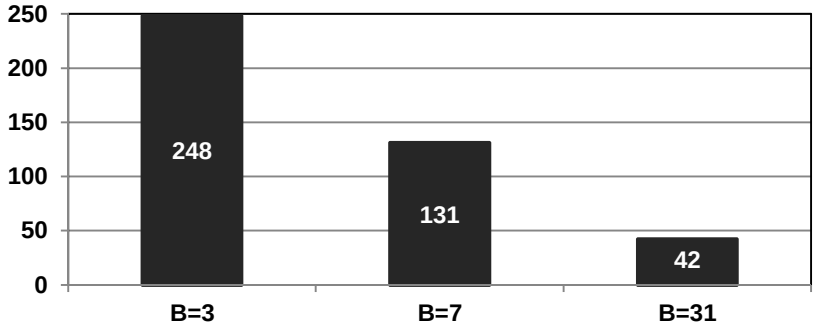
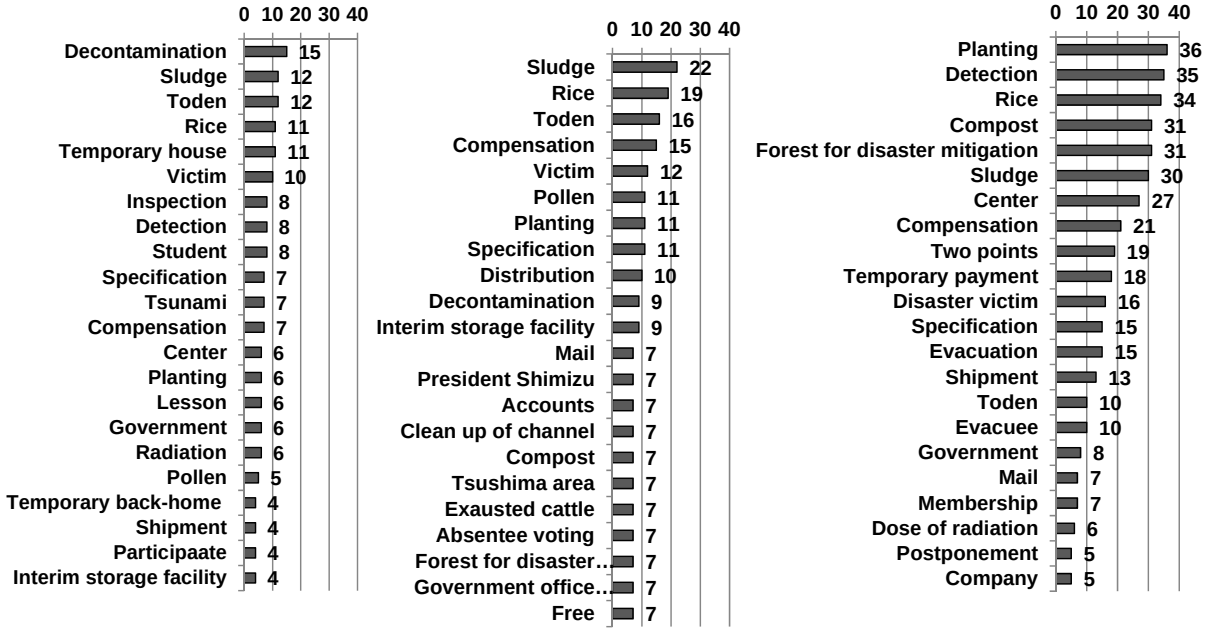


Figure 7 Comparison of items of keywords ranked No.1.



(a) B=3 (b) B=7 (c) B=31

Figure 8 Keywords ranked as No.1 and its frequency

Taking a look at the B=3 cases, frequently used keywords in this emergency period immediately after the quake include “tsunami”, “evacuation”, “disaster victim” and “debris”. “Blanket” was another important word since the earthquake occurred during the winter season and blankets were strongly required by the evacuees. On March 19th, due to worries about the spread of radiation from the nuclear power plant accident, the word “pregnant” was seen for the first time, On March 30th, “temporary home return” was ranked top. This was when the evacuees who had to leave their hometown for fear of radiation were allowed to pay a brief visit home just to bring their valuables.

The B=7 case, which is similar to the B=3 case, covers the time when the earthquake hit. Keywords described as emergency terms such as “tsunami”, “evacuation” and “debris” are seen. On March 16th and 17th, “pregnant” was ranked top indicating the serious concerns of radiation by pregnant women as in the B=7 case. As for B=31, “evacuation” and “refuge” were the most used keywords for some days during emergency period. From March 22nd, “election” was ranked high because the nationwide local elections in April were also another issue of attention.

2. *Effect of different time interval B*: Comparing the short and long time intervals in terms of “B” , we see that top ranked keywords change day by day in B=3 (in which the target time interval days are shorter). On the other hand, some specific keywords, such as “evacuation”, “refugee”, “acceptance” and “election”, tend to be ranked higher in the longer time intervals.

Table 2 Time-history of keywords that ranked as No.1 with its frequency

		B=3		B=7		B=31	
Year	Month	Keyword	Number of No.1	Keyword	Number of No.1	Keyword	Number of No.1
2011	3	Center	3	Last spring	3	Evacuation	15
		Pregrant	2	Student	3	Election	5
		Tsunami	2	Pregrant	2	Postponement	1
	4	Student	3	President Shimizu	7	Disaster victim	12
		Move in	3	Danger	4	Evacuee	5
		Vegetables	2	Move in	4	Request	5
	5	Japan Agreculture	3	Temporary payment	5	Temporary payment	18
		Temporary back-home	3	Toden	5	Government	8
		Temporary payment	3	Japan Agreculture	4	Toden	5
	6	Sludge	3	Sludge	7	Sludge	19
		Temporary house	3	Clean up of channel	7	Company	5
		Clean up of channel	3	Measurement	5	Temporary back-home	2
	7	Specification	4	Specification	9	Specification	15
		Participaate	3	Shipment	4	Shipment	13
		Ratio of adjustment	3	Beef cattle	4	Farmhouse	3
	8	Student	3	Sludge	3	Compensation	11
		Specification	3	Compensation	3	Evacuee	5
		Pension for survivor	2	Announcement	3	Refgue	5
	9	Reconciliation	3	Two points	6	Two points	16
		Prime minister Noda	3	Compensation	5	Compensation	6
		Mediation	3	Guardian	4	Temporary place	4
	10	Rice	3	Rice	7	Forest for disaster mitigation	23
		Landslide	3	Forest for disaster mitigation	7	Two points	3
		Forest for disaster mitigation	3	Interim storage facility	4	Compensation	3
	11	Wild boar	3	Compost	7	Compost	22
		Compost	3	Absentee voting	7	Forest for disaster mitigation	8
		Absentee voting	3	Government office building	7	–	–
	12	Golf course	3	Tsushima area	7	Rice	13
		Sludge	3	Bark	6	Compost	9
		Recycle	3	Membership	6	Membership	7
2012	1	Decontamination	6	Toden	7	Rice	21
		Hanami yama mountain	3	Rice	4	Planting	5
		Government	3	Decontamination	4	Donation	2
	2	Rice	4	Victim	7	Planting	29
		Subsidy for reconstrction	3	Pollen	6	–	–
		Planting	3	Subsidy for reconstrction	5	–	–
	3	Free	3	Accounts	7	Center	27
		Area where is difficult to return	3	Distribution	7	Planting	2
		Distribution	3	Free	7	Iodine	1
	4	Exausted cattle	3	Mail	7	Detection	12
		Mail	3	Exausted cattle	7	Mail	7
		Personnel	3	Pollen	4	Exausted cattle	5
	5	Cherry blossom	3	Sludge	7	Detection	23
		Sludge	3	Yanagisawa	7	Sludge	8
		Subsidy	3	Buying credit	4	–	–

Therefore, as the time interval B becomes longer, the analysis data is used from wide range period along with the smoothing effect.

The characteristics of the duration effect of time interval B can be explained by how many kinds of keywords were ranked No.1 at least once as shown in Figure 7. When observing different time intervals B = 3, 7 and 31 days, fewer keywords have been ranked in the longer time intervals of B. For example, the B=31 case shows only 42 kinds of keywords ranked No.1 while the B=3 case shows as many as 248.

3. *Keywords ranked No.1*: Figure 8 shows the keywords which were ranked No.1, and how many times the keyword has reached the No.1 position. The most frequently ranked as No.1 include: “decontamination” with 15 times for B=3 days, “sludge” with 22 times for B=7 days and “planting” with 36 times for B=31 days. From this result, we see that specific keywords were constantly listed high for the longer B due to the effect of soothing.

Table 2 shows the time-history of keywords that remained No.1 for a month. By reviewing this table, we can observe the timeline of events. Unfortunately, only the top three are shown in this table due to the limitation of paper space even though many keywords remained in the No.1 position for a month. Let us focus on the B=31 case as we look at the top keywords of the months in chronological order. “Evacuation” was the most important keyword in

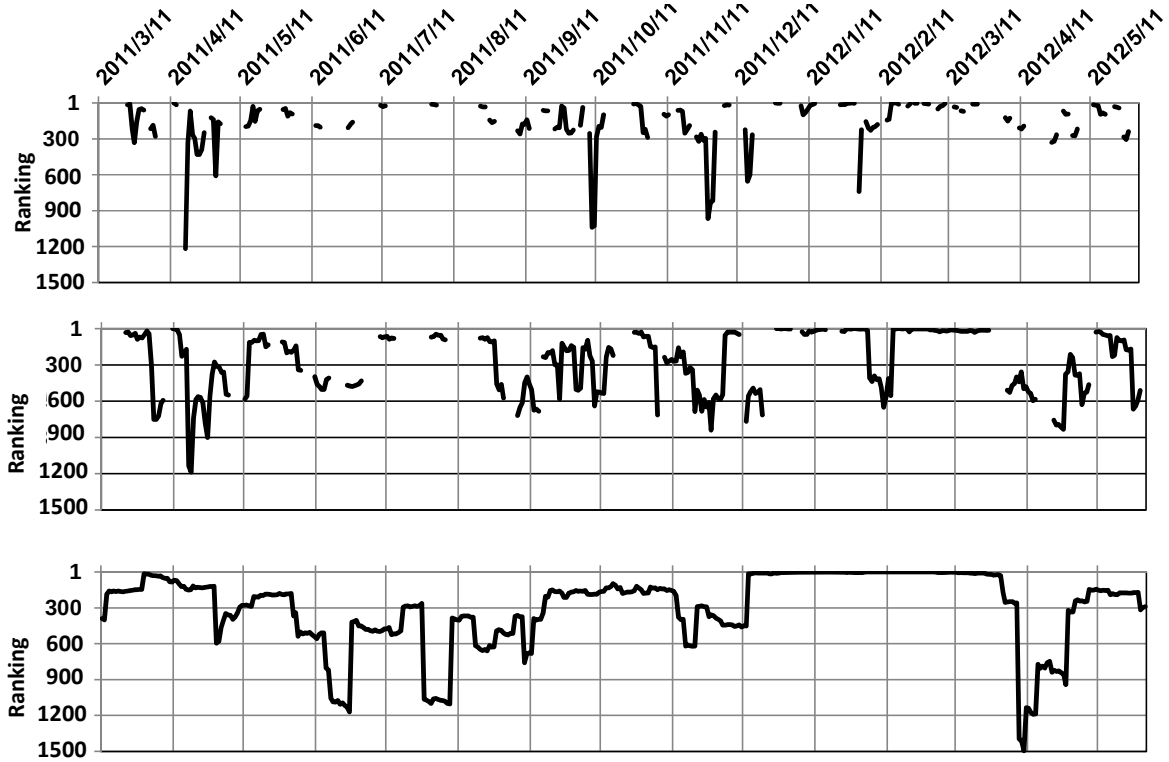


Figure 9 Time history of ranking of "Planting" (Top: B=3, Middle: B=7, Bottom: B=31)

March 2011, followed by "disaster victim" (April), "temporary payment" (May), "sludge" (June), "specification" (July), "compensation" (August), "two points" (September), "forest for disaster mitigation" (October), " compost" (November), "rice" (December). Moving onto 2012, "rice" (January), "planting" (February), "center" (March) and "detection" (April and May). By following the top keywords, we can see the outline and the stream of this complex disaster despite the intertwined problems and difficulties.

4. *Trend of each keyword*: This system also helps us see the trend of specific keywords that a system user might take interest in. Figure 9 shows the time history of the word "planting." The case B=3 shows high discontinuity, while continuity is clearly shown in B=31 due to the soothing effects. From around October 2011, the problems related to "planting" constantly emerge as shown in the B=31 case.

4. KEYWORD TIME CHART DATABASE

All results analyzed by this technique are collected into the database. A keyword, with its time history of weight value, can be easily and quickly searched by category and immediately visualized. The six categories: time, place, actor, society, space and event are prepared by the following WBS (Work Breakdown Structure) methodology. If you are interested in the trend of keywords related to society, the database can show the time history of the related keywords. "Planting" in Figure 9, belonging to the "society" category, suggests that a serious problem lies ahead in growing new rice and other farm products due to the nuclear power plant accident. The transition of ranking positions can also be visualized in graphs and charts.

5. CONCLUSIONS

We have proposed the running spectrum system for analyzing text data in the advanced society that has digital data delivery and storage environment. The news reported by Fukushima Minpo newspaper is used for the verification of the technique. The result shows the dynamic characteristics of the data that change in the time domain. As time goes on, more digital data/information on natural disasters will become available. Then, the proposed technique serves efficient and effective to analyze huge amount of digital information, thus providing appropriate understanding of the events and occurrences in chronological order.

REFERENCES

[1] Meliha Yetisgen-Yildiz, Wanda Pratt. (2009). "A new evaluation methodology for literature-based discovery systems." Journal of Biomedical Informatics, Vol. 42, Issue 4, pp. 633-643.

[2] Fukushima-Minpo Co. "Tohoku earthquake reports", http://www.fukushimaminponews.com/ about.html. [Acceded at 2012.6.28]

10CUEE CONFERENCE PROCEEDINGS
10th International Conference on Urban Earthquake Engineering
March 1-2, 2013, Tokyo Institute of Technology, Tokyo, Japan

THE IMPACT OF THE 2011 TOHOKU TSUNAMI DISASTER AND IMPLICATIONS TO TSUNAMI-RESILIENT COMMUNITY

Shunichi Koshimura[1], Satomi Hayashi[2], and Hideomi Gokon[3]

1) Professor, International Research Institute of Disaster Science, Tohoku University, Japan
2) Graduate student, Graduate School of Engineering, Tohoku University, Japan
3) Graduate student, Graduate School of Engineering, Tohoku University, Japan
koshimura@irides.tohoku.ac.jp, s_hayashi@geoinfo.civil.tohoku.ac.jp, gokon@geoinfo.civil.tohoku.ac.jp

Abstract: A comprehensive study was conducted to identify the impact of the 2011 Tohoku tsunami disaster and to understand the lessons towards the reconstruction of Tohoku to build tsunami-resilient community. Through an integrated investigation by field measurement, remote sensing and numerical modeling approaches with on spatial information sciences, the results lead to an implication for land use management and relocation planning to reconstruct tsunami-resilient coastal communities.

1. INTRODUCTION

On 11 March 2011, a devastating tsunami accompanied with M9.0 earthquake attacked the northern Pacific coast of Japan (Tohoku), and the coastal communities especially in Iwate, Miyagi, and Fukushima Prefectures were totally devastated. The total affected area by the tsunami was reported as 561 km2 along the Pacific coast of Japan (GSI, 2011), and the maximum tsunami run-up height reached up to 40 m in Iwate Prefecture (Mori et al., 2012). As of 27 June, 2012, National Police Agency reported 15,866 dead (4,671 in Iwate, 9,523 in Miyagi, and 1,606 in Fukushima) and 2,946 missing, 130,441 buildings/houses were collapsed or washed-away (National Police Agency, 2012). The economic impacts were estimated as 16 to 25 trillion yen (Cabinet Office, 2011), while FY2011 national budget of Japan was 92 trillion yen (Ministry of Finance Japan, 2011).

Having passed almost two years since the event occurred, the devastated areas have started moving forward to reconstruct their communities. Though the recovery process is still underway, local governments completed the draft of reconstruction plan including infrastructure design, transportation, land use management, urban design, relocation, and economic and industrial outlooks. This paper aims to summarize the impact of the 2011 Tohoku tsunami disaster with particular regard to structural damage, to understand the lessons towards reconstruction of Tohoku region. To identify the tsunami impact, we conducted an integrated studies of field measurement and aerial photo inspection with the approach of spatial information sciences. The findings lead to understandings structural vulnerability against the 2011 tsunami and to provide an implication for land use management and relocation planning to reconstruct resilient coastal communities.

2. MAPPING STRUCTURAL DAMAGE AND VULNERABILITY

2.1 Visual inspection of aerial photos

We conducted an effort of mapping structural damage through visual interpretation of aerial photos to identify the structural vulnerability against the 2011 tsunami. For visual inspection, we used the aerial photo archives of Geospatial Information Authority of Japan acquired in the devastated area (GSI, 2011b). The ortho photos of 80 cm/pixel resolution were composited with mosaic image processing. Combined with the ZENRIN building data (building shape files), the inspection was conducted for each building, by comparing pre- and post-tsunami aerial photos focusing on the existence of houses' roofs to add an attribution of classification "washed-away" or "surviving" as the damage status.

Figure 1 shows an example of the classification in Yuriage, Natori city. The result of mapping of structural damage in Miyagi Prefecture is summarized in Table 1 and the mapping results are on our web site (www.tsunami.civil.tohoku.ac.jp) to be used for field survey, land use management to understand vulnerable areas and reconstruction planning. Combined wit the results of mapping inundation zone, structural damage classification results enable to determine the number of exposed structures, then calculate P_D, as the proportion of the number of structure classified as "washed-away" and the number of exposed structure. Table 1 implies that almost 30 % of the structures in the tsunami inundation zone in Miyagi Prefecture were devastated and high proportion of devastated buildings are concentrated in the northern part of Miyagi Prefecture (Sanriku region). Sanriku coastline is particularly vulnerable to tsunamis, because it has many v-shaped bays that cause tsunami energy to converge and

amplify. In addition, the death ratio, which was obtained as a proportion of the number of death and exposed population, shows the correlation of with P_D.

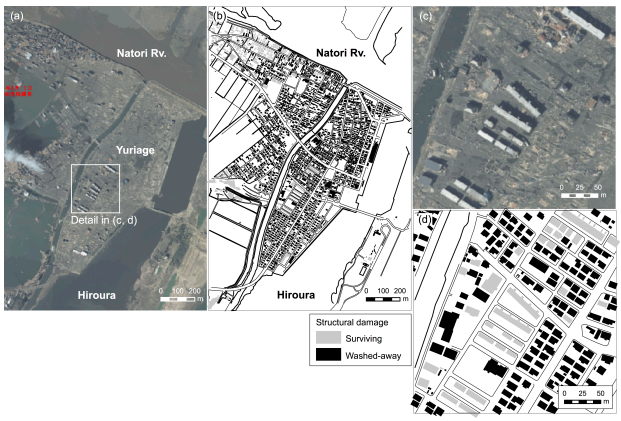


Figure 1 Example of mapping structural damage in Yuriage, Natori city, by inspection of post-event aerial photos.

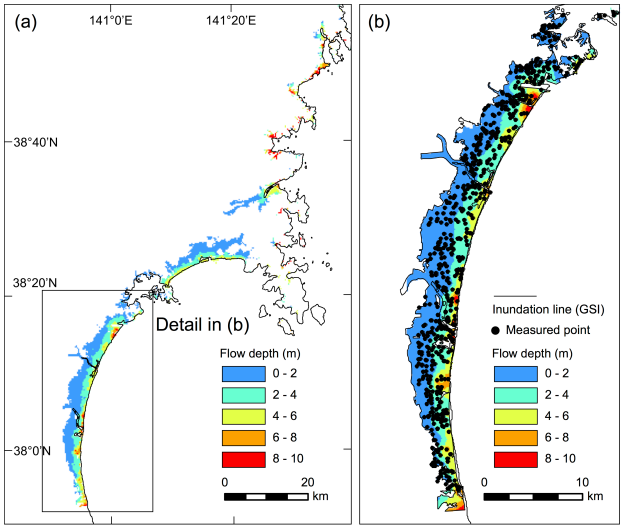


Figure 2 Mapping the tsunami flow depth measured by Miyagi Prefectural government and our survey team (Abe et al, 2011). Black dots indicate the measured points.

2.2 Structural vulnerability and tsunami fragility curves

Integrating structural damage mapping with field survey data, such as flow depths, lead to a new measure of identifying structural vulnerability against tsunami, as a form of tsunami fragility curve or tsunami fragility function. Tsunami fragility curve is defined as the structural damage probability or fatality ratio with particular regard to the hydrodynamic features of tsunami inundation flow, such as flow depth, current velocity and hydrodynamic force (Koshimura et al., 2009a).

Figure 2 shows the spatial distribution of flow depths measured in tsunami inundation zone. Spatial interpolation of measurement data (point data) to obtain raster data is combined with the structural damage mapping (Figure 1). The procedure of developing tsunami fragility curves is as follows.

1. Damage data acquisition: obtaining damage data from aerial photo interpretation.
2. Tsunami hazard estimation: estimating the hydrodynamic features of tsunami by field measurement.
3. Data integration between the damage data and tsunami hazard information: correlating the damage data and the hydrodynamic features of tsunami through the GIS analysis.
4. Calculating damage probability: determining the damage probabilities by counting the number of damaged or survived structures, for each range of flow depths.
5. Regression analysis: developing the fragility curves by regression analysis of discrete sets of damage probability and hydrodynamic features of tsunami.

Taking above procedure, the tsunami fragility curve is preliminary obtained as shown in Figure 3. The fragility curve shown in the figure indicates the damage probabilities of structural destruction equivalent to the flow depth. Structures in Miyagi Prefecture were especially vulnerable when the local flow depth exceeded 2 m, and 6 m flow depth would totally cause total devastation. This fact leads to a lesson to determine the land use plan which considers the effect of coastal protection.

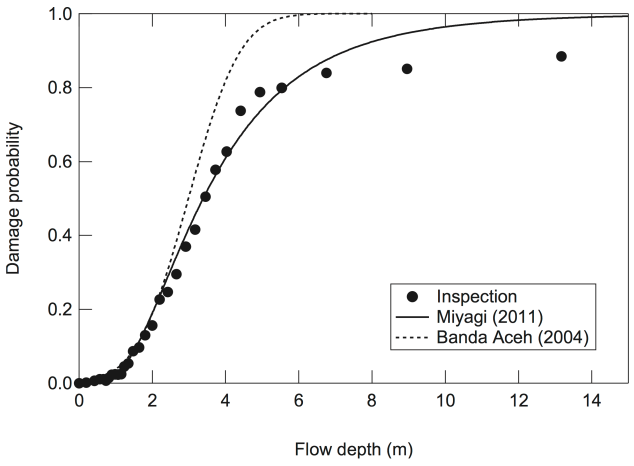


Figure 3 Tsunami fragility curve for structural destruction (washed-away). The solid line is obtained from Miyagi Prefecture (2011 event) and the dashed one is from Banda Aceh, Indonesia (2004 Indian Ocean tsunami).

3. EVALUATION OF RECONSTRUCTION PLAN

In April 2011, one month after the event occurred, the central government established the reconstruction policy council to develop a national recovery and reconstruction outlook for tsunami-resilient community. Besides, the central government decided the policy of coastal protection such as seawalls and break waters, which would be designed to ensure their performance to potential tsunami level of approximately 150 year recurrence interval. In this sense, the government policy of designing coastal protection is for

150-year tsunami level (this is called "Prevention Level") which ensures to protect lives and properties. And for the tsunami level more than 150-year recurrence interval, so-called extreme event, the government calls "Preparedness/Mitigation Level" to reduce the losses and damage by all of the efforts of coastal protection, urban planning, evacuation, and public education.

When the proposed reconstruction plan should be verified, numerical model becomes a powerful tool. Figure 4 shows the result of numerical modeling of the 2011 tsunami inundation in Sendai city (Maximum flow depth) based on the non-linear shallow water theories (Koshimura et al., 2009b). After the event occurred, the authors attempted to understand how the tsunami inundated to the Sendai coast by the tsunami inundation modeling using a 10 m topography grid, with a tsunami source model proposed by the authors. As shown in the figure, the tsunami penetrated more than 5 km inland to have caused devastation on the coast and to be consistent with the observed tsunami inundation extent. After several aspects of validations (Koshimura et al., 2009b) the tsunami numerical models can be used for evaluation of reconstruction plans from the view point of tsunami disaster mitigation.

Under the limitations and uncertain conditions of funding, prefectural and local governments have developed their own recovery and reconstruction plans, which assume 10 years to be completed. These plans consist of the combination of structural prevention/mitigation, urban planning, preparedness, and suggest their land use management, relocation, housing reconstruction and tsunami disaster mitigation plans. The key role of academia, in engineering point of view, is to verify and evaluate if these plans really work for future disaster reduction. For instance, based on the findings regarding the structural vulnerability (see Figure 3), Sendai city determined a reconstruction plan (Sendai city, 2011) to reduce the tsunami flow depth less than 2 m in the populated area with a conceptual image of multiple coastal protection (Figure 5). A significant feature of the Sendai city's reconstruction plan is integrating several coastal protection facilities such as seawalls, coastal forests, park (artificial hill) and elevated roads to minimize the potential losses. Figure 6 indicates the plan view of the multiple protection of Sendai city with a 7.2 m seawall and river dike and 6 m elevated prefectural road.

The authors conducted a tsunami numerical modeling under the 2001 tsunami source scenario, by incorporating the reconstruction plan, to evaluate how these protections will work in terms of tsunami reduction. Figure 7 shows one example from preliminary results. As indicated in the figure, we found that the multiple protection will contribute on substantial reduction of the tsunami inundation zone, and flow depth on Sendai plain especially at the western side of 6 m elevated prefectural road. Using this result, Sendai city determined the land used plan and the area of housing reconstruction and relocation. However, note that the tsunami (the 2011 scenario) will overtop even 7.2 m seawall and the 6 m elevated road. Here, the model assumes no destruction of structures. In this sense, the model cannot reproduce all the aspects of tsunami inland penetration. Coastal infrastructure such as breakwaters and seawalls cannot always protect life and property. Seawalls or coastal structures should be designed with the assumption of overtopping and resiliency, and communities should not rely on coastal infrastructures alone for protection.

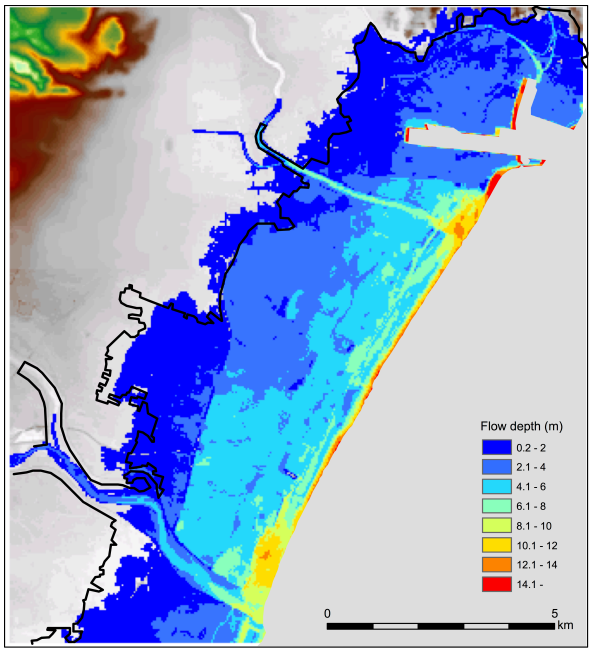


Figure 4 The result of numerical modeling of the 2011 tsunami inundation in Sendai city (Maximum flow depth). Black solid line is the tsunami inundation extent obtained by GSI (GSI, 2011b).

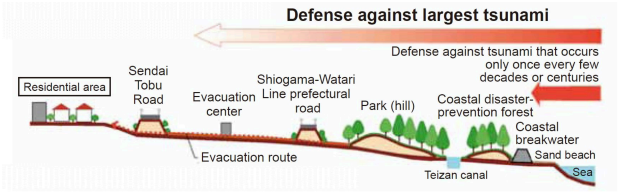


Figure 5 Conceptual image of tsunami-prevention facilities in Sendai city (Sendai city, 2011).

4. SUMMARY

Throughout the comprehensive studies based on the remote sensing, numerical models and spatial information sciences, the authors summarized the impact of the 2011 Tohoku earthquake tsunami disaster and discussed the lessons towards the reconstruction of Tohoku region. The 2011 event offers valuable lessons that should be applied, in order to build safer and more resilient coastal communities.

As observed in the devastated areas in Miyagi Prefecture, the tsunami flow depth over 2 m has potential to severely damage houses, and more than 6 m flow depth will cause total devastation. This finding can inform land use planning (zoning) or one goal of comprehensive tsunami disaster mitigation, so that residential areas will not be inundated more than 2m.

Since the 1896 Meiji Sanriku earthquake tsunami that killed 22,000 people, the 1933 Showa earthquake tsunami and since the more recent 1960 Chilean earthquake tsunami, Tohoku region has developed the coastal protection infrastructure of seawalls and breakwaters that have never been devastated throughout the history since 1934. Again, we need to note that coastal infrastructure cannot always protect life and property: even great seawalls may fail. Seawalls should be designed with the assumption of overtopping and resiliency, and communities should not rely on coastal infrastructures alone for protection.

Acknowledgements:

This research was funded by the IRIDeS grant (A-3) and the Grant-in-Aid for Scientific Research (Project Numbers : 24241059, 24651195 and 22681025) from the Ministry of Education, Culture, Sports, Science and Technology (MEXT) of Japan.

References:

Geospatial Information Authority of Japan (GSI) (2011a) , <http://www.gsi.go.jp/>

Mori, N., T. Takahashi and the 2011 Tohoku Earthquake Tsunami Joint Survey Group (2012), Nationwide post event survey and analysis of the 2011 Tohoku earthquake tsunami, Coastal Engineering Journal, Vol. 54, No. 1, 125001, doi: 10.1142/S0578563412500015.

National Police Agency (2012), Report of the damage caused by the 2011 Tohoku earthquake and tsunami (in Japanese), <http://www.npa.go.jp/archive/keibi/biki/higaijokyo.pdf>

Cabinet Office (2011), <http://www.bousai.go.jp/oshirase/h23/110624-1kisya.pdf>

Ministry of Finance Japan (2011), <http://www.mof.go.jp/english/budget/budget/fy2012/e20111224b.pdf>

Ministry of Land, Infrastructure, Transport and Tourism (2011), <http://www.mlit.go.jp/common/000138154.pdf>

Abe, I. et al. (2011), High resolution survey results for the inundation limit and height of the 2011 Tohoku earthquake tsunami, Abstract of Japan Geoscience Union Meeting 2011,MIS036-P120, <http://www2.jpgu.org/meeting/2011/yokou/MIS036-P120.pdf>.

Geospatial Information Authority of Japan (GSI) (2011b), aerial photo archives, <http://portal.cyberjapan.jp/denshi/index3_tohoku.html>.

Gokon, H. and S. Koshimura (2012), Mapping of building damage of the 2011 Tohoku earthquake tsunami in Miyagi Prefecture, Coastal Engineering Journal, Vol. 54, No. 1, 125006-1-12, doi: 10.1142/S0578563412500064.

Koshimura, S., Y. Namegaya and H. Yanagisawa, Tsunami Fragility, A new measure to assess tsunami damage, Journal of Disaster Research, Vol. 4, No. 6, pp.479-488, 2009.

Chock, G., I. Robertson, D. Kriebel, M. Francis, I. Nistor, Tohoku Japan Tsunami of March 11, 2011 Performance of Structures, ASCE/SEI Tohoku Tsunami Reconnaissance Report, 2012.

Koshimura, S., T. Oie, H. Yanagisawa and F. Imamura (2009), Developing fragility functions for tsunami damage estimation using numerical model and post--tsunami data from Banda Aceh, Indonesia, Coastal Engineering Journal, No.3, pp.243-273.

Sendai city (2011), Sendai City Earthquake Disaster Reconstruction Plan, Digest Version, 12 p.

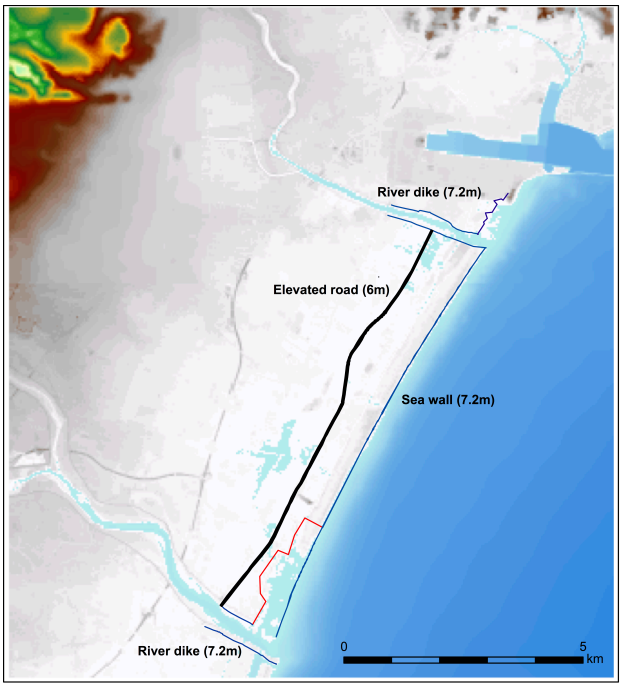


Figure 6 Setting of tsunami prevention facilities in Sendai city reconstruction plan.

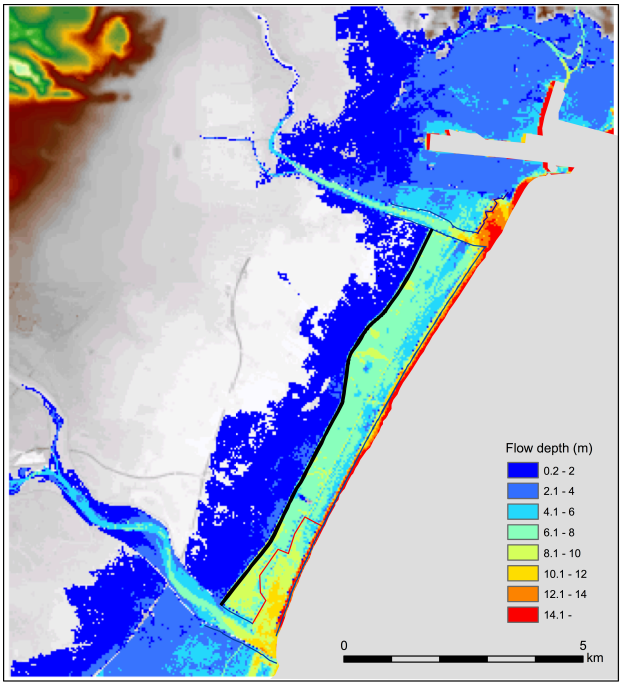


Figure 7 Preliminary result of tsunami numerical modeling to evaluate the effect of the proposed reconstruction plan in Sendai city (Maximum flow depth).

10CUEE CONFERENCE PROCEEDINGS
10th International Conference on Urban Earthquake Engineering
March 1-2, 2013, Tokyo Institute of Technology, Tokyo, Japan

COMPARISON OF SEVERAL COMMON TRANSFER FUNCTIONS FOR SITE EFFECT STUDY IN TAIPEI BASIN

Jyun-Yan Huang[1], Kuo-Liang Wen[2),3)], Chun-Te Chen[1)], Shuen-Chiang Chang[1)], and Hsien-Jen Chiang[4)]

1) PHD candidate, Department of Earth Science, National Central University, Taiwan
2) Professor, Department of Earth Science, National Central University, Taiwan
3) Division Head, National Center for Research on Earthquake Engineering, Taiwan
4) Post-Doc, Department of Earth Science, National Central University, Taiwan

Abstract: Detailed shallow velocity structure was very important for site effect study. One of the most accurate but expansive ways was P-S logging measurement from boreholes which could give us not only Vs30 to classify site class but also detailed velocity structure including P and S wave (Kuo et al. 2012). However, this technique was usually hard to widely obtain due to economy consideration for construct large amount of high cost boreholes. Otherwise, free field strong motion stations were much more densely than boreholes in Taiwan that give some chance to calculate transfer functions in many ways. From mid-later of 20th century, transfer function from spectral ratio method between rock and soil site started to consider site effect. Microtremor (Nakamura 1989) and earthquake H/V spectral ratio (Lermo and Chávez-García 1993) as a transfer function than became popular on late 20th century. Wen and Huang (2012) constructed a dense microtremor survey in whole Taiwan except mountain region which possible could apply to this objective. In this study, the characteristic comparison of above three methods was made to discuss the spectrum difference in many cases in Taipei basin.

1. INTRODUCTION

Taipei basin is one of the most important regions in Taiwan, over two million people lives in Taipei city which was the capital of Taiwan. Strongly site effect occurred in here due to deeply sedimentary basin environment which could induce highly seismic risk during large earthquake. For instance 1999 Chi-Chi, Taiwan and 2002 March 31 earthquake caused some disasters in Taipei basin which hypocenter distance was about 100 km far. Ground motion was enlarged and peak motion was higher than closer hypocenter distance region such as Taoyuan County from site amplification effect. Directly underneath earthquake below Taipei basin also been taken seriously recent year since Sanchiao fault was redefined as a secondary activity fault (Lin et al. 2007).

Traditionally attenuation equation was widely used to predict peak ground motion including acceleration (PGA), velocity (PGV), Fourier amplitude spectrum (FAS), acceleration response spectra (SA), velocity response spectra (SV) and displacement response spectra (SD) etc. for engineering purposes. Seismologists tried hard to provide fully time history from simulation technique that attenuation equation can't afford it. But peak motion was usually in high frequency band (>1 Hz) that need detailed shallow velocity structure to obtain.

One convenient wide frequency simulation tool call stochastic method (Beresnev and Atkinson 1998, Motazedian and Atkinson 2005, Boore 2009) can provide acceptable high frequency (up to 10 Hz) behavior for rock sites. Precisely frequency spectrum could be obtained if the accurate transfer function was considered.

One of the most accurate but expansive ways to derive shallow velocity structure was from P-S logging measurement from boreholes which could give us not only Vs30 to classify site class but also detailed velocity structure including P and S wave (Kuo et al. 2012). There were totally 68 strong motion stations been measured with about 5-10 km interval in Taipei basin (Figure 1).

Taiwan Strong Motion Instrumentation Program (TSMIP) had operated 119 strong motion stations since 1991 and collected several hundred earthquakes in Taipei region. The plentiful earthquake database could help to understand site effect in the basin. In mid-later of 20th century, spectral ratio between horizontal spectrum in soil site and reference rock site (hereafter denoted as H/H ratio) started to estimate site response (Borcherdt 1970). However, good reference rock site was not easy to find in many regions. Microtremor H/V (Nakamura 1989) and earthquake H/V spectral ratio method (Lermo and Chávez-García 1993) than become popular. Dense microtremor survey was completed with 589 measure points and 0.5 km interval in whole Taipei basin (Wen and Huang 2012) which provide detailed site information for whole basin.

In this study, spectrum difference between H/H, H/V, microtremor H/V and from Stochastic Method Simulation (SMSIM) was identified in order to apply these transfer functions to wide frequency simulation technique. Precisely shake map prediction and frequency behavior even full time history could be provided in the future.

2. METHODS AND DATA PROCESSING

2.1 Database

Seismic data used in this study were recorded at strong motion stations in Taipei basin of TSMIP from January, 1991 to December, 2009. Magnitude collect here was less than Mw 6.0 (3.65-5.98, total number of earthquakes: 333) to deal with simple source condition. Hypocenter distance from 14 to 309 km. Earthquake hypocenter most located eastern Taiwan and some 1999 Chi-Chi aftershock in central Taiwan (Figure 2).

2.2 H/H Spectral Ratio Method

Earthquake response could divided into source, path and site effect. The equation could express as follows:

$$\mathrm{R(f)} = S_0(f) \times P(f) \times S_i(f) \tag{1}$$

which R(f) was frequency spectrum of strong motion record, S_0(f) means source, P(f) means path and S_i(f) means site effect. When there were two closer stations with different site condition (i.e. rock and soil) and which were far from the hypocenter during earthquake. Source and path effect were almost the same and could eliminate to understand site effect:

$$\frac{R_s(f)}{R_r(f)} \approx \frac{S_{is}(f)}{S_{ir}(f)} \tag{2}$$

Rs means frequency spectrum of soil site and Rr means reference rock site.

Finely reference rock site was hard to obtain due to outcrop surface station usually accompany with thin regolith layer which could induce some amplification in different frequency band. Another problem was even large amount earthquake occurred but rock site usually hard to trigger than induce lack of data to analyze.

2.3 H/V Spectral Ratio Method

Spectral ratio from single station was developed through microtremor measurement in down-hole seismometer (Nakamura 1989). Vertical amplification motion A_s(f) was treated as a part of source effect and needed to eliminate from site consideration.

$$A_S(f) = \frac{S_V(f)}{B_V(f)} \tag{3}$$

where S_v was vertical spectrum of surface soil site and B_v was borehole rock site. Traditional H/H ratio S_E(f) could describe as:

$$S_E(f) = \frac{S_H(f)}{B_H(f)} \tag{4}$$

where S_H showed horizontal spectrum of surface soil site and B_H showed reference rock site. Divided Eq. (3) to (4):

$$S_M(f) = \frac{S_E(f)}{A_S(f)} = \frac{\frac{S_H(f)}{B_H(f)}}{\frac{S_V(f)}{B_V(f)}} = \frac{\frac{S_H(f)}{S_V(f)}}{\frac{B_H(f)}{B_V(f)}} \tag{5}$$

Nakarura (1989) found $\frac{B_H(f)}{B_V(f)}$ will within unity and simplify Eq. (5):

$$S_M(f) \approx \frac{S_H(f)}{S_V(f)} \tag{6}$$

which means site effect could find from microtremor data of single surface station.

Lermo and Chávez-García (1993) stretched H/V technique to shear wave part of seismogram in Mexico and prove the spectrum was consistent with H/H ratio.

2.4 Transfer Function From Stochastic Method Simulation (SMSIM)

Stochastic modeling technique first assumed the average spectrum of each part of seismogram will follow ω^2 model (Boore 1983). For acceleration spectrum A(ω) of rock site (didn't consider site effect):

$$A(\omega) = 2\omega^2 S(\omega) P(\omega) e^{-\omega R/2QB} \tag{7}$$

where ω: angular frequency, S: source spectrum which followed Brune (1970), P: path attenuation spectrum, R: hypocenter distance, Q: quality factor.

Stochastic modeling technique was developed including two different source type (point source and finite-fault) to deal with simple and complex source problem. In this study, point source approach was used to consider site effect in Taipei basin using small earthquake (Mw<6.0).

2.5 Data Processing

Strong motion records in Taipei basin were firstly eliminated higher peak ground acceleration (PGA) that only keeps PGA less equal to 60 gal in our database to avoid possible non-linear site response (Wen et al. 2006) in transfer function calculation. Magnitudes of earthquakes were set an upper bound Mw6.0 for transfer function calculated from SMSIM.

Shear wave part of acceleration records of each site was cut through a window function which window length set on 10.24 sec. for H/H, H/V and SMSIM transfer function in this study. Five percent cosine taper was obtained in front and

final portion for window function to avoid frequency leakage from truncation of time history. Afterward, cut window of S wave portion was transformed to frequency domain and applied five times smoothing for whole frequency content. North-south and East-west component were root-mean-squared (RMS) to obtain horizontal spectrum. Finally, horizontal spectrum from soil site divided to spectrum from rock give us H/H ratio and horizontal divided to vertical spectrum obtain H/V ratio (see flow-chart in Figure 3). Station TAP071 was selected to be reference rock site for H/H ratio due to the average H/V ratio was flat (Figure 4), site class was B (velocity of top 30 meter, VS30 was 831 m/s) and located on the edge of basin which could represent outcrop of Taipei basin.

Figure 5 was flow chart of constructed transfer function of SMSIM and parameter show in table 1. Average motion of 11 rock site (site class B) for SMSIM were calculated first (black bold dash line in Figure 6) and treated it as reference rock site for calculating basin response. Afterward, transfer function from each single strong motion (soil site) was computed, general transfer function for each site class could find from averaging all the transfer function from stations with same site classification (Figure 6). Detailed of constructed transfer function of SMSIM and the application could find from Wen et al. (2013).

Microtremor H/V ratio was collected from Wen and Huang (2012), measure points which was close to strong motion stations was selected to be comparison in this study.

3. RESULTS AND DISCUSSIONS

3.1 Comparison of Four Kinds of Transfer Functions

Four kinds of transfer functions were compared for totally 65 strong motion stations in Taipei basin. Figure 7 showed the examples for different site condition. The frequency with highest ratio was selected as dominant frequency for each spectrum (circles in Figure 7). Degree of Spectrum Difference (DSPD) was assumed to quantitatively describe difference between each spectral ratios, the equation was as followed:

$$DSPD = \sum_{0.2}^{10} \left(\left| \log_{10} \left(\frac{SP_1}{SP_2} \right) \right| * df \right) \qquad (8)$$

where SP_1 and SP_2 means two spectrum whom been compared (Denoted on Figure 7, four pairs of DSPD were calculated including earthquake H/V vs. microtremor H/V; earthquake H/H vs. H/V; earthquake H/H vs. microtremor H/V and H/H vs. SMSIM). df was sampling frequency. DSPD value could explain area between two spectral ratios on the figure. For these example stations, dominant frequencies and whole trend were similar from four kinds of method but amplification ratio had some difference especially compared to H/H ratio. The amplitude of H/H ratio usually small then the others seems due to spectrum of reference rick site TAP071 were not flat enough and values not close to 1 (Figure 4). But good reference rock site was hard to obtain confined with geology distribution in Taipei basin. Maybe H/H ratio was not easy to obtain in this region. Otherwise, Earthquake H/V had a good agreement with microtremor H/V in this study (with average 1.81 DSPD for all stations, Table 2), which means microtremor H/V mad good ability to explain site response and could applied in some location didn't have strong motion stations or didn't have enough seismic records. Simultaneously, due to the processing of transfer function of SMSIM was similar with H/H ratio, their value of DSPD were rather small (with average 1.74 DSPD for all stations, Table 2).

3.2 Space Difference of DSPD in Taipei Basin

Spectrum difference was larger between H/H, H/V and H/H, Micro H/V especially in site class B and C (Table 2). Distribution of spectrum difference in space was considered in this section (Figure 8). Large value of DSPD of H/H vs. H/V spread on the edge of basin, usually occurred in site class B and C. This might due to H/V ratio could still response some thin layer which amplified spectrum but these layer had similar response in two rock site induced small amplification show in H/H ratio (Figure 8 (a)). Meanwhile, there's seems no space difference between H/H, microtremor H/V (Figure 8 (b)) and between H/V, microtremor H/V (Figure 8 (d)). Otherwise, obvious space difference between H/H and SMSIM and appear a south-east north-west direction related to reference rock site TAP071 (Figure 8 (c)). Since average response in B class was used as denominator for transfer function of SMSIM which should assume no difference in space. This might suggest distance between soil site and reference rock site in north-west Taipei basin should be corrected in the future to makes the H/H ratio more consistence in whole region.

3.3 Average Transfer Function for Different Site Class in Taipei Basin

Site response in Taipei basin showed different phenomenon in stiff sediment (B and C class) and soft sediment (D and E class) stations between these four kinds of transfer function (Figure 7). H/H ratio had obvious difference with H/V and microtremor H/V in whole frequency band of stiff site and difference mainly occur in low frequency band for soft soil site. In order to classified these difference more precisely, unity DSPD was considered to check spectrum difference in high and low frequency band, equation described as followed:

$$\overline{DSPD} = DSPD / f_band \qquad (9)$$

where f_band means frequency band of summation in DSPD calculations. 3 Hz was used here to divide high and low frequency band for averaging spectrum for different site class (Figure 9). For stiff site, spectrum difference was close in low and high frequency band for each transfer functions. Unity DSPD showed decrease trend from low to high frequency for C and D class.

Finally, H/H, H/V and microtremor H/V showed some

difference between each other and different with transfer function from SMSIM. It suggests no matter which kind of transfer function was applied to simulation technique the systematic difference should be considered to get accurately frequency behavior.

4. CONCLUSIONS

Four kinds of transfer function was discussed in Taipei basin in this study included H/H, H/V, microtremor H/V and from SMSIM. All these transfer function showed some difference in amplitude with H/H ratio which might due to reference rock site was not easy to obtain in this region. Meanwhile, microtremor H/V showed a good agreement with H/V ratio in different site class with average DSPD 1.81 (Table 2, Figure 7, 9). It could be widely applied to different location which didn't have strong motion station or enough seismic record.

Otherwise, spectrum difference was not clear for microtremor H/V and H/H, H/V ratio in space distribution. But H/V ratio showed some variance in edge of the basin might relate to some thin layers amplified frequency domain. Finally, when simulation technique tried to apply site correction from these transfer functions the systematic difference should be considered first. The precisely high frequency simulation might be more easier obtain in the future.

Acknowledgements:

This study was supported by the National Science Council under grant numbers NSC-100-2116-M-008-023 and NSC-101-2116-M-008-023.

References:

Beresnev, I.A. and Atkinson, G.M. (1998), "FINSIM---a FORTRAN Program for Simulating Stochastic Acceleration Time Histories from Finite Faults," *Seism. Res. Lett.*, **69**(1), 27-32.

Boore, D.M. (1983), "Stochastic Simulation of High-Frequency Ground Motions Based on Seismological Models of the Radiated Spectra," *Bull. Seism. Soc. Am.,* **73**, 1865-1894.

Boore, D.M. (2009), "Comparing Stochastic Point-Source and Finite-Source Ground-Motion Simulations: SMSIM and EXSIM," *Bull. Seism. Soc. Am.*, **99**(6), 3202-3216.

Borcherdt, R.D. (1970), "Effects of Local Geology on Ground Motion Near San Francisco Bay," *Bull. Seism. Soc. Am.*, **60**, 29-61.

Brune, J. N. (1970), "Tectonic Stress and the Spectra of Seismic Shear Waves from Earthquakes," *J. Geophys. Res.,* **75**, 4997-5009.

Cheng, S.N., Wang, Z.B., L., Z.W. and Chiang, C.H. (2010), "Constructed Seismic Catalog in Taiwan Region (II)," *Technique report of Central Weather Bureau*, **57**, 483-502. (in Chinese)

D' Amico, S., Akinci, A. and Malagnini, L. (2012), "Predictions of High-frequency Ground-motion in Taiwan Based on Weak Motion Data," *Geophys. J. Int.*, **189**, 611-628.

Kuo, C.H., Wen, K.L., Hsieh, H.H., Lin, C.M., Chang, T.M. and Kuo, K.W. (2012), " Site Classification and Vs30 Estimation of Free-Field TSMIP Stations Using the Logging Data of EGDT," *Engineering Geology*, **129-130**, 68-75.

Lermo, J. and Chávez-García, F. J. (1993), "Site Effect Evaluation Using Spectral Ratios with Only One Station," *Bull. Seism. Soc. Am.*, **83**, 1574-1594.

Lin, C.W., Lu, S.T., Shih, T.S., Chen, Z.Y. and Lin, Y.H. (2007), "Activity Fault of Northern Taiwan," *Special Publication of the Central Geological Survey*, **19**, pp127. (in Chinese)

Motazedian, D. and Atkinson, G.M. (2005), "Stochastic Finite-Fault Modeling Based on a Dynamic Corner Frequency," *Bull. Seismol. Soc. Am.*, **95**, 995-1010.

Nakamura, Y. (1989), "A Method for Dynamic Characteristies Estimation of Subsurface Using Microtremor on the Ground Surface," *QR of RTRI*, **30**(1), 25-33.

Wen, K.L., Chang, T.M., Lin, C.M. and Chiang, H.J. (2006), "Identification of Nonlinear Site Response Using the H/V Spectral Ratio Method," *Terr. Atmos. Ocean. Sci.*, **17**(3), 533-546.

Wen, K.L. and Huang, J.Y. (2012), "Dense Microtremor Survey for Site Effect Study in Taiwan," 15th World Conference of Earthquake Engineering, 24-28 September, Lisbon, WCEE2012_1682.

Wen, K.L., Huang, J.Y. and Chen, C.T. (2013), "Empirical Site Correction For Ground Motion Simulation," 10CUEE Conference Proceedings, 10th International Conference on Urban Earthquake Engineering, March 1-2, Tokyo Institute of Technology, Tokyo, Japan. 01-317.

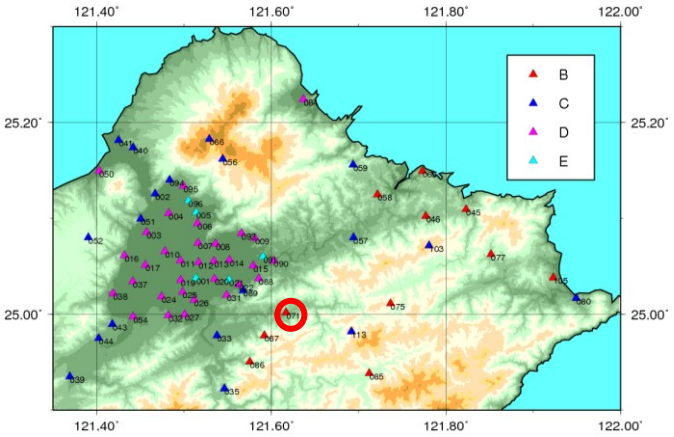


Figure 1 Distribution of Strong Motion Station in Taipei Basin. Color of Triangles Represents Different Site Class from Engineering Geological Database for TSMIP (EGDT, http://egdt.ncree.org.tw/) Database. Numbers Are Station Code, i.e. 001 Means TAP001. Circle Denote Reference Rock Site TAP071.

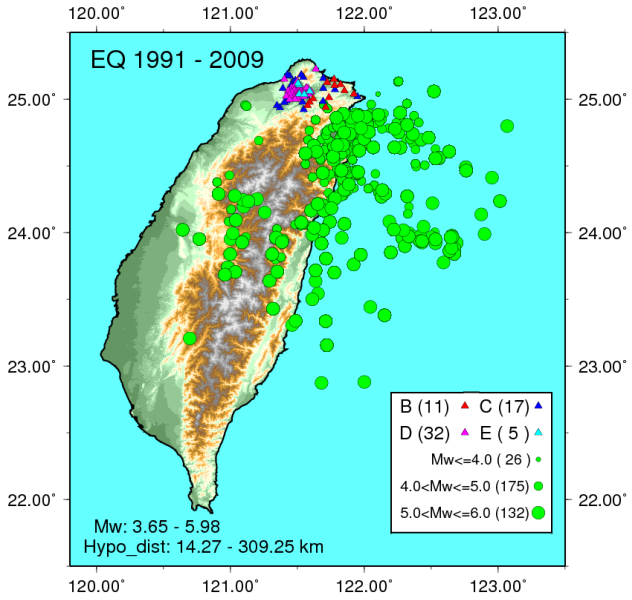


Figure 2 Earthquake Used in This Study, Number in Legend Denote Number of Stations and Earthquake with Different Site Class and Magnitude.

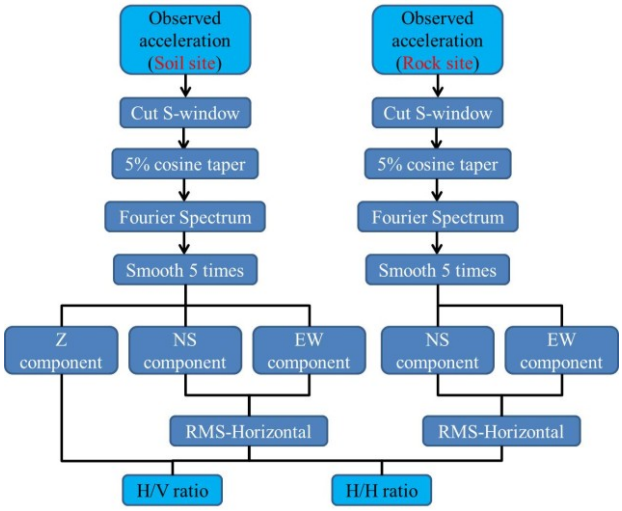


Figure 3 Flow-chart of Data Processing of H/H and H/V Ratio in This Study.

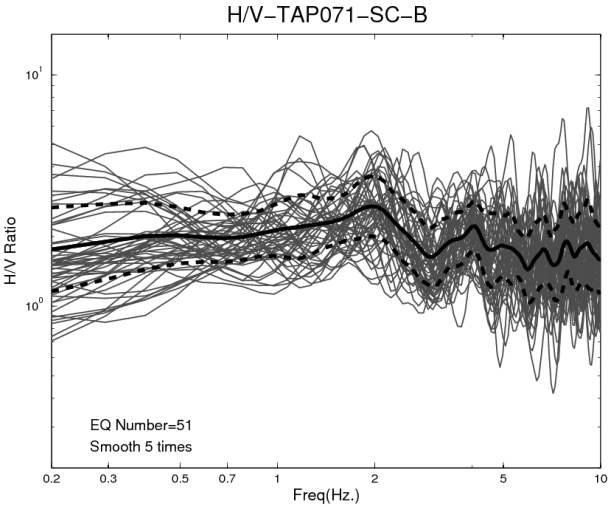


Figure 4 Average H/V Spectral Ratio of Reference Rock Site TAP071.

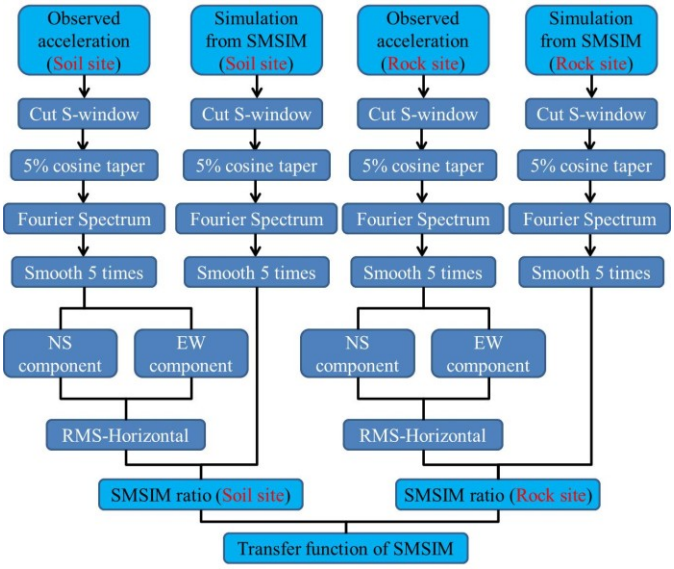


Figure 5 Flow-chart of Data Processing of Transfer Function from SMSIM Calculation in This Study.

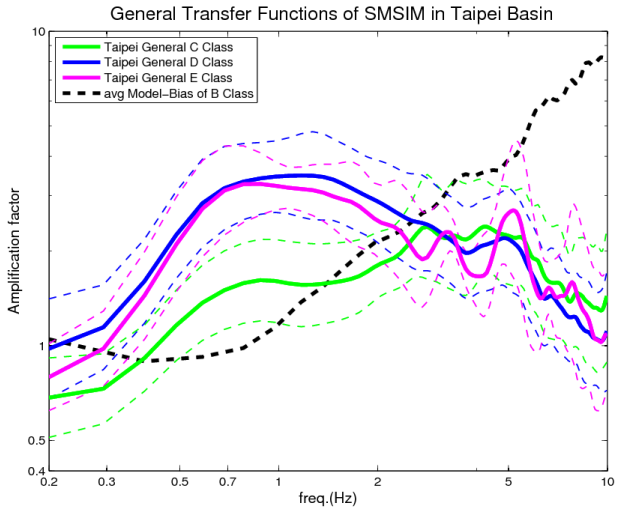


Figure 6 General Transfer Function from SMSIM in Taipei Basin.

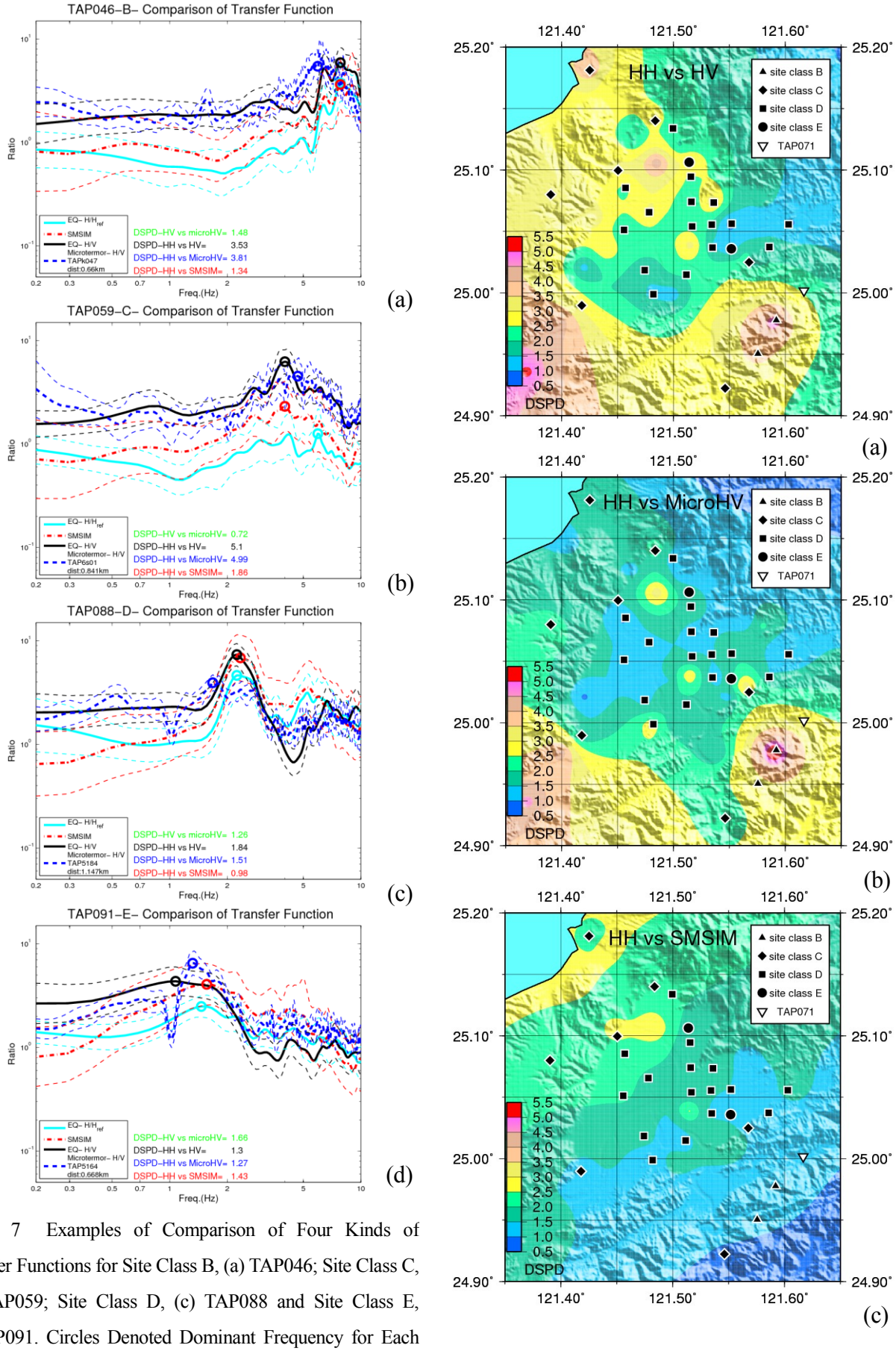
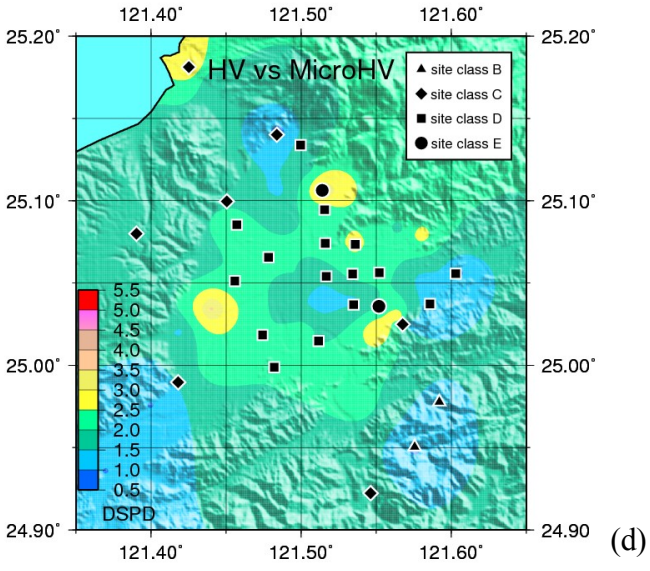
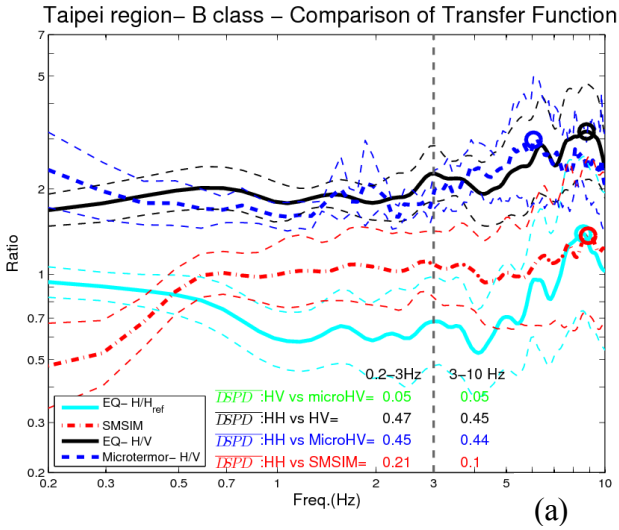


Figure 7 Examples of Comparison of Four Kinds of Transfer Functions for Site Class B, (a) TAP046; Site Class C, (b) TAP059; Site Class D, (c) TAP088 and Site Class E, (d)TAP091. Circles Denoted Dominant Frequency for Each Site.

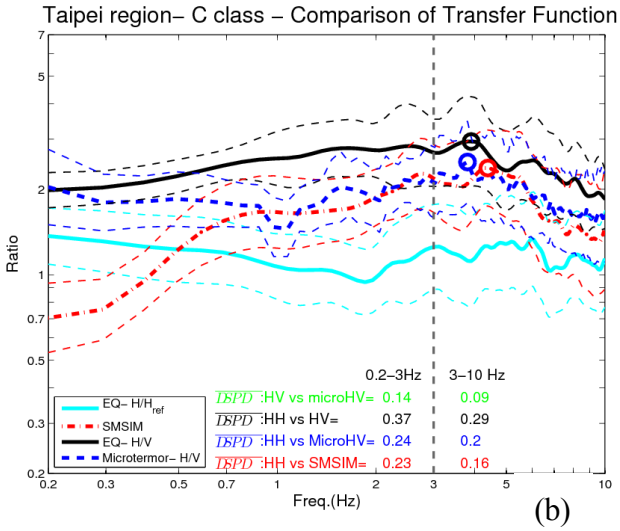


(d)

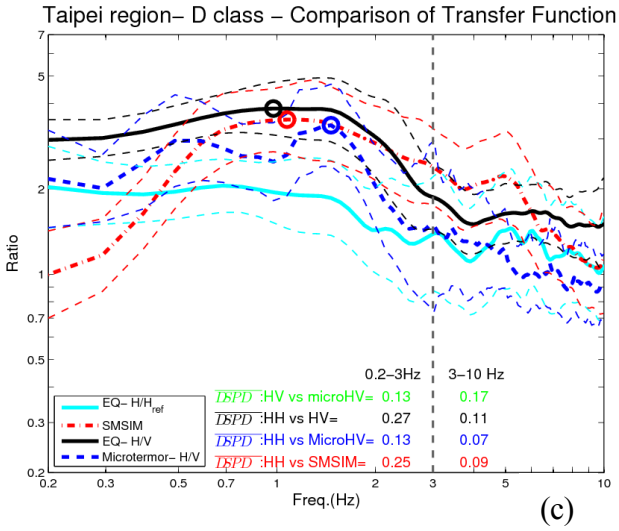
Figure 8 DSPD Difference in Space of Taipei Basin. (a) HH vs. HV, (b)HH vs. MicroHV, (c) HH vs. SMSIM and (d) HV vs. MicroHV.



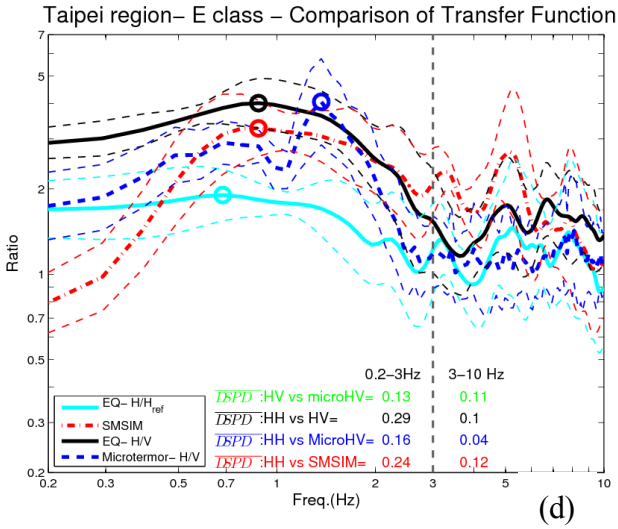
(a)



(b)



(c)



(d)

Figure 9 Average Spectrum for Four Kinds of Transfer Function in Taipei Basin. (a) Site Class B, (b) Site Class C, (c) Site Class D, (d) Site Class E.

Table 1 Parameters Use in SMSIM, Follows D'Amico et al. 2012. Magnitude Transform Equation for Small Earthquake Follows Cheng et al. 2010.

Shear-wave velocity (VS)	3.2 km/s
Density (ρ)	2.8gm/cm^3
Geometric spreading R^b: b	-1.2 (1–10 km) -0.7(10–40 km) -1.0(40-80 km) -0.5(>80 km)
Quality factor	$350f^{0.32}$
path duration	default
κ (kappa)	0.05 sec.
M_W	ML=1.961Mw+0.338+-0.256 , ML<=6.0; ML=5.115*(ln(Mw))-3.131+-0.379 , ML>=5.5 (Cheng et al., 2010)
Stress (bar)	30 , Mw<4.5; 50 , 4.5<=Mw<5.5; 70 , 5.5<=Mw<6.5; 80 , 6.5<=Mw<7.6;

Table 2 Average DSPD for Different Site Class for Four Kinds of Spectrum Pairs in This Study.

	HHvsHV	HHvsMicroHV	HHvsSM	HVvsMicroHV
B avg	5.00	4.91	1.53	1.19
C avg	3.33	2.60	1.87	1.51
D avg	2.10	1.64	1.69	2.03
E avg	2.18	1.84	1.84	2.02
all avg	2.73	2.25	1.74	1.81

10CUEE CONFERENCE PROCEEDINGS
10th International Conference on Urban Earthquake Engineering
March 1-2, 2013, Tokyo Institute of Technology, Tokyo, Japan

A SITE-SPECIFIC SEISMOLOGICAL MODEL WITHIN A BAYESIAN UPDATING FRAMEWORK

Alin Radu[1)], Mircea Grigoriu[2)]

1) PhD Student, School of Civil and Environmental Engineering, Cornell University, Ithaca, NY
2) Professor, School of Civil and Environmental Engineering, Cornell University, Ithaca, NY
acr99@cornell.edu, mdg12@cornell.edu

Abstract: Fragility analyses constitute the essential ingredients in performance-based seismic design of structures. To construct accurate seismic fragilities, a large number of ground-acceleration records capable to describe site seismicity is required. Since the number of site records is rather small, this number is augmented by, e.g. scaling real or artificial records. This approach provides limited information on structural performance since scaling does not change frequency content. Probabilistic models for the seismic ground acceleration process are usually calibrated to regional data so that they cannot provide detailed information on site seismicity.

It is proposed to combine the information provided by a seismological model with the site records within a Bayesian framework. The resulting model allows the simulation of an arbitrary number of ground motions that are consistent with all available information on seismic hazard at a site. The posterior model delivers spectral densities for seismic ground-acceleration processes at arbitrary sites as a function of earthquake magnitude and source-to-site distance. For illustration, a posterior model for the seismic hazard is constructed based on site ground-motion records.

1. INTRODUCTION

Earthquake hazards may have a catastrophic impact on human lives, environment and economy. Performance-based seismic design provides a balance between safety, functionality and life-time costs of structural systems. Seismic fragilities are response-based analyses which represent the probabilities of reaching a critical state under given characteristics of the ground motion. A large number of ground motions is required for their computation. Generally, the number of ground-motion records is insufficient to characterize the seismicity at a site which is vital for assessing seismic performance of structures. In practice, scaled versions of site records are used to calculate fragility curves as a function of selected intensity measures. Resulting fragilities provide limited information on structural performance, since scaling only affects the amplitude of the motion, but not its frequency content (Grigoriu 2011; Kafali and Grigoriu 2007; Baker and Cornell 2005; Baker and Cornell 2006).

Three types of models are currently used to characterize seismic hazard: models which use only real records selected by heuristic arguments (Douglas 2006) or by matching response spectral accelerations (Baker 2011; Ozer and Akkar 2012; Jayaram et al. 2011; Fengxin et al. 2006), models calibrated to recorded data which are used to generate artificial ground motions (Zentner and Poirion 2012) and models which combine real with artificial ground motions (Seyedi et al. 2009).

The Bayesian framework is employed in this study to construct a novel model which accounts for all available information on site seismicity. The proposed model is based on site ground-acceleration records and the specific barrier model (SBM). The SBM is a seismological model which delivers spectral densities of the ground motion as a function of moment magnitude m, source-to-site distance r and other parameters (Papageorgiou and Aki 1983b; Papageorgiou and Aki 1983a; Halldorsson and Papageorgiou 2005). The implementation of the Bayesian analysis requires to represent the ground-acceleration spectral density $g(\nu; m, r)$, given by the SBM, by a parametric model $\tilde{g}(\nu; \Theta, m, r)$, which depends on a vector Θ of uncertain parameters. The prior density for Θ is postulated such that the expectation of $\tilde{g}(\nu; \Theta, m, r)$ with respect to the prior distribution of Θ is equal to $g(\nu; m, r)$. The proposed methodology produces posterior versions of the specific barrier model, that is, updated versions of spectral densities for seismic ground-acceleration processes at arbitrary sites as a function of earthquake magnitude and source-to-site distance, under a well-defined probability law.

The paper also addresses another current problem. Models can only provide approximations for the physical phenomena and concerns are raised when dealing with extraordinary events which cannot be estimated by models in use. Events like the Tohoku Earthquake in Japan on March 11, 2011 and the 5.8-magnitude Virginia Earthquake in the USA on August 23, 2011 must be treated accordingly. The proposed hazard model can be updated sequentially

when new records become available. Updating hazard models to new data was considered before, in (Atkinson and Boore 2011) and (Wang and Takada 2009), in which the parameters of ground-motion prediction models are updated to new data available. The latter also employs Bayesian statistical methods for the update.

The model and the methodology proposed are tested and then used for various simulated seismic hazard scenarios. The posterior model for the spectral density is derived from simulated ground-motion accelerations. As the number of records increases, the output spectral densities converge to the SBM spectral densities and confidence intervals become narrower and concentrated around the SBM densities. When the sensitivity of the model is tested using data generated from other postulated spectral densities, the output of our model deviates from the SBM. The posterior data on the spectral densities stays within the range postulated by the prior information, but it departs from the prior mean depending on the type of data and on the number of records used in the analysis. Similar findings are reported for a simulated hazard scenario in Los Angeles.

2. SEISMIC HAZARD MODEL

The seismic model in this paper has two components: a seismological model calibrated to regional data and a site-specific model for the earthquake probabilities.

2.1 Model Description

We model the seismic ground motions as stochastic processes using a seismological frequency model, that is, the specific barrier model (SBM). This model produces spectral densities $g(\nu; m, r)$ for seismic ground motions as a function of m and r, considering also site effects and rupture mechanisms (Papageorgiou and Aki 1983b; Papageorgiou and Aki 1983a). The physical model of the source fault used in the SBM is a rectangular plane containing circular cracks with fixed diameters. A local stress drop $\Delta\sigma_L$ occurs in each crack and they spread radially outwards at sequential times until they reach their barriers. The most important output of the model is the amplitude spectrum shown in Eq. (1).

$$a(\nu; m, r) = cS(\nu; m, \Delta\sigma_L)F(\nu)Q(\nu; r)G(\nu) \qquad (1)$$

in which c is a scaling factor, S and F are the source and the frequency spectra, respectively, Q is a ground motion prediction model and G is a function which accounts for the soil effects. The key parameter in this model, $\Delta\sigma_L$, is fitted to global data (Halldorsson and Papageorgiou 2005; Foster et al. 2012) and it is assumed to be universally valid. Moreover, the SBM is calibrated to global data and it does not capture the variability in the seismic spectral densities at a site. Thus, we can refer to the output of the SBM as prior information means for the spectral densities depending on (m, r).

Seismic ground accelerations are complex processes which are caused by travelling seismic waves. Of these waves, surface waves are most relevant for civil engineers due to their damaging effects. These waves generate the so-called strong ground-motion part of the earthquake, which may be considered stationary (Li and Chen 2009). The time history model for simulating the strong ground-motion part is assumed to be a zero-mean, stationary Gaussian process $X(t)$ with the probability law described fully by the one-sided spectral density

$$g(\nu; m, r) = \left(2\pi t_f\right)^{-1} |a(\nu; m, r)|^2 \qquad (2)$$

Under the Gaussian model, the power spectral density in Eq. (2), depending only on the two parameters $(m,\ r)$, defines completely the probability law of the seismic hazard at a site. In practice, the stationarity assumption is relaxed by multiplying the stationary process with a modulation function (Rezaeian and Kiureghian 2010; Li and Chen 2009).

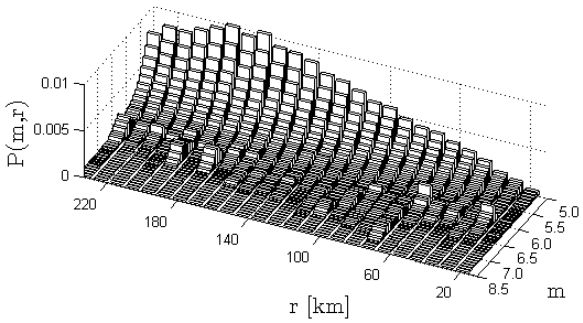


Figure 1 Seismic activity matrix for Los Angeles, CA

The second part of the hazard model is given by the seismic activity matrix, that is, a two-dimensional matrix defined in the (m, r) space, which provides the probability of occurrence of an earthquake of magnitude m and with an epicentral distance r. These matrices are calculated using the mean annual rates for earthquakes with coordinates (m, r), provided by the United States Geological Survey (USGS) for each zip code in the United States. The dimensions of the (m, r) space are flexible and they can be set up within the USGS database. Figure 1 illustrates the seismic activity matrix for Los Angeles, CA with ranges of the parameters $m \in [5; 8]$ and $r \in [5; 225] km$ and with a total number of cells $N = 875$. The two components of the seismic hazard for a specific site, that is, the spectral density $g(\nu; m, r)$ from the SBM and the seismic activity matrix, define completely the ground-acceleration process.

2.2 Model Approximation

The goal of this paper is to update the earthquake spectral density model using site records. The form of the spectral density, given by the SBM in Eqs. (1) and (2), is complicated and impractical since it is only available in an algorithmic form. To simplify calculations, a linear approximate model is sought. The singular value decomposition procedure (Chatterjee 2000) is used to construct a parametric model for $g(\nu; m, r)$.

Suppose the frequency band of $g(\nu; m, r)$ is discretized in n equal intervals $\Delta\nu$. Then, the spectral densities for a seismic activity matrix with N cells can be written in the form of a matrix A with n lines and N columns. The singular value decomposition of A is:

$$A = USV^T \tag{3}$$

where U and V are $n \times n$ and $N \times N$ orthogonal matrices, respectively and S is a $n \times N$ matrix with all off-diagonal elements equal to zero. The non-zero diagonal elements are arranged in ascending order $s_k = S_{kk}$, $k = 1, \dots, d$, where $d = \min(n, N)$. The values s_k are called singular values of A. We approximate A by

$$\tilde{A} = \sum_{k=1}^{\tilde{d}} s_k Q_k \tag{4}$$

where $\tilde{d} \leq d$ and $Q_k = u_k v_k^T$ is the modal matrix corresponding to the singular value s_k, and is the product between the $k-th$ column of U and the transposed $k-th$ column of V. The approximate representation of A in Eq. (4) improves as the number of modes $\tilde{d}$ increases.

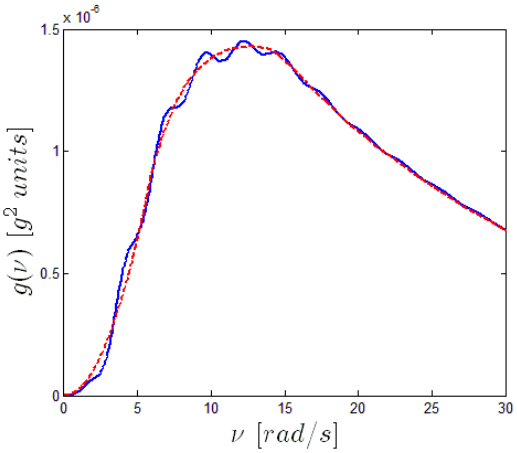


Figure 2 Power spectral density for cell $(m = 5.95, r = 85km)_{j=234}$

Each column j of A represents the power spectral density $g(\nu; (m, r)_j)$ for cell $(m, r)_j$ of the seismic activity matrix. Each column j of Q_k represents the $k-th$ mode of $g(\nu; (m, r)_j)$ and it is denoted by $\varphi_k(\nu; (m, r)_j)$. Figures 2 and 3 show the SBM and its singular value decomposition approximate representation with solid and dashed lines, respectively, for two cells, $(m = 5.95, r = 85km)_{j=234}$ and $(m = 8.05, r = 205km)_{j=771}$, using only the first $\tilde{d} = 6$ modes.

2.3 Bayesian Updating Framework

The Bayes' theorem is used to update the vector of unknown parameters Θ given the observed data X. According to the theorem, the posterior density $f(\Theta|X)$ of Θ is

$$f(\Theta|X) \propto f(\Theta) l(X|\Theta) \tag{5}$$

where $f(\Theta)$ is called the *prior* and the function $l(X|\Theta)$ is called the *likelihood* function. The likelihood accounts for the significance of the observed data X in the distribution of the unknown parameters Θ (Grigoriu 2012).

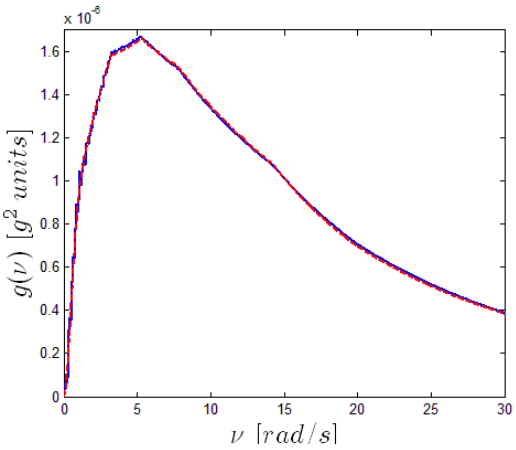


Figure 3 Power spectral density for cell $(m = 8.05, r = 205km)_{j=771}$

In this Bayesian framework, the singular values s_k are viewed as random variables θ_k with $E[\theta_k] = s_k$, with $k = 1, \dots, d$, where d is the number of singular values. They must also satisfy the existence condition of the spectral density, i.e. $g(\nu; \Theta, (m, r)_j) \geq 0$, for all $j = 1, \dots, N$, where N is the number of cells in the seismic activity matrix. Therefore, the uncertain model used in the Bayesian analysis is obtained from the discrete approximation for the spectral density and has the form

$$\tilde{g}(\nu; \Theta, (m, r)_j) = \sum_{k=1}^{d} \theta_k \varphi_k (\nu; \Theta, (m, r)_j) \tag{6}$$

where $\varphi_k(\nu; \Theta, (m, r)_j)$ is the $k-th$ mode in the $j-th$ cell of the seismic activity matrix. The spectral densities and the modes depend on $(m, r)_j$, but the unknown parameters $\theta_k, k = 1, \dots, d$, are global, i.e. they are unique for all cells of the seismic activity matrix. The notation $(m, r)_j$ is dropped and replaced by the index $j = 1, \dots, N$, denoting the $j-th$ cell in the seismic activity matrix.

Figure 4 illustrates the first seven singular values for the spectral densities matrix A for Los Angeles. The first couple of modes carry most of the weight in the approximation of A. Thus, to simplify the calculations, the representation in Eq. (6) is replaced by Eq. (7)

$$g_j(\nu; \Theta) = \theta_1 \varphi_{1,j}(\nu) + \theta_2 \varphi_{2,j}(\nu) + \theta^* \varphi_j{}^*(\nu) \tag{7}$$

where $\varphi_1(\nu), \varphi_2(\nu)$ are the first two modes of the decomposition and

$$\varphi_j{}^*(\nu) = \sum_{k=3}^{d} \theta_k \varphi_{k,j}(\nu) \tag{8}$$

is a cumulative mode, composed of all the other $d-2$ modes in the approximation of A.

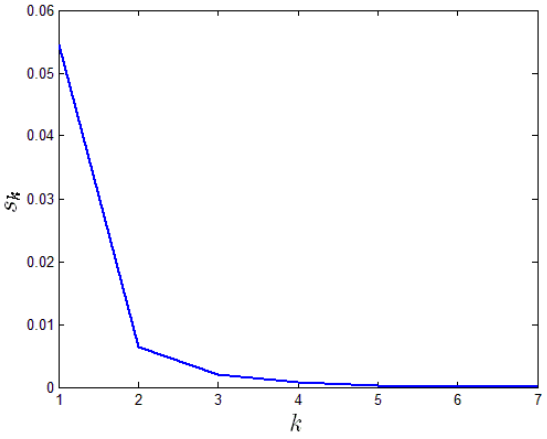


Figure 4 First seven singular values of $\boldsymbol{A}$

For calculations, the unknown parameters are normalized to have mean 1, by scaling modes $\varphi_{k,j}(\nu)$ by the corresponding s_k. The vector of unknown parameters is now $\Theta = (\theta_1, \theta_2, \theta^*)$, with a joint prior distribution $f(\Theta)$. In Figure 5 the three modes for cell $(m = 8.05,\ r = 205km)_{j=771}$ are shown.

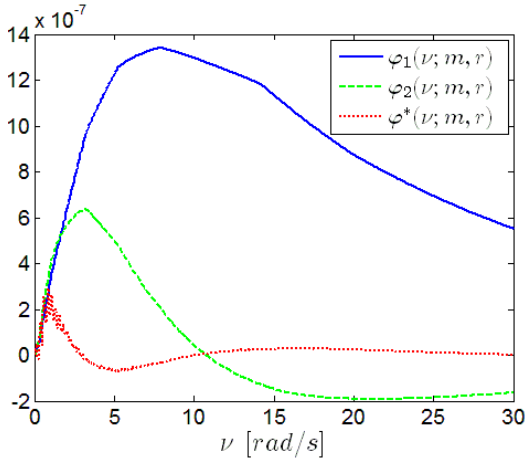


Figure 5 Modes for cell $j = 771$

The prior distribution $f(\Theta)$ of Θ must be postulated such that the two imposed conditions on Θ be satisfied. The joint prior probability density function proposed in the current analysis is

$$f(\theta_1, \theta_2, \theta^*) = f(\theta_1|\theta_2, \theta^*) f(\theta_2) f(\theta^*) \qquad (9)$$

in which θ_2, θ^* are independent, uniformly distributed and $f(\theta_1|\theta_2, \theta^*)$ is a $Gamma(\alpha, \beta)$ conditional prior probability density function centered around the mean $E[\theta_1]$=1, that is,

$$f(\theta_1|\theta_2, \theta^*) \propto (\theta_1 - E[\theta_1])^{\alpha-1} e^{-(\theta_1 - E[\theta_1])/\beta} \qquad (10)$$

where $\alpha > 0$ and $\beta > 0$ are the shape and the scale parameters, respectively.

The likelihood function $l(X|\Theta)$ depends on the recorded ground motions X and the unknown parameters Θ. As established before, X is only the strong-motion part of the ground-acceleration record, which is assumed to be a zero-mean, stationary, Gaussian process with spectral density $\tilde{g}_j(\nu; \Theta)$. Thus, we can write the likelihood function given the data time history X_i recorded in cell j as follows in Eq. (11)

$$l_j(X_i|\Theta) \propto \left|\Sigma_j(\Theta)\right|^{-\frac{1}{2}} \exp\left\{-\frac{1}{2} X_i^T \Sigma_j(\Theta)^{-1} X_i\right\} \qquad (11)$$

where $\left|\Sigma_j(\Theta)\right|$ is the determinant of the covariance matrix $\Sigma_j(\Theta)$, with components $\gamma_{u,v}^j$, calculated at all discrete times $u, v = 1, \dots, n_i$ with n_i being the number of discrete points in record X_i. The components of the covariance matrix are

$$\gamma_{u,v}^j(\Theta) = \sum_{k=1}^{q} \tilde{g}_j(\nu_k; \Theta) \cos(\nu_k (u - v))\, \Delta\nu \qquad (12)$$

where q is the number of discrete frequency points. Following standard practice, numerical calculations are based on the log-likelihood function given by

$$\log\left(l_j(X_i|\Theta)\right) \propto \log\left(|\Sigma_j(\Theta)|\right) + X_i^T \Sigma_j(\Theta)^{-1} X_i \qquad (13)$$

The posterior probability density of the unknown parameters is calculated from

$$f(\Theta|X_i) = \rho f(\Theta) l_j(X_i|\Theta) \qquad (14)$$

where ρ is a normalization constant, which assures that the posterior density function integrates to unity. The Bayesian updated model just illustrated is for a single record. For a larger set of ground-acceleration time histories $X_1, \dots, X_i, \dots, X_s$ recorded in cells $j(X_1), \dots, j(X_i), \dots, j(X_s)$ the same procedure should be used in a *cascade analysis*. This type of analysis is sequential and the posterior $f(\Theta|X_i)$ becomes the prior for the update with the following record X_{i+1}. The log-likelihood is then calculated as shown in Eq. (13). We can write the following recurrent upgrading relation:

$$f(\Theta|X_{i+1}) = \rho f(\Theta|X_i) l_{j(X_i)}(X_{i+1}|\Theta) \qquad (15)$$

for $i = 1, \dots, s-1$. Markov Chain Monte Carlo methods may be used for sampling Θ from the posterior density.

3. MODEL VALIDATION

The model proposed in the previous section is an updating model for the seismic spectral densities using the site records. Two important attributes of this model should be checked to validate it. The model should converge to the original values given by the SBM, when simulated data from the SBM are used in the analysis and yet be sensitive to exceptional ground-motion records. We show these properties by upgrading the spectral density model for a

single cell of the seismic activity matrix for Los Angeles, $(m = 8.05,\ r = 205km)_{j=771}$, rather than for the entire matrix.

3.1 Convergence

The parametric model $\tilde{g}(v;\Theta,(m,r)_j)$ is updated with samples generated from $g(v;\Theta,(m,r)_j)$ for a fixed, but arbitrary cell. Convergence means that the posterior spectral densities approach the SBM spectral densities as the number of samples increases indefinitely. Numerical results are shown for cell $j = 771$. The samples are generated as zero-mean, stationary normal processes using the spectral representation method (Grigoriu 1993; Kafali and Grigoriu 2007). Using the updating methodology presented in Eq. (15), the posterior density for the unknown parameters is obtained. As the number of data used in the analysis increases, the calculated means for all the uncertain parameters $\theta_1, \theta_2, \theta^*$ from the resulting posterior distributions converge to 1, the value corresponding to the SBM. Validating results are presented in Table 1.

Table 1 Convergence of the posterior means

Analysis	SBM	100 samples	1,000 samples	10,000 samples
$E[\theta_1]$	1	1.0236	1.0042	1.0001
$E[\theta_2]$	1	1.1109	1.0029	1.0017
$E[\theta_3]$	1	1.0011	1.0000	1.0000

Figures 6-9 show the marginal prior densities postulated in Eq. (10) and the marginal densities calculated for parameters $(\theta_1, \theta_2, \theta^*)$ for 100 and 1,000 samples, respectively. The spread of the posterior marginal density for parameter θ_1 narrows down more rapidly than for the other two parameters because both its weight in the model is higher and its prior $Gamma$ density postulated is much stronger than the non-informative uniform density used for the other two parameters.

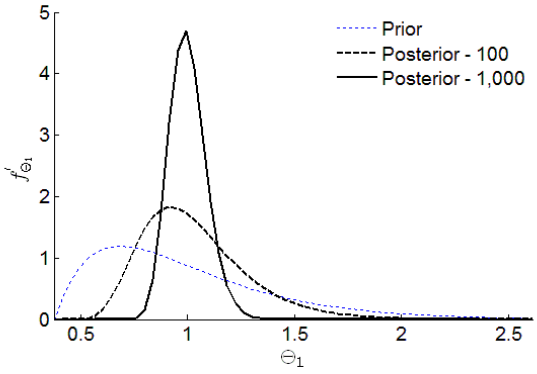


Figure 6 Posterior densities for $\boldsymbol{\theta_1}$

Each set of values $(\theta_1, \theta_2, \theta^*)$ corresponds to a spectral density function and has a probability mass given by the joint posterior density. Thus, we also have the probability law of the spectral densities at the specified site and in the cell or cells where the update was performed. Figures 9 and 10 illustrate the range of the spectral densities, the mean spectral density from the SBM and the 5-th and the 95-th percentiles, calculated for 100 and 1,000 samples, respectively. Since all the data in the analysis was generated using the SBM spectral density, the confidence intervals are concentrated around the SBM density. These intervals narrow down as the number of samples increases and they approach the mean spectral density.

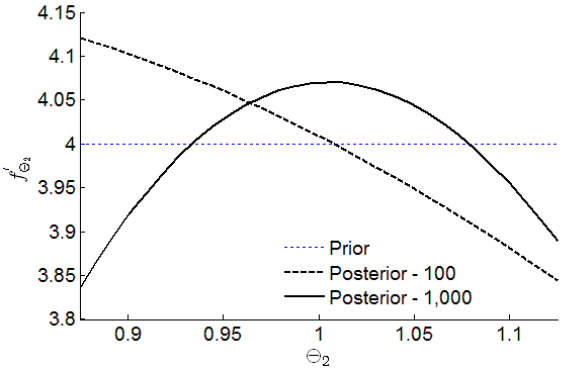


Figure 7 Posterior densities for $\boldsymbol{\theta_2}$

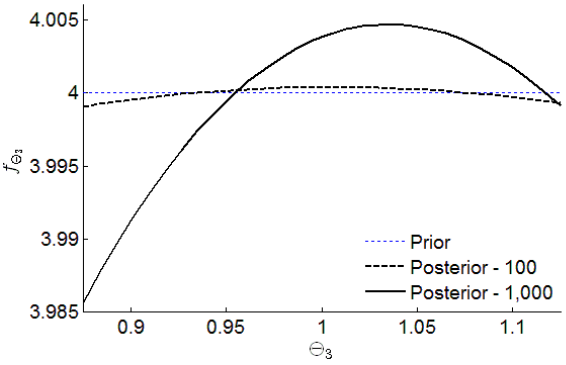


Figure 8 Posterior densities for $\boldsymbol{\theta_3}$

3.2 Sensitivity Analysis

Model sensitivity means that posterior spectral densities differ on average significantly from the SBM output if updated with records unlikely to be produced by $g(v;\Theta,(m,r)_j)$. The sensitivity of the model to uncommon earthquakes is important for updating the model with ground-motions records like the Tohoku earthquake in Japan.

In order to check this, we update the densities for the same cell $j = 771$, but using ground motion samples simulated by using the SBM spectral density for cell $(m = 5.95,\ r = 85km)_{j=234}$. The two cells used in the analysis have different frequency contents, as shown in Figures 2 and 3. Since the modes are cell dependent, we expect to see that the means of the unknown parameters diverge from the value 1 corresponding to the SBM spectral density.

The analysis is performed similarly to that in the previous section, using the sequential update methodology for 100 and 1,000 samples, respectively. In Figures 11 – 13, the marginal prior densities, and the two sets of marginal

posteriors are plotted for each of the three unknown parameters.

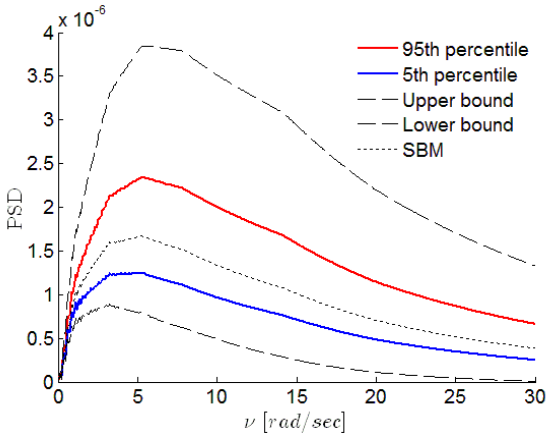


Figure 9 Statistics for the analysis with 100 samples

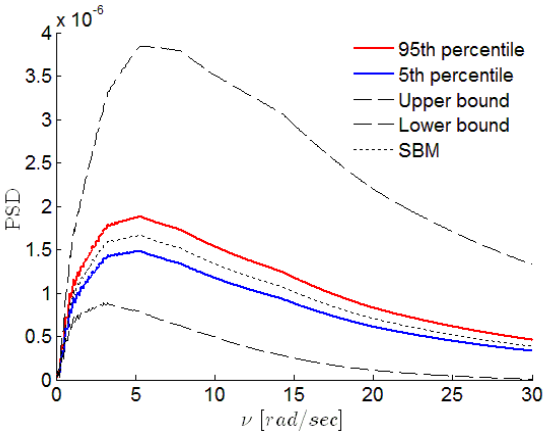


Figure 10 Statistics for the analysis with 1,000 samples

Using the same priors postulated before, just a slight deviation is noticed after the analysis with the first 100 samples, but after using all 1,000 samples, a conclusive deviation of the posterior mean from the mean 1 corresponding to the spectral density given by the SBM for cell $j = 771$ is noticed. Thus, we can state that the model is sensitive to unusual data. The information is processed through the Bayesian analysis, reflected in the posterior of the unknown parameters and implicitly in the posterior probability law of the spectral densities characteristic for that particular cell of the seismic activity matrix.

4. UPDATED SPECTRAL DENSITY FOR A SEISMIC SITE

The model responded as expected to the validation tests imposed in the previous section and it can be used for realistic applications. A posterior model for the spectral densities at a given site is developed by using the proposed methodology. For this purpose, we simulate a hazard scenario for Los Angeles. The updated posterior probability law for the spectral densities characteristic for this site is constructed in the Bayesian framework.

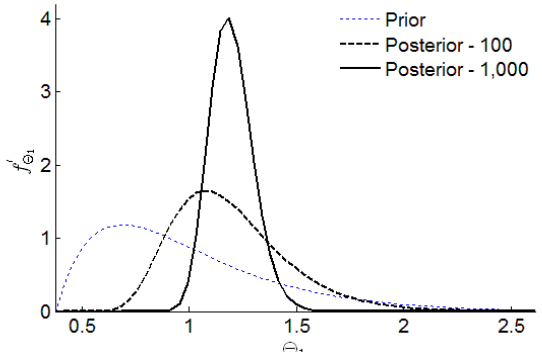


Figure 11 Sensitivity analysis for $\boldsymbol{\theta_1}$

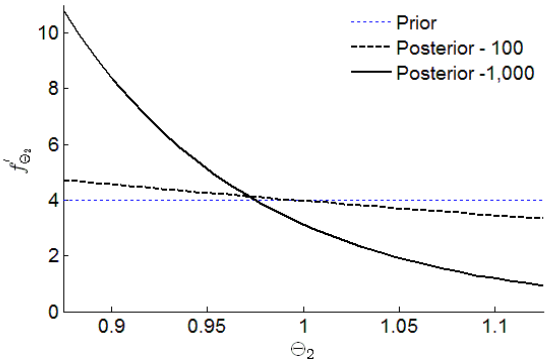


Figure 12 Sensitivity analysis for $\boldsymbol{\theta_2}$

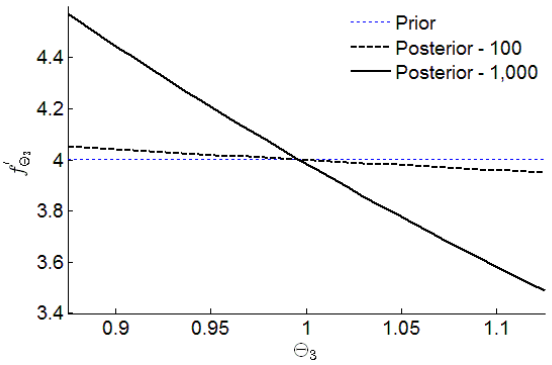


Figure 13 Sensitivity analysis for $\boldsymbol{\theta_3}$

4.1 Hazard Scenario

The hazard scenario is based on the seismic activity matrix shown in Figure 1 and the prior information on the spectral densities provided by the SBM. Unlike in the previous section, a global updated model is developed. The construction of the model in Eq. (6) allows for a global update since the uncertain parameters are global and match the SBM spectral densities for the entire seismic activity matrix.

The spectral density model for the entire seismic activity matrix can be updated for all cells in a single analysis. In practice, it is preferred to refer to seismic ground motions in relation to their corresponding seismic sources, which are characterized by location from the site and type of

earthquake magnitude produced. For the sake of this example, the seismic activity matrix is divided in four sub-matrices, each representing an imaginary source. We will refer to them as SAM1 corresponding to the seismic sources located at a distance $r < 100km$ from the site and which produce earthquakes of magnitudes $m < 6$, SAM2 for which $r < 100km, m \geq 6$, SAM3 for which $r \geq 100, m < 6$ and SAM4 with $r \geq 100km, m >= 6$.

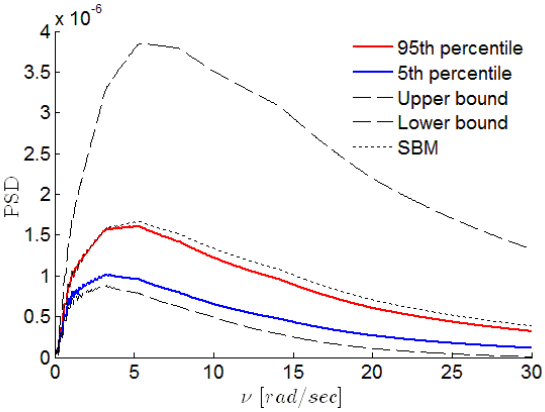


Figure 14 Statistics for densities in cell $\boldsymbol{j = 771}$ updated in SAM4

The priors for each sub-matrix are similar to the one described in Eq. (9), but their ranges are different to ensure the existence of the power spectral density for all combinations $(\theta_1, \theta_2, \theta^*)$ in all cells, for each individual sub-matrix. The likelihood function is calculated separately, for each ground motion record available, using the modes corresponding to the cell in which the record was registered.

Only 100 records are used in the analysis and they are simulated using the spectral densities provided by the SBM. The strong-motion ground acceleration time histories are generated in various cells chosen from the multinomial distribution described by the seismic activity matrix. As shown in Figure 1, the highest probability mass is concentrated in SAM4 and there is a lower probability mass concentrated in SAM1 and SAM3. According to the outcome of a 100-sample trial of this multinomial density, no ground motions are simulated in SAM3, 1 sample in SAM 1, 20 time histories are generated in SAM2 and the rest 79 motions are simulated in cells contained in SAM4.

4.2 Analysis

The update will be performed for each sub-matrix individually and using the ground motions corresponding to the cells belonging to each of them. Different posterior distributions are obtained for each sub-matrix because the ranges for the unknown parameters are different and number of available data used for each update is variable. Moreover, in SAM3 there is no update, since no data is available for the analysis. This suggests that the prior density is very important in the analysis. Thus, a non-informative uniform prior might be preferred to the $Gamma$ prior postulated. This assigns different probabilities to spectral density functions which cannot be corrected due to the lack of data.

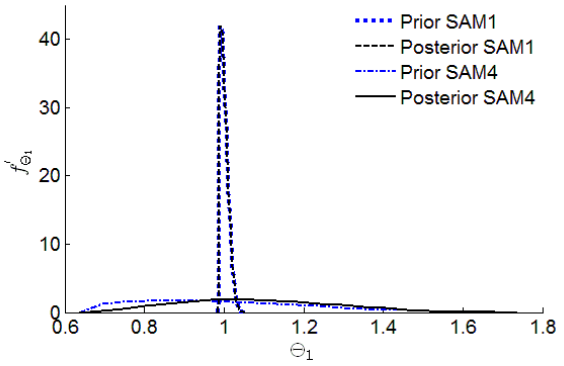


Figure 15 Posteriors for $\boldsymbol{\theta_1}$ in SAM1 and SAM4

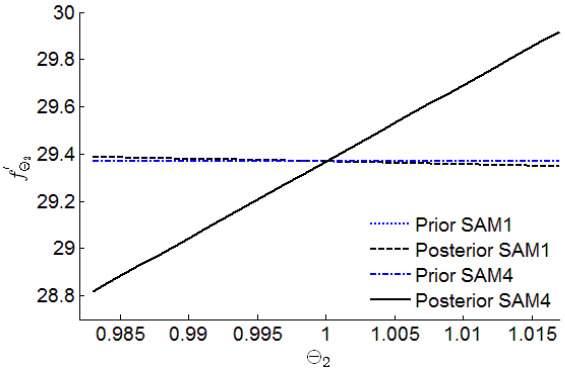


Figure 16 Posteriors for $\boldsymbol{\theta_2}$ in SAM1 and SAM4

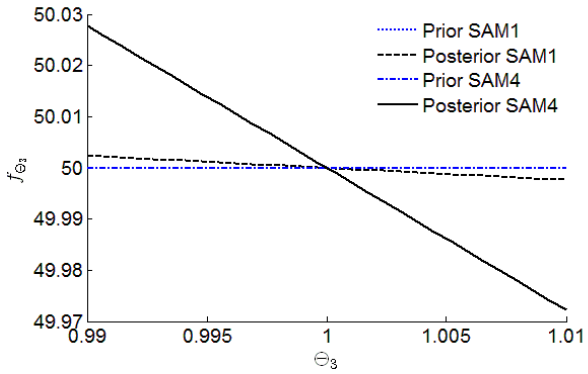


Figure 17 Posteriors for $\boldsymbol{\theta_3}$ in SAM1 and SAM4

For comparison with the results in the previous section, posterior statistics for cell j=771 are calculated again. Cell $(m = 8.05,\ r = 205km)_{j=771}$ belongs to SAM4 and only 2 samples from the 79 available for this sub-matrix belong to this cell. However, the update for the unknown parameters is performed using all 79 time histories available. Figure 14 shows the SBM density, the range and the 5-th and the 95-th percentiles, respectively. Unlike the results shown in Figures 9 and 10, where the update was done only using samples from the actual cell, the SBM spectral density is outside the confidence interval. This shows the importance in the variability of the ground motion and the necessity of using a site-specific model. The data suggests that the SBM

model overestimates the frequency content of the ground motions in this particular cell. It is also important to note that the confidence intervals stay within the limits of the prior range postulated.

The two cells used in our analyses, $j = 234$ and $j = 771$ correspond to SAM1 and SAM4, respectively. Figures 15-17 present the marginal priors and posterior densities of the unknown parameters of SAM 1 and SAM 4. For the two cells we keep the ranges for the parameters θ_2 and θ^* fixed, which leads to very different ranges for θ_1 for the two sub-matrices. Since only one sample is available for the analysis in SAM1, a very slight perturbation of the prior is noticed from the postulated prior, which emphasizes again the importance of the prior distributions. Since the number of samples of ground motion accelerations used in the analysis is very small, no convergence to the mean value 1 is observed in the posterior marginal distribution of the unknown parameters.

5. CONCLUSIONS

A novel model has been proposed for characterizing site seismicity. The model is based on the specific barrier model (SBM), a seismological model, which produces seismic power spectral densities as a function of moment magnitude and epicentral distance, and site records. A parametric representation of the SBM, depending on a vector of unknown parameters Θ, has been used to update the spectral densities provided by the original model, within a Bayesian framework using site records.

It was found that the proposed model converges to the SBM if it is updated with ground-acceleration records generated by the model as the sample size increases infinitely. If the ground-acceleration records are inconsistent with the SBM, the posterior version of the proposed model may differ significantly from the SBM. This is the most useful feature, which allows modifying the SBM to account for recent large seismic events.

Acknowledgements:

The authors acknowledge gratefully the support from the National Science Foundation under the NSF Award Number CMMI-0925714.

References:

Atkinson, G.M. & Boore, D.M. (2011), "Modification to existing ground-motion prediction equations in light of new data", *Bulletin of the Seismological Society of America*, **101**(3), 1121–1135.

Baker, J.W. (2011), "Conditional mean spectrum: tool for ground motion selection", *Journal of Structural Engineering*, **137**(3), 322–331.

Baker, J.W. and Cornell, C.A. (2005), "A vector-valued ground motion intensity measure consisting of spectral acceleration and epsilon", *Earthquake Engineering and Structural Dynamics*, **34**, 1193–1217.

Baker, J.W. and Cornell, C.A. (2006), "Spectral shape, epsilon and record selection", *Earthquake Engineering and Structural Dynamics*, **35**, 1077–1095.

Chatterjee, A. (2000), "An introduction to the proper orthogonal decomposition", *Current Science*, **78**(7), 808–817.

Douglas, J. (2006). "Strong-motion records selection for structural testing", *Proceedings of the First European Conference on Earthquake Engineering and Seismology*, Geneva, Switzerland.

Fengxin, Z., Yushan, Z. and Hongshan, L. (2006), "Artificial ground motion compatible with specified ground shaking peaks and target response spectra", *Earthquake Engineering and Engineering Vibration*, **5**(1), 41–48.

Foster, K.M. et al. (2012), "Calibration of the specific barrier model to the NGA dataset", *Seismological Research Letters*, **83**(3), 566–574.

Grigoriu, M (1993), "Simulation of stationary process via a sampling theorem", *Journal of Sound and Vibration*, **166**(2), 301–313.

Grigoriu, M (2012), "Stochastic systems. Uncertainty quantification and propagation", London, UK: Springer-Verlag Ltd.

Grigoriu, M (2011), "To scale or not to scale seismic ground accceleration records", *Journal of Engineering Mechanics*, **137**(4), 284–293.

Halldorsson, B. and Papageorgiou, A.S. (2005), "Calibration of the specific barier model to earthquake to different tectonic regions", *Bulletin of Seismological Society of America*, **95**(4), 1276–1300.

Jayaram, N., Lin, T. and Baker, J.W. (2011), "A computational efficient ground-motion selection algorithm for matching a target response spectrum mean and variance", *Earthquake Spectra*, **27**(3), 797–815.

Kafali, C. and Grigoriu, M. (2007), "Seismic fragility analysis : Application to simple linear and nonlinear systems", *Earthquake Engineering and Structural Dynamics*, **36**(13), 1885–1900.

Li, J. and Chen, J. (2009), "Stochastic dynamics of structures", Singapore: John Wiley Sons.

Ozer, B. and Akkar, S. (2012), "A procedure on ground motion selection and scaling for nonlinear response of simple structural systems", *Earthquake Engineering and Structural Dynamics*, **41**, 1693–1707.

Papageorgiou, A.S. and Aki, K. (1983a), "A specific barrier model for the quantitative description of inhomoeneous faulting and the prediction of strong ground motion. Applications of the model", *Bulletin of Seismological Society of America*, **73**(4), 953–978.

Papageorgiou, A.S. and Aki, K. (1983b), "A specific barrier model for the quantitative description of inhomoeneous faulting and the prediction of strong ground motion. Description of the model", *Bulletin of Seismological Society of America*, **73**(3), 693–722.

Rezaeian, S. and Kiureghian, A.D. (2010), "Simulation of synthetic ground motions for specified earthquake and site characteristics", *Earthquake Engineering and Structural Dynamics*, **39**, 1155–1180.

Seyedi, D.M. et al. (2009), "Development of seismic fragility surfaces for reinforced concrete buildings by means of nonlinear time-history analysis", *Earthquake Engineering and Structural Dynamics*, 39, 91–108.

Wang, M. and Takada, T. (2009), "A Bayesian framework for prediction of seismic ground motion", *Bulletin of the Seismological Society of America*, **99**(4), 2348–2364.

Zentner, I. and Poirion, F. (2012), "Enrichment of seismic ground motions databases using Karhunen-Loeve expasion", *Earthquake Engineering and Structural Dynamics*, **41**(14), 1945-1957.

10CUEE CONFERENCE PROCEEDINGS
10th International Conference on Urban Earthquake Engineering
March 1-2, 2013, Tokyo Institute of Technology, Tokyo, Japan

ANALYSIS AND STUDY OF SITE EFFECT IN KAOHSIUNG AND PINGTUNG AREA IN TAIWAN

H. J. Chiang[1], and K. L. Wen[2]

1) Post Doctor, Institute of Geophysics, National Central University, Taiwan
2) Professor, Institute of Geophysics, National Central University, Taiwan
s1642006@cc.ncu.edu.tw, wenkl@earth.ncu.edu.tw

Abstract: Kaohsiung city is the most important harbor and second large city in Taiwan. This study estimates the S-wave velocity structures by six microtremor arrays. We then conducted a research to study the site effects, which includes analyze three installed borehole seismometer arrays, and perform very dense microtremor measurements in the area. After carefully selection, we pick 705 records and use the H/V ratio method to get information of soil amplification. In this study, we select several frequencies to plot out the contour map for understanding the frequency responses in this area. For the 0.6 ~ 1.5 Hz, the contours show that main amplification effects occurred at the southern part of Kaohsiung area and most Pingtung plain. With the frequency increasing to 2.0 Hz, the main amplification area move from the plain area to the hill area. At the plain area, the dominant frequency is about 0.6 ~ 2.0 Hz, and the hill area is great than 2.0 Hz. We found that the basement structure can explain the contour very well. Yet, the H/V dominated frequency distribution map reveals more detail features. The Vs30 can't exactly respond the site effects in the plain area stations.

1. INTRODUCTION

Taiwan is located on the Circum-Pacific seismic belt. The seismicity in Taiwan area is very high (Hsu, 1961). Therefore, defense lives and possessions from disaster earthquakes are a major concern of the people in this region.

Amplification of strong ground motion by alluvial deposits during an earthquake has been documented on a lot of occasions and caused damage in recent large earthquakes, for example, 1985 Michoacan earthquake, 1989 Loma Prieta earthquake, 1994 Northridge earthquake, 1995 Kobe earthquake, and 1999 Chi-Chi, Taiwan earthquake. Many studies shown that the top alluvium layer will play an important role for site amplification effects (Boore et al., 1993; Boore et al.,1994; Anderson et al., 1996). Therefore, site effects study is very important for mitigating damage during an earthquake. Many methods have been used to characterize the site amplification. The Central Geological Survey had spent four years to bore more than 50 wells. And now, it is very clear to know the basement depth is changing from 120 to 40 meters for the western and eastern part of the Kaohsiung city. The harbor and commercial area locate at the western part of this area, and the eastern part is small hill area. In this study, we used the H/V ratio to analyze the site effect. The H/V ratio contours at some specific frequencies are selected to compare with the geological structures under the Kaohsiung area.

2. TSMIP NETWORK AND BOREHOLE ARRAYS

2.1 TSMIP Network

TSMIP is executed by the Seismological Observation Center of the Central Weather Bureau, Taiwan, ROC (Shin, 1993). The main purpose of this program is to study the characteristics of the ground motion in different geological conditions and the response of different types of man-made structures. All results can be used to improve the design spectrum and building codes of current use. The program installed up to 600 digital free field strong motion instruments and 400*3 digital channels of strong motion monitoring systems in nine metropolitan areas. The distribution of stations within the Kaohsiung and Pingtung area is shown in Figure 1 in triangle symbol.

2.2 Borehole Arrays

There had been installed three borehole seismometer arrays by the Central Geological Survey in the Kaohsiung area. Each array was installed three seismometers at different depth (surface, 50 m, 150 m). The location of the borehole arrays is shown in Figure 2 (KS001, KS002, KS003).

3. SHALLOW S-WAVE VELOCITY STRUCTURE

We had done microtremor array measurements at six different sites. Figure 2 also shows the distribution of the microtremor array in the study area in rhombus symbol. We set up 13 seismometers in several triangles at each microtremor array measurement, and receive microtremor at

the same time. The seismometer which we use to do microtremor measurements is made by the Tokyo Sokushin. The mode of the recorder is the SAMTAC-801B and the sensor is the VSE-311C. The sampling rate is 200 pps. There is a time shift between the pulse at each station. We use the F-K analysis to get a dispersion curve. Then we get the S wave velocity structure by using the Genetic Algorithm Search. Figure 3 shows the best 20 solutions at each microtremor array.

At the three borehole seismometer arrays, we had done the P-S velocity logging before the seismometer had installed in the deepest borehole (150 m). Comparing with the two methods, the shallow S-wave velocity structure can match well (Figure 4). After all the borehole seismometer arrays had been set up, we have received some earthquakes. We can use the earthquake records to calculate the transfer function between two different depths. We use the S wave velocity from the result of the P-S velocity logging and 1-D Haskell method to calculate the theoretical transfer function between two different depths and compare with the observed transfer function. Figure 5 shows the result of the Ks001 borehole seismometer array. We can find that the two results match very well, and it also reveals that the preciseness of the P-S velocity logging.

4. SITE EFFECT ANALYSIS

We perform a very dense microtremor survey in the study area. Most microtremor measurements were done during the midnight to reduce artificial effects in the urban area. The measurements are denser in the urban area than countryside. We measure about 18 minutes at each site. The sampling rate is 200 pps. After carefully selection, we pick 705 records and use the H/V ration method to study the soil amplification in the Kaohsiung and Pingtung area. Figure 6 shows the H/V ratio in different frequency. For the lower frequencies, the contours show that main amplification effects occurred at sedimentary area. For the higher frequencies, the main amplification area move from the harbor and coast area to the hill area. We pick the dominant frequency of each record and plot out the contour map (Figure 7). At the harbor and city area, the dominant frequency is about 0.5 ~ 0.9 Hz, and the hill part is about 3.0 ~ 5.0 Hz.

Then we use a very simple equation, that is V = 4 f x H, to transfer the dominant frequency to the thickness of the sediment. We get the S wave velocity of the top sediment which is about 250 m/s by using the P-S velocity logging. Then we can easily get the thickness of the sediment (Figure 8). Comparing with the true basement structure made by the drilling, the two results match very well. Yet, the H/V dominated frequency distribution map reveals more detail features.

Vs30 is a very important parameter in the Engineering. There are 41 TSMIP stations witch have been bored a well around 30 meters depth. The P-S velocity logging has been done at these stations. We use the S wave velocity from the result of the P-S velocity logging to calculate the theoretical transfer function and compare with the H/V ratio near the stations. At the hill area, the site classification is B type and the transfer function appears like a constant (Figure 9). At the edge of the plain, Vs30 can respond the geological condition and the transfer function can match the H/V ratio (Figure 10). But at the most plain stations, Vs30 can't respond the depth of the sediments which dominate the site effect. Figure 11 shows a quite different result at the plain stations.

5. CONCLUSION

We combine several methods to study the ground motion characteristics in this urban area. In the Kaohsiung area, with the frequency increasing, the main amplification area move from the harbor and the southern part of Kaohsiung area to the hill area, which locates at the eastern part of Kaohsiung area. For the higher frequency (3.0 Hz), there are no obvious high contour areas. In the Pingtung plain, the main amplification area moves around the Kaoping River at the frequency from 0.5 to 2 Hz. From the contour of the dominant frequency, We can find that the southwestern part of Kaohsiung city is about 0.5 ~ 0.9 Hz, and the northeastern part is about 1.3 ~ 1.7 Hz, and the basement structure can explain the site amplification result very well.

By comparing the 1-D Haskell method and H/V ratio, Vs30 is applied in the Engineering but sometimes can't respond the geological condition especially in the plain area.

Acknowledgements:

We would like to thank the Central Weather Bureau, Taiwan for releasing the strong motion data set. This study has been supported by the National Science Council, Taiwan, under the grant no. NSC 101-2116-M-008-021.

References:

Anderson, J. G., Lee, Y., Zeng, Y., and Day, S. (1996), "Control of strong motion by the upper 30 meters," *Bulletin of the Seismological Society of America*, **86**(6), 1749-1759.

Boore, D. M., Joyner, W. B., and Fumal, T. E. (1993), "Estimation of response spectra and peak accelerations from western United States earthquakes: an interim report," U.S. Geol. Surv. Open-File Rep. 93-509, 72pp.

Boore, D. M., Joyner, W. B., and Fumal, T. E. (1994), "Estimation of response spectra and peak accelerations from western United States earthquakes: an interim report, Part 2," U.S. Geol. Surv. Open-File Rep. 94-127, 40pp.

Hsu, M. T. (1961), "Seismicity of Taiwan (Formosa)," *Bull. Earthq. Res. Inst.,* Univ. of Tokyo, **39**, 831-847.

Shin, T. C. (1993), "Progress summary of the Taiwan Strong Motion Instrumentation Program," Symposium on Taiwan Strong Motion Instrumentation Program, 1-10.

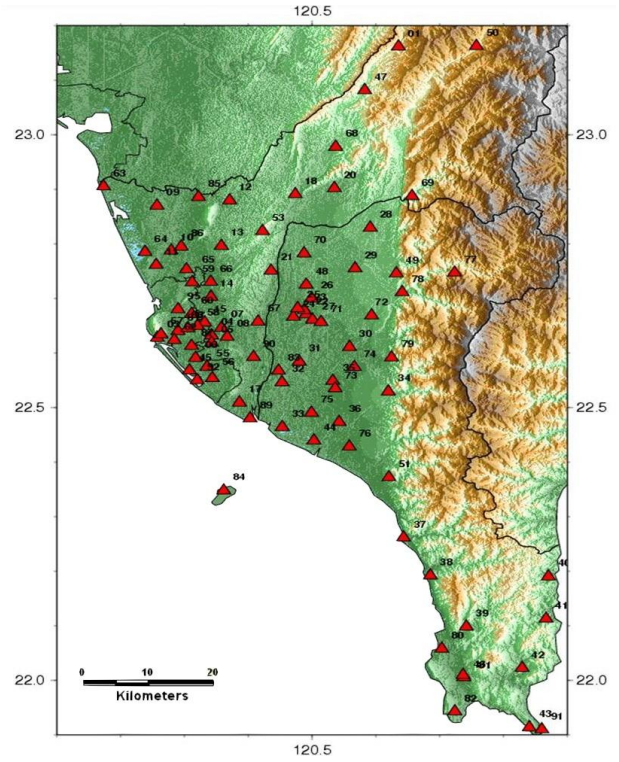


Figure 1 The distribution of TSMIP stations within the Kaoshiung and Pingtung area.

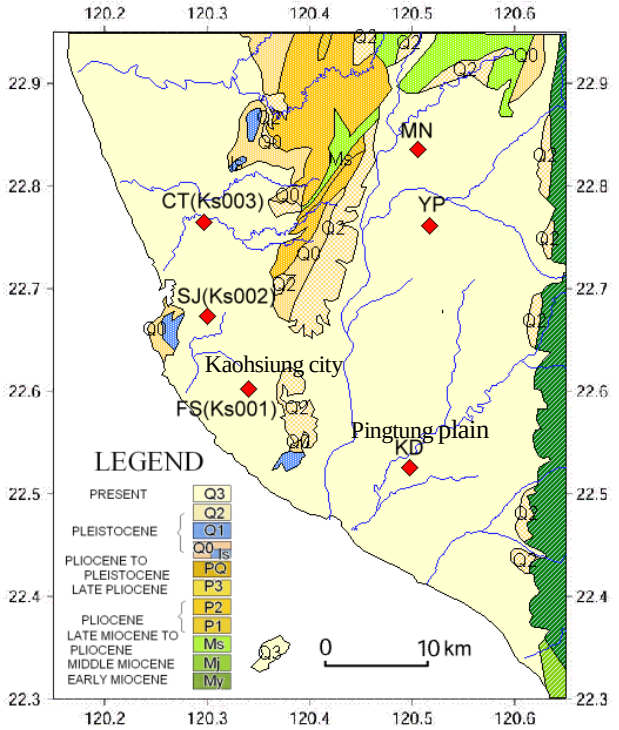


Figure 2 The distribution of the 6 microtremor arrays. The three borehole seismometer arrays are indexed as Ks001 ~ Ks003.

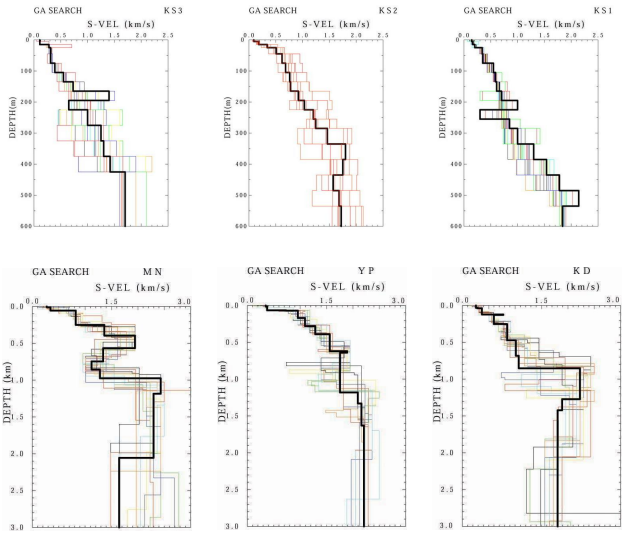


Figure 3 The best 20 solutions of the S-wave velocity structure at each microtremor array. The bold black line is the final velocity structure we use to do the 1-D Haskell method to calculate the theoretical transfer function.

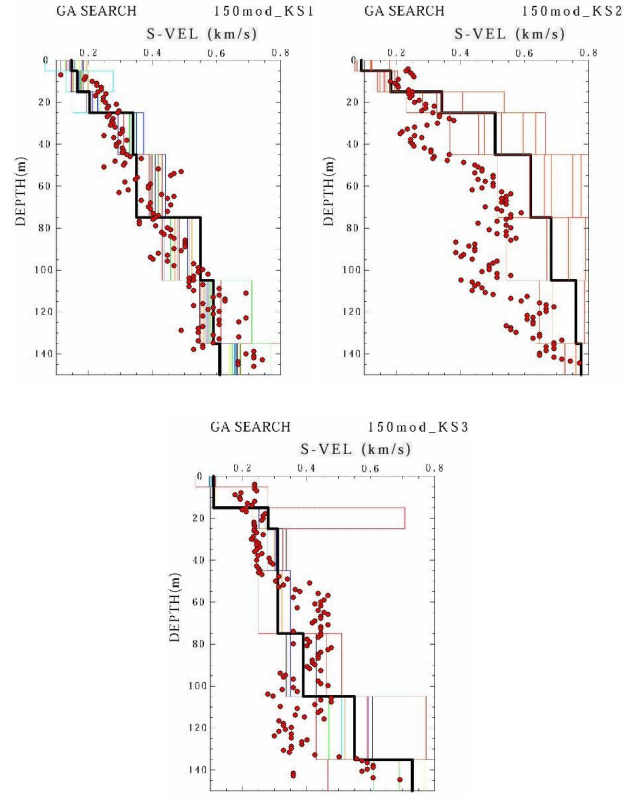


Figure 4 Comparison of the results of P-S velocity logging and microtremor array.

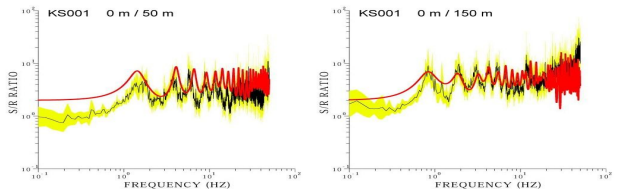


Figure 5 Comparison of the observed and theoretical transfer function by using the 1-D Haskell method and S wave velocity from the result of the P-S velocity logging.

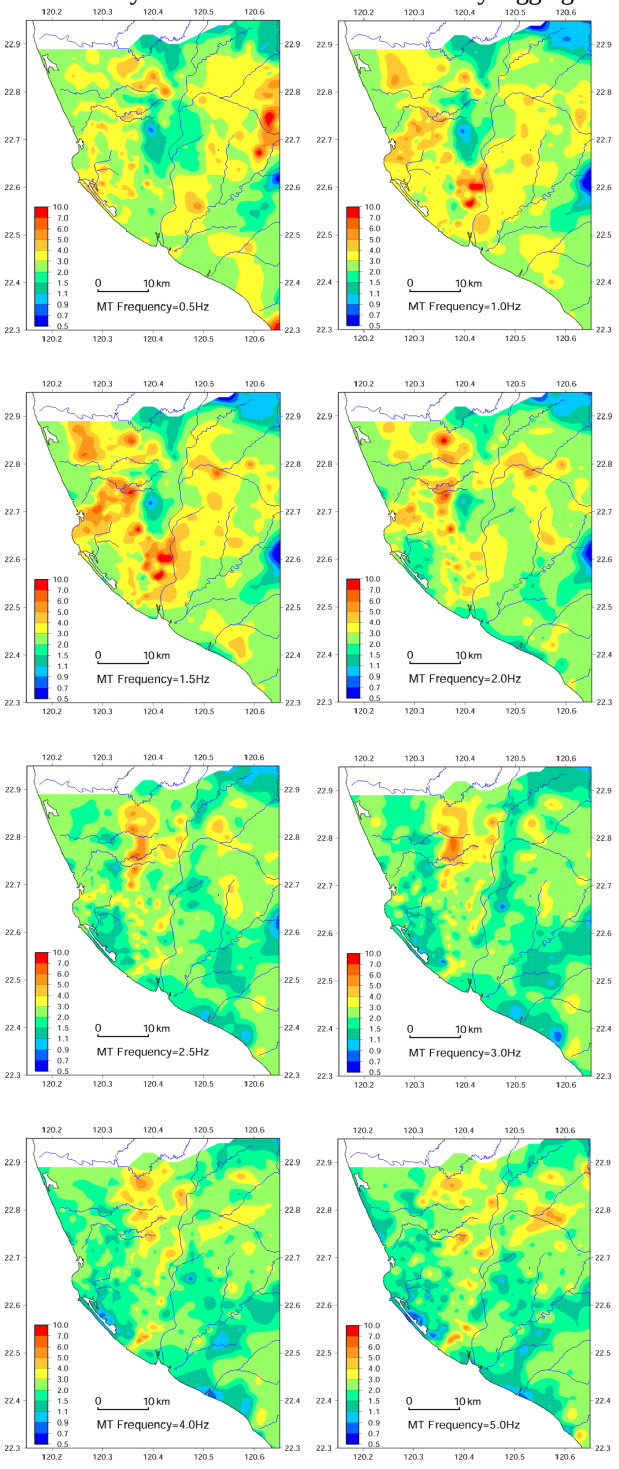


Figure 6 The H/V ratio in different frequency.

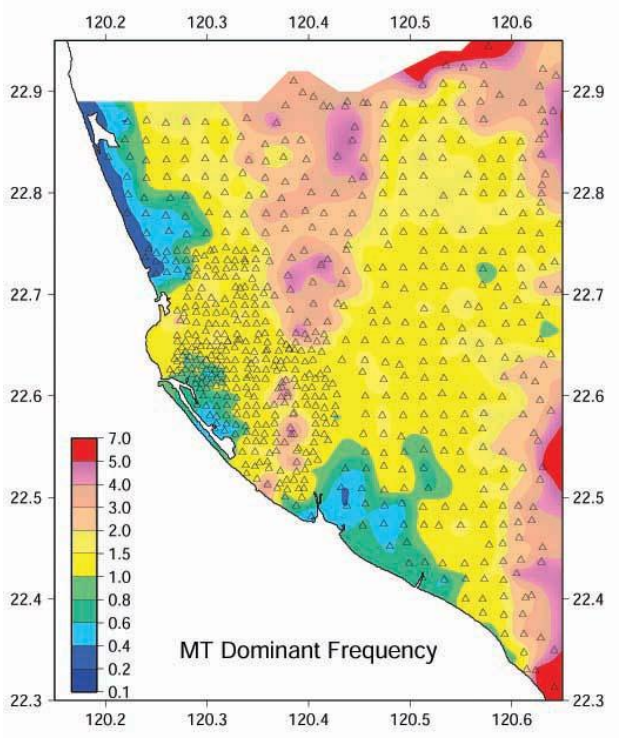


Figure 7 The dominant frequency in this area.

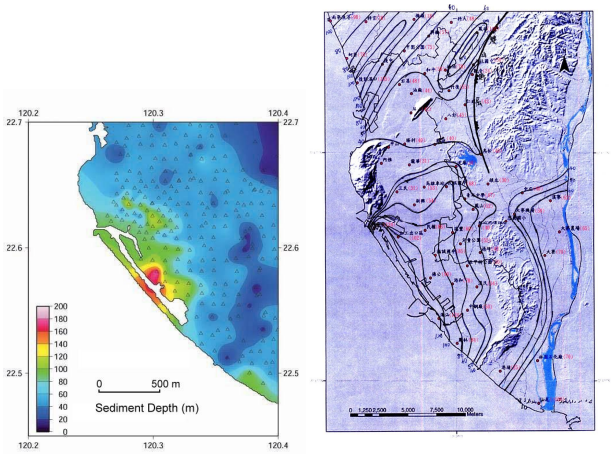
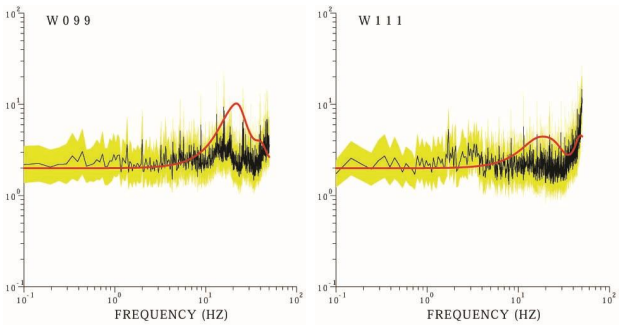
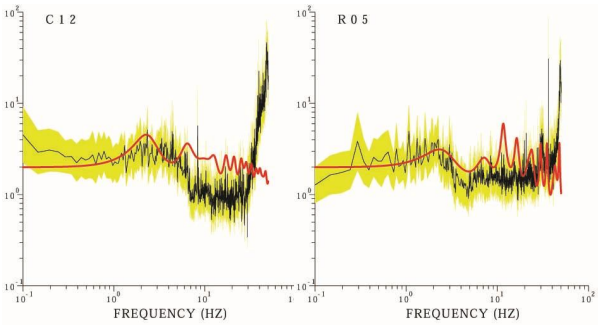


Figure 8 The thickness of the sediment converted from the dominant frequency and true basement structure made by the drilling.



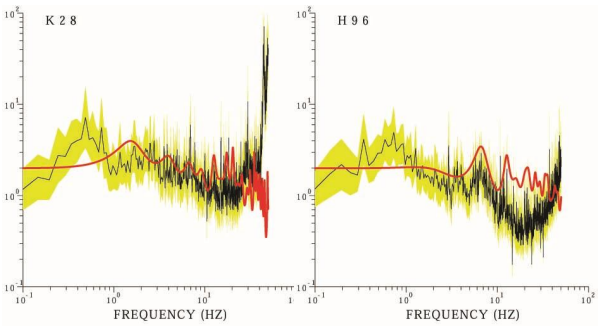
KAU034 KAU051

Figure 9 The transfer functions of the B type stations at the hill area.



KAU015 KAU030

Figure 10 The transfer functions of the TSMIP stations at the edge of the plain.



KAU011 KAU089

Figure 11 The transfer functions of the TSMIP stations in the plain.

10CUEE CONFERENCE PROCEEDINGS
10th International Conference on Urban Earthquake Engineering
March 1-2, 2013, Tokyo Institute of Technology, Tokyo, Japan

APPLICATION OF WAVEFORM INVERSION TO ACTUAL SEISMIC REFRACTION DATA FOR RETRIEVING SHALLOW 2D S-WAVE VELOCITY PROFILE

Amrouche Mohamed[1], Hiroaki Yamanaka [2]

1) Doctoral Student, Dept. of Environmental Science and Technology, Tokyo Institute of Technology, Japan
2) Professor, Dept. of Environmental Science and Technology, Tokyo Institute of Technology, Japan
amrouche.m.aa@m.titech.ac.jp,yamanaka @depe.titech.ac.jp

Abstract: We are attempting to develop a cheap and accessible seismic approach based on the inversion of the P-SV refraction data to retrieve the lateral variations of shallow soils. This method is based on the full wave field modeling based on a 2.5D Finite difference staggered formulation, source indepedent deconvolution is applied to boh observed and calculated waveforms to allow an inversion without requiring the knowledge of the source signature. The algorithm used for the inversion is the hybrid heuristic search method proposed by Yamanaka (2007). The current study aims to assess the applicability of the wave form inversion for 2D shallow soil profiling to actual refraction data. We conducted field survey in our university campus and tried to retrieve the lateral variations of the soil. Two soil profiles were inverted using shots at both ends of the survey line. The 2D soil profiles obtained by the inversion shows agreement with existing borehole data underling comparable soil structure. The inversion also allowed the detection of a lateral velocity gradient within the second layer of the soil.

1. INTRODUCTION

The near surface structural irregularities of soils may generate complex waves that interfere to disturb the expected response of buildings. Retrieving the two dimensional profile of shallow soils can have an important role to mitigate earthquake damage upon manmade structures. Many geophysical tools are available to profile the shallow soils such as the conventional seismic refraction method, or the multi-channel surface wave analysis (MASW) and each technique have its advantages and pitfalls.

We are proposing a new technique based on the wave form inversion of P-SV time series obtained from conventional seismic refraction, and the full wave field numerical modeling. The current study aims to verify the applicability of our method to actual refraction data and try to retrieve the two dimensional soil profiles.

2. METHODOLOGY

To simulate the behavior of waves inside a soil model, we used the Finite Difference P-SV staggered grid proposed by J.Virieux (1984), the classical 2D equations of motion implemented in the FD scheme to approximate velocity within the model are upgraded to 2.5D in order to include the three dimensional spreading in a 2D plan. To materialize our soil structure numerically, we use the combination of the tomographic cell and homogeneous layered model used by Takekoshi and Yamanaka (2009). This method allows dividing soil layers into several blocks with irregular interfaces. The inversion process consists then to attribute suitable values for depth and velocities at each block simultaneously in order to determine the adequate interface and the shear wave velocity.

The inversion algorithm used in this study is the hybrid heuristic search method proposed by Yamanaka (2007), this algorithm have shown excellent results on inverting phase velocity of Rayleigh waves in 1D soil profiles (Zaineh et al. 2011).

Since we are not supposed to know source frequency of the plank hammering during the data acquisition, it is important to get rid of the source effect from the signal. A source independent deconvolution was applied to the observed and calculated waveforms to delete source effect from our signal.

3. DATA ACQUISITION

We conducted a field survey in our university campus, Tokyo Institute of Technology Suzukakedai Campus in Yokohama city. We selected newly constructed parking lot as an investigation area because of the availability of a borehole data carried out previously for some geotechnical purposes. The availability of the borehole data allows correlating our 2D inverted soil model with existing one dimensional S wave velocity profile. It is very important to report that the parking area was modified after the drill of the borehole, the top surface layer was improved and a pavement layer with a thickness of around 20cm was constructed.

A conventional seismic refraction survey can be used to acquire waves generated by sledge hammering at the free surface. A line of receivers recorded the vertical component

of velocity. The survey line was spreaded nearby the borehole location. Fig.1 shows the location of the borehole as well as the survey line location. For polarity distinction, we will use the term upstream for the off shot near the borehole side, and downstream for the opposite side of the survey line.

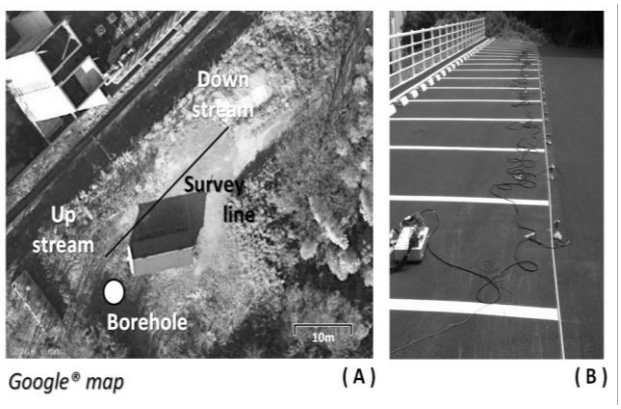


Figure 1 Location of the field data acquisition:
(A) Map of the investigated area before parking construction.
(B) Picture taken during survey after parking construction.

4. DATA PROCESSING AND INVERSION

The interception of the waves is carried out using 4.5Hz vertical geophones with a spacing of 2m covering the distance of 30m of the investigation area. Since we were performing the survey over a pavement, the geophones were fixed to the ground using artificial clay to ensure a correct transmission of the energy and reduce the coupling effect between the geophones and ground. Two vertical shots using a 5kg hammer excite the surface at both ends of the survey line; a wooden plate doubled with a sponge cushion is used to generate impacts without damaging the newly constructed pavement.

An auto-triggering system allows acquisition after the detection of the first motion at the nearest station from the shot; this station is considered as a triggering station and will not be included in the inversion. The geophones are connected to an amplificatory allowing tuning the appropriate amplification for analog recording along the survey line. The acquisition is performed using a 16 channels data logger with an acquisition window of 0.2s and a sampling rate of $5x10^{-5}$s.

We inverted the data from two shots at the upstream and downstream ends of the survey line independently. In data processing before the inversion, we applied a source deconvolution by dividing the whole signal by a reference station in the frequency domain; in our experiment we use the closest station to the source as a reference station. The division in frequency generates unwanted high frequencies, a band pass filter allows to keep the frequencies of interest and the frequency range used in the inversion is 20Hz-70Hz. Fig.2 shows the raw signal obtained from the upstream and the downstream shots and the processed waveforms.

A Finite Difference numerical grid of 400 x 200 grids is generated using a meshing of 0.1m to invert the two dimensional soil. A priori depth information obtained from the borehole data allows one to know the number of layers to be inverted and fixes the search limits for our inversion as in Table 3. Our target is to invert the two first layers of the soil, we divide each layer to 30 blocks, which brings it to a total of 120 unknown parameters. We set iteration number to 250 for 20 models at each generation. The P wave velocities obtained from the borehole data are utilized for the inversion.

Since many random numbers are used in the hybrid heuristic search inversion, the variation of the misfit function and the inverted parameters are more or less dependent on the random numbers used at each execution. In order to avoid any effect related to the initial models randomly generated, we conducted five inversions with different initial values of the random number generator for each inversion and average the models obtained to a single synthesis model.

Table1: inversion parameters of the real data.

	S-wave velocity (m/s)	P-wave velocity (m/s)	Depth(m)
Layer 01	100 – 450	480	0.2 – 4.0
Layer 02	100 – 450	725	4.5 – 7.0
Layer 03	Fixed (500)	1100	Half Space

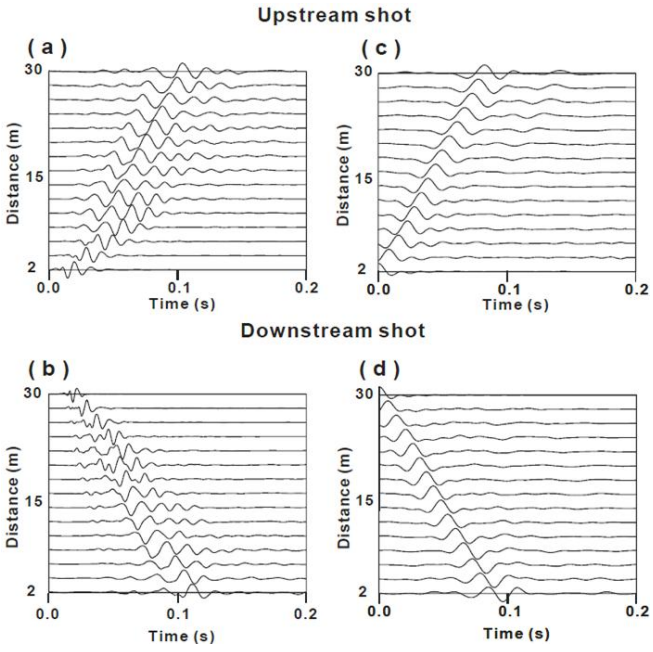


Figure 2 (a,b) Raw acquired data. (c,d) Deconvoluted and filtered waveforms.

The two dimensional averaged model from 5 inversions retrieved from each shot are displayed in Fig.3: The inverted waveforms of both shots show an acceptable fitting between the target waveform and the inverted ones, the main phase

arrivals at each station were well reproduced, except for some inaccuracies on the polarity of the initial breaks at the upstream shot.

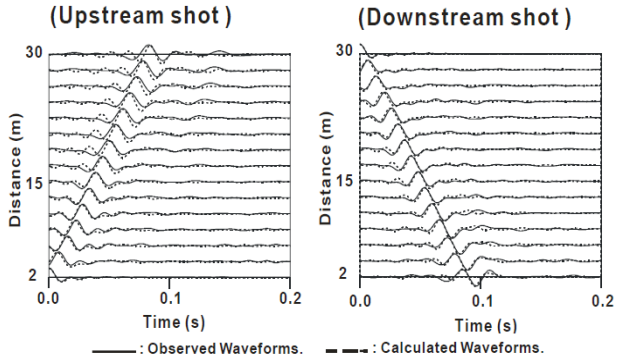


Figure 3 Comparison of the observed and final inverted waveforms.

5. INVERTED 2D PROFILES

The Figure 4 shows the 2D averaged inverted soil model from 5 inversions obtained from each shot. The source location is materialized by a black star and the black dashed lines in the profiles represents the area covered by receivers, zones outside the dashed lines do not enter the scope of observation and are out of our discussion.

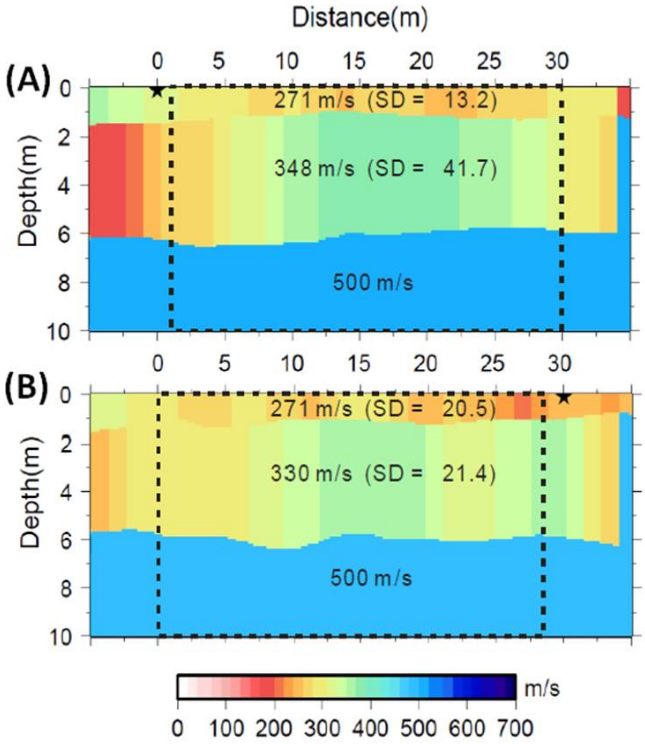


Figure 4 Two dimensional inverted soil models:
(A): Obtained from upstream shot.
(B): Obtained from downstream shot.

Comparing the 2D soil models inverted from each side of the survey line, we can clearly identify the layer boundaries around 1m and 6m depths respectively. The top layer was attributed a similar shear wave velocity of 271m/s. The second layer underlines a notable velocity variation, both profiles clearly underline a tendency of a velocity increasing between 12m and 22m, this lateral velocity is slightly pronounced in the upstream profile with velocities higher than the downstream profile, in fact the averaged velocities of the second layer are respectively 348m/s and 330m/s for both upstream and downstream profiles. This lateral velocity gradient may be explained by a local soil compaction carried out for construction purposes. We also calculated the standard deviation (SD) for block velocities at each layer, the values of the SD are displayed for each model in the Figure.

The detection of this lateral gradient among the second layer illustrates the utility of our approach; this kind of variation can never be detected if we just rely on a borehole data.

In order to validate our inverted models, we compared the inverted results with a borehole data located near the survey area (see Figure 01). To correlate the 2D inverted profiles with the borehole data, we sampled one dimensional profile from both upstream and downstream inverted models at 5m distance. Since our inversion targets are the two first layers of the profile, layers deeper than 6m are out of discussion. The comparison between the shear wave velocity of the borehole and the inverted velocities at 5m distance obtained from both upstream and downstream inversions are illustrated in Figure 5, the standard deviation from 5 inversions at 5m are also calculated and plotted in the figure.

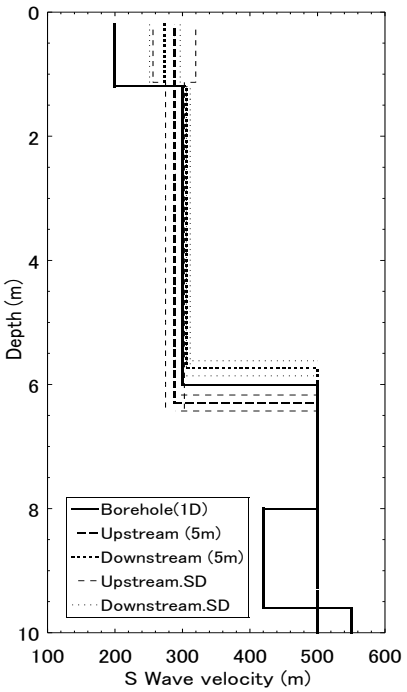


Figure 5 Comparison of the one dimensional Vs profile with standard deviation (SD) from 5 inversions for each shot.

The surface layer was attributed a velocity approximating 280m/s on the upstream profile, and 274m/s on the downstream profile while the borehole gives the surface layer a velocity of 200m/s. This over estimation can be explained by the improvements of the surface layer carried out before the construction. The Figure 6 displays a picture taken during the construction of the parking lot indicating a clear distinction between the original surface and the modified ground upon which the asphalt layer was constructed. The large standard deviation of the velocities from 5 inversions also underlines the difficulty of the algorithm to properly determine the velocity of the surface layer because of its complexity.

The second layer seems to be better estimated than the first layer and both profiles gives relatively close velocities to the borehole velocity.

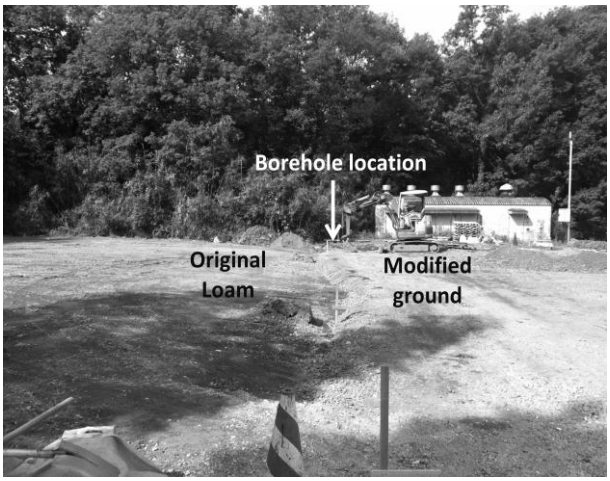


Figure 6 Picture taken during pavement construction.

6. CONCLUSIONS

We succeeded to deduce the two dimensional shallow soil using the full wave form inversion of actual refraction data. Two shots at the upstream and the downstream of the survey line gave models showing similar layer boundaries and approximated velocities, a lateral velocity gradient was revealed by both profiles in the second layer of the soil. Correlation of these profiles with an existing borehole profile showed acceptable agreements of the inverted soil structure except for shallow layer where improvements were carried out for construction purposes.

This method is still under development and the experiment discussed in this paper is just preliminary result. Further developments can be implemented by inverting several shots simultaneously in order to increase inversion precision.

Acknowledgements:

The authors acknowledge support from the Japan Ministry of Education, Culture, Sport, Science, and Technology (MEXT) for establishing the Center for Urban Earthquake Engineering (CUEE) in Tokyo Institute of Technology. This support makes possible the forthcoming international conference, as well as international joint research projects and exchange programs with overseas universities.

References:

Amrouche, M. and Yamanaka, H. (2012), "Determination of 2D shallow S wave velocity profile using waveform inversion of P-SV refraction data". Proceeding of the 15th world conference on Earthquake Engineering.

Aoi, S. Iwata, T and Irikura, K. (1995), "Waveform inversion for determining the boundary shape of the basin structure ". *Bulletin of the Seismological Society of America*, **85**, P1501-1506.

Narayan, J. (1998), "2.5D numerical simulation of acoustic wave propagation". Pure applied Geophysics,**151**,P47-61.

Takekoshi, M. and Yamanaka, H. (2009), "Waveform inversion of shallow seismic refraction data using hybrid heuristic search method". Exploration Geophysics,**40**,P99-104.

Virieux, J., (1984), "P-SV wave propagation in heterogeneous media: Velocity-stress finite difference method". Geophysics. **49**,No11:P1933-1957.

Yamanaka, H., (2007), "Inversion of surface-wave phase velocity using hybrid heuristic search method". Geophysical Exploration,**60**,No3:P265-275.

Yamanaka, H. and Yamauchi, H., (2010), "Waveform inversion of SH waves in seismic refraction exploration for 2D shallow S-wave velocity profile: numerical experiments and application to actual data". Geophysical Exploration,**63**,No4:P321-332.

Zaineh, H.E et al., (2012), "Estimation of Shallow S-Wave Velocity Structure in Damascus City Syria, Using Microtremor Exploration". Journal of Soil Dyn. and Earthq. Eng., **39**: 88–99

10CUEE CONFERENCE PROCEEDINGS
10th International Conference on Urban Earthquake Engineering
March 1-2, 2013, Tokyo Institute of Technology, Tokyo, Japan

RELIABILITY OF DISPERSION MEASUREMENT FROM MICROTREMORS WITH SEISMIC INTERFEROMETRY

Kosuke Chimoto[1], and Hiroaki Yamanaka[2]

1) Student, Interdisciplinary Graduate School of Science and Engineering, Tokyo Institute of Technology, Japan
2) Professor, Interdisciplinary Graduate School of Science and Engineering, Tokyo Institute of Technology, Japan
chimoto.k.aa@m.titech.ac.jp, yamanaka@depe.titech.ac.jp

Abstract: Since cross correlation of microtremor with seismic interferometry is known to give the Green's function between two stations, dispersion measurements with cross correlation functions of microtremors is expanding. However, the reason is still not clear why a cross correlation functions allow us a reliable dispersion measurements, and thus the constraint for the measurements is also not clear. In this work, we establish the reliability of dispersion measurements with cross correlation of microtremors observed in the Kanto region, Japan comparing with theoretical dispersion from estimated S-wave velocity structure. Since previous works shows the success in dispersion measurements only in the range of small wavelength, we compare the result of the measurements with wavelength.

1. INTRODUCTION

Seismic interferometry is known to reconstruct Green's function, and thereby it is extensively used for the dispersion measurements (e.g. Shapiro and Campillo, 2004). It is well known that seismic interferometry depends on the presence of sources in the zone of constructive interference, or stationary phase region by using a stationary phase approximation (Snider, 2004). Only the sources near the line connecting two stations will contribute to the signals observed in the cross correlation function (CCF). Sources at opposite side of the line will contribute to the signal at positive and negative lags in the CCF respectively, and many previous studies have showed that the amplitude of the CCFs become larger from the coastline to the continent (e.g. Gerstoft et al., 2006, Stehly et al., 2006). Therefore, the dispersion measurements with seismic interferometry are often constrained by the interstation distance larger than two or three wavelengths due to the source dependence (e.g. Bensen et al., 2008; Lin et al., 2008). The accuracy of dispersion measurements is also considered theoretically, suggesting the errors may be significant for relatively long-period waves and small station spacing (Tsai, 2009, Lin et al., 2008).

Here, we demonstrate that the reliability of the dispersion measurements with seismic interferometry by using observed microtremors in the Kanto, Japan, acquired with the temporal seismic networks constructed by the authours (Yamanaka et al., 2010). It is found that the errors are significant for long-period waves and small station spacing. Furthermore, we found that the errors become large even in the short-period range.

2. DATA AND DATA PRCESSING

2.1 Data

The authors have deployed the seismometers in the southern Kanto, Japan (Figure 1) for the long-term microtremor observation (Yamanaka et al., 2010). Microtremors were collected more than 1 year. We here use the data observed from August 2009 to July 2010. Unfortunately, the time series at some stations are less than yearlong due to the instrumental troubles.

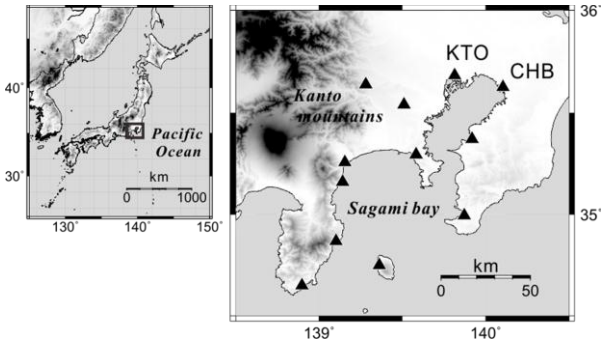


Figure 1. Locations of the long-term microtremor observations.

2.2 Data prcessing

We followed the data processing described in Prieto et al. (2011). The data processing applies no temporal normalization such as 1 bit normalization, which is commonly used in seismic interferometry (Bensen et al., 2007). Moreover, we did not apply filtering in the frequency domain for the microtremors, because it restricts the frequency range for the dispersion measurements. The

coherencies represented by equation 1 are calculated for the divided long-term microtremors with 1 hour segment. The coherencies for each segment are finally averaged and then Fourier inverse transform is performed to obtain the CCF.

$$\gamma_{xy}(\omega) = \left\langle \frac{u_x(\omega)u_y^*(\omega)}{\{|u_x(\omega)|\}\{|u_y(\omega)|\}} \right\rangle \Leftrightarrow C_{xy}(\tau) \quad (1)$$

where the brackets represent an ensemble average, the curly brackets { - } stand for a spectral average or spectral smoothing, the $\Leftrightarrow$ represents Fourier transform. $u_x(\omega)$ and $u_y(\omega)$ are the Fourier transformed ground motion at stations x and y, and C_{xy} represents the crosscorrelation function.

Figure 2 shows the CCFs with various durations of cross correlation time series which are band-pass filtered between 1 – 10 s for the averaged coherency between stations CHB and KTO shown in Figure 1. The waveforms become clearer with increasing the duration, suggesting the long duration gives the better results by reducing the noise.

Figure 3 is all the cross correlation functions estimated with yearlong microtremors with vertical components between all the possible stations pairs shown in Figure 1. The waveforms are filtered between 2 – 6 s periods for the averaged coherency. It is found that the waves are propagating with increasing the interstation distances.

3. FREQUENCY-TIME ANALYSIS

Dispersion can be measured with the frequency-time analysis (FTAN, Dziewonski, 1969). FTAN applies a series of Gaussian filter for the CCF. Figure 4 shows the results of the FTAN for the CCFs with various durations of the cross correlation time series for the positive and negative lags between the stations CHB and KTO shown in Figure 2. The result for the CCFs with the long duration clearly shows the dispersive features. On the other hand, the CCFs with the short duration does not clearly show such features. It indicates that the long duration makes it easier to measure the dispersion. And also the period range for dispersion measurements is broaden with the long duration. The difference between the positive and negative lags may be expected from the waveforms of CCFs as shown in Figure 2. The negative CCFs have much signal than the positive CCFs in both waveforms and the result of the FTAN. This difference is known to coming from the sources (e.g. Gerstoft et al., 2006; Stehly et al., 2006). Although the amplitudes between negative and positive have much difference, the traveltimes which can be observed at the period of about 5 s shows the similarity. This indicates that the seismic interferometry is able to extract the phase of Green's function but is has difficulty in reconstructing its amplitude.

4. DISPERSION MEASUREMENT

The dispersion of Rayleigh wave group velocity is also measured form the FTAN. Figure 5 is the measured dispersion from the CCFs with negative lags between stations CHB and KTO for the duration of 6890 hour illustrated in the bottom of Figure 2. Contour shows the normalized amplitude estimated with the FTAN. Circles are the velocities estimated from the lags of the CCF of which

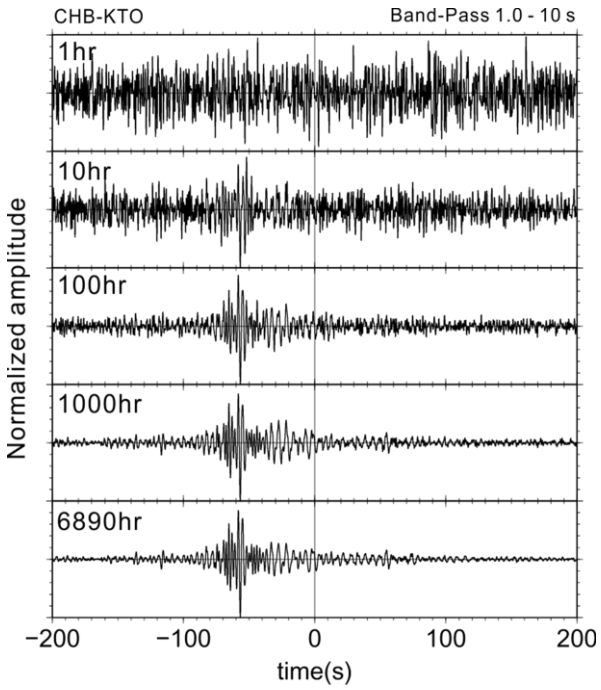


Figure 2. Cross correlation functions with various durations between stations CHB and KTO.

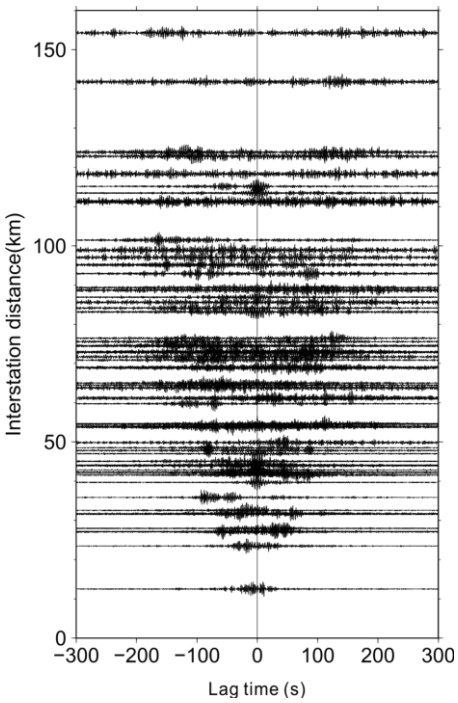


Figure 3. Cross correlation functions with vertical components estimated in the Kanto, Japan.

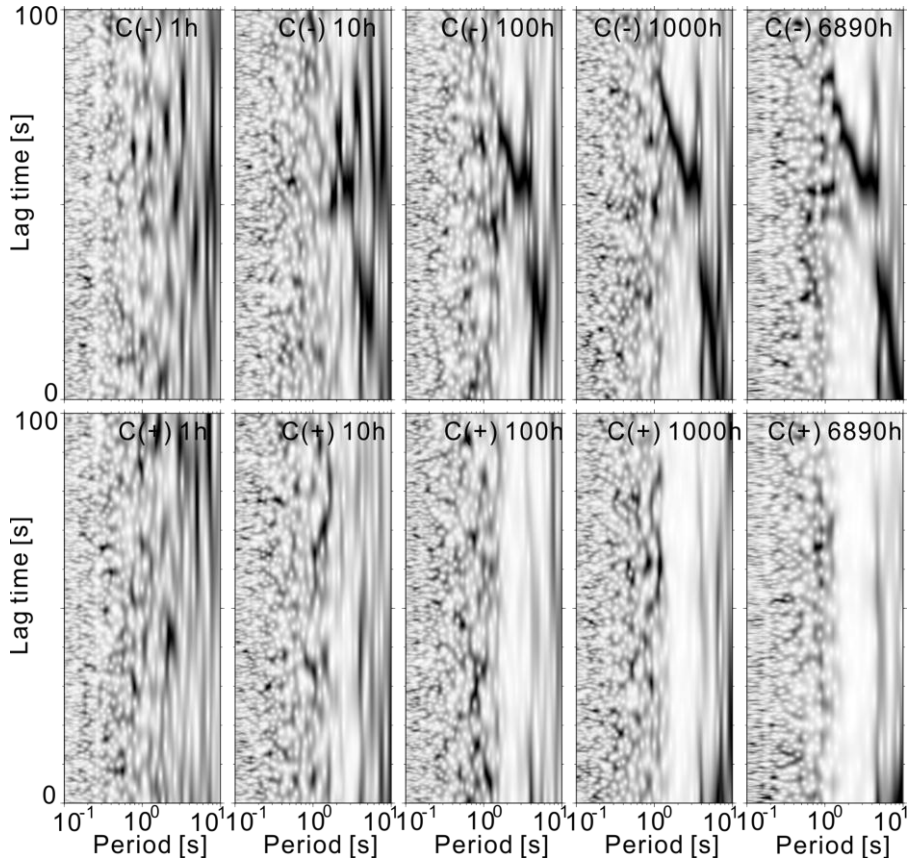


Figure 4. The results of the frequency-time analysis for the CCFs with various durations for the negative (top) and the positive (bottom) lags.

amplitudes attain the maximum value. For the comparison, we also plot the theoretical group velocities of fundamental mode of Rayleigh wave, which is calculated from the previous model of the region proposed by Yamanaka and Yamada (2006). The observed dispersion shows agreement with the theoretical dispersion in the period range from about 1 s to 7 s. However, observed group velocities at the periods above about 7 s are relatively large compared to the theoretical ones. At the period below about 1 s, group velocities are not well observed due to the fluctuation.

According to Aki and Richards (2002), the phase of Rayleigh wave is $i(kr+\pi/4)$, where i represents the imaginary, k and r are the wavenumber and the distance. It is also known that the phase of the cross correlation function is also described with kr (e.g. Snieder, 2004, Tsai, 2009). As mentioned above, the application of the dispersion measurements with seismic interferometry is often used the constraint criterion, minimum three wavelength interstation distance ($kr > 6\pi$). We here discuss about the observed dispersion of Rayleigh wave with kr. In Figure 5, we also illustrate the theoretical kr, which is calculated with the previous model in the region as described above. As we have observed, the errors of dispersion measurements is significant for long periods above about 7 s, which correspond to the kr of about 4π. It is well correspond to the theoretical consideration in Tsai (2009) Figure3, the error between the approximation and the exact velocity occurs

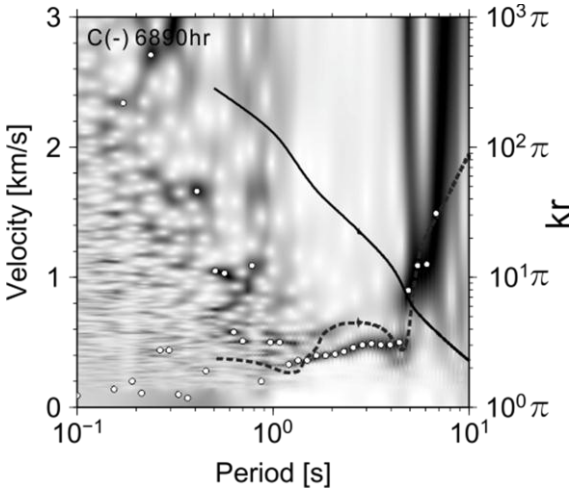


Figure 5. Contour shows the result of the dispersion measurement with the frequency-time analysis. Circles indicate the velocity which observed the maximum amplitude in the CCF. Broken and solid lines indicate the theoretical fundamental mode of Rayleigh wave group velocities and its kr.

about the *kr* below about 15. However, the error observed in the short period below about 1 s, which correspond to the *kr* of about 100π (Figure 5) is not clearly known.

5. RELIABILITY OF DISPERSION MEASURMENT

As we see in the last chapter, the reliability of the dispersion measurements depends on *kr*. In Figure 6, we plot the error of the estimation in the dispersion measurements between observed and theoretical dispersion given by equation 2.

$$Error = \left| \frac{V_{obs.} - V_{cal.}}{V_{cal.}} \right| \quad (2)$$

where $V_{obs.}$ is the observed group velocity and $V_{cal.}$ is the theoretical group velocity after Yamanaka and Yamada (2006). The $V_{obs.}$ is automatically measured as shown by circles in Figure 5 for only the signals can be observed in the dispersion measurements.

Figure 6 shows that the errors of the most of the CCFs are less than 100 percent in the *kr* range between about 5π and 100π. Even the errors of 100 percent are reasonable, because it is known that the Kanto region has three-dimensional high complexity, and the model accuracy is not clear especially around the Kanto basin (Yamanaka and Yamada, 2006). On the other hand, in the *kr* below about 5π and above about 100π, the errors are tremendously large, suggesting the measured dispersion is unreliable. The results shows the range for reliable dispersion measurements is between about 5π and 100π in the Kanto region.

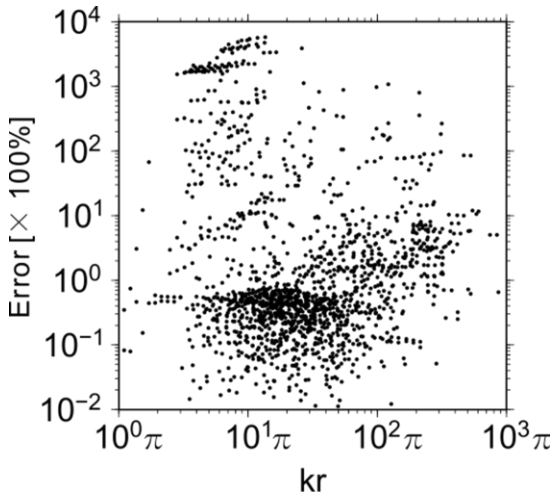


Figure 6. The errors between the observed and theoretical group velocities as a function of *kr*.

6. CONCLUSIONS

For the broad-band reliable dispersion measurements with seismic interferometry, we estimated the cross correlation functions by applying no filtering for the microtremors, acquired in the Kanto, Japan. The frequency-time analysis for the cross correlation functions with various durations of cross correlation time series showed the long duration makes it easier and broaden the period range for dispersion measurements. The comparison between the observed dispersion and theoretical dispersion showed the similarity in the *kr* range about 5π and 100π. However, the errors of measured dispersion out of the range become significant.

Acknowledgements:

We thank many cooperators for constructing the temporal seismic network in the Kanto region. This research was supported by Special Project for Earthquake Disaster Mitigation in Tokyo Metropolitan Area, JSPS KAKENHI Grant Number 22310108 and 23・56272. Kosuke Chimoto is grateful for support from the Japan Society for the Promotion of Science.

References:

Aki, K. and P. Richards, 2002, Quantitative seismology second edition, University Science Books.

Bensen, G. D., M. H. Ritzwoller, M. P. Barmin, A. L. Levshin, F. Lin, M. P. Moschetti, N. M. Shapiro, and Y. Yang, 2007, Processing seismic ambient noise data to obtain reliable broad-band surface wave dispersion measurements, Geophys. J. Int., 169, 1239-1260.

Bensen, G. D., M. H. Ritzwoller, and N. M. Shapiro, 2008, Broadband ambient noise surface wave tomography across the United States, J. Geophys. Res., 113, B05306, doi: 10.1029/2007JB005248.

Dziewonski, A., S. Bloch, and M. Landisman, 1969, A technique for the analysis of transient seismic signals, Bull. Seism. Soc. Am., 59, 427-444.

Gerstoft, P., K. G. Sabra, P. Roux, W. A. Kuperman, and M. C. Fehler, 2006, Green's functions extraction and surface-wave tomography from microtremors in southern California, Geophysics, 2006, 71, SI23-SI31.

Lin, F. C., M. P. Moschetti, and M. H. Ritzwoller, (2008): Surface wave tomography of the western United states from ambient seismic noise: Rayleigh and Love wave phase velocity map, Geophys. J. Int., 173, 281-298, doi:10.1111/j.1365-246X.2008. 03720.x.

Prieto, G. A., M. Denolle, J. F. Lawrence and G. C. Beroza, 2011, On amplitude information carried by the ambient seismic field, C. R. Geosci., 343, 600-614 doi:10.1016/j.crte.2011.03.006.

Shapiro, N. M., and M., Campillo, (2004): Emergence of broadband Rayleigh waves from correlations of the ambient seismic noise, Geophys. Res. Lett., 31, L07614, doi: 10.1029/2004GL019491.

Snieder., R. (2004): Extracting the Green's function from the correlation of coda waves: A derivation based on stationary phase, Phy. Rev. E,, 69, 046610.

Stehly, L., M. Campillo, and N. M., Shapiro, 2006, J. Geophys. Res.., 111, B1306, doi: 10.10290/2005JB004237.

Tsai, V. C., (2009): On establishing the accuracy of noise tomography travel-time measurements in a realistic medium, Geophys. J. Int., 178, 1555-1564, doi:10.1111/ j.1365-246X.2009.04239.x.

Yamanaka, H. and N. Yamada, 2006, Modeling 3D S-wave velocity structure of Kanto basin for estimation of earthquake ground motion, Butsuri-Tansa (Geophys. Explor.), 59, 549-560. (in Japanese)

Yamanaka, H., K. Chimoto, T. Moroi, T. Ikeura, K. Koketsu, M. Sakaue, S. Nakai, T. Sekiguchi, and Y. Oda, 2010, Estimation of surface wave group velocity in the southern Kanto area using seismic interferometric processing of continuous microtremor data, Butsuri-Tansa (Geophys. Expl.), 63, 409-425. (in Japanese)

10CUEE CONFERENCE PROCEEDINGS
10th International Conference on Urban Earthquake Engineering
March 1-2, 2013, Tokyo Institute of Technology, Tokyo, Japan

STUDY FOR SEISMIC MICROZONING IN DAMASCUS CITY, SYRIA, FROM STRONG MOTION SIMULATION CONSIDERING LOCAL SITE AMPLIFICATION

Hussam Eldein Zaineh[1)], Hiroaki Yamanaka[2)], and Yadab Prasad Dhakal[3)]

1) Doctoral candidate, Dept. of Environmental Science and Technology, Tokyo Institute of Technology, Japan.
2) Professor, Dept. of Environmental Science and Technology, Tokyo Institute of Technology, Japan.
3) Doctor, Dept. of Environmental Science and Technology, Tokyo Institute of Technology, Japan.
zaineh.h.ab@m.titech.ac.jp, yamanaka@depe.titech.ac.jp, dhakal.y.aa@m.titech.ac.jp

Abstract: Damage patterns in past earthquakes show that the local site conditions have a major effect on the level of ground shaking. Seismic microzonation, which is a methodology for mapping the seismic hazard at local scales to incorporate the effects of local site conditions, can provide input for urban planning and for assessment of the vulnerability of the building stock for different hazard levels. Site amplification factors were estimated following one dimensional shear wave propagation theory for vertical incident S-wave. We performed a multiple regression analyses with the averaged amplification factor as the criterion variable that defined by different topographic data in Damascus city. We found a good correlation between the site amplification and the elevation as well as the distance from Barada River. We simulated the strong ground motions using the source model of the 1759 Earthquake for a grid points system with 1.0 * 1.0 km in Damascus city. The microzonation maps with respect to peak ground velocity were estimated for the city. The highest values of *PGV* were concentrated at the central and eastern parts of the city. We also discussed the nonlinear amplification in the city following the equivalent linear approximation of nonlinear response of the 1-D soil strata. The non-linearity effects are more remarkable in the high frequency amplification for the central and eastern region of the city; this region suffered mainly from the foundation failure and slumping of the ground during the 1759 earthquake.

1. INTRODUCTION

1.1. Background

Damascus city is located about 30 km in the south-east of Serghaya Fault and might suffer a great damage in the case of big earthquakes along the fault. Serghaya Fault, as a branch of Dead Sea Fault System is considered as the main source of seismic risk potential for the city. Through the last 2000 years, many destructive earthquakes occurred in the region and caused much causality in the metropolitan of Damascus including the old city of Damascus (e.g. Poirier and Taher 1980; Guidoboni et al. 2004; Sbeinati et al. 2005). It is important to note that the seismic activity of DSFS during the last 100 years has been far lower than the historical one. Consequently, the public awareness on earthquake hazard as well as the government efforts toward urban risk mitigation is quite low in Syria.

In this study, site amplification factors were estimated and a multiple regression analysis was performed with the averaged amplification as the criterion variable and topographic data in Damascus city. Then, by using the source model of the November 1759 Earthquake (Zaineh et al. 2012b), the strong ground motions in Damascus city were simulated and the microzonation maps with respect to peak ground velocity were estimated and nonlinearity effects in the city were discussed.

1.2. Tectonic Settings

The Dead Sea Fault System forms the plate boundary that links the Arabian plate convergence in southern Turkey with the active seafloor spreading in the Red Sea. Figure 1(a) shows the plate tectonic settings of DSFS, (b) illustrates the tectonic settings of the northern Arabian plate, and (c) shows the active faults of the central part of the DSFS in Lebanon and southwest Syria. The recent relative motion between the Arabian and African plates is estimated to be 4-8 mm/yr, based on plate models (e.g. Joffe & Garfunkel 1987; Jestin et al. 1994) and recent GPS observations (e.g. McClusky et al. 2000, 2003). This is consistent with the geological estimates of Quaternary slip rates for the southern DSFS (e.g. Garfunkel et al. 1981; Klinger et al. 2000a).

The central part of the DSFS in Lebanon and southwest Syria is a ~ 200 km long northeast-southwest striking restraining-bend that strikes 25º-30º degrees from the main trend of the transform as illustrated in Fig. 1(b). At the southern end of this restraining-bend, the relatively simple trace of the southern DSFS branches into several distinct strike-slip faults (Walley 1988). Primary among these faults are (1) the Yammouneh Fault (YF), which is clearly observed beneath the Bekaa Valley (BV) between the Lebanon Mountains (LM) and the Anti-Lebanon Mountains (AL); (2) the Serghaya Fault (SF) in southwest Syria, which can be traced approximately 125 km through Anti Lebanon Mountains to the eastern edge of the Bekaa Valley; and (3) the Roum Fault (RouF) in southern Lebanon as shown in

Fig. 1(c).

The total length of Serghaya F. and the 2.0-2.5 m displacements, combined with the historical seismicity, suggest that the fault may be capable of generating large (M ~ 7) earthquakes. The results also suggest a slip rate of about 1.4 mm yr-1, with an average of approximately 2 m of slip per event at this location and a mean return period of about 1300 yr (Gomez et al. 2001 , 2003).

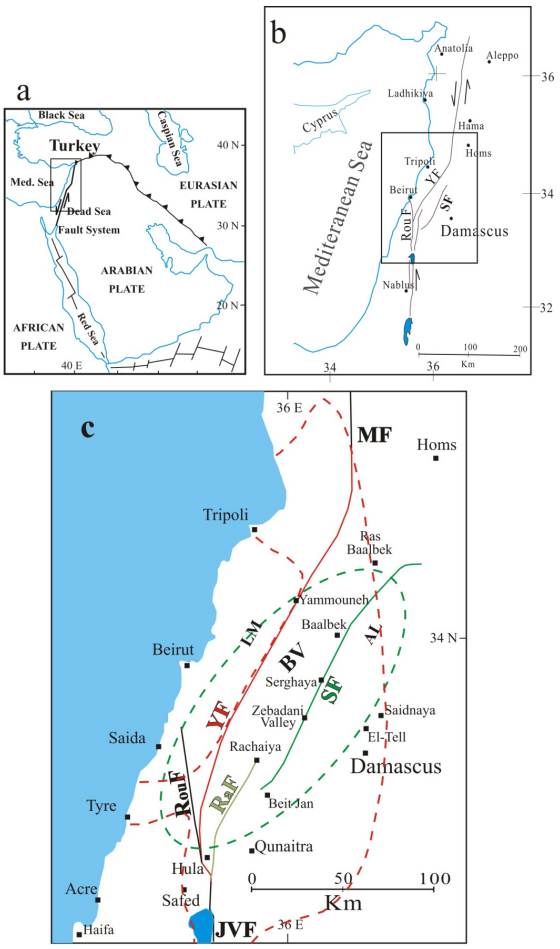


Figure 1(c) Plate tectonic context of DSFS. (b) Tectonic settings of the northern Arabian plate. (c) Active faults of the central part of the DSFS in Lebanon and southwest Syria.

1.3. Geology and Site Characterization of Damascus

Damascus city occupies the mostly part of Dimashq basin (Damascus basin), which is located to the south-western part of Syria. The north-western part of Damascus was formed after many tectonic evolutions that affected the region and started in Mesozoic period. As a result, many folding structures appear as Mt. Qasyoun and Mt. El-Qalamoun which bounded the basin at the north-west (Ponikarov, 1963). The south-eastern part of the area is quite different from the folded mountain system. It is a depression zone characterized typically by platform dislocations and intensive basaltic eruption (Ponikarov, 1963). The eruption of basalts in this area began in the middle Miocene and continued during the Pleistocene and as a result, some basalt flow reaches as far as about 20 km south of Damascus as Mt. El-Mane and Mt. El-Madani which bounded the basin at the south (Dubertret, 1929; 1940). Actually, the basin is filled by deposits of the surrounded heights and deposits carried by Barada River which flows through the basin and forms the lowland of the basin. Figure 2 shows the geological map of Damascus city, it is clear that the main part of the city lies on the sedimentary basin (Damascus Basin) and belong to the same geological category (Q_3). Single site Microtremor measurements were carried out for 300 sites in Damascus city. Horizontal to Vertical (H/V) spectral ratios were calculated and the results show big variations in H/V curves from area to area in Damascus city (Zaineh et al. 2010).

Zaineh et al. (2012a) estimated the shallow S-wave velocity structure at 30 sites in the city by using short-period microtremor explorations (sites locations are shown in Fig. 2). They estimated shear wave velocities and thicknesses of the layers down to the engineering bedrock (V_S ~750 m/s) by an inversion of Rayleigh wave phase-velocity data. Following a trial and error procedure, S-wave velocity of the deep soil layer (V_S ~1600 m/s) underline the engineering bedrock as well as the thickness of the engineering bedrock were assumed by fitting the theoretical ellipticities of Rayleigh wave with observed H/V of microtremors (Zaineh et al. 2012a). The deep soil layer was found to be uniform in the city. While the shallow structure (overlain the deep layer) is not uniform in Damascus city and there is a wide variation in the S-wave velocity and thickness of the shallow soil layers and the city can be divided into three different regions (***a, b***, and ***c***).

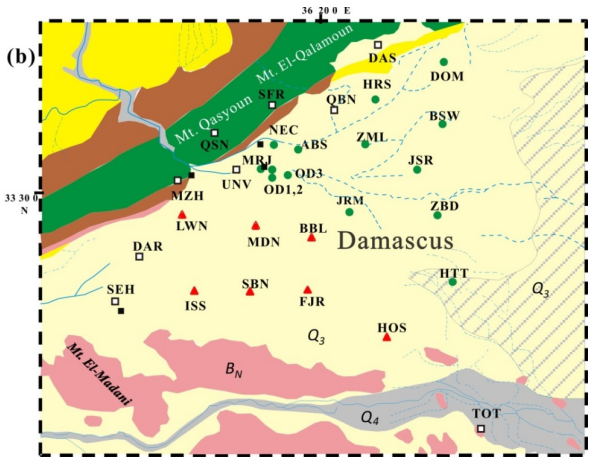


Figure 2 Geological Map of Damascus city (Ministry of Industry, 1963) with the locations of microtremor survey sites. Circles, squares, and triangles denote the sites of ***a, b***, and ***c*** regions respectively

2. SEISMIC MICROZONING OF SITE AMPLIFICATION

2.1 1-D site amplification factor

Site amplification factors were calculated by following

one-dimensional shear wave propagation theory for vertical incident S-wave using the resulted V_S structure (Zaineh et al. 2012a). We considered the uniform deep soil layer (V_S ~1600 m/s) as a half-space layer. Figure 3 shows the computed site amplification factors for the all sites of group ***a, b,*** and ***c***. The results show that region ***a*** has the highest site amplification among the regions due to the presence of a soft layer (V_S *~200 m/s*) near the surface which controls the site amplification in this region while the ***c*** region has the lowest site amplification.

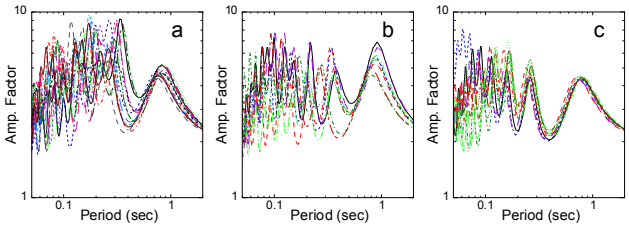


Figure 3 Computed site amplification factors for the all sites of group ***a, b,*** and ***c*** in Damascus city.

2.2. Amplification factor vs. topographic data

Since a topographic data are available for all areas with uniform sampling for the globe, while information about the surficial geology and shear wave velocity do not exist for many regions in the world. Intuitively, topographic data should be used as an indicator of the near-surface geomorphology and lithology to the first order, with steep mountains indicating the rock, nearly flat basins indicating the soil. Recently, many studies have confirmed a good correlations between the V_{S30} (V_{S30} internationally is well correlated with the site amplification) and the topographic conditions as well as the geomorphologic unit (Gallant J. C. et al. 2003; Matsuka M. et al. 2005; Chiou B. S. J. et al. 2006; David J.W. et al. 2007).

The averaged amplification factors (*AF*) for a period range (0.1s – 2.0s) for the 30 sites in Damascus city were estimated (Figure 3). The 30 sites have corresponding *AF* and elevation parameter (E_v) and we introduced the distance from the nearest river (D_r) as a possible geographic condition. For the elevation data, we used the SRTM data (3arcsec) to extract the elevation map of Damascus city. For the distance from river (D_r), it was calculated by considering the Barada River with its branches that shown in the blue lines in Fig. 2. We performed a multiple regression analyses with the average site amplification (*AF*) as the criterion variable that defined by E_v and D_r as independent parameters as shown in equation (1). In order that the numeric data are uniform (E_v and D_r), the data were standardized as shown in equation (2):

$$\log(AF) = 0.583 - 0.028 * \log(E_V') - 0.042 * \log(D_r') \quad (1)$$

$$X_i' = (X_i - \bar{X})/\sigma_x \quad (2)$$

Where, X_i is the original data, X_i' represents the standardized data, $\bar{X}$ is the mean value, σ_x is the standard deviation, and E_V' & D_r' are the standardized values of E_v and D_r. We found a good correlation between the site amplification and topographic conditions (E_v and D_r). This relationship can be used for seismic hazard assessment even though it needs to be improved. Figure 4 shows a comparison between the averaged amplification factors (*AF*) and the calculated ones (AF_{reg}) derived from the above equation (Eq. 1).

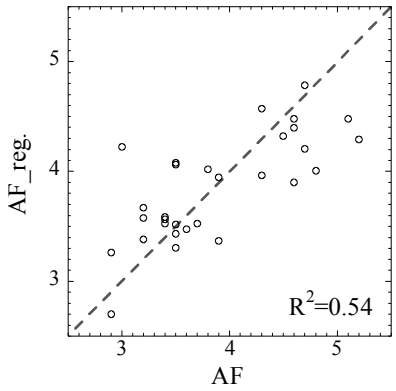


Figure 4 Comparison between the averaged amplification factors (*AF*) and the calculated ones derived from regression analysis (AF_{reg})

3. CHARACTERISTIC OF EARTHQUAKE GROUND MOTIONS IN DAMASCUS

Zaineh et al. (2012b) constructed a source model of the 1759 Earthquake and the appropriateness of their source Model was validated by comparing the calculated intensities with the observed ones by Ambraseys & Barazangi (1989). The strong ground motions in Damascus city were simulated and compared with the design requirements in the Syrian building code. Grid systems with 1.0 km * 1.0 km cells were adopted in Damascus city (Dashed lines in Fig. 6 and Fig. 7). We simulated the ground motions at the top layer of V_S = *1600 m/s* at each grid point using the source model of the 1759 Earthquake. Figure 5 shows the simulated velocity waveforms at the top layer of V_S = *1600 m/s* at some grid points in Damascus city. The horizontal peak ground velocity (PGV_{1600}) at each grid point was calculated from the root-mean-square combination of the two horizontal components. Figure 6 presents the distribution of PGV_{1600} at the top layer of V_S=*1600 m/s*. Generally, there is a decreasing in the values of PGV_{1600} from the north-western to the south-eastern sides of Damascus city. The largest values of PGV_{1600} (~45 cm/sec) were concentrated in the north-western sites that are the nearest to the central asperity in the proposed source model (Zaineh et al. 2012b). The smallest values (~15cm/sec) were concentrated in the south-eastern parts of Damascus city which are the farthest from the source.

Using the relationship between the averaged amplification factors (*AF*) with the elevation (E_v) and distance from river (D_r) (Eq. 1), we calculated the PGV_S at

the ground surface as follows:

$$PGV_S = PGV_{1600} * AF \qquad (3)$$

Figure 7 illustrates the distribution of PGV_S at the ground surface in the city of Damascus. Generally, the largest values of PGV_S were concentrated in the central and eastern parts of Damascus (region ***a***) due to the high site amplification in this area. And the smallest values were concentrated in the southern parts of the city (region ***b***).

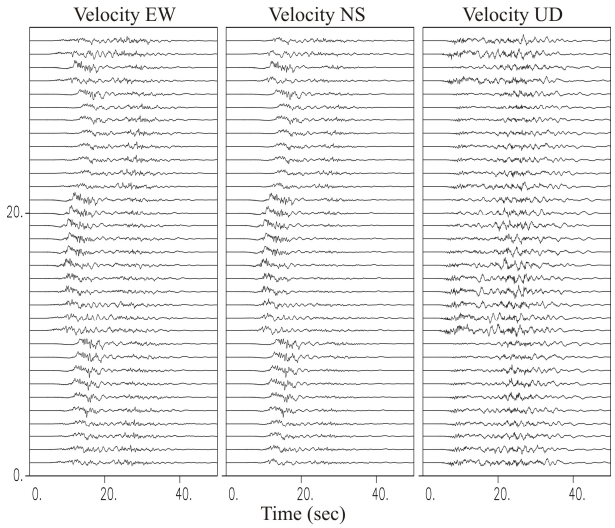


Figure 5 Simulated velocity waveforms at the top layer of V_S = *1600 m/s* at some grid points in Damascus city

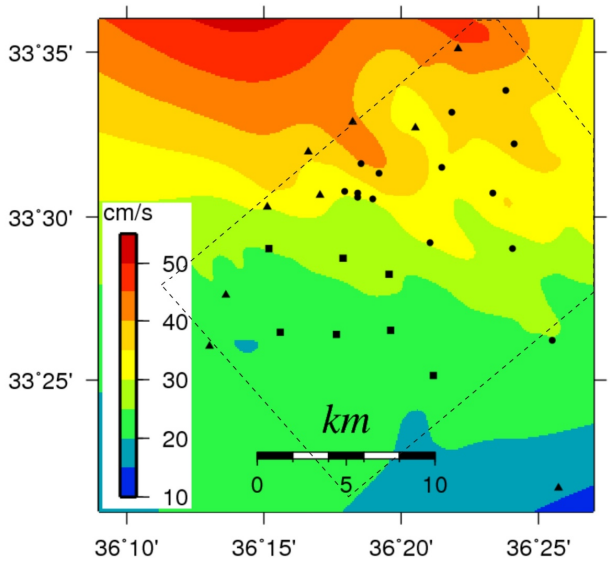


Figure 6 Distribution of PGV_{1600} at the top layer of V_S=*1600 m/s* in Damascus city, circles, squares and triangles represent the sites of groups ***a, b,*** and ***c*** respectively.

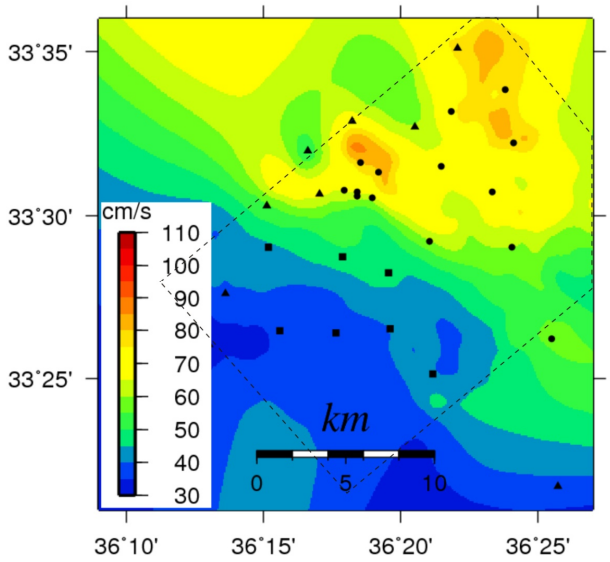


Figure 7 Distribution of peak ground velocities at the ground surface in Damascus city; circles, squares and triangles represent the sites of groups ***a,*** ***b,*** and ***c*** respectively.

4. NONLINEARITY EFFECTS IN DAMASCUS CITY

The simulated waveforms at the top layer of V_S=*1600 m/s* (Fig. 5) were used as input for 1-D site response analysis. Following the equivalent linear approximation of nonlinear response (Schnabel et al. 1972), we estimated the non-linear amplification factors. We used Koyamada's Model to express the nonlinear relations between the shear strain S_e with the shear modulus G, and the damping factor ***h*** (Miura et al. 2001). Figure 8 shows site amplification factors for some sites in Damascus city belong to different regions, the red doted lines represent the non-linear response and the solid lines represent the linear response of the soil strata at each site. The non-linearity effects are more remarkable in the high frequency amplifications of the sites of ***a*** region located in the central and eastern parts of the city than the sites of ***b*** and ***c*** regions due to the shallow soft layers in the ***a*** region sites. The non-linear transfer functions (amplification factors) of ***a*** region sites (DOM, ZBD, and HTT) were shifted toward lower frequencies as shown in Fig. 8. The non-linear effects are very small in the ***b*** and ***c*** regions where stiffer soil layers were observed.

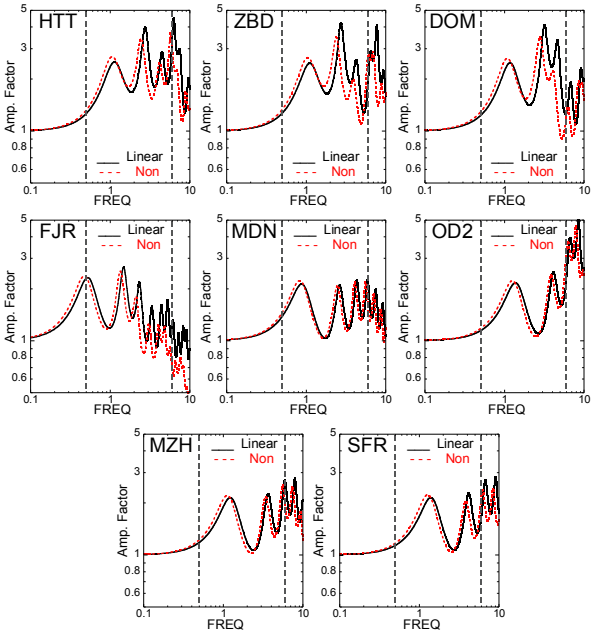


Figure 8 Site amplification factors for some sites in Damascus city belong to different regions, red doted lines represent the non-linear response and the solid lines represent the linear response of the soil strata at each site

5. CONCLUSIONS

Site amplification factors were calculated by one-dimensional shear wave propagation theory for vertically incident S-wave by using the resulted 1-D soil profiles (Zaineh et al. 2012a). The results show that region ***a*** has the highest site amplification among the regions due to the presence of a shallow soft layer (V_S *~200 m/s*) which controls the site amplification while the ***c*** region has the lowest site amplification.

We performed a multiple regression analyses with the average site amplification (*AF*) as the criterion variable that defined by different independent parameters in the case of Damascus city. We found a good correlation between the site amplification and topographic conditions (E_v, and D_r). The obtained relationship can be used for seismic hazard assessment even though it needs to be improved.

The microzonation maps with respect to peak ground velocity were estimated for Damascus city. The largest values of PGV_S were concentrated in the central and eastern parts of Damascus (region ***a***) due to the high site amplification in this area. And the smallest values were concentrated in the southern parts of the city (region ***b***).

We discussed the nonlinear amplification in the city following the equivalent linear approximation of nonlinear response of the 1-D soil strata. The non-linearity effects are more remarkable in the high frequency amplification for the central and eastern region of the city; this region was suffered mainly from the foundation failure and slumping of the ground during the 1759 earthquake.

Acknowledgements:

We are really indebted to Prof. Sasano, Prof. Seo, Dr. Foujita and Dr. Morita at Tokyo Institute of Technology for their highly intensive support. We also would like to express our thanks to Dr. Daoud, Miss. Dakkak, Mr. Ibrahim and Mr. Alchalbi for their help in discussion. Furthermore, we acknowledge a financial support of Center for Urban Earthquake Engineering (CUEE) under the G-COE program of the Ministry of Education, Culture, Sports, Science and Technology (MEXT) in Japan. Some of the figures in this paper were made using GMT software (Wessel P. and Smith WHF, 1991).

References:

Alhourani A. et al. (2012) Framework for performance-based seismic design approach for developing countries, Proceedings of the 32nd Conference on Earthquake Engineering, JSCE, Japan

Ambraseys N.N, and Barazangi M. (1989) The 1759 earthquake in the Bekaa Valley: implications for earthquake hazard assessment in the Eastern Mediterranean region. J. Geophys. Res., 94: 4007–4013

Chiou B. S.-J., and Youngs R. R. (2006) PEER-NGA empirical ground motion model for the average horizontal component of peak acceleration and pseudo-spectral acceleration for spectral periods of 0.01 to 10 seconds, Interim Report for USGS Review, 219 pp

David J. W., and Trevor A. I. (2007) Topographic Slope as a Proxy for Seismic Site Conditions and Amplification, Bull. Seism. Soc. Am. 97, 5, 1379–1395

Dubertret. L. (1929) Etudes des règions volcaniques du Haouran, du Djebel Druse et du Diret el Jouloul (Syrie). Reo. gèogr. phys. et gèol. dynam., 2: 275 – 321

Dubertret. L. (1940) Sur l'âge du volcanisme en Syrie et du Uban. C. r. Soc. géol. Fr., 55 – 57

Gallant J. C., and Dowling T. I. (2003) A multiresolution index of valley bottom flatness for mapping depositional areas, Water Resour. Res. 39, doi 10.1029/2002WR001426

Garfunkel Z et al. (1981) Active faulting in the Dead Sea rift, Tectonophysics, 80: 1–26

Gomez F et al. (2001) Coseismic displacements along the Serghaya fault: an active branch of the Dead Sea fault system in Syria and Lebanon. J. Geol. Soc. Lond., 158: 405–408

Gomez F et al. (2003) Holocene faulting and earthquake recurrence along the Serghaya branch of the Dead Sea fault system in Syria and Lebanon. Geophys. J. Int., 153: 658–674

Guidoboni E et al. (2004) The 1138-1139 and 1156-1159 destructive seismic crises in Syria, south-eastern Turkey and northern Lebanon. J. of Seism., 8: 105-127

Klinger Y et al. (2000a) Slip rate on the Dead Sea transform fault in the northern Araba Valley (Jordan). Geophys. J. Int., 142: 755–768

Jestin F et al. (1994) The Somalia plate and the Eastern Africa Rift System: present-day kinematics, Geophys. J. Int., 116: 637–654

Joffe S., and Garfunkel Z. (1987) Plate kinematics of the circum Red Sea—a re-evaluation, Tectonophysics, 141: 5–22

Matsuoka M. et al. (2005) Nationwide site amplification zoning using GIS-based Japan Engineering Geomorphologic Classification Map, in Proc. 9th Int. Conf. on Struct. Safety and Reliability, 239–246

McClusky S et al. (2000) GPS constraints on plate motion and deformation in the eastern Mediterranean: Implications for plate dynamics. J. Geophys. Res., 105: 5695–5719

McClusky S et al. (2003) GPS Constraints on Africa (Nubia) and Arabia plate motions. Geophys. J. Int., 155: 126–138

Miura K et al. (2001) Response spectrum method for evaluating nonlinear amplification of surface strata, Journal of Structural and Construction Engineering, Transaction of Architectural Institute of Japan, 539: 57-62

Ministry of Industry (1963) Geological map of Syria, I-36-XII I-37-VII, Dimashq Sheet scale 1:200,000

Poirier J P, and Taher M A (1980) Historical seismicity in the Near and Middle East, North Africa, and Spain from Arabic documents (VIIth–XVIIIth century). Bull. Seism. Soc. Am., 70: 2185–2201

Ponikarov V.P. (1963) Explanatory Notes on the Geological Map of Syria, Scale 1:500,000, Part 1 Stratigraphy, Igneous Rocks and Tectonics. Ministry of Geology, Russia

Sbeinati M R et al. (2005) The historical earthquakes of Syria: an analysis of large and moderate earthquakes from 1365 B.C. to 1900 A.D., Ann. Geofis., 48(3): 347-435

Schnabel P B et al. (1972) SHAKE: - a computer program for earthquake response analysis of horizontally layered sites. Report EERC72-12, Earthquake Engineering Research Center, Univ. of California, Berkeley

Walley C (1988) A braided strike-slip model for the northern continuation of the Dead Sea fault and its implications for Levantine tectonic. Tectonophysics, 145: 63-72

Wessel P Smith W H F (1991) Free software helps map and display data. EOS, Trans. Amer. Geophys. U., 72(441): 445-446

Zaineh H E et al. (2003) Classification of public buildings according to their resistance to earthquake loads. Tech. Report, General Est. of Geology and Mineral Resources, Syria. (In Arabic)

Zaineh H. E. et al. (2010) Preliminary Seismic Micro-Zoning Study for Damascus City by Using Microtremors, Proc. of the 14th European Conf. on Earthquake Engineering, Macedonia

Zaineh H. E. et al. (2012a) Estimation of Shallow S-Wave Velocity Structure in Damascus City Syria, Using Microtremor Exploration. J. of Soil Dyn. and Earthq. Eng. 39: 88–99

Zaineh H. E. et al. (2012b) Strong motion simulation during the November 1759 Earthquake along Serghaya Fault in the metropolitan of Damascus, Syria. Submitted to the Journal of Seismology (JOSE-S-12-00158)

10CUEE CONFERENCE PROCEEDINGS
10th International Conference on Urban Earthquake Engineering
March 1-2, 2013, Tokyo Institute of Technology, Tokyo, Japan

IMPROVED METHOD OF DATA ANALYSIS FOR THE GRAVITY AND MAGNETIC EXPLORATION SYSTEM

Satoshi Tokue[1)], Yumiko Ogura[1)], Hitoshi Morikawa[2)], Shigeo Matsuda[3)], Masayuki Saeki[4)], Takuya Suzuki[5)], and Eri Ohzawa [5)]

1) Graduate Student, Dept. of Built Environment, Tokyo Institute of Technology, Japan
2) Professor, Dept. of Built Environment, Tokyo Institute of Technology, Japan
3) Clover tech Inc., Japan
4) Associate Professor, Dept. of Civil Engineering, Tokyo University of Science, Japan
5) Graduate Student, Dept. of Civil Engineering, Tokyo University of Science, Japan
tokue.s.aa@m.titech.ac.jp

Abstract: Making a model of ground structure is one of the most important topics in aspect of the earthquake ground motion prediction of a certain area. For the purpose, we are now developing a gravity and magnetic exploration system for moving careers. To discuss the sensitivity and practicability of the exploration system, air-borne survey had been carried out in Oct. 15th, 2012. We set the system on the autonomous-cruise-type uninhabited helicopter and navigate it over a concrete gravity dam with some magnetic body. Data analysis method have been applied to the observed data, and compare them with theoretical gravity effect which calculated by the terrain model. Finally, the improvement in these methods has been discussed.

1. INTRODUCTION

It is important for the regional earthquake disaster prevention to make an estimation model of ground structure and clarify the non-fairing nature of the ground in detail. For this purpose, gravity and magnetic surveys can be used to estimate the deep and vast velocity and density structures of the ground because of quick observations.

To observe over a very large area, it is desirable that observation sensors are installed on moving careers. However, these careers such as airplane or ships usually make very large vibration noise that might mask the signal we want. Conventional airborne or shipboard gravimeter has such a complicated and huge system to shutout the disturbance and to retain the sensor vertical by means of stabilized platform which controlled by the mechanical or fiberoptic gyroscope for accurate gravity observation. Also, very accurate measurement of position is required for the correction of the Eotvos effect.

Nowadays, since these implements such as gyroscopes, accelerometers, computers and GPS measurement system are dramatically improved, observation system becomes much smaller and higher-performance. We now aspire to make observation system simple, which sensors installed directly on the career, then correct the observed data by post processing from the accurate posture data. Furthermore, the new accelerometer sensor "D-servo", which has enough dynamic range for the carrier disturbance and resolution for detection of gravity anomaly had been developed as shown in Yokoi et al. (2012).

To discuss the sensitivity and practicability of the exploration system, air-bone survey has been carried out. We set the observation system on an autonomous-cruise-type uninhabited helicopter and navigate it over a huge concrete gravity dam, which makes big gradient in gravity, with some magnetic body as flood spillway. By means of GPS data of each cruise, theoretical gravity is calculated from terrain model made of 50m-mesh rectangular parallelepiped which height is altitude. Effects of stored water and dam itself are also considered. Some data analysis methods is applied to the observed data, and then compared with the result of the theoretical calculation to evaluate the system performance. Finally, the improvement of the proposed methods is discussed.

2. AIRBORNE OBSERVATION

2.1 Summarize of the Observation

The air-borne survey carried out on Oct. 15th, 2012, at a concrete gravity dam of Shizuoka pref., Japan. This dam is 155.5m height, 293.5m length, and 326,848,000m^{3}of impoundment (Figure 1). There is a flood spillway made of steel, which is magnetic body, on the top of the dam.

Schema of observation is shown in Figure 2. The helicopter navigates upper and lower stream of the dam body for 500m each in constant velocity 2m/sec. The height of these cruise are fixed to 50m or 70m from the base station at each

cruise. We set 3 cruise courses as shown in Figure 3. Except for the arrival and departure, helicopter is controlled automatically by the program, so that it is possible to keep the height, speed and course during the cruise. At first, the helicopter flew up to the start point of the course in upper stream, then start cruise in constant velocity and height to the lower stream. After it reached to the end point of the course, it flew back the same course in same speed without changing the heading direction. At the end of each cruise, the helicopter came back to the base station for data logging and oiling.



Figure 1 Observation Site

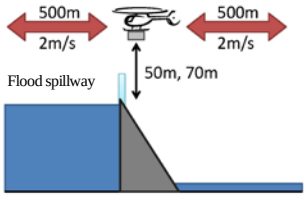


Figure 2 Schema of Survey

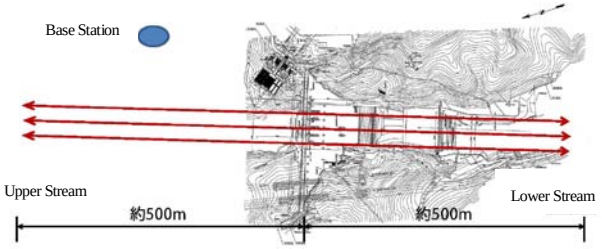


Figure 3 Cruise Course

2.2 Details of Exploration System

Sensors used for our exploration system are listed in Table 1. Since the helicopter cannot load heavy equipments, total weight of sensors and data loggers must be less than 10kg. We have 2 accelerometers for gravity detection; D-servo and VSE-156SG (both are made by Tokyo Sokushin; it is called VSE). These 2 sensors have enough resolution to detect gravity anomaly in mGal order, however VSE sensor has low dynamic range that cannot allow the large disturbance of the helicopter if the weather is too windy. In addition, there are 3-axis accelerometer, named hereafter Titan (Nanometrics) as inclinometers, Cesium magnetometer (Geometrics) for magnetic survey, and GPS & IMU unit (NovAtel, & Tamagawa Seiki) for the positioning detection system. These sensors and data loggers are set under the helicopter as shown in Figure 4. Cesium magnetometer is suspended under the helicopter since helicopter itself is also magnetized. Furthermore, GPS unit and Proton magnetometer had been set at the base station for reference. All data loggers are synchronized with GPS clock so that accurate time can be obtained in different sensors.

Table 1 Sensors of Exploration System

Sensor	Use	Range
D-servo (Tokyo Sokushin)	gravimeter	±992 [Gal]
VSE-156SG (Tokyo Sokushin)		±50 [Gal]
Titan (Nanometrics)	inclinometer	±4x980 [Gal]
Cesium Magnetometer (Geometrics)	magnetometer	-
GPS(NovAtel) & IMU (Tamagawa)	positioning	-

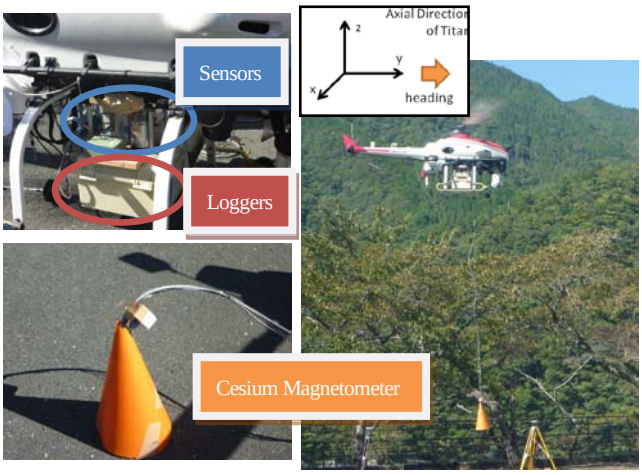


Figure 4 Exploration System

3. THEORETICAL CALCULATION

3.1 Gravity of Rectangular Prism

For calculation of the gravitational terrain effect, we assume geographical features as the set of rectangular prism whose height is an altitude. Exact solution of the gravitational attraction of a rectangular parallelepiped is obtained in Nagy (1966), and the formula simply deformed by Banajee and Das Gupta (1977). Let the coordinate of the measurement point(x_s, y_s, z_s), gravitational attraction caused by a rectangular prism whose base is rectangular with sides $x_{i+1} - x_i$ and $y_{j+1} - y_j$, height is h_{ij}, can be written as Eq.1 below:

$$g_{ij} = \frac{1}{2}G\rho\left[x\ ln\frac{R+y}{R-y} + y\ ln\frac{R+x}{R-x} - 2z\ tan^{-1}\frac{xy}{zR}\right]\Big|_{x_i - x_s}^{x_{i+1} - x_s}\Big|_{y_j - y_s}^{y_{j+1} - y_s}\Big|_{-z_s}^{h_{ij} - z_s},$$

where $R = \sqrt{x^2 + y^2 + z^2}$ and $[f(x,y)]\Big|_{x_1}^{x_2}\Big|_{y_1}^{y_2} = [f(x_2,y_2) - f(x_1,y_2)] - [f(x_2,y_1) - f(x_1,y_1)]$ (1)

Here, G is the gravitational constant and ρ is the density.

If we think that we can approximate the effect of the rectangular prism of horizontal cross-sectional area S with the effect of the center axis line of the prism which the density of the prism compressed into, that is, linear density approximation, we can rewrite Eq.1 into Eq.2 as follows:

$$g_{ij} = -G\rho S\left[\frac{1}{R}\right]\Big|_{h_{ij} - z_s}^{-z_s}$$
$$h_{ij} = \frac{z_{ij} + z_{(i+1)j} + z_{i(j+1)} + z_{(i+1)(j+1)}}{4} \quad (2)$$
$$R = \sqrt{\left(x_s - \frac{x_i + x_{i+1}}{2}\right)^2 + \left(y_s - \frac{y_j + y_{j+1}}{2}\right)^2 + {z_s}^2}$$

It is said that if the measurement point is too close to the prism, errors in Eq.2 cannot be neglected. At the observation in this study, since the measurement point is on the helicopter which parted from the ground surface, enough accuracy is satisfied in the calculation by means of Eq.2.

Either case using Eq.1 or Eq.2, since these gravity attractions are expressed in linear combination, total gravity of the whole model can be obtained as Eq.3:

$$g_{ALL} = \sum_i \sum_j g_{ij} \quad (3)$$

3.2 Terrain Model and Other Corrections

Flowchart of how to calculate theoretical gravity is shown in Fig.5. Terrain model is made from 50m-mesh altitude data provided by Geospatial Information Authority of Japan, as shown in Fig.6. Since x and y axis show numbers of meshes, size of the whole area we used at the calculation is 20 x 10km. However, the altitude data does not distinguish between ground and water surface, which difference of the density between these two elements must be considered for the calculation. Furthermore, gravitational effect caused by the dam body itself should be also considered. We make two layers, stored water layer and dam body layer above the field layer in the model. From Eq.3, we can calculate these 3 different layers apart and then sum up for the total gravity.

For the calculation, actual position of the helicopter is also required. GPS data are corrected and converted into latitude, longitude, height, velocity, and azimuth. Position data are converted into xyz coordinates to map on Fig.6, then gravitational terrain effects are obtained from Eq.2. Free air corrections and Eotvos corrections are also obtained here by using latitude, height, velocity and azimuth. Example of calculated reference gravity is shown in Fig.7. We can see that terrain gravitational effect is less than 10 mGal, and Eotvos effect is about 20 mGal during the flight.

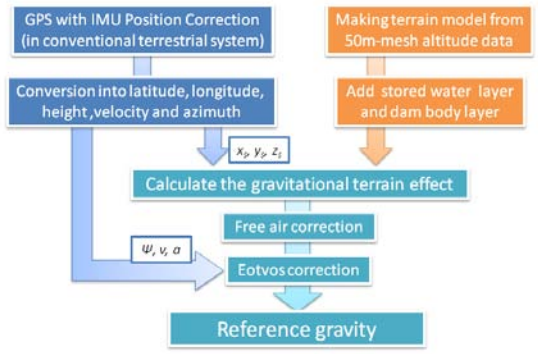


Figure 5 Flowchart of Theoretical Gravity Calculation

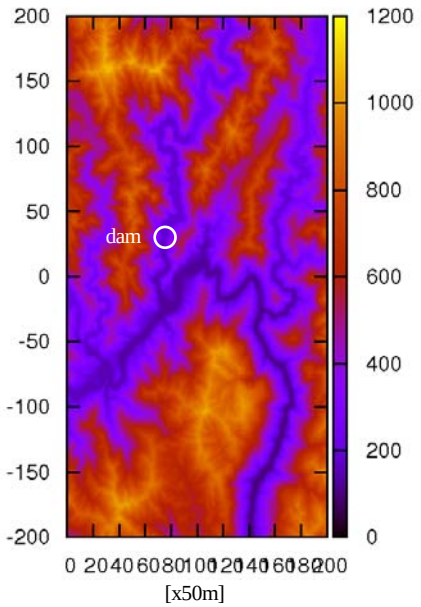


Figure 6 50m-mesh Field Data

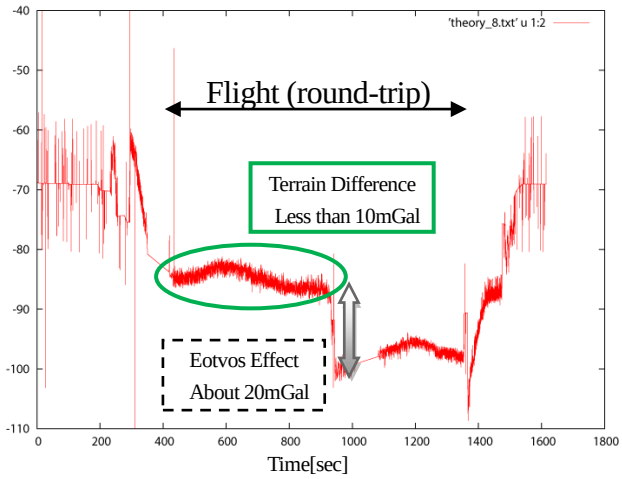


Figure7 Example of Obtained Reference Gravity

4. OBSERVED DATA

4.1 Magnetic Survey

Examples of observed magnetism are shown in Fig.8. These two figures show the magnetism of the same course, the center red line in Fig.3, which go through just over the magnetic body at the dam top, in different height, 50m and 70m from the level of the base station. Without any analysis, we can clearly see that sensors detect the magnetic body in stable. In addition, at different height, sensor only detect the magnetism intensity difference during the time pass through over the magnetic body, but almost same at other points. We can say that the sensor working very well to detect the effect of magnetic body.

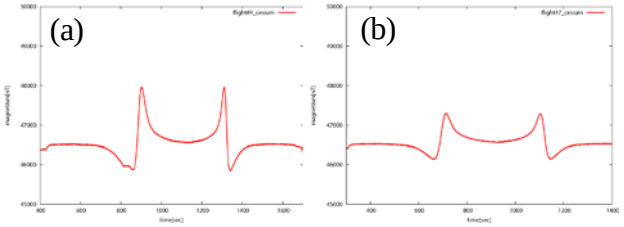


Figure 8 Magnetism in same course at different height (a)50m and (b)70m

4.2 Gravity Survey

Unlike magnetic data, effects of vibration or inclination of the career is much larger than gravity anomaly we want. Therefore, we can tell very few things from raw signals. To see details of gravity data, long-period low pass filter is required to ignore the short-term disturbance caused by careers. Fig.9 shows theoretical gravity obtained in Fig.7 and observed accelerometer data filtered by 5th Butterworth filter with cutoff 45 sec. Here, VSE and D-servo are gravimeters, and Titan is 3-axis accelerometer for detection of inclination, and positive direction of Z-axis is set downward so that gravitational effect is indicated in positive.

At a glance view of Fig.9, it seems that gravimeters describe main tendency of theoretical gravity in some extinct. However, their amplitude is quite different from calculated theoretical gravity. For example, we can note from Fig.7 that

amplitude of Eotvos effect is just about 20 mGal. On the other hand, difference we can see in the middle in gravimeters of Fig.9 is much larger, about 1Gal. It is clear that there are some other causes which make such a big difference in sensor outputs, that is, inclination of the career. Output of titan x and y, that are illustrated in Fig.9, also have a big difference at the same time. It suggests that there is long term inclination in cruise, during going and returning. Furthermore, fluctuation during going or returning cruise seems too large that we should correct before applying further analysis. Still more, large fluctuation before cruise or big change of inclination involves the trend when long-period filter is applied, that the effect might hide the gravitational terrain difference under a cover.

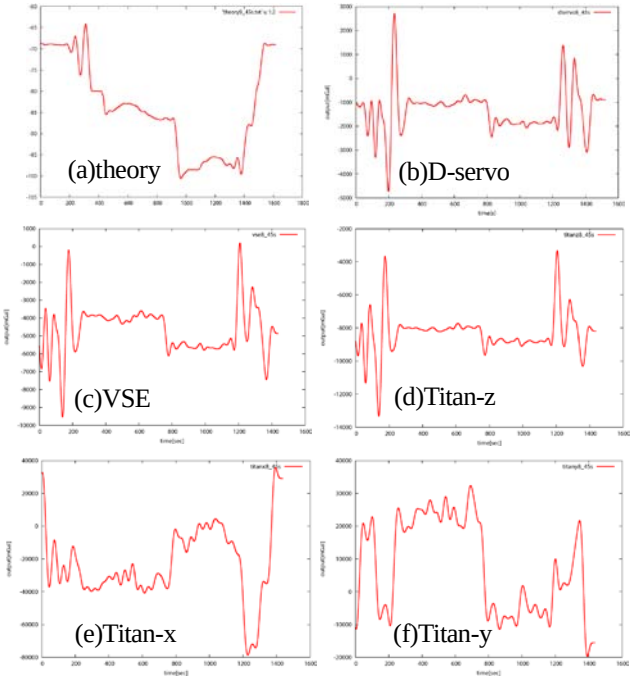


Figure 9 Theoretical Gravity and Data of Flight #8 (Filtered by Butterworth 45sec)

5. ANALYSIS OF GRAVITY DATA

5.1 Inclination Correction

Fig.10 shows a schematic figure of the inclination of the sensor. If we assume that inclined angle from horizontal plane to x or y axis as θ and output of Titan-x and y is 0 at horizontal plane, we can determine the angle θ from output of x or y and the gravity standard, $g = 980\mathrm{Gal}$, as follows:

$$\theta = sin^{-1}\frac{|x \text{ or } y|}{g} \qquad (4)$$

From Eq.4, we can calculate the inclination of the sensors. However, if we require more accuracy in this correction, accurate calibration of the whole sensors is quite important. In detail, 2 types of calibration of the sensor are required. At first, outputs of Titan-x and -y are adjusted to 0 at accurate horizontal plane so that assumption in Eq.4 is satisfied. Secondly, actual amount of change in output of all gravimeters and accelerometers must be measured just before the observation. Usually, outputs of sensors change with the angle as shown in Fig.11. It is clear from Fig.12, which is the raw signal of Titan-x, amplitude of going and returning cruise are different. This difference comes from Fig.11: if the fluctuation of the career is almost same during the whole cruise, difference in reference, that is, average angle in going or returning trip. This result also suggests that inclination correction is indispensable for the accurate gravity observation.

Inclination correction of gravity caused by x component which calculated by means of output of Titan-x and θ observed from Eq.4 are shown in Fig.13. Notice that we cannot calculate the amount of the correction from output of z-component because we usually adjust z with gravitational acceleration included, that is, output of z direction is not the absolute gravity. Even though the amplitude of the fluctuation in Fig.9 Titan-x has a little difference between going and returning cruise, difference in amount of correction in Fig.13 is much larger. This might suggest that Titan-x in this observation has some offset so that observed angle is slightly different from actual. We hardly detect these offset before or after the observation because environmental factor is dominant, such as temperature, air pressure, or how to load the system on different career. Since accuracy in angle is very sensitive to the output of gravity, we have to consider about suitable way for calibration during observation.

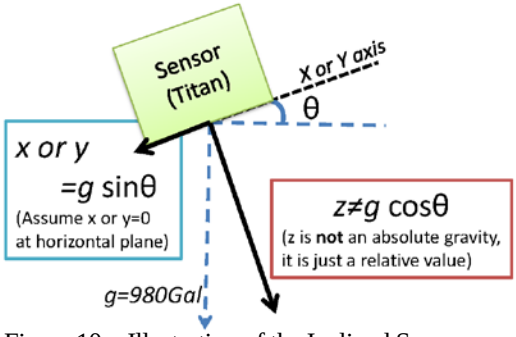


Figure 10 Illustration of the Inclined Sensor

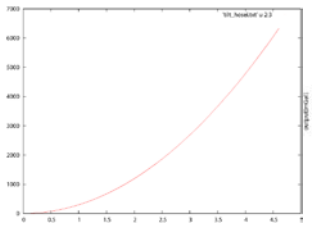


Figure 11 Output Difference with Angles[degree]

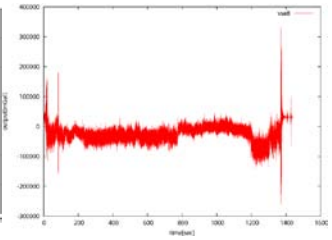


Figure 12 Raw Data of Titan-x (Flight #8)

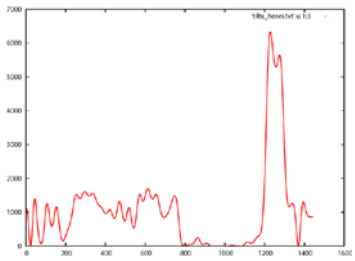


Figure 13 Inclination Correction (Titan-x)

5.2 Improvement of Gravity Analysis and Its Results

For detection of long-period components from the gravity data, Hilbert-Huang Transform (HHT) is used. Basic ideas of the method are described in Huang et al. (1998). HHT has an advantage in nonlinear and non-stationary data analysis, especially superior in long-term trend detection. On the other hand, this method is very susceptible for edge effect of the data. In addition, as we mentioned in section 4.2, long period filter tend to flatten the rapid change in the data, leaked effect sometimes cover up the signal we want. To ignore the short period disturbance for long-term inclination correction, we should pick out the data during the terrain difference should be detected from whole cruise data before apply filters. Moreover, to avoid the edge effect at HHT, we connected the same signal we picked out at head and tail of that data, namely we remade the picked out data as the same data repeated almost 3 times. Then, we tapered the data edge for 100 sec with linear declination. After the process, Butterworth filter is applied to remove the short-period disturbance and inclination correction is calculated. Finally, we divide the signal into some intrinsic mode functions (IMF) with different frequency by HHT, and look for the main term of the connected signal of objective frequency.

The procedure for analysis is summarized as follows:

1. Pick out the data during the term that we want to detect the gravity anomaly, then connect the picked out data at head and tail of the data itself. Apply the same procedure to all sensors.
2. Taper head and tail of the data for about 100sec each.
3. Apply a low-pass filter of Butterworth type with cutoff period of 30sec/45sec (hereafter, we call 30- or 45-sec filter) to remove the short-period disturbance.
4. By using filtered Titan-x and Titan-y data, calculate inclination correction of the z-components.
5. Apply HHT to divide the corrected output of the gravimeter into IMFs with different frequency. Then pick up the main term of the connected signal of objective frequency.

Results of the analysis of VSE and D-servo sensors during going cruise of flight #8 are shown in Figs.14 and 15, respectively. Fig.14 shows the sum of 10^{th} and 11^{th} IMF mode of the VSE signals and the analytical gravity of the corresponding term. In the same way, Fig. 15 shows the sum of 8^{th} and 9^{th} IMF mode of the D-servo signals. 30-sec and 45-sec filter is applied for the analysis. From both results, almost same signals have been detected, and they agree with the calculated analytical gravity very well in phase and period. Connecting the same data repeatedly make ease to pick up the IMF with constant frequency, such as the gravitational anomaly observed in constant career velocity. Furthermore, edge effect cannot reach to the main portion of the data by this process so that much clear trend in main portion can be separated by HHT. Same procedure for the analysis is also applied to Titan-z, yet the signal shown in Figs.14 or 15 cannot be detected. Titan accelerometer does not have enough resolution to detect the gravity anomaly, in other words, detected signals in Figs.14 and 15 seems to be the gravitaty anomaly.

Still, there are differences in amplitude. This might be the effect of inaccuracy in the inclination correction. For more detailed discussion, we should consider the calibration process, or devise some algorithm to determine the accurate inclined angle for the correction.

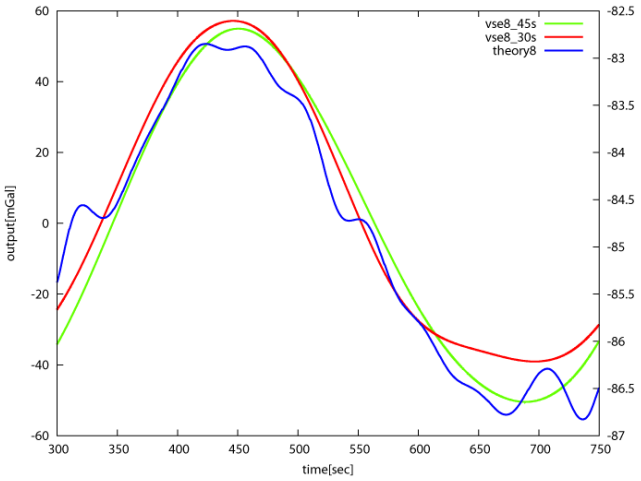


Figure 14 Result of Analysis (VSE)

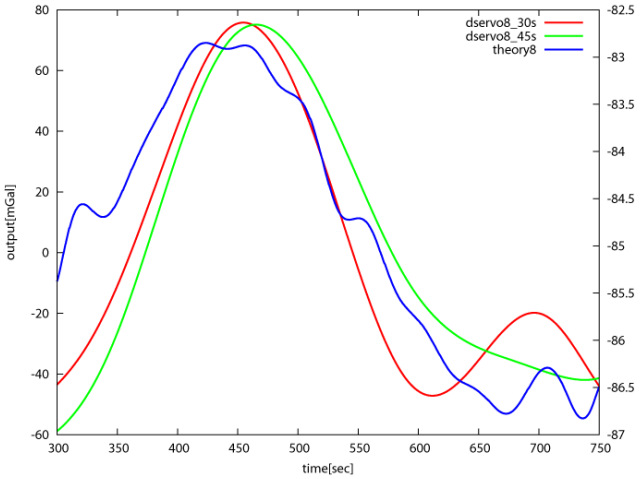


Figure 15 Result of Analysis (D-servo)

6. CONCLUSIONS AND FUTURE DEVELOPMENT

The exploration system had been tested at the airborne observation near a huge concrete dam. Theoretical gravity anomaly was calculated from terrain model. Sensitivity of the magnetic survey was quite well. On the other hand, inclination correction seems to be required in gravity survey. For the accurate correction, we should consider about suitable way of the calibration of sensors. Improved method for gravity analysis is proposed and the result has quite good agreement with theoretical gravity in phase and period of the signal, but there are still some disagreements in amplitude. Certain algorithm might be required to determine the accurate inclined angles for the correction. It will be also effective to apply the method to more stable career observation, such as shipboard observation.

Acknowledgements:

We are deeply grateful to dam operators whose kindness and cooperation were of help for the observation project. We are also indebted to project members of Yamaha Moter Co, Ltd. for preparations and operation of the unmanned helicopter system. This study is partially supported by Grant-in-Aid for Young Scientists (S) (No.21671003) of Japan Society for the Promotion of Science (JSPS).

References:

Yokoi, I., Ogura, Y., Suda, H., Kima, S., Matsuda, S., Tokue, S., Morikawa, H., Noguchi, T., and Ishida, Y. (2012), "Improvement of Digital Servo Sensor for Gravity Survey," *Proceedings of the 32nd Conference on Earthquake Engineering*, JSCE, ID 1-308.

Nagy, D. (1966) "The gravitational attraction of a right rectangular prism," *Geophysics*, **31**(2), 362-371

Banerjee, B. and Das Gupta, S. P. (1977), "Gravitational Attraction of a Rectangular Parallelepiped," *Geophysics*, **42**(5), 1053-1055

Huang, N. E., Z. Shen, S. R. Long, M. C. Wu, H. H. Shin, Q. Zheng, N. –C. Yen, C. C. Tung, and H. H. Liu (1998) "The empirical mode decomposition and the Hilbert spectrum for nonlinear and non-stationary time series analysis", *Proc. of the Royal Society of London A*, **454**, 903-995

10CUEE CONFERENCE PROCEEDINGS
10th International Conference on Urban Earthquake Engineering
March 1-2, 2013, Tokyo Institute of Technology, Tokyo, Japan

ESTIMATION OF GROUND STRUCTURE USING GRAVITY SURVEY METHOD AROUND FURUKAWA, JAPAN, WHERE WAS SEVERELY DAMAGED BY 2011 TOHOKU EARTHQUAKE

Sakkrawit Sripunyaphikhup[1], Hitoshi Morikawa[1], Hiroyuki Goto[2], Masayuki Inatani [2], Yumiko Ogura [1], Satoshi Tokue [1], Xinrui Zhang [1], Shohei Hamasaki [1], Masahiro Iwasaki [3], Masayuki Araki [4], and Sumio Sawada [2]

1) Department of Built Environment, Tokyo Institute of Technology, Japan
2) Disaster Prevention Research Institute, Kyoto University, Japan
3) Osaki City Government
4) aLab Company Limited
sripunyaphikhup.s.aa@m.titech.ac.jp, morika@enveng.titech.ac.jp, goto@catfish.dpri.kyoto-u.ac.jp

Abstract: In March 2011, there were huge earthquake ground motions in Tohoku region. Furukawa, Japan, was one of a few places in Japan where had severe damages caused by earthquake ground motion. However, the interesting point is that size of this ciy is quite small but the damages were totally different from places to places, in area of 2km x 2km. Therefore, investigation of the ground structure is necessary. Firstly, very dense seismometers have been installed to observe the ground motions. Nevertheless, gravity survey method was conducted later to confirm that the ground structures are indeed different within this small area. Gravity survey was carried out at the intervals of hundreds meter because there was an estimation that soft soil sediment is not thick. The Bouguer anomaly, as a result from gravity survey, has some significant variations in some places, which correspond to the most severely damaged places. Furthermore, residual anomaly as extracted from regional anomaly also states the similar fashion to both Bouguer anomaly and severe damaged places. Final 3-D map showing the altitude of basement presents the variations of the depth in 2km x 2km with the maximum different up to 67 meters.

1. INTRODUCTION

The 2011 earthquake off the Pacific coast of Japan caused severe damage to many parts of Japan, particularly, in the Northeastern of the country. Most of those damages came from the attacked Tsunami or liquefaction just after the earthquake; however, there were a few places where the damages were the results of hit by earthquake ground motions. Furukawa in Osaki city, Figure 1, is one of those a few places.

Nevertheless, the interesting point, which motivated the observation in this area, is that the damages were not uniformly distributed, in the other word, the damages were greatly different in the distance of a few kilometers or area of 2km x 2km.

First step of observation was to collect the recorded seismogram installed in the area, after the inspection, we found that recorded response spectrum of two adjacent stations, JMA-Furukawa and K-NET-MYG006, which are a few kilometers apart having the response difference about two times, around 1.5-sec period as shown in Figure 2. Then we carried out the observation using dense sensors (Goto, 2011), 19 sensors by the end of 2011 for 2 km x 2 km area, to better understand the anomaly of the damage distribution. As a result, the anomaly of the ground motion is large

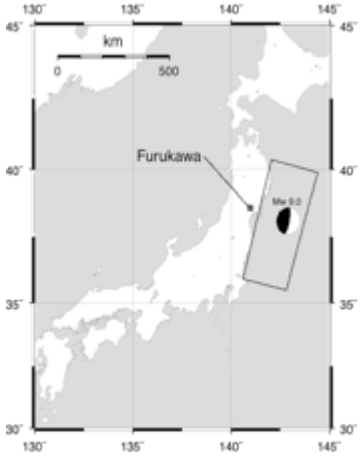


Figure 1 Location of the observation area, Furukawa, Osaki, Japan

beyond our consideration. The anomaly of ground motions should come from the anomaly of ground structure. Then we decided to carry out the gravity survey in this area. There is an estimated data suggesting that soft soil sediment is not so thick, or, depth to the engineering bedrock is less than 50 meters so very high resolution of gravity anomaly is required. Thus, we chose to do the gravity survey with the observing interval of a few hundred meters in the downtown area.

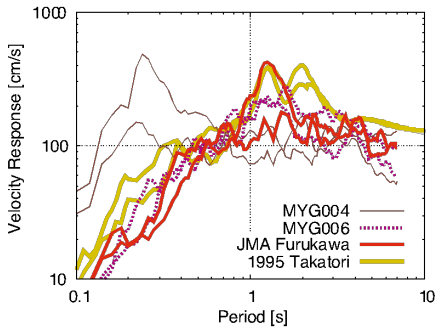


Figure 2 Velocity response spectrum of JMA-Furukawa and MYG006 stations, showing the recorded value different about 2 times, also comparing to 1995 Kobe earthquake (Goto, 2011).

2. PROCESSING OF GRAVITY SURVEY

2.1 Data Acquisition

Basically, gravity survey requires two kinds of data, which are gravitational value of the observed points and the exact location of those points i.e. latitude, longitude, and elevation. In this observation, we use the LaCoste and Romberg gravimeter (S/N:G911) to measure the gravity value, which can give the accuracy up to 3 microgals (approximation of gravitation field of the Earth is about 9.8 x 10^8 microgals). The gravitational acceleration of the Earth can be basically derived from the well-known Newton's equation: i.e.

$$F = Gm_1m_2/r^2 \qquad (1)$$

To position the exact location of the observed points, we measure by using Magellan GPS. In this study, we perform an observation 3 times i.e. September 2011, February 2012, and October 2012.

2.2 Data Processing

In order to analyze the gravity survey data, the absolute gravity value is necessary. Also, observation requires a loop survey, which we have to start and end at the same point, daily. So we designate absolute gravity value point, base point, in front of the JR Furukawa station by transferring the value from the closest known absolute gravity point in Tsukidate where is quite far from Furukawa and would consume a lot of time because gravity survey requires a loop survey daily, start and end at the same point. This known absolute gravity point, named as HRKB, has a value of 980098.8553 mgal with the latitude and longitude of 38.571339 and 140.967204, respectively, and the altitude is 59.483 meters.

The observed values must be corrected by many procedures because they contain several errors due to instruments, shape of the Earth, physical properties of surrounding area, and the location of observed points.

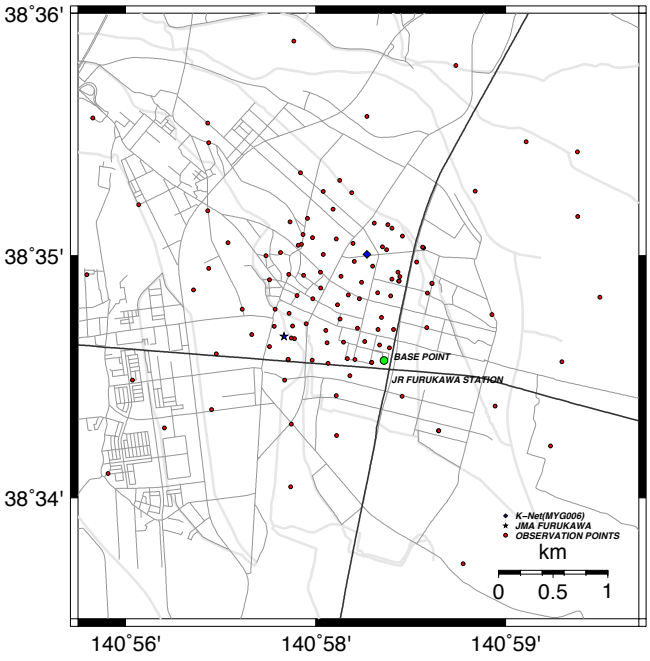


Figure 3 Map of the observed area with observed points (red dots) also JMA-Furukawa and K-NET-MYG006 stations. Bold-black lines show railway, thin-light lines show traffic way, and bold-light lines show stream way.

As the survey processes go on, of course, time passes by. Differences of time of reading the values from gravimeter have differences of gravitational value due to effect of attraction between moon and sun. This effect is called gravity tidal effect, which varies with time. There is another effect called drift, which comes from the gravimeter. Even the instrument is well controlled in every way; the spring and any connections inside the gravimeter are not perfectly stable and cause small error to the reading values. Latter effect is called drift. These tidal and drift effects must be corrected first before doing further analysis.

From the equation (1), gravity varies with elevation (distance from the center of the Earth), then any points those higher in elevation has lower gravitational acceleration comparing to those points with lower elevation. The gravity at a point on the surface of the Earth can be obtained by

$$g = GM / R^2 \qquad (2)$$

from this equation, if we take a derivative with the vertical direction, we will see that gravitational value varies with the elevation. In the other word, if the elevation correction of observed points were not made, a gravity map would be incorrect due to differences in elevation because we make a gravity map on a reference datum level. This effect is called free-air effect. The attraction of materials between a reference elevation and observed points also affects the reading values. This effect is called Bouguer effect and can be corrected by

$$g = 2\pi G\sigma h \qquad (3)$$

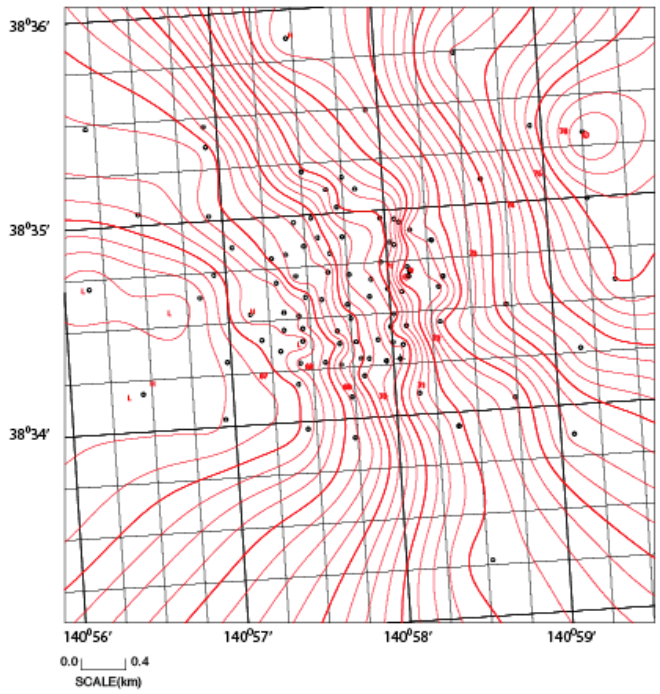


Figure 4 Bouguer anomaly map of the observed area, Furukawa, Osaki, Japan. Small black dots denote the observation points.

where σ is density of medium and h is thickness. In this study, we assume σ to be 1.90 g/cm^3.

Furthermore, owing to Earth is not a sphere, so gravitational values are not the same with difference of latitude. Gravitational acceleration is increased from equator to pole. This procedure is called latitude correction.

3. RESULTS FROM GRAVITY SURVEY IN FURUKAWA AREA

The primary goal of gravity survey method is to determine the ground structure beneath a survey area. By collecting and analyzing the observed gravitational values with corrections, we will yield a map called Bouguer anomaly map. In this study, we assume the density of engineering bedrock equal to 2.40 g/cm^3 together with the density of soft soil sediment equal to 1.90 g/cm^3 and the total numbers of observed points is 98. Obtained Bouguer anomaly map is shown in Figure 4.

From the above Bouguer anomaly map, it indicates that the gravitational value gradually decreased from the east to west. Figure 5 and Figure 6 show the regional gravity trend and residual gravity trend of observation area, respectively.

Regional gravity has the similar trend as the Bouguer anomaly map which is decreasing from east to west. This Regional anomaly trend gives the information on the regional geological structure, or, deep crustal features. While residual gravity map suggests that there are some small places where the gravitational value changes abruptly as indicated as loops due to the local gravity field, which is caused by local geological structures, or, shallow structure.

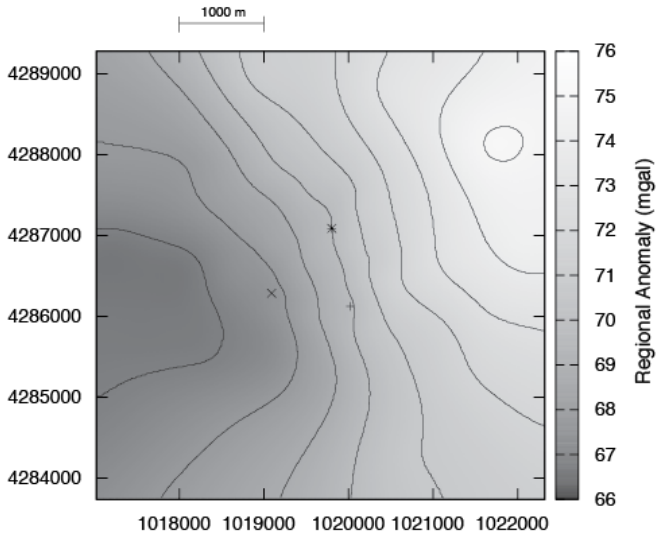


Figure 5 Regional gravity trend caused by regional geological structure shows that gravity value decreasing from east to west. The symbols +, ×, and * show the base point, JMA-Furukwa, and K-NET-MYG006 stations, respectively.

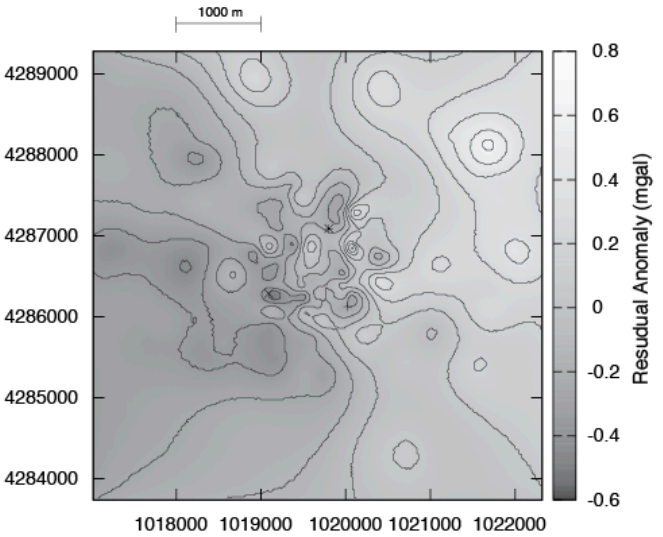


Figure 6 Residual gravity trend caused by local geological structure shows gravity variations due to local gravity field. Darker color suggests low gravity; which means soft soil sediment in shallow structure. The symbols +, ×, and * show the base point, JMA-Furukwa, and K-NET-MYG006 stations, respectively.

From those maps mentioned above, we estimate the basement map of the ground layer, Figure 7, showing the altitude of the boundary between surface sediments and engineering bedrock, which we set the values to be 1.90 g/cm^3 and 2.40 g/cm^3, respectively, together with the reference datum is set to be zero at the base point (HRKB). According to the simulated basement map, it can be seen that within the area approximately 5.0 km x 5.0 km, there are several places where the depth of soft soil sediment is quite deep relatively to surrounding area. The maximum different of depth to the bedrock is about 67 meters.

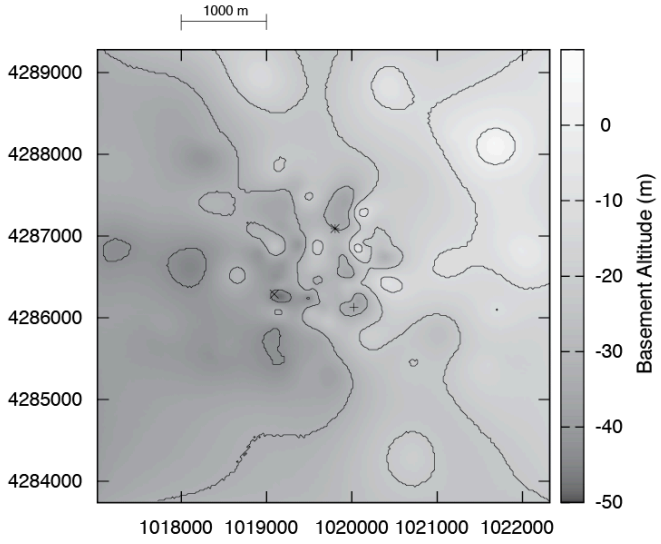


Figure 7 Basement map shows the thickness of soft soil sediment (1.90 g/cm^3) to the bedrock(2.40 g/cm^3). Engineering bedrock's altitude is deeper from east to west. The symbols +, ×, and * show the base point, JMA-Furukwa, and K-NET-MYG006 stations, respectively.

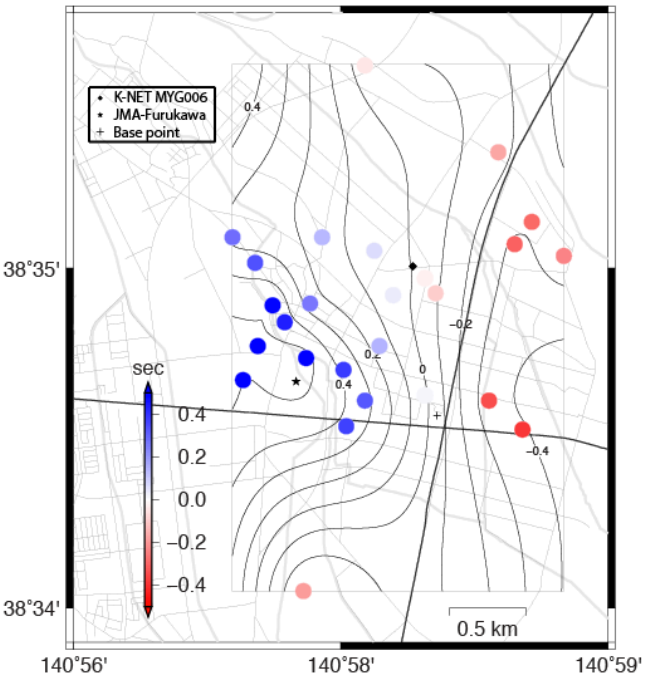


Figure 8 Arrival time at sensors installed in this area. Minus means prior arrive. Plus means later arrive, time delayed. Recorded waves came from east direction.

4. DISCUSSION

From the basement map, thickness of soft soil sediment, which we set to 1.90 g/cm3, is increasing from east of downtown to the western side, in other word; depth to the engineering bedrock is greater in the western side area. This information is corresponding to the real structural damaged data; which said that structures in the western side of Furukawa downtown were severely damaged; on the other hand, structures in the western side of downtown were little damaged or no damage. This result is not only matching with the structural damaged data, but also, corresponds to the pseudo-velocity response spectrum of the March 2011 aftershock event, which a record from JMA-Furukawa station that installed in the western side of downtown had a peak value about twice as a record from MYG006 K-NET installed in the north-eastern side of downtown.

Furthermore, on December 07, 2012, there was an earthquake event off the Pacific coast of Japan epicenter at 37.8N 144.2E with the magnitude of 7.3. Since we already installed seismometer densely (Goto, 2011) in this downtown area, so we have the information of the ground motion for this area. We did an analysis on the arrival time of surface wave, Rayleigh wave, because this surface wave travels in the surface layers, or, shallow layers, as we now have the information that ground structure beneath this area is not uniform, yet quite complicated. Analysis result of arrival time of Rayleigh wave is shown in Figure 8. This figure gives an information that if the ground structure was uniform in this small downtown, the arrival time at any sensors should be acted as a trend, parallel to each other, because the wave travels naturally as a straight-line so wave front must be parallel.

Cross line in the Figure 8 is the location of JR Furukawa station. Let us consider from the east side of figure vertically, the records at sensors from minus to zero have a trend of parallel, but when it passed 0-sec line, wave travelled with low velocity. Thus it suggests that those areas where wave travels with low speed comparing to adjacent areas should have soft soil layers because wave travels slower with low density of medium.

The results from Figure 7 and Figure 8 have similar trend for the shallow structure.

5. CONCLUSIONS

Shallow structures, or soft soil layers, underneath this downtown are not uniform and have some extremely soft soil basins distributed in the western side of downtown. This might be the reason that structures in this downtown suffered significantly level of damage even they are located near to each other within the range of few hundreds meters.

References:

Goto, H., Morikawa, H., Inatani, M. (2012), "Very Dense Seismic Array Observations in Furukawa District, Japan," *Seismological Research Letters,* **83**, 765-774.

Goto, H., Morikawa, H. (2011), "Ground Motion Characteristics During the 2011 off the Pacific Coast of Tohoku Earthqauke," *Soil and Foundation*, **52**, No.5

Nettleton, L. L. (1976), "Gravity and Magnetics in Oil Prospecting," *McGrawHill Book Company,* Part I.

Griffin W. R. (1948), "Residual Gravity in Theory and Practice," *Society of Exploration Geophysics*, Annual meeting of the society 1948

Murray, A. S., Tracey, R. M., "Best Practice in Gravity Surveying," *Australian Geological Survey Organization*, 43 pp.

10CUEE CONFERENCE PROCEEDINGS
10th International Conference on Urban Earthquake Engineering
March 1-2, 2013, Tokyo Institute of Technology, Tokyo, Japan

THE SIGNIFICANCE OF THE RATIO OF POWER SPECTRA BETWEEN TWO SITES IN THE WAVEFIELD OF MICROTREMOR

Xinrui ZHANG[1)] **and Hitoshi MORIKAWA**[1)]

1)Dept. Built Environment, Tokyo Institute of Technology

E-mail: zhang.x.aj@enveng.titech.ac.jp

ABSTRACT: In the SPAC method, the underground structure is assumed to be horizontal layers, which confines the accuracy of the estimation. On the other hand, the seismic interferometry theory makes it possible to identify the differnce of ground structure between each two sites by taking the ratio of power spectra respectively. Hence, we propose a method combining the conventional SPAC method and the concept of Green's function, which is known as the seismic interferometry. In order to show the availability of this combination, wavefield dominated by microtremors is simulated in which the SPAC method could be conducted effectively. Then the availability of seismic interferometry proposed previously is examined under the simulated wavefield and the need to take the ratio of the power spectra instead of using the power spectra itself directly is confirmed.

1. INTRODUCTION

Since Aki[1] proposed a new approach to estimate phase velocities of surface waves, spatial auto-correlation (SPAC) method has been a very useful tool to estimate ground structure because of its simple post-process. After that, many reseachers both in and out of Japan continued to publish papers on practical adaption of Aki's theory to microtremor exploration. However, in all those improved methods, the layers under surface can only be assumed to be horizontal through the SPAC method while in fact, the layers are likely to be inclined slightly with certain angle. Hence, it is expected to obtain more detailed information of ground structure such as inclination by making better use of the records.

In recent years, the seismic interferometry theory[2][3] has also been widely used to estimate ground structure. It is proved that in an elastic medium the Fourier transform of azimuthal average of the cross correlation of motion between two sites is proportional to the imaginary part of the exact Green's function between these sites[4]. Hence, it becomes possible to calculate the ratio of imaginary part of different Green's function by taking the ratio of corresponding cross correlation to analyze ground structure more particularly because Green's function indicates intrinsic property of the medium. Actually, seismic interferometry is conditionally consistent with the SPAC method[5] which offers the base of introducing seismic interferometry to SPAC method.

SPAC method requires the multiplification calculation of Fourier transformation of records at two sites of center of an array and a one site on the circular array. By taking the ratio of power spectral between two different sites, it is hoped to obtain the ratio of imaginary part of Green's function according to seismic interferometry theory correspondingly and analyze the difference of ground structure through the ratio. More information such as the inclination of layers could be obtained.

Since this new concept has been proposed[7][8], some problems has been pointed out and the availablity of the combination remains to be proved. Firstly, the ratio of power spectra is used to calculate the ratio of imaginary part of Green's function whicn means the wavefield is supposed to consist of mainly body wave[9] [10]. However, the SPAC method requires the wavefield to be dominated by microtremors. It seems to be paradox but it is believed that seismic interferometry theory itself satisfies wavefield of full wave[11]. It is hoped that by taking the ratio of power spectra between two sites, the surface wave content will be extinguished and the body wave content remains.

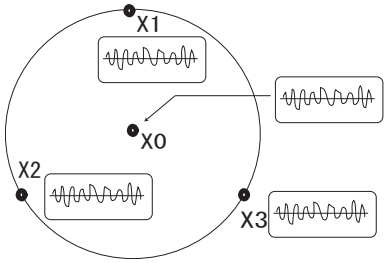


Figure 1. The equilateral-triangle array

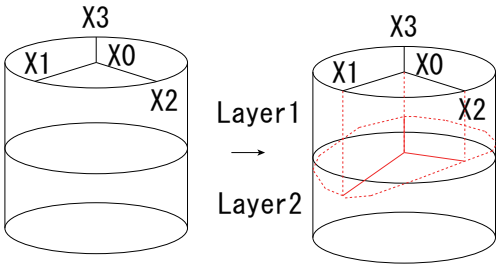


Figure 2. An example describing how the new method is expected to raise the accuracy of estimating ground structure.

Secondly, under the assumption of body wave being dominating, it is said that power spectra itself of each site could be used to analyze out the peak frequency of the ground structure (in simple case, the first layer) which tend to say that there is no need to take the ratio of them. Nevertheless, in wavefield dominated by microtremor and with the inclination of layers small enough, it is hard to extract useful information from each power spectra alone and to compare between them.

In this paper, the concept of SPAC method, interferometry and the combination of them are firstly proposed comprehensively. Then, in order to solve the two problems mentioned above, we use finite-difference method to simulate some 2-layered simple layered medium under the wavefield dominated by microtrmors. Next, SPAC method is applied to certain array of observation sites to examine if this wavefield is effective for SPAC method. Finally, the availability of seismic interferometry would be analyzed and the need to take the ratio of power spectra will be shown.

2. COMBINATION OF SPAC METHOD & SEISMIC INTERFEROMETRY

In this chapter, the basic knowledge of SPAC method and seismic interferometry will be introduced and the new concept of combining them will be proposed.

(1) SPAC method

Given an equilateral-triangle array as shown in Fig.1 and vertical time series records at four sites, the azimuthal-average of spatial auto-correlation coefficients $\rho(\omega,r)$ can be calculated as:

$$\rho(\omega,r)=\frac{1}{3}\sum_{j=1}^{3}\frac{S_{0j}(\omega)}{S_{00}(\omega)S_{jj}(\omega)}, \tag{1}$$

where ω and r are the angular frequency and radius of the circular array, respectively. $S_{jj}(\omega)$ and $S_{0j}(\omega)$ are the power spectra of vertical component of microtremors at site j ($j=0,1,2,3$) and the cross spectra of the vertical records between site j and 0. The site 0 is center of the array and sites 1, 2, and 3 are located on the circle.

Practically, $S_{jk}(\omega)$ is obtained by the product of Fourier transformation of records at two sites as

$$S_{jk}(\omega)=F(\omega,X_j)F^*(\omega,X_k), \tag{2}$$

where X_j is a location of site j and * stands for the complex conjugate.

Afterwards, a dispersion curve can be obtained and the property of under-surface layers are estimated using the curve.

(2) Green's function from correlation

It has been demonstrated[6][3] that in an elastic medium, the averaged cross correlation of motions at sites 1 and 2, whose locations are X_1 and X_2, can be written as:

$$\begin{aligned}&<F_\ell(\omega,X_1)F_m^*(\omega,X_2)>\\&\quad=-2\pi E_s k^{-3}\Im[G_{\ell m}(X_1,X_2,\omega)],\end{aligned} \tag{3}$$

where ℓ and m indicate one of three directions, (x,y,z). k and E_s are wave number of shear wave and the averaged energy density of shear wave, respectively. $<\cdot>$ stands for an expectation and $\Im[\cdot]$ for the imaginary part.

(3) Combination of SPAC method and Green's function

In the simpliest case using an equilateral-triangle array, ℓ and m are both set as vertical direction, which is z, and sites 1 and 2 as the same sites. Hence, it becomes

$$\begin{aligned}&<F_z(\omega,X_1)F_z^*(\omega,X_1)>\\&\quad=-2\pi E_s k^{-3}\Im[G_{zz}(X_1,X_1,\omega)]\end{aligned} \tag{4}$$

Therefore, let us take the ratio of the power spectra at center of the array and an azimuthal site so that the corresponding ratio of imaginary part of Green's function can be obtained as

$$\frac{S_{jj}(\omega)}{S_{00}(\omega)}=\frac{\Im[G_{zz}(X_j,X_j,\omega)]}{\Im[G_{zz}(X_0,X_0,\omega)]} \tag{5}$$

and it is expected to analyze the difference of ground structure between every two sites such as the inclination. The process is indicated simply in Fig.2.

In the simplist equilateral-triangle case, three ratios $\frac{S_{11}(\omega)}{S_{00}(\omega)}$, $\frac{S_{22}(\omega)}{S_{00}(\omega)}$, $\frac{S_{33}(\omega)}{S_{00}(\omega)}$ according to Eqn.5 can be obtained to analyze the difference between the corresponding two sites.

Table 1 Two-layered models of ground structure

Layer	P-wave velocity	S-wave velocity	Density	Thickness
	[m/s]	[m/s]	[t/m^3]	[m]
1	800	400	1.5	120
2	1800	1200	2.0	∞

Moreover, it is convenient and efficient to calculate this ratio because the power spectra is just the intermediate result in the process of SPAC method.

3. The VALIDITY OF SEISMIC INTERFEROMETRY IN THE WAVEFIELD DOMINATED BY MICROTREMORS

Since this new concept has been proposed, some preliminary research in order to confirm the availability of it has been done[7][8]. Through a smulation examination by finite difference method, the most compelling conclusion is drawn that Eqn.(5) is well satified in case of shallow ground structure[8]. However, until now, the SPAC method has not been taken consideration into the examination yet. Eqn.(5) is proved to be valid in diffused wavefield which is not necessarily an available one for SPAC method.

Besides, in terms of the assumption of SPAC method and Eqn.(5), the SPAC method requires the wavefield dominated by microtremor while the retrieval of Green's function from power spectra demands body wave's domination[10] [9]. The assumption seems to contradict with each other. Though, it is worth noticing that seismic interferometry itself is a full wave theory[11]. Though the power spectra should embody mainly surface wave, the ratio between them has the potential to contain information of body wave while the surface wave component diminishes through the division.

(1) A wavefield available for SPAC method

In order to show that SPAC method and seismic interferometry are both effective in the wavefield dominated by microtremor, firstly a wavefield available to apply SPAC method should be created. We still use Sakai's program[13] which is based on finite difference method as the tool to do simulation.

We assume the ground structure to be horizontally 2-layered medium, namely, no difference between each two sites. The inclined layered medium will be used afterward when adding the seismic interferometry theory. The property of each layer is shown in Table 1. To be ideal, we create the wavefield by exerting randomly distributed sources at random time surroundingly (as far away from the array as possible). Each source is on the surface or subsurface and with random force orientation. The source time function is a delta-like signal. The scope of simulation is $200 \times 200 \times 30$ with each mesh size of $20 \times 20 \times 20m$. The

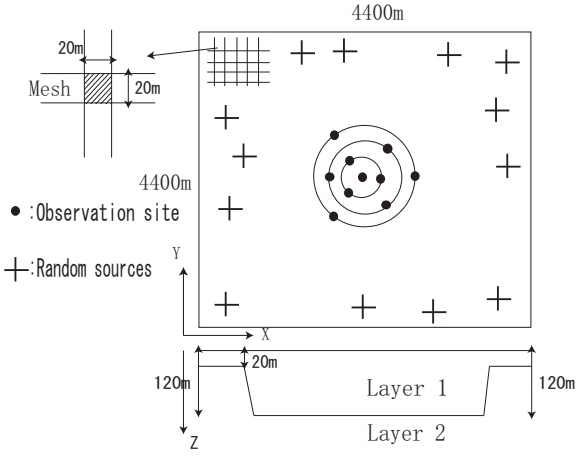


Figure 3. Plan and section plan of horizontally layered medium

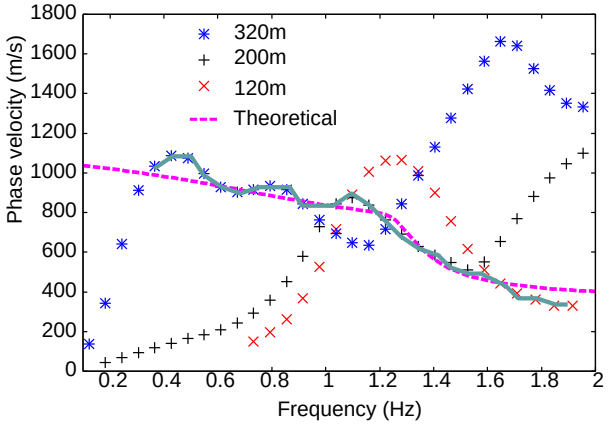


Figure 4. Dispersion curve

three observation arrays are set to be equilateral triangle with radius of 120*m*, 200*m*, 320*m* and 400*m* respectively. The plan and section plan are shown in Fig.3. The boderline of the first layer is set to be like a basin so as to help surface wave generate.

For simplicity, we use the vertical component of the record with duration of 64s and time step of 0.004s. Then the SPAC method metioned before is applied and the dispersion curve of 4 arrays is drawn as Fig.4 shows. The line is the theoretical phase velocity of rayleigh wave. The frequency range is limited because of the precision limit of Sakai's program[13] itself. We can see that the phase velocity disperses which means the wave field is

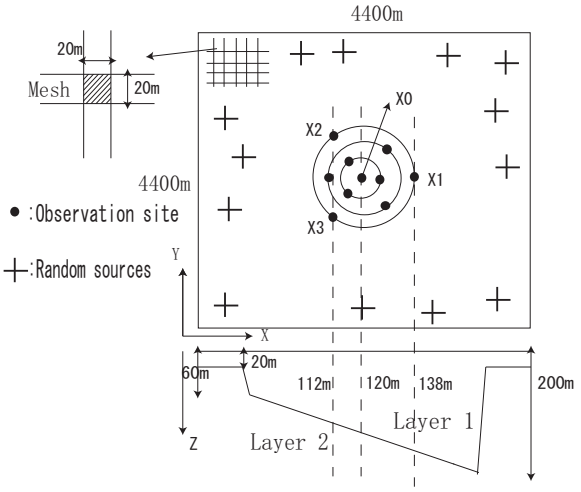


Figure 5. Plan and section plan of inclined layered medium

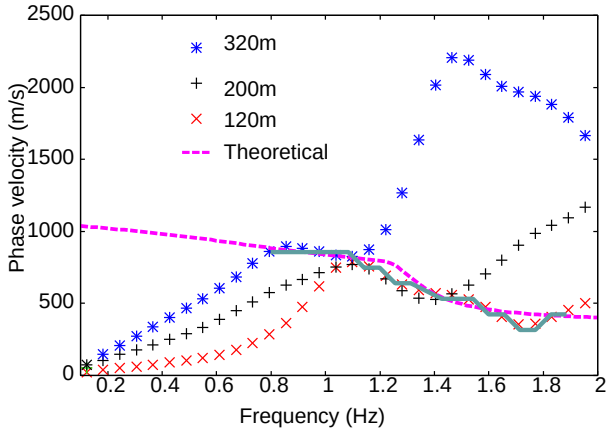


Figure 6. Dispersion curve

dominated by surface wave. Besides, the result from SPAC method coincides with theoretical one quite well which shows the wavefield is available to apply SPAC method.

(2) The availablity of seismic interferometry in the wavefield dominated by microtremor

As the way of creating wavefield available for SPAC method has been proved to be right, for the second simulation, the way to exert sources is the same while the model of ground structure is modified to be a inclined one. Because it is concluded the sensitivity and error will be large for deep structure[8], the first layer's thickness is set to be small value of around 120m. The plan and section plan of simulation are shown in Fig.5.

Then, in the same way, the SPAC method is applied using the records observed at the same 3 arrays of sites to see how it behaves when the layers are not horizontal but slightly inclined. The result is shown in Fig.6. It can be seen that the theoretical dispersion curve still matches with the result from simulation very well. Hence, even in slightly inclined layered medium, the SPAC method is still available.

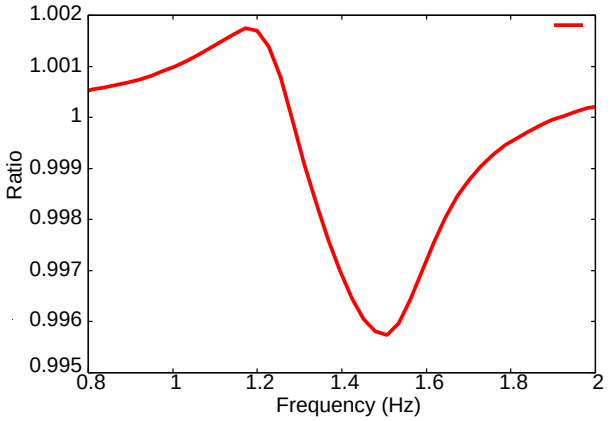


Figure 7. The theoretical ratio between site X1 and X2

Then, in order to examine if Eqn.(5) is satisfied, all the sites on the largest array are chosen as the examination sites as Fig.5 shows. For example, the site X1,X0 and X2(X3) corresponds to the depth of the first layer of 128m, 120m and 112m, respectively and the ratio is calculated between X1&X0, X1&X2, X1&X3, X0&X3 and X0&X2. The same thing is done for the other two arrays which means finally we obtain totally $5 \times 3 = 15$ ratios.

We use Hisada's program[14][15] to calculate the theoretical ratio of imaginary part of Green's function (the right hand side of Eqn.(5)) while the ratio of power spectra (the left hand side of Eqn.(5)) is easily calculated from the intermediate result (the power spectra of each site) just now. We use the frequency at which the ratio got the peak value (critical frequency) as the indicator to compare between them instead of comparing all over the whole range of frequency[8].

Because of the property of ground structure, even for the pair of sites (X1&X2) with the biggist difference in ground structure, the theoretical ratio of imaginary part of Green's function is quite small even at the critical frequency as shown in Fig.7. Besides, with the first layer's thickness varies in the small range, the shape of the ratio also changes quite slow. If we compare them one pair by another pair, the peak of simulation ratio will not be obvious for a part of pairs. In addition, the domination of microtremor and the system error of theoretical ratio[8] will exert bad influence on the result. Hence, we add all the ratios into one figure to see an comprehensive image. Accordingly, we choose 3 representative theoretical ratio in one figure to represent its rough moving scope. Finally, we compare them two as shown in Fig.8. We can see that for the theoretical ratio, there are two peaks which correspond to the two highest and densist peaks in simulatio ratio. They matches quite well which indicates that Eqn.(5) still works to certain degree in the wavefield dominated by microtremors.

(2) The neccessity of taking the ratio between

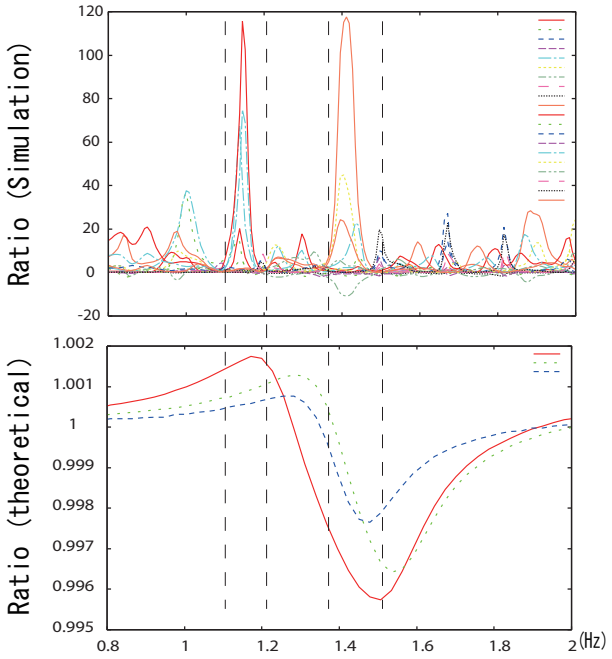


Figure 8. The comprehensive comparison between theoretical and simulation ratio

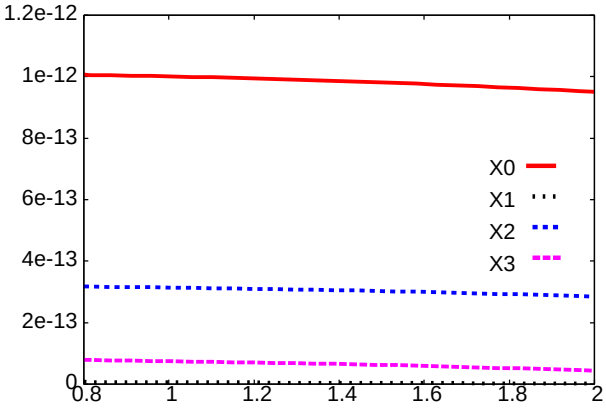


Figure 9. The power spectra of X0, X1, X2 and X3

two power spectra

This problem becomes easy to solve now. Fig.9 shows the power spectra of X1, X0, X2 and X3. It is obvious that there are almost no peak of power spectra over all the frequency range. In other words, it is hard to find the frequency at which the power spectra arrives at the peak. It is because that the microtremor takes on the main part of the power which makes it difficult to extract reflection response out.

However, by taking the ratio of X1 and X0, for example, the peak turns up and the peak coincides with the theoretical ratio of imaginary part of Green's function as Fig.10 shows. It indicates that the ratio contains the information of body waves. Therefore, taking the ratio of power spectra between two sites is necessary in order to get the critical frequency. This critical frequency denotes the differece between the reflection response of two sites.

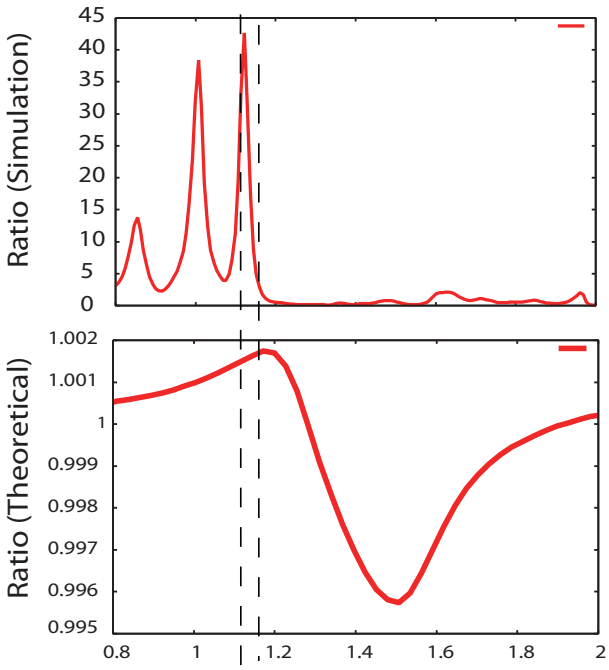


Figure 10. Comparison after taking the ratio of power spectra

4. CONCLUSIONS

We introduced the new method of combining SPAC method and seismic interferometry briefly and do the discussion mainly on the availability of seismic interferometry in wavefield dominated by microtremor. There are several conclusions.

(1) The SPAC method is available when the layers underground are slightly inclined in spite of the assumption of horizontally layered medium.
(2) Sesimic interferometry still works in the wavefield dominated by microtremor. In some case like the examination in this article, because of the property of ground structure, the peak value of theoretical ratio $\frac{\Im[G_{zz}(X_j,X_j,\omega)]}{\Im[G_{zz}(X_i,X_i,\omega)]}$ is quite small which causes the critical frequency hard to identify practically. Hence, we can make all the ratios in one figure to identify the most obvious peaks and do analysis. More work will be done on this in the future.
(3) It is necessary to take the ratio between power spectra of 2 sites because power spectra alone contains mainly microtremors and is hard to analyze.

ACKNOWLEDGMENT: Acknowledgement: This study was partially supported by KAKENHI (21671003).

REFERENCES

[1] Aki, K.: Space and time spectra of stationary stochastic waves, with special reference to microtremors, *Bull. Earthq. Res. Inst.*, University of Tokyo, 35, 415–456, 1957.

[2] Wapenaar, K., Draganov, D. and Robertson, J.: Introduction to the supplement on seismic interferometry. Geophysics, 71, SI1eSI 4, 2006.

[3] Sánchez-Sesma, F.J. and Campillo, M.: Retrieval of the Green's function from cross correlation: The canonical elastic problem, *Bulletin Seismological Society of America*, Vol. 96, No. 3, pp.1182-1191, 2006.

[4] Sánchez-Sesma, F.J., Pérez-Ruiz, J.A., Luzón, F., Campillo, M. and Rodríguez-Castellanos, A.: Diffuse fields in dynamic elasticity, *Wave motion*, 45, 641-654, 2008.

[5] Yokoi, T. and Margaryan, S.: Consistensy of the spatial autocorrelation method with seismic interferometry and its consequence, *Geophysical Prospecting*, 56, 435-451, 2008.

[6] Sánchez-Sesma, F.J.: A theory for microtremor H/V spectral ratio: Application for a layered medium, *Geophysical Journal International*

[7] ZHANG, X. and MORIKAWA, H.: A method to estimate ground structure combining SPAC method and seismic interferometry, *Proceedings of the 31st Conference on Earthquake Engineering, JSCE*, 1groundmotion-158, 2011

[8] ZHANG, X. and MORIKAWA, H.: An approach to estimate inclined layered medium by applying Green ' s function to SPAC method, *15th World Conference on Earthquake Engineering*, 2012

[9] Erica, G. and Andrew, C.: Generalised receiver functions and seismic interferometry, *Tectonophysics*, 1-26, 532-535, 2012

[10] Jan W. Thorbecke and Deyan Draganov: Finite-difference modeling experiments for seismic interferometry . *Geophysics*, V. 76, No. 6, H1-H18, 2011.

[11] Wapenaar K. amd Fokkema J.: Green's function representations for seismic interferometry. *Geophysics*, 71, SI33-SI46, 2006.

[12] Sakai, K.: A method to estimate ground structure with high accuracy applying the combination of microtremor data and gravity data

[13] Sakai, Y.: Assess seismic response in high-frequency range of Kyoto Basin using finite difference method, 2001

[14] Hisada, Y.: Efficient method for computing green's functions for a layered half-space with sources and receivers at close depths, *Bulletin of the Seismological Society of America*, V.84, 1994.

[15] Hisada, Y.: Efficient method for computing Green's functions for a layered half-space with sources and receivers at close depths (Part 2), *Bulletin of the Seismological Society of America*, V.85, 1995.

10CUEE CONFERENCE PROCEEDINGS
10th International Conference on Urban Earthquake Engineering
March 1-2, 2013, Tokyo Institute of Technology, Tokyo, Japan

USING STOCHASTIC FINITE-FAULT METHOD TO SIMULATE GROUND MOTION FROM 2010 JIASHIAN, TAIWAN, EARTHQUAKE

Fu-Ming Wu[2], Kuo-Liang Wen[1], Jyun-Yan Huang[3] and Chun-Te Chen[3]

1) Professor, Department of Earth science, National Central University , Chungli
2) Master student, Department of Earth science, National Central University , Chungli
3) Ph.D. candidate, Department of Earth science, National Central University , Chungli
taiwantaipei1319@hotmail.com, wenkl@earth.ncu.edu.tw, 986402005@cc.ncu.edu.tw, 956402004@cc.ncu.edu.tw

Abstract: The stochastic finite fault method is applied to simulate records of 2010 Jiashian, Taiwan, earthquake. This study used the method which can divide the fault plane of large event into subfaults, and each subfault is treated as each point source and assigned an ω^2 spectrum.

The method consists of two steps. First, class B stations (NEHRP) of free field in southern Taiwan are used to calibrate model and found an excellent model with smaller average model bias. Model bias defined as the logarithm of the ratio of the FAS (Fourier amplitude spectrum) of observation to that of simulation. Second, use calibrated model to multiply transfer function to derive synthetic acceleration waveform of soil sites.

The transfer function in this study is H/V ratio (Nakamura, 1989; Lerom and Chávez-García, 1993) of seismic event that derived by 1991 to 2009 from CWB (Central Weather Bureau) database. Then, we use the spectrum result from the calibrated model and multiply by the transfer function to get the simulated waveform of horizontal component. The result also compare with the observed record.

1. INTRODUCTION

The Jiashian earthquake occurred at 08:18:53 A.M. on March 4, 2010 and it was a large earthquake with magnitude M_L = 6.4 and focal depth was 22.6 km (from Central Weather Bureau) in southern Taiwan. It caused many buildings damage, soil liquefaction, and two high speed rails derailed.

We want to know the error range of the PGA (peak ground acceleration) from the observation and simulation in southern Taiwan.

So we based on the Jiashian earthquake parameter by Lee (2012) and determined the unknown parameter in reasonable range. And then, using "class B" (HEHRP) of KAU series to calibrate model with model bias. Finally, we compare the error range of PGA from observation and calibrated model.

2. DATA

In this study, the data we used is recorded by the Taiwan Strong Motion Instrumentation Program (TSMIP). So we chose KAU station series (Figure 1) which received Jiashian earthquake record. The data using H/V method is based on CWB (Central Weather Bureau) database from 1991~2009 with PGA (Peak ground acceleration) less than 60 gal to calculate the mean spectral ratio value.

3. STOCHASTIC FINITE FAULT MODEL

3.1 Stochastic Finite-Fault Model

In this study, we use the fortran program EXSIM (Extend Finite-Fault Simulation ; Motazedian and Atkinson 2005), which is base on the new concept "dynamic corner frequency" and motified by FINSIM. In this method, a large fault plane divided into *N* subfaults and each subfault is considered as a small point source. The ground motion of subfaults are summed with a proper time delay in time domain to calculate acceleration time series, *a(t)*, from the entire fault plane,

$$a(t) = \sum_{i=1}^{nl} \sum_{j=1}^{nw} a_{ij}\left(t + \Delta t_{ij}\right), \qquad (1)$$

where n_l and n_w are the number of subfaults along the strike and dip of the main fault ($n_l \times n_w = N$), respectively, and Δt_{ij} is the relative delay time for the radiated wave from the ijth subfault to reach the observation point. According to Motazedian and Atkinson (2005), the dynamic corner frequency is depended on the arrival time of each subfault, and the rupture process controls the frequency content of simulated time series of each subfault. The acceleration spectrum of the ijth subfault, $A_{ij}(f)$, as follows:

$$A_{ij}(f) = C\, M_{0ij} H_{ij} (2\pi f)^2 / \left[1 + \left(f/f_{0ij}\right)^2\right], \quad (2)$$

where M_{0ij} and f_{0ij} are seismic moment and dynamic comer frequency of ijth subfault and H_{ij} is scaling factor, as follow :

$$M_{0ij} = \frac{M_0 S_{ij}}{\sum_{l=1}^{nl} \sum_{k=1}^{nw} S_{kl}}, \quad (3)$$

$$H_{ij} = \left(N \sum \{f^2/[1 + (f/f_0)^2]\} / \sum \left\{f^2 / \left[1 + \left(f/f_{0ij}\right)^2\right]\right\}^{1/2}\right), \quad (4)$$

where S_{ij} is the relative slip weight of the ijth subfault; The constant C in equation (2) is,

$$C = R^{\theta\varphi} F V / 4\pi\rho\beta^3, \quad (5)$$

Where $R^{\theta\varphi}$ is radiation pattern (average value of 0.55 for shear wave) , F is free surface amplification (2.0), V is partition onto two horizontal components (0.71), ρ is density, and β is shear-wave velocity.

3.2 H/V Method

Single station spectral ratio method propose by Nakamura (1989). The first step is painting the waveforms of seismic events from 1991~2009. A 10-sec S-wave portion was selected to calculate the Fourier amplitude spectrum. After 5% cosine taper, each ratio was smoothed by using the three-point average method for the weightings of 0.25, 0.5, and 0.25. The root-mean-square spectrum from the NS component and EW component was calculated as the horizontal spectrum. Finally, the H/V spectral ratio was derived horizontal spectrum by vertical spectrum.

4. DATA PROCESSING

The Jiashian earthquake records of 71 stations was used in this study, and the simulating time series data was from the finite-fault program EXSIM (Extend Finite-Fault Simulation ; Motazedian and Atkinson, 2005) using source and path parameters for 2010 Jiashian earthquake (Table 1).

We use the model bias (logarithm of Fourier Amplitude Spectrum of observation over simulation) to examine the model better or worse, and the waveform and FAS (Fourier amplitude spectral) of the 4 B-class stations of KAU series showed in Figure 2.

Now, the model bias (Figure 3) is logarithm of observation of B-class stations over simulation of A-class because there is no A-class station in Taiwan. The result showed the FAS of simulation that is larger than observation because observation record had more attenuation.

Originally, KAU003 is a B classification from Engineering Geological Database for TSMIP, but we found the PGA and frequency content of KAU003 (Figure 4) which are not as other B-class stations. Finally, we found the drilling of KAU003 which is not around seismic instrument, and we don't use KAU003 to calibrate in this study.

5. CONCLUSIONS

The simulating waveforms of 71 stations used fast Fourier transform to frequency domain, and multiply transfer function, and IFFT to time domain. In this study, the transfer function is single H/V method. The best result in 71 stations is KAU009 (Figure 5), the spectral amplitude of observation (black line) and simulation (red line) is similar, and PGA had no larger difference.

However, we compare the PGA from 71station of simulation and observation in Figure 6. Mostly, the observations were larger than simulations, and maybe this transfer function H/V method can not response total effects.

The PGA of observation and simulation versus distances from 71stations showed in Figure 7. The more near-fault stations existed more difference, and better result was at long distance.

Finally, we discuss the error range ($\ln Err_i$) from observation and simulation, used this formula, as following:

$$\ln Err_i = \ln PGA_i - \ln \overline{PGA_i}$$

here, PGA_i is the observed PGA of ith station and $\overline{PGA_i}$ is the prediction from EXSIM multiplying transfer function. The result of Figure 8 can compare with Figure 6, and the standard deviation of $\ln Err$ is 0.67. In further, this finite-fault method with attenuation relationship will become better.

Acknowledgements:
We used the Jiashian observed record from TSMIP and re-calculate the H/V spectral ratio of KAU stations. This study was supported by the National Science Council ubder grant numbers NSC 101-2116-M-008-021. Thanks Dariush Motazedian very much to provide the finite-fault program EXSIM. (http://http-server.carleton.ca/~dariush/).

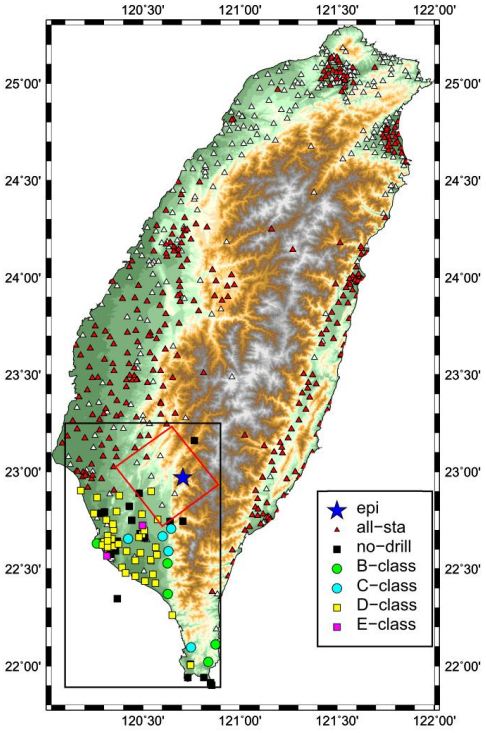
References:

Lee, S. J., Mozziconacci, L., Liang, W.-T., Hsu, Y.-J., Huang, W.-G., and Huang, B.-S. (2012). "Source complexity of the 4 March 2010 Jiashian, Taiwan, Earthquake determined by joint inversion of teleseismic and near field data," *Journal of Asian Earth Sciences*., Doi: http://dx.doi.org/10.1016/j.jseaes.2012.11.018.

Motazedian, D., and Atkinson, G., (2005). "Stochastic finite-fault model based on dynamic comer frequency," *Bulletin of the Seismological Society of America*., **95**(3), 995–1010.

Nakamura, Y., (1989), "A method for dynamic characteristics estimation of subsurface using microtremor on the ground surface," *QR of RTRI*, **30**(1), 25-33.

(a)



(b)

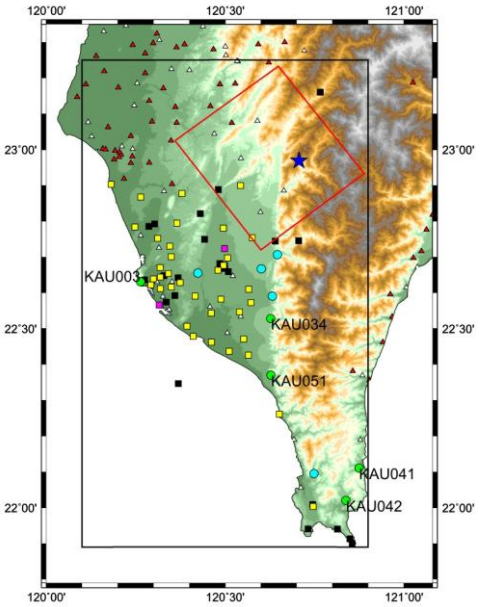
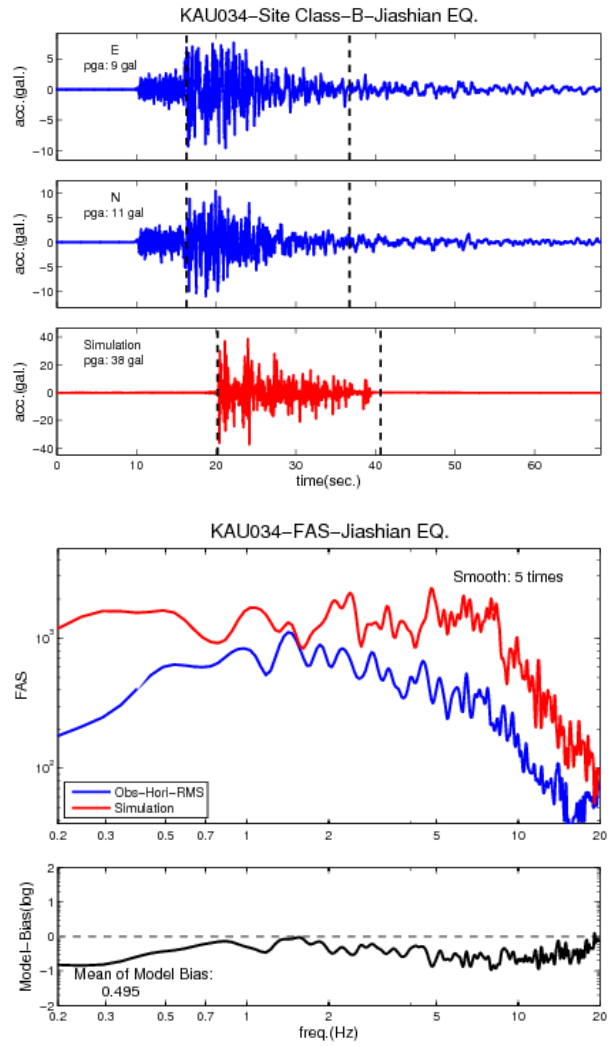
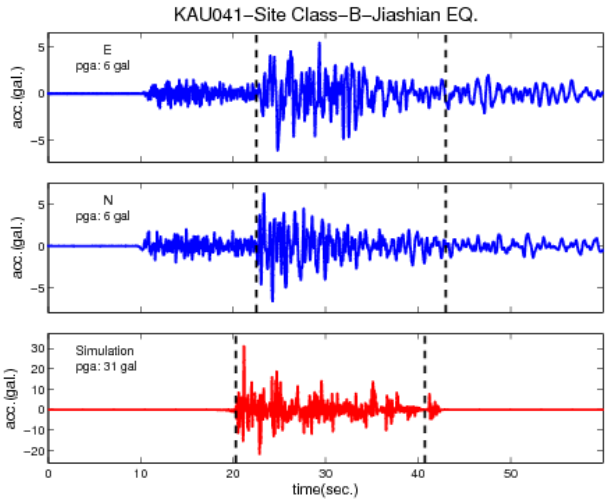


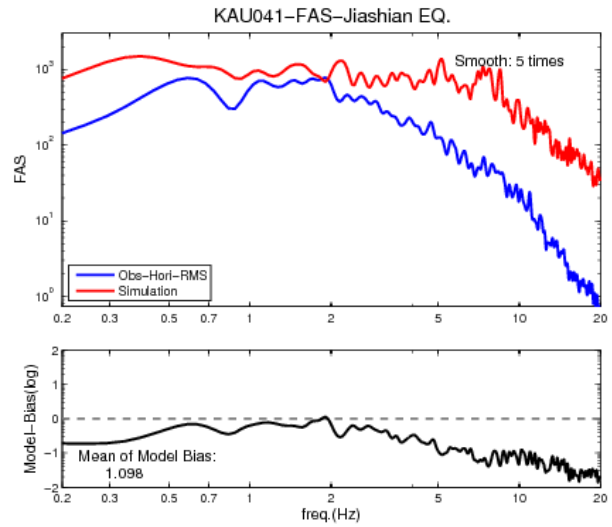
Figure 1 71 stations were used in this study. White and red triangle didn't use in this study; Green circles mean B classification (NEHRP) staions; Blue circles mean C classification stations; Yellow squares mean D classification stations; Purple squares mean E classification; Black squares mean stations without drilling (a) entire Taiwan , and (b) Kaohsiung area.

(a)

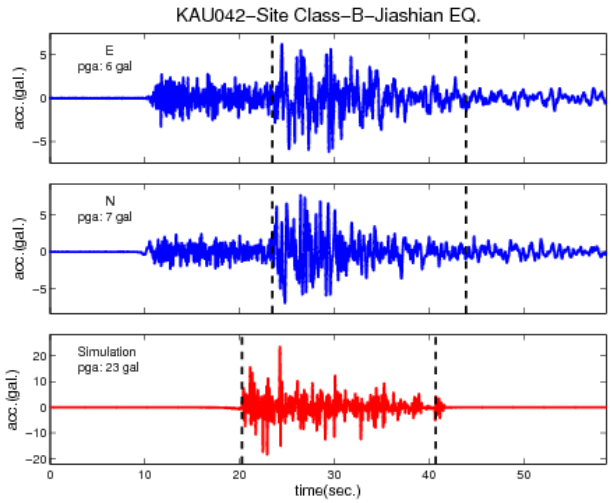


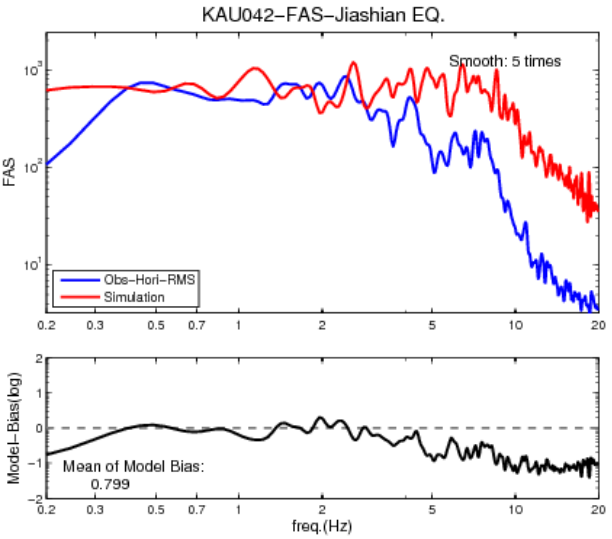
(b)



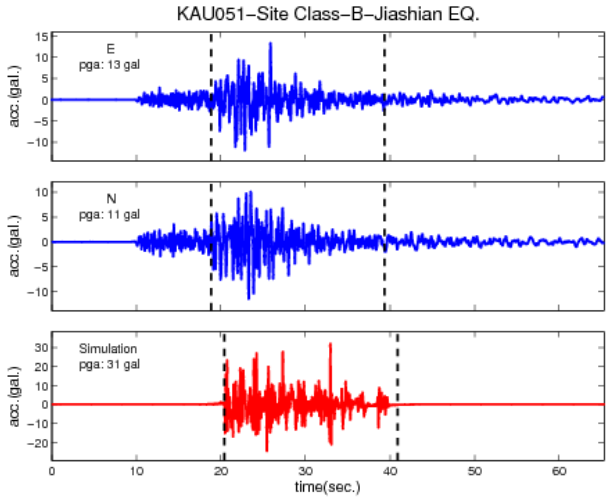


(c)





(d)



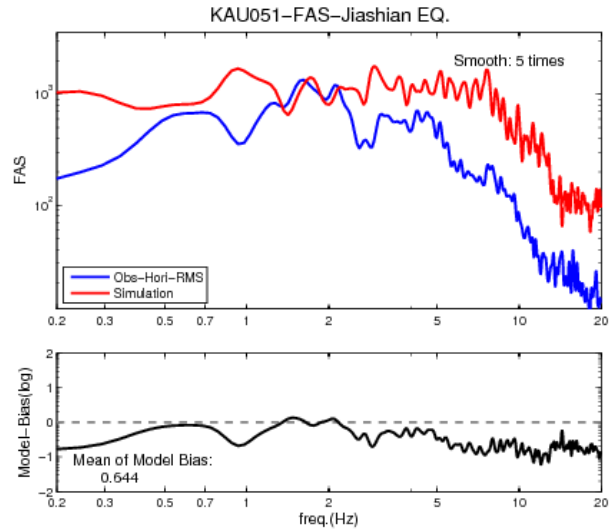


Figure 2 The four B-class (NEHRP) stations were used "Model Bias", which is equal to logarithm of Fourier Amplitude Spectrum (FAS) of observation over simulation. The waveform and FAS showed (a) KAU034, (b) KAU041, (c) KAU042, and (d) KAU051.

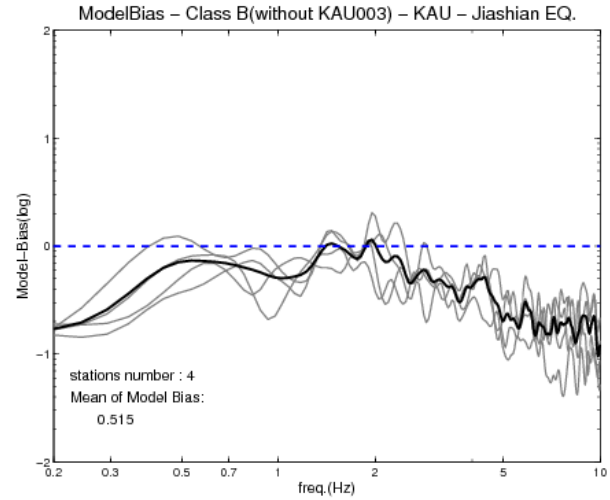


Figure 3 Mean of model bias from 4 B-class stations. KAU003 is B classification in NCREE database, but we found the drilling of KAU003 which is not near the station.

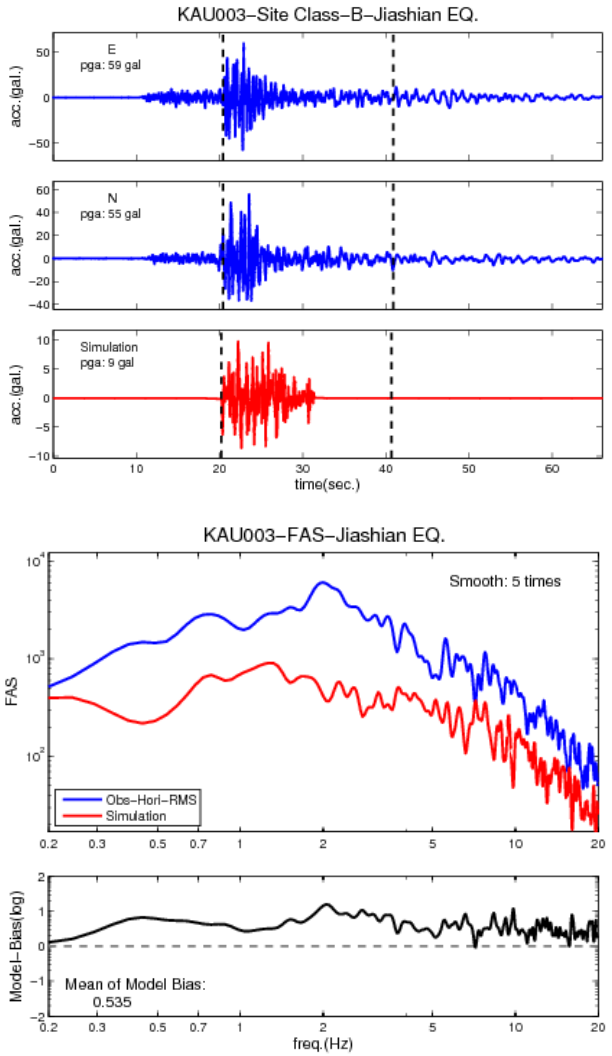


Figure 4 The waveform and FAS of KAU003 are not as B-class station. We don't use KAU003 to calibrate the model in this study.

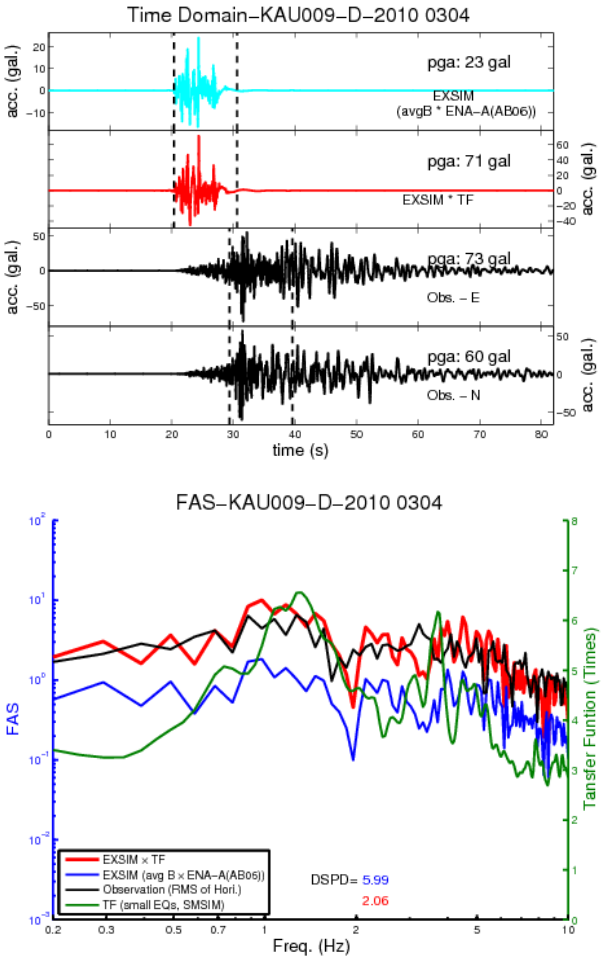


Figure 5 The good result KAU009 showed. The PGA of KAU009 from observation and simulation is similar, and the spectral amplitude multiplied transfer function (each H/V ratio in this study) is similar to FAS of observation.

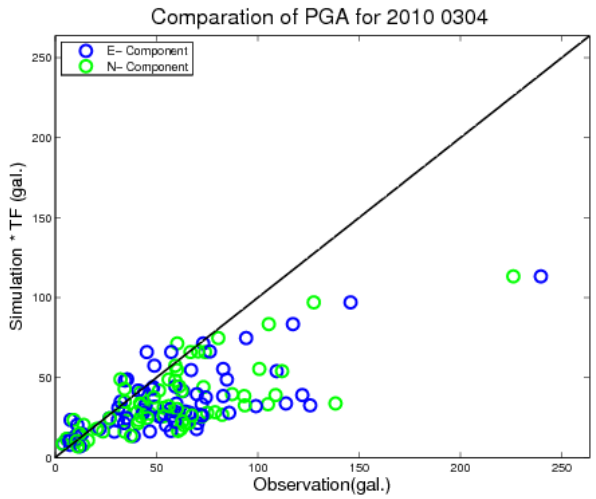


Figure 6 Comparison of PGA for 2010 Jiashian earthquake . Mostly, the PGA of observation is large than simulation. Blue and green circles showed E- and N-component, respectively.

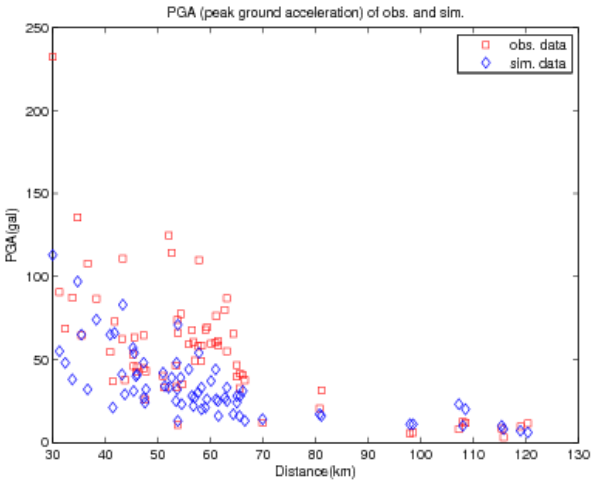


Figure 7 The PGA of observation and simulation versus distances from the 71 stations.

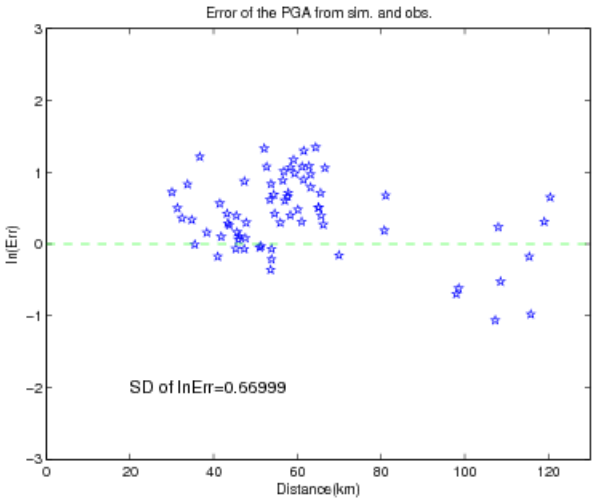


Figure 8 Comparison the error between observation and simulation. The standard deviation of $\ln_{Err}$ is 0.67.

Table 1
Source and Path Parameters for 2010 Jiashian Earthquake Model Implemented in Simulation

Parameter	Median value
M_w	6.47
Source depth(km)	22.6
Stress drop (bars)	12.3
Fault orientation(strike/dip)	324°/39°
Fault dimensions(km)	42 by 48
Subfault dimensions(km)	3 by 3
Number of subsources summed	224
Kappa (sec)	0.05
Q(*f*)	$80 \cdot f^{0.9}$
Geometric spreading R^b	b = -1.0, R < 50km
	b = 0.0, 50km ≦ R < 150km
	b = -0.5, R ≧ 150km
Crustal shear-wave velocity (km/sec)	3.2
Rupture velocity(km/sec)	0.8 × (shear velocity)
Crustal density (g/cm^3)	2.7
Windowing function	Saragoni-Hart taper
Low-cut filter	no filter
Crustal amplification	Atkinson and Boore (2006) generic hard rock site

10CUEE CONFERENCE PROCEEDINGS
10th International Conference on Urban Earthquake Engineering
March 1-2, 2013, Tokyo Institute of Technology, Tokyo, Japan

SIMULATION OF STOCHASTIC GROUND MOTION WITH SITE CORRECTION USING EQUIVALENT-LINEAR METHOD AT TAIPEI BASIN DOWNHOLE ARRAYS

Saifuddin[1], Kuo-Liang Wen[2], Jyun-Yan Huang[3], and Hsien-Jen Chiang[4]

1) Master student, Department of Earth Sciences, National Central University, Taiwan (R.O.C)
2) Professor, Department of Earth Sciences, National Central University, Taiwan (R.O.C)
3) PhD student, Department of Earth Sciences, National Central University, Taiwan (R.O.C)
4) Post-Doctoral student, Department of Earth Sciences, National Central University, Taiwan (R.O.C)
100622601@cc.ncu.edu.tw, wenkl@earth.ncu.edu.tw, 986402005@cc.ncu.edu.tw, s1642006@cc.ncu.edu.tw

Abstract: Attenuation relationship (peak ground acceleration, PGA) is widely used by engineers in seismic hazard estimation studies. This study was conducted by combining stochastic point-source (Boore 2003) and equivalent-linear (Idriss and Sun 1992) methods to simulate ground motion, and compared the results to attenuation relationship. The stochastic method was performed to obtain simulated waveforms in rock site (TAP086 station) near of Wuku downhole and Wuku downhole. It showed decent results in rock site, while underestimated result in Wuku downhole. Simulated waveforms in rock sites were used as input motions for site correction. Site correction was performed in Wuku downhole using equivalent-linear method. Shear wave velocity profile (Wen et al. 1995 and Wang et al. 2004), geological soil profile (Liu 1999) of Wuku downhole and input motions are required for equivalent-linear method to obtain simulated waveforms in soil surface of Wuku downhole. Equivalent-linear method can assist to correct simulated PGAs and model bias at Wuku downhole using simulated waveform at rock site as outcropping input motion.

1. INTRODUCTION

Taipei city and several satellite cities are located in Taipei basin. Taipei city is the political, economic, and cultural center of Taiwan and demands serious attention to seismic risk mitigation. Many earthquakes of moderate to large magnitude ($5.3 \leq M_L \leq 7.3$) occurred near the Taipei metropolitan area since1659 from the limited historical records (Huang et al. 2008). Several downhole stations were installed in Taipei basin in order to study the basin effects and seismic wave propagation to anticipate future large and catastrophic earthquakes.

This study is conducted by combining stochastic point-source (Boore 2003) and equivalent-linear (Idriss and Sun 1992) methods to simulate ground motion at Taipei downhole basin and compared the results to attenuation relationship. Simulated waveforms in outcropping rock (TAP086 station) are obtained using stochastic point-source method. The simulated waveforms in outcropping rock are used as input motion at basement of Wuku downhole (679 m) to obtain simulated waveforms on surface using equivalent-linear method (Figure 2). Equivalent-linear method is performed for site correction in order to yield decent simulated waveforms.

2. METHOD

2.1 Data

Figure 1 shows earthquakes distribution and location of TAP086 station and Wuku downhole. Seven earthquakes with local magnitude M_L=5.6-6.6 were selected based on peak ground acceleration (PGA) in surface station of Wuku downhole which had PGA more than 10 gal. EQ2, EQ4, EQ5, EQ6 were located in northeastern Taiwan, while EQ1, EQ3, and EQ7 were located in offshore. EQ1, EQ2, EQ4 and EQ7 were shallow earthquake (less 35 km) while EQ3, EQ5 and EQ7 were deep earthquake (more than 35 km). TAP086 (V_{s30}=942.80 m/s) is one of the closest stations of class B to Wuku downhole about 18.57 km. Wuku downhole has stations at 0, 30, 60, 90, 141 and 352 m. EQ1, EQ2, and EQ3 were recorded at stations of 0, 30, 60, 90 and 141, while EQ4, EQ5, EQ6, EQ7 were recorded at stations 0, 30, 60, 141, and 352 m.

2.2 Stochastic Point-Source Method (SMSIM)

SMSIM is simple and powerful method for simulating high frequency ground motions is to combine parametric or functional descriptions of the ground motion amplitude spectrum with a random phase spectrum modified such that the motion is distributed over a duration related to the earthquake magnitude and to the distance from the source (Boore 2003). Table 1 shows parameters for stochastic

point-source method.

SMSIM was performed to obtain simulated waveforms at TAP086 station and Wuku downhole. Figure 5 shows that 15 seconds of selected S-window and this selected waveform was transformed into Fourier amplitude spectrum (FAS) for analysis of frequency range from 0.2-10 Hz.

2.3 Equivalent-Linear Method (SHAKE91)

SHAKE91 has been applied routinely in engineering community to evaluate one-dimensional soil site response and considers nonlinear site response. It showed decent simulated waveforms for small and large input motion (Lee et al. 2006).

Shear wave velocity of soil profile (Figure 3), geological soil profile (Liu 1999) and input motion (Figure 6) are required for SHAKE91 to produce waveforms in different layers or depths (Figure 7).

3. RESULT AND DISCUSSION

In order to verify reliability of model and methods, comparison of observed and simulated PGAs were performed as well as the model bias which is formulated as:

$$\text{Model bias}=\log\left(\frac{FAS_O}{FAS_S}\right) \quad (1)$$

FAS_O: Fourier amplitude spectrum of observed waveform
FAS_S: Fourier amplitude spectrum of simulated waveform

3.1 Verification on Artificial Layers of Wuku Downhole

Wuku downhole has depth 760 m. It was found that the basement of Wuku area about 679 m (Wang et al. 2004). This 679 m was divided into 50 artificial layers and each layer is assumed to have shear modulus reduction and damping factor of clay, sand or rock (Figure 4). To verify the reliability of these artificial layers, observed waveforms at 0 m were used as input motion for SHAKE91 to obtain simulated waveforms for different depths (Figure 8-12). Figure 8 to 12 show decent result of PGAs comparison and model bias for different depth.

3.2 Simulated Waveforms at Wuku Downhole Using Observed Waveforms at TAP086 as Input Motion for SHAKE91

Observed waveforms at TAP086 station were used as outcropping input motion to simulate waveform at Wuku downhole. Figure 13 shows decent comparison of PGA and model bias, the PGA comparison close to target line with average model bias 0.151 and 0.184 for east and north component respectively.

3.3 Simulated Waveforms at TAP086 Station Using SMSIM

SMSIM was performed to obtain simulated waveforms, and compared against observed waveforms for EQ4, EQ5, EQ6, and EQ7. Figure 14 shows that simulated and observed PGA close to target line which shows a decent result as well as model bias also shows a decent result by having average model bias 0.111.

3.4 Simulated Waveforms at Wuku Downhole Using SMSIM

SMSIM was performed to obtain simulated waveforms, and compared against EQ1 to EQ7. Figure 15 shows that simulated PGAs are generally underestimated to observed PGAs as well as model bias from frequency 0.2 to 4 Hz and the value of average model bias 0.290.

3.5 Simulated Waveforms at Wuku Downhole Using SMSIM and SHAKE91

Simulated waveforms at TAP086 station were used as input motion to simulate in surface station of Wuku downhole. Figure 16 shows that comparison of simulated and observed waveform close to target line as well as decent model bias with value of average model bias 0.217. If comparing to Figure 15, it showed that SHAKE91 can assist to correct the simulated PGAs and model bias.

4. CONCLUSIONS

The artificial layers of Wuku downhole and Wuku velocity structure are reliable which was showed by decent comparison of observed and simulated waveforms and model bias at different depths.

TAP086 records can be used as outcropping input motion to simulate waveform at Wuku downhole. Simulated waveforms using SMSIM at TAP086 station showed decent result.

Simulated waveforms using SMSIM at Wuku downhole were underestimated compared to observed waveforms.

SHAKE91 can assist to correct simulated PGAs and model bias at Wuku downhole using simulated waveform at TAP086 station as outcropping input motion.

Further study is required for other Taipei downhole basin arrays, and compared the result to attenuation relationship.

Acknowledgements:

The authors used the earthquake data from TSMIP and earthquake downhole data from IES, Academia Sinica. This study was supported by the National Science Council under grand numbers, NSC101-2923-M-008-001 and NSC102-2923-M-008-001. The authors would like to grateful to David M. Boore for providing SMSIM program and I.M. Idriss and J.I. Sun for providing SHAKE91 program.

References:

Boore, D.M. (2003), "Simulation of Ground Motion Using the Stochastic Method," *Pure and Applied Geophysics* **160**(3), 635–676.

Huang, W.G., Huang, B.S., Chen, K.C., Liu, C.C., Lin, C.R., Tsao, S.H., Hsieh, Y.C. and Chen, C.H. (2008), "Observations Using

the Taipei Basin Broadband Downhole Seismic Network: The 26 December 2006, Pingtung Earthquake Doublet, Taiwan," *TAO*, **19**(6), 761-766.

Idriss, I.M. and Sun, J.I. (1992), "A Computer Program for Conducting Equivalent Linear Seismic Response Analyses of Horizontally Layered Soil Deposits," Center for Geotechnical Modeling, Department of Civil and Environmental Engineering, University of California, Davis, California.

Lee, C.P., Tsai ,Y.B., and Wen, K.L. (2006), "Analysis of Nonlinear Site Response Using the LSST Downhole Accelerometer Array Data," *Soil Dynamics and Earthquake Engineering* **26**(5), 435–460.

Liu, T.C. (1999), "Microzonation of Intensity and Construction of GIS System in Taipei Basin", Master Thesis of Institute of Civil Engineering, National Taiwan University (*in Chinese*).

Sokolov, V., Loh, C.H., and Wen, K.L. (2001), "Site Dependent Design Input Ground Motion Estimations for the Taipei Area: a Probabilistic Approach," *Probabilistic Engineering Mechanics* **16**(2), 177-191.

Sokolov, V., Loh, C.H. and Jean,W.Y. (2006), "Strong Ground Motion Source Scaling and Attenuation Models for Earthquakes Located in Different Source Zones in Taiwan," *4th International Conference on Earthquake Engineering*, Paper No. 003.

Tsai, C.C.P. (1997), "Relationship of Seismic Source Scaling in the Taiwan Region," *TAO*, **8** (1), 49-68.

Wang, C.Y., Lee, Y.H., Ger, M.L., Chen,Y.L. (2004), "Investigating Subsurface Structures and P- and S-wave Velocities in the Taipei Basin," *TAO*, **15**(4), 609-627.

Wen, K.L., Fei, L.Y., Peng, H.Y. and Liu, C.C. (1995), "Site Effect Analysis From the Record of the Wuku Downhole Array," *TAO*, **6**(2), 285-298.

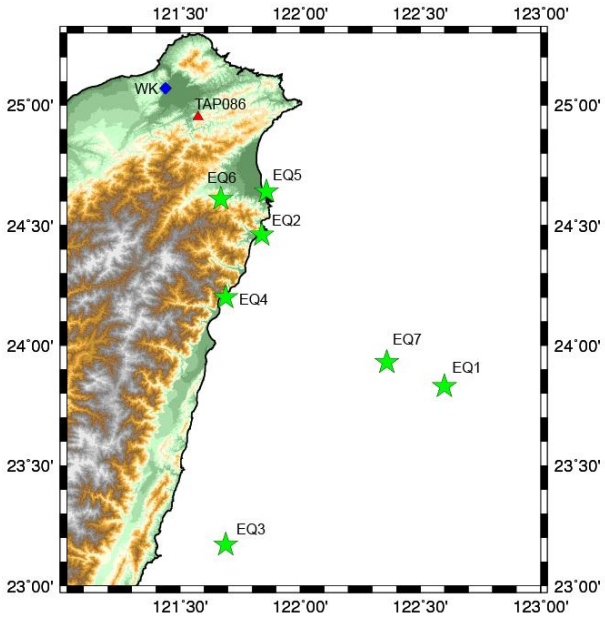


Figure 1 Earthquake Distribution and Wuku (WK) Downhole and TAP086 Location

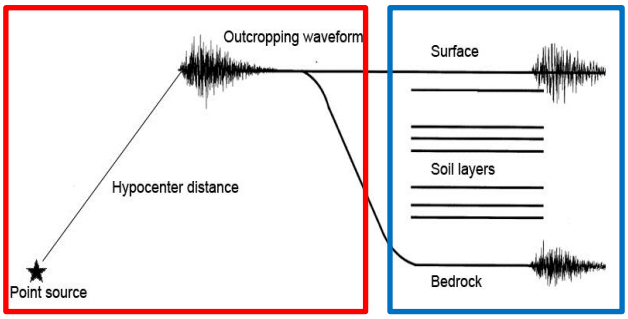


Figure 2 Simulation Proses Using SMSIM at TAP086 (Red Square) and SHAKE91 at Wuku Downhole (Blue square)

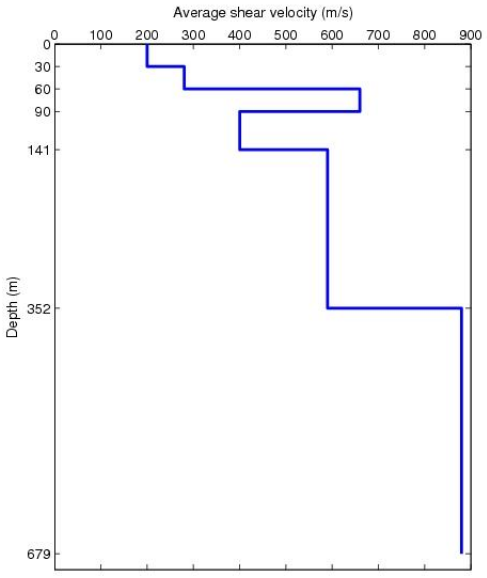


Figure 3 Average Shear Velocity of Wuku Area (Wen et al. 1995) with Modification for 352-679 m (Wang et al.2004)

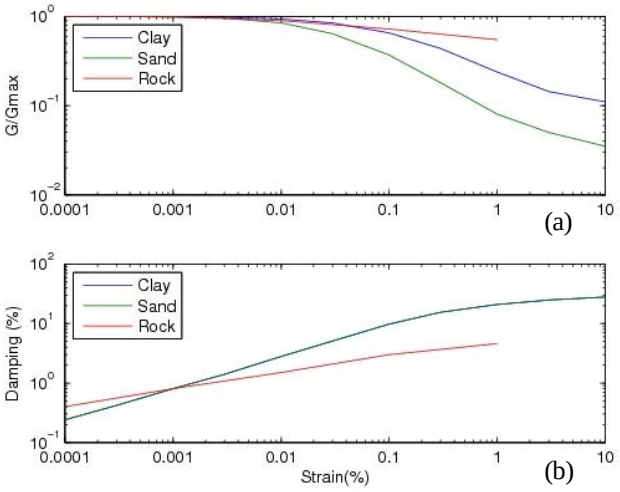


Figure 4 (a) Normalized Shear Modulus, and (b) Damping Factor Related to Strain for SHAKE91 (Default from SHAKE91, Idriss and Sun 1992)

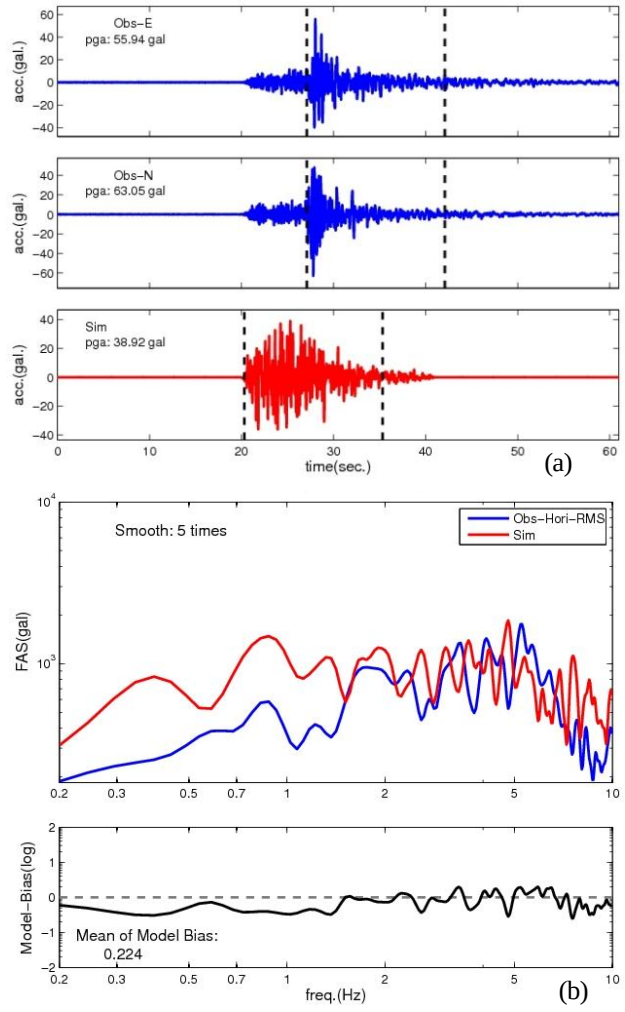


Figure 5 Comparison of Observation and Simulation Using SMSIM (a) 15 Seconds of S-window (b) FAS and Model Bias for EQ6

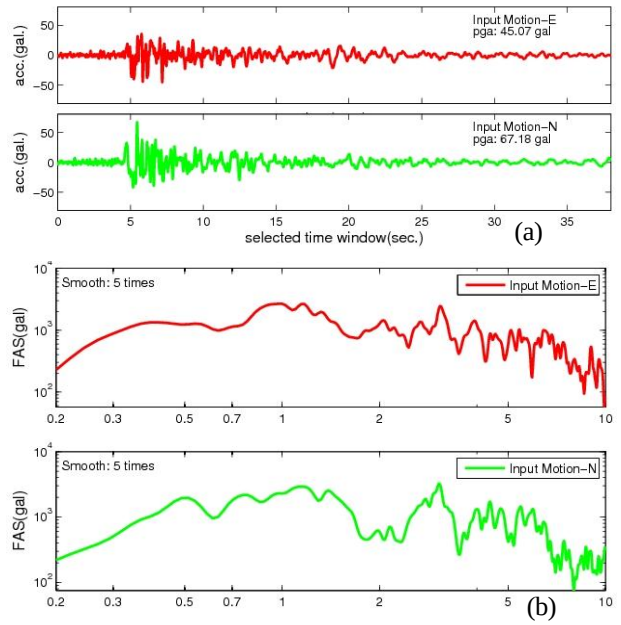


Figure 6 Input Motion for SHAKE91 at 0 m for EQ6: (a) acceleration (b) FAS

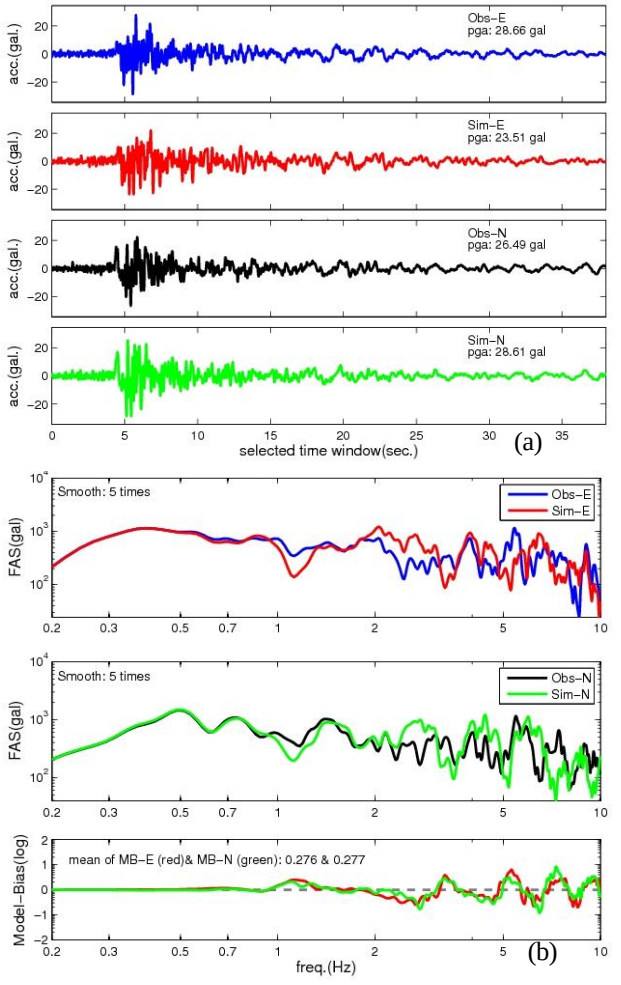


Figure 7 Comparison of Observation and Simulation Using SHAKE91 at 60 m for EQ6: (a) Acceleration (b) FAS and Model Bias

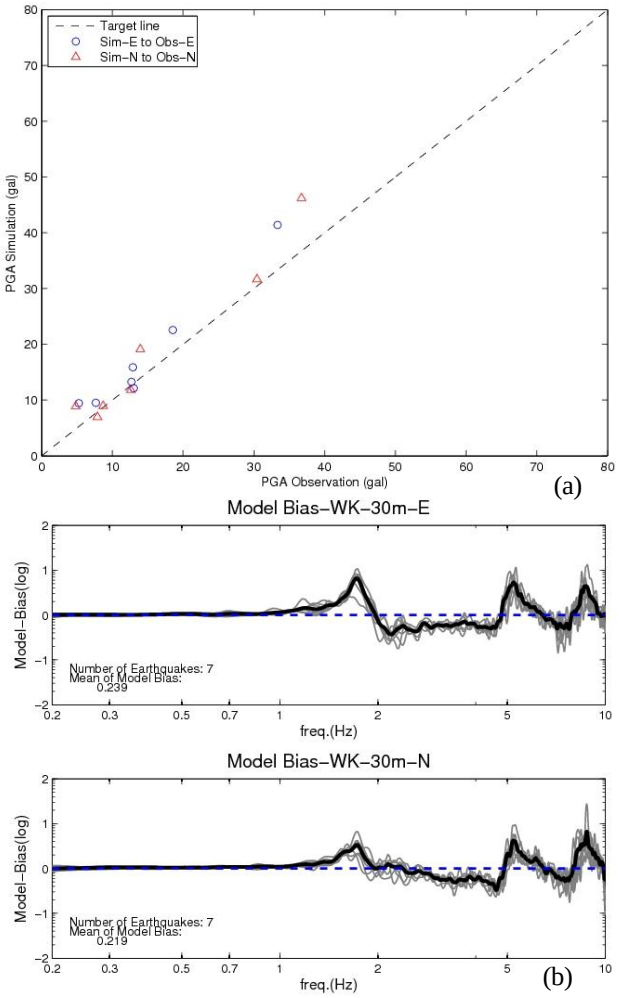
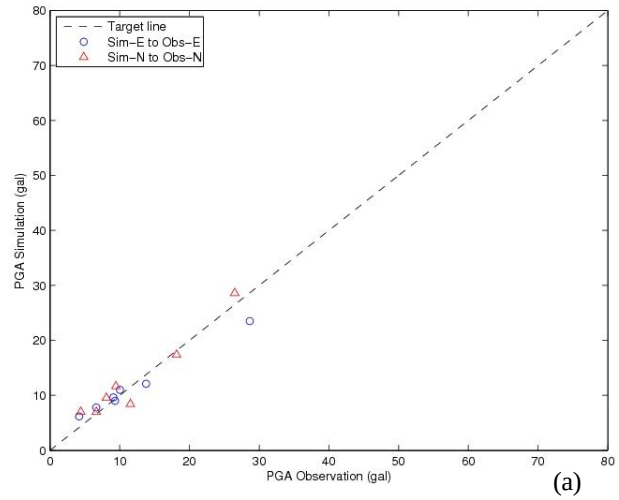


Figure 8 Comparison of Observation and Simulation Using SHAKE91 at 30 m: (a) PGA (b) Model Bias



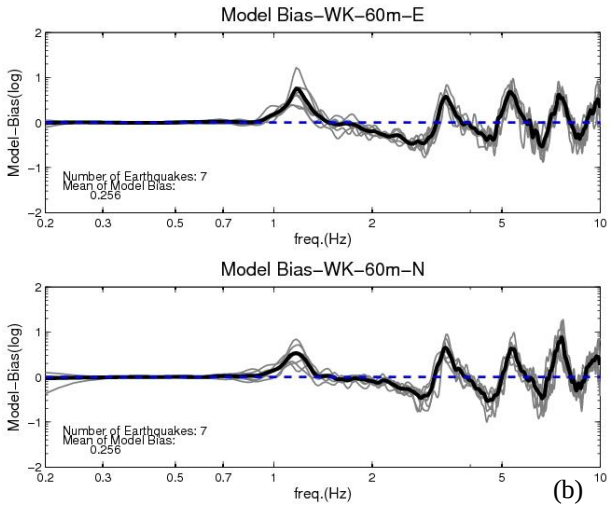


Figure 9 Comparison of Observation and Simulation Using SHAKE91 at 60 m: (a) PGA (b) Model Bias

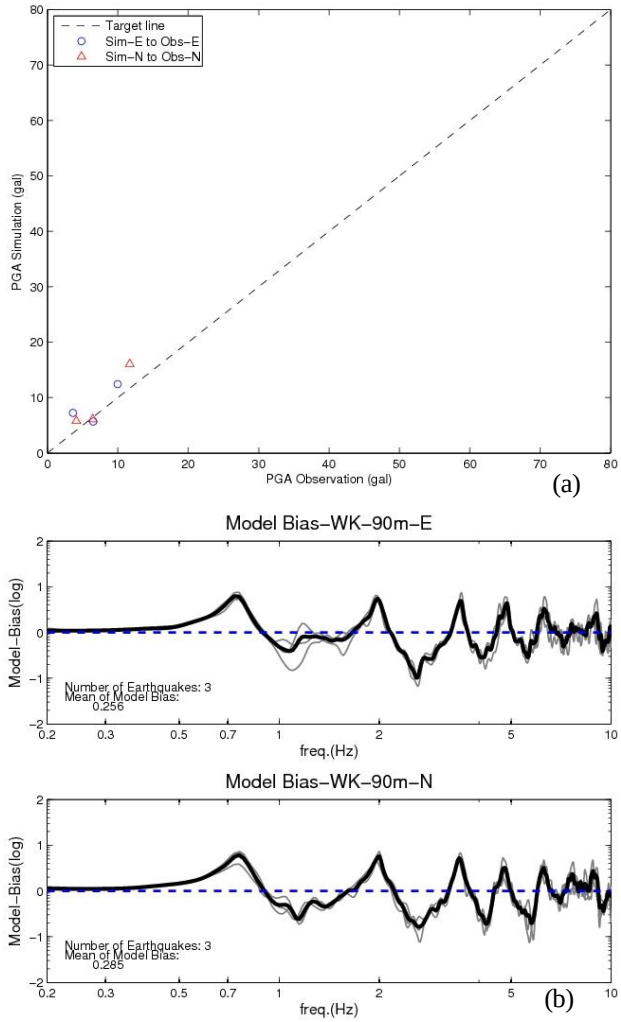


Figure 10 Comparison of Observation and Simulation Using SHAKE91 at 90 m (a) PGA (b) Model Bias

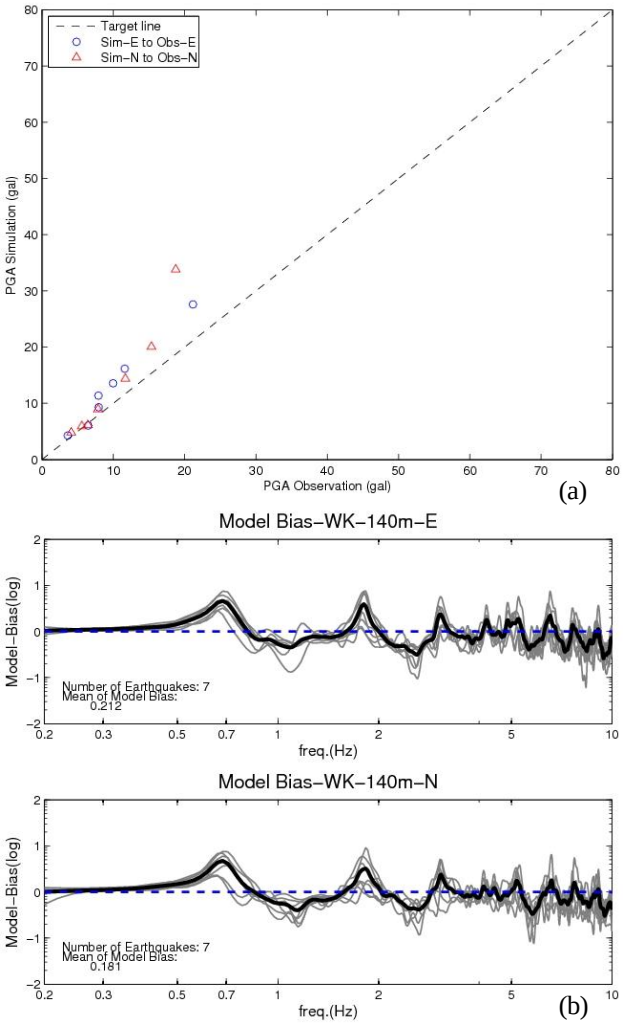
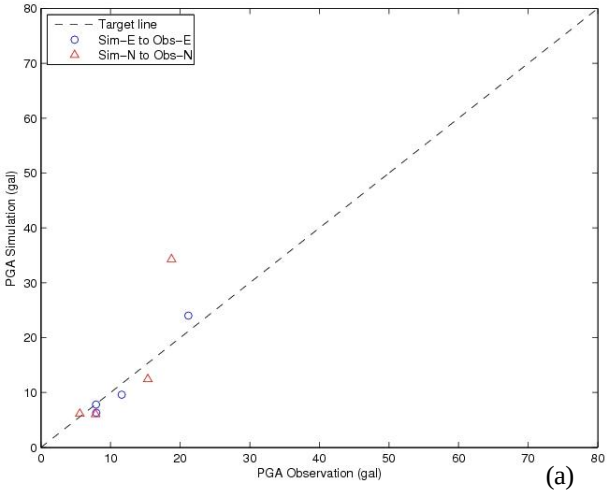


Figure 11 Comparison of Observation and Simulation Using SHAKE91 at 140 m (a) PGA (b) Model Bias



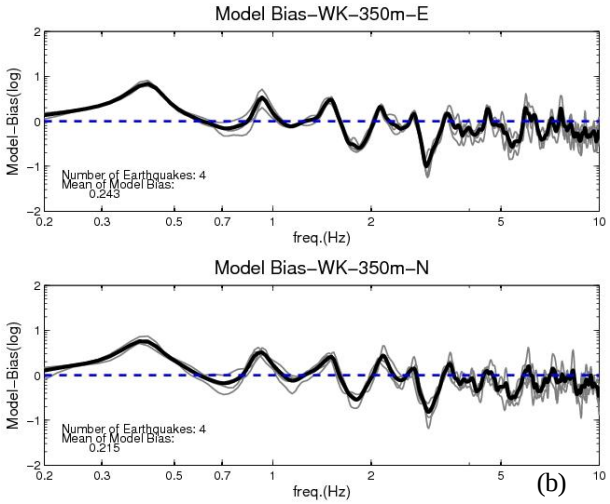


Figure 12 Comparison of Observation and Simulation Using SHAKE91 at 350 m (a) PGA (b) Model Bias

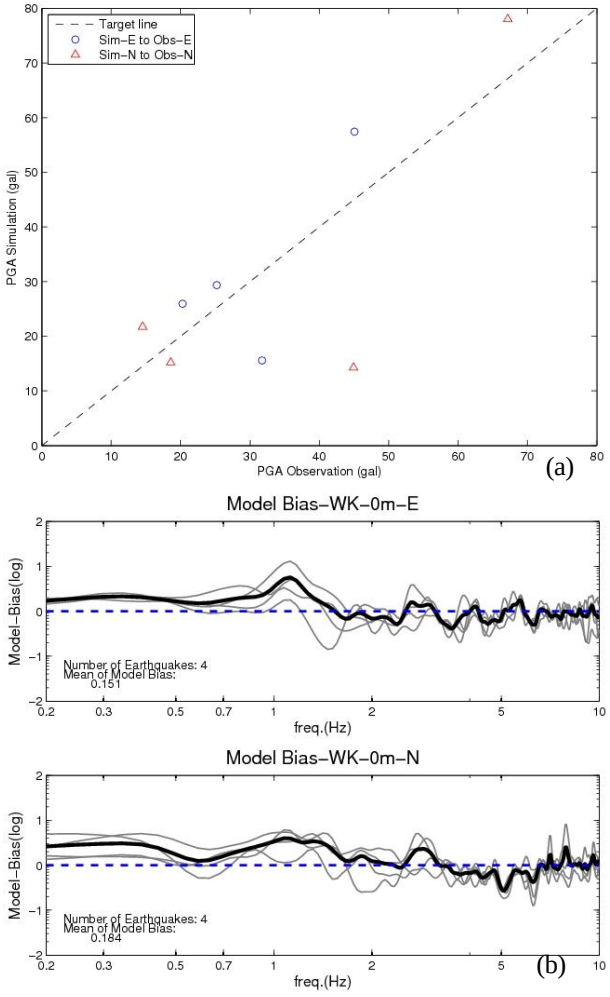
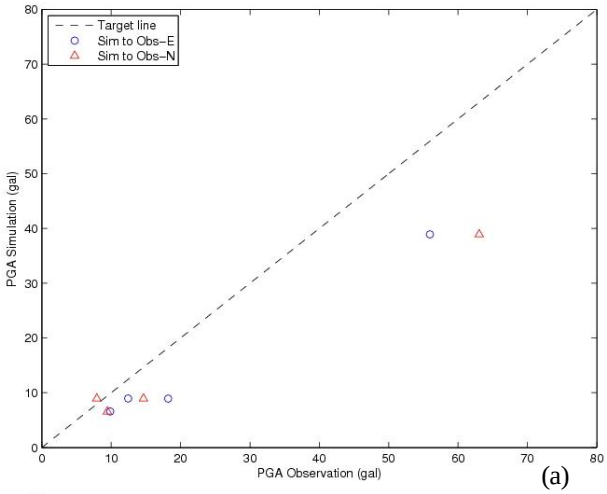
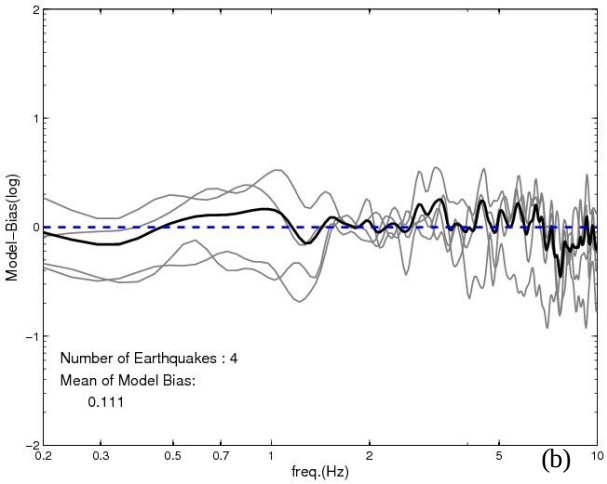


Figure 13 Comparison of Observation and Simulation Using Observed Waveform at TAP086 as Outcropping Input Motion for SHAKE91 at 0 m Station of Wuku Downhole (a) PGA (b) Model Bias

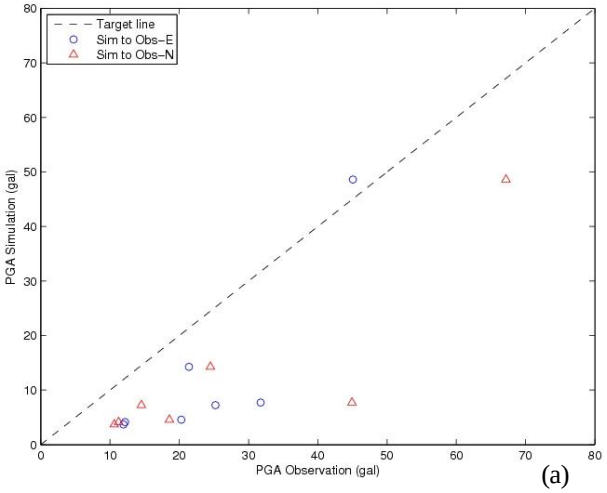


(a)

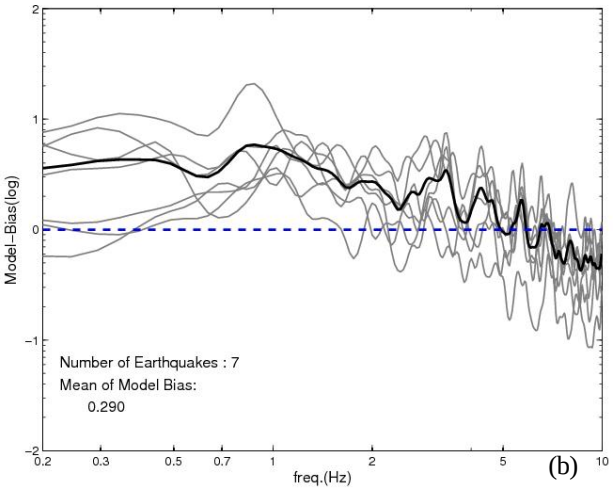


(b)

Figure 14 Comparison of Observation and Simulation Using SMSIM at TAP086 Station (a) PGA (b) Model Bias

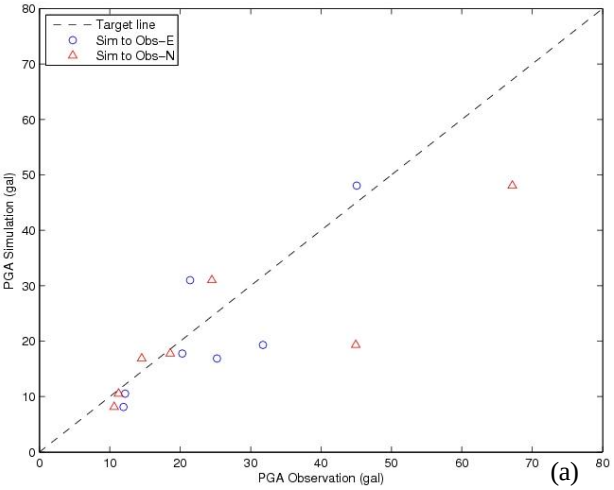


(a)

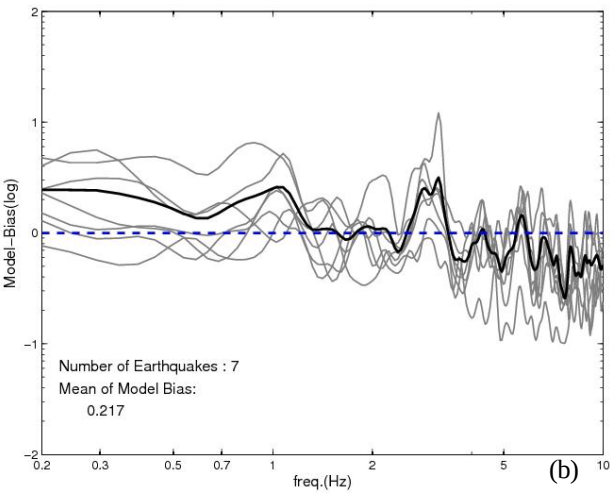


(b)

Figure 15 Comparison of Observation and Simulation Using SMSIM at Wuku Downhole (a) PGA (b) Model Bias



(a)



(b)

Figure 16 Comparison of Observation and Simulation Using Simulated Waveform at TAP086 as Outcropping Input Motion for SHAKE91 (a) PGA (b) Model Bias

Table 1 Parameters for SMSIM

Parameters	**Values**
Stress Drop (bar)	Northeastern Taiwan: $\log(\Delta\sigma) = -3.3976 + 0.2292\log(M_0) \pm 0.6177$ (Tsai 1997) Offshore: $\Delta\sigma = 100$ (Sokolov et al. 2006)
Shear Wave Velocity (km/s)	3.2
Density (g/cm^3)	2.7
Quality Value	Shallow Earthquake: $Q(f) = 125f^{0.8}$ Deep Earthquake: $Q(f) = 225f^{1.1}$ (Sokolov et al. 2001)
Geometrical Spreading	1/R for R<50 km 1/R^0 for 50 km ≤R<150 km 1/R$^{0.5}$ for R≥150 km (Sokolov et al. 2001)
Kappa (sec)	0.05

10CUEE CONFERENCE PROCEEDINGS
10th International Conference on Urban Earthquake Engineering
March 1-2, 2013, Tokyo Institute of Technology, Tokyo, Japan

LONG-PERIOD GROUND MOTION SIMULATIONS IN THE KANTO BASIN USING DIVERSE VELOCITY MODELS FOR THE HYPOTHETICAL TOKAI EARTHQUAKE

Yadab Prasad Dhakal[1)] and Hiroaki Yamanaka[2)]

1) Researcher, Department of Environmental Science and Technology, Tokyo Institute of Technology, Japan
2) Professor, Department of Environmental Science and Technology, Tokyo Institute of Technology, Japan
dhakal.y.aa@m.titech.ac.jp, yamanaka@depe.titech.ac.jp

Abstract: In this study, we used the velocity models, proposed by Headquarters for Earthquake Research Promotion (HERP, 2012) and Yamada and Yamanaka (2012), of the Kanto basin for long-period (2~20s) ground motion simulations for the hypothetical Tokai earthquake (Mw~8). We used already available source model for the earthquake. Previous studies showed that the velocity models performed nearly similarly in the period range of 2 to 10 s at most sites in the Kanto basin for moderate magnitude (Mw<6.0) earthquakes which occurred beneath the basin. In this study, we compared the synthetics only for the large magnitude Tokai earthquake, and found that the models performed quite differently from each other at recognizable areas in the Kanto basin. This suggests a further evaluation and modification of the existing velocity models for reliable prediction of long-period ground motions from future large earthquakes.

1. INTRODUCTION

Many high-rise buildings and large oil-storage tanks, which are susceptible to long-period ground motions, are located today on the deep sedimentary basins. The 3-D velocity structure of a sedimentary basin greatly controls the amplitude and duration of long-period ground motions during large earthquakes. Many institutes are involved in constructing and updating the 3-D velocity structure model of the deep sedimentary basins for the seismic disaster mitigation planning in Japan (e.g., Koketsu *et al*., 2008). As a result, several 3-D velocity models have been proposed for the Kanto basin, which is the largest basin in Japan. Although the objective of constructing such models is to accurately predict the long-period ground motions, the models are different because they have been constructed using different data sets.

Recently, Headquarters for Earthquake Research Promotion (HERP, 2012) released a new version of its previous velocity model. Similarly, Yamada and Yamanaka (2012) (here after YY) made available an updated version of their previous deep velocity model of the Kanto basin. The HERP model has been reconstructed by compiling a diverse suite of data, geological, geophysical, deep borehole profiles, microtremor explorations, and so on (e.g, Tanaka et. al., 2005; Fujiwara et al., 2006; HERP 2012). On the other hand, the YY model has been reconstructed using the Rayleigh wave phase velocities at periods from 0.5 to 5 s deduced from microtremor array observations at more than 250 sites in the area. Considering stronger long-period shakings likely to occur in the Kanto basin than those observed during the 2011 Mw 9 Tohoku-oki earthquake (e.g.,Yoshimi et al., 2012), it is urgent to evaluate the existing deep velocity models of the Kanto basin for reliable prediction of long-period ground motions from future large earthquakes.

Previous studies by us (Dhakal and Yamanaka, 2012) showed that the models performed nearly similarly in the period range of 2-10 s for moderate magnitude earthquakes that occurred just beneath the basin. In this study, we compare the synthetics from YY model to those from HERP model for the hypothetical Tokai earthquake. In this case, we cannot evaluate which model performed better, but we hope to get some idea how the models perform for a future large earthquake. We perform waveform simulations using a finite difference method, and compare the waveforms at period from 2 to 20 s (0.05-0.5 Hz) at the K-NET and KiK-net sites in the Kanto basin and adjacent areas. Finally, we discuss the results with respect to our previous studies (Dhakal and Yamanaka, 2012), and recent observed records from large earthquakes.

2. VELOCITY MODEL PARAMETERS

In this study, we use two different velocity models, namely, HERP (2012) and Yamada and Yamanaka (2012) (YY) of the Kanto basin for long-period ground motion simulation. The HERP models were reconstructed using diverse suite of data: the geological maps, seismic reflection and refraction surveys, gravity surveys, H/V inversions of earthquake coda waves, deep borehole profiles, and layer

boundaries estimated by microtremor exploration method (e.g., Tanaka et. al., 2005; Fujiwara et al., 2006; HERP 2012). On the other hand, the YY model was reconstructed using the Rayleigh wave phase velocities at periods from 0.5 to 5 s deduced from microtremor array observations at more than 250 sites in the area. Thus, the models differ primarily on the basic data used for the model reconstructions. The two models mentioned above are the updated versions of their previous ones by the respective institutions.

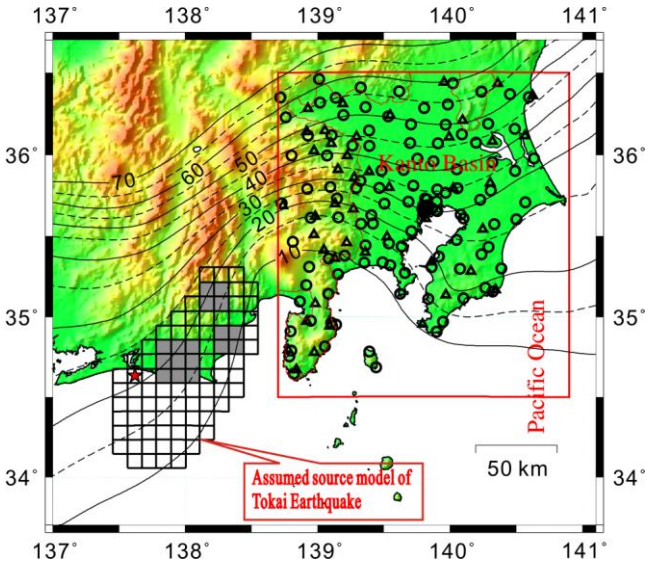


Figure 1. Index map showing the source model of Tokai earthquake (rectangular grids), and strong motion stations (circles: K-NET, and Triangles: KiK-net). A star denotes the hypocenter, and the shaded zones inside the fault plane indicate the location of asperities. The contours denote the depth to the upper surface of Philippine Sea plate. The red rectangle enclosing the stations indicates the model region for the Yamada and Yamanaka (YY) (2012) model. The thin red lines inside the YY model indicate the basin edge at the surface in the YY model.

The HERP model consists of twenty three layers in total (including the crustal and upper mantle layers). Among the twenty three layers, there are eleven layers above the seismic basement having Vs 3.2 km/s. However, we find that only three layers having Vs values of 0.5, 1.0, and 1.5 km/s above the seismic basement constitute the main sections of the Kanto basin in the HERP model. The YY model consists of only three layers above the seismic basement. The top layer comprises several sections of different Vs values (0.3 ~ 0.8 km/s), and the other two layers have Vs values of 1.0 and 1.5 km/s above the seismic basement. Outside the basin area, the velocity structures are adopted from the HERP model, so the velocity structures are same outside the basin for the both simulations using the HERP and YY models. All the layers overlying the Vs 2.9 km/s of the HERP model are removed in the Kanto basin area, and YY model is substituted. The depth of the layer having Vs 3.0 km/s of the YY model is set as a joining depth between the two models; the boundary depth of HERP model for the Vs 2.9 km/s layer is aligned with the depth of Vs 3.0 km/s of the YY model, and other layers in the HERP models are adjusted accordingly. The model regions are indicated in Fig. 1

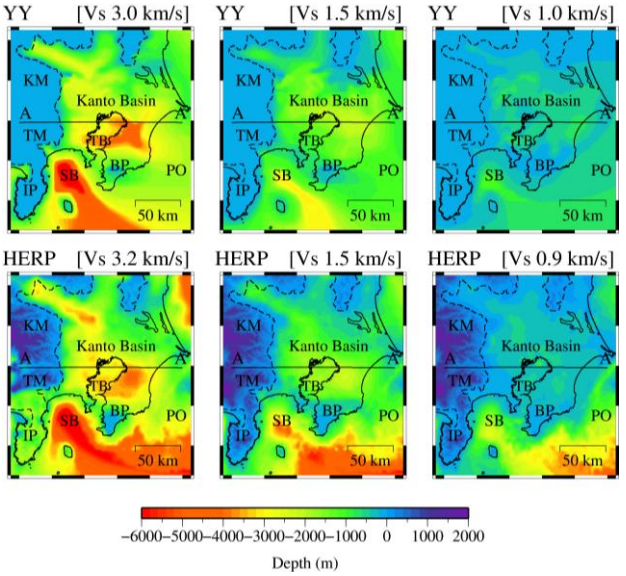


Figure 2. Maps showing depth to the top of three layers having similar S-wave velocities for the YY and HERP velocity structure models of the Kanto basin. The top panel depicts depth to the upper boundary of layers having S-wave velocity of 3.0, 1.5, and 0.9 km/s from left to right, respectively, for the YY model. Similarly, the lower panel depicts the depth to the upper boundary of layers having S-wave velocity of 3.2, 1.5, and 0.9 km/s from left to right, respectively, for the HERP model. A solid line AA' indicates a profile for the vertical section of the velocity structures, depicted in Fig. 3. A dashed line denotes the basin edge at the surface adopted in the YY model. The two letter codes TM, KM, IP, SB, TB, BP, and PO denote the Tanzawa Mountains, Kanto Mountains, Izu Peninsula, Sagami Bay, Tokyo Bay, Boso Peninsula, and Pacific Ocean, respectively.

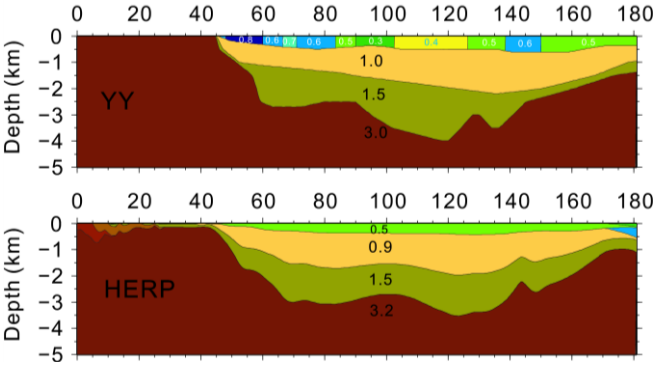


Figure 3. Vertical sections of the velocity structures along the profile A-A' depicted in Fig. 2 for the sedimentary layers in the Kanto basin in the YY (upper panel) and HERP (lower panel) models.

Figure 2 displays the depth to the upper boundary of three major layers having similar Vs values of about 1.0, 1.5, and 3.2 km/s in the two models. Vertical sections of the two

velocity structure models along an east-west profile are depicted in Fig. 3. It can be seen that the geometry of the interface between the seismic basement layer (Vs ~ 3.2 km/s; the lowest layer in the sections) and the overlying sedimentary layers is different between the two models. The location of the crests and troughs in the basement interface differ between the two models. The layer having Vs 1.5 km/s is almost missing at the western basin edge area in the YY model. Although the HERP model consists of some variations on the Vs values in the top layer, the vertical section illuminates that the top layer in the HERP model can be considered to be a single layer having a Vs value of 0.5 km/s. Since the models differ in the Vs values in the layers overlying the Vs 0.5 km/s layer in both the models, we adopt the top layer in the both models having Vs value of 0.5 km/s. The velocity model parameters are summarized in Tables 1 and 2 for the HERP and YY models, respectively.

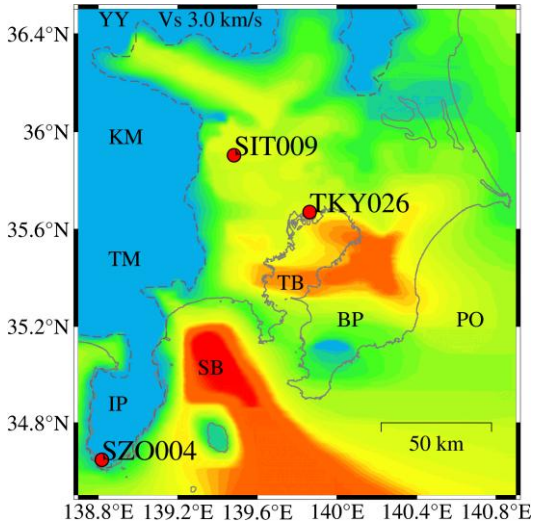


Figure 4. Location of strong motion sites where the synthetic ground motions are displayed in this paper. The background map indicates depth to the upper boundary of layer having S-wave velocity of 3 km/s in the YY model. For explanation on the two letter codes, see Fig. 2.

3. EARTHQUAKE SOURCE PARAMETERS

We used the characterized source model of the Tokai earthquake proposed by Headquarters for Earthquake Research Promotion (2009). The source fault area is depicted in Fig. 1. The asperities are shown by shaded rectangular areas, and, in total, three asperities are set. The fault is modeled with 91 point sources; 74 points as background point sources. In Fig. 1, the star denotes the rupture start point (hypocenter), and a uniform rupture propagation velocity of 2.7 km/s is used for the waveform simulation. We used triangle shaped moment rate functions for the waveform simulations. The rise time of the point sources are adopted from the source parameters table provided by HERP (2009). The orientation of the fault plane and seismic moments are also taken from HERP (2009).

4. WAVEFORM SIMULATION METHOD

We applied the staggered-grid finite difference method (Graves, 1996), with fourth-order accuracy in space and second-order accuracy in time, for the 3-D simulation. We used the method of discontinuous grids (Aoi and Fujiwara, 1999) to optimize computing time and memory. We divide the model region into two grid zones, namely the upper and lower grid zones, with different grid spacing. The upper and lower grid zones consist of grids with a uniform spacing of 0.15 and 0.45 km, respectively, in all three directions of the model region.

We consider a horizontal free-surface boundary condition for the top of the model space. The absorbing boundary condition of Clayton and Engquist (1977) and non-reflecting boundary condition of Cerjan et al. (1985) are implemented to eliminate artificially reflected waves from the other boundaries of the model space. We apply the method of Graves (1996) for the anelastic attenuation. According to Levander (1988), at least 5 grid points per wavelength are required for fourth order accuracy in the finite difference method. In our simulation more than six grid points per shear wavelength lie in the lowest velocity layer of 0.5 km/s at the maximum frequency of 0.5 Hz. Therefore, we limit our comparison between the synthetics from the two velocity models to the resolved frequency of 0.5 Hz in the simulations. We use a time increment of 0.008 s, which satisfies the stability criteria of the finite difference method for the entire grid used in our grid formulation (e.g., Aoi and Fujiwara, 1999).

Table 1. Material Parameters in the YY Model

No.	Vp (km/s)	Vs (km/s)	Density (g/cm^3)	Depth (km)	Qp, Qs
1	1.8-2.2	0.5-0.8	1.88-2.01	0.00	100
2	2.40	1.00	2.10	*variable*	100
3	3.20	1.50	2.25	*variable*	150
4	5.60	3.00	2.50	*variable*	300

5. RESULTS

In this section, we show the comparison of the velocity waveforms and their Fourier spectra in the frequency range of 0.05-0.5 Hz at selected sites (Fig. 4). We also show the comparison of the peak ground velocities at different frequency ranges between the two synthetics.

We show the comparison of the waveforms and Fourier spectra at the SZO004 site in Fig. 5. This site is located at the tip of the Izu Hanto peninsula. The ground motion at this site may be considered as an input motion to the Kanto basin. We can see that the waveforms are dominated by large amplitude phases of about 12-15s period, and the waveforms decay quickly after the body wave and surface waves propagated from the source. Since this site is located outside the basin, the synthetic waveforms for the both HERP and

YY models are similar as expected.

Table 1. Material Parameters in the HERP Model

No.	Vp (km/s)	Vs (km/s)	Density (g/cm^3)	Depth (km)	Qp, Qs
1	1.8	0.5	1.95	0.00	100
2	2	0.6	2	*variable*	120
3	2.1	0.7	2.05	*variable*	140
4	2.2	0.8	2.07	*variable*	160
5	2.3	0.9	2.1	*variable*	180
6	2.4	1	2.15	*variable*	200
7	2.7	1.3	2.2	*variable*	260
8	3	1.5	2.25	*variable*	300
9	3.2	1.7	2.3	*variable*	340
10	3.5	2	2.35	*variable*	400
11	4.2	2.4	2.45	*variable*	400
12	5	2.9	2.6	*variable*	400
13	5.5	3.2	2.65	*variable*	400
14	5.8	3.4	2.7	*variable*	400
15	6.4	3.8	2.8	*variable*	400
16	7.5	4.5	3.2	*variable*	500
17	5	2.9	2.4	*variable*	200
18	6.8	4	2.9	*variable*	300
19	8	4.7	3.2	*variable*	500
20	5.4	2.8	2.6	*variable*	200
21	6.5	3.5	2.8	*variable*	300
22	8.1	4.6	3.4	*variable*	500

We show the comparison of the waveforms and Fourier spectra at the TKY026 site in Fig. 6. We can see that the waveforms are dominated for a longer duration by the later phases, secondarily generated surface waves from the basin edges, and multiple reflections of the body waves from the sedimentary layers. It can be seen that the spectral amplitudes are larger for the HERP model in the periods from about 8s and over compared with those from the YY model. However, at periods smaller than about 8s, the spectral amplitudes are similar for both the models. The waveforms differ largely on the horizontal components. The vertical components are quite similar. A distinctive phase having a period of about 10s can be seen at time of about 130s using the HERP model.

We show the comparison of waveforms and Fourier spectra at the SIT009 site for the two models in Fig. 7. We can see that the waveforms obtained using the HERP model exceeds or tends to exceed the spectral amplitudes at periods over about 5s (>0.2 Hz), and the YY model exceeds or tends to exceed at frequencies smaller than 0.2 Hz. A similarity to this result is found at several other sites in the Kanto basin.

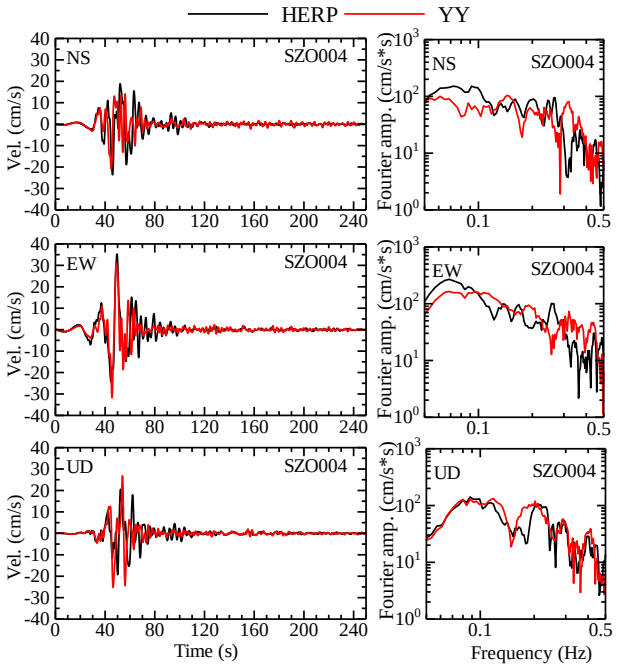


Figure 5. Synthetics at the SZO004 site. The waveforms were bandpass filtered at 0.05-0.5 Hz. The black and red traces are for the HERP and YY models, respectively.

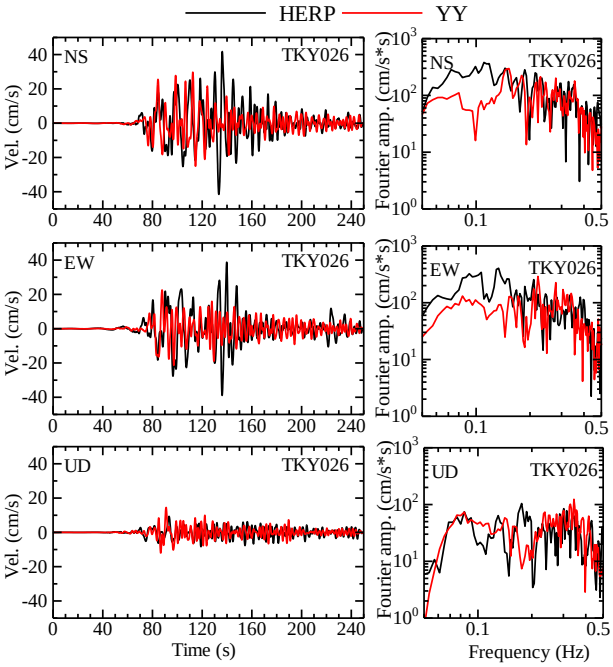


Figure 6. Synthetics at the TKY026 site. The waveforms were bandpass filtered at 0.05-0.5 Hz. The black and red traces are for the HERP and YY models, respectively.

We show a comparison of the peak ground velocities at four frequency bandwidths in Fig. 8. The frequency band-widths are 0.05-0.1 Hz, 0.05-0.2 Hz, 0.05-0.3 Hz, and

0.05-0.5 Hz from the top to the bottom of Fig. 8. The peak ground velocities were obtained at the K-NET and KiK-net sites depicted in Fig. 1.

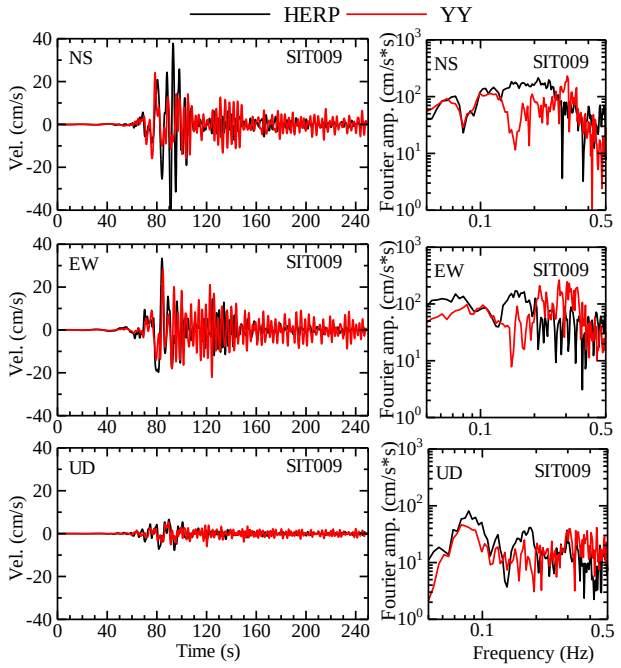


Figure 7. Synthetics at the SIT009 site. The waveforms were bandpass filtered at 0.05-0.5 Hz. The black and red traces are for the HERP and YY models, respectively.

In Fig. 8, it can be seen that the PGVs obtained using the HERP model are greater than those obtained using the YY model at frequencies 0.05 to 0.1 Hz at many stations. The PGVs between the two models scatter largely at frequencies 0.05 to 0.2 Hz, thus further indicating that the two models behave differently for the Tokai Earthquake. At increased frequency bandwidths, the scattering decreases, but the two models still differ noticeably.

6. DISCUSSIONS AND CONCLUSIONS

We performed 3-D FD simulations of long-period ground motions (2-20s) in the Kanto basin and adjacent areas using two different velocity models for the hypothetical Tokai earthquake. Since the models are reconstructed to predict long-period ground motions for future earthquake, we attempted to compare the ground motions in the Kanto basin using the HERP and YY models. The HERP model consists of velocity structure information not only of the sedimentary layers in the model region, but also the velocity structure information of the deeper crustal, and upper mantle structures. On the other hand, the YY model consists of velocity structure information of the sedimentary layers in the Kanto basin.

To simulate the ground motions using the YY model, we removed all the layers above Vs 2.9 km/s in the Kanto basin of the HERP model, and filled the basin with the layers from the YY model. The upper boundary of Vs value of 2.9 km/s in the HERP model is shifted up or down to match with the upper boundary of the Vs 3.0 km/s of the YY model. Outside the basin and beneath the layer having Vs value of 3.0 km/s, the HERP velocity structure is retained, and the ground motion simulations were performed. Some differences on the simulated ground motions might have resulted from using the above scheme, which causes modifications mainly just outside the basin, but within the YY model region, where the YY model is set to be a simplified structure of having Vs value of 3.0 km/s at the top.

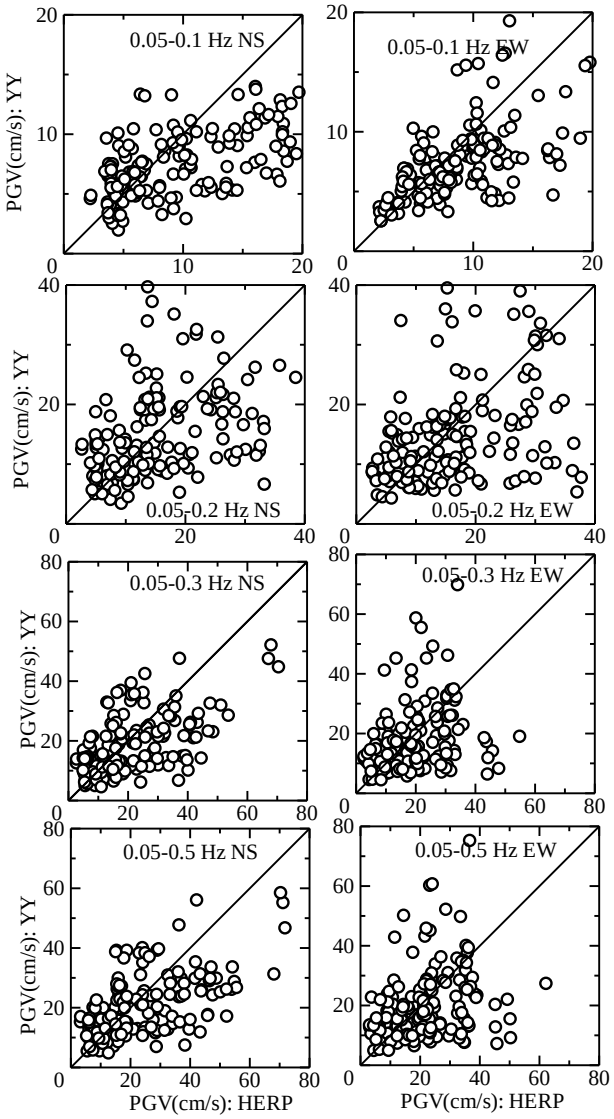


Figure 8. Comparison of PGVs at different frequency bandwidths obtained from using the HERP (along horizontal axis) and YY (along vertical axis) models. The frequency bandwidths and component names are indicated in each of subfigures.

Another source of difference between the two ground motions might be the removal of the layer having Vs value of 1.0 km/s in the HERP model inside the YY model region. Outside the YY model region, the layer extends as accretionary prism outside the YY model region. Further investigations on the velocity structures would make clear.

We show a comparison of the Fourier spectra at the

TKY026 site obtained for the records of Mw 9.0 off-Tohoku earthquake, the off-Ibaraki prefecture earthquake (Mw 7.8, the largest aftershock of the Tohoku earthquake), and the Tokai earthquake (Mw 8.0) in Fig. 9. Also shown are the Fourier spectra of the records obtained at the HKD129 site (Tomakomai) during the Mw 8.3, 2003 Tokachi-oki earthquake. It can be seen that the horizontal spectral amplitudes at the TKY026 site for the Tokai earthquake are much larger than those from the Mw 9.0 Tohoku earthquake at periods over about 7 s. For periods shorter than about 0.7 s, the spectral amplitudes for the Tokai earthquake match with those observed at the HKD129 site during the 2003 Tokachi-oki earthquake. Huge oil storage tanks were severely damaged at Tomakomai, which is located on thick sedimentary layers having total thickness over about 6 km. The spectral amplitudes from the off-Ibaraki prefecture earthquake are the lowest in the frequency range of analysis.

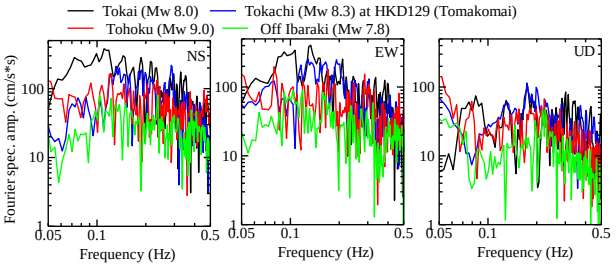


Figure 9. Comparison of velocity Fourier spectra at the TKY026 site between several earthquake records; black: hypothetical Tokai earthquake (Mw 8) (black), red: Off Tohoku earthquake (Mw 9), blue: Tokachi-oki earthquake record at HKD129 (Tomakomai site) (Mw 8.3), and green: Off Ibaraki prefecture earthquake (Mw 7.8).

In this study, we find that the two models generate ground motions differently for the Tokai earthquake at several sites, where the synthetic ground motions were more or less similarly reproduced during the smaller events that occurred just beneath the Kanto basin. This indicates that the two models differ primarily in the basin edge structure. Therefore, we conclude that further examination and tuning of the models are required for an improved prediction of long-period ground motions from future earthquakes.

Acknowledgements:

We are thankful to HERP, which provided us with the Tokai earthquake fault model, and the subsurface velocity model. We are also thankful to Prof. Hiroaki Yamanaka, Tokyo Institute of Technology, and Assoc. Prof. Nobuyuki Yamada, Fukuoka University of Education for providing us with their new velocity model of the Kanto basin. We acknowledge Wessel and Smith (1998) for providing us with the Generic Mapping Tool, which is used to draw some of the figures in this study. We are also thankful to NIED, which provided us with strong ground motion data at sites used in his study. Thanks are due to the Global COE (Centers of Excellence) Program of International Urban Earthquake Engineering Centre for Mitigating Seismic Mega Risk at Tokyo Institute of Technology for financial support to conduct this study.

References:

Aoi S, Fujiwara H (1999) 3-D Finite-difference method using discontinuous grids. Bull Seismol Soc Am, 89:918–930.

Cerjan C, Kosloff D, Kosloff R, Reshef M (1985) A nonreflecting boundary condition for discrete acoustic and elastic wave equations. Geophysics 50:705-708.

Clayton R W, Engquist B (1977) Absorbing boundary bonditions for acoustic and elastic wave equations. Bull Seismol Soc Am 67:1529-1540.

Dhakal Y P, Yamanaka H (2012) An evaluation of 3-D velocity models of the Kanto basin for long-period ground motion simulations. J Seismol (in press).

Fujiwara H, Kawai S, Aoi S, Ishii T, Okumura T, Hayakawa Y, Morikawa N, Senna S, Kobayashi K, Xian-Sheng Hao K (2006) Japan seismic hazard information station, J-SHIS. 4th Intl Conf on Earthq Engg, Taipei, Taiwan, Paper No. 274.

Graves R W (1996) Simulating seismic wave propagation in 3D elastic media using staggered-grid finite differences. Bull Seismol Soc Am 86:1091-1106.

HERP(2012) (Headquarters for Earthquake Research Promotion) http://www.jishin.go.jp/main /chousa /12_choshuki/index.htm.

Koketsu K, Miyake H, Fujiwara H, Hashimoto T (2008) Progress towards a Japan integrated velocity structure model and long-period ground motion hazard Map. 14th World Conf on Earthq Engg, China, Paper ID S10-038.

Levander A R (1988) Fourth order finite difference P-SV seismograms. Geophysics 53:1425-1436.

Tanaka Y, Koketsu K, Miyake H, Furumura T, Sato H, Hirata N, Suzuki H, Masuda T (2005) Integrated modeling of 3D velocity structure beneath the Tokyo metropolitan area. AGU Fall Meeting S21A-0200.

Wessel P, Smith W H F (1998) New improved version of the generic mapping tools released. Eos Trans Am Geophys U 79:579.

Yamada N, Yamanaka Y (2012) 3-D S-wave velocity model of Kanto basin for long period ground motion simulation with special focus on treatment of shallow near surface part. Exploration Geophysics 65(3): 139-150.

Yoshimi M, Sekiguchi H, Horikawa H (2012) Ground motion simulations for great interplate earthquakes around Japan: variability of ground motion resulted from complexity in source models. Proceedings of the Intl Symp on Engineering Lessons Learned from the 2011 Great East Japan Earthquake, March 1-4, Tokyo, Japan, pp 263-274.

10CUEE CONFERENCE PROCEEDINGS
10th International Conference on Urban Earthquake Engineering
March 1-2, 2013, Tokyo Institute of Technology, Tokyo, Japan

FUNDAMENTAL RESEARCH FOR ENHANCEMENT OF ESTIMATION ON EARTHQUAKE GROUND MOTION -DEVELOPMENT OF A METHOD FOR CRUSTAL DEFORMATION ANALYSIS USING HIGH-FIDELITY THREE-DIMENSIONAL CRUSTAL STRUCTURE MODEL-

Ryoichiro Agata[1)], Tsuyoshi Ichimura[2)], Mamoru Hyodo[3)], Takane Hori[3)], Kazuro Hirahara[4)] and Muneo Hori[5)]

1) Student, Department of Civil Engineering, University of Tokyo, Japan
2) Associate Professor, Earthquake Research Institute, University of Tokyo, Japan
3) Japan Agency for Marine-Earth Science and Technology, Japan
4) Professor, Earth and Planetary Science, Graduate School of Science, Kyoto University, Japan
5) Professor, Earthquake Research Institute, University of Tokyo, Japan
agata@eri.u-tokyo.ac.jp, ichimura@eri.u-tokyo.ac.jp, hyodo@jamstec.go.jp, horit@jamstec.go.jp, hirahara@kugi.kyoto-u.ac.jp, hori@eri.u-tokyo.ac.jp

Abstract: Estimation on earthquake ground motion and the associated damage is expected to be improved by estimating coseismic slip distribution accurately. Estimation of coseismic slip distribution can be improved by using large-scale analyses of the observed crustal deformation data based on detailed data of crustal structure. However, it has not been achieved because of the difficulty of generating high-fidelity models of crustal structure for numerical analyses. In this research, we developed a method for generating a high-fidelity three-dimensional finite element model for crustal structure whose degree-of-freedom of more than 100 million, and a method for crustal deformation analyses using the generated model. Crustal deformation analyses performed in Southwest Japan show that there may be a significant difference in estimation results of coseismic slip distribution, depending on whether the high-fidelity model is used or not.

1. Introduction

Enhancement of the estimation on earthquake ground motion and the associated damage could be made by estimating coseismic slip distribution accurately. Coseismic slip distribution is estimated by combining crustal deformation analysis in a large scale with the detailed data of the crust and the observation data of crustal deformation. Observation data with high accuracy have been accumulated owing to the development of observation technology. GEONET (operated by GSI: Geospatial Information Authority of Japan) is well known as a monitoring system of crustal deformation on the ground in the whole Japanese islands. Moreover, monitoring systems of crustal deformation on the seafloor such as DONET (operated by JAMSTEC: Japan Agency for Marine-Earth Science and Technology) have been launched recently. The errors of these monitoring systems are in cm-order at maximum. In addition, data of crustal structure themselves also have been accumulated. To be more specific, material data and geometry data in 1km grid of the crustal structure of the Japanese islands have been developed. However, there were difficulties in generating high-fidelity numerical models of crustal structure and computation using the model. As a result, in spite of the detailed crustal data, crustal deformation analyses have been performed by using a simplified crustal structure model such as homogeneous half-space.

Therefore in this research, by using accumulated data and the technique of high performance computing, we developed a method for generating a high-fidelity three-dimensional (3D) finite element (FE) model of crustal structure. A method for crustal deformation analyses with the generated model is also proposed. To show the advantage of our method, an application example of crustal deformation analyses in Southwest Japan will be shown.

2. Methodology

In this section, the analysis method and the numerical model generation method are briefly explained.

2.1 Formulation

We adopt a FE analysis as a numerical analysis method because it has an advantage in analyzing medium whose geometry is complex, such as crustal structure. We

investigate the crustal deformation resulting from the final coseismic slip distribution. Therefore, assuming crustal structure to be a linear elastic body, we perform a static analysis of crustal deformation due to fault dislocation. After taking boundary conditions into consideration, the target equation is as follows:

$$\mathbf{K}\,\mathbf{u} = \mathbf{f}$$

where **K**, **u**, **f** are the global stiffness matrix, displacement vector, and force vector, respectively. Fault slip is introduced by the split-node technique (Melosh and Rafesky 1981). The split-node technique can simply compute the effects of fault slip by virtually splitting the nodes on the fault plane. Infinite elements (Zienkiewicz *et. al.* 1983) are implemented on the side and bottom of the target domain to describe the infinite condition.

2.2 Model generation method

Conventionally, elasticity solution in a homogeneous half-space or numerical models with large approximation of the geometry has been used for estimating coseismic slip distribution. On the other hand, our method can automatically generate 3D FE model of crustal structure using background cell, which makes it possible to perform crustal deformation analyses taking complex geometry and heterogeneity of material of crust into consideration. The input data are layered crustal data (digital elevation model data and material data) with complex geometries of the ground surface and the layer interfaces (Figure 1 (left)). Tetrahedral elements are used near the surfaces to represent the geometries of the crust well, while voxel elements are used in the homogeneous areas, in order to achieve a good balance between reduction of the number of elements and reproduction of the geometry (Figure 1 (right)). This is an extension of the method proposed in Ichimura *et. al.* (2009). Its extension points improve the approximation of geometries, the control of multi-voxel generation, and the introduction of the infinite condition by an infinite element.

2.3 Computation method

Since the degree-of-freedom (DOF) of the generated models is large, the computation needs to be parallelized so that the computation is finished in a realistic time. We use shared memory parallelization (SMP) only, not using distributed memory parallelization. It is because using SMP only will have less communication overhead between each computer node when we compute many cases at once (as computation of Green's functions or Monte Carlo approach) with many computer nodes.

We need a memory-efficient method to solve the linear equation because the DOF of the target problem is large. The combination of Element-by-Element (EBE) method (Hughes *et. al.* 1983) and Conjugate Gradient (CG) method is used for that purpose. We don't need to store the entire **K** matrix on computer memory with this method, and the required memory space is largely reduced. As the preconditioning of CG method, Point Jacobi Method is used because it is memory-efficient, and relatively easy to be parallelized. Our code is verified by comparing the results with the elasticity solution in a homogeneous half-space (Okada 1985).

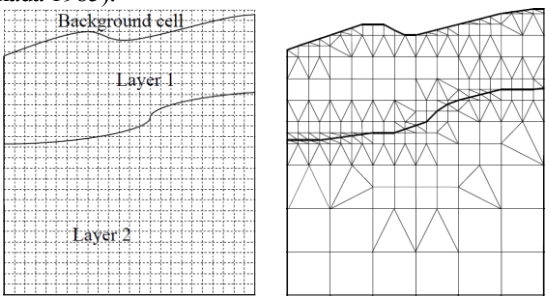


Figure 1 Schematic view of generating the 3D FE model: The target domain is covered by a uniform back ground cell (left); To generate a high-fidelity model of crustal structure, tetrahedral elements are used near the surfaces to represent the geometries of the crust well, while voxel elements are used in the homogeneous areas (right).

3. Application to crustal deformation analyses in Southwest Japan

As an application example, firstly 3D FE model of Southwest Japan is generated by the proposed method. Then, crustal deformation analyses in Southwest Japan are performed by inputting an estimated coseismic fault slip of Nankai Earthquake computed by an earthquake cycle simulation (Hyodo *et. al.* 2012) to the model. The target area for modeling is shown in Figure 2. The size of the area is 976km in *x* direction (east and west), 784km in *y* direction (north and south), and 400km in *z* direction (vertical). The crustal structure is modeled as a 4-layered structure, whose material properties are shown in Table 1. The generated model (we call it "our model") is shown in Figure 3. The DOF, the number of tetrahedral elements and voxel elements are 134,000,160, 44,713,627 and 36,405,531, respectively. To compare the result, we generate a model which considers neither of the surface geometry and the material heterogeneity (we call it "conventional model"). The solution obtained using this model is equivalent to the analytical elasticity solution in a homogeneous half-space. The average altitude of the ground surface in our model is used as the altitude of the ground surface in the conventional model. Its material property is the same as that of layer 1 in Table 1. The displacements on the ground computed by crustal deformation analyses using the 2 models are compared.

The computation was performed on one computer node with 12 computation cores (Intel(R) Xeon X5680×2) and 48GB computation memory. The computation time was 29650s (elapsed time). Figure 4 shows the distribution of surface displacement computed from the assumed fault slip shown in Figure 2. The relative difference of the surface displacement between our model and the conventional model is shown in Figure 5 and 6. The red points indicate the observation nodes of DONET. These figures show that

DONET observes crustal deformations in the area where the relative displacements are significantly large. The relative differences in the observation points located in those areas are shown in Table 2. In these points, the relative differences, which are up to 45%, are significantly large. From these analyses, we could find that the relative difference of the surface displacement is significantly large in the area where DONET monitors crustal deformation on the seafloor. It indicates that there is a significant difference in estimation results of coseismic slip distribution, if high-fidelity models as shown in this paper are not used.

4. Conclusion

In this research, aiming enhancement of the estimation on earthquake ground motion and damage it causes, we developed a method for generating a high-fidelity 3D FE model of crustal structure. Since the DOF of generated high fidelity model is large, fast computation method using memory-efficient solver and parallel computation is also developed. In the application example of crustal deformation analyses in Southwest Japan, significant differences are shown between the results of our model and the conventional model. Especially, larger differences could be seen near the observation area of DONET. These analyses indicate that there is a significant difference in estimation results of coseismic slip distribution, if high-fidelity models as shown in this paper are not used. We expect this method will contribute to setting more appropriate scenario fault rupture, and lead to enhancement of the estimation on earthquake ground motion.

As future work, we would like to apply our method to more appropriate estimation of coseismic slip distribution and stochastic approach to the ambiguity of crustal data. We also need to apply viscoelasticity to the model so that the model can be applicable to a longer time scale.

Acknowledgements:

I would like to thank Dr. Takuto Maeda for providing the crustal data of Southwest Japan and Dr. Yoshimitsu Okada for providing a subroutine for the verification. Part of the results is obtained by using the K computer at the RIKEN Advanced Institute for Computational Science (Proposal number hp120308).

References:

Melosh, H. J. and Rafesky, A. (1981), "A simple and efficient method for introducing faults into finite element computations," *Bulletin of the Seismological Society of America*, **71**, 1391-1400

Zienkiewicz, O. C., EMson, C. and Bettess, P. (1983), "A novel boundary infinite element," *International Journal for Numerical Methods in Engineering*, **19**, 393-404.

Ichimura, T., Hori, M. and Bielak, J. (2009), "A Hybrid Multiresolution Meshing Technique for Finite Element Three-Dimensional Earthquake Ground Motion Modeling in Basins Including Topography," *Geophysical Journal International*, **177**, 1221-1232.

Hughes, T. J. R., Levit, I. and Winget, J. (1983), An element-by-element solution algorithm for problems of structural and solid mechanics, *Computer Methods in Applied Mechanics and Engineering*, **36**, 241-254.

Okada, Y. (1985), "Surface deformation due to shear and tensile faults in a half-space," *Bulletin of the Seismological Society of America*, **75**, 1135-1154.

Hyodo, M., Hori, T. and Baba, T. (2012), "Reconsideration of Possible Earthquake Scenarios in the Nankai Trough," *AOGSAGU (WPGM) Joint Assembly*, Singapore.

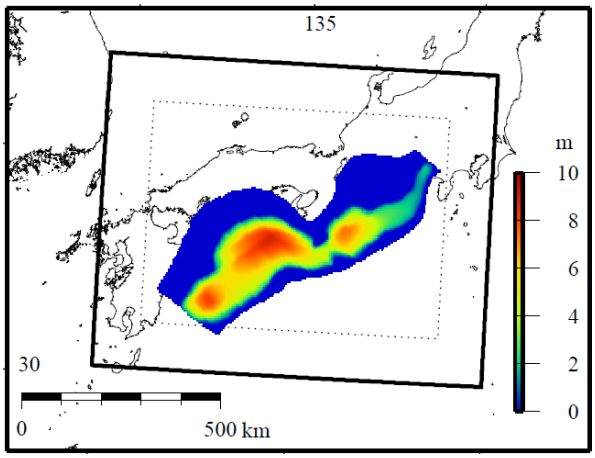


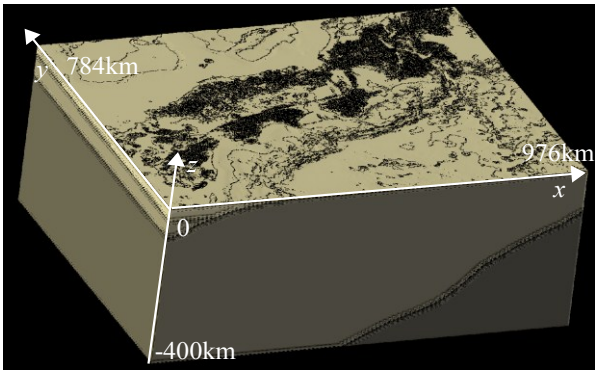
Figure 2 The target area for modeling (black line) and the estimated coseismic fault slip (Hyodo *et. al.* 2012) as an input. The dotted line indicates the area of 1% accuracy defined by the verification.

Table 1 The names and material properties of the 4 layers of Southwest Japan model. Layer 1: Crust; layer 2: Upper Mantle; layer 3: Philippine Plate; layer 4: Pacific Plate. V_p: P wave velocity (m/s); V_s: S wave velocity, ρ: density (kg/m^3); E: Young modulus (GPa); ν: Poisson ratio, respectively.

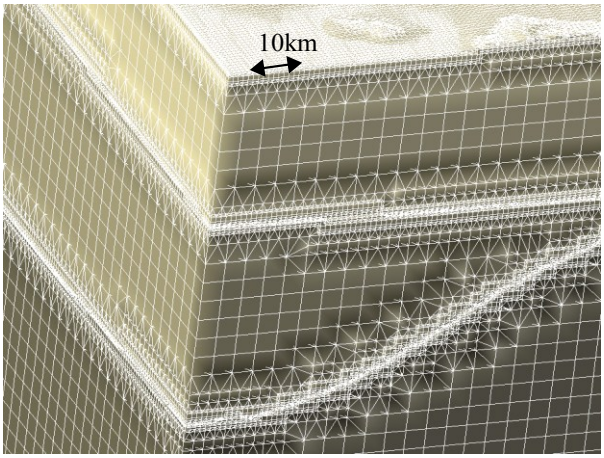
	Vp	*Vs*	ρ	E	ν
layer 1	5664	3300	2670	72.3	0.243
layer 2	8270	4535	3320	175	0.285
layer 3	6686	3818	2600	95.4	0.258
layer 4	6686	3818	2600	95.4	0.258

Table 2 The relative differences on the observation points shown in Figure 6. On these points, the relative differences are large, which are up to 45 %.

	longitude	latitude	norm of disp. (m)	relative difference
B-5	136.93	33.48	1.04	0.21
B-6	136.92	33.36	0.43	0.45
B-7	136.81	33.36	0.93	0.17
B-8	136.80	33.47	1.84	0.09
D-13	136.69	33.22	0.51	0.34
D-14	136.58	33.17	0.57	0.27
D-15	136.56	33.23	1.21	0.10
D-16	136.60	33.30	1.79	0.06



Full view



Close-up view

Figure 3 The overview of our model. The close-up view shows that the complex geometries of the ground surface and the interface are well represented.

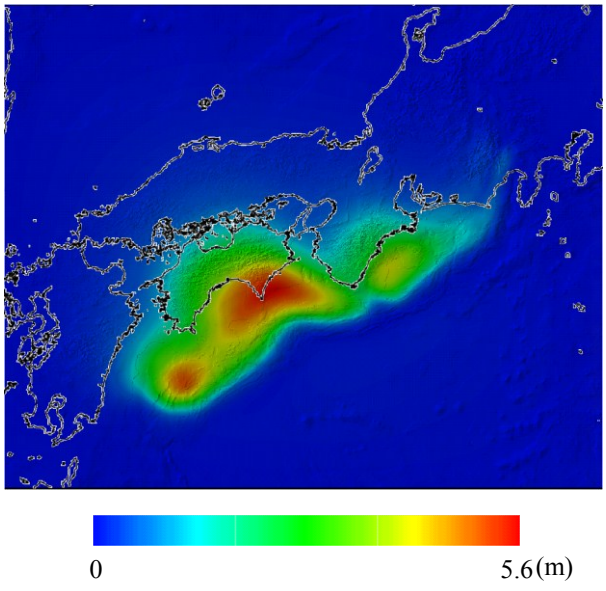


Figure 4 Distribution of the surface displacement due to the estimated coseismic fault slip computed using our model.

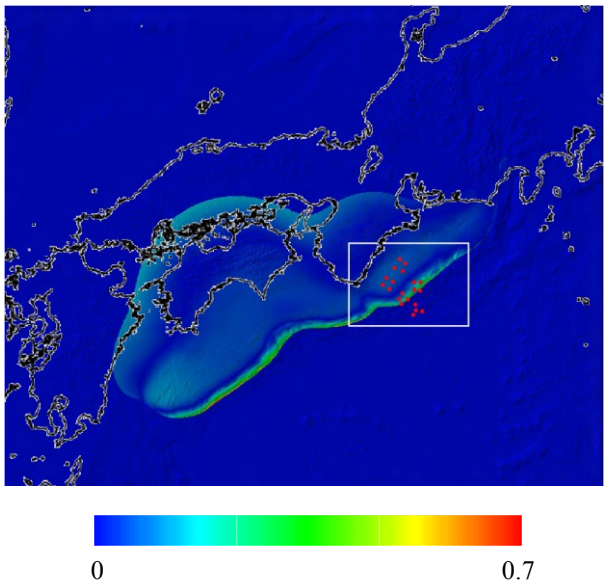


Figure 5 Relative differences of the magnitude of surface displacements between our model and the conventional model. The area whose magnitude of the surface displacement is less than 0.5m is visualized as its value is 0. The red points indicate the observation points of DONET. A close-up view of the area surrounded by the white lines is shown in Figure 6.

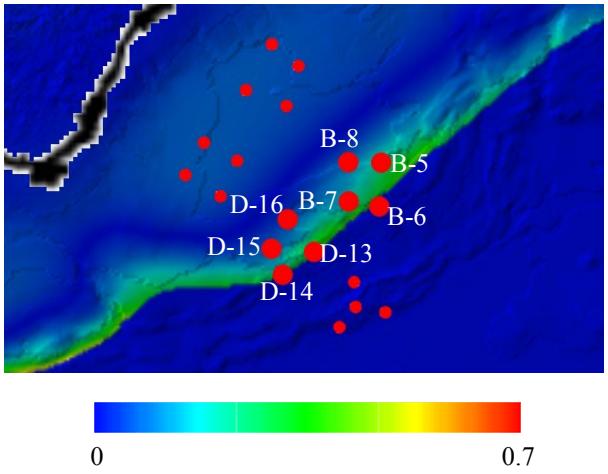


Figure 6 A close-up view of Figure 5. The large points indicate the observation points which are located in the area where relative differences are large. B-*n* and D-*n* (*n* is a natural number) are the names of the observation points.

10CUEE CONFERENCE PROCEEDINGS
10th International Conference on Urban Earthquake Engineering
March 1-2, 2013, Tokyo Institute of Technology, Tokyo, Japan

STOCHASTIC MODELING OF BHUJ (2001) EARTHQUAKE AND SYNTHESIS OF SEISMIC SCENARIOS FOR THE SURAT REGION, INDIA

T. P. Thaker[1] and K. S. Rao[2]

1) Assistant Professor, Dept. of Civil Engineering, Pandit Deendayal Petroleum University, Gandhinagar, Gujarat,India
2) Professor, Dept. of Civil Engineering, Indian Institute of Technology Delhi, Hauzkhas, New Delhi-110016, India
tej_p_thaker@yahoo.co.in, tpthaker.iitd@gmail.com, raoks@civil.iitd.ac.in

Abstract: In the absence of instrumental recordings, the present study intended to generate synthetic ground motions for the Surat region, Gujarat (India) considering probable earthquake scenarios using stochastic finite fault simulation technique. The simulations have been composed of two stages. In the first stage, attempt has been made to simulate Bhuj (2001) earthquake of Mw 7.7 which was recognized as most devastating event occurred in the last century in India. In the second stage, the simulated results have been validated through actual recordings and data from literature. Using the calibrated regional parameters, ground motions of 2001 event for the Surat city has been simulated at 66 sites and spatial variation in PGA has been presented. In addition, the ground motions of the same event have been simulated for the important cities in the state which may be very useful for carrying out numerous seismic studies in the region. The developed ground motions inferred from these simulations are of immense value for the proposed seismic microzonation and site specific studies in the region.

1. INTRODUCTION

The January 26, 2001 earthquake occured near Bhuj in the Kutch region of Gujarat, India was the largest intra-continental event struck in the past century and caused considerable damages even to the far off city like Surat along with other cities/towns in the state of Gujarat. With the fast increasing density of population and large infrastructural establishments in recent times, the vulnerability of Surat city to the damaging earthquakes is increasing alarmingly day by day. Therefore it is of great need to have a reliable estimation of seismic hazard due to probable damaging earthquakes occurring in and around Surat region. The good regional coverage of strong motion observations play vital role in achieving this purpose However with best of our knowledge, no instrumental record has been found in Surat region till this date and even very few records of strong motions from earthquakes surrounding Surat are available due to lack of instrumentation.

The quantified dataset even for the Bhuj earthquake is very limited and sparse; hence, the researchers presently face a daunting problem in predicting ground motion level for future events in the region. The Strong Motion Accelerogram (SMA) records at various locations are the most commonly used data from the engineering point of view. However, for the Bhuj earthquake, the only available such instrumental record was from the basement of a ten-storey building, approximately 240 km away from the epicentre at Ahmedabad (23.04 0N, 72.61 0E). In addition to that the other instrumental data useful for the engineering purpose are on an array of spectral response recorders (SRR) at 13 different locations in the State of Gujarat are available for the same earthquake. In lack of a robust database of strong-motion records, seismological modeling is a vital alternative until sufficient instrumental records become available in Gujarat.

With this background the present study motivated by the need, envisaged to estimate the ground motions on firm rock conditions for Surat city for an earthquake of magnitude Mw 7.7 occurred in Kutch region of Gujarat. An improved version of the one dimensional stochastic simulation model of Boore (1983) to account for a finite fault as proposed by Motazedian and Atkinson (2005) is used for simulating ground motions. In this method, the characteristics of seismic source, path attenuation and local soil conditions are taken into account, while generating the ground motions. Database of the model parameters have been prepared from the extensive review of the literature. Further, numbers of synthetic time histories are generated assuming the probable earthquake scenarios for the Surat region by adopting suitable model parameters.

2. STOCHASTIC SIMULATION MODEL

The prediction of earthquake ground motion for large earthquakes is a crucial problem in earthquake engineering. Engineering analysis for seismic performance of structures requires seismological input that describes amplitude, frequency content and duration of the expected ground motions. Stochastic modeling of earthquake radiation is widely used in prediction of strong ground motions (Hanks and McGuire, 1981; Boore, 1983; Boore and Atkinson, 1987; Atkinson and Boore, 1997; Toro et al. 1997, Atkinson

and Silva, 2000). In this method, high frequency earthquake motions are represented as band limited Gaussian noise having ω^2 mean spectrum, where, ω = angular frequency (Aki, 1967; Brune, 1970, 1971; Boore, 1983). In most commonly employed approach, earthquakes are treated as point sources. Point source modeling of earthquake ground motion may not be appropriate for large earthquake, because the effects of a large fault plane, including fault geometry and directivity which influence the amplitudes, frequency content and duration of ground motion.

To consider these finite-fault effects in ground-motion modeling, Hartzell (1978) proposed a discrete finite fault model that captures the salient features of radiation from large earthquakes. A finite fault plane is subdivided into elements (sub-faults), and radiation from a large earthquake is obtained as the sum of contributions from all elements, such of which acts as a small independent sub-source. In the typical implementation, the rupture starts at a hypocentral point on the fault and propagates radially from it, triggering the sub-faults as it passes them. The field from all sub-events are geometrically delayed and added together at the observation point. This basic idea has been implemented in many studies (Irikura, 1983; Irikura, 1992; Kamae and Irikura, 1992; Irikura and Kamae, 1994; Bour and Cara, 1997). Beresnev and Atkinson (1998) used the same concept and proposed stochastic finite fault simulation code FINSIM. Motezedian and Atkinson (2005) made a major modification to FINSIM to introduce the concept of "dynamic corner frequency" in order to overcome difficulties associated with this code. The improved and more realistic stochastic finite-fault model, described above has been included in the EXSIM code has been used in the present study to estimate the synthetic ground motions for Surat region.

3. STOCHASTIC SIMULATION OF BHUJ (2001) EARTHQUAKE OF Mw 7.7

As mentioned earlier, the Bhuj (2001) earthquake is the most damaging event occurred in the state of Gujarat. Several studies are reported in the literature to simulate the ground motion of Bhuj (2001) earthquake using different approaches. Hough et al. (2002) and Singh et al. (2003) used a finite source stochastic simulation model (Beresnev and Atkinson, 1997, 1998) to estimate the near source ground motions. Iyengar and Raghukanth (2004) used seismological model of Boore (1983) based on point source modeling to derive ground motion attenuation relations for Peninsular India. Further, Iyengar and Raghukanth (2006) used an empirical Green's function and an analytical method to simulate the ground motion at Bhuj city and the peak ground acceleration values in the region respectively. Recently, Chopra et al. (2010a) used stochastic finite fault model (Motazedian and Atkinson, 2005) to simulate Bhuj (2001) event. The models adopted by Hough et al. (2002), Singh et al. (2003) and Iyengar and Raghukanth (2004) have got many limitations since it is based on olden concepts of stochastic modelling which have been revised subsequently as discussed in the section 2.0. Further, most of the above study attempted to simulate only high frequency PGA and hardly any effort has been made to simulate spectral accelerations in the frequency domains even in the latest model of Chopra et al. (2010a). Therefore, systematic efforts have been made to assess suitable model parameters for Bhuj (2001) earthquake from large dataset reported in the earlier studies and validating to the extent possible with the available instrumental as well data reported in the literature including simulations in the frequency domain. These parameters are used to generated ground motions of the same event at base rock level for Surat region which may useful further for estimation of site specific response or any seismic studies in the region.

3.1 Selection of Model Parameters

Ground motion at the particular site is influenced by three main elements i.e., source, path and local site conditions. The source parameters include size, depth, stress drop, rupture process and fault geometry. Travel path parameters include geometrical attenuation, dissipation of seismic energy due to inelastic properties of the earth and scattering of elastic waves. Local site factors include the properties of most rock/soil and the effect of the surface topography near the recording site. The source parameters of Bhuj (2001) earthquake has been studied by numerous authors (Rastogi et al. 2001; Negishi et al. 2001; Antolik and Dreger, 2003; Singh et al. 2003; Bodin and Horton, 2004). Mandal and Johnston (2006) estimated the source parameters for the aftershocks of 2001 main event. The most important source parameter for the simulation is the stress drop, which controls the spectral amplitudes at high frequencies. The intra plate earthquakes are generally characterized by large stress drop values in comparison to the plate boundary earthquakes (Kanamori and Anderson, 1975; Mandal and Johnston, 2006).

The various studies reported in the literature (Rastogi et al. 2001; Negishi et al. 2001; Bodin and Horton, 2004; Antolik and Dreger, 2003; Singh et al. 2003) revealed large static stress drop in the range of 125-246 bars for the Bhuj (2001) earthquake. Negishi et al. (2002) estimated stress drop in the range of 126-246 bars from the aftershock analysis. Antolik and Dreger (2003) estimated the stress drop value of 210 bar for the fault length of 45 km. Singh et al. (2003) have estimated the stress drop of 200 bars on the basis of stochastic finite fault modeling using FINSIM (Beresnev and Atkinson, 1998). Bodin and Horton (2004) have calculated stress drop of 150-200 bars on the basis of stochastic point source modeling. Mandal and Johnston (2006) estimated the stress drop in the range of 6.3 to 207 bars for the earthquakes in the Kutch region after analysing the 213 aftershocks of the same event. Recently Chopra et al. (2010a) proposed stress drop of 125 bars using stochastic finite fault simulation (Motazedian and Atkinson, 2005).

These large variations in observed stress drop values from the literature necessitate the systematic estimation of this parameter for the Bhuj (2001) event. Hence, simulations were carried out for stress drop values in the range from 80 - 260 bars with an increment of 10 bars. In the actual

earthquake ruptures, the slip may only be occurring on some part of the fault, whereas the other areas on the fault are passive. According to Motazedian (2006), only the active area contributes to the dynamic frequency at a given moment in time and therefore the cumulative number of pulsing sub-faults would increase with time at the beginning of the rupture and become constant at some fixed percentage of the total rupture area. This percentage is referred to as the '% pulsing area'. The percentage pulsing area is taken as 50 %, which means that at most 50 % of the fault plane is slipping at any moment in time. Same value has been adopted by Chopra et al. (2010a) for the simulations of the Bhuj (2001) earthquake. This parameter does not exert a large influence on the simulated amplitudes at most frequencies; however it exerts a moderate influence at lower frequencies (Motazedian and Atkinson, 2005). For simplicity, the random slip distribution has been assumed.

Aftershock studies of the 2001 Bhuj earthquake revealed an E-W trending strong cluster covering an area of 60 km x 40 km that dips to the south (Negishi et al. 2001; Bodin and Horton, 2004; Mandal et al. 2004a). Yagi and Kikuchi (2001) estimated the fault dimensions of 75 km x 35 km based on the teleseismic wave inversion. Mori (2001) used fault dimensions of 50 km x 40 km from the distribution of aftershocks for inversion of teleseismic data whereas; Antolik and Dreger (2003) used fault dimensions of 80 km x 35 km through the inversion of teleseismic broadband waves. In this study simulations were tried on all four fault dimensions.

In the implementation of the stochastic method, the attenuation effects of the propagation path are modelled through the empirical 'Q' and geometric attenuation model. It is observed that at high frequency (> 1 Hz) Q increases with frequency and can be represented in the form of $Q(f) = Q_o f^n$, generally Q_o is Q(f) a frequency of 1 Hz and n is the coefficient of frequency dependence (Chopra et al. 2010b), represents the level of tectonic activity of the region. The regions of high seismic activity are characterized by less Q(f) value compare to stable region where as higher 'n' value represents that the regions with high seismic activity and vise a versa (Roecker et al. 1982; Rodriguez et al. 1983; Van Eck 1988; Havskov et al. 1989; Mandal et al. 2001). Various researchers estimated the Q(f) values for Indian seismic regions (Gupta et al. 1995; Gupta, 1999; Paul et al. 2001; Singh et al. 1999, 2003, 2004; Bodin and Horton, 2004; Mandal et al. 2004c; Nath et al. 2008a; Chopra et al. 2010b). We have tried three available frequency dependent relations for the region i.e., $Q = 102 f^{0.98}$ (Mandal et al. 2004c) estimated from local coda waves, $Q = 508 f^{0.48}$ (Singh et al. 1999, 2003) obtained from regional Lg wave of Jabalpur (1997) earthquake data recorded at 10 broadband stations and $Q = 790 f^{0.22}$ (Bodin et al. 2004) from their study of ground motion prediction. For the geometric attenuation, the geometic spreading operator of 1/Rb, where b = 1 for $R \leq 40$ km, b = 0.5 for $40 < R \leq 100$ km and b = 0.55 for $R > 100$ km is assumed following the work of Bodin et al. (2004) with some modifications. It has been reported that the Ground motion of the Bhuj event is very close to the events of central or eastern North America (Bodin et al. 2004, Chopra et al. 2010a). Therefore the duration model developed for eastern North America (Atkinson and Boore, 1995) was used by keeping same hinges as in the attenuation model. This model gives duration (T) as 1/fc for $R < 10$ km, $1/f_c + 0.16R$ for $10 \leq R \leq 40$ km, $1/f_c - 0.03R$ for $40 < R \leq 100$ km and $1/f_c + 0.04R$ for $100 < R < 1000$ km, following Chopra et al. (2010a) with slight modifications. Another factor which affects the shape of the spectra is the near surface attenuation factor 'k'. Mandal et al. (2007) proposed a kappa 'k' value of 0.025 for the Kutch region. In the present study values of 'k' varying between 0.020 and 0.030 have been adopted.

The material properties like shear wave velocity and crustal density are taken a value of 3.6 km/sec and 2.8 g/cc as recommended by Singh et al. (2003) for Indian shield. Other parameters such as crustal amplification factor, location, hypocenter depth, depth of top of rupture etc are taken from Chopra et al. (2010a).

3.2 Calibration of Parameters and Model Validation

As mentioned earlier, no instrumental observations are available for Bhuj (2001) event in the near source region except few reading from spectral response recorder (SRR) and one recording of strong motion accelerogram installed at Ahmedabad (Cramer and Kumar, 2003; Iyengar and Raghukanth, 2004). The SRR gives the peak response of a simple harmonic oscillator with known damping coefficient (η) and natural period (T). There are 13 such SRR stations recording the spectral accelerations at $\eta = 0.05$, 0.1 and T = 0.40, 0.75 and 1.25 s operating within the radius of 300 km from the epicenter of Bhuj (2001) earthquake. The recorded spectral accelerations along with NEHRP class and geology of SRRs sites are presented in Table 1. These are the same stations where the various researchers (Singh et al. 2003; Iyengar and Raghukanth, 2006; Chopra et al. 2010a) have carried out simulations using different approaches. These simulations provide an opportunity to calibrate model parameters and validation of stochastic models in the absence of direct recorded PGA at different sites in the state of Gujarat.

Table 1 SRR Values at Three Different Time Periods with 5 % Damping with Site Conditions

S No.	Site	Distnace from Epicentre	Geology	NEHRP Class	Spectral Accelerations (Sa) at 5 % Damping		
					0.4 s	0.75 s	1.25 s
1	Anjar	44	Tertiary	C	1.616	0.705	0.423
2	Kandla	53	Tertiary	C	0.863	0.572	-
3	Niruna	97	Quaternary	D	0.811	0.650	0.300
4	Naliya	147	Tertiary	C	0.720	0.216	-
5	Khambhaliya	150	Basaltic Rock	A	0.192	0.102	0.06
6	Jamjodhpur	166	Basaltic Rock	A	0.176	0.094	0.056
7	Dwarka	188	Quaternary	D	0.211	-	0.058
8	Porbandar	206	Quaternary	D	0.191	0.248	0.054
9	Junagarh	216	Basaltic Rock	A	0.176	0.094	0.056
10	Amreli	225	Basaltic Rock	A	0.176	0.094	0.056
11	Ahmedabad	238	Quaternary	D	0.288	0.230	0.219
12	Cambay	266	Quaternary	D	0.488	0.041	-
13	Anand	288	Quaternary	D	0.144	0.061	0.045

Previously Kumar et al. (2001) estimated PGA values using SRR data. These values refer to the recorders on

different soil conditions and hence can not compare directly with the simulation results. To circumvent this difficulty, Cramer and Kumar (2003) corrected these data for firm rock (B/C boundary, NEHRP) condition using correction factors Joyner and Boore (2000). Singh et al. (2003) used finite fault stochastic model (Beresnev and Atkinson, 1997), whereas Iyengar and Raghukanth (2006) used analytical model in their studies and simulated PGA values for hard rock sites with shear wave velocity of 3.6 and 2.88 km/s respectively. Iyengar and Raghukanth (2004) estimated the PGA values from SRR data using empirical equations developed by multivariate regression of global database and these values has been modified to B/C site condition following the Cramer and Kumar (2003). Recently Chopra et al. (2010a) simulated Bhuj (2001) event using finite fault simulation for B/C boundary conditions and also for the hard rock conditions. In order to compare the results with earlier studies, the simulations were carried out at hard rock sites and for NEHRP B/C site conditions with shear wave velocity of 2.9 km/s and 760 m/s respectively at these 13 SRR locations adopting model parameters presented in section 3.1. The PGA values estimated in the present study using best fit model parameters along with those obtained in the previous studies are presented in Figs. 1 and 2.

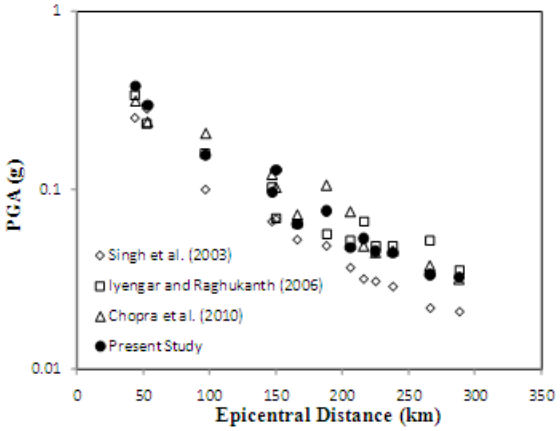


Figure 1 PGA Values Estimated in Present Study and Obtained in Literature for Hard Rock Site

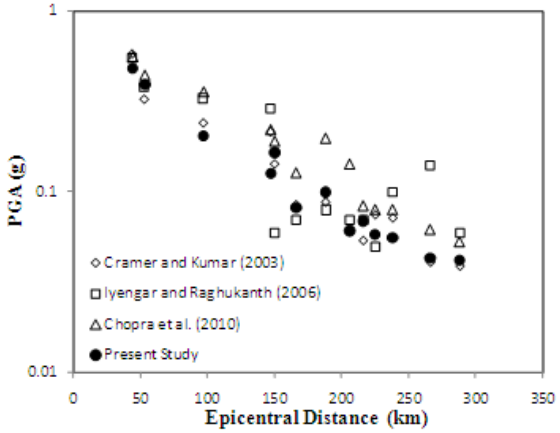


Figure 2 PGA Estimated in Present Study and Estimated from SRR Recordings for NEHRP B/C Site Condition (Vs = 760m/s)

It has been observed from Fig.1 that the PGA values obtained in the present study reconcile well with those obtained in the earlier studies for hard rock conditions except for Singh et al. (2003). The estimated PGAs in this study are higher in comparison to values predicted by Singh et al. (2003) for most sites, which is quite expected since the present PGA values are valid for NEHRP A conditions with Vs = 2.9 km/s whereas the results of Singh et al. (2003) are for rock outcrop with Vs = 3.6 km/s. The results presented in Fig. 2 reveal that, the PGA values obtained by Cramer and Kumar (2003) for the B/C site condition at SRR locations are in sound agreement with the simulated PGA in this study for majority of sites and provide slightly batter estimates than values predicted by Chopra et al. (2010a) whereas the values predicted by Iyengar and Raghukanth (2006) show comparatively scattered predictions.

The comparisons presented above are only in terms of PGA, and derived indirectly from seismological modeling or following empirical relations using SRR data. However, PGA alone does not provide complete representation of ground motion and question still arises as to the possibility of validating the simulated results by other means. Hence the spectral accelerations (Sa) at 5 % damping obtained from SRRs at three different natural periods such as 0.40, 0.75 and 1.25 s respectively corresponding to local site conditions as presented in Table 2 have been used simultaneously to calibrate model parameters in addition to PGA. First the simulations were tried for four hard rock (NEHRP A) sites. The comparisons of recorded and simulated spectral accelerations at hard rock sites are presented in Fig. 3 which indicates that the simulated values are in the favorable range with recorded values for most of the sites.

Table 2 Calibrated Model Parameters for the Simulations of Bhuj (2001) Earthquake

Parameter	Calibrated Parameters
Magnitude, Mw	7.7
Lat., Long.	23.36 0N, 70.34 0E
Hypocenter depth Strike, dip	22 km 780, 450
Fault Length and Width Rupture Depth	75 km x 35 km 10 km
Sub-fault size	5 km x 5 km
Stress drop, $\Delta\sigma$ Slip distribution	150 bar Random
Crustal Shear wave velocity, β Crustal Density, ρ	3.6 km/s 2.8 g/cc
Quality factor, Q(f)	Q = 508 f 0.48
Geometric Spreading Kappa 'k'	1/Rb b = 1 (R = 40 km) b = 0.5 (40 < R = 100 km) b = 0.55 (R > 100 km) 0.020
Duration (T) Pulsating %	1/fc (R < 10 km) 1/fc + 0.16R (10 = R = 40 km) 1/fc – 0.03R (40 < R = 100 km) 1/fc + 0.04R (>100 km) 50 %
Site Amplification	Boore and Joyner (1997) Atkinson and Boore (2006)

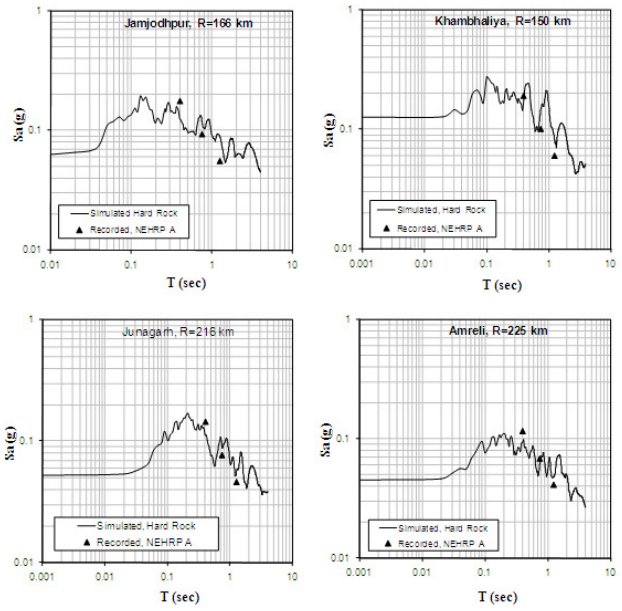


Figure 3 SRR Recordings and Simulated Response Spectra at 5% Damping for Hard Rock Sites

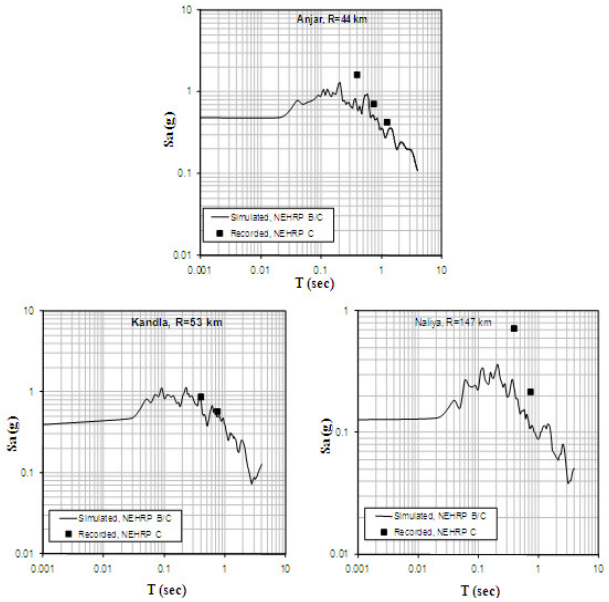


Figure 4 Simulated Response Spectra (5% Damping) at NEHRP B/C Site and SRR Recordings at NEHRP C Sites

Usually Class C and D sites are having relatively soft rock/Quaternary deposits over hard rock and large variations may be expected from site to site and hence the direct comparison might be difficult and more sound predictions may require extensive site specific analysis which is not in the scope of present study. Hence in lack knowing exact soil conditions, the SRR records on Tertiary sites (NEHRP C) and Quaternary sites (NEHRP D) compared qualitatively with simulated results of B/C sites as shown in Figs. 4 and 5. The comparisons indicate that the values predicted for class C and D sites are under predicted by model for most of the sites and it is also observed that the values predicted by the model showing much closer results for Class C in comparison to Class D sites. This is expected since model predicts the values for firm rock (B/C) site conditions. In and all, the model predicts the values reasonably well for most of site conditions. However, very limited recorded data, accuracy of this records and site conditions are also attributing to the variations and with more recorded data in future more accurate predictions can be made. The best fit calibrated model parameters are presented in Table 2.

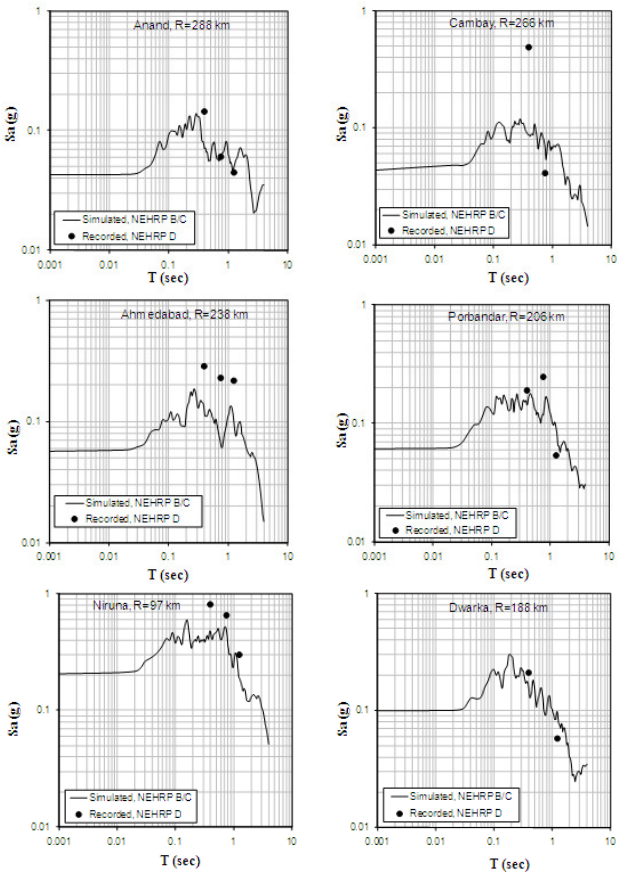


Figure 5 Simulated Response Spectra (5% Damping) at NEHRP B/C Site and SRR Recordings at NEHRP D Sites

Further, using the calibrated model parameters given in Table 2, simulations were carried out for 369 points in a grid of 0.4^0 x 0.4^0 spread all over Gujarat on B/C site condition, however slightly finer grid of 0.1^0 x 0.1^0 has been taken in near field region as decay rate is expected to be higher compare to other region. The spatial distribution of PGA values for the state of Gujarat is shown in the Fig. 6.

The PGA would have exceeded 0.60 g proximity to the epicenter of Bhuj (2001) event, reported by Iyengar and Raghukanth (2006) from the analytical results. According to Pervez et al. (2003), the design ground acceleration in epicenter zone reached up to 0.60 g and varies between 0.30 – 0.60 g and 0.08 – 0.15 g for the Kutch and Saurashtra regions respectively. Chopra et al. (2010a) estimated PGA variation from 0.20 to 0.62 g and 0.08g to 0.15 g for entire Kutch and Saurashtra region using similar approach. Present study yields PGA in the range of 0.20 g to 0.65 g for the Kutch and 0.05 g to 0.20 g for Saurashtra region. Iyengar and Raghukanth (2006) estimated PGA in the range of 0.31 - 0.37 g using empirical Green's functions to simulate ground

motion and 5 % damped response spectrum at Bhuj city. In the present analysis PGA varies from 0.30 to 0.35 g for the Bhuj. The above observations reveal that the results of present study are conciliate well with the earlier studies.

Now it would be interesting to see how well the PGA results correlate with field observation of damage after the earthquake. Several relations are available in literature (Trifunac and Brady, 1975; Wald et al. 1999) for estimating PGA from the intensity values. However it is recognized that the damage pattern and level depend on the vulnerability of the structures, which in turn varies from country to country (Raghukanth et al. 2008). Iyengar and Raghukanth (2006) addressed this issue and developed relation for Indian sub-continent using fourty three sampled data. Using this empirical relation given in Eqn. (1), the simulated PGA values have been converted into Modified Meracalli Intensity (MMI) values.

$$\ln(y) = 0.6782\,MMI - 0.8105;\ \text{where, } y = PGA\,(g) \qquad (1)$$

The simulated MMI values thus obtained have been contoured and compared with the reported intensity map following Chopra et al. (2010a) depicted in Fig. 7.

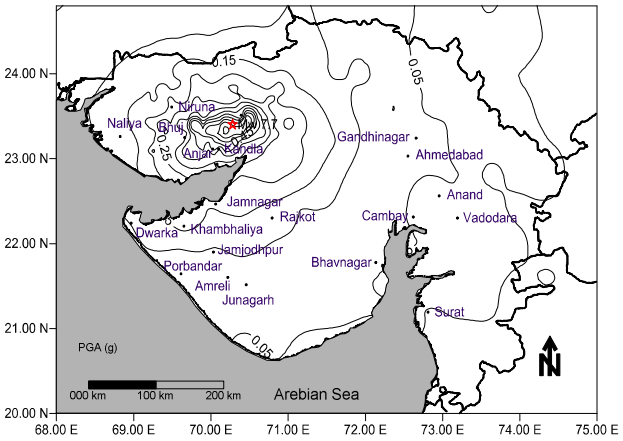


Figure 6 Predicted PGA (g) Model for Gujarat on NEHRP B/C Site Condition

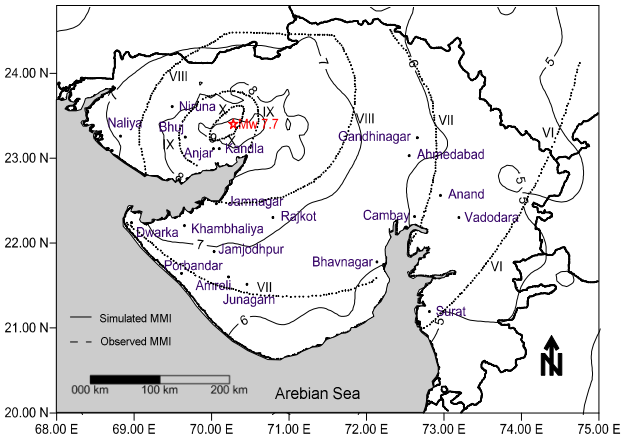


Figure 7 Simulated and Observed MMI Models

It has been observed from the Fig.7 that, the simulated MMIs ranges from 5 to 9 whereas the reported intensity values varied between VI and X. The reported intensity values are 1 unit greater than the simulated intensity values at most of the sites. This may be due to the fact that the simulated intensities were estimated from the PGA values computed at B/C site conditions whereas reported intensities are based on the many factors such as experience of the observant, damages and seismic hazards like, landslide, liquefaction, ground fissures etc (Richter, 1958).

As mentioned earlier, the only strong motion record of the 2001 event is available at Ahmedabad in the basement of the Passport Office; some 240km away from the epicenter. The recorded value of PGA at Ahmedabad is 0.10 g at site classified as NEHRP, D whereas simulated value at this site is 0.056 g for B/C boundary conditions (Fig. 2). This under prediction by the simulated model may be attributed to the local site effect. The same has been observed from Fig. 6.5 for Ahmedabad site therefore, the ground motion at surface has been computed adopting one dimensional ground response analysis. The ground response analysis has been carried out using DEEPSOIL program (Hashash et al. 2008).

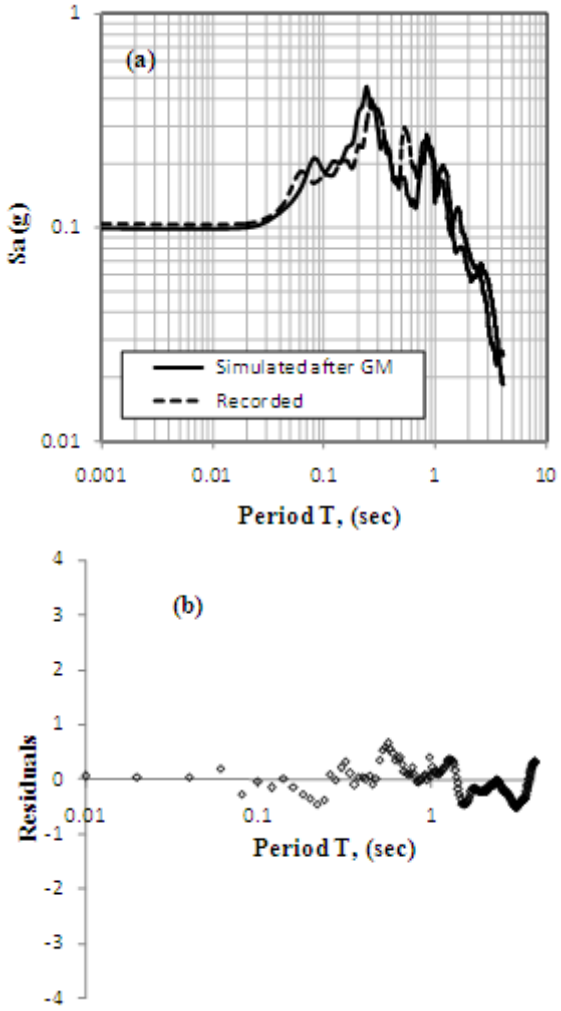


Figure 8 Recorded and Predicted Response Spectrum (b) Residual Plot at Ahmedabad

The detailed soil profile at the recording site including soil type, thickness of layer, shear wave velocity has been taken from the previous work (Trivedi et al. 2006; Trivedi, 2010).

A response spectrum of predicted ground motion at surface using ground response analysis has been compared with recorded one at the same site as shown in Fig. 8 (a). The Residual of the predicted and recorded spectral acceleration have been estimated for all the periods and presented in Fig. 8 (b). The comparison presented in the Fig. 8 indicates that the residuals are very close to the zero line and predicted spectral acceleration values reconcile considerably well with the recorded one for the most of the period ranges.

3.3 Generation of Ground Motion at Surat for Bhuj (2001) Event

The main purpose of the present study is to generate synthetic strong motion accelerogram records at Surat city in absence of actual recordings during 2001 event. It is observed that the stochastic model for the Bhuj (2001) earthquake has been reasonably validated using different approaches. Therefore calibrated finite fault model parameters given in Table 2 have been used to generate ground motion histories at important cities/towns in the state of Gujarat including Surat given Fig. 9.

In addition to that, the ground motions have been simulated at 66 sites in Surat region using the same model parameters. The results of these simulations indicate that the Bhuj (2001) earthquake may have generated PGA in the range of 0.026 g to 0.037 g for the Surat region. The spatial distribution of PGA for this region has been presented in Fig. 10. The ground motion generated here will be very useful for various seismic studies to be carried out in the region.

3. DISCUSSION AND CONCLUSIONS

In absence of recorded ground motion data, the seismological modeling seems to be a rational alternative in obtaining the ground motion during the significant event. The main aim of present investigations is to generate ground motions for the Surat region in absence of instrumental records which in turn useful for estimating future hazards in the region. First, the ground motions for Bhuj (2001) earthquake (Mw 7.7) were estimated using one dimensional stochastic finite fault modeling based on the dynamic corner frequency (Motazedian and Atkinson, 2005).

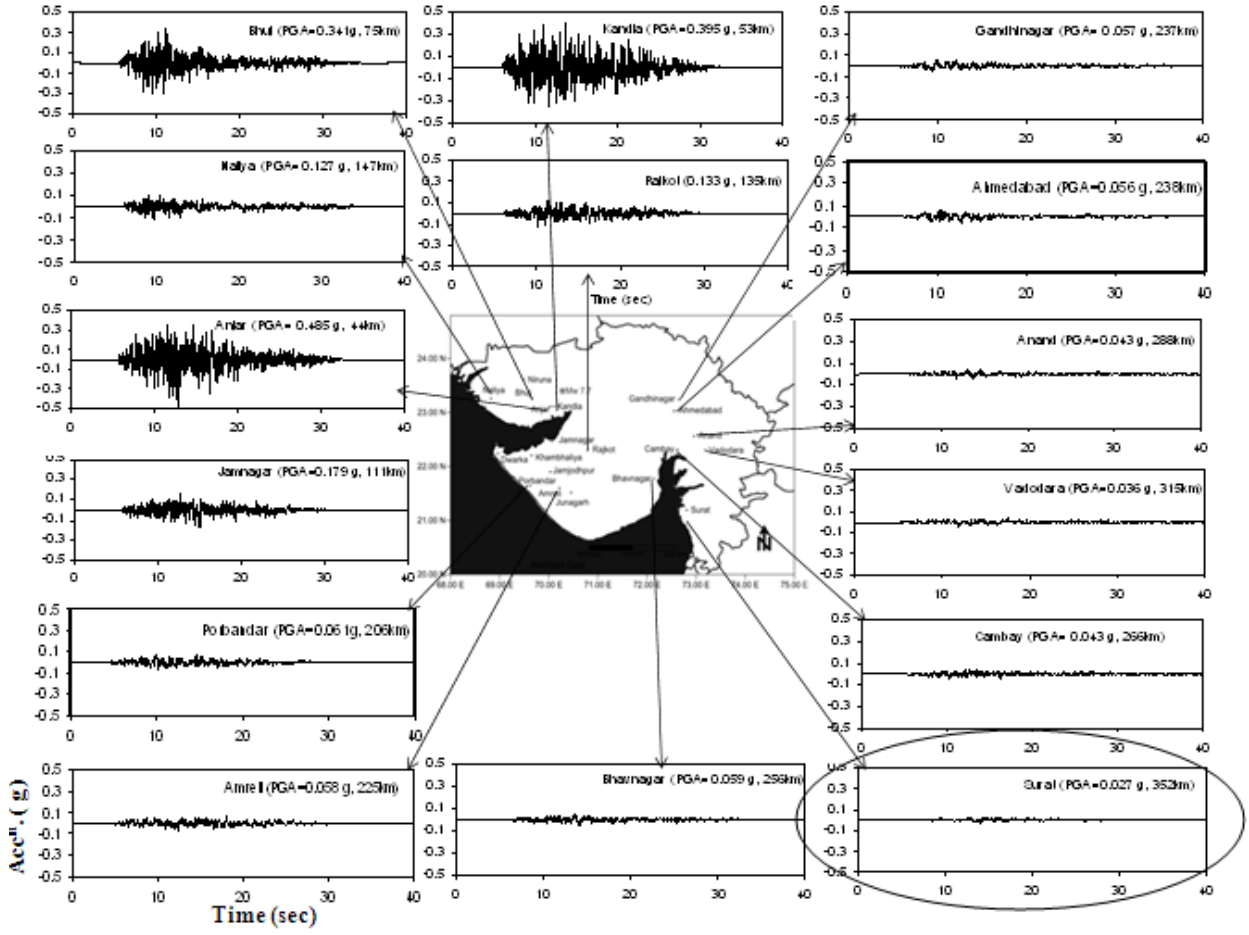


Figure 9 Simulated Ground Motions at Important Cities/ Towns in the State of Gujarat including Surat for B/C Site Condition

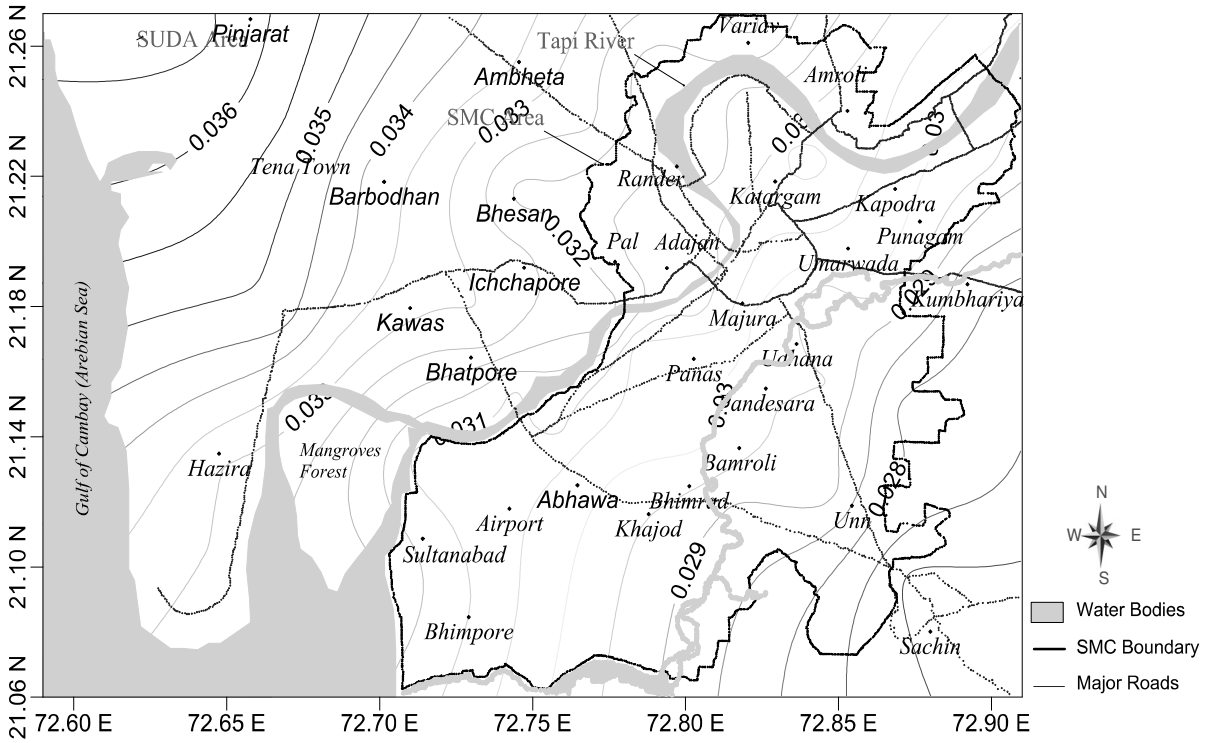


Figure 10 Simulated PGA of Bhuj (2001) Earthquake at Firm Rock (Vs = 760 m/s) sites for Surat Region

The results of simulations have been validated through different approaches. In the first approach, the ground motions were simulated at hard rock and NEHRP B/C boundary sites where SRR recordings are available.

The estimated PGA values at hard rock and B/C sites validated with those obtained in literature adopting different methodologies. The stress drop value of 150 bars estimated from above simulation which is in the range of the findings from earlier investigations carried out by Negishi et al. (2001) and Bodin and Horton (2004) for the same event whereas stress drop predicted by Antolik and Dreger (2003) and Singh et al. (2003) is quite high in comparison to the present study. On other hand, Chopra et al. (2010a) model underestimated the stress drop value in comparison to the present study. It is observed that the quality factor, $Q = 508f^{0.48}$ provides best fit estimations with available results. Hough et al. (2002) and Singh et al. (2003) adopted the same 'Q' value estimating near source ground motions of same event using a finite source stochastic modeling (Beresnev and Atkinson, 1997). Moreover, the same 'Q' has been used by Iyengar and Raghukanth (2004) for establishing the attenuation relations for western central region of India using extensive seismological modeling.

In the second approach, the predicted response spectrum has been compared with recorded spectral acceleration data from SRRs for different site conditions. The simulated spectra at hard rock site are in the close agreement with recorded accelerations for available period ranges. Whereas simulated spectra at B/C sites underestimates the recorded results of SRRs placed on NEHRP C and D sites on account local site effects. Further in third approach, the simulated PGA at B/C site conditions have been converted to MM Intensities using region specific empirical relation (Iyengar and Raghukanth, 2006) and validated with observed of Bhuj (2001) event in the state of Gujarat. The spatial distribution of PGA in Gujarat region brings out the western directivity effects on account of fault orientation and slip direction which is consistent with the observations of Chopra et al. (2010a). The PGA values are higher in the western side compare to east at comparable distances. The strong westward directivity has been observed towards the town Bhuj and Anjar, which are damaged extensively during the Bhuj (2001) earthquake. The estimated PGA values are also useful in understanding the ground motion attenuation with distance. It is observed that The PGA attenuating very fast up to the contour of 0.25 g, thereafter the rate of decay is reducing considerably on account of geometrical spreading function used in this study. Finally in the fourth approach, the influence of local site effects has been testified using site response analysis. The surface level ground motion has been obtained at Passport office, Ahmedabad using one dimensional ground response analysis validated with recorded time history at same sites.

The comparisons presented above highlights the importance of seismological modeling in the generation of ground motions. The simulated parameters have been used to predict ground motions of Bhuj (2001) event in the Surat region at 66 sites along with other important town/cities in the state of Gujarat. Generated synthetic ground motions will be very useful in assessing the performance of the structures in the state. The most probable earthquake scenarios have been selected considering the seismic hazard analysis and seismotectonic of the region.

References:

Chopra, S., Kumar, D., Rastogi, B.K. (2010a), "Estimation of strong ground motions for 2001 Bhuj (Mw 7.6) India earthquake", *Pure Appl. Geophys*. **167**, 1317-1330.

Motazedian, D. and Atkinson, G.M. (2005), "Stochastic finite-fault modeling based on a dynamic corner frequency", *Bull. Seismol. Soc. Am.* **95**, 995-1010.

Hanks, T.C. and McGuire, R.K. (1981), "The character of high frequency strong ground motion" *Bull. Seismol. Soc. Am*., **65**(3), 2071-2095.

Boore, D.M. (1983), "Stochastic simulation of high-frequency ground motions based on seismological models of the radiated spectra", *Bull. Seismol. Soc. Am*., **73**, 1865-1894.

Boore, D.M. and Atkinson, G.M. (1987), Stochastic prediction of ground motion and spectral response parameters at hard rock sites in Eastern North America, *Bull. Seismol. Soc. Am.*, **77**, 440-467.

Atkinson, G.M. and Boore, D.M. (1997), "Stochastic point source modeling of ground motions in the Cascadia region, *Seismol. Research Letters* **68**, 74-85.

Toro, G.R., Abrahamson, N.A. and Schneider, J.F. (1997), "A model of strong ground motions from earthquakes in central and eastern North America: Best estimates and uncertainties, *Seismol. Research Letters*, **68**, 41-57.

Atkinson, G.M. and Silva, W. (2000), "Stochastic modeling of California ground motions", *Bull. Seismol. Soc. Am*., **90**, 255-274.

Aki, K. (1967), Scaling low of Seismic Spectrum, *J. Geophys. Res.* **72**, 1217-1231.

Brune, J.N. (1970), "Tectonic stress and the spectra of seismic shear waves from earthquakes", *J. Geophys. Res*., **75**, 4997-5009.

Brune, J.N. (1971), "Correction", J. Geophys. Res., **76**, 5002.

Hartzell, S. (1978), "Earthquake aftershocks as Green's functions", *Geophys. Res. Letters*, **5**, 1-14.

Irikura, K. (1983), "Semi-empirical estimation of strong ground motions during last earthquakes", *Bull. Disaster Prevention Research Institute*, Kyoto Univ., **33**, 63-104.

Irikura, K. (1992), "The construction of large earthquake by a superposition of small events, *Proc. 10th World Conference on Earthquake Engineering*, **10**, 727-730.

Kamae, K. and Irikura, K. (1994), "Prediction of site-specific strong ground motion using semi-empirical methods, *Proc. 10th World Conference on Earthquake Engineering*, **2**, 801-806.

Irikura, K. and Kamae, K. (1994), "Estimation of strong ground motion in broad-frequency band based on a seismic source scalling model and an empirical Green's function technique; Earthquake source mechanics", *Ann. Geofis.,* **37**, 1721-1743.

Bour, M. and Cara. M. (1997), " Test of a simple empirical Green's function method on moderate sized earthquakes", *Bull. Seismol. Soc. Am.,* **87**, 668-683.

Beresnev, I. and Atkinson, G. (1998), "FINSIM- a FORTRAN program for simulating stochastic acceleration time histories from finite faults", *Seismol. Research Letters*, **69**, 27-32.

Hanks, T.C. (1982), "fmax", Bull. Seismol. Soc. Am., **71**, 1867-1879.

Anderson, J.G. and Hough, S.E. (1984), "A model for the shape of the Forier amplitude spectrum of acceleration at high frequencies", *Bull. Seismol. Soc. Am.*, **71**, 1969-1993.

Atkinson, G. (2004), "Empirical attenuation of ground motion spectral amplitudes in southeastern Canada and north eastern United States", *Bull. Seismol. Soc. Am.*, **94**, 1079-1095.

Hanks, T.C., and Kanamori, H. (1979), "A moment magnitude scales, J. Geophysical Research, 84, 2348-2350.

Beresnev, I. and Atkinson, G. (1997), "Modeling finite fault radiation from the wn spectrum", *Bull. Seismol. Soc. Am*., **87**, 67-84.

Motazedian, D. (2006), Region-specific key seismic parameters for earthquakes in Northern Iran", *Bull. Seismol. Soc. Am.*, **96**, 1383-1395.

Hough, S.E., Martin, S., Bilham, R. and Atkinson, G.M. (2002), "The 26 January 2001 M 7.6 Bhuj, India earthquake: Observed and predicted ground motions", *Bull. Seismol. Soc. Am*., **92**, 2061-2079.

Singh, S.K., Bansal, B.K., Bhattacharya, S.N., Pacheco, J.F., Dattatrayam, R.S., Ordaz, R.S., Suresh. M., Kamal, G. and Hough, S.E. (2003), "Estimation of ground motion for Bhuj (26 January 2001; Mw 7.6) and for future earthquake in India", Bull. Seismol. Soc. Am., 93, 353-370.

Iyengar, R.N. and Raghukanth, S.T.G. (2004), "Attenuation of strong ground motion in Peninsular India", *Seismol. Research Letters*, **72**, 530-540.

Rastogi, B.K. (2001), "Ground deformation study of Mw 7.7 Bhuj earthquake of 2001", Episode, 24, 160-165.

Negishi, H., Mori, J., Sato, T., Singh, R., Kumar, S. and Hirata, N. (2002), "Size and orientation of the fault plane for the 2001 Gujarat, India earthquake (Mw 7.7) from aftershock obsrvations: a high stress drop event", *Geophys. Research Letters,* **29**, 1949, doi: 10.1029/2002GL015280

Antolik, M. and Dreger, S.D. (2003), "Rupture process of the 26 January 2001 Mw 7.6 Bhuj, India earthquake from teleseismic broadband data, *Bull. Seismol. Soc. Am*., **93**, 1235-1248.

Bodin, P. and Horton, S. (2004), "Source parameters and tectonic implications of aftershocks of the Mw 7.6 Bhuj earthquake of January 26, 2001", *Bull. Seismol. Soc. Am*., **94**, 818-827.

Mandal, P. and Johnston, A. (2006), "Estimation of source parameters for the aftershocks of the 2001 Mw 7.7 Bhuj earthquake, India", *Pure and Appl. Geophys.,* **163,** 1537-1560.

Kanamori, H. and Anderson, D.L. (1975), "Theoretical basis of some empirical relations in seismology", *Bull. Seismol. Soc. Am*., **65**, 1073-1095.

Motazedian, D. (2006), "Region-specific key seismic parameters for earthquakes in northern Iran", *Bull. Seismol. Soc. Am*., **96**, 1383-1395.

Mandal, P., Rastogi, B.K., Satyanarayana, H.V.S., Kousalya, M., Vijayraghvan, R., Satyamurthy, C., Raju, I.P., Sarma, A.N.S. and Kumar, N. (2004a), " Characterization of causative fault system for the 2001 Bhuj earthquake of Mw 7.7, *Tectonophysics*, **378**, 105-121.

Yagi, Y. and Kikuchi, M. (2001), "Western India earthquake", http://wwweic.eri.utokyo.ac.jp/index-e.html

Mori, J., Sato, T. and Negishi, H. (2001), "Slip distribution of 2001 west India earthquake", Amer. Geophys. Union, 82, F915.

Chopra, S., Rao, K.M. and Rastogi, B.K. (2010), Estimation of sedimentary thickness in Kachchh basin", Gujarat using Sp converted phase", Pure and Appl. Geophys., **167**, 1247-1257.

Cramer, C.H. and Kumar, A. (2001), " Bhuj, India, earthquake engineering seismoscope recordings and eastern north America ground motion attenuation relations", Bull. Seismol. Soc. Am., **93**, 1390-1394.

10CUEE CONFERENCE PROCEEDINGS
10th International Conference on Urban Earthquake Engineering
March 1-2, 2013, Tokyo Institute of Technology, Tokyo, Japan

SIMULATION OF LIQUEFACTION-INDUCED VOID REDISTRIBUTION IN A CENTRIFUGE TEST

Ross W. Boulanger[1)], Ronnie Kamai[2)], and Katerina Ziotopoulou[3)]

1) Professor, Dept. of Civil and Environmental Engineering, University of California, Davis, CA, USA
2) Post-doctoral Researcher, Pacific Earthquake Engineering Research Center, University of California, Berkeley, CA, USA
3) Doctoral candidate, Dept. of Civil and Environmental Engineering, University of California, Davis, CA, USA
rwboulanger@ucdavis.edu, rkamai@berkeley.edu, kziotopoulou@ucdavis.edu

Abstract: Liquefaction-induced deformations for geotechnical structures can be significantly affected by the effects of pore pressure diffusion and the associated void redistribution. Numerical simulations using a critical-state compatible constitutive model are shown to reproduce the pattern of void redistribution that was observed in a centrifuge model test. The capabilities and limitations in our current abilities to account for void redistribution in nonlinear deformation analyses are discussed.

1. INTRODUCTION

Design and evaluation of geotechnical structures affected by soil liquefaction requires engineering procedures that can account for liquefaction-induced strength loss and deformations. Laboratory tests on field samples have been used to estimate undrained shear strengths (e.g., Poulos et al. 1985), but the application of such results assumes that the void ratio of in-situ soils either stays constant or decreases during diffusion of earthquake-induced excess pore water pressures. Empirical correlations based on back-analyses of liquefaction flow slide case histories have instead been preferred for practice because they implicitly account for pore pressure diffusion (and associated void redistribution) and other in-situ mechanisms of strength loss that standard laboratory element testing cannot recreate. Nonlinear deformation analyses have provided insights on the mechanisms of strength loss associated with pore water pressure diffusion and void redistribution (e.g., Seid-Karbasi and Byrne 2007), but the ability of such analysis methods to confidently predict void redistribution effects has not been adequately demonstrated. For this reason, the application of nonlinear deformation analyses to practical problems still relies on case history experiences for estimating the in-situ residual shear strength of liquefied soils.

The mechanism of strength loss due to void redistribution is illustrated in Figure 1 for a liquefied soil layer within an infinite slope (Kulasingam et al. 2004). The liquefied layer is overlain and underlain by lower permeability soils, as shown in Figure 1a (after Whitman 1985). The shear stress ratio, stress-path, and void ratio response at the top and bottom of the sand layer (points A and C, respectively) are illustrated in Figures 1b, 1c, and 1d, respectively. Earthquake shaking generates excess pore water pressures, which result in an upward hydraulic gradient that causes pore water to flow up toward the interface with the overlying low-permeability layer. A thin zone at the top of the sand layer dilates in response to the net inflow of water and develops shear strains that are related to the imposed volumetric strains through the sand's dilation angle. The progressive loosening of this thin zone results in a shear strain concentration and can result in the sand eventually reaching critical state (point i). Any further inflow of water then results in the thin zone shedding shear stress and the slope becoming unstable.

This paper describes numerical simulations of a centrifuge model test involving silt interlayers in a saturated sand slope. The experimentally observed pattern of void redistribution is described, followed by the results of the numerical simulations. The capabilities and limitations in the numerical models and the challenges in numerically simulating the details of these mechanisms are discussed.

2. PHYSICAL MODEL STUDIES

Malvick et al. (2008) used back-analyses of time series data from a dense array of pore pressure transducers within a saturated sand slope with embedded silt layers to quantify several aspects of the pore pressure diffusion and void redistribution process. The test was performed on a 9-m-radius centrifuge at a centrifugal acceleration of 45 g; results are presented in equivalent prototype units unless otherwise stated. The arrangement of pore pressure

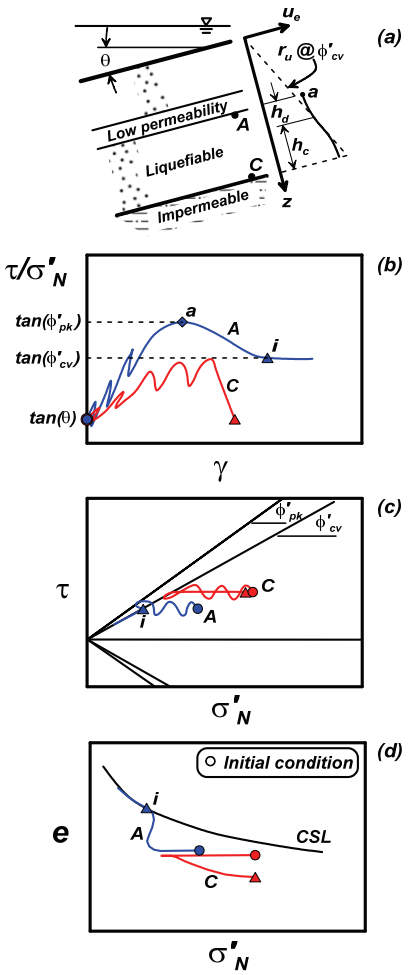


Figure 1. Schematic of soil responses near the top and bottom of a liquefiable sand layer overlain by low permeability soil (after Kulasingam et al. 2004)

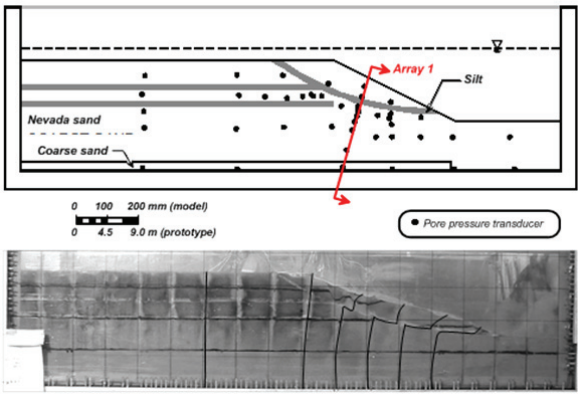


Figure 2. Localization along a lower permeability interlayer in a saturated sand slope tested in a 9-m-radius centrifuge (after Malvick et al. 2008)

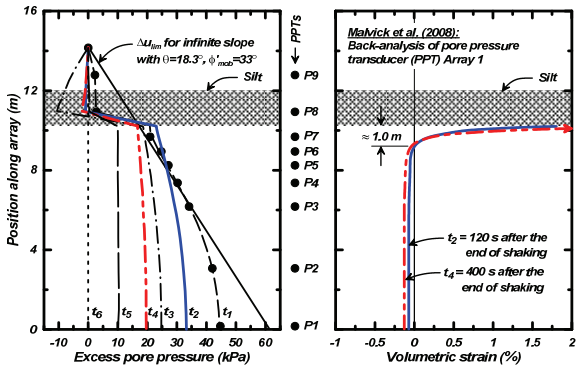


Figure 3. Results of back-analyses of data from the dense array of pore pressure transducers: Excess pore pressures and volumetric strains at different times (after Malvick et al. 2008)

transducers and a photograph of the post-testing deformed geometry of the model slope are shown in Figure 2. The pore pressures and volumetric strains calculated for Array 1 are shown in Figure 3. Hydraulic gradients were calculated by numerical differentiation of the measured pore pressure distribution with respect to position along the array. Flow rates were computed based on Darcy's Law and integrated with respect to time to obtain flow quantities, from which volumetric strains within specific intervals were computed. Their analysis results showed that a dilating (loosening) zone of about 1 m or greater thickness developed in the sand immediately beneath the embedded silt layer during diffusion of the excess pore pressures (Figure 3). They concluded that the dilating zone corresponded to regions where the mobilized friction angle exceeded the critical state friction angle, and that the dilating zone can be initially relatively thick before its size eventually diminishes to the thickness of a thin shear band.

Kamai and Boulanger (2010) obtained similar results from back-analyses for a dense array of pore pressure transducers within a dynamic centrifuge model test involving liquefaction-induced lateral spreading of a clay crust overlying a loose liquefying sand layer. Their results indicate that loosening occurred over an approximately 0.6-m-thick interval at the top of the sand layer, and that the greatest volumetric strains (a few percent) occurred immediately near the interface with the clay crust.

The results of these and other physical modeling studies have demonstrated that the effects of void redistribution depend on the initial D_R, slope geometry (e.g., low-permeability interlayers, sand layer thickness), shaking duration, shaking amplitude, and shaking history (e.g., Liu and Qiao 1984; Elgamal et al. 1989; Dobry and Liu 1992; Fiegel and Kutter 1994, Kokusho 1999, 2003, Kulasingam et al. 2004, Malvick et al. 2008, Kamai and Boulanger 2010).

3. SIMULATIONS

Simulations were performed for the centrifuge test by Malvick et al. (2008) shown previously in Figure 2. The simulations were performed using the finite different mesh shown in Figure 4, and included a sensitivity study covering a range of cyclic strengths, hydraulic conductivities, mesh size, and other parameters.

The constitutive model used in these analyses, PM4Sand, was developed by Boulanger (2010) and Boulanger and Ziotopoulou (2012). The model follows the basic framework of the stress-ratio controlled, critical state compatible, bounding-surface plasticity model for sand presented by Dafalias and Manzari (2004), with a number of modifications and additions as described in Boulanger and Ziotopoulou (2012). The model was implemented as a user-defined material for use with the commercial program FLAC (Itasca 2011). Details of the implementation for version 2 of the model, which was the version used for the simulations presented herein, are given in Boulanger and Ziotopoulou (2012).

The numerical simulations captured the trends and magnitudes of the recorded accelerations and pore pressures during shaking reasonably well. The simulations were in reasonable agreement with the final deformed geometry, but did not reproduce the delayed timing of the post-shaking slope deformations that were observed in the experiment. Details of the numerical modeling procedures are given in Kamai (2011); note that the simulation results in Kamai (2011) used version 1 of the PM4Sand model whereas the results shown here differ slightly because they were performed using version 2 (Boulanger and Ziotopoulou 2012).

The sand elements immediately below the silt arc in this mesh were generally about 200 mm thick, which is comparable to the expected dimensions of a potential shear band in this model. The median particle size for this sand is about 0.17 mm (model scale), such that a 10 to 20 grain diameter thick shear band would be 2 to 4 mm thick in model scale and thus 90 to 180 mm thick in the prototype scale used for the simulations. Analyses were also performed using a slightly more refined mesh, with the differences in results being consistent with those discussed previously. Considering the approximations involved in estimating the thickness of the localization zone, the values of the strains within the localized shear zone computed using the mesh in Figure 4 are expected to be reasonable for illustrating the mechanism of void redistribution.

Computed patterns of void redistribution for this model are illustrated by the results in Figure 5 for two different values of sand permeability. The sand permeability for the case shown in Figure 5a was set equal to the value obtained in laboratory element tests, whereas the sand permeability was increased by a factor of five for the case shown in Figure 5b. This variation of permeability was chosen in part because some studies have suggested permeability increases markedly when liquefaction is triggered (e.g., Haigh et al. 2012) and partly to examine the sensitivity of analysis

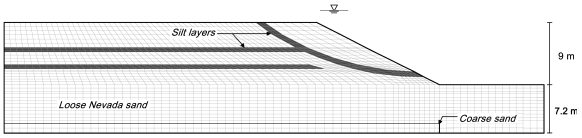
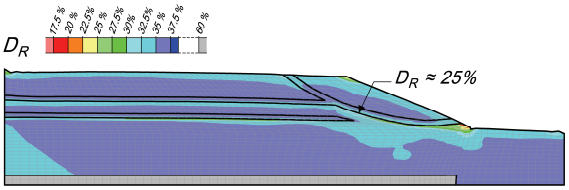
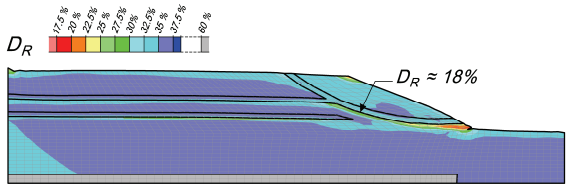


Figure 4. Model configuration and finite difference mesh for EJM02.



(a) sand permeability of 0.012 cm/s



(b) sand permeability of 0.06 cm/s

Figure 5. Deformed mesh and contours of D_R for two analysis cases that both start with an initial D_R = 35%:

results to the uncertainty in input parameters. These two numerical simulations produce patterns of void redistribution that are consistent with the patterns identified through back-analyses of the data from the dense array of pore pressure transducers (Figure 3). The simulation results are consistent in showing that there is an approximately 1.0 to 3.0 m thick zone (varies along the arc) of sand immediately beneath the silt arc that loosens as a consequence of a net inflow of pore water, and that the greatest degree of loosening occurs in a thin zone immediately beneath the silt arc. For the case shown in Figure 5a, the sand elements immediately beneath the silt arc near the middle of the slope loosen from D_R = 35% before shaking to $D_R \approx 29\%$ at the end of shaking and then to $D_R \approx$ 24.5% about 300 seconds after the end of shaking. For the case shown in Figure 5b, the same sand elements loosen more rapidly until they reach critical state at $D_R \approx 18\%$ just before the end of shaking; these elements do not experience significant changes in D_R after shaking for this case, since most of the excess pore pressure dissipates during shaking due to the higher permeability. Thus, the five-fold increase in permeability between the models in Figures 5a and 5b increased the volumetric strains from about 2.2% to 3.6% at this point in the slope, caused a greater proportion of the strains to occur during shaking versus after shaking, and also increased overall slope deformations by about 18%. These

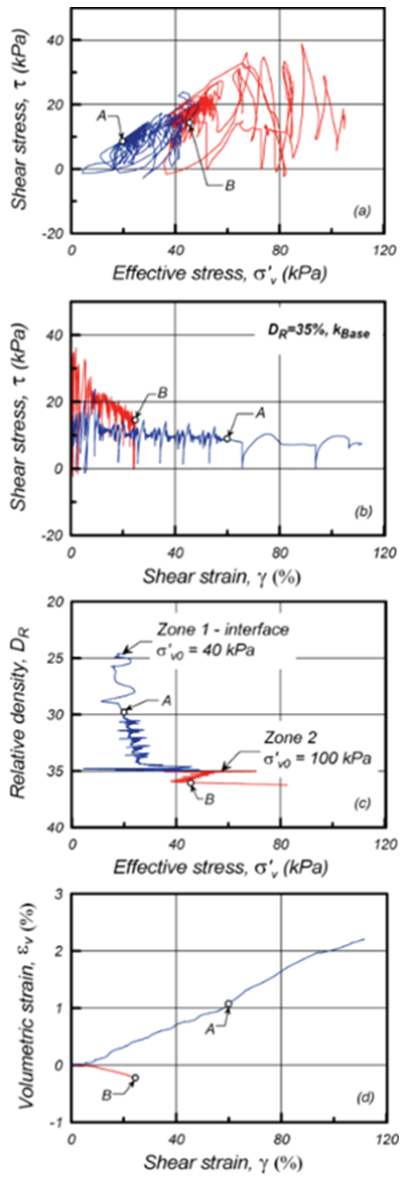


Figure 6. Stress and strain paths of two elements from one scenario simulation: Element 1 is in the sand just beneath the silt interlayer and Element 2 is about 6 m below Element 1. Points A and B represent the end of shaking for Elements1 and 2, respectively.

effects are consistent with the simpler analytical and dimensional analysis results obtained by Kulasingam (2004).

The stresses and strains that were computed for two elements in the mesh for the simulation with the lower sand permeability are shown in Figure 6. Element 1 is a sand element just beneath the silt arc near the middle of the slope, whereas Element 2 is a few meters below Element 1 (below the zone of dilation). Points A and B correspond to the end of shaking for Elements 1 and 2, respectively. The sand at Element 2 developed high excess pore pressures and shear strains of several percent during shaking, but then progressively contracted (densified) due to the net outflow of pore water from this zone both during and after shaking. The sand at Element 1 also develops high excess pore pressures during shaking, but it progressively loosens under the net inflow of pore water and accordingly develops very large shear strains under the combined effects of this pore water inflow and continued small levels of shaking. The simulation paths are very consistent with the expected patterns presented schematically in Figure 1 by Kulasingam et al. (2004).

4. CHALLENGES IN PRACTICE

There are a number of technical challenges that need to be addressed for improving the ability to numerically simulate the process of void redistribution and its effects on residual shear strengths and deformations. The length scale for any eventual localization needs to be consistently accounted for and better understood for conditions where geologic contacts are less distinct and/or have gradually varying soil properties (e.g., permeability in a fining-upward sequence). Constitutive models are also needed that can better simulate post-liquefaction reconsolidation strains because these volumetric strains directly affects the volume of water given off by consolidating zones. Existing elastic-plastic continuum models generally under-estimate post-liquefaction reconsolidation strains, which can be expected to cause an under-estimation of the magnitude of void redistribution and difficulties in simulating delayed slope deformations. In addition, there are numerical challenges in simulating localization processes using any continuum model, whether it is void redistribution or cracking of overlying crusts with associated graben formation during the sliding process. It follows that there remains an important need to evaluate the extent to which any numerical modeling procedure can differentiate between cases (e.g., physical model tests) where void redistribution has and has not led to significant concentrations of shear strains and contributed to the associated deformations.

Simulating void redistribution effects for field conditions involves even further challenges, including improving our ability to characterize geologic heterogeneities, geology contacts, in-situ soil properties, and ground motion characteristics. Geologic details can be expected to have a major influence on the thickness and/or continuity of any loosening zones and on the formation of ground cracks or soil boils that may reduce the progression of loosening in certain zones.

5. CONCLUSIONS

Physical model tests involving liquefiable sands with lower-permeability interlayers have demonstrated how various factors can influence the degree to which void redistribution can affect shear strength losses and slope deformations. The potential for void redistribution to cause

strain localizations and associated deformations in liquefied soil depends on the soil properties (initial relative density, cyclic resistance ratio, permeability), slope geometry (layer thicknesses, slope angle, continuity of interfaces), and ground motion characteristics (shaking intensity, shaking duration, shaking history).

Numerical simulations using the critical-state compatible constitutive model PM4Sand (Boulanger and Ziotopoulou 2012) with the commercial program FLAC (Itasca 2011) were shown to reasonably reproduce the patterns of void redistribution, but did not reproduce the delayed timing of the post-shaking scope deformations that were observed in the experiment. Numerical simulations provide additional insight on the mechanisms of void redistribution, although there remain several factors that currently limit our ability to simulate void redistribution effects in practice.

Acknowledgements:

Travel by the authors was supported by the Japan Ministry of Education, Culture, Sport, Science, and Technology (MEXT) through the Center for Urban Earthquake Engineering (CUEE). Funding for portions of this research was provided the U.S. Geological Survey through Award G09AP00121. Support for K. Ziotopoulou was provided by the 2008 International Fulbright Science and Technology Award from the Institute of International Education and the U.S. Department of State. The authors appreciate the above financial support and the assistance of numerous colleagues with various aspects of the work presented herein.

References:

Boulanger, R. W. (2010), "A sand plasticity model for earthquake engineering applications", Report No. UCD/CGM-10-01, Center for Geotechnical Modeling, Department of Civil and Environmental Engineering, University of California, Davis, California.

Boulanger, R. W. and Ziotopoulou, K. (2012). PM4Sand (Version 2): A sand plasticity model for earthquake engineering applications. Report No. UCD/CGM-12-01, Center for Geotechnical Modeling, Department of Civil and Environmental Engineering, University of California, Davis, California, 100 pp.

Dafalias, Y. F., and Manzari, M.T. (2004), "Simple plasticity sand model accounting for fabric change effects", Journal of Engineering Mechanics, ASCE, 130(6), 622-634.

Dobry, R., and Liu, L. (1992). "Centrifuge modeling of soil liquefaction." Proc. Tenth World Conference on Earthquake Engineering., Madrid, Spain. pp. 6801-6809.

Elgamal, A. W., Dobry, R., and Adalier, K. (1989). "Study of effect of clay layers on liquefaction of sand deposits using small-scale models." Proc. 2nd U.S.-Japan Workshop on Liquefaction, Large Ground Deformation and Their Effects on Lifelines. pp. 233-245. NCEER, SUNNY-Buffalo, Buffalo, NY.

Fiegel, G. L., and Kutter B. L. (1994). "Liquefaction mechanism for layered soils." J. Geotech. Engineering, ASCE, 120(4), 737–755.

Haigh, S. K., Eadington, J., and Madabhushi, S. P. G. (2012). "Permeability and stiffness of sands at very low effective stresses." Geotechnique, 62(1), 69-75.

Itasca (2011), FLAC – Fast Lagrangian Analysis of Continua, Version 7.0, Itasca Consulting Group, Inc., Minneapolis, Minnesota.

Kamai, R. (2011). Liquefaction-induced shear strain localization processes in layered soil profiles." Ph.D. dissertation, University of California, Davis.

Kamai, R. and R. W. Boulanger (2010), "Characterizing localization processes during liquefaction using inverse analyses of instrumentation arrays", Meso-Scale Shear Physics in Earthquake and Landslide Mechanics. Y. H. Hatzor, J. Sulem and I. Vardoulakis. The Netherlands, CRC Press/.Balkema: 219-238.

Kamai, R., and Boulanger, R. W. (2012). "Single-element simulations of partial-drainage effects under monotonic and cyclic loading." Soil Dynamics and Earthquake Engineering, 35, 29-40.

Kokusho, T. (1999). "Water film in liquefied sand and its effect on lateral spread." J. Geotechnical Eng., ASCE 125(10), 817–26.

Kokusho, T. (2003). "Current state of research on flow failure considering void redistribution in liquefied deposits." Soil Dynamics and Earthquake Engineering 23(7): 585-603.

Kulasingam, R. (2004). "Effects of void redistribution on liquefaction-induced deformations." Ph.D. thesis, University of California, Davis, California.

Kulasingam, R., Malvick, E. J., Boulanger, R. W., and Kutter, B. L. (2004). "Strength loss and localization of silt interlayers in slopes of liquefied sand." J. Geotechnical and Geoenvironmental Engineering 130(11): 1192-1202.

Liu, H., and Qiao, T. (1984). "Liquefaction potential of saturated sand deposits underlying foundation of structure." Proc. 8th World Conf. Earthquake Engineering, Vol. III, San Francisco. pp. 199-206.

Malvick, E. J., Kutter, B. L., and Boulanger, R. W. (2008). "Postshaking shear strain localization in a centrifuge model of a saturated sand slope." J. Geotechnical and Geoenvironmental Engineering, ASCE, 134(2), 164-174.

Poulos, S. J., Castro, G., and France, J. W. (1985). "Liquefaction evaluation procedure." J. Geotechnical Engineering, ASCE 111(6), 772–91.

Seid-Karbasi, M., and Byrne, P. M. (2007). "Seismic liquefaction, lateral spreading, and flow slides: a numerical investigation into void redistribution." Canadian Geotechnical Journal, Vol. 44, No. 7, pp 873-890.

Whitman, R. V. (1985). "On liquefaction." Proceedings, 11th International Conference on Soil Mechanics and Foundation Engineering, San Francisco, CA, A.A. Balkema, pp. 1923–926.

10CUEE CONFERENCE PROCEEDINGS
10th International Conference on Urban Earthquake Engineering
March 1-2, 2013, Tokyo Institute of Technology, Tokyo, Japan

LIQUEFACTION POTENTIAL EVALUATION: ENERGY-BASED METHOD VERSUS STRESS-BASED METHOD

Takaji Kokusho[1)]

1) *Professor, Department of Civil & Environment Engineering, Chuo University, Japan*

Abstract: A data set of undrained cyclic triaxial test for liquefaction parametrically changing relative density and fines content is reviewed and interpreted in scope of energy. It is found that the strain amplitude or pore-pressure buildup during cyclic loading is uniquely correlated not only to energy dissipated in soil specimens but also to strain energy given from outside. An energy-based method (EBM) is developed in which liquefaction potential can be evaluated by comparing the strain energy for liquefaction in a sand layer with upcoming seismic energy with no regard to the differences in seismic motions. Comparative studies in soil models demonstrate that the effect of various input motions is intrinsically included in EBM, whereas it has to be considered by choosing a proper coefficient in a conventional stress-based method (SBM). Another significant difference is that liquefaction potential tends to be higher for a shallower depth in EBM, while it is vice versa in SBM in a uniform sand deposit.

1. INTRODUCTION

From the dawn of the liquefaction research, a stress-based method (SBM), comparing undrained cyclic strength with seismically induced shear stress, was employed (Seed and Idriss 1971) and standardized in engineering practice for liquefaction potential evaluations in many design codes.

On the other hand, an energy-based method (EBM) was proposed by Davis and Berrill (1982) and Berrill and Davis (1984), assuming that the pore-pressure buildup is directly related to the amount of seismic energy dissipated in the soil. In order to demonstrate the energy-dependency of liquefaction, laboratory soil test was conducted (e.g. Figueroa et al. 1994), which showed that the dissipated energy per unit volume during undrained cyclic loading is closely connected to pore-pressure build-up.

Despite a close link between dissipated energy and pore-pressure build-up, the application of EBM has been very limited so far in engineering practice. In this paper, a systematic research is undertaken, in which laboratory tests and seismic energy evaluations are combined to propose an approach of EBM. It is then applied to a hypothetical sand deposit to compare the result with that of SBM under the same seismic motions.

2. SOIL TEST RESULTS ON DISSIPATED ENERGY DURING CYCLIC LOADING

In order to examine correlations between dissipated energy and excess pore-pressure as well as soil strain, a series of undrained cyclic triaxial test data obtained in the previous research (Kokusho et al. 2012) have been reviewed here. The test was carried out using reconstituted specimens of Futtsu beach sand (along the Tokyo Bay), with the mean grain size D_{50}=0.19 mm and the uniformity coefficient U_c=1.9, which consists of non-weathered sub-round particles. The size of the specimen was 10 cm in diameter and 20 cm

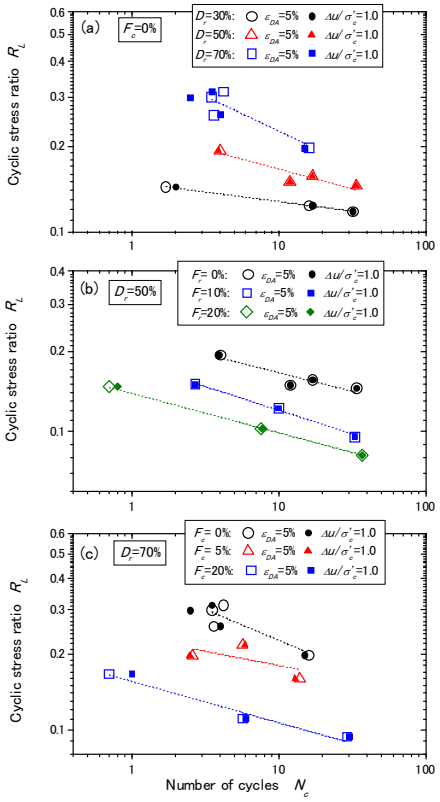


Figure 1 Cyclic stress ratio R_L versus number of cycles N_c

in height. The relative density was varied nominally in three steps; D_r≒30, 50 and 70%. In some cases, low-plasticity fines (the plasticity index I_p=6) was mixed to make sand samples with various fines content F_c.

The samples were isotropically consolidated to an effective stress of σ_c' =98 kPa, and cyclically loaded with frequency 0.1 Hz under a undrained condition with a constant axial cyclic stress amplitude σ_d . Number of cycles N_c to attain double-amplitude axial strains ε_{DA} =2, 5, 10% and the pore-pressure ratio $\Delta u/\sigma_c'$ =1.0 were measured under various cyclic stress ratios $R_L = \sigma_d / 2\sigma_c'$.

Fig. 1 shows cyclic stress ratios R_L versus number of load cycles N_c on the log-log chart for ε_{DA} =5% and $\Delta u/\sigma_c'$ =1.0 for a series of tests; (a) only clean sands (F_c=0%) with D_r ≒30, 50, 70%, (b) F_c=0~20% with D_r≒50% and (c) F_c=0~20% with D_r≒70%. The plots in the chart are approximated by an empirical formula with positive constants *a* and *b*;

$$R_L = aN_c^{-b} \qquad (1)$$

Despite data scatters, it may be said that the R_L-value for ε_{DA} =5% increases systematically with increasing D_r, and decreasing F_c.

Fig. 2 exemplifies a typical stress-strain relationship for D_r=51% and F_c=0%. The dissipated energy per unit volume in a test specimen is calculated in each stress cycle for

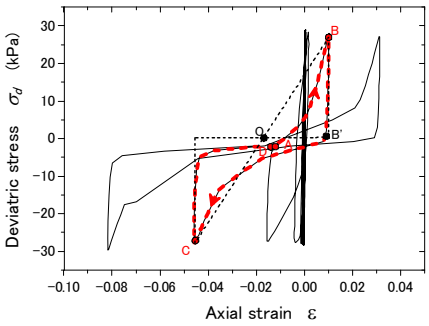


Figure. 2 Typical stress-strain relationship during undrained cyclic triaxial test.

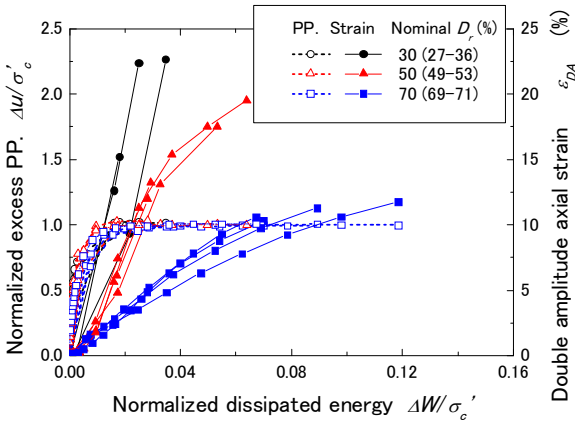


Figure 3 Relationships between normalized dissipated energy at each cycle and corresponding excess pore-pressure and double amplitude axial strain.

a hysteretic area ABCD shown in the figure with a thick dashed curve and summed up for all the cycles from the start to a particular cycle *k* as

$$\Delta W = \sum_k \left(\int_A^D \sigma_d d\varepsilon \right)_k \qquad (2)$$

In Fig. 3, the maximum values of ΔW are read off in individual loading cycles from time-histories for all the test data. The ΔW -values are plotted versus maximum values of pore-pressure Δu and double-amplitude axial strain ε_{DA} in the corresponding cycles with different symbols for sands of F_c=0 and nominal D_r-values 30, 50 and 70%. Here, the pore-pressure and the dissipated energy per unit volume is non-dimensionalized by the effective confining stress σ_c' . It is remarkable that the pore-pressure build-up occurs with increasing dissipated energy almost uniquely despite the difference in D_r, and approaches $\Delta u/\sigma_c'$ =1.0 at $\Delta W/\sigma_c'$ =0.02 or smaller.

In a good contrast, a dominant effect of D_r is visible on the strain amplitude versus energy relationship in Fig. 3. The induced strain ε_{DA} is almost in proportion to the normalized energy $\Delta W/\sigma_c'$ for each relative density D_r up to a certain strain around ε_{DA} = 10% even after the onset of liquefaction. Thus, the dissipated energy can be correlated consistently with strain amplitude depending on individual D_r-values up to the initial liquefaction (ε_{DA} =5%) and thereafter, and serve as an indicator for severity of liquefaction.

In Fig. 4, the normalized dissipated energies $\Delta W/\sigma_c'$ are plotted in the vertical axis versus the number of load cycles N_c in the horizontal axis on log-log charts to attain strain amplitudes, ε_{DA} =2, 5, 10%, and pressure build-up, $\Delta u/\sigma_c'$ =1.0. The plots in (a) are for clean sand (F_c=0) with parametrically varying nominal relative density D_r≒30, 50 and 70% and those in (b) are for sand containing parametrically changing fines content (F_c=5~20%) having relative densities, D_r≒50 and 70%. There are groups of 2 to 4 data-points with the same symbols for which the same prescribed strain ε_{DA} or pore-pressure $\Delta u/\sigma_c'$ were attained in different numbers of cycles N_c, because multiple tests for test specimens having the same F_c and nominal D_r were carried out with different cyclic stress amplitudes. The lines connecting them do not show consistent increasing or decreasing trend in $\Delta W/\sigma_c'$ -values with increasing N_c. They may be judged to be essentially flat in all the test cases, despite some lines for dense sands showing non-systematic up-down trends particularly for ε_{DA} =10%. The trends in Fig. 4 seem to indicate that the dissipated energy almost uniquely determines the strain amplitude or pore-pressure buildup during cyclic loading, no matter how many cycles N_c and how large the associated applied stress ratio R_L are required to attain a particular strain amplitude ε_{DA} or pressure buildup. This further indicates that a R_L-N_c line for particular strains or $\Delta u/\sigma_c'$ =1.0 drawn in Fig. 1, normally addressed as a basis for the stress-based approach of liquefaction potential evaluation, actually represents a line of equal-energy dissipation (Green and Terri 2005). This ob-

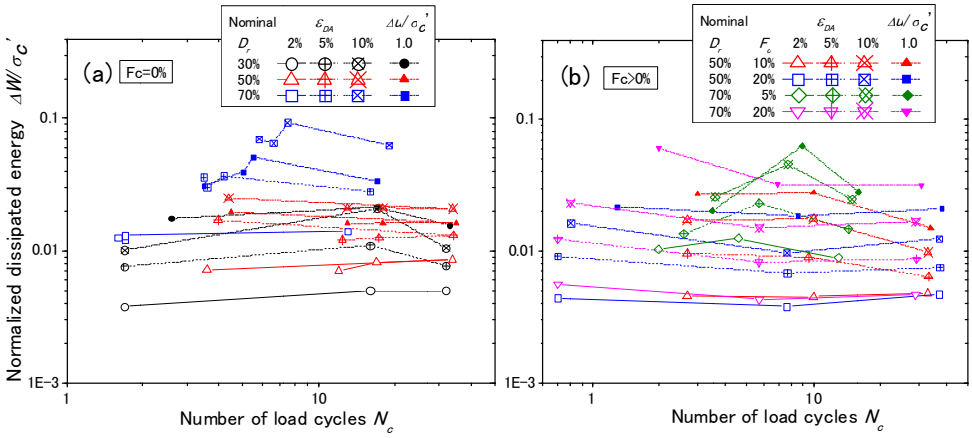


Figure 4 Normalized dissipated energy for ε_{DA}=2, 5, 10% and $\Delta u/\sigma'_c$=1.0 plotted versus number of load cycles.

servation paves a way to an energy-based method (EBM) using conventional soil data in the stress-based method (SBM).

Based on the test results in Figs. 1 and 4 for $D_r \fallingdotseq$30-70% and F_c=0-30%, a direct relationship between cyclic resistance ratio R_{L20} for N_c=20 and corresponding dissipated energy $\Delta W/\sigma'_c$ can be developed as shown in Fig. 5. Despite differences in relative density and fines content, the R_{L20}–values for the strain level ε_{DA}=5% (circles) may be uniquely correlated with $\Delta W/\sigma'_c$ and approximated by a parabolic function

$$\Delta W/\sigma'_c = 0.032 - 0.48R_{L20} + 2.40R_{L20}^2 \qquad (3)$$

for practically meaningful R_{L20}–values ($R_{L20} \geq 0.1$) with a regression coefficient RC=0.93. For ε_{DA}=2% and 10%, similar curves with the vertical coordinate 0.4 times and twice that of ε_{DA}=5%, respectively, are drawn in the chart. The curves seem to be compatible with the plots, because ε_{DA} is almost in proportion to the normalized energy $\Delta W/\sigma'_c$ up to around ε_{DA} = 10% as indicated in Fig. 3.

Because the relationship between R_{L20} and corresponding dissipated energy $\Delta W/\sigma'_c$ in Fig. 5 holds uniquely for sands with various densities and fines content, it may also be applicable to natural sands with different soil fabrics such as those reflecting long geological histories. This indicates that relationships between the cyclic resistance ratio R_{L20} and SPT N-value already established and practically used in SBM, may be transformed into a direct energy versus N-value correlation to be used in EBM.

Based on the research results combining undrained cyclic triaxial tests on intact samples recovered by in situ freezing technique and associated in situ SPT logging (Matsuo 1997), the following empirical formula giving R_L (ε_{DA}=5%) from normalized SPT blow counts N_1 was proposed for clean sand (F_c<10%) (Japan Road Association 2002).

$$R_L = \begin{cases} 0.0882\sqrt{N_1/1.7} & : N_1 < 14 \\ 0.0882\sqrt{N_1/1.7} + 1.6\times10^{-6}(N_1 - 14)^{4.5} & : 14 \leq N_1 \end{cases} \qquad (4)$$

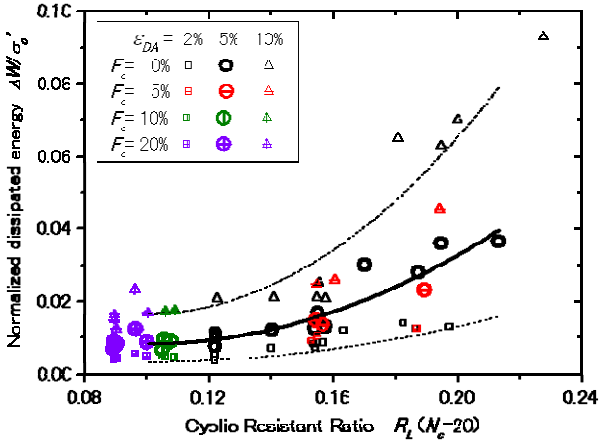


Figure 5 Normalized dissipated energy versus cyclic resistance ratio for ε_{DA}=2, 5, 10% for sand specimens with different fines content.

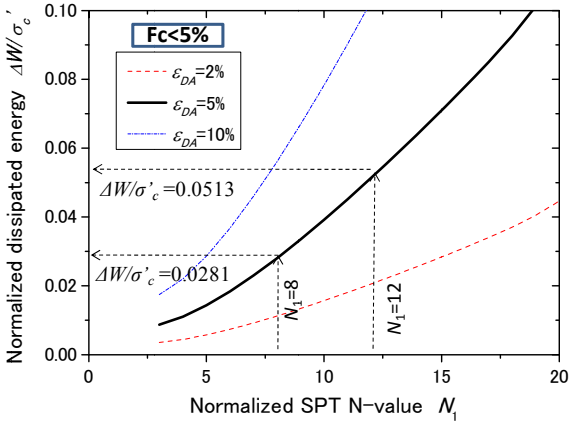


Figure 6 Direct relationship between normalized N-value (N_1) and Normalized dissipated energy $\Delta W/\sigma'_c$ for clean sand of F_c<5%.

Here, the value N_1 is calculated from SPT N-value and effective overburden stress σ'_v in the next equation (p_0=98 kPa).

$$N_1 = 1.7N/(\sigma'_v/p_0 + 0.7) \quad (5)$$

Fig. 6 shows a direct relationship between N_1 and $\Delta W/\sigma'_c$ thus developed using Eqs. (3) and (4). The curves are drawn not only for ε_{DA}=5% (normally considered as the onset of liquefaction) but also for ε_{DA}=2% and 10% by assuming the proportionality between ε_{DA} and $\Delta W/\sigma'_c$. Other relationships may readily be obtained if site-specific R_L versus N_1 curves other than that in Eq. (4) considering various effects (such as fines content, aging, and over-consolidation) is combined with the R_{L20} versus $\Delta W/\sigma'_c$ correlation in Fig. 5.

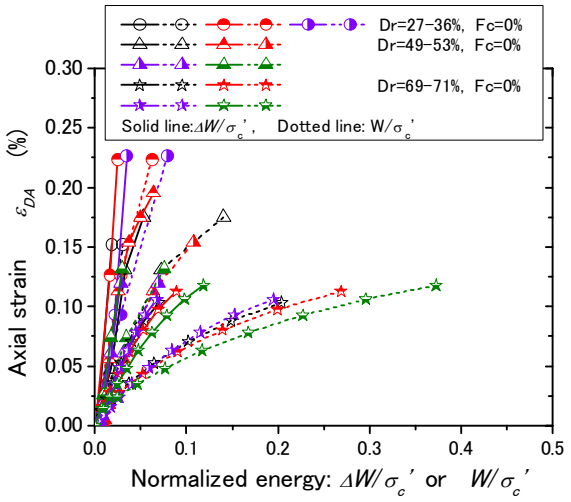


Figure 7 Relationships between normalized dissipated energy $\Delta W/\sigma'_c$ or normalized strain energy W/σ'_c versus axial strain obtained in the triaxial tests.

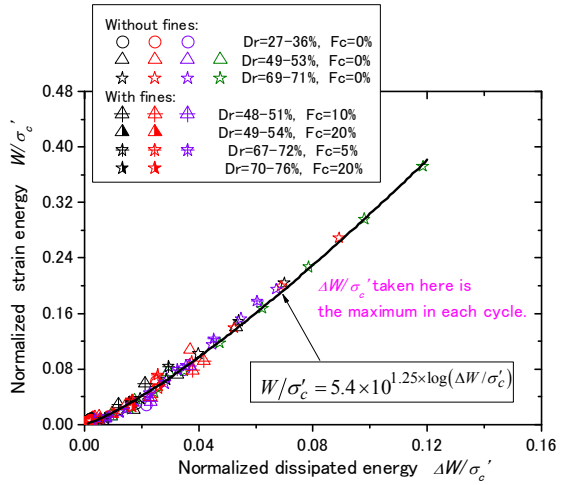


Figure. 8 Relationship between normalized dissipated energy $\Delta W/\sigma'_c$ versus normalized strain energy W/σ'_c for all triaxial test results.

In order to compare the dissipated energy with the wave energy in the field, it is necessary to know how much wave energy is needed for a certain amount of energy ΔW to be dissipated inside the soil for liquefaction. The wave energy may well be replaced by strain energy in laboratory tests. Hence, the strain energy W was evaluated together with the dissipated energy ΔW in the same triaxial test series already explained.

The strain energy per cycle in the triaxial test is defined as 4 times the area of a triangle OBB' illustrated in Fig.2, and the strain energy accumulated up to a certain cycle k is calculated as

$$W = \sum_k 4\left(\mathrm{OB'} \times \mathrm{BB'}/2\right)_k \quad (6)$$

In Fig. 7, strain energies defined in Eq.(6) and normalized by the effective confining stress as W/σ'_c is plotted versus axial strain and compared with corresponding normalized dissipated energy, $\Delta W/\sigma'_c$, of the same symbols for all the test results of clean sands (F_c=0%). Energies represented by symbols connected with dashed lines (W/σ'_c) are obviously larger than those by the same symbols connected with solid lines ($\Delta W/\sigma'_c$), and the ratio of the two energies seems to be almost constant despite large differences in the energy values.

In Fig. 8, the normalized strain energies W/σ'_c in the vertical axis directly compare with the normalized dissipated energies $\Delta W/\sigma'_c$ in the horizontal axis not only for clean sands but also for sands containing fines. Though the two energies are not proportional, it is remarkable that W/σ'_c and $\Delta W/\sigma'_c$ are uniquely correlated for sands with largely different relative densities and fines contents. This also indicates that the dissipated energy in sand in the liquefaction process is uniquely correlated to the energy given from outside regardless of the cyclic stress amplitude and the number of cycles. An empirical formula is obtained as

$$W/\sigma'_c = 5.4\times10^{1.25\times\log(\Delta W/\sigma'_c)} \quad (7)$$

and superposed on the plots in Fig. 8. This equation may presumably be applicable even to irregular cyclic stresses for in situ liquefaction evaluation to determine threshold seismic wave energy per unit volume for liquefaction.

3. UPWARD SEISMIC WAVE ENERGY EVALUATION

In order to evaluate a liquefaction potential based on the energy-based method, it is necessary to compare the threshold energy for liquefaction given by Eq. (7) with seismic wave energy coming upward at a site during design earthquakes. There may be two methods, (a) and (b), to determine the upward seismic energy.

In the first method (a), seismic energy can be estimated by a simple formula assuming spherical energy radiation of body waves from a source (a causative fault) as

$$E_{IP} = E_{Total} \Big/ \left(4\pi R^2\right) \tag{8}$$

where, E_{IP} is incident energy at a site per unit area (kJ/m^2), R is a distance (m) from a center of energy release. A total energy E_{Total} (kJ) in Eq. (8) to radiate from the center is calculated from an earthquake magnitude M (Gutenberg 1956) as;

$$\log E_{Total} = 1.5M + 1.8 \tag{9}$$

In the energy-based evaluation method proposed by Davis & Berrill (1982), the dissipated energy in liquefiable sand was directly correlated with seismic energy arriving at a site calculated by essentially the same formulas as Eqs. (8) and (9). In their method, however, it was not addressed at which depth the incident energy is given by the equations, or how it transmits upward from deep bedrock to liquefiable sand layer. Instead, the seismic energy thus evaluated was directly compared with liquefaction case histories to empirically draw a boundary separating plots of liquefied and non-liquefied sites on a SPT N-value versus energy charts (Berrill and Davis 1985).

Using vertical array records, Kokusho and Suzuki (2011, 2012) has demonstrated that the upward wave energy E_u starting from a base layer tends to decrease drastically with decreasing ground depth in most sites and the decreasing trend is almost in proportion to the power of 0.70 of the seismic impedance ratio between corresponding soil layers such as;

$$\beta = \alpha^{0.7}: \quad \alpha < 1, \quad \beta = 1.0: \quad \alpha \geq 1 \tag{10}$$

Here, values $\alpha = \left(\rho V_s\right)_i \Big/ \left(\rho V_s\right)_j$ and $\beta = E_{u_i} \Big/ E_{u_j}$ stand for impedance ratio (ρV_s = impedance) and upward energy ratio, respectively, between an upper layer i and a lower layer j at arbitrary levels. Thus the upward energy E_u at a layer shallower than the base layer may be determined from incident energy at the base E_{IP} and the impedance ratio α with respect to the base layer.

In the second method (b), if a site-specific design motion is available, the seismic energy can be evaluated from it based on the multiple reflection theory of SH wave. It is well known that upward and downward SH waves at arbitrary levels can be evaluated from a record at any level (e.g. Schnabel et al. 1972), provided that the soil profile is known and approximated to behave as linear or equivalent linear materials. The upward energy supplied to a liquefiable layer can be calculated from particle velocity of SH wave propagating upward $\dot{u}$ for a time interval, $t = 0 \sim t_1$ (Kokusho and Motoyama 2002) , as

$$E_u = \rho V_s \int_0^t \left(\dot{u}\right)^2 dt \tag{11}$$

In the present paper, the second method using the one-dimensional dynamic response analysis will be employed, assuming the soils behave as equivalent linear materials. In SBM, input earthquake motions are normally defined at a ground surface. In order to compare the results of EBM with the conventional SBM, the input motion is given at a ground surface in the equivalent linear analysis to calculate not only maximum shear stresses for SBM but also upward wave energies for EBM.

In the equivalent linear analysis, a strain-dependent damping ratio D iteratively decided is used in computing dynamic soil response. This indicates that the strain energy W to be evaluated in Eq. (7) can also be determined from ΔW by using the damping ratio D as

$$W/\sigma_c' = \left(\Delta W/\sigma_c'\right)/\left(\pi D\right) \tag{12}$$

This appears to be more consistent with the analysis. Unlike Eq. (7), however, Eq. (12), using hysteretic damping ratio D measured in normal cyclic loading tests for a small to medium strain range, may not properly reflect the energy dissipation on the process to liquefaction. Therefore, Eq. (7) is used in this paper for the strain energy evaluation in liquefying soils.

4. STUDY ON HYPOTHETICAL SAND DEPOSIT

A comparative study is undertaken here in which EBM is applied to a hypothetical site to compare with SBM. A level sand deposit 10 m thick underlain by a stiff base shown in Fig. 9 is considered. The sand is divided into 5 layers, 2 m thick each, numbered 1 to 5 from the top. The top 2 m (L1) is unsaturated with the density ρ_t =1.8 t/m^3 and the lower 8 m (L2 to L5) are saturated with ρ_{sat} =1.9 t/m^3. In Model-A, the sand is uniform with the normalized SPT N-value N_1=8. In Model-B, N_1=8 in the upper three layers (L1 to L3) and N_1=12 in the lower two layers (L4, L5). The corresponding S-wave velocity V_s (m/s) is determined from N-value, calculated from N_1 in Eq. (5), using the next equation (Japan Road Association 2002).

$$V_s = 80N^{1/3} \tag{13}$$

S-wave velocity of each layer is assigned at its middle depth to give V_s-distributions shown in Fig. 9 for the one-dimensional dynamic response analysis.

In order to make an equivalent linear analysis of the hypothetical ground, strain-dependency of shear modulus ratio G/G_0 and damping ratio D for the sand layer are given by the next equations.

$$G/G_0 = \frac{1}{1 + \left(\gamma/\gamma_r\right)^{\alpha}} \tag{14}$$

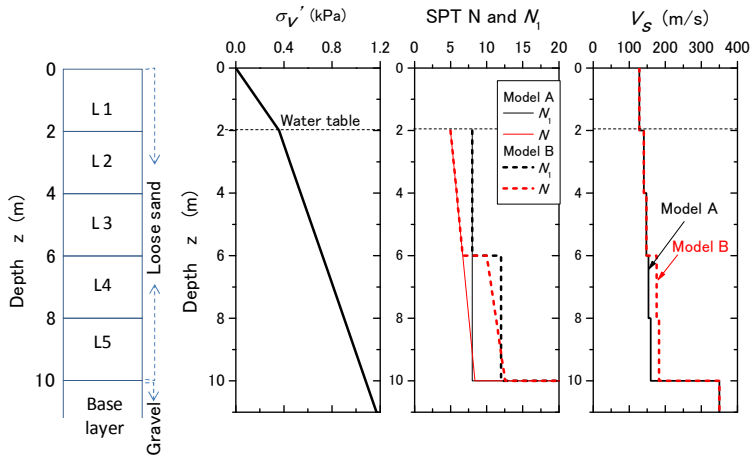


Figure 9 Hypothetical soil models A & B of 10 m thick loose sand underlain by a base layer

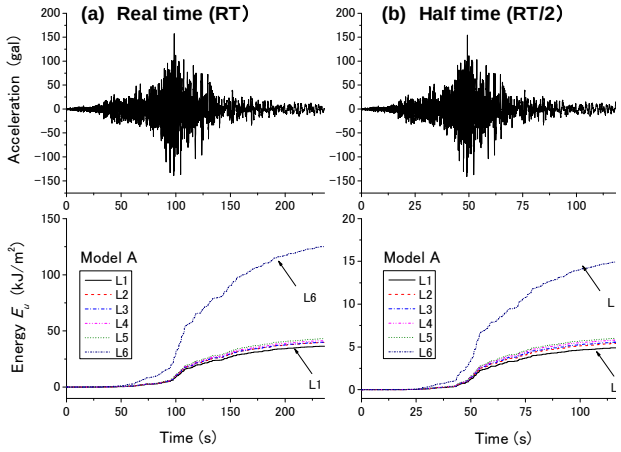


Figure 10 Input acceleration motions at ground surface at K-net Urayasu for the main shock during 2011 Tohoku earthquake (M=9.0) and corresponding upward energies for Real time (RT)(a) and Compressed half-time (RT/2) (b).

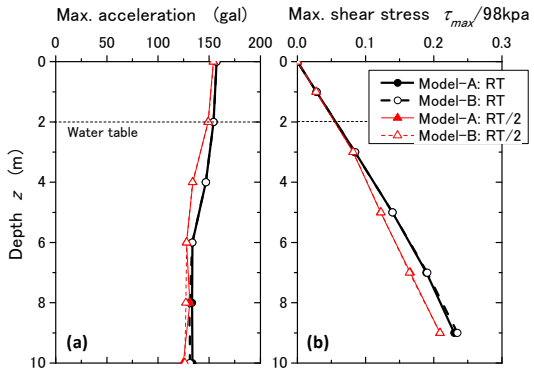


Figure 11 Maximum acceleration (a) and maximum shear stress (b) in the soil models A & B calculated along the depth.

$$\frac{D-D_0}{D_{\max}-D_0}=\left(1-\frac{G}{G_0}\right)^{\beta} \tag{15}$$

These equations are modified versions of the original formulas by Hardin-Drnevich (1972), by introducing power constants α, β as well as initial and maximum damping ratios, D_0 and $D_{\max}$, respectively, to have better fitting with measured data (Kokusho and Motoyama 1998). The reference strain γ_r in Eq. (14) corresponding to modulus degradation $G/G_0 = 0.5$ is proportional to the square root of the effective mean stress σ'_m (Hardin-Drnevich 1972).

A horizontal ground motion obtained during 2011 Tohoku earthquake (M_w=9.0) at a strong motion station, K-net Urayasu (EW direction), shown in the top of Figs. 10 (a) and (b) is given at a surface of the model ground to conduct a 1D equivalent linear analysis using SHAKE (Schnabel et al. 1972). The duration of the motion used in the analysis is 236 s, which covers from P-wave arrival to the end of major contribution of SH-wave. This motion is given either in the real time scale RT (a) with digitized time increment Δt =10 ms (duration 236 s) or in a compressed half time scale RT/2 (b) with Δt =5 ms (duration 118 s). Maximum accelerations and shear stresses along the depth obtained in the analyses for RT and RT/2 in Models-A and B are shown in Fig. 11 (a) and (b), respectively. Both the accelerations and stresses are almost identical in the two models, and slightly smaller for the compressed half time scale (RT/2) than for the real time scale (RT).

4.1 Stress-Based Method (SBM)

In a normal SBM, liquefaction is to occur if a factor F_L expressed in Eq. (16) is lower than unity.

$$F_L = R/L \tag{16}$$

Here in situ cyclic resistance ratio R is determined from R_L corresponding to isotropically consolidated triaxial test specimens as

$$R = R_L\left(1+2K_0\right)/3 \tag{17}$$

using in situ earth-pressure coefficient at rest K_0. Seismically induced cyclic stress ratio L at a certain depth is ob-

tained from the maximum seismic stress ratio $L_{\max} = \tau_{\max}/\sigma'_v$ as

$$L = r_n L_{\max} = r_n \tau_{\max}/\sigma'_v = \tau_0/\sigma'_v \tag{18}$$

The equivalent amplitude of cyclic stress τ_0 is determined by multiplying the maximum stress $\tau_{\max}$ by a constant r_n, where r_n is a reduction coefficient of stresses, $\tau_0 = r_n \tau_{\max}$, to replace a irregular motions with the maximum stress $\tau_{\max}$ to an equivalent sinusoidal motions with a given number of cycles of stress amplitude τ_0 (Seed and Idriss 1971). Here, the stress reduction coefficient r_n is given in the next empirical formula using an earthquake magnitude M proposed by Tokimatsu and Yoshimi (1983).

$$r_n = 0.1(M-1) \tag{19}$$

M=7.5 in Eq. (19) gives r_n =0.65 and if K_0=0.5 is assumed, then the factor F_L becomes as follows.

$$F_L = R/L = \frac{1+2K_0}{3r_n}\frac{R_L}{L_{\max}} \approx R_L/L_{\max} \tag{20}$$

However, if the earthquake magnitude of the 2011 Tohoku earthquake, M=9.0, is considered in lieu of M=7.5, r_n =0.80 in Eq. (19). If K_0=0.5 is used again, then

$$F_L = R/L \approx R_L/1.2L_{\max} \tag{21}$$

In Fig. 12, the R_L-values compare with L_{max} (r_u=0.65) or $1.2L_{max}$ (r_u=0.80) in (a) Model-A and (b) Model-B to evaluate liquefaction potential for RT and RT/2-motions. In Fig. 13, the F_L-value thus evaluated in Eq. (20) or Eq. (21) is illustrated along the depth for the two models.

In Model-A, the cyclic resistance ratio R_L is 0.191 constant in the uniform sand layer with N_1=8 from Eq. (4). For the RT-motion, if the R_L-value is compared in Eq. (20) with the maximum seismic stress ratios L_{max} for r_u=0.65 (M=7.5), F_L≈1.0 in L2 and F_L<1.0 in L3 to L5. If R_L is compared in Eq. (21) with 1.2 L_{max} for r_u=0.80 (M=9.0), F_L becomes still lower and F_L<1.0 in L2 to L5, hence all the saturated sand layers are to liquefy. For the RT/2-motion, though F_L-values become slightly higher, the results are not so much different from the RT-motion. It is noted that, in the uniform soil model (Model-A), the deeper the layer, the lower its F_L-value and the higher its liquefaction potential for both RT and RT/2-motions.

In Model-B, R_L is 0.191 and 0.234 in the upper and lower two layers with N_1=8 and 12, respectively, according to Fig. 8. For the RT-motion, if L_{max} for r_u=0.65 (M=7.5) is compared in Eq. (20) with the R_L-value, F_L<1.0 in L3 and F_L≈1.0 in other layers, indicating that only L3 is to liquefy obviously. If r_u=0.80 (M=9.0) is chosen, then F_L<1.0 in Eq. (21) for all the saturated sand (L2-L5) including the lower layers with higher N_1-values. If the RT/2-motion is considered, F_L≈1.0 for L3 and F_L >1.0 for other layers if r_u=0.65 (M=7.5) is chosen, whereas F_L<1.0 again for r_u=0.80 (M=9.0) similar to the RT-motion.

The above results in SBM may be summarized that the choice of r_u=0.65 or r_u=0.80 tends to have a great effect on the F_L-value, while the difference of input motions, RT or RT/2, seems to have a smaller effect, despite a considerable difference of energy in the two motions as will be mentioned later. It is also pointed out that liquefaction potential tends to be higher in deeper layers than shallower layers in a uniform sand deposit.

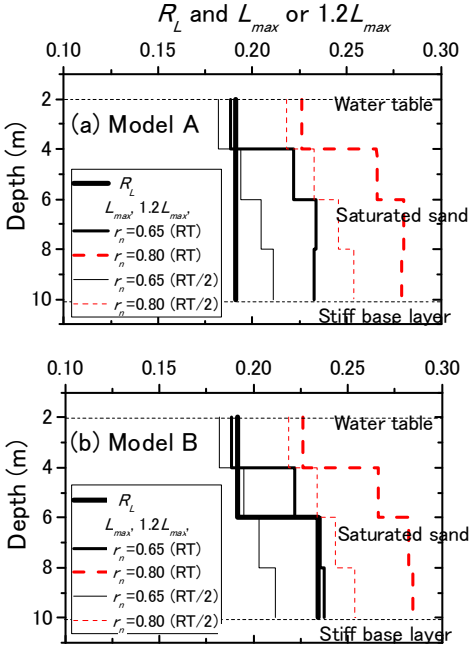


Figure 12 Depth-dependent R_L-profiles compared with L_{max}-profiles for RT & RT/2-motions: (a) Model-A & (b)Model-B

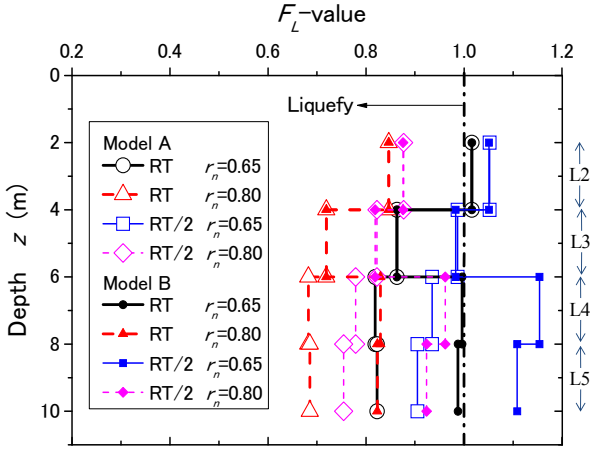


Figure 13 Depth-dependent F_L-profiles in Models-A & B for RT & RT/2-motions obtained by SBM.

4.2 Energy-Based Method (EBM)

Based on the same one-dimensional equivalent linear analyses using the same input motion, upward energies at the top of layers of 2 m thick each were calculated in Models-A and B using Eq. (11). At the bottom of Fig. 10, typical time-histories of upward energies E_u are shown together with the acceleration time histories at the top, for (a) the real time motion (RT), and (b) the compressed half time motion (RT/2), respectively. The energies E_u are not so much different in the sand layers (L1 to L5) after experiencing remarkable reduction at the boundary between the stiff base layer and the loose sand layer. Also note that the energy dramatically decreases if the time scale of the input acceleration is halved (RT/2), because, for the same absolute acceleration $\ddot{u}$, the particle velocity $\dot{u}$ and $(\dot{u})^2$ becomes 1/2 and 1/4 smaller, respectively, and the energy calculated by Eq. (11) for the time duration a half of RT becomes $(1/2)^3$=1/8 smaller. The final accumulated upward energy in each layer at the end of shaking denoted here as E_{uf} will be used in EBM.

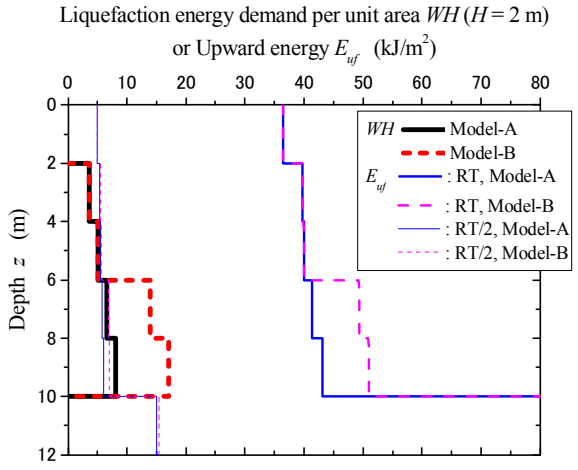


Figure14 Liquefaction energy demand WH compared with Upward energy E_{uf} along the depth in Models-A & B for RT & RT/2-motions

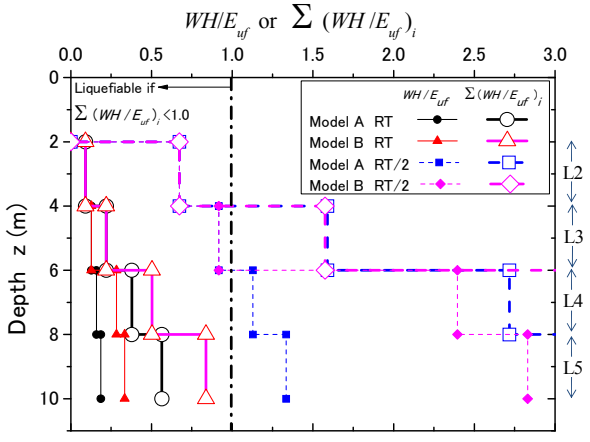


Figure15 Energy ratio WH/E_{uf} or accumulated energy ratio $\Sigma(WH/E_{uf})_i$ along the depth obtained by EBM in Models-A & B for RT & RT/2-motions.

The EBM procedure proposed in this paper to compare with SBM generally consists of following steps.

a) A soil model is divided into layers of a constant thickness H (H=2 m in this paper) in accordance with penetration test data of the same depth interval. The normalized dissipated energy $\Delta W/\sigma_c'$ for a soil of unit volume to liquefy is determined for each layer from penetration test results, using a relationship such as in Fig. 6. For the onset of liquefaction, $\Delta W/\sigma_c'$ corresponding to double amplitude axial strain ε_{DA}=5% in triaxial test data is chosen.

b) The normalized strain energy W/σ_c' given from outside corresponding to $\Delta W/\sigma_c'$ per unit volume of soil to liquefy is evaluated by Eq. (7).

c) Then the strain energy for a layer with a thickness H to liquefy WH (named here as liquefaction energy demand) is calculated. Here, the effective confining stress σ_c' is assumed to be equal to an average mean effective stress in the layer, $\sigma_m' = (1+2K_0)\sigma_v'/3$.

d) Upward energy E_u is calculated at each layer using an equivalent linear one-dimensional wave propagation analysis of a horizontally-layered soil model and the energy at the end of shaking E_{uf} is evaluated.

e) The liquefaction energy demand WH is directly compared with the upward energy E_{uf} in the corresponding layer by calculating an energy ratio WH/E_{uf}. It may well be interpreted that a layer with a smaller energy ratio WH/E_{uf} has higher liquefaction potential than others in a soil profile.

f) The energy ratios of individual layers are numbered sequentially starting from the lowest ratio (i=1) toward higher ones and summed up as $\Sigma\left(WH/E_{uf}\right)_i$.

g) Liquefaction occurs in that sequence and in those layers for which $\Sigma\left(WH/E_{uf}\right)_i$ <1.0, because the upward energy can liquefy individual sand layers in the above-mentioned sequence until it is totally consumed by the energy demands.

In Model-A, the normalized dissipated energy per unit volume to liquefy the uniform sand layer of N_1=8 can be read off from the curve in Fig. 6 corresponding to ε_{DA}=5% as $\Delta W/\sigma_c'$ =0.0281. Then, the corresponding normalized strain energy per unit volume is given as W/σ_c' = 0.0621 from Eq. (7). The liquefaction energy demand WH for H=2 m thick layer to liquefy is calculated using the corresponding average confining stress $\sigma_c' = \sigma_v'(1+2K_0)/3$, assuming the earth-pressure coefficient at rest K_0 is 0.5. In Fig. 14, the liquefaction energy demands WH (thick lines) are shown together with the upward energies E_{uf} along the depth for Models-A and B. As already mentioned, E_{uf} is quite different between the two input motions, RT (thin line) and RT/2 (very thin line).

In Fig. 15, the energy ratios WH/E_{uf} calculated in individual layers is shown along the depth with thin lines plus smaller symbols for Models-A and B. Because the energy ratio WH/E_{uf} is obviously smaller for layers with shallower depths both for RT and RT/2 motions even in the uniform sand deposit (Model-A), liquefaction tends to occur first in L2 and descend in sequence to the deeper layers. The thick

lines with larger symbols in the same figure are the accumulated energy ratio $\Sigma\left(WH/E_{uf}\right)_i$ calculated in the EBM procedure (f) explained above. For the RT-motion shown by thick solid lines, $\sum\left(WH/E_{uf}\right)_i$ <1.0 for the summation from L2 to L5, indicating that the upward energy is enough to liquefy all the saturated sand layers not only in Model-A but also in Model-B. In contrast, for the RT/2-motion shown by thick dashed lines, $\Sigma\left(WH/E_{uf}\right)_i$ <1.0 only for L2 (the shallowest saturated layer), indicating the upward energy is not enough to liquefy other than L2 in the two models. Thus, there exists a clear difference in liquefaction potential between the two input motions, reflecting the tremendous energy reduction in the RT/2-motion as mentioned before.

4.3 Comparison of EBM and SBM

If the results by EBM in Fig. 15 are compared with those by SBM in Fig. 16, the following observations may be made. First, the two results both in Model-A and B appear to be essentially consistent in that all the saturated sand layers are to liquefy by the RT-motion. This consistency gets better if the stress reduction coefficient in Eq. (19) is taken as r_n =0.80 considering the M=9.0 earthquake in SBM. If r_n=0.65 is used as in normal practice considering a smaller magnitude earthquake, the two results disagree partially, because L2 is hard to liquefy in SBM. In EBM, the effect of input motions due to different earthquake magnitude, which has to be considered by choosing the coefficient r_n properly in SBM, is intrinsically included.

The effect of the compressed half-time scale motion (RT/2) is far more evident in EBM because the upward energy E_u reduces to 1/8 of the RT-motion. The reduced upward energy is sufficient to liquefy only L2 both in Model-A and B in EBM. In contrast, the effect is minor in SBM with about 10% change in the seismic stress $\tau_{\max}$ and F_L as well, as indicated in Figs. 11 and 13, respectively. In Models-A and B, all the layers (L2 to L5) are to liquefy if r_n=0.80 is chosen, quite contradictory to the results of EBM. If r_n=0.65 is chosen considering that the RT/2-motion should represent an earthquake magnitude lower than 9.0 because of its shorter duration, only L2 are not to liquefy in Model-A and only L3 is on the verge of liquefaction in Model-B, which are contradictory more or less with EBM, again.

Another significant qualitative difference between the two methods is that liquefaction potential is higher in shallower layers than in deeper layers in a uniform sand deposit (Model-A) in EBM as shown in Fig. 15, whereas it is vice versa as indicated in Fig. 13 in SBM. In shake table liquefaction tests on uniform saturated sand, it is normally observed that liquefaction first starts near the ground surface and then moves down to deeper portion as shaking continues (e.g. Kokusho et al. 1980). This seems to indicate a higher liquefaction potential in shallower depth if sand is essentially uniform as obtained in the EBM evaluation, though more detailed study is needed considering the effects of various soil conditions and input motions.

Thus, a basic procedure of EBM has been developed and applied to soil models to compare with SBM. Further studies on its applicability to case histories with detailed soil investigations and seismic motions are certainly needed to show its reliability in actual site conditions.

5. CONCLUSIONS

In order to develop an energy-based method (EBM) for liquefaction potential evaluation, a series of undrained cyclic triaxial test data was examined from a viewpoint of energy, yielding following major findings;

1) Dissipated energy per unit volume accumulated to a given cycle, ΔW, is almost uniquely correlated with pore-pressure buildup $\Delta u/\sigma_c'$. The ΔW-value is almost proportional to axial strain for each relative density group up to a strain around $\varepsilon_{DA} \approx 10\%$.
2) The ΔW-value thus evaluated is quite insensitive to the number of load cycles N_c to induce a given strain under different cyclic stress ratio R_L, indicating that a R_L-N_c correlation addressed in the stress-based method (SBM) can be interpreted as an equal-energy line.
3) The ΔW-value may be uniquely correlated with a cyclic resistance ratio such as R_{L20} for N_c=20, irrespective of different fines content and soil fabrics. It paves a way to develop a direct relationship between ΔW and N_1 for EBM using a R_L -N_1 curve already available in SBM.
4) The ΔW-value is closely connected with associated strain energy W accumulated to a given cycle in the same soil test data. A correlation between ΔW and W is almost unique despite differences in relative density and fines content, and formulated as Eq. (7).
5) If a soil profile of a site is divided into layers of equal thickness H, the energy demand for each layer to liquefy is expressed as WH using the strain energy W corresponding to the onset of liquefaction. The WH-value thus obtained can be directly compared with upward seismic energy to evaluate liquefaction potential by EBM in the field.

Then, the liquefaction potential of sand deposit of 10 m thick (Model-A: uniform loose sand of N_1=8 and Model-B: loose sand of N_1=8 underlain by sand of N_1=12) was evaluated by EBM to compare with a conventional SBM. An input motion of a M=9.0 earthquake has been given at the ground surface in a real time scale (RT) or a compressed half-time scale (RT/2) to have following major findings.

6) The upward energy of RT-motion is enough to liquefy all the saturated sand layers not only in Model-A but also in Model-B. This evaluation by EBM is apparently consistent with that by SBM using the stress reduction coefficient r_n= 0.80 considering the M=9.0 earthquake. The effect of input motions of larger magnitudes is intrinsically included in the EBM, whereas it has to be considered by choosing proper coefficient r_n in SBM.
7) The effect of the compressed half-time scale motion (RT/2) is far more evident in EBM because the upward energy E_u reduces to 1/8 of the RT-motion. The re-

duced energy is not sufficient to liquefy more than L2 both in Model-A and B in EBM. In contrast, the effect is minor in SBM with only about 10% reduction in seismic shear stress, so that all the layers (L2 to L4) are still to liquefy if r_n=0.80 is chosen, and only L2 is unlikely to liquefy if r_n=0.65 is chosen in Model-A, more or less contradictory to EBM again.

8) A significant qualitative difference is recognized between the two methods that the liquefaction potential is higher in shallower layers than in deeper layers in a uniform sand deposit in EBM whereas it is vice versa in SBM. Observations in previous shake table tests on uniform soil models seem to be more compatible with the evaluation in EBM than SBM.

Thus, EBM seems to highlight some significant aspects of liquefaction potential evaluation from the viewpoint of energy demand versus energy supply, which may not be sufficiently taken into account by SBM. As already demonstrated, dissipated energy can be a good unique parameter to evaluate the pore-pressure buildup and induced strain. The key of the energy-based liquefaction evaluation is how to properly determine the upward energy to compare with the energy demand. In this paper, the upward seismic energy was calculated from one-dimensional dynamic soil response analyses, although it may also be determined in a more simple way from earthquake magnitude, a distance from earthquake energy source and site-specific seismic impedance ratios. More research on actual case histories is needed to improve the energy approach to be more reliable and applicable in actual engineering design.

Acknowledgments

Ex-graduate students Ryo Kato, Fumiki Ito and Yohta Nagao of Civil Engineering Department in Chuo University for past several years who conducted laboratory soil tests and data reduction in terms of energy for this research are appreciated. NIED, Tsukuba Japan, who disseminated valuable K-net data during the 2011 Tohoku earthquake Japan, is gratefully acknowledged. Scholars, Liam Finn, Peter Byrne, Ernest Naesgaard and Russell Green, with whom the present author discussed on how to compare the energies in EBM are also appreciated.

References

Berrill, J. B. and Davis, R. O. (1985), "Energy dissipation and seismic liquefaction of sands: Revised model", *Soils and Foundations*, Japanese Society of Soil Mechanics and Foundation Engineering, Vol.25, No.2, 106-118.

Davis, R. O. and Berrill, J. B. (1982), "Energy Dissipation and Seismic Liquefaction of Sands", *Earthquake Engineering & Structural Dynamics*, Vo.10, 59-68.

Figueroa, J. L., Saada, A. S., Liang, L. and Dahisaria, N. M. (1994), "Evaluation of soil liquefaction by energy principles", *Journal of Geotechnical Engineering*, ASCE, 120 (9), 1554-1569.

Green, R. A. and Terri, G. A. (2005), "Number of equivalent cycles concept for liquefaction evaluations-revisited", *Journal of Geotechnical & Geoenvironmental Eng*., ASCE, Vol.131, No.4.

Gutenberg, B. (1956), "The energy of earthquakes", *Quarterly Journal of the Geological Society of London*, Vol.CXII, No.455, 1-14.

Hardin, B. O. and Drnevich, V. P. (1972), "Shear modulus and damping in soils: measurement and parameter effects", *Journal of SMFD*, ASCE, Vol.98, SM6, 603-624.

Japan Road Association (2002), "Liquefaction potential evaluation method" *Design code for road bridges; Seismic design*, Maruzen Publishing Co. Ltd. , 65-66 (in Japanese).

Kokusho, T. and Motoyama, R. (1998), "Application of equivalent linear analysis to large strain problems (Formulation for strain-dependency of shear modulus ratio and damping ratio", *Proc. of 33rd National Geotechnical Annual Conference*, Japanese Geotechnical Society (in Japanese).

Kokusho, T. and Motoyama, R. (2002), "Energy dissipation in surface layer due to vertically propagating SH wave", Journal of Geotechnical and Geoenvironmental Engineering, ASCE, Vol.128, No.4, 309-318.

Kokusho, T. and Suzuki, T. (2011), "Energy flow in shallow depth based on vertical array records during recent strong earthquakes", *Soil Dynamics & Earthquake Engineering*, Vol. 31, 1540-1550.

Kokusho, T. and Suzuki, T. (2012), "Technical Note: Energy flow in shallow depth based on vertical array records during recent strong earthquakes (supplement)", *Soil Dynamics & Earthquake Engineering*, Vol.42, 128–131.

Kokusho, T., Ito, F., Nagao, Y. and Green, R. (2012), "Influence of non/low-plastic fines and associated aging effects on liquefaction resistance", *Journal of Geotechnical & Geoenvironmental Engineering,* ASCE, Vol.138, No.6, 747-756.

Matsuo, O. (1997), "Liquefaction potential evaluation method and earthquake resistant design", *Kisoko* (in Japanese), Vol.25, No.3, 34-49.

Schnabel, P. B., Lysmer, J. and Seed, H. B. (1972), "SHAKE – A Computer Program for Earthquake Response Analysis of Horizontally Layered Sites", *Report EERC* 72-12, University of California, Berkeley.

Seed, H. B. and Idriss, I. M. (1971), "Simplified procedure for evaluating soil liquefaction potential", *Journal of SMFE Div.* , ASCE, 97 (9), 1249-1274.

Tokimatsu, K. and Yoshimi, Y. (1983), "Empirical correlation of soil liquefaction based on SPT N-value and fines content", *Soils and Foundations*, 23 (4), 56-74.

10CUEE CONFERENCE PROCEEDINGS
10th International Conference on Urban Earthquake Engineering
March 1-2, 2013, Tokyo Institute of Technology, Tokyo, Japan

NUMBER OF EQUIVALENT CYCLIC SHEAR AND EFFECTIVE DURATION FOR SOIL LIQUEFACTION IN TOKYO BAY AREA DURING THE 2011 GREAT EAST JAPAN EARTHQUAKE

Hiroshi Arai[1)]

1) Senior Researcher, Building Dept., National Institute for Land and Infrastructure Management, MLIT, Japan
arai-h92ta@nilim.go.jp

Abstract: Number of equivalent cyclic shear N_{eq} and effective duration t_d for soil liquefaction at two sites in Tokyo bay area are estimated by using one-dimensional effective stress analyses for the 2011 Great East Japan earthquake (M_w = 9.0). Also estimated are those at liquefied and non-liquefied sites for the past earthquakes. On the basis of the estimated results and discussions on their relationships with earthquake magnitude M referring to the previous studies, the following conclusions are made: 1) The N_{eq} and t_d estimated in Tokyo bay area during the 2011 earthquake are about 20-60 and about 25 s, respectively, which might be about 2-6 times larger than those at the liquefied and non-liquefied sites during the past earthquakes. 2) The N_{eq} and t_d values could roughly be predicted for a huge earthquake with magnitude M > 8 by extrapolation of the existing M-N_{eq} and M-t_d relations for the past earthquakes with magnitude M < 8, respectively, those were empirically proposed in the previous studies.

1. INTRODUCTION

During the 2011 Great East Japan earthquake (M_w = 9.0), about 15000 residential houses were significantly settled and/or tilted with either no or slightly damage to their superstructures due to soil liquefaction in Tokyo bay area, where are located about 300-400 km away from the epicenter of the main shock (Ministry of Land, Infrastructure, Transport and Tourism, 2011). In the area, strong ground motions were recorded at a number of observatories during the main shock and aftershocks. The peak horizontal ground accelerations of the main shock were no more than 1.5-2.5 m/s^2 in the area, however, the whole durations of the ground motion records were over 2-3 minutes because of the huge earthquake magnitude.

Many reports have suggested that one of the causes for soil liquefaction in Tokyo bay area during the 2011 earthquake could mainly be due to the long durations of the ground motions during the main shock and subsequent aftershock (e.g., Architectural Institute of Japan, 2011; Tokimatsu *et al*., 2012). To verify that suggestion quantitatively, the number of equivalent cyclic shear N_{eq} and the effective duration t_d for soil liquefaction should properly be evaluated in the area during the main shock. The N_{eq} and t_d are the key parameters to control whether the liquefaction could occur or not in sandy soils at a site during earthquakes (e.g., Tokimatsu and Yoshimi, 1980; Seed *et al*., 1983).

The objectives of this article are to estimate the number of equivalent cyclic shear N_{eq} and the effective duration t_d for soil liquefaction in Tokyo bay area during the 2011 Great East Japan earthquake, and to examine their relationships with the earthquake magnitude M.

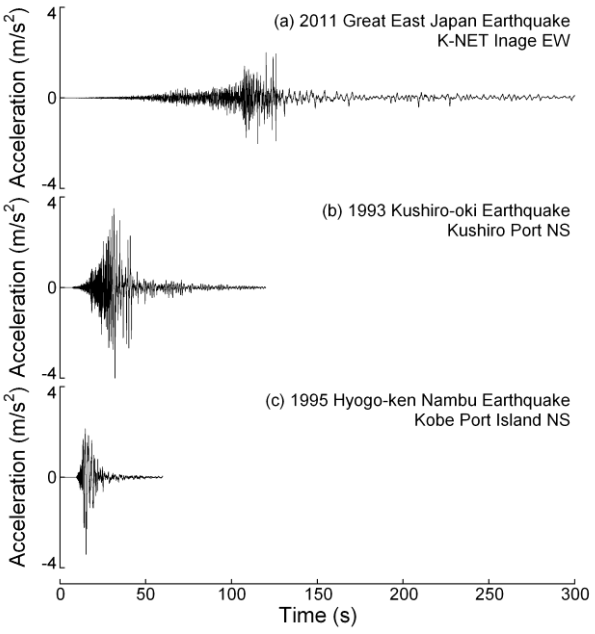


Figure 1 Typical strong ground motion records at liquefied sites in Japan

2. CHARACTERISTICS OF STRONG GROUND MOTIONS IN TOKYO BAY AREA DURING THE 2011 EARTHQUAKE

Figure 1(a) illustrates the acceleration time history of horizontal ground motions recorded at K-NET Inage station located in Tokyo bay area (National Research Institute for

Earth Science and Disaster Prevention, 2011), where sand boil and fountain were observed on ground surface during the main shock and subsequent aftershock. Also shown below the figure (as Figures 1(b) and 1(c)) are typical ones recorded at the liquefied zones in Kushiro and Kobe cities during the 1993 Kushiro-oki and the 1995 Hyogo-ken Nambu earthquakes, respectively (Iai *et al*., 1995; Architectural Institute of Japan, 1995). From the figures, it is revealed that the duration of strong ground motions in Tokyo bay area during the 2011 earthquake is much longer than those at the liquefied zones during the past earthquakes.

In Figure 1(a), the spiky acceleration waveforms are observed at a time of 120-130 s during the main shock. This might be caused due to cyclic mobility of sandy soils in K-NET Inage site. At that time, furthermore, the amplitude and predominant period of acceleration time history change drastically, suggesting that soil liquefaction could have been induced in sandy layers of the site.

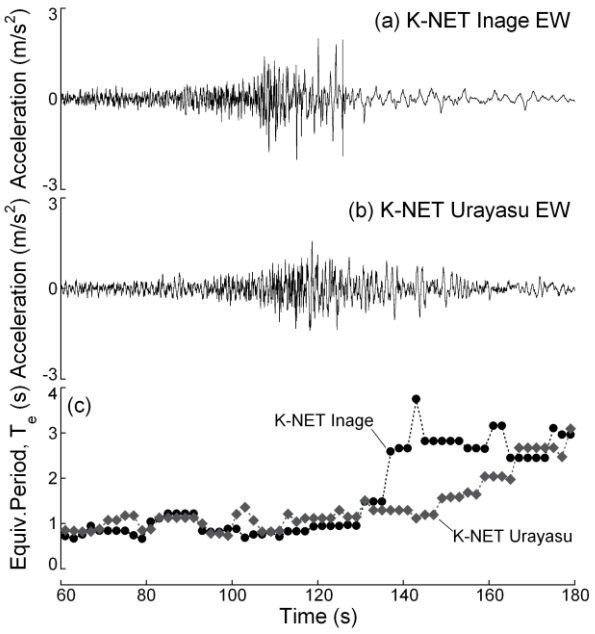


Figure 2 Time histories of acceleration and equivalent predominant period of horizontal ground motions at K-NET Inage and Urayasu stations during the 2011 earthquake

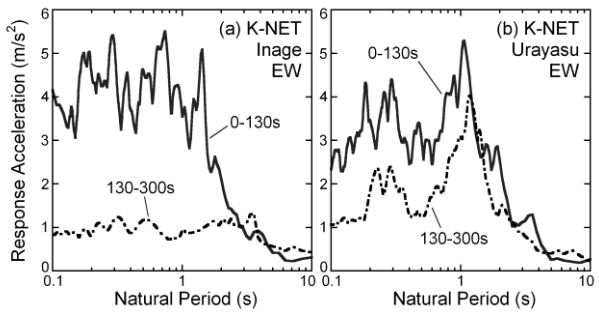


Figure 3 Acceleration response spectra with damping factor of 5 % for horizontal ground motions at K-NET Inage and Urayasu stations during the 2011 earthquake

Figures 2(a) and 2(b) indicate the acceleration time histories of horizontal ground motions recorded at K-NET Inage and Urayasu sites where were liquefied and not, respectively, in Tokyo bay area during the main shock and subsequent aftershock. From the figures, it is again suggested that the horizontal acceleration waveforms on ground could significantly change due to soil liquefaction. The equivalent predominant period at a time t, $T_e(t)$, of the horizontal ground motions recorded for the sites during the main shock are then computed through Eq. (1):

$$T_e(t) = 2\pi \frac{\max\left|v\left(\left|\tau - t\right| < T_w/2\right)\right|}{\max\left|a\left(\left|\tau - t\right| < T_w/2\right)\right|} \qquad (1)$$

in which T_w is the length of time window (= 5 s), $a(t)$ and $v(t)$ are the acceleration and velocity time histories of horizontal ground motions, respectively. In this study, $v(t)$ is determined from $a(t)$ by using the Fast Fourier Transformation (FFT) method.

The computed equivalent predominant period $T_e(t)$ at K-NET Inage and Urayasu sites during the main shock are shown in Figure 2(c). From the figure, $T_e(t)$ at the both sites vary from 1 to 3 s in a duration of 60-180 s, however, their variations with time are not similar. $T_e(t)$ for K-NET Inage site changes drastically at a time of 130-140 s, while that for Urayasu does gradually in the whole duration. Compared among Figures 2(a)-(c), this could be caused due to soil liquefaction occurred in K-NET Inage site (Architectural Institute of Japan, 2011; Tokimatsu *et al*., 2012).

The acceleration response spectra with damping factor of 5 % for horizontal ground motions in durations of 0-130 and 130-300 s are, furthermore, calculated at the both stations for the main shock, and are shown in Figure 3. In the figure, it is again confirmed that the strong ground motion characteristics could have changed drastically at a time of about 130 s in K-NET Inage site because of soil liquefaction.

3. NUMERICAL SIMULATIONS OF DOWNHOLE ARRAY RECORDINGS TO ESTIMATE SHEAR STRESS TIME HISTORIES IN TOKYO BAY AREA

To evaluate the number of equivalent cyclic shear and the effective duration for soil liquefaction at a site during an earthquake, the shear stress time histories of sandy soils at the site should properly be determined for the earthquake, for example, based on a nonlinear dynamic response analysis. In Tokyo bay area, the downhole array recordings during the main shock are available at two sites: Chiba port and Yumenoshima strong ground motion stations (Port and Airport Research Institute, 2011; Bureau of Port and Harbor, Tokyo Metropolitan Government, 2011). At the both sites, the PS velocity logging data and the results of in-situ laboratory tests on nonlinear dynamic properties including liquefaction for undisturbed soil samples are also disclosed (Chiba Port Office, Ministry of Transport, 1997; Ishihara *et al*., 1989). During the main shock and aftershocks, remarks of soil liquefaction, e.g., sand boil, fountain, ground lateral

Table 1 Soil layer model and parameters set for 1-D effective stress analyses at Chiba port site

Layer Thickness (m)	Unit Weight (t/m^3)	S-wave Velocity (m/s)	Soil Type	Ave. N-value	Fines Content	Reference Shear Strain	Maximum Damping Factor	Liquefaction Resistance at 20 Cycles	Inclination of Liquefaction Resistance Line on log-log Plot	Shear Resistance Angle (deg.)	Phase Transformation Angle (deg.)	Relative Density
1.50	1.80	120	Fill			4.E-04	0.22					
1.90	1.80	120	Fine Sand			5.E-04	0.24					
1.13	1.80	220	Fine Sand	13.0	0.065	5.E-04	0.24	0.30	-0.15	39	35	0.70
1.13	1.80	220	Fine Sand	23.0	0.043	5.E-04	0.24	0.60	-0.15	40	36	0.85
1.13	1.80	220	Fine Sand	21.0	0.070	5.E-04	0.24	0.50	-0.15	40	36	0.85
1.13	1.80	220	Fine Sand	21.0	0.104	5.E-04	0.24	0.65	-0.15	40	36	0.85
0.95	1.80	200	Fine Sand	7.0	0.106	5.E-04	0.24	0.24	-0.15	32	29	0.60
0.95	1.80	200	Fine Sand	8.0	0.093	5.E-04	0.24	0.24	-0.15	33	30	0.60
0.95	1.80	200	Fine Sand	5.0	0.116	5.E-04	0.24	0.22	-0.15	30	27	0.55
0.95	1.80	200	Fine Sand	3.0	0.210	5.E-04	0.24	0.22	-0.15	28	25	0.55
1.20	1.60	120	Silty Sand	1.0	0.441	8.E-04	0.22					
1.60	1.60	120	Silt			1.E-03	0.21					
3.00	1.60	120	Clay			2.E-03	0.20					
8.10	1.80	290	Fine Sand			5.E-04	0.24					
4.30	1.60	210	Clay			2.E-03	0.20					
7.92	1.90	420	Fine Sand			5.E-04	0.24					
–	1.90	420										

Water Table: 3.40m

Table 2 Soil layer model and parameters set for 1-D effective stress analyses at Yumenoshima site

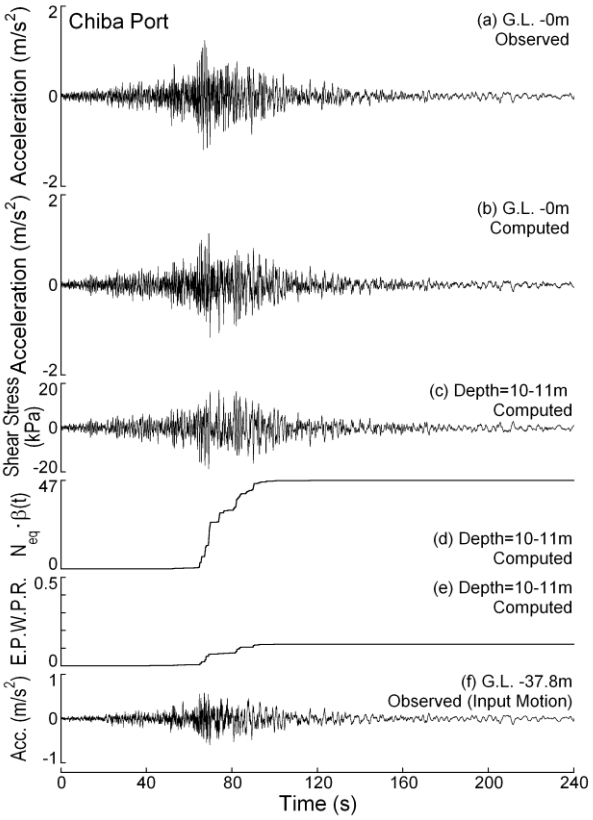
Layer Thickness (m)	Unit Weight (t/m^3)	S-wave Velocity (m/s)	Soil Type	Ave. N-value	Fines Content	Reference Shear Strain	Maximum Damping Factor	Liquefaction Resistance at 20 Cycles	Inclination of Liquefaction Resistance Line on log-log Plot	Shear Resistance Angle (deg.)	Phase Transformation Angle (deg.)	Relative Density
1.10	1.80	230	Sandy Silt			8.E-04	0.23					
4.30	1.80	230	Sandy Silt			8.E-04	0.23					
0.80	1.91	130	Fine Sand			5.E-04	0.24					
2.80	1.91	130	Fine Sand	19.0	0.170	5.E-04	0.24	0.22	-0.17	39	35	0.80
2.30	1.82	170	Fine Sand	20.0	0.070	5.E-04	0.24	0.22	-0.17	38	34	0.70
2.40	1.82	170	Fine Sand	21.0	0.100	5.E-04	0.24	0.22	-0.17	38	34	0.75
1.70	1.82	220	Silty Sand	10.0	0.330	8.E-04	0.23	0.22	-0.17	33	30	0.65
4.60	1.82	220	Silty Sand	11.0	0.330	8.E-04	0.23	0.22	-0.17	33	30	0.65
6.00	1.70	150	Silty Clay			1.E-03	0.21					
14.00	1.50	150	Silty Clay			1.E-03	0.21					
4.20	1.50	170	Silty Clay			1.E-03	0.21					
1.30	1.87	250	Silty Sand			8.E-04	0.23					
4.70	1.69	250	Silt			1.E-03	0.22					
9.30	2.10	560	Sandy Gravel									
14.30	1.87	330	Sandy Gravel									
9.80	1.79	330	Sandy Silt									
5.90	2.10	560	Sandy Gravel									
–	2.10	560										

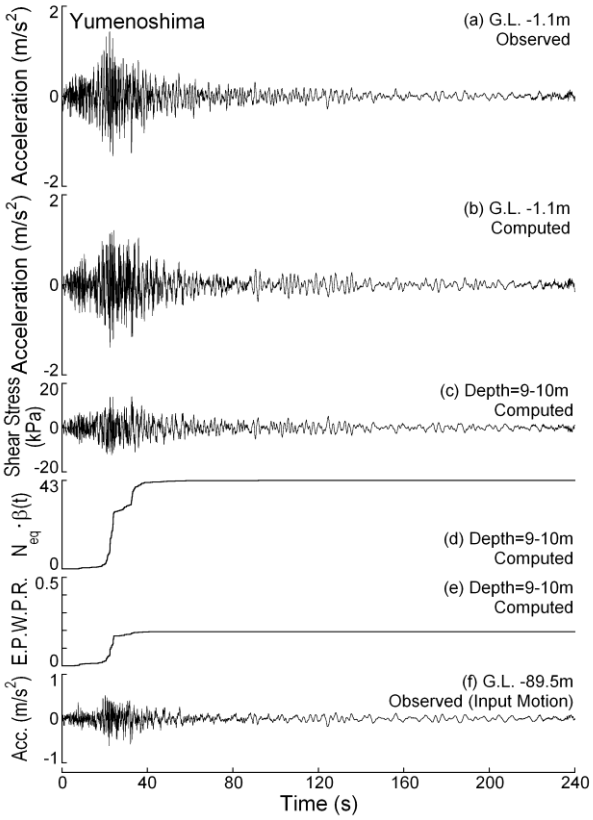
Water Table: 6.20m

deformation and/or settlement, were not observed on ground surfaces at the both sites.

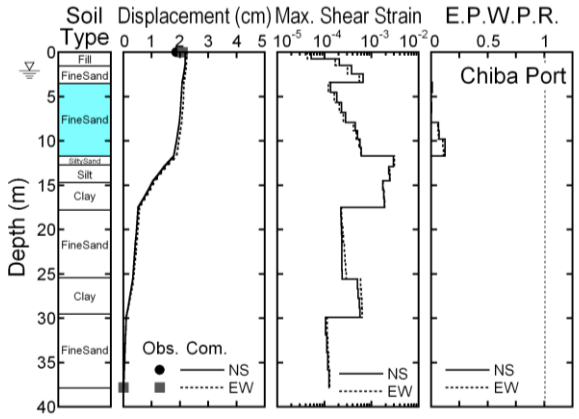
Thus, the one-dimensional (1-D) effective stress analyses are conducted for the soil profiles with the horizontal underground motions recorded at depths of 37.8 and 89.5 m in Chiba port and Yumenoshima sites, respectively, to estimate the shear stress time histories of liquefiable soils in Tokyo bay area during the main shock. The soil layer models and parameters employed in the analyses, which are set from the results of ground investigations stated previously, are listed as Tables 1 and 2 for Chiba port and Yumenoshima sites, respectively. In the analyses, the modified Ramberg-Osgood model is used for presenting the shear stress-strain relations of soils. The constitutive models to compute the excess pore water pressure induced by cyclic shear in sandy soils are those proposed by Shamoto *et al*. (1992, 1997) and Zhang *et al*. (1997), considering the effects of both cyclic mobility and post liquefaction. Further details of the effective stress analyses employed in this study can be found elsewhere (e.g., Shamoto *et al*., 1992).

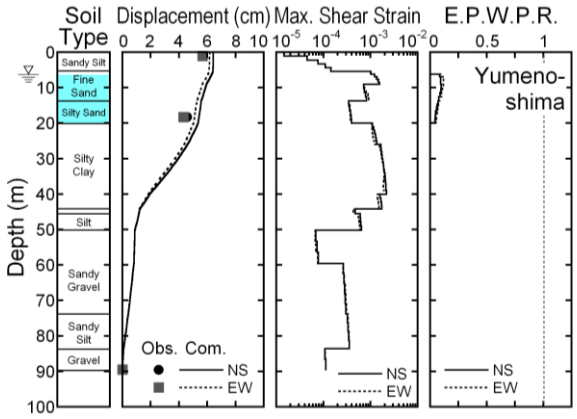
Figures 4 and 5 indicate the acceleration time histories of horizontal ground motions resulted from the effective stress analyses at Chiba port and Yumenoshima sites, respectively, compared to those from the observed records. Also shown in the figures are the time histories of shear stress and excess pore water pressure ratio in the liquefiable sandy layers estimated from the analyses. The variations of maximum values for lateral displacement, shear strain, and excess pore water pressure ratio with depth at Chiba port and Yumenoshima sites are shown in Figures 6 and 7, respectively. In the figures, the estimated ground responses during the main shock are in good agreement with the observed ones at each site. The maximum values of excess pore water pressure ratios are less than about 0.1-0.2 at the both sites, which seem to be consistent with the fact that no liquefaction remarks were observed on ground surfaces at the sites during the main shock. These suggest that the estimated shear stress time histories at the sites could reliably be reasonable.





Figures 4 (Left) and 5 (Right) Time histories of typical ground responses resulted from 1-D effective stress analyses at Chiba port and Yumenoshima sites for the 2011 earthquake (EW direction)





Figures 6 (Left) and 7 (Right) Variations of maximum ground responses with depth resulted from 1-D effective stress analyses at Chiba port and Yumenoshima sites for the 2011 earthquake

4. NUMBER OF EQUIVALENT CYCLIC SHEAR AND EFFECTIVE DURATION FOR SOIL LIQUEFACTION IN TOKYO BAY AREA

4.1 Number of Equivalent Cyclic Shear

Based on the textbook by Yoshimi (1991) and Figure 8, the number of equivalent cyclic shear for soil liquefaction N_{eq} can be computed by using Eq. (2):

$$N_{eq} = \frac{1}{2} N_e \sum_i N_i^{-1} = \frac{1}{2} \tau_e^{\frac{1}{C}} \sum_i \tau_i^{-\frac{1}{C}} \qquad (2)$$

in which τ_e is the effective shear stress (= 0.65× τ_{max}: τ_{max} is the maximum shear stress for a whole time history), τ_i is the peak shear stress at i th half cycle in the time history, and C is the inclination of liquefaction resistance line on a log-log scaled plot showing relationship between number of cyclic shear and shear stress ratio (see Figure 8).

Figures 9(a) and 9(b) illustrate the relationships between the number of equivalent cyclic shear for soil liquefaction N_{eq} and the effective shear stress ratio τ_e/σ'_{m0} computed by using Eq. (2) with the shear stress time histories derived from the effective stress analyses at Chiba

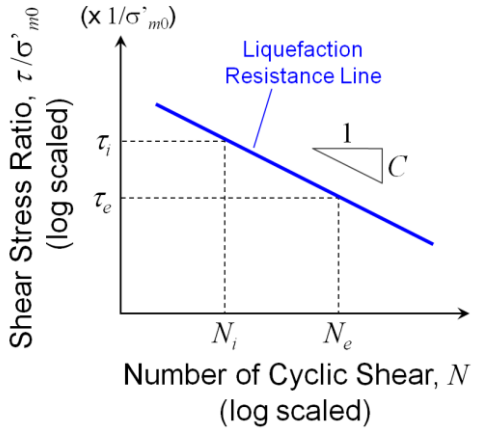


Figure 8 Schematic diagram showing relationship between number of cyclic shear and shear stress ratio on a log-log scaled plot to determine liquefaction resistance line of loose saturated sand under undrained condition

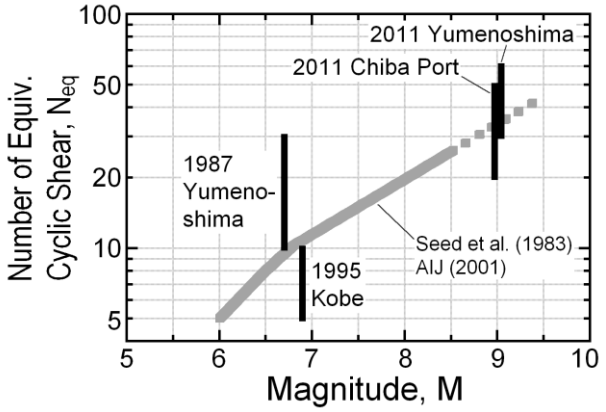


Figure 10 Relationship between earthquake magnitude M and number of equivalent cyclic shear for soil liquefaction N_{eq} resulted from this and previous studies

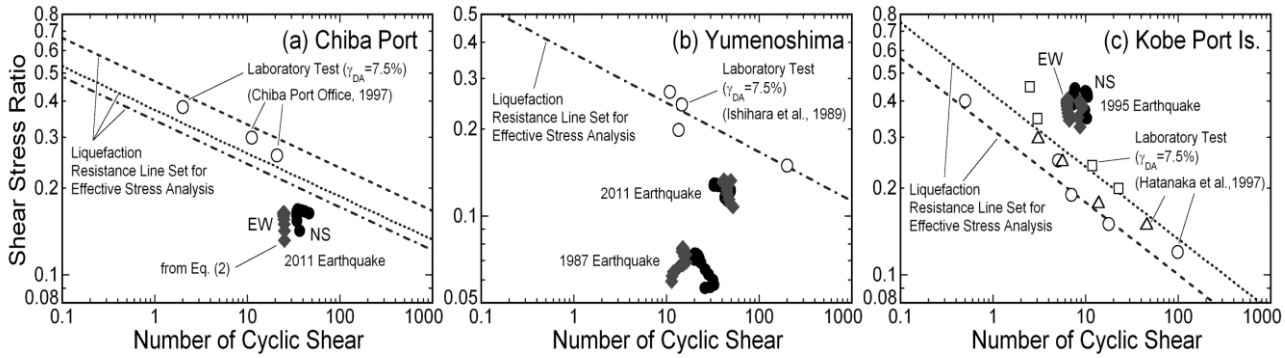


Figure 9 Relationships between number of equivalent cyclic shear for soil liquefaction N_{eq} and effective shear stress ratio τ_e/σ'_{m0} resulted from 1-D effective stress analyses compared to liquefaction resistance data from in-situ laboratory tests at (a) Chiba port, (b) Yumenoshima, and (c) Kobe port island sites

port and Yumenoshima sites, respectively. Also shown in Figures 9(b) and 9(c) are those computed similarly at Yumenoshima and Kobe port island sites for the 1987 Chiba-toho-oki and the 1995 Hyogo-ken Nambu earthquakes, respectively. Subsurface soils at Kobe port island site were heavily liquefied during the 1995 earthquake, while there were no liquefaction remarks on ground surface at Yumenoshima site during the 1987 earthquake (e.g., Architectural Institute of Japan, 1995; Ishihara *et al.*, 1989). Open circles, squares, and triangles shown in Figures 9(a)-(c) indicate the liquefaction resistance data from in-situ laboratory tests for undisturbed sandy soil samples at the sites (Chiba Port Office, 1997; Ishihara *et al.*, 1989; Hatanaka *et al.*, 1997). Comparison of these figures with the ground surface conditions observed during the earthquakes suggests the following:

i. The N_{eq}-τ_e/σ'_{m0} relations estimated from the effective stress analyses in this study are consistent with the facts whether subsurface soils were liquefied or not at the sites during the earthquakes.
ii. The N_{eq} in Tokyo bay area during the 2011 earthquake could be about 20-60, which might be about two times larger than that in the area during the 1987 earthquake.
iii. The N_{eq} in Kobe port island during the 1995 earthquake could be about 5-10, which might be about 1/4-1/6 times smaller than that in Tokyo bay area during the 2011 earthquake.

Figure 10 shows the relationship between the earthquake magnitude M and the number of equivalent cyclic shear for soil liquefaction N_{eq} estimated in this study as vertical black bars. The solid and broken gray lines in the figure indicate the existing M-N_{eq} relation for the past earthquakes with magnitude $M < 8$ (e.g., Seed *et al.*, 1983; Architectural Institute of Japan, 2001) and its extrapolation with a range of $M > 8$, respectively. The M-N_{eq} relation estimated in this study (the distribution of vertical black bars) seems to roughly be consistent with the both solid and broken gray lines. This indicates that the number of equivalent cyclic shear for soil liquefaction N_{eq} could roughly be predicted for a huge earthquake with magnitude $M > 8$ by extrapolation of the existing M-N_{eq} relation for the past earthquakes with magnitude $M < 8$, which was empirically proposed in the previous studies.

4.2 Effective Duration

To evaluate the effective duration for soil liquefaction t_d, Tokimatsu and Yoshimi (1980) have introduced the time history index $\beta(t)$ defined as Eq. (3):

$$\beta(t) = \frac{\text{Cumulative number of equiv. cycles at time } t}{N_{eq}} \qquad (3)$$

The t_d is then determined from the length of time for which the $\beta(t)$ value changes from 0 to 1.

Figure 11 indicates the $\beta(t)$ of the liquefiable sandy soils estimated from the effective stress analyses at Chiba port and Yumenoshima sites for the 2011 earthquake, compared to those evaluated at the liquefied sites for the past earthquakes with magnitude M < 8 (after Tokimatsu and Yoshimi, 1980). In the figure, the effective duration for soil liquefaction t_d in Tokyo bay area during the 2011 earthquake would be about 25 s, while those for the past earthquakes be less than about 10-15 s.

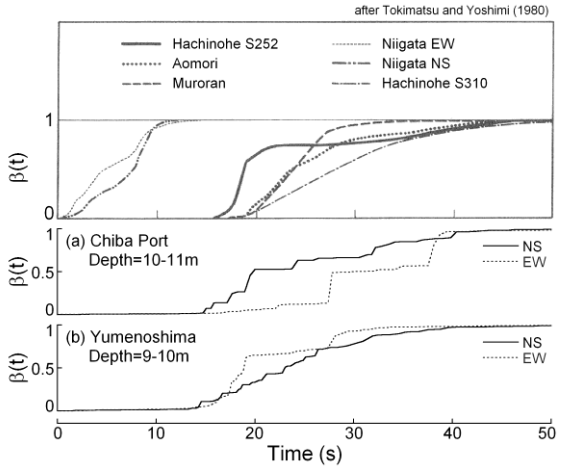


Figure 11 Time histories of cumulative index $\beta(t)$ defined as Eq. (3) to evaluate effective duration for soil liquefaction

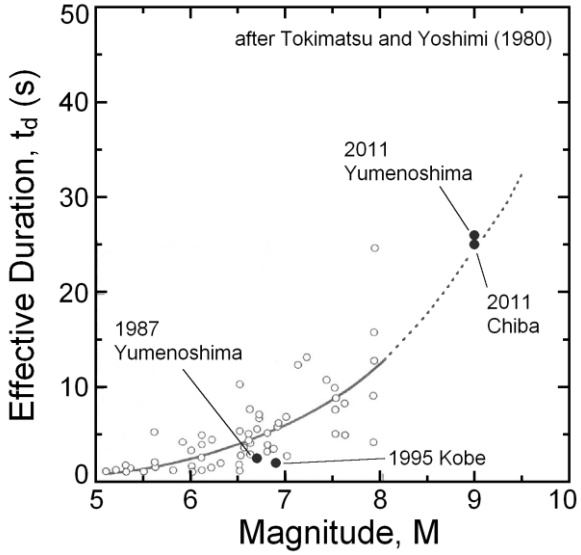


Figure 12 Relationship between earthquake magnitude M and effective duration for soil liquefaction t_d resulted from this and previous studies

Figure 12 shows the relationship between the earthquake magnitude M and the effective duration for soil liquefaction t_d estimated in this study as solid circles. Open circles and solid curve in the figure are the existing M-t_d relational data derived at the liquefied sites for the past earthquakes with magnitude M < 8 and their regression curve, respectively (after Tokimatsu and Yoshimi, 1980). The broken curve with a range of M > 8 is the extrapolation of the existing regression one in the figure. The M-t_d relation estimated in this study (the distribution of solid circles) seems to be consistent with the both solid and broken curves. This also suggests that the effective duration for soil liquefaction t_d might be forecasted for a huge earthquake with magnitude M > 8 by extrapolation of the existing M-t_d relation for the past earthquakes with magnitude M < 8, which was empirically proposed in the previous studies.

5. CONCLUSIONS

The number of equivalent cyclic shear N_{eq} and the effective duration t_d for soil liquefaction at Chiba port and Yumenoshima sites in Tokyo bay area are estimated by using the one-dimensional (1-D) effective stress analyses for the 2011 Great East Japan earthquake (M_w = 9.0). Also estimated are those at Yumenoshima and Kobe port island sites for the 1987 Chiba-toho-oki and the 1995 Hyogo-ken Nambu earthquakes, respectively. Based on the estimated results and discussions on their relationships with earthquake magnitude M referring to the previous studies, the following conclusions are made:

1. The N_{eq} and t_d estimated in Tokyo bay area during the 2011 earthquake are about 20-60 and about 25 s, respectively, which might be about 2-6 times larger than those at the liquefied and non-liquefied sites during the past earthquakes.
2. The N_{eq} and t_d values could roughly be predicted for a huge earthquake with magnitude M > 8 by extrapolation of the existing M-N_{eq} and M-t_d relations for the past earthquakes with magnitude M < 8, respectively, those were empirically proposed in the previous studies.

Acknowledgements:

The earthquake ground motion records used in this study were provided by National Research Institute for Earth Science and Disaster Prevention (NIED), Port and Airport Research Institute (PARI), Bureau of Port and Harbor, Tokyo Metropolitan Government, and Kobe city, Japan. The author would like to express his sincere thanks and appreciation to these organizations.

References:

Architectural Institute of Japan (1995), "Preliminary Reconnaissance Report of the 1995 Hyogo-ken Nambu Earthquake," English Edition.

Architectural Institute of Japan (2001), "Recommendations for Design of Building Foundations," 61-72 (in Japanese).

Architectural Institute of Japan (2011), "Preliminary Reconnaissance Report of the 2011 Tohoku-Chiho Taiheiyo-Oki Earthquake," 530-552 (in Japanese).

Bureau of Port and Harbor, Tokyo Metropolitan Government (2011), http://www.kouwan.metro.tokyo.jp/business/kisojoho/jishindou.html (in Japanese).

Chiba Port Office, Ministry of Transport (1997), "Report on Soil Investigations at Chiba Port," 1-51 (in Japanese).
Hatanaka, M., Uchida, A., and Ohara, J. (1997), "Liquefaction Characteristics of a Gravelly Fill Liquefied during the 1995 Hyogo-ken Nambu Earthquake," *Soils and Foundations*, **37**(3), 107-115.
Iai, S., Morita, T., Kameoka, T., Matsunaga, Y., and Abiko, K. (1995), "Response of a Dense Sand Deposit during 1993 Kushiro-oki Earthquake," *Soils and Foundations*, **35**(1), 115-131.
Ishihara, K., Muroi, T., and Towhata, I. (1989), "In-situ Pore Water Pressures and Ground Motions during the 1987 Chiba-toho-oki Earthquake," *Soils and Foundations*, **29**(4), 75-90.
Ministry of Land, Infrastructure, Transport and Tourism (2011), http://www.mlit.go.jp/ (in Japanese).
National Research Institute for Earth Science and Disaster Prevention (2011), "Strong-motion Seismograph Networks (K-NET, KiK-net)," http://www.kyoshin.bosai.go.jp/.
Port and Airport Research Institute (2011), http://www.eq.pari.go.jp/ (in Japanese).
Seed, H. B., Idriss, I. M., and Arango, I. (1983), "Evaluation of Liquefaction Potential Using Field Performance Data," *J. Geotechnical Engineering*, American Society of Civil Engineers, **109**(3), 458-482.
Shamoto, Y., Tokimatsu, K., and Ariizumi, K. (1992), "Applicability of a One Dimensional Effective Stress Analysis to an Existing Soil Deposit," *J. Structural and Construction Engineering*, Architectural Institute of Japan, **433**, 113-119 (in Japanese with English abstract).
Shamoto, Y., Zhang, J. M., and Goto, S. (1997), "Mechanism of Large Post-Liquefaction Deformation in Saturated Sand," *Soils and Foundations*, **37**(2), 71-80.
Tokimatsu, K. and Yoshimi, Y. (1980), "Effects of Vertical Drains on the Bearing Capacity of Saturated Sand during Earthquakes," *Proc., Int'l Conf. on Engineering for Protection from Natural Disasters*, Asian Institute of Technology, Bangkok, 643-655.
Tokimatsu, K., Tamura, S., Suzuki, H., and Katsumata, K. (2012), "Geotechnical Problems in the 2011 Tohoku Pacific Earthquake," *Joint Conf. Proc., 9th Int'l Conf. on Urban Earthquake Engineering / 4th Asia Conf. on Earthquake Engineering*, Tokyo Institute of Technology, Tokyo, 49-61.
Yoshimi, Y. (1991), "Liquefaction of Sandy Soils," Second Edition, Gihodo Publisher Co. Ltd, 54-59 (in Japanese).
Zhang, J. M., Shamoto, Y., and Tokimatsu, K. (1997), "Moving Critical and Phase-Transformation Stress State Lines of Saturated Sand during Undrained Cyclic Shear," *Soils and Foundations*, **37**(2), 51-59.

10CUEE CONFERENCE PROCEEDINGS
10th International Conference on Urban Earthquake Engineering
March 1-2, 2013, Tokyo Institute of Technology, Tokyo, Japan

EFFECT OF GRAIN SIZE DISTRIBUTIONS ON LIQUEFACTION RESISTANCE FOR A LARGE NUMBER OF LOADING CYCLES

Jun IZAWA[1] and Yoshitaka MURONO[2]

1) Assistant Senior Researcher, Earthquake and Structural Engineering, Structures Technology Division, Railway Technical Research Institute, Japan
2) Manager, Earthquake and Structural Engineering, Structures Technology Division, Railway Technical Research Institute, Japan
izawa@rtri.or.jp, murono@rtri.or.jp

Abstract: This paper describes the results of the hollow cylindrical cyclic torsion shear tests on effects of grain size distributions on liquefaction resistance for a large number of loading cycles, which is considered to affect soil liquefaction due to a long duration earthquake with low acceleration, for example, observed in the Tokyo Bay area in the 2001 Great East Japan Earthquake. The test results clearly show that the tendency of decrease of liquefaction resistance for a large number of loading cycles is influenced by mean grain size, inclination of grain size distribution and so on. Finally, the effect of liquefaction resistance curve characteristics on assessment of liquefaction potential was examined using the cumulative damage theory.

1. INTRODUCTION

Liquefaction of saturated non-cohesion soils was observed in the past severe earthquakes in Japan, such as 1995 Hyogo-ken Nambu earthquake, 1964 Niigata earthquake and so on. Such liquefaction areas were located near the epicentre of the earthquakes, and are considered to have been heavily vibrated by strong earthquake motions. On the other hand, in the 2001 Great East Japan Earthquake, severe liquefaction was observed in the Tokyo Bay area, which is far from the epicenter, and acceleration observed there was less than 200 Gal. One of the possible reasons for such liquefaction due to low acceleration earthquake is considered to be very long shaking duration, which was longer than 300 seconds. Additionally, according to the report of Ino et al. (2011), silty soils with relatively small particle size and relatively gentle inclination of particle size distribution curve, which seem to have relatively large liquefaction resistance as compared with that of layers composed of uniform grain size soils, liquefied in the same area. In view of these aspects, it is considered that liquefaction observed in the Tokyo Bay area in t the 2001 Great East Japan Earthquake might have a relationship with both characteristics of the earthquake and grains size distributions of the layer.

Liquefaction potential is generally assessed with F_L method. F_L method determines factor of safety by comparing the shear stress ratio acting on the soil layer, L and the liquefaction resistance, R. In many case, R_{20} is used as the representative value of liquefaction resistance, which is the shear stress ratio for soils to liquefy by 20 loading cycles with the same stress amplitude in the soil test samples. Effect of characteristics of input earthquakes cannot be considered by the method, which uses R_{20}. Thus, design standard for Japan Highway Bridges (Japan Road Association 2012) uses the correction factor for irregularity of input earthquake, C_w, which is calculated by ccumulative damage degree method (D value) with liquefaction resistance curve of Toyoura sand (Azuma et al. 1997). By using C_w, the liquefaction resistance can be increased against near-field earthquakes, which may have large acceleration and short duration. On the contrary, $C_w = 1.0$ is used for ocean trench earthquakes. This means that R_{20} indicates almost the same resistance mobilized against ocean trench earthquakes, which have relatively low acceleration but long duration. Some researchers studied the value of C_w for ocean trench earthquqkes. Yashiro et al. (2003) suggested $C_w = 0.9$ from the results of the effective stress analyses and assessment of liquefaction potential with the cumulative damage degree. Yoshida et al. (2009) determined $C_w = 0.5$, which was also obtained from the comparative studies between effective stress analyses and assessment of liquefaction potential for 236 grounds. In the design standard for railway structures (Railway Technical Research Institute 2012), effect of characteristics of input earthquakes on soil liquefaction resistance is directly evaluated with cumulative damage degree method for liquefaction layers and the design earthquakes, which is described by Annaki & Lee (1976) for example. The authors verified the applicability of this method from the comparative studies on effective stress analysis and the cumulative damage degree method against some earthquakes (Izawa et al. 2012). Furthermore, it was found that the liquefaction potential against long duration earthquake with low acceleration greatly depends on the accuracy of the liquefaction resistance curve especially for a

large number of loading cycles. This means that not only R_{20} but also the shape of the liquefaction resistance curve should be considered in assessment of liquefaction potential in view of soil characteristics.

In this study, then, a series of hollow cylindrical cyclic torsion shear tests was conducted to investigate the effects of particle size distributions on liquefaction resistance for a large number of loading cycles, which is considered to affect soil liquefaction due to long duration earthquakes with low acceleration.

2. CYCLIC TORSION SHEAR TESTS

2.1 Outline of the tests

A series of hollow cylindrical cyclic torsion shear tests were conducted, especially focusing on the effects of grain size distribution on liquefaction resistance for a wide range of loading cycles, which ranged from about a few cycles to about 1000 cycles. The size of the test pieces was 200 mm in outer diameter, 120 mm in inner diameter and 300 mm in height. After the samples were consolidated with the constraint pressure of 98 kPa (back pressure was 200 kPa), 5 or 6 test data of the liquefaction resistance were obtained. The occurrence of liquefaction was defined as the moment when the shear strain reached 7.5%.

4 soil samples were chosen in this study, which were the samples A, B, C and DL Clay, whose properties are summarized in Table 1. The samples A, B and C were artificially prepared by mixing the Fujinomori Clay with Silica sand No. 6 and 7, to obtain the target particle size distributions. The grain size distributions of Sample A, B and C are plotted in Figure 1, in which the grain size distribution of Toyoura sand is also plotted for comparison. The target grain size distribution of the sample A was set so as to have the smallest mean grain size, D_{50}, and to be the most well-graded soil among the boiled sands taken by Ino et al. The sample B has almost the same shape of grain size distribution as that of the sample A, but its D_{50} is about 0.1 mm larger than that of the sample A. That is, if the grain size distribution of the sample A is moved so as to have larger grain size, the target grain size distribution of the sample B can be obtained. The sample C and Toyoura sand have almost the same D_{50} as that of the sample B, but they are poorly-graded in the order of the sample C and Toyoura sand as shown in Figure 1. Finally, DL Clay has the smallest grain size among all the samples, and poorly-graded equivalent to that of Toyoura sand. The target distributions were obtained in general, although there are some discrepancies between the idealized distribution and the obtained one as shown in Figure1.

Table 2 lists the test cases conducted in this study. Target relative densities, Drs, of the sample A and DL clay, which are as dense as possible by the air pluviation method, are about 90 % and 80 % respectively,. Unit weight of the sample B was set so as to be the same as that of the sample A, resulting in the fact that Dr was 60%. The sample B with relative density of 84% was also made to investigate effect of unit weight. Relative density of the sample C was set at 80%, to obtain almost the same dry density as that of the

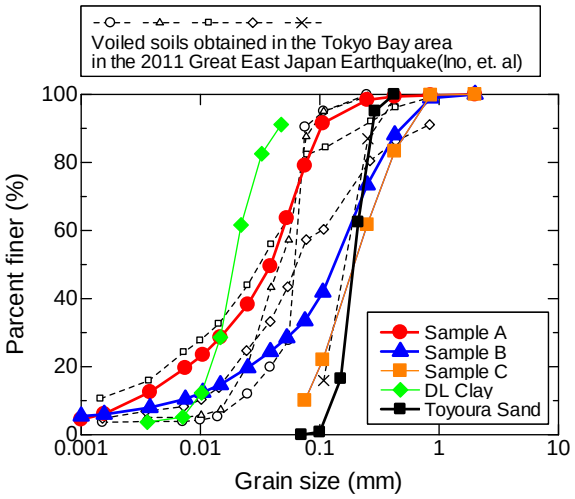


Figure 1 Grain size distributions

Table 1 Properties of the soil samples

Sample	Gs	D_{50}(mm)	Uc	Uc'	Fc(%)	Pc(%)	e_{max}	e_{min}
A	2.62	0.039	17.4	1.82	79.1	15.3	1.50	0.765
B	2.64	0.133	25.9	3.29	33.5	8.90	1.18	0.623
C	2.65	0.190	5.46	1.76	22.0	3.20	1.19	0.635
DL Clay	2.65	0.151	2.81	1.11	99.1	5.70	1.68	0.695
Toyoura sand[4)]	2.65	0.180	1.32	—	0	0	0.989	0.615

Table 2 Test conditions

Test case	Dr(%)	Unit weight (kN/m^3) Dry, γ_d	Unit weight (kN/m^3) Saturated, γ_{sat}	Void ratio
Sample A	91.2	14.1	18.6	0.832
Sample B	60.0	14.0	18.5	0.846
	84.0	15.1	19.2	0.712
Sample C	85.8	15.1	19.2	0.720
DL clay	77.0	13.5	18.2	0.920

sample B(Dr=84%). The test pieces of DL Clay were prepared so as to be as dense as possible. The test results for Toyoura sand conducted by Aono et al. (1986) were used in this study.

2.2 Results and Discussions

Figure 2 shows the relationships between the liquefaction resistance and the number of loading cycles of the samples A, B (Dr=60%) and DL clay, whose dry unit weight are almost the same. Regarding the samples B and C whose average particle sizes, D_{50}, are almost the same, their liquefaction strength curves are shown in Figure 3. Results of Aono et. al. were plotted in the figure for comparisons. It should be noted that the liquefaction resistances of the Toyoura sand were increased by 1.2 times so as to be able to be compared with the results obtained from the torsion shear tests referring to the past study(Tanaka et al. 1999), as these data were obtained from cyclic triaxial tests.

The solid lines in the figures are approximated by the following equation (1) with a liquefaction strength at 20 cycles, R_{20}, and a coefficient α, which are summarized in Table 3.

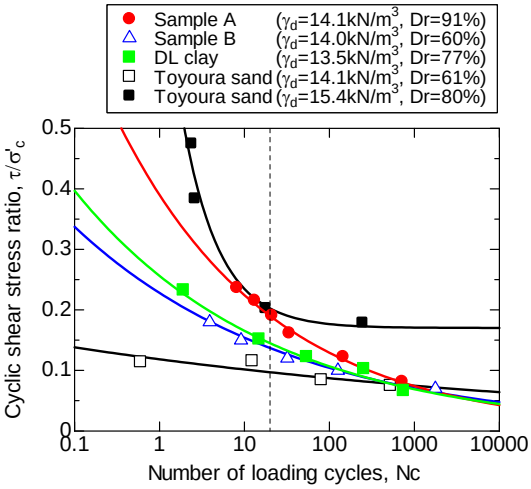


Figure 2 Cyclic shear stress ratio versus number of loading cycles reaching to shear strain of 7.5% for samples with almost the same unit weight.

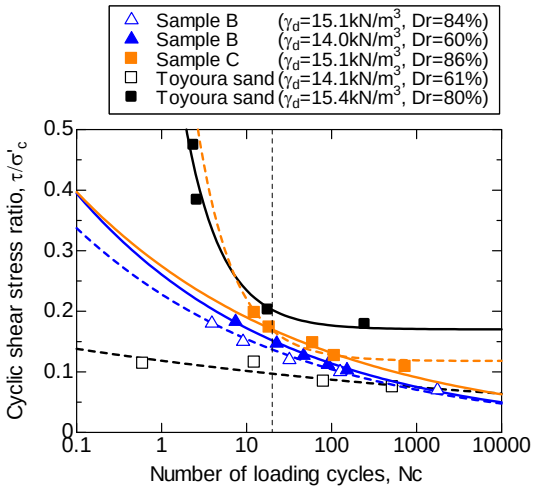


Figure 3 Cyclic shear stress ratio versus number of loading cycles reaching to shear strain of 7.5% for samples with almost the same mean grain size.

Table 3 Summary of the liquefaction tests

	Dr(%)	R_{20}	R_{1000}	α
Sample A	91.2	0.190	0.074	0.24
Sampe B	60.0	0.137	0.070	0.17
	84.0	0.152	0.074	0.18
Sample C	85.8	0.170	0.095*	0.16*
DL clay	77.0	0.145	0.070	0.19
Toyoura sand[4)]	80.0	0.200	0.17	-
	61.0	0.134	0.109	0.05

*The coefficient for approximation with the Equation (1)

$$R_i = R_{20}\left(\frac{N_c}{20}\right)^{-\alpha} \quad (1)$$

As shown in Figure 2, the sample A, which has smaller grain size and the well-graded distribution, shows the largest R_{20} among all the samples, but the liquefaction resistance decreases to almost the same resistance as those of the sample B and DL clay with an increase of loading cycles. On the other hand, Toyoura sand with relative density of 80%, whose R_{20} is almost the same as that of the sample A, did not show decrease after the cyclic number of about 100. Since the liquefaction resistance curve of Toyoura sand with Dr=80% is very different from those of the other samples and could not be fitted with the equation (1), the curve was approximated with a hyperbolic curve, as indicated by the equation (2).

$$R_i = \frac{0.643}{Nc} + 0.171 \quad (2)$$

DL clay, which has very small grain sizes, shows relatively large decrease for a large number of cycles, although it is very poorly-graded soil similar to Toyoura sand. Similarly, the results of the sample B shows relatively large decrease for a large number of cycles as shown in Figure 3, and then the liquefaction resistance curve can be fitted with the equation (1). The results of the sample C, whose properties are in between that of the sample B and Toyoura sand, did not show large decrease, and the liquefaction resistance curve can be fitted with the equation (3) as indicated with broken line in Figure 3.

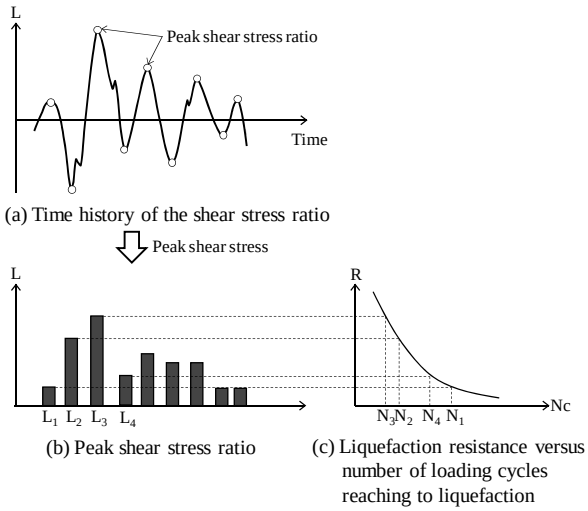


Figure 4 Procedure for determining the *D* value used in the assessment of liquefaction potential.

$$R_i = \frac{1.02}{Nc} + 0.118 \quad (3)$$

There is large discrepancy of liquefaction resistance curves between Toyoura sand with Dr = 80 % and 60%. On the other hand, such large discrepancy cannot be observed between the case of the sample B with Dr = 84% and that with Dr = 60%. It is considered that effect of the relative density on the liquefaction resistance is influenced if the soil is poorly-graded.

3. EFFECT OF LIQUEFACTION POTENTIAL

It is found that the shape of liquefaction resistance curve may be influenced by the grain size distribution of soils. Effect of such difference of the shape of liquefaction resistance curves on liquefaction potential was evaluated by the cumulative damage degree method as it is used in the design of Japanese Railway structures. Procedure of the method is simply explained as follows.

Firstly, the liquefaction resistance for cyclic number of 20, R_{20} is determined from the laboratory tests or estimated with N value indicated in the Japanese railway standard.

Then, the liquefaction resistance curve, which shows the relationship between liquefaction resistance, R_i and number of cycles, N_c can be estimated by the following equations (4) and (5), where relative density, Dr is also estimated from N value.

i) $N_c \leqq 20$

$$R_{(i)} = R_{20}\left(\frac{Nc}{20}\right)^{-1.35\exp(-3.64+0.037\,Dr)} \quad (4)$$

ii) $N_c > 20$

$$R_{(i)} = R_{20}\left(\frac{Nc}{20}\right)^{-0.23} \quad (5)$$

Secondly, peak accelerations at the ground surface are picked up with zero crossing method and peak values of shear stress acting on soil layers are calculated by the following equation.

$$L = (1.0 - 0.015z)\frac{a}{g}\frac{\sigma'_v}{\sigma_v} \quad (6)$$

where L: peak shear stress ratio, z: depth of ground(m), a: surface peak acceleration(Gal), g: garavity(Gal), σ_v:total vertical stress(kN/m^2), σ'_v: effective vertical stress(kN/m^2). The largest peak shear stress ratio, L_{max} is used as the representative shear stress ratio in the assessment. The required cyclic number for the soil to liquefy with each peak shear stress can be obtained based on the liquefaction strength curve as shown in Figure 4. Then, the cumulative damage degree, D is calculated by the equation (7).

$$D = \sum \frac{1}{2Nc} \quad (7)$$

When the cumulative damage degree, D reaches 1.0, it can be considered that the soil layer liquefied. Then, the peak shear stress ratio is repeatedly corrected until D becomes just 1.0. When D is equal to 1.0, the largest peak shear stress ratio, $L'_{\max}$ is set to be R_D, which is the liquefaction resistance corrected with the cumulative damage degree. Finally, the liquefaction resistance, R_L which is corrected in consideration of stress anisotropy in natural ground, is determined by the equation (8).

$$R_L = \frac{1+2K_0}{3} R_D \quad (8)$$

Liquefaction potential can be assessed with the following equation.

$$F_L = \frac{R_L}{L_{\max}} \quad (9)$$

If the $F_L < 1.0$, the ground is assessed as liquefaction ground. Degree of liquefaction of the ground can be evaluated with P_L value obtained by the following equation.

$$P_L = \int_0^H (1 - F_L)(10 - 0.5z)dz \quad (10)$$

where H: length of liquefaction layer (m), z: depth(m), and z is less than 20m. If $P_L \geqq 5$, the ground is assessed as liquefaction ground. If $P_L \geqq 20$, severe liquefaction may occur.

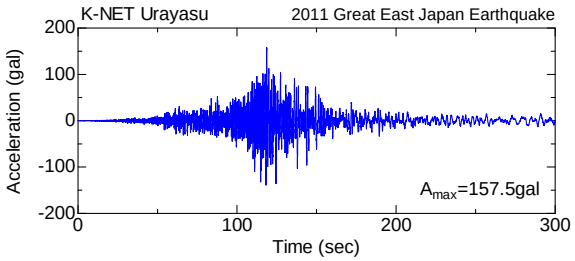


Figure 5 The input wave used for the assessment of liquefaction potential.

Table 4 Results of assessment of liquefaction potential

	Dr	R_{20}	L	R_D	R_L	F_L	P_L
Sample A	—	0.190	0.330	0.290	0.193	0.587	31.0
Sample B	84.0%	0.152	0.310	0.229	0.153	0.494	38.0
	60.0%	0.137	0.323	0.205	0.138	0.426	43.1
Sample C	85.8%	0.170	0.310	0.252	0.168	0.542	34.3
DL clay	77.0%	0.145	0.330	0.220	0.146	0.444	41.7
Toyoura sand	80%	0.200	0.321	0.345	0.230	0.716	21.3

R_D: Liquefaction resistance corrected with the cumulative damage degree.
R_L : Liquefaction resistance corrected in consideration both of stress anisotropy in natural ground and properties of input wave.

In the sensitivity analysis of the liquefaction resistance curve, a layer with depth of 10m composed of sample A or B or Toyoura sand respectively is used. K-NET Urayasu wave shown in Figure 5 is used, which is a typical long duration earthquake with low acceleration observed in the 2001 Great East Japan Earthquake. Table 4 shows the results of the assessment of liquefaction potential. The layer composed of the sample A shows about 20% smaller F_L value than that of Toyoura sand, whose R_{20} is almost the same as that of the sample A. Consequently, about 1.5 times larger P_L value is calculated. Figure 6 shows the liquefaction resistance curve obtained in this study and the time history of peak shear stresses used in determining D value in the assessment. The greater part of the shear stress ratio is under 0.20, which corresponds to about R_{20} of Toyoura sand and Sample A. Therefore, characteristics of the liquefaction resistance for a large number of loading cycles greatly affected to the assessment of liquefaction potential against a long duration earthquake with low acceleration. This result clearly shows that the shape of the liquefaction resistance at a number of cycles may influence liquefaction potential.

4. Summary

This paper describes the effect of grain size distribution on the liquefaction resistance for a large number of loading cycles, which may influence liquefaction potential against a long duration earthquake with low acceleration based on the results of liquefaction resistance tests together with the torsion shear tests. As a result, the following trend can be obtained.

1) Well-graded soils may show large decrease of liquefaction resistances for a large number of loading cycles, even although they can have a large liquefaction

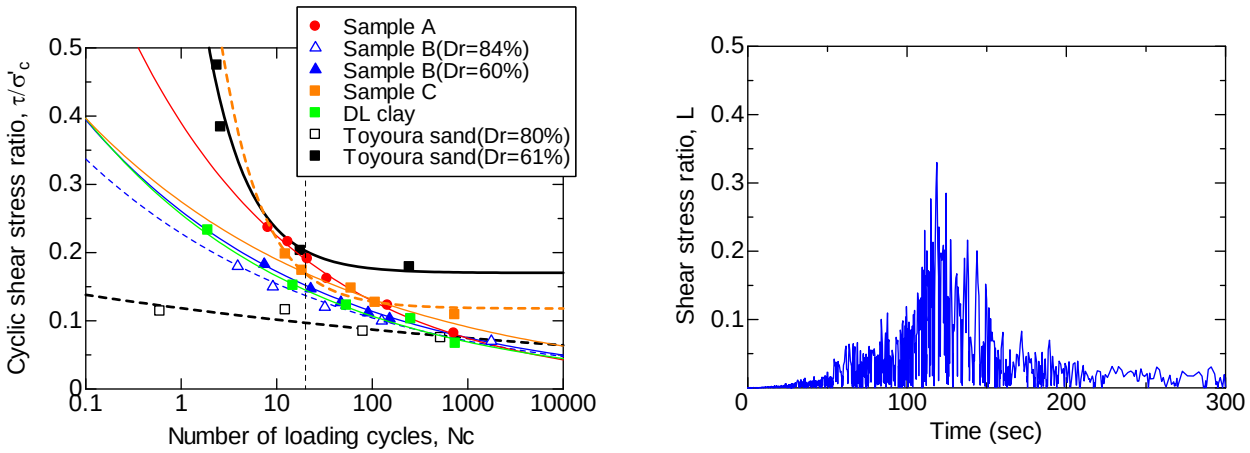


Figure 6 Cyclic shear stress ratio versus number of loading cycles reaching to shear strain of 7.5% and shear stress ratio used for assessment of liquefaction potential.

resistance at 20 loading cycles, R_{20}. Additionally, effect of relative density on the liquefaction resistance curve is small if the soil is well-graded.

2) Poorly-graded soils with relatively large particle size didn't show large decrease of liquefaction resistances for a large number of loading cycles. On the other hand, poorly-graded soils with small particle size may show decrease of liquefaction resistances for a large number of loading cycles.
3) Difference of the liquefaction resistance curve for a large number of loading cycles may affect results of assessment of liquefaction potential by the cumulative damage degree method.

AKCNOWLEDGEMENT

The K-NET record used in this paper was observed by the National Research Institute for Earth Science and Disaster Prevention.

References:

Annaki, M. and Lee, K. L. (1976), "Equivalent uniform cycle concept for soil dynamics", Journal of Geotechnical Engineering, Vol. 103, No. GT6, pp. 549-564.

Aono, T., Miura, S., Toki, S. and Yamashita, S. (1986), "The limit liquefaction resistance of saturated soils", Proceeding of the 41th Annual Conference of Japanese Society of Civil Engineering.(in Japanese)

Azuma, T., and Tamura, K. (1997). Estimation of the Liquefaction Strength Considering Ground motion Characteristics, Doboku Gijutu Siryo, Vol. 39-9, pp. 50-55. (in Japanese)

Ino, K., Yasuda, S., Watanabe, T., Aoyagi, T. and Ozawa, N.(2011), "Investigation of liquefaction occurred at the Tokyo Bay area in the 2011 Great East Japan Earthquake", Proceeding of the 66th Annual Conference of Japanese Society of Civil Engineering.(in Japanese)

Izawa, J., Tanoue, K. and Murono, Y. (2012), "Soil Liquefaction due to Long Duration Earthquakes with Low Acceleration", Proc. of the 15th World Conference on Earthquake Engineering, Paper No. 2075.

Railway Technical Research Institute. (2012). "The Design Standards for Railway Structures and Commentary (Seismic Design)", Supervised by Ministory of Land, Infrastucture and Transportaion, Maruzen. (in Japanese)

Japan Road Association. (2012). *Specification for Highway Bridges*. (in Japanese)

Tanaka, Y., Matsumoto, M., Kawashima, A. and Kawasaki, K. (1999), "Comparison of Liquefaction Strengths as Obtained from Triaxial Test and Torsional Hollow Cylinder Test", Report of the Research Center for Urban Safety and Security in the Kobe University, Vol. 3, pp. 129-135. (in Japanese)

Yashiro, K., Sugito, S., Yashima, A., Furumoto, Y. and Uzuoka, R.(2003), "On the assessment of Liquefaction potential in consideration of duration of seismic wave", Proceeding of the 27th Japanese Workshop on the Earthquake Engineering, Paper No. 111. (in Japanese)

Yoshida, N., Ohya, Y., Sawada, S. and Nakamura, S. (2009), "Simplified procedure for evaluating liquefaction potential under ocean trench type long period earthquake", Journal of the Japan Association for Earthquake Engineering, Vol. 9, No. 3, pp. 28-47. (in Japanese)

10CUEE CONFERENCE PROCEEDINGS
10th International Conference on Urban Earthquake Engineering
March 1-2, 2013, Tokyo Institute of Technology, Tokyo, Japan

COMPARISON BETWEEN DAMAGE DISTRIBUTION AND ESTIMATED LIQUEFACTION POTENTIAL IN CHIBA CITY

Toru Sekiguchi[1)], and Shoichi Nakai[2)]

1) Assistant Professor, Dept. of Urban Environment System, Chiba University, Japan
2) Professor, Dept. of Urban Environment System, Chiba University, Japan
tsekiguc@faculty.chiba-u.jp, nakai@faculty.chiba-u.jp

Abstract: Liquefaction potentials estimated by some methods based on boring logs were compared with damage distribution of sand boiling in Mihama ward of Chiba city. Horizontal surface displacements estimated by simplified method are in roughly good agreement with damage distribution of sand boiling. Despite the fact that horizontal surface displacements estimated by integrating shear stress calculated by equivalent linear analysis are totally small, those seem to correlate with damage distribution of sand boiling.

1. INTRODUCTION

The 2011 Tohoku earthquake (MW 9.0) that struck the east area of Japan on March 11 caused Tsunami and extensive damage. In Mihama ward of Chiba city that is located in the east of Tokyo, more than 300 km away from the epicenter and consists entirely of reclaimed ground along Tokyo Bay, a huge number of liquefaction damage, such as sand boiling, ground deformation and floor incline of buildings including 23 fully destroyed houses, occurred, and strong motions at the grounds with peak ground accelerations (PGA) of more than 3 m/s^2 were recorded.

Although small sand boiling was found on the main road, narrower streets inside a block were almost completely covered with sand boiling as thick as 45 cm. One of the interesting phenomena, however, is that there are some no-damage blocks right next to heavily damaged blocks.

The objective of this study is to compare the damage distribution and estimated liquefaction potential based on boring logs in Mihama ward of Chiba city.

2. LIQUEFACTION DAMAGE DISTRIBUTION

The liquefaction damage distribution was surveyed on public roads in Mihama ward immediately after the earthquake from March 12 to 20 (Sekiguchi and Nakai, 2012). The target area of the investigation is all the public roads and parks which could be entered in the ward. The damage of sand boiling is classified into 3 levels ; heavy, minor and none.

Figure 1 shows distribution of sand boiling using 50 m square grids. Heavy sand boiling is densely distributed in coastal area when compared to inland area. On the other hand, there are some districts where little sand boiling was found in coastal area.

3. ESTIMATED LIQUEFACTION POTENTIAL

3.1 Simplified Method

Horizontal surface displacements due to liquefaction (D_{cy}) were estimated for 540 boring logs in the ward based on simplified method (AIJ, 2001). The peak ground acceleration was set with 2.5 m/s^2 based on strong motion record in the ward. The magnitude of earthquake was set with 9.0. Because almost all boring logs have no data of

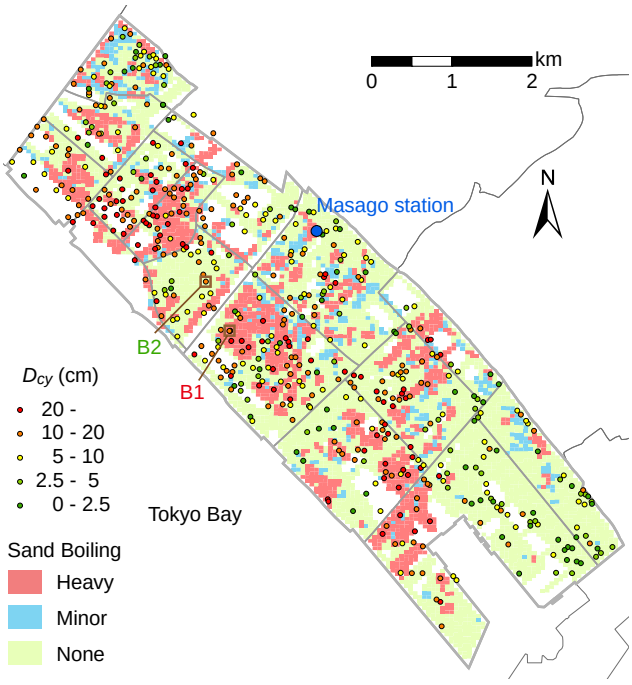


Figure 1 Distribution of Sand Boiling and Estimated Horizontal Surface Displacements due to Soil Liquefaction

soil test, fine fraction contents (F_c) of each layer were set depending on the soil type based on reference (Yamanaka et. al,2010). Minimum F_c of sand is supposed to be 10 % corresponding to fine sand.

In figure 1, estimated horizontal surface displacements for boring logs are also plotted by circle. The displacements in heavy damage area tend to be relatively large.

Figure 2 shows frequency distribution of estimated horizontal surface displacement classified into three liquefaction damage level of the surrounding area. At area with heavy damage of sand boiling, about 80 % of estimated displacements are more than 10 cm. On the other hand, about 60 % of estimated displacements are less than 10 cm at area with none damage.

3.2 Method with Equivalent Linear Analysis

The shear wave velocity structure models of surface soils were made using boring logs in Mihama ward. The one-dimensional shear wave velocity profiles to a depth of engineering bedrock were estimated based on 314 boring logs. The shear wave velocities were estimated from the soil types and *N*-values by empirical equations in Chiba prefecture (Nagata et al. 2008).

One-dimensional equivalent linear dynamic response analyses with frequency dependent damping (Schnabel at al., 1972, Sugito et al., 1993) were conducted using the estimated soil profiles from boring logs. The nonlinear dynamic soil properties used for the analysis are based on the study by Imazu and Fukutake (1986). The acceleration record of the EW component at Masago station shown in Figure 1 during the Tohoku earthquake was used as the input ground surface motion to compute the outcrop bedrock motion at the engineering bedrock layer.

Calculated shear stresses of sand layers were used as $(\tau_{max})_d$ for simplified method estimating horizontal displacement. Figure 3 shows distribution of estimated horizontal surface displacements using shear stress calculated by equivalent linear analysis. A tendency same as figure 1 is seen.

Figure 4 shows frequency distribution of estimated horizontal surface displacement using shear stress calculated by equivalent linear analysis. The tendency seems to be same as figure 2.

Figure 5 shows boring logs, estimated shear wave velocity profiles, depth distribution of shear stress ratios, factor of safety for liquefaction (F_L), and shear strain calculated from equivalent linear analysis at B1 with heavy damage and B2 with no damage in figure 1. At B1 with heavy damage, there are soft sand layers to the depth of 6 m, and factor of safety for liquefactions are low around a depth of 5m. The estimated horizontal surface displacement is, therefore, relatively large. At B2 with no damage, although there is no soft sand layer to a depth of 8m, estimated displacement is not so small. The reason is that shear strains at a depth from 8 to 18 m might affect the surface displacement. Liquefaction at such a large depth, however, might not affect damage at ground surface such as sand boiling.

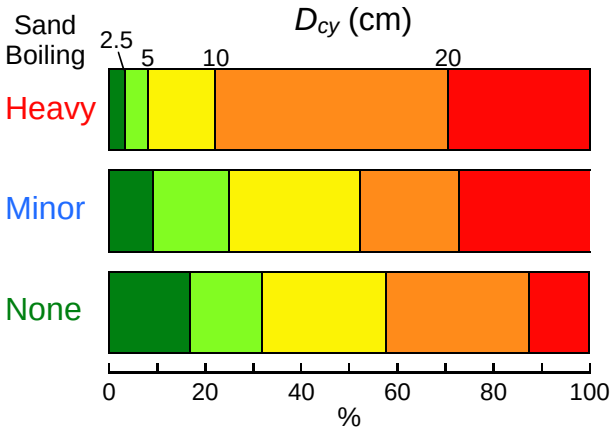


Figure 2 Frequency Distribution of Estimated Horizontal Surface Displacements due to Soil Liquefaction



Figure 3 Distribution of Estimated Horizontal Surface Displacements using Shear Stress Calculated by Equivalent Linear Analysis

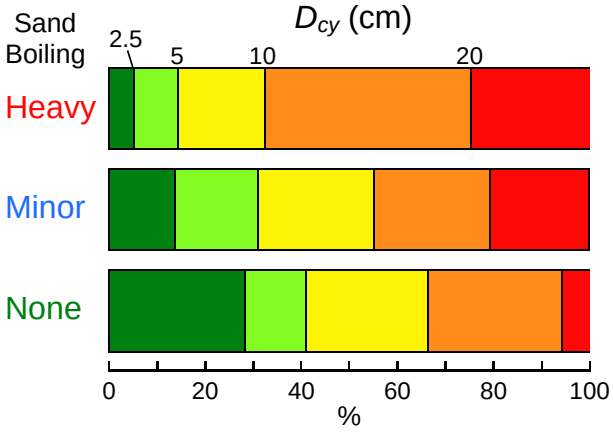


Figure 4 Frequency Distribution of Estimated Horizontal Surface Displacements using Shear Stress Calculated by Equivalent Linear Analysis

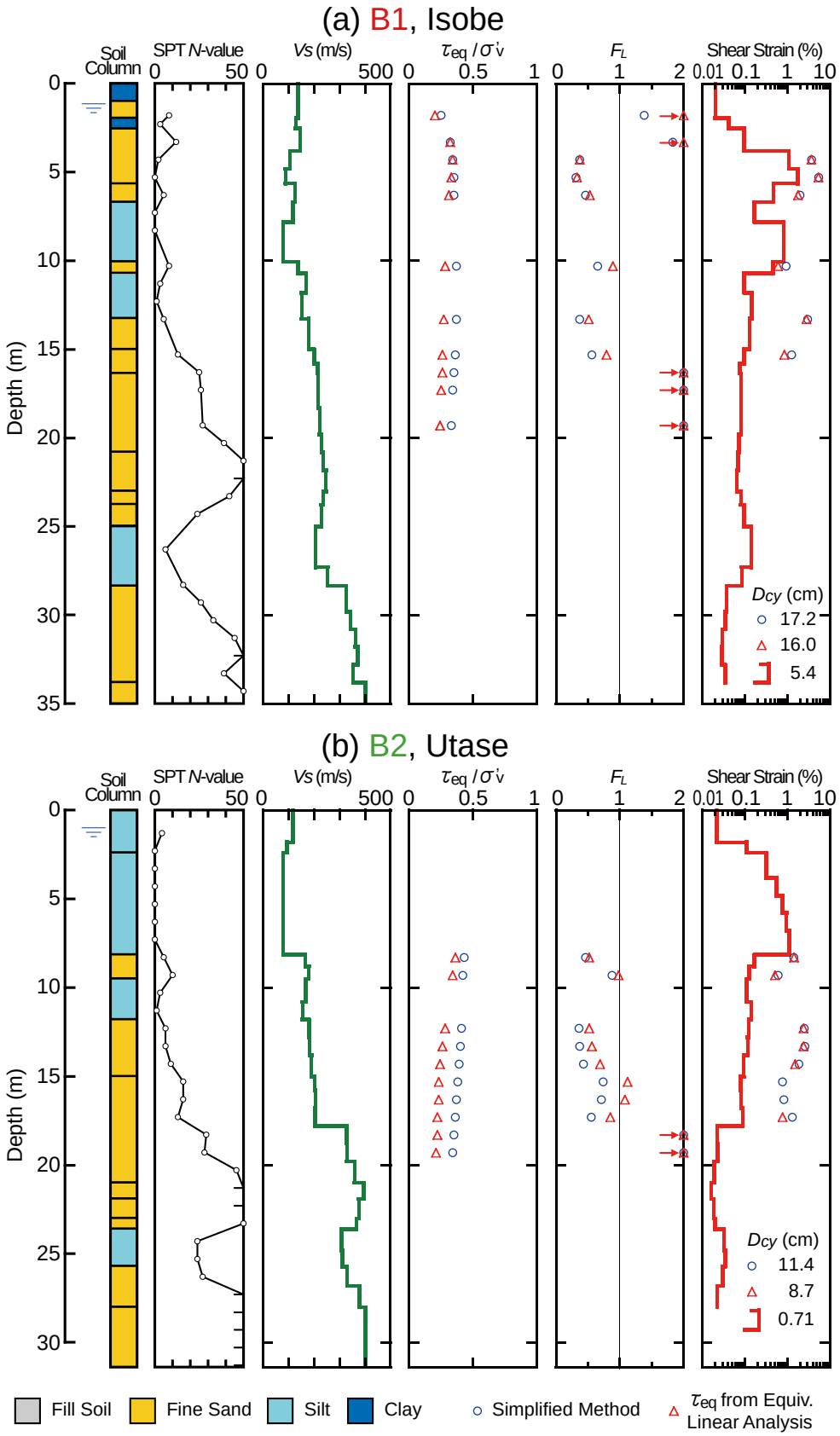


Figure 5 Boring Logs, Estimated Shear Wave Velocity Profiles, Depth Distribution of Shear Stress Ratios, Factor of Safety for Liquefaction (F_L), and Shear Strain Calculated from Equivalent Linear Analysis at B1 and B2



Figure 6 Distribution of Estimated Horizontal Surface Displacements by Integrating Shear Strain of Sand Layers

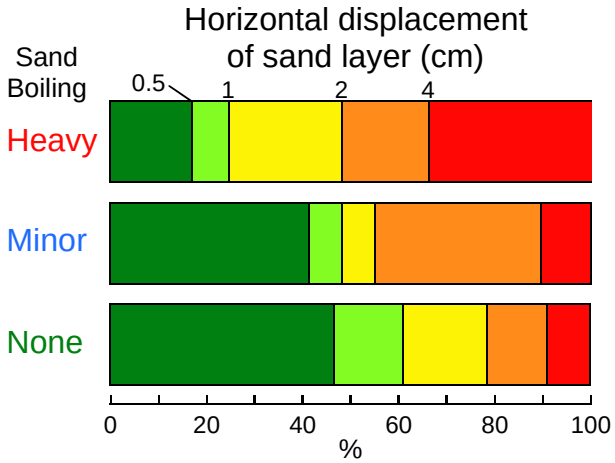


Figure 7 Frequency Distribution of Estimated Horizontal Surface Displacements by Integrating Shear Strain of Sand Layers

3.3 Integration of Shear Strain from Equivalent Linear Analysis

In terms of shear strain in figure 5, those at sand layers around a depth of 5 m at B1 are relatively large, and those at sand layers at B2 are small. Horizontal surface displacements were estimated by integrating the shear strain of sand layers calculated by equivalent linear analysis.

Figure 6 shows distribution of estimated horizontal surface displacements by integrating the shear strain of sand layers. Figure 7 shows frequency distribution of estimated horizontal surface displacement by integrating the shear strain of sand layers. At points with large displacement estimated by simplified method in spite of no damage such as B2, displacements become relatively small. Despite the fact that estimated displacements are totally small, those seem to correlate with damage distribution of sand boiling.

4. CONCLUSIONS

Liquefaction potentials estimated by some methods based on boring logs were compared with damage distribution of sand boiling in Mihama ward of Chiba city. The following conclusions can be made through this study:

1. Horizontal surface displacements estimated by simplified method are in roughly good agreement with damage distribution of sand boiling.
2. Despite the fact that horizontal surface displacements estimated by integrating shear stress calculated by equivalent linear analysis are totally small, those seem to correlate with damage distribution of sand boiling.

Acknowledgements:

The boring data and the strong motion records at Masago station were provided by Chiba city and Chiba prefecture.

References:

Sekiguchi, T., and Nakai, S. (2012), "Liquefaction Damage Distribution in Mihama Ward of Chiba City during 2011 Tohoku Earthquake," *Proc. of the 15th World Conference on Earthquake Engineering*, 10pp.

Architectural Institute of Japan (2001), "Recommendations for Design of Building Foundations," 61-66 (in Japanese).

Yamanaka, H., Tokimatsu, K., Ohmachi, T., Morikawa, H., and Midorikawa, S. (2010), "Evaluation of Earthquake and Tsunami Hazard," Asakura Publishing Co., Ltd., 24 (in Japanese).

Nagata, Y., Nakai, S., and Sekiguchi, T. (2008). "S-Wave Velocity of Surface soils in Northwest Region of Chiba Prefecture, " Jounal of Technology and Design, Architectural Institute of Japan **14**(28), 429-432 (in Japanese).

10CUEE CONFERENCE PROCEEDINGS
10th International Conference on Urban Earthquake Engineering
March 1-2, 2013, Tokyo Institute of Technology, Tokyo, Japan

DYNAMIC BEHAVIOR OF A STRUCTURE ON DESATURATED SAND UNDER RELATIVELY LONG SHAKING

Jiro Takemura[1)], Ippei Yoshimura[2)], and Tatsuya Yamanashi[3)]

1) Associate Professor, Department of Civil Engineering, Tokyo Institute of Technology, Japan
2) Engineer, CTI Engineering Co. Ltd. Tokyo, Japan3
3) Graduate Student, Department of Civil Engineering, Tokyo Institute of Technology, Japan
jtakemuri@cv.titech.ac.jp,ip-yoshimura@ctie.co.jp, yamanashi.t.ab@m.titech.ac.jp

Abstract: A series of centrifuge model test has been conducted to investigate the dynamic behavior of the desaturated sand with a super structure under relatively long period shaking. In the centrifuge tests, two desaturation methods were employed, one is lowering and raising ground water table, which can make wider desaturation area, and the other air injection with a limited desaturation area under the structure. A shaking table test of the model was conducted to discuss the effects of shaking time and method of desaturation.

1. INTRODUCTION

Liquefaction is a phenomenon commonly observed in saturated sandy soils at almost every past moderate to large earthquakes. Since liquefaction has caused serious damage to many structures, a large number of researches have been conducted, particularly for the development of its countermeasures, for example, sand compaction piles as a densification method, deep cement mixing as a solidification method, and gravel drains as a method for excess pore pressure dissipation. However, these countermeasures are often costly and difficult to apply due to surrounding environment especially for the long or large scale structures, such as coastal dykes and housings in residential area. Considering these limitations, soil desaturation has been considered as an inexpensive liquefaction countermeasure without large disturbance in the environment in its execution.

The degree of saturation, S_r, has a significant effect on liquefaction resistance (Yoshimi et al, 1989; Okamura et al., 2006; Okamura and Soga, 2006; Ueno et al., 2008). Entrapped air in the soil is considered to be utilized for an economical countermeasure against liquefaction in suppressing the buildup of excess pore water presure, if the air bubbles in the pore of the soil introduced by the desaturation process can be sustained below ground water table.

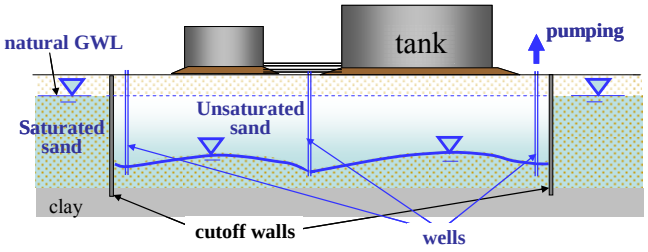
Okamura and Soga (2006) found a unique relationship between the liquefaction resistance ratio (R_u/R_s, where R_u and R_s are liquefaction resistance of unsaturated and saturated soils respectively) and the potential volumetric strain, ε_v^* as given in the following equations:

$$R_u/R_s=\log(6500\varepsilon_v^*+10) \qquad (1)$$

$$\varepsilon_v^* = \frac{\sigma_c'}{p_0+\sigma_c'}(1-S_r)\frac{e}{1+e} \qquad (2)$$

where σ_c', p_0, e denote effective confining pressure, absolute pressure of the pore fluid and void ratio of soil respectively.

Centrifuge modeling has been used as a useful approach in the study of soil liquefaction, especially for verification of countermeasures against liquefaction (e.g., Kimura et al, 1995). In particular, considering eq.(2), the dependence of effective confining pressure on the stress level implies that the effect of the degree of saturation cannot be represented



Figire1(a) Desaturation of liquefiable soils by groundwater lowering.

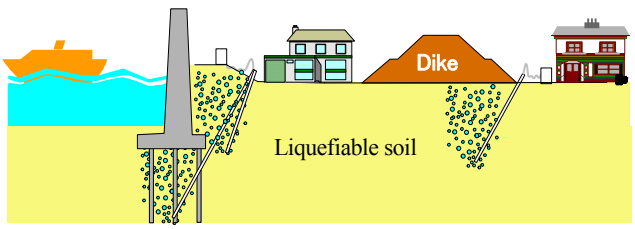


Figure1(b) Desaturation of liquefiable soils by air injection.

Table 1 Properties of silica sands used

	No.8	No.3
Specific gravity: G_s	2.65	2.56
Mean particle size: D_{50} (mm)	0.100	1.47
Particle size: D_{10} (mm)	0.041	1.21
Coefficient of uniformity: U_c	2.93	1.26
Max. void ratio: e_{max}	1.333	0.971
Min. void ratio: e_{min}	0.703	0.702
Permeability coef.: k (m/sec)	2.0×10^{-5}	4.6×10^{-3}
(k in prototype scale with 50g)	(1.0×10^{-3})	(2.3×10^{-1})

well in small scale models under laboratory floor conditions.

From a series of centrifuge model tests, Takemura et al. (2009, 2010, 2012) confirmed that soil desaturation is effective as a liquefaction countermeasures. The methods of soil desaturation considered by Takemura are air injection and groundwater lowering and raising respectively as illustrated **Figures 1**. However, the shakings applied in these models were relatively short about 15sec in a prototype scale under 50g. The dynamic behavior of desaturated sand subjected to a long seismic motion, like the one observed in the 2011 Earthquake off the Pacific Coast of Tohoku has not been well studied.

In this study, an attempt was made to prepare partially saturated model sand by the two methods, i.e., lowering and raising ground water table and air injection. The former method can make wider desaturation area with over-consolidation history, while the latter one makes the desaturation area limited under the structure. A shaking test was then conducted for the desaturated sand with a gravity type footing by applying relatively long sinusoidal shaking motion of 1 minute in a prototype scale. From the test results, discussed are dynamic behavior of the desaturated sand during the long shaking motion and the applicability of soil desaturation as a liquefaction countermeasure.

2. CENTRIFUGE MODEL TESTS

2.1 Soils used in the tests

Silica sand No.8 was used to make the model ground and Silica No.3 was for the drainage layer beneath the model ground. Properties of the sands are given in **Table 1**. Water was used for pore fluid in the model. Silica sand No.8 is fine sand with relatively small permeability. Although the permeability in a prototype scale under 50g is 50 times larger when water is used, it is still small enough to create liquefaction phenomena in the model. As seen in **Figure 2**, this fine sand has high residual degree of saturation and can hold air bubbles in the pore to make a relatively small degree of saturation in submerged condition especially under large buoyancy force in high centrifugal accelerations.

Figures 3 show liquefaction curves of Silica sand No.8 obtained from cyclic triaxial tests. The effect of decreasing S_r from 100% to 90 is similar to that of increasing D_r from 60 to 80% (Figures 3(a) and (b)). Overconsolidation also has the effect of increasing liquefaction strength (Figure 3(c)). It should be noted that the changes of relative density by the

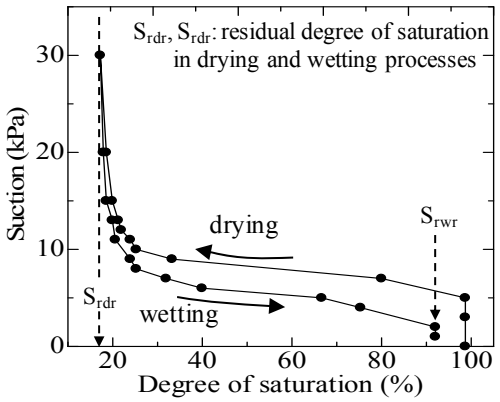


Figure 2 Capillary pressure and degree of saturation curve : Silica sand No.8.

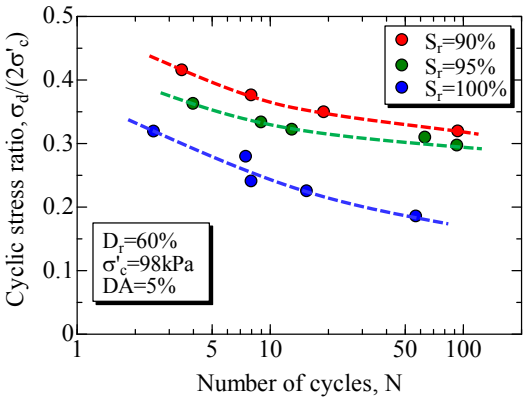


Figure3(a) Liquefaction curves of silica sand No.8: effects of degree of saturation.

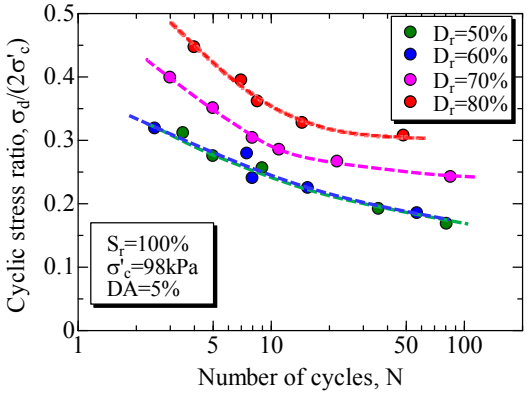


Figure 3(b) Liquefaction curves of silica sand No.8: effects of relative density.

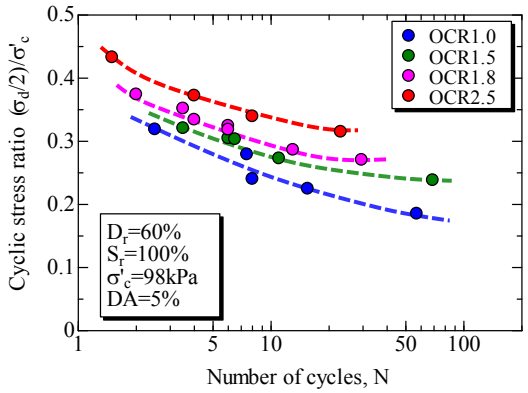


Figure3(c) Liquefaction curves of silica sand No.8: effects of over-consolidation.

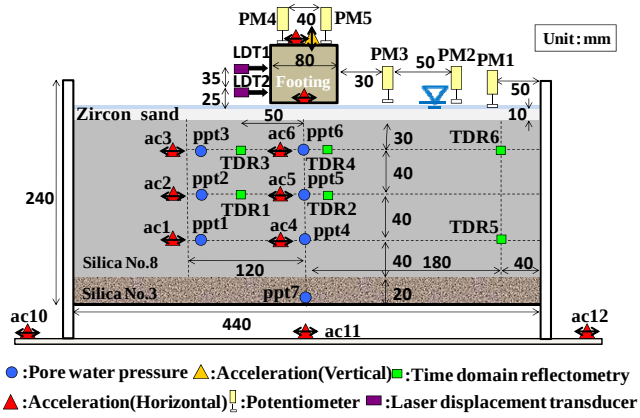


Figure 4 (a) Test setup and implementations of centrifuge model test.: Ground water lowing (GWL) case.

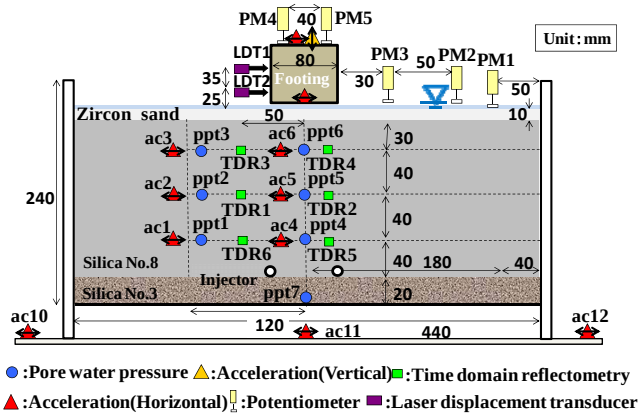


Figure 4 (b) Test setup and implementations of centrifuge model test.: Air Injection (AI) case.

desaturation and the preconsolidation with relatively large pressure are both very minute and the increases of the strength should be exclusively introduced by the effect of air in the pore and the overconsolidation respectively.

2.2 Model preparation

A laminar type shear box made of aluminum with inner sizes of 440mm in width, 150mm in length and 240mm in depth (Kimura et al, 1995) was used in the tests. Test setups employed are shown in **Figures 4**. In the model preparation Silica sand No.3 was first placed as the bottom drainage layer by compaction with a wooden rod. Then, layer of dry Silica sand No.8 was made by air pluviation in a loose condition (Dr=64%). 10mm thick Zircon sand was laid on the top surface of the model ground to give the surcharge pressure of 10kPa in 50g. A model footing made of solid aluminum with the dimensions of 80mm in width, 80mm in height and 150mm in breadth was then placed on the center of the ground surface carefully. Mass of the footing is 2.5kg, giving the base contact pressure, p_f=100kPa in 50g. The model ground was fixed on a mechanical type shaker (Kimura et al, 1988) and then put into a vacuum tank with the shaker to saturate the sand by introducing deaired water from the bottom of the box. After saturating the sand, the shaker was then mounted on Tokyo Tech Mark III Centrifuge and displacement sensors were placed at locations shown in **Figures 4(a) and (b)**. Having completed the test setup, the centrifugal acceleration was gradually increased up to 50g.

2.3 Test cases and shaking tests

a) Saturated model

As a reference of the desaturated model, shaking test was conducted for saturated model sand without desaturation process.

After confirming the equilibrium condition of the model sand in 50g, a shaking test was conducted by applying a sinusoidal motion using the shaker in about 1.0 second with the frequency of 40Hz (**Figure 5**). The prototype duration and frequency of the input motion are 50sens and 0.8 Hz respectively. During the shaking test, accelerations, excess

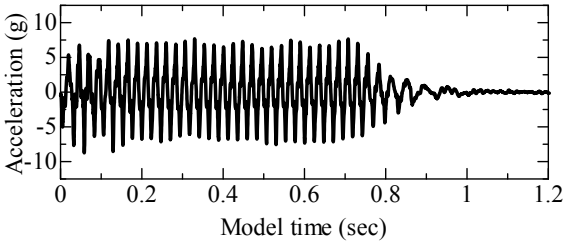


Figure 5 Input base acceleration of the centrifuge test.

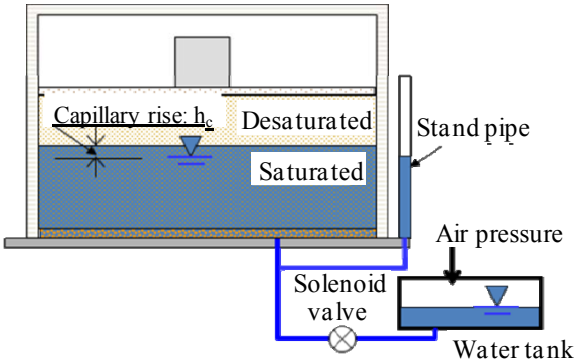


Figure 6(a) Desaturation process by ground water lowing and rising: GWL.

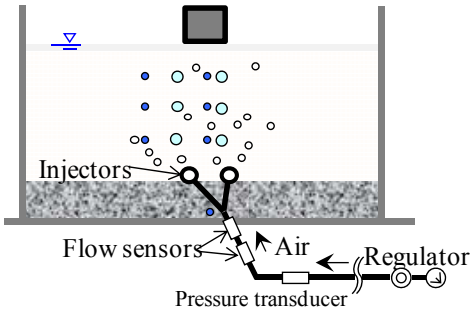


Figure 6(b) Desaturation process by air injection: AI .

pore water pressures and settlements were measured by the sensors shown in **Figure 4(a)**.

b) Desaturation by lowering and raising ground water (GWL)

In 50g, the water was drained from the bottom to the water tank by opening the solenoid valve (**Figure 6(a)**). The valve was closed when the groundwater level (GWL) in the standpipe lowered to the bottom of the Silica sand No.8 layer. Achieving a stationary reading in the Time Domain Reflectometry (TDR) sensor, the water was recharged from the bottom by applying air pressure to the water tank and opening the valve.

Confirming no change in the reading of TDR sensors and PPTs after the water table recovered to the original level, a shaking test was conducted by applying the same input motion as the saturated case.

c) Desaturation by air injection (AI)

In 50g field, the air was injected through the injector by increasing air pressure gradually. This injector is made by porous ceramics, which produces very minute air bubbles. Air pressure transducer and flow sensors were positioned along pressure line as shown in **Figure 6(b)**.

Air pressure transducer provided continuous measurements of the air pressure at the bottom of test box prior to the onset of injection. Flow sensors measured the rate of injected air. The air injection was stopped when TDR sensors reached a stationary state.

Confirming no reading change in TDR sensors and PPTs after stopping air injection, the shaking was conducted as described earlier.

Conditions of test cases are summarized in **Table 2**.

Table 2 Test cases and conditions

Test code	Saturated	GWL	AI
Relative density: Dr	64%	64%	64%
Desaturated area	Non	whole	Below footing
Degree of saturation	100 %	89-95 %	95-98 %
Input accel. amplitude	8g	8g	8g

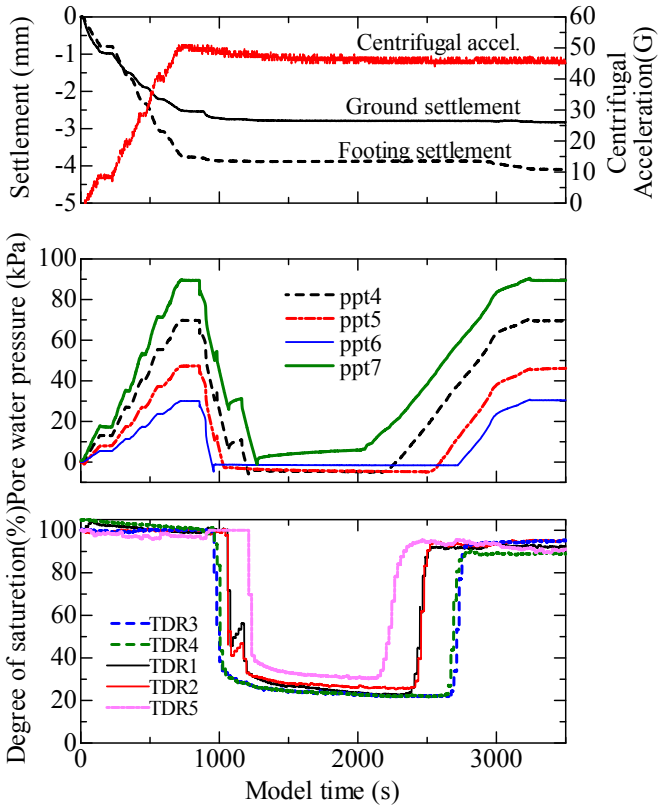


Figure 7 Variation of settlement, pore water pressure and degree of saturation in G-increase and desaturation process: GWL.

3. TEST RESULTS AND DISCUSSIONS

In the following discussion, test results are given in prototype scales except for **Figures. 7, 8 and 9.**

3.1 Desaturation process

1) Lowering and raising groundwater (GWL)

Figures 7 show observed settlements, pore water pressures and degrees of saturation observed during the desaturation process of GWL. Depth profiles of the minimum S_r and the S_{r_res}, which were observed during and after desaturation process, are depicted in **Figure 9**. The degrees of saturation in the desaturation process were calculated from the water volumetric content measured by TDRs assuming full saturation before lowering the water table. For the case of GWL, S_{r_res} was observed to increase with depth. By lowering the GWL, S_r decreased to about 20% and plateaued to 87% to 92% after the GWT returned to its original position.

R_u/R_s estimated by equations (1) and (2) with σ_c', p_0 and e, together with those for different S_{r_res}s range from 1.8 to 2.2. The liquefaction resistance increased with a decrease in the degree of saturation. For the same S_{r_res}, R_u/R_s increases with depth due to the effects of effective confined pressure. But this effect could be cancelled by the increase of S_{r_res} with depth for the GWL case, giving the less variation of R_u/R_s with depth. On top of that, it should be noted that the sand was overconsolidated by the increase of effective unit weight in GWL process and suction induced by the desaturation to the relatively small S_r (see **Figure 2**). Considering the high suction with smaller S_{r_min} and smaller vertical stress σ_c', it is expected that the overconsolidation ratio was larger at the shallow depth than the deep depth.

2) Air injection (AI)

Figures 8 shows the variation of injection pressure and air flow rate with time in the AI case. Observed variations of S_r are also shown in the figure.

Observed S_{r_min} and S_{r_res} of AI case are shown in **Figure 9**. The minimum degrees of saturation of AI case were much higher compared to those of GWL case. As a

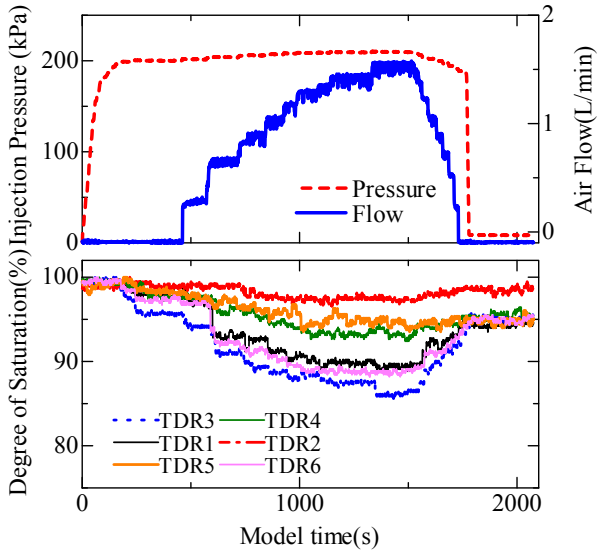


Figure 8 Variation of air flow rate, injection pressure and degree of saturation during air injection: AI

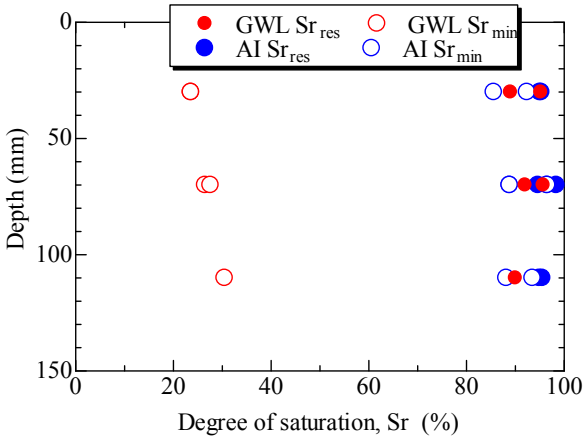


Figure 9 Minimum and residual degrees of saturation obtained in GWL and AI tests.

result, the residual degrees of saturation of AI were higher than those of GWL case. As for the area to which the air bubbles reached, it could not be confirmed by the TDR sensor, as all sensors responded similarly except of the TDR 2, middle depth below footing. However, from the pore water pressure behavior during the shaking, it could be inferred that the air could horizontally reached between the locations of TDR1 and ppt2 at the middle depth and the location of ppt3 at the shallow depth.

3.2 Shaking test

1) Acceleration response

Horizontal accelerations which were observed by the accelerometers at the upper free ground are compared for 3 cases in **Figure 10.** Clear attenuation was observed in the saturated case and the air injection case but not in the groundwater lowering and raising case. **Figure 11** shows variations of the accelerations measured at the top and bottom of the footing. For AI case, large noise in data was

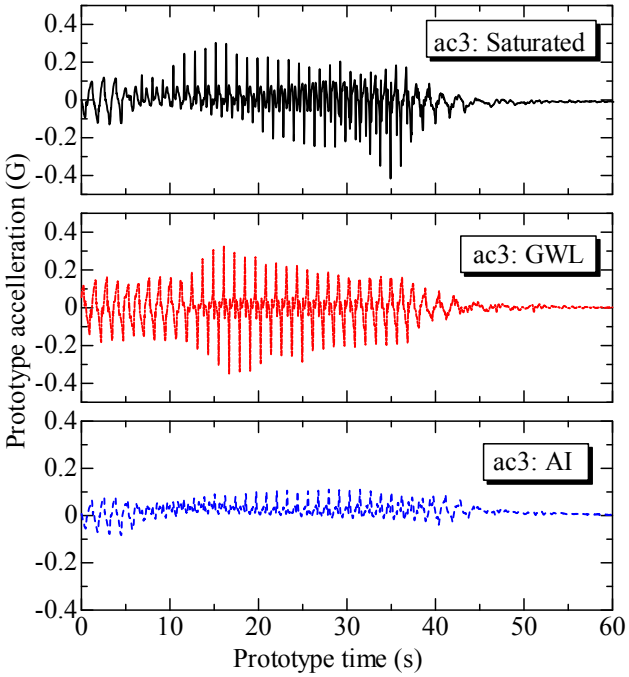


Figure 10 Observed acceleration at the shallow depth in level ground (ac3).

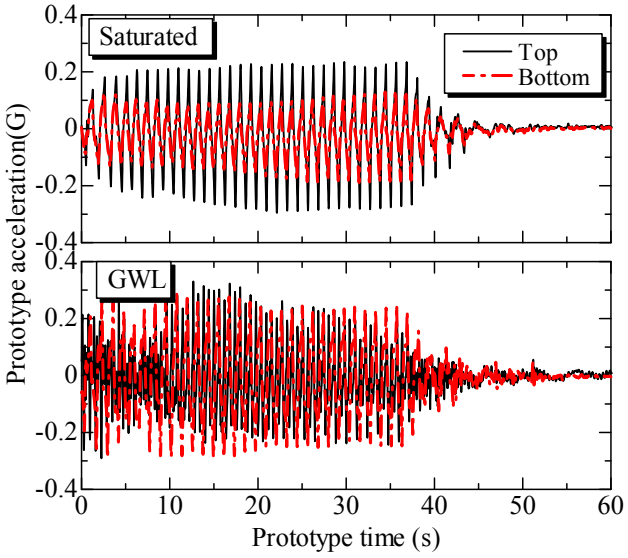


Figure 11 Observed accelerations at top and bottom of the footing.

observed, thus was not included in the presentation of results. In Saturated case, the amplitude at the top was larger than that at the bottom, showing a clear rocking motion. While in GWL case, the similar accelerations were observed at the bottom and top, but they are amplified larger than the input acceleration.

2) Pore water pressure behavior

Figure 12 compares the generated excess pore water pressure (Δu) during shaking, as measured by different pore pressure transducers (ppt) for all the cases. In this figure, effective vertical stress (σ'_{v0}) and effective vertical stress due to footing pressure (σ'_{vf}) are also shown. Generally the

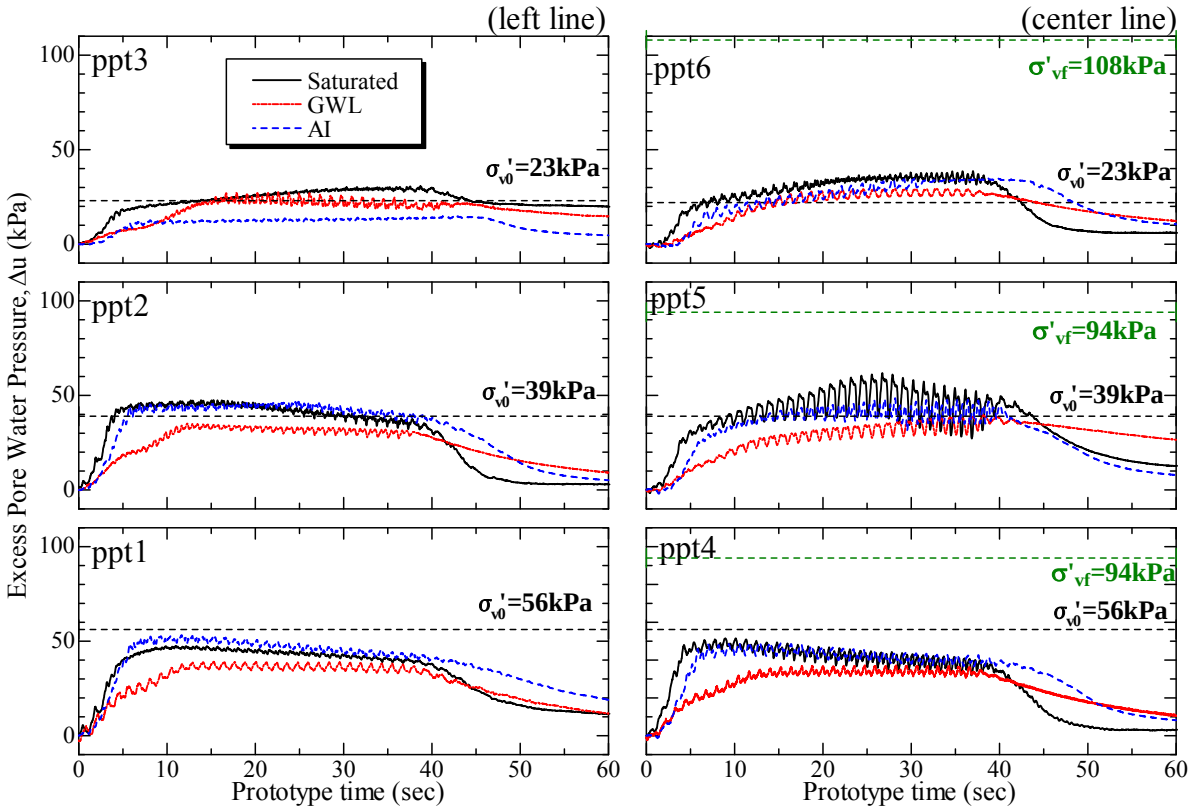


Figure 12 Excess pore water pressures observed during shaking . σ'_{v0} is the effective vertical stress in free field ; σ'_{vf} the effective vertical stress underneath the footing.

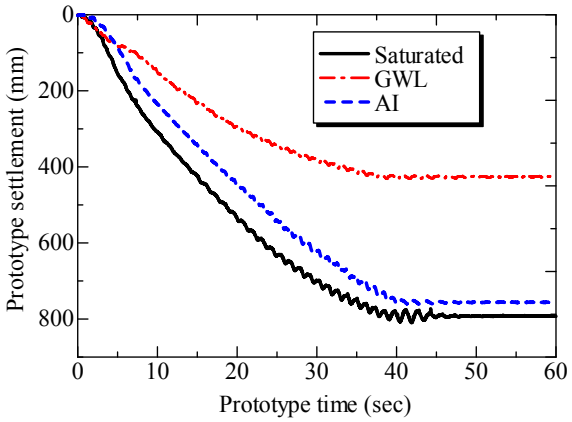


Figure 13 (a) Footing settlements observed during the shaking.

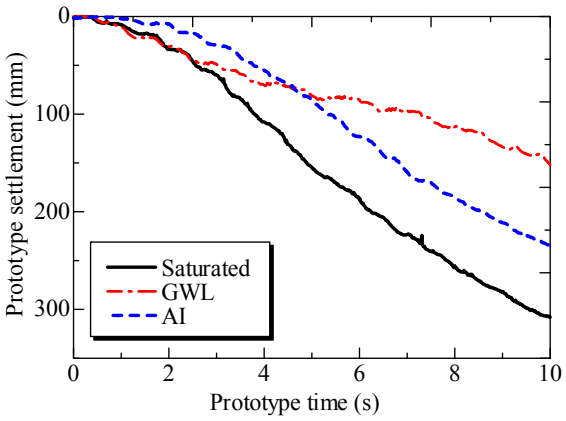


Figure 13 (b) Footing settlements observed in the early stage of shaking.

excess pore water pressures were smaller for the desaturated cases than for the saturated case. However Δus observed at ppt1 and ppt2 are almost the same, which indicates the extent to which air propagated and inhibited the generation of pore water pressure. Thus, the effectiveness of AI could be limited in the region enclosed by ppt3 to ppt6.

The excess pore water pressures generated in GWL case are smaller compared to Saturated and AI, except of AI case in the early stage of shaking before 4-5 secs. This difference in the efficiency of preventing Δu generation could be attributed to the higher S_r of AI case than GWL case and overconsolidation effect introduced in GWL case. Both desaturated cases show less amplitudes of excess pore water pressure change in the cyclic behavior, indicating the effect of air compression in the soil pore. Furthermore the dissipation of Δu after the shaking was slower for the desaturated case than the saturated case especially for GWL case, which also implies the effects of high compressibility on the coefficient of consolidation.

It should be note that even in GWL case Δu gradually increased with time and got close to the values of the other cases in the later stage of shaking.

3) Settlement behavior

Observed settlements of the footing during shaking tests are shown in **Figure 13(a).** Marked efficiencies of desaturation in preventing the footing settlement can be confirmed especially for GWL case. The footing settlement of GWL is about 390 mm (50%) smaller than that of saturated case. Such clear improvement effect in reducing the settlement cannot be confirmed for AI case. However, from the settlement behavior in the early stage of shaking (**Figure 13(b)**), the settlement of AI case is found delayed and smaller than that of Saturated case.

In **Figure 14**, settlement rates of the footing during shaking are shown together with the excess pore water pressure ratio obtained at ppt5. Some correlation between the rate and Δu can be confirmed in the period of rapid increase of Δu. But the rate gradually decreases after the rapid increase of Δu. Due to the delay of the Δu increase the time at the peak of the rate of GWL was also delayed. The rate of AI case became larger than that of Saturated case in the later stage of the shaking.

Total footing settlements of three models are compared by bar chart in **Figure 15**. The settlements in different time period are shown in the figure with the ratio of the settlement in each period to that of Saturated case. From the figure it can be reconfirmed the effect of desaturation in the different loading periods. The desaturation in the limited area underneath the structure by air injection could have limited efficiency for reducing the settlement in the beginning of the shaking and the settlement in the subsequent shaking is almost the same or even larger than the saturated case. On the hand the desaturation by GML has efficiency for long time.

The above mentioned effect of desaturation in wide area can be more clearly confirmed in preventing the inclination of the footing (**Figure 16**). Very small inclination took place by the shaking for GWL case, but the very large inclinations were observed in Saturated and AI cases. Although, the accumulated inclinations are comparable for the two cases, the amplitude of AI case was larger than that of Saturated case. This observation implies that the larger amplification of the footing took placed in AI case than Saturated case, could be a reason why the settlement rate of AI case became larger than that of Saturated case in the later stage of shaking (**Figure 14**). Although the stiffness of the sand under the footing was deteriorated but the reduction of stiffness is expected smaller than that of Saturated case. This is attributed to the difference in the dynamic response between Saturated and AI cases.

4. CONCLUSIONS

From the centrifuge done in this study, the following conclusions can be drawn about the dynamic behavior of the desaturated sand with a super structure during relatively long shaking motion.

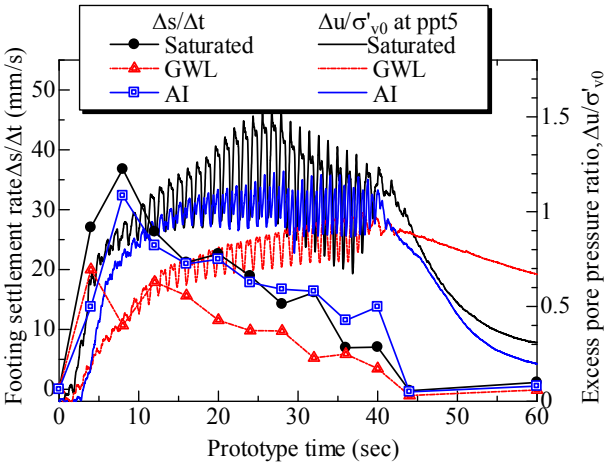


Figure 14 Variation of settlement rate of the footing and excess pore water ratio $\Delta u/\sigma'_{vo}$. of ppt5.

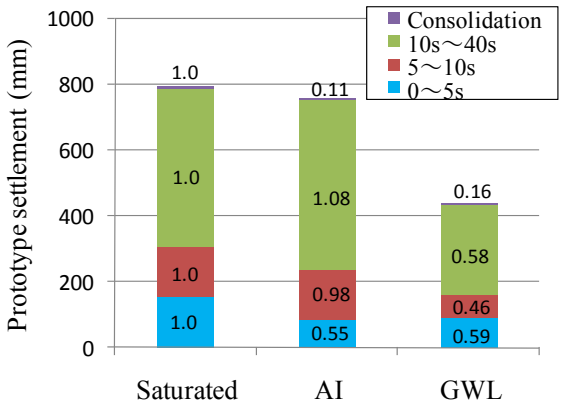


Figure 15 Comparison of settlement at various shaking period..

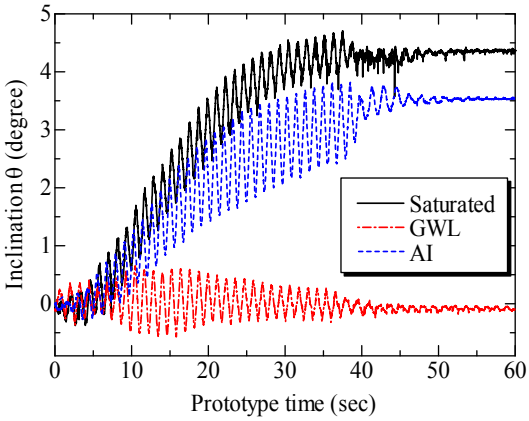


Figure 16 Inclination of the footing during the shaking.

1) Air injection (AI) and ground water lowering and raising (GWL) processes were able to inhibit the generation of excess pore water pressures especially for the latter process.
2) GWL process can securely provide the desaturation in a wider area of the ground and introduce overconsolidation. Because of these combined effects the GWL process can have a wide-ranging effect in terms of prohibiting the occurrence of liquefaction. However, even for the GWL process, the excess pore water pressures gradually increase with time and reach to those for the saturated case. The prevention of pore water pressure generation by GWL process can contribute to the reduction of the settlement of the structure, especially to the reduction of the differential settlement.
3) Air injection can make desaturation in the area of interest below the structure. If the injected area is small, the effect of AI process is very limited for very short period of shaking. After the level of pore water pressure at the mid-depth reached to that of the saturated case, settlement rate became the same of that of the saturated case and even larger.

References

Kimura, T., Takemura, J. and Saitoh, K.: Development of a simple mechanical shaker using a cam shaft, *Proc. Centrifuge 88*, Paris, pp.107-110, 1988.

Kimura, T., Takemura, J., Hirooka, H. and Okamura, M. (1995): Countermeasures against liquefaction of sand deposits with structures, *Proc. Int. Conf. Earthquake Geotechnical Engineering, IS Tokyo 95*, Vol.3, pp.1203-1224.

Okamura, M., Ishihara, M. and Tamura, K. (2006): Degree of saturation and liquefaction resistances of sand improved with sand compaction pile, *Journal of Geotechnical and Geoenvironmental Engineering, Proc. ASCE*, Vol.132, No.2, pp.258-264.

Okamura, M. and Soga, Y. (2006): Effects of pore fluid compression on liquefaction resistance of partially saturated sand, *Soils and Foundations*, Vol.46, No.5, pp.695-700.

Takemura, J. Igarashi, R. Izawa, J., Okamura, M. and Masuda, M. (2008): Centrifuge model tests on soil desaturation as a liquefaction countermeasure, *Procs. 17th Intn. Conf. SMGE.*, Vo.2, Egypt, pp.502-505.

Takemura,J., Komatsumoto, N., Seki, S. and Izawa, J. (2010): Seismic Stability of Gravity Type Quay Wall on Desaturated Loose Sand, *Joint Conf. Proc. 7th Intn. Conf .Urban Earthquake Engineering (7CUEE) & 5th Intn. Conf. on Earthquake Eng. (5ICEE),* Vol.1, pp. 467-472.

Takemura,J., Komatsumoto, N., Seki, S. and Ittichai, B.(2012): Seismic Stability of Gravity Type Quay Wall on Loose Sand with desaturation processes, *Proc. 9th Intn .Conf.Urban Earthquake Engineering (9CUEE)* ,Vol.1, pp. 645-651.

Ueno, T., Kazama, M. Uzuoka, R. and Sento, N. (2008): Liquefaction of unsaturated sand considering the pore air pressure and volume compressibility of the soil particle skelton, Soils and Foundations, Vol.48, No.1, pp.87-99.

Yoshimi, Y., Tanaka, K. and Tokimatsu, K. (1989): Liquefaction resistance of a partially saturated sand, *Soils and Foundations*, Vol.29, No.3, pp.157-162.

10CUEE CONFERENCE PROCEEDINGS
10th International Conference on Urban Earthquake Engineering
March 1-2, 2013, Tokyo Institute of Technology, Tokyo, Japan

Development of Soil Pressures under Lateral Loading

Anne Lemnitzer[1)] and Albert Luu[2)]

1) Assistant Professor, University of CA, Irvine
2) Graduate Student, University of CA, Irvine
alemnitz@uci.edu, albert.luu@hotmail.com

Abstract: Underground structures are typical infrastructural components in mega cities around the world and range from tunnels, underground parking facilities, storage units, industrial/service structures to shopping centers as well as entertainment and sports facilities. In seismic active areas those underground systems are particularly vulnerable to earthquake damage. In order to better understand the behavior of underground structures and the soil - structure interaction when subjected to various levels of earthquake shaking, a large scale shake table experiment was conducted at E-Defense in Miki, Japan in February of 2012. With the aim of gaining insight in the interactive behavior between underground structures and surrounding soil, a set of innovative load cell based pressure sensors was developed and installed along a vertical shaft of 6.5m depth. Measurements of seismic soil pressures for various levels of shaking (50% & 80% Kobe 1995) were recorded and evaluated to be compared with traditional theories and current design methods. Consistent with classical observations, the pressure distribution was found to increase linearly with depth. A strong dependency of pressures on the level of acceleration was noticed. While classical methods significantly under-predicted measured pressures at small accelerations (<0.2g), pressures at accelerations larger than 0.4g tended to be smaller than theoretical methods suggest.

1. INTRODUCTION

Underground structures are typical infrastructural components in mega cities around the world and range from tunnels, underground parking facilities, storage units, industrial/service structures to shopping centers as well as entertainment and sports facilities. In seismic active areas, underground systems are particularly vulnerable to earthquake damage with consequences extending from minor structural damages (e.g., repairable crackings) and temporary closure (economical loss) to superstructure collapse and loss of lives. Typical lateral design of foundation systems and retaining structures often relies on classical (static) earth pressure theories and frequently tends to neglect seismic effects due to the lack of understanding thereof and the shortcoming of experimental data. While this assumption can be accurate for foundation systems exposed to small levels of seismic shaking, stronger accelerations due to larger magnitude earthquakes as observed during the past three years (Chile 2010, New Zealand 2010, Haiti 2010, Japan 2011) can cause significant damage to the foundations and the superstructures.

Retaining structure failures due to large lateral pressures (resulting from wall damage, post liquefaction lateral spreading or a combination of excessive lateral impact loads and soil displacement) are often observed during reconnaissance efforts, in particular, in port regions and urban areas with condensed underground construction. With the aim of gaining insights in the interaction between underground structures and the surrounding soil, as well as the soil pressures developed against the retaining structure, a set of newly developed load cell based pressure sensors was exported to Japan to be installed in an experiment that investigated the behavior of underground structures during a variety of seismic events. The project was conducted the Hyogo Earthquake Engineering Research Center (E-Defense) in Miki, Japan (Lead Principle Investigator) in collaboration with the Network for Earthquake Engineering Simulation (NEES).

2. LITERATURE REVIEW

2.1 Classical Approaches

In 1776, Charles Coulomb was the first scientist to study the static lateral earth pressures on retaining structures (Kramer, 1996). Using the concept of an imaginary planar surface inside the backfill where the weight of the soil above this surface created the lateral earth pressure acting on the structure, Coulomb determined the magnitude of the soil thrust acting on the retaining structure for both minimum active and maximum passive earth pressures using the principle of force equilibrium. Rankine (1875) simplified Coulombs approach by making assumptions about the stress conditions and strength envelope of the backfill soil as well as by neglecting the wall soil interface friction angle to obtain minimum and maximum lateral pressures on the wall. Extending Coulombs theory further, Okabe (1926) along with Mononobe and Matsuo (1929) developed a method of estimating seismic soil pressures following the 1923 Great Kanto Earthquake in Japan. Known as the M-O method, the

Mononobe-Okabe approach is currently the most widely used method in practice for estimating seismic soil pressures. The total active dynamic thrust per M-O can be expressed as

$$P_{AE} = \frac{1}{2} K_{AE} \gamma H^2 (1 - k_v) \quad (1)$$

where P_{AE} is the seismic active earth pressure, K_{AE} is the dynamic active earth pressure coefficient, γ is the unit weight of the soil, H is the height of the backfill material and k_v is the vertical acceleration in the soil mass in g. The point of application of the M-O active resultant force is assumed to be at a height of *H/3* above the base of the wall. The total pressure on the retaining system can be determined by adding the static (P_A) and dynamic (P_{AE}) active thrust as

$$P_A + P_{AE} = P_{TOT} \quad (2)$$

Seed and Whitman (1970) adapted the M-O method in predicting the seismic earth pressures, but suggested that the point of application of the dynamic increment thrust should be between 1/2 to 2/3 the wall height above its base. In particular, Seed and Whitman recommended that the dynamic component acts at approximately 0.6H from the base. This introduced a concept of inverted triangle where the base of the triangle is inverted to be on the top. Seed and Whitman expressed the seismic active earth pressure as:

$$P_{AE} = \frac{1}{2} \gamma H^2 \left(k_A + \frac{3}{4} k_h \right) \quad (2)$$

where k_A is the active static earth pressure coefficient per Coulomb and k_h is the horizontal seismic acceleration.

2.2 Recent Numerical & Experimental Studies

Gazetas *et al.* (2004) presented a numerical study of dynamic stresses imposed on a variety of retaining systems under short-duration and impulsive base excitation. Rigid and flexible systems were modeled using FEM analysis and subjected to ground motions such as the 1999 Athens earthquake. In general results showed that total shear force and overturning moment acting at the base of the wall were smaller than those computed with the M-O theory for the same acceleration.

Psarropoulos *et al.* (2005) developed a general finite-element method that specifically focused on the distribution of dynamic earth pressures on rigid and flexible walls. The analytical model investigated the effects of wall rigidity and the rocking base compliance, combined with both: homogeneous and inhomogeneous backfill, as well as backfills with a multi-layer soil system. By trial analyses of numerical modeling, this study observed that the magnitude of the wall pressures was proportional to the wall height. Results from this experiment also confirmed the general agreement between M–O and elasticity-based solutions for structurally or rotationally flexible walls.

Madabhushi and Zeng (2007) conducted centrifuge tests accompanied by numerical simulations to investigate the seismic response of cantilever retaining walls under earthquake loading backfilled with dry and saturated soil material. Earthquake effects were more severe on the retaining system with saturated backfill than that with dry backfill due to the combined effects of increased inertial force, hydrodynamic pressures, and excess pore pressure in the backfill material.

Al-Atik and Sitar (2010) conducted a combined analytical (FEM) and experimental (centrifuge) research program to evaluate the magnitude and distribution of seismically induced lateral earth pressures on cantilever retaining structures with dry medium dense sand backfill. Two centrifuge tests with a flexible and a stiff retaining wall placed in a soil container filled with a two-layer sand model with varying stiffness were performed under various ground motions. The observed pressure distribution can be reasonably approximated as triangular with the resultant force located approximately 1/3 above the base of the wall, as suggested by Mononobe-Okabe. The measured dynamic pressure magnitudes were generally inconsistent with the M-O assumptions and maximum values did not occur in phase with inertial forces. The measured dynamic pressures on both stiff and flexible walls were about 65% of what was estimated by Mononobe-Okabe. The experiment also observed that dynamic effects at the maximum dynamic wall moments were not significant when the peak ground acceleration did not exceed 0.4g, that is, for peak ground accelerations less than 0.4g, the maximum dynamic wall moment was mainly due to the inertia of the wall itself and seismic soil pressures are generally negligible.

Sitar et al. (2012) expanded the centrifuge testing program to braced and un-braced, U-shaped, underground structures interacting with a free standing cantilever wall placed in a flexible shear beam container. Results showed that the seismic earth pressure increments increased with depth, which is consistent with the static earth pressure distribution. Pressures predicted using the M-O approach formed the upper limit for the results. The inverted triangle of dynamic earth pressure increment, computed using the Seed and Whitman (1970) solution, was not observed during the experiment. However; results showed that the Seed and Whitman (1970) approximation represented a reasonable upper limit for the value of the seismic earth pressure increment for both fixed base cantilever structures (U-shaped walls) and cross-braced, basement-type walls. For the case of the free standing cantilever walls, small amounts of rotation and translation significantly decreased the forces acting in the retaining structure. This data was consistent with the suggestion by Seed and Whitman (1970), that well designed retaining structures should be capable of withstanding ground motions with PGA of 0.3g without the need for specific seismic design provisions.

3. Experimental Setup

3.1 Test Specimen

The test specimen consisted of a 40-ring laminar container with dimensions of 6.5 m in height and 8.0 m in

diameter, as shown in Figure 1. The soil container was mounted on the shake table as empty container and then furnished with underground test structures and filled with soil material. The underground system consisted of two shield tunnels in horizontal direction at the bottom of the soil container, two vertical shafts and a cut-and-cover tunnel connecting the vertical shafts via a rigid and a flexible joint (see Figure 2). All structures were aluminum constructions scaled at a ratio of 1/20 to approximate the stiffness/flexibility of the prototype model.



Figure 1: Laminar Soil Box mounted on E-Defense's Shake Table (Photo: Y. Kawamata)

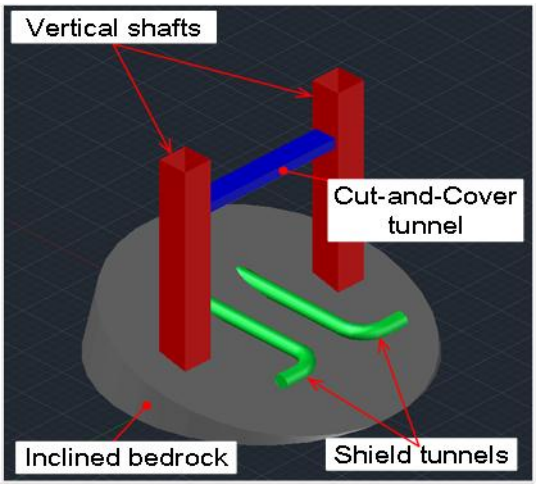


Figure 2: Model of Underground Structures placed inside the Laminar Soil Box (Source: Kawamata et al., 2012)

The two independent shield tunnels embedded in soil material at a lower elevation in the container (green) represent typical underground transportation systems. Both tunnels were placed partly in stiffer (cemented) soil and partly in softer soil as indicated in Figure 2. The tunnels had a diameter of 0.4 m and were located at approximately 1.1 m from the bottom of the container. The two vertical shafts represent vertical infractructure components such as elevators, station buildings, emergency exits, maintainance facilities etc. The vertical shafts were built as 0.8 m square hollow sections and were fixed to the bottom of the contained via bolts, as well as embedded in the stiff cemented soil that was placed underneath the sand fill. The upper horizontal cut-and-cover tunnel system is used to model underground structures such as shopping centers, transit stations, possibly office or maintainance/storage facilities. The horizontal tunnel was connected to the vertical shafts via flexible and rigid joints and were 0.6 m wide and 0.3 m high. The tunnel was located at an elevation of 5.3 m from the bottom of the container and was covered by a 0.4 m thick layer of soil fill (soil surface elevation).

3.2 Instrumentation

The test specimen was instrumented with sensors consisting of strain gauges, LVDTs, accelerometers, soil-pressure sensors and optical devices to monitor the specimen behavior during test conduction. US funding through the Natioanl Science Foundation (NSF) was provided to develop and install load cell based soil pressure sensors on one of the vertical shafts. The selected shaft was the vertical shaft with the rigid cut and cover tunnel connection and is shown as the shaft on the left side in Figure 6. Pressure sensors were developed by AFB Engineered Test Systems and modified for this particular application. The sensors (shown in Figure 3) have a surface area of 78.54 cm^2 (Diameter of 10 cm) and a capacity of 144kPa (3ksf) and 288 kPa (6ksf) respectively. Higher capacity sensors were installed at lower shaft elevations. The sensors were manufactured with aluminum cases to comply with the shaft material and attached using special ring adapters from the inside of the shaft. In this manner the sensor surface and the vertical shaft surface were one continous flush area and localization effects around the sensors were avoided. As shown in Figure 4, a total of 20 pressure sensors were installed by US collaborators distributed over 3 shaft sides. Readings of the pressure sensors were recorded at a frequency of 200 Hz.

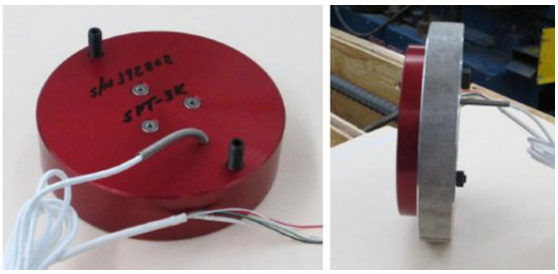


Figure 3: Soil Pressure Sensor installed along the vertical shaft

3.3 Soil Material

The soil consisted of fine sand (#48 Albany Silica Sand) and was placed in multiple layers in the laminar container. Approximately 1000 tons of material were used and compacted to about 35% relative compaction using vibratory equipment as well as via mechanically dropping of weights. Soil properties were investigated via laboratory testing in Japan (Kawamata *et al.*, 2012, and personal communication) and revealed a unit weight γ of 1.616 g/cm^3, an average relative density D_R of 55%, and a water content w

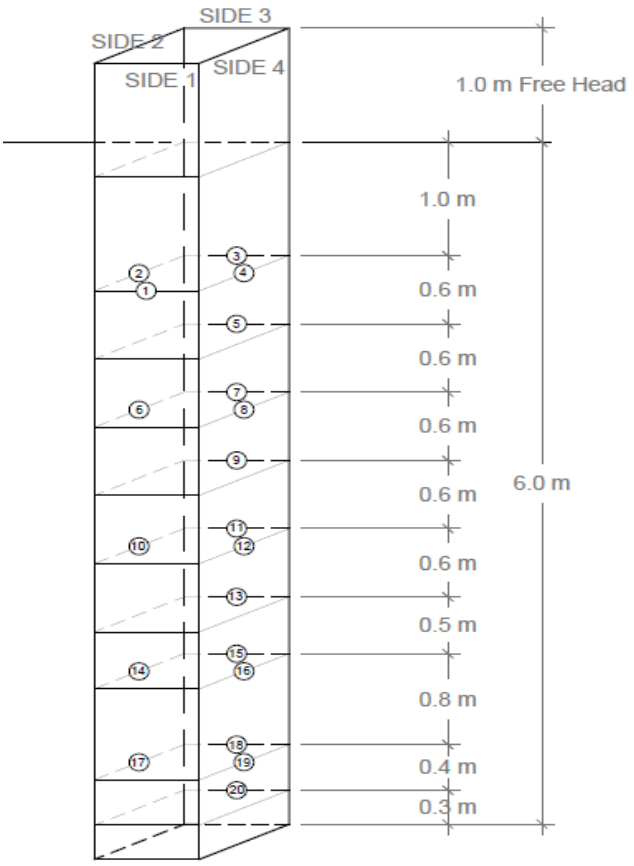


Figure 4: Installation location of pressure sensors

of about 5.1%. Triaxial shear tests (CU) for soils at D_R of 40% revealed a friction angle ϕ of 31.7° and a cohesion *c* of 31.8 kPA. A second soil sample tested at D_R of 60% showed a friction angle of 35.5° and a cohesion of 18 kPA.

The soil material at the bottom of the soil container was mixed with cement to create a stiff layer at the container bottom that could simluate a bedrock layer in the prototype model. Figure 5 shows the soil material in storage at the E-Defense facility and Figures 6 and 7 show the test specimen in plan and section view and indicate the "bedrock" layer and its geometry in the soil container.



Figure 5: Albany Silica Sand used as Fill Material (Photo: Y. Kawamata)

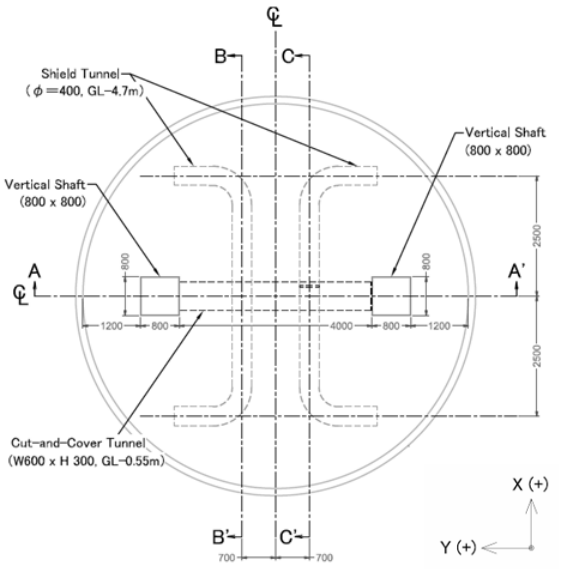


Figure 6: Plan View of Soil Container with Underground Structures (Drawing: Y. Kawamata)

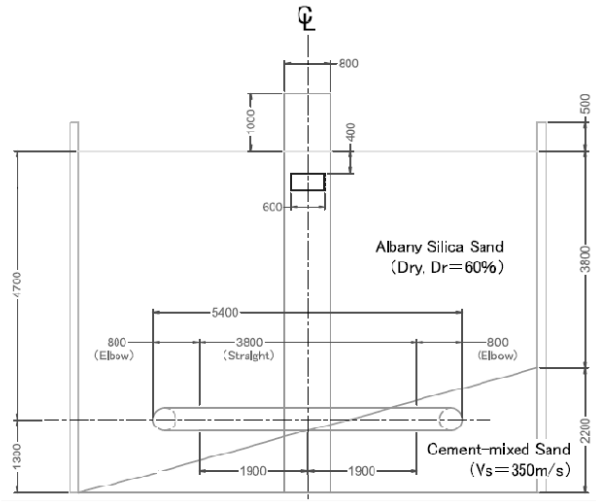


Figure 7: Section View (B' – B') of Soil Container (Drawing: Y. Kawamata)

3.4 Input Motions

The experiment was performed using input ground motions of the 1995 Kobe earthquake scaled to 50% and 80% of the accelerations measured at the JR Takatori station in Kobe, Japan. Table motions were observed to vary slightly from the target input due to noise in the hydraulic system, the interaction between the table and the test specimen and the nonlinar behavior of the test specimen itself (Kawamata *et al.*, 2012). Table accelerations were measured at four location on the shake table and are presented in Figure 8 for the 80% scaled Takatori record. The input motions were two- dimensional (x & y only), however a vertical (z) acceleration was recorded in the accelerometers that can be addressed to table rocking during the experiment conduction. Vertical accelerations showed a magnitude of only 4-6 % of the horizontal acceleration and are therefore negligible. The NS component of the Jakatori

earthquake was input in the specimen's y-axis and the EW component was applied to the specimen's x-axis.

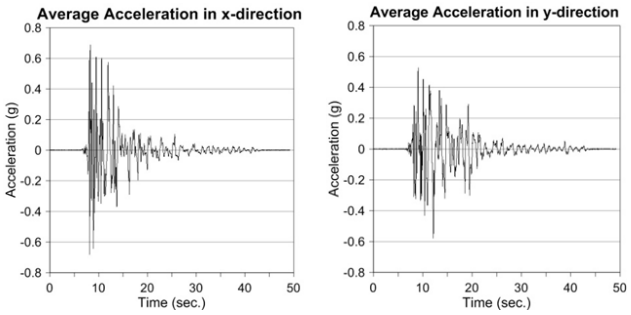


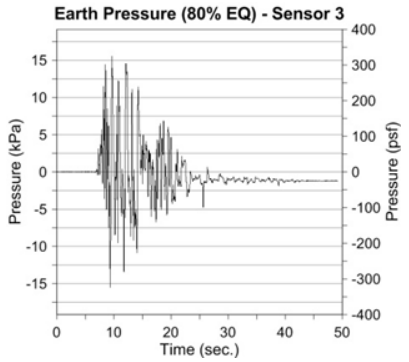
Figure 8: Table Records of Input Motion: 80% Takatori Station, 1995 Kobe Earthquake

A series of step sine motions gradually increasing from 1-20 Hz was conducted on every test day prior to the actual shake table experiment to better quantify the obtained test results. Sine sweep results are not shown for briefty of this paper.

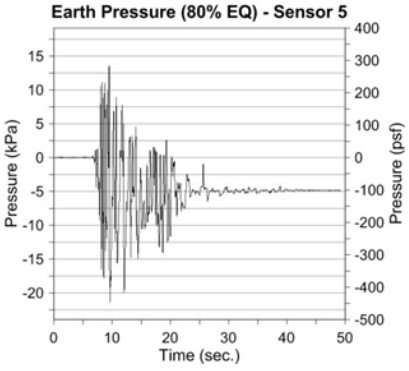
4. PRELIMINARY RESULTS

4.1 Soil Pressure Time Histories

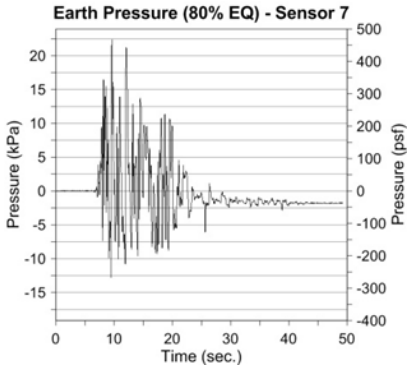
Figures 9a-i show exemplarily the seismic increments of the pressure-time histories along side 3 of the vertical shaft during the 80% Takatori input motion. Side 3 has the densest instrumentation and faces the laminar soil box in (-)x direction in Figure 6. It can be observed that the soil pressures increase with depth up to the embedment of the vertical shaft in the cemented soil (sensors 18 & 20). Pressures reduce significantly as the shaft and the cemented soil move together (likely as "*rigid*" body) at the bottom of the container. To reiterate, the graphs shown in Figure 9 (a-i) only present the seismic pressure increment since all instrumentation installed in the test specimen was "zeroed" before test begin.



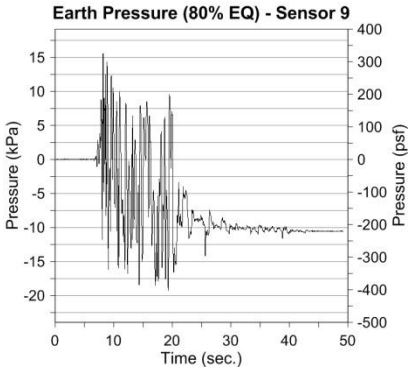
@ -1.0m



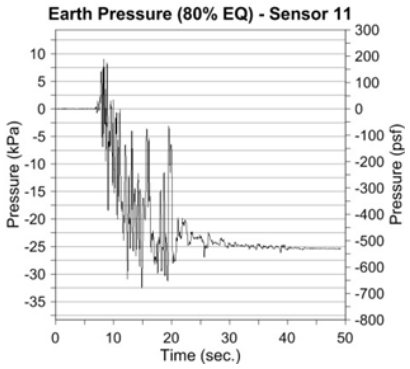
@ -1.6m



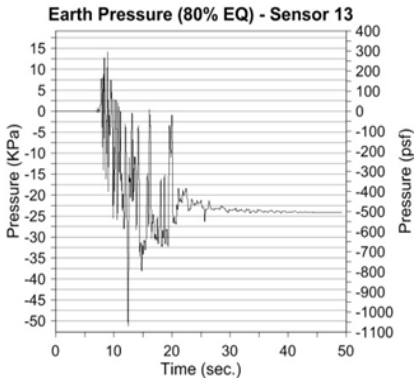
@ - 2.2m



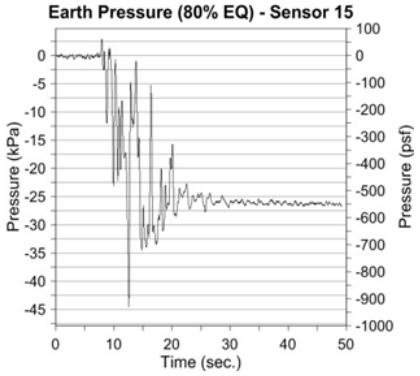
@ - 2.8m



@ -3.4m



@ -4.0m



@ -4.5m

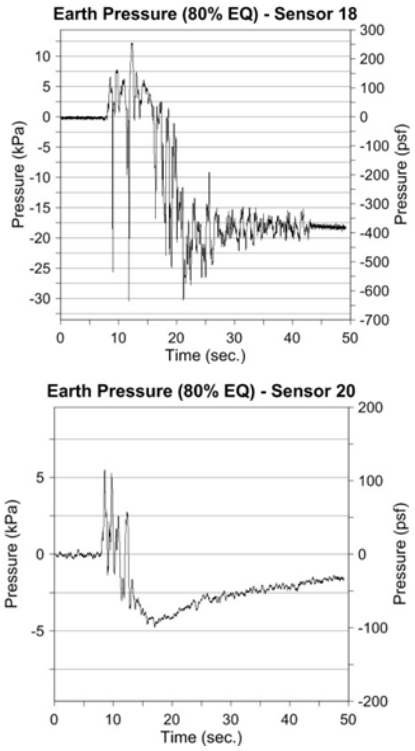


Figure 9a-i: Soil Pressure Time Histories at Various Locations along the Vertical Shaft

The time histories indicate a permanent shift of the measured seismic pressures with residual values up to 24 kPa (500 psf). Residual pressures increase with depth up to the point of fixity of the shaft into the cemented material. The same trend was observed during the 50% shaking with only slightly smaller residual pressures. Settlement of the soil material occurred during both tests (50% and 80%), with a stronger settlement noticed during Test 1 (50%), in particular underneath the cut and cover tunnel. This observation was expected given the relative low percentage of relative compaction of the soil material (RC ~ 35%) and led to significant densification of the soil towards the bottom of the laminar container.

4.2 Earth Pressure Distribution

The vertical earth pressure distribution along side 2, 3 and 4 for the vertical shaft with the rigid joint is shown for selected accelerations in Figures 10, 11 and 12. Data measurements are currently still being processed and more results will be available for publication in the near future to provide a detailed insight into both, ground motion tests and sine sweeps.

The pressure versus depth distribution is relatively similar in magnitude and shape for all continuously instrumented sides. Side one had only one sensor installed at the top and therefore does not provide any meaningful data. The soil pressures increase approximately linearly with depth up to a depth ratio of *z/H* of 0.7, where *z* is the depth of the sensor inside the soil taken from the top surface, and *H* is the total depth of the soil inside the laminar box. Beyond depths of 4.5 m from the surface, the soil pressures reduce significantly as the shaft is fixed into the cemented material and moved along with the cemented material similar to a rigid body motion. The "*fixity*" at the bottom leads to a parabolic shape of the total pressure distribution as indicated in Figures 10-12. The total active seismic pressure resultant occurs at a height of 0.4 – 0.44 H from the bottom of the shaft.

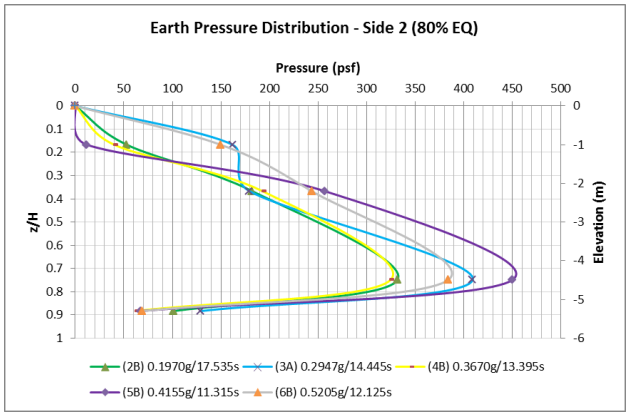


Figure 10: Pressure distribution vs. depth along side 2 of the US- instrumented vertical shaft

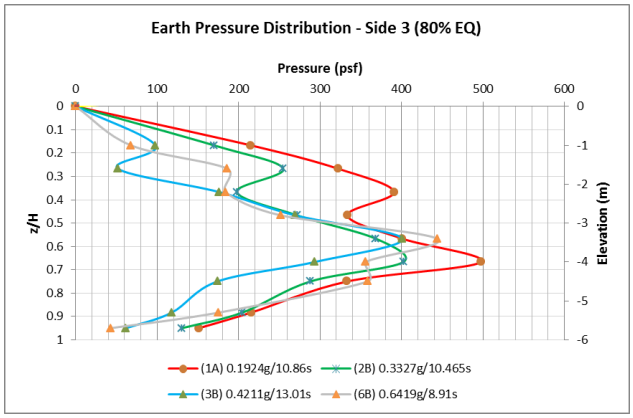


Figure 11: Pressure distribution vs. depth along side 3 of the US- instrumented vertical shaft

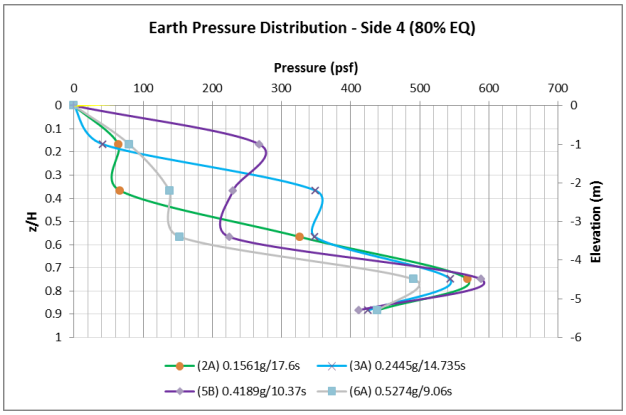


Figure 12: Seismic pressure distribution vs. depth along side 4 of the US- instrumented vertical shaft

The soil pressure at the bottom of the shaft does not return to

zero pressure but recorded small pressures between 2 – 7 kPA (50 – 150 psf) due to slight movement of the vertical shaft. Post test excavations revealed that part of the fixed connection at the bottom of the container was loosened (during Test 1 at 50% ground motion) allowing for small rotations of the shaft starting at the bottom of the container (personal communication with Dr. Kawamata). This rotation (pounding against the cemented materials) may be reflected in the non-zero pressures at the depths greater than z/H > 0.75. Straing gauge data are currently being processed by our Japanese colleagues to account and correct for this effect.

4.3 Comparison of Measured and Calculated Earth Pressures

The seismic increment of the vertical earth pressure distribution is compared to the M-O and Seed & Whitman methods for a range of accelerations using equations (1) and (3). The vertical acceleration was taken as constant value using the measured vertical records of the table motions (as explained in section 3.4). Accelerometer readings from sensors placed inside the soil mass are not publicly available at this moment per E-Defense data sharing regulations and will not allow further processing until 2 years following test completion (i.e. February 2014). The presented pressure distributions are collected from both tests (50% and 80%) to present a better range of accelerations and pressures measured therein. All pressure distributions are presented for side 3. The comparisons of interest in Figures 13 - 18 are the red line labeled Dynamic 1 which represents the seismic pressure calculated using the M-O method and the green line labeled Dynamic 3 which represents the Seed and Whitman method. In both methods the seismic soil pressure was determined by calculating the total pressure and subtracting the static portion using the Coulomb theory.

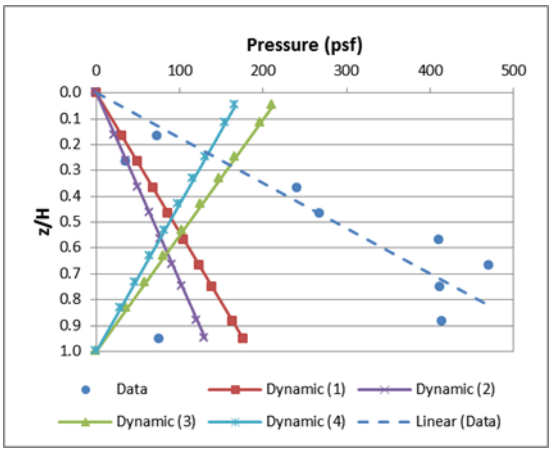


Figure 13: Comparison of measured pressures with the M-O (Dynamic 1) and S & W (Dynamic 3) methods at an acceleration of 0.1495 g

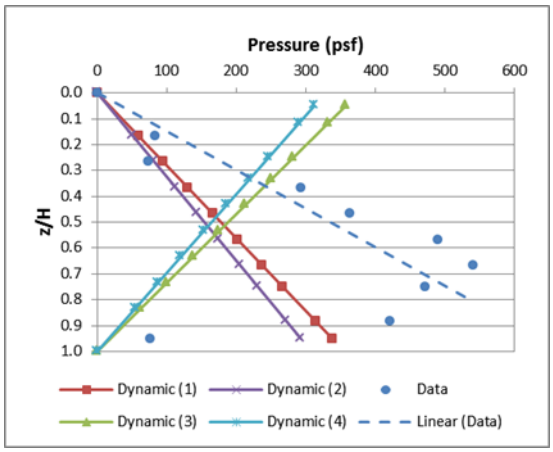


Figure 14: Comparison of measured pressures with the M-O (Dynamic 1) and S & W (Dynamic 3) methods at an acceleration of 0.2523 g

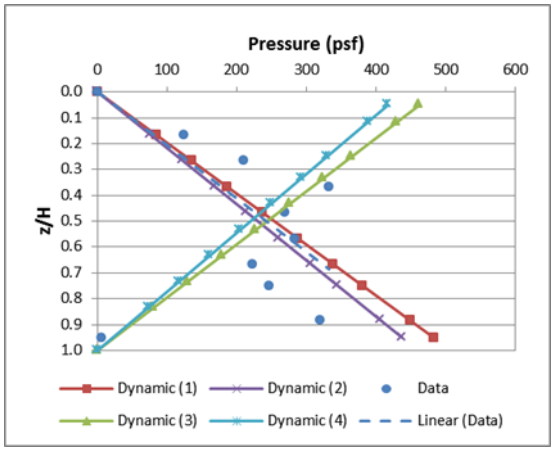


Figure 15: Comparison of measured pressures with the M-O (Dynamic 1) and S & W (Dynamic 3) methods at an acceleration of 0.3627 g

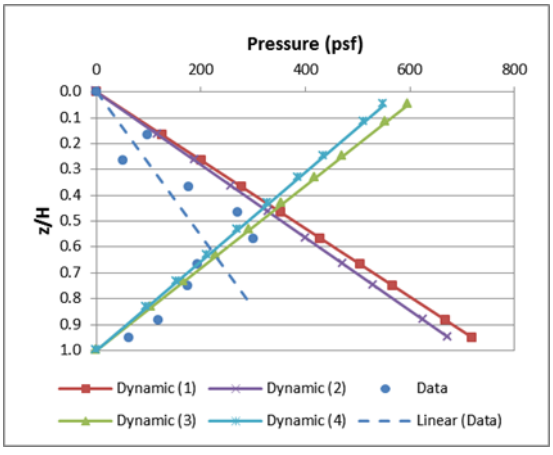


Figure 16: Comparison of measured pressures with the M-O (Dynamic 1) and S & W (Dynamic 3) methods at an acceleration of 0.4211 g

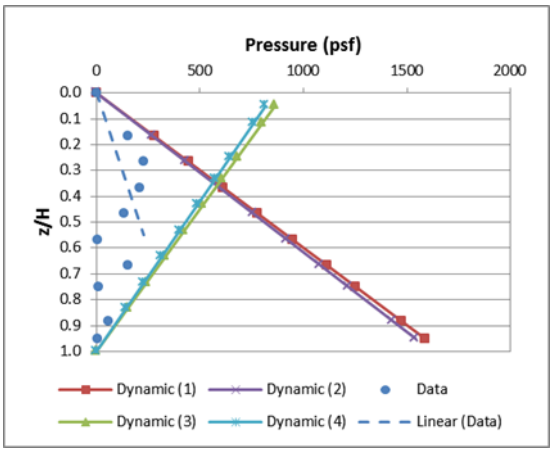


Figure 17: Comparison of measured pressures with the M-O (Dynamic 1) and S & W (Dynamic 3) methods at an acceleration of 0.6093 g

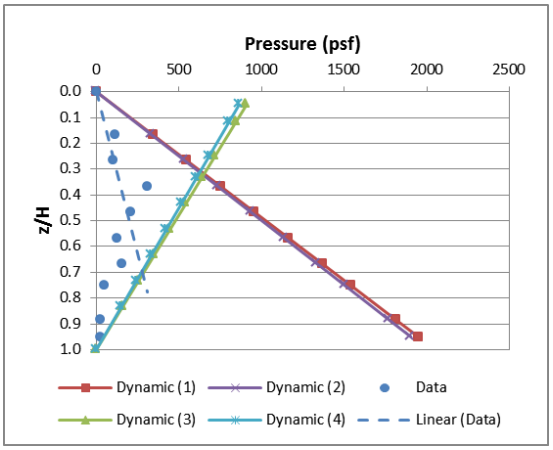


Figure 18: Comparison of measured pressures with the M-O (Dynamic 1) and S & W (Dynamic 3) methods at an acceleration of 0.6423 g

Figures 13- 18 present the variation of the seismic pressure increments along the shaft for table accelerations ranging between ~ 0.15g – 0.64g. For accelerations below 0.3g the measured results showed much larger earth pressures (2-3 times) than estimated using the M-O method (Figure 13 & 14). An approximate linear fit was added to the measured data; however, earth pressures at small accelerations did not show a consistent trend in shape. Measured results and analytical approximations matched comparably well for accelerations around 0.3g – 0.4g (Figure 15). This was observed for both shake table tests and is consistent with findings of other researchers (Seed and Whitman, 1970, Sitar *et al*, 2012). At accelerations beyond 0.4g, measured pressures were only slightly lower than the analytical solutions. Large differences in pressures were observed for accelerations beyond 0.45 g, as shown in Figures 17 and 18 for accelerations > 0.6g. M-O overestimated pressures with magnitudes of almost 10 times compared to test observations, S & W's maximum pressure overestimated the measured values by a factor of 3- 4.

It is important to mention that the observations presented in this manuscript can not be easily generalized since the test structure shows a somewhat different structural behavior than a typical reinforced concrete retaining structure subjected to similar ground motions. In particular, the observed larger pressures at smaller accelerations may be attributed to the flexibility of the vertical aluminum shafts and the relatively loose soil material. This effect is likely not to occur for a stiff retaining wall. While the pressure measurements at small accelerations contradict with previous experimental research findings (e.g. Al-Atik & Sitar, 2010); results observed at larger accelerations agree well with studies found in literature (Seed & Whitman 1970, Sitar *et al*. 2012) and general observations in practice.

Since the test structure is subjected to a much stronger 3-dimensional effect than the implemented analytical methods consider, the authors anticipate to continue and expand this study upon release of further data (e.g. accelerometer readings in the soil mass over the depth of the laminar soil box, strain gauge data along the vertical shaft). Test data should be compared with analytical solutions that consider the effects of wave propagation inside the soil mass, dynamic properties of the soil (e.g. shear wave velocity), the frequency content of the input motion and the acceleration distribution along the vertical height of the test specimen as studied by researchers like Wood (1973), Veletsos et al., (1994) and Ostadan (2005).

3. CONCLUSIONS

A large scale shake table experiment was conducted at the E-Defense facility in Miki Japan to investigate the behavior and interaction of underground structures subjected to scaled ground motions from the Kobe 1995 earthquake. The system of underground structures consisted of 2 vertical shafts connected by a cut and cover tunnel, and 2 horizontal shafts at a lower elevation. The bottom of the container was furnished with cemented soil material at a slope of 2:1 and filled thereafter with Albany Silica sand to a total height of 6.0m. The test structures were heavily instrumented. Measurements from soil pressure sensors installed at one of the vertical shafts are presented in this paper and compared to classical analytical methods such as Monobe-Okabe (M-O) and Seed & Whitman (S & W). Pressures were observed to increase linearly with depth up to the "*point of fixity*" (i.e. the point where the shaft is embedded in the cemented material). Pressures exceeded estimates of the M-O method for accelerations less than 0.3g possibly due to the flexibility of the shaft structure and the properties of the soil material. More work is needed at this point to fully quantify the observed experimental behavior. Measured data and analytical predictions matched reasonably well for accelerations between 0.3g and 0.4g. Seismic pressures at high accelerations (e.g. 0.6g) were significantly lower than analytical methods suggest. The point of application of the dynamic earth pressure resultant was calculated to be between 0.4 – 0.44H from the bottom of the vertical structure. Further studies integrating the dynamic soil

properties and the acceleration distribution / wave length propagation in the soil mass are suggested at this time to fully understand the specimen behavior under a wider range of ground motions.

Acknowledgements:

The authors would like to thank the National Science Foundation (NSF) for providing partial support for the conducted research under award # CMMI 1201213. We highly appreciate the assistance and collaboration of our Japanese colleagues Dr. Kawamata and Dr. Nakayama at E-Defense in Miki, Japan for providing and sharing their facilities and test instruments for the collection of data. Their willingness to accommodate our requests and provide additional data and figures (photographs and graphics shown in this paper) is gratefully recognized. We would like to thank Steve Keowen from AFB Engineered Test Systems and Dr. Alberto Salamanca from NEES@UCLA for their assistance with the sensor manufacturing and calibration. Dr. Akio Abe of Tokyo SOIL is acknowledged for installing the sensors at the test specimen in Japan.

References:

Al-Atik, L. and Sitar, N. (2010). "Seismic Earth Pressures on Cantilever Retaining Structures," *Journal of Geotechnical and Geoenvironmental Engineering*, America Society of Civil Engineers, 136 (10), 1324 – 1333.

Gazetas, G., Psarropoulos, P.N., Anastasopoulos, I., and Gerolymos, N. (2004). "Seismic behaviour of flexible retaining systems subjected to short-duration moderately strong excitation," *Soil Dynamics and Earthquake Engineering*, 24, 537 - 550

Kawamata, Y., Nakayama, M., Towhara, I., Yasuda, S., and Tabata, K. (2012). "Large-scale experiment using E-Defense on dynamic behaviors of underground structures during strong ground motions in urban areas," *Proceedings of the15th World Conference on Earthquake Engineering, Lisbon, Portugal*, Paper No.4582.

Kramer, S. L. (1996). "Geotechnical Earthquake Engineering," Prentice Hall, NJ.

Madabhushi, S.P.G. and Zeng, X. (2007). "Simulating seismic response of cantilever retaining walls," *Journal of Geotechnical and Geoenvironmental Engineering*, America Society of Civil Engineers, 133 (5), 539 – 549.

Mononobe, N. and Matsuo, H. (1929). "On the determination of earth pressure during earthquake," *Proceedings World Engineering Congress*, 9, 179-187.

Mononobe, N. and Matsuo, M. (1932). "Experimental investigation of lateral earth pressure during earthquakes," Earthquake Research Institute and Research Office of Public Works, 884 - 902

Ostadan, F. (2005). "Seismic soil pressure for building walls-An updated approach," *Soil Dynamics and Earthquake Engineering*, 25, 785 - 793

Psarropoulos, P.N., Klonaris, G., and Gazetas, G. (2005). "Seismic earth pressures on rigid and flexible retaining walls," *Soil Dynamics and Earthquake Engineering*, 25, 795 - 807

Seed, H. B. and Whitman, R. V. (1970). "Design of earth retaining structures for dynamic loads," *Proc., ASCE Specialty Conference on Lateral Stresses in the Ground and Design of Earth Retaining Structures*, Vol. 1, Cornell Univ., Itahaca, N.Y., 103 – 147.

Sitar, N., Mikola, R. G. and Candia, G. (2012). "Seismically induced lateral earth pressures on retaining structures and basement walls," *Proc. ASCE Geo-Congress*,

Veletos, A. and Younan, A.H. "Dynamic soil pressure on rigid vertical walls". *Soil Dynamics and Earthquake Engineering*, 23, 275 – 301

Wood, J.H. (1973). "Earthquake induced soil pressures on structures". Doctoral Dissertation, EERL 73-05. California Institute of Technology, Pasadena, CA.

10CUEE CONFERENCE PROCEEDINGS
10th International Conference on Urban Earthquake Engineering
March 1-2, 2013, Tokyo Institute of Technology, Tokyo, Japan

DYNAMIC CENTRIFUGE MODEL TEST OF BUILDING WITH EMBEDDED FOOTING ON SEMI-RIGIDLY CONNECTED PILE HEADS IN LIQUEFIABLE SOIL

Sadayuki Ishizaki[1)], Kohji Tokimatsu[2)], and Toshiaki Nagao[3)]

1) Research Engineer, Technology Center, Taisei Corporation, Japan
2) Professor, Center for Urban Earthquake Engineering, Tokyo Institute of Technology, Japan
3) Chief Research Engineer, Technology Center, Taisei Corporation, Japan
sada.ishizaki@sakura.taisei.co.jp, kohji@o.cc.titech.ac.jp, toshiaki.nagao@sakura.taisei.co.jp

Abstract: Dynamic centrifuge model tests are conducted to investigate the influence of embedded footing on the seismic behavior of a pile-supported building with semi-rigid pile head connections in liquefiable soil. The test results show the followings. (1) The earth pressure acting on an embedded footing with semi-rigid pile head connections works as a reaction force to the inertia force, whereas that with rigid pile head connections acts as an external force during liquefaction. (2) The maximum acceleration of a superstructure with semi-rigid pile head connections becomes smaller than that with rigid pile head connections during liquefaction. (3) The pile damage reducing effect of the semi-rigid pile head connection method is enhanced in liquefiable ground as compared with that in non-liquefiable ground, because the lateral force on pile heads with semi-rigid pile head connections is considerably reduced because of conclusion (1) and (2).

1. INTRODUCTION

In these days, various semi-rigid pile head connection methods have been developed that permit the rotation of pile heads as more effective pile design methods (Umeno 2005, Kitagawa 2007). The static structural properties of these pile heads have been verified through structural tests such as bending tests and shear tests, confirming that the new methods offer good deformation capacity (e.g., Yasuda et al. 2006 , Aoshima et al. 2006). And the dynamic interaction between a building with semi-rigid pile head connection methods and soil has previously been investigated by numerical analysis, in which the rotational characteristic at the pile heads is modeled using a rotational spring element (e.g., Muramatsu et al. 2002, Funahara et al. 2003). But there have been few experimental studies using a whole building and soil. Especially in liquefied soil, the influence of the dynamic interaction on pile damage reduction and superstructure response has yet to be elucidated. Shaking table tests of a pile-supported building model with a semi-rigid pile head connection method in dry sand were conducted by the authors to examine the dynamic interaction (Ishizaki et al. 2006). Further, Ishizaki et al. (2011) conducted centrifuge model tests to investigate the seismic behavior of buildings with semi-rigid pile head connections in liquefiable soil. The test results showed the followings. (1) The semi-rigid pile head connections effectively reduced the bending moment of piles both before and during liquefaction. (2) The acceleration of a superstructure with semi-rigid pile head connections decreased during liquefaction. But in these studies, the influence of embedded footing was not considered. In this study, dynamic centrifuge model tests are conducted to investigate the influence of embedded footing on the seismic behavior of a pile-supported building with semi-rigid pile head connections in liquefiable soil.

2. TEST OUTLINE

Dynamic centrifuge model tests were performed at 50g centrifugal acceleration using a geotechnical centrifuge at the Technology Center of Taisei Corporation. Two soil-pile-structure models were used: a building model with either rigid pile head connections (Model RB) or semi-rigid pile head connections (Model SB). The models were prepared in a laminar shear box measuring 560×210×400mm (L×W×D).

2.1 Physical Models

Figure 1 shows the soil-pile-structure models used in the tests. The soil profile consists of three layers: two saturated sand layers and a top dry sand layer. The saturated layers were created using Toyoura sand with a target relative density of 90% in the lowest layer and 60% in the middle layer. These two layers were saturated with silicone oil 50 times more viscous than water. And, the dry silica sand No.3 was further pluviated to form non-liquefiable layer around the footing.

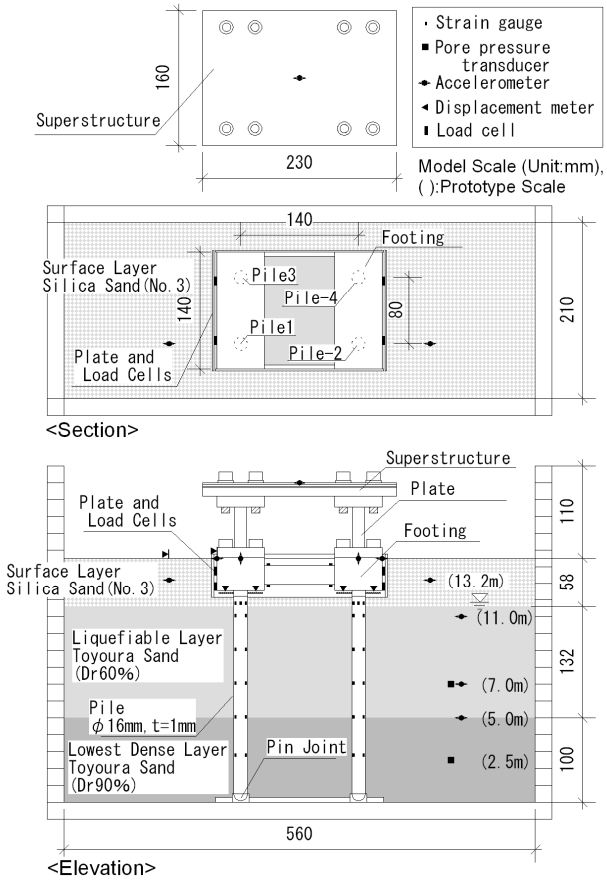


Figure 1 Model Layout

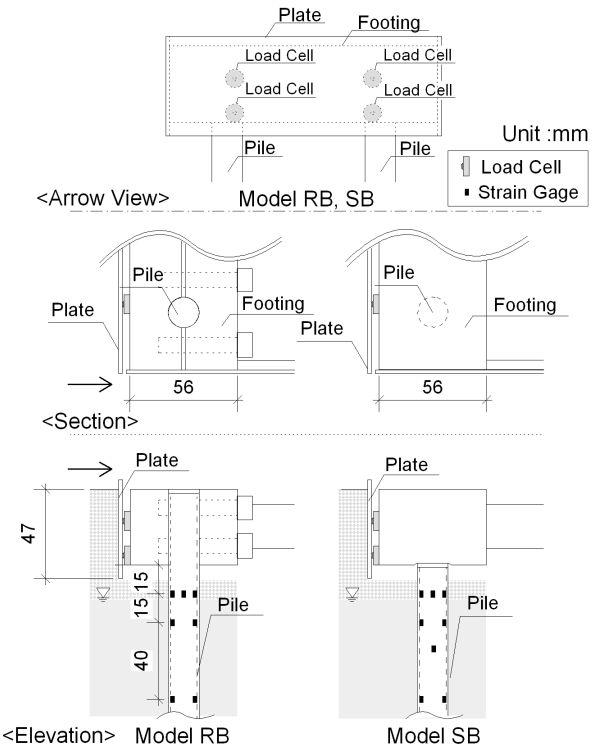


Figure 2 Models of Pile Heads and Footings

The mass of the superstructure was 5.2 kg and that of the foundation was 3.0 kg. The natural period of the superstructure at small excitation was 0.003 s (0.15 s in the prototype scale). The pile groups consisted of 2×2 stainless steel pipes, each of 16 mm diameter and 1mm wall thickness. The elastic coefficient of the pipe was 1.97×10^8 kN/m^2. The pile tips were connected to the base of the laminar box with pin joints.

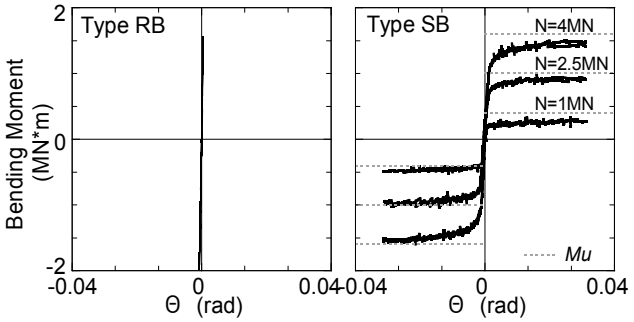


Figure 3 Rotational Characteristics of Pile Heads

The pile head models are shown in Figure 2. The pile heads were connected to the footing either rigidly or semi-rigidly according to the model type. In Type RB, the pile heads were sandwiched between individual sections of the footing and fastened by bolts, while in Type SB, the footing simply rested on the pile heads. The rotational characteristics at the pile head connections were identified by preliminary static bending tests. Figure 3 shows the relations between the bending moment and rotation angle at pile heads for both types of connections. In Type SB, the initial rigidity was small, and the rotation angle increased drastically as the bending moment increased. The relation curve was almost the same either in loading or unloading (non-linear elastic behavior). In Type SB, the relations vary according to the axial force. The maximum resistance of moment M_u is given by:

$$M_u = N/2D \qquad (1)$$

where, D is pile diameter and N is axial force. M_u at each axial force is also shown in Figure 3.The bending moment at the semi-rigid pile head connections are close to M_u for the respective axial forces. The rotational characteristic of the actual semi-rigid pile head connection (Aoshima et al. 2006) is mostly reproduced in the model.

The model of the embedded footing is also shown in Figure 2. Plates supported by four load cells each were set up on the right and left sides of the footing to evaluate the earth pressure acting on it. Teflon sheets were pasted on the sidewalls of footing, parallel to the shaking direction, to reduce sidewall friction. There was a clearance between the base of the footing and the underlying soil. Hence the sidewall friction and base friction were negligible.

2.2 Measurement

The measurement parameters are also shown in Figure 1. The horizontal accelerations of the soil and structure, vertical accelerations of the footing, strains in the piles, pore water pressures in the soil, and the earth pressures acting on both sides of footing were measured. The displacements of

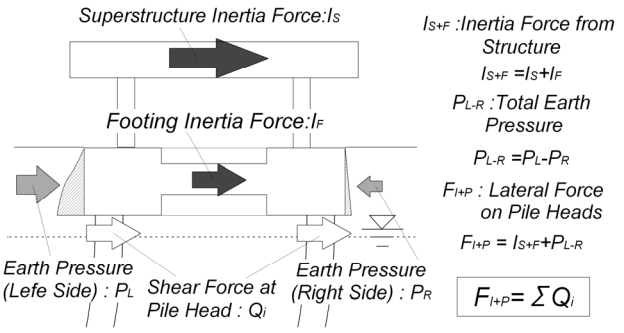


Figure 4 Forces acting on Structure and Pile Heads

the structure and soil were calculated by double integration of the accelerations with respect to time.

Figure 4 is a schematic figure showing the forces acting on the pile heads, the embedded footing, and the superstructure.

The inertia forces imposed by the superstructure and footing were evaluated from their respective masses and the measured accelerations. The total of the inertia force from the structure (I_{S+F}) was then calculated by summing these individual inertia forces from the superstructure (I_S) and the footing (I_F). The total earth pressure acting on the footing (P_{L-R}) is calculated by the difference between earth pressure on the left side (P_L) and that on the right side (P_R), because the side wall friction and base friction were almost negligible. And then, in Type B, the total force acting on the pile head (F_{I+P}) calculated by the summation of I_{S+F} and P_{L-R} is equal to ΣQi.

3. TEST RESULTS

This section consists of analysis and discussion of the results of main excitations for Model SB and RB. All data presented in this sections are of prototype scale.

3.1 Response of Soil

The time histories of accelerations of the soil and shaking table, soil displacements, and excess pore water pressures in the soil, in Model SB and RB, are shown in Figure 5. The excess pore water pressures at heights of 7.0 m above the base of the laminar box reach the initial effective vertical stresses, and the middle layers then liquefy in both models.

3.2 Response of Structure

Figure 6 shows the time histories of superstructure accelerations, footing displacements, bending moments and rotational angles at the pile heads.

Prior to 14s, at which time instant the excess pore water pressures in the liquefiable layers are rising, the superstructure acceleration in Model SB is similar to that in Model RB. After 25s, by which time the soil in the liquefiable layer has almost liquefied, the accelerations in both models show similar oscillation in periods when the superstructure acceleration in Model RB is relatively small, such as 64.5 to 67 s and 99 to 107 s. But in periods when the superstructure acceleration in Model RB is large, such as 50 to 55 s, 77 to 83 s, and 93 to 98 s, the superstructure acceleration in Model SB tends to be smaller and somewhat delayed as compared with that in Model RB. Furthermore, the maximum acceleration of the superstructure in Model SB is about 60% of that in Model RB. The further effect of semi-rigid pile head connections on reducing superstructure acceleration is identified not only in the model with non-embedded footing (Ishizaki et al. 2011) but also in the this model with embedded footing.

The footing displacements in both models increase during liquefaction. It is confirmed that the footing displacements correspond to the respective surface soil displacements which are not illustrated in this paper.

3.3 Lateral Force on Pile Heads

The time histories of I_{S+F}, P_{L-R}, and F_{I+P} are shown in Figure 7. P_{L-R} in Model SB is a little larger but shows similar oscillation to that in Model RB prior to 13.5 s (Fig. 7(b)). But during liquefaction (after 25 s), P_{L-R} in Model SB tends to be smaller and delayed as compared with that in Model RB. In the periods from 50 to 55 s and from 77 to 83 s, in

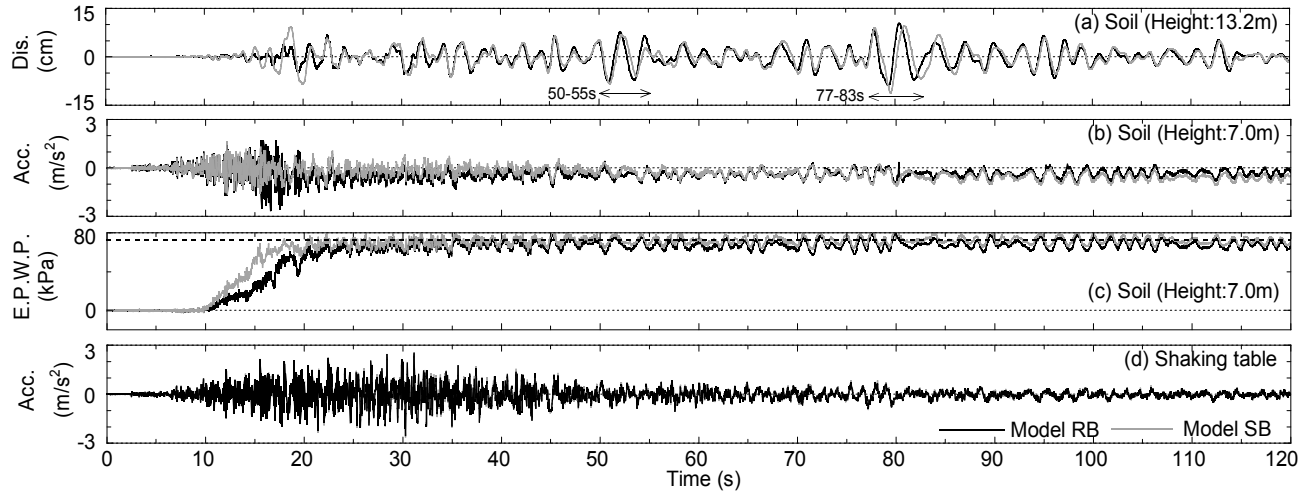


Figure 5 Time Histories of Accelerations of Soil and Shaking Table, Displacements of Soil, and Excess Pore Water Pressures of Soil

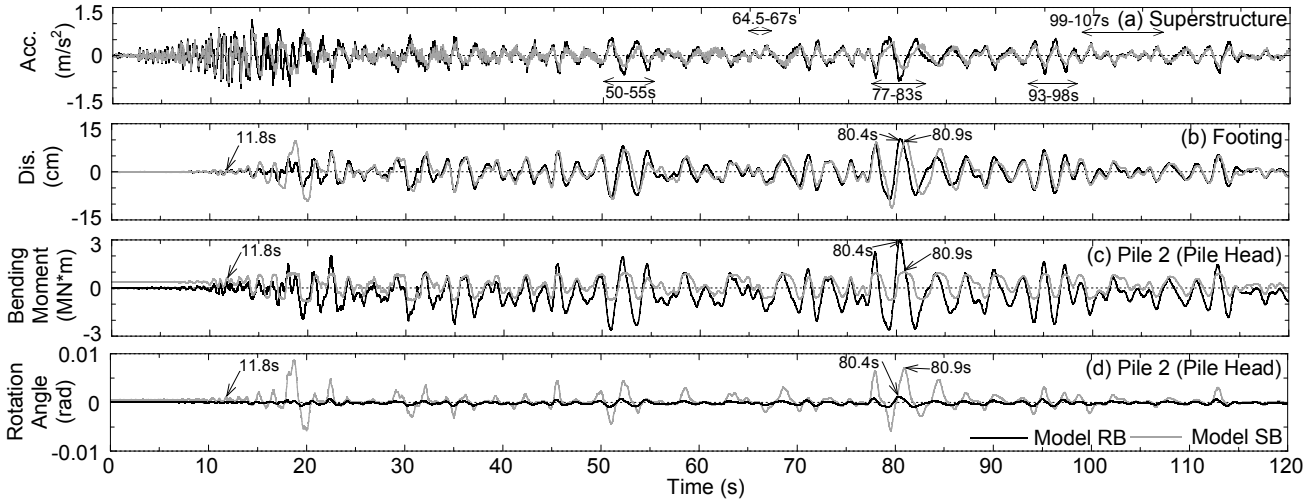


Figure 6 Time Histories of Accelerations of Structures, Displacements of Footings, and Bending Moments and Rotation Angles at Pile Heads

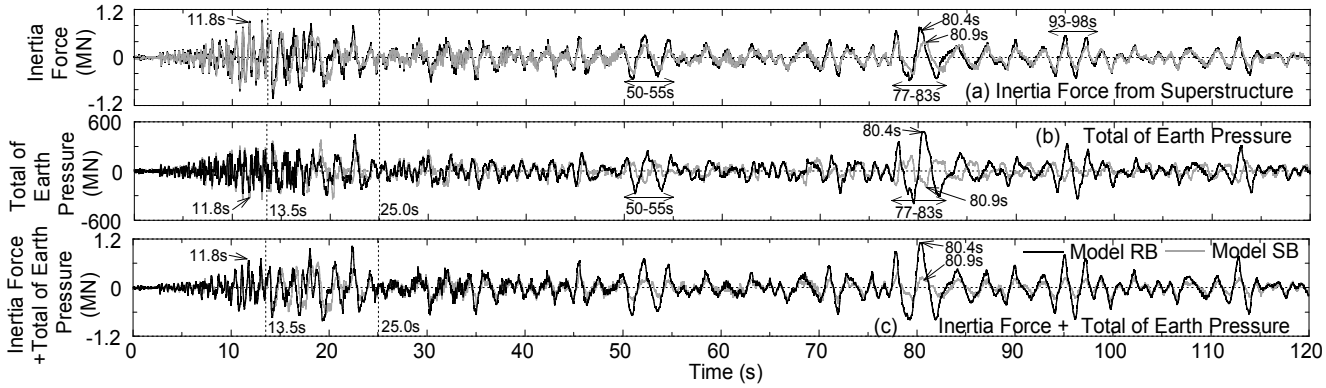


Figure 7 Time Histories of Inertia Forces from Structures, Total Earth Pressures Acting on Footing, and Total Lateral Force on Pile Heads

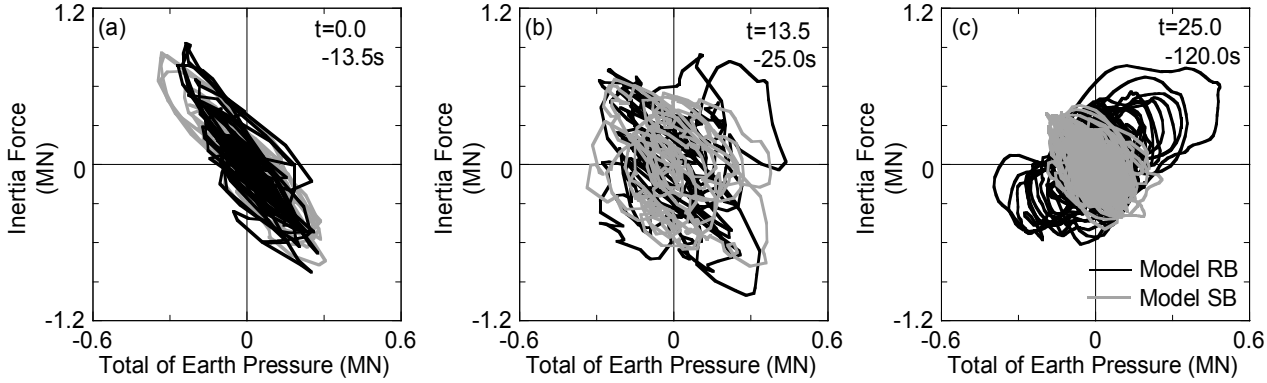


Figure 8 Relations Between Inertia Force from Structure and Total Earth pressure Acting on Footing

particular, the sign of $P_{L\text{-}R}$ in Model SB tends to be opposite to that in Model RB.

During liquefaction, the maximum value of I_{S+F} in Model SB is smaller than that in Model RB because the maximum superstructure acceleration in Model SB is smaller than that in Model RB (Fig. 7(a), 6(a)).

Figure 8 shows the relations between I_{S+F} and $P_{L\text{-}R}$ in the period from 0.0 to 13.5 s (the early process of liquefaction), in the period from 13.5 to 25.0 s (later process of liquefaction), and after 25.0 s (during liquefaction).

In the early process of liquefaction, $P_{L\text{-}R}$ in each model is negatively correlated with I_{S+F}; i.e., the total earth pressure acting on the embedded footing works as a reaction force against the inertia force imposed by the structure. Therefore, the total lateral force on the pile heads (F_{I+P}) decreases due to the embedment effect, a mechanism that is recognized in the seismic design of pile foundation in non-liquefiable ground (AIJ 2001).

In the later process of liquefaction, the differences in phases between I_{S+F} and $P_{L\text{-}R}$ in both models become

distinctive as the excess pore water pressure rises.

During liquefaction, $P_{L\text{-}R}$ in Model RB is positively correlated with I_{S+F}; that is, $P_{L\text{-}R}$ acts as the external force and F_{I+P} increases due to the influence of the embedded footing (Fig. 8(c), 7(c)). In contrast, in Model SB, $P_{L\text{-}R}$ is negatively correlated with I_{S+F}; that is, $P_{L\text{-}R}$ acts as a reaction force to I_{S+F}. Therefore, in Model SB, the embedment effect which reduces the total lateral force on the pile heads is observable not only before liquefaction but also during liquefaction (Fig. 7(a), (c)).

In Model SB, F_{I+P} is a little smaller than that in Model RB before 13.5 s (Fig. 7(c)). It tends to decrease with increasing excess pore water pressure and is considerably smaller than that in Model RB during liquefaction.

3.4 Effect on Pile Damage Reduction

Figure 9 shows distributions of bending moments along the piles at 11.8 s (the time instant during the early process of liquefaction when F_{I+P}s are almost the same in the both models), 18.7/22.4 s (when the bending moments at the pile heads take a peak during the later process of liquefaction), and 80.4/80.9 s (when the bending moments at the pile heads take a peak during liquefaction). In the early and later process of liquefaction (Figs. 9(a), (b)), the maximum bending moment along the pile in Model SB, which occurs within the soil, is greater than the peak bending moment in the soil in Model RB. And the maximum bending moments in Model SB are about 60 to 75% of those that occur at the pile heads in Model RB. In contrast, during liquefaction, the peak value of bending moment of the pile in the soil in Model SB is smaller than that in Model RB. And the maximum bending moments along the piles in Model SB occur at the pile heads and are about 20 to 35% of the maximum bending moments in Model RB. Therefore, the effect on pile damage reducing of semi-rigid pile head connection method is enhanced during liquefaction.

The reasons for the considerably smaller maximum bending moments along the piles during liquefaction in Model SB are considered as follows. The natural own periods of the superstructures are shorter than those of the liquefied soil. Therefore, the soil deformation tends to acts the same direction as the inertia force from the structure (Tamura et al. 2002). In Model RB, the deformation performance of the pile foundation is inferior because the pile heads are connected rigidly to the footing. Hence, the soil deformation is larger than that of the pile foundation. And the relative displacement between the pile/footing and the liquefied soil increases, leading to the increase in both earth pressure acting on the embedded footing and subgrade reaction acting on the piles (Fig. 7(b)). Moreover, during liquefaction, the earth pressure acting on the footing in Model RB acts as an external force which increases the lateral force on pile heads (Fig. 8(c), 7(c)). Consequently, the maximum bending moments along the piles in Model RB become particularly high during liquefaction, especially when the soil displacement especially increases (Figs. 9(a) to (c)). On the other hand, in Model SB where rotation of the pile heads is allowed, the deformation performance of the pile foundation is superior from the beginning and the pile foundation follows the deformation of soil during liquefaction. The earth pressure acting on the embedded footing and the subgrade reaction for the piles does not increase because there is no increase in relative displacement. Furthermore, the earth pressure works as a reaction force to the inertia force at the moment when the inertia force increases, whereas that in Model RB acts as an external force (Fig. 7(b), 8(c)). In addition, the acceleration of the superstructure with semi-rigid pile head connections tends to be smaller than that with rigid pile head connections; that is, the inertia force imposed by the structure with semi-rigid pile head connections is smaller than the inertia force that with rigid pile head connections (Fig. 7(a)). Consequently, the lateral force on piles with semi-rigid pile head connections is considerably smaller than

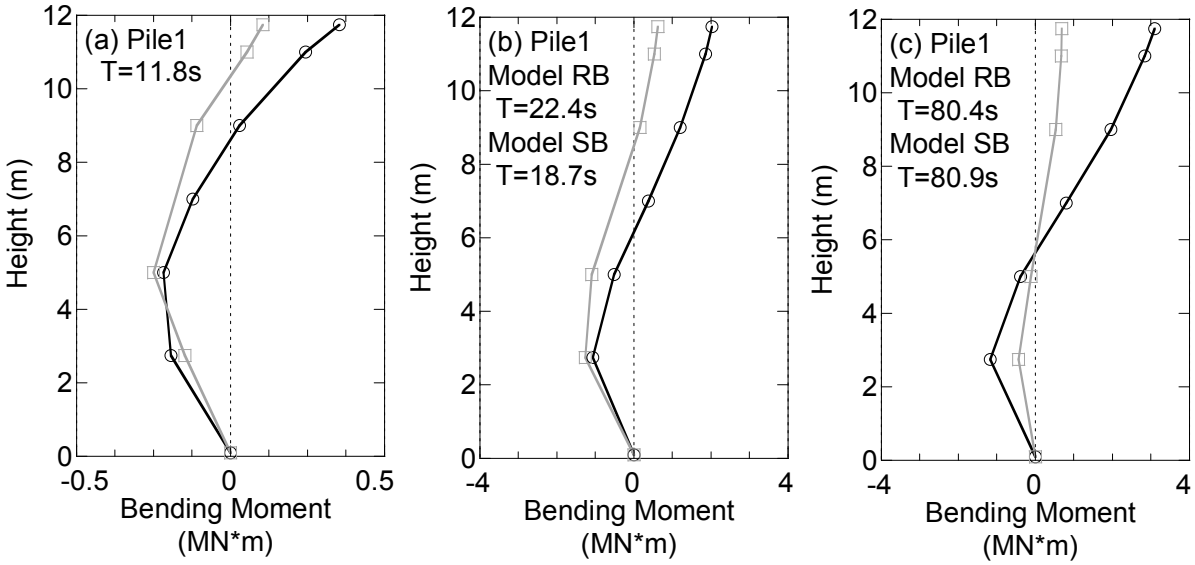


Figure 9 Distributions of Bending Moment along Piles at About 11.8s (Before Liquefaction), 18.7 or 22.4s (Later Process to Liquefaction), and 80.4 or 80.9s (during Liquefaction)

that with rigid pile connections (Fig. 7(c)) because of the above mentioned three reasons: no increase in the total earth pressure and the subgrade reaction, the total earth pressure working as a reaction force against the inertia force, and the decreasing inertia force. Therefore, the pile damage reduction effect of semi-rigid pile head connection method is enhanced in liquefiable ground as compared with that in non-liquefiable ground (Fig. 9(a) to (c)).

4. CONCLUSIONS

Dynamic centrifuge model tests were conducted to investigate the influence of embedded footing on the seismic behavior of a pile-supported building with semi-rigid pile head connections in liquefiable soil. Based on the test results and analysis, the following effects of adopting the semi-rigid pile head connection method in liquefiable soil have been demonstrated.

1. The earth pressure acting on an embedded footing with semi-rigid pile head connections is smaller than that with rigid pile head connections when the soil is liquefied. Furthermore, the earth pressure works as a reaction force to the inertia force, whereas that with rigid pile head connections acts as an external force during liquefaction.
2. The maximum acceleration of a superstructure with semi-rigid pile head connections becomes smaller than that with rigid pile head connections during liquefaction. To paraphrase this finding, the inertia force imposed by the structure on the pile heads is reduced.
3. The main reason for conclusions 1) and 2) is that the pile foundation with semi-rigid pile head connections has superior deformation performance compared to that with rigid pile head connections and this characteristic becomes more evident during liquefaction.
4. The semi-rigid pile head connections effectively reduce the maximum bending moment along piles both before and during liquefaction. Furthermore, the pile damage reducing effect of the semi-rigid pile head connection method is enhanced in liquefiable ground as compared with that in non-liquefiable ground, because the lateral force on pile heads with semi-rigid pile head connections is considerably reduced because of conclusion 1) and 2).

In order to fully verify these effects in liquefiable ground, it is important to accumulate more experimental data for various conditions of soil-profile, superstructure, rotational characteristic of pile head, input motion, and so forth. Furthermore, an analytical approach able to simulate the dynamic interactions between a building with semi-rigid pile head connections and liquefied soil is also awaited.

References:

Umeno, T. (2005), "Removal Methods and Connection Methods at Pile Heads for Cast-in-place Reinforced Concrete Piles", The Foundation Engineering & Equipment, 33(2), 26-29 (in Japanese).

Kitagawa, M. (2007), "Pile Head Connection Methods for Precast Concrete Piles", The Foundation Engineering & Equipment, 35(7), 32-36 (in Japanese).

Yasuda, S., Komuro, T., Soya, K., Muramatsu, K., Korenaga, T. and Kawabata, I. (2006), "Development of Flexible Connection of Pile Head" Journal of Technology and Design, Architectural Institute of Japan, 23, 131-136 (in Japanese).

Aoshima, K., Shimada, H. and Komuro, T. (2006), "Mechanical Characteristics of Pile Head Joint with Improved Simplified Connection Method for Precast Concrete Piles", Journal of Structural and Construction Engineering, Architectural Institute of Japan, 607, 125-132 (in Japanese).

Muramatsu, A., Morita, H., Hara, T., Komuro, T., Tatsuno, S. and Soya, K. (2002), "Seismic Performance of Reinforced Concrete Pile without Anchorage of Pile Rebar", Summaries of Technical Papers of Annual Meeting, Architectural Institute of Japan, B-1, 191-194 (in Japanese).

Funahara, H., Aoshima, K., Majima, M., Ishizaki, S. and Fujii, S. (2003), "Numerical Study on Seismic Behavior of Building with Semi-rigid Pile Heads", Summaries of Technical Papers of Annual Meeting, Architectural Institute of Japan, B-1, 693-694 (in Japanese).

Ishizaki, S., Majima, M., Nagao, T., Funahara, H. and Aoshima, K. (2006), "Shaking Table Tests on Soil-pile-structure Models with Semi-rigid Pile Head Connections", Journal of Structural and Construction Engineering, Architectural Institute of Japan, 602, 171-177 (in Japanese).

Ishizaki, S., Tokimatsu, K. and Nagao, T. (2012), "Dynamic Centrifuge Model Test of Pile-supported Building with Semi-rigid Pile Head Connections in Liquefiable Soil", International Journal of Geotechnical Engineering, Volume 6, Issue 2, pp.231-238, April, 2012.

Architectural Institute of Japan (2001), "Recommendations for Design of Building Foundations" (in Japanese).

Tamura, S., Tokimatsu, K., Uchida, A., Funahara, H., and Abe, A. (2002), "Relation between Seismic Earth Pressure Acting on Embedded Footing and Inertial Force Based on Liquefaction Test using Large Scale Shear Box", Journal of Structure and Construction Engineering, Architectural Institute of Japan, 559, 129-134 (in Japanese).

10CUEE CONFERENCE PROCEEDINGS
10th International Conference on Urban Earthquake Engineering
March 1-2, 2013, Tokyo Institute of Technology, Tokyo, Japan

USE OF PRE-SHAKING FOR SOIL-PILE SYSTEM IDENTIFICATION IN CENTRIFUGE SHAKING TABLE TESTS

C. J. Lee[1], W. Y. Hung[2], C.H Tsai[3], T. Chen[3], Y. C. Tu[3], and Meng-Hsiu Hsieh[4]

1) Professor, Department of Civil Engineering, National Central University, Jhongli, Taiwan
2) Associate technologist, National Center for Research on Earthquake Engineering, Taipei, Taiwan.
3) Research Assistant, Department of Civil Engineering, National Central University, Jhongli, Taiwan
4) Associate Engineer, Institute of Nuclear Energy Research, Atomic Energy Council, Longtan, Taiwan
cjleeciv@ncu.edu.tw, wyhung@ncree.narl.org.tw, tegcc@hotmail.com,marshall94216@iner.gov.tw

Abstract: In this paper, the pre-shaking technique is presented for both measuring the V_s profile of soil deposit and determining the fundamental frequencies of both the soil deposit and the soil-structure system in a centrifuge model tested at an acceleration of 80 g. The pre-shaking is a non-destructive test, use of the shaker as a wave source and a vertical array of accelerometers embedded in the sand bed and the accelerometers attached on the pile as receivers. Accordingly the method of pre-shaking can be easily used for both the in-flight subsurface exploration (measurements of V_s profile) and the in-flight SI on the soil-structure systems. A soil-pile centrifuge model is used to demonstrate the application of pre-shaking in a routine centrifuge shaking table test. The testing setup, testing procedures, and the related system identification techniques and signal processing for the soil-pile system are discussed. The natural frequencies measured from the pre-shaking tests are consistent with those derived from the theoretical basis.

1. INTRODUCTION

The damage caused by earthquakes is strongly dependent upon the local site condition, and thereby site characterization has become an important role in earthquake-resistant design and must be taken account of. Several system identification (SI) techniques have been developed for estimation of in situ soil properties and local site parameters (i.e., shear wave velocity profile of soil, fundamental frequencies of soil and structure), using recorded earthquake data (Oskay and Zeghal, 2011).

An alternative approach to geotechnical earthquake engineering small-scale dynamic centrifuge modeling has been used to provide insights into the behavior of soil-structure interaction during shaking. Thus an inexpensive and non-destructive technique for model soil bed characterization as those used in situ, that is capable of performing both the in-flight subsurface exploration and the in-flight SI on a model soil bed and/or on a model structure any time, is urgently required.

In geotechnical earthquake engineering the shear wave velocity of soil, V_s, can be used to evaluate in-flight dynamic soil properties in centrifuge models as well as in situ dynamic soil properties. Centrifuge modelers have developed several methods for in-flight V_s measurements. Brandenberg et al. (2006), Gohl and Finn (1991), and Lei et al. (2004) used a pair of bender elements to generate (transmit) and detect (receive) shear waves in geotechnical centrifuges. Arulnathan et al. (2000) used a miniature air hammer to generate shear waves, and the propagating shear waves were recorded using a vertical array of four accelerometers positioned at different depths. More recently, Rammah et al. (2006) and Kim & Kim (2010) developed bender element tomography systems to investigate in-flight shear wave velocity distributions in centrifuge models.

2. TECHNIQUES OF PRE-SHAKING

Several SI techniques have been performed on the measured output (response) and input (excitation) in order to gain insight into the system properties of soil stratum and structure. Transfer functions, or ratios of amplitude spectra of input and out acceleration pairs, have employed to estimate fundamental frequencies of geotechnical systems and associated shear wave velocities of deposit in geotechnical earthquake engineering practice. Adopting these SI techniques in the centrifuge test, however, the saturated loose sand bed even subjected to the smaller but the longer duration vibration may generate considerable amount of excess pore water pressure and consequently results in disturbing the sand fabric of and in reducing the stiffness of sand bed.

In this paper, the pre-shaking technique is presented for both measuring the V_s profile of soil deposit and determining the fundamental frequencies, f, of both the soil deposit and the soil-structure system in a centrifuge model. The pre-shaking is a non-destructive test, use of the shaker as a wave source and a vertical array of accelerometers as

receivers. Accordingly the method of pre-shaking can be easily used for both the in-flight subsurface exploration (measurements of V_s profile) and the in-flight SI on the soil-structure systems. A soil-pile centrifuge model is used to demonstrate the application of pre-shaking in a routine centrifuge shaking table test. The testing setup, testing procedures, and the related system identification techniques for the soil-pile system are discussed as follows.

3. GEOTECHNICAL CENTRIFUGE MODELING

This experimental work was undertaken in the Centrifuge at the National Central University (NCU), Taiwan. The NCU Geotechnical Centrifuge has a nominal radius of 3 m and equips a 1-D servo-hydraulically controlled shaker integrated into a swing basket. The shaker has maximum nominal shaking force 53.4 kN with maximum table displacement of ±6.4 mm and operates at up to 80 *g* centrifugal acceleration. The nominal operating frequency range is 0 - 250 Hz. A laminar container with inside dimensions of 711 mm x 356 mm x 353 mm (L×W×H) is constructed from 38 light-weight aluminum alloy rings arranged in a stack. The laminar container is designed for dry or saturated soil models. The boundary effects of the laminar container used in the study is minimal; hence the container permits development of stresses and strains associated with one dimensional shear wave propagation (Lee et al., 2012). Fig. 1 shows the laminar container resting on the NCU Geotechnical Centrifuge Shaker.

Three instrumented model bending piles (L-Pile, B-Pile, and S-Pile) were fabricated with the same aluminum-alloy tubes of 9.6 mm outer diameter and 8 mm internal diameter. The embedment depth of model pile was 330 mm. Strain gauges were placed externally at eight positions to measure the distribution of bending moment along the pile depths. Resin was coated on the surface of model pile for waterproofing. The model piles after coating were designed to replicate 0.96 m diameter circular pile with an embedment depth of 26.4 m if tested at an acceleration of 80 g and they have flexural stiffness (*EI*) of 725848 kN-m^2 in prototype scale. Here *E* and *I* are the Young's modulus and the moment of inertia of the pile. The instrumented bending piles with pin joints at each pile tip were calibrated for establishing the relation of the output voltage and the bending moment prior to the model tests. A tip mass was attached on each pile head to simulate the dead weight of superstructure. Three different tip masses were attached on the pile heads for simulating seismic response of the piles with different weights of superstructures as shown in Fig. 2. Table 1 lists the basic characteristic of tip masses attached on the L-Pile, the B-Pile, and the S-Pile.

A fine quartz sand was used to prepare the uniform sand deposit. The characteristics of the quartz sand are summarized in Table 2. The instrumented bending piles attached with different tip masses on the pile head were first connected to the container base with pin joints and then the quartz sand was pluviated with a regular path into the container from a hopper at a constant falling height and at a constant flow rate for preparing fairly uniform sand deposits having the relative density of about 60%. After finishing the preparation of saturated sand bed the centrifuge was then accelerated at a 10 *g* per step until it reached the centrifugal acceleration of 80 *g*.

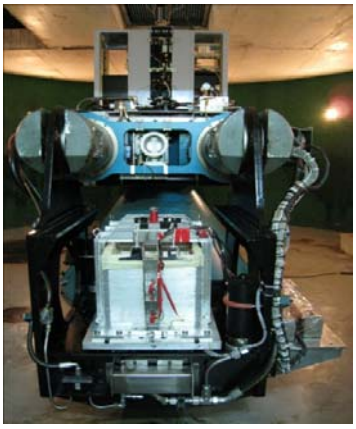


Figure 1 Laminar container and the NCU Geotechnical Centrifuge Shaker.

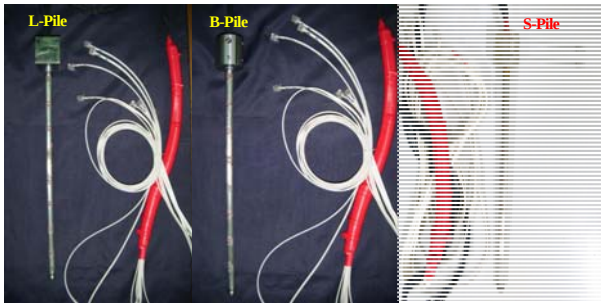


Figure 2 photos of L-Pile, B-Pile, and S-Pile

Table 1 Characteristics of tip masses on the pile head

	[1]Dimensions (cm)	[2]Weight (kN)	Rotation Inertia (kg-m^2)
L-Pile	4.5×4.5×4.5	3179.52	1716952
B-Pile	Φ4.5×4.5	2421.76	1242363
S-Pile	Φ4.5×4.5	343.03	170029

[1]Model scale; [2]Prototype scale.

Table 2 Characteristics of fine quartz sand

	G_s	D_{50} (mm)	D_{10} (mm)	[1]ρ_{max} (g/cm^3)	[1]ρ_{min} (g/cm^3)
Quartz sand	2.65	0.193	0.147	1.66	1.44

Fig. 3 presents a typical setup to show the dimensions of tested sand bed, the position of piles, and the types and the positions of instrumentations used in the model tests. Each model contained two piles those which were attached with different tip mass on the pile heads as listed in Table 1. The model dimensions are in centimeters, and the prototype dimensions in parentheses are in meters. The thickness of model sand bed is 33.9 cm in model scale, simulating a 27.2-m thick and 56.8-m long sand deposit if tested in an acceleration of 80 *g*. The sand bed was instrumented with

eight vertical spaced accelerometers (A#) to record the shear wave propagating from the base to the ground surface as shown in Fig.3. At the same elevations close to the accelerometers eight pore water pressure transducers (P#) were instrumented as well in the saturated sand deposit. No pore water pressure transducer was instrumented in the dry sand model. One LVDT (Linear variable differential transformer) was installed at the top of ground surface to measure the time histories of surface settlement. All the measuring points are far from the boundary of laminar container to prevent from the boundary effects (Lee et al., 2012).

Two LVDTs and two accelerometers were also instrumented on the tip mass for each pile to measure the horizontal displacements and the horizontal accelerations at two different levels. Consequently the time histories of the angular acceleration and the angular displacement for the tip masses can be calculated. The bottom of tip mass was clear of the surface of sand. Thus the model piles had translation fixity but rotational free at the pile tips and free to rotation and sway at the pile heads as shown in Fig. 3.

Three LVDTs were attached on the side wall of laminar container to measure the free field soil lateral deformations along the depths during shaking and after shaking. Eight strain gauges on each pile were used to measure the profiles of bending moment along the pile depths. This comprehensive instrumentation and detailed measurements are necessary to understand the seismic behavior of pile embedded in a liquefiable sand deposit. All the measurements are presented in prototype units unless specially noted otherwise.

A series of centrifuge shaking table tests at the acceleration of 80 g was conducted; the test conditions for each model are listed in Table 3. Totally seven models were conducted in the study. Test P-D-1, P-D-2, and P-D-3 were the dry sand models, whereas Test P-W-1, P-W-2, P-W-3, and P-W-4 were all the sand models having relative densities of about 60%. The elevation of the water table in the saturated sand models was at the ground surface. Two instrumented piles with various tip mass were embedded for each sand model. Each model was first subjected to one cycle of smaller sinusoidal vibration (pre-shaking) with different frequencies (1 *Hz*, 2 *Hz*, and 3 *Hz*) for the in-flight subsurface exploration and the in-flight SI to determine the shear wave velocity profile along depths and the nature frequencies of both the sand deposit and the piles. Subsequently each model was subjected to multiple earthquake events for evaluating the seismic response of the pile embedded in the sand deposit. In this paper only the test results of pre-shaking are reported and discussed.

4. TEST RESULTS AND INTERPRETATIONS

Most centrifuge models are instrumented with vertical arrays of accelerometers for monitoring the dynamic response of the soil bed and thereby the accelerometers are the requisite transducers. In the study the model sand bed was subjected to pre-shaking driven by the shaker as listed in Table 3 to measure the profile of the shear wave velocity and to identify the fundamental frequencies in terms of the vertical accelerometer array. The shaker fired one cycle of smaller controlled amplitude sinusoidal wave (around 0.01 *g* in amplitude and 1, 2, and 3 *Hz* in frequency, both in the prototype scale) that provided a source of vibrations. A higher sampling rate of 30k samples/sec was used to acquire the acceleration time histories of the vertical accelerometer array. The instrumented accelerometers registered identifiable signals with a higher sampling frequency so that the sampling interval was sufficiently small relative to the travel times to avoid low-resolution V_s estimates.

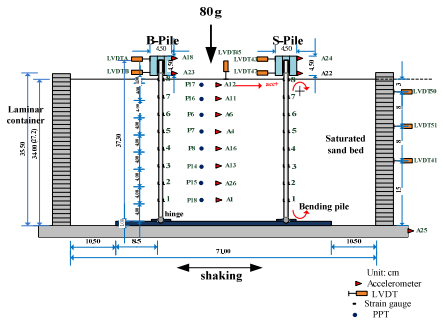


Figure 3 Typical testing setup and instrumentations.

Table 3 Test conditions in the study

Test No.	Relative density, D_r (%)	Pre-shaking Event	Tested pile	Remark
P-D-1	63	S1-1Hz S1-2Hz S1-3Hz	L-Pile and B-Pile	Dry sand bed
P-D-2	66	S1-1Hz S1-2Hz S1-3Hz	L-Pile and B-Pile	Dry sand bed
P-D-3	60	S1-1Hz S1-2Hz S1-3Hz	B-Pile and S-Pile	Dry sand bed
P-W-4	63	S1-1Hz S1-2Hz S1-3Hz	L-Pile and B-Pile	Saturated sand bed
P-W-9	62	S1-1Hz S1-2Hz S1-3Hz	B-Pile and S-Pile	Saturated sand bed

The shear waves were picked up by the array of embedded accelerometers. Each pair of adjacent accelerometers registered the arrival time of the first wave, the time difference between two accelerometers allowed the average shear wave velocity in the sand layer to be calculated. Figure 4 shows the signals acquired on the accelerometer array, with band pass filtering (0.1-10 *Hz*), for Test P-W-9 after the shaker fired a one-cycle smaller amplitude sinusoidal wave (around 0.01 *g* in amplitude and 2 *Hz* in frequency). The first peak on each time history of acceleration could be selected. The measured first peak amplitudes of the acceleration varied from 0.015 *g* (0.15 m/s^2) at the bottom of the sand bed to 0.03 *g* (0.3 m/s^2) at the top of sand bed. Each signal exhibited a pronounced first peak, as shown in Fig. 4. The traveling time was determined

by the first peak to the first peak criterion on the accelerometer pairs (A1 and A16; A16 and A11; and A4 and A11). Accordingly, the average shear wave velocity, V_s , of the soil stratum between the accelerometer pairs could be calculated as follows:

$$V_s = \Delta S/\Delta t \quad (1)$$

where ΔS and Δt are the distance between adjacent accelerometers and the registered time difference between the first peaks of accelerometer pairs, respectively. Fig. 5(a), 5(b), and 5(c) display the profiles of measured shear wave velocity for the tests as listed in Table 3. Although the dry sand beds (P-D-1, P-D-2, and P-D-3) and the saturated sand Beds (P-W-4, and P-W-9) have the similar relative density ($D_r \fallingdotseq 60\%$), the measured V_s values from the dry sand beds are higher than those from the saturated sand beds as shown in Fig. 5(a) and 5(b) because of the higher effective overburden pressure developing in the dry sand bed. The measured average shear wave velocities for the tested sand beds are summarized in Table 4.

Consider a uniform layer of isotropic, liner elastic soil deposit overlying rigid rock, which is subjected to a 1-D vertically propagating shear wave from the bedrock. The nature frequency of deposit, f_n, which depends only on the thickness and shear wave velocity of the deposit, provides a useful indication of the frequency of vibration at which the most significant amplification can be expected. The nature frequency is given by

$$f_n = \frac{V_s}{4H} \quad (2)$$

where H = thickness of uniform sand deposit. Substituting the measured average shear wave velocity of the tested sand deposit into Eq. (2), the nature frequency is calculated and listed in Table 4.

As described previously the nature frequency of vibration system is the frequency at which a system naturally vibrates once it has been set into motion. Figures 6(a) and 6(b) display the typical time histories of acceleration measured at the depths of 10.4 m and 12.6 m for Test P-W-9 during pre-shaking which was excited with 2 *Hz*. The start time of the free vibration are also pointed at in the figures. Fig. 7 displays the Fourier amplitude spectra for Test P-W-9, those which were computed from the time histories of acceleration (A16 and A7) measured at the sand deposit in the period of free vibration as shown in Fig. 6(a) and 6(b).

The maximum peak amplitude measured with the accelerometers of A1, A16, A4, and A11 all appears at the same frequency of 1.5 *Hz*. This frequency is defined as the calculated nature frequency of sand deposit. Moreover, the same value of calculated nature frequency is obtained no matter which exciting frequency used in the pre-shaking. The measured nature frequencies of the sand deposit are also listed in Table 4. The nature frequencies measured from the Fourier amplitude spectra are lower than those calculated with Eq. 2 in terms of the measured shear wave velocities. Both the measured and the calculated nature frequencies of dry sand deposit have the higher than those obtained from the saturated sand deposits. These consistent results of the nature frequency may illustrate that the use of pre-shaking is a convenient tool for the SI on the tested sand bed.

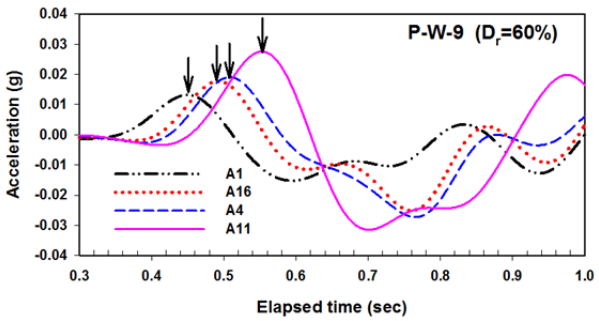


Figure 4 Time histories of acceleration measured during pre-shaking (exciting frequency of 2 *Hz*)

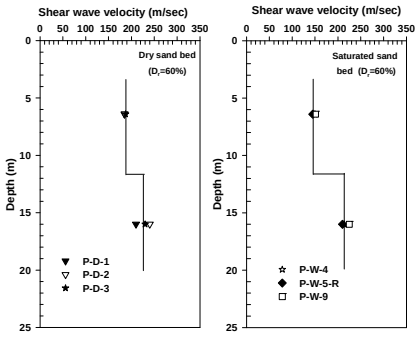


Figure 5 The profiles of measured shear wave velocity: (a) dry sand bed ($D_r \fallingdotseq 60\%$); (b) saturated sand bed ($D_r \fallingdotseq 60\%$)

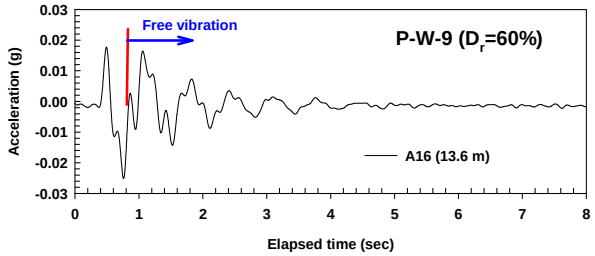
Table 4 Summary of average shear wave velocities, calculated and measured nature frequencies of sand beds

Test No.	Average V_s (m/sec)	Calculated f_n (Hz)	Measured f_n (Hz)
P-D-1	210	1.9	1.6
P-D-2	210	1.9	1.7
P-D-3	210	1.9	1.7
P-W-4	170	1.6	1.5
P-W-9	170	1.6	1.54

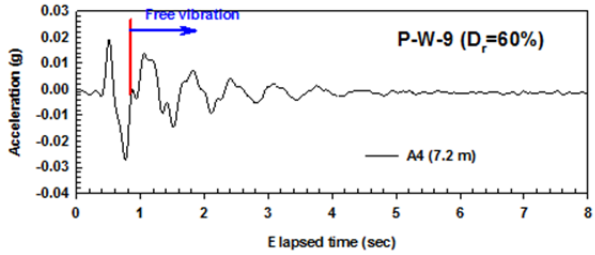
The accelerometers attached on the top and the bottom of tip mass of the pile can measure the time histories of acceleration during pre-shaking. Figures 8(a) and 8(b) display the typical time histories of acceleration measured at the top and bottom of tip mass attached on the B-Pile and S-Pile during pre-shaking which was excited with 2 *Hz* for Test P-D-3. The start time of the free vibration are also pointed at in the figures.

Fig. 9 displays the Fourier amplitude spectra for Test P-D-3, those which were computed from the time histories of acceleration (A18 and A24, A22 and A23). The same results are obtained from the other model tests in the study. The Fourier amplitude spectrum of each pile has two maximum peak amplitudes. One is the nature frequency of sand deposit the pile is embedded, the other is the nature frequency of pile. Table 5 gives the summary of the nature

frequencies of piles. The pile with the largest tip mass (L-Pile) has the lowest nature frequency (≒0.82 *Hz*), the pile with the second large tip mass (B-Pile) has the second low nature frequency (≒1 *Hz*), the pile with the lowest tip mass (S-Pile) has the highest nature frequency (≒3.2 *Hz*).

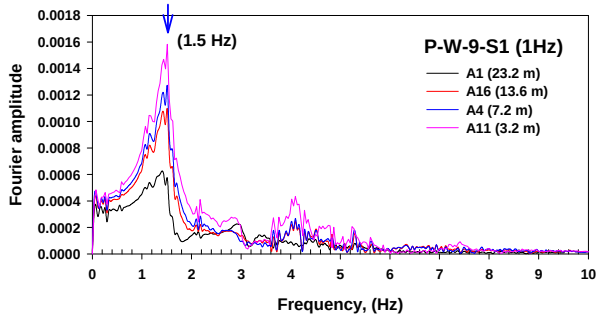


(a) A16 measured at depth of 13.6 m

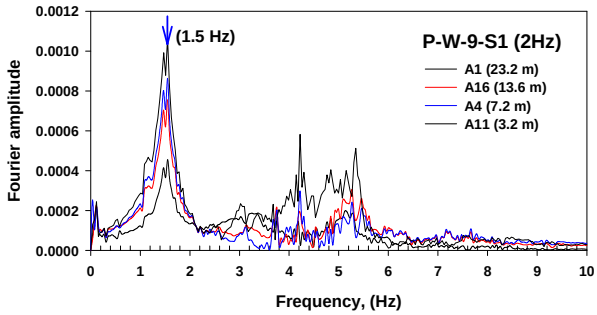


(b) A4 measured at depth of 7.2 m

Fig. 6 Time histories of acceleration in the sand deposit during pre-shaking (exciting frequency of 2 *Hz*) for P-W-9: (a) A16 measured at depth of 13.6 m; (b) A4 measured at depth of 7.2 m.

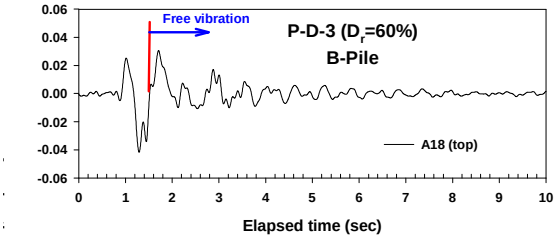


(a) exciting frequency of 1 *Hz*

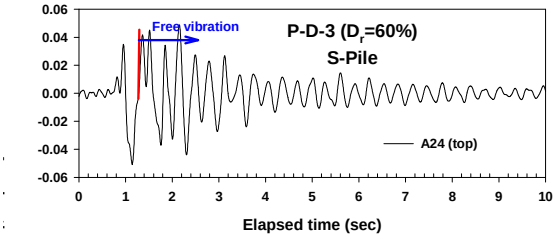


(b) Exciting frequency of 2 *Hz*.

Figure 7 Fourier amplitude spectra of sand bed in the period of free vibration for Test P-W-9 (S1): (a) exciting frequency of 1 *Hz*; (b) exciting frequency of 2 *Hz*.



(a) A18 measured at the top of tip mass of B-Pile



(b) A24 measured at the top of tip mass of S-Pile

Figure 8 Time histories of acceleration during pre-shaking (exciting frequency of 2 *Hz*) for P-D-3: (a) A18 measured at the top of tip mass of B-Pile; (b) A24 measured at the bottom of tip mass of S-Pile.

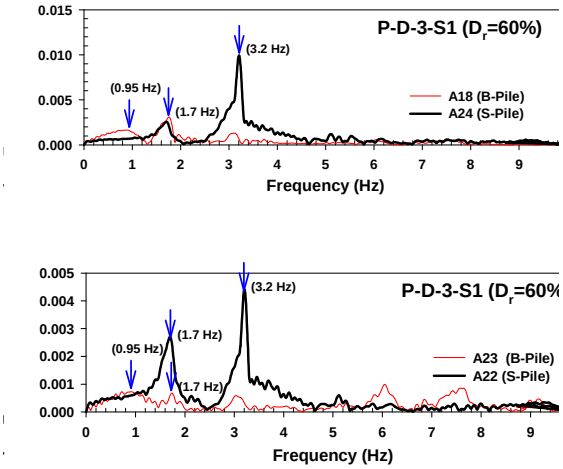


Fig. 12 Fourier amplitude spectra of B-Pile and S-Pile computed from the time histories of acceleration in the period of free vibration for Test P-D-3.

Table 5 Summary of the nature frequencies of piles

Test No.	1st nature frequency (*Hz*)			2nd nature frequency (*Hz*)		
	L-Pile	B-Pile	S-Pile	L-Pile	B-Pile	S-Pile
P-D-1	1.62	1.60		0.82	1.01	
P-D-2		1.74	1.78		0.96	3.2
P-D-3		1.5	-	0.80	0.96	
P-W-4		1.5	1.5		1.0	3.2
P-W-9		1.5			0.96	3.2

5. CONCLUSIONS

The pre-shaking technique is capable of measuring the V_s profile of soil deposit and determining the nature frequencies of both the soil deposit and the soil-structure system in a centrifuge model tested at an acceleration of 80 g. The pre-shaking is a non-destructive test, use of the shaker as a wave source and a vertical array of accelerometers embedded in the sand bed and the accelerometers attached on the pile as receivers. Accordingly the method of pre-shaking can be easily used for both the in-flight subsurface exploration (measurements of V_s profile) and the in-flight SI on the soil-structure systems. The natural frequencies measured from the pre-shaking tests are consistent with those derived from the theoretical basis. This technique can be conducted at any time before and after major earthquake events are fired.

Acknowledgements:

The authors express their gratitude for the financial supports from the Institute of Nuclear Energy Research (INER), Atomic Energy Council (NSC993113Y042A004 & NL1010367). These supports make this study and future researches possible.

References:

Arulnathan, R, Boulanger, RW, Kutter, BL, Sluis, WK (2000) New tool for shear wave velocity measurements in Model Test. Geotechnical Testing Journal 23(4): 444-453.

Brandenberg, BJ, Choi, S, Kutter, BL, Wilson, DW, Santamarina, JC (2006) A bender element system for measuring shear wave velocities in centrifuge models. In: proceedings of Physical Modeling in Geotechnics – 6th ICPMG: 160-165.

Corte, J.F., Garnier, J., Cottineau, L.M, and Rault, G. (1991) Determination of model soil properties in the centrifuge. Proc. Of International Conference Centrifuge 91, Boulder, CO, 13-14 June : 607-614.

Dyvik R, Madshus C. (1985) Lab measurements of G_{max} using bender elements. In: Proceedings of advances in the art of testing soils under cyclic conditions. Detroit, MI: ASCE Geotechnical Engineering Division: 186–196.

Gohl, WB, Finn, W.D. (1991) Use of piezoceramic bender in soil dynamic testing. In K.B. Shobha & W.B. Geoffrey (eds) Recent Advances in instrumentation, data accquision and testing in soil dynamics, Geotechnical Special Publication No.29: 118-133.

Hardin BO, Drnervich, VP (1972) Shear modulus and damping ratio in soils: design equations and curves. J. Soil Mech Foundations Div, ASCE 98(7): 667-691.

Kim NR, Kim. DS (2010) Development of V_s tomography testing system for Geotechnical Centrifuge Experiments. 7th Physical Modeling in Geotechnics, 7th ICPMG,. Springman, Laue and Seward (eds). L(1): 349-354.

Lee, C.J., Huang, H.Y. (2007) Wave velocities and their relation to fabric evolution during the shearing of sand. Soil Dynamics and Earthquake Engineering 27(1):1-13.

Lee, C.J., Wei, Y.C., and Kuo, Y.C. (2012). "Boundary effects of a laminar container in centrifuge shaking table tests," *Soil Dynamics and Earthquake Engineering*, Vol.34(1), 37-51.

Lee, C.J., Wang, C.R., Wei, Y.C., Hung, W.Y. (2012). "Evolution of the shear wave velocity during shaking modeled in centrifuge shaking table tests," *Bulletin of Earthquake Engineering*, Vol.10(2), 401-420.

Lei, F., Zeng, X. Figueroa, JL (2004) Shear Wave Velocity measurement in Centrifuge Using Bender Elements. International Journal of Physical Modeling in Geotechnics, 4(2):1-11.

Oskay, C., and Zeghal, M. (2011) A survey of Geotechnical system identification techniques. Soil Dynamics and Earthquake Engineering 31(4):568-582.

Rammah, KI, Ismail, MA, Fahey, M (2006) Development of a centrifuge tomography system at UWA. Proc. Physical Modelling in Geotechnics, 6th ICPMG, Ng, Chang and Wang (eds). L(1): 229-234.

10CUEE CONFERENCE PROCEEDINGS
10th International Conference on Urban Earthquake Engineering
March 1-2, 2013, Tokyo Institute of Technology, Tokyo, Japan

A CASE STUDY ON MULTIPLE MECHANISM MODEL IN THREE DIMENSIONAL SOIL-STRUCTURE INTERACTION ANALYSES

Ryo Ueda[1] and Ariyoshi Yamada[2]

1) Kobori Research Complex .inc, Japan
2) Kajima Corporation, Japan
uedar@kobori-takken.co.jp

Abstract: Directional nonlinear interaction in non-linearity of soil is an essential issue especially in three dimensional soil-structure interaction analyses. The multiple mechanism model is a rigorous method which is able to represent it, but it is seldom studied in details for practical adaptation so far. This study describes the effects of directional nonlinear interaction on dynamic response behavior of soil and structure, using three dimensional finite element analyses with multiple mechanism model. The results show that structural response subjected to two-directional input is analytically consistent with response to one directional synthesized input.

1. INTRODUCTION

Recently, some structures are constructed on relatively soft soil site, and their shape of foundation become complicated according to requirement of building design. Accurate computation is desired in such intricate cases. Multiple mechanism model is a rigorous method used for representing a soil non-linearity. In the method, polyhedron model is often introduced for the non-linear behavior, where the three dimensional stress and strain on virtual plains interact to each other.

The strain space multiple-mechanism model is originally proposed by Iai (Iai et al., 1993). The stress and stiffness is given by combining all the partial stress contributions from the virtual plain strain shear mechanisms over the entire directions of the axes.

Authors (Ueda et al., 2012) studied validity and accuracy of multiple mechanism model based on several case studies with a simple layered soil model, in which two directional responses were tested. It is shown that the response of soil subjected to two directional input is consistent with response to one directional synthesized input, and 8 plains model is comparable to 20 plains model in their accuracy. This implied that 8 plains model is expected to be applicable to execute three dimensional analyses under limited computational resources. However the effect of directional interaction in three dimensional model is not yet known in details so far.

2. COORDINATE TRANSFORMATION THEORY

Iai represents the theory of coordinate transformation for three dimensional analysis with reference to Cook,1981. With some mathematical and engineering background, coordinate transformation between original coordinate and transformed one is conducted a series of manipulations of matrix. In the three dimensional space the stress and strain vectors are written by

$$\{\varepsilon\}^T = \{\varepsilon_x \varepsilon_y \varepsilon_z \gamma_{xy} \gamma_{yz} \gamma_{zx}\} \tag{1}$$

The stress and strain vectors on transformed coordinates on virtual plain will given as

$$\{\tilde{\varepsilon}\}^T = [T_\varepsilon]\{\varepsilon\} \tag{2}$$

in which

$$[T_\varepsilon] = \begin{bmatrix} a_1^2 & b_1^2 & c_1^2 & a_1b_1 & b_1c_1 & c_1a_1 \\ a_2^2 & b_2^2 & c_2^2 & a_2b_2 & b_2c_2 & c_2a_2 \\ a_3^2 & b_3^2 & c_3^2 & a_3b_3 & b_3c_3 & c_3a_3 \\ 2a_1a_2 & 2b_1b_2 & 2c_1c_2 & (a_1b_2+a_2b_1) & (b_1c_2+b_2c_1) & (c_1a_2+c_2a_1) \\ 2a_2a_3 & 2b_2b_3 & 2c_2c_3 & (a_2b_3+a_3b_2) & (b_2c_3+b_3c_2) & (c_2a_3+c_3a_2) \\ 2a_3a_1 & 2b_3b_1 & 2c_3c_1 & (a_3b_1+a_1b_3) & (b_3c_1+b_1c_3) & (c_3a_1+c_1a_3) \end{bmatrix} \tag{3}$$

On the equation (3), components a_i ,b_i ,c_i (i=1,2,3) are direction cosines between original coordinate and transformed coordinate. Now let us define the directions of the axes with the angles ψ and ζ of a spherical coordinate shown in Figure1. The components are given by

$$\begin{bmatrix} a_1 & b_1 & c_1 \\ a_2 & b_2 & c_2 \\ a_3 & b_3 & c_3 \end{bmatrix} = \begin{bmatrix} \cos\psi\cos\zeta & \sin\psi\cos\zeta & -\sin\zeta \\ -\sin\psi & \cos\psi & 0 \\ \cos\psi\sin\zeta & \sin\psi\sin\zeta & \cos\zeta \end{bmatrix} \tag{4}$$

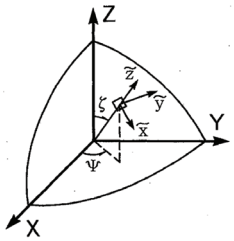


Figure 1 Spherical Polar Coordinate (Iai et al.1993)

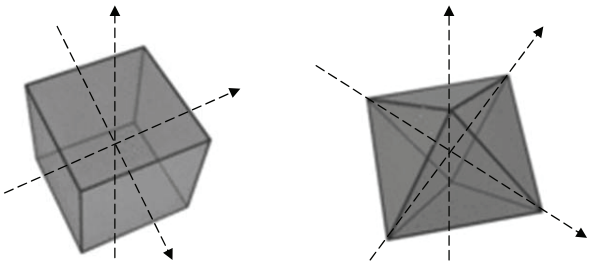
Transformed strains on each virtual plain are moreover transformed and decomposed into an assembly of simple shear strains on multi-spring model. Constitutive equation of relationship between strain and stress is adopted on each spring on all virtual plains.

The shape of virtual plain is theoretically arbitrary in general. Once the shape of virtual plain is decided the angles of spherical polar coordinates can be determined.

3. DIRECTIONAL NONLINEAR INTERATION

Directional nonlinear interaction, or simply "directional interaction," is explained as below. When a shear strain γ_{zx} is considered, the shear stiffness μ_{zx} should decrease due to non-linear effect. Then it should also affect other component μ_{yz}. The shear strain γ_{yz} affects γ_{zx}, vice versa. In order to consider this effect, multiple mechanism model combines all the partial stress contributions from the virtual plain strain shear mechanisms

As written in beginning in introduction, virtual plains for coordinate transformation are often defined as polyhedron, which has mathematical symmetry. Shapes of polyhedron are shown in Figure 2. The first is 6-plains model, what is called "cube". Cube has, needless to say, plains parallel to absolute coordinate. It is simple and easy to understand but it cannot follow the directional interaction behavior of x and y direction because virtual plains on any direction are independent to each other. The second is 8-plains model, "Octahedron". It can follow the directional interaction obviously.



6 Plains (Cube) 8 Plains (Octahedron)

Figure 2 Polyhedrons

4. ANALYSIS MODEL

A three dimensional soil-structure interaction model for case study is shown in Figure 3. It consists of 8-node solid elements of soil, rigid foundation, and shear spring model of structure. Analytical dimension is 200m in width and 80m in depth. The structure is 35-storied typical high-rise building with embedded raft foundation. Side and bottom boundary surfaces are supported with viscous boundary, and interaction correction force is considered adequately.

For more details, see also Figure 4. This is an enlarged view of octagonal foundation. In this case study, the shape of foundation must be axial-symmetric along the axis of input wave, because its soil impedance has to be equal in each direction of input wave.

Characteristic of soil is shown in Figure 5. Soil is composed of three layers. The foundation is built on second layer of 300m/s in S-wave velocity, and engineering bedrock at the bottom is 500m/s.

Input wave is shown in Figure 6. It is one of the waves defined by seismic design code in Japan. Its amplitude is normalized to 0.1G. One directional input case with $\sqrt{2}$ times amplitude as a benchmark, and 6 and 8 plains model for two directional input were computed.

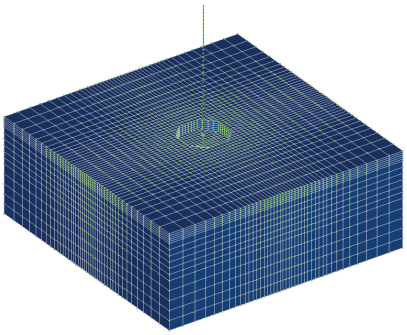


Figure 3 Model for Case Study

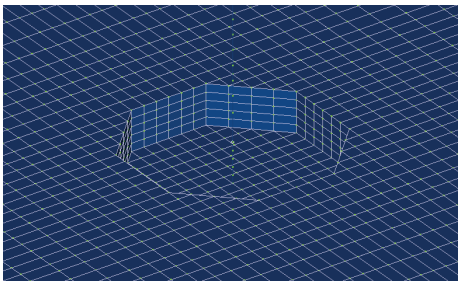


Figure 4 Model (Enlarged View of Foundation)

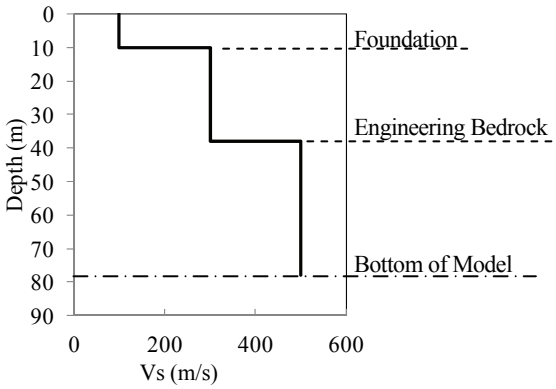


Figure 5 Characteristic of Soil

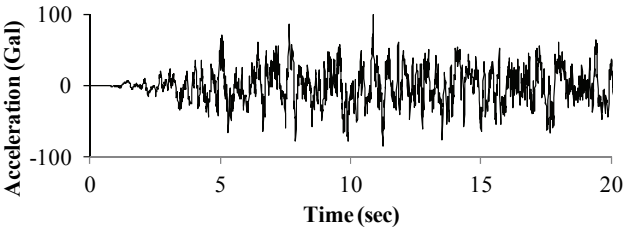


Figure 6 Acceleration of Input Wave

4. RESULTS

For grasping the result, figure 7 shows deformation and strain contour of three dimensional model. The building and surface of soil are deformed, while the boundary keeps semi-infinite condition. This implies that analysis is executed with sufficient numerical accuracy.

4.1 Validation of 8 Plains Model

Figure 8 shows response accelerations at 35th floor, foundation, and ground surface. Here the acceleration of benchmark model of one directional input is normalized in its amplitude with divided by $\sqrt{2}$. 8-plains model is almost consistent to the benchmark. To the contrary, 6-plains model is different in the wave form and its maximum acceleration. The case of 6-plains model overestimates the acceleration. The difference is larger in the ground surface and less in the top of structure.

The difference can be seen clearer in the acceleration spectrum shown in Figure 9. The predominant period of structure is about 2.0 sec. The difference is relatively small at period domain longer than 1.0 sec. It implies that directional interaction effect becomes larger on low-rise building.

Distribution of displacement on the ground surface and foundation at the time of 15sec is shown in Figure 10. The outline of foundation is represented by a dotted line. The figure of 8-plains model with two directional input is almost consistent to the benchmark if it is rotated by 45 degrees, while the figure of 6-plains model shows smaller values than benchmark obviously.

These results show that the 8-plains model is successful to compute the directional nonlinear interaction.

4.2 More Improvement of Accuracy

Let us examine the case of another direction of input. Figure 11 shows displacement orbits of ground surface, in which the waves are input in the direction of 45 degrees and 22.5 degrees, also axial symmetric, toward the x-axis. Theoretically displacement orbit should draw a straight line independently to direction of input. It is confirmed in the case of 45 degrees. Nevertheless it is found that the orbit of 22.5 degrees input is irregularly fluctuating in the 6-plains model case. Comparing 8-plains model, its fluctuation is lessened, even though not perfect. Now an additional case of 20-plains model, shown in Figure 12, is introduced here. Its fluctuation is even slighter than other former cases.

These results show that the accuracy could be improved by increasing the number of plain.

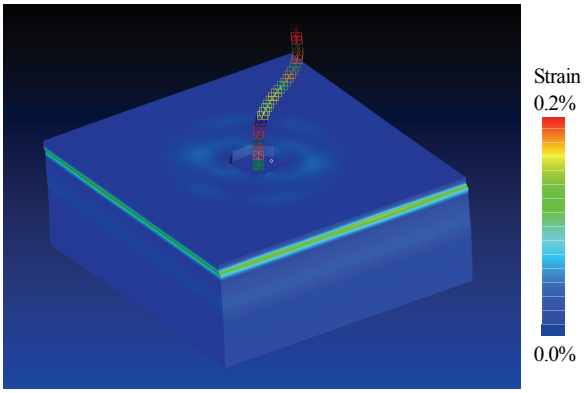
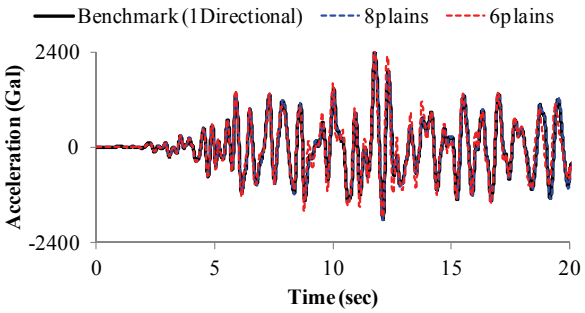
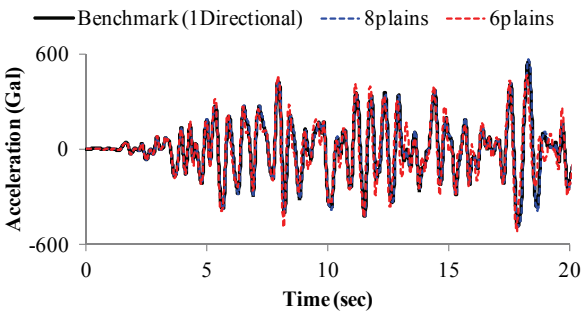


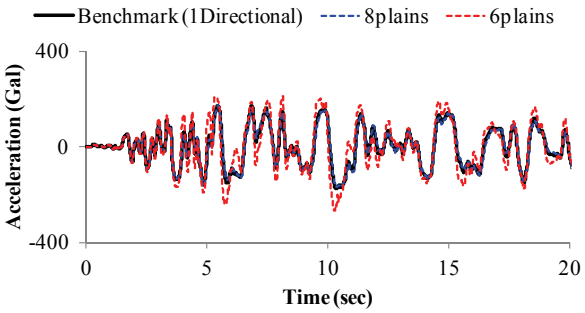
Figure 7 Deformation and Strain Contour Snap Shot at 15 sec



(a) 35th Floor

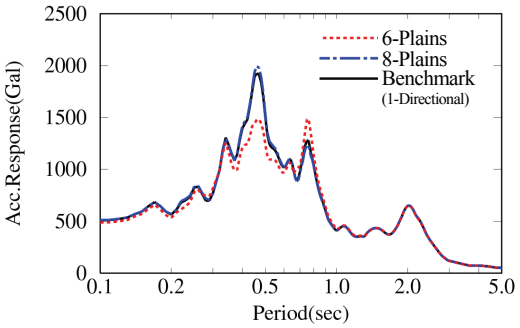


(b) Foundation



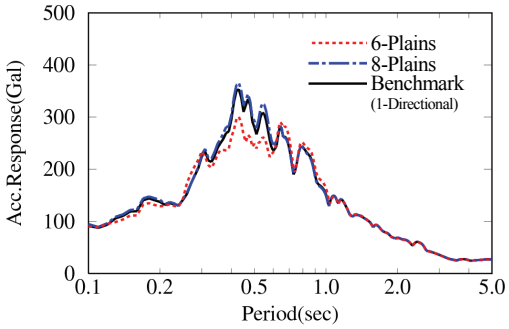
(c) Ground Surface

Figure 8 Acceleration Time History



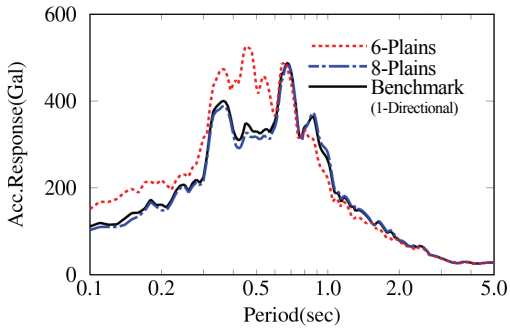
Acc. Response Spectrum (Damp=5%)

(a) 35th Floor



Acc. Response Spectrum (Damp=5%)

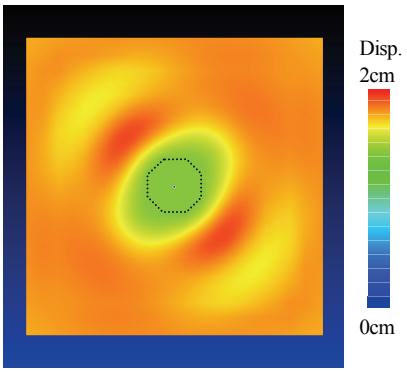
(b) Foundation



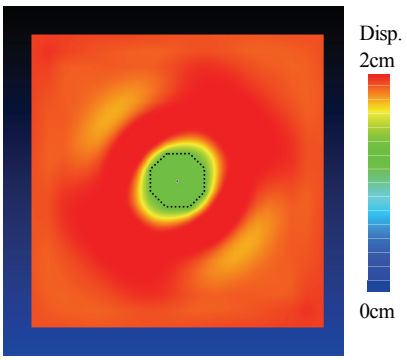
Acc. Response Spectrum (Damp=5%)

(c) Ground Surface

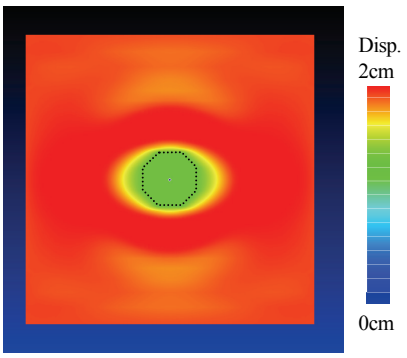
Figure 9 Acceleration Response Spectrum



(a) 6-plains

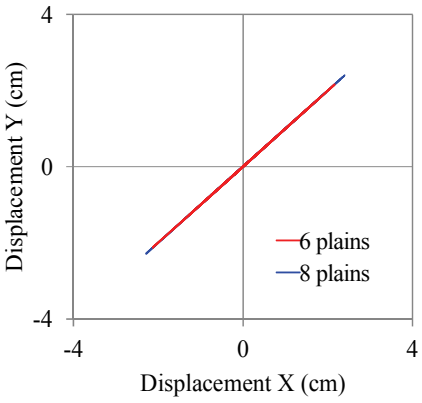


(b) 8-plains

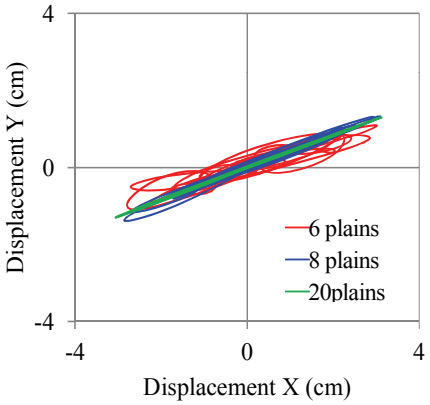


(c)Benchmark (one directional)

Figure 10 Distribution of Displacement on Ground Surface and Foundation at 15sec



(a) Response to Input of 45 Degrees



(b) Response to Input of 22.5 Degrees

Figure 11 Displacement Orbit of Ground Surface

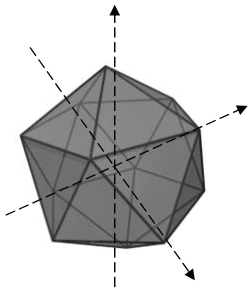


Figure 12 20 Plains (Icosahedron)

5. CONCLUSIONS

This paper represents a case study on three dimensional soil-structure interaction analyses using multiple mechanism model. The directional nonlinear interaction is computed successfully and applicability of multiple mechanism model to three dimensional analysis is demonstrated.

Meanwhile, the accuracy of calculation could be improved by increasing the number of plain, which is approximating to the ideal sphere. 8 plains model gives practically sufficient accuracy in consideration with engineering purpose and computational cost. However, when more detailed examine is required for such as highly complicated structure, liquefiable soil, severe earthquake, and so on, it would be better to refer to results obtained by using more than 8 plains model.

References:

Iai,S., Matsunaga, Y. and Kameoka, T. (1992): "Strain Space Plasticity Model for Cyclic Mobility", *Soils and Foundations*, Vol. 32, No.2, pp. 1-15.

Ueda,R., Yamada A., Koyamada K. and Okano, H. (2012): "A Case Study on Polyhedron Model of a Strain Space Multiple Mechanism Model", *9CUEE Conference Proceedings*, 9th International Conference on Urban Earthquake Engineering/ 4th Asia Conference on Earthquake Engineering, pp.469-472.

Cook.,R.D. (1981): "Concepts and Applications of Finite Element Analysis", John Wiley & Sons.

Ueda,R. et al. (2012): "Evaluation of Input Motions for High-Rise Buildings Based on the Observed Data, part1-4", *Proceedings B2*, Conference of Architectural Institute of Japan, pp.633-640.

Yamada.A., Nagano, M., Yamazoe, M., Miura, K.,(2002) : "Earthquake Response Analytical Method for 3-Dimentional Large Scale Soil Model Considering Multi-Volumes with Variable Mesh Size and Integral Time Increment", *Journal of Structrure and Constrution Engineering*, Transaction of Architectural Institute of Japan, No.561, pp.73-80.

Chen H. et al (2012): "Numerical Investigation on Seismic Responses of A Liquefiable Sandy Soil Stratum with Multiple Silt Layers", *9CUEE Conference Proceedings*, 9th International Conference on Urban Earthquake Engineering/ 4th Asia Conference on Earthquake Engineering, pp.473-478.

10CUEE CONFERENCE PROCEEDINGS
10th International Conference on Urban Earthquake Engineering
March 1-2, 2013, Tokyo Institute of Technology, Tokyo, Japan

LONG-TERM SETTLEMENT OF HOLOCENE CLAY GROUND AFTER THE 2011 GREAT EAST JAPAN EARTHQUAKE

Naohiro Nigorikawa[1] and Yoshiharu Asaka[2]

1) Researcher, Institute of Technology, Shimizu Corporation, Japan
2) Senior Research Engineer, Institute of Technology, Shimizu Corporation, Japan
n.nigorikawa@shimz.co.jp, yoshiharu.asaka@shimz.co.jp

Abstract: The aim of the study reported in this paper is to reveal the long-term settlement of Holocene clay ground after the 2011 Great East Japan Earthquake. The authors have taken level readings five times across Urayasu City, Chiba prefecture, during the period from April 2011 to April 2012. The result is a chronological record of changes in settlement of first-order benchmarks and survey points showing that long-term ground settlement is taking place due to the earthquake. The settlement rate is shown to be 7 mm/year, more than 2.5 times the rate of settlement before the earthquake. However, no such subsidence is observed where reclaimed land has been improved using the sand drain and fill preloading methods. Further, the alluvial lowland has also not settled since the earthquake.

1. INTRODUCTION

Until now, on the types of ground-related disaster receiving most attention tends to have been those caused by liquefaction of sandy ground and liquefaction-induced deformation. Liquefaction was observed in the 2011 Great East Japan Earthquake (termed the 3.11 Earthquake in this paper), with coastal reclaimed areas of Tokyo Bay, including Urayasu City in Chiba Prefecture, suffering extensive damage over a wide area. Many studies and experiments related to liquefaction were carried out in the wake of the 1964 Niigata Earthquake, with the result that the public is now well aware of the liquefaction problem.

On the other hand, cohesive ground behaves rather differently in an earthquake; there is no instantaneous deformation, as occurs with sandy grounds, so no seismic capacity problem has been noted. As a result, design and construction methods related to architectural and civil engineering structures do not allow for any consideration of the co-seismic and post-seismic behavior of cohesive ground. Yet detailed observations of disaster areas as well as centrifuge model tests (Hotta et al., 1998) carried out in recent years have shown that land subsidence might occur over a long period of time following an earthquake, particularly in soft cohesive ground. Thus an essential consideration in the design of foundations not directly supported by stiff ground layers or embankments is the evaluation of post-seismic residual ground deformation. But with a scarcity of accumulated measurements of cohesive ground settlement, there has been little effort to investigate or analyze this phenomenon (ex. Koishi et al., 2012).

In this paper, data on the long-term ground settlement of Holocene clay in Urayasu City following the 3.11 Earthquake is obtained by taking levels and trends in settlement based on the measurements are reported.

2. GEOLOGICAL CONDITIONS IN URAYASU CITY

2.1 STRATAL ORGANIZATION

Figure 1 shows the location of Urayasu City in the west of Chiba Prefecture. The southern part of Urayasu was formed from reclaimed land along the shores of Tokyo Bay, and three-quarters of the city stands on reclaimed land. The reclamation was carried out mainly with sand excavated from the seabed off Urayasu. Reclamation began in 1964 and was completed in 1980, with the work taking place in phases: the first phase ran from 1964 through 1971, with the rest of the reclamation taking place in the second phase from 1975 through 1980. The upper layer at the surface consists of sandy fill in most areas, underlain by Holocene sand with an N-value between 2 and 20, below that is Holocene clay

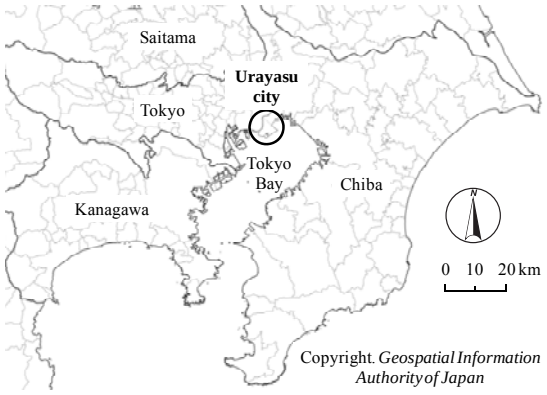


Figure 1 Location of Urayasu city

with an N-value between 0 and 5. Pleistocene sand with an N-value of 50 or greater is deposited below these Holocene layers. In addition, there is humus soil underlain by Pleistocene sand in some places.

Figure 2 shows the history of this land reclamation as well as two geological sections through Urayasu. The data in this figure was obtained on the basis of borehole investigations. Buried valleys and buried terraces are present below Urayasu, causing complex variations in the thickness of the Holocene clay. Along line A-A' the clay is 30 to 40 meters thick, while along B-B' it is 10 meters thick near the old coastline to the northern end and 40 meters thick at the seaward end, with a marked thickening toward the sea (in the southeast direction).

As this makes clear, there are thick layers of Holocene clay under Urayasu. In fact, there were concerns about consolidation of Holocene clay layer from the beginning of the reclamation work. According to a contemporary report on foundation improvement work, the eastern side of the area reclaimed in the second phase was improved using the sand drain and/or fill preloading methods as a solution the problem. The improved area is indicated in Fig. 2.

2.2 LEVEL FLUCTUATION OF FIRST-ORDER BENCHMARKS MEASURED BY THE PREFECTURAL GOVERNMENT

The Chiba prefectural government takes levels every year in order to observe ground level fluctuation in the prefecture. Figure 3 shows recent level changes of first-order benchmarks near the cross sections in Fig. 2, illustrating ground displacement in this part of Chiba Prefecture before the 3.11 Earthquake. Vertical ground displacement has been close to zero overall at benchmarks U1 and U14. On the other hand, benchmarks U3A and U16 have settled. These points are located in areas reclaimed in the first phase. This means that post-reclamation consolidation has been continued until the present. Figure 4 shows linear approximate equations fitted to the settlement measurements for benchmarks U3A and U16 before the 3.11 Earthquake. The settlement is linear at a rate of 0.004-0.008 mm/day (or approximately 1.4-3.0 mm/year).

3. OUTLINE OF LEVEL SURVEYS BY THE AUTHORS

3.1 SURVEY LINES AND SURVEY POINTS

The authors began by establishing two survey lines across Urayasu. Figure 5 shows the locations of the survey lines, survey points, and first-order benchmarks (as managed by Chiba prefecture). Line-A connects Maihama with Chidori. It has a total length of about 3 kilometers. Line-B, taking Urayasu Station (on the Tozai subway line) as its starting point, links Kitasakae and Nekozane with Hinode and Akemi. It has a total length of about 5 kilometers. These lines were chosen to cross the alluvial lowland and reclaimed land from northwest to southeast in order to look squarely at the relation between long-term settlement after the 3.11 Earthquake and the reclamation history.

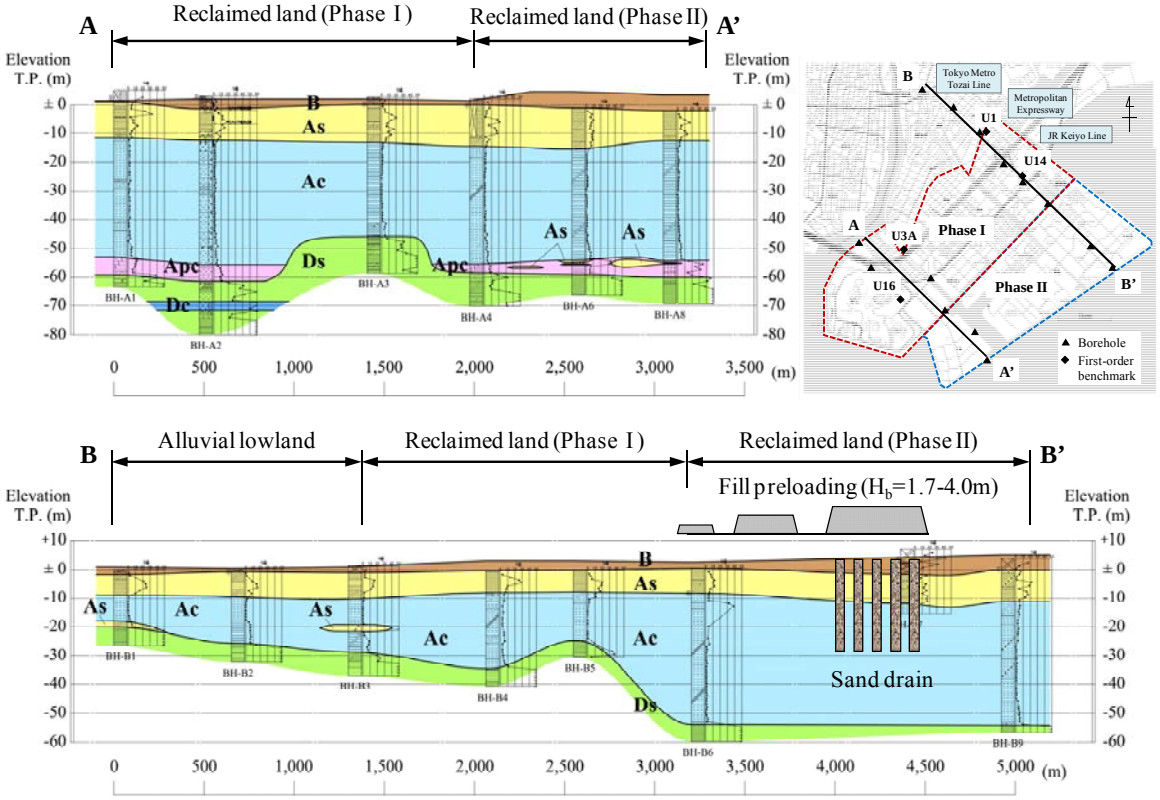


Figure 2 History of the land reclamation and geological sections through Urayasu

Neighborhoods toward the southern ends of these lines lie on comparatively new ground.

Eight survey points were selected on Line-A and twelve on Line-B. The interval between these points ranges from 150 to 800 meters. The points were selected as having a small chance of being redeveloped, demolished, removed,

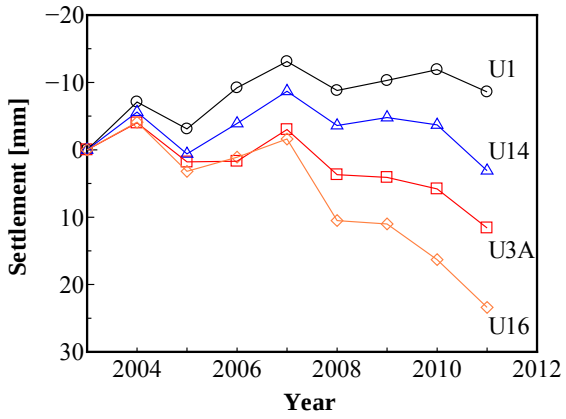


Figure 3 Level changes for first-order benchmarks before the 3.11 earthquake

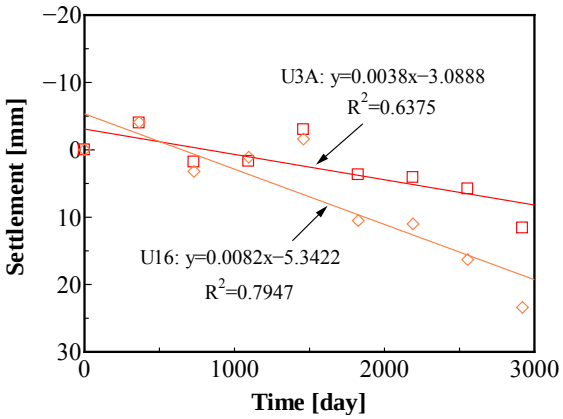


Figure 4 Linear approximate equations fitted to the settlement measurements for benchmarks U3A and U16 before the 3.11 Earthquake

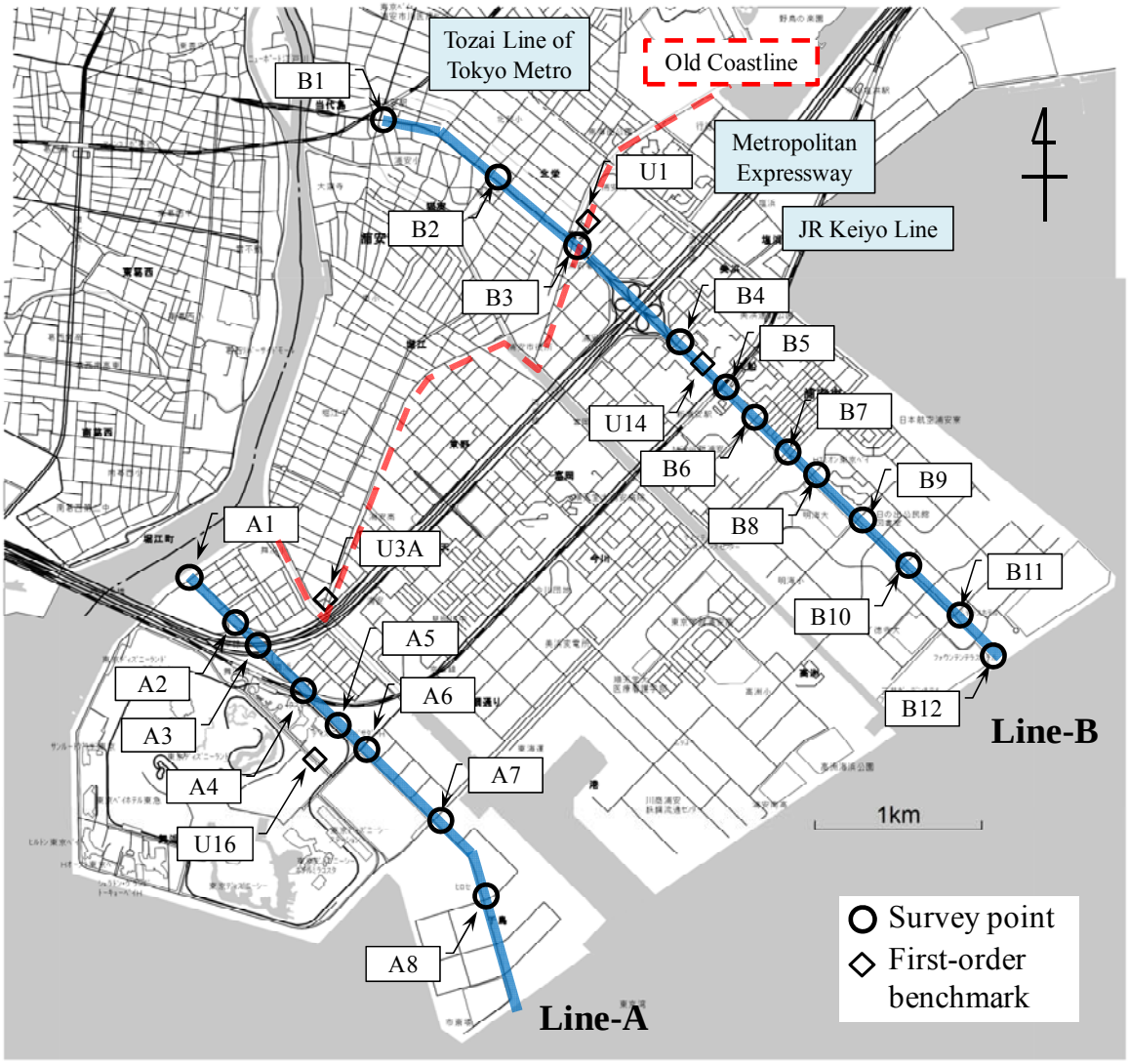


Figure 5 Location of survey lines, survey points, and first-order benchmarks

and suffering local subsidence since the intention is to obtain accurate level data over a long period. The same points were surveyed in each set of level readings. As examples of the survey points chosen, Photo 1 shows point A2, the foundation of a street lamp, and Photo 2 shows point B4, a metal marker.

All reference marks, which would not be affected by ground level fluctuation, were set up on structures supported by bearing piles or on elevated bridge piers. The type of foundation was identified by company or public records of construction.

3.2 LEVEL READINGS

The authors used the following procedure to obtain the level readings:

(1) Measure level of the reference mark (Photo 3);

(2) Relay the reference level to a location close to the survey point (Photo 4). Relay points are at intervals of 30-40 meters;

(3) Measure the relative elevation of the survey point as seen from the reference mark (Photo 5).

To control the accuracy of the observations, measurements were made out and back between three or four survey points. The difference at closure is less than 2 millimeters.

Measurements began in April 2011 and survey point levels have been taken five times as of April 2012 (including measurement of the initial levels). In addition, the first-order



Photo 3 Observation of level of the reference point



Photo 1 Example of the survey point (A2: a foundation of a street lump)



Photo 4 Setting of a rely point



Photo 2 Example of the survey point (B4: a metal marker)



Photo 5 Observation of level of the survey point

benchmarks (U1, U14, and U16) were measured each time.

4. RESULT OF LEVEL SURVEYS BY THE AUTHORS

4.1 SETTLEMENT OF FIRST-ORDER BENCHMARKS

Figure 6 shows the measured settlement of the first-order benchmarks with respect to the initial April 2011 elevations recorded after the 3.11 Earthquake. Benchmark U1, sited above the alluvial lowland of the old coastline, has fallen and risen and there is no overall trend in the subsidence. On the other hand, benchmarks U14 and U16 located centrally in the phase I reclaimed land show a monotonic downward settlement. For the purpose of investigating the long-term settlement trend following the earthquake, fitted lines obtained by calculation are shown in Fig. 7. The two lines have almost the same gradient and the settlement rate is 0.02 mm/day (or 7 mm/year).

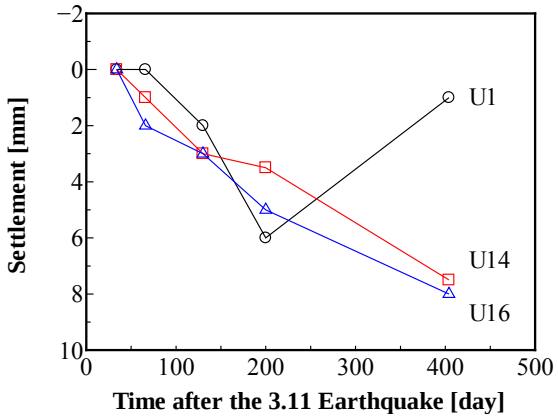


Figure 6 Level changes of the first-order benchmarks measured by the authors after the 3.11 Earthquake

Table 1 compares the settlement rate before and after the 3.11 Earthquake. The vertical strain rate, defined as the amount of settlement divided by the total thickness of the Holocene clay layer, is taken as an index of settlement in this paper because it is well known that settlement is closely linked to the Holocene clay thickness. In the case of benchmark U14, consolidation settlement by reclamation had been convergent before the earthquake. However, subsidence has re-occurred since the earthquake. As for benchmark U16, the post-earthquake vertical strain rate is 2.5 times its value before the earthquake.

Figure 8 shows the overall time history of the settlement of benchmark U16. This shows the displacement of the horizontal ground surface, which includes the following components: consolidation settlement following reclamation before the earthquake; immediate post-earthquake settlement caused by liquefaction; and long-term settlement of the Holocene clay following the earthquake. The amount of liquefaction settlement is based on an investigation of liquefaction damage (Fukutake et al., 2011) carried out seven days after the earthquake. The slope

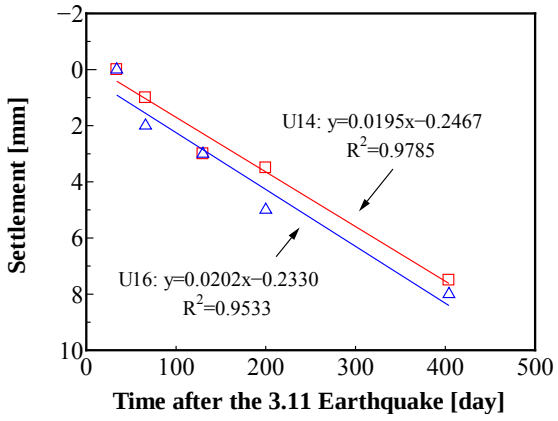


Figure 7 Linear approximate equations fitted to the settlement measurements for the first-order benchmark after the 3.11 Earthquake

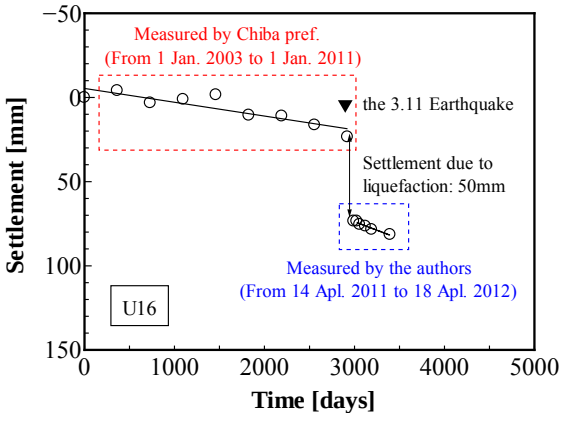


Figure 8 Overall time history of the settlement of the first-order benchmark U16

Table 1 Settlement rates before and after the 3.11 Earthquake

Bench-mark	Before the 3.11 Earthquake			After the 3.11 Earthquake			Ratio of vertical strain rates (After/Before)
	Settlement rate		Vertical strain rate	Settlement rate		Vertical strain rate	
	[mm/day]	[mm/year]	[/year]	[mm/day]	[mm/year]	[/year]	
U14	0.000	0	—	0.02	7	1.6E-04	—
U16	0.008	3	8.8E-05	0.02	7	2.2E-04	2.5

of the settlement line is clearly steeper after the earthquake; as noted above, the ratio of pre- and post-earthquake settlement strain rates is 2.5 times.

4.2 SETTLEMENT OF SURVEY POINTS

This section discusses the settlement of the survey points, which exhibit a characteristic behavior.

Figure 9 shows the vertical displacement of survey points B1 to B3 following the 3.11 Earthquake. None of these points have settled significantly. As seen in Fig. 5 previously, these three survey points are located to the south of Line-B and lie above the alluvial lowland ground which has been deposited for over ten thousand years and therefore compacted more than reclaimed ground. From this it is considered that the post-earthquake settlement rate at these points is not greater than before the earthquake.

Figure 10 shows the settlement of survey points B8 to B11 after the 3.11 Earthquake. These points are all located on the phase II reclaimed land. Nevertheless, the ground settlement behavior of each point is different. Survey points B8 and B9 have settled, while the other two have not. As already noted in section **2.1**, eastern areas of the phase II reclaimed ground were improved using both the sand drain and fill preloading methods. It is assumed that survey points B10 and B11 lie within this improved area, so they have not exhibited any settlement yet. On the other hand, survey point B8 and B9 are located in improved areas using only fill preloading, so they have seen significant settlement.

These results demonstrate that the long-term settlement behavior of the Holocene ground since the earthquake differs according to whether the area was reclaimed or reclaimed and then improved.

Figures 11 and 12 shows the chronological changes in settlement along the two survey lines. It is clear in this figure that subsidence occurs predominantly above thick Holocene clay layers.

5. CONCLUSIONS

The authors have carried out level surveys with the aim of observing the long-term settlement of Holocene clay in

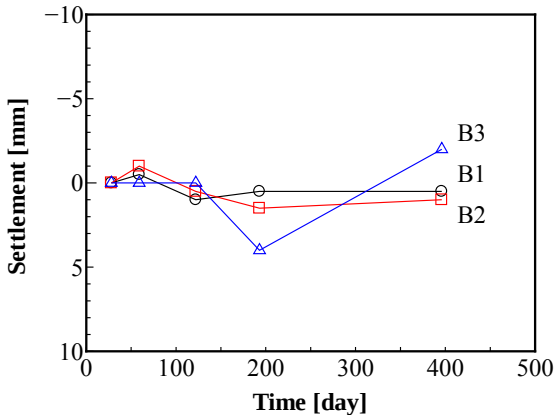


Figure 9 Settlement of survey points B1 to B3 following the 3.11 Earthquake

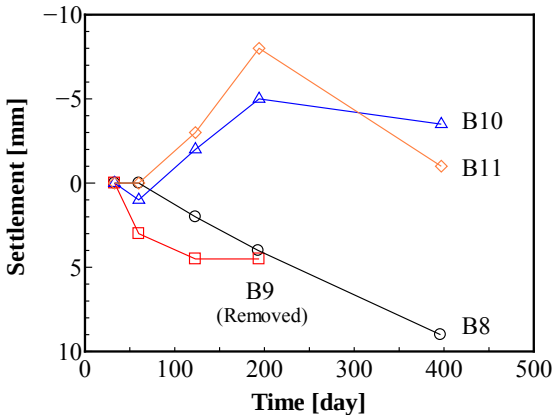


Figure 10 Settlement of survey points B8 to B11 following the 3.11 Earthquake

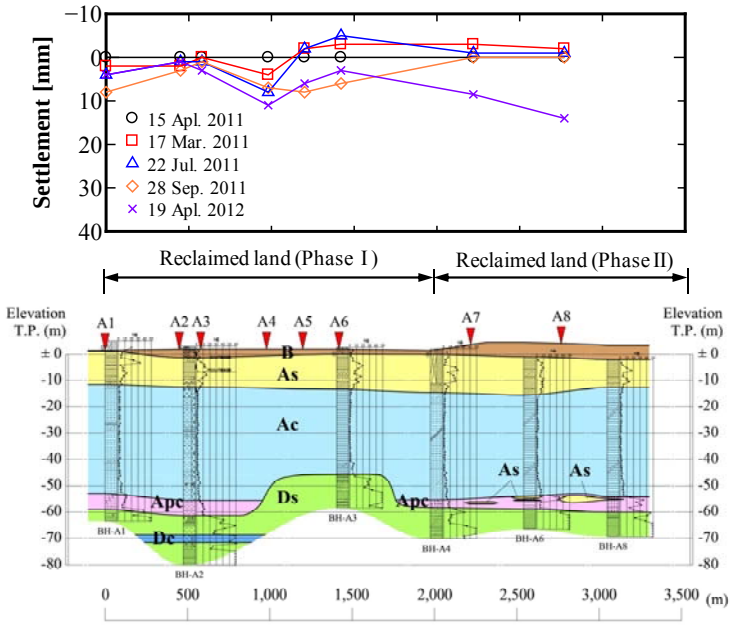


Figure 11 Chronological changes in settlement along the survey line: Line-A

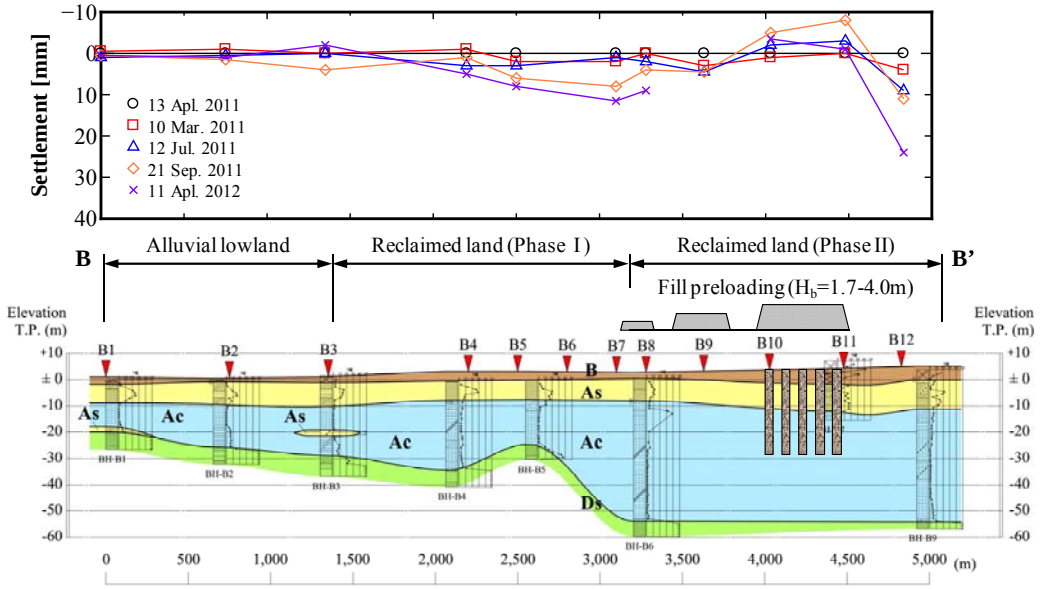


Figure 12 Chronological changes in settlement along the survey line: Line-B

Urayasu, Chiba Prefecture, following the 3.11 Earthquake. The results of the investigations can be summarized as follows:

(1) Long-term settlement of Holocene clay following the 3.11 Earthquake was observed at the first-order benchmarks and the survey points on reclaimed ground;

(2) The settlement rate observed at phase I reclaimed land after the earthquake was 7 mm/year. This is 2.5 times the settlement rate observed before the earthquake. That is, the earthquake has accelerated the subsidence of Holocene clay ground;

(3) The long-term post-earthquake settlement behavior is different according to whether the reclaimed land has been improved or not. Post-earthquake subsidence was not observed in the case of reclaimed land that had been improved using both the sand drain and preloading methods. The alluvial lowland ground also has not settled since the earthquake.

The results reported in this paper are based on ground displacement data collected by the authors in the year following the earthquake. However, there is concern that settlement of the Holocene clay may continue, so the authors plan to continue level surveys on a regular basis.

Acknowledgements:

The authors are grateful to Dr. Kiyoshi Fukutake of Shimizu Corporation for the information about the 3.11 earthquake damage in Urayasu. Also the insightful advice of Dr. Yasuhiro Shamoto and Mr. Tadashi Sakamoto of Shimizu Corporation on establishing survey points is highly appreciated. Additional data for this study was quoted from boring logs and level fluctuations of first-order benchmarks published by Chiba prefecture.

References:

Chiba prefecture, "*Information bank of geological environment*," available from http://wwwp.pref.chiba.lg.jp/pbgeogis/servlet/infobank.index (accessed 7 Dec. 2012).

Chiba prefecture, "*Result of annual leveling*," available from http://www.pref.chiba.lg.jp/suiho/jibanchinka/torikumi/seikaomote.html (accessed 7 Dec. 2012).

Urayasu city, "*Information book of urban environment*," available from http://www.city.urayasu.chiba.jp/menu3183.html (accessed 7 Dec. 2012).

Fukutake, K. and Jang, J. (2011): "Studies on Soil Liquefaction and Settlement in the Urayasu District Using Effective Stress Analyses for the 2011 East Japan Great Earthquake," *Journal of Structural Mechanics and Earthquake Engineering*, Vol. 68, No. 4, pp. I_293- I_304 (in Japanese).

G.L.Fiegel, B.L.Kutter, I.M.Idriss (1998): "Earthquake-induced Settlement of Soft Clay," Centrifuge 98, pp. 231-236.

Hotta, H., Shamoto, Y., Tamura, T., Narikawa, M., Ohshima, Y. and Kishino, Y. (1998): "Study on Settlement and Seismic Behavior of Spread Foundation on Thick Cohesive Stratum: Part 2 Centrifuge Model Test," *Report of the Annual Meeting of the Architectural Institute of Japan*, pp. 557-558 (in Japanese).

Japan Railway Construction Public Corporation (1991): "Construction record of JR Keiyo Line," 1241p.

Jinbo, H. and Kimura, T. (1994): "Foundation improvement for land reclamation (waterfront area), -Eastern area of Urayasu and Minato Mirai 21 Area-," *Monthly Magazine Dobokugijutsu*, pp. 56-63, Dobokugijutsusha.

Koishi, Y., Tomobuchi, M., Ohtsuka, S. and Isobe, K. (2012): "A Study on Long-term Settlement of Holocene Clay Ground Following an Earthquake," *Report of the Annual Meeting of the Japanese Geotechnical Society*, pp. 265-266, (in Japanese)

Tohno, I. and Yasuhara, K. (1991): "Lectures: Repeated consolidation of the soil, 3. Case study of repeated consolidation of ground (1),"*Tsuchi-To-Kiso*, Vol. 39, No. 7, pp. 85-91 (in Japanese).

Yasuhara, K. and Tohno, I. (1991): "Lectures: Repeated consolidation of the soil, 4. Case study of repeated consolidation of ground (2)," *Tsuchi-To-Kiso*, Vol. 39, No. 8, pp. 73-80 (in Japanese).

Yasuhara, K., Tokida, K., Matsuo, O. and Nasu, M. (1998): "Lectures: Dynamical property of cohesive soil, 3. Case history of cohesive soil dynamic problems and phenomenon mechanism." *Tsuchi-To-Kiso*, Vol. 46, No. 7, pp. 57-62 (in Japanese).

10CUEE CONFERENCE PROCEEDINGS
10th International Conference on Urban Earthquake Engineering
March 1-2, 2013, Tokyo Institute of Technology, Tokyo, Japan

ESTIMATION OF BEARING CAPACITY AND PULL-OUT RESISTANCE OF A PILE WITH OR WITHOUT A WING PLATE IN ALTERNATELY CYCLIC LOADING BASED ON CENTRIFUGAL MODEL TESTS

Hiroko Suzuki [1], Kei Inamura[2], Kohji Tokimatsu [3], Masatoshi Wada[4] and Hideyuki Mano[5]

1) Assistant Professor, Architecture and Building Engineering, Tokyo Institute of Technology, Japan
2) Former Graduate Student, Architecture and Building Engineering, Tokyo Institute of Technology, Japan
3) Professor, Architecture and Building Engineering, Tokyo Institute of Technology, Japan
4) Group Manager, Building Construction & Steel Structures Division, Nippon Steel & Sumikin Engineering, Japan
5) Group Manager, Institute of Technology, Shimizu Corporation, Japan
hsuzuki@arch.titech.ac.jp

Abstract: In order to estimate the effects of alternately cyclic loading on bearing capacity and pull-out resistance of piles, monotonic and cyclic vertical loading tests were conducted on a pile with or without a wing plate near the pile tip under a centrifugal force field of 30 G. In the test model, a pile model penetrated a dry sand deposit prepared in a rigid box. Both the pull-out shaft friction and wing resistance decrease with increasing amplitude and number of cyclic loadings. In contrast, the pushing shaft friction also decreases but the pushing wing and tip resistances increase with increasing amplitude and number of cyclic loadings.

1. INTRODUCTION

Piles supporting a structure suffer cyclic vertical loading due to overturning moment from the structure. In cases of tower-like structures and/or tall buildings, the vertical load induced by the overturning moment is considered to be large. The cyclic vertical loading lowers frictional resistance of piles, which might have affected the bearing capacity and pull-out resistance of piles. In the field survey made after the 2011 Tohoku Pacific Ocean Earthquake, it was found that the damaged piles were pulled out with toppled structures in the coastal areas that tsunami attacked. It is possible, when soil liquefaction and/or cyclic loading had lowered the frictional resistance of piles, horizontal and buoyant forces of the tsunami were applied to the building, pulling the piles out of the ground (Architectural Institute of Japan, 2011). It is hence important to investigate the frictional resistance in such a case, where soil liquefaction and/or cyclic loading occur.

To investigate the bearing capacity and pull-out resistance of piles, in-situ alternately cyclic loading tests have been conducted on full-scale pile models. Yajima et al. (1992) have suggested that the maximum shaft friction of a pile is larger in the pushing direction than in the pulling direction. Nonomura et al. (2004) have suggested that the maximum shaft friction is smaller in alternately cyclic loading than in cyclic axial compressive loading. In cases of a pile with a wing plate near the pile tip, the wing resistance could act against vertical load (Kokuda et al., 2006). Komatsu et al. (2003) have confirmed that, in the pulling direction, the wing resistance acts against vertical load instead of the shaft friction after the shaft friction is lowered. However, in-situ tests need large-scale apparatus, and therefore many in-situ tests were not conducted.

To estimate the bearing capacity and pull-out resistance of piles, centrifugal model tests were conducted. In the tests, for a pile with or without a wing plate, alternately vertical cyclic loading, monotonic compressive loading and monotonic tensile loading were conducted. In this study, the effects of alternately cyclic loading on shaft friction, wing resistance and tip resistance are investigated based on the centrifugal model tests.

2. CENTRIFUGAL MODEL TESTS ON PILES WITH OR WITHOUT A WING PLATE

To investigate the effects of alternately cyclic loading on bearing capacity and pull-out resistance of piles, centrifugal model tests were conducted on piles with or without a wing plate. Fig. 1 shows a test model. In the test, a pile model was set in a dry sand deposit constructed in a cylindrical rigid box with an inner diameter of 500 mm and a height of 500 mm. To

carry out loading, a hydraulic actuator was jointed with the pile model. Fig. 2 shows pile models with or without a wing plate. The pile models were made of stainless steel pipes having a diameter of 21.7 mm and a thickness of 3 mm. In the case of a pile with a wing plate, a wing plate with a diameter of 33.6 mm and a thickness of 3 mm was welded to the pipe near the tip. Both the piles had strain gauges on the inner surface and a load cell at the tip, as shown in Figure 2. The gauges were placed at seven depths, which were named SG1 to SG7. To increase the shaft friction on the pile surface, dry sand was applied on the pile surface. To prepare a dry sand deposit in a cylindrical box, Toyoura sand (e_{max} = 0.982, e_{min} = 0.604) was used. The sand layer had a relative density of 90 % and a height of 400 mm. The sand was air-pluviated to form a uniform layer. When the height of the sand layer reached the designated height (160 mm), the pile model was set with a penetration of 10 mm into the sand layer.

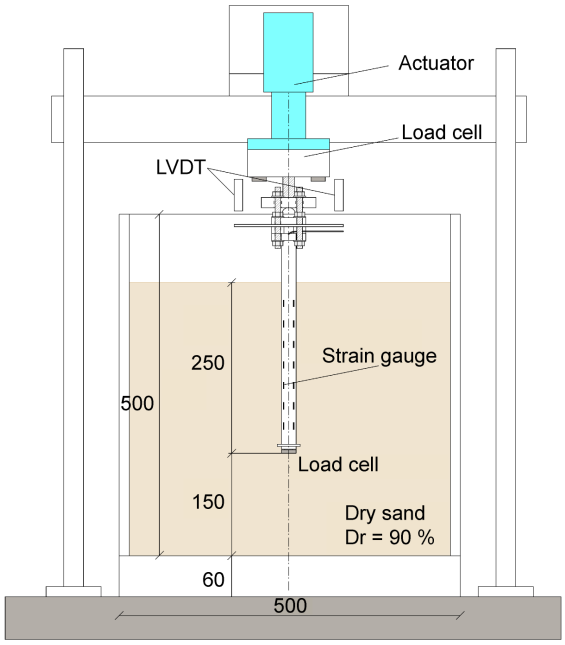


Figure 1 Test model

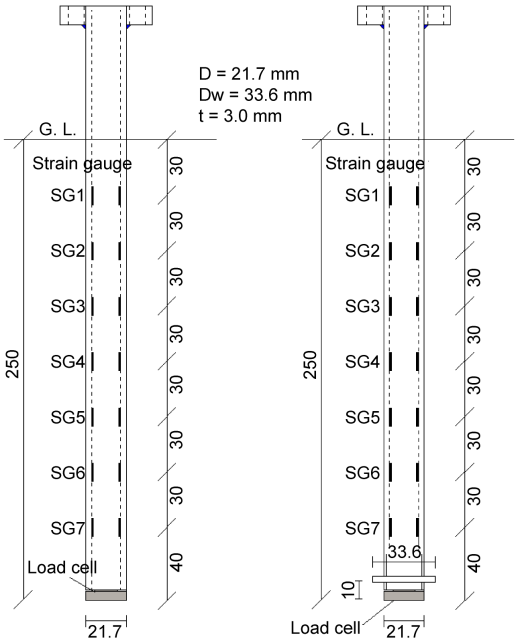


Figure 2 Pile models

All tests were performed under a centrifugal acceleration of 30G. Table 1 and Figure 3 show test series conducted in this study. Alternately cyclic loading and monotonic loading for piles with or without a wing plate were conducted under displacement control with a loading rate of about 1.0 mm/min. In Table 1, a subscript of "d" stands for percentage (%) of pile displacement with respect to a pile diameter. The maximum loading displacement was equal to a pile diameter (21.7 mm) or a wing plate diameter (33.6 mm) in the monotonic compressive loading tests and was equal to 25 % of a pile diameter (5.0 mm) in the monotonic tensile loading test. In the alternately cyclic loading tests, the loading amplitude was gradually increased in four steps (1, 5, 10 and 15 % of a pile diameter). In each step, the loading was repeated three times, as shown in Figure 3(b). In the tests, vertical load and vertical displacement at the pile head, tip resistance and axial strains at seven depths of piles were observed. Henceforth, a pile without a wing plate is called Pile-S and that with a wing plate is called Pile-W, respectively.

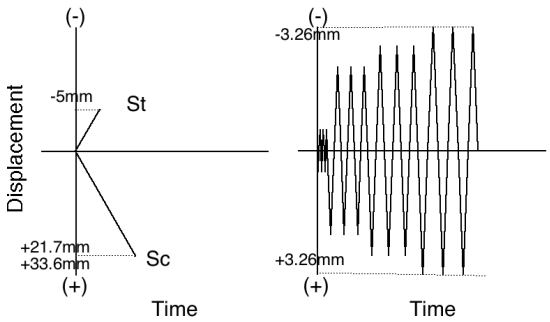
To estimate the bearing capacity and pull-out resistance of piles, P, forces acting on the piles are defined by the following equations:

$$\text{Pile-S} \quad \text{<pushing>} \quad P = R_p + R_f \tag{1}$$

$$\text{<pulling>} \quad P = R_f \tag{2}$$

$$\text{Pile-W} \quad \text{<pushing>} \quad P = R_p + R_f + R_w \tag{3}$$

$$\text{<pulling>} \quad P = R_f + R_w \tag{4}$$



(a) Cases S_Sc, W_Sc & W_St (b) Cases S_C1 & W_C1

Figure 3 Loading displacement

Table 1 Test cases

	Pile model	Loading	Loading displacement (mm)
S_Sc	Pile-S	Compressive loading	+21.7
W_Sc	Pile-W		+33.6
W_St	Pile-W	Tensile loading	-5.0
S_C1	Pile-S	Alternately cyclic loading	±0.217(d_1), ±1.09(d_5), ±2.17(d_{10}), ±3.26(d_{15})
W_C1	Pile-W		

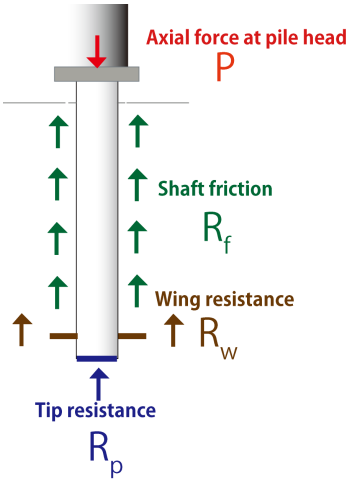


Figure 4 Forces acting on pile

in which R_p, R_f and R_w stand for tip resistance, entire shaft friction and resistance of wing plate (wing resistance), respectively. In this study, P and R_p correspond to the vertical load observed at the pile head and at the pile tip. R_f is estimated from the difference between the vertical load at the pile head and the axial force observed at strain gauge SG6. R_w is estimated from the difference between the tip resistance and the axial force observed at strain gauge SG6. The reason why strain gauge SG7 is not used is because SG7 was located closely to a device for setting a load cell and its observed values might have been inaccurate (Figure 2). In this study, positive values stand for compressive force or displacement in the pushing direction, while negative values stand for tensile force or displacement in the pulling direction. The values shown in the following part correspond to the observed values in the model scale and not in the prototype scale.

3. EFFECTS OF ALTERNATELY CYCLIC LOADING ON BEARING CAPACITY AND PULL-OUT RESISTANCE OF PILES

3.1 Bearing capacity and pull-out resistance of piles in monotonic loading

Figure 5 shows the relations of pile displacement with axial force at the pile head, tip resistance, shaft friction and wing resistance for monotonic loading tests. In the figures, the relations for Pile-S are presented in black lines and those for Pile-W are presented in gray lines. The shaft friction is significantly smaller than other forces because the pile length is relatively short (7.5 m in the prototype scale). The tip resistance does not reach the ultimate value under a large loading displacement (Figure 5(b)). In contrast, the shaft friction reaches the ultimate value with a displacement of 1-2 mm, and then it gradually decreases with increasing displacement (Figure 5(c)). The wing resistance does not reach the ultimate value in the pushing direction but reaches the ultimate value in the pulling direction (Figure 5(d)).

The yield displacement of the shaft friction (1-2 mm) corresponds to 30-60 mm in the prototype scale. This is larger than the yield displacement presented in the AIJ Recommendation (Architectural Institute of Japan, 2001), in which the yield displacement is 5-20 mm. The previous study has shown that the yield displacement is larger in cases of gravel than in cases of fine sand (Isemoto et al., 2000). The difference in the yield displacement between reduced scale and prototype scale might have been induced by the scale effect.

3.2 Bearing capacity and pull-out resistance of piles in alternately cyclic loading

To estimate the effects of alternately cyclic loading on bearing capacity and pull-out resistance of piles, Figure 6 shows the relations between pile displacement and axial force at the pile heads in black lines. In the figures, grey lines indicate the relations for monotonic loading tests. In the pushing direction, the axial force at the pile head increases with increasing amplitude and number of cyclic loading. In contrast, in the pulling direction, the axial force at the pile head decreases. This suggests that alternately cyclic loading might have increased bearing capacity but decreased the pull-out resistance. The pull-out resistance becomes close to zero with amplitude of 2.17 mm (d_{10}) in the case of Pile-S and of 3.26 mm (d_{15}) in the case of Pile-W.

To estimate the decrease in pull-out resistance, normalized load in the cyclic loading tests is determined.

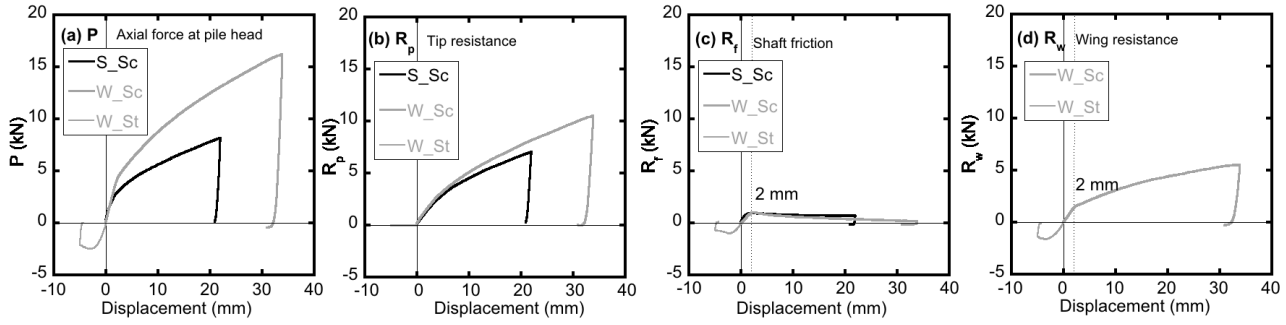


Figure 5 Relation of resistance with vertical pile displacement in monotonic loading tests

The normalized load is given as a ratio of the value in cyclic loading tests with respect to that in monotonic loading test with the same loading displacement. A monotonic tensile loading test on Pile-S was not conducted. Further, in the case of Pile-S, the shaft friction is assumed to be the same between the pushing and pulling directions as the shaft friction of Pile-W is almost the same between the pushing and pulling directions. Namely, the pull-out resistance of Pile-S is equal to the observed shaft friction in the pushing direction, as shown in Eq. (2). Henceforth, the subscripts "mono" and "cyc" indicate the values in the monotonic loading tests and in the cyclic loading tests respectively.

Figure 7 shows the normalized pull-out resistance of the first and third cycle in each step. The normalized pull-out resistance decreases with the cyclic loading when the loading amplitude is greater than 1.09 mm (d_5). A comparison in the normalized resistance in the third step with amplitude of 1.09 mm (d_5) between Pile-S and Pile-W shows that a ratio with respect to the monotonic loading is 30 % in Pile-S and 50 % in Pile-W. Further, with amplitude of 3.26 mm (d_{15}), the pull-out resistance becomes as low as 20 % of that in the monotonic loading tests.

To estimate the increase in bearing capacity in the pushing direction, Figure 8 shows the relations of tip resistance with pile displacement. The tip resistance increases with increasing amplitude and number of cyclic loading in both the cases of Pile-S and Pile-W. These trends are related to those in the axial force at the pile head (Figure 6), indicating that the increase in the axial force at the pile head is induced by the increase in the tip resistance. To notice a displacement, at which the tip resistance develops in pushing, the displacement is shifted from 0 mm at the initial stage to the negative side after cyclic loading. In the final loading step, the tip resistance develops with a displacement of -2.0 mm (Figure 8(b)). These findings indicate that the sand might have moved beneath the pile tip in pulling and might have been densified by the pile tip in pushing, as shown in Figure 9.

To estimate the effects of alternately cyclic loading on the shaft friction, Figure 10 shows the relations of shaft friction with pile displacement. With increasing amplitude and number of cyclic loading, the shaft friction becomes smaller than that in the monotonic loading in both the cases of Pile-S and Pile-W. The normalized shaft friction is computed as a ratio of the shaft friction with respect to that with the same loading displacement in monotonic loading tests. Figures 11 and 12 show the normalized shaft friction for the first and third cycles in each loading step. The normalized shaft friction significantly decreases when loading amplitude is greater than 1.09 mm (d_5). The ratio of shaft friction in cyclic loading with respect to that in monotonic loading is 50 % in the pushing direction and 20 % in the pulling direction.

Figure 13 shows the distributions of axial force for the first and third cycles with loading amplitude of 1.09 mm (d_5). It is to be noted that the axial force decreases at around 180 mm depth in Pile-W; this is because the wing resistance acts against the axial force. The difference between the first and third cycles is more significant in the pulling direction than in the pushing

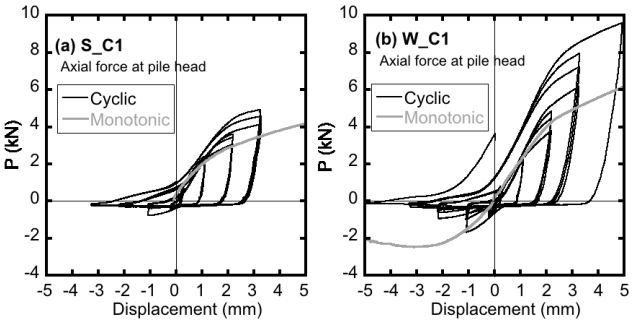


Figure 6 Relation of axial force with pile displacement

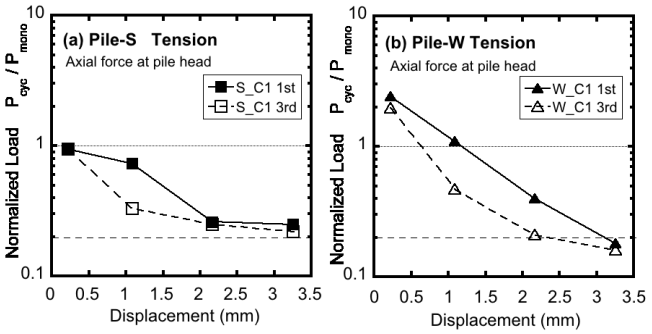


Figure 7 Relation of normalized axial force with loading amplitude in pulling

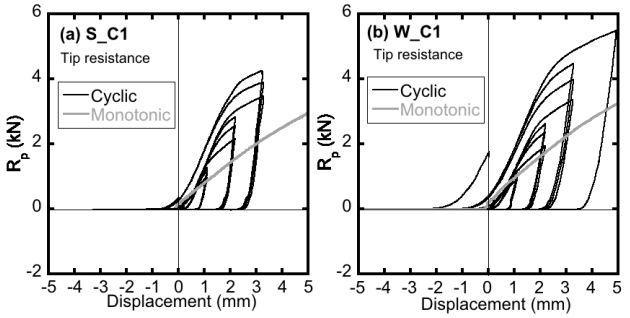


Figure 8 Relation of tip resistance with pile displacement

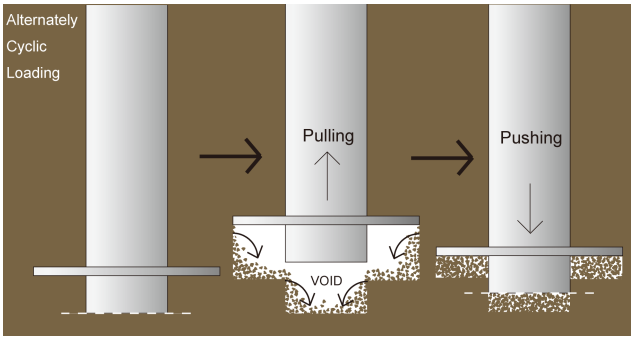


Figure 9 Increase in sand density beneath pile tip due to alternatively cyclic loading

direction, confirming that the decrease in shaft friction is more significant in the pulling direction than in the pushing direction. This is probably because the shaft friction depends on the overburden load. The shear deformation caused by pushing a pile acts to increase the overburden load in the soil around the pile. In contrast, the shear force caused by pulling a pile acts to decrease the overburden load in the soil around the pile.

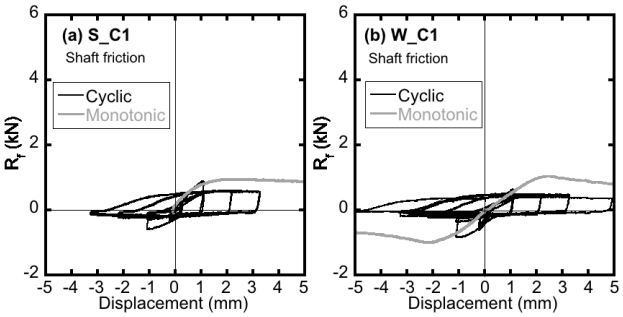


Figure 10 Relation of shaft friction with pile displacement

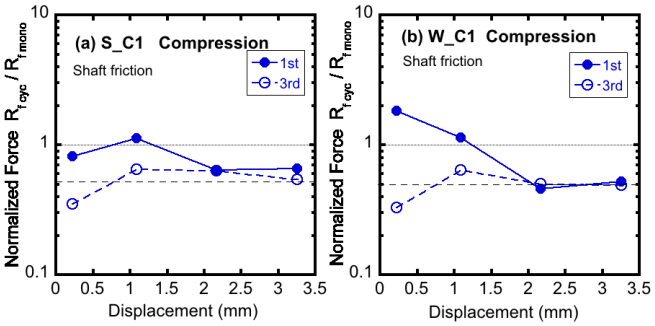


Figure 11 Relation of normalized shaft friction with loading amplitude in pushing direction

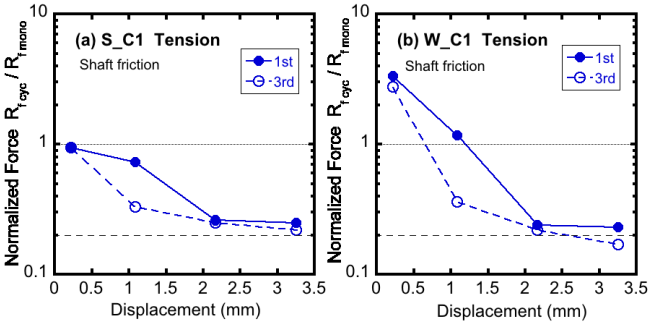


Figure 12 Relation of normalized shaft friction with loading amplitude in pulling direction

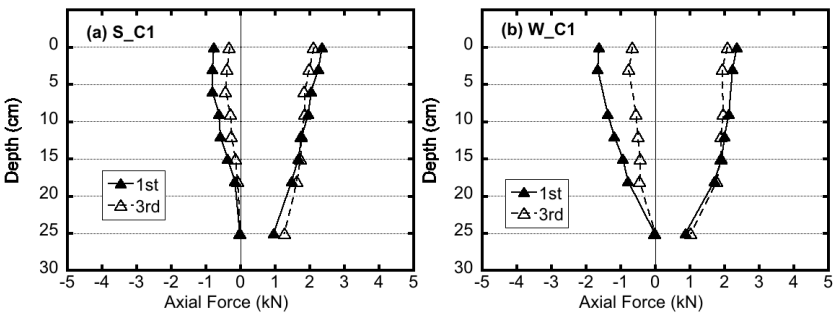


Figure 13 Distribution of axial force with depth under loading amplitude of 1.09 mm

To estimate the effects of a wing plate, Figure 14 shows the relations of wing resistance with pile displacement. The wing resistance in the pushing direction increases with increasing amplitude and number of cyclic loading, the trend of which is similar to that in the tip resistance shown in Figure 8. A displacement, at which the wing resistance develops in the pushing direction, is shifted from zero to the negative side. Namely, the wing plate tends to move and increase the density of the soil beneath the wing plate, similarly to the pile tip. In contrast, in the pulling direction, the wing resistance decreases with increasing amplitude and number of cyclic loading.

Figure 15 shows the normalized wing resistance for the first and third cycles in each loading step in the pulling direction. It is given as a ratio of the wing resistance in cyclic loading with respect to that in monotonic loading. The wing resistance decreases after the loading amplitude exceeds 1.09 mm (d_5), and finally it becomes as low as 20 % of that in monotonic loading. This is probably induced by a disturbance and a decrease of density of the soil above the wing plate. A comparison of the trends between the shaft friction and the wing resistance in pulling shows that the decrease is more significant in the shaft friction than in the wing resistance. As a result, the wing resistance dominates over the shaft friction in resisting pull-out loading.

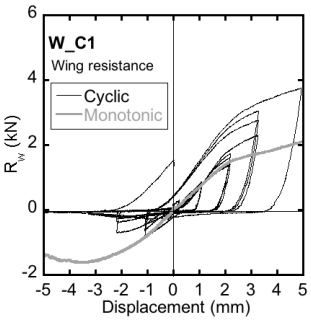


Figure 14 Relation of wing resistance with pile displacement

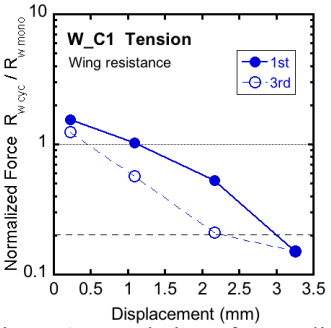


Figure 15 Relation of normalized wing resistance with loading displacement

4. CONCLUSIONS

To estimate the bearing capacity and pull-out resistance of a pile with or without a wing plate, monotonic loading tests and alternately loading tests were conducted under centrifugal acceleration of 30 G. The test results and discussions have led to the following conclusions:

1) When the cyclic loading amplitude exceeds 5-10 % of pile diameter, the bearing capacity increases but the pull-out resistance decreases. This is because the pushing and pulling shaft friction and the pulling wing resistance decreases but the pushing tip and wing resistances increase with increasing amplitude and number of loading displacement.

2) The increase in the tip resistance might have been induced by a phenomenon in which the pile tip tends to move and to densify the soil beneath the pile tip.

3) The shaft friction decreases when the cyclic loading amplitude becomes greater than 1.0 mm. The shaft resistance in the pullout direction decreases to as low as 1/5 of the peak value in the monotonic loading, whereas that in the pulling direction decreases to 1/2. This is because the shear deformation of the soil around a pile induced by loading increases overburden load in pushing but decreases overburden load in pulling.

4) The pushing wing resistance increases with increasing amplitude and number of cyclic loading, the trend of which is similar to that of the tip resistance. In contrast, the pull-out wing resistance decreases with cyclic loading. The decrease in the pulling direction is more significant in the shaft friction than in the wing resistance. As a result, in the case of a pile with a wing plate, the wing resistance dominates over the shaft friction in resisting pull-out loading.

References:

Architectural Institute of Japan (2011), "Preliminary reconnaissance report of the 2011 Tohoku-Chiho Taiheiyo-Oki Earthquake" (in Japanese).

Architectural Institute of Japan (2001), "Recommendations for design of building foundations" (in Japanese).

Isemoto, N., Katsura, Y. and Yamada, T. (2000), "Bearing capacity of cast-in-place concrete pile (Part 2: Relation between skin-friction and displacement)", *Proc. of Japan National Conference on Architecture and Building Engineering*, 727-728 (in Japanese).

Kokuda, M., Sato, H., Osakabe, T., Kunishi, H., Nagata, M., Hirata, H. and Tamura, M. (2006), " Fundamental study on penetration and bearing capacity of screw pile with helical wing", *Journal of Structural and Construction Engineering*, No. 601, 91-98 (in Japanese).

Komatsu, A., Aoki, H., Tanamura, S., Nishioka, H. and Hirashima, Y. (2003), "Static axial reciprocal load test of screwed pile (Part 1) (Part 2)", *Proc. of 38th Japan National Conference on Geotechnical Engineering*, 1487-1490 (in Japanese).

Nonomura, Y., Otsuka, M., Ishida, M. and Fukui, J. (2004), "Bearing capacity of piles for static axial reciprocal load test", *Proc. of 45th Japan National Conference on Geotechnical Engineering*, 1469-1470 (in Japanese).

Yajima, J., Aoki, Y. and Shibazaki, F. (1992), "Pulling friction and pushing friction of piles", *Proc. of Japan National Annual Conference on Architecture and Building Engineering*, 1283-1284 (in Japanese).

10CUEE CONFERENCE PROCEEDINGS
10th International Conference on Urban Earthquake Engineering
March 1-2, 2013, Tokyo Institute of Technology, Tokyo, Japan

APPLICABILITY OF EQUIVALENT LINEAR SEISMIC RESPONSE ANALYSIS UNDER LARGE EARTHQUAKES

Nozomu Yoshida[1)]

1) Professor, Department of Civil and Environmental Engineering, Tohoku Gakuin University, Japan

Abstract: Equivalent linear analysis and truly nonlinear analysis are compared at 268 sites under 11 earthquake motions in order to grasp general feature of the applicability of the equivalent linear method. SHAKE and YUSAYUSA are used for equivalent linear and truly nonlinear methods, respectively. The stress-strain relationships are modeled into the hyperbolic model whose elastic modulus and shear strength are evaluated based on the soil profiles and the SPT-*N* value. SHAKE shows larger peak acceleration and smaller peak displacement than YUSAYUSA, but other indices such as instrumental seismic intensity, peak velocity, and spectral intensity are nearly same to each other. In conclusion, equivalent linear analysis is applicable when truly nonlinear analysis is applicable except the case that peak acceleration and/or peak displacement are important. Even in this case, however, since peak acceleration is overestimated, it is a conservative side evaluation for the design of structures.

1. INTRODUCTION

Seismic response analysis of ground is one of the frequently used tools for the design of various structures. Various methods and computer programs have been proposed. One of the frequently used computer programs is SHAKE (Schnabel et al., 1972), which uses equivalent linear techniques. The name SHAKE is now used as if it is a common noun, and it is also used as common noun in this paper. Unlike the name "equivalent", however, it is an approximate method. Therefore, it is believed that it cannot be applied at large strains. For example, Ishihara (1982) suggests constitutive models and methods of the seismic response analysis related to different shear strain ranges and soil properties as shown in Figure 1.

On the other hand, input earthquake motion has increased significantly in Japan, especially after the 1995 Kobe earthquake and more after 2007 Niigataken-chuetsu-oki earthquake. Magnitude of the design earthquake motion, for example, exceeds 1 G in the design of a nuclear power plant. Design input earthquake motion with maximum acceleration more than 0.5 m/s^2 is not an extraordinary case, but frequently appears in the practical design of civil and building structures. In these situations, maximum shear strain frequently reaches a few percent or more. Regardless of the applicable range in Figure 1, however, SHAKE is still used in many engineering practice partly because of the easy handling and stable numerical integration.

There are not a few researches comparing the SHAKE and truly nonlinear analysis, and some of them pointed that they agree to each other well and some are not. This difference comes from various reasons. At first, there are shortages in SHAKE because it is an approximated method, which is discussed in detail by the authors (Yoshida et al.,

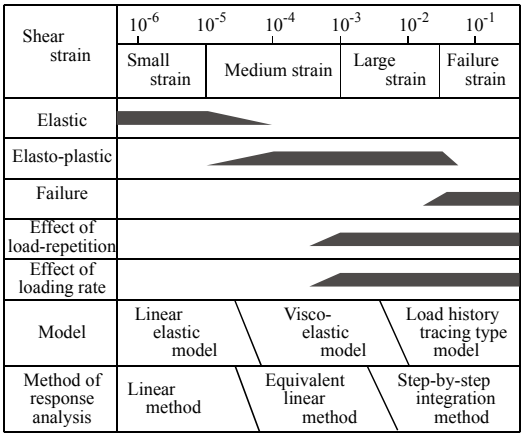


Figure 1 Change in soil properties with shear strain and corresponding modelling principle and method of response analysis (Ishihara, 1982)

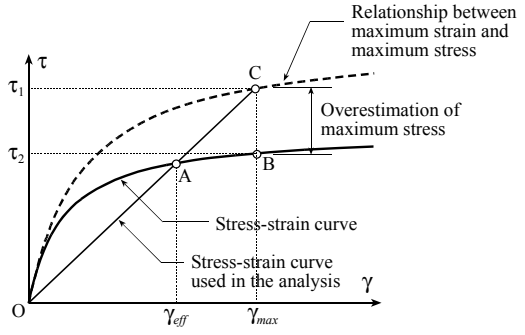


Figure 2 Mechanism of overestimation of maximum shear stress (Yoshida et al., 2002)

2002). There are two shortages in addition to the fact that it cannot express the accurate stress-strain behavior because it is produced by the complex moduli.

The first shortage is overestimation of the maximum acceleration. The mechanism is shown in Figure 2. Since stress-strain relationships is a linear line passing the point A (γ_{eff}, $\tau=G\gamma_{eff}$), maximum stress at $\gamma=\gamma_{max}$ (τ_1 at point C) is larger than actual stress (τ_2 at point B), which overestimation of maximum shear stress result in overestimation of maximum stress.

The second shortage is typically seen in Figure 3. Amplification is significantly underestimated at high frequency. Maximum acceleration is underestimated by this mechanism.

These two factors work in the opposite way. The first mechanism overestimates maximum acceleration and the second mechanism underestimates maximum acceleration. Degree of effects depends on the degree of nonlinearity. This

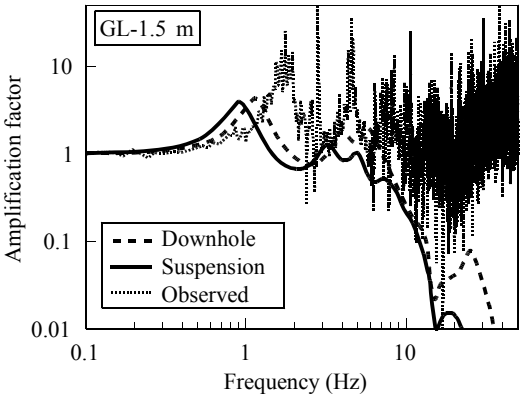


Figure 3 Underestimation of amplification at high frequencies (Yoshida et al., 2002)

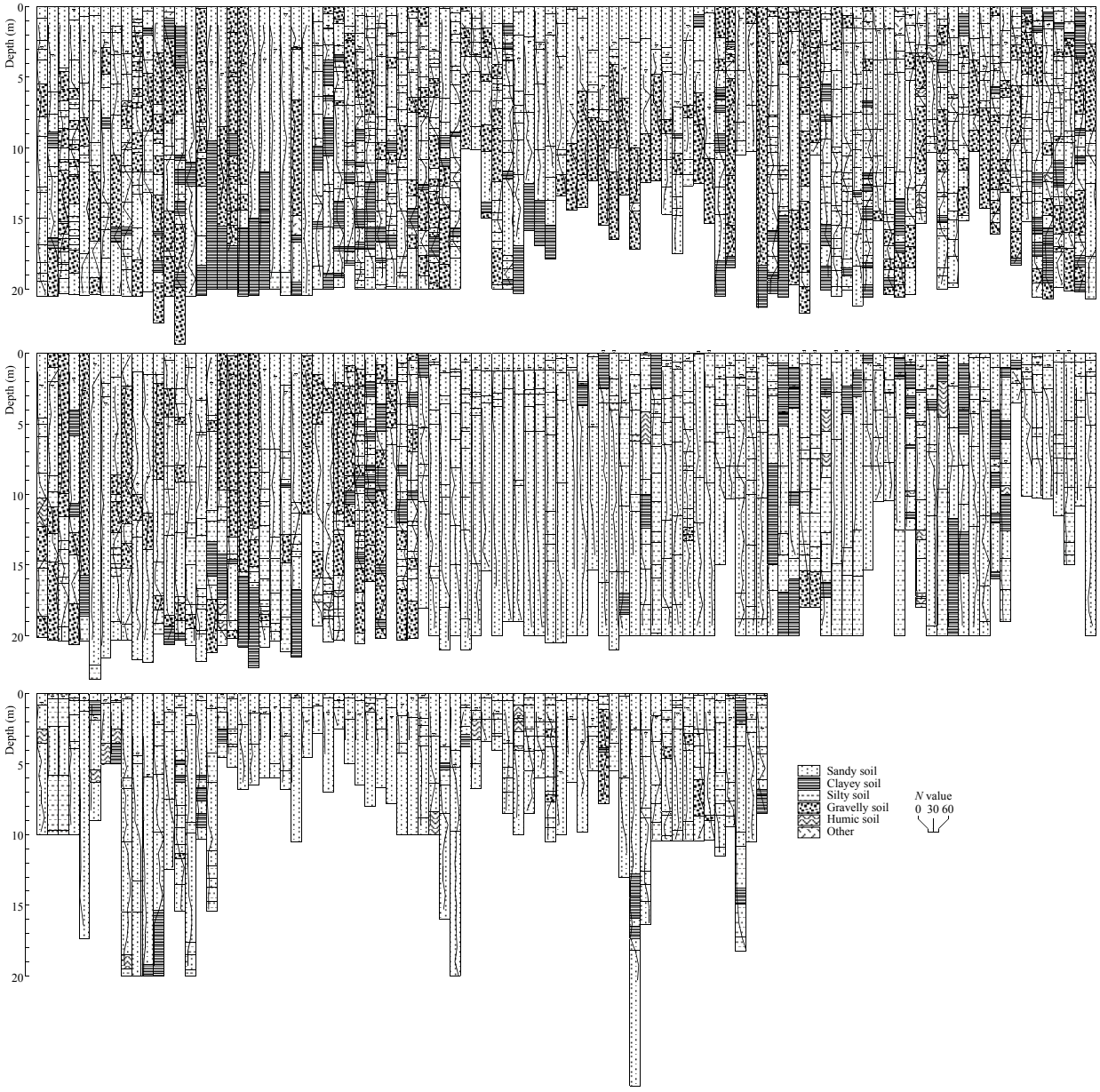


Figure 4 Soil profiles

may be one of the reasons why evaluations of SHAKE scatter.

Another reason of scatter of the evaluation is the method how to evaluate the applicability or the accuracy of the seismic response analysis. Agreement of the maximum acceleration was sometimes used and sometimes frequency characteristics were used, and sometimes others. It means that indices convenient for the purpose have been used.

There are many indices that express intensity of the earthquake motion, which also makes the evaluation of applicability difficult. In addition, only a small number of ground model and./or small number of earthquake motion were used in the past researches. In addition, difference may appear depending on earthquake motions.

In this paper, accuracy of SHAKE is evaluated by comparing the truly nonlinear method for more than 200 sites and under various types of input earthquake motions.

2. GROUND AND MODELING

Figure 4 shows soil profiles and SPT-*N* value of the ground used in this paper; in total, 268 sites are used. These sites were the sites used to evaluate applicability of the conventional method to evaluate onset of identification during the 1995 Kobe earthquake (Public Work Research Institute, 1996). Among them, 137 sites are related to the Kobe earthquake and the rest to other earthquakes.

Soils are classified into 6 categories, i.e., sand, silt, clay, gravel, humus, and others. Here, others include concrete and cobble, etc. In the modeling, humus soil are treated same as clay, and others are set same as soil below. The SPT-*N* values are averaged in the same soil layer. If there is no *N* value data in a layer, it is set same with the below layer. These modeling may not be good if actual behavior of the ground is investigated, but are not because the purpose of this paper is to investigate different ground model.

Unit weight of each layer was included in the original data. The shear wave velocity V_s is evaluated based on the specifications for highway bridges (JRA, 2012), i.e.,

$$V_s = 100N^{1/3} \quad \text{(clayey soil)} \tag{1}$$

$$V_s = 80N^{1/3} \quad \text{(soil other than clay)} \tag{2}$$

Shear strength of the clayey soil is evaluated as an average value suggested by JGS (2004)

$$\tau_f = 19N \quad \text{(kPa)} \tag{3}$$

On the other hand, the internal friction angle ϕ is evaluated based on Hatanaka and Uchida (1996) as

$$\phi = 20 + \sqrt{20N_1} \quad \text{(degree)} \tag{4}$$

where N_1 is corrected *N* value considering the effective over burden stress, and is evaluated as (JRA, 2012)

$$N_1 = \frac{170N}{\sigma'_v + 100} \quad (\sigma'_v \text{ in kPa}) \tag{5}$$

The hyperbolic model

$$\tau = \frac{G_0\gamma}{1 + \tau_f\gamma / G_0} \tag{6}$$

is used for shear stress τ- shear strain γrelationships, and the Masing's rule is used to obtain hysteresis curve.

3. EARTHQUAKE MOTION

Input earthquake motion must have various and typical nature in order to obtain the general feature of the response. Eleven recorded earthquake motions which have different characteristics are employed so as to confirm this requirement. They are as follows.

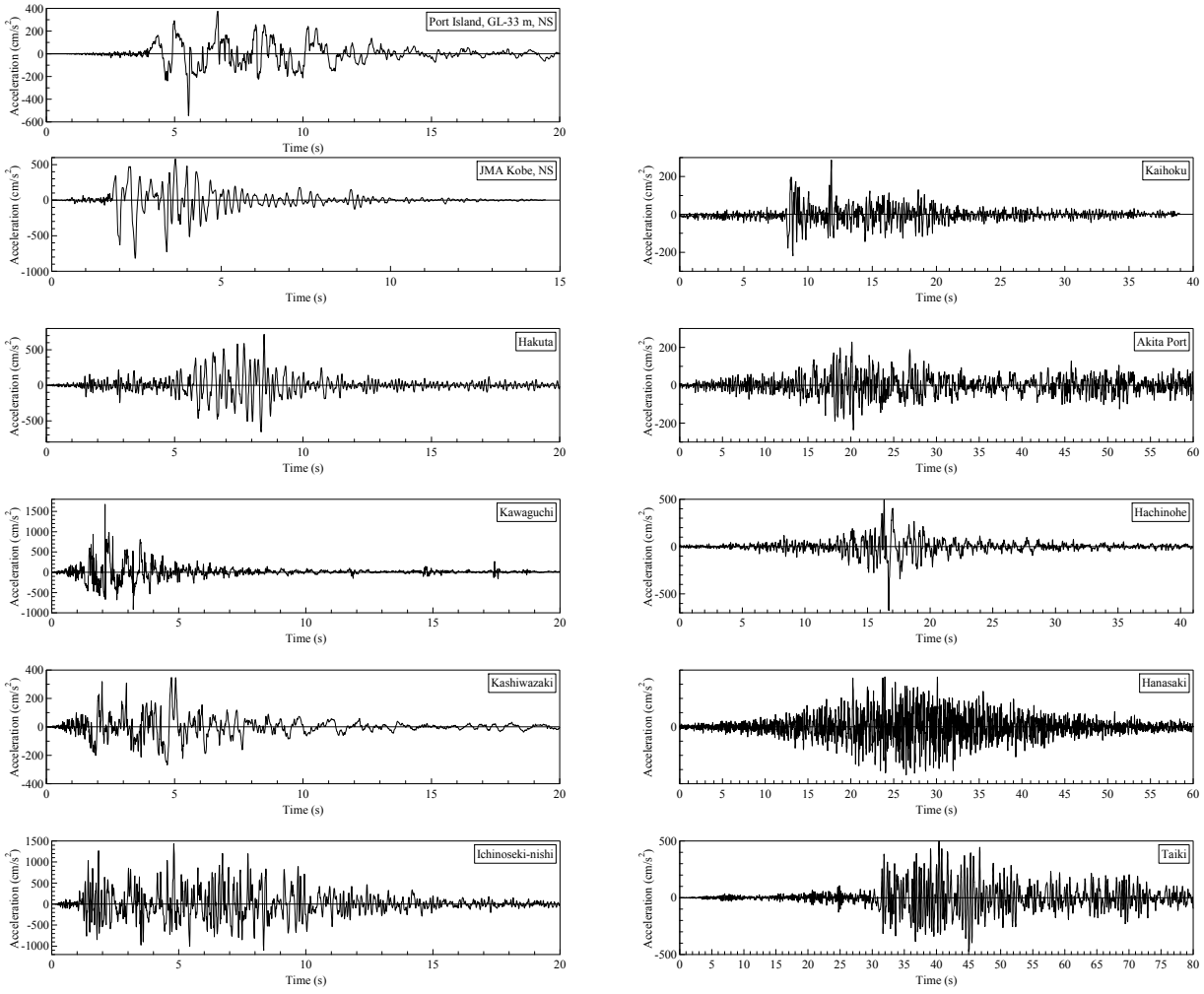
1) Inland earthquake
   Port Island GL-33 m, NS, 1995 Kobe eq.
   JMA Kobe, NS, 1995 Kobe eq.
   Hakuta, NS, 1999 Tottoriken-seibu eq.
   JMA Kawaguchi, EW, 2004 Niigataken-chuetsu eq.
   TEPCO Kashiwa-Kariwa Service hole SG1, NS, 2007 Niigataken-chuetsu-oki eq.
   Ichinoseki-nishi, EW, 2008 Iwate-Miyagi-nairiku eq.
2) Ocean trench earthquake
   Kaihoku bridge EW, 1978 Miyagiken-oki eq.
   Akita port, 1983 Nihonkai-chubu eq.
   Hachinohe office, EW, 1994 Sanriku-haruka eq.
   Hanasaki, EW, 1994 Hokkaido-toho-oki eq.
   Taiki, EW, 2003 Tokachi-oki eq.

These waves are applied as the earthquake motion of the outcropped base. Layers with V_s=300 m/s is added at the bottom of the ground in Figure 4 in the SHAKE analysis. The shear wave velocity of the base layer is confirmed not to affect the behavior in the subsoil (Usami et al., 2009)

Waveforms of the input motion are shown in Figure 5. Generally speaking, duration of the earthquake is shorter in the inland earthquakes. Figure 6 shows response spectra of the input motions under 5% damping.

4. METHOD OF ANALYSIS

Two different methods, equivalent linear method and truly nonlinear method, are used to evaluate applicability of SHAKE. A computer program DYNEQ (Yoshida, 1995) is used for the equivalent linear analysis. DYNEQ is an open source program that has various functions based on complex moduli method, among which technique same with SHAKE is used in the calculation, and is referred as SHAKE. A computer program YUSAYUSA-2 (Yoshida and Towhata, 1991), which is also an open source program, is used for the



(a) Inland earthquakes (b) Ocean trench earthquakes

Figure 5 Input earthquake motions

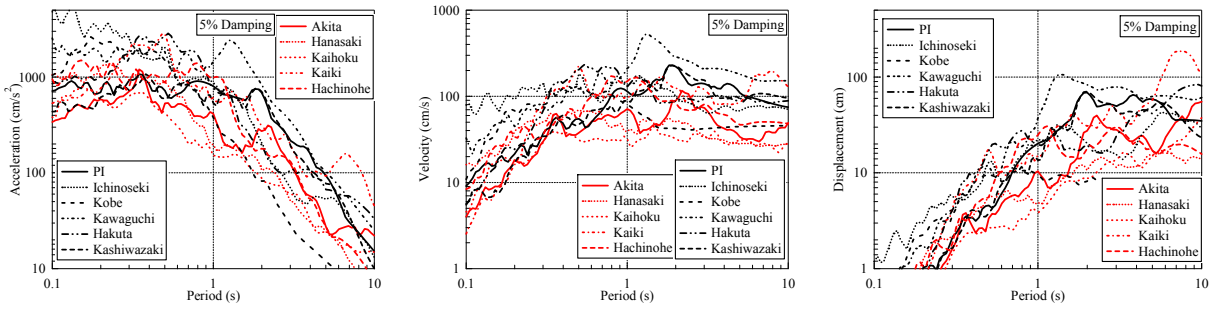


Figure 6 Response spectra of input motion

truly nonlinear analysis. It will be referred as YUSAYUSA.

These two programs are examined under the same condition, i.e., the same ground model and the same stress-strain relationships. The only difference is that velocity proportional damping is considered in YUSAYUSA for the stability of numerical integration. Since the Rayleigh damping is employed, viscous coefficient matric [c] is calculated from the mass matrix [m] and stiffness matrix [k] as

$$[c] = \alpha[m] + \beta[k] \tag{7}$$

where α and β are constants and are set 0.090, 0.00091 so that average damping ratio between 0.5 Hz and 6 Hz becomes 1.43 % (Q=35).

5. COMPARISON AND DISCUSSION

5.1 Earthquake motion index

Many earthquake motion indices have been proposed, which indicates difficulty to express the intensity of the ground motion in one index. In this paper, several frequently used indices are used.

1) Peak acceleration

Peak acceleration is the most frequently used index because it directly related to inertia force of the structure. However, it is sometimes too sensitive.

2) Peak velocity

Applicability of the peak acceleration as an earthquake motion index becomes less for longer period structure. Instead of it, peak velocity becomes a good index. Here, this velocity is absolute velocity, but not relative velocity from the base although relative velocity is frequently used as output because it is directly obtained by solving the equation of motion.

3) Peak displacement

Displacement is a very important index for the design of the underground structures. Comparison of relative displacement with recorded one is very difficult to evaluate them from the earthquake record because vertical array records are necessary and because it depends on the method of integration as will be seen in in Figure 11. However, it can be done between analyses.

4) Instrumental seismic intensity

Seismic intensity has been used to express the degree of damage or ground shaking. Because of its nature, it takes time to evaluate the seismic intensity. After the 1995 Kobe earthquake, Japan Meteorological Agency made an seismic intensity which can be calculated from the acceleration time history and which is consistent with traditional JMA seismic intensity (Muramatsu, 1996). Evaluation of seismic intensity can be done very quickly. Instrumental seismic intensity I_{JMA} is evaluated as

$$I_{JMA} = 2\log a_0 + 0.94 \tag{8}$$

where a_0 is the acceleration in cm/s^2 that sum of duration in which acceleration exceeds a_0 is 0.3 s in the filtered acceleration-time history. It is defined by using three directional component, but only one-directional component is used in this paper.

5) Spectral Intensity

Spectral intensity SI is first proposed by Housner (1965) by integrating the response spectrum from 0.1 s to 2.5 s. It is modified to divide 2.4 s in order to make the dimension of the seismic intensity to be same with velocity. Then it is calculated as

$$SI = \frac{1}{2.4}\int_{0.1}^{2.5} S_{v,0.2}\,dt \tag{9}$$

where $S_{v,0.2}$ is a velocity response spectrum under 20 % damping. Equation (9) indicates that SI is an average of velocity spectrum between 0.1 and 2.5 s. Pseudo velocity spectrum is sometimes used instead of velocity spectrum, but velocity spectrum is used in this paper.

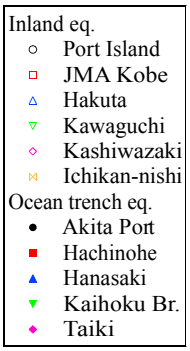


Figure 7 Legend to distinguish input earthquake

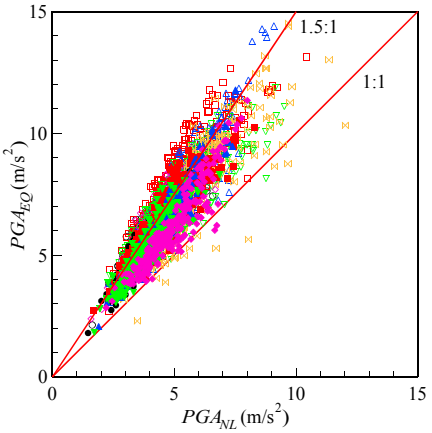


Figure 8 Comparison of peak ground accelerations

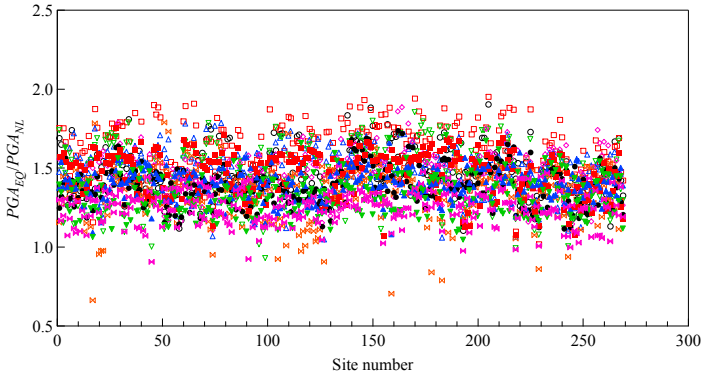


Figure 9 Acceleration ratios (SHAKE/YUSAYUSA)

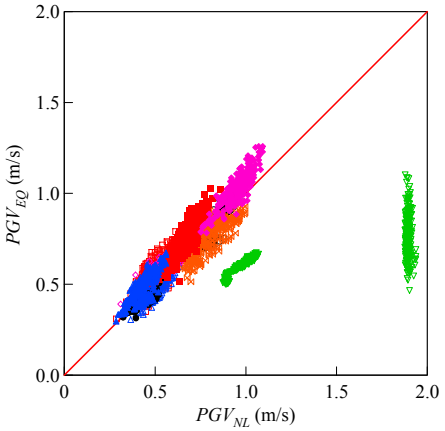


Figure 10 Comparison of peak ground (absolute) velocity

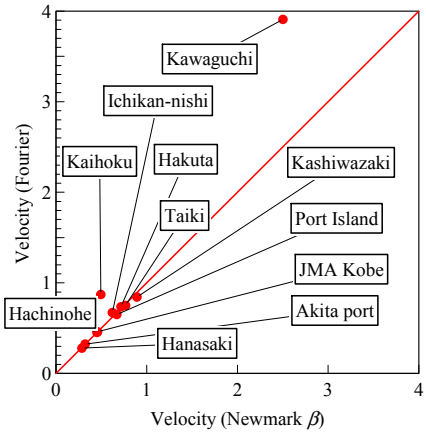


Figure 11 Maximum velocity of input earthquake motions

5.2 Comparison of indices

Result under 11 earthquake motions are shown in one figure in the followings. Result of each earthquake motion is distinguished by the symbols in Figure 7.

Figure 8 compares PGAs by all analyses, where subscript *EQ* indicates equivalent linear method (SHAKE) and *NL* indicates nonlinear method (YUSAYUSA). Two lines are drawn in the figure whose gradients are 1:1 and 1.5:1. PGA by SHAKE is always larger than that by YUSAYUSA except only several cases. PGA is overestimated more than 1.5 times in SHAKE in many cases. The mechanism of this overestimation is already pointed out by Yoshida et al. (2002).

Figure 9 shows ratio of PGA in each soil profile. The same symbols seem to lie nearly horizontally although PGA scatters widely as seen in Figure 8.

Peak ground velocity, PGA, is compared in Figure 10. Both PGV's are nearly the same although that by the equivalent linear method seems to be a little larger than that by the nonlinear analysis. There are, however, two exceptions. PGV by nonlinear method shows much larger value than that of equivalent linear method under Kawaguchi (△) and Kaihoku (▼). This is not caused from the difference of the analytical methods but other reason.

Input earthquake motions are integrated to obtain absolute velocity by Fourier transform in SHAKE and Newmark's β method (β=0.25) in YUSAYUSA, respectively. Zero-th order or constant term is neglected in SHAKE, but is also integrated in YUSAYUSA. Figure 11 compares maximum velocity integrated by the Fourier transform and by the Newmark's β method. Almost all earthquake motion shows the same maximum velocity in two methods, but maximum velocity by the Newmark's β method is much larger than that by Fourier transform for Kaihoku and JMA Kawaguchi, which is the reason why PGV's by YUSAYUSA are much larger than those by SHAKE in Figure 10.

Considering these it can be concluded that PGV's are nearly the same for both SHAKE and YUSAYUSA although those by SHAKE is a little larger than those by YUSAYUSA.

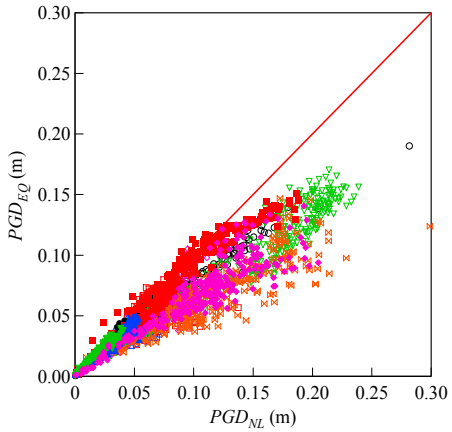


Figure 12 Comparison of PGD

Figure 12 compares displacements at the ground surface relative to base, PGD. PGD by SHAKE is in general smaller than that by YUSAYUSA. This behavior can be explained by the mechanism in Figure 2. Since stiffness is estimated large in SHAKE, resulting stress becomes small. It is also seen that degree of difference depends on the earthquakes as the same symbol shows similar tendency. Both analyses, for example, show similar PDG under Kaihoku. PDG's under Hachinohe also seem similar although PGD by SHAKE becomes smaller when PDG becomes larger than 0.1 m. In addition, agreement is better under the ocean type earthquake than under the inland earthquake, except under Taiki.

Figures 13 and 14 compare JMA seismic intensity I_{JMA} and spectral intensity *SI*, respectively. Same with PGV, both indices are nearly the same although those by SHAKE are a little larger than that by YUSAYUSA. It is also pointed out that data under the same earthquake motion show similar characteristics

Figure 15 shows comparison of maximum stresses by both methods. Here, the largest strain in each ground is used as the maximum strain. Therefore, it may not be the same layer. If the mechanism shown in Figure 2 works, the shear

strain by SHAKE is smaller than that by YUSAYUSA. Validity of this mechanism was confirmed through Figure 2 and Figure 12 in general. However, there are many data that strains by SHAKE are larger than those by YUSAYUSA. It may indicate that vibration mode are different under each analysis.

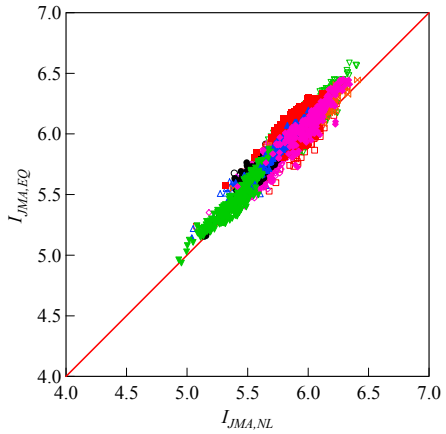


Figure 13 Comparison of JMA seismic intensity

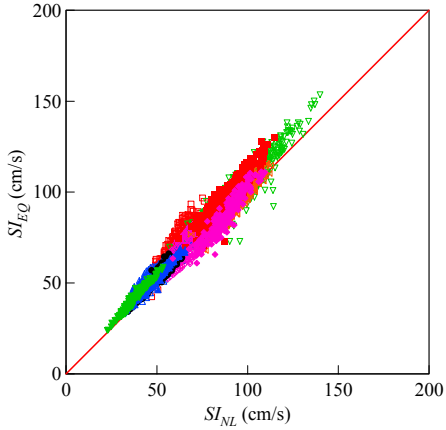


Figure 14 Comparison of SI value

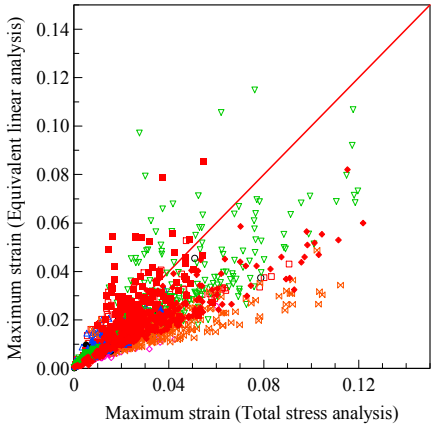


Figure 15 Comparison of maximum strains

6. CONCLUDING REMARKS

Applicability of the equivalent linear analysis (SHAKE) under large earthquakes is examined by using more than 200 sites and 11 earthquakes. The following conclusions are obtained.

1) PGA is overestimated by the equivalent linear method. Sometimes, it is more than 1.5 times larger than that by the truly nonlinear method.

2) PGD is underestimated by the equivalent linear method. It is frequently less than a half compared with that by the truly nonlinear method.

3) Other indices such as PGV, seismic intensity, and spectral intensity are nearly the same between the equivalent linear method and truly nonlinear method although evaluation by the equivalent linear method is a little larger than that by the truly nonlinear method.

4) Vibration modes may be different between the equivalent linear method and the truly nonlinear method.

5) Amplification characteristics are affected by the input earthquake motion.

Considering these, equivalent linear method is applicable in many fields because it shows a little conservative result, except the case that maximum displacement and maximum acceleration are interested at.

References:

Housner, G. W. (1965): Intensity of earthquake ground shaking near the causative fault, Proc., 3WCEE, Vol. I, pp. III-94-III-115

Hatanaka, M. and Uchida, A. (1996): Empirical correlation between penetration resistance and internal friction angle of sandy soils, Soils and Foundations, Vol. 36, No. 4, pp. 1-9

Ishihara, K. (1982): Evaluation of soil properties for use in earthquake response analysis, Proc., 9th International Symposium on Numerical Models in Geomechanics, Zurich, pp. 237-259

JGS (2004): Japanese standards for geotechnical and geoenvironmental investigation methods -standards and explanations-, 889pp.

JRA (Japan Road Association) (2012): Specifications for highway bridges, Part V (seismic design) (in Japanese)

Muramatsu, I. (1996): On JMA instrumental seismic intensity, JSEEP NEWS, No. 150, pp. 27-36 (in Japanese)

Public Work Research Institute (1996): Report on accuracy of method to identify liquefaction during the Hyogoken-nambu earthquake (in Japanese)

Schnabel, P. B., Lysmer, J. and Seed, H. B. (1972): SHAKE A Computer program for earthquake response analysis of horizontally layered sites, Report No. EERC72-12, University of California, Berkeley

Usami, Y., Sasaki, T. and Yoshida, N.. (2009):Effect of velocity structure under seismic base layer on earthquake response, Proc., Meeting of Tohoku Branch of JSCE, pp. pp. 317-318 (in Japanese)

Yoshida, N. and Towhata, I. (1991): YUSAYUSA-2 and SIMMDL-2, theory and practice, revised in 2003 (version 2.1), Tohoku Gakuin University and University of Tokyo; http://www.civil.tohoku-gakuin.ac.jp/yoshida/computercodes/eqcode.html

Yoshida, N. (1995): A computer program for DYNamic response analysis of level ground by EQuivalent linear method, Revised in 2004 (version 3.25), Tohoku Gakuin University; http://www.civil.tohoku-gakuin.ac.jp/yoshida/computercodes/eqcode.html

Yoshida, N., Kobayashi, S., Suetomi, I. and Miura, K. (2002): Equivalent linear method considering frequency dependent characteristics of stiffness and damping, Soil Dynamics and Earthquake Engineering, Elsevier, Vol. 22, No. 3, pp. 205-222

10CUEE CONFERENCE PROCEEDINGS
10th International Conference on Urban Earthquake Engineering
March 1-2, 2013, Tokyo Institute of Technology, Tokyo, Japan

EFFECT OF INPUT MOTION CHARACTERISTICS ON SEISMIC DEFORMATION OF A RIVER LEVEE

Ryosuke Uzuoka[1], Jorge Shimabukuro[2] and Masumitsu Kuse[3]

1) Professor, Dept. of Civil and Environmental Engineering, The University of Tokushima, Tokushima, Japan
2) Senior Engineer, Disaster Prevention and Environmental Division, Kouzou Keikaku Engineering Inc., Tokyo, Japan
3) Associate Professor, River Basin Research Center, Gifu University, Gifu, Japan
uzuoka@ce.tokushima-u.ac.jp, shimabuku@kke.co.jp, kuse@gifu-u.ac.jp

Abstract: The 2011 off the Pacific Coast of Tohoku Earthquake caused large deformation of river levees in Miyagi, Fukushima and Ibaraki Prefectures in eastern Japan. The river levees along Naruse River in Miyagi Prefecture settled largely about 30 km far from the river mouth. Liquefaction of the bottom part of river levee underneath ground water caused the deformation of levees on soft clayey ground. On the other hand the river levees along Naruse River close to the river mouth did not deform largely although the levees settled over 30cm in 1978 off Miyagi-ken earthquake and had large cracks on the top in 2003 Miyagi-ken inland earthquake. It was possible that liquefaction of sandy foundation ground caused the damages in 1978 and 2003 earthquakes. The river levees showed different performance dependent on earthquake motions. This study discusses the effect of input motion characteristics on seismic deformation of the river levee on liquefiable ground using two practical effective stress analyses.

1. INTRODUCTION

River levees on soft ground have often suffered from severe damages in past earthquakes. The 2011 off the Pacific Coast of Tohoku Earthquake caused large deformation of many river levees in Miyagi, Fukushima and Ibaraki Prefecture in eastern Japan (Sasaki et al. 2013, Oka et al. 2013). The river levees along Naruse River in Miyagi Prefecture settled largely about 30 km far from the river mouth. Liquefaction of the bottom saturated part of river levee caused the deformation of levees on soft clayey ground. On the other hand the river levees along Naruse River close to the river mouth did not deform largely although the levees settled over 30cm in the 1978 off Miyagi-ken earthquake (JSCE 1980) and had large cracks on the top in the 2003 Miyagi-ken inland earthquake (JGS 2003). It was possible that liquefaction of sandy base ground caused the damages in the 1978 and 2003 earthquakes (JSCE 1980). The river levees showed different performance dependent on earthquake motions. This study discusses the effect of input motion characteristics on seismic deformation of the river levee on liquefiable ground using two practical effective stress analyses.

Two numerical codes of 2-D soil-water coupled dynamic analysis code "LIQCA" (Oka et al. 1999) and "FLIP" (Iai et al. 1992) are used in this study to avoid the effect on the results of differences in the numerical codes. Both of numerical methods have been validated through numerical simulation of model tests and damage cases and have been used for practical prediction of seismic deformation of river levees for over ten years. The analyses use two observed motions of 2003 and 2011 earthquakes. The 2011 earthquake motion has the long duration and the large number of cycles, and the amplitude of acceleration is middle range. In comparison with the 2011 earthquake, the 2003 earthquake motion has the shorter duration and the smaller number of cycles, and the amplitude of acceleration is larger. The material parameters of soil layers are empirically determined based on the sounding tests.

2. DAMAGED LEVEE

2.1 Earthquake and Damage

The damaged "Hamaichi" levee is located on the left bank at the distance of 1.55 km from the mouth of the Naruse River in Figure 1. Table 1 shows damage overview after three major earthquakes around Hamaichi levee. This embankment was severely damaged during the 1978 off Miyagi-ken earthquake on 12 June 1978. The Japan Meteorological Association (JMA) assigned M_{JMA} of 7.4 to this earthquake. The epicenter and the focal depth were estimated about 60 km off Miyagi coast and about 40 km deep respectively. We call the earthquake "1978 Eq." hereafter. The embankment top settled about 30 – 50 cm, and a number of longitudinal cracks were observed on the top in Figure 2. Revetments on the surface of embankment and sheet pile were installed as the restoration after the earthquake.

The second earthquake occurred at an inland north area of Miyagi Prefecture at 7:13, local time, on 26 July, 2003.



Figure 1 Location of damaged levee

Table 1 Damage overview after three earthquakes at Hamaichi levee

Eq.	Location	Damage	Restoration
1978	0.2k+33m -1.4k+185m	Severe Settlement of top: 30-50cm	Revetment, Sheet pile
2003	0.3k - 0.7k	Moderate Longitudinal crack: max. 20 cm width	
2011	1.1k - 1.4k	No major cracks on the top Erosion at landside by overtopped tsunami	

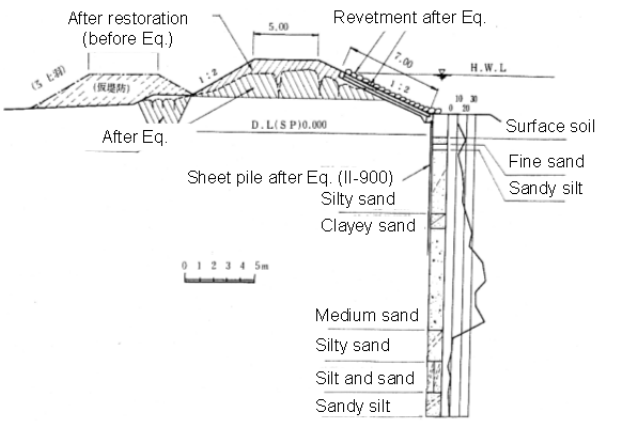


Figure 2 Damage, restoration and soil profile at Hamaichi levee after 1978 Eq. (JSCE 1980)



Photo 1 No major damage on the top at Hamaichi levee after 2011 Eq. (23 Nov. 2011)

We call the earthquake "2003 Eq." hereafter. The National Research Institute for Earth Science and Disaster Prevention

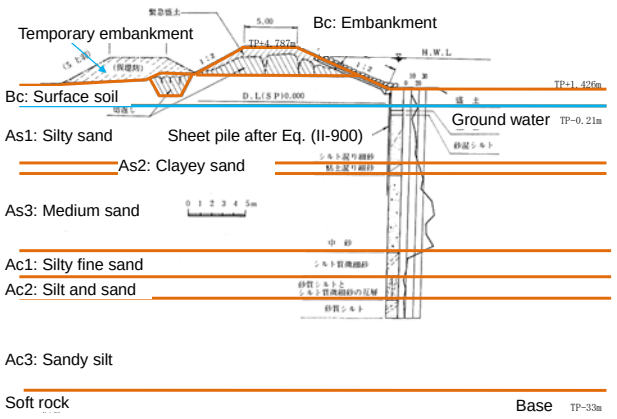
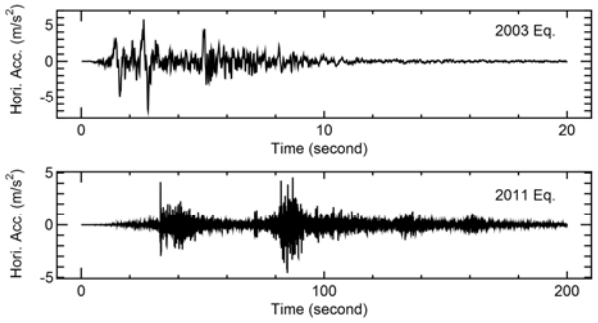
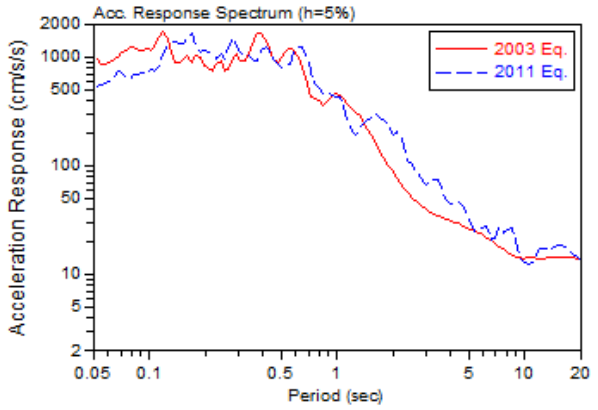


Figure 3 Soil profile at the damaged site



(a) Acceleration time histories



(b) Acceleration response spectra

Figure 4 Input acceleration histories and acceleration response spectra in 2003 Eq. and 2011 Eq.

(NIED) assigned M_w of 6.1 to this earthquake, with about 12.9-km focal depth. After the earthquake longitudinal cracks with the width of about 20 cm were observed on the top of embankment at 0.3 km – 0.7 km from the river mouth. The damage degree was not severe as in 1978 Eq.

The third earthquake is the 2011 off the Pacific Coast of Tohoku Earthquake at 14:46, local time, on 11 March, 2011. JMA assigned M_w of 9.0 to this earthquake, with about 24 km focal depth. We call the earthquake "2011 Eq." hereafter. No major cracks on the top of embankment was observed after 2011 Eq. The overtopped tsunami water eroded the toe of embankment slope at landside in Photo 1. Detailed

damage investigation was difficult due to tsunami disaster.

2.2 Ground Condition

Figure 3 shows the soil profile under the levee. The shallow layers (As1) with the depth of about 5 m consist of fine sand and silt with the SPT N-value of 10 – 20. The shallow layers were inferred to be liquefied during 1978 Eq. The deep layers (As2, As3) with the depth of 5 – 11 m consist of medium sad with the SPT N-value of over 30. The deeper layers (Ac1, Ac2, and Ac3) consist of silt mainly. The base layer of soft rock is located at GL – 34 m.

2.3 Earthquake Motion

During 2003 Eq. and 2011 Eq., vertical array records were observed at at Nakashimo strong motion station in Fig. 1. The Nakashimo site is about 900 meters apart from the Hamaichi levee. Figure 4 shows the deconvoluted acceleration histories and acceleration response spectra at the soft rock base layer. The duration of 2011 Eq. is much longer than 2003 Eq., and the predominant period of 2011 Eq. is slightly longer than 2003 Eq. The deconvoluted acceleration at soft rock base layer were calculated waves from the observed waves at GL -13 m by using elastic wave propagation analysis. In 1978 the strong motions site was not established; therefore we performed seismic analyses with acceleration histories during 2003 Eq. and 2011 Eq.

3. NUMERICAL DATA

The two-dimensional finite element model in Fig. 5 was made based on the cross section in Fig. 2 and 3. The soil was modeled by plain strain elements and the sheet pile (II-900) was modeled by beam elements. The soil at the bottom boundary was viscous boundary where the horizontal accelerations in Fig. 4 were input. The lateral boundaries in LIQCA were periodical boundaries which were tied to reproduce the same displacement at the same depth. The lateral boundary in FLIP was viscous boundary with free field motion. The bottom and lateral boundaries were impermeable. The ground water level was located on TP -0.21 m. Pore water migration in FLIP was not considered. The numerical results of self-weight analysis were considered in the dynamic analysis as the initial effective stress and pore water pressure. The coefficients in Newmark implicit time integration were 0.6 and 0.3025 in LIQCA. The time increments were 0.001 and 0.005 seconds in LIQCA and FLIP respectively.

The As1 layer only was assumed to be liquefiable soil layer because there is no detailed soil investigation at this site. Most material parameters in Table 2 were empirically determined from SPT N-value in Fig. 2. Figure 6 shows the liquefaction strength curves of As1 soil in LIQCA and FLIP.

4. NUMERICAL RESULTS

Figure 7 shows the deformed configurations and distributions of excess pore water pressure ratio after 2003 Eq. The excess pore water pressure ratio is defined the

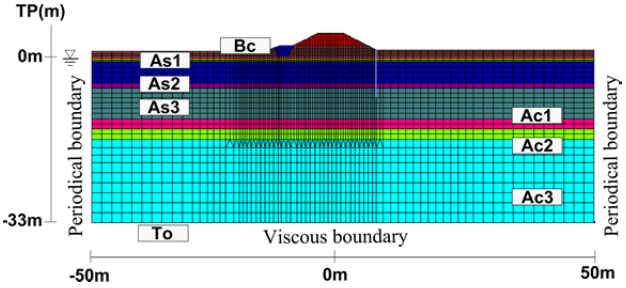


Figure 5 FE model at the damaged site

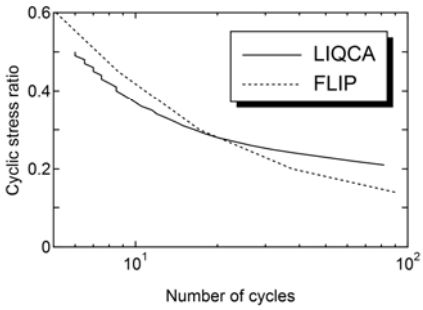
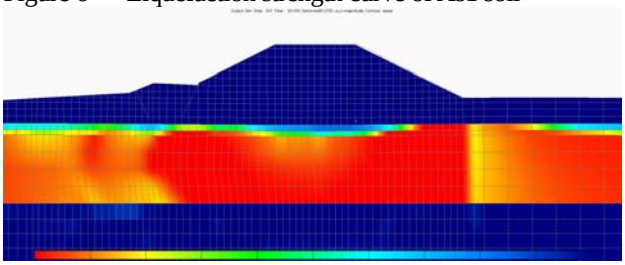
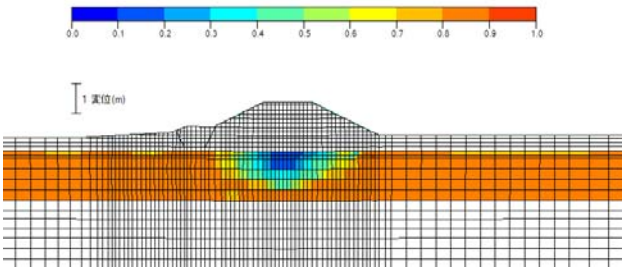


Figure 6 Liquefaction strength curve of As1 soil



(a) LIQCA



(b) FLIP

Figure 7 Deformed configurations and distributions of excess pore water pressure ration after 2003 Eq.

excess pore water pressure divided by initial effective overburden pressure. Both of numerical methods showed partial liquefaction in As1 layer, and the settlement at the top of embankment after the earthquake was less than 10 cm. The results by LIQCA showed slightly larger excess pore water pressure ratio, and the settlement was also larger than FLIP. These results reproduced the actual minor damage in Table 1.

Figure 8 shows the deformed configurations and the distributions of excess pore water pressure ratio after 2011 Eq. Both of numerical methods showed complete liquefaction in As1 layer, and the settlement at the top of embankment after the earthquake was about one order larger than 2003 Eq. The different results between two earthquakes

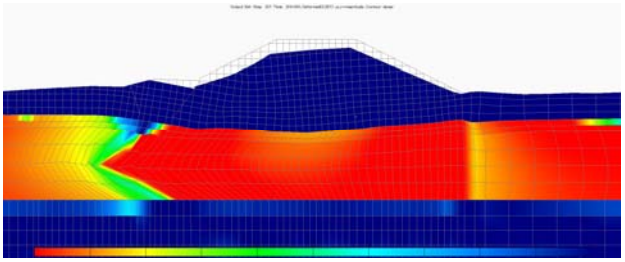
are due to the input motions. The number of cycles of input motion in 2011 Eq. was much larger than 2003 Eq. although the maximum acceleration responses were almost same in Fig. 4. The results by LIQCA showed larger deformation in As1 layer at the left side (land side) than FLIP. However no major cracks on the top of embankment was observed after 2011 Eq. although the overtopped tsunami water eroded the toe of embankment slope at landside in Photo 1. It is possible that large number of cycles of the input motion does not always cause large deformation of river levee. We need further investigation with detailed soil properties.

5. CONCLUSIONS

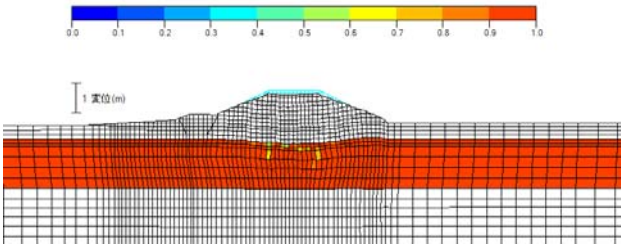
The Hamaichi levee near the mouth of the Naruse River showed different performance after three major earthquakes in 1978, 2003 and 2011. This study discussed the effect of input motion characteristics on seismic deformation of the river levee on liquefiable ground using two practical effective stress analyses. Both of numerical methods reproduced the different damage of river levee with different earthquake motions. The numerical results suggested that large number of cycles of the input motion does not always cause large deformation of river levee.

Acknowledgements:

The authors acknowledge the National Institute for Land and Infrastructure Management, Ministry of Land, Infrastructure, Transport and Tourism, Japan for providing earthquake records at Nakashimo strong motion station. Prof. Masata Sugito and others of JSCE committee on earthquake motion and structural damage gave us useful suggestions. This study is financially supported by JSPS, Japan Society for the Promotion of Science, for Grants-in-Aid for Scientific Research under Contract No. 23360195.



(a) LIQCA



(b) FLIP

Figure 8 Deformed configurations and distributions of excess pore water pressure ration after 2011 Eq.

References:

Iai, S., Matsunaga, Y. and Kameoka, T. (1992), "Strain space plasticity model for cyclic mobility," *Soils and Foundations*, 32(2), 1-15.

Japanese Geotechnical Society (JGS), Tohoku Branch (2003), "Reconnaissance report on damage by the 2003 Miyagi earthquake," JGS. (in Japanese)

Japanese Society of Civil Engineers (JSCE), Tohoku Branch (1980), "Reconnaissance report on damage by the 1978 off Miyagi earthquake," JSCE. (in Japanese)

Oka, F., Yashima, A., Tateishi, A., Taguchi, Y. and Yamashita, S. (1999), "A cyclic elasto-plastic constitutive model for sand considering a plastic-strain dependence of the shear modulus,"

Table 2 Material parameters

(a) LIQCA

Name of soil profile		Bc	As1	As2	As3	Ac1	Ac2	Ac3	To
Soil type		Embankment	Sand	Sand	Sand	Silt	Silt	Silt	Base
Model type		EPC	EPS	RO	RO	RO	RO	RO	-
Density	ρ (t/m^3)	1.53	1.84	1.84	1.84	1.84	1.84	1.84	2.04
Initial void ratio	e_0	0.80	0.80	0.80	0.80	0.80	0.80	0.80	-
Coefficient of permeability	k (m/s)	1.0×10^{-5}	1.0×10^{-5}	1.0×10^{-5}	1.0×10^{-5}	1.0×10^{-8}	1.0×10^{-8}	1.0×10^{-8}	-
Initial shear velocity	V_s (m/s)	222	229	251	298	219	208	200	300
Initial shear modulus	G_0	75628	96215	115579	163293	87983	79390	73394	-
Poisson's ratio	ν	-	-	0.33	0.33	0.33	0.33	0.33	-
Compression index	λ	-	0.025	-	-	-	-	-	-
Swelling index	κ	-	0.005	-	-	-	-	-	-
Failure stress ratio	M^*_f	-	1.16	-	-	-	-	-	-
Phase transformation stress ratio	M^*_m	-	0.91	-	-	-	-	-	-
Cohesion	c (kPa)	80	-	0	0	80	80	80	-
Internal friction angle	ϕ (deg)	0	-	36	38	0	0	0	-
Hardening parameter	B^*_0	7000	7000	-	-	-	-	-	-
	B^*_1	140	140						
Control parameter of anisotropy	C_d	-	2000	-	-	-	-	-	-
Reference strain parameter	γ^{P*}_r	-	0.002	-	-	-	-	-	-
	γ^{E*}_r	-	0.2	-	-	-	-	-	-
Dilatancy parameter	D^*_0	-	1.0	-	-	-	-	-	-
	n	-	4.0	-	-	-	-	-	-
R-O parameter	h_{max}	-	-	0.24	0.24	0.20	0.20	0.20	-
	γ_r	-	-	4.6×10^{-4}	4.2×10^{-4}	9.1×10^{-4}	1.0×10^{-3}	1.1×10^{-3}	-

Notes: EPC: Elasto-plastic model for clay, EPS: Elasto-plastic model for sand, RO: Ramberg-Osgood model

Table 2 Material parameters (continued)
(b) FLIP

Name of soil profile		Bc	As1	As2	As3	Ac1	Ac2	Ac3	Rock
Soil type		Embankment	Sand	Sand	Sand	Silt	Silt	Silt	Base
Model type(*1)		MS	MS+EPWS	MS	MS	MS	MS	MS	-
Density	ρ (t/m^3)	1.53	1.84	1.84	1.84	1.84	1.84	1.84	2.04
Bulk modulus of water	Kf(kPa)	-	2.2×10^6	-	-	-	-	-	-
Initial shear velocity	V_s (m/s)	222	229	251	298	219	208	200	300
Initial shear modulus	G_0	75628	96215	115579	163293	87983	79390	73394	-
Poisson's ratio	ν	0.33	0.33	0.33	0.33	0.33	0.33	0.33	-
Cohesion	c (kPa)	-	-	0.0	0.0	80.0	80.0	80.0	-
Internal friction angle	ϕ' (deg)	-	-	36.0	38.0	0.0	0.0	0.0	-
Porosity	n	-	0.45	-	-	-	-	-	-
Phase transformation angle	ϕ_p(deg)	-	25.00	-	-	-	-	-	-
Paramters for EPWS model									
Overall cumulative dilatancy	w1	-	10.00	-	-	-	-	-	-
Initial phase of cumulative dilatancy	p1	-	0.50	-	-	-	-	-	-
Final phase of cumulative dilatancy	p2	-	0.83	-	-	-	-	-	-
Threshold limit dilatancy	c1	-	1.00	-	-	-	-	-	-
Ultimate limit of dilatancy	s1	-	0.005	-	-	-	-	-	-
Maximum damping coefficient	h_{max}	0.20	0.24	0.24	0.24	0.20	0.20	0.20	-
Note: MS: Multi-Spring model,Excess Pore Water Pressure model									

Geotechnique, 49(5), 661-680.

Oka, F., Tsai, P., Kimoto, S. and Kato, R. (2013), "Damage patterns of river embankments due to the 2011 off the Pacific Coast of Tohoku earthquake and a numerical modeling of the deformation of river embankments with a clayey subsoil layer," *Soils and Foundations*, DOI: 10.1016/j.sandf.2012.11.010. (in press)

Sasaki, Y., Towhata, I., Miyamoto, K., Shirato, M., Narita, A., Sasaki, T. and Sako, S. (2013), "Reconnaissance report on damage in and around river levees caused by the 2011 off the Pacific coast of Tohoku earthquake," *Soils and Foundations*, DOI: 10.1016/j.sandf.2012.11.018. (in press)

10CUEE CONFERENCE PROCEEDINGS
10th International Conference on Urban Earthquake Engineering
March 1-2, 2013, Tokyo Institute of Technology, Tokyo, Japan

MEASUREMENTS OF TRANSLATIONAL AND ROTATIONAL DYNAMIC STIFFNESS FOR A MODEL LEVEE ON PEAT

Edward T. Reinert[1)], Scott J. Brandenberg[2)], and Jonathan P. Stewart[3)]

1) PhD Candidate, Department of Civil and Environmental Engineering, UCLA
2) Associate Professor and Vice Chair, Department of Civil and Environmental Engineering, UCLA
3) Professor and Chair, Department of Civil and Environmental Engineering, UCLA
etrein@gmail.com, sjbrandenberg@ucla.edu, jpstewart@seas.ucla.edu

Abstract: An eccentric mass shaker mounted to the crest of a model levee resting on very soft peat soil was used to measure dynamic base shear-displacement and base moment-rotation relations. The model levee rotated and translated visibly during testing, exhibiting a response that deviates significantly from the one-dimensional wave propagation assumption often used to analyze the seismic response of levees. We evaluate complex-valued stiffness and damping of the levee-foundation soil interaction for translational and rotational modes of vibration. The damping is strongly dependent on frequency, indicating that it is controlled by radiation of energy away from the vibrating levee. These radiation damping effects are dominant even at low frequencies that are well within the range of engineering interest for ground failure evaluations. Interestingly, the levels of radiation damping are roughly comparable, when expressed as percentage of critical, to predictions from classical models for impedance functions of rigid rectangular foundations on an elastic half-space. More research is needed to generalize these observations for application to seismic analysis of levees resting on peat.

1. INTRODUCTION

The seismic response of levees is a crucial issue for flood control and water distribution systems. Levees are often founded atop soft soils that have the potential to perform poorly during earthquakes. Peat is the softest and most compressible type of soil on which levees are founded, but very little is known about its seismic performance. Levees resting atop peat have been observed to fail during past earthquakes (e.g., Sasaki 2009), but it is often difficult to separate the contribution of the peat from the contribution of other problematic soils such as liquefiable sands.

Seismic stability of levees is a particularly important issue in the Sacramento / San Joaquin Delta, which is the hub of California's water distribution system. Unlike typical flood control levees that are intermittently loaded, the Delta levees constantly convey water and protect land that is below sea level due to subsidence of peaty organic soil. A recent seismic risk analysis predicts that a moderate earthquake in the region would simultaneously breach many levees, thereby flooding multiple islands and drawing saline water from the bay (DRMS 2009). This event is projected to halt water delivery for a period of years, causing tens of billions of dollars in direct losses. A significant limitation for this type of loss estimation analysis is lack of knowledge regarding the seismic response of peaty organic soils.

This paper presents results from a large-scale field test of a model levee resting atop very soft and compressible peat. An eccentric mass shaker imposed earthquake-level motions on the levee, and the response was recorded using dense sensor arrays. This paper focuses on the seismic interaction between the soft peat and the comparatively stiff levee fills using soil-structure interaction concepts.

2. MODEL CONFIGURATION

A photo of the model levee and eccentric mass shaker is shown in Fig. 1. The model levee was composed of compacted clay reinforced with geogrids. The levee was



Figure 1. Model levee with MK-15 eccentric mass shaker mounted on crest.

1.8m tall, 12m long at the base (from left-to-right in Fig. 1), and 3.7m wide. The clay was compacted in six 0.3m thick lifts that were wrapped with geogrid to form vertical side walls, thereby modeling a slice of levee. A sturdy timber frame was embedded in the upper three lifts, and the nees@UCLA MK-15 eccentric mass shaker was attached to the frame.

The model levee was constructed on the interior of Sherman Island, near Antioch, CA. Deposition of the peat began about 11,000 years ago at the end of the last ice age. Following reclamation of Delta lands beginning in 1850, the peat has subsided at a rate as high as 10 cm/year, and many islands now lie more than 5m below sea level. The soil profile beneath the model levee consisted of 2m of unsaturated desiccated peat overlying 9m of soft fibrous peat overlying a deposit of Pleistocene dune sand (Fig. 2). The saturated fibrous peat exhibited water contents as high as 500%, and shear wave velocities near 25 m/s. At a depth of 2m, the peat is nearly entirely organic, with very little visible evidence of inorganic minerals, with increasing content of inorganic clay minerals deeper in the deposit. Details of the laboratory testing program that accompanies the test can be found in Shafiee et al. (2013).

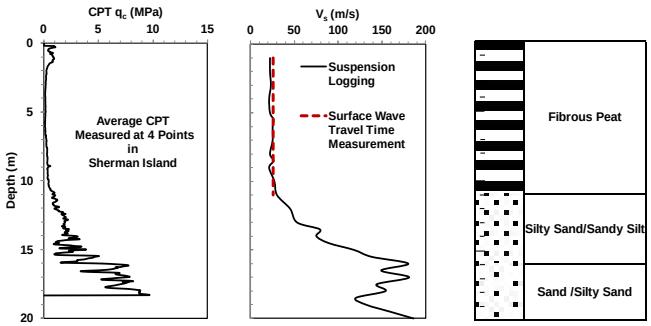


Figure 2. Cone tip resistance and shear wave velocity profiles for free-field Sherman Island site (Shafiee et al. 2013). Suspension log conducted by GeoVision (2000) at a similar site near the test site.

3. DATA PROCESSING AND ANALYSIS

This section explains the procedures used to calculate the base shear, base moment, average base displacement, and average base rotation of the model test levee for the purpose of defining the stiffness and damping of levee-foundation soil interaction. A schematic of the levee and the accelerometers used to calculate these values can be seen in Fig. 3. Eight EpiSensor triaxial accelerometers were placed on each side of the embankment: four along the base, two at mid-height, and two on the crest. Sixteen total accelerometers were mounted on the levee (eight on each side) and additional accelerometers were placed on the ground surface away from the levee, and subsurface accelerometers and piezometers were placed in the peat beneath the levee, though these sensors are beyond the scope of the paper. The embankment was then divided into sixteen tributary wedges, and the centroid, volume, and weight of each wedge was calculated. The test data used to calculate desired quantities consisted of the x and z components of acceleration of the accelerometers on the embankment and the shaker force F_{shk} [see Reinert et al. (2012) for details on F_{shk} calculation].

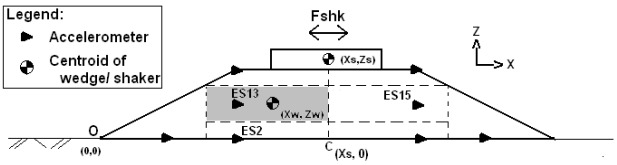


Figure 3. Schematic of model levee including shaker and instrumentation.

The first step was interpolating acceleration at the centroid of each wedge from the measured accelerations. For example, consider the shaded wedge in Fig. 3. The z-component of acceleration at the centroid was interpolated between ES13 and ES15 since vertical acceleration is anticipated to vary horizontally due to rotation of the levee. The x-component of acceleration was taken as being equal to ES13 in this case since the elevation of the centroid is equal to the elevation of ES13. For some wedges, the elevation of the centroid is not identical to the elevation of any accelerometer, in which case the centroid acceleration is interpolated vertically between the nearest two sensors.

Once the representative accelerations for each wedge were computed, we then calculated the base shear and moment of the embankment by (*i*) computing inertia force for each wedge in the horizontal and vertical directions, (*ii*) summing horizontal inertia forces plus shaker force to obtain base shear, and (*iii*) summing horizontal inertia force multiplied by vertical moment arm, vertical inertia force multiplied by horizontal moment arm, and shaker force multiplied by the height to the centroid of the shaker. Moments were computed about the center of the base [i.e., at point (x_s,0) in Fig. 3]. Shear is positive from left-to-right, and moment is positive clockwise. Steps (ii) and (iii) are explicitly defined in Eqs. 1 and 2.

$$V_{base} = F_{shk} + \sum_{i=1}^{16} -m_i a_{x,i} \tag{1}$$

$$M_{base} = z_s \cdot F_{shk} + \sum_{i=1}^{16} -m_i a_{x,i} z_{w,i} + \sum_{i=1}^{16} m_i a_{z,i} (x_{w,i} - x_s) \tag{2}$$

The final step of calculations was to compute a representative base displacement and rotation, which are combined with the shear and moment to evaluate frequency-dependent stiffness. First, displacements were

computed by double-integrating the acceleration records in time. The Fourier transform of each record was computed, and the real and imaginary components were multiplied by a Butterworth filter with an order of 5 and a corner frequency of 0.2 Hz. Note that this filter is acausal (i.e., it does not alter the phase of the signals) since the real and imaginary components are both multiplied by the same scalar. The filter was required to remove low frequency noise that would otherwise cause erroneous drift in the displacement records. The representative base displacement was then computed as the average of the x-component of displacement from the eight accelerometers along the base of the levee. Very little variation in these motions was observed, and an equally-weighted average is therefore reasonable.

The representative rotation is complicated by flexibility of the model levee. Fig. 4 shows undeformed and deformed positions of the accelerometers during positive and negative loading cycles. The base of the levee is clearly nonlinear, which indicates that the rotation varies along the length of the levee. The representative rotation in this case was computed using a weighted least squares regression approach in which the weights for the two sensors nearest to the center of the levee were three times larger than the weights of the sensors nearest to the toes of the levee slopes. The motivation for using a weighted least squares procedure is that more mass lies near the center of the levee, therefore the rotation near the center should be more representative of the flexible levee response.

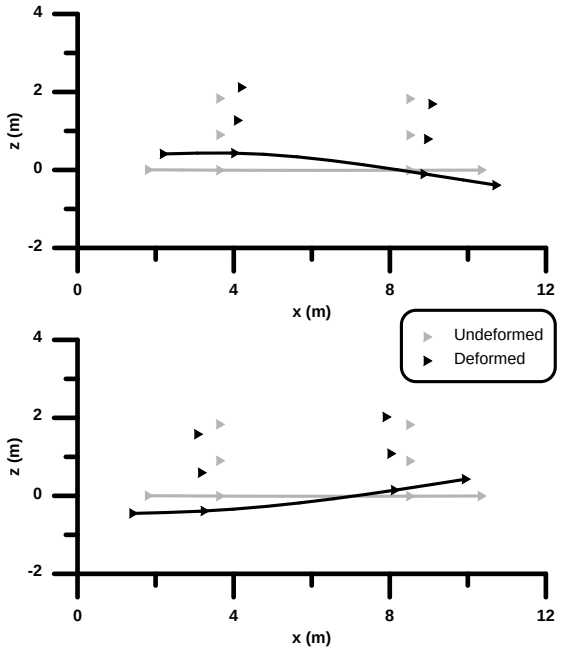


Figure 4. Deformed and undeformed displaced positions of sensors during a positive and negative loading cycle (displacements amplified × 100).

4. MEASURED SHEAR-DISPLACEMENT AND MOMENT-ROTATION RESPONSES

Measured levee-foundation soil responses are presented in Figs. 5 and 6 in terms of base shear versus horizontal translation and base moment versus representative rotation. The results in Fig. 5 apply for a medium intensity motion that resulted in a maximum horizontal crest acceleration of 0.04g. At 1Hz, the moment-rotation relation is essentially linear with no measurable damping, while the horizontal force-displacement relation exhibits a small amount of damping. Radiation damping and hysteretic damping are likely present in the measurement, though separating the relative contribution of each is not possible from the measured data. As the frequency increases, the damping increases as well, and the force-displacement curves are essentially circular at 3Hz. Damping also increases for moment-rotation, but not as significantly as for force-displacement. This trend was also observed by Tileylioglu et al. (2011) for a rigid concrete foundation on stiff soil.

Fig. 6 presents the measured responses for a high intensity motion that resulted in a maximum crest acceleration of 0.27g. The curves for f=3Hz are not presented because the shaker capacity was mobilized during this motion, and could not reach frequencies higher than 2.6Hz. For a given frequency, more damping is apparent in the responses for the high intensity motion compared with the medium motion. This trend is likely the result of higher shear strains mobilized in the soil by the high intensity motion, which would cause (i) increased hysteretic damping, and (ii) increased radiation damping due to the reduction in shear modulus (and reduction of equivalent shear wave velocity) of the peat and associated increase in dimensionless frequency, $a_o = \omega B/V_s$, where ω = angular frequency = $2\pi f$, and B = footing half-width. The non-harmonic features in the shear-translation and moment-rotation responses for the higher frequency motions were caused by pounding between the timber frame and the model levee.

The dramatic increase in damping with frequency is consistent with analytical solutions for rigid footings on an elastic halfspace. For example, consider B = 1.85m, V_s = 25m/s, and f = 3Hz. The dimensionless frequency is $a_o = 2\pi(3\text{Hz})(1.85\text{m})/(25\text{m/s}) = 1.4$. The radiation damping for a rigid rectangular footing with L/B = 12m/3.7m = 3.2 is 86% for translation and 108% for rotation using the solutions suggested by Pais and Kausel (1988). These very high radiation damping values at low frequencies are caused by the peat's extraordinarily low shear wave velocity.

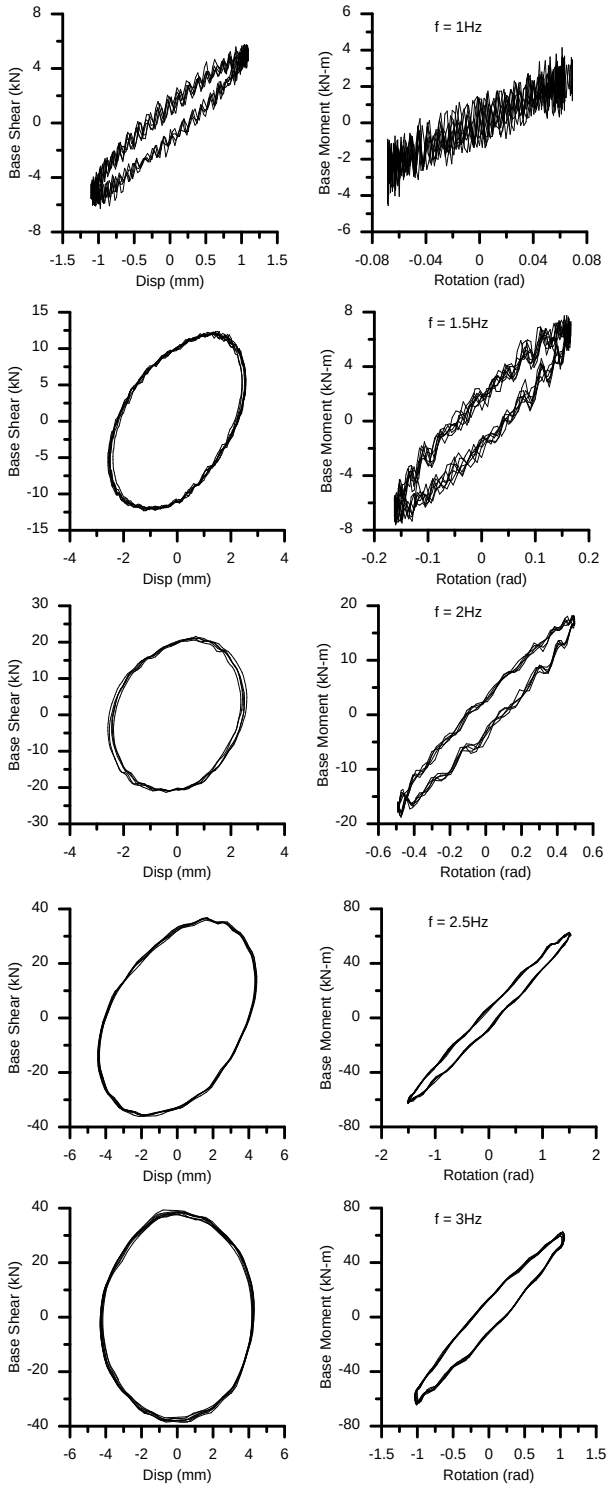


Figure 5. Impedance relations for a medium intensity motion that resulted in peak horizontal crest acceleration of 0.04g.

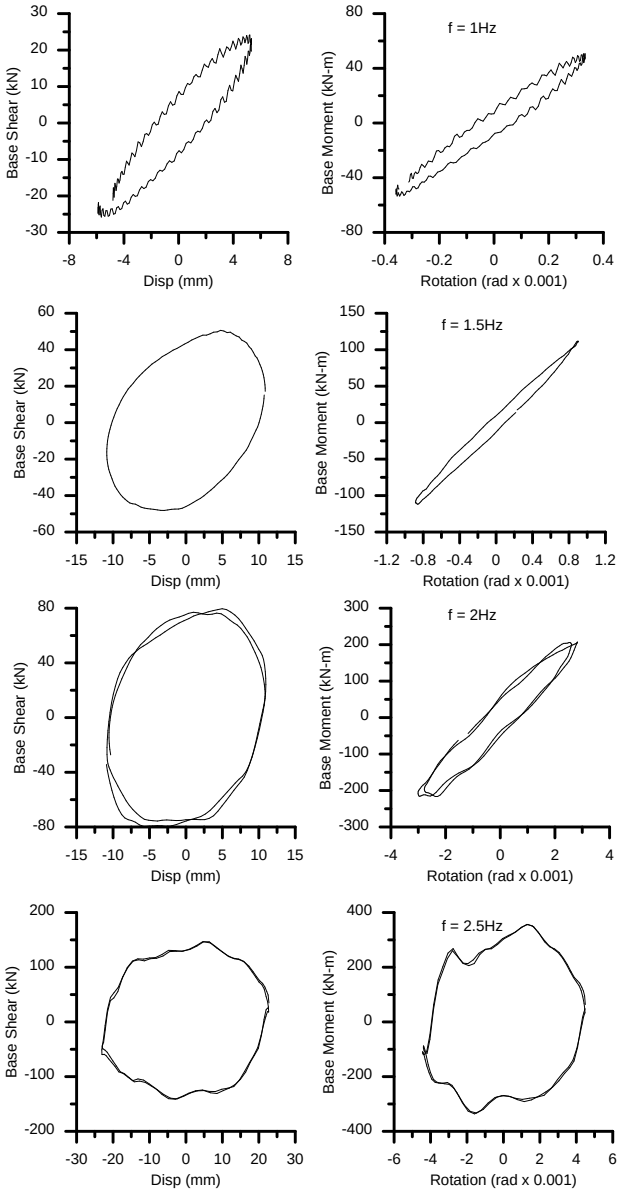


Figure 6. Impedance relations for a large intensity motion that resulted in peak horizontal crest acceleration of 0.27g.

4. CONCLUSIONS

A dynamic test of a model levee on very soft peat soil was interpreted herein using soil-structure interaction concepts. This approach is reasonable because the levee fill is significantly stiffer than the underlying peat, which had a shear wave velocity of only 25m/s. Measurements of V_s for the levee fill have not yet been processed, but we anticipate that V_s was at least 150 m/s based on visual/manual observations of the unsaturated clay fill. The model levee translated and rotated significantly during shaking. The response of the levee indicates that seismic analysis of levees using one-dimensional wave propagation theory may be inappropriate when the foundation conditions are very soft. For example, a one-dimensional site response analysis of a profile below the levee crest could not possibly capture the rotational response, and may result in erroneous prediction of crest acceleration. Furthermore, rotational deformation of the levee causes rotations of principal shear stresses, resulting in a stress path that is different from simple shear, particularly near the levee toes. Liquefaction of saturated cohesionless levee fill is a significant concern for many levees, including those in the Sacramento / San Joaquin Delta, and modifications to traditional liquefaction triggering procedures may be needed for levees on peat. More research is required to develop such modifications.

Relations for the complex shear-translation and moment-rotation responses were computed from a dynamic test of a model levee on very soft peat soil. The results indicate a significant amount of radiation damping at frequencies that are well within the bandwidth of typical earthquake ground motions and that are of interest for ground failure analysis. Whether this conclusion can be generalized to the earthquake behavior of levees resting on peat is currently unclear for a number of reasons. First, the model levee was shaken at the crest in a top-down configuration, which is different from the bottom-up propagation of seismic waves during an earthquake. Second, the model levee was smaller than typical levees, and a scale effect is possible due to the size of the levee relative to the thickness of the peat, and the higher consolidation pressures (and associated lower void ratios and higher stiffness) that would exist in the peat beneath a larger levee. Third, the model levee was a three-dimensional slice rather than a long two-dimensional earth structure that would be more consistent with a real levee. Nevertheless, the test data identified an important fundamental issue that requires further study.

Acknowledgements:

The authors would like to acknowledge the following people for assistance during the test: co-PI Robb E.S. Moss from Cal Poly, San Luis Obispo; Mike Driller, Bryan Brock, David Mraz, and Nancy Vogel from the Department of Water Resources; the nees@UCLA group including Bob Nigbor, Steve Keowen, Alberto Salamanca, Sophia Poulos, and Jackson English, and UCLA students Pavlo Chrysovergis and Sean Ahdi. This research was supported by the National Science Foundation under award number 0830081 through the George E. Brown Network for Earthquake Engineering Simulation Research (NEESR) program in coordination with cognizant program official for this grant is Richard J. Fragaszy. Any opinions, findings, and conclusions or recommendations expressed in this material are those of the author(s) and do not necessarily reflect the views of the National Science Foundation.

References:

GeoVision (2000). “Department of water resources boreholes DHP-4D and DHP-5J3 suspension P&S velocities” prepared for California Water Department Resources.

Pais, A and E Kausel (1988). “Approximate formulas for dynamic stiffnesses of rigid foundations,” Soil Dyn. & Eqk. Engrg., 7(4), 213-227.

Sasaki, Y. (2009). "River dike failures during the 1993 Kushiro-oki earthquake and the 2003 Tokachi-oki earthquake," Earthquake geotechnical case histories for performance-based design - Kokusho (ed), 2009 Taylor & Francis Group, London, pp. 131-157, 2009.

Shafiee, A., Brandenberg, S.J., and Stewart, J.P. (2013). “Laboratory investigation of the pre- and post-cyclic volume change properties of Sherman Island peat,” 2013 Geo Congress, San Diego.

Tileylioglu, S, JP Stewart, and RL Nigbor (2011). “Dynamic stiffness and damping of a shallow foundation from forced vibration of a field test structure,” J. Geotech. & Geoenv. Engrg., 137 (4), 344-353.

URS Corporation, Jack R. Benjamin and Associates (2009). "Delta Risk Management Strategy (DRMS) Phase 1 Report." California Department of Water Resources.

10CUEE CONFERENCE PROCEEDINGS
10th International Conference on Urban Earthquake Engineering
March 1-2, 2013, Tokyo Institute of Technology, Tokyo, Japan

CONFINING EFFECT OF BEARING PLATE AND HELIX ON SLIDING RESISTANCE OF REINFORCED SLOPE USING STEEL PIPE PILES

Akihiro Takahashi[1], and Yohei Nakamichi[2]

1) Associate Professor, Department of Civil Engineering, Tokyo Institute of Technology, Japan
2) Graduate Student, Department of Civil Engineering, Tokyo Institute of Technology, Japan
takihiro@cv.titech.ac.jp, nakamichi.y.ab@m.titech.ac.jp

Abstract: To examine confining effect of bearing plate and helix on sliding resistance of reinforced slope using steel pipe piles, a series of centrifuge tests were conducted. Test results reveal that (1) installation of the inclined preventive piles increases the frictional resistance at the interface between the sliding and stable layers, (2) confinement provided by bearing plate at pile head or helix along the pile increases the sliding resistance of reinforced slope by 20~50% within the scope of tests, (3) the bearing plate makes the tensile resistance of the pile notably larger, and (4) marked effectiveness of pre-stressing is confirmed at the beginning of loading.

1. INTRODUCTION

Preventive pile against slope failure is a major reinforcement method. The reinforcement mechanism of the preventive pile is very complicated, because it is designed to prevent slope failure with its passive resistance induced by the interaction between the pile and the ground. Preventive piles had been usually constructed in vertical direction because of the limitation of construction methods. However recently, it is becoming available to construct the piles in any direction, i.e., non-vertical direction, and there is a possibility to design the preventive pile more effectively.

Takahashi and Morikawa (2012) demonstrated that the preventive pile inclined toward the downslope direction with respect to the sliding surface shows the larger resistance against sliding through a series of the centrifuge tests. In their tests, increase of the sliding resistance is attributed not only to the shearing and axial resistance of piles, but also to confining effect of piles, i.e., existence of piles increases the shearing resistance of soil.

When a slope is reinforced by ground anchors, bearing plates play an important role in providing pressure to increase sliding resistance. If such a bearing plate is fitted with the head of the preventive pile, we can expect increase of the sliding resistance. Probably use of helical piles as preventive piles may have similar effects to increase shearing resistance at the interface between the sliding and stable layers.

Objective of this study is to examine confining effect of bearing plate and helix on sliding resistance of reinforced slope using steel pipe piles through a series of centrifuge tests. Model slopes are similar to those tested by Takahashi and Morikawa (2012), but by considering capacity of the loading system; tests were conducted at 15g, which is half of that applied by Takahashi and Morikawa (2012).

2. OUTLINE OF CENTRIFUGE TESTS AND TEST CONDITINOS

A schematic view of the experiment system is illustrated in Fig.1. Experiment system that can impose the ground movement with the prescribed sliding surface is used. The model stable layer and mobile (or sliding) layer were made in a steel rigid box with the sliding layer size 630mm in width, 300mm in depth, and 250mm in thickness. All experiments were conducted under 15g of centrifugal acceleration. Thus, the thickness of the sliding soil mass

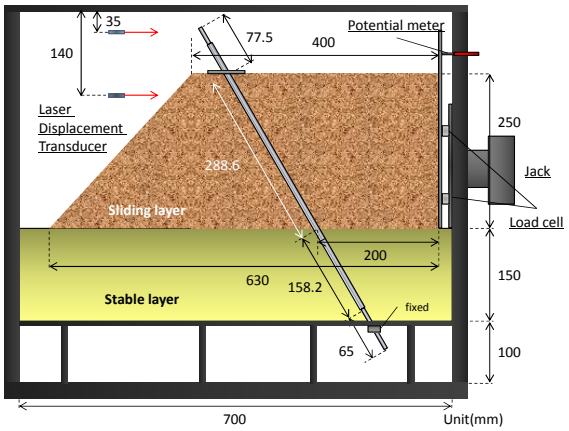


Figure 1 Experiment system (Dimensions are in model scale)

Table 1 Test cases

Case	Num. piles	Bearing plate	Helical piles
1	–	–	–
2	3	–	–
3		60mm-square	–
4		90mmm-square	–
5		60mm-square (Pre-stress = 0.175kN/pile)	–
6		–	Helix dia. = 18mm

corresponds to 3.75m in the prototype scale.

The stable layer was modelled as a relatively stiff layer having the SPT N-value of around 20. Stiffness of the stable layer was estimated by the empirical relationship between the Young's modulus and SPT N-value (NERI, 2010). The stable layer was made of urethane rubber whose Young's modulus was about 20MPa. The stable layer have holes that model pile could be installed, and the pile tip can be fixed at the bottom of the stable layer, i.e., the tip of the piles could be regarded as the fixed end. Three model piles were arranged in a row with equally spaced for all the cases (Distance between the piles = 1.5m (≈ 11 *D*) in the prototype scale). In the tests, the stable layer was covered with Teflon sheet so that friction between the stable and sliding layers could be minimized.

The sliding layer made of Edosaki sand (Takahashi & Izumi, 2010) was constructed on the stable layer by compacting the soil with a water content of 15% to achieve a degree of compaction of 90%. The displacement was given only to the sliding layer by the jack through the loading plate. Slip of the sliding surface occurred at the interface between the sliding and stable layers in all the cases.

Model pile is a hollow steel pipe made of ferritic stainless steel. The outer diameter is 9mm and the thickness is 0.5mm. The corresponding pile in the prototype scale was 135mm in outer diameter. The model pile had 28 strain measurements inside the steel pipe for monitoring axial strain or bending strain along the pile. Six test cases were conducted as shown in Table.1. In the case with pre-stressing (Case 5), prescribed tension of the pile was given by means of spring attached on the bearing plate before spinning the centrifuge. In case 6, spacing of the helix on the pile was 18mm and the thickness of the helix was 1mm.

3. TEST RESULTS

Figure 2 shows relationships between the load measured with the load cells and normalised horizontal displacement of the slope nearby the pile. From the figure, definite reinforcement effects of piles against sliding are confirmed by comparing the cases with piles to that without piles (Case 1). In Case 1 (without preventive piles), the load reaches steady state with 3kN when the horizontal displacement is around 2mm (≈ 20% *D*). This corresponds to the frictional resistance arise from the interface between the sliding and stable layers.

In Cases 2 (with straight piles) and 3 (with straight piles capped by small bearing plate), there is no large difference compared to Case 1 at the beginning of loading (before yielding), while the load continuously increases even after Case 1 had reached the steady state. This increase of the load is regard as a reinforcement effect of the piles on the slope. Unexpectedly, Cases 4 (with straight piles capped by large bearing plate) and 6 (with helical piles) show softer response at the beginning of loading, compared to Cases 1~3. This may be attributed to disturbance of the ground near the piles when the piles were installed.

By comparing Case 2 to Case 3, Case 3 shows the larger load than that for Case 2. Case 2 shows plateau in the load-displacement curve after reaching the displacement of 60% *D*, while the load continuously increases in Case 3 because of the confining effect of the bearing plate. As expected, the case with the larger bearing plate (Case 4) exhibits larger resistance when the larger displacement is imposed compared to the case with the smaller plate (Case 3). The pre-stressing has marked confining effect at the

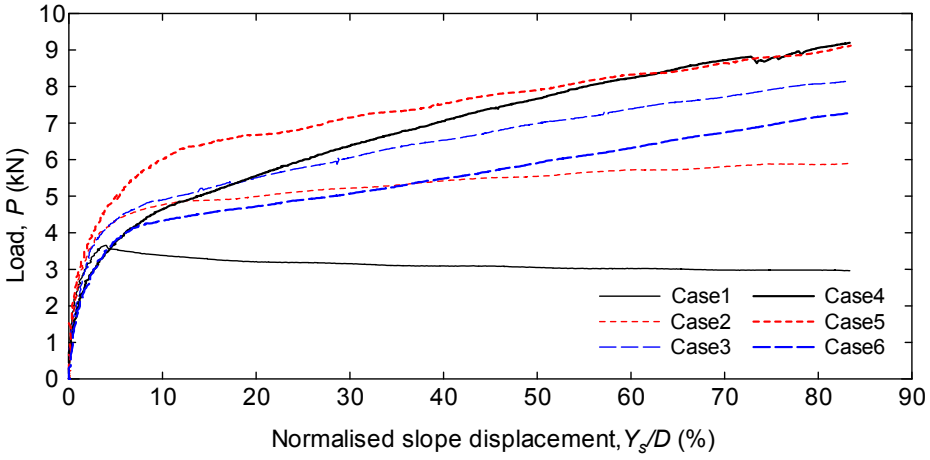
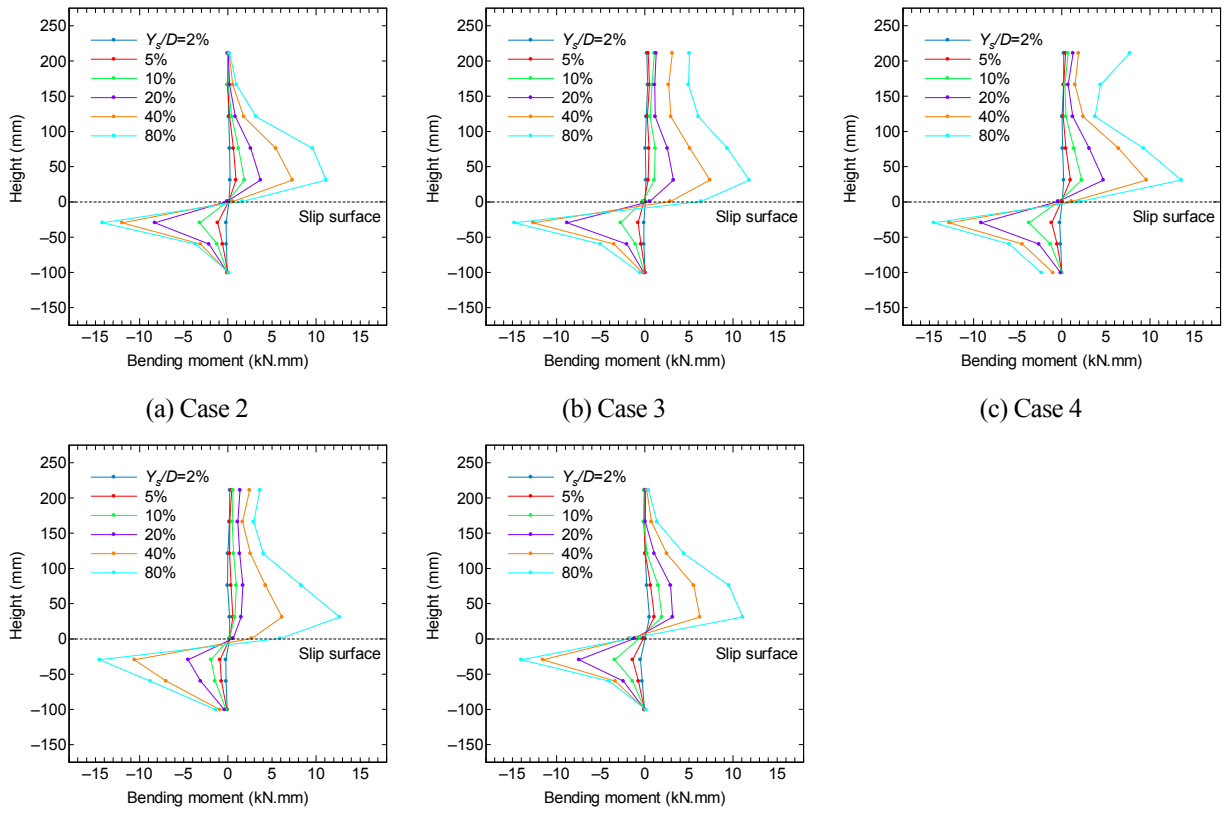


Figure 2 Load-displacement curves for all cases



(a) Case 2 (b) Case 3 (c) Case 4

(d) Case 5 (e) Case 6

Figure 3 Bending moment profiles

beginning of the loading (see Cases 5 and 3). The confining effect in the case with the helical piles (Case 6) is somewhat weak, but the marked difference can be seen in contrast to Case 2. The confining provided either by bearing plate or by helix had an effect on enhancement of sliding resistance of reinforced slope and it increased the resistance by 20~50% by compared to the case with the straight piles (Case 2).

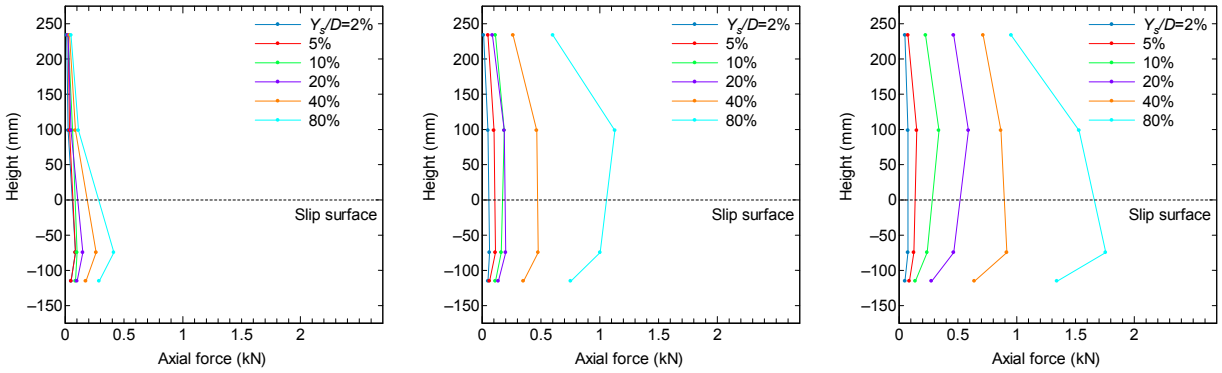
Figure 3 shows distributions of bending moment of the pile in all the cases. Large positive bending moment is observed just above the interface between the sliding and stable layers, while the large negative bending moment appears in the stable layer. Magnitude of the minimum bending moment in the stable layer is larger than that of the maximum bending moment in the sliding layer for all the cases. In the cases where the bearing plate is attached to the pile head (Cases 3~5), a certain amount of bending moment appeared around the pile head, since rotational movement of the pile head was restrained by the bearing plate.

Figure 4 shows distributions of axial force of the pile in all the cases. In the cases where the bearing plate is attached to the pile head (Cases 3~5), very large axial force is observed. Among them, in Case 5 where pre-stressing was given before loading, due to the better contact of the bearing plate with the ground surface from the beginning, magnitude of the axial force was large from the beginning of the loading. Case 6 (with helical piles) shows relatively large axial force by comparison with Case 2, but not that much compared to the cases where the bearing plate is attached to the pile head (Cases 3~5).

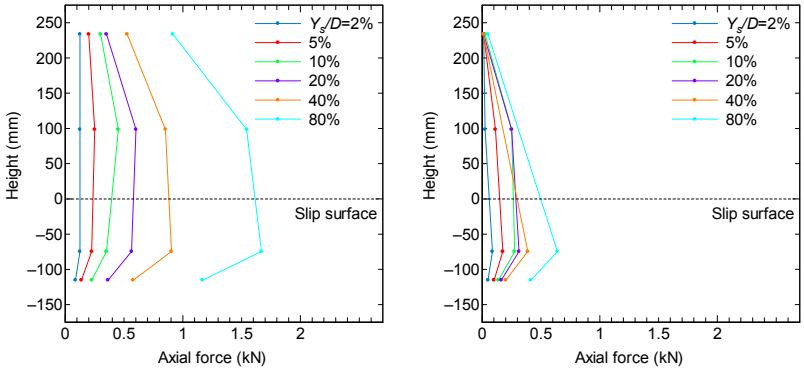
Considering equilibrium of forces in the experiment system, the load can be expressed by the sum of the resistance of piles and the friction at the interface. The sum of the horizontal components of shear and axial forces at the sliding surface is the horizontal resistance induced by piles. Figure 5 shows the share of the horizontal resistances for Cases 2, 4 and 5. The line of filled circle in the figure is the measured load–displacement curve, while the lines with open triangle and open square are horizontal component of shear force and axial force, respectively. Consider the equilibrium of force mentioned above, the resistance induced by the ground friction can be calculated. Difference between the calculated frictional component and Case 1 (see Fig. 2) should correspond to the increase of the frictional resistance at the interface between the sliding and stable layers as a result of the sliding layer – pile interaction. From this figure, it can be said that (1) installation of the inclined preventive piles increases the frictional resistance at the interface, (2) the bearing plate makes the tensile resistance of the pile notably larger, and (3) marked effectiveness of pre-stressing is confirmed at the beginning of loading.

4. SUMMARY

To examine confining effect of bearing plate and helix on sliding resistance of reinforced slope using steel pipe

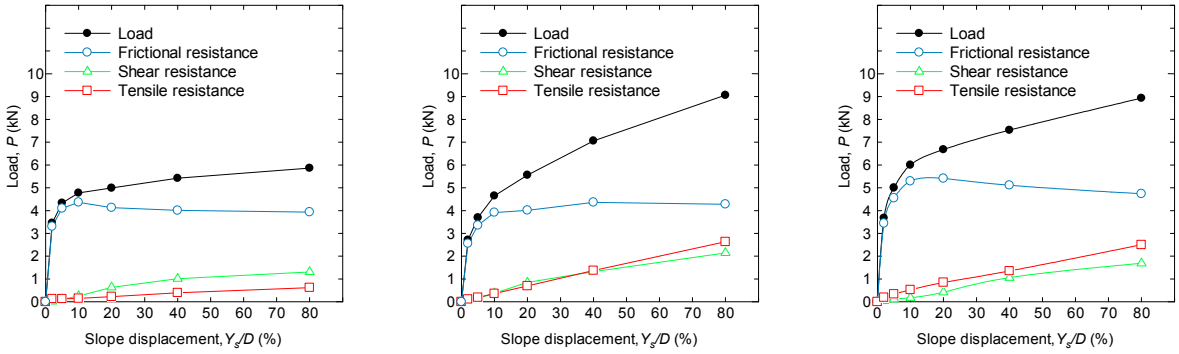


(a) Case 2 (b) Case 3 (c) Case 4



(d) Case 5 (e) Case 6

Figure 4 Axial force profiles



(a) Case 2 (b) Case 4 (c) Case 5

Figure 5 Share of horizontal resistances

piles, a series of centrifuge tests were conducted. Test results reveal that (1) installation of the inclined preventive piles increases the frictional resistance at the interface between the sliding and stable layers, (2) confinement provided by bearing plate at pile head or helix along the pile increases the sliding resistance of reinforced slope by 20~50% within the scope of tests, (3) the bearing plate makes the tensile resistance of the pile notably larger, and (4) marked effectiveness of pre-stressing is confirmed at the beginning of loading.

Acknowledgements:

The work presented in this paper is a part of the collaborative research with the Nippon Steel & Sumikin Engineering Co., Ltd.

References:

Nippon Expressway Research Institute (2010), "Design Specification for Expressway," 2 (in Japanese.)

Takahashi, A. & Izumi, N. (2010), "Effects of pre-existing cracks and deformation caused by earthquake on rainfall-induced slope failure," Proc. 2010 Taiwan-Japan Symposium on Advancement of Urban Earthquake Hazard Mitigation Technology, 37-40.

Takahashi, A. & Morikawa, N. (2012), "Experimental Study on Reinforced Slope using Steel Pipe Piles," Proc. 2012 Taiwan-Japan Symposium on Advancement of Urban Earthquake Hazard Mitigation Technology, 60-63.

10CUEE CONFERENCE PROCEEDINGS
10th International Conference on Urban Earthquake Engineering
March 1-2, 2013, Tokyo Institute of Technology, Tokyo, Japan

A STUDY ON THE CHARACTERISTICS OF THE GROUND SURFACE DEFORMATION INDUCED BY THE REVERSE FAULT SLIP

Y.Y, Chang [1], C.J, Lee [2], W.C, Huang [3], W.Y, Hung [4]

1) Doctoral Student, Department of Civil Engineering. National Central University, Taiwan
2) Professor, Department of Civil Engineering. National Central University, Taiwan.
3) Professor, Department of Civil Engineering. National Central University, Taiwan.
4) Associate technologist, National Center for Research on Earthquake Engineering, Taiwan.
93342004@cc.ncu.edu.tw, cjleeciv@cc.ncu.edu.tw, wenchaoh@gmail.com, wyhung@ncree.narl.org.tw

Abstract:

This paper presents the results between centrifuge modeling test and numerical simulations of propagation of an active dip-slip fault rupture through a dense, uniform sand soil layer which is covering the rigid bedrock. A series of centrifuge modeling (dip angle=60°) in the conditions of acceleration of 1g, 40g and 80g were performed to investigate the ground surface deformation trough due to reverse faulting. Sets of test datum were obtained during the period of increasing gravity and uplifting the fault throws, The datum of increasing gravity of centrifuge modeling test were used to calibrate the parameters of PFC^{2D} (Particle Flow Code) modeling, and the calibration parameters were used in the PFC^{2D} main program to simulated the ground surface deformation, After comparison of the results between centrifuge modeling test and PFC^{2D} numerical simulations, It shows that, the ground surface deformation of centrifuge modeling test and PFC^{2D} numerical simulation were quite agreement. A sigmoid(Probability Density Function ,PDF) curve equation was used to fit the ground surface deformation of centrifuge test data, and extend study for underground rupture path propagation were simulated by PFC^{2D}, the growth of rupture path can be seen and the primary influence zone can be obtained.

1. INTRODUCTION

Ground movement due to the dip-slip faulting has been considered as a significant affecting to the man-made structure, in year of 1999, three majors earthquake were occurred in Turkey (Kocaeli and Duzce) [Ulusay et al., 2001] and Taiwan (Chi-Chi). Several man-made structures were destroyed due to foundation displacement in which fault rupture occurs on the ground surface [Dong et al., 2000]. Eurcode EC8 (1994) banned the structure adjacent to the active fault and may request some set-back distance from fault trace. After 1999 Chi-Chi earthquake, the evidence shows that the set-back distance of seismic code is not so conservative, and the issue of ground surface deformation become important, some field observations [Chen et al., 2000], small scale tests [Lin et al., 2006], centrifuge experiments of normal/reverse fault [Bransby et al., 2008] and numerical analysis [Anastasopoulos et al., 2007; Dimitrios et al., 2009]results were published, and they are showing the very good results for understanding the ground surface deformation.

In order to observe deformation zone of the ground surface which was induced by reverse faulting, the centrifuge modeling tests of reverse fault were performed, the ground surface deformation datum were recorded and interpreted. A PFC2D simulation was used to conduct the numerical results of underground deformation and rupture path propagation in this study.

2. Centrifuge modeling test

The capacity of NCU centrifuge is 100 g-ton , the nominal radius is 3 meters, the dimensions of centrifuge platform are 100 cm×55 cm×72 cm (length × width ×height) and the maximum payload of platform is 400 kg [Lee et al., 2012]. The centrifuge was accelerated at an acceleration of 10 g per step until it reached the target acceleration or the acceleration of 80 g. In each step the surface profile scanner was trigged to scan the surface of soil bed for measuring the changes in the surface elevations. Once the target acceleration was achieved, normal faulting or reverse faulting was carried out. The fault throw was increased with a constant velocity of 2 mm/min by the motor for both normal faulting and reverse faulting. The surface profile scanner was driven once to scan the surface elevations per 2.5 mm increment throw. The fault displacement was increased until a final throw of 5 cm (corresponding to 4 m at prototype scale) was actuated. The testing program is detailed in Table 2-I, and the test results of 80g were shown on figure 2-I (a) and (b).

Table 2-I Reverse fault testing program

test number	height of specimen (mm)	relative density (%)	acceleration (*g*)	fault throws (mm)
R_200_70_1*g*	200	70	1	50
R_200_70_40*g*	200	70	40	50
R_200_70_80*g*	200	70	80	50

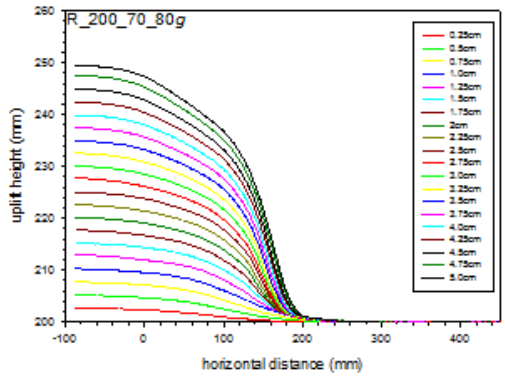


Figure 2-I(a) ground surface deformation profiles at various throws

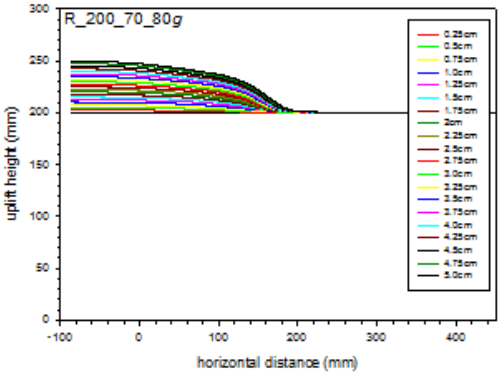


Figure 2-I(b) ground surface deformation profiles at various throws

3.PFC^{2D} modeling

PFC^{2D} (Particle Flow Code-2 dimension) models the movement and interaction of circular particles by the distinct element method [Cundall et al., 1979]. The particle model was used to understand uniform element behavior, and used to solve real problems that involve complicated deformation patterns.

In PFC^{2D}, the relative parameters are density (ρ, kg/m^3), normal stiffness (K_n, N/m^2), Shear stiffness (K_s, N/m^2), friction coefficient (tanφ), wall property and the radius of the particle. For the test sand, the radius of quartz particle (D_{50}=0.193 mm) are too small, for the modeling of 200mm x 1000mm (Figure 3-I) may need about 680,000 particles. In general, the standard computer can't afford such a heavy duty or may need a long time to deal with a simple question; it seems not so realistic and economy to use real particle size in the PFC^{2D} modeling. In this study, the same particle distribution curve but shift to 20 time of real particle size was used as a fundamental size, by means of random and pluviation method to create element particles and to stack the sand soil layer. In Figure 3-I, wall 2 and wall 3 were considered as a fixed wall, wall 1,wall 4 and wall 5 can be moving uplift, and its moving vector is along the direction of fault plane angle, all the wall were considered as a rigid and frictionless element. X_0 denotes the width from fault tip to point of maximum ground surface inclination and X_{tot} denotes the width of the overall ground surface distortion zone (influence zone) in Figure 3-I.

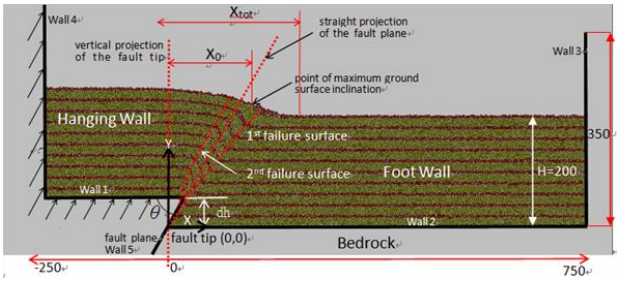


Figure 3-I PFC modeling

4. Comparing with centrifuge test and PFC^{2D}results

Kn=0.5e7N/m^2, Kn/Ks=3, tanØ = 36°, m=0.4 were used as parameters of PFC^{2D} simulations, comparison of PFC^{2D} simulation and centrifuge 1g, 40g, 80g test results were shown on the Figure 4-I(a)~(c), where the dot line is PFC^{2D} simulation results, continuous line is centrifuge modeling test results. In 1g simulation Figure 4-I (a), shows the trends of ground surface deformation is similar, Figure 4-I (b)~(c) show the 40g , 80g fitting condition, they show the good agreement of PFC^{2D} simulation results and centrifuge test data. Figure 4-I (a),(b),(c) show the results of ground surface deformation in the condition of 1g,40g and 80g which the throws are 1cm, 2cm, 3cm, 4cm and 5cm, that means the ratio of dh/H are 5%,10%,15%,20% and 25% respectively. By means of regression, the probability density function (PDF) curve can be used to fit the shape of ground surface deformation, the equation of PDF curve and differential equation of PDF curve were shown on the equation (1) and equation (2).

$$f = y_0 + \frac{a}{1+e^{-\left(\frac{x-x_0}{b}\right)}} \quad (1)$$

$$f' = \frac{ae^{-\left(\frac{x-x_0}{b}\right)}}{b}\left(1+e^{-\left(\frac{x-x_0}{b}\right)}\right)^{-2} \quad (2)$$

f : height of probability density function (PDF) curve
f' : slope of PDF curve
y_0 : average elevation of original ground surface
X : horizontal distance from fault tip
X_0 : the expected value
b : parameter of the shape of the curve, minus sign

represents the curve is from left hand side down to right hand side, and the smaller the b value, the deeper the shape of the curve.

a : distance from original ground surface elevation to the ground surface elevation of hanging wall.

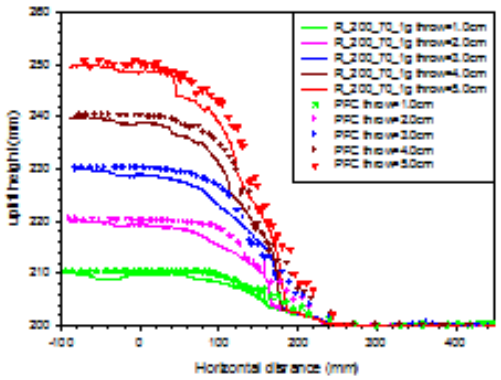


Figure 4-I(a) comparison of PFC^{2D} simulation and centrifuge test_ 1g,

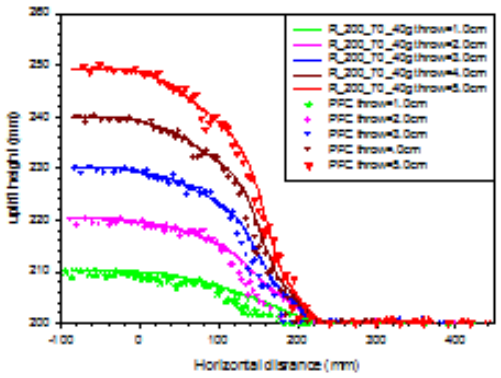


Figure 4-I(b) comparison of PFC^{2D} simulation and centrifuge test_ 40g

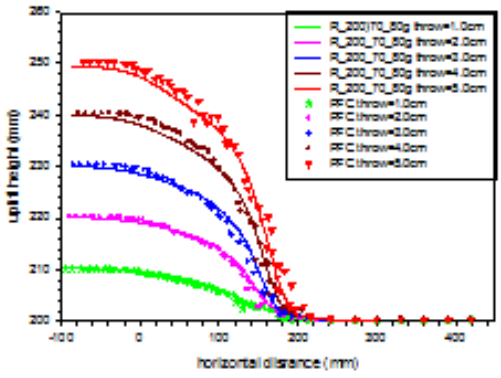


Figure 4-I(c) comparison of PFC^{2D} simulation and centrifuge test_ 80g

5 PFC^{2D} simulation for rupture path propagation and influence zone

Figure 5-I(a) ~ (b) show the original dh/H=0% (throws=0m) mesh and dh/H=25% (throws=4m) mesh deformation during the reverse faulting, figure 5-I (b) shows that, the larger mesh deformation concentrates on the fault rupture path. When the fault rupture dislocated, the particle that around the rupture path will rotate in terms of counter clockwise or clockwise, in the lager distortion area the particles may cause more rotation. According to the particle rotation, PFC^{2D} simulation shows the growth of rupture path in the condition of 80*g*. Figure 5-II (a) ~ (h) shows the growth of rupture path in the different dh/H ratio from 1.25% to 25%. When the dh/H ratio is less or equal to 1.25%, the 1strupture path is beginning to form from the bedrock (fault tip) in the vertical direction, the height of rupture is about 30% of the soil disposal height. While dh/H ratio is equal to 2.5%, 2nd rupture were formed on the right hand side of the 1st rupture, the rupture path direction is same as fault plane angle (dip angle), in the same time, the 1st rupture height extended to about 50% of the soil disposal height. In the condition of dh/H ratio is equal to 3.75%, the 2nd rupture extended to the ground surface. The 1st rupture extended to the ground surface, while the dh/H ratio is equal to 5%, in the same time, the shear zone were developed on the left hand side of the 2nd rupture path. During the dh/H ratio is from 6.25% to 25% the distortion zone were enlarged both side of the rupture. since the rupture force direction is 60 degree from the down-left side to the up-right side, the soil layer in the hanging wall will squeeze the 2nd rupture path, and forced 2nd rupture to the right hand side, so the slope of the top rupture is smoothing than the rupture in the bottom side. during the range of dh/H is 15%~20%, the 2nd rupture is gradually stopping extend to the right hand side, in the mean time, the rupture force still acting on the footwall, the rupture squeeze by the hanging wall, the distortion zone were suffered more disturbs, and main distortion zone are concentrate on the area of 2nd rupture and maximum inclination point. From Figure 4-II (h), in the condition of the ratio of dh/H is equal to 25%, the primary influence zone was measured, and it shows the length of the primary influence zone about 1.25H under the condition of particle rotation is larger than 15 degree.

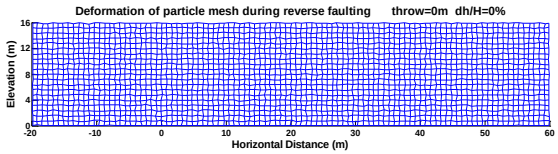


Figure 5-I(a)

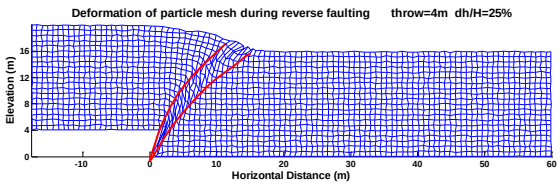


Figure 5-I(b)

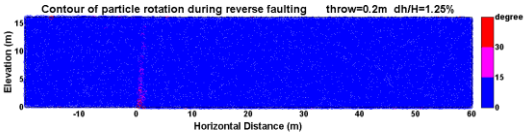


Figure 5-II(a)

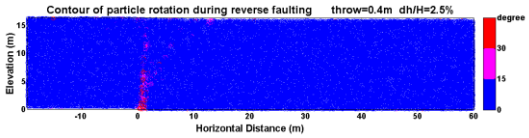


Figure 5-II(b)

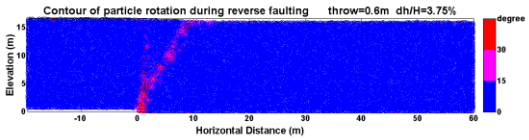


Figure 5-II(c)

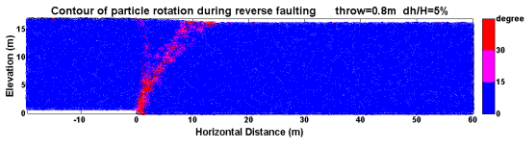


Figure 5-II(d)

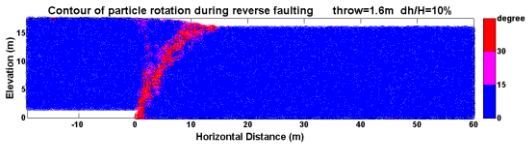


Figure 5-II(e)

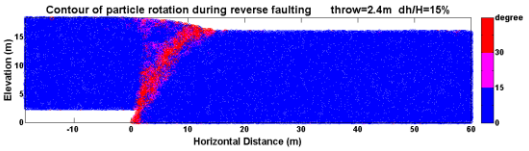


Figure 5-II(f)

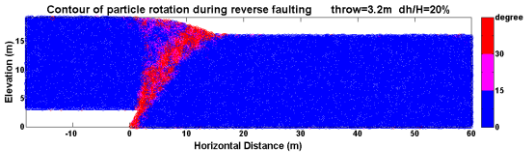


Figure 5-II(g)

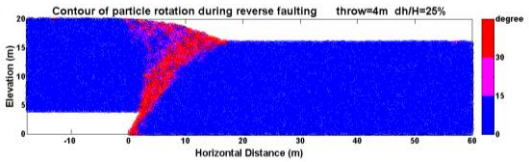


Figure 5-II(h)

6. Conclusions

1. A probability density function (PDF) curve can simulate the different ground surface deformation profile for the various thickness of soil formation after the reverse faulting, and the influence zone can be predicted by using the technique of regression.
2. According to the PFC^{2D} simulation, the rupture path were formed in the stage of dh/H is less or equal to 1.25%, and 2 rupture paths extended to the ground surface in the dh/H ratio is 3.75%~5%. In the dh/H=25%, the primary length of influence zone is about 1.1 times of soil disposal (H).
3. In this paper, the sand deposit of relative density Dr=70%, dh/H=1.25%~25% and dip angle is 60 degree were used to perform the physical model test only, different dip angle centrifuge test or PFC^{2D} simulation results can be analyzed by means of the regression of the probability density function curve, and ground surface deformation and influence zone can be predicted.

Acknowledgements

This research was sponsored by Central Geological Survey, MOEA, series number of report "100-5226904000-05-01".

References

Ulusay R, Aydan Ö, Hamada M. (2001), "The behaviour of structures built on active fault zones: examples from the recent earthquakes in Turkey," Seismic fault-induced failures, 1–26.

Dong J.J., Wang C.D., Lee C.T., Liao J.J., Pan Y.W. (2004), "The influence of surface ruptures on building damage in the 1999 Chi-Chi earthquake: a case study in Fengyuan City, " Engineering Geology , 71(1–2), 157–179.

Chen C.C., Huang C.T., Cherng R.H., Jeng V. (2000), "Preliminary investigation of damage to near fault buildings of the 1999 Chi-Chi earthquake," Earthquake Engineering and Engineering Seismology ,2(1), 79–92.

Lin M.L., Chung C.F., Jeng F.S. (2006), "Deformation of

overburden soil induced by thrust fault slip," Engineering Geology, 88(1–2), 70–89.
Bransby M.F., Davies M.C.R., EI Nahas A. (2008), "Centrifuge modeling of normal fault–foundation interaction," Bulletin of Earthquake Engineering, 6(4), 585–605.
Anastasopoulos I., Gazetas G. (2007), "Foundation–structure systems over a rupturing normal fault: part II. Analysis of the Kocaeli case histories," Bulletin of Earthquake Engineering, 5(3), 277–301.
Loukidis D., Bouckovalas G. Papadimitriou A. (2009), (2009), "Analysis of fault rupture propagation through uniform soil cover," Soil Dynamics and Earthquake Engineering, 1389-1404.
Lee C.J., Wang C.R., Wei Y.C., Hung W.Y. (2012), (2009), " Evolution of the shear wave velocity during shaking modeled in centrifuge shaking table tests," Bulletin of Earthquake Engineering, 10(2),401-420.
Cundall P.A., Strack O.D.L. (1979), " A discrete numerical model for granular assemblies," Geotechnique, 29(1), 47-65.

10CUEE CONFERENCE PROCEEDINGS
10th International Conference on Urban Earthquake Engineering
March 1-2, 2013, Tokyo Institute of Technology, Tokyo, Japan

METHODOLOGY FOR COMBINING MICROTREMOR MESUREMENTS AND SIMPLIFIED GROUND RESPONSE ANALYSIS

Atsushi Mikami[1)]

1) Associate Professor, Dept. of Civil and Environmental Engineering, The University of Tokushima, Japan

Abstract: For the evaluation of seismic performance of line structures such as tunnels, levees, etc, it is necessary to evaluate seismic ground response as well as to conduct soil investigation over a wide area. This study proposes a method of combining simple soil investigation and three dimensional ground response analysis. Assuming to conduct microtremor measurement on a ground surface as the soil investigation, a best-simplified ground model that is in congruity with the simplicity and accuracy of the simple soil investigation is derived. Eigenvalue analysis of a soil deposit on undulating bedrock showed that similar results were obtained from the proposed method and three dimensional finite element method with detailed soil data provided.

1. INTRODUCTION

Line structures such as tunnels and levees are different from other structures such as buildings and dams in a sense that they extend over a very long distance. In order to give input motions to such structures, it is of necessity to evaluate surface level ground motions taking into account three-dimensional topographical and geological conditions. It would be ideal if we could use some numerically sophisticated methods such as the three dimensional finite element method together with densely investigated PS soil logging data that provides all the three-dimensional mesh properties for the analysis. However, this is usually cost-prohibitive.

This paper proposes a method that combines three component microtremor measurements conducted on a ground surface and a three dimensional ground model used for ground response analysis. The major emphasis of this study is placed on derivation of a best-simplified ground model that is in congruity with the simplicity and accuracy of simple soil investigation. The method of microtremor measurement used in this study is both a work and cost saving investigation as is described in the following. Two horizontal and one vertical components are observed on a ground surface for approximately ten minutes, and the ratio of these orthogonal components are taken to calculate the H/V spectral ratio. As mentioned above, this method has an advantage that it is quite simple, hence, it can be applicable for a wide area soil investigation without the need for the heavy and costly work.

2. MICROTREMOR MESUREMENTS

2.1 Method of Soil Investigation

As a simple soil investigation that can be applicable to a wide area, microtremor measurement is assumed to be employed. Three component microtremor measurements are carried on the ground surface, and horizontal to vertical spectral ratio (H/V spectrum, known as Nakamura's method, 1989) is calculated. This is quite a simple and cost-effective investigation without the need for heavy work, thus, it has the potential to be applicable to a wide area.

2.2 Estimation of Predominant Frequency at a Site

Microtremor observations were conducted at sites where PS-logging information is available (such as K-NET and KiK-net sites). Three component servo type velocity meters (Tokyo Sokushin VSE-15D) with a portable vibration observing system (SPC-35) were used. At each site, microtremors were observed for approximately ten minutes with a sampling frequency of 100 Hz.

Observed three component microtremor time histories were Fourier transformed, then, power spectra was calculated. Smoothing with Parzen window that has bandwidth of 0.4(Hz) was applied. By taking the ratio of smoothed horizontal and vertical spectrum of microtremors, H/V spectral ratio is calculated. H/V spectral ratios calculated by using NS and EW components were eventually averaged to obtain the H/V spectral ratio.

Figure 1 shows an example of H/V spectral ratio. Five different segments (approximately 20 seconds data for each) are extracted from the horizontal and vertical components of microtremor time histories to calculate each H/V spectral ratio. Then, they are averaged to obtain the final result (red curve). It seems that consensus has been formed on the point that the peak frequency of H/V spectral ratio indicates predominant frequency at the site.

Figure 2 shows the relationship between predominant frequency of S wave calculated based on the

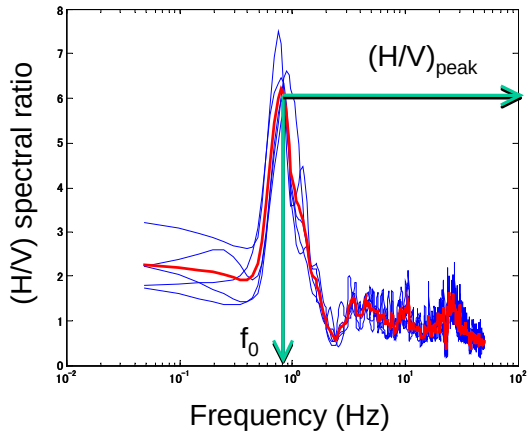


Figure 1 An Example of H/V Spectral Ratio (KiK-net Sendai)

quarter-wavelength rule and peak frequency of H/V spectral ratio, respectively. They show significant agreement with each other. This result indicates that fundamental frequency at a site can be evaluated from microtremor measurement on a ground surface. Similar results can be seen in previous research such as Ohmachi et al. (1994).

In addition, similarity of frequency characteristics of H/V spectral ratios calculated from microtremor and seismic records was confirmed by Okuma et al. (2002). Hence, if there are some seismometers near the construction site, the observed records can also be utilized for the purpose of ground modeling. Figure 3 shows a comparison of H/V spectral ratio calculated from microtremor and seismic records at KiK-net Tokushima site where contrast in soil stiffness between surface soil and bedrock is high. Similar H/V spectral ratios were also calculated at this site.

However, we can not identify each of the Vs and H only from the H/V spectral ratio because there is a trade-off between Vs and H (i.e. fundamental frequency can be expressed by the ratio of Vs and H). Hence, we assume here that depths of the base rock can be ascertained from soil boring (such as the standard penetration test) information which recently has been becoming available nationwide to the public (such as KuniJiban (Public Works Research Institute, 2008)). Averaged Vs of the surface soil deposit can then be estimated from microtremor measurement. In the following section, a multi-layered surface soil is replaced with a homogeneous soil overlying bedrock, and amplification characteristics are estimated.

3. EVALUATION OF 1D SITE RESPONSE BY AN EQUIVALENT GROUND MODEL

3.1 Replacement of multi-layer ground with an equivalent homogeneous ground

Knowing the predominant frequency of a multi-layered ground from microtremor measurement, the multi-layered ground is replaced with an equivalent homogeneous soil

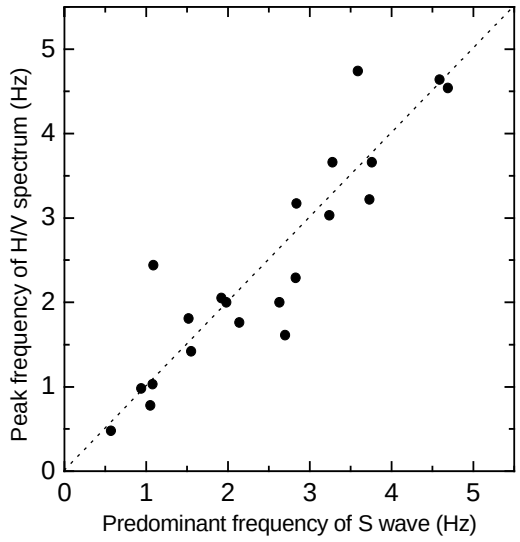


Figure 2 Predominant Frequency

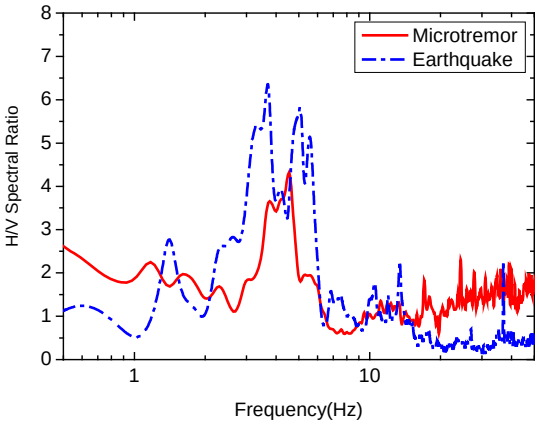


Figure 3 H/V spectral ratio calculated from microtremor and seismic records

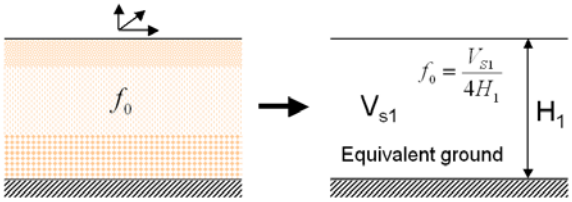


Figure 4 Replacement of Multi-layer Ground with an Equivalent Homogeneous Ground

overlying bedrock as shown in Figure 4. “Equivalent” indicates that the replaced homogeneous soil model has an identical predominant frequency as that of multi-layered ground.

3.2 Site Amplification Characteristics

In order to investigate site amplification characteristics

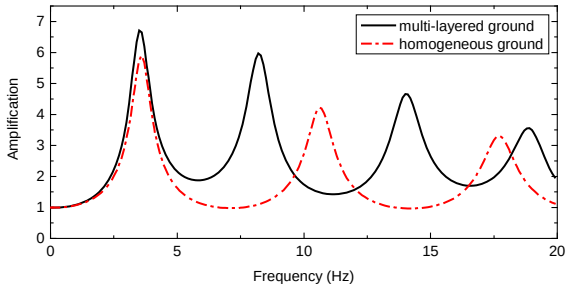


Figure 5 Site Response Functions (model ground)

Table 1 Properties of Sample Ground

Layer	Depth (m)	Soil	Thickness (m)	Density (kg/m^3)	Shear Modulus (N/m^2)
1	0-3.8	Clay	3.8	1500	1.18×10^7
2	3.8-7	Sandy Clay	3.2	1670	2.84×10^7
3	7-10.9	Sand	3.9	1850	5.59×10^7
4	10.9-	Soft Rock	-	1950	4.90×10^8

of the replaced ground, Figure 5 compares one dimensional site response functions of a sample ground shown in Table 1 (Osaki, 1994). Complex shear modulus G^* and damping constant h, which are expressed as below, are incorporated in both multi-layered ground and homogeneous ground model.

$$G^* = G(1+2ih) \tag{1}$$

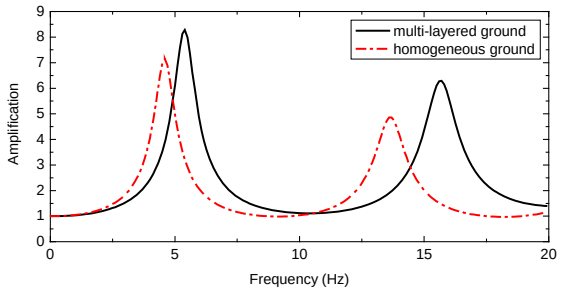
$$h = \frac{\alpha}{\omega} + \beta \tag{2}$$

where α and β are damping coefficients of the ground. They are assumed to be 2 and 0.02, respectively, for all the soil layers.

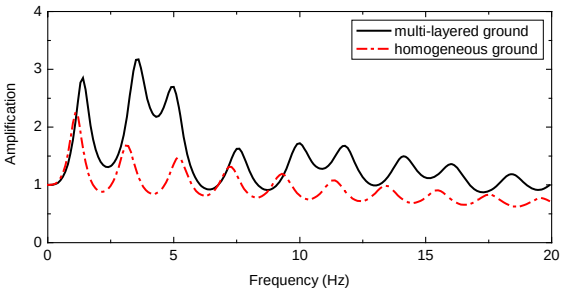
The thick line shows site response function of multi-layered soil and the dotted line indicates that of equivalent homogeneous ground. The response function calculated with homogeneous soil shows a good fit with the multi-layered soil in a relatively low frequency range. This result implies a reasonable approximation and further simplification that the soil model uses only the first mode along the depth of homogeneous soil.

3.3 Site Amplification Characteristics at Several Sites

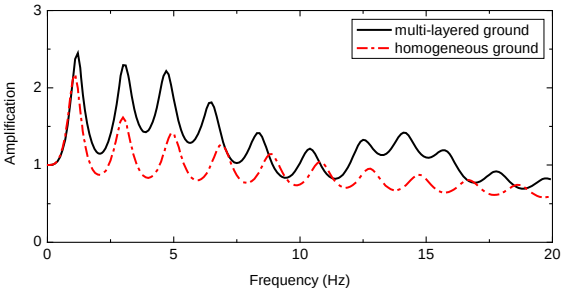
Site responses are calculated for several actual sites where microtremor measurements were conducted in the past by the author as shown in Figure 6. The same damping model and damping coefficients are assumed in the analysis. Figure 6(a) shows site response function from KiK-net



(a) KiK-net Tokushima



(b) Tokushima University



(c) A Certain Place in Koto-Ward, Tokyo

Figure 6 Site Response Functions

Tokushima which is located in the edge of Tokushima plain. Thickness of the surface soil deposit is approximately 15(m) underlain by bedrock. Slight difference can be seen in the peak frequency of the first mode.

Site response functions are also compared for Tokushima University sites (located in the middle of Tokushima plain) and for a certain place in Koto-Ward, Tokyo as shown in Figure 6 (b) and (c). They are consistent with each other near the first mode frequency, however, difference becomes larger for the higher mode responses.

4. FURTHER SIMPLIFIED MODEL

4.1 Derivation of further Simplified Ground Model

At the end of the previous section, a simplified soil model that considers only the first mode along the depth of equivalent homogeneous soil was suggested as being further simplified but efficient modeling, taking into account the site

amplification characteristics of the equivalent homogeneous ground derived as reasonable model to utilize microtremor measurements. Referring to previous work by Nogami et al.(2001), further simplified model is derived in the followings starting from the three dimensional governing equation.

The governing equation for three dimensional soil is given as shown below.

$$\rho\frac{\partial^2 u}{\partial t^2}=\frac{\partial\sigma_{xx}}{\partial x}+\frac{\partial\sigma_{xy}}{\partial y}+\frac{\partial\sigma_{xz}}{\partial z} \tag{3}$$

$$\rho\frac{\partial^2 v}{\partial t^2}=\frac{\partial\sigma_{yx}}{\partial x}+\frac{\partial\sigma_{yy}}{\partial y}+\frac{\partial\sigma_{yz}}{\partial z} \tag{4}$$

$$\rho\frac{\partial^2 w}{\partial t^2}=\frac{\partial\sigma_{zx}}{\partial x}+\frac{\partial\sigma_{zy}}{\partial y}+\frac{\partial\sigma_{zz}}{\partial z} \tag{5}$$

where σ_{ij} = stress components, ρ = soil density, u, v, w = displacements in the x, y, z direction.

Converting the equilibrium equations to the equation with respect to displacement, and ignoring vertical motion,

$$\rho\frac{\partial^2 u}{\partial t^2}=\frac{\partial}{\partial x}\left[\lambda\left(\frac{\partial u}{\partial x}+\frac{\partial v}{\partial y}\right)+2\mu\frac{\partial u}{\partial x}\right]+\frac{\partial}{\partial y}\left[\mu\left(\frac{\partial u}{\partial y}+\frac{\partial v}{\partial x}\right)\right]+\frac{\partial}{\partial z}\left[\mu\frac{\partial u}{\partial z}\right]$$
$$\rho\frac{\partial^2 v}{\partial t^2}=\frac{\partial}{\partial y}\left[\lambda\left(\frac{\partial u}{\partial x}+\frac{\partial v}{\partial y}\right)+2\mu\frac{\partial v}{\partial y}\right]+\frac{\partial}{\partial x}\left[\mu\left(\frac{\partial u}{\partial y}+\frac{\partial v}{\partial x}\right)\right]+\frac{\partial}{\partial z}\left[\mu\frac{\partial v}{\partial z}\right]$$

(6),(7)

Separation of variables as $u=U(x,y,t)\phi(z)$, $v=V(x,y,t)\phi(z)$ is applied.

$$\rho\frac{\partial^2 U}{\partial t^2}\phi=(\lambda+\mu)\phi\frac{\partial}{\partial x}\left(\frac{\partial U}{\partial x}+\frac{\partial V}{\partial y}\right)+\mu\phi\left(\frac{\partial^2}{\partial x^2}+\frac{\partial^2}{\partial y^2}\right)U+\mu U\frac{\partial^2\phi}{\partial z^2}+\frac{\partial\mu}{\partial z}\frac{\partial\phi}{\partial z}U$$
$$\rho\frac{\partial^2 V}{\partial t^2}\phi=(\lambda+\mu)\phi\frac{\partial}{\partial y}\left(\frac{\partial U}{\partial x}+\frac{\partial V}{\partial y}\right)+\mu\phi\left(\frac{\partial^2}{\partial x^2}+\frac{\partial^2}{\partial y^2}\right)V+\mu V\frac{\partial^2\phi}{\partial z^2}+\frac{\partial\mu}{\partial z}\frac{\partial\phi}{\partial z}V$$

(8),(9)

Galerkin's method is applied along the z direction as Nogami (2001),

$$\int_0^H\left(-\rho\frac{\partial^2 U}{\partial t^2}\phi+(\lambda+\mu)\phi\frac{\partial}{\partial x}\left(\frac{\partial U}{\partial x}+\frac{\partial V}{\partial y}\right)+\mu\phi\left(\frac{\partial^2}{\partial x^2}+\frac{\partial^2}{\partial y^2}\right)U+\mu U\frac{\partial^2\phi}{\partial z^2}+\frac{\partial\mu}{\partial z}\frac{\partial\phi}{\partial z}U\right)\phi dz=0$$
$$\int_0^H\left(-\rho\frac{\partial^2 V}{\partial t^2}\phi+(\lambda+\mu)\phi\frac{\partial}{\partial y}\left(\frac{\partial U}{\partial x}+\frac{\partial V}{\partial y}\right)+\mu\phi\left(\frac{\partial^2}{\partial x^2}+\frac{\partial^2}{\partial y^2}\right)V+\mu V\frac{\partial^2\phi}{\partial z^2}+\frac{\partial\mu}{\partial z}\frac{\partial\phi}{\partial z}V\right)\phi dz=0$$

(10),(11)

Applying integration by parts to the last two terms, the following equations are finally obtained.

$$\rho^*\frac{\partial^2 U}{\partial t^2}+k^*U=(\lambda+\mu)^*\frac{\partial}{\partial x}\left(\frac{\partial U}{\partial x}+\frac{\partial V}{\partial y}\right)+\mu^*\left(\frac{\partial^2}{\partial x^2}+\frac{\partial^2}{\partial y^2}\right)U$$
$$\rho^*\frac{\partial^2 V}{\partial t^2}+k^*V=(\lambda+\mu)^*\frac{\partial}{\partial y}\left(\frac{\partial U}{\partial x}+\frac{\partial V}{\partial y}\right)+\mu^*\left(\frac{\partial^2}{\partial x^2}+\frac{\partial^2}{\partial y^2}\right)V$$

(12),(13)

where $\rho^*, k^*, (\lambda+\mu)^*, \mu^*$ are expressed as follows.

$$\rho^*=\int_0^H\rho\phi^2 dz \tag{14}$$

$$k^*=\int_0^H\mu\left(\frac{\partial\phi}{\partial z}\right)^2 dz \tag{15}$$

$$(\lambda+\mu)^*=\int_0^H(\lambda+\mu)\phi^2 dz \tag{16}$$

$$\mu^*=\int_0^H\mu\phi^2 dz \tag{17}$$

These resulting model is basically the same as the Quasi-Three-Dimensional Ground Model (Q3DGM) developed by Tamura et al. (1991). Incidentally, the governing equation for a two dimensional case is given as can be seen below.

$$\rho\frac{\partial^2 u}{\partial t^2}=(\lambda+\mu)\frac{\partial}{\partial x}\left(\frac{\partial u}{\partial x}+\frac{\partial v}{\partial y}\right)+\mu\left(\frac{\partial^2}{\partial x^2}+\frac{\partial^2}{\partial y^2}\right)u$$
$$\rho\frac{\partial^2 v}{\partial t^2}=(\lambda+\mu)\frac{\partial}{\partial y}\left(\frac{\partial u}{\partial x}+\frac{\partial v}{\partial y}\right)+\mu\left(\frac{\partial^2}{\partial x^2}+\frac{\partial^2}{\partial y^2}\right)v$$

(18),(19)

Comparing these equations, the only difference is k^*U and k^*V terms which work as restoring force regarding relative horizontal displacement along z direction.

4.2 Finite Element Modeling

Governing equation for the Q3DGM is given as shown below.

$$\frac{\partial\sigma_{xx}}{\partial x}+\frac{\partial\sigma_{xy}}{\partial y}=\rho\frac{\partial^2 u}{\partial t^2}+ku$$
$$\frac{\partial\sigma_{yx}}{\partial x}+\frac{\partial\sigma_{yy}}{\partial y}=\rho\frac{\partial^2 v}{\partial t^2}+kv \tag{20},(21)$$

The governing equation is multiplied by weight functions w_x, w_y, and integrating over the area,

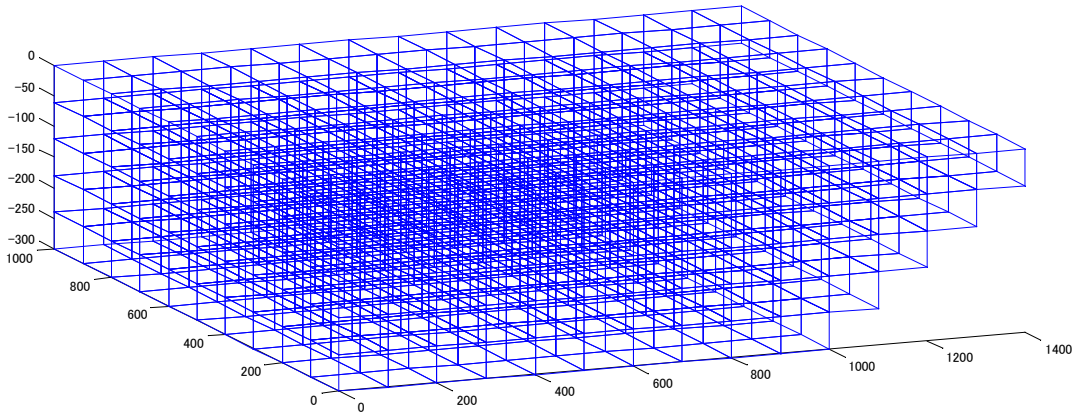


Figure 7 Soil Deposit on Undulating Bedrock

$$\int_S w_x \frac{\partial \sigma_{xx}}{\partial x} dS + \int_S w_x \frac{\partial \sigma_{xy}}{\partial y} dS = \int_S w_x \rho \frac{\partial^2 u}{\partial t^2} dS + \int_S w_x k u dS$$

$$\int_S w_y \frac{\partial \sigma_{yx}}{\partial x} dS + \int_S w_y \frac{\partial \sigma_{yy}}{\partial y} dS = \int_S w_y \rho \frac{\partial^2 v}{\partial t^2} dS + \int_S w_y k v dS$$

(22),(23)

Introducing Green-Gauss theorem,

$$\int_S w_x \sigma_{xx} n_x dS - \int_V \frac{\partial w_x}{\partial x} \sigma_{xx} dV + \int_S w_x \sigma_{xy} n_y dS - \int_V \frac{\partial w_x}{\partial y} \sigma_{xy} dV = \int_V w_x \rho \frac{\partial^2 u}{\partial t^2} dV + \int_V w_x k u dV$$

$$\int_S w_y \sigma_{yx} n_x dS - \int_V \frac{\partial w_y}{\partial x} \sigma_{yx} dV + \int_S w_y \sigma_{yy} n_y dS - \int_V \frac{\partial w_y}{\partial y} \sigma_{xy} dV = \int_V w_y \rho \frac{\partial^2 v}{\partial t^2} dV + \int_V w_y k v dV$$

(24),(25)

Then, rearranging the equations,

$$\int_V \left(\frac{\partial w_x}{\partial x} \sigma_{xx} + \frac{\partial w_x}{\partial y} \sigma_{xy} \right) dV = \int_S w_x t_x dS - \int_V w_x \rho \frac{\partial^2 u}{\partial t^2} dV - \int_V w_x k u dV$$

$$\int_V \left(\frac{\partial w_y}{\partial x} \sigma_{yx} + \frac{\partial w_y}{\partial y} \sigma_{yy} \right) dV = \int_S w_y t_y dS - \int_V w_y \rho \frac{\partial^2 v}{\partial t^2} dV - \int_V w_y k v dV$$

(26),(27)

Addition of these equations yields,

$$\int_V \{\nabla w\}^T \{\sigma\} dV = \int_S \{w\}^T \{t\} dS - \int_V \{w\}^T \{\rho \ddot{u}_i\} dV - \int_V \{w\}^T \{k u_i\} dV$$

(28)

Displacement vector is approximated by using a shape function $[N]$, and the weight function is expressed as well, by the following equation.

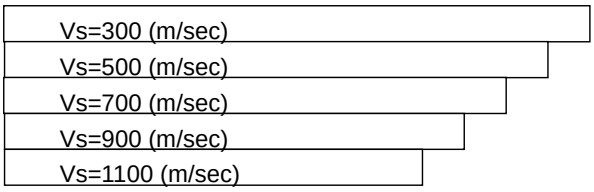


Figure 8 Soil Profile

$$\{u\} = [N]\{a\}$$
$$\{w\} = [N]\{c\}$$

(29),(30)

Finally, the following equation is obtained.

$$\int_V \rho [N]^T [N] dV \{\ddot{a}_i\} + \int_V [B]^T [D] [B] dV \{a\} + \int_V k [N]^T [N] dV \{a_i\} = \int_S [N]^T \{t\} dS$$

(31)

5. COMPUTATIONAL RESULTS

The proposed simplified ground model is verified in this section. Eigenvalue problem of multi-layered irregular shaped ground was solved by the three dimensional finite element method and by the proposed method. Fundamental vibration modes calculated by these methods are compared.

5.1 Soil Deposit on Undulating Bedrock Used for the Analysis

Irregular shaped ground model was prepared as shown in Figure 7. The boundary of the ground model varies three dimensionally; it consists of a flat and inclined bedrock section. The bottom and four sides are fixed boundaries. The surface soil deposit consists of horizontal layers of 60m

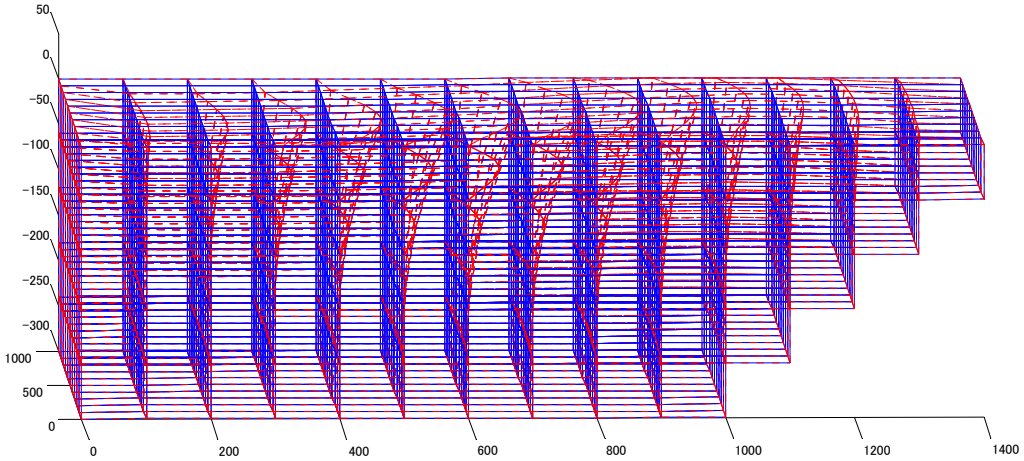


Figure 9 Vibration mode along depth by 3D FEM (unit in meters)

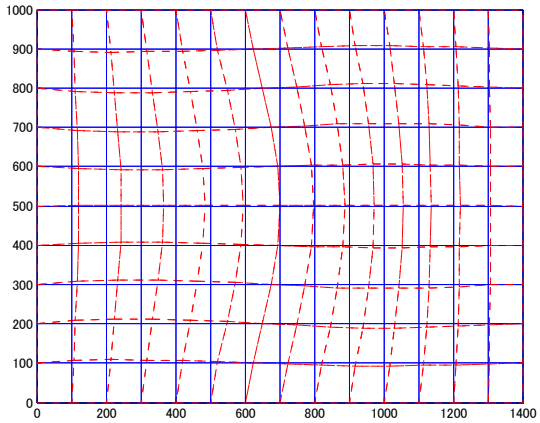


Figure 10 Top view of fundamental mode by 3D FEM (unit in meters)

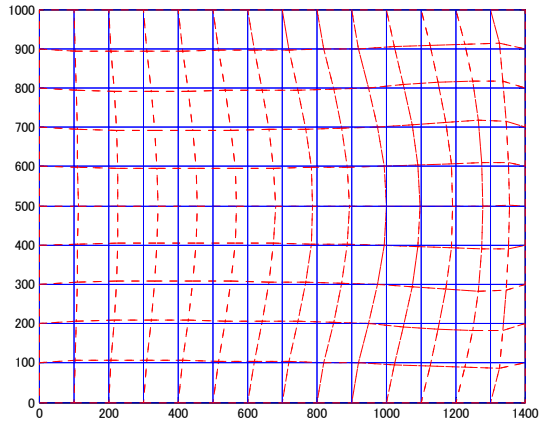


Figure 11 Top view of fundamental mode by Q3DGM (unit in meters)

thickness each with different soil properties as shown in Figure 8. Soil density and Poisson's ratio are assumed to be constant over the volume; they are 1800(kg/m^3) and 0.4, respectively.

5.2 Results by Three Dimensional Finite Element Method

The three dimensional finite element method with 8 nodes solid element is used. Fundamental vibration mode along the depth is shown in Figure 9. Fundamental frequency of the model became 0.7618(Hz). Vertical motion can also be found in this analysis. Figure 10 shows computational results at the surface (top view) for the first mode frequency. From these results, we can clearly recognize that ground vibration dominates in the flat bedrock section near the irregular bedrock section.

5.3 Results by the Simplified Ground Model Proposed in this Study

Each soil column which consists of horizontal layers is modeled with homogeneous soil column that has the identical fundamental frequency. Hence, the replaced surface soil is no longer three dimensional; it is a two dimensional model in which three dimensional topographical effects are reflected.

Similar result was obtained from the proposed method as shown in Figure 11, even though computation time is much shorter. The calculated fundamental frequency became 0.8608(Hz). No vertical motion exists in this case since vertical motion is neglected in this model. There was similar horizontal displacement mode in the short direction (perpendicular to the direction of sloping bedrock).

6. CONCLUSIONS

This study proposed a method of combining simple soil investigation with microtremor measurements and simple ground response analysis. Assuming to conduct microtremor measurements on a ground surface while assuming that the depths of bedrock are known, and utilizing H/V spectral ratio evaluated from microtremor measurements, multi-layered surface soil deposit is replaced with a homogeneous soil deposit overlying bedrock. A

best-simplified ground model that is in congruity with the simplicity and the accuracy of the microtremor measurement is derived in the following steps. Showing a result that the simple soil model is suitable to be used in a low frequency range, the model is attributed to a further simplified ground model, which is basically the same model as the Quasi-Three-Dimensional-Ground Model proposed by Tamura et al. Similar computational results were obtained by dynamic analysis of multi-layered, irregular-shaped ground model between the proposed method and the three dimensional finite element method with detailed soil data provided. Hence, the proposed approach may be rational and cost effective when ground response analysis is needed for a wide area.

Acknowledgements:

Support for this project was provided by Japan Science and Technology Agency (Grant No.13-014). This support is greatly acknowledged. The author also acknowledges National Research Institute for Earth Science and Disaster Prevention, Japan who provides soil profile data at K-NET and KiK-net sites. Thanks are also due to former students who helped conducting microtremor measurements.

References:

Nakamura, Y. (1989), "A method for dynamic characteristics estimation of subsurface using microtremor on the ground surface," *Quarterly report of RTRI*, **30**(1), 25-33. (in Japanese).

Nogami, T., Konagai, K. and Mikami, A. (2001), "Simple formulations of ground impedance functions for rigid surface foundations," *Soil Dynamics and Earthquake Engineering* **21**(6), 475-484.

Okuma, Y., Matsuoka, M., Yamazaki, F. and Harada, T. (2002), "Estimation of Earthquake Ground Motion in Miyazaki Prefecture Using the H/V Spectral Ratio of Microtremor," *Journal of Structural Engineering and Earthquake Engineering, JSCE*, No.696/I-58, 262-272.

Omachi, T., Konno, K., Endoh, T. and Toshinawa, T. (1994), "Refinement and application of an estimation procedure for site natural periods using microtremor," *Journal of Structural Engineering and Earthquake Engineering, JSCE*. I-27:489, 251-260.

Ohsaki, Y. (1994), "Introduction to Spectral Analysis of Ground Motions," Kajima Publishing, Tokyo, Japan. (in Japanese)

Public Works Research Institute (2008), KuniJiban, http://www.kunijiban.pwri.go.jp/en/index.html.

Tamura, C., Konagai, K. and Suzuki, T. (1991), "Earthquake response analysis of soft soil deposit on undulating bedrock," Report of the Institute of the Industrial Scinence, The University of Tokyo. **36**(5), 227-261.

Tamura, C. and Suzuki, T. (1987), "A Quasi-Three-Dimensional Ground Model for Earthquake Response Analysis of Underground Structures – Construction of Ground Model - ," *Seisan Kenkyu*. **39**(1), 37-40. (in Japanese).

10CUEE CONFERENCE PROCEEDINGS
10th International Conference on Urban Earthquake Engineering
March 1-2, 2013, Tokyo Institute of Technology, Tokyo, Japan

IMPLICIT STRESS-UPDATE ALGORITHM FOR THE CONSTITUTIVE MODEL TO DESCRIBE CYCLIC BEHAVIOR BASED ON FINITE DEFORMATION THEORY

Tomohide Takeyama[1)], Shinya Tachibana[2)]

1) Assistant Professor, Dept. of Civil Engineering, Tokyo Institute of Technology, Japan
2) Assistant Professor, Geosphere Research Institute, Saitama University, Japan
takeyama@cv.titech.ac.jp, stachi@mail.saitama-u.ac.jp

Abstract: The elasto-plasticity based on the finite deformation theory is roughly classified two types which are the formulation by the additive decomposition of deformation rate using the hypo-elastic constitutive model and the formulation by the multiplicative decomposition of deformation gradient using hyper-elastic constitutive model. The latter formulation is becoming main stream recently, because the elastic energy dissipation does not occur and the objectivity is kept since it is not necessary to transform the rate form of constitutive model into incremental form. In this research, the implicit stress-update algorithm by using exponential return-mapping method for the extended sub-loading Cam-Clay model with the hardening/softening due to shear deformation is proposed in the framework of the finite deformation theory based on the multiplicative decomposition of deformation gradient. The accuracy of the proposed method is validated by comparing the stress updated by large deformation and small deformation.

1. INTRODUCTION

The relationship between the stress and the deformation of geo-material based on the finite deformation theory has both of the material nonlinearity and the geometric nonlinearity. Therefore a method that can implicitly integrate the stress-deformation relationship is needed. The stress update algorithm based on return mapping method have been developed to solve such a problem by Simo and Ortiz (1985), Simo and Taylor (1985), Ortiz and Simo (1986). The elasto-plasticity based on the finite deformation theory is roughly classified two types which are the formulation by the additive decomposition of deformation rate using the hypo-elastic constitutive model and the formulation by the multiplicative decomposition of deformation gradient using hyper-elastic constitutive model. The former one is widely used because the formulation is relatively easy although the constitutive model is complicated. The latter formulation is becoming main stream recently, because the elastic energy dissipation does not occur and the objectivity is kept since it is not necessary to transform the rate form of constitutive model into incremental form. Yamakawa et al. (2010) formulated extended sub-loading Cam-Clay model in the framework of the finite deformation theory based on the multiplicative decomposition of deformation gradient and developed the stress-update algorithm by using return mapping method. In this research, the implicit stress-update algorithm by using exponential return-mapping method for the extended sub-loading Cam-Clay model with the hardening/softening due to shear deformation (Hashiguchi et al. (1998)) is proposed in the framework of the finite deformation theory based on the multiplicative decomposition of deformation gradient. The accuracy of the proposed method is validated by comparing the stress updated by large deformation and small deformation.

2. ALGORITHM FOR STRESS UPDATE

2.1 multiplicative decomposition of deformation

Two material points $\mathbf{X}$ and $\mathbf{X}+d\mathbf{X}$ move to $\boldsymbol{x}=\phi(\mathbf{X})$ and $\boldsymbol{x}+d\boldsymbol{x}=\phi(\mathbf{X}+d\mathbf{X})$ in the current configuration respectively from the reference configuration to the current configuration due to motion of the continuum as shown in Fig. 1. By applying Taylor expansion to the motion $\phi(\mathbf{X}+d\mathbf{X})$, the infinitesimal vector $d\boldsymbol{x}$ is obtained as

$$d\boldsymbol{x}=\mathbf{F}\cdot d\mathbf{X} \tag{1}$$

where $\mathbf{F}$ is deformation gradient tensor which is defined as

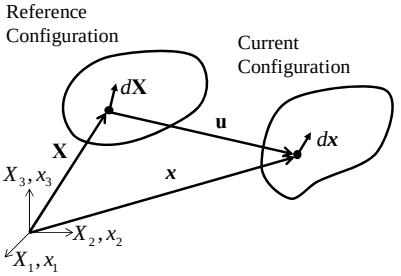


Fig. 1. Movement of infinitesimal vector $d\mathbf{X}$ near a material point $\mathbf{X}$

$$\mathbf{F} = \frac{\partial \boldsymbol{x}}{\partial \mathbf{X}}. \tag{2}$$

Equation (1) represents that the infinitesimal vector $d\mathbf{X}$ near the material point $\mathbf{X}$ is transformed to $d\boldsymbol{x}$ due to the motion of continuum. In order to formulate motion of continuum in the framework of hyper elasto-plasticity, the intermediate configuration is adopted. The intermediate configuration is imaginary configuration defined near an individual material point which is removed stress and elastic deformation from the current configuration. A schematic figure explained the multiplicative decomposition of deformation gradient is shown in Fig. 2. Plastic deformation gradient $\mathbf{F}^p$ describes deformation from the reference configuration to the intermediate configuration. Elastic deformation gradient $\mathbf{F}^e$ describes deformation from the intermediate configuration to the current configuration. In this research, the multiplicative decomposition of deformation gradient proposed by Lee (1969) is employed.

$$\mathbf{F} = \mathbf{F}^e \cdot \mathbf{F}^p \tag{3}$$

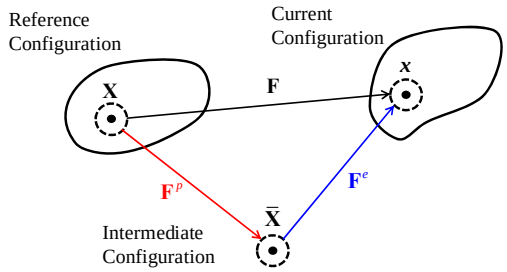


Fig. 2. Schematic figure explained the multiplicative decomposition of deformation gradient

2.2 Return mapping algorithm

Since the relationship between stress and deformation of geo-material generally has nonlinearity, a method to solve nonlinear equations implicitly is needed. The return mapping algorithm (Simo and Ortiz (1985); Ortiz and Simo (1986)) is employed to update the stress. This section summarizes the return mapping algorithm for finite deformation theory. A schematic figure explained the procedure of return mapping algorithm is shown in Fig. 3.

Considering a problem to obtain the stress at the time $t = t_{n+1}$ when an increment of displacement $\Delta\mathbf{u} = \boldsymbol{x}_{n+1} - \boldsymbol{x}_n$ from the time $t = t_n$ to the time $t = t_{n+1}$ is given, the deformation during the time step is described as

$$f_{[n,n+1]} = \frac{\partial \boldsymbol{x}_{n+1}}{\partial \boldsymbol{x}_n} = \frac{\partial\left(\boldsymbol{x}_n + \Delta\mathbf{u}\right)}{\partial \boldsymbol{x}_n} \tag{4}$$

where $f_{[n,n+1]}$ is the relative deformation gradient. The deformation gradient from the reference configuration to the current configuration at the time $t = t_{n+1}$ is described as

$$\mathbf{F}_{n+1} = f_{[n,n+1]} \cdot \mathbf{F}_n \tag{5}$$

The stress-update algorithm using the return mapping method is divided into two operations. One is "elastic predictor" and the other one is the "plastic corrector". In the "elastic predictor", we assume that the given deformation is totally caused by elastic deformation. The assumed elastic deformation gradient is called as the trial elastic deformation gradient and described as

$$\mathbf{F}^{e,trial}_{n+1} = \mathbf{F}_{n+1} \cdot \mathbf{F}_n^{p^{-1}} \tag{6}$$

By substituting the trial elastic deformation gradient to the hyper elastic constitutive equation, the stress can be updated on trial. By substituting the stress updated on trial to the yield function which the internal plastic variables are fixed at the time $t = t_n$, the elasto-plastic state can be judged. If yield function is negative, i.e. the stress is within the yield surface, the stress updated on trial is the stress at the time $t = t_{n+1}$ and we can proceed to the next step. On the other hand, if yield function is zero or positive, the elasto-plastic constitutive equations including plastic development rules is solved iteratively to update the stress by Newton-Raphson method in "plastic corrector" because the assumption that the given deformation is totally caused by elastic deformation is wrong. The detail procedure in the "plastic corrector is described in the next section.

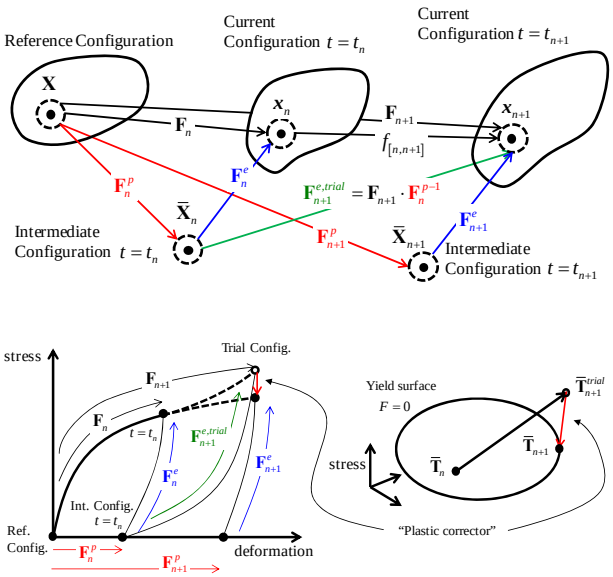


Fig. 3. Schematic figure explained the procedure of return mapping algorithm

2.3 Governing equations

The governing equations describing elasto-plastic behavior based on the fi

nite deformation theory are the multiplicative decomposition of deformation gradient (Eq.(3)), the hyper-elastic constitutive equation (Eq.(13)), the sub-loading function of the modified Cam-Clay type (Eq.(18)), the associated flow rule (Eq.(19)), the isotropic hardening rule (Eq.(20)), the development rule of hardening parameter

(Eq.(21)), the development rule of similarity ratio (Eq.(22)) and the development rule of similarity center (Eq.(23)). The hyper-elastic constitutive equation is

$$\bar{\mathbf{S}} = 2\frac{\partial \mathcal{W}^e}{\partial \bar{\mathbf{C}}^e}. \tag{7}$$

$\bar{\mathbf{S}}$ is second Piola-Kirchhoff stress referenced the intermediate configuration and is defined as

$$\bar{\mathbf{S}} = J\mathbf{F}^{e^{-1}} \cdot \boldsymbol{\sigma} \cdot \mathbf{F}^{e^{-T}} \tag{8}$$

where $J = \det \mathbf{F}$ is the volume change. $\boldsymbol{\sigma}$ is the Cauchy stress. $\mathcal{W}^e$ is hyper-elastic potential function. In elastic model of the modified Cam-Clay model, elastic bulk modulus and elastic shear modulus usually depend on the pressure so that the linear relationship of $\ln v - \ln p$ is represented. In this research, the hyper-elastic constitutive model depends on pressure proposed by Yamakawa et al. (2010) is employed. The hyper-elastic potential is defined as

$$\mathcal{W}^e(J^e, \hat{\bar{\mathbf{C}}}^e) = \bar{\mathcal{W}}^e(J^e) + \hat{\mathcal{W}}^e(J^e, \hat{\bar{\mathbf{C}}}^e), \tag{9}$$

$$\bar{\mathcal{W}}^e(J^e) = -\bar{P}_0 \tilde{\kappa}^* \left(\frac{J^e}{J_0^e} \right)^{-1/\tilde{\kappa}^*}, \tag{10}$$

$$\hat{\mathcal{W}}^e(J^e, \hat{\bar{\mathbf{C}}}^e) = \frac{1}{2}\mu^e \left(tr\hat{\bar{\mathbf{C}}}^e - 3 \right), \tag{11}$$

where J^e is an elastic volumetric change which is determinant of an elastic deformation gradient tensor $\mathbf{F}^e$. J_0^e and $\bar{P}_0$ are an elastic volumetric change and a pressure in the reference configuration respectively. $\hat{\bar{\mathbf{C}}}^e$ is a constant volume component of elastic right Cauchy-Green deformation tensor $\bar{\mathbf{C}}^e := \mathbf{F}^{e^T} \cdot \mathbf{F}^e$. $\tilde{\kappa}^*$ is elastic compression index. μ^e is a elastic shear modulus depend on pressure:

$$\mu^e = \mu_0^e + \frac{\alpha}{\tilde{\kappa}^*} \bar{\mathcal{W}}^e \left(J^e \right) \tag{12}$$

where μ_0^e is constant component of elastic shear modulus. α is a coefficient concerning with pressure dependency of elastic shear modulus. Second Piola-Kirchhoff stress referenced the intermediate configuration $\bar{\mathbf{S}}$ is derived by differentiating Eq.(9) with respect to $\bar{\mathbf{C}}^e/2$:

$$\bar{\mathbf{S}} = \bar{P}_0 \left(\frac{J^e}{J_0^e} \right)^{-1/\tilde{\kappa}^*} \left[1 + \frac{\alpha}{2\tilde{\kappa}^*} \left(tr\hat{\bar{\mathbf{C}}}^e - 3 \right) \right] \bar{\mathbf{C}}^{e^{-1}} + J^{e^{-2/3}} \mu^e \left(\mathbf{1} - \frac{1}{3} tr\hat{\bar{\mathbf{C}}}^e \bar{\mathbf{C}}^{e^{-1}} \right). \tag{13}$$

The normal yield function of the modified Cam-Clay model is employed.

$$F\left(\bar{\mathbf{T}}, \bar{P}_c\right) = \frac{\bar{Q}^2}{\mathrm{M}^2} + \bar{P}\left(\bar{P} - \bar{P}_c\right) = 0 \tag{14}$$

where $\bar{\mathbf{T}}$ is Mandel stress tensor referenced the intermediate configuration defined as

$$\bar{\mathbf{T}} = J\mathbf{F}^{e^{-1}} \cdot \boldsymbol{\sigma} \cdot \mathbf{F}^{e^{-T}} = \bar{\mathbf{C}}^e \cdot \bar{\mathbf{S}}. \tag{15}$$

Mandel stress is work-conjugate with plastic rate of deformation tensor $\bar{\mathbf{L}}^p$ defined as

$$\bar{\mathbf{L}}^p = \dot{\mathbf{F}}^p \cdot \mathbf{F}^{p^{-1}}. \tag{16}$$

$\bar{P}$ and $\bar{Q}$ are mean Mandel stress and deviatoric Mandel stress respectively. M is critical state parameter. The subscript c indicates the variable in pre-consolidated state. Hashiguchi et al. (1998) proposed the extended sub-loading surface which is always inside the normal yield surface in stress space. The sub-loading surface has similar figures and position to the normal yield surface. After Hashiguchi et al. (1998), modified Mandel stress defined by following equation is adopted.

$$\bar{\mathbf{T}}_{\mathrm{mod}} = \bar{\mathbf{T}} - (1 - R)\bar{\mathbf{A}} \tag{17}$$

where R is called similarity ratio expressed the ratio of size of the normal yield surface to the sub-loading surface. $\bar{\mathbf{A}}$ is called similarity center. The extended sub-loading function is described as

$$f\left(\bar{\mathbf{T}}, \bar{\mathbf{A}}, \bar{P}_c, R\right) = \frac{\bar{Q}_{\mathrm{mod}}{}^2}{\mathrm{M}^2} + \bar{P}_{\mathrm{mod}}\left(\bar{P}_{\mathrm{mod}} - R\bar{P}_c\right) = 0. \tag{18}$$

The associated flow rule is described as

$$\bar{\mathbf{L}}^p = \dot{\gamma}\bar{\mathbf{M}} \tag{19}$$

where $\dot{\gamma}$ is the plastic consistent parameter. $\bar{\mathbf{M}}$ is the first derivative of sub-laoding function with respect to Mandel stress. The isotropic hardening law is

$$\frac{\dot{\bar{P}}_c}{\bar{P}_c} = -\Theta\dot{\chi}. \tag{20}$$

Θ is defined as $1/\left(\tilde{\lambda}^* - \tilde{\kappa}^*\right)$. $\tilde{\lambda}^*$ is elasto-plastic compression index. χ is the hardening parameter. The development rules of hardening parameter, similarity ratio and similarity center are as follows.

$$\dot{\chi} = tr\bar{\mathbf{L}}^p + \sqrt{\frac{2}{3}}\mu \left\| \bar{\mathbf{L}}^{p(dev)} \right\| \left(\frac{\bar{Q}}{\bar{P}} + \mathrm{M}_d \right) \tag{21}$$

$$\dot{R} = -u_0 \ln R \left\| \bar{\mathbf{L}}^p \right\| \tag{22}$$

$$\dot{\bar{\mathbf{A}}} = c\left(\bar{\mathbf{T}} - \bar{\mathbf{A}}\right)\left\| \bar{\mathbf{L}}^P \right\| + \frac{\dot{\bar{P}}_c}{\bar{P}_c}\bar{\mathbf{A}} \tag{23}$$

where μ, M_d, u_0 and c are material parameters.

Assuming that plastic rate of deformation tensor $\bar{\mathbf{L}}^p$ is constant during a time step Δt and integrating Eq.(16) with respect to time from t_n to t_{n+1}, the following equation is derived:

$$\mathbf{F}^p_{n+1} = \exp\left(\Delta t \bar{\mathbf{L}}^p_{n+1}\right) \cdot \mathbf{F}^p . \tag{24}$$

Making dot product Eq.(24) and $\mathbf{F}^e_{n+1}$, $\mathbf{F}^{p^{-1}}_n$ and taking account that inverse tensor of $\exp\left(\Delta t \bar{\mathbf{L}}^p_{n+1}\right)$ is $\exp\left(-\Delta t \bar{\mathbf{L}}^p_{n+1}\right)$, Eq. (24) yields

$$\mathbf{F}^e_{n+1} = \mathbf{F}^{e,trial}_{n+1} \cdot \exp\left(-\Delta t \bar{\mathbf{L}}^p_{n+1}\right) \tag{25}$$

where $\mathbf{F}^{e,trial}_{n+1} := \mathbf{F}_{n+1} \cdot \mathbf{F}^{p^{-1}}_n$ is trial elastic deformation gradient tensor assumed plastic deformation is not occurred during a time step Δt. By backward Euler approximation, Eq.(19) takes the form:

$$\bar{\mathbf{L}}^p_{n+1} = \frac{\Delta\gamma_{n+1}}{\Delta t}\bar{\mathbf{M}}_{n+1} . \tag{26}$$

Substituting Eq.(26) to Eq.(25), the following equation is derived:

$$\mathbf{F}^e_{n+1} = \mathbf{F}^{e,trial}_{n+1} \cdot \exp\left(-\Delta\gamma_{n+1}\bar{\mathbf{M}}_{n+1}\right). \tag{27}$$

The stress is updated by substituting the elastic right Cauchy-Green deformation tensor at the time $t = t_{n+1}$: $\bar{\mathbf{C}}^e_{n+1}$ to the hyper-elastic constitutive equation (Eq.(13)), therefore it is more convenient transforming Eq.(27) to the folloing equation.

$$\bar{\mathbf{C}}^e_{n+1} = \bar{\mathbf{Q}}^{p\ T}_{n+1} \cdot \bar{\mathbf{C}}^{e,trial}_{n+1} \cdot \bar{\mathbf{Q}}^p_{n+1} \tag{28}$$

where $\bar{\mathbf{Q}}^p_{n+1} := \exp\left(-\Delta\gamma_{n+1}\bar{\mathbf{M}}_{n+1}\right)$. By backward Euler approximation and using Eq.(26), Eq.(22) and Eq.(23) take the forms:

$$R_{n+1} - R_n = -u_0 \Delta\gamma_{n+1} \ln R_{n+1} \left\| \bar{\mathbf{M}}_{n+1} \right\| \tag{29}$$

$$\bar{\mathbf{A}}_{n+1} - \bar{\mathbf{A}}_n = c\Delta\gamma_{n+1}\left(\bar{\mathbf{T}}_{n+1} - \bar{\mathbf{A}}_{n+1}\right)\left\| \bar{\mathbf{M}}_{n+1} \right\| + \frac{\bar{P}_{c.n+1} - \bar{P}_{c.n}}{\bar{P}_{c.n+1}}\bar{\mathbf{A}}_{n+1} \tag{30}$$

In the iterative process, the unknown variables $\bar{\mathbf{C}}^e_{n+1}$, $\Delta\gamma_{n+1}$, R_{n+1} and $\bar{\mathbf{A}}_{n+1}$ are calculated by solving simultaneously Eq.(28), Eq.(18), Eq.(29) and Eq.(30). The pre-consolidated stress $\bar{P}_{c.n+1}$ is obtained from the isotropic hardening law (Eq.(20)) and development rule of hardening parameter (Eq.(21)). By integrating Eq.(20) with respect to time, the following equation is derived:

$$\bar{P}_{c.n+1} = \bar{P}_{c.n} \exp\left(-\Theta\Delta\chi\right) \tag{31}$$

where

$$\Delta\chi = \Delta\gamma_{n+1} tr\bar{\mathbf{M}}_{n+1} + \Delta\gamma_{n+1}\sqrt{\frac{2}{3}}\mu\left\| \bar{\mathbf{M}}^{(dev)}_{n+1} \right\|\left(\frac{\bar{Q}_{n+1}}{\bar{P}_{n+1}} + \mathrm{M}_d \right) \tag{32}$$

The equations to solve by return mapping method are summarized as follows:

$$\mathbf{Y}_{\bar{\mathbf{C}}^e} = \bar{\mathbf{C}}^e_{n+1} - \bar{\mathbf{Q}}^{p\ T}_{n+1} \cdot \bar{\mathbf{C}}^{e,trial}_{n+1} \cdot \bar{\mathbf{Q}}^p_{n+1} = 0 \tag{33}$$

$$Y_f = f\left(\bar{\mathbf{T}}_{n+1}, \bar{\mathbf{A}}_{n+1}, \bar{P}_{c.n+1}, R_{n+1}\right) = 0 \tag{34}$$

$$Y_R = R_{n+1} - R_n + u_0\Delta\gamma_{n+1}\ln R_{n+1}\left\| \bar{\mathbf{M}}_{n+1} \right\| = 0 \tag{35}$$

$$\mathbf{Y}_{\bar{\mathbf{A}}} = \bar{\mathbf{A}}_{n+1} - \bar{\mathbf{A}}_n - c\Delta\gamma_{n+1}\left(\bar{\mathbf{T}}_{n+1} - \bar{\mathbf{A}}_{n+1}\right)\left\| \bar{\mathbf{M}}_{n+1} \right\| - \frac{\bar{P}_{c.n+1} - \bar{P}_{c.n}}{\bar{P}_{c.n+1}}\bar{\mathbf{A}}_{n+1} = 0 \tag{36}$$

By defining the unknown vector $\mathbf{X}$ and the residual vector $\mathbf{Y}(\mathbf{X})$ as

$$\mathbf{X} = \left(\bar{\mathbf{C}}^e_{n+1}, \Delta\gamma_{n+1}, R_{n+1}, \bar{\mathbf{A}}_{n+1}\right)^T \tag{37}$$

$$\mathbf{Y}(\mathbf{X}) = \left(\mathbf{Y}_{\bar{\mathbf{C}}^e}, Y_f, Y_R, \mathbf{Y}_{\bar{\mathbf{A}}}\right)^T , \tag{38}$$

The equations to solve yields

$$\mathbf{Y}(\mathbf{X}) = 0 . \tag{39}$$

By linearize Eq. (39) to solve iteratively by Newton-Raphson method, the following equation is deribed.

$$\mathbf{Y}\left(\mathbf{X}^{(k)}\right) + \frac{\partial\mathbf{Y}}{\partial\mathbf{X}}\left(\mathbf{X}^{(k)}\right)\cdot\delta\mathbf{X} = 0 \tag{40}$$

The blanketed superscript indicates the number of iteration. By solving Eq. (40), we can correct the unknown vector at the time t_{n+1} by

$$\mathbf{X}^{(k+1)} = \mathbf{X}^{(k)} + \delta\mathbf{X} . \tag{41}$$

In differentiate the residual vector by the unknown vector, the exponential tensor have to be differentiate, because exponential tensor is included in Eq. (33). The derivative of exponential tensor is derived by Neto (2001).

3. NUMERICAL EXAMPLES

In this chapter, the simulation of constant volume shear test and the cyclic loading test with constant strain amplitude are carried out to confirm the accuracy of the implicit stress-update method using return mapping algorithm based on finite deformation theory described in the previous chapter. The simulation of cyclic loading test with constant stress amplitude is also carried out to confirm the ability to express the cyclic behavior of the constitutive model.

3.1 Simulation of constant volume shear test

In order to confirm the accuracy of the stress-update method, the result of simulation which is input large deformation is compare with the result which is input small deformation. In the simulation, deformation gradient is given as

$$\mathbf{F} = \mathbf{F}^* \cdot \mathbf{F}_0, \quad \mathbf{F}^* = \begin{bmatrix} 1 & F_s & 0 \\ 0 & 1 & 0 \\ 0 & 0 & 1 \end{bmatrix} \tag{42}$$

where $\mathbf{F}_0$ is an initial deformation gradient. $\mathbf{F}^*$ is deformation from initial configuration. The shear component of deformation gradient F_s is set to be 0.2. The given deformation gradient is divided evenly into 1000 steps and 5 steps. The initial stress state is set following three cases. In case 1, the initial stress state is isotropic normally consolidated state and pre-consolidated stress in terms of Mandel stress is -100kPa. In case 2, the initial stress state is isotropic over-consolidated state and initial mean stress in terms of Cauchy stress is -100kPa. The pre-consolidated stress in terms of Mandel stress is -400kPa i.e. over consolidation ratio is 4.0. In case 3, the initial stress state is anisotropic over consolidated state and initial mean stress in terms of Cauchy stress is -66.7kPa. The pre-consolidated stress in terms of Mandel stress is -200kPa i.e. over consolidation ratio is about 1.6. The material parameter used in the simulation is summarized in Table. 1. The results of simulations are shown in Fig. 4.

Table 1. Material parameter used in the simulation

Critical state parameter	M	1.05
Elastic compression index	$\tilde{\kappa}^*$	0.06
Elasto-plastic compression index	$\tilde{\lambda}^*$	0.20
Constant of elastic shear modulus (kPa)	μ_0^e	1000.0
Parameter for pressure dependency of μ^e	α	0.0
Reference pressure (kPa)	$\bar{P}_0$	-100.0
Reference elastic volumetric change	J_0^e	1.00
Evolution parameter of similarity ratio	u_0	10.0
Evolution parameter of similarity center	c	10.0
Evolution parameter of shear hardening/softening	μ	0.5
Stress ratio of shear boundary surface	M_d	0.7
Initial value of similarity center	$\bar{\mathbf{A}}_0$	**0**

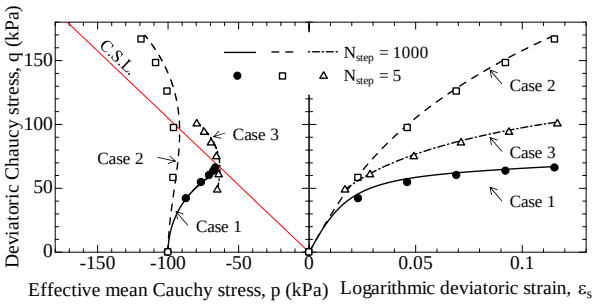


Fig. 4. Simulation results of constant volume shear test

Though the simulation results of case1, case2 and case 3, the stress updated by large deformation (5 steps) is not different from the stress updated by small deformation (1000steps). Therefore it can be said that the accuracy of the stress-update method is sufficient high for the simulation of constant volume shear test.

3.2 Simulation of cyclic loading test

The simulation of cyclic lading test with constant strain amplitude is carried out. The shear component of deformation gradient F_s is changed within the range: $-0.015 \le F_s \le 0.015$ and two cycle of cyclic loading test is simulated. The initial stress state is isotropic normally consolidated state and pre-consolidated stress in terms of Mandel stress is -100kPa. In order to validate the accuracy of the solution, two case of simulation which the total deformation is divided into 45 steps and 900 steps. The parameter used in the simulation is identical with the simulation of the constant volume shear test except elastic shear modulus. The elastic shear modulus is set to be 5000kPa in this simulation. The result of simulation is shown in Fig. 5. In the case of the cyclic loading, the stress-update method has high accuracy as well as the case of the constant volume shear.

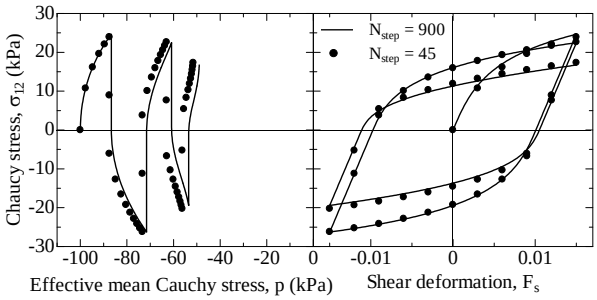


Fig. 5. Simulation result of cyclic loading with constant deformation amplitude

The simulation of cyclic loading test with constant stress amplitude is carried out. The material parameter used in the simulation is summarized in Table 2. The initial stress state is isotropic normally consolidated state and pre-consolidated stress in terms of Mandel stress is -400kPa. Initial mean stress in terms of Cauchy stress is -100kPa. The amplitude of the stress is 12kPa. The result of simulation is

shown in Fig. 6. It is found that the behavior so-called cyclic mobility can be expressed by incorporating the hardening/softening due to shear deformation to the constitutive model as plastic development rule.

Table 2. Material parameter used in the simulation

Critical state parameter	M	1.05
Elastic compression index	$\tilde{\kappa}^*$	0.025
Elasto-plastic compression index	$\tilde{\lambda}^*$	0.082
Constant of elastic shear modulus (kPa)	μ_0^e	800.0
Parameter for pressure dependency of μ^e	α	0.0
Reference pressure (kPa)	$\bar{P}_0$	-100.0
Reference elastic volumetric change	J_0^e	1.00
Evolution parameter of similarity ratio	u_0	10.0
Evolution parameter of similarity center	c	10.0
Evolution parameter of shear hardening/softening	μ	3.0
Stress ratio of shear boundary surface	M_d	0.7
Initial value of similarity center	$\bar{\mathbf{A}}_0$	**0**

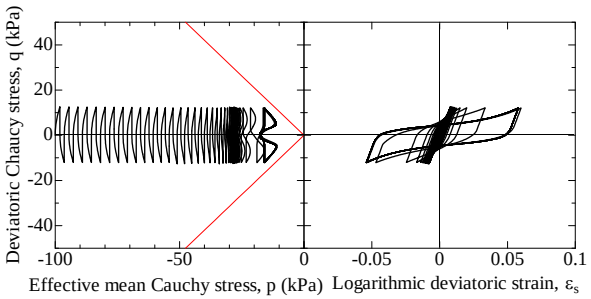


Fig. 6. Simulation result of cyclic loading with constant deformation amplitude

4. CONCLUSIONS

In this paper, the implicit stress-update method by using return-mapping method for the extended sub-loading Cam-Clay model with the hardening/softening due to shear deformation is formulated in the framework of the finite deformation theory based on the multiplicative decomposition of deformation gradient. The simulations of constant volume test and the cyclic loading test are carried out by formulated stress-update method. Through the simulations, it is confirmed that the accuracy of the method is sufficient high and it is able to express the cyclic behavior of geo-material such as cyclic mobility.

Acknowledgements:

The authors acknowledge support from the Japan Ministry of Education, Culture, Sport, Science, and Technology (MEXT) for establishing the Center for Urban Earthquake Engineering (CUEE) in Tokyo Institute of Technology. This support makes possible the forthcoming international conference, as well as international joint research projects and exchange programs with overseas universities.

References:

de Souza, Neto, E.A. (2001), "The exact derivative of the exponential of an unsymmetric tensor," *Computational Methods in Applied Mechanics and Engineering*, **190**, pp.2377-2383.

Hashiguchi, K., Chen, Z. P. (1998), "Elastoplastic constitutive equation of soils with the subloading surface and the rotational hardening," *International Journal of Numerical and Analytical Methods in Geomechanics*, **22**, pp.197-227.

Ortiz, M., Simo, J.C. (1986), "An analysis of a new class of integration algorithms for elastoplastic constitutive relations," *International Journal of Numerical Methods in Engineering*, **23**, pp.353-356.

Simo, J.C., Ortiz, M. (1985), "A unified approach to finite deformation elastoplastic analysis based on the use of hyperelastic constitutive equations," *Computational Methods in Applied Mechanics and Engineering*, **49**, pp.221-245.

Simo, J.C., Taylor, R.L. (1985), "Consistent tangent operators for rate-independent elastoplasticity," *Computational Methods in Applied Mechanics and Engineering*, **48**, pp.101-118.

Yamakawa, Y., Yamaguchi, Y., Hashiguchi, K. and Ikeda, K., (2000), "Formulation and implicit stress-update algorithm of extended subloading surface Cam-clay model with kinematic hardening for finite strains," *Journal of Applied Mechanics, JSCE*, **13**, 411-422.

10CUEE CONFERENCE PROCEEDINGS
10th International Conference on Urban Earthquake Engineering
March 1-2, 2013, Tokyo Institute of Technology, Tokyo, Japan

SEISMIC EARTH PRESSURE AND SIDE FRICTION ACTING ON EMBEDDED PILE CAP AND PILE'S STRESS

Shuji Tamura[1] and Takenori Hida[2]

1) Associate Professor, DPRI, Kyoto University, Japan
2) Assistant Professor, Science University Tokyo, Japan
tamura@sds.dpri.kyoto-u.ac.jp

Abstract: To estimate a pile's bending moment and shear force accurately, a response displacement method was developed with consideration of the seismic earth pressure and side friction acting on an embedded pile cap. Sensitivity of the coefficients of horizontal subgrade reactions for piles on the pile's shear force and bending moments and the effects of structure inertia and soil displacement on the pile's bending moment were examined using numerical parameter studies. Estimated seismic earth pressure and side friction on the pile cap, pile cap displacement, bending moment and shear force of the piles showed good agreement with the experimentally obtained results that were varied considerably with the piles' bending rigidity and relative density of soil models. The estimated shear force and bending moment at the pile head were affected slightly by variation of the coefficient of horizontal subgrade reaction. The bending moments of the low bending stiffness pile are smaller than those of the high bending stiffness pile, especially in the dense sand case.

1. INTRODUCTION

The seismic earth pressure and side friction acting on an embedded pile cap affect pile stress (Sugimura et al., 1984; Fujii et al., 1998). Therefore, the embedment effects of the pile cap, the amplitude of the resultant force of earth pressure and side friction, and the phase difference between the resultant force and the structure inertia force are important for the seismic design of pile foundations in conformity to their performance.

Garde and Dobry (1998) reported, based on cyclic lateral loading centrifuge tests with relative density of D_r=75%, that the contribution of the passive side accounts for more than half of the total capacity of an embedded pile cap. Tamura et al. (2007) demonstrated that the total earth pressure in the dense sand case plays an important role in reducing the shear force at pile heads based on dynamic centrifuge tests in a superstructure–footing model supported by piles in sand deposits of different relative densities of D_r=45%, 75% and 95%. Tamura et al. (2005) also reported that the phase difference between a structural inertia force and total earth pressure can be estimated by considering the natural period of the superstructure, the predominant period of the ground, the ground displacement, and the pile cap displacement. However, estimating pile stress with the embedment effects remains difficult.

The objectives of this study are 1) to estimate the amplitudes of the earth pressure and side friction acting on an embedded pile cap supported by pile foundation during an earthquake, 2) to evaluate the bending moment and shear force of a pile considering the earth pressure and side friction, and 3) to evaluate the sensitivity of the coefficients of horizontal subgrade reactions for piles on the pile's shear force and bending moment, and the effects of structure inertia and soil displacement on the pile bending moment. To achieve these objectives, a response displacement method was developed with earth pressure and side friction. To verify the method's effectiveness, dynamic centrifuge tests were conducted on a superstructure-footing model supported by 2×2 piles in a dry sand layer on liquefied soil. Furthermore, numerical parameter analyses were conducted.

2. CENTRIFUGE TESTS

Six dynamic centrifuge tests were conducted with centrifugal acceleration of 40 × *g* using the geotechnical centrifuge at the Disaster Prevention Research Institute, Kyoto University. A pile–footing–superstructure model was prepared in a laminar shear box with inner dimensions of 450 mm (length) × 150 mm (width) × 200 mm (height). Table 1 presents all test cases in which the piles' bending stiffness, the natural period of a superstructure, and the soil relative density were varied.

For the tests, 2×2 pile models of two types were used. Table 2 and Fig. 1 respectively present the pile conditions, the model setup, and the sensor location. The lid-shaped footing was modeled with rigid brass of 90 mm (shaking direction) × 68 mm (width) × 55 mm

(height). The pile heads were linked rigidly to the upper plate of the pile cap. Their tips were also linked rigidly to the laminar shear box. The strain gauges at the pile heads were not in contact with the soil. Four plates supported by small load cells were set up on the active and passive sides and shearing sides of the pile cap. The resultant forces of the earth pressure and side friction are defined as the sum of the earth pressure acting on the active and passive sides of the pile cap and the shearing forces acting on the pile cap's side parallel to the shaking direction. The baseline of the earth pressure and wall friction amplitudes was set to zero before the centrifuge test. Toyoura sand was pasted on active and passive sides and on shearing sides of the pile cap models to increase friction between the pile cap surface and the soil. The pile cap was embedded 44 mm into the dry sand before tests.

The natural period of the superstructure in Cases 1, 2, 5, and 6, supported by plate springs under the fixed pile cap condition, was 0.0075 s. The natural period of the superstructure in Cases 3 and 4, supported by ball bearings, was 0.125 s, which was adjusted by rubber sheets between the superstructure and the panel fixed on the pile cap. The respective masses of the superstructure and pile cap were 2.0 kg and 0.99 kg.

Dry sand was air-pluviated to prepare a uniform soil layer with relative density D_r of 30% in Cases 1–4 and 80% in Cases 5 and 6. Toyoura sand (D_{50}=0.21 mm) was used. The water table was set to 54 mm below the ground surface for all tests. Excitation for the test used Hachinohe 1968 NS. The peak acceleration was scaled to about 120 m/s^2 (3 m/s^2 in prototype scale). In addition to the earth pressure and the side friction acting on the pile cap, the horizontal accelerations of the superstructure, the pile cap, the soil and the shear box base, and the excess pore water pressure were measured. All data presented in the following sections are of prototype scale. Details of the test results were reported by Tamura and Hida (2012).

3. RESPONSE DISPLACEMENT METHOD CONSIDERING EARTH PRESSURE AND SIDE FRICTION

3.1 Analytical Model for Estimating Pile Stress with Embedment Effects

Response displacement methods for estimating pile stress incorporating the seismic earth pressure and side friction on a pile cap have been developed. Figure 2 presents the proposed analysis model. The earth pressure and side friction on a pile cap can be evaluated by the nonlinear spring between the pile cap and the free-field soil. Details of the nonlinear spring are described in Sections 3.2–3.4. To incorporate consideration of the degree of fixation at pile head and pile tip, rotation springs were set up on the pile head and pile tip. The superstructure and pile cap inertias and the soil deformation were applied to the pile–footing model simultaneously using an incremental method, considering the combination of their phase differences based on the natural period of the superstructure, the predominant period of the ground, the ground displacement, and the pile cap displacement

Table 1 Test cases

	Case 1	Case 2	Case 3	Case 4	Case 5	Case 6
Piles' bending stiffness	High	Low	High	Low	High	Low
Natural period of superstructure	0.0075 s (0.3s)		0.125 s (5.0 s)		0.0075 s (0.3s)	
Relative density of soil model	30%				80%	

(Prototype scale)

Table 2 Pile's condition

	Pile with high bending stiffness	Pile with low bending stiffness
Pile materials	Stainless steel bar	Aluminum pipe
Diameter, Thickness (Prototype scale)	ϕ=8 mm (ϕ=32 cm)	ϕ= 8mm, t=0.8 mm (ϕ=32 cm,t=3.2 cm)
Bending stiffness (Prototype scale)	3.85 × 10^5 Ncm^2 (9.86 × 10^4 kNm^2)	0.84 × 10^5 Ncm^2 (2.14 × 10^4 kNm^2)

(Prototype scale)

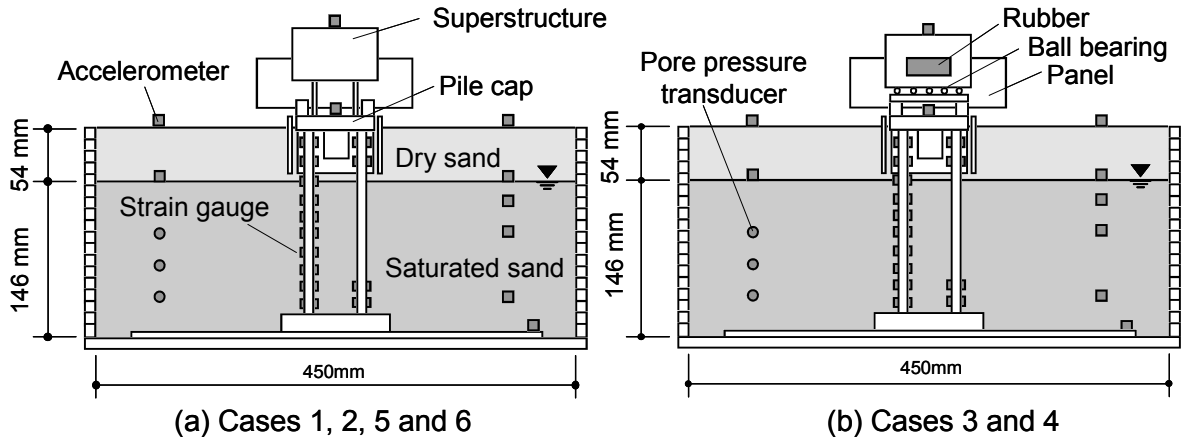


Figure 1 Test setup and instrumentation

(Tamura and Tokimatsu, 2005).

3. 2 Estimation of Seismic Earth Pressure

The relation between the total earth thrust and the relative displacement was evaluated based on the seismic earth pressure theory considering the sign (positive or minus) of the horizontal seismic coefficient, k_h. The total earth thrust acting on a pile cap, P_E, is estimated as

$$P_E = P_{EL} - P_{ER} = \frac{1}{2}\gamma H^2 B(K_{EL} - K_{ER}) \quad (1)$$

in which P_{EL} and P_{ER} respectively signify the left and right sides' earth pressure, γ denotes the soil's unit weight, H represents the embedment depth of the pile cap, B stands for the left and right sides' pile cap width, and K_{EL} and K_{ER} respectively represent the seismic earth pressure coefficients (Zhang et al., 1998) of the pile cap's left and right sides. The seismic earth pressure coefficients depend not only on the relative displacement between the pile cap and the free-field soil but also on seismic coefficient and its sign. The effect of the sign of the horizontal seismic coefficient on the seismic earth pressure can be determined by soil displacement, ΔS and pile cap displacement, ΔB (Tamura and Tokimatsu, 2005) based the assumption that the soil wedge inertia is in phase with the soil displacement because the acceleration and displacement of a sinusoidal wave have mutually opposite signs and the acceleration and horizontal seismic coefficient also have opposite signs. When the pile cap displacement is less than the soil displacement, the passive side wedge increases its size with decreasing size of the active side wedge, as depicted in Fig. 3(a). Therefore, the passive side earth pressure increases and the active side earth pressure decreases, as depicted in Fig. 3 (c). Consequently, the total earth thrust increases continuously with increasing k_h. When the pile cap displacement is greater than soil displacement, the passive side wedge decreases its size with increasing size of the active side wedge, as depicted in Fig. 3(b). Therefore, the passive side earth pressure decreases and the active side earth pressure increases as depicted in Fig. 3(d). Thus the total earth thrust decreases concomitantly with increasing k_h.

The input parameters for calculating seismic earth pressure were determined from previous studies and observed data. The minimum relative displacement requiring development of the active state was assumed as 0.5% and 0.1% of the pile cap's embedment depth for Cases 1–4 (D_r=30%) and Cases 5 and 6 (D_r =80%), respectively, based on results of a previous study (Zhang et al., 1998). The minimum relative displacement demanded development of the passive state, respectively as 4% and 2% of the pile cap's embedment depth for Cases 1–4 (D_r =30%) and Cases 5 and 6 (D_r =80%) (Fang et al., 2002; Rollins and Sparks, 2002). The respective internal friction angles for Cases 1–4 (D_r =30%) and Cases 5 and 6 (D_r =80%) were 34 deg and 42 deg. The wall friction angle between the soil and pile cap was set to 18 deg for all cases based on experimentally obtained results. The

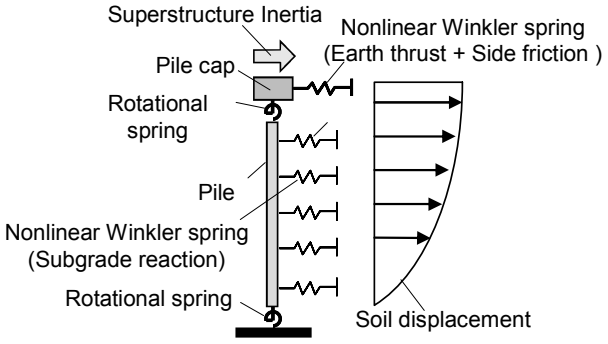


Figure 2 Analysis model for pile considering embedment effects

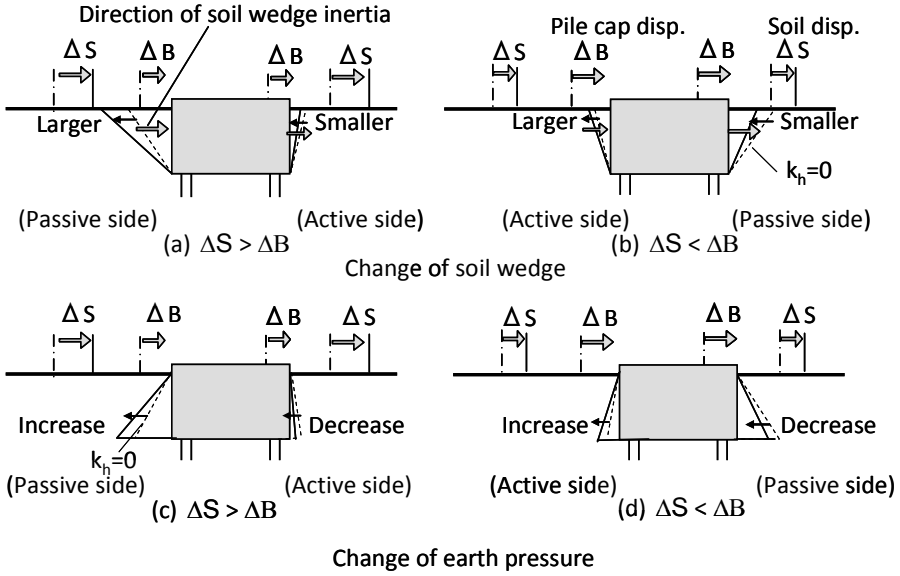


Figure 3 Effects of direction of soil wedge inertia on seismic earth pressure

horizontal seismic coefficients, k_h, were assumed to be -0.2, 0, and 0.2 in which k_h was a positive value when soil displacement was greater than the pile cap displacement.

Fig. 4 shows that the estimated total earth thrusts compared with the test results. The estimated total earth thrust with k_h=0.2 showed good agreement with the test results for Cases 1–4, which corresponded to the estimation on the effects of k_h on the total earth thrust, as depicted in Fig. 3 because the soil displacement tended to be greater than the pile cap displacement. In Cases 5 and 6, the soil displacement was less than the pile cap displacement, indicating that the total earth thrust decreases concomitantly with increasing k_h based on the proposed method. The estimated total earth thrust with k_h= -0.2, 0 and 0.2 also showed good agreement with test results because k_h had slight effects on the earth thrust for extremely small relative displacement.

3. 3 Estimation of Side Friction

Side friction was evaluated using the bilinear model considering the shear strength of soil around the sidewall (Tamura et al., 2009). The side friction, P_F was estimated as

$$P_F = \mu P_0 D_{re} / D_{\max} \qquad (D_{\mathrm{re}} \leq D_{\max}) \qquad (2)$$

$$P_F = \mu P_0 \qquad (D_{\mathrm{re}} > D_{\max}) \qquad (3)$$

$$P_0 = \frac{1}{2}\gamma H^2 L K_0 \qquad (4)$$

in which μ denotes the friction coefficient between the soil and the pile cap's surface, P_0 is the earth pressure at rest, D_{re} signifies the relative displacement between the pile cap and the soil, $D_{\max}$ represents the relative displacement at which the side friction reaches its maximum, L stands for the length of the pile cap (shaking direction), and K_0 is the earth pressure coefficient at rest, as estimated using Jaky's formula. Considering that the friction depends on the shear strength of the soil when the pile cap's surface is rough (Uesugi, 1986), the friction coefficient, μ is estimated as

$$\mu = \tan(\phi) \qquad (5)$$

where ϕ is the internal friction angle of the soil.

Fig. 5 shows that the estimated side frictions were compared with the test results to clarify the validity of the proposed method. The minimum relative displacement at which the side friction reached its maximum was assumed as 10 mm for Cases 1–4 and 3 mm for Cases 5 and 6 based on test results. The estimated side frictions agreed with the experimental data for all cases when the relative displacements were less than 2 cm, but were less than the experimental value when the relative displacements were greater than 2 cm because the positive dilatancy of sand increases the lateral pressure acting on the side when the relative displacement becomes large (Tamura et al., 2009). The effects of dilatancy demand further study, but errors are admitted in practical cases when the relative displacement is large because the side friction amplitude is smaller than the earth thrust amplitude.

3.4 Estimation of Resultant Force of Seismic Earth Pressure and Side Friction

The estimated resultant force of earth pressure and side friction, the nonlinear spring between the pile cap and the free-field soil of the proposed analysis, was verified with the test results depicted in Fig. 6. The horizontal

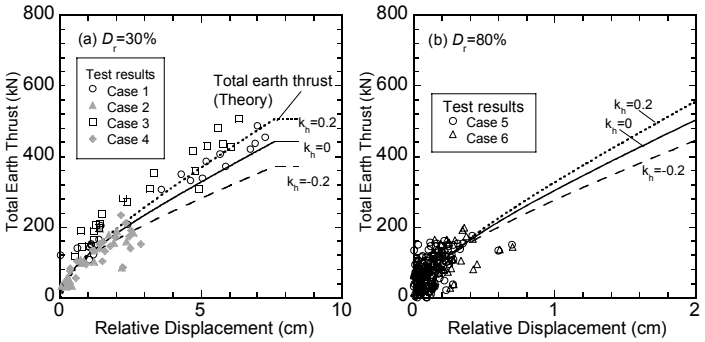


Figure 4 Relative displacement and total earth thrust

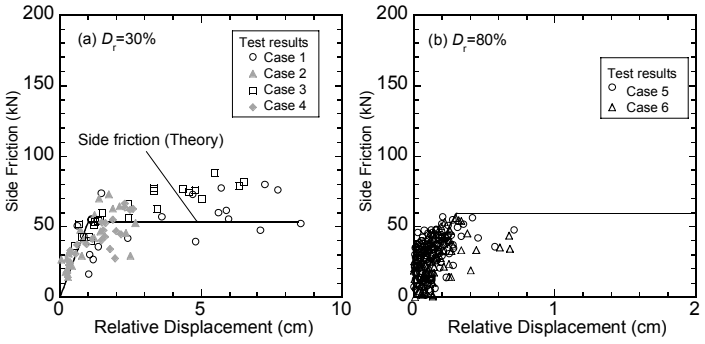


Figure 5 Relative displacement and side friction

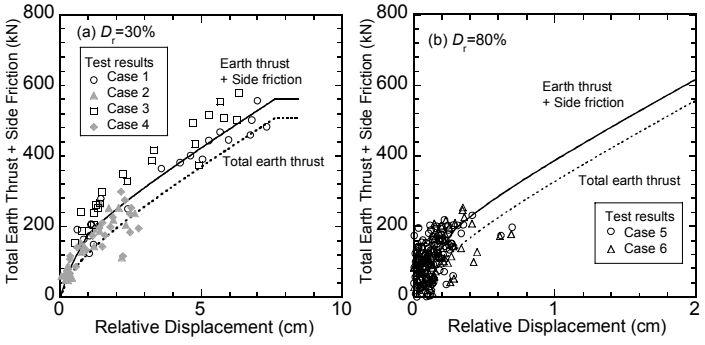


Figure 6 Relative displacement and the resultant force of earth pressure and side friction

seismic coefficients k_h were assumed as 0.2 for Cases 1–4 and -0.2 for Cases 5 and 6, considering soil and pile cap displacements. The estimated resultant force showed good agreement with the test results. The broken line in the figures shows the estimated total earth thrust (without the side friction), which was dominant in the resultant forces. The estimated resultant force (with the side friction) showed better agreement with the observed data.

4. PILE STRESS ESTIMATED USING THE PROPOSED METHOD

4.1 Calculation Conditions

The pile cap displacement, the resultant force of earth pressure and side friction, the pile's bending moment, and the shear force were evaluated based on calculation conditions as follows. The nonlinear spring corresponding to the resultant force of earth pressure and side friction was evaluated using Eqs. (1)–(5). The direction of soil wedge inertia was estimated using the soil displacement and pile cap displacement (Fig. 3). The rotation springs at the pile head and tip were 1.41×10^5 kNm/rad for the high-stiffness pile model and 1.65×10^5 kNm/rad for the low-stiffness pile model, which were evaluated using the relation between the pile cap displacement and the horizontal load acting on the pile cap based on static horizontal loading tests without soil. The subgrade reaction of a pile was evaluated using the nonlinear spring based on recommendations for design of building foundations in Japan (AIJ, 2001) using the N-value estimated from the shear wave velocities (Tamura and Hida, 2012). The soil displacements from the ground surface to GL -3 m in Cases 1–4 and GL -1 m in Cases 5 and 6 were assumed to be constant and equal to the ground surface displacement. Then the soil displacement decreased concomitantly with increasing depth as a cosine function. The superstructure and pile cap accelerations and the ground surface displacement were used as the observed values. The estimated and measured data presented hereinafter were examined when the bending moment at the pile head reached its maximum after soil liquefaction. That is because the vertical distribution of the subgrade reaction of piles and soil displacement are dramatically changed before and after soil liquefaction.

The observed superstructure acceleration, pile cap acceleration and ground surface displacement used for the numerical analyses are shown in Table 3. The minus sign of the pile cap acceleration implies that the pile cap acceleration is greater than 180 deg with the superstructure acceleration. The superstructure accelerations, where the natural period of the superstructure is greater than the predominant period of the ground surface acceleration, were much smaller than the pile cap accelerations for Cases 3 and 4. To investigate the sensitivity of the coefficients of the subgrade reaction on the numerical results, the reductions in the ultimate subgrade reaction, α and in the subgrade reaction modulus, β on liquefaction were assumed respectively to be 0.01, 0.1 and 0.2.

4.2 Estimated Pile Cap Displacement

Pile cap displacements, as estimated using the proposed method, were compared with observed data for all cases, as portrayed in Fig. 7. The observed pile cap displacements were distributed from 2.5 cm (Case 5) to 26 cm (Case 2), indicating that the pile cap displacements were markedly affected by the relative density of the soil and the bending stiffness of piles. The black circles in the figure show the observed soil displacements. The soil displacements in Cases 1–4 were greater than the observed pile cap displacement. In contrast, the soil displacements in Cases 5 and 6 were smaller than the observed pile cap displacements. The estimated pile cap displacements increased concomitantly with increasing α , β for Cases 1–4 because the soil displacements tended to be greater than pile cap's and pile's displacements. The estimated pile cap displacements showed fairly good agreement with the observed values, especially when α, β were 0.1–0.2. Estimated pile cap displacements also increased concomitantly with increasing α, β for Cases 5 and 6, although the soil displacements were smaller than the pile cap displacements because the soil displacements were larger than the pile displacements at the lower part of piles and soil layer. The estimated pile cap displacements showed excellent agreement with observed data with any α, β for Cases 5 and 6.

4.3 Estimated Earth Pressure and Side Friction

Figure 8 shows that the estimated resultant forces of earth pressure and side friction per pile are compared with the test results. The respective positive and negative

Table 3 Superstructure and pile cap accelerations and ground surface displacement when bending moments at pile head were maximum after soil liquefaction

	Case 1	Case 2	Case 3	Case 4	Case 5	Case 6
Superstructure acceleration (cm/s^2)	150	116	42	34	247	276
Pile cap acceleration (cm/s^2)	137	117	-141	-125	189	216
Ground surface displacement (cm)	20.5	26.1	18.2	25.7	2.3	6.2

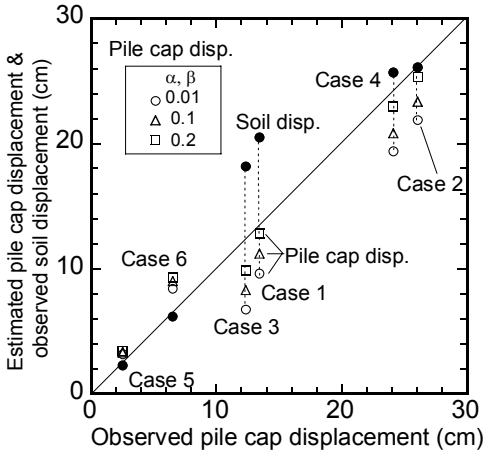


Figure 7 Estimated and observed pile cap displacement and observed soil displacement

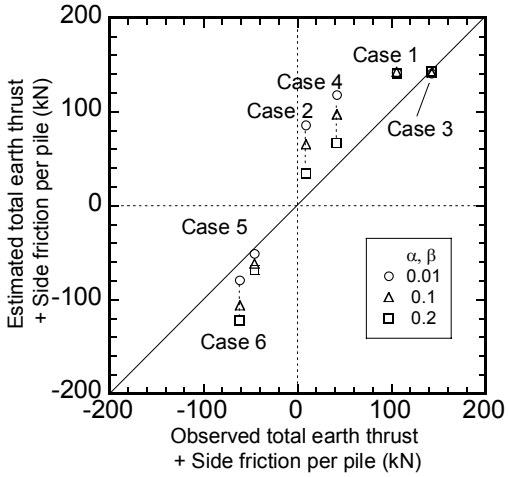


Figure 8 Estimated and observed resultant force of total earth thrust and side friction

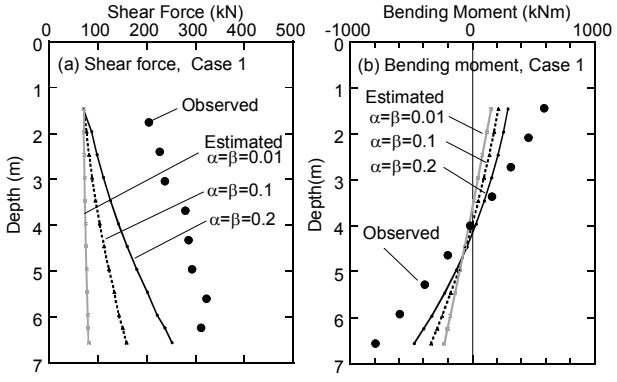


Figure 9 Vertical distribution of bending moment and shear force of pile without the resultant force of earth pressure and side friction

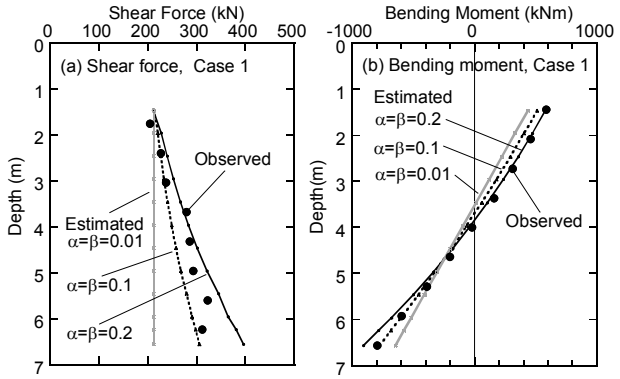


Figure 10 Vertical distribution of bending moment and shear force of pile with the resultant force of earth pressure and side friction

resultant forces show that the resultant forces are in phase and out of phase by 180 deg with the structure inertia. The observed resultant forces were in phase with the structural inertia for Cases 1–4 but were out of phase by 180 deg with structural inertia for Cases 5 and 6. The estimated resultant forces showed fairly good agreement with the experimentally obtained results, not only in terms of the amplitude but also in terms of the phase difference between the resultant forces and the structural inertia. The resultant forces for Cases 1 and 3 were unaffected by α, β because the earth pressure almost reached the passive state with any α, β. The resultant forces for Cases 2 and 4 decreased concomitantly with increasing α , β because the relative displacement between the soil and pile cap decreased. In contrast, the resultant forces for Cases 5 and 6 increased concomitantly with increasing α , β because the relative displacement between the soil and pile cap increased. These results indicate that the effects of the coefficients of subgrade reaction on the resultant force varied according to the soil, pile cap and pile displacements.

4.4 Estimated bending moment and shear force of piles

Figures 9 and 10 show the vertical distributions of pile's bending moment and shear force in Case 1, as respectively estimated without and with the earth pressure and side friction. The observed shear force increased continuously with increasing depth, indicating that the soil acted on the pile as an external force. This phenomenon resulted from the soil, for which the displacement was greater than the pile. The estimated shear force and bending moment amplitudes neglecting the earth pressure and side friction were much smaller than the test results with any α, β. In contrast, the estimated shear force and bending moments considering the earth pressure and side friction showed fairly good agreement with the observed data when α, β=0.1 and 0.2. These results indicate that the piles' shear force and bending moment cannot be estimated accurately without the earth pressure

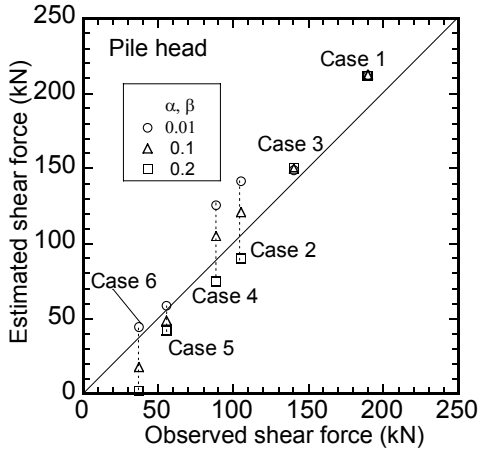


Figure 11 Estimated and observed shear force at pile head

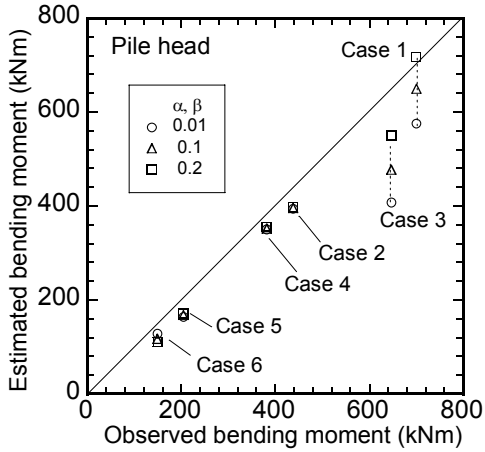


Figure 12 Estimated and observed bending moment at pile head

and side friction when a pile cap is embedded. The earth pressure and side friction are regarded as estimating the piles' stress hereinafter.

Figure 11 shows the estimated shear forces at the pile head compared with the test results. The estimated shear force at the pile head for Cases 1 and 3 did not depend on α, β because the earth pressure almost reached the passive state. The estimated shear force at pile head with α, β=0.1 and 0.2 showed good agreement with the observed data for all cases.

Figure 12 shows the estimated bending moments at the pile head compared with the test results. The estimated bending moments at the pile head with any α or β showed fairly good agreement with observed data in Case 2 and Cases 4–6. In Cases 1 and 3, the estimated bending moment with α, β=0.2 showed good agreement with the observed data.

5. EFFECTS OF STRUCTURE INERTIA AND SOIL DISPLACEMENT ON THE PILE BENDING MOMENT

The pile cap displacement, the resultant force of earth pressure and side friction and the bending moment at a pile head were examined in numerical parameter studies to investigate the effects of structure inertia and soil displacement on pile stress quantitatively. The parameters are bending stiffness of piles, relative soil density, structure inertia, and soil displacement. The pile and soil conditions for the numerical analysis are the same as those of the experiments. The reduction factors of subgrade reaction, α and β , were assumed as 0.2. The ground surface displacement D_s was assumed as 0, 10, 20, 30 cm in D_r=30% and 0, 5, 10, 15 cm D_r=80%. The soil displacement distribution was inferred using the same method as that described in Section 3.2. The horizontal equivalent seismic coefficient k_h is assumed as 0.2 for D_r=30% and -0.2 for D_r=80%. The structure inertia, assumed to be in phase with the soil displacement, changed from 0 to 300 kN. The circles in the following figure show the observed data when the pile's bending moment became the maximum for Cases 1–6. The observed and estimated data show good agreement corresponding to the structure inertia and ground surface displacement, suggesting high reliability of the numerical results.

5.1 Pile Cap Displacement

The relations between the structure inertia, the soil displacement and the pile cap displacement are presented in Fig. 13. The pile cap displacement is affected not only by the structure inertia but also by the soil displacement. For example, the pile cap displacement when the soil displacement is 30 cm and the structure inertia is 0 kN is equivalent to that when the soil displacement is 10 cm and the structure inertia is 300 kN in the case of high bending stiffness pile and D_r=30%. The inclinations of the lines showing inertia-displacement for D_r=30% are greater than those for D_r=80%, indicating that the pile cap displacements for D_r=30% are strongly affected by the structure inertia.

5.2 Earth Pressure and Side Friction

The relations between the structure inertia, the soil displacement, and the resultant force of earth pressure and side friction are presented in Fig. 14. The plus sign of the resultant force reflects that the resultant force is out of phase by 180 deg with the structure inertia. For D_r=30%, the resultant force of the high bending stiffness pile is in phase with the structure inertia except for the small soil displacement, indicating that the earth thrust and side friction tend to increase pile stress. The resultant force amplitude of D_s=30 cm is almost constant, about –150 kN, because the earth pressure reaches the passive state. In contrast, the resultant force of the low bending stiffness pile is out of phase by 180 deg with the structure

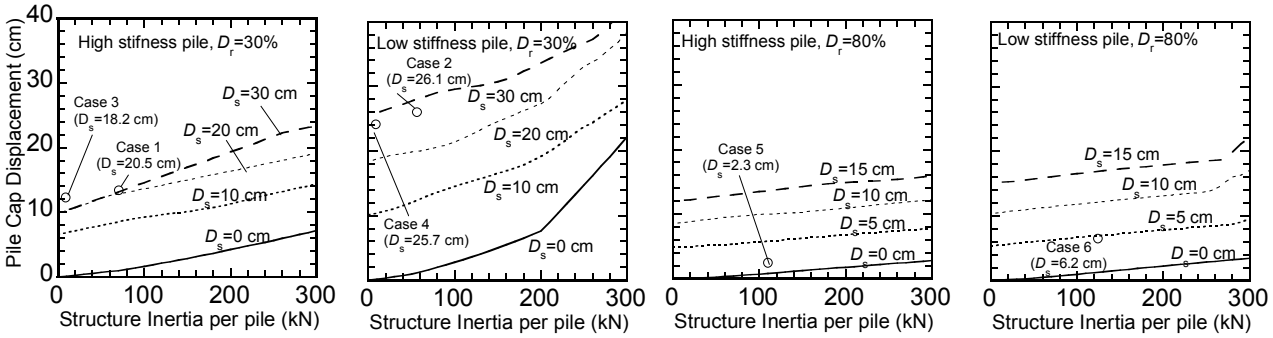


Figure 13 Effects of structure inertia and soil displacement on pile cap displacement

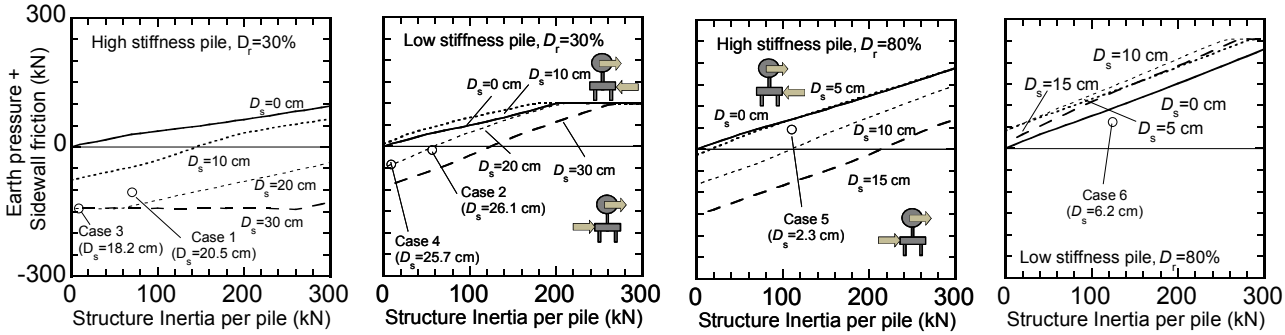


Figure 14 Effects of structure inertia and soil displacement on the resultant force of earth pressure and side friction

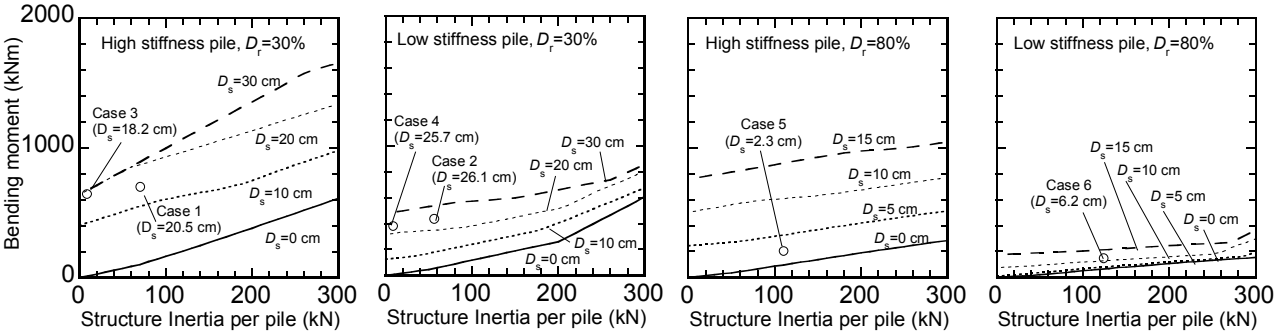


Figure 15 Effects of structure inertia and soil displacement on bending moment at pile head

inertia except for the large soil displacement and small structure inertia, indicating that the earth thrust and side friction tend to decrease the pile stress. The resultant forces when the structure inertia is large become constant, reflecting that the earth pressure reaches the passive state. The resultant force amplitude, about 100 kN, is smaller than that of the high bending stiffness pile. This difference results from the direction of the soil inertia.

For D_r=80%, the resultant force of the high bending stiffness pile is out of phase by 180 deg with the structure inertia when the soil displacement is small and the structure inertia is large, but it is in phase when the soil displacement is large and the structure inertia is small. The resultant force of the low bending stiffness pile is out of phase by 180 deg with the structure inertia with any structure inertia and soil displacement.

5.3 Bending Moment at Pile Head

The relations between the structure inertia, the soil displacement, and the bending moment at the pile head are presented in Fig. 15. The bending moment increases concomitantly with increasing structure inertia. For D_r=30%, the bending moment of the low bending stiffness pile is about half that of the high bending stiffness pile. The bending moment of the high stiffness pile is less affected by the structure inertia in D_s=20 cm than in D_s=30 cm. The resultant force of D_s=30 cm, in phase with the structure inertia, is large and almost constant for any structure inertia because the large relative displacement causes the passive state. In contrast, the resultant forces of D_s=20 cm are also in phase but decrease with the structure inertia. Therefore, the bending moment of

D_s=20 cm is less affected by the structure inertia. The bending moment of the low stiffness pile is also affected strongly by the structure inertia when the structure inertia is greater than about 200 kN because the resultant force, out of phase 180 deg with the structure inertia, reaches the passive state. It is noteworthy that the mechanism of the effects of the resultant force which reaches a passive state on the bending moment differs between the high stiffness pile and the low stiffness pile.

For D_r=80%, the bending moment of the low bending stiffness pile is about a quarter of that of the high bending stiffness pile because the resultant force of the earth pressure and side friction of the low stiffness pile reduced the shear force at pile head more efficiently than that of the high stiffness pile.

5.4 High Bending Stiffness Pile vs. Low Bending Stiffness Pile

The bending moments of the low bending stiffness pile are smaller than those of the high bending stiffness pile for both soil models, especially in the dense sand cases, because the resultant force is out of phase by 180 deg and its amplitude becomes large with small relative displacement. The pile's stress reduction effects in the loose sand case are limited when the structure inertia and/or the soil displacement are large. As described above, the effects of the structure inertia and the soil displacement on the pile's bending moment are extremely complicated, but they can be evaluated quantitatively using the proposed method.

6. CONCLUSION

A response displacement method was developed to estimate pile stress with consideration of the seismic earth pressure and side friction acting on an embedded pile cap. Sensitivity of the coefficients of subgrade reactions of piles on a pile's shear force and bending moment, and the effects of structure inertia and soil displacement on a pile's bending moment were examined in numerical parameter studies. The following conclusions were drawn.

(1) Estimated amplitudes of the resultant force of seismic earth pressure and side friction and the estimated phase difference between the resultant force and the structure inertia force showed good agreement with experimentally obtained results. The resultant forces were greater for loose sand cases but were smaller for dense sand cases with increasing coefficients of subgrade reactions of piles.

(2) Estimated amplitudes of the shear force and bending moment at the pile head agreed well with the observed results. The shear forces and bending moment were affected slightly by the variation of the subgrade reactions on piles.

(3) The bending moments of the low bending stiffness pile are smaller than those of the high bending stiffness pile, especially in the dense sand case, because the resultant force is out of phase by 180 deg and its amplitude becomes large with small relative displacement.

References:

Fang, Y., Ho, Y., and Chen, T. (2002), "Passive Earth Pressure with Critical State Concept," *J. Geotech. Geoenviron. Eng.,* **128**(8), 651-659.

Fujii, S., Isemoto, N., Satou, Y., Kaneko, O., Funahara, H., Arai, T., and Tokimatsu, K. (1998), "Investigation and analysis of a pile foundation damaged by liquefaction during the 1995 Hyogoken-Nambu earthquake," *Soils and Foundations* – Special issue on Geotechnical Aspects of the 1995 Hyogoken Nambu Earthquake, No. 2, 179–192.

Gadre, A. and Dobry, R. (1998), "Lateral Cyclic Loading Centrifuge Tests on Square Embedded Footing," *J. Geotech. Geoenviron. Eng*., **124**(11), 1128-1138.

Rollins, K. and Sparks, A. (2002), "Lateral Resistance of Full-Scale Pile Cap with Gravel Backfill," *J. Geotech. Geoenviron. Eng*., **128**(9), 711-723.

Sugimura, Y. and Hirade, T. (1984), "Experimental study of reduction effect of horizontal force due to embedment of the foundation," *Summaries of Technical Papers of Annual Meeting,* AIJ, Structures II, 2409–2410. (in Japanese)

Tamura, S. and Tokimatsu, K. (2005), "Seismic earth pressure acting on embedded pile cap based on large-scale shaking table tests," *Geotechnical Special Publication*, No. 145, ASCE, 2005, 83–96.

Tamura, S., Imayoshi, T., and Sakamoto, T. (2007), "Earth pressure and side friction acting on an embedded pile cap in dry sand based on centrifuge tests," *Soils and Foundations*, Japan Geotechnical Society, **47**(4), 811-819.

Tamura, S., Sakamoto, T., Hida, T., and Maeda N. (2009): "Evaluation of seismic earth pressure and wall friction acting on embedded pile cap based on centrifuge test," *Proceedings of the International Conference on Performance-Based Design in Earthquake Geotechnical Engineering* (IS-Tokyo2009), 517-521

Tamura, S. and Hida, T.(2012): Evaluation of Pile Stress Based on Response Displacement Method Considering Earth Pressure and Sidewall Friction Acting on Embedded Footing – Case of Dry Sand Layer on Liquefied Soil –, *15th World Conference on Earthquake Engineering*, Paper ID 2889.

Uesugi, M. and Kishida, H. (1986), "Influential factors of friction between steel and dry sands," *Soils and Foundations*, **26**(2), 33-46.

Zhang, Jian-Min, Shamoto, Y., and Tokimatsu, K. (1998), "Evaluation of earth pressure under any lateral deformation," *Soils and Foundations*, Japan Geotechnical Society, 38(1), 15-33.

10CUEE CONFERENCE PROCEEDINGS
10th International Conference on Urban Earthquake Engineering
March 1-2, 2013, Tokyo Institute of Technology, Tokyo, Japan

EVALUATION OF COLLAPSE AND NON-COLLAPSE OF PARALLEL BRIDGES AFFECTED BY LIQUEFACTION AND LATERAL SPREADING

Benjamin Turner [1], Scott Brandenberg [2], and Jonathan Stewart [3]

1) Graduate Student Researcher, Department of Civil and Environmental Engineering, University of California, Los Angeles.
2) Associate Professor and Vice Chair, Department of Civil and Environmental Engineering, University of California, Los Angeles.
3) Professor and Chair Department of Civil and Environmental Engineering, University of California, Los Angeles.
bjturner@ucla.edu, sjbrandenberg@ucla.edu, jstewart@seas.ucla.edu

Abstract: An overview is presented of the authors' ongoing investigation of the performance of a railroad bridge and adjacent highway bridge during the 2010 El Mayor-Cucapah earthquake in Baja California, Mexico. A span of the pile-supported railroad bridge collapsed due to movement of a pier from lateral spreading. The highway bridge, supported on drilled shafts, suffered moderate structural damage but did not collapse. An overview of the site, structural details of the bridges, and the proposed geotechnical explorations and analyses are presented. The Pacific Earthquake Engineering Research Center (PEER) recently published "Recommended Design Practice for Pile Foundations in Laterally Spreading Ground," which synthesizes the last decade of research on the topic. Using the results from planned geotechnical investigation, the authors intend to analyze the bridges according to the PEER guidelines. The case studies will provide valuable insight for validating the recommended guidelines.

1. INTRODUCTION

On April 4, 2010, the M_w 7.2 El Mayor-Cucapah earthquake occurred southwest of Mexicali in northern Baja California, Mexico (USGS 2010). Liquefaction-related damage to irrigation and transportation infrastructure, buildings, and agricultural land was widespread throughout the region (GEER 2010). This paper focuses on an ongoing study of two parallel bridges located about 60km southeast of Mexicali that were subjected to liquefaction-induced lateral spreading and vertical settlement during the El Mayor-Cucapah earthquake.

Although the two bridges were subjected to the same level of lateral spreading demand, their performance levels were different, making this a valuable case study. An overview of the observed damage and structural details of the bridge along with the authors' planned site investigations and analyses are presented in the following sections. The primary focus of the investigation and analyses will be to model the highway bridge in an effort to understand why it exhibited desirable performance while the railroad bridge collapsed.

2. REGIONAL GEOLOGY AND SEISMICITY

The Mexicali Valley and its counterpart on the USA side of the border, the Imperial Valley, are located in the Salton Trough, an extensional basin formed by tectonic activity along the transform boundary between the Pacific and North American plates (Figure 1). To the southeast, the Gulf of California represents further extension due to divergent fault step-over at the plate margin, while movement to the northwest is primarily strike-slip along the San Andreas Fault system. The Colorado River enters the east side of the basin near the Mexico-USA border, depositing alluvium over marine deposits for a total soil thickness up to 2,400m thick (GEER 2010). High groundwater levels from the river and agricultural activity combined with the loose alluvial deposits create a high liquefaction hazard throughout the valleys.

Several faults cross the region, primarily accommodating strike-slip movement in the northwest-southeast direction and extension in the northeast-southwest direction. The El Mayor-Cucapah earthquake occurred mainly along the Pescadores and Borrego faults northwest of the epicenter and the previously unknown Indiviso Fault to the southeast, which was buried beneath sediments of the Colorado River delta prior to the earthquake. The offset was oblique with the primary component being strike-slip (GEER 2010).

The northern Baja California region is known to be seismically active, with several major earthquakes occurring in recent history. The El Mayor-Cucapah earthquake was the largest recorded event in the region since an estimated Mw 7.2 event in 1892 (Hough and Elliot 2004).

3. SITE DESCRIPTION

Immediately following the earthquake, a team of researchers from the Geotechnical Extreme Events Reconnaissance (GEER) Association visited the Mexicali and Imperial Valleys to collect perishable geotechnical data

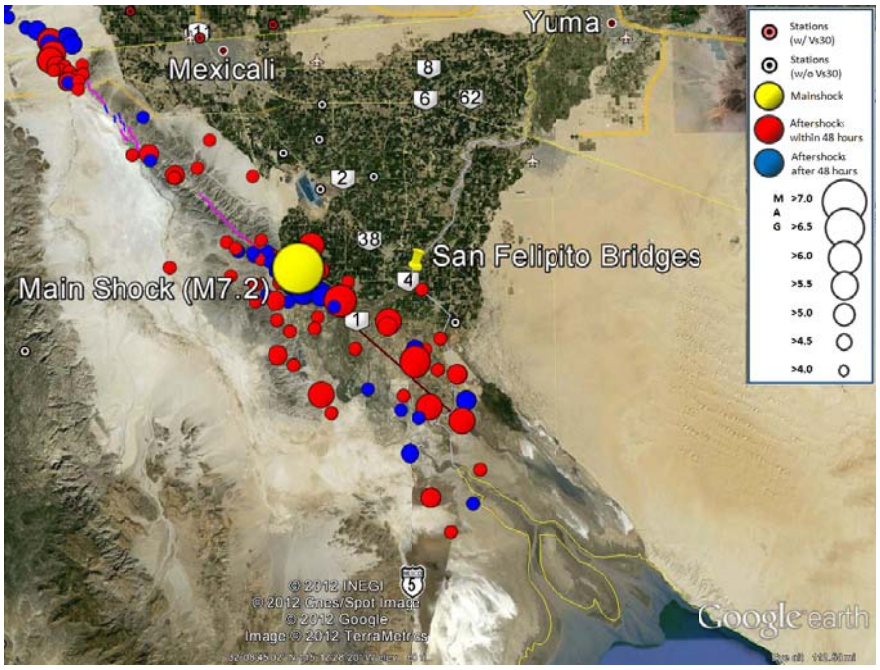


Figure 1: Regional map showing main event, aftershocks, and site location. After GEER Report (2010).

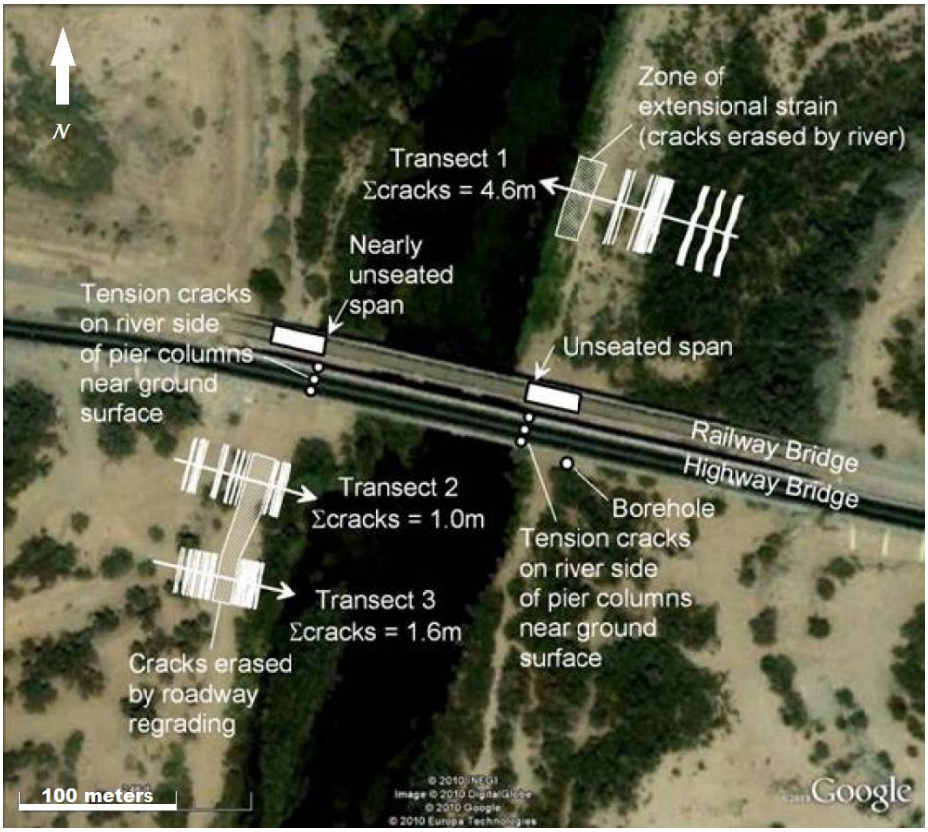


Figure 2: Site map showing lateral spreading and observed structural damage to bridges. After GEER Report (2010).

and observe structural damage associated with geotechnical issues. Except as noted, the following information in Sections 3 and 4 is adapted from the report of their reconnaissance effort, available on the GEER website (GEER 2010).

Two closely-spaced, parallel bridges span the Colorado

River at the site, a railroad bridge and a highway bridge, collectively called the "San Felipito Bridges" (see Figure 2). The river is flanked on both sides by relatively flat agricultural land with gently sloping banks. The nearest ground motion station to the site, located in Riito approximately 12km to the southeast, recorded a peak ground acceleration of approximately 0.4g.

3.1 Geotechnical Conditions

The near-surface soil profile at the site generally consists of recent alluvial deposits of loose sand with varying amounts of silt. The Secretaría de Comunicaciones y Transportes (Secretariat of Communications and Transportation) de México (SCT), the government agency with jurisdiction over the highway bridge, conducted a soil boring during the GEER reconnaissance trip. The soil profile inferred from their boring log consist of 6m of silt overlying approximately 5.5m of loose sand, underlain by dense sand, with the groundwater table at a depth of 2m. The location of the boring is shown in Figure 2. Further site investigations including subsurface testing are planned as described in Section 5.0.

3.2 Ground Failures

As shown in Figure 2, lateral spreading cracks were observed on the river banks both north and south of the bridges in the non-liquefied silt crust that overlays the liquefiable sand. It was not evident from the initial reconnaissance whether or not the approximately 4m of silt below the groundwater table liquefied during the earthquake. The sum of the measured lateral spreading cracks was as much as 4.6m along a transect about 60m north of the bridge, although not all the deformation could be directly measured due to heavy vegetation cover and erosion of cracks by the river prior to the arrival of the GEER team.

Measured lateral spreading deformation was greater on the east bank of the river than the west bank, possibly because the river currently flows along the western margin of its floodplain so the alluvial sediments on the east bank are younger and hence looser and more susceptible to liquefaction. This observation could have implications for estimates of potential lateral spreading deformations at similar sites.

Vertical settlement of up to 0.5m was observed, likely due to a combination of reconsolidation following liquefaction and deviatoric deformation. At the location of the largest measured vertical ground settlement, the bridge pier settled approximately 0.5m, likely due to static loads, down-drag forces mobilized during liquefaction, and a loss of axial resistance.

4. BRIDGE DAMAGE AND STRUCTURAL DETAILS

Both bridges have precast-prestressed concrete simply-supported spans on elastomeric bearings resting atop reinforced concrete, pile-supported piers. Although both bridges were founded on deep foundations, the railroad bridge suffered unseating collapse of one span and near collapse of two other spans, while the highway bridge suffered only moderate structural damage without collapsing. Further structural details of the bridges are provided in the following two sections.

4.1 Railroad Bridge

Constructed in 1962, the railroad bridge consists of a single track supported on three approximately 1.0m-deep T-shaped girders. The simply-supported spans rest on elastomeric bearings atop reinforced concrete pier walls which are supported on driven pile foundations. No other positive structural connection between the girders and the pier walls was observed, e.g. shear keys and diaphragm anchorage as described below for the highway bridge. The research team has not obtained construction plans for the railroad bridge at this time, although we anticipate receiving these drawings through coordination with Mexican colleagues.

Damage to the railroad bridge consisted of collapse of a span on the eastern side of the river as lateral spreading translated and rotated the pier at the western end of the span towards the river, exceeding the lateral capacity of the elastomeric bearing and leading to unseating of the girders. The superstructure also displaced in the transverse direction relative to the pier. Similar movement of piers on the west bank of the river nearly led to collapse of two additional spans. Temporary steel trestles were erected to replace the collapsed span and support the nearly-collapsed spans.

4.2 Highway Bridge

The following structural details are based on the bridge construction plans (1998) provided to the research team by SCT.

The highway bridge consists of approach fills up to 6m thick leading to ten 20m-long simply-supported spans (Figure 3). Each span consists of seven precast-prestressed 1.15m-deep I-shaped girders spaced approximately 1.6m on-center in the transverse direction. Precast slab panels rest on the top flanges of adjacent girders, covered by a cast-in-place deck slab. The deck slabs are cast continuously across spans 1-2-3, 4-5-6-7, and 8-9-10, i.e. in three separate sections. The girders are supported on 60cm-wide concrete masonry plates on 1.6m-wide pier caps, which are in turn supported on four extended shaft columns. The elastomeric bearings are 20cm wide in the longitudinal direction.

Vertical diaphragms connect the ends of the girders in the transverse direction. A prestressing strand in the transverse direction passes through the diaphragms and ducts in the girder-ends across the entire 11m width of the bridge, forming a continuous member to provide lateral force resistance in the transverse direction.

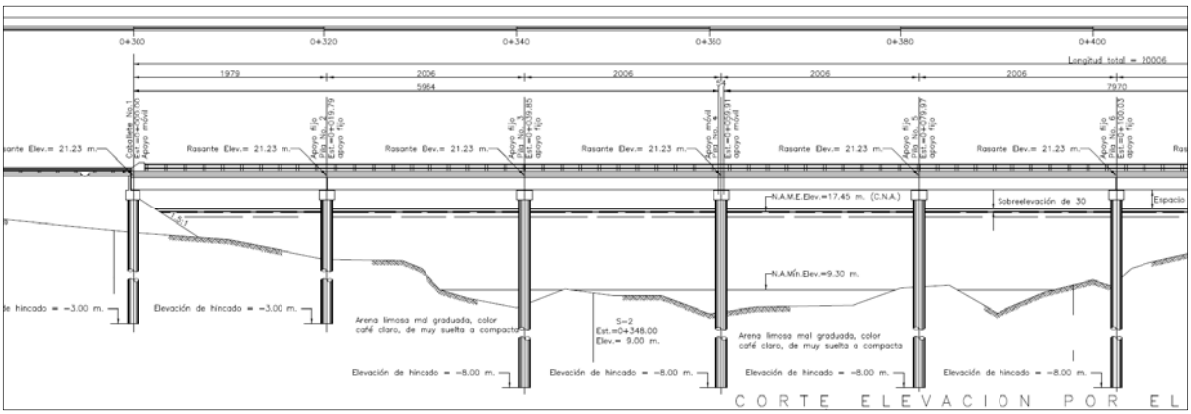


Figure 3: Western half of highway bridge, from original construction plans (SCT 1998).



(a)



(b)



(c)

Figure 4: (a) shear key damage at pier cap (photo Richard Woods), (b) vertical ground settlement relative to columns (photo Jim Gingery), and (c) column flexural concrete cracking at base (photo Richard Woods).

The girder-to-pier-cap connections are a mix of "pinned" and "roller bearing" types. At the piers between spans 3-4 and 7-8, as well as at the end supports at the abutments, the only connection between the girders/diaphragm and the pier cap is the laminated neoprene elastomeric bearing. The bearing transfers axial load and allows for rotation and translation of the girders by compressing and deforming in shear, respectively. A polymer-filled expansion joint is constructed in the deck slab at these locations to allow for thermal expansion and contraction.

At the remaining piers, the deck slab is continuous over the joint and translation of the girders is restrained by anchorage via two rectangular blocks that extend from the base of the diaphragm into the pier cap. The anchorage blocks fit into a rectangular slot cast into the pier cap such that translation is restrained in both the longitudinal and transverse directions. There is no positive connection between the diaphragm anchorage blocks and the pier cap via reinforcing bars that are continuous across the joint; an asphaltic felt pad is placed between the two elements. A

small amount of rotation is allowed at these "pinned" type connections. The end conditions of all ten spans are considered simply-supported.

The four 1.2m diameter extended shaft columns are continuous with four drilled shaft foundations of the same diameter at each pier. There are no pile caps, although the shafts are connected with a transverse beam near the ground level for the shafts in the river, likely to prevent erosion (visible in Figure 4c). The 1.5m high abutment walls are supported on three 1.2m diameter drilled shafts. The foundations in the river extend to the deepest elevation, approximately 14m below the pile cap, while the foundations nearest the abutments and beneath the eastern spans where flow is seasonal are shorter by 3m to 6m. Assuming horizontal stratigraphy at the site, the deepest foundations extend about 10m into the dense sand layer.

Three separate zones of damage were observed on the highway bridge, shown in Figure 4 (GEER 2010; Meneses et al. 2010):

1. 30-cm-tall shear key "retainers" extending up from the ends of the pier caps to provide lateral restraint of the edge girders were cracked and spalled, but did not fail, indicating that the bridge was loaded in the transverse direction. The shear keys on the western abutment pier cap were damaged in a similar manner. Transverse offset of the elastomeric bearings was also observed.
2. Flexural cracking was observed on the inward (river side) of the columns at the column-to-pile-cap connection of the piers on both sides of the river crossing. The flexural demand indicates horizontal movement of the foundations and pile cap towards the center of the river due to lateral spreading. The bridge deck was cracked above these damaged piers.
3. Vertical settlement of approximately 0.5m of one of the piers resulted in vertical displacement and cracking of the bridge deck immediately above the pier. This pier was adjacent to the span of the railroad bridge that collapsed, on the east river bank.

4.3 Performance Comparison

The desirable performance of the highway bridge appears to be due at least in part to the presence of the diaphragm anchorage blocks connecting the pier caps to the spans, which allowed the load acting on the foundations to be transferred to and resisted by the superstructure acting in compression along the longitudinal axis of the bridge. Lacking this positive structural connection, the railroad bridge piers had minimal translational restraint once the shear capacity of the elastomeric bearings was exceeded. The force exerted on the bridge foundations also differed due to the different layout and type of foundation elements. The highway bridge foundations may extend further into the dense sand layer, which would give them additional lateral resistance.

Although the reconnaissance team was not able to directly measure the lateral spreading deformation along the axis of the bridges due to ongoing repair efforts, it was visually evident that the deformation near the bridges was less than the measured deformation in the free field to the north and south. This indicates that the foundations of the bridges influenced lateral spreading soil displacements in the vicinity of the bridge. Furthermore, this indicates that the each bridge may have influenced the response of the other.

5. FURTHER RESEARCH

The authors plan to conduct cone penetration tests (CPT) at the site during the spring of 2013 in collaboration with the Mexican authorities in order to obtain detailed geotechnical data. Shear wave velocity and porewater pressure will be measured during the CPT.

The highway bridge will be analyzed using the finite element program OpenSEES (McKenna 1997) according to the Ashford et al. (2011) guidelines (i.e., the "PEER approach"), and the performance predicted by the analyses will be compared to the observed bridge performance. Foundation elements will be modeled as beam on nonlinear Winkler foundations using displaced p-y springs to model the ground deformation due to lateral spreading. The primary emphasis of the analyses will be to model the highway bridge that did not collapse.

6. CONCLUSIONS

Structural details of a pair of parallel bridges crossing the Colorado River are presented, with a description of their performance during the 2010 M_W 7.2 El Mayor-Cucapah Earthquake in Baja California, Mexico. The authors' proposed geotechnical site investigations and analyses are described. Results of the modeling will be reported in future publications.

Acknowledgements:

The authors acknowledge support from Dr. Raúl Flores Berrones of the Mexican Institute of Water Technology (IMTA) and Luis Humberto Ibarrola Diaz, General Director of Technical Services at SCT for assistance in obtaining the bridge plans and coordinating site activities.

References:

Ashford, S.A., Boulanger, R.W., and Brandenberg, S.J. (2011), "Recommended Design Practice for Pile Foundations in Laterally Spreading Ground," Pacific Earthquake Engineering Research Center, Report No. PEER 2011/04, 44 p.

Geotechnical Extreme Event Reconnaissance (GEER) (2010) Stewart, J., Brandenberg S. (eds). "Preliminary Report on Seismological and Geotechnical Engineering Aspects of the April 4 2010 M_w 7.2 El Mayor-Cucapah (Mexico) Earthquake", Report No. GEER-023, available: http://www.geerassociation.org/GEER_Post%20EQ%20Reports/Baja%20California_2010/Baja_Cover_2010.html

Hough, S. E. and A. Elliot (2004), "Revisiting the 23 February 1892 Laguna Salada Earthquake," *Bull. Seis. Soc. Amer.*, **94**(4), 1571-1578.

McKenna, F.T. (1997), "Object-Oriented Finite Element Programming: Frameworks for Analysis, Algorithms and Parallel Computing," PhD Thesis, Department of Civil

Engineering, University of California, Berkeley.
Meneses, J. (ed.), et al. (2010), "The El Mayor-Cucapah, Baja California Earthquake April 4, 2010, An EERI Reconnaissance Report," Earthquake Engineering Research Institute, Oakland, California. Available: http://www.eqclearinghouse.org/20100404-baja/general-information/eeri-recon-report
Secretaría de Comunicaciones y Transportes de México (SCT) (1998), "Puente San Felipito," Construction Plans, State Government of Baja California, Mexico, Ministry of Human Settlements and Public Works, Design by Sigma Ingenieria Civil S.A. de C.V., 6 sheets.
United States Geological Survey (USGS) (2010), "Magnitude 7.2 - Baja California, Mexico, 2010 April 04 22:40:42 UTC," Available: http://earthquake.usgs.gov/earthquakes/eqinthenews/2010/ci14607652/.

10CUEE CONFERENCE PROCEEDINGS
10th International Conference on Urban Earthquake Engineering
March 1-2, 2013, Tokyo Institute of Technology, Tokyo, Japan

NUMERICAL EVALUATION OF FAILURE MECHANISMS OF PILE FOUNDATION IN LIQUEFIABLE SOILS

Mohammad Reza Salami[1)], Katsuichiro Goda[1)], and Subhamoy Bhattacharya[2)]

1) Department of Civil Engineering, University of Bristol, United Kingdom
2) Division of Civil, Chemical and Environmental Engineering, University of Surrey, United Kingdom
cezms@bristol.ac.uk, katsu.goda@bristol.ac.uk, s.bhattacharya@surrey.ac.uk

Abstract: Traditionally, piles in seismic regions are designed to withstand horizontal loads caused by lateral spreading of liquefied soils. This is focused upon stability/safety of pile foundation against a bending failure mechanism, and is prevalent in current design codes. In contrast, recent research indicates that the bending mechanism cannot explain all historical cases of pile failure and suggests buckling failure as an alternative mechanism. A further investigation is warranted to evaluate potential failure mechanisms of piles in liquefiable soils. This study assesses dynamic behavior of liquefiable soils by using an advanced finite-element tool, which adopts a two-surface critical state plasticity sand model and implements a so-called *u-p* formulation to account for soil-fluid interaction and pore-pressure build-up realistically. Numerical simulation of pile failures (either due to bending or buckling) is conducted by considering different pile and soil parameters as well as different ground motions in terms of amplitude and frequency content. Moreover, temporal evolution of liquefaction at depth and time-varying effects of inertia and kinematic forces acting on piles are examined in detail. In general, parametric results indicate that slender end-bearing piles have potential to buckle, while in the same condition large-diameter piles remain safe against buckling (thus are likely to fail due to bending). The results are in agreement with field investigations and experimental test results.

1. INTRODUCTION

Pile foundation failure due to liquefaction was recognized as one of the most dramatic failure mechanisms of structures and bridges after the 1964 Niigata and 1995 Kobe earthquakes. Extensive investigations have been conducted to understand the main cause of pile failures (Tokimatsu *et al*., 1996, 1997; Hamada, 1992, 2000; Abdoun and Dobry, 2002). A well-established theory of pile failure is based on a bending mechanism, where lateral loads are induced by inertia of a superstructure due to ground shaking and lateral spreading of the surrounding soils. In this mechanism, piles are regarded as laterally-loaded beams, and several design criteria related to strength of piles (e.g. yield moment M_y and plastic moment capacity M_p) need to be checked to prevent bending failure of piles. For instance, the Japanese Highway code (JRA, 2002) adopted a concept of pile failure proposed by Ishihara (1997), known as 'top-down and bottom-up effects'. In this theory, in pre-liquefaction phase, the maximum bending moment along a pile is caused by inertia forces of a superstructure which are transferred to the pile head and eventually to soil (i.e. top-down effect). On the other hand, in post-liquefaction phase when pore pressure becomes excessive and soil stiffness drops dramatically, the effects due to the lateral spreading of liquefied sloped ground become dominant. In such situations, the maximum bending moment within the pile occurs at lower portion of the pile head (i.e. bottom-up effect).

The recent studies of piles embedded in liquefiable soils by Bhattacharya (2003), Knappett and Madabhushi (2005), and Kimura and Tokimatsu (2007) provided a new insight into a possible failure mechanism of piles. In cases soils surrounding a pile liquefy completely and the axially-loaded pile becomes unsupported laterally, piles may fail due to buckling. In other words, piles in liquefied soils may be better regarded as slender columns carrying axial and lateral loads, rather than laterally-loaded beams. The bucking mechanism depends on stiffness of a pile rather than strength. It could result in sudden instability, if the axial load approaches the critical value (P_{cr}), based on Euler's equation:

$$P_{cr} = \frac{\pi^2}{L_{eff}^2} EI \quad (1)$$

where L_{eff} is the effective length of the column, which depends on the length and boundary condition of the column ends, and EI is the column stiffness. The ground shaking increases pore pressure of saturated cohesion-less soils and thus effective stress of soils is decreased over the pile length. Consequently, soil skeleton loses resistance against shear and liquefied soils behave like liquid. This post-liquefaction phase renders piles laterally unsupported; with the increase of L_{eff}, piles become susceptible to buckling failure rapidly under axial loads (dead, live, and dynamic loads). It is noteworthy that the considerable force acting on structures is due to gravity; vertical load may be further amplified by ground shaking.

Recently, Bhattacharya *et al.* (2005) have proposed a simple safety assessment procedure against buckling. The assessment involves the comparison of two key parameters, critical depth of a pile against buckling (capacity) and laterally-unsupported length of a pile (demand). The former can be determined as a function of axial load, flexural stiffness, and pile boundary condition, while the latter is determined in terms of ground motion characteristics and soil profile. Furthermore, Bhattacharya and Goda (2013) have extended this procedure based on a probabilistic concept by taking into account uncertainty associated with input ground motion, liquefaction occurrence, and pile properties. The critical aspects of the procedure requiring further improvement include the effects of liquefied soils on piles in terms of lateral support and the temporal evolution of dynamic loads due to inertia with respect to liquefaction of the surrounding soils along the pile length. They have significant influence on the estimation of the critical depth of a pile against buckling.

In this study, pile bucking failure is investigated through numerical simulation of dynamic soil-pile behavior subjected to ground shaking. The focus is to provide better understanding of pile foundation failure (bending or buckling) in liquefiable soils; the key parameters involved are pile diameter, pile material, soil parameters, and ground shaking. For this, finite-element (FE) models of a single pile passing through liquefiable soils are developed (note: pile end is embedded into engineering bedrock and thus fixed). Two material types, concrete and steel, are considered for piles. Critical buckling loads of the concrete/steel piles are calculated based on Euler's buckling equation and three different masses, representing a superstructure, equivalent of $0.3P_{cr}$, $0.5P_{cr}$, and P_{cr}, are attached to the pile head to evaluate the effects of axial loads on pile performance before and after liquefaction. To account for nonlinear behavior of liquefied soils and soil-fluid interaction accurately, an advanced soil constitutive model by Dafalias and Manzari (2004), implemented in fully-coupled *u-p* elements, is adopted. Soil properties are varied by considering three different relative densities (Dr = 30%, 50%, and 80%). Depth of liquefaction and shear strength drop are assessed via FE simulations. This facilitates the better understanding of the buckling failure mechanism in comparison with previous studies (Bhattacharya *et al.*, 2005; Bhattacharya and Goda, 2013), where empirical equations were adopted to calculate the critical depth of liquefaction. Two ground motions with scaled ground acceleration amplitudes of 0.1g and 0.2g are used as input motion. They have different frequency content; thus the effects of ground motion characteristics on pile performance in liquefiable soils can be investigated. All FE models are three dimensional, and *P-Δ* effect of pile is considered. Prior to the simulations, numerical validation of the FE models is provided by considering dynamic centrifuge test data by Wilson (1998).

2. FINEITE ELEMENT AND SOIL CONSTITUTIVE MODELS

A fully-coupled *u-p* formulation is used to model soil skeleton and pore fluid interaction (Zienkiewich and Shiomi, 1984). In this formulation, variables are soil particle displacement *u* and pore fluid (water) pressure *p*. FE spatial discretization of *u-p* formulation for dynamic problems is given by:

$$\boldsymbol{M\ddot{U}} + \int_V \boldsymbol{B^T}\sigma' dV - \boldsymbol{QP} - \boldsymbol{f^{(s)}} = \boldsymbol{0} \tag{2}$$

$$\boldsymbol{Q^T\dot{U}} + \boldsymbol{HP} + \boldsymbol{S\dot{P}} - \boldsymbol{f^{(p)}} = \boldsymbol{0} \tag{3}$$

where $\boldsymbol{M}$ is the mass matrix, $\boldsymbol{U}$ is the solid displacement vector, $\dot{U}$ is the vector of relative velocity, $\ddot{U}$ is the vector of relative acceleration, $\boldsymbol{B}$ is the strain-displacement matrix, $\boldsymbol{\sigma'}$ is the effective stress tensor (derived from a soil constitutive model), and $\boldsymbol{Q}$ is the discrete gradient operator, coupling the motion and flow equations. $\boldsymbol{P}$ is the pore pressure vector, $\boldsymbol{S}$ is the compressibility matrix, and $\boldsymbol{H}$ is the permeability matrix. The vectors $\boldsymbol{f^{(s)}}$ and $\boldsymbol{f^{(p)}}$ represent the effects of external loads (and body forces) and fluxes, respectively. Newmark's algorithm is used to numerically solve the above equations, which is implemented in OpenSees (McKenna and Fenves, 2001).

Soil is a complex material that behaves non-linearly when subjected to large strain exceeding 10^{-5} (Hardin and Drnevich, 1972). It often shows anisotropic and time-dependent behavior. In addition, soil is hysteretic, behaving differently in primary loading, unloading, and reloading phases. Advanced soil constitutive models based on a concept of plasticity are able to capture important features of soil, such as nonlinearity, hardening, softening, anisotropy, pore water pressure generation, contraction, and dilation. To simulate liquefaction phenomena, a comprehensive material model proposed by Dafalias and Manzari (2004) is used; this is available from a University of California at Davis computational geomechanics toolset and is implemented in OpenSees. This model was originally proposed by Manzari and Dafalias (1997) as a two-surface critical state plasticity model for sand. It presents well-established mechanisms for predicting softening/hardening as well as dilative/contractive response of sand with different loose and dense states. The model has been updated by Dafalias and Manzari (2004). The new version incorporates the fabric-dilatancy tensor, which has a significant effect on the contractive unloading response. This version also takes into account the effect of a modified Lode angle associated with a flow rule, which produces more realistic response in non-triaxial stress conditions. The developed constitutive models and FE elements were validated extensively by Jeremic *et al.* (2008), Cheng and Jeremic (2009), and Shahir and Pak (2010). The model is well-calibrated for Nevada sand; typical model parameters are listed in Table 1. These material parameters are used throughout this study; an investigation of calibrating individual Dafalias-Manzari soil parameters for actual soil data is beyond the scope of this study.

Table 1 Dafalias-Manzari parameters for Nevada sand

Parameter	Symbol	Value
Elasticity	G_0	150
	ν	0.05
Critical state	M	1.14
	c	0.78
	λ_c	0.027
	e_0	0.83
	ξ	0.45
Yield surface	m	0.02
Plastic modulus	h_0	9.7
	c_h	1.02
	n^b	2.56
Dilatancy	A_0	0.81
	n^d	1.05
Fabric-dilatancy	z_{max}	5.0
	C_z	800

3. NUMERICAL MODEL VALIDATION

Dynamic centrifuge tests of pile-supported structures in liquefiable sand performed by Wilson (1998) are used to validate a developed FE model for a soil-pile system. The soil profile consists of two horizontal layers of saturated, fine uniformly graded Nevada sand. The lower dense layer (Dr = 80%) is 11.4 m thick, whereas the upper medium dense layer (Dr = 55%) is 9.1 m thick at the prototype scale. A highly-instrumented single steel pipe with a diameter of 0.67 m and wall thickness of 19 mm at the prototype scale is selected to model a pile. It is extended 3.8 m above the ground level and carries superstructure weight of 480 kN; the embedded length of the pile is about 16.8 m. A layout of the centrifuge test model is shown in Figure 1. The laminar box containing the soil-pile-superstructure system was spun at a centrifuge acceleration of 30g, and the pile remained elastic during the tests.

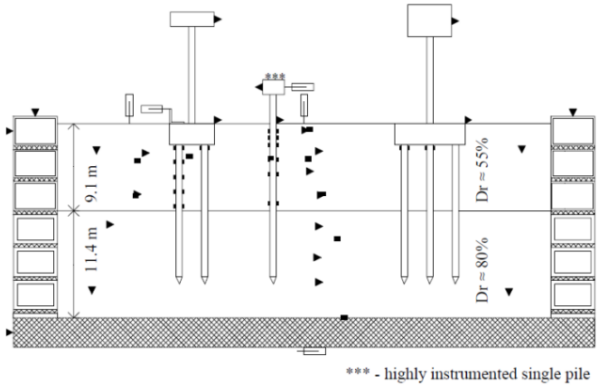


Figure 1 Layout of the centrifuge test model by Wilson (1998)

Figure 2 shows the schematics of FE meshes, consisting of 896 cubic eight-node soil elements and 16 beam-column elements. Each soil node has 4 degrees of freedom (DOFs), 3 for translation of soil skeleton and 1 for pore pressure, while the pile node has 6 DOFs. A beam-column element is used for the pile, and details of soil-pile nodal connection is shown in Figure 2, which was proposed by Cheng and Jeremic (2009). The physical modeling of the pile is implemented by using rigid connecting elements with the same material parameters of the pile. The beam-column elements connect each pile node to the surrounding nodes of a soil element at the same depth and transfer the forces from soil to pile and vice versa. Material parameters used in this validation are presented in Table 2. The modified 1995 Kobe acceleration record, scaled to peak acceleration of 0.22g, is used as a base input motion. Figure 3 shows the acceleration time history and Fourier amplitude of the input motion.

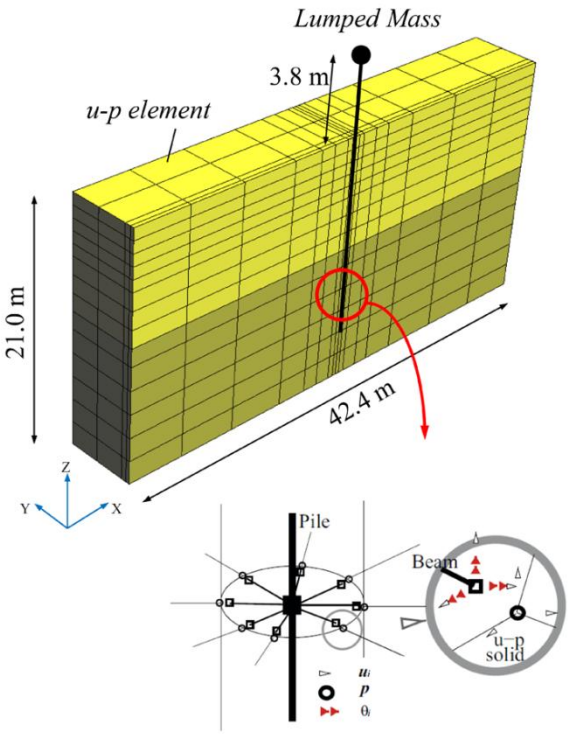


Figure 2 Finite-element mesh and diagram showing coupling of displacement DOFs of a beam-column element (pile) with displacement DOFs of *u-p* elements (soil).

Table 2 Material parameters for Nevada sand (Popesco and Prevost, 1993)

Parameter	Dr = 55%	Dr = 80%
Porosity	0.409	0.377
Saturated unit weight (kN/m^3)	19.87	20.41
Permeability coefficient (m/s)	6.05×10^{-5}	3.70×10^{-5}
Permeability coefficient at prototype scale (m/s)	1.82×10^{-4}	1.11×10^{-4}

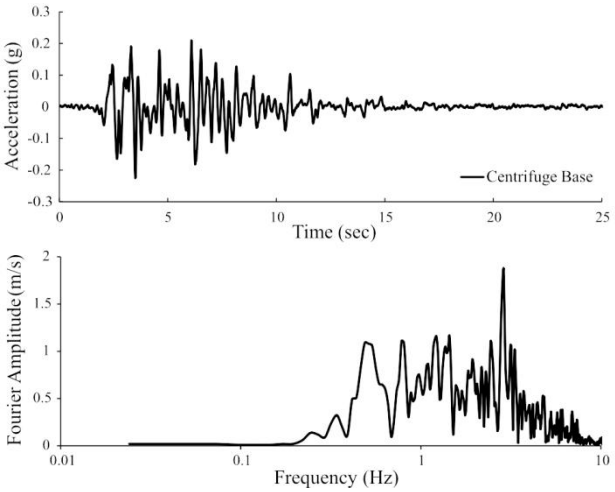


Figure 3 Acceleration time history (top) and Fourier amplitude (bottom) of the scaled Kobe record

Time histories of measured and computed acceleration of soils at different depths are presented in Figure 4. Generally, reasonable agreement between the test and simulation results is obtained, except for some spikes. It is well-known that liquefiable soil deposits show a pronounced reduction in high-frequency amplitude and increase low-frequency amplitude following the initial liquefaction. The change in frequency content corresponds to the dramatic reduction in soil stiffness and strength. However, ground motion data and soil experiments often show several isolated spikes of high acceleration. The spikes can be attributed to the influence of dilated soil above the phase transformation line (i.e. soil is stiffened), increasing transmission of high frequency motions. This also leads to the constructive interference of waves traveling upward through the liquefied soil; the resulting waves have been termed de-liquefaction shock waves (Kutter and Wison, 1999). Considering the fact that the Dafalias-Manzari model is highly dependent on position of the phase transformation line, it may overestimate the soil strength and stiffness near this line. This may be the reason for the differences between simulation and experiments, and suggests that further improvements are necessary in soil constitutive modeling.

Figure 5 shows time histories of measured and computed excess pore pressure ratios at approximately the same depths as in Figure 4. The excess pore pressure ratio (r_u) is defined as the ratio of the difference of current pore pressure and hydrostatic pore pressure over the initial effective vertical stress: $r_u = \Delta u/\sigma'_{v0}$. Comparison of the results shows that the FE model is capable of simulating the experiment accurately, except at the depth of 5 m. In the current study, permeability is considered to be constant during liquefaction, although in reality, it varies due to changes in soil skeleton; in some cases it increases up to 6-7 times greater than its initial value. The difference between the experimental and numerical results may be related to the constant value of permeability used in the analysis, noting that a variable permeability can improve the numerical prediction of excess pore pressure as well as lateral/vertical soil displacement (Rahmani and Pak, 2012).

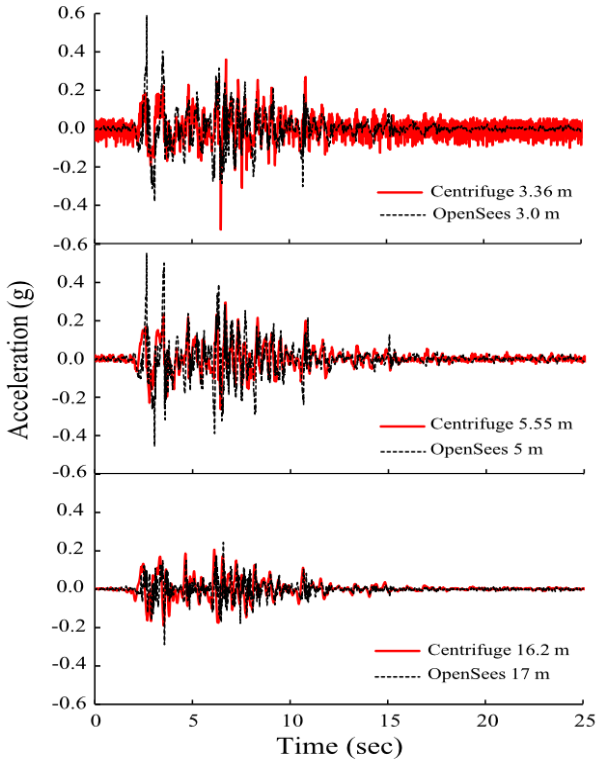


Figure 4 Comparison of simulated and measured acceleration time histories of soils at about 3 m depth (top), about 5 m (middle) and about 17 m depth (bottom)

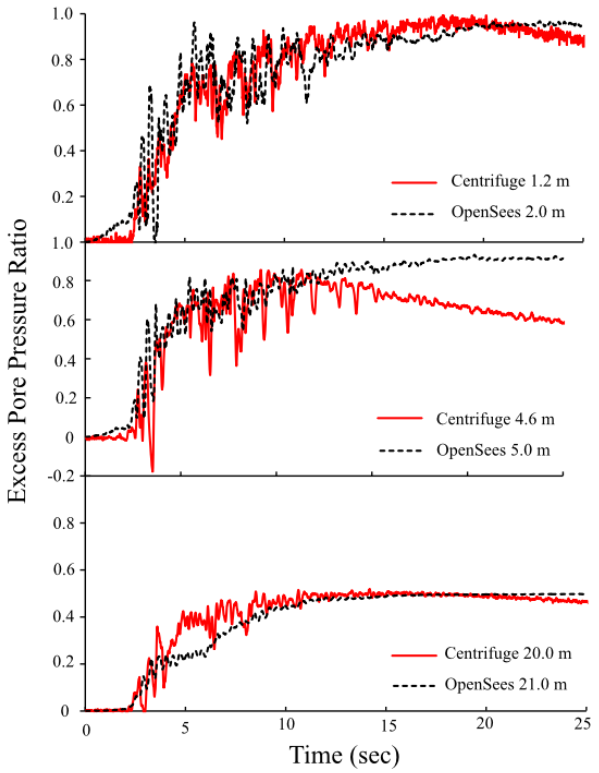


Figure 5 Comparison of time histories of simulated and measured excess pore pressure ratios at about 2 m depth (top), about 5 m (middle) and about 20 m depth (bottom)

Finally, Figure 6 shows time histories of computed and measured acceleration responses of the superstructure. The FE model is capable of predicting acceleration responses of the superstructure accurately, especially for the first few cycles (before full liquefaction). The differences between the experiment and simulation are due to temporary increase in soil stiffness, which results in large acceleration spikes transmission from ground to superstructure.

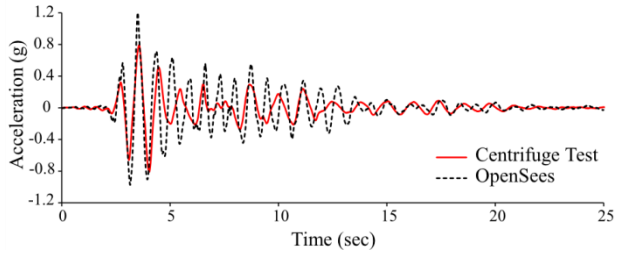


Figure 6 Comparison of time histories of simulated and measured acceleration response of superstructure

4. PARAMETRIC ANALYSIS FOR PILE FOUNDATION FAILURE MECHANISM

To investigate a pile failure mechanism in detail (e.g. temporal evolution of liquefaction at depth and time-varying effects of inertia and kinematic forces acting on piles), a parametric study is carried out by developing FE models for a pile foundation, surrounded by saturated liquefiable soils. In particular, the focus is given to axial load carried by pile, properties of pile and soil, and ground motion characteristics.

4.1 Model Set-up

A two-layer soil system is considered; a top layer represents liquefiable soil with Dr = 30% or 50%, while a bottom layer represents dense sand with Dr = 80%, providing sufficient fixity for the pile end. A single pile of 25 m long is considered with 4 m above the ground surface and 21 m below the surface. For the embedded pile part, 4 m of the pile is in the dense bottom layer and 17 m of the pile passes through the loose liquefiable layer. Figure 7 shows the geometry of the adopted model and pile boundary condition. In the FE model, soil parameters for Nevada sand (Table 1) are used. Parameter values for porosity, density, permeability, and $(N_1)_{60}$ from standard penetration tests (SPT) are listed in Table 3. Two pile material types, concrete and steel, with different diameters of 0.5 and 1.0 m are considered in the analysis. Euler's elastic buckling load P_{cr} is calculated for each case. To investigate pile performance under different axial loads, the equivalent mass on the tip of the pile, representing a superstructure, is adjusted such that the corresponding axial loads equal the critical buckling load multiplied by a factor of 0.3, 0.5, and 1.0. *P-Δ* effect is taken into account in the analysis and all models are three dimensional with 1020 *u-p* elements. The pile properties, used in the FE models, are summarized in Table 4. The values resemble materials used in practice closely. Ground motion characteristics, such as maximum acceleration amplitude and frequency, have significant effects on pile (Carvajal *et al.*, 2002; Rahmani and Pak, 2012). Two ground motions with different dominant frequencies and scaled peak acceleration of 0.1g and 0.2g are considered in the parametric analysis. Table 5 provides a summary of the two ground motion records, while Figure 8 shows unscaled input ground motion acceleration time histories and their Fourier amplitude spectra.

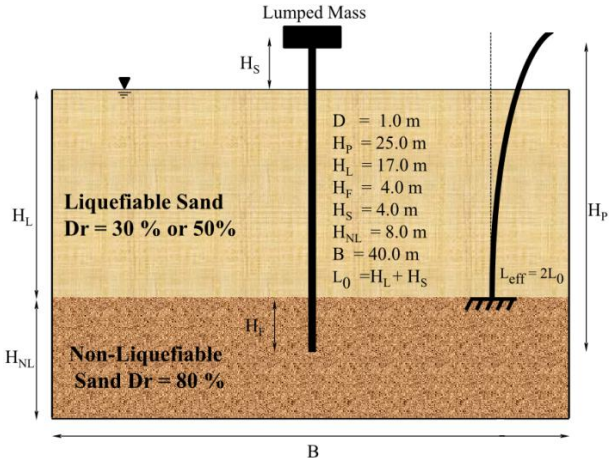


Figure 7 Schematic diagram of soil-pile system used in the parametric study

Table 3 Material parameters for Nevada sand

Parameter	Dr = 30%	Dr = 50%	Dr = 80%
Porosity	0.438	0.415	0.370
Saturated unit weight (kN/m^3)	19.38	19.98	20.05
Permeability coefficient (m/s)	7.5×10^{-5}	5.9×10^{-5}	3.7×10^{-5}
$(N_1)_{60}$	4	11	28

Table 4 Pile properties for parametric analysis

Properties	Concrete pile		Steel pipe (16 mm-thick)	
Diameter (m)	0.5	1.0	0.5	1.0
Density (kg/m^3)	2500		7800	
Flexural strength f_y (kPa)	1.78×10^4		5.0×10^5	
Modulus of elasticity E (kPa)	2.96×10^7		2.1×10^8	
Yield moment M_y (kNm)	215	1740	1400	6000
Moment of inertia I (m^4)	0.003	0.049	0.0007	0.006
Cross section area (m^2)	0.196	0.785	0.024	0.049

Table 5 Ground motion data for parametric analysis

Earthquake	Station	M_w	Dominant frequency (Hz)
1995 Kobe	Port Island	6.93	3.0
1999 Kocaeli	Duzce	7.5	0.3

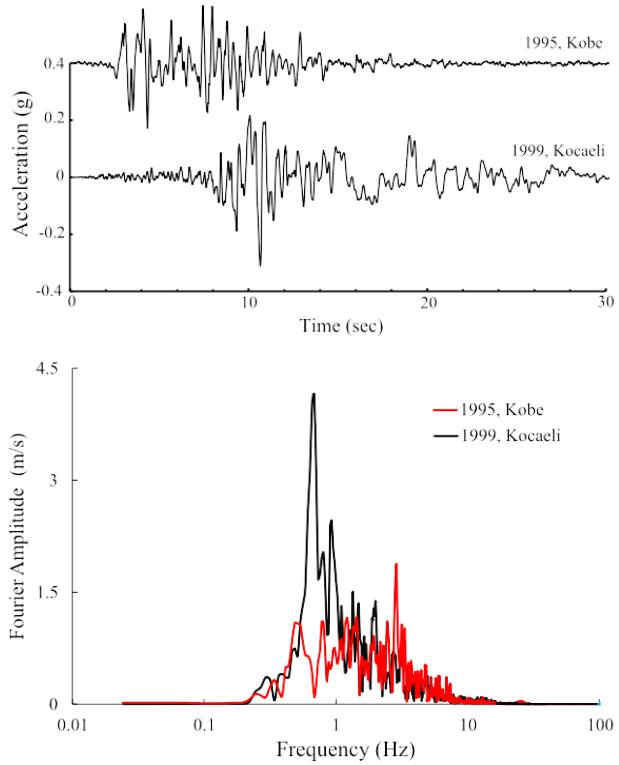


Figure 8 Acceleration time histories (top) and Fourier amplitude (bottom) of the input ground motions

4.2 Soil Residual Strength

In this section, it will be shown that pile buckling in liquefiable sands occurs if the shear strength around the pile, subject to significant axial load, drops remarkably to a negligible value (i.e. loss of lateral support).

To calculate P_{cr}, the unsupported length of the pile (liquefaction depth H_L in Figure 7) needs to be calculated. Depth of liquefaction could vary depending on the relative density of soil and input acceleration.

Figure 9 shows the temporal changes of acceleration, excess pore pressure ratio (r_u), and shear strength at depths of 2, 6, and 10 m for the scaled Kobe record with the peak amplitude of 0.2g. By considering post-liquefaction as a condition where the excess pore pressure reaches 1.0, undrained residual strength of soil drops dramatically to a negligible value, leading to an unsupported pile condition. The post-liquefaction phase is identified and distinguished by a red line in Figure 9. It is noted that post-liquefaction starts at different times over depth of the pile, generally, from shallower to deeper layers.

Evaluating undrained residual strength of liquefied soils is a challenging issue in geotechnical engineering, as it involves the complex nonlinear soil behavior due to dynamic loading. Numerous investigations have been conducted to assess in-situ undrained residual strength (S_r). For example, Seed (1986) proposed a method for evaluating in-situ undrained residual strength based on SPT. He presented the results of back-analysis of several liquefaction failure case histories from which values of S_r were estimated for sites with available SPT data. The empirical correlation between S_r and $(N_1)_{60}$ is shown in Table 6. He also proposed that owing to the limited number of case studies and uncertainty associated with available information, the lower-bound of the curves should be considered. Cyclic stress-strain curves derived from FE analysis (Figure 9) show that for the specific case, the residual undrained shear strength at various depths drops near zero at post-liquefaction phase (i.e. red line); for comparison, the broken horizontal lines corresponding to S_r = +/-5 kPa are included in the stress-strain plots. This result is in agreement with the correlation of SPT data with residual undrained strength (i.e. lower bound case in Table 6). It can be concluded that a liquefiable soil deposit has potential to lose its strength and consequently piles in liquefied soils are forced to carry axial and inertial loads without sufficient lateral support from the surrounding soils.

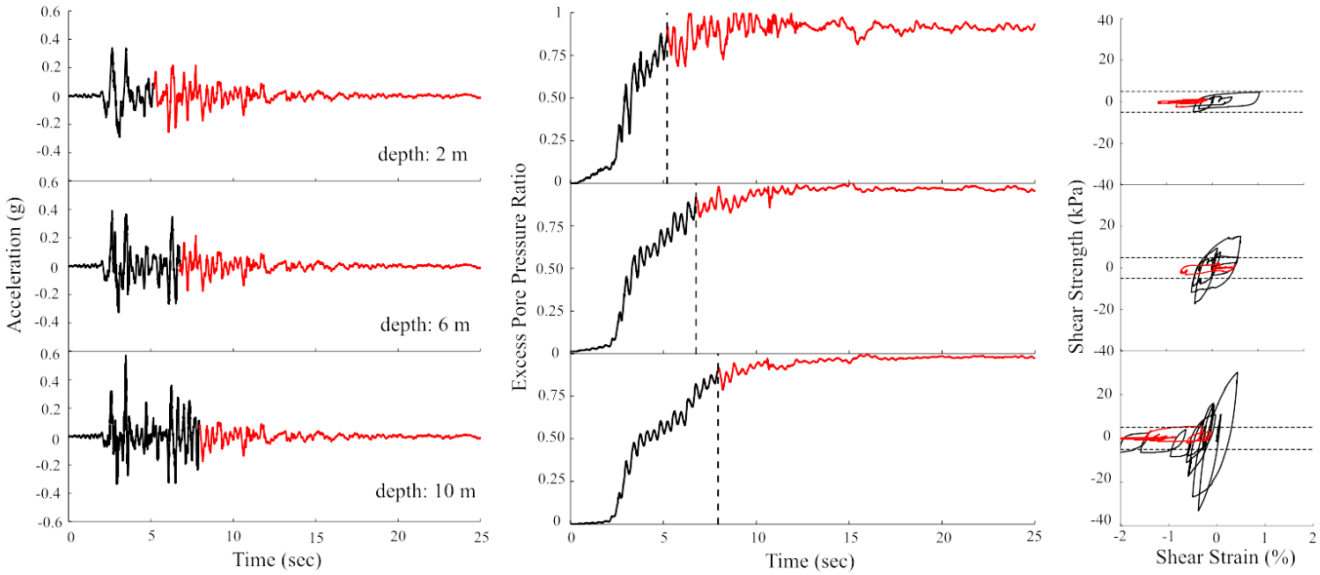


Figure 9 Acceleration time history (left), excess pore pressure ratio (center), and shear stress-strain relationship (right) at three depths (2, 6, and 10 m) for the 0.5 m concrete pile subject to the Kobe ground motion, scaled to 0.2g

Table 6 Recommended undrained residual strength (S_r) (Seed and Harder, 1990)

SPT-based N value $(N_1)_{60}$	Shear strength (kPa)	
	Upper bound	Lower bound
4	11	0
8	20	2
12	32	10
16	-	25

4.3 Buckling Analysis Results

Having reliable estimates of the unsupported length of the pile, bending and buckling criteria can be checked. Timoshenko and Gere (1961) showed that in analyzing stability of elastic columns, lateral displacement caused by lateral loads is greatly amplified in the presence of axial loads. If δ_0 is the displacement of a cantilever column due to lateral loads alone, the final displacement δ is amplified due to axial load (P) by the following expression:

$$\frac{\delta}{\delta_0} = \frac{1}{\left(1-\frac{P}{P_{cr}}\right)} \quad (4)$$

Figure 10 shows amplification of lateral displacement of a column due to applied axial loads. It is evident that for P/P_{cr} = 0.33 (i.e. ratio of the applied axial load to Euler's elastic buckling load), the lateral displacement amplification is almost twice of static lateral displacement due to lateral loads alone. For axial loads exceeding $P/P_{cr} \geq 0.33$, the failure mechanism is likely to be governed by buckling. Considering this criterion, three ratios of applied axial loads to Euler's elastic buckling load are considered in the parametric analysis; the case with P/P_{cr} = 0.3 is regarded as safe against buckling, while the cases with P/P_{cr} = 0.5 and P/P_{cr} = 1.0 may be unsafe, if the top soil layer is fully liquefied. It is also noteworthy that the applied axial loads in this study do not take into account dynamic inertia effects caused by superstructure mass (note: dynamic response of the superstructure affects pile and soil responses significantly and is taken into account). Such dynamic effects can be included in the assessment by using a rigid base foundation with multiple pile rows (such that lateral motions of a superstructure are transformed into dynamic axial forces along the piles).

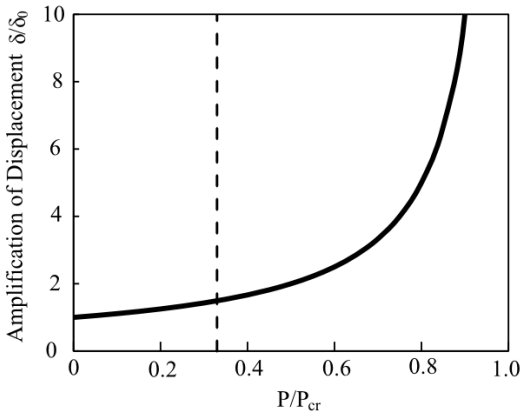


Figure 10 Amplification of lateral displacement versus normalized axial load

In addition to buckling failure mode, bending failure may occur when the maximum bending moment along the pile exceeds the yield moment of pile, ($M_{max}/M_Y \geq 1.0$). Table 4 shows the yield moment capacity for each pile. Therefore, bending-buckling interaction could occur, if both criteria are exceeded ($M_{max}/M_Y \geq 1.0$ and $P/P_{cr} \geq 0.33$), whereas the designed pile may be judged as safe if $P/P_{cr} < 0.33$ and $M_{max}/M_Y < 1.0$.

Figure 11 shows bending moment, shear force, and displacement diagrams of the 0.5 m concrete pile due to the Kobe record with the maximum acceleration scaled to 0.2g. The yield moment for this case is 215 kNm (Table 4). The predominant failure mechanism for two cases ($P = 0.5P_{cr}$ and $P = P_{cr}$) are due to bending-buckling interaction (i.e. $M_{max}/M_Y \geq 1.0$ and $P/P_{cr} \geq 0.33$). The plastic hinge is placed at about 1.0 m below the ground level where the maximum bending moment occurs along the pile. The maximum bending moment along the pile increases dramatically with greater applied axial forces. The pile with $P = 0.3P_{cr}$ is considered to be safe both under the bending and buckling criteria ($M_{max}/M_Y < 1.0$ and $P/P_{cr} < 0.33$). However, if dynamic effects due to superstructure are included, the buckling failure mechanism might be developed. Figure 11 also provides a comparison between kinematic soil-pile interaction (red line) and inertia interaction. Kinematic pile response in liquefaction is significantly different from inertia interaction, especially in terms of maximum value, location, and occurrence timing. In kinematic interaction, pile follows the imposed movement of liquefied soils, thus the maximum bending moment and shear force may dominates during post-liquefaction phase at greater depth.

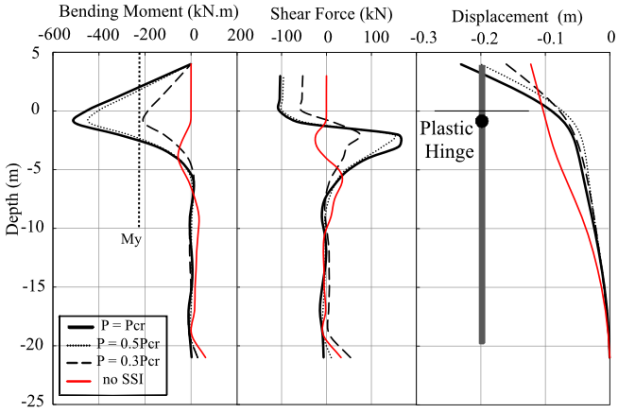


Figure 11 Bending moment (left), shear force (center), and displacement (right) of the 0.5 m concrete pile subject to the Kobe ground motion, scaled to 0.2g

4.4 Effects of pile properties and input ground motions

The detailed analysis of pile foundation failure mechanisms was presented in the previous two subsections for the 0.5 m concrete pile subjected to the Kobe record, scaled to 0.2g. In this subsection, to draw general observations/conclusions, more results are discussed by considering different pile properties and input ground motions (Tables 4 and 5).

Figure 12 shows the bending-buckling interaction diagrams for the 1999 Kocaeli and 1995 Kobe records, scaled to 0.1g and 0.2g, for 0.5 m and 1.0 m concrete and steel piles. The bending-buckling diagram plots a data point of M_{max}/M_Y and P/P_{cr} from numerical simulation of a specific analysis case (in terms of pile property and input ground motion), and is useful to identify a possible failure mode of a pile foundation. Based on the values of M_{max}/M_Y and P/P_{cr}, four domains are identified: safe domain for $M_{max}/M_Y < 1.0$ and $P/P_{cr} < 0.33$; buckling failure domain for $M_{max}/M_Y < 1.0$ and $P/P_{cr} \geq 0.33$; bending failure domain for $M_{max}/M_Y \geq 1.0$ and $P/P_{cr} < 0.33$; and buckling-bending failure domain for $M_{max}/M_Y \geq 1.0$ and $P/P_{cr} \geq 0.33$.

Figure 12(a) shows a bending-buckling interaction diagram of steel and concrete piles for the Kocaeli record with different peak acceleration amplitudes. Generally, the maximum bending moment of piles increases by applying greater axial loads (i.e. higher ratios of P/P_{cr}). This is due to elastic instability (buckling) and *P-Δ* effect. The bending capacity of a pile can be remarkably improved by increasing the flexural strength (using steel instead of concrete). However, the capacity against buckling failure is not changed significantly because it is related to the geometry of pile section. Reliable estimation of possible pile failure modes facilitates the effectiveness in seismic design of piles in liquefiable soils (i.e. selecting an appropriate combination of material strength and pile cross-section property to avoid bending and buckling failure modes). It is also noted that ground motion acceleration amplitude can have significant influence on pile performance; higher acceleration increases the inertia forces acting on pile and results in a higher maximum bending moment along the pile.

Figure 12(b) shows a bending-buckling interaction diagram for the 0.5 m concrete pile subject to two input ground motions with different peak acceleration amplitudes. It can be observed that variability of the results is significant (although the sample size of the input records is rather small). As the liquefaction induces dramatic changes of the soil properties (Figure 9), the frequency content of the input ground motion is likely to have significant influence. Different dynamic forces may be caused within pile, depending on the natural frequency of a pile-superstructure system and the properties of liquefied soils. Rigorous assessment of the bending-buckling failure modes in terms of ground motion characteristics is warranted.

Finally, Figure 12(c) represents a bending-buckling interaction diagram of concrete piles with different diameters (0.5 m and 1.0 m) subjected to the Kocaeli record (scaled to 0.1g). The result indicates that two curves for different pile diameters in the bending-buckling interaction diagram are similar. This is because in the current analysis set-up, the superstructure mass at the pile tip is determined such that a certain ratio of the axial force in terms of the critical buckling load is achieved. It is noteworthy that in real situations, the thick pile (1.0 m) has Euler's elastic buckling load 16 times greater than the slender pile (0.5 m). Hence, the result shown in Figure 12(c) may be interpreted that the pile buckling failure in liquefiable soils is less likely by using a thicker pile.

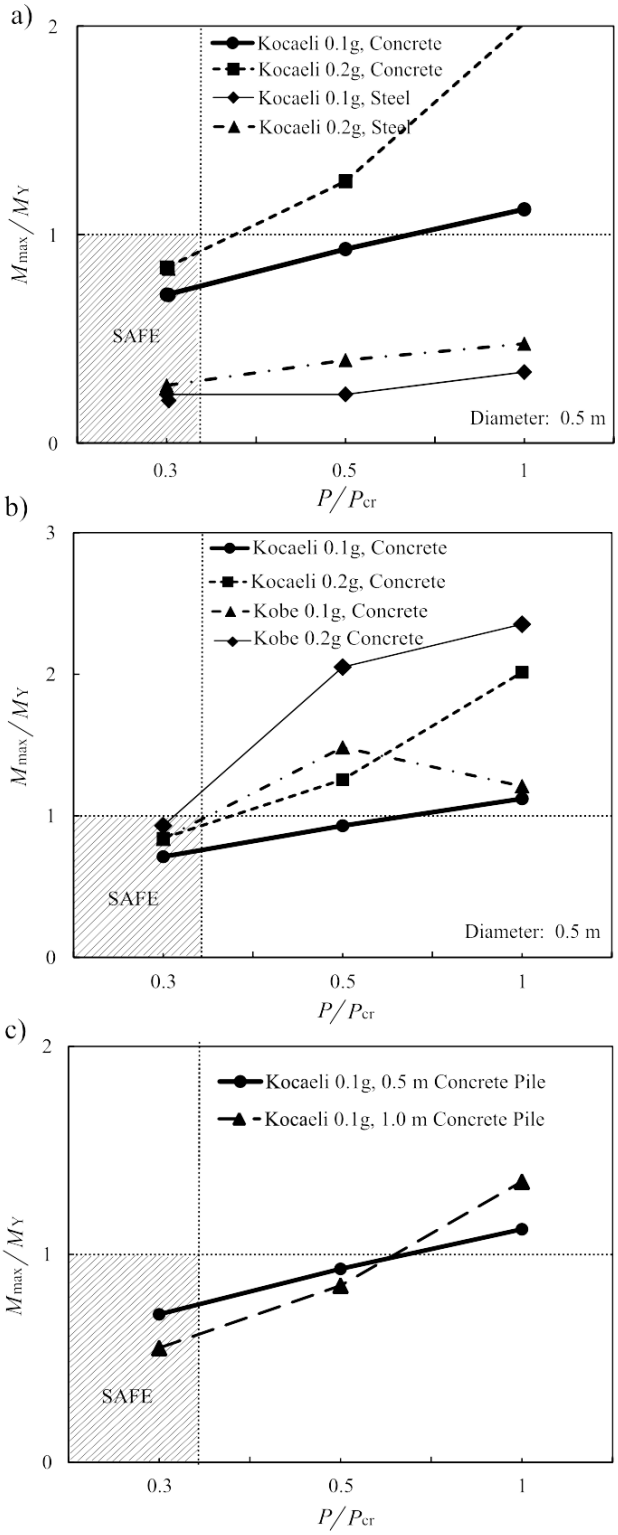


Figure 12 Bending-buckling interaction diagrams of concrete and steel piles due to the 1999 Kocaeli and 1995 Kobe records, scaled to 0.1g and 0.2g

5. CONCLUSIONS

In this paper, failure mechanisms of slender end-bearing pile in

liquefiable soils were evaluated. Historical evidences, experimental tests, and numerical results have shown that laterally unsupported piles could fail in buckling, in cases where axial loads on the pile exceed a certain fraction of Euler's critical buckling load (a factor of 0.33 is adopted in this study). Moreover, a combination of bending and buckling could be a plausible cause for actual failure mechanism of pile foundation due to liquefaction. The analysis showed that the maximum acceleration amplitude, frequency content, and pile stiffness have significant influence on the failure mechanism. Consideration of different boundary conditions of a pile, dynamic effects of superstructure inertia on axial forces, and various input ground motions is worthy of further investigations. Based on the results obtained in this study, it is recommended that the elastic instability of slender piles in liquefiable soils should be checked in addition to bending failure to achieve a safe and reliable seismic design of pile foundation.

6. REFERENCES

Abdoun, T.H., Dobry, R. (2002), "Evaluation of pile foundation response to lateral spreading," *Soil Dynamics and Earthquake Engineering*, **22**(8):1051–1058.

Bhattacharya, S. (2003), "Pile instability during earthquake liquefaction," *PhD Thesis*, University of Cambridge, Cambridge, United Kingdom.

Bhattacharya, S., Bolton, M.D., Madabhushi, S.P.G. (2005), "A reconsideration of the safety of the piled bridge foundations in liquefiable soils," *Soils and Foundation*, **45**(4):13–26.

Bhattacharya, S., Goda, K. (2013), "Probabilistic buckling analysis of axially loaded piles in liquefiable soils," *Soil Dynamics and Earthquake Engineering*, **45**(2):13–24.

Carvajal, J.C., Taboada-Urtuzuastegui, V.M., Romo, M.P. (2002), "Influence of earthquake frequency content of soil dynamic properties at CAO site," *Soil Dynamics and Earthquake Engineering*, **22**(4):297–308.

Cheng, Z., Jeremic, B. (2009), "Numerical modeling and simulation of pile in liquefiable soil," *Soil Dynamics and Earthquake Engineering*, **29**(11):1405–1416.

Dafalias, Y.F., Manzari, M.T. (2004), "Simple plasticity sand model accounting for fabric change effects," *Journal of Engineering Mechanics*, **130**(6):622–634.

Hamada, M. (1992), "Large ground deformations and their effects on lifelines: 1964 Niigata earthquake," *Technical Report NCEER, 92–0001, National Centre for Earthquake Engineering Research*, Buffalo, NY, United States of America.

Hamada, M. (2000), "Performances of foundations against liquefaction-induced permanent ground displacements," In: *Proceeding of the 12th World Conference on Earthquake Engineering*, Auckland, New Zealand, Paper 1754.

Hardin, B.O., Drnevich, V.P. (1972). "Shear modulus and damping in soils: measurement and parameter effects," *Journal of Soil Mechanics and Foundations Division*, **98**(6):603–624.

Ishihara, K. (1997), "Terzaghi oration: geotechnical aspects of the 1995 Kobe earthquake," In: *Proceeding of International Conference on Soil Mechanics and Geotechnical Engineering, Hamburg*, Germany, 2047–2073.

Jeremic, B., Cheng, Z., Taiebat, M., Dafalias, Y.F. (2008), "Numerical simulation of fully saturated porous materials," *International Journal for Numerical and Analytical Methods in Geomechanics*, **32**(13):1635–1660.

JRA (2002), "Specification for highway bridges: part V - seismic design," *Japanese Road Association*, Tokyo, Japan.

Kimura, Y., Tokimatsu, K. (2007), "Buckling stress of slender pile with lateral displacement at the pile head in liquefied soils," *Journal of Structure and Construction Engineering*, **617**:169–175.

Knappett, J.A., Madabhushi, S.P.G. (2005), "Modelling of liquefaction-induced instability in pile groups," In: *ASCE Geotechnical Special Publication No 145 on Seismic Performance and Simulation of Pile Foundations in Liquefied and Laterally Spreading Ground*, University of California, Davis, California, United States, 255–267.

Kutter, B.L., Wilson, D.W. (1999), "De-liquefaction shock waves," In *Proceeding of 7th U.S.-Japan Workshop on Earthquake Resistant Design of Lifeline Facilities and Countermeasures against Soil Liquefaction*, Seattle, WA, United States of America, 295–309.

Manzari, M.T., Dafalias, Y.F. (1997), "A critical state two-surface plasticity model for sands," *Geotechnique*, **47**(2):255–272.

McKenna, F., Fenves, G.L. (2001), "The OpenSees command language manual: version 1.2," PEER Center, University of California at Berkeley, Berkeley, CA, United States of America.

Popescu, R., Prevost, J.H. (1993), "Centrifuge validation of a numerical model for dynamic soil liquefaction," *Soil Dynamics and Earthquake Eng*ineering, **12**(2):73–90.

Rahmani, A., Pak, A., (2012), "Dynamic behavior of pile foundation under cyclic loading in liquefiable soils," *Computers and Geotechnics*, **40**(3):114–126.

Seed, H.B. (1986), "Design problems in soil liquefaction," *Journal of Geotechnical Engineering*, **113**(8):827–845**.**

Seed, R.B., Harder, L.F. (1990), "SPT-based analysis of cyclic pore pressure generation and undrained residual strength," In: *Proceeding of the H.B. Seed Memorial Symposium*, Bi-Tech Publishing Ltd, **2**:351–391.

Shahir, H., Pak, A. (2010), "Estimation of liquefaction-induced settlement of shallow foundations by numerical approach," *Computers and Geotechnics*, **37**(3):267–279.

Timoshenko, S.P., Gere, J.M. (1961), "Theory of elastic stability," *McGraw-Hill*, New York, NY, United States of America.

Tokimatsu, K., Mizuno, H., Kakurai, M. (1996), "Building damage associated with geotechnical problems," *Soils and Foundations*, Special Issue 1:219–234.

Tokimatsu, K., Ohoka, H., Satake, K., Shamoto, Y., Asaka, Y. (1997), "Failure and deformation modes of piles due to liquefaction-induced lateral spreading in the 1995 Hyogoken-Nanbu earthquake," *Journal of Structural and Construction Engineering*, **495**:95–100.

Wilson, D.W. (1998), "Soil pile superstructure interaction in liquefying sand and soft clay," *Ph.D. Thesis*, University of California at Davis, Davis, CA, United States of America.

Zienkiewicz, O.C., Shiomi, T. (1984), "Dynamic behaviour of saturated porous media; the generalized Biot formulation and its numerical solution," *International Journal for Numerical Methods in Engineering*, **8**(1):71–96.

10CUEE CONFERENCE PROCEEDINGS
10th International Conference on Urban Earthquake Engineering
March 1-2, 2013, Tokyo Institute of Technology, Tokyo, Japan

LIQUEFACTION-INDUCED GROUND DEFORMATION OBSERVED AT GOHNO-IKE POND IN KAMISU CITY DURING 2011 GREAT EAST JAPAN EARTHQUAKE

Shigeru Kanemitsu[1], Yoshimichi Tsukamoto[2], and Shohei Kawabe[3]

1) Graduate student, Department of Civil Engineering, Tokyo University of Science, Japan
2) Professor, Department of Civil Engineering, Tokyo University of Science, Japan
3) Assistant professor, Department of Civil Engineering, Tokyo University of Science, Japan
j7612610@ed.tus.ac.jp, ytsoil@rs.noda.tus.ac.jp, s-kawabe@rs.tus.ac.jp

Abstract: The earthquake reconnaissance investigations were carried out at one of the illustrative sites where the soil liquefaction induced ground deformation of cracks and subsidence as well as sand boils was observed at Gohno-ike Pond of Kamisu city during 2011 Great East Japan Earthquake. A series of Swedish weight sounding tests were carried out at this site, and the soil profiles were estimated. It was found that soil liquefaction must have occurred within the reclaimed deposits overlying the soft sedimentary "pond-bed" soil deposits.

1. INTRODUCTION

Soil liquefaction induced during 2011 Great East Japan Earthquake left a numerous number of scars on the ground surfaces, causing damages to lifelines, infrastructures and residential houses. Most of the ground failures were found associated with soil liquefaction, in Kanto region including metropolitan Tokyo. The authors' research group visited frequently to the liquefaction affected areas, and conducted a multiple series of field Swedish weight sounding tests at the areas located along the lower stream of Tonegawa river, including Sawara of Katori city, Hinode of Itako city, and Fukashiba of Kamisu city, (Tsukamoto et al. 2012a&b, Kawabe et al. 2012).

One of the illustrative sites that the authors had investigated was located at Gohno-ike pond in Kamisu city. When the authors' research group visited this site on October 14 to 16, 2011, the clear indications of soil liquefaction induced ground deformation of cracks and subsidence as well as sand boils were observed. The authors' research group decided to visit this site again on November 21 to 23, 2012, to reexamine the effects of soil liquefaction, and conducted a series of Swedish weight sounding tests. The results of the field investigations are described below.

2. SITE INVESTIGATION

Kamisu city is located at the lower stream area of Tonegawa river, as shown in Fig. 1, and is one of the areas seriously affected by soil liquefaction. The shaded zones indicated in Fig. 2 show the areas affected by soil liquefaction in Kamisu city. At the bottom-right side of Fig. 2 is located Gohno-ike pond. From the comparison with the old map of the 1880's shown in Fig. 3, (Tonegawa River Lower Stream Office 2011), the round shaded zone of soil liquefaction at the bottom-right side of Fig. 2 coincides with the old Gohno-ike pond. The old Gohno-ike pond was

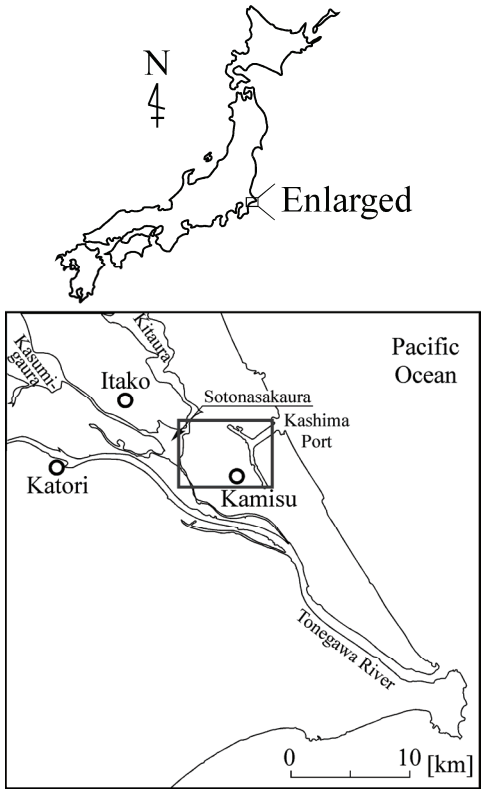


Figure 1 Location of Kamisu city

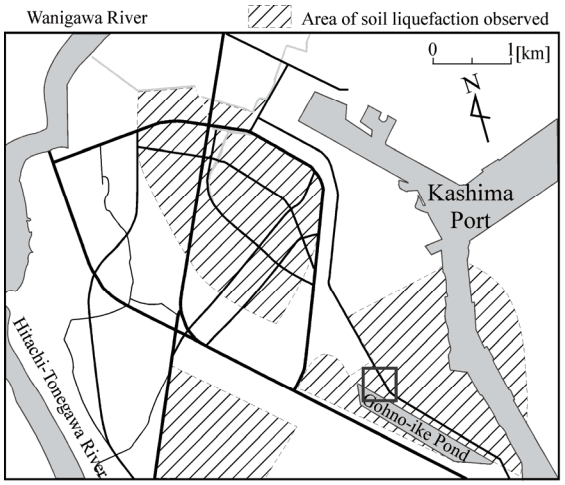


Figure 2 Location of Gohno-ike pond of Kamisu city

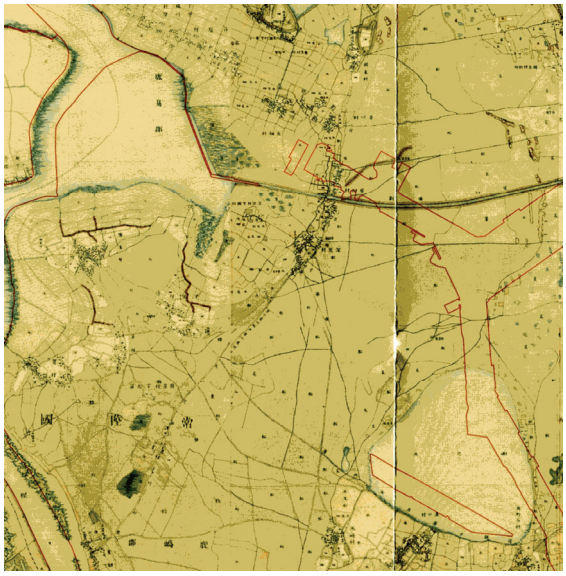


Figure 3 Old map of 1880's locating the current Gohno-ike pond, (after TRLSO 2011), (Red lines indicate current waterside lines.)

reclaimed for development of nearby industrial estates in 1969, and the current Gohno-ike pond was formed.

The authors' research group visited this area on October 14 to 16, 2011, and investigated the effects of soil liquefaction on the reclaimed land. At the foot of the steel tower for high-voltage electric cables can be observed a series of cracks on the ground surface, as shown in Fig. 4. In addition, the ground subsidence was also observed as shown in Fig. 5. At the walking street relatively close to the steel tower can be seen some remains of sand boils, as shown in Fig. 6. Some sand boils were also found near the current Gohno-ike pond, as shown in Fig. 7. The positions of ground cracks and subsidence as well as sand boils are indicated in the plan view of this area, as shown in Fig. 8.

3. SWEDISH WEIGHT SOUNDING TESTS

A series of Swedish weight sounding (SWS) tests were carried out at this area when the authors' research group



Figure 4 Cracks observed near the pylon



Figure 5 Subsidence observed near the pylon



Figure 6 Sand boils observed on the reclaimed hill



Figure 7 Sand boils observed near Gohno-ike pond

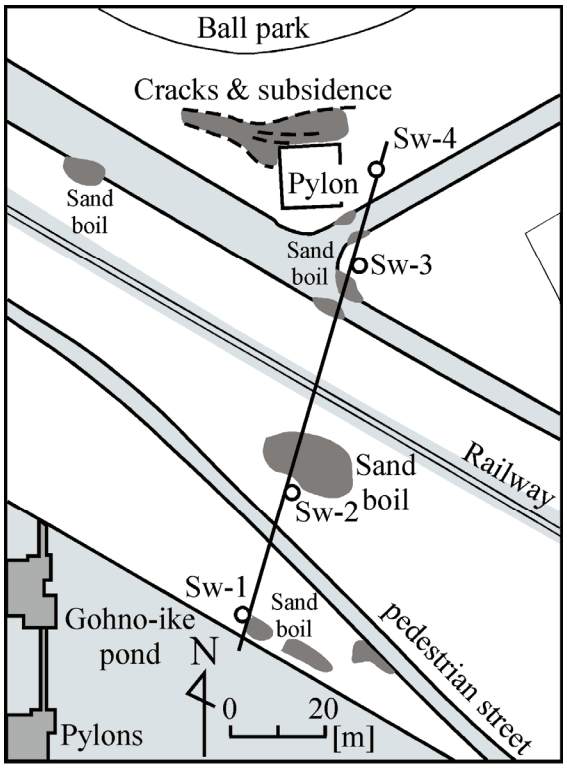


Figure 8 Location of SWS tests and ground deformation

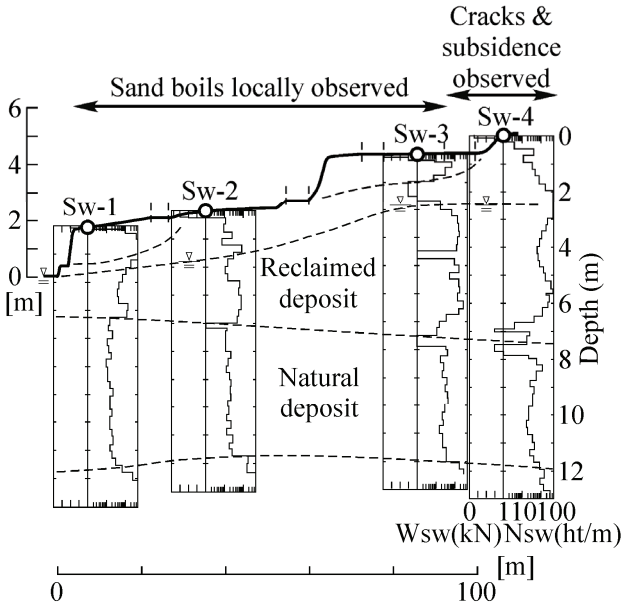


Figure 9 Results of SWS tests and estimated soil profile

revisited this site on November 21 to 23, 2012. The positions of SWS tests are shown in Fig. 8. The details of the testing equipment and procedure and the data reduction for SWS tests are described by Tsukamoto et al. (2004) and Tsukamoto (2009).

The results of SWS tests are summarized as a cross section, as shown in Fig. 9. The groundwater level was not monitored during the SWS tests, and the estimated level of the groundwater is shown in Fig. 9. The reclaimed deposit might be found overlying the loose "old pond"-bed deposit, which should have been reclaimed in 1969. The area that the

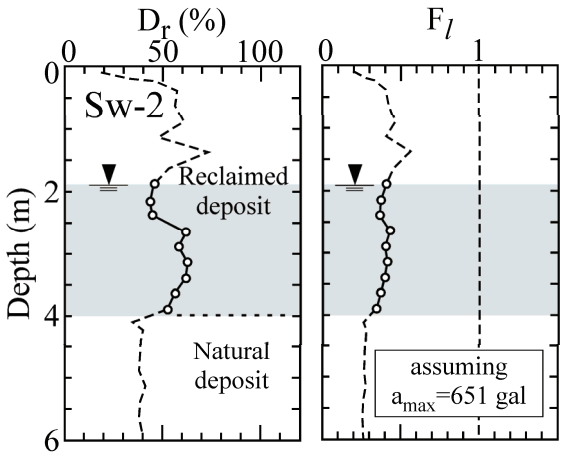


Figure 10 Estimated depth-wise profile of relative density D_r and factor of safety against liquefaction F_l at the position Sw-2

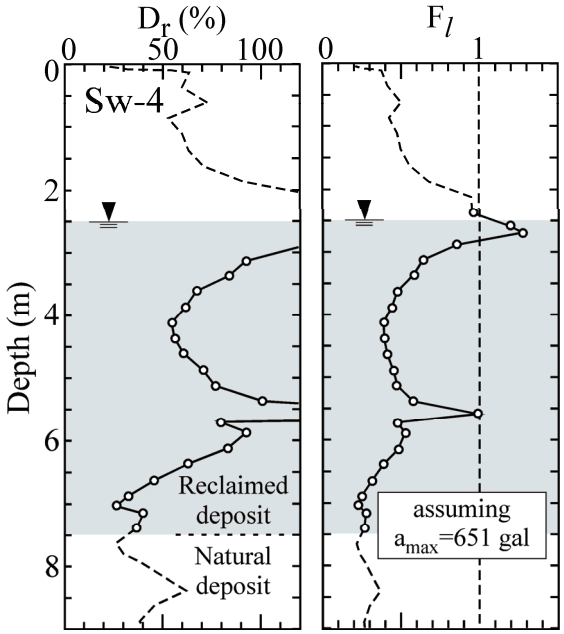


Figure 11 Estimated depth-wise profile of relative density D_r and factor of safety against liquefaction F_l at the position Sw-4

sand boils were observed is indicated on top of Fig. 9, so is indicated the area that the cracks and subsidence were observed. When the authors' research group revisited this site on November 21 to 23, 2012, the remains of sand boils had already been removed, and it was not possible to retrieve any samples of sand boils. Therefore, any physical properties of sand boils were not obtained. However, since the authors' research group had obtained the sand boil samples at the other end of Gohno-ike pond when they visited this site on October 14 to 16, 2011, it would be reasonable to assume that the physical properties of this sand boil sample are similar to each other at this site. By holding this bold assumption and employing the soil liquefaction analysis proposed and exercised by Tsukamoto et al. (2011), the depth-wise profiles of relative density D_r and factor of safety against liquefaction F_l are estimated as shown in Figs. 10

and 11. The profile for Sw-2 is shown in Fig. 10 ,and that for Sw-4 is shown in Fig. 11. Herein, the maximum ground surface acceleration of as high as 651 gal at east-west component was assumed, which was observed at the K-Net station of Kashima.

4. CONCLUSIONS

The earthquake reconnaissance investigations were conducted at Gohno-ike pond in Kamisu City, where the liquefaction-induced ground deformation and sand boils were observed. A multiple series of Swedish weight sounding tests were carried out and the subsurface soil profiles were estimated. The liquefied soil layers responsible for surface exposed ground deformation were identified.

Acknowledgements:

The authors would like to acknowledge Professors K. Ishihara and T. Kokusho for their continued support. Thanks are also extended to the kind assistance from the staff members of Kamisu City. The acceleration records discussed in the present study were obtained from K-Net database. The financial assistances provided by J-Rapid of Japan Science and Technology Agency are also acknowledged. The Swedish weight sounding tests described in the present study were conducted with a help of M. Takemura, S. Hagiwara and K. Hanawa.

References:

Kawabe, S., Tsukamoto, Y., Kokusho, T. and Takahashi, R. (2012) "Soil liquefaction observed at Katori City located along the lower stream of Tonegawa River during 2011 Great East Japan Earthquake", Proceedings of One Year after 2011 Great East Japan Earthquake – International Symposium on Engineering Lessons Learned from the Giant Earthquake.

Tonegawa River Lower Stream Office (2011) "Leaflets on Tonegawa River lower stream at the beginning of Meiji era (No.1)", Ministry of Land, Infrastructure and Transport, (in Japanese).

Tsukamoto,Y., Ishihara,K. and Sawada,S. (2004) "Correlation between penetration resistance of Swedish weight sounding tests and SPT blow counts in sandy soils", Soils and Foundations, Vol.44, No.3, 13 - 24.

Tsukamoto, Y. (2009) "Determining the undrained residual strength of soils from field penetration tests with some case history studies", Performance-Based Design in Earthquake Geotechnical Engineering - from case history to practice – (eds. T. Kokusho, Y. Tsukamoto & M. Yoshimine), CRC Press/Balkema : Theme Lecture, Proceedings of IS-Tokyo2009 (Tsukuba, Japan, June 15 – 18, 2009), 179 – 192.

Tsukamoto, Y. and Ishihara, K. (2011) "Use of field penetration tests in evaluating occurrence of soil liquefaction at reclaimed deposits during 2000 Tottori-ken Seibu earthquake", Proceedings of 5th international conference on earthquake geotechnical engineering, Santiago, Chile, January 10-13, 2011, CD Paper No. UOFTS.

Tsukamoto, Y., Kawabe, S., Kokusho, T. and Araki, K. (2012a) "Soil liquefaction observed at areas located along the lower stream of Tonegawa River during 2011 Great East Japan Earthquake", Proceedings of International Symposium on Engineering Lessons Learned from the Giant Earthquake, One Year after the 2011 Great East Japan Earthquake, March 1-4, 2012, Kenchiku-kaikan, Tokyo, Japan, CD.

Tsukamoto, Y., Kawabe, S., Kokusho, T. and Araki, K. (2012b) "Observed performance and estimated soil profiles of reclaimed and natural deposits at Kamisu City during 2011 Great East Japan Earthquake", Joint Conference Proceedings, 9th International Conference on Urban Earthquake Engineering/ 4th Asia Conference on Earthquake Engineering March 6-8, 2012, Tokyo Institute of Technology, Tokyo, Japan, Paper ID 02-285, pp.143 – 146.

10CUEE CONFERENCE PROCEEDINGS
10th International Conference on Urban Earthquake Engineering
March 1-2, 2013, Tokyo Institute of Technology, Tokyo, Japan

EFFECTS OF DRAINAGE AND DEWATERING ON DIFFERENTIAL SETTLEMENT OF WOODEN HOUSES FOUNDED ON LIQUEFIABLE SOILS

Yasutsugu Suzuki[1)], Kohji Tokimastu[2)], Takahiko Hidekawa[3)], Naohito Adachi[1)]

1) Chief Research Engineer, Kajima Technical Research Institute, Kajima Corporation, Japan
2) Professor, Dept. of Architecture and Building Engineering, Tokyo Institute of Technology, Japan
3) Research Engineer, Kajima Technical Research Institute, Kajima Corporation, Japan
Suzuki-y@kajima.com, kohji@o.cc.titech.ac.jp, hidekawa@kajima.com, adachina@kajima.com

Abstract: Dynamic centrifuge tests were conducted to investigate the effects of drainage and dewatering as remedial measures to mitigate damage to wooden houses founded on liquefiable soils. The results showed that: (1) drainpipes, if properly installed, can maintain the tilting angle of wooden houses less than 6/1000; (2) dewatering the groundwater level from G.L.-1.0m to G.L.-4.0m can reduce absolute structure settlement by about 50% and relative settlement by almost 100%; (3) combined method using both drainage and dewatering could have significant effects on reducing differential settlement of houses.

1. INTRODUCTION

In off the pacific coast of Tohoku Earthquake on March 11, 2011, many single-family houses built on reclaimed land of Tokyo Bay and the Tone River basin were suffered from differential settlement and tilting of their foundations due to liquefaction (Tokimatsu et al., 2011). In particular, about 9000 single-family houses were damaged in Urayasu city in Chiba Prefecture (Urayasu city, 2012). The same type of damage to single-family houses built on reclaimed land occurred in the Hyogoken-Nambu Earthquake on January 17, 1995 (Editorial Committee for the Report on the Hanshin-Awaji Earthquake Disaster, 1998). Since then, many types of liquefaction remedial measures have been developed and used in construction of new buildings and structures. Liquefaction remedial measures for existing buildings and single-family houses, in contrast, have not been widely developed and used because of the cost. The national and local governments have, therefore, been developing inexpensive liquefaction countermeasures for existing single-family houses since the Tohoku Earthquake.

Urayasu city and other local governments, together with residents, have developed new system for liquefaction remediation of a district rather than a single house, in which governments implement countermeasures for roads, and residents implement countermeasures for their houses.

New liquefaction countermeasures for existing houses using both drainage and dewatering have been proposed. It is difficult to lower groundwater level greatly, because settlement and tilt of houses occurs due to consolidation of the deep clay layer. Thus, lowering groundwater level is not sufficient on its own. Therefore, a combined method using both dewatering and drainage seems promising.

This paper presents a study on liquefaction countermeasures using both dewatering and drainage method. Dynamic centrifuge tests were conducted to investigate the effects of dewatering and drainage on settlement and tilt of wooden houses founded on liquefiable soils.

2. OUTLINE OF CENTRIFUGE SHAKING TESTS

Figure 1 shows the centrifuge test models with the positions of measuring instruments within a laminar box (inside dimensions of length L=700mm, width W=220mm, and height H=300mm). The shaking table tests were carried out under a centrifugal acceleration of 50 g. Structures were set on upper dry and lower saturated sand layers with relative density of about 50%. Figure 2 shows grain size distribution curves of silica sand sizes No. 7 and No. 8. The upper dry sand layer comprised silica sand size No. 8 and the lower saturated sand layer comprised silica sand size No. 7. Horizontal and vertical acceleration, horizontal and vertical displacement in structures, horizontal acceleration, excess pore water pressure and vertical displacement in ground were measured.

The test cases are shown in Table 1. In the shaking table tests, the two types of liquefaction countermeasures, drainage and lowering of groundwater level, were tested. Two structural models, small and large, were used in the tests. Two of the same structures were set on both the left side (I-side) and right side (N-side). Groundwater was set to three levels, 20mm, 50mm and 80mm (1.0m, 2.5m and 4.0m

in prototype scale) for the small models, and to two levels, 20mm and 50mm (1.0m and 2.5m in prototype scale), for the large models. Two drain types, large and small, were used in the tests. The drains were set 5mm (0.25m in prototype scale) from the models and 100mm (5.0m in prototype scale) below ground level. For the small models using 12 drains and the large models using 24 drains, the drains were set at a pitch of 30mm (1.5m in prototype scale). For the large models using 12 drains, the drains were set at a pitch of 60mm (3.0m in prototype scale). For the small models using 4 drains, the drains were set at the four corners. For the models with groundwater levels at 50mm and 80mm, the sensors in the ground were set a little lower than that with groundwater level at 20mm, as shown in Figure 1. Measurements were conducted in the same way.

Photo 1 shows the two types of structural models and Table 2 shows the physical properties. The structures were made of MC nylon and composed of superstructure, foundation, flat spring and eccentric mass. The flat spring connected the superstructure with the foundation. A metallic mass was set on the foundation to induce differential settlement as eccentric load. The large and small structural models imposed the same contact ground pressure. The mass and natural frequency of the structural models were about the same as those of common single-family wooden houses in Japan.

Photo 2 shows the two types of drain models. They were made of stainless-steel mesh (100 wires per inch, wires 0.1mm in diameter), rolled into cylinders. In order to adjust the amount of water dissipation due to liquefaction, two drain models were used. The large one was 5.0mm in diameter (250mm in prototype scale), and the small one was

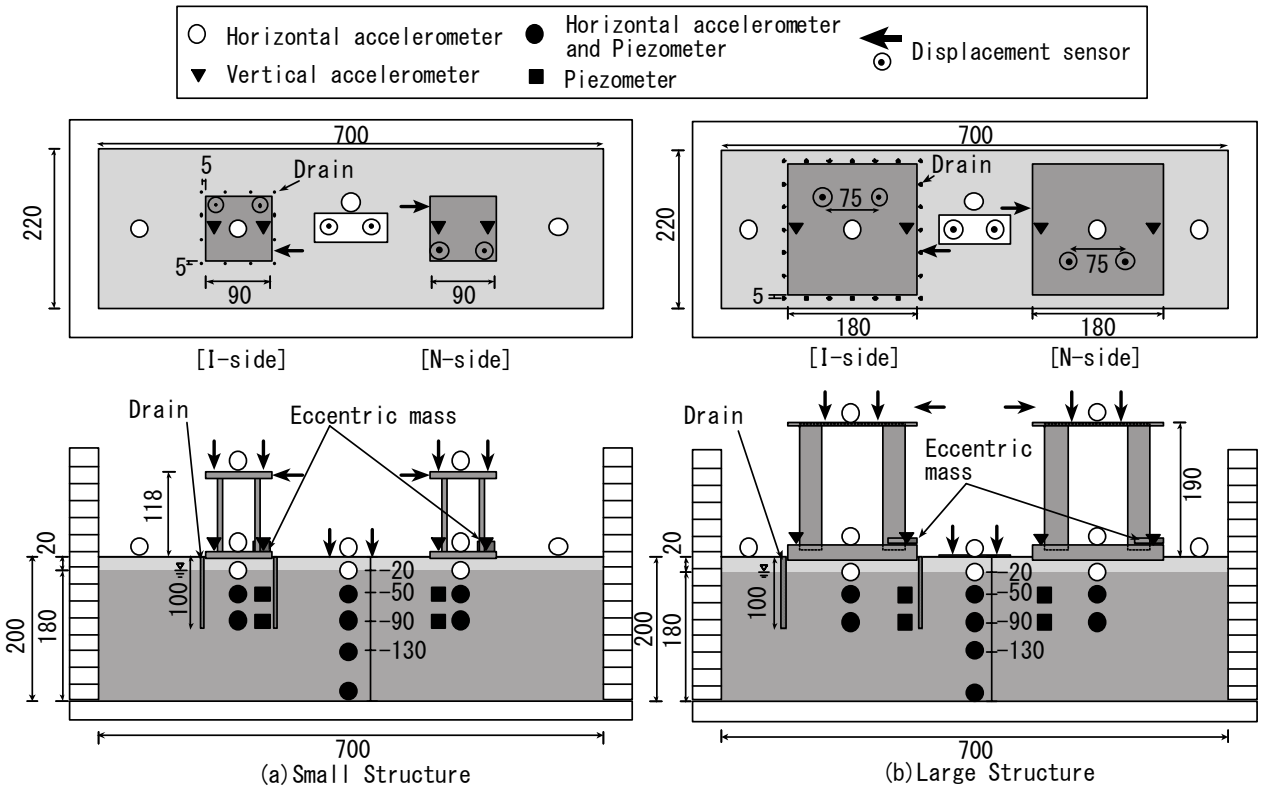


Figure 1 Tests setup and instrumentation for groundwater level with 20mm in model type (unit mm) [Case-S1, Case-L1]

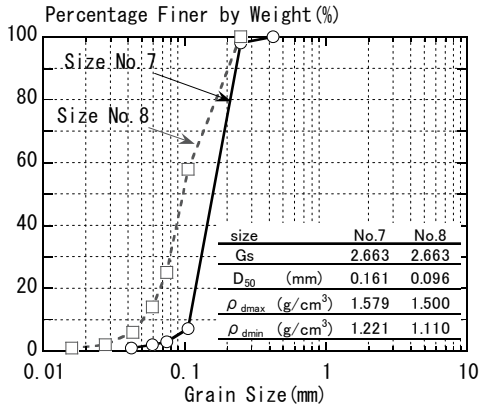


Figure 2 Grain size distribution curve

Table 1 List of test cases

	Structure	Groundwater level※	I-side	N-side
Case-S1	Small	G.L.-20mm (-1.0m)	12 Drains (Large)	No
Case-S2	Small	G.L.-50mm (-2.5m)	12 Drains (Large)	No
Case-S3	Small	G.L.-80mm (-4.0m)	12 Drains (Large)	No
Case-S4	Small	G.L.-20mm (-1.0m)	12 Drains (Small)	No
Case-S5	Small	G.L.-20mm (-1.0m)	4 Drains (Large)	4 Drains (Small)
Case-L1	Large	G.L.-20mm (-1.0m)	24 Drains (Large)	No
Case-L2	Large	G.L.-50mm (-2.5m)	24 Drains (Large)	No
Case-L3	Large	G.L.-20mm (-1.0m)	24 Drains (Small)	12 Drains (Small)
Case-L4	Large	G.L.-50mm (-2.5m)	12 Drains (Small)	No

※ Model (Prototype)

2.5mm in diameter (125mm in prototype scale). In order to examine the countermeasure effect of drainage, shaking table tests were carried with various numbers and diameter of drains.

Figure 3 shows the test procedure. First, a dry sand layer of relative density 50% was made by air pluviation from the bottom of a laminar box to groundwater level. Second, sand was saturated by slowly pouring in silicon oil with 50 times the viscosity of water from the bottom of the laminar box in a vacuum. After that, drains were set in the saturated sand as shown in Photo 3, and the dry sand layer was made by the same method. Finally, two structures were set on the ground.

The artificial earthquake wave shown in Figure 4 was applied as the input acceleration wave (Niwa et al., 1993). First, the test model was shaken using a maximum acceleration of 400cm/s^2 as a main shock. Next, a maximum acceleration of 200 cm/s^2 was used as an aftershock after

Table 2 Physical properties of model structures

Small Structure		Model	Prototype
Superstructure	Mass	140g	17.5t
	Frequency	130Hz	2.6Hz
Foundation	Mass	130g	16.3t
	Area	90mm × 90mm	4.5m × 4.5m
Eccentic Mass	Mass	50g	6.3t
Total	Height	118mm	5.9m
	Mass	320g	40.1t

Large Structure		Model	Prototype
Superstructure	Mass	250g	31.3t
	Frequency	100Hz	2.0Hz
Foundation	Mass	780g	97.5t
	Area	180mm × 180mm	9.0m × 9.0m
Eccentic Mass	Mass	140g	17.5t
Total	Height	190mm	9.5m
	Mass	1170g	146.3t

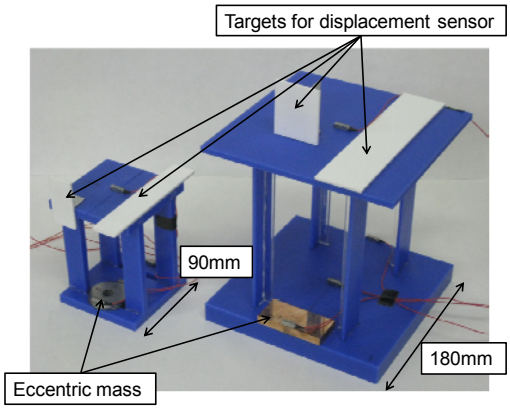


Photo 1 Small (left) and Large (right) structure models

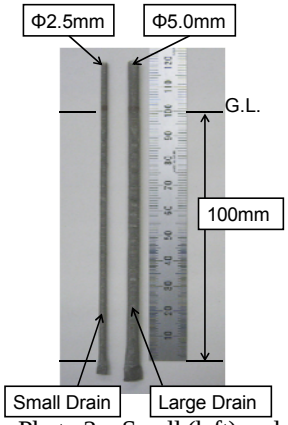


Photo 2 Small (left) and Large (right) drains

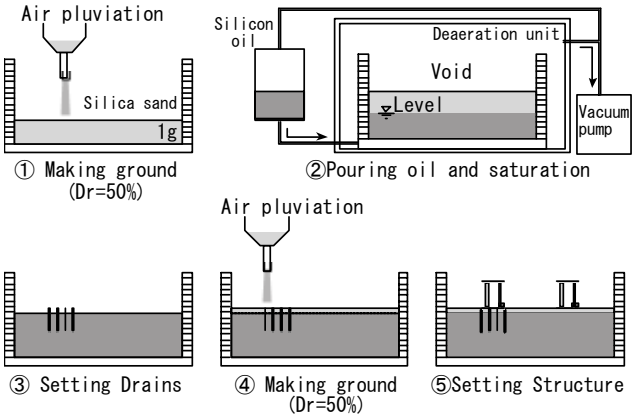


Figure 3 Procedure of test models

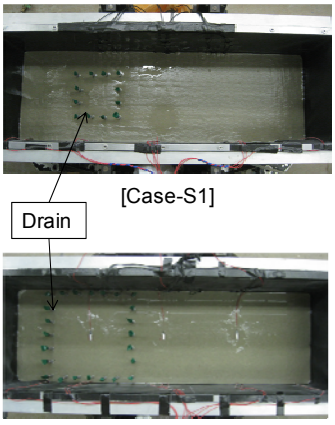


Photo 3 View after drains set up

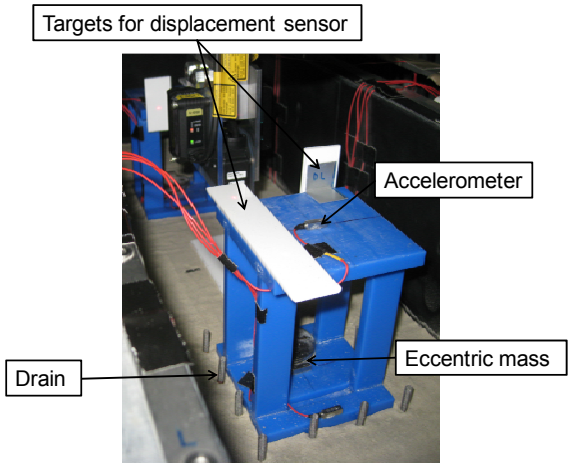


Photo 4 View before first shaking for Case-S1

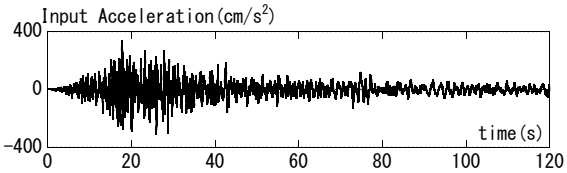


Figure 4 Input acceleration

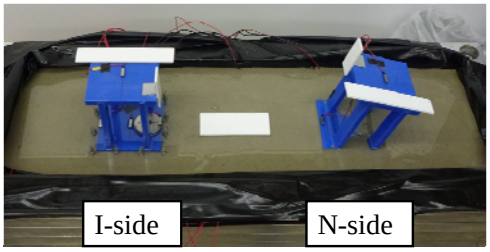


Photo 5 View after third shaking for Case-S1

excess pore water pressure due to the main shock completely dissipated. After that, the maximum acceleration of 400 cm/s^2 was used once or twice again.

Photo 4 shows the view before the first shaking for Case-S1. The structure in the front in photo 4 is on the I-side. The drains can be seen sticking up from the ground. Photo 5 shows the view after the third shaking for Case-S1. In Photo 5, the structure without drains on the N side was significantly tilted, but the structure with 12 large drains on the I side was only slightly tilted and settled down only after the third shaking.

In this paper, we show only the result of the first main shock in prototype scale.

3. TEST RESULTS

3.1 Soil and Structure Responses for Case-S1

As an example of response results for the small structure, Figure 5 shows the time histories of Case-S1 with 12 large drains and without drains. Input acceleration of shaking table, horizontal acceleration of center ground surface, and horizontal acceleration of superstructure and foundation in both I and N side are shown on the left side of Figure 5. Excess pore water pressure of the center ground and just under the structures at G.L.-4.5m, absolute settlement of the ground and both structures, and rotation angle of both structures are shown on the right side of Figure 5. All histories in Figure 5 are shown for 120 seconds after the start of vibrations.

Excess pore water pressure at G.L.-4.5m was constant after about 15 seconds, indicating that the saturated sand layer liquefied. The peak accelerations were about 80cm/s^2 on the ground surface and both foundations, and about 180cm/s^2 on both superstructures at about 10 seconds. The amplitudes of those accelerations were smaller than the input acceleration after 10 seconds. There was little difference between the acceleration time histories of the superstructures and foundations for the structure with 12 large drains on I side and the structure without drains on N side. However, there was a difference between the excess pore water pressures just under the structures. The drains were very effective because excess pore water pressure on I side was smaller than the others. Excess pore water pressure on N

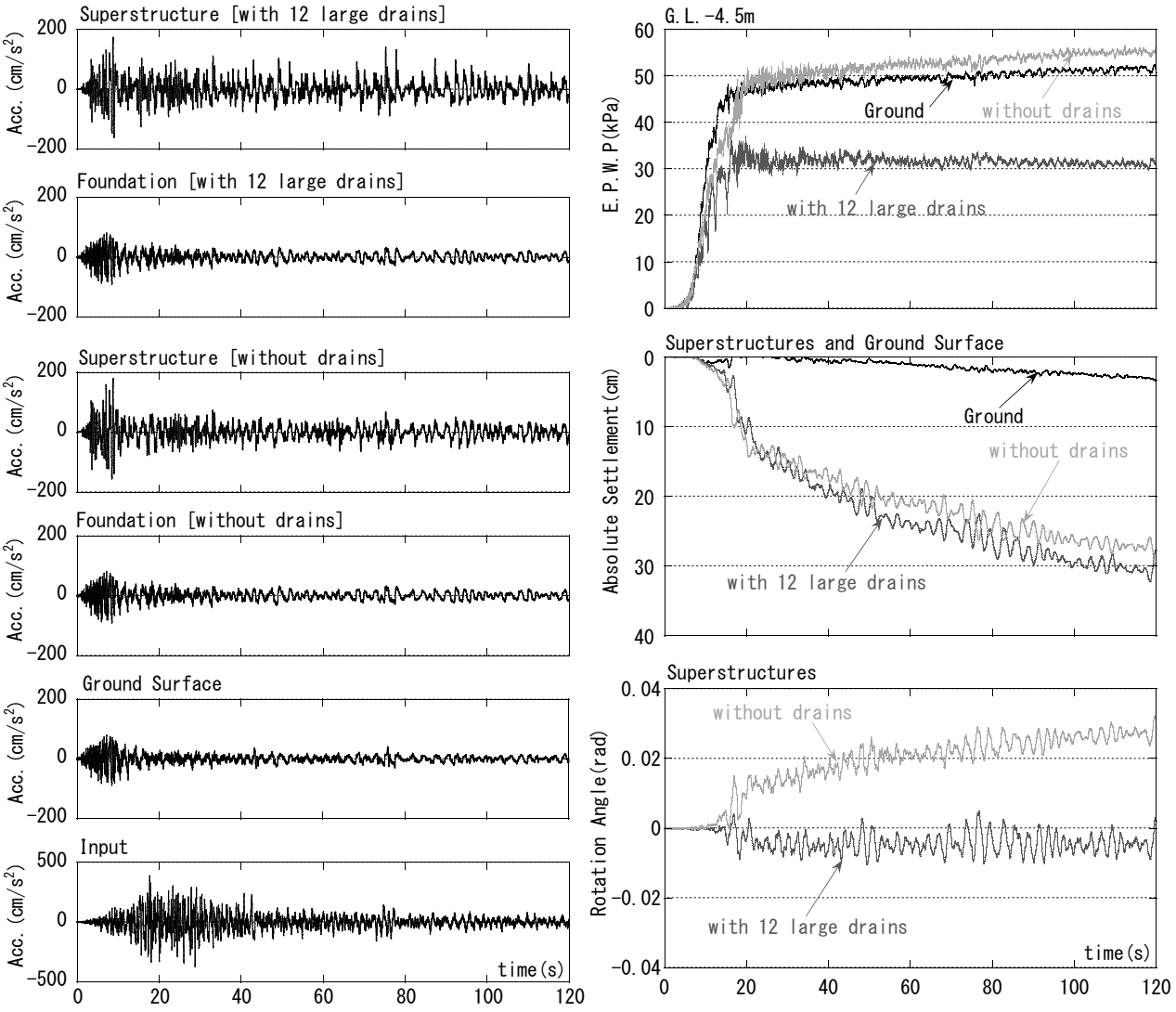


Figure 5 Time histories of structures and soil response for Case-S1

side was larger than that of the center ground because of increasing confining pressure of the ground by the weight of the structure.

Absolute settlements of both structures were clearly larger than that of the ground surface. The absolute settlement of the structure with 12 large drains on I side was slight larger than that of the structure without drains on N side, because excess pore water pressure on I side was dissipated to the ground surface more rapidly by the drains. However, the settlement on N side was subsequently slightly larger than that on I side as shown in Figure 7.

Although the rotation angle of the N-side structure increased in the direction of the eccentric mass during shaking, the rotation angle of the I-side structure was suppressed. Because the effective stress of the ground was maintained by the effect of dissipation by the drains, one-way structure tilt due to dynamic rocking motion could be suppressed simultaneously.

3.2 Soil and Structure Responses for Case-L1

As an example of response results for the large structure, Figure 6 shows the time histories of Case-L1 with 24 large drains and without drains in the same form as Figure 5.

Excess pore water pressure at G.L.-4.5m was constant after about 15 seconds, indicating that the saturated sand layer liquefied. The peak accelerations were about 80cm/s^2 at ground surface and at both foundations, and about 300cm/s^2 in both superstructures at about 10 seconds. The amplitudes of those accelerations were smaller than the input acceleration after 10 seconds. The ratio of peak accelerations of the large and small superstructures was nearly equal to their structure height ratio. Although the responses of the large structures were larger than those of the small structures, they showed similar responses under liquefaction as Case-S1. As for Case-S1, there was little difference between the acceleration time histories of the superstructures and the foundations for the structure with 24 large drains on I side and the structure without drains on N side. However, there was a difference between the excess pore water pressures. The drains were mostly effective, because the excess pore water pressure on I side was smaller than those of the others. However, the effect of the drains for Case-L1 was smaller

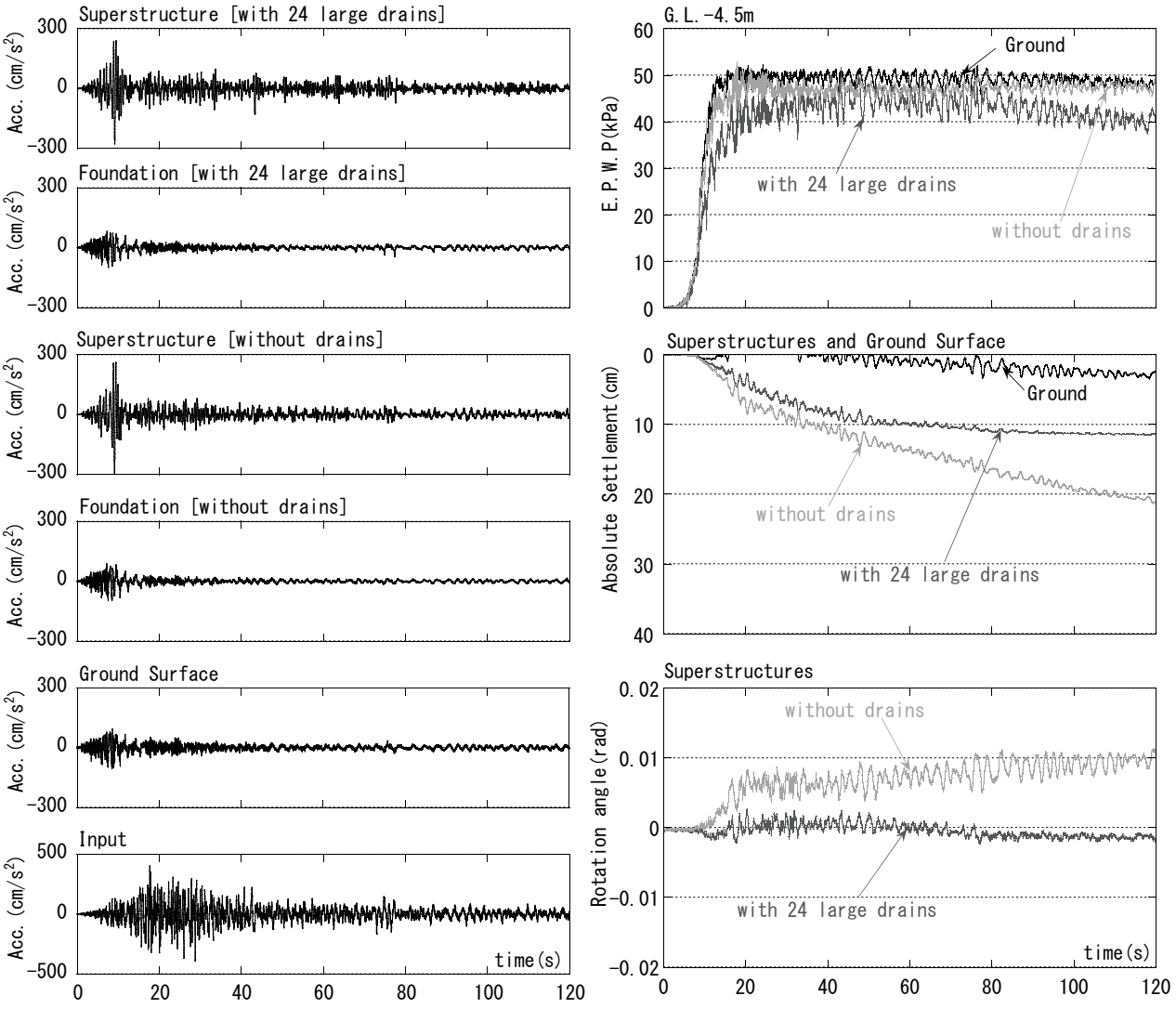


Figure 6 Time histories of structures and soil response for Case-L1

than that for Case-S1.

As for Case-S1, the absolute settlements of both structures were larger than that of ground. However, the difference between them was smaller than for Case-S1. The absolute settlement of the structure with 24 large drains on I side was remarkably smaller than that of the structure without drains on N side, in spite of the smaller dissipation effect due to drains compared with Case-S1. That was a different phenomenon from Case-S1.

Although the rotation angle of the N-side structure increased in the direction of the eccentric mass during shaking, the rotation angle of the I-side structure was suppressed. As for Case-S1, because the effective stress of the ground was maintained by the dissipation effect of the drains, one-way structure tilt due to dynamic rocking motion could be suppressed simultaneously.

3.3 Effect of Drains for Small Structural Model

Figure 7 shows the results of different numbers and diameter of drains with groundwater level -1.0m using the small structural model in Case-S1, Case-S4 and Case-S5. This figure shows excess pore water pressure at G.L.-4.5m, absolute settlement of ground surface and structures, and rotation angle of structures for 600 seconds. The excess pore water pressure of the ground under the center of the structures is shown at the upper left, and that under the end of structure near the drains is shown at the upper right.

The excess pore water pressure of the ground rose rapidly for about 10 seconds in each case, remained almost constant until the end of shaking, and then dissipated. The maximum excess pore water pressures under the center of the structure with drains were smaller than that without drains during shaking. In particular, the maximum excess pore water pressures with 12 drains reduced to about 60% of that without drains, and it also tended to dissipate faster. The maximum pore water pressure using 12 large drains was less than that using 12 small drains. The maximum excess pore water pressures using 4 drains were almost the same. The maximum pore water pressures under the end of the structure near the drains were slightly smaller than those under the center of the structure.

The absolute settlements of the structures were larger than that of the ground in each case. The absolute settlements of the structure with drains were larger than that without drains, because the excess pore water pressure dissipated to the ground surface more rapidly. However, the absolute settlement of the structure without drains was larger than that with drains at the time of 600 seconds because a complete liquefaction state was maintained for a long time in the case without drains.

The rotation angle of the structure with 4 small drains was similar to that of the structure without drains. The rotation angle of the structure with drains in other cases was remarkably small.

3.4 Effect of Drains for Large Structural Model

Figure 8 shows the results for different numbers and diameter of the drains with groundwater level -1.0m using the large structural model for Case-L1 and Case-L3. This figure has the same form as Figure 7.

Excess pore water pressure of the ground rose rapidly for about 10 seconds in each case, remained almost constant

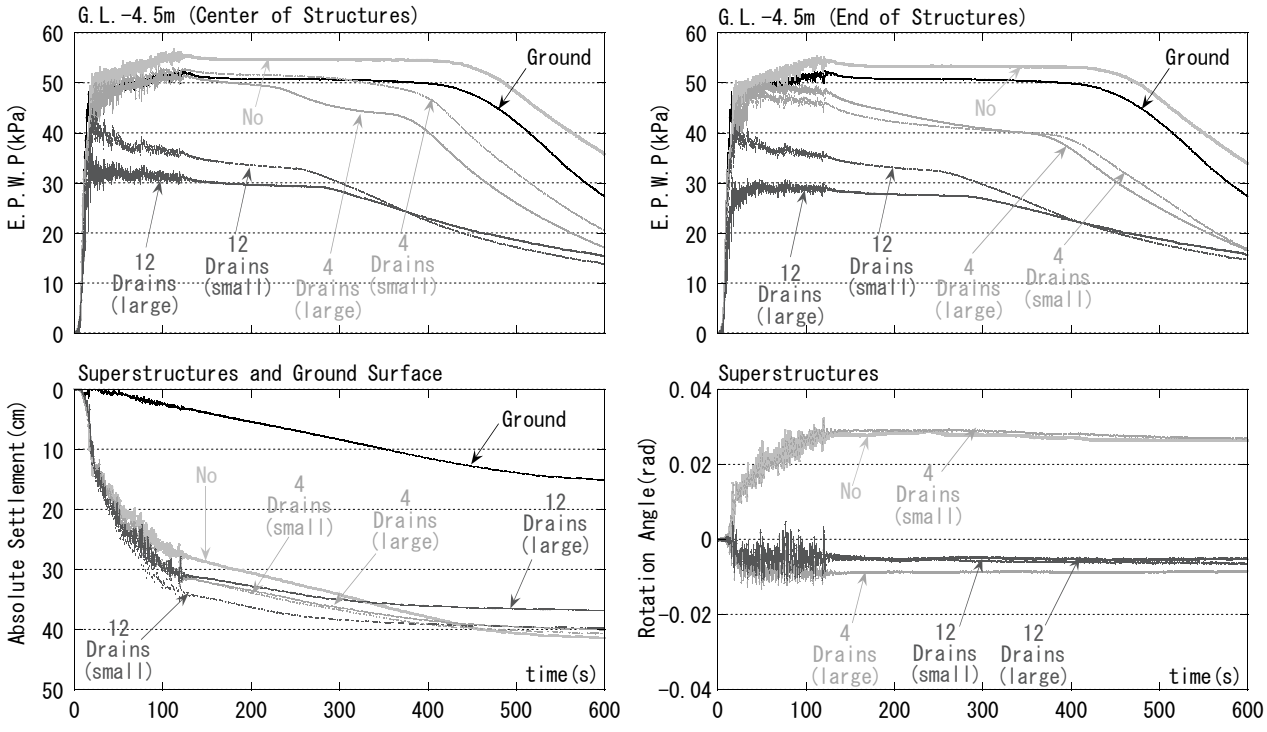


Figure 7 Time histories of excess pore water pressure, absolute settlement and rotation angle for small structure models with groundwater level -1.0m

for a period and then dissipated. However, this effect was less remarkable than that shown in Fig.7 using small structural models. The maximum excess pore water pressure of the ground under the center of the structure with 24 large drains was slightly smaller than for the other cases. The dissipation of excess pore water pressure under the center of the structure with drains was faster than that without drains. However, the excess pore water pressure and its dissipation in the ground under the end of the structure near the drains were varied with number and diameter of drains, because the distance between the center and end of the structure was about twice that for the small structural models.

The absolute settlements of the structures were larger than that of the ground in each case. The absolute settlements of the structure with drains and without drains were initially almost the same in each case. However, the difference between the absolute settlements increased with number and diameter of drains after a period of shaking.

The rotation angle of the structure with 12 small drains was similar to that of the structure without drains. The rotation angle of the structure with drains in other cases was very small.

4. STRUCTURE SETTLEMENT AND ROTATION

The relationships between the absolute settlements and rotation angles of structures, and the numbers and diameter of drains, are shown in Figure 9 for the time 1200 seconds from the start of vibration. The test cases are shown on the horizontal axis in the increasing order of the drainage effect. Test results for the small structure with groundwater level -1.0m are shown at the top of Figure 9, those for the large structure with groundwater level -1.0m are shown at the middle, and those for the large structure with groundwater level -2.5m are shown at the bottom.

The suppression of the absolute settlements and rotation angles of the structure depends on the numbers and diameter of the drains. There was a large difference between the small structure rotation angles with 4 small drains and with 4 large drains. There was also a large difference between the large structure rotation angles with 12 small drains and with 24 large drains. Thus, the effect on the structure rotation angle was clearly reflected by the numbers and diameter of drains, i.e., the dissipation capacity.

The relationships between absolute structure settlements and rotation angles, and the groundwater level are shown for the small and large structural models in Figure 10. These values are shown for a time of 1200 seconds from the start of vibration.

The ground settlements were almost constant regardless of groundwater level. The structure settlements decreased with lowering groundwater level. It was possible to suppress about 50% of the absolute structure settlement or almost 100% of structure settlement relative to the ground by lowering the groundwater level from G.L.-1.0m to G.L.-4.0m. For the large structural model, the settlements of the structure with drains were smaller than those without drains, and were almost the same as those of the ground. The rotational angles of the structures with drains were smaller than those without drains for both small and large structural models. It is therefore possible to suppress the differential

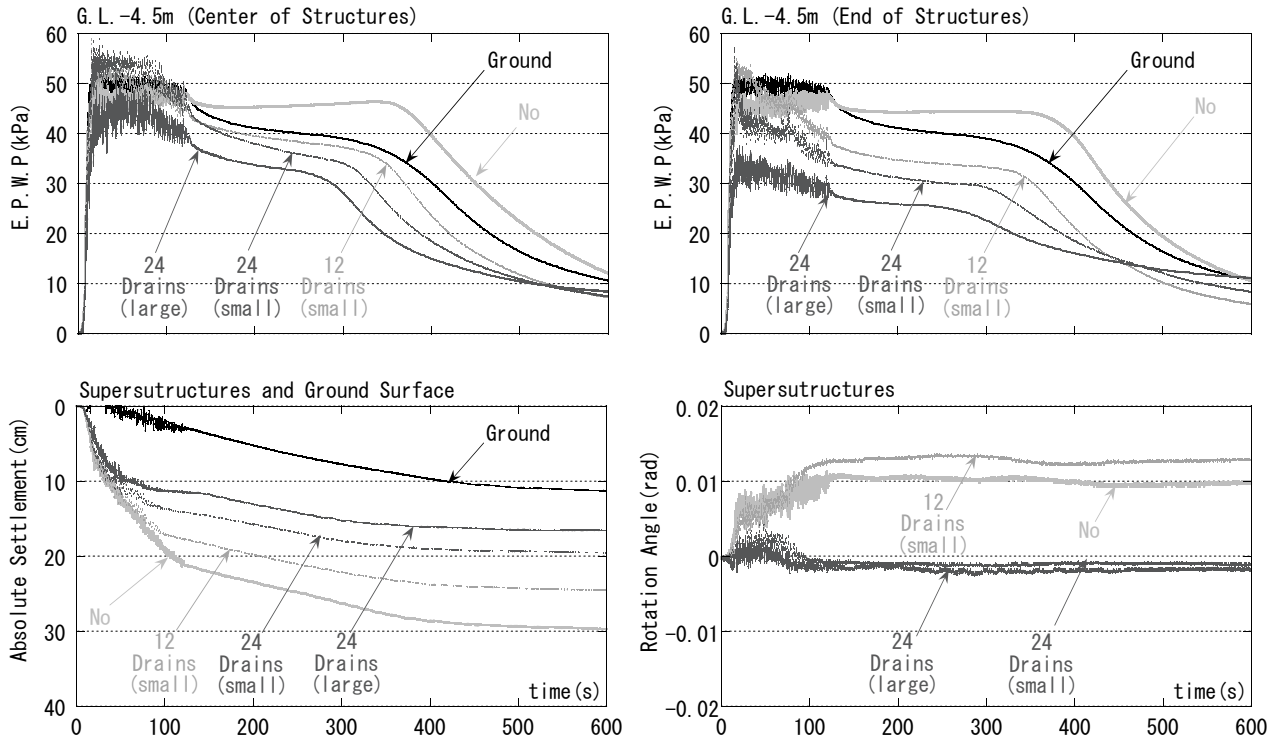
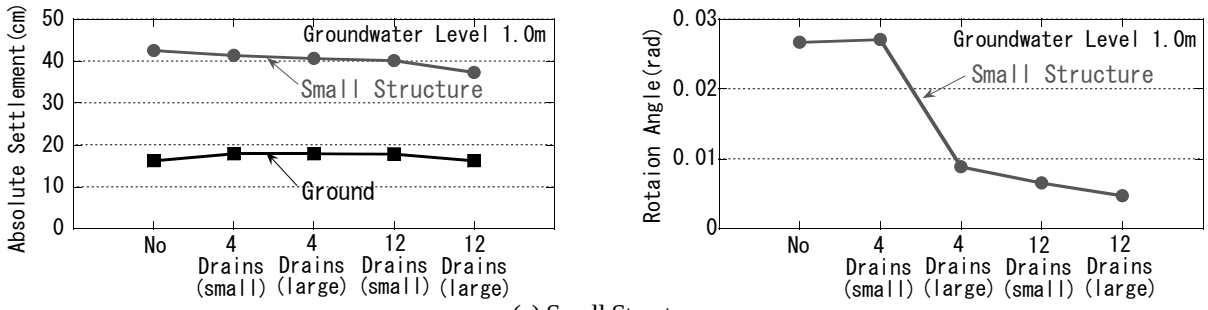
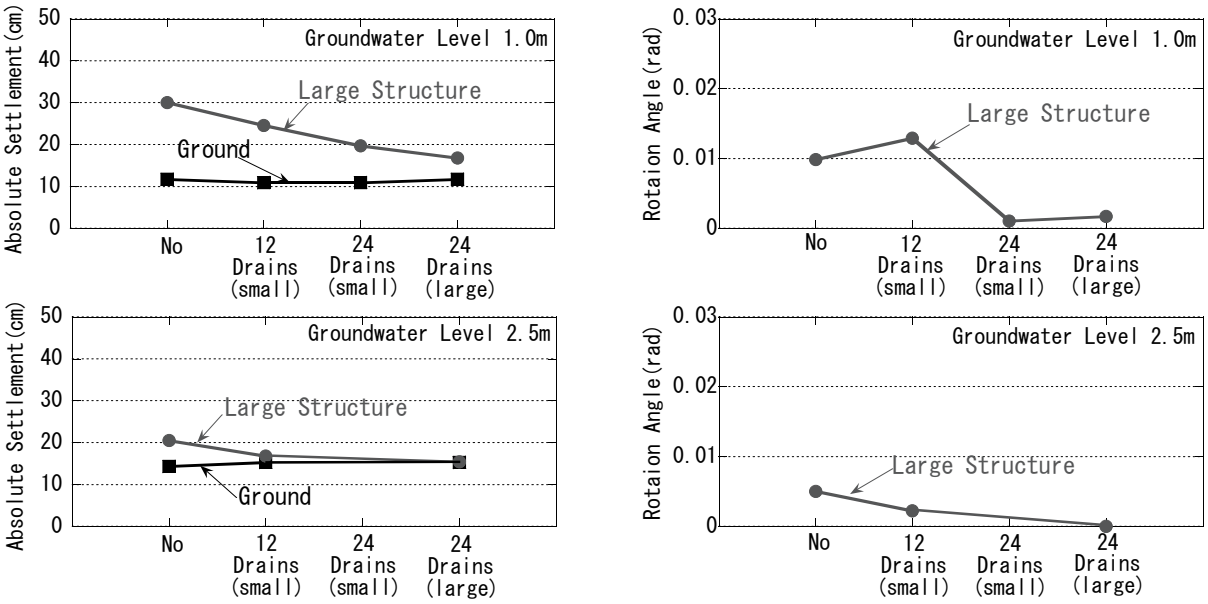


Figure 8 Time histories of excess pore water pressure, absolute settlement and rotation angle for large structure models with groundwater level -1.0m

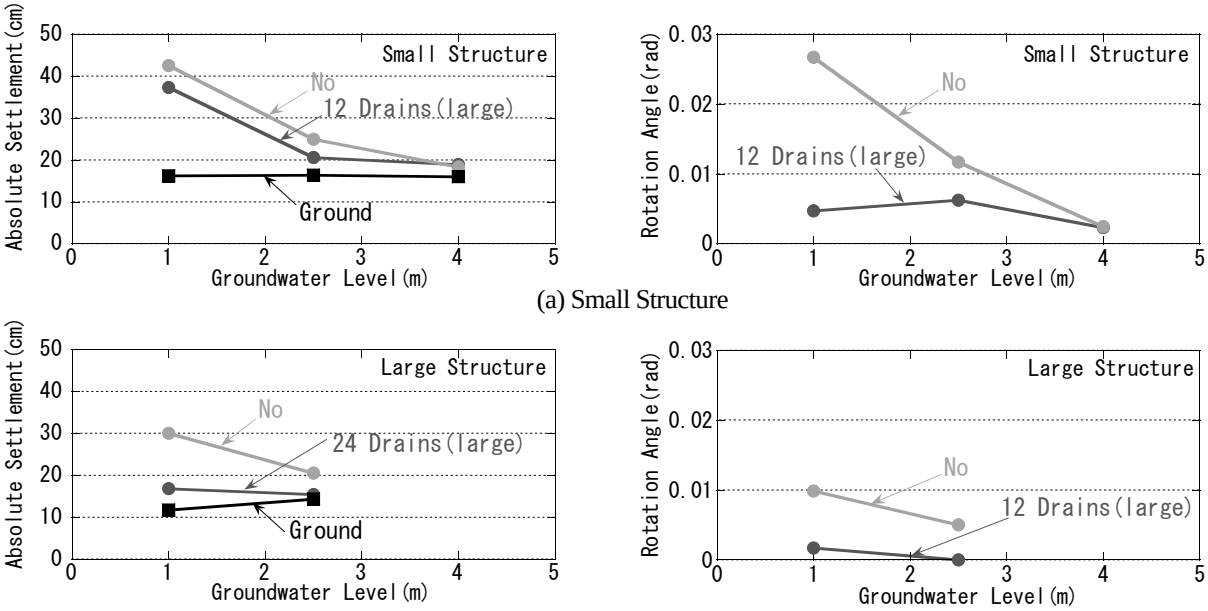


(a) Small Structure



(b) Large Structure

Figure 9 Absolute structure settlement and rotation angle classified by number and diameter of drains



(a) Small Structure

(b) Large Structure

Figure 10 Absolute structure settlement and rotation angle classified by groundwater level

settlement by reducing to less than 6/1000 the rotation angle of the structure. Therefore, the combined method using both drainage and dewatering could be an effective measures to mitigate differential settlement of houses founded on liquefiable soils.

5. CONCLUSIONS

Dynamic centrifuge tests were performed to investigate the effect of dewatering and drainage on liquefaction induced damage to structures such as single-family houses. The conclusions drawn from this study may be summarized as follows.

1) The relative settlement and tilting angle of a structure due to soil liquefaction decrease with lowering groundwater table, regardless of the size of the structure.

2) The relative settlement and tilting angle of a structure due to soil liquefaction decrease with increasing number and diameter of drainpipes installed around the structure, probably because the excess pore water pressure below the structure generated by earthquake shaking can dissipate rapidly and the ground stiffness was maintained due to the presence of drainpipes. The effects appear more pronounced as the size of the structure increases.

3) The combined method using dewatering and drainage could be effective for reducing damage to wooden houses founded on liquefiable soil.

Acknowledgements:

This study was supported by research and development program of construction technology in Ministry of Land, Infrastructure, Transport and Tourism. We would like to thank their program.

References:

Tokimatsu, K., Tamura, S., Suzuki, H., and Katsumata, K. (2011), "Geotechnical Damage during the 2011 off the Pacific Coast of Tohoku Earthquake, *Research reports on earthquake engineering by Center for Urban Earthquake Engineering*, Tokyo Institute of Technology, No.118, 21-48 (in Japanese)

Urayasu city (2012), "The Final Report in Research Committee of Liquefaction Countermeasure Technology in Urayasu City" (in Japanese)

Editorial Committee for the Report on the Hanshin-Awaji Earthquake Disaster (1998), "Report on the Hanshin-Awaji Earthquake Disaster, Building Series Volume 4, Damage to Building Foundations", Architectural Institute of Japan (in Japanese)

Niwa, M., Yokota, H., Tohdo, M. (1993), "Design of Input Earthquake Motion for Dynamic Design", *Building Disaster Prevention*, No. 182, 4-17 (in Japanese)

10CUEE CONFERENCE PROCEEDINGS
10th International Conference on Urban Earthquake Engineering
March 1-2, 2013, Tokyo Institute of Technology, Tokyo, Japan

NUMERICAL MODELING ISSUES IN PREDICTING POST-LIQUEFACTION RECONSOLIDATION STRAINS AND SETTLEMENTS

Katerina Ziotopoulou[1], and Ross W. Boulanger[2]

1) PhD Candidate, Dept. of Civil & Environmental Engineering, University of California, Davis, U.S.A.
2) Professor, Dept. of Civil & Environmental Engineering, University of California, Davis, U.S.A
kziotopoulou@ucdavis.edu, rwboulanger@ucdavis.edu

Abstract: Volumetric strains and settlements that develop during post-liquefaction reconsolidation of sand are difficult to numerically model using the conventional constitutive separation of strains into elastic and plastic components since a large portion of the post-liquefaction reconsolidation strains are due to sedimentation effects which are not easily incorporated into either the elastic or plastic components of behavior. Single element simulations using various constitutive models show that they generally predict post-liquefaction reconsolidation strains that are an order of magnitude smaller than observed in various experimental studies. Accurate prediction of post-liquefaction volumetric strains can also be important for numerically simulating post-shaking pore pressure redistribution and its effect on slope deformations. This paper describes modifications to the bounding surface plasticity constitutive model PM4Sand that provide a means for improved modeling of post-liquefaction reconsolidation strains after the end of strong shaking in a nonlinear deformation analysis. The methodology of the approach along with the calibration is presented, followed by a comparison of the response computed for a field case history.

1. INTRODUCTION

Settlement caused by one-dimensional reconsolidation of liquefied soils, along with any settlement caused by lateral spreading, is an important possible consequence of liquefaction. Settlement caused by post-liquefaction reconsolidation results from volumetric strains that develop throughout the underlying soil profile. Such volumetric strains are not easy to numerically model. The conventional numerical separation of strains into elastic and plastic components cannot capture post-liquefaction volumetric strains that are due to sedimentation under essentially zero effective stress. For this reason, it is common for numerical models to underestimate liquefaction-induced one-dimensional settlements.

The ability to numerically model post-liquefaction reconsolidation strains can also be important for predicting deformation and stability of slopes. Diffusion of the earthquake-induced excess pore water pressures leads to outward seepage from zones that are reconsolidating. If this transient seepage is impeded by an overlying lower permeability soil layer, the accumulation of water near such an interface can lead to void redistribution and subsequent localized loosening, strength loss and possibly water film formation (e.g., Kokusho 1999, Kulasingam et al. 2004). These mechanisms can all locally diminish the shear resistance in a loosening zone leading to greater deformations and possibly instability.

In this paper, modifications to an elastic-plastic constitutive model are presented for improving the numerical prediction of post-liquefaction reconsolidation strains and settlements. The modifications were made to the PM4Sand model (Boulanger and Ziotopoulou 2012) as implemented in the numerical platform FLAC (Itasca 2011). PM4Sand, like other elastic-plastic models, significantly underestimates post-liquefaction reconsolidation strains. A phenomenological modification was added to PM4Sand that enabled the constitutive model to reproduce realistic volumetric strains during the post-liquefaction reconsolidation phase. The following sections of this paper provide: a review of laboratory data, a description of the constitutive equations, results of direct simple shear single element simulations, and the analysis of a case history.

2. LABORATORY DATA

Ishihara and Yoshimine (1992) observed that the volumetric strains that occur during post-liquefaction reconsolidation of sand samples were directly related to the maximum shear strains that developed during undrained cyclic loading and to the initial relative density (D_R) of the sand. They compiled laboratory results and developed the relationships shown in Figure 1. The experimental data show post-liquefaction reconsolidation volumetric strains ranging from 1 to 4% for most relative densities. Their results also showed that a significant portion of the reconsolidation strains occurred early in the reconsolidation phase when the effective stresses were still small.

Other laboratory studies of post-liquefaction reconsolidation strains (e.g., Tokimatsu and Seed 1987, Sento et al. 2004) produced results similar to those of Ishihara and Yoshimine (1992). Sento et al. (2004), however, showed that post-liquefaction reconsolidation strains are more uniquely related to

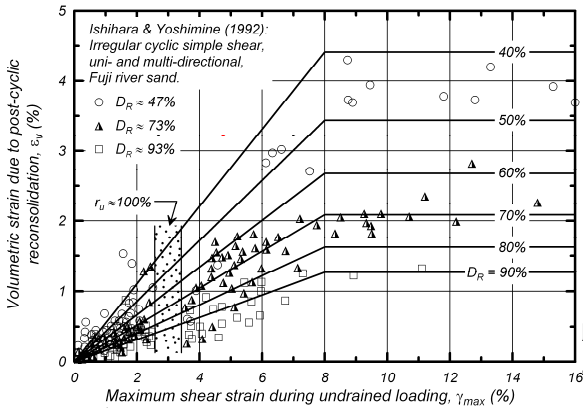


Figure 1 Relationship between post-liquefaction volumetric strain and the maximum shear strain induced during undrained cyclic loading of clean sand (after Ishihara and Yoshimine 1992; redrawn in Idriss and Boulanger 2008).

the accumulated shear strain (summing the absolute magnitude of shear strain increments) that develops during the undrained cyclic shearing process than to the maximum shear strain that develops during undrained shearing. In practice, experimental results for post-liquefaction reconsolidation strains are unlikely to be available for an individual site but any numerical model should at least give results that are consistent with the range of experimental data in the literature.

3. CONSTITUTIVE MODELING

3.1. Elastic – Plastic Component

Constitutive models are most often based on the additive decomposition of strains (or strain rates) into elastic and plastic components. For example, volumetric strain increments $d\varepsilon_v$ are composed of an elastic volumetric strain increment $d\varepsilon_{vol}^{el}$ and a plastic volumetric strain increment $d\varepsilon_{vol}^{pl}$:

$$d\varepsilon_{vol} = d\varepsilon_{vol}^{el} + d\varepsilon_{vol}^{pl} \tag{1}$$

Elastic strains are computed from Hooke's law and the stress increment, and plastic strains are computed from the yield criterion and flow rule. For PM4Sand, the elastic volumetric strain increment $d\varepsilon_{vol}^{el}$ is equal to the mean effective stress increment dp' divided by the bulk modulus K and the plastic volumetric strain increment $d\varepsilon_{vol}^{pl}$ is equal to the dilatancy D multiplied by the plastic shear strain increment $d\gamma_{vol}^{pl}$:

$$d\varepsilon_{vol} = d\varepsilon_{vol}^{el} + d\varepsilon_{vol}^{pl} = \frac{dp'}{K} + D \cdot \left| d\gamma^{pl} \right| \tag{2}$$

One-dimensional post-liquefaction reconsolidation strains are the result of integrating volumetric strain increments as the vertical effective stress σ_v' recovers from zero (i.e., the liquefied state) to its initial value prior to cyclic loading (σ_{vo}'):

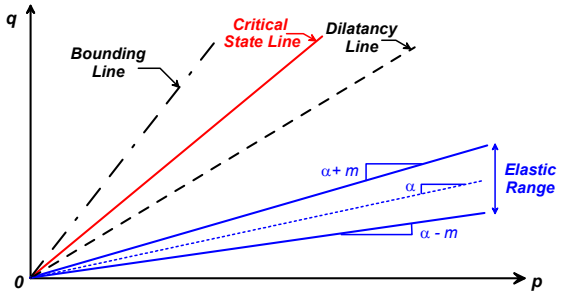


Figure 2 Schematic of the yield, critical, dilatancy, and bounding lines in q-p space (after Dafalias and Manzari, 2004)

$$\varepsilon_{vol-1D} = \int_0^{\sigma_{vo}'} \left(\frac{d\varepsilon_{vol}}{d\sigma_v'} \right) d\sigma_v' \tag{3}$$

The nature of this integration depends on the details of the constitutive model.

3.1.1. Stress-Ratio Based Models

Stress-ratio controlled models, like PM4Sand, use a narrow open cone-type yield surface with its apex at the origin and obeying rotational hardening. This means that only changes of the stress ratio (i.e. the ratio of deviatoric stress q over the mean effective stress p') can cause plastic shear and volumetric strains, while constant stress-ratio loading induces only elastic strains. The stress-ratio based dilatancy, critical state and bounding surfaces of the Dafalias and Manzari (2004) model, upon which PM4Sand was developed, are illustrated in Figure 2. Other examples of stress-ratio based models include the ones developed by Papadimitriou et al. (2001), Andrianopoulos et al. (2010) and Yang et al. (2003).

In simulations of one-dimensional reconsolidation of a liquefied sand, the stress-ratio will remain constant for a stress-ratio based constitutive model with a constant Poisson's ratio v. Reconsolidation strains, as computed using Equation 3, will therefore be integrated along the K_o consolidation line. The bulk modulus K will vary with confinement and thus, the reconsolidation response will be non-linear elastic.

The one-dimensional post-liquefaction reconsolidation volumetric strains obtained by constitutive models using the above framework are illustrated by the following analytical calculation. One-dimensional volumetric strain increments are equal to the vertical stress increment $d\sigma_v'$ divided by the constrained modulus M:

$$d\varepsilon_{vol} = \frac{d\sigma_v'}{M} \tag{4}$$

The constrained modulus M is related to the shear modulus G and Poisson's ratio v as:

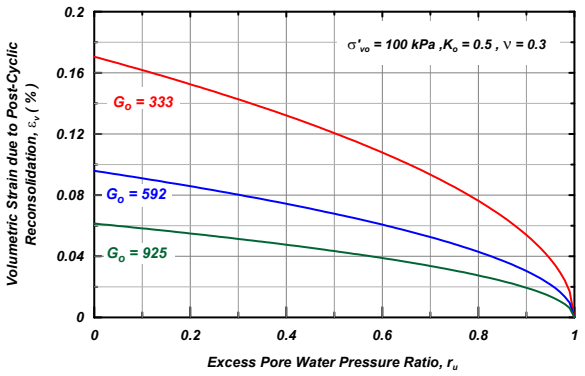


Figure 3 Volumetric strain versus r_u curves with different G_o's obtained through analytical integration of elastic volumetric strain increments.

$$M = \frac{2G(1-\nu)}{(1-2\nu)} \tag{5}$$

The shear modulus G of sand is approximately proportional to the square root of the confinement p' and thus can be expressed as:

$$G = G_o P_{atm} \sqrt{\frac{p'}{P_{atm}}} \tag{6}$$

where G_o is the shear modulus coefficient and P_{atm} is the atmospheric pressure.

The above equations can be used to analytically solve for the volumetric strains that are obtained as the vertical effective stress is recovered during reconsolidation. For example consider reconsolidation from a liquefied state ($\sigma'_v = 0$, $r_u = 1$) back to an initial vertical effective stress of $\sigma'_{vo} = 100kPa$ ($\sigma'_v = \sigma'_{vo}$, $r_u = 0$). The Poisson's ratio is assumed to be constant at a value of 0.3. G_o values of 333, 592, and 925 are considered, which would correspond to in-situ shear wave velocities V_s of 120, 160 and 200 respectively prior to earthquake loading. The volumetric reconsolidation strains computed for these values of G_o are plotted versus r_u in Figure 3. The final volumetric strains range from 0.06 to 0.17% which is about an order of magnitude lower than expected based on experimental data (e.g., Figure 1). This simple example illustrates the order of magnitude of the discrepancy that is often observed in the reconsolidation strains computed using a number of different sand constitutive models.

3.1.2. Other model considerations

Other constitutive models include plastic strains during mean stress increases at a constant stress ratio by the introduction of additional plastic loading mechanisms, such as a cap type of loading surface or a more generalized yield surface (e.g., Taiebat and Dafalias 2008; Wang et al. 1990). These features may, or may not, improve predictions of post-liquefaction volumetric strains because they are not necessarily formulated to account for sedimentation strains. In any event, single element simulations can be used to evaluate the ability of these models to reproduce the range of post-liquefaction volumetric strains observed in laboratory element tests.

3.2. PM4Sand (Boulanger and Ziotopoulou 2012)

The sand plasticity model PM4Sand presented and modified herein for the effects of post-liquefaction reconsolidation follows the basic framework of the stress-ratio controlled, critical state compatible, bounding-surface plasticity model for sand presented by Dafalias and Manzari (2004). The Dafalias and Manzari (2004) model extended the previous work by Manzari and Dafalias (1997) by adding a fabric-dilatancy related tensor quantity to account for the effect of fabric changes during loading. Dafalias and Manzari (2004) provide a detailed description of the motivation for the model framework, beginning with a triaxial formulation that simplifies its presentation and then followed by a multi-axial formulation. Boulanger and Ziotopoulou (2012) provide detailed descriptions of all PM4Sand constitutive equations and terms, along with simulated element responses for a broad range of conditions. PM4Sand follows the conventional additive decomposition of strains, so that it cannot naturally capture reconsolidation settlements.

Modifications to PM4Sand were performed by developing an approximate phenomenological method of accounting for sedimentation strains during reconsolidation. The method has been incorporated in the model to provide more realistic estimates of reconsolidation strains by reducing the post-earthquake elastic shear modulus G (and hence the elastic bulk modulus K). Reducing the elastic moduli increases the post-liquefaction reconsolidation strains (e.g., Equations 2 and 4), thereby compensating for the sedimentation strains which are not explicitly modeled. The user may activate this feature after the end of strong shaking, such that post-liquefaction reconsolidation strains are better approximated in the remainder of the simulation.

The elastic shear and bulk moduli's reduction is based on the maximum fabric parameter z_{max} (a model input parameter), the cumulative fabric z_{cum} (a damage measure), the current stress-ratio M_{cur} and the slope of the dilatancy line M_d. Detailed descriptions of these parameters are given in Boulanger and Ziotopoulou (2012). A sedimentation mean effective stress p'_{sed} is introduced which controls the range of mean effective stresses over which reconsolidation strains are enhanced (i.e., elastic moduli are reduced):

$$p'_{sed} = p'_{sed_o} \cdot \left(\frac{z_{cum}}{z_{cum} + z_{\max}} \right) \cdot \left\langle 1 - \frac{M_{cur}}{M_d} \right\rangle^{0.25} \tag{7}$$

where the MacCauley brackets return zero if the argument is negative, and the sedimentation coefficient p'_{sedo} was calibrated to 20 kPa.

The elastic moduli reduction factor F_{sed} is calculated as a function of p' and p'_{sed}:

$$F_{sed} = F_{sed,min} + (1 - F_{sed,min}) \cdot \left(\frac{p'}{20 \cdot p'_{sed}} \right)^2 \leq 1 \quad (8)$$

where the constant $F_{sed,min}$ represents the smallest value that F_{sed} can attain. The value of F_{sed} progressively reduces from unity toward the value of $F_{sed,min}$ as z_{cum} progressively increases and provided that M_{cur} is less than M_d. The constant $F_{sed,min}$ was calibrated to a value of 0.04 for the results shown later.

The elastic shear G and bulk K moduli that will be applied to the soil during the post-liquefaction reconsolidation modeling phase are calculated by multiplying the reduction factor F_{sed} by the corresponding elastic moduli of the soil computed using the original constitutive relationships:

$$G_{(reduced)} = F_{sed} \cdot G \quad (9)$$

$$K_{(reduced)} = F_{sed} \cdot K \quad (10)$$

4. SINGLE ELEMENT SIMULATIONS

Performance of the PM4Sand constitutive model has been evaluated using single element and boundary value problem simulations. PM4Sand has been implemented as a user defined material for use with the commercial finite difference program, FLAC 7.0 (Itasca 2011). PM4Sand's numerical implementation scheme was developed to comply with the mixed discretization scheme used in FLAC's architecture (Marti and Cundall 1982). The goal of the generalized calibration of the model has been to produce drained and undrained, monotonic and cyclic responses under a broad range of stress conditions that are reasonably consistent with the range of behaviors observed for numerous sands as described in the technical literature and embodied in engineering design correlations (e.g., as commonly correlated to in-situ test data such as SPT, CPT and V_s data). The constitutive model has been shown to be relatively easy to calibrate and provide reasonable responses.

A similar calibration approach was followed for the modifications presented herein. Single element simulations of direct simple shear tests with a post-cyclic loading reconsolidation phase were used to calibrate the p_{sedo} and G_{sed} parameters so that the model provided a reasonable approximation of the progressive accumulation of volumetric strains during the post-cyclic reconsolidation phase and provided final reconsolidation strains that are consistent with the ranges observed experimentally (e.g., Figure 1). The resulting ability of the model to produce reasonable relationships between volumetric strains and maximum shear strain experienced during cyclic loading is illustrated in Figure 4 where results are presented for two cases: the first case was using the implementation of PM4Sand described in Boulanger and Ziotopoulou (2012), which does not include the modifications described in this paper, while the second case included the modifications presented in this paper. For both cases, Figure 4 illustrates the ultimate volumetric strain plotted versus the maximum shear strain γ (%) experienced during the undrained cyclic simple shear loading for three different relative densities of D_R = 35%, 55%, and 75%. Using the original PM4Sand implementation, the computed reconsolidation strains shown in Figure 4 are about an order of magnitude smaller than the laboratory results of Ishihara and Yoshimine (1992) presented in Figure 1. Using the modifications presented herein, the reconsolidation strains are in reasonable agreement with the laboratory results presented in Figure 1, both in their trends and magnitudes.

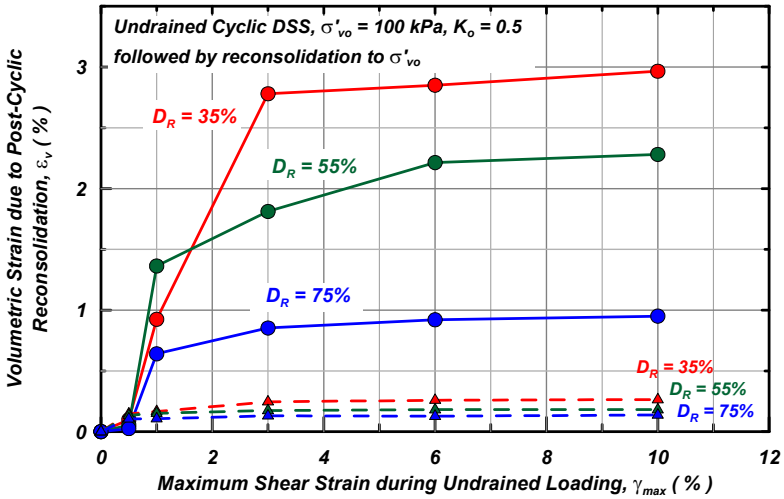


Figure 4 Volumetric strain due to post-cyclic reconsolidation versus the maximum shear strain induced during undrained cyclic DSS loading. Dashed lines correspond to PM4Sand before any modifications and solid lines correspond to PM4Sand implemented with the modifications for post-liquefaction volumetric reconsolidation strains.

5. RESPONSE OF PORT ISLAND LIQUEFACTION ARRAY

Port Island is a man-made island in Kobe city that experienced liquefaction damage during the 1995 M=6.9 Kobe earthquake (e.g., Ishihara et al. 1996). The soil profile and the SPT blowcounts N reported by Ishihara et al. (1996) are shown in Figure 6. The liquefiable layer was the approximately 18-m-thick Masado soil (decomposed granite). The water table was located at a depth of 3 m. Damage included ground surface settlements ranging from 20 to 50 cm across the island (Ishihara et al. 1996). Peak horizontal accelerations of 0.35g and 0.58g were recorded at the ground surface and at a depth of 16 m during the earthquake.

One-dimensional site response analyses of the site subjected to the north-south component of motion were performed using PM4Sand with the modifications presented in this paper in the program FLAC (Itasca, 2011). The liquefiable layer (i.e., submerged Masado fill) was modeled with PM4Sand while all other soil layers were modeled with a hysteretic damping model in FLAC. All model input parameters are reported in Ziotopoulou (2010).

Results are presented in Figure 6 for two analysis cases: the first case was using the implementation of PM4Sand described in Boulanger and Ziotopoulou (2012) which does not include the modifications described in this paper. The ground surface settlements versus time are shown in Figure 6 and the final reconsolidation volumetric strains are plotted versus depth in Figure 5. The final ground surface settlement of 0.03 m after the full dissipation of the earthquake-induced excess pore water pressures is about an order of magnitude smaller than what was observed. This final settlement corresponds to volumetric strains that are about 0.01% to 0.04% in the saturated Masado fill, which are consistent with the corresponding element simulations shown in Figure 4, which in turn are an order of magnitude smaller than commonly observed in laboratory element tests (Figure 1).

The second analysis case included the modifications to PM4Sand presented in this paper. The reduction in elastic moduli was applied to the PM4Sand materials at the end of strong shaking (at 46 sec). The ground surface settlements are shown in Figure 6 versus time and the final reconsolidation volumetric strains are plotted versus depth in Figure 5. In this case the settlements up to the end of shaking (at 46 sec) are identical to the ones obtained in the first analysis case because the reduction to the elastic moduli was not applied until that time. The settlements before 46 sec are limited by the rate at which water can seep out of the soil profile during shaking. The

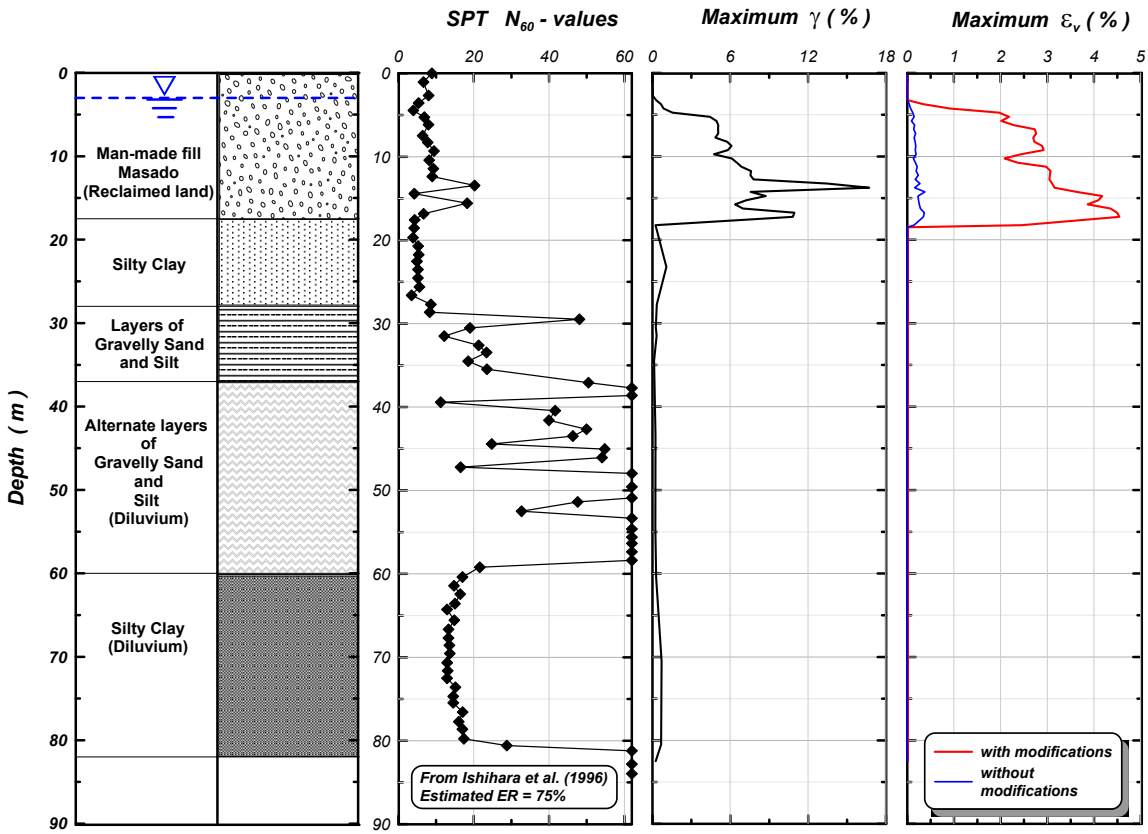


Figure 5 Port Island Array profile. Depth plots of SPT blow count N values (Ishihara et al. 1996) and distribution of maximum shear strains and maximum volumetric strains that developed during the dynamic and the post-liquefaction reconsolidation analyses respectively of the profile with and without the modifications presented in this paper.

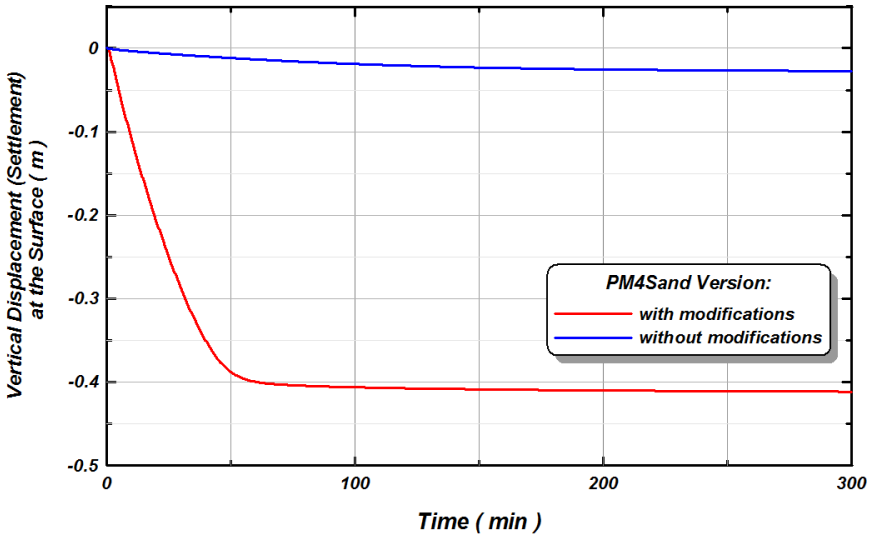


Figure 6 Comparison of vertical displacement time histories at the ground surface of the Port Island liquefaction array for PM4Sand with and without the modifications presented in this paper.

final ground surface settlement of 0.41 m after the full dissipation of the earthquake-induced excess pore water pressures is consistent with the observed settlements of 0.2 to 0.5 m. This final settlement corresponds to volumetric strains that are about 2.0% to 4.5% in the saturated Masado fill, which are consistent with the corresponding element simulations shown in Figure 4, which in turn are consistent with the ranges observed in laboratory element tests (Figure 1).

6. CONCLUSIONS

Modifications were implemented to the bounding surface plasticity constitutive model PM4Sand that provide a practical means for improved modeling of post-liquefaction reconsolidation strains after the end of strong shaking in a nonlinear deformation analysis. The modifications involve a reduction of elastic moduli (shear and bulk modulus) at low effective stresses by a factor that accounts for the soil's loading history through a cumulative fabric term; the reduction is elastic moduli is applied after the end of strong shaking (or cyclic loading) at a time specified by the user. The modified and calibrated model was shown to provide reconsolidation strains that are consistent with the ranges observed experimentally (e.g., Ishihara and Yoshimine 1992), and thus overcomes a common limitation of elastic-plastic soil models. The modified model was applied to a case history and shown capable of significantly improving predictions of liquefaction-induced ground surface settlements. Additional work is needed, however, to develop constitutive and numerical modeling approaches that can more mechanistically simulate post-liquefaction reconsolidation strains without distinguishing between the strong-shaking and post-strong shaking portions of a simulation.

Acknowledgements:

Travel by the authors to this event was supported by the Japan Ministry of Education, Culture, Sport, Science, and Technology (MEXT) through the Center for Urban Earthquake Engineering (CUEE). Support for K. Ziotopoulou was provided by the 2008 International Fulbright Science and Technology Award from the Institute of International Education and the U.S. Department of State. Additional support was provided by the California Division of Safety of Dams. The authors appreciate the above support and the assistance of numerous colleagues with various aspects of the work presented herein.

References:

Andrianopoulos, K. I., Papadimitriou, A. G., and Bouckovalas, G. D. (2010), "Bounding surface plasticity model for the seismic liquefaction analysis of geostructures," *Soil Dynamics and Earthquake Engineering,* 30, 895–911.

Boulanger R. W., and Ziotopoulou K. (2012), "PM4Sand (Version 2): A sand plasticity model for earthquake engineering applications," Report No. UCD/CGM-12/01, *Center for Geotechnical Modeling*, Department of Civil and Environmental Engineering, University of California, Davis, CA, 2012; 100 pp.

Dafalias, Y. F., and Manzari, M. (2004), "Simple plasticity sand model accounting for fabric change effects," *Journal of Engineering Mechanics*, ASCE, 130(6), 622-634.

Idriss, I. M., and Boulanger, R. W. (2008), "Soil liquefaction during earthquakes," Monograph MNO-12, *Earthquake Engineering Research Institute*, Oakland, CA, 261pp.

Ishihara, K., Yasuda, S., and Nagase, H. (1996), "Soil characteristics and ground damage," *Special Issue of Soils and Foundations*, January, 109−118.

Ishihara, K., and Yoshimine, M. (1992), "Evaluation of Settlements in Sand Deposits Following Liquefaction during Earthquakes," *Soils and Foundations*, Vol. 32, No. 1, pp. 173-188.

Itasca (2011), "FLAC – Fast Lagrangian Analysis of Continua, Version 7.0," Itasca Consulting Group, Inc., Minneapolis, Minnesota 2011.

Kokusho, T. (1999), "Water film in liquefied sand and its effect on lateral

spread," *Journal of Geotechnical and Geoenvironmental Engineering*, 125(10), 817–826.

Kulasingam, R., Malvick, E. J., Boulanger, R. W., and Kutter, B. L. (2004), "Strength loss and localization at silt interlayers in slopes of liquefied sand," *Journal of Geotechnical and Geoenvironmental Engineering*, ASCE, 130(11), 1192-1202.

Manzari M. T., and Dafalias Y. F. (1997), "A critical state two-surface plasticity model for sand," *Géotechnique*; 47(2): 255-272.

Marti J., and Cundall P. A. (1982), "Mixed discretization procedure for accurate solution of plasticity problems," *International Journal on Numerical Methods and Analytical Methods in Geomechanics*, 6, 129-139.

Papadimitriou, A. G., Bouckovalas, G. D., and Dafalias, Y. F. (2001), "Plasticity model for sand under small and large cyclic strains," *Journal of Geotechnical and Geoenvironmental Engineering*, 127(11), 973–983.

Sento, N., Kazama, M., Uzuoka, R., Matsuya, A., and Ishimaru, M. (2004), "Liquefaction-induced volumetric change during re-consolidation of sandy soil subjected to undrained cyclic loading histories," in *Cyclic Behaviour of Soils and Liquefaction Phenomena,* Proceedings of the International Conference, Bochum, Germany, 31 March-2 April, ed. Th. Triantafyllidis, Taylor & Francis, pp. 199-206.

Taiebat, M., and Dafalias, Y. F. (2008), "SANISAND: simple anisotropic sand plasticity model," *International Journal for Numerical and Analytical Methods in Geomechanics*, 32(8), 915–948.

Tokimatsu, K., and Seed, H. B., (1987), "Evaluation of settlements in sands due to earthquake shaking", *Journal of Geotechnical Engineering*, ASCE 113(GT8), 861–78.

Wang, Z. L., Dafalias, Y. F., and Shen, C. K. (1990), "Bounding surface hypoplasticity model for sand." *Journal of Engineering Mechanics,* 116(5), 983–1001.

Yang, Z., Elgamal, A., and Parra, E., (2003), "A Computational Model for Liquefaction and Associated Shear Deformation," *Journal of Geotechnical and Geoenvironmental Engineering*, ASCE, 129(12), 1119-1127.

Ziotopoulou, K. (2010), "Evaluating model uncertainty against strong motion records at liquefiable sites," Masters thesis, University of California, Davis, 294 pp.

10CUEE CONFERENCE PROCEEDINGS
10th International Conference on Urban Earthquake Engineering
March 1-2, 2013, Tokyo Institute of Technology, Tokyo, Japan

MODELING OF EARTHQUAKE INDUCED UPLIFT OF TUNNELS IN LIQUEFIABLE SOIL

Siau Chen Chian[1], and Kohji Tokimatsu[2]

1) Research Fellow, Center for Urban Earthquake Engineering, Tokyo Institute of Technology, Japan
2) Professor, Department of Architecture and Building Engineering, Tokyo Institute of Technology, Japan
chian@cuee.titech.ac.jp, kohji@o.cc.titech.ac.jp

Abstract: Tunnels buried in liquefiable sand deposits may suffer uplift following a major earthquake. Numerical modeling supported with centrifuge experiment on shallow circular tunnels were conducted and have shown to be capable of replicating such uplift failure mechanism with similar excess pore pressure and uplift displacement of a circular buried structure. The uplift of the tunnel was initiated following the rapid excess pore pressure generation. After the soil had liquefied, the rate of uplift came to a constant value despite further uniform cyclic shearing produced by the shaking. This substantiates the presence of a shear modulus degradation limit. Minimal uplift displacement of the tunnel was observed after shaking despite the retention of high excess pore pressure. This implied that the duration of cyclic shearing has a direct influence on the accumulation of uplift displacement of the tunnel. In addition, this refutes the hypothesis that liquefied soil can be assumed as a viscous fluid. Soil dilation near the face of the tunnel as observed in the centrifuge experiment was successfully produced in the numerical analysis. Given the general matching results between the numerical and centrifuge models, it is evident that the constitutive soil model was effective in replicating the floatation response of the structure in the centrifuge test.

1. INTRODUCTION

Faced with the growing demand for effective transportation network, coupled with the scarcity of land in urban areas, underground highway and railway construction has been increasingly popular in the past few decades. Many of these transportation facilities, such as the George Massey Tunnel in Vancouver and the Bay Area Rapid Transit (BART) Tunnel in San Francisco lie in soil deposits which are highly susceptible to soil liquefaction in the event of a major earthquake. Each of these large scale underground structures carries thousands of commuters and evidently poses extreme concerns to public safety. Large diameter natural gas pipelines in New Mexico, Japan and Canada are similarly confronted with likelihood of damage following an earthquake. It is therefore imperative to conduct in-depth research to ensure such seismic risks are mitigated.

This paper presents a section of the numerical and experimental studies carried out on the uplift of tunnels buried in liquefied sand deposits. Verification on the performance of the constitutive soil model was also conducted based on the Wildlife Liquefaction Array recording of the 1987 Superstition Hills Earthquake.

2. SIMPLIFIED UPLIFT MECHANISM

Underground structures such as tunnels are generally subjected to a buoyant force due to their lower submerged unit weight than the surrounding soil. This buoyancy force (F_B) governed by Archimedes Principle is counteracted by the weight of the tunnel (F_T), effective surcharge of the overlying soil (F_{WS}) and the shear resistance from the soil (F_{SP}). The force equilibrium is illustrated in Figure 1.

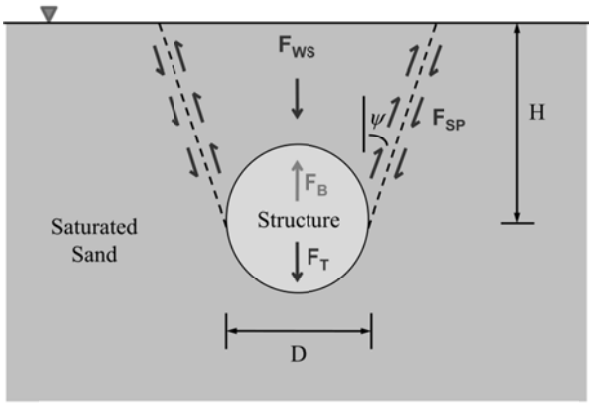


Figure 1 Forces Acting on Tunnel at Static Condition

In the event of soil liquefaction, the shear strength of the soil is significantly reduced, which in turn decreases the shear resistance from the soil inhibiting the uplift of the tunnel. In addition, the generation of excess pore pressure may also induce an upward force at the invert of the tunnel which encourages the floatation of the tunnel.

3. NUMERICAL MODELLING

3.1 Background

Numerical analyses were performed using FLAC (Fast Lagrangian Analysis of Continua), a finite difference program code developed by Itasca Consulting Group. The program has been widely used in various geotechnical problems such as slope stability, embankment, deep excavation and tunneling. It is also capable of simulating yielding and flow of materials at large strain (Itasca, 2011), and hence suitable for soil liquefaction problems.

A user-defined continuum soil model, Wang model (Wang *et al.*, 1990) was applied to the analysis to simulate soil liquefaction properties and response. The Wang model is a non-linear, fully-coupled bounding surface plasticity constitutive model for sand, specifically formulated to capture the contraction and dilation induced by shear stress applied to the soil. Figure 2 illustrates the failure surface, maximum pre-stress surface and phase transformation line considered in the model.

The constitutive model-dependent parameters, namely the modulus coefficient defining the small strain elastic shear modulus (G_0), the reduction of shear modulus with increasing strain amplitude (h_r) and the blow count related parameters (k_r and d) were calibrated to produce similar contractive and dilative responses as typical cyclic laboratory tests of loose saturated sand (e.g. Toyoura sand). Details of the calibration procedure and conformance of the constitutive model with cyclic laboratory tests were discussed by Wang *et al.* (1990, 2006) and Wang and Makdisi (1999).

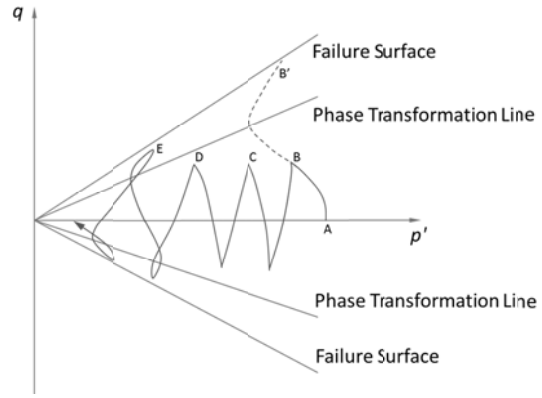


Figure 2 Effective Stress Paths under Monotonic (Path ABB´) and Cyclic Undrained Triaxial Loading (Path ABCDE) (from Wang *et al.*, 1990).

The numerical analyses presented in this paper were carried out as a plane strain condition and the tunnel lining was assumed as rigid. The boundary condition at the sides of the model must account for the semi-infinite free-field condition. Given the application of only a simple 1-D input wave, the free-field condition was achieved by applying a one-dimensional free-field calculation in parallel with the main-grid analysis, and applied to the sides of the main-grid analysis. Absorbing boundaries were also applied to the sides of the main-grid to ensure minimal seismic wave reflections (Cundall *et al.*, 1980).

3.2 One-Dimensional Soil Analysis

In order to verify the suitability of the constitutive soil model for soil liquefaction analysis, the site response of the Wildlife Liquefaction Array was simulated. The Wildlife Liquefaction Array is located in the Imperial Valley desert of southern California. The most significant recording was the soil liquefaction following the 1987 Superstition Hills Earthquake (Holzer and Youd, 2007). Figure 3 illustrates the soil profile of the site. The soil profile was kept simple as the key objective of this simulation was to assess the soil response between a liquefied and non-liquefied site produced by the constitutive model, rather than to obtain accurate depiction of the observation on site. The absence of Love waves in the numerical analysis, which contributed 13 to 35% of the excess pore pressure generation following the earthquake (Holzer and Youd, 2007), also meant that it was even more difficult to obtain exact replication of the observations on site. As such, the soil profile was merely used as a basis for the numerical simulation on a real site. The input acceleration to the numerical model was based on the deepest accelerometer recording at 7.5m depth of soil in the NS direction. In order to assess the response of a non-liquefied soil deposit, an identical numerical model was subjected to a weaker input acceleration of 0.1 times the amplitude of the former input acceleration. Figures 4 and 5 show the results obtained from the above mentioned simulations.

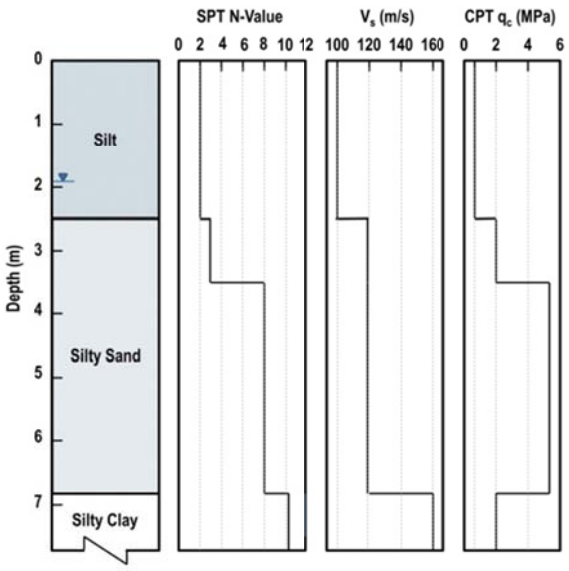
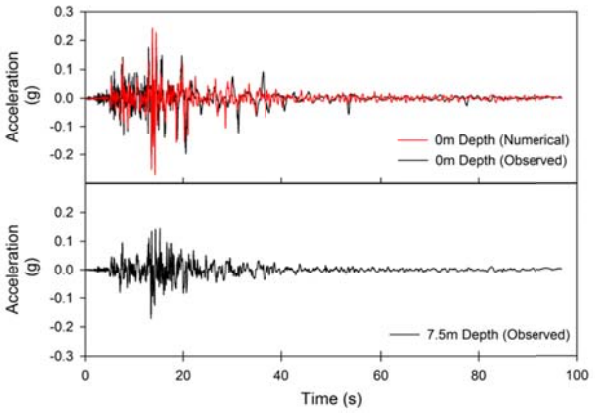


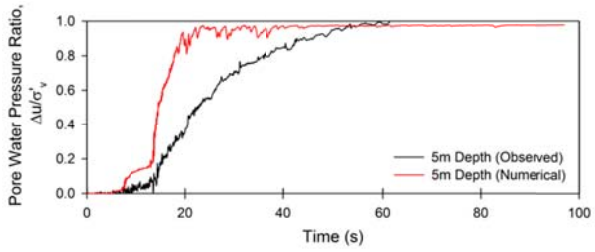
Figure 3 Simplified Wildlife Liquefaction Array Soil Profile and Properties (adapted from Bennett *et al.*, 1984)

In Figure 4, soil liquefaction was achieved in both the numerical analysis and observed data sometime past 20 seconds of earthquake shaking. This was supported by the presence of sharp spikes of acceleration spaced at long periods and excess pore pressure ratio near 1.0. The differences between the observed and numerical results were likely due to the simplified soil profile and the absence of long period Love waves in the numerical analysis. Nevertheless the numerical analysis was able to replicate the response spectra especially at the period range before 0.5 seconds where the natural period of the site lies

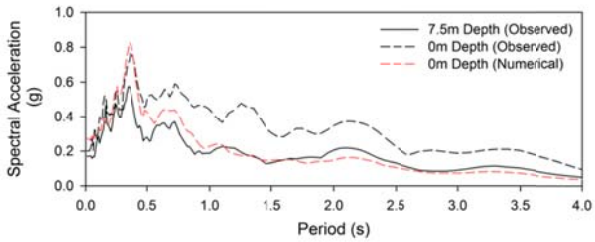
(approx. 0.28 seconds). The lower spectral acceleration predicted at longer period could possibly be due to absence of the long period Love waves which produced large (approx. 1.5%) cyclic shear strains after the strong shear wave abated (Holzer and Youd, 2007) as discussed earlier . Such significant cyclic shear strain would also affect the process of soil softening and thereby altering the long period response of the soil. Such hypothesis was inferred by several publications which similarly predicted lower than observed response spectra at long periods of the response spectra (Youd and Carter, 2003; Ziotopoulou *et al.*, 2012).



(a) Acceleration



(b) Excess Pore Pressure Ratio

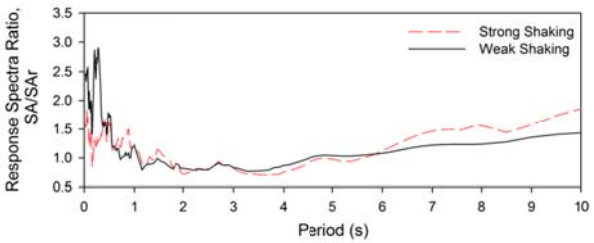


(c) Response Spectra

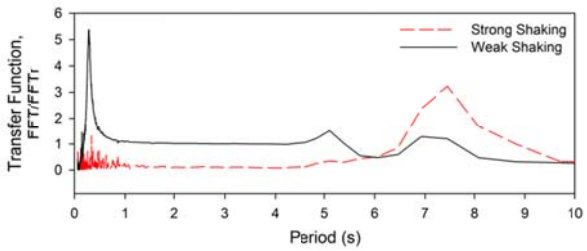
Figure 4 Wildlife Liquefaction Array Simulation on the 1987 Superstition Hills Earthquake

The constitutive soil model was further verified with response spectra ratio and transfer function plots in Figure 5. In the case of the site response between liquefied and non-liquefied soil, it was anticipated that shear wave propagation through a liquefied soil would be inhibited due to the loss of shear stiffness of the soil. As such, low period wave recordings at the soil surface would be attenuated. This is portrayed in the numerical analysis between a strong shaking (the actual 1987 Superstition Hills Earthquake) and a weaker shaking (0.1 times of the same Superstition Hills Earthquake) as shown below in Figure 5. A lower response spectra ratio at the initial natural period of the site (approx. 0.28 seconds) was produced in the case of the strong shaking. The loss of shear stiffness due to soil liquefaction also amplified the longer period waves, hence indicating a shift in the dominant peak of the response spectra ratio plot as evident in Figure 5a.

The above findings were further substantiated by the transfer function which was computed as the ratio of the Fast Fourier Transform at the surface and the base of the numerical models. The weaker shaking produced a natural period of about 0.26s for the 7.5m thick soil deposit (shear wave velocity, V_s of 115m/s) as indicated at the dominant peak in Figure 5b. However, the peak was no longer obvious in the case of the strong shaking. Instead, the dominant peak was located at about 7.4s (V_s of approx. 4m/s), hence confirming a sensible effect of soil liquefaction.



(a) Response Spectra Ratio



(b) Transfer Function

Figure 5 Liquefied and Non-Liquefied Site Responses

4 NUMERICAL AND CENTRIFUGE SIMULATION OF TUNNEL UPLIFT IN LIQUEFIABLE SOIL

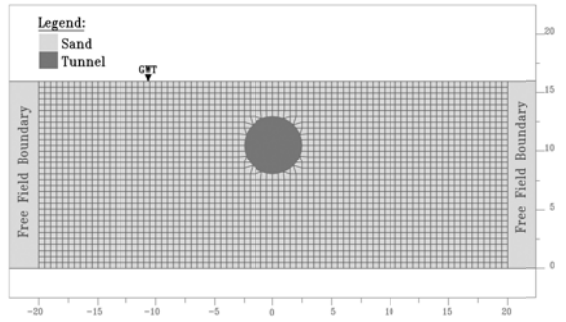
Based on the above Wildlife Array simulation, the FLAC program accompanied with the Wang constitutive soil model has demonstrated its suitability in simulating soil liquefaction condition. A numerical analysis on the uplift of tunnel was subsequently carried out and supported with a centrifuge experiment. The material properties of the sand in centrifuge test are shown in Table 1. Figure 6 shows the soil model layout for the numerical analysis and the centrifuge test.

In order to reduce reflecting incident stress waves due to the rigid boundary of the centrifuge model container, 25mm of moldable Duxseal was placed on the sides of the container to

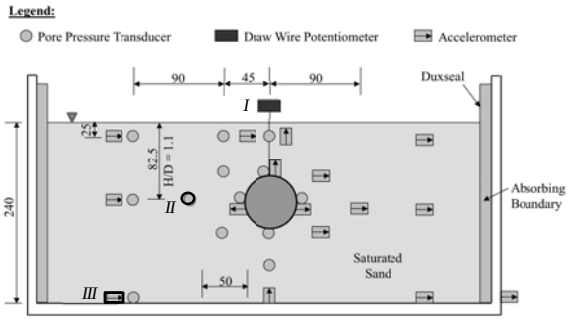
reduce reflecting incident stress waves by at least 65% (Steedman and Madabhushi, 1991), as well as achieving semi-infinite boundaries given its compressibility properties (Cheney *et al.*, 1988). The Duxseal remained stable and did not show any unusual deformation after each centrifuge testing. This substantiates optimum molding of the Duxseal to achieve the desired boundary condition.

Table 1 Material Properties of Hostun Sand

Properties	Hostun sand
ϕ_{crit}(°)	33
D_{10}(mm)	0.209
D_{50}(mm)	0.335
e_{min}	0.555
e_{max}	1.01
G_s	2.65



(a) Numerical Model



(b) Centrifuge Test

Figure 6 Soil Model Layout: for Numerical and Centrifuge Models

An automatic sand pourer, which relied on the concept of sand pluviation by gravity, was used to achieve a 45% relative density of the sand. A circular hollow structure with closed ends was buried in the sand at a depth of 1.1 times of its diameter. The sand was subsequently saturated with high viscous fluid of kinematic viscosity (in cSt) equivalent to the centrifuge g-level. By increasing the viscosity of the pore fluid in the sand, the rate of excess pore pressure generation (due to earthquake loading) and the rate of dissipation (due to soil consolidation) are both matched. Centrifuge g-level of 66.7g was used to scale the model tunnel of 75mm in diameter to the prototype scale of 5m in diameter. The mass of the tunnel including attached instruments at prototype scale was about 6 tons (specific gravity, G_s of 0.3). Near sinusoidal earthquake shaking of about 27 seconds at 0.75 Hz at prototype scale was applied at the base of the soil model while it was in-flight.

Figure 7 shows the results obtained from the numerical analysis and the centrifuge test. It was observed that both results were comparable. Excess pore pressure was generated rapidly with the application of shaking and attained near full liquefaction in about 4 cycles of shaking. As discussed earlier, the simplified theoretical floatation mechanism suggests that a buoyant structure may float when the soil's shear strength from its inter-particle frictional contact is reduced with the generation of excess pore water pressure. Floatation of the tunnel is hence assumed to be initiated due to build-up of high pore water pressure. This is substantiated with the commencement of the uplift as observed in the numerical analysis and centrifuge test in Figure 7.

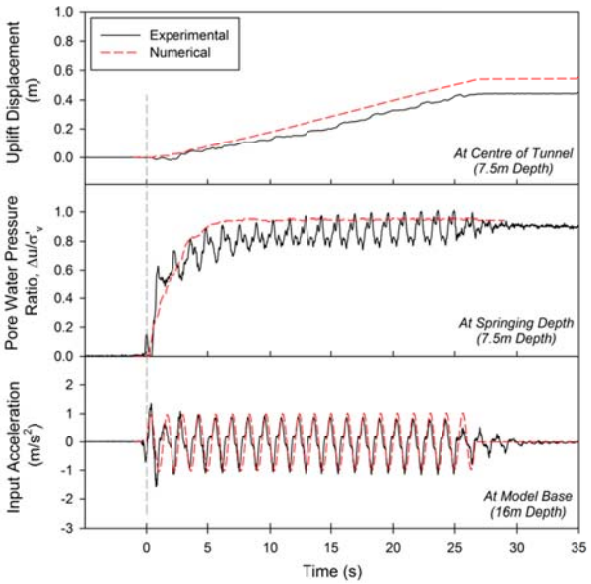


Figure 7 Tunnel Uplift Displacement (*I*), Far Field Pore Water Pressure Ratio (*II*) and Input Acceleration (*III*) Time Histories

Some differences were present between the numerical analysis and centrifuge test result. The far field excess pore pressure obtained from the numerical analysis was slightly higher than the mean values from the centrifuge test after the initial few cycles of shaking. This led to the higher rate of uplift of the tunnel during that time frame, thereby resulting in a higher final uplift displacement of the tunnel. This infers that the rate of uplift of the tunnel was highly dependent on the excess pore pressure. The generation of excess pore pressure leading to soil liquefaction was due to cyclic shearing of the soil which also led to degradation of the soil's shear modulus. A lower shear modulus encourages the uplift of the tunnel. However, a limit of the shear modulus degradation exists where cyclic degradation no longer takes place with further shearing (Lo Presti *et al.*,

2004). As such, the rate of uplift of the tunnel would arrive at a constant value after the soil had liquefied. This is supported by both the numerical analysis and the centrifuge test result in Figure 7. Given the general matching results between the numerical and centrifuge models, it is evident that the constitutive soil model was effective in replicating the floatation response of the structure in the centrifuge test.

After the end of the shaking, minimal uplift displacement of the tunnel was observed in both the numerical analysis and centrifuge experiment, despite retaining high excess pore pressure. This implied that the duration of cyclic shearing has a direct influence on the accumulation of uplift displacement of the tunnel, in addition to the liquefied soil condition. As such, the uplift displacement of an underground structure can be estimated based on the knowledge of the cyclic shear modulus degradation, excess pore pressure generation and the duration of the shaking.

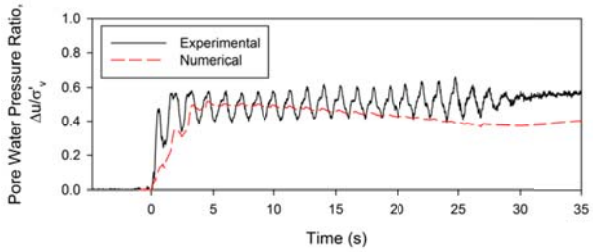


Figure 8 Near Field Pore Water Pressure Ratio at Springing Depth of Tunnel

At the near field (i.e. face) of the tunnel, studies have shown that soil dilation arising from the cyclic displacement of the tunnel relative to the surrounding soil exists around an uplifting tunnel (Chian and Madabhushi, 2012). Figure 8 shows the near field pore water pressure ratio measured at the springing (i.e. mid-depth) of the tunnel. In the figure, soil liquefaction was not pronounced at the face of the tunnel despite attaining near full liquefaction in the far-field as shown in Figure 7. In addition, the numerical analysis produced a decreasing pore water pressure ratio as compared to the centrifuge test as shown in Figure 8. Such reduction in pore pressure is likely due to the increased shearing of the soil at the tunnel interface. This hypothesis is supported by the higher rate of uplift of the tunnel after 5 seconds of shaking in the numerical analysis as observed in Figure 7. These observations clearly demonstrate that the numerical analysis was capable of producing the dilative effect inferred by the lower excess pore pressure. Such reduction in excess pore pressure near the tunnel would inevitably have consequences in the design and performance of underground structures against seismic uplift in liquefiable soil deposits.

5. CONCLUSIONS

Liquefaction induced uplift failure of tunnels was investigated with numerical and centrifuge modeling. The FLAC program accompanied with the Wang constitutive model for soil liquefaction was applied to the study. The performance of the numerical package was assessed with the Wildlife Liquefaction Array case study and has shown to be capable of producing soil liquefaction responses and properties. The uplift of shallow circular tunnels was investigated with numerical modeling and centrifuge testing. Both modeling techniques were capable of replicating such uplift failure mechanism with similar excess pore pressure and uplift displacement of a circular buried structure. Rapid excess pore pressure generation was followed by the uplift of the tunnels. The rate of uplift of the tunnel was found to be highly dependent on the excess pore pressure, and came to a constant value after the soil had fully liquefied. This substantiates that a limit of the shear modulus degradation exist where cyclic degradation no longer takes place with further shearing. Minimal uplift displacement of the tunnel was observed after shaking despite retaining high excess pore pressure, thereby implying that the duration of cyclic shearing has a direct influence on the accumulation of uplift displacement of the tunnel. This observation also refutes the hypothesis that liquefied soil can be assumed as a viscous fluid. Soil dilation near the face of the tunnel as observed in the centrifuge experiment was produced in the numerical analysis. These consistencies undoubtedly demonstrate and pave the prospects of applying similar numerical analyses and centrifuge tests for geotechnical problems associated with the uplift of underground structures in liquefiable soil deposits.

Acknowledgement:

The authors are grateful for the support from the Japan Ministry of Education, Culture, Sport, Science, and Technology (MEXT) via the "International Urban Earthquake Engineering Center for Mitigating Seismic Mega Risk" program at Tokyo Institute of Technology, and the Cambridge Trust at the University of Cambridge.

References:

Bennett, M.J., McLaughlin P.V., Sarmiento, J.S. and Youd, T.L. (1984), "Geotechnical Investigation of Liquefaction Sites, Imperial Valley, California," *U.S. Geological Survey*, Open-File Report 84-252.

Cheney, J., Hor, O., Brown, R. and Dhat, N. (1988), "Foundation Vibration in Centrifuge Models," *Proceedings of Centrifuge 88*, 481–486.

Chian, S.C. and Madabushi, S.P.G. (2012), "Excess Pore Pressures Around Underground Structures Following Earthquake Induced Liquefaction," *International Journal of Goetechnical Earthquake Engineering* **3**(2), 25-41.

Cundall, P.A., Hansteen, H., Lacasse, S. and Selnes, P. (1980), "NESSI – Soil Structure Interaction Program for Dynamic and Static Problems," *Norwegian Geotechnical Institute*, Report 51508-9.

Holzer, T.L. and Youd, T.L. (2007), "Liquefaction, Ground Oscillation, and Soil Deformation at the Wildlife Array, California," *Bulletin of the Seismological Society of America* **97**(3), 961-976.

Itasca Consulting Group, Inc. (2011), "FLAC (Fast Lagrangian Analysis of Continua), Version 7," Minneapolis, U.S.A.

Lo Presti, D., Lai, C. and Foti, S. (2004), "Geophysical and Geotechnical Investigations for Ground Response Analyses," *Proceedings of the Recent Advances in Earthquake Geotechnical Engineering and Microzonation*, 101-138.

Steedman, R.S. and Madabhushi, S.P.G. (1991), "Wave Propagation in Sand Medium," *Proceedings of the International Conference on Seismic Zonation*, Vol. II, 253-260.

Wang, Z.L., Dafalias, Y.F. and Shen, C.K. (1990), "Bounding Surface Hypoplasticity Model for Sand," *Journal of Engineering Mechanics*, **116**(5), 983-1001.

Wang, Z.L. and Makdisi, F.I. (1999), "Implementing a Bounding Surface Hypoplasticity Model for Sand into the FLAC Program," *Proceedings of the International Symposium on Numerical Modeling in Geomechanics*, 483-490.

Wang, Z.L., Makdisi, F.I. and Egan, J. (2006), "Practical Applications of a Non-Linear Approach to Analysis of Earthquake-Induced Liquefaction and Deformation of Earth Structures," *Soil Dynamics & Earthquake Engineering*, **26**, 231-252.

Youd, T.L. and Carter, B.L. (2003), "Influence of Liquefaction on Response Spectra at Wildlife, California and Port Island, Japan Instrument Sites," *Proceedings of the Eighth U.S.-Japan Workshop on Earthquake Resistant Design of Lifeline Facilities and Countermeasures Against Liquefaction*, 613-624.

Ziotopoulou, K., Boulanger, R.W. and Kramer, S.L. (2012), "Site Response Analysis of Liquefying Sites," *Proceedings of the GeoCongress*, 1799-1808.

10CUEE CONFERENCE PROCEEDINGS
10th International Conference on Urban Earthquake Engineering
March 1-2, 2013, Tokyo Institute of Technology, Tokyo, Japan

EFFECTS OF NON-HOMOGENEITY ON LIQUEFACTION IN STRATIFIED SOIL DEPOSITS

Manika Maharjan[1] and Akihiro Takahashi[2]

1) Graduate Student, Department of Civil and Environmental Engineering, Tokyo Institute of Technology, Japan
2) Associate Professor, Department of Civil and Environmental Engineering, Tokyo Institute of Technology, Japan
maharjan.m.aa@m.titech.ac.jp ,takihiro@cv.titech.ac.jp

Abstract: Natural sand deposit normally consists of many sub layers with different soil particles and properties, ranging from soft sand lenses to stiff cohesive clay and coarse sand layers, referred as non-homogeneous soil deposits. The actual soil profile characterized by various patterns of layering and lensing is very complex, which may have great effect on geotechnical engineering problems at a site. The effects of non-homogeneity on liquefaction in stratified soil deposits are investigated by carrying out a series of dynamic centrifuge tests and numerical simulations. Non-homogeneity in the tests is incorporated by including the periodically distributed silt patches. The centrifuge tests were also conducted on uniform homogeneous and continuous layered soil deposits for the comparison purposes. Two dimensional finite element analyses based on extended sub-loading surface model are carried out. Simulation results are compared to the centrifuge test measurements and observations. The experimental and numerical results shows that more excess pore water pressure remains for a longer period of time at discontinuous region in non-homogeneous soil deposits compared to the uniform and continuous layered soil deposits. The dissipation of excess pore water pressure becomes the dominant mechanism for non-uniform settlement after the seismic excitation as the pore pressure generation ceases the supply of new mass of water. The rapid dissipation of excess pore water pressure through the discontinuous part in the non-homogeneous soil deposits manifest a larger settlement at the corresponding part, causing non-uniform settlements.

1. INTRODUCTION

Liquefaction has been reported as a cause of severe damage to foundations of buildings, bridges and other structures, as well as to ports and buried lifelines during past major earthquakes. During earthquakes, saturated sandy soils are characterized by substantial rise in excess pore water pressure, leading to dramatic loss of strength and stiffness. When this excess pore pressure reaches a value equal to the initial effective stress, soil particles do not support each other, referred to as a zero effective stress condition; a state of initial liquefaction (NRC 1985; Ishihara and Yoshimine 1992; Fiegel and Kutter 1994; Kramer 1996; Brennan and Madabhushi 2005). Following the two devastating earthquakes viz. the 1964 Niigata and 1964 Great Alaska Earthquakes, many geotechnical earthquake engineering research programs on liquefaction were initiated in Japan and North America. These have provided researchers with better insight into the liquefaction phenomenon and associated failures. Initially, the study was only focused on assessing the triggering factors for liquefaction in clean, sandy soils. As the years passed, physical model studies on layered soil deposits evolved. Various experimental studies based on the physical model tests, such as one dimensional column tests (Kokusho 1999; Tohumcu Özener et al. 2008), shaking table tests (Liu and Qiao 1984; Kokusho 1999), and centrifuge model tests (Dobry and Liu 1992; Fiegel and Kutter 1994; Balakrishnan and Kutter 1999; Kulasingam et al. 2004; Brennan and Madabhushi 2005) as well as site investigations (Kokusho and Fujita 2002) and numerical analyses (Yoshida and Finn 2000; Seid-Karbasi and Byrne 2007; Lu and Cui 2010) have been conducted to examine the effects of liquefaction in stratified sands. All of the studies concluded that the presence of relatively impermeable layer (silt) within the liquefiable deposits results in the formation of a water film beneath it. The excess pore water squeezed from the liquefied sand is trapped by a relatively impermeable sub-layer and forms a water film beneath it, which has a key role in the extent of lateral deformations in the sloping surface (Kokusho 1999; Kokusho 2000; Kokusho and Kojima 2002).

It is noted that the real soil profile is complex and a soil deposit is neither uniform nor consists of continuous layers. Natural sand deposit normally consists of many sub-layers with different soil particles and properties, ranging from soft sand lenses to stiff cohesive clay and coarse sand layers. Ghosh et al. (2005) performed a series of centrifuge tests to analyze the effects of localized loose sand in a dense sand deposit subjected to seismic loading. It was found that the soft layer has significant influence on the overall response of the layered strata. Chakrabortty and Popescu (2012) also conducted a series of centrifuge tests on homogeneous and heterogeneous soil deposits followed by numerical simulation, where the heterogeneous model consisted loose pockets of same sand with lower relative density. The results showed more excess pore water pressure is generated in a heterogeneous soil deposits than in corresponding

homogeneous soil. However, the stratification of soil profile is not only limited to soft layers involving one type of soil material as considered by Chakrabortty and Popescu (2012); it consists of many discontinuous layers ranging from highly permeable liquefiable to impermeable non-liquefiable layers. The patterns of layering and lensing in an actual soil profile can be extremely complex and have great effect on geotechnical engineering problems at a site (NRC 1985). In order to systematically predict the earthquake response of saturated porous media it is essential to correctly simulate the generation, redistribution, and dissipation of excess pore water pressure during and after earthquake shaking, which are the major mechanisms in case of real soil profile (Taiebat et al. 2010). To the best knowledge of authors, numerical or experimental studies related to the presence of discontinuous less permeable layer in the liquefiable soil have not been carried out. Therefore, liquefaction potential of non-homogeneous soil profile is not well understood, though many liquefaction case histories exist.

In this study, the effects of non-homogeneity in stratified soil deposits are investigated by carrying out four dynamic centrifuge tests and numerical simulations. Two of the model tests were conducted on non-homogenous soil deposits. Non-homogeneity was incorporated by including periodically distributed silt patches with a lower permeability than the liquefiable soil specimen with the same length of discontinuities in each layer, which will be referred as drainage layer hereafter. For reference, tests on a uniform soil deposits and continuous layered soil deposit were also conducted. Laminar containers were used in all the tests to properly simulate the boundary conditions. Two dimensional finite element analyses based on extended sub-loading surface model were carried out. Simulation results are compared to the centrifuge test measurements and observations. The main objective of the study is to enhance the understanding of liquefaction mechanism in non-homogenous soil deposits and to systematically study the effects of non-homogeneity of the soil deposit on the amount of excess pore water pressure, drainage path, and settlement of the liquefiable soils.

2. CENTRIFUGE MODEL TEST PROCEDURES AND CONDITIONS

2.1 Soil and pore fluid

Toyoura sand and Silica sand No.8 were used in all four centrifuge tests (Table 1). The difference between the permeability of the sands is of order 1; Silica sand No. 8, referred as silt, being less permeable, was employed to create the continuous relatively impermeable layer in Model 2 and discontinuous relatively impermeable layer in Models 3 and 4, creating non-homogeneity in soil deposits.

The models were saturated with a viscous fluid in order to ensure accurate simulation of prototype soil permeability. The viscous fluid was a mixture of water and 2% Metolose (Hydroxypropylmethyl cellulose from Shin-Etsu Chemical Company) by weight of water to achieve a viscosity of about 40 times the viscosity of water. It has also been shown in previous research that this type of viscous fluid neither disturbs nor adversely affects the dynamic properties of cohesionless soil (Okamura et al. 2001). The density and surface tension of this solution is practically identical to that of water. Therefore, the highly viscous Metolose solution ensured accurate simulation of prototype soil permeability of a fine sand and silt when the models were tested at centrifugal acceleration of 40g.

Table 1 Index properties of soils

Property	Toyoura sand	Silica sand No. 8(Silt)
Specific gravity, G_s	2.65	2.65
D_{50}(mm)	0.19	0.10
D_{10} (mm)	0.14	0.041
Maximum void ratio, e_{max}	0.973	1.333
Minimum void ratio, e_{min}	0.609	0.703
Permeability, k (m/s)at Dr=50%	2×10^{-4}	2×10^{-5}

2.2 Model preparation

Models were constructed in a flexible laminar container with dimensions of 500×200×450 mm in length, width, and height, respectively, which allows the container to deform dynamically with the soil layer. The models were prepared by air pluviation method to the depth of 225 mm in model scale, where sand was poured from a hopper which was moved manually back and forth along the longest dimension of the box, and the falling height was kept constant to obtain the desired relative density. Accelerometers and pore pressure transducers were installed at the desired locations during model preparation. The colored noodles 'somen' were placed at the sand-silt interface to trace the deformation pattern. During the preparation of non-homogeneous soil deposits, Toyoura sand was deposited first by the help of two light weighted blocks placed on both sides (Fig. 1). Then, the remaining parts were filled with Silica sand No.8 by air pluviation method. The de-aired Metolose solution was dripped slowly from the top of the container under a vacuum of 760 mmHg until the solution level reached the desired elevation. The saturation process for all the tests required approximately 30 hours. After saturation, the sand was again poured by air pluviation method to make the total height equal to 245 mm in model scale so that the water table was 20 mm below the surface in model scale and finally laser displacement transducers and potentiometers were placed at the surface. After preparation, the models were placed in Tokyo Tech Mark III centrifuge (Takemura et al. 1999) and spun at centrifugal acceleration of 40g.

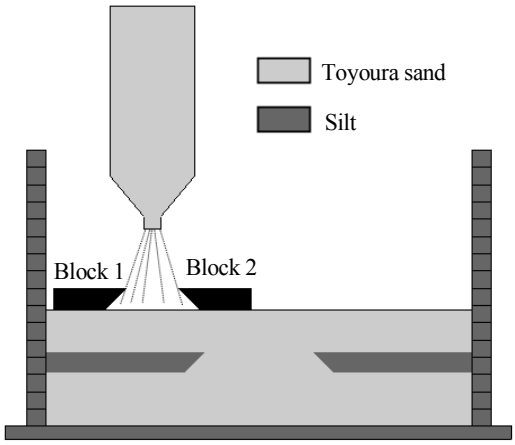


Figure 1 Model preparation of non-homogeneous soil deposits.

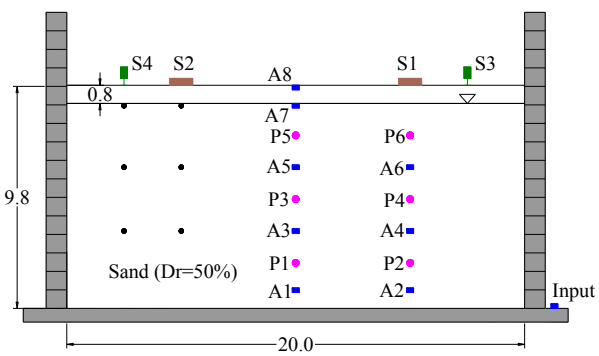
2.3 Test conditions

Four dynamic centrifuge model tests were conducted on the Tokyo Tech Mark III centrifuge (Takemura et al. 1999) at a centrifugal acceleration of 40g. The model configurations and the entire test results are presented and discussed in prototype scale units, unless indicated otherwise.

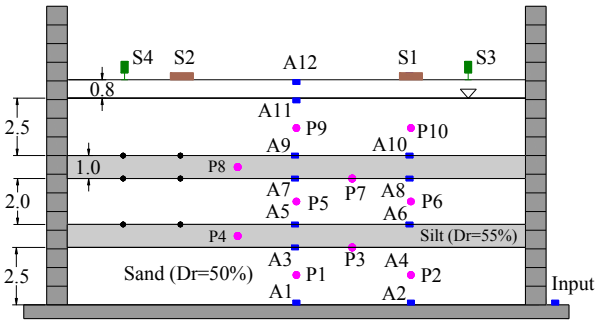
Table 2 Model configurations

Test code	Model series	Model details
Model 1	Uniform sand	D_{r1}=50-55%
Model 2	Continuous silt interlayered sand	D_{r1}=50-55%
		D_{r2}=55-60%, H_{silt}=1 m
		No discontinuity
Model 3 and Model 4	Discontinuous silt interlayered sand	D_{r1}=50-55%
		D_{r2}=55-60%, H_{silt}=1 m
		Drainage length = 5 m

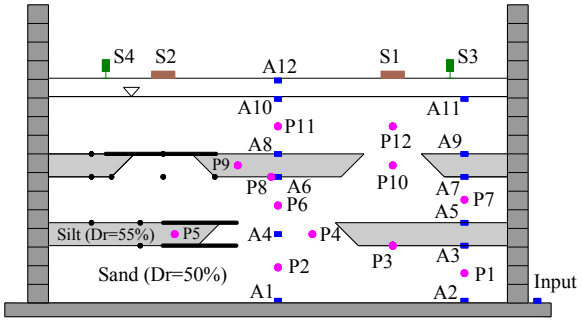
Figure 2 and Table 2 depict the model configurations. Model 1 is a homogeneous uniform sand profile, consisting of Toyoura sand only (Fig. 2(a)); Model 2 is a five layered homogeneous soil profile, consisting of three layers of sand and two continuous sandwiched silt layers of thickness 1.0 m (Fig. 2(b)); Model 3 and Model 4 are non-homogeneous soil profiles consisting of sand layers with two discontinuous silt layers of thickness 1.0 m (Fig. 2(c)). (d)). In Model 3, lower silt layer consists of one 5.0 m long (referred to as



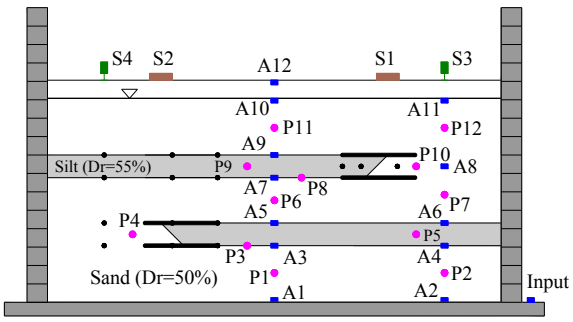
(a) Model 1



(b) Model 2



(c) Model 3



(d) Model 4

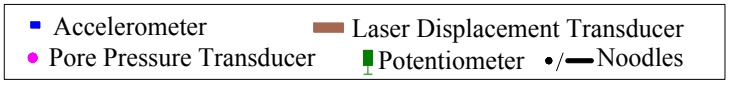


Figure 2 Model test configurations. All the units are in m in the prototype scale.

average length of discontinuity) i.e. the drainage layer is 5.0 m, dividing the silt layer into two equal portions of length 7.5 m each, and upper silt layer consists of two discontinuities at the quarter line of average length, i.e. drainage layer is 2.5 m each (Fig. 2(c)). In Model 4, lower and upper silt layers consist of only one average length of discontinuity in each layer at the edge near the left and right boundary, respectively (Fig. 2(d)).

For the entire centrifuge model tests, earthquake ground motion recorded at the Hachinohe Port in 1968 Tokachi-Oki earthquake (NS component) was applied at the base of the model parallel to the long sides of the container (Fig. 3). The ground motion applied to the shaker is plotted with a dotted line, and the input motions recorded at the base of the laminar container for each tests are plotted with solid lines. During the experiments, the accelerations were recorded by accelerometer and pore pressure transducers installed at different locations measured excess pore water pressures generated during dynamic loading. Laser displacement transducers and potentiometers measured the surface settlements.

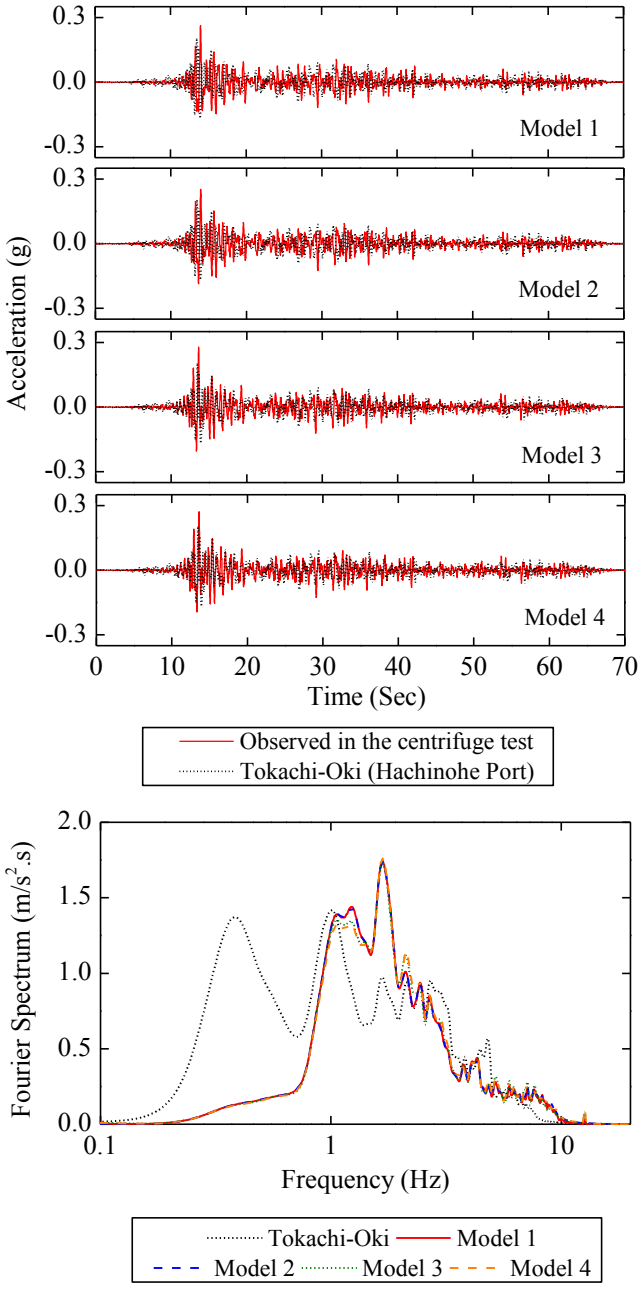


Figure 3 Acceleration time histories and Fourier spectra of input waves for Hachinohe Port record of 1968 Tokachi-Oki earthquake (NS component).

3. FINITE ELEMENT MODELING AND ANALYSIS

Two dimensional finite element analyses were conducted under the plain strain condition (Takahashi 2002). The extended sub-loading surface model proposed by Hashiguchi and Chen (1998) was adopted for the soil layers. Geo-material parameters of the soil layers are listed in Table 3 where G_S, specific gravity; e_0, initial void ratio; κ and λ, tangent of swelling and compression line; ν, poisson's ratio; σ_{ij0}, initial stress; $\sigma_{m0} = \sigma'_{ij}(1+\chi_0^2)/3, \delta_{ij}$, Kronecker's delta, K_0, coefficient of earth pressure at rest; k, hydraulic conductivity, and the other parameters represent the specific parameters for the constitutive model used. These parameters were determined so that numerical simulations on a single element fitted cyclic undrained triaxial test results. The acceleration recorded during the centrifuge tests were applied as earthquake motion. In order to

Table 3 Material parameters for numerical analysis

Parameter	Toyoura Sand	Silica No. 8
G_S	2.65	2.65
e_0	0.791	0.98
κ	0.0013	0.0029
λ	0.0072	0.015
ν	0.33	0.33
ϕ	40°	35°
ϕ_d	25°	27°
μ	0.9	1
ϕ_b	30°	27°
b_r	100	100
u_1	4	8
m_1	1	1
c	30	30
K_0	0.7	0.7
$F_0/(-\sigma_{m0})$	1.2	1.2
s_{ij0}	$0.2\sigma_{ij0}$	$0.2\sigma_{ij0}$
k (m/s)	2.0×10^{-4}	2.0×10^{-5}

obtain the numerical solution, the differential equations were integrated along time. System damping was represented by stiffness proportional damping, and the damping ratio used was 1% in the first mode of free vibration of the system

Numerical simulations of the centrifuge model tests were carried out. Modeling and results of Model tests 1 and 4 are discussed here for brevity. Figure 4 shows the finite element discretization and boundary conditions of the test specimens. Model 1 and Model 4 consist of 800 and 880 quadrilateral elements, respectively. During the numerical simulations, acceleration time histories were sampled at A3, A5, and A7 locations for Model 1 and at A1, A3, A5, and A9 locations for Model 4, excess pore water pressure time histories were sample at P3, P4, P5, and P6 locations for Model 1 and at P6, P7, P11, and P12 locations for Model 4 and settlements were sampled at S1 and S2 locations for Model 1 and at S1, S2, S3, S4, and S5 locations for Model 4 (Fig. 4). P6, P7, and P12 were selected for Model 4 to observe the pore water pressure responses along the drainage path and are compared with the responses at P11, which lies far from the drainage path. At these key locations, computed accelerations, pore pressures and vertical settlement are compared to the corresponding experimental measurements.

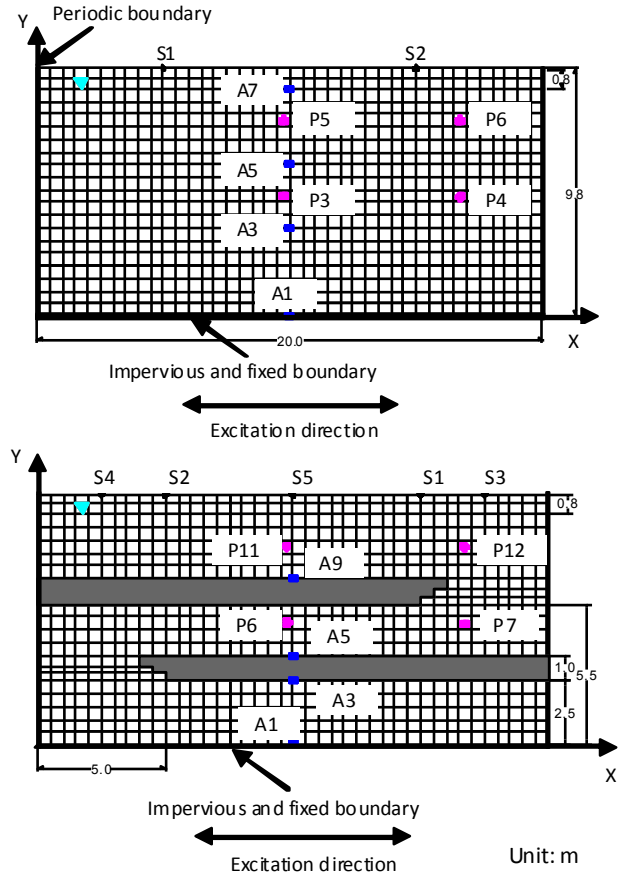
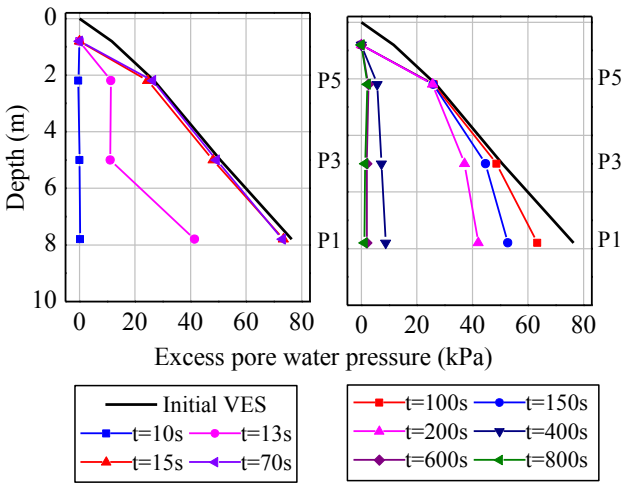


Figure 4 Finite element discretization and boundary conditions of centrifuge model test: (a) Model 1; and (b) Model 4).

4. EXPERIMENTAL RESULTS

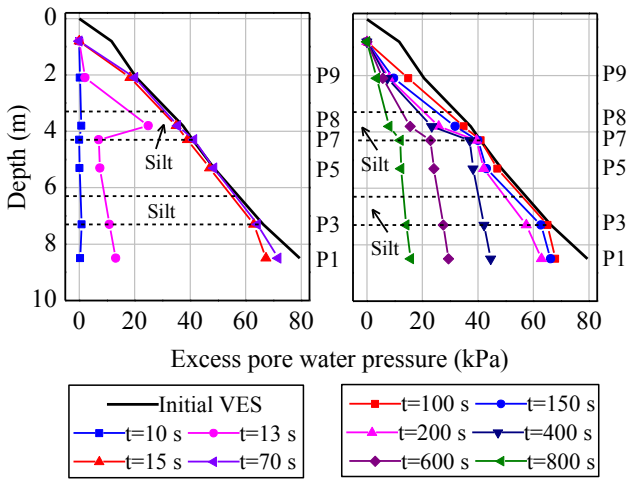
4.1 Excess pore water pressure (EPWP) responses

The excess pore water pressure, when reaches a value equal to the initial vertical effective stress (VES), indicates the occurrence of liquefaction; a state of initial liquefaction. The changes of excess pore water pressure at the centerline during shaking and after shaking for Models 1 and 2 are illustrated in Figs. 5 and 6. Results are also presented for PPTs located at centerline and quarter line after shaking for Models 3 and 4 (Figs. 7 and 8). Also shown in these figures are the positions of silt layers with dashed lines. In case of uniform homogeneous profile, excess pore water pressure generated rapidly, reaching liquefaction between 13-15 s at all the depths followed by rapid dissipation, shown by changes of excess pore water pressure isochrones for PPTs P1, P3, and P5 aligned at the centerline in Fig. 5.



(a) During shaking (b) After shaking

Figure 5 Excess pore water pressure isochrones measured on centerline in Model 1.



(b) During shaking (b) After shaking

Figure 6 Excess pore water pressure isochrones measured on centerline in Model 2. Dotted lines distinguish the sand and silt layer in the model.

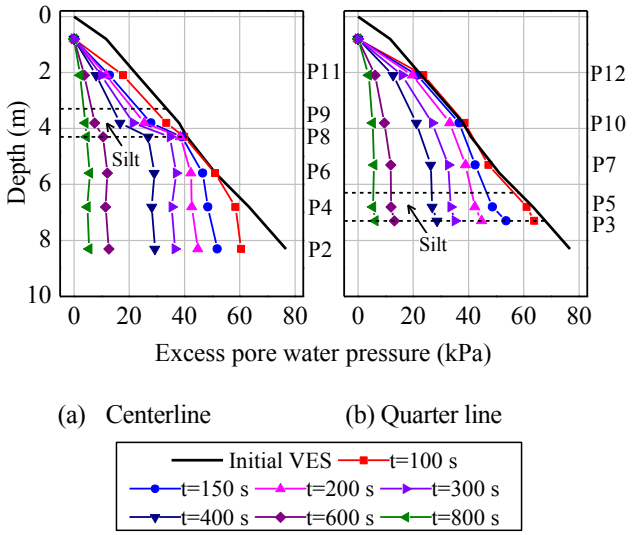


Figure 7 Excess pore water pressure isochrones measured in Model 3 after shaking.

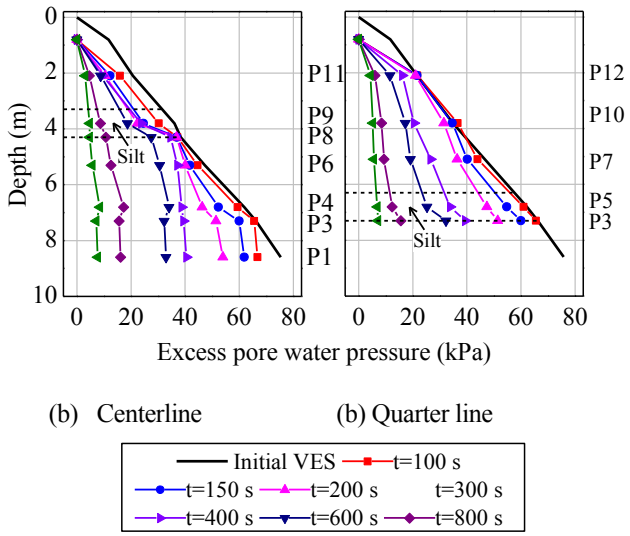


Figure 8 Excess pore water pressure isochrones measured in Model 4 after shaking.

The elapsed time for complete dissipation of excess pore water pressure is about 400 s (Fig. 4(b)). Excess pore water pressure generated rapidly in sand and silt in case of continuous and discontinuous layered soils, but the elapsed time for dissipation is quite different. The excess pore water pressures beneath the upper silt layer remain equal to the initial effective stress for a longer time even after the cessation of dynamic motion, indicating the trapping of pore water as shown by PPT P7 for Model 2 and PPT P8 for Models 3 and 4 (Figs. 6-8). It can be seen that the excess pore water pressures measured below the upper silt layer have nearly the same rate of dissipation after a certain time, which is about 400 s for continuous layered and 300 s for discontinuous layered soils (Figs. 6-8). The faster dissipation in discontinuous layered soils might be due to the presence of discontinuity in silt layer, allowing the pore pressure at high pore pressure region easily find a path to be drained out and transmit to the low pore pressure region through that path.

When the pore water pressures build-up during shaking, dissipation starts mainly towards the ground surface through the shortest path as possible (Ishihara and Yoshimine 1992). The silt layer being relatively impermeable hinders the upward movement of pore water, thus the possible shortest drainage path being the path through P4, P6, P10, and P12 for Models 3 and 4 (see Figs. 1(c) and 1(d)) and finally towards the ground surface. A comparison between EPWP for PPTs lying along the drainage path (i.e., P6, P10, and P12) and those lying away from the drainage path (i.e., P7, P9, and P11) for Models 3 and 4 is shown in Figs. 7 and 8. Excess pore water pressure is larger at PPTs lying along the drainage path than PPTs away from the drainage path. The difference in EPWP between PPTs lying along the drainage path and away from the drainage path is more pronounced at the shallow depths (for example at 2.1 m depth in Figs. 7 and 8). The difference in EPWP around the discontinuous region and below the upper silt layer creates a hydraulic gradient pointing towards the discontinuous region which led to the migration of pore water towards the discontinuity region. This causes the excess pore water pressure at discontinuity in silt layer, i.e., drainage layer remain larger for a longer period of time during its dissipation. As a result, the excess pore water pressure responses at P12 for Models 3 and 4, which lies above the discontinuity at 2.1 m depth, is significantly larger than that at P11, above the silt layer at the same depth (Figs. 7 and 8). Excess pore water pressure dissipates as soon as shaking stops at P11 while it remains equal to the initial vertical effective stress until 200 s at P12 (Figs. 7 and 8). The excess pore water pressure at P12 remains equal to the initial vertical effective stress until t=150 s for Model 3 and until t=200 s for Model 4. This is due to the effect of length and number of discontinuities in the silt layer. Model 4 consists of only one discontinuity in silt layer at the right part of length 5 m in upper silt layer, i.e., drainage layer of length 5 m, while Model 3 consists of two discontinuities in upper silt layer of length 2.5 m each. The presence of several discontinuities can accelerate the rate of dissipation. The excess pore water can easily transmit from the liquefied sand beneath silt layer (high pore pressure region) to the upper sand layer through the highly permeable discontinuities in silt layer (i.e., both drainage layers) due to seepage flow or migration of pore water.

4.2 Settlement responses

Settlement time histories at the surface measured by laser displacement transducers (LDTs) and potentiometers for all the tests are presented in Fig. 9. Two LDTs and two potentiometers were aligned along the centerline at the surface. An acrylic base plate was used as a target for LDTs so that they would not sink into the liquefied sand. Similarly, plexiglass was used to support the potentiometers. Potentiometers for the Models 1 and 4 malfunctioned; therefore, the records are not presented. A significant part of settlement takes place in all the tests during the initial process of pore pressure build-up, at the time when seismic

shaking is applied (up to 70 s). Nonetheless, a part of the settlement during seismic shaking might also be due compression of dry sand and penetration of target base plates, which was observed during the tests. The dissipation of excess pore water pressure becomes the dominant mechanism after seismic loading as the pore pressure generation ceases the supply of new mass of water, which is manifested as settlement. Therefore, the settlement induced during dissipation of EPWP after shaking is of great importance for assessing the uneven settlement induced by non-homogeneity of soil deposits and therefore is further compared in terms of rate of settlement.In case of homogeneous continuous profile, the rate of settlement is nearly the same at different locations (see for example, S1 and S2, Fig. 10(a)). In case of non-homogeneous soils, the rate of settlement is significantly larger above the discontinuity part than that above the silt layer (S1 and S2 Fig. 10(b)).

Figure 11 shows the rate of settlement after shaking at S1 for all the model tests for different time windows. It can be seen that the rate of settlement is presumably greater in Model 1 until 160 s. This reveals the rapid dissipation of excess pore water pressure within a shorter period of time due to a large value of permeability of Toyoura Sand and consequently more settlement is induced in Model 1. The continuous dissipation of excess pore water pressure in Model 3 and 4 for a longer period of time causes the rate of settlement quite significant for a longer period of time. Moreover, the rate of settlement for Model 3 and 4 is significantly larger for all the time windows than that for Model 2. In Model 3 and 4, there is a continuous supply of pore water pressure at the discontinuous part due to seepage flow or migration of pore pressure from the surrounding soil of high pore pressure, resulting in dissipation of excess pore water pressure for a longer period of time (P12, Figs. 7 and 8) and finally causing the rate of settlement greater at S1 in Model 3 and 4. It can be concluded that soil settlement is incorporated by the increment in the amount of pore pressure generation and drainage. However, the rate of

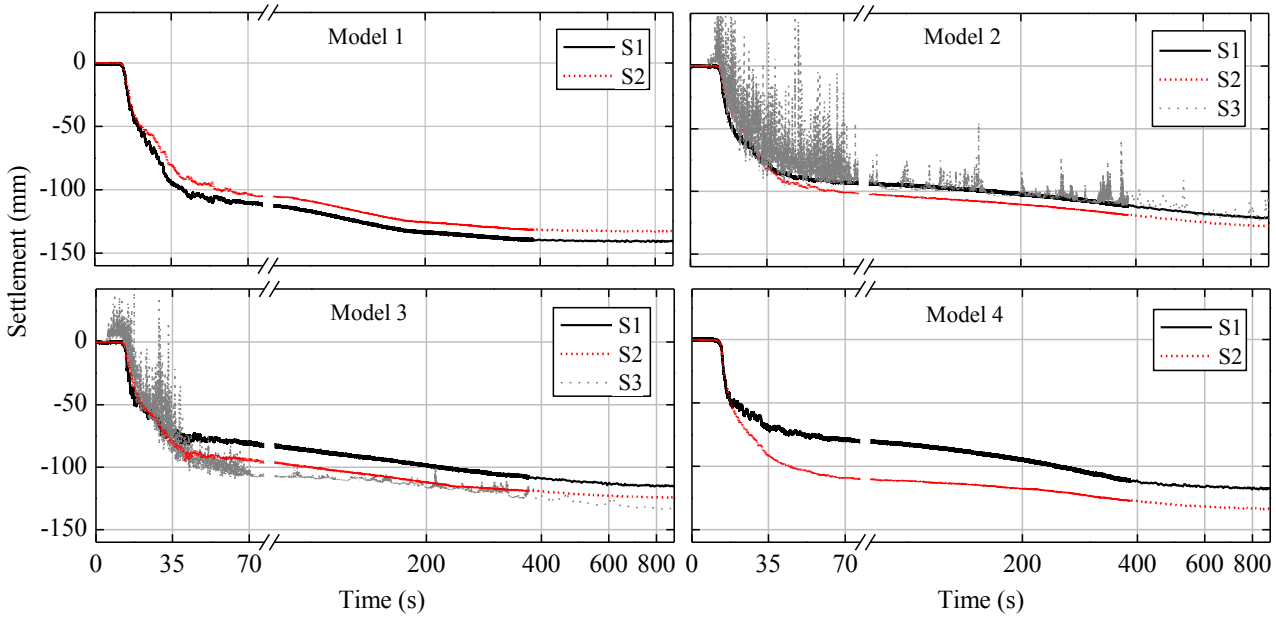


Figure 9 Settlement time histories for all the model tests.

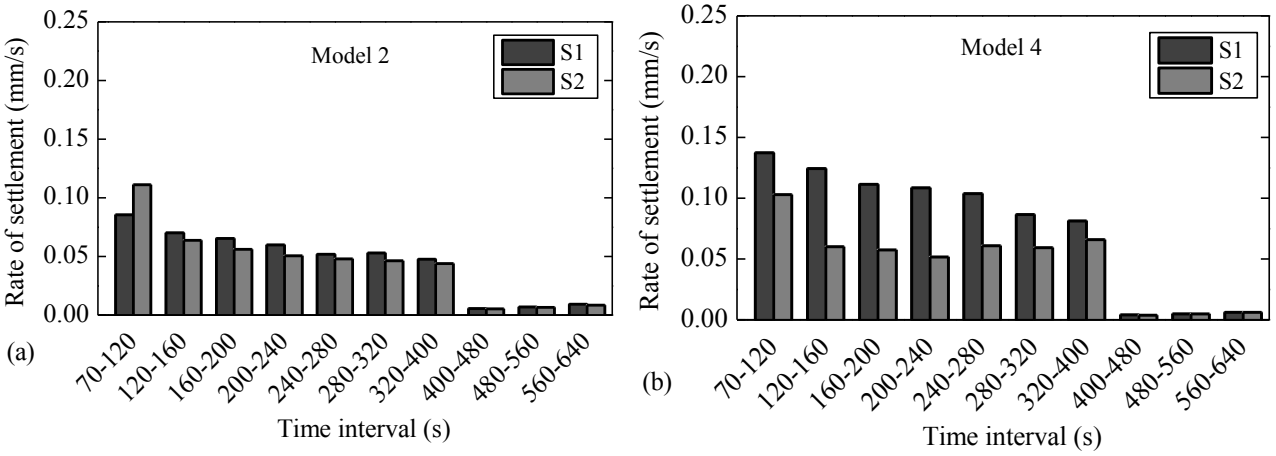


Figure 10 Variation of rate of settlement: (a) Model 2 and (b) Model 4

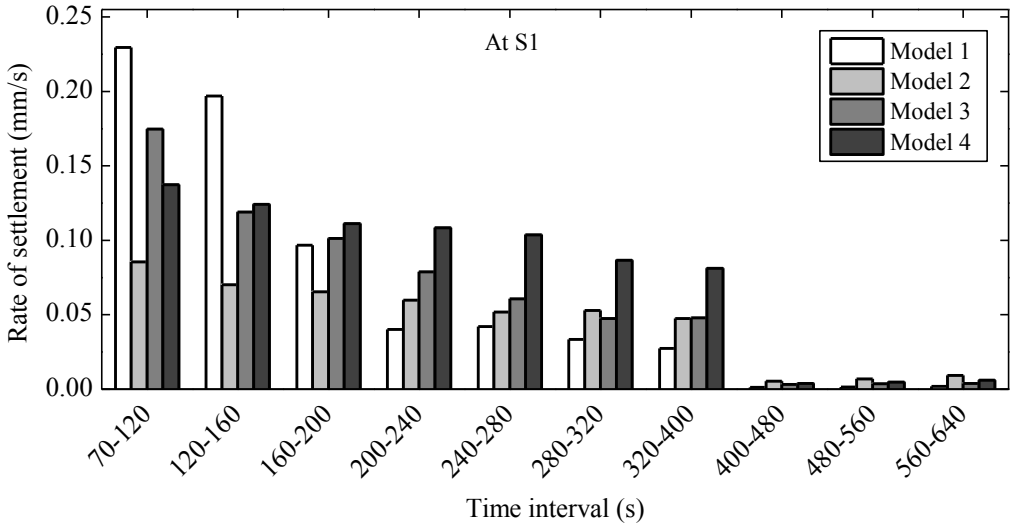


Figure 11 Variation of rate of settlement at S1 for all the tests.

settlement for Model 4 and Model 3 is fairly the same until 200 s, while it is substantially larger after 200 s for Model 4 than that for Model 3, indicating the larger rate of dissipation of excess pore water pressure at P10 in Model 4 (Figs. 8 and 11). The presence of only one discontinuity in silt layer concentrates the flow of excess pore water pressure from high pore pressure region to the permeable drainage layer.

The settlement induced by seepage flow after the earthquake at S1, S2, and S3, lying on the ground surface for all Models is presented in Table 4. The settlements at S1, S2, and S3 for Models 1 and 2 indicate the uniform settlement. The larger settlements at S1 and S2 for Model 3 and S1 for Model 4 and the smaller settlement at S3 for Model 3 and S2 for Model 4 indicate the uneven settlement. Meanwhile, the settlement at S1 is significantly larger for Model 4 than that for Model 3 and the settlement at S2 for Model 4, which is above the silt layer, is significantly smaller than that for Models 2 and 3. This shows that in Model 4, the excess pore water pressure is forced to drain through only one discontinuity layer, inducing the larger settlement at the discontinuity region, while in Model 3, the excess pore water is drained out through two discontinuities, reducing the volume of dissipation, inducing the smaller settlement difference.

Table 4 Settlement induced by seepage

Test code	S1 (mm)	S2 (mm)	S3 (mm)
Model 1	30.6	30	
Model 2	29	28.3	30.2
Model 3	35	32	27
Model 4	39.5	24.9	

5. NUMERICAL RESULTS

During liquefaction, a significant increase in soil permeability occurs by seismic excitation (Taiebat et al. 2010; Shahir et al. 2012). It is important to take an account of the permeability increase in the course of simulation of liquefaction. The actual variation of permeability incorporates the accurate simulation of excess pore water pressure generation and dissipation. Assuming a constant increased permeability is a common method for taking permeability variation into consideration in the process of liquefaction modeling (Shahir et al. 2012). Balakrishnan (2000) and (Taiebat et al. 2010) increased the permeability coefficient equal to 3.67 and 4 times the initial value, respectively for the simulation of the centrifuge experiment. In order to determine the effects of permeability of sand on the responses of excess pore water generation and dissipation and consequent settlement during liquefaction in non-homogeneous soil deposits, several numerical analyses were conducted by varying the coefficient of permeability of both liquefiable soil and relatively impermeable soil, i.e., constant permeability values of liquefaction of $k_{initial}$, 2.5 $k_{initial}$, and 5 $k_{initial}$. The coefficient of permeability ($k_{initial}$) of Toyoura sand and Silica No. 8 are 2×10^{-4} and 2×10^{-5} m/sec, respectively. The permeabilities of both soils were increased by 2.5, and 5 times the value mentioned above. The computed excess pore water pressures for all the permeabilities are similar to the centrifuge model tests in terms of the generation of excess pore water pressure, while the dissipation of excess pore water is quite different for differentpermeabilities. It can be seen that the dissipation of excess pore water pressure is quite faster with the increase in permeabilities. Moreover, the overall excess pore water pressure response was adequate when the permeability of $2.5k_{initial}$ was used.

Figure 12 shows the time histories of the excess pore

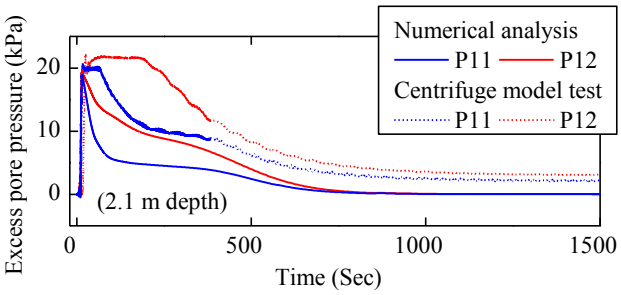


Figure 12 Excess pore water pressure time histories for Model 4.

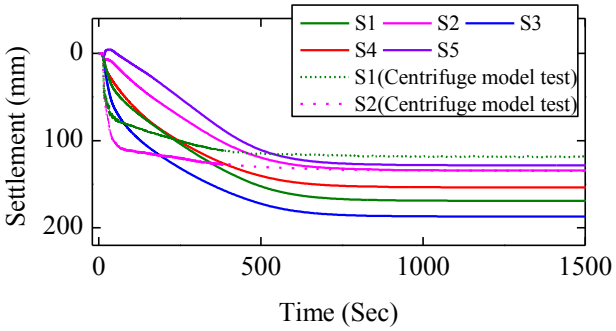


Figure 13 Settlement time histories for Model 4.

water pressure for P11 and P12 computed from numerical analysis when $2.5k_{initial}$, and centrifuge model tests for Model 4. Both numerical analysis and centrifuge model tests indicate that the excess pore water pressure is larger for longer period of time after shaking at the discontinuity part. Figure 13 presents the time histories of the vertical displacement at the selected locations for the numerical analysis when $k=2.5k_{initial}$ and the centrifuge model tests for Model 4. The final settlement is larger at S3, which lies completely above the discontinuity region, while the settlement at S1, which is at the adjacent of the discontinuity region, is also larger than that above the silt layer (S2, S4, and S5).

The permanent deformations of the model ground computed from numerical analysis along with the contours of excess pore water pressure distribution at t=354 sec are presented in Figure 14. The deformation at the discontinuity part is larger than that in the silt layer at the sand silt interface. The colored noodles placed at the sand-silt interface in the centrifuge model tests also showed the same deformation pattern. The permanent vertical displacement above the discontinuity part at the ground surface was found to be larger than that above the silt layer. Moreover, the contours of excess pore water pressure distribution shows the larger amount of excess pore water pressure above the discontinuity region.

6. CONCLUSIONS

This paper presents the centrifuge model test results and

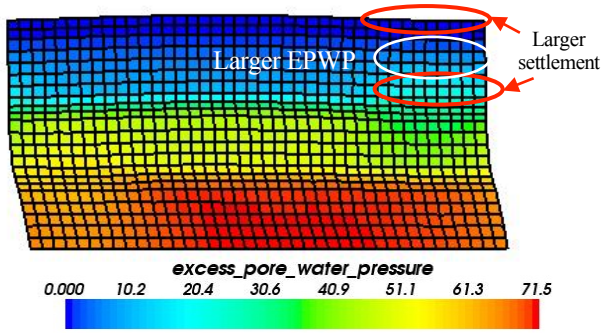


Figure 14 Permanent deformations of model ground with contours of excess pore water pressure distribution.

numerical simulation results, which investigated the effects of non-homogeneity on liquefaction in stratified soil deposits. Stratified soil consists of many sub layers of soil of different properties, which was defined by including periodically distributed discontinuous silt patches with lower permeability than the surrounding soil during centrifuge model tests. For comparison purposes, tests were also conducted on a model of continuous layered soil deposit and a model of uniform soil deposit.

It was found that, in stratified soil deposits the pore water was trapped beneath or within less permeable siltpatches due to the local migration of pore water and difference in permeability of the soils, restricting its upward movement. This indicates that the pore water finds a path to drain from high pore pressure region to low pressure region, which reveals that the presence of the discontinuous less permeable layer can have significant effects on the pore water pressure dissipation mechanism and drainage. It is determined that the presence of discontinuity of higher permeability in the less permeable soil layer can act as the drainage layer, through which the excess pore water pressure can be drained out during shaking and dominantly after shaking, as the dissipation of pore water becomes the dominant factor for settlement. Excess pore water pressure was accumulated for a longer period of time after shaking in non-homogeneous soil deposits compared with the uniform and continuous layered soil deposits, especially at shallow depths. The settlement induced by seepage at the surface above the discontinuity part was found to be larger than that above the silt layer, resulting in non-uniform settlements.

The modeling of liquefaction in field is complicated by the various uncertainties in stratigraphic details and geological non-uniformities. It is impossible to model the real soil profile exactly the same considering all the geological non-uniformities and taking into the account of uncertainties and various soil properties. Attempts have been made to model the multi-layered soil profile consisting of discontinuous relatively impermeable layer in order to enhance the understanding of the complicated mechanisms of liquefaction in non-homogeneous soil during earthquake loading and to improve the ability to account for them in practice.

Acknowledgements:

The first author is pleased to acknowledge a Monbukagakusho (Ministry of Education, Culture, Sports, Science and Technology, Japan) scholarship for graduate students. The work presented in this paper is a part of the research and development project on safety measure for levee, commissioned by Ministry of Land, Infrastructure, Transport and Tourism, Japan.

References:

NRC (1985). Liquefaction of soils during earthquakes report. Washington, DC, National Academy Press.

Ishihara, K. and Yoshimine, M. (1992). "Evaluation of settlements in sand deposits following liquefaction during earthquakes." *Soils and Foundations* **32**(1): 173-188.

Fiegel, G. L. and Kutter, B. L. (1994). "Liquefaction mechanism for layered soils." *Journal of Geotechnical Engineering* **120**(4): 737-755.

Kramer, S. L. (1996). Geotechnical earthquake engineering, Prentice Hall.

Brennan, A. and Madabhushi, S. (2005). "Liquefaction and drainage in stratified soil." *Journal of Geotechnical and Geoenvironmental Engineering* **131**: 876-885.

Kokusho, T. (1999). "Water film in liquefied sand and its effect on lateral spread." *Journal of Geotechnical and Geoenvironmental Engineering* **125**(10): 817-826.

Tohumcu Özener, P., Özaydın, K. and Berilgen, M. M. (2008). "Investigation of liquefaction and pore water pressure development in layered sands." *Bulletin of Earthquake Engineering* **7**(1): 199-219.

Liu, H. and Qiao, T. (1984). Liquefaction potential of saturated sand deposits underlying foundation of structure. *Proceedings of 8th World Conference on Earthquake Engineering*, San Francisco.

Dobry, R. and Liu, L. (1992). Centrifuge modeling of soil liquefaction. *Tenth World Conference on Earthquake Engineering*.

Balakrishnan, A. and Kutter, B. L. (1999). "Settlement, sliding, and liquefaction remediation of layered soil." *Journal of Geotechnical and Geoenvironmental Engineering* **125**(11): 968-978.

Kulasingam, R., Malvick, E. J., Boulanger, R. W. and Kutter, B. L. (2004). "Strength loss and localization at silt interlayers in slopes of liquefied sand." *Journal of Geotechnical and Geoenvironmental Engineering* **130**: 1192-1202.

Kokusho, T. and Fujita, K. (2002). "Site investigations for involvement of water films in lateral flow in liquefied ground." *Journal of Geotechnical and Geoenvironmental Engineering* **128**(11): 917-925.

Yoshida, N. and Finn, W. D. L. (2000). "Simulation of liquefaction beneath an impermeable surface layer." *Soil Dynamics and Earthquake Engineering***19**(5): 333-338.Seid-Karbasi, M. and Byrne, P. M. (2007). "Seismic liquefaction, lateral spreading, and flow slides: a numerical investigation into void redistribution." *Canadian Geotechnical Journal* **44**(7): 873-890.

Lu, X. B. and Cui, P. (2010). "A study on water film in saturated sand." *International Journal of Sediment Research* **25**(3): 221-232.

Kokusho, T. (2000). "Mechanism for water film generation and lateral flow in liquified sand layer." *Soils and Foundations* **40**(5): 99-111.

Kokusho, T. and Kojima, T. (2002). "Mechanism for postliquefaction water film generation in layered sand." *Journal of Geotechnical and Geoenvironmental Engineering* **128**(2): 129-137.

Ghosh, B., Klar, A. and Madabhushi, S. P. G. (2005). "Modification of Site Response in Presence of Localised Soft Layer." *Journal of Earthquake Engineering* **9**(6): 855-876.

Chakrabortty, P. and Popescu, R. (2012). "Numerical simulation of centrifuge tests on homogeneous and heterogeneous soil models." *Computers and Geotechnics* **41**: 95-105.

Taiebat, M., Jeremic, B., Dafalias, Y. F., Kaynia, A. M. and Cheng, Z. (2010). "Propagation of seismic waves through liquefied soils." *Soil Dynamics and Earthquake Engineering* **30**(4): 236-257.

Okamura, M., Abdoun, T. H., Dobry, R., Sharp, M. K. and Taboda, V. M. (2001). "Effects of sand permeability and weak aftershocks on earthquake-induced lateral spreading." *Soils and Foundations* **41**(6): 63-77.

Takemura, J., Kondoh, M., Esaki, T., Kouda, M. and Kusakabe, O. (1999). "Centrifuge model tests on double propped wall excavation in soft clay." *Soils and Foundations* **39**(3): 75-87.

Takahashi, A. (2002). "Soil-pile interaction in liquefaction-induced lateral spreading of soils." *PhD dissertation*, Tokyo Institute of Technology, Tokyo, Japan

Hashiguchi, K. and Chen, Z. P. (1998). "Elastoplastic constitutive equation of soils with the subloading surface and the rotational hardening." *International Journal for Numerical and Analytical Methods in Geomechanics* **22**(3): 197-227.

Shahir, H., Pak, A., Taiebat, M. and Jeremić, B. (2012). "Evaluation of variation of permeability in liquefiable soil under earthquake loading." *Computers and Geotechnics* **40**: 74-88.

Balakrishnan, A. (2000). "Liquefaction remediation at a bridge site." *PhD dissertation*, University of California, Davis, Davis, CA.

10CUEE CONFERENCE PROCEEDINGS
10th International Conference on Urban Earthquake Engineering
March 1-2, 2013, Tokyo Institute of Technology, Tokyo, Japan

CENTRIFUGE MODEL STUDY ON THE EFFECT OF SHIELD TUNNELING ON ADJACENT PILE FOUNDATION

Ittichai Boonsiri[1)], Jiro Takemura[2)], and Sakae Seki[3)]

1)Graduate Student, Dept. Civil and Environmental Engineering, Tokyo Institute of Technology, Japan
2) Associate Professor, Dept. Civil and Environmental Engineering, Tokyo Institute of Technology, Japan
3) Technical Staff, School of Engineering, Tokyo Institute of Technology, Japan
Boonsiri.i.aa@m.titech.ac.jp, jtakemur@cv.titech.ac.jp, seki@cv.titech.ac.jp

Abstract: A series of centrifuge model tests has been carried out to study the effects of tunnel-induced soil movements of both surface and subsurface area by Potentiometers and Particle Image Velocimetry (PIV) software respectively. The tunneling process was simulated by reducing the diameter of the model tunnel for various ground loss values in 100g centrifugal acceleration. Two model acrylic pile groups which consist of four piles each with the different lengths were embedded in a dry sandy ground at either side of a tunnel. The effects of the horizontal distance between pile and tunnel (Xp), the relative pile tip position and tunnel (Zpe), and cover depth ratio (C/D) were investigated in this study. The horizontal and vertical movements and inclination of the pile cap, together with the observed soil movements is discussed.

1. INTRODUCTION

Ground settlements and movements are inevitably caused by the tunnel construction in soft ground and are the vital concern especially in urban areas. Therefore, the tunneling-induced soil movements have been long studied by many researchers not only ground surface settlement, but also subsurface settlement (Mair (1996)). The potential effects of the ground movements associated in the tunnel construction must be properly considered in the design and construction of tunnel to avoid the adverse effects, i.e., damages of the adjacent structures.

Several researchers have proposed numerical methods for evaluating the behavior of existing piles and inverse effects of nearby tunneling on them. However, there are still some uncertainties and the validation of the proposed methods are required, especially for the effects of many factors, such as, types of soil, types of tunneling and imposed soil movement or ground loss by tunneling, tunnel depth, types of piles (single and group piles), pile construction methods, depth and location of piles, initial pile bearing resistance, load supported by piles, and so on (Chen et al. (1999)).

Physical modeling, especially centrifuge modeling is a useful tool to tackle these problems with its capability of creating the similar stresses in a small scale model to those of the full scale prototype. This similitude is the critical condition in a model in which most of stresses and their changes are caused by weight of soils, e.g., excavation of soil in tunneling process. In the early stage of tunneling study using the centrifuge, rubber bags with air pressure or liquid pressure were mainly used to investigate the stability of tunnel and deformation of soils (Mair (1979) & Takemura et al. (1999)). The rubber bag method has some uncertainty in the induced tunnel deformation and pressure acting on the tunnel. To control the tunnel perimeter displacement more accurately, mechanical tunneling simulator was developed in which a tapered inner core is pulled to decrease the diameter of outer tunnel (Katoh et al (1998)).

In this study, a series of centrifuge model tests were carried out to scrutinize the tunneling induced soil movement and its effect on adjacent group pile. In the tests, mechanical type 2D tunneling machine was used to impose the ground deformation in dry sand. From the observed bending moment and axial force of the piles, and the horizontal and vertical movement and inclination of the pile cap, together with the observed ground displacements, the tunnel-soil-pile interaction is discussed.

2. CENTRIFUGE MODEL TESTS

2.1 Shield model tunnel

To simulate tunneling process in a centrifuge models, various techniques have been applied. Loganathan and Poulos (2000) described an oil volume control technique. A syringe pump was fabricated to control the volume of silicone oil in the aluminum. Similarly, Mair (1979) introduced the air pressure method by using the reinforced rubber bag. This rubber bag can maintain its diameter and circular shape before the air pressure was lowered to reduce the model tunnel diameter.

Table1 Specification of model piles

Properties	Model	Prototype
Material	Acrylic	RC Concrete
Diameter	10mm	0.5m
Thickness	1mm	Solid
Young's Modulus	3.2 Gpa	20-28 Gpa
Embedment depth	140mm 210mm	14m 21m
Bending rigidity EI (GNm^2)	$9.3x10^{-10}$	$(6.2\text{-}8.6)x10^{-2}$

In this study, the Mechanical type of shield tunneling machine is employed. This machine is composed of a steel ring and a wedge shaped shaft as shown in Figure 1. The ring is divided longitudinally into six parts, and covered with a steel sleeve (t=0.5 mm) and a rubber membrane (t=0.2mm). The machine is located at the central part of a model container. The wedge shaped shafts are connected to a screw jack behind the container, which can move horizontally inward and outward. This process will change the position of the ring in the radial direction.

As a result, this model tunnel covered with rubber can expand or contract its diameter. This rubber is used for a consistent circular shape transformation of the tunnel when it reduces or increases the diameter. Moreover, this rubber membrane also prevents sand intrusion inside the model tunnel. The initial diameter of the shield model is 70 mm. The diametrical velocity of expansion and contraction is controlled from 0.1 mm/sec to 1.3 mm/sec.

2.2 Model pile and pile cap

Model piles were designed to replicate a circular concrete pile (Table1). By using the relation of flexural rigidity of prototype (E_pI_p) equal to N^4 of the model (E_mI_m), where N is the model linear scale (in these tests N = 100), or the centrifuge acceleration ratio, E is Young's modulus, I is the area moment of inertia, and the subscripts m and p denote prototype and model respectively.



(a) (b)

Figure 1 Group piles model : (a) Short pile ; (b) Long pile

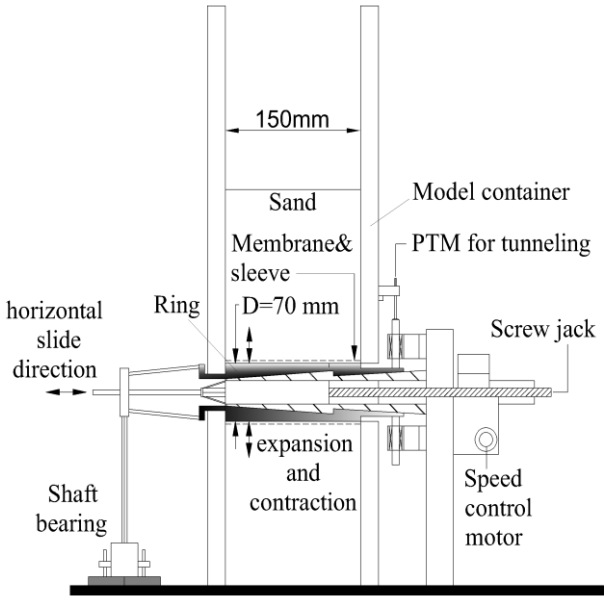


Figure 2 Shield tunneling machine equipped in the model

An acrylic material with Young's modulus of 3.2 GPa was selected to make model piles of 10 mm outer diameter and 8 mm internal diameter with an embedded length of 210 mm and 140 mm (Figure 3). One group pile consists of two strain gauges piles in the front row and two dummy piles in the rear row as described in Figures 2&3. Inside the hollow acrylic pile, three types of strain gauge were placed, namely, axial strain type (to directly measure axial strain at the pile end), bending strain type (to directly measure bending strain along a pile) ,and strain gauge which can measure both axial forces and bending moment as shown in Figure 3.

20 mm thick stainless steel made pile cap rigidly held the piles vertically at a center-to-center spacing of 50 mm. Acrylic or aluminum made plate was fixed on top of the pile cap to add an extra-weight on the pile group.

2.3 Sample preparation

Tokyo Tech Mark III Centrifuge was used for the experiments.

Models were placed and tested in an aluminum box which had an internal plan area of 150 mm by 550 mm and an internal height of 600 mm. Front wall of the container is made of acrylic plate, through which the ground movement can be observed.

Two assemble group piles were placed on either side of the tunnel at the predetermined vertical and horizontal locations. Dry Toyoura sand (Table 2) was pluviated with a hopper at a constant falling height and flow rate. The sand was poured by layers in 20 mm thickness each until it reached the designed depth. The target relative density (D_r) of the sand was about 80%. The minimum distance between container sidewall and the model pile is 120 mm which is considered adequately enough to minimize the boundary effects (Lee and Chaing (2007)).

Table2 Specification of Toyoura sand

Specific gravity (G_s)	2.65
Mean particle diameter (D_{50})	0.19
Coefficient of uniformity	1.62
Maximum void ratio (e_{max})	0.973
Minimum void ratio (e_{min})	0.609

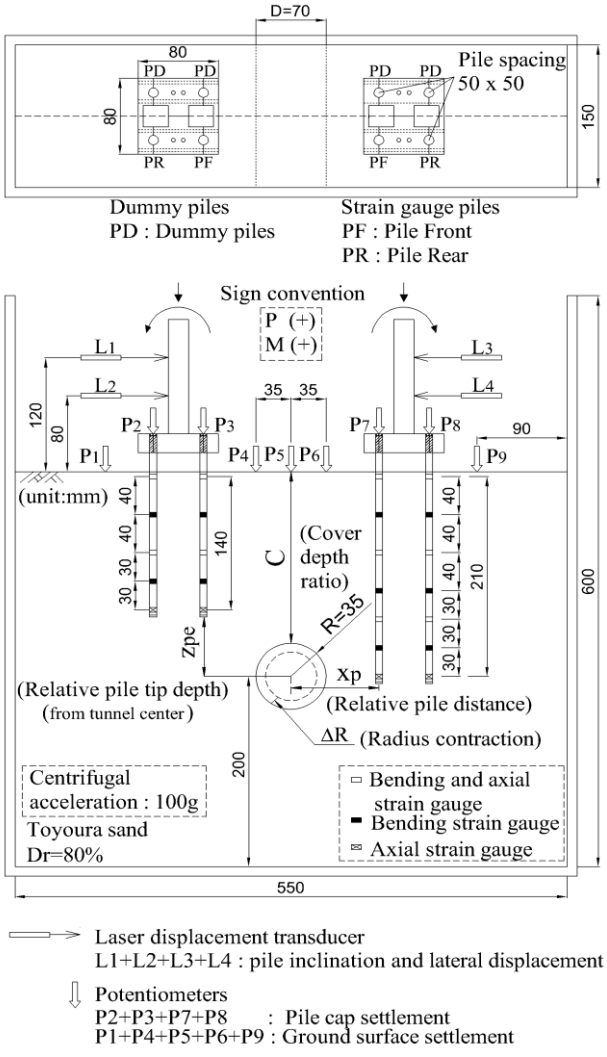


Figure 3 Test setup and instrumentations

After the sand preparation, the box was mounted on the centrifuge platform. Pair of potentiometers and laser displacement transducers were placed to measure the displacement (horizontal and vertical movements, and inclination) of each pipe cap and potentiometers were placed on the sand surface to measure the surface settlements as shown in Figure 3. A digital camera was fixed at the front of the box to capture the image of ground surface movement.

2.4 Test procedures and test conditions

Centrifuge model was accelerated to 100g. After confirming the steady condition of each measurement, the tunneling test was started reducing the diameter from 70 mm to 60 mm for simulating the tunneling process two dimensionally.

Particle Image Velocimetry (PIV) technique was used (White et al. (2003)) to measure the soil movements. Geo-PIV was applied for the data processing (White (2003)). The radius contraction of the tunnel was measured by potentiometer, which is converted to ground loss ratio ($\Delta V/V_o$), where ΔV is a volume of tunnel contraction, and V_o is an initial volume of model tunnel (D=70 mm).

Under 100g centrifugal acceleration, the model used in this study has a tunnel model of 7m diameter and pile group with the length of 14m and 21m depths in a prototype scale at either side of the tunnel.

In the following section, test results are presented using model scale. The displacement, axial force and bending moment of the prototypes are 100, 10^4, and 10^8 times those of the model.

The series of tests can be divided into three series (Table 3). The test conditions of the eleven cases are the distance of piles from the tunnel (X_p), the relative pile tip position and tunnel (Z_{pe}), and the tunnel cover depth (C/D),which determines the relative depth of pile to the tunnel for the given pile length. In Table 3 the test conditions are given by normalized values, C/D, X_p/R, Z_{pe}/R, where R is the tunnel radius as shown in Figure 3.

3. TEST RESULTS AND DISCUSSIONS

3.1 Soil surface settlement

Surface settlements was measured by potentiometers resting on the pile cap and soil surface of the dry Toyoura sand sample. The ground surface settlement is slightly different by the cases.

In the Figure 4, PMG and PMP mean potentiometer on the ground surface and on the pile cap respectively. The value after these abbreviations denotes a horizontal location of potentiometer from the center line of the model tunnel. The positive and negative values mean the position of potentiometers are on the right-hand side and left-hand side respectively. The settlement increases with increasing the ground loss ratio. In addition, the graph displayed nonlinearity between the settlement and ground loss ratio. In the small value of ground loss ratio less than (5 %), rate of increment is higher than a large number of ground loss ratio. The pile group models tend to show less settlement in the case in which a horizontal distance is far from the tunnel model (Figure 4b). In addition, when a pile tip level of long pile below the model tunnel, the pile cap settlements were reduced (Figure 4c).

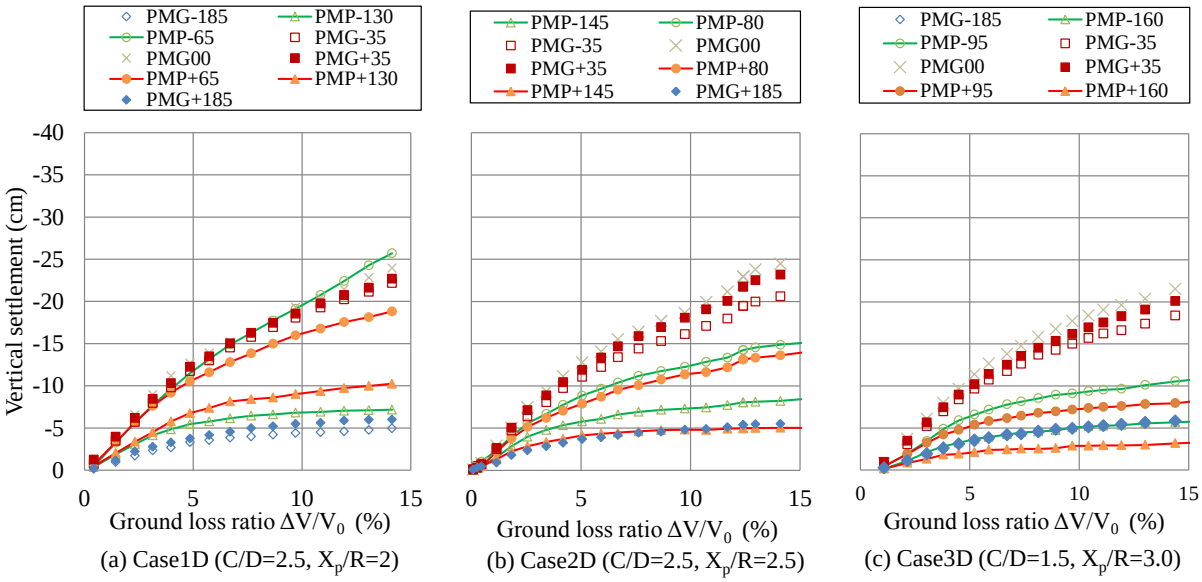
3.2 Shield model tunnel

By using PIV technique, soil subsurface movement is able to investigate. The sequence pictures which were captured during the reduction of tunnel diameter were used in GeoPIV program. This program was computed by module in matlab software.

The soil layers above a tunnel model were divided by the center of patches in GeoPIV software as shown in Figure 5(a).

Table 3 Test conditions

Test Series	Case	C/D	X_p/R short pile	Z_{pe}/R short pile	Z_{pe}/R long pile	Weight short pile (g)	S.F. short pile	Weight long pile (g)	S.F. long pile	D_r (%)
A	Case0D	2.5	-	-	-	-	-	-	-	80%
	Case0S	1.5	-	-	-	-	-	-	-	
B(1)	Case1D	2.5	2.0	-2	0	1040	2.0	2030	1.5	
	Case2D	2.5	2.5	-2	0	1040	2.0	2030	1.5	
	Case3D	2.5	3.0	-2	0	1040	2.0	2030	1.5	
B(2)	Case4D	2.5	2.0	-2	0	760	3.0	1040	3.0	
	Case5D	2.5	2.5	-2	0	760	3.0	1040	3.0	
	Case6D	2.5	3.0	-2	0	760	3.0	1040	3.0	
C	Case1S	1.5	2.0	0	2	760	3.0	1040	3.0	
	Case2S	1.5	2.5	0	2	760	3.0	1040	3.0	
	Case3S	1.5	3.0	0	2	760	3.0	1040	3.0	



(a) Case1D (C/D=2.5, X_p/R=2) (b) Case2D (C/D=2.5, X_p/R=2.5) (c) Case3D (C/D=1.5, X_p/R=3.0)

Figure 4 Ground surface settlement and pile cap settlements in various ground loss ratio measured by potentiometer

The displaced vector (Figure 5 (b)) show a corresponding trend for Gaussian distribution profile where the highest movement is concentrated in the center-line above the tunnel. The resolution from digital camera of canon power-shot G7 is 180 pixels per 1 inch. Therefore, this range is converted to 0.14 mm/pixels in real object displacement. The patch size which used in this analysis was 128 pixels or 18 mm In addition, the search zone length area between sequence images was imposed to 12 pixels. The first layer was at 12 mm from the ground surface level and the deepest layer was at 138 mm and 84 mm for C/D ratio of 2.5 and 1.5respectively.

The settlement profile slightly decreased as a position of potentiometers far from the tunnel axis. Furthermore, the deepest layer showed the highest vertical soil movement into opening tunnel

3.3 Pile displacement and ground loss ratio

The safety of structure is one of the most important for designation of all buildings. For this reason there is highly recommend for predicting the movement of the structure not even the vertical settlement but also the lateral movement and the inclination of the designed building.

The effect from a relative horizontal distance (X_p) is showed in Figure 6 in which this parameter is divided by radius of tunnel. The induced settlement is significantly influenced by the position of pile and tunnel.

The rate of settlement profile significantly increased in the interval value of X_p/R equal to 2.0 - 2.5. In contrast, the interval value of X_p/R equal to 2.5-3.0 showed small settlement value. In the small ground loss value, the induced settlement showed a small value compare to the large ground loss value.

This result is different from Lee and Chaing (2007) who propose that the settlement of single pile is significantly large even a small magnitude of ground loss value.

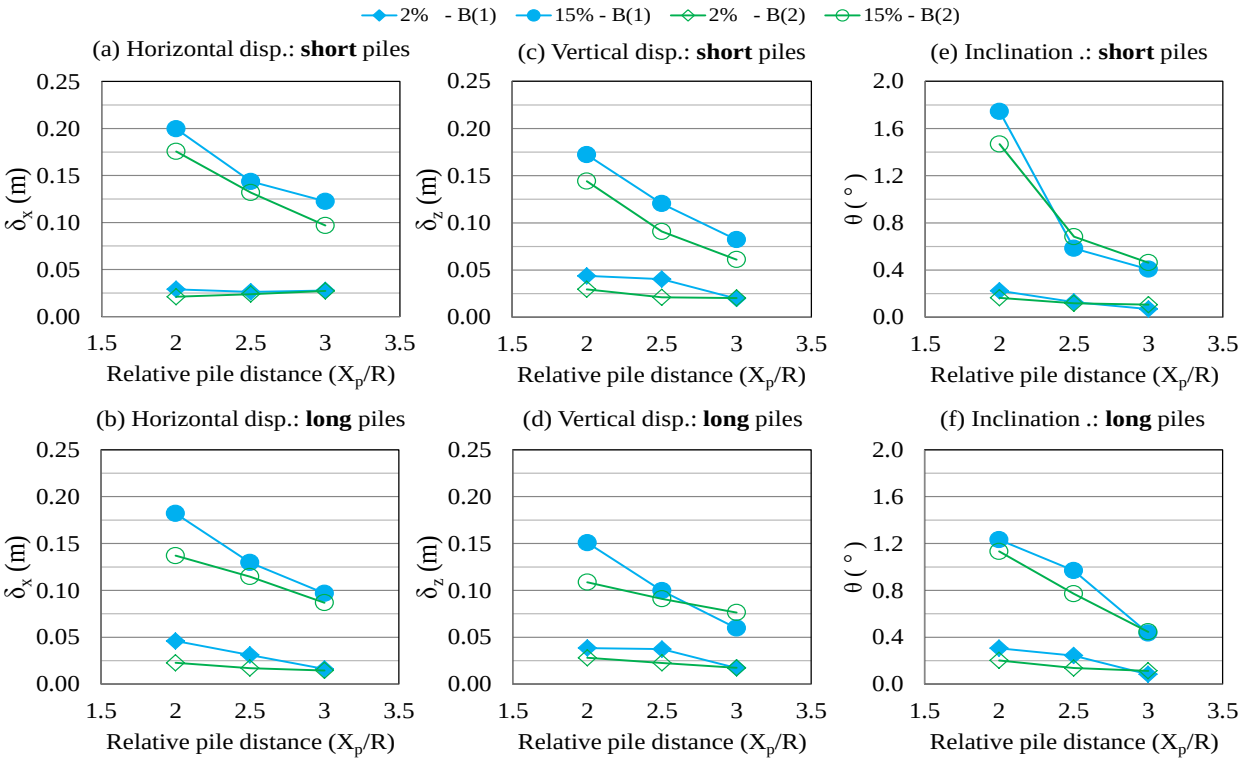


Figure 6 Comparison of displacement in term of relative distance (X_p/R): (a).(b) horizontal displacement; (c),(d) vertical displacement; (e),(f) inclination angle

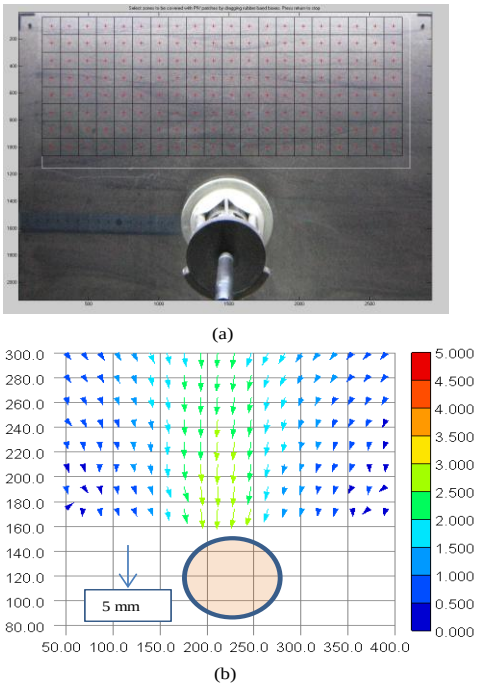


Figure 5: PIV analysis: (a) divided patches of series pictures; (b) vectors of soil movement

The result may come from the pile group which can distribute extra loads to another pile reducing the settlement into small value. The short group pile of different working load showed the normal trend of settlement.

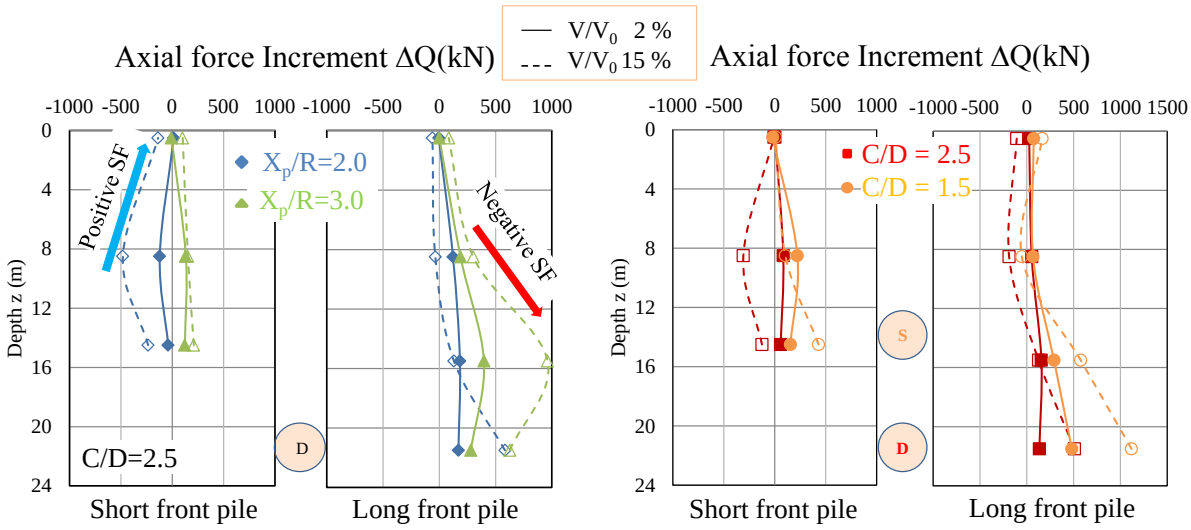
3.4 Axial force and bending moment

Tunneling process causes the soil movement which reacts with the pile foundation. As a result, the existing pile will develop extra bending moments and extra axial forces on the pile. Ground loss ratio of 2% and 15% were selected for working load and failure conditions respectively. The axial loads on the pile are attributed to the mobilization of the relative displacements between the surrounding soil and the pile during tunneling process. The upper part of pile in the nearest case, with $X_p/R=2$, showed a positive skin friction which is caused by larger pile settlement than the subsurface settlement. Although, this magnitude become less when the pile is far from the tunnel as shown in Figure 7(a). Pile groups which have cover and depth ratio equal to 1.5 develop negative skin friction since a pile settlement become less when the value of relative pile tip level is increased (Figure 7(b)).

4. CONCLUSIONS

The following conclusions were summarized in this study.

1.) Tunnel induced subsurface settlement can be approximated by a Gaussian distribution curve. The settlements above the tunnel are larger for the deeper depth than the shallower depth, but the settlements at outside from the tunnel are smaller for the deeper depth than those of the shallower depth.



(a) (b)

Figure 7 Comparison of axial force development at front pile positions with 2% and 15% ground loss: (a) horizontal distance effect; (b) relative pile tip depth effect

2.) The pile groups embedded above the tunnel shows large displacements, which increase as the pile closes to the tunnel. The inclination rapidly increase for the horizontal distance of the front pile from the tunnel center less than 2.5 tunnel radius, especially for the large ground loss.

3.) The mobilized pile shaft friction is negative due to the large soil movement relative to the pile, except of the front pile with shallower depth than the tunnel and closer to the tunnel.

4.) The fixity of pile by the cap of pile group creates the largest bending moment at the pile top.

Acknowledgements:

The authors acknowledge the support to this research by the DaiDaiToku Project from the Japan Ministry of Education, Culture, Sports, Science and Technology (MEXT)

References:

Mair, R. J. (1996). "Settlement effects of bored tunnels", Proc. of Intn. Sympo, Geotechnical Aspects of Underground Construction in Soft Ground, London, pp. 43-53.

Chen, L. T., Poulus, H. G. and Loganathan, N. (1999). "Pile responses caused by tunneling", Journal of Geotechnical and Geoenvironmental Engineering, ASCE, Vol.125, No.3, pp. 207-215.

Mair, R. (1979). "Centrifuge modelling of tunnel construction in soft clay", PhD. thesis, University of Cambridge, UK.

Takemura, J., Kondoh, M., Esaki, T., Kouda, M. and Kusakabe, O. (1999). "Centrifuge model tests on double propped wall excavation in soft clay", Soils and Foundations, Vol.39, No.3, pp. 75-87.

Katoh, Y., Miyake, M. and Wada, M. (1998). "Ground deformation around shield tunnel", Proc. Centrifuge 98, Vol.1, pp.733- 738.

Loganathan, N., Poulos, H.G. and Stewart, D.P. (2000). "Centrifuge model testing of tunnelling-induced ground and pile deformations", Geotechnique, Vol. 50, No.3, pp.283-294.

Lee, C.J. and Chiang, K.H. (2007). "Responses of single piles to tunneling-induced soil movements in sandy ground", Canadian Geotechnical Journal, Vol.44, No.10, pp.1224-1241.

White, D. J., Take, W. A., and Bolton, M. D. (2003). "Soil deformation measurement using particle image velocimetry (PIV) and photogrammetry", Geotechnique, Vol.53, No. 7, pp.619-635

10CUEE CONFERENCE PROCEEDINGS
10th International Conference on Urban Earthquake Engineering
March 1-2, 2013, Tokyo Institute of Technology, Tokyo, Japan

STRESS REDUCTION EFFECT OF STRUCTURE DUE TO BASEMAT UPLIFT AND SOIL YIELDING

Takafumi Inoue[1] and Atsushi Mikami[2]

1) Graduate Student, Department of Civil & Environmental Engineering, The University of Tokushima, Japan
2) Associate Professor, Department of Civil & Environmental Engineering, The University of Tokushima, Japan
tinoue@ce.tokushima-u.ac.jp, amikami@ce.tokushima-u.ac.jp

Abstract: In order to verify seismic performance of a structure, it is necessary to evaluate the effect of dynamic soil-structure interaction appropriately. One of the reliable models that can account for basemat uplift as well as soil yielding is the macro-element model for shallow foundations. This paper studies stress reduction effects induced in structures (such as bridge piers) due to basemat uplift and soil yielding by the use of a macro-element model for foundations placed on sands. A superstructure is modeled by a lumped mass and Bernoulli-Euler beam. A foundation-soil system is modeled as four cases; (1) fixed base, (2) elastic soil, (3) elastic soil with basemat uplift and (4) elasto-plastic soil with basemat uplift. Time histories that have different frequency characteristics are considered as input motions to the models. Response comparisons of the models show remarkable reduction of section force due to basemat uplift and soil yielding. Therefore, it may be concluded that the degree of base shear reduction depends on the frequency characteristics of the input motions relative to the system.

1. INTRODUCTION

As the design method shifts to performance-based design, it becomes more important to accurately estimate the response of superstructure accompanied by foundation rotation and basemat uplift. Basemat uplift is reportedly induced even by weak to medium ground motions (Fukui et al., 1999), hence, it is necessary to incorporate the effect of basemat uplift into a design code.

Hayashi (1996) assessed slightly damaged buildings standing on the most severely damaged area during the 1995 Hyogoken-Nanbu Earthquake. By using numerical simulation, he has studied damage reduction effect due to basemat uplift of buildings which were subject to strong ground motions, and showed that the damage reduction effect sometimes becomes remarkable depending on structural parameters and input motions. The finite element model was used in his analysis treating soil as a linear or equivalent linear medium.

This paper studies the reduction effect of a section force induced in the structure due to basemat uplift and soil yielding by the use of a macro-element model considering four kinds of foundation-soil models such as (1) fixed base (2) elastic soil (3) elastic soil with basemat uplift and (4) elasto-plastic soil with basemat uplift. Time histories which have different frequency characteristics are considered as input motions in the model.

2. MACRO-ELEMENT MODEL

In this study, a macro-element model developed by Nakatani et al. (2008) is employed to study stress reduction effect of structures due to basemat uplift and sand soil yielding. A brief overview is described in this section. Details can be referred to in Shirato et al. (2008).

2.1 Relationship between displacements and loads of a macro-element model

In the macro-element model, the foundation is assumed to be rigid, and foundation-soil model which is subjected to combined loads is modeled as one element. Displacements and loads at the center of the footing are defined as shown in Figure 1 and the following equations.

$$x = \begin{pmatrix} v & u & \theta \end{pmatrix}^T \tag{1}$$

$$F = \begin{pmatrix} V & H & M \end{pmatrix}^T \tag{2}$$

where the superscript T stands for transposition. The relationship between incremental displacements and loads is expressed by

$$dF = \left(D^{el} + D^{up} + D^{pl} \right)^{-1} dx \tag{3}$$

where D^{el}, D^{up} and D^{pl} are elastic compliance, uplift compliance and plastic compliance, respectively.

2.2 Elastic compliance

In order to determine elastic compliance, equivalent elastic spring coefficients corresponding to the vertical, translational, and rocking component are used based on Gazetas(1991). The coefficients for a rectangular foundation are expressed by

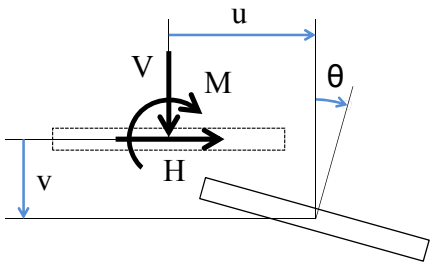


Figure 1 Definition of displacements and loads for the macro-element model

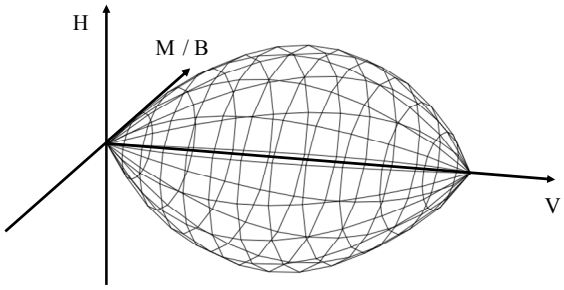


Figure 2 Schematic of bearing capacity surface

$$K_v = \frac{4.54G(B/2)}{1-v} \tag{4}$$

$$K_h = \frac{9G(B/2)}{2-v} \tag{5}$$

$$K_r = \frac{3.6G(B/2)^3}{1-v} \tag{6}$$

where G and v are shear modulus and Poisson's ratio of the underlying soil and B is the footing length. Frequency dependence of the coefficients is ignored.

2.3 Uplift compliance

Uplift compliance is determined based on the following model for uplift. $\theta^{up} - M$ relationship is expressed by

$$\theta^{up} = 0 \ \ (M \le M_\alpha) \tag{7}$$

$$\theta^{up} = \left\{ \frac{4}{(3 - M/M_\alpha)^2} - \frac{M}{M_\alpha} \right\} \theta_0 \ \ (M > M_\alpha) \tag{8}$$

where M_α and θ_0 are moments that are influenced by soil plasticity and rotation at which the uplift initiates. Then $v^{up} - M$ relationship is expressed by

$$v^{up} = 0 \ \ (M \le M_\alpha) \tag{9}$$

$$v^{up} = -\frac{B}{2} \left\{ \frac{4}{(3 - M/M_\alpha)^2} - \frac{4}{(3 - M/M_\alpha)} + 1 \right\} \ \ (M > M_\alpha) \tag{10}$$

2.4 Plastic compliance

In order to determine plastic compliance, bearing capacity surface is used. A schematic diagram of this is shown in Figure 2 Shirato et al. (2008) assumed following expression for bearing capacity surface.

$$f_{cr} = h^2 + m^2 - \xi^2 (1 - \xi)^{2\zeta} = 0 \tag{11}$$

where $\xi = V / V_m$, $h = H / (\mu V_m)$, $m = M / (\psi B V_m)$ and V_m is bearing capacity in terms of centered vertical loading. Parameters μ and ψ are tangents at the origin on the $V - H$, $V - M$ planes, respectively. To describe plastic deformations, a yield function is defined based on Nova and Montrasio (1991) as follows:

$$f_y = h^2 + m^2 - \xi^2 (1 - \xi / \rho_c)^{2\zeta} = 0 \tag{12}$$

where ρ_c is the hidden parameter that specifies instantaneous size of the yield surface and translates instantaneous combined loads into the norm of an equivalent vertical force. In order to relate size of the yield surface and incremental displacements, the hardening rule and flow rule are required. As for the hardening rule, isotropic hardening, which defines similar bearing capacity surface and yield surface, is assumed. The hardening function is expressed by

$$\rho_c = 1 - exp\left(-\frac{R_0 v_c}{V_m} \right) \tag{13}$$

where R_0 is initial gradient of the $V - v^{pl}$ curve. v_c is expressed by

$$v_c = \left\{ \left(v^{pl}\right)^2 + \left(\alpha_M u^{pl}\right)^2 + \left(\gamma_M B \theta^{pl}\right)^2 \right\}^{0.5} \tag{14}$$

where α_M and γ_M are non-dimensional parameters that incorporate the contribution of horizontal displacement and rotation into hardening. As for the flow rule, a non-associated flow rule is adopted. Regarding such a non-associated flow rule, a plastic potential function is defined as follows:

$$g = \lambda^2 h^2 + \chi^2 m^2 - \xi^2 (1 - \xi / \rho_g)^{2\zeta} = 0 \tag{15}$$

where $\lambda = \mu / \mu_g$, $\chi = \varphi / \varphi_g$, μ_g and φ_g are parameters that

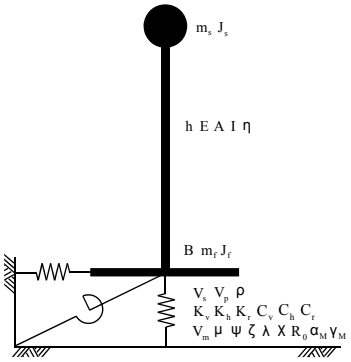


Figure 3 Schematic of structure-foundation-soil system

Table 1 Parameters of structure-foundation-soil system

Parameter	Unit	Value
Lumped mass m_s	t	500
Moment of inertia of the structure J_s	$t \cdot m^2$	4167
Height h	m	10
Young modulus E	kN/m^2	24500000
Section area A	m^2	4.423
Second moment of area I	m^4	1.557
Damping factor η	s	0.05
Footing length B	m	10
Mass of the foundation m_f	t	100
Moment of inertia of the foundation J_f	$t \cdot m^2$	833
Shear wave velocity V_s	m/s	230
Primary wave velocity V_p	m/s	356
Ground density ρ	t/m^3	1.539
Vertical elastic spring coefficient K_v	kN/m	2640110
Translational elastic spring coefficient K_h	kN/m	2155052
Rocking elastic spring coefficient K_r	$kN \cdot m/rad$	52300000
Vertical damping coefficient C_v	kNs/m	50953
Translational damping coefficient C_h	kNs/m	35397
Rocking damping coefficient C_r	$kNsm$	1.0
Bearing capacity of centered vertical loading V_m	kN	51503
Parameter of yield functon μ		0.9
Parameter of yield functon ψ		0.48
Parameter of yield functon ζ		0.95
Parameter of plastic potential λ		0.45
Parameter of plastic potential χ		0.45
Parameter of hardening function R_0		26742
Parameter of hardening function α_M		2.8
Parameter of hardening function γ_M		1.7

specify the shape of the plastic potential surface.

3. STRESS REDUCTION AGAINST A REAL EARTH QUAKE

Here, stress reduction effects of a structure-foundation-soil system against real earthquakes is reviewed. The system was subjected to different types of acceleration-time histories. A foundation-soil system is modeled as four cases; (1) fixed base, (2) elastic soil, (3) elastic soil with basemat uplift and (4) elasto-plastic soil with basemat uplift.

3.1 Structure-foundation-soil system

Schematic and parameters of the structure-foundation-soil system is shown in Figure 3 and Table 1. The parameters were set based on Nova and Montrasio (1991) and Nakatani et al. (2008). A superstructure was modeled by a lumped mass and Bernoulli-Euler beam. The total degrees of freedom of the system were six; consisting of three degrees of lumped mass and three degrees of the macro-element. A foundation-soil system is modeled as four cases; (1) fixed base, (2) elastic soil, (3) elastic soil with basemat uplift and (4) elasto-plastic soil with basemat uplift. Frequency dependence of elastic compliances was ignored.

3.2 Stress reduction against a real earthquake

The degree of stress reduction effects of a structure was studied. The aforementioned structure-foundation-soil system is subjected to input motions in the time domain. Two kinds of ground motions are considered as the input motions here; subduction type earthquake (acceleration time history that was recorded at a port in Hachinohe during the 1968 Tokachi-Oki Earthquake) and inland type earthquake (acceleration time history observed at JR Takatori station during the 1995 Hyogoken-Nanbu Earthquake). These time histories are shown in Figure 4 and 5. For conducting nonlinear analysis with the macro-element model, time step for seismic response analysis was set at 0.0001 seconds by interpolating the input time histories which were originally recorded at 0.02 second intervals. A linear acceleration method was used for the numerical integration.

The time history of base shear that occurred in the structure for subduction zone type earthquake is shown in Figure 6. The thin black line, the thin blue line, the thick red line and the thick green line correspond to responses for fixed base case, elastic soil case, elastic soil with basemat uplift case and elasto-plastic soil with basemat uplift case, respectively. The case (1) show different time responses from other cases (this difference implies the wave radiation effect). However, linear case and nonlinear cases show similar time responses. This means that significant stress reduction effect due to basemat uplift and soil yielding are not apparent in this case.

Secondly, an inland type earthquake is considered as input motion into the system. Calculated responses are shown in Figure 7. Meanings of curves are the same as Figure 6. Responses show significantly different waveforms. The fixed base case and elastic soil case show similar time responses (this difference implies the wave radiation effect). However, when basemat uplift is considered, the base shear becomes significantly different from linear cases. Nonlinear cases show drastic reduction of base shear, thus longer period motions are implied. When soil yielding is considered, the period of the motion becomes even longer.

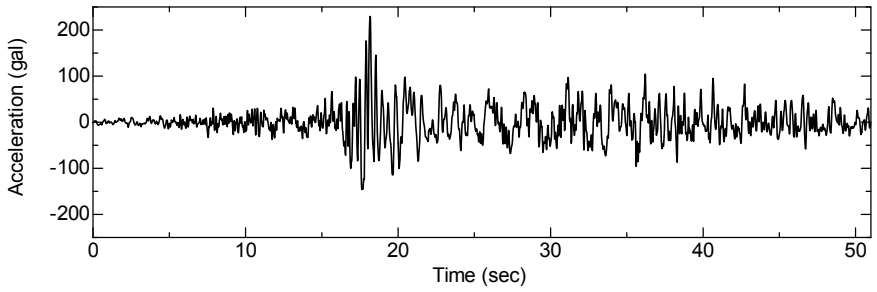


Figure 4 Acceleration time history

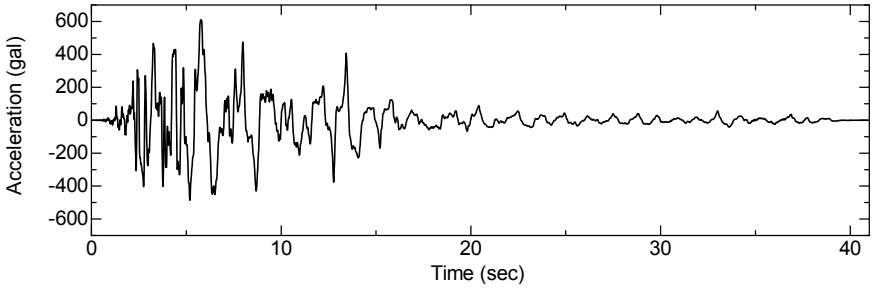


Figure 5 Acceleration time history

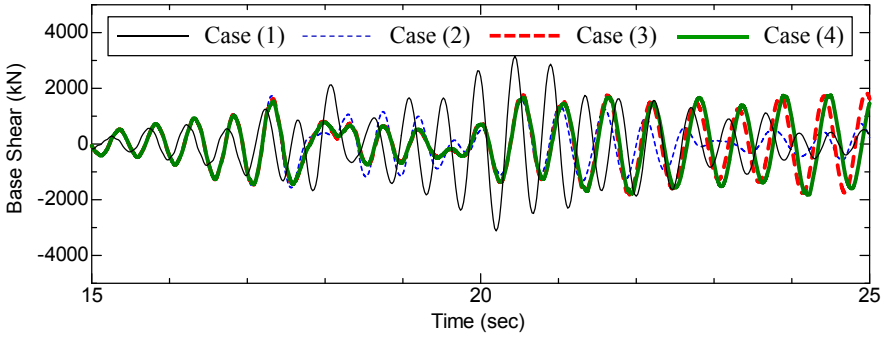


Figure 6 Base shear time history

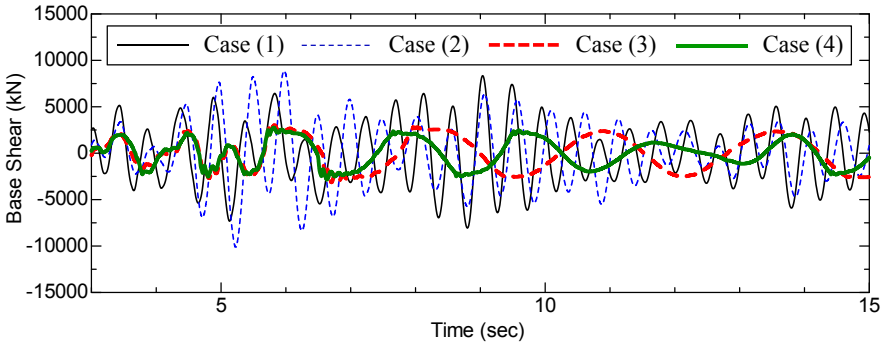


Figure 7 Base shear time history

We can recognize from these results that stress reduction of structures due to basemat uplift and soil yielding can occur in some cases depending on input ground motions. In order to examine factors that might bring a differences in the level of stress reduction, some artificial input motions that have different frequency characteristics are considered in the next section.

4. STRESS REDUCTION OF STRUCTURE FOR INPUT MOTIONS OF DIFFERENT FREQUENCY CHARACTERISTICS

The same structure-foundation-soil system is considered. As the input motion, harmonic waves that have different frequency characteristics are given. An example of the harmonic seismic wave which has a natural frequency of 1.78Hz is shown in Figure 8. The amplitude gradually increases until it reaches to the amplitude of 500gal. As the former section, foundation-soil system is modeled as four cases; (1) fixed base, (2) elastic soil, (3) elastic soil with basemat uplift and (4) elasto-plastic soil with basemat uplift. Three cases of different excitation frequencies are considered: (a) excitation frequency fe is lower than the natural frequency of the elastic soil system fn (fe/fn=0.9) (b) excitation frequency is the same as the natural frequency of the elastic soil system (fe/fn=1.0) and (c) excitation frequency is higher than the natural frequency of the elastic soil system (fe/fn=1.1). The natural frequency of the elastic soil system is 1.98(Hz).

4.1 Stress reduction for case (a)

The time history of base shear induced in the structure is shown in Figure 9. The meanings of the curves are the same as before. The base shear responses of fixed base and elastic soil model are larger than nonlinear cases. When basemat uplift effect is incorporated in the model, the base shear reduced significantly. Any clear difference can not be seen by the soil yielding effect.

4.2 Stress reduction for case (b)

Calculated responses are shown in Figure 10. In this case, the base shear of the elastic soil model becomes much larger than others. This is because the elastic soil system reached resonance with excitation frequency becomes system frequency. Compared to the elastic soil case, base shear of the models that incorporated basemat uplift effect reduced significantly.

4.3 Stress reduction for case (c)

The result is shown in Figure 11. In this case, excitation frequency is higher than the elastic soil system and closer to the fixed base model. For this reason, base shear of the fixed base model is largest. Owing to radiation damping effect, base shear of the elastic soil model reduced significantly. Furthermore, basemat uplift effect

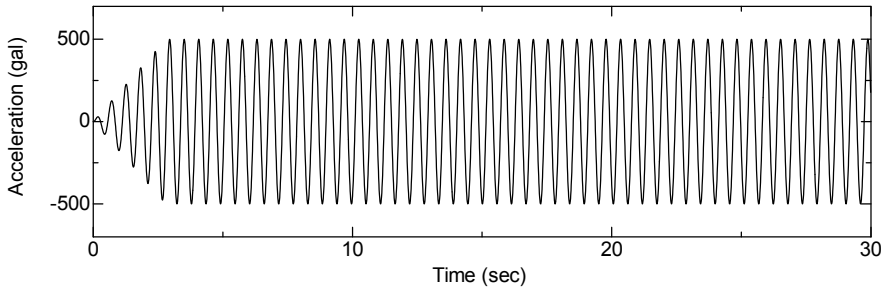


Figure 8 Acceleration time history

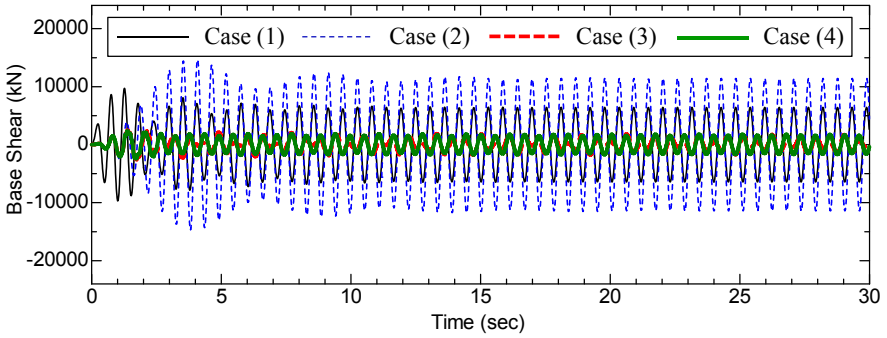


Figure 9 Base shear time history (Case (a))

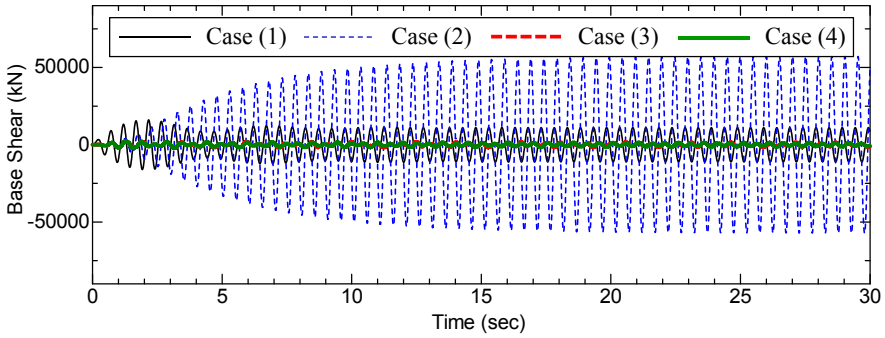


Figure 10 Base shear time history (Case (b))

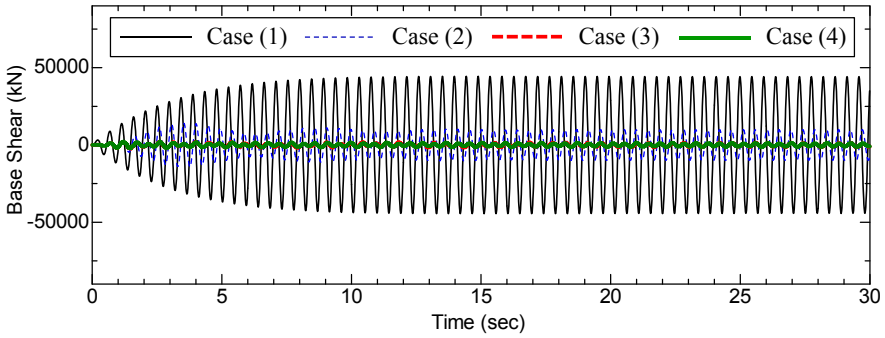


Figure 11 Base shear time history (Case (c))

works to drastically reduce the base shear of the structure in this case.

5. CONCLUSIONS

This study examined stress reduction effects induced in a structure due to basemat uplift and soil yielding by the use of a macro-element model for foundations placed on sands. The foundation-soil system is modeled as four cases; (1) fixed base, (2) elastic soil, (3) elastic soil with basemat uplift and (4) elasto-plastic soil with basemat uplift. Time histories with different frequency characteristics were considered as input motions to the models. Comparisons of responses for the models showed remarkable reduction of section force due to basemat uplift and soil yielding. Therefore, it may be concluded that the degree of base shear reduction depends on the frequency characteristics of the input motions relative to the system.

Acknowledgements:

Authors acknowledge the Public Works Research Institute, Tsukuba, Japan, for providing the analysis program.

References:

Fukui, J., Kimura, Y., Ishida, M. and Kishi, Y. (1999), "An investigation on the response of shallow foundations to large earthquakes," *Technical Memorandum of PWRI*, Public Works Research Institute, (3627), (in Japanese).

Gazetas, G. (1991), "Foundation vibrations, " *Foundation Engineering Handbook*, Fang HY (ed.), van Nostrand Reinhold: NY.

Hayashi, Y. (1996), "Damage reduction effect due to basemat uplift of buildings," *Journal of Structural and Construction Engineering (Transactions of AIJ)*, **485**:53-62, (in Japanese).

Japan Road Association. (2012), *Specifications for Highway Bridges*, Maruzen, (in Japanese).

Nakatani, S., Shirato, M. and Kouno, T. (2008), "Development of a numerical model for the seismic nonlinear behavior and irreversible displacement of a shallow foundations," *PWRI Report*, Public Works Research Institute, (4101), (in Japanese).

Nova, R. and Montrasio, L. (1991) , "Settlement of shallow foundations on sand," *Géotechnique*, **41**(2), 243-256.

Shirato, M., Paolucci, R., Kouno, R., Nakatani, S., Fukui, J., Nova, R., di Prisco, C. (2008) , "Numerical simulation of model tests of pier-shallow foundation systems subjected to earthquake loads using an elasto-uplift-plastic macro element," *Soils and Foundations*, **48**(5), 693-71.

10CUEE CONFERENCE PROCEEDINGS
10th International Conference on Urban Earthquake Engineering
March 1-2, 2013, Tokyo Institute of Technology, Tokyo, Japan

EVALUATING ONE DIMENSIONAL SITE RESPONSE ANALYSIS USING BOREHOLE ARRAYS

Georgios Zalachoris[1], Ellen M. Rathje[2]

1) Graduate Student Researcher, University of Texas at Austin, Austin, TX, USA
2) Professor, University of Texas at Austin, Austin, TX, USA.
gzalachoris@gmail.com, e.rathje@mail.utexas.edu

Abstract: Numerical techniques commonly used to compute the response of soil and rock media under earthquake shaking are investigated by analyzing the observations provided by instrumented borehole arrays. Using a selected subset of the Kiban-Kyoshin (NIED KiK-net, Japan) database along with recordings from the La Cienega (California) and Lotung (Taiwan) arrays, site amplification predictions using 1-D linear elastic analysis, equivalent linear (EQL) analysis and equivalent linear analysis with frequency-dependent soil properties (EQL-FD) are compared with borehole observations. Specifically, 13 sites are investigated using over 800 recorded ground motions characterized by low (less than 0.05 g) to high (greater than 0.3 g) recorded peak ground accelerations at the downhole sensor. Low intensity motions are used to investigate the appropriate boundary conditions at the base sensor, as well as to quantify the average misfit (i.e. bias) between the simulations and observations. Larger intensity motions are used to investigate the ability of the numerical models to predict site amplification at moderate to large strain levels. Our analyses indicate that the appropriate boundary conditions for analysis of a borehole array depend on the depth of the borehole sensor. Comparisons with the observed motions indicate that the misfit of simulations can be significant. However, at low intensities, the average bias across all sites analyzed is close to zero, indicating that 1-D wave propagation does not systematically over-predict or under-predict site amplification. However, at large intensities the EQL approach generally under-predicts site amplification at periods less than 0.4 s due to over-damping at large strains. On the contrary, the EQL-FD approach over-predicts of site amplification, due to the utilization of small strain damping values at high frequencies.

1. INTRODUCTION

Local soil conditions play a significant role in the nature and characteristics of ground shaking during earthquakes. The influence of local soil conditions on ground shaking is typically evaluated using numerical modeling techniques, all of which involve the propagation of earthquake waves from the base rock through a model of the soil layers to the ground surface. The various properties of the soil layers are the primary input into the modeling process, while the surface motion, in terms of an acceleration time series or response spectrum, is the primary output. The existing site response approaches differ from each other based on the way they address: 1) the complexity of the seismic wave propagation pattern, and 2) the nonlinearity of the soil response. Thus, 1-D, 2-D and 3-D models have been developed to simulate the directional effects of the passing seismic waves on the soil response, while equivalent-linear (EQL) and fully nonlinear (NL) models provide the numerical tools by which the nonlinear soil behavior may be approximated.

In cases where major topographic and basin effects are minimal, one-dimensional ground response analysis has been considered adequately representative of the actual wave propagation conditions (Figure 1). That is, it can be reasonably assumed that all boundaries are horizontal and extend infinitely, and thus, the response is dominated by vertically propagating and horizontally polarized shear waves (SH-waves). Moreover, in engineering practice the nonlinear and inelastic soil behavior is approximated most commonly by the equivalent-linear approach. That is, once the modeling parameters such as the shear wave velocity profile and shear modulus reduction and damping curves have been specified, linear analysis is performed with iteratively adjusted soil properties. Within the general framework of an equivalent-linear analysis, two major formulations are prevalent. The most widely accepted approach is the traditional equivalent-linear formulation (EQL), as first introduced by Schnabel *et al.* (1972). Based on this approach, the shear modulus and damping are iteratively adjusted to be consistent with an effective level of shear strain induced in each soil layer (Figure 1). More recently, a new formulation, namely an equivalent-linear analysis with frequency dependent soil properties (EQL-FD) (e.g. Assimaki and Kausel, 2002; Yoshida *et al.*, 2001) has been proposed. These phenomenologically-based algorithms address the inability of the traditional EQL formulation to accurately predict site amplification at high frequencies at large input intensities. The EQL-FD iterative procedure, instead of targeting a single-valued effective shear strain to select strain-compatible soil properties, takes advantage of the complete shear strain frequency spectrum to select strain-compatible properties at each frequency (i.e. frequency-dependent properties, Figure 1).

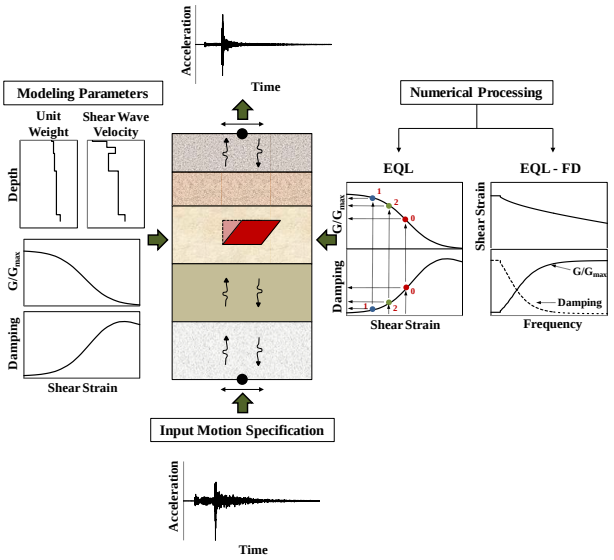


Figure 1 Schematic of the aspects associated with 1-D equivalent-linear (EQL, EQL-FD) numerical models

In this study, one-dimensional linear-elastic (LE) analyses are performed initially to evaluate key assumptions associated with one-dimensional site response. Then, using the obtained information, we investigate the ability of both 1-D equivalent-linear formulations (EQL and EQL-FD) to accurately predict the ground response under moderate to strong shaking. This evaluation is achieved by comparing the theoretically computed response with observations obtained from vertical strong motion borehole arrays. Our ultimate goal is to: 1) evaluate the performance of the numerical algorithms at different levels of earthquake shaking, and 2) quantify the uncertainty associated with the theoretical models.

2. SITE AND GROUND MOTION SELECTION

2.1 Data from strong motion borehole arrays

Geotechnical strong motion borehole arrays consist of vertically distributed, strong-motion accelerometers and they have been installed in numerous locations around the globe. Borehole arrays provide critical information to better understand the physical mechanisms associated with the response of soil and rock media under earthquake shaking. The continuously increasing number of strong-motion recordings from these arrays has been driving more rigorous studies on the assumptions and accuracies of numerical models commonly used to compute site response (e.g., Borja *et al.*, 1999; Kottke, 2010; Kaklamanos *et al.*, 2012).

Specifically, the Kiban-Kyoshin (NIED KiK-net) network in Japan is one of the largest sources of strong motion recordings from borehole arrays. It consists of more than 650 sites where surface-borehole pairs of sensors are available. For each site, shear and compression wave velocity profiles are provided along with basic soil and rock classifications and descriptions. Despite the fact that the site characterization is not extensive, the breadth and the number of strong motion recordings is large and diverse, something that makes the database suitable for the evaluation of site response methodologies.

2.2 Factors for site selection

Towards an effort to select the most suitable sites and associated strong ground motion recordings for the purposes of the present study, site characterization information and strong motion data obtained through the KiK-net database were processed and classified. For each site in the database, information was compiled regarding the time-averaged shear wave velocity over the top 30 m (V_{s30}) of the array, the number of recorded motions, their respective peak accelerations, and the depth to the downhole sensor. In Figure 2, the distribution of sites relative to their NEHRP site classification and the distribution of recordings relative to their peak ground acceleration at the downhole sensor (PGA_{base}) are shown. These data show that the majority of sites are Site Class C (V_{s30} = 360 - 750 m/s) and the majority of the recordings have PGA_{base} < 0.1 g. Specific criteria were established to select appropriate KiK-net sites for further investigation. These factors included: 1) the stiffness of the site based on the available in-situ shear wave velocity measurements, 2) the number of the recorded motions, 3) the range of PGA_{base} values, and 4) the availability of high intensity motions as recorded at the downhole sensor. Sites characterized by low V_{s30} were preferred due to the fact that these sites typically exhibit strong nonlinearity during intense ground shaking. Understandably, sites with such a characteristic along with the availability of high intensity recordings represent the ideal combination.

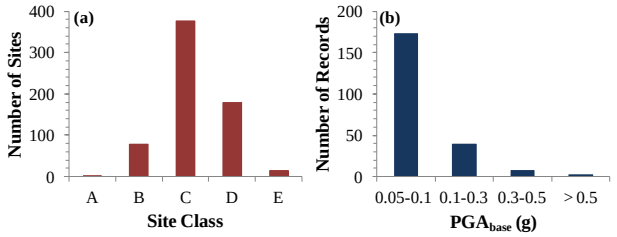


Figure 2 a) Number of sites per NEHRP site classification, and b) number of records per PGA_{base} range

Consequently, 11 KiK-net sites were identified to be most suitable for this study. The selected sites are presented in Tables 1 and 2, where information on the site characteristics and the number of the recorded motions can be found. To supplement this study in terms of softer sites with smaller V_{s30}, we also made use of two additional vertical borehole arrays, namely the La Cienega and Lotung arrays. The V_{s30} for the 13 selected sites ranges from 184 m/s to 371 m/s, while the depth to the downhole sensor varies from "shallow" (≤ 100 m) to "deep" (> 200 m). In Figure 3, the V_S profiles of the selected sites are presented, as reported by the KiK-net database and by Kottke (2010) for the La Cienega and Lotung sites. The KiK-net profiles, obtained through in-situ suspension logging measurements, often do not extend to the depth where the downhole sensor is located and thus extrapolation of the measured shear wave velocity profile was required. Some of the sites (FKSH19, IBRH11, IBRH13 and KSRH10) also exhibit a strong impedance contrast within the top 50 m of the profile (Figure 3).

Table 1 Site characteristics of the selected borehole arrays

Site	$V_{s,30}$ (m/sec)	$V_{s,min}$ (m/sec)	$V_{s,"base"}$ (m/sec)	z_{1000} (m)
FKSH19	338	170	3060	> 40
FKSH20	350	350	610	> 60
IBRH11	242	130	2100	30
IBRH13	335	170	3000	34
IWTH26	371	130	680	> 36
KSRH06	326	90	660	> 170
KSRH07	204	100	510	> 82
KSRH10	212	190	1700	36
MYGH05	305	120	1080	260
MYGH10	348	110	770	> 114
TTRH02	310	210	790	> 42
La Cienega	250	140	644	> 249
Lotung	184	114	256	> 50

Table 2 Number of recordings per PGA_{base} range

Site	< 0.05g	0.05g - 0.2g	> 0.2g
FKSH19	132	1	1
FKSH20	41	10	1
IBRH11	187	16	1
IBRH13	54	16	2
IWTH26	22	6	2
KSRH06	34	12	-
KSRH07	36	-	2
KSRH10	30	4	-
MYGH05	13	13	1
MYGH10	83	20	1
TTRH02	13	1	2
La Cienega	6	1	1
Lotung	10	6	-

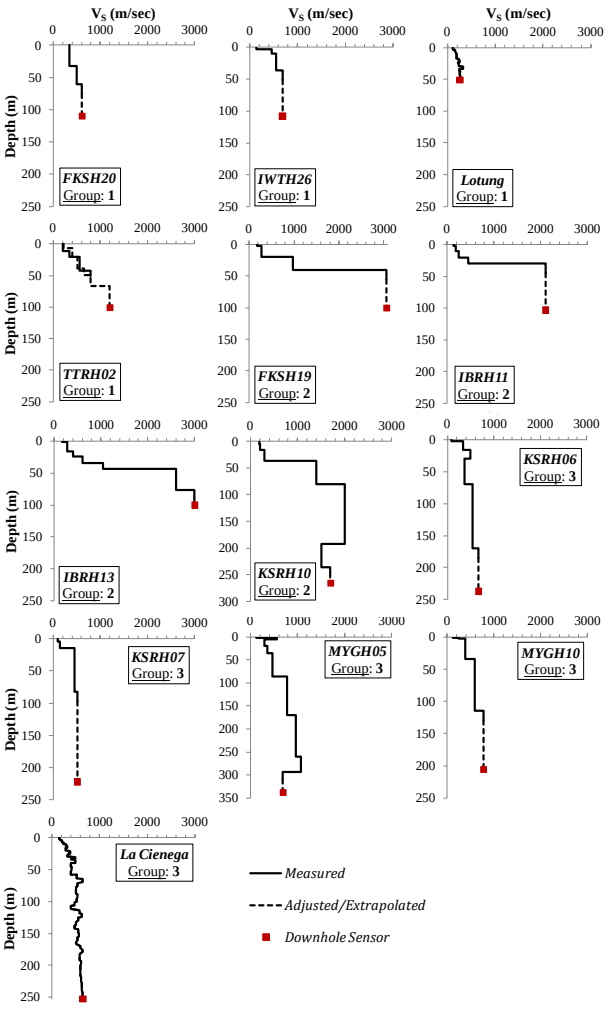


Figure 3 Shear wave velocity (V_S) profiles of the borehole arrays used in this study

2.3 Signal processing of recorded motions

After the borehole arrays were selected, the horizontal (East-West and North-South) components of the recorded motions, both at the downhole sensor and the ground surface, were processed in a unified manner. A fifth-order Butterworth, time-domain, acausal filter with a low-pass cut-off frequency of 30 Hz and a high-pass cut-off frequency of 0.15 Hz was applied to all motions. Subsequently, the recordings were baseline corrected and post-processed, i.e. response and Fourier amplitude spectra were calculated. The obtained transfer functions, i.e. the ratios of surface to "base" Fourier amplitude spectra, were smoothened using a logarithmic triangular window with a width equal to one-fifth of a decade.

3. IDENTIFICATION OF BOREHOLE WAVEFIELD

3.1 Uncertainty in the borehole wavefield

In a one-dimensional layered model, the wave propagation pattern typically consists of an up-going (A) and a down-going (B) seismic wave (Kramer, 1996), as shown in Figure 4. These waves are complex valued and differ from each other within each layer, except for the free surface layer. A certain degree of uncertainty exists in the actual wave propagation field (i.e., boundary condition) present at the depth of base recording within a borehole array (e.g., Bonilla *et al.*, 2002). That is, the down-going (B) wave may or may not be present at the base of the borehole, a remark that leads to two potential assumptions regarding the motion recorded at depth. One possible assumption is that the dowhole response includes both up-going and down-going waves (A+B). This assumption is often referred to as a "within" motion. The alternative assumption, namely an "incoming only" motion, refers to wavefields where only the up-going (A) wave is present. The assumption that best simulates the actual wave propagation conditions at a site of a borehole array is not known a priori. Therefore, a separate set of analyses was performed for each borehole array to evaluate the wavefield that best models the observed responses.

3.2 Evaluation of appropriate borehole wavefield

Identification of the most suitable borehole wavefield is achieved by comparing the observed frequency domain transfer function swith the theoretical transfer functions computed based on the velocity profile and the different wavefield assumptions. The assumption yielding results most similar to the observations can be considered to be most representative. In the past, other researchers (Bonilla *et al.*, 2002; Thompson *et al.*, 2009) have

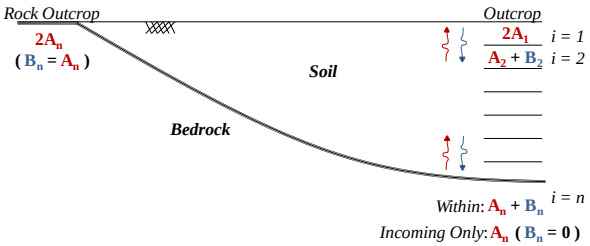


Figure 4 Common assumptions regarding wavefield pattern throughout a 1-D layered system (after Kottke, 2010)

made similar efforts to investigate and explain the physical mechanisms associated with the selection of the appropriate wavefield for a given borehole array.

Within the framework of the present study, 1-D linear-elastic analyses (LE) were performed assuming both "within" and "incoming only" wavefields at the base of the arrays. The observed transfer functions for the lowest levels of shaking (PGA_{base} < 0.05 g) were compared with the computed transfer functions for the two boundary conditions. The soil layers at the sites were modeled as linear-elastic with damping values assigned in two ways. First, a minimum damping (D_{min}) value, as obtained by the Darendeli (2001) model for the modulus reduction and damping curves, was assigned to each layer. The Darendeli (2001) model models damping as confining stress dependent, with larger damping values (generally ~ 1.0-1.5 %) close to the ground surface and smaller values (~ 0.5 %) at depth. Because the damping values from Darendeli (2001) are based on laboratory testing, they only account for material damping and do not account for other mechanisms of energy dissipation in the field such as wave scattering. To investigate the influence of incorporating these other mechanisms of energy dissipation, an increased damping value of 2.5 % was considered. The utilization of two different damping profiles was essential in order to address the uncertainty concerning: 1) the assumed level of damping experienced by soil materials at low levels of induced shear strain, and 2) the potential attenuation of the down-going seismic wave (B).

Analyses assuming both wavefields and damping profiles were performed. In Figure 5, theoretical transfer functions computed based on both the "within" and "incoming only" assumptions are compared with the observed transfer functions. Because the "within" transfer functions using D_{min} generally had excessively large peaks, the "within" transfer functions in Figure 5 are shown with damping values set to 2.5 %. The "incoming only" transfer functions are shown for damping profiles based solely on D_{min}. In general, the "within" wavefield produces very peaked transfer functions, even with the increased damping, due to the destructive interference between the upgoing and downgoing waves at the modal frequencies of a velocity profile. This phenomenon is more profound at lower frequencies, which are related to the response of deeper strata of the soil profile. The "incoming only" transfer functions are much smoother than the "within" transfer functions because the downgoing wave is ignored. It is clear from Figure 5 that some sites are better modeled by the "within" transfer function while others are better modeled by the "incoming only" transfer function.

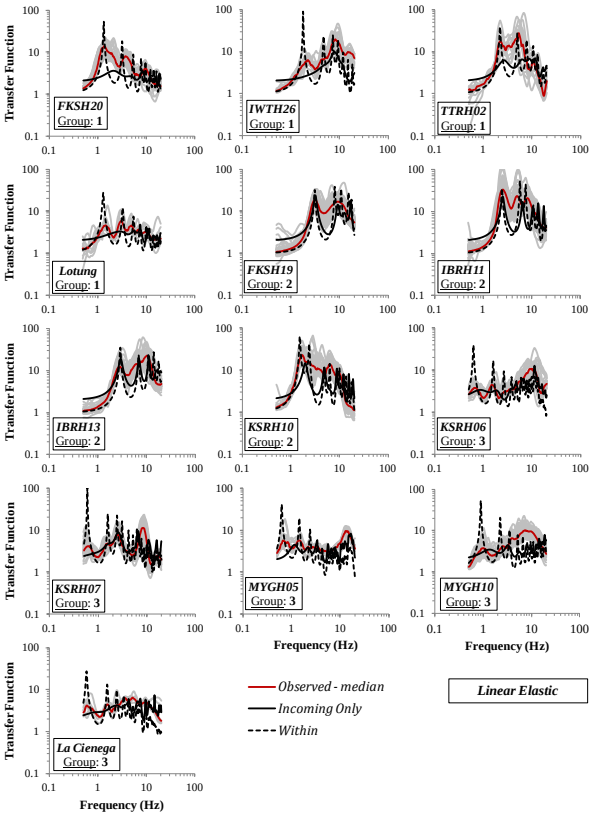


Figure 5 Comparison of theoretical linear-elastic transfer functions and observed transfer functions for low intensity motions

Based on these observations, the borehole arrays can be subdivided into three groups based on the appropriate wavefield and the physical justification for this wavefield (Table 3). Group 1 sites are best-fit by the "within" wavefield, most likely because the downhole sensor is positioned at relatively shallow depths (i.e., ≤ 100 m) such that the downgoing wave is present at the downhole sensor. Group 2 sites are best-fit by either the "within" or "incoming only" wavefields because both wavefields produce similar responses (Figure 5). The similarity in the transfer functions for the two wavefields is caused by a strong shear wave velocity contrast within the top 50 m of the profile (Figure 3) which traps the downgoing wave in the softer layers near the surface. Because the "within" boundary condition is most commonly used in engineering practice when analyzing borehole arrays, subsequent analyses of Group 2 will utilize the "within" wavefield boundary condition. Finally, Group 3 sites are best fit by the "incoming only" wavefield. This wavefield provides the best fit because the borehole sensor is relatively deep (i.e., ≥ 200 m), such that the downgoing wave is not present at the borehole sensor due to attenuation/damping in the upper layers. It should be noted that the theoretical transfer functions are not able to fully capture the observed transfer functions at all frequencies. The discrepancies are most likely attributed to simplifications associated with 1-D wave propagation, as well as to potential bias in the utilized material properties.

Table 3 Grouping of arrays based on site characteristics and appropriate wavefield boundary condition

Site	Downhole Sensor depth (m)	Selected Wavefield	Damping for LE analyses (%)	Group*
FKSH20	109	Within	2.5	1
IWTH26	108	Within	2.5	1
TTRH02	100	Within	2.5	1
Lotung	50	Within	2.5	1
FKSH19	100	Within/Incoming	2.5 / D_{min}	2
IBRH11	103	Within/Incoming	2.5 / D_{min}	2
IBRH13	100	Within/Incoming	2.5 / D_{min}	2
KSRH10	255	Within/Incoming	2.5 / D_{min}	2
KSRH06	237	Incoming Only	D_{min}	3
KSRH07	222	Incoming Only	D_{min}	3
MYGH05	337	Incoming Only	D_{min}	3
MYGH10	205	Incoming Only	D_{min}	3
La Cienega	265	Incoming Only	D_{min}	3

*Group	Characteristics / Description
1	Downhole Sensor Depth: approx. < 100 m
2	Strong impedance contrast within the profile
3	Downhole Sensor Depth: approx. > 200 m

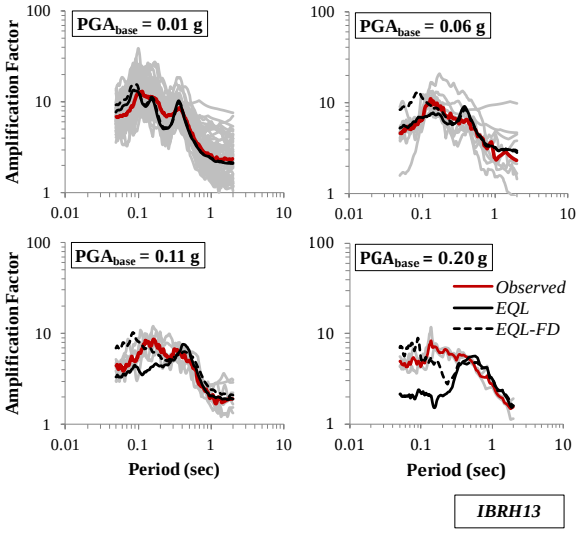


Figure 6 Observed and computed Amplification Factors for the IBRH13 borehole array

4. ASSESSMENT OF SITE RESPONSE METHODS

4.1 General framework

The assessment of the performance of the 1-D equivalent linear site response methodologies (EQL and EQL-FD) is based on site amplification factors, defined as the acceleration response spectrum of the surface motion divided by the acceleration response spectrum of the recorded base motion. This evaluation is different than used for the evaluation of boundary conditions in Section 3, but it is deemed appropriate because most site response analyses are aimed at producing acceleration response spectra rather than Fourier Amplitude Spectra. Analyses were performed using the selected wavefield assumption for each site (Table 3). Modulus reduction and damping curves based on the Darendeli (2001) model were assigned to all soil layers. Subsequently, the results from the analyses were classified according to their corresponding level of shaking, as depicted by the peak acceleration of the input motions (PGA_{base}). Because the PGA_{base} values range from low (less than 0.05 g) to high (greater than 0.3 g), the effect of input intensity on the accuracy of the predictions is investigated.

Figure 6 illustrates the comparison between observed and computed *median* amplification factors for borehole array IBRH13 at different input level intensities. Results are shown for four ranges of PGA_{base}, with median values of 0.01 g, 0.06 g, 0.11 g, and 0.20 g, respectively. The performance of both the EQL and EQL-FD models strongly depends on the level of shaking, and thus implicitly on the magnitude of the induced shear strains. At low intensity levels, namely for PGA_{base} less than 0.05 g, there is strong agreement between observations and theoretical results at all frequencies. A slight over-prediction occurs at periods less than 0.1 s and a slight under-prediction at a period of about 0.25 s, but still the agreement is quite good. As input intensity increases, the computed amplifications factors from the EQL and EQL-FD methods deviate from each other, as well as from the observations, at periods less than about 0.3-0.4 s. In general, the EQL model strongly under-predicts amplification at shorter periods because of over-damping of high frequencies due to the large peak strain used to select the frequency-independent properties (i.e. damping). The EQL-FD analysis seems to better predict the response at periods between 0.1 s and 0.3 s, with the exception of highest input intensities (PGA_{base} ~ 0.20 g). Here, some under-prediction is observed. However, at periods below 0.1 s the EQL-FD approach systematically over-predicts the site amplification. At these very high frequencies, which are associated with very small strains during unloading-reloading cycles, the EQL-FD approach utilizes damping close to or equal to the minimum damping values incorporated in the damping curve. Consequently, the EQL-FD analysis predicts a near-linear-elastic response and high amplification at these frequencies. This is an attribute of the model that can be seen throughout our analyses.

The discussion above involves only one out of the thirteen sites analyzed, although many of the observations are valid for the other borehole arrays. To compare results across sites and quantify the accuracy and uncertainty of the different approaches, a unifying framework is used. The framework is based on a model developed by Abrahamson *et al.* (1990) for the quantification of the goodness-of-fit between seismological ground motion observations and simulations. Abrahamson *et al.* (1990) quantified the misfit between numerically simulated and recorded strong ground motions in terms of the natural log of the response spectral values. In the present study, we quantify the misfit (or bias) as the difference between the natural log of the observed and calculated amplification factors (AF) at each frequency. This modification is solely semantic, because the calculated bias is the same in either case. Therefore, for the i^{th} site and j^{th} recording, the residual (y) between the natural log of the observed amplification factor ($\ln AF^{obs}$) and the natural log of the theoretically calculated amplification factor ($\ln AF^{calc}$) is given by:

$$y_{i,j}(f) = ln\ AF_{i,j}^{obs}(f) - ln\ AF_{i,j}^{calc}(f) \quad (1)$$

where f is frequency. Positive bias represents under-prediction by the model, while negative bias represents over-prediction by the model. For example, residuals with values 1.0, 0.5, -0.5 and -1.0 correspond to ratios of AF^{obs}/AF^{calc} equal to 2.71, 1.65, 0.61 and 0.36, respectively. Figure 7 presents the calculated residuals for IBRH13 site. The results in Figure 7 are the direct equivalent of the results in Figure 6, with the EQL approach producing large positive residuals (i.e., under-prediction) at high frequencies and large input intensities and the EQL-FD producing negative residuals (i.e., over-prediction) at high frequencies and large input intensities.

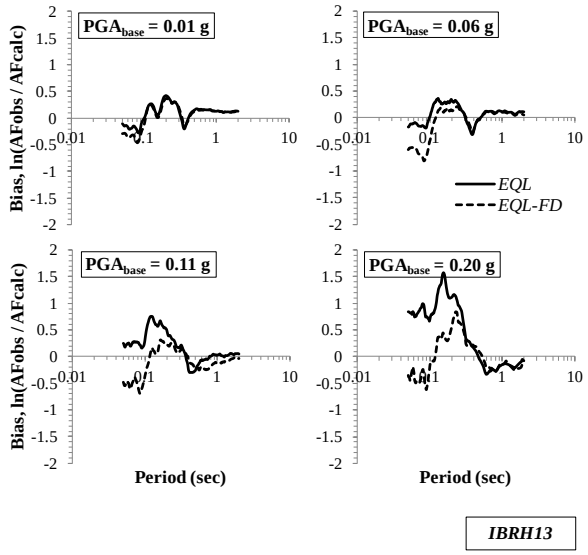


Figure 7 Calculated bias for EQL and EQL-FD methods for IBRH13 borehole array

4.2 Identification of sources of uncertainty

Examining site response models for a specific site gives us insight into the effects of particular site characteristics. However, uncertainty assessment requires the combination of observations from several sites, such that statistically significant measures can be established and evaluated. Within the framework of our efforts, we tried to identify sources of uncertainty by using models proposed by several researchers in the context of either ground motion prediction equations (GMPEs) (e.g., Lin *et al.*, 2011; Rodriguez-Marek *et al.*, 2011) or site response analysis (e.g., Kaklamanos *et al.*, 2012). In this study, the notation utilized by Kaklamanos *et al.* (2012) is adopted.

Assuming that the observation residuals at a specific frequency, $y_{i,j}$, as previously introduced, represent a normally distributed random variable with mean μ_y and standard deviation σ_y, we can separate the residuals into different components, as:

$$y_{i,j} = \alpha + \eta_{s,i} + \varepsilon_{i,j} \quad (2)$$

where α is the "fixed effect", $\eta_{s,i}$ is the inter-site residual, and $\varepsilon_{i,j}$ is the intra-site residual. The "fixed effect", α, represents the mean bias across all sites and recordings. The inter-site residual, $\eta_{s,i}$, quantifies the "site-specific" bias and is assumed to be a normally distributed random variable with, ideally, a zero mean ($\mu_{\eta_s} = 0$) and standard deviation τ_s. For the i^{th} site, $\eta_{s,i}$ represents the misfit between the mean residual of the site and the "fixed effect", α. The intra-site residual, $\varepsilon_{i,j}$, expresses the "within-site" variability and is a normally distributed random variable with zero mean ($\mu_\varepsilon = 0$) and standard deviation σ. $\varepsilon_{i,j}$ represents the difference between a single observation, $y_{i,j}$, and the site-corrected mean residual ($\alpha + \eta_{s,i}$).

Considering the model of equation (2), the mean (μ_y) and standard deviation (σ_y) of the observation residuals can be split into three components, namely: the fixed effect, α; the inter-site standard deviation, τ_s; and the intra-site standard deviation, σ. Specifically, the uncertainty measures of $y_{i,j}$ are given by:

$$\mu_y = \alpha \quad (3)$$

$$\sigma_y = \sqrt{\tau_s^2 + \sigma^2} \quad (4)$$

The mean inter -site residual (μ_{η_s}), could have been included in equation (3) to fully represent the actual linear model, as developed based on the observations of the present study. However, although μ_{η_s} has been assumed to be zero-valued, this assumption is not fully achieved in this study because the number of borehole arrays considered is relatively limited (13) and the number of recordings is not evenly distributed among the sites. Therefore, the computed values of μ_{η_s} are not zero, although generally they were close to zero (~0.1).

4.3 Uncertainty evaluation across sites

As shown in the evaluation of single-site bias (Figures 6 and 7), one of our main goals was to examine the effect of increasing levels of shaking on the site response predictions. When evaluating a single site, PGA_{base} was an appropriate parameter upon which to classify the different responses. For the uncertainty analysis across sites with different shear wave velocity characteristics, the maximum calculated shear strain (γ_{max}) was established as a more appropriate parameter to use. The magnitude of the induced shear strains is the parameter mostly influencing the results because it directly influences the damping used in the site response analysis. Five different ranges of γ_{max} values were considered; γ_{max} < 0.01 %, 0.01-0.1%, 0.1%-0.3%, 0.3%-1.0%, and > 1.0%. The number of sites and number of input motions yielding γ_{max} values within each of these shear strain ranges varied substantially. For example, 407 motions from 13 sites are included in the γ_{max} < 0.01 % bin, 24 motions from 9 sites are included in the γ_{max} of 0.1%-0.3% bin, and 25 motions from 8 sites are included in the γ_{max} > 1.0 % bin. It should be noted that γ_{max} is computed as part of the analysis and thus is not an independent assessment of the strain that can be predicted a priori. Nonetheless, the computed γ_{max} best explains the deviations of the site response results from the observations and it should be proportional to the actual induced strains in the soil deposit.

By combining the observations and numerical results from all borehole arrays using equation (2) and grouping the results

based on the computed γ_{max}, we are able to quantify the across-site accuracy of the EQL and EQL-FD methods at different strain levels and provide estimates of the uncertainty associated with the site amplification predicted by these models. Figures 8 and 9 summarize the uncertainty modeling for the EQL and EQL-FD methods, respectively. Figures 8a and 9a illustrate the mean residuals, while Figures 8b and 9b present the corresponding standard deviations. Results are shown for calculated maximum shear strain ranges of: $\gamma_{max} \leq 0.01\%$, $0.1\% < \gamma_{max} \leq 0.3\%$, and $\gamma_{max} > 1.0\%$. The mean observation residuals (μ_y) are represented by the "fixed effect" α, while the total standard deviations (σ_y) include inter and intra-site standard deviations (τ_s and σ, respectively).

Figure 8a, demonstrates that the accuracy of the EQL approach strongly depends on the level of the induced strains. At small strain levels ($\gamma_{max} \leq 0.01\%$), the EQL yields mean residual values (μ_y) relatively close to zero across almost the entire frequency range. When the induced strain level increases, the responses from the EQL approach deviate from observations, with μ_y becoming large and positive. Indeed, at periods smaller than approximately 0.4 s, the EQL approach under-predicts the response by as much as factors of 1.5 to 3.0. Under-prediction

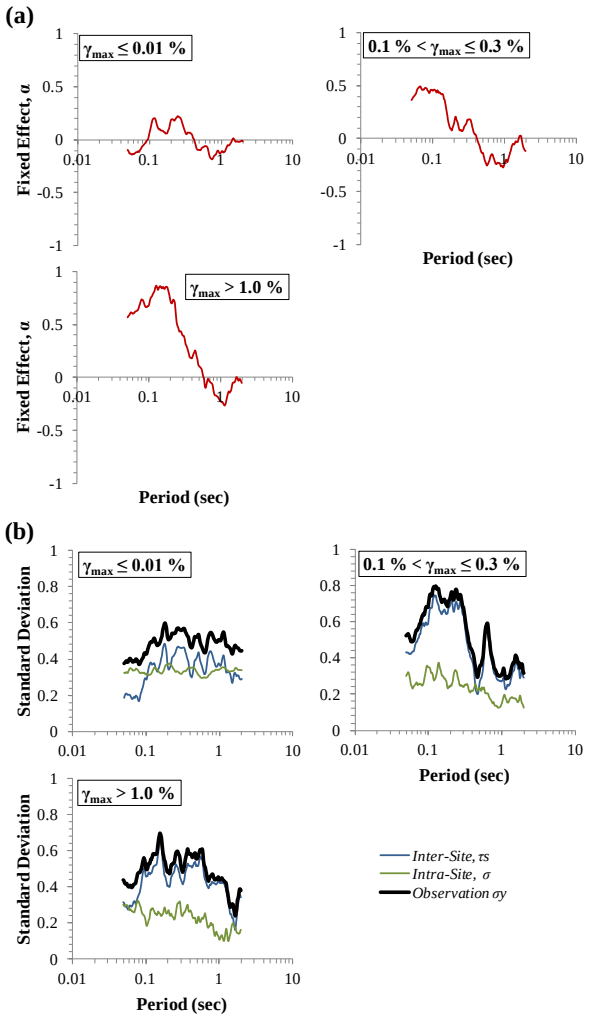


Figure 8 (a) Mean residuals, and (b) standard deviations for amplification factors computed by the EQL approach

of the response can be attributed to the inability of the numerical model to deal with excessive nonlinearities caused by strong shaking. The total observational standard deviation (σ_y, Figure 8b) at small strains is approximately 0.4 at periods less than 0.1 s and it is about 0.55 at larger periods. The inter-site and intra-site standard deviations contribute almost equally (~0.3 to 0.4) to the total standard deviation. At larger strains, σ_y increases to about 0.65-0.8 at periods less than about 0.4 s, and the inter-site component dominates with the intra-site standard deviation being relatively small (0.2-0.3). At these levels of shaking the calculated maximum strain, and not input motion characteristics, predominantly influences the performance of the theoretical model, which may explain the observed low intra-site variability. Moreover, the greater contribution of the inter-site variability (τ_s) to the total variability (σ_y) is most likely attributed to the fact that analyses resulting in large shear strains include fewer sites and motions per site, making the estimate of τ_s unreliable.

As shown in Figure 9, at low strain levels ($\gamma_{max} \leq 0.01\%$), the residuals and standard deviations from the EQL-FD approach are very similar to those for the EQL approach. This similarity occurs because the soil properties do not vary significantly with frequency at small strains. In contrast, as the magnitude of the induced strains increases, the mean residuals for the EQL-FD approach become systematically negative at periods less than about 0.3 s. These residuals indicate an over-prediction of the amplification by factors as large as 1.5 to 2.0. As previously discussed, the over-amplification of high frequencies is caused by the utilization of the minimum damping value at high frequencies. In terms of the variability in the calculated residuals for the EQL-FD approach (Figure 9b), the total standard deviation at small strains is similar to that for the EQL approach. At larger strains there is some increased variability across some periods but the effect is not clearly identified. As for the EQL method, at larger strains the inter-site variability is the primary contributing factor to the total standard deviation, with the corresponding intra-site standard deviation taking relatively small values (0.2-0.3). However, the fewer number of sites and motions included in the analyses at large strains makes the computed inter-site standard deviation less reliable.

Figure 10 summarizes the mean observation residuals (μ_y) and total standard deviations (σ_y) for the EQL and EQL-FD approaches across the five shear strain bins considered. For the EQL approach, the mean residual stays close to zero (+/- 0.1 which represents +/-10%) across all periods for strains less than about 0.1%. At strains larger than 0.1%, the residuals become increasingly positive for periods less than 0.4 s and indicate an under-prediction of the response. For the EQL-FD approach, the residuals become increasingly negative for periods less than 0.4 s at strains greater than 0.01%, which is a smaller strain threshold than for the EQL approach. Nonetheless, the over-prediction by the EQL-FD approach appears to be generally less than the under-prediction by the EQL approach. With the exception of slightly lower values at small strains, total standard deviations (Figure 10b) seem to be unaffected by the level of

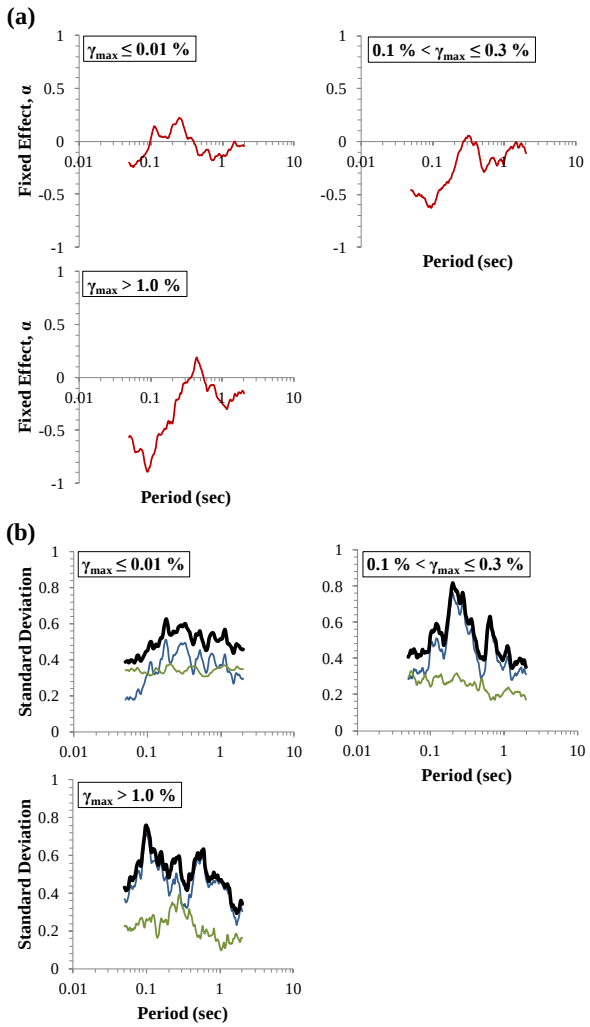


Figure 9 (a) Mean residuals, and (b) standard deviations for amplification factors computed by the EQL-FD approach

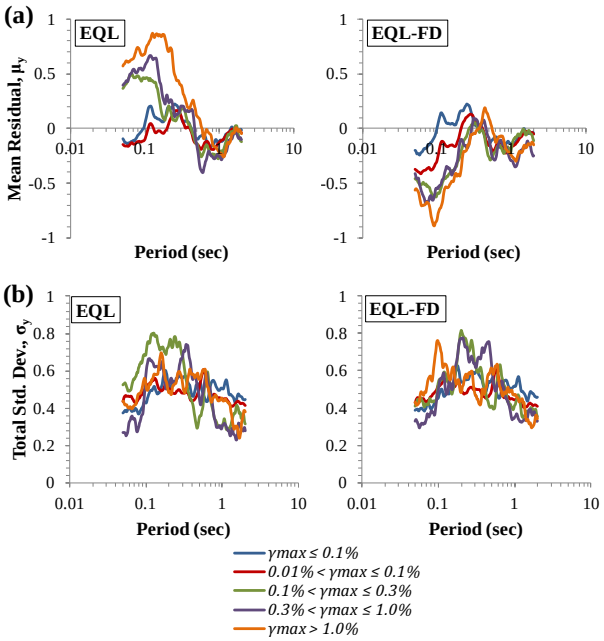


Figure 10 (a) Mean residuals, μ_y, and (b) total standard deviations, σ_y, across different induced shear strain levels

shaking. Moreover, they are, for all practical purposes, similar for both numerical models. Site response variability seems to be smaller at periods less than 0.1 s and periods greater than 1.0 s.

5. CONCLUSIONS

Observations from 13 selected strong-motion borehole arrays have been studied and compared with results from numerical site response analysis. Site response analyses were performed using two main approaches: equivalent-linear (EQL) and equivalent linear with frequency-dependent soil properties (EQL-FD). Using the recordings and theoretical calculations we evaluated the appropriate boundary conditions at the base of each borehole array, the accuracy of the site amplification computed by the two site response approaches, and the associated variability in the computed site amplification.

Results from linear-elastic analyses were utilized to identify the boundary conditions (i.e., borehole wavefield) as captured by the recordings at each array. The borehole wavefield that most accurately models the recorded surface motions strongly depends on the depth to the downhole sensor. Sites with depths to the base sensor greater than about 200 m are better analyzed using an "incoming only" assumption, while sites with shallower base sensor depths (less than about 100 m) seem to be better characterized by a "within" wavefield. Borehole arrays with a strong impedance contrast within the upper 50 m of their profile can be analyzed using either wavefield assumption.

Amplification factors computed by the EQL and EQL-FD approaches were compared with those observed, both on a site-by-site basis as well as within an across-site context. At low levels of shaking and induced shear strain levels, both the EQL and EQL-FD methods yield mean residuals across all sites close to zero, indicating no systematic bias in the site amplification predictions at small strains. As input intensity and the induced shear strain increases, the computed responses from both the EQL and EQL-FD methods deviate from the observations. The misfit is typically exhibited at periods less than 0.4 s. In this frequency range the EQL approach systematically under-predicts the response, while EQL-FD method consistently over-predicts site amplification. In both cases, the differences can be as large as a factor of 1.5 to 3.0.

A model was used to quantify the variability associated with both EQL and EQL-FD methods. Inter and intra-site contributions to the total variability were evaluated. Both approaches appear to be characterized by similar levels of variability. When performed at a single site, the intra-site standard deviation is generally frequency-independent with values on the order of 0.2 to 0.3. When evaluated across sites, the total standard deviations are larger with values around 0.5 to 0.7 and are practically independent of the level of shaking.

Acknowledgements:

Financial support for this work was provided by the Nuclear Regulatory Commission under grant NRC-04-09-134. This support is gratefully acknowledged.

References:

Abrahamson, N. A., Somervill, P., G., and Cornell, C. (1990), "Uncertainty in Numerical Strong Motion Predictions," *Proceedings of the Fourth US National Conference on Earthquake Engineering*, volume **1**, 407-416.

Assimaki, D., and Kausel, E. (2002), "An Equivalent Linear Algorithm with Frequency-and-Pressure-Dependent Moduli and Damping for Seismic Analysis of Deep Sites," *Soil Dynamics and Earthquake Engineering*, **22**, 959-965.

Bonilla, L. F., Steidl, J. H., Gariel J.-C., amd Archuleta, R. J. (2002), "Borehole Response Studies at the Garner Valley Downhole Array, Southern California," *Bulletin of Seismological Society of America*, **92**(6), 3165-3179

Borja, R. I., Chao, H. Y., Montans, F., J., Lin, C. (1999), "Nonlinear Ground Response at Lotung LSST site," *Journal of Geotechnical and Geoenvironmental Engineering*, **125**(3), 187-197.

Darendeli, M. B. (2001), "Development of a New Family of Normalized Modulus Reduction and Material Damping Curves," *Ph.D Dissertation, The University of Texas at Austin*, Austin, Texas, 396 pp.

Kaklamanos, J., Bradley, B., A., Thompson, E., M., and Baise, L., G. (2012), "Critical Parameters Affecting Bias and Variability in Site Response Analyses using Kik-net Downhole Array Data," *Technical Report, Department of Civil and Environmental Engineering, Tufts University*, Medford, Massachusetts, 45 pp.

Kottke, A. (2010), "A Comparison of Seismic Site Response Methods," *Ph.D Dissertation, Unverisity of Texas at Austin*, Austin, Texas, 396 pp.

Kottke, A., and Rathje, E. (2008), "Technical Manual for Strata," *Report 2008/10, Pacific Earthquake Engineering Research (PEER) Center*, Berkeley, California, 2008b

Kik-net, *Kiban-kyoshin network*, URL http://kik.bosai.go.jp/.

Lin, P.-S., Chiou, B., Abrahamson, N., Walling, M., Lee, C.-T., and Cheng, C.-T. (2011), "Repeatable Source, Site, and Path Effects on the Standard Deviation for Ground-Motion Prediction," *Bulletin of Seismological Society of America*, **101**, 2281-2295

Rodriguez-Marek A., Montalva G., A., Cotton, F., and Bonilla, F. (2011), "Analysis of Single-Station Standard Deviation using the Kik-net data," *Bulletin of Seismological Society of America*, **101**, 1242-1258.

Schnabel, P. B., Lysmer, J., and Seed H. B. (1972), "SHAKE: A Computer Program for Earthquake Response Analysis of Horizontally Layered Sites," *Report UCB/EERC-71/12, Earthquake Engineering Research Center, University of California*, Berkeley, California, 102 pp.

Thompson, E., Baise L., Kayen R., and Guzina, B. (2009), "Impediments to Predicting Site Response: Seismic Property Estimation and Modeling Simplifications," *Bulleting of Seismological Society of America*, **99**(5), 2927-2949

Yoshida, N., Kobayashi, S., Suetomi, I., and Miura, K. (2002), "Equivalent Linear Method Considering Frequency Dependent Characteristics of Stiffness and Damping," *Soil Dynamics and Earthquake Engineering*, **22**, 205-222.

10CUEE CONFERENCE PROCEEDINGS
10th International Conference on Urban Earthquake Engineering
March 1-2, 2013, Tokyo Institute of Technology, Tokyo, Japan

EVALUATION OF LOCAL SITES EFFECTS IN LIMA CITY, PERU FROM GROUND MOTION DATA

Selene Quispe[1], Hiroaki Yamanaka[2], Hernando Tavera[3], Fernando Lazares[4] and Zenon Aguilar[4]

1) Doctoral Student, Tokyo Institute of Technology, Japan
2) Professor, Dept. of Environmental Science and Technology, Tokyo Institute of Technology, Japan
3) Researcher, Department of Seismology, Geophysical Institute of Peru, Peru
4) Professor, Fac. of Civil Engineering, National University of Engineering, Peru
selene.q.aa@m.titech.ac.jp, yamanaka@depe.titech.ac.jp, hernando.tavera@igp.gob.pe, f_lazares@uni.edu.pe, zaguilar@uni.edu.pe

Abstract: The present study aims to examine thoroughly the relation between the local site effects and the local subsurface conditions in Lima city, due to the fact that there is little information related to the seismic amplification in this city. Using ground motion records, the amplification effects are studied empirically, in the frequency range from 0.1 to 20 Hz. This study analyzes the seismic events observed along the Pacific coast of Lima city, which were recorded by 10 stations. Because of the limitation in data, site amplification factors are evaluated by using three different methods: the standard spectral ratio, the spectral inversion method and the H/V ratio, so as to identify the significant peaks and troughs at all sites. Results show that most of the stations present relatively large amplifications in the high-frequency range over 3 Hz, moreover RIN station. Nonetheless, CAL site has a different behavior of amplification.

1. INTRODUCTION

A future large earthquake is expected to occur in Lima city, the capital and most densely-populated city of Peru. According to several works (Okal et al. (2006) and Pulido et al. (2010)) the seismic gap that has been identified near coast of Lima city might generate a gigantic magnitude ~9.0 Mw event, which could occur any time within the next 20 years.

During the 1974 October 3 Mw8.0 earthquake – the last event of considerable magnitude that Lima city has been subjected – with focal depth about 13 km, few areas outside of Lima center were severely damaged, such as La Campiña (Chorrillos), La Molina and Callao – La Punta (Repetto et al. 1980). Works described by Husid et al. (1977), Espinoza et al. (1977), Repetto et al. (1980) and Stephenson et al. (2009) refer that these areas were affected by the influence of local surface conditions. For example, in La Molina district it was possible to observe the collapse of reinforced concrete structure during the October 3, 1974, earthquake.

The present study uses ground motion records observed along the Pacific coast of Lima city, Peru, in which the seismic events were recorded by 10 stations, including stations installed both at La Molina and Callao districts. The relation between local subsurface conditions and the local site effect in some areas of Lima city are discussed based on the results obtained from three empirical methods.

2. GROUND MOTION DATA AND ACCELEROMETER STATIONS

Data from 2003 to 2008 was used in this study so as to analysis the site effects at 10 stations. Table 1 gives pertinent information on the 17 events used in this work, and Figure 1 shows their locations relative to our recording sites. These seismic events are superficial and intermediate earthquakes, with Local Magnitude ML from 3.8 to 7.0. The epicentral distances range between ~55 and ~200 km. Because the PGAs were mostly small, we can assume linear site responses, even during the 2007 August 15th Pisco earthquake (Mw 8.0) the influence of non-linearity on the site response was not detected (Quispe 2010).

In addition, from the ten stations used in this work, four stations (CSM, CAL, MOL and CDLCIP) are maintained by CISMID Accelerometer Network, nonetheless MOL site was removed after Pisco earthquake struck, three stations (CER, RIN and PUCP) deployed by the South American Regional Seismological Centre (CERESIS) and three stations (MAY, LMO and NNA) deployed by the Geophysical Institute of Peru (IGP).

All the observation sites are shown in Figure 1 on the geological map of Lima city (Martinez et al. 1975). According to this map, basically most of the stations (sites MAY, CER, RIN, CAL, CDLCIP, CSM, MOL and PUCP) are located on alluvial soil deposits belonging to the Quaternary Holocene (Figure 1), however sites LMO and NNA are located on cretaceous intrusive rock (Figure 1).

Table 1 Event Information (* Means the Event Was Recorded).

Date yyyy/mm/dd	Hour hr:min	Long. (deg)	Lat. (deg)	Mag. (ML)	Depth (km)	Site CSM	Site CAL	Site MOL	Site CDLCIP	Site CER	Site RIN	Site PUCP	Site MAY	Site LMO	Site NNA
2003/05/08	16:33	-77.40	-12.98	5.4	51	*	-	-	-	-	-	*	-	-	*
2003/05/28	21:26	-77.01	-12.48	5.3	51	*	-	-	-	-	-	-	-	-	-
2005/01/17	11:26	-76.78	-12.10	3.8	54	-	-	-	-	-	-	-	-	-	*
2005/03/02	13:48	-76.14	-11.86	5.7	124	-	-	-	-	*	-	-	-	-	*
2005/07/25	6:51	-77.33	-12.24	4.0	42	*	-	*	-	-	-	-	-	-	-
2005/11/10	16:38	-76.22	-12.26	4.0	71	-	*	-	-	-	-	-	-	-	-
2005/12/27	17:02	-76.57	-12.22	4.5	99	*	-	-	-	-	-	-	-	-	-
2006/05/12	3:45	-77.40	-11.96	4.3	80	-	-	-	-	-	-	-	-	*	-
2006/10/20	10:48	-77.02	-13.55	6.2	43	*	-	*	-	-	*	*	*	-	*
2006/10/22	22:14	-77.60	-12.05	3.8	30	-	-	-	-	-	-	-	-	-	*
2006/10/26	22:54	-76.92	-13.44	5.8	42	-	-	-	-	-	-	-	*	*	-
2006/12/11	21:53	-77.37	-11.64	4.2	54	-	-	*	-	-	-	-	-	*	*
2007/08/15	23:40	-76.76	-13.67	7.0	40	*	*	*	*	*	*	*	*	*	*
2007/08/17	13:18	-76.85	-13.61	5.5	23	*	-	-	-	-	-	-	-	*	-
2008/03/29	6:40	-77.73	-12.17	4.3	48	-	*	-	*	-	-	-	-	-	-
2008/03/29	12:51	-77.25	-12.25	5.3	51	*	*	-	*	-	*	-	-	*	-
2008/06/07	13:06	-77.29	-12.48	5.0	67	*	*	-	-	*	-	-	-	*	-

Source parameters were determined by the Geophysical Institute of Peru (IGP)

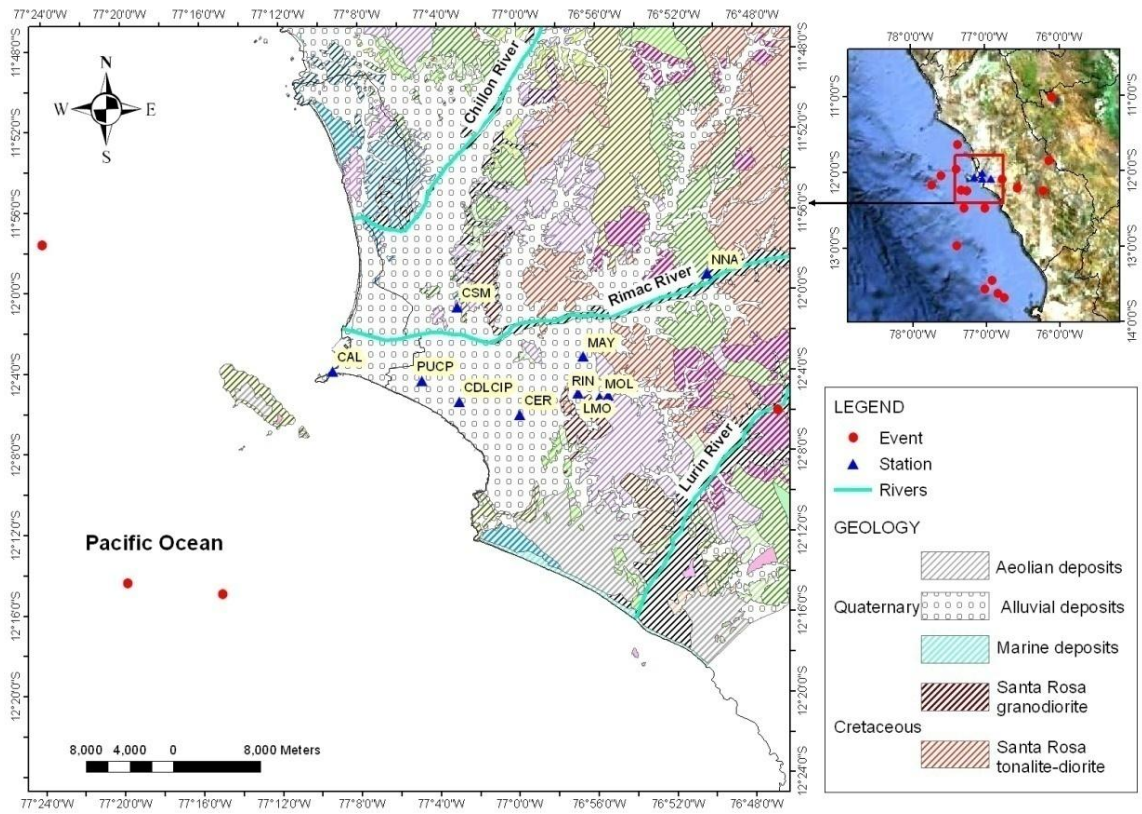


Figure 1 Red circles show the epicenter of events used for this work. Blue triangles represent the stations which are located on the geological map of Lima city (Martinez et al. 1975).

All the observation sites are shown in Figure 1 on the geological map of Lima city (Martinez et al. 1975). According to this map, basically most of the stations (sites MAY, CER, RIN, CAL, CDLCIP, CSM, MOL and PUCP) are located on alluvial soil deposits belonging to the Quaternary Holocene (Figure 1), however sites LMO and NNA are located on cretaceous intrusive rock (Figure 1).

3. SITE RESPONSE ESTIMATION TECHNIQUES

Because of the fact that not all the analyzed events were recorded at all the ten sites as well as the limitation on data, three different empirical methods have been applied in order to get reliable information about the relevant frequencies on seismic amplification factors, such methods are the standard spectral ratio technique (Borcherdt 1970), the spectral inversion method (Iwata and Irikura 1988) and the horizontal-to-vertical spectral ratio technique (Nakamura 1988, Lermo and Chavez-Garcia 1993, Field and Jacob 1995).

The traditional spectral ratio assumes that the site response is estimated by a simple division of the amplitude spectrum calculated from a record at the analyzed station with the amplitude spectrum from a record of the same component at the reference site. However from a practical point of view, the spectral inversion method offers the advantage that records from some events can be included in the inversion even if records at the reference site are not available. This offers the advantage of a more complete exploitation of the data set (Riepl et al 1998). In addition, the inversion method simultaneously gives source, path, and site factors; nonetheless in this article, our concern is to determine the site factor and not to go into details on the other effects. The horizontal-to-vertical spectral ratio in comparison to the other techniques estimates the empirical transfer function using spectral ratios between horizontal and vertical components of motion, so no reference site is needed. For this study, NNA rock site was used as the reference site, because its spectral response shows lesser amplification levels in comparison to LMO site (Cabrejos 2009). As a constraint condition for the spectral inversion method, we set the site amplification factor for NNA to be 2, irrespective of frequency.

The processing sequence for the data set to compute the spectral ratios relative to a reference site or relative to the vertical component was as follows. From each record we selected a window of 20 sec, beginning at the shear-wave arrival. In order to recognize the onset time of S-wave, particle motion plots for two components of motion, EW component on the horizontal axis and NS component on the vertical axis (Figure 2), and Husid plots (Husid et al. 1969), where the horizontal axis is the time and vertical axis is the accumulated horizontal component square for each horizontal component (Figure 3), are realized. After that, the time window of 20 sec was cosine tapered (10%), using the same criterion took by Takemura et al. (1990), and Fourier transformed. The spectral amplitudes were then smoothed by Parzen windows of 0.6-Hz widths. Both for the standard spectral ratio and the horizontal-to-vertical spectral ratio, horizontal value is calculated by taking the geometrical average of the north-south and east-west components. For the inversion method, the Fourier acceleration amplitude spectra of two horizontal components are computed and summed vectorially.

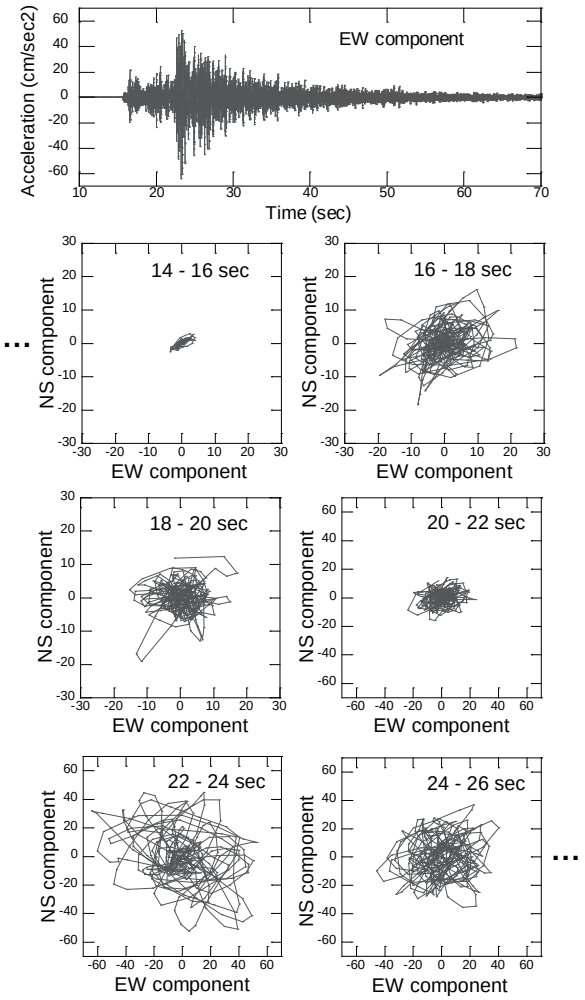


Figure 2. Particle motion plots for two components of motion (CSM station, seismic event 2008/03/29 12:51).

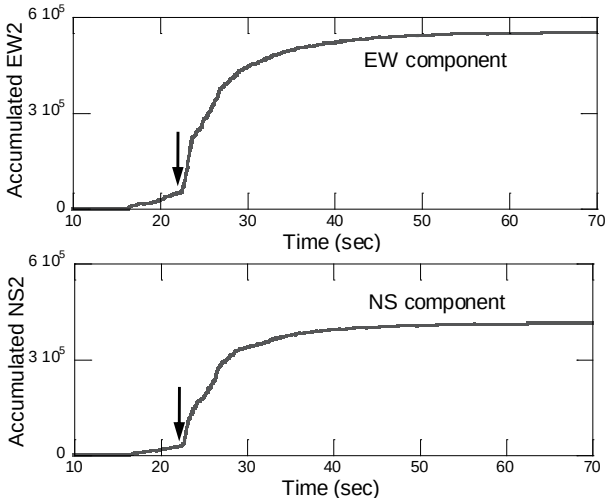


Figure 3. Husid plots to recognize the onset time of S-wave. Black arrows indicate the S-wave onset time (CSM station, seismic event 2008/03/29 12:51).

In order to take advantage that the rupture process of Pisco earthquake was composed of two major events, separated by 60 to 70 seconds (Bernal and Tavera 2007), the

first and the second main events are analyzed for this work, nonetheless the 2nd main event was not recorded by LMO station. For taking a window of 20 sec starting just before the direct S-wave arrival for these two major events, the same procedure as we previously explained was applied.

4. COMPARISON AMONG DIFFERENT EMPIRICAL METHODS

The different estimates of site amplification factors for the stations are compared in Figure 4. Those obtained from the Standard Spectral Ratio (SSR) are shown by thick solid lines, site factors estimated by Spectral Inversion Method (SIM) are shown by thin lines, and amplitude factors calculated from the Horizontal-to-Vertical Spectral Ratio (HVSR) are shown by dotted lines. The SSR for LMO site is not presented for this work given that we do not count on enough seismic events that were simultaneously recorded both for LMO and NNA sites.

According to Figure 4, the geometrical averages of SSR are very similar with inversion results in the analyzed frequency range from the analysis of small and large events. Results show that the amplification level obtained by the SIM are slightly larger in comparison to the traditional approach introduced by Borcherdt (1970) as we can see for CSM, MAY, CDLCIP, PUCP, CAL, and LMO sites. This may be due to the time window of 20 sec that tend to increase slightly the inversion results with the length of the time window because of the effects of later arrivals of surface waves in the case of a long time window (Uetake and Kudo 2005), since as part of this work but results do not show, a time window only taking the S-wave portion was analyzed and inversion results coincided with SSR at many sites in the frequency range higher than 1 Hz.

On the other hand, the geometrical averages of HVSR are also compared with the reference site methods by using the same time window. Results indicate a similarity in the shape of the curves, but HVSR fails for the estimation of the amplification level, since according to Figure 4 most of the sites have much lower amplification in comparison to the other methods. This method assumes that vertical component is expected to be free of amplification, however results obtained by other studies show that subsurface structure influences the vertical component in the same order of magnitude as the horizontal components (Riepl et al. 1998).

For CSM, MAY, CER and CDLCIP stations, even though the amplification level does not fit very well among the analyzed empirical methods, the same peaks and troughs can be identified by the three methods for these four stations. Site effects on these curves (Figure 4) show several peaks of amplification between 3 and 8 Hz as well as a small bump that occurs between 1 and 2 Hz, which is more evident for CER station. Furthermore, relatively large ratios at high frequencies of 10 Hz, moreover for CSM station that has the highest amplification in comparison to the other three sites. There is also a significant trough at about 9 Hz, for CDLCIP site the prominent trough varies in the frequency range between 6 and 10 Hz.

The different estimates for PUCP station show that several peaks of amplification can clearly be distinguished in the frequency range between 1 and 8 Hz, at least four peaks, as well as a trough at about 9 Hz as the previously mentioned stations.

For MOL station, the amplification level both for the SSR and the inversion method are in good agreement for the frequency range investigated. Higher amplifications occur at frequencies larger than 3 Hz as we can see in Figure 4. Amplification effects evaluated by the HVSR do not coincide well with the other methods, however the shape of the site spectra is similar, even a prominent trough at about 12 Hz is identified. This result suggests that the frequency response of vertical component at this site amplifies at the same level as the horizontal components.

The site response at RIN site is dominated by three prominent peaks which are well predicted in the three methods, even though the HVSR predicts lower amplitude in comparison to the reference site methods. The strongest peaks of amplification occur between 3-4 Hz, 7-8 Hz, and frequencies larger than 10 Hz.

For CAL station in comparison to the other sites which amplification levels are larger at higher frequencies, this site shows clearly that strongest amplifications appear at frequencies lower than 3 Hz for the three methods, however amplifications at higher frequencies also occur but are comparatively low. In addition, a trough at about 9-10 Hz has also been detected.

The station located on a rock outcrop, LMO site, has relatively small variations against frequency given that rock sites have local site response (Uetake and Kudo 2005).

Finally, the result of horizontal-to-vertical spectral ratio for NNA site, the reference station, shows that the average transfer function is flat for frequencies lower than 3 Hz, nonetheless no significant trends appear but values are around one. Furthermore, the frequency response at NNA site has a trough, and the trough makes the peaks at frequencies larger than 10 Hz for soft soil sites. That is why, sediment sites show peaks at frequencies larger than 10 Hz that are attributed to the spectral response of NNA given that a relatively strong trough is found.

5. EVALUATION OF LOCAL SURFACE CONDITIONS AND LOCAL SITE EFFECTS

According to the Figure 1, most of the stations are located on Quaternary alluvial deposits with the exception of the rock sites LMO and NNA. CSM, MOL, CER and CDLCIP sites are installed on alluvial gravel deposits that cover a large portion of Lima city, and present a good geomechanic behavior locally named “Lima Conglomerate” (Repetto et al. 1980 and Aguilar 2005). The site response at these stations are characterized by relatively large peaks at around 3-8 Hz, which represent the resonant modes between the poorly graded gravel deposit and other shallow materials that overlie this deposit. PUCP site is also placed on alluvial gravel deposits (Figure 5) nonetheless this site shows several

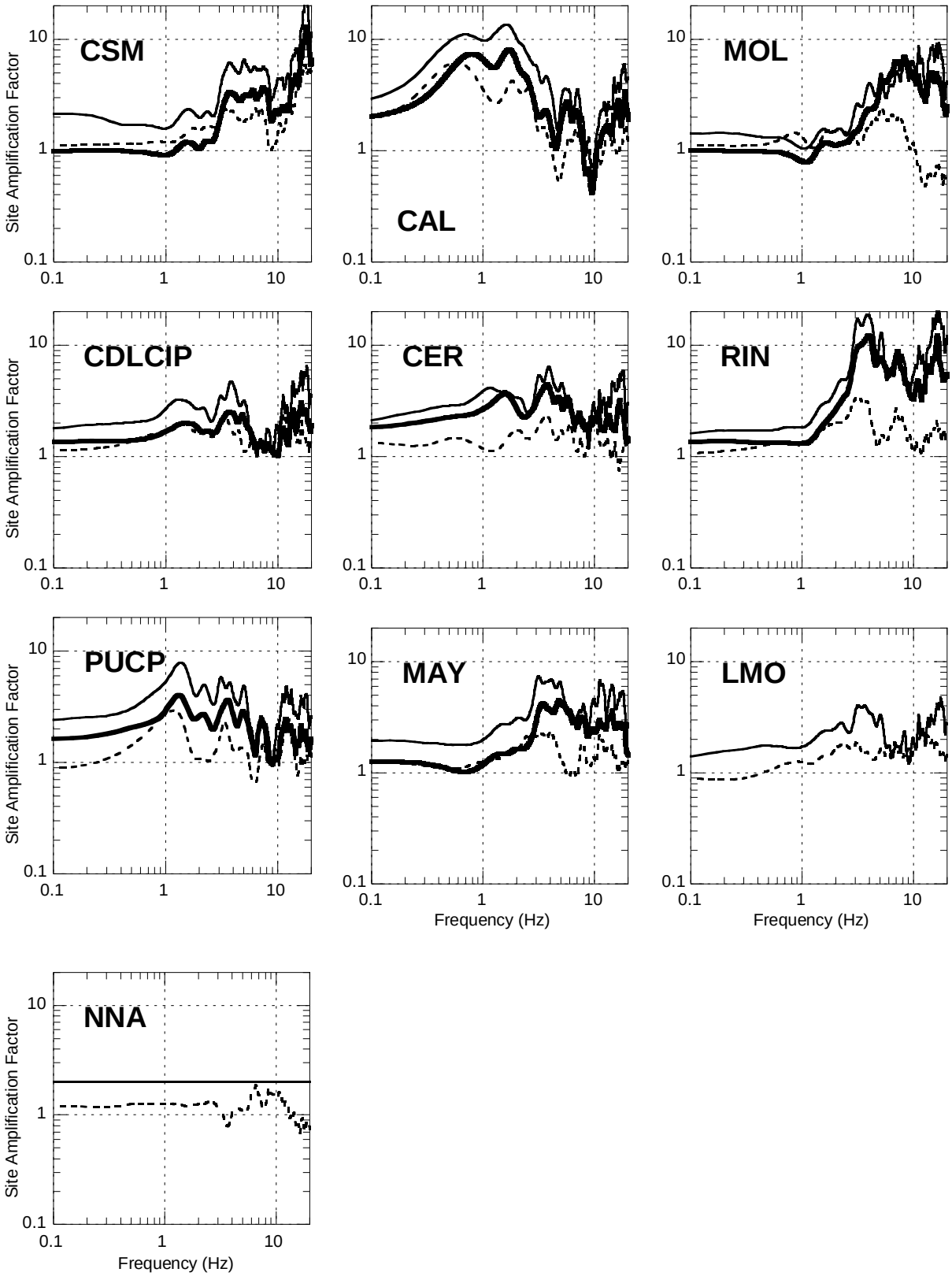


Figure 4. Comparison between spectral ratios from the horizontal components with reference to NNA, the Spectral Inversion Method and the Horizontal-to-Vertical Spectral Ratio. Thick solid lines show the geometrical average of two horizontal spectral ratios. Thin solid lines represent the results obtained by the Spectral Inversion Method. Dotted lines show the geometrical average estimated by applying the HVSR.

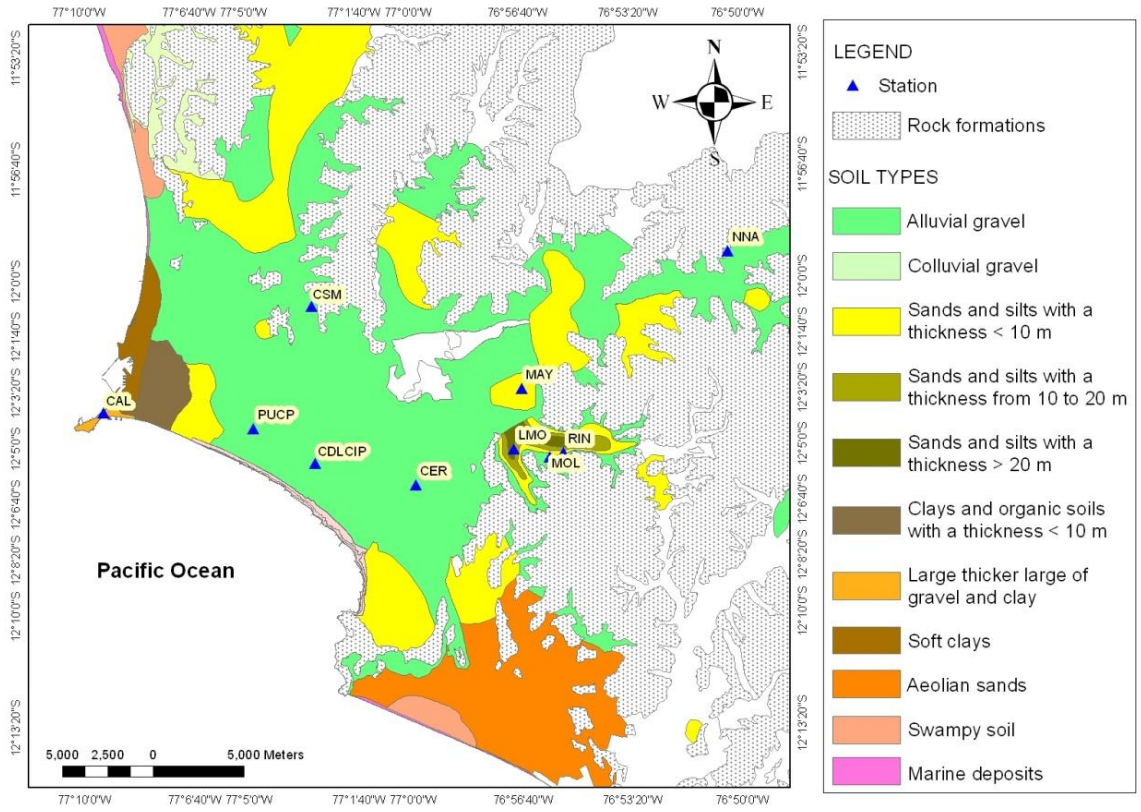


Figure 5. Soil type map of Lima city.

prominent peaks being the most significant at about 1-2 Hz (Figure 4). Our results suggest the presence at the surface of relatively softer soil layers that might contribute to the local response at this site, so it is required to carry out further studies in order to have a better understanding.

MAY and RIN sites are installed on sand and sill deposits with a thickness less than 10 m (Figure 5). At MAY station, spectral ratios show slightly large amplitudes at about 3-5 Hz due to the presence at the surface of these relatively soft layers but with a thickness less than 5 m that overlie on alluvial gravel. However, the site response at RIN station is dominated by a prominent peak between 3 and 4 Hz, which represents the first resonant mode at this site. This station shows the largest amplification factor in comparison to the other sites in this frequency range due to the medium dense sand deposits with a thickness larger than 5 m according to a soil pit near at this site. This significant peak that responds at about 3 Hz has also been detected by Stephenson et al. (2009) but by analyzing velocity response spectra.

On the other hand, CAL station shows a different behavior of amplification since important amplifications appear in the range frequency lower than 3 Hz due to the fact that this station is placed on gravel layer that overlies on a thick clay deposit.

6. DISCUSSION

Even though most stations are located on alluvial soil deposits belonging to the Quaternary Holocene, the presence of thin soft layers that overlying the Lima Conglomerate influence in the site response, dominated by several relatively small peaks in the frequency range between 3 and 6 Hz, as we can see in the CSM, MOL, CER and CDLCIP sites (Figure 4). However, RIN station has the highest amplification levels in the same frequency range because of the fact that this site is located in La Molina district, place that back in time has been reported to be affected by the influence of local subsurface conditions (Repetto et al. 1980 and Stephenson et al. 2009).

Works developed by Lee and Monge (1968) and Stephenson et al. (2009) report that this place has a complex subsurface structure that might contribute to the local site response at La Molina. In terms of our results, the horizontal-to-vertical spectral ratio for both stations present much lower amplitudes in comparison to the reference site methods, Riepl et al. (1998) reports that it is probably the complex subsurface structure that influences the vertical component in a similar manner to the horizontal components, that makes the amplification level lower.

On the other hand, small peaks at about 6-10 Hz are commonly found for all the sediment sites, which we interpret this amplification as the predominant frequency of Lima Conglomerate. Calderon (2012) gathered information about the one-point microtremor measurements (Figure 6), and such points represent the H/V ratio peak period. So on the basis of this information, we interpret that Lima Conglomerate has a dominant period of ~0.1 sec, period or frequency that has also been identified in our results. Several

researchers have pointed out that Lima city underlies by a deposit consisting of a medium dense to very dense coarse gravel and sand with cobbles, extending from the ground surface to rock, with a thickness larger than 80 m (Repetto et al 1980, Le Roux et al. 2002, Martinez A. 2007 and Aguilar et al. 2009).

The site response for CAL station shows highest amplifications for frequencies lower than 3 Hz in accordance to the gravel layer that overlies by a thick clay deposit. Our results are also consistent with the H/V peak period distribution map (Figure 6). According to this map, the predominant period at Callao-La Punta district lies in the range of 0.41 to 0.6 sec.

In addition, MOL, RIN and CSM sites show strong peaks at frequencies larger than 10 Hz, this may be because these stations are installed very close to a hill, so further studies are needed to have a better understanding.

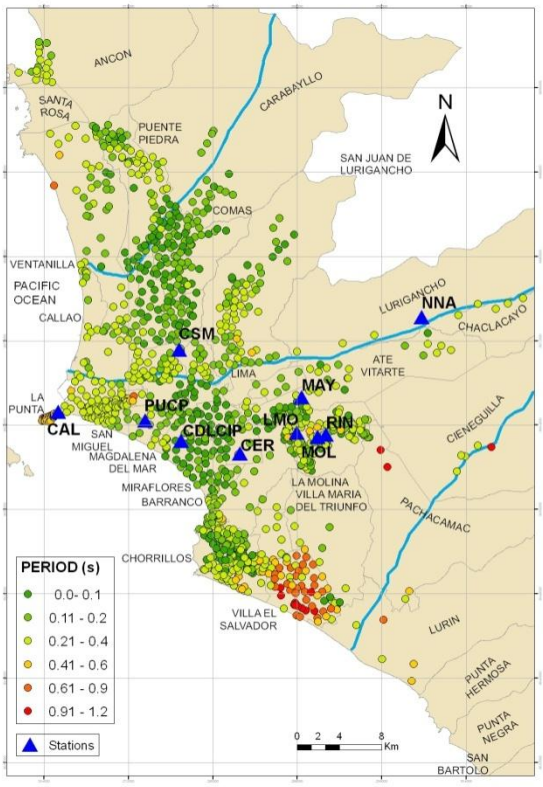


Figure 6. Location of seismic stations over the predominant period distribution map obtained from the H/V spectrum of single-point microtremor measurements (Calderon 2012).

7. CONCLUSIONS

In spite of the limitation of data, the application of the three empirical methods has allowed to evaluate the site effects on examined sites, since information about frequencies at which important amplification might appear have been provided for the study area.

Our results indicate that sediment sites show prominent peaks in the frequency range at 3-6 Hz, due to the surface layers that overlie on the alluvial gravel deposits. Most of these stations show relatively high amplification levels. Nonetheless, CAL site shows a different behavior of amplification because of soft clay layer that underlies on this site.

Last but not least, according to our results and the predominant period distribution map (Calderon 2012), we conclude that one the dynamic site characteristics of soils in Lima city is its predominant period of ~0.1 sec.

Acknowledgements:

The authors thank the Geophysical Institute of Peru (IGP) for supplying information on instrument locations belonging to IGP, as well as for providing the accelerograms data recorded by these instruments. We are likewise grateful to the research assistants at CISMID who helped in the completion of this study.

References:

Aguilar, Z. (2005), "Seismic Microzonation of Lima City," Japan-Peru Workshop on Earthquake Disaster Mitigation, Japan Peru Center for Earthquake Engineering and Disaster Mitigation (CISMID), Faculty of Civil Engineering, National University of Engineering, Lima, Peru.

Aguilar Z, Martínez A. y Basurto D. (2009), "Diseño e Implementación de un Equipo de Corte Directo para Suelos Gravosos en el Laboratorio," XVII Congreso Nacional de Ingeniería Civil, Instituto de la Construcción y Gerencia (ICG), Lima, Perú (in spanish).

Bernal, I. and Tavera, H. (2007), "Aceleraciones Máximas Registradas en la Ciudad de Lima: Sismo de Pisco del 15 de Agosto del 2007 (7.0 ML), Informe Preliminar," (in Spanish).

Borcherdt R. D., "Effects of local geology on ground notion near San Francisco Bay," *Bull. Seismol. Soc. Amer.*, 60, 29–81, 1970.

Cabrejos, J. (2009), "Amplificación Sísmica en la ciudad de Lima aplicando la Técnica de Cocientes Espectrales," Facultad de Ingeniería Civil, Universidad Nacional de Ingeniería, Lima, Perú (in spanish).

Calderon, D. (2012), "Dynamic Characteristics of the Soils in Lima, by estimating Shallow and Deep Shear-Wave Velocity Profiles," Ph.D. Thesis, Chiba University, Japan.

Espinoza A. F., Husid L. R., Algermissen S. T. and De Las Casas J. (1977), "The Lima earthquake of October 3, 1974: Intensity Distribution," *Bull. Seism. Soc. Amer.* 67(5), 1429-1439.

Field, E. H. and Jacob, K. H. (1995), "A comparison test of various site response estimation techniques, including three that are not reference site dependent," *Bull. Seism. Soc. Amer.* 85, 1127–1143.

Husid L. R. (1969), "Características de terremotos – análisis general," Revista del IDIEM 8, 21-42 (in spanish).

Husid, L. R., Espinoza, A. F. and De Las Casas J. (1977), "The Lima earthquake of October 3, 1974: Damage Distribution," *Bull. Seismol. Soc. Amer. 67(5)*, 1441-1472.

Iwata T. and Irikura K. (1988), "Source parameters of the 1983 Japan Sea earthquake sequence," *J. Phys. Earth* 36, 155–184.

Le Roux, J.P., Tavares, C., and Alayza, F. (2002), "Sedimentology of the Rimac-Chillon alluvial fan at Lima, Peru, as related to Plio-Pleistocene sea-level changes, glacial cycles and tectonics," *Journal of South American Earth Sciences*, 13, 499–510.

Lee, K. L. and Monge, J. (1968), "Effect of soil conditions on damage in the Peru earthquake of October 17, 1966," *Bull. Seismol. Soc. Amer.* 58, 937-962.

Lermo J. and Chavez-Garcia F. J. (1993), "Site effects evaluation using spectral ratios with only one station," *Bull. Seismol. Soc. Amer*. 83, 1574–1594.

Martínez, A. and Porturas, F. (1975), "Planos Geotécnicos para

Lima, Perú. Análisis y Visión en Ingeniería Sísmica," Pontificia Universidad Católica del Perú, Lima, Perú (in spanish).

Martínez, A. (2007), "Conglomerado de Lima Metropolitana en Cimentaciones", Conferencia Internacional en Ingeniería Sísmica, Centro Peruano Japonés de Investigaciones Sísmicas y Mitigación de Desastres (CISMID), Facultad de Ingeniería Civil (FIC), Universidad Nacional de Ingeniería (UNI), Lima, Perú (in spanish).

Nakamura, Y. (1988), "Inference of seismic responses of surface layer based on Microtremor measurement," Quarterly Report on Railway Research 4, 18–27 (in Japanese).

Okal, E.A., Borrero, J.C., and Synolakis C.E. (2006), "Evaluation of tsunami risk from regional earthquakes at Pisco, Peru," *Bull. Seismol. Soc. Amer.*, 96, 1634-1648.

Pulido N., Tavera H., Aguilar Z., Nakai S., and Yamazaki F. (2010), "Estimation of the seismic hazard for the Lima Metropolitan region: Earthquake scenarios and strong motion simulation," *XV Peruvian Geological Congress*, Cusco, Peru.

Quispe, S. (2010), "Preliminary Analysis for Evaluation of Local Site Effects in Lima City, Peru from Strong Ground Motion Data by the Spectral Inversion Method," Studies by participant at the IISEE 45, 1-32.

Repetto, P., Arango, I., and Seed, H. B. (1980), "Influence of site characteristics on building damage during the October 3, 1974 Lima earthquake," Report-Earthquake Engineering Research Center, College of Engineering, University of California, Berkeley, California, NTIS, 80–41.

Riepl J., Bard P.-Y., Hatzheld D., Papaionnou C., and Nechtschein S. (1998) "Detail evaluation of site response estimation methods across and along the sedimentary valley of Volvi (EURO-SEISTEST)." *Bull. Seism. Soc. Am.* 88, 488–502.

Stephenson, W.R., Benites, R.A. and Davenport, P.N. (2009), "Localized coherent response of the La Molina basin (Lima, Peru) to earthquakes, and future approaches suggested by Parkway basin (New Zealand) experience," *Solid dynamics and earthquake engineering*, 29(10), 1347-1357.

Takemura, M., Kato, K., Ikeura, T., and Shima, E. (1991), "Site Amplification of S-Waves from Strong Motion Records in Special Relation to Surface Geology", *J. Phys. Earth*, 39, 537-552.

Uetake, T. and Kudo, K. (2005), "Assessment of Site Effects on Seismic Motion in Ashigara Valley, Japan," *Bull. Seismol. Soc. Amer.* 95, 4 2297–2317.

10CUEE CONFERENCE PROCEEDINGS
10th International Conference on Urban Earthquake Engineering
March 1-2, 2013, Tokyo Institute of Technology, Tokyo, Japan

CENTRIFUGAL MODELING OF UNDERCUT SLOPES SUBJECTED TO PSEUDO-STATIC LOADING

Mohammad Hossein Khosravi[1], Jiro Takemura[2], and Thirapong Pipatpongsa[3]

1) Post-doctoral research fellow, Department of Civil and Environmental Engineering, Tokyo Institute of Technology, Japan
2) Associate Professor, Department of Civil and Environmental Engineering, Tokyo Institute of Technology, Japan
3) Associate Professor, Global Scientific Information and Computing Center, Tokyo Institute of Technology, Japan
khosravi.m.ab@m.titech.ac.jp, jtakemur@cv.titech.ac.jp, pthira@gsic.titech.ac.jp

Abstract: In this study the stability of undercut slopes subjected to pseudo-static loading was investigated through centrifugal modeling, in which pseudo-static horizontal load was applied by a tilting table. Moist Edosaki sand was used as the modeling material with a series of miniature pressure cells and accelerometers embedded into the model. Furthermore the movement of the slope was monitored through a series of potentiometers placed at the top edge of the slope model. Special attention in this study was focused on the failure mechanism of the undercut slopes and redistribution of the earth pressure in the model due to arch action. Model deformation was monitored and analyzed using particle image velocimetry (PIV) and image processing software. It was concluded that the failure mechanism in the undercut slopes involves a passive condition where the major principal stresses dominate the force supporting the arches over the excavated area.

1. INTRODUCTION

Excavation in front of a slope can cause some slope stability problems especially in the existence of a potential failure plane through the slope body. The potential failure plane may be a clay seam or an oblique fault exists in the soil/rock mass or any other type of weak planes which initiates the failure of the slope. This kind of problem can be arisen during excavation stage for various kinds of geotechnical projects such as, foundations, cutting through a mountain for road or railway construction and surface mining. The most unstable case is that the potential failure plane be exposed totally along the excavated area. Some of the huge slope failures during coal mining reported by Electricity Generating Authority of Thailand (EGAT, 1985) are evidences of this kind of problem. Doing more research on the above mentioned coal mining projects, Pipatpongsa et al. (2009) reported that stable scarps observed on the slopes after a failure. They explained that those stable scarps remained stable because of the passive arch action on the slope body. The phenomenon of arch action has been initially defined by Terzaghi (1936), as a load transfer mechanism from the yielding part of the material to the adjacent stationary parts.

The problem of undercut slopes was investigated and studied through theoretical, numerical and physical considerations (Khosravi et al. 2011, Khosravi et al. 2012a, Leelasukseree et al. 2012, Pipatpongsa et al. 2012). The existence of passive arch action was confirmed by the authors through a series of 1G physical model tests (Khosravi et al., 2011). They confirmed a performance of counterweight balance on the two sides of the excavated area (Khosravi et al. 2012a) in an attempet to stabilize the undercut slopes. Later the instability phenomena of undercut slopes were developed by the authors (Khosravi 2012) based on the Jenike's (1961) theory of cohesive arching in hoppers. The problem of undercut slopes under pseudo-static loading was studied later considering the effect of earthquakes (Khosravi et al. 2012b).

Pseudo-static slope stability method is a simple method for simulation of dynamic loads of an earthquake applying on a slope by assuming additional static loads. This first application of this method is attributed to Terzaghi (1950). The pseudo-static load then has components in both horizontal and vertical directions; however, the vertical component has insignificant effect on the stability of slope and is ignored usually in stability analysis (Kramer 1996). A well known experimental apparatus for applying a pseudo-static horizontal body force to the model is a tilting table in which the horizontal seismic coefficient (k_h) can be calculated from the tilted angle of the model.

In this study the stability of undercut slopes is investigated through centrifugal tilting table model tests. Moist Edosaki sand was used as the modeling material. Change of pressure distribution inside the model body was measured by a series of earth pressure cells. Furthermore the slope deformation was monitored and analyzed using particle image velocimetry (PIV) and image processing software.

2. MATERIAL PROPERTIES

Edosaki sand as a well graded material was used in this study with the grain size distribution shown in Figure 1.

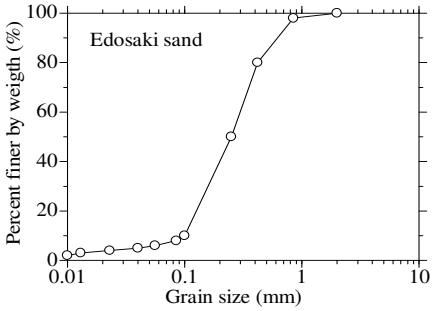


Figure 1 Grain size distribution of Edosaki sand

Moist sand with an optimum water content of w=15.4% was compacted inside the model container to achieve a bulk density of ρ=1630 kg/m^3. The basic properties of moist Edosaki sand are shown in Table 1.

Table 1 Basic properties of moist Edosaki sand

Average particle diameter (D_{50})	0.25 mm
Uniformity coefficient (Cu)	3.1
Specific gravity (G_s)	2.69
Optimum water content (w)	15.4 %
Unit weight (γ)	16 kN/m^3
Relative density (D_r)	92 %
Maximum void ratio (e_{max})	1.29
Minimum void ratio (e_{min})	0.87

In the undercut slope model, a Teflon sheet was used to simulate the potential failure plane due to its relatively low surface friction. A direct shear apparatus was employed to measure the shear strength parameters of moist Edosaki sand as well as the interface shearing resistance of sand and Teflon sheet. As shown in Figure 2, internal friction angle and cohesion for moist Edosaki sand was obtained 39.9^o and 6.5 kPa respectively. Interface friction between the sand and Teflon sheet was obtained 17^o with almost zero adhesion.

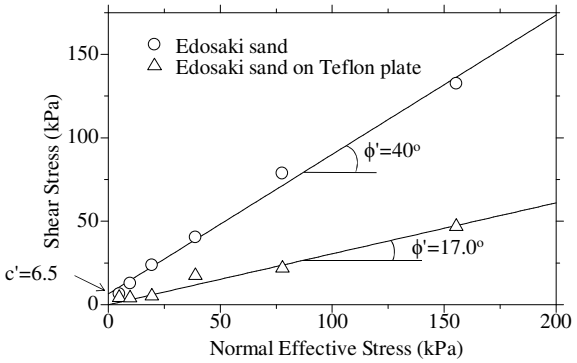
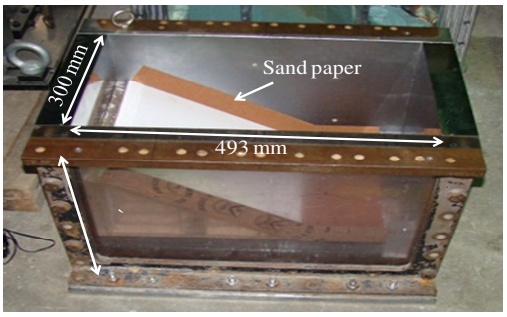


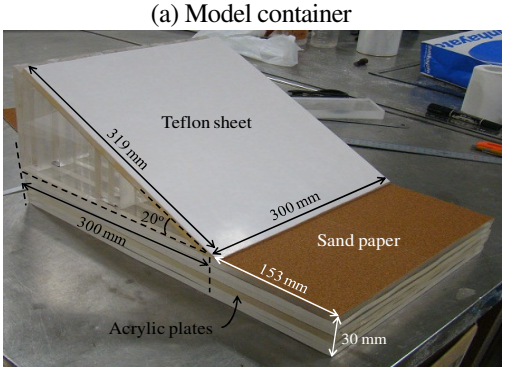
Figure 2 Shear strength parameters of moist Edosaki sand and its interface with Teflon sheet

3. EXPERIMENTAL SETUP

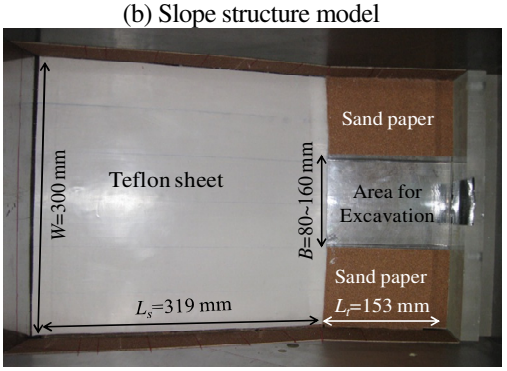
A strong metallic model container with a transparent side was used as the container of the model (Figure 3(a)). The slope structure model was made from rigid Acrylic plates as illustrated in Figure 3(b). The slope was covered by Teflon sheet to simulate a low friction interface as a potential failure plane beneath the sand layer. The part in front of the slope was covered with sandpaper to make a fully rough base surface. Furthermore, in order to realize to the assumption of fully rough side supports, the sides of both slope and base parts were covered with sand papers as shown in Figure 3(a-c).



(a) Model container



(b) Slope structure model



(c) Slope structure model inside the container

Figure 3 Model container and the slope structure

The model container was placed on a tilting table which is installed on the platform of the centrifuge as shown in Figure 4. The tilting table used in this study was developed by Nikken Sekkei Nakase Geotechnical Institute in 1995 (Saitoh et al., 1995). The specifications of this tilting table are listed in Table 2.

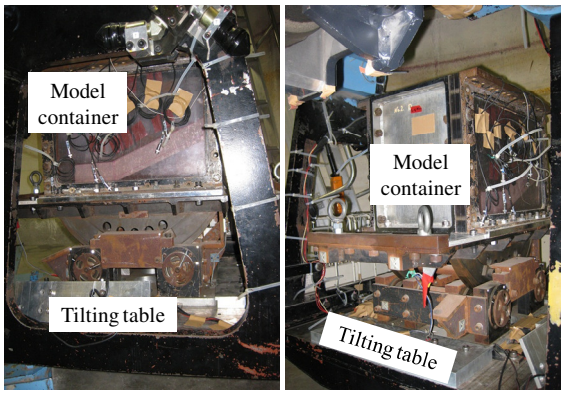


Figure 4 The model container and the tilting table placed on the centrifuge platform

Table 2 Specifications of this tilting table (Izawa & Kuwano, 2010)

weight	230 kg
Max. pay load	80 ton
Table size	
Width	920 mm
Beneath	450 mm
Max. tilting angle	20° (Corresponding k_h=0.36)
Max. tilting velocity	5°/min
Electric motor (Oriental motor, MSM590-501K)	
Voltage	AC 100 V
Power current	2.3 A
Max. power	90 W
Speed controller (Oriental motor, MSP301 N)	

Mark 3 centrifuge of the Tokyo Institute of Technology (Takemura et al., 1999) which is a beam type in-house centrifuge machine was used in this study. This type of centrifuge has two arms which one of them holds the platform for the model container and the other one holds a weight equal to the model container for counterbalance.

4. MODEL PREPARATION AND INSTRUMENTATION

Moist Edosaki sand was compacted inside the model container with a uniform relative density of 92%. Depending on the model test an area was excavated in front of the slope to make an initial undercut span as shown in Figure 5. Two model tests were conducted in this study where the geometry of the slope model is summarized in Table 3.

Table 3 Geometry of the slope model

Model test		1	2
Slope angle (α)		20°	
Slope length (L_s)		319 mm	
Pillar length (L_t)		153 mm	
Width (W)		300 mm	
Height (H)		50 mm	
Undercut span (B)	Bottom	80 mm	120 mm
	Top	120 mm	160 mm
	Average	100 mm	140 mm

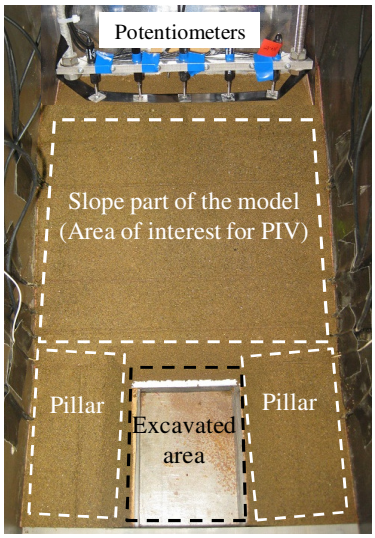
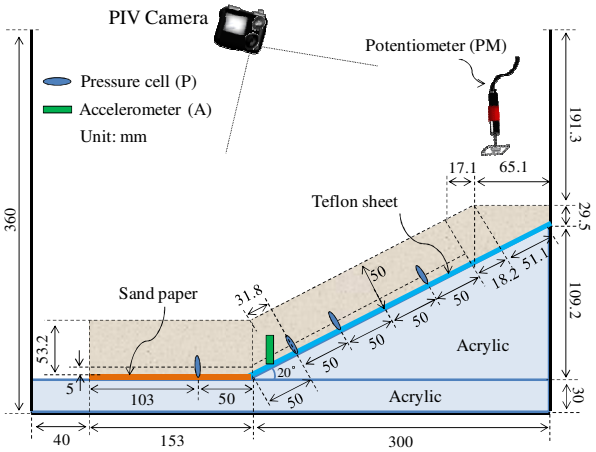
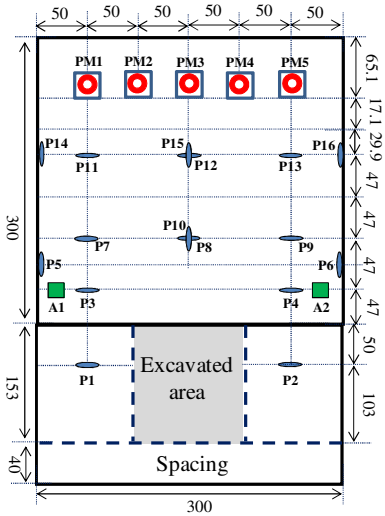


Figure 5 Moist Edosaki sand prepared in the model container

A total number of 16 pressure cells are buried in the moist sand during model preparation as illustrated in Figure 6.



(a) Side view



(b) Plan

Figure 6 The instrumented undercut slope model

Pressure cells type PS-1KC, class ZC with the capacities of 100kPa and 200kPa are used for this model. All of the pressure cells are buried 5 mm above the bottom of the sand layer, in other words, underneath a 45 mm-thick layer of sand. Furthermore, a row of 5 potentiometers type MLT-38000201 with the range of 60 mm installed at the top edge of the slope to record the slope movement during the test as shown in Figures 5 and 6.

5. EXPERIMENTAL RESULTS AND DISCUSSIONS

By tilting the table during the test a pseudo-static horizontal body force was applied to the model. The maximum tilting angle of the table was 20° corresponding to a horizontal seismic coefficient of 0.36 where the horizontal seismic coefficient was calculated by the following equation (Izawa & Kuwano, 2010). where k_h is horizontal seismic coefficient and β is the tilting angle.

$$k_h=\tan\beta \quad (1)$$

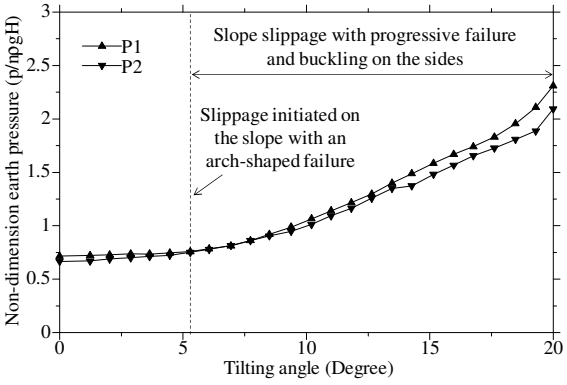
In this study the tilting velocity of the tilting table was about 3°/min and digital images for deformation analysis were captured every 20 second. Therefore, for every one degree of tilting the model, one image was captured. The results of earth pressure distribution in the model through pressure cells and deformation analysis through particle image velocimetry (PIV) are discussed individually in the two following subsections.

5.1. Earth pressure distribution

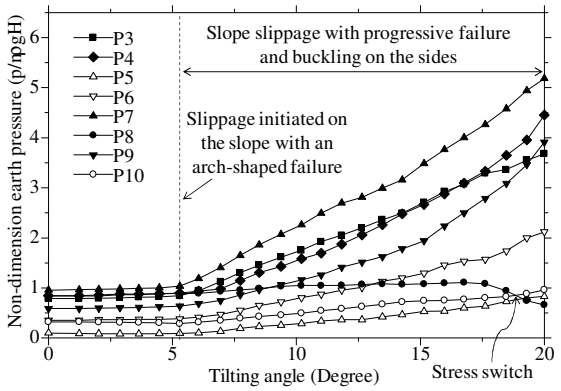
During the model tilting, the earth pressures inside the model were monitored and recorded by pressure cells. This data are normalized by $n\rho gH$ and plotted as a function of tilting angle in Figures 7 and 8 respectively for model tests 1 and 2. Where n is centrifugal acceleration, ρ is a bulk density of the sand, g is a gravity of Earth and H is a height of the model. In these figures, data measured along the dip and transverse directions are shown in close and open symbols respectively. By tilting the model, earth pressure in the pillars started to increase by slippage initiation of the slope and steadily increased until the total failure of the model (Figure 7(a) and 8(a)). The earth pressure on two sides of the slope model (P3, P4, P7 and P9) also increased gradually while the earth pressure at the center of the slope (P8) decreased. This behavior is consistent with that of 1G undercut slope physical model tests reported by authors which shows the development of passive arch action in the slope model as explained in details in Khosravi et al. (2011).

Due to symmetric geometry of the model, the centerline of the model can be assumed as a zero shear line where there is no relative displacement along the two sides; therefore, the dip and transverse directions along the centerline of the slope can represent the directions of principal stress.

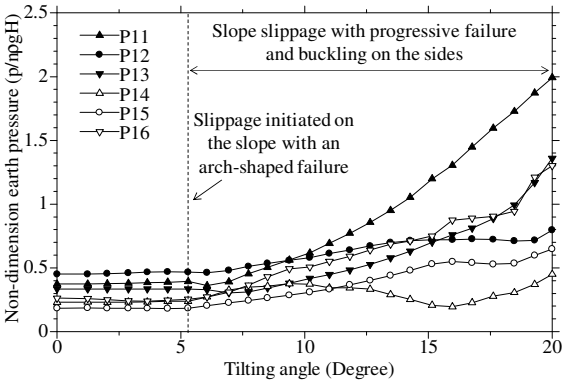
According to Figures 7 and 8 at the initial condition, where tilting was not started yet, the slope was in active condition as shown schematically in Figure 9(a). That's because the earth pressure along the dip direction (P8 and P12) was larger than that along the transverse direction (P10 and P15) at the centerline initially. By tilting the model, the status of the earth pressure along the center at the lower portion of the slope was gradually changed to passive condition where the earth pressure in dip direction (P8) became smaller than that along the transverse direction (P10). The intersection of P8 and P10 signify the isotropic stress condition where the state of earth pressure switched from active to passive. These intersections are indicated in Figures 7(b) and 8(b) as stress switch. Therefore the state of stress at the lower part of the slope was gradually changed to passive condition as shown schematically in Figure 9(b).



(a) Pillars

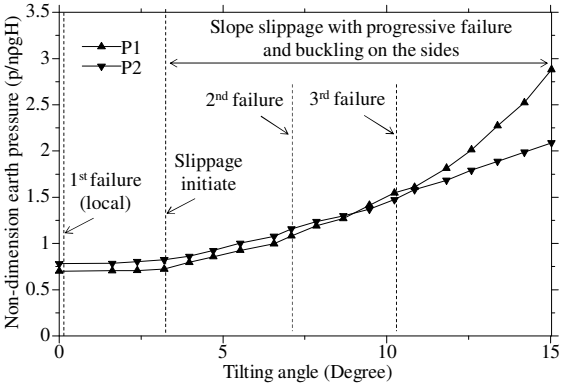


(b) Lower portion of the slope

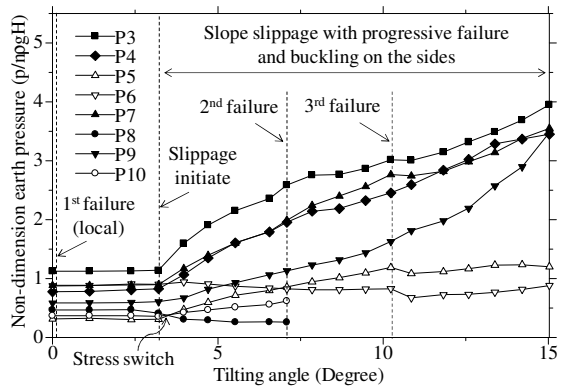


(b) Upper portion of the slope

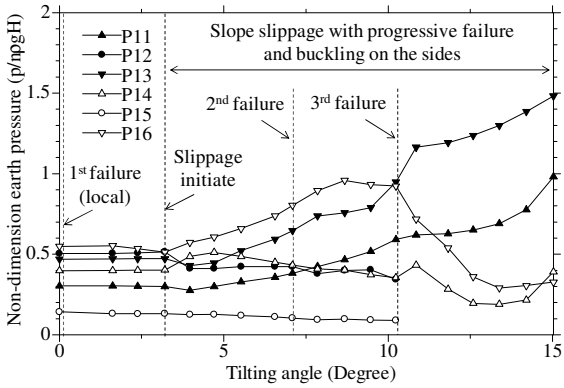
Figure 7 Measured earth pressure vs. tilting angle (Test 1_ B/W=0.33)



(a) Pillars



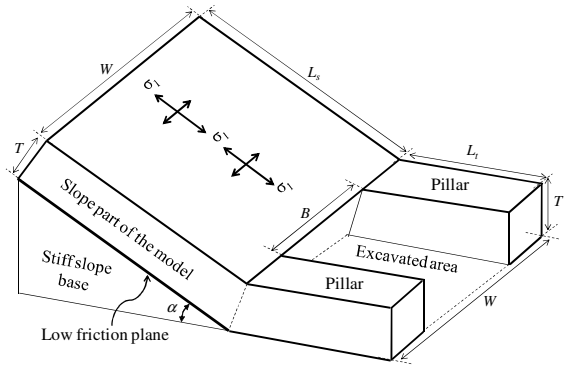
(b) Lower portion of the slope



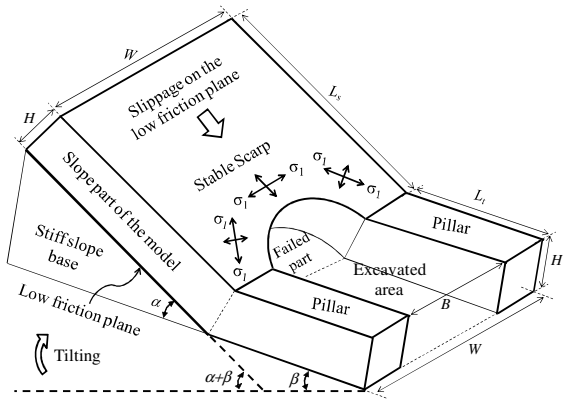
(b) Upper portion of the slope

Figure 8 Measured earth pressure vs. tilting angle (Test 2_ B/W=0.47)

In model test 1, where undercut span was relatively narrow (*B/W*=0.33), the slope slippage was initiated with an arch-shaped failure in front of the slope (Figure 10(a)). By tilting the model progressive failures were observed in front of the slope. As shown in Figures 10(b) and 11, sand buckled on the sides on the lower portion of the slope while the upper portion of the slope slipped down along the Teflon sheet almost uniformly. On the other hand in model test 2, where undercut span was relatively larger (*B/W*=0.47), an initial arch-shaped failure occurred in front on the slope just when the centrifuge acceleration reached to 50G before tilting the model (Figure 12(a)). Figure 9 obviously indicates that after this failure and even until the tilting angle of about β=3°, the pressure cells did not record any movement for the model. Therefore, this initial failure did not trigger the slope slippage and can be considered as a local failure. At the tilting angle of about β=3°, the slope slippage was initiated while pressure cells record changes in earth pressures. By tilting the model, progressive failures were occurred in the model with buckling on the sides and two noticeable stacks of arch-shaped failures in the center part of the slope (Figures 12 and 13).



(a) Initial condition (stable slope before tilting)



(b) Final condition (failure during tilting)

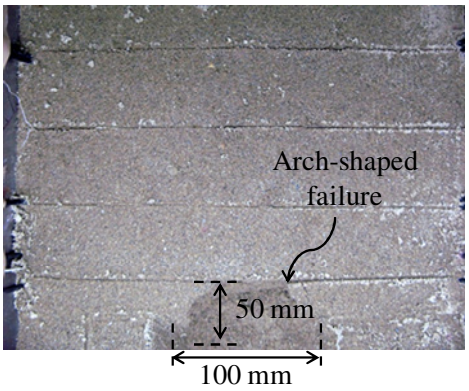
Figure 9 Schematization of the earth pressure distribution in an undercut slope

5.2. Slope deformation

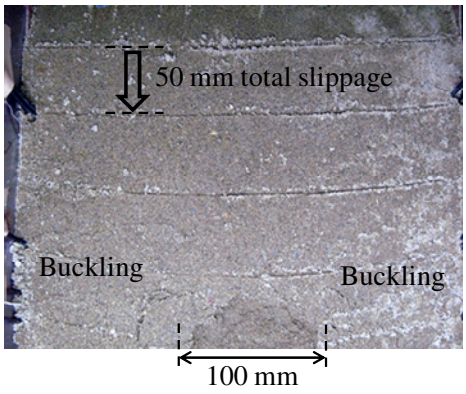
Particle image velocimetry (PIV), as a non-destructive optical method (White et al., 2003), was used in this study. Sequential digital images were captured during tilting of the model and used to determine the model's deformation through GeoPIV software (White & Take, 2003).

Results of PIV analysis for the model tests 1 and 2 are shown in Figures 14 and 15 respectively in the form of displacement vectors and contours of volumetric and deviatoric strain. Figure 14 shows the deformation in the model test 1 from when the tilting was started until a failure observed on the slope. In the model test 2 the first failure occurred before tilting started. Furthermore, as explained in the previous section, this failure did not trigger the slope slippage and was considered as a local failure. Then the

images for PIV analysis were captured from tilting initiation until the second failure occurred.



(a) Initial arch-shaped failure (β=5o)



(b) Total failure (β=5o~20o)

Figure 10 Arch-shaped and total failures occurred in Model test 1

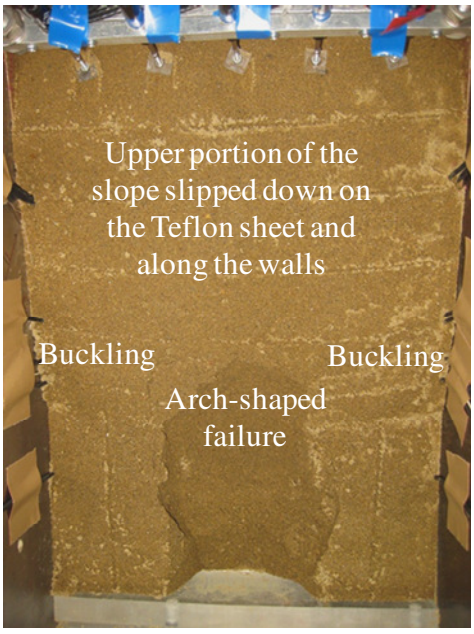
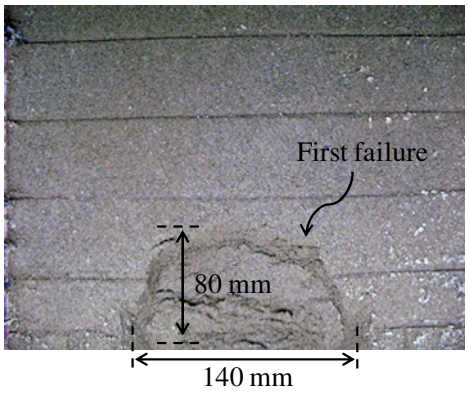
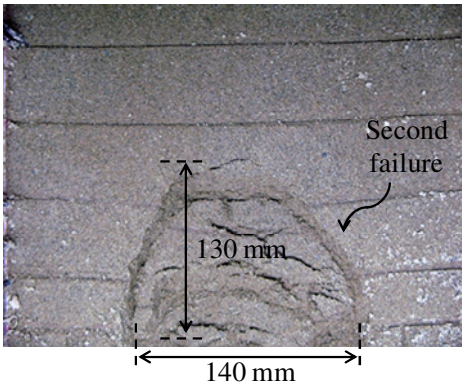


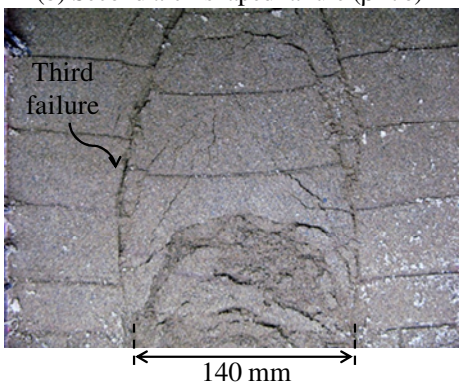
Figure 11 Final mode of failure in Model test 1



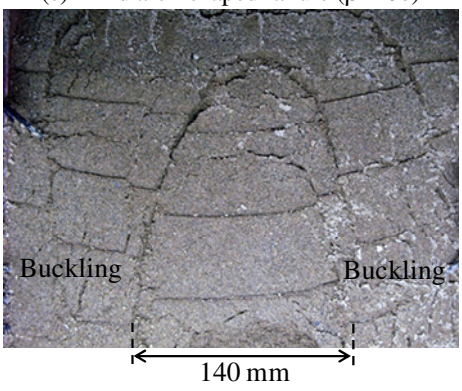
(a) Initial arch-shaped failure (β=0o)



(b) Second arch-shaped failure (β=7o)



(c) Third arch-shaped failure (β=10o)



(d) Total failure (β=0o~15o)

Figure 12 Arch-shaped and total failures occurred in Model test 2

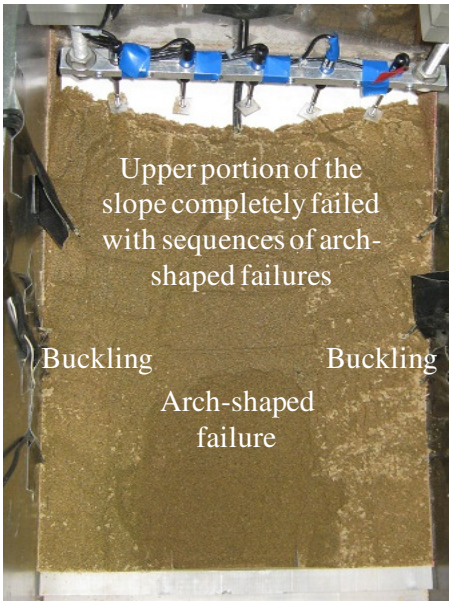
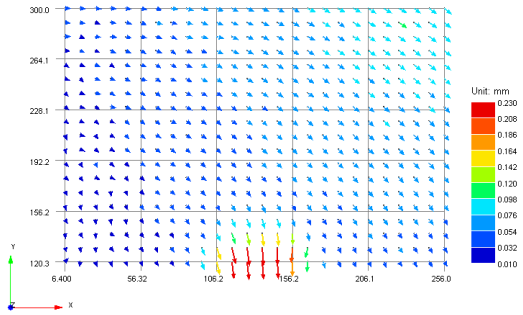
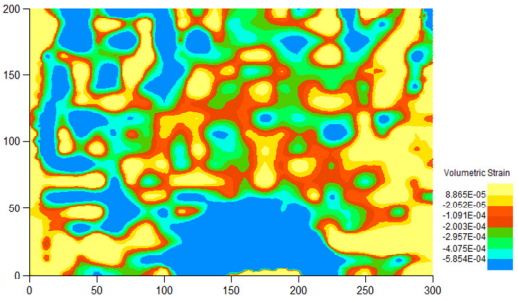


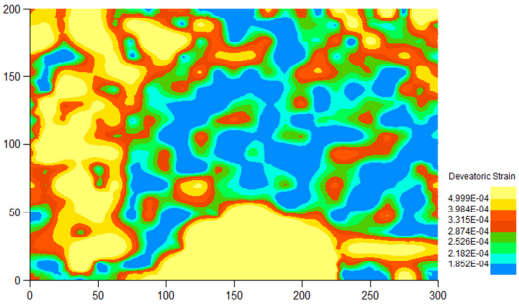
Figure 13 Final mode of failure in Model test 2



(a) Displacement vectors

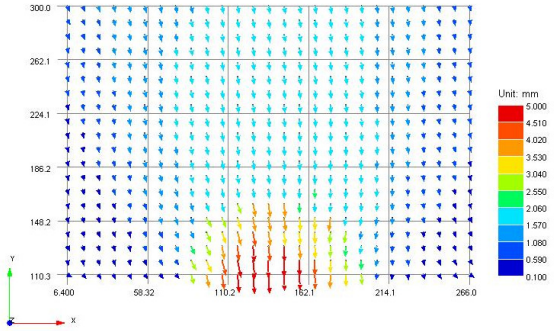


(b) Volumetric strain

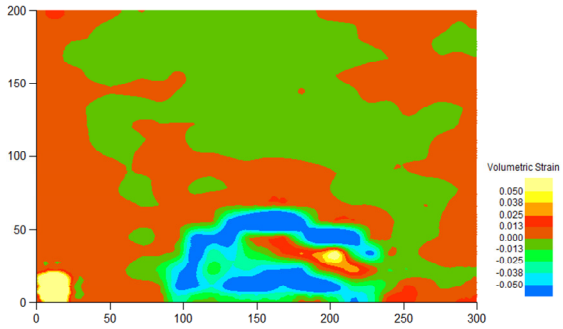


(c) Deviatoric strain

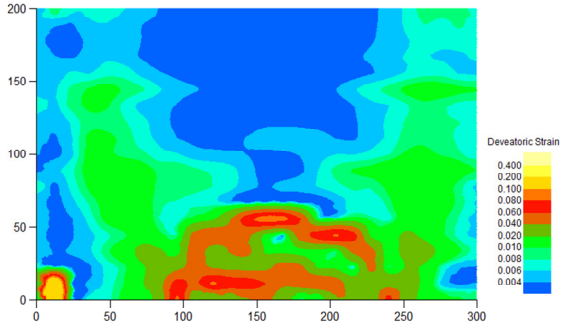
Figure 14 Results of PIV analysis (Model tests 1)



(a) Displacement vectors



(b) Volumetric strain



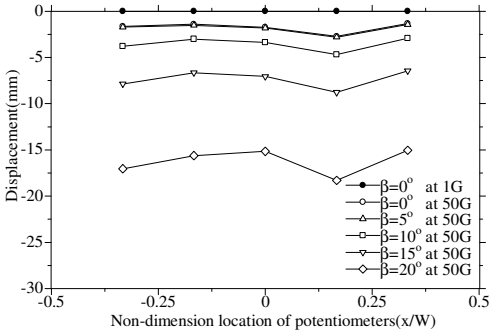
(c) Deviatoric strain

Figure 15 Results of PIV analysis (Model tests 2)

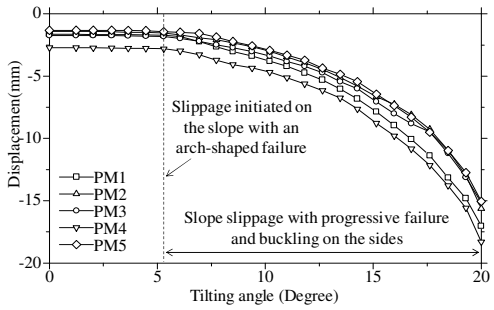
The negative values in volumetric strain (Figure 14(b) and Figure 15(b)) indicate dilation while the positive values indicate compression in the soil. From changes in volumetric strain even before failure, it can be seen that by tilting of the model the soil immediately above the excavated area dilate while the soil on the sides compress. This behavior is consistent with the earth pressure analysis explained in previous chapter where by tilting of the model the load from center part gradually transfers to sides.

The maximum values of deviatoric strain (Figure 14(c) and Figure 15(c)) indicate the part of the model with the maximum deformation in which the failure may be initiated from. Note that the holes existing in down left corner of Figures 15(b) and 15 (c) are considered as analysis error and should be ignored.

Furthermore displacements recorded by potentiometers for model tests 1 and 2 are plotted in Figures 16 and 17 respectively.

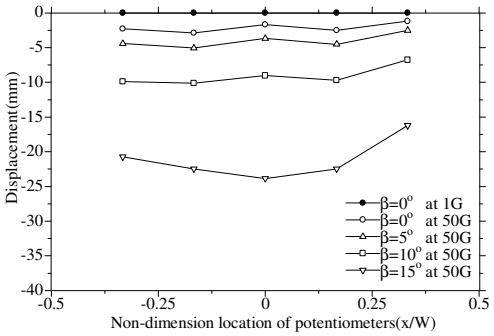


(a) Profile of the slope top edge

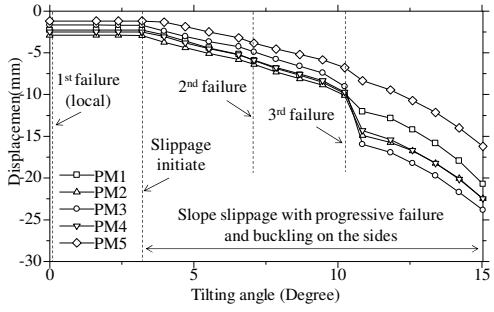


(b) Slope displacement vs. tilting angle

Figure 16 The slope displacement monitored by potentiometers (Model test 1)



(a) Profile of the slope top edge



(b) Slope displacement vs. tilting angle

Figure 17 The slope displacement monitored by potentiometers (Model test 2)

Attention is paid to Figure 16 (a), in model test 1. By increasing the centrifugal acceleration up to 50G, potentiometers showed some small relative displacements; however, the profile of the slope top edge during tilting of the model hardly changed. This implies that no relative displacements found between potentiometers and the slope top edge wholly moved down. It is also noticeable that during tilting process, until the tilting angle of β=5° there was no displacement recorded. After that, an arch-shaped failure occurred in the lower portion of the slope and the whole slope started to slip down on the low friction Teflon sheet.

In the model test 2, as shown in Figure 17 (b), the first failure happened when the centrifugal acceleration reached to 50G before tilting the model. However, this failure seems to be a local failure because subsequent slope failure was not observed. By increasing the tilting angle, the slippage was initiated on the slope at a tilting angle of β=3° as shown in Figure 17 (b). Later, two more failures occurred on the slope at tilting angles of about β=7° and β=10°. The relative displacement between the potentiometers gradually increased and the maximum displacement occurred at the center part of the slope top edge as shown in Figure 17 (a).

6. COMPARE TO THEORY

For the problem of a undercut slope under pseudo-static loading the relation between the slope angle (α_f) and the undercut span (B_f) at failure and the horizontal pseudo-static seismic coefficient (k_h) was defined through the following equation (Khosravi et al. 2012b).

$$\alpha_f = \phi_i - \tan^{-1} k_h + \sin^{-1}\left(\left(k\frac{\sigma_c}{\gamma B_f} + \frac{c_i}{\gamma H}\right)\frac{\cos\phi_i}{\sqrt{1+k_h^{\,2}}}\right) \qquad (2)$$

Where

σ_c: unconfined compressive strength of the material (σ_c=2c(1+sin(ϕ))/cos(ϕ))

ϕ: internal friction angle of the material

c: internal cohesion of the material

ϕ_i: interface friction angle

c_i: interface adhesion

γ: bulk unit weight of the material

H: thickness of the material

k: arching coefficient (k=1 for mild undercut slopes (α<45°) and k=4/π for steep undercut slopes (α>45°))

The horizontal pseudo-static seismic coefficient (k_h) is obtained for every model test by using of Eq. (1). Where the values of tilting angle (β) at the instant of first arch-shaped failure on the slope were used. Note that, as explained in the previous section, the first failure in model test 2 occurred before initiation of the slope slippage and also did not trigger the slope slippage; therefore, this local failure is unlikely to be the first failure in test 2 but the second failure was considered as the real first arch-shaped failure.

It was difficult to measure an accurate value for the internal cohesion of moist sand. A value evaluated from the free

standing height of the moist soil under 50G of centrifugal acceleration was compared to the value obtained from direct shear test (Figure 2). The stable height of the material was observed at least 3 cm which is equivalent to 1.5 m at prototype. For this free standing soil height, the internal cohesion of 3kPa was obtained through limit analysis solution (Hsai-Yang Fang 1991) which is almost the half of the value obtained from direct shear tests (6.5 kPa).

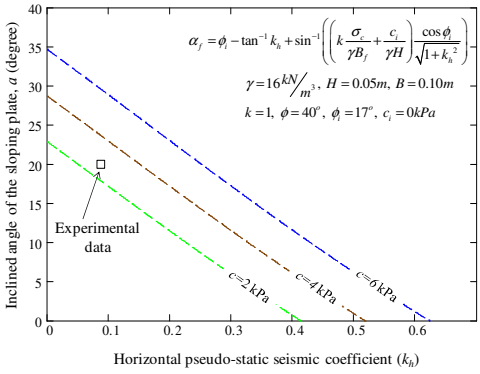
The experimental data are compared with the theory for various values of cohesion in Figures 18 and 19. It can be concluded from these figures that a value of the material's internal cohesion back calculated from the free standing height of the moist soil under centrifugal field is more reliable that the value obtained from direct shear test.

In order to show all the experimental data in a unique plot the horizontal pseudo-static seismic coefficient (k_h) removed from Eq. (2) and instead the tilting angle (β) was added as in Eq. (3).

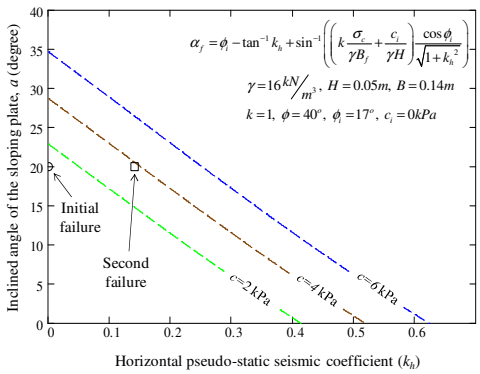
$$(\alpha+\beta)_f = \phi_i + \sin^{-1}\left(\left(k\frac{\sigma_c}{\gamma B_f}+\frac{c_i}{\gamma H}\right)\cos\phi_i\right) \qquad (3)$$

Where $(\alpha+\beta)_f$ represents the inclined angle of the slope at failure including the initial slope angle plus the tilting angle.

Figure 20 compares all the experimental data with theory where for comparison, the result of a previous centrifugal undercut slope test under static condition (Khosravi 2012) was also shown.

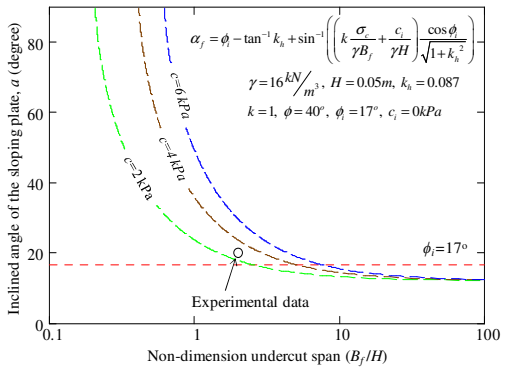


(a) Model test 1

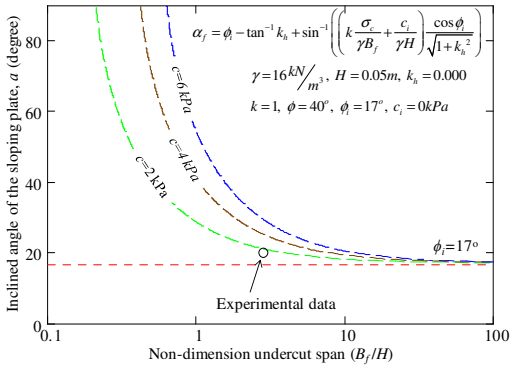


(b) Model test 2

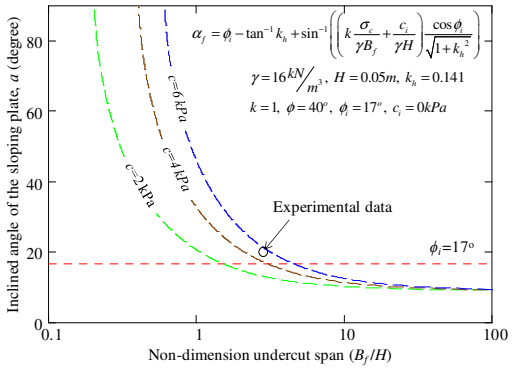
Figure 18 Slope angle versus horizontal pseudo-static seismic coefficient



(a) Model test 1



(b) Model test 2-first failure



(c) Model test 2-second failure

Figure 19 Slope angle versus undercut span

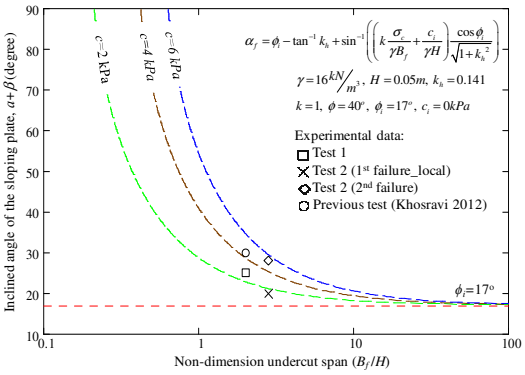


Figure 20 All the experimental data compared with theory in a unique plot

7. CONCLUSIONS

This work describes the pseudo-static stability of undercut slopes using centrifuge tilting table tests. Slope models with a specific undercut span were subjected to pseudo-static loading under a centrifugal acceleration of 50G. The earth pressure distribution inside the model was recorded through a series of earth pressure cells. The deformation of the slope was monitored through analysis of sequential digital images captured during the test by particle image velocimetry technique. A row of potentiometers were also placed at the top edge of the slope to record the slope displacement.

By applying a pseudo-static loading to a certain level, the slope initiated to slip down and the earth pressure transferred from the center to sides. Furthermore, the stress condition in the slope was changed from active to passive gradually. These results are in agreement with those reported by authors on a series of 1G undercut slope model tests (Khosravi et al. 2011) conforming that arching effect in undercut slope is a scale-independent phenomenon.

An acceptable agreement between the experimental data and the theory under pseudo-static approach convinces that the concept of passive arching effect can assess the seismic stability of undercut slopes. Though arching typically involves a monotonic loading, the undercut slopes subjected to a cyclic loading could be considered by means of shakedown analysis because both phenomena of arching and shakedown are associated to the adaptation of load bearing structure.

Acknowledgements:

This work was supported financially by Global COE Program, Center for Urban Earthquake Engineering (CUEE). The helpful assistance of Mr. Seki during conducting the centrifugal model tests is appreciated.

References:

EGAT. (1985), "Thailand-Australia Lignite Mines Development Project," Geotechnical Report, Mae Moh Mine, Volume 3.

Fang, H.Y. (1991), "Foundation Engineering Handbook," 2nd edition.

Izawa, J. and Kuwano, J. (2010), "Centrifuge modelling of geogrid reinforced soil walls subjected to pseudo-static loading," *International Journal of Physical Modelling in Geotechnics*, 10(1), 1–18.

Jenike, A.W. (1961), "Gravity Flow of Bulk Solid," *Bulletin of the Utah Engineering Experiment Station 108*.

Khosravi, M.H., Pipatpongsa, T., Takahashi, A., and Takemura, J. (2011), "Arch Action over an Excavated Pit on a Stable Scarp Investigated by Physical Model Tests," *Soils and Foundations*, 51(4), 723-735.

Khosravi, M. H. (2012), "Arching Effect in Geomaterials with Applications to Retaining Walls and Undercut Slopes," Department of International Development Engineering, Graduate School of Science and Engineering, Tokyo Institute of Technology. *PhD dissertation*.

Khosravi, M.H., Tang, L., Pipatpongsa, T., Takemura, J. and Doncommul, P. (2012a), "Performance of Counterweight Balance on Stability of Undercut Slope Evaluated by Physical Modeling," *International Journal of Geotechnical Engineering*, 6(2): 193-205.

Khosravi, M. H., Pipatpongsa, T., and Takemura, J. (2012b), "Pseudo-Static Analysis of Passive Arch Action in Undercut Slopes against Earthquake," *9th International Conference on Urban Earthquake Engineering/ 4th Asia Conference on Earthquake Engineering*. Tokyo Institute of Technology, Japan.

Kramer, S.L. (1996), "Geotechnical Earthquake Engineering."

Leelasukseree, C., Pipatpongsa, T., Khosravi, M.H. and Mavong, N. (2012), "Stresses and a failure mode from physical and numerical models of undercut slope lying on inclined bedding plane," *The 7th Asian Rock Mechanics Symposium (ARMS 2012)*, Seoul, Korea.

Pipatpongsa, T., Khosravi, M.H., Doncommul, P., and Mavong, N. (2009), "Excavation Problems in Mae Moh Lignite Open-pit Mine of Thailand," *Proceedings of Geo-Kanto*, Tochigi, 459-464.

Pipatpongsa, T., Khosravi, M.H., Stathas, D., Leelasukseree, C. and Takemura, J. (2012), "Cohesive Arch Action in Laterally Confined Block of Moist Sand Placing on an Inclined Bedding Plane," *The 7th Asian Rock Mechanics Symposium (ARMS 2012)*, Seoul, Korea.

Saitoh, K., Katakami, N., Ishii, T., Tanaka, M., Nomoto, K. and Sugimoto, K. (1995), "Development of the simulator for the pseudo static method," *Proc. 50th Annual Conf. Jap. Soc. Civil Engrs*, 816–817, in Japanese.

Takemura, J., Kondoh, M., Esaki, T., Kouda, M. and Kusakabe, O. (1999), "Centrifuge model tests on double propped wall excavation in soft clay," *Soils and Foundations*, 39(3), 75-87.

Terzaghi, K. (1936), "Stress Distribution in Dry and Saturated Sand above a Yielding Trap-door," *Proceedings of First International Conference on Soil Mechanics and Foundation Engineering*, Harvard University, Cambridge, 307-311.

Terzaghi, K. (1950), "Mechanisms of Landslides," *Engineering Geology (Berkey) Volume*, Geological Society of America.

White, D. J. and Take, W. A. (2003), "GeoPIV," 7.6 ed, Cambridge University Engineering Department.

White, D. J., Take, W. A., and Bolton, M. D. (2003), "Soil deformation measurement using particle image velocimetry (PIV) and photogrammetry," *Geotechnique*, 53(7), 619-631.

10CUEE CONFERENCE PROCEEDINGS
10th International Conference on Urban Earthquake Engineering
March 1-2, 2013, Tokyo Institute of Technology, Tokyo, Japan

PULLOUT RESISTANCE OF GEOCELL PLACED AS REINFORCEMENT IN GRAVELLY SOIL BACKFILL

Xinye HAN[1)], Takashi KIYOTA[2)], and Fumio TATSUOKA[3)]

1) Graduate student, Institute of Industrial Science, University of Tokyo, Japan
2) Associate professor, Institute of Industrial Science, University of Tokyo, Japan
3) Professor, Department of Civil Engineering, Tokyo University of Science, Japan
hanxinye@iis.u-tokyo.ac.jp, kiyota@iis.u-tokyo.ac.jp, tatsuoka@rs.noda.tus.ac.jp

Abstract: To increase the pullout resistance of geocell, a square-shaped geocell was developed and pullout tests were conducted on small scaled models placed in gravelly soil backfill. A preloading method was applied to enhance a high initial stiffness of square-type geocell. Significant effects of in-plane geometry and height of geocell on the pullout resistance were found. Analysis of the tests results indicates noticeable particle size effects that can be explained by a conceptualized pullout interaction mechanism. It is shown that the pull-out resistance is composed of two factors: the shear resistance along the shear bands developed at the top and bottom interfaces between the geocell and the adjacent backfill and the anchorage resistance induced by passive pressure inside the aperture of the geocell, which increases and becomes more dominant in the total pull-out resistance with an increase in the height of geocell.

1. INTRODUCTION

Geosynthetic-reinforced soil structures are now widely used for different civil engineering applications, including earth retaining walls, bridge abutments, slopes, embankments, pavements and erosion control. Geocell, as a three-dimensional soil confinement system, has more attractive features than other planar geosynthetic reinforcements such as geotextles and geogrids (Yuu and Han, 2008).

Most of the previous studies of geocell were mainly focused on the function as base reinforcements subjected to vertical loads, such as roads, embankments, light houses. The influencing factors for the performance of geocell-reinforced bases, such as geometric structures and dimensions, properties of geocell material and properties of infilled soil, loading methods, etc., were investigated by many researchers including Rea and Mitchell (1978), Shimizu and Inui (1990), Mhaiskar and Mandal (1992b, 1994), Dash et al. (2001a, 2001b, 2003, 2004), etc.

For the last two decades, geosynthetic-reinforced soil retaining walls (GRS RWs) with a stage-constructed full-height rigid (FHR) facing have been constructed for railways, highways and other facilities and have shown greater seismic resistance than conventional retaining wall structures (Tatsuoka et al., 2009). Geogrids and geotextiles are commonly used as planar reinforcements to tensile-reinforce the backfill of RWs, embankments and other soil structures. However, the application of geocell as tensile reinforcement to these soil tructures is relatively new due to the lack of related research. Ling et al. (2009) investigated the seismic performance of several soil RWs having a geocell facing by shake table tests. The results showed that walls having a geocells facing are flexible exhibiting much better seismic performance than conventional type RWs. In addition, the performance of a RW with the backfill reinforced with geocell layers was better than a RW with the backfill reinforced by geogrid layers.

One of the important advantages of geocell is an ability of three-dimensionally confining large particles in the cells exhibiting a large anchorage capacity when pulled laterally. Kiyota (2009) and Kuroda (2012) conducted a series of pullout tests using diamond-shaped geocell models and several different types of geogrid to investigate whether or not the geocells can be used as tension reinforcement. It was found that, although the diamond-type geocell shows higher pullout resistance than geogrids, the global stiffness is not better than the geogrids due to progressive large deformation of diamond-shaped cells. In the present study, in order to increase the initial stiffness and pullout resistance of geocell, a new type geocell having square cells were developed and evaluated by pull-out tests.

2. TEST APPARATUS, PROCEDURES AND MATERIALS

2.1 Pullout test apparatus

Figure 1 shows the schematic diagram of pullout test apparatus that was developed at Tokyo University of Science (TUS). The tests were carried out on under plane strain conditions. The sand box was 700 mm (length) ×400mm (width) × 800mm (height). The main part of the apparatus was made of steel, while the longitudinal side walls were made of hard glass plates to reduce sidewall friction. The front wall to retain the backfill was composed of separate plates accommodating small load cells to measure the lateral earth pressure activated to the back face of the front wall. An opening with a height of 30 mm was provided at the front wall for pulling out the geocell specimen from the backfill.

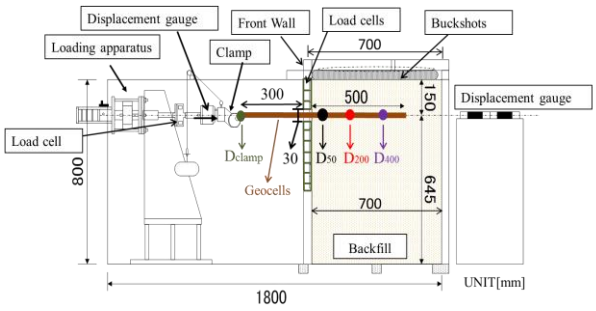
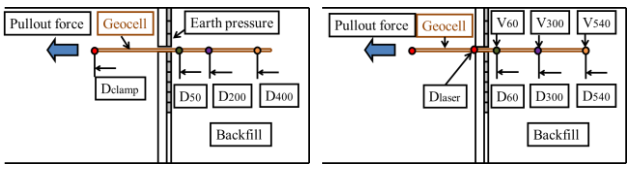


Figure 1. Pullout test apparatus at TUS

A similar apparatus was also developed at the University of Tokyo (UT).

2.2 Pullout test procedures

Gravels were poured into the soil box and compacted in 30 cm-thick sub-layers arranging a geocell model at the prescribed level in the backfill. The target relative density of the backfill was 90%. As listed in Tables 1 and 2 and indicated in Figure 2, the pullout displacements at the clamping device of the geo cell (D_{clamp}) were measured with two displacement gauges and the displacements at distances of 50 mm (D_{50}), 200 mm (D_{200}), and 400 mm (D_{400}) from the back face of the front wall were measured with three displacement gauges. In addition, the vertical displacements at distances of 60 mm (V_{60}), 300 mm (V_{300}), and 540 mm (V_{540}) from the back face of the front wall were also measured with three displacement gauges in UT. A surcharge of 1 kPa of lead shots was applied on the crest of the backfill. The tests were conducted by pulling out the geocell at a constant speed of 5 mm/min using a precision jack driven by a motor. The pullout force was measured with a load cell.



(a) (b)

Figure 2. Schematic diagram of measurements in the tests at (a) TUS; and (b) UT

Table 1 Physical quantities measured in the tests at TUS

Measured physical quantities	Symbols
Displacement at clamp	D_{clamp}
Horizontal displacements	D_{50}, D_{200}, D_{400}
Pullout force	F
Shear stress on the wall	τ
Horizontal pressure on the wall	σ

Table 2 Physical quantities measured in the tests at UT

Measured physical quantities	Symbols
Displacement near wall	D_{laser}
Horizontal displacements	D_{50}, D_{200}, D_{400}
Vertical displacements	V_{50}, V_{200}, V_{400}
Pullout force	F

2.3 Backfill and geocells

The backfill soils used in this study are poorly graded sub-round gravelly soils, Gravel No.1 and Gravel No.3 (Figure 3). Their particle sizes are 3~5 mm and 7~10 mm, respectively. As shown in Figure 4, the geocell reinforcement was 480 mm (length) × 350 mm (width), having eight cells in the longitudinal direction and seven cells in the transverse direction. The geocell was made of polyethylene terephthalate (PET) covered with PVC for protection, having a square aperture of 60 mm (length) ×50 mm (width) and a thickness of 1 mm. The longitudinal members have a common height which is 20mm higher than transversal members. The ultimate tensile strength of the material is 56 kN/m at a strain of 20 %. Four geocell models with different heights were prepared. The full height (H) of transverse members is 25 mm (SG-1); 12.5 mm (SG-2); 40 mm (SG-3); and 60 mm ((SG-4). The test cases are summarized in Table 3.



(a) (b)

Figure 3. Soil material: (a) Gravel No.1; (b) Gravel No.3

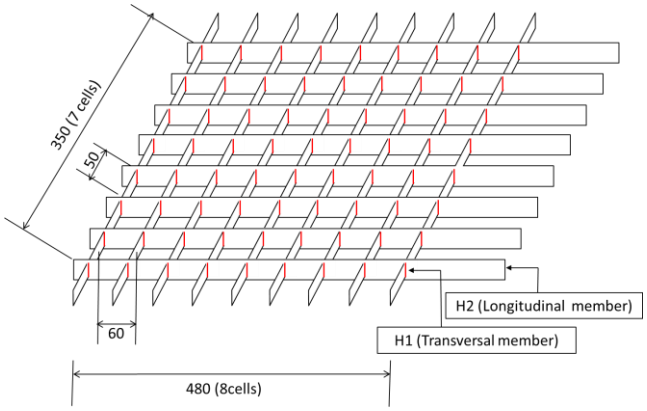


Figure 4. Schematic diagram of square-shaped geocell

Geocell	Height (transversal)	Height (longitudinal)	Backfill material	Test place
SG-1	25 mm	40mm	Gravel No.1	TUS
SG-2	12.5 mm	25mm	Gravel No.1	TUS
Tensar	5mm	5mm	Gravel No.3	TUS
SG-1	25 mm	40mm	Gravel No.1	UT
SG-2	12.5 mm	25mm	Gravel No.1	UT
SG-3	40 mm	60mm	Gravel No.1	UT
SG-2	25 mm	40mm	Gravel No.3	UT
SG-3	40 mm	60mm	Gravel No.3	UT
SG-4	60 mm	80mm	Gravel No.3	UT

reinforcement

Table 3 Test cases

3. RESULTS AND DISCUSSIONS

3.1 Effects of geometry of geocell

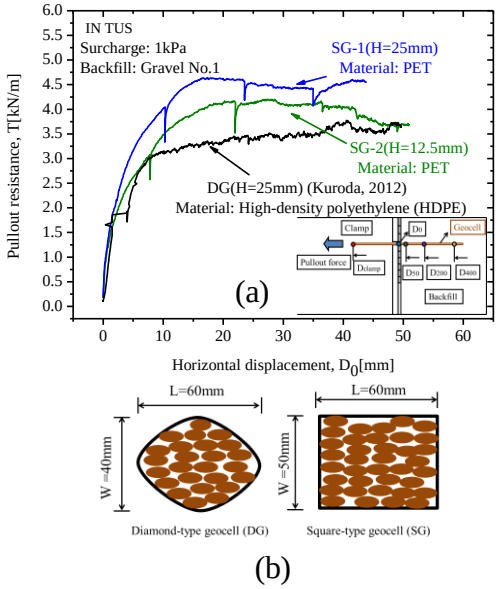


Figure 5. a) Relationships between pullout force and displacement D_0 for various types of geocell; and b) schematic diagrams of single geocell

Figure 5a shows the relationships between the pullout force (T) and the displacement (D_0) of square-shaped geocells (SG-1and SG-2) and diamond-shaped geocell (DG), which has the same height as SG-1, from the tests conducted on the same conditions (Kuroda, 2012). Geocell DG starts obvious yielding at the smallest displacement (8 mm) and does not exhibit strain-softening. Geocells SG-1 and SG-2 exhibited higher peak strengths at larger displacements, followed by noticeable strain-softening. This difference is due likely to the different geometries of the geocells, in particular the shape of aperture (Figure 5b). The fact that, despite a lower peak strength, geocell DG has the nearly the same initial stiffness as geocell SG-1 and SG-2 may be due to much thicker therefore much stiffer members of geocell DG (by a factor of >>1/6).

Figure 6 compares the results of earth pressures on the front wall during the pulling out of the geocells from soil. As shown in Figure 6, the earth pressure induced by geocell DG was higher than that by geocell SG-1 and SG-2. This fact indicates that the confining pressure developing around geocell DG was higher than those developing around geocell SG-1 and SG-2, despite that the peak strength is smaller.

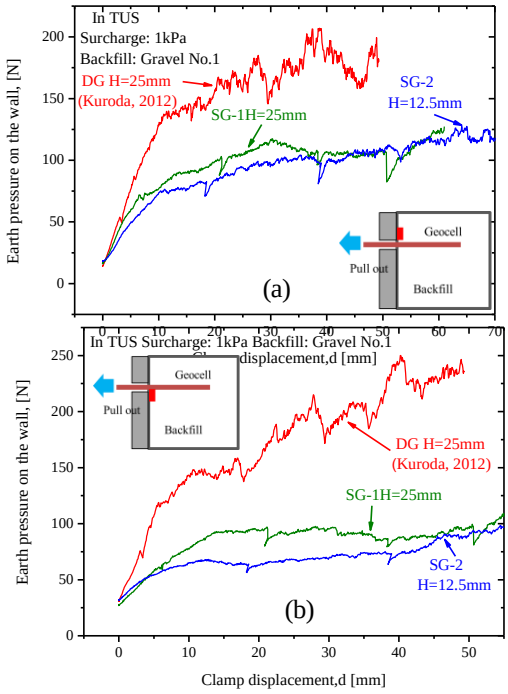


Figure 6. Earth pressures on the front wall: (a) above; and (b) below the opening

The complicated trends of behavior described above may be due to a larger deformability of the whole structure of geocell DG due to its specific shape of aperture despite thicker and stiffer members. That is, the soil in the diamond-shaped cells can be pushed out much more easily than with the square-shaped geocells, which results in a more progressive deformation of geocell DG than geocells SG-1 and SG-2, as shown in Figure 7.

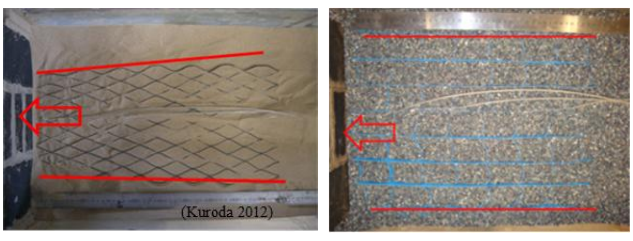
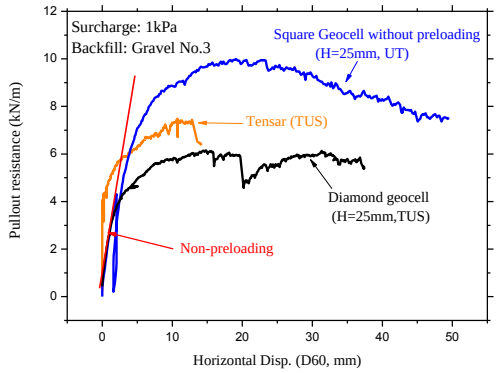


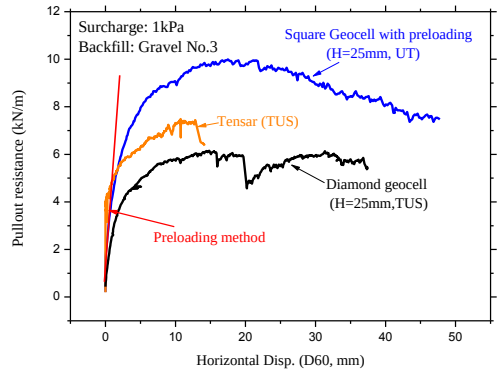
Figure 7. Deformation characterics of geocell: (a) diamond-type geocells; (b) square-type geocells

3.2 Enhancement of initial stiffness

With square-shaped geocells, the initial stiffness increases with an increase in the stiffness of transverse ribs. Tensar has a very high value of this stiffness, therefore it exhibits a very high initial stiffness as seen from Figure 8. It may also be seen from Figure 8 that, with geocell SG-1, the initial stiffness increases by applying preloading of pull-out load up to 4.3kN/m. This may be due to that preloading decreased the slackness of the initial arrangement of the transversal ribs.



(a)

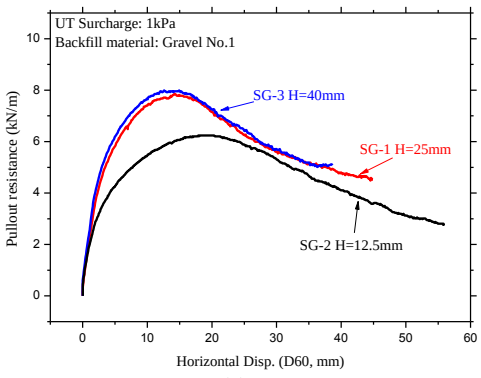


(b)

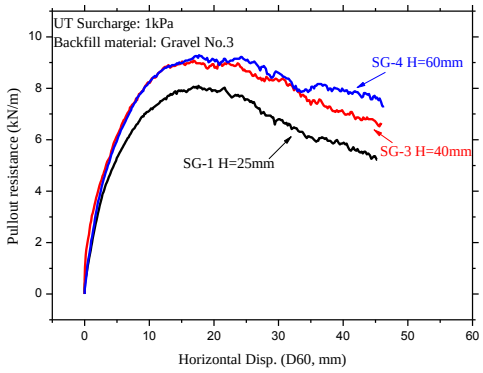
Figure 8. Relationship between pullout force and horizontal displacement among square- and diamond-shaped geocells and Tensar: (a) without and (b) with preloading

3.3 Effects of particle size relative to aperture size

The relative particle size effect was investigated by using square-type geocells with different heights arranged in backfill Gravels No.1 (the particle diameter is 3~5 mm) and No. 3 (7~10 mm). It may be seen from Figure 9 that, with an increase in the particle size, the peak strength increases while the amount strain softening decreases: i.e., the residual strength increases with an increase in the particle size to a more extent than the peak strength.



(a)



(b)

Figure 9. Pullout behavior of square-type geocells with different heights: (a) Gravel No.1; (b) Gravel No.3

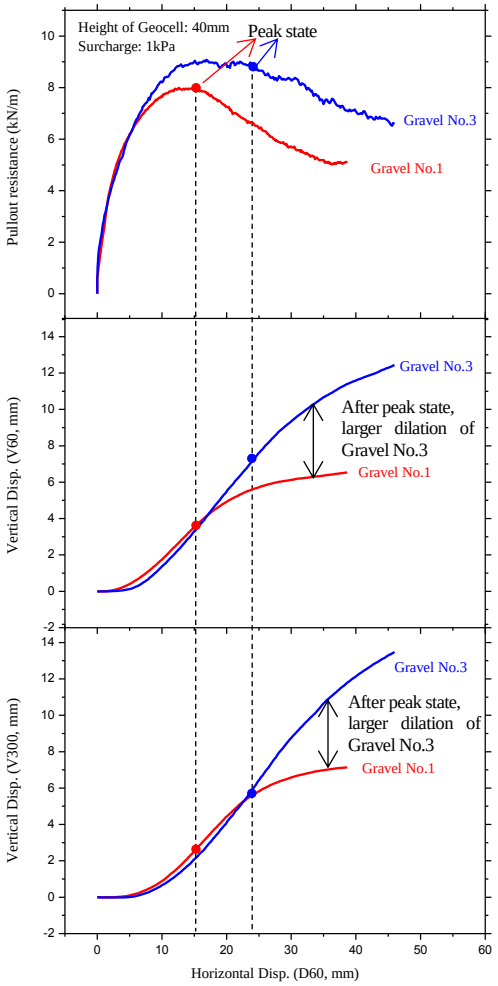


Figure 10. Relationship between horizontal displacement and pullout resistance, local vertical displacement (V_{60} and V_{300}) of SG-3 (H=40mm)

Figure 10 compares the effects of backfill particle size on the pull-out resistance and the local vertical displacements (i.e. V_{60}, V_{300}) measured above the geocell SG-3 (shown in Figure 2-b) plotted against the pullout displacement (D_{60}). In the post-peak regime, the rate of

dilatancy per horizontal displacement was larger while the strain-softening was smaller with Gravel No.3 (larger particles) than with Gravel No.1 (smaller particles). This result indicates that, with an increase in the backfill particle size, the shear band that develops at the interfaces between the geocell and the backfill becomes thicker, therefore the ultimate amount of dilatancy becomes larger, which results in a larger increases in the local vertical stress activated to the geocell, therefore larger pull-out resistance at large pull-out displacements.

The pull-out resistance increases with an increase in the rib height from 12.5 mm to 25 mm in Figure 9a and from 25 mm to 40 mm in Figure 9b. However, with further increase in the rib height, the pull-out resistance exhibits only a very small increase in both cases. To analyze this trend, Figure 11a summarizes the pull-out resistance of square-shaped geocells SG-1, SG-2, SG-3 & SG-4 embedded in Gravel No.1 and Gravel No.3 and diamond-shaped geocells DG embedded in Toyoura sand (Kuroda et al. 2012). It may be seen that, under otherwise the same conditions, the pull-out resistance increases with an incease in the rib height with the square-shaped geocells or the member height with the diamond-shape geocells. However, there exists an upper limit with the pullout resistance that is reached when the height of rib or member becomes a certain value that increases with an increase in the backfill particle diameter. The line presented in Figure 11a indicates this upper-limit state.

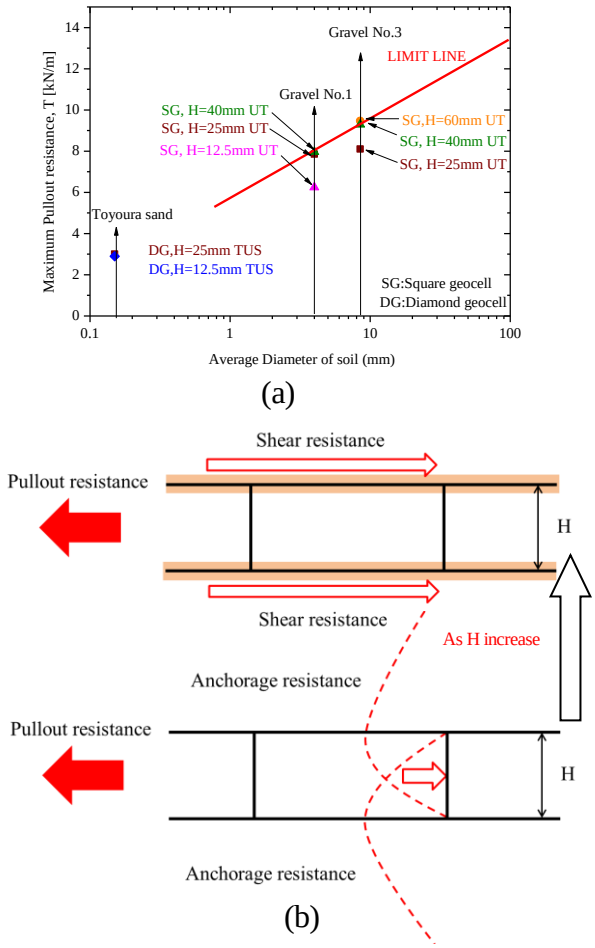


Figure 11. (a) Particle size effect on maximum pullout resistance; and (b) two mechanism of pullout resistance of reinforcement embedded in the backfill

These test results suggest the following fundamental mechanism. As shown in Figure 11b, the pullout resistance is equal to the smaller one of the following two types of resistance: 1) the shear resistance of the shear bands that develop along the upper and bottom faces of a geocell and the backfill, which is independent of the height of rib or member (i.e., the height of geocell); and 2) the anchorage resistance induced by passive pressure developing inside the cells, which increases with an increase in the height of geocell. Therefore, as the height of geocell increases, the total pullout resistance is first determined by the anchorage resistance and increases with an increase in the height of geocell. When the height of geocell reaches a certain value, the anchorage resistance reaches the shear resistance. Then, the pull-out resistance does not increase with further increase in the height of geocell. Both shear resistance and anchorage resistance increase with an increase in the backfill particle size, therefore the pull-out resistance does so. This trend becomes stronger at larger pull-out displacements. The test results show that the limit of the height of geocell at which the two types resistance become the same increase in the backfill particle size.

4. CONCLUSIONS

A geocell having square-shaped apertures was developed to increase the pull-out resistance. A series of pullout tests were conducted on small scaled models of square-shaped geocell arranged in backfill of gravelly soil. By analyzing the data from these tests and previous tests, the effects of the shape of cell and the height of transversal members (ribs) and the backfill particle size on pullout resistance were evaluated. The main conclusions from this study are as follows:

1. The effects of cell shape increases with an increase in the pull-out displacement. Under otherwise the same conditions, the square-shaped geocell exhibit higher peak pull-out resistance than the diamond-shaped geocell and higher residual strength to a more extent.
2. The initial pull-out stiffness of a geocell increases by reducing the initial slackness of the geocell by preloading.
3. The pullout resistance is equal to the smaller value of: the shear resistance of the shear bands along the upper and bottom faces of a geocell, which is independent of the height of geocell; and the anchorage resistance induced by passive pressure developing inside the cells, which increases with an increase in the height of geocell. Therefore, as the height of geocell increases, the total pullout resistance is equal to the anchorage resistance and increases with an increase in the height of geocell. When the height of geocell reaches a certain value, the pull-out resistance becomes the same as the shear resistance and does not increase with further increase in the height of geocell. Both shear resistance and anchorage resistance, therefore the pull-out

resistance, increase with an increase in the backfill particle size.

The tests results presented in this paper are rather limited. More tests to evaluate the effects of the stiffness and height of geocell and the particle diameter of backfill, the vertical pressure and so on should be tested in the future.

Acknowledgements:

The author sincerely appreciates the help of Mr. Michiyuki HARATA in TOKYO PRINTING INK MFG. CO., LTD to provide the geocell models, which can make the experiments proceed smoothly.

References:

Dash, S.K., Krishnaswamy, N.R., and Rajagopal, K. (2001a). "Bearing capacity of strip footings supported on geocell-reinforced sand." Geotextiles and Geomembranes, 19(4), 235-256.

Dash, S.K., Rajagopal, K., and Krishnaswamy, N.R. (2001b). "Strip footing on geocell reinforced sand beds with additional planar reinforcement." Geotextiles and Geomembranes, 19(8), 529-538.

Dash, S.K., Rajagopal, K. and Krishnaswamy, N.R . (2004). "Performance of different geosynthetic reinforcement materials in sand foundations." Geosynthetics International, 11(1), 35-42.

Dash, S.K., Sireesh, S., and Sitharam, T.G. (2003). "Model studies on circular footing supported on geocell reinforced sand underlain by soft clay." Geotextiles and Geomembranes, 21(4), 197-219.

Kiyota, T., Soma, R., Munoz, H., Kuroda, T., Ohta, J., Harata, M., and Tatsuoka, F. (2009). "Pullout behaviour of geo-cell placed as reinforcement in backfill." Geosynthetics Engineering Journal 24(0), 75-82. (In Japanese).

Kuroda, T., (2012). " Evaluation of static and seismic stability of bridges with reinforced backfill and integrated structural (New type and Rehabilitated type bridges) by model tests." Master thesis, Department of civil engineering, Tokyo University of Science. (In Japanese).

Ling, H.I., Leshchinsky, D.,Wang, J.P., Mohri, and Y., Rosen, A. (2009). Seismic response of geocell retaining walls: experimental studies. ASCE Journal of Geotechnical and Geoenvironmental ngineering 135, 515-524.

Mhaiskar, S.Y. and Mandal, J.N. (1992). "Comparison of a geocell and horizontal inclusion for paved road structure." Proceedings of the International Symposium on Earth Reinforcement Practice, 1, 641.

Mhaiskar, S.Y. and Mandal, J.N. (1994). "Three dimensional geocell structure: performance under repetitive loads", 5th International Conference on Geotextile, Geomembranes and Related products, Singapore, 155-158.

Rea, C. and Mitchell, K. (1978). "Sand reinforcement using paper grid cells." Proceedings, Symposium on Earth Reinforcement, ASCE Annual Convention, Pittsburgh, PA, 644-663.

Shimizu, M. and Inui, T. (1990). "Increasing in the bearing capacity of ground with geotextile wall frame." Geotextiles, Geomembranes and Related Products, 254.

Tatsuoka, F., Koseki, J., and Tateyama, M. (2009). "Seismic behaviour of geosynthetic-reinforced structures: Lessons from recent earthquakes and from recent earthquakes and design approaches." The 12th Italian Conference on Geosynthetics, Italy.

Yuu, J., Han, J., Rosen, A., Parson, R., Leshchinsky, D. (2008). Technical review of geocell-reinforced base courses over weak subgrade. International Proceeding of First Pan American Geosynthetics Conference and Exhibition, Cancun, Mexico: 1022-1030.

CONFERENCE PROCEEDINGS
The 10th International Conference on Urban Earthquake Engineering
March 1-2, 2013, Tokyo Institute of Technology, Tokyo, Japan

CENTRIFUGE MODEL TESTS ON FAILURE PATTERN OF CEMENT STABILIZED GROUND

Yuki Yoshida[1], Tomohide Takeyama[2] and Masaki Kitazume[3]

1) Bachelor student, Department of Civil Engineering, Tokyo Institute of Technology, Japan
yoshida.y.am@m.titech.ac.jp
2) Assistant Professor, Department of Civil Engineering, Tokyo Institute of Technology, Japan
takeyama@cv.titech.ac.jp
3) Professor, Department of Civil Engineering, Tokyo Institute of Technology, Japan
kitazume@cv.titech.ac.jp

Abstract: Cement stabilized soil is characterized by the brittle property in which high compression strength and small strain at failure and low tensile strength. It has been well recognized that the failure pattern of the stabilized soil is quite different from those of ordinary cohesive soils. A series of centrifuge model tests was conducted to investigate the failure pattern and stability of cement stabilized clay ground having an unsupported vertical slope. The model ground was subjected to monotonically increasing centrifugal acceleration until it failed due to the enhanced self-weight. It was found from the test results that the model ground failed with a combination of a vertical tensile crack and a straight shear failure plane, which was much different from the failure phenomenon of sandy or clayey ground. A new calculation incorporating the failure pattern of stabilized soil should be necessary to investigate its critical height and the failure zone precisely.

1. INTRODUCTION

Because of economical and environmental concerns it has become more difficult in recent years to obtain enough soil to make reclamation for airports, electric power plants, manufacture plants and so on. On the other hand, it has become difficult to find and construct disposal sites for waste subsoil or dredged soil. These circumstances have caused geotechnical engineers at present to use these poor quality materials as filling materials more than they were used one or two decades ago. Several soil admixture methods have been developed to improve their properties and to manufacture high quality fill materials. Actually, Horiuchi *et al*. (1992) and Kawasaki *et al*. (1992) manufactured fly ash and cement mixtures as a fill material to construct a man-made island for a bridge in Hokkaido, Japan. Tsuchida *et al*. (1996) manufactured lightweight soil, a mixture of dredged clay, cement and fine air form, to fill behind a sea revetment. Recently a cement soil mixture manufactured by the Pneumatic Flow Mixing Method as shown in Fig. 1 has been used to construct a man-made island for a new international airport (Kitazume *et al*., 2000, Kitazume and Sato, 2002).

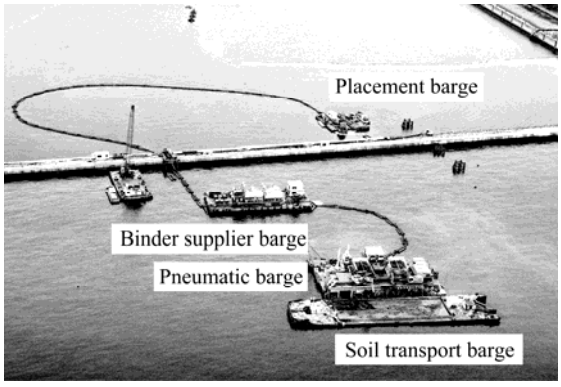


Fig. 1. Pneumatic Flow Mixing Method.

The deformation and strength characteristics of cement stabilized soils have been investigated in Japan, which have revealed that the stabilized soil is characterized by a brittle behavior with quite high compressive strength and quite small strain at failure, and the stabilized soil with relatively high strength shows tensile failure instead of shear failure, as exemplified in Fig. 2. Regarding to evaluate the stability of structures adjacent to or buried in the stabilized ground, Kitazume (1998) and Kitazume et al. (2003) investigated the earth pressure of cement stabilized ground by the centrifuge model tests. And The emphasized that the failure pattern of the cement stabilized ground was much different from that of ordinary ground. After the Hyogoken-Nambu earthquake in 1995, many design codes for the seismic stability were revised in Japan, so that seismic stability must be evaluated more precisely. The dynamic earth pressure of ordinary grounds is usually calculated by a pseudo-static limit equilibrium method based on the Mononobe-Okabe's method (Okabe 1924, Mononobe and Matsuo 1929). This calculation method is also applied to the cement stabilized ground, although its applicability has not been thoroughly clarified.



(a) relatively low strength (b) relatively high strength

Fig. 2 Failure pattern of cement stabilized soil.

In order to investigate the failure pattern of cement stabilized ground, the authors started a research project where a series of model tests and analyses is carried out on the above subject. In this paper, the failure pattern of the cement stabilized clay ground subjected to monotonic increase of self-weight was investigated in the Tokyo Institute of Technology Mark III geotechnical centrifuge apparatus. A series of centrifuge model tests was carried out on the cement stabilized clay ground having an unsupported vertical slope. The model ground was subjected to monotonically increasing centrifugal acceleration until it failed due to the enhanced self-weight. The applicability of the conventional limit equilibrium method based on Coulomb method to the cement stabilized ground was examined based on the model test results, where the calculated critical height of the ground did not coincide well with the model test results. A new calculation incorporating the failure pattern of stabilized soil should be necessary to investigate its critical height and the failure zone precisely.

In this paper, the model test procedure and test results are briefly introduced.

2. CENTRIFUGE MODEL TESTS

Centrifuge Apparatus

A static loading technique has also been employed to investigate the stability and failure pattern of cement stabilized ground where the model ground is subjected to enhanced self-weight. The centrifuge used for the tests was the Tokyo Institute of Technology Mark III Geotechnical centrifuge. The centrifuge has a maximum acceleration of 150 G, a maximum effective radius of 2.3 m and a maximum payload of 330 kg.

Model ground preparation and testing procedure

The model ground set up for the test is schematically shown in Fig. 3. A rigid specimen box had inside dimensions of 70 cm in length, 15 cm in width and 45 cm in height. The box had a Polycarbonate resin window to observe the model ground behavior. The inner surfaces of the box were lubricated with a mixture of silicone grease and silicone oil to minimize the friction between the box and the model ground.

The model ground was prepared as follows. Kaolin clay was thoroughly mixed with de-aired water for 60 minutes to make a uniform slurry with a water content of 120%, whose physical properties are summarized in Table 1. Then, binder factor *aw* of 5 or 10% of normal Portland cement was added to the slurry and mixed for 10 minutes, where the cement factor, *aw* was defined as the ratio of dry weight of cement to that of soil. The soil cement mixture was poured into the specimen box. Three mold specimens were also prepared with the same stabilized soil as the model ground for the unconfined compression test. The model ground and the mold specimen were sealed tightly to minimize water evaporation from the model ground and cured for the prescribed days in the laboratory. After curing, the model ground thus prepared was mounted on the centrifuge, and a potentiometer was placed at the crown of the model ground to measure the vertical displacement during the loading. The ground was subjected to monotonically increasing centrifugal acceleration until it failed due to the enhanced self-weight. During the flight, the vertical displacement at the crown of the model ground was measured and the ground deformation was observed by the TV camera mounted on the centrifuge. After the test, the failure pattern of the ground was carefully observed. At each test, unconfined compression tests were conducted on the mold specimen to estimate the unconfined compressive strength of the model ground. Three model tests were conducted by changing the strength of the model ground, as summarized in Table 2.

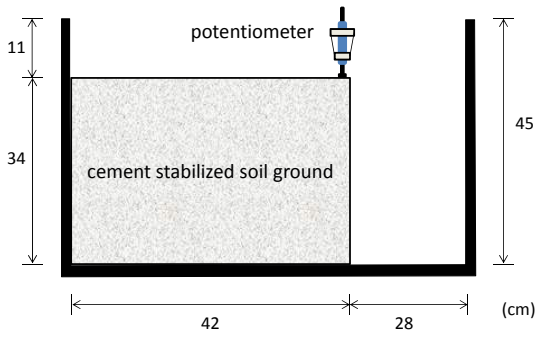


Fig. 3. Model ground setup.

Table 1. Properties of Kaolin clay.

Item	Value
Specific gravity, G_s	2.61
Liquid limit, w_L (%)	77.5
Plastic limit, w_P (%)	30.3
Plastic index, I_P	47.2
Compression index, C_C	0.56
Swelling index, C_S	0.10
C_u/p	0.24

Table 2. Test cases.

	CASE1	CASE2	CASE3
Cement factor, *aw* (%)	10	5	10
Water content, *w*(%)	120	120	120
Water/cement ratio, *w/c*	12	24	12
Curing days, *t* (day)	7	12	13
Unconfined compressive strength, q_u (kPa)	142.6	46.2	120.9
Height of ground (cm)	34.6	34.0	33.5
Unit weight (kN/m^3)	13.5	13.6	13.7
Centrifuge acceleration at failure (G_f)	46.5	17.7	46.5

3. TEST RESULTS

Displacement and centrifugal acceleration

During the test, the vertical displacement of the model ground was measured at its crown. Figure 4 shows the ground settlement, *S* in a model scale against the centrifugal acceleration *G* measured in the CASE3, where the unconfined compressive strength of 120.9 kPa. It can be seen that the *S* value increases very slightly at first as the *G* increases but suddenly jumps up to around 40 to 50 mm due to ground failure just after *G* reaches about 46 *G*. Similar test results were obtained in the CASEs 1 and 2. This phenomenon indicates that the entire ground failure suddenly took place without an pre-failure progressive deformation.

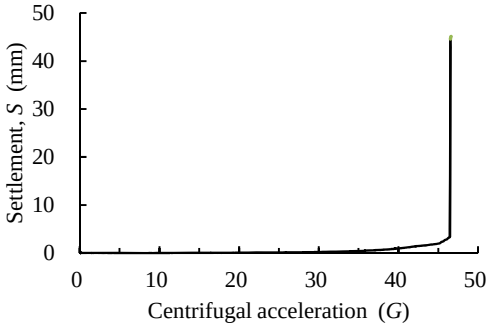


Fig. 4. Displacement and centrifugal acceleration curve (CASE3)

Failure pattern of ground

A typical failure pattern of the ground is shown in Fig. 5, which was obtained in the CASE3. For ease of detecting the failure pattern, the side surface of the model ground was painted as a grid pattern. In the figure, a tensile crack developed almost perpendicular to the ground surface. A shear failure plane also developed from the bottom end of the tensile crack toward the bottom of the ground base immediately after the tensile crack formed. A similar failure pattern was also found in the cement stabilized fly ash ground (Kitazume 1998). The failure pattern obtained in this study is much different from those of soft clayey ground or sandy ground (e.g. Japanese Soil Mechanics Society 1994, Zeng 1998). The features of the failure pattern is due to the considerably small ratio of tensile strength to compressive strength of cement stabilized soil.

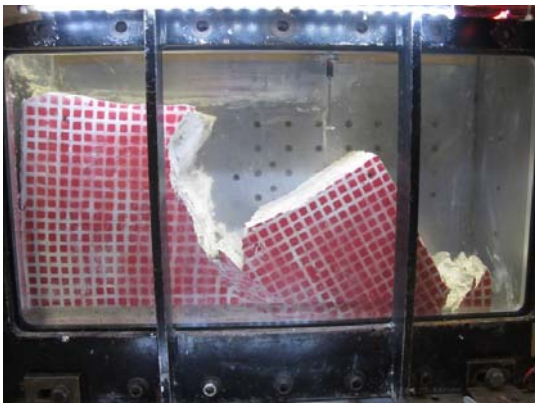


Fig. 5. Model ground failure (CASE3)

4. DISCUSSIONS

Critical height

The centrifugal acceleration at ground failure, G_f, was defined as the acceleration when the ground settlement jumped up as shown in Fig. 4. The G_f values thus obtained are summarized in Table 2 together with the test condition. The normalized critical height, H_c of the ground is calculated by Eq. (1) and plotted against the unconfined compressive strength, , q_u in Fig. 6.

$$H_c = \frac{\gamma \cdot H_m \cdot G_f}{q_u} \quad (1)$$

where

G_f : gravity at failure (*G*)
H_c: normalized critical height of model ground
H_m: height of model ground (m)
q_u : unconfined compressive strength of model ground (kN/m^2)
γ: unit weight of model ground (kN/m^3)

In the figure, similar test results (Kitazume *et al*., 2003) are plotted together. Although there is a scatter in the data, it is found that the normalized critical height, H_c decreases gradually with the strength of stabilized ground. The critical height calculated by the static limit equilibrium method, Coulomb theory, is plotted as chain line in the figure. The calculation gives a constant value of 2 irrespective of the strength of model ground. It can be seen that the calculation

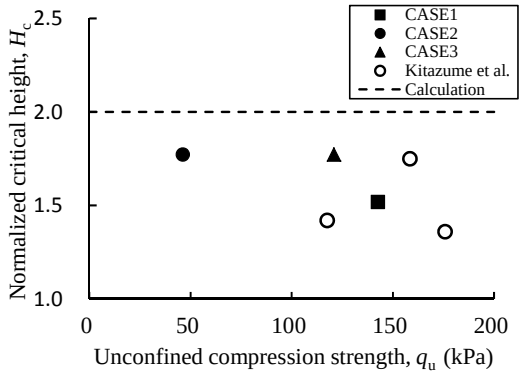


Fig. 6. Normalized critical height and strength of ground.

overestimates the measured values and the overestimation increases with increasing strength. This is because the failure pattern assumed in the theory, a straight shear failure plane alone, is much different from that obtained in the tests.

Failure zone

The normalized failure zone B_m/H_m is plotted against the G_f in Fig. 7, where B_m is the horizontal distance of the tensile crack plane measured from the front face of the ground. Again, the measured data by Kitazume *et al.* (2003) and the calculation of Coulomb theory are plotted together in the figure. The calculation is constant of 1.0 along the q_u, while the B_m/H_m value is smaller than the calculation and decreases with the increasing q_u. This difference also suggests that the conventional static limit equilibrium method cannot evaluate the failure zone of the cement stabilized ground. A new calculation incorporating the failure pattern of stabilized soil should be necessary to investigate its critical height and the failure zone precisely.

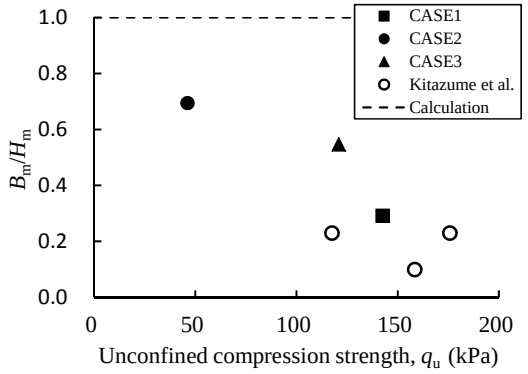


Fig. 7. Normalized failure zone and strength of model ground.

5. CONCLUSIONS

A series of model tests was conducted on the geotechnical centrifuge apparatus to investigate the stability and failure pattern of cement stabilized ground having an unsupported vertical slope. The test results show the unique feature of failure pattern that is characterized by a combination of a vertical tension crack and a shear failure plane. The conventional static limit equilibrium method based on Coulomb theory cannot evaluate the critical height and the failure zone of the ground obtained in the tests accurately. new calculation incorporating the failure pattern of stabilized soil should be necessary to investigate its critical height and the failure zone precisely.

REFERENCES

Horiuchi, S., Taketsuka, M., Odawara, T. and Kawasaki, H. (1992): Flyash slurry island: I. Theoretical and experimental investigations, *Journal of Materials in Civil Engineering*, ASCE, 4 (2), 117-133.

Japanese Soil Mechanics Society (1994): *Introduction to model tests for geotechnical engineering*, 165 (in Japanese).

Kawasaki, H., Horiuchi, S., Akatsuka, M. and Sano, S. (1992): Flyash slurry island: II. Construction in Hakucho Ohashi project, *Journal of Materials in Civil Engineering*, ASCE, 4 (2), 134-152.

Kitazume, M. (1998): Centrifuge model tests on failure of cement stabilized fly ash ground, *Soils and Foundations*, 38 (3), 143-152.

Kitazume, M., Yoshino, N., Shinsha, H., Horii, R. and Fujio, Y. (2000): Field test on pneumatic flow mixing method for sea reclamation, *Proc. of the International Conference on Coastal Geotechnical Engineering in Practice* (Nakase, A. and Tsuchida, T. eds.), 647-652.

Kitazume, M. and Sato, T. (2002): Development of pneumatic flow mixing method and its application to Central Japan International Airport construction, *Proc. of the 4th International Conference on Ground Improvement Techniques*, Kuala Lumpur, 1-14.

Kitazume, M., Hayano, K. and Hashizume, H. (2003): Seismic stability of cement treated ground by titling and dynamic shaking table tests, *Soils and Foundations*, 43 (6), 125-140.

Tsuchida, T., Takeuchi, D., Okumura, T and Kishida, T. (1996): Development of light-weight fill from dredgings, *Proc. of 2nd International Congress on Environmental Geotechnics*, 415-420.

Zeng, X. (1998): Seismic response of gravity quay walls. I: centrifuge modeling, *Journal of geotechnical and geoenvironmental Engineering*, 406-417.

10CUEE CONFERENCE PROCEEDINGS
10th International Conference on Urban Earthquake Engineering
March 1-2, 2013, Tokyo Institute of Technology, Tokyo, Japan

EXPERIMENTAL INVESTIGATION ON DEWATERING AND DRAINAGE METHODS TO MITIGATE LIQUEFACTION DAMAGE TO EXISTING HOUSES

Kohji Tokimatsu [1], Kazushi Tohyama[2], Hiroko Suzuki[3] and Yasutsugu Suzuki[4]

1) Professor, Architecture and Building Engineering, Tokyo Institute of Technology, Japan
2) Graduate Student, Architecture and Building Engineering, Tokyo Institute of Technology, Japan
3) Assistant Professor, Architecture and Building Engineering, Tokyo Institute of Technology, Japan
4) Chief Research Engineer, Kajima Technical Research Institute, Kajima Corporation, Japan
kohji@o.cc.titech.ac.jp

Abstract: To estimate effectiveness of dewatering and drain method for liquefaction remediation, a series of centrifuge shaking table tests were conducted. The following conclusions may tentatively be made: 1) The absolute and relative settlements as well as tilting angle of structures can decrease with lowering groundwater table. When it is lowered at a depth of 4m, the absolute settlement approximately becomes equal to the ground settlement, but both relative settlement and tilting angle of structures become almost zero. This claims that dewatering could be an effective method for reducing liquefaction-induced damage to existing houses; 2) Although the absolute settlement of structures may not be reduced by drain method, both relative settlement and tilting angle of structures can decrease with increasing drainpipe diameter and with decreasing spacing between drainpipes. This suggests that the installation of drainpipes around a structure in an appropriate manner is promising; 3) The tilting angle of structures founded on liquefiable soils decreases with increasing factor of safety with respect to the moment equilibrium, in which both dewatering and drainage effects are taken into account. This suggests that the dynamic overturning moment might have significant effects on the tilting of structures founded on liquefiable soils.

1. INTRODUCTION

The 2011 Tohoku Pacific Earthquake induced extensive soil liquefaction along the coast of Tokyo Bay and the floodplain of the Tone River (Architectural Institute of Japan, 2012). Accompanied by numerous sand boils and large ground settlements over 50 cm, soil liquefaction caused settlement/tilting of wooden and reinforced concrete buildings supported on spread foundations. Especially in Urayasu city, about 1/3-1/2 of wooden houses in reclaimed residential districts tilted more than 1/100 (Tokimatsu et al., 2012). There is a strong need to jack up to level the tilted buildings as well as to mitigate future liquefaction occurrence and associated damage. Although various restoration and remedial methods are available to tilted buildings as well as to buildings before construction, there seem no economically feasible measures for existing wooden houses.

To reduce liquefaction-induced damage to existing structures such as wooden houses, port facilities and embankments, dewatering and drainage methods have been occasionally used. Dewatering increases the thickness of the non-liquefiable surface layer and decreases the thickness of liquefiable underlying layer, thereby reducing potential damage induced by liquefaction; however, it is very difficult to use when the consolidation settlement of underlying clay layers is a matter of concern or when the lifetime cost including construction and maintenance becomes very expensive. The drainage method accelerates dissipation of excess pore water pressures during earthquakes using high permeability materials driven in liquefiable soils. Because of its installation cost, drain method may not be economical and realistic measures for existing houses. A small diameter plastic drainpipe (Photo 1), which has been developed recently and applied as remedial

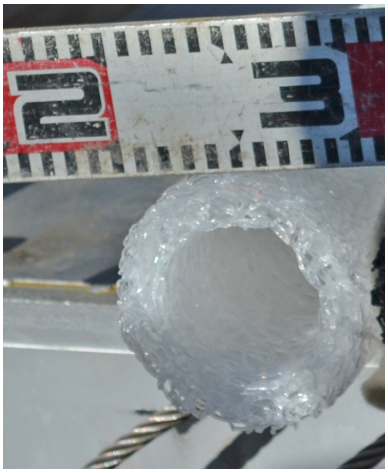


Photo 1 Plastic drainpipe

measures against uplift of existing manholes, is relatively cheap and easy to push into the ground, promising cost effective measures for existing houses.

To estimate effectiveness of drain method for liquefaction remediation, a series of centrifuge shaking table tests were conducted, in which drainpipes were installed around a house with its diameter and spacing as well as groundwater table being varied. The tests conducted with different groundwater table enables us to examine the effects of dewatering on mitigation of liquefaction damage. Detailed test procedures and results have been described elsewhere (Suzuki et al., 2013). On the basis of the result, this paper further investigates factors influencing tilting and settlement of houses founded on liquefiable soils having different groundwater table and with/without drainpipes.

2. Outline of centrifugal model tests

Shaking table tests were conducted on various soil-structure models with/without drainpipes under centrifugal acceleration of 25 or 50G, i.e., a reduced scale of 1/25 or 1/50. Pipe diameter and spacing, groundwater table and sizes of structure were varied in the test. Table 1 summarizes the soil-structure models tested and Table 2 shows the location of drainpipes placed around a house. Numerals in parentheses in the tables stand for the prototype scale. Each case ID consisting of four characters in Table 1 specifies both soil and structure conditions. The first numeral indicates the groundwater table in the prototype scale (1: 1.0m, 2: 2.0m, 3: 2.5m and 4: 4.0m), the second one the structure dimensions (S: 4.5m x 4.5m, L': 8.0m x 8.0m and L: 9.0m x 9.0m in a plan in the prototype scale), the third one the drainpipe diameter (0: without drain, 1: 130mm and 2: 250mm in the prototype scale) and the forth one the spacing between drainpipes (0: without drain, 1: 5.0m, 2: 3.0m, 3: 1.5m and 4: 1.0m in the prototype scale). Case IDs with an asterisk in Table 1 (1S00 and 3L00) were shaken twice to confirm reproducibility of the model tests.

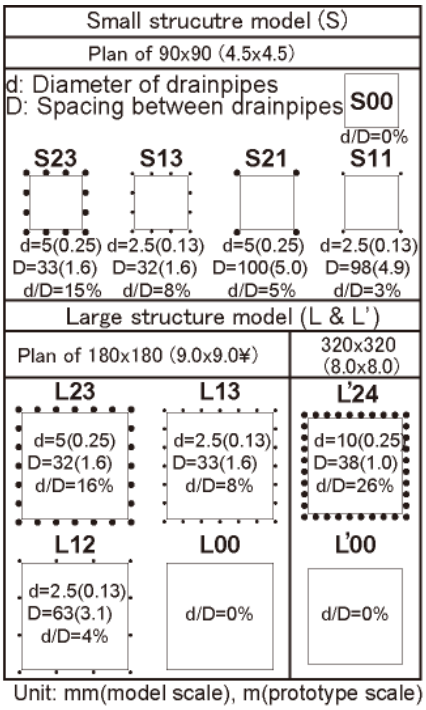
Figure 1 shows a typical test setup (e.g., cases IS00 and 1S23) conducted under a centrifugal acceleration of 50G. All the soil-structure models run with a centrifugal acceleration of 50G were constructed in a laminar box with a height of 300mm, a width of 220mm and a length of 700mm (Suzuki et al., 2013). In each container, two structures with/without drainpipes were founded on a sand deposit consisting of two layers. The lower layer was Silica sand #7 having a thickness of 180mm, which was overlain by finer Silica sand #8 with a thickness of 20mm. A relative density for both layers was about 50%. Dry Silica sand #7 was firstly air-pluviated in the box. When the height of the sand layer reached the groundwater table (20mm, 50mm or 80mm), the sand layer was saturated using silicon oil with 50cst under vacuum. The layer above the groundwater table was then prepared by air-pluviation. The coefficient of permeability of the liquefiable layer below the groundwater table (Silica sand #7) was 2.8×10^{-4} cm/s.

After completion of sand layer, a pair of either small or large structure models was placed on the sand layer with an embedment of 3mm. The small structure model (S) had a plan dimension of 90mm x 90 mm, a height of 118mm and a weight of 323g and the large

Table 1 Case ID

G	Water Table	Case ID
50	20mm (1.0m)	1S23
		1S21
		1S13
		1S11
		1S00
		※1S00
		1L23
		1L13
		1L12
		1L00
	50mm (2.5m)	3S23
		3S00
		3L23
		3L12
		※3L00
		3L00
	80mm (4.0m)	4S23
		4S00
25	80mm (2.0m)	2L'24
		2L'00

Table 2 Location of drainpipes



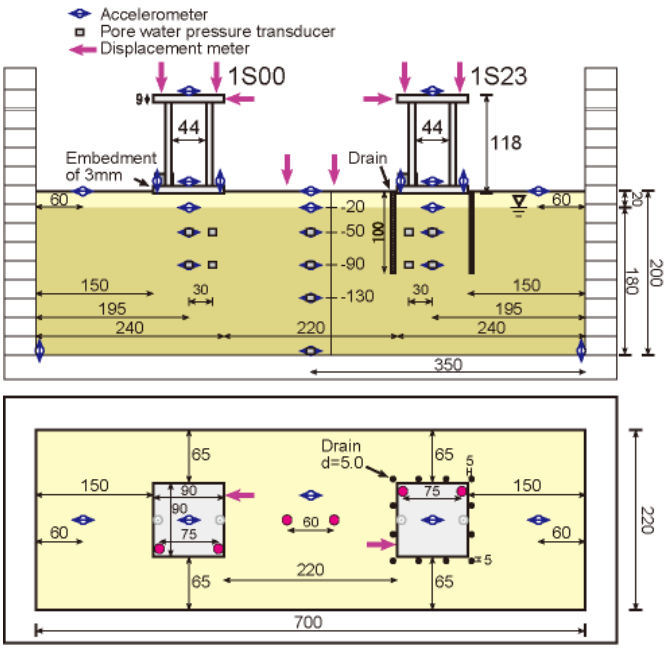


Figure 1 Typical test setup (50G)

one (L) had a plan dimension of 180mm x 180mm, a height of 190 mm and a weight of 1.043g. Both structures had an eccentric mass (52g or 139g) on their foundations with an eccentric distance of 25mm or 75mm from the center. These structure models had an average contact pressure of 15-18kN/m^2 between the foundation and the soil, a natural period of 0.3-0.4s and a height of gravity center of 2.5m in the prototype scale, representing a typical two-story wooden house in Japan. After placement of a pair of structures, drainpipes were push into the soil around a structure if needed, as specified in Table 2. Drainpipes were made of stainless-steel mesh (100 wires per inch, wires 0.1mm in diameter), having a diameter of 2.5mm or 5.0mm and a length of 100mm. During the preparation of soil structure models, displacement meters, accelerometers and pore water pressure transducers as well as displacement meters were installed in the soil as well as on the structures.

Soil-structure models tested under a centrifugal acceleration of 25G were prepared in a similar manner but in a larger laminar box with a height of 600mm, a width of 800mm and a length of 1950mm. A surface layer in this case was also Silica sand #8 having a thickness of 40mm but an underlying layer was Toyoura sand with a thickness of 360mm. A relative density for both layers was about 60%. Silicon oil with 25cst was used for saturating the soil. The coefficient of permeability of the liquefiable layer (Toyoura sand) was 9.2×10^{-4} cm/s. A structure model (L') had a plan of 320mm x 320mm, a height of 170 mm and a weight of 5.340kg. An eccentric mass (860g) was placed on the foundation with an eccentric distance of 120mm from the center. Its average contact pressure, natural period and height of gravity center in the prototype scale were almost the same as those of model structures S and L tested under 25g. Drainpipes used in this case were made of brass mesh (100 wires per inch, wires 0.1mm in diameter), having a diameter of 10mm and a length of 200mm.

A pair of structure models such as shown in Figure 1 was shaken, either under 50g or 25g, using an artificial ground motion called Rinkai as an input motion. The outputs from the installed sensors were recorded until the excess pore pressure in the ground had dissipated completely. This shaking and observation process was then repeated up to four times until one of the structures tilted largely. The maximum acceleration (in the prototype scale) was adjusted to 4.0m/s^2, 2.0m/s^2, 4.0m/s^2 and 4.0m/s^2 in the sequence order. This paper discusses the results only from the first shaking for a pair of structure models. Henceforth, the test results were shown in the prototype scale.

3. Estimation of effectiveness of drainage method through shaking table tests

3.1 Comparison in behavior between structures with and without drains

Figure 2 shows time histories of major outputs from cases 1S00 and 1S23 (with and without drainpipes). Straight lines in Figure 2(c)(d)(k)(l) stand for the initial effective stress, in which the initial overburden pressure from the structure is taken into account based on Boussinesq's formulas. The accelerations of the ground, footings and superstructures are significantly smaller than that of the shaking table (Figure 2 (e)-(h)(m)-(p)). Although the acceleration of the footing is almost the same between the two cases but the acceleration of the superstructure is slightly larger in model 1S23 (with drainpipes) than in model 1S00 (without drainpipes). The excess pore water pressures below the centers of footings in both cases increase with cyclic loading (Figure 2(c)(d)(k)(l)). The excess pore water pressures in case 1S00 (without drains) become approximately equal to the initial effective stresses at depths of both 2.5 m and 4.5 m. In contrast, those in case 1S23 (with drains) do not reach the initial effective stress at both depths and are kept as low as a half of those in case 1S00, probably because of the effects of drainpipes. As a result, the tilt angle in case 1S23 with drains becomes as small as 5/1000, which contrasts well

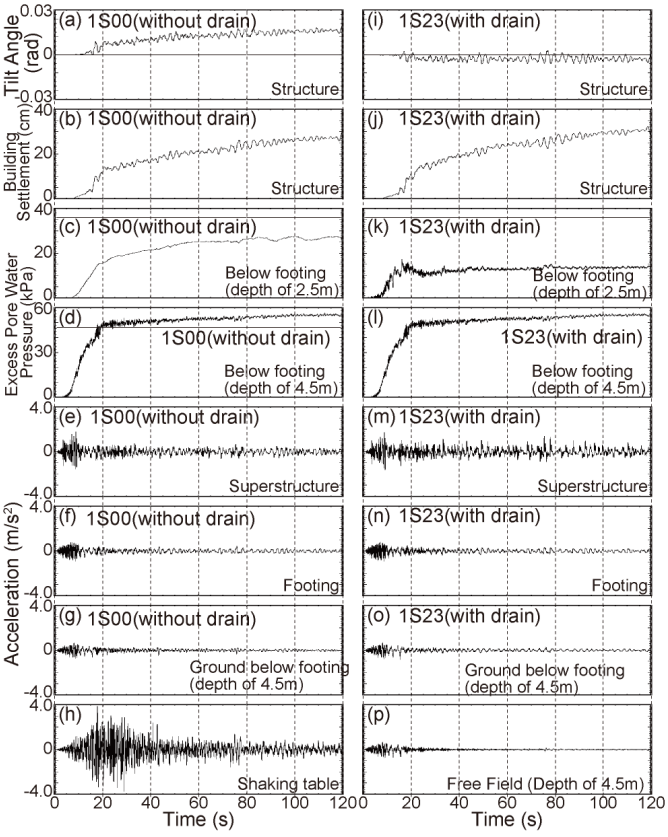


Figure 2 Time histories of major values for 1S00 and 1S23

with a larger value of 1/40 in case 1S00 without drains (Figure 2(a)(i)). It is interesting to note further that, despite its smaller angle of tilt, the absolute structure settlement in case 1S23 with drains is almost the same as that in case 1S00 without drains and significantly larger than that of the ground (Figure 2(b)(j)). This suggests that the installation of drainpipes around a structure be effective for reducing tilting angle but ineffective for reducing absolute settlement of the structure.

3.2 Effects of groundwater table on tilting and settlement of structures

Figure 3 shows the relationship between the groundwater table and the absolute settlements of both structure and ground surface for all cases after the dissipation of excess pore water pressures developed in the ground. Triangle symbols standing for the absolute settlements of the ground surface, suggest that the ground settlement is 150-170mm regardless of the groundwater table. The absolute settlement of structures decreases and approximates the order of the ground settlement with lowering groundwater table.

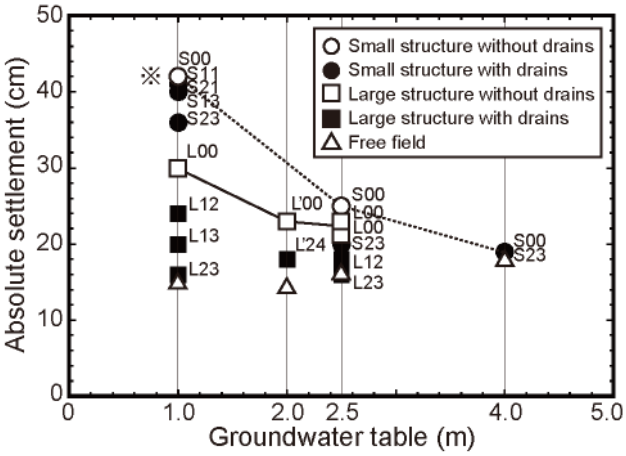


Figure 3 Relation of groundwater table with absolute settlement

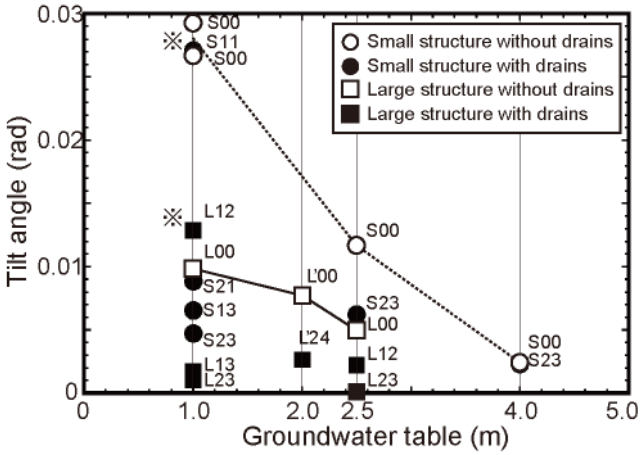


Figure 4 Relation of groundwater table with tilting angle

For example, in the case with the groundwater table of 4.0m, the settlement of structures with and without drains becomes almost equal to the ground settlement. This confirms that the dewatering is effective for reducing relative settlement of structure. Figure 3 shows that the absolute settlement tends to be larger in small structures (S) than in large structures (L). The difference in plan dimension might have affected the liquefaction degree of the soil below the structure and resulted in the different settlement between the two cases. Figure 3 also shows that the absolute structure settlements are almost the same regardless of the presence of drainpipes if their groundwater tables are the same. This confirms the finding in the previous section that the installation of drainpipes around a structure is ineffective for reducing absolute settlement of the structure.

Figure 4 shows the relationship between the groundwater table and the tilt angle of structure for all cases after the dissipation of excess pore water pressures. There is a strong trend in which the tilting angle of structure decreases with lowering groundwater table and becomes almost zero at 4.0 m regardless of the presence of drainpipes (cases 4S23 and 4S00). This claims that dewatering could be an effective method for reducing liquefaction-induced tilting of existing houses. There is another strong trend in which the tilting angle of the structure becomes significantly smaller when drainpipes are installed. However, the tilt angle of structures with drains varies from case to case, i.e., it becomes smaller with increasing drainpipe diameter and/or with decreasing drainpipe spacing.

3.3 Factor influencing tilt angle of structures

To estimate effects of spacing and diameter of drains on tilt of structures, normalized diameter is defined as a ratio between diameter, d, and spacing, D, of the drainpipes installed around a structure. It is assumed that d/D is zero in the case without drainpipes. Figure 5 shows the titling angle for the cases with the groundwater table of 1.0m with respect to the normalized diameter (d/D). There is a strong trend in which the tilt angle increases with decreasing the normalized diameter (d/D), suggesting the effects of drainpipes on reducing tilting of structures. Figure 6 shows the excess pore water pressure ratio at a depth of 2.5m below the edge of the footing with respect to the normalized diameter (d/D). The excess pore water pressure ratio increases with decreasing the normalized diameter (d/D), suggesting that both drainpipe diameter and spacing might have contributed to reduce the excess pore water pressure generation. Figure 7 shows the tilt angle of structures with respect to the excess pore water pressure ratio. As might be expected, the tilt angle of structures decreases with decreasing excess pore water pressure ratio.

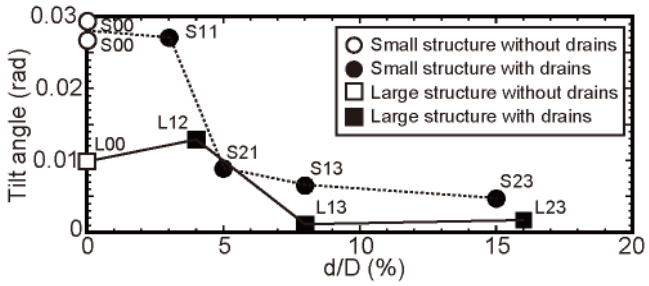


Figure 5 Relation of normalized diameter with tilting angle

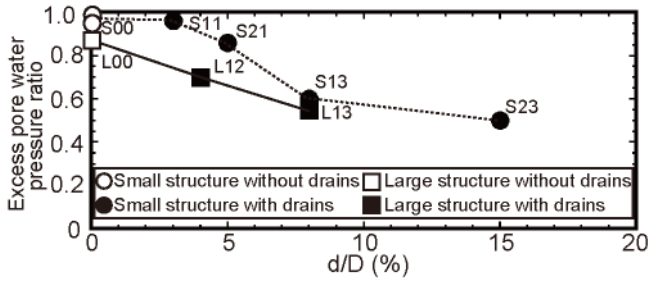


Figure 6 Relation of normalized diameter with excess pore water pressure ration

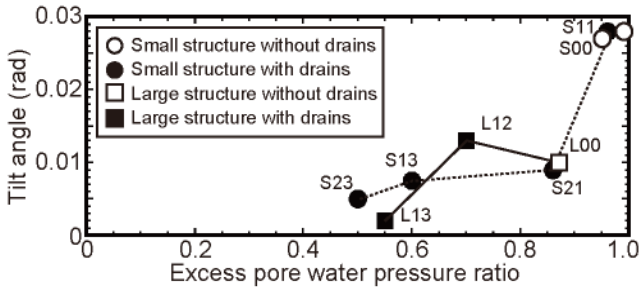


Figure 7 Relation of excess pore water pressure ratio with tilting angle

3.4 Estimation of safety factors against tilting

To estimate how the tilting and settlement of structures occur, equilibrium of load and moment acting on structures is examined. Figure 8 shows the failure conditions of a structure found on a non-liquefiable layer having a thickness of H, which overlies a liquefied layer with drainpipes. Assuming that only the shear force of the soil above the groundwater table can act against the weight of and the overturning moment from the structure in cases without drains but that the remaining effective stress in cases with drainpipes can resist the driving force and moment to some extent. The factor of safety with respect to vertical force equilibrium, F_{SW}, may be therefore given by:

$$F_{SW} = \frac{R_W}{L_W} \tag{1}$$

in which R_W is the resistant force from the ground and L_W is the entire weight of the structure, defined as:

$$R_W = 2\left(K\frac{H^2}{2}\gamma\tan\phi\right)(B+L) + \sum_{i=1}^{n}\int\sigma'_i dA \tag{2}$$

F_{s1}: Resultant force of shear stress in cross plan against shaking direction
F_{s2}: Resultant force of shear stress in horizontal plan against shaking direction
F_p: Resultant force of effective stress

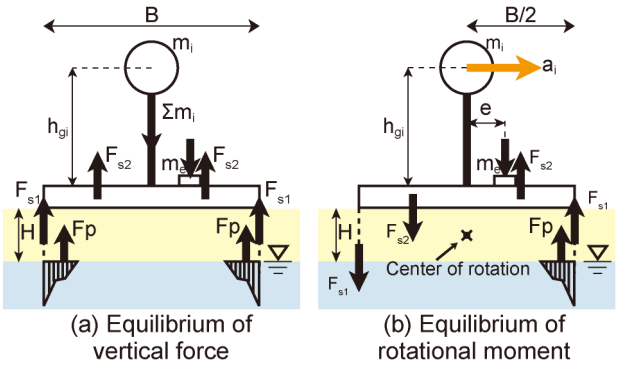


Figure 8 Equilibrium of vertical force and rotational moment

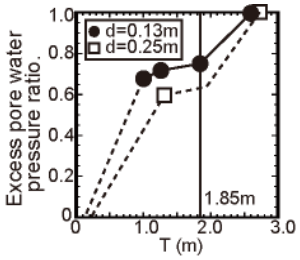


Figure 9 Excess pore water pressure ratio with distance from sensors

$$L_W = (m_1 + m_2 + m_e)g \tag{3}$$

in which K is the coefficient of earth pressure, γ is unit weight of non-liquefiable soil, H is the height of the surface layer above the groundwater table, ϕ is internal friction angle of the non-liquefied soil, B is the width of structure, L is the length of structure, n is the number of drainpipes, A is the area located within the effective radius of drains and below the footing, σ'_i is the effective stress of the soil within an effective radius of drains; and m_1, m_2 and m_e are masses of superstructure, foundation and additional eccentric mass added on the foundation, respectively; and g is gravity acceleration.

The safety factor with respect to moment equilibrium, F_{SM}, may be given by:

$$F_{SM} = \frac{R_M}{L_M} \tag{4}$$

in which R_M is the resistant moment, L_M is the overturning moment from structures, defined as:

$$R_M = \left(K\frac{H^2}{2}\gamma\tan\phi\right)\left(\frac{B}{2}+L\right)B + \sum_{i=1}^{n/2} l_i\int\sigma'_i dA \tag{5}$$

$$L_M = m_1 a_1 h_{g1} + m_2 a_2 h_{g2} + m_e g e \tag{6}$$

in which, l_i is a distance of drainpipes from the center, a_1 and a_2 are accelerations of superstructure and footing, h_{g1} and h_{g2} are heights of gravity of center of

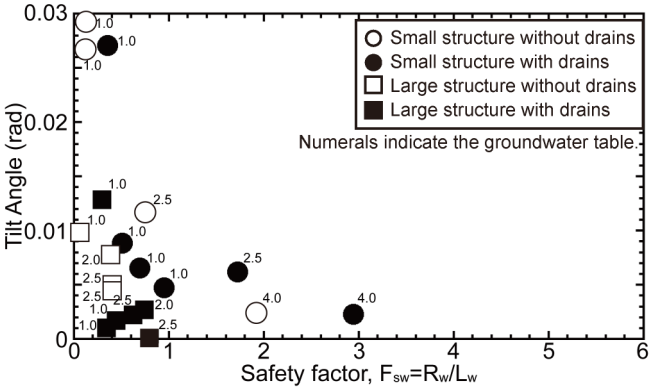


Figure 10 Relation of tilting angle with safety factor, F_{SW}

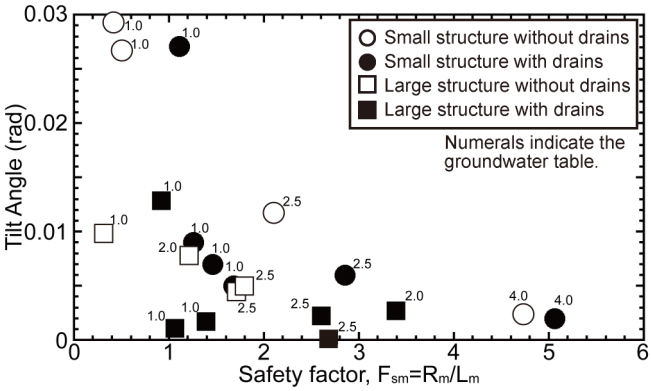


Figure 11 Relation of tilting angle with safety factor, F_{SM}

superstructure and footing, and *e* is eccentric distance of eccentric mass.

Figure 9 shows the maximum pore water pressure ratio plotted at the distance from the center of the nearest drainpipe. As expected, the pore water pressure ratio decreases with decreasing distance from the drainpipe. The trend is more significant for the drainpipes with a larger diameter. It is assumed that the effective radius is 1.85 m and the effective stresses within the effective radius are those shown in Figure 9.

Figure 10 shows the relationship between factor of safety factor with respect to force equilibrium and tilting angle of structures. The tilting angle of structures generally decreases with increases factor of safety; however, it seems that the trend is somewhat different depending the plan dimension of the footing. Figure 11 shows the relationship between factor of safety with respect to moment equilibrium and tilting angle of structures. Although F_{SM}=1 may not be a good boundary separating damaged from undamaged structures, there seems a fairly well defined trend in which the tilting angle of structures decreases with increasing factor of safety regardless of the plan dimension of foundations. This suggests that the dynamic overturning moment might have significant effects on the tilting angle of structures.

4. Conclusions

A series of centrifuge shaking table tests were conducted, in which drainpipes were installed around a house with its diameter and spacing as well as groundwater table being varied. On the basis of the result, the following conclusions may tentatively be made:

1) The absolute and relative settlements as well as tilting angle of structures can decrease with lowering groundwater table. When it is lowered at a depth of 4m, the absolute settlement approximately becomes equal to the ground settlement, but both relative settlement and tilting angle of structures become almost zero. This claims that dewatering could be an effective method for reducing liquefaction-induced damage to existing houses.

2) Although the absolute settlement of structures may not be reduced by drain method, both relative settlement and tilting angle of structures can decrease with increasing drainpipe diameter and with decreasing spacing between drainpipes. This suggests that the installation of drainpipes around a structure in an appropriate manner is promising.

3) The tilting angle of structures founded on liquefiable soils decreases with increasing factor of safety with respect to the moment equilibrium, in which both dewatering and drainage effects are taken into account. This suggests that the dynamic overturning moment might have significant effects on the tilting of structures founded on liquefiable soils.

References:

Architectural Institute of Japan (2011), "Preliminary reconnaissance report of the 2011 Tohoku-Chiho Taiheiyo-Oki Earthquake" (in Japanese).

Suzuki, Y., Tokimatsu, K., Hidekawa, T. and Adachi, N. (2013), "Effects of drainage and dewatering on differential settlement of wooden houses founded on liquefiable soils", Proc. of 10th International Conference on Urban Earthquake Engineering.

Tokimatsu, K., Tamura, S., Suzuki, H. and Katsumata, K. (2012), "Building damage associated with geotechnical problems in the 2011 Tohoku Pacific Earthquake", Soils and Foundations, Vol. 52, No. 5.

10CUEE CONFERENCE PROCEEDINGS
10th International Conference on Urban Earthquake Engineering
March 1-2, 2013, Tokyo Institute of Technology, Tokyo, Japan

BASIC PHYSICAL MODEL TEST ON SEISMIC PERFORMANCE OF FILL INDUCED BY SUFFUSION

Kazuki Horikoshi[1], Lin Ke[1], and Akihiro Takahashi[2]

1) Graduate Student, Department of Civil Engineering,, Tokyo Institute of Technology, Japan
2) Associate Professor, Department of Civil Engineering, Tokyo Institute of Technology, Japan
horikoshi.k.aa@m.titech.ac.jp, ke.l.aa@m.titech.ac.jp, takihiro@cv.titech.ac.jp

Abstract: Suffusion is a potential risk for the long-term stability of the hydraulic structure, such as dams and levees. Suffusion is transport or migration of fine fractions inside the void of coarse skeleton. When suffusion occurs, the hydraulic and mechanical characteristics of soil are altered. In addition, suffusion has implications with valley fill in catchment topography as well as hydraulic structure. If the suffusion occurs and soil skeleton is intact in spite of fine fractions are eroded by seepage flow, the soil structure is probably unstable due to evolution of loose zone under phreatic surface. In this situation, soil structure is more vulnerable to large-scale earthquake.
For this reason, we performed a series of seepage tests on the small-scaled levees, followed by bearing capacity tests on levees. In this paper, extent of erosion-induced deterioration of shearing resistance of levee against external load is discussed through comparisons of bearing capacity at top of the slope before and after the suffusion. As a result, we noted out that suffusion has the potential to change the seismic stability of soil structure depending on the amount of eroded fine fraction and distribution of the fine fraction in the structure.

1. INTRODUCTION

The 2007 Noto Hanto Earthquake caused significant damages of fills built on catchment topography. In recent earthquakes, such as the 2011 off the Pacific coast of Tohoku Earthquake, in the mountain area, vulnerability of valley fills have been underscored. The reasons why fills damage concentrated on catchment topography are that the water table is typically high and major part of the fill is saturated. Moreover, the strong ground motion caused pore pressure increase, so that shear resistance of embankment decrease. However, poor quality fills, which are constantly high water table, are subject to suffusion, which is transport or migration of fine particles inside the void of coarse skeleton. This phenomenon is also expected one of the reason of collapse of fills. Foster and Spanngle (2000) reported that 46% of dams' failure or damage is related to internal erosion. Internal erosion (suffusion is one of the modes of the internal erosion) is one of the major causes of failure or damage of fill dams. Kenney and Lau (1985) developed index using grain size distribution appertains to internal stability of filter fill dam. Several elemental experiments result broadly confirmed this criterion by using well graded and gap-graded sand gravel soils (e.g. Skempton and Brogan 1994, Kokusho and Fujikura 2008). Skempton and Brogan (1994) also expressed internally unstable soils categorized by Kenny's criterion has significantly lower critical hydraulic gradient than well-known Terzaghi's theory. Kokusho and Fujikura (2008) approached how to determination of seepage failure mode by using Kenney's criterion and coefficient of uniformity Cu. Recent studies of suffusion have suggested the phenomenon is affected by fine fraction content, hydraulic gradient and confining pressure (Bendahmane *et al.* 2008, Moffat *et al.* 2011). Furthermore, much research are carried out about change of hydraulic characteristics of soil structure. Sterpi (2003) established an empirical equation governing internal erosion. Fujisawa *et al.* (2010), Cividini and Goida (2004), Cividini *et al.* (2009) simulated the internal erosion model through numerical analyses. However, these experimental and numerical approaches considered adsorption of erosion particle, but do not considered stability as exemplified by seismic performance of fills induced by internal erosion, such as suffusion.

If the suffusion occurs and soil skeleton is intact in spite of fine fractions are eroded by seepage flow, the soil structure is inferred unstable due to evolution of loose zone under phreatic surface. In this situation, soil structure is more vulnerable to large-scale earthquake. To address this issue, a series of seepage tests were conducted on the small-scaled levees, followed by bearing capacity tests on levees. In this paper, extent of erosion-induced deterioration of seismic performance of levee against external load is discussed through comparisons of bearing capacity at top of the slope before and after the suffusion.

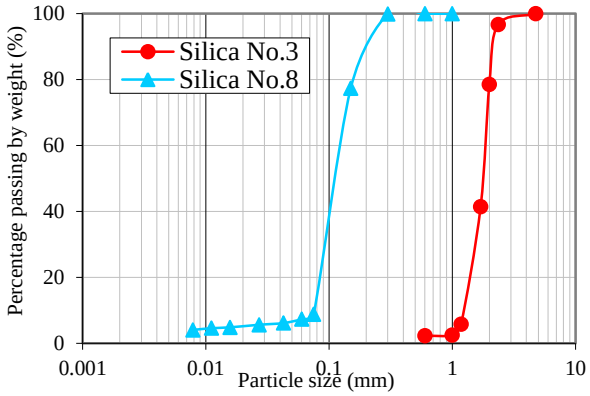


Figure 1 Grain size distribution curves of Silica sand

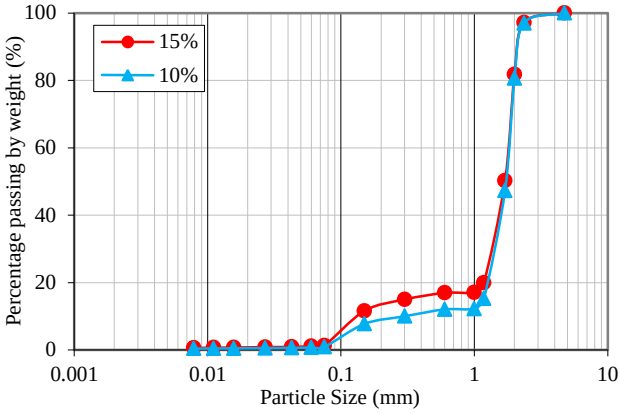


Figure 2 Grain size distribution curves of mixtures

Table 1 Basic properties of Silica sand

Property	Silica No.3	Silica No.8
Median grain sizeD_{50} (mm)	1.72	0.16
Effective grain size D_{10} (mm)	1.37	0.087
Uniformity Coefficient C_u	1.29	2.09
Curvature Coefficient C_c	0.99	2.34
Maximum void ratio (e_{max})	1.009	1.333
Minimum void ratio (e_{min})	0.697	0.703

Table 2: Basic properties of mixtures

Fine content of mature (%)	15%	10%
Median grain size D_{50} (mm)	1.77	1.73
Effective grain size D_{10} (mm)	0.27	0.25
Uniformity Coefficient C_u	15.5	18.0
Specific gravity	2.63	2.63
Maximum void ratio, e_{max}	0.678	0.704
Minimum void ratio, e_{min}	0.505	0.543
Void ratio range (e_{max}- e_{min})	0.173	0.161

2. EXPERIMENTAL DEVICE

2.1 Soil materials

To simplify the phenomenon, mixtures of fine and coarse fractions are used for the model slopes. Furthermore by using the cohesionless coarser soil than the prototype embankment material, phenomenon can also be macroscopically observed and occur in a short time. For this reason, the Silica No. 3 and Silica No.8 sands are used as model materials. The grain size distribution curves of each Silica sand and basic properties of the materials are summarized in Fig. 1 and Table 1. Silica No. 3 sand models soil skeleton, while Silica No.8 sand is used as the erodible fine particles, in the void of the coarse skeleton. Silica No. 8 sand is not categorized as fine fraction in the Japanese Industrial Standards. However, in this research, Silica No. 8 is considered as fine fraction because the grain size is relatively finer than Silica No. 3 sand that forms the soil skeleton. The chosen fine fractions of mixture are 10 %, 15 %. The grain size distribution curves of mixtures and basic properties of each mixtured material are shown in Fig. 2 and Table 2, respectively. According to Kenney's criterion which expresses internal stability of filter all the mixtures are internally unstable.

2.2 Experimental apparatus and procedure

Side view of the experimental system is schematically illustrated in Fig. 3. The steel box with inner dimensions of 450 mm (length) × 150 mm (width) × 350 mm (height). The embankment model is made in this box. The box has two tanks at both sides, named "water supply tank" and "drainage tank", respectively. Vertical sidewalls between the drainage tank and embankment model provide a metal gauze so that only water and fine fraction can flow through. By pouring the water in water supply tank, seepage flow in model ground could be realized. From the running off seepage water and sediment from toe of slope to drainage tank, the fine fraction was collected by sieve of size 0.075mm. Here, the effect of particles smaller than 0.075mm was not considered due to the very small amount. To prevent material separation during preparation of the model embankment, partially saturated soil is used. Water contents of model ground with fine fraction content of 10%, 15% area are 2%, 3%, respectively. The sand is compacted layer by layer with 20mm thickness. Then, the model ground is scraped off with a shaped frame and formed to be a 230.5mm high model embankment. The model embankment was composed of two areas, "Base zone" and "Slope zone". The Base zone is the 50mm-thick horizontal layer and the Slope zone is the embankment with the slope of 1 : 1.8. The target density is the minimum density of each mixture. Boundary condition at the upstream side is constant head

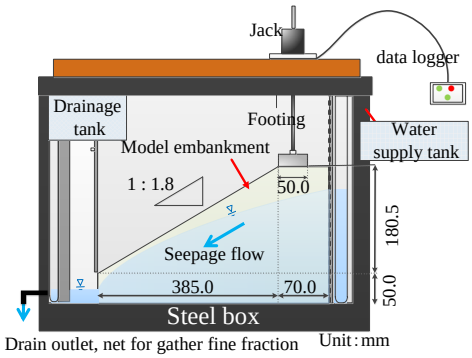


Figure 3 Side view of experimental model and Setting for bearing capacity test

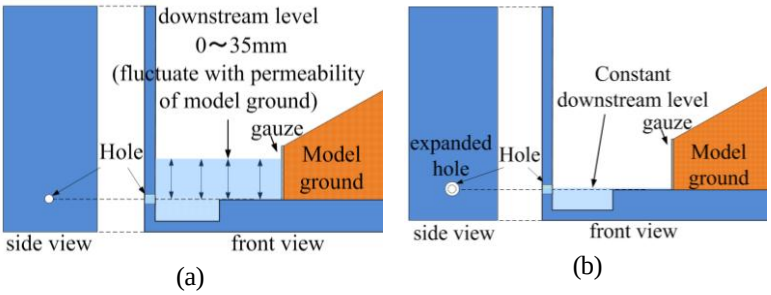


Figure 4 Boundary condition at the downstream site
(a) Type A (Case10%H-A), (b) Type B (Case10,15%H-B)

Table 3 Test cases

Case		Content of Silica sand No. 8 (%)	Boundary condition of toe of slope	Loading location	Loading speed (mm/min)	Dry density (g/cm^3)	Seepage time (min)
10%-A	Initial	10	A	top of slope	62.50	1.535	30
	10140					1.535	10140
10%-B	Initial	10	B	20mm from the edge of a slope	11.75	1.549	30
	5760					1.554	5760
	22850					1.544	22850
15%-B	Initial	15	B	20mm from the edge of a slope	11.75	1.551	30
	20670					1.558	20670

(172mm). Boundary condition at the downstream side has two patterns: In Type A, the water level is set at a height of 35mm from the bottom, while it is set at the bottom in Type B. Since the size of the outlet for Type A is small, the water level can change (initial height is 0mm, maximum height, approximately, 35mm) if flow rate exceeds threshold value (approx.3000ml/min). Boundary condition at the downstream site of each type is schematically illustrated in Fig. 4.

In this study, three series of bearing capacity test on spatially-eroded soil structure by suffusion are conducted to discuss a destabilization of fill at each degradation stage after seepage test as shown in Table 3. For comparison, bearing capacity tests at initial state are also conducted. Within the scope of this study, at the beginning of the seepage test, position of the phreatic surface and unsaturated zone does not change much depending on the material used. Temporal position change of phreatic surface was estimated based on the visual observation using photographic images. During the loading test, seepage flow of the model ground has been kept constant.

Figure 3 also shows the schematic illustration of the case in which the installation location of model footing is top of slope and 20mm from the edge of a slope. The model footing made of duralumin (50mm in width, 150mm in breadth) whose bottom was roughened by attaching a sand paper is used. The loading device consists of a 50kN capacity actuator and an H-beam frame which is firmly bolted on the web of the steel box. Vertical load is measured by a load cell of 50kN capacity attached to the loading rod. The model footing is loaded at the rate of 62.5mm/min or 11.75mm/min until the failure occurs. A digital video camera in front of the side wall of the steel box is used for monitoring of the ground movement.

After the experiments, the grain size analyses for each part of model embankment were conducted to confirm position of distribution of fine fraction.

3. RESULT AND DISCUSSIONS

In Case 10%-A, 15.1% of the fine fraction was eroded by seepage test which was done before bearing capacity test on top of slope. On the other hand, in Cases 10%-B and, 15%-B, 5.3% and 5.4% of the fine fraction was eroded, respectively. The grain size analysis for each part of embankment after the experiments as shown in Table 4. The value of fine fraction content is relatively small in the upstream side (distance from the toe: 289-385 mm) due to

Table 4 Condition fine fraction content distribution before bearing capacity test

Case	Initial state	Distance from the slope toe (mm)			
		0-96	96-193	193-289	289-385
10%-A	9.94	7.69	10.82	10.46	5.22
10%-B	9.98	8.91	10.28	11.46	8.99
15%-B	15.03	12.91	16.03	16.01	11.93

no supply of fine particles from the upper stream side.

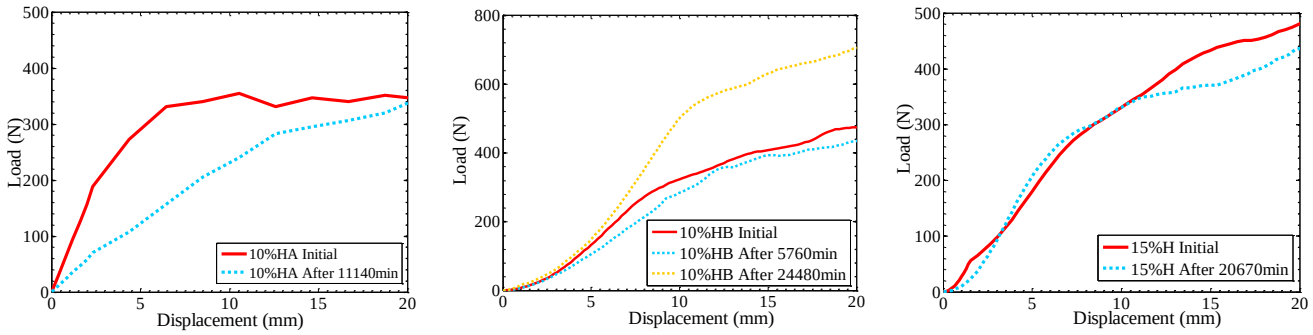
Figure 5 shows the load-displacement curves before and after the seepage tests for Cases 10%-A, 10%-B and Case 15%-B, respectively. In Case 10%-A where cross-sectional area of the drainage boundary becomes large with increase of flow rate, relatively large amount of fine fraction is internally washed out due to seepage flow. Owing to suffusion, failure mode of the slope is general shear failure and the peak appears in the load-settlement curve, while the slope exhibited local shear failure and no clear peak is seen in the curve after 10140 min (Fig. 5(a)). In the latter, 15 % of the fine fraction was eroded by seepage test. In the former, the slip surface appeared around the phreatic surface (Fig. 6(a)), while the large deformation zone was extended well below the phreatic surface due to the suffusion-induced strength reduction of the soil in the latter. As a result of the strength reduction of the soil, decrease in the bearing capacity was observed for the embankment with suffusion. This indirectly suggests decrease of seismic performance.

In Cases 10%-B and, 15%-B, amount of fine fraction loss is small due to the difference in the hydraulic boundary condition around the toe as shown in Fig. 4. In these cases, no clear difference in failure mode before and after suffusion is observed. Decrease in the bearing capacity is not observed after suffusion in these cases as shown in Fig. 5 (b) and 5 (c). Location of the slip surface are also observed little to change Fig. 6 (b) and 6 (c). The result of case of rinsed in water 24480 min in Fig. 5 (b) indicate larger bearing capacity than initial state. This fact indicates that the suffusion does not necessarily cause the strength reduction of the soil and the bearing capacity of the embankment. These can either increase or decrease depending on amount of eroded soil of the seepage flow, i.e., progress of the internal erosion.

4. CONCLUSIONS

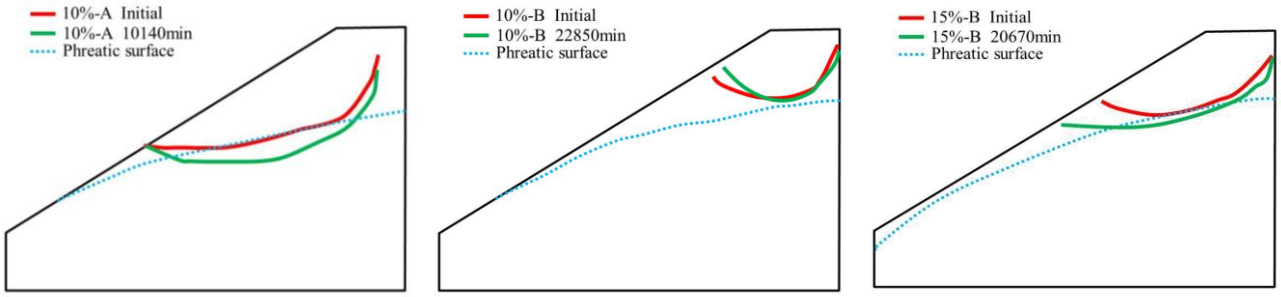
In this paper, extent of erosion-induced deterioration of seismic performance of levee against external load is discussed through comparisons of bearing capacity at top of the slope before and after the suffusion.

By considering effects of amount of fine fraction and hydraulic boundary condition on soil erodibility, the suffusion-induced destabilization of the embankment is examined and the following conclusions are drawn:



(a) Case10%A-H (b) Case10%B-H (c) Case15%B-H

Figure 5 Result of bearing capacity tests



(a) Case10%A-H (b) Case10%B-H (c) Case15%B-H

Figure 6 Comparison slip surface between before and after the suffusion

Suffusion can change the stability (e.g. seismic performance) of soil structure depending on the amount of eroded fine fraction and distribution of the fine fraction in the structure. When relatively large amount of fine fraction is eroded, the soil structure can be destabilized. Note, these facts indicate that the suffusion does not necessarily cause the strength reduction. Therefore, this result needs to be tested one step further by conducting some parametric experiments.

References:

Bendahmane, F., Marot, D., and Alexis, A. (2008), "Experimental parametric study of suffusion and backward erosion," *Journal of Geotechnical. and Geoenvironmental. Engineering,"* **134**(57), 57-67.

Cividini, A. Gioda, G. (2004), "Finite-element approach to the erosion and transport of fine particles in granular soils," *International Journal Geomechanics*, **4**(3), 191-198.

Cividini, A., Bonomi, S., Giulio, C.V., and Gioda, G. (2009), "Seepage-induced erosion in granular soil and consequent settlements," *International Journal Geomechanics*, **9**(4), 187-194.

Foster, M.R. and Spanngle, M. (2000), "The statistics of embankment dam failures and accidents," *Canadian Geotechnical Journal*, **37**(5), 1000-1024.

Fujisawa, K., Murakami, A., & Nishimura, S. (2010), "Numerical analysis of the erosion and the transport of fine particles within soils leading to the piping phenomenon," *Soils and Foundations*, **50**(4), 471-482.

Kenny, T.C. and Lau, D. (1985), "Internal stability of granular filters," *Canadian Geotechnical Journal*, **22**(2): 215-225.

Kokusho, T. and Fujikura, Y. (2008), "Effect of particle gradation on seepage failure in granular soils," 4th *International Conference on Scour and Erosion, Tokyo, Japan*, 497-504.

Moffat, R. Fannin, R.J. and Garner, S.J. (2011), "Spatial and temporal progression of internal erosion in cohesionless soil," *Canadian Geotechnical Journal*, **48**(3), 399-412.

Skempton A.W. and Brogan J. (1994), "Experiments on piping in sandy gravels," *Geotechnique*, **44**(3), 440–460.

Sterpi, D. (2003), "Effects of the erosion and transport of fine particles due to seepage flow," *International Journal Geomechanics*, **3**(2), 191-198.

10CUEE CONFERENCE PROCEEDINGS
10th International Conference on Urban Earthquake Engineering
March 1-2, 2013, Tokyo Institute of Technology, Tokyo, Japan

CRITERIA FOR DETERMINING G_{MAX} IN LABORATORY ELEMENT TESTS USING DISK TYPE PIEZOELECTRIC TRANSDUCERS

Muhammad Irfan[1], and Taro Uchimura[2]

1) PhD Candidate, Department of Civil Engineering, The University of Tokyo, Japan
2) Associate Professor, Department of Civil Engineering, The University of Tokyo, Japan
mirfan1@msn.com, uchimura@civil.t.u-tokyo.ac.jp

Abstract: Correct determination of shear wave velocity is pivotal in reliable estimation of small strain shear modulus (G_{max}). Discussed herein is the determination of small strain shear modulus (G_{max}) in triaxial tests using disk type piezoelectric transducers. A laboratory investigation for the measurement of shear wave velocity was carried out to examine the effects of electromagnetic coupling (crosstalk), shape of input waveform, excitation frequency, and isotropic confining pressure on measurement of shear wave travel time. The evaluation showed that the distortion of shear wave signals caused by electromagnetic coupling between source and receiver can effectively be removed by proper grounding of transmitter and receiver disk transducers. Using sinusoidal input waveform and increasing the number of wavelengths between source and transmitter was observed to diminish near field effects and improve the reliability of shear wave travel time determination.

1. INTRODUCTION

The small strain shear modulus of soil, G_{max}, is a fundamental parameter in several static and dynamic analyses involving deformational calculations (Jardine, 1986; Richart et al., 1970). It provides valuable soil information relevant to various engineering applications including liquefaction assessment, foundations subjected to dynamic loading, and soil improvement control, etc. The value of G_{max} is commonly determined by well-established laboratory experimental techniques such as resonant column, and cyclic torsional shear tests. Besides, determination of G_{max} by using elastic wave propagation velocity in soil is gaining popularity due to its procedural simplicity. In such tests, an elastic shear wave generated by a piezoelectric transducer located at one end of a confined soil specimen is received by another piezoelectric transducer located at the other end of soil specimen. The travel time of elastic wave between the source and transmitter, t, and travel distance, L, are used to compute the wave propagation velocity defined as;

$$V = L/t \tag{1}$$

After determining the shear wave velocity by using the above mentioned expression, small strain shear modulus, G_{max}, can be determined by using the relationship from elastic continuum mechanics;

$$G_{max} = \rho V_S^2 \tag{2}$$

where, Vs is the shear wave velocity, and ρ is the total mass density of soil specimen.

The correct determination of shear wave velocity is therefore critical in reliable estimation of G_{max}. Although there is considerable agreement among researchers to use tip-to-tip distance between transmitter and receiver bender element for determination of Vs (Dyvik & Madshus, 1985; Leong et al., 2005; Viggiani & Atkinson, 1995); there is however no consensus on the shape of excitation waveform, and determination of first arrival of shear wave. The intent of this paper is to discuss the determination of correct shear wave arrival time by using a flat-shaped disk transducer. Ambiguities involved in the determination of correct arrival time due to electromagnetic coupling, shape of input waveform, and near-field effect are discussed hereinafter.

2. EXPERIMENTAL SETUP

Disk type piezoelectric ceramic plates manufactured by

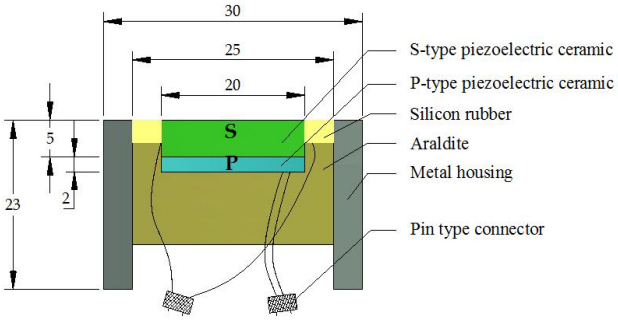


Figure 1: Schematic diagram of disk transducer.

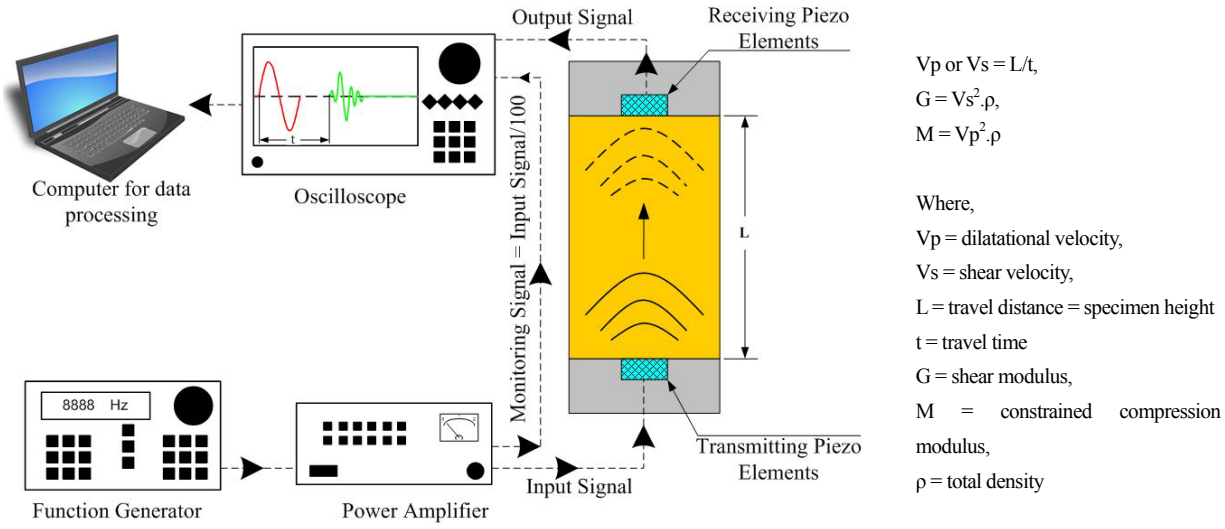


Figure 2: Schematic configuration of disk type piezoelectric ceramic transducers and associated electronics.

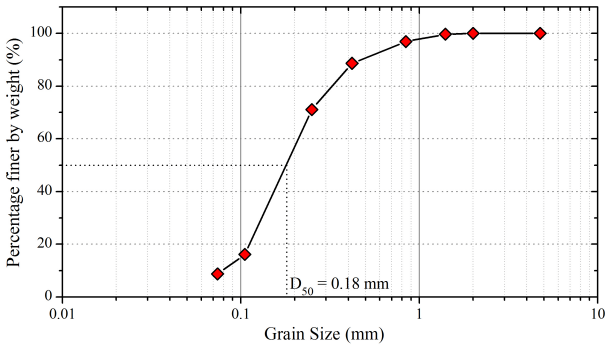


Figure 3: Edosaki sand – particle size analysis.

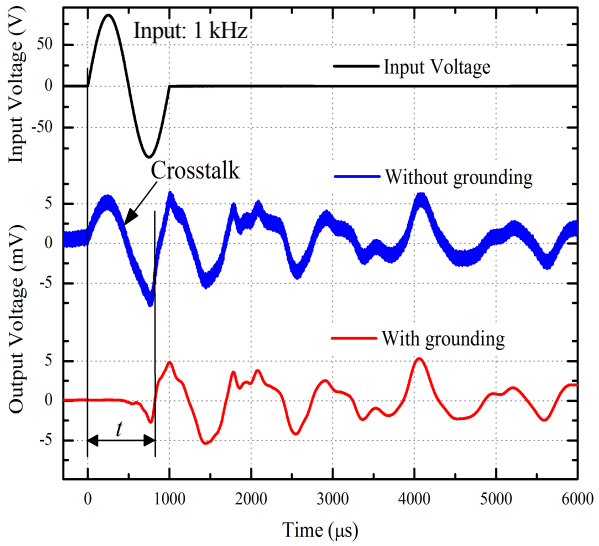


Figure 4: Crosstalk affecting shear wave receiver signals in Edosaki sand at isotropic confining stress of 150 kPa.

Fuji ceramics corp. were employed in this study. The ceramic disks ware 20 mm in diameter with a thickness of 2 mm and 5 mm for P and S type respectively. Both P and S type disks were bonded together with araldite (a two-component epoxy glue) and were encapsulated in a metal housing. Space in the top of metal housing was filled with silicon rubber to make the transducer more ductile and to allow easy movement of transducer. A thin layer of araldite was also coated on the surface of transducer to protect it against direct exposure of testing material and also to make it waterproof. Figure 1 shows schematic representation of disk transducer used for this study. The metal housing supporting the disk transducer was then fixed at the center of triaxial cell base pedestal by means of an O-ring.

The transmission system to excite the transmitter disk transducer consisted of function generator (Tektronix, AFG3022B) and power amplifier (NF Corp. model HSA4012). The function generator produced an excitation voltage of 4.5 *Vpp* (*Vpp = peak-to-peak voltage*) which was amplified to 90 *Vpp* by power amplifier and applied to the transmitter disk transducer. The excitation voltage was limited to 90 *Vpp* in order to avoid deterioration of piezoelectric elements due depolarization. The receiving system consists of a digital oscilloscope (HIOKI model 8860 with Hioki 8957 high resolution input module). The wave transmitted through the soil specimen was received at the top cap by receiver disk transducer which transferred the signal to oscilloscope to be digitally displayed. Input signal from the power amplifier was fed to the oscilloscope through a monitoring channel. The digital oscilloscope thus records both the input and output signals simultaneously. A schematic diagram of measurement system is show in Fig. 2.

3. MATERIALS AND METHODOLOGY

Test material used for this study was Edosaki sand (natural sand with around 10% fines). Particle size distribution of Edosaki sand is shown in Fig. 3; and Table 1 summarizes its basic material properties. A 70% saturated

triaxial specimen (*height = 150 mm, diameter = 75 mm*) was prepared at an initial relative density of 87%. Isotropic confining pressure was increased from an initial value of 15 kPa to 300 kPa at a rate of 0.4 kPa/min. During this stress increment shear wave velocity readings were taken at 50 kPa, 100 kPa, 200 kPa and 300 kPa respectively. Courtesy nondestructive nature of the test, on a single specimen, several elastic wave measurement readings can be taken by varying fundamental parameters like input waveform, excitation frequency, applied voltage, isotropic stress level, etc.

Table 1: Basic properties of Edosaki sand.

Property	*Value*
Specific gravity, Gs	2.639
Minimum void ratio, e_{min}	0.647
Maximum void ratio, e_{max}	1.160
Fines (%)	9
Maximum dry density (g/cm^3)	1.762
Optimum moisture content (%)	14.6

4. CROSSTALK AND GROUNDING

Electromagnetic coupling between source and receiver piezoelectric transducer causes the deterioration of output signal in the form of an early component which is quasi-simultaneous with the input signal. This electromagnetic coupling, which is often referred as "crosstalk", can be very important in conductive soils such as wet clays on seafloor sediments (J. Lee & Santamarina, 2005). Crosstalk significantly affects the determination of correct arrival time when testing with low input frequencies, which are often required while studying nearly saturated sands. In such cases, deterioration of signal due to crosstalk masks the actual arrival of received signal. Figure 4 shows crosstalk deterioration in shear wave signals obtained in 70% saturated Edosaki sand specimen at isotropic confining

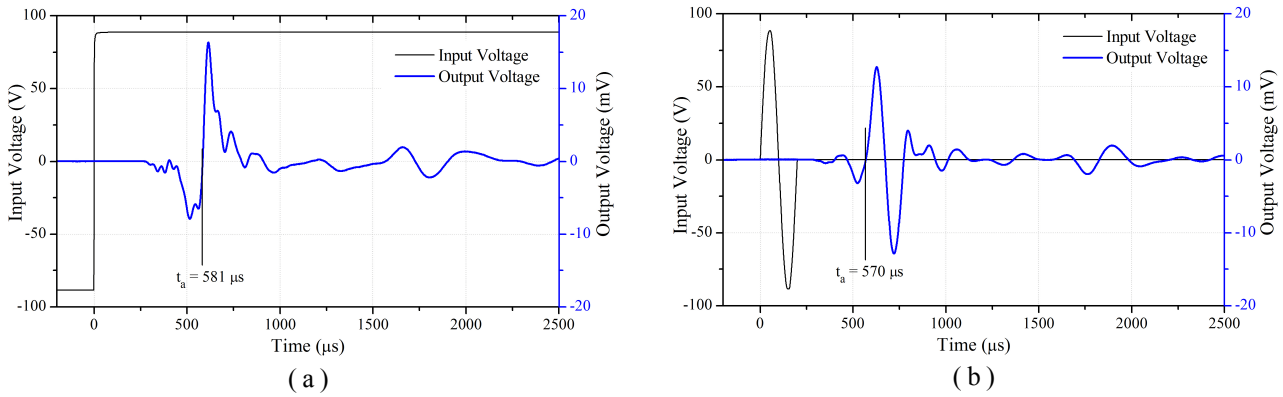


Figure 5: Effect of input waveform on receiver signals; (a) square pulse (b) sine pulse.

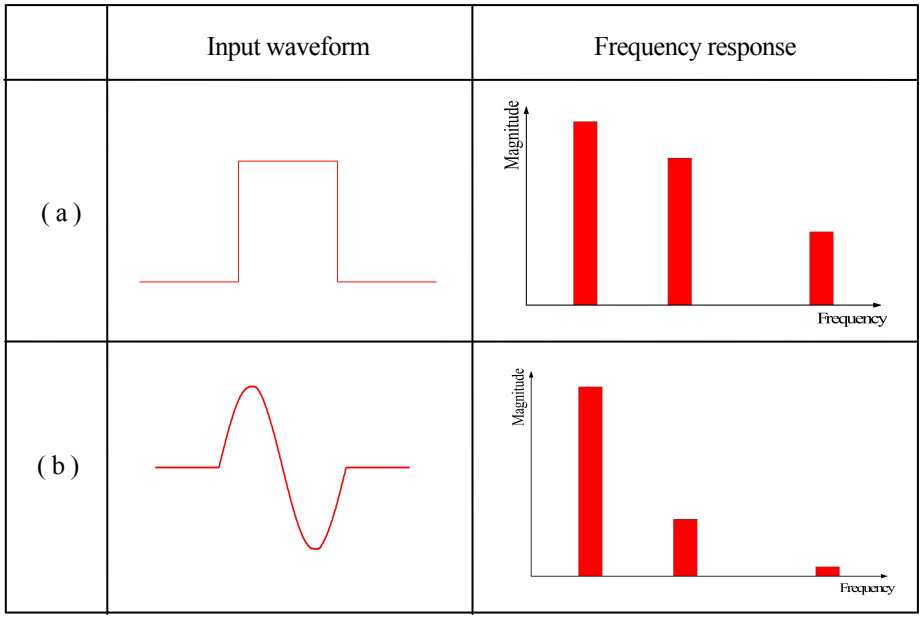


Figure 6: Frequency response of commonly used driving waveforms; (a) square pulse (b) sine pulse (after Blewett et al. (2000))

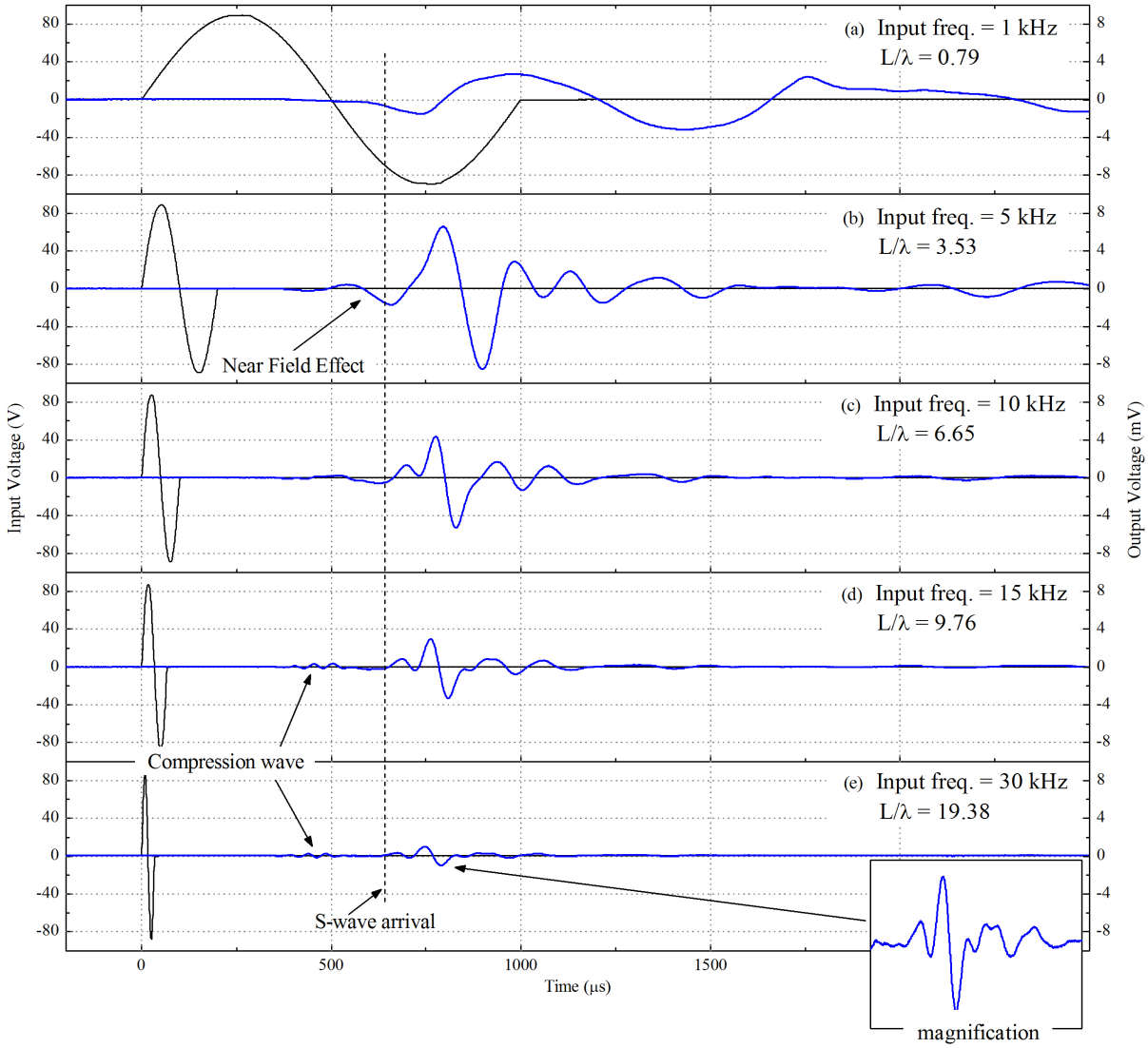


Figure 7: Effect of excitation frequency on shear wave receiver signals in Edosaki sand specimen at isotropic confining stress of 150 kPa; (a) f_{in} = 1 kHz; (b) f_{in} = 5 kHz; (c) f_{in} = 10 kHz; (d) f_{in} = 15 kHz; (e) f_{in} = 30 kHz.

pressure of 150 kPa. As the actual arrival point of received signal is masked by crosstalk, the first arrival would appear at a time later than the actual arrival time; consequently the computed wave velocity is lower than the actual value. Crosstalk in disk transducers is found to be removed by grounding the transmitter disk transducer. Received signal is also influenced by 50 Hz noise from commercial power supply, as can be observed from increased thickness of received signal in Fig. 4. Grounding the receiver disk transducer ensures removal of noise caused by commercial power supply. Both transmitter and receiver disk transducers are therefore, properly grounded in all subsequent tests conducted in this study.

5. INPUT WAVEFORM

Two types of input waveforms are commonly used by researchers; square (Bates, 1989; Dyvik & Madshus, 1985; Lohani et al., 1999; Rodríguez & Moreno-Carrizales, 2001), and sinusoidal (Blewett et al., 2000; C. J. Lee & Huang, 2007; Leong et al., 2005; Pennington et al., 2001; Viggiani & Atkinson, 1995). Response of both square and sinusoidal waves is evaluated in this study. Figure 5 shows receiver signals for square and sinusoidal wave in 70% saturated Edosaki sand specimen. In case of square input, more distortion was observed before the actual arrival causing greater ambiguity in determination of travel time (Fig. 5(a)). Also the received signal does not resemble the input signal; this observation is consistent with the observations made by Jovicic et al. (1996), Blewett et al. (2000), and Leong et al. (2005). High distortion for square wave input can be explained on the basis of large number of frequency components contained within it (Fig. 6(a)). Group velocity dispersion within the specimen leads to separation of different frequency components within the voltage-edge waveform. These propagate at different speeds, arriving at different times, and producing a severely distorted receiver waveform (Blewett et al., 2000). Conversely, sinusoidal wave input causes comparatively less distortion due to the presence of fewer frequency components (Fig. 6(b)).

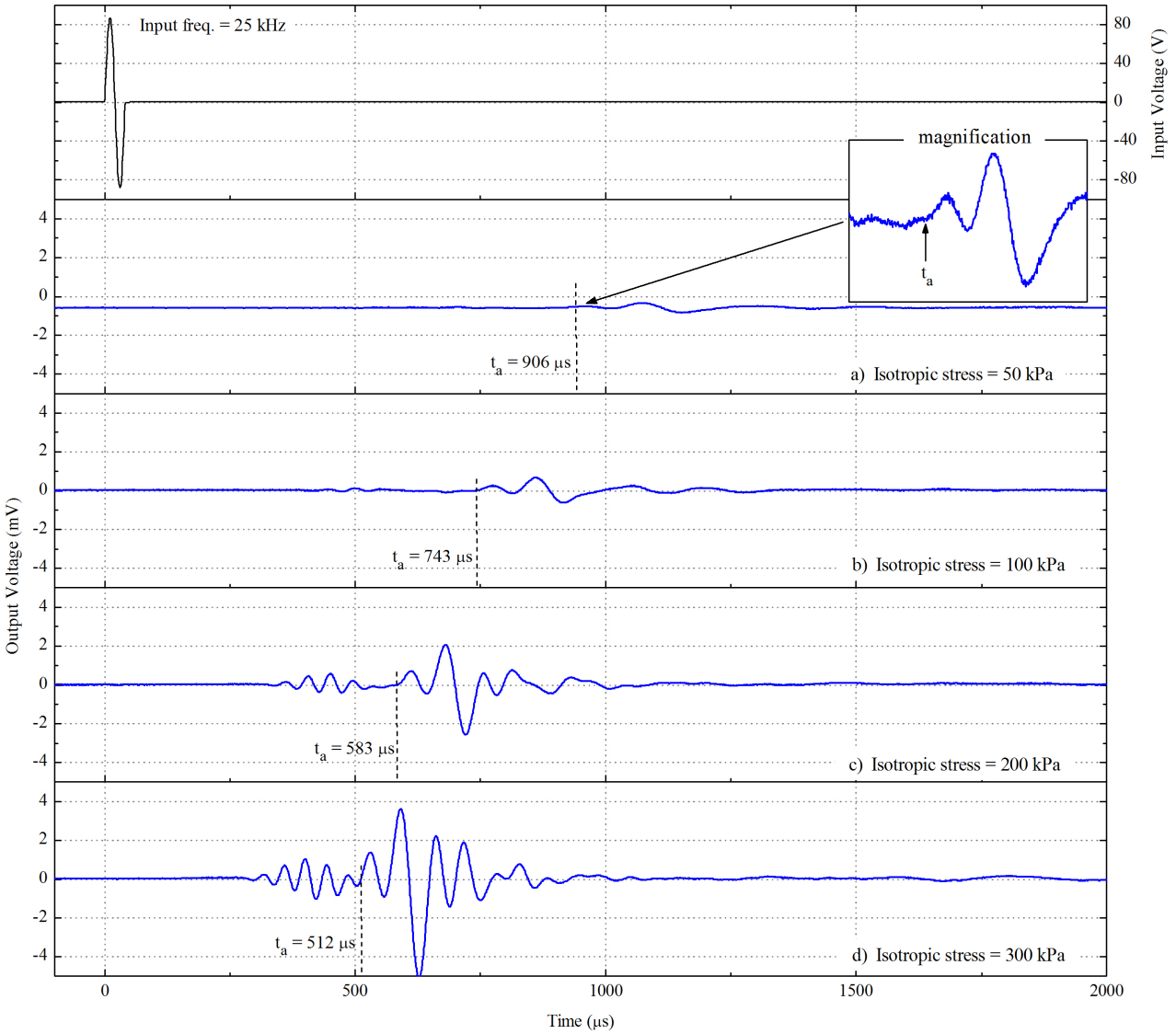


Figure 8: Effect of isotropic confining stress on shear wave receiver signals in Edosaki sand specimen; (a) Isotropic stress = 50 kPa; (b) Isotropic stress = 100 kPa; (c) Isotropic stress = 200 kPa; (d) Isotropic stress = 300 kPa.

Receiver signals for sinusoidal wave input resembled the input signal and less distortion observed at the beginning of signal, made travel time determination comparatively easy (Fig 5(b)). Sinusoidal input waveform is therefore, used for all subsequent tests in this study.

6. NEAR-FIELD EFFECT

During shear excitation, disk transducer, generates two P-wave side lobes parallel to its plane of vibration. These lobes are generated due to the compression effect associated with shear vibration. Difference in travel velocity prevents interference of shear and compression waves. However, test result of shear waves show some traces of distorted P-waves making the identification of first arrival ambiguous. Sanchez-Salinero et al. (1986) showed that the S-wave signal is always accompanied by propagation of another signal of opposite polarity travelling with the velocity of P-waves. This so-called "near-field" effect is quantified in terms of wave path length *(L)* to wavelength *(λ)* ratio. Inverting the polarity of input voltage does not help in removing near-field effect as by doing so the polarity of whole signal, including the near-field component is reversed (Mancuso & Vinale, 1988).

In this study, the effects of excitation frequency on shear wave receiver signals are evaluated by testing 70% saturated Edosaki sand triaxial specimen. Figure 7 shows typical test results of varying input frequency from 1 kHz to 30 kHz at isotropic confining pressure of 150 kPa. Maximum amplitude of shear wave signal is received at f_{in} = 5 kHz. J. Lee and Santamarina (2005) suggested that the excitation frequency of strongest signal gives the approximate resonant frequency of the system. The magnitude of near-field effect is found to decay considerably with increasing L/λ, i.e. number of wavelengths between transmitter and receiver (Fig. 7(a) to (e)). This observation is consistent with several other researchers including Sanchez-Salinero et al. (1986), Brignoli et al. (1996),

Arulnathan et al. (1998), and Leong et al. (2005), etc. Also, for sufficiently high excitation frequencies, the compression wave component can visibly be separated from shear wave as can be observed in Fig. 7 (d) and (e). However, increased wave attenuation (Fig. 7 (a) to (e)) and overshooting of signals (J. Lee & Santamarina, 2005; Wang et al., 2007) at high frequencies limits the maximum excitation frequency and hence the L/λ ratio.

Figure 8 shows the effect of stress level on received signals. A high excitation frequency of 25 kHz was used in order to minimize near-field effects. The number of particle contact points within the specimen increase with higher isotropic stress. It not only increases the shear wave velocity but also the amplitude of received signal. However, at higher isotropic stress the amplitude of compression wave component is also found to increase (Fig. 8 (c) & (d)). This strong compression wave component, having very low attenuation, thus interferes with shear wave signal, making it further difficult to distinguish the first arrival of shear wave (Fig. 8 (d)). Thus, a higher excitation frequency may not be a good choice at high confining pressures.

7. CONCLUSIONS

Accurate determination of shear wave velocity is essential for reliable evaluation of G_{max}. In this study, disk type piezoelectric transducers capable of measuring shear wave velocity in laboratory triaxial apparatus were fabricated. Ambiguities involved in the correct determination of shear wave travel time are discussed. The main conclusions drawn from this study are summarized in the following points;

- Electromagnetic coupling between source and receiver piezo-transducer, commonly known as crosstalk, was found to distort the shear wave receiver signals. Crosstalk could effectively be removed by grounding both transmitter and receiver piezoelectric transducers.
- Large number of frequency components contained within square excitation leads to exceedingly distorted receiver signals. Interpretation of first arrival and determination of shear wave travel time is considerably easy when sinusoidal excitation waveform is used.
- The S-wave signals are affected by near-field effects. Near-field effect diminishes with an increase in L/λ ratio, i.e. increasing excitation frequency.

References:

Arulnathan, R., Boulanger, R. W., & Riemer, M. F. (1998). Analysis of Bender Element Tests. *Geotechnical Testing Journal, GTJODJ, 21*(2), 120-131. doi: 10.1520/GTJ10750J

Bates, C. (1989). Dynamic soil property measurements during triaxial testing. *Geotechnique, 39*(4).

Blewett, J., Blewett, I. J., & Woodward, P. K. (2000). Phase and amplitude responses associated with the measurement of shear-wave velocity in sand by bender elements. *Canadian Geotechnical Journal, 37*(6), 1348-1357. doi: 10.1139/t00-047

Brignoli, E. G. M., Gotti, M., & Stokoe, K. H. (1996). Measurement of Shear Waves in Laboratory Specimens by Means of Piezoelectric Transducers. *Geotechnical Testing Journal, GTJODJ, 19*(4), 384-397. doi: 10.1520/GTJ10716J

Dyvik, R., & Madshus, C. (1985). *Lab Measurements of Gmax Using Bender Elements.* Proceedings, Advances in the art of testing soils under cyclic conditions.

Jardine, R. J. (1986). Studies of the Influence of Non-Linear Stress-Strain Characteristics in Soil-Structure Interaction. *Geotechnique, 36*(3), 377-396.

Jovicic, V., Coop, M., & Simic, M. (1996). Objective criteria for determining Gmax from bender element tests. *Geotechnique, 46*(2), 357-362.

Lee, C. J., & Huang, H. Y. (2007). Wave velocities and their relation to fabric evolution during the shearing of sands. *Soil Dynamics and Earthquake Engineering, 27*(1), 1-13. doi: http://dx.doi.org/10.1016/j.soildyn.2006.05.006

Lee, J., & Santamarina, J. (2005). Bender Elements: Performance and Signal Interpretation. *Journal of Geotechnical and Geoenvironmental Engineering, 131*(9), 1063-1070. doi: doi:10.1061/(ASCE)1090-0241(2005)131:9(1063)

Leong, E. C., Yeo, S. H., & Rahardjo, H. (2005). Measuring shear wave velocity using bender elements. *ASTM geotechnical testing journal, 28*(5), 488-498. doi: 10.1520/GTJ12196

Lohani, T., Imai, G., & Shibuya, S. (1999). Determination of shear wave velocity in bender element test. *Earthquake Geotechnical Engineering*, 101-106.

Mancuso, C., & Vinale, F. (1988). Propagazione delle onde sismiche: teoria e misure in sito. *Atti del Convegno Nazionale del Coordinamento per gli Studi di Ingegneria Geotecnica*, 115-138 [In Italian].

Pennington, D. S., Nash, D. F. T., & Lings, M. L. (2001). Horizontally mounted bender elements for measuring anisotropic shear moduli in triaxial clay specimens. *ASTM geotechnical testing journal, 24*(2), 133-144. doi: 10.1520/GTJ11333J

Richart, F. E., Hall, J. R., & Woods, R. D. (1970). Vibrations of soils and foundations.

Rodríguez, J. a. D., & Moreno-Carrizales, P. (2001). A study of soil microstructure using bender element tests. *Proceeding, IVth International Conference on Recent Advances in Geotechnical Earthquake Engineering and Soil Dynamics*, Paper No. 1.39.

Sanchez-Salinero, I., Roesset, J. M., Stokoe, I., & Kenneth, H. (1986). Analytical studies of body wave propagation and attenuation. Texas Univ at Austin Geotechnical Eengineering Center Report GR 86-15: DTIC Document.

Viggiani, G., & Atkinson, J. (1995). Stiffness of fine-grained soil at very small strains. *Geotechnique, 45*(2), 249-265.

Wang, Y., Lo, K., Yan, W., & Dong, X. (2007). Measurement Biases in the Bender Element Test. *Journal of Geotechnical and Geoenvironmental Engineering, 133*(5), 564-574. doi: doi:10.1061/(ASCE)1090-0241(2007)133:5(564)

10CUEE CONFERENCE PROCEEDINGS
10th International Conference on Urban Earthquake Engineering
March 1-2, 2013, Tokyo Institute of Technology, Tokyo, Japan

COMPARISON BETWEEN CPT AND SDS DATA FOR SOIL CLASSIFICATION IN CHRISTCHURCH

Yasin Mirjafari[1)], Rolando P. Orense[2)], and Naoaki Suemasa[3)]

1) PhD Student, Department of Civil and Environmental Engineering, University of Auckland, New Zealand
2) Associate Professor, Department of Civil and Environmental Engineering, University of Auckland, New Zealand
3) Professor, Tokyo City University, Japan
smir332@aucklanduni.ac.nz, r.orense@auckland.ac.nz, nsuemasa@tcu.ac.jp

Abstract: A large number of civil engineering structures were damaged due to liquefaction during huge recent earthquakes in Christchurch and need to be reconstructed. Prior to reconstruction, properties of soils in different areas should be identified and, based on behavior of underlying soils, appropriate foundation for structures should be designed. Cone Penetration Test (CPT) is one of the most common in-situ tests for soil characterization. However, this test is relatively expensive and needs skilled operator. Therefore, Swedish Weight Sounding (SWS) test has become popular for ground investigation as it does not occupy large space and it is simpler and faster compared to other methods. Nevertheless, using SWS has some disadvantages such as low accuracy of soil classification and rod friction is excluded in the test results. The Screw Driver Sounding (SDS) test developed in Japan is a new operating system for SWS consisting of a machine that drills a rod into the ground at different steps of loading while being rotated. This machine can continuously measure the required torque, load, speed of penetration and rod friction during the test, so can give a better overview of the soil profile along the depth of penetration. In this paper, based on the test conducted in Christchurch adjacent to a borehole and a CPT site, a comparison of the accuracy of soil classification based on CPT and on SDS method is discussed. The results confirm the advantages of SDS over the CPT method in terms of accuracy for soil classification.

1. INTRODUCTION

It is well understood that huge earthquakes can cause severe damage to civil engineering structures. Following the devastating earthquakes in Christchurch, a significant part of the structures was either destroyed or badly damaged and need to be reconstructed. A significant part of such damage was related to ground failures associated with liquefaction. Liquefaction is a phenomenon that occurs in saturated, sandy soils during earthquakes, which results in a loss of soil strength and bearing capacity. The city of Christchurch is situated on the east coast of the South Island of New Zealand, which borders the Pacific and Indian-Australian tectonic plates. Adequate knowledge of ground conditions is very important for analyses, design and construction of geotechnical systems. For preventing similar damages in the future, physical and mechanical properties of soils in different areas should be identified prior to reconstruction and based on the behavior of underlying soils, appropriate foundation for structures should be designed.

Recently, the use of in-situ soil testing has increased in geotechnical engineering practice. This is because of the rapid development of in-situ instruments, improved understanding of soil behavior and the subsequent realization of the limitations and inadequacies of some conventional laboratory testing (Eslami, 2006). Several in-situ tests obtain direct measurements of soil properties and geotechnical parameters (AASHTO, 1988). The most common tests include: standard penetration test (SPT), cone penetration test (CPT), Piezo-cone (CPTu), Swedish weight sounding (SWS), flat dilatometer (DMT), pressure meter test (PMT), and vane shear test (VST). Each test applies specific loading patterns to measure the corresponding soil response in an attempt to evaluate material characteristics, such as strength and/or stiffness (AASHTO, 1988).

In this study after a review of CPT, SPT and SWS, a new in-situ test called Screw Driver Sounding (SDS) method is introduced and the results of soil classification by this test in Christchurch is compared to CPT-based soil classification.

2. POPULAR IN-SITU TESTS FOR SOIL CLASSIFICATION

The Standard Penetration Test (SPT) is still the most popular in-situ test (Eslami, 2006). However, plenty of

problems and limitations exist for this test, with respect to performance, interpretation and repeatability. These are due to the uncertainty of the energy delivered to the rod, test procedures and operator-equipment effects. On the other hand, the Cone Penetration Test (CPT) is simple, fast, and it gives continuous records with respect to depth. The results are interpretable on both empirical and analytical basis and a variety of sensors can be incorporated by using a cone penetrometer (Eslami, 2006). However this test needs skilled operator to perform (AASHTO, 1988).

Swedish weight sounding (SWS) is another in-situ test that is popular in Japan and Nordic countries. It is estimated that about 20,000 SWS tests are carried out annually in Sweden alone (Broms and Flodin, 1988). The test has also been used in countries like Singapore, Algeria and some east European countries (Bergdahl et al., 1988). Also Habibi et al. (2006) reported the use of SWS in estimating the bearing capacity of foundation for some buildings in southern areas of Tehran, Iran. The key advantages of this test are that it is highly portable, low cost and, similar to CPT, provides a continuous profile of the soil. SWS consists of some pieces of weights (a 5kg clamp, two 10kg and three 25kg weights), a screw-shaped point, 22mm extension rods and a handle (or a motor) for rotating the rods (Habibi, 2006). Figure 1 shows a schematic view of the apparatus and its screw-shaped point.

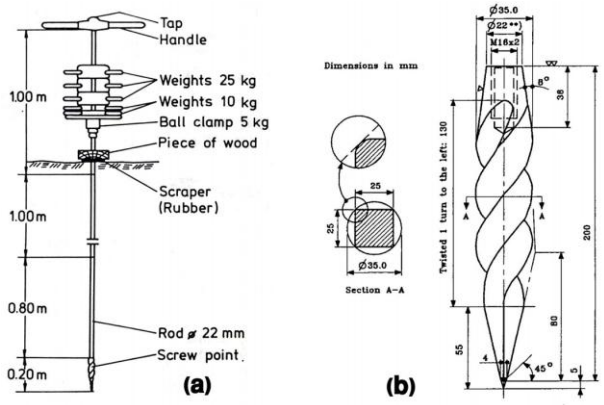


Figure 1 Swedish weight sounding equipment: (a) schematic view of apparatus (Bergdahl et al., 1977); (b) screw-shaped point (ENV19 97:3, 2000).

The penetration resistance of soil can be estimated ether by measuring the required load or the number of half-turns that the screw point is rotated to penetrate to a planned depth. When sounding is performed in soft soil, the penetration resistance is typically measured only through the weight required for penetration of the rods. This means that the weight is increased up to the weight which could penetrate the soil. The levels of static loading used in the test are 0, 5, 25, 50, 75 and 100kg. If the penetration does not occur with 100kg loading, the rod is rotated by using a handle. Although the SWS test is highly portable and simpler than other sounding tests, this test has some disadvantages such as low accuracy in classifying soils. As SWS is usually conducted without soil sampling, soil classification is estimated from the test results, local circumstances at the site and experience of operator. Furthermore, SWS cannot penetrate into very dense soils and the usual depth of penetration is limited to 10-15 m. The other problem associated with the SWS test is that the result is fairly influenced by rod friction, which may affect the measured results. Especially, in case where the soil contains gravel, the required load to penetrate, number of half-turns and consequently soil resistance from the SWS tends to be over-estimated as the rod friction becomes large.

3 SCREW DRIVER SOUNDING TEST

3.1 Background and test procedure

A new operation system for the SWS, the Screw Driver Sounding test, called as SDS, has been recently developed in Japan to minimize the disadvantages of the SWS as well as to incorporate a procedure to measure the rod friction. The machine originally used for the SWS test has been improved to be suitable for the SDS test. In the usual SWS test, there are two loading stages. In the first stage, a vertical load (W_{sw}) is applied to the rod in 4 incremental steps up to a load of 1kN. If the settlement of the rod does not reach 25cm depth, the rod is penetrated by rotating the rod into the soil in the second stage. In the SDS test, on the other hand, a static loading system is used and the number of load steps is increased to 7, while the rod is always rotated at a constant rate during the test. The step loads are 0.25, 0.38, 0.5, 0.63, 0.75, 0.88, 1kN in this order and the load is increased at every complete rotation of the rod. Measured items in the test are maximum torque (Max.*T*), average torque (Av.*T*), minimum torque of rod (Min.*T*), penetration length (*L*), penetration velocity (*V*) and number of rotations of rod (*N*). The data are measured at every complete rotation of the rod. In the SDS as well as the SWS, a set of loading is conducted at every 25cm for penetration and after each 25cm penetration, the rod is lifted up by a few centimeters and then rotated to measure the rod friction. Figure 2 shows the SDS machine during testing in Christchurch.



Figure 2 SDS machine during operation

3.2 Plasticity model for the SDS test

To clarify the interaction between the torque and the vertical force, a plasticity theory analogy model for the Swedish weight sounding by using the results of a SWS miniature test was proposed by Suemasa et al (2005). The summary of the model is described below for better understanding of the SDS result. Further details are provided by Suemasa et al (2005).

An incremental work done by torque and vertical force is given by

$$\delta E = \pi T \delta n_{ht} + W \delta s_t \tag{1}$$

where T is the required torque to rotate the screw point, W is the required vertical load, δn_{ht} is the number of incremental half turns and δs_t is the incremental settlement caused by the load. The penetration load, W_p, is defined as a the load by which the screw point is penetrated into ground without rotation. The incremental work is normalized by the penetration load as shown in equation 2.

$$\frac{\delta E}{W_p D} = \frac{\pi T}{W_p D}\delta n_{ht} + \frac{W}{W_p}\frac{\delta s_t}{D} = T_n \delta n_{ht} + W_n \frac{\delta s_t}{D} \tag{2}$$

In the above equation, D is diameter of the screw point, and T_n and W_n are the normalized T and W, respectively. From the observations of the test results, an elliptical yield locus centered on the origin is assumed in this model, i.e.

$$c_y T_n^2 + W_n^2 = 1 \tag{3}$$

where c_y is the coefficient of yield locus. A function of plastic displacement potential is also assumed to be elliptical, i.e.

$$c_p T_n^2 + W_n^2 = 1 \tag{4}$$

where c_p is a coefficient of plastic potential. If the associative flow rule is adopted, c_p must be equal to c_y. Differentiating this plastic potential function gives the displacement incremental vector as

$$N_{sw} D = \frac{\delta n_{ht}}{\delta s_t / D} = c_p \frac{\pi T}{W D} \tag{5}$$

where $N_{sw}D$ is the number of normalized half turns. From these results, it is found that each soil category has different values of c_p. Thus, by measuring the applied torque in SWS, soils can be classified by using the theory developed for SWS (Tanaka, 2012).

3.3 Estimation of rod friction

Due to the effects of rod friction during penetration, the measured load and torque for penetration are more than the required ones at screw point. The rod friction can be divided into a vertical component (W_f) and a horizontal component (T_f) as the rod is rotated and penetrated into the ground (Tanaka, 2012).

The applied load (W_a) and applied torque (T_a) by the SDS machine are defined as follows:

$$W_a = W_f + W \tag{6}$$

$$T_a = T_f + T \tag{7}$$

where W and T are load and torque at the screw point, respectively. The maximum shear stress acting on the rod surface is computed as,

$$\tau_{\max} = \frac{T_m}{2\pi r^2 \cdot L} \tag{8}$$

where T_m is the torque resisting the rod friction measured at the end of a loading set, r is a radius of the rod and L is a total penetrated length. Assuming that the direction of rotation velocity (V_θ) and of settlement velocity (V_z) are equal to those for horizontal shear stress (τ_θ) and vertical shear stress (τ_z) on rod surface, respectively, the formulas can be given as follows:

$$\tau_\theta = \tau_{\max}.\sin\theta \tag{9}$$

$$\tau_z = \tau_{\max}.\cos\theta \tag{10}$$

By substituting eq. (8) into eqs. (9) and (10), the vertical and the horizontal components of the rod friction are obtained as

$$\tau_f = 2\pi r^2 L \frac{v_\theta}{\sqrt{v_v^2 + v_\theta^2}} . \frac{T_m}{2\pi^2 L} \tag{11}$$

$$W_f = 2\pi r L \frac{v_v}{\sqrt{v_v^2 + v_\theta^2}} . \frac{T_m}{2\pi^2 L} \tag{12}$$

4. SOIL CLASSIFICATION USING SDS DATA IN JAPAN

Soils can be classified in different ways using SDS data. For instance, changes in measured torque which are caused by increasing the applied load are not equal for different types of soils. Per the classification proposed by Tanaka et al. (2012), the slope of the corrected torque against corrected load graph (dT/dW) tends to have a positive value for sand or loam, and a negative value or zero for clay and silt. Depending on the density and soil friction, the slope would change. Denser materials with more friction show higher value of dT/dW. For peat or organic soil, as well as other frictional soil, the corrected load is very small and the corrected torque increases as the corrected load increases. As these types of soils include plant roots and leaves that can be entangled at the screw point, the corrected torque has a tendency to increase. For tuff clay, the corrected torque tends to be constant or to decrease while the corrected load is increased. Tuff clay is compressible and shows brittle response in shear due to the many large gaps inside it. In the tuff clay, even with high SPT N value, it is thought that the corrected torque would be small due to the changes in soil fabric by the rotation of the screw point.

The slope of an approximate line obtained from the relationship between the number of normalized half turns ($N_{sw}D$) and normalized torque ($\pi T/WD$) is the coefficient of plastic potential (c_p). The relationship between c_p and dT/dW is shown in Figure 3 for different types of soils. The values of c_p for loam, loamy clay and tuff clay categorized as diluvial layer is more than 1 (Section A). On the other hand, for silt, this parameter changes between 0.3 and 1 (Section B). c_p for peat and organic soil is less than 0.3 (Section C). For diluvial layer, c_p is more than 1 and dT/dW is positive; c_p is less than 1 for alluvial layer and less than 0.3 for peat layer (Tanaka, 2012).

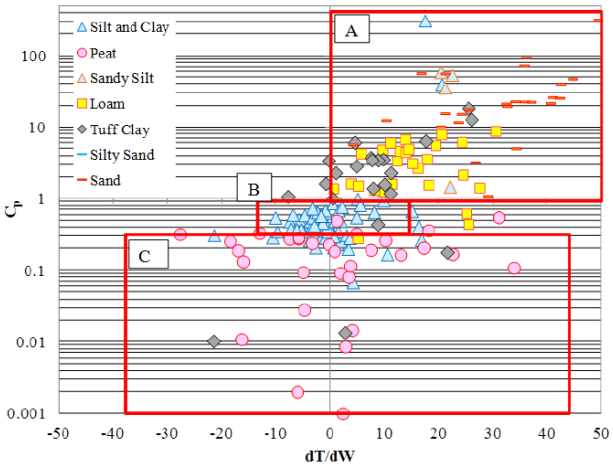


Figure 3. Relationship between c_p and dT/dW defining soil types (Tanaka, 2012).

5. SOIL CLASSIFICATION USING SDS DATA IN CHRISTCHURCH

A SDS test was conducted in Christchurch near a CPT site and borehole in order to make a comparison between the results of soil classification from these two tests. The selected site was located in Avonside Drive. This area liquefied during 2010 earthquake in Christchurch. Figure 4 shows the location of the selected site. The SDS test was conducted within a two meter distance from the CPT test and borehole. The borehole and CPT data was obtained from the Canterbury Geotechnical Database.

Figure 5 illustrates the CPT profile of the soil and the changes in SDS parameters along the depth. Based on Japanese data which has been presented in Section 3, soils can be classified by using dT/dW, average required torque and c_p. As shown in Figure 5, dT/dW is positive along the soil profile which means the soil is coarse-grained. From a depth of 1.0-2.75m, the average values of corrected torque and c_p are around 20 and 3, respectively; because of these low values, the soil in this region can be classified as sandy silt. Below 2.75m, the value of dT/dW gradually increases and this trend continues until 4m. Similarly, the average required torque for penetration increased from 35Nm to 45Nm, indicating an increase in soil friction or density. In



Figure 4 Location of test site in Christchurch.

this region, the value of c_p also gradual increased from 3 to 13. It can be predicted that between 2.75m and 4m, the percentage of fines in sand dropped or the soil becomes more frictional. From 4m to 5m, dT/dW increased gradually. The required torque for penetration in this part of the deposit was approximately 50Nm and average value for c_p was around 8. An increase in dT/dW in this section of the soil profile indicates a soil type with medium sand profile. There was a drop in dT/dW between 5 and 6 m referring to an increase in percentage of fines which reduced the friction of the soil. Below depth of 6m, an upward trend for dT/dW and c_p again continued, indicating a reduction in percentage of fines. Soil in this section of the profile can be classified as fine to medium sand.

The obtained soil classification from SDS is next compared to that obtained from CPT. For this purpose, the CPT soil behavior type classification used in this study is based on Robertson (1990) soil behavior type chart. Note that the CPT-based charts are for soil behaviour type (SBT), since the cone responds to the in-situ mechanical behavior of the soil and not directly to soil classification criteria based on grain-size distribution and soil plasticity. Robertson (1990) proposed using normalized (and dimensionless) cone parameters, Q_{t1}, F_r, and B_q, where

$$Q_{t1} = (q_t - \sigma_{vo})/\sigma'_{vo} \quad (13)$$

$$F_r = [f_s/(q_t - \sigma_{vo})]100\% \quad (14)$$

$$B_q = (u_2 - u_0)/(q_t - \sigma_{v0}) = \Delta u/(q_t - \sigma_{v0}) \quad (15)$$

where σ_{v0} is the in situ total vertical stress; σ'_{v0} is the in situ effective vertical stress; u_0 is the in situ equilibrium water pressure; u_2 is the pore pressure measured at cone shoulder; Δu is the excess penetration pore pressure and q_t is cone resistance corrected for pore water pressure on cone shoulder. In the original paper by Robertson (1990), the normalized cone resistance was defined using the term Q_t. The term Q_{t1} is used here to show that the cone resistance is the corrected cone resistance, and the stress exponent for stress normalization is 1.0.

Jefferies and Davies (1993) identified that a soil behavior type index, I_c, could represent the SBT in zones in the Q_{t1}–F_r

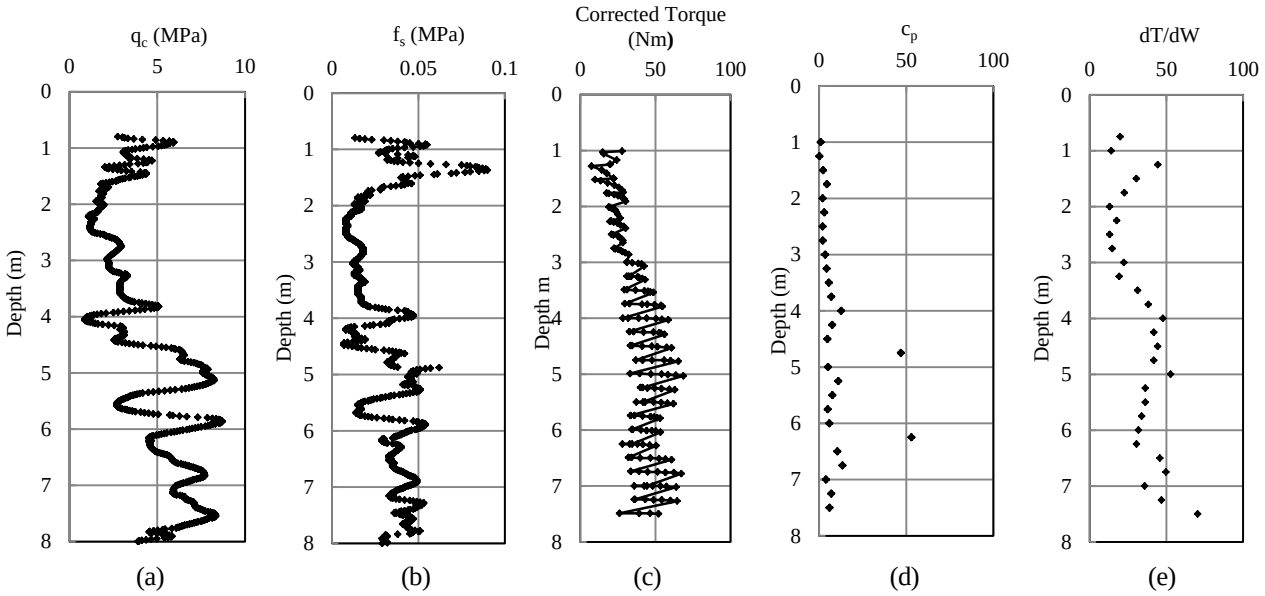


Figure 5 Variation with depth of: (a) cone resistance of CPT; (b) sleeve friction of CPT; (c) changes in corrected torque in SDS; (d) changes in c_p in SDS; (e) changes in *dT/dW* in SDS.

chart, where I_c is essentially the radius of concentric circles that define the boundaries of soil type. Robertson and Wride (1998) modified the definition of I_c to apply to the Robertson (1990) Q_{t1}–F_r chart as defined by,

$$I_c = [(3.47 - \log Q_{t1})^2 + (\log F_r + 1.22)^2]^{0.5} \qquad (16)$$

Contours of I_c on the Q_{t1}–F_r chart are shown in Fig. 6. The contours can be used to approximate the SBT boundaries. The chart identifies numbered areas that separate the soil types in twelve zones, as shown in table 1.

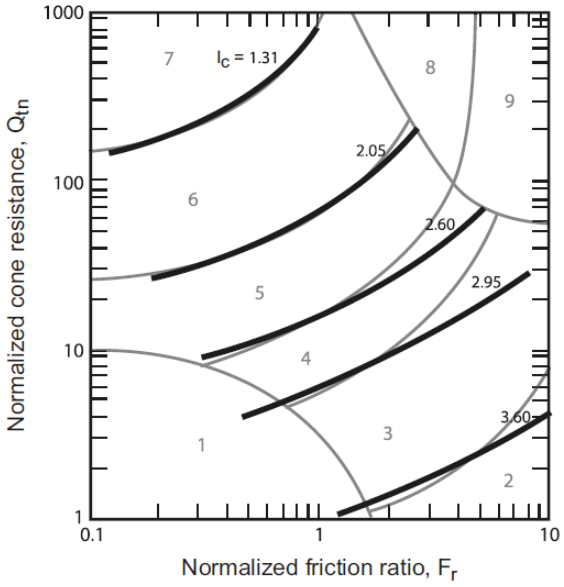


Figure 6 Contours of soil behavior type index, I_c (thick lines), on normalized SBTn Q_{t1}–F_r chart (SBT zones based on Robertson, 1990).

Table 1 Profiling chart for use in soil classification (Robertson 1990)

Zone	**Soil Behaviour Type (SBT)**
1	Sensitive fine-grained
2	Clay - organic soil
3	Clays: clay to silty clay
4	Silt mixtures: clayey silt & silty clay
5	Sand mixtures: silty sand to sandy silt
6	Sands: clean sands to silty sands
7	Dense sand to gravelly sand
8	Stiff sand to clayey sand
9	Stiff fine-grained

Table 2 shows the comparison of the results of soil classification using SDS, CPT and borehole. As seen from the table, the results obtained from SDS are very close to those indicated in the borehole description. Thus, even without sampling, SDS can classify soils with acceptable degree of accuracy.

It should be mentioned though that the SDS-based classification was formulated from a database of Japanese soils. Thus, more tests are currently being planned in New Zealand to increase the range of soil types in the database and to further refine/improve the proposed classification scheme. Moreover, it is planned to make use of the SDS parameters to identify regions of high liquefaction potential using the Christchurch experience as benchmark. Indeed, the

Table 2 Results of soil classification using SDS, CPT and borehole data

CPT Soil description	SDS Soil description	Borehole		Depth (cm)
		Strength/ Density	Soil description	
-	-	Loose	FILL: Fine sand, dry, poorly graded	0-80
Silty sand- Sandy silt	Sandy Silt	Soft	Sandy silt, Moist, low plasticity, sand is fine	80-275
Sand and Silty sand	Silty Sand	Loose	Fine sand with trace silt, wet, poorly graded	275-300
Silty sand-Sandy silt	Silty Sand	Soft	Sandy silt, moist, low plasticity, sand is fine	300-350
Silty sand-Sandy silt	Sand	Loose	Fine sand with trace silt, Wet, poorly graded	350-375
Sand and Silty sand	Sand			375-470
Sand and Silty sand	Sand	Loose	Fine to medium sand with trace silt, wet, well graded	470-525
Silty sand	Silty sand			525-600
Silty sand- Sand	Sand			600-750

SDS method has a very good potential in geotechnical in-situ investigation.

6. CONCLUSIONS

In this study, a comparison between the most common field tests was made and a new in-situ test, called Screw Driver Sounding (SDS) was introduced. Based on a large number of tests conducted in Japan, it was shown that soils can be classified using SDS parameters, such as c_p, average corrected torque and *dT/dW*. For a site located in Christchurch, SDS was performed and the results of soil classification using SDS parameters were compared with those obtained from a borehole and a CPT site located less than 2m. It was shown that both methods, i.e. SDS and CPT, give almost similar results, indicating that SDS provides accurate soil classification.

More tests are currently planned in New Zealand to refine the current method of soil classification. As a future research, it is planned to evaluate the liquefaction potential of sites based on SDS parameters.

Acknowledgments

The authors would like to acknowledge Nitto Seiko Company for providing the SDS machine and the Japan Home Shield (JHS) Company for providing assistance for this research. We also would like to acknowledge the Canterbury Geotechnical Database for providing the borehole data and CPT records in Christchurch, as well as the Christchurch City Council for providing access to the test site.

References:

American Association of State Highway and Transportation Officials, AASHTO, (1988). *Manual on Subsurface Investigations*, Washington, D.C.

Bergdahl, U., Broms, B.B. and Muromachi, T. (1988). "Swedish Weight Sounding Test: International Reference Test Procedure," *Penetration Testing*, ISOPT-1, De Ruiter (ed.), A.A. Balkema Inc., 71-90.

Broms, B.B. and Flodin, N., (1988). "History of Soil Penetration Testing" *Penetration Testing*, A.A. Balkema Inc.

Canterbury Geotechnical Database (2012). https://canterbury geotechnicaldatabase.projectorbit.com

Campanella, R. G. and Robertson, P. K. (1988). "Current status of the piezocone test," *Proceedings of First International Symposium on Penetration Testing*, ISOPT-1, Orlando, March 22 - 24, Vol. 1, pp. 93 - 116.

ENV 1997:3-2000 (2000). *Euro Code 7: Geotechnical Design Assisted by Field Testing*, 146.

Eslami, A. and Gholami, M. (2006). "Analytical model for the ultimate bearing capacity of foundations from cone resistance", *Scientia Iranica*, Vol. 13, No. 3, pp 223-233, Sharif University of Technology.

Habibi, M. Cheshomi, A. and Fakher, A. (2006). "A case study of liquefaction assessment using Swedish weight sounding" *4th International Conference on Earthquake Engineering*, Taipei, Taiwan.

Jefferies, M.G., and Davies, M.P. (1993). "Use of CPTU to estimate equivalent SPT N60," *Geotechnical Testing Journal*, 16(4): 458– 468. doi:10.1520/GTJ10286J.

Robertson, P.K. (1990). "Soil classification using the cone penetration test," *Canadian Geotechnical Journal*, 27(1): 151–158. doi:10.1139/t90-014.

Robertson, P.K., and Wride, C.E. (1998). "Evaluating cyclic liquefaction potential using the cone penetration test," *Canadian Geotechnical Journal*, 35(3): 442–459. doi:10.1139/ cgj-35-3-442.

Suemasa, N., Shinkai, K., Suzawa, T., and Tamura, M (2005), " A plasticity model for Swedish weight sounding test," *4th Japan – Philippines Workshop on Safety and Stability of Infrastructure against Environmental Impacts*, Univ. of the Philippines, pp 169-177.

Tanaka,T., Suemasa, N. and Ikegame, A. (2012), "Classification of strata using screwdriver sounding test" *Proceedings of the Twenty-second International Offshore and Polar Engineering Conference Rhodes*, Greece.

10CUEE CONFERENCE PROCEEDINGS
10th International Conference on Urban Earthquake Engineering
March 1-2, 2013, Tokyo Institute of Technology, Tokyo, Japan

EFFECTS OF INTERNAL EROSION ON CYCLIC RESISTANCE OF GAP-GRADED COHESIONLESS SOIL

Lin Ke[1)] and Akihiro Takahashi[2)]

1) Graduate Student, Department of Civil Engineering, Tokyo Institute of Technology, Japan
2) Associate Professor, Department of Civil Engineering, Tokyo Institute of Technology, Japan
ke.l.aa@m.titech.ac.jp, takihiro@cv.titech.ac.jp

Abstract: The phenomenon that amount of internally eroded soil structures were prone to fail during Noto Peninsula Earthquake of Japan in 2007 draws the attention on the influence of seepage induced internal erosion on the cyclic resistance characteristics of the soil structures. Seepage induced internal erosion is defined as the gradual migration of fine particles in soils through the voids between the coarse particles. Gap-graded soil is vulnerable to internal erosion due to its deficiency in certain particle size. Internal erosion would cause the significant changes in void ratio, hydraulic conductivity and shear strength of soils. This paper concentrates on the influence of internal erosion on the cyclic resistance of gap-graded cohesionless soils by experimental investigations. A series of one-dimensional seepage tests are conducted inside of a newly developed triaxial cell, capable of applying constant rate seepage flow into soil specimens. Undrained cyclic shear tests are performed after seepage tests to evaluate the cyclic resistance change. It is noted that the internal erosion indicated by fine particle loss causes significant increase of hydraulic conductivity. The volumetric deformation of soil specimens is associated with the process of internal erosion. The cyclic resistance ratio is influenced by the internal erosion.

1. INTRODUCTION

Seepage-induced transfer of soil grains is observed widely both in natural soil deposits and in earth structures. Gap-graded soils, like sandy gravels or silty sands, are especially vulnerable to internal erosion due to its deficiency in certain particle size. The phenomenon that those zones of valleys, which may have been suffered from years of internal erosion, failed during Noto Peninsula Earthquake of Japan in 2007 raises the concern about the possible influence of internal erosion on the soil microstructure change and, consequently, the strength change. In literature, “internal erosion” refers to the phenomenon that small soil grains are eroded through the voids between the coarse grains by seepage flow. It develops chronically, usually accompanying with constant quantities of seepage flow over years.

The study on internal erosion originates from the phenomenon that base soil or filter, composed by those “poor graded” soils (i.e., gap-graded or coarse widely graded soils), could fail because of internal erosion of fine grains (Skempton and Brogan, 1994; Tomlinson and Vaid, 2000; Moffat and Fannin, 2006; among others). In those experimental investigations, various factors, such as the soil geometric characteristics, flow velocity, flow direction, hydraulic gradient and possible chemical reactions are taken into consideration. This phenomenon could be undertood from two perspectives: hydraulic mechanism and soil mechanics.

From hydraulic point of view, it is of significance to understand that (I) the factors governing the onset of internal erosion, (II) the amount of soil grains passing through the soil matrix and, correspondingly, (III) the variation of hydraulic parameters during internal erosion. The onset of internal erosion is governed by two constrains, geometrical constraint and hydro-mechanical constraint. Instinctively, geometrical constraint refers to the size of fines should be smaller than the size of voids in soil. Following the basic idea, many evaluation methods have been proposed to assess the internal stability of soil based on the grain size distribution (US Army Corps of Engineers, 1953; Istomina, 1957; Lubochkov, 1962, 1965; Kezdi, 1979; Kenney and Lau, 1985, 1986; Burenkova, 1993; Skempton and Brogan, 1994, among others). Kovacs (1981) defined the hydro-mechanical constraint as “the critical velocity or hydraulic gradient, above which the fine grains start to move”, which is found closely related with the effective stress level in soil. Skempton and Brogan (1994) firstly analyzed the influence of effective stress level on soil internal stability. A reduction factor was proposed to note that the soil internal stability will intrigue at a hydraulic gradient significantly lower than the anticipated from theory. Based on the results of series of permeameter tests, Moffat and Fannin (2011) demonstrated the effective stress level dependent hydraulic gradient characteristics and proposed the concept of a hydromechanical path in stress ~ gradient space. Li and Fannin (2012) proposed a linear

hydromechanical envelope in stress ~ gradient space. The envelope is governed by the proportion of effective stress in fines.

From soil mechanics point of view, the sand behavior is largely dependent on the friction along grain contacts. With the progress of soil erosion, the sand microstructure would suddenly change to another mode at certain hydraulic gradient, which is called "hydraulic gradient at failure" (Chang and Zhang, 2011). Correspondingly, the mechanical behavior of soil would greatly vary with this process. The study of the erosion dependent soil behavior is still on progress in literature. Wood *et al.* (2010) attempt to model the mechanical consequences of internal erosion by two-dimensional discrete element analysis. The simulation indicates that the erosion could intrigue the soil state change, from "dense" (below the critical state line) to "loose" (above the critical state line), with corresponding available strength lower than the critical state strength. Scholtès *et al.* (2010) consider the internal erosion as the progressive removal of the finest grains and conclude that the soil strength is strongly influenced by the erosion: the soil behavior changed from a dilatant to a contractant when extracting the fine grains. Those zones in the soil structure where internal erosion occurs would be more prone to fail. By the seepage tests in newly developed triaxial apparatus, Chang and Zhang (2011) prove that the mechanical behavior of tested specimens becomes contractive, which originally is dilative, after the loss of a significant amount of fine grains due to internal erosion.

The primary purpose of this paper is to experimentally show the influence of internal erosion on the cyclic behavior of gap-graded cohesionless soil. A multi-stage test procedure is applied to assess the condition necessary to trigger the internal erosion. The hydraulic conductivity change and volumetric strain of the tested soil specimen during seepage test are demonstrated. The cyclic resistance ratio change of the soil subjected to internal erosion is evaluated by a series of undrained cyclic tests.

2. TEST APPARATUS

The newly developed triaxial internal erosion apparatus could directly investigate not only the hydraulic characteristics of soils during onset and progress of internal erosion but also the mechanical behaviors subjected to internal erosion. It is applicable for testing non-cohesive soils. It mainly consists of a constant-flow-rate control unit, an automated triaxial system and eroded soil collection unit. In this apparatus, the hydraulic control is by constant-rate-of-flow. The unit is composed of a flow pump with the maximum flow rate of 1360mL/min for controlling flow rate through the specimen and a Differential Pressure Transducer (DPT) for measuring the pressure drop from the top to the bottom of tested specimens. The whole system allows independently synchronous control of the hydraulic condition and stress state of the tested specimens. The schematic illustration of the overall system is shown in Fig.1.

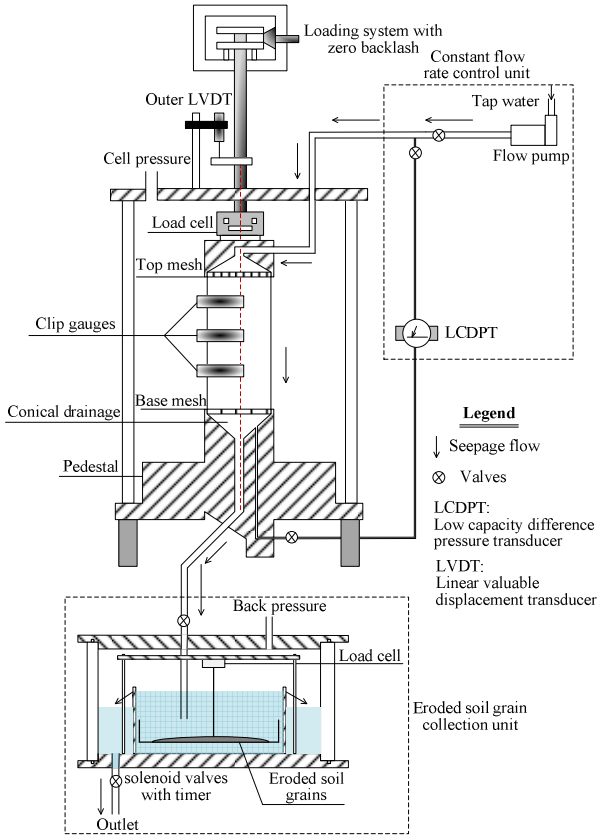


Figure 1 Schematic diagram of triaxial seepage test

3. TEST SPECIMENS

In this study, the tested specimens are the binary mixtures of two types of Silica sands (Silica No.3 and No.8) with different dominant grain sizes. With larger grain size, the Silica No.3 works as the soil skeleton in the mixtures while the fine Silica No.8 is the erodible fines. The mass fraction of Silica No.3 and No.8 in the mixture is determined considering the geometrical restriction: the volume of fines should be less than that of the voids between coarse grains. In this paper, the fine content of 35% is adopted. The grain size distribution and the physical properties of the mixture are shown in Fig.2.

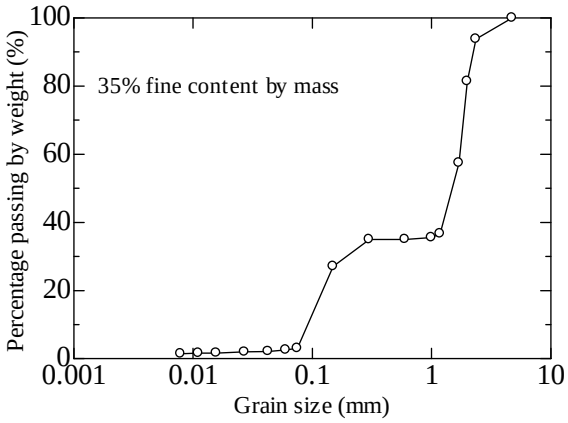


Figure 2 Grain size distribution curve of specimens

The tested specimen is 70mm in diameter and 150mm in height. The technics of moist tamping (Ladd, 1978) is implemented to prevent the segregation of the two different sized grains. The sample preparation procedures are as follows: determine the oven-dried weights of clean Silica No.3 and No.8 for a test according to the fine content and relative density. Thoroughly mix the soils with de-aerated water to make sure the distribution of fine grains in a specimen is uniform. Equally separate the wet mixture into 10 pieces and keep them in a zipped bag to equalize moisture at least 16 hours before use. The specimen is prepared layer by layer. Weigh the amount of material required for each layer, and place it into the mold by scoop. Each layer is compacted to the required density. The initial weight could not be directly checked after preparation. Therefore, the after-test oven-dry weight of the specimen together with the eroded soil weight should be checked.

4. SEEPAGE TEST & CYCLIC TEST

Those prepared soil specimens are firstly fully saturated (B>0.9) and then isotropically consolidated until mean effective stress reaches 50kPa. Depending on the test cases, Seepage tests are conducted while maintaining p'=50kPa (mean effective stress) and q=0kPa (deviatoric stress). After seepage test, the soil specimens are subjected to a cyclic shear stress in axial direction under the same effective stress as that of seepage test. The cyclic strength in terms of the cyclic resistance ratio (CRR) is defined as $\sigma_d/2\sigma_c'$ (σ_d: cyclic shear stress; σ_c': effective stress) that produces an axial strain of 5% in double amplitude in 20 cycles (N_c) of uniform load application. Three cyclic tests are performed with various values. The axial strain rate is set at 0.5%/min. Companion soil specimens at the same stress state without erosion are tested for the comparison purpose. A summary of the test cases is shown in Table 1.

5. TEST RESULTS & DISCUSSIONS

5.1 Seepage test results

In seepage test, the flow rate is increased gradually from 0 to 310mL/min. The measured hydraulic gradient is shown in Fig.3. Due to internal erosion, soil specimen would experience transferring of fines through the voids of coarse grains resulting in an increase of the void volume. Correspondingly, the hydraulic gradient would decrease. As is shown in Fig.3, at approximate 1500s, internal erosion initiates, indicated by the sudden decrease of hydraulic gradient. If Darcy's law is assumed to be applicable, it could be inferred that hydraulic conductivity of soil specimen increases due to internal erosion. Moreover, fines would be

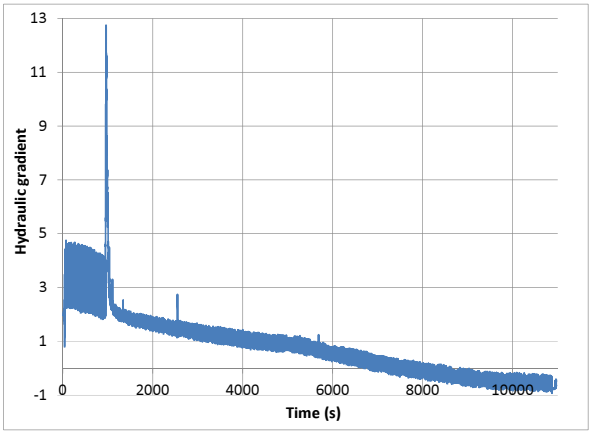


Figure3 Measured hydraulic gradient

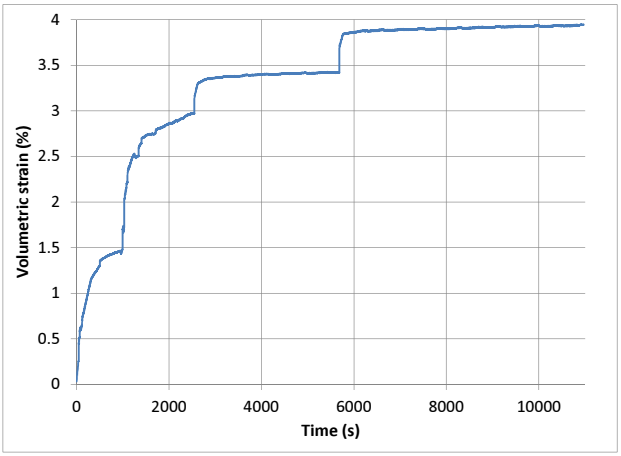


Figure 4 Volumetric strain of soil specimen in seepage test

Table 1 Summary of test cases

Specimen	Fine content (%)	Initial relative density (%)	Mean effective stress (kPa)	Erosion	CRR
50N0.07	35	30	50	N.A.	0.07
50N0.1	35	30	50	N.A.	0.1
50N0.12	35	30	50	N.A.	0.12
50E0.1	35	30	50	Y	0.1
50E0.15	35	30	50	Y	0.15
50E0.2	35	30	50	Y	0.2

Note: N.A. means no erosion; Y means erosion;

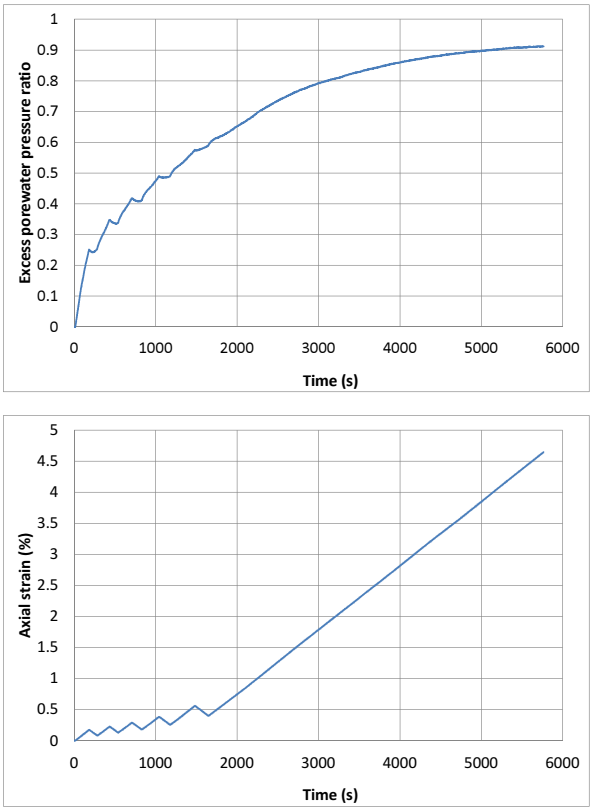


Figure 5 Pore pressure and Axial strain response of uneroded soil specimen (CRR=0.12)

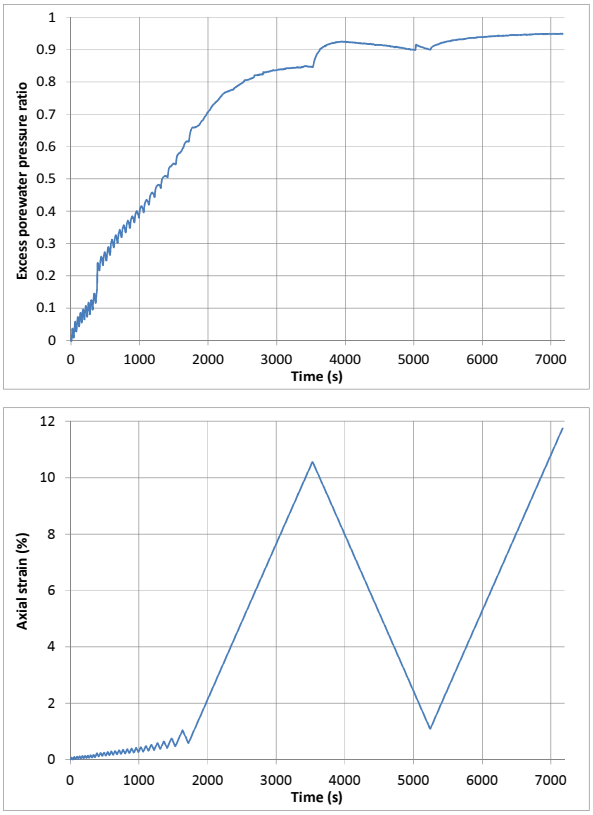


Figure 6 Pore pressure and Axial strain response of internally eroded soil specimen (CRR=0.12)

eroded away by the seepage flow, resulting in the increasing

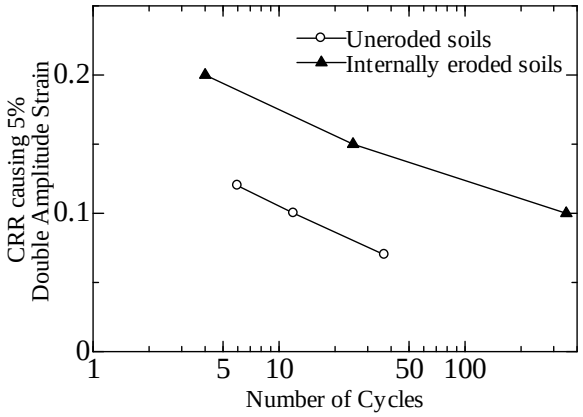


Figure 7 Cyclic Resistance of soil specimens

of volumetric strain of the tested specimen, as is shown in Fig.4. It can be observed that a dramatic change of soil volume occurs as soon as internal erosion initiates. With the progress of erosion, the volume change becomes moderate and reaches at a constant value. By weighing the mass of eroded soil grains, nearly half of the fines in soil specimens are eroded away.

5.2 Undrained cyclic test results

The typical pore pressure and axial strain response of the uneroded soil specimen under the cyclic resistance ratio of 0.12 are shown in Fig.5. That response of the internally eroded specimen under the same cyclic resistance ratio is shown in Fig.6. The test specimen without erosion shows liquefaction behavior of moderately loose sand. Pore pressure cumulates gradually at the early stage and reaches 0.9 of pore pressure ratio when liquefaction occurs. The axial strain increases linearly with the number of cycles which indicates that the soil specimen would produce a progressive or gradual failure. Fall *et al.* (1997) observed a similar behavior on gravels, which they referred as “ratchet” phenomenon. For the internally eroded soil specimen, pore pressure and axial strain response exhibit a similar behavior. Liquefaction occurs when pore pressure ratio is approximately 0.9. The axial strain increases with the number of cycles. A plot of cyclic resistance ratio versus number of cycles required to cause 5% double amplitude strain for uneroded and eroded soil respectively is shown in Fig.7. It indicates that the CRR causing 5% double amplitude strain in 20 cycles increases from 0.08 to 0.16 due to internal erosion.

6. CONCLUSIONS

Influence of internal erosion on soil cyclic behavior is experimentally studied through a series of triaxial seepage tests at designated stress state and undrained cyclic tests. By giving downward seepage flow to the gap-graded soil specimens, internally eroded soils are created. Undrained cyclic tests are performed on those internally eroded soils. The hydraulic conductivity of soils drastically increases with progress of the internal erosion. A large amount of fines would be eroded away with seepage flow. Soils would

greatly deform due to the loss of fines. The undrained cyclic test conducted on the eroded soils indicates that due to internal erosion CRR causing 5% double amplitude strain in 20 cycles would increase.

References:

Burenkova, V.V. (1993), "Assessment of suffosion in non-cohesive and graded soils. Proceedings, the First International Conference of 'Geo-Filters'," Karlsruhe, Germany, Oct. 1992, *Filters in Geotechnical and Hydraulic Engineering*, Brauns, Heibaum & Schuler, Eds., Balkema, Rotterdam, 357-360

Chang, D.S. and Zhang, L.M. (2011), "A stress-controlled erosion apparatus for studying internal erosion in soils," *Geotechnical Testing Journal*, **34**(6), 579-589

Fall, M., Tisot, J.P. and Cisse, I.K. (1997), "Undrained behavior of compacted gravel lateritic soils from western Senegal under monotonic and cyclic triaxial loading," *Engineering Geology*, **47**, 71-87.

Istomina, V.S. (1957), "Filtration Stability of Soils," Gostroizdat, Moscow, Leningrad.

Kenney, T.C. and Lau, D. (1985), "Internal stability of granular filters," *Can. Geotech. J.*, **22**, 215-225

Kenney, T.C. and Lau, D. (1986), "Internal stability of granular filters: Reply," *Can. Geotech. J.*, **23**, 420-423

Kezdi, A. (1979), "Soil Physics: Selected Topics (Developments in Geotechnical Engineering)," Elsevier Science Ltd.

Kovacs, G. (1981), "Seepage hydraulics," Elsevier Scientific Publishing Company, Amsterdam, Netherlands

Ladd, R.S. (1978), "Preparing test specimens using undercompaction," *Geotechnical Testing Journal*, **1**(1), 16-23

Li, M. and Fannin, R.J. (2012), "A theoretical envelope for internal instability of cohesionless soil," *Géotechnique*, **62**(1), 77-80

Lubochkov, E.A. (1962), "The self-filtering behavior of non-cohesive soils," *Izvestia VNIIG*, **71**

Lubochkov, E.A. (1965), "Graphical and analytical methods for the determination of the properties of non-cohesive soils characterizing suffusion," *Izvestia VNIIG*, **78**

Moffat, R.A. and Fannin, R.J. (2006), "A large permeameter for study of internal stability in cohesionless soils," *Geotechnical Testing Journal*, **29**(4), 273-279

Moffat, R.A. and Fannin, R.J. (2011), "A hydromechanical relation governing internal stability of cohesionless soil," *Can. Geotech. J.*, **48**, 413-424

Scholtès, L., Hicher, P.Y. and Sibille, L. (2010), "Multiscale approaches to describe mechanical responses induced by particle removal in granular materials," *Comptes Rendus Mecanique*, **338**, 627-638

Skempton, A.W. and Brogan, J.M. (1994), "Experiments on piping in sandy gravels," *Géotechnique*, **44**(3), 449-460

Tomlinson, S.S. and Vaid, Y.P. (2000), "Seepage forces and confining pressure effects on piping erosion," *Can. Geotech. J.*, **37**, 1-13

U.S. Army Corps of Engineers (1953), "Filter experiments and design criteria," *Technical Memorandum 3~360*, Waterways Experiment Station, Vicksburg.

Wood, D.M., Maeda, K. and Nukudani, E. (2010), "Modeling mechanical consequences of erosion," *Géotechnique*, **60**(6), 447-457

10CUEE CONFERENCE PROCEEDINGS
10th International Conference on Urban Earthquake Engineering
March 1-2, 2013, Tokyo Institute of Technology, Tokyo, Japan

RELATIONSHIPS BETWEEN DAMAGE TO RAILWAY STRUCTURES AND SEISMIC INTENSITY IN THE 2004 NIIGATA-KEN CHUETSU EARTHQUAKE AND THE 2007 NIIGATA-KEN CHUETSU-OKI EARTHQUAKE

Shuichi TAYA[1] and Saburoh MIDORIKAWA[2]

1) Graduated Student, Department of Built Environment, Tokyo Institute of Technology, Japan
2) Professor, Department of Built Environment, Tokyo Institute of Technology, Japan
sh-taya@jr-central.co.jp,smidork@enveng.titech.ac.jp

Abstract: In order to examine a relationships between damages of railway structures by earthquake and seismic intensity, the damage survey data of railway structures in the 2004 Niigata-ken Chuetsu earthquake and the 2007 Niigata-ken Chuetsu-oki earthquake are collected and compiled. Damage rates of different railway structures(earth structures, bridges, tunnels) are calculated at each JMA seismic intensity level. The results indicate that (1) the damaged embankments are found at the JMA seismic intensity 5- or larger, (2) the damaged bridges and tunnels are found at the JMA seismic intensity 5+ or larger, and (3) damage rates of all the structural types become higher with increase of the JMA seismic intensity.

1. INTRODUCTION

Better understanding of a relationship between damages of railway structures by earthquake and seismic intensity is needed for the optimized decision method of train operation control after an earthquake . If railway structures are damaged by earthquake and the train enters the damaged point, the train might be derailed. Therefore, if observations of ground motion in the wayside seismometers are larger than a certain level, train operation is suspended and the track is inspected. Suspended train operation by earthquake will affect the social activities. It is required to reduce unnecessary control. Therefore, it is important to know exactly relationships between damage to railway structures and seismic intensity, and to set reasonable criteria of train operation control after an earthquake.

Criteria of train operation control after an earthquake is determined based on the case histories of damage to railway structures by past earthquakes. Previous studies show that railway structures in the area where the JMA seismic intensity is larger than 5+ are damaged (Suzuki et al. 2003, Itoh and Taya 2006). However, damage rates for each the JMA seismic intensity level are unclear.

For damage assessment, Saitama prefecture and Tokyo metropolis constructed seismic seismic vulnerability functions based on the damage survey data in the 1978 Miyagi-ken-oki earthquake and the 1995 Hyogo-ken Nambu earthquake, respectively. These vulnerability functions, however, is applicable only in limited intensity levels, because these vulnerability functions were made based on earthquake damage survey data of a single earthquake. Takahama and Midorikawa constructed vulnerability functions that can be applied in the range of the JMA seismic intensity 4 to 7 based on the damage survey data in the 1978 Miyagi-ken-oki earthquake, the 1995 Hyogo-ken Nanbu earthquake, and the 2004 Niigata-ken Chuetsu Earthquake.

Railway structures can be classified into earth structures, bridges, and tunnels. It is thought that seismic capacity is different for each structural type. However, previous studies do not show relationships between railway structure damage and JMA seismic intensity for different structural types.

In this paper, we propose damage rates of different railway structural types at each the JMA seismic intensity level based on the 2004 Niigata-ken Chuetsu earthquake and the 2007 Niigata-ken Chuetsu-oki earthquake.

2. FLOW OF THIS STUDY

Fig.1 shows the flow of this study. To calculate damage rate of different railway structural types at each the JMA seismic intensity level, "the total length (or total number) of each JMA seismic intensity level" and "the number of damage of each JMA seismic intensity level" (divided into structural types) are needed. First, the total lengths of different structural types are measured for all lines surveyed. Tunnels and bridges are counted. Next, to grasp the number of damage of each structural type, damage survey data of railway structures in the 2 earthquakes are collected and compiled.

To calculate damage rates at each the JMA seismic intensity level, it is necessary to estimate the seismic

intensity at each point along the lines. In this study, spatial distributions of the JMA seismic intensity in 2 earthquakes are estimated based on seismometer data of JR, JMA, local government, JH, and K-Net.

The total numbers of different structural types and the total numbers of damaged structures at each the JMA seismic intensity level are grasped. Damage rates of different structural types at each the JMA seismic intensity level are calculated.

3. CONPILING DAMAGE SURVEY DATA OF RAILWAY STRUCTURES

Fig.2 shows all lines surveyed (6 lines, approximately 500 km). It is difficult to count earth structures. Therefore, the total length of earth structures is measured. It is easy to count tunnels and bridges. Therefore, the total numbers of tunnels and bridges are counted.

To measure the total length of earth structures, “the 100m points” are set for every 100m along lines. The structural type of each 100m point is picked up from the map symbol using “cyberjapan” by GSI. The numbers of 100m point of each structural type are counted. The total length of earth structures is calculated dividing the total number of 100m point of earth structures by 10.

Earth structures can be classified into "Embankments", "Cuttings", and "Natural ground or Lower embankments". The symbols of railway structure on “cyberjapan” are classified into tunnels, bridges, embankments, cuttings, and station yards. If the symbol on the 100m point means embankments or cuttings, the structural type is interpreted as the symbol. If the symbol on the 100m point is nothing, the structural type is interpreted as natural ground or lower embankments. Table 1 shows the total lengths of each structural type.

The total number of tunnels is found by counting the symbols on “cyberjapan”.The total number of bridges is found by counting the point crossing railway and road, or river. Table 2 shows the numbers of tunnels and bridges

Latitude and Longitude of a point can be picked up by clicking on the “cyberjapan”. Then latitude and longitude of each 100m point is picked up at the same time picking up the structural type. When estimating the JMA seismic intensity of each 100m point, latitude and longitude of the 100m point are required.

Damage survey data, such as kilometer post, structure name, and detail of damage, are described in the articles by the JR East. The number of damaged structures of each structural type is counted referring to these data. Damages which do not affect obviously trains are excluded. Table 3 shows the numbers of damaged structures dividing into structural types in the 2004 Niigata-ken Chuetsu earthquake and the 2007 Niigata-ken Chuetsu-oki earthquake.

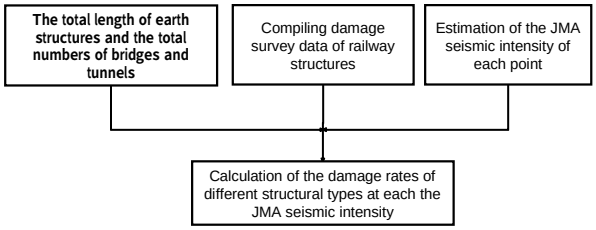


Figure 1 The flowchart of this study

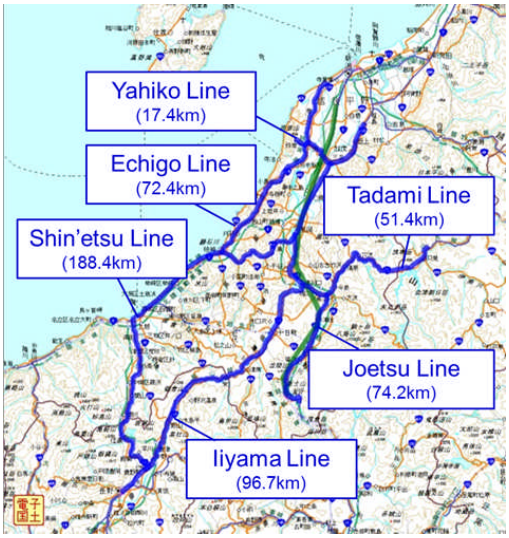


Figure 2 Surveyed lines

Table 1 The lengths of earth structures (km)

Line Name	Natural ground or Lower embankments	Embankments	Cuttings
Echigo	64.1	2.5	0.4
Joetsu	27.3	32.2	4.6
Shin'etsu	123.9	36	8.6
Iiyama	61.3	14.0	7.0
Yahiko	10.4	2.3	0.2
Tadami	25.2	7.2	0.4
Total	312.2	94.2	21.2

Table 2 The numbers of tunnels and bridges

Line Name	Tunnels	Bridges
Echigo	0	78
Joetsu	9	126
Shin'etsu	15	196
Iiyama	29	70
Yahiko	0	21
Tadami	13	67
Total	66	558

Table3 The numbers of damaged structures

Structural type	2004 Chuetsu	2007 Chuetsu-oki
Natural ground or Lower embankment	22	19
Embankments	47	12
Cuttings	6	6
Bridges	17	7
Tunnels	18	4

4. ESTIMATION OF THE JMA SEISMIC INTENSITY AT EACH POINT

Estimating the JMA seismic intensity for all lines surveyed including sections without damage is required. Then the spatial distributions of the JMA seismic intensity for all area surveyed are estimated from recorded values. The JMA seismic intensity of each 100m point is picked up from the estimated spatial distributions. The JMA seismic intensity of damaged point is referred from the JMA seismic intensity of nearest 100m point.

The method to estimate the spatial distribution of the JMA seismic intensity, same as Yamazaki et.al (1998) and Maruyama et.al (2008), is as follows: (1) the observed values on the ground surface are converted to the estimated values on the bedrock by applying amplification ratios (2) the spatial interpolation on the base rock level is carried out (3) the amplification ratio is again introduced and the spatial distribution of the estimated values on the ground surface is obtained (Fig. 3). Table 4 shows the calculation condition in this study. Fig.4 and fig.5 shows the result of the estimation of the spatial distribution of the JMA seismic intensity in the 2 earthquakes.

5. CALCULATION OF DAMAGE RATES OF DIFFERENT RAILWAY STRUCTURES AT EACH SEISMIC INTENSITY LEVEL

5.1 Calculation of damage rates of earth structures at each seismic intensity level

The number of damaged earth structures are divided by the section length of each the JMA seismic intensity level. Then the damage rates at each seismic intensity level (locations/km) are calculated (Fig6-9).

The damaged embankments are found at the JMA seismic intensity 5- or larger. The damage rate of the JMA seismic intensity 5- is only 0.01(locations/km). The damage rates are higher with increase of the JMA seismic intensity. The Trends are not significantly different in the 2 earthquakes. Comparing between three structural types, the damage rate of embankments are the highest in any the JMA seismic intensity level. The natural ground and lower embankment is next, the cuttings is lowest. This is consistent with the empirical knowledge that higher embankments are vulnerable.

5.2 Calculation of damage rates of bridges at each seismic intensity level

The number of damaged bridges are divided by the total number of bridges of each the JMA seismic intensity level. Then the damage rates at each the JMA seismic intensity level are calculated (Fig. 10).

Damaged bridges are found at the JMA seismic intensity 5+ or larger. Not more than the JMA seismic intensity 6+, damage rates become higher with increase of the JMA seismic intensity. The damage rate at the JMA

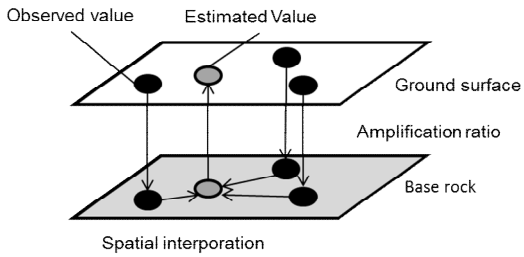


Fig. 3 Schematic figure for interpolation of seismic intensity

Table 4 The calculation condition in this study

	2004 Chuetsu	2007 Chuetsu-oki
Observated values	Converted the JMA seismic intensity to velocity, applied Fujimoto and Midorikawa (2010)	the JMA seismic intensity
Amplification ratio	Converted from AVS30 of J-SHIS, applied Fujimoto and Midorikawa(2006)	Converted from AVS30 of J-SHIS, Midorikawa et. al (2008)
The method of spaial interporation on the base rock	The Kridgeing method	IDW method
Fault model	The model of AIST	–

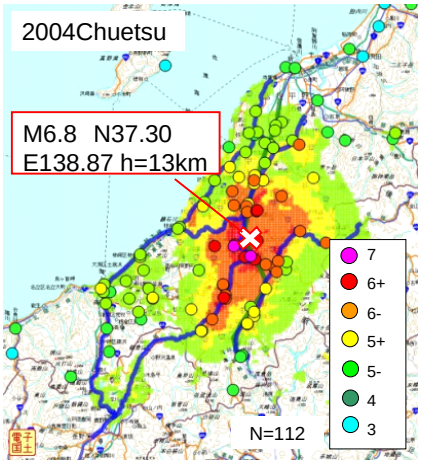


Fig. 4 the spatial distribution of the JMA seismic intensity in the 2004 Niigata-ken Chuetsu earthquake

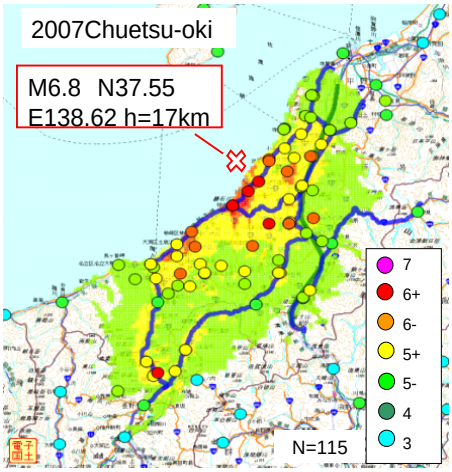


Fig. 5 the spatial distribution of the JMA seismic intensity in the 2007 Niigata-ken Chuetsu-oki earthquake

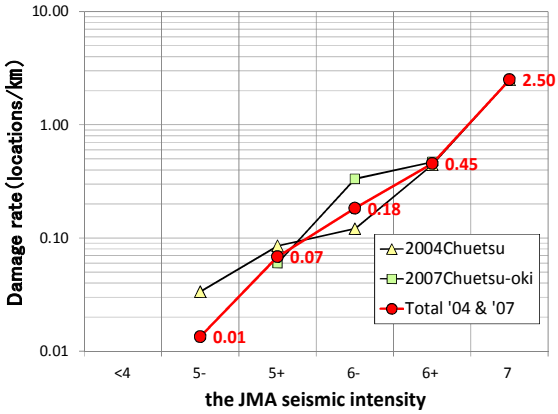


Fig. 6 The damage rate of each the JMA seismic intensity of natural ground or lower embankments

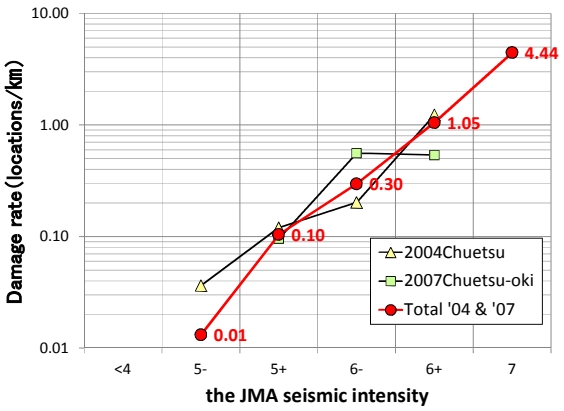


Fig. 9 The damage rate of each the JMA seismic intensity of all earth structures

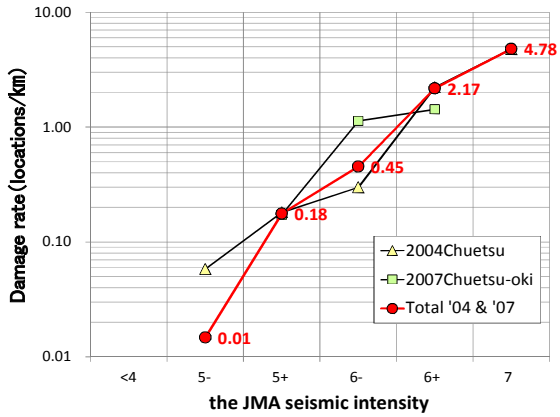


Fig. 7 The damage rate of each the JMA seismic intensity of embankments

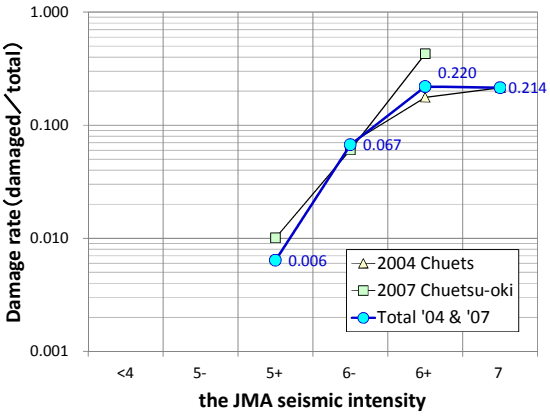


Fig. 10 The damage rate of each the JMA seismic intensity of bridges

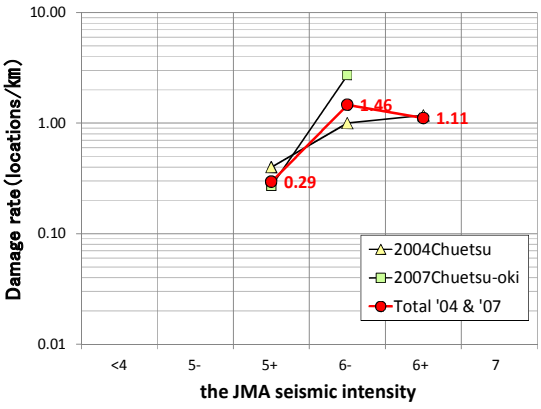


Fig. 8 The damage rate of each the JMA seismic intensity of cuttings

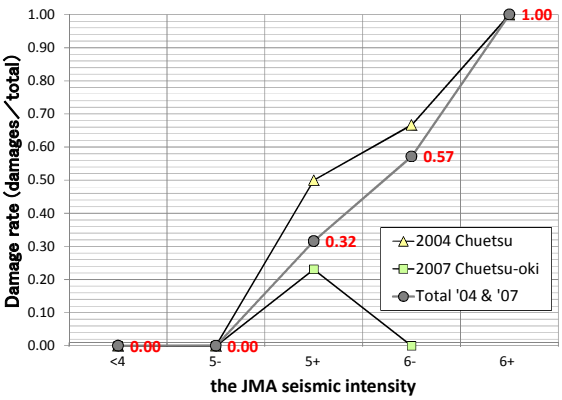


Fig. 11 The damage rate of each the JMA seismic intensity of tunnels

seismic intensity 6+ and 7 are comparable. Most of bridges in the area the JMA seismic intensity 7 are over-road bridges with short span. For this reason, it is thought that the damage rate at the JMA seismic intensity 7 is calculated lower.

5.3 Calculation of damage rates of tunnels at each seismic intensity level

The number of damaged tunnels are divided by the total number of tunnels of each the JMA seismic intensity level . Then the damage rates at each the JMA seismic intensity level are calculated (Fig. 11). The JMA seismic intensity of both entrance are compared. The JMA seismic intensity of the tunnel is applied the larger one.

Damaged tunnels are found at the JMA seismic intensity 5+ or larger. Damage rates become higher with increase of the JMA seismic intensity. All tunnels are damaged more or less at the JMA seismic intensity 6+.

Comparing between the 2 earthquakes, the damage rates of the JMA seismic intensity 6- are quite different. This is because the total number of tunnels at the JMA seismic intensity 6- in the 2007 Chuetsu-oki earthquake was only 2.

6. CONCLUSIONS

Damage survey data of railway structures in the 2004 Niigata-ken Chuetsu earthquake and the 2007 Niigata-ken Chuetsu-oki earthquake are collected and compiled. The damage rates of different structural types (earth structures, bridges, tunnels) at each the JMA seismic intensity level are calculated.

The results indicate that (1) the damaged embankments are found at the JMA seismic intensity 5- or larger, (2) the damaged bridges and tunnels are found at the JMA seismic intensity 5+ or larger, and (3) damage rates of all the structural types become higher with increase of the JMA seismic intensity.

The result will be available to optimize the decision method of train operation control after an earthquake.

Acknowledgements:

The strong motion data used in this study are provided by JH, JMA, JR East, local governments, NIED. The amplification factor data of surface layers used in this study are provided by J-SHIS.

References:

Itoh, Y. and Taya, S. (2006), "Optimizing train operation control after an earthquake" *The Journal of Japan Railway Civil Engineering Association* (in Japanese).

Suzuki, H and Shimamura, M. (2003), "A Study of a Method of Train Operation Control after an Earthquake", *JR EAST Technical Review No.3*, pp.53-60 (in Japanese)

Saitama prefecture (1982), "Saitama-ken Jishin Higai Soutei Chousa Kekka ni tsuite",(in Japanese)

Tokyo metropolis (1997), "Damage Estimates of an Earthquake with an Epicenter in the Tokyo Metropolitan Area" (in Japanese)

Takahama, T. and Midorikawa, S., "Seismic Vulnerability Functions of Railway Structures for Different Geomorphologic Conditions Derived from Damage Survey Data", *The Journal of JAEE*, Vol.9, No.5, pp.57-72

GSI website, http://portal.cyberjapan.jp/index.html

Maruyama, Y., Yamazaki, F., Yogai, H., Tsuchiya, Y. (2008), "Relationship between Damage Ratio of Expressway Embankment and Seismic Intensity Based on the Actual Damage Data in the Mid-Niigata Earthquake", *Journal of JSCE*, 64(2), 208-216

JR East (2005), "Railway Structures and the 2004 Niigata-ken Chuetsu Earthquake", STRUCTUAL ENGINEERING DATA, Vol.24

Yamazaki, F.;Motomura, H., Hamada, T. (2000), "Damage Assessment of Expressway Network in Japan Based on Seismic Monitoring", *Proc. of 12th World Conference on Earthquake Engineering*, CD-ROM, 2000; Paper No. 0551

Fujimoto, k. and Midorikawa, S. (2010), "Empirical Relationship between JMA Instrumental Seismic Intensity and Ground Motion Parameters Considering the Effect of Earthquake Magnitude", *Journal of JAEE*, 10(2).

J-SHIS website, http://www.j-shis.bosai.go.jp/

Fujimoto, k. and Midorikawa, S. (2006), "Relationship between Average Shear-Wave Velocity and Site Amplification Inferred from Strong Motion Records at Nearby Station Pairs", *Journal of JAEE*, 6(1).

AIST website, http://staff.aist.go.jp/h.horikawa/2004Chuetsu/source.html

Midorikawa, S., Komazawa, M., Miura, H. (2008), "Relationships between Average Shear-Wave Velocity and Site Amplification Factors Obtained by Records from Yokohama Dense Strong-Motion Network", *Journal of JAEE*, 8(3).

10CUEE CONFERENCE PROCEEDINGS
10th International Conference on Urban Earthquake Engineering
March 1-2, 2013, Tokyo Institute of Technology, Tokyo, Japan

EXPERIMENTAL INVESTIGATION OF THE STRESSES IN A TANK SHELL RESULTING FROM UPLIFT DURING EARTHQUAKES

Miguel Ormeño[1], Tam Larkin[2], and Nawawi Chouw[3]

1) PhD Candidate, Department of Civil and Environmental Engineering, The University of Auckland, New Zealand
2) Senior Lecturer, Department of Civil and Environmental Engineering, The University of Auckland, New Zealand
3) Associate Professor, Department of Civil and Environmental Engineering, The University of Auckland, New Zealand
morm010@aucklanduni.ac.nz, t.larkin@auckland.ac.nz, n.chouw@auckland.ac.nz

Abstract: Storage tanks are critical lifelines that generally supply water or fuel. For this reason, it is very important that these structures remain undamaged or functional after an earthquake. However, previous investigations have demonstrated that strong earthquakes can cause severe damage or collapse of storage tanks. Theoretical studies by other researchers have shown that allowing the tank to uplift (separation of the tank base from the foundation) generally reduces the base shear and the base moment. This paper supplements and enhances the theoretical work performed by others. This paper reports on a series of experiments using a shake table of a model tank made of PVC containing water . A comparison of the seismic behaviour of a fixed base system (tank with anchorage) with a system free to uplift (tank without anchorage) is presented. The experiments were performed using stochastically simulated ground motions based on a Japanese design spectrum and two different tank aspect ratios (height/radius). Measurements were made of the stresses in the tank shell and the horizontal displacement of the top of the tank. Whereas the top displacement and the tank shell acceleration increased when uplift was allowed, axial compressive stresses decreased when the tank was able to uplift.

1. INTRODUCTION

Storage tanks are lifelines that store essential supplies such as potable water or fuel. For this reason, it is important that these structures remain operational after an earthquake. However, evidence in the literature (Haroun 1983, Manos and Clough 1985, Cooper 1997) has shown that large earthquakes can cause severe damage to storage tanks or even collapse in some cases (Figure 1). For these reasons, many studies have been carried out to investigate the seismic behaviour of storage tanks (Housner, 1957, Wozniak and Mitchell, 1978, Veletsos, 1984). A number of standards and design guides have been developed.



Figure 1 Steel tank collapsed during Darfield earthquake, New Zealand (2010)

Current standards for seismic design are based mainly on the spring-mounted masses analogy proposed by Housner (1957) (Figure 2). This model establishes that liquid storage tanks behave mainly in two vibration modes. The portion of the liquid contents which moves rigidly with the tank shell is known as the impulsive mass M_i. The portion of the contents which moves by developing a sloshing motion is called the convective mass M_c.

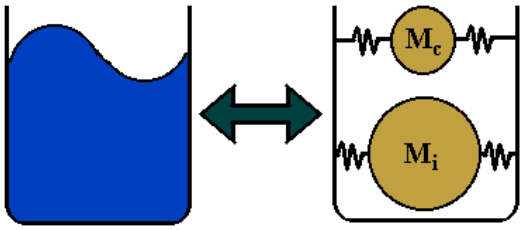


Figure 2 Spring-mounted masses analogy after Housner (1957)

A phenomenon that has been little studied is uplift of the base of the tank. Uplift is the physical separation of the tank base from the tank foundation. The first studies of liquid tanks assumed the structure to be fixed to the base. However, many storage tanks are not anchored to the base and thus these structures are able to uplift. Current design

guidelines for storage tanks (API650 2007, NZSEE 2009) give a conservative seismic design for unanchored tanks (Ormeño et al., 2012). These documents consider that uplift of structures has the potential to lead to structural collapse. Lack of investigation in this matter has established the belief that structural uplift is harmful for structures.

In the case of storage tanks, a few theoretical studies have been carried out concerning the uplift of the base plate. Ishida and Kobayashi (1988) and Malhotra and Veletsos (1994a) used small deflection beam theory to model the bottom plate of the tank and in this way they studied the behaviour of unanchored tanks. Malhotra (2000) utilised the moment-rotation relationship given by Malhotra and Veletsos (1994b) to carry out a simplified nonlinear analysis for performance-based seismic design of tanks. In the example presented by Malhotra (2000), the seismic forces were reduced by more than 70% from that of the equivalent fully anchored tank. Ormeño et al. (in print) investigated the effect of uplift on the displacement and acceleration of the tank shell. However, there is no experimental investigation about the effect of uplift on the tank shell stress which is the parameter that controls the design of this type of structure.

The objective of this work is to quantify the effect of uplift on storage tanks in terms of tank shell acceleration, of the top displacement of the tank and the axial stresses in the tank wall. The study entails the use of a PVC model tank that is subjected to earthquake motion on a shake table.

2. METHODOLOGY

2.1 Tank Model

A PVC tank is utilised to model a prototype steel tank (Figure 3). Two different aspect ratios (H/R: Liquid level to radius ratio) were studied. The properties of the model and prototype are shown in Table 1. Two different fixity conditions were tested, free base and fixed base. Figure 4 shows both cases. Dynamic properties were computed by using NZSEE (2009). Scale factors are shown in Table 2.

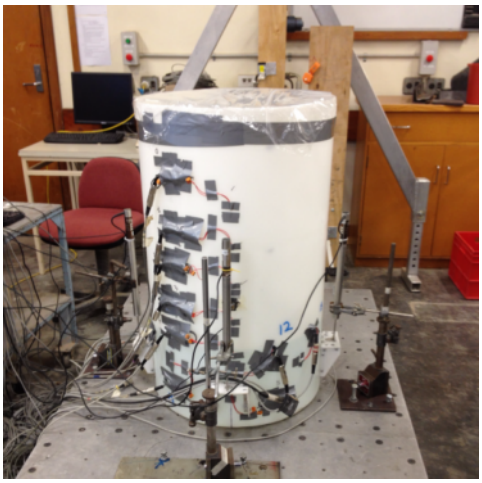


Figure 3 PVC tank model

Table 1 Dimensions and properties of tank model and prototype

	Model	Prototype
Material	PVC	Steel
Young's modulus (MPa)	$1.6*10^3$	$2.068*10^5$
Diameter (m)	0.50	10.00
Height (m) (#)	0.75	15.00
Wall and base thickness (mm)	4	10
Mass of the contents (kg) (#)	147	1178097

(#) These values correspond to an aspect ratio of 3

Table 2 Scale Factors

Dimension	Scale factor
Length	20
Mass (liquid content only)	8000
Time	4.64
Stiffness	369.5
Acceleration	0.93
Force	7440

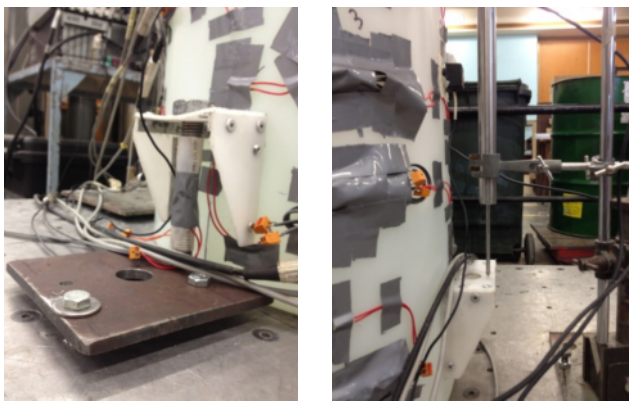


Figure 4 Fixed base case (left) and free base case (right)

2.2 Setup

Strain gauges were implemented on the tank wall to measure the axial distribution of stresses. A wire transducer was attached to the top of the tank to measure the horizontal displacement of the tank shell. An accelerometer was located at a height of 400 mm to measure the tank wall acceleration. Figure 5 shows the setup used.

2.3 Ground Motions

A set of 4 stochastically generated earthquake records based on the Kobe Japanese spectra were used in testing the tank model (Chouw and Hao, 2005). The similitude requirement was met by applying the scale factors shown in Table 2. Time-History of the Ground Motion 1 (GM1) is shown in Figure 6.

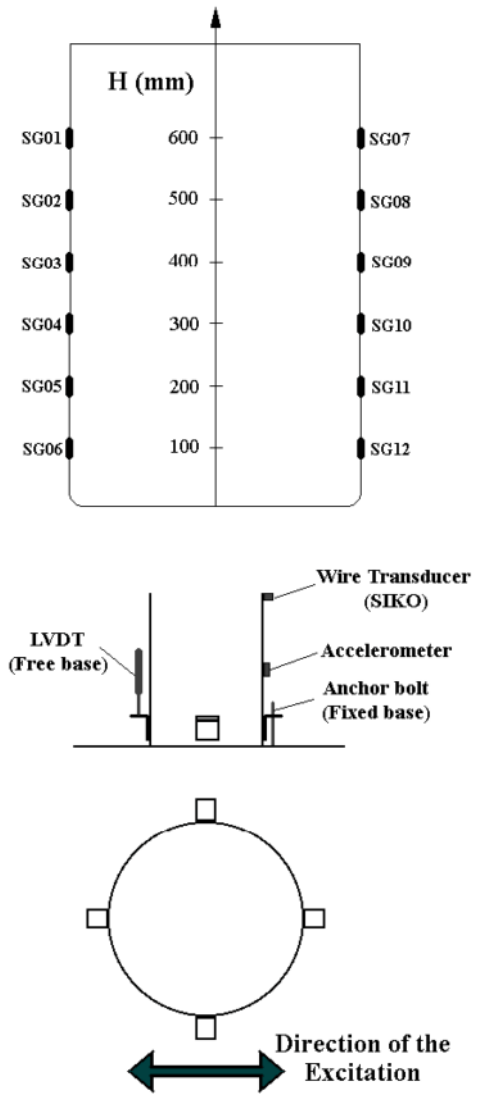


Figure 5 Experimental Setup. Strain Gauges distribution (top), locations of the devices utilised (centre) and plan view of the model (bottom).

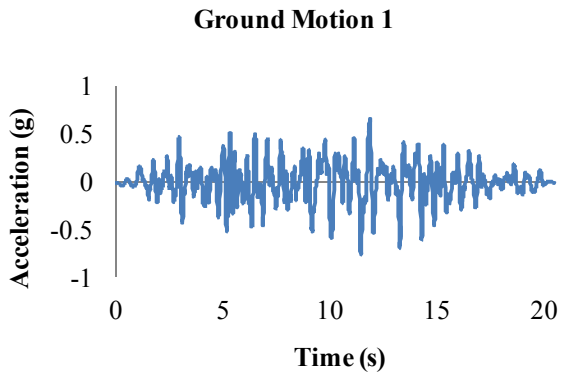


Figure 6 Ground Motion 1 (GM1)

3. RESULTS

Table 3 shows the ratio between the maximum displacement of the top of the tank shell for the free base condition to the one obtained for the fixed base condition. Table 4 shows the ratio between the maximum acceleration of the tank shell for the free base condition to the one obtained for the fixed base condition.

Table 3 Maximum top displacement ratio

Ground Motion	H/R=1	H/R=3
GM1	0.995	1.013
GM2	0.977	1.018
GM3	1.009	1.064
GM4	1.000	1.020

Table 4 Maximum tank shell acceleration ratio

Ground Motion	H/R=1	H/R=3
GM1	1.006	1.098
GM2	1.074	1.194
GM3	1.137	1.027
GM4	1.028	0.934

It is noticeable from the values shown in Tables 3 and 4 that higher values of displacement and acceleration are generally obtained for the free base case, i.e., maximum values of tank shell acceleration and top displacement are higher when the tank is able to uplift. This trend is observed in 13of 16 ratios shown in Tables 3 and 4.

However, the parameter that largely controls the design of liquid storage tanks is the stress in the tank shell. Figures 7 and 8 show the maximum axial compressive stress obtained for GM1 and for both aspect ratios.

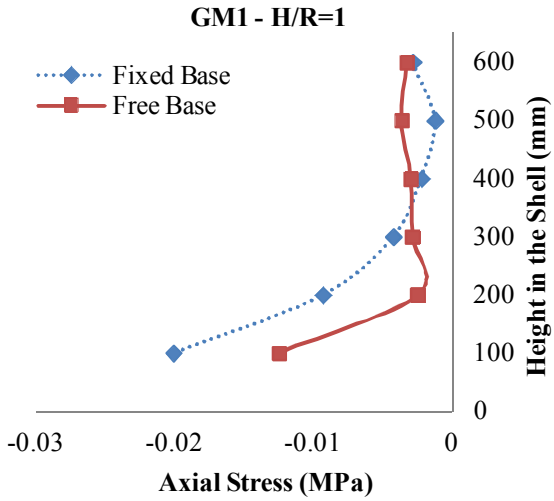


Figure 7 Maximum axial compressive stresses for Ground Motion 1 and H/R = 1

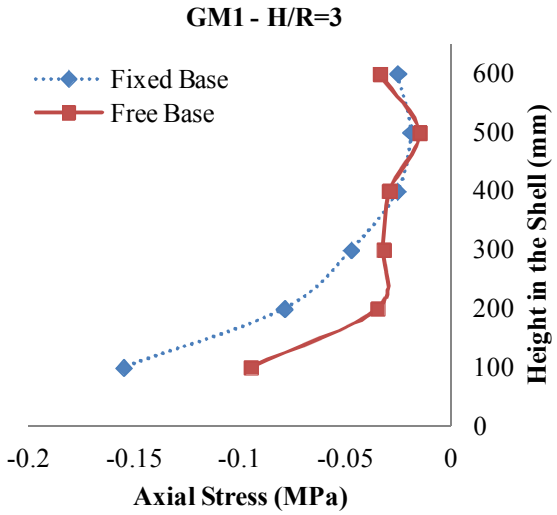


Figure 8 Maximum axial compressive stresses for Ground Motion 1 and H/R = 3

From Figures 7 and 8 it is noticeable that the axial compressive stresses decreased when the tank is able to uplift. To provide an overview of the effect of uplift on the axial compressive stresses, the bottom value (which is the maximum) will be considered. Table 5 shows the ratio between the maximum axial stress at the bottom of the tank wall for the free base condition to that obtained for the fixed base condition.

Table 5 Ratio of maximum axial compressive stress ratio

Ground Motion	H/R=1	H/R=3
GM1	0.622	0.612
GM2	0.713	0.751
GM3	0.599	0.740
GM4	0.553	0.802

It is noticeable from Table 5 that for all the cases analysed (4 ground motions and 2 aspect ratios) the maximum value of axial compressive stress in the tank shell decreased when the tank was able to uplift. The results obtained from Table 5 seem to contradict the results given by Tables 3 and 4. This apparent contradiction can be explained by analysing Figure 9. In Figure 9 the tank-liquid system for the free base case is modeled as a single degree of freedom (SDOF) system. Equation 1 defines the displacement of the SDOF system.

Among the terms shown in the right side of Equation 1, only the horizontal displacement due to the tank shell deformation, u, causes axial stresses in the tank shell. For this reason, the results shown in Tables 3, 4 and 5 are not contradictory, i.e., it is perfectly possible to obtain higher displacements (or accelerations) when the tank is able to uplift because the horizontal displacement (or acceleration) due to the rotation of base plate is included. This component has no role in the fixed base case. However, the axial compressive stress, which is the parameter that controls the design, decreases when the tank is able to uplift.

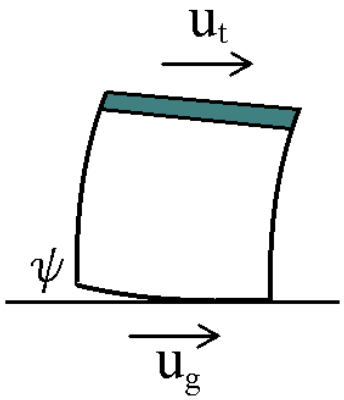


Figure 9 SDOF system for the free base condition

$$u_t = u_g + \Psi \cdot h + u \quad (1)$$

where: u_t = total displacement of the equivalent SDOF system;
u_g = ground displacement;
Ψ = base rotation due to uplift;
h = height of the equivalent SDOF system; and
u = displacement of the SDOF due to the tank shell deformation.

4. CONCLUSIONS

A series of experiments were carried out to determine the effect of base plate uplift on the axial compressive shell stresses in liquid storage tanks. The results showed that uplift has a beneficial effect on the axial compressive stresses in the tank shell. For the 4 ground motions and 2 aspect ratios utilised the maximum compressive stress decreased by approximately 20% to 40% when the tank was able to uplift. These results contradict the current design practice of unanchored tanks. Standards and design guides, API650 (2007) and NZSEE (2009), give a conservative procedure to compute the required tank shell thickness when the tank is able to uplift, considering that uplift has the potential to increase the axial stresses in the tank shell.

With respect to the values of maximum tank wall acceleration, these increased in 88% of the cases analysed when uplift was allowed. Similarly in 75% of the cases analysed the maximum top displacement was higher when the tank was placed on a free base than when the tank was on fixed base. At first sight these results seem to be contradictory to the results obtained for the axial stresses, but in fact, it is possible to get higher displacements and accelerations of the tank wall and lower induced wall stresses. The explanation of this feature of tank response is that it is only the component of the total displacement due to the tank wall deformation that causes stresses in the shell. The horizontal displacement due to the base plate uplift has no impact on the tank shell stresses.

Finally, it is recommended that the current standards and design guides be reviewed with respect to the procedures of design concerning the seismic design of storage tanks when uplift is included.

Acknowledgements:

The authors wish to thank the Chilean Government for awarding the first author with the scholarship "Becas Chile" for his doctoral study at the University of Auckland.

References:

API (2007). Welded steel tanks for oil storage. API Standard 650, 11th Edition, American Petroleum Institute.

Chouw, N., Hao, H. (2005). "Study of SSI and non-uniform ground motion effect on pounding between bridge girders", *Soil Dynamics and Earthquake Engineering*, **25**, 717-728

Cooper, T. W. (1997) "A study of the performance of petroleum storage tanks during earthquakes, 1933–1995", NIST No. GCR 97-720, U.S. Dept. of Commerce, National Institute of Standards and Technology, Gaithersburgh, Md.

Haroun, M. A. (1983), "Behavior of Unanchored Oil Storage Tanks: Imperial Valley Earthquake", *Journal of Technical Topics in Civil Engineering*, ASCE, **109(**1), 23-40.

Housner, G. W. (1957), "Dynamic pressures on accelerated fluid containers", *Bulletin of the Seismological Society of America*, **47**, 15-35.

Ishida, K., and Kobayashi, N. (1988), "An effective method of analyzing rocking motion unanchored cylindrical tanks including uplift", *J. Pressure Vessel Technology*, ASME, **110**, 76-87.

Malhotra, P. K. (2000), "Practical nonlinear seismic analysis of tanks", *Earthq. Spect.*, **16**(2), 473–492.

Malhotra, P. K. and Veletsos, A. S. (1994a), "Beam model for base uplifting analysis of cylindrical tanks", *J. Struc. Eng.*, ASCE, **120**(12), 3471-3488.

Malhotra, P. K. and Veletsos, A. S. (1994b), "Uplifting analysis of base plates in cylindrical tanks", *J. Struc.Eng.*, ASCE, **120**(12), 3489-3505.

Manos, G. C. and Clough, R. W. (1985), "Tank damage during the May 1983 Coalinga earthquake", *J. Earthq. Eng.. Struct. Dyn.*, **13(**4), 449-466.

NZSEE (2009). Seismic design of storage tanks - Recommendations of a study group of the New Zealand National Society for Earthquake Engineering.

Ormeño, M., Larkin, T., and Chouw, N. (2012), "Comparison between standards for seismic design of liquid storage tanks with respect to soil-foundation-structure interaction and uplift", *Bulletin of the New Zealand Society for Earthquake Engineering*, **45**, 40-46.

Ormeño, M., Larkin, T., and Chouw, N. (in print), "Influence of uplift on liquid storage tanks during earthquakes", *International Journal of Coupled Systems Mechanics*

Veletsos, A. S. (1984), "Seismic response and design of liquid storage tanks", *Guidelines for the seismic design of oil and gas pipeline systems*, Technical Council on Lifeline Earthquake Engineering, ASCE, New York, 255–370.

Wozniak, R. S. and Mitchell, W. W. (1978), "Basis of seismic design provisions for welded steel oil storage tanks", API Refining 43rd

10CUEE CONFERENCE PROCEEDINGS
10th International Conference on Urban Earthquake Engineering
March 1-2, 2013, Tokyo Institute of Technology, Tokyo, Japan

EVALUATION OF GAS DISTRIBUTION PIPELINES NETWORK SUBJECTED TO SEISMIC WAVE PROPAGATION IN GREATER TEHRAN AREA, IRAN

Danesh Nourzadeh[1)], Khosrow Bargi[2)], and Shiro Takada[3)]

1) Research Assistant, Dept. of Civil & Environmental Engineering, Carleton University, Canada
2) Professor, School of Civil Engineering, University of Tehran, Iran
3) Adjunct Professor, School of Civil Engineering, University of Tehran, Iran
danesh_nourzadeh@carleton.ca, kbargi@ut.ac.ir, takada_smartinfra@kobe.zaq.jp

Abstract: In this paper, total behavior of The Greater Tehran gas distribution pipelines during seismic wave propagation is evaluated. By synchronizing and adjustment of distribution maps of the pipelines, ground conditions and seismic inputs, various different cases for evaluation are selected. These cases are analyzed by precise finite elements method. In the numerical evaluations, different pipe specifications including material, size, end conditions and bends, soil conditions and seismic wave attributes including peak ground acceleration, time history and directivity are considered. After comparison of the numerical results and simpler formulas, the basic criteria for damage assessment of the pipelines are created, which are used for network analysis. The results showed a relatively satisfying overall performance for the network; however, in several cases, some countermeasures for rehabilitation and improvement of the system reliability and safety are suggested and discussed.

1. INTRODUCTION

Pipelines are one of the most widespread lifelines in urban life, which have so many different usages in the contemporary days. Obviously gas distribution systems are among the most important types because of their purpose, yet vulnerability and high risks and consequences of the accidents and failures. This importance urges the stakeholders and decision makers to take all the significant natural and manmade hazards into the consideration for the risk management of these major lifelines.

Arguably the most significant and destructive natural hazards for the buried pipelines is the seismic activity, while this hazard can affect the structure in different ways as seismic transient wave, faulting, liquefaction, and landslide. Among all the mentioned effects of the earthquake, the seismic wave propagation is the phenomenon that occurs globally in a wide area; while the others are likely to happen locally in the vicinity of faults, problematic soils or the unstable slopes.

In this paper, the risk of gas distribution pipelines in the Greater Tehran area capital of Iran, during seismic wave propagation is subject of the study. The risk of this network was previously assessed for the liquefaction hazard by the authors (Nourzadeh et al. 2011-a, 2011-b), and this research is a continuation and follows the same procedure. In the previous research, it was proven that the gas distribution pipelines of Tehran has relatively low risk during the occurrence of liquefaction, and the only methodology suggested for boosting the performance of the network was planning several monitoring stations and implementation of a synchronized control and monitoring system, known as SCADA (supervisory control and data acquisition), to mitigate the risks of the network. In this research, first the seismicity of the area is reviewed, then several selected cases are analyzed numerically, of which the results are used to determine the network performance during the seismic wave propagation hazard.

2. SEISMICITY OF TEHRAN

The seismicity of Tehran Greater Area has been analyzed previously by different methodologies including deterministic seismic scenarios, and probabilistic seismic hazard analysis (PSHA). It is mostly advised to use the former assessments results in a risk assessment research (Klügel et al. 2006), while the latter leads to type of results mostly used in new designs. In this regard, the seismic scenarios of the area are used in the current research, which are described in the following.

The seismic scenarios are derived deterministically for causing the most destructive effect regardless of the probability of occurrence. In this method, different classes of the ground motions are considered in the area including historic and prehistoric earthquakes and also the maximum credible level of the shaking related to the known major faults. In the case of the Tehran Greater Area, the last strong ground motion happened back to more than 150 years ago, and the major active faults are shown in Figure 1.

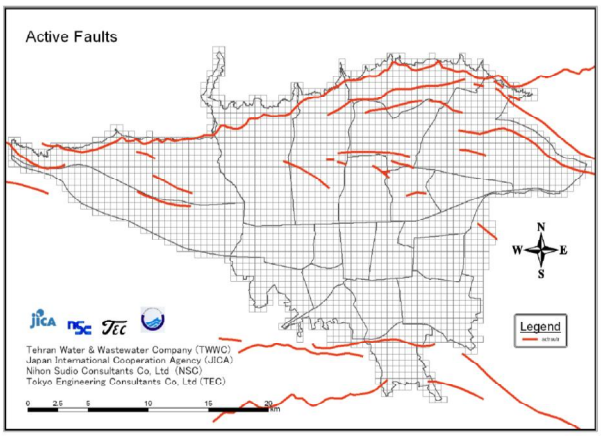


Figure 1 Major Active Faults in the Tehran Greater Area (after JICA, 2000)

Four different scenarios were derived for the area in the previous studies based on three major active faults, namely Mosha, North Tehran and Ray Faults along with a floating fault model to take the hidden faults under the alluvial layers. The mechanism for most of these faults is strike slip as it was verified later (Ashtari et al. 2005), and the length of the faults exceed 68 km. The specifications of the faults and the resulted ground motions are shown in Table 1.

Table 1 Selected Significant Faults and Resulted Ground Motion Scenarios

	Mosha Fault	N. Tehran Fault	Ray Fault	Floating Fault
Length (km)	68	58	26	13
Width (km)	30	27	16	10
Depth (km)	0	0	5	5
Magnitude (M_w)	7.2	7.2	6.7	6.4
Max. PGA (g)	0.3	0.4	0.6	0.6

3. SEISMIC RESPONSE ANALYSIS OF GAS PIPELINES

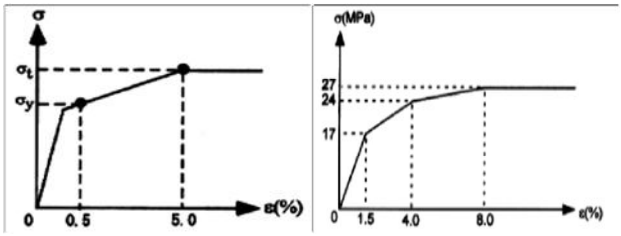
3.1 Pipelines Specifications

The exact data on gas transmission and distribution pipelines in the Greater Tehran Area were gathered and used in the numerical simulations as shown in Table 2. Also the sizes and dimensions of the pipelines were gathered based on the construction manuals and standards, and considered respectively in the analyses.

Table 2 Specificaions of the Pipelines Network

	Main Transmission Network	Local Distribution Network
Internal Pressure	250 psi	60, 100 psi
Pipe Material	Steel: API 5L- Gr. B	Steel: API 5L- Gr. B
	Steel: API 5L- X 42	PE: HDPE 80, 100
Pipe Diameters	2- 48 inches	Steel: 2- 12 inches
		PE: 63- 160 mm
Burial Depth	1- 1.20 m	1- 1.20 m
Coating	Tar or 3 layered PE	Tar or 3 layered PE

As mentioned in the table above, the materials used in the pipeline network are steel and polyethylene (PE), so different numerical models for representing these materials were selected for the analysis. The mathematical models were selected to consider the nonlinear behavior of the pipe materials as shown in Figure 2.



(a) (b)

Figure 2 Material Models for (a) Steel Pipes, and (b) PE pipes (after Pezeshki et al, 2004)

3.2 Analytical Models

Based on the specification of the pipelines used in the gas distribution network in Tehran, different cases were selected for study to represent the overall response of the system. In this regard, 12 different pipes including 8 steel pipes (4 high pressure transmission pipes), and 4 different sizes of PE pipes were selected to be analyzed. The lengths of the continuous pipelines were selected as 700 and 1400 m for all cases, taking the findings and suggestion of the previous studies (JWWA, 1997, Lee et al. 2009) into the consideration.

Based on the soil distribution maps and properties of the dominant types in the greater Tehran area, 3 different soil types were selected as the surrounding soil model for the pipelines. The properties of soil types were selected as dense sand (DS) with internal friction angle (ϕ) of 35º, loose sand (LS) with ϕ of 25 º, and soft clay (SC) with cohesion (C) of 16.8 kPa. According to these assumptions, surrounding soil was modeled as nonlinear springs in three dimensions using

the basic formulation in the American codes (ALA, 2001).

The finite element model was generated using beam elements for the pipes, and three dimensional soil springs. The earthquake excitations were applied to the other end of the mentioned soil elements as displacement time-histories. For this analysis, time-histories of 3 major earthquakes of Tabas 1978, Northridge 1994, and Kobe 1995 were selected (data obtained from www.usgs.gov) and scaled to the selected PGAs for the analysis ranging from 0.3 to 0.65g. After generating design acceleration records, the time-histories were converted to the displacement records by the numerical integration in time, of which examples are shown in Figure 3 for scaling PGA of 0.65g.

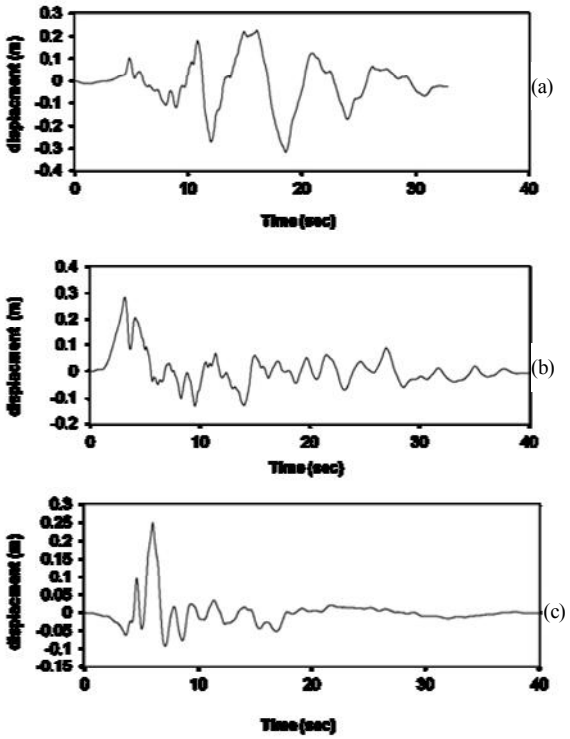


Figure 3 Displacement Time-histories of (a) Tabas, (b) Northridge, and (c) Kobe Earthquakes Scaled for 0.65g PGA

The earthquake excitations were assumed to act on the pipelines as the combined effect of surface and body (shear) waves. In this regard, the ground motions in 3 dimensions were applied to the pipelines with the incident angle of 0 and 45 degrees, and in both types the vertical component of the motion was scaled to 2/3 of the horizontal magnitude. The destructive effect of the seismic wave propagation on the pipeline is inducing differential displacements in the length as the result of phase delay of the received wave along the pipeline. Therefore the minimum seismic wave length of 100m was selected for the ground motions and the seismic inputs were assigned correspondingly.

3.3 Numerical Analysis and Results

The numerical simulations were conducted by the finite elements method using ABAQUS v6.10 software. In the analyses, the straight and bended (90º and 135º) pipelines with lengths of 700 and 1400m were discretized into 10m length beam models connected to 3D nonlinear soil springs at the nodes. Also the effect of soil and internal pressures were neglected in the analysis, as the effects are examined to be small (also in Lee et al. 2009).

The end conditions of the pipelines were assumed as combinations of fixed and pinned, however by a simple sensitivity analysis, it was found that the fixed-fixed assumption leads to more critical responses. The analyses started from the highest seismic action level (PGA of 0.65g), and continued until the pipelines are safe. The acceptance criteria for the pipeline safety were defined as strain levels under the allowable strains shown in Table 3. In the table, t and R refer to the thickness and radius of the pipes.

Table 3 Allowable Strains for Pipelines in Seismic Wave Propagation (ALA 2001, JGA 2000)

Failure Mode	Allowable Strain
Low-Cycle Fatigue, Buckling	0.175 t/R
Tension	3% for Steel Pipe
	20% for PE Pipes

Based on the described model assumptions, more than 340 FE analyses were conducted and the results were gathered in a database. The total behavior of the pipes were deterministically considered to be the most critical response during 3 time-histories, and therefore the overall results are shown in Table 4.

Table 4 Finite Elements Analysis Results for the Selected Cases

Pipe Mat.	Pipe Diameter	Bend Angle	Soil Type	PGA range	Response Level
Steel-Gr B	8" 12"	0	all	≥ 0.65 g	Major Damage
Steel-X42	12" to 30"	0	all	≥ 0.65 g	Major Damage
Steel-Gr B	4" to 12"	0	all	≥ 0.5 g	Moderate Damage
Steel-X42	12" to 30"	0	all	≥ 0.5 g	Moderate Damage

Pipe Mat.	Pipe Diameter	Bend Angle	Soil Type	PGA range	Response Level
Steel-Gr B	12”	90	all	≥ 0.65 g	Moderate Damage
Steel-X42	12” to 30”	90	all	≥ 0.65 g	Moderate Damage
Steel-Gr B	6” to 12”	45	all	≥ 0.6 g	Moderate Damage
Steel-X42	12	45	all	≥ 0.6 g	Moderate Damage
PE	all	all	all	≤ 0.65 g	Safe

In the table above, “Major Damage” is assumed the failure in tension, while “Moderate Damage” corresponds to the buckling and wrinkling failure in the pipes. As it is understood from the above mentioned results, the soil conditions do not play a major role in the response of the pipelines; also the PE pipes have shown very desirable behavior during this seismic action.

4. Damage Assessment of Gas Distribution Network

After response analysis of the buried pipelines during the selected seismic activities, the total network reliability and overall response should be assessed. In this regard, the damage distribution maps were produced in GIS environment. The final result of the analysis is shown in Figure 4.

In this map, the greater Tehran Area is divided into blocks and the PGA distribution corresponding each of the seismic scenarios were assigned. Comparing the PGA distributions, soil properties and pipeline network map gives the damage locations in the network as it is shown in the figure.

As it was shown in Table 4 and Figure 4, in some cases there will be a major damage in the gas distribution pipelines despite relatively satisfying performance of the system. It is also demonstrated that the main transmission pipelines will probably experience significant damages during the high seismic activities, which will lead to catastrophic events. Therefore it is essential to implement mitigation and retrofit plans for improving the performance of the network.

There are several mitigation and retrofit options for this matter as it is briefly discussed as following:

1- It is advised to use a central monitoring and spontaneous action station for automatic shut down of the system flow in case of disaster. This suggestion by the authors led to starting a preliminary SCADA system with an array of seismographs for real-time monitoring and immediate measures in the cases of earthquake occurrence for Tehran lifeline networks.

2- As the main transmission pipelines are believed to suffer the earthquake effects, it is suggested to implement secondary and alternative routes in north and south of the greater Tehran area to improve the redundancy in the system.

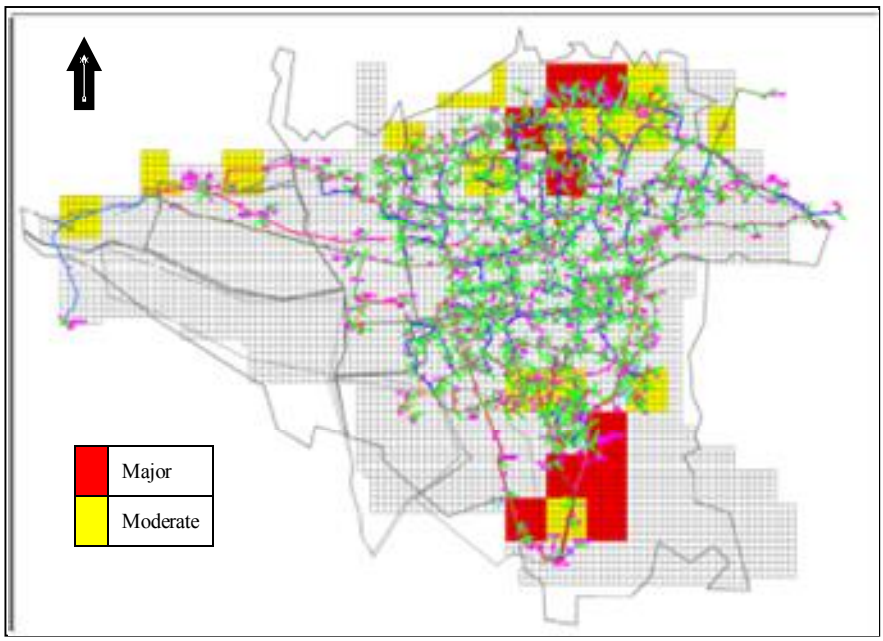


Figure 4 Damage Distribution Map in Tehran Gas Distribution Network

3- In all areas with moderate and major damage indexes, it was advised to use automatic shutoff valves for the pipelines to mitigate the secondary effects of the pipeline failures as the internal pressure of the pipelines are high, which could lead to probable explosions after the leakage.

4- It could be suggested to replace the vulnerable medium pressure pipelines with PE pipes in a long term plan, but in the short term the best mitigation plan could be using the monitoring systems and automatic shutoff valves.

5- It is advised to consider some emergency stations for field patrol and also post earthquake countermeasures in the highlighted areas.

5. CONCLUSIONS

In this paper, response of buried gas pipelines was analyzed during seismic wave propagation in the greater Tehran area in Iran. Using the fragility analyses of the individual structures, the overall performance and damage distribution in the system were derived and several mitigation and retrofit plans were discussed to boost the performance and mitigate the risk of the pipelines network during the seismic activity.

Acknowledgements:

This paper was based on a research project funded by Tehran Province Gas Company (TPGC). The authors would like to acknowledge the kind supports of the members of this organization.

References:

American Lifeline Alliances (ALA), (2001), "Guidelines for Design of Buried Steel Pipes", ASCE, USA.

Ashtari, M., Hatzfeld, D. and Kamalian, N. (2005),"Microseismicity in the Region of Tehran" *Journal of Tectonophysics*, Elsevier, **395**, 193-208.

Japan Gas Association, (2000), "Seismic Design Guideline for High Pressure Gas Pipelines". (Written in Japanese)

Japan International Cooperation Agency (JICA), (2000), "The Study on Seismic Microzoning of the Greater Tehran Area in the Islamic Republic of Iran", Main Report to Tehran Municipality.

Japan Water Works Association (JWWA), (1997), "Seismic Design Specifications for Water Facilities", Japan. (Written in Japanese)

Klügel, J.U., Mualchin, L. and Panza, G.F. (2006), "A Scenario-based Procedure for Seismic Risk Analysis" *Journal of Engineering Geology*, Elsevier, **88**, 1-22.

Lee, D.H., Kim, B.H., Lee, H. and Kong, J.S. (2009), "Seismic Behavior of a Buried Gas Pipeline under Earthquake Excitations" Journal of Engineering Structures, Elsevier, 31, 1011-1023.

Nourzadeh, D., Bargi, K. and Takada, S. (2011), "Reliability Assessment of Tehran Province Gas Distribution Pipeline System during Liquefaction", *Proceedings of 8th International Conference on Urban Earthquake Engineering*, Japan.

Nourzadeh, D., Bargi, K. and Takada, S. (2011), "Evaluation of Tehran Province Gas Distribution Pipelines during Liquefaction", *Proceedings of 6th International Conference on Seismology & Earthquake Engineering*, Iran.

10CUEE CONFERENCE PROCEEDINGS
10th International Conference on Urban Earthquake Engineering
March 1-2, 2013, Tokyo Institute of Technology, Tokyo, Japan

COLLAPSE VULNERABILITY ASSESSMENT OF EXISTING CONCRETE BUILDINGS

K.J. Elwood [1], M. Baradaran Shoraka[2], and T.Y. Yang [3]

1) Associate Professor, Dept. of Civil Engineering, University of British Columbia, Vancouver, Canada
2) Graduate Student, Dept. of Civil Engineering, University of British Columbia, Vancouver, Canada
3) Assistant Professor, Dept. of Civil Engineering, University of British Columbia, Vancouver, Canada
elwood@civil.ubc.ca, majidbs@gmail.com, yang@civil.ubc.ca

Abstract: Existing reinforced concrete buildings lacking details for ductile response during earthquake shaking represent a prevalent construction type in high seismic zones around the world. The poor seismic performance of these non-ductile concrete buildings is evident from recent earthquakes in Chile, New Zealand and Japan. Seismic rehabilitation of these existing buildings plays an important role in reducing urban seismic risk; however, with the massive inventory of existing concrete buildings and the high costs of seismic rehabilitation, it is necessary to start by identifying and retrofitting those buildings which are most vulnerable to collapse. Numerous sources of uncertainty complicate the ability to identify buildings which are vulnerable to collapse. For this reason, it is important to develop estimates of collapse probability to account for all significant sources of uncertainties. This paper will introduce the concept of collapse indicators, design and response parameters that are correlated with "elevated" collapse probability. The methodology for identifying collapse indicators is based on results of comprehensive collapse simulations. Appropriate collapse indicators and corresponding limits are evaluated by seeking trends between probability of collapse and collapse indicators. This paper will discuss significant challenges which pose a barrier to the assessment of collapse indicators that are applicable for the wide range of existing concrete buildings.

1. INTRODUCTION

In the mid-1990s new seismic rehabilitation guidelines (e.g. FEMA 273 [10]) were introduced to the world, providing the structural engineering profession with the first generation of 'performance-based' procedures for seismic assessment and rehabilitation design. These documents revolutionized the assessment of existing buildings by encouraging the use of nonlinear analysis, by enabling the engineer to select project-specific performance objectives, and perhaps most importantly, by recognizing that structural collapse was limited by both strength and deformation capacity. The past 15 years has seen modest improvements to this first-generation performance-based design procedure as FEMA 273 [10] has evolved into of ASCE/SEI 41 [3], including updated acceptance criteria for concrete components based on new experimental data [8]. However, the overall framework remains essentially deterministic and inconsistent conservatism in specified deformation capacities throughout the document may impact the reliability of the predicted performance of a building structure. Furthermore, the component-based assessment procedures (i.e. once one component is determined to have exceeded a performance level, the entire structure is deemed to have exceeded the performance level) ignore the ability of a structural system to redistribute loads as damage accumulates and will tend to lead to conservative assessments of collapse vulnerability. Seismic evaluation documents based on checklist assessments (e.g. ASCE/SEI 31 [2]) are also generally conservative to ensure dangerous buildings are not misdiagnosed. As currently formulated, ASCE/SEI 31 and ASCE/SEI 41 are not capable of reliably determining the relative collapse risk between different non-ductile concrete buildings. From a public policy standpoint, the ability to economically make this distinction across the large inventory of existing concrete buildings is a critical need and a necessary next step in the evolution of seismic rehabilitation documents.

ATC-76-5 [16] identified the following critical needs for addressing the collapse risk associated with older concrete construction:

- Improved procedures for identifying building systems vulnerable to collapse, including simple tools that do not require detailed analysis.
- Updated acceptance criteria for concrete components based on latest research results.
- Identification of cost-effective mitigation strategies to reduce collapse risk in existing concrete buildings.

To address the first critical need, ATC-76-5 proposed a methodology for identifying parameters, termed collapse indicators, correlated with an elevated probability of collapse based on results of comprehensive collapse simulations and estimation of collapse probabilities for prototypical concrete buildings. Ideally there should be a variety of collapse indicators, ranging from those appropriate for rapid

assessment to others used to identify collapse potential based on results of detailed nonlinear analysis. Collapse indicators for rapid assessment must be very simple parameters which can be established based on basic information available from a quick survey of the building or engineering drawings. Collapse indicators for detailed collapse prevention assessment can make use of the results from building analyses. This paper will demonstrate a methodology to identify collapse indicators and discuss challenges to be overcome in the identification of collapse indicators representative of a general inventory of buildings. The methodology discussed below was initially proposed as part of the ATC-76-5 project [16] funded by NIST, and will be further developed in ongoing projects (ATC-78 and ATC-95) funded by NIST and FEMA. This paper does not provide specific recommendations for collapse indicator limits, but instead focuses on the development of the methodology. The goal of the ongoing ATC projects is to refine the methodology and ultimately lead to simplified practical guidance for engineers on how to identify collapse vulnerable buildings based on limits for selected collapse indicators.

2. POTENTIAL COLLAPSE INDICATORS

The identification of collapse indicators appropriate for engineering practice, and establishing limits on these indicators, is best accomplished through detailed analytical studies such as those described in Section 3. However, before embarking on the analytical studies, it is essential to come up with a list of potential collapse indicators from which the recommended collapse indicators will be selected. Engineering judgment and experience with collapse analyses were used to select the preliminary list of potential collapse indicators below. It is anticipated that this list will evolve as further experience is gained from the analyses described in Section 3.

Ideally there should be a spectrum of collapse indicators, ranging from those appropriate for rapid assessment to others used to identify collapse potential based on results of detailed nonlinear analysis. Collapse indicators for rapid assessment must be very simple parameters which can be established from basic information available from a quick survey of the building or engineering drawings. Conversely, collapse indicators for detailed collapse prevention assessment can make use of the results from nonlinear analyses. It is proposed to categorize collapse indicators into two fundamental types:

Design parameter collapse indicators: These collapse indicators are determined based on design features of a concrete building, including reinforcement details, structural system layout, and relative strength and stiffness of members. These indicators can be further sub-categorized as "rapid assessment" (RA) or "engineering calculation" (EC) collapse indicators, where the former can be determined from a quick survey of the building or engineering drawings and the latter requires some calculation of capacities and demands based on engineering drawings. RA and EC collapse indicators will be useful for refining the seismic evaluation procedures in ASCE/SEI 31 [2].

Response parameter collapse indicators: These collapse indicators reflect the response of the structure based on results from building analysis (BA). Generally the most refined collapse indicators are expected to be derived from results of nonlinear analysis and provide system-level acceptance criteria for the Collapse Prevention performance level.

Table 1 provides a list of potential collapse indicators to be considered for investigation in the analytical studies discussed in Section 3. These collapse indicators have been grouped based on the classification described above, and further grouped as component or system-level parameters. Component Building Analysis indicators shown in Table 1 (BA – C#) can be interpreted as equivalent to component acceptance criteria in ASCE/SEI 41 [3]. It is anticipated that relationships may exist among the indicators, as vectors of indicators may be found to provide a better indication of collapse potential than any one indicator. For example, if the average minimum transverse reinforcement ratio (RA-C1) is less than a specific value and the column-to-floor area ratios (RA-S1) are greater than a specific value, then collapse potential is expected to be high.

3. COLLAPSE SIMULATION

In order to better understand and define the collapse potential for concrete buildings, model building prototypes are developed for nonlinear analyses using OpenSees [17]. These models, capable of capturing onset of structural collapse, enable the selection of collapse indicators having strong correlation with collapse potential. Using the prototypes, the Design Parameter collapse indicators listed above, including geometric and mass properties (e.g. plan dimensions, building height), can be varied to explore the effects on collapse probability. Sophisticated building prototype models allow explicit consideration of collapse probability considering both loss of vertical load carrying capability and lateral dynamic instability; uncertainty in modeling and ground motion are also accommodated.

Collapse of real buildings is highly dependent on the complex behavior and interaction among individual components. The analyses to refine the selection of collapse indicators utilize building models to explore characteristic behavior and the effects of parametric variations.

In contrast to ductile structural systems, non-ductile concrete buildings will typically experience gravity-load collapse resulting from loss of vertical load carrying capacity in critical components prior to experiencing a "side-sway" collapse resulting from degradation in lateral resistance [5]. The nonlinear building models used for this study incorporate elements capable of approximately capturing the loss of vertical load carrying capacity for critical gravity-load supporting components (e.g. columns [4,7] and slab-column connections [12]) and account for P-delta effects. It should be noted that these models provide a relatively simple representation of a very complex phenome-

Table 1: Examples of collapse indicators

Type of Collapse Indicator		System-level		Component-level	
Design Parameters	**Rapid Assessment (RA)** *Quantities that can be determined from a quick survey of the building or engineering drawings.*	*RA-S1.*	Maximum ratio of column-to-floor area ratios for two adjacent stories.	*RA-C1.*	Average minimum column transverse reinforcement ratio for each story.
		RA-S2.	Maximum ratio of horizontal dimension of the SFRS in adjacent stories.	*RA-C2.*	Minimum column aspect ratio.
		RA-S3.	Maximum ratio of in-plane offset of SFRS from one story to the next to the in-plane dimension of the SFRS	*RA-C3.*	Misalignment of stories in adjacent buildings.
		RA-S4.	Plan configuration (L or T shape versus rectangular)		
		RA-S5.	Minimum ratio of column area to wall area at each story**		
	Engineering Calculations (EC) *Quantities that require some calculation of capacities and demands based on engineering drawings, but do not require structural analysis results from computer modeling.*	*EC-S1.*	Maximum ratio of story stiffness for two adjacent stories	*EC-C1.*	Maximum ratio of plastic shear capacity ($2M_p/L$) to column shear strength, V_p/V_n .
		EC-S2.	Maximum ratio of story shear strength for two adjacent stories.	*EC-C2.*	Maximum axial load ratio for columns with $V_p/V_n > 0.7$.
		EC-S3.	Maximum ratio of eccentricity (distance from center of mass to center of rigidity or center of strength) to the dimension of the building perpendicular to the direction of motion.	*EC-C3.*	Maximum ratio of axial load to strength of transverse reinforcement (45 deg truss model).
		EC-S4.	Portion of story gravity loads supported by columns with ratio of plastic shear demand to shear capacity > 0.7.	*EC-C4.*	Maximum ratio of joint shear demand (from column bar force at yield) to joint shear capacity for exterior joints.
				EC-C5.	Maximum gravity shear ratio on slab-column connections.
Response Parameters	**Building Analysis (BA)** *Quantities for detailed collapse prevention assessment using the results from nonlinear building analyses.*	*BA-S1.*	Maximum degradation in base or story shear resistance.	*BA-C1.*	Maximum drift ratio.
		BA-S2.	Maximum fraction of columns at a story experiencing shear failures.	*BA-C2.*	Maximum ratio of deformation demands to ASCE/SEI 41 limits for columns, joints, slab-column connections and walls.
		BA-S3.	Maximum fraction of columns at a story experiencing axial failures.		
		BA-S4.	Minimum strength ratio (as defined in ASCE/SEI 41).		

* Collapse indicator notation: RA = Rapid Assessment; EC = Engineering Calculation; BA = Building Analysis; S=System; C = Component.

** May not result in collapse but could help prevent collapse if a mechanism forms.

Table 2: Four and seven story non-ductile RC frame structures

Num. of Stories	Num. of Bays	Story Height (m)	Bay Width (m)	Framing System	Period (s)
4[1]	3	3.96	7.62	Space	1.98
7[2]	8	4.12	5.72	Perimeter	1

[1] [14]; [2] [13]

non at the point of gravity-load failure, and hence, may lack some sophistication required to accurately capture the behavior of the building to the point of total collapse. In particular, given the lack of data available for validation, modeling of three dimensional gravity load redistribution through a slab floor system after gravity load failure of a single component should be considered approximate at best. Despite possible inaccuracies, the failure models provide good estimates of observed collapse behavior of simple 2D frames [6,9,20].

One significant challenge that must be overcome to undertake this analysis is the distinction between the "true" point of gravity-load collapse and non-convergence due to numerical instability of the model. In this study, collapse is detected based on a comparison of floor-level gravity load demands and capacities (adjusted at each time step to account for member damage and allow for load redistribution) [5,6,9]. The first point when floor-level vertical load demands exceed the total vertical load capacity at that floor is defined as gravity-load collapse for the building system. Non-convergence of the analysis prior to significant degradation in the capacity to resist gravity loads and not associated with large lateral displacements (side-sway collapse) will not be considered as collapse, and the results of such analysis will be omitted from the calculation of collapse probabilities.

The following sections briefly describe the scope for the analytical studies. First, the key elements of the numerical models are introduced. In this paper, four- [14] and seven-story [13] non-ductile reinforced concrete frame buildings located in Los Angeles, California, are used as example structures to illustrate the methodology. Next, the model and ground motion uncertainties are briefly explained. Finally, the two approaches used to establish limits on the collapse indicators (design and response parameters) are discussed.

3.1 Numerical Model

Two-dimensional finite element models are used to simulate the seismic response of the buildings using OpenSees [17]. A fixed-base model is used in the analysis; as a result soil-structure foundation interaction is neglected. The frame elements are modeled using the force-based beam–column model with distributed nonlinear fiber sections. The joints are modeled using the Alath and Kunnath model [1] which includes the pinching hysteric behaviour to account for the degradation usually seen in these non-ductile elements. Axial failure of joints is not considered in this example. The shear and axial response in the columns are modeled using the modified Limit State material model [4,7] recently implemented in OpenSees. Key characteristics of the structures are summarized in Table 2.

3.2 Record- to-record and model uncertainty

Performance-based earthquake engineering enables probabilistic prediction of structural response, incorporating key sources of uncertainty in the process. By using a suite of earthquake records, nonlinear dynamic analyses (via incremental dynamic analysis, IDA [19], and/or multiple stripe analysis, MSA [11]) directly incorporates information about variability in ground motions in the collapse performance assessment. However, nonlinear dynamic analysis alone does not account for how well the structural model represents the collapse behavior of the building; hence, model uncertainties should also be accounted for in the process of collapse simulation. These modeling uncertainties are especially important in predicting collapse, because of the high degree of empiricism and uncertainty in predicting deformation capacity and other critical parameters.

In this methodology the uncertainty for each random variable is explicitly considered in the analysis and reflected in the final probabilities of collapse. The random variables selected with the respective probability distribution should have the capability of capturing the major uncertainties inherent in non-ductile reinforced concrete frames. Uncertainty in the shear and axial failure models for non-ductile columns are considered as the main sources of model uncertainty for the example buildings. The shaded area shown in Fig. 1, presents the entire outcome of failure model variability considered for these non-ductile columns. The variability in the drift at column shear and axial load failure is represented by a lognormal distribution with a mean equivalent to the limit-state material failure models and a coefficient of variation of approximately 0.3 [9].

In addition to model variability, record to record variability is considered in the process. Accounting for record to record uncertainty is possible by selecting an appropriate suite of ground motions specific for the building site and the anticipated hazard level with a good fit to the conditional mean spectrum. Ten ground motions for each hazard level are considered using MSA in this example.

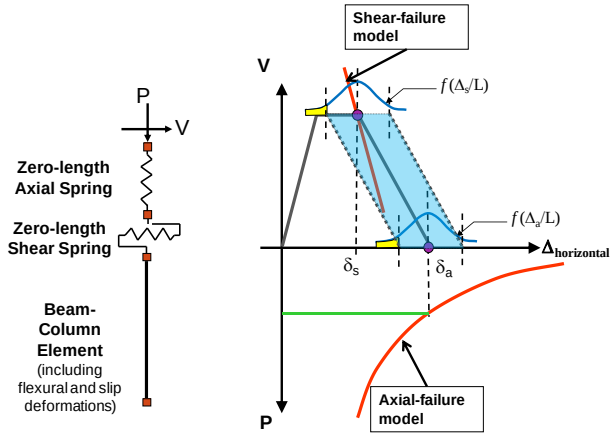
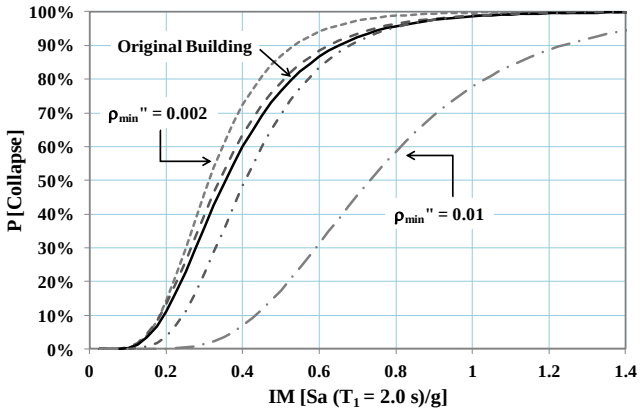


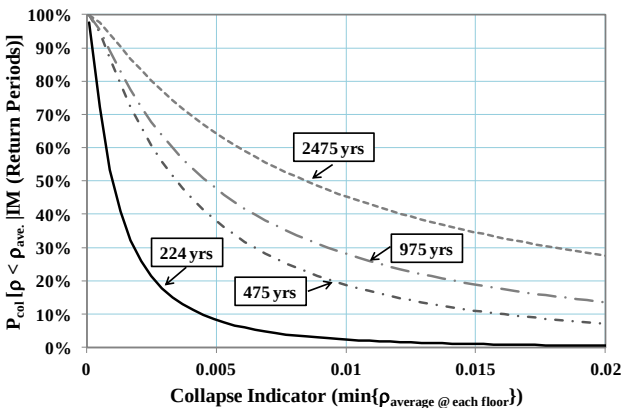
Fig. 1 Structural model uncertainty in shear and axial failure models [7]

3.2 Assessment procedure for design parameters

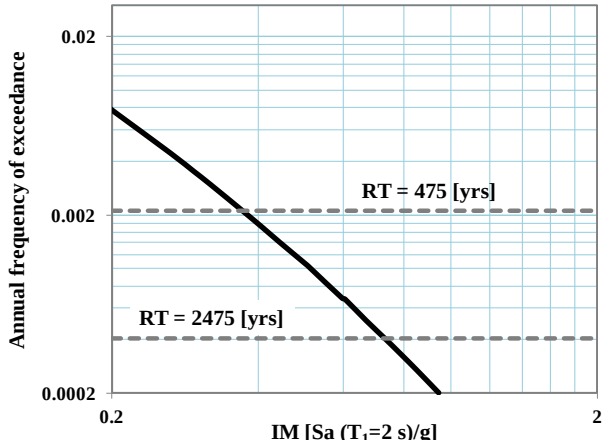
The nonlinear models will be used to estimate the probability of collapse considering ground motion and model uncertainties. The procedure is to first build the complete nonlinear model of a building prototype and



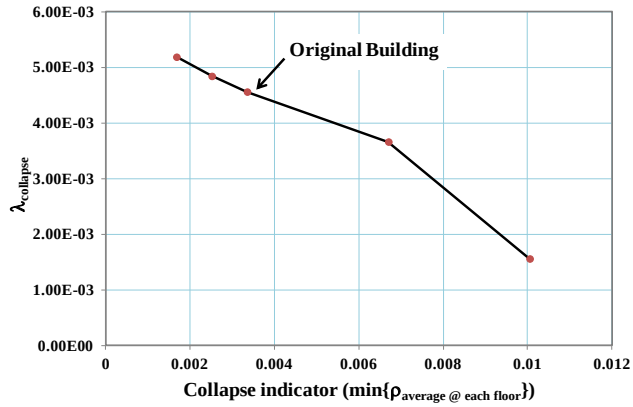
(a) Develop collapse fragilities for a range of the selected collapse indicator (*e.g. RA-L1*)



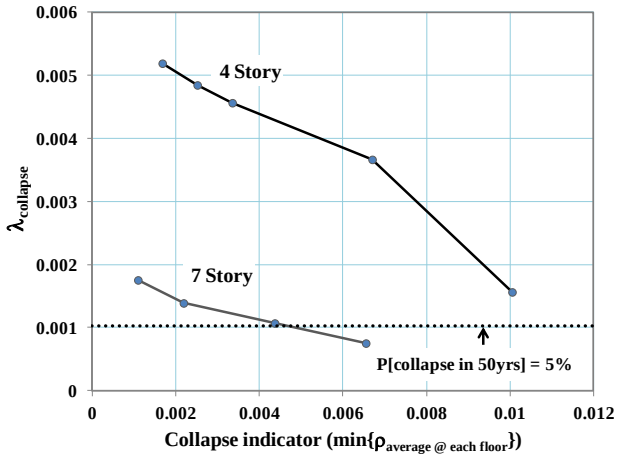
(b) Develop collapse fragilities for a range of selected return periods (*e.g. 475 yrs, ...*)



(c) Estimate mean annual rate of collapse ($\lambda_{collapse}$) integrating the collapse fragility curves with the hazard curve



(d) Seek trends in $\lambda_{collapse}$ for changes in collapse indicator



(e) Repeat for "several" building prototypes and choose an appropriate risk and determine the range for the collapse indicator

Fig. 1 Procedure for establishing collapse indicator limits, design parameters

evaluate the building collapse fragility [5,6]. Two- and three-dimensional analytical models can be used. Then a selected collapse indicator parameter (e.g. RA-L1, average minimum column transverse reinforcement ratio) will be altered in the building model and the collapse fragility will be reassessed for each realization of the collapse indicator (Fig. 2.a). Fig. 2.a shows the variation of the collapse fragilities for the four-story example building with the average column transverse reinforcement ratio, RA-L1. As expected, collapse probability increases as the average column transverse reinforcement ratio decreases. The same figure can be represented by grouping the collapse fragility into different bins of hazard intensities as shown in Fig. 2.b. The variation of the collapse fragilities can be multiplied with the slope of the hazard curve shown in Fig. 2.c to estimate the mean annual frequency of collapse ($\lambda_{collapse}$) as a function of the design parameter (Fig. 2.d). The assessment illustrated in Fig. 2.a through Fig. 2.d can be repeated several times to access the sensitivity of the design parameters for several different building types (Fig. 2.e).

Limits on the collapse indicators can be selected based on a "suitable" mean annual frequency of collapse ($\lambda_{collapse}$) (Fig. 2.e). For instance, $\lambda_{collapse}$ could be selected to be consistent with the new risk-targeted ground motions used for new design [15], i.e. a uniform collapse risk of 1% in 50 years. To be consistent with current seismic rehabilitation practice and to encourage economical retrofits, it is reasonable to relax the target collapse risk compared to that used for new buildings; for example, a mean annual of frequency of collapse of 0.001, equivalent to a probability of collapse of 5% in 50 years. To achieve this selected risk level, Fig. 2.e indicates that the transverse reinforcement ratio should not be below, approximately 0.0043 and 0.012 for the seven- and four-story example buildings, respectively. It should be noted that an ideal collapse indicator would have only limited variation in the collapse indicator limit suggested by the different building types. The results shown in Fig. 2 suggest that transverse reinforcement ratio by itself may not be an ideal collapse indicator for frame buildings as the number of columns and stories also influence the results. Future research will consider how to determine appropriate limits for combinations of collapse indicators.

3.2 Assessment procedure for response parameters

As shown in Table 1, response parameters considered as collapse indicators could be related to the deformations (e.g. global/interstory drift ratios) or forces (e.g. minimum strength ratio) extracted from the nonlinear analysis. These response parameters are also referred as engineering demand parameters (EDPs). Since the performance level considered in this study is collapse prevention, the damage states are discrete and binary and it is assumed that the collapse observation is an ordinary Bernoulli random variable (i.e., a value of unity whenever the structure sustains collapse and zero in all other cases).

The variability in building responses can be accounted for using cumulative distribution functions (CDFs) to approximate the probability of each response parameter (e.g. maximum interstory drift ratio) occurring. For each building response (BR) and intensity measure (in this study the return period, RT, is used to represent the intensity measure), cumulative distribution functions are developed based on nonlinear dynamic analysis. The objective is to develop a CDF for the probability of collapse given BR and RT, P(Collapse| BR, RT). The probability of exceeding the collapse state conditioned on a particular building response and return period is modeled using a lognormal probability distribution, given by the following equation:

$$P(Collapse|\, BR, RT) = \Phi\left[\frac{Ln(BR) - Ln(\overline{BR})}{\sigma_{LnBR}}\right] \qquad (1)$$

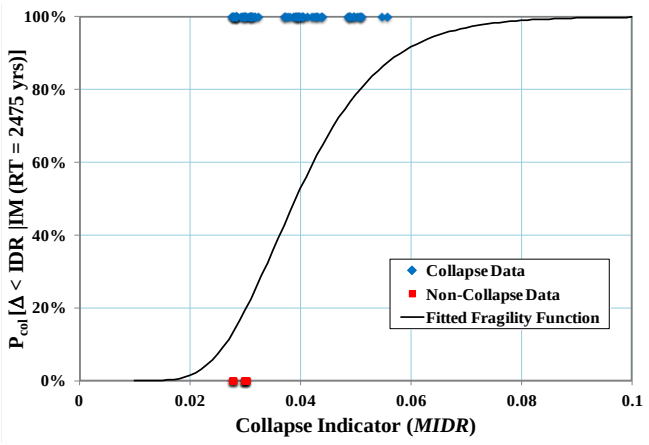
where P(Collapse| BR, RT) is the probability of achieving the collapse state, $\overline{BR}$ is the median of the BRs at which the probability of collapse is observed, and $\sigma_{\mathrm{Ln}BR}$ is the standard deviation of the natural logarithm of the BRs. As suggested by Ramirez [18] different methods could be used to determine the statistical parameters of the lognormal distribution for the CDF, for example, least square methods and the maximum likelihood method. The maximum likelihood method is used in this study to estimate the median ($\overline{BR}$) and standard deviation ($\sigma_{\mathrm{Ln}BR}$). CDFs for building prototypes are developed and related to a selected collapse indicator (e.g. BA-C1 - maximum drift ratio at collapse). Fig. 3.a shows a fitted curve of the response parameter. As shown in this figure, the results of the collapse indicator are either collapse or no collapse from response history analyses.

Using the methodology presented in the previous section, CDFs (Fig. 3.b) are multiplied with the slope of the hazard curve shown in Fig. 2.c to estimate the annual frequency of collapse ($\lambda_{collapse}$). Similar collapse fragilities would be determined for different building prototypes and trends in the probabilities of collapse are compared. Potential limits for the collapse indicator are estimated, similar to the design parameters, for a selected mean annual of frequency of collapse, such as 0.001. Using this limit, Fig. 3.c indicates the maximum interstory drift should not exceed 4.5% for the seven story building and 4% for the four story building.

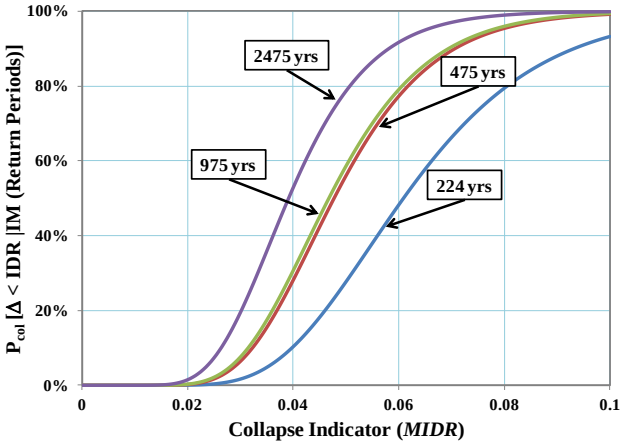
4. SUMMARY AND FUTURE CHALLENGES

The risk associated with older non-ductile concrete buildings internationally is significant, and the development of improved technologies for mitigating that risk is a large and costly undertaking. Considering the limited funding available for seismic retrofit, to achieve a meaningful reduction in the collapse risk it is essential to be able to identify the very worst buildings and fix these first. A potential methodology for identifying collapse indicators based on results of comprehensive collapse simulations and estimation of collapse probabilities for a collection of building prototypes is described.

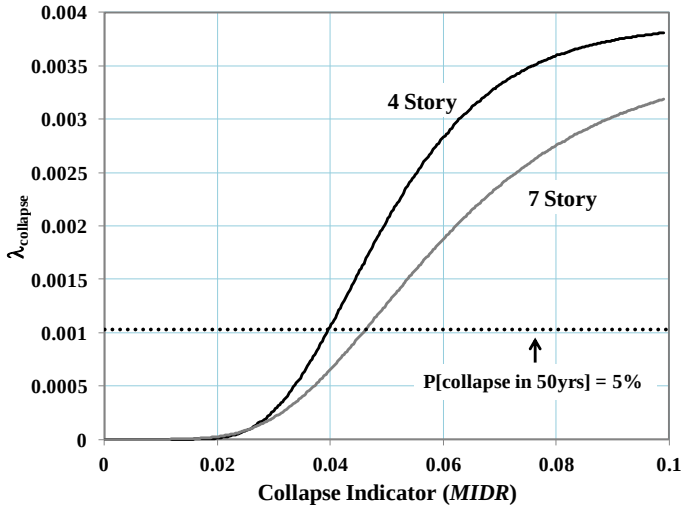
Although only demonstrated here for frames, the probabilities of collapse must be considered for a broad



(a) Determine *CDF* for prototype building



(b) Develop *CDF*s for range of selected return periods



(c) Repeat for "several" building prototypes and choose an appropriate risk and determine the range for the collapse indicator

Fig. 2 Procedure for establishing collapse indicator limits, response parameters

cross section of building types to ensure the selected limits for the collapse indicators are appropriate for the large varied inventory of existing buildings. Methodologies for selecting sample design (e.g. average column transverse reinforcement ratio) and response (e.g. maximum interstory drift ratio) parameter are explained. Limits on the collapse indicators can be selected based on a suitable mean annual frequency of collapse ($\lambda_{collapse}$). In this paper, $\lambda_{collapse}$ is selected based on a target collapse risk. An alternative to this method could be to compare $\lambda_{collapse}$ for the prototype buildings with the $\lambda_{collapse}$ of a "good" existing building, for which seismic rehabilitation is not required to achieve a collapse prevention performance level.

Additional research is required to establish limits for use in design practice and to improve the methodology to address the interaction of multiple collapse indicators. Ongoing studies funded by FEMA and NIST through the ATC-78 and ATC-95, respectively, are expected to result in specific guidance for practicing engineers based on some of the concepts presented in this paper.

Acknowledgements:

This work is supported in part by the National Institute of Standards and Technology through the NEHRP Consultants Joint Venture Program and National Sciences and Engineering Research Council of Canada through the Canadian Seismic Research Network. Any opinions, findings, and conclusion or recommendations expressed in this work are those of the authors and do not reflect those of the organizations noted here.

The authors acknowledge support from the Japan Ministry of Education, Culture, Sport, Science, and Technology (MEXT) for establishing the Center for Urban Earthquake Engineering (CUEE) in Tokyo Institute of Technology. This support makes possible the forthcoming international conference, as well as international joint research projects and exchange programs with overseas universities.

References:

1. Alath S, Kunnath SK. Modeling inelastic shear deformation in RC beam-column joints. Part 1 (of 2), May 21, 1995 - May 24, ASCE, Boulder, CO, USA, 822-825.
2. ASCE/SEI, 2003, Seismic Evaluation of Existing Buildings,

ASCE Standard ASCE/SEI 31-03, American Society of Civil Engineers, Reston, Virginia.
3. ASCE/SEI, 2006, Seismic Rehabilitation of Existing Buildings, ASCE Standard ASCE/SEI 41-06, American Society of Civil Engineers, Reston, Virginia.
4. Baradaran Shoraka, M., and Elwood, K. J., 201x, "Mechanical model for non-ductile reinforced concrete columns," Journal of Earthquake Engineering, Manuscript submitted for review.
5. Baradaran Shoraka, M., Yang, T. Y., and Elwood, K. J., 2012, "Seismic loss estimation of non-ductile reinforced concrete buildings," Earthquake Engineering and Structural Dynamics, DOI: 10.1002/eqe.2213..
6. Baradaran Shoraka, M., 2013. "Collapse Assessment of Existing Concrete Buildings", PhD Thesis, Department of Civil Engineering, University of British Columbia, Vancouver, Canada.
7. Elwood, K.J., 2004, "Modeling failures in existing reinforced concrete columns". Canadian Journal of Civil Engineering; 31(5): pp.846–859.
8. Elwood, K.J., Matamoros, A., Wallace, J.W., Lehman, D.E., Heintz, J.A., Mitchell, A., Moore, M.A., Valley, M.T., Lowes, L. Comartin, C., and Moehle, J.P., 2007, "Update of ASCE/SEI 41 Concrete Provisions", Earthquake Spectra, Earthquake Engineering Research Institute, August 2007, vol. 23, no. 3, pp. 493-523.
9. Elwood, K.J., and Moehle, J.P., 2008, "Dynamic Collapse Analysis for a Reinforced Concrete Frame Sustaining Shear and Axial Failure", Earthquake Engineering and Structural Dynamics, vol. 37, no. 7, pp. 991-1012.
10. FEMA, 1997, NEHRP Guidelines for the Seismic Rehabilitation of Buildings, FEMA 273, Federal Emergency Management Agency, Washington, D.C.
11. Jalayer F, Cornell CA., 2009, Alternative non-linear demand estimation methods for probability-based seismic assessments. Earthquake Engineering and Structural Dynamics; 38 (8): 951-972.
12. Kang T. H.-K., Wallace J. W. and Elwood, K. J., 2009, "Nonlinear Modeling of Flat Plate Systems," Journal of Structural Engineering, ASCE, vol. 135, no. 2.
13. Krawinkler, H. "Van Nuys Hotel Building Testbed Report: Exercising Seismic Performance Assessment. PEER Report 2005/11." College of Engineering, University of California, Berkeley 2005.
14. Liel, A. B., Haselton, C. B., and Deierlein, G. G. (2011). "Seismic collapse safety of reinforced concrete buildings. II: Comparative assessment of nonductile and ductile moment frames." J. Struct. Eng., 137(4), 492–502.
15. Luco, N., B. Ellingwood, R.O. Hamburger, J.D. Hooper, J.K. Kimball and C.A. Kircher, 2007, "Risk-targeted vs. current seismic design maps for the coterminous United States." Proc., Annual SEAOC 2007 Conference, Structural Engineers Association of California.
16. NIST GCR 10-917-7 (ATC-76-5), 2010, Program Plan for the Development of Collapse Assessment and Mitigation Strategies for Existing Reinforced Concrete Buildings, National Institute of Standards and Technology (NIST).
17. OpenSees. "Open system for earthquake engineering simulation _OpenSees_ framework-Version 2.1.0." Pacific Earthquake Engineering Research Center, Univ. of California, Berkeley, <http://opensees.berkeley.edu> [10 September 2010].
18. Ramirez, C. M., 2008, Building-Specific Loss Estimation Methods & Tools for Simplified Performance-Based Earthquake Engineering, Doctoral Dissertation, Stanford University.
19. Vamvatsikos D, Allin Cornell C., 2002, Incremental dynamic analysis. Earthquake Engineering and Structural Dynamics; 31 (3): 491-514.
20. Yavari, S., Elwood, K.J., and Wu, C.L., 2009, "Collapse of a Nonductile Concrete Frame: Evaluation of Analytical models," Earthquake Engineering and Structural Dynamics, vol. 38, no. 2, pp. 225-241.

10CUEE CONFERENCE PROCEEDINGS
10th International Conference on Urban Earthquake Engineering
March 1-2, 2013, Tokyo Institute of Technology, Tokyo, Japan

LOW DUCTILITY CONCRETE WALL TEST CONSIDERING PERPENDICULAR WALL ACTION

Carlos Zavala[1)], Patricia Gibu[2)], Luis Lavado[3)], Jenny Taira[4)], Lourdes Cardenas[4)] and Luis Ceferino[5)]

1) Professor, Structural Laboratory, CISMID-FIC National University of Engineering (UNI), Lima, Peru
2) Associate Professor, Structural Laboratory, CISMID-FIC National University of Engineering (UNI), Lima, Peru
3) Assistant Professor, Structural Laboratory, CISMID-FIC National University of Engineering (UNI), Lima, Peru
4) Assistant Researcher, Structural Laboratory, CISMID-FIC National University of Engineering (UNI), Lima, Peru
5) Research Student, Structural Laboratory, CISMID-FIC National University of Engineering (UNI), Lima, Peru

Abstract: Low ductility wall buildings became part of the Peruvian construction boom of the first decade of the 21st century. Government promote under the Program named Mi Vivienda (My house in English), the construction of low rise buildings of 5 stories using walls with wire mesh reinforcement, provide part of a solution of the apartment deficit, with reasonable cost. However, the height of the buildings started to grow and grow, reaching 12 to 16 stories. In the design of this walls, provisions recommend the confinement of the corners of the walls, due the action of the walls ensemble will give a limited ductility under seismic behavior. In this paper the comparison of the action of perpendicular wall with a one plane wall is presented. Here experimental test has been performed by a cyclic loading test considering the action of a constant axial load of 40 kN, where the elastic stiffness of H shape wall is higher than one plane wall. Also resistant of the H shape wall increase, however ductility remains almost similar in both walls, due to the slip during the H wall test.

1. INTRODUCTION

Low ductility buildings appears at the middle of 1997 in Peru. As an initiative of Professor Galvez from graduate school of FIC-UNI, the promotion of the first multifamily building of four stories with the concept of replacing the masonry on a confines wall by a thin concrete wall reinforce with electrowelded wire mesh, will produce a compose material with similar better characteristics than the masonry. First experiments on this kind of wall where successfully developed at structural laboratory of CISMID-FIC-UNI (Zavala et. al 2003), considering a low stress concrete (100 kg/cm^2) a wall of 10 cm. thickness, 250 cm. height, 300 cm. length and reinforce on corners of 3 bars #3 with wall reinforce of Q91 wire mesh of 3 mm. diameter @ 10 cm. The result was a low ductility wall with low drift, even lower than the masonry limit (where Peruvian standards demands maximum drift of 1/200), with maximum drift near 1/400.

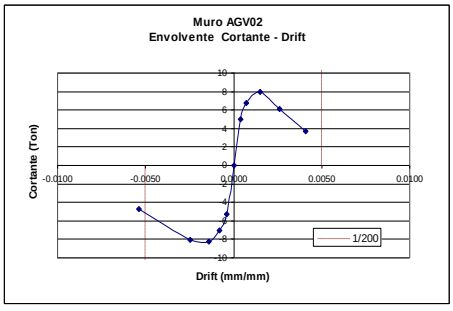


Figure 1: Behavior curve (Zavala et. al 1997)

This took the attention for the design of this kind of wall since the reinforce has upper yield point (65 to 70 ksi) than regular A60 bars (60 ksi), which is one of the reasons of the less ductility.

The Ministry of Housing invest in the research of the behavior of this kind of wall, so configuration variable and reinforce variable area presented(Zavala et. al 2003).

Since 1999 the use of this walls starts to grow on buildings projects. Government, through Ministry of Housing, promote under the Program named Mi Vivienda (My house in English), the construction of low rise buildings of 5 stories, provide part of a solution of the apartment deficit in the country, with reasonable cost.

However constructors started to grow in altitude the buildings to 8 stories, 12, stories and 16 stories, using the same reinforce, without research the behavior as a middle high building.

Therefore, on 2003 the Ministry of Housing introduce an recommendation for the design of low ductility walls on the Peruvian Concrete Standards.

The investigations of this kind of wall continue at UNI during the following years. On 2004 Medina and Zavala produce a research considering ideal conditions on material, construction process and standards. As an example a wall reinforce with normal concrete (210 kg/cm^2), 10 cm. thickness 250 cm. height, 300 cm. length and reinforce of 3 bars #4 with wall reinforce of QE257 wire mesh of 5.7 mm diameter @ 10 cm. gave results with a drift limit similar than confined masonry and upper stress.

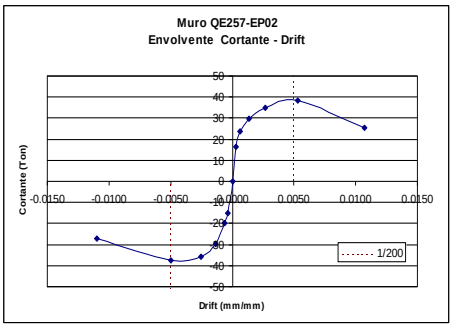


Figure 2:Behavior Curve Medina et. al 2004

Since 2004 investigation has been performed on in plane walls, however non investigation considering this kind of walls have been developed in Peru.

Under the SATREPS Peru - Japan joint research project and using the new jack system of capacity of 500 kN and 400 mm. stroke investigation of low ductility wall with the action of a perpendicular has been performed. In this paper preliminary results are presented showing the tendency of the contribution of the perpendicular wall to the in plane wall.

2. ABOUT THE EXPERIMENTAL TEST CONSIDERING PERPENDICULAR WALL ACTION

In order to investigate in experimentally the influence of the perpendicular wall on and H shape configuration against one plane wall, two experiments were performed: an experiment on a one plane wall, and an experiment with a perpendicular wall that produce an H shape wall.

2.1 About Test specimen

Both walls (one plane and H wall) will has the same dimensions: 2500 mm. length with 2600 mm. height and 100 mm. thickness. In the case of H wall, a flange with a total dimension (Bf) of 2500 mm. is incorporated to the one plane wall, in order to investigated it influence by the measured stresses.

The walls have a reinforce on the corners as confinement 3 bars #4. Wire mesh appears as reinforcement of the web and flange with electro welded mesh Q-158 (5.5 mm. diameter @ 0.15m As=1.58 cm2/m). Is common use of 600 mm. dowels between stories on buildings, but in the case of the specimens dowels are same growing from the footing base. Figure 3 presents the configuration of both specimens, one plane and H shape wall, notice that there is a horizontal border beam of 300 mm. by 300 mm. section on the top of each beam. Also foundation of 900 mm. by 300 mm. is on the bottom part of the specimen.

The construction process tried to replicate as near the real environment on the site area. So wire mesh from the footing was fixed with the wire mesh of the wall and three ductile bars #4 were placed on the corners of the specimens. Wood forms were used to encase the reinforcement and set the fluid mix of concrete inside to produce the concrete wall.

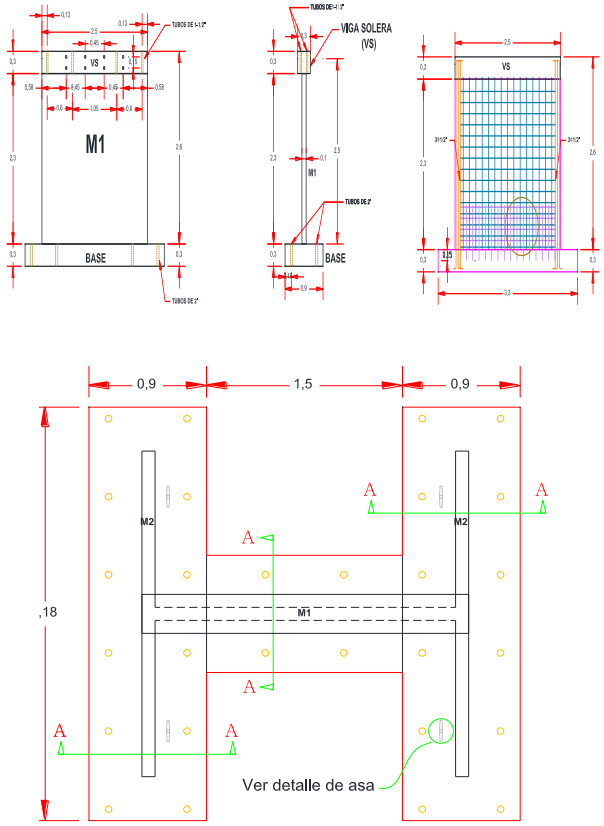


Figure 3: Test specimen configuration for H shape wall

On the top of each wall a loading beam is build to be use for setting of the loading steel frame. Figure 3 presents four stage of the constructions of the specimens.

2.2 About test performance

For the test execution 2 jacks and one actuator were used for the application of the loads. Axial load equivalent to 200 kN that approximately represents the load of four stories over the wall.



Figure 4: Test Setup on Plane and H walls.

During the execution of the test, this load will be applied at the beginning of the load process, and after reaching 200 kN, the load will remain constant during the whole test. To simulate the lateral action such a earthquake

movement, an increasing cyclic displacement will be applied to the specimen in order to start the movement of the wall and measure in each step the load.

For the measure of the displacements a set of transducer were placed to measure displacement in different locations on the walls. In the one plane wall and web wall (on H shape specimen), displacements transducers were set on the positions presented on Figure 5, here sensors on the body of the wall were setting on the diagonal, vertical and horizontal in order to reproduce the displacement on all directions. For the measure of the stress on points strain gauges were glued to the surface of the concrete and to the reinforce bars. All the sensors and gauges, were connected to an scanning box and data logger Tokyo Sokki TDS 530.

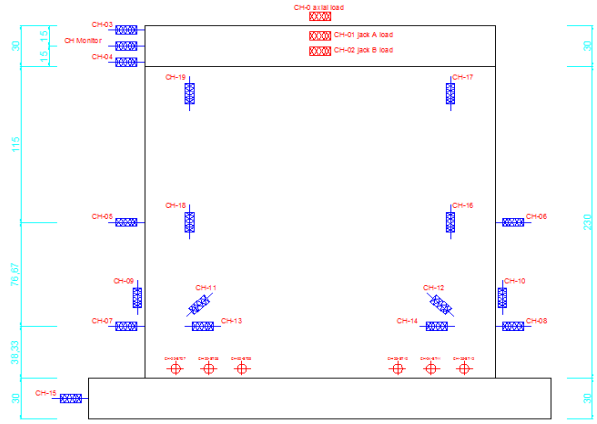


Figure 5: Displacement transducer setting

On Figure 4, the test setup of both specimens are presented. Here is possible to notice the difference on the setup due to need of application of the axial load and lateral load simultaneously in special in the case of the H shape wall were space is quite narrow to applied both loads. In the case of H shape wall the perpendicular wall (flange wall) has three lines of sensors in order to investigated the displacement on that positions and the dissipation of the stress. Also strain gages were set for the same purpose.

2.3 Test results

The cyclic displacement versus base shear on the experimented walls are presented on

Figure 6, where hysteresis curves of the development of each test are presented. It is possible to read that both specimens had almost the same level of maximum stress, but in different failure mode. The reason of this similitude of stress level is due to an slip on the foundation occurs after 4 mm displacement. In the case of the one plane wall, shear cracking appears on the base of the experiment. Then flexural cracks starts to appear on both borders elements, propagation horizontally. Finally diagonal cracks appear and a combination of shear failure with slip failure of the base, is the final failure pattern.

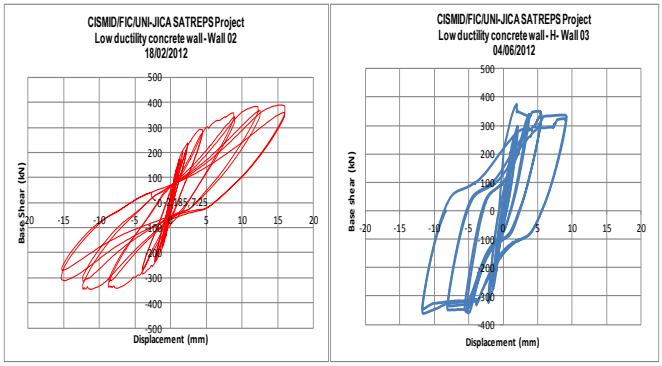


Figure 6: Hysteresis curves of one plane wall and H shape wall

Due to the slip of the specimen, we will consider the behavior of the H wall previous to the slip and compare the behavior curves of both specimens for this condition. The slip of the specimen occurred for 1/1600 drift, just after the cracking starts on the specimen. Figure 7 presents the behavior curve showing that both curves almost reached the same capacity. However, considering the first stage of the test, when drift is less than 1/1600, the behavior will introduce a difference on the resistant.

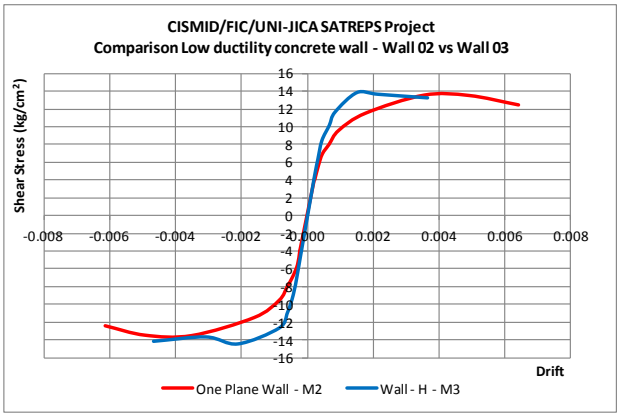


Figure 7: Behavior curves plane wall and H shape wall

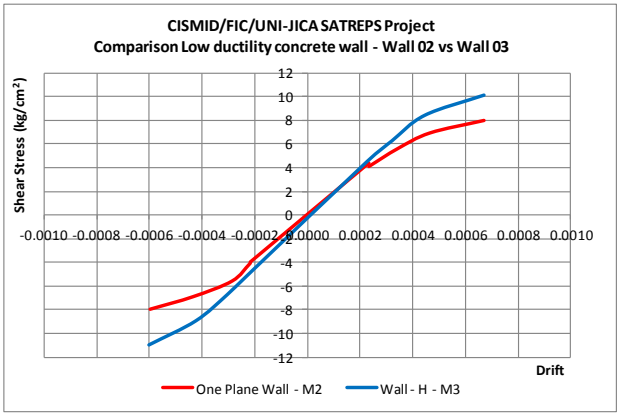


Figure 8: Behavior curves plane wall and H shape wall for drift less than 1/1600

On Figure 8 is presented the behavior curve prior the slip of the specimen. There is a notorious contribution of the perpendicular wall on the behavior.

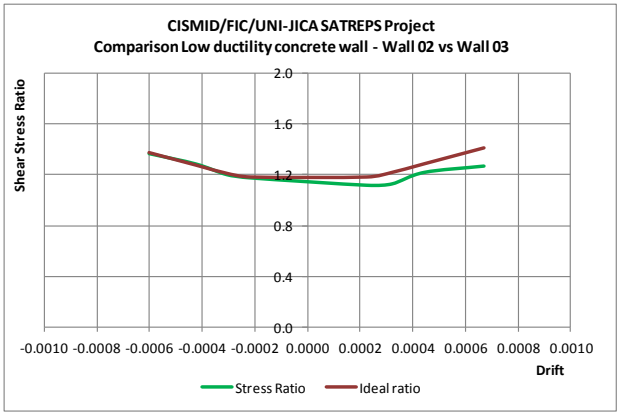


Figure 9: Stress ratio between H wall and plane wall

On green color is presented the shear stress ratio between the H wall and plane wall, that was compute from the test results. It is possible to the that when jack is pushing the curve shows a very defined ratio, however when jack is pull, the capacity of the system gave lower values. It is possible to recognize that ideal behavior on a simulation is given when jack is pushing the specimen. On red color in Figure 9, is presented ideal shear stress ratio for the wall. Here we can see that till behavior is elastic the ratio is about 1.18, so perpendicular wall action will increase 18% of shear stress capacity. After cracking of the specimen the increment became higher and reach a value of 1.40, so it means an increment of 40% in the shear resistance due to the perpendicular wall action.

A preliminary formula for the variation of the shear stress to evaluate the contribution of the perpendicular walls to the plane wall is the following:

$$\tau_H/\tau_{plane} = 552.98\gamma + 1.039 \qquad (1)$$

where τ_H/τ_{plane} is the shear stress ratio between the H wall with the plane wall and γ is the interstory drift.

3. CONCLUSIONS

Low ductility walls are an alternative to build middle rice buildings in Peru. Many research has been performed on plane walls however non research has been performed on this kind of wall to measure the perpendicular wall action. Therefore the present research present the first contribution in Peru for the knowledge of this action.

Two walls were investigate: one in plane and the other with H shape where the contribution of the flange to the in plane wall intend to be measure.

Unfortunately the H specimen slip occurs at 1/1600 drift during the test, after cracking occurs so test was completed showing similar results for the capacity of the walls.

Therefore, considering the behavior prior of the slip of the specimen shows a notorious difference between plane and H wall shear resistance.

This difference was evaluated in terms of ratio of both stresses for the same drift. Results shows that during elastic stage of the specimen, perpendicular walls contribute 18% to the shear resistance, but after cracking stress ratio increase till 40%. So the contribution of the perpendicular wall will be very important during the inelastic behavior of the wall

We need to continue the study in order to verify the spread of stress on perpendicular flange wall and web wall. We need to consider more study for the perpendicular action on the non linear behavior developing more test to prove the tendency of the preliminary formula (1) presented in this paper.

Acknowledgements:

The authors would like to express our gratitude to the Ministry of Education of Japan, thorough the Japan Science and Technology Agency (JST) and the Japan International cooperation Agency (JICA) for the support the Japan-Peru SATREPS Project for the support to this research. Also our gratitude to Dr. Fumio Yamazaki PI investigator of the SATRPES project and promoter of this investigation.

References:

Zavala, C., Medina G. and Proaño, R. (2005), "Behavior of Concrete walls reinforce with electrowelded wire mesh," Research Report CISMID-FIC-UNI (In Spanish).

Medina G. and Zavala C. (2004), "Study of the behavior of low ductility and one story scale model reinforce with electrowelded wire mesh ", Graduate Thesis FIC-UNI (In Spanish).

10CUEE CONFERENCE PROCEEDINGS
10th International Conference on Urban Earthquake Engineering
March 1-2, 2013, Tokyo Institute of Technology, Tokyo, Japan

CFD ANALYSIS OF WIND PRESSURE ON THE COMPLEX HIGH-RISING STRUCTURE

Qiong Xing[1)],Jiang Qian [2)]

1) Phd Student, State Key Laboratory of Disaster Reduction in Civil Engineering, Tongji University, P. R. China
2) Professor, State Key Laboratory of Disaster Reduction in Civil Engineering, Tongji University, P. R. China
jqian@tongji.edu.cn *804119414@qq.com*

Abstract: The complex high-rising structures are more with increasing heights and more complicated shapes. Wind load is the control lateral load. Now wind tunnel test is an effective method of predicting the wind pressure distributions on the complex high-rising structures. But the similarity coefficients of the wind tunnel test can not be satisfied, and the model making and test conditions are limited. Having Shanghai TV tower as an engineering background, the CFD numerical model was built, and the surface roughness heights of the cylinders and spheres were determined. Numerical results are found to have good agreement with experimental results. On the basis, the influence of surface roughness on the wind pressure of the sphere and three cylinders was discussed. The results show that : when the surface roughness is not symmetrical, the symmetry of the wind pressure distribution on the sphere changes a little; when the surface roughness of the three cylinders are different, the phenomenon of drift flow around three cylinders still exists.

High-rising structures are used more widely, e.g. electricity, communication technology and office building. The high-rising structures are more with increasing height and more complex shape. Wind load is a dominant lateral fore, but Load code for the design of building structure only gives the shape coefficient with simple and regular shapes in the uniform flow. This can not be satisfied with the engineering practice need. Wind tunnel test is an effective method of predicting the wind pressure distributions on the complex high-rising structures, for the flow pattern is complicated. Li (1997) did the wind tunnel test of Shanghai TV tower, discussed the wind load distribution and lift coefficient of the middle and upper spheres, and analyzed interference effects of the cylinder group and spheres and internal interference effects of the cylinder group. Gu (2009) did the wind test of Guangzhou new TV tower. Guanzhou TV tower body is a peripheral framework composed of steel tubes, horizontal annular members, and spiral diagonals. A new experimental technique of dividing the entire tower into sections is proposed for the wind load distribution. But wind tunnel tests have many limitations. The models and working conditions are limited for some unsatisfied similarity coefficient, long periods and high cost. With the development of computational fluid dynamics, Numerical simulation is adopted in predicting wind loading distribution. Chen (2006) presented the details of the numerical simulations of Henan TV tower. Wind load distribution, shape coefficient and wind velocity distribution are in good agreement with experimental results. Shanghai TV tower as the engineering background, simulations were done to get the static wind distribution of the tower. The wind tunnel test results done by Li (1997) shows that the wind load distributions of cylinder groups and spheres are asymmetric under symmetrical incoming flow which is called “bias phenomenon”. The phenomenon has not given the explicit explanation. In this paper, simulations of Shanghai TV tower were done to get the preliminary explanation and calculation.

1. INTRODUCTION

Shanghai TV tower called the oriental pearl TV tower is located in Pudong Park surrounded by the Huangpu River. The wind environment of the tower is complicated. The members of Shanghai TV tower are simple, so it is easier to get the interference effects of members. Shanghai TV tower is 454 meters high. The main part of the tower is composed of three nine-meter columns and spheres with diameters of 45m and 50m. The tower is supported by three stanchions with slanting angle 58°. The tower pictures are shown in Fig. 1. The three big circular cylinders are in equilateral-triangular arrangements. Spacing between cylinders is varied from 2 to 3 cylinder diameters. The interference between the three cylinders and between the three cylinders and spheres is very strong and complex.



Figure 1 pictures of Shanghai TV tower

2. NUMERICAL METHOD

The Realizable k- ε model is adopted for simulations of the tower. Based on finite volume method, SIMPLE is a guess-and-correct procedure for decoupling and solution of the discretised equations.

Boundary conditions: At the inlet, the mean velocity is 30m/s as the wind tunnel test. The turbulent intensity at the inlet of the computational domain is specified as 5% for the turbulent intensity is relatively small at the uniform velocity inlet. The pressure-outlet condition is used at the outlet of the computational domain. Symmetric plane boundary condition is employed at the top and the sides of the computational domains. Wall function boundary conditions are used for the cylinders and ground.

Data processing: the pressure coefficient of the tower is specified as (Bencai Huang, 2008) :

$$Cp = \frac{P - P_{\infty}}{\frac{1}{2} r V_{\infty}^{2}} \qquad (1)$$

Where P is the wind loading pressure; P_{∞} is the aerostatic pressure; r is the air density; V_{∞} is the inlet velocity.

3. SIMULATION OF THE TOWER SURFACE ROUGHNESS

3.1 Simulation of Cylinder Surface Roughness

The inlet conditions, Reynolds number and the surface roughness are the key factors in flows around circular cylinders (Emil Simiu et al., 1978). In real structures, the circular cylinders and spheres are in the super-critical regime. In numerical simulations, the surface roughness is the determined factor to get the cylinders and spheres in the super-critical regime, for the diameters of cylinders and spheres and the inlet velocity is already known.

In numerical simulations of the cylinder and sphere surface roughness, the turbulent model, boundary conditions and data handling were used as mentioned above. In this way, the surface roughness could be adopted in the numerical simulation of the tower.

In numerical simulations, diameters of cylinders and spheres are used as the ones in the tower. The diameter of the cylinder is 9m, and 270m in height. The diameter of the sphere is 50m. According to the wind tunnel test of the single circular cylinder (Huizhi Li, 2002), the surface roughness of cylinders determined by the wind tunnel test was adopted in numerical simulations. The non-dimensional roughness height (ratio of roughness height and the diameter) is 1.5×10-4. Given the similar coefficient of wind tunnel tests, the surface roughness height of cylinders is 0.00135m (full scale) (Bert Blocken et al.,2007). The numerical simulated model is shown in Fig. 2.

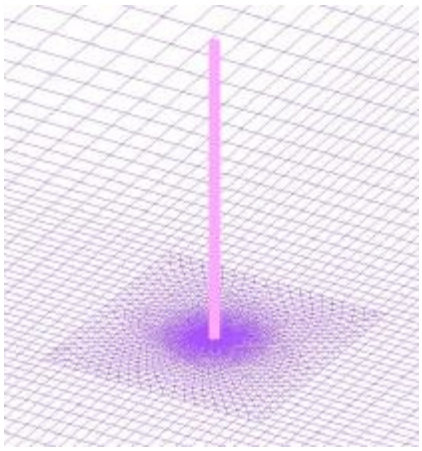


Figure 2 Numerical model of one cylinder

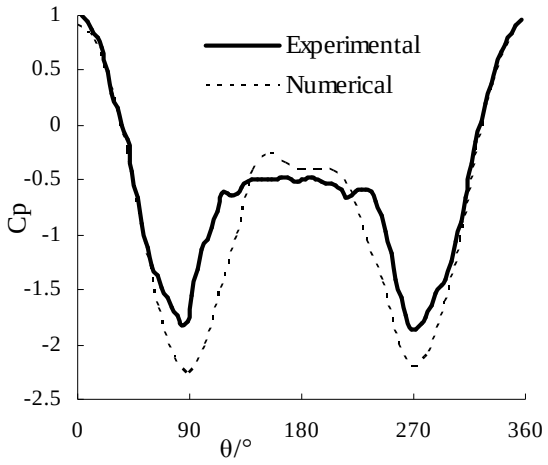


Figure 3 Comparison of numerical results and wind tunnel test results of one cylinder

To avoid three dimensional effects (Guochao Chen et al.,2011), results of the mid-section are adopted for comparison with the wind tunnel test results of one single cylinder (Huizhi Li,1997). Fig. 3 describes the comparison. The results show good agreement with experiments on the windward cylinder surface. The maximum Cp on the windward surface is 1. On the leeward surface ($90^\circ < \theta < 270^\circ$), the minimum Cp appears. The experiment result is near to -2. The numerical result is -2.26 within the experimental accuracy. The separation occurs approximately at 110° in experiment and 130° in simulations. On the leeward surface, there is a regime mean pressure coefficient is nearly uniform. The profiles of experiments and simulations are in the same trend. As mentioned above, the cylinder surface roughness satisfies the numerical simulation need of flow around cylinders in the super-critical regime.

3.2 Simulation of the Sphere Surface Roughness

In the wind tunnel test, the sphere model was made of wood covered by wire mesh (Huizhi Li,1997). There is not detailed data of the sphere surface roughness or the diameter of the wire in relative literatures. The surface roughness of spheres is an important factor in wind loading distribution of the tower. According to the diameters of wire and similar coefficient used in wind tunnel test, several roughness heights of the sphere were tested in numerical simulations. The roughness height of the sphere ranges from 0.04m to 0.2m. Fig. 5 reports the wind loading distributions of the sphere with different roughness heights.

As shown in Fig. 5, on the windward sphere surface, the wind load distributions of the sphere with different roughness heights are almost the same. The maximum Cp value is near to 1. The minimum mean pressure occurs at 90°. The separation point shifts from 110° to 130°. The absolute value of the minimum mean pressure decreases with increase of roughness height. The minimum mean pressure ranges from -1.085 to -0.849. On the leeward surface, the pressure coefficient decreases from 0.08 to -0.159 with increase of the surface roughness height. The sphere with roughness heights ranging from 0.04m to 0.2m is in the super-critical regime. The wind load distributions of the sphere with roughness heights ranging from 0.04m to 0.2m change slightly. All this indicates the wind loading distribution of the sphere is insensitive to surface roughness.

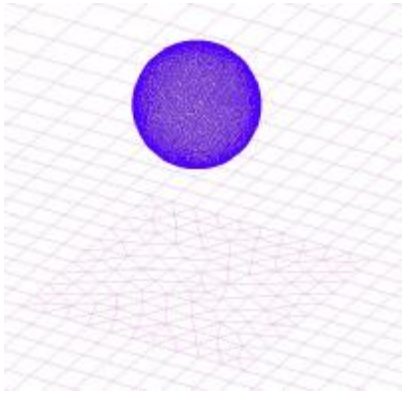


Figure 4 Numerical model of the sphere

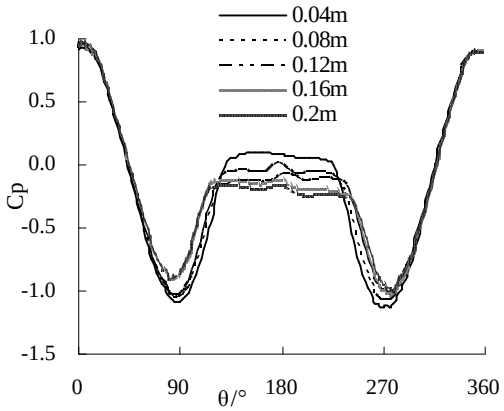


Figure 5 Pressure coefficient distribution of sphere with different roughness heights

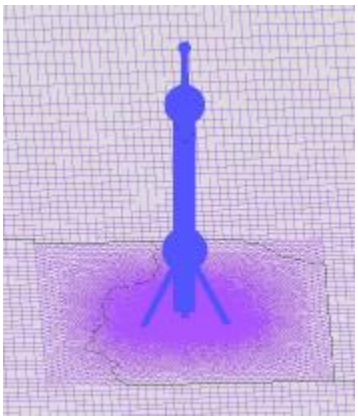
4. SIMULATION OF SHANGHAI TV TOWER

4.1Geometric Model

The structures above the space module are relatively small and their effect on wind load is negligible. So the structures above the space module are not included in the geometric model to reduce mesh amount and the computing time. In order to study interference effects of three cylinders, the small beams between the cylinders are omitted.



(a) Computational grid of the tower



(b) Computational grid of the vicinity of the tower

Figure 6 Mesh of numerical model of the tower

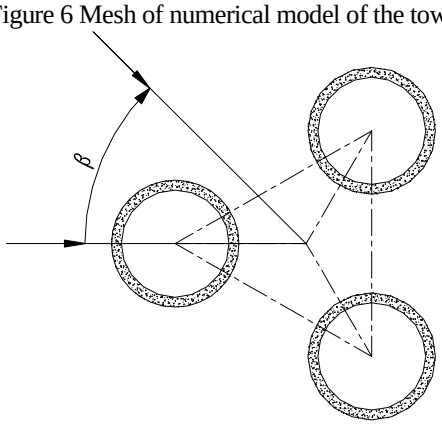


Figure 7 Schematic showing of the wind direction

4.2 Numerical Simulation Model

The computational domain is 2240m×4520m×1000m, in the span wise direction, the stream wise direction and normal to the ground wall. The tower is placed at 1/3 of the domain upstream. The tower is placed in a 320m×320m×500m rectangular sub domain(Guochao Chen et al.,2011). In the areas close to the tower, fine tetrahedral elements were used, whereas coarse hexahedron elements were used far away from the tower, as shown in Fig. 6. This handling can improve the computational accuracy and reduce the amount of mesh. The turbulent model, boundary conditions and data handling were used as the above. The cylinder surface roughness height is 0.00135m and the sphere surface roughness height ranges from 0.04m to 0.2m. The final surface roughness height is 0.1m according to comparison with the experimental results.

4.3Computing Conditions and Aata Handling

The calculating wind directions are 0° ,15° ,30° ,45° ,60° . Schematic showing of the wind direction is shown in Fig. 7. Fig. 7 shows 0° wind angle of attack.

4.4 Analysis of Computation Results

4.4.1 Analysis of Wind Load Distribution of the Spheres

In wind direction angle of 60, the wind loading distributions of the diameter surface at 75m in height and at 262.5m in height are compared with the experiment results done by Li(1997), as shown in Fig. 8 and Fig. 9.

On the windward and leeward surface of the lower sphere, the numerical results show good agreements with experiments. The maximum pressure coefficient reaches 1 on the windward surface. The pressure coefficients of the leeward surface range from -0.25 to 0.35. The minimum pressure coefficient reaches -1.12 and occurs at 90° approximately in numerical simulation and at 80° in the wind tunnel test. The separation point occurs at 110° in wind tunnel test and 130° in numerical simulation. The mean pressure distribution of the sphere is symmetric, and in contrast, the experiment result is not symmetric. There is deviation between the experimental and numerical results in the lateral direction on the windward surface.

On the windward surface, the numerical results fit better with experiments. The maximum pressure coefficient reaches 1 on the windward surface. The minimum pressure coefficient is nearly -0.9 in wind tunnel tests and -1.09 in numerical simulation and occurs at nearly 90° . On the leeward surface, the pressure coefficients of numerical results range from -0.2 to -0.26, and of the wind tunnel test results are nearly -0.45. But the numerical and experimental results are nearly in the same trend.

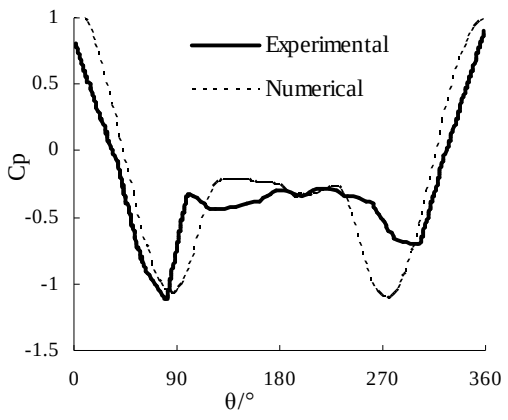


Figure 8 Pressure coefficient distribution of the sphere below

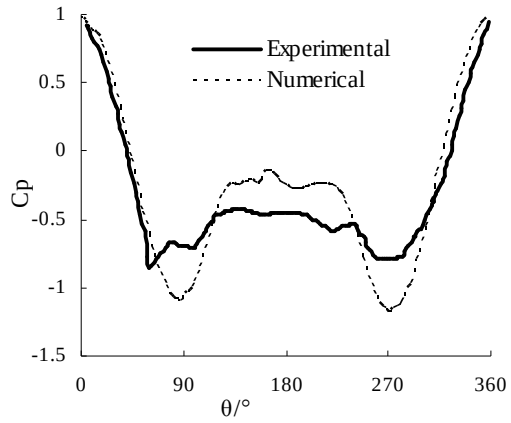


Figure 9 Pressure coefficient distribution of the sphere above

4.4.2 Analysis of Wind Load Distribution of the Cylinders

The mid-sections of the three cylinders are influenced little by the upper and lower spheres. Fig. 10, Fig. 11 and Fig. 12 report the wind loading distributions of the cylinders with cylinder 1 front and cylinder. As shown in Fig. 10, the maximum pressure coefficient is 0.9 and the minimum pressure coefficient is -3.37. The experimental minimum pressure coefficient is in the range of -2 to -2.5. The numerical wind loading distributions show good agreements with experiments in the same trend, except a little difference at 90° .

For cylinder 2 and cylinder 3, the wind loading distribution fits better with experiments on the windward surface and the difference between the numerical and experimental results is obvious on the windward surface. The wind loading distribution of the cylinder changes with different Reynolds numbers and different surface roughness heights. The minimum pressure coefficient ranges from -1.5 to -3. This can be concluded by literature (Huizhi li,1997; Zhifu Gu et al.,2001). The numerical results of cylinder 2 and cylinder 3 are within the range of -1.5 to -3. The numerical results are accepted according to relative literatures.

The numerical results show good agreements with experiments with the same trend. CFD numerical simulation can be a method of predicting wind load distribution of high-rising structures.

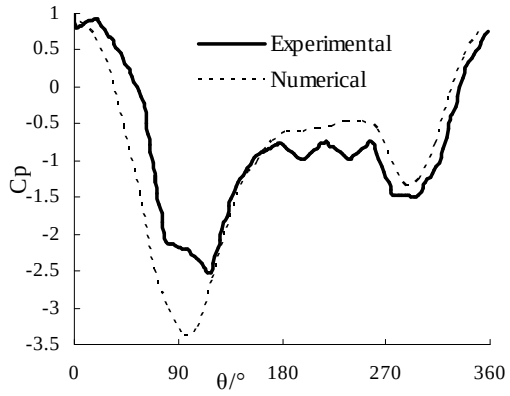


Figure 10 Pressure coefficient distribution of cylinder1

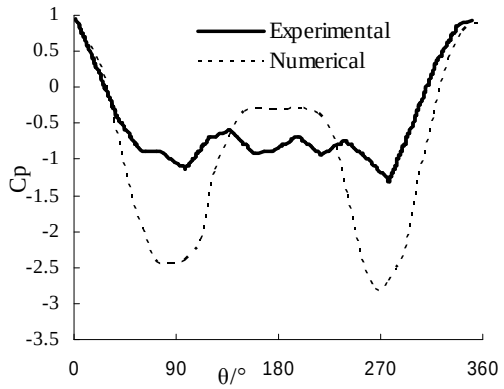


Figure 11 Pressure coefficient distribution of cylinder 2

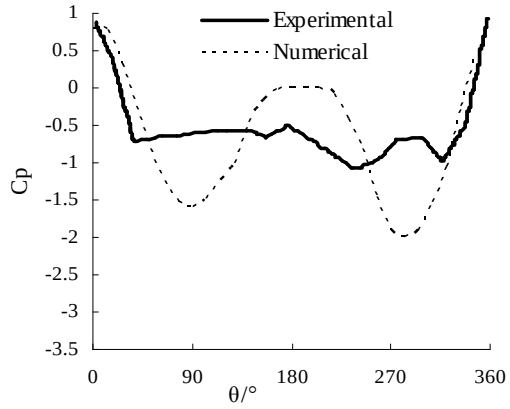


Figure 12 Pressure coefficient distribution of cylinder 3

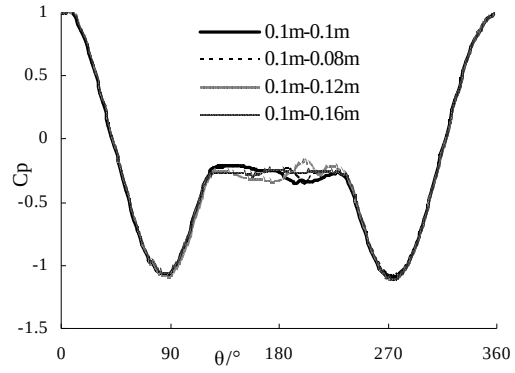


Figure 13 Pressure coefficient distribution of the lower sphere with different asymmetric surface roughness heights

5. SURFACE ROUGHNESS INFLUENCES ON WIND LOAD DISTRIBUTION OF THE TOWER

5.1 Influence on Symmetry of the Wind Loading Distribution of the Sphere

The wind load distribution of a single sphere should be symmetric in symmetric flow. As shown in Fig. 5, the wind load distributions of spheres with different surface roughness heights are symmetric. In contrast, Fig.7 and Fig. 8 show the asymmetric wind loading distribution of the sphere in symmetric flow. This is inconsistent with empirical speculation. Some literatures predicted that the asymmetric wind load distribution of the sphere was probably related to the asymmetric surface roughness height and asymmetric interference of the cylinders. The numerical simulation model of the sphere with asymmetric surface roughness was made in FLUENT to study the asymmetric surface roughness influence. In numerical simulations, a part of the sphere surface is with 0.1m roughness height, and the left is with 0.08m, 0.12m, and 0.16m, respectively. Fig. 13 reports comparison of wind load distributions of the sphere with asymmetric and symmetric surface roughness. The profiles of wind load distribution of spheres with different surface roughness are almost the same, except a little discrepancy on the leeward surface. The profiles are symmetric as a whole. This means the asymmetric surface roughness has little influence on the wind loading distribution of the sphere. Finally, it is suggested that future studies can focus on the factors of the asymmetric wind loading distribution of the sphere.

5.2 Influences on Symmetry of the Wind Loading Distribution of the Group of the Cylinders

The wind loading distributions of the three cylinders are not symmetric in symmetric flow. The unsteady bias phenomenon is found in experiments and numerical simulations done by Gu (2001), K.Lam(1988), S. G. Pouryoussefi(2011) and Yan(2010), et al. Literatures did not give the explicit explanation of the bias phenomenon so far. Some literature predicted that the bias phenomenon was related to the surface roughness. The numerical simulation model of the cylinder under three different working conditions was built to study surface roughness influence. Working condition 1, the surface roughness height of three cylinder is all 0.00135m. Working condition 2, the surface roughness heights of cylinder 1, cylinder 2 and cylinder 3 are 0.00135m, 0.0018m and 0.0018m, respectively. Working condition 3, the surface roughness heights of cylinder 1, cylinder 2, and cylinder 3 are 0.00135m, 0.0018m and 0.0027m, respectively. Fig. 14, Fig. 15 and Fig. 16 report the comparison of wind distribution of the three cylinders under three working conditions.

The distributions of the three cylinders are almost the same under working condition 2 and 3. The separation point shifts toward 10°. The pressure coefficient at 90° under working condition 2 and 3 is 0.5 bigger than the one under working condition 1. The pressure coefficient at 270° under working condition 2 and 3 is 0.9 smaller than the one under working condition 1. The asymmetry of wind load distribution of cylinder 3 is improved under working condition 3. It suggested the bias phenomenon still exists when the three cylinders are with different roughness heights but the bias extent decreases. Further study of the bias phenomenon needed to be done.

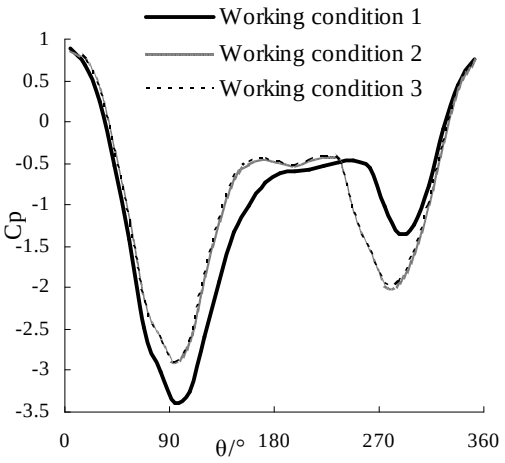


Figure 14 Pressure coefficient distributions of cylinder 1 under three working conditions

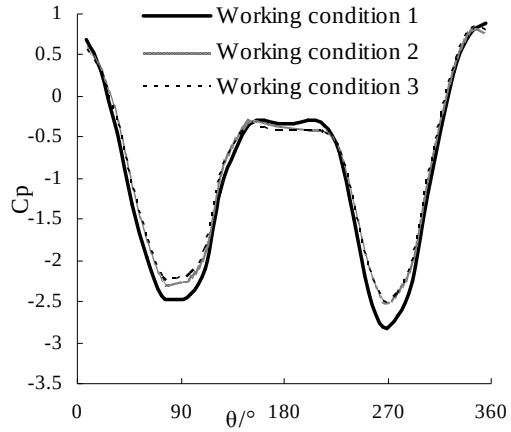


Figure15 Pressure coefficient distribution of cylinder 2 under three working conditions

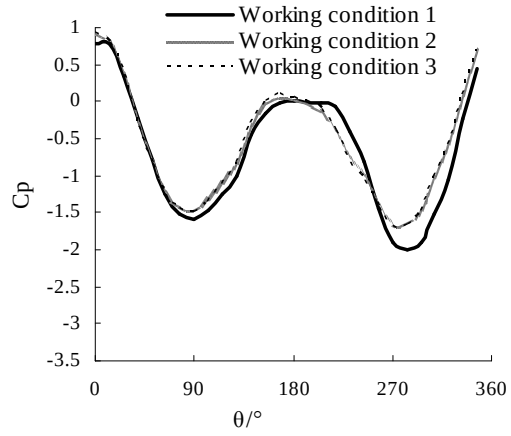


Figure 16 Pressure coefficient distribution of cylinder 3 under three working conditions

6. CONCLUSIONS

The main results may be summarized as follows:

(1) In comparison with the experimental and numerical loading distribution of the upper and lower spheres and the group of three cylinders, the numerical results show good agreements with experiments on the windward surface. Small differences are found between numerical and experimental results on the leeward surface within experimental error. CFD numerical simulation can be an effective method of predicting wind load distribution of high-rising structures.

(2) The surface roughness plays an important part in turbulent flow around spheres and cylinders. According to experimental and empirical surface roughness heights, the spheres and cylinders are in the sup-critical regime. The wind loading distribution of the sphere changes slightly in a specific range of surface roughness heights.

(3) In comparison of the wind load distributions of the sphere with symmetric and asymmetric surface roughness, the symmetry of the wind load distribution of the sphere changes a little in a specific range of surface roughness heights.

(4) Bias phenomenon still exists among the three cylinders when the surface roughness of the cylinders changes, but the extent of the bias decreases.

References:

LI Huizhi, XIE Changtian,(1997), "Wind Load on Shanghai Television Tower," Experiments and Measurements in Fluid Mechanics, 11（4）, 30-34.

LI Huizhi, ZHANG Liangliang,(1997), "Pressure Distributions and Aerodynamic Forces on the Shanghai TV Tower'spheroids," Journal of Experimental Mechanics, ,12（3）, 416-420.

LI Huizhi, XIE Changtian,(1997), "Pressure Distribution and Aerodynamic Force of Three Cylinders at High Reynolds Number," Experiments and Measurements in Fluid Mechanics, 11（2）, 44-47.

GU Ming, HUANG Peng, ZHOU Xuan-yi, etal,(2009), "Wind Tunnel Force Balance Test and Wind-induced Responses of the Guangdong New TV Tower Structure Ⅰ:wind tunnel test," China Civil Engineering Journal, 42（7）, 8-13.

ZHOU Zhiyong, CHEN Airong, ZENG Yong, etal,(2006), "Numerical Analysis of Shape Coefficient of CFD Simulation and Wind Induced Random Vibration Response of Henan TV Tower," 23（3）, 5-7.

SUN Xiaoying, WU Di, WU Yue, etal,(2010), "Wind-induced Interference Effects on Long-span Spherical shell for Coal Storage," Journal of Vibration and Shock, 29（2）, 39-42.

Huang Bencai, Wang Congjun,(2008), "Principles and Applications of Sructures Wind Analysis," Shanghai: Tongji University Press

Emil Simiu,Robert H.Scanland,(1978), "Wind Effects on Structures,"New York:John Wiley

LI Huizhi, FAN Youjing, WU Yizhang, et al,(2002), "Wind Tunnel Test of Pressure Distribution on Cylinders with Various Surface Roughness," Engineering Mechanics, 19(2), 129-131.

Bert Blocken, Jan Carmeliet, Ted Stathopoulos,(2007), "CFD Evaluation of Wind Speed Conditions in Passages Between Parallel Buildings--effect of Wall-function Roughness Modifications for the Atmospheric Boundary Layer Flow," Journal of Wind Engineering and Industrial Aerodynamics, (95)948-950:

DONG Guochao, CHEN Zhengqing, LUO Jianhui, et al,(2011) ,"Effects of Surface Roughness on the Mean Pressure Coefficient of Concrete Cooling Tower," Journal of Hunan University(Natural Sciences),38（7）, 6-9.

SHEN Qi, WAGN Guoyan, GU Ming,(2008), "Numerical Smulation of Wind Loads on High-rise Buildings and Disaster Analysis," Journal of Tongji University(Natural Science), 36（5）, 592-597.

Zhifu Gu, Tianfeng Sun,(2001), "Classifications of Flow Pattern on Three Circular Cylinders in Equilateral-triangular Arrangements," Journal of Wind Engineering and Industrial Aerodynamics, (95)553-568.

K.Lam, W.C.Cheung,(1988), "Phenomena of Vortex Shedding and Flow Interference of Three Cylinders in Different Equilateral Arrangements," J. Fluid Mech. (196)1-26.

S. G. Pouryoussefi(2011), "Force Coefficient and Strouhal Numbers of Three Circular Cylinders Subjected to a Cross-flow," Arch Appl Mech81:1725-1741.

Yan Bao, Dai Zhou,(2010), "Numerical Simulation of Flow over Three Circular Cylinders in Equilateral Arrangements at Low Reynolds Number by a Second-order Characteristic-based Split Finite Element Method," Computers&Fluids:882-899.

10CUEE CONFERENCE PROCEEDINGS
10th International Conference on Urban Earthquake Engineering
March 1-2, 2013, Tokyo Institute of Technology, Tokyo, Japan

DYNAMIC ANALYSIS OF EXISTING NON-CONFORMING CONCRETE GYMNASIA WITH STEEL ROOF

Tetsuya Ohmura[1] and Shizuo Hayashi[2]

1) Associate Professor, Engineering Faculty, Tokyo City University, Japan
2) Professor, Materials and Structures Laboratory, Tokyo Institute of Technology, Japan
tohmura@tcu.ac.jp, hayashi.s.ac@m.titech.ac.jp

Abstract: Numerous gymnasiums were damaged at the 2011 Tōhoku earthquake and tsunami. Much of them were built before the Japanese building standard was revised. There are many gymnasiums besides Tohoku region and they should be strengthened to prepare to a large earthquake which might occur in the near future. However, it is often hard to strengthen them, because they have concrete posts to support their steel roof. Some of them were retrofitted by buttresses in the past, while the conventional method using buttresses needed much space to construct it and have a cost problem. We suggested a new retrofit method for them based on our dynamic analyses results.

1. INTRODUCTION

The Japanese building standards act was revised in 1981 based on experience gained from past earthquake disasters. However, there are still numerous school buildings and gymnasia built before 1981 that lack sufficient seismic performance. The seismic strengthening of these buildings has been promoted but there are many problems preventing it, including the cost and time required for the work. Advanced seismic strengthening methods have been expected to minimize the construction expense and to shorten the construction period.

When the Japanese building standard act was revised in 1981, not only the allowable stress design method for DBE but also the limit design method considered plastic hinges mechanism for MCE were shown. So buildings built before the revised were designed based on the former method, and there are a lot of existing non-conforming buildings which had the low control level of the work and the quality. The Hanshin Awaji earthquake of 1995 increased public awareness of the lack of sufficient seismic performance for existing non-conforming buildings. The law promoting the strengthening of buildings was enforced in that year, and numerous existing nonconforming buildings have been strengthened.

Public school buildings are often put to practical use as evacuation locations and earthquake resilience footholds, and seismic assessments and strengthening have been performed for concrete school buildings and steel gymnasia with the goal of ensuring the safety of students. Thus, the ratio of buildings with sufficient seismic performance has been steeply increased.

Generally, the codes by The Japanese Building Disaster Prevention Association (BDPA) are used for the seismic assessment and strengthening of concrete buildings. On the other hand, various strengthening methods that consider construction conditions have been developed and used in different social backgrounds.

In addition, school gymnasia have been done seismic assessment and strengthened based on codes by BDPA and the education ministry. If it is determined that steel gymnasia or combined concrete and steel gymnasia lack sufficient seismic performance, they should generally be strengthened by the addition of braces in the longitudinal direction and knee braces in the span direction.

However, to strengthen the two-story concrete school gymnasia with steel roofs shown in Figures 1 to 3, it would be easier to be strengthened in the longitudinal direction because they contain moment frames with shear walls, whereas being strengthened in the span direction would be harder because they contain concrete posts.

Figure 4 shows a sample of seismic strengthening for an independent concrete post. Their seismic performance depends on their ultimate moment strength of the bottom column or the rotation strength of the base, because they should be a cantilever during an earthquake. A strengthening method that involves the construction of a buttress after a pile and base were constructed was often used for buildings that lack base rotation strength. This strengthening method requires some room around the building and a longer construction period, which tends to increase the construction cost.

Although the above mentioned strengthening would be needed if the lack of sufficient seismic performance of an

independent concrete post was found after being assessed based on the codes, a longitudinal concrete girder has actually expected to be effective for an independent concrete post. Thus, there have been no heavily damaged or overturned independent concrete posts in past disasters.

In this study, three-dimensional static nonlinear analyses for two-story concrete gymnasia with steel roofs were performed and the hysteretic characteristics of each member were determined. Then, three-dimensional time history response analyses were performed in the span direction. The effect of longitudinal concrete girders was examined. The ultimate moment strength of these girders was increased, and the seismic performance of the building was studied. These results could be used as the basic data for a design to strengthen concrete gymnasia.

2. BUILDING

The building for our analyses is shown in Figure 1 to 3 as mentioned before. It has a stage in the west, an entrance in the east, an arena for basketball in the center. There are some gallery at the second floor level consist of some cantilever slab from the longitudinal concrete girders at the second floor.

Longitudinal concrete girders were also used at the roof level. The roof, which consisted of steel girders and horizontal braces, was supported at the top of independent concrete posts, but the lateral force at the roof could not be transferred via horizontal braces because of a lack of strength.

There are some concrete walls with opening in the longitudinal direction at the first floor and a moment frame in the second floor, as shown Figure 2. The seismic index of structure in their seismic assessment based on the BDPA was 1.12 at the first floor, and 0.87 at the second floor.

The stiffness and strength values in frames X1 to X2 and X7 to X8 were higher because there are many concrete walls around the stage in the west and the entrance in the east. The seismic index of the structure was 2.05. On the other hand, the stiffness of the independent concrete posts in frames X3 to X6 was lower and the seismic index of the structure was 0.47 because they were cantilever posts.

The independent concrete posts were located 6 meter apart in X3 to X6, the span in the Y direction was approximately 20 m, and the height of the eaves was approximately 9 m. Figures 5 and 6 show the statistics for the span and eave heights. This statistics included 26 gymnasia with the same structure.

The painted plot in the Figure means the gymnasia for our analyses. Independent concrete posts were located 5.0 to 7.5 m apart, the spans in the Y direction were 17.5 to 31.0 m, and the eave heights were 7.2 to 10.0 m in the statistics. The span and eave heights of the gymnasia in our analyses were typical.

Figure 7 shows component of the gymnasia. The depth in the span direction of the independent concrete post was 700mm, and the width was 600mm. 18 rebar D22 (#7) was located at the first floor, and rebar was decreased at the second floor.

The hoop diameter and interval were 9 mm and 100 mm, respectively. The widths of the girders were 350 mm at the second floor and 300 mm at the roof level. Their depth was 600mm. The compressive concrete strength was 32 N/mm^2, and the yield strength of the rebar was 343 N/mm^2.

3. ANALYSIS

Push over analysis was performed using 3 dimensional non-linear analyses at first. Next, their hysteretic characters of columns, posts, shear walls and girders were respectively determined by the modified Takeda model. Then three dimensional time history dynamic analyses were performed.

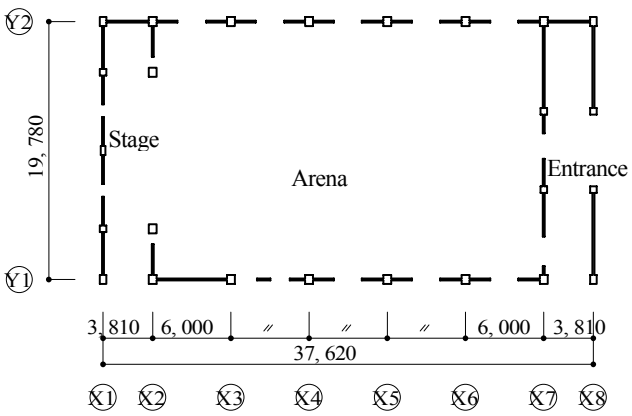


Figure 1 Plan (unit mm)

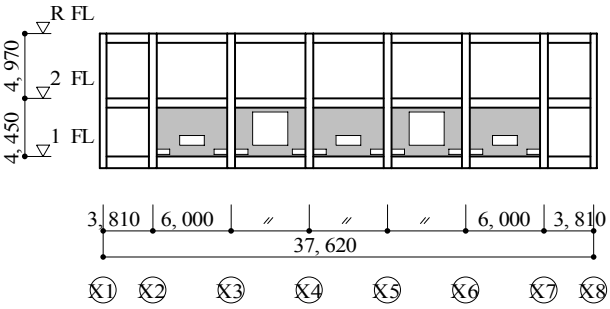


Figure 2 Y2 frame Elevation (unit mm)

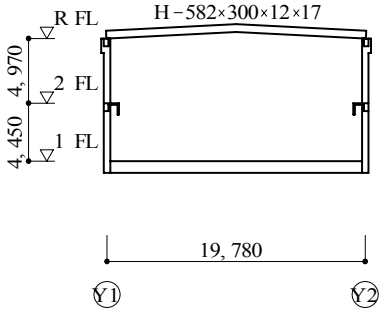


Figure 3 X4 to 6 frame Elevation (unit mm)

3.1 Modeling

Figure 8 shows models of the columns and girders. The model of the girder used two moment springs to consider cracking at both ends, along with a shear spring. The in-plane and out-of-plane moments were considered, but they were independent of each other. The combined moment effect was ignored.

It was assumed that the only rebar at the corner of the section was effective for the out-of-plane moment strength of the girders. The bending shape at the end of the hoop was 90°, but the effect of it was ignored.

The model of the columns has multi-springs at the both ends considered cracking and a shear spring.

The rotation strength of the base is considered, and they are modeled as the moment strength of the foundation girder.

As mentioned above, the horizontal braces at the roof could not transfer the lateral force of the roof, and the displacements of the independent concrete posts were different respectively.

The static earthquake load is determined by Ai in the Japanese building standard act. Masses were located at the second floor and roof level in our dynamic analyses, as shown in Figure 8.

Pin supports are located under the foundations, and the vertical and horizontal displacements of the foundations are ignored. Pushover analyses were stopped when any drift angle reached to 4%.

Figure 9 shows the ultimate moment strength of the longitudinal concrete girder in each run. Four runs were performed. Run #1 was performed for the original model for the existing gymnasia, and runs #2, #3, and #4 were performed for models with girders that have 9, 13, and 41 times the moment strength.

3.2 Earthquake motion input

Figure 10 shows the acceleration response spectra for the earthquake motion input. Five earthquake motions were input in the horizontal direction in the span direction. Their phases for the target spectra by BRI were based on El Centro NS (1940), Hachinohe NS (1968), JMA Kobe NS (1995), Taft EW (1952), and an artificial earthquake wave (BCJ-L2).

The target spectra were the acceleration response spectra, BRI-L2, which are represented by the horizontal motion normalized response spectra times the response equivalent ratio of the damping.

4. PUSH OVER ANALYSIS RESULTS

4.1 Hysteresis curve

Figure 11 and 12 show the hysteresis curve of the original model #1. Only frame Y2 are focused, because

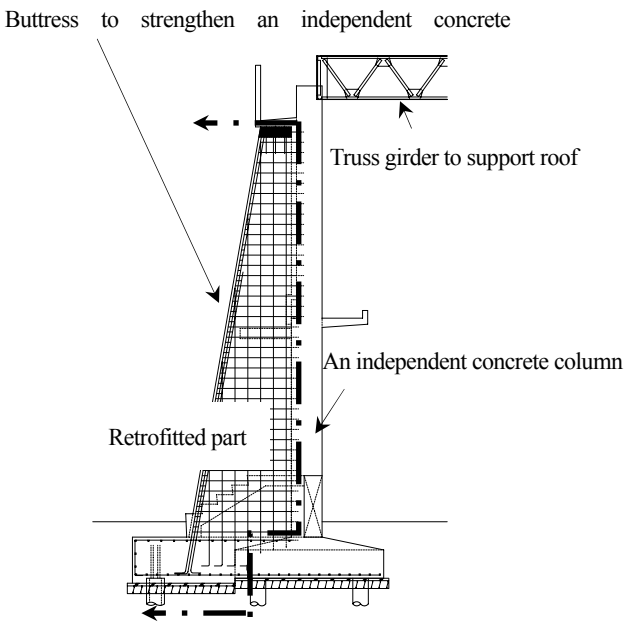


Figure 4 A detail of buttress

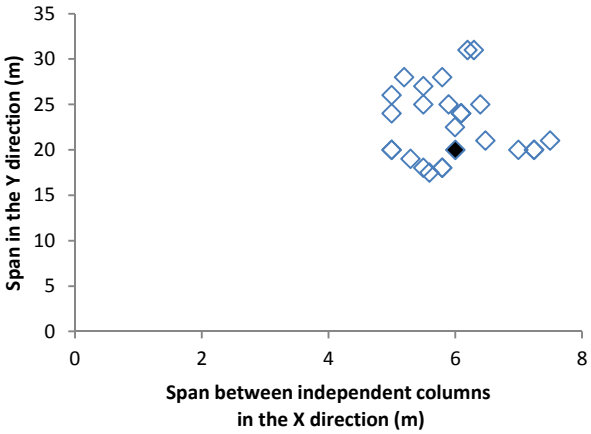


Figure 5 Statistics of span

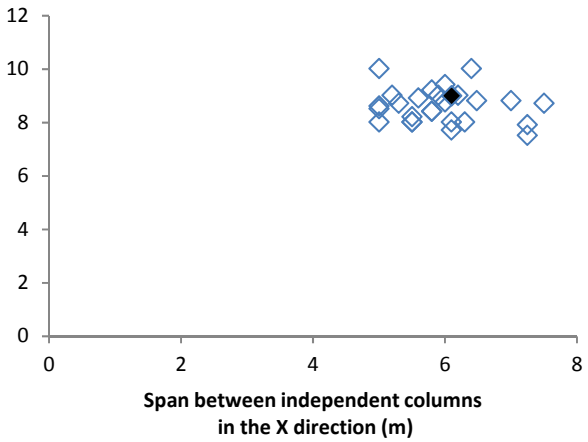


Figure 6 Statistics of eaves

the model is approximately symmetric.

Frames X1 to X2 with concrete walls are stiffer and have higher lateral strengths than frames X3 to X4 with the independent posts. The pushover analyses were stopped after a collapse mechanism was formed at frames X3 to X6 with the independent concrete posts and reached a sufficient drift angle.

The stiffness of frames X3 to X4 declined after a drift angle of about 0.3% at the second floor and at about 0.2% at the first floor, and a collapse mechanism formed at about 1.3% at the second floor and at about 1.1% at the first floor. Then, the lateral force was about 50 kN at the second floor and about 90 kN at the first floor.

The drift angle of frame X1 to X2 at the final step is about 3.1×10^{-3}% at the second floor and about 2.3×10^{-3}% at the first floor, and there is no stiffness reduction. They have high stiffness and strength because of concrete walls.

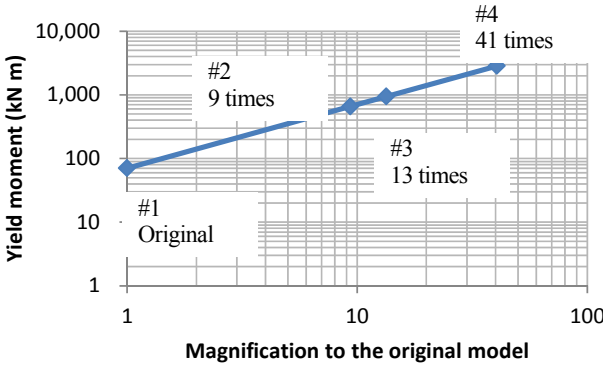


Figure 9 Ultimate moment strength of girder for four cases

2nd floor	700, 600	R floor	600, 300
Bar	10 - D22 6 - D19	Upper	5 - D19
Hoop	□- 9φ @ 100	Bottom	3 - D19
1st floor	700, 600	Stirrup	□- 9φ @ 200
Bar	18 - D22	2nd floor	600, 350
Hoop	□- 9φ @ 100	Upper	4 - D22
		Bottom	3 - D22
		Stirrup	□- 9φ @ 200

Figure 7 Column and girder section (unit mm)

Notes : D22 and D19 were #7 and #6.

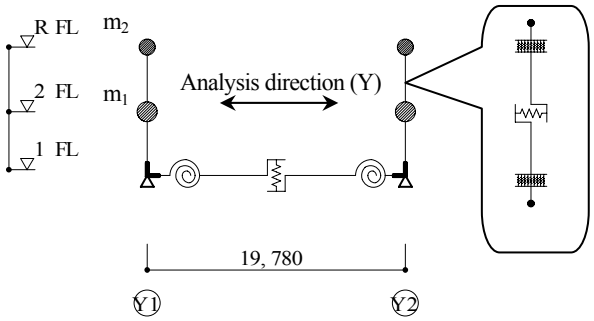


Figure 8 Column and girder model

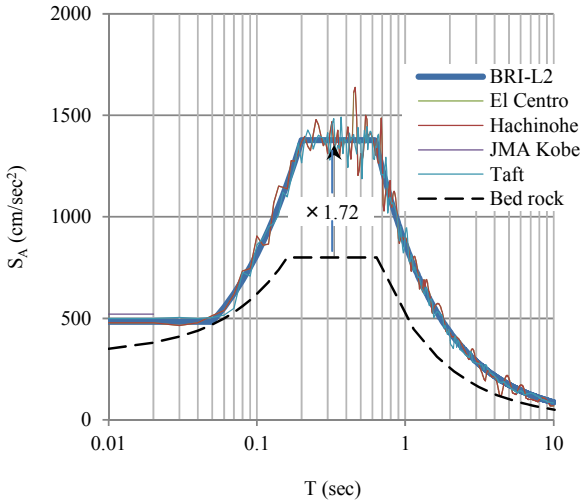


Figure 10 Acceleration response spectra

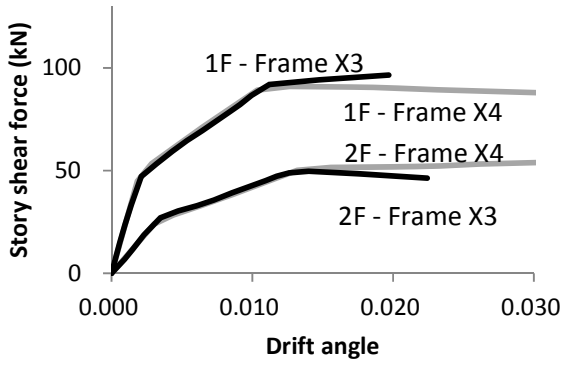


Figure 11 Hysteresis curve

4.2 Moment and hinge diagram

Figure13 shows a moment and collapse mechanism diagram for the original model #1. The moment diagram of the independent concrete posts in frame X3 to X6 is the same as that of a cantilever.

The out-of-plane moment at the longitudinal concrete girders occurred at the second floor and roof level. This means the longitudinal concrete girders were effective for the independent concrete posts with the application of a lateral load.

The moment diagram of the longitudinal concrete girder was the same as that of a long span girder that has both ends fixed. Moment hinges were formed at the center and at both ends of the girder. The independent concrete posts resist for lateral load as a cantilever supported by longitudinal concrete girders.

5. TIME HISTORY RESPONSE ANALYSIS RESULTS

The three dimensional static analysis was performed in the section 4, their skeleton curves for the dynamic analysis were determined based on the modified Takeda model. Then, three-dimensional time history response analyses were performed in the span direction, and analysis results were discussed.

5.1 Maximum response shear force and coefficient

Figure 14 and 15 show maximum response shear force and shear coefficient of the original model #1. They represented analysis results of the elastic model and the non-linear model. The solid and dash line mean the first floor and the second floor.

The analysis results for the five earthquake waves were different respectively, but the analysis results for frame X4 were approximately the same as those for frame X5. The analysis results for frame Y2 were focused upon because frames Y1 and Y2 were approximately symmetric and the analysis results for their independent concrete posts were approximately the same.

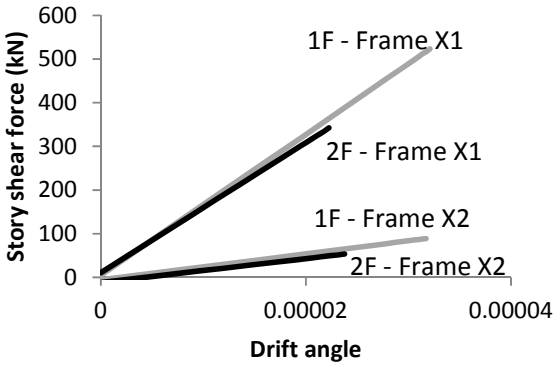


Figure 12 Hysteresis curve

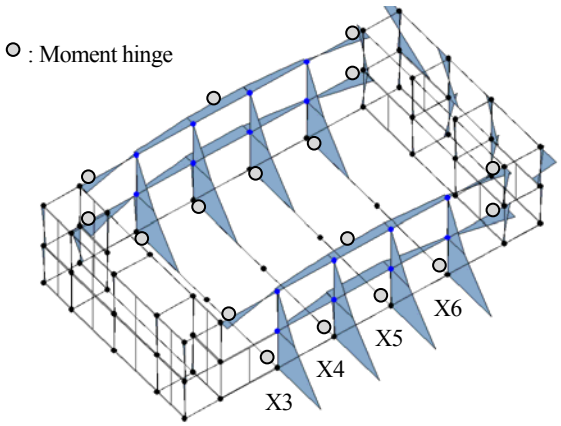


Figure 13 Moment and hinge diagram

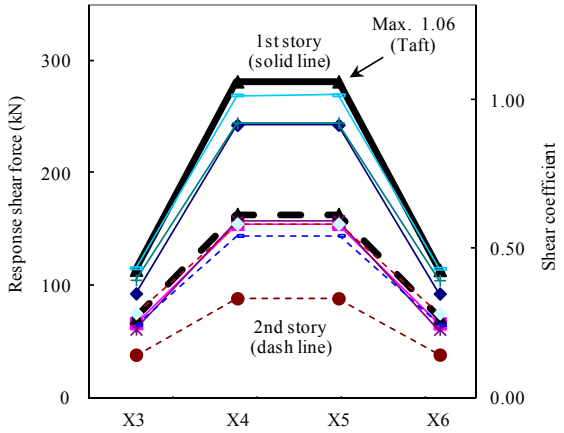


Figure 14 Response shear force (Y2 frame, elastic model)

(The original model)

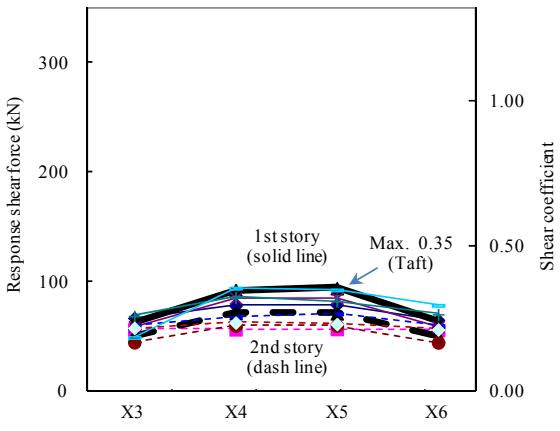


Figure 15 Response shear force (Y2 frame, non-linear model)

Maximum response shear coefficients of the elastic and non-linear models are 1.06 and 0.35. Maximum response shear coefficient is declined, because of plasticity of the frames.

Figure 16 shows the maximum response shear force and coefficient of model #3, where the out-of-plane moment strength of the longitudinal concrete girders was increased by 13 times. The maximum response shear coefficient of 0.36 was increased to 0.46 because the lateral strength of the independent concrete posts depended on the out-of-plane moment strength of the longitudinal concrete girders.

5.2 Maximum response inter story displacement and drift angle

Figure 17 shows maximum response displacement and drift angle at the roof floor. They were 220 mm and 2.3%.

Figure 18 shows maximum response displacement and drift angle of the model #3 which had 13 times the out of plane moment strength of the longitudinal concrete girders to the original model #1..

The maximum response displacement was decline to 81mm.

5.3 Effect of longitudinal girders for seismic performance

Maximum response shear coefficient was increased and maximum response displacement was declined in case out of plane moment strength of the longitudinal concrete girders was increased.

The method of seismic strengthening that the out of plane moment strength of the longitudinal concrete girders was increased was effective.

Figure 19 shows the relationship between the magnified ratio of the out of plane moment strength of the longitudinal

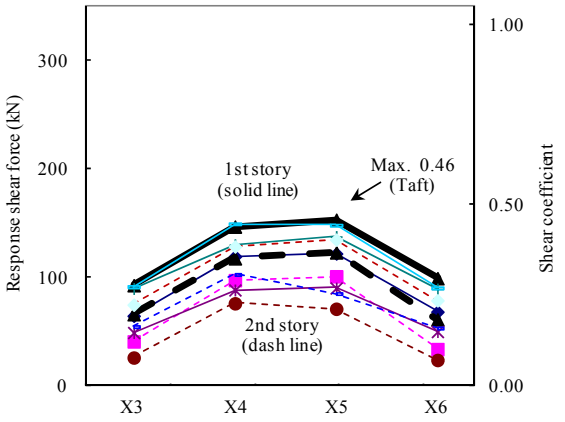


Figure 16 Response shear force (Y2 frame, non-linear model)

(Girder yield moment increased by 13 times to the original

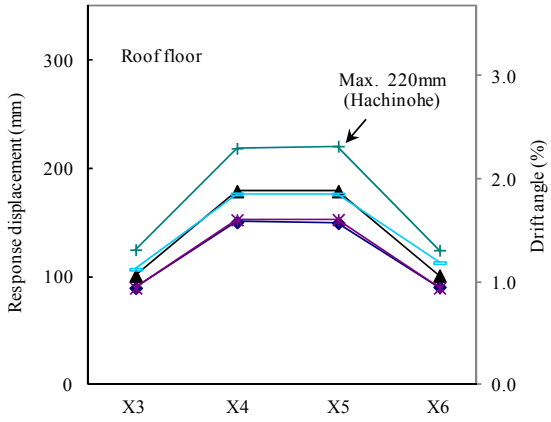


Figure 17 Response displacement (Y2 frame, non-linear model)

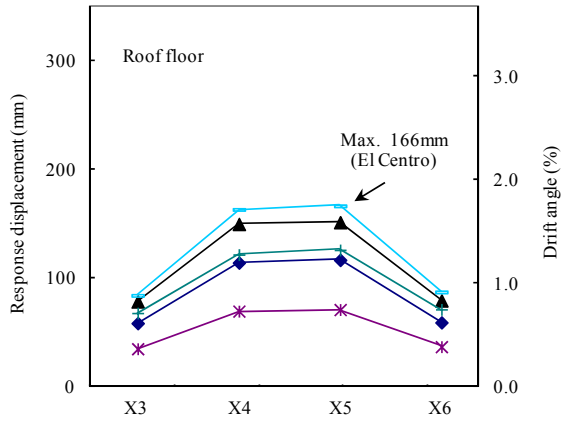
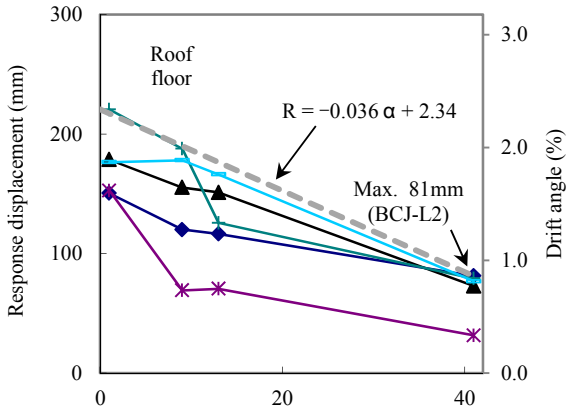


Figure 18 Response diplacement (Y2 frame, non-linear model)

(Girder yield moment increased by 13 times to the original



Magnification to ultimate momnet strength of girders

Figure 19 Relationship between magnification and drift angle

concrete girder and maximum response drift angle. The increment of the magnified ratio made maximum response drift angle decreased.

Maximum response drift angle could be calculated by using equation (1)

$$R = -0.036 \cdot \alpha + 2.34 \cdots\cdots\cdots\cdots (1)$$

where,

α = the magnified ratio of the out of plane moment strength of the longitudinal concrete girder

R = maximum response drift angle

6. CONCLUSION

1. An existing non-conforming gymnasium which had typical spans and eaves heights was modeled. The three dimensional static analysis results showed the effect of the longitudinal concrete girders for seismic performance, because moment hinges were formed at along them in the out of plane direction.
2. The three-dimensional time history response analyses results showed that the maximum response shear coefficient was 1.06 in the elastic model and 0.35 in the non-linear model.
3. The maximum response displacement was declined following increase of the out-of-plane moment strength of the longitudinal concrete girders.
4. The regression equation to calculate the maximum response drift angle using magnification ratio of longitudinal concrete girders.

Acknowledgements:

Professor Toru Takeuchi is thanked for giving much valuable advice to us. The support of NTT DATA staff is deeply appreciated.

References:

Eduardo N. B. S. Julio and Fernando A. B. Branco, "Reinforced Concrete Jacketing--Interface Influence on Cyclic Loading Response", *ACI Structural Journal*, Vol.104, 471-477, July 1, 2008

Dionysios A. Bournas and Thanasis C. Triantafillou, "Flexural Strengthening of Reinforced Concrete Columns with Near-Surface-Mounted FRP or Stainless Steel", *ACI Structural Journal*, Vol.106, 495-505, July 1, 2009

Ioannis Vrettos, Efstathia Kefala, and Thanasis C. Triantafillou, "Innovative Flexural Strengthening of Reinforced Concrete Columns Using Carbon-Fiber Anchors", *ACI Structural Journal*, Vol.110, 63-70, January 1, 2013

Tetsuya Ohmura, Shizuo Hayashi, Kazuhiro Kanata, Toshiharu Nakamura, Yasuhiro Nishikawa, Yumi Suzuki, Tashiro Fujimura, "Shear Transfer Mechanism of Seismic Strengthened Frames by Steel Braces without Dowel Anchors", *AIJ Journal of Structural and Construction Engineering*, Vol.616, 73-80, Jun 2007

Hiroshi Kuramoto, Ryosuke Haga, Tomoya Matsui, Takashi Taguchi, "Dynamic Loading Test on RC Frame Externally Retrofitted by CES Frame", *AIJ Journal of Structural and Construction Engineering*, Vol.630, 1265-1272, August 2008

Tetsuo Yamakawa, Md. Nafiur Rahman, Yoichi Morisita, "Experimetntal Investigation and Analytical Approach for Seismic Retrofit of RC Column with Wing Wall", *AIJ Journal of Structural and Construction Engineering*, Vol.608, 109-117, October 2006

10CUEE CONFERENCE PROCEEDINGS
10th International Conference on Urban Earthquake Engineering
March 1-2, 2013, Tokyo Institute of Technology, Tokyo, Japan

FRP-RETROFITTED T-BEAM-WIDE-COLUMN JOINTS UNDER CYCLIC LOADING

Kiang Hwee Tan[1], and Aziz Ahmed[2]

1) Professor, Department of Civil & Environmental Engineering, National University of Singapore, Singapore
2) PhD Candidate, Dept. of & Environmental Engineering, National University of Singapore, Singapore
tankh@nus.edu.sg, azizahmed@nus.edu.sg

Abstract: This paper presents an investigation on the seismic behavior of T-beam-wide-column joints. First, a practical fiber-reinforced polymer (FRP) retrofit was proposed to enhance the lateral load capacity of such joints, and tests were carried out on both nun-retrofitted and retrofitted specimens. The applied retrofit increased the yield load by 18 to 28 percent and the ultimate capacity by 3 to 7 percent; however, enhancement in ductility was not observed. A finite element model using ABAQUS was next formulated and verified the behavior of the test specimens. The numerical model was then used to examine the effectiveness of an enhanced FRP retrofit scheme, which was found to increase the lateral load capacity of the joints by 47 to 70 percent, with ductile post-peak behavior.

1. INTRODUCTION

Beam-column joints play an important role in the seismic response of building structures. In major cities in Asia, many buildings are gravity-load designed and they may be susceptible to the damaging effect of far-field earthquakes (Tan et al. 2012). In Singapore, in particular, columns in residential buildings often have a cross-section with a larger aspect ratio. As a result, beam-column joints are typically in the form of a T-beam wide column joint.

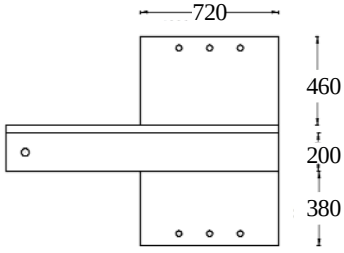
The behaviour of gravity-load designed T-beam-wide column joints under cyclic loading is not well understood. A study was therefore carried out to examine the lateral load capacity of T-beam-wide column joints. Both interior and exterior joints with and without FRP retrofit were tested. The results were used to verify a finite element model that was developed using ABAQUS (Dassault Systemes Simulia Corp., 2010) to predict the joint behaviour. An enhanced retrofit scheme was then established based on the test results of the retrofitted joints, and the verified model.

2. TEST PROGRAM

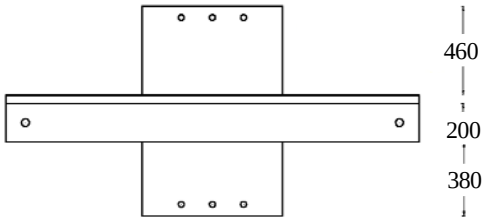
Exterior and interior T-beam-wide column joints were selected from the first/second stories of a 15-storey residential building. The first storey height is typically about 25% longer than upper storeys. The joints are designed without seismic provisions to BS8110 (BSI 1985) which resulted in the longitudinal reinforcement at the bottom of the beam being about half of that at the top. The transverse steel ratio in the column was 0.2%, and consisted of mild steel links with characteristic yield strength of 250 MPa. Longitudinal steel ratio in the column was 2.4%, and comprised high strength steel bars having characteristic yield strength of 460 MPa. No transverse reinforcement was provided in the joint region.

2.1 Test Specimens

The test specimens were two-fifth scaled models of the prototype joints, and the dimensions are shown in Figure 1.



(a) Exterior joint



(b) Interior joint

Figure 1 Dimensions of test specimens (*in mm*)

In total, four joint specimens were prepared and tested. They are labelled EU, ER, IU and IR, as shown in Table 1, with E denoting an exterior joint and I an interior joint.

The symbols U and R indicated unretrofitted and retrofitted specimens, respectively. In each specimen, the column segment has a height of 1040 mm, with a length of 460 mm above the top face of the T-beam and 380 mm below the soffit of the beam. It has a cross-section measuring 720 mm by 120 mm. The T-beam has a flange width of 400 mm, flange thickness of 40 mm, web width of 120 mm and overall depth of 240 mm. The beam protrudes a length of 600 mm on one or both sides of the column in the direction of the longer section dimension.

Table 1 Description of joint specimens

Designation	Type	Condition	f_c'(MPa)*
EU	Exterioir	Un-retrofitted	29.2
ER	Exterior	Retrofitted	21.3
IU	Interior	Un-retrofitted	27.4
IR	Interior	Retrofitted	27.7

*concrete compressive strength at day of testing joint, based on average of three cylinders

All joint specimens have similar arrangement of steel reinforcement as shown for an interior joint in Figure 2. The column had sixteen 13 mm diameter (deformed) bars as longitudinal reinforcement, and 6 mm diameter (smooth) closed links at 90 mm spacing as transverse reinforcement. The flange of the beam had 6 mm diameter (deformed) bars at 130 mm spacing in two orthogonal directions at the top acting as negative reinforcement. The beam was further reinforced with four 10 mm diameter (deformed) longitudinal bars at the top and two 10 mm diameter (deformed) bars at the bottom, with 6 mm diameter (smooth) closed links at 90 mm spacing as transverse reinforcement.

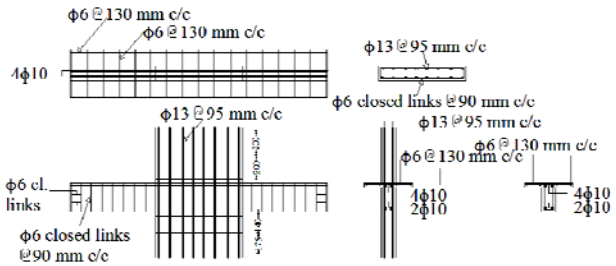


Figure 2 Steel reinforcement details

The concrete had a target cylinder compressive strength of 25 MPa at 28 days. Ordinary Portland cement, natural sand (fine aggregate), crushed granite of 10 mm maximum size (coarse aggregate) and water were mixed in ratio of 1: 3.08: 3.14: 0.79 by weight. The cement content was 289 kg/m^3.

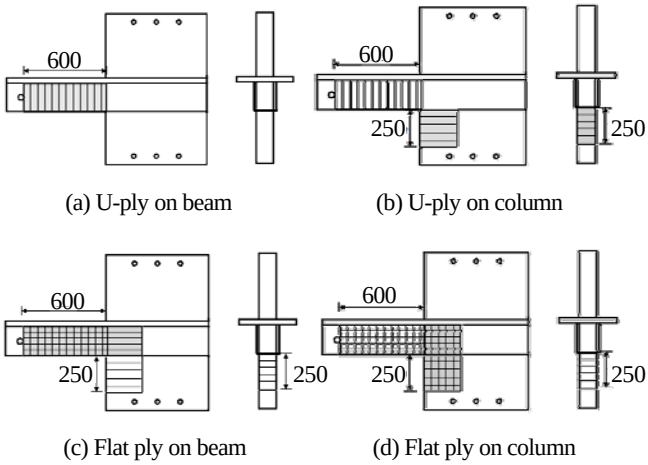
The average yield strengths for 6 mm (smooth), 6 mm (deformed), 10 mm (deformed) and 13 mm (deformed) bars were 245, 375, 482 and 528 MPa, respectively.

Carbon FRP sheets were used to retrofit the joint specimens. They had a design thickness of 0.176 mm/ply and a fibre weight of 300 g/m^2, with an elastic modulus of 240 GPa, tensile strength of 3800 MPa and elongation at rupture of 1.55%, according to the manufacturer's specifications. A three-part resin with the main component, hardener, and powder, mixed in the portional of 2 : 1 : 2 by weight was to bond the FRP sheets.

2.2 Fabrication of Joint Specimens

The reinforcement cage was assembled and concrete cast. Holes were provided at the ends of the beam and column components (see Figure 1) to facilitate the passing of through bolts to simulate pin connection during testing of joints. The specimens were stripped off the mould 24 hours after casting, and then placed under wet gunny sacks for at least 28 days. After that, the specimens were left inside the laboratory.

FRP sheets were applied only on the part below the flange of the beam to simulate actual condition. The surface of the specimen was first grinded to remove dust, grease, disintegrated materials and other bond inhibiting materials. Then, resin was applied on the required surface using a roller, followed by installation of the carbon FRP sheets. Figure 3 illustrates the procedure in which the FRP sheets were applied for Specimen ER. The same FRP system was applied to Specimen IR. After the installation of the FRP system, the joint specimens were left in the laboratory for a week before testing.



(a) U-ply on beam (b) U-ply on column

(c) Flat ply on beam (d) Flat ply on column

Figure 3 FRP retrofit of joint specimen

2.3 Test Set-up, Instrumentation and Procedure

The joint specimens were tested with the column in an upright position, as shown in Figure 4. The column pin support was considered as the point of contraflexure for the bottom column, while the centre of actuator was considered as the point of contraflexure for the top column. The beam ends were connected to the test floor by means of C-channels on each side, with high strength G 8.8 bolts forming the pin and roller joints.

Axial load was applied on un-retrofitted exterior joint specimen, that is, EU, only, using prestressing strands that were tensioned between stiffened plates mounted at the top and bottom of the column.

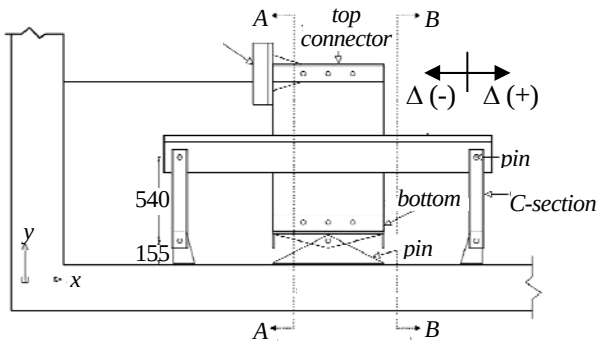


Figure 4 Test set-up (*dimensions in mm*)

The axial load ratio was 0.10. It was however found that the axial load ratio up to 0.5 (Ahmed 2013) has little effect on the response of the joint to lateral loading. Consequently, axial load was not applied to the remaining three specimens.

Each test specimen was instrumented with strain gauges to monitor strains in concrete, steel and FRP sheets in the vicinity of the joint. Linear variable displacement transducers (LVDTs) were used to measure the lateral displacement at top and bottom of the column segment as well as ends of beam segments, and vertical and horizontal displacements at the beam-column interfaces.

The un-retrofitted specimens, EU and IU, were tested under static pushover loading, for which the rate of loading was 0.02 mm/min throughout. On the other hand, the FRP retrofitted specimens, ER and IR, were tested under cyclic loading with the loading cycles shown in Figure 5.

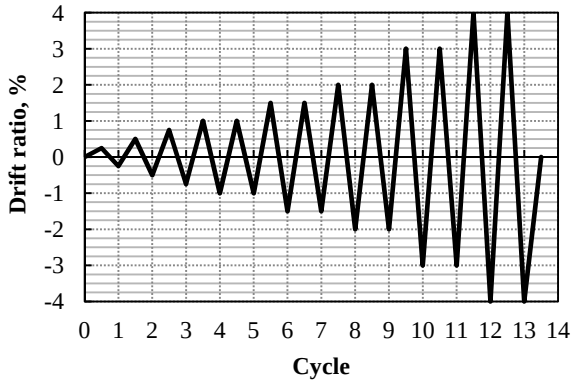


Figure 5 Loading cycles for retrofitted specimens

The rate of loading for the FRP retrofitted specimens was 0.01 mm/s for the first three cycles with maximum drift ratios of 0.25%, 0.50% and 0.75%, respectively. The drift ratio was defined as the lateral displacement of the top relative to the bottom of the specimen, divided by the specimen height. From the fourth cycle onwards, the loading rate was 0.02 mm/s.

The loading was paused after every full cycle to locate the regions of FRP debonding and rupture and the crack pattern. The test was stopped after the load had dropped 20% below the peak value.

3. TEST RESULTS AND DISCUSSION

Figure 6(a) shows the observed load versus lateral displacement at the top of specimen (corresponds to point of contraflexure in the upper column) for exterior joints, while Figure 6(b) shows the same for interior joints.

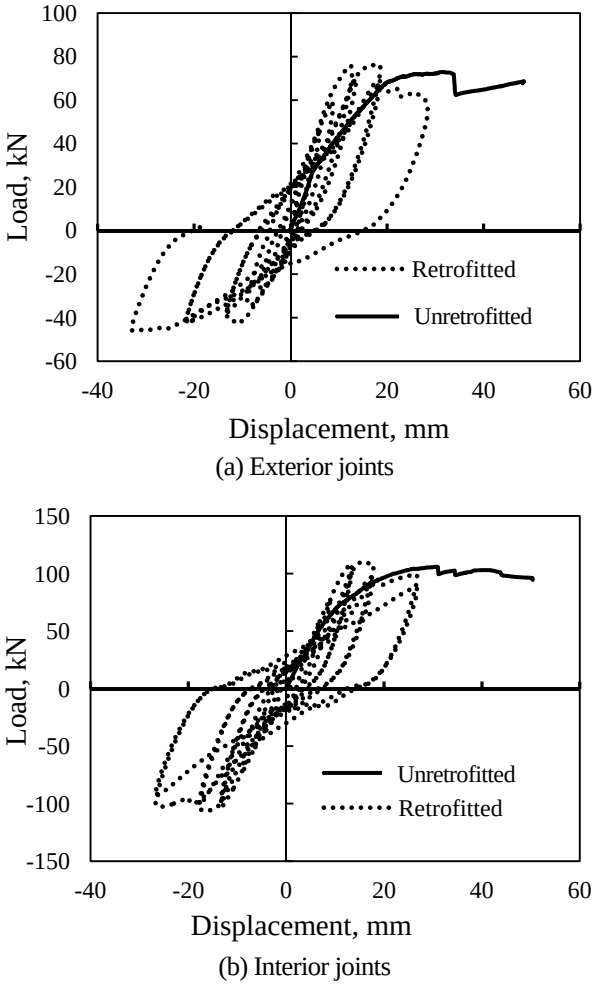


Figure 6 Load-lateral displacement relations

3.1 Unretrofitted Joints

The exterior joint [Figure 6(a)] experienced first flexural cracking at the top of the slabs at a load of 25.2 kN and a displacement of 4.3 mm. Inclined shear cracks began to form from the bottom of slabs at a load of 40.1 kN and discplacement of 8.8 mm.

The cracks subsequently propagated towards the beam-column joint and first yielding of longitudinal steel occurred in the top beam bars under tension at a load of 64.3 kN and displacement of 18.1 mm. Concrete began to crush at about 68.6 kN and 19.6 mm. Due to crushing and spalling of concrete, failure occurred at 72.4 kN and a displacement of 33.1 mm. Finally, the slab was completely cracked under tension near the beam-column joint. Thus, most of the damage occurred in the beam near the beam-column joint, resulting in shear-compression failure of the beam. There was negligible damage in the column or

the joint although some inclined cracks formed at the joint.

Similar behaviour was observed for the interior joint. Flexural cracks first appeared at the top of the slabs, load of 25.8 kN and a lateral displacement of 3.22 mm. Cracks began to form from the bottom of the beam on one side of the beam column joint at 37.1 kN and a displacement of 4.77 mm. At 46.1 kN and 6 mm, these cracks had propogate4d to the bottom of the slabs and subsequently towards the joint region.

Yielding of steel reinforcement first occurred at bottom of the beam near the joint at 80.1 kN and 13.1 mm, then on top of the beam on the other side of the joint at 94.8 kN and 18.9 mm. Concrete began to crush at the bottom of the beam near the beam-column joint at about 98.2 kN and 21.1 mm, and failure finally occurred at 105.9 kN at a lateral displacement of 30.8 mm.

Most of the damage was found in the beam near the beam-column joint. There was negligible damage on the column or the joint although some diagonal cracks formed in the joint. Shear compression failure was observed in the beam on one side and flexural tension failure on the other side of the joint.

3.2 FRP-Retrofitted Joints

Both FRP retrofitted exterior and interior joints were tested under cyclic loading (refer Figures 4 and 5). The push direction is referred as the positive (+) direction and the pull direction as the negative (-) direction.

The retrofitted exterior joint ER experienced first flexural cracking in the slabs during the second cycle at a load of 24.1 kN and a lateral displacement at the top of the specimen of 3.1 mm [Figure 6(a)]. These cracks propagate with subsequent cycles. There was however no significant stiffness degradation up to the third cycle.

The longitudinal bars at the bottom of the beam first yielded at the 4^{th} cycle under a load of 40.1 kN and a displacement of -9.25 mm. Rupture of FRP sheets happed in the 5^{th} cycle at 42.9 kN and -11.2 mm. The specimen maintained its strength under positive loading throughout the next two cycles but lost stiffness and began to experience a drop in load-carrying capacity in the negative direction.

Next, yielding of the top longitudinal bars of the beam occurred in the push direction of the 7^{th} cycle, at 75.8 kN and +12.4 mm. The maximum lateral load capacity was attained with concrete crushing at 76.3 kN and +17.9 mm in the same cycle.

The test was terminated after 10^{th} cycle due to extensive damage of the specimen. Most of the damage again occurred near the beam column joint. Some shear cracks which initiated in the non-retrofitted regions, formed at the top and bottom of the columns and in the joint. FRP debonding was also observed in the beam and the joint, mainly due to compressive forces, but also partly due to poor bond between the FRP sheets and concrete in the joint region.

The retrofitted interior joint exhibited first flexural cracking at the top of the beam flange during the second cycle at 24.3 kN and +2.8 mm. Although the crack propagated subsequently, there was no stiffness degradation up to the 5^{th} cycle.

Yielding of the bottom longitudinal bars in the beam bottom occurred on both sides of the joint during the 6^{th} cycle, at 102.7 kN and +13.4 mm, and 97.3 kN and -12.3 mm. The maximum lateral load capacity was reached in the 7^{th} cycle due to rupture of FRP sheets on both sides of the joint followed by concrete crushing, at 108.1 kN and +18.2 mm, and 105.6 kN and -17.1 mm. The flanges on both side of the joint were found to be completely cracked across. The test was terminated after 10^{th} cycle due to extensive damage of the specimen.

Similar to the retrofitted exterior joint, most of the damage occurred near the beam-column connection, and some diagonal cracks formed at the top and bottom of the columns and in the joint. FRP debonding was also observed in the beam and the joint.

3.3 Effectiveness of Applied Retrofit

Figure 6(a) compares the lateral load response of un-retrofitted and etrofitted exterior joint, while Figure 6(b) shows the comparison for interior joints. The behaviour of retrofitted joint was similar to that of the un-retrofitted joint in the first cycle up to 30 kN for exterior joints, and 45 kN for interior joints, at which cracking occurred in the un-retrofitted joints. However, due to earlier cracking and subsequent yielding, the un-retrofitted joints exhibited more ductile behaviour at failure.

The displacement ductility, defined as the ratio of the lateral displacement at concrete crushing of the critical section to that at first yield of steel reinforcement, was 1.83 for the un-retrofitted exterior joint EU, and 2.35 for the un-retrofitted interior joint IU.

For FRP-retrofitted exterior joint ER, the failure mode was actually more brittle with debonding followed by concrete crushing while being loaded in positive direction and FRP rupture while being loaded in negative direction. The strength increase was only 5% and the displacement ductility was 1.44. It should however be noted that the concrete strength was much lower than that for the un-retrofitted joint (see Table 1). Also, the applied retrofit had delayed the yielding of steel reinforcement, with the first yield load increased by 18%, compared to the un-retrofitted joint, and hence a lower displacement ductility.

Similarly, for the FRP-retrofitted interior joint IR, the failure mode was more brittle with debonding followed by concrete crushing and FRP rupture. The first yield load was increased by 28% while the maximum load by only 2%. The displacement ductility was 1.36.

The retrofit technique investigated herein resulted in a higher first yield load but not so much the ultimate load capacity and tthe displacement ductility. A finite element model was thus formulated and verified using these test results, and subsequently used to propose an enhanced practical FRP retrofit method for the joints which would lead to increased ultimate strength while maintaining adequate displacement ductility of the joints.

4. FINITE ELEMENT ANALYSIS

A finite element analysis of the tested joints under lateral load was carried out using ABAQUS (DSSC. 2010). Steel reinforcing bars were modelled as one-directional strain elements with elastic-perfectly plastic properties in both tension and compression. Concrete was modelled by 8-node solid brick elements, and Concrete Damaged Plasticity Model was used to simulate the behaviour of concrete. Bond-slip and dowel action were modelled by considering "tension stiffening" effect in concrete. Further details are given in the reference (Aziz 2012).

FRP reinforcement was modelled using 3-D, four node shell elements. The elements were superimposed on the solid brick elements, and perfect bond between the FRP reinforcement and concrete elements was assumed. The FRP material is assumed to be linearly elastic. In-plane stress-based failure theory was used to specify failure of the FRP material, assuming that all the compressive stresses were taken by the saturant.

4.1 Verification of Finite Element Analysis

Figures 7(a) to (d) compare the observed lateral load response with the predictions of the FE analysis. The predicted ultimate load capacities were within 5% of the observed values. However, the predicted displacements were 6 to 10 mm smaller that the observed displacements, due to some slippage at the connections.

In general, the ABAQUS model was found to predict the increase in yield load and ultimate load capacity as observed in the tests. It also predicted a loss in displacement capacity due to FRP retrofit as observed in the tests. It can also be seen that failure of the FRP retrofitted exterior joint specimen by concrete crushing was more gradual than the retrofitted interior joint due to rupture of FRP reinforcement. The finite element analysis further indicated a strain greater than 0.004 at the location of FRP rupture, which agreed with recorded gauge readings.

4.2 Suggestion for Enhanced Retrofit Scheme

Based on the test results and comparison with finite element analysis, and using the same modeling technique, the effect of various ply lengths and thicknesses on the joint performance was investigated. An enhanced retrofit scheme was established and shown in Figure 8.

For the exterior joint, a long flat FRP ply going around the end of the column instead of a flat ply ending 250 mm inside the joint is proposed. Additionally, a second flat ply extending from 200 mm before the pin connection (contraflexure point) in the beam to 250 mm inside the joint is applied. The additional plies are meant to improve the bond anchorage of the FRP sheets. They will help distribute the yielding of steel reinforcement over the length of the beam, thus providing better ductility.

A similar scheme is proposed for interior joints, in which two flat plys are provided across the whole width of the joint.

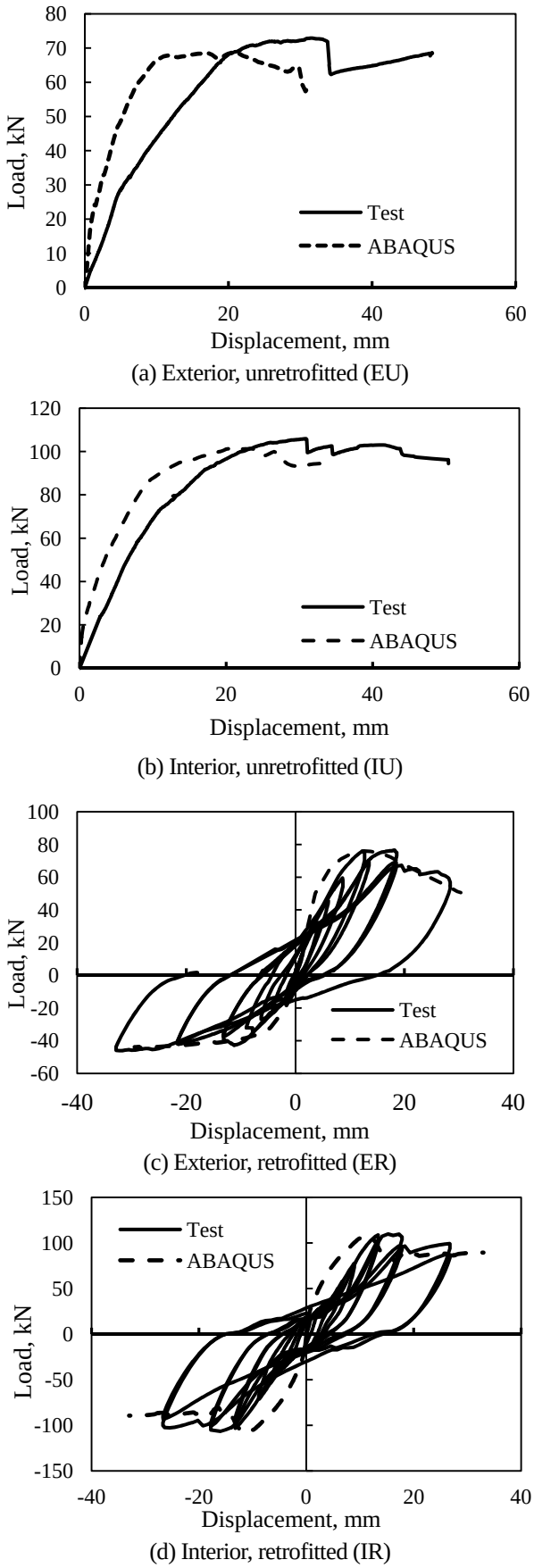
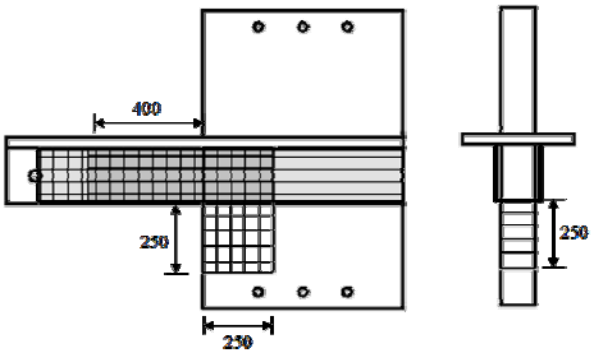
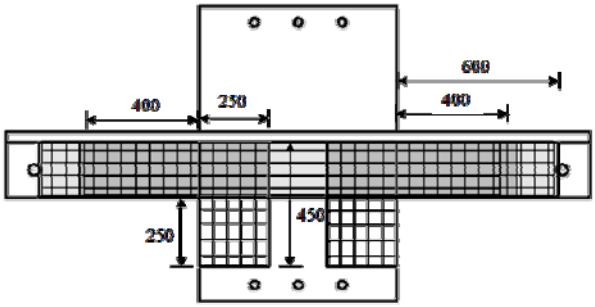


Figure 7 Comparison of FEA results with tests



(a) Exterior joint



(b) Interior joint

Figure 8 Enhanced retrofit scheme

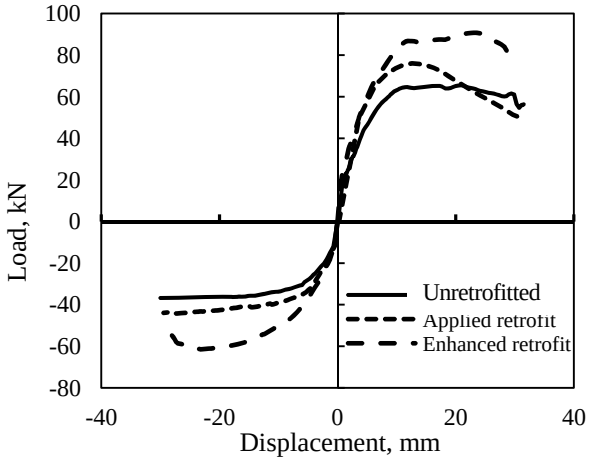
Figure 9 compares the load-displacement curves for the retrofitted joints under lateral loading using the original (applied) and suggested (enhanced) schemes with the un-retrofitted joint, based on the finite element analysis. The concrete strength was assumed the same and equal to that of the un-retrofitted joint shown in Table 1.

While the applied retrofit for exterior joint resulted in 17% increase in ultimate strength with respect to the unretrofitted joint in the positive loading direction, the enhanced retrofit scheme led to a strength increase of about 40%, and the capacity is maintained up to the ultimate displacement, that is similar to the un-retrofitted joint. In the negative loading direction, the applied retrofit resulted in 17% increase in ultimate strength whereas the enhanced retrofit increased the strength by about 70%.

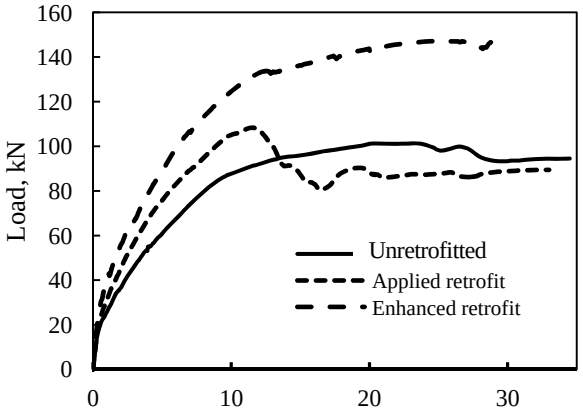
For the interior joint, enhanced retrofit resulted in about 47% increase in the ultimate strength compared to 7% increase for the applied retrofit. The capacity was also maintained up to the ultimate displacement that is close to that of the un-retrofitted joint.

5. CONCLUSIONS

The tests showed that the T-beam-wide-column joints do not suffer much damage in the joint region under lateral loading. They were found to fail by flexural tension and shear-compression in the beam at the joint interface.



(a) Exterior joints



(b) Interior joints

Figure 9 FEA of unretrofitted and retrofitted joints

The experimentally investigated FRP retrofit scheme delayed the yield of steel reinforcement, and increased the lateral load capacity marginally. By adopting an enhanced FRP technique established from finite element analysis that was verified with the test results, it was shown that the lateral load capacity could be increased substantially without reduction in ductility of the joint.

Acknowledgements:

The authors thank Basler & Hofmann Singapore Pte Ltd for providing the FRP reinforcement. Support from the staff of Structural Engineering Laboratory, National University of Singapore in carrying out the experiments is gratefully acknowledged.

References:

Ahmed, A. (2012), "Seismic Vulnerability and Retrofitting of Gravity Load Designed RC Structures," *PhD* Thesis, National University of Singapore.

British Standard Institution (1985). "*Structural Use of Concrete, Parts 1, 2 and 3 (BS8110),*" BSI, London, UK.

Dassault Systemes Simulia Corp. (2010), "*ABAQUS Standard User's Manual,*" **6**.10, Providence, RI, USA.

Tan, K.H., Balendra, T. and Ahmed, A. (2012), "Seismic Vulnerability of Gravity-Load Designed Buildings", Invited Paper, *11th International Symposium on New Technologies for Urban Safety of Mega-Cities in Asia*, Ulaanbataar, Mongolia.

10CUEE CONFERENCE PROCEEDINGS
10th International Conference on Urban Earthquake Engineering
March 1-2, 2013, Tokyo Institute of Technology, Tokyo, Japan

SEISMIC PERFORMANCE OF REINFORCED CONCRETE BUILDINGS INCORPORATING SOIL-STRUCTURE INTERACTION

Wanchai Yodsudjai[1)], Sarawoot Charoensuttikul[2)], and Piya Chotickai[3)]

1) Assistant Professor, Department of Civil Engineering, Kasetsart University, Thailand
2) Graduate Student, Department of Civil Engineering, Kasetsart University, Thailand
3) Assistant Professor, Department of Civil Engineering, Kasetsart University, Thailand
fengwcy@ku.ac.th, pokparkdee@hotmail.com, fengpyc@ku.ac.th

Abstract: The paper presents the seismic performance of 10-story reinforced concrete buildings with various structural configurations in Bangkok area. The nonlinear dynamic analyses were conducted according to the guideline provided in ATC-40. The influence of the foundation configurations and structural systems on the seismic performance was evaluated. The simplified and refined analytical models for various foundation configurations were developed and compared. Nonlinear pile foundations were modeled using the load-transforms method for vertical displacement and p-y curves for horizontal movement. The analytical results revealed that the foundation configuration and structural system had significant effects on the seismic responses and performance. The refined analytical model with soil-structure interaction could provide realistic estimate of the structural responses under earthquake excitation and was crucial to be used in the analysis for the buildings with a flexible foundation system.

1. INTRODUCTION

Awareness for a seismic risk in Bangkok area due to remote-distance earthquakes from the active faults on the northern and western regions of the country has raised a concern on the safety and performance of old reinforced concrete buildings built before the release of the seismic design regulations in Thailand. These buildings were designed to mainly resist gravity and wind loads. Several structural configurations were generally used depending on the functional requirements. Some residential buildings were constructed using slab on ground without tie beam on the 1st floor level to reduce loads on foundation and provided a parking space. Without tie beams or structural members to provide a diaphragm action at the base, the buildings would have a flexible foundation system for lateral loads. Additionally, many of these buildings were designed using bored pile with deep pile tip to increase in the load capacity per pile and had only one pile per footing. These flexible base conditions caused the buildings to be vulnerable to the seismic excitations.

The paper was therefore aimed to evaluate the seismic performance of typical reinforced concrete buildings with various structural configurations. The effect of foundation flexibility on base shear, natural frequency, and seismic performance was examined using nonlinear static pushover analysis.

2. NONLINEAR STATIC PUSHOVER ANALYSIS

Nonlinear static pushover analysis can be used for the performance analysis of new and existing buildings. It is an efficient analysis method to trace the structural responses from the elastic range, though yielding and cracking, up to complete failure. Pushover analysis can be described as the method applying lateral loads in a pattern that represent the relative inertia forces at each floor level. A building is pushed laterally under lateral loads until a target displacement is obtained. The target displacement used in the analysis can be the displacement corresponding to the one expected for design earthquake or the displacement causing collapse mechanisms. Generally, both force distribution and target displacement are based on the assumption that the response is controlled by a fundamental mode throughout the analysis (Pinho et. al., 2007). Although the assumption is incorrect, the analysis results obtained from this simplification have been shown to provide rather good estimates of seismic performance (Krawinkler and Seneviratna, 1998).

By utilizing the analysis, the sequence of yielding and failure can be traced. The strength degradation or reduction in stiffness of members for each increment of lateral loads is monitored during the analysis and used to update the analytical model for the next incremental load. Nonlinear behaviors of structural members are commonly considered using a plastic hinge concept which the degradation is concentrated at critical locations. Figure 1 presents a general shape of the flexural plastic hinge provided in ATC-40. By combining many step loads, the relationship between base shear and top roof displacement or a capacity curve can be developed. The curve generally exhibits saw tooth characteristic corresponding to overall strength degradation. The capacity curve is then used to compare with the seismic demand required by a specific earthquake to obtain the

performance point of the structure.

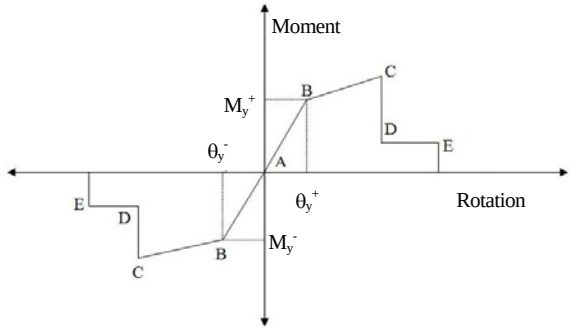


Figure 1 Relationship between Moment and Rotation of Flexural Plastic Hinge (ATC-40)

3. FOUNDATION MODELING

Buildings are commonly supported by pile foundations in areas with soft soil condition. During an earthquake excitation, these foundations provide restraints for vertical and lateral movements at the base of the structures. Sufficient load carrying capacity of the foundations is therefore required to prevent an excessive displacement and instability of the structures. The relationship between the resistant load in pile and vertical movement can be modeled using the load transfer approach (Seed and Reese, 1957). With this simplification approach, piles can be modeled as a series of elements with nonlinear springs, as presented in Figure 2, to represent the interaction between friction force on pile's surface and settlement, called T-Z spring, and the relationship between the resisting force at pile tip and settlement, call Q-Z spring. Based on this concept, several spring models are available in the literatures, including Vijayvergiya (1977), McVay (1989), Pando (2003), API (2000), and FHWA (2010).

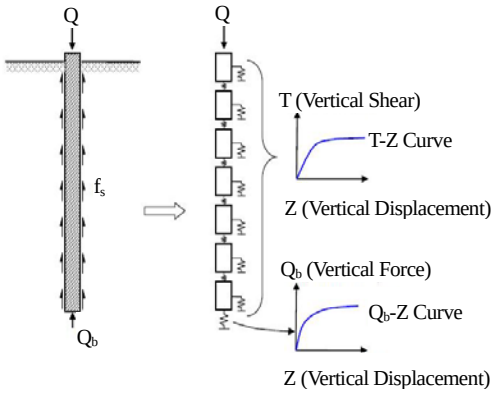


Figure 2 Load Transfer Approach for Vertical Movement of Pile

In this study, the most suitable model was selected based on a comparison of the available proposed models and the experimental results of static pile load tests for driven and bored piles of fourteen construction projects in Bangkok area. The comparative study revealed that the model proposed by Vijayvergiya (1977) gave the best estimate of the pile responses. The relationships between the friction on pile surface (f_s) and settlement (z) for clay and sand can be expressed as:

$$f_s = f_{s,\max} \cdot \left(2 \cdot \sqrt{\frac{z}{z_c}} - \frac{z}{z_c} \right) \quad (for \quad z \le z_c) \tag{1}$$

$$f_s = f_{s,\max} \quad (for \quad z \ge z_c) \tag{2}$$

Where z_c is the movement required to mobilize $f_{s,\max}$.

The relationships between bearing resistant (q) at pile tip and settlement (z) can be expressed as:

$$q = \left(\frac{z}{z_c} \right)^{\frac{1}{3}} \cdot q_{\max} \quad (for \quad z \le z_c) \tag{3}$$

$$q = q_{\max} \quad (for \quad z \ge z_c) \tag{4}$$

Where z_c is the movement required to mobilize $q_{\max}$.

Piles resisting lateral loads can be modeled as an elastic beam on elastic foundation. The interaction of soil and pile can be represented by elastic springs on the front and back of the pile being considered, as shown in Figure 3. The relationship between spring force and lateral displacement can be presented using p-y curve. Based on the available p-y curves in the literatures and a comparative study with the experimental results of fifteen lateral pile load tests, the models proposed by Matlock (1970), Reese and Welch (1975), and Reese et. al. (1974) were used in this study for soft clay, stiff clay and sand, respectively.

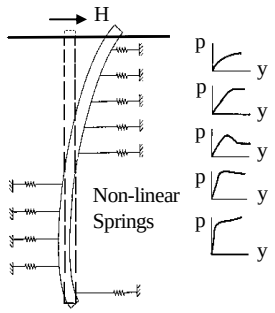


Figure 3 p-y Curve for Lateral Movement of Pile

Pile group effect can be included in the analysis by means of P-multiplier. The p-y curve of single pile is adjusted by multiplying with a reduction factor to account for a pile group effect. The P-Multipliers for a pile group with spacing between piles of 3 times of a pile diameter were equal to 0.80, 0.55 and 0.45 for the front, second and third rows, respectively (Rollins, 2006).

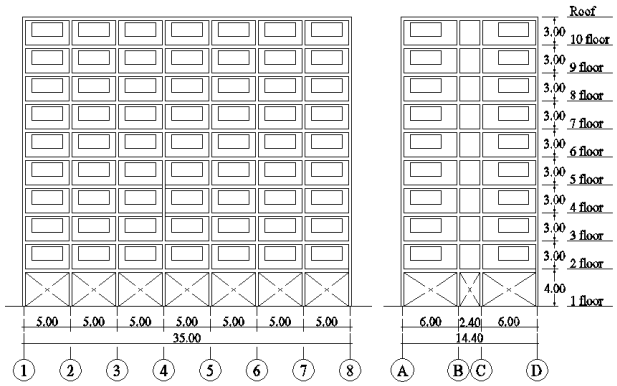
4. STRUCTURE MODEL

The seismic responses and performance of typical 10-story reinforced concrete buildings with various foundation configurations and structural systems were examined. Table 1 presents the variation of foundation configurations and structural systems included in this study. All buildings were designed for gravity loads with concrete compressive strength of 24 MPa and yield strength of 400 MPa for reinforcing steel. Two structural systems, namely Building Type A and Building Type B, were the buildings with beam-column structure and slab-column-shear wall structure, respectively, as presented in Figure 4.

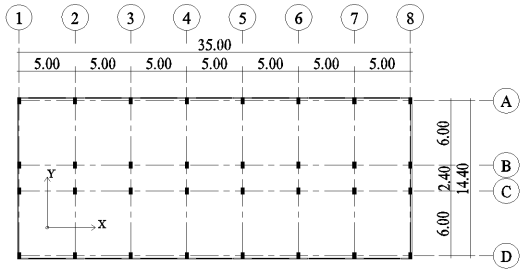
For each Building Type, several structural systems at the 1st floor level were considered, including precast slab on ground beam, flat slab, and slab on ground without tie beam. With the specified design live load of 200 kg/m^2, typical dimensions of reinforced concrete members were equal to 0.35x0.60 m for column, 0.25x0.50 m for beam, and 0.175-m thickness for flat slab. Two foundation configurations included a fixed-base condition and nonlinear soil-pile systems with soil properties corresponding to typical soil layers in Bangkok area, as presented in Figure 5. For the foundation systems with bored piles, the bored piles of size 0.6-m in diameter and 0.8-m in diameter were used for the exterior and interior columns, respectively. With these pile sizes, one bored pile had sufficient capacity to resist gravity loads and was assigned for each column. In the case of driven pile, the pile sizes of I-0.30x0.30 m and I-0.35x0.35 m were employed. According to the applied gravity loads, four driven piles were used for each footing. By comparing the analysis results of the buildings with similar structural systems at the 1st floor level but having different pile types, the effect of number of piles per footing on the seismic responses could be examined.

Table 1 Structural Configuration of Building Models

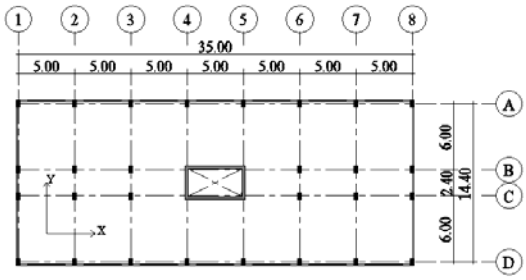
Building Type	Structural System at First Floor	Foundation	Pile Type
A1	-	Fixed Base	-
A2	Precast Slab with Beam	Nonlinear	Bored Pile
A3	Flat Slab	Nonlinear	Bored Pile
A4	Slab on Ground without Tie Beam	Nonlinear	Bored Pile
A5	Slab on Ground without Tie Beam	Nonlinear	Driven Pile
B1	-	Fixed Base	-
B2	Slab on Ground without Tie Beam	Nonlinear	Bored Pile
B3	Flat Slab	Nonlinear	Bored Pile
B4	Precast Slab with Beam	Nonlinear	Bored Pile
B5	Slab on Ground without Ties Beam	Nonlinear	Driven Pile



a) Elevation View



b) Typical Floor Plan for Building Type A



c) Typical Floor Plan for Building Type B

Figure 4 Building Configurations

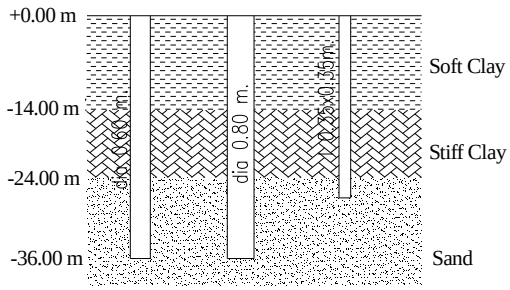


Figure 5 Soil Layer and Pile Depth

Three-dimensional finite element models were developed for each structural configuration using the commercial finite element software SAP 2000. Beams and columns were modeled using line elements having linear elastic properties along the length with nonlinear hinges to represent the nonlinear flexural behavior of beams and both

axial and flexural behaviors of columns. The nonlinear hinges in beams and columns were modeled as lumped plasticity at the start and end of each element and assigned according to the guidelines provided in FEMA-356. The diaphragm action of flat slab at the 1st floor level for Building A3 and B3 was modeled using elastic linear shell elements. An interaction between internal forces and nonlinear behavior of shear wall under earthquake was incorporated in the model using available nonlinear shell elements. Piles were modeled by line elements with nonlinear T-Z and Q-Z springs to represent the resisting force for vertical displacement and nonlinear p-y springs for lateral displacement.

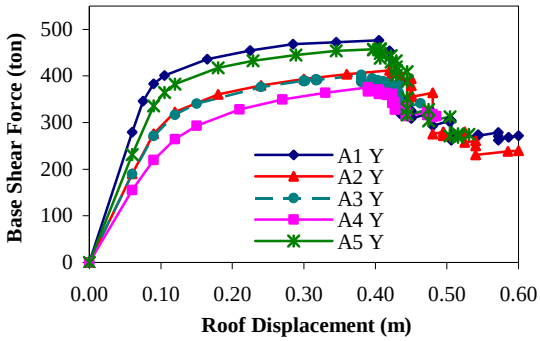
5. ANALYSIS RESULTS

Nonlinear static pushover analysis was conducted to evaluate the effect of foundation configurations and structural systems on the seismic performance of the buildings. The soil-structure interaction of each building was investigated and presented in terms of dynamic characteristics and a relationship between base shear force and roof lateral displacement. The performance level of buildings was determined using the design earthquake provided by the Uniform Building Code (1997).

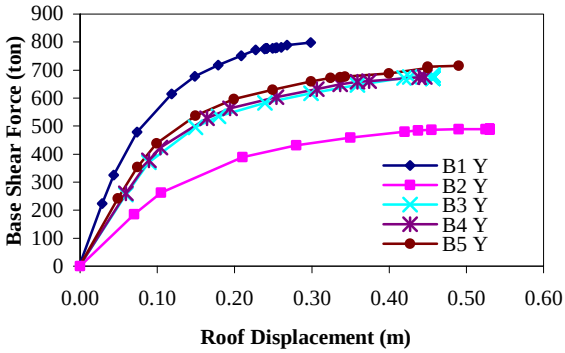
5.1 Pushover Curve

A nonlinear static pushover analysis was performed using three-dimensional finite element models. The seismic performances of the buildings in both X- and Y-directions were evaluated. The capacity curves were plotted between base shear and top roof displacement, as presented in Figure 6. The analysis results revealed that the building models with the consideration of soil-structure interaction had the capacity to resist lateral load of 5-25 percent lower than the fixed-base model for Building Type A and 10-40 percent lower than the fixed-base model for Building Type B. Building Type A failed in shear mode with inflection points located on the 2nd to 4th floors, while Building Type B failed in flexural mode. The failure mechanisms were different, depending on the foundation system. In the elastic range, the relationship between roof displacement and base shear was linear. With an increase in lateral force, beams on the 2nd to 4th floors started to yield and then the structural failure progressed to the columns on the 1st floor level.

The acceleration-displacement response spectra (ADRS) were plotted using the capacity curves obtained from the pushover analysis, as presented in Figure 7. The capacity spectra were compared with the demand spectra given by the Uniform Building Code (1997) for seismic Zone 1. An intersection between the capacity and demand spectra represented the performance point, where the capacity of structure matched the demand given by the earthquake force. The analysis results indicated that the structural responses of all buildings at the performance point were in a nonlinear region.

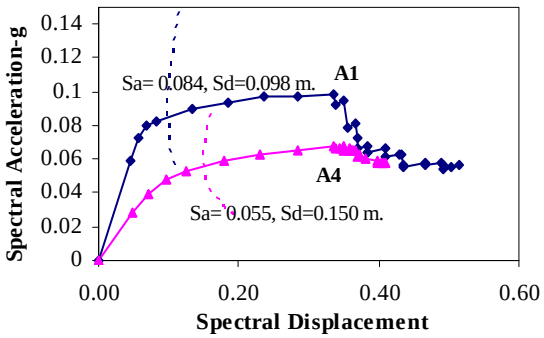


a) Building Type A

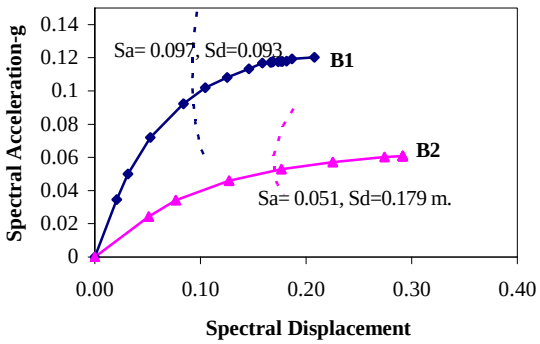


b) Building Type B

Figure 6 Capacity Curves in Y-Direction



a) Building Type A



b) Building Type B

Figure 7 Acceleration-Displacement Response Spectra

5.1 Dynamic Characteristics

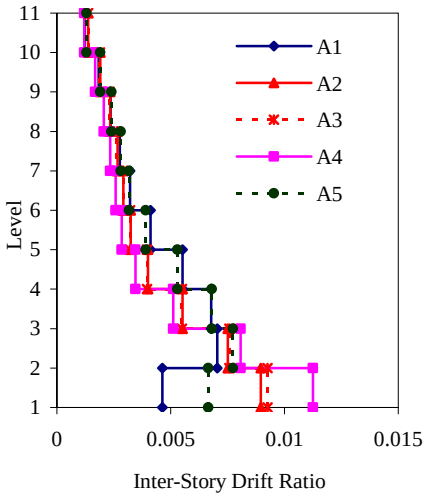
A comparison of the natural periods of buildings with various foundation configurations and structural systems is presented in Table 2. The natural periods were obtained from modal analysis of the finite element models. For the same structural systems, the natural period increased considerably when the flexibility conditions at the 1st floor level were included in the model. The buildings with flexile structural conditions at the 1st floor level had natural periods of 15-42 percent and 25-70 percent longer than the ones with a fixed based condition for Building Type A and Type B, respectively. The buildings with flat slab at the 1st floor level (A3 and B3) were found to have the natural period relatively close to the ones with precast slab on ground beam (A2 and B4).

The base shear and top roof displacement corresponding to the design earthquake of UBC (1997) were determined and are presented in Table 2. The analysis results indicated that the buildings with flexible foundations had lower base shear but higher lateral displacement than the building with a fixed base. The base shear forces in the buildings with a fixed base (A1 and B1) were 33-56 percent greater than the buildings with a very flexible base condition (A4 and B2). These higher values of shear force resulted in a greater amount of reinforcement required for the earthquake resistance design. Additionally, a number of piles per footing were found to affect the natural period and base shear at the performance point. When a group of piles was employed, the natural period and base shear of the buildings without tie beams (A5 and B5) were relatively close to the buildings with a fix base condition.

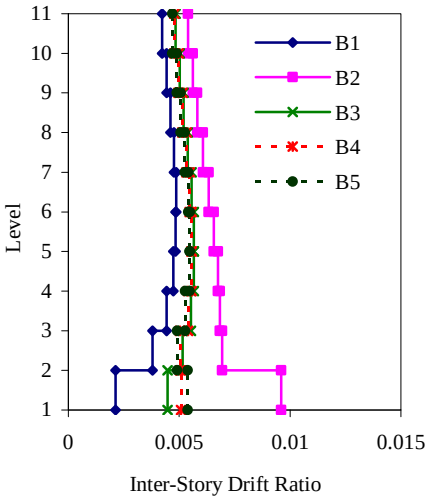
Table 2 Dynamic Characteristics and Seismic Responses for Various Structural Configurations

Building Type	Natural Period (second)	Base Shear (ton)	Lateral Displacement (cm)	Percentage of Base Shear in Shear Wall
A1	1.75	412	12.30	-
A2	2.21	348	16.00	-
A3	2.22	345	16.20	-
A4	2.49	310	17.80	-
A5	1.98	395	14.10	-
B1	1.82	643	13.20	81.42
B2	3.11	412	24.40	46.07
B3	2.38	536	18.00	88.34
B4	2.35	542	17.70	71.77
B5	2.29	565	17.30	49.73

The lateral roof displacements of Buildings Type A with flexible base conditions were in a range of 14.1 to 17.8 cm, which were greater than the displacement of 12.3 cm obtained from the building with a fixed base condition. Similarly, the lateral roof displacements of Building Type B with flexible base conditions were varied from 17.3 to 24.4 cm and greater than the displacement of 13.2 cm given by the building with a fixed base condition. Figure 8 shows the inter-story drift along Y direction. The Building Type A1 and B1 with a fixed base condition had maximum inter-story drift of 0.46 and 0.22, respectively. These inter-story drifts were found to increase significantly as the flexibility condition at the base was considered. The maximum inter-story drifts of building with flexible base were in a range of 0.58-1.14 percent for Building Type A and 0.55-0.96 for Building Type B. It should be noted that buildings that had slab on ground without tie beam had the inter-story drift greater than the allowable limit for immediate occupancy performance level of 1 percent. However, all buildings had the maximum drift less than the limit of 2 percent for the life safety performance level.



a) Building Type A



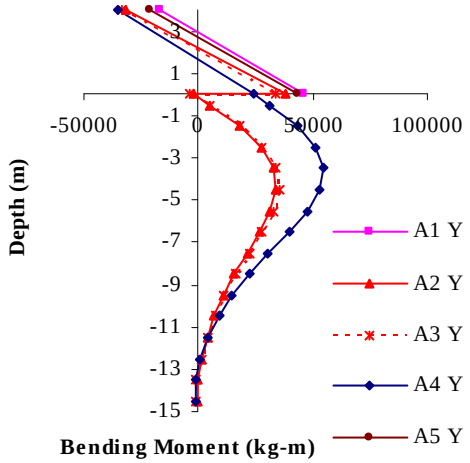
b) Building Type B

Figure 8 Inter-Story Drift along Y-Direction

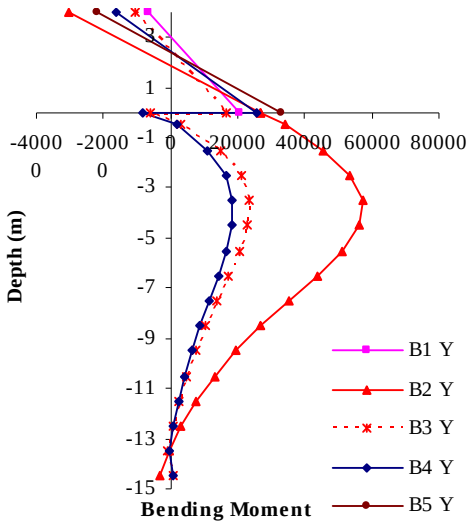
5.2 Internal Force Distribution

The effect of foundation flexibility on the distribution of shear force in the structures was investigated. The building models with a fixed base condition provided base

shear forces greater than the building models with flexible base conditions. The base shear forces were decreased by 25-35 percent when slab on ground without tie beam was used, instead of a fixed base condition. For Building Type B with shear wall, the distribution of base shear in columns and wall considerably depended on flexibility at the base. Most of the shear force was resisted by shear wall when a fixed base condition was assumed. However, the distribution of base shear in shear wall was decreased by 10-44 percent, when a soil-structure interaction was considered in the models.



a) Building Type A



b) Building Type B

Figure 9 Bending Moments in Column at 1st Floor Level and in Pile

Figure 9 presents the variation of bending moment in column at the 1st floor level and in pile for Building Type A and Type B. Shear and bending moment forces were varied depending on the structural configurations. The buildings with high flexural stiffness at the 1st floor level had a high value of bending moment at the pile cap. For the buildings with a flexible base condition, the maximum bending moment in pile was located at the depth approximately equal to five times of a pile diameter.

6. CONCLUSION

The effect of foundation flexibility and structural system on the seismic responses and performance of typical 10-story reinforced concrete buildings in Bangkok area was examined using nonlinear static pushover analysis. Nonlinear material property and nonlinear soil-structure interaction were considered. Based on the analysis results, the following conclusions were drawn:

1. The seismic responses and performance of the buildings were affected by a number of piles per footing and structural system at the 1st floor level.

2. The model with a fixed based condition overestimated the overall lateral stiffness of the buildings with flexible bases, resulting in relatively low values of natural period and roof displacement. This could lead to an overestimated design base shear and underestimated inter-story drift at the performance point.

3. The distribution of internal forces in structural members and piles was influenced by the flexibility at the base and foundation.

4. The refined analytical model with soil-structure interaction was essential to be used in the analysis for the buildings with a flexible foundation system.

Reference:

API. (2007), "Recommended Practice for Planning, Designing and Constructing Fixed Offshore Platforms," American Petroleum Institute.

Applied Technology Council (1996), "Seismic Evaluation and Retrofit of Reinforced Concrete Buildings," ATC-40 report, California Seismic Safety Commission.

FEMA 356. (2000), "Prestandard and Commentary for the Seismic Rehabilitation of Building," American Society of Civil Engineers, Federal Emergency Management Agency.

FHWA (2010), "Drilled Shafts: Construction Procedures and LRFD Design Methods," Publication No. FHWA-NHI-10-016, National Highway Institute U.S. Department of Transportation.

Krawinkler, H. and Seneviratna, G. (1998), "Pros and Cons of Seismic Performance Evaluation," *Engineering Structures*, 20(4-6), 452-464.

Matlock, H. (1970), "Correlations for Design of Laterally Loaded Piles in Soft Clay," *2nd Annual Offshore Technology Conference*, Paper No. OTC 1204, 577-594.

McVay, M. C., Towsend, F. C., and Bloomquist, D. G. (1989), "Numerical Analysis of Vertical Loaded Pile Groups," *Proceedings of the Foundation Engineering Congress*, North Western University, Illinois.

Pando M. A. (2003), "A Laboratory and Field Study of Composite Piles for Bridge Substructures," the Virginia Polytechnic Institute and State University.

Pinho, R., Casarotti, C., and Antoniou, S. (2007), "A Comparison of Single-Run Pushover Analysis Techniques for Seismic Assessment of Bridges," *Earthquake Engineering and Structural Dynamics*, 36, 1347-1362.

Reese L. C., Cox W. R., and Koop F. D. (1974), "Analysis of Laterally Loaded Piles in Sand," *5th Annual Offshore Technology Conference*, Paper No. OTC 2080, 473-485.

Reese, L.C. and Welch, R.C. (1975), "Lateral Loading of Deep Foundations in Stiff Clay," *Journal of Geotechnical Engineering*

Division, American Society of Civil Engineers, 101(GT7), 633-649.
Rollins K.M., Olsen R.J., Egbert J.J., Jensen D.H., Olsen K.G., and Garrett B.H. (2006) "Pile Spacing Effects on Lateral Pile Group Behavior." *Geotechnical and Geo-Environmental Engineering*, ASCE, 132(10), 1262-1271.
Seed, H. B., and Reese, L. C. (1957), "The Action of Soft Clay along Friction Piles," American Society of Civil Engineers, New York, NY, 122, 731-753.
UBC (1997), "Uniform Building Code," International Code Council.
Vijayvergiya V. N. (1977), "Load-Movement Characteristics of Piles," *Port 77 Conferences*, American Society of Civil Engineers, New York, NY.

10CUEE CONFERENCE PROCEEDINGS
10th International Conference on Urban Earthquake Engineering
March 1-2, 2013, Tokyo Institute of Technology, Tokyo, Japan

RESIDUAL STRUCTURAL CAPACITY OF RC SUPERSTRUCTURE OF OPEN-TYPE WHARF DAMAGED BY EARTHQUAKE MOTION

Mitsuyasu Iwanami [1], Yuichiro Kawabata [2], Ema Kato [3], and Takahiro Nishida [4]

1) Professor, Department of Civil Engineering, Tokyo Institute of Technology, Japan
2) Senior Researcher, Structural Mechanics Division, Port and Airport Research Institute, Japan
3) Head of Structural Mechanics Division, Port and Airport Research Institute, Japan
4) Research Associate, Department of International Development Engineering, Tokyo Institute of Technology, Japan
iwanami@cv.titech.ac.jp, kawabata-y@pari.go.jp, katoh-e@pari.go.jp, nishida@ide.titech.ac.jp

Abstract: Through the Great East Japan Earthquake, port facilities have been strongly recognized as transportation base for emergent supply in order to provide assistance for rehabilitation of disaster-affected areas. A practical method to evaluate residual structural capacity of damaged port facilities is required to establish to judge whether the facilities can be used for emergent purpose such as transportation base or not. This paper deals with residual structural capacity of reinforced concrete (RC) superstructure of pile-supported open-type wharf damaged by earthquake actions. In the experiment, reversed cyclic horizontal loading was conducted on 1/4 scaled models of pile-supported open-type wharf in order to cause different levels of damage in steel pipe piles. Thereafter, bending loading tests were carried out on superstructures of the damaged models to investigate the failure process and the residual load carrying capacities of RC superstructure of pile-supported wharf damaged by earthquake actions. The result of the bending loading tests on damaged RC superstructures can be utilized as a reference for judging whether RC superstructure can be used for emergent purpose after earthquake.

1. INTRODUCTION

Among berthing facilities in port areas, a pile-supported pier structure is superior to other types of structures, such as a gravity type quaywall, from the viewpoint of seismic performance. Therefore, there are only few examples of structural damage in pier structures due to earthquake so far. One of the examples was reported that a pier at Kobe Port was damaged due to Great Hanshin Awaji Earthquake, 1995 (Inatomi et al. 1997). In this example, it was considered that steel pipe piles were buckled by increased soil pressures due to liquefaction, not by seismic motion itself (Minami et al. 1997). Also, considerable damages were not observed in pier structures even after Great East Japan Earthquake, 2011 (Takahashi et al. 2011), indicating their high performance against seismic motions.

On the other hand, through the experiences of Great East Japan Earthquake, it was strongly recognized that port facilities are very important for urgent restoration of disaster-affected areas after the earthquake. It is because port facilities can be used as transportation base for urgent materials and rescue activities.

In the present design of port facilities (The Ports and Harbours Association of Japan. 2007), partial damages are allowed against seismic actions in order to obtain rational cross-sections of structural members. The limit state against the L1 seismic motion is yielding of steel pipe piles and cross-section failure of reinforced concrete (RC) superstructure, and the limit state against the L2 seismic motion is designated by the number and position of plasticity of steel pipe piles. However, in case that structural components of pier are damaged due to earthquake, there is no method to judge whether the damaged pier can be used and to judge whether usage restriction is necessary. Hence, it is essential to establish residual performance evaluation methods of pile-supported pier structures damaged by earthquake in order to assist the disaster-affected areas, as well as those for other type berthing facilities.

There are lots of research works on structural behavior of pile-supported pier structures during earthquake (Yokota et al. 1999). However, most of the research focused on elastic and plastic behavior and residual capacity of steel pipe piles, while no research was conducted on residual performance of RC superstructure of damaged pier. The RC superstructure directly supports vertical loads of cargos and vehicles on the apron, so that it is important to appropriately evaluate residual structural capacity of RC superstructure of damaged pier to judge the possibility of usual or restricted use. Furthermore, in evaluation of residual structural capacity of damaged RC superstructure on site, it is also required to establish urgent inspection system after earthquake.

In this paper, the relationship between damage state and residual structural capacity of RC superstructure of

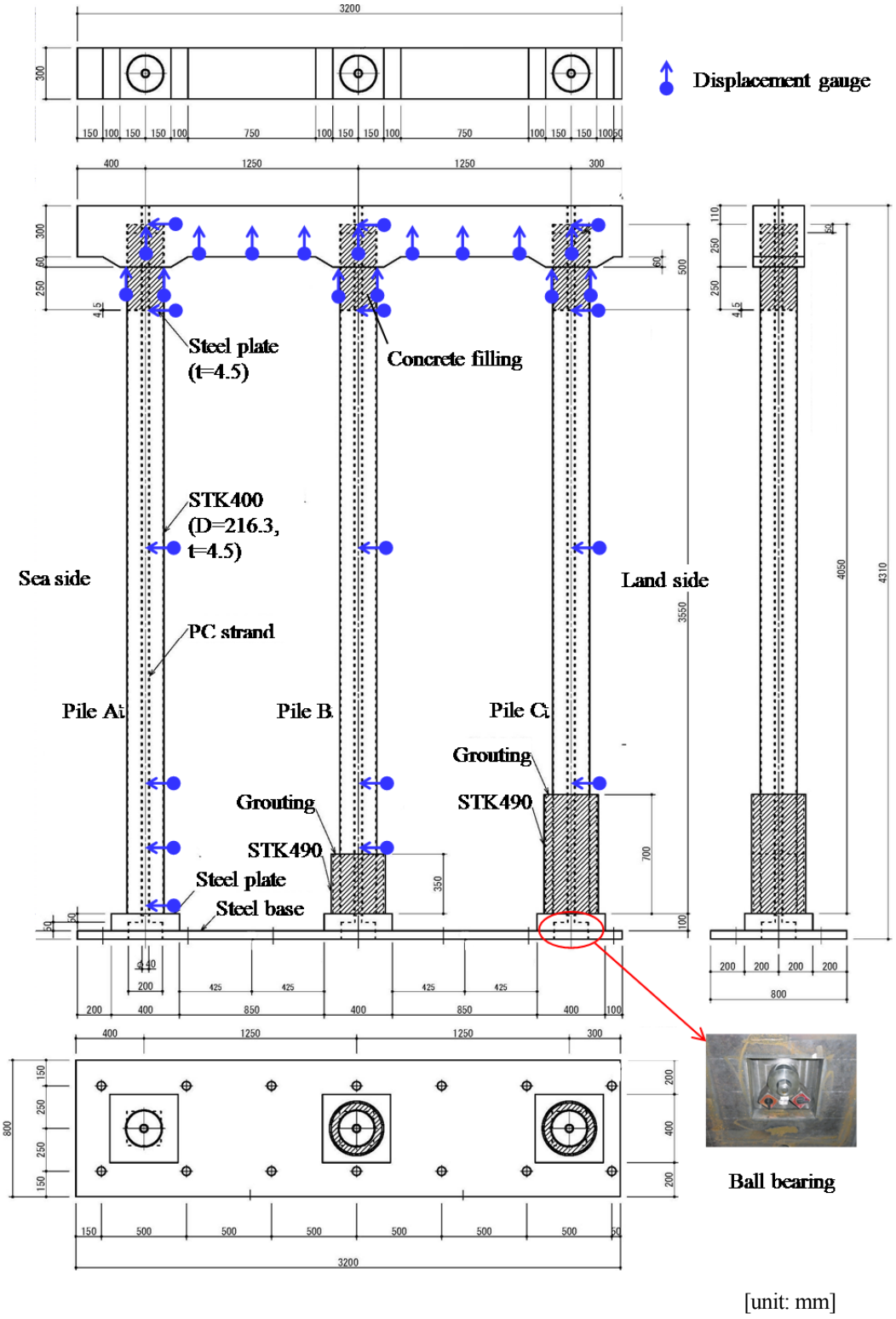
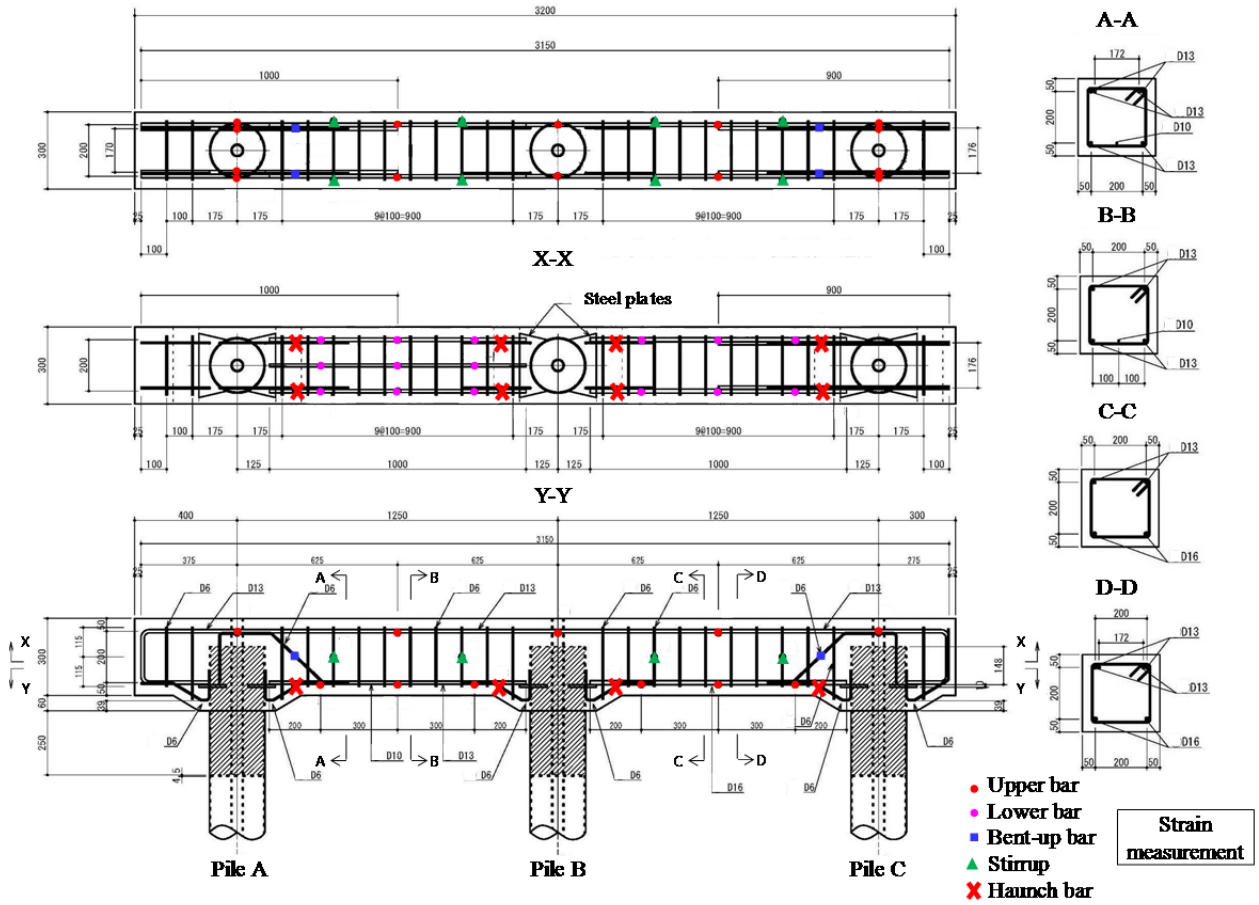


Figure 1 Test Model

pile-supported pier structures damaged by seismic motion was experimentally investigated as a first step of series of research works. In the experiment, models of pile-supported pier structures were damaged by reversed cyclic horizontal loading, and bending loading tests on damaged RC superstructures were conducted to examine the residual structural capacity of concrete members. By changing the degree of damage caused by reversed cyclic horizontal loading on each model of pier structure, the relationship between the degree of overall damage of pier structure and residual structural capacity of RC superstructure was made clear.



[unit: mm]

Figure 2 Steel Bars Arrangement of RC Superstructure

2. EXPERIMENTAL OUTLINE

2.1 Test Model

Figure 1 shows the shape and dimensions of 1/4 models of a pier structure. The original pier structure was a typical pile-supported open-type wharf in Japan, of which front water depth was -10m. The model consisted of one reinforced concrete beam and 3 steel pipe piles. Pile A was located in the sea side, and Pile C was in the land side. Below the fixed points of piles under the seabed, larger steel pipes were set around the piles and grouting was made between them to simulate the design supporting condition of piles under the seabed. Similar to the actual pier, concrete was fulfilled into the top of steel pipe piles in order to rigidly connect between piles and superstructure.

Figure 2 shows the steel bars arrangement of RC superstructure. The steel bars arrangement was decided so that the ratios of bending capacity and shear capacity of RC superstructure to the plastic moment of steel pipe piles were almost the same as those of the original pier structure. Main bars were welded to steel plates connected to steel pipe piles at the heads.

Mechanical properties of concrete, grout, steel pipe piles and steel bars are listed in Table 1. The yield strain of

Table 1 Mechanical Properties

	Compressive strength (N/mm^2)	Young's modulus (kN/mm^2)
Concrete	55.9	33.1
Filling concrete	58.6	33.1
Grout	69.5	-

	Yield strength (N/mm^2)	Tensile strength (N/mm^2)	Yield strain (μ)	Young's modulus (kN/mm^2)
D6	339	526	1892	179
D10	375	521	2093	179
D13	350	488	1957	179
D16	383	559	2128	180
STK400	407	493	-	

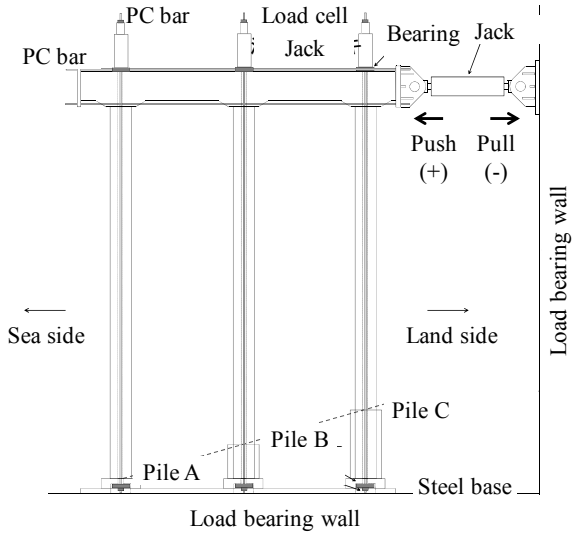


Figure 3 Reversed Cyclic Horizontal Loading

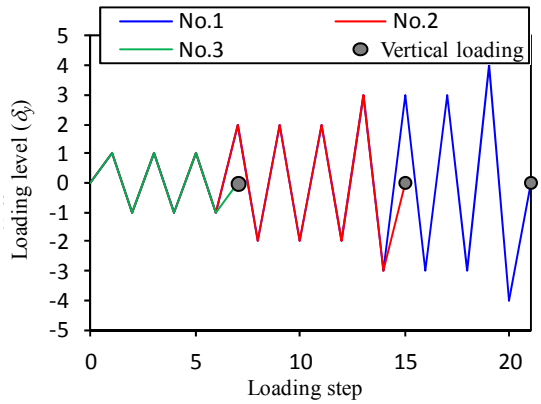


Figure 4 Loading Step

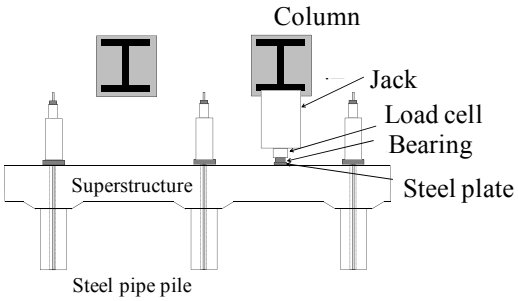


Figure 5 Bending Loading

steel pipe piles was assumed to be 2000μ.

The positions of measurement of displacement and strain during loading are also indicated in Figure 1 and Figure 2.



Photo 1 Bending Loading Test

2.2 Loading Method

Figure 3 illustrates the method of reversed cyclic horizontal loading on the model, simulating seismic motions. To fix the model to a load-bearing wall, steel pipe piles were welded to steel plate and base, which was rigidly connected to the load-bearing wall by PC bars. PC strands were inserted into inside of piles to apply axial forces to the piles simulating the design dead load and surcharge. During the loading, the axial forces were monitored by load cells, and adjusted to be the designated values by using hydraulic jacks. The designated axial forces were 10% of the yield load in compression of the piles for Pile A and Pile C, and 5% for Pile B. Horizontal forces simulating seismic motions were applied by a hydraulic jack connected to the load-bearing wall. The horizontal loading was conducted based on the fundamental horizontal displacement, δ_y, which was defined as the displacement when the maximum strain in steel pipe piles reached the yielding in the first horizontal loading. Figure 4 shows the loading step for each test model. In Model 1, the loading was continued up to $4\delta_y$ after the peak, while the loading in Model 2 and Model 3 was finished at the peak load, $3\delta_y$, and the yielding of steel pipe pile, $1\delta_y$, respectively. By the horizontal loading, the test models were damaged at different degrees.

After the horizontal loading, bending loading tests on the damaged RC superstructures of the test models were conducted in order to investigate the relationship between the degree of overall damage of pier structure and residual structural capacity of RC superstructure. In the bending loading test, steel rigid columns were installed onto a load-bearing floor so as to set a hydraulic jack for the bending loading to RC superstructure, as shown in Figure 5. The width of loading plate inserted between the superstructure and the jack was 100mm. The axial forces to the steel pipe piles were kept to be applied to the same values as the horizontal loading. The hydraulic jack for the horizontal loading was released from the test model in order not to restrain the superstructure from the load-bearing wall. The bending loading test was conducted on the beam between Pile B and Pile C (Beam BC), and then the beam between Pile A and Pile B (Beam AB). The view of the bending loading test is shown in Photo 1.

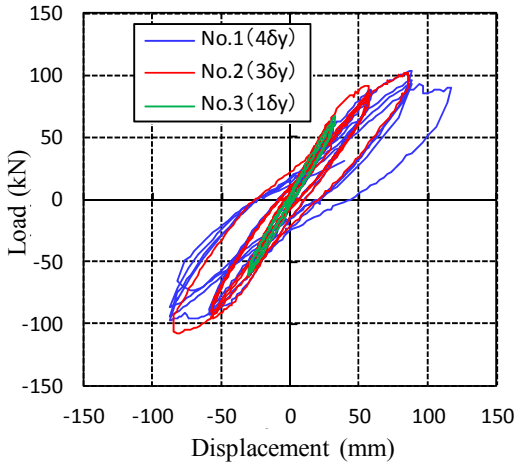


Figure 6 Result of Reversed Cyclic Horizontal Loading

3. RESULTS AND DISCUSSION

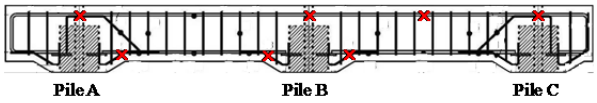
3.1 Damage Process of Pile-supported Pier Structure During Earthquake

Figure 6 shows the relationship between the horizontal load and the horizontal displacement of RC superstructure during the reversed cyclic horizontal loading on the test models. The fundamental horizontal displacement was 29mm for Model 1, 28mm for Model 2, and 30mm for Model 3, respectively.

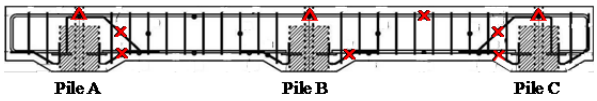
In Model 1, the horizontal load reached the peak of 103.7kN at the loading step of $3\delta_y$. After the peak, the horizontal loads were decreased gradually, and the ultimate state was reached at the loading step of $4\delta_y$, due to breakage of welded part between Pile A and the steel base. The damage process observed in Model 2 and Model 3 was similar to that in Model 1.

With increase in the damage degree of the model as a whole, damage in the RC superstructure was progressed as follows: Figure 7 shows the positions of yielding of steel bars in RC superstructure of Model 1 and Model 2 during the reversed cyclic horizontal loading. In Model 3, yielding of steel bars was not apparently detected during the loading. From this figure, it was found that steel bars near the pile heads were yielded in cased that the pier structure suffered from the maximum horizontal load, $3\delta_y$.

Figure 8 shows crack patterns observed in side surface and bottom surface of RC superstructure of test models after the reversed cyclic horizontal loading. The number of cracks around the midspan of the beam was small, and the width was narrow. Cracks were concentrated near the pile heads, and spalling of concrete cover was observed in Model 1 and Model 2. In comparison between Model 1 and Model 2, more cracks occurred near the head of Pile B in Model 1. This coincided with the state of yielding of steel bars mentioned above. Focusing on Model 3, many cracks occurred near the head of Pile C, even though the maximum experienced horizontal displacement was $1\delta_y$. It was because

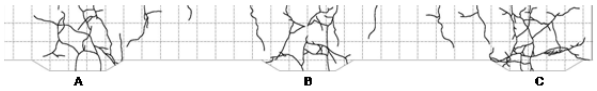


(a) Model 1

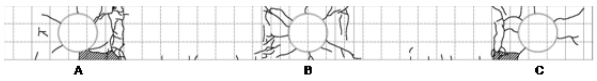


(b) Model 2

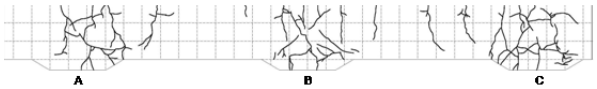
Figure 7 Positions of Yielding of Steel Bars



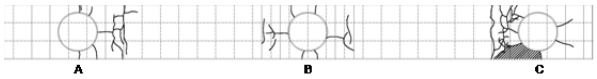
(a) Model 1, Side Surface



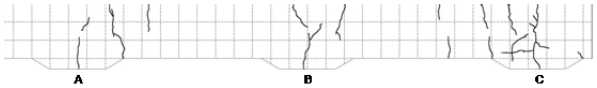
(b) Model 1, Bottom Surface



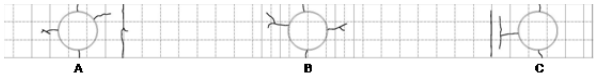
(c) Model 2, Side Surface



(d) Model 2, Bottom Surface



(e) Model 3, Side Surface



(f) Model 3, Bottom Surface

Figure 8 Crack Patterns

Pile C was located on landside, being the shortest. Based on the test result, the damage process of RC superstructure was summarized as follows: many cracks first occurred near the pile head on landside, and then the pile head on seaside was damaged. Finally, cracks near the pile head in between became dominant after the maximum horizontal capacity of pier structure was reached. This tendency was similar to the previous research result (Yokota et al. 1999).

From the test result, it can be said that the degree of overall damage of pier structure is able to be qualitatively evaluated by checking crack patterns of RC superstructure at urgent inspection after earthquake. However, in actual conditions, it might be necessary to consider influence of

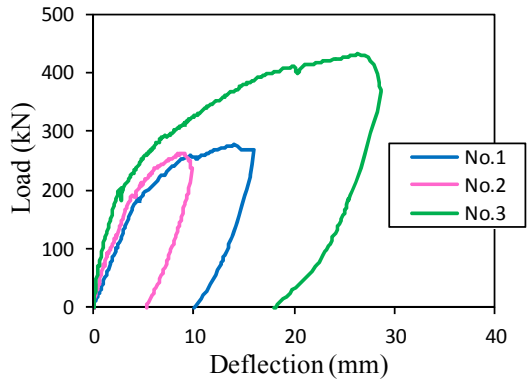


Figure 9 Result of Bending Loading on Beam BC

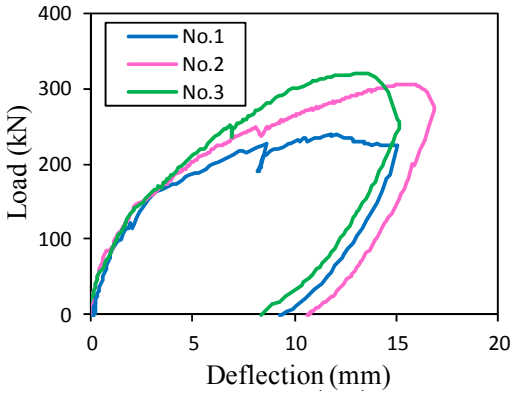
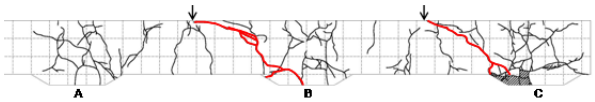
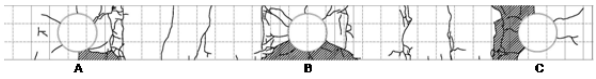


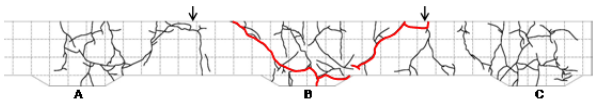
Figure 10 Result of Bending Loading on Beam AB



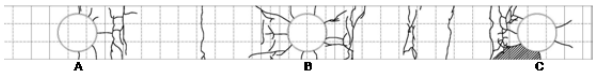
(a) Model 1, Side Surface



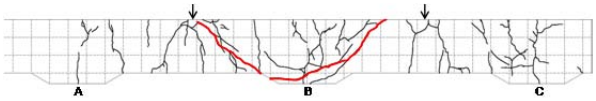
(b) Model 1, Bottom Surface



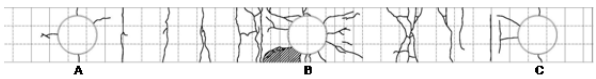
(c) Model 2, Side Surface



(d) Model 2, Bottom Surface



(e) Model 3, Side Surface



(f) Model 3, Bottom Surface

Figure 11 Crack Patterns after Bending Loading Tests on RC Superstructure

materials deterioration such as steel bar corrosion on structural behavior of RC superstructure, necessitating further research works in the future.

3.2 Result of Bending Loading Tests on Damaged RC Superstructures

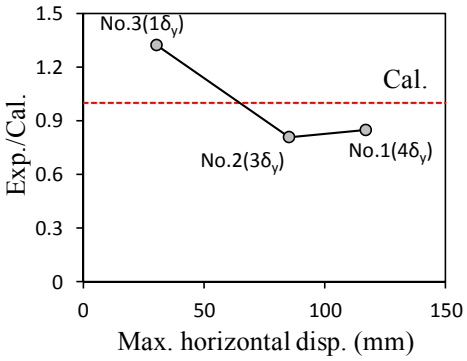
Figure 9 shows the relationship between load and midspan deflection during the bending loading tests on Beam BC. Model 3 had the largest residual structural capacity of RC superstructure, since the model was not heavily damaged due to the preceding reversed cyclic horizontal loading, that is, the experienced maximum horizontal displacement was $1\delta_y$. The residual structural capacities of RC superstructure of Model 1 and Model 2 were almost the same, because both the models suffered from the maximum horizontal capacity of pier structure.

Figure 10 shows the load-deflection relationship obtained from the bending loading tests on Beam AB, which was conducted after the test on Beam BC. The residual structural capacities of Beam AB were smaller than those of Beam BC, since damage due to the preceding bending loading on Beam BC affected structural behavior of Beam AB. In particular, the constraint conditions at the head of Pile B were different between Beam BC and Beam AB. Focusing on the influence of the degree of overall damage on residual structural capacity of RC superstructure, Model 3 had the largest capacity among three models, similar to the tendency observed in Beam BC.

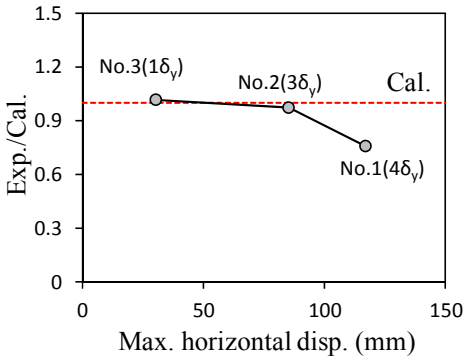
Crack patterns of RC superstructure after the bending loading tests on Beam BC and Beam AB are illustrated in Figure 11. The red lines in the figure indicate dominant cracks occurring during the bending loading tests, which caused the ultimate failure of beams. The failure mode of the beams was shear failure after yielding of steel bar in concrete in all the cases. The heavier the degree of overall damage of pier structure, the less the number of bending cracks and the number of cracks near the pile head. On the contrary, crack widths were larger in case of RC superstructure with heavier damage due to the preceding loading.

3.3 Residual Structural Capacity of Damaged RC Superstructure of Pile-supported Pier Structure

In judging whether RC superstructure can be used for emergency purpose after earthquake and whether the



(a) Beam BC



(b) Beam AB

Figure 12 Residual Structural Capacity of Damaged RC Superstructure of Pile-supported Open-type Wharf

restriction is necessary for temporary use, information about residual structural performance of RC superstructure damaged by seismic motions is surely required. Based on the test result of the bending loading tests on damaged RC superstructure, the following method can be proposed to roughly evaluate the residual structural capacity of RC superstructure damaged by seismic actions. Since all the beams failed in shear, shear capacity of concrete beam was focused on. The ratios of the maximum load obtained from the bending loading tests on concrete beams to their shear capacities calculated according to Japanese standard specifications (Japan Society of Civil Engineers. 2007) were introduced to evaluate the residual structural capacity. Figure 12 shows the relationships between the capacity ratio and the experienced maximum horizontal displacement during the reversed cyclic horizontal loading, which expresses the degree of overall damage of pier structure during earthquakes. From this figure, even though the pier structure suffered from heavy damage such as $4\delta_y$, residual structural capacity of RC superstructure was more than 70% of sound one.

4. SUMMARY

In this study, residual structural capacity of RC superstructure of pile-supported open-type wharf damaged by seismic motions was investigated through the experimental approach. The result will be useful to judge whether the structure can be used for emergency purpose after the earthquake. Also, it can be one of the references to examine if usage restriction or urgent repair is necessary or not.

This study is the first step of series of wide-ranged research projects, leaving lots of issues to be solved. From now on, a system for urgent restoration of port facilities after earthquake should be established by conducting intensive researches regarding evaluation methods of residual structural performance of damaged facilities, judgment criteria for temporary use, urgent repair technique for damaged facilities.

Acknowledgements:

A part of this work was supported by JSPS Grant-in-Aid for Scientific Research (B) Grant Number 23360192.

References:

Inatomi, T. et al. (1997), "Damage to Port and Port-related Facilities by the 1995 Hyogoken-nanbu Earthquake," *Technical Note of The Port and Harbour Research Institute*, **857**.

Minami, K. et al. (1997), "Damage Observation of Open-type Wharf in Kobe Port and its Dynamic Analysis of Interaction," *Proceedings of the 24 JSCE Earthquake Engineering Symposium*, 693-696.

Takahashi, S. et al. (2011), "Urgent Survey for 2011 Great East Japan Earthquake and Tsunami Disaster in Ports and Coasts," *Technical Note of The Port and Airport Research Institute*, **1231**.

The Ports and Harbours Association of Japan. (2007), "Technical Standards and Commentaries for Port and Harbour Facilities in Japan."

Yokota, H. et al. (1999), "Ultimate Structural Performance of Steel-pile Supported Wharves," *Report of The Port and Harbour Research Institute*, **38**(2), 223-255.

Japan Society of Civil Engineers. (2007), "Standard Specifications for Concrete Structures -Design-."

10CUEE CONFERENCE PROCEEDINGS
10th International Conference on Urban Earthquake Engineering
March 1-2, 2013, Tokyo Institute of Technology, Tokyo, Japan

STUDY ON BOND PROPERTY OF CORRODED REINFORCING BAR UNDER CYCLIC LOADING

Tomohiro Miki [1] and Takuya Shiomi[2]

1) Associate Professor, Department of Civil Engineering, Kobe University, Japan
2) Graduate Student, Department of Civil Engineering, Kobe University, Japan
mikitomo@port.kobe-u.ac.jp, 116t124t@stu.kobe-u.ac.jp

Abstract: Cyclic loading during an earthquake affects on the bond behavior between reinforcing bar and concrete. The final goal of this study is to investigate the effect of corrosion on the bond behavior between reinforcing bar and concrete subject to cyclic loading. First, accelerated corrosion tests were carried out for the reinforced concrete specimens and positive and negative cycle loading tests were performed for all the specimens. The results of loading tests indicate that the maximum bond stress of corroded specimens in which more than 2% of cross-sectional loss of reinforcing bar is observed is larger than that of non-corroded specimens. In the pre-peak behavior, the initial stiffness of bond stress-slip relationship becomes larger as the corrosion proceeds, and the specimens without corrosion cracks show small influence due to the corrosion under cyclic loading.

1. INTRODUCTION

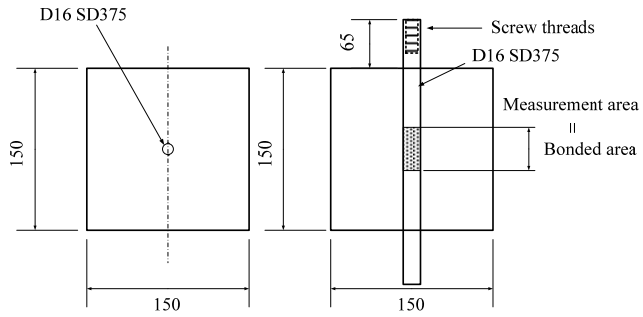
An appropriate maintenance management system has been required with the deteriorated of existing reinforced concrete (RC) structures. For the rational operation in the maintenance of the structures, it is required to evaluate the residual mechanical performance of the deteriorated structures appropriately. In the analysis for these structures, not only the material deterioration itself but also the interaction between concrete and steel reinforcing bar should be considered. In this point of view, the bond property is very important. One of the problems in the bond property of RC structures is corrosion of reinforcing bar. The bond stress due to the significant expansion pressure by the corrosion products decreases when the steel corrosion occurs in the RC structures (Fang, 2006). Herein, the bond property between the reinforcing bar and concrete is greatly affected by cyclic loading during an earthquake (Morita and Kaku, 1975). The final goal of this research framework is to comprehend the bond property between reinforcing bar corrosion and concrete under cyclic loading experimentally.

2. TEST PROGRAMS

2.1 Specimens

The schematic diagram of the specimen is shown in Figure 1 and the specified mix of concrete used is shown in Table 1 (Shiomi and Miki, 2012). The size of the specimen is a cube of 150 × 150 × 150 mm, and the D16 reinforcing bar is arranged at the center of the square section. The test program consisted in a total number of 16 RC specimens. To avoid the disorder of bond condition on the concrete edge, the bond in 55mm from the concrete edge side was removed by wrapping the vinyl tape around the reinforcing bar. The measurement area was in the range of 40 mm at the center. Only this area was located at the corrosion area of the corrosion specimen. In this study, a concrete with a designed compressive strength of 30 N/mm^2 was obtained. Maximum size of coarse aggregate was 20 mm. Early-strength Portland cement was used with an air entraining agent (Pozzolith No.70) in the concrete mixes.

The experimental case is shown in Table 2. The experimental parameters were the bond length of bonded area, the degree of corrosion and the level of cyclic. In the degree of corrosion of the corrosion specimen, the ratio of cross-sectional loss of reinforcing bar was the range 0% (un-corroded specimen) and between 0.9% and 6.3%. The level of cyclic was subjected to three types of once, three and ten times. Still, the way of loading is explained later.



(a) Section View (b) Side View in the Middle Section

Figure 1 Schematic Diagram of Specimen: all dimensions in mm

Table 1 Mix Proportion

G_{max} (mm)	W/C (%)	s/a (%)	kg/m^3				ml/m^3
			W	C	S	G	AE
20	64.9	48	179	278	884	945	552

Table 2 Experimental Cases

Specimens ID	Number of cycle	Bond area (mm)	Corrosion (%)
No.1	0	40	0
No.2		30	
No.3		20	
No.4		40	2.1
No.5		30	2.8
No.6		20	2.3
No.7		40	3.7
No.8	1		0
No.9			1.1
No.10			4.2
No.11	3		0
No.12			1
No.13			2.1
No.14			2.5
No.15			6.3
No.16	10		0
No.17			0.9
No.18			1.7
No.19			2.1
No.20			3.7

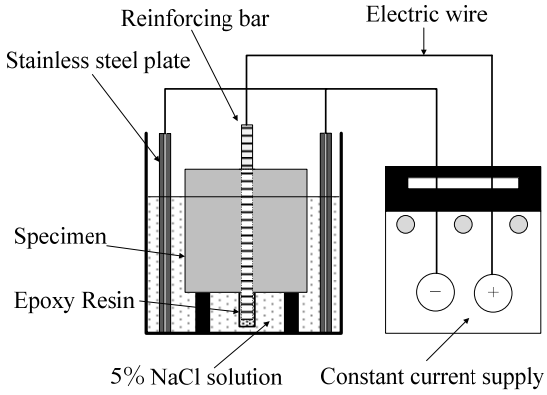


Figure 2 Electrochemical Corrosion System

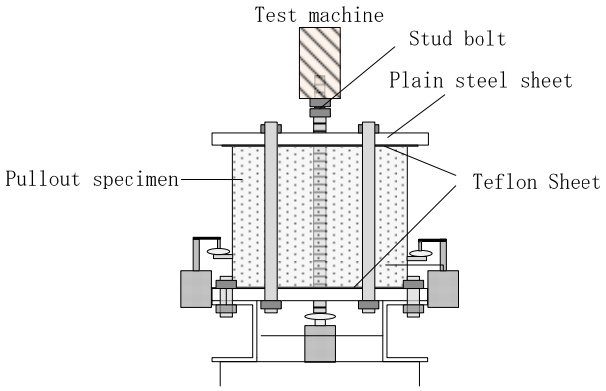


Figure 3 Loading Test Setup

2.2 Accelerated Corrosion Tests

In this study, accelerated corrosion tests were performed to corrode the reinforcing bar of the corroded specimen within a short time. The schematic diagram of the electrolytic corrosion test is shown Figure 2. To corrode only the bonded area, the reinforcing bar in the concrete was covered with a vinyl tape excluding 40 mm of the center in the measurement area and the reinforcing bar of the portion outside the specimen was coated by epoxy resin. The specimen was soaked in electrolytic solution (5% sodium chloride, NaCl by the weight of water). The reinforcing bar was set as an anode and the stainless plate was as a cathode. Then the amount of corrosion was managed by weld time.

After loading tests, reinforcing bar was taken from the demolished RC specimens. To remove the corrosion product on the reinforcing bar, the bars were immersed in the 10% solution of diammonium hydrogen citrate at room temperature for 1 day. After removing the corrosion products, reinforcing bars were divided into samples with the length of 40mm. In order to evaluate the corrosion level of reinforcing bar the ratio of cross-sectional loss is used. The corrosion ratio is defined as a ratio of the weight-loss of corroded reinforcing bar from its initial weight to that of non-corroded reinforcing bar and calculated by using Eq. (1).

$$C = \frac{\Delta w}{w} \times 100 \quad (1)$$

where, Δw: weight difference between the samples of non-corroded and corroded reinforcing bars (g/mm), w: weight of non-corroded reinforcing bar (g/mm)

2.3 Loading Tests

The positive and negative cyclic loading tests were performed for all pullout specimens. A servo motor drive screw type loading machine was used for loading test. The screw was carved for the edge of the loading side exposure reinforcing bar of the pullout specimen, and it was connected with the crossing head of the loading machine. The schematic diagram of the loading test setup is shown in Figure 3.

Load and slip displacement in the direction to pulling out is defined as positive, while that in the opposite direction is defined as negative. The loading speed was set as 1.5mm/min and controlled at the cross head of the testing machine. The loading tests were performed by setting the controlled displacement acting at reinforcing bar; the test machine displacement at the cross head. The slip displacements of the reinforcing bar to be reversed the loading direction were set to be 0.02 mm, 0.2 mm, 0.5 mm, 1.0 mm, 2.0 mm and 3.0 mm, respectively.



(a) No.9 (Corrosion 1.1%)



(b) No.14 (Corrosion 2.5%)



(c) No.15 (Corrosion 6.3%)

Figure 4 Corroded Reinforcing Bars

3. TEST RESULTS AND DISCUSSION

3.1 Accelerated Corrosion Tests

The amount of cross-sectional loss of reinforcing bar is summarized in Table 2. Various amount of corrosion can be seen as this table. The photos of corroded reinforcing bar after electrolytic accelerated corrosion test are shown in Figure.4. The corrosion condition of reinforcing bar in the bonded area indicates that the cross sectional loss due to corrosion is concentrated around rib in the reinforcing bar. This is because the corrosion action became active due to bleeding water that stands around rib. It is found that the reinforcing bars in No.14 and No.15 specimens had pitting corrosion at around the rib.

3.2 Results of Loading Tests

3.2.1 Bond Stress-Reinforcing Bar Slip Relationships

The relationships between the bond stress and slip of reinforcing bar of No.9, No.13 and No.19 specimens are shown in Figure 5, respectively. Here the bond stress τ and the reinforcing bar slip S can be calculated by using following equations.

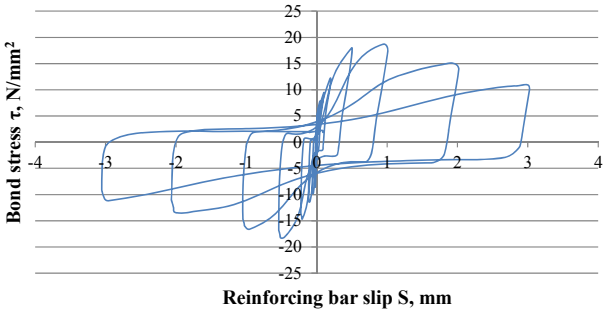
$$\tau = \frac{P}{\pi\, Dl} \qquad (2)$$

where, τ: bond stress, P: the axial tension acting reinforcing bar (N), D: the diameter of reinforcing bar (D16: D = 15.9 mm), l: the measurement area (Corrosion area in case of corrosion specimens =40mm)

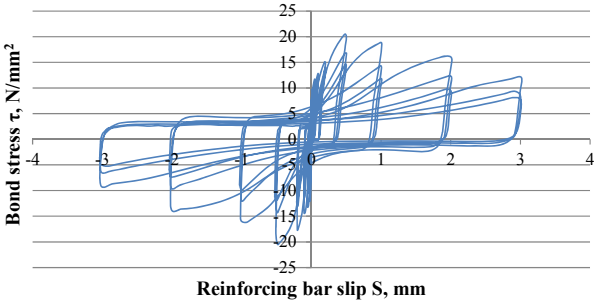
$$S = ① - \left(\frac{② + ③}{2}\right) \qquad (3)$$

where, S: the reinforcing bar slip (mm), ①～③: the displacement measured by displacement gage ①～③ (mm) as shown in Figure 6.

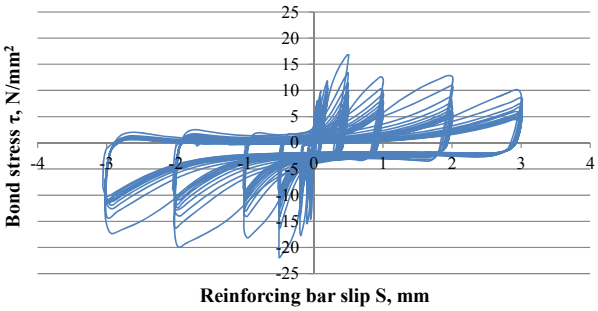
For the bond stress in the vertical axis in Figure 5, an upward load (the direction of pulling) was defined as positive while downward load (the direction of compressing) was defined as negative. As for the slip of reinforcing bar in the cross axis in the figure, the displacement of upward was defined as positive, while that of downward was defined as negative. Values of ② and ③ during loading was significantly small compared with displacement of ①.



(a) No.9 (1 loading cycles, Corrosion 1.1%)



(b) No.13 (3 loading cycles, Corrosion 2.1%)



(c) No.19 (10 loading cycles, Corrosion 2.1%)

Figure 5 Bond Stress-Reinforcing Bar Slip Relationships

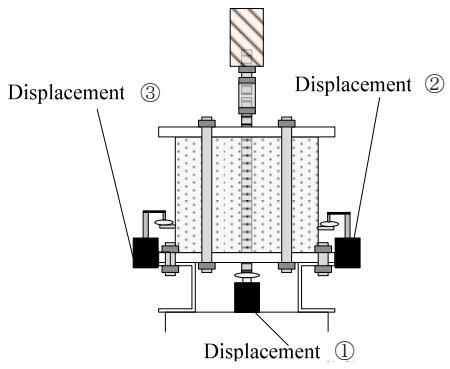


Figure 6 Displacement Measurement Setup



(a) No.7 (0 loading cycle, Corrosion 3.7%)



(b) No.10 (1 loading cycle, Corrosion 4.2%)



(c) No.14 (3 loading cycles, Corrosion 2.5%)



(d) No.19 (10 loading cycles, Corrosion 2.1%)

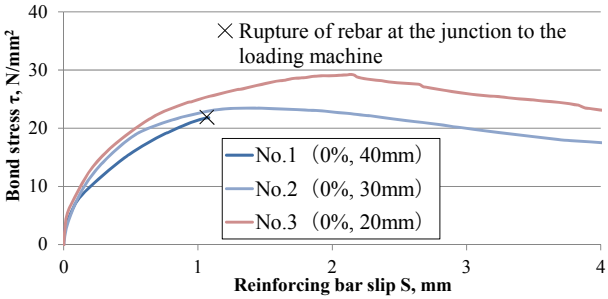
Figure 7 Bonded Surface of Concrete after Loading Test

3.2.2 Bonded Surface of Concrete after Loading Tests

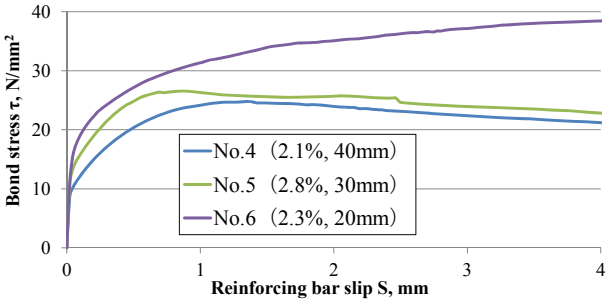
After loading tests, the specimens were demolished and the measurement area was visually observed. The photos of the concrete surface are shown Figure 7. The surface of the bonded concrete in the specimens subjected to more than three loading cycles seems to be smooth. The concrete among between adjoining transverse ribs of reinforcing bar resisted the slip deformation, and the fracture surface of concrete was finally formed as connecting at a tip of transverse rib to the adjoining rib.

3.2.3 Influence of Bonded Length of Reinforcing Bar

Figure 8 shows envelope curves of the bond stress-slip of reinforcing bar under monotonic loading. In these specimens the bonded length of the reinforcing bar which corresponds to the corrosion area of the rebar was changed in the range from 20 mm to 40 mm. The bonded lengths of 20 mm, 30 mm and 40 mm which are 1.3, 1.8 and 2.2 times the diameter of the D16 rebar, respectively are significantly shorter than a development length of the deformed bar that is used in the test. Although the maximum bond stress of the specimen of 20 mm bonded length was largest among these specimens in the both cases of sound and corroded reinforcing bar, the difference of these bond stress-slip of the rebar relationships seems to be not significant. Therefore, the following discussion is focused on the bond stress-slip relationships of the specimens in which the bonded length of rebar is set to be 40 mm.



(a) Corrosion Ratio: 0%



(b) Corrosion Ratio: around 2.5%

Figure 8 Envelope Curves of Bond Stress-Reinforcing Bar Slip Relationship under Monotonic Loading

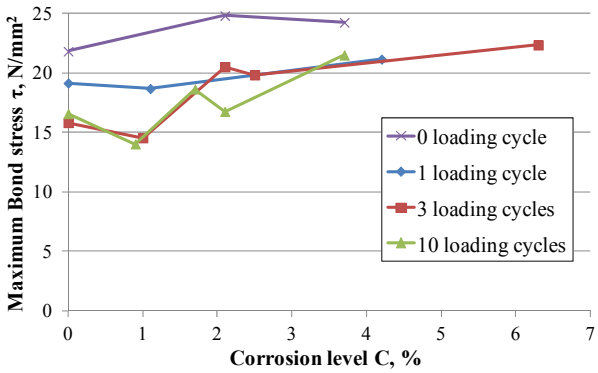


Figure 9 Maximum Bond Stress with Different Corrosion Levels and Loading Cycles

3.2.4 Influence of Corrosion Level of Reinforcing Bar

The relationships between the corrosion level and the maximum bond stress of specimen subjected to the monotonic or cyclic loading are shown in Figure 9. The results in the figure indicates that the maximum bond stresses of the specimens for more than around 2% cross-sectional loss due to the corrosion were larger than that of non-corroded specimens. This is because of an expansion pressure due to the corrosion products and the bond stress increases by the reaction force of surrounding concrete.

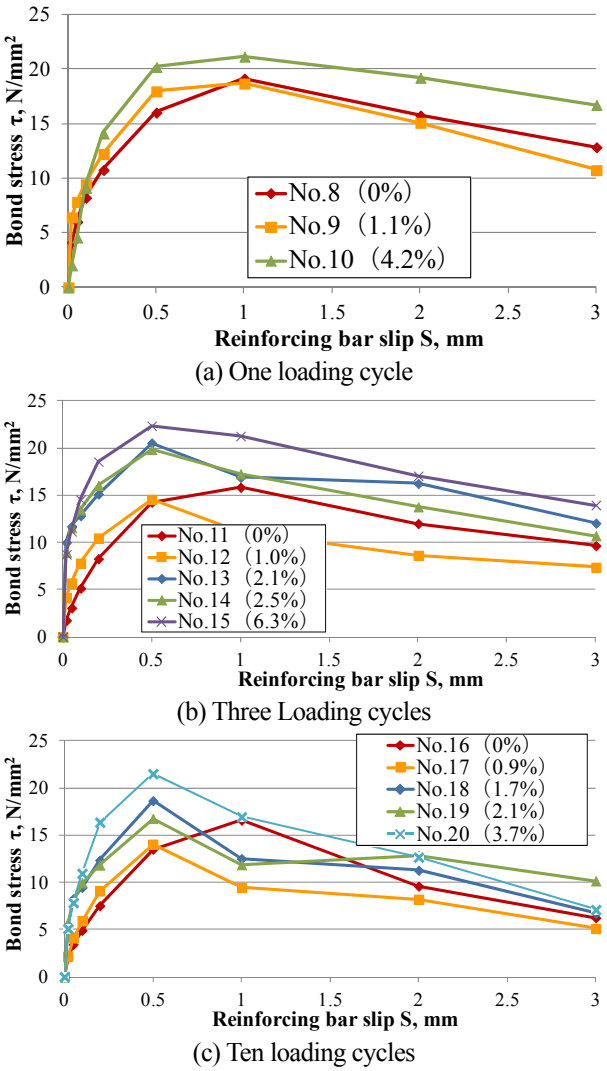
On the other hand, the maximum bond stress generally decreases when corrosion level greatly increases since the crack in the concrete along with a rebar occurs due to the expansion pressure of significant corrosion products. It should be noted that there is no crack in the specimen after the accelerated corrosion test was carried out in which the

corrosion level was set as until around 6% in this study.

Figure 10 shows the envelope curves of the relationship between the bond stress and slip of reinforcing bar under cyclic loading. The bond-slip relations under each loading cycle can be compared in these figures. The results indicate that the initial stiffness in the bond stress-slip relationship increases as the increase in the corrosion ratio. On the other hand, the post peak behavior in the bond stress-slip curve is similar in the each case although the maximum bond stress increases when the corrosion proceeds.

3.2.5 Influence of Number of Loading Cycles

The envelope curves of the bond stress-slip of reinforcing bar relationship are shown in Figure 11. The parameter compared with in the figures is the difference in the number of cyclic loading. The experimental results show that the bond stress becomes smaller as the increase in the loading cycles at all the corrosion level. The specimen subjected to cyclic loading of more than three times indicates that the maximum bond stress reaches at 0.5 mm of the slip. This behavior is caused by the bond deterioration under cyclic loading due to the concrete cracking along with the reinforcing bar and smoothed the bonded surface of the concrete as previously shown in Figure 7. It can be found that the decrease in the bond stress in the post peak is significantly observed in the specimen of around 4% of the corrosion.

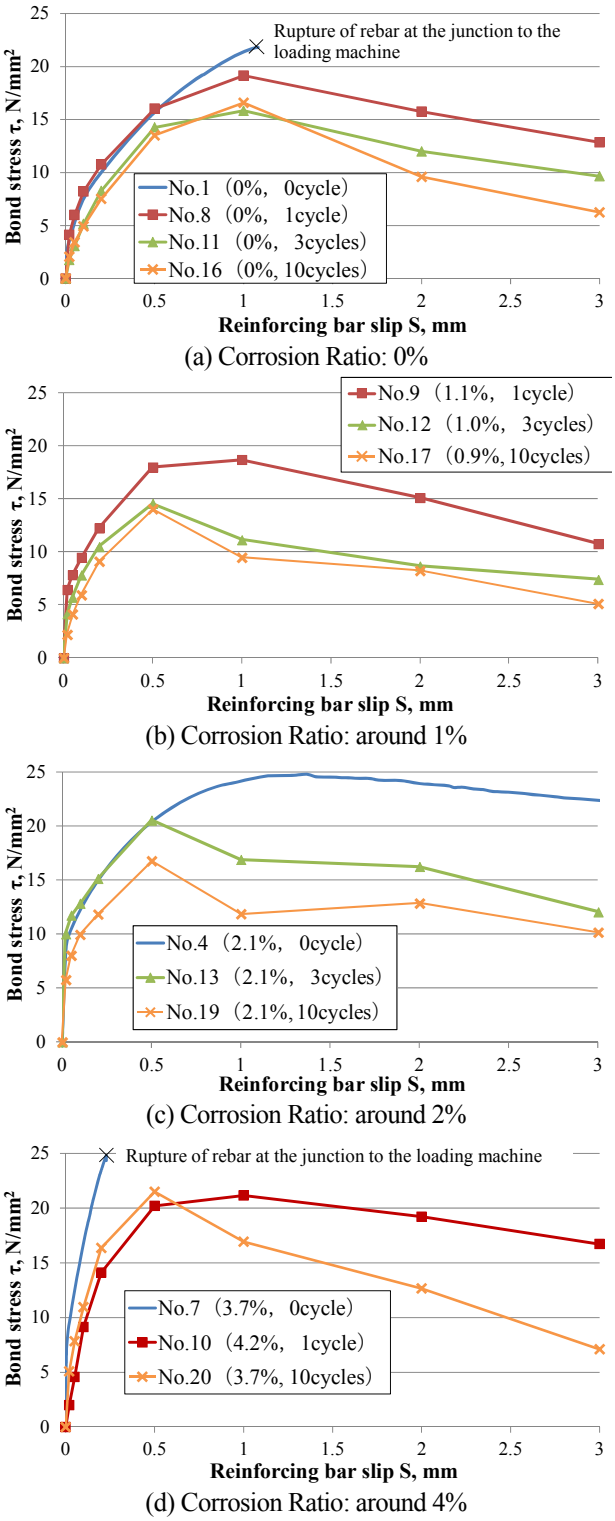


(a) One loading cycle

(b) Three Loading cycles

(c) Ten loading cycles

Figure 10 Envelope Curves of Bond Stress-Reinforcing Bar Slip Relationship at Each Loading Cycles



(a) Corrosion Ratio: 0%

(b) Corrosion Ratio: around 1%

(c) Corrosion Ratio: around 2%

(d) Corrosion Ratio: around 4%

Figure 11 Envelope Curves of Bond Stress-Reinforcing Bar Slip Relationship at Each Corrosion Ratio

3.2.6 Bond Stress Deterioration during Loading Cycles at Constant Slip Displacement of Reinforcing Bar

A decrease ratio of bond stress during loading cycles at the constant slip displacement of 0.02 mm, 0.5 mm and 2.0 mm are shown in Figure 12, respectively. Here, the decrease ratio of bond stress is defined by using Eq. (4) as follows,

$$\alpha_{i-N} = \frac{\tau_{i-N}}{\tau_{i-1}} \qquad (4)$$

where, $\tau_{i\text{-}N}$: the bond stress at the slip i mm and the N^{th} cycles, $\tau_{i\text{-}1}$: the bond stress at the slip i mm and the first cycle, i: the slip displacement of reinforcing bar at free end (i = 0.02, 0.5 and 2.0 mm), N: the number of load cycles (N = 1, 2···10, during 10 times loading cycles)

When a constant slip displacement is applied, the change of the bond stress as increase in the number of cycles can be confirmed from Figure 12. The experiment shows that the bond stress in the No.16 specimen decreases at 0.02 mm of the slip of rebar as shown in Figure 12(a) while the bond stress of corroded specimens remains constant. The bond stress in the No.16 specimen decreases to around 70% of initial value during loading cycles. It is also found that the bond of corroded specimens doesn't deteriorate when the slip of rebar is relatively small.

At the slip displacement of 0.5 mm, the bond stress of No.16 decrease to 55% of the bond stress at this slip displacement during 10 times cycles while the bond stress of corroded specimens significantly decreases to 30-40% of the peak stress at this slip displacement. In the post-peak range in which the slip of rebar reaches at 2.0 mm, the decrease ratio of all specimens indicates similar. Consequently, specimens without corrosion crack have a little influenced of the corrosion even when the number of cycles is increased.

4. CONCLUTIONS

The cyclic loading tests were performed for all pullout specimens where a D16 reinforcing bar was embedded in the concrete. In the experiment the bonded length of rebar was set as within 20 mm to 40 mm and the corrosion level was evaluated by the ratio of cross-sectional loss which ranged between 0.9% and 6.3%. The conclusions obtained in present study are as follows;

(1) The maximum bond stress of the corroded specimens in which the cross-sectional loss of rebar is more than around 2% becomes larger than that of non-corroded specimens.

(2) In the pre-peak behavior where the slip of rebar is less than 0.5 mm, the initial stiffness in the bond stress-rebar slip relationship increases as the increase in the corrosion ratio.

(3) The specimen subjected to cyclic loading of more than three times but less than ten indicates that the maximum bond stress is reached at 0.5 mm of the slip of rebar.

(4) At the slip displacement in which the peak bond stress is reached, the bond stress of the non-corroded specimen decreases 55% of the initial value during 10 times cycles while the bond stress of corroded specimens significantly decreases to 30-40% of the peak stress. On the other hand, in the post peak where the slip of rebar reaches 2.0 mm the decrease in the bond stress indicates similar to that of the non-corroded specimen, consequently, specimens without corrosion cracks have a little influence of the corrosion even when the number of cycles is increased.

References:

Fang, C., Gylltoft, K., Lundgren, K. and Plos, M. (2006), "Effect of Corrosion on Bond in Reinforced Concrete under Cyclic Loading," *Cement and Concrete Research*, **36**, 548-555.

Morita, S. and Kaku, T (1975), "Bond-slip Relationship under Repeated Loading," *Transactions of Architectual Institue of Japan*, **229**, 15-24.

Shiomi, T. and Miki, T (2012), "Experimental Study on Bond Behavior between Corroded Reinforcing Bar and Concrete Subjected to Cyclic Loading," *Proceedings of the Concrete Structure Scenarios*, **12**, 425-430.

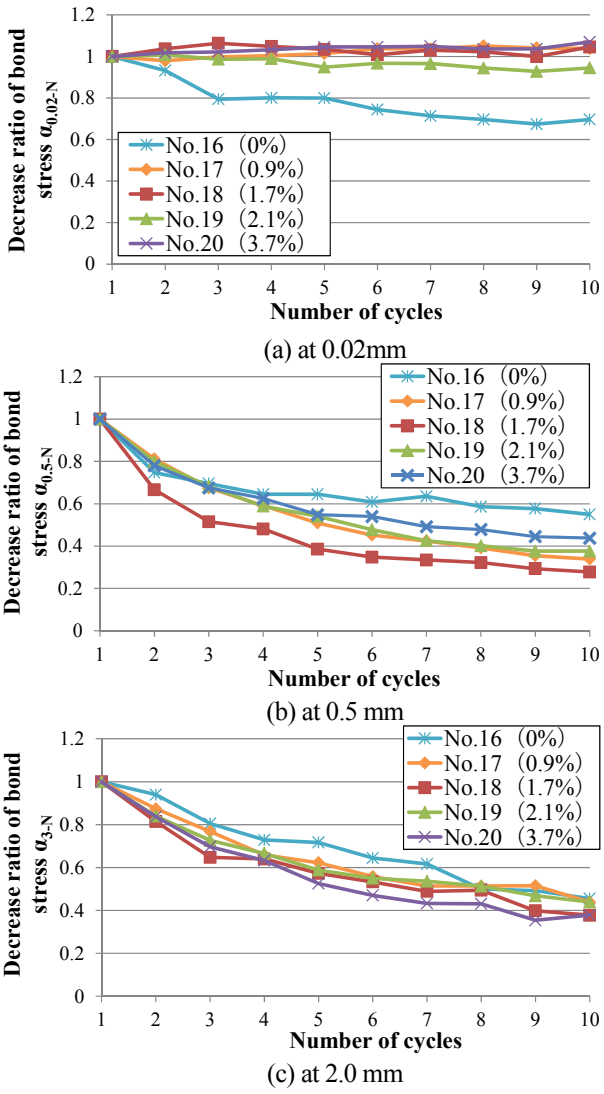


Figure 12 Decreasing Ratio of Bond Stress during Loading Cycles of Constant Rebar Slip

10CUEE CONFERENCE PROCEEDINGS
10th International Conference on Urban Earthquake Engineering
March 1-2, 2013, Tokyo Institute of Technology, Tokyo, Japan

MECHANICAL BEHAVIOR AND STRENGTHENING METHODS OF RC BEAMS DAMAGED BY CORROSION IN ANCHORAGE PART OF REBARS

Koji Matsumoto[1], Makoto Mori[2], and Junichiro Niwa[3]

1) Assistant Professor, Department of Civil Engineering, Tokyo Institute of Technology, Japan
2) Master Course Student, Department of Civil Engineering, Tokyo Institute of Technology, Japan
3) Professor, Department of Civil Engineering, Tokyo Institute of Technology, Japan
matsumoto.k.ar@m.titech.ac.jp, mori.m.ah@m.titech.ac.jp, jniwa@cv.titech.ac.jp

Abstract: To investigate strengthening methods for anchorage part of rebars damaged by corrosion, beam type bond test apparatus representing anchorage part of RC beams was prepared and pull out tests of anchorage part of rebars damaged by corrosion strengthened by restraint force and FRP sheets were conducted. As a result of the experiment, non-strengthened specimen failed in bond splitting failure, however, failure mode of the strengthened specimens shifted to rebar yielding and their pull out strength recovered to the level of the non-damaged specimen. In addition, loading tests of corroded RC beam whose anchorage parts were strengthened by restraint force and FRP sheets were carried out. As a result, failure mode shifted from anchorage failure to flexural failure and load carrying capacity significantly increased.

1. INTRODUCTION

Recently, the number of deteriorated reinforced concrete (RC) structures due to corrosion of steel rebars has been increasing in many countries. Degradation of mechanical performance of RC structures due to corrosion of steel rebars is one of the seismic risks in urban societies. The rebars in the beams of RC structures may suffer corrosion throughout the length or may partially corrode localized portions such as mid span, shear span and anchorage part. If the corroded rebars with insufficient anchorage strength is subjected to a tensile force near the supports of beams, the anchorage failure occurs and the load carrying capacity significantly decreases. Hence, to prevent the anchorage failure of corroded RC beams, development of repairing and strengthening method for anchorage portion is immediately needed.

In order to recover or improve the load capacity of RC structures, strengthening of whole beam is not economical as it requires huge amounts of time, labor and materials. So, the more realistic countermeasure to prevent anchorage failure is to repair and strengthen only the anchorage portion. Many studies have been conducted to deal with the mechanical properties of the corroded RC beams (Matsuo et al. 2004, Tsunoda et al. 2007). However, the study on the RC beams with corroded anchorage part and its strengthening methods has not been investigated yet. Hence, this study focuses on the strengthening of the corroded anchorage part which highly influences the mechanical performance of the RC beams.

To investigate the mechanical characteristics of corroded rebars in the anchorage part of RC beams and to develop the strengthening methods of anchorage part, corroded specimens which represent the anchorage part of RC beams were prepared and pull-out tests of corroded rebars were conducted on non-strengthened and strengthened specimens. In addition, the loading tests of corroded RC beams strengthened in anchorage part of rebars were also conducted. In this study, three different strengthening methods by using transverse reinforcement, restraint force and continuous fiber sheet were investigated.

2. EXPERIMENTAL PROGRAM

2.1 Outline of the specimens

This study consists of two series of experiments. Series 1 is the pull-out tests of corroded rebars, and series 2 is the loading tests of RC beams. In series 1, a beam-type bond testing apparatus shown in Figure 1 was used to represent the anchorage part of a beam. Pull out force was applied to the rebars in terms of bending moment acting between loading and supporting points. The outline of the testing part is shown in Figure 2. Unbonded part of 65 mm in length was provided at the end of loading part and the bond length was 350 mm. Steel rebars were deformed bars with nominal diameter of 15.9 mm and Table 1 shows the mechanical properties of the rebar.

In series 2, in order to simulate the structures with corroded rebars throughout the span and partially

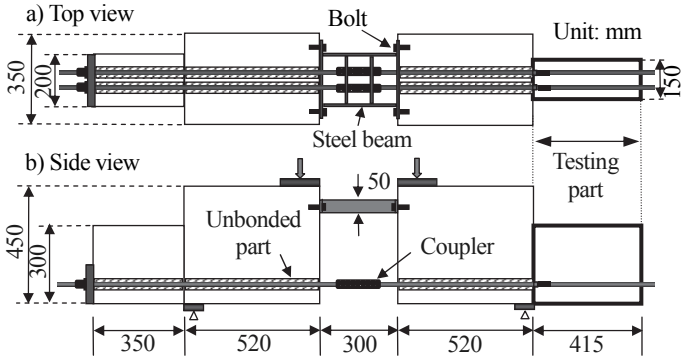


Fig. 1 Outline of beam-type testing apparatus

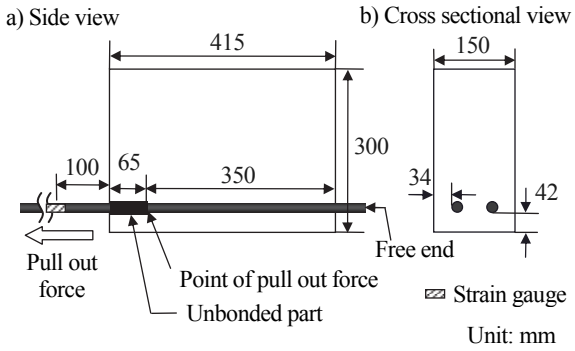


Fig. 2 Detail of testing part (Series 1)

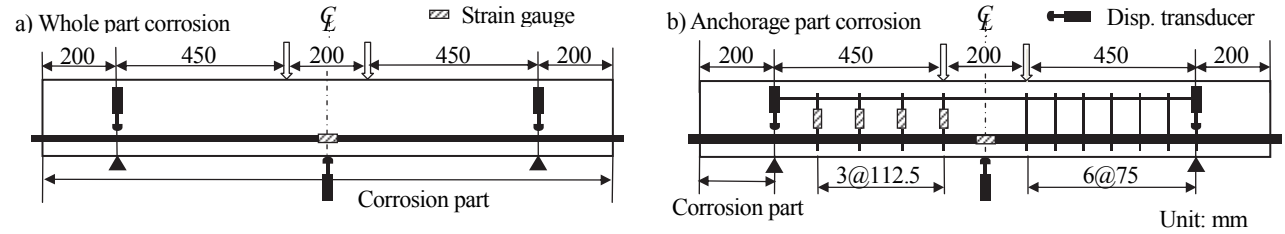


Fig. 3 Outline of RC beam (Series 2)

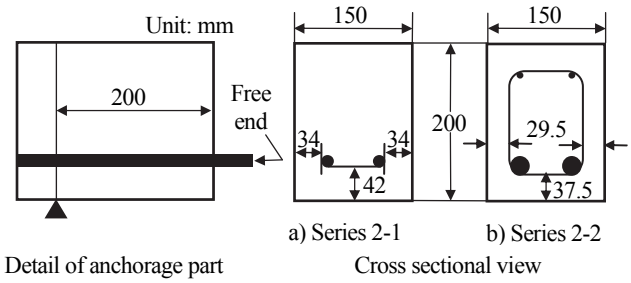


Fig. 4 Detail of anchorage and cross sectional view (Series 2)

Table 1 Properties of steel rebars

Series		Nominal diameter (mm)	Yield strength (N/mm^2)
1	Longitudinal rebar	15.9	341
2-1		15.9	465
2-2		25.4	461
	Stirrup	6.35	328

Table 2 Specifications of RC beams

Term	Notation	Unit	Value	
			Series 1	Series 2
Cross sectional area of longitudinal rebars	A_s	mm^2	397.2	1013.4
Longitudinal reinforcement ratio	p_w	%	1.77	4.50
Stirrup ratio	r_w	%	—	0.38
Width	b_w	mm	150	
Shear span	a	mm	450	
Effective depth	d	mm	150	
a/d ratio	a/d	—	3.0	

Table 3 Mix proportion of concrete

G_{max} (mm)	W/C (%)	s/a (%)	Unit weight (kg/m^3)				
			W	C	S	G	Ad
20	60	45	177	296	838	963	0.443

G_{max}: Maximum size of coarse aggregate, s/a: sand percentage, W: water, C: cement, S: sand, G: gravel, Ad: AE water-reducing admixture

corroded rebars at the anchorage part, six RC beam specimens having corrosion throughout the rebars, i.e. whole part corroded beam (series 2-1) and three RC beam specimens having corrosion at anchorage part (series 2-2) were prepared. Figures 3 and 4 show the outline and the cross sectional view of series 2, respectively. Table 1 shows the mechanical properties of rebars. Table 2 shows the specifications of the RC beams. Concrete of design compressive strength 30 N/mm^2 was used and the mix proportion of concrete is shown in Table 3. Shear reinforcements were provided in only series 2-2 and in order to assume the failure of test span, larger amount of stirrups was provided in the other span.

The shear capacity V_u of RC beams was calculated by adding the shear carried by concrete which was assumed to be the same as shear capacity of RC beams without stirrups and stirrups (Niwa et al. 1987), and is given by,

$$V_u = V_c + V_s \tag{1}$$

$$V_c = 0.2 \cdot \sqrt[1/3]{f_c'} \cdot \sqrt[1/4]{\frac{1000}{d}} \cdot \sqrt[1/3]{p_w} \cdot \left(0.75 + 1.4\frac{d}{a}\right) \cdot b_w d \tag{2}$$

$$V_s = A_w f_{wy} (z/s) \tag{3}$$

where, V_c is shear carried by concrete (kN), V_s is shear carried by stirrups (kN), f_c' is compressive strength of concrete (N/mm^2), d is effective depth (mm), p_w is

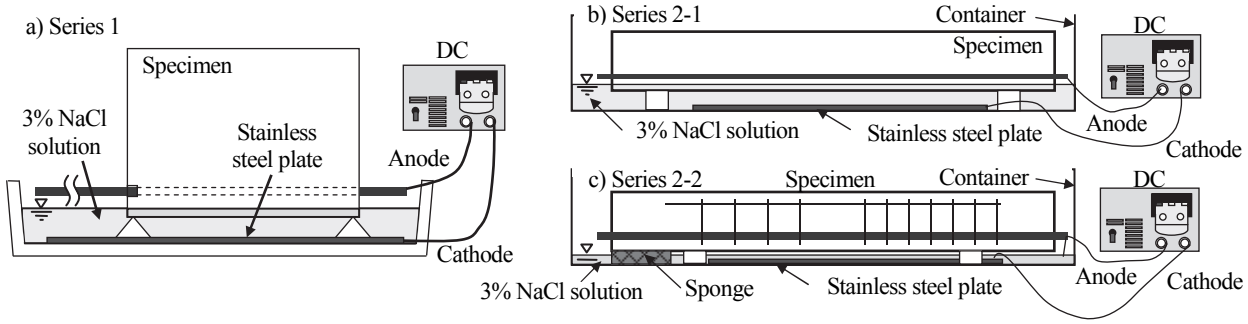


Fig. 5 Outline of electric corrosion test

Table 4 Experimental cases and results of loading tests

Series	Name	Strengthening method		AC (A×h)	C (%)	P_{cal} (kN)	Results of loading tests		
							f_c' (N/mm^2)	Failure mode	P_{max} (kN)
Anchorage specimens (Series 1)	N			0	0		35.5	Steel yielding	67.7
	C11			180.0	11.4		38.0	Bond splitting	42.3
	C14T	Transverse reinforcement (r_w=0.95%)		376.6	13.6		36.3	Bond splitting	67.0
	C10R2.5	Restraint force	2.5 N/mm^2	173.9	9.7		39.3	Steel yielding	67.7
	C13R5		5.0 N/mm^2	179.2	12.9		37.1	Steel yielding	67.7
	C8C-O	Continuous fiber sheet	High elasticity carbon	171.8	7.7		41.8	Steel yielding	67.7
	C13C-U			180.7	12.6		36.1	Steel yielding	67.7
	C8G-O		Glass	168.9	7.8		35.8	Steel yielding	67.7
	C13G-U			170.9	12.8		36.1	Bond splitting	66.8
Whole part corrosion RC beams (Series 2-1)	W-0			0	0	65.4	29.1	Diagonal tension	71.7
	W-12			750	12.5	73.4	41.2	Anchorage	98.5
	W-16			925	16.4	68.1	32.9	Anchorage	75.7
	W-21			1100	21.2	71.3	37.7	Anchorage	24.0
	W-16R	Restraint force (5 N/mm^2)		931	16.5	70.0	35.6	Flexure	70.7
	W-16C	Carbon fiber sheet		898	16.7	75.6	45.0	Flexure	66.0
Anchorage part RC beams (Series 2-2)	A-0			0	0	139.2	30.4	Diagonal tension	156.3
	A-9			250	8.8	146.7	38.6	Diagonal tension	173.8
	A-13			350	13.1	146.3	38.1	Anchorage	134.5

r_w: Reinforcement ratio, AC: Accumulated current (Ampere × Hour), C: Average corrosion degree of two rebars, f_c': Compressive strength of concrete

longitudinal reinforcement ratio (%), A_s is cross sectional area of longitudinal rebars (mm^2), b_w is width of the beam (mm), s is spacing of stirrups (mm), A_w is total cross sectional area of stirrups in the range of s (mm^2), f_{wy} is yield strength of stirrups (N/mm^2), z is moment arm length (mm).

2.2 Steel corrosion acceleration method

Following the procedure given by Tsunoda et al. (2007), electric corrosion tests were conducted to corrode steel rebars. The outlines of the electric corrosion test in each series are shown in Figure 5. In this method, the steel rebars and the stainless steel plate were set to anode and cathode. In series 1 and series 2-1, about 20 mm in height from the bottom of the specimen was soaked in 3% NaCl solution and corrosion was induced in the whole part of steel rebars. In series 2-2, water level of 3% NaCl solution was below the bottom of the specimen. To induce corrosion in the steel rebars at the anchorage part, the bottom of the anchorage part of the beam was connected to 3% NaCl solution through a sponge (Figure 5(c)). The corrosion degree in each specimen was controlled by using accumulated current given by the product of an electric current and time. The target corrosion degree in all specimens of series 1 was 10%.

2.3 Experimental cases

Table 4 lists the experimental cases of both series. In series 1, a non-corroded control specimen N was prepared to compare the difference of bond behavior between corroded and non-corroded specimens. Three different strengthening methods using transverse reinforcement, restraint force and continuous fiber sheet were implemented to strengthen the specimens. The arrangement of transverse reinforcements is shown in Figure 6. Closed stirrups of steel rebars with nominal diameter of 9.53 mm were provided as the transverse reinforcement. Restraint force was introduced by using four PC bars and two steel plates as shown in Figure 7. High elasticity carbon fiber sheet and glass fiber sheet were wrapped in the specimens as

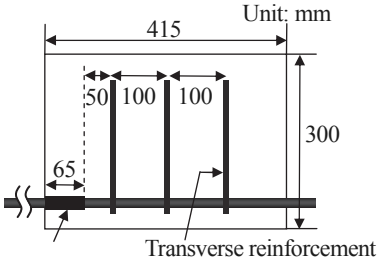


Fig. 6 Arrangement of transverse reinforcements

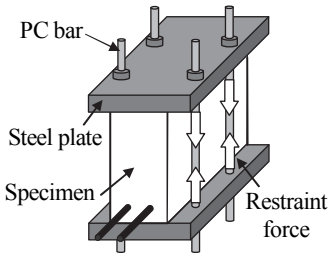


Fig. 7 Method to introduce restraint force

Table 5 Material properties of fiber sheet

Sheet	Thickness (mm)	Tensile strength (N/mm^2)	Elastic modulus (kN/mm^2)
Carbon	0.143	1900	640
Glass	0.118	1500	73

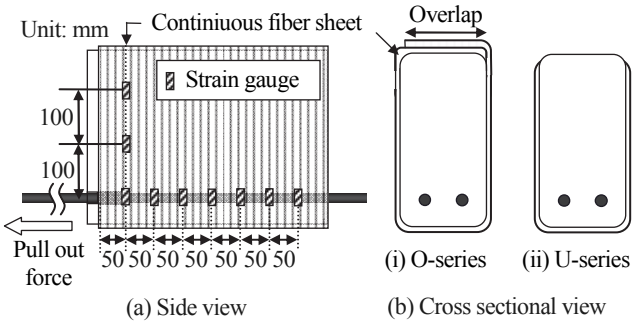


Fig. 8 Continuous fiber sheet and location of strain gauges

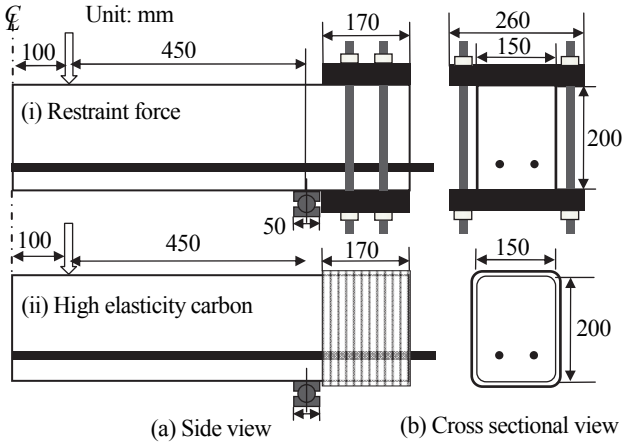


Fig. 9 Outline of strengthened specimens

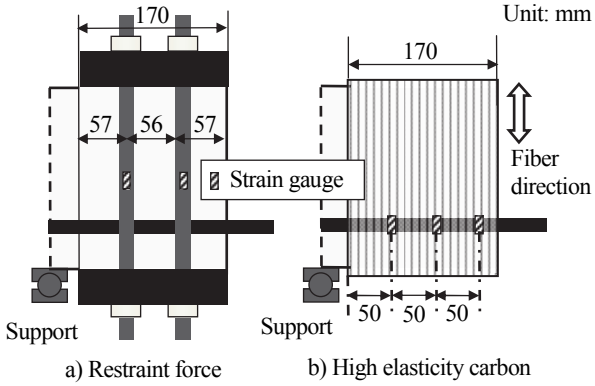


Fig. 10 Details of strengthened parts

shown in Figure 8. The corners of the specimen were chamfered before wrapping the fiber sheet. Table 5 shows the material properties of each continuous fiber sheet. The fiber sheets were wrapped in two different ways. The first way was to wrap all around (O-series), and the other way was to wrap the specimen in only sides and bottom (U-series) as shown in Figure 8(b).

In series 2, before investigating the strengthening effect of RC beams, non-strengthened specimens were prepared to compare the mechanical characteristic to RC beams having steel corrosion at whole part and anchorage part. The parameter of non-strengthened specimens was the corrosion degree. Similarly, the specimens strengthened by the restraint force and high elasticity carbon fiber sheet were prepared. The corrosion degree in both strengthened specimen was 16%. Strengthening was introduced only at the anchorage part of RC beams in series 2-1. The outline of strengthened specimen is shown in Figure 9. The each strengthening method was introduced in the same process as in series 1. Restraint force was introduced by using four PC bars and two steel plates. During the application of restraint force, strain in each PC bars were monitored to confirm the equal tensile forces in all PC bars (Figure 10(a)). To avoid the disturbance to the support plates, strengthening length was set to 170 mm, which was 30 mm shorter than anchorage part.

2.4 Instrumentations and loading method

In series 1, the slip of rebars at the location where the pull out force is applied was measured by using the attachment equipment shown in Figure 11. The attachment equipment was connected to the longitudinal rebars through a 15 mm square duct of depth equal to cover concrete (Figure 12). The duct was created in the sides of the beams during casting. Thus, the measured displacement of the aluminum plate in attachment equipment provides the slip of rebars. To measure the strain in unbonded portion of rebar, one strain gauge was attached at the point 100 mm away from the testing part (Figure 2(a)). In the specimens strengthened by fiber sheet, installation of π-gauges and visual observation cannot confirm the crack propagation and widening in concrete as fiber sheet is wrapped on surface of specimen. Thus, in order to evaluate the crack propagation and widening, strain gauges were attached to the surface of fiber sheet at 50 mm interval as shown in Figure 8.

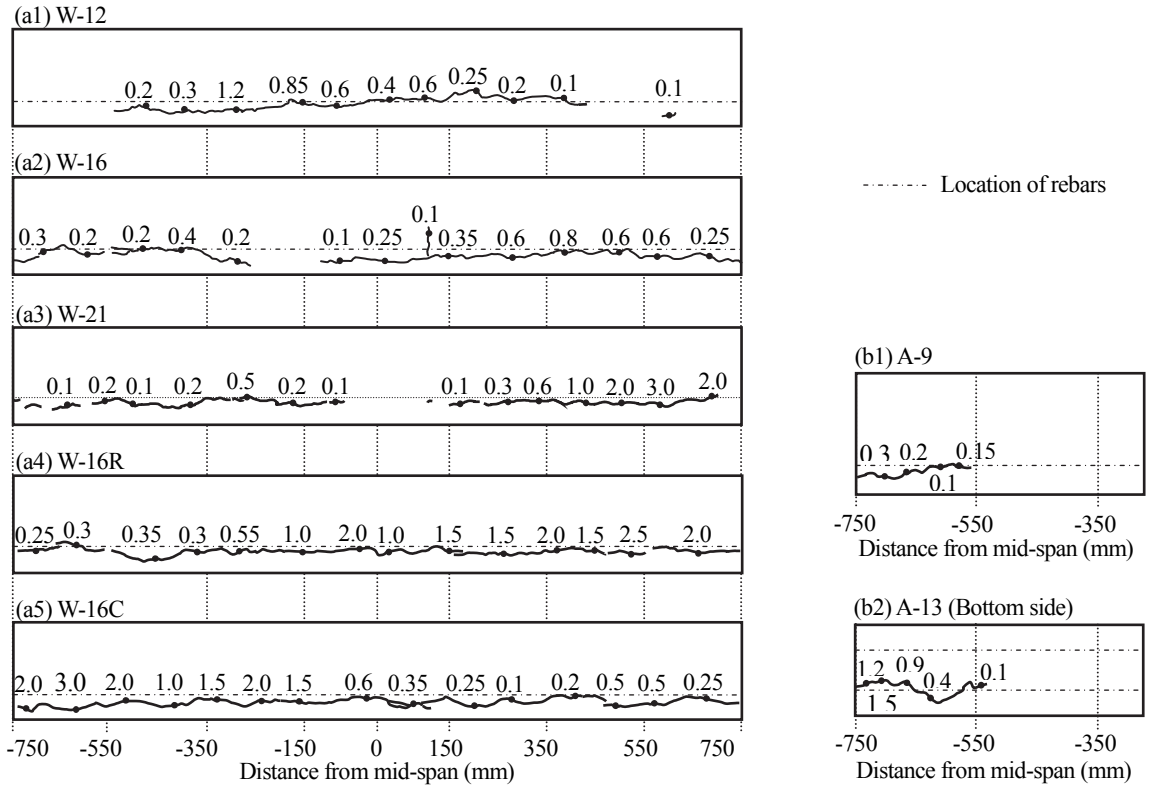


Fig. 11 Corrosion crack conditions

In series 2, mid-span and support displacement were measured by using displacement transducer and the strain in rebars at the mid-span of non-corroded specimens W-0 and A-0 was measured by strain gauges. Also, strain gauges were attached to the stirrups in the specimens of series 2-2. Strain gauges were also attached to the surface of fiber sheet at 50 mm interval as shown in Figure 10.

For loading tests in both series, four-point bending tests were conducted. Teflon sheets sandwiching the grease were inserted between the specimen and the supports to prevent the horizontal friction.

3. RESULTS OF ELECTRIC CORROSION TESTS

3.1 Corrosion crack condition

Figures 11 shows the location of corrosion cracks in all the specimens of series 2. In all series, some corrosion cracks caused by the steel corrosion acceleration test propagated along the longitudinal rebars on the surface of specimens. The values in the figure represent the crack width in mm and the bold ones represent the maximum corrosion crack width. The corrosion crack width tended to increase with increase of accumulated current in all the cases except in specimen W-16 (Table 4 and Figure 11(a)).

3.2 Steel damage condition

After the loading test, rebars were taken out from the specimens and the rust on the rebars were removed using wire brushes. The cleaned rebars were soaked in 10% diammonium hydrogen citrate for two days at 60 degrees Celsius to clean up the remaining corrosion products following to the recommendation by JCI (2004)[4]. Then, the rebars in series 1 and 2-1 were cut into pieces with 50 mm length. In series 2-2, the rebars at the anchorage part was cut to 200 mm length and 100 mm long rebar was taken from the portion beyond the anchorage part.

To evaluate the amount of steel corrosion, the mass reduction ratio C was calculated and is given by,

$$C = (w_0 - w_c)/w_0 \times 100 \quad (4)$$

where, w_0 is the mass per unit length of an original rebar (g/cm), w_c is the mass per unit length of a corroded rebar (g/cm).

The corrosion degree of rebars was defined as the average value of C at each section of two rebars. Table 4 shows the results of corrosion degree. In series 2-2, the corrosion in rebars at 100 mm from supporting point of the specimen A-9 and A-13 were 2.8% and 3.1%, respectively and the corrosion degree in the rebars beyond 100 mm away from the supporting point was almost 0%.

4. RESULTS OF PULL OUT TESTS OF ANCHORAGE SPECIMENS (SERIES 1)

4.1 Result of the maximum pull out force

Table 4 shows the results of the loading test, where the maximum pull out force (P_{max}) was calculated by using the strain in the unbonded part of the rebars. When the specimen failed in the bond splitting, the pull out force was calculated by multiplying a cross sectional area and the elastic modulus of a rebar to the measured strain. However, when the measured strain exceeded the yielding strain, the pull out force was calculated by multiplying a cross sectional area of a rebar to the yield strength. The corroded specimen C11 failed in the bond splitting at 60% of the maximum pull out force of the non-corroded specimen N. It shows that the anchorage strength decreased due to the steel corrosion. The maximum pull out force of all the strengthened specimens was almost same as that of the specimen N. Hence, the effectiveness of the applied strengthening methods to recover the anchorage strength was confirmed.

4.2 Result of slip and strain of FRP sheet

Figure 12 shows the change of slip measured by the attachment equipment. In this figure, the specimen C14T which was strengthened by transverse reinforcements is not shown because the slip could not be measured. Here, value of slip under 14, 28, 42, 56, 60 and 64 kN of pull out force are shown. The bond between rebars and concrete decreased due to corrosion, consequently, the slip of the corroded specimen C11 was larger compared to that of non-corroded specimen even though the pull out force was small. The slip of all the strengthened specimens decreased compared to the specimen C11. This shows the application of each strengthening method prevented corroded rebars from pulling out.

Figure 13 shows the strain distribution of each fiber sheet when the pull out force was 14, 28, 42, 56, 64, 67 kN and peak load. Positive value means tensile strain. In all specimens strengthened by fiber sheet, the strain at distant point from the point of the pull out force increased with the increase in the pull out force. It indicates that the tensile force acted in the sheet because cracks along the rebars were widened. Since the elastic modulus and thickness of carbon fiber sheet were larger, the strain in the specimens strengthened by high elasticity carbon fiber sheet was larger than that of the specimens strengthened by glass fiber sheet. Therefore carbon fiber sheet was more effective to prevent cracks from widening. Moreover, comparing specimens having different wrapping way, the strain in the specimens which had larger corrosion degree was larger than that of the specimen having smaller corrosion degree. In this experiment, two strain gauges were also attached at 100 mm interval in height direction as shown in Figure 8, however, measured strain in these gauges were very small in all the specimens. Also, the corrosion degree of the specimen C13C-U and C13G-U was 3% larger than that of the specimen C8C-O and C8G-O. Hence, it can be said that the tensile force acted on the fiber sheet was affected by corrosion degree but not by the wrapping way of fiber sheets.

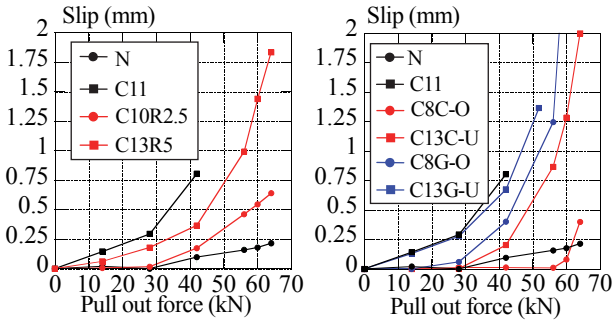


Fig. 12 Slip at the point of pull out force

5. RESULTS OF LOADING TESTS OF RC BEAMS (SERIES 2)

5.1 Failure mode and the peak load

The compressive strength of concrete, the calculated shear capacity of RC beam (P_{cal}), the observed peak load P_{max} and the failure mode are tabulated in Table 4. P_{cal} was calculated considering no

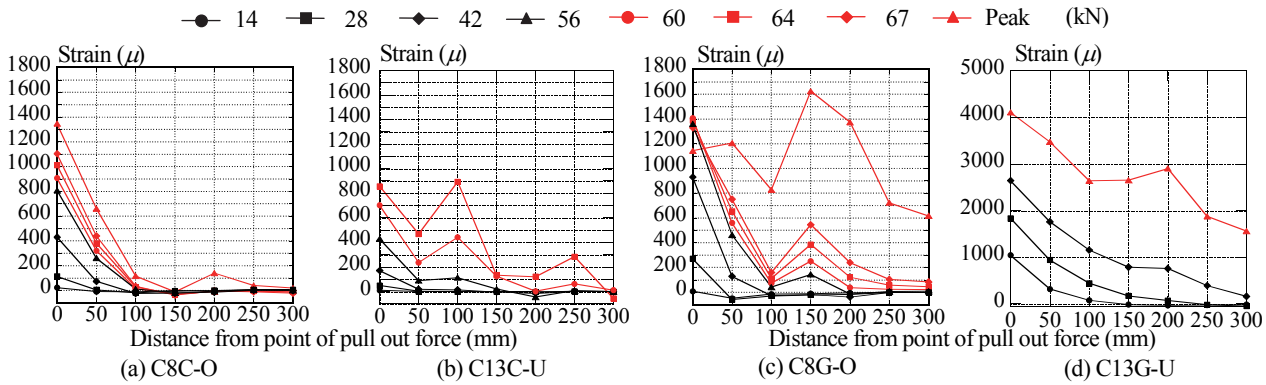
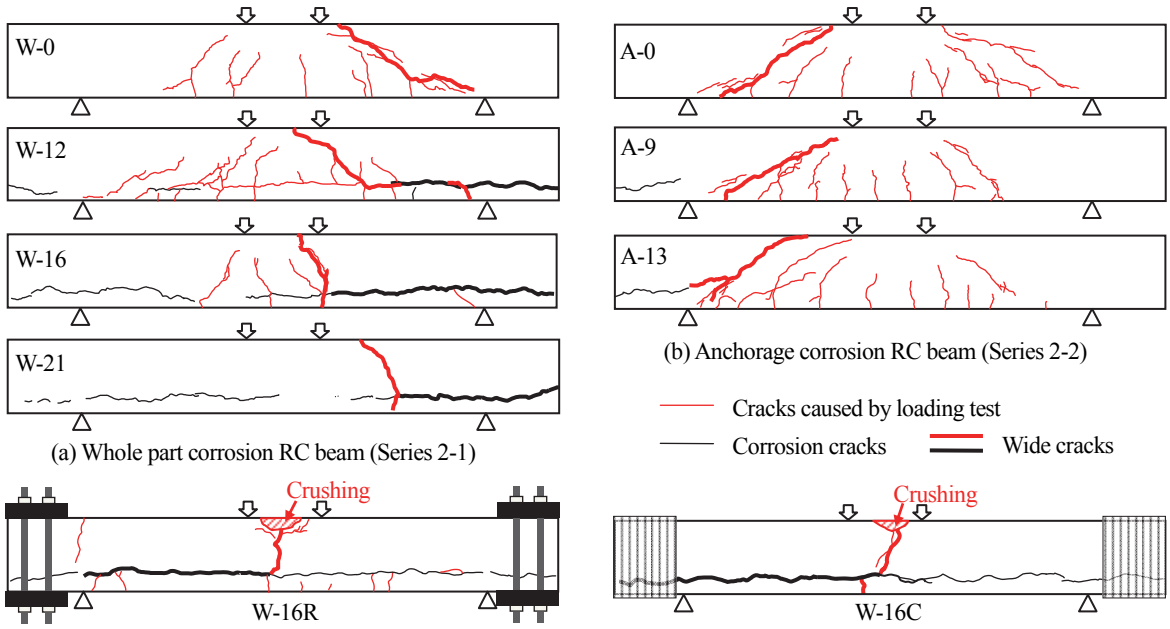


Fig. 13 Strain distribution in fiber sheet



(a) Whole part corrosion RC beam (Series 2-1)

(b) Anchorage corrosion RC beam (Series 2-2)

(c) Strengthened RC beam (Series 2-1)

Fig. 14 Crack conditions at the maximum load

corrosion in the rebars.

(1) Non-strengthened RC beams (Series 2-1 and 2-2)

Figures 14(a) and (b) show the crack pattern in non-strengthened beams at the peak load. In the non-corroded specimen W-0 and A-0, diagonal cracks occurred and propagated from loading point to support and finally failed in shear. The shear capacity of corroded specimen W-12 increased by 37% compared to W-0 because of formation of arch action caused by the corrosion of longitudinal rebars[3]. In all the corroded specimen of series 2-1, the corrosion of the rebars deteriorated the bond between concrete and rebars leading to the anchorage failure. Moreover, the peak load decreased with the increase of corrosion degree. In particular, the corroded specimen W-21 in which corrosion degree was more than 20% failed in anchorage before flexural cracks occurred and the peak load was about 30% of non-corroded specimen W-0.

In series 2-2, the corroded specimen A-9 failed in shear similar to the non-corroded specimen A-0. Because the anchorage strength of rebars did not decrease much when corrosion degree was 9% and pull out capacity was enough not to be failed in anchorage. The corroded specimen A-13 failed in anchorage and the maximum load decreased 13% compared to non-corroded specimen A-0. The pull out force acted on the rebars of anchorage exceeded the pull out capacity when corrosion degree reached to 13%.

(2) Strengthened RC beams (Series 2-2)

In corroded specimens W-16R and W-16C strengthened by restraint force and high elasticity carbon fiber sheet, flexural cracks dominated and finally failed in flexure due to crushing of concrete in compression zone at the mid span as shown in Figure 14(c). The corrosion cracks inside the span gradually widened with increasing the load level. However, in the specimen W-16R, the cracks at the anchorage portion did not widened even though the load reached to the peak. It shows that the application of restraint force can prevent the cracks from widening.

Compared to the corroded specimen W-16, the maximum load of strengthened specimens W-16R and W-16C decreased by 6.6% and 12.8%, respectively in spite of strengthening. These behaviors seemed to be related to the corrosion crack width. The maximum corrosion crack width in the specimen W-16 was 0.8 mm. Whereas, those of the specimens W-16R and W-16C were 2.5 mm and 3.0 mm, respectively (Figure 11(a)). It is reported that the bond is affected more by the corrosion crack width along the longitudinal rebars than by the corrosion degree[1]. Hence, there is a possibility that load capacity of the specimen W-16R and W-16C before strengthening was close to the specimen W-21 in which maximum corrosion crack was 3.0 mm rather than the specimen W-16. Since the peak load of the strengthened specimens W-16R and W-16C was almost three times as much as that of W-21, it can be confirmed that the applied strengthening methods have significant effect on the load capacity of corroded RC beams.

5.2 Load-displacement curves

(1) Non-strengthened RC beams (Series 2-1 and 2-2)

Figure 15 shows the load-displacement curves of all the non-strengthened RC beams. In the specimen W-0, a diagonal crack occurred when the load was 62 kN and the load slightly decreased. Then, the load increased again. Finally, at the peak load (71.7 kN), the

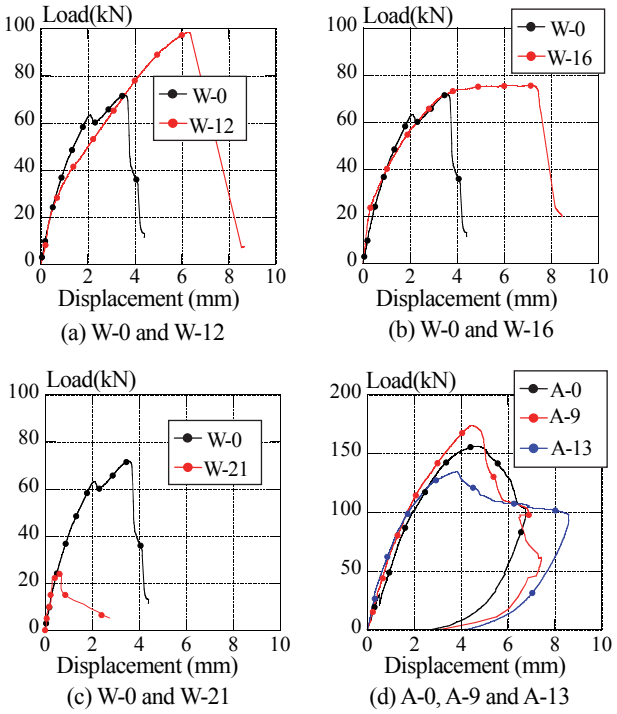


Fig. 15 Load-displacement curves (Non-strengthened specimens)

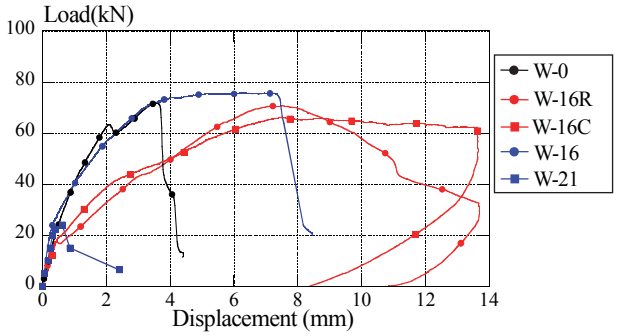


Fig. 16 Load-displacement curves (Strengthened specimens)

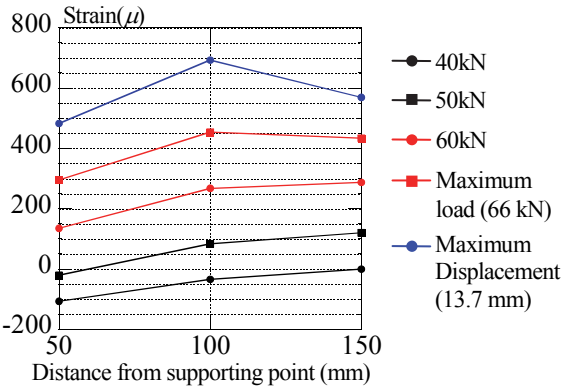


Fig. 17 Strain distribution of fiber sheet (W-16C)

diagonal crack widely opened and the load decreased rapidly. In the specimens W-12 and W-16 which failed in anchorage, a rapid drop of the load was confirmed after failure. In particular, in the specimen W-12 which had the largest pull out force among the corroded specimens, the load suddenly dropped from the peak load (98.5 kN) to 7.2 kN exhibiting the brittle failure.

In all cases of series 2-2, the load increased after a diagonal crack occurred because of the presence of stirrups. Finally, the stirrups yielded and the diagonal tension failure occurred in the specimen A-0 and A-9. The specimen A-13 failed in anchorage before all stirrups yielded.

(2) Strengthened RC beams (Series 2-2)

Figure 16 shows the load displacement curves of two strengthened specimens along with those of the specimens W-0, W-16 and W-21 to compare the response of strengthened and non-strengthened specimens. After the load reached to about 20 kN, stiffness of two strengthened specimen gradually decreased compared to the other non-strengthened specimens. In the specimen W-16R, after the peak load, the load gradually decreased. In contrary, the load suddenly dropped after the peak load in the specimens W-0 and W-16. In the specimen W-16C, the load did not decrease much after the peak load. Flexural failure is supposed to occur because crushing of concrete in compression zone at mid span was observed at 10 mm of displacement.

Compared to the specimen W-21 in which the maximum corrosion crack width was almost same as that in two strengthened specimens, the peak load and the deformation performance of the specimen W-16R and W-16C were improved substantially. On the other hand, compared to the non-corroded specimen W-0, the stiffness of two strengthened specimens decreased significantly. Although the load capacity was recovered by strengthening, the stiffness was not recovered when strengthening was applied only to the anchorage portion.

5.3 Strain of FRP sheet

In order to evaluate the crack propagation and widening of cracks, strain gauges were attached in the fiber direction of the fiber sheets (Figure 10(b)). Figure 17 shows the strain distribution in high elasticity carbon fiber sheet when load was 40, 50, 60 kN, the peak load (66 kN), and the maximum displacement (13.7 mm). Positive value means tensile strain.

When the load was 40 kN and 50 kN, due to the compressive force acted on concrete from the vertical support reaction, compressive strain was observed particularly at the point 50 mm from the support. On increasing load, the crack widened and tensile force acted on the fiber sheet to resist widening of cracks, that resulted tensile strain in all the strain gauges. After the peak load, the strain also became larger until the maximum displacement. Moreover, the strain at the 50 mm from the supporting point was the smallest among the three gauges throughout the loading test. The support reaction was dominant at that point because the location of strain gauge was the nearest from the support.

6. CONCLUSIONS

1) The anchorage part specimen in which mass reduction ratio was 11% failed in bond splitting with 38% reduction in pull out strength. However, pull out strength recovered to the level of non-corroded specimen after restraint force and continuous fiber sheet were provided. By applying these methods, mechanical performance of anchorage parts of rebars having corrosion can be improved.
2) The anchorage part specimen strengthened by high elasticity carbon fiber sheet in which elastic modulus and thickness were comparatively larger prevented cracks from widening than that strengthened by glass fiber sheet. Strengthening effect of the continuous fiber sheet wrapped in U-shape (only sides and bottom) was almost same as that wrapped to whole section. Strengthening effect of continuous fiber sheet on anchorage parts of rebars is not affected by the wrapping way but stiffness of the sheet.
3) Shear capacity of the RC beam specimen having corrosion in whole part of longitudinal rebars increased due to the arch action when mass reduction ratio was about 12%. However, anchorage failure occurred and load capacity decreased when mass reduction ratio was more than 16%. Load capacity of RC beams having corrosion in whole part of longitudinal rebars decreases when the amount of corrosion exceeds certain degree.
4) In RC beams having corrosion only in the anchorage part of longitudinal rebars, pull out force starts to act on the rebars in anchorage part after the formation of a diagonal crack. The specimen with mass reduction ratio of 13% failed in anchorage and the load capacity decreased. Reduction of load capacity and failure mode are supposed to be determined by magnitude of the pull out force at the anchorage as well as the corrosion degree.
5) By providing restraint force or continuous fiber sheet, failure mode shifted from anchorage failure to flexural failure and load capacity significantly increased compared to the specimen in which width of the corrosion cracks was the same. However, member stiffness was smaller than that of the non-corroded specimen. By strengthening anchorage parts of rebars, load capacity of RC beams can be improved. In order to save cost and time, strengthening of only anchorage parts is supposed to be effective for maintaining safety of structures.

Acknowledgements:

The authors acknowledge support from the Center for Urban Earthquake Engineering (CUEE) in Tokyo Institute of Technology.

References:

Matsuo, T., Sakai, M., Matsuura, T. and Kanazu, T. (2004), "An Experimental Study on Shear Resisting Mechanism of RC Beams with Corroded Reinforcement," *Journal of Concrete Research and Technology*, **15**(2), 69-77. (in Japanese)

Tsunoda, M., Watanabe, K. and Niwa, J. (2007), "Shear Failure Behavior of RC Liner Members Having Partially Corroded Longitudinal Bras," *Proceedings of Japan Concrete Institute*, **31**(2), 1561-1566. (in Japanese)

Niwa, J., Yamada, K., Yokozawa, K. and Okamura, H. (1987), "Revaluation of the Equation for Shear Strength of Reinforced Concrete Beams without Web Reinforcement," *Concrete Library of JSCE*, **9**, 65-84.

Japan Concrete Institute (2004), JCI Standards (1977-2002). (in Japanese)

10CUEE CONFERENCE PROCEEDINGS
10th International Conference on Urban Earthquake Engineering
March 1-2, 2013, Tokyo Institute of Technology, Tokyo, Japan

STRATEGY FOR SEISMIC UPGRADING OF PUBLIC SCHOOLS

Hsiao, F. P. [1], Hwang, S. J. [1)*], Chung, L. L. [1], Yeh, Y. K. [1], Jean, W. Y. [1], Shen, W. C. [1], Chiou, T. C. [1], Chow, T. K. [1], Yang, Y. S. [1], and Chao, Y. F. [1]

1) National Center for Research on Earthquake Engineering, Taiwan (R.O.C.)
**)sjhwang@ntu.edu.tw*

Abstract: School buildings of all types of construction were seriously damaged by the 921 Chi-Chi Earthquake. Seismic evaluation and retrofit of these numerous vulnerable school buildings is an important societal issue to be resolved. The National Center for Research on Earthquake Engineering (NCREE) assisted the Ministry of Education with the arrangement of the program to accelerate the retrofit and rebuilding of elementary school, junior high school, senior high school and vocational school buildings, as part of the Economic Recovery Act. Currently, the program plans to spend 18.27 billion NTD between 2009 and 2012, and has proceeded with the seismic evaluation and retrofit of school buildings in Taiwan. In addition, NCREE established a School Project Office for this program to ensure that the work will be carried out in the most economic and effective manner. The purpose of the office is to provide administrative and technical supports, and to hold training programs and workshops for school administrators and professional engineers. A three-stage strategy for screening with existing school buildings also has been proposed by NCREE for execution of this program.

1. INTRODUCTION

Taiwan is located on the circum-pacific seismic zone. Earthquakes are common experiences for people in Taiwan. There were lots of heavy earthquakes happened and often caused schools to be destroyed seriously in the past years. In 1999, the Chi-Chi Earthquake caused nearly half of the school buildings in the central area of Taiwan to collapse or damage seriously. As many as 656 primary and secondary school buildings were damaged in that earthquake. This disaster told us the seismic capacities of existing school buildings in Taiwan are probably not sufficient. Significant casualties and property losses could be resulted from the collapse of these school buildings under strong earthquakes. Furthermore, school buildings might have to be assigned as emergency shelters immediately after a severe earthquake. To avoid casualties in the future earthquakes is the most important job in Taiwan. To retrofit these bad seismic performance school buildings is one solution to reduce the probable casualties.

The global economy went into a slump in 2008 as the impact of the international financial crisis spread. The whole economy has been heavily affected by this turn of events, and the unemployment rate has risen swiftly. On December 30 in 2008, the government announced that it will directly inject NT$858.5 billion to rescue Taiwan's economy over the next four years. The project involves 20 key public works projects and 64 special investment plans, and aims to achieve 6 major objectives. A total of NT$500 billion will be invested under the project. The focus of the policy will be on expanding public works projects, promoting major private investment projects, and fostering developing of industries that display a high degree of competitiveness. One of these projects is about the retrofitting or reconstruction of school buildings which is superintended by the Ministry of Education. Before the retrofitting the seismic capacity of school buildings should be evaluated with a reliable method. A three-stage strategy for screening with existing school buildings (Fig.1) was proposed by NCREE. These three stages are simple survey, preliminary evaluation and detailed evaluation. Simple survey is conducted by school administration while preliminary and detailed evaluations by professional engineers.

After a stage is completed, a summary report is submitted through internet to NCREE where a data base is established (Hwang, 2008). Based on the statistical analysis result from the data base, decision on seismic upgrading of school buildings can be made by the executives. Moreover, it is a good reference for the engineering community. Through the processes of preliminary evaluation, detailed evaluation, retrofit design and retrofit implementation, seismic upgrading of school buildings will be completed.

2. SEISMIC DEFICIENCY OF PUBLIC SCHOOL IN TAIWAN

Most school buildings in Taiwan were designed based upon the standard floor plan developed in 1966. Typically there is a corridor outside of the classrooms. The floor or roof above the corridor is often cantilevered without columns, and classrooms have been configured side by side in a row. Based on the damage statistics, a lack of seismic

resistance appears to be a common problem in the existing school buildings in Taiwan. Some of the major characteristics of seismic deficiency in school buildings are: (1) lack of integral planning; (2) collapse along corridor; (3) effect of short columns; (4) imbedded pipelines; and (5) lack of transverse reinforcement.

2.1 Lack of integral planning

In Taiwan, a large number of old buildings in elementary and secondary schools appear lacking of an integral planning in advance (Chung, 2000). Instead, many old school buildings have been constructed and later on expanded in a patchy way. It was due to the population growth in the school district and the rising of multifarious branches of teaching, the number of existing classrooms was no longer enough. Hence the school authorities had strived for funding from year to year. When the budget allowed, new classrooms were added to the existing ones in the horizontal or vertical directions at different times in order to solve the problems of under-supply of classrooms. If the new classrooms were added horizontally, the structural system of the old school building could be spoiled. If the new classrooms were built on top of the old ones, seismic and gravity load demands on the old classrooms would be significantly increased. The new classrooms expanded in the horizontal direction are rather closely adjacent, if it is not connected, to the old ones so as to maintain the continuity of activity space for pupils and teachers. Having constructed at different times, the old and the new classrooms could be different in height, weight or stiffness. Thus, the two structures may possess different fundamental vibration periods. When an earthquake occurred, the old and new classrooms would vibrate not in-phase. Under this circumstance, if the adjacent seismic gaps were not wide enough, those classrooms could have pounded each other. The pounding could cause the complete failure and collapse of columns in the adjacent building.

2.2 Collapse along corridor

Most school buildings in Taiwan were designed based upon the standard floor plan developed in 1966. According to the standard floor plan, classrooms have been configured side by side in a row. Typically there is a corridor outside of the classrooms. The floor or roof above the corridor is often cantilevered without columns. Transverse to the corridor, classrooms are typically partitioned by using brick walls which are continuous in the gravity direction. However, along the direction of the corridor, doors and windows have been constructed for entrance and natural light. Only small amount of walls could be continuous. The noted cantilevered corridor may be convenient for students' activities on the first floor. Thus, it often leaves only 2 reinforced concrete frames along the corridor direction. Unfortunately, these two frames typically consist of short columns. These short columns are resulted from the concrete or brick windowsill constructed between the columns. The adverse effects of the short column on the seismic performance of RC frame structures will be highlighted later in this article. Based on the worldwide observations on school building damages, there is strong evidence that school buildings tend to collapse along the corridor. There seems no case recorded that school buildings collapse transverse to the corridor direction.

2.3 Effect of short columns

In order to gain lighting and ventilation, the two exterior sides of the classrooms have been built with windows and doors. At the upper portion of the columns, it is often constrained by concrete or brick lintel above the window. At the lower portion of the columns, it is typically constrained by the noted infill below the windowsill. Thus, the effective length of the column has been significantly shortened. During an earthquake, the shear demand on the shortened column is therefore greatly increased. Unfortunately, these columns have been constructed with poor concrete and without sufficient shear reinforcement. Consequently, the columns have been found frequently failed in the shear mode, with X-shape cracks commonly observed. As a matter of fact, if a seismic gap had been cut between the column and the infill, the effective length of the column would not be shortened. In this manner, a more desirable flexural failure mode could be achieved. The seismic gap could be filled with compressible but watertight material.

2.4 Imbedded pipelines

Utility lines, including water supply, drainage and electricity have been embedded inside the columns. Consequently, the effective area of the columns is substantially reduced. The cross-sectional area of the columns is typically about 25 to 30 cm square. After a 5-cm diameter minimum drainage pipe is embedded, the column cross-sectional area is greatly reduced. The strength of the column has been evidently reduced and was never carefully taken into account. It is obvious that a complete separate space for running the utility lines is needed.

2.5 Lack of transverse reinforcement

The spacing of column transverse steel reinforcement in many old buildings has been found exceeding 20 cm. Transverse steel reinforcement is essential in confining core concrete, prolonging buckling of longitudinal reinforcement and prohibiting shear failure. The lack of lateral reinforcement should help to explain why the school building columns have often been failed in a brittle shear failure mode. The ductility of this kind of columns can be effectively enhanced by seismic retrofit using steel or carbon fiber jacketing.

3. STRATEGY AND STATISTICS OF SEISMIC UPGRADING

3.1 Three-stage strategy for screening

In order to effectively tackle the seismic deficiency problems for school buildings in Taiwan, three stages have

been proposed for screening, including simple survey (Chung, 2005), preliminary evaluation (Chung, 2004) and detailed evaluation (Chung, 2008). The simple survey is conducted by school administrators. In a simple survey, a chart has been developed for collecting school data and building data. School data include street address of the school, the number and the identification of school buildings. Building data include the number of stories, the year of design or construction, condition of the building, floor dimension, number of columns and the cross-sectional dimension of the typical column in each frame, number of walls and the cross-sectional dimension of the typical wall in each frame. After the survey chart is filled, data entries are submitted through internet. Before the extensive simple survey was launched across all school districts, workshop has been held to train school administrators responsible for conducting the survey.

The second stage of screening, preliminary evaluation is conducted by professionals. In a preliminary evaluation, a chart has been developed for the professionals to carry out the evaluation. In addition to the identification of the school and the building, the data include design ground acceleration, number of stories, floor area above the first story, cross-sectional areas of columns, reinforced-concrete walls, four-side and three-side bounded brick walls, and conditions of the building.

The third stage of screening is the detailed evaluation conducted by professional engineers. The push-over method using commercial computer program such as ETABS has been adopted in Taiwan. Seismic retrofit design is conducted by professional engineers. Four seismic retrofit techniques for school buildings have been verified experimentally in NCREE. It includes reinforced concrete jacketing of columns, steel jacketing of columns, wing walls addition adjacent to columns and composite columns addition to partition brick walls. The proposed strategy of seismic evaluation and retrofit of these school buildings has been accepted and implemented by the Ministry of Education. It has been recommended by NCREE research team that detailed evaluation and retrofit design of a school building be conducted by the same professional engineer so that the responsibility can be clearly defined. Moreover, it is also suggested that the detailed evaluation and retrofit design must be reviewed by a panel so that the engineering work quality can be guaranteed. In the final stage of retrofit construction, inspection has been prescribed.

The seismic performance of school buildings can be evaluated from its seismic capacity to demand ratio. The seismic capacity of the school buildings is computed by superimposing the shear strength of various vertical members such as walls and columns. The seismic demand is determined from the weight and location of school buildings. The seismic performance is further modified according to the conditions of the buildings. Simple survey has been conducted by school administrators such as director of general affairs, section chief of general services, or teacher with knowledge on civil engineering or building maintenance. The information of the survey has been submitted to the computer server in NCREE through internet.

3.2 Statistics of seismic database for school buildings in Taiwan

In Taiwan, there are 3,497 elementary and junior high schools. Among them, 3,419 schools (about 98%) completed the simple survey and submitted school data and building data to NCREE. The data base possesses data for 12,650 school buildings and the data for 11,060 school buildings (about 87%) are valid.

According to the statistics analysis, the means of the length and depth for the floor plans of school buildings are 52.9m and 11.5m, respectively. The mean of the number of stories for school buildings is 2.8. The mean of the floor area of the first floor for school buildings is 616m^2. The mean of the spans along the corridor for school buildings is 4.0m. The mean of the ratio of column area to floor area for school buildings is 57.0cm^2/m^2. The seismic design codes of buildings were revised in 1982 and 1997. 39% of school buildings were built before 1982, 41% between 1982 and 1997, 15% after 1997 and 5% unknown. 80% of the school buildings scored with fundamental seismic performance less than 80, 18% between 80 and 100, 38% above 100. After consideration of the conditions for the school buildings through modification factor, 55% of the school buildings scored with seismic performance indices less than 80, 16% between 80 and 100, 29% above 100.

4. ACTIVITIES IN SEISMIC UPGRADING PROJECT

The School buildings of all types of construction were seriously damaged by the 921 Chi-Chi earthquake. Soon after, NCREE started to develop technologies for seismic evaluation and retrofit. As a result of the achievements of laboratory and in-situ experiments, NCREE developed several seismic technologies, including a simple survey method, a preliminary evaluation process, a detailed evaluation process, and a retrofit design method. NCREE then used these research results in their "Technology Handbook for Seismic Evaluation and Retrofit of School Buildings (Chung, 2008)." By holding training programs and workshops, NCREE provides professional training in those technologies to school administrators and professional engineers in Taiwan.

During the past several years, NCREE assisted the Ministry of Education with establishing a seismic database for the assessment and retrofit of school buildings, and with collecting basic information as well as the results of the evaluation and retrofitting for all school buildings in Taiwan. By establishing the actual seismic capacity of all school buildings in Taiwan, this internet database has become the foundation of the plan for their seismic capacity improvement. In addition, NCREE assisted the Ministry of Education with the arrangement of the program to accelerate the retrofit and rebuilding of elementary school, junior high

school, senior high school and vocational school buildings, as part of the Economic Recovery Act. Currently, the program plans to spend 18.27 billion NTD between 2009 and 2012 (Table 1), and has proceeded with the seismic evaluation and retrofit of elementary school, junior high school, senior high school and vocational school buildings in Taiwan (Table 2). In addition, NCREE established a School Project Office for this program to ensure that the work will be carried out in the most economic and effective manner. The purpose of the office is to provide administrative and technical support, and to hold training programs and workshops for school administrators and professional engineers.

To date, NCREE held 37 training programs in 2009, including preliminary evaluations, detailed evaluations, retrofit designs and review committee conferences (with 2,666 people participating). NCREE also held 15 training workshops, authored and produced a technology handbook, developed a seismic evaluation method (Capacity Spectrum Method) and developed seismic rehabilitation method for school buildings, in cooperation with 1,246 professionals. Finally, NCREE assisted the Ministry of Education with conducting 1413 peer reviews of retrofit designs, with 453 school buildings passing the final reviews. Of these, 100 buildings have completed their retrofit. Additionally, three observation/evaluation workshops held in Wan-Fang elementary school and Da-Tong elementary school by NCREE showcased the advantages of retrofit implementation.

5. CONCLUSIONS

In Taiwan, the Ministry of Education has launched a project on upgrading the seismic performance from 2009 to 2012. A three-stage strategy for screening with existing school buildings has been proposed by NCREE. These three stages are simple survey, preliminary evaluation and detailed evaluation. Preliminary evaluation of school buildings is conducted in sequence according to the seismic performance indices of school buildings from simple survey. Detailed evaluation of school buildings is carried out in sequence according to the seismic performance indices of school buildings from preliminary evaluation. Retrofit design and implementation of school buildings are executed in sequence according to the capacity and demand ratios from detailed evaluation. In this project, thousands of school buildings will be beneficial through the processes of preliminary evaluation, detailed evaluation, retrofit design and retrofit implementation to compete against the next seismic hazard.

References:

Chung, L.L. and Hsu, T.Y. (2000), "Seismic damage of school buildings in Taiwan," *Proceedings of First International Conference on Structural Stability and Dynamics*, Taipei, Taiwan, pp. 647-652. (in Chinese)

Chung, L.L., Sheu, D.Y., Jean, W.Y., Liao, W.I., Chiu, C.K., and Chow, T.K. (2004), "Preliminary seismic evaluation of primary and secondary school buildings," *International Conference in Commemoration of 5th Anniversary of the 1999 Chi-Chi Earthquake*, Taiwan, pp. 100. (in Chinese)

Chung, L. L., Chien, W. Y., Yeh, Y. K., Hwang, S. J. and Sher, C. W. (2005), "Simple Seismic Survey for Typical Building Structures of Primary and Secondary Schools," *NCREE Report*, NCREE-05-007. (In Chinese)

Chung, L. L., Yeh, Y. K., Chien, W. Y., Chai, J. F., Hsiao, F. P., Shen, W. C., Chiou, T. C., Chow, T. K., Chao, Y. F. and Yang, Y. S. (2008), "Technology Handbook for Seismic Evaluation and Retrofit of School Buildings," *NCREE Report*, NCREE-08-023. (In Chinese)

Hwang, S. J., Yeh, Y. K., Chung, L. L., Jiang, W. G., Chien, W. Y., Chen, H. M., Chao, Y. F., Chow, T. K., Shen, W. C. and Kao, W. K. (2008), "Database for Seismic Assessment and Retrofit of School Buildings," *NCREE Report*, NCREE-08-035. (In Chinese)

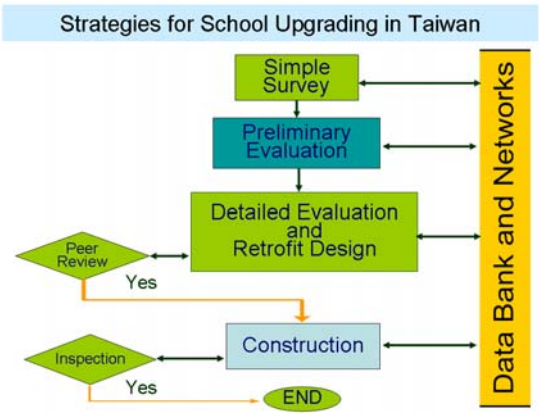


Figure 1 Strategy of Screening Buildings

Table 1 Budgets (in Million NTD)

Year	2009	2010	2011	2012
Preliminary Evaluation	36	----	----	----
Detailed Evaluation	238	306	135	99
Retrofit Design	71	162	70	32
Retrofit Implementation	3155	4032	1795	1469

Table 2 Number of School Buildings in Various Stages

Year	2009	2010	2011	2012
Preliminary Evaluation	6,000	----	----	----
Detailed Evaluation	660	850	375	276
Retrofit Design	198	450	195	88
Retrofit Implementation	171	420	187	153

10CUEE CONFERENCE PROCEEDINGS
10th International Conference on Urban Earthquake Engineering
March 1-2, 2013, Tokyo Institute of Technology, Tokyo, Japan

SUBSTRUCTURE PSEUDO-DYNAMIC TESTS OF REINFORCE CONCRETE FRAMES WITH SOFT-FIRST-STORY

Hideto Kanno[1], Naofumi Teramoto[2], Tetsuya Nishida[3], and Jun Kobayashi[3]

1) Associate Professor, Dept. of Architecture and Environment Systems, Akita Prefectural University, Japan
2) Associate Professor, Dept. of Civil and Environmental Engineering, Akita National College of Technology, Japan
3) Professor, Dept. of Architecture and Environment Systems, Akita Prefectural University, Japan
kanno@akita-pu.ac.jp

Abstract: Soft-first-story structures such as pilotis buildings are known as vulnerable structures against earthquakes. In this paper, a simple scheme for reducing the structural damage of such buildings is proposed, and its effectiveness is experimentally examined through substructure pseudo-dynamic tests. In the proposed method, low yield strength steel devices are applied as elasto-plastic damper on the first story of the buildings. The six stories single-span pilotis model with or without steel damper were provided for the test. The behavior of the two side columns at the first story and the steel damper are tested experimentally. The substructure pseudo-dynamic tests are successfully performed to investigate the elasto-plastic behavior of the damper and the reinforced concrete columns placed on the soft-first-story, as well as the total structural performance. The experimental results indicate that the seismic damage of pilotis buildings can be reduced since the steel dampers work effectively as expected. Especially, the steel dampers provide good performance during the largest ground motion and followed large aftershocks. The maximum response displacement has a stronger correlation with maximum momentary input energy than the amount of total input energy, because of the characteristics of the elasto-plastic behavior of reinforce concrete structure during earthquake.

1. INTRODUCTION

Soft-first-stories structures such as pilotis buildings are vulnerable structure against earthquake. Especially, in Kobe earthquake 1995, some pilotis buildings designed with current design codes as well as many old buildings had suffered the serious structural damages. Most of those damages were concentrated on the first story due to the change in lateral stiffness and strength compared to the upper portion of the structures. One of the ways to reduce the seismic damage of such structures is to increase column section on the first story in order to improve their stiffness discontinuity. However this has also constructive problem causing discontinuity of main bars of columns. Another way is to dissipate seismic response energy of the soft-first-story using dynamic damper taking advantage of concentration on structural deformation on the soft-first-story.

A simple scheme for reducing the structural damage of such pilotis buildings using low yield strength steel devices as elasto-plastic damper set on the first story is proposed in this paper. Detailed response of such buildings should be discussed based on precise elasto-plastic behavior of steel dampers. Especially, the shape of hysteresis loop of steel damper including fatigue behavior is important. A full size test seems to be almost impossible; therefore we conceived a scaled model and substructure pseudo-dynamic testing method for the purpose. In this study, the six stories pilotis reinforced concrete (RC) frames were experimentally tested in order to examine the effectiveness in reducing the structural damage using steel damper. Two sets of structural models were compared with each other through substructure pseudo-dynamic tests.

2. OUTLINES OF TESTS

Figure 1 shows outlines of the building model in this study. That is the six stories single span pilotis frame and also one-directional in-plane loading in transverse direction is taken into account. Its transverse span is 9,000mm. The height of the first story is 3,500mm and the height of the upper floors is all assumed to be 3,100mm. The steel damper is set between the lower and the upper beam on the first story of this frame, where the damper support member is assumed to be rigid so that deformation or stiffness of the support member can be neglected.

In substructure pseudo-dynamic test, a model structure is divided into two portions. One is actual specimen which is tested experimentally so that elasto-plastic behavior of the critical portion of the structure is realistically represented. The behavior of another portion, which would not critically affect on the total response of the structure, is numerically calculated in conventional elasto-plastic computational method. Substructure pseudo-dynamic test is developed on a basis of pseudo-dynamic test, which is an experimental

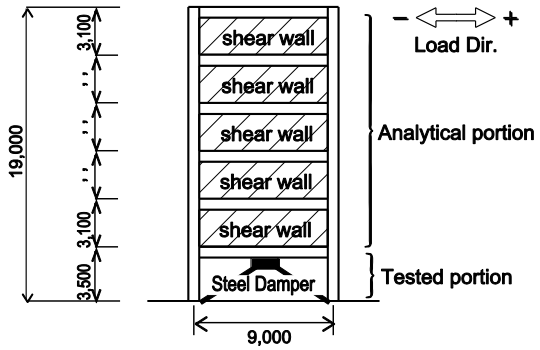


Figure 1 Outlines of model frame

technique for simulating a seismic response of the structural component. In these tests, two side columns and one steel damper on the first floor are the tested portion, which are replaced into three specimens. Figure 2 shows the diagram of pseudo-dynamic testing system which was developed in our laboratory. The system consists of the main management part (Main PC), data acquisition part and hydraulic pump control part. The main management part controls the total system and executes the numerical analysis during the tests. The main PC sends command signals such as the target displacement assigned for each tested portions to the hydraulic pump control unit so that the target displacement can be reached. Then the measured information such as the restoring forces and moments of the tested portion is sent back to Main PC together with analytical results of numerical models to calculate the total structural behavior. The loading conditions for the tested portion, the deformations, axial loads and rotational angles of beam-column connections are calculated step by step prior to the next step loading. Thus, the loading is carried out with accuracy of 1/100 mm using servo-controlled hydraulic jacks. Also loads in the two directions, that is, horizontal and axial loads, as well as rotational moment at the column top, are measured simultaneously.

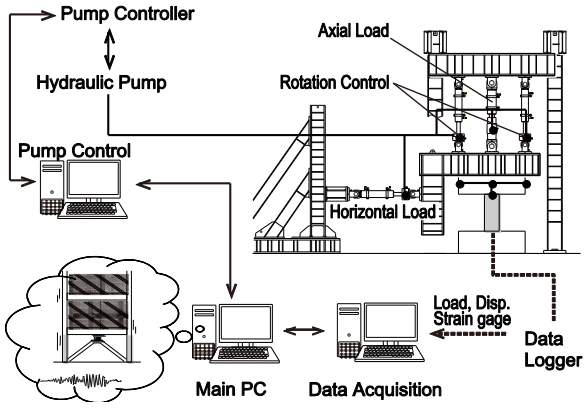


Figure 2 Schematic diagram of testing system

The integration method using the operator-splitting (OS) method was applied in these tests. This method has been used in many substructure pseudo-dynamic experiments, and made it possible to calculate seismic response under the interaction between the specimen and the whole frame [Nakashima et al. 1990]. The formulations of this method are follows:

$$Ma_{n+1} + Cv_{n+1} + K^I d_{n+1} + K^E_{n+1} d_{n+1} = P_{n+1} \quad (1)$$

$$\tilde{d}_{n+1} = d_n + v_n \Delta t + a_n \left(\Delta t/2\right)^2 \quad (2)$$

$$d_{n+1} = \tilde{d}_{n+1} + a_{n+1} \left(\Delta t/2\right)^2 \quad (3)$$

$$v_{n+1} = v_n + \left(a_n + a_{n+1}\right) \left(\Delta t/2\right) \quad (4)$$

Here, K^I and K^E_{n+1} are the linear and non-linear stiffness matrices, M and C are mass and viscous damping matrices, $\tilde{d}$ and d are predictor and corrector displacement vectors, v and a are velocity and acceleration vectors, and Δt is the integration time interval, respectively.

The characteristic of this method is to divide the stiffness of the whole structure into a linear and a non-linear stiffness. For the non-linear tested part, the explicit predictor-corrector method is used.

The Newmark's β method, the linear stiffness integration method, is also applied to take account of the non-linear portion of the whole structure. When the linear stiffness is much larger than the non-linear stiffness, the integration method is unconditionally stable. In this work, the equations were transformed into the incremental equations. It was confirmed that even when the incremental form equations were applied, the condition where the linear stiffness is larger than the non-linear tangent stiffness, provides that the integration method gives stable solutions.

The procedures of the substructure pseudo-dynamic tests in this study are as follows:

1. By using the integration method (OS method), the target predictor displacement $\tilde{d}$ at the next step is calculated. The Main PC (as shown in Figure 2) is used in this calculation.
2. The main PC sends the target displacement (horizontal displacement and rotational angle at the top of the column and steel damper) to the PCs for Pump Control of each specimen (two RC columns and the steel damper).
3. Until the current displacement reaches the target value, the specimens are loaded by the four jacks (one jack, in the case of damper) under the control.
4. The restoring forces (horizontal load and moment at the top of the column) are measured when the displacements reach the target value by the load cells attached to the jacks, and the values are fed back to the Main PC.

5. After the restoring forces are fed back to the Main PC, it sends a command to the PC for Data Acquisitions.
6. After the data acquisition is completed, procedure 1 is performed using the data on the restoring force and input acceleration.

In this study, two RC specimens and one steel damper on the first floor were tested. Therefore two kinds of test loading systems were prepared. Here, each specimen must be loaded simultaneously with up-per portion (analytical part) as a part of the frame. Therefore four static hydraulic jacks (in the case of damper, one jack) were installed to each column specimen so that loading with three degree of freedom (in the case of damper, single degree of freedom) could be performed. In the case of RC column, the central jack in the vertical direction had a loading capacity of 2,000kN and the force capacity of the other two vertical jacks and one horizontal jack were 500kN. The force capacity of horizontal jack set for damper was 500kN.

Specimens of RC columns are shown in Figure 3. The dimension of the column was 300 x 300 mm in section and 1,050mm in clear height, which was 3/8 scale of the building model. The main reinforcements were deformed 13mm bars, which had averaged yield strength of 377 N/mm^2. The shear reinforcements were deformed 6mm high strength bars, which had averaged strength of 1,100N/mm^2. The compressive strength of the concrete was 38.8 N/mm^2.

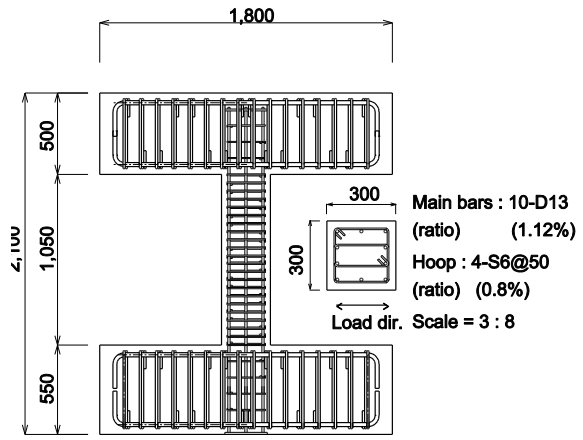


Figure 3 Details of the RC column

The steel damper was designed so that about 10% of the damping factor for the building model can be achieved. Figure 4 shows details of the low yield steel damper. The steel damper was panel shapes and its dimension was 262mm squared and 6mm thickness. In the case of damper portion, full-scale model was prepared to provide realistic elasto-plastic hysteresis behavior. The low yield strength steel had the average yield strength of 154 N/mm^2.

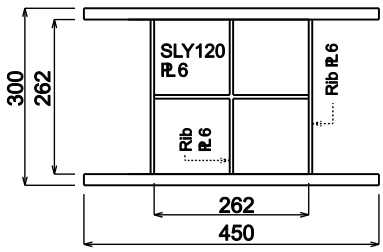


Figure 4 Details of the low yield steel damper

Two series of substructure pseudo-dynamic tests have been conducted. One is for pilotis frame with the steel damper set on the soft-first-story. The other one is only pilotis frame without the steel damper to confirm the damper effect. In these tests, the integration time interval was 0.01s. The Rayleigh damping was applied and the viscous damping ratio was set at 3%. Simulated earthquake ground motions as shown in Figure 5 have been used. The simulated motions are based on the phase characteristics of the El Centro 1940. And the target spectral characteristic is based on the design spectrum specified in the Japanese building design code. Both series of the tests, with damper or without damper, have been divided into 3 steps, which are from weak elastic response (RUN1) to the strong plastic level (RUN3). After RUN3 (the maximum level tests), the second step level test have been carried out again as RUN4 in order to discuss the aftershock response.

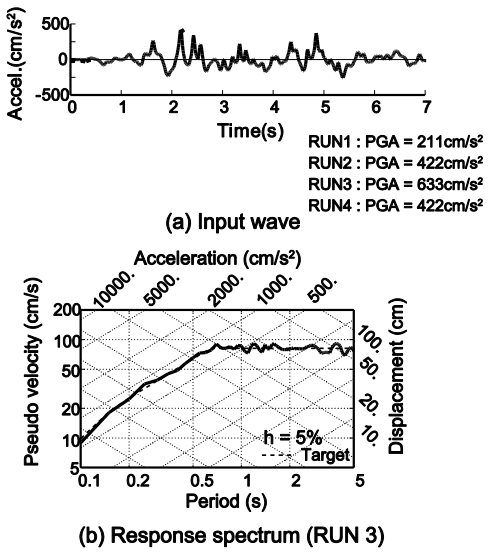


Figure 5 Input ground motion

3. TESTS RESULTS

Figure 6 shows base shear versus story drift hysteresis loops obtained through the tests. Figure 7 shows the shear force versus deformation relationships of tested members during RUN3. In these figures, upper show the case of bared

pilotis frame without damper and bottom show the case with damper. It can be seen that damper set on the soft-first-story worked enough and indicated good performance for the pilotis frame, especially in larger level excitation.

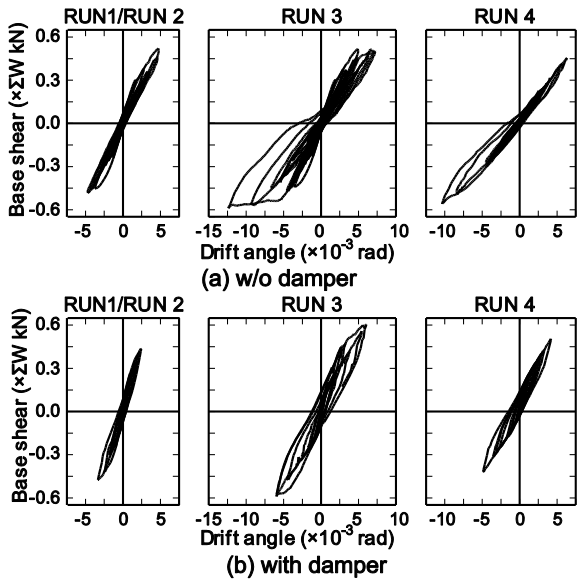


Figure 6 Base shear – drift angle relationships

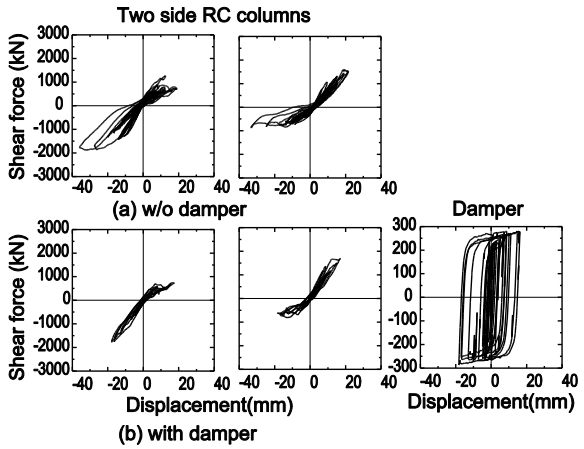


Figure 7 Shear force – deformation relationships of tested members during RUN3

During RUN1, both models (with or without damper) showed almost elastic behavior. In the case of model without damper, some main bars yielded at the bottom of RC column during RUN2. Then in the following loading RUN3, all of reinforcements yielded and story drift angle reached about 1/80. Contrarily, the model with damper, some of main bars yielded during RUN3, its maximum displacement remained within the half of the model without damper. During RUN4, which represents the behavior in aftershock, both models showed larger response than RUN 2; however the model with damper had much less displacement than the model without damper.

The maximum lateral load distributions in both tests are shown in Figure 8. Re-cent studies [e.g. Yong 1999] suggest that in pilotis structures, the maximum lateral load on each floor would be uniformly distributed, because most of displacement tends to concentrate on the first story due to the change in lateral stiffness and strength on the floor. In this research, also the maximum lateral load distribution is same as the recent research results even if the damper is set into the soft-first-story.

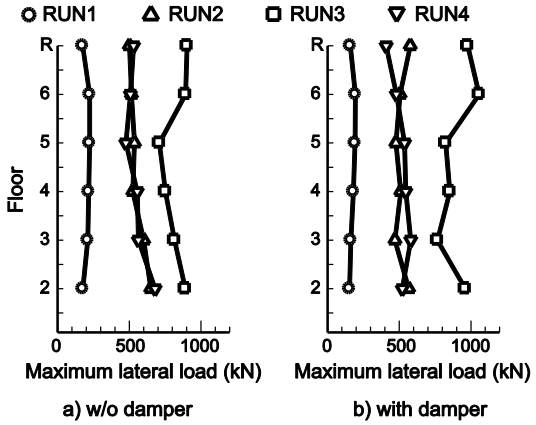


Figure 8 Maximum lateral load distributions in both tests

4. ENERGY RESPONSE

To discuss energy response during earthquake is helpful in designing building structure. In this study, seismic response energy of soft-first-story frame is discussed based on results of substructure pseudo-dynamic tests. Total input energy *EI* and momentary input energy ΔE are discussed dividing input energy into hysteretic energy dissipation (lateral and axial direction) of RC columns at the soft-first-story and the upper portion (shear wall), viscous damping and energy dissipation of damper set on the first story. Here, momentary input energy means increment of input energy, which is defined as seismic energy inputted during a half cycle of response [Inoue *et al.*1998]. Figure 9 shows time histories of displacement and seismic energy response ΔE and *EI* during RUN3, which is the maximum level loading of the tests.

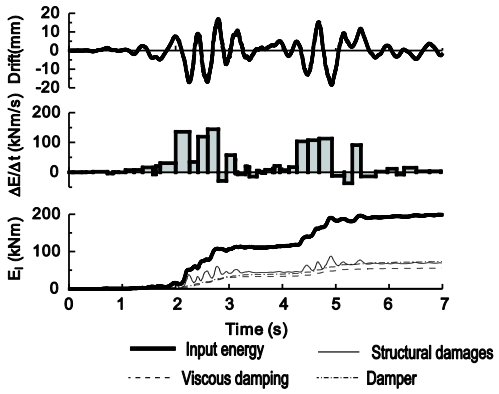


Figure 9 Time history of energy response during RUN3 (the model with damper)

It can be seen that ΔE is large when displacement is increased in both tests. Figure 10 shows relationships between the maximum momentary input energy ΔE_{max} and the maximum story drift of first story. It suggests that ΔE_{max} reflects a kind of intensity of energy input, related with the maximum response displacement which is developed during transient responses.

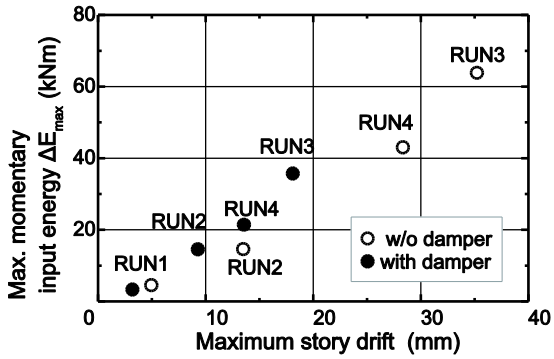


Figure 10 Maximum moment input energy – maximum story drift relationships

Table 1 and 2 show the each ratio of dissipated energy to seismic input in each step of tests. The model without damper, dissipated energy due to RC columns damages are about 40 to 50% of all the input energy, and the viscous damping energy is about 30 to 40%. This tendency is observed in all the step of input level.

Table 1 Energy dissipation ratio (total input)

(a) w/o damper

	CH	CA	U	D	V
RUN 1	64%	4%	5%	N/A	37%
RUN 2	45%	6%	9%	N/A	40%
RUN 3	49%	6%	6%	N/A	39%
RUN 4	42%	6%	5%	N/A	47%

(b) with damper

	CH	CA	U	D	V
RUN 1	26%	4%	7%	38%	25%
RUN 2	25%	2%	6%	43%	24%
RUN 3	27%	3%	5%	37%	28%
RUN 4	17%	4%	5%	47%	27%

CH : Column damage (Horizontal)
CA: Column damage (Axial)
U: Upper wall damage
D: Damper dissipation
V: Viscous damping

Table 2 Energy dissipation ratio of ΔE_{max}

(a) w/o damper

	CH	CA	U	D	V
RUN 1	63%	11%	10%	N/A	16%
RUN 2	65%	0%	0%	N/A	35%
RUN 3	70%	6%	5%	N/A	19%
RUN 4	61%	7%	8%	N/A	24%

(b) with damper

	CH	CA	U	D	V
RUN 1	56%	8%	9%	18%	9%
RUN 2	45%	5%	12%	19%	19%
RUN 3	58%	9%	9%	14%	10%
RUN 4	53%	9%	7%	20%	11%

CH : Column damage (Horizontal)
CA: Column damage (Axial)
U: Upper wall damage
D: Damper dissipation
V: Viscous damping

In the case with damper, the energy dissipation of steel damper is so large (about 40%). And as a result, the energy dissipation due to column damages and viscous damping are less than cases without damper. Especially, the energy dissipation ratio during RUN4 shows that the steel damper worked enough even for comparatively large aftershocks.

5. CONCLUSIONS

Substructure pseudo-dynamic tests are successfully performed to investigate the dynamic behavior of the damper and the reinforced concrete columns placed on the soft-first-story, as well as the total structural performance. Experimental results indicate that the seismic damage of pilotis buildings can be reduced since the steel dampers work effectively as expected. Especially, the steel dampers provide good performance during the largest ground motion and followed large aftershocks. The maximum response displacement has a stronger correlation with maximum momentary input energy ΔE_{max} than the amount of total input energy, because of the characteristics of the elasto-plastic behavior of RC structure during earthquake.

References:

Farzad Naeim and Marshall Lew (2000) The 1999 Earthquake Disasters Worldwide: How Many Times Do We Have to Relearn the Fundamentals of Seismic Engineering?, *The Structural Design of Tall Buildings*, **9** (2):161-182

Hemant B. Kaushik, Durgesh C. Rai, and Sudhir K. Jain (2009) Effectiveness of Some Strengthening Options for Masonry-Infilled RC Frames with Open First Story, *Journal Structural Engineering*, ASCE, **135**, (925) :925-937

Iqbal A. (2006) Soft First Story with Seismic Isolation System, *NZSEE Conference*, Napier, New Zealand, CD-ROM PaperID 36

Mezzi M. and Parducci, A. (2005) Preservation of Existing Soft-First-Story Configurations by Improving the Seismic Performance, *3rd Specialty Conference on the Conceptual Approach to Structural Design*, CD-ROM

Nakamura T., Hori N. and Inoue N. (1998). Evaluation of Damaging Properties of Ground Motions and Estimation of Maximum Displacement based on Momentary Input energy. *Journal of Structural and Construction Engineering* (*in Japanese*), **513** :65-72.

Nakashima M., Kaminosono T., Ishida M. and Ando K.(1990) Integration techniques for sub-structure pseudo-dynamic test, *4th US National Conference on Earthquake Engineering*, **2**:512-524

Okamoto H. and Ishimaru T.(1997) Relationship between Response Spectrum of Pseudo Velocity and That related to Energy Input Rate, *Summaries of Tech. Papers of Annual Meeting AIJ* (*in Japanese*) B-2:453-454

Teramoto N., Testuya Nishida T., Jun Kobayashi.J(2008)Structural Performance of Side Columns Subjected to Varying Axial Load,The *14th World Conference on Earthquake Engineering*, paper-ID 05-03-0234

Todorovska M. I.(1999)Base isolation by a soft first story with inclined columns, *Journal of Engineering Mechanics*, ASCE, **1254**:448-457

Yong Lu, T. P. Tassios, G.-F. Zhang, and Elizabeth Vintzileou (1999) Seismic Response of Reinforced Concrete Frames with Strength and Stiffness Irregularities, *ACI Structural Journal*, **96,** (2):221-229

10CUEE CONFERENCE PROCEEDINGS
10th International Conference on Urban Earthquake Engineering
March 1-2, 2013, Tokyo Institute of Technology, Tokyo, Japan

EARTHQUAKE-RESISTANT DESIGN OF LIGHTLY-REINFORCED AND LOW-RISE CONCRETE WALLS

Julian Carrillo

Assistant Professor, Department of Civil Engineering, Universidad Militar Nueva Granada, Colombia
wjcarrillo@gmail.com

Abstract: Low-rise housing units made of reinforced concrete walls are a common type of construction in many Latin American countries. These walls are often 100 mm thick with concrete compressive strengths of 15 to 20 MPa, and require a minimum or lower amount of web reinforcement. Existing requirements in current codes are not directly applicable and led to excessive costs. To study the seismic behavior of thin, lightly-reinforced and low-rise concrete walls and to develop a guideline for design of typical housing, an extensive research program was carried out. The experimental program included 39 quasi-static and shaking table tests of walls with different height-to-length ratios (0.5, 1.0 and 2.0) and walls with openings. Variables studied were the type of concrete (normalweight, lightweight and self-consolidating), web steel ratio (0%, 0.125% and 0.25%) and the type of web reinforcement (deformed bars and welded-wire mesh). Using a performance-based seismic design approach, recommendations for predicting the shear strength, displacement capacity, as well as acceptance limits of the structural response, are proposed. Taking into account the practical approach of the recommendations, they provide a robust tool for designers and code-developers to assess the adequacy of current design procedures and to promote a safe and economic housing.

1. INTRODUCTION

Over the last ten years, in order to satisfy housing demand, the number of new housing units in several Latin America countries, such as Mexico, Peru and Chile, has increased considerably. A significant portion of these housing units is one to two stories high and has been constructed with reinforced concrete (RC) walls. Because of the typical large wall-to-floor area ratio of these housing units, seismic force and displacement demands are, most of the times, relatively low. This phenomenon has prompted housing developers to use walls with low concrete compressive strengths (between 15 and 20 MPa) and small thickness (100 mm). For these cases, the minimum wall reinforcement prescribed by the American Concrete Institute's Building Code (ACI 318-11), appears to be excessive for controlling wall diagonal tension cracking. The use of thin walls, web reinforcement in ratios smaller than the minimum code-prescribed values, and web shear reinforcement made of welded-wire mesh are also the consequence of the hasty construction and cost-cutting practiced by developers in order to be competitive in the housing market.

Aimed at studying the seismic behavior of lightly reinforced, thin concrete walls and developing guides for the analysis and design of low-rise housing, a large research program was carried out. The experimental program comprised 39 quasi-static and dynamic loading tests of walls with different height-to-length ratios (0.5, 1.0 and 2.0) and door and window openings, three web steel ratio (0%, 0.125% and 0.25%), three types of concrete (normalweight, lightweight and self-consolidating) and two types of web shear reinforcement (deformed bars and welded-wire mesh).

The aim of this paper is to report on the development of a backbone model for typical RC walls, as well as to discuss and introduce acceptance limits of structural response as they relate to the expected wall damage. A performance-based seismic design (PBSD) approach was considered so that suitable limit states could be taken into account. Acceptance limits were derived for different damage levels (performance levels), within a PBSD framework. Selected performance indicators were allowable story drift ratios and residual cracking. Allowable story drift ratio is a common performance indicator in structural design. Residual cracking was expressed in terms of residual crack width and residual damage index.

2. EXPERIMENTAL PROGRAM

The experimental program comprised testing of 39 isolated cantilever walls. Main characteristics and failure modes of the 39 wall specimens are presented in Table 1.

2.1 Variables Studied

Variables studied were those obtained from current design and construction practice for low-rise housing in Latin America. A detailed description of the experimental program may be found elsewhere (Carrillo and Alcocer, 2013, 2012a-d). The following variables were studied:

Table 1 Main Characteristics of Wall Specimens

Type of testing	Wall	Type of concrete	f_c MPa	Type of web reinforcement	f_y MPa	$\rho_h = \rho_v$ %	t_w mm	h_w mm	l_w mm	h_w/l_w	Failure mode **
Quasi-static: monotonic	MCN0M	N	18.8	---	---	0	101	2412	2403	1.00	DT
	MCN50M	N	18.8	D	447	0.14	102	2415	2402	1.01	DT
	MCN100M	N	18.8	D	447	0.28	101	2417	2402	1.01	DC-DT
	MCL0M	L	16.3	---	---	0	101	2428	2398	1.01	DT
	MCL50M	L	16.3	D	447	0.14	102	2427	2397	1.01	DT
	MCL100M	L	16.3	D	447	0.28	101	2425	2398	1.01	DC-DT
	MCS0M	S	19.4	---	---	0	102	2425	2398	1.01	DT
	MCS100M	S	19.4	D	447	0.28	102	2424	2397	1.01	DT-DC
Quasi-static: reversed-cyclic	MCN50C	N	17.5	D	447	0.14	102	2431	2399	1.01	DT
	MCN100C	N	17.5	D	447	0.28	101	2432	2397	1.01	DC-DT
	MCS50C	S	22.0	D	447	0.14	102	2424	2403	1.01	DT
	MCS100C	S	22.0	D	447	0.28	103	2426	2401	1.01	DT-DC
	MCL50C	L	10.8	D	447	0.14	101	2426	2398	1.01	DT
	MCL100C	L	10.8	D	447	0.28	101	2424	2399	1.01	DC
	MRN100C	N	16.2	D	447	0.28	100	2433	2400	0.45	DC-SL
	MEN100C	N	16.2	D	447	0.28	100	2435	1240	1.96	DC-DT
	MRN50C	N	16.2	D	447	0.14	100	2425	2400	0.45	DT
	MEN50C	N	16.2	D	447	0.14	100	2421	1240	1.95	DT
	MRL100C	L	5.2	D	447	0.28	101	2423	5413	0.45	SL
	MRN50mC	N	20.0	W	605	0.12	103	2401	5396	0.44	DT
	MCN50mC	N	20.0	W	605	0.12	103	2396	2398	1.00	DT
	MEN50mC	N	20.0	W	605	0.12	101	2399	1239	1.94	DT
	MRL50mC	L	5.2	W	605	0.12	106	2419	5415	0.45	DT
	MCL50mC	L	26.0	W	605	0.12	100	2423	2403	1.01	DT
	MEL50mC	L	26.0	W	605	0.12	100	2435	1221	1.99	DT
	MVN100C	N	16.0	D	447	0.26	110	2397	3826	*	DT-DC
	MVN50mC	N	16.0	W	605	0.11	110	2397	3826	*	DT
	MCN50C-2	N	20.0	D	447	0.14	100	2400	2398	1.00	DT
	MCS50C-2	S	27.1	D	447	0.14	104	2404	2402	1.00	DT
	MCL50C-2	L	26.0	D	447	0.14	100	2426	2441	0.99	DT
	MCL100C-2	L	5.2	D	447	0.29	98	2432	2407	1.01	DC
	MCNB50mC	N	8.9	W	605	0.12	102	2404	2401	1.00	DT
	MRNB50mC	N	8.9	W	605	0.13	100	2401	5400	0.44	DT
Dynamic: shake table	MCN50mD	N	24.7	W	630	0.11	83	1923	1916	1.00	DT
	MCN100D	N	24.7	D	435	0.26	84	1924	1921	1.00	DT-DC
	MCL50mD	L	21.0	W	630	0.11	82	1917	1917	1.00	DT
	MCL100D	L	21.0	D	435	0.27	82	1918	1912	1.00	DT-DC
	MVN50mD	N	24.7	W	630	0.11	83	1924	3042	*	DT
	MVN100D	N	24.7	D	435	0.26	84	1926	3042	*	DT-DC

D = deformed bar, W = welded-wire mesh, * wall with openings, ** DT = diagonal tension, DC = diagonal compression, SL = sliding.

Height-to-length ratio: walls with height-to-length ratio (h_w/l_w) equal to 0.5, 1.0 and 2.0, and walls with openings (door and window openings) were tested. Full-scale wall thickness, t_w, and clear height, h_w, were 100 mm and 2.4 m, respectively. Then, to achieve the height-to-length ratio, length of walls was varied.

Concrete type: normalweight (N), lightweight (L) and self-consolidating (S) concrete were included in the test series. Nominal concrete compressive strength, f_c', was 15 MPa for all types of concrete. Ranges of measured mechanical properties of concrete for the 39 specimens are presented in Table 2.

Table 2 Mechanical Properties of Concrete

Property	Normal-weight, N	Light-weight, L	Self-consolidating, S
Compressive strength, f_c, MPa	16.0 - 24.7	10.8 - 26.0	22.0 - 27.1
Modulus of elasticity, E_c, MPa	8430 - 14750	6700 - 10790	8900 - 11780
Tensile splitting strength, f_t, MPa	1.55 - 2.20	1.14 - 1.76	1.58 - 1.98
Flexural strength, f_r, MPa	2.32 - 3.75	1.43 - 3.29	2.27 - 2.48
Specific dry weight, γ, kN/m^3)	18.8 - 20.3	15.2 - 18.3	18.9

Web steel ratio: 100% of ρ_{min} (0.25%), 50% of ρ_{min} (0.125%), 0% of ρ_{min} = without reinforcement (for reference only) were used. Minimum web steel ratio (ρ_{min}) was that prescribed by ACI 318-11. Web reinforcement was placed in a single layer at wall mid-thickness and same ratios of horizontal and vertical reinforcement ($\rho_h = \rho_v$) were used.

Type of web reinforcement: deformed bars (D) and welded-wire mesh made of small-gage wires (W) were used. Nominal yield strength of bars and wire reinforcement, f_y, was 412 MPa (for mild steel) and 491 MPa (for cold-drawn wires), respectively. Ranges of measured mechanical properties of steel reinforcement for the 39 specimens are presented in Table 3. In the cold-drawn wire reinforcement used in this study, the loading branch between onset of yielding and maximum deformation capacity (at fracture) was much shorter than that of mild-steel reinforcement. The behavior of wire reinforcement was characterized by fracture of material with a slight increment of strain (see the Elongation row in Table 3).

Table 3 Mechanical Properties of Steel Reinforcement

Location in the wall	Boundary: deformed bar	Web: deformed bar, D	Web: welded-wire, W
Type	Mild	Mild	Cold-drawn
Yield strength, f_y, MPa	411 - 456	435 - 447	605 - 630
Ultimate strength, f_{su}, MPa	656 - 721	659 - 672	687 - 700
Elongation, %	9.1 - 16.0	10.1 - 11.0	1.4 - 1.9

Boundary elements: because of their aspect ratio, the behavior of the RC walls tested was expected to be controlled by shear deformations. Therefore they were likely to exhibit a brittle failure mode governed by shear demands. Since the aim of this program was to study the shear behavior of the walls, the longitudinal boundary reinforcement was purposely designed and detailed to prevent flexural failure prior to achieving a shear failure. Thickness of boundary elements was equal to web thickness. Typical geometry and reinforcement layout of some of the full-scale wall specimens are shown in Figure 1.

2.2 Test Setups

Quasi-static (monotonic and reversed-cyclic) and dynamic (shaking table) testing series were included. In quasi-static testing, loading protocol consisted of a series of increasing amplitude cycles. For each increment, two cycles at same amplitude were applied (Sánchez, 2010). Owing to limitations in the payload capacity of the shaking table equipment, lightly-reduced scale models were designed and built for shaking table testing. During dynamic testing, models were subjected to a series of base excitations represented by earthquake records associated to three limit states (Carrillo and Alcocer, 2012b).

An axial compressive stress of 0.25 MPa was applied on top of the walls and was kept constant during testing. This value corresponded to an average axial stress in the first floor walls of a two-story prototype house.

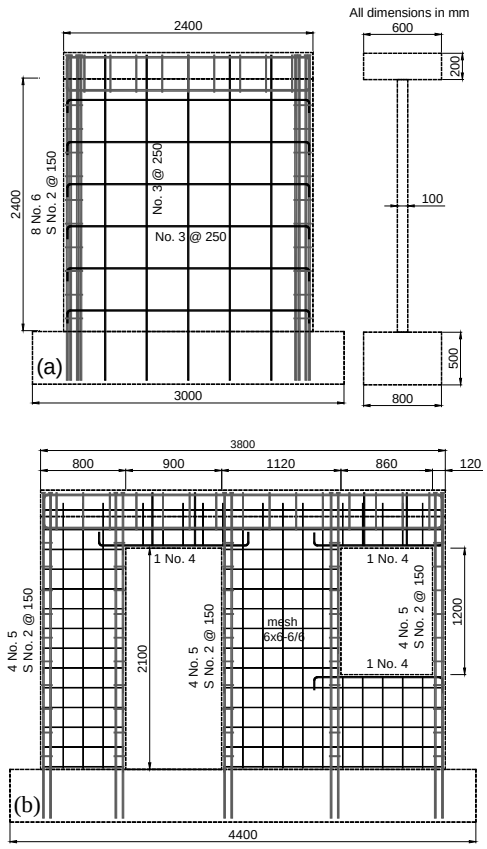


Figure 1 Geometry and Reinforcement Layout of Some Wall Specimens: (a) h_w/l_w = 1.0, 100% of ρ_{min} and Using Deformed Bars; (b) Wall with Openings, 50% of ρ_{min} and Welded-Wire Mesh.

2.3 Failure Modes

For evaluating the observed wall behavior, three failure modes were defined: (i) when yielding of the majority of the web shear reinforcement and no web crushing of concrete was observed, a diagonal tension failure (DT) was defined; (ii) when yielding of some steel bars or wires, and noticeable web crushing and spalling of concrete was observed, a diagonal compression failure (DC) was defined, and, (iii) when yielding of the majority of the web steel reinforcement and noticeable web crushing of concrete was observed, a mixed failure mode (DT-DC) was defined. Test results indicated that the contribution of wall sliding to the whole deformation was negligible for all tests. Therefore, wall sliding at the base (SL) was not purposely included.

Walls reinforced with 50% of the minimum code prescribed web steel reinforcement ratio and using deformed bars or welded-wire mesh, exhibited DT failure. Failure mode was governed by web inclined cracking of concrete at approximately 45° and yielding of most of web shear reinforcement prior to severe strength and stiffness decay. In walls reinforced with welded-wire mesh, fracture of wires after plastic yielding of web shear reinforcement was observed. Failure was brittle because of the limited elongation capacity of the wire mesh itself (see Table 3). In

contrast, walls reinforced using deformed bars and the minimum web steel ratio, exhibited DT-DC failure. Typical final crack patterns of walls during shaking table testing are shown in Figure 2.

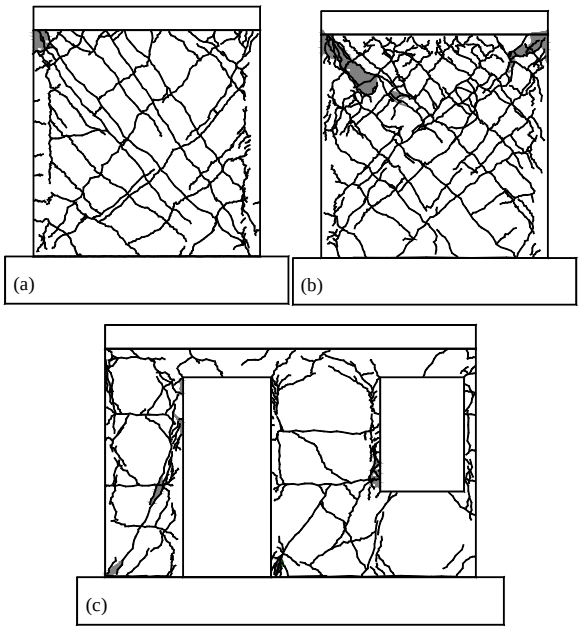


Figure 2 Typical Final Crack Patterns: (a) Wall with h_w/l_w = 1.0, 50% of ρ_{min} and Using Welded-Wire mesh (DT Failure), (b) Wall with h_w/l_w = 1.0, 100% of ρ_{min} and Using Deformed Bars (DT-DC Failure), (c) Wall with Openings, 50% of ρ_{min} and Using Welded-Wire Mesh (DT Failure).

3. BACKBONE MODEL

Most seismic codes, including the American Concrete Institute's ACI 318-11, rely mainly on conventional force-based limit states (i.e. ultimate limit state) and on serviceability limit state, but they do not include an explicit relationship between displacement demand and capacity. In contrast, modern design procedures set more emphasis to the deformation capacity of a system. For example, Performance Based Seismic Design (PBSD) requires the explicit consideration of lateral displacement as a performance indicator, besides verifying the structural design through an essentially force-based procedure (Priestley 2000). PBSD has been applied to systems failing under flexural mode, but its implementation for systems under shear failure is still limited. According to a literature review (Carrillo and Alcocer, 2013), to date there is no methodology for performance-based design of low-rise RC walls failing in shear. One of the main obstacles hindering the implementation of PBSD in these cases is the absence of suitable models for predicting the load-displacement curve of elements failing in shear.

Several analytical models have been proposed for predicting the peak shear strength. Nevertheless, due to the particularities of the RC walls in low-rise housing, most of the design recommendations and equations in the existing models are not directly applicable. In general, the main limitations are: (i) previous models have been developed on the basis of a much wider range of parameters controlling the shear behavior of walls; in contrast, in typical low-rise housing, parameters vary in a narrower range (low concrete strength, thin walls, low axial stress, low steel ratios); (ii) the behavior of walls with web shear reinforcement made of welded-wire mesh is not explicitly included in previous models; in the walls tested in this study, the low strain capacity (elongation) of the cold-drawn wire reinforcement, which significantly reduces the displacement capacity of walls, is a key parameter for PBSD; (iii) previous models have been calibrated on the basis of results observed from quasi-static tests only, that is, loading rate effects, low-cycle fatigue, cumulative parameters (Carrillo and Alcocer 2012d), and the dynamic effect of the vertical axial stress on the wall shear strength have been excluded, and finally, (iv) some previous models are not readily practical and versatile for design purposes.

3.1 Limit States

From the shape of the envelope of measured hysteresis of specimens described in Table 3, it was decided that a tri-linear backbone model was suitable for describing the performance of walls for low-rise housing (Carrillo and Alcocer, 2012a). The backbone model for PBSD is shown in Figure 3. The model is described using parameters associated to three limit states: diagonal shear cracking (V_{cr}, R_{cr}), peak shear strength (V_{max}, R_{max}) and ultimate deformation capacity (V_u, R_u).

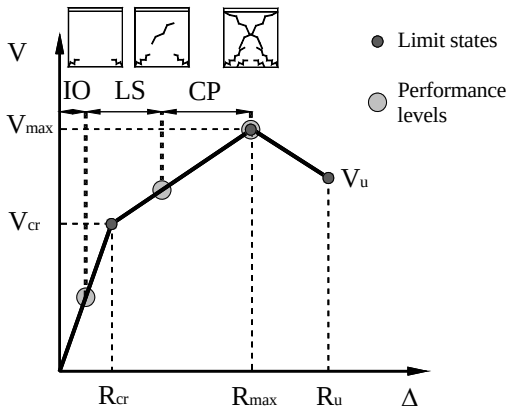


Figure 3 Backbone Model

Diagonal cracking limit state is attained when the initial inclined web cracking is observed. Strength limit state corresponds to peak shear strength. Ultimate deformation capacity limit state is associated to any of the two following scenarios: when a 20% drop to the peak shear strength is reached or when web shear reinforcement made of welded-wire mesh fractures. In the specimens studied, the first scenario occurred in walls reinforced with deformed bars; the second scenario was observed in walls with web shear reinforcement made of welded-wire mesh.

3.2 Objectives and Levels of Performance

A performance objective is the description of an acceptable damage level (performance level) of a structure when it is subjected to an earthquake motion associated to a specific intensity (hazard level). In a PBSD context, performance levels are introduced as limiting values of performance indicators that can be measured in the structural response (Guljas and Sigmund, 2006). When performance levels are established, associated limiting values (performance indicators) became the acceptance criteria whose compliance ought to be verified during subsequent design stages.

Following the procedure recommended in Vision 2000 (SEAOC, 1995), three performance levels were selected in this study: immediate occupancy (IO), life safety (LS) and collapse prevention (CP). Performance levels and corresponding damage stages of walls for low-rise housing are shown descriptively in Figure 3.

3.3 Shear Strength Capacity

Eq. (1) is proposed for estimating the peak shear strength of the RC walls used in typical low-rise housing. The functional form of the equation is similar to that of current design methodologies. The equation was proposed by Carrillo and Alcocer (2013) and was calibrated using the 39 isolated walls described in the experimental program (Table 1). Eq. (1) assumes that shear strength is made up by the contribution of concrete, V_c, plus that of the web steel reinforcement, V_s.

$$V_{\max} = V_c + V_s = [\alpha_1 \sqrt{f_c'} + \eta_h \rho_h f_{yh}] A_w \leq \alpha_2 \sqrt{f_c'} A_w \quad (1)$$

where α_1 and α_2 are coefficients defining the relative contribution of the concrete to diagonal tension and diagonal compression strength, respectively. Such contributions are calculated using Eqs. (2) and (3), respectively.

$$\alpha_1 = 0.21 - 0.02\left(\frac{M}{V l_w}\right) \text{ (MPa)} \quad (2)$$

$$\alpha_2 = 0.40 \text{ (MPa)} \quad (3)$$

where M/Vl_w is the ratio between bending moment and shear force times wall length. In Eq. (1), f_c' is the specified concrete compressive strength, ρ_h is the horizontal web steel ratio, f_{yh} is the yield strength of the horizontal web shear reinforcement, and η_h represents the efficiency of ρ_h and should be calculated using Eq. (4). Eq. (1) was calibrated on the basis of the gross area of a concrete wall section, A_w, that is, wall thickness (t_w) times wall length (l_w).

$$\eta_h = 0.8 \quad \text{For deformed bars} \quad (4a)$$

$$\eta_h = 0.7 \quad \text{For welded-wire mesh} \quad (4b)$$

Shear strength at distributed diagonal web cracking corresponds essentially to the shear force at which the principal tension stress of concrete is reached. Thus, it is assumed that V_{cr} is similar to the contribution of concrete to shear strength, then:

$$V_{cr} = V_c = \alpha_1 \sqrt{f_c'} A_w \quad (5)$$

As mentioned earlier, the ultimate deformation capacity limit state is associated with a 20% drop in the peak strength, or to the fracture of web shear reinforcement made of welded-wire mesh. For the former case:

$$V_u = 0.8 V_{\max} \quad (6)$$

3.4 Displacement Capacity

The equations for calculating displacement parameters were developed in terms of drift ratio (as a percentage), as it is a very common performance indicator used in code-based design. Drift ratio, R, was obtained by dividing the relative displacement measured at mid-thickness of the top slab by the height at which the displacement was measured (h). The proposed relationships are based on a model in which the total displacement is calculated as the sum of contributions related to flexure and shear. The contribution of wall sliding at the base was omitted because the sliding displacements measured during the tests were minimal (Carrillo and Alcocer, 2012b).

On the basis of observed trends from experimental results, and considering the findings of similar studies, it was assumed that the displacement associated with diagonal cracking was independent of the ratio and type of web steel reinforcement. Thus, using the diagonal cracking shear strength (V_{cr}), calculated via Eq. (5), and the cracked initial stiffness (K_{cr}), Eq. (7) is proposed for calculating R_{cr}.

$$R_{cr}(\%) = \left(\frac{V_{cr}}{K_{cr}}\right)\frac{100}{h} \quad (7)$$

where K_{cr} includes both shear and flexural deformations. According to Ghobarah (2004), realistic drift calculations should be made using a reduced gross inertia due to the properties of the cracking section. For walls tested in cantilever, K_{cr} is calculated from conventional theory of materials using Eq. (8).

$$K_{cr} = \left(\frac{h^3}{c_1 3 E_c I_g} + \frac{h}{c_2 G_c A_c}\right)^{-1} \quad (8)$$

where A_c is the shear area of the wall cross section (A_w/1.2), E_c is the modulus of elasticity of concrete, I_g is the moment of inertia of gross concrete section about the centroidal axis, G_c is the shear modulus of concrete and, c_1 and c_2 are factors for including cracking of concrete prior to the reinforcement yielding. Carrillo and Alcocer (2012b) have recommended the use of $c_1 = c_2 = 0.5$ for the practical seismic design of walls used in typical low-rise housing.

Eqs. (9) and (10) are proposed for estimating R_{max} and R_u. The equations were derived from observed trends and

iterative nonlinear regression analyses. Constants a_1, a_2, b_1, b_2, c_1 and d_1 depend on the type of web shear reinforcement. The proposed values for these constants are presented in Table 4.

$$R_{\max}(\%) = \frac{V_{\max}}{t_w\sqrt{f_c'}}\frac{1}{a_1}e^{b_1(M/Vl_w)} \quad \text{For deformed bars} \qquad (9a)$$

$$R_{\max}(\%) = \frac{V_{\max}}{t_w\sqrt{f_c'}}\frac{1}{a_2}\left(\frac{M}{Vl_w}\right)^{b_2} \quad \text{For welded-wire mesh} \qquad (9b)$$

Table 4 Constants for Calculating Drift Capacity

At peak shear strength, $R_{\max}$		At ultimate, R_u
Deformed bars (MPa)	Welded-wire mesh (MPa)	Deformed bars (MPa)
$a_1 = 5200$	$a_2 = 1450$	$c_1 = 3650$
$b_1 = 1.30$	$b_2 = 1.60$	$d_1 = 1.35$

Because of the brittleness of the failure mode observed in walls reinforced with welded-wire mesh, R_u was considered to be equal to R_{max} (Equation 10a). Like R_{cr}, R_{max} and R_u include the contributions of both shear and flexural deformations.

$$R_u(\%) = \frac{V_{\max}}{t_w\sqrt{f_c'}}\frac{1}{c_1}e^{d_1(M/Vl_w)} \quad \text{For deformed bars} \qquad (10a)$$

$$R_u(\%) = R_{\max}(\%) \quad \text{For welded-wire mesh} \qquad (10b)$$

4. PERFORMANCE LEVELS

Definition of comprehensive and realistic quantitative acceptance limits that are associated to well-known damage stages has been the subject of research and discussion. Considering that PBSD has been mainly applied to systems failing under flexure, most studies include performance indicators for walls exhibiting a ductile failure mode. According to Ghobarah (2004), available story drift limits are conservative for ductile structures, but may be unsafe for non-ductile structures.

To evaluate seismic damage of concrete walls in low-rise housing, whose response is governed by shear deformations, performance indicators related to story drift ratio (R_{allow}) and residual cracking were used (Carrillo and Alcocer, 2012c). Residual cracking was, in turn, analyzed in terms of residual crack width (w_{res}) and a residual damage index (I_{cracks}). For establishing the limiting values of selected performance levels, the following was considered: (i) for low-income population, housing unit is the main patrimony; therefore, housing rehabilitation should be economical and easily attainable, especially for IO and LS performance levels; (ii) consistent with the latter, safety levels of walls failing in shear, associated to threshold values of performance indicators should be higher than those used for medium- and high-rise concrete buildings dominated by flexural deformations; and (iii) response measured during testing indicated that strength and stiffness degradation of concrete walls was rapid as soon as peak shear strength was reached (Carrillo and Alcocer, 2012d); therefore, drift values close to those at peak shear strength should not be permitted for PBSD of low-cost housing.

Based on technical and economic facts, the immediate occupancy (IO), life safety (LS) and collapse prevention (CP) performance levels for low-rise concrete housing are related to initial inclined web cracking, to extension of web inclined cracks to wall edges without penetration into boundary elements, and to wall peak shear strength, respectively. Expected damage for the three performance levels is described in more detail in Table 5. The prescribed damage stages roughly corresponded to design strengths of 25%, 75% and 100% of the peak shear strength for IO, LS and CP performance levels, respectively. Note that CP performance level was defined to that at peak shear strength, that is, strength degradation was purposely excluded for the reasons explained above.

Table 5 Performance Indicators

Performance level	Expected damage	Indicator	Type of web shear reinforcement		
			Deformed bars	Welded-wire mesh	Wall without reinforcement
IO	*Minor damage:* - Flexural cracking at the boundary elements and minor web inclined cracks.	R_{allow}	0.15 Safety level = 1.8 *CV* = 17.0 %	0.10 Safety level = 2.3 *CV* = 27.2 %	0.05 Safety level = 5.6 *CV* = 16.5 %
		w_{res}, mm	0.10	0.08	0.05
		I_{cracks}, %	---	---	---
LS	*Moderate damage:* - Extension of web inclined cracks to the wall edges without penetration into the boundary elements.	R_{allow}	0.40 Safety level = 1.9 *CV* = 17.8 %	0.25 Safety level = 2.1 *CV* = 24.6 %	0.10 Safety level = 4.9 *CV* = 34.1 %
		w_{res}, mm	0.50	0.20	0.07
		I_{cracks}, %	0.10	0.04	---
CP	*Significant damage:* - Noticeable web diagonal cracking and/or yielding of some web steel bars/wires. - Moderate web crushing of concrete and damage around openings.	R_{allow}	0.65 Safety level = 2.4 *CV* = 32.9 %	0.35 Safety level = 1.3 *CV* = 24.8 %	0.15 Safety level = 5.4 *CV* = 21.7 %
		w_{res}, mm	2.50	0.40	0.10
		I_{cracks}, %	0.30	0.08	---

Typical residual crack patterns associated to performance levels of walls reinforced with 100% of ρ_{min} and using web shear reinforcement made of deformed bars, as well as of walls reinforced with 50% of ρ_{min} and using welded-wire mesh are shown in Figure 4.

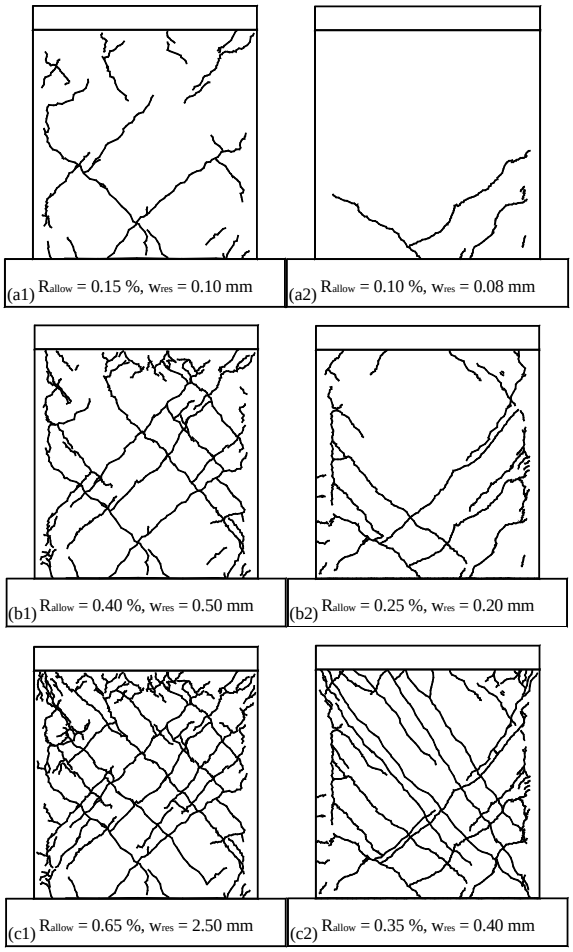


Figure 4 Residual Cracking Stage for Walls Reinforced with 100% of ρ_{min} and Using Deformed Bars: (a1) IO, (b1) LS and (c1) CP; and with 50% of ρ_{min} and Using Welded-Wire Mesh: (a2) IO, (b2) LS and (c2) CP.

Acceptance limits in terms of allowable story drift ratios (R_{allow}) and residual crack width (w_{res}) are indicated in Figure 4. Considering that some crack propagation was observed while maintaining the peak load during intervals of quasi-static testing protocol (Carrillo and Alcocer, 2012d), the expected damage level and limiting values of residual cracking were described and defined exclusively from damage observed during shaking table testing of concrete walls.

Although the final damage level of walls (Figure 2) was significantly larger than that associated to the CP performance level (Figure 4), walls reinforced with 50% of ρ_{min} and web shear reinforcement made of welded-wire mesh were suitably rehabilitated using jacketing made of steel fiber reinforced concrete. In general terms, the observed and measured performance of rehabilitated walls was satisfactory because strength and displacement capacities measured in the original walls were adequately restored. Further information may be found elsewhere (Avila et al., 2011).

4.1 Allowable Story Drift Ratios

Similarly to findings reported by Ghobarah (2004), Duffey et al. (1994) stated that allowable story drift limits specified by most seismic codes are generally unconservative for concrete walls with low aspect ratio with characteristics similar to those investigated herein, because such code-based drift limits are likely more directed toward medium- and high-rise structures than for low-rise shear walls.

Allowable drift ratios were determined from hysteresis curves measured during shaking table and quasi-static tests of RC walls. Typical measured hysteresis curves for walls with web shear reinforcement made of deformed bars and with web steel ratio equivalent to 50% and 100% of the minimum web steel ratio prescribed by ACI 318-11 are shown in Figures 5 and 6, respectively. Similar results for walls with web shear reinforcement made of welded-wire mesh are presented in Figure 7. In the graphs, limits proposed for IO, LS and CP performance levels are also indicated. Results for walls with h_w/l_w ratios equal to 0.5, 1.0 and 2.0 are included in these figures. The hysteresis curves were expressed in terms of the normalized shear strength (V/V_{normal}), shear stress (in the right-hand ordinate axis), and lateral drift ratio expressed in percentage. Shear strength predicted using equations proposed as a result of this program (Carrillo and Alcocer, 2013), V_{normal}, was utilized to normalize the measured lateral force, V. Calculated shear strength was computed using as-built wall dimensions and measured mechanical properties of materials (see Tables 1, 2 and 3). The mode of failure is also indicated in the graphs.

Analyzing trends for determining R_{allow}, it was evident that the type of web shear reinforcement and the h_w/l_w ratio (or M/Vl_w ratio) were the main factors affecting R_{allow}. For example, for walls with h_w/l_w = 2.0 it would be feasible to define story drift limiting values higher than those for walls with h_w/l_w = 0.5 or 1.0 (Figures 5 to 7). However, for code purposes, it is unwise to propose R_{allow} values that depend on h_w/l_w or M/Vl_w ratios. This statement is based on the fact that, at the same story, all walls are subjected to practically the same value of story drift demand. With regards to the type of concrete used, significant differences among walls made of normalweight, lightweight and self-consolidating concrete were not observed.

As it was indicated above, one of the objectives of this research program was to develop analysis and design guidelines for RC low-rise housing. From the results of this program, it was apparent that shear strength of walls reinforced with 50% of ρ_{min} was comparable to that of walls reinforced with 100% of ρ_{min}. It was also found that minimum web reinforcement is overly conservative for controlling diagonal tension cracking, especially for structures located in low seismic hazard zones.

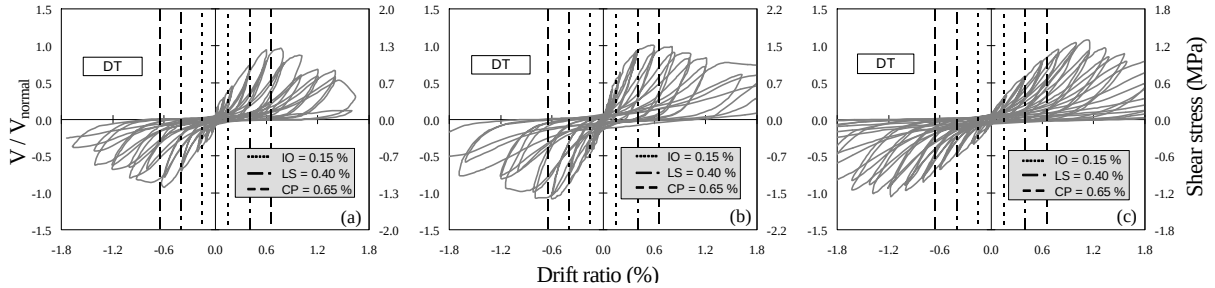


Figure 5 Hysteresis Curves and Allowable Story Drift Ratios for Walls Reinforced with 50% of ρ_{min} and Using Deformed Bars: (a) h_w/l_w = 0.5 (Normalweight), (b) h_w/l_w = 1.0 (Lightweight) and (c) h_w/l_w = 2.0 (Normalweight Concrete).

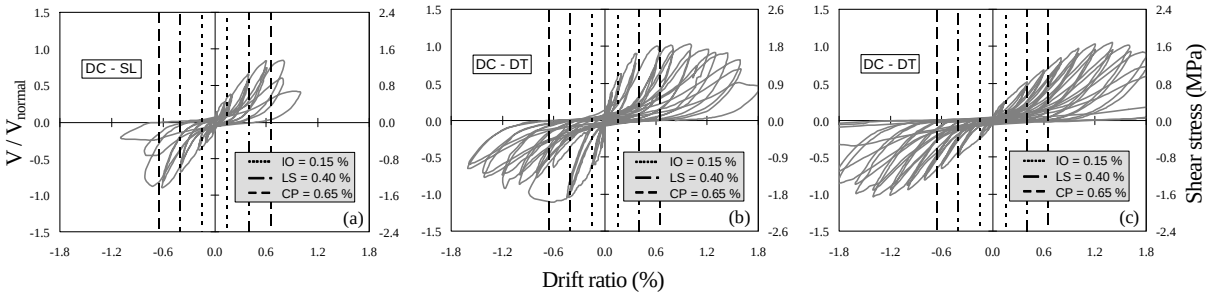


Figure 6 Hysteresis Curves and Allowable Story Drift Ratios for Walls Reinforced with 100% of ρ_{min} and Using Deformed Bars: (a) h_w/l_w = 0.5 (Normalweight), (b) h_w/l_w = 1.0 (Normalweight) and (c) h_w/l_w = 2.0 (Normalweight Concrete).

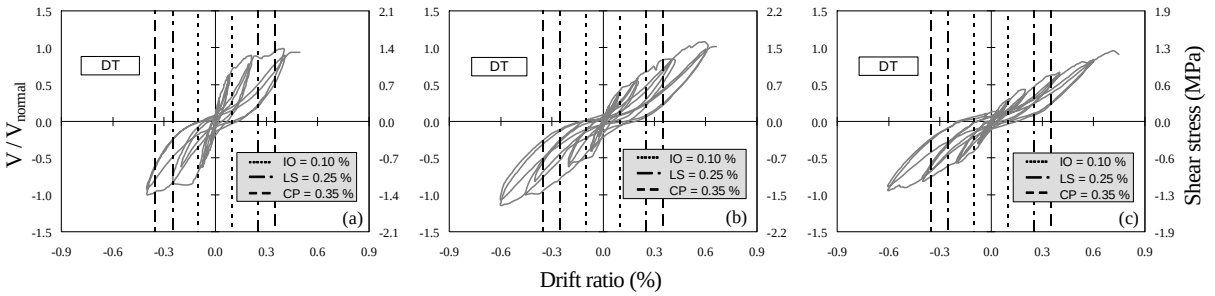


Figure 7 Hysteresis Curves and Allowable Story Drift Ratios for Walls Reinforced with 50% of ρ_{min} and Using Welded-Wire Mesh: (a) h_w/l_w = 0.5 (Normalweight), (b) h_w/l_w = 1.0 (Lightweight) and (c) h_w/l_w = 2.0 (Normalweight Concrete).

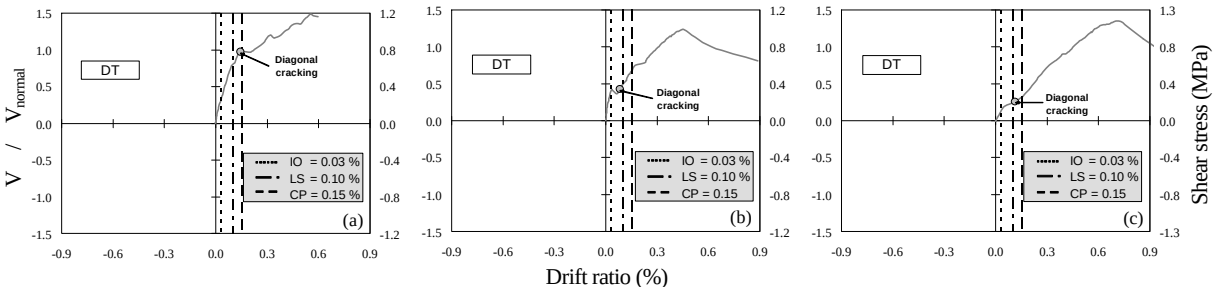


Figure 8. Hysteresis Curves and Allowable Story Drift Ratios for Walls without Web Shear Reinforcement (h_w/l_w = 1.0): (a) Normalweight, (b) Lightweight and (c) Self-Consolidating Concrete.

For the design methodology, three zones were identified. For low-hazard zones, walls without web shear reinforcement are allowed. For medium-hazard, walls with 50% of ρ_{min} can be used. For high seismic hazard zones, 100% of ρ_{min} should be used. For the low seismic hazard zone, shrinkage cracking should be controlled. Also, more stringent drift ratios for limiting inclined cracking of concrete should be applied. For this case, performance levels are related to the same damage stages defined for walls with web shear reinforcement made of welded-wire mesh and

deformed bars. Expected damage for the three performance levels are shown in Table 5. The envelopes curves for walls without web reinforcement are shown in Figure 8. In the graphs, the limits proposed for IO, LS and CP performance levels are indicated. Prescribed damages stages roughly corresponded to design strengths of 15%, 40% and 50% of the peak shear strength, for IO, LS and CP performance levels, respectively.

Based on measured hysteresis curves, proposed allowable story drift limits and description of the expected damage for the three performance levels are presented in Table 5. The maximum crack width measured after unloading, w_{res}, is also indicated in the table. As it was mentioned earlier, proposed values only depended on the type of web shear reinforcement. A single value for walls with web shear reinforcement made of deformed bars was established because differences in behavior between walls with 100% and 50% of ρ_{min} were not significant (Figures 6 and 7). The corresponding damage stages of the walls are shown in Figure 4.

Limiting values of allowable story drift ratio (R_{allow}) specified by seismic codes are not necessarily associated to the maximum capacity of structural elements or systems. These limiting values are typically associated to prescribed safety levels so that they can be used in practical structural engineering design. The safety level of an allowable drift ratio value for a particular performance level was calculated as the ratio between the measured drift capacity at a defined limit state and the measured drift ratio of the performance level (Carrillo and Alcocer, 2012c). Mean values and coefficients of variation (mean–*CV*) of the safety levels of allowable drift ratios for IO, LS and CP performance levels of walls are presented in Table 5. It was considered that a safety level of 2 was appropriate for seismic design of reinforced walls. For unreinforced walls, a safety level of 6 was selected as a target value.

Safety levels are dependent on the steel reinforcement ratio and characteristics of web shear reinforcement. For instance, safety levels were higher for walls with web shear reinforcement made of welded wire mesh than those for walls with deformed bars. An exception was observed for the CP performance level of walls with web shear reinforcement made of welded-wire mesh because displacement capacity at failure of these walls was almost equal to displacement capacity at peak shear strength. In addition, for walls where web shear reinforcement was not used, safety levels are roughly three times higher than those of walls with web shear reinforcement. In all cases, variation of safety levels was high (around 20%). This can be explained by the fact that results from tests of walls having different h_w/l_w ratios were used.

4.2 Residual Cracking

Limiting values of residual cracking (w_{res}, I_{cracks}) associated to the defined limiting values of story drift ratios were established using the damage observed during shaking table tests of RC walls. In this research, index I_{cracks} was calculated using Eq. (1).

$$I_{cracks} = \frac{\sum (l_{crack} \times w_{crack})}{A_{facade}} \times 100 \qquad (11)$$

where l_{crack} and w_{crack} are the length and maximum width of a residual crack measured at the end of an earthquake record, and A_{facade} is the wall surface area on one side. The maximum value of w_{crack} was also calculated and was labeled as w_{res}. For each wall tested, the relationship between w_{res}, or I_{cracks}, and maximum story drift measured during testing stages was plotted and evaluated in Figure 9. It was noted that the rate of increase of residual cracking was not significantly influenced by the type and amount of web shear reinforcement.

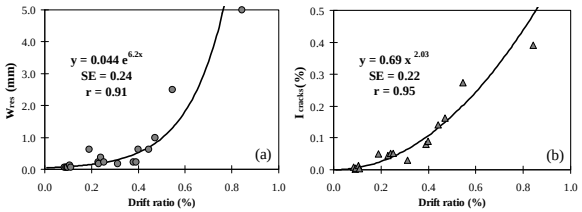


Figure 9 Residual Cracking: (a) Measured Residual Crack Width, (b) Residual Damage Index.

Also shown in Figure 9 are curves obtained from nonlinear regression. In this study, two commonly used measures of "goodness-of-fit" of results of nonlinear regression analyses were computed: the correlation coefficient (r) and the standard error of the residuals (SE). Fitted curves showed a very good agreement with test data, i.e. r is close to 1.0 and SE is around 20%. Applying the equations developed, for a story drift ratio equal to 0.5%, w_{res} and I_{cracks} are equal to 0.98 mm and 0.17%, respectively. For instance, for a RC wall with h_w/l_w = 1.0 and h_w = 2.4 m, the total area of residual cracks is roughly equal to 9800 mm^2 (2400 mm × 2400 mm × 0.17%), and thus, the total length of cracks with a crack width equal to 0.98 mm is roughly equal to 10 m (9800 mm^2 / 0.98 mm). In this way, the length of cracks to be repaired can be estimated. To determine the limiting values of w_{res} and I_{cracks}, equations of nonlinear regression analysis depicted in Figure 9 were used. Results are also included in Table 5.

5. DISCUSSION

5.1 Scope and Evaluation of the Recommendations

Up to date, PBSD has been applied basically to systems with a prevailing failure mode under flexure; thus, its implementation for systems failing by shear is still limited. This is the case of RC walls failing under shear. One of the main obstacles hindering the implementation of PBSD is the absence of suitable models for predicting the load-displacement curve, as well as of the lack of appropriate acceptance limits. Analysis of test data and experimental programs revealed that walls with the characteristics of those studied herein had not been tested

extensively.

In this study, a backbone model for estimating the load-displacement curve of the RC walls and acceptance limits in terms of story drift ration and residual cracking in typical low-rise housing were developed. The variables included were obtained from the design and construction practices of low-rise economic housing in several Latin American countries. The recommendations have also been calibrated on the basis of results observed from quasi-static and dynamic tests. The latter are considered a more suitable testing method as shake table testing includes the dynamic effects experienced by real structures when subjected to actual earthquake loads, i.e. loading rate effects, low-cycle fatigue, and cumulative parameters (Carrillo and Alcocer, 2012d).

5.2 Limitations

The applicability of the recommendations is limited to walls with the characteristics of typical RC walls in one- and two-story economic housing, i.e. prismatic walls with $M/Vl_w \leq 2.0$ and walls with door and window openings, thickness of boundary elements equal to web thickness, response governed by shear deformations, a specified concrete compressive strength that varies between 15 MPa and 25 MPa, axial stress that is less than 0.03 f_c', a web steel ratio smaller than or equal to 0.25%, wall web reinforcement made of deformed bars or welded-wire mesh, and same amounts of horizontal and vertical web reinforcement. Normalweight ($19 \leq \gamma \leq 21$ kN/m3), lightweight ($15 \leq \gamma \leq 19$ kN/m^3) and self-consolidating ($19 \leq \gamma \leq 21$ kN/m^3) concrete was used in the experimental program.

6. CONCLUSIONS

In order to improve design methods toward safer and more economical housing, a backbone model and acceptance limits for PBSD were developed. The semi-empirical model included three different limit states (diagonal cracking, peak strength and ultimate deformation capacity) and is intended to capture the average response from the experiments. Limit states include prediction of shear strength and displacement capacity. The proposed model has been developed to be included in design guidelines. Due to this feature, the proposed model may be implemented in conventional force-based design, as well as in PBSD. For PBSD, the tri-linear backbone model may be used for estimating the global load-displacement capacity curve of the housing in order to be compared to acceptance limits at selected performance levels.

Within a performance-based seismic design framework, and due to the lack of acceptance limits of performance indicators for shear-dominated walls, a series of acceptance limits were also developed. Selected acceptance limits were story drift ratios, residual crack width and residual damage index. These limits were developed for immediate occupancy, life safety and collapse prevention performance levels. Because of the inherent brittle nature of the mode of failure of walls tested, acceptance limits were purposely developed to be conservative, i.e. limits are smaller than those measured at peak strength. These values provide an adequate level of safety against rapid deterioration of stiffness and strength after reaching peak lateral load capacity.

The outcome of this research could contribute to the development of more accurate models and guidelines for improving current provisions. By adopting the recommendations proposed herein, safer and more economical housing may be designed. More economical housing also has the indirect benefit of facilitating the reduction of housing deficits.

Acknowledgements:

The author gratefully acknowledges the guidance of my supervisor during doctoral studies, Professor Sergio M. Alcocer, the financial support of Grupo CEMEX and the extensive assistance in the experimental testing of staff and students of the Structural Engineering Laboratories of the Instituto de Ingenieria at UNAM.

References:

ACI Committee 318 (2011). "Building code requirements for structural concrete and commentary (ACI 318-11)," *American Concrete Institute*, Farmington Hills, MI, 465 pp.

Ávila, O., Carrillo, J. and Alcocer, S. (2011), "Rehabilitation of concrete walls using steel fiber reinforced concrete (SFRC): Shaking table tests," *Concreto y Cemento, Investigación y Desarrollo*, **2**(2), 2-17. (in Spanish)

Carrillo, J. and Alcocer, S. (2013), "Shear strength of RC walls for seismic design of low-rise housing," *ACI Structural Journal*, In Press.

Carrillo, J. and Alcocer, S. (2012a), "Backbone model for performance-based seismic design of RC walls for low-rise housing," *Earthquake Spectra*, **28**(3), 943-964.

Carrillo, J. and Alcocer, S. (2012b), "Seismic performance of concrete walls for housing subjected to shaking table excitations," *Engineering Structures*, **41**, 98-107.

Carrillo, J. and Alcocer, S. (2012c), "Acceptance limits for performance-based seismic design of RC walls for low-rise housing," *Earthquake Engineering and Structural Dynamics*, **41**, 2273-2288.

Carrillo, J. and Alcocer, S. (2012d), "Experimental investigation on dynamic and quasi-static behavior of low-rise reinforced concrete walls," *Earthquake Engineering and Structural Dynamics*, DOI: 10.1002/eqe.2234.

Duffey, T., Goldman, A. and Farrar, C., 1994. Shear wall ultimate drift limits, *Earthquake Spectra*, **10**(4), 655-674.

Ghobarah, A. (2004), "On drift limits associated with different damage levels," *Proceedings of the International Workshop on Performance-based Seismic Design Concepts and Implementation*, Bled, Slovenia.

Guljas, I. and Sigmund, V. (2006), "Performance domain design procedure for wall buildings," *Proceedings of the 1st European Conference on Earthquake Engineering and Seismology*, Geneva, Switzerland, Paper 454.

Priestley, M. (2000), "Performance based seismic design," *Proceedings of the 12th World Conference on Earthquake Engineering*, New Zealand. Paper 2831.

Sánchez, A. (2010), "Seismic behavior of housing with concrete walls," Technical Report, Institute of Engineering, *National University of Mexico*, UNAM, Mexico (in Spanish).

SEAOC (1995), "Vision 2000: Performance-based seismic engineering of buildings," Report, *Structural Engineers Association of California, Sacramento*, California.

10CUEE CONFERENCE PROCEEDINGS
10th International Conference on Urban Earthquake Engineering
March 1-2, 2013, Tokyo Institute of Technology, Tokyo, Japan

EXPERIMENTAL STUDY ON CRACKING STRENGTH OF CONFINED MASONRY WALLS SUBJECTED TO SHEAR FORCE

Koshiro Nishimura[1], Yasuaki Goto[2], and Shintaro Murai[3]

1) Associate Professor, Faculty of Engineering, Hokkaido University, Japan
2) Professor, Faculty of Engineering, Hokkaido University, Japan
3) Graduate Student, Graduate School of Engineering, Hokkaido University, Japan
nishimura.koshiro@eng.hokudai.ac.jp, gottsu@ eng.hokudai.ac.jp, s-murai@ eng.hokudai.ac.jp

Abstract: An object of this study is to evaluate strength of confined masonry walls. Eleven confined masonry wall specimens were tested under cyclic lateral load in the previous study. The walls were constructed with brick and joint mortal and no reinforcements in the walls. Two reinforced concrete columns of both side confined the wall. In this paper, results of these specimens were classified into three failure modes and two transition mode those were shear failure, slipping failure, flexural failure, and those combinations. And strengths of the specimens could be roughly estimated by calculations of flexural strength and cracking strength. However, brick strength isn't used in these calculations nevertheless cracks were observed on bricks. Therefore, two kind of shear-loading tests were conducted to verify the cracking strength formula. One is shear-loading test of prism specimen consisted with brick and mortar. The other is shear-loading test of brick in order to obtain strength when the brick cracks.

1. INTRODUCTION

Confined masonry buildings are commonly constructed in many countries. In these structures, masonry walls are confined with reinforced concrete columns and beams. Because of these low-cost buildings, various constructing methods, problem of skill level, and so on, a simple evaluation method for strength of the confined masonry wall is desirable.

An objective of this study is to propose simple and logical evaluation method for strength of the confined masonry wall without opening. Eleven one-story and one-span specimens of confined masonry walls were tested under cyclic lateral load in previous studies (Toge et al. 2006, Sakaitani et al. 2008, Hayashi et al. 2009, Sugai et al. 2010, Murai et al. 2011, Tanabe et al. 2012). In this paper, failure modes of these specimens are classified firstly. Next, strengths of test results are compared with calculations of strengths for the failure modes. Then, two kind of shear-loading tests were conducted to verify the cracking strength formula. One is shear-loading test of prism specimen consisted with brick and mortar. The other is shear-loading test of brick.

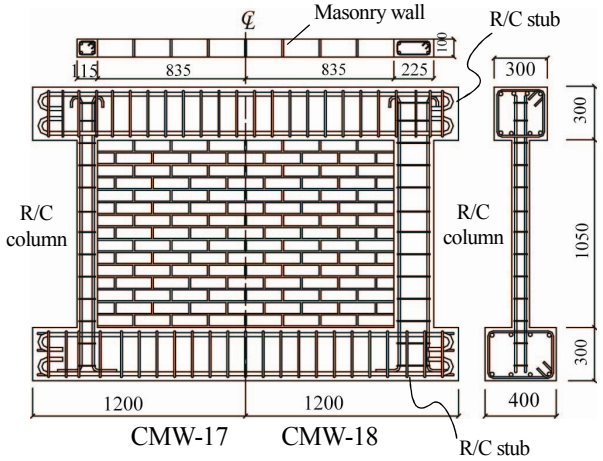


Figure 1 Details of Specimens

2. CYCLIC LOADING TEST OF CONFINED MASONRY WALLS

2.1 Outlines of Experiments

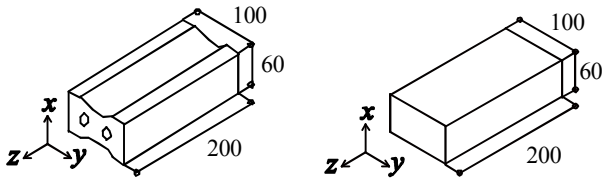
Eleven confined masonry wall specimens without opening were prepared in the previous studies. Figure 1 shows detail of two of these specimens. The specimen was one-story and one-span wall. The wall was confined with two reinforced concrete columns, hereafter R/C columns, at both sides. The specimens were modeled ground-story in three-story building, and were half scale. Therefore, the specimen of masonry wall with R/C columns was fixed by two R/C stub beams at top and bottom.

Table 1 shows list of the eleven specimens. Primary parameters were strength of joint mortar, brick, and longitudinal bars in column. The bricks were gardening bricks at retail in Japan, and had hole or no hole as shown in Figure 2. Compressive strengths of the bricks are shown in Table 1, and its loading direction is shown in Figure 2. The

Table 1 List of Confined Masonry Wall Specimens and Material Properties

Specifics		Name of specimens	Masonry wall part			Column part						Constant axial load [kN]
Brick and bonding	F_{mor}		f_{br}' [N/mm^2]		f_{mor}' [N/mm^2]	Width x Depth [mm^2]	f_c' [N/mm^2]	Main reinforcement		Shear reinforcement		
			X dir.	Z dir.				Arr.	σ_y [N/mm^2]	Arr.	σ_y [N/mm^2]	
Special brick, Straight joint	30	CMW-01	15.0	45.9	32.1	100 x 225	31.7	6-D13	1020	6ϕ@50	380	100
		CMW-04			39.0	100 x 115	34.9	4-D13	1020			52
		CMW-08	17.1	49.0	33.3	100 x 115	30.1	6-D13	1080	6ϕ@50	346	100
Cuboid brick, Breaking joint		CMW-11	17.9	19.9	39.2	100 x 115	23.9	4-D13	352	D6@50	335	100
		CMW-13			32.5	100 x 115	31.5	6-D13	853			100
	10	CMW-14	71.6	53.5	11.0	100 x 115	25.6	4-D13	373	D6@50	351	100
		CMW-15			13.7	100 x 115	24.5	4-D6	351	4ϕ@125	336	100
		CMW-17	16.0	14.1	15.9	100 x 115	23.1	4-D13	988	4ϕ@125	547	100
		CMW-18			15.9	100 x 225	22.7	4-D13	988			100
		CMW-19	20.9	26.7	8.5	100 x 115	23.8	6-D10	474	4ϕ@100	500	100
		CMW-20			8.3	100 x 115	23.6	6-D10	349			100

F_{mor}: target compressive strength of joint mortar, f_{br}': brick compressive strength, f_{mor}': compressive strength of mortar cylinder, f_c': compressive strength of concrete cylinder, σ_y: yield stress of reinforcing bar.



Special brick Cuboid brick

Figure 2 Dimension of Bricks

bricks were cut in 100mm of length on x-directional compression test. Target compressive strengths of joint mortar, F_{mor}, were 10 and 30 N/mm^2. Mortar compressive strengths, f_{mor}', are also shown in Table 1 those are given by compression tests of mortar cylinders. The mortar cylinders have 50mm in diameter and 100mm in height.

Figure 3 shows a loading setup. The bottom stub was fixed, and a lateral load and a vertical load were applied through universal joints. The specimen was subjected to static cyclic load. The vertical load was transferred through steel plates those were placed between a steel beam and the top stub above the columns. The vertical load shown in Table 1, which acts on the specimen as axial force, kept constant during the test. Lateral displacement at the top stub, δ in Figure 3, was measured by displacement transducers. Rotation of the specimen, hereinafter R, is equal to δ/H, which H is equal to 1050 mm of clear span.

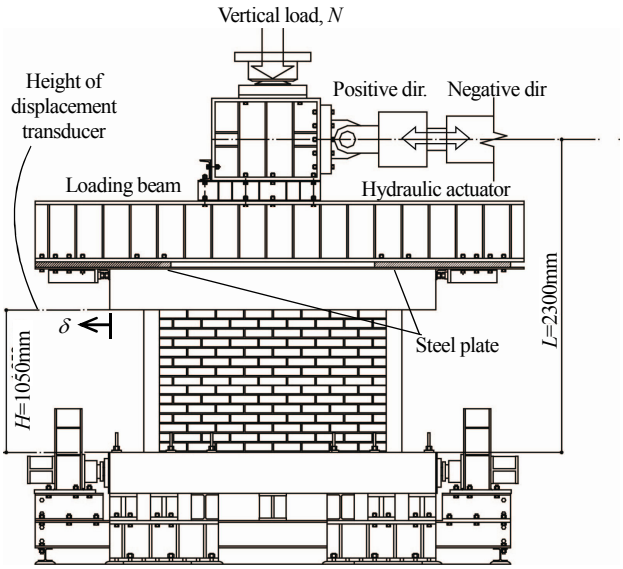


Figure 3 Loading Setup

2.2 Test Results and Failure Mode

Figure 4 shows representative test results, which are lateral load - rotation curves and damages after the loading. As shown in this figure, test results were classified into three failure mode and two transition mode; shear failure mode, flexural failure mode, slipping failure mode, flexural failure mode after slipping, and slipping failure mode after flexural yielding.

Performances of those failure modes are as follows. The shear failure mode: it could be observed diagonal cracks extending, and then shear resistance declined brittlely. The flexural failure mode: the wall yielded in flexure due to yielding of longitudinal bars in the column, and showed ductile behavior. The slipping failure mode: the wall failed due to cracking in joint mortar. Bricks also cracked at compression part in the wall, but major crack could be observed in the joint mortar. The flexural failure mode after slipping: first peak of shear resistance occurred by cracking in the joint mortar, and then second peak was due to yielding of the longitudinal bars in the column. The slipping failure mode after flexural yielding: first peak of shear resistance was due to yielding of longitudinal bars in column, and then the resistance declined because of cracks in the joint mortar.

3. EVALUATION OF STNREGTH

3.1 Concept of Evaluation

In this paper, a design concept is assumed that the confined masonry wall resists earthquake by its strength, and ductility of the wall isn't taken into account. The strength of

confined masonry wall is evaluated by cracking strength in the wall because cracks in masonry wall must weaken resistance against lateral force in out-of-plane direction. And a flexural strength is adopted for evaluation in case of short reinforcements in columns.

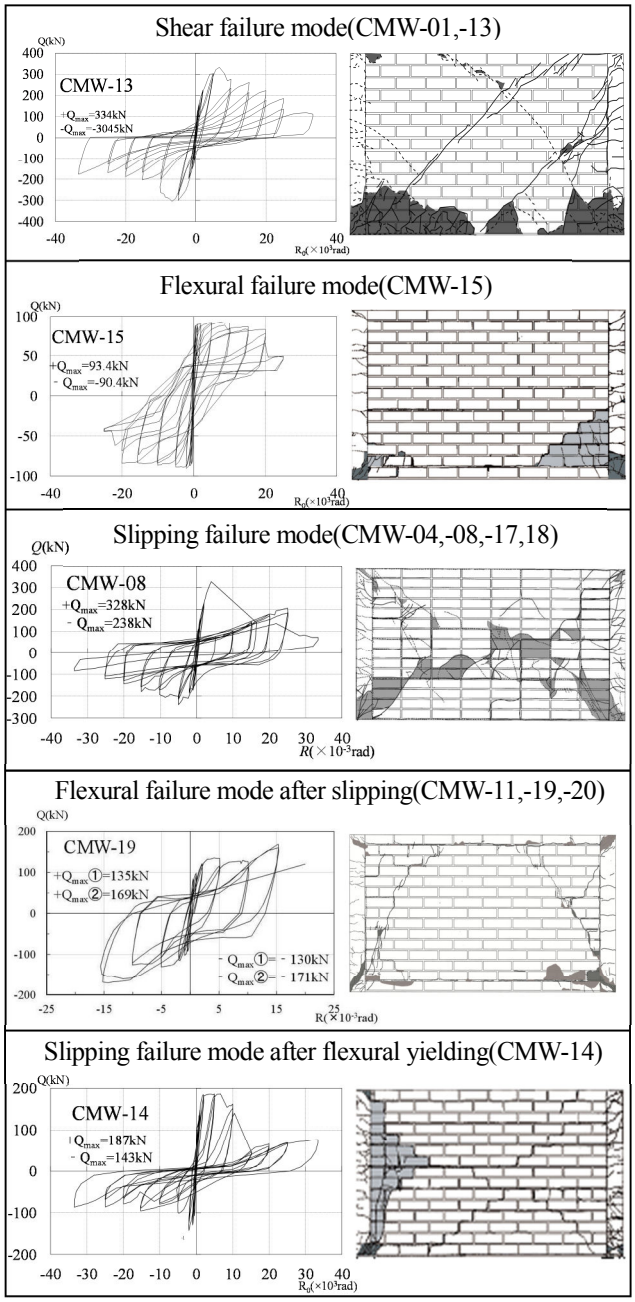


Figure 4 Failure Mode

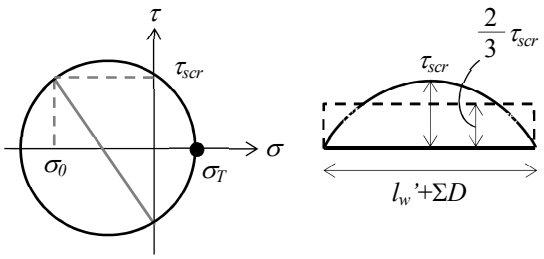


Figure 5 Stress in Horizontal Section of wall

3.2 Cracking Strength

A shear cracking strength for R/C shear wall written in AIJ guideline (Architectural Institute of Japan 1999), which is the following equation, is applied to the cracking strength of masonry wall in this paper.

$$V_C = \frac{t_w l_w}{\chi_w}\tau_{scr} \tag{1}$$

$$\text{where } \chi_w = \frac{3(1+u)\left\{1-u^2\left(1-\frac{t_w}{b}\right)\right\}}{4\left\{1-u^3\left(1-\frac{t_w}{b}\right)\right\}} \tag{2}$$

$$u = \frac{l'_w}{l'_w+\sum D} \tag{3}$$

$$\tau_{scr} = \sqrt{\sigma_T^2 + \sigma_T\sigma_0} \tag{4}$$

t_w: thickness of a wall panel;
l_w: distance between centers of boundary columns;
σ_0: axial stress per unit area;
σ_T: concrete tensile strength ($0.33\sqrt{\sigma_B}$ can be used.);
σ_B: concrete compressive strength;
b: width of columns;
D: depth of columns;
l'_w: clear span of a wall panel.

This strength is decided by assuming the maximum principal stress in concrete reach the tensile strength of concrete as shown in Figure 5. An object of this formula is a shear wall having larger width of column than wall thickness. In this paper, the confined masonry walls have the same column width as wall thickness. The following equation can be given from Eq. (1) by assuming conditions that concrete strength is replaced by mortar strength, and b is equal to t_w.

$$V_{cr} = \frac{2}{3}t_w(l'_w + \sum D)\tau_{cr} \tag{5}$$

$$\tau_{cr} = \sqrt{\sigma_{mT}^2 + \sigma_{mT}\sigma_0} \tag{6}$$

t_w: thickness of wall;
D: depth of columns;
l'_w: clear span of a wall panel;
σ_o: axial stress per unit area
σ_{mT}: mortar tensile strength ($0.33\sqrt{f_{mor}}$ can be used.)
f_{mor}: mortar compressive strength

As shown in Eq.(5), this model is given by assuming parabola shear stress distribution shown in Figure 5.

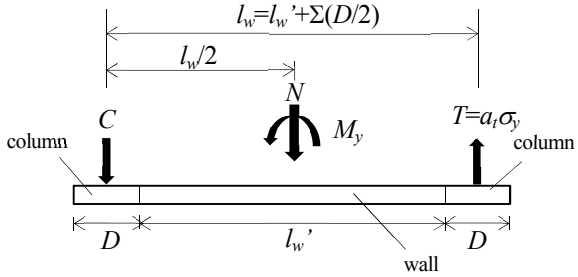


Figure 6 Section of Bottom End

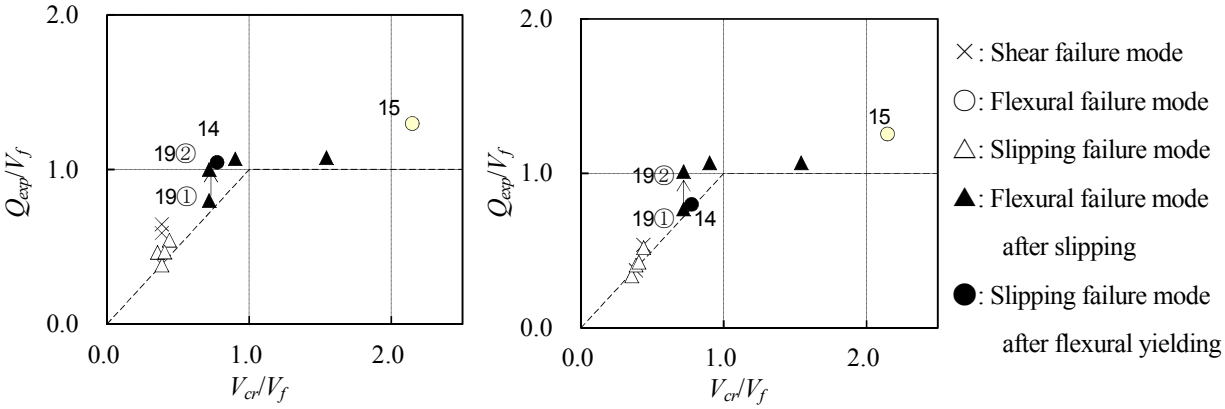


Figure 7 Comparison between Test Results and Calculations of Strength of Confined Masonry Wall Specimens

3.3 Flexural Strength

The flexural strength of confined masonry wall is based on a flexural strength of R/C shear wall (Architectural Institute of Japan 1990), as follows.

$$M_y = l_w(a_t\sigma_y + 0.5N) \quad (7)$$

$$V_f = M_y/L \quad (8)$$

a_t: gross sectional area of longitudinal bars in tensile column;
σ_y: yield strength of reinforcing bars;
D: depth of columns;
l_w: distance between centers of boundary columns;
N: axial force;
L: shear span of a wall.

Above equation is assumed a stress distribution at a bottom end of the wall as shown in Figure 6. This formula has no effects of vertical reinforcements in wall because the specimens have no reinforcements in wall. The effects of reinforcements in wall must be examined separately.

3.4 Comparison between Test Results and Calculation

Figure 7 shows comparison between test results and calculation of strength. A left figure shows comparison of positive side of loading, and a right one is negative side. Q_{exp} expresses the maximum shear load in the test, only the first peak of shear load of CMW-19 is also drown together. V_{cr} and V_f are calculations of cracking strength and flexural strength, respectively. The V_{cr} is calculated with a condition σ_o=0 by assuming columns support all the axial force. A vertial axis is Q_{exp}/V_f, and a horizontal axis is V_{cr}/V_f. In this graph, a point is plotted near to Q_{exp}/V_f=1 or Q_{exp}/V_f=V_{cr}/V_f if the test result is close to the flexural strength or the cracking strength, respectively.

As shown in Figure 7, the calculations of strengths show good agreement with the maximum shear force and the failure mode of test results. A tendency can be seen that the specimen fail in shear or slipping when V_{cr}/V_f is less than 1.0, and fail in flexure when V_{cr}/V_f is greater than 1.0.

The specimen CMW-14, as shown in Figure 4, yielded in flexure under positive side loading, and the maximum load under negative side loading was lower than that of positive side. The CMW-14 was classified into slipping failure mode after flexural yielding. As shown in Figure 7, the maximum loads under positive and negative side loadings of CMW-14 almost agreed with V_f and V_{cr}, respectively. The maximum load of CMW-15 was greater than V_f, because, according to strain gages, work hardening of longitudinal bars in tensile column was observed. CMW-19 showed two peaks of load as shown in Figure 4, which was classified into the flexural failure mode after slipping. The first and second peaks of load of the CMW-19 agreed with V_{cr} and V_f, respectively.

As results of the comparison, the strength of specimens can be roughly evaluated by V_{cr} and V_f, and the failure mode is distinguishable by comparing V_{cr} and V_f,. However, some problems remain in this method. In this paper, the following problems are aimed; V_{cr} doesn't evaluate two types of cracking those are crack in joint mortar and crack through brick and mortar; brick strength isn't included in this method; a cracking criterion of masonry wall that is composite material wall doesn't solved. In order to examine these problems, two kinds of shear-loading tests were conducted.

4. SHEAR-LOADING TESTS OF PRISMS AND BRICKS

4.1 Objectives of Shear-loading Tests

Two types of cracking are aimed those are crack in joint mortar and crack through brick and mortar. In order to examine cracking criteria of masonry wall, material properties of brick and mortar are needed at least. In this study, two kinds of shear-loading tests were conducted. One is shear-loading test of prism specimen consisted with brick and mortar whose object is to be occurred the two types of cracking. The other is shear-loading test of brick. The test is conducted to obtain strength when the brick cracks. Tensile strength of mortar can be obtained by a splitting test of cylinder, and compression tests of mortar cylinder and brick give those compressive strengths.

Table 2 List of Prism Specimens and Test Resuls

Phase	f_{br}' [N/mm^2] X dir.	f_{br}' [N/mm^2] Z dir.	f_{mor}' [N/mm^2]	Name of specimens	No.	Sectional area [mm^2]	P_V [kN]	P_H [kN]	crack in middle part	τ_{exp} [N/mm^2]	σ_{exp} [N/mm^2]	σ_{1exp} [N/mm^2]
I	20.1	13.9	12.5	EM10-I	1	2.05 x 10^4	59.7	N/A	brick & joint	2.91	N/A	N/A
					2	2.05 x 10^4	51.5	64.3	joint	2.51	2.76	1.49
					3	2.08 x 10^4	54.8	70.0	brick & joint	2.64	3.37	1.46
			31.2	EM30-I	1	2.05 x 10^4	58.6	N/A	brick	2.86	N/A	N/A
					2	2.06 x 10^4	62.1	79.0	brick	3.01	3.83	1.67
					3	2.05 x 10^4	57.5	64.3	brick & joint	2.80	3.13	1.65
II	15.2	12.7	8.8	EM10-II	1	2.08 x 10^4	56.1	70.8	brick	2.70	3.41	1.49
					2	2.08 x 10^4	55.7	67.0	brick & joint	2.67	3.22	1.51
					3	2.10 x 10^4	54.9	64.5	brick	2.62	3.08	1.50
			26.0	EM30-II	1	2.08 x 10^4	54.9	63.2	brick & joint	2.64	3.04	1.53
					2	2.08 x 10^4	61.2	66.1	brick	2.94	3.18	1.73
					3	2.10 x 10^4	54.9	N/A	brick	2.62	N/A	N/A

f_{br}': brick compressive strength, f_{mor}': compressive strength of mortar cylinder.

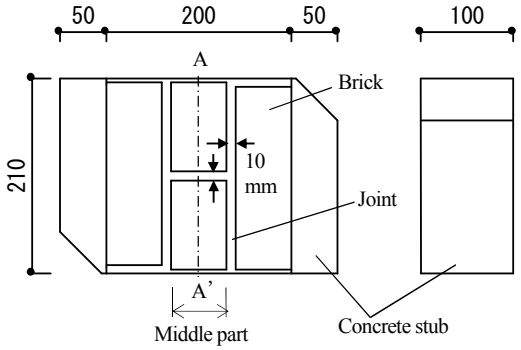


Figure 8 Detail of Prism Specimen

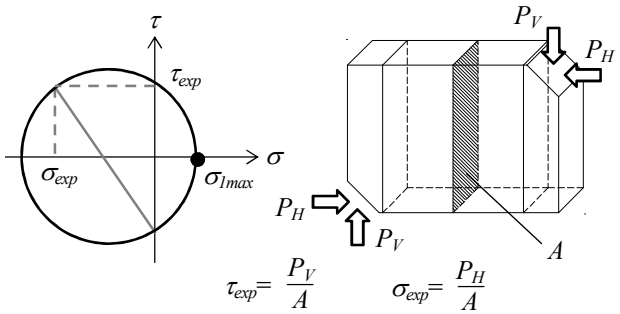


Figure 10 Stress in Prism Specimen

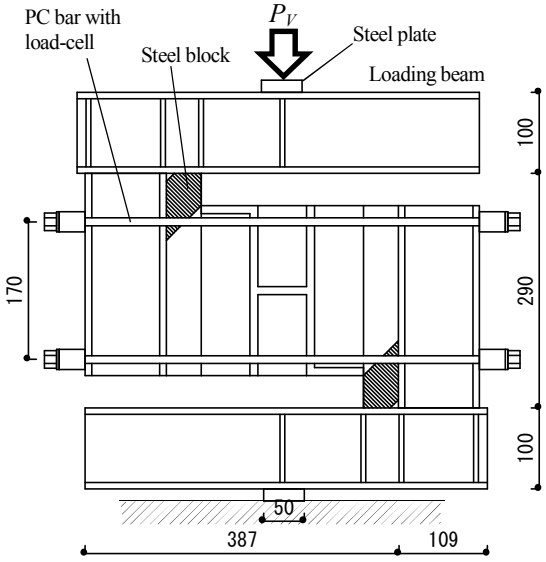


Figure 9 Loading Setup of Prism Specimen



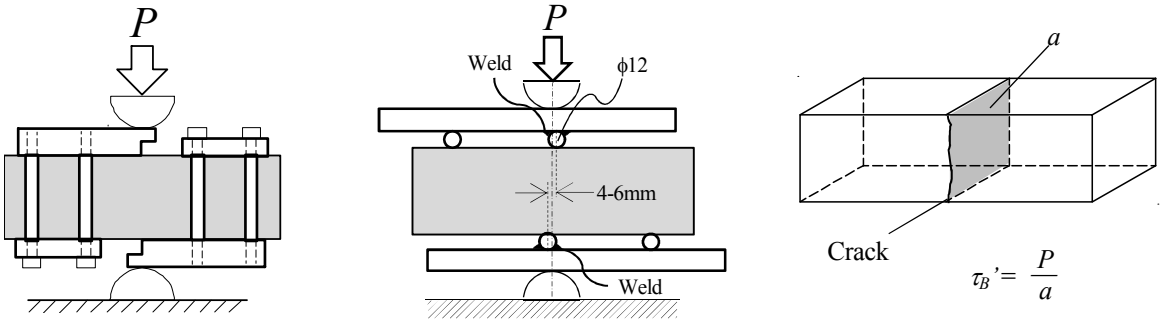
EM10-I EM30-I

Figure 11 Photo after the Tests

4.2 Prism Specimens and Test Results

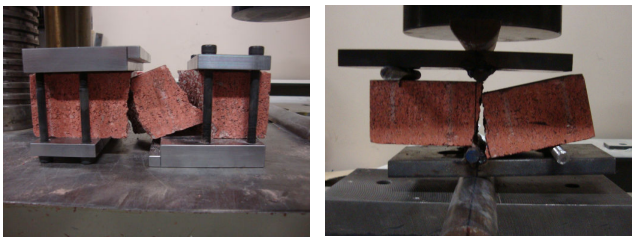
Figure 8 shows the prism specimen that is consisted with three pieces of brick, joint mortar, and stub concrete. The specimen had breaking joint, and was constructed as the joint is placed at center of the prism. Table 2 shows list of the specimens and those material properties. A parameter of this test is mortar strength, which target strengths are 10 and 30 N/mm^2. Two production lots of bricks were used in this test. The shear-loading tests in which the first and second lots of bricks were used, were called phase I and II, respectively, as shown in Table 2. Strength of the stub concrete is about 40 N/mm^2. Three specimens were prepared per four combination of mortar and brick strengths, and totally twelve prism specimens were tested.

Figure 9 shows loading setup. The prism specimen was fixed on loading beam with four PC bars. The specimen was subjected to shear, bending, and axial force by vertical load and tension in the PC bars. The PC bars have load cells, and were adjusted as tension in the bars was equal to zero before loading. Shear force and axial force transmit from the loading beams to steel blocks, concrete stubs, and masonry part. Bending moment is equal to zero at section A-A' shown



Type A Type B Stress in Brick

Figure 12 Detail of Shear-Loading Test of Brick



Type A Type B

Figure 13 Photos after Shear-Loading Tests

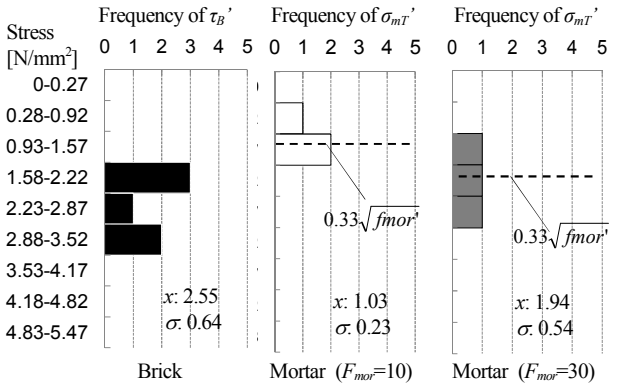
in Figure 8, and shear stress at the center is largest in the section A-A'. Therefore, target of this test is crack in middle part shown in Figure 8. As shown in Figure 10, normal stress and shearing stress on the section A-A' are assumed as values given by dividing axial force and shear force by sectional area at A-A', respectively. The axial force and shear force are equal to the total tension in PC bars and the vertical load, respectively. The normal stress and shearing stress when a crack occurs at middle part of prism, is named σ_{exp} and τ_{exp} in this paper.

Figure 10 also shows Mohr's stress circle with σ_{exp} and τ_{exp}. The maximum principal stress, σ_{1exp}, can be given from a test result. In Eq. (5), the strength is decided by assuming the maximum principal stress reach the tensile strength of mortar. In order to examine this assumption, σ_{1exp} is compared with mortar tensile strength and brick strength associated with crack.

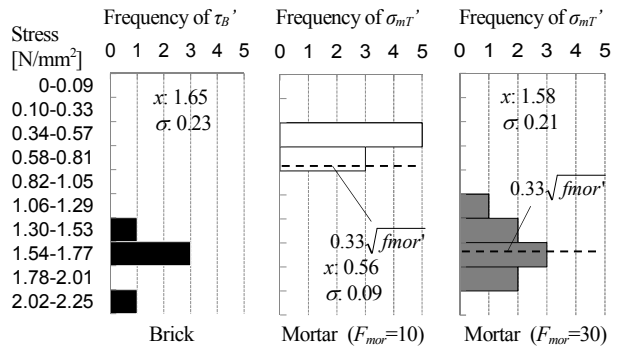
Figure 11 shows photos after the tests. All the specimens failed immediately after cracking. Therefore it can be considered that the maximum load was equal to load of cracking. As shown in Figure 11, at the middle parts of the specimens, crack was in joint mortar of EM10-I, and went through brick and joint of EM30-I. The results could be obtained that different strength of joint mortar caused different cracks in the masonry prisms. Table 2 also shows test results. In a column of "crack at middle part" in this table, "joint" and "brick and joint" means that a crack passed through almost on the center, and "brick" means that a crack was a little distant from the center. σ_{1exp} is the maximum principle stress mentioned above.

4.3 Shear-Loading Test of Brick and Test Results

As shown in Figure 12, two types of shear-loading



Phase I (EM10: $_{mean}\sigma_{1exp}$=1.47, EM30: $_{mean}\sigma_{1exp}$ =1.66)



Phase II (EM10: $_{mean}\sigma_{1exp}$=1.50, EM30: $_{mean}\sigma_{1exp}$ =1.63)

Figure 14 Strengths of Brick and Mortar

system of brick were tried. The both types were aimed that bricks failed with single crack plane at the center. The Ohno system of anti-symmetric bending, which was published in 1956 in Japan, was applied to the type B. Figure 13 shows test results of the both types. The type A wasn't good system because the brick failed with two cracks. It was supposed that bending caused the crack distant from the center. Regarding the type B, the brick failed with single crack plane. Therefore, the type B was adopted in this study. τ_B' is a value given by dividing the maximum load by sectional area of a brick as shown in Figure 12.

4.4 Considerations

Figure 14 is histograms of the test results, whose vertical axis is strength and horizontal axis is frequency.

Table 3 τ_B' and σ_{mT} of CMW speimens

Failure mode	Specimens	V_{cr}/V_f	Stress[N/mm^2] 0 1 2 3 4 5 6
Shear failure mode	CMW-01	0.39	○ ▲
	CMW-13	0.44	○ ▲
Flexural failure mode	CMW-15	2.15	○ ▲
Slipping failure mode	CMW-04	0.44	○ ▲
	CMW-08	0.36	○ ▲
	CMW-17	0.39	○ ▲
	CMW-18	0.41	○ ▲
Flexural failure mode affter slipping	CMW-11	1.54	○
	CMW-19	0.72	○ ▲
	CMW-20	0.90	○ ▲
Slipping failure mode after flexural yielding	CMW-14	0.77	○ ▲

○: $0.33\sqrt{fmor'}$ ▲: τ_B'

Interval of the vertical axis is equal to a standard deviation of τ_B' that is the test result of shear-loading test of brick, and mean of τ_B' is at the center of interval. Results of splitting test of mortar cylinder, σ_{mT}', are shown together. The mortar cylinders for splitting test had 100mm in diameter and 200mm in height. A broken line is $0.33\sqrt{f'_{mor}}$, which is adopted in Eq. (5) as mortar tensile strength. In Figure 14, x is a mean value, and σ is a standard deviation of each data. $_{mean}\sigma_{1exp}$ is the mean of σ_{1exp} shown in Table 2, which is the results of shear-loading tests of prism specimens.

As shown in Figure14, because τ_B and σ_{mT}' have wide variation in those results, it is difficult to conclude a cracking criterion of masonry wall in this paper. However, the following tendencies can be seen: σ_{1exp} is obtained between τ_B' and σ_{mT}'; σ_{1exp} of the specimen cracked in joint is close to σ_{mT}'; σ_{1exp} of the specimen cracked through brick and joint is close to τ_B'. In this study, two types of cracking couldn't be distinguished by comparing between τ_B' and σ_{mT}'.

4.5 Shear-Loading Test of Brick used in Confined Masonry Wall Specimens

Shear-loading tests were conducted with bricks those were used in the confined masonry wall specimens shown in Table 1. Table 3 shows comparison between τ_B' and σ_{mT}. The τ_B' is an average of shear-loading test results of bricks, and the σ_{mT} is equal to $0.33\sqrt{f_{mor}'}$, which was calculated with mortar compressive strength f_{mor}'. As shown in Figure 7, Eq. (5) showed good agreement with the test results, though brick strength wasn't used in Eq. (5). As shown in Table 3, τ_B' are close to mortar tensile strength in the specimens of shear failure mode and slipping failure mode. Therefore, in spite of no brick strength in Eq. (5), it is supposed that the cracking strength gave good agreement with the test results of loading test of the confined masonry wall specimens. Regarding the failure mode of the confined masonry wall specimens, in spite of difference between τ_B' and σ_{mT}, the specimens can be classified into flexural failure mode if V_{cr}/V_f is larger than 1.0.

5. CONCLUSIONS

In this paper, failure modes of eleven confined masonry wall specimens were classified into three failure modes and two transition modes those were shear failure, slipping failure, flexural failure, and those combination. And strengths of the specimens could be roughly estimated by calculations of flexural strength and cracking strength. Two kinds of shear-loading tests with a prism specimen and a brick were conducted in order to verify the cracking strength. In the shear-loading test of brick, strength τ_B' could be obtained when the brick failed with single crack plane. As results of the shear-loading tests of prism specimens, the maximum principal stresses in the specimens with crack in joint mortar and crack through brick and mortar, are close to mortar tensile strength and τ_B', respectively. And as results of the shear-loading tests of bricks those were used in the confined masonry wall specimens, τ_B' are close to mortar tensile strength on the specimens of shear failure mode and slipping failure mode. Therefore, in spite of no brick strength in the cracking strength formula, the cracking strength gave good agreement with the test results of loading test of the confined masonry wall specimens.

References:

Architectural Institute of Japan. (1999), "Design Guidelines for Earthquake Resistant Reinforced Concrete Buildings Based on Inelastic Displacement Concept", AIJ, (in Japanese).

Architectural Institute of Japan. (1990), "Ultimate Strength and Deformation Capacity of Buildings in Seismic Design", AIJ, (in Japanese).

Hayashi, T., Hoken, M., Kitano, A., Kobayashi, H., Goto, Y., and Joh, O., (2009), "Experimental Study on Influence of Brick Properties and Failure Type of RC Columns on Shear Resistance of Confined Masonry Walls: Part 1 and Part 2," *Summaries of Technical Papers of Annual Meeting*, AIJ, **IV**, 901-904, (in Japanese).

Murai, S., Houken, M., Kitano, A., and Goto, Y., (2011), "Experimental Study on Evaluation for Seismic Performance of Confined Masonry Walls Considering Column Behavior: Part 1 and Part 2," *Summaries of Technical Papers of Annual Meeting*, AIJ, **IV**, 919-922, (in Japanese).

Sakaitani, K., Toge, T., Inbe, T., Goto, Y., Kitano, A., and Joh, O., (2008), "Experimental Study on Shear Resistance of Confined Masonry Walls: Part 1 and Part 2," *Summaries of Technical Papers of Annual Meeting*, AIJ, **IV**, 977-980, (in Japanese).

Sugai, M., Inbe, T., Miyauchi, J., Goto, Y., Kitano, A., and Joh, O., (2010), "Experimental Study on Influence of Joint Strength between Brick and Column Failure Type on Seismic Performance of Confined Masonry Walls: Part 1 and Part 2," *Summaries of Technical Papers of Annual Meeting*, AIJ, **IV**, 909-912, (in Japanese).

Tanabe, S., , M., Kitano, A., and Goto, Y., (2012), "Experimental Study on Strength and Failure of Confined Masonry Walls – Influence of Wall and Column Strength–," *Proceedings of AIJ Hokkaido Architectural Research Conference*, AIJ Hokkaido Chapter, **85**, 59-62, (in Japanese).

Toge, T., Kaneko, M., Hayasaki, N., Goto, Y., Kitano, A., and Joh, O., (2006), "Experiments on Shear Resistance of Confined Masonry Walls with Variation in Opening Shapes of Shear-Span Ratio: Part 1 and Part 2," *Summaries of Technical Papers of Annual Meeting*, AIJ, **IV**, 791-794, (in Japanese).

10CUEE CONFERENCE PROCEEDINGS
10th International Conference on Urban Earthquake Engineering
March 1-2, 2013, Tokyo Institute of Technology, Tokyo, Japan

CALCULATION OF LOAD-CAPACITY OF RC BEAMS BY LATTICE MODEL ARRANGED BY EXPERIMENT RESULTS

Yuki Nakata[1)], Ken Watanabe [2)], Tadatomo Watanabe [3)], and Junichi Abe [4)]

1) Researcher, Concrete Structures, Railway Technical Research Institute, Japan
2) Assistant Senior Researcher, Concrete Structures, Railway Technical Research Institute, Japan
3) Vice President, Hokubu Consultant Co., Ltd., Japan
4) Engineer, Engineering Department, Hokubu Consultant Co., Ltd., Japan
nakata@rtri.or.jp, wataken@rtri.or.jp, chuho@hokubu-c.co.jp, j-abe@hokubu-c.co.jp

Abstract: The lattice model is the method which can easily demonstrate the load-displacement relationship of reinforced concrete (RC) beams. This model functioned by both the arch action and the truss action can calculate the load-capacity, and indicates the bearing mechanism of loads. The existing discretized method of lattice model shows the non-linearity by changes in both areas of arch and compressive truss elements. However, this method cannot decide the areas of these elements for beams with small shear-span effective ratio. In this research, we consolidated the development of damages caused by many factors to the areas of all elements, and proposed all process as a method for the calculation of load-capacity of RC beams by lattice model arranged by experiment results.

1. INTRODUCTION

The design code in the field of civil engineering (JSCE 2007) describes some calculation equation such as: the design shear capacity (V_{yd}), the shear compression capacity (V_{dd}), the web compression capacity (V_{wcd}). The failure mode of the RC beams was classified as above three types; and equations was described according to the assumption of the load bearing mechanism. According to the verification system, these calculation equation need to calculate the shear capacity of beam with small differences among V_{yd}, V_{dd}, and V_{wcd}, because a failure phenomenon changes gradually according to its specification. However, each equation consists of contributions by concrete and by stirrups has been developed separately. This history made the differences among V_{yd}, V_{dd}, and V_{wcd} large. Figure 1 shows the calculation of V_{yd} and V_{dd} of RC beams with high dense stirrups as a function of a/d. There is not crossing point between curves of V_{yd} and V_{dd}. The gap between curves of V_{yd} and V_{dd} was caused by, such as the accuracy of the equations. In addition, the value of V_{yd} is corresponding to the yield of stirrups, on the other hands; the value of V_{dd} is corresponding to the maximum load. Therefore, with considering failure type, the calculation method which does not depend on failure type will solve the problem of the gap.

One of the methods for demonstrating the load-bearing capacity as well as load-displacement relationship is the lattice model. The lattice model can express the load-bearing mechanism easily and clearly. The previous study (Niwa et al. 1995) develops the lattice model for slender RC beams with changing the cross-section area and stress-strain relationship of each strut. The cross-section area was decided by calculating the minimum potential energy. According to the trial for the RC beam with smaller a/d by authors, however, the cross-section area was not decided by the method.

The objective of this study is to develop the discretization method for RC beam including the range of smaller a/d. By fixing the stress-strain relationship applied to each strut, the cross-section area of each strut was controlled according to the experimental results. Then, the contribution of each strut changing by specimen design was discussed.

2. CONTRIBUTION OF ARCH AND TRUSS MEMBERS BASED ON CROSS-SECTION AREA

2.1 Concept of Anlayses

Figure 2 describes the lattice model used in this study. The model discretizes RC beams as the flexural compression

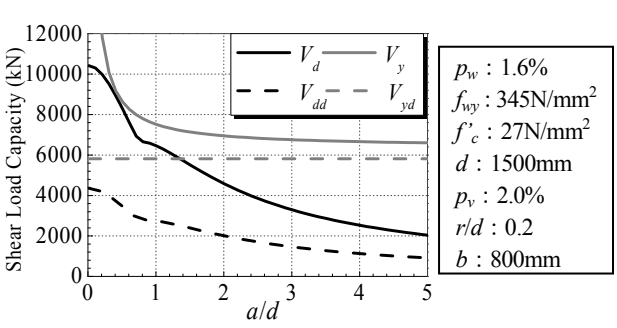


Figure 1 Continuity between V_{yd} and V_{dd} as a Function of a/d

member, flexural tension member, diagonal compression member, diagonal tension member, arch member, horizontal member for longitudinal rebar, and vertical member for stirrups. The previous study (Niwa et al. 1995) decreases the strength of concrete for compression member with considering to the lateral strain of concrete proposed by Collins. The propagation of damage by increment of loading was expressed by changing the stress-strain relationship. On the other hands, this study considered the propagation of damage by controlling the cross-section area of each strut according to the experimental results. This section focuses on t-value corresponding to the ratio of area between arch and truss members.

2.2 Analytical Method

This paper referred RC beam having a/d=0.5, 2.0 (Tanimura et al. 2004). This paper discretized these specimens as Figures 2, 3. The stress-strain relationship is used as follows: bilinear-type for rebars, parabola involving compressive fracture energy for concrete in compression, one-forth model for concrete in tension, and Okamura-Maekawa model involving the effect of bond between rebar and concrete for flexural tension members.

2.3 Analytical Results

Figures 4 and 5 compare the load-displacement relationships of specimen No.31 and No.3 (Tanimura et al. 2004) as a function of t-value. Four t-value were used as 0.2, 0.4, 0.6, and 0.8. These figures indicate that maximum load was increased with the increase in t-value. The calculation result seems to be corresponding to the experimental value when t=0.8 at No.31, and t=0.4 at No.3. Table 1 tabulates the vertical component of load carried by each member at maximum load. The table indicates the same load generating the diagonal member in both model with different a/d, but the contribution by arch and stirrup member. Even so, the load started to be decreased when the arch member reached its peak. This result implies that the contribution of arch member increased with the decrease in a/d. On the other hands, the cross-section area of the arch needs some enough when a/d become larger, resulting in t=0.8 at a/d =2.0, and t=0.4 at a/d =0.5.

3. LATTICE MODEL DISCUSSED BY THE EXPERIMENTAL RESULTS

3.1 Analytical Concept

This section decides the cross-section area of each member according to the experimental results, and discusses the contribution of each member.

3.2 Analytical Method

The stress-strain relationship used in this section was corresponding to the chapter 2. The cross-section area of diagonal compressive member, diagonal tension member, and arch member was decided according to the experimental data (Tanimura et al. 2004), of which specimen has p_w of 0.21, 0.48, 0.84%, and a/d of 1.5. Table 2 summarizes the

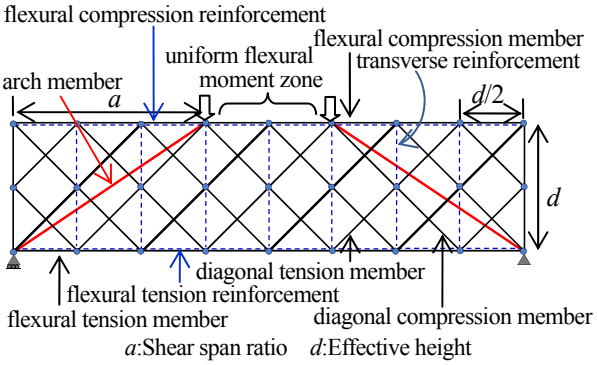


Figure 2 Concept of Lattice Model (a/d=1.5)

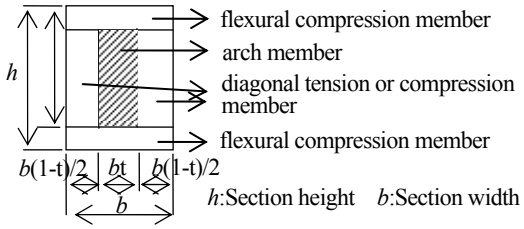


Figure 3 Section of Lattice Model

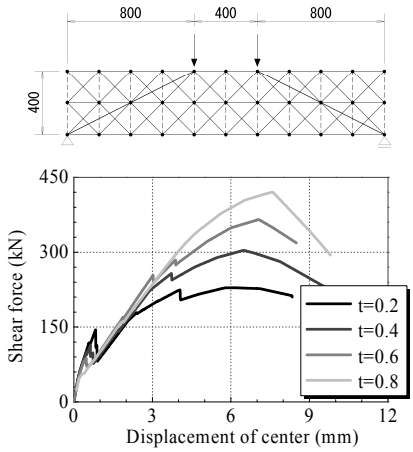


Figure 4 Analytical Model and Results (No.31)

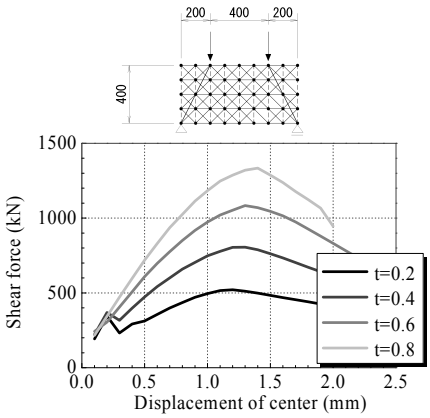


Figure 5 Analytical Model and Results (No.3)

Table 1 Contribution Ratio of Shear Force

member	No.31	No.3
diagonal compression member	49.98	41.03
diagonal tension member	0.08	7.67
arch member	18.18	28.19
transverse reninforcement	32.76	21.15

method for setting the cross-section area of each member, and Table 3 compares the experimental value referred for this study and analysis data. The stiffness of the shear force-displacement curve decreased after a diagonal crack was observed. The cross-section area of the diagonal tensile member was adjusted to obtain the first bending point of load-displacement curves obtained by the specimen and the lattice model.

The stiffness as well as cross-section area of the diagonal compression member will affect the load carried by stirrups. The cross-section area of the diagonal compression member was decided by fitting the load carried by stirrups in the specimen with that in the lattice model. This means the average stress $\sigma_{s.ave}$ of all stirrups in the shear span was identical. Figure 6 shows the relationship between the average stress by stirrups and shear force. Even some of the stirrups were yielded, $\sigma_{s.ave}$ become smaller with the increase in p_w (Table 2).

Finally, the cross-section area of the arch member was decided when the maximum load of the specimen and the lattice model were identical. The height of flexural compression member was fixed as 200 mm, and the cross-section area of the other member was decided as the previous study (Niwa et al. 1995).

3.3 Analytical Results

Figures 7 show the shear force-displacement relationship. According to 3.2, the lattice model can demonstrate the load-displacement curve as well as the load bearing capacity.

Figure 8 the cross-section area of arch, compression, and tension members as a function of p_w. The cross-section areas of arch and compression members were increased with the increase in p_w. The previous study (Tanimura et al. 2004) reported that the localized compressive failure zone was increased by the lateral force, which was also affected by the arrangement of stirrups. This is one of the reasons the increment of cross-section area of arch member. On the other hands, there was no tendency in the diagonal tension member by p_w because the member was set as expressing the diagonal cracking.

Figure 9 shows the hysteresis of force carried by each member in No.12, which was calculated at the cross-section identified by dash-line in Figure 1. The diagonal tension member did not carry when the displacement reached 2 mm. The summation of load carried by the arch and the diagonal

Table 2 Determination of Areas of Each Member

members	arch member*	diagonal compression member*	diagonal tension member*
areas	the maximum value of shear force in experiments	the average stress of transvers reinforcement with shear span	shear force of stffness change point by diagonal crack occur in experiment
members	flexulal compression reinforcement	flexulal tension member	transverse reninforcement
areas	200mm	c×2	$A_{w.a}=A_{w.e}\times S_{.a}/S_{.e}$
members	flexulal tension	flexulal compression	
areas	the same areas to experiments		

c : cover, A_w : area of transverse reinforcement, S : interval of transverse reinforcement (Index .a and .e mean analyses and experiment in A_w and S, respectively)

*Experiments to match for determination of areas

Table 3 Results of Experiments and Analyses

specimens (2004)	p_w	Experiments			Analyses		
		V_{crack}	V_{max}	$\sigma_{s.ave}$	V_{crack}	V_{max}	$\sigma_{s.ave}$
	%	kN		N/mm^2	kN		N/mm^2
No.10	0.21	160	464	304	161	461	328
No.11	0.48	160	491	249	158	494	256
No.12	0.84	160	570	189	162	565	183

p_w : shear reinforcement ratio (%), V_{crack} : shear force of stiffness change point by diagonal crack occur, V_{max} : maximum value of shear force, $\sigma_{s.ave}$: the average stress of transvers reinforcement with shear span

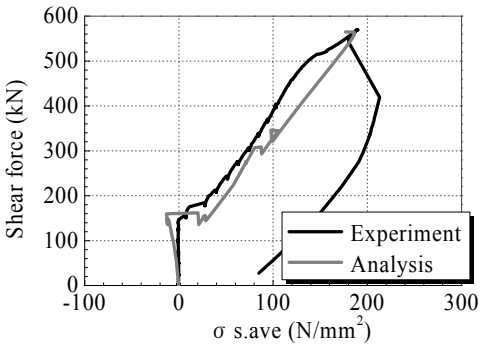
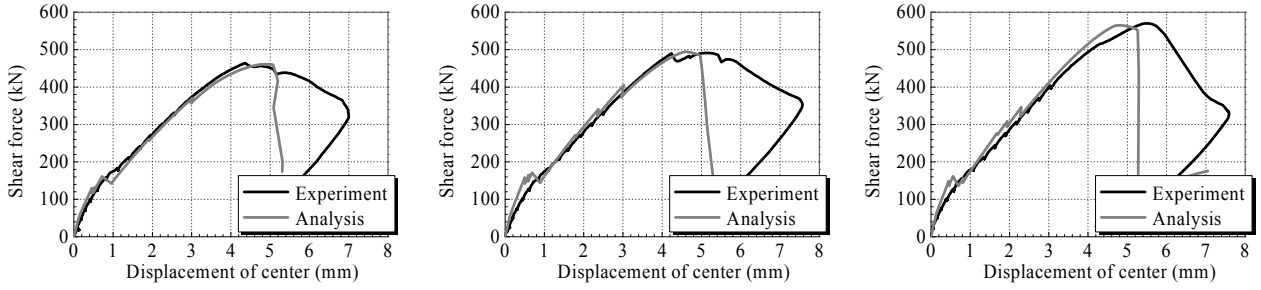


Figure 6 Average Stress of Transverse Reinforcement (No.12)



(a) No.10 (b) No.11 (c) No.12

Figure 7 Shear Force – Displacement of Center Relationships

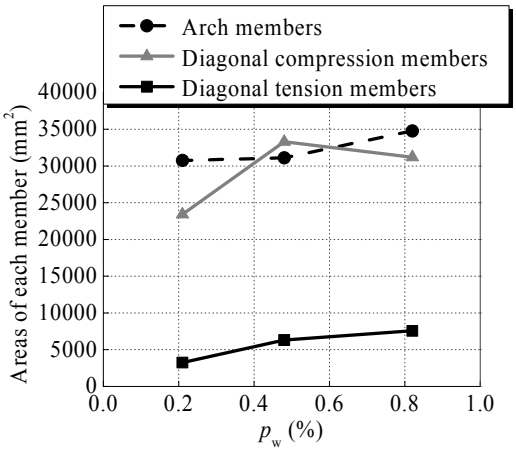


Figure 8 Distributions of the Areas of Each Member

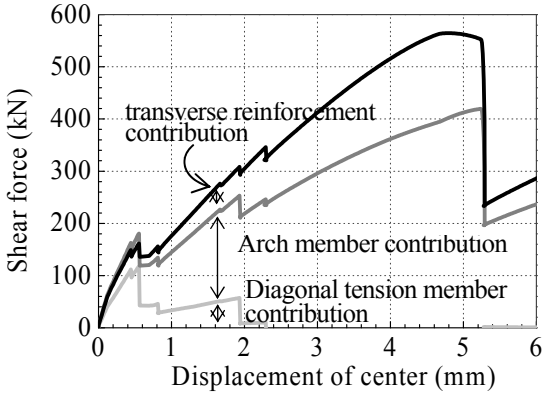


Figure 9 Contributions of Shear Forces of Each Eember and Transverse Reinforcement (No.12)

tension members was corresponding to the shear carried by concrete (V_c) in slender RC beams (JSCE 2007). On the other hands, the summation of both in this study, of which a/d being smaller, was increased with the increase in the displacement.

4. CONCLUSIONS

This study developed the lattice model, which demonstrated the load carrying mechanism by changing the cross-section area of each member. In the range of this study, the cross-section member of arch, diagonal tension members were increased with the increased in p_w. The developed model demonstrated the load-displacement relationship in pre-peak region.

References:

Japan Society of Civil Engineers (JSCE) (2007), "Standard Specifications for Concrete Structures (Design),"Maruzen.

Junichiro, N., Choi, I.C. and Tada-aki, T., (1995), "Analytical study on the shear resisting mechanism of reinforced concrete beams, " Journal of Japan society of Civil Engineering, Concrete Structures and Pavements, JSCE, 508, 79-88. (in Japanese)

Yukihiro, T., Tsutomu, S., Tadatomo, W., and Shigeru, M., (2004), "Shear strength of deep beams with stirrups, " Journal of Japan society of Civil Engineering, Concrete Structures and Pavements, JSCE, 760, 29-44. (in Japanese)

10CUEE CONFERENCE PROCEEDINGS
10th International Conference on Urban Earthquake Engineering
March 1-2, 2013, Tokyo Institute of Technology, Tokyo, Japan

THREE-DIMENSIONAL NONLINEAR BEAM-TRUSS MODEL FOR NON-PLANAR REINFORCED CONCRETE WALLS

Yuan Lu[1] and Marios Panagiotou[2]

1) Graduate Student Researcher, Dept. of Civil and Environmental Engineering, University of California at Berkeley, Berkeley, CA, USA
2) Assistant Professor, Dept. of Civil and Environmental Engineering, University of California at Berkeley, Berkeley, CA, USA

Abstract: This paper presents a three-dimensional (3D) nonlinear cyclic model which uses a coarse grid of beam and truss elements in order to capture the behavior of non-planar reinforced concrete walls including shear-flexure interaction and diagonal crushing failure. 3D nonlinear Euler-Bernoulli fiber-section frame elements are used to represent steel and concrete in the vertical direction, nonlinear trusses are used to represent the steel and concrete in the horizontal direction, and nonlinear biaxial trusses are used to represent the diagonal field of concrete in compression. The model represents the effects of shear- flexure interaction by accounting for strains in the horizontal direction and the biaxial effects, the effect of normal tension strain on the compressive strength of concrete, of the concrete diagonals. The model is validated by comparing the experimentally measured and numerically computed response of three reinforced concrete wall specimens which have T-, C-, and I-shape sections, respectively; the response of the latter two specimen are characterized by crushing of the concrete in the diagonal direction. The overall force-deformation and local strain responses are presented.

1. INTRODUCTION

Reinforced concrete (RC) walls are one of the most common elements used in structures to resist loads and develop deformations expected during earthquake excitation. The computation of their nonlinear cyclic response is of significant interest to both practicing engineers and researchers. This task is particularly challenging for non-planar RC walls, which are commonly used in medium- and high-rise construction, when subjected to uni-axial or multi-axial loading representative of earthquake excitation. The computation of the response of non-planar RC walls can be even more challenging when it is significantly affected by flexure shear interaction (FSI). Here, FSI is described as the combination and coupling of axial, flexural, and shear load on structural elements, resulting in a multi-axial stress-strain state and coupling of nonlinearities that affect the behavior of concrete in compression. The FSI may significantly affect the cyclic behavior of RC non-planar walls in terms of strength, stiffness, deformation capacity, softening response, and strains developed in steel and concrete.

Nonlinear modeling approaches for non-planar RC walls may be divided into five main categories: (i) fiber-section beam-column element (termed beam elements in this paper) models; (ii) wide column models known also as equivalent frame models; (iii) truss or lattice models; (iv) models with beams and trusses; and (v) finite element (FE) models using either plane stress or solid elements.

Fiber-section beam models (sometimes called "stick" models) typically use a linear shear force – deformation and torsional moment – twist angle relationship (Mazars et al. 2006, Orakcal and Wallace 2006), and have been altered to consider the inelastic behavior of the transverse steel reinforcement and represent FSI using equilibrium, specific assumptions for the shear strain field, and bi-axial concrete material laws (Petrangeli 1999, Petrangeli et al. 1999, Martinelli 2008). However, these models use the plane-sections-remain-plane assumption of beam theory, which can significantly differ from the section response of non-planar walls in reality.

Beyer et al. (2008b) presented a nonlinear equivalent frame model using nonlinear Euler-Bernoulli (no shear deformation) fiber-section vertical beam elements and rigid horizontal beam elements connected with linear shear and torsional springs. This model did not account for the inelastic response of steel in the horizontal direction as well as for the bi-axial behavior of the concrete diagonals.

Three-dimensional truss models (also called lattice models) have been used to model hollow square RC columns (Miki and Niwa 2004) but have not been used to model any non-planar wall or hollow section member that experienced diagonal concrete crushing.

Barbosa (2011) presented a 3D model for planar RC walls consisting of Euler-Bernoulli fiber-section beams that represented the boundary elements of the walls, and nonlinear truss elements to model the concrete and steel in the horizontal direction and the inner regions of the walls in the vertical direction. Nonlinear concrete trusses were used in the diagonal direction and elastic beams were used in parallel with vertical elements for out-of-plane stiffness.

Nonlinear cyclic 3D FE models using plane stress elements or solid (block) elements that use smeared crack

and/or plasticity models have been developed and used to analyze the cyclic behavior of RC non-planar walls or RC components with hollow sections (Sittipunt and Wood, 1993; Ile and Reynouard, 2000; El-Tawil et al. 2002; Palermo and Vecchio 2002; Maekawa 2003; Hassan and El-Tawil 2003; Balkaya and Kalkan 2004; Ile and Reynouard 2005; Kotronis et. al. 2005). Three-dimensional FE models using only plane-stress elements do not model the out-of-plane flexural rigidity of segments comprising a non-planar wall. The complexity and computational effort required in nonlinear 3D FE modeling using solid elements increases significantly compared to 2D models.

This paper describes a nonlinear beam-truss modeling approach for non-planar RC walls subjected to cyclic uni-axial or multi-axial loading that requires moderate computational effort. The main objective of the proposed model is to compute the post-cracking 3D behavior of non-planar RC walls, considering FSI and mesh-size effects. The model, which uses a nonlinear truss element developed herein, applies a bi-axial material model for concrete in the diagonal direction, as well as existing nonlinear truss and Euler-Bernoulli fiber-section beam elements. The model accounts for the effect of normal tensile strain on the stress-strain relationship of concrete in compression [as reported by Vecchio and Collins (1986)], but also incorporates mesh-size effects as proposed by Panagiotou et al. (2012) for planar walls in 2D. Compared to the beam-truss model of Barbosa (2011), the model developed herein features different placement of beam and truss elements, and also accounts for the instantaneous bi-axial effects in the behavior of concrete in the diagonal direction in compression. Compared to the beam-truss model presented in the report by Lu and Panagiotou (2012), the model presented in this paper uses nonlinear truss elements in parallel to the horizontal linear beam elements in the horizontal directions.

To test the efficacy of the model, the experimentally measured and computed response of three case studies were considered: (i) a wall with a T-shape section subjected to uni-axial cyclic loading with significant contribution of the flange to the response; (ii) a U-shape section wall subjected to multi-axial cyclic loading, which failed by crushing of concrete in the diagonal direction; and (iii) an I-shape section wall subjected to uni-axial loading, which failed with diagonal crushing of the web. The global responses in terms of lateral force-lateral displacement as well as the more localized strain responses are presented.

2. BEAM-TRUSS MODELING APPROACH

Consider the T-section wall shown in Figure 1(a) where its length along the *X*- and *Y*-axis is L_X and L_Y, respectively. The thickness of the rectangular-section segments of the wall parallel to the *X*- and *Y*-axes is t_X and t_Y, respectively. The height of the wall is *H*. Figure 1(b) shows the model of this wall, which consists of four type of elements: (1) nonlinear fiber-section Euler-Bernoulli beam elements – called nonlinear beam elements herein – in the vertical direction (*Z*-axis); (2) nonlinear truss elements in the two horizontal directions (along *X*- and *Y*-axes); (3) linear Euler-Bernoulli beam elements – called herein linear beam elements – in parallel to the truss elements in the horizontal directions; and (4) nonlinear truss elements in the diagonals of the panels formed by the horizontal and vertical elements.

The points where at least one vertical and one horizontal element intersect with a diagonal truss comprise

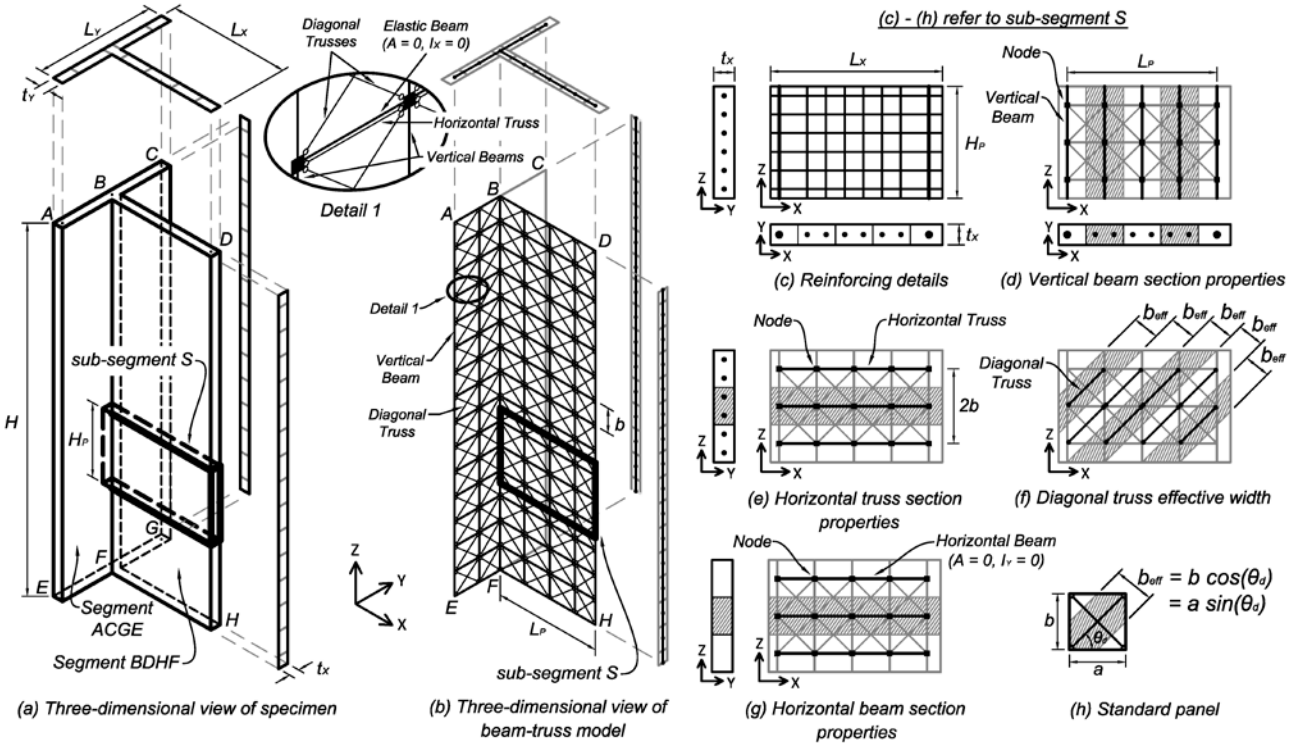


Figure 1. Schematic description of the beam-truss model approach for a T-shape section wall.

the nodes of the model, shown in Figure 1(d) and (e). Each node has six degrees of freedom (DOFs), with all DOFs fixed at the base. Nine lines of vertical beam elements were used (five in each of the two segments of the T-wall) and line BF was common for the two segments. Fifteen lines of horizontal trusses and linear beams were used along the height of the wall. As an example of the determination of section properties, considered sub-segment S of segment ACGE of the wall [see Figure 1(a)], the reinforcing details of which are shown in Figure 1(c). The vertical beam elements and horizontal truss elements model the concrete and steel included in the section areas each element represents. Figures 1(d) and (e) show the section properties (area of concrete, area and layout of steel) of each of the vertical beams and horizontal trusses, respectively. For the vertical nonlinear beam elements, a fiber-section with 24 fibers in a 6 × 4 grid is used to represent the concrete and a single fiber to represent each reinforcing steel bar. The linear beam elements in the horizontal directions [shown in Figure 1(g)] have flexural rigidity E_cI_Z (to model the out-of-plane stiffness of the segments of the wall), zero axial rigidity, and zero in-plane flexural rigidity. Gross section properties are used to calculate I_Z. Both the vertical nonlinear fiber-section beams and horizontal linear beams, have torsional rigidity GJ equal to 10% of the gross section torsional rigidity, GJ_g. E_c is the initial concrete modulus and $G = 0.38E_c$, the concrete shear modulus.

In addition to the vertical and horizontal elements, concrete truss elements were used for all diagonals to model the compressive field of concrete in the corresponding direction. The angle of the diagonals with respect to the horizontal elements is θ_d [see Figure 1(h)]. In this study, θ_d ranged between 40° and 50°, and the effect of the truss angle was investigated in Case Study 3 presented below. The area of each diagonal is the product of the effective width b_{eff} [see Figure 1(f)] and the thickness of the panel t_X. The effective width of the diagonal is $b_{eff} = a \sin(\theta_d)$, where a is the length of the panel [see Figure 1(h)].

3. MATERIAL CONSTITUTIVE STRESS-STRAIN RELATIONSHIPS

3.1 Concrete Model for Vertical and Horizontal Elements

The stress-strain relation of concrete used in the vertical beam and horizontal truss elements is shown in Figure 2, where f_c' is the peak compressive strength of unconfined concrete occurring at strain ε_o = 2%. The compressive stress-strain relation up to f_c' is based on the Fujii concrete model (Hoshikuma et al. 1997):

$$f(\varepsilon)=\begin{cases} E_c\varepsilon + 0.5\cdot\left(\dfrac{f_c' - E_c\varepsilon_o}{\varepsilon_o}\right)\cdot\varepsilon^2 & \varepsilon \le \varepsilon_o \\ \left(\dfrac{f_c' - f_{cc}}{(\varepsilon_o - \varepsilon_{co})^3}\right)\cdot(\varepsilon-\varepsilon_{co})^3 + f_{cc} & \varepsilon_o < \varepsilon \le \varepsilon_{co} \end{cases} \quad (1)$$

The initial concrete modulus was $E_c = 5000$ sqrt(f_c') (MPa). For unconfined concrete, after reaching f_c', the compressive stress decreased linearly to zero at strain ε_u. The value of ε_u accounted for mesh-size effects base on the notion of concrete fracture energy in compression (Bazant and Planas 1998), with $\varepsilon_u = (1 - \Lambda)\,\varepsilon_o + (L_R/L)(0.2\% + \Lambda\,\varepsilon_o)$ where L is the length of the truss element or the length corresponding to each integration point of the beam element (Coleman and Spacone 2001), L_R = 600 mm is the reference length considered in this study, and $\Lambda = f_c'/[0.5\,(E_c\varepsilon_o + f_c')]$, a factor that considers the effect of unloading on the concrete fracture energy in compression. For $L = L_R$, ε_u = 0.4%. See Bazant and Planas (1998), Coleman and Spacone (2001), Panagiotou et al. (2012), Lu and Panagiotou (2012) for additional discussion on how the degrading branches of material constitutive laws account for mesh-size effects in FE, fiber-section beam, truss models, and beam-truss models respectively.

For confined concrete, the peak compressive stress f_{cc} occurring at strain ε_{co}, and the strain ε_{cs} at which softening initiates was calculated based on Mander et al. (1988). The stress-strain relation of confined concrete is described in Equation 1and was the same as the unconfined during loading up to f_c'. The confined concrete stress remains constant and equal to f_{cc} for strains between ε_{co} and ε_{cs}. For strains larger than ε_{cs}, the stress softens linearly to zero at a strain ε_{cu}. Accounting for mesh size effects $\varepsilon_{cu} = (1 - \Lambda)\,\varepsilon_{cs} + (L_R/L)(0.2\% + \Lambda\,\varepsilon_{cs})$, where $\Lambda = f_{cc}/[0.5\,(E_c\varepsilon_{cs} + f_{cc})]$. For L_R = 600 mm, $\varepsilon_{cu} = \varepsilon_{cs} + 0.2\%$.

The concrete tension stress-strain relationship during loading is linear with tangent modulus E_c until it reaches the tensile strength of concrete $f_t = 0.33$ sqrt(f_c') in MPa. After this point, the concrete softens [see Stevens et al. (1991)]:

$$f = f_t \cdot [(1-M)e^{-\lambda_r(\varepsilon-\varepsilon_{cr})} + M] \quad (1)$$

where the parameter $M = C_t\rho_l / d_b$, λ_t = 540 / sqrt(M), and C_t = 75mm, ρ_l is the steel ratio in the direction parallel to the axis of the beam element, and d_b the diameter of the rebar of interest.

Upon unloading from a compressive strain, the tangent

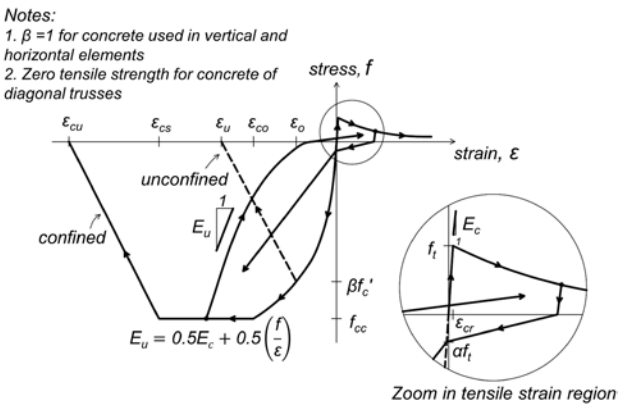


Figure 2. Stress-strain relationship of concrete material models

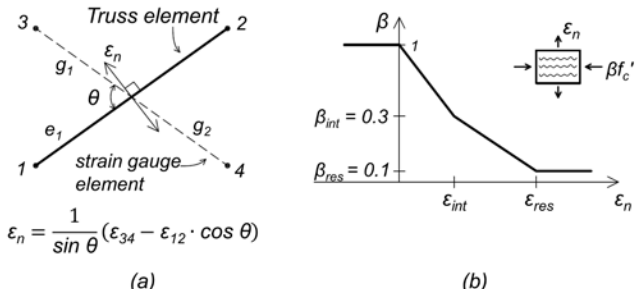


Figure 4. (a) Truss element accounting for biaxial effects in the compressive stress-strain behavior of concrete. (b) Relation between concrete compressive stress reduction factor, β, and normal strain, ε_n.

modulus is $E_u = 0.5\,E_c + 0.5(f/\varepsilon)$ until reaching zero stress, then reloads linearly to the point with the largest tensile strain that occurred before. The unloading from a tensile strain is linear with a tangent modulus E_c until reaching zero stress. After this, the material loads in compression and targets a stress equal to $\alpha \cdot f_t$ at zero strain with $\alpha = 0.5$. Thereafter, the material loads linearly to the point where the peak compressive strain occurs. In the case where the stress of this target point is less than $\alpha \cdot f_t$, the material reloads directly to the point where peak compressive strain occurred without passing through the point with stress $\alpha \cdot f_t$ at zero strain.

3.2 Concrete Model for Diagonal Truss Elements

The concrete material model used for the truss elements has two differences compared to that used for the vertical and horizontal elements: it has zero tensile strength and accounts for the bi-axial strain field on the concrete compressive behavior as described by Vecchio and Collins (1986). Thus, the compressive stress-strain behavior is dependent on the strain, ε_n, normal to the axis of the truss element. For truss element e_1 extending from node 1 to node 2 [shown in Figure 3(a)], ε_n is computed using the zero-stiffness gauge element extending from the mid-length of the element to nodes 3 and 4, g_1 and g_2, respectively. The instantaneous compressive stress of element e_1 is multiplied by the factor β determined from the instantaneous normal strain ε_n, which is the average of the strain measured with the gauge elements g_1 and g_2. The angle θ is the angle formed between the undeformed truss and the gauge elements; values of θ close to 90° are suggested. When $\varepsilon_n > 0$, the relationship between β and ε_n is tri-linear, as shown in Figure 3(b). otherwise $\beta = 1$. For this study, the relation between β and ε_n depends on the length of the gauge elements, as first proposed by Panagiotou et al. (2012). Here, $\varepsilon_{int} = (600 / L_g)\cdot 1\%$ and $\varepsilon_{res} = (600 / L_g)\cdot 2.5\%$, where L_g is the total length of gauge elements g_1 and g_2, as shown in Figure 3(a). In this paper, $\beta_{int} = 0.3$ is used, and the sensitivity of computed response to the value of β_{int} was investigated in Case Study 3 presented below. For the truss elements, the same equations described in the previous section are used to determine ε_u and ε_{cu}, with L being the length of the truss element (Panagiotou et al. 2012).

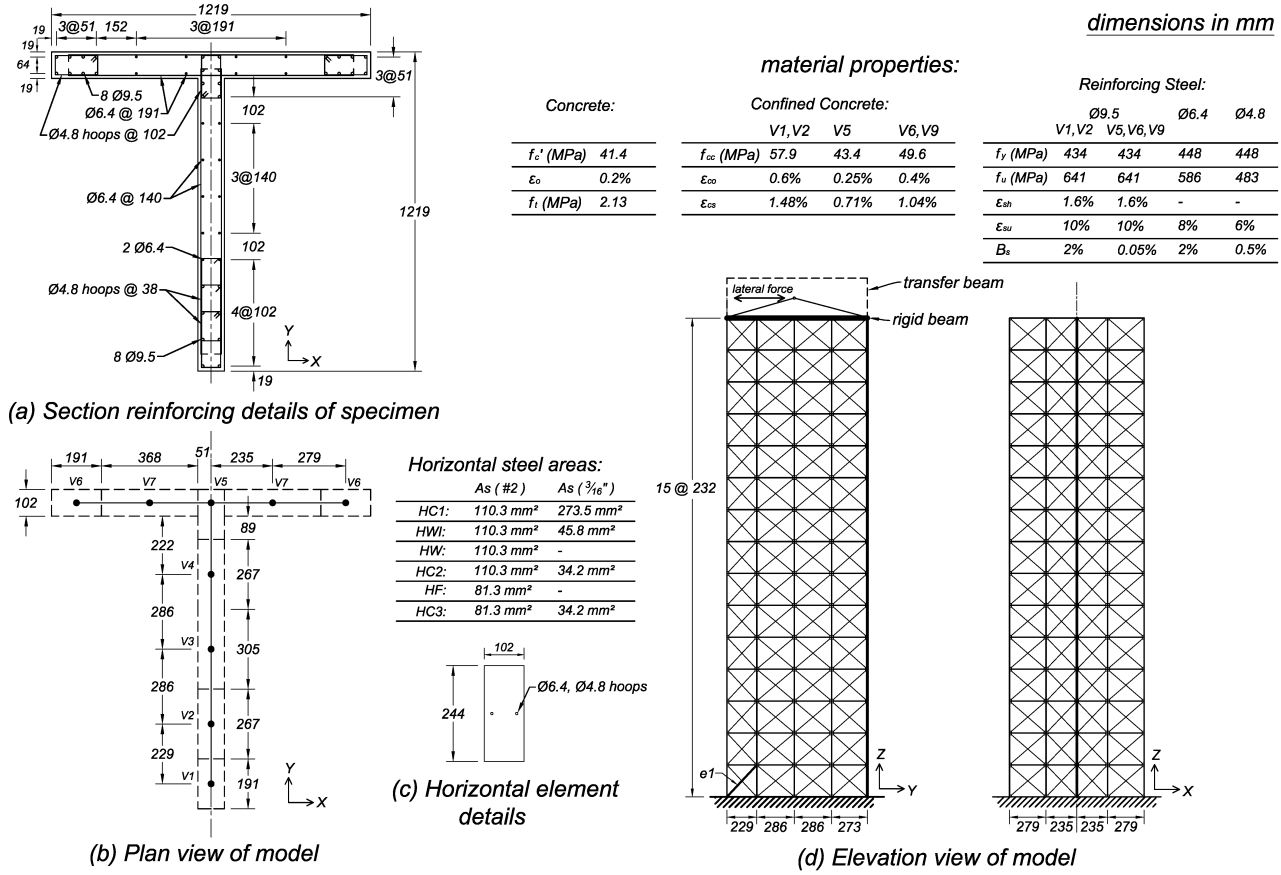


Figure 3. Case study 1 – TW2: Description of the specimen and TW2-9 beam-truss model.

3.3 Reinforcing Steel Model

The Giuffré-Menegotto-Pinto model (GMP) was used to model the reinforcing steel. The initial elastic modulus was E_c = 200 GPa, the yield strength was f_y, and the post-yield hardening ratio was B_s. Values of B_s used in the different bars of the three case studies are given in Figures 4, 8, and 9, respectively. These values were determined based on steel coupon monotonic tension test results reported in each case study. The values of B_s were calibrated for the regions of the walls where peak strains were computed so that the maximum computed stress at peak computed strain matched the stress at the same strain in the experimental coupon-test results. The parameters controlling the transition between the elastic to plastic branches (Filippou et al. 1983) were as follows: R_0 = 20, cR_1 = 0.925, and cR_2 = 0.15 with 5% isotropic strain hardening in compression only (a_1 = 5%). The effects of geometric nonlinearity (bar buckling) and bond slip between reinforcing steel and concrete as well as of strain penetration in the base anchorage blocks were not considered in this study.

4. MODEL VALIDATION

4.1 Case Study 1: Thomsen and Wallace (1995, 2004) – Specimen TW2

In this case study, a T-shape section RC wall - called TW2 - was considered (see Figure 4). The shear span ratio was M / VL_w = 3, where M is the bending moment at the base of the wall, V the base shear force, and L_w the length of the wall in the direction of loading. The length of both the web and the flange of this wall was 1219 mm. The axial load ratio of the wall was $N / f_c'A_g = 0.074$, where N is the vertical load applied at the centroid of the section and A_g is the gross T-shape section area. The vertical load remained constant during all cycles. The loads were applied through a steel beam that was placed at the top of the web in the direction of loading. The average longitudinal steel ratio ρ_l was 1.2% and the transverse steel ratio ρ_t in the web equal to 0.44%. Boundary elements were used at both ends of the web and the flange.

Figure 5(a) shows the experimentally measured lateral force versus lateral displacement response of TW2. Positive displacement is the direction in which the flange is in compression, and negative displacement is the direction in which the flange is in tension. The specimen was tested up to drift ratio Θ = 2.5%. The drift ratio is defined as Δ /H, where Δ is the lateral displacement, and H is the height where the lateral load is applied. The specimen experienced lateral strength degradation during the second and third cycles, at peak drift ratio Θ = 2.5% in the negative direction due to out-of-plane buckling of the confined core of the boundary region at the end of the web. Figure 6 shows the profile of experimentally measured (using strain gauges attached on the reinforcing steel bars 51 mm from the base of the wall) steel tensile strains along the flange for the negative direction of loading where the flange was in tension. The profiles were uniform for Θ = 1%, while larger strains were concentrated near the mid-length of the flange for Θ = 2% and 2.5%.

Two beam-truss models (BTM) were developed for this case study. The first BTM, shown in Figure 4, was termed TW2-9. As shown in Figure 4(b), the BTM TW2-9 had nine nodes at its base with θ_g ranging from 40° to 47°. Details for the concrete and steel section areas in the vertical, horizontal,

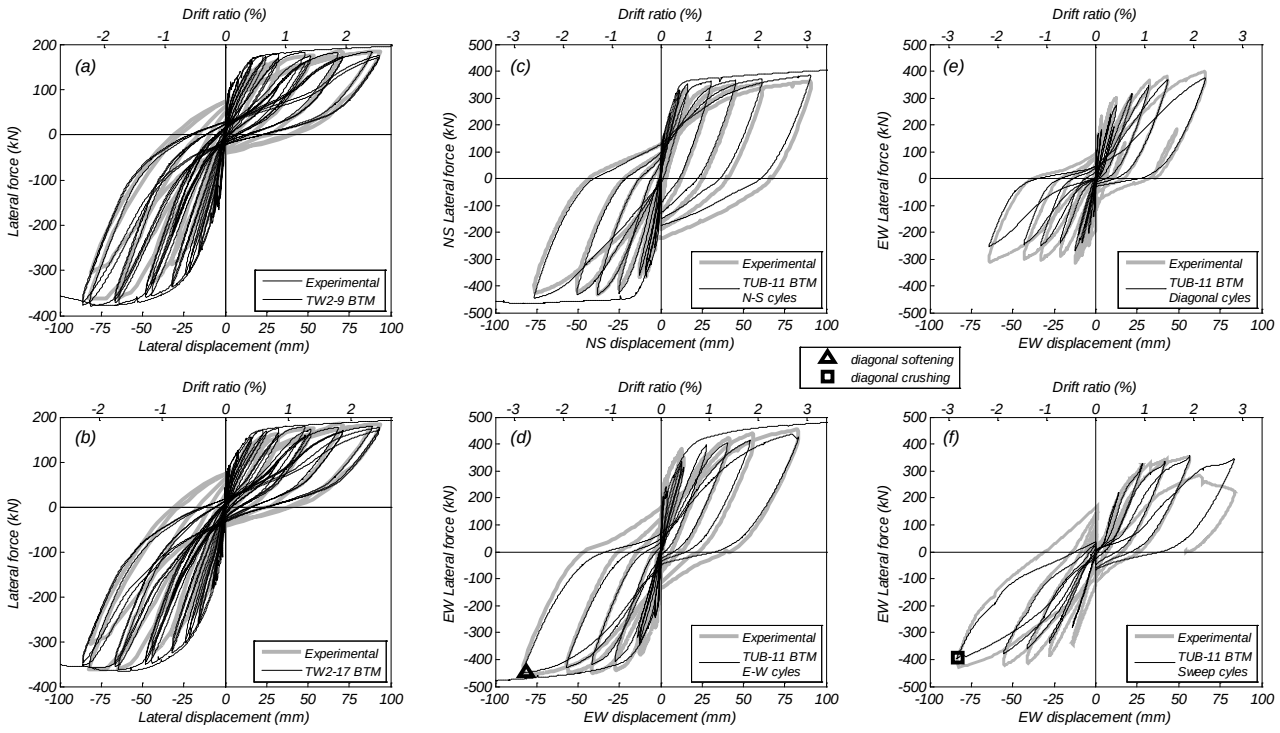


Figure 5. Results of BTMs for Case Studies 1 and 2: (a) TW2-9, (b) TW2-17; (c) TUB-11 N-S direction, (d) TUB-11 E-W direction, (e) TUB-11 diagonal cycle for the E-W direction, (f) TUB-11 sweep cycle for the E-W direction.

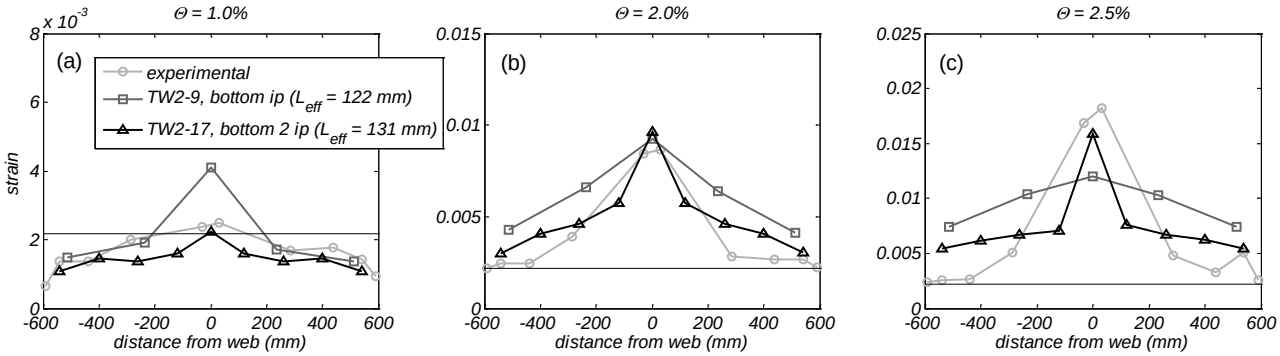


Figure 6. Case study 1 – TW2: Comparison of measured and computed tensile strains of the reinforcing steel along the base of the flange for drift ratios: (a) 1.0%; (b) 2.0%; (c) 2.5%.

and diagonal elements are presented in Lu and Panagiotou (2012). The second BTM was termed TW2-17, with two times finer mesh than TW2-9 [see Lu and Panagiotou (2012) for more details on this model]. The BTMs TW2-9 and TW2-17 had 881 and 2857 DOFs, respectively, and required 36 and 190 minutes, respectively, to run the cyclic analysis consisting of 3565 mm of total applied displacement.

Figure 5(a) compares the experimentally measured and numerically computed response using the TW2-9 model. The numerical model computed the force-displacement response satisfactorily. For both directions the computed peak lateral strength was in excellent agreement with the experimentally measured response. The computed lateral strength at Θ = 1.0% was 1.17 times the experimentally measured response. For drift ratios larger than 1.5%, the computed lateral strength did not exceed 1.09 times the experimentally measured. This model did not account for buckling of the sections, which was the predominant mode of failure of this wall. The peak diagonal compressive strain of the web computed for negative displacement was 0.14%, measured in element e_1, shown in Figure 4(d). This was in good agreement with the observed response in the experiment where no crushing of the diagonal compression field was observed. Model TW2-17 computed a similar force-displacement cyclic response to that computed by TW2-9 [see Figure 5(b)], resulting in a computed lateral strength that was 1.14 times the measured strength at 1.0% drift ratio.

Using models TW2-9 and TW2-17, Figure 6 compares the experimentally measured and numerically computed steel tensile strain profiles along the flange near its base. The numerically computed strains shown are the strain of the bottom integration points of the bottom elements of the flange of TW2-9 and the average computed strains of the two integration points of the bottom elements of the flange of TW2-17. These computed values correspond to a smeared strain over a length 122 mm and 131 mm, respectively. For 2.0% and 2.5% drift, model TW2-9 computed a smoother strain profile than that measured; however, using this model, the computed strain for Θ = 2.5% at the mid-length of the flange was 0.66 times the experimentally measured strain. Overall, the computed strains using model TW2-17 (two times finer mesh than TW2-9) was in very good agreement, with the experimentally measured strains; the computed strain values at the mid-length of the flange were between 0.85 and 1.15 times the experimentally measured strains, and computed strain at mid-length of the flange was 1.15 times the experimentally measured strain for Θ = 2.5%. This comparison demonstrates the effect that the level of mesh refinement can have on the magnitude of computed strains.

4.2 Case Study 2: Beyer et al. (2008a) – Specimen TUB

The test specimen of Case Study 2 – called TUB – was a U-shape section wall with M / VL_w = 2.8 in the E-W direction and 2.6 in the N-S direction, see Figure 7. The axial load ratio was $N / f_c'A_g$ = 0.04. The load remained constant during the cyclic load reversals and was applied through a steel beam parallel to the E-W direction passing from the centroid of the section. To apply the lateral load, a collar was used at the top of the wall. One actuator was used in the E-W direction and two in the N-S direction. The reinforcing steel ratios ρ_l and ρ_t were equal to 1.0% and 0.45%, respectively. Boundary elements were used at the ends of each of the three segments of the wall. At each level of lateral displacement, the specimen was tested with one cycle in each of the E-W, N-S, and diagonal (SW - NE) directions as well as a sweep cycle. The force-displacement responses were plotted separately in each of the E-W and N-S directions for each cycle and are shown in Figure 5(c) to (f). The specimen failed due to crushing of concrete compression diagonals at about 260 mm from the base of the segment of the wall parallel to the E-W direction during the sweep cycle at peak drift ratio Θ = 3%. The peak lateral force in the E-W direction was $5.4A_w\text{sqrt}(f_c')$, where A_w is the total cross-sectional area of segment of the wall parallel to the EW direction, and f_c' in psi. This is only 54% of the peak shear force that ACI (2011) allows.

Figure 7 shows the beam-truss model – termed TUB-11 – which had eleven lines of vertical elements in total and with θ_g ranging from 41° to 44°. The collar was also modeled with a BTM [see Figure 7(e)], and elastic linear beam was used to model the steel spreader beam, see Figure 7(b). The BTM TUB-11 had 924 DOFs and required 99 minutes to run the cyclic analysis consisting of 4095 mm of total displacement.

For the N-S and E-W cycles, the computed response using TUB-11 was in excellent agreement with the measured response, see Figure 5(c) and (d) respectively. The model

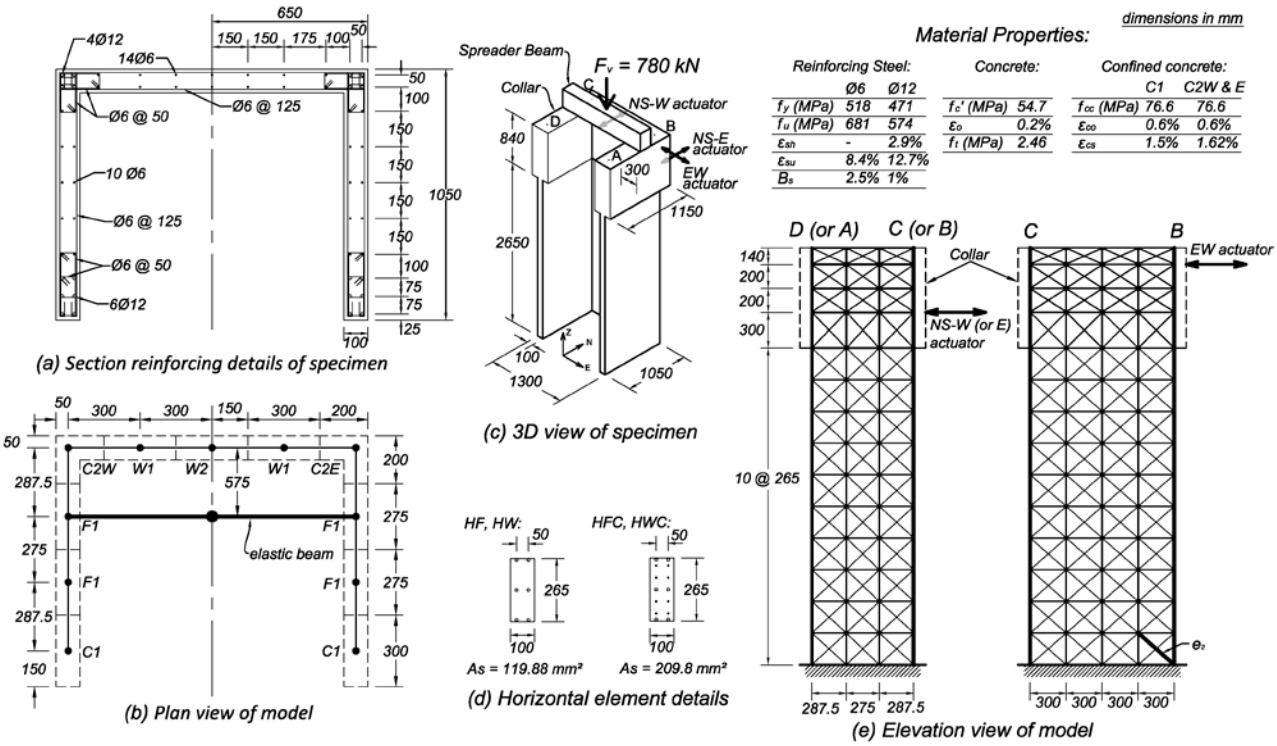


Figure 7. Case study 2 – TUB: Description of specimen and the TUB-11 beam-truss model.

computed a peak lateral force that is 1.06 and 0.98 times the experimentally measured peak lateral force for the N-S and E-W cycles, respectively. In the diagonal and sweep cycles, the computed peak lateral forces in the E-W direction were 0.94 and 0.92 times the experimentally measured, respectively, see Figure 5(e) and (f). The cyclic computed response in all directions considered was in very good agreement with the experimentally measured for all cycles. In very good agreement with the experimentally observed diagonal crushing, the model computed crushing of the concrete 265 mm from the base at element e_2, see Figure 7(e), in the segment of the wall parallel to the EW direction during the sweep cycle at drift ratio Θ = 3.0%.

4.3 Case Study 3: Oesterle et al. (1976) – Specimen F1

Case Study 3 considered the I-shape section wall with M / VL_w = 2.4, which is shown in Figure 8. The two parallel segments of this wall (termed flanges) were 914 mm long, while the third segment perpendicular to them (termed the web) was 1905 mm long. The specimen was subjected to uni-axial load reversals in the direction of the web. A 203-mm-thick slab was cast at the top of the specimen. No axial load was applied on the specimen. The lateral load was applied at 4572 mm from the base of the wall. The flanges were very heavily reinforced with longitudinal steel ratio of 3.8%, while the corresponding ratio for the web was 0.28%. The transverse steel ratio was 0.65% both in the web and the flange. Figure 9 shows the experimentally measured force-displacement response of F1. The specimen was tested up to Θ = 2.2% with 3 cycles at each level of displacement. Spalling in the diagonal direction was first observed during the second cycle at 1.1% peak drift ratio. The specimen experienced significant loss of the lateral strength during the first cycle of 2.2% drift ratio due to crushing of concrete of the web in the diagonal direction at 300 mm from the base of the wall. The peak lateral strength of this specimen was $8.6A_w\text{sqrt}(f_c')$, where A_w is the section area of the web.

Two numerical BTMs were developed. The first BTM - termed F1-11-45 - is shown in Figure 8; it had eleven lines of vertical beams, see Figure 8(b), with horizontal elements every 298 mm and θ_g ranging from 44° to 46°. The top slab of the BTM was modeled with elastic linear beam elements. The second BTM - termed F1-11-50 - also had 11 lines of vertical beams but had horizontal elements every 373 mm, resulting in θ_g around 50°. The BTMs F1-11-45 and F1-11-50 had 991 and 793 DOFs, respectively, requiring 45 minutes (each) to run the cyclic analysis of 2722 mm of total displacement.

Figure 9(a) compares the experimentally measured and numerically computed response using F1-11-45 model. The computed response was in very good agreement with the experimental response in terms of peak strength and the general hysteretic response up to the point where major strength degradation was computed, with the computed peak strength being 0.95 times the experimentally measured strength. In good agreement with the experimentally observed response, the model computed diagonal crushing of concrete [in the diagonal truss element, e_3, at the base of the web, as shown in Figure 8(c)] followed by a strength degradation of 0.5 times the computed peak strength at 2.0% drift in the first cycle with peak drift ratio Θ = 2.2%; this was in fair agreement with the experimental response, where crushing occurred at -2.0% drift during the same cycle. The point of crushing was very sensitive to the relation between β and ε_n: the same BTM F1-11-45 using β_{int} = 0.3, 0.4, and 0.5 computed crushing in the diagonal direction at 2.0%,

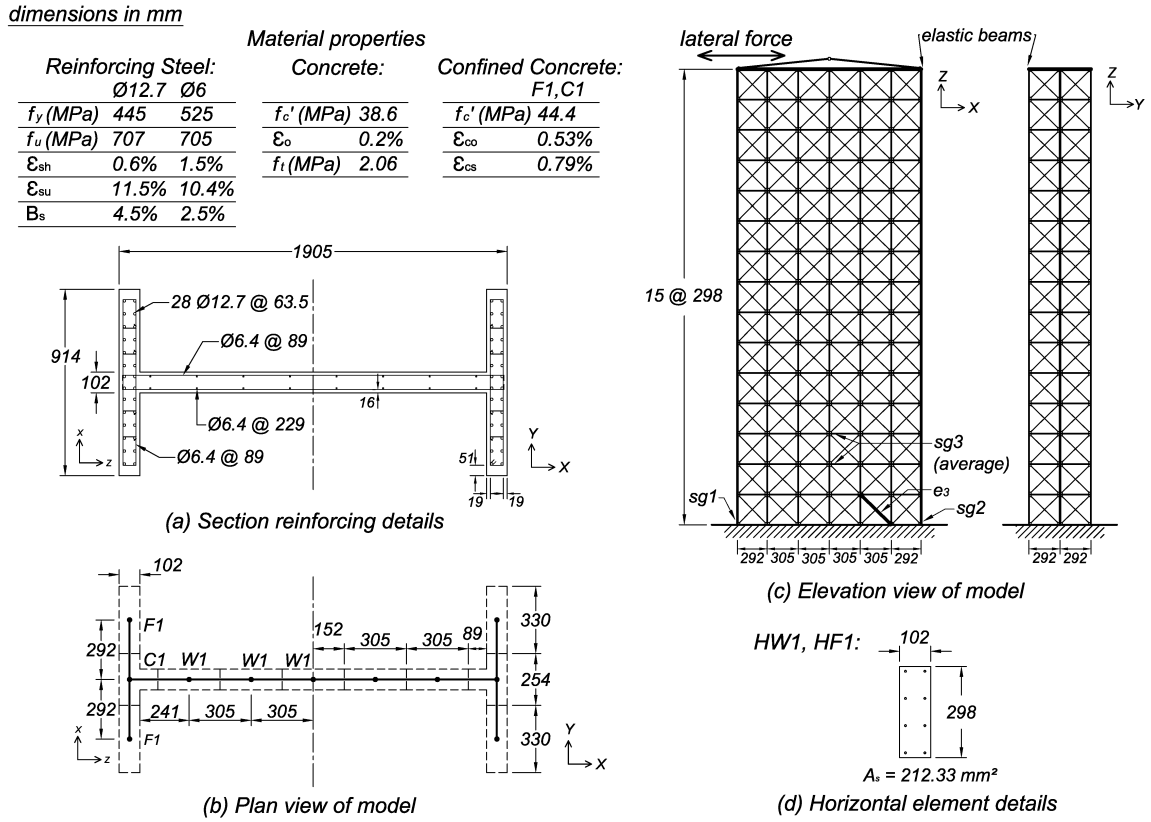


Figure 8. Case study 3 – F1: Description of specimen and the F1-11-45 beam-truss model.

2.2%, and -1.6% drift, respectively, of the first cycle with peak drift ratio Θ = 2.2% [see Figures 10(a) and (b)], with the computed response with β_{int} = 0.5 to be closer to the experimentally measured response. As shown in Figure 9(b), the value of β_{int} had practically no effect on the part of the computed response before the initiation of softening in the diagonal direction.

F1-11-50 computed a peak strength that was 0.95 times that computed by F1-11-45 and computed crushing of concrete in the diagonal direction at Θ = 1.3% during the first cycle with peak drift ratio of 2.2%, see Figure 9(c). After the first crushing of the diagonal trusses, the computed strength of this model dropped to 0.38 times the peak strength. Similar observations that the increase of the angle of the diagonals resulted in initiation of strength degradation and crushing of concrete in the diagonal direction at smaller displacement level were made in the 2D model of Panagiotou et al. (2012).

Figure 10 shows the experimentally measured response using strain gauges attached on the steel rebars and computed strains versus lateral force. The response was plotted up to the first cycle of Θ = 2.2% (where experimentally measured strain data exist). The locations of the strain gauges are shown in Figure 8(c). The strains computed from this model were in very good agreement with the measured longitudinal and transverse strains at the base for the cycles with peak drift ratio up to and including 1.1%, with less agreement (for one of the three locations considered) in the cycle with peak drift ratio equal to 2.2%. For the third cycle at Θ = 1.1%, the maximum computed strains at the locations of *sg1*, *sg2*, and *sg3* were 0.77, 0.81, and 1.12 times the measured strains, respectively. For the

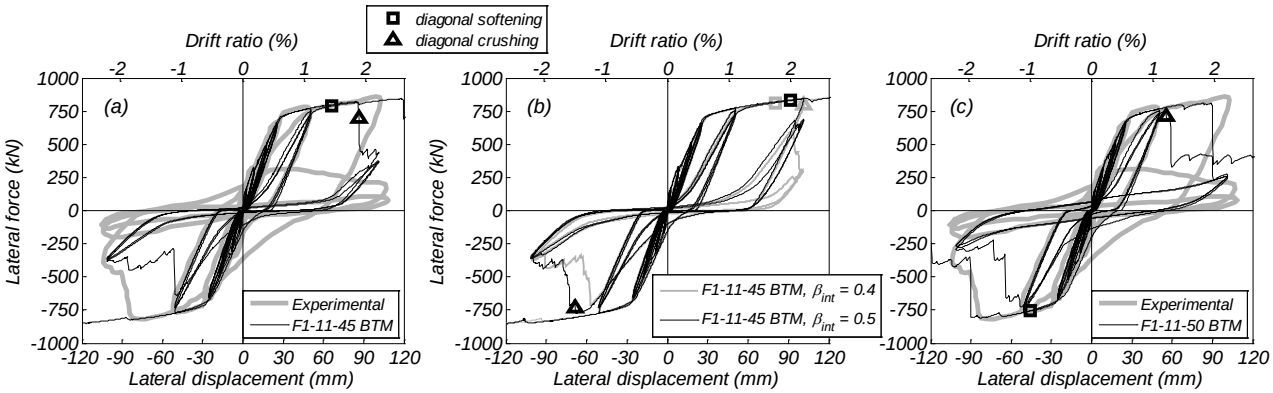


Figure 9. Results of BTMs for Case Study 3: (a) F1-11-45 (β_{int}=0.3), (b) F1-11-45 (β_{int} = 0.4 and 0.5) (c) F1-11-50 (β_{int}=0.3).

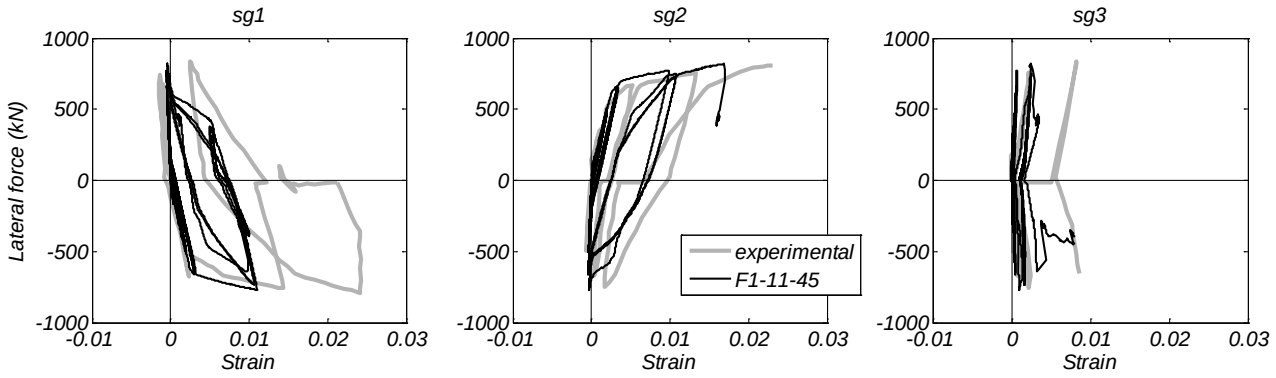


Figure 10. Case Study 3: Comparison of measured and computed lateral force vs. strain using BTM model F1-11-45. The locations of strain gauges are shown in Figure 8.

first cycle at Θ = 2.2%, where the diagonal web crushing occurred, the maximum computed strains at the locations of *sg1*, *sg2*, and *sg3* were 0.45, 0.74, and 1.07 times the measured strains, respectively. The length corresponding to the integration point used for the computed strains were 149 mm for *sg1* and *sg2*, and 153 mm for *sg3*.

5. CONCLUSIONS

This paper described a three-dimensional (3D) beam-truss model (BTM) for non-planar reinforced concrete walls. The model used nonlinear fiber-section Euler-Bernoulli beam elements in the vertical direction and nonlinear truss elements in the horizontal direction to represent concrete and reinforcing steel. Linear beams were used in parallel with the horizontal truss elements to model the out-of-plane flexural rigidity of the wall segments. Nonlinear truss elements were used to represent the diagonal field of concrete in compression. The model represents the effects of flexure-shear interaction by computing the stresses and strains of steel and concrete in the vertical, horizontal, and diagonal directions, and by accounting for the effect of normal tensile strain on the compressive behavior of the concrete in the diagonal direction. The model accounted for mesh-size effects by considering the strength degrading branches of the concrete stress-strain material models dependent on the length of the elements.

The efficacy of the model was investigated comparing the computed response using the BTM with the experimentally measured response of three non-planar RC walls subjected to cyclic loading having a T- U-, and I-shape section, respectively. The experimentally observed failure mode of the latter two walls was due to diagonal web crushing. The response of the three walls using existing nonlinear fiber-section Euler-Bernoulli beam models was also computed. The following conclusions were drawn:

1. The beam-truss models computed very satisfactorily the post-cracking cyclic force-displacement response of the three specimens. The computed peak lateral strength was between 0.92 and 1.1 times the experimentally measured for all three case studies. In very good agreement with the experimentally measured response, the model computed crushing of concrete diagonals of the U- and I-shape section walls of Case Studies 2 and 3, respectively, for cycles with maximum drift ratios equal to 3% and 2.2%, respectively.

2. Models TW2-17 and F1-11-45 computed strain histories that were in good agreement with the experimentally measured response for all the cycles (apart from one location of F1-11-45 during the last cycle of the response). The authors believe that the computation of strains (local response) is more sensitive to model parameters than the overall force-displacement response; the lower level of accuracy in the computation of strains is assumed to be due to a combination of the following reasons: (a) the strains computed were averaged over a specific length while the experimentally measured were local strains of the steel (no experimentally measured data using displacement transducers were available); (b) the formulation of the model was using constant-angle diagonals of width equal to b_{eff}; (c) the steel model used did not model the yield plateau and nonlinear hardening explicitly; and (d) the model did not account for the effects of bond slip and strain penetration of steel in the anchorage blocks.

3. For the T-shape section wall, the models TW2-9 and TW2-17 computed peak strength 1.05 and 1.01 times the experimentally measured for the direction of the response with flange in tension, respectively. The models computed the lateral strength at 1.0% drift to be 1.17 and 1.14 times the experimentally measured, respectively. The overestimation at 1% drift was assumed to be due to the overlap of areas of concrete in the vertical, horizontal, and diagonal elements of this model as well as due to the use of constant-angle diagonals of width equal to b_{eff}. Overestimation of strength and stiffness was also observed in the other two Case Studies, but it was negligible for drift ratios larger than 0.5%.

4. The effect of mesh refinement [considered in Case Study 1] was found to be negligible on the overall force–displacement response but was important for the magnitude of computed strains. The ratio of length of the vertical beams to the height of the wall was equal to 6.7%, and 3.6% in models TW2-9 and TW2-17, respectively. The latter resulted in much better agreement between computed and measured strains along the flange of the T-shape section wall.

5. The effect of the angles of the diagonals was investigated in Case Study 3. Models F1-11-45 and F1-11-50 had diagonal elements at 45^o and 50^o with respect

to the horizontals, respectively. F1-11-45 computed initiation of degradation at 2.0% drift ratio, which was in better agreement with the experimental data. As expected, the level of drift at which crushing of the diagonal concrete was computed was found to be sensitive to the relation of concrete compressive strength and normal tensile strain (values of β_{int} = 0.3 to 0.5 were considered in Case Study 3).

References:

Newmark, N.M. and Rosenblueth, E. (1971), "Fundamentals of Earthquake Engineering," Prentice-Hall Inc.

Trifunac, M.D. and Brady, A.G. (1975), "A Study on Duration of Strong Earthquake Ground Motion," *Bulletin of the Seismological Society of America*, 65(3), 581-626.

Kasai, K., Fu, Y., and Watanabe, A. (1998), "Passive Control Systems for Seismic Damage Mitigation," *Journal of Structural Engineering*, American Society of Civil Engineers, 124(5), 501-512.

MacRae, G. A. and Kawashima, K. (2001),"Seismic Behavior of Hollowed Stiffened Steel Bridge Columns," *Journal of Bridge Engineering*, American Society of Civil Engineers, 6(2), 110-119.

Fujimoto, K. and Midorikawa, S. (2000), "Simplified Method for Predicting Ground Motion Intensity Map Considering Effect of Irregular Deep Underground Structure," *Proceedings of the 6th International Conference on Seismic Zonation*, Paper No. 2-23B.

American Concrete Institute (ACI). (2011). "Building code requirements for structural concrete," *ACI 318-11*, Farmington Hills, Mich., 503 pp.

Balkaya, C., and Kalkan, E. (2004). "Three-dimensional effects on openings of laterally loaded pierced shear walls." *Journal of Structural Engineering*, 130(10), 1506-1514.

Barbosa, A. R. (2011). "Simplified vector-valued probabilistic seismic hazard analysis and probabilistic seismic demand analysis: application to the 13-story NEHRP reinforced concrete frame-wall building design example." Ph.D. Thesis, Department of Structural Engineering, University of California, San Diego.

Bazant, Z. P. and Planas, J. (1998). "Fracture and size effect in concrete and other quasibrittle materials." Boca Raton, FL: CRC Press.

Beyer, K., Dazio, A., and Priestley, M. J. N. (2008a). "Quasi-static cyclic tests of two U-shaped Reinforced Concrete Walls." *Journal of Earthquake Engineering*, 12(7), 1023-1053.

Beyer, K., Dazio, A., and Priestley, M. J. N. (2008b). "Inelastic Wide-Column Models for U-Shaped Reinforced Concrete Walls." *Journal of Earthquake Engineering*, 12(S1), 1-33.

Coleman, J. and Spacone, E. (2001). "Localization issues in force-based frame elements." *Journal of Structural Engineering*, 127(11), 1422-1425.

El-Tawil, S., Kuenzli, C. M., and Hassan, M. (2002). "Pushover of hybrid coupled walls. I: design and modeling." *Journal of Structural Engineering*, 128(10), 1272-1281.

Filippou, F. C., Popov, E. P., and Bertero, V. V. (1983). "Effects of bond deterioration on hysteretic behavior of reinforced concrete joints". Report EERC 83-19, Earthquake Engineering Research Center, University of California, Berkeley.

Hassan, M. and El-Tawil, S. (2003). "Tension flange effective width in reinforced concrete shear walls." *ACI Structural Journal*, 100(3), 349-356.

Hoshikuma, J., Kawashima, K., Nagaya, K., and Taylor, A. W. (1997). "Stress-strain model for confined reinforced concrete in bridge piers." *Journal of Structural Engineering*, 123(5), 624-633.

Ile, N., and Reynouard, J. M. (2000). "Non-linear analysis of reinforced concrete shear wall under earthquake loading." *Journal of Earthquake Engineering*, 4(2), 183–213.

Ile, N. and Reynouard, J. M. (2005). "Behaviour of U-shaped walls subjected to uniaxial and biaxial cyclic lateral loading." *Journal of Earthquake Engineering*, 9(1), 67-94.

Kotronis, P., Mazars, J., Nguyen, H., Ile, N., Reynouard, J. M., Bisch, P., and Coin A. (2005) "The seismic behavior of reinforced concrete structural walls: experiments and modeling." *250th anniversary of the 1755 Lisbon earthquake, International conference proceedings*, Lisbon, Portugal.

Lu, Y. and Panagiotou, M. (2012). "Three-Dimensional Nonlinear Cyclic Beam-Truss Model for Non-Planar Reinforced Concrete Walls." Report UCB/SEMM-2012/01, Earthquake Engineering Research Center, University of California, Berkeley.

Maekawa, K., Pimanmas, A., and Okamura H. (2003). "Nonlinear mechanics of reinforced concrete." New York, NY: Spon Press. 721 pp.

Mander, J. B., Priestley, M. J. N., and Park, R. (1988). "Theoretical stress-strain model for confined concrete," *Journal of Structural Engineering*, 114(8), 1804-1826.

Martinelli, L. (2008). "Modeling shear–flexure interaction in reinforced concrete elements subject to cyclic lateral loading." *ACI Structural Journal*, 105(6), 675-684.

Mazars, J., Kotronis, P., Ragueneau, F., and Casaux G. (2006) "Using multifiber beams to account for shear and torsion. Applications to concrete structural elements." *Computer Methods in Applied Mechanics and Engineering*, 195(52), 7264-7281.

McKenna, F., Fenves, G. L., Scott, M. H., and Jeremic, B. (2000). "Open system for earthquake engineering simulation." <http://opensees.berkeley.edu>

Miki, T. and Niwa, J. (2004). "Nonlinear analysis of RC structural members using 3D lattice model," *Journal of Advanced Concrete Technology*, 2 (3), 343-358.

Oesterle, R. G., Fiorato, A. E., Johal, L. S., Carpenter, L. S., Russell, H. G., and Corley, W. G. (1976). "Earthquake-resistant structural walls - tests of isolated walls." Report to the National Science Foundation, Construction Technology Laboratories, Portland Cement Association, Skokie, Illinois.

Orakcal, K., and Wallace, J. W. (2006). "Flexural Modeling of Reinforced Concrete Walls - Experimental Verification." *ACI Structural Journal*, 103(2), 196-206.

Palermo, D. and Vecchio, F. J. (2007). "Simulation of cyclically loaded concrete structures based on the finite-element method." *Journal of Structural Engineering*, 133(5), 728-738.

Panagiotou, M., Restrepo, J.I., Schoettler, M., and Kim G. (2012). "Nonlinear cyclic truss model for reinforced concrete walls." *ACI Structural Journal*, 109(2), 205-214.

Petrangeli, M., Pinto, P. E., and Ciampi, C. (1999). "Fiber element for cyclic bending and shear of RC structures. I: Theory." *Journal of Engineering Mechanics*, 125(9), 994-1001.

Petrangeli, M. (1999). "Fibre element for cyclic bending and shear of RC structures. II: verification." *Journal of Engineering Mechanics*, 125(9), 1002-1009.

Sittipunt, C. and Wood, S. L. (1993). "Finite element analysis of reinforced concrete shear walls." *Civil Engineering Studies*, Structural Research Series No. 584, University of Illinois, Urbana.

Stevens, N. J., Uzumeri, S. M., Collins, M. P., and Will, T. G. (1991). "Constitutive model for reinforced concrete finite element analysis." *ACI Structural Journal*, 88(1), 49-59.

Thomsen, J. H. and Wallace, J. W. (1995). "Displacement-based design for reinforced concrete structural walls: an experimental investigation of walls for rectangular and T-shaped cross-sections." Report No. CU/CEE-95-06, Clarkson University.

Thomsen, J. H. and Wallace, J. W. (2004). "Displacement-based design of slender reinforced concrete structural walls - experimental verification." *Journal of Structural Engineering*, 130(4), 618-630.

Vecchio, F. J., and Collins, M. P. (1986). "The modified compression field theory for reinforced concrete elements subjected to shear." *Journal of the American Concrete Institute*, 83(2), 219-231.

10CUEE CONFERENCE PROCEEDINGS
10th International Conference on Urban Earthquake Engineering
March 1-2, 2013, Tokyo Institute of Technology, Tokyo, Japan

INFLUENCE OF POST-TENSIONED ROPES ON THE DYNAMIC RESPONSE OF INNOVATIVE MORTAR-FREE INTERLOCKING STRUCTURES

Majid Ali[1)], and Nawawi Chouw[2)]

1) PhD student, Department of Civil and Environmental Engineering, The University of Auckland, New Zealand
2) Associate Professor, Department of Civil and Environmental Engineering, The University of Auckland, New Zealand
mali078@aucklanduni.ac.nz, n.chouw@auckland.ac.nz

Abstract: An innovative technology for affordable earthquake-resistant houses consisted of movable interlocking blocks is introduced. It is anticipated that the mortar-free construction can facilitate more energy dissipation during an earthquake because of the relative movability at the block interface. As part of the development process, a mortar-free interlocking column with rope reinforcement is tested under harmonic and earthquake loadings to understand the dynamic response. The un-grouted ropes are post-tensioned with a magnitude of 200 N. A mass of 150 kg is placed at the top of the column to simulate the mass of diaphragm. To enhance the ductility and material damping of the whole structure, the novel interlocking blocks are made with coconut fibre reinforced concrete. The influence of rope reinforcement on the development of relative displacement, base shear, overturning moment and block uplift is investigated. The results confirm that the proposed construction technology has a potential for earthquake prone regions, especially in developing countries.

1. INTRODUCTION

Economical earthquake-resistant housing is desirable in seismically active rural areas of developing countries. These regions often suffer a significant loss of life during strong ground motion because of lack of seismic-resistant housing. To enable an efficient and cost-effective structural solution, a new concept of construction was investigated utilizing structures consisting of (i) newly developed interlocking blocks with relative movability at the block interface and (ii) coconut-fibre rope reinforcement. The interlocking blocks were prepared with coconut fibre reinforced concrete (CFRC). An up-to-date history of the interlocking blocks, developed by other researchers, is summarized in Ali et al. (2012). Most of these blocks are hollow (Anand and Ramamurthy, 2000 and 2003; Jaafar et al. 2006), some are solid (Nazar and Sinha, 2007) and curved (Dedek et al. 2012), and in few cases, with provisions of holes for reinforcement. These blocks can be prepared mechanically or manually, but in some cases, it requires very complicated moulds and manual casting. Usually, the material is concrete (Anand and Ramamurthy, 2000 and 2003; Jaafar et al., 2006); stabilized soil [Dedek et al., 2012; Smith, 2012] and with fly ash (Nazar and Sinha, 2007; Uygunoglu et al, 2012). The thickness of these blocks also varies, making them suitable either for load bearing, partition or cladding wall. Interlocking mechanism is provided either by horizontal, vertical or both interconnecting keys for in-plane and out-of-plane directions. The main purpose of these blocks is to make precise alignment and quick construction. It may be noted that the interlocking keys of hollow blocks alone are normally not sufficient to resist stresses of design load for an assembled wall in a structure due to elimination of mortar layers (Thanoon et al., 2004). This might be because of limited key projection. To overcome this problem, normal reinforced concrete is used at regular intervals in the holes provided in hollow blocks. This makes the structure a little bit expensive. In some cases, relatively lesser mortar (as compared to that required in normal brick masonry) is used with the interlocking blocks (Smith, 2010). Their main objective considered so far is an easy, fast and cost-effective construction mainly for resisting static loading. Therefore, other interlocking blocks, except Elvin and Uzoegbo's blocks, are not discussed here.

Elvin and Uzoegbo (2011) studied the response of a full-scale dry-stack masonry structure (3.9 m x 3.9 m x 2.76 m high) under the scaled earthquake and harmonic loadings. The structure was made of interlocking bricks and minimum steel reinforcement with a 2560 kg top mass to simulate the roof loading. It was observed that the bricks were shifted and damaged in the plane of the wall to such an extent that brick-sized gaps opened up. Many bricks were split, cracked, crushed or even misplaced. The cracking of plaster and spalling also occurred. Despite this severe damage, the test structure remained standing, successfully carrying the roof load. The energies of the earthquake and harmonic loadings

were dissipated through inter-brick friction and in some cases by brick cracking and crushing. The bricks were dry-stacked, which allowed them to move and, hence, dissipate energy. The ability of the test structure to withstand the applied earthquakes relied heavily on energy dissipation through inter-block friction. It should be noted that only horizontal ground motion was considered. If the vertical component of the ground accelerations was considered, the friction between the bricks may be reduced.

The following points are carefully noted from Elvin and Uzoegbo study: 1. use of minimum steel reinforcement in the structure; 2. blocks made of soil, which resulted in splitting and crushing of bricks during dynamic loading; 3. insufficient longitudinal interlocking key height and lack of transverse keys; and 4. earthquakes with vertical components may have an adverse effect on energy dissipation. These observations may indicate some of the shortcomings for achieving an efficient performance of the proposed mortar-free structures. By comparison, the interlocking blocks presented here have following characteristics: 1. there is no use of steel reinforcement, only coconut-fibre ropes are used in mortar-free structures; 2. blocks are made of CFRC, which avoids splitting and crushing of materials and also gives additional material damping; 3. sufficient interlocking key heights in both directions; and 4. earthquakes with vertical components are considered in the design of interlocking blocks as energy is dissipated through uplift (i.e. the relative movement at the interface).

To the best of the author's knowledge, the investigation of mortar-free construction without steel reinforcement for resisting earthquake loading has not been reported so far. The dynamic characteristics of mortar-free structures comprising the newly developed interlocking CFRC blocks are discussed in the following sections.

2. EXPERIMENTAL PROCEDURES

2.1 Preparation of blocks, foundation and column

As concluded in Ali et al. (2012), the optimized CFRC properties was obtained with a mix design ratio (cement: sand: aggregates: water) of 1:4:2:0.64, 5 cm long fibres and 1% fibre content by mass of concrete materials. Therefore, the same mix design is used for preparing blocks for the current study. For testing of CFRC mortar-free structures, a footing with a size of 1500 mm long, 600 mm wide and 200 mm deep was also prepared with CFRC (having a mix design ratio of 1:4:2 and 5 cm long fibres) but with a low fibre content (0.25%) because of the presence of steel reinforcement (ϕ10mm@100mmc/c in both directions at the bottom layer and ϕ5mm@100mmc/c in both directions at the top layer). The reason for using CFRC in the foundation was to observe the damage (if any) due to friction between the blocks and the foundation. Steel reinforcement was used so that the foundation could easily be shifted on and off the shake table; otherwise, steel reinforcement was not required. The holes were provided in the foundation for the insertion of the ropes (i.e. to anchor the ropes in the foundation) so that the same foundation could be used for all structures to be tested; otherwise, the holes in the foundation were not required. There was no damage to the foundation after all structures had been tested, however it had been planned to repair any damage from one test before the start of next. The depth of foundation would be governed by the rope tension (i.e. pullout load) generated during the dynamic loading. A groove (1200 mm long, 200 mm wide and 75 mm deep) was also provided in the foundation for holding the interlocking blocks. All specimens were cured for 28 days, then dried for 48 hours and finally whitewashed before testing to enable clear identification of cracks. Coconut fibre ropes of ~36 mm diameter were used as vertical reinforcement of the structures. The tensile strength of these ropes was 15.3 MPa, reported in Ali and Chow (2013). The mortar-free column with ropes is shown in Figure 1. The column consisted of a stack of 13 single standard blocks with an overall height of 1.92 m. A mass of 150 kg was placed at the top of the column to simulate the roof mass. A post-tension force of 200 N was applied in the ropes for the column with vertical reinforcement. The column was tested under harmonic and earthquake loadings. The column without ropes was also tested in a similar manner and reported in a separate paper. However, the outcome of the testing of column without ropes is briefly presented here to compare the results with that of column with ropes so that the influence of post-tensioned un-grouted ropes on the dynamic behavior can be clarified.

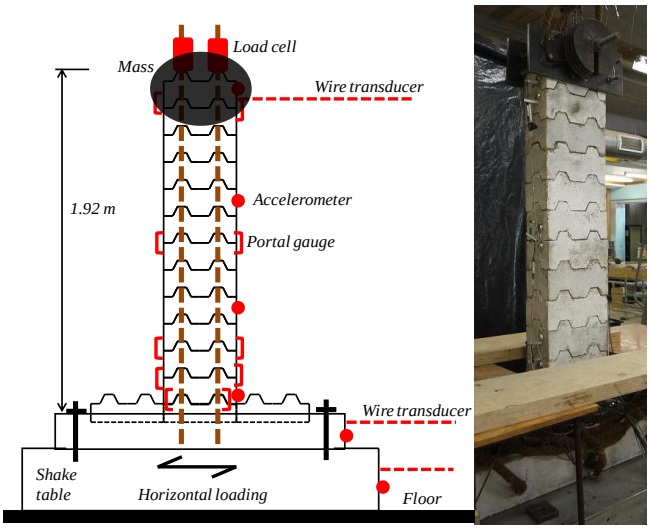


Figure 1: Instrumentation of mortar-free column with ropes, schematic (left) and actual (right).

2.2 Instrumentation

The experimental setup for the mortar-free column with ropes mounted on the shake table along with the details of the following instrumentation for measuring its response is shown in Figure 1:

(i) Six accelerometers along the structure height for determining induced accelerations (at shake table, at foundation, one each at blocks 2, 5, 9 and the top block of the structure)

(ii) Ten portal strain gauges for quantifying the block relative movement, i.e. uplift (five on left and five on right sides)
(iii) Three wire displacement transducers (one at the structure top, one on the foundation and one on the shake table)
(iv) Two load cells at the structure top for measuring the rope tension.

2.3 Testing

Using the shake table, the loadings employed on the structure were in the following sequence:

a. Harmonic loading with constant amplitude and varying frequencies passing through the fundamental frequency. Three levels of amplitudes (i.e. 5, 10 and 15 mm) were applied. Each of these amplitudes was applied with exciting frequencies ranged from 1 Hz to 2 Hz with an increment of 0.25 Hz. The corresponding peak table accelerations ranged from 0.02 g (for 5 mm and 1 Hz) to 0.24 g (for 15 mm and 2 Hz).
b. Earthquake loadings (Tabas 1978, Llolleo 1985, El Centro 1940, and Kobe 1995). These were applied from 0.05 g to 0.20 g with an increment of 0.05 g.
c. Harmonic loading with a constant frequency (1.5 Hz and varying amplitudes, beginning from 20 mm and increasing until structure failure. The selection of the constant frequency was based on the experience of test (a) as the structure at the selected frequency responded in resonance.

It is important to note that the structure was tested through the whole sequence of loading and the damage occurred at any stage was cumulative. The readings of the wire displacement transducers at the foundation and shake table confirmed that the shake table was capable of simulating the load accurately.

3. RESULTS AND ANALYSIS

3.1 Structural response under harmonic loading with constant amplitudes and a varying frequency

3.1.1 Fundamental frequency and damping ratios

The half bandwidth method was used to determine the damping ratio and the fundamental frequency in spite of the fact that the considered structure behaved nonlinearly. The applied ground motion, u_g, of 5 mm and the corresponding top displacement, u_t, time histories of the column without ropes are shown in Figure 2 for the exciting frequency of 1.5 Hz. The column response is divided into three phases: A. when the column started its vibration until it attained the steady-state condition, B. steady-state response of the column, and C. free vibrations of the column. The duration of phase A varied considerably for different amplitudes and frequencies. The steady-state response is used for the calculation of transmissibility TR_d and TR_a using displacement and acceleration readings, respectively. The damping ratio and the fundamental frequency calculated from the displacement and acceleration readings are close to each other. A comparison of TR_d vs f/f_n curves for all amplitudes of the harmonic loading is shown in Figure 3. f and f_n are the excitation frequency and the structural fundamental frequency, respectively. It may be noted that the curves become relatively flatter for high amplitude loading showing higher damping of the structure. As expected, the structure without ropes has more damping compared to the structure with rope (Figure 4). The structure with ropes have, as expected, a higher average fundamental frequency (1.57 Hz) compared to the structure without ropes (1.47 Hz).

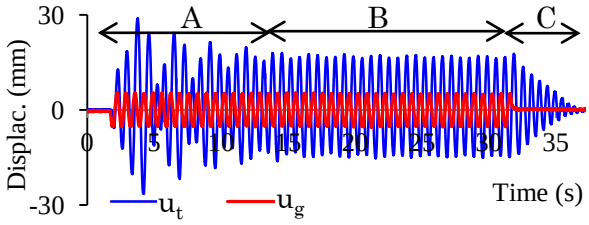


Figure 2: Displacement time history due to a harmonic loading of 5 mm and 1.5 Hz for column with ropes.

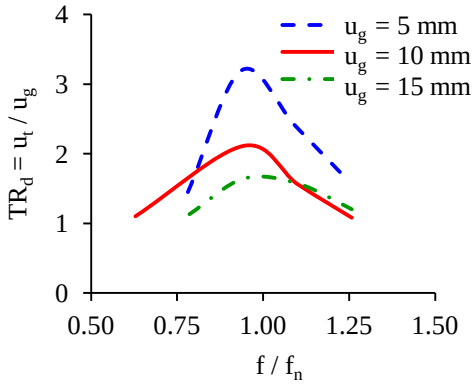


Figure 3: TR_d vs f/f_n curves due to harmonic loadings for column with ropes.

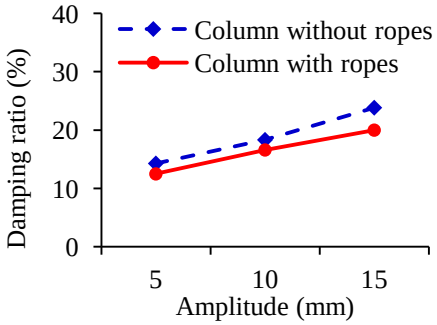


Figure 4: Comparison of the damping ratios from different amplitudes of harmonic loadings.

3.1.2 Base shear – displacement curves, energy dissipation and overturning moment

Base shear 'Q' is calculated as $\Sigma(m_i.\ddot{u}_i)$, where $\ddot{u}_i$ are the accelerations at the considered locations and m_i are the

contributing masses corresponding to $\ddot{u}_i$. The column mass is divided into the contributing masses in such a way that, along the structure height, the centre of each mass is close to $\ddot{u}_i$. The purpose of this approximate calculation of base shear is to obtain the base shear - displacement relationship. Displacement, u, is top in-plane relative horizontal displacement which is taken as the difference between the top displacement and the base displacement as measured by the wire displacement transducer. The base shear – displacement (Q-u) curves obtained from different frequencies under 10 mm harmonic loading are shown in Figure 5. The magnitudes of the base shear and the displacement are generally larger for the structure without ropes compared to the structure with ropes.

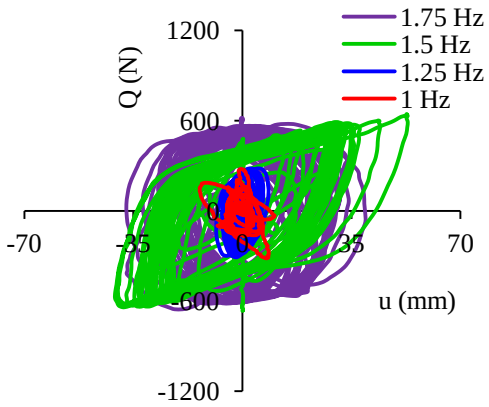


Figure 5: Q-u curves obtained from harmonic loadings for column with ropes.

The Q-u curves are further divided into the structure responses in the periods A, B and C, as defined in Figure 3, to highlight the behaviour during steady-state response. The area within one loop of a Q-u curve of the steady-state response is taken as the energy dissipated for whole system per cycle. Energy dissipation increased up to a frequency near the resonant frequency and then decreased (Figure 6). It also increased with increasing amplitude. The column without ropes had more energy dissipation compared to the column with ropes.

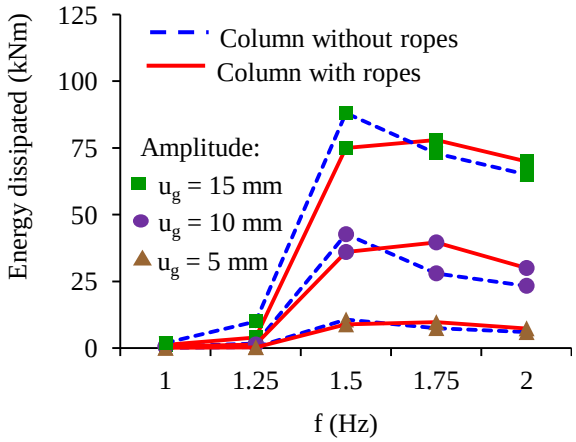


Figure 6: Comparison of energy dissipation due to harmonic loadings.

The maximum overturning moment of the structures is calculated by multiplying the maximum base shear with the height from the base of the groove in the foundation to the centre of the mass taken in the calculation of the base shear. The comparison of overturning moment for the structures is shown in Figure 7. The maximum overturning moment generally first increases up to a frequency near to the resonant frequency and then decreases with an increase in the exciting frequency. It also increased with an increasing input amplitude. The incremental trend in overturning moment is more non-linear at strong excitations compared to that due to the low excitations. Generally, the structures without ropes had a higher overturning moment compared to the structures with ropes because of larger top relative displacement in the former structure.

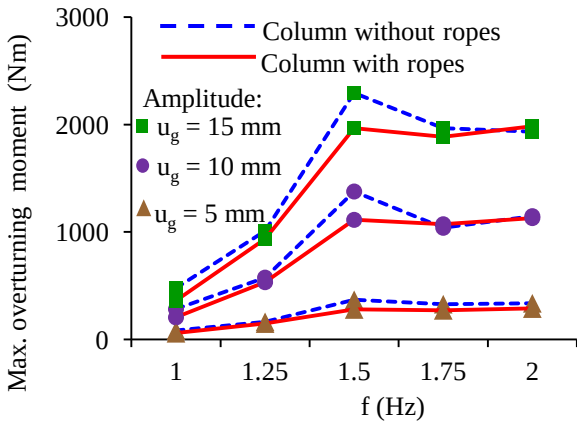


Figure 7: Comparison of overturning moment due to harmonic loadings.

3.1.3 Block uplift and rope tension

The mortar-free column allows vertical relative movement at the block interface during the applied harmonic loadings. The block uplifts along the column height during one cycle is shown in Figure 8. When the column deflected towards one side (say left side, as shown in the figure), uplifts are observed at the right side and the top relative displacement is to the left. Regarding the rope stresses, considerably more tension is observed in the right rope compared to the left rope. It may be noted that for a higher load, there will be some tension in the left ropes because of significant uplift at the right side. All these observations are reversed when the column is deflected to the other side (i.e. the right side). The magnitude of the uplift (at edges as shown in Figure 9) along the column height decreases from bottom to top, with the maximum uplift at the column base.

The uplifts between blocks 1 and 2 due to the 1.5 Hz and 10 mm harmonic loading are shown in Figure 9. The left and right uplifts occurred alternately. As expected, the time history of the rope tension corresponds to the development of uplift. The rope tension time history is presented in Figure 10. The tension in the left and right ropes also occurred alternately.

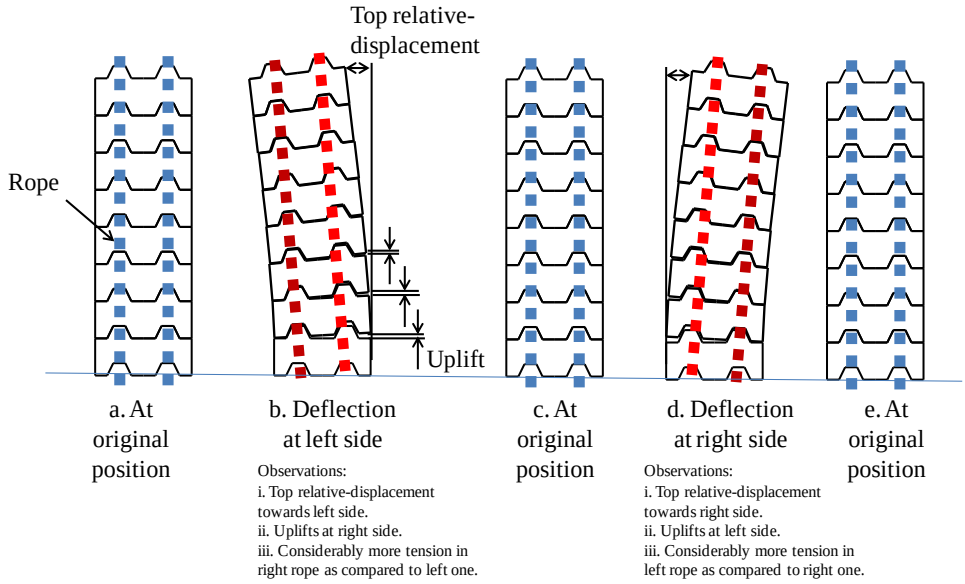


Figure 8: Observations during deflections under harmonic and earthquake loadings.
(Note: Foundation and top-mass are not shown for clarity)

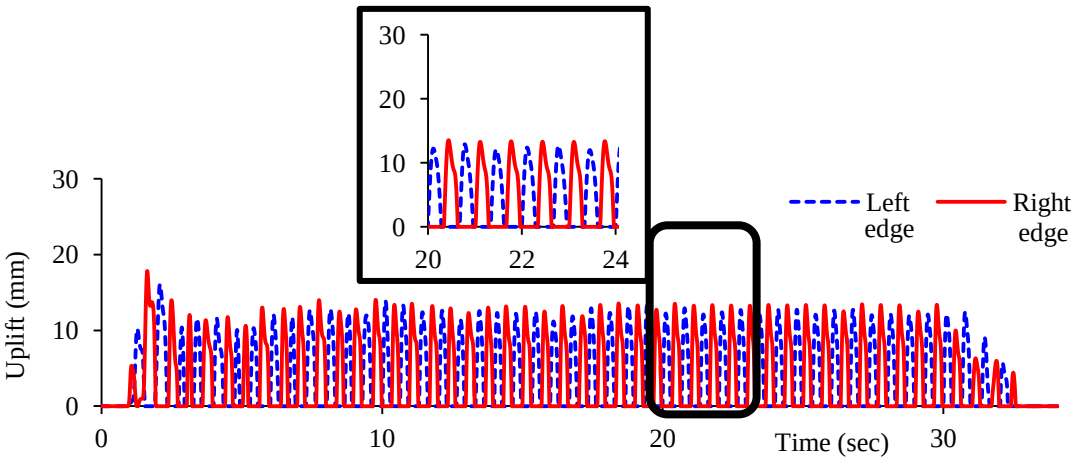


Figure 9: Maximum uplifts for 1.5 Hz and10 mm harmonic loading for column with ropes.

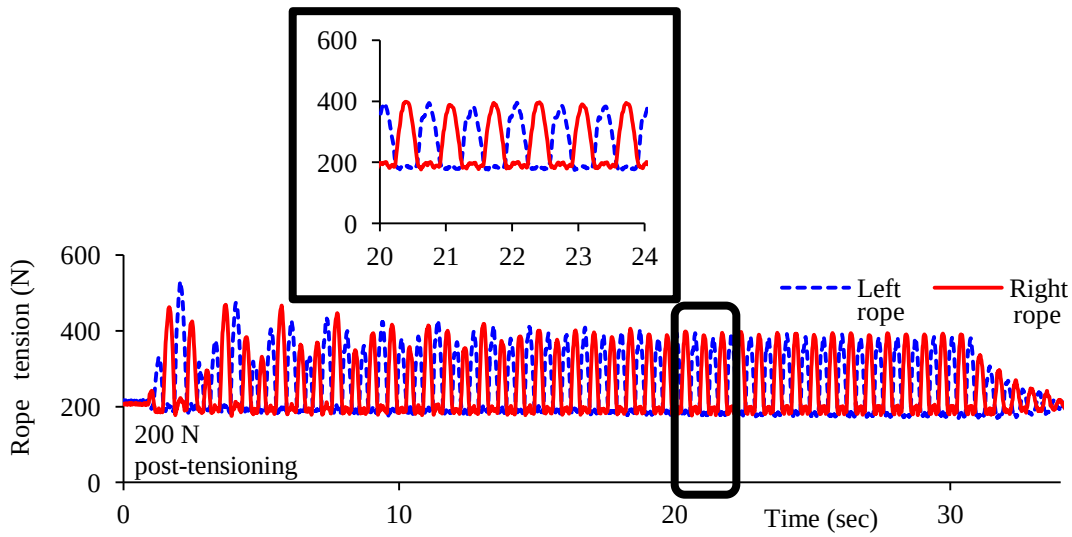


Figure 10: Rope tension – time history due to the 1.5 Hz and10 mm harmonic loading for column with ropes.

It is observed that the number of uplifts increased with a higher frequency. The maximum uplifts between blocks 1 and 2 at different frequencies under steady state of 10 mm harmonic loading are shown in Figure 11. The magnitude of uplift increased up to a frequency near to the resonant frequency and then decreased. As expected, the structure without ropes had more uplift compared to the structure with ropes. This has lead to a higher damping and consequently higher energy dissipation in the former structure.

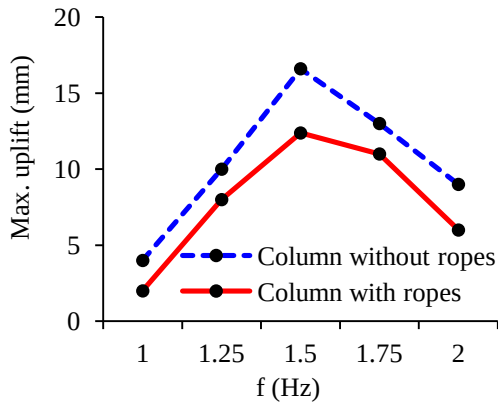


Figure 11: Comparison of maximum uplift due to harmonic loadings.

The relationship between the rope tension and relative displacement is presented in Figure 12. The number of times the ropes underwent tensioning increased as the frequency increased. The maximum rope tension during steady-state response with different amplitudes of harmonic loadings is shown in Figure 13. The magnitude of rope tension increased up to a frequency near to the resonant frequency and then it decreased. The tension developed in the rope was far less than the pull out load determined in a previous study (Ali and Chouw, 2013). This indicates that the ropes would not be pulled out due to the harmonic loadings considered if the ropes were embedded in the foundation. The rope tension was also less than the rope ultimate tensile load, ensuring no possibility of the rope breaking. As determined in Ali and Chouw (2013), a force of 1625 N is required to pull out ropes from a 100 mm deep foundation. The rope of 36 mm diameter is capable of taking a tensile load of 14 kN.

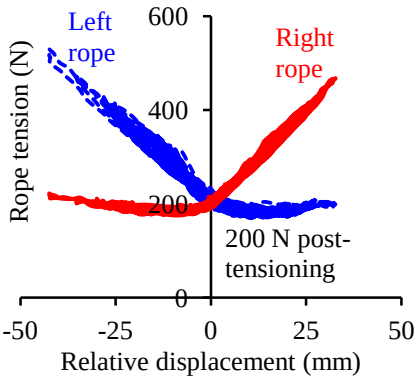


Figure 12: Rope tension – horizontal relative displacement.

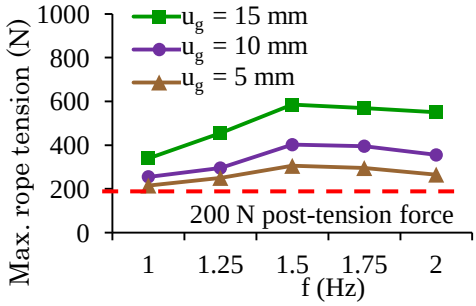


Figure 13: Maximum rope tension during steady-state response of the column with ropes to the harmonic loading.

3.2 Structural response under earthquake loadings

The considered earthquake loadings with the PGA scaled to 0.2 g are shown in Figure 14. The fundamental frequency of the column is marked in the enlarged view of the response spectrum (Figure 15) to enable an estimation of the impact of the load considered on column tested. It is noted that the response spectrum is for linear structures. For a structure with a fundamental frequency of 1.57 Hz, the response acceleration due to El Centro and Kobe earthquake loadings would be close (i.e. 0.40 g and 0.41 g, respectively), and the response acceleration (0.36 g) due to Llolleo earthquake loading would be larger than that (0.24 g) due to Tabas earthquake loading. However, the response of the considered mortar-free structures was expected to be nonlinear. It could be anticipated that the Kobe earthquake loading would be critical, followed by the EL Centro, Llolleo and Tabas earthquake loadings for the considered structures and that the increment in the considered response parameters (i.e. induced acceleration, base shear, overturning moment, block uplift and rope tension) would also be nonlinear. This is being observed in the considered parameters explained in the following sub-sections:

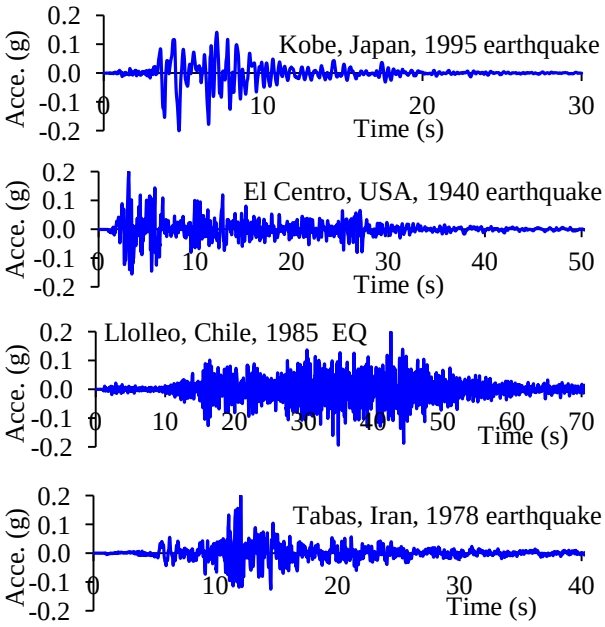


Figure 14: Earthquake loadings with PGA = 0.2 g.

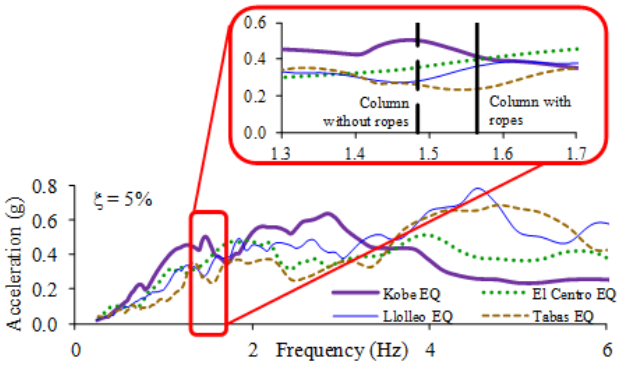


Figure 15: Response spectrum with marked fundamental frequencies of columns.

3.2.1 Induced accelerations

Induced vibrations were recorded using accelerometers attached along the height of the structure. The accelerations recorded at the blocks 2, 5, 9 and the column top (notated as $\ddot{u}_2$, $\ddot{u}_5$, $\ddot{u}_9$ and $\ddot{u}_t$, respectively) under the El Centro 1940 loading are shown in Figure 16. It can be observed that the maximum induced top acceleration was higher than the peak ground acceleration. The increase in the peak response accelerations at any considered location, due to the applied incremental peak ground acceleration, was nonlinear for the structures with and without ropes. The reason for this could be the variation of the inertial force within the column due to the applied ground motions.

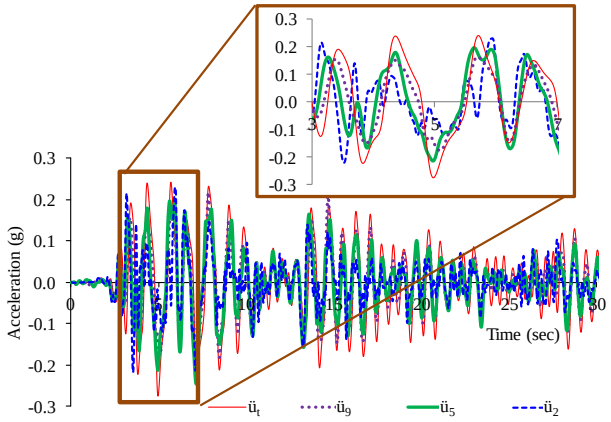


Figure 16: Induced accelerations in column with ropes.

3.2.2 Base shear – displacement curves and maximum overturning moments

Base shear, displacement and overturning moments were calculated in the same manner as those of the harmonic loading. The base shear – displacement curves are shown in Figures 17. It is observed that the structures without ropes have relatively wider hysteretic loops compared to the structures with ropes. This shows more energy dissipation for the former structures. The structure without ropes experience larger lateral displacement in comparison to the structure with ropes. The maximum overturning moment for column with ropes due to the earthquake loadings is shown in Figure 18. The maximum overturning moment is not proportional to the applied incremental earthquake loading. The Kobe earthquake loading generated the highest overturning moment followed by El Centro, Llolleo and Tabas loadings.

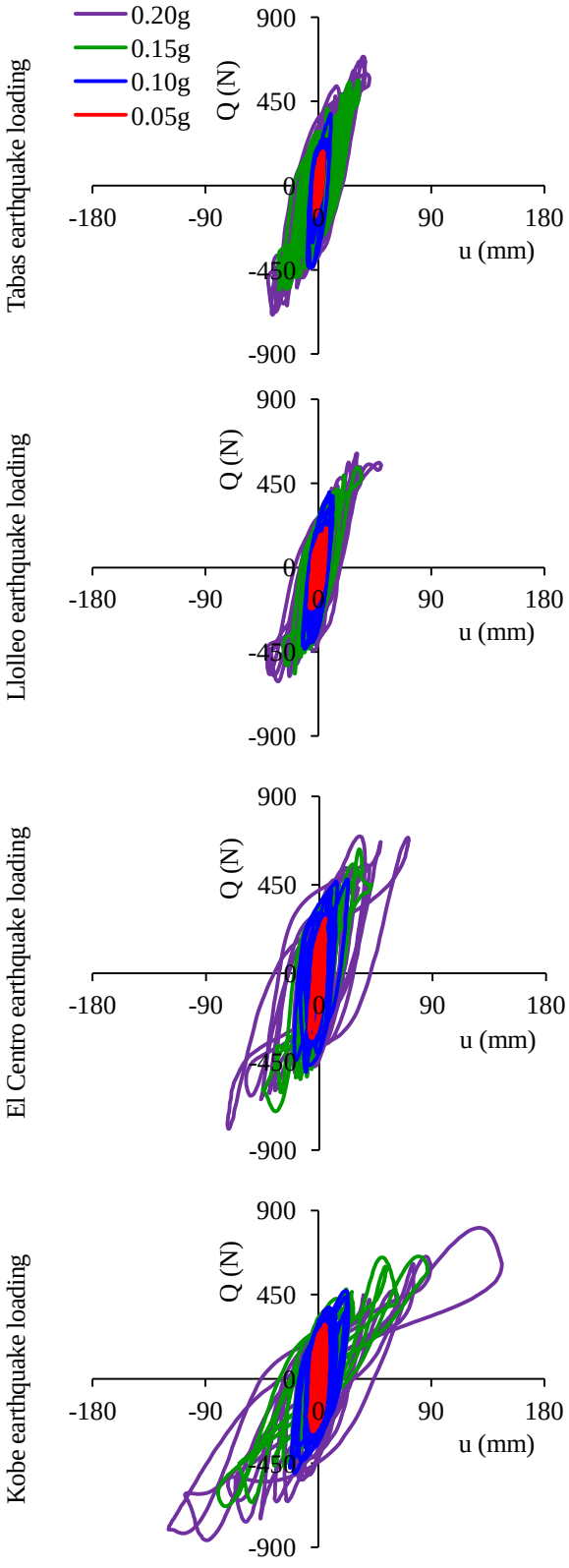


Figure 17: Q-u curves obtained from earthquake loadings for column with ropes.

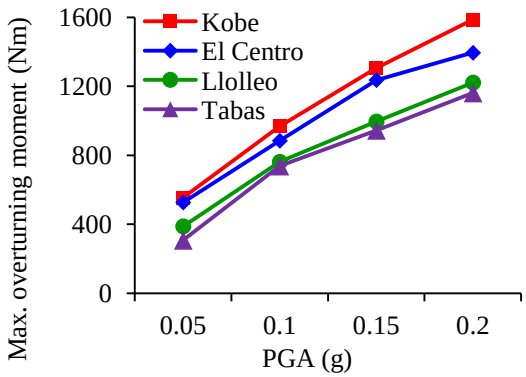


Figure 18: Comparison of overturning moments due to earthquake loadings for column with ropes.

3.2.3 Block uplift and rope tension

Left and right uplifts occurred alternately. As expected, more uplifts were observed in the structure without ropes than in the structure with ropes. The maximum block uplift due to the earthquake loadings is shown in Figure 19. The maximum block uplift is not proportional to the applied incremental earthquake loading. The reason for this could be the non-linear activation of inertial force along the column height. Kobe earthquake loading generated the largest uplift, followed by El Centro, Llolleo and Tabas earthquake loadings.

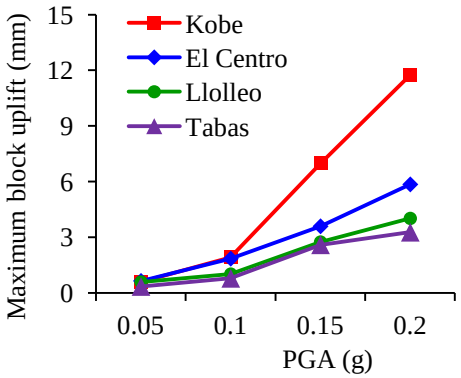


Figure 19: Comparison of uplifts due to earthquake loadings for column with ropes.

The rope tension due to 0.2g El Centro 1940 earthquake loading is shown in Figure 20. As expected, the left and right ropes were activated alternately. It can be observed that there was some magnitude of tension in one rope when the other was in full tension. This observation is already explained in Figure 8 (see stages b and d). The maximum rope tension due to the earthquake loadings is shown in Figure 21. Corresponding to the nonlinear uplift development along the column height, the maximum rope tension is also nonlinear. Kobe earthquake loading generated the highest tension, followed by El Centro, Llolleo and Tabas earthquake loadings.

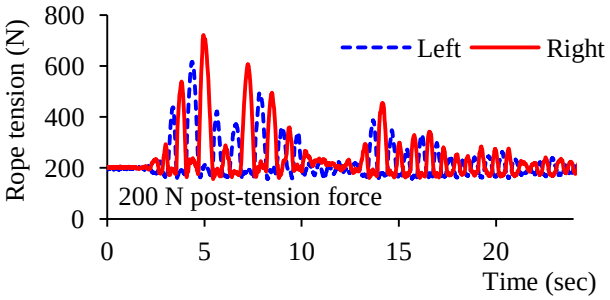


Figure 20: Rope tension due to 0.2g El Centro 1940 earthquake loading.

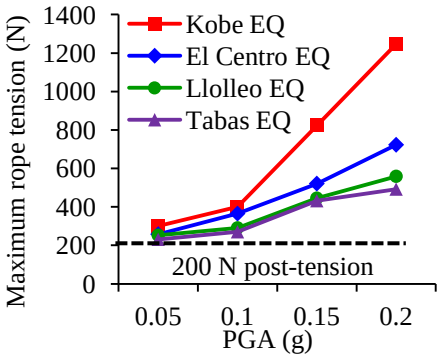


Figure 21: Maximum rope tension due to earthquake loadings.

3.3 Structural response under harmonic loading with constant frequency and varying amplitudes

As mentioned earlier, the structure was tested under successive loading, and any damage occurring at any stage was cumulative. No damage was observed even after all earthquake loadings had been applied. Finally, harmonic loadings with a constant frequency (1.5 Hz) and varying amplitudes (20, 30, 40, 50, 60 and 70 mm) were employed to introduce damage in the structure. As expected, the block uplifts and top relative displacements increased with increased input load. The columns without and with ropes failed during harmonic loading of 50 mm and 60 mm, respectively. The column failed in bending in the out-of-plane direction because one of the bottom interlocking keys cracked and partially shear off, causing instability in the structures. The column failure and damaged interlocking key of the block are shown in Figure 22. From the discussion of block testing (Ali et al., 2012), it was predicted that the main cause of structural failure would be the damage in one of the bottom interlocking keys of the block. It is recommended that a careful compaction in the bottom interlocking keys can result in higher capacity/strength of the block. The mechanically prepared blocks may also avoid such damage.

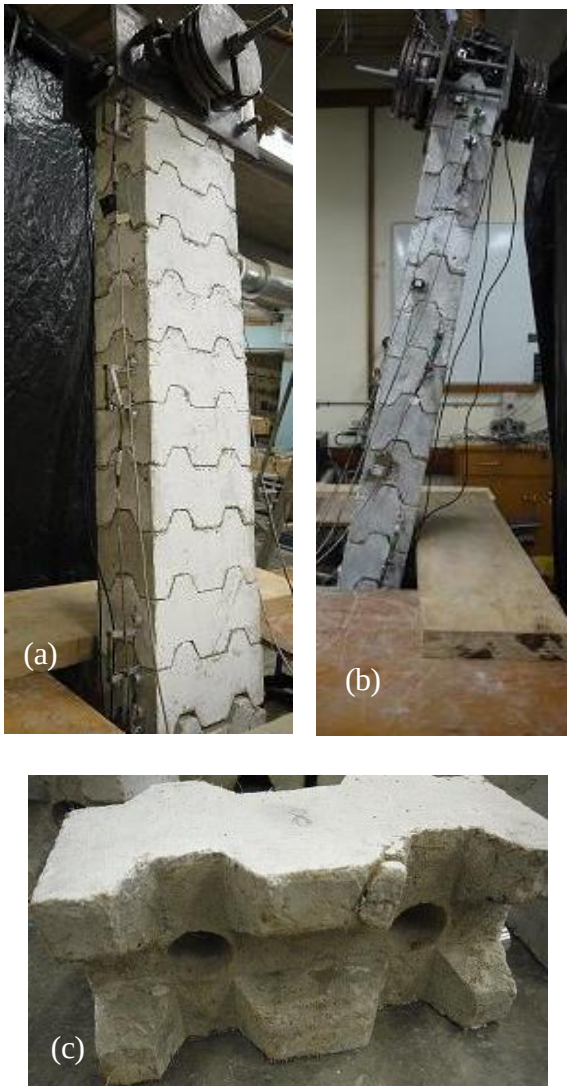


Figure 22: Typical column failure; (a) isometric view, (b) side view, and (c) damage in the bottom interlocking key.

3. CONCLUSIONS

A new approach to construct economical earthquake-resistant houses has been described. The mortar-free columns consisted of an innovative CFRC interlocking blocks. CFRC was prepared with a mix design ratio (cement: sand: aggregates: water) of 1:4:2:0.64, 5 cm long fibres and 1% fibre content by mass of concrete materials. Columns were tested without and with the coconut-fibre rope reinforcement. The un-grouted ropes were utilized as the vertical reinforcement to limit the lateral displacement of the columns. On the other hand, the column without ropes yielded a higher damping due to greater relative movement of the blocks compared to the column with ropes. There is a need to find a balance between the lateral displacement and damping so that the maximum benefit in terms of energy dissipation while avoiding structural collapse can be achieved. A mass of 150 kg was placed at the top of the columns to simulate a roof mass. The results presented in this paper can only be considered indicative, confirming that the proposed construction technology has the potential for a wide use in earthquake prone regions.

Even though the columns performed in a nonlinear manner, linear methods were employed to estimate the damping and the fundamental frequency. The following conclusions can be drawn from this investigation:

- As expected, the fundamental frequency and stiffness of the column with post-tension ropes were higher than those of the column without ropes. However, the difference was small because of low post-tension force (i.e. only 200 N).
- The damping of the column without ropes was higher than that of the column with ropes because the relative movements of the blocks in the former column were large compared to those of the latter column.
- The higher damping was observed for all columns when harmonic loading was employed with amplitude of 15 mm compared to amplitude of 5 mm.
- The energy dissipation in columns was high at a frequency close to proximity of the resonant frequency. The same trend was observed for the maximum overturning moment, uplift and rope tension.
- The column with ropes had smaller relative top displacements and block uplifts compared to the column without ropes.
- The base shear of the column with ropes was smaller than that of the column without ropes. This is due to smaller top relative displacements.
- During the harmonic and earthquake loading, the induced accelerations at the top of the columns were generally higher than the ground accelerations, while smaller accelerations were observed at the other locations considered.
- The maximum rope tension recorded in any shake table test was significantly smaller than the force required to pull the ropes out of a 100 mm embedment.
- The maximum rope tension generated due to any dynamic loading was also less than the tensile load of the rope by a very considerable margin.

This work was the first step towards exploring the behaviour of the deemed technology. Full-scale walls having a top mass (or a diaphragm) should be investigated for a better understanding of their seismic performance. The loss in post-tension stress of ropes over a long period should also be studied.

Acknowledgements:

The authors would like to thank all who helped throughout the research, particularly Golden Bay Cement and Winstone Aggregates for support of this research. The authors also wish to thank Pakistan Higher Education Commission for supporting the PhD study of the first author at the University of Auckland.

References:

Ali M, Gultom R.J. and Chouw N. (2012). "Capacity of innovative interlocking blocks under monotonic loading". *Construction and Building Materials*, **37**, 812-821.

Ali M. and Chouw N. (2013). "Experimental investigations on coconut-fibre rope tensile strength and pullout from coconut fibre reinforced concrete". *Construction and Building Materials*, (Under review).

Anand KB and Ramamurthy K. (2000). "Development and performance evaluation of interlocking-block masonry". *Journal of Architectural Engineering*, **6**(2), 45-51.

Anand KB and Ramamurthy K. (2003). "Laboratory-Based Productivity Study on Alternative Masonry Systems". *Journal of Construction Engineering and Management*, **129**(3), 237-42.

Dedek KP, Claude MAM and Kumaran GS. (2012). "Feasibility study of low cost concrete products as an appropriate: Alternative construction material in the Rwandan construction industry". *Advanced Research Materials*, **367**, 55-62.

Elvin A. and Uzoegbo H.C. (2011). "Response of a full-scale dry-stack masonry structure subject to experimentally applied earthquake loading". *Journal of the South African Institution of Civil Engineers*, **53**(1), 22 -32.

Jaafar MS, Thanoon WA, Najm AMS, Abdulkadir MR and Ali ABA. (2006). "Strength correlation between individual block, prism, and basic wall panel for load bearing interlocking mortarless hollow block masonry." *Construction and Building Materials* , **20**, 492-98.

Nazar ME and Sinha SN. (2007). "Fatigue Behaviour of interlocking grouted stabilised mud-fly ash brick masonry". *International Journal of Fatigue*, **29**, 953-61.

Smith E. (2010). "Interlocking stabilised soil blocks: Appropriate technology that doesn't cost the earth". *The Structural Engineer*, **88**(15/16), 25-29.

Thanoon WA, Jaafar MS, Kadir MRA, Ali ABA, Trikha DN and Najm AMS. (2004). "Development of an innovative interlocking load bearing hollow block system in Malaysia". *Construction and Building Materials*, **18**: 445-54.

Uygunoglu T, Topcu IB, Gencel O and Brostow W. (2012). "The effect of fly ash content and types of aggregates on the properties of pre-fabricated concrete interlocking blocks (PCIBs)." *Construction and Building Materials*, **30**, 180-87.

10CUEE CONFERENCE PROCEEDINGS
10th International Conference on Urban Earthquake Engineering
March 1-2, 2013, Tokyo Institute of Technology, Tokyo, Japan

SHEAR BEHAVIOR OF POLYPROPYLENE FIBER REINFORCED ECC BEAMS WITH REDUCTION OF SHEAR REINFORCEMENTS

Rui Zhang[1], Koji Matsumoto[2], and Junichiro Niwa[3]

1) PhD Candidate, Department of Civil Engineering, Tokyo Institute of Technology, Japan
2) Assistant Professor, Department of Civil Engineering, Tokyo Institute of Technology, Japan
3) Professor, Department of Civil Engineering, Tokyo Institute of Technology, Japan
zhang.r.ab@m.titech.ac.jp, matsumoto.k.ar@m.titech.ac.jp, jniwa@cv.titech.ac.jp

Abstract: The substantial strain capacity and crack control capacity of ECC makes it an ideal material for earthquake-resistant structural members. In this study, the effects of reducing shear reinforcing ratio in polypropylene fiber reinforced cementitious composites (PP-ECC) beams were investigated. A normal RC control beam was prepared with providing amount of shear reinforcements. Further, fibe specimens using PP-ECC were fabricated with monotonic reducing shear reinforcing ratio from the level of RC control beam to zero. And there was also another RC beam without shear reinforcement within shear span was prepared for comparison. Based on the experimental results obtained, it was found that PP-ECC beam with 71% reduction of shear reinforcements can still reach the shear carrying capacity of RC control beams.

1. INTRODUCTION

Polypropylene Fiber Reinforced Engineered Cementitious Composites (PP-ECC, referred herein after), as one kind of ECCs, exhibits multiple fine cracking, pseudo strain hardening behavior and high ductility under uniaxial tensile loading. It has higher tensile strength compared to normal concrete and has capability of reaching ultimate tensile strain between 1 and 5% under monotonic loading. Its pseudo strain-hardening behavior results from its unique multiple fine cracking mechanism, in which closely spaced fine cracks forms because of the bridging action of fibers (Maalej and Li, 1994; Li, 1998). Different from the normal concrete in mixture, ECCs generally use fine aggregates and relatively low volume fractions of short and random fibers (approximately 2 to 3%). Since the absence of coarse aggregate, the elastic modulus of ECC is comparatively lower than that of normal concrete while its compressive strength does not have significant difference from normal concrete.

So far, various types of fiber have been utilized to produce ECCs, including steel, carbon and polymer fibers (Li, 1998). Most structural and retrofit application of ECC reported in the literature use ultra-high molecular weight polyethylene (PE) and polyvinyl alcohol (PVA) fibers. Compared with widely used PVA fibers, polypropylene (PP) fiber is softer, lower cost and easier dispersing which results in better workability. In addition, because of hydrophobic and non-polar nature of PP fiber, PP-ECC has better durability in alkaline environment. In this research, a cementitious composite combined with fabricated polypropylene fibers with improved bond properties (**Figure 1**) that exhibits the pseudo strain hardening and multiple fine cracking of ECCs (Hirata et al., 2009) was used. The properties of PP fiber are shown in **Table 1**.

Although the steel reinforced ECC (R/ECC) structural members such as column and beam-column joints with reduction of shear reinforcements (Li and Fischer, 2002; Parra-Montesinos et al., 2005) has been confirmed in previous study, the shear behavior of ECC beam with reduction of shear reinforcements has not been completely clarified yet. Therefore, Shimuzu et al. (2004) have done several experimental programs on evaluating the shear behavior of PVA-ECC by conducting Ohno shear beam tests and uniaxial tensile tests. The shear strength of tested beams was predicted by employing truss-and-arch model with reduced tensile strength which was obtained from uniaxial tensile tests. However, Kabele et al. (2007) revealed that only a fraction of ECC's tensile strength and strain capacity might be utilized in shear elements due to possible damage of bridging fibers on sliding crack surfaces. Therefore, determining reduction factor for ECC tensile strength is the key to predict shear strength of beam precisely.

In this research, totaling five PP-ECC and two normal RC beams with various shear reinforcing ratios were tested to clarify shear behavior. The tensile properties of ECC was obtained from uniaxial tensile tests.

2. EXPERIMENTAL PROGRAM

2.1 Steel Reinforcements

A regular deformed steel reinforcing bar with nominal

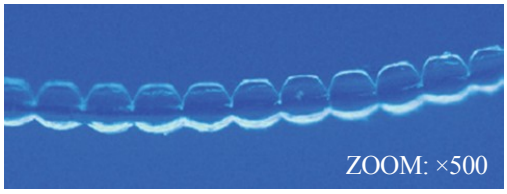


Figure 1 Cross Section of PP Fiber

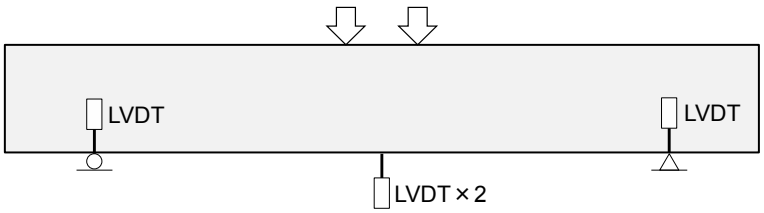


Figure 2 Test Setup

Table 1 Properties of Polypropylene (PP) Fiber

Fiber type	Length (mm)	Diameter (μm)	Young's modulus (MPa)	Tensile strength (MPa)
PP	12	36	5000	482

Table 2 Properties of Steel Reinforcements

Steel bars	Diameter (mm)	f_y (MPa)	f_u (MPa)	ε_u	ε_y
Rebar in tension	25.4	400	577	0.22	0.002000
Shear reinforcements	6.35	323	499	0.17	0.001615
Rebar in compression	6	277	434	0.33	0.001385

Table 3 Mix Proportion of PP-ECC

W/C	Unit (kg/m^3)			
(%)	Water	Cement	PP Fiber	AE
27	371	1400	27	7

Table 4 Mix Proportion of Concrete

W/C	Unit (kg/m^3)				
(%)	Water	Cement	Fine aggregate	Coarse aggregate	AE
60	176.6	294.3	829.9	970.3	2.943

Table 5 Summary of Beam Specimens

Specimen designation	Length L (mm)	Shear reinforcements		Longitudinal bar		Matrix type
		r_w (%)	s (mm)	A_s (mm^2)	p_w (%)	
RC-Ref	2100	0.42	100	1013.4	2.7	Concrete
RC-00		0	700			
RE-42		0.42	100			ECC
RE-30		0.3	140			
RE-24		0.24	175			
RE-12		0.12	350			
RE-00		0	700			

r_w is shear reinforcing ratio. s is the spacing of shear reinforcements. A_s is the total cross sectional area of longitudinal reinforcements. p_w is the longitudinal reinforcing ratio.

diameter of 25.4 mm and yield strength of 400 MPa was used in all beam specimens for longitudinal reinforcement in tension. The shear reinforcement was adopted deformed bar with nominal diameter of 6.35 mm and yield strength of 323 MPa. The round steel bar with diameter of 6 mm and yield strength of 277 MPa was used for longitudinal reinforcement in compression. The type and properties of all steel bars used in these seven beam specimens is summarized in **Table 2**.

2.2 PP-ECC and Concrete

PP-ECC material used in this research is a class of short-fiber, randomly distributed cementitious composites with 3% fiber volume fraction. The polypropylene fiber has a diameter of 36 μm and a length of 12 mm. The modulus of elasticity and tensile strength of this fiber are 5 GPa and 480 MPa, respectively. This fibrillated polypropylene fiber with rugged surface results in improvement of bond properties and exhibits the pseudo strain hardening and multiple fine cracking of ECC under tensile stress (Hirata et al., 2009). The mixture proportion of PP-ECC used in this study is shown in **Table 3**.

For the normal concrete beams, concrete with a design compressive strength of 27 MPa was used. Mixture components include 20 mm maximum size coarse aggregate, fine aggregate and high-early strength cement. **Table 4** gives the mixture proportion of normal concrete for control beam.

2.3 Test Specimens

Two different types of matrixes, totaling seven beams, including one control beam (RC-Ref), one RC beam without shear reinforcement within the shear span (RC-00) and five PP-ECC beams varying shear reinforcing ratio from the level of control beam to zero, summarized in **Table 5**, were tested by four-point loading method as shown in **Figure 2** The designations of these seven specimens are selected according to its matrix type and shear reinforcing ratio. 'RC' and 'RE' indicates that the matrix type of the specimen is 'Reinforced Concrete' or 'Reinforced ECC'. Except the case of control beam (RC-Ref), the latter digit in specimen designations indicates the shear reinforcing ratio, e.g. RE-24 means the specimen with shear reinforcing ratio of 0.24%

using steel reinforced ECC.

All beam specimens have the same cross-sectional dimension (150×300 mm), longitudinal reinforcements and shear span-depth ratio. The normal concrete beam, RC-Ref is designed following JSCE code, providing an amount of shear reinforcements (six stirrups in one shear span) which satisfied an under-reinforced condition, is used as a control beam. The beam specimen corresponding RC-Ref using PP-ECC, namely RE-42, having identical shear reinforcing ratio to normal concrete control beam RC-Ref, was also prepared for comparisons. The dimension and reinforcement details of these two beam specimens are as shown in **Figure 3**. To evaluate the shear behavior without shear reinforcements, another normal concrete beam specimen RC-00 without shear reinforcements was designed to compare shear capacity with beam specimen RE-00 with identical reinforcement but using matrix of PP-ECC. The dimension and reinforcement arrangement is shown in **Figure 4**. Whereas the rest three PP-ECC beam specimens, the shear reinforcing ratios vary from 0.30 to 0.12%, which means the shear reinforcements within one shear span decreases from four to one. All shear reinforcements were uniformly arranged distributed within the shear span as shown in **Figure 5**.

2.4 Test Setup and Procedure

The arrangement of test setup is shown in **Figure 2**. The beam was subjected to a four-point bending load. The distance of 200 mm between two loading points was fixed for all specimens. The shear span-depth ratio *a/d* for all specimens was 2.8. Two linear variable differential transformers (LVDTs) were used to monitor the deflection in the mid-span, and another two LVDTs were attached to the supporting points at two sides of specimen to measure the deformation. As for all steel reinforcements, two strain gauges were attached to two longitudinal reinforcements in tension. For every shear reinforcement within shear span, there were strain gauges attached at the region where diagonal crack was expected to occur. The locations of strain gauges are shown in **Figure 3**, **Figure 4** and **Figure 5**. All specimens were applied with a monotonic load up to failure.

3. TESTS RESULTS AND DISCUSSIONS

3.1 Load-Deflection Behaviors and Failure Modes

The experimental load versus mid-span deflection curves for all specimens involved in this study as well as their failed span at the ultimate stage are shown in **Figure 6** through **Figure 8**. The results of all specimens including material tests are summarized in **Table 6**. The shear carrying capacity by comparing ECC specimens with RC control beam is shown in **Figure 9**.

As for the steel reinforced concrete beam RC-Ref, the first crack appeared in the center span at a load of 54 kN, then inclined shear cracks were induced and propagated with increasing load. The ultimate load capacity of RC-Ref was

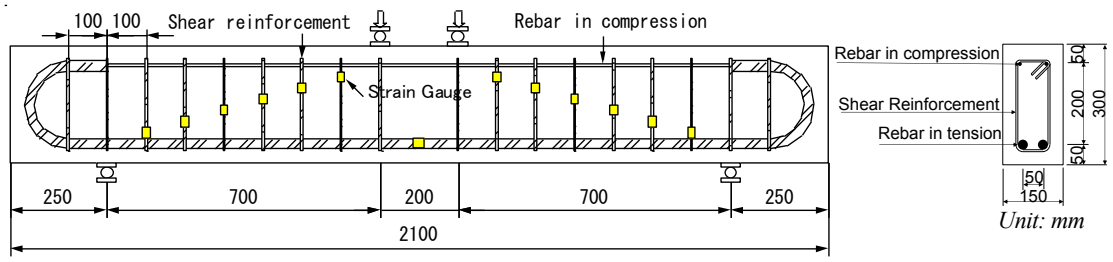


Figure 3 Dimension and reinforcement details of RC-Ref and RE-42

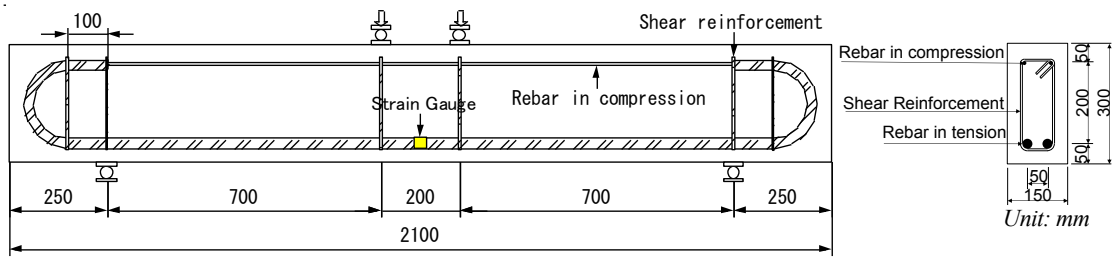


Figure 4 Dimension and reinforcement details of RC-00 and RE-00

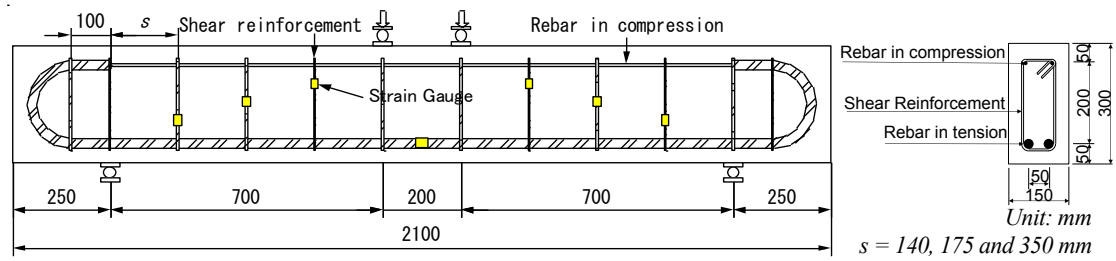


Figure 5 Dimension and reinforcement details of RE-30, RE-24, and RE-12

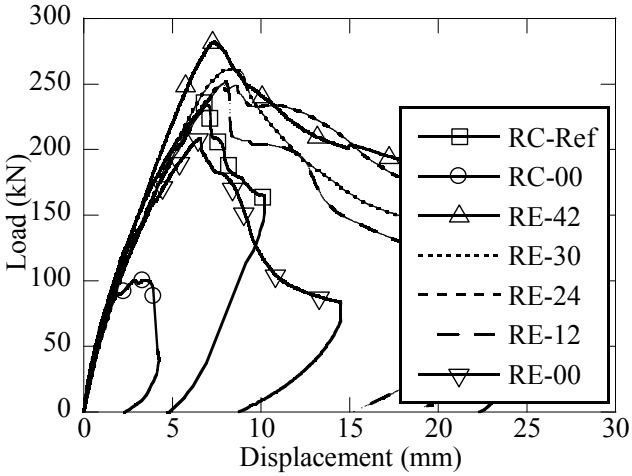


Figure 6 Load and Displacement Curves for All Specimens

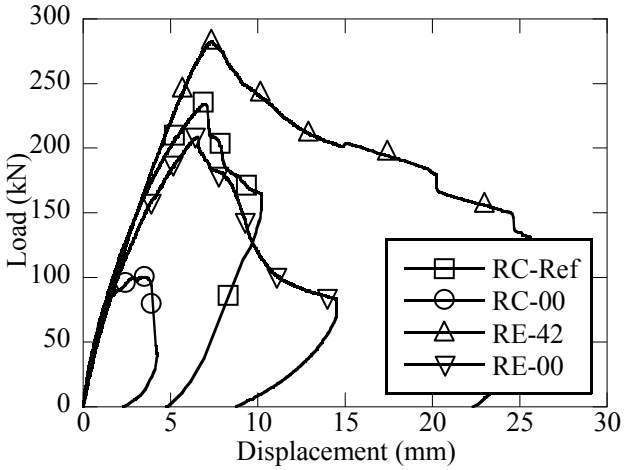
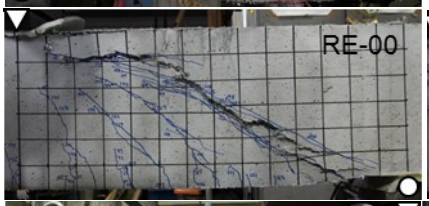


Figure 7 Load and Displacement Curves for RC-Ref, 00 and RE-42,00













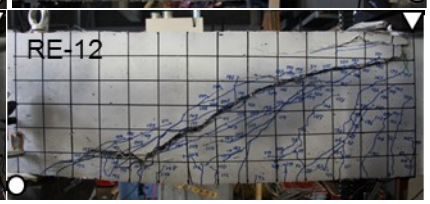


Figure 8 Ultimate Stage of All Specimens

Table 6 Summary of Beam Tests

Specimen	V_{exp} (kN)	Translational angle (10^{-3} rad)	f'_c (MPa)	f_t (MPa)
RC-Ref	117.03	8.72	29.1	2.53*
RC-00	50.27	4.42	34.9	2.88*
RE-42	141.09	9.23	30.4	3.67
RE-30	130.56	10.55	33.1	3.56
RE-24	125.24	9.87	31.5	3.39
RE-12	126.05	10.02	35.6	3.68
RE-00	104.38	8.19	32.8	3.71

*Tensile strength was obtained by split compression method. The rest were tested by direct tensile tests.
V_{exp} is the peak shear force taken by specimens during tests.

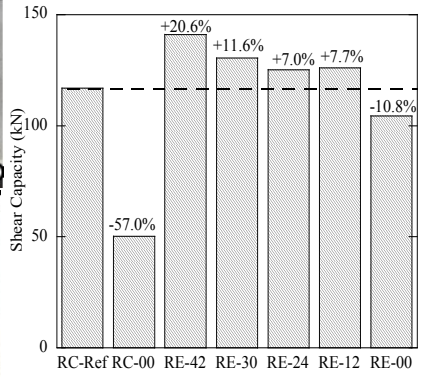


Figure 9 Shear Carrying Capacity Compared with RC-Ref

234.06 kN. After the peak load, the beam finally failed in crushing and spalling of the concrete in the compression zone of shear span closing to loading point. Flexural failure was prevented by providing sufficient longitudinal bars.

Beam RE-42 has an identical reinforcement layout to that of RC-Ref, except a different matrix, however, the ultimate load capacity was 20.6% higher than that of RC-Ref, achieved 282.18 kN. The first crack load of RE-42 is 86 kN, which is 32 kN greater than that of RC-Ref. Beyond the cracking load, the flexural stiffness decreased slightly but kept almost constant up to failure. Several diagonal cracks were developed in shear span, forming as extension of flexural cracks. These shear cracks bent following the compressive stress trajectory with increase of

load. Because of the lower shear span-depth ratio *a/d* (2.8 for all specimens), the beam flexural capacity cannot be fully developed, and then shear capacity dominates the ultimate load-carrying capacity. The failure of RE-42, similar to that of RC-Ref, was initiated by crushing of ECC at the top compression side of main shear crack.

RC-00 and RE-00 is a pair of counterpart beam specimens without shear reinforcements compared to the rest of specimens. RE-00 exhibits similar load-displacement behavior to that of RC-00 before diagonal cracking. Compared with commonly known brittle mode of shear failure such as occurred in RC-00, the shear failure of RE-00 was ductile. This is due to the bridging effect resulting from PP fiber. At the beginning, vertical flexural cracks firstly appeared at the tensile side of beam. When principle tensile stress within shear span exceeded the cracking strength of ECC, a diagonal crack propagated through the beam web. Instead of appearance of several wide cracks, numerous fine cracks developed in the ECC beams and spread throughout large area. The shear resistance of ECC beam was significantly increased by bridging force carried by fibers. The large deformation capacity was provided by multi fine cracking. The peak load of RE-00 was 208.76 kN, compared with that of equivalent concrete beam with shear reinforcements (RC-Ref) wherein the load and deflection capacity just decreased by 10.8% and 6%, respectively. However, if compared with another concrete beam without shear reinforcements (RC-00), the load and deflection capacity of RE-00 increased by 107.6% and 85.2%, respectively.

With various shear reinforcing ratios between the level of control beam and zero, RE-30, 24 and 12 are specimens failed in shear compression similar to that of RE-42. The stiffness of these three beams was found to be slightly higher than that of RE-00 but lower than that of RE-42. The peak load of RE-30, 24 and 12 were 261.12, 250.48 and 252.1 kN, respectively.

3.2 Cracking Pattern

Figure 10 presents the cracking pattern of all specimens at the peak load as well as critical crack developed after peak load as shown with red line. The strain of longitudinal rebars for five specimens in tension just reached yielding strain at their peak loads but soon decreased as increase of load. Meanwhile, the localized diagonal crack was gradually developed after the peak load and cracks in compression zone closing to loading points in shear span appeared.

As has been confirmed by previous research (Suryanto et al. 2010), in conventional reinforced concrete, any slide movement at a crack develops a significant degree of shear resistance because of the aggregate interlock and rough planes of crack. However, in ECC, while the crack opening is small, both crack-shear friction between crack surfaces and fiber bridging contribute to the shear transfer resistance. As the crack opening increases, the frictional resistance diminishes, while the contribution of fiber bridging remains, resulting in a significantly less shear resistance compared to normal concrete due to the absence of coarse aggregate. **Figure 11** shows significant crack slip observed after the peak load during the tests.

3.3 Proportion of Shear Resisting Forces

Considering the force acting at the diagonal crack in a ECC beam subjected to point loads (**Figure 2**), the shear force is resisted by shear carried by ECC (V_{ECC}) or concrete (V_c) and the shear carried by stirrups (V_s). As a result, the shear capacity of beam specimens (V) can be simplified by **Eq. 1** for ECC and **Eq. 2** for RC.

$$V = V_{ECC} + V_s \quad (1)$$

$$V = V_c + V_s \quad (2)$$

where, V_{ECC} is the shear carried by ECC for R/ECC specimens, V_c is the shear carried by concrete for RC beams

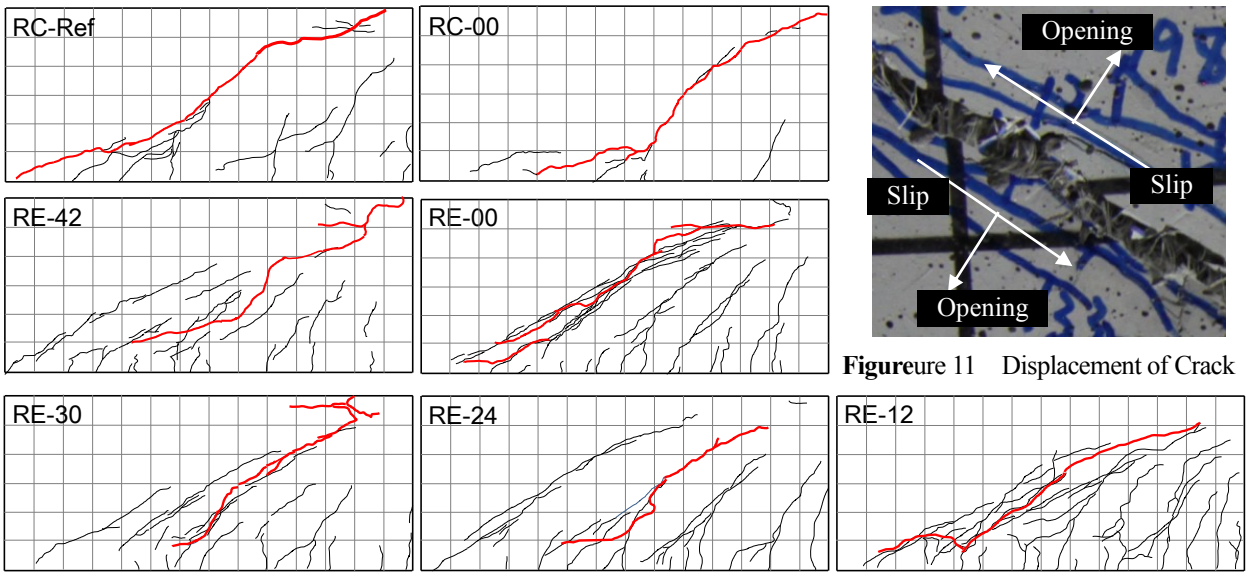


Figure 10 Cracking Pattern at the Peak Load

Figureure 11 Displacement of Crack

Table 7 Experimental Shear Carried by ECC/Concrete and Stirrups

Specimens	V_{exp} (kN)	V_{ECC}/V_c* (kN)	V_s (kN)	V_{ECC}/V_c (%)	V_s (%)
RC-Ref	117.03	49.99	67.04	43%	57%
RC-00	50.27	50.27	0	100%	0%
RE-42	141.09	100.17	40.92	71%	29%
RE-30	130.56	90.05	40.51	69%	31%
RE-24	125.24	86.39	38.85	69%	31%
RE-12	126.05	105.59	20.46	84%	16%
RE-00	104.38	104.38	0	100%	0%

V_{ECC}/V_c refers to the shear carried by ECC for ECC beam or concrete by RC beam.

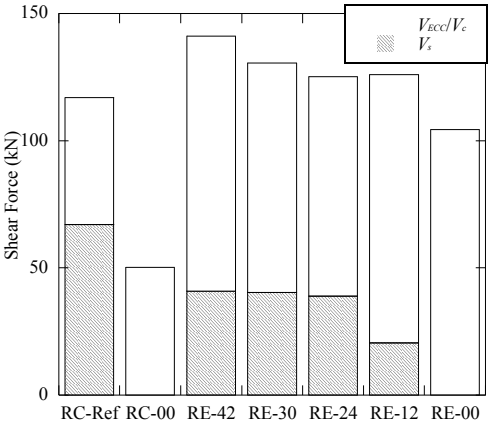


Figure 12 Shear Force Carried by ECC and Shear Reinforcements

and V_s is the shear carried by stirrups.

So far, since there are different simple models utilized for accounting for shear strength of ECC beam, V_{ECC}, shear carried by ECC has not been determined yet. The shear carried by stirrups (V_s) can be calculated from the strain of stirrups which diagonal crack crossed. The strain of stirrups was recorded by prepared strain gauges attaching on the stirrups during the tests. Thus, the shear carried by stirrups (V_s) can be formulated by **Eq. 3** and **Eq. 4**.

$$V_s = \sum \sigma_{si} \tag{3}$$

$$\sigma_{si} = \begin{cases} A_w E_s \varepsilon_s \left(\varepsilon_s < \varepsilon_y\right) \\ A_w f_{wy} \left(\varepsilon_s \geq \varepsilon_y\right) \end{cases} \tag{4}$$

where, σ_{si} is the stress of shear reinforcement crossing critical cracks at the peak load, A_w is cross sectional area of one shear reinforcement within s (mm^2), E_s is the elastic modulus of stirrups, ε_s is the stirrup strain recorded in the tests, ε_y is the yielding strain of shear reinforcements listed in **Table 2**, and f_{wy} is the yield stress of stirrups. As **Eq. 1** through **Eq. 4** presented above, the V_{ECC} and V_c can be calculated by **Eq. 5** and **Eq. 6**, respectively:

$$V_{ECC} = V_{exp} - V_s \tag{5}$$

$$V_c = V_{exp} - V_s \tag{6}$$

where, V_{exp} is the maximum shear force taken by specimens in experiments, V_{ECC}, V_c and V_s at the peak load were listed in **Table 7** and plotted in **Figure 12**.

4. UNIAXIAL TENSILE TESTS OF PP-ECC

4.1 Specimen and Test Method

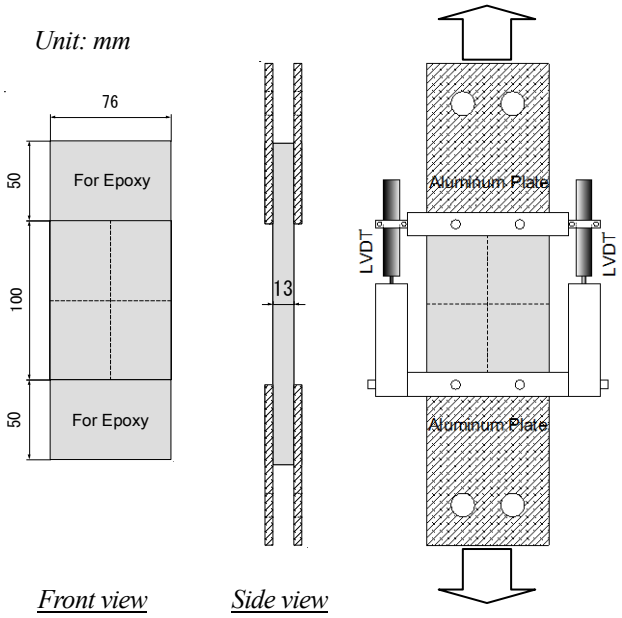
Tensile properties of PP-ECC were also inspected by employing uniaxial tensile method. The specimens for uniaxial tensile tests were plates with cross sectional size of 76×13 mm, as shown in **Figure 13(a)**. The epoxy was used to glue both sides of plate specimens with aluminum plates which were used for setting specimen into test facility. Two LVDTs set parallel to axial direction at both sides, as shown in **Figure 13(b)**, were used to measure axial deformation. 0.1 mm/min was selected as the head speed of loading facility.

4.2 Test Results

Tensile stress vs. strain curves of three specimens are shown in **Figure 14**. The test result clearly shows typical pseudo strain hardening behavior of ECCs. From the beginning of tests, stress continued to increase until occurrence of the first crack. The stress suddenly decreased a little at the time when first crack occurred, whereas it continued to increase after the occurrence of first crack. As the loading continued, the increase and sudden drop of stress continued to happen. Meanwhile, more and more fine cracks were observed on the surface of specimen. At the strain around 3%, a localized crack gradually formed and the stress began to decrease slowly. If according to Shimizu et al. (2004)'s definition that ultimate strain is at the point where stress becomes half of maximum stress after peak stress, this test result shows that PP-ECC has strain capacity greater than 3%. The tensile strength is greater than 3 MPa.

5. EVALUATION OF SHEAR STRENGTH

Several researchers attempted to develop simplified model to evaluate shear strength of steel reinforced ECC structural member. Up to date, the truss-and-arch model recommended by AIJ for RC design of RC structural members, and modified truss model recommended by JSCE are utilized. In this study, the equation in Recommendations for Design and Construction of HPFRCC by JSCE (2008) was used to evaluate the shear strength. JSCE recommendations evaluate the shear strength of steel reinforced ECC beam based on a modified truss model for design of RC structural members. The equation incorporates three parts and the total shear carried by structural member is



(a) Dimension of specimen (b) Setup of tests

Figure 13 Uniaxial Tensile Tests of PP-ECC

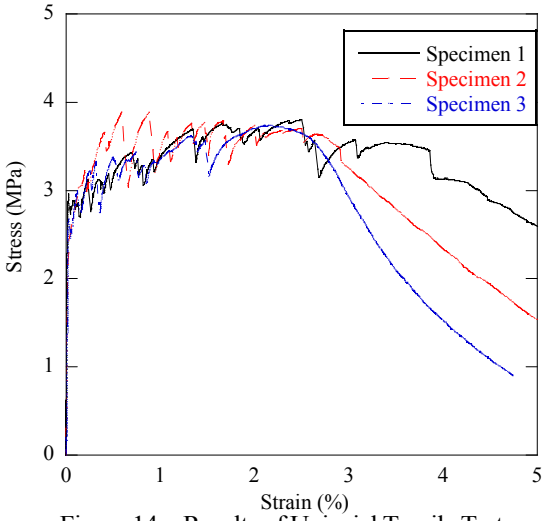


Figure 14 Results of Uniaxial Tensile Tests

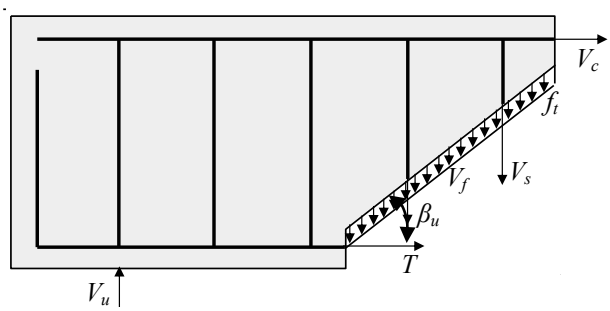


Figure 15 Shear Resistance Mechanism Defined by Modified Truss Model

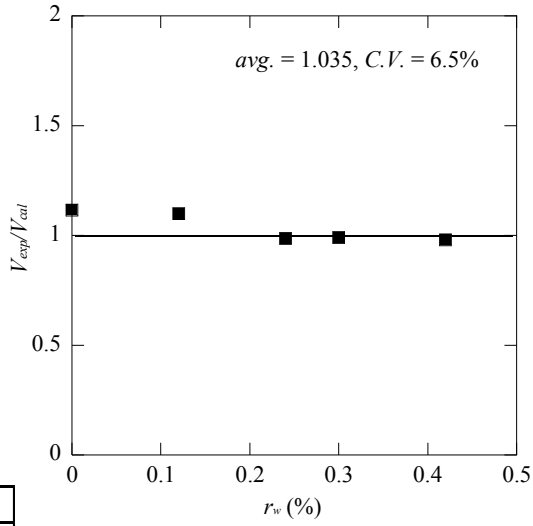


Figure 16 Comparison of Calculated Strength

Table 8 Results of v_t by Reverse Calculation

ID	RE-42	RE-30	RE-24	RE-12	RE-00
v_t	0.45	0.47	0.51	0.55	0.49

expressed by **Eq. 7** and shown in **Figure 15**.

$$V_{cal} = V_c + V_s + V_f \tag{7}$$

where, V_{cal} represents calculated total shear strength of ECC structural member, V_c, V_s and V_f represents shear carried by cement matrix, shear reinforcements and fiber, respectively. V_c is similar to the equation for RC structural members, but with a reduction factor of 0.7 due to the absence of coarse aggregate, which is expressed by **Eq. 8**.

$$V_c = 0.7 \times 0.20 \sqrt[3]{f'_c} \cdot \sqrt[4]{1/d} \cdot \sqrt[3]{100 p_w} \cdot b_w \cdot d \tag{8}$$

where, f'_c is compressive strength of ECC (N/mm^2), d is effective depth (mm), p_w is longitudinal reinforcing ratio and b_w is the web thickness (mm).

V_s is exactly the same as that for design of RC structures, which is presented by **Eq. 9**.

$$V_s = A_w f_{wy} \left(\sin\alpha_s + \cos\alpha_s\right) / s \cdot z \tag{9}$$

where, α_s is angle of shear reinforcements to the member axis, which is 90° in this study. s is the spacing of shear reinforcements and z is the distance from location of compressive stress resultant to centroid of tensile steel, taken as d/1.15.

V_f, the shear carried by fibers, is assumed to be uniformly distributed force in the vertical direction along the inclined crack due to the tensile property of ECC, which is presented by **Eq. 10**.

$$V_f = \left(f_t / \tan\beta_u\right) \cdot b_w \cdot z \tag{10}$$

where, f_t is the tensile strength of ECC (N/mm^2), β_u is the angle of diagonal crack surface to the member axis, taken

here as 45°.

However, according to the previous research, Kabele et al. (2007) revealed that only a fraction of ECC's tensile strength and strain capacity might be utilized in shear elements due to possible damage of bridging fibers on sliding crack surfaces. It is proposed that f_t with a reduced value will be adopted to evaluate the shear strength of these ECC specimens in this study. Therefore, the modified V_f can be expressed by **Eq. 11**.

$$V_f = \left(v_t \cdot f_t / \tan\beta_u\right) \cdot b_w \cdot z \qquad (11)$$

where, v_t is reduction factor for tensile strength of ECC. The value of v_t can be obtained by reverse calculation by using experimental results of specimens. The reverse calculation is shown in **Table 8**. Since there is no obvious tendency by factors, such as shear reinforcing ratio, tensile and compressive strength of ECC, and the average value for all specimens is 0.50, therefore, it was determined that v_t equal to 0.50 in this study. Then, according to **Eq. 8**, **Eq. 9** and **Eq. 11** presented above, the experimental value of maximum shear force in the beam tests is plotted with calculated shear strength given by **Eq. 7** in **Figure 16**. The average (*avg.*) and the coefficient of variation (*C.V.*) of the ratio of experimental to calculated value (V_{exp}/V_{cal}) are1.035 and 6.5%, respectively, which indicates that calculated results using v_t show good agreement with experimental results.

6. CONCLUSIONS

This paper describes the shear behavior of PP-ECC beam specimens with various shear reinforcing ratios by experimental investigation. Totaling seven beams, two normal steel reinforced concrete and five steel reinforced PP-ECC beams, were tested under static monotonic loading condition. In general, all beam specimens with the same longitudinal reinforcements and dimensions were failed in shear. However, PP-ECC beams had significantly large load-carrying capacity than do the counterpart RC beams. Especially the load-carrying capacity of PP-ECC beam without shear reinforcements within shear span almost achieved that of normal RC beam provide with an amount of shear reinforcements and was two times of that of RC beams without the shear reinforcements. Even the shear reinforcement was reduced from the level of control beam, the load-carrying capacity did not decreased significant, in particular three specimens with shear reinforcing ratio between level of control beam and zero, load-carrying capacity were not affected significantly by reduction of shear reinforcements, which is different from the case of RC.

The uniaxial tensile tests for PP-ECC were also performed to confirm the strain-hardening and multiple fine cracking behaviors, which are characteristics of ECC. Based on the test results, PP-ECC exhibited obvious strain-hardening and multiple fine cracking during the tests. The tensile strain capacity achieved 3% above and tensile strength was 3MPa above.

The evaluation method on shear strength of PP-ECC beams were proposed based on modified truss model by adding a tensile reduction factor. The calculated results show good agreement with experimental results.

Acknowledgements:

The authors acknowledge Young Researcher Fund from the Center for Urban Earthquake Engineering (CUEE) in Tokyo Institute of Technology and Obayashi Corporation for providing PP-CC material.

References:

Li, V. (1998) "Engineered Cementitious Composites (ECC) – Tailored Composites through Micromechanical Modeling," *Fiber Reinforced Concrete: Present and the Future*, eds. N. Banthia, and A. Mufti, Canadian Society of Civil Engineers, 64-97.

Maalej, M. and Li, V. (1994) "Flexural/Tensile-strength Ratio in Engineered Cementitious Composites," *Journal of Materials in Civil Engineering, ASCE*, 6(4), 513-528.

Hirata, T., Kawanishi, T., Okano, M. and Watanabe, S. (2009) "Study on Material Properties and Structural Performance of High-Performance Cement Composites Using Polypropylene Fiber", *Proc. of Japan Concrete Institute,* 31(1), 289-294. (Japanese)

Kesner, K. and Billington, S. L. (2004) "Tension, Compression and Cyclic Testing of Engineered Cementitious Composite Materials," *Technical Report MCEER-04-0002*.

Li, V. and Fischer, G. (2002) "Effect of Matrix Ductility on Deformation Behavior of Steel Reinforced ECC Flexural Members under Reversed Cyclic Loading Conditions," *ACI Structural Journal*, 99(6), 781-790.

Shimizu, K., Kanakubo, T., Kanda, T. and Nagai, S. (2004) "Shear Behavior of Steel Reinforced PVA-ECC Beams," *13th World Conference on Earthquake Engineering*, Canada.

JSCE, (2008) "Recommendations for Design and Construction of High Performance Fiber Reinforced Cement Composites with Multiple Fine Cracks (HPFRCC)," Japan Society of Civil Engineers.

Kanakubo, T., Shimizu, K., Kanda, T. and Nagai, S. (2007) "Evaluation of Bending and Shear Capacity of HPFRCC Members Toward the Structural Application" *Proc. of Hokkaido University COE Workshop on High Performance Fiber Reinforced Composites for Sustainable Infrastructure System-Material modeling,* Structural Design and Application, Sapporo, Japan.

Suryanto, B., Nagai, K. and Maekawa, K. (2010) "Modeling and Analysis of Shear-critical ECC Members with Anisotropic Stress and Strain Fields," *Journal of Advanced Concrete Technology, JCI,* 8(2), 239-258.

Kabele, P., and Kanakubo, T., (2007) "Experiential and Numerical Investigation of Shear Behavior of PVA-ECC in Structural Elements," *Proc. of 5th International RILEM Workshop on High Performance Fiber Reinforced Cement Composites (HPFRCC 5)*, Reinhardt and Naaman, eds., 137-146.

Parra-Montesinos, J. G., Peterfreund, W. S., and Chao, S., (2002) "Highly Damage-Tolerant Beam-Column Joints Through Use of High-Performance Fiber-Reinforced Cement Composites" *ACI Structural Journal*, May-June 2005

10CUEE CONFERENCE PROCEEDINGS
10th International Conference on Urban Earthquake Engineering
March 1-2, 2013, Tokyo Institute of Technology, Tokyo, Japan

SHEAR BEHAVIOR OF STEEL AND SYNTHETIC FIBER REINFORCED CONCRETE BEAMS

Pitcha Jongvivatsakul[1], Koji Matsumoto[2], and Junichiro Niwa[3]

1) Ph.D. Candidate, Department of Civil Engineering, Tokyo Institute of Technology, Japan
2) Assistant Professor, Department of Civil Engineering, Tokyo Institute of Technology, Japan
3) Professor, Department of Civil Engineering, Tokyo Institute of Technology, Japan
jongvivatsakul.p.aa@m.titech.ac.jp, matsumoto.k.ar@m.titech.ac.jp, jniwa@cv.titech.ac.jp

Abstract: Including short fibers into concrete is one of the alternatives for improving seismic performance of concrete structures. The researches on fiber reinforced concrete (FRC) beams; however, has been focused mainly on steel fibers. In addition, the shear resisting mechanism of FRC beams has not yet been clarified. This paper aims to investigate the shear carried by steel and synthetic fibers of FRC beams with stirrups based on tension softening curves. FRC beams with various types of fibers, which were 30-mm steel, 60-mm steel, polypropylene, polyvinyl alcohol and polyethylene terephthalate fibers were tested. The shear carried by fibers was investigated from stress transferred across the crack and area of crack surface. The experimental results revealed that steel fibers could transfer more stress than synthetic fibers. However, synthetic fibers provided longer length and flatter angle of the diagonal crack, thereby increasing the area that stress can transfer. Finally, the evaluated shear carried by fibers based on tension softening curves showed good agreement with experimental results even types of fibers are varied.

1. INTRODUCTION

Fiber reinforced concrete (FRC) structures are superior to ordinary reinforced concrete (RC) structures because of their high shear strength coming from the bridging effect of fibers. Short fibers are proper to add in the structures to enhance the seismic performance. The use of fibers as shear reinforcement; however, has focused exclusively on steel fibers (Sharma 1986, Narayanan et al. 1987 and Kwak et al. 2002). Recently, synthetic fibers have become more attractive because of the effectiveness with which they improve shear strength (Li et al. 1992) and their relatively less cost when compared with that of steel fibers. Nevertheless, the influence of steel and synthetic fibers on the shear resisting mechanism of FRC beams with stirrups has not been completely understood. In the Japanese design guidelines for reinforced concrete piers with steel fibers (1999), steel fibers have been considered for the shear reinforcement of concrete structures. However, the design guidelines have not considered the post-cracking behavior of FRC beams in detail.

The method to evaluate the shear carried by steel fibers of FRC beams with stirrups was proposed by the authors (Jongvivatsakul et al. 2011). The tension softening curve—one of the parameters in fracture mechanics—was used to explain the post-cracking behavior of FRC beams. The stress transferred across the diagonal crack of the FRC beams was calculated using the relationship between the tension softening curve and crack surface displacement. The shear force carried by fibers was calculated. However, only 30-mm steel fibers were tested in the previous study. The proposed method has not been applied to various types of fibers yet.

The objective of this study is to investigate the shear carried by steel and synthetic fibers of FRC beams with stirrups by using tension softening curves. The shear resisting mechanism of five FRC beams with stirrups and various types of fibers (i.e. material type and length) was examined. In addition, the diagonal cracking behavior (i.e. the crack surface displacement, diagonal crack length and angle of diagonal cracks) and tensile stress transferred across the diagonal crack were discussed. The method to evaluate the shear carried by fibers using tension softening curves was verified to confirm the applicability of those curves in investigating the shear capacity of FRC beams with stirrups and various fibers.

2. EXPERIMENTAL PROGRAM

2.1 Specimens

A total of five specimens with different types of fibers were prepared and tested. The experimental cases are listed in Table 1. The specimens were named according to the type of fibers used in the beams. Figure 1 shows the dimension and reinforcing bar arrangement of a FRC beam. The shear span (a) was 700 mm and the effective depth (d) was 250 mm. The ratio of shear span to the effective depth (a/d) was 2.8. The longitudinal reinforcement ratio (p_w) was 2.7%. All specimens were controlled such that they would fail in the left shear span by providing fewer stirrups in the left shear span, as shown in Fig. 1. The stirrup ratio in the test span (r_w) was 0.30% in all specimens.

Table 1 Experimental Cases

Specimen	Material type of fiber	Fiber volume ρ_f (%)	Properties of fibers						p_w *4 (%)	f_y *5 (MPa)	r_w *6 (%)	f_{wy} *7 (MPa)	s *8 (mm)
			L_f *1 (mm)	D_f *2 (mm)	Density (kg/m^3)	Strength (MPa)	E *3 (GPa)	Shape of the end					
SF30	Steel	1.0	30	0.62	7850	1050	210	Hooked	2.7	1022	0.3	325	140
SF60	Steel		60	0.90	7850	1050	210	Hooked					
PP	Polypropylene		30	1.6×0.6	910	470	15	Straight					
PVA	Polyvinyl alcohol		30	0.66	1300	960	23	Straight				315	
PET	Polyethylene terephthalate		30	0.70	1370	460	5.8	Straight					

*1 fiber length, *2 diameter of fiber, *3 elastic modulus, *4 longitudinal reinforcement ratio, *5 yield strength of longitudinal reinforcement, *6 stirrup ratio, *7 yield strength of stirrups and *8 spacing of stirrups in test span.

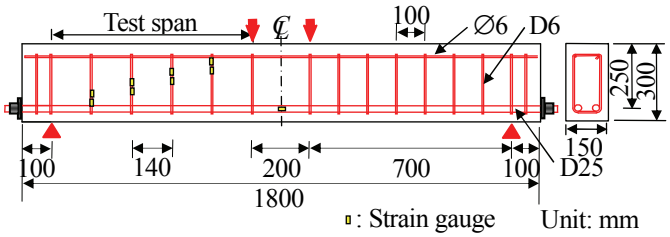
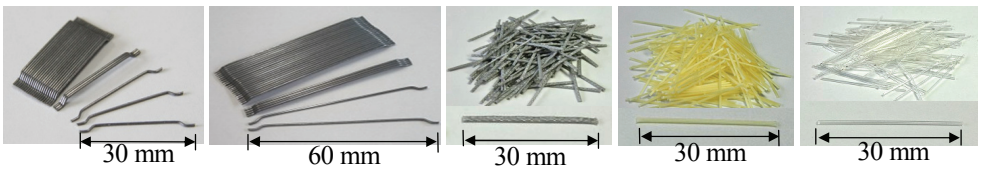


Figure 1 Detailed Diagram of a FRC Beam

Table 2 Mixture Proportion for Concrete

G_{max} (mm)	W/C	Unit weight (kg/m^3)				
		W	C	S	G	SP
20	0.35	165	471	917	790	5.2

G_{max} = maximum size of the coarse aggregate, W = water, C = cement, S = fine aggregate, G = coarse aggregate, SP = high-performance air-entraining (AE) water-reducing agent



(a) SF30 (b) SF60 (c) PP (d) PVA (e) PET

Figure 2 Fibers

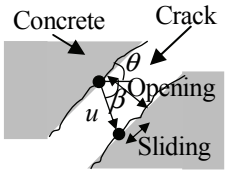


Figure 3 Definition of u

2.2 Material

The materials used in this study were high-early strength Portland cement, fine aggregates, coarse aggregates, and high-performance air-entraining (AE) water-reducing agent. Table 2 shows the mixture proportion for concrete.

Five types of fibers were incorporated into concrete, including steel fibers with lengths of 30 mm (SF30) and 60 mm (SF60), polypropylene fibers (PP), polyvinyl alcohol fibers (PVA) and polyethylene terephthalate fibers (PET). Pictures of the fibers are shown in Fig. 2 and their properties are summarized in Table 1. The volume fraction of fibers was equal to 1.0% of the full volume of the concrete in all specimens.

The longitudinal reinforcing bars were made of deformed steel having 25.4-mm nominal diameter. The stirrups made of deformed steel that was 6.35 mm in nominal diameter were arranged as the shear reinforcement. The yield strengths are listed in Table 1. Two round bars of 6-mm diameter were used as compression bars with yield strength of 304 MPa.

2.3 Loading Setup and Instrumentation

Specimens were subjected to a four-point bending with a simply-supported condition, as illustrated in Fig. 1. Steel plates were placed on the pin-hinge supports and loading points. Figure 1 shows the detailed loading arrangement along with the locations of loading points and strain gauges. The measuring parameters were the applied load, displacements of mid-span and supporting points using four transducers and the strain of the longitudinal steel bars and stirrups.

2.4 Measurement of Crack Surface Displacement and Diagonal Crack Length

Crack surface displacement (u) was measured from the image analysis system developed by Watanabe et al. (2009). Crack surface displacement (u) is defined as the total displacement of cracks in the direction of principal tensile strain (β), which is the direction of the crack's movement, as shown in Fig. 3. In order to analyze the images, red targets of 5-mm diameter were attached on the specimen surface with an interval of 20 mm. During the loading test, photographs of the specimen were captured for every 5 kN of shear force by using three digital cameras fixed on tripods. The image analysis system can investigate the coordinates of the red targets throughout the test span. As a result, the crack surface displacement can be calculated. Because the diagonal crack was expected to open rapidly

near the peak load, some photographs were captured near the peak load with short time intervals to capture the exact behavior at the peak.

Moreover, the length (L) and angle of the diagonal crack (θ) were measured from the visible diagonal crack at the peak load by using the software system, which supports analytical functions ranging from the image measurement to statistical data processing. Calibration was performed to define the length of one pixel in the image for converting the measurement data in pixels to actual lengths. In addition, the images captured for the measurements of crack surface displacements were used to measure crack length and the angle of diagonal cracks at the peak.

3. TENSION SOFTENING CURVES

The tension softening curves were used to investigate stress transferred across the diagonal crack of FRC beams. The curves were obtained from the bending tests of notched beams with a dimension of $100 \times 100 \times 400$ mm, following the standard of the Japan Concrete Institute (2003). Table 3 lists the compressive strength and fracture energy (G_F) of the concrete measured by notched beam tests. Using a least-squares data-fitting procedure, the shape of bilinear curves of the tension softening diagram can be obtained as shown in Table 3. The tension softening curves of five types of fiber reinforced concrete are shown in Fig. 4.

The tension softening behavior varied depending on the type of fibers. SF30 showed the highest peak stress. However, SF60 resisted the highest stress across the crack after $u \geq 0.12$ mm. It is because fiber length increased; thus, the bonding strength improved. At the identical crack opening displacement, steel fibers (SF30 and SF60) transferred higher stress than that by synthetic fibers (PP, PVA and PET) due to their high tensile strength and anchorage. There were two mechanisms in which the stress transferred between crack surfaces was lost. SF30, SF60 and PP failed in the pull-out mechanism, whereas PVA and PET exhibited both pull-out and cut-off mechanisms. Because the tensile strength of fibers was comparatively greater than their bond strength, pull-out failure occurred.

4. CALCULATION OF SHEAR FORCES

From the free body diagram of a part of the shear span of a FRC beam subjected to point load (Fig. 5), the shear capacity (V) of FRC beams can be considered as:

$$V = V_c + V_s + V_f \tag{1}$$

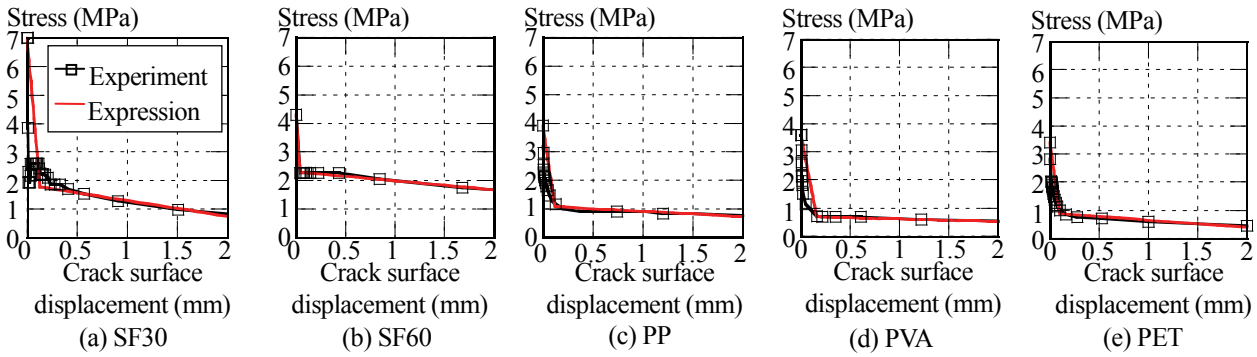


Figure 4 Tension Softening Curves

Table 3 Properties and Expression of Tension Softening Curves

Type	f_c' *1 (MPa)	f_t *2 (MPa)	G_F *3 (N/mm)	Expression
SF30	56.6	3.6	4.24	$\sigma = \begin{cases} 7.0 - 40.2u & \text{for } u < 0.13 \text{ mm} \\ 1.85 - 0.55u & \text{for } u \geq 0.13 \text{ mm} \end{cases}$
SF60	55.9	3.4	8.82	$\sigma = \begin{cases} 4.3 - 50.5u & \text{for } u < 0.04 \text{ mm} \\ 2.3 - 0.31u & \text{for } u \geq 0.04 \text{ mm} \end{cases}$
PP	58.8	3.9	3.02	$\sigma = \begin{cases} 3.9 - 23.5u & \text{for } u < 0.12 \text{ mm} \\ 1.1 - 0.18u & \text{for } u \geq 0.12 \text{ mm} \end{cases}$
PVA	59.9	3.6	2.34	$\sigma = \begin{cases} 3.6 - 18.2u & \text{for } u < 0.16 \text{ mm} \\ 0.7 - 0.09u & \text{for } u \geq 0.16 \text{ mm} \end{cases}$
PET	61.5	3.3	2.89	$\sigma = \begin{cases} 3.4 - 25.2u & \text{for } u < 0.10 \text{ mm} \\ 0.9 - 0.25u & \text{for } u \geq 0.10 \text{ mm} \end{cases}$

*1 compressive strength, *2 tensile strength and *3 fracture energy

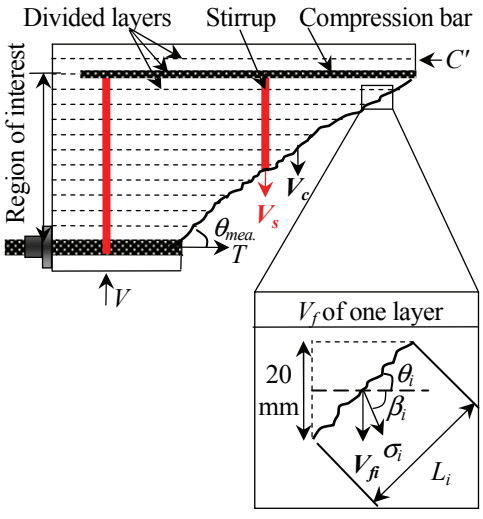


Figure 5 Free Body Diagram of a FRC Beam

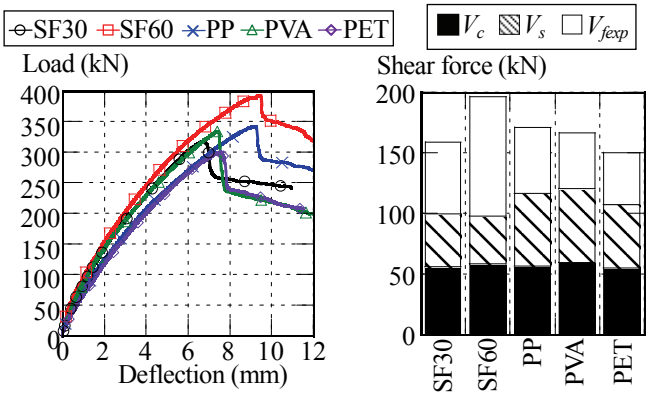


Figure 6 Load-Deflection Curves

Figure 7 Shear Contributions

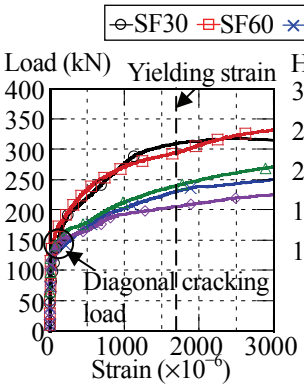


Figure 8 Stirrups Strain

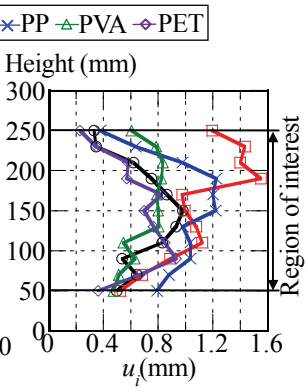


Figure 9 u_i at Peak Load

$$V_c = 0.2 \cdot \sqrt[3]{f_c'} \cdot \sqrt[4]{1000/d} \cdot \sqrt[3]{100 p_w} \cdot b_w \cdot d \quad (2)$$

$$V_s = A_w f_{wy} (z \cot\theta / s) \quad (3)$$

where V_c is shear capacity of members without stirrups (N), V_s is shear carried by stirrups (N), V_f is shear carried by fibers (N), f'_c is the compressive strength of the concrete (MPa), d is effective depth (mm), p_w is longitudinal reinforcement ratio, b_w is web thickness (mm), s is stirrup spacing (mm), A_w is the total cross-sectional area of stirrups provided in the range of s (mm^2), f_{wy} is the yield strength of stirrups (MPa), z is distance from the location of compressive stress resultant to the centroid of tension steel (z = 7d/8) (mm) and θ is angle between the diagonal crack and horizontal line measured from the observed diagonal crack (=$\theta_{mea.}$) (degree).

The experimental value of shear carried by fibers (V_{fexp}) can be obtained from Eq. (4).

$$V_{fexp} = V_{exp} - V_c - V_s \quad (4)$$

Furthermore, according to the JSCE design guidelines (1999), the shear capacity of FRC members can be predicted by using Eq. (5). Thus, the experimental value of κ(= κ_{exp}) can be calculated by Eq. (6). However, Eq. (5) was proposed only for steel fiber reinforced concrete members having 1.0–1.5% fiber out of full concrete volume.

$$V_{JSCE} = (1+\kappa) \cdot V_c + V_s \quad (5)$$

$$\kappa_{exp} = V_{fexp} / V_c \quad (6)$$

where V_{JSCE} is the predicted shear capacity from JSCE equation and κ is the coefficient representing the effect of fibers (κ= 1.0).

5. EXPERIMENTAL RESULTS AND DISCUSSIONS

5.1 Influence of Fiber Types on Shear Behavior

The relationship between the applied load and the mid-span deflection is presented in Fig. 6. The load-deflection response was linear prior to cracking. After the initiation of the first flexural cracking, the load-deflection response became nonlinear. Later, the diagonal crack was observed in the test span and it propagated to the loading point and support. In the pre-peak region, the propagation of the diagonal crack stopped and the inclination of the load-deflection curve decreased. Then, diagonal tension failure occurred and the concrete in the compression zone was crushed. The same behavior of the load-deflection response could be observed in all specimens.

Table 4 summarizes the concrete properties, information regarding diagonal cracks, calculated shear forces and shear forces obtained from the loading tests of FRC beams. Furthermore, Fig. 7 presents the shear contributions of concrete, stirrups and fibers. The shear capacity (V_{exp}) of SF60 was the highest among all specimens. The difference in V_c between each specimen was small because the compressive strength of the concrete did not significantly vary as shown in Fig. 7. On the other hand, V_s was different in each specimen due to the deviation in the angle of between diagonal crack and horizontal line, which was measured from the observed diagonal crack ($\theta_{mea.}$ in Fig. 5). The values of $\theta_{mea.}$ are given in Table 4. Steel fibers provided steeper angles of diagonal cracks than synthetic fibers. Figure 8 shows the average strain of stirrups in the test span. Stirrups in the test span were yielded before the ultimate load. Synthetic fibers (PP, PVA and PET) led the early yielding of stirrups before SF30 and SF60. Considering the shear carried by fibers from the experiment (V_{fexp}), V_{fexp} of SF60 was the greatest as observed in Fig. 7. The specimens including steel fibers showed higher V_{fexp} than synthetic fibers. In addition, V_{fexp} increased with the increase in fiber lengths from 30 to 60 mm. The κ_{exp} of SF30 and SF60 were greater than 1.0, which are the value recommended in the design guidelines (1999), whereas those of PP, PVA and PET were less than 1.0. In case that enough anchorage and bond are provided, steel fibers are the most effective to enhance the shear carried by fibers.

5.2 Crack Distribution Along the Depth of Diagonal Crack

In order to measure the crack surface displacement, the image analysis was performed. The specimens were divided

Table 4 Summary of the Calculation and Experimental Results of FRC Beams

Beam	Concrete properties			Results of diagonal crack						Calculation and experimental results						
	f'_c [*1] (MPa)	f_t [*1] (MPa)	G_F [*2] (N/mm)	u [*3] (mm)	σ [*4] (MPa)	L [*5] (mm)	β [*6] (°)	θ [*7] (°)	$\theta_{mea.}$ [*8] (°)	V_{exp} (kN)	V_c (kN)	V_s (kN)	V_{fexp} (kN)	κ_{exp}	V_{fcal} [*9] (kN)	V_{fexp}/V_{fcal}
SF30	55.3	3.0	4.24	0.67	1.48	387.3	63.3	34.0	36.8	158.8	56.3	43.0	59.5	1.06	72.6	0.82
SF60	61.9	3.7	8.82	1.08	1.97	378.3	64.6	41.6	38.2	196.3	58.4	39.6	98.3	1.68	96.2	1.02
PP	57.0	3.1	3.02	0.94	0.93	428.1	69.2	32.2	27.5	170.8	56.9	59.8	54.1	0.95	53.6	1.01
PVA	65.4	3.0	2.34	0.69	0.64	490.6	63.7	27.8	27.0	166.8	59.5	61.1	46.1	0.78	40.4	1.14
PET	51.8	3.0	2.89	0.62	0.75	427.3	64.8	26.5	31.0	149.9	55.1	51.9	43.0	0.78	43.0	1.00

[*1] measured from specimens prepared together with FRC beams, [*2] fracture energy from notch beams test, [*3] average crack surface displacement at the peak, [*4] average stress at the peak, [*5] total crack length at the peak, [*6] average angle of principal tensile strain at the peak, [*7] average angle of diagonal crack at the peak, [*8] measured angle between the diagonal crack and horizontal line and [*9] calculated shear carried by fibers based on tension softening curves (Eq. (7)).

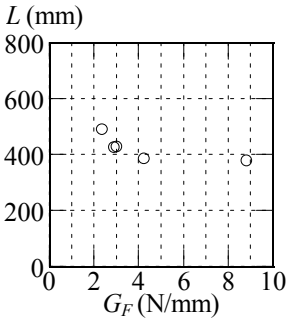


Figure 10 Effect of G_F on L

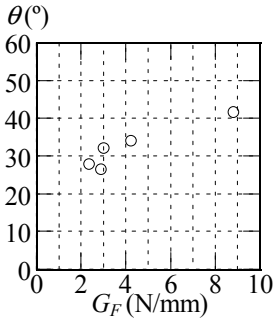


Figure 11 Effect of G_F on θ

into 15 layers. The pictures of specimens at the peak load were used to measure the information of diagonal crack of each layer (i.e. crack surface displacement (u_i), length of diagonal crack (L_i), angle of principal tensile strain (β_i) and angle of diagonal crack (θ_i)) (see Fig. 5). The region of interest for investigation of the shear carried by fibers is the part between location of compression bars and tensile reinforcing bars, where is 50-250 mm from the bottom of the specimens as indicated in Fig. 5. The region of interest is where fibers show their tensile performance.

The value of crack surface displacement (u_i) along the height of the diagonal crack is shown in Fig. 9. Generally, u_i was greater at approximately the middle height of specimens when compared with u_i at the top and the bottom of specimens because of the compression zone at the top of specimens and restraint by longitudinal reinforcing bars at the bottom part of the specimens. u_i differed depending on the types of fibers. u_i at the peak load was in the parabolic shape and was varied in the range from 0.2 to 1.55 mm as observed in Fig. 9. The average values of u_i in the region of interest (u) are listed in Table 4. SF60 had the widest u among all specimens.

5.3 Diagonal Crack Length

The crack length (L) is the summation of L_i in the region of interest. The values of L are listed in Table 4. PP, PVA and PET provided longer L than those by specimens with steel fibers (SF30 and SF60), as shown in Table 4, because of the relatively flatter angle of diagonal cracks. In addition, there was a relation between L and G_F. L decreased with the increase in G_F as shown in Fig. 10. This tendency conforms to the effects of r_w and ρ_f on L as reported in the previous study by the authors (Jongvivatsakul et al. 2011). This implies that G_F can be one of the indicators for the efficiency of fibers as a shear reinforcement.

5.4 Angles of Principal Tensile Strain and Diagonal Crack

The angles of principal tensile strain (β_i) and diagonal crack (θ_i) of each layer were measured. Table 4 gives the average value of β_i in the region of interest (β). β did not change significantly among these specimens. On the other hand, by considering the average of θ_i (=θ), θ was varied from 26.5° to 41.6°. The specimens with higher G_F revealed steeper θ than those of low G_F (see Fig. 11).

6. SHEAR CARRIED BY FIBERS

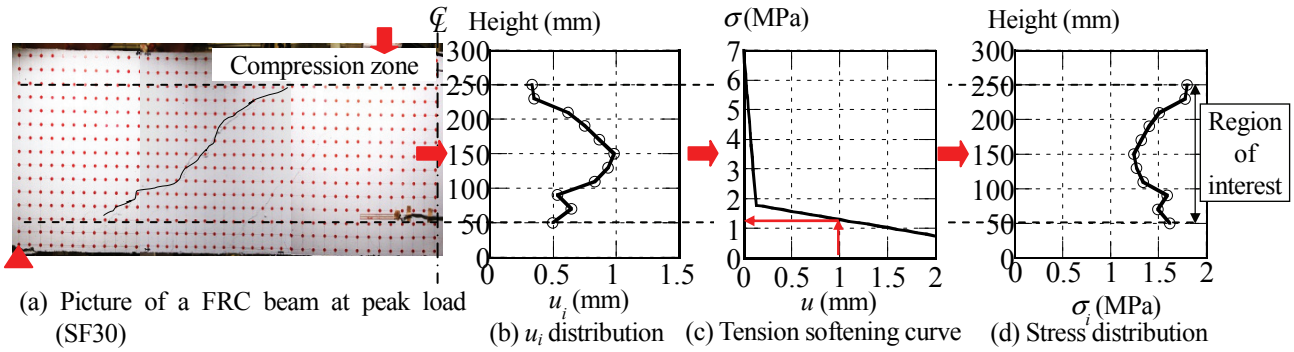
6.1 Review of the Evaluation Method

The authors (Jongvivatsakul et al. 2011) have proposed a method for evaluating the shear carried by steel fibers by using tension softening curves. Tensile stress transferred across the diagonal crack (σ_i) can be converted from crack surface displacement (u_i) by using the relationship between tensile stress and crack opening displacement of the tension softening curves as shown in Fig. 12.

By considering the force acting at the diagonal crack in a FRC beam due to the effect of fibers (Fig. 5), the shear carried by fibers (V_{fcal}) is the summation of forces in the region of interest, where is the heights of 50-250 mm from the bottom of the specimens, and can be calculated from Eq. (7).

$$V_{fcal} = \sum_{i=1}^{n} \left(\sigma_i \cdot b_w \cdot L_i \cdot \cos\left(\beta_i + \theta_i - 90\right) \cdot \sin\beta_i \right) \qquad (7)$$

where n is the number of layers in the region of interest (n = 11), σ_i is the tensile stress of the layer i (MPa), L_i is the length of the diagonal crack of the layer i (mm), β_i is the angle of the principal tensile strain of layer i (degree) and θ_i is the angle of the diagonal crack of the layer i (degree).



(a) Picture of a FRC beam at peak load (SF30) (b) u_i distribution (c) Tension softening curve (d) Stress distribution

Figure 12 Investigation of Tensile Stress Transferred Across the Diagonal Crack

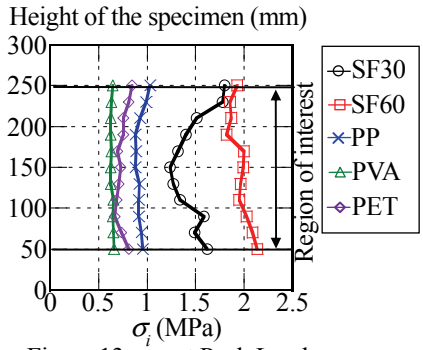


Figure 13 σ_i at Peak Load

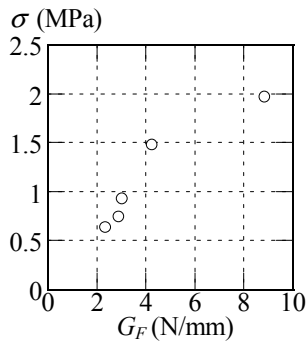


Figure 14 Effect of G_F on σ

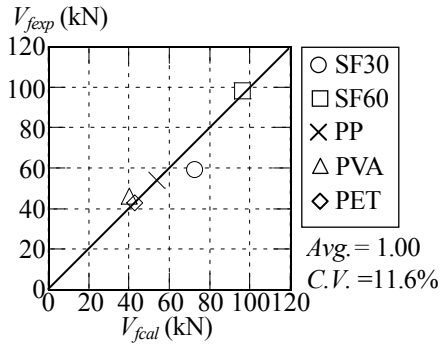


Figure 15 Comparison between V_{fexp} and V_{fcal}

This method was validated for evaluating the shear carried by steel fibers of FRC beams varying ρ_f, r_w and d with high accuracy. However, only steel fibers having length of 30 mm have been investigated in the previous research. It has not yet been extended to FRC beams with various types of fibers.

6.2 Calculated Shear Carried by Fibers

The tensile stress transferred across the diagonal crack at the peak load was evaluated from crack surface displacement and the relationship between the tension softening curves listed in Table 3. The results of stresses (σ_i) are shown in Fig. 13. The larger stress could be resisted to the top and bottom parts of the specimens because of the smaller u_i. Although u_i of the specimens was varied depending on the fiber types without the clear tendency, the value of σ_i was significantly different and a tendency was observed. It is because each fiber reinforced concrete transferred the different stress at the identical crack surface displacement as observed in tension softening curves. SF60 resisted the highest σ_i resulting in the largest V_{fexp}. Synthetic fibers resisted relatively low and uniform σ_i at the peak load due to their flat slope of the second branch of tension softening curves (i.e. when $u \geq 0.12$, 0.10 and 0.16 mm for PP, PVA and PET, respectively). The average value of σ_i in the region of interest (σ) is listed in Table 4. With the increase in G_F, σ increased as observed in Fig. 14.

Shear carried by the fibers (V_{fcal}) was calculated using Eq. (7) and was summarized in Table 4. Figure 15 shows the comparison between the experimental results and calculated values. The ratio of the mean of the experimental value to the calculated value of shear carried by fibers was 1.00 with a coefficient of variation (*C.V.*) of 11.6%. The proposed method can be used to evaluate shear carried by fibers of FRC beams. Moreover, this method can be used when the material types and lengths of fibers were varied because the tension softening curves can reflect the characteristic of each fiber.

7. CONCLUSIONS

(1) Shear capacity of FRC beams with steel fibers was greater than that of specimens having synthetic fibers. Steel fibers are the most effective to enhance the shear carried by fibers when there is enough fiber length and bonding strength due to high tensile strength of steel fibers.

(2) The specimen with 60-mm steel fibers provided the widest crack surface displacement at the peak load because of the effects of the fiber length and shape of ends. However, it was most effective for transferring stress across the crack because it resisted the highest stress in post-cracking behavior as indicated by the tension softening curve. Therefore, the post-cracking behavior in the curve is essential for investigating the shear resisting mechanism of FRC beams.

(3) Stress transferred across the diagonal crack and the angle of the diagonal crack increase with the increase in the fracture energy, while the length of diagonal crack becomes shorter. However, the angle of principal tensile strain was not varied in this study.

(4) The method to evaluate the shear contribution of fibers was presented. The calculated shear carried by fibers

showed a good agreement with experimental results, even for various material types and fiber lengths.

Acknowledgements:

The authors acknowledge support from the Center for Urban Earthquake Engineering (CUEE) in Tokyo Institute of Technology.

References:

Japan Concrete Institute (JCI) (2003), "Method of Test for Fracture Energy of Concrete by Use of Notched Beams," JCI Standard.

Japan Society of Civil Engineers (JSCE) (1999), "Guidelines of Design for RSF Piers," Concrete Library 97, JSCE. (in Japanese)

Jongvivatsakul, P., Watanabe, K., Matsumoto, K. and Niwa, J. (2011), "Evaluation of Shear Carried by Steel Fibers of Reinforced Concrete Beams Using Tension Softening Curves," *Journal of Materials, Concrete Structures and Pavements*, Japan Society of Civil Engineers, **67**(4), 493-507.

Kwak, Y.-K., Eberhard, M. O., Kim, W.-S. and Kim, J. (2002), "Shear Strength of Steel Fiber-Reinforced Concrete Beams without Stirrups," *ACI Structural Journal*, American Concrete Institute, **96**(4), 530-538.

Li, V. C., Ward, R. and Hamaza, A. M. (1992), "Steel and Synthetic Fibers as Shear Reinforcement," *ACI Structural Journal*, American Concrete Institute, **89**(5), 499-508.

Narayanan, R. and Darwish, I. Y. S. (1987), "Use of Steel Fibers as Shear Reinforcements," *ACI Structural Journal*, American Concrete Institute, **84**(3), 216-227.

Sharma, A. K. (1986), "Shear Strength of Steel Fiber Reinforced Concrete Beams," *ACI Structural Journal*, American Concrete Institute, **83**(4), 624-628.

Watanabe, K., Higashi, H. and Niwa, J. (2009), "Real-Time Image Analyzing System for Evaluating the Shear Failure Mechanism of Reinforced Concrete Beams," *The 4th International Conference on Construction Materials: Performance, Innovations and Structural Implications* (*ConMat'09*), 1477-1482.

10CUEE CONFERENCE PROCEEDINGS
10th International Conference on Urban Earthquake Engineering
March 1-2, 2013, Tokyo Institute of Technology, Tokyo, Japan

BEHAVIOR OF PRESTRESSED CONCRETE BEAMS HAVING RUPTURED STRANDS STRENGTHENED IN FLEXURE BY EXTERNALLY BONDED CFRP SHEETS

Thi Thu Dung Nguyen[1], Koji Matsumoto[2], Yuji Sato[3], Asami Iwasaki[3] and Junichiro Niwa[4]

1) PhD. Candidate, Department of Civil Engineering, Tokyo Institute of Technology, Japan
2) Assistant Professor, Department of Civil Engineering, Tokyo Institute of Technology, Japan
3) Engineering Division, Civil Engineering Design Section, Fuji P.S. Corporation
4) Professor, Department of Civil Engineering, Tokyo Institute of Technology, Japan
dungnguyen.aa@m.titech.ac.jp, matsumoto.k.ar@m.titech.ac.jp, y.sato@fujips.co.jp, a.iwasaki@fujips.co.jp, jniwa@cv.titech.ac.jp

Abstract: Recently, the deterioration of prestressed concrete (PC) girders that leads to the ruptures of strands or tendons has become a concern in many countries. There are urgent needs of investigating as well as retrofitting the damaged members, particularly for seismic resistance, enhancement in strength, stiffness are required. This paper presents the experimental works of flexural strengthening for PC beams having ruptured strands using different amounts of externally bonded Carbon Fiber Reinforced Polymer (CFRP) sheets. The damaged PC beam had 50% of tensile prestressing strands were ruptured at middle of the span. Then, CFRP sheets were bonded to the tension surface for flexural strengthening with different amount of sheet layers. The flexural capacity of the strengthened beams was recovered up to 91.5% of the original PC beam. The increase in number of the bonded sheets resulted in the reduction of tensile stress carried by the remaining prestressing strands. The failure changed from debonding in the constant moment region to debonding from the end of the bonded sheets. The predicted flexural capacity based on ACI 440.2R guidelines tends to be overestimated when greater than three layers bonded because the failure modes were different from the predictions.

1. INTRODUCTION

Recently, the deterioration of prestressed concrete (PC) beams because of chloride attack, insufficient grout or external impacts that lead to the ruptures of strands or tendons has become a concern in many countries. These damages cause an excessive reduction of flexural capacity and decrease the stiffness of not only the damaged members but also the whole structures. As a result, the structures become high vulnerability to earthquakes. Hence, there are urgent needs of retrofitting the damaged members, particularly for seismic resistance, the improvement in the strength and member stiffness are required. The traditional strengthening methods (strand splices, external post-tensioning tendons or steel plate jackets), however, have drawbacks because they require large equipments, consume much time, labors. Moreover, the strengthening materials themselves may not be protected from future corrosion.

Meanwhile, the application of fiber reinforced polymers (FRPs) in structural repair and strengthening has been increased in the last decades. A various types of FRP materials (carbon fiber, glass fiber, aramid fiber, etc.,) have been commonly used in different types such as bars, sheets, laminates or meshes. While bars and grids are commonly used for substitute of internal steel bars in new structures, FRP sheets are applied for repair and strengthening of existing structures. Carbon fiber reinforced polymer (CFRP) sheets with the advantages of high strength to weight ratio, excellent corrosion resistance, ease and short time of construction have been adopted widely in strengthening of existing reinforced concrete (RC) members. To date, there have been many studies focusing on the application of CFRP sheets in flexural strengthening of RC beams. Besides, the provisions of the guidelines for design and construction of structural members strengthened by externally bonded FRP sheets in many countries like USA (ACI 440.2R-08) and Japan (JSCE recommendation 2002) prove the great contribution of those countries to broadening the application of a new strengthening method. Even though, there have been a few studies on the behaviors of damaged PC beams strengthened by externally bonded CFRP sheets. Moreover, because of difficulties in predicting the failure modes, the current design guidelines have not reflected all the factors; therefore, predicting the flexural strength of concrete members, particularly, PC members with ruptured strands externally bonded by FRP sheets has been still conservative.

Hence, this study aims to investigate the behaviors of PC beams having ruptured strands strengthened in flexure by externally bonded CFRP sheets. The object of strengthening was PC beams having 50% of strands ruptured. CFRP sheets were externally bonded to the bottom side of PC beams with different number of sheet layers. Furthermore, the experiment outcomes were compared with the predicted values based on the guideline of ACI (ACI 440.2R-08).

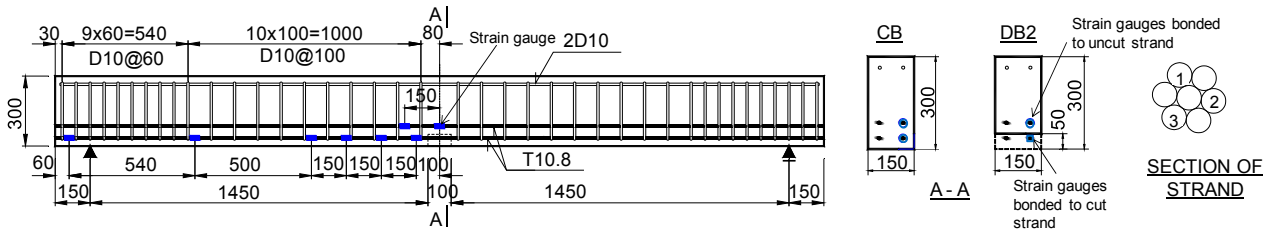


Figure 1 Details of specimens (Unit: mm)

Table 1 Mixing proportion of concrete

Unit quantity (kg/m^3)					
Water	C	S	G	Water reduce agent	AE agent
155	388	824	967	2.13	3.69

C: early strength Portland cement, density = 3.14 g/cm^3
S : fine aggregate, density = 2.65 g/cm^3, F.M. = 2.81
G: coarse aggregate, density = 2.65 g/cm^3, F.M. = 6.38
AE agent: air entraining agent

2. OUTLINE OF EXPERIMENTS

2.1 Details of PC beams

The details of the specimens are shown in Fig. 1. In the figure, CB denotes the control beam or undamaged beam. DB2 donotes the PC beams which had 50% of the prestressing strands were cut at middle of span. The specimens had a rectangular section of 150 mm wide and 300 mm high. The total length was 3.3 m while the beam span was 3.0 m. Four prestressing strands were arranged in two layers in tension zone. The prestressing strand had the nominal diameter of 10.8 mm, consisted of seven wires. The cross-section area of each strand was 70.08 mm^2. The prestressing strands were pre-tensioned with the initial stress of 1,075 N/mm^2. Two deformed bars diameter of 10 mm were set in compression zone. Also, the stirrups were provided to prevent shear failure. The stirrup spacing is shown in the figure.

For the damaged PC beams, to duplicate the rupture of prestressing strands, a portion of concrete with 100 mm long and 50 mm high was left at the middle of the span. Two of four strands were exposed at the bottom side span at this portion (section A-A, Fig. 1). The exposed prestressing strands, then, were cut using a steel cutting blade. In terms of strengthening, the concrete sections at the midspan were restored to the original rectangular shape by a high strength cementitous mortar.

2.2 Material properties

The mixing proportion of concrete is given in Table 1. The concrete was designed with the average 28-day cylinder compressive test of 55 N/mm^2. The tensile strength and yielding strength of prestressing strands were 1,894 N/mm^2 and 1,722 N/mm^2, respectively. The deformed bars used for stirrups and compression reinforcement had yielding strength of 370 N/mm^2. The design 28-day compressive strength of mortar was 50.2 N/mm^2.

Table 2 Experimental cases

No.	Name	CFRP sheets				
		t_f (mm)	n_f	b_f (mm)	l_f (mm)	w_f (mm)
1	CB	-	-	-	-	-
2	DB2	-	-	-	-	-
3	DB2-100-1	0.111	1	125	1,000	-
4	DB2-100U-2b	0.333	2	125	1,000	180
5	DB2-100U-3b	0.333	3	125	1,000	180
6	DB2-100U-4b	0.333	4	125	1,000	180
7	DB2-100U-5b	0.333	5	125	1,000	180

t_f: thickness of one layer CFRP sheet; n_f: number of longitudinal CFRP sheet layers; b_f: width of CFRP sheet; l_f: length of CFRP sheet; w_f: width of U-shaped transverse sheet

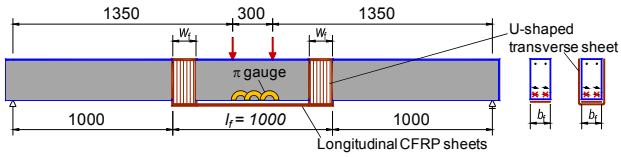


Figure 2 Layout of externally bonded CFRP sheets (Unit: mm)

2.3 Layout of externally bonded CFRP sheets

Table 2 lists the experimental cases. CB and DB2 were the reference cases, the other specimens were strengthened in flexure by attaching unidirectional CFRP sheets to the bottom face of the damaged PC beams. The attaching layout of CFRP sheets is illustrated in Fig. 2. The number of CFRP sheet layers was varied from one to five layers in the strengthened beams while the width and lengths of CFRP sheets were constant values of 125 mm and 1,000 mm respectively. Except DB2-100-1, the additional U-shaped transverse sheets were wrapped at the end of the longitudinal sheets in order to prevent the debonding of the longitudinal sheets. The name of specimen indicates the damaged beam - the length of the longitudinal CFRP sheets, presence of U-shaped anchorage sheets - number of CFRP sheet layers.

The CFRP sheet with the thickness of 0.111 mm was adopted in DB2-100-1. In the other specimens, CFRP sheets having the thickness of one layer of 0.333 mm were used.

CFRP sheets were bonded to concrete surface by wet-layup procedure. First, bottom faces of concrete were ground slightly to make them smooth. Then, a primer was

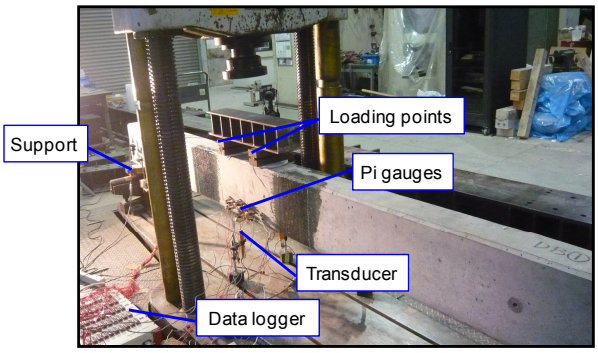


Figure 3 Instrument settings for loading test

applied to the concrete surfaces. In the next stage, each layer of CFRP sheet was impregnated with an epoxy-resin to concrete surface. After all the layers of CFRP sheets were pasted, a finishing coat of the same epoxy resin was externally covered. The strengthened specimens were cured in the room temperature for at least seven days before the loading tests.

2.4 Loading method and measured items

The specimens were tested as simply supported beams with the effective span of 3,000 mm. Loads were applied at two points at a space of 150 mm on either side of the midspan (Fig. 3). Load was applied by a 1000 kN loading machine.

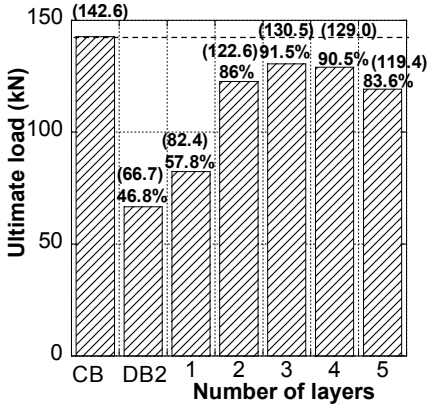
In Fig. 1, the solid rectangles present the locations of the strain gauges in the strands. The strain gauges were bonded to the strands before casting concrete. There were two measuring locations in uncut prestressing strands and six locations in the cut ones. The values of these strain gauges were monitored before, after cutting the strands and during the loading test. Besides, in order to measure the tensile strains in the surface of the bonded CFRP sheets, the strain gauges were attached along the sheets. In the top of concrete section, the gauges were attached to obtain the compressive strains at the midspan.

The linear variable differential transducers were used to monitor the vertical displacement of the specimens. Two transducers were set at the middle of the beam span, and the other two were located at each support. Moreover, the crack widths in the constant moment region were measured by π-gauges. The applied load and all measurements were recorded automatically through a data logger with the time interval of three seconds. The crack propagations during the loading were marked with the load levels.

3. EXPERIMENTAL RESULTS

3.1 Flexural capacity and stiffness

Figure 4 presents the effect of the number of layers of the bonded CFRP sheets on the ultimate load of the strengthened beams compared to CB and DB2. It can be seen clearly, the rupture of 50% of the prestressing strands at the middle of span led to a reduction in the flexural capacity of 53.2% in the damaged beam DB2. The ultimate loads was



( ) Experimental ultimate load, P_u.
% : P_u/P_u^{CB}

Figure 4 Comparison in ultimate loads

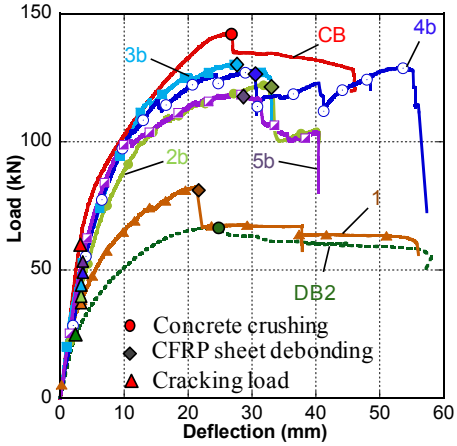


Figure 5 Load-deflection curves

recovered up to around 91.5% (130.5 kN) of CB in the beam strengthened by three layers. However, the ultimate load of the beams strengthened with four and five layers were not greater than that. The ultimate load of the beam strengthened by five layers slightly reduced in comparison to the load capacity of the beam strengthened with three layers. Likely, the debonding of CFRP sheets occurred earlier with the increase in the number of CFRP layers. Therefore, those CFRP sheets did not effectively utilize their full strength to the flexural capacity of the beams.

Figure 5 shows the relationship between the applied load and the deflection at midspan. As the slopes of the curves represent the flexural stiffness, the stiffness of the damaged beams DB2 decreased significantly compared to CB in post-cracking region. When CFRP sheets were bonded to the tension surface (DB2-100-1), the deflections in post-cracking region at same load levels was much smaller than that of DB2. Up to three layers bonded, the decrease in the midspan deflections was accompanied by the increase in number of CFRP sheet layers. Hence, the curves became steeper and get closer to that of CB. However, when the number of the sheets greater than three layers, the large difference in the stiffness between the strengthened and un-strengthened portions accelerated the widening of the cracks at the sheet ends. As a result, the beam stiffness was

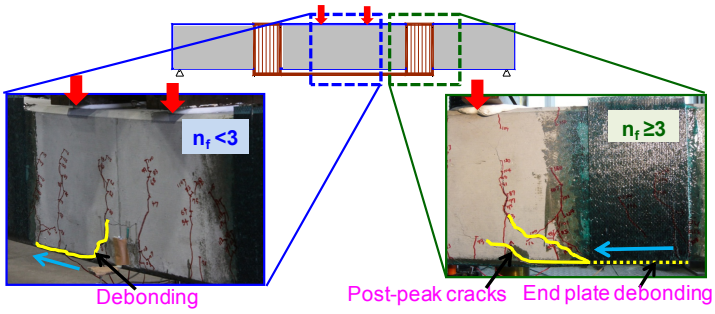


Figure 6 Failures occurred at different portions in strengthened beams

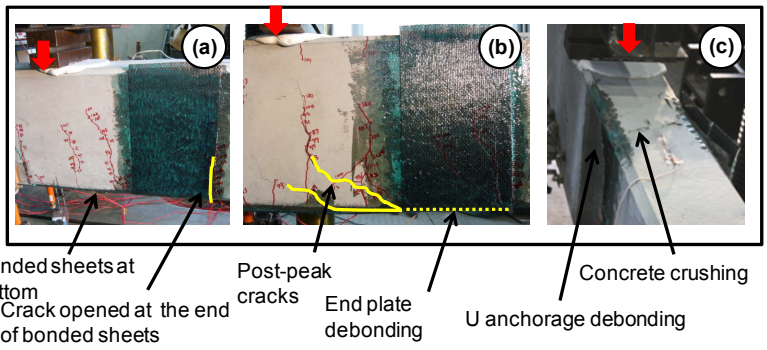


Figure 7 Typical failure of PC beams strengthened with greater than three layers

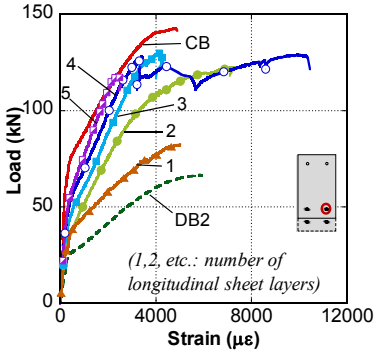


Figure 8 Load-tensile strain increment at midspan

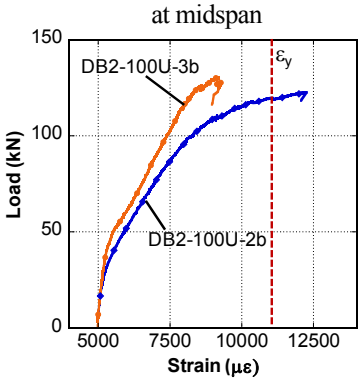


Figure 9 Strain development in strands

decreased, that led to a larger deformation in the beams strengthened with four and five layers.

3.2 Failures of composite sections

Figure 6 shows the failures occurred at different portions of the strengthened PC beams when the amount of CFRP sheets was increased. When the amount of the bonded sheets was less than three layers, the debonding of the bonded sheets was initiated from the flexural cracks in the constant moment region. However, in case the amount of the bonded sheets was greater than three layers, the sheets were debonded from the sheet ends. Likely, the critical sections in the strengthened PC beams were shifted from the constant moment region to the portion near the sheet ends when the amount of the bonded sheets was increased. Figure 7 details the general behaviors in the beams strengthened by more than two layers of CFRP sheets. At first, the flexural cracks were formed in the constant moment region. After that, as the gradual increase of the applied load, the cracks were formed in the shear span, in the portion from the loading points to the end of the bonded CFRP sheets. When the cracks at the ends of the bonded sheets opened (Fig. 7(a)), the beam stiffness was reduced. Consequently, although the deflection grew fast, the load carrying capacity increased slowly. Figure 7(b) shows the debonding of the longitudinal sheets in DB2-100U-4b. As can be seen, the debonding of the sheets was initiated from the sheet end, which propagated towards the loading point in the post-peak loading. As the debonding occurred from the sheet ends, the sections near the end of the sheets became more critical because the sheets terminated to carry the tensile stress. The debonding between the bonded CFRP sheets and concrete, then, was followed by the crushing of concrete at the top fiber of the section near the sheet end as shown in Fig. 7(c).

In general, the strengthened PC beams were failed by debonding of CFRP sheets. However, the failure behaviors were affected by the amount of the bonded CFRP sheets to the damaged PC beams.

3.3 Effects of amount of CFRP on tensile strains of internal prestressing strands and debonding mechanisms

Figure 8 illustrates the relationship of the applied load and the increment of the tensile strains at midspan of the uncut prestressing strands which is a circled in the section. It was apparent that the increase in tensile strains in the prestressing strands became smaller at the same load level when the number of CFRP layers was increased. The effect on the strain reduction in the remaining prestressing strands possibly resulted in the decrease of yielding load of strands. The evidence is given in Fig. 9. The tensile strain reached yielding strain (ε_y) when the beam was strengthened with two layers of CFRP sheets. Nevertheless, when the amount of CFRP sheets was increased to three layers, the tensile strain in the prestressing strands was still far to reach the yielding strain even the ultimate load was greater in case of three layers of the sheets were bonded.

Likely, the different failure behaviors (discussed in section 3.2) were influenced by this effect. When small amount of CFRP sheets bonded (e.g. two layers, Fig. 9), the strands yielded at the middle of the span. Hence, flexural cracks opened widely in the constant moment region and propagated around the mortar portion. This caused some displacements in vertical and horizontal directions at the interface between concrete and the bonded sheets. These

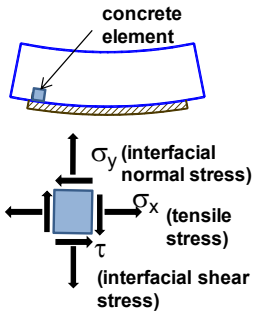


Figure 10 Stresses acting on concrete element near the interface

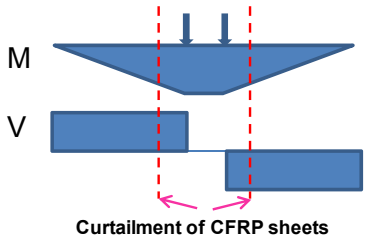


Figure 11 Moment and shear force diagram

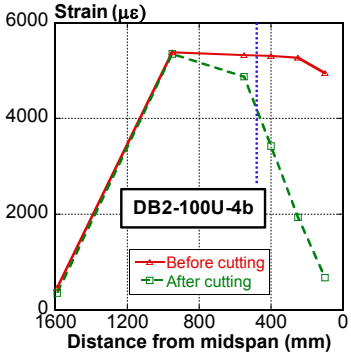


Figure 12 Strain losses in ruptured strands

displacements induced a shear and normal stresses at the crack mouth. When the principal stress at this location exceeded the bond strength, debonding started and propagated towards the sheet end. In this case, the debonding failure was generated from the cracks in the constant moment region. However, when a larger amount of CFRP sheets was bonded (e.g. three layers, Fig. 9), the tensile strain in the remaining strands did not reach yielding strain. Thus, the width of flexural cracks in the constant moment region remained small and the stresses did not rise at the middle of the span. Even though, debonding was started from the end of the bonded sheets because of high concentration of the interfacial stresses near the sheet ends.

Figure 10 introduces the stresses acting in a concrete element near the interface between concrete and bonded sheets, which are interfacial shear stress (τ), interfacial normal stress (σ_y), and the tensile stress (σ_x). The tensile stress at the bottom of concrete section is due to a bending moment at a considered section, while the interfacial stresses shows the high concentration at the end of the bonded sheets because the discontinuity in member rigidity. According to previous studies, the interfacial stresses are highly related to the distance between a support and the sheet end, elastic modulus and thickness of the bonded plate, elastic modulus of the adhesive layers and concrete compressive strength (Sayed-Ahmed et al. 2009 and Smith et al. 2001). If the combination of three stress components, the principal stress, exceeds the strength of the weakest element, the debonding occurs. As explained in the section 2.3, the lengths of the bonded CFRP sheets in the experiments were constant. Moreover, the curtailments of the bonded CFRP sheets were 350 mm shifted from the loading points, which located in the high moment and shear region (Fig. 11). In addition, Fig. 12 illustrates the typical behavior of the strain in the cut prestressing strand before and after it was cut. The horizontal axis shows the locations of the strain gauges while "zero" (0) corresponds to the midspan where the strands was cut. The vertical axis shows the measured values of the strain gauges. As can be seen, the strain dropped suddenly to approximately zero near the cutting point. For the gauges whose locations were further from the cutting point, the values of strain drops were gradually smaller. The curtailment of the bonded CFRP sheets is shown in the figure as the dot line. Clearly, the curtailment of the sheets was within the length in which the strains dropped.

Therefore, the debonding from the end of the bonded sheets in this study can be explained by the concentration of the stresses near the sheet ends. First, this referred to the increase in total thickness of the bonded CFRP sheets larger amount of sheet layers was used. Second, the curtailments of the bonded sheets located not only in high shear and moment regions but also within the length that strains in prestressing strands were lost, that led to the high tensile stress at the sheet ends. Moreover, it is certain that the behaviors of prestressing strands are highly related to the effective stress in the strands. Thus, the effects of prestressing stress level to debonding behavior in PC beams need to be further taken into account.

3.4 Comparison with the predicted load capacities based on the guidelines of ACI

The experimental results were compared with the calculated values based on the recent guideline of ACI (ACI 440.2R-08). In this guideline, the flexural section analysis was adopted and the flexural capacity was computed based on the stress and strain compatibility and equilibrium. For the PC beams strengthened with externally bonded FRP sheets, in case non-prestressed reinforcement is not provided, the flexural capacity consists of two components which are carried by prestressing strands and fiber sheets as shown in the below equation:

$$M_n = A_p f_{ps}\left(d_p - \frac{\beta_1 c}{2}\right) + \psi A_f f_{fe}\left(h - \frac{\beta_1 c}{2}\right) \quad (1)$$

Where:

A_p: area of prestressing steel
f_{ps}: stress in prestressing steel at beam failure
d_p: effective depth to centroid of prestressing steel
f_{fe}: stress in fiber sheet at beam failure
A_f: area of FRP sheets
h: height of beam section
c: distance from extreme compression fiber to neutral axis
β_1: ratio of depth of equivalent rectangular stress block to depth of the neutral axis
ψ: partial reduction factor, $\psi = 0.85$

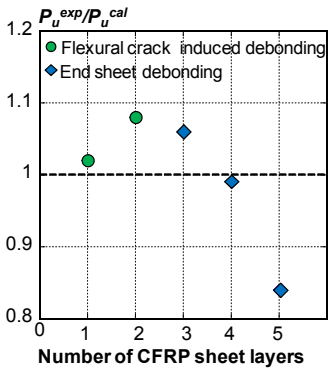


Figure 13 Comparison of ultimate loads between experimental and predicted values

The stress in fiber sheets at the beam failure (f_{fe}) in Eq. (1), is determined from the assumption of the failure modes. It takes the maximum strain in the FRP sheets at the sections computed from the case of whether crushing of concrete, debonding of FRP sheets or rupture of FRP sheets occurs. In the guideline, Eq. (2) is given to predict the effective strain of the bonded sheets in case the debonding of the bonded FRP sheets induced by an immediate cracks. In this equation, the debonding strain of the bonded sheets depends on compressive strength of concrete and properties of bonded sheets.

$$\varepsilon_{fd} = 0.418\sqrt{\frac{f'_c}{n_f E_f t_f}} \le 0.9\varepsilon_{fu} \qquad (2)$$

Where:
f'_c: *compressive strength of concrete (N/mm^2)*
n_f: *number of FRP layers*
E_f: *elastic modulus of FRP sheet (N/mm^2)*
t_f: *thickness of FRP sheet (mm)*
ε_{fu}: *ultimate strain of FRP sheet*

Figure 13 represents the comparison of the ultimate loads of the strengthened PC beams between experimental data and the calculations based on ACI guideline. In case the flexural cracks induced debonding occurred in the strengthened beams, the experimental results showed a good agreement with the calculation based on ACI. However, in case the debonding from the sheet ends occurred, even the reduction factor $\psi = 0.85$ was employed in the calculations, the calculated values tended to overestimated. This is because of the differences of failure modes when the amount of CFRP sheets were increased which have not been considered. The debonding from the sheet ends occurred in the experiments; however, there is no available method to to predict the flexural capacity of the strengthened beams failed in end sheet debonding in the recent guideline of ACI.

Moreover, as discussed previously, the failure behaviours of composite actions were influenced by not only the amount of the bonded sheets but also the location where the sheets are curtailed.

4. CONCLUSIONS

In this study, the effects of the externally bonded CFRP sheets on the pre-tensioned PC beams having strands ruptured were investigated in terms of flexural capacity, stiffness, strains in the remaining prestressing strainds and failure behaviors. Moreover, the failure mechnisms were explained, which was affected by the amount of the bonded sheets.

First, the strand ruptures in the PC beams lead to the reductions in both flexural capacity and member stiffness. The strengthening method in which CFRP sheets are bonded externally to tension surface of the damaged PC beams shows the effective performance in improvement of the flexural capacities, the stiffness in post-cracking region and decrease the stress carried by the remaining strands. The enhancement of the post-cracking stiffness and decrease of strains in strands are associated with the increase in number of CFRP sheet layers. The ultimate load was enhanced up to 91.5% of the ungamaged beam by bonding three layers of CFRP sheets.

Second, with the same sheet lengths provided, the failure modes tend to change from debonding induced by flexural cracks in the constant moment region to debonding from the sheet ends when the damaged PC beams are strengthened with larger amount of CFRP sheets. While the first failure mode results from the opening of the flexural cracks, the second one causes by the high concentration of stresses near the sheet ends. The concentration of stresses near the end of the bonded sheets is because of a larger amount of CFRP sheets bonded and the curtailment of the bonded sheets in a high shear and moment. Moreover, the lengths of CFRP sheets in this study did not cover the lengths in which the prestress in the prestressing strands were lost due to the ruptures. Hence, to utilize the strength of CFRP sheets with a large amount of CFRP sheets effectively, sufficient lengths of CFRP sheets need to be further investigated.

Finally, the recent guideline of ACI are insufficient to predict the debonding from the ends of the bonded sheets. Therefore, the calculated flexural capacities of the PC beams strengthened by externally bonded CFRP sheets tend to overestimate when this failure occurs.

Acknowledgements:
The authors acknowledge the research fund support from the Center for Urban Earthquake Engineering (CUEE) in Tokyo Institute of Technology.

References:

ACI 440.2R-08 (2008), "Guideline for design and construction of externally bonded FRP systems for strengthening concrete structures", ACI Committee 440.

JSCE recommendations (2002), "Recommendations for Upgrading of Concrete Structures with Use of Continuous Fiber Sheets", JSCE.

Sayed-Ahmed E.Y., Bakay R. and Shrive N.G. (2009), "Bond strength of FRP laminates to concrete: State-of-the-art Review", *Electronic Journal of Structural Engineering*, **9**, 45-61.

Smith S.T and Teng J.G. (2001), "Interfacial stresses in plated beams", *Engineering Structures*, **23**, 857-871.

10CUEE CONFERENCE PROCEEDINGS
10th International Conference on Urban Earthquake Engineering
March 1-2, 2013, Tokyo Institute of Technology, Tokyo, Japan

EVALUATION OF SHEAR CAPACITY OF RC BEAMS USING UFC PERMANENT FORMWORK WITH DIFFERENT SHEAR SPAN TO EFFECTIVE DEPTH RATIO

Puvanai Wirojjanapirom[1], Koji Matsumoto[2], Katsuya Kono[3] and Junichiro Niwa[4]

1) Ph.D. candidate, Department of Civil Engineering, Tokyo Institute of Technology, Japan
2) Assistant Professor, Dept. of Civil Engineering, Tokyo Institute of Technology, Japan
3) Research Scientist, Research and Development Center, Taiheiyo Cement Corporation, Japan
4) Professor, Department of Civil Engineering, Tokyo Institute of Technology, Japan
Wirojjanapirom.p.mm@m.titech.ac.jp, matsumoto.k.ar@m.titech.ac.jp, katsuya_kono@taiheiyo-cement.co.jp, jniwa@cv.titech.ac.jp

Abstract: Shear failure in RC beams is well known as brittle nature. This failure can be prevented by the application of Ultra High Strength Fiber Reinforced Concrete (UFC). UFC provides highly advanced mechanical properties, such as high compressive strength as 150 MPa, high durability and high ductility. The use of UFC as a permanent formwork of RC structures is one of the alternatives to enhance the shear resistance and ductility of the structure. However, the available studies on the mechanical performance of RC beams using UFC permanent formwork is insufficient and the effect of shear span to effective depth (*a/d*) ratio has not been considered. The objective of this paper is to evaluate the shear capacity of RC beams using UFC permanent formwork considering the effect of *a/d.* The specimens were subjected to four-point bending. The experimental results indicated that UFC permanent formwork enhanced shear capacity of RC beams significantly. Moreover, failure mode changed depending on *a/d*. Finally, the shear carried by a UFC permanent formwork was investigated. Computational values showed good agreement with experimental values.

1. INTRODUCTION

The improvement of seismic performance of infrastructures is required, in order to mitigate the social damage and seismic risk. Prevention of shear failure in reinforced concrete (RC) members is one of the significant factors. Shear failure in RC members is well known as brittle nature. As methods for shear retrofitting and strengthening of RC members, cross-sectional restoration, steel plate attachment and FRP sheet attachment have been started to be used. However, these methods have some problems such as corrosion of steel plate and brittle failure of FRP material. This demand can be achieved by the utilization of developed Ultra High Strength Fiber Reinforced Concrete (UFC). UFC is an advanced cementitious material which has outstanding properties, such as more than 150 MPa compressive strength, high ductility and high durability.

The permanent formwork for RC structures is one of the applications of UFC. The definition for permanent formwork derived from CIRIA C558 is, the permanent formwork is a structural element of whatever material that is used to contain the placed concrete, mold it to the required dimensions and remain in place for the life of the structure (Wringley 2001). Shirai et al. (2008) reported application of UFC permanent formwork for repairing of Tedorigawa Bridge in Ishikawa prefecture, Japan. It shows that UFC formwork left in-place increased durability against chloride attacks, abrasion and impact wear. Moreover, The U-shaped UFC permanent formwork with shear keys and screws and bolts system which provided to fix the UFC permanent formwork to the inside RC was introduced by the authors (Wirojjanapirom et al., 2012). The results show that the shear capacity of RC beams using UFC U-shaped permanent formwork increased drastically. However, the available studies on the mechanical performance of RC beams using UFC permanent formwork is insufficient and the effect of shear span to effective depth (*a/d*) ratio has not been considered. Therefore, the objective of this paper is to evaluate the shear capacity of RC beams using UFC permanent formwork with considering the effect of *a/d.* The specimens were subjected to four-point bending. Shear capacities, crack patterns and failure mechanism were investigated.

2. EXPERIMENTAL PROGRAMS

2.1 Experimental Parameters and Specimens

To determine the effect of *a/d* on shear behavior of a RC beam with U-shaped UFC permanent formwork, the loading test of four specimens listed in Table 1 was conducted. Table 1 summarizes the testing variables and

Table 1 List of the experimental cases

No.	Name	Thickness of UFC formwork (mm)	Stirrup ratio (%)	*a/d*
1	UFC20-KB	20	0	3.27
2	UFC20-KB-ad1	20	0	1.00
3	UFC20-KB-ad21	20	0	2.16

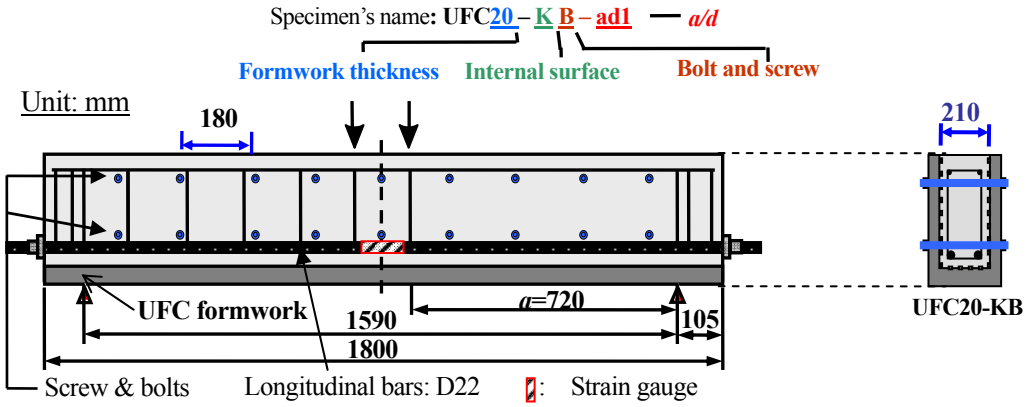
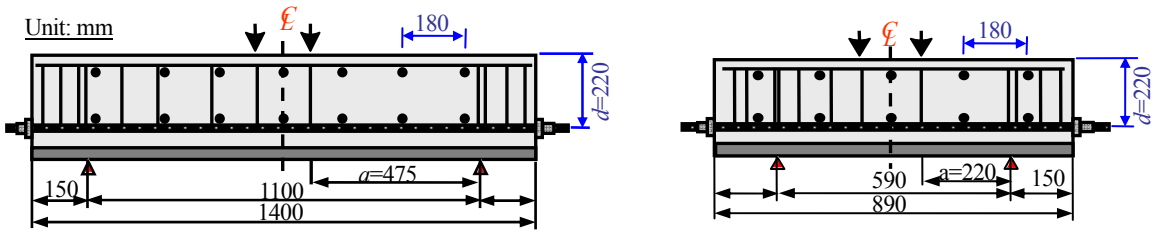


Figure 1 Specimens detail



a) UFC20-KB-ad21 (*a/d*=2.16) **b)** UFC20-KB-ad1 (*a/d*=1.0)

Figure 2 Detail of UFC20-KB-ad21 and UFC20-KB-ad1

specimen's name.

Figure 1 shows dimension, reinforcing steel bar arrangement and cross section of UFC20-K specimen. As constant variables for all specimens, effective depth, width, height and tension reinforcement ratio are d=220 mm, b=250 mm, h=300 mm and p_w =1.41%, respectively. In order to control a shear span of failure, a number of stirrups were provided in one span. Three specimens with different shear span. Effective depth of the beams was same, but the shear span was varied. The original specimen was UFC20-KB with a/d= 3.27. The a/d of UFC20-KB-ad1 and UFC20-KB-ad21 were 1.00 and 2.16, respectively. Figure 2 shows the dimension of UFC20-KB-ad21 and UFC20-KB-ad1 specimen. Specimens were subjected to a four-point bending with the load applied to both the UFC and RC at the same time. The applied load was measured. Mid-span deflection was measured by using transducers. Strain gauges were used for measuring the strain of tension steel bars at mid-span and concrete on the top fiber at mid of shear span. Moreover, four π-gauges were used to measure the diagonal crack opening width along the diagonal line between the loading point and support.

2.2 Materials

The self-compacting concrete was used in this experiment, and detail of mix proportion is summarized in Table 2. The materials used in the concrete mixes were high-early strength cement, lime stone powder, fine aggregates, coarse aggregates, viscosity improver and superplasticizer, which was high-performance air entrained (AE) water reducing agent. The designed compressive strength of 7-day age concrete was 35 MPa.

The steel short fibers with 0.2 mm diameter and 15 mm length were used for UFC. Mix proportion of UFC forms is shown in Table 3. The volume fraction of steel fibers in all specimens was 2.0%.

The longitudinal reinforcing bars used in this research were deformed steel bar with 21.6 mm nominal diameter. The yield strength was 1026 MPa. The deformed steel bar of 10 mm in diameter was arranged as compression reinforcement. The yield strength was 339 MPa.

3. RESULTS AND DISCUSSIONS

3.2 Load-displacement relationships and failure patterns

Table 2 Mix proportion of concrete

G_{max}	W/C	Unit weight (kg/m^3)						
[mm]	[%]	*W*	*C*	*L*	*S*	*G*	*SP*	*V*
13	57	165	292	249	718	857	4.38	0.25

W: Water, *C*: Cement, *L*: Lime stone powder, *S*:Sand,
G: Coarse Aggregate, *SP*: Superplasticizer, *V*: Viscosity improver

Table 3 Mix proportion of UFC

Flow (mm)	Unit weight (kg/m^3)			
	Water	Premix binder	Steel fiber	Water reducing agent
260±20	180	2254	157	24

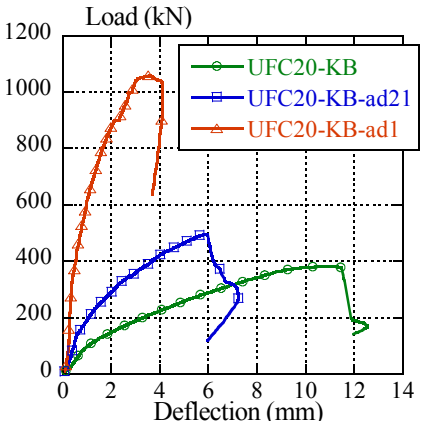
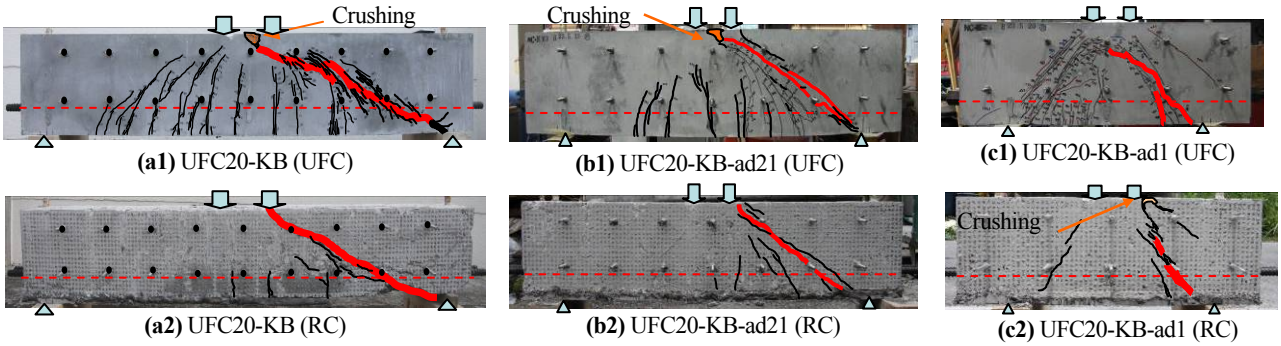


Figure 3 Load-deflection relationships

Table 4 Mechanical properties of concrete and UFC, and the result of loading tests

Name	Mechanical Properties of concrete		Mechanical Properties of UFC		Results of loading test			
	f'_c (MPa)	f_t (MPa)	f'_{c_UFC} (MPa)	f_{t_UFC} (MPa)	Flexural cracking load (kN)	Peak load (kN)	V_u (kN)	Failure mode
UFC20-KB	40.4	2.1	184.2	11.9	82.1	384.0	192.0	Diagonal tension
UFC20-KB-ad21	33.1	2.2	182.7	12.6	142.8	496.2	248.1	Shear compression
UFC20-KB-ad1	30.6	2.3	177.8	10.8	334.2	1058.6	529.3	Shear compression

f'_c: Compressive strength of concrete, f_t: Tensile strength of concrete, f'_{c_UFC}: Compressive strength of UFC, f_{t_UFC}: Tensile strength of UFC, V_u: Shear capacity



(a1) UFC20-KB (UFC) **(b1)** UFC20-KB-ad21 (UFC) **(c1)** UFC20-KB-ad1 (UFC)

(a2) UFC20-KB (RC) **(b2)** UFC20-KB-ad21 (RC) **(c2)** UFC20-KB-ad1 (RC)

Figure 4 Crack patterns

Table 4 shows the mechanical properties of concrete and UFC, and the result of loading tests. Figure 3 shows the relationships between the load and the mid-span deflection. Figure 4 shows the crack patterns of UFC20-KB-ad21, UFC20-KB-ad1 and UFC20-KB which the first two specimens failed in shear compression failure mode. After the loading test, UFC formwork was removed and diagonal crack of inside RC part was observed. The red lines in Fig. 4 represent the critical cracks.

In UFC20-KB specimen, flexural cracks on the UFC formwork appeared when the load was 82 kN. When the load reached to the peak (384 kN), the critical diagonal crack was propagated and widened, and the crushing of UFC under the loading point occurred as shown in Fig. 4(a1). Figure 4(a2) shows the diagonal crack of inside RC part. It seems that the diagonal crack of inside RC part occurred at the same location of that in the UFC permanent formwork.

In UFC20-KB-ad21 specimen, the diagonal crack on the UFC formwork initiated at 347.3 kN but the load was still increasing. Then, crushing of UFC under the loading point occurred at the peak load as shown in Fig. 4(b1). Figure 4(b2) shows the diagonal crack of inside RC part.

In UFC20-KB-ad1 specimen, the flexural crack on the UFC formwork initiated at 334.2 kN. After that, many cracks propagated in the direction from the support to the loading point with increasing in load as shown in Fig. 4(c1). After the loading test, the debonding failure of RC and UFC formwork and the crushing of inside RC part under the loading point were observed as shown in Fig. 4(c2).

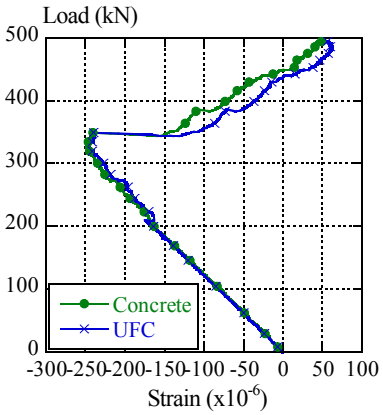


Figure 5 Load-strain at the upper surface (UFC20-KB-ad21)

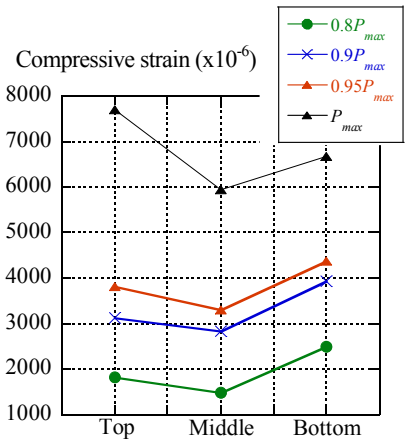


Figure 6 Maximun compressive strain of concrete

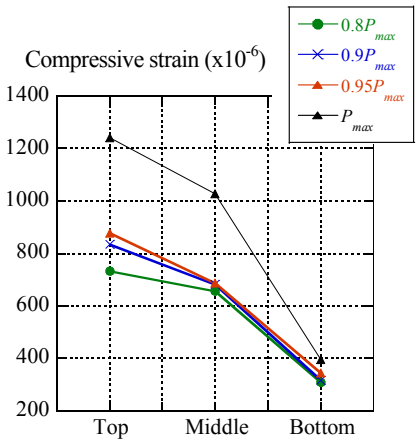


Figure 7 Maximun compressive strain of UFC

3.3 Effect of shear span to effective depth ratio (*a/d*)

For UFC20-KB, firstly, a diagonal crack initiated in RC part, however, failure did not occur because UFC on the sides of the RC part prevented the opening of the diagonal crack and the aggregate interlock in RC part remained. After that, as the load increased, the diagonal crack in RC part attempted to widen and UFC formwork was still resisting by forces, which were generated at the top and bottom of bolts and from the shear key interface. As a result, many cracks were observed on the UFC formwork as shown in Fig. 4(a1). Then, the main diagonal crack on UFC occurred at 70 percentage of peak load ($0.7P_{max}$) but load was still increasing, while the opening width of diagonal crack was increasing. Then, the load reached to peak and failure occurred.

For UFC20-KB-ad21, although a diagonal crack on UFC formwork initiated, the diagonal tension failure did not occur since UFC prevented widening of diagonal crack inside RC part. Consequently, the compressive stress acted above the diagonal crack. As a result, the top fiber strains of both UFC and concrete which measured at the top surface of mid of shear span were changed into the reverse direction as shown in Fig. 5. Here, the tensile strain is shown as positive, conversely, negative shows the compressive strain. The flexural tension stress occurred at the upper edge of both UFC and RC. After that, the load reached to the peak because of the crushing of UFC near the loading point as shown in Fig. 4(b1).

From the descriptions above, it can be said that when the *a/d* ratio changed from 3.27 to 2.16, the failure mode changed from the diagonal tension failure to the shear compression failure because of the compression stress acted above the diagonal crack and crushing of the UFC occurred near the loading point.

3.6 Compressive strain of concrete in the strut formation of UFC20-KB-ad1

UFC20-KB-ad1 also failed in the shear compression mode. The failure mechanism was examined by using the strains measured in the compressive strut of both concrete and UFC. The strains of concrete and UFC were measured by using the acrylic bars and concrete strain gauges, respectively. Figure 8(a) shows the arrangement of acrylic bars inside concrete. Concrete strain gauges were attached at the same position of those on acrylic bars. According to the method by Nakamura and Higai (1999), acrylic bars were fixed by making dents and set at the center of the cross section width in the direction of compressive stress flow from the loading point to the supporting point. Five acrylic bars were set at 17 mm intervals. Three strain gauges were attached on each acrylic bar, in order to measure the strain near the loading point, center of the compressive strut and the supporting point.

Figures 6 and 7 show the development of the maximum compressive strain of concrete near the loading point (Top), center of the strut (Middle) and near the supporting point (Bottom) of concrete and UFC, respectively. In both concrete and UFC, compressive strains increased drastically near the peak load because the compression struts were formed in both concrete and UFC formwork. Therefore, the compressive strains reached ultimate strain and crushing of concrete occurred. It should be noted that the distribution of compressive strain of both concrete and UFC seems to be different. This is because the compatibility between RC and UFC permanent formwork cannot be secured.

4. INVESTIGATION OF SHEAR CARRIED BY U-SHAPED UFC PERMANENT FORMWORK

4.1 Shear Carried by UFC Permanent Formwork Failed in Diagonal Tension

The shear carried by UFC permanent formwork failed in diagonal tension was investigated.

The shear carried by UFC formwork was calculated by subtracting the shear carried by concrete and stirrups from the total shear capacity obtained from the loading test as calculated from Eq. (1)

$$V_{UFC} = V_u - V_c - V_s \quad (1)$$

where, V_{UFC} is the shear carried by UFC formwork, V_c is the

Table 5 Shear carried by UFC formwork observed in the experiment and obtained in the calculation

Specimens	Thickness of UFC, t (mm)	Angle, θ (°)	tensile stress, σ_{UFC} (N/mm^2)	$V_{UFC\text{-}exp}$ $=V_{exp}$-V_c-V_s (kN)	$V_{UFC\text{-}cal}$ (kN)	Exp/Cal
UFC20-KB	20	22.1	3.8	127.3	118.8	1.07

shear carried by concrete, V_s is the shear carried by stirrups.

In this research, the shear carried by concrete was obtained by Eq. (2)

$$V_c = 0.2(f_c')^{1/3}(p_w)^{1/3}(\frac{1000}{d})^{1/4}(0.75+\frac{1.4}{a/d})b_w d \quad (2)$$

where, V_c is shear capacity of normal RC beam without stirrups (kN), f'_c is compressive strength of concrete (MPa) , p_w is tension reinforcement ratio (%), b_w is web thickness (mm) and d is effective depth (mm).

.

The shear carried by UFC formwork was computationally obtained based on a simplified shear carrying model. The crack length of permanent formwork and the angle of diagonal crack are represented by l and θ, respectively. Therefore, the shear carried by UFC formwork based on this model is given by Eq. (3).

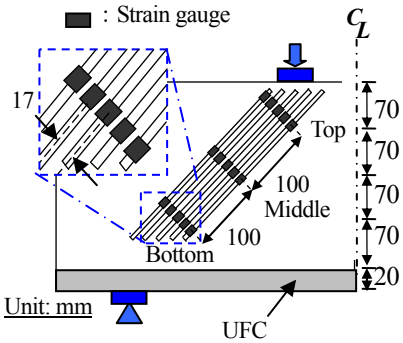
$$V_{UFC} = \frac{2 \cdot t \cdot \sigma_{UFC} \cdot d}{\tan\theta} \quad (3)$$

where, t is the thickness of UFC permanent formwork, and d is effective depth.

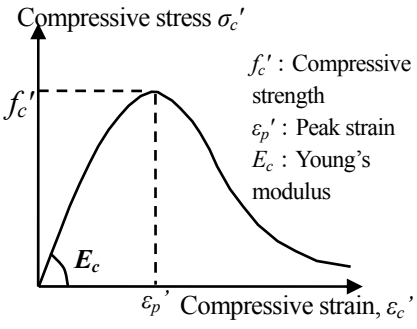
The tensile stress (σ_{UFC}) was determined by the diagonal crack width measured by using π-gauge along the diagonal crack line from support to loading point and using the tension softening curve of UFC measured by Kakei et al. (Kakei et al. 2003).

4.2 Result of the Calculation

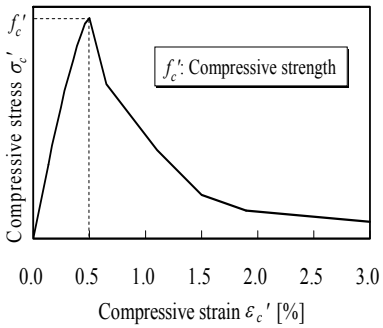
Table 5 summarizes the results of experimentally observed and computationally obtained shear carried by UFC formwork by Eq. (1) and Eq. (3), respectively. In all three specimens, the ratio of experimentally observed shear carried by UFC formwork to computationally obtained value shows good agreement. Thus, the model was able to give a reasonable result. This is because the diagonal crack on both



(a) The location of strain point

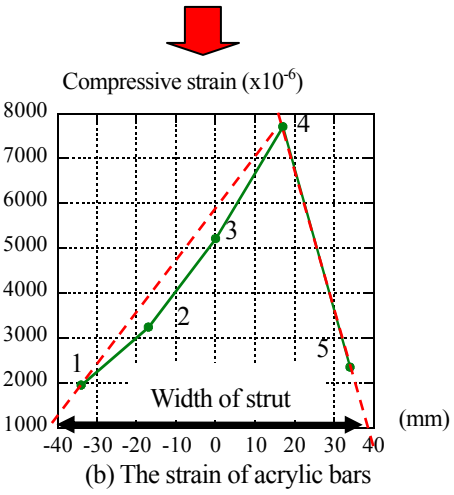


(a) Concrete (Thorenfeldt's model)



(b) UFC (Kakei's model)

Figure 9 Stress-strain relationship for concrete and UFC in compression



(b) The strain of acrylic bars

Figure 8
Definition of the compressive strut

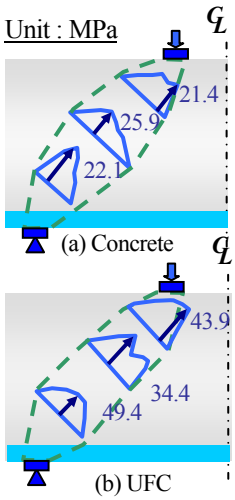


Figure 10 Compressive stress distributions

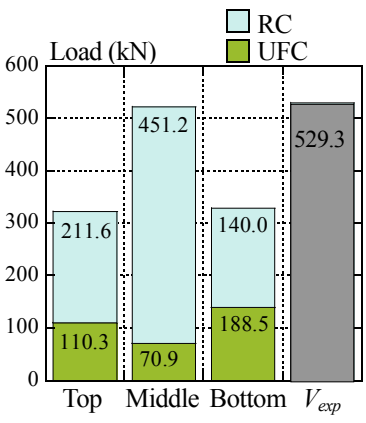


Figure 11 Comparison of calculation and experimental value of shear resisting force

UFC formwork and RC part was located to almost the same position, and also the diagonal crack width of UFC was measured.

4.3 Shear Carried by UFC Permanent Formwork Failed in Shear Compression

As mentioned, UFC20-KB-ad1 specimen failed in the shear compression failure mode. The shear carried by UFC permanent formwork failed in the shear compression failure mode is examined in this session.

Figure 8 presents the method for determining width of the compressive strut. The maximum strain point and both minimum strain points at $0.95P_{max}$ were connected by straight dashed lines as shown in Fig. 8 (b) and the width of compression strut was assumed to be the distance between the points where the strains equal to 0 as shown in Fig. 8 (b). Assuming that the strains of acrylic bars and concrete were the same and the stress state was assumed as uni-axial compression and the strain that measured on UFC was considered also in the same way. The compressive stress acting on the concrete was calculated by using the strain of acrylic bars, and the compressive stress of UFC was calculated by the strain measured by a strain gauge. From stress-strain model, the measured strains of both concrete and UFC were transformed to stress. For concrete, the stress-strain model proposed by Thorenfeldt et al. (1987) shown in Fig. 9(a) was used to calculate the compressive stress. For UFC, the stress-strain model of UFC based on the experimental results proposed by Kakei et al. (2003) shown in Fig. 9(b) was used to calculate the compression stress. Figure 10(a) and (b) show the compressive stress distributions of concrete and UFC permanent formwork, respectively. In concrete part, the strut width at the middle was wider than that near the loading point and near the support. It means that the stress concentrations were observed in both near loading and supporting points. This is because the constraint effect of UFC permanent formwork confined RC with screws and bolts.

4.3 Calculation of the compressive force

The stress distributions of both concrete and UFC were converted to the vertical component of the compressive force acting on the concrete strut and UFC strut by using Eq. (4) and (5).

$$F_{st} = D \times b_i \quad (4)$$

$$F' = F_{st} \times \sin\alpha \quad (5)$$

where, F_{st} is the compressive force acting on the concrete or UFC strut, D is the force per unit width under the compressive stress distribution curve, b_i is the width of cross section of concrete or both of UFC formwork thickness, F' is the vertical component of F_{st}, α is the angle of the strut with respect to the longitudinal axis of beams.

Figure 11 shows the comparison of the summation of calculated value F' from RC and UFC with the experimental shear capacity V_{exp}.

The summation of F' at the middle provided the good agreement with V_{exp}. However, the summation of F' underestimated V_{exp} at the top and bottom location. It is because the uni-axial stress-strain model (Thorenfeldt's model) was used while the compression strut of inside concrete was constrained by the UFC formwork with screws and bolts.

5. CONCLUSIONS

(1) Failure mode of RC beams using a UFC U-shaped permanent formwork changed depending on the shear span to effective depth ratio. Compression strut was formed in a UFC formwork in the case of *a/d* equal to 2.16 and 1.0.

(2) The shear carried by a UFC formwork in RC beams failed in the diagonal tension mode was investigated by assuming and using the tensile stress obtained from the tension softening curve. The computational values showed the good agreement with the experimental values.

(3) Compression forces of a UFC formwork and RC part in the specimen with *a/d* 1.0 calculated by using uni-axial stress-strain model did not show the good agreement near the screwed bolts. It indicated that the constraint effect of screwed bolts should be considered to evaluate the shear compressive capacity.

Acknowledgements:

The authors acknowledge financial support from the Center for Urban Earthquake Engineering (CUEE) at Tokyo Institute of Technology.

References:

Wringley R G. (2001), "Permanent Formwork in Construction (CIRIA C558)", CIRIA/Concrete Society, 13-16.

Shirai, K., Matsuda, K. and Tanaka, S. (2008), "Durability of UFC Formwork Left In-Place and Its Application", *Proceedings of 8th International Symposium on Utilization of High-Strength and High-Performance Concrete*, 870-875.

Wirojjanapirom, P., Matsumoto, K., Kono, K., and Niwa, J. (2012) "The Experimental Study on Shear Behavior of RC Beams using U-Shapped UFC Permanent Formwork", *Joint conference proceeding of 9th International Conference on Urban Earthquake Engineering/ 4th Asia Conference on Earthquake Engineering,* 935-940.

Nakamura, H. and Higai, T. (1999), "Compressive Fracture Energy and Fracture Zone Length of Concrete", *JCI-C51E Seminar on Post-Peak Behavior of RC Structures Subjected to Seismic Loads*, Vol. 2, 259-272.

Thorenfeldt, E., Tomaszewicz, A. and Jensen, J. J. (1987), "Mechanical Proporties of High-Strength Concrete and Application in Design", *Proceeding of the Symposium on Utilization of High-Strength Concrete*, Tapir, Trondheim, 149-159.

Kakei, T., Kawaguchi, T., Niwa, J. and Hyodo, H. (2003), "Fracture Properties of Ultra High Strength Steel Fiber Reinforced Cementitious Composites", *Proceedings of Cement and Concrete*, Vol. 57, 230-231. (in Japanese)

10CUEE CONFERENCE PROCEEDINGS
10th International Conference on Urban Earthquake Engineering
March 1-2, 2013, Tokyo Institute of Technology, Tokyo, Japan

BOND STRENGTH AND BOND-SLIP BEHAVIOR OF STEEL REINFORCEMENT IN HIGH-PERFORMANCE FIBER-REINFORCED CEMENTITIOUS COMPOSITES

Matthew J. Bandelt[1] and Sarah L. Billington[2]

1) Graduate Research Assistant, Dept. of Civil and Environmental Engineering, Stanford University, Stanford, CA, USA
1) Associate Professor, Dept. of Civil and Environmental Engineering, Stanford University, Stanford, CA, USA
mbandelt@stanford.edu, billington@stanford.edu

Abstract: High-performance fiber-reinforced cementitious composites (HPFRCC) are emerging materials that exhibit enhanced tensile behavior and ductility as compared to traditional concrete. Consequently, these materials are under investigation by researchers for use in a variety of structural components that are expected to dissipate energy during earthquakes. Developing an understanding of the bond created between HPFRCC materials and mild steel reinforcement is necessary to improve performance predicting tools and design guidelines for these novel materials. On-going research on characterizing the bond strength and bond-slip behavior of steel reinforcement in HPFRCC materials will be presented. Beam specimens with reinforcement splices were tested with varying amounts of cover and transverse steel to examine the bond characteristics of HPFRCC materials relative to ordinary concrete. Experiments completed thus far show that HPFRCC provides a confining effect that can substantially increase bond strength and bond-slip ductility. Future research on additional experiments of reinforced HPFRCC members will also be discussed.

1. INTRODUCTION

High-performance fiber-reinforced cementitious composites (HPFRCC) have been studied over the last two decades and proposed for a number of applications to improve the resilience of structures under earthquake loading. These materials exhibit a unique pseudo tensile strain hardening behavior that results in increased component ductility, energy dissipation and damage tolerance. Potential applications for HPFRCC materials include hinge regions for bridge piers (Rouse and Billington 2003), hybrid beam-column joints (Parra-Montesinos and Wight 2000), coupling beams (Lequesne et al. 2010) and many other related areas for increased structural performance under seismic demands.

In order to develop adequate design guidelines and performance predicting tools for HPFRCC materials, it is necessary to understand the bond that develops between HPFRCCs and steel reinforcement. Previous experimental studies on bond in HFPRCC materials have used the direct pull-out test and test results show a substantial increase in bond strength due to the mechanical properties of these materials (Chao et al. 2009). However, the pull-out test method is recognized as an inadequate method to fully characterize bond strength due to the simplified stress state (ACI Comittee 408 2003). Instead, a beam specimen with lap splices is the preferred experiment since a more realistic stress state can be obtained. Traditional strain softening fiber reinforced concrete (FRC) materials have been tested using beam splice specimens (Harajli et al. 2002), but there are no experimental results available, to date, on tensile strain hardening HPFRCC materials.

On-going research is being conducted by the authors to characterize bond between HPFRCC materials and steel reinforcement for future model development. In this paper, the results of experiments on beam specimens containing lap splices are presented for two different mixture types.

2. EXPERIMENTAL PROGRAM

2.1 Materials

Two cement based mixes were used to fabricate the specimens in this study; a normal weight concrete and an Engineered Cementitious Composite (ECC).

The normal weight concrete consisted of Type II/V Portland cement, water, fine aggregate and coarse aggregate. The fine aggregate had a fineness modulus of 3.1 and the coarse aggregate had a maximum size of 9.5 mm.

Engineered Cementitious Composites are one type of HPFRCC that do not use coarse aggregate. The ECC mix consisted of Type II/V Portland cement, Class F fly ash, silica sand, a viscosity modifying admixture, super-plasticizer and 2.0% by volume polyvinyl alcohol (PVA) fibers. The silica sand had a 0.13 mm particle size and the PVA fibers were 12 mm long. The proportions for 1 cubic meter of the concrete and ECC mixes are shown in

Table 1.

Table 1 Proportions for 1m^3 of Concrete and ECC Mixes

Mix	Binder		Water	Aggregate		Admixtures		PVA Fibers
	Cement (kg)	FA (kg)	(kg)	Fine (kg)	Coarse (kg)	SP (kg)	VMA (kg)	(kg)
Concrete	653	-	249	602	802	-	-	-
ECC	547	656	312	438	-	2.7	0.6	26

FA = Fly Ash; SP = Superplasticizer; VMA = Viscocity Modifying Agent

2.2 Specimen Design

As previously noted, beam specimens with lap splices were fabricated and tested in this study since they are considered the preferred specimen type for bond experiments. All specimens were designed to ensure that a bond failure would occur prior to yielding of the reinforcement. The specimens were designed in this manner so that the maximum bond stress could be measured.

The beams were 1473 mm in length and had a height of 229 mm. Shear stirrups, with a diameter of 10 mm, were placed in the maximum shear region and spaced at 89 mm to guarantee that the beams failed due to insufficient bond strength rather than shear.

Two steel longitudinal reinforcing bars with a diameter (d_b) of 16 mm were used throughout the cross section. At mid-span two bars were lap spliced to another another two bars as shown in Figure 1. Two of the bars were debonded for the remaining length of the beam using a thin wall PVC pipe so that reinforcement slip could be measured at the end of the beam. The reinforcement that was debonded was extended outside of the beam so that instrumentation to measure reinforcement slip could be installed. A splice length (L_s) of 10d_b (160 mm) was chosen to ensure that the specimens would fail due to bond rather than flexure.

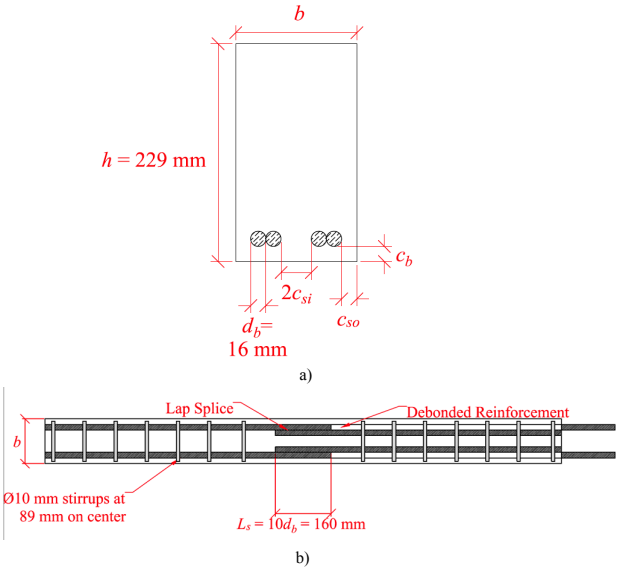


Figure 1 a) Specimen Cross Section within Splice Region b) Specimen Plan View

In addition to the mechanical properties of a material, there are two other important factors that affect bond behavior between steel reinforcement and a cementitious mix (Orangun et al. 1977). The first is the ratio of concrete cover to bar diameter (c/d_b), where the term "cover" refers to bottom cover (c_b), side cover (c_{so}) and cover between bars (c_{si}) as shown in Figure 1a. The second important factor is the presence of confinement (i.e., stirrups) in areas where bond is critical.

Four specimen types were designed with these factors in mind to examine how these two parameters (c/d_b ratio and presence of confinement) affected bond strength in HPFRCC materials. Specimens with two different cover to bar diameter ratios were studied, 1.0 and 1.5, and specimens with and without confinement in the splice region were tested for each mix type. The compressive strengths for ECC and concrete were 50 MPa and 45 MPa, respectively. The test matrix and compressive strengths of each material are outlined in Table 2.

Table 2 Test Matrix and Compressive Strengths

Specimen Name	Mix	b (mm)	c (mm)	c/d_b	Confinement	f'_c (MPa)
CON-1-UC	Concrete	127	16	1.0	-	45
CON-1-C	Concrete	127	16	1.0	2 #10	45
CON-1.5-UC	Concrete	159	24	1.5	-	45
CON-1.5-C	Concrete	159	24	1.5	1 #10	45
ECC-1-UC	ECC	127	16	1.0	-	50
ECC-1-C	ECC	127	16	1.0	2 #10	50
ECC-1.5-UC	ECC	159	24	1.5	-	50
ECC-1.5-C	ECC	159	24	1.5	1 #10	50

$c = c_b = c_{si} = c_{so}$

Confinement = number of stirrups in splice region

2.3 Test Setup and Procedure

The simply supported beams had a span length of 1372 mm and were loaded in four-point bending to create a constant moment region. A 245 kN universal testing machine applied force to a load distribution element, which then loaded the beam at the third points. The testing machine was set to displacement control at a rate of 0.5 mm/min. The test was paused at certain points during testing (i.e., just after first cracking, just before the expected bond failure load, after bond failure and at other intermittent points) to investigate and map crack patterns. All specimens were coated in a lime wash so that crack propagation could be easily identified. An overview of the test setup can be seen in Figure 2.

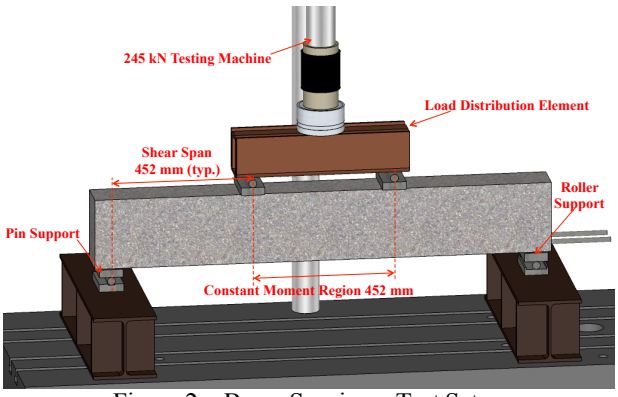


Figure 2 Beam Specimen Test Setup

Strain gages were installed to calculate bond stresses. The gages were placed on all four pieces of reinforcement 6 mm outside of the splice region. Linear variable

differential transducers (LVDTs) were positioned at mid-span to monitor vertical displacement.

LVDTs were also installed at the ends of the two reinforcing bars that were debonded. These LVDTs, shown in Figure 3, measured displacement (slip) of the reinforcement as the specimens were loaded.

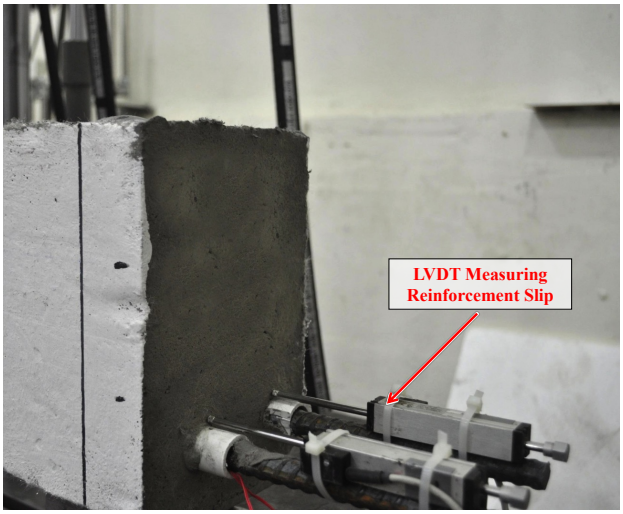


Figure 3 LVDTs Used for Slip Measurement

3. EXPERIMENTAL RESUTLS

3.1 Failure Mechanisms and Crack Propagation

Initial cracks were mapped after a change in stiffness was detected during testing. These first flexural cracks, shown in Figure 3, were well distributed throughout the constant moment region. ECC and concrete specimens both showed similar initial crack patterns within the constant moment region.

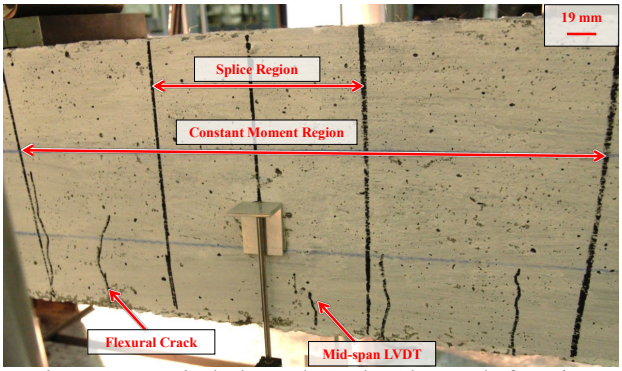


Figure 3 Typical Flexural Cracks Observed after First Cracking

A bond failure was observed when a drop in load carrying capacity occurred. The ECC specimens exhibited more distributed cracking; however, cracks localized in the splice region for both ECC and concrete specimens causing a bond failure. The bond cracks were observed on the vertical and bottom faces of the beams as shown in Figures 4 and 5, respectively.

While testing ECC-1.5-UC, a bond crack on the underside of the beam developed in the splice region. This crack then propagated towards a flexural crack outside of the splice region. As the experiment continued, the flexural crack widened and a portion of the beam began to separate out of plane as shown in Figure 6. It is important to note that this was the only specimen where this was observed.

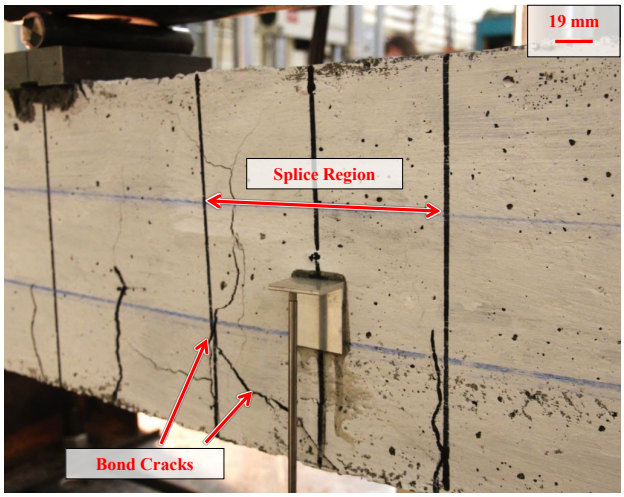


Figure 4 Typical Bond Cracks on Vertical Side of Beam

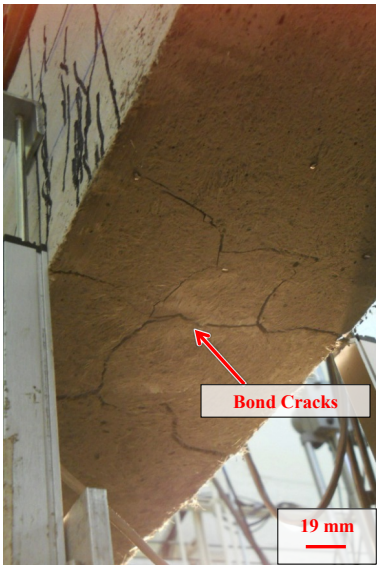


Figure 5 Typical Bond Cracks on Underside Side of Beam

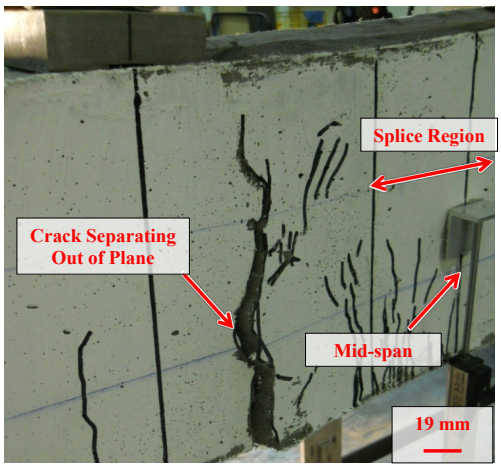


Figure 6 Separating Crack from ECC-1.5-UC

3.2 Bond Strength

Bond strength was calculated from the strain data collected during testing using Equation 1; where u is the bond stress, T_s is the tension force in the steel reinforcement, d_b is the diameter of the steel reinforcement, L_s is the splice length, A_b is the area of the reinforcement, E_s is the modulus of elasticity of the reinforcing steel and ε_s is the strain in the reinforcing steel. It should be noted that the average strain from the four gages was used.

$$u = \frac{T_s}{\pi d_b L_s} = \frac{A_b E_s \varepsilon_s}{\pi d_b L_s} \quad (1)$$

The peak bond strengths from all of the experiments are summarized in Table 3. The ECC specimens had higher maximum bond strengths than their concrete specimen counterparts. The increase in bond strength from ECC ranged from 22 to 64 percent.

There was an increase in bond strength by changing the c/d_b value from 1.0 to 1.5 for the concrete specimens, but little to no increase was observed for the ECC specimens. A substantial increase in bond strength was observed for the c/d_b value of 1.5 when confinement was added to the concrete specimens; however, there was little to no increase in bond strength by confinement otherwise.

Table 3 Maximum Bond Strengths in Concrete and ECC Specimens

Confinement	c/d_b	$u_{max,Concrete}$ (MPa)	$u_{max,ECC}$ (MPa)	Percent Increase
Unconfined	1.0	5.4	8.6	61%
Unconfined	1.5	5.8	8.3	42%
Confined	1.0	5.2	8.4	64%
Confined	1.5	7.0	8.5	22%

3.3 Bond-Slip Behavior

The bond stress vs. slip responses of the unconfined and confined specimens are shown in Figures 7 and 8. In general, the bond-slip curves have three distinct segmentss:

1. An initial branch where bond strength and reinforcement slip increase until the maximum bond stress is reached
2. A descending branch, after the maximum bond stress is reached where bond stress decreases as reinforcement slip increases
3. A final branch where bond stress remains relatively constant while reinforcement slip increases

Concerning the initial branch of the bond-slip curve, the ascending stiffness was similar for both materials. However, as noted in Section 3.2, the peak bond strengths for the ECC specimens were much higher.

After the maximum bond stress was reached, the bond strength of the ECC specimens decreased at a lower slip rate than the concrete specimens. When confinement was added to the concrete specimens, the descending portion of the bond-slip slip curve was less brittle than when confinement was not present. This was also true for the ECC specimens, but to a lesser degree.

The ECC residual bond strengths were substantially higher than the residual concrete bond strengths. Additionally the ratio of residual bond strength to maximum bond strength was higher for ECC specimens.

One important observation is that the residual bond strength of ECC-UC-1.5 was lower than that of ECC-UC-1.0. This was unexpected since bond strengths are expected to increase with increasing c/d_b ratios. However, one explanation for the decrease in residual strength is that the separating crack that developed in ECC-UC-1.5, as previously discussed in Section 3.1 and shown in Figure 6, resulted in a lower residual bond capacity. Additional specimens are planned to further investigate the distinct behavior of ECC-UC-1.5.

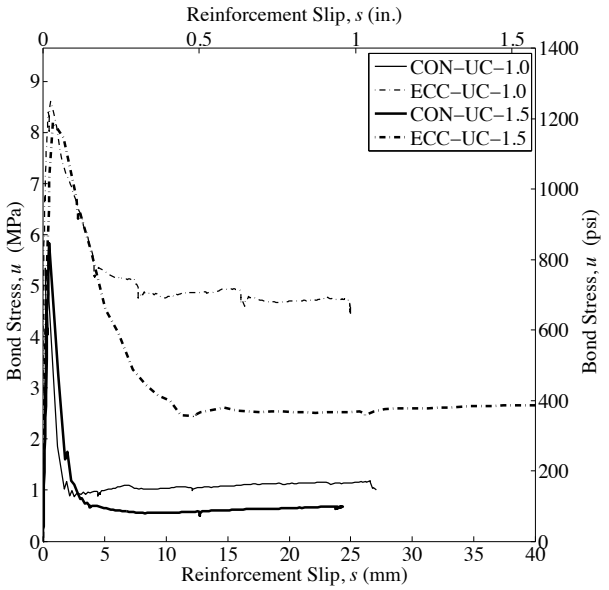


Figure 7 Bond Stress vs. Reinforcement Slip of Unconfined Specimens

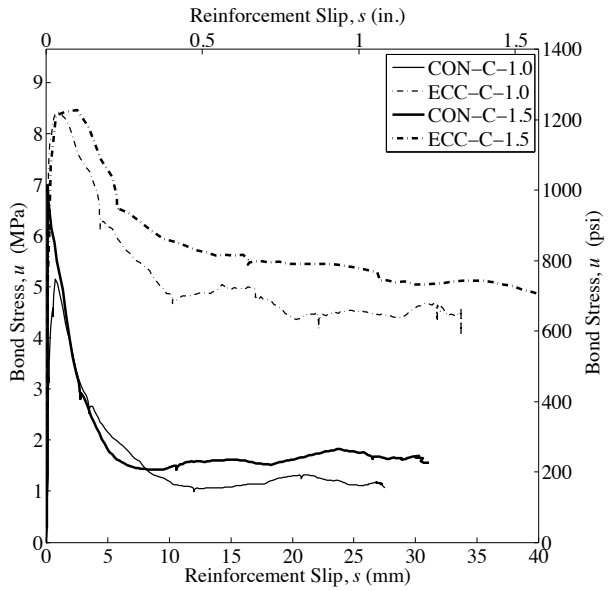


Figure 8 Bond Stress vs. Reinforcement Slip of Confined Specimens

4. CONCLUSIONS AND FUTURE WORK

4.1 Conclusions

Four variations of beam splice specimens were studied to examine the bond behavior in Engineered Cementitious Composites (ECC), one type of HPFRCC, as compared with traditional normal weight concrete. Eight beam specimens were tested in four-point bending with constant moment and shear regions. The parameters varied were cover to bar diameter ratios and amount of confinement in the splice region. Bond stresses were calculated from strain data, and reinforcement slip was measured using LVDTs attached to the reinforcement.

The ECC specimens had higher bond strengths than the concrete specimens in all of the experiments. Additionally, the concrete specimen failures were significantly more brittle since there was a more sudden drop in bond strength after the maximum bond stress was reached. Residual bond strengths were higher in ECC than concrete. Bond-slip data also showed that after the maximum bond strength was reached, bond strengths decreased at a lower slip rate for ECC than concrete.

4.2 Future Work

Additional specimens are being fabricated using two other HPFRCC mix types; a Hybrid Fiber Reinforced Concrete (HyFRC) which utilizes steel fibers and PVA fibers, and a High-Performance Fiber-Reinforced Concrete which uses steel fibers. These three mixes (ECC, HyFRC and HPFRC) represent a range of emerging materials that will help characterize bond in HPFRCCs.

Since the primary application of HPFRCC materials is for earthquake resistant construction, future experiments are planned to examine bond strength deterioration under cyclic loads. The results of these experiments will be used to develop theoretical bond-slip curves for different HPFRCC materials. These bond-slip curves will then be implemented in finite element programs to develop robust analytical models for HPFRCC materials.

Acknowledgements:

The authors gratefully acknowledge funding from the John A. Blume Earthquake Engineering Center and the National Science Foundation (NSF) Graduate Research Fellowship Program (GRFP). Travel support from the Pacific Earthquake Engineering Research (PEER) Center for the first author to attend the 10 CUEE is appreciated. The assistance of undergraduate researcher Albert Alix, Stanford University, is gratefully acknowledged.

References:

ACI Comittee 408 (2003). *Bond and development of straight reinforcing bars in tension*. Farmington Hills, Michigan, 49.

Chao, S.-H., Naaman, A. E., and Parra-Montesinos, G. J. (2009). "Bond behavior of reinforcing bars in tensile strain-hardening fiber-reinforced cement composites." *ACI Structural Journal*, 106(6), 897–906.

Harajli, M. H., Hamad, B. S., and Karam, K. (2002). "Bond-slip response of reinforcing bars embedded in plain and fiber concrete." *Journal of Materials in Civil Engineering*, 14(6), 503–511.

Lequesne, R., Setkit, M., Parra-Montesinos, G. J., and Wight, J. K. (2010). "Seismic detailing and behavior of coupling beams with high-peformance fiber-reinforced concrete." *ACI Spring 2008 Convention*, American Concrete Institute, University of Michigan, Ann Arbor, MI, United States, 205–222.

Orangun, C. O., Jirsa, J. O., and Breen, J. E. (1977). "A Reevaluation of Test Data on Development Length and Splices." *Journal of the American Concrete Institute*, 74(3), 114–122.

Parra-Montesinos, G. J., and Wight, J. K. (2000). "Seismic response of exterior RC column-to-steel beam connections." *Journal of Structural Engineering*, 126(October), 1113–1121.

Rouse, M., and Billington, S. L. (2003). "Behavior of Bride Piers with Ductile Fiber Reinforced Hinge Regions and Vertical , Unbonded Post-Tensioning." *Fib Symposium, Concrete Structures in Seismic Regions*.

10CUEE CONFERENCE PROCEEDINGS
10th International Conference on Urban Earthquake Engineering
March 1-2, 2013, Tokyo Institute of Technology, Tokyo, Japan

LARGE-SCALE TESTING AND ANALYSIS OF CONCRETE-ENCASED STEEL COUPLING BEAMS UNDER LARGE DUCTILITY DEMANDS

Christopher J. Motter[1], John W. Wallace[2], David C. Fields[3], John D. Hooper[3], and Ron Klemencic[4]

1) Graduate Student Researcher (GSR), Dept. of Civil and Environmental Engineering, University of California, Los Angeles
2) Professor, Dept. of Civil and Environmental Engineering, University of California, Los Angeles
3) Principal; Magnusson Klemencic Associates, Seattle, Washington
4) President; Magnusson Klemencic Associates, Seattle, Washington
motter@ucla.edu, wallacej@ucla.edu, dfields@mka.com, jhooper@mka.com, rklemencic@mka.com

Abstract: Reinforced concrete coupling beams with embedded structural steel sections are an alternative to diagonally-reinforced concrete coupling beams. Because prior testing has been conducted on relatively small steel sections, testing of large-scale specimens was conducted to validate analytical models used to determine the required embedment length. The test set-up included reversed-cyclic shear loading applied to the tip of a cantilevered coupling beam containing a structural steel section embedded into a concrete shear wall, which was simultaneously subjected to reversed-cyclic lateral loading to create alternating tension and compression fields across the embedment zone. To assess the degree of potential conservatism in the previously published embedment equations, tests were conducted on two composite coupling beams with varying embedment length, one beam with embedment length expected to result in good performance and a second beam with an embedment length of 75% of the first beam. Both test beams maintained shear coupling loads above 75% of the peak value up to a 6% rotation, although the beam with longer embedment displayed less strength degradation and less pinching.

1. INTRODUCTION

Reinforced concrete shear walls provide an efficient lateral system for resisting seismic and wind loads. Coupling beams connect adjacent colinear shear walls to create larger shear wall assemblages which more efficiently resist lateral loads. The coupling action of these beams reduces the overturning demand within individual wall piers, and imparts vertical forces to the walls via beam shear, thereby creating axial tension-compression couples between coupled wall piers. During significant seismic events, coupling beams are often the first elements to yield. For this reason, coupling beams act as fuses which dissipate earthquake energy through large inelastic rotations, and help control the magnitude and pattern of forces felt by the coupled walls.

ACI 318-11 code provisions require the use of diagonal reinforcement in reinforced concrete coupling beams when shear demand is high and length to depth ratio is low. Testing shows that beams constructed with this reinforcement maintain reliable strength during larger rotations (Naish et al, 2009). Such beams are frequently used in mid- and high-rise buildings in high seismic zones. Coupling beams are typically located between vertically stacked door or corridor openings, putting limitations on beam depth. The congestion associated with embedding diagonal reinforcement into boundary zones of reinforced concrete shear walls creates constructability challenges, thereby increasing construction time and cost.

The use of concrete-encased steel coupling beams provides a viable design alternative and potentially decreases congestion in the wall boundary zone. Embedded steel sections transfer coupling forces to shear walls through a bearing mechanism, which avoids the need for welded and bolted connections while benefiting from the ductility of properly-selected structural steel sections. Steel wide-flange sections encased in concrete are provided further stability against buckling, which results in increased beam ductility. The concrete encasement also provides fire-proofing for the steel beam.

2. BACKGROUND

2.1 Embedment Length

For reinforced concrete coupling beams with embedded steel sections, the strength of the beam-to-wall connection is dependent on the embedment length of the steel section. Adequate embedment length may be defined as the length necessary to create reliable transfer of forces from the beam to the wall without excessively damaging the wall. Mattock and Gaafar (1980) and Marcakis and Mitchell

(1982) developed load transfer models to determine the required embedment length. Although these embedment models govern the transfer of forces from unencased cantilevered steel sections to reinforced concrete columns, the mechanism is parallel to the transfer of forces from steel coupling beams to concrete shear walls.

The Marcakis and Mitchell (1980) and Mattock and Gaafar (1982) embedment models both assume a linear strain distribution in the embedment region, with a strain of ε_c = 0.003 at the outer face of the connection, as shown in Figure 1. A uniform magnitude stress block is used to approximate the bearing stress distribution at the front of the embedment region, while a parabolic stress-strain relationship (Hognestad, 1955) is used to determine the bearing stress distribution along the deeper portion. Based on the applied beam forces, equilibrium is achieved through iteration of the strain gradient. In lieu of iteration, simplifying assumptions were used to develop design equations. Because both embedment models were based on the same assumptions (leading to identical stress diagrams), use of the Marcakis and Mitchell (1980) and Mattock and Gaafar (1982) design equations yield nearly identical results.

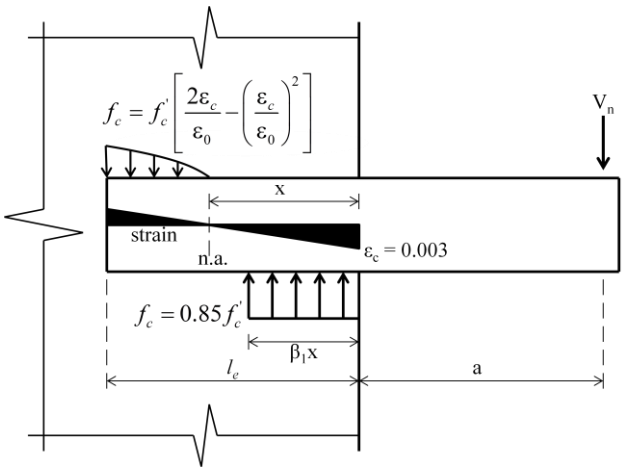


Figure 1. Embedment Model

Harries et al (2000) recommended that both the Marcakis and Mitchell (1980) and the Mattock and Gaafar (1982) embedment equations be modified to include the effects of concrete spalling at the face of the embedment. The Marcakis and Mitchell (1980) embedment equation modified to including spalling is as follows:

$$V_n = \frac{0.85 f_c' b(l_e - c)}{1 + 3.6\left(\frac{e}{(l_e - c)}\right)} \qquad (2.1)$$

where $e=a+(l_e - c)/2$. V_n is the ultimate beam load, a is the cantilever length, l_e is the embedment length, c is the distance of spalling, b is the effective width, and f'_c is the maximum compressive stress of concrete. The distance of spalling at the face of the connection is typically assumed to be equal to the depth of wall cover. During testing, Marcakis and Mitchell (1980) observed spalling of cover concrete to the outside of the column confining ties in the connection region, indicating load spreading to this effective width. The effective width, b, is thus taken as the width of the confined region, not to exceed 2.5 times the width of the embedded member.

The Mattock and Gaafar (1982) embedment equation modified to including spalling is as follows:

$$V_n = 4.5\sqrt{f_c'}\left(\frac{t}{b}\right)^{0.66} \beta_1 b(l_e - c)\left(\frac{0.58 - 0.22\beta_1}{0.88 + (a+c)/(l_e - c)}\right) \qquad (2.2)$$

where f'_c is in MPa, t is the wall thickness, b is the bearing width, equal to the flange width for wide-flange sections, and β_1 is the ACI stress block factor, defined as the ratio of the uniform stress block depth to the neutral axis depth.

Based on test results for shear-controlled concrete-encased steel coupling beams, Gong and Shahrooz (2001b) recommend computing the embedment length necessary to develop the full expected capacity of the composite coupling beam, including the effects of encasement on shear strength. Significant energy dissipation due to inelastic connection deformation occurred for members in which encasement was neglected when determining the member capacity for computing embedment length.

2.2 Embedment Detailing

As shown in Figure 2, the 2010 AISC *Seismic Provisions for Structural Steel Buildings* (referred to as the "2010 AISC Seismic Provisions" from this point forward) require the use of auxiliary transfer bars (welded to the beam flanges) and face bearing plates within the embedment zone

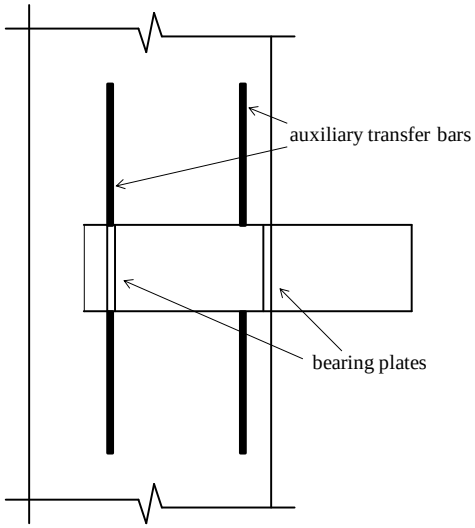


Figure 2. Embedment Detailing Requirements of 2010 AISC Seismic Provisions

of the embedded steel section. Transfer bars are required to be attached via welding to the top flange and bottom flange at the front and back of the member. A pair of web stiffener plates are required at the location of the back transfer bars, and a pair of face-bearing plates are required at the beam-wall interface.

The role of the auxiliary transfer bars is to aid in the transfer of load from the coupling beam to the shear wall. These bars are required to be developed into the shear wall, enabling the transfer of load via bond. The bearing plates also provide an additional force-transfer mechanism by allowing the formation of a diagonal strut between the two plates. These plates also act as web stiffeners, since the welded transfer bars create concentrated loads on the steel section.

3. TEST SET-UP AND SPECIMEN DESIGN

Because prior testing was often conducted on small-scale specimens (Gong and Shahrooz, 2001a; Gong and Shahrooz, 2001b), this research study strives to assess the reliability of the embedment equations at the largest scale possible based on laboratory constraints (determined to be ~one-half scale). Prior tests were often conducted for steel sections embedded into either uncracked (sometimes unstressed) walls or reaction blocks (Harries et al, 1993; Harries et al, 1997; Gong and Shahrooz, 2001a; Fortney, 2005). Because local stress/strain fields could impact the required length of embedment, the test was designed to include a wall subjected to lateral loading and overturning moment such that the wall strains/stresses at the embedment location represented realistic conditions, as shown in Figure 3.

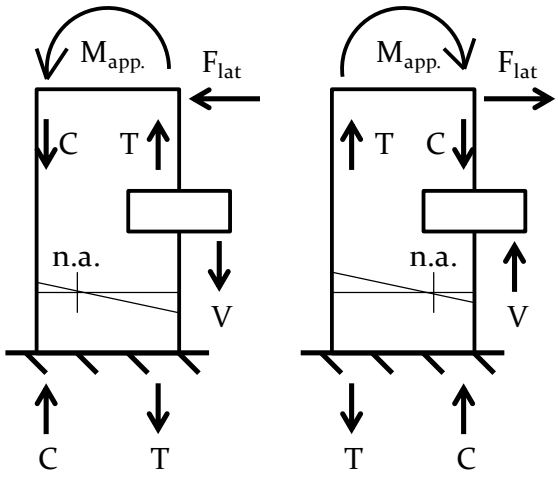


Figure 3. Wall Strains at Embedment Zone

The overall test set-up is shown in Figure 4. The test specimen included a reinforced concrete shear wall with two one-half-length composite coupling beams (one on each side of the wall), which were tested individually. The only difference between the two coupling beams was the embedment length. The point of load application represented the midpoint, which is also an inflection point, in a full-length coupling beam.

To generate wall overturning moment, two 1780-kN (max.) actuators with +/- 457 mm stroke were used to apply equal and opposite vertical loads. The wall lateral shear force (and additional moment) was applied by a 1335-kN (max.) actuator with +/- 305 mm stroke. To support the lateral reaction from the 300-kip actuator, reaction blocks were stacked, grouted at the interfaces, and post-tensioned to the laboratory strong-floor with 31.75 mm diameter high-strength Dywidag rods. The "top beam" in Figure 4 refers to a thickened portion at the top of the wall (poured continuously with the upper wall) constructed to facilitate anchorage to the loading beam. The top beam and footing were post-tensioned to the steel section at the top of the specimen and the laboratory strong floor, respectively.

3.1 Coupling Beams

Figure 5 shows cross-sections for the beams (same for both) and the shear wall. The embedded steel section was a (AISC) W12x96 (d = 322.6 mm, t_w = 14.0 mm, b_f = 309.9 mm, and t_f = 22.9 mm) with flanges trimmed to a width of 139.7 mm, which is an approximation of a one-half-scale (AISC) W24x250 (d = 668.0 mm, t_w = 26.4 mm, b_f = 335.3 mm, and t_f = 48.0 mm). The use of a built-up section for the embedded member was also considered in order to achieve precise scaling. However, due to differences in fabrication and material properties for wide flanges and built-up sections, the use of a built-up test section to represent a WF prototype section was deemed undesirable.

The aspect ratio of the test beams was 3.33, which is typical for office buildings in the U.S. Due to the high aspect ratio, the beams were flexure-controlled. Because the contribution of concrete shear strength was not essential to ensure flexure-critical behavior, coupling beam stirrups (6.35 mm dia. @ 76.2 mm spacing) were detailed as two U-bars rather than individual hoops for ease of constructability. Longitudinal bars (9.525 mm dia.), used as placeholders for shear reinforcement, were not developed in the shear wall, thereby contributing no flexural strength to the coupling beam to better control the moment transferred to the embedment region.

Because the beams were flexure-controlled, the maximum expected shear load was obtained by dividing the ultimate flexural capacity by the cantilever length (including wall spalling, i.e. wall cover). This approach assumes that the intended yield and failure mechanism is entirely within the beam rather than the connection, meaning that beam failure occurs at the face of the embedment rather than in the connection. Based on the maximum expected shear load, the required embedment length was determined using both the Marcakis and Mitchell (1980) and Mattock and Gaafar (1982) embedment equations corrected to include the effects of wall spalling per the recommendation of Harries et al (2000).

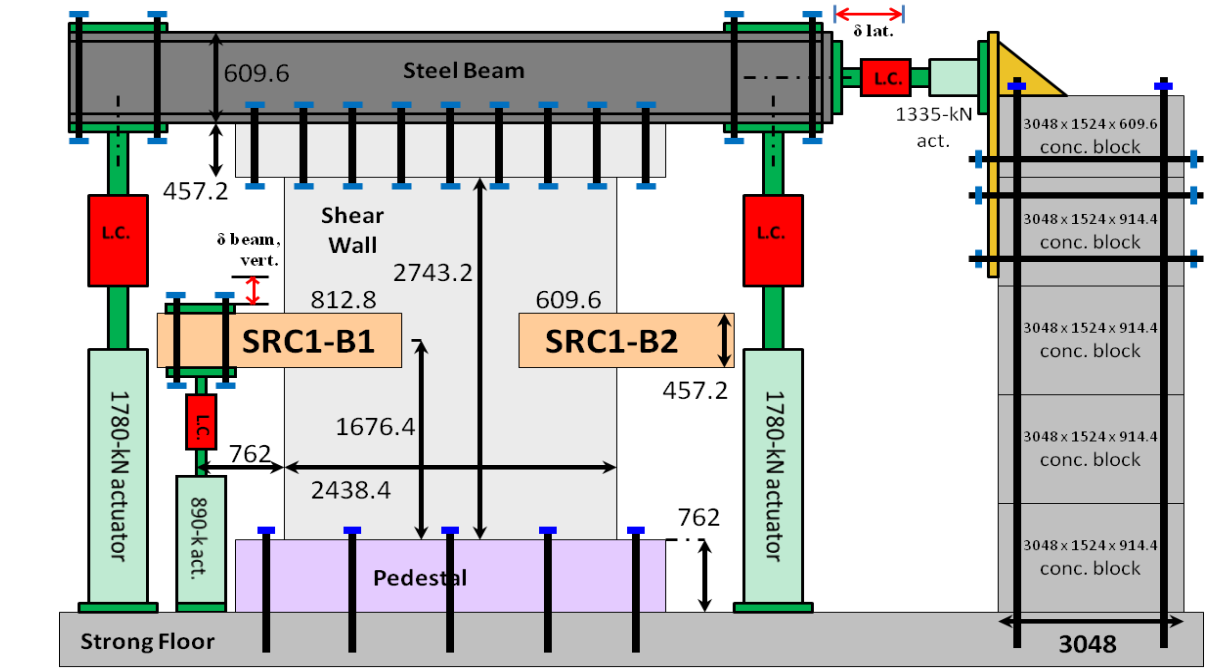


Figure 4. Test Set-Up

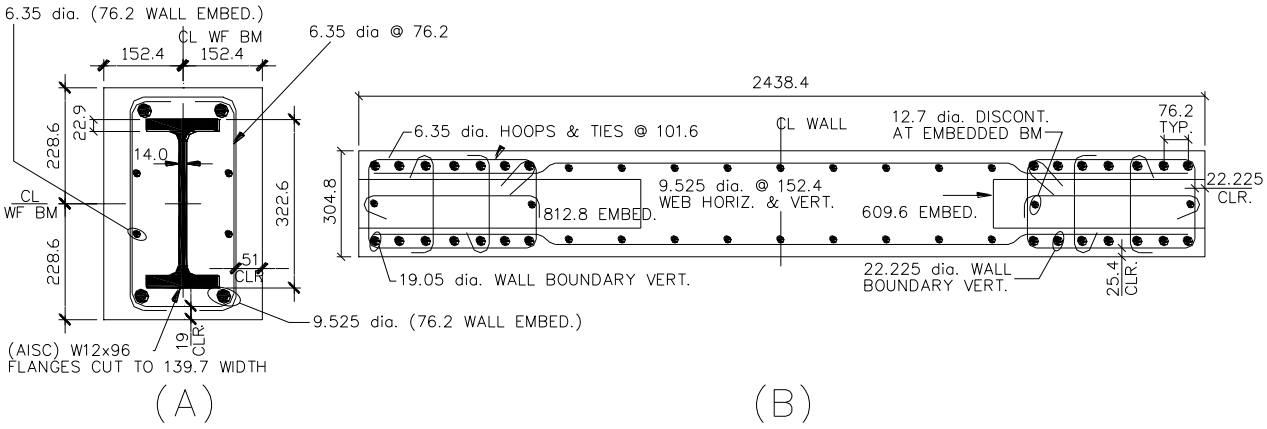


Figure 5. Beam (A) and Wall (B) Cross-Sections (all dimensions in mm)

Table 1. Member Capacity and Corresponding Embedment Length

			μ-2σ	μ-σ	μ	μ+σ	μ+2σ	min	max	des. w/o ϕ	des. w ϕ
BIAX	Vn	kN	807	839	871	903	934	811	959	810	900
	Embed. (M&M)	mm	686	704	719	734	752	688	762	688	734
	Embed. (M&G)	mm	673	704	706	721	737	676	749	676	721
AISC, Fy	Vu	kN	696	730	763	797	830	702	854	702	780
	Embed. (M&M)	mm	627	645	663	681	699	630	711	630	673
	Embed. (M&G)	mm	615	632	650	668	686	617	696	617	660
AISC, Fu	Vu	kN	908	942	977	1011	1045	892	1099	884	982
	Embed. (M&M)	mm	737	754	772	787	805	729	831	726	775
	Embed. (M&G)	mm	724	742	759	775	792	716	818	711	762

The 2010 AISC Seismic Provisions for Structural Steel Buildings supports the use of either an AISC-based or ACI-based approach to determine the flexural capacity of a concrete-encased steel coupling beam. When using the AISC-based approach, the ultimate flexural capacity of the beam is computed based on a fully plastic steel section and a uniform stress block for concrete in compression. The ACI-based approach requires strain compatibility of the cross-section. In this case the steel section was converted into an equivalent area of reinforcement and reinforced concrete beam analysis (strain compatibility fiber analysis) was performed using BIAX software (Wallace and Ibrahim, 1996) to determine the ultimate capacity. The steel properties of the A992 wide-flange used in all analyses were obtained from the test results of Liu et al (2007), which were used in the 2005 AISC Seismic Provisions. These test results provide a mean and standard deviation, as well as a maximum and minimum, for actual yield stress, F_y, and ultimate tensile stress, F_u, of structural steel wide flange sections tested under cyclic loading. For the AISC plastic analysis approach, values for both F_y and F_u were considered.

Both the AISC and ACI methods used to determine beam flexural capacity assume monotonic loading and the development of full composite action (i.e. no slip) between the concrete and steel. Since cyclic loading was applied and shear studs were not provided, these analysis methods were expected to over-predict the actual member capacity, which is conservative for computing minimum embedment lengths.

Based on the range of required embedment lengths obtained from the range of structural steel properties (Liu et al 2007) and the two analysis methods (AISC-based and ACI-based), shown in Table 1, a conservative embedment length of 813-mm was selected for the first coupling beam. An embedment length of 610-mm was selected for the second coupling beam, in order to assess the degree of conservatism inherent in the embedment equations and better understand the limitations of the connection. From this point forward, the beams with 813-mm and 610-mm embedment lengths are referred to as Beam 1 and Beam 2, respectively.

3.2 Shear Wall

Figure 5(b) shows the shear wall cross-section. ACI 318 Chapter 21 and Appendix A (strut-and-tie modeling) code provisions were used to guide the design of the shear wall. Within the embedment zone, bearing forces were assumed to transfer into wall vertical reinforcement. Because the bearing forces were computed to be larger for the section with shorter embedment length, local stresses in wall vertical boundary bars were expected to be larger than those associated with the longer embedment length. For this reason, 14#7 (22 mm dia.) wall verticals were used on the side with Beam 2, and 14#6 (19 mm dia.) wall verticals were used on the side with Beam 1. Horizontal and vertical web bars were selected to satisfy the ACI 318-11 code minimum.

An intermediate level of wall boundary confinement is representative of a mid-to-upper-level story for a high-rise reinforced concrete building in a zone of moderate to high seismic risk. Transverse reinforcement at the wall boundary was provided to satisfy provisions for an intermediate level of boundary confinement (often referred to as an "ordinary boundary element") per ACI 318-11 Section 21.9.6.5, which requires a 203.2 mm maximum spacing. Assuming 12.7 mm hoops and ties at 203.2 mm spacing for the prototype suggested 6.35 mm hoops and ties at 101.6 mm spacing.

ACI 21.9.6.5 also requires that $h_x \leq 355.6$ mm (per ACI 21.6.4.2 as mandated within ACI 21.9.6.5), which scaled to $h_x \leq 177.8$ mm. h_x is defined as the maximum center-to-center spacing of cross-ties or hoop legs. Two cross-ties were used for the test specimen in the short direction as shown in Figure 5; therefore, $h_x = 181.0$ mm for the 22.225 mm (dia.) verticals (deemed close enough to 177.8 mm). A central cross-tie was also needed in the long direction. Discontinuous 12.7 mm (dia.) vertical bars were used as placeholders for this cross-tie, but were not embedded into the footing or the concrete top beam in order to avoid adding wall flexural strength.

For horizontal and vertical web bars the code minimum reinforcing ratio is ρ=0.0025 per ACI 318-08 Section 21.9.2.1. At one-half-scale, 19.05 mm (dia.) @ 304.8 mm spacing (ρ=0.0031) scaled to 9.525 mm (dia.) @ 152.4 mm spacing (ρ=0.0031).

3.3 Embedment Detailing

Figure 6 and Figure 7 show the wall boundary detailing at the connection zone. Due to the presence of the embedded steel section, standard hoops and cross-ties could not be placed. In order to maintain wall boundary confinement through the depth of the embedded beam, pre-drilled holes through the web of the steel section allowed the use of threaded rods and steel plates to achieve the desired level of confinement.



Figure 6. Photo of Embedment Detail

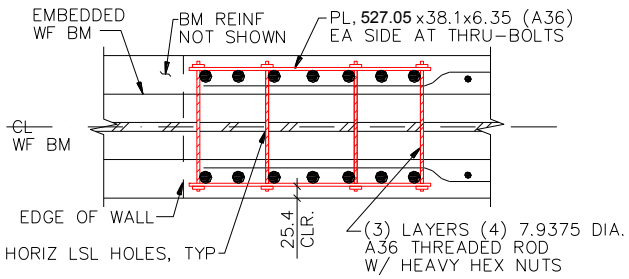


Figure 7. Drawing of Embedment Detail

Despite the detailing requirements of the 2010 AISC Seismic Provisions, auxiliary transfer bars and bearing plates (Figure 2) were not provided in the embedment zone. Transfer bars and bearing plates provide load transfer mechanisms in addition to bearing. This study is intended to assess the reliability of the embedment equations without the added benefit of additional load-transfer mechanisms.

4. TESTING PROTOCOL

The testing protocol is shown in Figure 8. The coupling beam actuator controlled the test. The three wall actuators were slaved to this actuator based on the force ratios shown in Figure 8. For Beam 1 the wall forces were large enough to exceed the wall cracking moment at the embedment zone. For Beam 2 the wall forces were 2.5 times larger than Beam 1 in order to approach wall yield at the embedment zone. Larger wall loads in combination with shorter embedment length were expected to create the more critical scenario for the coupling beam connection.

The calculated shear force at flexural yield, $V@M_y$, (based on BIAX strain compatibility fiber analysis using the average steel yield stress, F_y = 379 MPa, and the average steel ultimate stress, F_u = 502 MPa from Liu et al (2007)) for the composite coupling beam was computed to be 712 kN. Load-controlled cycles were performed at increments of $(V@M_y)/8$, $(V@M_y)/4$, $(V@M_y)/2$, and $3(V@M_y)/4$ (89 kN, 178 kN, 356 kN, and 534 kN). For the remainder of this paper the term "rotation" refers to the chord rotation of the cantilevered coupling beam, which was computed as the beam displacement at the point of load application divided by the 762 mm cantilevered length. Based on the observed stiffness at $3(V@M_y)/4$, the yield rotation was estimated and the test proceeded as displacement-controlled. For Beam 1 the yield rotation was estimated to be 1.67%, and subsequent cycles were carried out at rotations of 1.67%, 2.25%, 3.0%, 4.0%, 6.0%, 8.0%, 10.0%, and 13.0%. Despite very little strength degradation, the test was stopped at 13.0% rotation, which was deemed larger than any practical performance goal.

The difference in stiffness between the positive (upward) and negative (downward) loading direction was significant for Beam 2. Therefore, during load-controlled cycles, loading in the negative direction was carried out under displacement-control based on the actual displacement for the positive direction (which was load-controlled). Yield rotation in the positive direction was estimated to be 0.6%, and the displacement-controlled cycles were carried out at rotations of 0.67%, 1.0%, 1.5%, 2.0%, 3.0%, 4.0%, 6.0%, 8.0%, and 10.0%.

5. TEST RESULTS

5.1 Observed Damage

For both beam tests, damage concentrated primarily at the beam-wall interface. Figure 9 shows damage photos for both tests after the completion of loading cycles at 3% and 6% rotation. After 3% rotation Beam 1 showed significant cracking but minimal spalling at the interface. Comparatively, Beam 2 showed more spalling and wider cracking at the interface. After the cycles at 6% rotation, significant spalling was evident for both beams, with Beam 2 displaying more extensive spalling than Beam 1. Aside

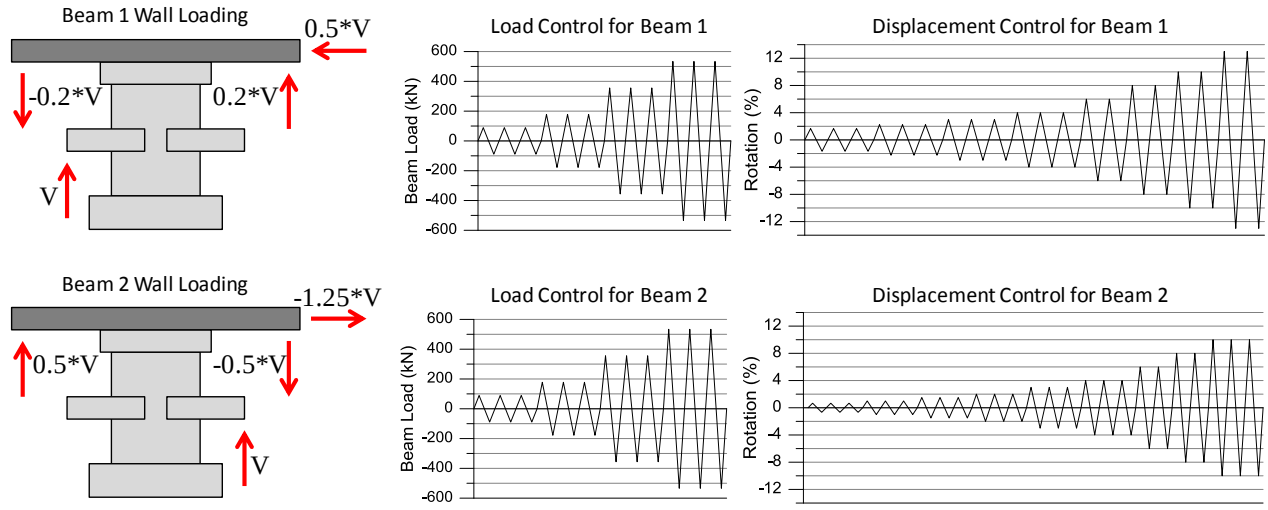


Figure 8. Testing Protocol



Beam 1 after 3% rotation *Beam 2 after 3% rotation* *Beam 1 after 6% rotation* *Beam 2 after 6% rotation*

Figure 9. Damage Photos

from the damage at the beam-wall interface, only minor hairline cracking was observed in the beam span for both tests. Cracking in the embedment region was evident during both tests, and was more extensive for Beam 2; however, there was no spalling in the embedment region during either test.

Although significant outward slip of the steel section was observed during the test, in actual structures, outward slip of the steel section is restrained at some level by a floor slab as well as embedment into an adjacent shear wall, which creates axial load on the coupling beam. Because axial load is dependent on structural lay-out, geometry, etc, it was not simulated for this test due to the lack of a specific prototype structure.

5.2 Load-Displacement

Figure 10 shows load-displacement plots for Beam 1 and Beam 2. Both plots display large ductility with minimal strength degradation. The plot for Beam 1 is symmetric, with very minimal strength degradation up to 13% rotation. The plot for Beam 2 displays more pinching, greater strength degradation, and noticeable asymmetry, including reduced capacity in the negative loading direction. The pinching is consistent with the formation of a gap between the steel flange and the concrete in the connection zone, which was observed during testing.

Although the Beam 2 embedment length was initially designed to be less than required, it is interesting to note that based on the observed capacity of the test beams and the as-tested concrete compressive strength of 51.0-MPa the minimum required embedment length computed for both the Marcakis and Mitchell (1980) and Mattock and Gaafar (1982) embedment equations is 584 mm, suggesting that the provided 610 mm embedment length for Beam 2 is adequate.

The asymmetry in the load-displacement plot for Beam 2 is attributable to the stress field created at the embedment zone due to wall loading. During positive (upward) beam loading, the wall loads created a vertical compression field in the embedment region, while a tension field was induced in the embedment region of the wall during negative (downward) beam loading. The Beam 2 connection was softer and also developed less capacity when in tension compared to compression. This effect appears less pronounced for Beam 1, due to lower-magnitude wall loading.

Throughout testing of Beam 1, a correction to the measured displacement was made to account for beam displacement due to wall rotation. This was also done for the early phases of Beam 2 testing; however, the data were not reliable and the idea of correcting for this was abandoned. Test data for Beam 1 were adjusted to neglect the correction in order to provide a direct comparison with Beam 2 test data in Figure 10. For this reason, the load-rotation plot for Beam 1 shows rotation levels that differ slightly from those used to control the test.

The performance of both coupling beams was favorable, characterized by minimal strength degradation at large ductility demands and observed damage concentration

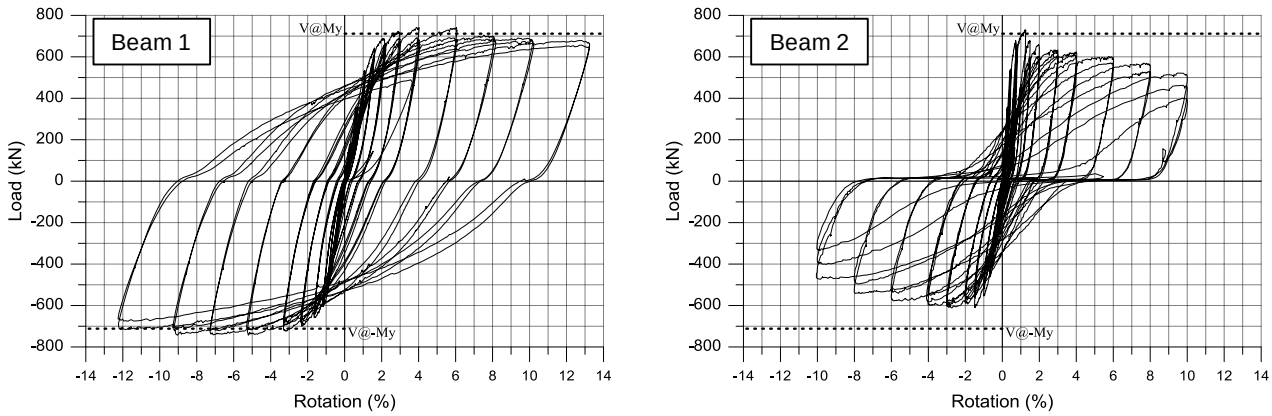


Figure 10. Load-Displacement

(indicative of plastic hinge formation) at the beam-wall interface. Favorable performance of these two members suggests that in this particular instance the embedment length was adequate to transfer the loads via bearing without the added benefit of additional force-transfer mechanisms. Changes to the 2010 AISC Seismic Provisions that would eliminate the need for face bearing plates and auxiliary transfer bars may be considered, although additional testing is needed to provide further evaluation.

5.3 Backbone Curves

Backbone curves are show in Figure 11. The backbone curves for the test data are comprised of load and displacement pairings at the peak of the first cycle of each loading increment. Note that the AISC Seismic Provisions do not explicitly provide backbone parameters. The backbones curves shown in Figure 11 were generated by combining AISC recommendations for stiffness, flexural capacity, and required ductility demand. To determine the initial stiffness for concrete-encased steel coupling beams, provisions H4.3.1 and H5.3.1 in the 2010 AISC Seismic Provisions refer to ACI 318-11 Chapter 10. Presumably this is a reference to ACI 318-11 Chapter 10 Section 10.10.4.1 which specifies an effective moment of inertia of $0.35I_g$ for beams, where I_g is the gross moment of inertia of the concrete section. Neither ASCE 41-06 nor FEMA 356 provide the rotational ductility parameters for steel coupling beams that are needed to generate backbone curves for modeling. However, section H5.5c of the seismic provisions indicates that steel coupling beams need not be designed to exceed a rotation of 0.08 radians (8.0%). The AISC backbone plots shown in Figure 11 were based on an initial stiffness of $0.35E_cI_g$ and a loss of all load-carrying capacity at 0.08 radians.

For the AISC backbone curves, the flexural capacity of the composite section was computed using a plastic analysis approach, including a uniform stress block for concrete in compression. This approach is supported by section H4.2.1 in the 2010 AISC Seismic Provisions. A plastic stress of F_y, the design yield stress of steel, was used. For the AISC expected capacity indicated in Figure 11, the plastic stress of structural steel was taken as R_y*F_y, where R_y is 1.1 for F_y = 345 MPa (50 ksi) in keeping with standard seismic design. The AISC backbone curves in Figure 11 considered fixity at the beam-wall interface as well as fixity within the connection, i.e. at $L_e/3$ from the beam-wall interface as suggested by Harries et al (2000) for modeling purposes. Moving the effective point of fixity to $L_e/3$ from the interface increases the effective cantilever length, thereby reducing the shear-carrying capacity of a flexure controlled-section.

Based on good agreement with test results, it appears reasonable to compute the design flexural capacity of composite coupling beams using the AISC approach. Referring again to Figure 11, the capacity of the AISC backbone curve matches well with the Beam 1 backbone. The AISC with fixity at $L_e/3$ backbone agrees well with the observed performance for Beam 2 negative (-), a case for which larger applied wall moment produced larger tension across the connection compared to Beam 1. Beam 2 positive (+) reaches a capacity that matches the AISC backbone but strength degrades to a residual capacity that better matches an AISC with fixity at $L_e/3$ backbone. The strength degradation is likely a result of the behavior in the negative loading direction, i.e. local yielding of vertical wall reinforcement allows the formation of gapping between the flange of the steel section and the surrounding concrete. Reliable strength for both positive and negative loading should be based on a fixity point at $L_e/3$ inside the beam-wall interface, whereas peak beam load for positive loading should be based on a fixity point at the depth of concrete spalling (wall edge minus concrete cover). More research is needed to further quantify the relationship between effective fixity and wall tension/compression across the connection.

Referring again to Figure 11, because the expected AISC capacity (including R_y) is slightly larger than the observed capacity for both beams in both loading directions, using the expected AISC capacity to determine the embedment length is slightly conservative and recommended for design. Note that for cases in which the beam capacity is reduced in the negative direction, the larger

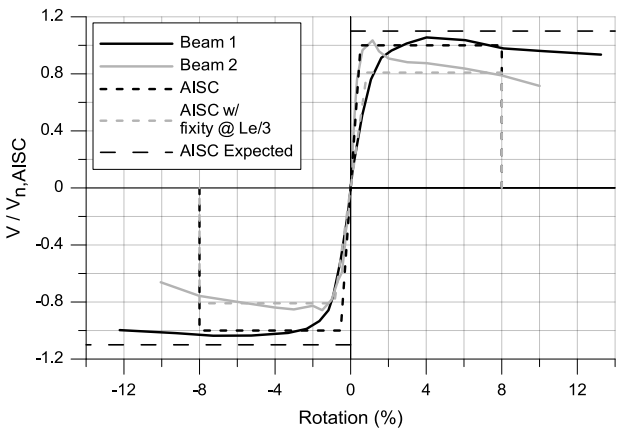


Figure 11. Backbone Curves

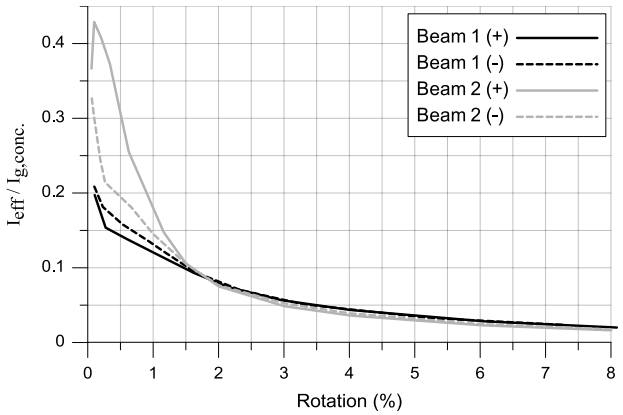


Figure 12. Effective Secant Stiffness

capacity in the positive direction governs the computation of the required minimum embedment length.

5.4 Effective Secant Stiffness

The effective secant stiffness was evaluated using the elastic stiffness relationship for a point load on a fixed-end cantilever, re-arranged to be expressed in terms of an effective moment of inertia, normalized by the gross moment of inertia. Figure 12 shows effective secant stiffness plots generated based on $E_cI_{g,conc.}$, where $I_{g,conc.}$ is the moment of inertia for the gross concrete section neglecting steel, and E_c is the elastic modulus of concrete. The plots in Figure 12 are based on data at the peak of the first cycle at each load/displacement increment. For comparative purposes, the absolute value of peak rotation is used, putting all data in the first quadrant.

Referring to Figure 12, there is minimal difference in the effective secant stiffness beyond rotations of about 1.5%. For rotations less than 1.5%, the difference between positive and negative stiffness values for Beam 2 is attributable to the embedment stresses in the wall, which produce compression for positive loading and tension for negative loading. The effective stiffness appears largest for Beam 2 loaded in the positive direction. Based on good agreement with the AISC backbone in Figure 11, using an initial stiffness of $0.35E_cI_{g,conc.}$ appears reasonable for Beam 2 positive (+). Referring to Figure 12, it appears reasonable to use an initial stiffness of $0.2E_cI_{g,conc.}$ for other cases, i.e. Beam 1 and Beam 2 negative (-). It also appears reasonable to use an initial stiffness of $0.35E_cI_{g,conc.}$ with fixity at $L_e/3$ (Figure 11) for cases with tension across the connection (i.e. in the negative loading direction).

Note that the larger negative stiffness for Beam 2 compared to Beam 1 may be somewhat misleading. Wall loading creates rotation that generates beam tip displacements that oppose the measured beam displacements reflected in Figure 12. Therefore, the relative cantilever displacement includes the measured displacement plus any additional opposing displacement due to wall rotation. Because the plot in Figure 12 does not reflect the effect of wall rotation, the stiffness values appear larger. Since the wall loads for Beam 2 were 2.5 times larger than for Beam 1, the effect is more pronounced for Beam 2. Due to local deformations in the embedment zone, obtaining reliable data for wall rotation was difficult; however, measured wall deformations were small compared to beam deformations, suggesting that the effect of wall rotation on beam tip displacements was relatively minor.

6. CONCLUSIONS

A testing program was undertaken to assess the performance of concrete-encased steel coupling beams embedded into reinforced concrete shear walls at large-scale and for realistic loading and boundary conditions. Moment and shear load were applied to the wall to generate stress/strain fields in the coupling beam embedment zones that were representative of conditions in actual structures; simultaneous reversed, cyclic loading was applied to the coupling beams. Two tests were conducted on structural steel wide-flange sections to investigate the role of embedment length and detailing on beam strength, stiffness, and deformation capacity. The embedment models proposed by Marcakis and Mitchell (1980) and Mattock and Gaafar (1982) were used to compute the required embedment length needed to transfer bearing forces from the beam to the wall. The embedment length for Beam 1 was selected to represent a conservative design, with longer embedment, whereas the embedment length for Beam 2 was selected to be a minimum value (75% of the value used for Beam 1). Wall loads were also varied, with the wall moment for the shorter embedment (Beam 2) approaching the wall yield moment in the embedment region, or approximately 2.5 times larger than the wall moment for Beam 1. Excellent performance was observed for Beam 1, with beam rotation capacity exceeding 10% with negligible strength loss. Damage at the beam-wall interface led to lower strength and deformation capacity for Beam 2, and also more pinching of the load-deformation response. Based on the study, the following conclusions were reached:

1) The design moment strength of concrete-encased steel coupling beams may be computed using a plastic section analysis in which the plastic steel stress is taken as the design yield stress, F_y, concrete in compression is modeled as a uniform stress block, and concrete tensile strength is neglected.
2) The effective point of fixity may be taken at the depth of wall spalling (i.e. wall cover) at the beam-wall interface for long embedment and lower applied wall moment (Beam 1). For Beam 2 (positive beam load), with shorter embedment and larger wall demands, the point of fixity varied between the depth of wall spalling (concrete cover) at yield to $L_e/3$ inside the beam-wall interface at 6% rotation. It appears that damage at the beam-wall interface for negative loading results in subsequent strength loss for positive loading. Therefore, reliable strength for both positive and negative loading over a range of plastic rotations typically expected for coupling beams (up to 6% rotation) should be based on a fixity point at $L_e/3$ inside the beam-wall interface, whereas peak beam load for positive loading should be based on a fixity point at the depth of concrete spalling (wall edge minus concrete cover). Two additional tests will be conducted to further assess these issues.
3) Embedment performance was adequate for both beam tests; therefore, either the Marcakis and Mitchell (1980) or Mattock and Gaafar (1982) embedment equations, modified to account for spalling as recommended by Harries et al (2000), may be used to compute the minimum required embedment length of the embedded steel section.

The embedment equation in the 2010 AISC Seismic Provisions is based on the Mattock and Gaafar (1982) embedment equation. Although Beam 2 was initially designed to examine behavior for an embedment length slightly less than required, the provided embedment length actually satisfied embedment equations based on the as-tested concrete compression strength and the observed beam capacity. For flexure-controlled sections, the expected shear force used to compute the minimum required embedment length may be determined based on the expected flexural capacity and effective point of fixity. The calculation for the expected flexural capacity differs from the calculation of the design flexural capacity in that the expected yield stress, R_y*F_y (with R_y taken as 1.1 for F_y = 345 MPa = 50 ksi), is used as the plastic stress.

4) The initial bending stiffness of a concrete-encased steel coupling beam depends on the stress/strain field across the connection. The effective bending stiffness was $0.35E_cI_{g,conc.}$ for Beam 2 positive (+), with the larger applied wall moment creating compression across the connection. The effective bending stiffness was $0.2E_cI_{g,conc.}$ for other cases, where $I_{g,conc.}$ is the moment of inertia computed for the gross concrete section.
5) The 2010 AISC Seismic Provisions require the use of auxiliary transfer bars welded to the flange of the embedded steel section and bearing plates welded near the end of the embedded steel section as well as at the beam-wall interface. The steel sections tested in this study did not use transfer bars and face-bearing plates; however, sufficient wall boundary vertical steel was provided to satisfy load paths for bearing forces. Test results indicated favorable performance for these members, suggesting that in this particular instance the embedment length was adequate to transfer the loads via bearing without the added benefit of additional force-transfer mechanisms. Changes to the 2010 AISC Seismic Provisions that would eliminate the need for face bearing plates and auxiliary transfer bars may be considered. More testing is needed to provide further evaluation.

Acknowledgements:

The work presented in this paper is supported by funds from the Charles Pankow Foundation. This research was performed in a collaboratory renovated with funds provided by the National Science Foundation under Grant No. 0963183, which is an award funded under the American Recovery and Reinvestment Act of 2009 (ARRA). Any opinions, findings, and conclusions expressed in this material are those of the authors and do not necessarily reflect those of the National Science Foundation.

References:

ACI Committee 318 (2011), "Building Code Requirements for Structural Concrete (ACI 318-11) and Commentary," American Concrete Institute, Farmington Hills, MI.

AISC (2005), "Seismic Provisions for Structural Steel Buildings," ANSI/AISC 341-05, American Institute of Steel Construction, Chicago, IL.

AISC (2010), "Seismic Provisions for Structural Steel Buildings," ANSI/AISC 341-10, American Institute of Steel Construction, Chicago, IL.

American Society of Civil Engineers (2007), "ASCE/SEI Standard 41-06, Seismic Rehabilitation of Existing Buildings," Reston, VA.

Federal Emergency Management Agency (2000), "Prestandard and Commentary for the Seismic Rehabilitation of Buildings (FEMA-356)," Washington, D.C.

Fortney, P.J. (2005). "The Next Generation of Coupling Beams," *PhD Dissertation*, University of Cincinnati.

Gong, B. and Shahrooz, B.M. (2001a), "Concrete-Steel Composite Coupling Beams. I: Component Testing," *Journal of Structural Engineering*, 127(6), 625-631.

Gong, B. and Shahrooz, B.M. (2001b), "Concrete-Steel Composite Coupling Beams. II: Subassembly Testing and Design Verification," *Journal of Structural Engineering*, 127(6), 632-638.

Harries, K.A., Gong, B. and Shahrooz, B.M. (2000), "Behavior and Design of Reinforced Concrete, Steel, and Steel-Concrete Coupling Beams," *Earthquake Spectra*, 16(4), 775-798.

Harries, K.A., Mitchell, D., Cook, W.D., and Redwood, R.G. (1993), "Seismic Response of Steel Beams Coupling Concrete Walls," *Journal of Structural Engineering*, 119(12), 3611-3629.

Harries, K.A., Mitchell, D., Redwood, R.G., Cook, W.D. (1997), "Seismic Design of Coupled Walls – A Case for Mixed Construction," *Canadian Journal of Civil Engineering*, 24, 448-459.

Hognestad, E., Hanson, N.W. and McHenry, D. (1955), "Concrete Stress Distribution in Ultimate Strength Design," *ACI Journal Proceedings*, 52(12), 455-479.

Liu, J., Sabelli, R., Brockenbrough, R.L. and Fraser, T.P. (2007), "Expected Yield Stress and Tensile Strength Ratios for Determination of Expected Member Capacity in the 2005 AISC Seismic Provisions," *Engineering Journal*, First Quarter, 15-25.

Marcakis, K. and Mitchell, D. (1980), "Precast Concrete Connections with Embedded Steel Members," *PCI Journal*, 25(4), 88-116.

Mattock, A.H. and Gaafar, G.H. (1982), "Strength of Embedded Steel Sections as Brackets," *ACI Journal*, 79(9), 83-93.

Motter, C.J., Wallace, J.W., Field, D.F., Hooper J.D., and Klemencic, R. (2012), "Large-Scale Testing and Analysis of Concrete-Encased Steel Coupling Beams Under High Ductility Demands," *Proceedings of the 15th World Conference on Earthquake Engineering*, Paper No. 1514.

Naish, D., Wallace, J.W., Fry, J.A. and Klemencic, R. (2009), "Reinforced Concrete Link Beams: Alternative Details for Improved Construction," *UCLA – SGEL Report 2009/06*.

Shahrooz, B.M., Remetter, M.E. and Qin, F. (1993), "Seismic Design and Performance of Composite Coupled Walls," *Journal of Structural Engineering*, 119(11), 3291-3309.

Wallace, J.W. and Ibrahim, Y.A. (1996), "BIAX: Strength Analysis of Reinforced Concrete Sections," Computer Program.

10CUEE CONFERENCE PROCEEDINGS
10th International Conference on Urban Earthquake Engineering
March 1-2, 2013, Tokyo Institute of Technology, Tokyo, Japan

BEHAVIOR OF REINFORCED CONCRETE FLAT SLAB SYSTEMS UNDER CORNER AND CENTER SUPPORT FAILURE SCENARIOS

Saurabh Prasad[1] and Tara C. Hutchinson[2]

1) Graduate Student, Department of Structural Engineering, University of California, San Diego, USA
2) Professor, Department of Structural Engineering, University of California, San Diego, USA
saprasad@ucsd.edu, tara@ucsd.edu

Abstract: Seismic design philosophy emphasizes that structures should be able to deform under repeated cyclic loading yet not sustain severe damage and maintain structural stability. However, reinforced concrete structures built prior to the introduction of new seismic codes are susceptible to severe structural damage, particularly the columns. Poorly confined columns subject to cyclic loading have repeatedly demonstrated shear failure, resulting in reduced axial load carrying capacity and creating a discontinuous load path. It is believed that beam-slab subsystems, being an integral load transfer component in a structure, could help mitigate collapse by load redistribution in event of a support failure. This paper presents the results from tests conducted on two 1/3rd-scale pre-1960's designed beam-slab subsystems under simulated column removal at corner and center-edge column locations. Performance of the specimens was evaluated based on the load deflection relationship, post yield behavior, and observed damage to the specimen.

1. INTRODUCTION

1.1 Background

Reinforced Concrete (RC) slabs are an integral part of a structure and are required to transfer gravity loads to columns, shear walls, or beams. In modern design codes, e.g. ACI 318 (2011), slabs are designed to carry gravity and lateral loads through flexure and shear. Floor level slabs in buildings are particularly important service load carrying components and have been the focus of study by several researchers. Several studies (e.g. Hopkins and Park, 1971; Hung and Nawy, 1969; Park 1970 and 1971; Christiansen and Frederiksen, 1983; Guice et. al. 1989; Muthu et. al. 2006) have been performed to understand the behavior of slabs and the effect of membrane forces on the ultimate load carrying capacity. In particular prior efforts have compared experimental ultimate loads to predictions of Yield Line Theory (Johansen, 1962 and 1972). It has been suggested by researchers that the load enhancement realized via membrane effects could be used as a secondary load carrying mechanism to prevent progressive collapse after initial failure (e.g. Hawkins and Mitchell, 1979; Mitchell and Cook, 1984).

Owing to the importance of the beam-slab subsystem in mitigating structural failure, it is important to understand its performance under different loading scenarios. Several researchers have performed numerical and analytical studies on progressive collapse (e.g. Alashker et al., 2010; Alashker and El-Tawil, 2010 and 2011; Alashker et al. 2011; Mohamed, 2009; Bao et al., 2008; Sasani and Kropenlnicki, 2008; Sadek et al., 2011), however, only a few studies have been conducted on older RC structures (e.g. Sasani et al. 2007; Sasani and Sagiroglu, 2010; Sasani, 2008; Sasani et. al., 2011). Though these studies indicate the beam-slab subsystem demonstrates stable structural response under different support failure scenarios, they fail to investigate the role played by the beam-slab subsystem in mitigating structural collapse after initial support failure. To study and mitigate the collapse risk of older RC construction, it is necessary to understand the performance of this critical subsystem under a support failure scenario. It is envisioned that the large deflections and ensuing load redistribution that occur when a slabs support fails may help minimize the potential for system level failure under extreme seismic loading conditions.

1.2 Scope of Study

To understand and mitigate structural collapse of older construction, it is necessary to study the behavior of beam-slab subsystems designed based on older design codes. This paper describes the results obtained from an experimental investigation of two 1/3rd scale beam-slab subsystems under simulated support failure at different locations. The specimens were evaluated based on their load deflection behavior, post yield behavior and observed damage due to simulated column failure.

2. EXPERIMENT DETAILS

Two four panel (2x2 configuration) reinforced concrete specimens were constructed and tested under simulated column failure. Failure of three corner support location was

simulated on the first specimen, and failure of two center-edge columns were simulated on the second specimen.

2.1 Details of The Specimens

Specimen details were based on review of older construction typically found on the West coast of the United States and in consultation with a professional practice committee (2010). Each specimen was 6.45 m in both directions with supports at every 3.05 m. Spandrel beams, 7.62 cm x 30.48 cm (width x height), were present on two adjacent edges on specimen 1 and on one edge on specimen 2. Drop panels were provided at each support location as commonly observed in older construction. Both specimens were supported at nine support locations, i.e. a 3x3 support configuration, or a 2x2 panel configuration. Figure 1 (a) and (b) present a schematic of specimens 1 and 2, respectively and the corresponding test locations. Specimen 1 was tested at three corner support locations, namely (i) beam-beam corner, (ii) slab-slab corner, and (iii) beam-slab corner. Specimen 2 was tested at two center-edge support locations, namely (i) slab edge, and (ii) beam edge as shown in Figure 1 (b).

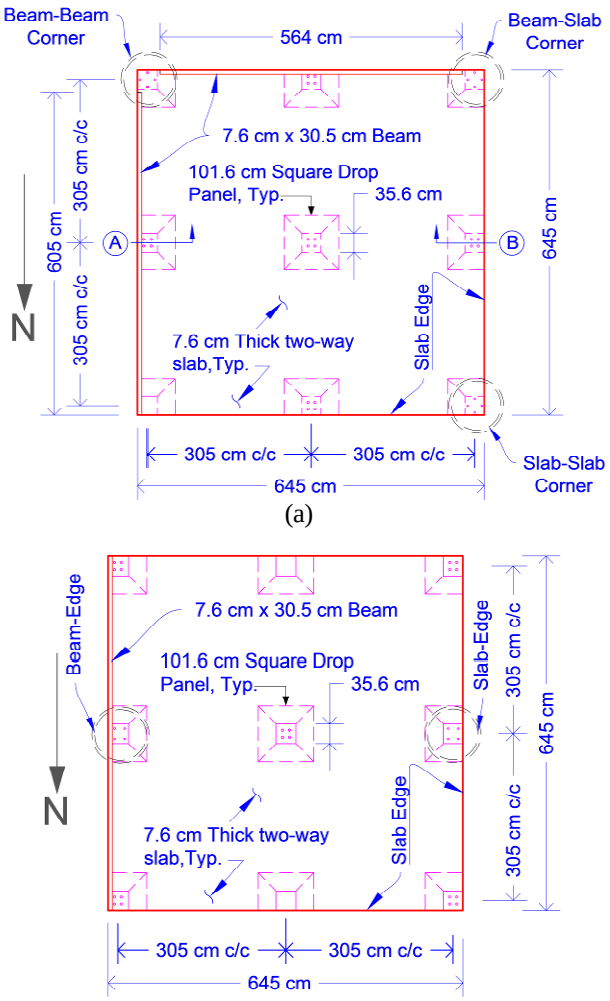


Figure 1 : Schematic of the test specimens, (a) plan view of specimen 1, and (b) plan view of specimen 2.

It is to be noted that in specimen 1, spandrel beams were curtailed, where present, near the test locations to facilitate mounting of actuators.

Both specimens were cast in place using a single pour of Type II concrete. Day of test uniaxial compressive strengths were 45.4 and 38.0 MPa for specimen 1 and 2, respectively. Reinforcement in the slab was provided using Grade 40 - M10 (9.52 mm diameter, 275 MPa) deformed bars and Grade 60 - M13 (12.7 mm diameter, 415 MPa) deformed bars were used for the spandrel beam longitudinal reinforcement. Grade 36 - M6 (6.3 mm diameter, 250 MPa) smooth rebar were used to provide shear stirrups on the spandrel beam at 12.7 cm spacing on center. Figures 2 and 3 provide a schematic of the slab and beam reinforcing in specimen 1, respectively.

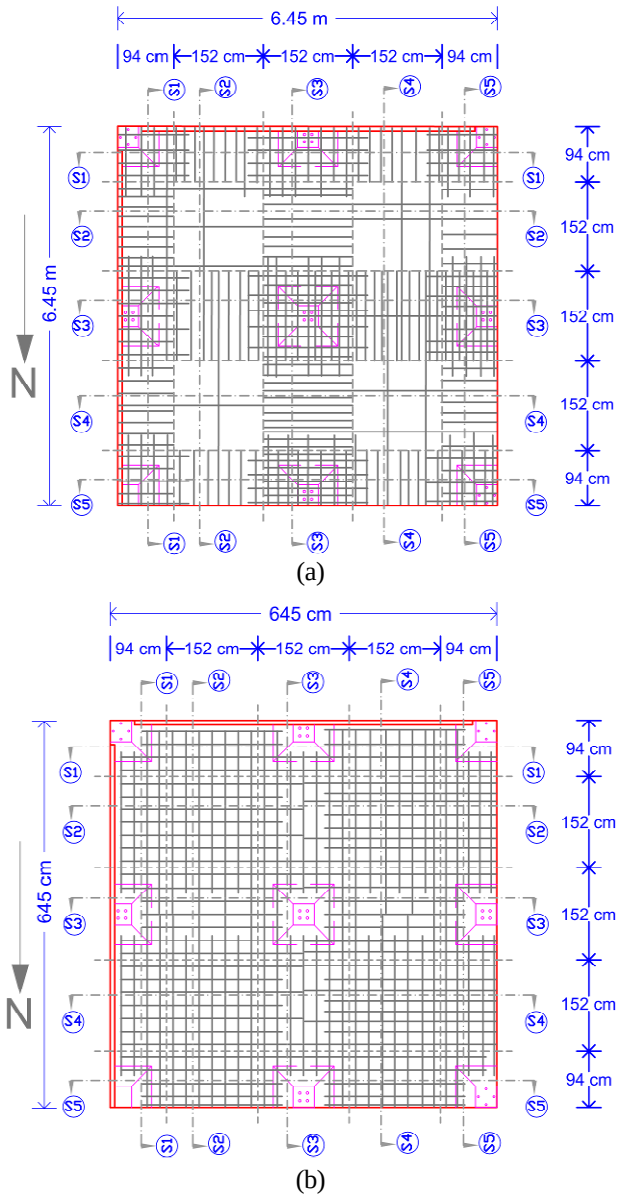


Figure 2 : Reinforcement detail of slab: (a) top rebar and (b) bottom rebar (refer to Table 1 for reinforcing ratios of top and bottom steel at cross sections S1-S5).

Other reinforcement details including, curtailment; rebar spacing; embedment details were provided based on ACI-318 (1956). A summary of slab reinforcing ratios is provided in Table 1.Reinforcing details in specimen 2 were similar to specimen 1. Additional details of the specimens may be found in test reports by Prasad and Hutchinson (2012).

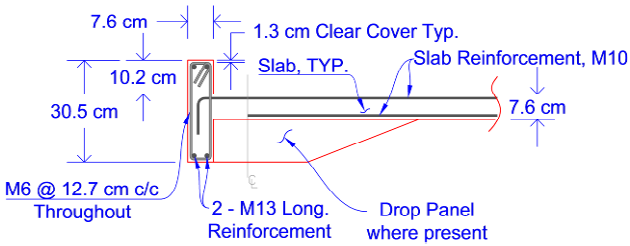


Figure 3 : Schematic of beam reinforcement detail.

Table 1: Summary of reinforcing steel ratios at different sections of specimen 1

	Top Reinforcing Ratio, ρ(%)	Bottom Reinforcing Ratio, ρ(%)
S1	0.51 - 0.66	0.51 - 0.59
S2	0.00 - 0.15	0.51 - 0.59
S3	0.51 - 0.88	0.51 - 0.59
S4	0.00 - 0.73	0.51 - 0.59
S5	0.51 - 0.66	0.51 - 0.59

2.2 Test Setup and Loading Protocol

Specimens were elevated above the reaction floor using concrete pedestals to provide sufficient clearance for load cell placement, inspection and push down. Figure 4 shows a schematic of the test setup for specimen 2.

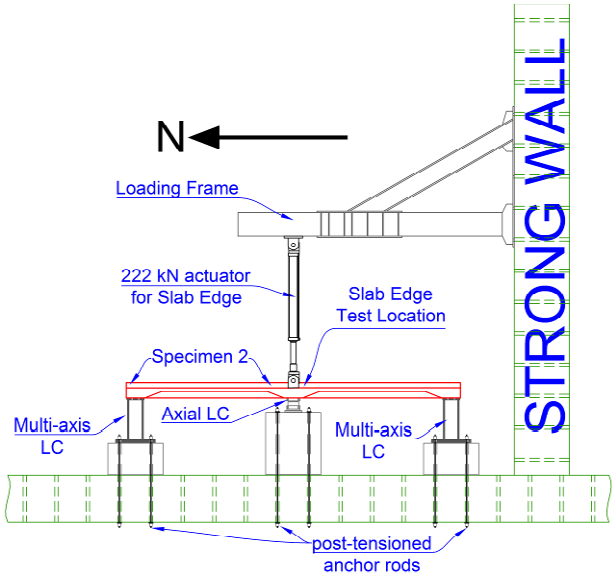


Figure 4 : Profile view of specimen 2 showing load cells at support locations and actuator for push down. Note: The axial load cell below the actuator was removed before the push test. (LC = load cell).

Both specimens were initially loaded under a uniform gravity load of 4.31 kN/m^2, which comprised of 3.35 kN/m^2 of uniform load to simulate prototype mass and 0.96 kN/m^2 to represent a uniform live load. This uniform gravity load was applied using concrete blocks, which were directly poured on specimen 1, and subsequently reused on specimen 2.

Specimens were tested under quasi-static push, in displacement control at the simulated column failure locations using a 222 kN actuator. Each location was tested one at a time with load cells in place at other push locations. After removal of the load cell at the test location and attachment of the actuator, specimen 1 was pushed (downward) to approximately 23 cm vertical displacement. Once the maximum displacement was attained, the actuator was retracted to zero load and detached from the specimen before moving it to the next test location. Figure 5 shows a photograph of the specimen with attached actuator before the test at the beam-beam corner location on specimen 1. A similar approach was used during the simulated support failure test locations on specimen 2. The slab edge was pushed monotonically to 26.7 cm before coming back to zero load, whereas the beam edge was pushed to a vertical deformation of 45.7 cm. It should be noted that once the test was complete at a given location, the respective load cell was unable to be moved back in place due to the accumulated large plastic deformation.

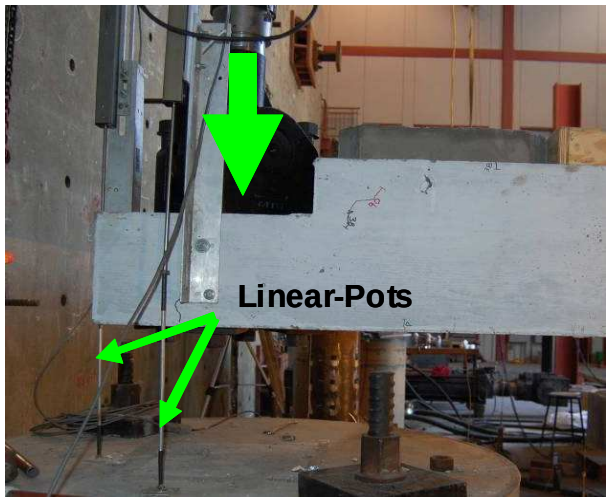


Figure 5 : Test setup at slab-edge push location on the second specimen before the test.

3. EXPERIMENTAL RESULTS

3.1 Load-Deflection Behavior

Figure 6 presents the vertical load deflection behavior at the three corner locations measured on specimen 1. Note that the negative load of approximately 8.9 kN at initial zero displacement is due to the self-weight of the specimen and the superimposed uniform loads.

The specimen was able to resist its largest vertical load at the beam-beam corner due to the presence of spandrel

beams on both edges adjacent to the simulated support failure test position. At this locations maximum load had an amplitude of 41.4 kN and occurred at a vertical displacement of 11.4 cm. It is to be noted that during the test at the beam-beam corner, the actuator inadvertently retracted back

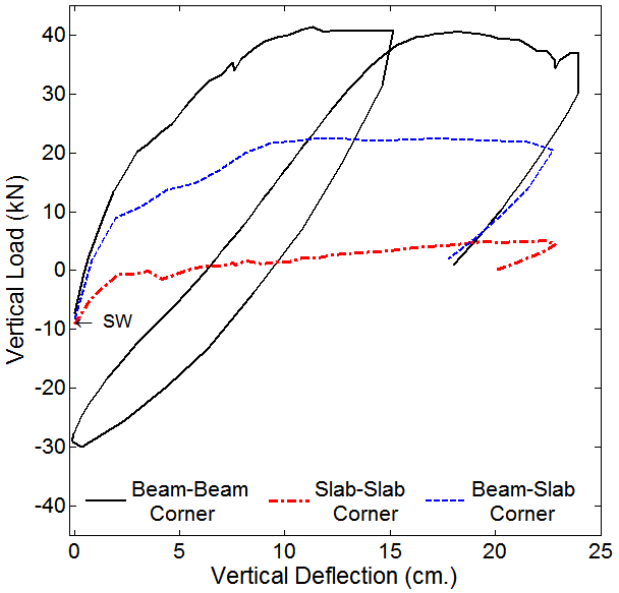


Figure 6 : Load deflection behavior at corner test locations on specimen 1 (SW = Self Weight)

to zero displacement due to error in actuator control, as a result a single recovery cycle is observed in the load-deflection response. At the beam-slab corner location, the specimen was able to achieve a maximum load of 22.7 kN at a vertical displacement of 10.2 cm. For both test locations, the beam-beam corner and the beam-slab corner, the specimen continued to deform plastically after initial yield with little strength degradation. During the test at the slab-slab corner on specimen 1, the maximum load was only 5.1 kN which was achieved at a displacement of 23 cm.

Specimen 2 was tested at two center-edge locations, namely the slab edge and the beam edge. Figure 7 presents the measured load-deflection behavior for specimen 2 at each of these simulated support failure locations. Similarly, initial negative loads at zero displacements are the initial reactions on the respective load cell at the test locations due to self-weight and superimposed uniform gravity loads. During the test at the slab edge, the specimen deformed approximately 12.5 mm under the gravity load itself. It was able to attain a maximum load of 40.9 kN at a vertical displacement of 27.3 cm. During the test at the beam edge, the specimen initially attained a large vertical load of nearly double that of the slab edge test location, with an amplitude of 74.2 kN at 6.35 cm vertical displacement. Beyond this, the vertical load abruptly decreased to 66.7 kN and remained nearly constant until a displacement of 12.7 cm. Subsequently, the specimen gained strength until a vertical displacement of approximately 31.8 cm where it attained its maximum vertical load of 83.6 kN. At approximately 32 cm vertical displacement, the drop panel at the test location

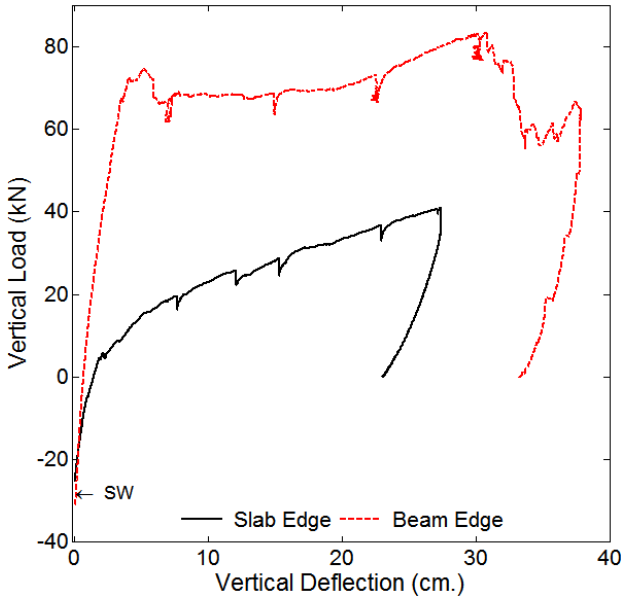


Figure 7 : Load deflection behavior at center-edge test locations on specimen 2 (SW = Self Weight)

failed in shear as shown in Figure 8, resulting in a dramatic reduced load capacity. Additional vertical displacement imposed on the specimen was mostly due to the rotation of the failed drop panel zone, which did not introduce significant vertical displacement on the beam itself. At the end of tests on specimen 2, significant plastic deformation was observed at both test locations.



Figure 8 : Shear failure at test location during the test at beam edge on specimen 2.

3.2 Observed Physical Damage

Figure 9 (a) and (b) present a schematic of observed damage on specimen 1 at the end of the simulated support failure tests. Tension cracks on the top follow the failure pattern as predicted by yield line theory. Although the yield lines were well defined along large cracks, the region of cracking was broad and spread over a width ranging from 10 to 18 times the thickness of the slab. Due to the smaller stiffness at the slab-slab edge, tension cracks on the top of the specimen were more tightly spaced as compared to the

other two sections where spandrel beams provide extra stiffness to the system.

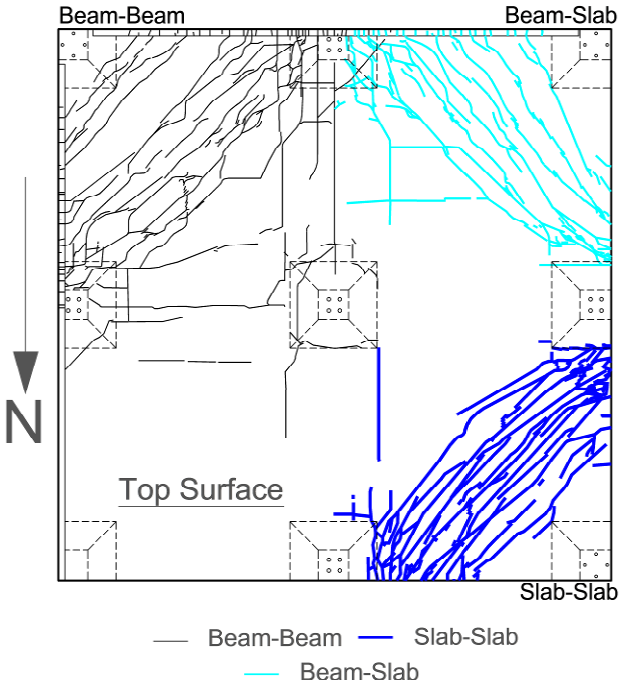


Figure 9 : Observed cracking at the end of each test on specimen 1 : (a) cracks on the top surface, and (b) cracks on the bottom surface and sides.

Cracks at the bottom of the specimen radiated outwards from the push location and were bounded by the yield lines that form along the adjacent support locations. Few cracks were observed inwards of the specimen due to the large membrane forces developing between supports in case of beam-beam and beam-slab corner.

A significant number of cracks were observed on the spandrel beams during the test at the beam-beam and beam-slab corner locations. Shear cracks formed near the push location, which transformed to flexure-shear cracks away from the push location. Near the adjacent supports, large flexure demand on the spandrel beam caused compression failure and rebar buckling at the bottom of the spandrel beams as shown in Figure 10.

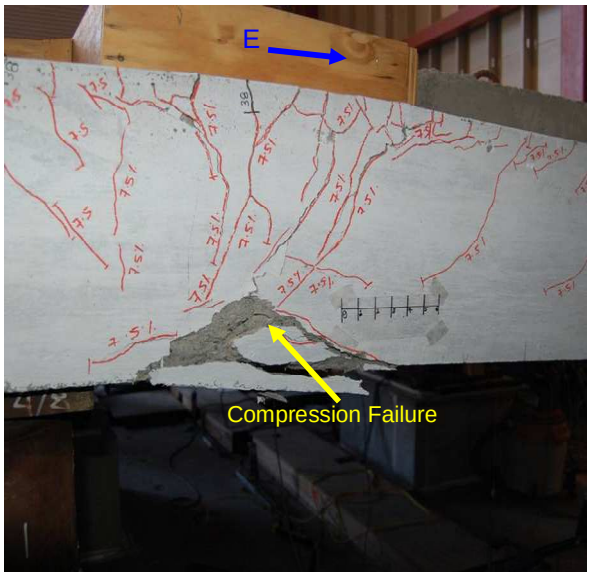
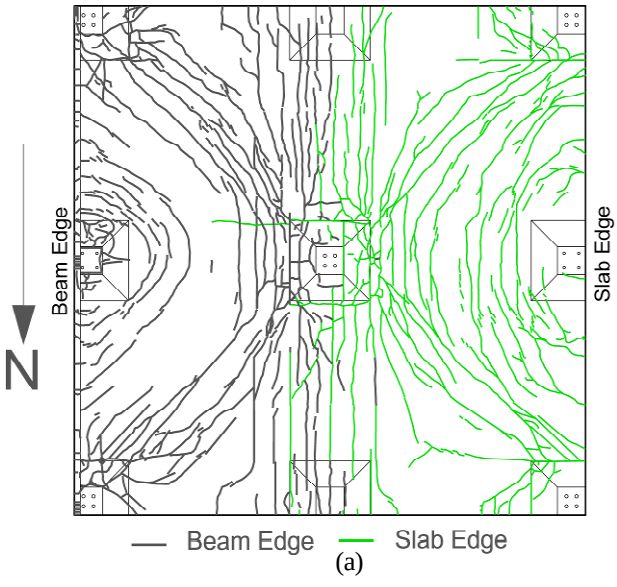
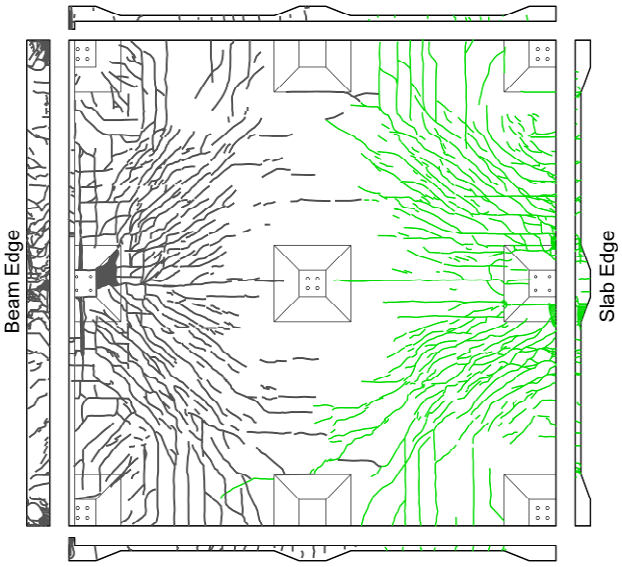


Figure 10 : Compression failure in EW spandrel beam near adjacent support at the end of test at beam-beam corner.

Figure 11 (a) and (b) presents a schematic of the damage observed on specimen 2 at the end of simulated support failure tests at slab edge and beam edge locations. Tension cracks on the top follow the predicted yield line patterns. However, region of cracking was broad and spread over a width of 35 to 50 times the slab thickness. Cracks on the top were more localized during the test at beam edge due to the increased stiffness compared to the cracking observed during the test at slab edge location. Large cracks were observed at adjacent corner support locations due to the large moment demands imposed at these locations.





(b)

Figure 11 : Observed cracking at the end of each test on specimen 2 : (a) cracks on the top surface, and (b) cracks on the bottom surface and sides.

Similar to specimen 1, cracks at the bottom radiated away from the push locations bounded by the yield lines on the top during the tests on specimen 2. Few cracks were observed inward of the specimen due to the large membrane forces that developed during each test.

Flexure and flexure-shear cracks were observed along the length of the beam and the slab edge during the tests. Flexure cracks were prominent near the adjacent corner supports and flexure shear cracks formed near the mid-span during each test. During the test at beam edge location, large moment and deflection demands at the ends of the spandrel beams caused rebar pullout hindering the beam from achieving is moment capacity, Figure 12. At the end of test at the beam edge location, large deflection and moment demands caused concrete spalling and beam rebar buckling at the test location as shown in Figure 13.



Figure 12 : Rebar pull out and concrete spalling at end of spandrel beam during the test at beam edge location.

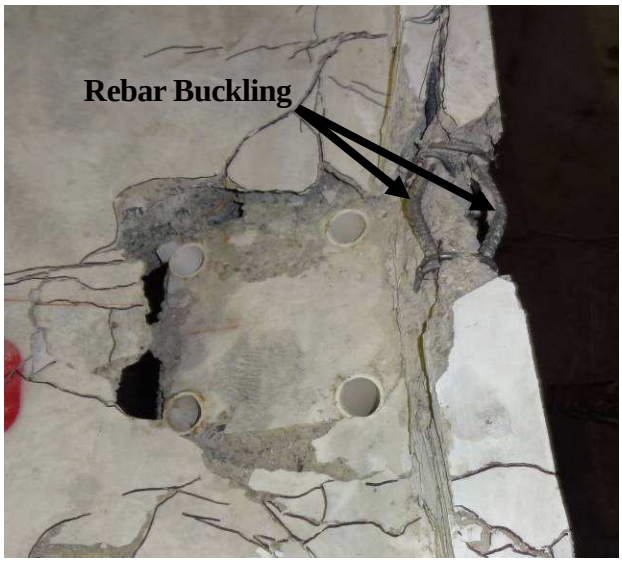


Figure 13 : Concrete spalling and rebar buckling at beam edge test location. Drop panel failure at the test location is also visible.

4. CONCLUSIONS

With advancements in understanding of seismic response of reinforced concrete (RC) structures over the past few decades, recent design codes have introduced several changes, including guidelines for reinforcement detailing to ensure safer structures under seismic events. Lack of these provisions in older codes renders some components of old buildings, such as columns for example, highly susceptible to shear failure. This in turn would result in a significant reduction in their axial load carrying capacity, compromising structure safety and increasing collapse risk. Being an integral part of a buildings load carrying mechanism, beam-slab subsystems have the potential to provide secondary load carrying capacity in the event of column failure. To study and mitigate the collapse risk in older construction, it is necessary to understand the performance of the beam-slab subsystem under support failure.

Simulated support removal tests were performed on two-1/3rd scale reinforced concrete beam-slab subsystems with details mimicked by pre-1960's construction. In total, three corner and two center-edge displacement-controlled push down tests were performed. For all column removal scenarios, the performance of the specimens was found to be satisfactory based on their maximum measured vertical load and stable post yield behavior. Test locations with spandrel beams were able to carry significantly larger loads compared to other locations due to large flexural strength of the beam. Although the failure pattern of each test conformed with predicted yield line theory, observed cracking was spread over a wide width. Severe damage was observed along the yield lines, with remainder of the slab experiencing little or no damage. Specimen edges were severely damaged at the end of each test with most severe damage observed during the test at the beam edge on specimen 2.

Acknowledgements:

This study is supported through the National Science Foundation (NSF)-NEESR project entitled: Mitigation of Collapse Risk in Vulnerable Concrete Buildings, where Professor Jack Moehle is the Principal Investigator. Funding is provided through NSF grant number: CMMI-0618804. The authors would also like to acknowledge the staff at the University of California, San Diego Charles Lee Powell Laboratory; in particular, Mr. Andrew Gunthardt, Mr. Paul Greco; Mr. Noah Aldrich and Mr. Darren Mckay for their technical assistance during the tests. In addition, the input of the professional practice committee, composed of Bill Holmes, Elie Elkhoury, Michael Mehrain, and Nabih Youssef, are greatly appreciated. Opinions and findings of this study are of the authors and do not necessarily reflect those of the sponsor.

References:

ACI 318 (1956). "Building Code Requirements for Structural Concrete and Commentary (ACI 318-56)." American Concrete Institute, Farmington Hills, Michigan.

ACI 318 (2011). "Building Code Requirements for Structural Concrete and Commentary (ACI 318-11)." American Concrete Institute, Farmington Hills, Michigan.

Alashker, Y. and El-Tawil, S. (2010), "Design model for collapse capacity of composite floors", Structures Congress.

Alashker, Y. and El-Tawil, S. (2011), "A design-oriented model for the collapse resistance of composite floors subjected to column loss", Journal of Constructional Steel Research, 67(1), 84-92.

Alashker, Y., Li, H., El-Tawil, S. and Sadek, F. (2010), "Progressive collapse resistance of steel-concrete composite floors", Journal of Structural Engineering, ASCE, 136(10), 1187-1196.

Alashker, Y., Li, H. and El-Tawil, S. (2011), "Approximations in progressive collapse modeling", Journal of Structural Engineering, ASCE, 137 (9), 914-924.

Bao, Y., Kunnath, S. K., El-Tawil, S. and Lew, H. S. (2008), "Macromodel-based simulation of pregressive collapse: RC frame structures", Journal of Structural Engineering, ASCE, 134 (7), 1097-1091.

Christiansen, K. P., Frederiksen, V. T. (2006), "Experimental investigation of rectangular concrete slabs with horizontal restraints", Material and Structures, 16(3), 179-192.

Elkhoury, E. (Nabih Youssef and Associates); Holmes, W. (Rutherford and Chekene); Mehrain, M. (URS Corp.); Nabih, Y. (Nabih Youssef and Associates), Professional Practice Advisory Committee, 2010.

Guice, L.K., Slawson, T.R., Rhomberg, E.J. (1989), "Membrane analysis of flat plate slabs." American Concrete Institute (ACI) Structural Journal, 83–92.

Hawkins, N. M., Mitchell, D. (1979), "Progressive Collapse of Flat Plate Structures." Journal of the American Concrete Institute (ACI), 76(7), 775-808.

Hopkins, D.C. and Park, R., (1971), " Test on a Reinforced Concrete Slab and Beam Floor Designed with Allowance for Membrane Action" ACI Special Publication - 30, 223-250

Hung, T. Y., Nawy, E. G. (1971). "Limit strength and serviceability factors in uniformly loaded, isotropically reinforced two-way slabs." American Concrete Institute, SP-30, Detroit, 301-24.

Johansen, K. W. (1962). "Yield-line theory", Cement and Concrete Association, London, 181 pp.

Johansen, K. W. (1972). "Yield-line formulae for slabs", Cement and Concrete Association, London, 106 pp.

Mitchell, D., Cook, W. D. (1984), " Preventing Progressive Collapse of Slab Structures." Journal of Structural Engineering, 110(7), 1513-1532.

Mohamed, O. A. (2009), "Assessment of progressive collapse potential in corner floor panels of reinforced concrete buildings", Engineering Structures, 31, 749-757.

Muthu, K. U., Amarnath, K., Ibrahim, A. and Mattarneh, H. (2006), "Load deflection behavior of partially restrained slab strips", Engineering Structures, 29(5), 663-674.

Park, R. (1970), "The behavior of a model slab and beam floor designed by limit design." Civil Engineering Transactions, Institution of Engineers, Australia, 12(1), 1-6.

Park, R. (1971), "Further test on a reinforced concrete floor designed by limit procedures." American Concrete Institute, SP -30, 251(70).

Prasad, S., and Hutchinson, T., (2012). "Experimental Evaluation of a 1/3rd scale Lightly Reinforced Concrete Slab under uniform, pattern and concentrated pull down load: Corner Conditions." University of California, San Diego, Department of Structural Engineering, Structural Systems Research Project (SSRP) Report No. 12/11, 2012

Sadek, F., Main, J. A., Lew, H. S. , and Bao, Y. (2011), "Testing and Analysis of Steel and Concrete Beam- Column Assemblies under a Column Removal Scenario", Journal of Structural Engineering, ASCE, 137 (9), 881-892.

Sasani, M. (2008), " Response of a reinforced concrete infille-frame structure to removal of two adjacent columns", Engineering Structures, 30, 2478-2491

Sasani, M., Bazan, M. and Sagiroglu, S. (2007), " Experimental and analytical progressive collapse evaluation of actual reinforced concrete structures", ACI Structural Journal, 104(6), 731-739.

Sasani, M. and Sagiroglu, S. (2010), " Gravity Load Redistribution and Progressive Collapse Resistance of 20- story Reinforced Concrete Structure following loss of interior column." ACI Structural Journal, 107(6), 636-644.

Sasani, M. and Kropelnicki, J., (2008), "Progressive Collapse Analysis of an RC Structure." Structural Design of Tall and Special Buildings, 17, 757-772.

Sasani, M., Kazemi, A., Sagiroglu, S. and Forest, S., (2011), " Progressive Collapse Resistance of an actual 11-story structure subjected to severe initial damage", Journal of Structural Engineering, ASCE, 137(9), 893-902.

10CUEE CONFERENCE PROCEEDINGS
10th International Conference on Urban Earthquake Engineering
March 1-2, 2013, Tokyo Institute of Technology, Tokyo, Japan

SEISMIC PERFORMANCE AND MODELING OF POST-TENSIONED, PRECAST CONCRETE SHEAR WALLS

Ahmet Can Tanyeri[1)], Jack P. Moehle[2)], and Takuya Nagae[3)]

1) PhD Candidate, Department of Civil and Environmental Engineering, University of California, Berkeley, USA
2) Professor, Department of Civil and Environmental Engineering, University of California, Berkeley, USA
3) Senior Researcher, National Research Institute for Earth Science and Disaster Prevention, Japan
actanyeri@berkeley.edu, moehle@berkeley.edu, nagae@bosai.go.jp

Abstract: A three-dimensional earthquake simulation test on a full-scale, four-story, prestressed concrete building was conducted using the E-Defense shaking table facility. The seismic force-resisting system of the test building comprised two post-tensioned (PT) frames in one direction and two unbonded PT precast walls in the other direction. The test building was subjected to several earthquake ground motions, ranging from serviceability level to near collapse. The behavior of the wall direction of the building under several ground motions is simulated using nonlinear response history analysis of practical structural engineering models, and the 2D simulation results are compared with the test results. Conducted numerical simulations are in good correlation with the test results for the important engineering parameters with some discrepancies.

1. INTRODUCTION

Past earthquakes have shown examples of unsatisfactory performance of buildings using reinforced concrete structural walls as the primary lateral force-resisting system. In the 1994 Northridge earthquake examples can be found where walls possessed too much overstrength, leading to unintended failure of collectors and floor systems, including precast and post-tensioned construction. In the 2010 Chile and 2011 Christchurch earthquakes, many structural wall buildings sustained severe damage. Although some differences in detailing practices exist between those countries and the U.S., the failure patterns raise concerns about how well conventionally reinforced structural walls in U.S. buildings will perform during the next earthquake. Past research efforts, including the PREcast Seismic Structural Systems (PRESSS) program (Priestley 1991) and subsequent studies, have explored alternative design approaches using post-tensioned (PT) precast structural walls to better control yielding mechanisms and promote self-centering behavior. These studies have provided excellent guidance on design and construction requirements, but examples of full-scale, three-dimensional dynamic tests to demonstrate behavior in realistic structural systems have been lacking. Such demonstrations are important to identify complex interactions that occur in complete building structures. Such demonstrations also are useful to serve as a vehicle for acceptance by the engineering community.

In December 2010, the National Research Institute for Earth Science and Disaster Prevention (NIED) in Japan conducted a three-dimensional earthquake simulation test on a full-scale, four-story building using the E-Defense shaking table. Design, instrumentation, preliminary numerical studies, and testing of the building were a collaboration among researchers from Japan and the U.S. The seismic force-resisting system of the test building comprised two bonded PT frames in one direction and two unbonded PT precast walls in the other direction. The building was designed using the latest code requirements and design recommendations available both in Japan and the U.S., including ACI ITG-5.2-09. The test building was subjected to several earthquake ground motions, ranging from serviceability level to near collapse.

Three-dimensional earthquake simulation testing of full-scale specimens is rare. Data from this test give a unique opportunity to understand the behavior of the unbonded PT walls and their interaction with other structural elements during an earthquake. In this study, the authors developed practical structural engineering models for the wall direction of the building. A comparison of the simulation and test results is done to assess the capability of currently available models to simulate the response of a real PT building under gradually increasing earthquakes.

2. OVERVIEW OF THE TEST

2.1 Test Specimen

The test specimen was a full-scale, four-story, post-tensioned precast concrete building. It had a rectangular plan (Figure 1), with dimensions 7.2 m in the Y (transverse) direction and 14.4 m in the X (longitudinal) direction. Height of each floor was 3 m, resulting in total building

height of 12 m. The lateral-load-resisting system in the Y direction was two precast unbonded PT shear walls and one bay unbonded PT center frame at B Axis. In the X direction the structural system consisted of two-bay bonded PT frames. All the structural elements were precast off-site and installed and post-tensioned on-site. Post-tensioning tendons of beams and columns in the X direction were bonded with grouting after installation. On the other hand, PT tendons of shear walls and beams in the Y direction were constructed to be unbonded from concrete.

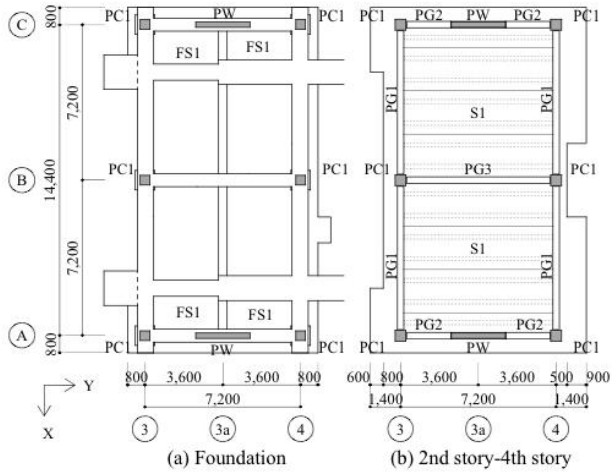


Figure 1 Plan View of the Specimen (Unit: mm)

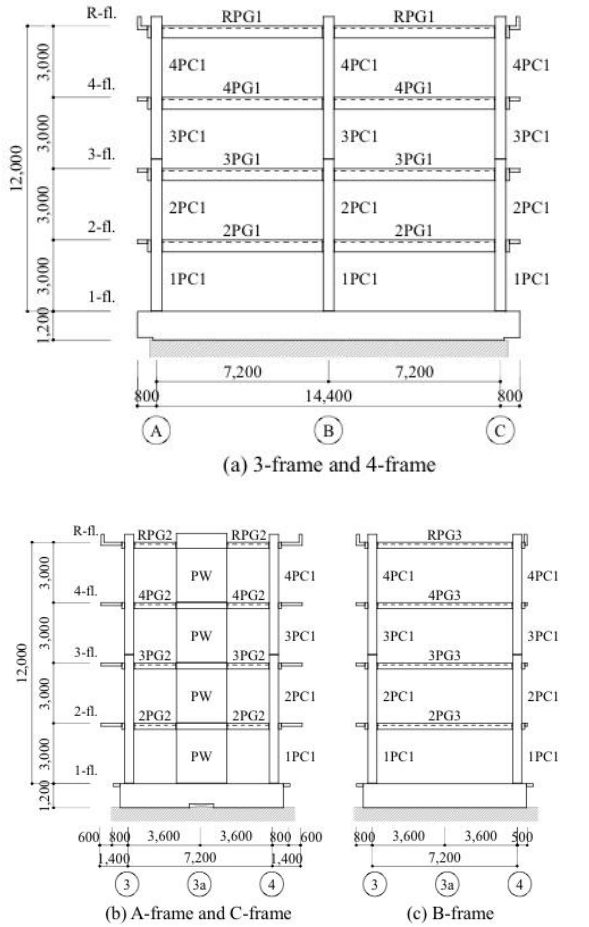


Figure 2 Elevation View of the Specimen (Unit: mm)

Shear walls had a rectangular cross section with a length of 2500 mm and a thickness of 250 mm. PT walls were 12 m high, and therefore had a slenderness ratio of H_w/l_w =4.8. Columns (PC1) had 450-mm square cross sections. Beams (PG2 & PG3) were partially precast, with the top 100 mm of the 300 mm by 300 mm section cast in place with the slab. The slab was 130 mm thick with the top 100 mm cast in place monolithically with the beams. The slab was supported by pretensioned joists with 1 m interval in the transverse direction. See Table 1 for additional details (Nagae et al. 2011).

Concrete design strength was 60 MPa for precast parts and 30 MPa for cast-in-place parts. The design strength of the grout mortar was 60 MPa. The first two floors of the north wall were constructed using FRCC (fiber reinforced cement composite). Nominal strength of the generic steel bar was 345 MPa. Transverse reinforcement of beams and walls in the Y direction was high strength steel bars with nominal strength of 785 MPa. Although columns were designed for required shear reinforcement by the Japanese Building Standard Law, the column core was not intentionally confined. PT rods of the columns were high strength steel with 1080 MPa design strength. PT strands used in walls and beams had design strength of 1600 MPa. Test results of the materials are shown in Table 3.

Reinforcement details of the PT walls and wall-to-beam joint details are shown in Figure 3. Eight D22 (22 mm diameter) steel energy dissipation bars were unbonded through the lower 1.5 m of the first story and connected to the foundation with mechanical couplers. Effective prestressing of the PT tendons was 0.6 times the yield strength for the walls and PG2 beams, and 0.8 times the yield strength for the other beams and columns.

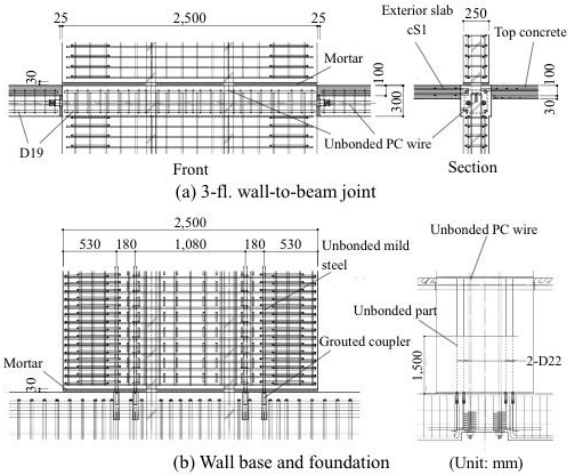


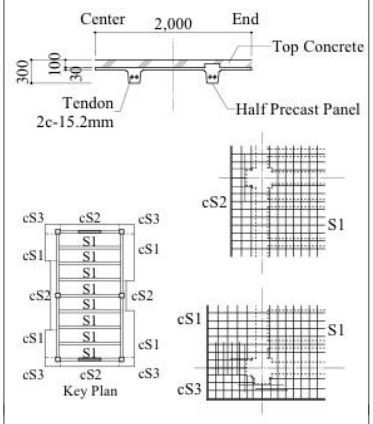
Figure 3 Reinforcement Details of Walls (Unit: mm)

The total weight of the specimen was 5592 kN. The weight of each floor was 996 kN for Roof, 813 kN for 3rd floor, 806 kN for 2nd floor, and 804 kN for the 1st floor.

Table 1 Member Cross-Sections

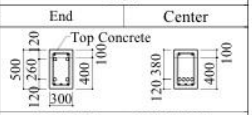
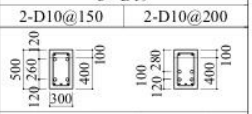
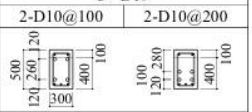
List of Column		
		PC1
All	Section	
	Tendon	8-21mm(SBPR1080/1230)
	Rebar	4-D19
	Hoop	D10@100

List of Slab Depth: 130mm



		Shorter direction	Longer direction
S1		D10@200	D10@200
cS1	Top	D13@200	D10@250
	Bottom	D10@200	D10@250
cS2	Top	D10@200	D10@250
	Bottom	D10@200	D10@250
cS3	Top	D13@200	D13@200
	Bottom	D10@200	D10@200

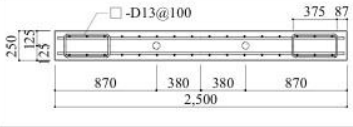
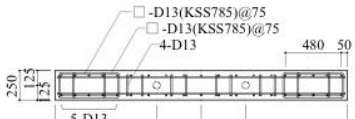
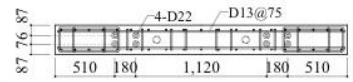
List of Girder

		PG1	
	Location	End	Center
R-fl.	Section		
	Tendon	4C-1-17.8mm(SWPR19L)	
	Top	2 - D19	
	Bottom	3 - D19	
	Stirrup	2-D10@150	2-D10@200
4-fl.	Section		
	Tendon	4C-1-19.3mm(SWPR7BL)	
	Top	2 - D19	
	Bottom	3 - D19	
	Stirrup	2-D10@100	2-D10@200
3-fl. 2-fl.	Section		
	Tendon	4C-3-15.2mm(SWPR7BL)	
	Top	2 - D19	
	Bottom	3 - D19	
	Stirrup	2-D10@90	2-D10@200

List of Girder

		PG2	PG3
All	Section		
	Tendon	2C-1-17.8mm(SWPR19L)	2C-1-17.8mm(SWPR19L) 1C-17mm(SBPR930/1080)
	Top	2 - D19	2 - D19
	Bottom	2 - D19	2 - D19
	Stirrup	2-D10@100(KSS785)	2-D10@150

List of Wall

		PW
4-fl. 3-fl. 2-fl.	Section	
	Tendon	3-10-15.2mm(SWPR7B)
	V bar	D13@150(double)
	H bar	D13@100(double)
1-fl.	Top Section	
	Bottom Section	
	Tendon	2-10-15.2mm(SWPR7B)
	V bar	D13@150(double)
	H bar	D13@75(double)

(Unit: mm)

Table 2 Effective prestress and permanent axial load

	P_e [kN]	N_L [kN]
1PC1 (B-axis)	2274	733
1PW	2666	176
2PG1	1822	-
2PG2	338	-
2PG3	338	-

Table 3 Material Test Results

(a) Concrete

	σ_B [N/mm^2]
PCa	83.2
PCa (F)	85.5
Top	40.9

(b) Grout

	σ_B [N/mm^2]
Mortar	135.6
Mortar (F)	120.3
Milk cement	63.4

(c) Steel

	σ_y [N/mm^2]	σ_t [N/mm^2]
PC bar ϕ21 (Column, SBPR1080/1230)	1194	1277
D22 (Wall, SD345)	385	563
D19 (Column and beam, SD345)	389	561
D13 (Wall, SD295A)	347	501
D13 (Slab, SD295A)	372	522
D10 (Column and beam, SD295A)	361	518
D10 (Slab, SD295A)	388	513
D13 (Wall and PG2, KSS785)	938	1107
	F_y [kN]	F_t [kN]
PC wire ϕ15.2 (Wall, SWPR7BL)	250	277
PC wire ϕ15.2 (Beam, SWPR7BL)	255	279
PC wire ϕ17.8 (Beam, SWPR19L)	356	404
PC wire ϕ19.3 (Beam, SWPR7BL)	429	481

2.2 Input Motions

Input ground motions were scaled JMA-Kobe and JR-Takatori records from 1995 Kobe earthquake. The motions were applied in two horizontal and vertical directions simultaneously. Firstly, JMA-Kobe motion was applied with wave amplitude scale factor of 10%, 25%, 50%, and 100%, respectively. Lastly, 40% and 60% JR-Takatori were applied. This paper considers the 25%, 50% and 100% excitations only. Figure 4 shows time records and acceleration response spectra of input motions.

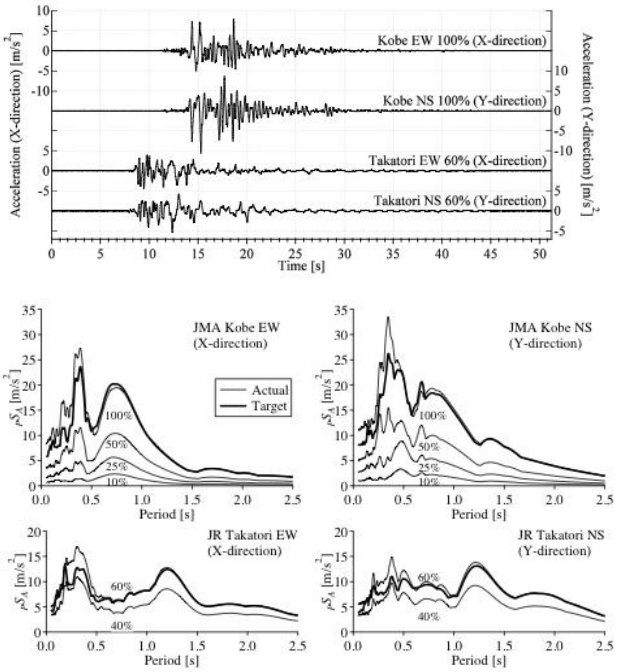


Figure 4 Time Records and Acceleration Response Spectra of the Input Motions

3. NUMERICAL SIMULATION

A three-dimensional numerical model of the Y direction of the specimen was implemented using the computer program Perform 3D (CSI). Figure 5 shows a 3D view of the model.

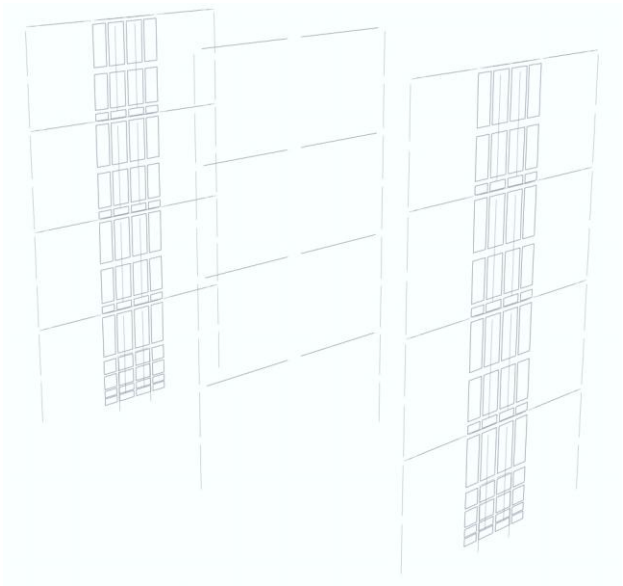


Figure 5 3D View of the Perform 3D model

3.1 Shear Wall Model

Structural walls were modeled using 4-noded "Shear Wall Elements" (CSI) with fiber cross sections. In this implementation, all interconnected planar wall segments at any level are assumed to remain plane when deformed. In the first story, where inelastic actions were expected to concentrate, shear wall elements were meshed so that each element had a height of $2b_w$ (b_w = wall thickness). This value is established from post-earthquake observations of the typical height of spalled regions. For the rest of the building, larger sized elements are used. Due to anticipated low shear demands, an elastic shear material was used for walls, with effective shear stiffness defined as $G_cA_w = 0.4E_cA_w$ /20 (PEER/ATC-72-1), in which G_c is shear modulus, E_c is Young's modulus of concrete (taken as $4700\sqrt{f_c'}$, MPa), and A_w is web area. Rocking behavior of wall segments is implemented for wall elements at each floor level. This behavior is achieved by inserting fiber sections at the interfaces having representative compressive behavior but zero tensile strength.

The constitutive material model for concrete is a trilinear idealization of material test results (Figure 6). The stress-strain relationship for confined concrete is implemented using the confinement model for high-strength concrete developed by Razvi & Saatcioglu (1999). Tension resistance of concrete is modeled except for the rocking sections.

Similarly, the reinforcing steel stress-strain relation was a simplified trilinear curve with a descending portion (Figure 7). The ultimate strain of reinforcing steel in tension was limited to 0.05 in consideration of cyclic fatigue (PEER/ATC-72-1). Behavior in compression was checked according to the ratio s/d_b (s = spacing of transverse

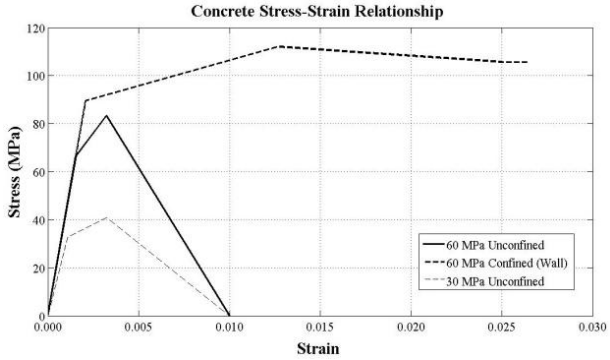


Figure 6 Concrete Stress-Strain Relation

reinforcement and d_b = diameter of longitudinal bar) in consideration of longitudinal bar buckling (Monti and Nuti, 1992). The adequately small s/d_b ratio is such that reinforcing bars are unlikely to buckle prematurely. The ultimate strain of reinforcing steel under compression nonetheless is limited to 0.02 because of potential buckling at large strains (PEER/ATC-72-1).

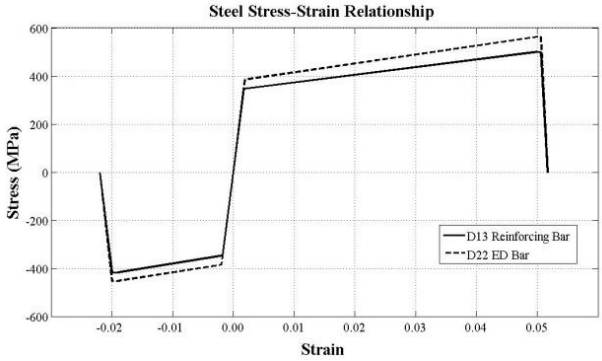


Figure 7 Reinforcing Bar Stress-Strain Relation

PT tendons and energy dissipation (ED) bars are modelled using truss elements with nonlinear material properties. Truss elements are connected to shear wall elements through rigid beams extending to locations of tendons and ED bars in the cross section. Lateral displacements of PT tendons are slaved to shear wall elements at each floor level, which is analogous to the effect of the tendon ducts. Truss elements representing the ED bars are modelled along the unbonded length of the bars. Bar slip (strain penetration) effects are considered for modelling of the ED bars. The ED bar trusses are extended below the top of the foundation to mimic the extra elongation caused by slip of the ED bars. Post-tensioning loads on tendons are applied as initial strains concurrently with gravity loads in analysis.

3.2 Beam and Column Models

Beams and columns are modelled using nonlinear beam-column elements with rigid end zones. Nonlinear fiber sections are assigned through the length of elements with distributed plasticity. Similar to the shear wall elements, a simplified trilinear curve with a descending portion is used to model concrete and steel materials. Due to adequate shear design of the members, an elastic shear material was used for beams and columns, with effective shear stiffness defined as $G_cA_w = 0.4E_cA_w$ (Elwood et al. 2007). Similar to rocking sections of wall elements, opening between precast elements is simulated by assigning a "rocking section" to beam element integration points closest to wall and columns). The aforementioned "rocking section" has the same cross section and fiber locations as at other integration points. However, materials assigned to this section are modified to have no tension resistance.

Upper portions of half-precast beams were cast monolithic with the slabs. Beam effective flange widths are calculated using ACI 318 equations. Unlike column elements, for which forces are resisted with fiber sections in both transverse directions, beam elements in Perform 3D use fiber sections only in the major bending axis. Bending stiffness of the minor bending axis is defined with effective bending stiffness $0.5E_cI_g$, in which I_g is gross section moment of inertia according to the minor bending axis.

Unbonded PT tendons of beams (PG2 & PG3) are modelled with parallel truss elements with nonlinear material properties. Their vertical displacements through beams and walls are slaved to parallel elements similar to modelling of ducts for walls. Similar to PT tendons of walls, post-tensioning loads on tendons are applied as initial strains. In contrast, bonded PT rods of columns (PC1) are included in the fiber cross-section. Post-tensioning loads on columns are approximated by applied point loads (in the same direction with gravity).

3.3 Miscellaneous Notes on the Numerical Model

Rayleigh damping is used for nonlinear response history analysis, with parameters set to produce 2 percent damping at periods $T_1/8$ and $1.25T_1$, where T_1 = 0.29 seconds. All analyses were in the Y direction; therefore, X-direction displacements of all nodes are restrained. After the application of gravity and prestressing loads, the model is excited with 25%, 50%, and 100% Kobe motions, respectively.

4. COMPARISON OF SIMULATION AND TEST RESULTS

Prior to application of earthquake motions, the test building was excited with white noise. Fundamental periods of the building were 0.29 s in the Y direction and 0.45 s in the X direction. Modal analysis of the numerical model resulted a fundamental period of 0.29 s in the Y direction.

Base shear versus roof drift ratio responses of the numerical model and test specimen under 25%, 50%, 100% Kobe excitations are shown in Figures 8, 10, and 12. Comparisons of roof drift ratio versus time responses of numerical model and test specimen are shown in Figures 9, 11, and 13. Flag-shaped hysteresis typical of unbonded post-tensioned concrete is apparent. The numerical model and test results are in very good agreement for important engineering parameters, such as stiffness, maximum base shear, and maximum roof drift. For all excitations, energy dissipated during the earthquake (area inside the hysteresis curve) is estimated with a good accuracy.

Although estimated maximum roof drift ratios are very close to the test results, phase shifts in roof drift ratio versus time are significant for some parts of the response. The roof drift ratio response history estimate for the 25% Kobe motion shifts out-of-phase after 19 s. The vibration period of the test specimen is increasing after 19 s, but the numerical model does not identify this increase in period.

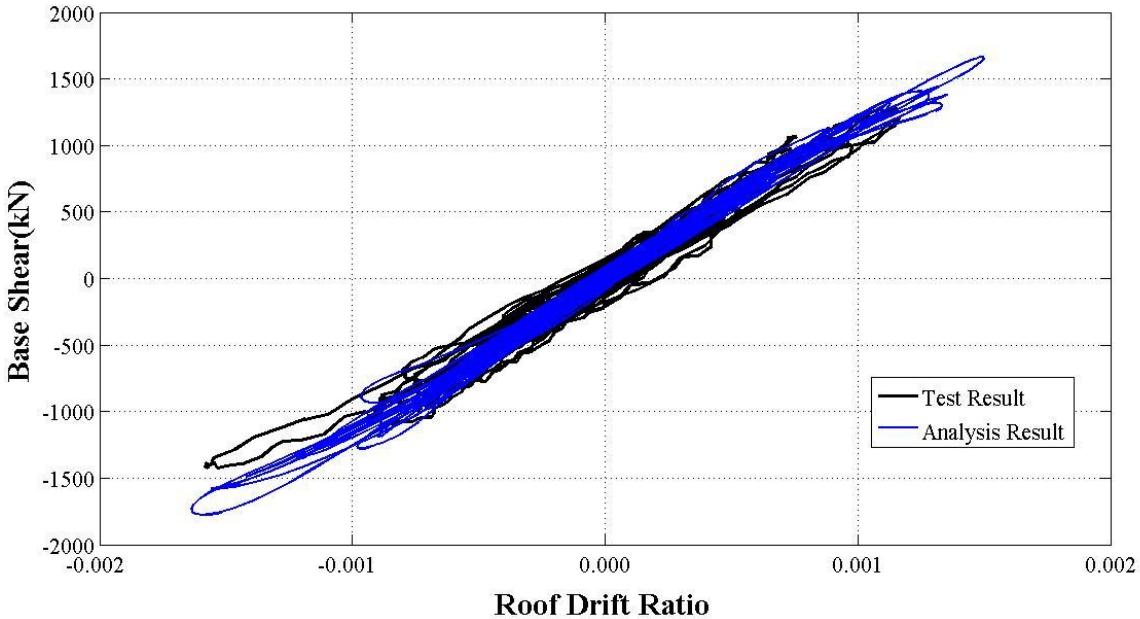


Figure 8 Base Shear-Roof Drift Ratio Comparison of Results for 25% Kobe Motion

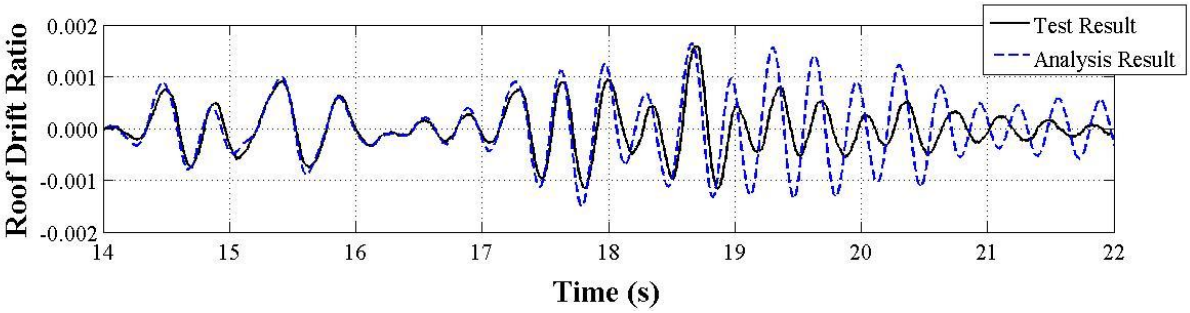


Figure 9 Roof Drift Ratio-Time Comparison of Results for 25% Kobe Motion

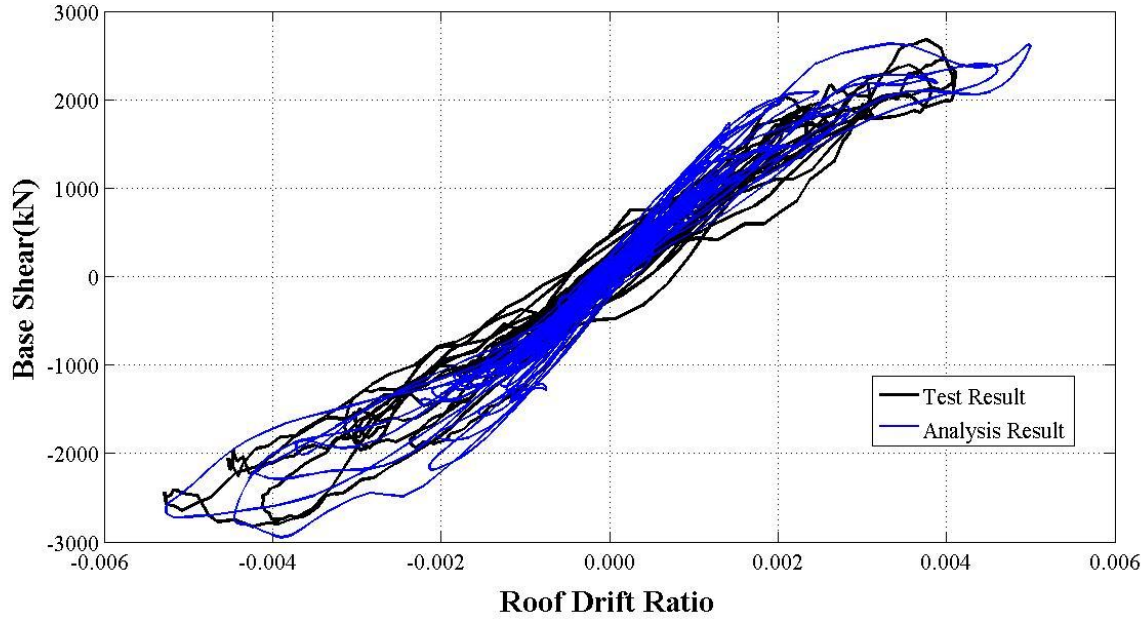


Figure 10 Base Shear-Roof Drift Ratio Comparison of Results for 50% Kobe Motion

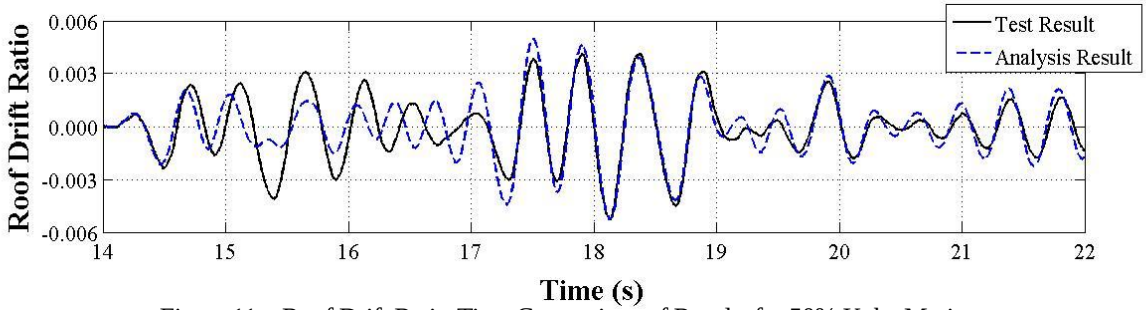


Figure 11 Roof Drift Ratio-Time Comparison of Results for 50% Kobe Motion

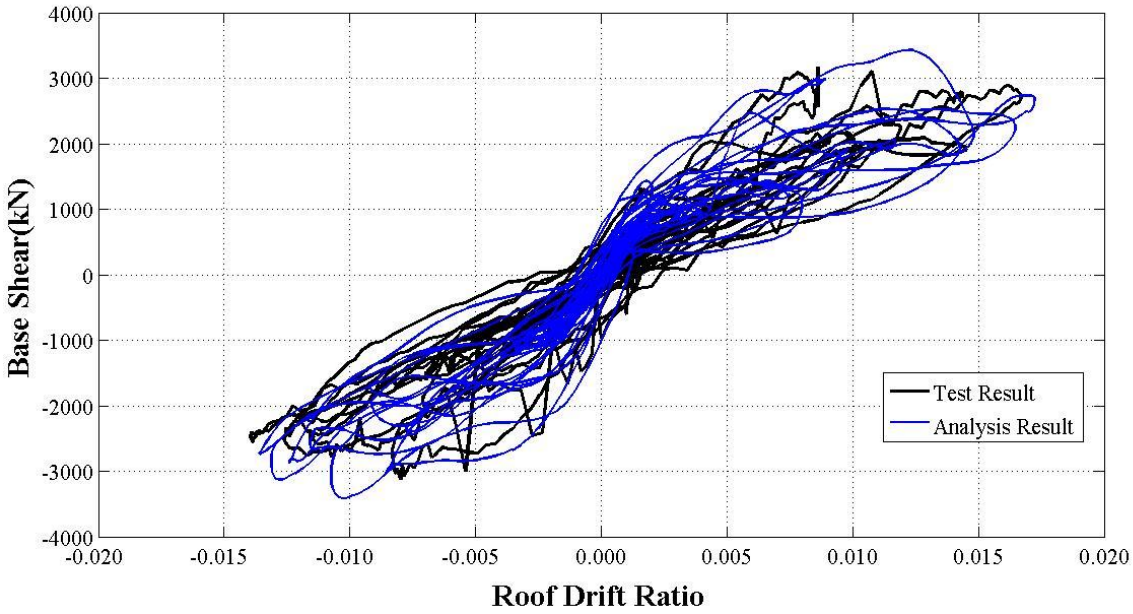


Figure 12 Base Shear-Roof Drift Ratio Comparison of Results for 100% Kobe Motion

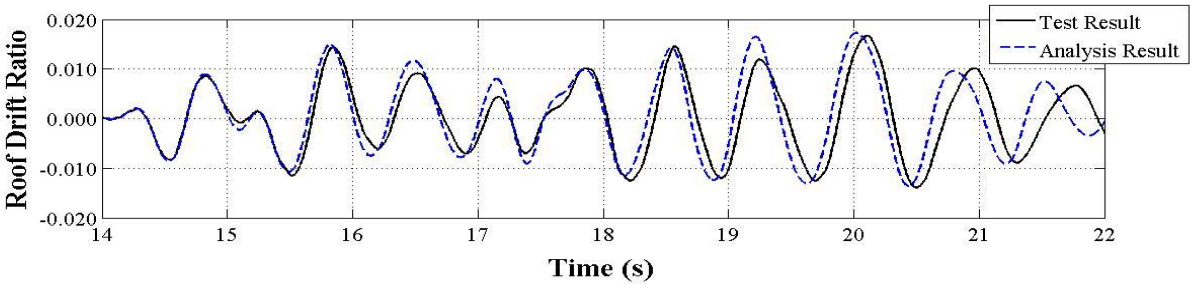


Figure 13 Roof Drift Ratio-Time Comparison of Results for 100% Kobe Motion

The calculated roof drift ratio history for the 100% motion also does not estimate the increase in vibration period after 21 s. Measured and calculated response decay near the end of the test match fairly closely for the 50% and 100% Kobe motion, suggesting the damping is modeled reasonably. For the 25% motion response, calculated response damps out more slowly than the test results.

5. CONCLUSIONS

A three-dimensional earthquake simulation test on a full-scale, four-story, prestressed concrete building is conducted using the E-Defense shaking table facility. The seismic force-resisting system of the test building comprised two post-tensioned (PT) frames in one direction and two unbonded PT precast walls in the other direction. The test building was subjected to several earthquake ground motions, ranging from serviceability level to near collapse. The wall direction (Y direction) of the building is modeled using the computer program Perform 3D, with emphasis on a model that would be practical for design-office implementation. This model is subjected to several base motions to explore the accuracy of the numerical model.

Important engineering parameters such as fundamental vibration period, stiffness, hysteresis shape, maximum base shear, and maximum roof drifts are adequately simulated using the numerical model. There are, however, some discrepancies in variation of these responses with time. These results indicate that, while further improvements may be desirable, the selected modelling approach is capable of producing seismic response estimates of sufficient accuracy to be used for detailed design of unbonded post-tensioned, precast structural wall systems.

Acknowledgements:

The writers acknowledge the funding provided to participate in the tests by the U.S. National Science Foundation. Funding for this study provided by Pacific Earthquake Engineering Research (PEER) Center and Precast/Prestressed Concrete Institute (PCI) Daniel P. Jenny Fellowship is gratefully acknowledged. The writers also thank Computers & Structures, Inc. (CSI) for providing the computer software used for this study. Lead participation of T. Nagae, T. Matsumori, H. Shiohara, T. Kabeyasawa, S. Kono, K. Tahara, and M. Nishiyama from Japan side and J. Wallace, W. Ghannoum, and R. Sause from the U.S side is gratefully acknowledged.

References:

ACI 318-08 (2008), "Building Code Requirements for Structural Concrete (ACI 318-08) and Commentary," American Concrete Institute, Farmington Hills, Michigan.

ACI ITG-5.2-09 (2009), "Requirements for Design of Unbonded Post-Tensioned Precast Shear Wall Satisfying ACI ITG-5.1 (ACI ITG-5.2-09) and Commentary," American Concrete Institute, Farmington Hills, Michigan.

Computers and Structures, Incorporated (CSI), "Perform 3D, Nonlinear Analysis and Performance Assessment for 3D Structures,"

Monti, G., and Nuti, C. (1992), "Nonlinear Cyclic Behavior of Reinforcing Bars Including Buckling," *Journal of Structural Engineering*, American Society of Civil Engineers, **118**(12), 3268-3284.

Nagae, T. A., Tahara, K., Matsumori, T., Shiohara, H., Kabeyasawa, T., Kono, S., Nishiyama, M., Wallace, J., Ghannoum, W., Moehle, J.P., Sause, R., Keller, W., and Tuna, Z. (2011),"Design and Instrumentation of the 2010 E-Defense Four-Story Reinforced Concrete and Post-Tensioned Concrete Buildings," *Technical Report 2011/104*, Pacific Earthquake Engineering Research Center, University of California, Berkeley.

PEER/ATC-72-1 (2010), "Modeling and Acceptance Criteria for Seismic Design and Analysis of Tall Buildings," Applied Technology Council, Redwood City, CA.

Priestley, M.J.N. (1991), "Overview of the PRESSS Research Program," *PCI Journal*, Precast/Prestressed Concrete Institute, **41**(2), 22-40.

Razvi, S., and Saatcioglu, M. (1999), "Confinement Model for High-Strength Concrete," *Journal of Structural Engineering*, American Society of Civil Engineers, **125**(3), 281-289.

Tanyeri, A.C., Moehle, J.P., Nagae T. (2012), "Seismic Performance and Modelling of Post-Tensioned, Precast Concrete Shear Walls", *15th World Conference on Earthquake Engineering, Lisboa 2012*

10CUEE CONFERENCE PROCEEDINGS
10th International Conference on Urban Earthquake Engineering
March 1-2, 2013, Tokyo Institute of Technology, Tokyo, Japan

EFFECT OF ELECTRO-WELDED WIRE MESH ON THE SEISMIC VULNERABILITY OF THIN RC SHEAR WALLS IN LIMA, PERU

Luis G. Quiroz[1)], and Yoshihisa Maruyama[2)]

1) PhD candidate, Department of Urban Environment Systems, Graduate School of Engineering, Chiba University, Japan
2) Associate Professor, Department of Urban Environment Systems, Graduate School of Engineering, Chiba University, Japan
lgquiroz@uni.edu.pe, ymaruyam@tu.chiba-u.ac.jp

Abstract: The probability of damage states with respect to a ground motion index is predicted through the seismic fragility curves. Using fragility curves, it is possible to estimate the vulnerability of structures to seismic hazard. In this study, an analytical approach was adopted to construct fragility curves for thin RC shear walls that are the vertical components of the lateral-force-resisting system to earthquakes typically used in Lima, Peru since 1998. The main characteristic of these walls is the use of electro-welded wire mesh as main reinforcement instead of conventional rebar. The thin RC shear walls were modeled based on the results of experiments. A series of non-linear dynamic response analyses was performed using strong motion records obtained in Lima, Peru and the damage ratios were estimated with respect to damage states. The fragility curves for the walls were constructed assuming that the damage ratios follow lognormal distributions. The fragility curves constructed in the present study are helpful for predicting the damage state of buildings composed of the thin RC walls especially in Lima, Peru.

1. INTRODUCTION

The study of seismic loss is a matter of research in many countries located in seismic-prone regions. Every study follows a similar flowchart during the process of loss estimation: estimation of intensity measures, structural responses, damage estimation, statistical analysis, construction of fragility curves and finally loss assessment. To evaluate the damage to structures, fragility curves are widely employed and developed for RC buildings (Jovanoska 2000), bridges (Karim and Yamazaki 2001), expressway embankments (Maruyama et al. 2010), and other types of structures (Chiou et al. 2011).

Withman (1973) defined the damage probability matrices, and the ATC Project (1985) also defined damage probability matrices for 78 categories of structures. Jaw and Hwang (1988) introduced the fragility curves, and Nocevski (1993) developed empirical and analytical fragility curves. Similar approaches to construct fragility curves are presented by Karim and Yamazaki (2001) and others.

During the 2010 Chile Maule earthquake, some buildings, which resist lateral seismic forces with thin walls, suffered from severe damage and in some cases collapsed (EERI 2010). In Lima City, many similar types of buildings have been built since 1998, and the number of these types of buildings has been increasing over the years. However, the last big earthquake that hit Lima city occurred in 1974. Therefore, it is difficult to know the actual behavior of these buildings during an earthquake and the loss associated with their fails.

The fragility curves can be developed based on analytical, empirical, expert's opinion and combinational approaches. The objective of this study is to develop analytical fragility curves based on numerical simulations and evaluate the influence of the use of electro-welded wire mesh as main reinforcement instead of conventional rebar for the thin RC shear walls. Fragility curves describe the conditional probability of a certain damage state for a given intensity of ground motion index and can be expressed as

$$P_{ik} = P\left[X \geq x_i \middle| Y = y_k\right] \quad (1)$$

where P_{ik} is the conditional probability of a certain damage level x_i for a given ground motion intensity y_k. X is the variable that reflects the damage state and Y is the variable that reflects the ground motion intensity.

The response characteristics of the thin RC shear walls were evaluated in the previous study (Quiroz et al. 2012). These walls were regarded as the prototype of those used in low-rise and mid-rise buildings in Lima, Peru. The numerical model of the wall is developed using a multi degree-of-freedom system and macro models that represent the overall behavior of the RC elements. A series of non-linear dynamic response analyses is carried out using Peruvian records. Regression analyses are performed to reveal the relationship between the damage ratios of the walls and the ground motion index to construct fragility curves. Finally, the influences on the fragility curves due to the type of material used as main reinforcement of the wall

are discussed and the probabilities of a certain damage state for three hazard levels areis estimated.

2. PROTOTYPES AND NUMERICAL MODEL

A thin RC shear wall was selected as a prototype of those used in low-rise and mid-rise in Lima, Perú. The dimensions of the prototypes were a height of 2400 mm (per floor), a length of 2650 mm and a thickness of 100 mm. The walls present the edge reinforcement consisted of conventional rebar. In the case of main reinforcement, two types of models are considered. The first wall is called MQE257EP and it presents electro-welded wire mesh, which is made of non-ductile material, as main reinforcement. The second wall is called MFIEN3EP and it presented conventional rebar as main reinforcement. A single layer of main reinforcement is used in both directions for both cases. Figure 1 shows a general view of the walls and Table 1 shows the distribution of reinforcement. The number of stories considered in the analysis is five.

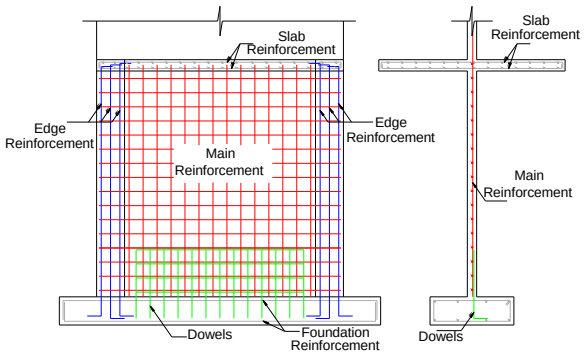


Figure 1 General characteristics of the specimens considered in the study

Table 1 Distribution of reinforcement in walls

Prototype	Main Reinforcement	ρ_h and ρ_v	Dowels	Edge Reinforcement
MQE257EP	QE257	0.257%	QE84/257	3 #4
MFIEN3EP	#3 @ 250	0.284%	#3 @ 250	

As can be observed from Table 1, the horizontal reinforcement ratio (ρ_h) and vertical reinforcement ratio (ρ_v) is almost similar for both walls. The wall MQE257 has the main reinforcement called QE257, which is formed by wires of 7 mm in the horizontal and vertical direction spaced at 150 mm. This wall has dowels which consists of a mesh QE84/257 formed by wires with a diameter of 4 mm in the horizontal direction and wires with a diameter of 6 mm in the vertical direction, both spaced at 150 mm. In case of the wall MFIEN3EP, the main reinforcement consists of corrugated bars with a diameter of 9.5 mm (#3) spaced at 250 mm in both directions. The dowels present a similar configuration as the wall MQE257 (#3 @ 250 mm) but they are distributed only in vertical direction.

The randomness of the structural characteristics is usually considered through the variation of the built-in materials properties, but in the present study, this effect has not been considered. Then, uncertainty in the capacity of the structural element was reduced by selecting material strengths based on the experiments and an appropriate inelastic model.

The compression strength of concrete was set to be 17.16 MPa that is typically used in these walls. The following properties were considered for the reinforcement based on the test (Quiroz et al. 2012). In case of the conventional reinforcement, the yielding stress was set to be 450 MPa with an associated strain of 0.002. As for the electro-welded wire mesh, the yield strain was 0.0035 with a yield stress of approximately 485 MPa. The main difference between these two types of reinforcement is the strain at the maximum strength. The strain of conventional reinforcement is 4.5 times larger than that of electro-welded wire mesh. Figure 2 shows a comparison of the two types of reinforcement.

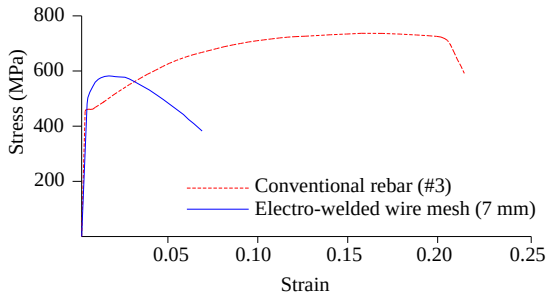


Figure 2 Schematic comparisons of conventional reinforcement and electro-welded wire mesh

The numerical model represents the effect of non-linearity of walls by modeling with the concentrated springs idealized by a trilinear backbone curve and hysteretic rules.

The definition of the bearing characteristics and their modeling of the hysteretic behavior of the cross-sections is of particular importance in defining damage under seismic motions. The bearing characteristics of a cross-section are given through the moment-curvature relationship. The three-parametric model proposed by Park et al. (1987), which is based on a tri-linear curve, was adopted to model the relationship. The three parameters α, β, and γ were estimated in the previous study (Quiroz et al. 2012).

To predict the hysteretic curve of the prototypes, the nonlinear behaviors of materials should be modeled numerically. In the case of concrete, unconfined concrete is assumed because the thickness of the walls is small and does not allow any type of confinement. The Kent and Park model was considered in this study (Kent and Park 1971). The tensile strength of concrete was neglected. The ultimate strain was set to be 0.0035 and the other parameters have been estimated using the expressions of Kent and Park (1971). For reinforcement, the uniaxial behavior of conventional reinforcement and electro-welded wire mesh is modeled by the trilinear model. The behavior is considered to be the same for compressive and tensile stresses.

3. DAMAGE LEVELS

To construct the seismic fragility curves, it is necessary to define structural damage levels. Many approaches have been used to define damage indices, e.g. one of those approaches considers three categories: non-cumulative, cumulative and combined damage indices. The structural parameters related to the categories mentioned before are the maximum deformation, hysteric behavior, and deformation/energy absorption. The first category has the advantage of simplicity in estimation process. Typical structural responses used in that category are drifts and displacement ductility ratios.

Because the damage to structure is related to local deformations, the drift can be used to show different damage states. The drift is calculated as the ratio between the relative displacement of a story and the height of the story. In the literature, it is possible to find many drift limits for walls. Farrar et al. (1993) proposed that the failure occurs with the drifts of 0.85 - 1.50% for low-rise walls with reinforcement ratio of smaller than 0.25%. Duffey et al. (1994) established that an 80% of reduction in ultimate capacity occurs at the drift of 1.34%, and a reduction of 50% occurs at the drift of 1.84% based on statistical analysis of their experimental results on light reinforced low-rise walls. Ghobarah (2004) stated that structural collapse of buildings with low-rise walls with low ductility can occurs at the drift of more than 0.80%.

For the present study, the maximum drift among at the all stories is considered as damage index and the definition of damage states by Ghobarah (2004) was employed because the drifts associated with the damage states are close to those observed during the experiments of Zavala (2004). Table 2 shows the definition of damage states proposed by Ghobarah based on the amount of drift.

Table 2 Definition of damage states with respect to the drift proposed by Ghobarah (2004)

State of damage	Drift limit (%)
No damage (ND)	0 – 0.1
Light (L)	0.1 – 0.2
Moderate (M)	0.2 – 0.4
Severe (S)	0.4 – 0.8
Collapse (C)	> 0.8

4. EARTHQUAKE GROUND MOTIONS

In order to consider the uncertainty of the ground motion, a way to overcome this is considering various records that reflect the seismicity of a specific place.

In the present study, a dataset of Peruvian records was used. This dataset consists of nineteen acceleration time histories recorded by Japan Peru Center for Earthquake Engineering and Disaster Mitigation, National University of Engineering, Peru (CISMID) and Geophysical Institute of Peru (IGP). The number of events is 14, and each record consists of the two horizontal components and one vertical component. The acceleration records of horizontal components are applied to the numerical models. All the records have been recorded in dense gravel soil, which represents the typical soil of Lima, and most of them consist of very high frequency contents. The dataset includes the ground motion record during the severe earthquake occurred in Lima after 1951. The magnitudes vary from 4 to 8. The magnitudes of the earthquake events are shown in Table 3. The origin of several of the records is associated withto the process of subduction between the Nazca and South American plates and presents a wide range of magnitudes and epicentral distances.

Table 3 Dataset of Peruvian ground motion records

Event	Year	M_W	M_S	M_L
Lima Eq.	1951	-	5.5	6
Ancash Eq. [1]	1970	-	7.8	-
Nov-71	1971	5.6	-	-
Jan-74	1974	6.5	6.6	-
Lima Eq. [1]	1974	-	7.6	-
Lima & Callao Eq. [1]	1966	8.1	8	-
Nov-74	1974	-	7.2	-
Mar-04	2004	-	-	5
Jul-04	2004	-	-	5.4
Mar-05	2005	-	-	5.7
Feb-06	2005			5.4
Lamas Eq.	2005	-	-	7
Pisco & Ica Eq.	2007	7.9	-	7
Callao Eq.	2008	5.3	-	5.3

In the Table 3, the superscript 1 indicates the records used to draw the inelastic design spectrum of the Seismic Peruvian standard E.030 (Ministry of Housing Peru 2003).

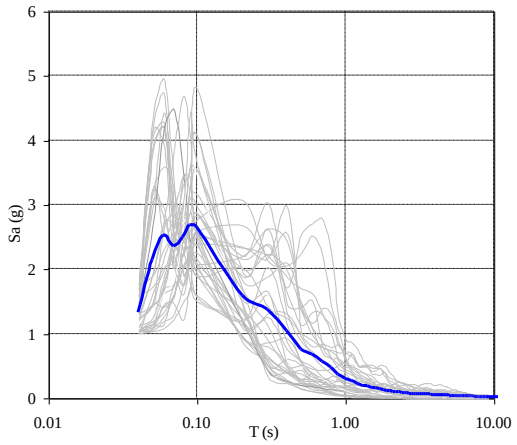


Figure 3 Acceleration response spectra (normalized to have PGA of 1g) with 5 percent damping ratio for Peruvian records

Figure 3 shows the acceleration response spectra for Peruvian earthquakes, which are normalized to have PGA of 1g, with the damping ratio of 5%. The mean amplitude is also shown with a thick line. Although the large variations in the spectral shape can be caused by many factors, such as

soil conditions and source-to-site distance, the mean amplitude of spectral shapes is different from event to event. Based on Figure 3, the ground motion records in Peru mainly consist of shorter period contents.

5. FRAGILITY CURVES

A difficult task in the analysis of structures is the determination of their structural response. IDARC2D (Reinhorn et al. 2009), a macro-element program, is used in the simulation of the structural response. IDARC2D has been extensively validated against laboratory testing of structural systems and components types, and it is used for the inelastic static and dynamic response analysis of RC structures.

The non-linear dynamic analysis is carried out using a combination of the Newmark-Beta integration method and the pseudo-force method. In the numerical analysis, the values for time increment step, damping value and damping type are 0.005 s, 5% and Rayleigh damping, respectively.

As is mentioned before, the fragility curves can be constructed with respect to different ground motion indices, e.g. PGA, PGV, AI, duration time, etc. In the present study, PGA was selected as the ground motion index because this parameter presented a better correlation with the drift than others. The damage ratio for each damage state under a certain excitation level is obtained. Base on these data, fragility curves for the walls are constructed assuming a lognormal distribution. This distribution was used by other researchers (Mehanny, and El Howary 2010).

The cumulative probability P_R of occurrence of the damage equal or higher than a damage state is given by

$$P_R = \Phi\left[\frac{\ln Y - \lambda}{\zeta}\right] \quad (2)$$

where Φ is the standard cumulative normal distribution, Y is the ground motion index (PGA), λ and ζ are the mean and standard deviation of ln Y. These two parameters of the distribution are obtained by the least-squares method on a lognormal probability paper.

The values of PGA for all records were scaled to have different excitation levels. Hence, the PGA for the records was scaled from 100 cm/s^2 to 1500 cm/s^2 with the interval of 100 cm/s^2. The scaled records were applied to the numerical model to obtain the damage index (maximum drift). Using the damage indices, the number of occurrence for each damage state was estimated under each excitation level. Finally, the damage ratio was obtained for every damage state. As an example, Figure 4 shows the number of occurrences of each damage state under different excitation levels for the wall MQE257EP and MFIEN3EP.

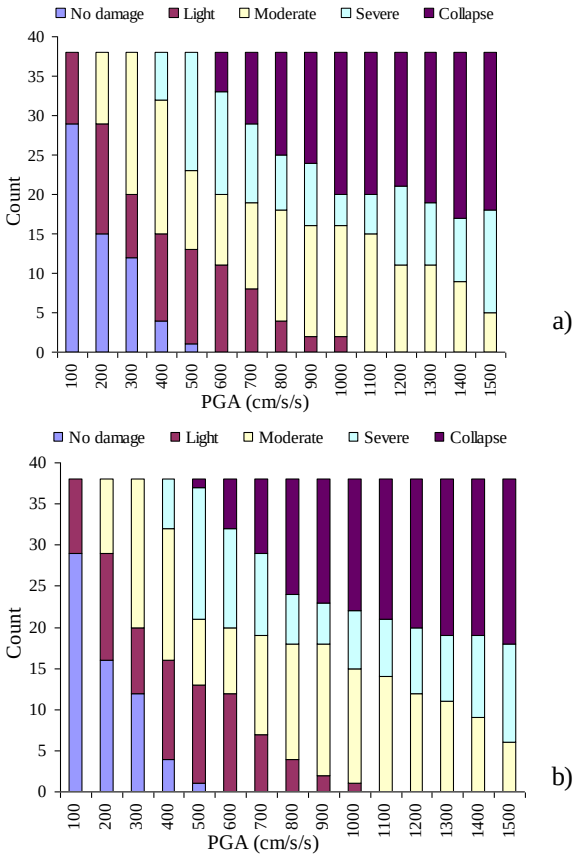


Figure 4 Number of occurrences of each damage state under the Peruvian records for the walls a) MQE257EP and b) MFIEN3EP

5.1 Influence of material used as main reinforcement

The use of electro-welded wire mesh as main reinforcement is a subject of controversy in the last years in Peru. From 1998 to 2004, many buildings were built whose lateral resistance system to earthquake consist of thin RC shear walls reinforced with electro-welded wire mesh as main reinforcement. For this reason, the influence of the use electro welded-wire mesh instead of conventional reinforcement as the main reinforcement in the fragility curves is evaluated.

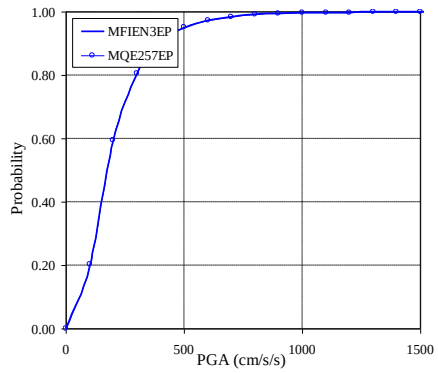
The fragility curves obtained for the walls MFIEN3EP and MQES57EP are presented. As can be observed, the amount of main reinforcement is almost the same for those walls but the material used in the every wall is different. Table 4 shows the parameters of fragility curves for thin RC shear walls.

Table 4 Parameters of fragility curves for the thin RC shear walls

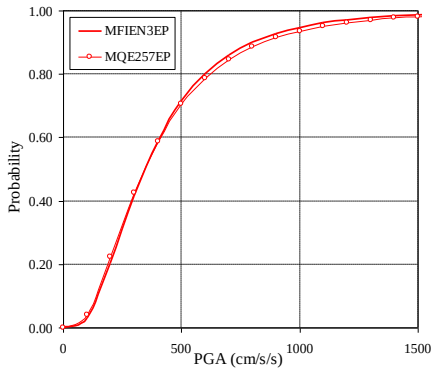
Prototype	Damage state							
	D > Light		D > Moderate		D > Severe		D = Collapse	
	λ	ξ	λ	ξ	λ	ξ	λ	ξ
MQE257EP	5.14	0.65	5.83	0.70	6.62	0.83	7.13	0.82
MFIEN3EP	5.16	0.65	5.84	0.66	6.61	0.88	7.13	0.65

Figure 5 presents the fragility curves for the walls with respect to PGA considering Peruvian records for different damage states. As can be observed, the change in the

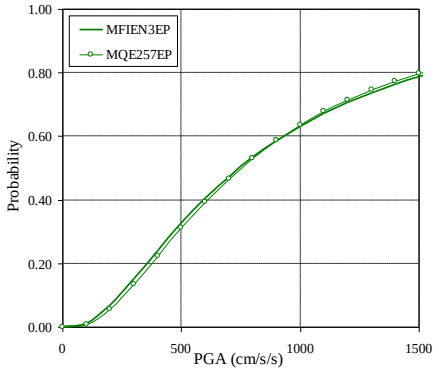
probability of exceeding a damage state with respect to the material used as main reinforcement is rather small. It is also observed that the slope of the curves gets steeper for first damage levels.



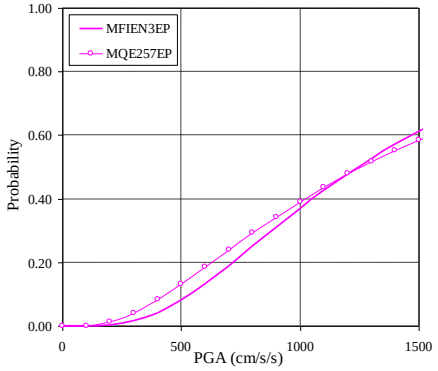
(a)



(b)



(c)



(d)

Figure 5 Comparison of the fragility curves for the walls MFIEN3EP and MQE257EP with a) light, b) moderate, c) severe and d) collapse damage states

5.2 Seismic performance

Finally, in order to evaluate the probability of being in each damage state, it is important to evaluate representative values of intensity. In the work of Silva (2008), the three levels of peak ground accelerations are presented (Table 5).

Table 5 Levels of hazard presented by Silva (2008)

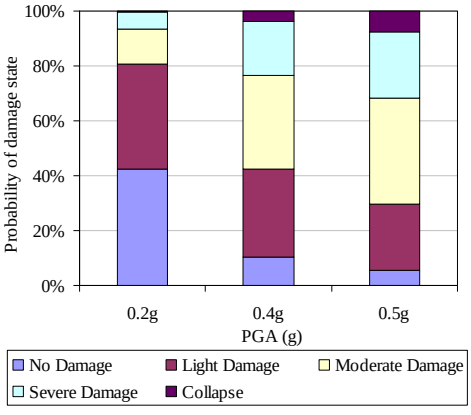
Ground Motion	Return Period (Years)	PGA (g)
Frequent	50	0.2
Rare	475	0.4
Very rare	970	0.5

Based on the fragility curves presented before, the probability of being in each damage state at each specified hazard level is obtained. Table 6 shows the comparison for the walls MFIEN3EP and MQE257EP. Figure 6 shows the damage probabilities for PGA equal to 0.2g, 0.4g, and 0.5g for the same walls.

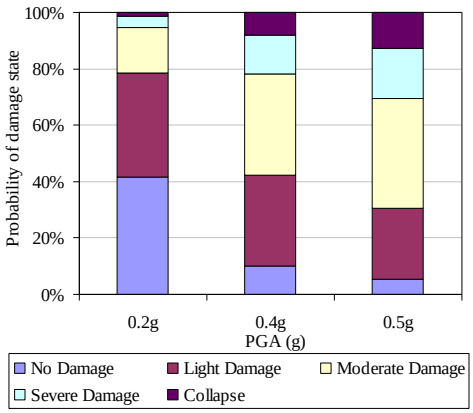
Table 6 Comparison of probability of each damage state for the three levels of seismic intensity

Damage State	PGA					
	MFIEN3EP			MQE257EP		
	0.2g	0.4g	0.5g	0.2g	0.4g	0.5g
No Damage	42.4%	10.3%	5.4%	41.7%	10.1%	5.3%
Light Damage	38.2%	32.0%	24.3%	36.8%	32.1%	25.1%
Moderate Damage	12.9%	34.3%	38.5%	16.2%	36.0%	39.1%
Severe Damage	6.3%	19.5%	24.1%	4.1%	13.9%	17.8%
Collapse	0.2%	3.9%	7.8%	1.2%	7.9%	12.7%

From Table 6, it is observed that in case of frequent earthquake, the damage is around 42% in no damage, 37% in light damage level and 14% in moderate damage for both walls. For a rare earthquake event, approximately 67% of the walls show light and moderate damage states and 10% of them without damage. In case of a very rare earthquake, approximately 63% of the wall MFIEN3EP and 57% of the wall MQE257EP show moderate and severe damage states. The probability of collapse is approximately 8% for the wall MFIEN3EP and 13% for the wall MQE257EP.



(a)



(b)

Figure 6 Damage probabilities for PGA equal to 0.2g, 0.4g, and 0.5g for the walls a) MFIEN3EP and b) MQE257EP

6. CONCLUSIONS

The use of fragility curves is a useful tool to estimate the structural damage in a certain type of structures due to the effect of future events. In the present study, the fragility curves for thin RC shear walls for low-rise and mid-rise buildings constructed in Lima is constructed thorough a series of numerical simulations. The PGA was selected as a seismic index, and the variation of the types of material used as main reinforcement were considered. The damage index is defined with respect to the drift, and it was classified into 4 damage states. The fragility curves presented in this study help to predict the damage that buildings composed of thin RC walls especially in Lima, Peru. From the analysis of the fragility curves obtained, the following conclusions can be drawn:

It was observed that the use of electro-welded wire mesh as main reinforcement gives similar damage probability compared with the wall consisted of the conventional reinforcement. This indicates that the use of electro-welded wire mesh is acceptable with the viewpoint of seismic resistance. The use of electro-welded wire mesh as main reinforcement can reduce the price of buildings.

The walls behave practically in moderate and light damage (94%) under the moderate earthquake. In case of the severe earthquake, the walls behave in severe and moderate damage (94% in average). The probability of collapse is approximately 6% in average for the both walls.

Acknowledgements:

The authors acknowledge the support from the Japan Science and Technology Agency (JST) and Japan International Cooperation Agency (JICA) under the SATREPS project "Enhancement of earthquake and tsunami disaster mitigation technology in Peru."

References:

ATC-13 (1985), "Earthquake damage evaluation date for California," Applied Technology Council, Redwood City, CA.

Chiou J.S., Chiang C.H., Yang H.H. and Hsu S.H. (2011), "Developing fragility curves for a pile-supported wharf," *Soil Dynamics and Earthquake Engineering*; **31**: 830–840.

Duffey, T.; Farrar, C. y Goldman, A. (1994), "Low-rise shear wall ultimate drift limits," *Earthquake Spectra*, V.10.

EERI (2010), "The Mw 8.8 Chile Earthquake of February 27, 2010," Special Earthquake Report - June 2010.

Farrar, C., Reed, J. and Salmon, M. (1993), "Failure modes of low-rise shear walls," *Journal of Energy Engineering*, V.119.

Ghobarah, A. (2004), "On drift limits associated with different damage levels," Bled Conference, Slovenia.

Jaw J.W. and Hwang H.M. (1988), "Seismic fragility analysis of shear wall structures," Technical Report NCEER-88-0009, State University of New York at Buffalo.

Jovanoska, E.D. (2000), "Fragility curves for reinforced concrete structures in Skopje (Macedonia) region," *Soil Dynamic and Earthquake Engineering*; **19**(6):455–66.

Karim K.R. and Yamazaki F. (2001), "Effect of earthquake ground motions on fragility curves of highway bridge piers based on numerical simulation," *Earthquake Engineering and Structural Dynamics*; **30**(12):1839 –1856.

Kent, D.C. and Park, R.R. (1971). "Flexural members with confined concrete". *Journal of the Structural Division, ASCE*, **97**:7, 1969-1990.

Maruyama Y., Yamazaki F., Mizuno K., Tsuchiya Y. and Yogai H. (2010), "Fragility curves for expressway embankments based on damage datasets after recent earthquakes in Japan," *Soil Dynamics and Earthquake Engineering*; **30**:1158–67.

Mehanny, S.S.F. and El Howary, H.A. (2010), "Assessment of RC moment frame buildings in moderate seismic zones: Evaluation of Egyptian seismic code implications and system configuration effects," *Eng. Struct.*, **32**: 2394-2406.

Ministry of Housing Peru (2003), "National Technical Standard E-030 - Earthquake Resistant Design," Lima, Peru. (In Spanish)

Nocevski N.K. (1993), "Definition of empirical and theoretical models for assessment of vulnerability level in high rise buildings," Doctoral thesis. IZIIS, Skopje.

Park, Y.J.; Reinhorn, A.M. and Kunnath, S.K. (1987), "IDARC Inelastic Damage Analysis of Reinforced Concrete Frame-Shear-Wall Structures," Technical Report NCEER-87-0008, State University of New York at Buffalo.

Quiroz L., Maruyama Y. and Zavala C. (2012), "Numerical simulation of the cyclic behavior of full-scale thin RC shear walls developed in Peru," *Proceedings of the First International Symposium on Earthquake Engineering*, Japan Association for Earthquake Engineering, pp. 445-454.

Reinhorn A.M., Roh H. Sivaselvan M., Kunnath S.K., Valles R.E., Madan A., Li C., Lobo R. and Park Y.J.. (2009), "IDARC2D Version 7.0: A Program for the Inelastic Damage Analysis of Structures," Technical Report MCEER-09-0006, State University of New York at Buffalo.

Silva, H. (2008), "Application of probabilistic methodology for damage estimation of mid-rise RC building in Lima," *Proceedings of the 14th World Conference on Earthquake Engineering*. Paper No 10-0004. 9p.

Whitman R.V., Reed J.W. and Hong S.T. (1973), "Earthquake damage probability matrices," *Proceedings of the Fifth WCEE*, Rome, Italy.

Zavala, C. (2004), "Test on walls and a one-floor house reinforced with electro-wire mesh UNICO/FORSA/PRODAC," Research report. Japan-Peru Center for Earthquake Engineering Research and Disaster Mitigation. Lima, Peru (in Spanish).

10CUEE CONFERENCE PROCEEDINGS
10th International Conference on Urban Earthquake Engineering
March 1-2, 2013, Tokyo Institute of Technology, Tokyo, Japan

SHAKING TABLE TEST OF A LARGE-SCALE SELF-CENTERING REINFORCED CONCRETE FRAME

Xilin Lu[1], Ye Cui[2], Jingjing Liu[2) 3)], Ying Zhou[1], and Wensheng Lu[1]

1) Professor, State Key Laboratory of Disaster Reduction in Civil Engineering, Tongji University, Shanghai, P.R.China
2) Ph.D. student, State Key Laboratory of Disaster Reduction in Civil Engineering, Tongji University, Shanghai, P.R.China
3) Ph.D. student, Faculty of Forestry, University of British Columbia, Vancouver, Canada
lxlst@tongji.edu.cn, 2010_yecui@tongji.edu.cn, jingjing.liu@ubc.ca, yingzhou@tongji.edu.cn, wenshenglu@vip.163.com

Abstract: A 1/2 scale model of a two-story self-centering reinforced concrete frame model was designed and tested on the shaking table in State Key Laboratory of Disaster Reduction in Civil Engineering at Tongji University to study the seismic performance of self-centering reinforced concrete frames. The interfaces in the joints can undergo compression but no tension by relaxing the constraints between structure and base or components. The forces for self-centering are provided by the post-tensioned prestressed reinforcement when the structure rocks under the earthquake. In this paper, the dynamic characteristics, displacement and joint responses of the model structure under different earthquake levels are discussed. The location and process of structural damage are summarized. The self-centering capability of the structure is analyzed. Test results indicate that the designed reinforced concrete frame has satisfying seismic performance and self-centering capacity subjected to earthquakes; self-centering structures can undergo large deformation with minor residual displacement after the earthquakes; more researches on energy dissipation members and the stiffness of columns and beams are expected.

1. INTRODUCTION

As an innovative branch of the seismic structural design, earthquake resilient structures have gained widespread concern in both academia and industry during the past few decades. This new system not only protects life safety by preventing structural failure in an earthquake, but also restores its structural function immediately after the earthquake (Lu *et al.* 2011). Earlier researches indicate that rocking of structure lowers the seismic excitation and ductility requirement of structures. Relaxing the constraints between structure and base or components, the interfaces in the joints can undergo compression but no tension. Post-tensioned prestressed reinforcement provides the forces for self-centering when the structure rocks under the earthquake (Zhou and Lu 2011). By controlling residual deformation of structures effectively, time and economic cost are saved. Little experimental research (Priestley 1991; Priestley and Tao 1993; El-Sheikh *et al.* 1999) on self-centering systems has been generated by far, most of which focused on steel frame structures (Christopoulos and Folz 2002; Garlock *et al.* 2007). Therefore, it is of significance to study the seismic performance of reinforced concrete self-centering structures.

This paper presents a 1/2 scale model of a self-centering reinforced concrete frame based on an one bay one span two stories prototype (Liu *et al.* 2012). It was designed and tested on the shaking table in State Key Laboratory of Disaster Reduction in Civil Engineering at Tongji University as the first shaking table test of large scale self-centering reinforced concrete structures in China. Focusing on the self-centering capability, the dynamic characteristics of the structure as well as the dynamic responses and damage under different levels of earthquakes are investigated. This provides the experimental basis for further study on self-centering reinforced concrete structures.

2. DISCRIPTION OF TEST

2.1 Model Design

In this experiment, a 1/2 scale model, with plan dimensions of 3.0 m × 1.5 m and a story height of 1.5 m was used. Columns were fixed in the base pits by prestressed strands. Rubber was placed in between the column and base. Top and seat angle connections were applied at the short beam and column joints. Prestressed strands were also used in the short beams. Figure 1 shows the plan and elevation of the model. Figure 2 shows a photograph of the test structure on the shaking table. The total height of the model including the base was 4.0 m while the weight was 13.0 t. The model was shaken in the short axis of the structure.

The model was fabricated under the similitude law (Lu *et al.* 2009; Zhou *et al.* 2006). Fine aggregate concrete with the characteristic strength of 40 MPa was used. HRB335 and HPB 235 were selected for the longitudinal reinforcement and stirrups, respectively. Two types of prestressed strands, Φ15.2 and Φ12.7 were adopted. The characteristic strength

of the angle steel was 345MPa. No slab was put on the floor. Two steel beams were hinged on the main beam to support the rigid mass above. Table 1 shows the similitude scale factors of the test model.

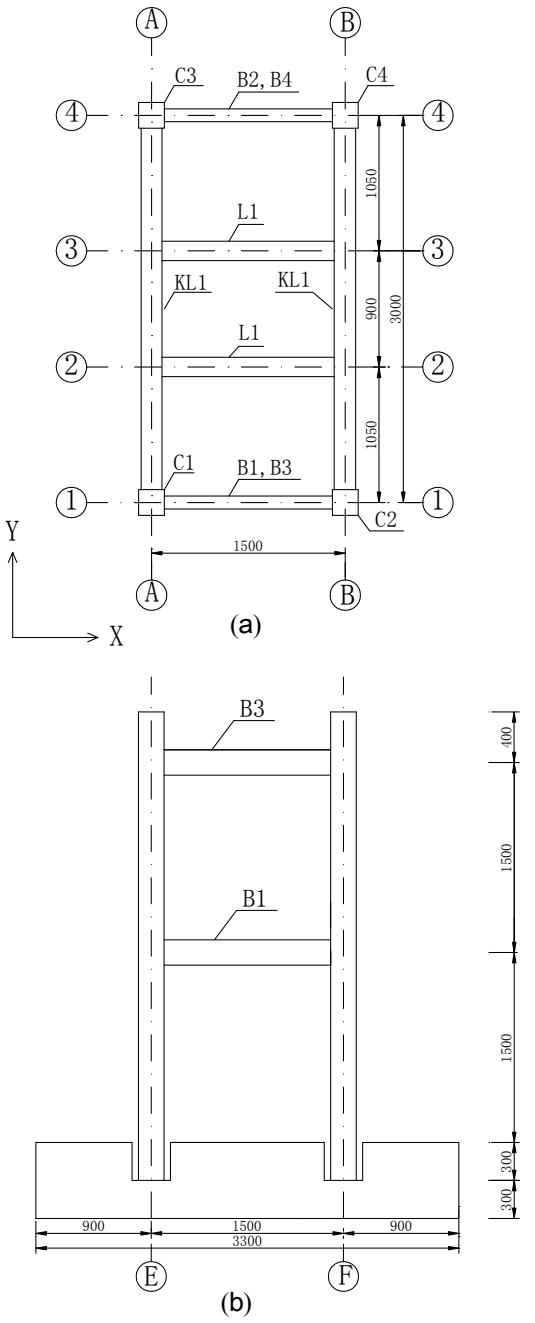


Figure 1 Plan and evalation view of test structure: (a) plan view, and (b) evalation view

Figure 3 shows the details of column base joints. Steel plates at the bottom of the columns were welded to the longitudinal bars. The interfaces between them and those in the base were separated. Rubber was placed in the interspace of columns and the base. Those construction measures were applied to prevent the local failures of concrete. The parameters of prestressed reinforcement in columns are shown in Table 2. The joints were expected to open at the interfaces under design excitation.

Table 1 Similitude scale factors

Parameter	Similitude scale factor	Parameter	Similitude scale factor
S_ε	1.000	S_M	0.125
S_σ	1.000	S_q	0.500
S_E	1.000	S_p	1.000
S_μ	1.000	S_m	0.250
S_ρ	2.000	S_K	0.250
S_l	0.500	S_T	0.707
S_S	0.250	S_f	1.414
S_δ	0.500	S_c	0.354
S_φ	1.000	S_v	0.707
S_F	0.250	S_a	1.000



Figure 2 Test model

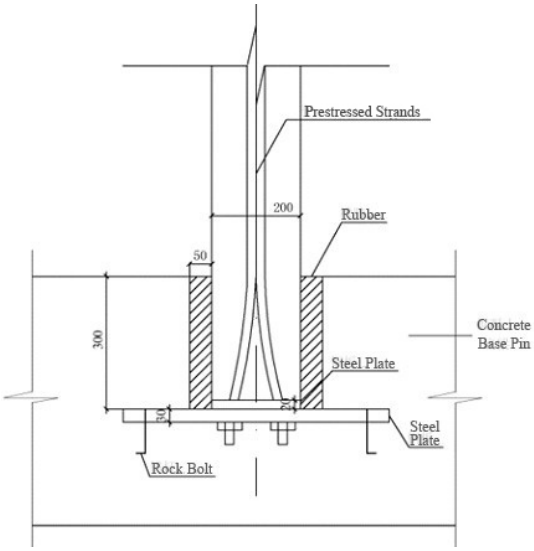


Figure 3 Details of column base joints

Table 2 Parameters of prestressed reinforcement in columns

Column size	Prestressed reinforcement ratio	Prestressed strands	Prestressed force in each strand
200mmx200mm	0.69%	2Φ^{s}15.2	40kN

Figure 4 shows the details of beam-column joints in the direction of short dimension. Beams and columns were connected by prestressed strands. Steel plates were set at the end of beams and the sides of columns to prevent local failures. Top and seat angle connections were used to enhance the shear strength and stiffness of the joints. Meanwhile, they worked as energy dissipation devices after the joints opened. The joints were designed using the same criteria as the base joints. The parameters of prestressed reinforcement in beams are shown in Table 3.

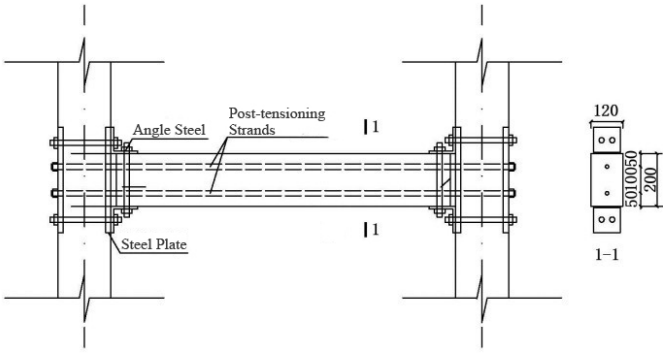


Figure 4 Details of beam-column joints

Table 3 Parameters of prestressed reinforcement in beams

Beam size	Prestressed reinforcement ratio	Prestressed strands	Prestressed force in each strand
100mmx200mm	0.99%	2Φ^{s}12.7	40kN

2.2 Test Plan

Two historical ground motions were used for the shaking table tests, 1940 El Centro (NS) and 2008 Wenchuan waves. The model was subjected to two alternate series of excitation, (1) white noise tests to assess the damages after previous tests by evaluating the fundamental frequency of vibration, and (2) seismic tests to obtain the structural response under different levels of earthquake. The input ground motions were loaded at increments of peak acceleration by 0.05g starting from 0.05g. The maximum level test was the El Centro 0.60g test and the Wenchuan 0.80g test.

2.3 Sensors

Five types of sensors were used to record the response of the model: (a) four string potentiometers to measure the displacement of each storey; (b) eight linear variable differential transformers (LVDT) fixed on the beams ends and column bases to measure local displacement; (c) eight load cells to measure axial force of the prestressed strands in the beams (B1, B3) and columns (C1, C2); (d) eight accelerometers to measure horizontal and vertical floor accelerations; (e) four strain gauges to measure the strain of angle steel on C2.

3. TEST RESULTS

3.1 Dynamic Characteristics

Figure 5 shows the first and second frequency of vibration in the *X* direction estimated from each white noise test. The initial first frequency was 4 Hz. After the tests, the first frequency fell to 1.75 Hz. The change in frequency was mainly due to the damage of non-self-centering components and the yield of angle steel.

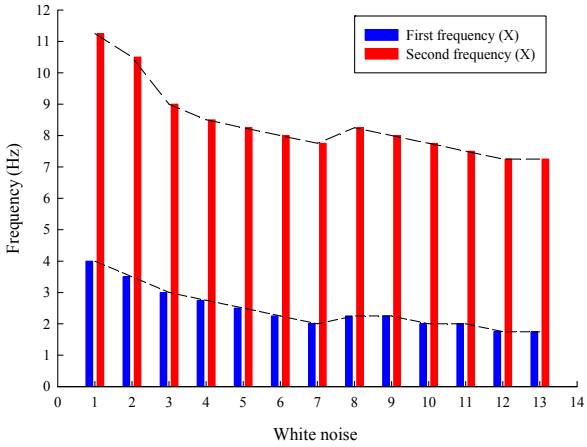


Figure 5 Change in frequency

3.2 Displacement Responses

Under seismic loads, the maximum floor displacement was 122.594mm for the first floor and 166.677mm for the second. Figure 6 shows the maximum inter-story drift ratio for each test. It reached 1/15 for the first floor and 1/26 for the second during the El Centro 0.60g test. The results demonstrate great ductility of the system.

Figure 7 shows the top floor displacement time history curve under the El Centro 0.60g test. The residual displacements were minimal respectively.

3.3 Joint Responses

The uplifts or openings are assumed to occur when the interfaces of self-centering joints reach a minimum gap of 1 mm. First, they were observed under the El Centro 0.20g test and the Wenchuan 0.30g test. When the El Centro 0.60g test

was loaded, the maximum uplift for column was 9.183 mm and the maximum opening for beam was 9.579 mm. Figure 8 shows the maximum uplift and opening under the El Centro 0.60g test. Figure 9 shows a picture of the uplift at the base and the opening at beam ends under the El Centro 0.40g test. Figure 10 shows the column uplift time history curve and beam opening time history curve under the El Centro 0.60 test.

The initial ratio of post-tentioning (PT) stress and yield stress were 0.16 and 0.23 for prestressed strands in columns and beams, respectively. The maximum stress of prestressed strands in columns were 473.185 MPa and 865.691 MPa for beams. The minimum stress of prestressed strands in columns were 248.829 MPa and 247.468 MPa for beams. These are shown in Figure 11. The prestressed strands were under linear elastic state across the test, providing the self-centering capability of the structure after the earthquake.

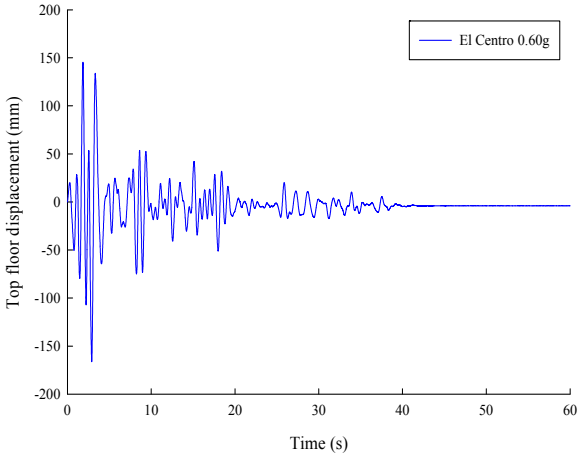
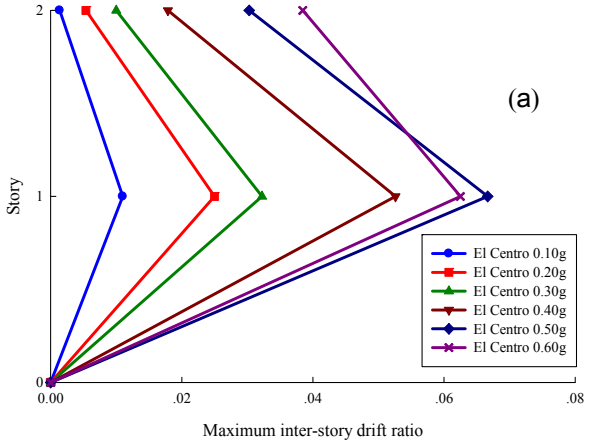


Figure 7 Top floor displacement time history curve



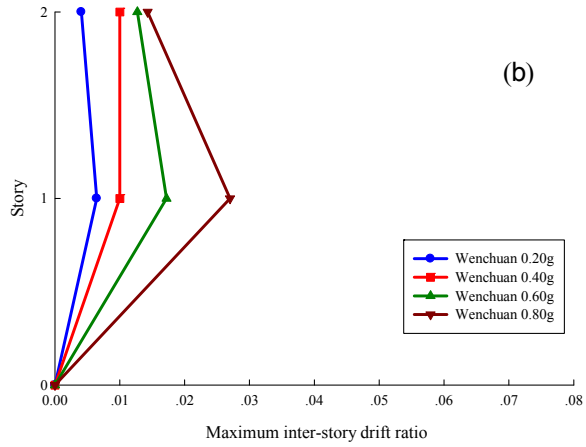
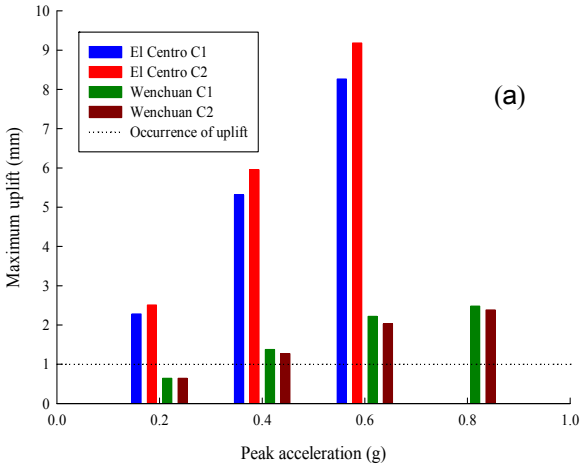


Figure 6 Maximum inter-story drift ratio under different earthquakes: (a) El Centro tests, and (b) Wenchuan tests



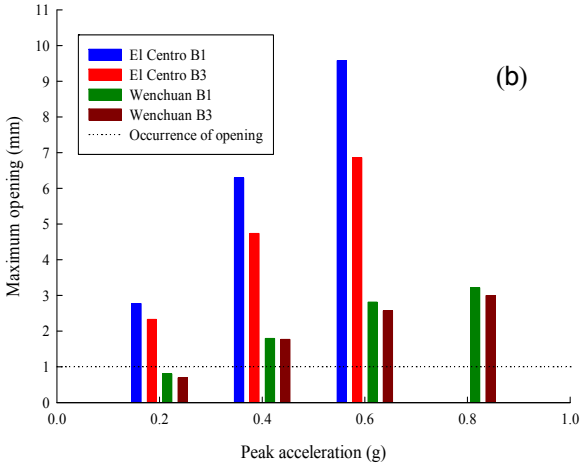


Figure 8 Maximum uplift and opening: (a) Column uplift, and (b) Beam opening

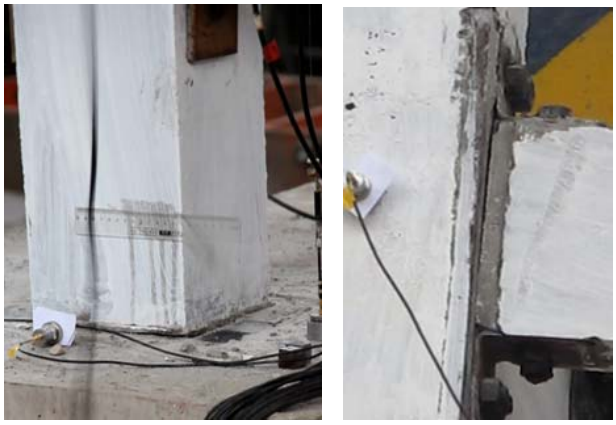


Figure 9 The uplift at the base and the opening at beam ends under El Centro 0.40g test

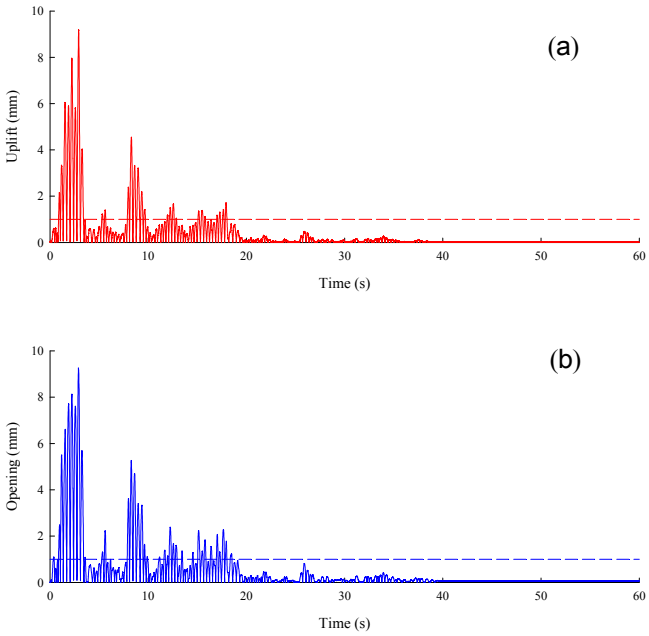


Figure 10 Time history curves of the uplift at the base and the opening at beam ends under El Centro 0.60g: (a) the uplift at the base, and (b) the opening of beam ends

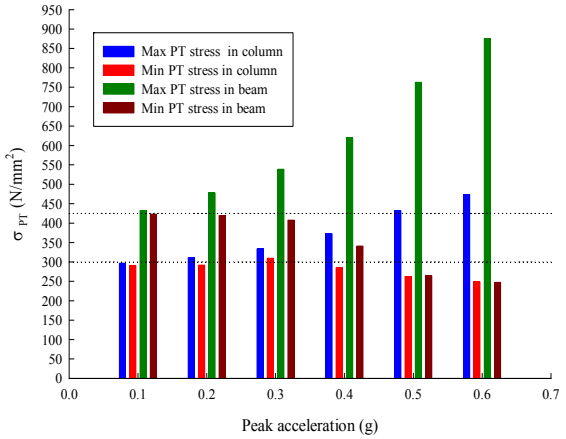


Figure 11 Maximum and minimum stress in prestressed strands under different earthquakes

The rubbers between the column and base were consistently elastic. Four strain gauges were used to measure the strains in the angle steel. The characteristic strength of the angle steel was 345MPa. The yielding strain is expected to be 1505με. As shown in Table 4, the angle steel was firstly considered yielded during the El Centro 0.25g test.

Table 4 Strain of the angle steel (με)

Test	B3T	B3B	B1T	B1B
El Centro 0.20g	1299	878	1112	1108
El Centro 0.25g	1725	1439	1740	1672

B1: beam B1; B3: beam B3; T: top; B: bottom.

4. CONCLUSIONS

This large-scale shaking table test validates that well designed self-centering reinforced concrete frame systems have satisfying seismic performance, especially under severe earthquakes. The structure with minimal residual displacement after the earthquake not only protects the lives and property but also saves great reconstruction time and cost. Below are the conclusions obtained from this study:

(1) The self-centering reinforced concrete frame has excellent seismic behavior. The tested model stayed elastic under excitation with maximum peak ground acceleration (PGA) of 0.20g. Small pieces of concrete cover fell down until the maximum PGA reached 0.45g. The structure kept in good condition without structural damage even after it went to 0.60g.

(2) The expected self-centering capacity was achieved in the test. The first uplift of columns and opening of beams happened at the El Centro 0.20g test. After the maximum PGA increased to 0.40g, the uplift of columns and opening of beams had been very obvious to observe. Large deformation of structure was obtained under the El Centro 0.60g test. However, no signal of collapse or structural damage appeared. The maximum uplift of columns reached 9.183mm while the maximum opening of beams 9.579mm. The structure went back to its initial position with negligible residual deformation.

(3) The major damage happened at the interfaces between angle steel and concrete. No damage was observed on the self-centering elements. The angle steel dissipated energy with large deformation as expected. It was noticed that yield of angle steel firstly happened at the El Centro 0.25g test, which could not be considered as a severe excitation. Higher strength of angle steel should be applied to achieve more ideal anticipation. However, rotational stiffness will also affect the self-centering capacity of structures.

(4) During the tests, bending deformation of both columns and beams were observed. To obtain better uplift and opening effect, columns and beams with higher stiffness should be selected.

Ongoing related studies involve numerical modeling and reliability analysis to characterize the self-centering reinforced concrete system. More research on energy dissipation devices and stiffness of elements is expected. It is hoped that an alternative of traditional seismic force resisting systems with better seismic performance and controllable post-quake repair could be provided.

Acknowledgements:

The authors acknowledge support from the National Natural Science Foundation of China under grant No. 51021140006. Any opinions, findings, and conclusions expressed in this material are those of the authors and do not necessarily represent those of the sponsors.

References:

Lu, X.L., Chen, Y. and Mao, Y.J. (2011), "New concept of structural seismic design: earthquake resilient structures", *Journal of Tongji University (Natural Science)*, 39(7), 941-947.

Zhou, Y. and Lu, X.L. (2011), "State-of-the-art on rocking and self-centering structures", *Journal of Building Structures*, 32 (9), 1-10.

Priestley, M.J.N. (1991), "Overview of PRESSS research program", *PCI Journal*, 36(4), 50-57.

Priestley, M.J.N. and Tao, J.R. (1993), "Seismic response of precast prestressed concrete frames with partially debonded tendons", *PCI Journal*, 38(1), 58-69.

El-Sheikh, M.T., Sause, R. and Pessiki, S. (1999), "Seismic behavior and design of unbonded post-tensioned precast concrete frames", *PCI journal*, 44(3), 54-71.

Christopoulos, C., and Folz, B. (2002), "Posttensioned energy dissipating connections for moment-resisting steel frames", *Journal of Structural Engineering*, 128, 1111.

Garlock, M.M., Sause, R. and Ricles, J.M. (2007), "Behavior and design of posttensioned steel frame systems", *Journal of structural engineering*, 133, 389.

Liu, J.J., Lu, X.L., and Zhou, Y. (2012), "Design and construction for a large-scale seismic model of self-centering reinforced concrete frame", *Science paper Online*.

Lu, W.S., Su, N.F., and Ding, K. (2009), "Shaking table test on super high-rise building with setback in elevation", *Journal of Earthquake Engineering and Engineering Vibration*, 29(3), 39-44.

Zhou, Y., Lu, X.L., and Lu, W.S. (2006), "Shaking table test model design in different structures", *Structural Engineers*, 22(4), 37-40.

10CUEE CONFERENCE PROCEEDINGS
10th International Conference on Urban Earthquake Engineering
March 1-2, 2013, Tokyo Institute of Technology, Tokyo, Japan

EXPERIMENTAL INVESTIGATION OF LARGE REINFORCED CONCRETE SPECIAL MOMENT RESISTING FRAME BEAMS

Tea Visnjic[1)], Marios Panagiotou[2)], Jack Moehle[3)], Grigoris Antonellis[4)]

1) Ph.D. Candidate, Dept. of Civil and Environmental Engineering, University of California – Berkeley, USA
2) Assistant Professor, Dept. of Civil and Environmental Engineering, University of California – Berkeley, USA
3) T.Y. and Margaret Lin Professor, Dept. of Civil and Environmental Engineering, University of California – Berkeley, USA
4) Graduate Student Researcher, Dept. of Civil and Environmental Engineering, University of California – Berkeley, USA
tea@berkeley.edu, panagiotou@berkeley.edu, moehle@berkeley.edu, antonellis@berkeley.edu

Abstract: A laboratory test program was conducted at University of California - Berkeley to assess the response capabilities of large reinforced concrete special moment resisting frame (SMRF) beams. The size of the test beams is representative of modern high-rise construction in the seismically active west coast of the United States and is larger than was typical in the past practice. When the 2008 ACI 318 requirements for SMRF beams are applied to these large beams, the beam hoop spacing can be as great as 305 millimeters in the plastic hinge region. This raised a concern that such SMRF beams may not be able to meet the performance expectations during an earthquake and motivated the experimental study. In order to address the adequacy of the code hoop spacing requirements, the test program evaluated the response of two full-scale beam models tested under reversed-cyclic loading. In the first specimen, the transverse hoops were placed at a maximum spacing allowed by the 2008 Code. In the second, the hoop spacing was reduced to satisfy the updated 2011 Code requirements. The responses of the two specimens are discussed, especially noting differences in performance.

1. INTRODUCTION

Reinforced concrete special moment resisting frames (SMRFs) are commonly selected seismic load resisting systems in the United States. These systems, referred to as "special moment frames" in ACI 318 (ACI, 2011), are designed around the strong column-weak beam design philosophy whereby the majority of inelastic flexural deformations are intended to occur in the columns of the bottom of the first story and in the beams along the height of the building. The yielding of reinforcing steel and concrete cracking in the beams that occur in the plastic hinge regions are also the main source of energy dissipation in the reinforced concrete moment frames. Previous studies of generic reinforced concrete SMRF buildings (Visnjic et al., 2012) showed that mean rotation amplitudes of the beams along the building height were 2% for the design basis earthquake and 3% for the maximum considered earthquake levels. Therefore, for a structure subjected to multiple large displacement cycles at levels consistent with the building code design provisions, it is important that the beams are capable of sustaining deformation reversals in a stable manner and without significant loss of strength.

In taller buildings, SMRF beams can be as deep as 1200mm and are generally larger than what was used in the past practices. The provisions of the ACI 318 code prior to the 2011 edition when applied to such large beams could result in a maximum spacing of transverse reinforcement reaching 305mm in the plastic hinge region. This raised a question whether such beams would be able to realize the stable inelastic flexural behavior under large deformation cycles during seismic events. The concern motivated the undertaking of the experimental program to evaluate the response capabilities of large reinforced concrete SMRF beams satisfying the existing code requirements of 2008 ACI 318 (ACI, 2008). The findings prompted the reduction of the maximum allowed transverse hoop spacing to 152mm in the 2011 ACI 318 code and are presented in the subsequent sections.

2. EXPERIMENTAL PROGRAM

2.1 Beam Specimens

The experimental program included two 4115mm-long cantilever reinforced concrete beams anchored to a common reaction block (Figure 1). Both beams were 762mm wide and 1219mm deep (Figure 2) and were longitudinally reinforced with five No. 36 bars (d_b = 36mm) at both the top and bottom. Transverse reinforcement hoops consisted of three pieces: a stirrup with seismic hook, a crosstie at the top to close the hoop, and an additional vertical crosstie bracing the longitudinal bars along the top and bottom faces. Each piece was made of No. 16 bar. The crossties were alternated end for end along the length of the beam, as specified in the ACI 318 code. The beams also contained the longitudinal skin reinforcement made up of No. 15 bars.

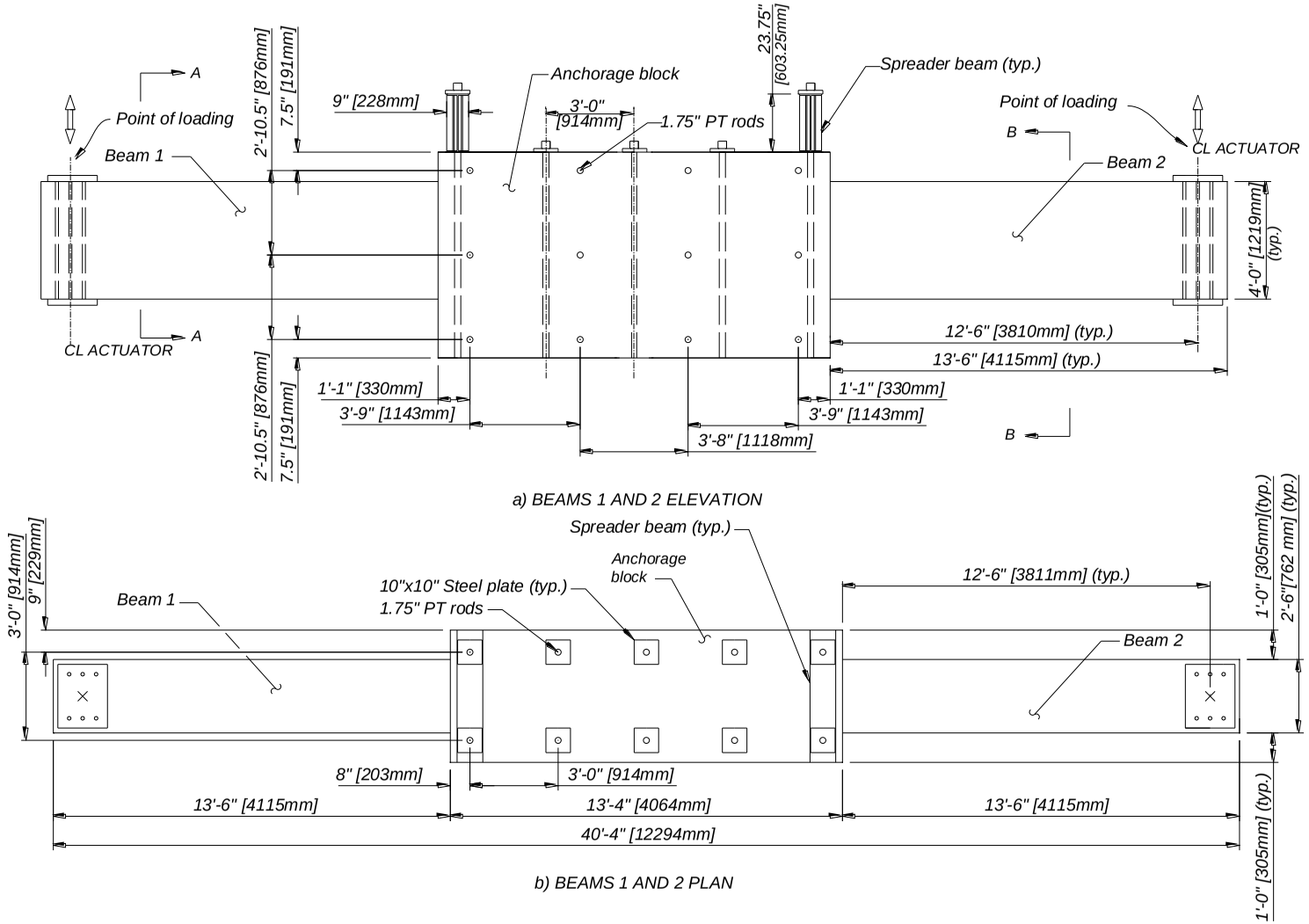


Figure 1 Laboratory Setup of Beams 1 and 2: (a) Elevation, and (b) Plan View

The only design parameter differing between the two beams was the spacing of the transverse hoops. Beam 1 hoops were spaced at s_h = 279mm to satisfy the provisions of the 2008 ACI 318 code. Beam 2 hoop spacing was reduced to s_h = 152mm and satisfies the current ACI 318 code provisions (ACI, 2011). This arrangement of beam hoops resulted in volumetric confinement ratios of ρ" = 0.31% and 0.57% for Beam 1 and Beam 2, respectively.

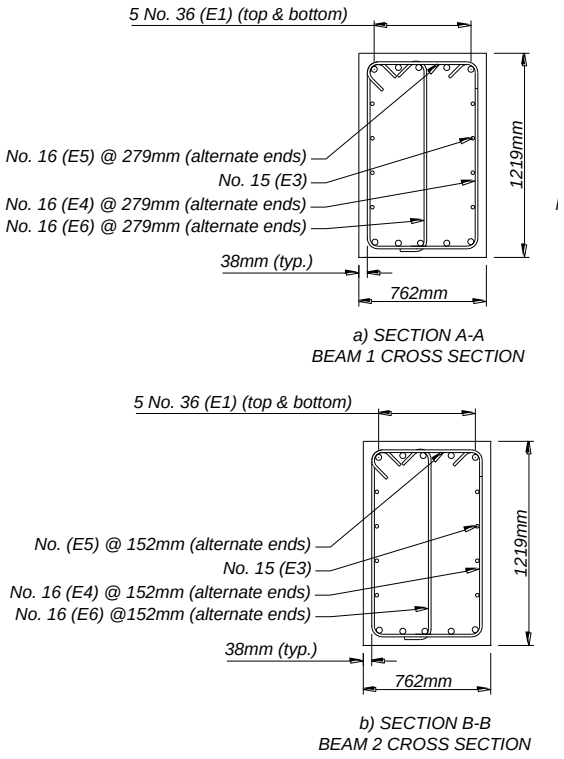


Figure 2 Cross Section of Beams 1 and 2

The specified compressive strength of normal weight concrete for the beams was f'_c = 34MPa. The concrete cylinders of sample from each batch used were tested on the day of the experiments for both beams. For Beam 1, the average compressive strength of concrete was 40.1MPa, while for Beam 2, it measured at 42.3 MPa.

ASTM A706 Grade 60 steel was used for the both the longitudinal No. 36 bars and transverse No. 16 bars with specified yield strength of f_y = 413MPa. Tension tests of three steel coupons constructed from No. 36 bars revealed the actual average yield strength to be f_y = 455 MPa with average maximum stress of f_u = 723 MPa. A well-defined yield plateau developed for the No. 36 specimens tested with the average strain at the onset of strain hardening equal to ε_{sh} = 1.2%. Average maximum measured stress in steel was f_u = 723 MPa. The coupons did not display a yield plateau. For the No. 16 bars, the average yield stress measured in three sample coupons was f_y = 503 MPa.

2.2 Loading Protocol

The beams were tested by imposing downward and upward displacement cycles simulating the effects of deformation reversals that occur during a major earthquake. Displacement history shown in Figure 3 was imposed by an actuator with a point of loading located 3810mm from the face of the anchorage block (Figure 1). Positive beam tip displacement and reaction forces correspond to downward beam deflection. A downward displacement and an upward displacement of equal amplitude followed with returning the beam tip to neutral position constitute a complete cycle. Cycles of equal amplitude were grouped into steps so that each new step contained cycles with different displacement amplitude from those in the preceding step. This is shown in Figure 3.

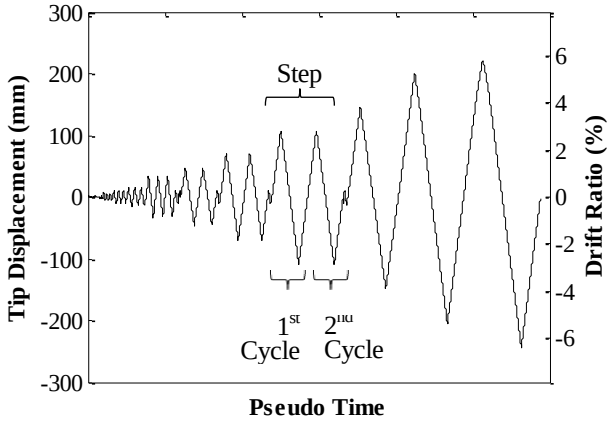


Figure 3 Loading Protocol for Beams 1 and 2

2.3 Instrumentation

The instrumentation of the test specimens included linear variable differential transformers (LVDTs) connected between steel rods that were embedded in the specimen along the top and bottom face of the beams. LVDTs were also placed between the bottom face of the beam at the point of loading and the strong floor to measure total beam deflection. In addition, strain gauges were attached to both the longitudinal bars and hoops at selected locations. During the testing of Beam 1, an error in data acquisition system resulted in permanent loss of measurements from few strain gauges and LVDTs, however, most important information could be gathered from the remaining instruments.

3. TEST RESULTS

3.1 Beam 1 Response Overview

Figure 4 shows the relation between the computed resisting moment and the measured beam drift ratio for Beam 1. The moment was calculated from the measured force applied at the beam tip and includes the self-weight of the beam. The initial deflection due to beam self-weight is deemed negligible and is not accounted for in the reported drift values. Cycles with amplitude lower than 0.28% are omitted from the graph for clarity.

Computed probable flexural strength M_{pr} = 2970 kN-m is also shown in Figure 4. This value was calculated in accordance with ACI 318 assuming the specified concrete compressive strength f'_c = 34 MPa and elasto-plastic steel stress-strain relation with maximum steel stress taken equal

to 1.25 times the specified yield stress, that is f_{pr} = 517 MPa. The M_{pr} calculation ignored the contribution of skin reinforcement, because the No.15 longitudinal bars were not fully developed into the anchorage. These bars, if accounted for, would result in 9% increase in M_{pr}. The peak measured moment was equaled to 2850 kN-m and was within 5% of the computed value.

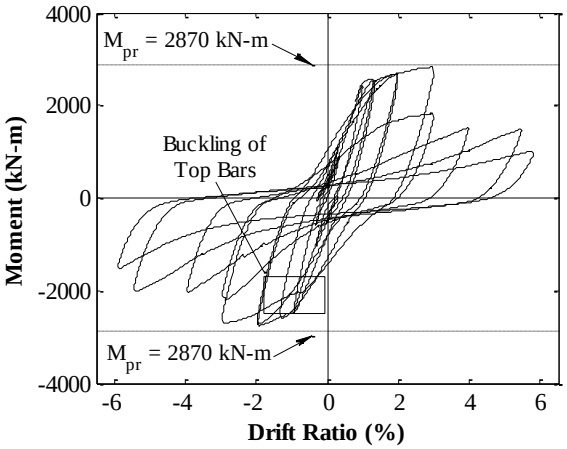
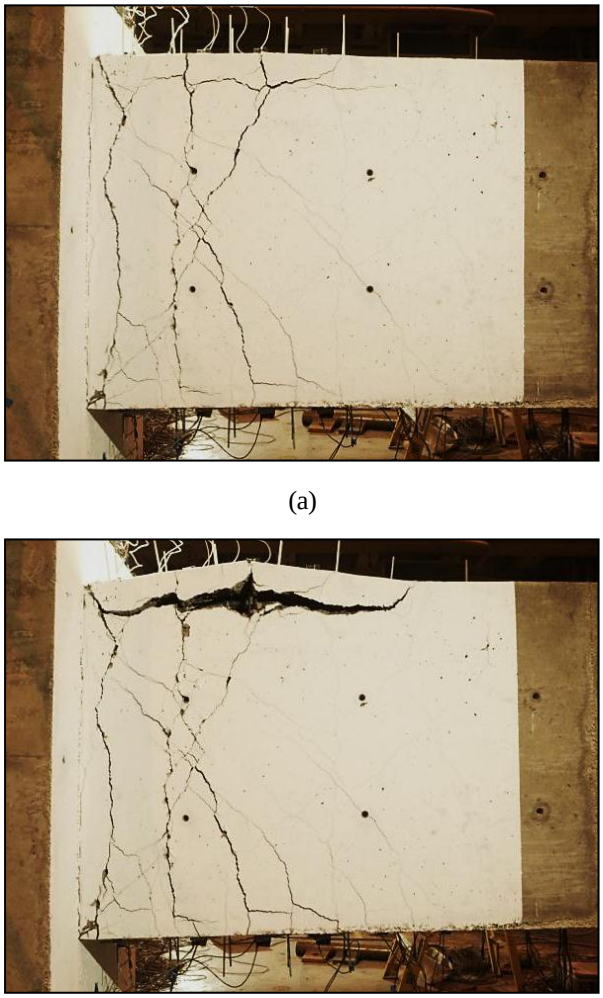


Figure 4 Moment-drift ratio history of Beam 1

The specimen displayed relatively stable response to load reversals with no apparent strength loss upon the completion of the cycles with 1.8% peak drift. During the first cycle with -2.7% peak drift, top longitudinal bars buckled, as shown in Figure 6, opening a "crack cave". This is also evident in the moment-drift ratio curve where a slight instantaneous drop in strength occurred (Figure 4). Buckling of longitudinal bars caused a 30% loss of flexural resistance during a second cycle with peak positive drift of 2.7% (Figure 4). During each subsequent cycle, Beam 1 showed progressive loss of stiffness and strength, with resistance of only 50% of the peak measured resistance during the last displacement cycle. Buckling also occurred in the bottom longitudinal bars, as can be seen in Figure 6(b).

Beam 1 developed large vertical cracks, attributable to flexure, which were spaced at about 250mm in the plastic hinge region. This is close to the spacing of the hoops and as can be seen in Figure 6(b), the locations of the cracks roughly coincide with the hoop locations. Diagonal cracks, attributable to shear, notably increased upon longitudinal bar buckling. The observed shear deformations contributed majorly to the total beam displacement in the last couple of cycles. In the last downward cycle with peak drift of 6.4%, Beam 1 exhibited signs of impending shear failure which can be observed in Figure 7, where the entire specimen moved in a translating mode.



(a)

(b)

Figure 6 Damage State of Beam 1during the First Cycle with Peak Drift Ratio θ = 2.7%: (a) Horizontal Cracks Indicating Onset of Top Longitudinal Bars Buckling (Instantaneous θ = -0.9%), and (b) Buckling of the Top Longitudinal Bars (Instantaneous θ = -2.7%)

3.2 Beam 2 Response Overview

The relationship between the computed resisting moment and the drift ratio for Beam 2 is plotted in Figure 8, with cycles of drift ratio amplitude lower than 0.28% omitted for clarity. Peak resisting moment for this specimen was 3148 kN-m, which was 10% higher than maximum resisting moment of Beam 1. Contrary to the first specimen (Beam 1), Beam 2 showed no evidence of significant strength loss upon completion of all cycles up to and including the peak drift ratio of 2.9%. Pinching of the moment-drift ratio curve became more pronounced in the second cycle with peak drift ratio of 2.9%. During this cycle horizontal cracks associated with initiation of bar buckling and top bar dowel action grew noticeably.



(a)



(b)

Figure 7 Beam 1 at the Maximum Positive Displacement Cycle (Instantaneous θ = 5.5%): (a) Overview, and (b) Plastic Hinge Region with Large Apparent Shear Deformation

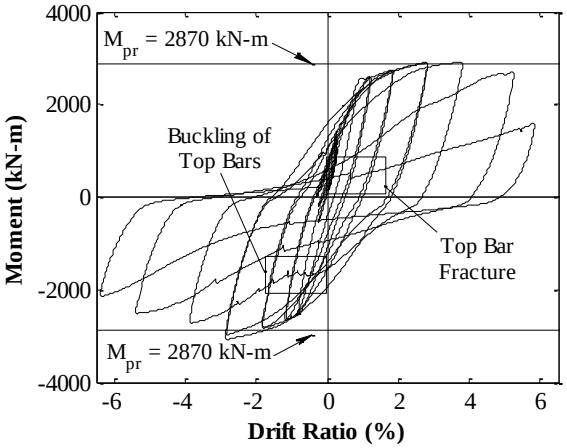


Figure 8 Moment-drift ratio history of Beam 2

Buckling of longitudinal bars in the top face became apparent during the upward displacement phase of cycle with peak θ = -3.9%, (Figure 9[a]). Instantaneous loss of strength can also be noted in the moment-drift curve due to the excessive buckling (Figure 8). Progressive reduction of resisting force followed during the subsequent cycles. Buckling of bottom longitudinal reinforcement became obvious during a cycle with a peak drift ratio of 5.3% (Figure 9[b]).



(a)



(b)

Figure 9 Beam 2 Plastic Hinge Region: (a) Buckling of the Top Longitudinal Reinforcement (Instantaneous θ = -3.9%), and (b) Buckling of the Bottom Longitudinal Reinforcement (Instantaneous drift ratio equal to peak cycle θ = 5.3%)

During the last loading cycle, corresponding to a 5.8% drift ratio, one of the top corner bars fractured at a beam drift ratio of 0.7%. This resulted in a sudden strength loss in the beam of approximately 38%. The peak resistance for this cycle was 43% lower than for the preceding downward cycle and 48% lower than the peak strength for loading in this direction. The condition of Beam 2 at the peak downward displacement is shown in Figure 10.



Figure 10 Overview of Beam 2 at the Maximum Positive Displacement (Instantaneous θ = 5.8%)

3.3 Shear Deformations

The relationship between the resisting shear and the shear deformation in the plastic hinge region of the two specimens is shown in Figure 11. For Beam 1, this relationship is plotted only for the cycles with peak drift ratio less than and including 1.8%, after which buckling occurred and measurements in the LVDTs were distorted. The peak measured shear force was 739 kN, corresponding to a nominal shear stress of 0.83 MPa, or $0.13\sqrt{f_c'}$ MPa using measured compressive strength. Although nominal shear strength V_n computed as defined in the ACI 318 was 1870 kN and more than twice the peak resisting shear value, significant deterioration of shear stiffness is notable as the cycles progress (Fig. 11). During the positive (downward) loading phase in the second cycle with peak drift θ = 1.8% shear deformations almost doubled from those measured in the preceding deformation cycle of the same drift amplitude. The shear stiffness deterioration is also evident in progressively larger pinching in the moment-drift ratio curves for the subsequent cycles of the same displacement amplitude (Fig. 4).

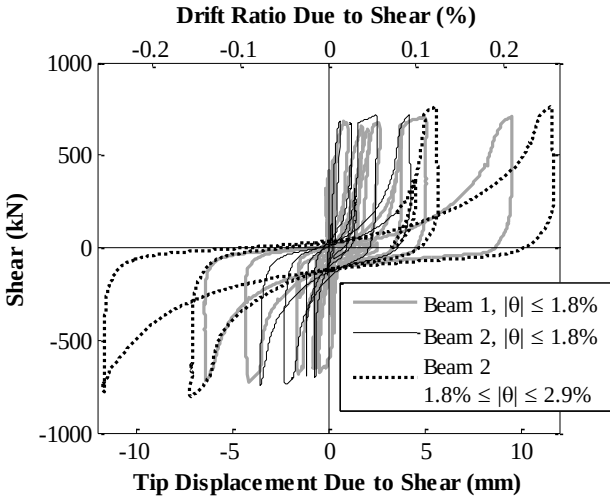


Figure 11 Measured Force vs. Shear Deformation Curve for Beams 1 & 2 and Cycles Preceding the Bar Buckling

The peak measured resisting force for Beam 2 was 805 kN, which corresponds to shear stress of $0.14\sqrt{f_c'}$ MPa, where f'_c is the measured compressive strength of concrete. The nominal shear capacity of Beam 2 computed according to ACI 318 was V_n = 2720 kN. Figure 11 shows the relationship between the resisting shear and shear deformation in the plastic region for Beam 2 for the cycles prior to the observed bar buckling. Shear stiffness degradation can be noted through the progression of cycles. Although Beam 2 was loaded to less than 30% of the computed nominal shear capacity, up to 10% of the total beam displacement was attributable to shear deformations. Beam 2 exhibited smaller shear deformations compared to Beam 1 at the cycles of equal displacement amplitude, which can be seen in Fig. 11. The solid gray and black lines depict approximate shear deformations for Beam 1 and Beam 2, respectively, up to a drift ratio of θ = 1.8%. During the last cycle with this drift ratio, approximate measured shear deformation in Beam 2 was roughly 50% of that measured during the equivalent cycle in Beam 1.

3.4 Measured Crack Widths

Both specimens developed large diagonal cracks associated with shear deformations and vertical cracks associated with flexural deformations. For Beam 2, crack widths were recorded at peak beam tip displacements for a first cycle in a step (refer to Section 2.3 and Figure 3 for definition) and upon completion of a step, that is, when the beam tip was brought back to zero displacement. Crack widths were not systematically recorded during the Beam 1 test; nevertheless, the measurements available provide a valuable insight in its response.

Figure 12 shows the diagonal (shear) crack widths measured at peak positive displacement of each leading cycle in a step. Crack widths in Beam 2 increase linearly with increasing drift ratio prior to cycle with θ = 1.8% amplitude. After this point, the cracks grow at an increased rate, though still in almost linear fashion. Few measurements recorded during Beam 1 test indicate that diagonal crack widths are roughly twice those of Beam 2 for drift ratios smaller than 2.7%. This is consistent with the shear deformation measurements (Figure 11) where Beam 1 displays twice the shear deformations of Beam 2. Largest recorded diagonal crack for Beam 1 was 25mm wide at 3.6% drift ratio, which is the instance when impending shear failure was initiated.

Vertical (flexural) crack width measurements are plotted as a function of peak drift ratio in Figure 13. The size of cracks increases approximately linearly with increasing peak drift ratio for Beam 2. The few measurements recorded for Beam 1 indicate similar trends, but slightly larger crack widths are recorded compared to those in Beam 2. Figure 13 also shows residual crack sizes for Beam 2 which can provide a measure of post-earthquake serviceability level and repairs required. Upon completing all of the cycles with drift ratio smaller than and including 3.9%, the largest residual crack measured on the Beam 2 was 15mm. It should be noted that the absolute largest residual crack was

recorded at the interface and it measured 20mm for this cycle.

3.5 Fixed-End Rotation

Rigid beam (fixed-end) rotation was measured by two pairs of LVDTs placed at the beam interface – two LVDTs were located at the top surface of each specimen and two were located at the bottom surface. The instruments were positioned to span a very short length (50mm) of the beam so as to minimize the flexural and shear deformation components in the measurement. Figure 14 shows the relationship between the fixed-end rotation and the total beam drift ratio for Beam 2. The curve is plotted only for the cycles prior to longitudinal bar buckling. As can be observed, fixed-end rotation contributes to roughly 40% of the total beam tip deflections for Beam 2. A 50% increase in fixed-end rotation is noted for the second cycle of 2.9% drift ratio, which is likely attributable to bond deterioration between the longitudinal reinforcement and surrounding concrete within the anchorage and the beam.

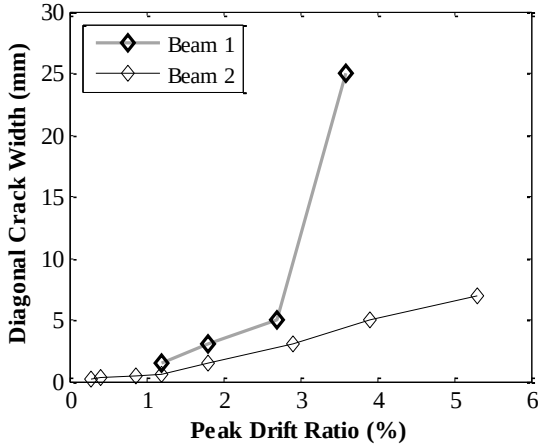


Figure 12 Diagonal Crack Width vs. Drift Ratio for Peak Positive Displacement of Each Cycle

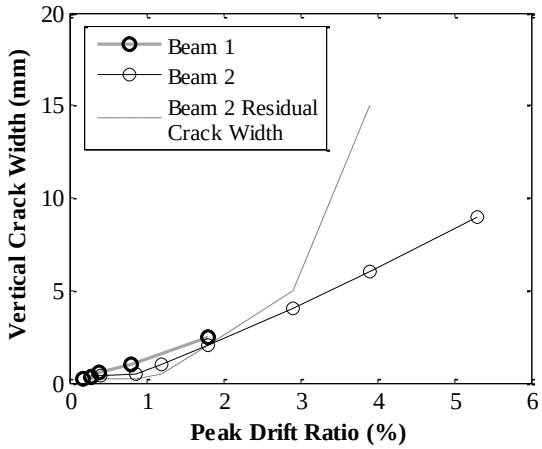


Figure 13 Vertical Crack Size vs. Drift Ratio for Peak Positive Displacement of Each Leading Cycle (Beams 1 & 2) and Residual Crack Size (Beam 2 Only)

Measurements from several instruments in Beam 1 were not acquired due to computer error during the experiment and as a result, only data from one of the top LVDTs measuring the deformation at the Beam 1 interface was recorded. Although this is not sufficient to compute the rigid beam rotations for Beam 1, the data available provide an approximate measurement of interface crack opening which offer an insight into level of fixed-end rotations of the specimen.

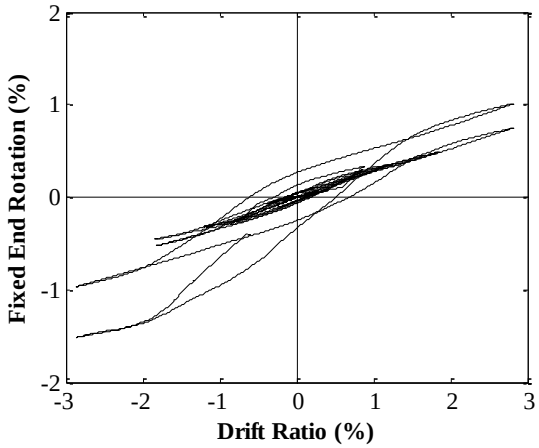


Figure 14 Fixed-End Rotation vs. Drift Ratio for Beam 2

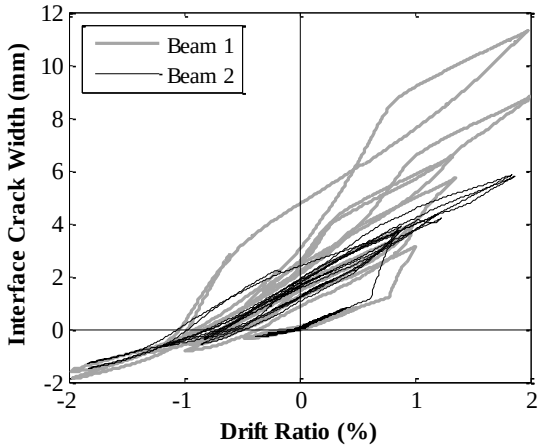


Figure 15 Elongation of LVDT Located at the Beam Interface with Reaction Block (Approximately Equal to Interface Crack Width) vs. Drift Ratio ($|\theta| \leq 2.9\%$)

The variation of the interface crack size with the beam drift ratio in Beam 1 is plotted in Figure 15 and compared to that of Beam 2, by plotting the data from the LVDT positioned at the corresponding location of Beam 2. Measurements from this instrument indicate approximately the same interface crack size when the top surface of beams where the instruments are located is in compression, that is, for the negative drift ratio.

During the cycles with positive drift ratio, interface cracks are similar for cycles with peak drift ratio less than roughly 0.7%. Beyond this point, interface crack size increases more quickly in Beam 1 (Fig. 15). At the maximum positive displacement of second cycle with peak drift ratio $\theta = 1.2\%$, interface crack in Beam 1 is roughly 1.5 times the size of interface crack of Beam 2. Crack widths at

the interface increase in both specimens during the following displacement cycle with θ =1.8% and Beam 1 again exhibits 50% larger interface crack. Upon displacing the beams to the same drift ratio for the second time (θ=1.8%) crack size in Beam 2 remains almost constant, while that of Beam 1 increases by another 30%. In other words, at the peak positive displacement for the second cycle with 1.8% drift ratio amplitude, Beam 1 interface crack was about 1.9 times the size of that in Beam 2. It may be plausible that same relationship holds for the rigid beam rotation attributable to slip between the two specimens, assuming the neutral axis depth at the same beam deflection does not differ significantly between the two specimens.

3.6 Plastic Hinge Elongation

Figure 16 shows the measured elongation in the plastic hinge region for the two specimens. The curve plotted corresponds to the elongation along the centerline of the beam, computed by averaging the elongations measured along the top and bottom face of the beams. This calculation excluded the contribution of bar slip at the interface with reaction block. Measurements of wire potentiometers beyond the point of longitudinal bar buckling were not considered. Interestingly, Beam 1 exhibited smaller growth for the cycles investigated. This may be due to larger contribution of fixed-end rotations for a given drift ratio, compared to Beam 2. Figure 16 indicates that upon completion of cycles with peak drift ratio of 2.9% the elongation of Beam 2 is 25mm.

A rule of thumb for estimating beam elongation is to multiply the beam drift ratio with half the height of the beam (e.g. Kabeyasawa et al., 2000). With this simple calculation, estimated beam elongation corresponding to drift ratios of 1.8% and 2.9% are 11mm and 17mm, respectively. The measurements reported in Figure 16 for the 1.8% drift ratio are almost identical to the estimated elongation. At the first cycle to 2.9% peak drift ratio, the measurements fall within 15% of the calculated value, while for the last cycle to 2.9% peak drift, the elongation measured is 50% higher than what was estimated by this rule of thumb.

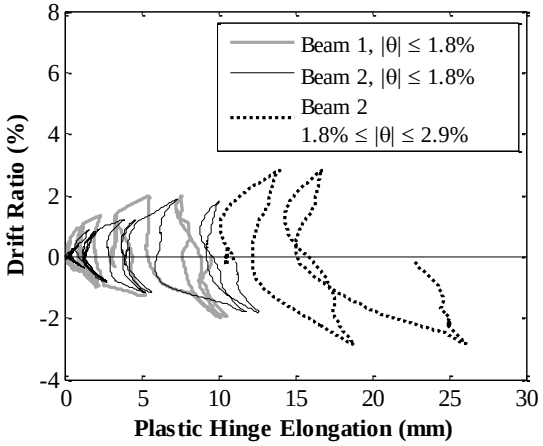


Figure 16 Axial Elongation of Plastic Hinge Region in Beams 1 and 2 Prior to Buckling of Longitudinal Steel

4. SUMMARY AND CONCLUSIONS

Two large reinforced concrete special moment resisting frame beams were tested in the laboratory program under reversed cyclic displacements of increasing amplitude (Section 2.2). Both beams had identical size (1219mm deep and 762mm wide), specified material properties, and size and arrangement of longitudinal reinforcement (Section 2.1). First specimen, Beam 1, contained No. 16 hoop sets spaced at 279mm (Figure 2[a]), corresponding to s_h/d_b = 7.8, and satisfying the requirements of ACI 318 (2008). The second specimen, Beam 2, contained hoops of identical components and reinforcement size as Beam 1, but spaced at 152mm (Figure 2[b]), which corresponds to s_h/d_b = 4.25. The transverse spacing of hoops in Beam 2 conforms to the provisions of ACI 318 (2011). The experimental investigation resulted in the following findings:

1. In both specimens, bar buckling of the longitudinal reinforcement was a primary source of damage initiation and progress. Longitudinal bar buckling initiated during a cycle with a peak drift ratio of 1.8% for Beam 1, while for Beam 2, bar buckling was delayed until the first cycle with a peak drift ratio of 2.9%.
2. Bars located at the top face were the first to buckle for both beams where the local concrete strength was expected to be the lowest, while longitudinal bars along the bottom face buckled in the subsequent cycles. A most likely cause of top bars buckling first, however, was the arrangement of the hoop components. In the absence of the top slab, the presence of the cap ties that closed the hoops at the top of the beam creates a weakness and this should be considered when detailing the transverse reinforcement in beams that are expected to deform into the inelastic range.
3. Beam 2 with reduced hoop spacing was capable of sustaining more displacement cycles and larger displacement amplitude than Beam 1. While Beam 1 lost 38% of its peak resistance during a second cycle to peak drift ratio of 2.7%, which occurred suddenly, Beam 2 strength loss was more gradual and did not occur until the cycles with peak drift ratio of 3.9%.
4. Although the beams had 2-3 times larger nominal shear capacity than the resisting shear induced during the tests, gradual degradation of shear stiffness was noted in both beams. Shear deformations in Beam 2 contributed to roughly 10% of the total beam displacement. Shear deformations measured in Beam 1 were roughly twice those in Beam 2 prior to cycles with longitudinal bar buckling. Larger shear deformations in Beam 1 were also evident from measured crack widths that were roughly twice those recorded in Beam 2. Apparent increase in shear deformations was exhibited during cycles after longitudinal bar buckling occurred, but the data was not quantified due to potential distortion of the instrument measurements.
5. Fixed-end rotations attributable to longitudinal bar slip constituted approximately 40% of the total beam displacement in Beam 2. Beam 1 rigid body rotation was not directly computed, however Beam 1 displayed larger interface crack widths than Beam 2, which indicates larger

fixed-end rotations.

6. During the displacement cycles that caused longitudinal bar yielding, plastic hinge zones of both specimens exhibited axial elongation of similar magnitudes. Beam 1 displayed slightly smaller elongation, possibly due to rigid body rotation contributing to a larger portion of the total beam displacement compared to Beam 2. Simple rule of thumb proves adequate for estimating beam elongation over most of the cycles prior to bar buckling.

Acknowledgements:

The authors acknowledge support from the Pankow Foundation, Webcor Builders, ACI Foundation's Concrete Research Council, and the CRSI Foundation, which provided the capability for constructing the test specimens and conducting the laboratory study. The work was conducted under the auspices of the Pacific Earthquake Engineering Research Center and using the laboratory test facilities of the Department of Civil and Environmental Engineering of the University of California, Berkeley. The study was guided by Robert Tener, Exective Director of Pankow Foundation, and by an expert Industry Advisory Committee. The opinions, findings, conclusions, and recommendations expressed in this publication are those of the authors and do not necessarily reflect the views of the study sponsors or the Pacific Earthquake Engineering Research Center.

References:

American Concrete Institute (ACI) (2008), *Building Code Requirements for Structural Concrete, ACI 318*, Farmington Hills, MI.

American Concrete Institute (ACI), (2011), *Building Code Requirements for Structural Concrete, ACI 318*, Farmington Hills, MI.

Kabeyasawa, T., Sanada, Y., and Maeda, M., (2000), "Effect of Beam Axial Deformation on Column Shear in Reinforced Concrete Frames", *Proceedings of the 12th World Conference on Earthquake Engineering*, Auckland, New Zealand.

Visnjic, T., Panagiotou, M., and Moehle, J.P., (2012), "Numerical Seismic Response of 20-Story Tall Reinforced Concrete Special Moment Frames Design with Current Code Provisions," University of California Berkeley Research Report No. UCB/SEMM-2012/02.

10CUEE CONFERENCE PROCEEDINGS
10th International Conference on Urban Earthquake Engineering
March 1-2, 2013, Tokyo Institute of Technology, Tokyo, Japan

NONLINEAR RESPONSE ASSESSMENT AND SEISMIC RETROFITTING OF REINFORCED CONCRETE BUILDINGS

Jason P. Palacio[1)], Alem Jay A. Pablo[2)], Eric Augustus J. Tingatinga[3)], William L. Mata[4)]

1) Graduate Student , Institute of Civil Engineering, University of the Philippines, Diliman, Philippines
2) Undergraduate Student, Institute of Civil Engineering, University of the Philippines, Diliman, Philippines
3) Assistant Professor, Institute of Civil Engineering, University of the Philippines, Diliman, Philippines
4) Instructor, Institute of Civil Engineering, University of the Philippines, Diliman, Philippines
jason_palacio@yahoo.com, aljempablo@yahoo.com, eating@up.edu.ph, william.mata@yahoo.com

Abstract: This study presents a performance-based design and assessment approach that captures a more realistic response of buildings when subjected to earthquakes and capable of incorporating target performance in the building design. The proposed method utilizes 3D nonlinear dynamic analysis of buildings with the objective of achieving predictable seismic performance and optimizes strengthening that translates to the owners' expectation. The frame model assumes that the nonlinear behavior of the structure is concentrated in plastic hinges, modeled as spring systems located at element ends. The building model is verified via agreement of elastic and nonlinear behavior with that obtained using conventional software. The ground acceleration data used in dynamic analyses is selected to be compatible with the design spectrum calculated at an assumed site. The method allows analysis of progressive collapse providing ease in the assessment of performance and identification of critical members of the building that needs retrofitting. This paper analyzes a building using the proposed method and shows that it is capable of simulating the building's nonlinear response and potential collapse mechanisms. Results show that the increase in member dimensions and/or the use of FRPs addresses the inadequacy and prevents the building to collapse.

1. INTRODUCTION

1.1. Background

In the past couple of years, several strong earthquakes occurred in countries such as Chile, Haiti, China, New Zealand, Japan, etc. that claimed thousands of lives and destroyed millions worth of infrastructure including ruptured roads, toppled bridges, and collapsed buildings. Similarly in the Philippines, a magnitude 6.9 earthquake shook Negros-Cebu area last February 2012 affecting about 64,000 families and causing major damages to roads, bridges, and buildings. The estimated cost of damage to the infrastructure was about 383 million pesos and 25% of it was on buildings. Reportedly, at least 15 thousand houses were either partially damaged or collapsed. Additionally, commercial buildings, government offices, schools, hospitals, malls, and churches were also damaged. The casualties reached at least 200 people, some of which were caused by collapsed concrete and debris. The local government advised a post-earthquake assessment to evaluate the extent of damage and urged to strengthen the existing structural policies as the buildings did not respond well to natural impacts (NDRRMC 2012). Thus, it is imperative to analyze the response of a building during earthquakes and predict its potential collapse mechanism.

This study proposes an approach that is capable of assessing and improving the structural response incorporating performance criteria when the building is subjected to seismic loads with the objective of optimizing safety. Performance based regulation often include performance criteria such as immediate occupancy, life safety and collapse prevention (Krawinkler 2004). Adopting this approach establishes a certain level of client-engineer agreement assuring compliance with the set criteria entailing to a more client oriented engineering as compared to the traditional approach.

Performance based approach in earthquake engineering emphasizes on the simulation of nonlinear response since earthquake loads often push the structure to its inelastic range. Moreover, nonlinear analysis is more reliable in capturing the material degradation or loss of strength thus providing a more realistic representation of structural response.

The proposed method of assessment uses an open-source program capable of performing 3D nonlinear dynamic analysis. This program is originally coded to simulate physically based rigid body systems and can correctly handle dynamics of rigid objects which includes motion, collision, interaction between object, etc. It was further developed to perform earthquake response analysis by introducing nonlinear links

(springs and dampers) with user-specified hysteresis rules.

1.2. Objective and Limitation

This study aims to analyze a residential house that is traditionally designed. The simulation of the house intends to identify the critical points or failing members and observe the potential collapse mechanism. This paper also aims to present the applicability of the method to strengthen the said building after the assessment via retrofitting assuming that the house is existing and redesigning if it is not yet constructed.

The study focuses on the collapse prevention of the building as its performance target. The analysis will only deal with the flexural behavior and failure of the structural members. It follows that the strengthening of the building will focus on the flexural capacities of the failing members.

1.3. Significance of the Study

Strengthening of identified critical members prior to earthquake is a necessary intervention to prevent damage to properties, personal injuries, and cost of repair. The end beneficiary of the study would be the owner of building since a thorough evaluation which gives them the knowledge on how strong their building is or how it would respond to earthquakes. Additionally, strengthening scheme will be prepared should they choose to implement in the future to improve their building and prevent potential collapse.

1.4. Related Study

Traditional design methodologies are being adopted in evaluating existing buildings. Using the strength based approach, the condition of the buildings are analyzed and checked if deficiencies are found. The deficiencies are determined by comparing members' capacity to the demands from the analysis. In seismic analysis, structural codes specify that the nonlinearity of elements should be considered. Current codes provide minimum provision for design with the objective of safeguarding against earthquake induced structural failures and loss of life, not to limit damage or maintain function (NSCP 2010). These current codes are being developed to eliminate a level of ambiguity particularly in quantifying damage states (UC Berkeley 2003).

Sung et al., (2006) used performance-based damage assessment on RC buildings. In general, performance-based earthquake assessment has the objective of determining the nonlinear performance of a building under different scales of strong earthquakes for safety and retrofitting considerations. They discussed several approaches for performance-based seismic evaluation provided by Applied Technology Council (ATC), Federal Emergency Management Agency (FEMA), etc. and extended these approaches to assess a low rise RC building through the results of pushover analysis and hysteresis relations.

Modelling Approaches

Giberson (1976) introduced nonlinear rotational springs at locations where bending moment reaches plasticity. Under earthquake loads, he used these springs at member ends assuming that inelastic deformation are concentrated at these locations and the middle part remain elastic. The spring stiffness properties were derived from the material properties and geometry of the member. This simple model is very viable to nonlinear analysis since any hysteresis relation can be assigned to the springs. The results using this method was found to be reasonable for a relatively low rise frame structure wherein the inflection points of the members does not deviate much from the middle.

Discrete element models overcome the variability of stiffness along member. This method sub-divides the member into several segments. Wen and Janssen (1965), presented discrete spring model in analyzing plane frame. It consists of segmented rigid elements connected by springs where flexibility is lumped as tributary basis where shorter segments are recommended in region of high bending moment.

Numerical approximations are expected to be more reliable as the number of segments or sub-elements increase. Most common numerical analysis method in structural analysis is the Finite Element Method (FEM). In FEM, the structure is represented by a finite number of elements connected by pre-selected number of nodal points. FEM's applicability in structures includes static, dynamic, linear and nonlinear analysis. In spite of its accuracy and wide range of application, it lacks the ability to deal with the separation between elements when subjected to large deformation since it assumes that the nodes connecting two or more elements have same displacements. Hence, it cannot simulate the potential collapse of the structure.

Meguro, K. and Tagel-Din, H. S. (2002) developed the Applied Element Method (AEM) to simulate highly nonlinear behaviour of structure under static and cyclic loadings. It discretizes the member into an assembly of elements connected by normal and shear springs which represent stresses and deformation. This method is capable of simulating large displacement, separation of elements and progressive collapse.

2. METHODOLOGY

The general procedure of the study is shown in the diagram in Figure 1 and is explained in the subsequent sections.

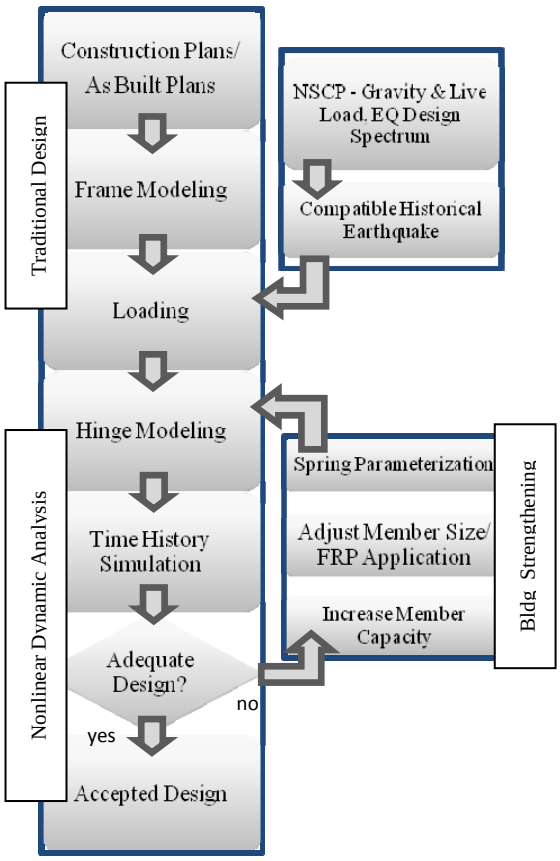


Figure 1. Conceptual Framework

2.1. Modelling

The building will be modeled as beam column space frame with inelastic hinges situated at end of each member to capture the concentration of plasticity of the material as shown in Figure 2

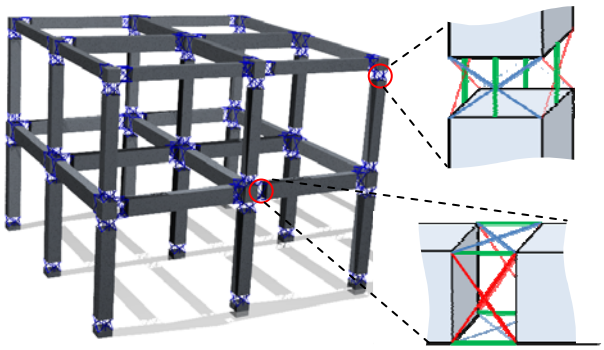


Figure 2. Proposed Building Model and Spring Configuration of Plastic Hinge at End of Beams and Columns

These hinges are modeled as a spring system capable of simulating the axial, shear, and flexural behavior of the members. The spring system configuration for beams consists of twelve springs which includes four parallel springs (axial spring in green) connected at each corner and two diagonal in-plane springs at each of the four sides of the beam (along the height and base of the member in red and in blue respectively.). On the other hand, spring configuration for columns is similar to that of beams but the four parallel springs are connected to the mid-edge of the member. This is to isolate the biaxial moment behavior of the column.

These spring configuration are optimally chosen to minimize the number of spring parameters to be determined in the succeeding section. Each spring has a load-deformation behaviour that may be elastic, elastoplastic, bilinear, tri-linear, etc.

2.2. Loading

Gravity and live loads are established using the information about the building and the minimum loads specified by the National Structural Code of the Philippines (NSCP).

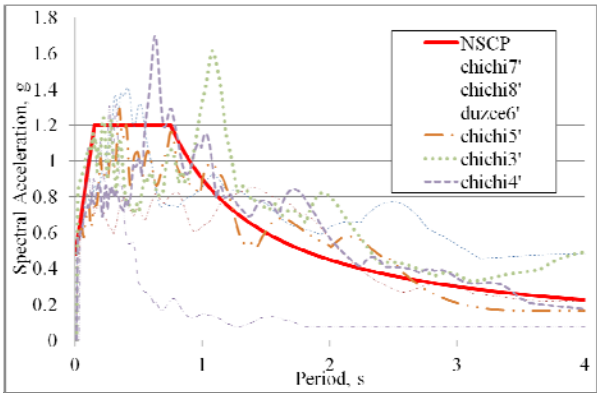


Figure 3. Selection of Design Spectrum-Compatible Earthquake Ground Motion used in Analyses

Earthquake loads are inputted as three dimension time histories and converted to inertial mass lateral loads. The selection of historical earthquake to be used is based on its compatibility with the design response spectrum provided by the NSCP using the data specific to the site, proximity to the fault line and soil conditions. In this research, the site is assumed to be on the University of the Philippines Diliman campus since it is relatively near the West Valley fault line which is a major fault found in Metro Manila. The response spectra of several earthquakes, namely 1995 Kobe, 1989 Loma Prieta, 1999 Chi chi, 1999 Duzce, 1979 Imperial valley, etc. (PEER 2010) were superimposed to the design spectra of the site. For brevity, only few earthquakes that is relatively close to the design spectra are shown on Figure 3. The repetition of Chichi earthquake in the figure corresponds to the data recorded from different stations. From this figure, it can be seen that chichi5 is a good representative of the design spectrum, hence, it will be used as the earthquake load in the succeeding time history analyses.

2.3. Spring Parameterization

Spring parameters are determined so that the resultant load-deformation curve is equivalent to the members' actual moment curvature depending on the section and reinforcements at the location of the hinge.

Beams

The assumptions in solving the spring parameters for beams are the following:

1. The load-deformation curve of the parallel (or longitudinal) springs under monotonic load is defined to be bilinear. Diagonal springs along the height is defined to be elastoplastic. Diagonal springs along the base are defined to be elastoplastic or elastic depending on the value ultimate point of deformation.
2. Actual beams' moment curvature relation is defined to be tri-linear having three critical stages namely, cracking point, yielding point, and ultimate point.
3. Deformation of the spring system is assumed to behave same as shown in Figure 4 when subjected to flexural loads.



Figure 4. Assumed Spring System Deformation under Flexure

4. Cracking of concrete of the actual beam is simulated by the simultaneous yielding of the parallel springs.
5. Yielding of the actual beam is dictated by the simultaneous yielding of the diagonal springs along the base.
6. Failure of the actual beam at ultimate point corresponds to the simultaneous failure of all springs.
7. Primary slope for the diagonal spring along the height depends on the vertical load to minimize static displacement.

Using these assumptions, all spring deformation parameters can be solved independently. Stiffness parameter can be also solved given the assumed loads transferred to the beam. The remaining unknown stiffness parameters are determined via system of linear equations by using the flexural deformation assumption (in Figure 4) and equating the sum of moments induced by each springs to the actual values of the flexural moment.

Columns

1. Similar to the beam, the load-deformation curve of the parallel springs along the base and height are defined to be bilinear but with different set of parameters. Diagonal springs along the base and height are both defined to be elatoplastic but also with different set of parameters.
2. Actual columns' moment curvature relation for both axis are defined to be tri-linear having three critical stages namely, cracking point, yielding point, and ultimate point.
3. Cracking of actual column to bending along x is dictated by the simultaneous yielding of the parallel springs along the base, thus
4. Cracking due to bending along y is controlled by the simultaneous yielding of the parallel springs along the height, thus
5. Yielding of actual column due to bending along x is simulated by the simultaneous yielding of the diagonal springs along the base.
6. Yielding of column due to bending along y is dictated by the simultaneous yielding of the diagonal springs along the height.
7. Failure of the actual column at ultimate point corresponds to the simultaneous failure of all springs.

Similar to the beam spring parameterization, all column springs' deformation parameters can be solved independently using the column assumptions in section 2.3(3)-(7) while the stiffness parameters are determined using summation of moments.

2.4. Time History Simulation and Building Assessment

The building model will be subjected to the earthquake load selected in section 2.2 in different directions to deal with the uncertainty of ground motion direction. It will be subjected to an incidence of 0°, 45°, 90°. This procedure will confirm the presence of critical member/s that can be used to check whether or not these members are the same as identified using static nonlinear pushover analysis.

After entering the building configuration data, i.e. node incidences, member connectivity, member dimension, rebar information, superimposed loads, and time history data, the program will internally solve for the displacement of each object at a time step as well as the strains induced per springs. The method will generate a graphical simulation showing the frame model being subjected to seismic loads for each direction. It will present a realistic shaking and readily observable interaction of members and structural response.

As the simulation progress, the state of the springs are identified for every critical points such as cracking, yielding and, flexure failure. The accumulation of yielding or failing springs within a joint will represent the state of the corresponding member. The sequence of failing members will be examined to identify the critical stages of the building's collapse mechanism. This procedure can also be used to efficiently isolate the members that need strengthening.

2.5. Retrofit/Redesign

Based on the assessment, the identified failing members are locally strengthened by adjusting the springs parameters. The amount of adjustment will be based on the increase in the actual members' capacity which correspond increase in member size and/or additional reinforcement which is applicable for newly designed building wherein the structural plans can still be revised. In case of an existing building, Carbon Fiber Reinforced Polymers (CFRP) will be used as the retrofit scheme to strengthen the members. The calculation will use CFRP specification in the will follow the provisions in ACI 440 (Guide for the Design and Construction of Externally Bonded FRP Systems for Strengthening Concrete Structures). The increase in capacity will be based on the amount of material used and its specification (FYFE Co. LLC. USA 2004). The enhanced building will then be simulated again to test whether the improvement is adequate and able to prevent collapse.

3. RESULTS AND DISCUSSION

3.1. Building and Moment Curvature

The building that will be used has 3 bays in *x* and *z* directions and has 3 levels. Column to column spacing is 3.5m and floor to floor height is 3m. All columns (C1) have 300x300mm section with 12-d16mm. Beams' specifications are summarized in the table below.

Table 1 Beam Schedule

Designation	Dimension	Top/Bottom Bars
B1 (2F Interior Beams)	300x400mm	6-d16mm/ 3-d16mm
B2 (2F Perimeter Beams) (Roof Interior Beams)	250x400mm	4-d16mm/ 3-d16mm
B3 (Roof Perimeter Beams)	200x300mm	3-d16mm/ 3-d16mm

The rendered model is shown in the Figure 2 illustrating the beams, columns, and the springs located at the ends of each members. The derived spring parameters for B1 and are shown in Figure 5 which follow the spring assumptions in section 2.3.

To check whether the spring system behaves like the member, its flexural response is calculated and is plotted with the actual section's moment-curvature diagram. Figure 6 illustrates moment-curvature relations of each spring, of the spring system, and of the actual section for the member B1. It can be seen here that response of the spring system agrees very well to that of the actual section. Also, the critical strain points on the moment curvature of the spring system coincides to the corresponding yield points of each springs as presented in section 2.3.

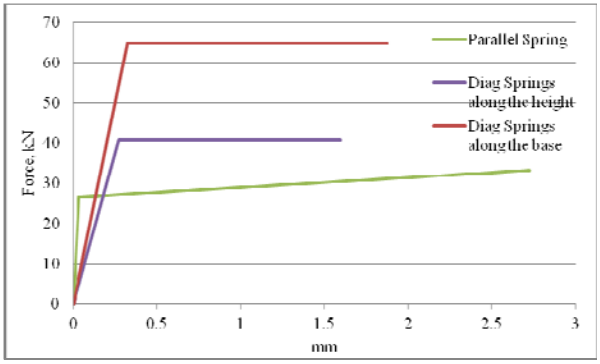


Figure 5. Sample Nonlinear Spring System Parameters of an RC Beam

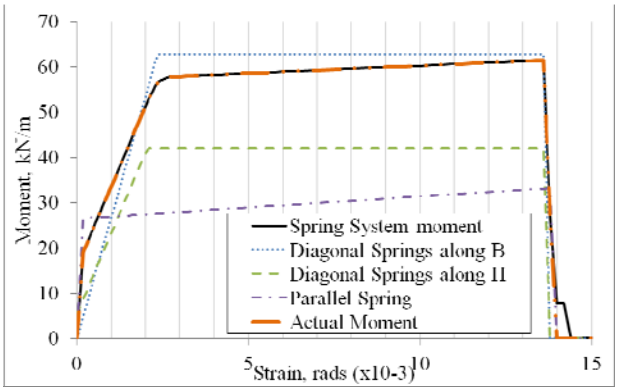


Figure 6. Agreement of Assumed and Computed Moment - Curvature Relations of a Plastic Hinge

3.2. Numerical Validation

1. Hysteresis Test

The observed hysteresis of the spring system generally follows the slopes of the curve envelope as the curvature increases. Figure 7 shows the general behavior of the spring system under increasing cyclic load. The figure also shows that the calculated moment curvature of the section (broken line) envelopes the hysteresis.

If unloading occurs before it reaches the cracking curvature point, it moves along the first slope hence behaving elastically. If the rotation reverses where the curvature is in between cracking point and ultimate (failing) point, the unloading slope is equivalent to the first slope and then followed by the second slope once it covers double the magnitude of the cracking point value. It will then follow the third slope when it attains a curvature magnitude equal to the yielding value from the unloading point. In cases where reloading takes place after unloading, the reloading slope will always track the first slope. If the reloading occurs before double the cracking point (along the first slope), it will traverse its existing path until it reaches its original unloading point. However, if reloading occurs after this point (along the second or third slope), it will not trace its existing path but will follow the first slope and then the second slope before reaching the unloading point. The spring system will follow this rule in any initial loading direction or in any load reversal.

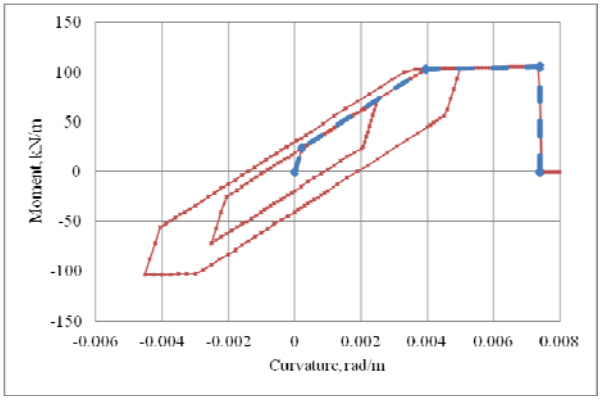


Figure 7. Hysteresis Behavior of a Plastic Hinge with assumed Nonlinear Spring Parameters

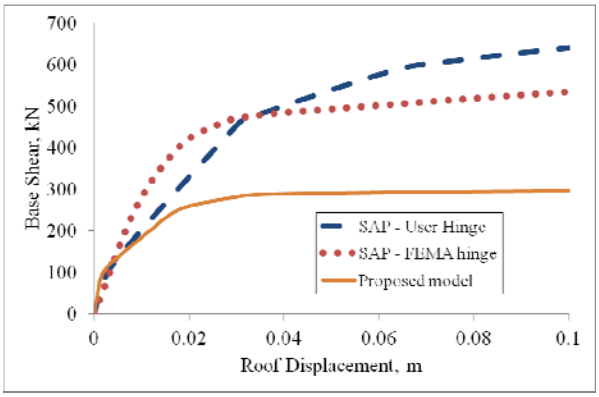


Figure 8. Comparison of Pushover Curves of Proposed Building Model and Corresponding SAP2000® models

2. Pushover Test

To evaluate the response model, a parallel runs are conducted by creating the same building configuration in SAP2000®. Two SAP2000® models are created differing only in the inelastic hinge properties, one has the default FEMA property and the other one has user-defined property same as in the proposed model. Push-over curves are derived for all models and is shown in Figure 8. It can be observed from the figure that in small displacements, the models are elastically behaving and relatively close to each other. The proposed model a steeper initial slope however it yields earlier. The figure shows that the strength of the proposed model is underestimated but the yield points for all models are relatively close. This may be due to the spring deformation assumptions made in section 2.3 where the diagonal springs contribute to the flexural resistance of the spring system. The steeper initial slope may be the effect of the rigidity of each member and the concentration of flexibility at the ends of the member, thus consistent to the general flexibility assumption.

3.3. Simulation Output

Simulating the model under 1999 Chi-chi earthquake in three incident directions, the program produced the output scenes shown in Figure 9. This figure shows the progression of the earthquake response with an incident angle of 45°. It can be observed here that springs start to yield 7 seconds after the earthquake started which coincides to the first significant increase in ground acceleration of Chi-chi time history data. This yielding of springs corresponds to the cracking and then steel yielding of the actual members. From here onwards, the number of yielding springs steadily rises and as the earthquake reaches its peak ground acceleration at about 10 seconds, the springs of the first floor columns begin to reach their ultimate deformation limit hence the failure of the columns. It can also be observe here the presence of yielding springs at the roof level due to amplified vibration causing larger forces at that level. On the 13th second, all springs connected to the first floor columns are at its ultimate point as they cannot resist lateral force anymore resulting to the full collapse of the building.

Shown in Figure 10 is a summarized chart of the number of elastic, yielding and failing springs colored as shades of green and red respectively describing the state of the springs at each floor per time-step as illustrated in Figure 9. The x-axis represents the number of springs, while the y-axis pertains to the beams and columns at a specific time frame. It can be seen here the formation of yield springs on beams and columns on all floors after 7 seconds. Failing springs are formed after the 10th second on the first floor columns and increases up until the full failure just before the 14th second. It was observed that the first columns that exhibited failure are the ones located at the mid and center columns followed by the failure of the corner columns.

For the cases of 0° and 90° earthquake incidence, no collapse is observed during the entire duration of the earthquake. But similar to the previous case, the yielding of springs starts on the 7th second. Also, there are failing springs formed at the first floor columns after the 10th second however it is not enough to generate a collapse.

3.4. Building Strengthening

1. Redesigning of Members

To address the failure of several members signified by the connected springs failure, the member dimension and/or the number of rebars is increased to adjust the springs' capacity. The adjusted columns are the ones identified from the previous section. Initially, the mid and center columns are adjusted from 300x300 mm to 350x350 mm while the corner columns are left unadjusted. This first trial also led to a full collapse. Continuing this iteration of redesigning, the final dimensions that attained a stable output is 400x400 mm for the mid and center columns and 350x350 mm for the edge columns.

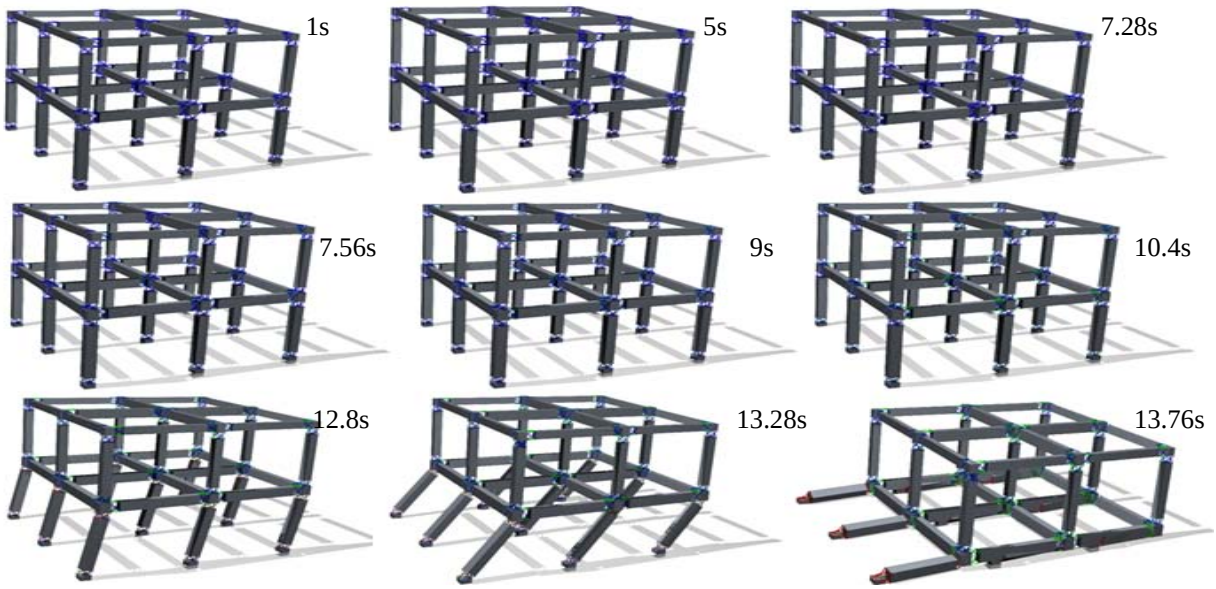


Figure 10. Progressive Collapse Sequence of a Two-Storey RC Building Subjected to 1999 Chi-chi Earthquake

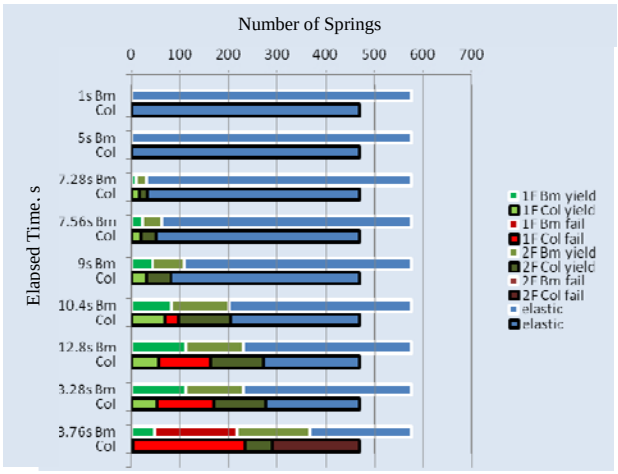


Figure 11. Progress of Yielding and Failure of Springs in Beams and Columns of Sample Building

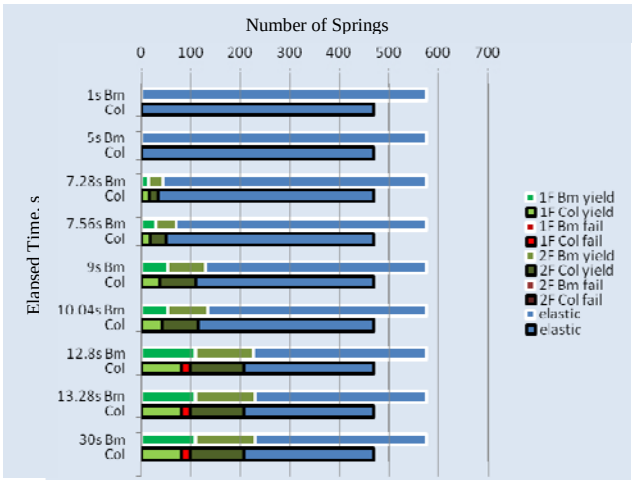


Figure 9. Progress of Yielding and Failure of Springs in Beams and Columns of Redesigned Building

Shown in Figure 11 is the state of springs of the improved building at the specified time frame. It can be seen here the significant decrease in the number of failing springs as compared to the original model. The presence of failing springs indicate the occurrence of damage on the member but insufficient to induce collapse even after 30 seconds of earthquake.

2. Retrofit by CFRP Application

Generally, the procedure of the design based on ACI 440 is similar to that of the reinforcing steel but with reduction factors to account for the material deterioration, bond-slip prevention between interface, and environment exposure. The assumptions used in the design is that there is a perfect bonding between different materials, shear deformation of the adhesive layer is neglected and it has linear elastic stress-strain relationship to failure. Figure 12 shows the computed capacities of an unreinforced section and sections with 1 to 5 plies of CFRP reinforcement.

To determine the amount of CFRP needed, the ultimate capacity of the composite section is derived from the improved final section calculated in the previous section. The calculated capacity of the 400x400 mm and 350x350 mm column is 178.9 kNm and 144.3 kNm respectively. The existing column will require 5 plies of CFRP to be equivalent to that of the 400x400 mm column while 3 plies are required to that of the 350x350 mm column. Each ply is 1 mm(0.04in) thick having a width equal to the width of the member. Therefore, the retrofitted columns will be 300x300 mm with 5 plies each face for the mid and center columns and 300x300 mm with 3 plies each face for the edge columns.

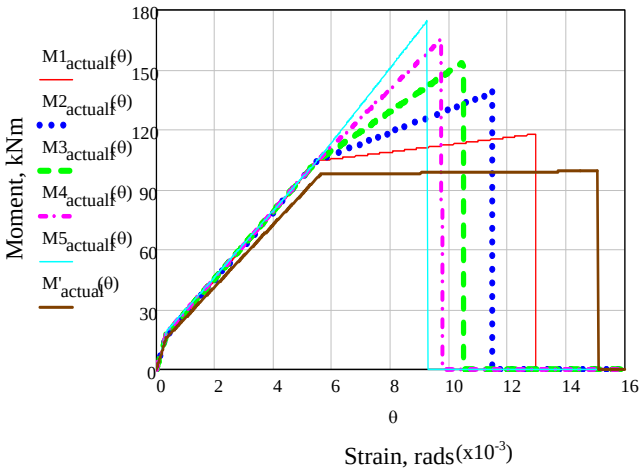


Figure 12. Improvement of Capacity of Beam Section with CFRP Reinforcement

4. CONCLUSION

The computed moment-curvature relation of the actual section is derived using the general concrete theories and this is the main basis of each of the spring parameters that makes up the member hinges. The calculated moment-curvature relation of the spring system is established to be virtually equivalent to that of the actual section. Also, this relation envelopes the hysteresis behavior of the spring system. The general behavior of the hysteresis traces the first slope at any point during unloading and/or reloading and then changes its slope once the deformation reaches its corresponding limit, namely the magnitude of the cracking and yielding curvature point. In small displacements, the test models in SAP2000® and in the proposed method are comparable in the elastic region. Push over curves substantiate the difference in lateral resistance and verify the effect of the spring system deformation assumptions. Also, the initial slope of push over curve derived from the proposed model demonstrates the distribution of the model's flexibility and shows the consistency using the one-component member model.

The time history analysis of the response confirms that the building model is inadequate when subjected to 1999 Chi-chi Earthquake and this earthquake load is chosen among others based on its compatibility with the design spectrum provided by the NSCP. The simulation proper for the 0° and 90° incident earthquake produce numerous members with yielding reinforcing steels indicated by the yielding of springs but no collapse is observed. However for the 45-degree incident case, full collapse is generated in 14 seconds of earthquake. The columns and beams exhibit yielding and failing as the ground acceleration increase significantly. The inadequacy is addressed by revising the member dimension or applying CFRP to increase the capacity of the section. The improved building requires 400x400 mm mid and center columns and 350x350 mm edge columns from the original 300x300 mm section. Using CFRP on the other hand, the composite section requires 5 and 3 plies per face of 1mm thick CFRP at the mid and center and edge columns, respectively.

References:

Wen, R. K. and Jansses, J. G. (1965), Dynamic Analysis of Elasto-Inelastic Frames, *Proceedings, 3rd World Conference on Earthquake Engineering.*

Giberson, M. F. (1967), "The Response of Nonlinear Multi-story Structures subjected to Earthquake Excitations", *Report in Earthquake Engineering Research Laboratory, California Institute of Technology.*

American Concrete Institution (2002), Guide for the Design Construction of Externally Bonded FRP Systems for Strengthening Concrete Structures ACI 440.2R-02

Otani S. (2002), "Nonlinear Earthquake Response Analysis of Reinforced Concrete Buildings", *Lecture notes in Department of Architecture, University of Tokyo* .

UC Berkeley (2003), "Basic Concepts in Performance Based Engineering", Notes in CEE227 Earthquake Engineering.

FYFE Co. LLC. USA (2004), "Tyfo Fibwrap System", *Brochure distributed by EC Structural Composites Inc.*

Krawinkler, H., and Miranda, E. (2004), "Performance-Based Earthquake Engineering : from Engineering Seismology to Performance-Based Engineering", Edited by Bozorgnia, Y. and Bertero, V. V., CRC Press.

Sung, Y. C., Su, C. K., Wu, C. W., and Tsai, I. C. (2006), "Performance-Based Damage Assessment of Low-Rise Reinforced Concrete Buildings", *Journal of the Chinese Institute of Engineers*.

Tingatinga, E.A. (2008), "Three-Dimensional Seismic Damage Simulation Using Rigid Body-Spring Method", *The Open Construction and Building Technology Journal*, 116-123.

Pacific Earthquake Engineering Research Center (2010), PEER ground motion database, *http://peer.berkeley.edu/peer_ground_motion_database/*

Association of Structural Engineers of the Philippines (2010), National Structural Code of the Philippines (NSCP) Vol.1 2010, ASEP.

National Disaster Risk Reduction and Management Council (2012), NDRRMC Updates, Effects of the 6.9 Earthquake in Negros Oriental, SiteRep no.22.

10CUEE CONFERENCE PROCEEDINGS
10th International Conference on Urban Earthquake Engineering
March 1-2, 2013, Tokyo Institute of Technology, Tokyo, Japan

Experimental Evaluation of Out-of-Plane Wall-to-Beam Connections under Cyclic Loading

Saman Abdullah[1], David Naish[2], Nagi Abo-Shadi[3]

1) Graduate Student, California State University, Fullerton, CA, USA
2) Assistant Professor, California State University, Fullerton, CA, USA
3) President, Structural Engineering Center, Inc, Brea, CA, USA
samaali@csu.fullerton.edu, dnaish@fullerton.edu, nagi@structuralec.com

Abstract: Connections between gravity framing (non-participating in resisting seismic forces) and the lateral force-resisting system need to be given considerations in building design. Studies of seismic behavior of the out-of-plane wall-to-beam joints are limited in literature. Furthermore, ACI 318 provisions with regard to seismic detailing of these joints are incomprehensive. The common practice is to provide a concealed column and/or a concealed beam where a gravity beam frames into a web of a structural wall. This research has a twofold objective. First, it is meant to assess the performance of these joints. Second, it will assess the impact of concealed columns on the overall performance of these joint. To accomplish these objectives, three half-scale reinforced concrete interior beam-wall joint specimens will be tested under quasi-static cyclic loading to simulate earthquakes. All test specimens have the same level of axial load, $0.2A_g$ f'c. These walls are designed to satisfy ACI 318 seismic provisions for structural walls loaded in the in-plane direction. These beams are designed as gravity members based on ACI 318 provisions.

1. INTRODUCTION

Where a beam frames into a web of a seismic structural wall (Fig. 1), it is common practice to provide a concealed column that has the wall width. Structural engineers consider that this addition would increase the wall's axial load capacity and the joint strength. The effect of these members on the performance of the joint and out-of-plane behavior of the wall needs further study. With a cursory review of literature with regards to reinforced concrete joints, it can be seen that the focus of the vast majority of research has been on the performance evaluation and design of beam-column joints and slab-column joints. Great advance has been made worldwide on their seismic design. Very little attention is given to the seismic performance of out-of-plane wall-beam joints. Furthermore, the ACI 318 seismic provisions are incomprehensive with regards to detailing of these joints. ACI 318 seismic provisions require members that are not designed as seismic force-resistant members to be designed and detailed for the demand imposed by the design displacement, which is inelastic displacement that the structure would experience during an earthquake. This implies that these joints should be designed to withstand forces imposed by the design displacement.

It appears that the only experimental studies done on out-of-plane beam-to-wall (or beam-wall like column) joints were conducted by Li et al (2002) and Li et al (2009). Li et al (2002) performed quasi-static tests on four full-scale non-seismically and limited seismically detailed joints. Two of the specimens were out-of-plane wall-like column-to-beam joints with column to beam width ratio of 3. They studied the influence of joint transverse reinforcement, lap splice of longitudinal beam and column reinforcement. Their test results showed that due to presence of limited joint transverse reinforcement, displacement ductility increased by nearly 50%. Also, the joint shear stress in these interior joints were $0.15f'_c$.

Li et al (2009) carried out experimental tests on six full-scale interior beam-to-wall-like columns and beam-to-wall joints. They investigated the impact of compressive axial load level on the overall performance of the joints. The results indicated that the axial load did not greatly influence the energy dissipation capacity, stiffness, and nominal shear in the joint but caused significant bond deterioration through the joint and, consequently, reduced lateral load capacity. Their test results also showed that these joints can withstand 2.0% drift ratio without significant strength and stiffness degradation.

Even though there have been some studies conducted on performance evaluation of non-ductile beam-column joints, the results may not reliably been considered since the joint strength deterioration is greatly influenced in relative thin walls due to bond slip (Kurose et al, 1988).

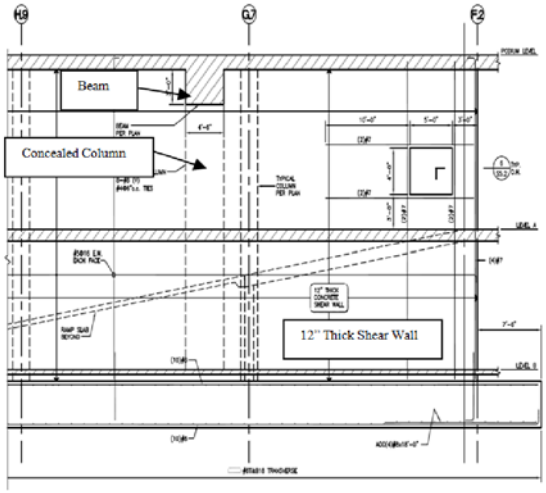


Fig. 1- Typical framing detail for concealed column

2. EXPERIMENTAL PROGRAM

2.1 Test Specimen Description

Three one-half scale interior out-of-plane wall-to-beam specimens, hereafter referred to as WB1, WB2, and WB3, are being constructed and will be tested under quasi-static cyclic loading. All the specimens have the same geometry but different wall sectional reinforcement and are subjected to the same level of axial compressive load, $0.2A_g f'c$. The length of the wall was controlled by the test setup space limits. The ratio of wall length to beam width is 3 for all test specimens. Each test specimen is a part of a structural wall system, where structural walls are used to resist earthquake induced lateral loads, with story height of 6' (1.83m) and span length of 10'-6" (3.2m)(Fig 2) to represent one-half scale connections of a building having 12' (3.658m) story height and 21' (6.40m) beam span length. Each test specimen consists of a 6" (152.4mm) thick, 24" (609.6mm) long, and 72" (1828.8mm) tall wall and 8"x13" (203.2x330.2mm) beams framing into the web of the wall. Fig. 2 shows the schematic illustrations of the specimens.

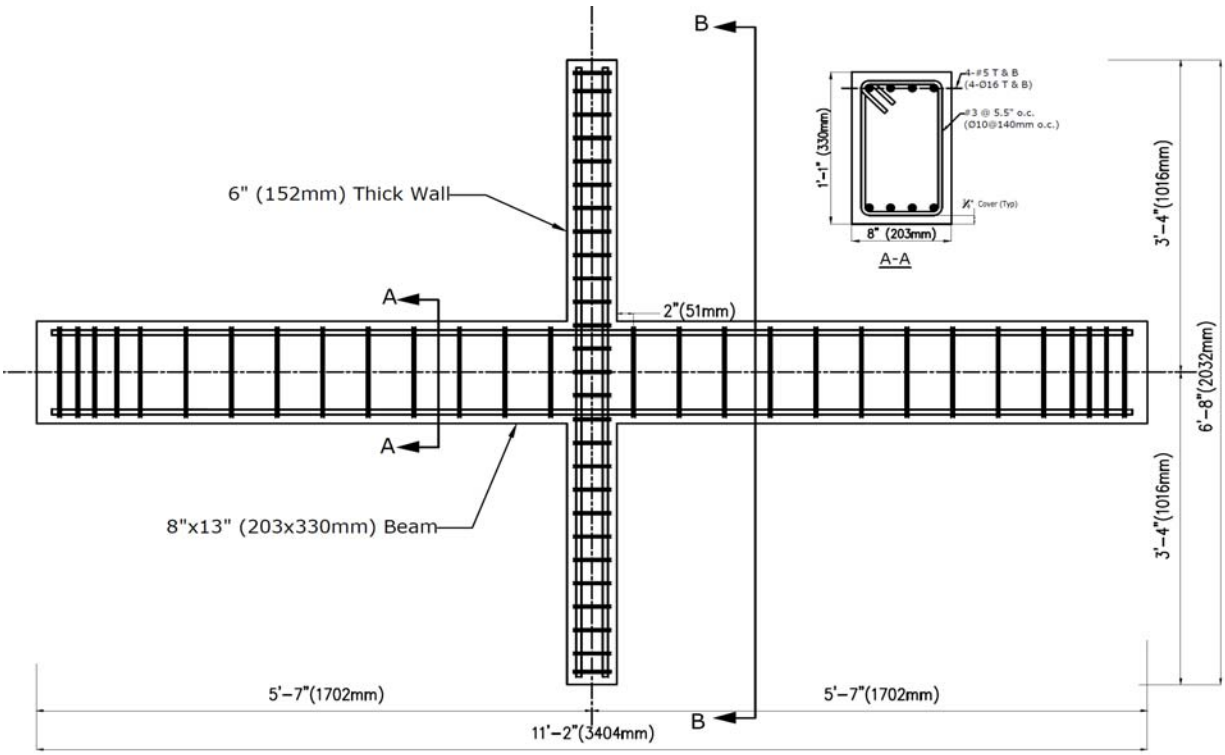


Fig.2- Test Specimens: WB1, WB2, and WB3

The first specimen, WB1, is a bare reference wall-beam connection, meaning that the joint is not strengthened with a concealed column. Furthermore, the joint has no lateral reinforcement except the wall horizontal reinforcement (Fig. 3). The second test specimen, WB2, is similar to WB1, except that a concealed column is made out of the web vertical bars, (Fig. 4). The concealed column is designed as gravity column to support the axial load with cross sectional dimension of 6"x7" (152.4x177.8mm). For WB3, in addition to the reinforcement provided in WB1, a concealed column is incorporated.

The walls were designed and detailed, in the in-plane direction, to satisfy the ACI 318 seismic provisions for structural walls. The wall web vertical reinforcement is the only parameter in the test specimens. All the test specimens have the same boundary elements in terms of both geometry and reinforcement. The first specimen, WB1, is a regular structural wall with two 6"x7" (152.4x177.8mm) boundary elements reinforced with 4-#5 (4-Ø16) bars each. The concrete in the boundary elements is confined using #3 (Ø10) seismic ties at 3" (76.2mm) on center. to satisfy requirements stipulated by ACI 318, as shown in Fig. 3. The web is reinforced horizontally and vertically using two curtains of #3 (Ø110) bars. Horizontal reinforcement is provided at 4.5" (114.3 mm) on center, resulted in a reinforcement ratio of 0.0081, whereas two bars are provided for vertical reinforcement per each face, yielding a reinforcement ratio of 0.0073. The web vertical bars are located outside the beam cage. Two horizontal wall bars pass through the joint core on each face of the wall, Fig 3. In WB2, the wall web vertical bars (4-#3 (4-Ø10)) are used as a concealed column passing through the joint core. The concealed column is transversely reinforced with #3 (Ø10) bars at 5" (127mm) on center with two ties located inside the joint. As for WB1, two of the web horizontal bars are passing through the joint, Fig. 4. Wall reinforcement in WB3 is identical to WB1 with two differences. First, a 6"x7" (152.4x177.8mm) concealed column, reinforced with 4-#4 (4-Ø12) longitudinal bars and #3 (Ø10) ties at 5" (127mm), is incorporated into the wall. Second, the two web vertical bars on each side are displaced slightly towards the boundary elements, Fig. 5. The concealed column longitudinal bars pass through the beam cage. As for WB2 and WB3, two of the web horizontal bars are passing through the joint.

The objective of this study is to observe and document the cracks and damage in the joint and its vicinity. Thus, the beams were designed to ensure that the majority of the damage and cracking would occur in the joint region and the wall near to the joint. The beams represent gravity beams in structural wall building systems. All test specimens have the same beam longitudinal and transverse reinforcement, 4-#5 (4-Ø16) bars at top and bottom and #3(Ø10) ties spaced at 5.5" (139.7mm) on center, respectively.

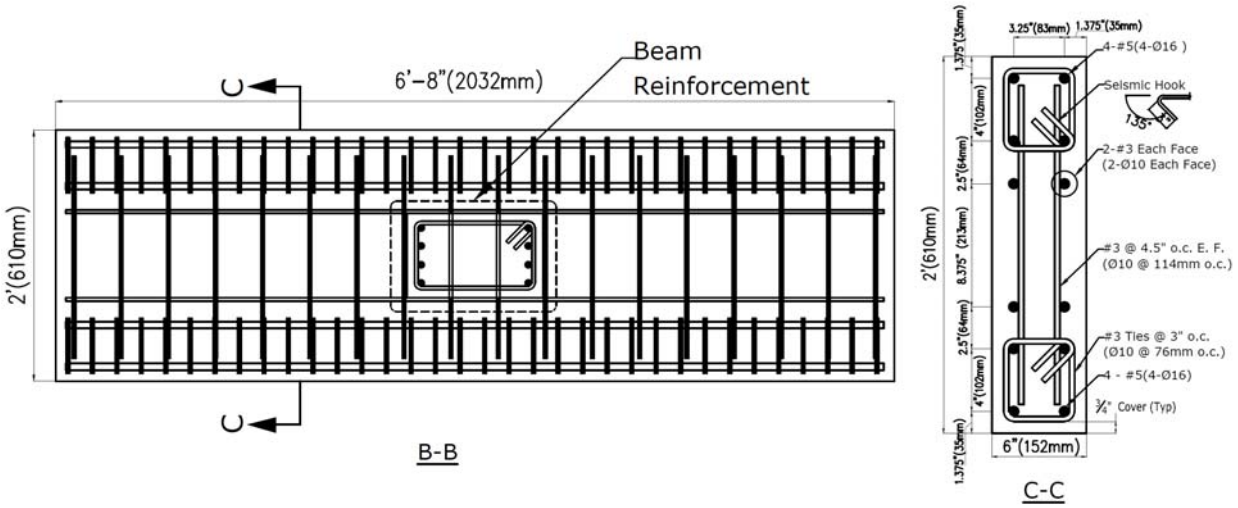


Fig. 3- Wall section reinforcement for WB1

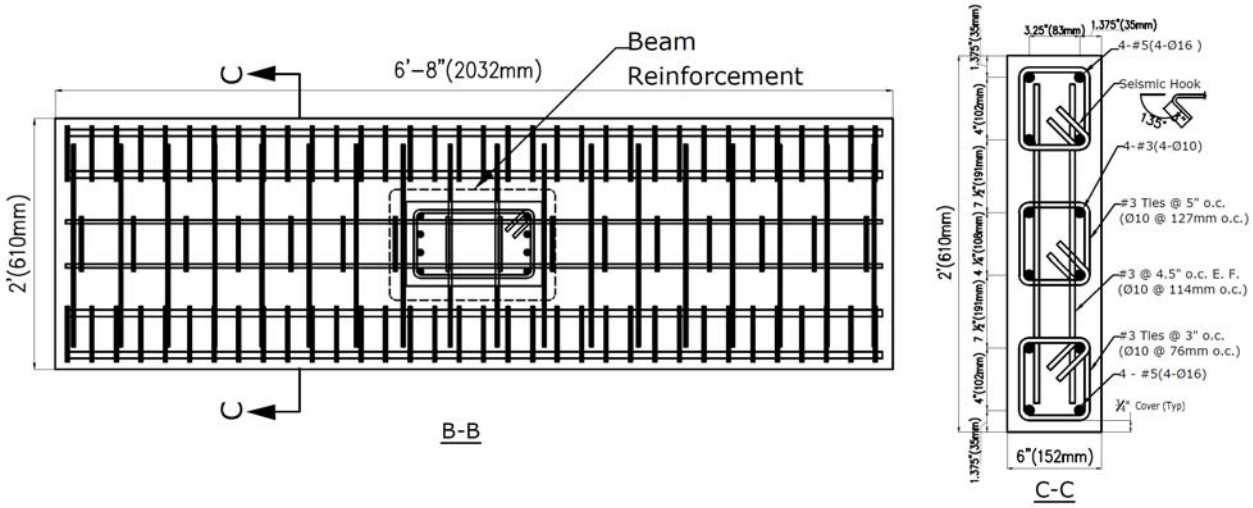


Fig. 4- Wall section reinforcement for WB2

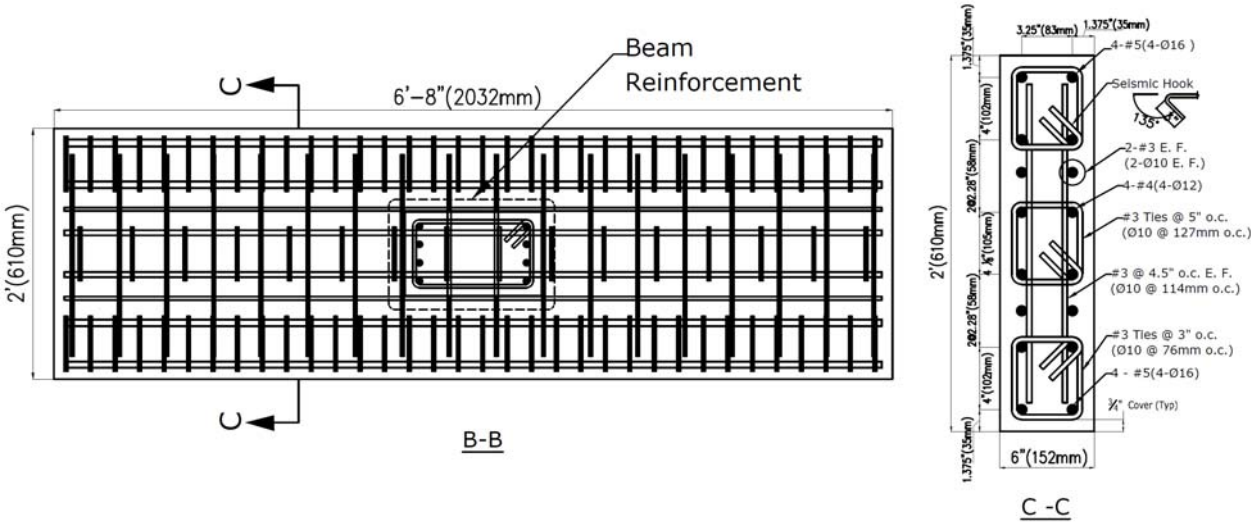


Fig. 5- Wall section reinforcement for WB3

The ratio of beam longitudinal bar diameter to wall thickness is 0.1 which is twice of what is required by ACI 318 code for beam-column connections in special moment resisting frames. The beam cross section and reinforcement details are shown in Fig. 2. Reinforcement details of the test specimens are shown in Fig. 2 through Fig. 5, and a summary is provided in Table 1.

2.2 Test Setup

The test arrangement used to apply cyclic loading consists of a two-dimensional steel frame as shown schematically in Fig. 6. The cyclic loading is applied by two 50-kip vertical hydraulic actuators acting simultaneously in opposite directions at each beam end. The actuators are connected to both the test rig and the transfer beams using pin connections to allow free rotation, Fig. 6. The lower end of the wall specimen is pinned to the test rig, while its top is restrained using roller-like support that allows rotation and vertical movement.

Table 1: Test Specimen Reinforcement Details

Test Specimen			WB1	WB2	WB3
Beam		Size, *b* x *h*, in (mm)	8”x13” (203x330)	8”x13” (203x330)	8”x13” (203x330)
		Top Reinf.	4-#5 (4Ø16)	4-#5 (4Ø16)	4-#5 (4Ø16)
		Top Rein. Ratio, ρ	0.01192	0.01192	0.01192
		Bottom Reinf.	4-#5 (4Ø16)	4-#5 (4Ø16)	4-#5 (4Ø16)
		Bot. Reinf. Ratio	0.01192	0.01192	0.01192
		Transverse Reinf.	#3@5.5” o.c. (Ø10@140mm)	#3@5.5” o.c. (Ø10@140mm)	#3@5.5” o.c. (Ø10@140mm)
Wall		Size, *h* x *l* x *t*, in (mm)	72”x24”x6” (1829x610x152)	72”x24”x6” (1829x610x152)	72”x24”x6” (1829x610x152)
	Wall Web	Vertical Reinf.	2-#3(2Ø10) E.F.		2-#3(2Ø10) E.F.
		ρ_v	0.0073		0.0073
		Horizontal Reinf.	#3 @ 4.5” o.c. (Ø10@114mm)	#3 @ 4.5” o.c. (Ø10@114mm)	#3 @ 4.5” o.c. (Ø10@114mm)
		ρ_h	0.0081	0.0081	0.0081
	B. Elem-ent	Longi. Reinf	4-#5 (4Ø16) Ea	4-#5 (4Ø16) Ea	4-#5 (4Ø16) Ea
		Transverse Reinf.	#3@3” o.c. (Ø10@76mm)	#3@3” o.c. (Ø10@76mm)	#3@3” o.c. (Ø10@76mm)
Concealed Column		Size, *b* x *h* (mm)		6”x7”(152x178)	6”x7”(152x178)
		Longi. Reinf.		4-#3 (4Ø10)	4-#4 (4Ø12)
		Transverse Reinf.		#3 @ 5” o.c. (Ø10@127mm)	#3 @ 5” o.c. (Ø10@127mm)

Note: 1in. = 24.5 mm; #3 bar = 10 mm dia. bar; #4 bar = 12 mm dia. bar; #5 bar = 16 mm dia. bar.

The cyclic loading is applied to the test specimen through the end of the specimen beam. The test protocol is load controlled up to 70% of yield load of wall and displacement controlled to the failure point of the specimen. Two complete loading cycles are applied at each displacement ductility level. The axial load is applied using 5-1/2” diameter, 270-kip 7-wire post tensioned strands passing through the wall section. The intension is to keep the axial load constant throughout the testing.

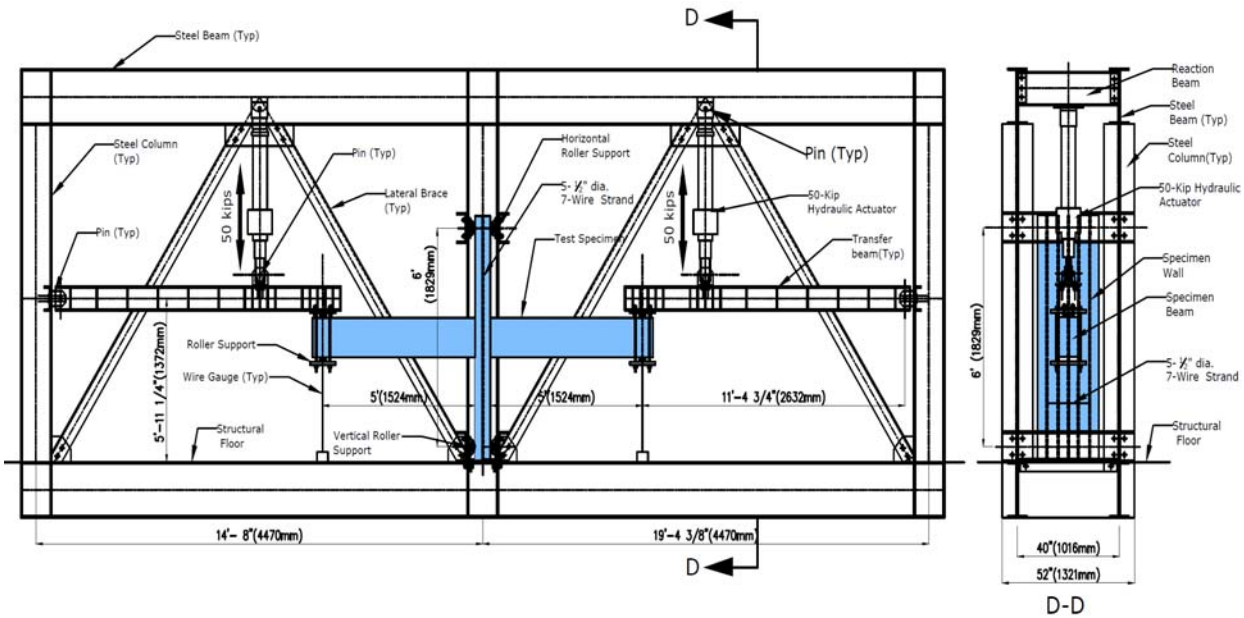
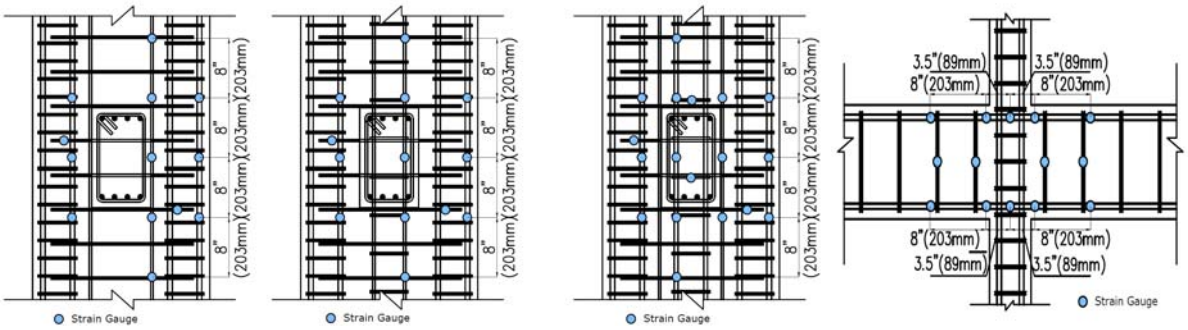


Fig. 6- Test Setup

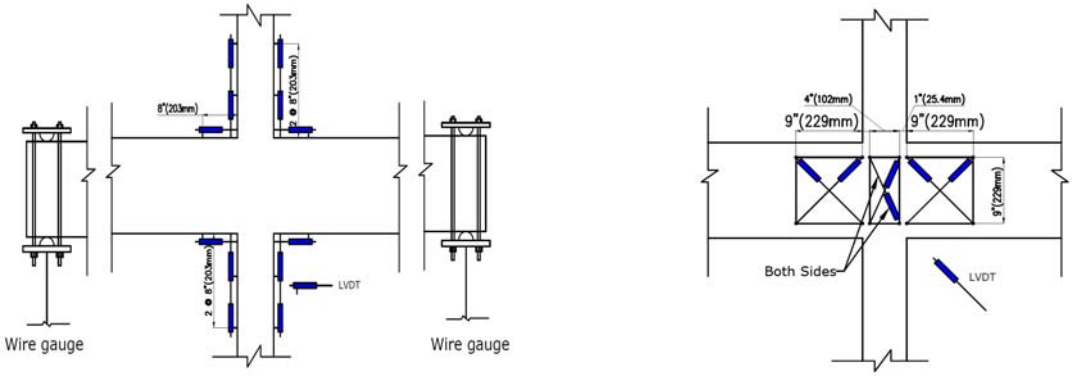
Instrumentation

In order to record the applied load, the specimen beam and wall deformation, and the strains in the reinforcing bars, the test specimens are instrumented with build-in load cells, LVDTs (linear variable displacement transducers), wire gauges, and strain gauges, as shown in Figures7 and 8. To collect data from these instruments instantaneously, they are connected to a computer-based data acquisition system. The strain in the reinforcing bars is monitored in each specimen using a minimum of 27 strain gauges, Fig. 7. The lateral load is applied to the transfer beam (Fig. 6) and is recorded using built-in load cells on the 50kip (222 KN) hydraulic actuators. Other load cells are mounted on the top end of the wall to measure the axial load. Two wire gauges are used to record the imposed displacements at the beam ends, Fig 8a. Two more wire gauges are used to measure slippage and the horizontal movement at the wall supports. A total of 20 LVDTs are mounted on the joint and its vicinity. Flexural deformation is determined based on the displacement measured by eight LVDTs, as illustrated in Fig 8a, while the shear deformation in the beam and the joint is measured by eight LVDTs, as shown in Fig. 8b. Four LVDTs are provided to measure crack width at the beam-wall interface, Fig 8a. All the test specimens have the same LVDT arrangement. Besides using the above electronic instrumentations, visual observations are recorded using photograph and videotaping.



(a) *(b)* *(c)* *(d)*

Fig. 7- Strain gauge distribution: (a) WB1 wall, (b) WB2 wall, (c) WB3 wall, and (d) WB1, WB2, and WB3 beams



(a) *(b)*

Fig. 8- Schematic illustration of LVDT: (a) LVDTs for flexure deformation and (b) LVDTs for Shear deformation

3. CONCLUSIONS

Test specimens are currently under construction and are scheduled to be tested this spring. The seismic response of the beam-wall joints will be determined and evaluated. Analytical study will be conducted to confirm the validity of the experimental study. Design recommendations will be developed based on results of both the experimental and analytical studies.

References

ACI Committee 318, ”Building Code Requirements for Structural Concrete (ACI 318-11) and Commentary,” American Concrete Institute, Farmington Hills, MI, 2011, 503 pp.

Li, B.; Wu, Y. N.; and Pan, T.-C.(2002), “Seismic Behavior of Non-seismically Detailed Interior Beam-Wide Column Joints—Part I: Experimental Results and Observed Behavior,” *ACI Structural Journal*, V. 99, No. 6, Nov.-Dec. 2002, pp. 791-802.

Bing Li, Tso-Chien Pan, and Cao Thanh Ngoc Tran.(2009),“Seismic Behavior of Non-seismically Detailed Interior Beam-Wide Column and Beam-Wall Connections,” *ACI Structural Journal*, V. 106, No. 5, September-October 2009

Kurose, Y.; Guimaraes, G. N.; Liu, Z.; Kreger, M. E.; and Jirsa, J. O. (1988), “Study of Reinforced Concrete Beam-Column Joints under Uniaxial and Biaxial Loading,” PMFSEL Report No. 88-2, Department of Civil Engineering, University of Texas at Austin, Austin, Tex., Dec. 1988, 146 pp.

10CUEE CONFERENCE PROCEEDINGS
10th International Conference on Urban Earthquake Engineering
March 1-2, 2013, Tokyo Institute of Technology, Tokyo, Japan

SEISMIC VULNERABILITY ASSESSMENT METHOD OF LOW-RISE RC BUILDINGS WITH MASONRY INFILL WALLS

Hamood Alwashali [1] and Masaki Maeda [2]

1) Master student, Department of Architecture and Building Science, Tohoku University, Japan,
2) Professor, Department of Architecture and Building Science, Tohoku University, Japan,
hamood@sally.str.archi.tohoku.ac.jp, maeda@archi.tohoku.ac.jp

Abstract: A practical seismic evaluation method that is more effective especially in developing countries is proposed. The proposed method is a recalibration of Shiga figure (Shiga, et al) to be applicable to RC buildings with masonry infill using mathematical models analysis. The damage evaluated by the proposed method is applied to the fragility curves of HAZUS and probability of damage is studied. Average structural damage and economic loss of a whole city could be easily estimated in a short time based on the probability of damage of each zone in the proposed method. Finally, the proposed method is then compared to actual earthquake damage which showed quite good agreement.

1. INTRODUCTION

RC buildings with masonry infill are a common practice in many developing countries. Poor performance of RC buildings with masonry infill was noticed in many earthquakes, recently in China 2008 Wenchuan earthquake and Haiti earthquake 2010; see Figure 1.The performance of these buildings could be improved by special detailing of frames, strengthen walls by reinforcement and other retrofitting techniques. However, the problem is that existing buildings makes a huge considerable number therefore seismic evaluation method is necessary to screen vulnerable buildings.



Figure 1 Damage of Building with masonry infill in China 2008 Wenchuan earthquake

In developing countries, the main issue is usually economic cost. Professional engineers and the time needed to seismically evaluate a whole city will be of a high cost. In addition, if almost all buildings are considered unsafe then the possible action of the government and people is no action because building a new city seems much easier. Therefore a proposed method should filter buildings into categories according to their vulnerability level. In other words, buildings with higher possibility of collapse and severe danger are filtered and have higher priority to be retrofitted. From the above points it is concluded that a simple, low cost and fast seismic screening method is needed as a first screening method.

The original concept of the method proposed in this study is not new and was introduced first by Shiga (Shiga 1968) for the Japanese buildings. The Shiga map screens the buildings into zones with different vulnerability levels according to their column sectional area, wall sectional area and floor area. This method was based on actual data of damaged buildings from Tokachi-Oki earthquake in 1968. A similar method was presented by Hasan and Sozen (Hasan 1997) using the damage data from Erzincan earthquake in 1992 in Turkey. Certainly there isn't better than a detailed analysis of each building and judgment of professional engineers. However, issues such economic costs and the time needed that were mentioned before makes these methods practical for preliminary screening of vulnerable building. The problem is that this method is only applicable to its region because of different seismicity level, material properties and structural details. Actual earthquake damage data is needed to construct Shiga map. As for countries with infrequent earthquakes (return period of 50~100 years), damage data is usually unavailable. Waiting for an earthquake to construct such method is not an option, 2010 Haiti disaster is a recent example. This paper presents a recalibration of Shiga`s method to be suitable to RC buildings with infill walls in different seismic regions. To make this study more realistic, a case study of RC buildings with masonry infill walls in Jordan is considered.

2. PROPOSAL OF SEISMIC EVALUATION METHOD

2.1 Method Flowchart:

The main Flowchart of the proposed method is shown in Fig. 9 Jordan will be used as an example for the proposed method

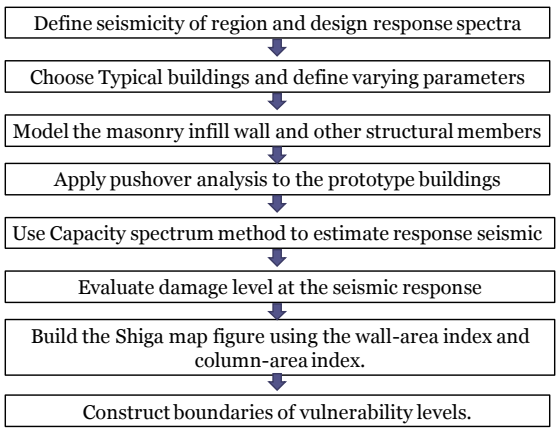


Figure 2 Flowchart of the proposed method

2.2 Define seismicity of Jordan

Jordan is a Middle East country located along the seismically active Dead Sea Transform Fault that extends 1000 km from the Red Sea to Turkey. The seismicity in Jordan is thought to be as moderate. Seismic hazard of Jordan with maximum PGA of about ~0.25g near the Dead Sea is shown in figure 3 (Earthquake hazard report 2007). Current estimates predict a major earthquake in the region roughly every 200 years. During the past ten years, an earthquake of magnitude Mw = 5.1 occurred in the Dead Sea basin on February 11th, 2004 and followed by an Mw = 4.7 earthquake on July 7th, 2004.

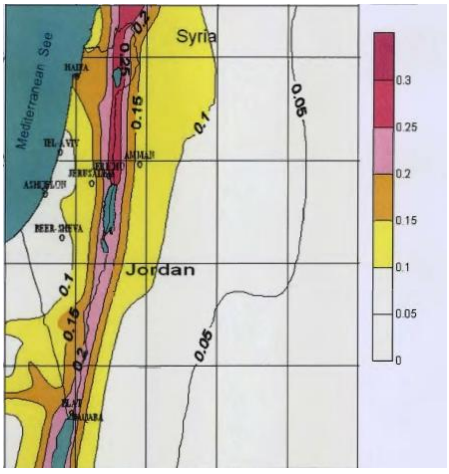


Figure 3. Hazard map with probability of occurrence of 10% in 50 years (Earthquake hazard report 2007)

Different regions have different seismicity levels in Jordan. UBC code (UBC 1997) is used to construct the design response spectrum for two soil types for PGA=0.2g, soil Type SB (rock) and soil Type Sc (very dense soil and soft rock), shown in Fig. 4. In this study, the response spectra of Sc Soil type were used.

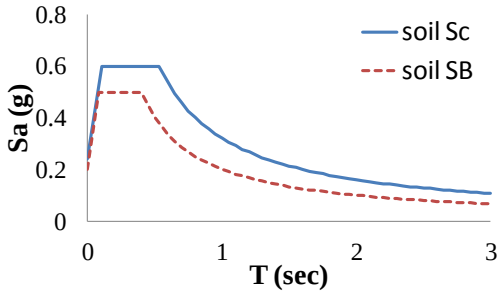


Figure 4 Design response spectra for two soil types Jordan

2.3 Typical buildings in Jordan

RC structures are widely used in Jordan. Typical building plan is shown in Fig. 5. The exterior infill walls are composed usually of 3 layers; stone facing, plain concrete and hollow concrete blocks as shown in Fig. 6. The exterior walls are of thickness ranging from 300~350 mm. These walls are bounded by slender RC columns. The interior columns are usually more reinforced than exterior columns. Exterior masonry walls are sometimes allowed to work as a bearing wall for buildings less than 12 m in height. This resulted in a large number of low rise buildings with masonry infill used usually as residential and commercial buildings in the main cities. This practice is not based on a structural analysis; it is based on past experiences and practices in surrounding countries. As for the partition walls inside the building, hollow concrete blocks of thickness ≈100mm is used. This partition walls are placed randomly and might not be bounded by any columns. The influences of the partition walls are ignored in this paper, only their weight were included. Slabs are ribbed slab (One-way joists) of thickness of 250mm~300mm. Typical beam and column sizes and reinforcement are shown in figure 7. RC walls are commonly used around stair cases and elevators in recently designed buildings (after 2000), see Fig. 4. These RC walls are usually placed in one direction which is mainly the transverse direction.

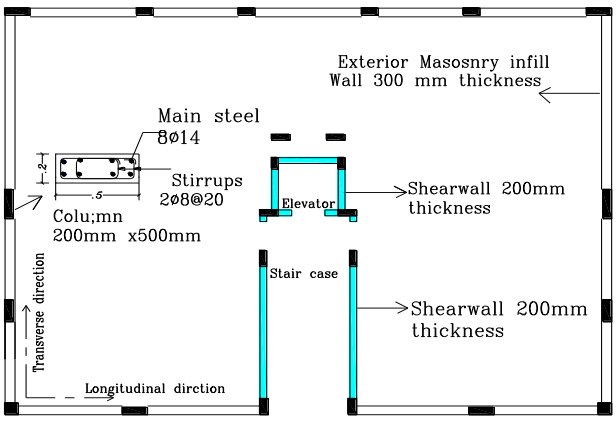


Figure 5 Typical plan for existing building

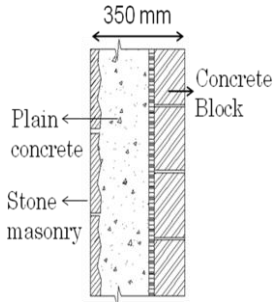


Figure 6 Masonry infill wall in exterior frames

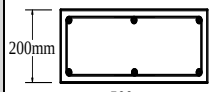
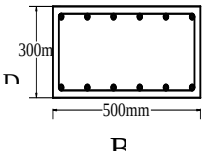
	Typical Column	Typical Beam
Dimension		
Main Bars.	6D16	Top&Bottom 12D16
Hoop	Ø8@200mm	Ø10@200mm

Figure 7. Typical column and beam

2.4 Prototype buildings characteristics

3 prototype buildings with different floor areas were used for analysis. Figure 8 shows the structural plan of prototype building B. Analysis was done for the X- direction (direction with no RC walls in the staircase) which is usually the weakest direction. Many cases were assumed for each building, assuming number of stories ranging from 1 till 4 stories and varying the places and number of masonry infill walls. Since exterior facings of buildings have usually many opening, exterior infill walls with opening of 1m^2 in each wall and thickness 300 mm were assumed, see Fig. 9. The interior partition walls were ignored in this paper, only their weight was included. Exterior columns (bounded by infill walls) and Interior columns are assumed to have dimensions of 200mm x 500mm and 300mm x 500mm respectively

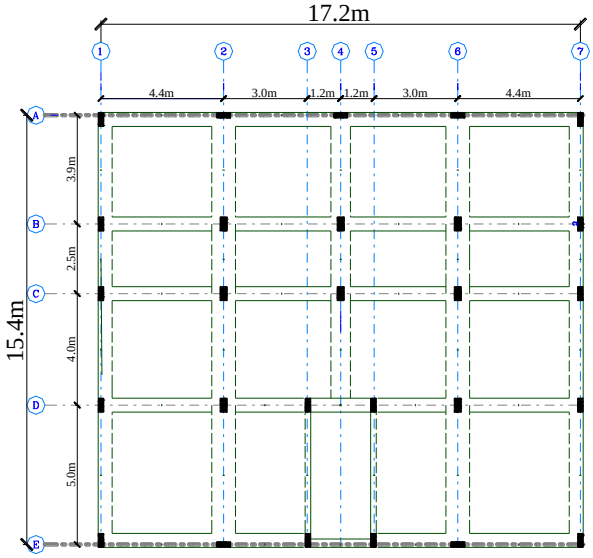


Figure 8 structural plan of prototype building B

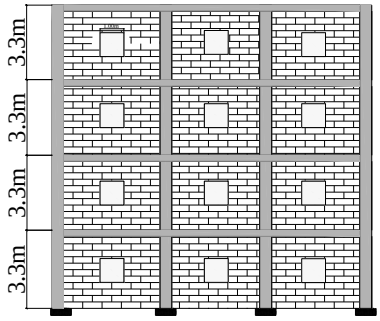


Figure 9 Typical elevation plan of exterior frame

2.5 Modeling of structure

In this study a simple two-dimensional pushover analysis using computer program SNAP is used. Infill walls are idealized as diagonal strut, beams and columns are idealized by two nonlinear rotational springs at their ends, a nonlinear shear spring in the middle and a linear axial spring, see Figure 10 and Figure 11. A tri-linear relation is used for rotational and shear springs, see Figure 12 and Figure 13. The contribution of slab to the beams flexural strength was ignored. The beam-column connection is assumed to be rigid. The distribution of lateral forces along the height in the pushover analysis is based on the Ai distribution prescribed in the AIJ provision (AIJ 1999). The cracking and yield moment of rotational spring and shear spring of columns and beams are estimated using AIJ standard (AIJ 1999). The infill wall is modeled as an equivalent diagonal compression strut with width, W_{ef}, calculated using Eq(1) and Eq(2) which are based on recommendations given in FEMA 356 (FEMA 2000). The equivalent struts have the same thickness and modulus of elasticity as the infill wall it represent.

$$W_{ef} = 0.175(\lambda_h H)^{-0.4}\sqrt{H^2 + L^2} \qquad (1)$$

$$\lambda_h = \left[\frac{E_w t_w \sin(2\theta)}{4E_c I_c H_{\inf}}\right]^{\frac{1}{4}} \qquad (2)$$

Where: E_w and E_c are the moduli of elasticity of the infill wall and the concrete .H_{inf}, H and L are the net height of the infill wall, the storey height, and the bay length of the frame. θ = arctan(H/L) (the inclination of the diagonal). t_w = is the thickness of the infill wall, I_c = moment of inertia of the column of the frame,

The axial strength of the equivalent strut of the infill panel is determined by dividing the expected infill shear strength, V_{ine} , by Cosθ (θ= arctan(H/L). The expected infill shear strength (V_{ine}) is determined by Eq(3) and Eq(4) using the methodology given in Section 7.5.2.2 in FEMA 356 (FEMA 2000) :

$$V_{ine} = V_{me}.An \qquad (3)$$

$$Vme = \frac{0.75\left(Vte + \frac{P}{An}\right)}{1.5} \qquad (4)$$

Where; V_{me} :bed joint shear strength, P : gravity load, An : area of net mortared of infill wall and V_{te} : Average bed-joint shear strength. Due to lack of research on the wall infill properties used Jordan, bed joint shear strength, V_{te}, is assumed 0.7 N/mm^2 and Elasticity of infill wall, E_W, of 9500N/mm^2. These values could be easily acquired in future research. To account for the influence of openings in the walls, initial stiffness and maximum force were reduced using the factor $\lambda_{opening}$ calculated using Eq(5) based on the work of Dawe and Seah (Dawe1988).

.

$$\lambda_{opening} = 1 - \frac{1.5 L_{opening}}{L\,\text{inf}}; \lambda_{opening} \geq 0 \qquad (5)$$

Figure 14 shows the backbone curve of infill wall. The d value shown in the Figure 14 is taken using Table 7-9 in FEMA356 (FEMA 2000) for assumed ratio of frame to infill strengths ≤ 0.7 (the frame is assumed to have small strength compared to the infill panel).

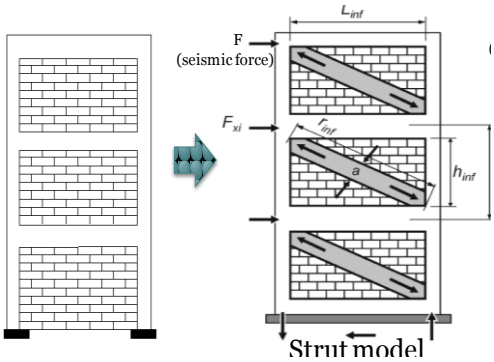


Figure10 Strut model for masonry infill walls

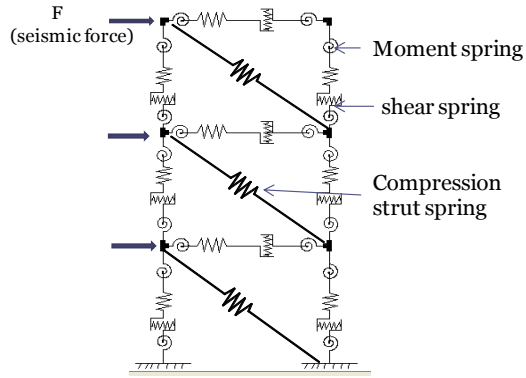


Figure 11 Model of Pushover analysis

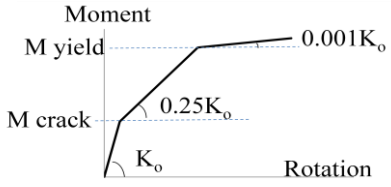


Figure 12 Rotational spring backbone curve

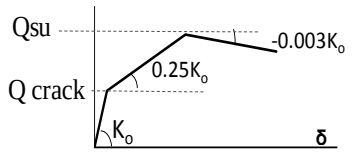


Figure 13 Shear spring backbone curve

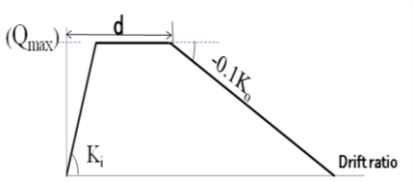


Figure 14 Strut spring back bone curve

2.6 Seismic response and damage evaluation:

The seismic response of the structure is calculated using methodology for calculating target displacement given in Section 3.3.3.3.2 in FEMA 356(FEMA 2000).

The damage evaluation is judged by approximating the amount and level of damage in the infill walls and columns in the first and second story of each building at the seismic response displacement given by the pushover analysis. The damage states employed are similar to those proposed in HAZUS99 (FEMA 1999) with some modification for the severe damage in which total and partial collapse is added. Where *Slight Structural Damage*: Diagonal (sometimes horizontal) hairline cracks on most infill walls; cracks at frame-infill interfaces. *Moderate Structural Damage*: Most infill wall surfaces exhibit larger diagonal or horizontal cracks; some walls exhibit crushing of brick around beam-column connections. Diagonal shear cracks may be observed in concrete beams or columns. *Extensive Structural Damage* (named as *severe damage* in this paper): Most infill walls exhibit large cracks; some bricks may dislodge and fall; some infill walls may bulge out-of-plane; few walls may fall partially or fully; few concrete columns or beams may fail in shear resulting in partial collapse and in imminent danger of collapse. Structure may exhibit permanent lateral deformation.

However, it is difficult to state when exactly the masonry infill wall could be called moderately damage or severely damaged in the backbone curve of figure 14. In figure 15 a suggested figure for damage evaluation is proposed. The elastic region till about 0.8 Q_{max} is considered with none damage, from 0.8Qmax till about half of C value is considered having slight damage. Severe damage starts from the point where the wall drops to 80% of its maximum shear strength.

The d value shown in figure 14 in many prototype buildings were calculated to be about 0.4% of inter-story drift using Table 7-9 in FEMA356. The moderate damage in many cases studied in this paper starts at drift of about 0.25%. This values quite well agrees with many experiments carried by (Merhabi et al 1996) were the first major crack occurred at drift between 0.17%~0.36% for strong infill and weak frame specimens.

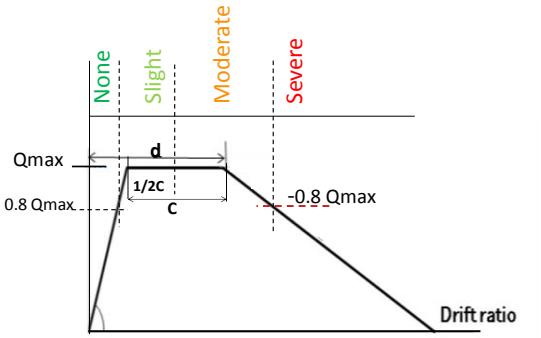


Figure 15 Proposed damage states of masonry infill

When more than half of the masonry infill walls strength degrades to 80% of its shear strength the buildings is considered severe. This might be quite conservative for buildings having strong frames which could carry the seismic demand even after the masonry walls are crushed. However, it is thought to be appropriate in the case study of Jordan where the masonry infill walls support part of the gravity load and the surrounding RC frame is lightly reinforced and weak, therefore the degradation and crushing of masonry infill walls could cause instability of structure and imminent danger of partial or total collapse.

To make the method clear, the proposed method is illustrated by example using one of the cases of the prototype buildings shown in figure 8:

This case is of a four storied structure having masonry infill walls in all its exterior axes. Axes A and E (see figure 8) have masonry walls with openings of 1m^2, columns and beams are modeled as stated previously. Axes B, C and D have no infill and modeled as moment frames. A displacement-controlled pushover analysis is applied to the longitudinal direction. The bilinear idealization of the capacity curve represented by base-shear and roof displacement is shown in figure 16. The total weight of the building was calculated to be 12900 kN with average weight per unit area of 12.5 kN/m^2.

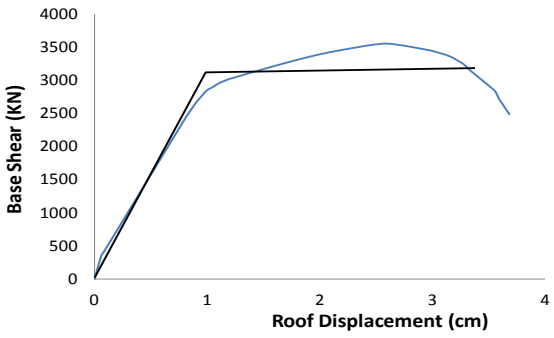


Figure 16 Bilinear idealization of the capacity curve

The performance point was calculated using the target displacement method for nonlinear analysis to be of 3.28cm of roof displacement. At this performance point more than 90% of the number of walls in the 1st floor has degraded to less than 80% of their maximum shear strength. Force-Displacement curve of strut spring of one of the walls in 1st floor is shown in figure 17. In additional, plastic hinges were formed on both ends of few columns of 1st floor. As for the 2nd floor all walls has reached the moderate region proposed in figure 15. Upper floors are still in their slight region. Since most of the infill walls of 1st story are evaluated as severe at performance point, this building is considered as severe.

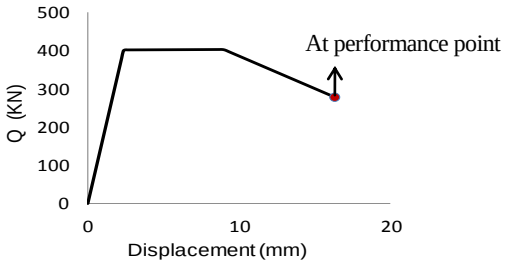


Figure 17 Force-Displacement curve of one of the masonry infill walls of 1st floor in the illustrated example

The Total area of floors, total cross sectional area of columns of 1st floor and total cross sectional area of masonry infill walls of this case (cross sectional area of openings in walls are deducted) of 1st floor are 1059.5m^2, 3.1m^2 and 6.63 m^2 respectively. The Column index, CI, which is percentage ratio of the cross sectional area of columns in 1st floor to the total floors area, is 0.29. The Wall index, WI_{inf} which is the percentage ratio of the cross sectional area of infill walls in 1st floor to the total floors area is 0.63.

3. Results:

Properties and results of the prototype buildings are shown in Table 1. The Column index, CI, is percentage ratio of the cross sectional area of columns of 1st story to the total floors area of the prototype buildings. The Wall index, WI_{inf} is the percentage ratio of the cross sectional area of infill walls (the length of the openings in infill walls are deducted from the total infill length) of the total of 1st floor to the total floors area of the prototype buildings.

The Column index, Wall index (WI) and damage expected of each building are shown in Figure 18. Fig. 18 is based on the concept of Shiga map. Hasan and Sozen (Hasan1997) used a similar figure for actual damage of buildings in Erzincan earthquake. The figure 18 is divided into vulnerability zones by the lower boundary line and upper boundary line. There are 3 Vulnerability Zones, for which zone A (danger zone) is the most vulnerable and zone C (safe zone) is the least. The boundary lines here are assumed based on the damage evaluated. However, the boundary lines assumed here could be adjusted based on the probability of expected damage and acceptable seismic hazard which are discussed in next section (section of probability of damage)

Thinking of results as capacity provided by the building versus seismic demand by earthquake, then capacity is thought to be provided by columns and infill walls strength, which is product of the shear stress and cross sectional area of columns and walls shown of the left side of Eq (6). The

Table 1 Properties and results of the prototype buildings

Building No.	Total Column area m^2	Total Infill Wall area m^2	Total Area m^2	Column index%	Infill Wall index %	Evaluated Damage level
Building A- 1 stories (case 2)	3.8	11.04	438	0.87	2.52	none
Building A- 1 stories (case 3)	3.8	4.44	438	0.87	1.01	slight
Building A- 2 stories (case2)	3.8	11.04	876	0.43	1.26	slight
Building A -2 stories (case 1)	3.8	13.92	876	0.43	1.59	Slight
Building A- 2 stories (case 3)	3.8	4.44	876	0.43	0.51	moderate
Building A- 3 stories (case 1)	3.8	13.92	1314	0.29	1.06	moderate
Building A- 3 stories (case 2)	3.8	11.04	1314	0.29	0.84	moderate
Building A- 4 stories (case 1)	3.8	13.92	1752	0.22	0.79	severe
Building A- 4 stories (case 2)	3.8	11.04	1752	0.22	0.63	severe
Building A- 4 stories (case 3)	3.8	4.44	1752	0.22	0.25	severe
Building B- 1 stories (case 1)	3.1	6.63	271.44	1.14	2.44	none
Building B- 1 stories (case 2)	3.1	3.72	271.44	1.14	1.37	slight
Building B- 2 stories (case 1)	3.1	6.63	542.88	0.57	1.22	slight
Building B- 2 stories (case 2)	3.1	3.72	542.88	0.57	0.69	moderate
Building B- 3 stories (case 1)	3.1	6.63	794.64	0.39	0.83	moderate
Building B- 3 stories (case 2)	3.1	3.72	794.64	0.39	0.47	severe
Building B- 4 stories (case 1)	3.1	6.63	1059.52	0.29	0.63	severe
Building B- 4 stories (case 2)	3.1	3.72	1059.52	0.29	0.35	severe
Building C- 1 stories (case 2)	1.48	3.48	101.2	1.46	3.44	none
Building C- 2 stories (case 1)	1.48	3.48	202.4	0.73	1.72	slight
Building C- 3 stories (case 2)	1.48	3.48	303.6	0.49	1.15	moderate
Building C- 4 stories (case 2)	1.48	3.48	404.8	0.37	0.86	moderate

demand needed is the product of the total weight of the building and response acceleration coefficient of earthquake (marked as C_a) and reduction factor (marked as D_s) to account for the ductility which the building posses.

Capacity ≥ Demand

$$\tau_c . A_C + \tau_w . A_W \geq W . C_a . D_s \qquad (6)$$

Where A_c: is the area of columns(mm^2), τ_c: is the shear strength of columns (N/mm^2), A_w: is the area of masonry infill (mm^2), τ_w: is the shear strength of masonry infill walls (N/mm^2) , W: is total weight of building, Ca: response acceleration coefficient of earthquake.

Total weight of the buildings (W) is the product of total area of floors (A_f) and average weight per unit area. The average weight per unit ranged for the studied cases between 12 kN/m^2~14 kN/m^2. Taking 13 kN/m2 as the average weight per unit area and assuming reduction factor Ds = 1 Therefore;

$$\tau_c . A_C + \tau_w . A_W \geq 0.013 N/mm^2 . A_f . C_a \qquad (6)$$

The response acceleration coefficient for Soil C spectra used in this case study for buildings with short periods (low-rise buildings) is 0.6g. Dividing both sides by A_f (area of floor), Therefore:

$$\tau_c . \frac{A_C}{A_f} + \tau_w . \frac{A_w}{A_f} \geq 0.0078 N/mm^2 \qquad (7)$$

Eq(7) is expressed in terms of column index (CI percentage ratio of column area to total floor area) and Wall index (WI_{inf}: percentage ratio of infill wall area to total floor area) and shown in Eq (8):

$$\tau_c . CI + \tau_w . WI_{inf} \geq 0.78 N/mm^2 \qquad (8)$$

The column shear strength τ_c and Wall shear strength τ_w of lower boundary shown in figure 18, are $1N/mm^2$ and $0.6N/mm^2$, respectively

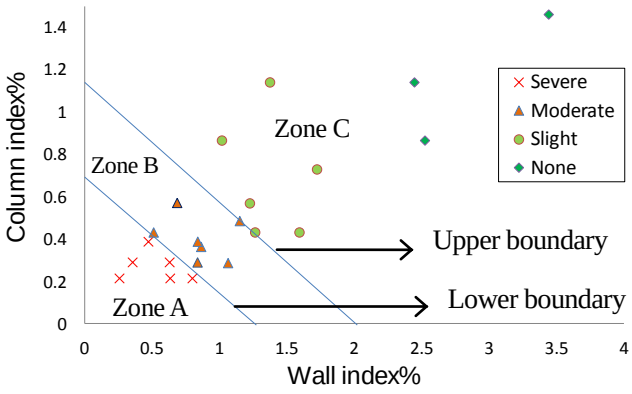


Figure 18 Proposed evaluation map

To make this method more practical; Eq (9) and Eq (10) are proposed. The inventory buildings having CI and WI_{inf} in index *less than 0.78N/mm²* are more vulnerable and therefore have higher priority to undergo a detailed analysis and seismic retrofit. Buildings having CI and WI_{inf} index *more than 0.78* N/mm^2 in Eq (10) have lower priority to be

checked. This boundary lines could be changed based on probability of damage and resources available for the seismic evaluation discussed later.

$$1.0\ CI+0.6\ WI_{inf} \geq 0.78\ N/mm^2 \quad (9)$$

$$0.65\ CI+0.37\ WI_{inf} \geq 0.78\ N/mm^2 \quad (10)$$

It should be noted here that Jordan has regions with different seismicity levels and soil condition. Therefore, different regions have different vulnerability zones and boundaries.
It is suggested that infilled frames with openings exceeding 50 percent of the panel area should be ignored.

4. Damage Probability:

Buildings evaluated to be in zone A (danger zone) does not imply that all buildings would be severely damage but it means that buildings in zone A are more probable to have severe damage. Vice versa is also true, a building in zone C (safe zone) does not imply that it would not be damaged but means that it less likely to be severely damaged.
Probability of damage could be checked using varies of methods; one of the most widely used is fragility curves. Fragility curves for the case of buildings in Jordan are still in its early stages of research. In this paper, HAZUS fragility curves are used to estimate damage probability.

4.1 Introduction of HAZUS fragility curves

HAZUS is a project conducted for the National Institute of Building Science (NIBS), under a cooperative agreement with the Federal Emergency Management Agency (FEMA). HAZUS is an estimation methodology for loss estimates from hazards and economical damage for structures and infra-structures in the United States. The probabilities of structural and non-structural damages to structures and life-lines as well as direct and indirect economical losses induced by natural disasters such as earthquake, flood and storm can be estimated.

In this paper, fragility curves for ground shaking damage for Low-rise RC buildings with masonry infill and pre-code design level is used. Pre-code damage functions was selected since it was recommended by HAZUS for older buildings that were not designed for seismic loads which is similar to the case of Jordan buildings built before seismic code was implemented in 2005. However, the fragility curves of HAZUS are derived for US buildings, thus the applicability of it to buildings in Jordan needs further research.

The fragility curves of HAZUS uses for 4 levels of damage states of structural damage; slight damage, moderate damage, extensive damage (severe damage) and complete damage. The description of slight damage and moderate damage of this paper are the same of that of HAZUS as stated before. The Complete damage state in HAZUS is defined as buildings which have collapsed or have partial collapse. The fragility curves are characterized in terms of spectral displacement as shown in figure 19.

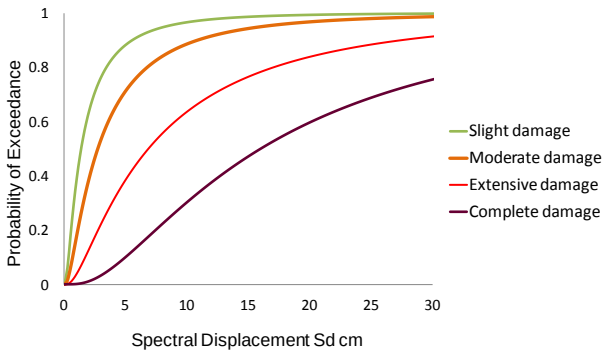


Figure 19 Fragility curves of Pre-code Low-rise RC buildings with unreinforced masonry infill

The performance point of each of the previous prototype buildings are transferred into spectral displacement using of Eq (11)

$$\Delta(Sd) = \frac{\Sigma(m_i \cdot \delta_i^2)}{\Sigma(m_i \cdot \delta_i)} \quad (11)$$

Where m_i is the weight of each floor and δ_i is displacement of each floor at the response point.
Figure 20 shows the damage state probability for the example building mentioned in the previous section which had performance spectral displacement of 2.9cm (3.24 cm roof displacement).

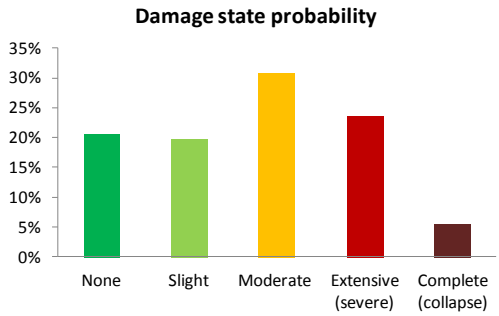


Figure 20 Damage probability of illustrated example

Using the fragility curves the damage state probability is studied for all selected buildings` cases in each zone. The four buildings just below the lower boundary that are in red circle marked as (a) in figure21 had an average probability of severe damage and collapse damage of *25.3% and 6.7%* respectively. This means that if you have about 100 buildings having similar Column index and wall index similar to those in circle(a) then 25 buildings will be heavily damaged and 7 buildings will collapse. Obviously, the weaker the building (smaller column and wall indices) than those in circle (a), then severe damage and collapse probability increases.

As for buildings in the orange circle marked as (b) in figure 21, the average probability of severe damage and collapse are *17.4% and 2.5%* respectively. This means that many buildings in this region can be heavily damaged, but only less than 2.5% will collapse.

As for buildings in the green circle marked as (c) in figure 21, the average probability of severe damage and collapse are *5.2% and 0.2 %* respectively. Buildings in this region are unlikely to collapse or partially collapse.

All the low-rise RC buildings with masonry infill walls in the city could be screened in a short time using only the column and wall indices. Those buildings then are checked are plotted proposed Shiga map for case of Jordan and classified into zones. Based on the percent of number of buildings in each zone then average structural damage and economic loss could be easily estimated. In additional, screening the city using this study helps to estimate roughly the resources needed for buildings` retrofit and risk mitigation.

The lower and upper boundaries proposed here could be modified easily based on the philosophy of the acceptable damage in the risk mitigation project and also based on the available resources for seismic evaluation and retrofit.
Understanding the probability of damage of each zone is an indispensable part of the proposed method

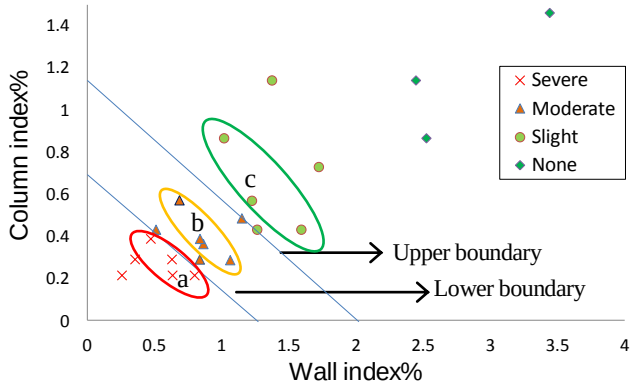


Figure 21 selected buildings for checking damage probability

5. Comparison with earthquake damage:

There is no recent major earthquake in Jordan. The nearest country with earthquake damage data is Turkey. RC buildings with masonry infill walls are commonly used in Turkey. Jordan and Turkey are Middle Eastern countries and they also shares the dead fault which runs through Jordan till the south-eastern part of Turkey (see figure 22). However, similar structure detailing and material quality in both countries is Not checked yet.



Figure 22 Dead Sea fault passing Jordan

5.1 Erzincan Earthquake Turkey; Data and Comparison

Erzincan 1992 earthquake is of magnitude 6.8 and PGA of ≈0.5g. The acceleration time history for NS and EW direction is shown in figure 23 and figure 24. The Architecture institute of Japan, AIJ, investigated a heavily damaged area in Erzincan earthquake (AIJ Report1993). It was reported that out of the 424 buildings investigated 28 (6.6%) collapsed and 68 (16.8%) were heavily damaged.
Erzincan`s response spectra (see figure 25) at short period is NS≈0.8g and EW ≈ 1.2g *which is much larger* than response spectra of 0.6g used in the proposed method especially in EW direction.

The damaged buildings data are collected by METU (Middle East Technical University) and AIJ and were mentioned by Hasan and Sozen (Hasan1997). Data contain also buildings with RC walls; therefore the data are filtered for buildings having only RC columns and Infill walls. The proposed boundaries are compared and plotted with data of damaged buildings by Erzincan earthquake 1992 in Turkey, see fig ure26.

The METU definition of damage state is different from the one used in this paper. Definitions of the damage state in the METU data as follows: Light: Reinforcement exposed but not buckled near joint faces. Fine flexural cracks in structural and nonstructural elements, Moderate: Reinforcement buckled near joint faces and/or inclined cracks in structural walls. Severe: Structural failure of individual elements.

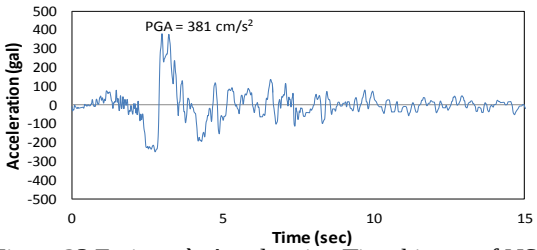


Figure 23 Erzincan`s Acceleration Time history of NS

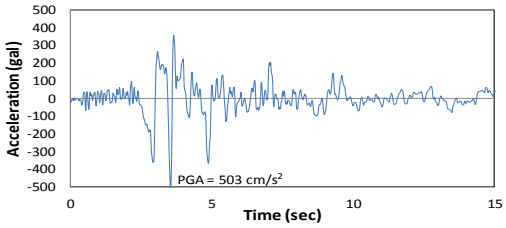


Figure 24 Erzincan`s Acceleration Time history of EW

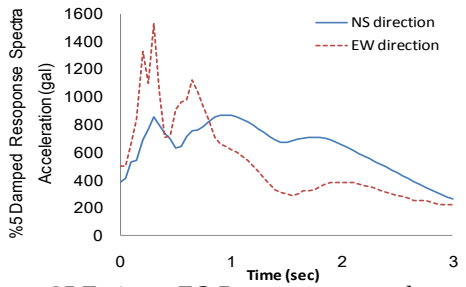


Figure 25 Erzincan EQ Response spectra damped 5%

The boundaries from the proposed buildings showed good agreement with damage of the Erzincan`s buildings. However, the Erincan`s response spectra (about 1g) is much larger than the response spectra in Jordan (about 0.6g). Then why good correlation was observed?

First the METU definition of damage state is different from the one used in this paper. Definition of the damage state of moderate state in METU indicates the reinforcement bars could be seen and they have already buckled. This moderate damage state of METU is thought to be as severe damage states used in this study and therefore the moderate damaged buildings in figure 26 could be considered severe by damage states of this study.

Another possible reason is that the duration time for major ground shaking of Erzincan EQ is less than 10 seconds (very short) & only one displacement cycle of large amplitude as shown in figure 23 and figure 24. Therefore cyclic degradation of masonry walls was not significant which helped to show good performance.

In addition, the strength of materials used in Erzincan building is unclear and could be much stronger the strength values assumed for buildings in Jordan.

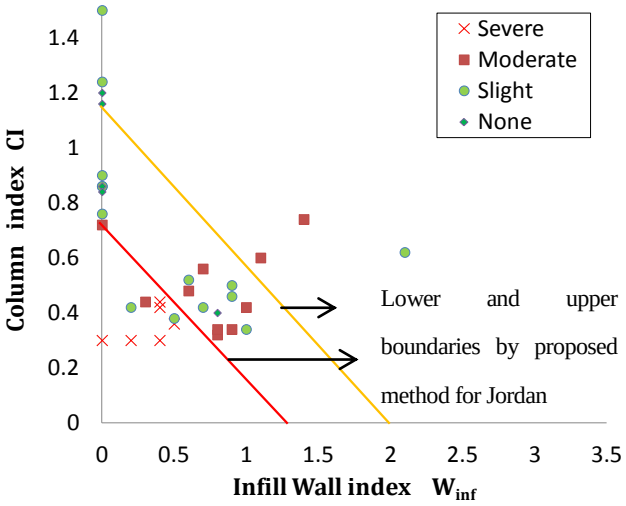


Figure 26 Comparison with data of damaged RC buildings with masonry infill of Erzincan earthquake 1992

6. CONCLUSIONS

Due to economical and time problems, a first screening method that is more practical and simple was introduced. The proposed method is fast and could be adjusted to be suitable to other regions with different seismicity and structural detailing. Buildings identified as vulnerable should undergo a more detailed procedures for further seismic evaluation.

An average structural damage and economic loss of a whole city could be easily estimated in a short time based on the probability of damage of each zone in the proposed method. In additional, screening the city using this study helps to estimate roughly the resources needed for buildings` retrofit and risk mitigation.

In future research, more prototypes with different Column and Wall indices should be checked to increase the accuracy of constructing the vulnerability zones.

Further improvements needs to be studied in further research such as adding regularity reduction index for buildings with irregular shapes. Material quality index should also be introduced to account for buildings construction quality and deterioration after construction. Even though captive columns are not commonly observed in Jordanian buildings, but captive columns should also be investigated in further research. In addition, Jordan`s material properties experiments are needed to account for the assumed values in this paper.

References:

AIJ standard for structural calculations of reinforced concrete structure. 1999 .(in Japanese)

AIJ Report (1993) ,on the damage investigation of the 1992 Turkey earthquake (in Japanese)

Dawe JL, Seah CK. *" Lateral load resistance of masonry panel in flexible steel frames".* Proceedings of the eighth international brick and block masonry conference. Trinity College; 1988.

Earthquake seismic hazard assessment for seismic for building codes, Final report 2007, submitted to : U.S. agency for international development . The principal investigators ; Geophysical Institute of Israel. The collaborators ; Natural Resources Authority of the Hashemite Kingdom of Jordan, Najah national University , Nabulus Palestinian National Authority and University for North Carolina. March 2007.

Federal Emergency Management Agency FEMA-356 (1999). HAZUS99 Technical Manual. Washington, DC, U.S.A: Federal Emergency Management Agency.

Federal Emergency Management Agency (FEMA) (2000), *"Prestandard and Commentary for the Seismic Rehabilitation of Buildings,"* FEMA 356, Washington, D.C.

Japan Building Disaster Prevention Association (JBDPA). (2001b). "*Standard for Seismic Evaluation of Existing Reinforced Concrete Buildings*".

Hassan, A.F., and. Sozen, M.A. "*Seismic Vulnerability Assessment of Low-Rise Buildings in Regions with Infrequent Earthquakes. "*ACI Structural Journal, Jan-Feb 1997; 94(1): 31-39.

Merhabi, A. B., and Shing, P.B., Schuller, M., and Noland, J. 1996. "Experimental evaluation of masonry-infilled RC frames." Journal of Structural Engineering, Vol. 122, No. 3, March 1996, pp. 228-237

Shiga, T., Shibata, A. and Takahashi, T., *"Earthquake Damage and Wall Index of Reinforced Concrete Buildings,"* Proceedings, Tohuku District Symposium, Architectural Institute of Japan, No. 12, Dec.1968, pp. 29-32. (in Japanese)

Uniform Building Code , UBC1997. Volume 2. 1997

10CUEE CONFERENCE PROCEEDINGS
10th International Conference on Urban Earthquake Engineering
March 1-2, 2013, Tokyo Institute of Technology, Tokyo, Japan

PROCESS OF COLLAPSE FOR RC FRAME INCLUDING SHEAR COLUMN

Kazuto Matsukawa[1)], Xiu Liu[2)], and Masaki Maeda[3)]

1) Doctoral Student, Dept. of Architecture and Building Science, Tohoku University, Japan
2) Graduate Student, Dept. of Architecture and Building Science, Tohoku University, Japan
3) Professor, Dept. of Architecture and Building Science, Tohoku University, Japan
matsukawa@sally.str.archi.tohoku.ac.jp, liu@ sally.str.archi.tohoku.ac.jp, maeda@archi.tohoku.ac.jp

Abstract: In this paper, experimental study for axial collapse of reinforced concrete structure composed of shear and flexural member was conducted. From the experiments and equilibrium of force when column failed by axial load, axial capacity analysis model of failed shear column was proposed. Idealized backbone curve of failed shear column was also constructed from the model. This model showed good agreement with shear column of specimens. After that, pushover collapse analyses of frame model of specimens were conducted. The model mentioned above was installed to the frame model. From the results, collapse analysis method and model are almost valid in comparison with especially more brittle specimens.

1. INTRODUCTION

Some of old reinforced concrete structures might have shear critical members. Failure of shear critical columns may cause a total collapse of building because of rapid degradation of horizontal and axial capacity. In Japanese seismic code and design standards (AIJ.2004), deterioration in shear resistance in column has not been considered because of complexity and unclearness of such behavior. Therefore, safety limit state of buildings (maximum deformation point of buildings to prevent collapse) is generally taken at the first occurrence of shear failure of a structural member.

However, this safety limit state is conservative because buildings might not collapse directly after shear failure if the horizontal and vertical forces can be redistributed from failed members to surrounding members. In addition, previous research (Mukai et.al 2010) showed that redistribution behavior was observed in experiment of RC frame including shear and flexure columns.

Main goal of this paper is to estimate that kind of behavior of RC frame. In this paper, an analytical model of residual axial capacity of column was constructed. After that, static cyclic loading experiments of reinforced concrete frames composed of brittle shear and ductile flexural columns were conducted to confirm suitability of the model.

2. MODEL OF RESIDUAL CAPACITY OF BRITTLE SHEAR COLUMN

2.1 Review of Previous Model

For reasonable collapse assessment, analytical model of deterioration of shear and axial capacity is needed. In past, models to assess the backbone characteristics of such brittle members considering shear-axial interaction were proposed by Elwood and Moehle (2004) and Yoshimura (2008), and the authors (2012).

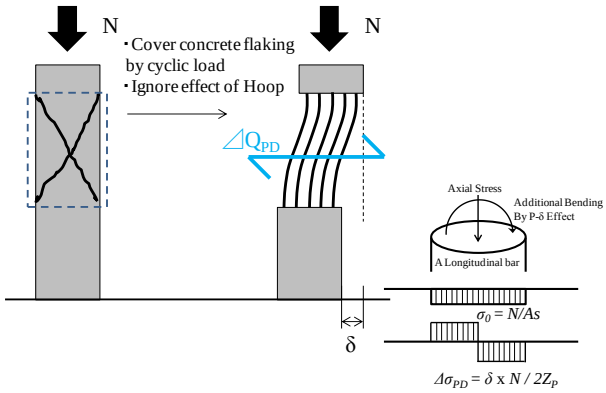


Figure1 Residual axial capacity model

Residual axial capacity model in authors' previous paper (2012) is shown in Figure1. And EQ.(1) is constructed from equilibrium of stress when longitudinal bars yield and column reaches axial collapse.

$$N_{R_L} = \frac{As \cdot \sigma_y}{\left(1 + \frac{As \cdot \delta}{2Z_p}\right)} \quad (1)$$

Where; N_{R_L}: residual axial capacity by longitudinal bars, Z_p: plastic section modulus of longitudinal bars, As: total area of longitudinal bars, σ_y: yield stress of longitudinal bars, δ: lateral drift of column.

As shown in Figure1, P-δ effect to longitudinal bars was considered in Eq.(1). Basic assumption of this model is

as follows;

1) Cover concrete was totally removed due to shear failure and cyclic loading
2) The influence of transverse reinforcements is small and therefore ignorable
3) Horizontal force of column is assumed to reach zero by capacity deterioration when vertical load N exceeds vertical capacity of column

In this paper, the effect of transverse reinforcement (mentioned assumption 2)) will be taken into consideration and is thoroughly studied.

2.2 Effects of transverse reinforcement

Transverse reinforcement contributes to residual capacity of column by confining crushed concrete. This effect is illustrated in Figure 2. After shear failure, wedge shaped area (see figure 2) is formed top and bottom of the damaged area. Transverse reinforcement resists the axial load N by confining the crushed concrete area. When vertical collapse occur, transverse reinforcements yield and equilibrium of force is constructed as shown in Eq.(2). Eq.(2) and Eq.(1) are added to form Eq.(3).

$$N_{R_T} \cdot \tan\gamma = \frac{2D_e \cdot A_{sw} \cdot \sigma_{wy}}{s \tan\phi} \tag{2}$$

$$\begin{aligned} N_R &= N_{R_L} + N_{R_T} \\ &= \frac{A_s \cdot \sigma_y}{\left(1 + \frac{A_s \cdot \delta}{2Z_p}\right)} + \frac{2D_e \cdot A_{sw} \cdot \sigma_{wy}}{s \tan\phi \tan\gamma} \end{aligned} \tag{3}$$

Where; N_R: total residual axial capacity, N_{R_T}: residual axial capacity by transverse reinforcement, D_e: effective width of the column, A_{sw}: total area of transverse bars, s: space of transverse bars, φ:angle of shear crack, γ:angle of wedge shaped area.

In previous research by Yoshimura (2008), backbone characteristics of residual shear and axial capacity were proposed (as shown in Figure3). In the backbone curve, collapse displacement is defined as R_u which is the point where shear capacity reaches zero and axial load N exceeds axial capacity N_R. Based on Eq.(3), the collapse displacement R_{u0} could be calculated by Eq.(4). Referring to Yoshimura model and Eq.(4), backbone curve of residual capacity could be calculated.

$$R_{U0} = \delta / h_0 = \frac{2Z_p}{A_s \cdot h_0} \left(\frac{A_s \cdot \sigma_y}{N - \frac{2D_e \cdot A_{sw} \cdot \sigma_{wy}}{s \tan\phi \tan\gamma}} - 1 \right) \tag{4}$$

Where; h_0: internal height of column.

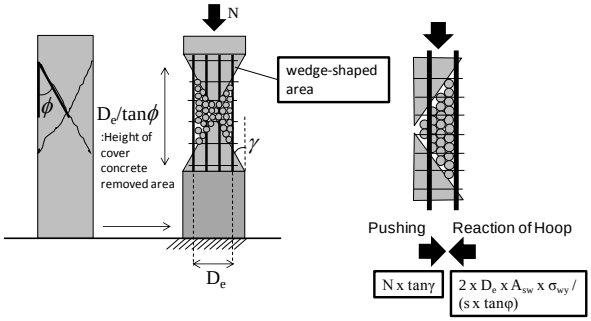


Figure2 Confinement effect of transverse bars

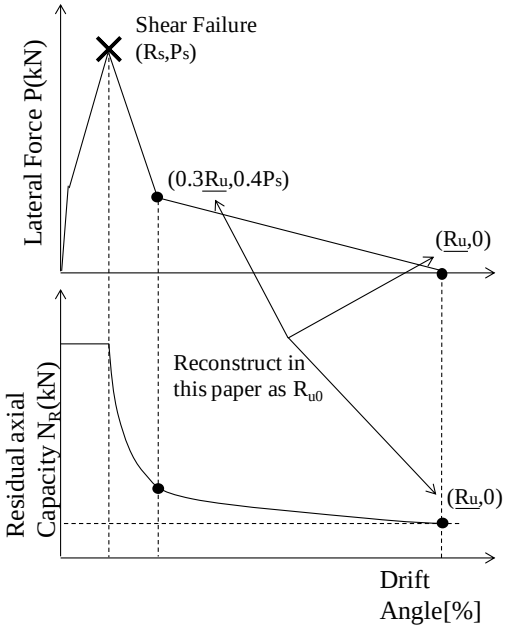


Figure3 Backbone curve of shear and axial capacity

3. EXPERIMENTAL STUDY OF RC FRAME INCLUDING SHEAR COLUMN

3.1 Test Specimen

Tests were conducted for five specimens; the example drawings are shown in Figure 4 and 5. These specimens are single story and two bays frame structures. Specimen F0101 (conducted with Fukuyama et al (2011)) was designed as a one-half scale and the others were designed as a 3/8 scale of typical building in Japan. Every member except for center column was designed so that flexure yielding precedes shear failure. Center columns were not provided with adequate transverse reinforcement and they were designed to demonstrate shear failure. Material properties of the specimens are shown in Table 1.

Main parameters of these specimens are p_w which is the area of transverse reinforcement normalized by the hoop spacing and column width and $N/A_s\sigma_y$ which is applied axial load divided by capacity of longitudinal reinforcement of center column. $N/A_s\sigma_y$ is index of axial capacity carried by longitudinal bars. Table2 shows the basic properties of center

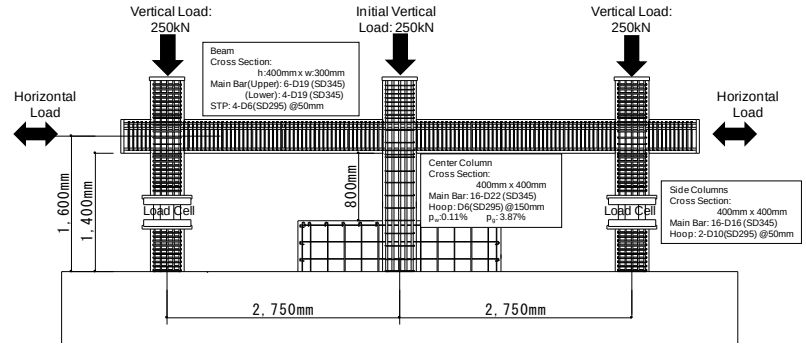


Figure 4 Drawing of specimen F0101

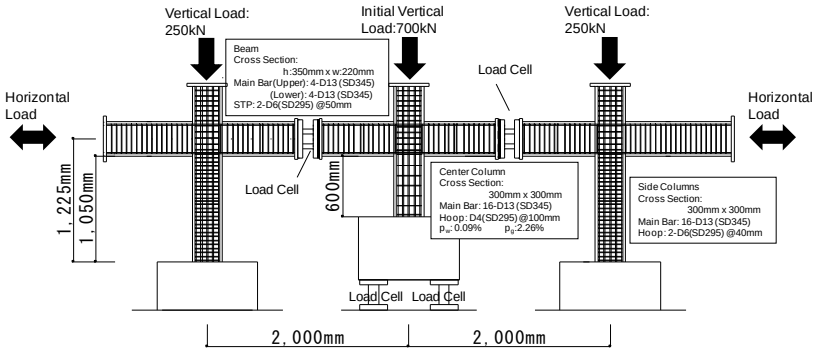


Figure 5 Drawing of specimen F0109

Table1 Material properties

	Concrete	
	Compressive Stress[N/mm^2]	Elastic modulas [N/mm^2]
F0101	34.7	$2.56x10^4$
F0109	26.9	$2.60x10^4$
F0103 F0203 F0102	29.2	$2.25x10^4$
		Yeld stress [N/mm2]
F0101	D6	370
	D10	318
	D16	378
	D19	379
	D22	396
F0109	D4	352
	D6	295
	D13	349
F0103 F0203 F0102	D4	365
	D13	381
	D16	366
	D19	382

Table2 Basic properties of center columns

Name	F0101	F0109	F0203	F0103	F0102
Cross Section[mm]	400x400	300x300	300x300	300x300	300x300
Longitudinal Reinforcement	16-D22(SD345)	16-D13(SD345)	12-D16(SD345)	12-D16(SD345)	12-D19(SD345)
p_g[%]	3.87	2.26	2.65	2.65	3.83
Transeverse Reinforcement	D6@150(SD295)	D4@100(SD295)	D4@40(SD295)	D4@100(SD295)	D4@100(SD295)
p_w[%]	0.11	0.08	0.21	0.08	0.08
Initial Vertical Load[kN]	250	700	300	300	250
η	0.05	0.29	0.12	0.12	0.10
N/Asσ y	0.10	0.99	0.34	0.34	0.20
R_{u0}[%]	10.71	1.18	2.42	1.96	4.81

columns. Center column of F0101 specimen has higher axial capacity as shown in Table2. Specimen F0109 has the poorest lateral reinforcement, therefore, expected to have brittle axial collapse. F0203 and F0103 are almost identical specimen except for transverse reinforcement. These specimen has designed to confirm effects of N_{R_T} (residual axial capacity by transverse reinforcement). F0102 has almost same longitudinal reinforcement ratio (p_g: section area of longitudinal bars normalized by cross section area of each column) with F0101 although axial load is two times larger than F0101.

In addition, side columns and half of beams of F0109 were reused at F0103, F0203 and F0102 because these members were less damaged.

3.2 Measurement and Loading Cycles

Horizontal cyclic loads are applied by two hydraulic jacks fixed at the ends of beams. Load cells to measure axial stress and shear stress are installed at middle of side columns of F0101 (see Figure4), bottom of center column and middle of beams of the other specimens (see Figure5).

F0101 was subjected to three cycles of 1/800rad, 1/400rad, 1/200rad, 1/100rad, 1/50rad and 1/33rad of story drift angle which are calculated as average horizontal displacement of the side columns divided by story height which is the height from top of stub to center of top joint of the each column. The others were subjected to two cycles of 1/800rad, 1/400rad, 1/200rad, 1/100rad and 1/67rad of story drift angle.

In addition, although cyclic loading were conducted until specimens showed axial collapse, additional axial load was applied to center column of specimens which didn't show axial collapse.

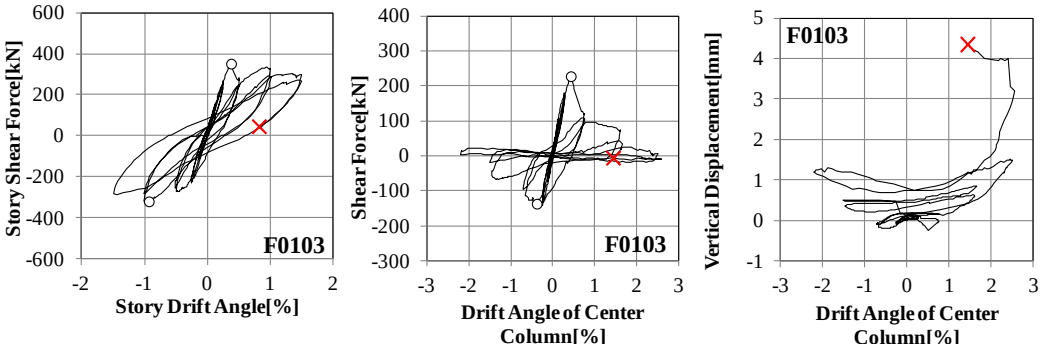


Figure6 Results of F0103

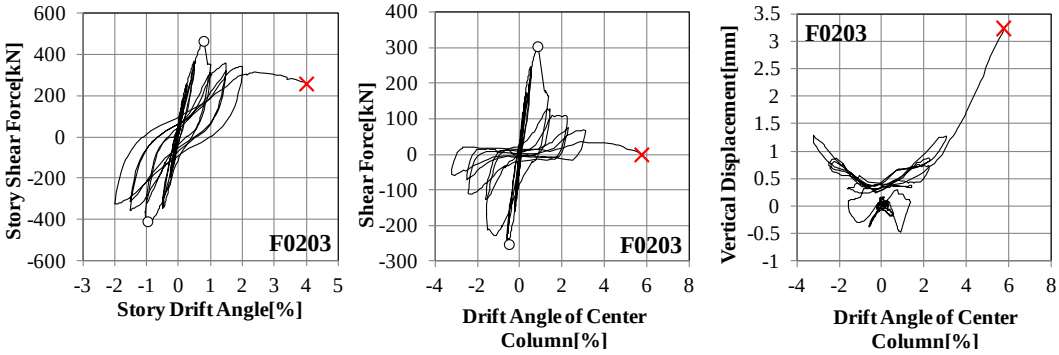


Figure7 Results of F0203

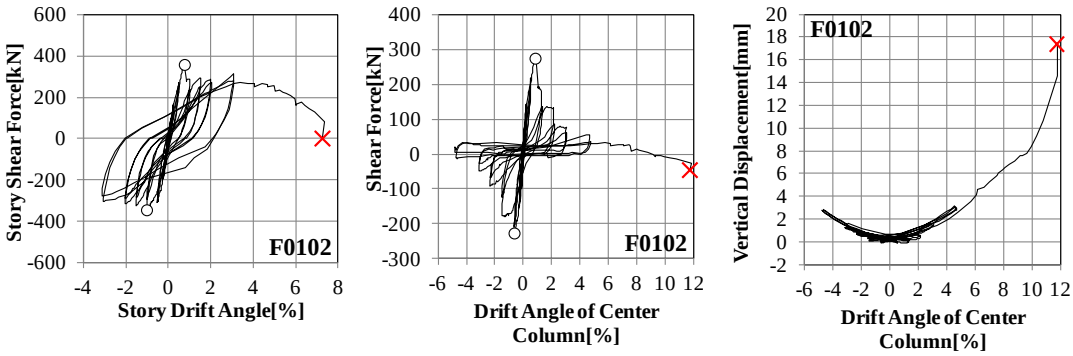


Figure8 Results of F0102

3.3 Test Results

In this paper, results of F0203, F0103 and F0102 will be mentioned in detail and refer to authors' previous paper (2011) for F0101 and F0109. Results of F0103, F0203 and F0102 are shown in Figure6, Figure7 and Figure8, respectively.

F0103 specimen showed about 350kN of maximum story shear force at 0.36% of story drift angle (see Figure6). After that, shear failure of center column occurred and shear capacity of the column and story rapidly decreased. After the cycle of 1/67rad, vertical displacement (downward direction as +) rapidly increased and vertical collapse (3hinges in the beams) was observed. In addition, at the point of vertical collapse, shear capacity of the center column reaches almost zero.

F0203 showed more ductile behavior than F0103(see Figure7). About 450kN of maximum story shear force was shown at 0.8% of story drift angle. Gradual decreasing of shear capacity was observed after shear failure of center column. In the process of decreasing, although vertical displacement was increased, vertical collapse was not observed until 4% of story drift angle. Ductility of F0203 was significantly improved by comparing F0103 which was given a half of transverse reinforcement.

In specimen F0102, at 0.75% of story drift angle, about 350kN of maximum story shear force and shear failure of center column were observed (see Figure8). Shear capacity of story decreased until 2% of story drift angle, after that, it raised until 4% of story drift angle. The reason is that shear force of side columns raised at that region regardless of decreasing of shear capacity of the center column. In region of over 4% of story drift angle, story shear capacity was decreased because side columns also showed shear failure (see Figure9). Vertical displacement of a side column significantly increased, therefore, relative vertical displacement of center column which means deformation of a beam wasn't increased. It is the reason why vertical displacement when F0102 collapsed such a large vertical

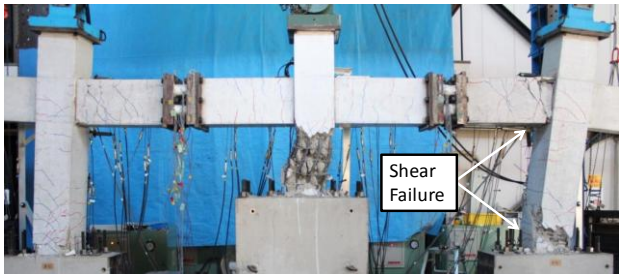


Figure9 F0102 at 6% of story drift angle

displacement (see Figure8). Then horizontal loading was stopped and additional axial load was applied to center column. Because of additional loading, vertical displacement of the column is rapidly increased and specimen showed vertical collapse.

3.4 Observation of Pictures

Figure10 shows pictures when shear failure occurs. Angles of shear crack are almost 30° on average, therefore, 30°was taken as φ.

After the loading, for center column of F0103, F0203 and F0102, broken concrete was raked from the core of columns to observe the wedge shaped area mentioned above as shown in Figure11. The angles of wedge shaped area is also shown in Figure11, they ranged from 24° to 57° and 40°on average, therefore, 40°is taken as γ.

In addition, referring Figure11, although snapped transverse reinforcements were observed, all the bars are may not be effective to resist to axial load. On average, half of transverse reinforcements were snapped and they're estimated to work as confinement, therefore, the effect of transverse reinforcements are considered as half(see Eq.(5),(6)).

$$N_R = \frac{A_s \cdot \sigma_y}{\left(1+\frac{A_s \cdot \delta}{2Z_p}\right)} + \frac{2D_e \cdot A_{sw} \cdot \sigma_{wy}}{s \tan 30° \tan 40°} \frac{1}{2} \qquad (5)$$

$$R_{U0} = \frac{2Z_p}{A_s \cdot h_0}\left(\frac{A_s \cdot \sigma_y}{N - \frac{D_e \cdot A_{sw} \cdot \sigma_{wy}}{s \tan 30° \tan 40°}} - 1\right) \qquad (6)$$

4. PUSHOVER ANALISYS

4.1 Analytical model and method

Pushover analyses are carried out to check suitability of the model mentioned above and estimate vertical collapse of structures. Structural model is shown in Figure12. First, members were distinguished as flexure members or shear members. Flexure members consist of an elastic shear spring, an elastic axial spring and inelastic flexure springs. Tri-linear model is applied to inelastic flexure springs based on AIJ standard (2010). Shear members have elastic flexure springs,

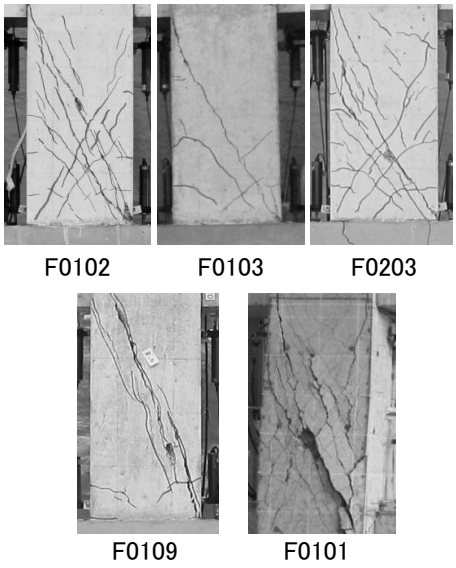


Figure10 Pictures at shear failure

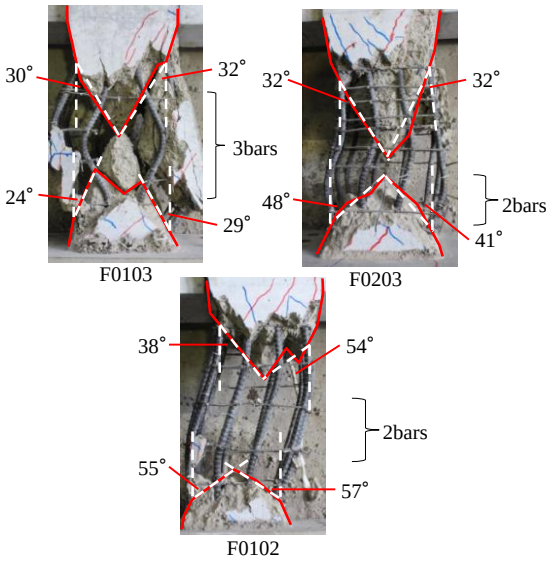


Figure11 Angles of wedge shaped area and snapped transverse reinforcement

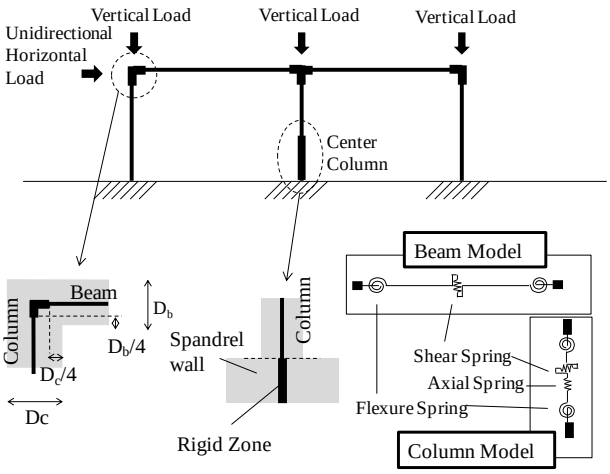


Figure12 Structural modeling

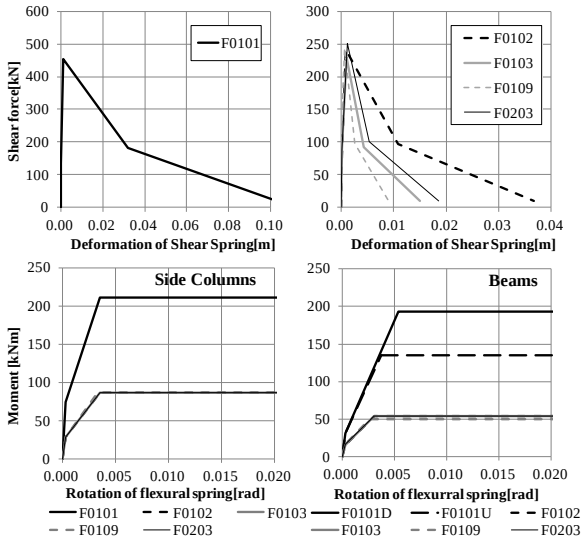
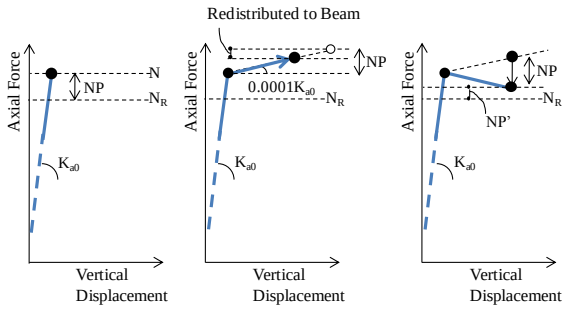


Figure 13 Backbone curve of inelastic springs



(a)Calculate NP (b) Calculate Force to Beams (c)Cancel NP

Figure14 Calculation of inelastic axial spring

an inelastic shear spring and an inelastic axial spring. quad-linear model similar to Figure 3 is applied to inelastic shear spring assuming 10kN as minimum shear capacity. Inelastic shear springs and flexure springs used in the analysis are shown in Figure13.

Calculation methodology of stress and displacement of inelastic axial spring is a bit complicated. As shown in Figure 14, residual axial capacity shown in Eqn.(5) and axial force carried by column is compared step by step. When former becomes lower than later, unbalanced load NP is calculated (Figure14(a)). To calculate vertical load carried by beams, then, stiffness of axial spring of the column was changed to 0.0001Ka (Ka: elastic axial stiffness) and NP was applied as vertical load to node at top of the column (Figure14(b)). After that, as shown in Figure14(c), NP was canceled from the column and NP' was calculate as residual unbalanced load (if NP' is not negligible, back to Figure14(a)).

Moreover, for F0101 and F0102 which were applied additional axial load in the middle of experiment, additional cases of pushover analysis are carried out because increasing vertical load in the middle of pushover is difficult. In these

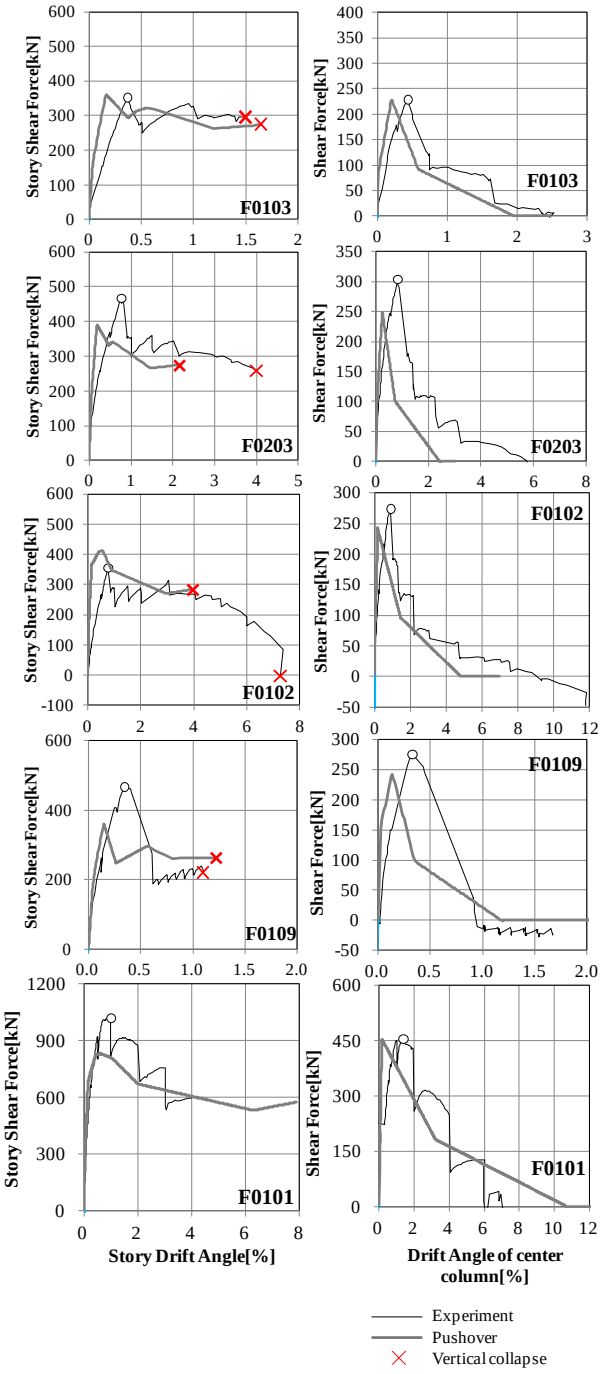


Figure 15 Comparison of experimental with analytical results

cases, maximum vertical load observed in the experiment was applied in the analysis (initial vertical load was applied in basic cases). If the model and analytical method are valid, experimental results expect to range between basic case and additional case.

4.2 Analytical Results

Figure15 shows analytical results and backbone curve of experimental results. As for Figure15, analytical results show good agreement with experiment especially their capacity degradation slope. Magnitude of correlation of

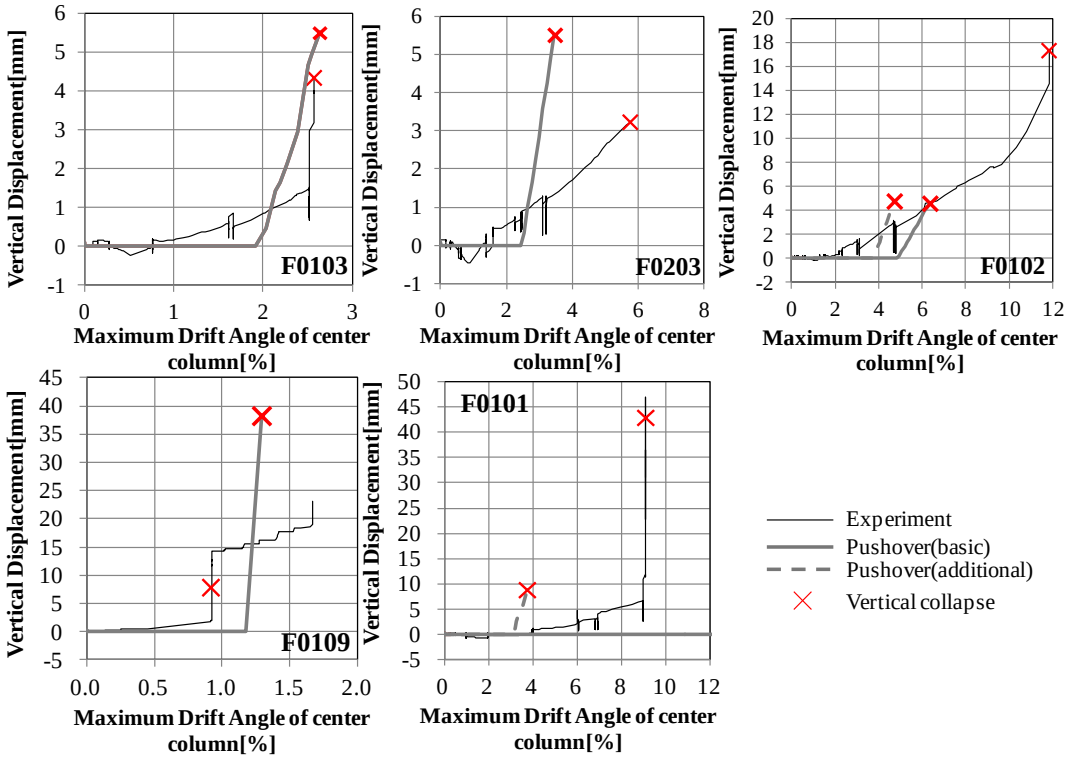


Figure16 Comparison of vertical displacement

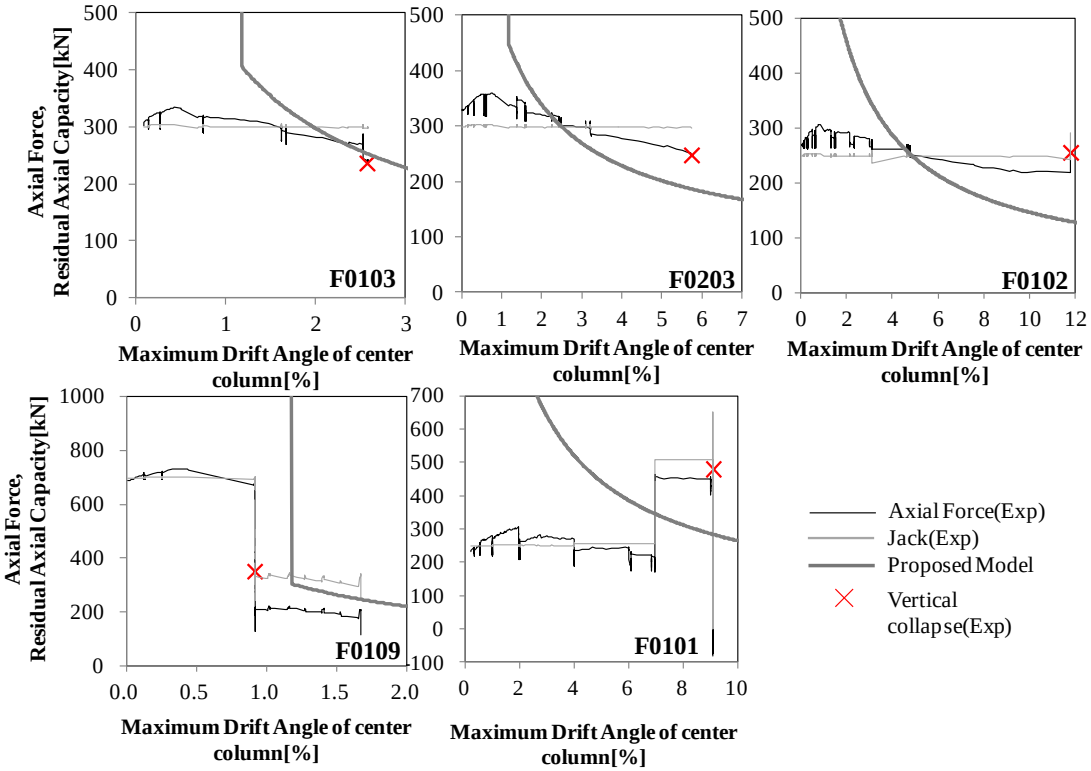


Figure17 Comparison of axial load (experimental with analytical model)

ductility of center column calculated by the model is also shows higher suitability. However, their maximum capacity were almost underestimated and elastic stiffness of analysis was more or less higher (but these are not main point of these studies).

Vertical displacement and maximum lateral drift of center column was shown in Figure16. In addition, for F0102 and F0101, the results of additional cases are also shown in Figure16. Analysis of more brittle specimens such as F0103 and F0109 shows higher suitability with the experiment especially point of vertical collapse and tendency of increment of vertical displacement. Although the other

specimens are not good to estimate point of vertical collapse, all these analyses could estimate as safe side of experiment. In addition, collapse displacement of F0102 was significantly larger than both basic case and additional case of pushover.

Figure17 shows that residual axial capacity of the model and vertical loading process of the experiment. Vertical load to center column applied by jack in the experiment was also shown in Figure17, difference between axial load and vertical load by jack is distributed to beams as shear force. Axial capacity degradation and vertical load redistribution behavior was observed.

As shown in Figure17, All the specimens except F0103 and F0109 collapsed at higher axial force than residual axial capacity by the model. On the contrary, for more brittle specimen such as F0103 and F0109, residual axial capacity of specimens at collapse shows good agreement with the model. These results suggest that residual axial capacity by the model is almost valid for brittle specimens although tend to underestimate ductility for other specimens.

5. CONCLUSIONS

Contributions of this paper are shown in as follows;

1) From the Equilibrium of force, model to estimate the residual capacity of the column was constructed
2) Experimental study of RC frame including shear and flexure column was carried out. Vertical collapse was observed in the experiment.
3) Capacity degradation slope estimated by proposed model showed good agreement with experiment.
4) Displacement that vertical collapse occurred could be estimated by pushover analysis especially for more brittle specimens.

Acknowledgements:

This work was supported by KAKENHI 23360238, Grant-in-Aid for Scientific Research (B). Experimental study of F-01 specimen was carried out with Building Research Institute of Japan for research topic titled "Study on explicit criteria for technical decision necessary for structural calculation of general buildings". The authors express gratitude to them and all who assisted him in this research.

References:

AIJ.(2004). "Guidlines for Performance Evaluation of Earthquake Resistant Reinforced Concrete Buildings (Draft) ". (in Japanese).

Mukai, T., Saito T., Fukuyama, H. and Kinugasa, H. (2010), "Experimental Study on Structural Performance Evaluation for R/C frame witha Brittle Column" AIJ annual meeting 2010(in Japanese).

ELWOOD, Kenneth, J. and MOEHLE, Jack, P. (2004). "Evaluation of Existing Reinforced Concrete Columns". The 13th World Conference Earthquake Engineering, Paper No. 579.

Yoshimura, M.(2008). "Formulation of Post-Peak Behavior of old Reinforced Concrete Columns until Collpase" The 14th World Conference Earthquake Engineering.

Matsukawa, K., Maeda, M., Al-Washali, Hamood. and Takahashi,K. (2012), "Research For Collapse of R/C Frame Composed of Shear And Flexure Column" , 15th World Conference Earthquake Engineering.

Fukuyama,H., Mukai,T., Kabeyasawa,T., Suwada,H., Maeda,M., Kinugasa,H,. Takahashi,N,. Nakano,Y., Seki,M., Ota,T.(2011). "Experimental Test on Structural Performance for RC Frame with Brittle Column Part.1 Outline of Experimental Test". Proceedings of Annual Convention of Architectural Institute of Japan(AIJ). pp.807-808. (in Japanese)

AIJ.(2010).AIJ "Standard for Structural Calculation of Reinforced Concrete Structures. " (in Japanese).

10CUEE CONFERENCE PROCEEDINGS
10th International Conference on Urban Earthquake Engineering
March 1-2, 2013, Tokyo Institute of Technology, Tokyo, Japan

EXPERIMENTAL STUDY ON REINFORCED CONCRETE FRAMES WITH BUCKLING RESTRAINED BRACES

Yusuke Maida[1], Zhe Qu[2], Shoichi Kishiki[3], Toshio Maegawa[4], Makoto Hamada[4], Hiroyasu Sakata[5],and Akira Wada[6]

1) JSPS Research Fellow, Graduate Student, Department of Built Environment, Tokyo Institute of Technology, Japan
2) Post-Doctoral Research Fellow, Center for Urban Earthquake Engineering, Tokyo Institute of Technology, Japan
3) Lecturer, Department of Architecture, Osaka Institute of Technology, Japan
4) Technical Research & Development Institute, KUMAGAIGUMI Co., Ltd., Japan
5) Professor, Structural Engineering Research Center, Tokyo Institute of Technology, Japan
6) Professor Emeritus, Tokyo Institute of Technology, Japan
maida.y.aa@m.titech.ac.jp, qu.z.aa@m.titech.ac.jp, kishiki@archi.oit.ac.jp, tmaegawa@ku.kumagaigumi.co.jp, mhamada@ku.kumagaigumi.co.jp, sakata.h.aa@m.titech.ac.jp, wada@akira-wada.com

Abstract: Cyclic loading test of subassemblies of continuously buckling restrained braced RC frames is conducted to evaluate the behavior of the connection details of BRBs and its influence on the surrounding RC components. Each subassembly consists of a RC beam-to-column joint with two columns (lower and upper stories), a beam framing into it and a set of BRBs that are diagonally connected to the beam-to-column joint. To achieve necessary boundary conditions, the specimen is rotated 90 degrees and is loaded with two displacement-controlled horizontal actuators at the column bottom and the beam end. It was observed that for all the specimens, BRBs yield and start to dissipate energy at an early stage with story drift ratios much smaller than those at beam yielding. The concrete corbels and the pre-stressing anchor bolts provide not only sufficient strength but also large stiffness to minimize the deformation loss in the BRB connections.

1. INTRODUCTION

In recent years, applications of BRBs in reinforced concrete (RC) frames have attracted much attention, in which, the connection of BRBs to RC frames is important. However, there are not commonly accepted details of installing BRBs on RC frames. The authors suggested a continuously buckling restrained braced frame system in which the BRBs are arranged in the form of a Warren truss (Maida et al, 2011). The corresponding BRB connection detail in the proposed system, which consists of anchor bolts and RC corbels, has been confirmed effective through component tests and subassemblage tests with BRBs simulated by force-controlled jacks (Qu et al, 2011). However, some other important issues, such as the performance of the BRBs in the proposed system, need to be investigated. To do this, subassemblies consisting of RC beam, column and BRBs of the proposed system were subjected to cyclic loading. The major parameter of this test investigation was the proportion of the yield strength of the BRBs in the upper and the lower stories. This experiment confirmed the influence of the unbalanced BRB force in the upper and the lower stories on the performance of the BRB connection.

2. EXPERIMENTAL PROGRAM

The specimens were 1/2 scale RC beam and column subassemblies with BRBs that resembles the trial design of a high-rise RC building (Kikuta et al, 2010). The details of the specimens are shown in Fig. 2.1 and 2.2. Specimen properties are shown in Table 2.1. For each specimen, BRBs in the upper and the lower stories were attached to the beam-to-column joint through a single gusset plate. The inclination angle of the BRBs was 40.4 deg. A group of eight anchor bolts fastened the gusset plate to the concrete joint and high strength non-shrink grout was filled between the gusset plate and the two RC corbels projecting from the column. Mortar filled steel tubes were used to restrain the buckling of the core of the BRBs (Fujimoto et al, 1988).

The major difference among the specimens was in the proportion of the yield strengths of the BRBs in the upper and the lower stories, and in the mechanism of resisting the horizontal force on the gusset plate. Four specimens were tested. These were '75-75N' of 750 kN BRBs for both the upper and the lower story; '50-75N' of a 500 kN BRB in the upper and a 750 kN BRB in the lower story, which resembled the case for a middle story of a high-rise building where the yield strength of the BRBs is changed; '0-75N' of only a 750 kN BRB in the lower story, which resembled the top story of a building. In the above three specimens, the

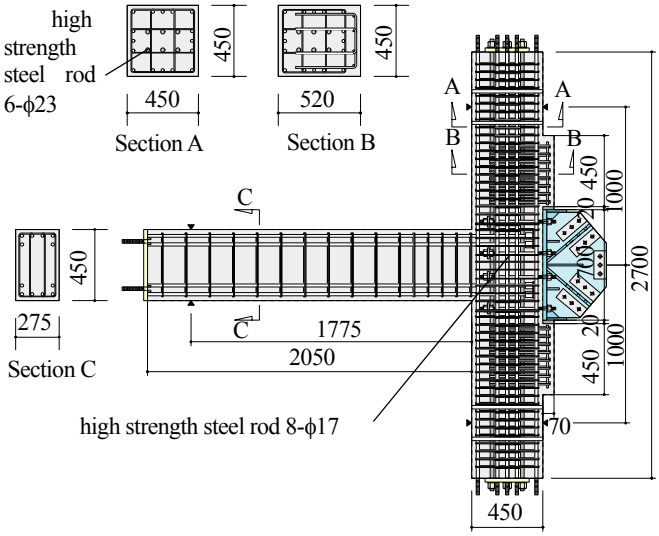


Figure 2.1. Details of specimens

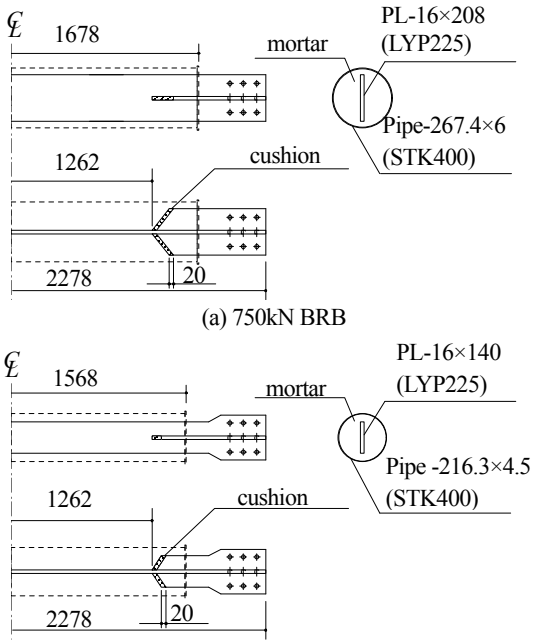


Figure 2.2. Details of BRBs

Table 2.1. Specimen Specifications

	75-75N	50-75N	0-75N	0-75S
Beam dimensions (mm)	275×450			
Beam longitudinal rebar	6-D19			
Stirrups in corbels	D10@50 - 8 legs			
Pre-tension per bolt (PC rod6-ϕ17) (kN)	571.2	571.2	571.2	0
Column dimensions (mm)	450×450			
Column longitudinal rebar	12-D19			
Column hoop	D10@70 - 4 legs			
Beam stirrup	D10@70 - 2 legs			
Yield strength of upper BRB (kN)	750	500	0	0
Yield strength of lower BRB (kN)	750	750	750	750
Presence of strut	no	no	no	yes

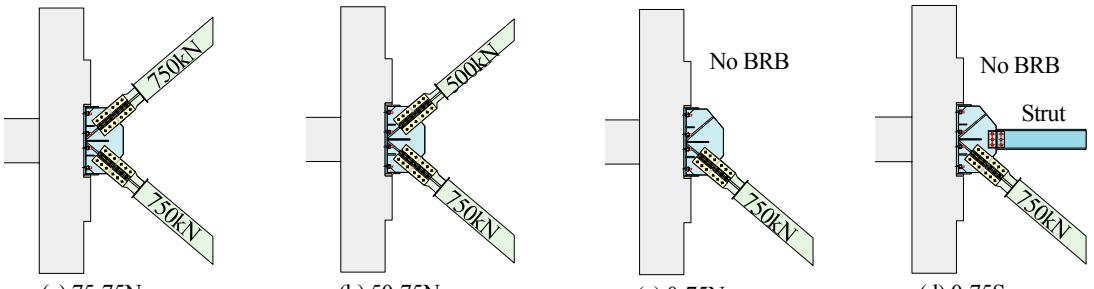


Figure 2.3. Configuration of BRBs and strut

anchor bolts for fastening the gusset plate was pre-tensioned to increase the stiffness of the connection. In the fourth specimen, namely '0-75S' in which only a 750 kN BRB was installed in the lower story, the anchor bolts were not pre-tensioned. Instead, a steel strut was installed to help resisting the horizontal force on the gusset plate (see Fig. 2.3).

High strength steel rods of 17 mm diameter were used for the anchor bolts. For each of the first three specimens, the group of eight steel rods was prestressed to provide 571.2 kN pre-tension, which equals the horizontal component of the yield strength of a single 750kN BRB, that is, $P_y\cos\alpha$, where P_y is the yield strength and α is the inclination angle of the BRB. In other words, each anchor bolt in the group was prestressed to 71.4 kN.

The test setup is shown in Fig. 2.4 and Photo 2.1. The

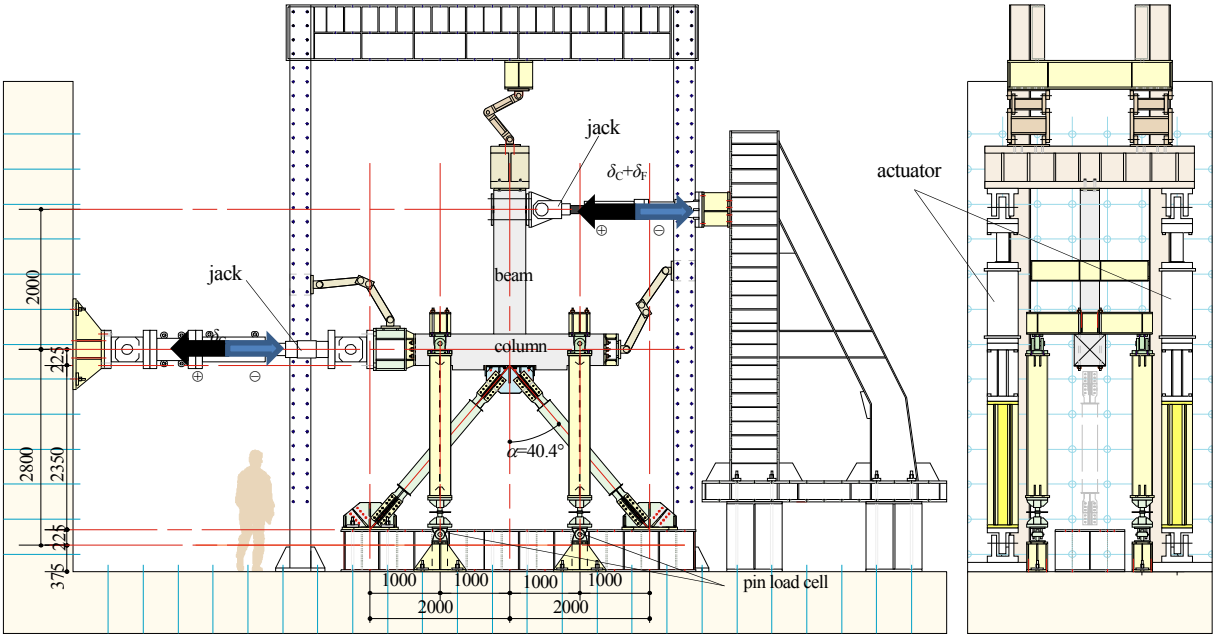


Figure 2.4. Experimental setup



Photo 2.1. Experimental setup

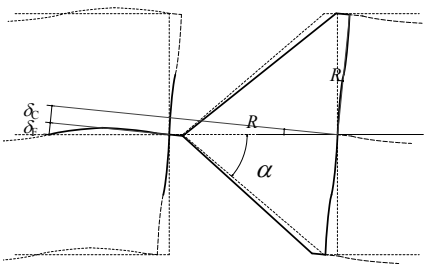


Figure 2.5. Deformation of building

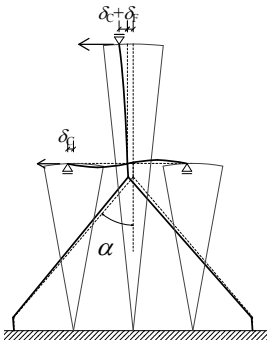


Figure 2.6. Deformation in experiment

specimen was rotated 90 degrees clockwise. The top and the bottom of the column were supported by pin rollers that allow for horizontal movement. The beam was restrained at its free end by two actuators in its axial direction. The bottom of the column and the beam free end were driven by two horizontal displacement-controlled jacks to impose deformation to the specimen.

The displacement of the two horizontal jacks kept a certain proportion during the loading. When the column was displaced by δ_C, resulting in a story drift ratio R, the beam end should be displaced by $\delta_C+\delta_F$ in order to create the deformation pattern as shown in Fig. 2.5. The two vertical actuators were also displacement-controlled to exhibit zero displacement during the test. Cyclic loading with increasing displacement amplitudes was conducted. For each specimen, two cycles were carried out for story drift ratio amplitudes of 1/1600, 1/800, 1/400, 1/200, 1/100. After that, only one cycle was carried out for amplitudes of 1/50 and 1/33.

3. EXPERIMENTAL RESULTS

3.1 Global response

The crack patterns at story drift ratio R = -1/100 of all specimens are shown in Fig. 3.1. For all specimens, flexural cracks occurred on the beam ends at an early stage. Afterwards, flexural-shear cracks accompanied the increase of the story drift ratio. The longitudinal rebar of beam yielded at R = 1/120 for the '75-75N' specimen, and shear cracks were observed at R = 1/100 on the beam-to-column joint.

The story drift ratio versus shear force relationship of the '75-75N' specimen is shown in Fig. 3.2(a). The story shear force can be separated into two parts, that is, the contribution of the RC part in the subassembly, θ_F, and that of the BRBs, which is directly related to the axial force of the BRBs, N_{BRB}. The hysteresis of the RC part and the BRB

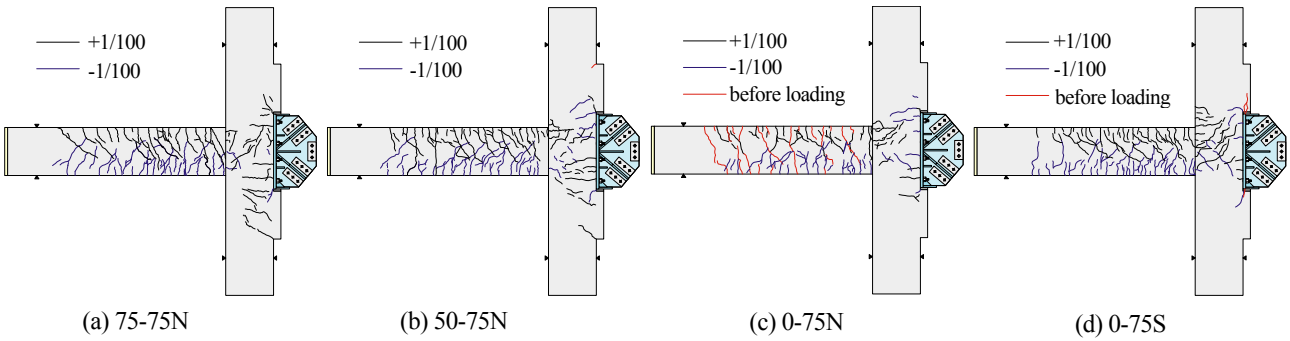


Figure 3.1. Cracks of RC part at R=+1/100 and R=-1/100

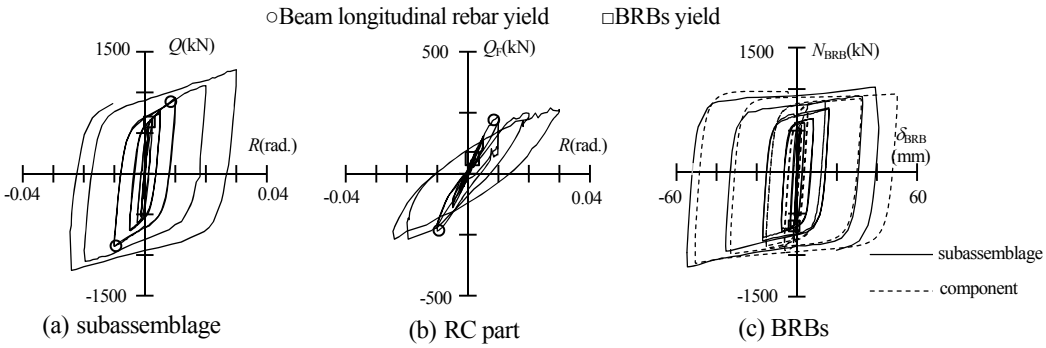


Figure 3.2. Behavior of '75-75N' specimen

in the lower story is shown in Fig. 3.2(b) and (c). Compressive force was acted on the beam in positive loading because of the difference in the yield strength of the upper and the lower BRBs for '50-75N', '0-75N' and '0-75S' specimens. As a result, the yield strength of the beam was a little bit increased for these specimens. The accumulative hysteretic energy dissipation of the RC part, W_F, and that of the upper BRB, W_{DU}, and the lower BRB, W_{DL}, for '75-75N' specimen are shown in Fig. 3.3. At R = -1/100, the energy dissipated by the lower BRB, W_{DU} = 98.6kNm, by the upper BRB, W_{DL} = 96.0kNm, and by the RC part, W_F = 9.2kNm. It is evident that the BRBs are very effective in dissipating energy in a RC frame by the fact that the energy dissipation in each BRB was approximately 10 times that in the RC part. Only the results for '75-75N' specimen is shown here as an example. Similar observations were made for all the other specimens.

The development of the crack width of the beam of '75-75N' specimen is shown in Fig. 3.4. The crack width was measured on the beam surface at the projecting position of the longitudinal rebars. The total and the maximum width is the sum and the maximum of the width of all the cracks on the beam surface going through the longitudinal rebars, respectively. For all the specimens, the total crack width was about 2 mm and the maximum one was about 0.2 mm at R = -1/100.

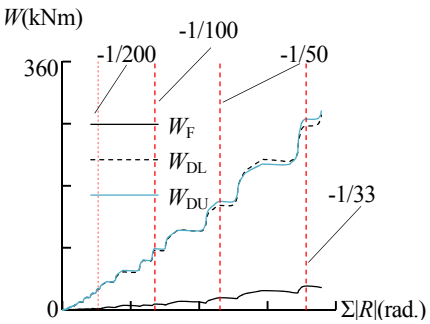


Figure 3.3. Hysteretic energy dissipation

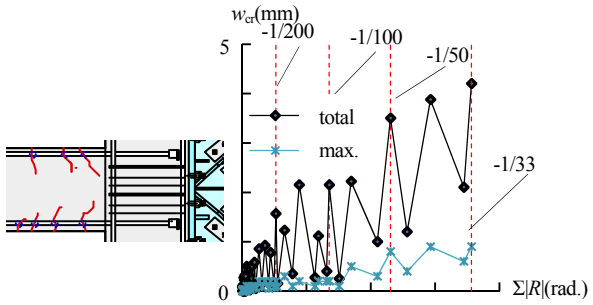
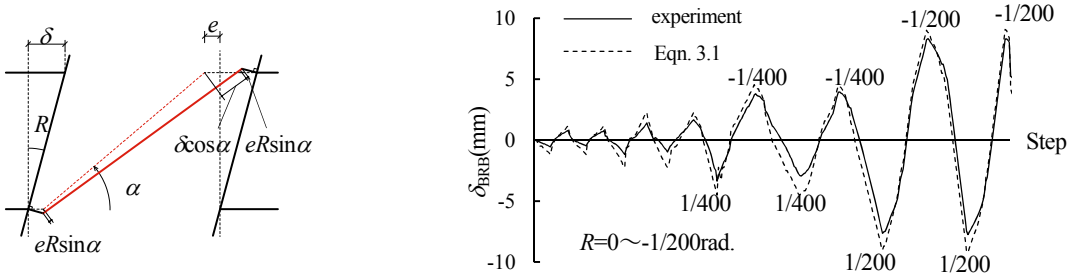


Figure 3.4. Crack width on beam

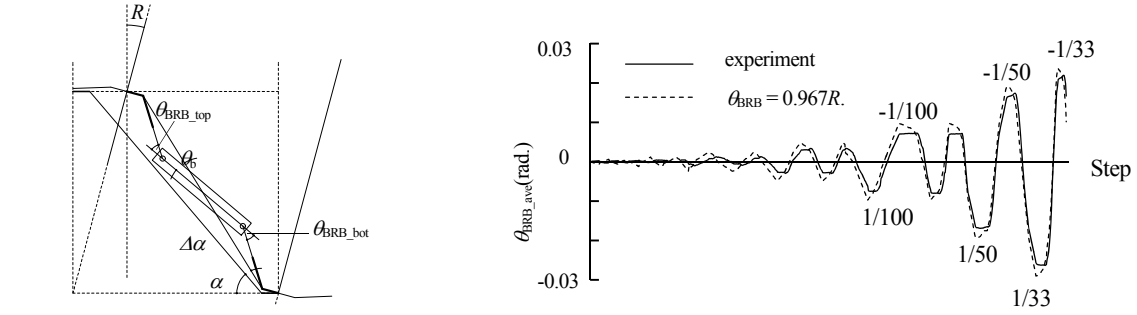
3.2 Behavior of BRBs

The axial deformation of BRBs measured in the experiment is compared with the ideal work point-to-work point deformation calculated from the story drift ratio (Eqn. 3.1) in Fig. 3.5. The latter can be regarded as a maximum deformation a BRB should be able to sustain if the connection is rigid. In the experiment, however, it was observed for '0-75N' and '0-75S' specimens that the measured axial deformation of the BRB was only 40 ~ 50% of the ideal displacement when the deformation of the subassembly was small, for example, the story drift ratio is less than 1/400. When the story drift ratio became larger, the ratio of the measured BRB deformation and the ideal brace



(a) work point-to-work point deformation calculated (b) Comparison between experiment and Eqn. 3.1

Figure 3.5. Axial deformation of BRBs '75-75N'



(a) plastic rotations at both ends calculated (b) Comparison between experiment and $\theta_{BRB} = 0.967R$.

Figure 3.6. Rotation of BRB end of '75-75N' specimen

displacement increased significantly. It is no less than 90 % for story drift ratio greater than 1/200 for all the specimens.

$$\delta_{BRB} = \delta \cos\alpha + 2eR \sin\alpha \qquad (3.1)$$

where e is eccentricity of the BRB work point with respect to the column and beam centerlines.

Different from component test of a single BRB subjected to uniaxial loading, the BRBs in the subassembly test sustained obvious plastic rotations at both ends (Fig. 3.6(a)). The measured end rotation is shown in Fig. 3.6(b). The rotation θ_{BRB_ave} is taken as the average of θ_{BRB_top} and θ_{BRB_bot} as shown in Fig. 3.6(a). It increased with the increase of the story drift ratio of the subassembly. This rotation can be estimated by the equation proposed by Kozai Club. (1998) from the story drift ratio R. For the present test, $\theta_{BRB} = 0.967R$. The estimated rotation is compared with the measured one in Fig. 3.6(b).

3.3 Behavior of BRB connection

The relationship of the horizontal displacement of the gusset plate, δ_H, versus the horizontal force on the gusset plate, P_{DH} (see Fig. 3.7), for '0-75N' and '0-75S' specimens are compared in Fig. 3.8. The tensile force on the gusset plate of the two specimens was almost the same. Notwithstanding, the maximum horizontal displacement of '0-75S' specimen was about 1.1 mm in both the pulling and the pushing direction, while that of '0-75N' specimen was only about 0.25 mm in the pulling and negligible in the pushing direction. The pre-tension of the anchor bolts seems more effective than installing a strut for resisting the tensile force on the gusset plate.

The relationship of the vertical displacement of the

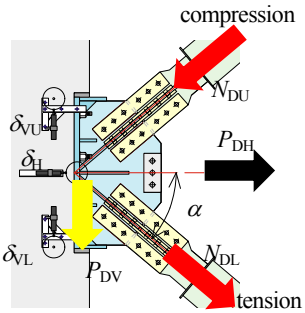


Figure 3.7. Location of displacement transducers

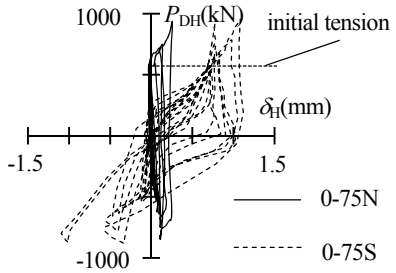


Figure 3.8. Horizontal displacement of gusset plate - tension of gusset plate relations

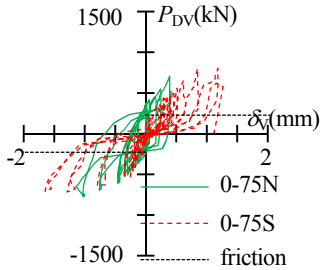


Figure 3.9. Vertical displacement of gusset plate - shear force of gusset plate relations

gusset plate, δ_V, versus the shear force on the gusset plate, P_{DV}, for '0-75N' and '0-75S' specimens are compared in Fig. 3.9. The vertical displacement δ_V is taken as the average of δ_{VU} and δ_{VL} as shown in Fig. 3.7. The possible friction force between the gusset plate and the underneath concrete in '0-75N' specimen is also shown as dashed lines in the figure, assuming a coefficient of friction of 0.4 (AIJ, 2011). For the '0-75N' specimen, the gusset plate has no vertical displacement until the shear force exceeds the friction force and the corbel begins to carry the extra shear force. As a result, the shear force carried by the corbel in the '0-75N' specimen was much smaller than that in the '0-75S' specimen, where there was much less friction force on the gusset plate-to-concrete interface. Accordingly, the shear deformation, δ_V, in the '0-75N' specimen is much smaller than that in the '0-75S' specimen during the positive loading, as can be seen in Fig. 3.9. In this sense, the pre-tensioning of the anchor bolts also has an effect on the shear resistance of the BRB connection.

4. CONCLUSIONS

In this study, cyclic test of the subassemblies of continuously buckling restrained braced RC frame was conducted. It is confirmed by the test results that both the RC frame and the BRBs in the system exhibit stable hysteretic behavior. In addition, the performance of the horizontal resistance of the BRB connection was investigated. It seems more effective to introduce initial tension into the anchor bolts to resist the horizontal force than to install a steel strut.

Acknowledgements:

This work was supported by the Grants-in-Aid for Scientific Research (A) (22246070). Part of the experimental results represented in this paper is a part of a research project entitled 'Feasibility of applying buckling restrained braces in high-rise residential buildings' sponsored by Kumagai Gumi Co., Ltd.

References:

Maida, Y, Qu, Z, Kishiki, S, Sakata, H, Wada, A, et al. (2011). Applications of buckling restrained braces in reinforced concrete frames. Summaries of technical papers of AIJ annual meeting. C-2:667-678.

Qu, Z, Maida, Y, Nonoyama, M, Kishiki, S, Sakata, H, Wada, A. (2011), Hybrid control test of connections for buckling restrained braces in RC continuously braced frames, Proc. 4th Intl. Conf. on Advances in Experimental Structural Engineering, Italy, in CD-ROM.

Kikuta, S, Hamada, M, et al. (2010), "Structural Performance of RC High-rise Buildings under Long Period Seismic Ground Motion : Part 10 Experimental study on the beam column sub-assemblages with different safety margin coefficient of bond and shear, "Summaries of technical papers of AIJ annual meeting, C-2:729-730.

Fhjimoto, M, Wada, A, Saeki, E, Watanabe, A, Hitomi, Y. (1988). A study on the unbonded brace encased in buckling-restraining concrete and steel tube. Journal of Structural Engineering. Vol.35B: Architectural Institute of Japan,249-257.

Kozai Club. (1998). The earthquake response and Seismic Design Method of Steel Frames with Hysteretic Dampers, Japanese Society of Steel Construction

Architectural Institute of Japan. (2011). Stress transferring mechanism and resistance mechanism of steel-reinforced concrete joints, Architectural Institute of Japan

10CUEE CONFERENCE PROCEEDINGS
10th International Conference on Urban Earthquake Engineering
March 1-2, 2013, Tokyo Institute of Technology, Tokyo, Japan

EXPERIMENTAL STUDY ON INFLUENCE OF BENDING RADIUS OF MAIN TENSILE BARS ON STRESS TRANSMISSION IN REINFORCED CONCRETE KNEE JOINTS WITH PRACTICAL DETAIL

Tuvshin Batjargal[1)] and Hisato Hotta[2)]

1) Graduate student, Dept. of Architecture and Building Engineering, Tokyo Institute of Technology, Japan
2) Professor, Dept. of Architecture and Building Engineering, Tokyo Institute of Technology, Japan
batjargal.t.aa@m.titech.ac.jp, hotta@arch.titech.ac.jp

Abstract: In Japan, the stress transmission of R/C column and beam joints is calculated differently depending on their type of joint.In interior joints, main bars are continued through the joint panel both vertically and horizontally. Thus, the ultimate strength of interior joints is more reliable.However, in knee joints main bars are not continued. Additionally, since there is no load on knee joints from above, frictional force between concrete and main bars weakens and makes the joint panel relatively easy to break under stress transmission.In the previous studies Hotta and Nishizawa (2012), it's concluded that the sufficient inside radius of the main tensile bars that were continuously arranged through the panel from beam to column improves structural performance and prevents bearing failure of the joint panel when the joints were tested in closing direction.The objective of this following study is to show the influence of the inside radius of the main tensile bars which is separated in the joint panel as a practical design under stress transmission by conducting closing load.

1. INTRODUCTION

In Japan, the stress transmission of R/C column and beam joints is calculated differently depending on their type of joint. This calculation does not take into account the various arrangements of main tensile bars. However, the way main tensile bars are arranged is quite important because their bending radius affects the bearing failure of joint panel under stress transmission. In the previous studies Hotta and Nishizawa (2012), the objects of the studies were main tensile bars whose arrangement was continued. It was concluded that the bigger the bending radius of main tensile bars in joint panels under stress transmission, the bigger the shear strength of joint panels.

The objective of this following study is to show the influence of the inside radius of the main tensile bars which is separated in the joint panel as a practical design under stress transmission by conducting closing load.

2. OUTLINE OF TESTS

2.1 Specimens

As shown in Figure 1, there are four specimens that were made and tested. Each specimen's column and beam dimensions were the same. Column's dimension is 200x100mm. Beam's dimension is 200x80mm. All main tensile bars were separated in the joint panels.But their bending radiuses were different and thus, categorized into two types: LB26 type and LB80 type.

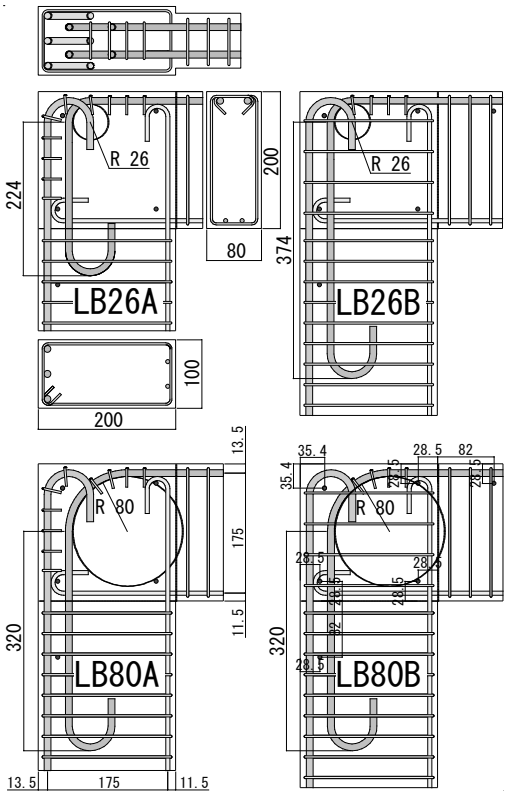


Figure 1. Dimension and detail of bar arrangement

As shown in Table 1,D10 deformed bars were used for main

tensile bars and D6 deformed bars were used for compressive bars. The columns and the beams were laterally strengthened by sufficient hoop reinforcements which were round bars with diameter of 3mm.

Table 1. Mechanical properties of reinforcing bars

Bar	Yield strength [N/mm^2]	Tensile strength [N/mm^2]	Young`s modulus $\times 10^5$[N/mm^2]
D10	459(457)	640(633)	1.92(1.83)
D6	387(381)	546(537)	1.93(1.86)
φ3	554(541)	617(627)	1.97(1.89)

In Table 2, mechanical properties of concrete are shown. First values are of LB26B, LB80A and LB80B specimens. Values in brackets indicate that of LB26A specimen.

Table 2. Mechanical properties of concrete

Comp strength [N/mm^2]	Splitting tensile strength [N/mm^2]	Young`s modulus $\times 10^4$[N/mm^2]
30.7(34.9)	2.54(2.68)	2.48(3.05)

2.1.1*LB26 type*

As illustrated in Figure 1, in joint panel, beam's main tensile bars were bent at 26 mm radius and their tails were anchored in column.In LB26A specimen, the length of the anchor was 224 mm. In joint panel, there was no lateral reinforcement.In LB26B specimen, the length of the anchor was 374 mm. In the joint panel, there were four lateral reinforcement bars placed at 45 mm span.

2.1.2*LB80 type*

As illustrated in Figure 1, in joint panel, beam's main tensile bars were bent at 80 mm radius and their tails were anchored in column. The length of anchor was 320 mm.In LB80A specimen, there was no lateral reinforcement in the joint panel.In LB80B specimen, there were four lateral reinforcement bars placed at 45 mm span in the joint panel.

2.2 Loading method and measuring method of deflection

All dimensions of specimens and loading method are outlined in Figure 2. The specimens were set to the pin and pin-roller blocks of a loading apparatus at both end plates by PC bars. The external load *P* was horizontally applied from the roller block in closing direction. The lengths of column and beam are the same and symmetrical, therefore, the axial force *N* and the shear force *V* are the same. Measurement apparatuses were set to both sides of specimens at measurement terminal points which are shown in Figure 3. These measurement apparatuses were to measure elongation of the beams and the columns, their end rotations, and shear deformation of the joint panel. Strain of reinforcing bars was not measured in the test at all because putting strain gauges influences bond characteristics of the bars

Figure 4 shows the arrangement of pi gauges to measure elongation between the measurement terminals set at the tensile region of the joint panel and the members near the critical section.

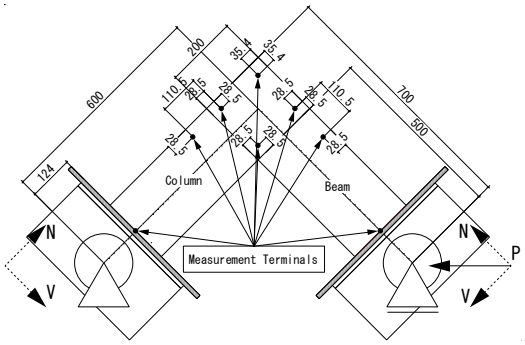


Figure 2. Method of loading

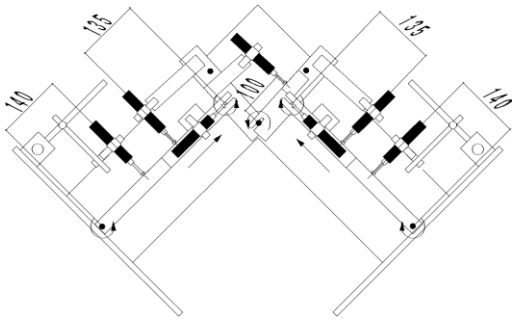


Figure 3. Apparatus for measuring deformation

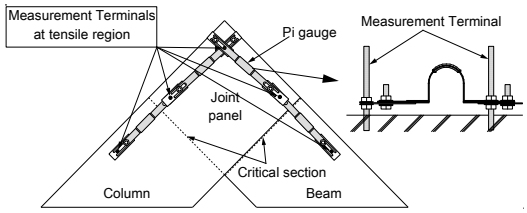


Figure 4. Pi gauges for measuring member's displacement

3. TEST RESULTS

3.1 Load deflection curves

Figures 5 and 6 show load versus deflection curves for all four specimens.Vertical axes stand for horizontal force applied to the roller end and horizontal axes stand for horizontal displacement of pin points and member's angle/joint shear strain.

There are four curves shown in each figure. The bold curve represents the relationship between horizontal displacement and horizontal load. The other three curves show each member's angle and shear strain of the joint panel.

As illustrated in Figures 5 and 6, there is horizontal line "Diagonal crack load" which was calculated by the Eq. (1).

$$V_{cr} = f_t b_j l_{dh} \quad (1)$$

Where f_t is tensile strength of concrete of which value is

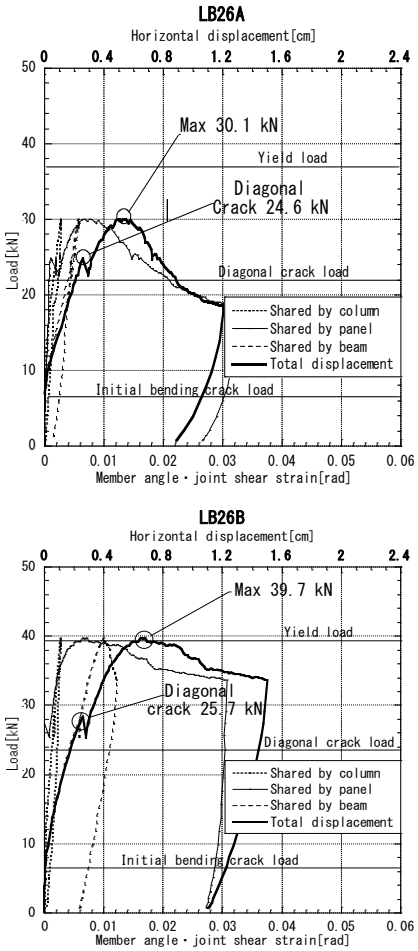


Figure 5. Load-deflection curves for LB26 type

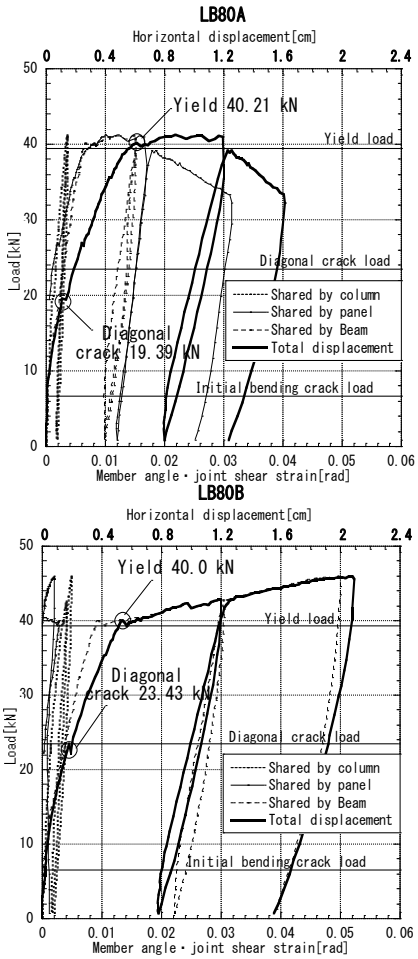


Figure 6. Load-deflection curves for LB80 type

indicated in Table 2 as splitting strength. b_j is effective breadth of joint panel and l_{dh} is distance between critical section of the beam and the end tensile reinforcing bars.

There is "Initial bending crack load" horizontal line which was calculated by Eq.(5) based on elastic section analysis of beams and occurs when the tensile strength of concrete reaches the splitting strength. As shown in Figure 2, when horizontal force*P* is applied, axial force*N* and shear force*V* are loaded to the beams and columns. Because the length of beams and columns is the same, *N* is equal to *V*.

$$V = N = \frac{P}{\sqrt{2}} \tag{2}$$

The moment*M*at critical section of beam is equal to shear force of beams *V* multiplied to the length of beams *l*.

$$M = Vl = Nl = \frac{Pl}{\sqrt{2}} \tag{3}$$

When axial force *N* is loaded to the beam, the tensile stress of concrete is calculated by following Eq. (4):

$$\sigma_t = \frac{M}{Z_e} - \frac{N}{A_e} \tag{4}$$

Substituting for Eq.(4) from Eq.(2) and Eq.(3) the initial bending crack load P_{cr} is solved for, when the tensile strength of concrete σ_t reaches the splitting strength f_t.

$$P_{cr} = \frac{\sqrt{2} \cdot f_t \cdot A_e \cdot Z_e}{A_e l - Z_e} \tag{5}$$

Where, A_e is equivalent sectional area of critical section of the beams and Z_e is equivalent section modulus of critical section of the beams.*l*is the length of the beam which is from critical section of the beam to pin roller end. The calculated value of the initial bending crack load is equal to 6.51kN. In the case of LB26A specimen, compared to other specimens, materials used had different strength. Therefore, LB26A specimen's initial bending crack load resulted in 6.9kN. LB26A's observed initial bending crack load was 8.77kN. LB26B's was 9.74kN. LB80A and LB80B were 10.77kN. Since initial bending crack loads were observed visually, observed values were slightly higher than calculated values.

Also, there is "Yield load" line which was calculated by plastic section analysis of beams and occurs when the tensile

stress of reinforcing bars reaches to the yield strength at the critical section of the members.The value of yield load was calculated as 39.9kN. In the case of LB26A, calculated yield load was 37kN.

Diagonal crack due to splitting failure of concrete occurred near the calculated crack load in all specimens and all specimens except LB26A reached calculated yield load.

Figures 7 and 8 show first diagonal crack and crack that occurred when horizontal force reached the maximum load respectively.

In the case of LB26A, many cracks around the corner where tensile bars of the beam and the column were lapped could be observed. Cracks might have been caused due to crushing of concrete. When it reached maximum load, a greater deformation was observed in the joint shear strain than member's angles (see Figure 5).

In the case of LB26B, because of the presence of lateral reinforcement in the joint panel, it had better performance results than LB26A.

Before the horizontal force reached the maximum load, beam's angle was increasing at a greater rate than joint shear strain. But once it reached the maximum load, joint shear strain started to increase rapidly and joint panel hardnessstarted to weaken gradually.Thus, it is difficult to determine whether the main tensile bars of the beam yielded or not by just looking at the figure, even though the maximum load exceeded calculated yield load. As shown in Figure 8, cracks that occurred during the maximum load are concentrated mostly where the main tensile bars of the beam bend at 90 degrees. It can be concluded that while there is lateral reinforcement, main tensile bars' smaller radius resulted in the bearing failure.

In the case of LB80A, there was no lateral reinforcement, but bending radius was bigger than LB26 type specimens. As illustrated in Figure 6, the corner lapping (where bending radius is approximately three times bigger) distributed the compressive pressure in the joint panel evenly. Thus, joint panel's strength improved and the beam yielded.

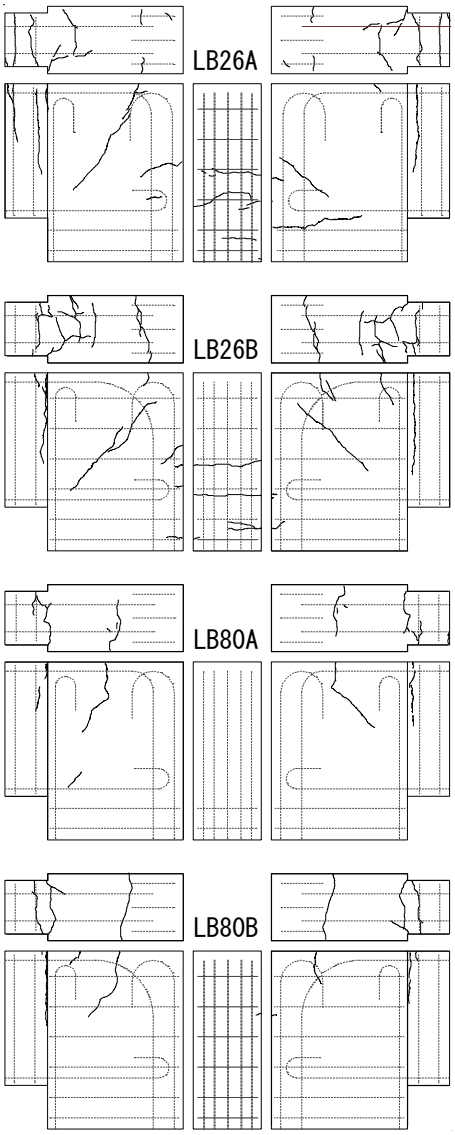


Figure 7. First splitting crack of joint panel for all specimens

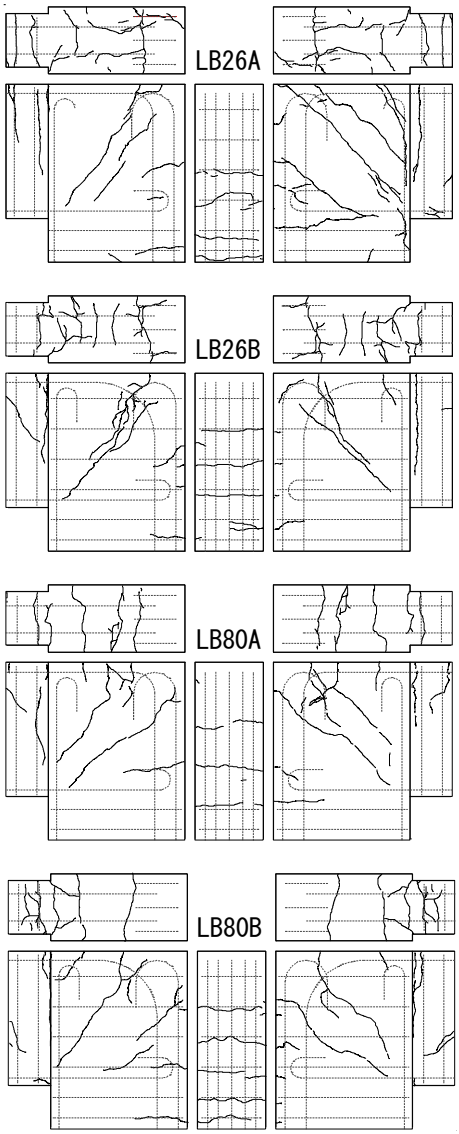


Figure 8. The crack that occurs during the maximum load for all specimens

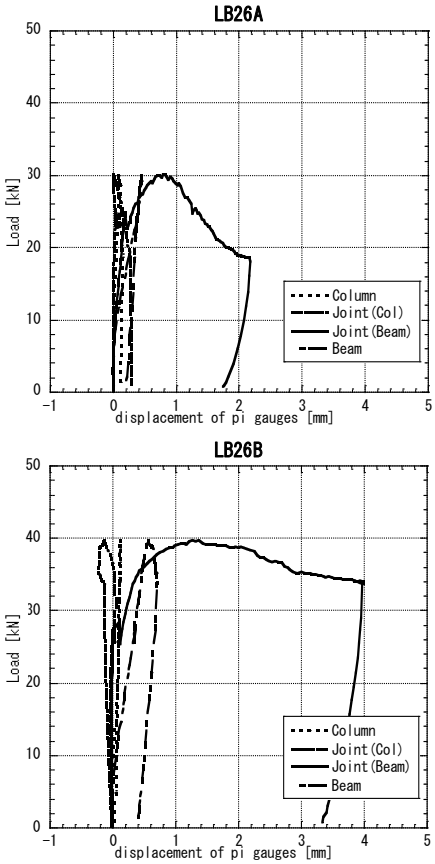


Figure 8. Pi gauge's displacement for LB26 type

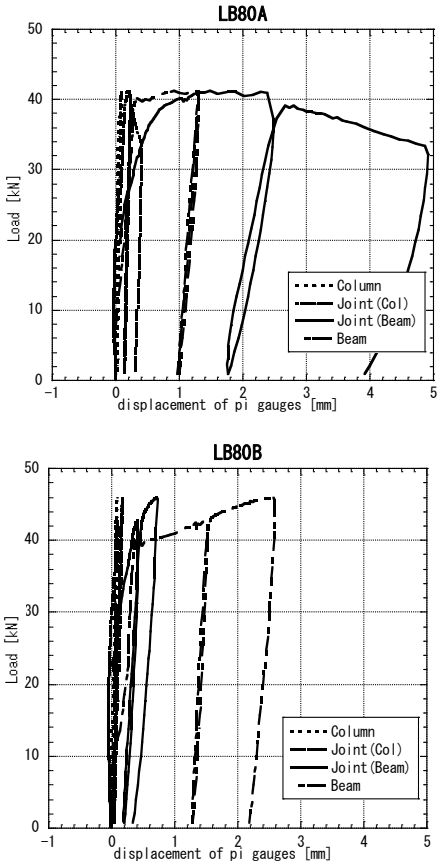


Figure 9. Pi gauge's displacement for LB80 type

In the case of LB80B, there were lateral reinforcements in the joint panel such as LB26B. The maximum load exceeded yieldload. As shown in Figure 6, there was no deformation in the joint panel, but angle of the beam changed parallel to horizontal displacement. Both the presence of the lateral reinforcement and the bigger bending radius have influenced to result in a better shear strength and to prevent any bearing failure.

3.2 Pi gauge curves

Figures 9 and 10 show pi gauge curves for all four specimens.Vertical axes stand for horizontal force applied to the roller and horizontal axes stand for pi gauge displacement. There are four curves in each figure.These figures show which member was displaced the most.

LB80B's beam displacement was the greatest compared to the other members.

In the case of LB26A, LB26B, LB80A, beam side displacement of joint panels were the greatest. This indicates that both LB80B's lateral reinforcement and bigger bending radius influenced, therefore the deformation in the joint panel was minimal.

4. CONCLUSION

Based on the test results, it is concluded that bending radius of main tensile bars of the beam in the joint panel affect shear strength of joint panel. More specifically, bending radius and shear strength of joint panel have a positive relationship.Also, adding lateral reinforcement in the joint panel increases shear strength performance of joint panel.

References:

Architectural Institute of Japan (AIJ) (2010), "AIJ Standards for Calculation of Reinforced Concrete Structures"

Hotta, H. and Nishizawa, H. "Experimental Study on Influence of Arrangement of Main Bars on Stress Transmission in Reinforced Concrete Beam-Column Knee Joints without Lateral Confinement"*Proceeding of the 15th World Conference on Earthquake Engineering*, Paper reference No.3428, Lisbon, Portugal 2012.

AIJ (1997)."Design Guidelines for Earthquake Resistant Reinforced Concrete Buildings Based on Inelastic Displacement Concept"

10CUEE CONFERENCE PROCEEDINGS
10th International Conference on Urban Earthquake Engineering
March 1-2, 2013, Tokyo Institute of Technology, Tokyo, Japan

A STUDY ON STRUCTURAL PERFORMANCE OF CES SHEAR WALLS WITH ECCENTRICALLY ARRANGED WALL PANEL:

Suguru SUZUKI[1)], Hiroshi Kuramoto[2)], and Tomoya Matsui[3)],

1) Dept. of Architectural Eng., Osaka University., Japan
2) Professor, Dept. of Architectural Eng., Osaka University., Japan
3) Associate Prof., Dept. of Architecture and Civil Eng., Toyohashi University of Technology, Japan
suzuki_suguru@arch.eng.osaka-u.ac.jp, matsui@ace.tut.ac.jp, kuramoto@arch.eng.osaka-u.ac.jp

Abstract: The objective of this study is aimed to develop the shear walls in composite CES structures composed of steel and fiber reinforced concrete. In this study, cyclic loading tests were conducted on CES shear walls with eccentrically arranged wall panel, and the structural performance, such as strength, deformability and failure modes, were investigated. The experimental variables were the position of wall panel and shear span ratio. As the result, it was clarified that the position of wall panel on the maximum shear force of CES shear walls had little effect. The deformability of CES shear walls was reduced by effect of eccentrically arranged wall panel. It was confirmed that the ultimate strength can be evaluated by the equation given by AIJ standard for structural calculation of SRC structure.

1. INTRODUCTION

Steel reinforced concrete (SRC) structures are typical composite structural systems consisting of steel and reinforced concrete (RC), which have an excellent earthquake resistance and deformability. However, the design process and construction work are more complicated than those for steel structures and RC structures. In order to solve these problems, Concrete Encased Steel (CES) structural system consisting of fiber reinforced concrete (FRC) and encased steels only, have been proposed by the authors as a new composite structural system (Kuramoto et al. 2007, Matsui et al. 2009), and continuous and comprehensive studies have being conducted to make it practical. Cyclic loading tests were also carried out on CES shear walls with different anchorage methods for the CES frame and FRC wall panel (Suzuki et al. 2011), and the basic structural performances, such as strength and failure modes, of the CES shear walls were investigated. As a result, it was confirmed that the effect of anchorage condition of wall longitudinal reinforcement on shear strength and flexural strength of CES shear walls is small. In addition, the deformability of CES shear walls improves by omitting anchorage of wall longitudinal reinforcement.

In practical use, on the other hand, a shear wall facing outside of the building was arranged eccentrically to boundary columns. In RC shear walls with eccentrically arranged wall panel, the position of wall panel has little effect on maximum shear force as shown in the existing study by Mochizuki et al. (2005). However, in CES shear walls, confinement effect from the steel to the wall panel was decreased, because the centre position of the wall panel and the position of the steel in column were different. Therefore, it is considered that the deformability of eccentric wall specimen is lower than that of non-eccentric wall specimen.

In this study, cyclic loading tests were carried out on CES shear walls with eccentrically arranged wall panel. The basic structural performance, such as ultimate strength, deformability and failure modes, of the CES shear walls were investigated.

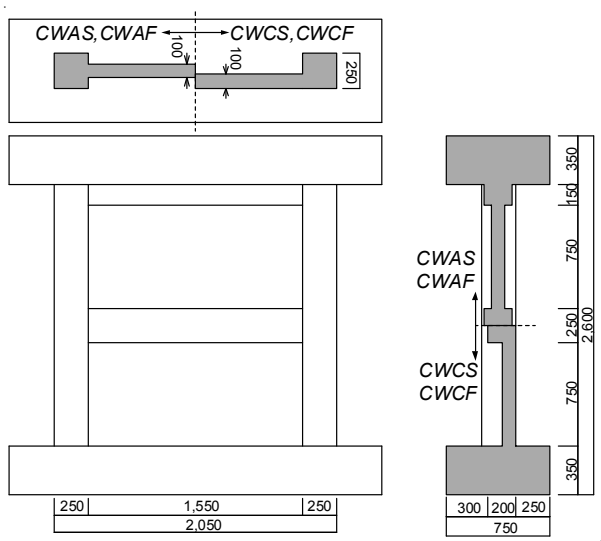


Figure 1 Test Specimen

Table 1 Detail of Specimens

Specimens		*CWAS*	*CWAF*	*CWCS*	*CWCF*
Column	*B* x *D*	250x250 (mm)			
	Steel	H-170x120x6x9 ($_sp$=4.9%)			
Beam	*B* x *D*	200x250 (mm)			
	Steel	H-148x100x6x9 ($_gp$=5.2%)			
Wall	Thickness	100 (mm)			
	Longitudinal bar	D6@75 zigzag ($_wp$=0.42%)			
	Transverse bar				
Shear span ratio		1.1	1.65	1.1	1.65
Position of wall panel		Non-Eccentric		Eccentric	
Axial force		1,260 kN		1,135 kN	

Table 2 Mechanical Properties of FRC

Specimen		σ_B (MPa)	E_C (GPa)	ε_{c0} (μ)
CWAS	1 story	38.6	24.8	2814
	2 story	36.4	26.7	2550
CWBS	1 story	42.0	25.7	2587
	2 story	30.6	29.5	2558
CWAF	1 story	41.2	25.5	2457
	2 story	38.6	27.6	2423
CWBF	1 story	40.1	24.9	2765
	2 story	35.9	24.8	3160

σ_B: Compressive strength, E_C: Elastic modulus,
ε_{c0}: Strain at compressive strength

Table 3 Mechanical Properties of Steel

Type	Specimen		σ_y (MPa)	E_S (GPa)	σ_u (MPa)
PL-6 Web (SS400)	*CWAS, CWAF*		260	190	420
	CWCS, CWCF	Column	300	197	422
		Beam	338	201	457
PL-9 Flange (SS400)	*CWAS, CWAF*		282	197	418
	CWCS, CWCF	Column	297	209	442
		Beam	317	197	448
D6 (SD295A)	*CWAS, CWAF*		345	190	501
	CWCS, CWCF		396	192	518

σ_y: Yield strength, E_s: Elastic modulus,, σ_u: Tensile strength

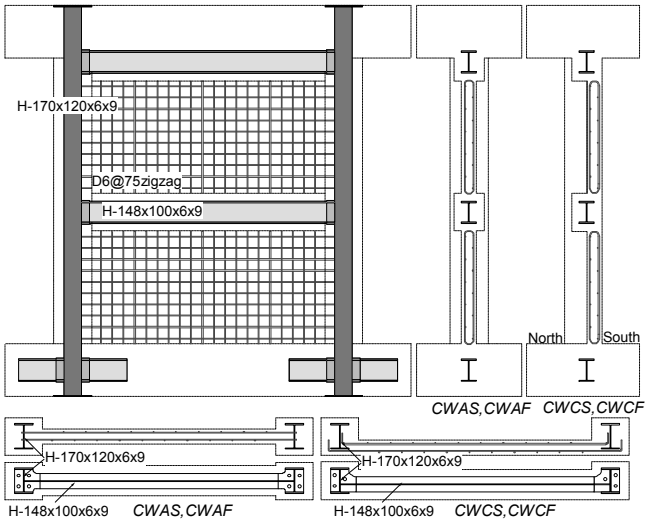


Figure 2 Bar Arrangement

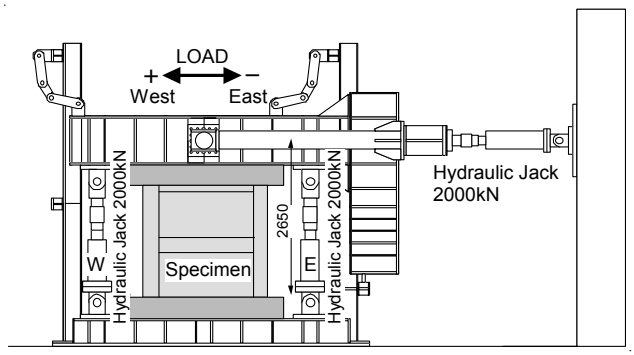


Figure 3 Loading Apparatus

2. TEST PROGRAM

2.1 Description of Specimen

The specimens were designed to simulate the lower two stories of a multi-story shear wall in a medium rise building, and were one-third-scale of prototype walls. Four specimens were prepared for this test.

The configurations and bar arrangements of the specimens are shown in Figures 1 and 2. Details of the sections are shown in Table 1. The column had a 250mm square cross-section, and the beam section was 200 mm x 250 mm. The column span length was 1,800 mm, and the wall thickness was 100 mm. The experimental variables were the shear-span ratio and the position of wall panel. The shear-span ratio was 1.1 in Specimens CWAS and CWCS, and it was 1.65 in Specimens CWAF and CWCF. Specimens CWAS and CWCS were expected to be shear failure mode. Specimens CWAF and CWCF were expected to be flexural failure mode. The position of wall panel for Specimens CWAS and CWAF were at the centre of the boundary column. On the other hand, the position of wall panel for Specimens CWCS and CWCF were arranged on the outside of the boundary column section (Figure 2). The longitudinal wall reinforcing bars in all specimens were bent into the wall panel. The transverse wall reinforcing bars for Specimens CWAS and CWAF were fixed by welding them to the steel web in the boundary columns. On the other hand, the transverse wall reinforcing bars for Specimens CWCS and CWCF were fixed by 90-degree hook in the boundary columns. In addition, the H-section steels of the boundary columns were anchored to the upper and lower stabs in all specimens.

The mechanical properties of the FRC and steel used are shown in tables 2 and 3, respectively. Poly vinyl alcohol (PVA) fibers with a diameter of 0.66 mm and length of 30 mm were used for FRC. The volumetric ratio of the fibers was 1.0 %.

2.2 Loading Program

The loading apparatus used is shown in Figure 3. The specimens were loaded with horizontal cyclic shear forces using a hydraulic jack with a 2,000 kN capacity, while applying a constant axial force ratio of 0.2 (N/N_0=0.2, where N=axial load, N_0=axial load capacity including steel of boundary columns) using two vertical manual jacks, each of which had a 2,000 kN capacity. During the testing, additional moment was also applied to the top of the

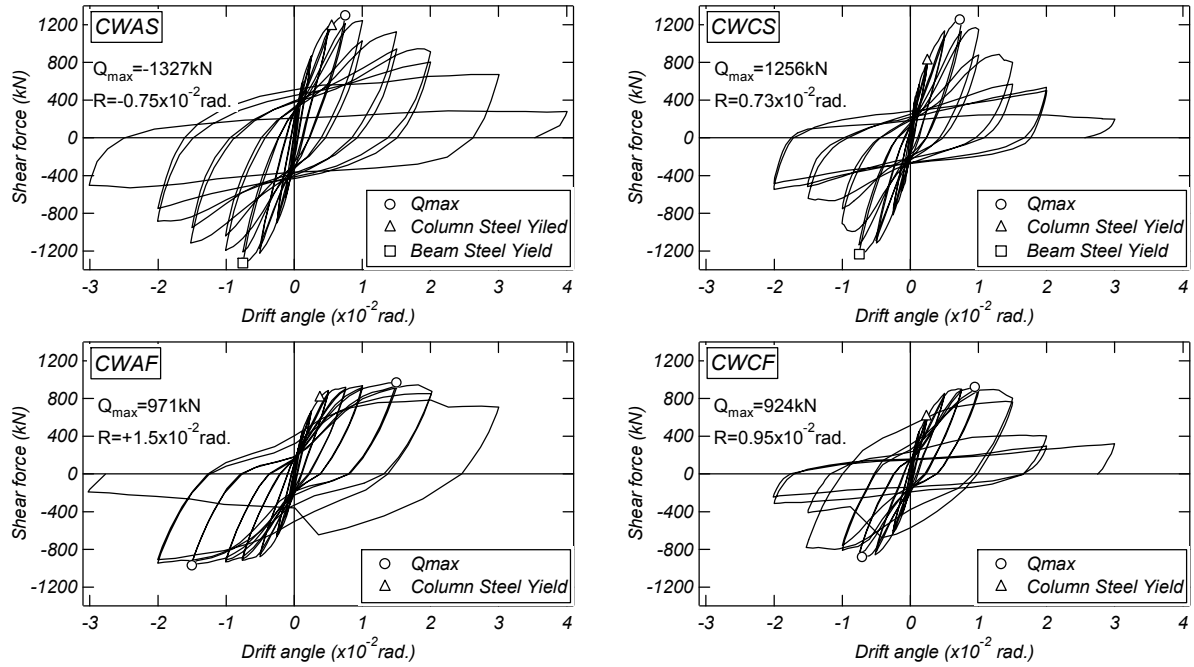


Figure 4 Shear Force Versus Drift Angle Relation Ships

specimen using the two vertical jacks to maintain the prescribed shear-span ratio of 1.1 or 1.65, using the following equations.

$$N_e = \frac{N_c}{2} - \frac{Q}{l}(h-a) \quad N_w = \frac{N_c}{2} + \frac{Q}{l}(h-a) \quad (1)$$

where, N_e: axial force of east side jack, N_w: axial force of west side jack, N_c: constant axial force, Q: shear force, l: distance between vertical jack, h: assumed height of applied shear force, and a: actual height of applied shear force.

The loading was conducted by controlling the relative drift angle R, given by the ratio of the height corresponding to the measuring point for the horizontal displacement at the top of the specimen, h_0 (2,050 mm), to the horizontal deformation δ, i.e., $R=\delta/h_0$. The horizontal load sequences consisted of one cycle for R of 0.0625 x 10^{-2} rad. and 0.125 x 10^{-2} rad. respectively, and after this from R of 0.25 x 10^{-2} rad. two cycles for each relative drift angle were applied.

3. EXPERIMENTAL RESULTS

3.1 Hysteresis Characteristics and Failure Modes

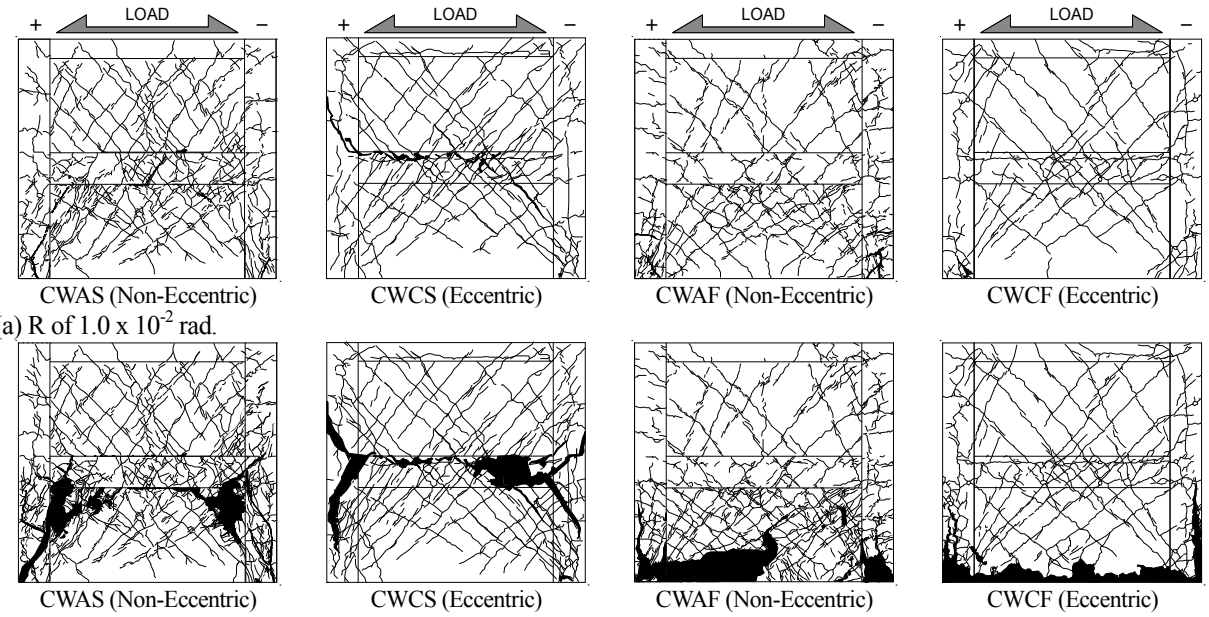
Shear force versus drift angle relationships of all specimens are shown in Figure 4. Cracking patterns of all specimens are shown in Figure 5 after the loading cycle of 0.75 x 10^{-2} rad. and after final loading cycle.

In all specimens, flexural cracks at the bottom of column occurred in the cycle of 0.0625 x 10^{-2} rad. Shear cracks at the first story wall panel occurred in the cycle of 0.125 x 10^{-2} rad.

In Specimen CWAS with non-eccentrically arranged wall panel, the maximum shear force reached -1,328 kN at R of -0.75 x 10^{-2} rad. In Specimen CWCS with eccentrically arranged wall panel, the maximum shear force reached 1,256 kN at R of 0.73 x 10^{-2} rad. It is found that the maximum shear force of Specimen CWAS was slightly larger than that of Specimen CWCS, because the concrete strength of Specimen CWAS was larger than that of Specimen CWCS. The deformability of Specimen CWAS and CWCS was different after reaching the maximum shear forces. While the shear force of Specimen CWAS decreased gradually, that of Specimen CWCS decreased drastically.

In Specimen CWAS with non-eccentrically arranged wall panel, slip between wall panel and beam was observed after the maximum shear force. Therefore, the damaged area was concentrated at the upper corner of the first story wall panel. On the other hand, in Specimen CWCS with eccentrically arranged wall panel, the damaged was concentrated on the boundary beam, especially in the cover concrete. This is because the eccentricity of the wall panel left a portion of the beam without protection of reinforcing bars.

In Specimen CWAF with non-eccentrically arranged wall panel, the maximum shear force reached 971 kN at R of 1.5 x 10^{-2} rad. In Specimen CWCF with eccentrically arranged wall panel, the maximum shear force reached 924 kN at R of 0.95 x 10^{-2} rad. It is found that the maximum shear force of Specimen CWAF was larger than that of Specimen CWCF, because the steel of the column for Specimen CWAF occurred strain hardening. However, hysteresis characteristics of both specimens were almost the same until the maximum shear force. The deformability of Specimens CWAF and CWCF were rather different after reaching the maximum shear force. Specimen CWAF showed significant strength deterioration at R of 3.0 x 10^{-2} rad. On the other hand, Specimen CWCF showed significant strength deterioration at R of 1.5 x 10^{-2} rad. These situations



(a) R of 1.0 x 10^{-2} rad.

(b) After Final Loading Cycle

Figure 5 Cracking Patterns (pictures show south side)

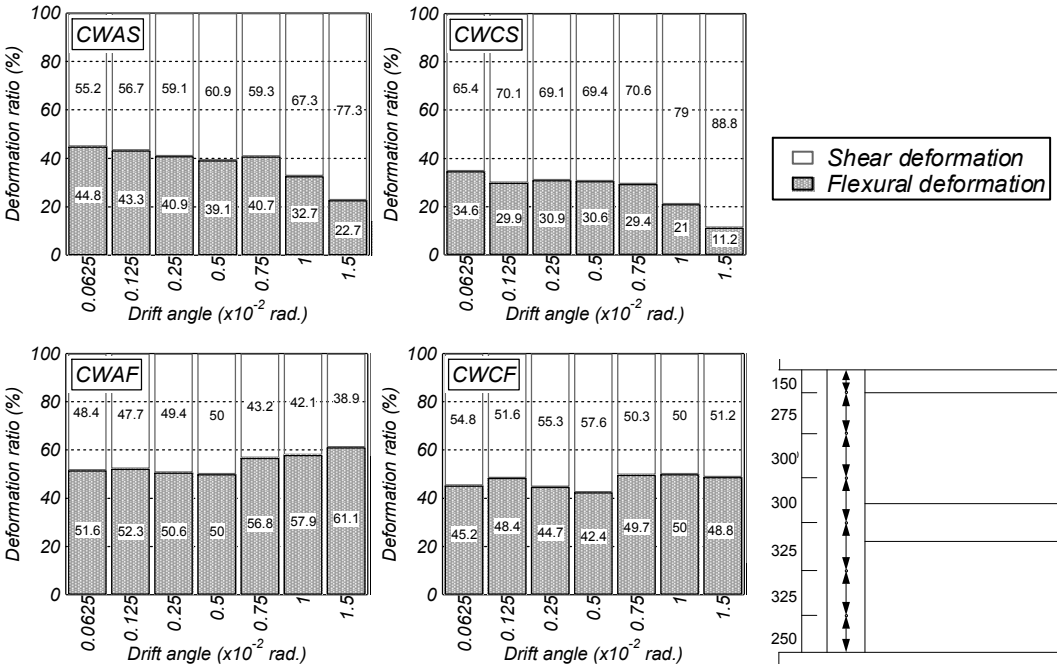


Figure 6 Deformation Components

Figure 7 Measured Displacements

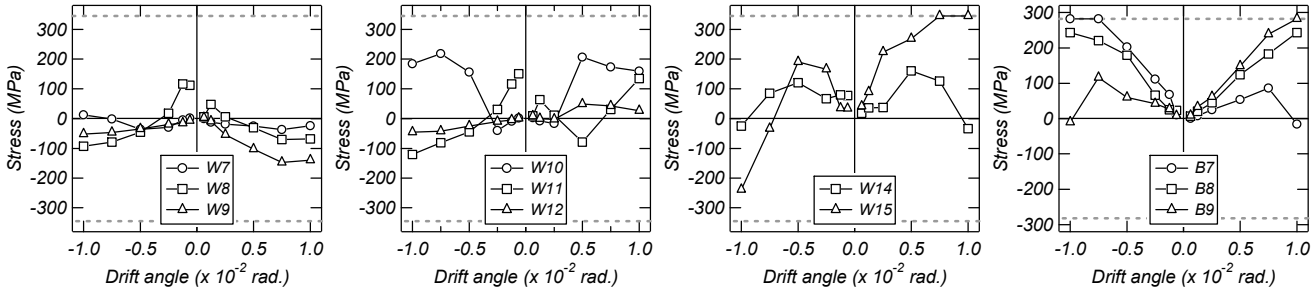
are corresponding to the failure process of both specimens. In Specimen CWAF with non-eccentrically arranged wall panel, the compressive failure of the wall panel occurred in the cycle of 1.5 x 10^{-2} rad. In Specimen CWCF with eccentrically arranged wall panel, the compressive failure of the wall panel occurred in the cycle of 3.0 x 10^{-2} rad. It was found that the deformability of Specimen CWCF was less than that of Specimen CWAF.

Thus, it is confirmed that the position of wall panel had little effect on the maximum shear force of the CES shear walls and that the eccentricity of wall panel reduce the deformability of CES shear walls.

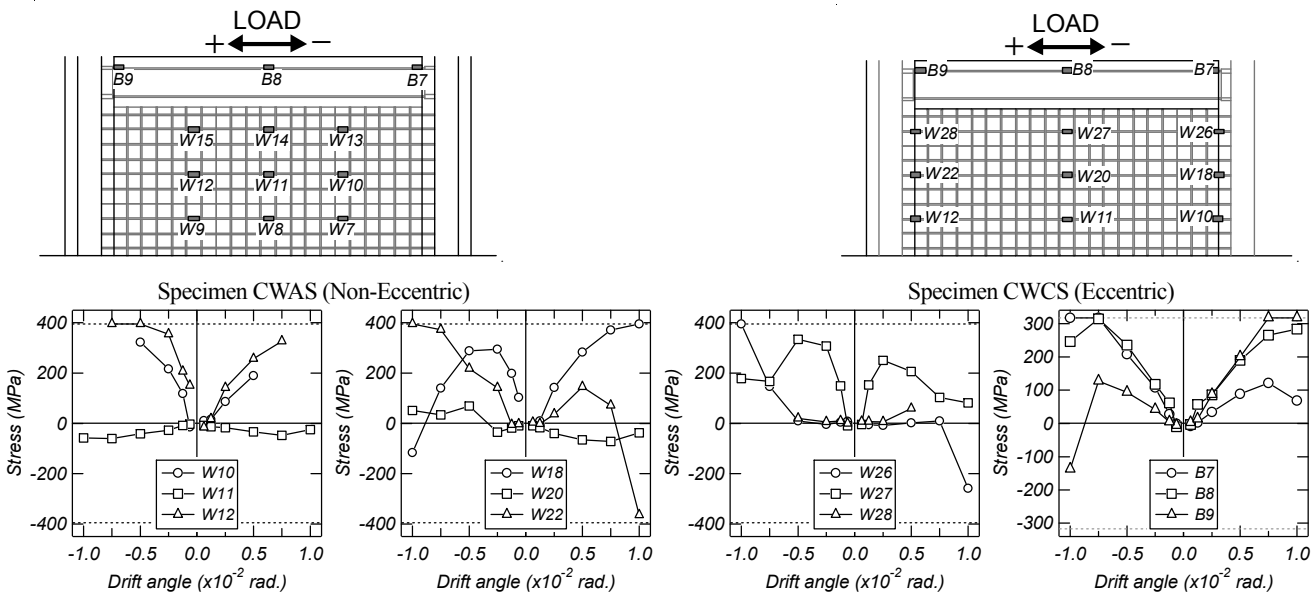
3.2 Deformation Components

Figure 6 shows the contribution of shear deformation and flexural deformation to the total deformation of the all specimens until R of 1.5 x 10^{-2} rad. Flexural deformation was calculated using the axial displacement of boundary columns, as shown in Figure 7, while shear deformation was calculated by subtracting the flexural deformation from the total deformation.

The results for Specimens CWAS and CWCS which



(a) Specimen CWAS (Non-Eccentric)



(b) Specimen CWCS (Eccentric)

Figure 8 Yield Situations for Transverse Wall Reinforcing Bars and Steel of Beam

had the shear failure mode showed that the shear deformation increased at R of 1.0 x 10^{-2} rad. after maximum shear force. The results for Specimens CWAF and CWCF which had the flexural failure mode showed that the deformation ratios were almost the same. However, the shear deformation in Specimens CWCS and CWCF with eccentricity was larger than that for Specimens CWAS and CWAF without eccentricity of the wall panel. One of the reasons is that the deformability of eccentric wall specimen was less than that of non-eccentric wall specimen.

3.3 Transition of Stresses in Wall Transverse Reinforcing Bars and Beam Steel

Figure 8 shows the stresses of the transverse wall reinforcing bars and steel flange of the beam in Specimens CWAS and CWCS, which exhibited shear failure. The stresses were calculated using the measured strain and the bilinear hysteresis assumption for the steel. The strains were measured on the reinforcement of the wall panel, and the upper flange of the beam.

In Specimen CWAS, the transverse reinforcement at the position W15 of the wall panel yielded at R of 0.75 x 10^{-2} rad. In Specimen CWCS, the transverse reinforcement at the position W12 of the wall panel yielded until R of 0.75 x 10^{-2} rad. However the stresses on the wall reinforcement hardly yielded in both specimens.

As for steel in the beam, the stresses increased with increase of drift angle in both specimens. In addition, the upper flange in the beam was near to the yielding at R of 0.75 x 10^{-2} rad. in both specimens. It was confirmed that the steel in the beam effectively contributed to resist the shear force.

4. EVALUATION OF ULTIMATE STRENGTH

The calculation results of the ultimate strengths for all specimens are listed in Table 4. The flexural strength was calculated using Eq. (2), which is equation given in the"AIJ Standards for Structural Calculation of Steel Reinforced Concrete Structures" omitting the term of the reinforcing bars in the boundary column. Moreover, the wall longitudinal reinforcing bars were not considered in the calculation for the Specimens without wall reinforcement anchorage.

The shear strength was calculated using the Truss-Arch Equation (Eq. (3)). It is assumed that the flexural capacity of the boundary column contribute to the shear strength of the CES shear walls, as expressed, ${}_{CS}M_U$, Eq. (4). The shear strength was calculated by adding the lower steel flange of the beam to the transverse wall reinforcement, because it was observed that the steel flange of the beam yielded at the

Table 4 Calculated Strength and Maximum Shear Force

Specimens			*CWAS*	*CWCS*	*CWAF*	*CWCF*
Maximum shear force		Q_{exp} *(kN)*	1,328	1,256	971	924
Flexural strength		Q_{mu} *(kN)*	1,178	1,183	786	789
Shear strength	Truss-Arch Eq	Q_{su} *(kN)*	1,319	1,295	1,202	1,208
Ratio of maximum shear force to calculated strength	Flexural strength	Q_{exp}/Q_{mu}	-	-	1.24	1.17
	Truss-Arch Eq	Q_{exp}/Q_{su}	1.01	0.97	-	-

maximum strength of the wall, as shown in Eq. (6).

Flexural strength equation

$$Q_{mu} = \left(\frac{N_U}{2} + {}_{sCS}A \cdot {}_s\sigma_y\right) {}_W l / h_w \tag{2}$$

Shear strength by Truss-Arch equation

$$Q_{su} = {}_W t \left\{ {}_W l_t \cdot p_{se} \cdot {}_W\sigma_Y \cot\phi + \tan\theta(1-\beta) {}_W l_a \cdot \nu \cdot {}_c\sigma_B \frac{}{2} \right\} \tag{3}$$

$$ {}_W l_a = {}_W l + \frac{1}{\cos\theta} \sqrt{\frac{2 {}_{CS}M_U}{\nu \cdot \sigma_B \cdot {}_W t(1-\beta)}} \tag{4}$$

$$\beta = \frac{2 p_{se} \cdot {}_W\sigma_Y}{\nu \cdot {}_c\sigma_B} \tag{5}$$

$$p_{se} = {}_w p + \frac{a_f \cdot \sigma_{fy}}{{}_W t \cdot h_w \cdot {}_W\sigma_y} \tag{6}$$

$$\tan\theta = \sqrt{\left(\frac{h_w}{{}_W l + D}\right)^2 + 1} - \frac{h_w}{{}_W l + D} \tag{7}$$

where N_U: total axial force in the boundary columns (N); ${}_{sCS}A$: cross section of the steel in the boundary column (mm^2); ${}_s\sigma_y$: yield strength of the steel in the boundary column (MPa); ${}_W l$: distance between the centres of the boundary columns of the wall (mm); h_w: assumed height of applied lateral force (mm); ${}_W t$: thickness of wall; ${}_W l_t$: equivalent wall length of truss mechanism (=l); p_{se}: lateral reinforcement ratio; a_f: cross section of the steel flange in the boundary beam (mm^2); σ_{fy}: yield strength of the steel flange in the boundary beam (MPa); ϕ: angle of truss mechanism ($\cot\phi = 1$); θ: angle of arch mechanism; β: contribution ratio of the compressive concrete in the truss mechanism; ν: effective factor for the compressive strength of concrete; ${}_c\sigma_B$: concrete strength (MPa); ${}_W l_a$: equivalent wall length of arch mechanism; ${}_{CS}M_U$: ultimate flexural moment of the boundary column.

As for Specimens CWAS and CWCS with shear failure mode, the ratios of the maximum shear force to the calculated by Truss-Arch Equation were about 1.0. Therefore, good agreements were obtained between the maximum strength and the calculated strength.

As for Specimens CWAF and CWCF with flexural failure mode, the ratios of the maximum shear force to calculated flexural strength was about 1.2. Thus it is showed that the flexural strength of CES shear walls can be approximately estimated by Eq. (2).

5. CONCLUSIONS

In this study, cyclic loading tests of CES shear walls with eccentrically arranged wall panel were conducted. The failure mode, lateral load carrying capacity and deformation capacity of the CES shear walls were examined. The following conclusions can be drawn.

1) Regardless of failure mode, the position of wall panel had little effect on the maximum shear force of CES shear walls.
2) The shear deformation for eccentric wall specimens was larger than that for non-eccentric specimens, and then a reduction of the deformability of CES shear walls with eccentrically arranged wall panel was observed.
3) It was confirmed that the steel in the beam effectively contributed to resist the shear force.
4) In the CES shear walls with eccentrically arranged wall panel, it was confirmed that the ultimate flexural strength can be evaluated by the equation in the AIJ design standard for SRC structure, and that the ultimate shear strength can be evaluated using the Truss-Arch Equation.

References:

Matsui, T. and Kuramoto, H. (2009), "Static Loading Test on CES Columns with H-Shaped Steel under Different Axial Force Levels and Shear-Span Ratios," *Proceedings of the Eleventh Taiwan-Korea-Japan Joint Seminar on Earthquake Engineering for Building Structures* **25**(2), 289-294.

Nagata, S., Matsui, T. and Kuramoto, H. (2007), "A Fundamental Study on Structural Performance of CES Beam-Column Joints," *Proceedings of the Japan Concrete Institute* **28**(2), 1279-1284.

Suzuki, S., Matsui, T. and Kuramoto, H. (2011), "Effect of Anchorage Condition of Wall Reinforcement on Structural Performance of CES Shear Walls," *Proceedings of the Japan Concrete Institute* **32**(2), 1189-1194.

Kanehira, U., Onozato, N., Simoyama, T. and Mochizuki, J. (2005), "Experiment of Structural Performance of Reinforced Concrete Framed Shear Walls which has a Wall in Same Surface as Column," *Proceedings of the Japan Concrete Institute* **27**(2), 463-468

Architectural Institute of Japan (2001), "AIJ Standards for Structural Calculation of Steel Reinforced Concrete Structures"

10CUEE CONFERENCE PROCEEDINGS
10th International Conference on Urban Earthquake Engineering
March 1-2, 2013, Tokyo Institute of Technology, Tokyo, Japan

NONLINEAR FINITE ELEMENT ANALYSIS OF REINFORCED CONCRETE STRUCTURE CONSIDERING MULTIPLE CRACKING FAILURE

Fangtao Sun[1], Seizo Tanaka[2], Muneo Hori[3] , Tsuyoshi Ichimura[4] , and Maddegedara Lalith[5]

1) PhD candidate, Department of Civil Engineering, University of Tokyo, Japan
2) Assistant Professor, Earthquake Research Institute, University of Tokyo, Japan
3) Professor, Earthquake Research Institute, University of Tokyo, Japan
4) Associate Professor, Earthquake Research Institute, University of Tokyo, Japan
5) Associate Professor, Earthquake Research Institute, University of Tokyo, Japan
sun@eri.u-tokyo.ac.jp, stanaka@eri.u-tokyo.ac.jp, hori@eri.u-tokyo.ac.jp, ichimura@eri.u-tokyo.ac.jp, lalith@eri.u-tokyo.ac.jp

Abstract: This paper studies the applicability of nonlinear solid-element finite element analysis (FEA) for reinforced concrete (RC) structures considering cracking failure. A highly advanced parallel FEM program, ADVENTURECluster, combined with a reformulated nonlinear concrete constitutive relationships and particle discretization scheme (PDS) for cracking simulation, is used to conduct nonlinear analysis for a RC column. Results are presented and applicability of the FEA is discussed.

1. INTRODUCTION

Reinforced concrete, as the main construction material, is most widely used for civil infrastructures, which encompass both aboveground buildings and underground tunnels. Design of these RC structures or their functional parts, usually requires nonlinear structural analysis to accurate estimate their mechanical behavior subjected to various kinds of static and dynamic loads. Such nonlinear analysis is especially important for the ultimate state design. However, with complex nonlinear response such as softening and cracking, the nonlinear behavior of RC structures is particularly difficult to be accurately evaluated, resulting in difficulties for their design.

Typically, experimental analysis using scale-down models is a standard approach to evaluate the nonlinear response of RC structures. However, for large and complex civil infrastructures, such experiments are generally costly, labor-intensive and time-consuming, and they are usually restricted to a few critical case studies, which may not be sufficient to represent the true response of real structures.

Recently, owing to the rapid development of computer technology and numerical schemes, large-scale computations based on finite element method (FEM) using an enormous number of solid elements can be easily and accurately carried out via high-performance computing. The ease and accuracy of such numerical simulations make it a prominent alternative for the traditional experimental analysis. Besides, for numerical computations, solid-element FEA offers advantages in constructing a numerical model, since it requires only material properties, and no structural member experiments are needed. Therefore, FEA using solid elements is much easier to tune material parameters than that using structural member.

In this paper, we seek to examine the applicability of nonlinear FEA with more than 1,000,000 solid elements to evaluate the nonlinear response of RC structures including cracking failure. A highly advanced parallel FEM program, ADVENTURECluster, is used to conduct such nonlinear FEA with solid elements. The program is enhanced with two essential features for numerical simulation of RC structures: nonlinear concrete constitutive relationships, and the ability to model brittle failure due to multiple-cracking. Since solid-element FEA with successful implementation of these two features entails an essential validation process, especially for its applicability to the complex seismic response of large civil infrastructure with composite materials. We focus our presentation in this paper on such a validation process.

2. NONLINEAR CONCRETE CONSTITUTIVE RELATIONSHIPS

Maekawa and his colleagues (Maekawa et al. 2003) have been developing original concrete elasto-plastic constitutive relationships which are attaining the highest reputation in the field of concrete engineering. Therefore, we employ Maekawa's concrete constitutive relations as the model of concrete. Though Maekawa's concrete relations

are well validated, its formulation is less transparent to be implemented in a general purpose FEM code. In this section, we reformulate the concrete relations so that it becomes easier to be implemented.

Maekawa's concrete constitutive relationships are rationally formulated in terms of elastic strain and its invariants. Denoting elastic/plastic strain and stress by $\boldsymbol{\epsilon}^{E/P}$ and $\boldsymbol{\sigma}$, respectively, a set of the original relations can be expressed as follows:

$$\boldsymbol{\sigma} = \mathbf{c} : \boldsymbol{\epsilon}^{E}, \tag{1}$$

$$\mathrm{d}\boldsymbol{\epsilon}^{P} = \boldsymbol{\ell} : \mathrm{d}\boldsymbol{\epsilon}^{E}. \tag{2}$$

Here, $\mathbf{c}$ is isotropic elasticity tensor, which is a forth-order tensor-valued function of elastic strain invariants. d- stands for the incremental of -, and $\boldsymbol{\ell}$ is another forth-order tensor.

From Eq. (1) and Eq. (2), $\mathrm{d}\boldsymbol{\sigma}$ can be expressed in terms of $\mathrm{d}\boldsymbol{\epsilon}$ as:

$$\mathrm{d}\boldsymbol{\sigma} = \mathbf{c}^{EP} : \mathrm{d}\boldsymbol{\epsilon},$$

here, $\mathbf{c}^{EP}$ is forth-order elasto-plastic tensor expressed as:

$$\mathbf{c}^{EP} = (\mathbf{c} + \nabla\mathbf{c} : \boldsymbol{\epsilon}^{E}) : (\mathbf{I} + \boldsymbol{\ell})^{-1}. \tag{3}$$

where, $\nabla\mathbf{c}$: $\boldsymbol{\epsilon}^{E}$ is a forth-order tensor with its component being $(\partial c_{ijpq}/\partial\varepsilon^{E}_{kl})\varepsilon^{E}_{pq}$. $(.)^{-1}$ denotes inverse of (.). $\mathbf{I}$ is forth-order symmetric unit tensor.

From Eq. (3), the calculation of elasto-plastic tensor $\mathbf{c}^{EP}$ includes complicated derivative of $\mathbf{c}$, namely $\nabla\mathbf{c}$, as well as inverse tensor $(\mathbf{I} + \boldsymbol{\ell})^{-1}$. When a problem with a large number of DOFs is solved, heavy computational loads are required. This formulation of concrete constitutive relationships is difficult to be implemented into a general FEM code.

In order to simplify the computation of elasto-plastic tensor $\mathbf{c}^{EP}$ and to reduce numerical loads, we reformulate Maekawa's concrete constitutive relationships to a more transparent form.

Regarding the damaging progress as a yield condition, we reformulate Maekawa's constitutive relations in a form similar to non-associated flow rule. Denoting dg and $\mathbf{d}$ as the incremental quantity and the direction respectively, the plastic strain increment $\mathrm{d}\boldsymbol{\epsilon}^{P}$ can be expressed as,

$$\mathrm{d}\boldsymbol{\epsilon}^{P} = dg\mathbf{d}.$$

In Maekawa's concrete constitutive relations, the second-order tensor $\mathbf{d}$ is given as,

$$\mathbf{d} = DP\boldsymbol{\delta} + \boldsymbol{\epsilon}^{E}/J_2^{E}$$

Here, D and P are functions of $\boldsymbol{\epsilon}^{E}$; $\boldsymbol{\delta}$ is Kronecker's delta; and J_2^{E} is the second invariant of deviatoric elastic strain.

The shear plastic relation between the second invariant of plastic strain and the second invariant of elastic strain in Maekawa's constitutive relations is introduced as the yield function (Yamashita et al. 2011), which can be written as:

$$f(J_2^{P}, J_2^{E}) = J_2^{P} - H(J_2^{E}) = 0,$$

Here, H is an empirical polynomial function of J_2^{E}. According to the consistency condition, that is $\mathrm{d}f = 0$, we simplify the plastic strain increment and elasto-plastic tensor $\mathbf{c}^{EP}$ as:

$$\mathrm{d}\boldsymbol{\epsilon}^{P} = \mathbf{L} : \mathrm{d}\boldsymbol{\epsilon} \tag{4}$$

$$\mathbf{c}^{EP} = (\mathbf{c} + \nabla\mathbf{c} : \boldsymbol{\epsilon}^{E}) : (\mathbf{I} - \mathbf{L}). \tag{5}$$

Here, $\mathbf{L} = \mathbf{d} \otimes (H'/2(1 + H'))(\mathbf{e}^{E}/J_2^{E})$, H' is the derivative of H with respect to J_2^{E}.

The reformulated plastic strain increment in Eq. (4) can now be explicitly calculated from strain increment $\mathrm{d}\boldsymbol{\epsilon}$ and this reformulation results in a more transparent form of elasto-plastic tensor $\mathbf{c}^{EP}$ described in Eq. (5), which no longer involves inverse tensor. Computational loads are reduced in the calculation process of elasto-plastic nonlinear FEA. Also, in order to further reduce the numerical load, we derived an explicit expression of the gradient of the elasticity tensor $\nabla\mathbf{c}$. Indeed, with the above reformulation, it becomes much more straightforward to implement the constitutive relationships into a general FEM program.

3. NUMERICAL ALGORITHM

As explained in Section 2, we obtained a more transparent form of concrete constitutive relationships which allow straightforward implementation into a general FEM framework. However, the elasto-plastic tensor of concrete is still non-symmetric and non-positive definite during the softening stage. The global stiffness matrix constructed from such an elasto-plastic tensor is thus non-symmetric and non-positive-definite, posing difficulties for nonlinear FEA of RC structures using a fast solver based on CG method.

In order to tackle this essential difficulty and to make the fast solver based on CG method applicable, we developed a numerical algorithm to solve a matrix equation with a non-symmetric and non-positive-definite coefficient matrix. In this algorithm, the non-symmetric and non-positive-definite matrix is replaced by a suitable symmetric and positive-definite matrix, and an additional term is added to the original equation so that the replacement is compensated.

The original governing equation of elasto-plastic FEM analysis for nodal displacement increment $\mathrm{d}\boldsymbol{u}$ is written as:

$$\boldsymbol{K}^{EP}\mathrm{d}\boldsymbol{u} = \mathrm{d}\boldsymbol{f}. \tag{6}$$

where, $\boldsymbol{K}^{EP}$ is global stiffness matrix constructed from elasto-plastic tensor $\boldsymbol{c}^{EP}$ as $\boldsymbol{K}^{EP} = \sum_e \boldsymbol{B}_e^{T}\boldsymbol{c}^{EP}\boldsymbol{B}_e$, it is neither symmetric nor positive-definite. $\mathrm{d}\boldsymbol{f}$ is external

nodal force increment.

Here, we use the following constitutive relation for deriving an alternative governing equation:

$$\mathrm{d}\boldsymbol{\sigma} = \mathbf{c} : \mathrm{d}\boldsymbol{\epsilon} + \mathrm{d}\boldsymbol{\sigma}^*, \tag{7}$$

in which $\mathrm{d}\boldsymbol{\sigma}^*$ is a second-order tensor given as:

$$\mathrm{d}\boldsymbol{\sigma}^* = (\mathbf{c}^{EP} - \mathbf{c}) : \mathrm{d}\boldsymbol{\epsilon} = -\mathbf{c} : \mathrm{d}\boldsymbol{\epsilon}^P + (\boldsymbol{\nabla}\,\mathbf{c} : \mathrm{d}\boldsymbol{\epsilon}^E) : \boldsymbol{\epsilon}^E. \tag{8}$$

Eq. (6) is accordingly replaced by:

$$\boldsymbol{K}\mathrm{d}\boldsymbol{u} = \mathrm{d}\boldsymbol{f} + \mathrm{d}\boldsymbol{f}^*. \tag{9}$$

Here, $\boldsymbol{K} = \sum_e \boldsymbol{B}_e^T\, \mathbf{c}\boldsymbol{B}_e$, $\mathrm{d}\boldsymbol{f}^*$ corresponds to the compensated term $\mathrm{d}\boldsymbol{\sigma}^*$.

In Eq. (9), $\mathrm{d}\boldsymbol{f}^*$ is computed directly from $\mathrm{d}\boldsymbol{\sigma}^*$ rather than being computed from the complex elasto-plastic tensor $\mathbf{c}^{EP}$. Furthermore, as shown in Eq. (8), $\mathrm{d}\boldsymbol{\sigma}^*$ can be obtained explicitly since $\mathrm{d}\boldsymbol{\epsilon}^P$ can be computed explicitly from $\mathrm{d}\boldsymbol{\epsilon}$ of the previous step (see Eq. (4)). Therefore, there is no need to compute $\mathbf{c}^{EP}$ and $\boldsymbol{K}^{EP}$. Better computational performance can be expected. Meanwhile, since $\mathbf{c}$ is symmetric and positive-definite, it is guaranteed that the global stiffness matrix $\boldsymbol{K}$ is symmetric and positive-definite, hence a fast solver based on CG method can be applied.

4. CRACKING SIMULATION METHOD

It is essential to consider cracking that takes place in concrete to evaluate failure patterns and ultimate capacity of RC structures. Currently, cracking functionality has been implemented in modern FEM packages. However, targeting at analyzing the initiation and propagation of a single or a few cracks, they are not suitable to analyze the complicated cracking process in concrete.

Cracking that occurs in concrete forms non-smooth facets accompanying many branching surfaces. Determining such multiple-crack configurations becomes the main difficulty for simulating cracking propagation in concrete. Since a crack is treated as a discontinuity in displacement field in numerical simulation, special treatment should be made to deal with the numerous and scattered displacement discontinuities.

In this study, we employ an alternative which is capable of determining multiple-crack configuration in concrete in a straightforward manner, based on strain/strength of concrete. This alternative, however, needs a new discretization scheme which is applicable to displacement filed with numerous discontinuities. Particle Discretization Scheme (PDS) (Hori et al. 2005) is a candidate of such a discretization scheme. In PDS, two sets of non-overlapping characteristic functions of Voronoi blocks and Delaunay blocks are employed to discretize displacement field and its derivatives.

Denoting $\phi^\alpha(\boldsymbol{x})$ and $\psi^\beta(\boldsymbol{x})$ as non-overlapping characteristic functions of Voronoi block Φ^α and Delaunay block Ψ^β respectively, the field variables is expressed as:

$$u(\boldsymbol{x}) = \sum_\alpha f^\alpha\, \phi^\alpha(\boldsymbol{x}),\ \ \boldsymbol{\nabla}u(\boldsymbol{x}) = \sum_\beta q^\beta\, \psi^\beta(\boldsymbol{x})$$

where $u(\boldsymbol{x})$ is the displacement function, $\boldsymbol{\nabla}u(\boldsymbol{x})$ is the derivative of $u(\boldsymbol{x})$. The non-overlapping characteristic function satisfy $\phi^\alpha(\boldsymbol{x}) = 1$ for $\boldsymbol{x} \in \Phi^\alpha$, $\phi^\alpha(\boldsymbol{x}) = 0$ for $\boldsymbol{x} \notin \Phi^\alpha$, $\psi^\beta(\boldsymbol{x}) = 1$ for $\boldsymbol{x} \in \Psi^\beta$, and $\psi^\beta(\boldsymbol{x}) = 0$ for $\boldsymbol{x} \notin \Psi^\beta$.

PDS can easily simulate multiple-crack configuration because cracks can be straightforwardly expressed along the boundaries of discontinuities between Voronoi blocks.

5. NUMERICAL APPLICATION

In order to exam the applicability of the enhanced code, a simple reinforced concrete cantilever column with qausi-static loading is simulated. The dimensions and layout of the reinforcements inside the column are shown in Figure 1. The RC cantilever column is a 500 x 500 x 1350 mm^3 structure member. There are 5 main reinforced bars with a diameter of 22 mm located in both two sides and equally spaced stirrups with a diameter of 10 mm in the vertical direction.

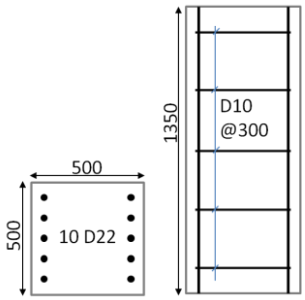


Figure 1 Layout of Reinforcements inside RC Column

5.1 Numerical Model

Figure 2 shows the numerical model and mesh model of the RC cantilever column. It is a detailed reasonably detailed model preserving all the reinforcements in the real body. The model is meshed with 3D tetrahedral solid elements which share nodes on the interface between concrete and steel bars. In total, there are 178,903 nodes, 1,068,331 elements and 536,709 DOFs.

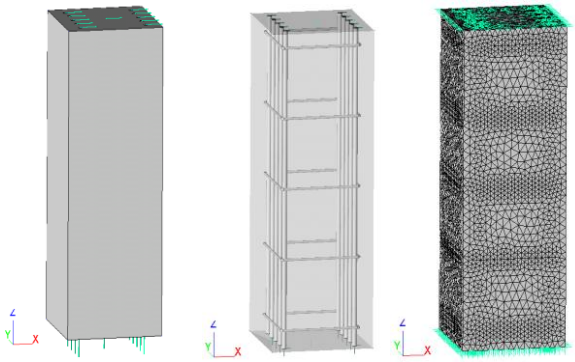


Figure 2 Numerical Model and Mesh Model of the RC Cantilever Column

Von Mises isotropic hardening constitutive model is adopted for reinforced bars, and the reformulated Maekawa's concrete constitutive relationships are employed to model concrete. The material properties are shown in Table 1. Load is increasingly applied in x direction on the top surface of the column, and the bottom surface is fixed in x, y and z directions.

Table 1 Material Properties

Material	Young's Modulus	Poisson's Ratio	Yield Stress	Compressive Strength
Concrete	20GPa	0.2	-	31.3MPa
Main bars	210GPa	0.3	442.3MPa	-
Stirrups	210GPa	0.3	385MPa	-

5.2 Results and Discussions

Using ADVENTURECluster combined with reformulated concrete constitutive relations and PDS, numerical simulation was carried out. Figure 3 compares the load-displacement curves of the numerical and experimental results. The localized pull out effect of reinforcing bar was observed, in the experiment, when load reaches around 140kN. Due to the current limitation of the code, simulation stopped when this level of load is reached. The comparison in Figure 3 shows that the numerical result agrees quite well with the experimental one (Nakajima et al. 1997).

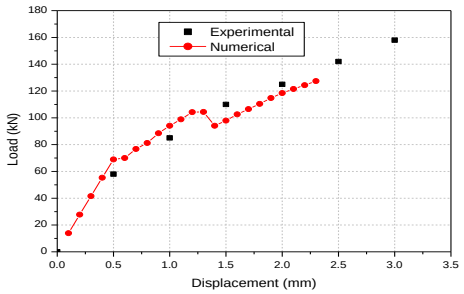


Figure 3 Load-displacement Curves

Figure 4 shows the cracking pattern and deformation with a factor of 20 of the RC column. In order to let the calculation run to a higher load level, a smaller Young's modulus is employed for concrete. Figure 5 shows the cracking pattern and deformation, using the smaller Young's modulus. As expected, the cracking pattern clearly indicates shear failure identical with the experimental result..



Figure 4 Cracking pattern of RC Column (127kN)



Figure 5 Failure Pattern of RC Column

As mentioned, cracking can only occur along the boundary of the Voronoi blocks in PDS. If the nodes of tetrahedral elements are shared on the interface between concrete and steel bars, cracking is not allowed along this interface, since full Voronoi blocks here contain both materials and the Voronoi boundaries do not coincide with the interface. In order to allow this interface cracking and improve the numerical results in the local areas, we employed different mesh for concrete and steel materials respectively. This simple treatment results in broken Voronoi blocks which contain single material and their boundaries are along the interface so that cracking can occur between concrete and re-bars. With the latter way of meshing, the total number of nodes, elements and DOFs are 246,198, 1,079,174 and 738,594, respectively.

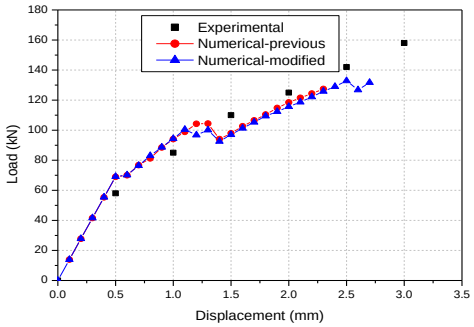


Figure 6 Comparison of Load-displacement Curves

Figure 6 shows the total load-displacement curves of the two mesh patterns. It indicates the total behavior of the RC column, using broken Voronoi blocks along the material interface, does not differ much from that of the original model. However, when we focus on the local area around the boundary of concrete and steel, we can see big difference. Figure 7 compares the stress distribution of concrete at the same load level for the two mesh cases. We can see that if cracking is not allowed to occur along the interface, the maximum tensile stress and compressive stress on the bottom surface of concrete reach 216.7MPa and 53.7MPa, respectively. This is obviously incorrect. While if we separate the meshes of the two materials so that cracking is allowed along their interface, the values are reduced to 4.6MPa and 19.9MPa respectively, showing a significant improvement of local stress prediction.

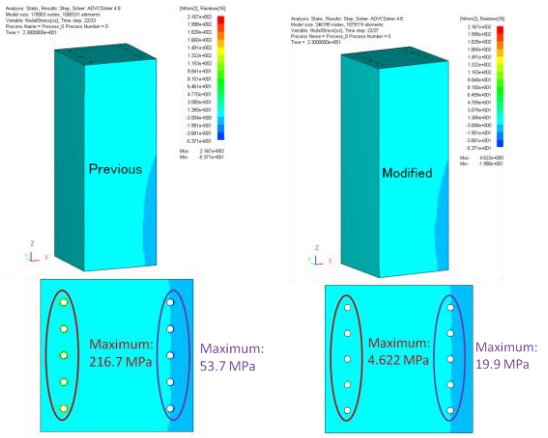


Figure 7 Comparison of Nodal Stress Distribution of Concrete

On the other hand, stress of the reinforcing bars increased, in the latter case, due to the released stress from cracked concrete. These results can be seen from Figure 8-9. It is also because cracking is allowed along the material boundary, stress of the reinforcing bars is not uniformly distributed, and stress concentration on the bars can be seen from Figure 9.

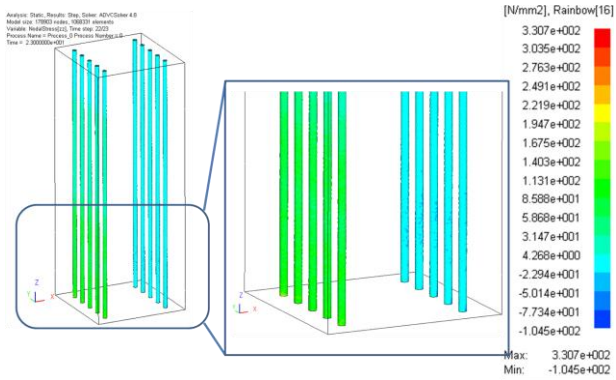


Figure8 Nodal Stress Distribution of Reinforcing Bars

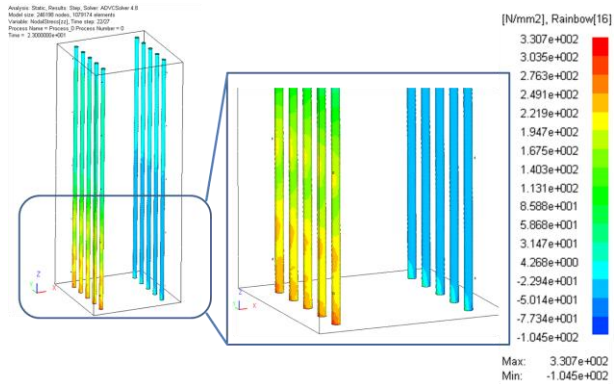


Figure9 Nodal Stress Distribution of Reinforcing Bars Using Modified Mesh

From the results discussed above, we can see that the reformulated nonlinear concrete constitutive relationships and PDS were successfully implemented into ADVENTURECluster. The nonlinear solid-element FEA is demonstrated capable of analyzing the nonlinear response and cracking behavior of RC structural member.

5. CONCLUDING REMARKS

We have implemented reformulated nonlinear concrete constitutive relationships and PDS into a highly advanced parallel FEM program, ADVENTURECluaster, for the nonlinear FEA of RC structures. As a numerical example to demonstrate its applicability, a RC cantilever column was simulated for its nonlinear response with multiple cracking failure under static load. The numerical results showed reasonable agreement with the experimental results, indicating a preliminary success of the enhanced program. However, further efforts are still needed to examine its applicability to more complex and larger RC structures.

References:

Maekawa, K., Pimanmas, A. and Okamura, H. (2003), "Nonlinear Mechanics of Reinforced Concrete," Taylor & Francis Group.

Yamashita, T., Hori, M., Oguni, K., et al. (2011), "Reformulation of Non-linear Constitutive Relations of Concrete for Large-scale Finite Element Method Analysis," *Journal of Japan Society of Civil Engineers*, **67**(1), 145-154.

Hori, M., Oguni, K. and Sakaguchi, H. (2005), "Proposal of FEM Implemented with Particle Discretization for Analysis of Failure Phenomena," *Journal of the Mechanics and Physics of Solids*, **53**, 681-703.

Wijerathne, M. L. L., Oguni, K. and Hori, M. (2009), "Numerical Analysis of Growing Crack Problems Using Particle Discretization Scheme," *International Journal for Numerical Methods in Engineering*, **80**, 46-73.

Nakajima, Y., Suzuki, A., Mishima, T., Watanabe. (1997), "A Study for Strength of Reinforced Concrete Pier by Pre-cast Panel," *Proc. of JCI Symposium on Seismic Retrofitting Techniques for Concrete Structures, JCI, 229-236.*

ADVENTURECluster, http://www.alde.co.jp/index.html

10CUEE CONFERENCE PROCEEDINGS
10th International Conference on Urban Earthquake Engineering
March 1-2, 2013, Tokyo Institute of Technology, Tokyo, Japan

ASSESSMENT OF SEISMIC COLLAPSE SAFETY OF REINFORCED CONCRETE FRAME BUILDINGS DESIGNED BY TWO GENERATIONS OF CHINESE SEISMIC PROVISIONS

Wenwen Luo[1], Yingmin Li[2], Zhe Qu[3], Hiroyasu Sakata[4], Heping Zhong[5], and Jun Han[6]

1) PhD Candidate, College of Civil Engineering, Chongqing Univ., China
2) Professor, College of Civil Engineering, Chongqing Univ., China
3) Post-Doctoral Research Fellow, CUEE, Tokyo Institute of Technology, Japan
4) Professor, Structural Engineering Research Center, Tokyo Institute of Technology, Japan
5) Engineer, China CTDI Engineering Corporation, China
6) Associate Professor, College of Civil Engineering, Chongqing Univ., China
luowenwen@cqu.edu.cn, liyingmin@cqu.edu.cn, m.quzhe@gmail.com, hsakata@serc.titech.ac.jp, zhp1210@126.com, hanjun@cqu.edu.cn

Abstract: Compared to the Chinese seismic code GB50011-2001, the strong-column weak-beam (SCWB) ratios and other seismic fortification measures have been largely modified in the new version GB50011-2010. However, the rationality and effectiveness of these modifications in GB50011-2010 for collapse safety of reinforced concrete (RC) frame buildings haven't been quantitatively checked. This study applies probabilistic assessment to assess the seismic collapse risk of RC frame buildings of varying height that are designed according to GB50011-2001 and GB50011-2010, respectively, in high seismic region. The probabilistic assessment relies on collapse fragility analysis based on incremental dynamic analysis (IDA), accounting for uncertainties in ground-motion characteristics and structural modeling. The influence of building height and an increase in the SCWB ratios introduced in GB50011-2010 on seismic collapse safety are investigated. The results can provide reference for building design and seismic code revise.

1. INTRODUCTION

The new version of Chinese seismic code, GB50011-2010 still follows the three level performance objectives and two stages seismic design procedure. The three level performance objectives require that the building should sustain a minor earthquake without any damage, a moderate earthquake with repairable damage, and a strong earthquake without collapsing (GB 50011, 2001 and GB50011, 2010). The third performance objective is the last defense line to protect the safety of life and property. For both the current seismic code and the former one, this performance level is achieved through internal forces adjustment under a minor earthquake level in the first design stage and checking the building deformation under a strong earthquake level in the second design stage. But only the deformation of important buildings or irregular buildings will be checked in the second design stage. The ordinary buildings try to meet this performance level by seismic concept design and details of seismic design which are lack of quantitative evaluation.

Current seismic design methods in seismic codes follow the capacity-ductility rule. For RC frame buildings, the SCWB is one of the most important seismic fortification measures in ensuring the preferred failure mode under strong earthquakes. Increasing the SCWB ratio delays column hinging, thereby increasing the deformation capacity of the entire building and the number of structure components involved in the collapse mechanism. The SCWB ratios have been substantially increased in the new seismic code, but the influence of these revisions on the seismic collapse safety haven't been quantitatively investigated.

Therefore, two sets of RC frame buildings which locate in high seismic region (intensity 8) are designed according to GB50011-2010 and GB50011-2001, respectively in this paper. The seismic collapse risk of these two sets is quantitatively assessed through seismic collapse fragility analysis. The influence of both the building height and an increase in the SCWB ratios introduced in GB50011-2010 are considered.

2. MODEL DESIGN

Two sets of RC frame buildings are designed according to GB50011-2001 and GB50011-2010, respectively. The stories of these buildings are 1, 2, 4, 6, 8 and 10. The plan of the buildings is shown in Figure 1(a). This kind of buildings is common in the teaching buildings and office buildings. The elevation of the buildings is shown in Figure 1(b). The height of the first floor is 4.2m, and the upper floors are 3.6m. The floor characteristic dead load is 5.0 kN/m^2 and the characteristic live load is 2.0 kN/m^2. These buildings are

located in intensity 8 area, the earthquake group is the first, and the site class is the 2nd.

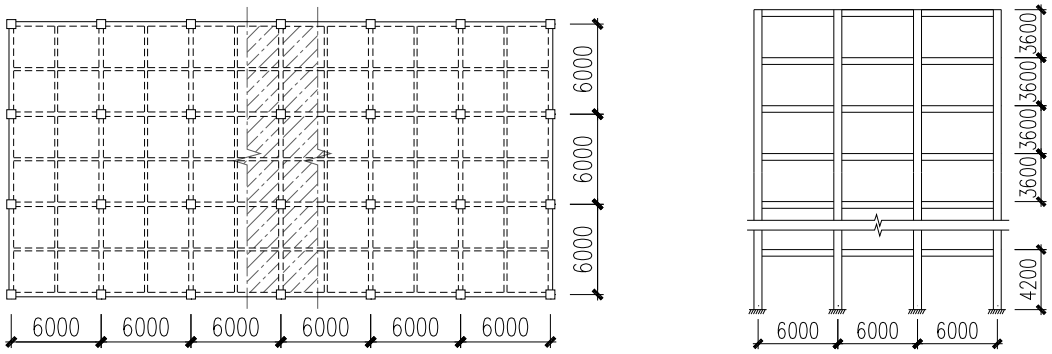
Table 1 Seismic Fortification Measures (μ_{max} = limit value for the design axial compression ratio of column, ρ_{min}= minimum longitudinal reinforcement ratio in column)

Seismic Code	Height(m)	SCWB	μ_{max}	ρ_{min}
GB50011-2010	≤24	1.5(1.5)	0.75	0.85
	24~30	1.7(1.7)	0.65	1.05
	>30	1.7(1.7)	0.65	1.05
GB50011-2001	≤24	1.2(1.25)	0.80	0.70
	24~30	1.2(1.25)	0.80	0.70
	>30	1.4(1.5)	0.70	0.90

The related seismic fortification measures for the two sets of buildings are listed in Table 1. The SCWB is ratio between the required sum of design column end moment and the sum of design beam end moment. The numbers in the brackets are the SCWB ratios of the lower end of column at the first story. When the height of the buildings designed according to GB50011-2010 or GB50011-2001 is higher than 24m or 30m, the required sum of design column end moment should also be 1.2 times of the sum of the actual beam end moment. The longitudinal slab rebar near the top of the beam is considered when calculate the actual beam end moment in GB 50011-2010.

Table 1 illustrates that for buildings whose height is less than 24 or higher than 30m, the SCWB ratios, the minimum reinforcement ratio of column and the limit value of design axial compression ratio in GB50011-2010 are about 1.2 times greater, 0.15% larger and 0.05 stricter than those in GB50011-2001, respectively. If the height of the building is between 24m and 30m, stricter seismic fortification measures should be used in GB50011-2010, Comparing with GB50011-2001.

The building design is carried out by using the code-conforming PKPM (version 2005 and 2010) procedure. The column section size of 1, 2, 4, 6-story buildings is primarily controlled by the limit value of elastic story drift ratio under a minor earthquake. While, the column section size of 8, 10-story buildings is mainly controlled by the limited value of design axial compression ratio. Try to make the maximum design axial compression ratio and elastic story drift of the buildings close to the limited value of the related codes, which means these buildings just meet the minimum requirements of the related codes. The influence of slab on beam stiffness is also considered during the design. The earthquake force is determined by CQC method. The characteristic value of cube compression strength obtained from standard test on 150mm side long cube specimen is 35MPa. The characteristic yield strength of longitudinal reinforcement is 400MPa. And the characteristic yield strength of the stirrup used in GB50011-2001 and GB50011-2010 is 235 MPa and 300MPa, respectively. The details of the buildings design are listed in Table 2.



(a) (b)

Figure 1 Building Layout (Unit: mm): (a) Plan of Building, and (b) Elevation of Building

3. SEISMIC COLLAPSE FRAGILITY ANALYSIS

3.1 Seismic Collapse Fragility Analysis Process

The collapse safety is evaluated by using seismic collapse fragility analysis method. Seismic collapse fragility is the probabilistic relationships between structure collapse probability and ground motion intensity. The process of the collapse fragility analysis basing on IDA analysis method (Vamvatsikos and Cornell, 2002) is listed below:

1) Establish the structure numerical analysis model which can accurately simulate the seismic response of structures.

2) Select a group of ground motion records which can represent the characteristic of ground motion of the building site. The number of the selected ground motion records should be enough to reflect the ground motion randomness. And a proper IM (Intensity Measure) should be used to normalize the ground motion.

3) For one of the ground motion record, gradually increase the IM and do the nonlinear time history analysis until the structure collapsed.

4) Repeat the step 3) for all the ground motion records.

5) Take the structure collapse capacity, the ground motion intensity when the structure collapsed, as random variable, and then estimate the parameters by assuming it follows lognormal distribution model. At last, the collapse

fragility curve can be obtained.

6) Properly adjust the collapse fragility results considering the structure model uncertainty.

Table 2 Design Characteristics of the Buildings (μ = maximum design axial compression ratio of column, θ = elastic story drift ratio, θ≤ 1/550, B = width, H = height, ρ_l = longitudinal reinforcement ratio, ρ_l'= compression reinforcement ratio, ρ_t = transverse reinforcement ratio)

Seismic Code	Design ID	Total Stories	Height (m)	μ	θ	Column					Beam					
						Stories	B(mm)	H(mm)	ρ_l(%)	ρ_t(%)	Stories	B(mm)	H(mm)	ρ_l(%)	ρ_l'(%)	ρ_t(%)
GB50011-2001	101	1	4.2	0.15	1/884	1	400	400	1.27	0.50	1	300	500	0.81	0.72	0.34
	201	2	7.8	0.29	1/559	1	450	450	1.99	0.45	1	300	500	0.89	1.34	0.34
						2	450	450	1.19	0.45	2	300	500	0.72	0.67	0.34
	401	4	15	0.51	1/558	1	500	500	1.82	0.40	1	300	550	0.73	1.46	0.34
						2	500	500	1.05	0.40	2	300	550	0.73	1.21	0.34
						3	450	450	1.30	0.45	3	300	550	0.65	0.89	0.34
						4	450	450	1.19	0.45	4	300	550	0.60	0.49	0.34
	601	6	22.2	0.64	1/558	1	550	550	1.33	0.73	1-2	300	600	0.81	1.46	0.34
						2-3	550	550	0.87	0.47	3	300	600	0.60	1.15	0.34
						4	500	500	1.05	0.40	4-5	300	600	0.60	0.89	0.34
						5-6	500	500	0.96	0.40	6	300	600	0.47	0.45	0.34
	801	8	29.4	0.71	1/558	1	600	600	1.05	0.67	1-3	300	600	0.81	1.59	0.34
						2-3	600	600	0.73	0.67	4-5	300	600	0.60	1.33	0.34
						4-8	550	550	0.80	0.47	6-7	300	600	0.53	0.89	0.34
						-	-	-	-	-	8	300	600	0.47	0.47	0.34
	1001	10	36.6	0.67	1/585	1	700	700	1.28	0.67	1-5	300	600	0.89	1.72	1.05
						2-3	700	700	1.03	0.56	6-7	300	600	0.60	1.33	1.05
						4-10	650	650	0.96	0.60	8-9	300	600	0.53	0.89	1.05
						-	-	-	-	-	10	300	600	0.47	0.47	1.05
GB50011-2010	110	1	4.2	0.15	1/884	1	400	400	1.91	0.50	1	300	500	0.81	0.72	0.34
	210	2	7.8	0.29	1/559	1	450	450	2.91	0.45	1	300	500	0.89	1.25	0.34
						2	450	450	1.19	0.45	2	300	500	0.72	0.67	0.34
	410	4	15	0.51	1/558	1	500	500	2.36	0.40	1	300	550	0.73	1.38	0.34
						2	500	500	1.51	0.40	2	300	550	0.73	1.21	0.34
						3	450	450	1.86	0.45	3	300	550	0.73	0.89	0.34
						4	450	450	1.19	0.45	4	300	550	0.60	0.49	0.34
	610	6	22.2	0.64	1/558	1	550	550	1.95	0.57	1-2	300	600	0.81	1.46	0.34
						2-3	550	550	1.09	0.37	3	300	600	0.60	1.15	0.34
						4	500	500	1.32	0.40	4-5	300	600	0.60	0.89	0.34
						5-6	500	500	1.05	0.40	6	300	600	0.55	0.45	0.34
	810	8	29.4	0.62	1/590	1	650	650	1.39	0.48	1-3	300	600	0.81	1.59	1.05
						2-3	650	650	1.05	0.48	4-5	300	600	0.66	1.33	1.05
						4-8	600	600	1.05	0.52	6-7	300	600	0.53	0.96	1.05
						-	-	-	-	-	8	300	600	0.47	0.47	1.05
	1010	10	36.6	0.59	1/602	1-3	750	750	1.08	0.52	1-5	300	600	0.89	1.59	1.05
						4-10	700	700	1.05	0.56	6-7	300	600	0.60	1.33	1.05
						-	-	-	-	-	8-9	300	600	0.53	0.94	1.05
						-	-	-	-	-	10	300	600	0.47	0.47	1.05

3.2 Nonlinear Analysis Model

Accurate numerical structural analysis model is the basis of the collapse fragility analysis. Because the structure becomes highly nonlinear during the collapse analysis, the numerical analysis model should not only seize the main strong nonlinear feature, but also have robust convergence ability. The lumped plasticity beam-column elements are used to simulate the nonlinear behavior of the columns and beams. The lumped plastic hinges are modeled by using a nonlinear hinge model with degrading strength and stiffness proposed by Ibarra et al, as shown in Figure 2 (Ibarra and Medina, 2005). Key parameters of this model include the plastic rotation capacity $\theta_{cap,pl}$, the post capping rotation θ_{pc} , the ratio of maximum to yield moment Mc/My and an energy-based degradation λ. The key parameters are predicted from a series of empirical relationships relating design characteristics to model parameters and calibrated to experimental data (Haselton and Deierlein, 2007). The axial compression ratio and transverse reinforcement ratio are the two important design parameters to determine these model parameters. As the decreasing of the axial compression ratio, the deformation capacity and the energy dissipation of the component increase, so the four key parameters will increase. The $\theta_{cap,pl}$, θ_{pc} and λ increase with the increase of transverse reinforcement ratio. To account crack action the effective component stiffness are determined on the basis of deformations at 40% of the yield strength. The influence of slab in the width of 600mm on each side of the beam is considered, when establish the beam model. The axial-flexure-shear interaction isn't accounted during the analysis.

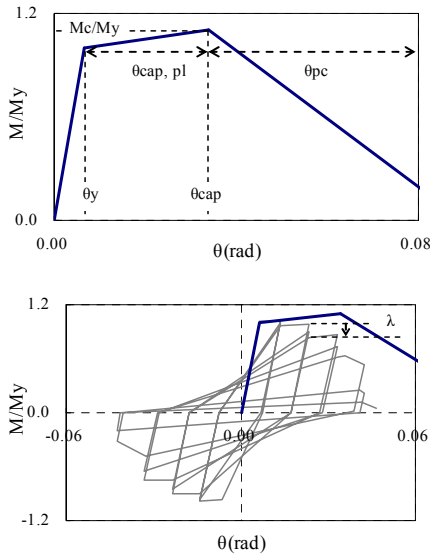


Figure 2 Monotonic and Cyclic Behavior of RC Beam-Column Hinge Model

The shade part of frame in Figure 1(a) is taken out to represent the entire building. So a two-dimensional three-bay nonlinear analysis frame model is created for each building by using the OpenSees structural analysis platform (OpenSees, 2012) with robust convergence algorithms developed by Haselton and Goulet (2007). The Rayleigh damping corresponding to 5% of critical damping in the first and third modes is applied.

3.3 Ground Motion Record

A lot of ground motion records will be used as input in IDA analysis to consider the randomness of the ground motions. A set of 22 pair of ground motions for Far-Field are suggested by ATC-63 (FEMA P695, 2009). Each pair of records has two components. To approximately account for three-dimensional ground motion effects (i.e., the maximum ground motion component), the lower collapse capacity from each pair of ground motions is recorded as the structure collapse capacity.

According to ATC-63, Shome and Cornell (1998) and Luco and Cornell (2007), the spectral acceleration response at the structure's estimated first-mode period $Sa(T_1)$ is a useful IM, with efficiency and sufficiency comparable or superior to other available scalar IMs such as PGA that can be calculated independently of the structure. So the IM selected for this paper is the 5% damped $Sa(T_1)$.

3.4 Collapse Criteria

There are several potential local and global collapse mechanisms of RC frame structures, notably (1) loss of gravity-load-carrying capacity of a column, (2) local collapse of beam-slab system, and (3) global side-sway collapse caused by dynamic instability in one or more stories (Haselton and Goulet, 2007). It is assumed that the detailing provisions of the design code will effectively prevent local collapse modes (1) and (2). The collapse point of collapse mode (3) is defined as the point of dynamic instability (not numerical non-convergence) when any further increase in the intensity of the record causes the drifts to increase without bound (Haselton and Goulet, 2007). The IDA curve becomes flat in this point.

3.5 Adjustment of Structure Collapse Fragility Analysis Results

The largest uncertainty of collapse fragility analysis results lies in characterizing the earthquake ground motion and simulating the structural response. If it is assumed that the structure collapse capacity follows the lognormal distribution model, the uncertainty introduced by ground motion can be considered by using the fitted logarithmic standard deviation ($\sigma_{ln,\,RTR}$) obtained from section 3.1 step 5). The uncertainty of simulating the structural response is mainly result from the modeling uncertainty. Lie et al. (2009) and Haselton and Deierlein (2007) have shown how to deal with this uncertainty in collapse fragility analysis. In this paper, the modeling uncertainty is calculated as $\sigma_{ln,\,modeling}$= 0.5 (Haselton and Deierlein, 2007). Then combined this two types of uncertainty, the resulting total uncertainty is $\sigma_{ln,\,total}^2=\sigma_{ln,\,RTR}^2+\sigma_{ln,\,modeling}^2$.

4. COLLAPSE FRAGILITY ANALYSIS RESULTS

4.1 Result of Collapse Risk

Collapse fragility analysis results for the two sets of buildings are summarized in Table 3. The collapse risks are described by the collapse margin ratio (CMR) and conditional collapse probability for the 2% in a 50-year level of ground motion intensity P[C|$Sa_{2/50}$].

Table 3 Summary of Collapse Risks of RC Buildings

Seismic Code	Design ID	Fist-mode period (T1) (s)	Sa,c(g)	$\sigma_{ln,RTR}$	CMR	P[C|$Sa_{2/50}$] (%)
GB50011-2001	101	0.43	2.15	0.41	2.55	7.84
	201	0.63	1.83	0.36	3.07	3.27
	401	1.07	1.00	0.36	2.70	5.21
	601	1.40	0.78	0.40	2.68	6.46
	801	1.75	0.59	0.35	2.48	6.24
	1001	2.00	0.66	0.30	3.19	1.72
GB50011-2010	110	0.43	2.80	0.40	3.32	3.14
	210	0.63	2.10	0.32	3.52	1.68
	410	1.07	1.22	0.38	3.29	2.92
	610	1.40	0.93	0.42	3.20	3.72
	810	1.67	0.86	0.35	3.46	2.11
	1010	1.95	0.72	0.28	3.33	1.78

The collapse margin ratio is the ratio between the median collapse capacity Sa,c and the 2% in a 50-year ground motion level $Sa_{2/50}$, CMR= Sa,c/$Sa_{2/50}$. The CMRs for GB50011-2001-conforming buildings range from 2.48 to 3.19, with an average of 2.78. While, the CMRs for GB50011-2010-conforming buildings range from 3.20 to 3.52, the average value is 3.35.

The GB50011-2001-conforming buildings, have an average P[C|$Sa_{2/50}$] of 5.12%, ranging from 1.72 to 7.84%. In contrast, GB50011-2010-conforming buildings, have an average P[C|$Sa_{2/50}$] of 2.56%, which are approximately 0.57 times smaller than that of GB50011-2001-conforming buildings, ranging from 1.68 to 3.72%. All buildings can sustain a strong earthquake without collapsed, according to the recommendation of ATC-63 that the building can achieve the no collapsing with strong earthquake object, if the collapse probability is less than 10%.

4.2 Collapse Mechanisms

Figure 3 illustrates the primary collapse mechanisms for all buildings and also provides the proportion of ground motions that caused the primary collapse mechanisms. Figure 4 shows the predominant collapse mechanisms for each building and corresponding percentage. The size of the circles shows the magnitude of the plastic deformation in each plastic-hinge. The blue plastic hinge means $\theta_{cap,pl} \leqslant$ plastic rotation $< \theta_{pc}$, and red plastic hinge means the plastic rotation $\geqslant \theta_{pc}$.

Figure 3 and Figure 4 indicate that the collapse mechanisms for GB50011-2001-conforming and GB50011-2010-conforming 1-story building are almost the same. 2-story building designed according to GB50011-2001 and GB50011-2010 are quite different. As the GB50011-2001-conforming 2-story building collapses in a single first-story mechanism, while the collapses for the GB50011-2010-conforming 2-story building occurs in a stories 1-2 mechanism and a single second-story mechanism. However, the collapses primarily occur in the bottom 2 stories for 4, 6, 8-story building. And there is little difference between these two sets. For 10-story building designed by GB50011-2001, the bottom 2 stories are mainly involved in the collapse mechanism. In contrast, for 10-story buildings designed by GB50011-2010 the bottom 3 stories are involved.

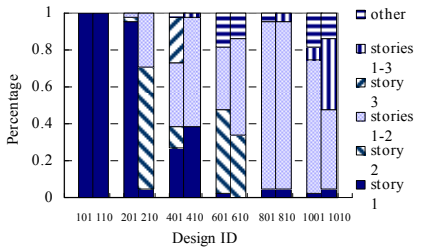
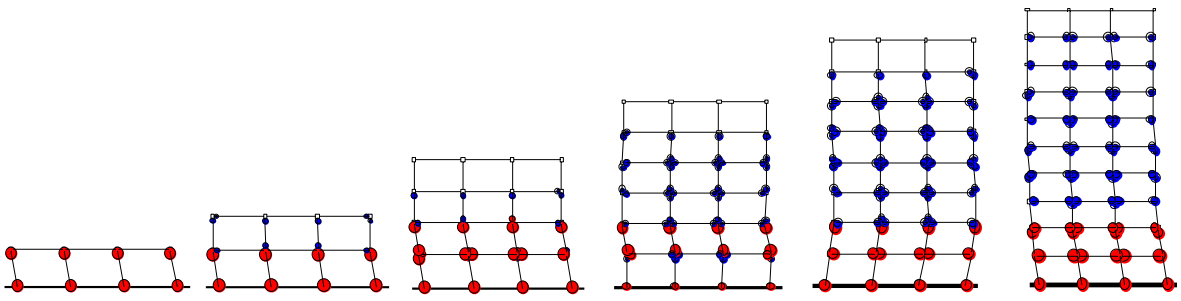
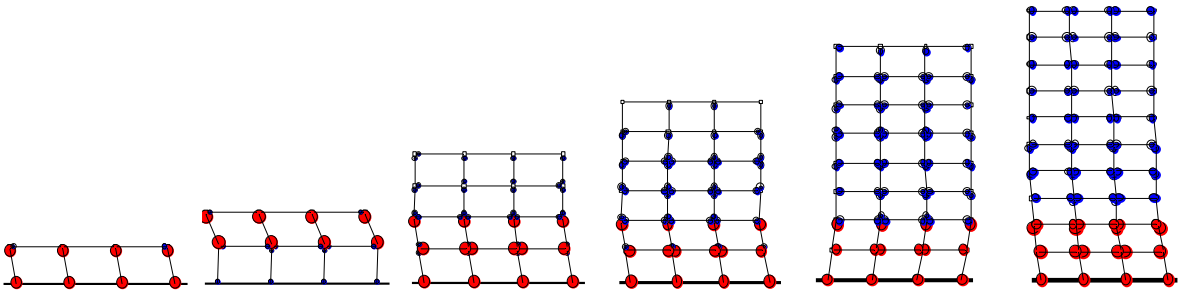


Figure 3 Summary of Collapse Mechanisms



(a)



(b)

Figure 4 Primary Collapse Mechanisms for Buildings of Various Heights: (a) Buildings designed according to GB50011-2001, and (b) Buildings designed according to GB50011-2010

4.3 Influence of Building Height on Collapse Safety

Figure 5 illustrates the relationship between building height and $P[C|Sa_{2/50}]$. It indicated that even designed by the same version of seismic code, the collapse risk of buildings with different height is different from each other. The results suggest that GB50011-2001-conforming 1, 6 and 8-story building have slightly higher collapse risk compared with buildings with other height. While, the collapse risk of GB50011-2010-conforming 1 and 6-story building are a little higher. The high collapse risk of 1-story buildings is result from the lack of plastic redistribution of internal forces. And the stricter seismic fortification measures (larger SCWB, lower maximum axial compression ratio and larger minimum longitudinal reinforcement ratio of column) result in increased collapse safety for taller buildings.

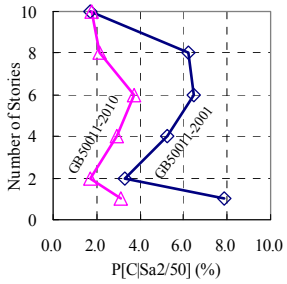


Figure 5 Collapse Risk as A Function of Building Height

4.4 Influence of Increase SCWB on Collapse Safety

The SCWB ratios used for 1, 2, 4 and 6-story buildings for GB50011-2001 and GB50011-2010 is 1.2(1.25) and 1.5(1.5), respectively. And the maximum axial compression ratio of the same height of buildings designed by GB50011-2001 and GB50011-2010 are almost the same. So the difference between the SCWB ratios of GB50011-2001 and GB50011-2010 is the only reason resulting in the different collapse risk of buildings. The ratio of $P[C|Sa_{2/50}]$ for GB50011-2010-conforming buildings ($P[C|Sa_{2/50}]_{10}$) to GB50011-2001-conforming buildings ($P[C|Sa_{2/50}]_{01}$) is shown in Figure 6. The average $P[C|Sa_{2/50}]$ of the four buildings designed according to GB50011-2010 is just 0.51 times of that for the four buildings designed according to GB50011-2001. For low-rise and mid-rise buildings increasing the SCWB ratios, introduced in GB50011-2010 can dramatically reduce the collapse risk.

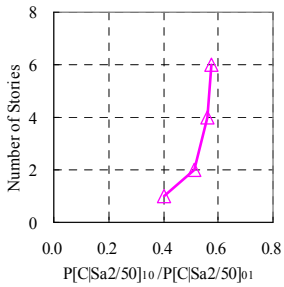


Figure 6 The Ratio Between $P[C|Sa_{2/50}]_{10}$ and $P[C|Sa_{2/50}]_{01}$

5. CONCLUSIONS

The probabilistic assessment based on nonlinear dynamic analysis is applied to quantitatively evaluate the seismic collapse safety of RC frame buildings of varying height that are designed according to GB50011-2001 and GB50011-2010. The results are summarized below:

1) The buildings designed either by GB50011-2001 or GB50011-2010 can sustain the 2% in a 50-year level of ground motion intensity without collapsed.

2) An increase in the SCWB ratio in GB50011-2010 does not significantly improve the building collapse mechanisms. Only the bottom two stories (or one story for 1-story building) are mainly involved in resisting the earthquake.

3) Even designed by the same version of seismic code the collapse risk of buildings with different height is different from each other.

4) For low-rise and mid-rise buildings increasing the SCWB ratios, introduced in GB50011-2010 dramatically reduce the collapse risk of buildings.

Acknowledgements:

This work was financially supported by Specialized Research Fund for the Doctoral Program of Higher Education (Project No. 20100191110028) and Chinese National Natural Science Foundation (Project No. 51108486).

References:

GB50011. (2001), "Code for seismic design of buildings," Ministry of Construction of the People's Republic of China.

GB50011. (2010), "Code for seismic design of buildings," Ministry of Construction of the People's Republic of China.

Vamvatsikos, D. and Cornell, C.A. (2002), "Incremental dynamic analysis," Earthquake Engineering and Structure Dynamics, **31**(3): 491-514.

Ibarra, L.F., Medina R.A., and Krawinkler, H. (2005), "Hysteretic models that incorporate strength and stiffness deterioration," Earthquake Engineering and Structure Dynamics, **34**(12): 1489-1511.

Haselton, C.B. and Deierlein, G.G. (2007), "Assessing Seismic Collapse Safety of Modern Reinforced Concrete Moment-Frame Buildings," PEER Report 2007/08: 69-111.

OpenSees (2012). Open System for Earthquake Engineering Simulation. http://opensees.berkeley.edu. Pacific Earthquake Engineering Research Center, University of California, Berkeley

Haselton, C.B. and Goulet, C.A. et al. (2007), "An Assessment to Benchmark the Seismic Performance of a Code-Conforming Reinforced Concrete Moment-Frame Building," PEER Report 2007/12: 130-131.

FEMA P695. (2009), "Quantification of building seismic performance factors," Federal Emergency Management Agency.

Shome, N. and Cornell, C.A. (1998), "Normalization and Scaling Accelerograms for Nonlinear Structural Analysis," Proceedings of the 6th U.S. National Conference on Earthquake Engineering, Paper NO.243.

Luco, N. and Cornell, C.A. (2007), "Structure-Specific Scalar Intensity Measures for Near-Source and Ordinary Earthquake Ground Motions," Earthquake Spectra, **23**(2): 357-392.

Liel, A.B., Haselton, C.B., Deierlein, G.G. and Baker, J.W. (2009), "Incorporating modeling uncertainties in the assessment of seismic collapse risk of buildings," Structural Safety, **31**(2), 197–211.

10CUEE CONFERENCE PROCEEDINGS
10th International Conference on Urban Earthquake Engineering
March 1-2, 2013, Tokyo Institute of Technology, Tokyo, Japan

EFFECT OF SOIL-FLEXIBILITY ON NONLINEAR RESPONSE OF HIGH-RISE BUILDINGS DURING COLLISIONS UNDER THE EL-CENTRO EARTHQUAKE

A. Abd-Elhamed[1], and S. Mahmoud[2]

1) Ph.D. Candidate, Faculty of Engineering at Mataria, Helwan University, Cairo, Egypt
2) Assistant Professor, Department of Civil Engineering, Faculty of Engineering, Gulf University, Kingdom of Bahrain
aymanm79@hotmail.com, elseedy@hotmail.com

Abstract: This paper presents the seismic response analysis of multi-storey reinforced concrete (RC) frame buildings with 15-storey and 3-bay during collisions considering the horizontal, vertical and rotational movements of the supporting soil through incorporating spring-damper systems at the foundation level. Both buildings are designed according to the Egyptian Code of Practice (ECP). The finite element software ETABS has been used to perform the analysis using the well-known earthquake motion named the El-Centro to excite the buildings model. Nonlinear spring impact elements are applied to simulate the induced pounding force at the points of contact of the colliding frames. To investigate the effect of soil-structure interaction (SSI) on the seismic response in terms of stories displacements, drifts, accelerations, shearing and pounding forces, two types of analysis are performed: first, the developed model is analyzed assuming rigid base soil and second, the analysis is carried out with the consideration of SSI effect. The results of the three dimensional finite element analysis with and without SSI are compared to each other. Based on the obtained results, it has been found that the performance of the RC multi-storey buildings frames is substantially influenced by SSI incorporation during collisions.

1. INTRODUCTION

Interactions between adjacent structures that do not have appropriate separation gaps have been repeatedly observed during strong earthquakes. In most of the seismic pounding analyses, buildings are considered to be fixed bases. These analyses have been proved to be valid only for buildings founded on hard and very stiff soil. In the reality, the underlying soil affects the seismic response of the buildings, whereas the consideration of underlying soil adds extra degrees of freedom at the foundation level and also allows energy dissipation, in additional to decrease the global stiffness of structural system especially for massive and stiff structures constructed on relatively soft soil (Wakabayashi 1985, Wolf 1987 and Stewart et al. 1999a). Although many analytical, numerical and experimental studies have been conducted into the pounding phenomenon, the numbers of those which take into account the effects of the underlying soil flexibility on the dynamic response of the pounding structures are very limited.

The SSI and its influence on the pounding of the adjacent buildings have been studied by Rahman et al. (2001), Chouw (2002) and Shakya and Wijeyewickrema (2009). Rahman et al. (2001) studied the pounding behavior of two 6-story and 12-story moment-resistant, reinforced concrete frame structures incorporating the effects of the soil flexibility considering impacts at different story levels. In their studies, the adjacent buildings and underlying soil were modeled using the FEM-BEM method with the RUAUMOKO software package; the seismic responses to the El-Centro earthquake were obtained via an inelastic dynamic analysis, and the Hertz contact force model was used to represent the pounding between the adjacent buildings. Rahman et al. (2001) found that the shift of period due to the underlying soil altered the time at which the first impact occurred, which had consequences on the subsequent poundings. Chouw (2002) performed an analysis on impacting two buildings linked by a pedestrian bridge taking into account the effect of soil flexibility by employing the boundary element in the Laplace and the time domain. The effects of SSI on mid-column seismic pounding in reinforced concrete buildings of unequal heights under near-field and far-field earthquakes were also studied by Shakya and Wijeyewickrema (2009). They used the SAP 2000 software to model the adjacent buildings and the underlying soil.

A review of the above cited few papers indicates that the analyses have performed using two dimensional finite element analysis for collisions between buildings of unequal heights.The purpose of the present study is to investigate the coupled effect of both supporting soil flexibility and pounding phenomenon on the response of multi-storey RC frame buildings with 15-storey and 3-bay during collisions considering the horizontal, vertical and rotational movements of the supporting soil through incorporating spring-damper systems at the foundation level using ETABS

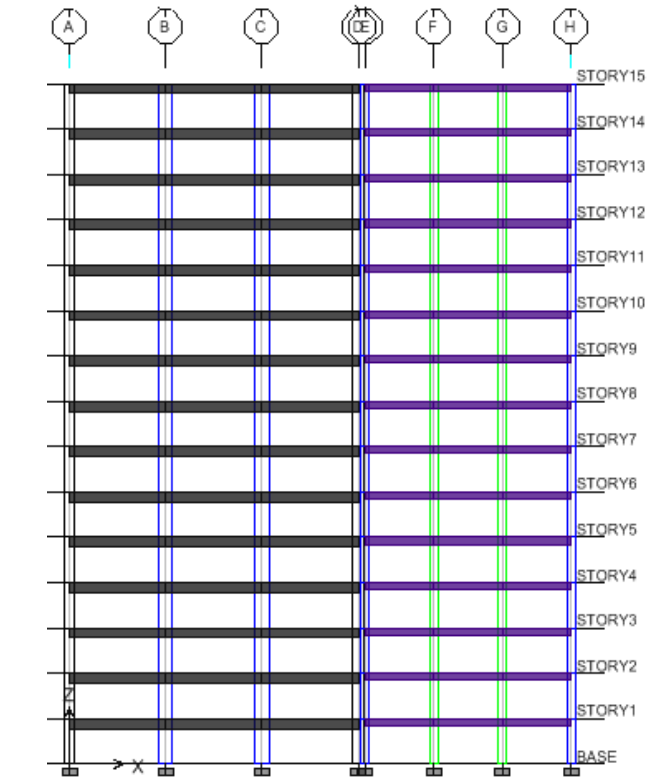
software. The first fifteen seconds of the N-S component of the 1940 El Centro earthquake (peak ground acceleration PGA = 0.348g) is utilised as the external dynamic excitation. Impact forces and acceleration time-histories of colliding buildings with respect to different gaps size between the colliding structures, in additional to envelopes of maximum story shears and storeys drift have been considered as the parameters to investigate the effects of soil on seismic pounding.

2. BUILDING MODEL

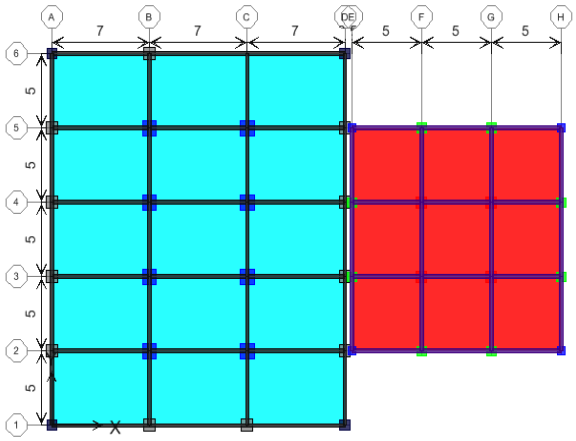
This study investigates pounding of adjacent multi-storey reinforced concrete frame buildings with 15-storey and 3-bay during collisions as shown in figure 1. A three-dimensional finite element model has been defined incorporating the effects of soil flexibility and non-linear time-history analyses have been performed. A heave building is assumed to collide with adjacent light building, as shown in figure 1. The fundamental periods of the buildings with different conditions are shown in table 1. The model has coincident Rigidity/stiffness Center and Mass Center that is located at the geometric center of the floor [from symmetry as shown in floor plan 1(c)]. The two buildings having story height 3.2m for all floors [figure 1(b)]. Concrete with compressive strength f_c' = 3500 t/m^2, unit weight γ_c = 2.5t/m^3, modulus of elasticity E_c = 2.1x10^6 t/m^2, which is determined according to ECP-2003 and Poisson's ratio υ = 0.2 and reinforcing steel with yield strength f_y = 3.6x10^4 t/m^2 are used for analysis and design. The design process requires the determination of the loads that act on the RC buildings. In general, these loads are categorized as gravity loads, which include dead loads (DL) and live loads (LL); and lateral loads, which include earthquake loads.

The dead loads include the own weight of the structural elements, the weight of flooring cover (0.2 t/m^2 for heave building and 0.15 t/m^2 for light building). According to EGP-2008, the live load for heave building is 0.4 t/m^2, and for light building is 0.2 t/m^2. The heave building is provided with 0.22 m thick floor slabs which are considered as rigid floor diaphragms, and also 0.16 m thick slabs for light building. The dimensions of all frame members which used in the parametric study are shown in table 2. Both buildings are designed according to the ECP. The finite element software ETABS has been used to perform the analysis considering 5% damping ratio using the well-known earthquake motion named the El-Centro to excite the buildings model.

The buildings under study here are residential buildings with a mass of 500 tons and 120 tons per story for heave and light building, respectively; and a lateral stiffness in compliance with ECP-2003. The fundamental period of the buildings can be found from their mass and stiffness.



(a)



(b)

Figure1 Two 15-storey Buildings of 3 Bay:
(a) Typical Floors Elevation (b) Typical Floors Plan

Table 1 Fundamental Periods of the Buildings with Different Conditions

	Fundamental Period (s)	
	Heave building	Light building
Without SSI	1.8537	2.319
With SSI	2.2342	2.402

Table 2 Dimension of Members for Collide Buildings

	Heave Building	Light Building
Interior Column Dimension (cm)	100x100	75x75
Edge Column Dimension (cm)	80x80	65x65
Corner Column Dimension (cm)	70x70	55x55
Beam Dimension (cm)	25x70	25x50

3. STRUCTURAL POUNDING MODEL

To simulating pounding force, Connection modeling was done using a GAP joint element, which has only got pressing behavior as shown in Fig. 2. The behavior of the element is such that it behaves nonlinearly with bilinear hardness, i. e. in the case the two adjacent buildings are touching each other, the hardness of gap element is active otherwise, the hardness is considered to be zero. The force-deformation relationship of the gap element is given by:

$$f_G = \begin{cases} K_G[(U_i - U_j) - gap] & \text{if } (U_i - U_j) > gap \\ 0 & \text{if } (U_i - U_j) < gap \end{cases} \quad (1)$$

Where f_G is the force, K_G is the spring constant, U_i and U_j are the displacements of the element's nodes i and j and gap is the initial gap opening. The axial stiffness of the gap element must be selected large enough to transfer compression forces across the gap with a minimum of deformation within the gap element compared to the stiffness of the nodes on the surface. Accordingly, the stiffness of gap element K_G is set to be 100 times higher than that of linear element so that it works nearly rigid when the gap is closed.

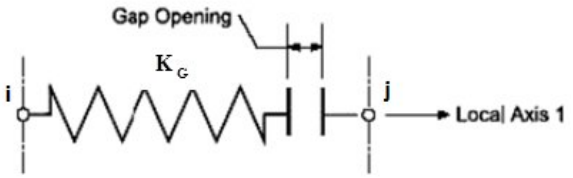


Figure 2 GAP Element and its Function

4. SOIL MODELLING

The discrete model has been formulated for the mat foundations embedded in the halfspace and located at the base of the structure to represent the soil and interaction mechanisms (Richart and Whitman, 1967). Springs and dashpots have been employed in the model in order to account for the transitional, rotational and vertical movements of the soil including damping. For a raft of length L and width B , The parameters of springs and dashpots for sway, rocking and vertical, which represent the SSI, are computed using the following expressions (Whitman and Richart. 1967):

$$k_h = 2(1-\nu)G\beta_x\sqrt{BL}, \quad c_h = 0.576k_h r_h\sqrt{\frac{\rho}{G}}$$

$$k_r = \frac{G}{1-\nu}\beta_\phi BL^2, \quad c_r = \frac{0.3}{1+\beta_\phi}k_r r_r\sqrt{\frac{\rho}{G}} \quad (2)$$

$$k_v = \frac{G}{1-\nu}\beta_z\sqrt{BL}$$

where ν is the Poisson's ratio of the soil, G is the shear modulus, β_x β_ϕ and β_z are the correct constants of swaying and rocking springs, respectively; ρ is the density of soil. The maximum shear modulus at low strain, G_{max}, is related to the shear wave velocity,V_s , according to the following expression (Richart and Whitman, 1967):

$$G_{max} = \rho(V_s)^2 \quad (3)$$

The shear modulus used in the analysis incorporating the SSI has been reduced in order to maintain closer behaviour of the soil. The modulus reduction curves (G/G_{max} - γ) are often used to solve dynamic problems when shear strains, γ, drive the soil beyond its elastic range. As the soil enters into the inelastic stage, the shear modulus of the soil is reduced substantially what is correspondingly related to the decrease in the shear wave velocity. In the case of the study conducted, the reduced shear modulus G has been assumed to be 50% of G_{max} calculated according to Eq. 3 (see Richart and Whitman, 1967).

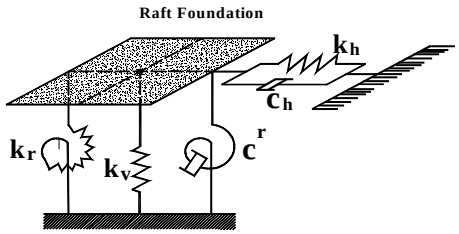


Figure 3 Equivalent Soil Springs to Model Horizontal, Vertical, and Rotational Soil Movements

5. NUMERICAL RESULTS

The effects of soil flexibility on the nonlinear seismic response of two 15-storey adjacent buildings with equal heights and insufficiently separated by several gap distances is considered and the response of the buildings to the El-Centro earthquake record is obtained during the occurrence of pounding. The mat size under the heavy building is of 21.7mx25.7m while under the light building is of 15.55mx15.55m. The supporting soil properties used to calculate the coefficient of frequency independent springs are shown in Table 3.

Table 3 Sandy Soil Type with Different Densities and Shear Wave Velocities at Depth of 15 m

Sandy Soil density γ (kg/m^3)	1.89×10^3
Poisson's ratio ν	0.3
Shear wave velocity V_s (m/sec)	150

The nonlinear dynamic analyses have been carried under the El-Centro earthquake record (Imperial Vally Irrigation Station, N-S component, PGA = 0.342g) for three different gaps of 20mm, 50mm, and 100mm. Two cases have been studied using the same parameters: (a) colliding buildings without incorporating the soil flexibility and (b) colliding buildings incorporating the horizontal, vertical and rotational movements of the supporting base soil.

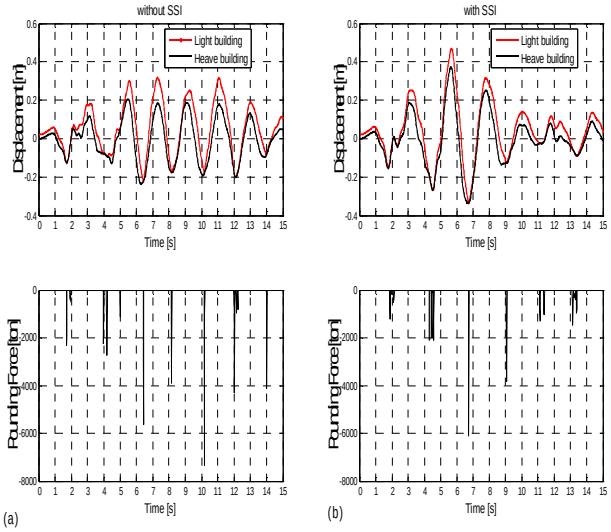


Figure 4 Displacement, and Pounding Force Time-Histories of the Top Floor (a) without SSI and (b) with SSI under the El-Centro Earthquake for Gap Size of 20 mm

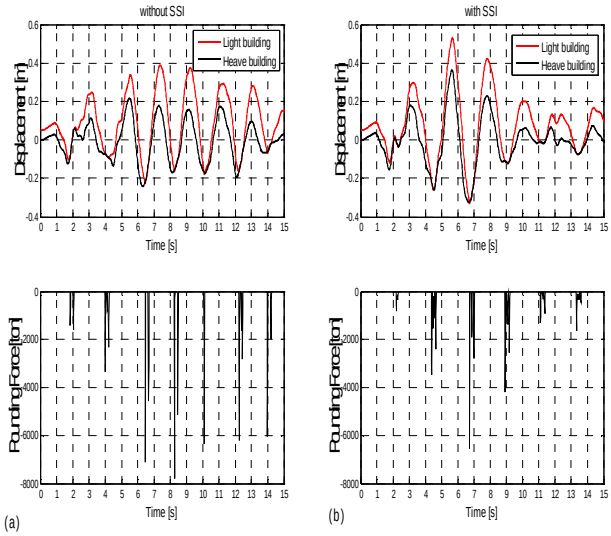


Figure 5 Displacement, and Pounding Force Time-Histories of the Top Floor (a) without SSI and (b) with SSI under the El-Centro Earthquake for Gap Size of 50 mm

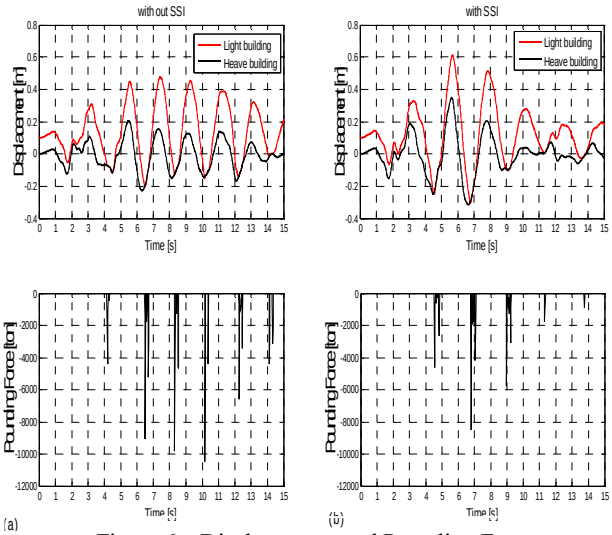


Figure 6 Displacement, and Pounding Force Time-Histories of the Top Floor (a) without SSI and (b) with SSI under the El-Centro Earthquake for Gap Size of 100 mm

Figures 4,5,6 show the sequence of collision forces at the top floors of the heavy and light buildings, (because the top floors experience the most critical condition) during the response to the Elcentro ground motion records. It can be seen that a reduction in the values of the induced pounding forces in the case of SSI inclusion compared with the case of assuming that the supporting soil exhibits as a rigid base for all the considered separation distances. Consequently, the SSI inclusion reduces the value of the peak pounding force. It has also been noticed that considering soil flexibility effect causes slight decreases in the number of impacts compared with the case of ignoring it as can be seen in Figures 4, 5, and 6. In addition, the inclusion of soil flexibility leads to change in pounding forces locations compared with the locations of the induced impact forces considering rigid base soil. The obtained nonlinear displacements for the storeys of adjacent buildings during collisions with and without considering soil flexibility effect for 20mm, 50mm and 100mm gaps are presented in Figures 4, 5, and 6 respectively. The results show that SSI effect during collisions increases the storeys displacements compared to the case for SSI exclusion.

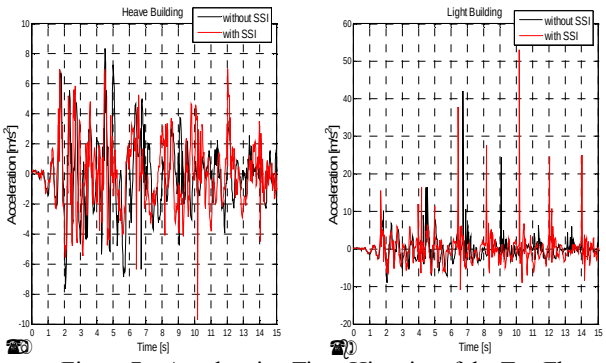


Figure 7 Acceleration Time-Histories of the Top Floor without and with SSI for: (a) Heave Building Storeys; (b) Light Building Storeys under the Elcentro Earthquake for Gap Size of 20 mm.

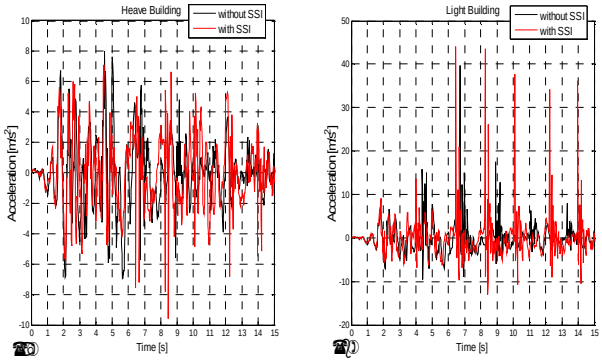


Figure 8 Acceleration Time-Histories of the Top Floor without and with SSI for: (a) Heave Building Storeys; (b) Light Building Storeys under the Elcentro Earthquake for Gap Size of 50 mm.

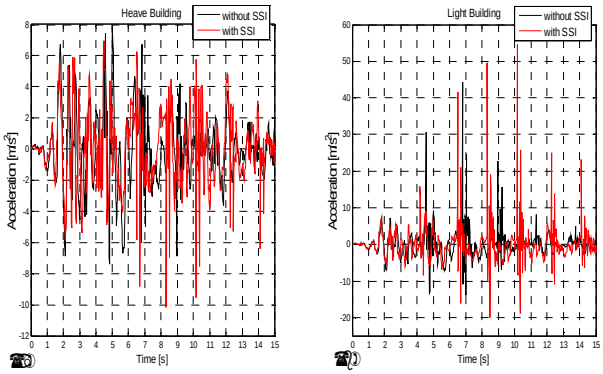


Figure 9 Acceleration Time-Histories of the Top Floor without and with SSI for: (a) Heave Building Storeys; (b) Light Building Storeys under the Elcentro Earthquake for Gap Size of 100 mm.

Figures 7, 8, and 9 give the acceleration time-histories of the colliding two buildings without and with SSI at the top floors of the heave and light buildings, for different gap sizes, under the El-Centro earthquake record. An increase in the peak acceleration can be observed as a result of soil flexibility incorporation, for all the considered separation distances. Those peak accelerations for both buildings occur at the time of impact (compare Figures 4, 5, and 6 and Figure 7, 8, and 9) for the case without and with SSI.

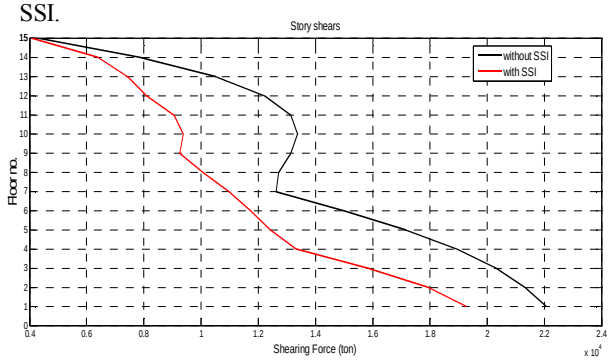


Figure 10 Envelopes of Maximum Story Shears of the Heave Building without and with SSI under Elcentro Earthquakes

The envelopes of maximum story shears of the heave building due to collisions with the light building under the El-Centro earthquake motion without and with SSI for 2cm gap are shown in Figure 10. It can be seen from the figure that interactions between adjacent structures incorporating the soil flexibility effects result in the decrease in the obtained maximum shearing forces for the storeys of the heavy building compared with those obtained ignoring the soil flexibility effect.

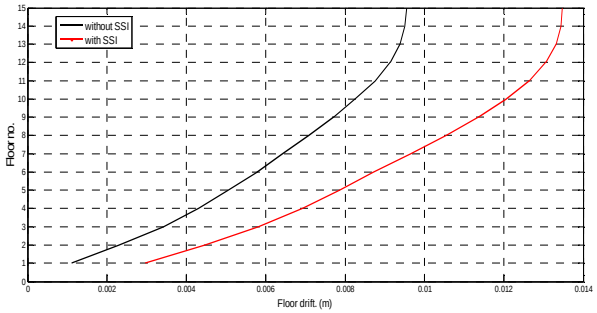


Figure 11 Story Drift of the Heave Building without and with SSI under Elcentro Earthquakes

The envelopes of maximum story shears of the heave building due to collisions with the light building under the El-Centro earthquake motion without and with SSI for 2cm gap are shown in Figure 11. It can be seen from the figure that interactions between adjacent structures incorporating the soil flexibility effects result in the decrease in the obtained maximum shearing forces for the storeys of the heavy building compared with those obtained ignoring the soil flexibility effect.

6. CONCLUSIONS

The current research work investigates the effect of soil flexibility on the nonlinear response time-history analysis of colliding two 15-storey adjacent buildings under the El-Centro ground motion record. Three different gap sizes are used in the study. The nonlinear seismic response of the highest stories of the colliding buildings considering and ignoring SSI effect in terms of displacement, acceleration and pounding force time-histories as well as the storeys peak shearing forces and peak drifts are presented and compared with the associated time-histories results excluding the SSI effects. The results of the study indicate that the SSI inclusion amplifies the obtained displacement and acceleration time-histories while pounding force time-history is reduced due to such inclusion of SSI. For the stories of both heavy and light buildings compared with the obtained values ignoring the SSI effect. In addition, the soil flexibility incorporation significantly reduces the stories peak shearing force during collisions. However, it has been found that the SSI effect increases the drift of all the stories of the buildings during collisions compared to the induced drifts during collisions of rigid base buildings. The study indicates the necessity of considering base soil flexibility during the nonlinear analysis of colliding buildings.

References:

Wakabayashi, M. (1985), "Design of earthquake-resistant buildings," Mc Graw-Hill, TX.

Wolf, J.P. (1987), "Dynamic soil-structure interaction, " Prentice Hall: Englewood Cliffs, N.J.

Stewart, J.P., Fenves, G.L., Seed, R.B. (1999a), "Seismic soil-structure interaction in buildings, " I: analytical methods. Geotechnical and Geoenvironmental Engrg., **125**(1), 26–37.

Rahman A.M., Carr A.J., Moss and P.J. (2001), "Seismic Pounding of a Case of Adjacent Multiple-Storey Buildings of Differing Total Heights Considering Soil Flexibility Effects," *Bulletin of The New Zealand Society for Earthquake Engineering,* 34:40–59.

Chouw N. (2002), "Influence of Soil-Structure Interaction on Pounding Response of Adjacent Buildings due to Near-Source Earthquakes.," *Journal of Applied Mechanics,* 5:543–553.

Shakaya K, Wijeywickrema A.C. (2009), "Mid--Column Pounding of Multi-Story Reinforced Concrete Buildings Considering Soil Effects," *Advances in Structural*, 12:71–85.

Richart, F.E. and Whitman, R.V. ASCE (1967), "Soil Mech Found Div," ASCE Vol. 93.SM6,), 143–168.

10CUEE CONFERENCE PROCEEDINGS
10th International Conference on Urban Earthquake Engineering
March 1-2, 2013, Tokyo Institute of Technology, Tokyo, Japan

ELASTIC LOCAL BUCKLING STRENGTH OF RECTANGULAR HOLLOW SECTION COLUMN UNDER BIAXIAL BENDING SHARE

Kikuo Ikarashi[1], Kosuke Sato[2] and Tao Wang[3]

1) Associate Professor, Department of Architecture and Building Engineering, Tokyo Institute of Technology, Japan
2) Graduate Student, Department of Architecture and Building Engineering, Tokyo Institute of Technology, Japan
3) Associate Professor, Department of Civil Engineering, School of Civil Engineering and Architecture, Ningbo Institute of Technology, Zhejiang University, Ningbo, China
ikarashi.k.aa@m.titech.ac.jp, sato.k.am@ m.titech.ac.jp, wanntao2@gmail.com

Abstract: The purpose of this paper is to evaluate the elastic local buckling strength of rectangular hollow section member subjected to axial force and biaxial bending. The effects of parameters such as axial force ratio and loading angle on the plate buckling coefficient are also clarified. It is shown that the buckling strength takes minimum when one axial bending acts on the column and the strength takes maximum when diagonal axial bending acts on the column. By considering the stress in the member, it is possible to enlarge the Japanese width-thickness ratio limit of the plate elements. This study is also intended to understand the elasto-plastic behavior of rectangular hollow section column under biaxial bending precisely.

1. INTRODUCTION

In Japan, rectangular hollow section column is commonly used in steel structures. In addition to axial force, biaxial bending acts on the column by seismic force and wind force. Although a lot of studies about the column have been conducted, there are few studies about the column under biaxial bending. Those studies about biaxial bending (for instance, Kojima et al. 2009 Ishida et al. 2011) have revealed the post local buckling behavior and the plastic deformation capacity of the column under biaxial bending.

However, in most of the previous studies, the local buckling characteristic and the property of the column material such as residual stress are intermingled. Thereby, it is difficult to specify how well each the local buckling characteristic and the property of the material affects the elasto-plastic behavior of the column. Since the buckling strength relating to the shape of the column has not been examined in detail, the effects of parameters such as loading angle and axial force ratio on the buckling strength are not clarified sufficiently. Because of this, in the current Japanese design criteria (AIJ 2005), the boundary conditions and the stress distributions of the plate elements constituting the column are simplified and the width-thickness ratio limit may be evaluated on an excessive safe side.

The purpose of this paper is to evaluate the elastic local buckling strength of rectangular hollow section column under biaxial bending by theoretical analysis with energy method (Timoshenko 1961) and numerical analysis with FEM. The effect of each parameter on the elastic buckling coefficient is also clarified. Moreover, the width-thickness ratio limit of the plate elements is calculated by basing on the buckling coefficient obtained by analysis. The calculated limitation is compared to the current limiting value in Japanese design criteria.

According to previous study by Wang and Ikarashi (2010), it is possible to predict plastic deformation capacity if elastic buckling strength is clarified in the case of H-shaped beam. This study is also intended to reveal the elasto-plastic behavior of the column under biaxial bending precisely.

2. OUTLINE OF ELASTIC LOCAL BUCKLING ANALYSIS OF RECTANGULAR HOLLOW SECTION COLUMN UNDER BIAXIAL BENDING

2.1 Analytical model

Figure 1 shows the analytical model of this study. In this paper, as shown in Figure 1, the elastic local buckling strength of rectangular hollow section column subjected to constant axial force P and biaxial bending with loading angle θ is evaluated by theoretical analysis and numerical analysis. In theoretical analysis, the buckling strength is derived from energy equation based on classical theory (Timoshenko 1961). In this paper, the buckling strength is clarified by energy method when loading angle θ is 0 or 45 [deg.]. The buckling strength is also clarified by FEM when θ is 0, 5, 10, 15, 20, 25, 30, 35, 40 or 45 [deg.].

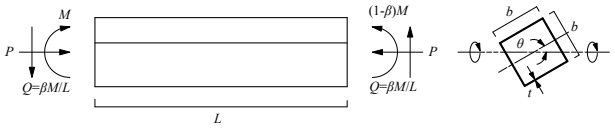


Figure 1 Analytical model

Elastic local buckling stress σ_{cr} in Eq. (1) is defined as a summation of bending stress σ_b and compressive stress σ_c. The elastic local buckling stress σ_{cr} means the elastic local buckling strength in this study. The buckling stress σ_{cr} is the maximum value of normal stress of the column when elastic local buckling occurs. As shown in the following equation, σ_{cr} can be expressed with plate buckling coefficient. The buckling strength is evaluated with buckling coefficient in this paper. Buckling coefficient is not affected by width-thickness ratio but affected by aspect ratio, boundary conditions and stress distributions. Variable $k_\sigma(\theta,p)$ expresses the buckling strength with the value of loading angle θ and the value of axial force ratio p.

$$\begin{aligned}\sigma_{cr} &= \sigma_b + \sigma_c \\ &= \left\{ {}_b k_\sigma(\theta,p) + {}_c k_\sigma(\theta,p) \right\} \frac{\pi^2 E}{12\left(1-\nu^2\right)} \frac{1}{\left(b/t\right)^2} \\ &= {}_n k_\sigma(\theta,p) \frac{\pi^2 E}{12\left(1-\nu^2\right)} \frac{1}{\left(b/t\right)^2}\end{aligned} \quad (1)$$

In this study, the analytical parameters are end moment ratio β, aspect ratio λ, loading angle θ and axial force ratio p. As shown in Eq. (2), aspect ratio λ is the dimensionless number of length divided by width. Variable p is the ratio of compressive stress to the buckling stress with a plate whose 4 edges are simply supported under pure compressive force. Axial force ratio p can be expressed by Eq. (3).

$$\lambda = \frac{L}{b} \quad (2)$$

$$p = \frac{{}_c k_\sigma(\theta,p)}{4} = \frac{k_n \, {}_b k_\sigma(\theta,p)}{4} \quad (3)$$

2.2 Outline of elastic local buckling analysis with energy method

In theoretical analysis, the elastic local buckling strength with loading angle θ 0 or 45 [deg.] is evaluated by energy method. An essential factor of local buckling of rectangular hollow section column is a buckling of the plate elements so that the elastic local buckling strength of the plate elements is clarified by energy method. In this section, the part of derivation process of the buckling strength under diagonal axial bending is shown.

Figure 2 is the normal stress and shear stress distribution of the compressive plate element constituting rectangular hollow section column under diagonal axial bending. The out-of-plane displacement function of the plate element w, normal stress distribution function $f(x,y)$ and shear stress distribution function $g(y)$ are expressed as Eq. (4), (5) and (6) respectively. Variable m, n, M and N in Eq. (4) are natural numbers and k_n in Eq. (5) is the ratio of compressive stress to bending stress. When diagonal axial bending acts on the column, local buckling of both two compressive plate elements is likely to occur around the compressive edge. Thereby, the boundary condition on the compressive edge can be assumed as simple support. On the other hand, the rotation on the edge where bending stress does not occur should be restricted by the plate element of tensile side. Hence, the boundary condition on the side of neutral axis is regarded as fixed support. Thus, the boundary conditions on the three edges are assumed as fixed support and the boundary condition on the one edge is assumed as simple support when the column is subjected to diagonal axial bending. Note that these boundary conditions hold only when compressive stress is sufficiently small compared to bending stress. If compressive stress is dominant, the boundary condition of the long edge regarded as fixed support can be assumed as simple support.

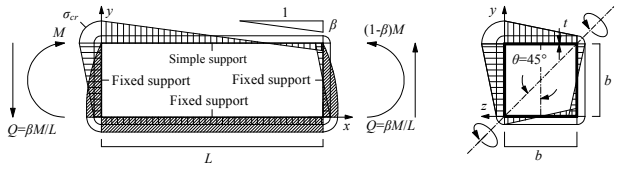


Figure 2 Normal stress and shear stress distribution of plate element under diagonal axial bending

$$\begin{aligned}w = \sum_m^M \sum_n^N a_{mn} &\left\{ \cos\frac{(m-1)\pi x}{L} - \cos\frac{(m+1)\pi x}{L} \right\} \\ &\cdot \left\{ \sin\frac{n\pi y}{b} - \frac{n}{n+1}\sin\frac{(n+1)\pi y}{b} \right\}\end{aligned} \quad (4)$$

$$f(x,y) = \frac{y}{b}\frac{L-\beta x}{L} + k_n \quad (5)$$

$$g(y) = -\frac{3}{2b^2}y^2 + \frac{3}{2} \quad (6)$$

Buckling conditional expression is Eq. (7). ΔU is the strain energy and ΔT is the work done by the external forces.

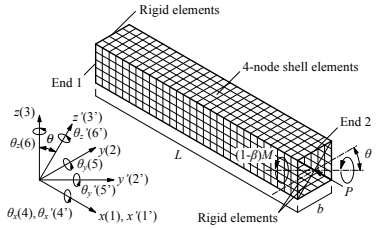
$$\frac{\partial \Delta U}{\partial a_{mn}} = \frac{\partial \Delta T}{\partial a_{mn}} \quad (7)$$

Eq. (7) is a system of homogeneous linear equations in assistant variable a_{mn}. Solving Eq. (7) as eigenvalue problem gives plate buckling coefficient.

2.2 Outline of numerical analysis with FEM

In numerical analysis, the elastic buckling stress σ_{cr} is evaluated when one end bending (β=1.0) or antisymmetric bending (β=2.0) acts on the column. Figure 3 shows the model of numerical analysis in this study. This model is mainly composed of 4-node shell elements. Rigid elements are set at the both ends of the column. The each number of axes in Figure 3 expresses degree of freedom corresponding

to the displacement and the rotation. The boundary conditions at the ends of the column are listed in the table of Figure 3. General-purpose FEM program Abaqus/Standard Version 6.8-4 is used to conduct numerical analysis in this study.



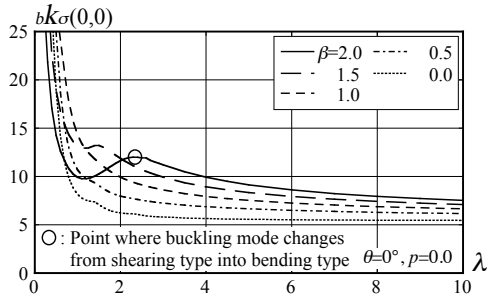
β	Boundary	Constraind degrees of freedom
1.0	End 1	1, 2, 3, 4, 5, 6
	End 2	2', 6'
2.0	End 1	1, 2, 3, 4, 5, 6
	End 2	2', 4', 5', 6'

Figure 3 Numerical analysis model

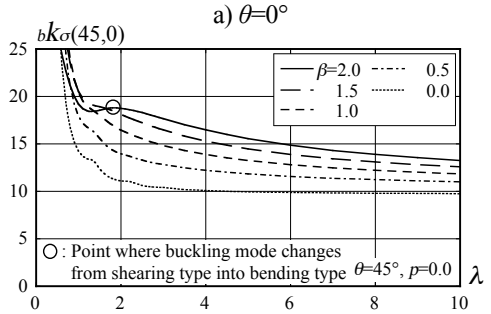
3. EVALUATION OF ELASTIC LOCAL BUCKLING STRENGTH OF RECTANGULAR HOLLOW SECTION COLUMN UNDER BIAXIAL BENDING

3.1 Evaluation of elastic local buckling strength without axial force

Figure 4 is the relationship between elastic buckling coefficient obtained by theoretical analysis and aspect ratio when rectangular hollow section column is not subjected to axial force but only subjected to biaxial bending. Figure 4 a) shows the elastic local buckling strength with the column under one axial bending and b) shows the buckling strength with the column under diagonal axial bending. The buckling coefficient corresponding to bending stress, ${}_bk_\sigma(\theta,0)$, is shown in Figure 4.



a) θ=0°

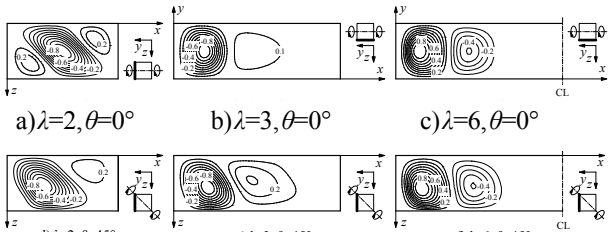


b) θ=45°

Figure 4 Effects of end moment ratio on elastic local buckling strength

According to Figure 4 a) and b), each ${}_bk_\sigma(0,0)$ and ${}_bk_\sigma(45,0)$ converges at a specific value as aspect ratio λ increases. It can be also seen that ${}_bk_\sigma(0,0)$ and ${}_bk_\sigma(45,0)$ become larger with the increase of end moment ratio β. If the column has large aspect ratio, the effect of β on the buckling strength is small. This is because the effect of shear stress on the buckling strength is small and the effect of bending stress is dominant at the large range of λ. In contrast, buckling coefficient becomes small with the decrease of λ in the small range of λ when the column is under antisymmetric bending (β=2.0). This is because the effect of shear stress on the buckling strength increases when λ decreases, compared to the effect of bending stress.

Figure 5 shows the buckling form of the plate element constituting rectangular hollow section column when the column is under antisymmetric bending (β=2.0). The buckling forms illustrated in the following figures are those of λ=2, 3 or 6 and θ=0 or 45 [deg.] when the column is subjected to the bending described on the right of each figure. The buckling form of the plate element expressed by bold line is shown in Figure 5. The elastic local buckling mode of a) is shearing type and the modes of b), c), e) and f) are bending type. The reason why buckling form of d) is close to the bending type, compared to a), is that the plate element of d) is affected by both bending and shear. As shown in Figure 5, the elastic local buckling mode of the column under antisymmetric bending changes from shearing type into bending type with the increase of λ. In Figure 4, ○ expresses the point where the local buckling mode changes when the column is under antisymmetric bending. Shearing type appears only when λ is less than 3. Therefore, the mode becomes bending type regardless of β if column has aspect ratio designed generally.



a) λ=2, θ=0° b) λ=3, θ=0° c) λ=6, θ=0°

d) λ=2, θ=45° e) λ=3, θ=45° f) λ=6, θ=45°

Figure 5 Buckling forms of plate element

Figure 6 shows the relationship between the buckling coefficient obtained by both theoretical and numerical analysis with aspect ratio. Bold lines express the results of theoretical analysis and thin lines express the results of numerical analysis. Figure 6 a) shows the buckling coefficient with the column under loading at one end (β=1.0). Figure 6 b) shows the buckling coefficient with the column subjected to antisymmetric bending (β=2.0). As shown in Figure 6 a) and b), it can be seen that the larger the angle θ is, the larger the elastic local buckling strength is. In other words, the bending stress becomes the largest when diagonal axial bending acts on the column and becomes the smallest when one axial bending acts. When the column is under

diagonal axial bending, the results of analysis with energy method are larger than the results of numerical analysis. This result indicates that the realistic boundary condition of the edge around neutral axis is not strictly fixed support.

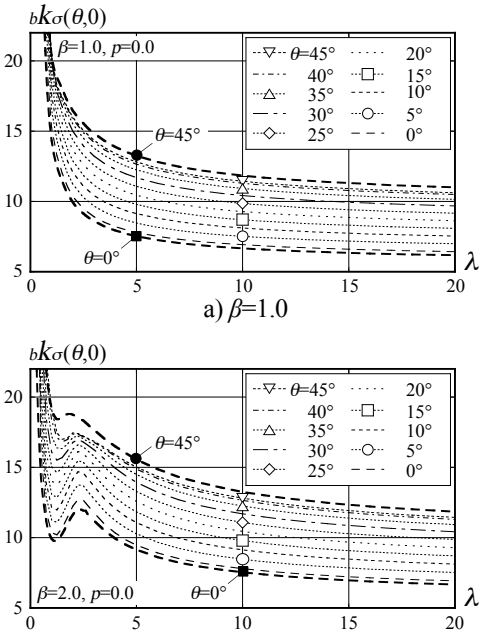


Figure 6 Effects of loading angle on elastic local buckling strength

3.2 Effects of axial force on elastic local buckling strength

Figure 7 shows the relationship between $_ck_\sigma(\theta,p)$ and $_bk_\sigma(\theta,p)$ when rectangular hollow section column is subjected to both constant axial force and biaxial bending. Variable $_ck_\sigma(\theta,p)$ is bucking coefficient corresponding to compressive stress in the column. According to Figure 7 a) and b), $_ck_\sigma(\theta,p)$ converges at a specific value with the decrease of $_bk_\sigma(\theta,p)$ regardless of loading angle θ. When variable k_n is large as possible, $_bk_\sigma(\theta,p)$ is 0.0, the convergence value is larger than 4.0. This result means that the edges of the plate elements of the column are not simply supported. It can be also seen that the larger the angle θ is, the larger the coefficient $_bk_\sigma(\theta,p)$ is while axial force ratio p is constant. Buckling coefficient $_bk_\sigma(\theta,p)$ takes maximum value when θ is 45 [deg.] and takes minimum value when θ is 0 [deg.] regardless of p.

Figure 8 shows the relationship between normalized $_ck_\sigma(0,p)$ and $_bk_\sigma(0,p)$. Plate buckling coefficient $_ck_\sigma(0,p)$ of the vertical axis is divided by the $_ck_\sigma(0,p_{max})$. Variable p_{max} is the maximum value of axial force ratio. On the other hand, $_bk_\sigma(0,p)$ of the horizontal axis is divided by the $_bk_s(0,0)$. According to Figure 8, the correlation curve of compressive stress and bending stress approaches straight line when the effect of shear stress on the column decreases.

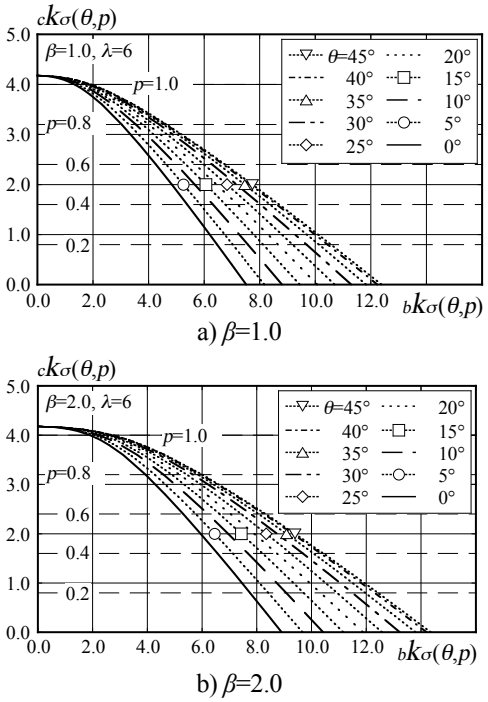


Figure 7 Effects of loading angle on interaction between compressive stress and bending stress

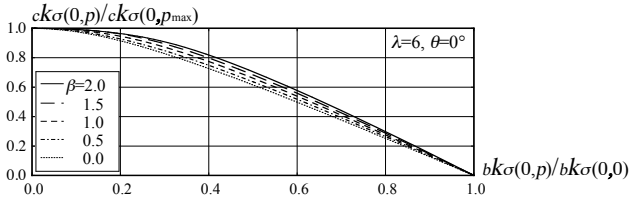
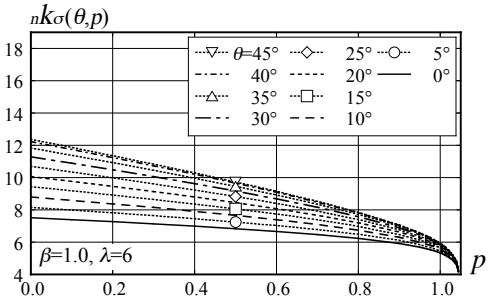


Figure 8 Effects of end moment ratio on interaction between compressive stress and bending stress

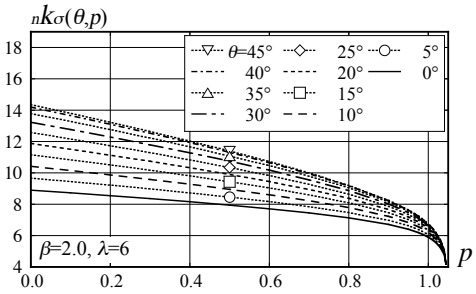
Figure 9 shows the relationship between $_nk_\sigma(\theta,p)$ and axial force ratio p. Elastic buckling coefficient $_nk_\sigma(\theta,p)$ is corresponding to the maximum value of normal stress in the member. The elastic local buckling strength of the column under both axial force and biaxial bending is indicated in Figure 9. According to Figure 9 a) and b), $_nk_\sigma(\theta,p)$ decreases when p becomes larger regardless of end moment ratio β. It can be also seen that $_nk_\sigma(\theta,p)$ becomes larger as loading angle θ increases. The buckling strength takes maximum value when the column is under diagonal axial bending and the strength takes minimum value when the column is under one axial bending regardless of p.

Figure 10 shows the decrease rate of the elastic local buckling strength by axial force ratio p. The vertical axis in Figure 10 is normalized buckling coefficient divided by the buckling coefficient without axial force. According to Figure 10, the decrease rate of the buckling strength by p becomes minimum when θ is 0 [deg.] and this rate becomes maximum when θ is 45 [deg.]. In particular, the buckling coefficient with the column subjected to pure compressive force is about 0.3 times as large as the buckling coefficient with the column only subjected to diagonal axial bending.

This result indicates that the buckling strength with the column under bending is larger than the strength with the column under axial force.

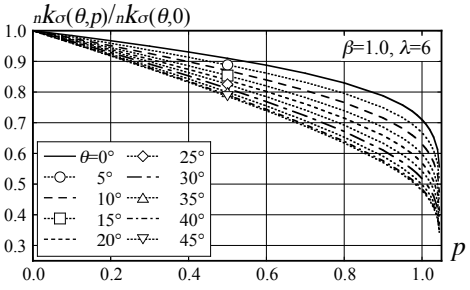


a) β=1.0

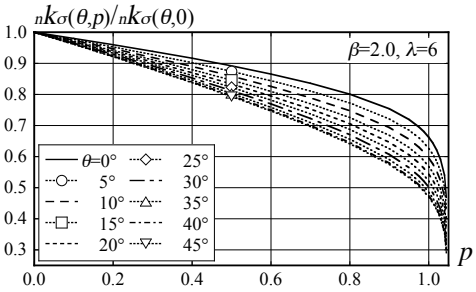


b) β=2.0

Figure 9 Relationship between elastic local buckling strength and axial force ratio



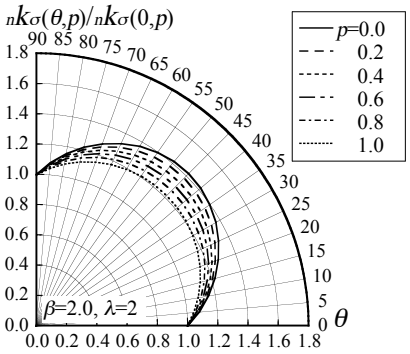
a) b=1.0



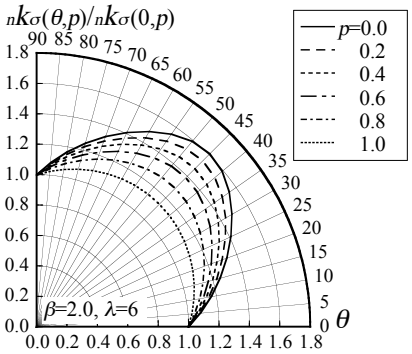
b) b=2.0

Figure 10 Decrease rate of elastic local buckling strength by axial force

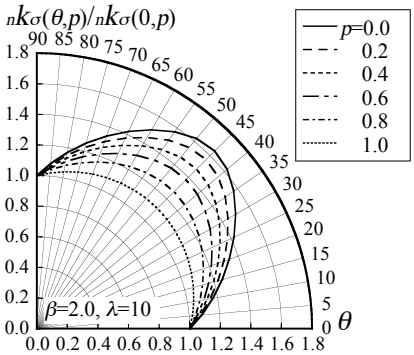
Figure 11 is the relationship between $_nk_\sigma(\theta,p)$ and loading angle θ on the polar coordinate. The radial lines in Fig.ure 11 are the normalized buckling coefficient divided by the buckling coefficient with θ=0 [deg.]. According to Figure 11, it can be confirmed that the buckling strength takes maximum when θ is 45[deg.] regardless of axial force ratio p. In particular, as shown in Figure 11 b), the buckling strength under diagonal axial bending is about 1.4 times than the buckling strength under one axial bending when p is 0.6. It can be also seen that the curve has a tendency to spread outside with the increase of aspect ratio λ. This means that the effect of θ on the buckling strength becomes larger when λ increases. In addition, the curve approaches circle with the increase of p. This means that the effect of θ on the buckling strength becomes smaller when p increases.



a)λ=2



b)λ=6



c)λ=10

Figure 11 Relationship between elastic local buckling strength and loading angle

According to Figure 12 b), although width-thickness ratio limitation decreases with the increase of axial force ratio p, the current Japanese limiting value is smaller than the calculated limitation even when p is 1.0. This indicates that the capacity of rectangular hollow section column is underestimated in the Japanese current criteria. The buckling coefficient with the column subjected to both axial force and bending is larger than the buckling coefficient with the column subjected only to axial force. In the current Japanese criteria, 4.0 is used for the value of ${}_nk_\sigma(\theta,p)$ in Eq. (8). Buckling coefficient becomes 4.0 when a plate simply supported around is under pure compressive stress. However, the realistic boundary conditions of the plate elements constituting the column are not strictly simple support. It is possible to enlarge the limiting value of width-thickness ratio if the stress distributions in the member are considered.

4. CONCLUSIONS

In this study, the elastic local buckling strength of rectangular hollow section column under biaxial bending is evaluated. In addition, the effect of each parameter on buckling coefficient is clarified:
The main conclusions are:

1. The elastic local buckling mode of rectangular hollow section column under antisymmetric bending changes from shearing type into bending type with the increase of aspect ratio. In particular, the mode becomes bending type regardless of end moment ratio if the column has aspect ratio designed generally;
2. The elastic local buckling strength becomes larger with the increase of loading angle regardless of axial force ratio. The buckling strength becomes minimum when one axial bending acts on the column and becomes maximum when diagonal axial bending acts on the column;
3. It is possible to enlarge the Japanese width-thickness ratio limit of rectangular hollow section column by considering the stress distributions in the member.

Notation

b	Width
t	Thickness
L	Length
M	Bending moment
Q	Shear force
P	Axial force
σ_{cr}	Elastic buckling stress
σ_b	Bending stress
σ_c	Compressive stress
${}_nk_\sigma(\theta,p)$	Plate buckling coefficient corresponding to normal stress with value of loading angle θ and value of axial force ratio p
${}_bk_\sigma(\theta,p)$	Plate buckling coefficient corresponding to bending stress with value of loading angle θ and value of axial force ratio p
${}_ck_\sigma(\theta,p)$	Plate buckling coefficient corresponding to compressive stress with value of loading angle θ and value of axial force ratio p
β	End moment ratio
λ	Aspect ratio
θ	Loading angle
p	Axial force ratio
k_n	Compressive stress ratio to bending stress
E	Young's module
ν	Poisson's ratio
σ_y	Yield stress
F	Design strength

References:

Kojima, D., Saito, Y., Shimada, Y. and Yamada, S. (2009), "Elasto-plastic behavior of RHS column under bi-axial bending: part-1 experiment and FEM", *Summaries of Technical Papers of Annual Meeting*, C-1, Architectural Institute of Japan, 591-592.

Ishida, T., Shimada, Y. and Yamada, S. (2007), "Hysteresis of RHS-columns under bi-axial bending", *Proceedings of Constructional Steel*, Japanese Society of Steel Construction, **19**, 691-696.

Architectural Institute of Japan, (2005), "*Design Standard for Steel Structures -Based on Allowable Stress Concept-*", 68-71.

Timoshenko, S. P., Gere, J. M. and Young, D. H. (1961), "*Theory of Elastic Stability*", Second edition, McGraw-Hill Book Co. Inc.

Wang, T. and Ikarashi, K. (2010), "Elasto-plastic buckling behavior of H-shaped beam with large depth-thickness ratio under cyclic loading", *Proceedings of SDSS's Rio 2010*, International Colloquium Stability and Ductility of Steel Structures, **1**, 377-384.

10CUEE CONFERENCE PROCEEDINGS
10th International Conference on Urban Earthquake Engineering
March 1-2, 2013, Tokyo Institute of Technology, Tokyo, Japan

METHOD OF SMALL-SCALE SHAKING TABLE TEST OVERCOMING THE SCALING EFFECT

Yuko Shimada[1], Kenta Takahashi[2], and Satoshi Yamada[3]

1) Assistant Professor, Faculty of Engineering, Chiba University, Japan
2) Graduate student, Structural Engineering Research Center, Tokyo Institute of Technology, Japan
3) Associate Professor, Structural Engineering Research Center, Tokyo Institute of Technology, Japan
yshimada@faculty.chiba-u.jp, kenta.t.aa@m.titech.a.jp, naniwa@serc.titech.ac.jp

Abstract: Shaking table test is great effective methods in seismic engineering field. However, shaking table tests generally conduct with small-scale frames to clear its behavior under dynamic loading because full-scale shaking table test is difficult to conduct by limit of experimental device. In small-scale test, there is the severe problem that the effect of gravity does not match the full-scale buildings by the scaling-effect, therefore, small-scale test is not corresponded to full-scale test. Our study proposes a new method of shaking table test with small-scale model that is able to overcome the scaling effect at the general experimental site. The method subsumes the concept of 'inverted shaking table'. This paper shows validly the new test method through the examination of dynamic test with single frame model.

1. INTRODUCTION

It is important to grasp the detail of collapse behavior of buildings under earthquakes in evaluation of structural safety. Shaking table test on real-scale structure is known as most effective method to achieve collapse behaviors of buildings. However, full-scale tests are able to conduct only few facilities; such as E-Defense, and cost great money and labor to execute. Full-scale tests are not easy to execute, while, small-scale tests with reduced-model are comparative easy. Small-scale test is not perfectly corresponded to full-scale test because it has some severe problems; (1) Reduced-model has quite small gravity and has less P-△ effect than real buildings (scaling effect), (2) Connection details and characteristics of section in reduced columns and beams are different from real building's, (3) The natural period of reduced model is small, therefore, it is necessary to special facilities with high-speed dynamic actuators, and the natural period of input wave needs to change. It has been not to develop a test method to overcome all these problems because it is very hard.

Our study proposes a new method of shaking table test with reduced-model that is able to overcome the problems of scaling effect and the national period between specimen and input wave. The method is based on the concept of 'inverted shaking table'. The concept is developed that shaking table test with reduced-model is able to conduct more easily and effectively in a general experimental site.

This paper shows the concept, experiment system based on the concept, and a series of dynamic test with the system.

2. TEST PROCEDURE

2.1 Inverted Shaking Table System and Specimen

Weight of reduced building model is small. It means vertical load of reduced model does not act to collapse the model as shown in Figure1. While, if vertical load as same as full-scale building is added to reduced model, the model is unstable and hard to set up in experiment system (Figure 2). Due to overcome this issue, a new experiment system (Inverted shaking table system) as shown in Figure 3 is developed.

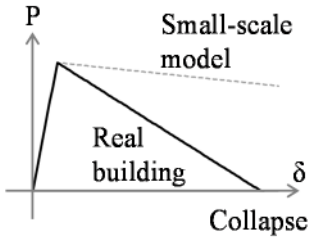


Figure 1 Difference of Behavior by P-△ effect

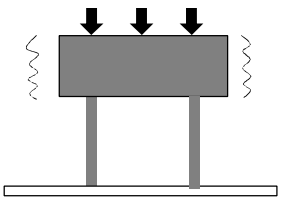


Figure 2 Unstable Model

In inverted shaking table system, specimen is set upside down at fix plate. Inertial mass of specimen connect to counter weights through a wire lope and some pulleys. This means that load from counter weights use as vertical load inputted specimen. Here, the wire lope is set not to touch other member or parts through a hole on the fix plate. Fix plate is connected dynamic actuators. This system is able to set vertical load freely by changing counter weights though initial horizontal force and the natural period keep the values. Enough height between specimen and pulley makes keeping the load from counter weights almost vertical when specimen has large deformation. Moreover, specimen is able to set with a stable position because specimen suspended to jigs.

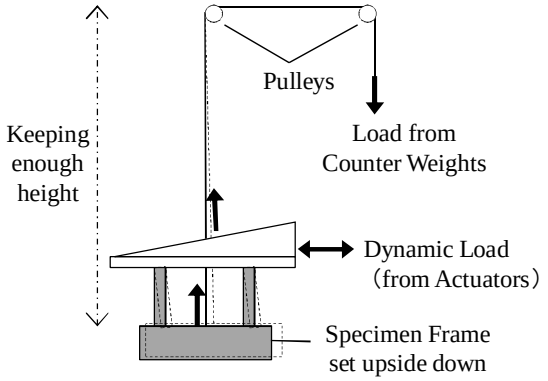


Figure 3 Inverted Shaking Table System

Specimen and jigs in this small-scale test shows in Figure 4. Specimen is a three-dimensional 1x1 span frame with inertia mass and four columns. All of the specimen parts in this test have weights under almost 20kgf for easy carrying. Specimen has 300mm height and inertia mass have changing from 100 to 140kg by the number of mass plate. Each column is a steel bar and the connection between column and other part is a pair of clevises due to pin joint. Stiffness of specimen is added by stiffness element which is separate to inertia mass and columns. Specimen is able to change inertia mass or stiffness, so that it is possible to shaking table test without adjusting time of input earthquake records. The connection between frame and stiffness element is made of combining some rod ends and screw bars.

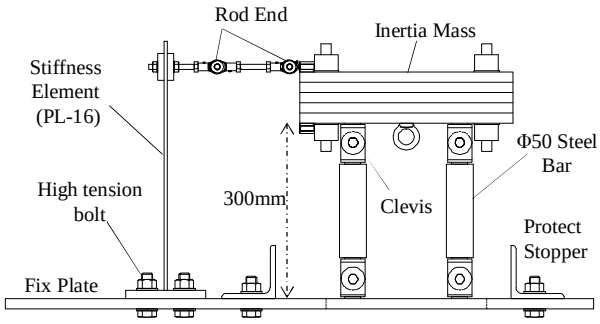


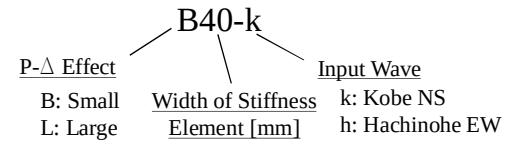
Figure 4 Detail of Specimen

Table 1 shows specimen list. Parameters of this test are the national period, vertical load for P-△ effect, and input earthquake record. The national period of each specimen is during 0.4sec to 1.2 sec due to simulate dynamic behavior of general steel building. Figure 5 shows detail of stiffness elements. The national period is set by changing width or length of stiffness elements; basic type is B40, long-period types are B40s and B60, and short-period type is B30.

W in Table 1 means vertical load given by subtracting M1 from M2. Here, M1 in Table 1 means inertia load, and M2 in Table 1 means value of counter weights. W is set two value; 392N and 588N. Input waves are JMA Kobe NS record in 1995 Kobe earthquake (Kobe NS in following) and Hachinohe EW record in1968 Tokachi-oki earthquake (Hachinohe EW in following).

Table 1 Specimen List

Stiffness Element	Specimen	Input Wave	M1 [kg]	M2 [kg]	W [N]	T_1 [sec]	Base Shear
B40	B40-k	Kobe NS	100	140	392	0.80	0.26
	L40-k			160	588		
	B40-h	Hachinohe EW		140	392		
B40s	B40s-k	Kobe NS	100	140	392	0.49	0.36
	L40s-k			160	588		
B60	B60-k	Kobe NS	100	140	392	0.40	0.54
	L60-k			160	588		
B30	B30-k	Kobe NS	140	160	392	1.24	0.18
	B30-h	Hachinohe EW					



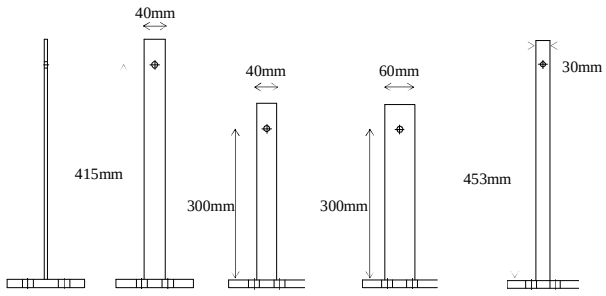


Figure 5 Stiffness Elements

2.2 Test Set-up and Measurement

Test set-up shows Figure 6 and Figure 7. Horizontal dynamic load is input by two 2,000kN actuators. Specimen is set at jig upside down, moreover, jigs and loading block are combined by PC steel bar.

Measurement in this test are follows; (1) Four accelerators ware set on the jigs and specimen for absolute acceleration, (2) Four potentiometer-type displacement transducers ware set near the jigs and specimen for absolute

horizontal displacement, (3) Two laser-type displacement transducers ware set for absolute vertical displacement, (4) Two strain gauges were glued on the stiffness element for grasping force added to stiffness element. Here, measurement is located at bilateral symmetry to loading dimension due to check torsion of specimen and backup.

Excitation list shows Table 2. In each specimen, free vibration was firstly added in order to check measurement system and measure the national period and damping factor. After the check earthquake record was input. Elastic excitation is the acceleration level that specimen was keeping within elastic area by pre-analysis. From the third excitation, earthquake record was added original, 1.25 times to original, 1.5 times to original by acceleration level. Maximum level in Kobe NS was 1.25 times as original record because spec of actuator is limited. Each excitation was finished in case that specimen collapsed

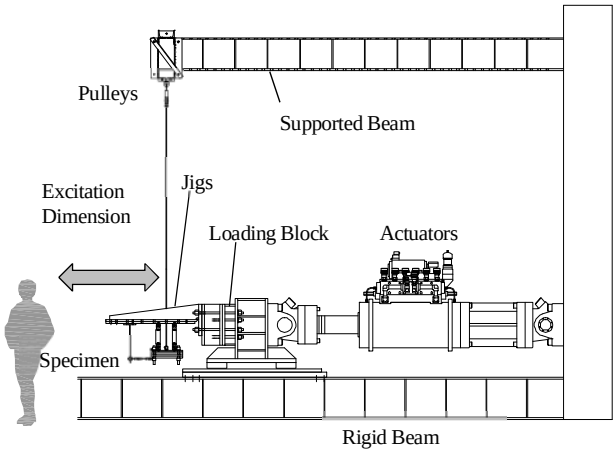


Figure 6 Test Set-up

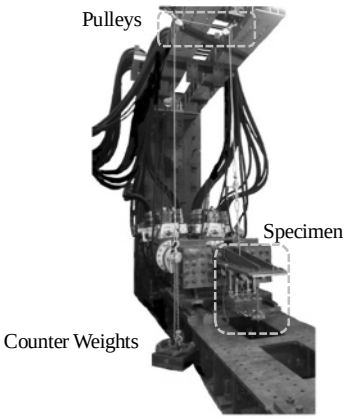


Figure 7 Specimen and Counter Weights

Table 2 Excitation List

	Kobe NS		Hachinohe EW	
	Input Level	Max. Acc.	Input Level	Max. Acc.
Free Vibration	-	-	-	-
Elastic Excitation	Kobe NS×0.1	82 gal	Hachinohe EW×0.6	107 gal
×1.0	Kobe NS×1.0	802 gal	Hachinohe EW×1.0	179 gal
×1.25	Kobe NS×1.25	1003 gal	Hachinohe EW×1.25	224 gal
×1.5	-	-	Hachinohe EW×1.5	269 gal

3. TEST RESULTS

Figure 8 shows Fourier spectrum in order to check wheatear earthquake record was able to input in each excitation as expected. 'Expected' in Figure 8 means input wave, and 'Response' means measurement value by accelerators on jigs. The left graph shows Kobe NS x1.25, the right graph shows Hachinohe EW x1.5, vertical line in both graph shows the national period of each specimen. Response value is not corresponded to expected value at the area that the national period is around 0.1 sec or over 3.0 sec in Kobe NS, while at the area that the national period is over 5.0 sec in Hachinohe EW. However, Response value is well corresponded to expected value at the area that the national period is during 0.2 sec to 2.0 sec in both input wave.

Table 3 shows test result list. *T* and *h* in the table are each the national first period and damping factor measured at elastic excitation. *Ke* in the table is unloading stiffness at elastic excitation. *h* varied in each specimen especially B30 series, although *T* and *Ke* are almost corresponded to calculated value.

Figure 9 shows Q_h versus δ relationships. δ in the figure is relative displacement calculated by horizontal measured displacement value of jigs and specimen. Q_h is horizontal shear force as shown in Figure 10. Bending moment at the point of stiffness element (M_G) is calculated by strain gauge. According to force balance around gauge, M_G is given by Eq. (1) below:

$$M_G = Q_h \times V \pm Q_v \times h \quad (1)$$

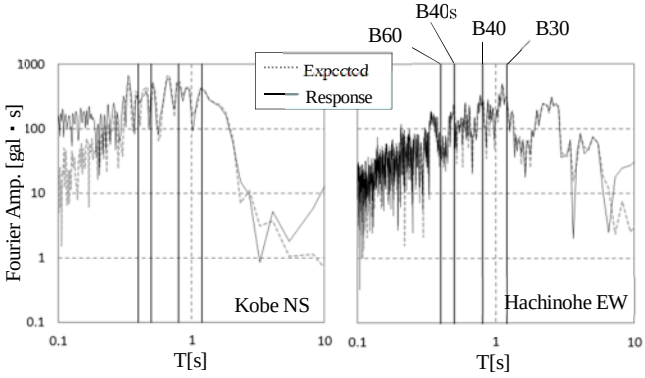


Figure 8 Fourier Spectrum

Table 3 Test Results

Specimen	T [sec]	h [%]	Ke [N/mm]	Kobe NS x1.0				Kobe NS x1.25				Kobe NS x1.25 (Second)			
				δmax (+) [mm]	δmax (-) [mm]	Qmax (+) [N]	Qmax (-) [N]	δmax (+) [mm]	δmax (-) [mm]	Qmax (+) [N]	Qmax (-) [N]	δmax (+) [mm]	δmax (-) [mm]	Qmax (+) [kN]	Qmax (-) [kN]
B40-k	0.86	2.9	6.2	118.9	-178.2	360.4	-331.5	-70.3	-182.3	5.4	-313.3				
L40-k	0.69	5.5	6.3	109.3	-132.4	401.5	-300.0	-21.7	-178.3	138.5	-303.8				
B40s-k	0.52	5.8	17.3	138.3	-34.6	484.3	-440.8	171.1	43.2	526.5	-476.5				
L40s-k	0.57	7.8	14.4	147.5	-39.0	599.9	-407.2	181.1	108.3	579.8	-217.2				
B60-k	0.45	3.7	22.8	114.9	-27.3	848.3	-573.9	149.6	32.6	924.2	-608.4	152.6	67.8	947.6	-601.2
L60-k	0.42	5.2	22.7	67.6	-42.4	789.1	-606.4	140.1	-25.9	951.9	-623.0	153.4	74.2	949.2	-566.0
B30-k	0.93	22	3.6	79.8	-192.4	224.5	-195.7								

Specimen	T [sec]	h [%]	Ke [N/mm]	Hachinohe EW x1.0				Hachinohe EW x1.25				Hachinohe EW x1.5			
				δmax (+) [mm]	δmax (-) [mm]	Qmax (+) [N]	Qmax (-) [N]	δmax (+) [mm]	δmax (-) [mm]	Qmax (+) [N]	Qmax (-) [N]	δmax (+) [mm]	δmax (-) [mm]	Qmax (+) [N]	Qmax (-) [N]
B40-h	0.88	10	6.4	42.3	-99.7	259.5	-291.2	6.7	-133.5	170.6	-303.8	-2.1	-166	27.0	-312.0
B30-h	1.14	14.2	3.5	40.4	-99.75	149.4	-187.8	-10.6	-161.4	32.2	-192.4	-146.7	-172.8	-148.6	-170.6

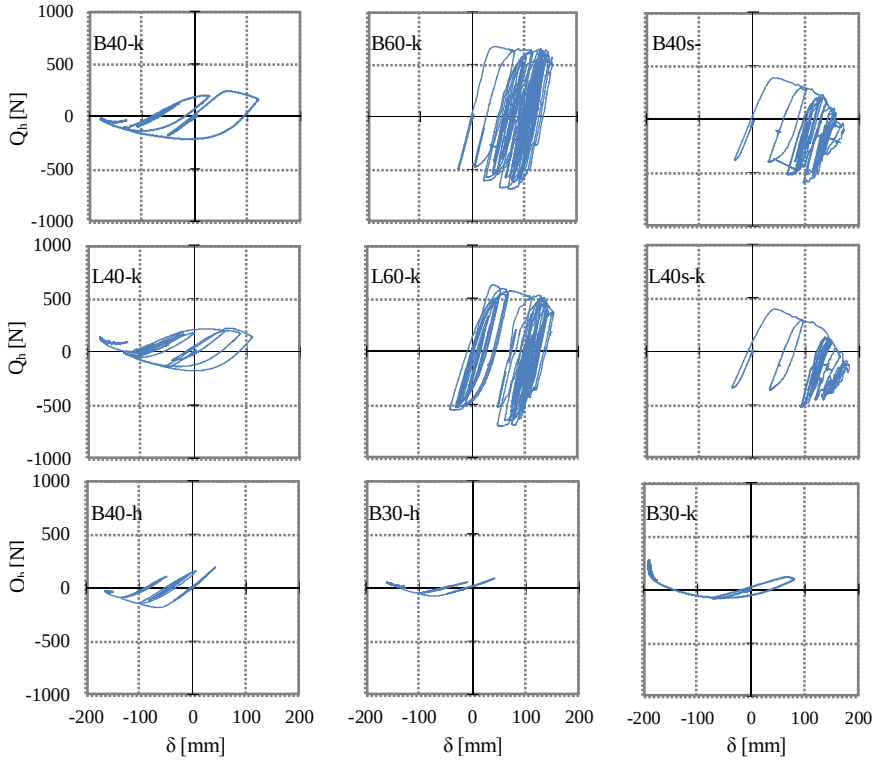


Figure 9 Q_h versus δ Relationship

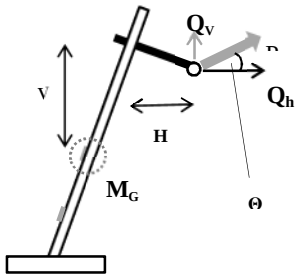


Figure 10 Force Balance around Stiffness Element

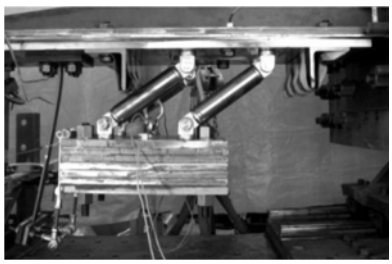


Figure 11 Collapse of B30-k

Q_h is given by Eq. (2) is changing Eq. (1);

$$Q_h = \frac{M_G}{V \pm \tan\theta \times h} \tag{2}$$

Here, the sign of *Qv* (positive or negative) in Eq. (1) changes according to displacement dimension of specimen because bending dimension caused by *Qv* is not always same to bending dimension caused by *Qh* when specimen have large deformation.

Collapse in this test is decided at the time of unloading stiffness changes negative, not to collapse perfectly by running columns into a protect stopper. The reason is that deformation of specimen is limited according that the wire lope which linked up counter weights to inertia mass touched fix plate when specimen has a large deformation. The solution of this trouble is only making longer the length of hole through the fix plate and jigs than present. This is one of our future works.

Showing Figure 9 again, specimen B40-k, L40-k, and B30-k collapsed at the excitation of Kobe NS x1.0, specimen B40-h collapsed at the excitation of Hachinohe EW x1.25. Figure 11 shows a picture after B30-k which had maximum displacement in all specimens collapsed. In this picture, collapse shows inertia mass close upper fix plate. On the other hand, specimens of B60 and B40s series did not collapse even inputting the excitation of Kobe NS x1.25 (2nd). These specimens has finished because displacement did not increase.

Figure 12 shows deformation of specimen. In case that specimen frame deformed the side of stiffness element as shown in Figure 12 (a), specimen was able to have large displacement by acting rod end and screw bar in the connection between frame and stiffness element. However,

in case that specimen frame deformed the opposite side of stiffness element as shown in Figure 12 (b), deformation of specimen was limited because the connection between frame and stiffness element stretched. Also, short stiffness elements of specimens have small horizontal deflection. This is the reason that specimens of B60 and B40s series stopped deformation without collapse.

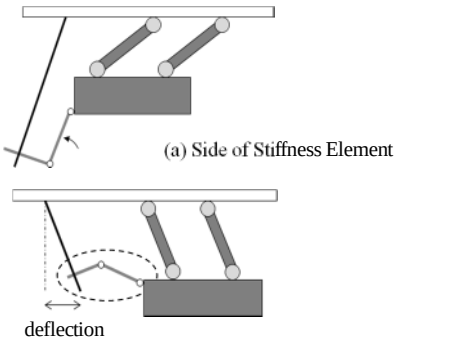


Figure 12 Deformation of Specimen

4. APPLICATIONS OF TEST RESULTS

4.1 Comparison to Response Analysis

Due to verify the test results obtained by new method of small-scale shaking table test, a series of response analysis inputting earthquake record is executed. Analysis model is single degree of freedom system and its hysteresis model is bi-linear type. Elastic stiffness of bi-linear uses the value of *Ke* as shown Table 3. Plastic stiffness (the second stiffness) k_2 and yield shear force *Qy* are calculated by way as shown in Figure 13 in each specimen. In analysis, k_2 and *Qy* of bi-linear uses average value to each k_2 and *Qy*.

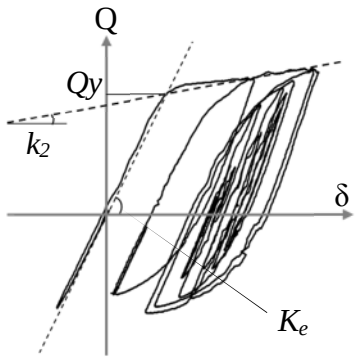


Figure 13 Modeling way of Bi-linear

Figure 14 shows some examples comparison between response analysis results and test results. Break line is shear force brought by P-△ effect. Response analysis results are almost corresponded to test results. This means new method of small-scale shaking table test is able to reproduce behavior of building under earthquake. Table 4 shows acceleration level when specimen collapsed both in analysis and shaking table test. Here, the decision of collapse in analysis is shown in Figure 15. Both specimens in shaking table test and in response analysis collapsed at almost similar excitation.

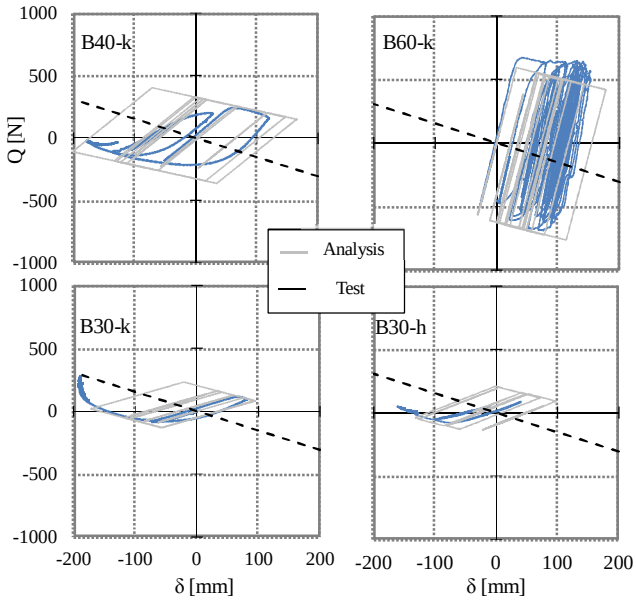


Figure 14 Comparison between Analysis and Test

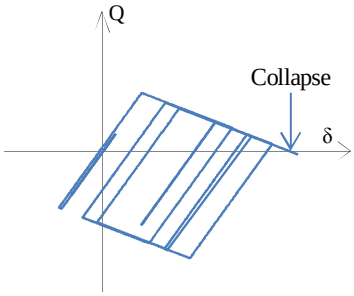


Figure 15 Definition of Collapse in Analysis

Table 4 Level when Specimen collapsed

Specimen	Response Analysis	Shaking Table Test
B40-k	Kobe NS x1.25	Kobe NS x1.0
L40-k	Kobe NS x1.0	Kobe NS x1.0
B60-k	Kobe NS x1.5	-
L60-k	Kobe NS x1.25	-
B40s-k	Kobe NS x1.0	-
L40s-k	Kobe NS x1.0	-
B30-k	Kobe NS x1.0	Kobe NS x1.0
B40-h	Not collapse even x1.5	Hachinohe EW x1.5
B30-h	Hachinohe EW x1.5	Hachinohe EW x1.25

4.2 Influence to Results caused by Vertical Load

Inversed shaking table system has a merit that vertical load is able to change with keeping the spec of specimen. In case of changing vertical load, displacement of specimen also changes by P-△ effect. Figure 16 shows comparison of displacement between B60-k and L60-k. The horizontal axis means cumulative time from excitation of Kobe NS x1.0 to the excitation of Kobe NS x1.25 (2nd). The vertical axis is horizontal relative displacement (δ). L60-k has small δ at

the excitation of Kobe NS x1.0 because damping factor of this specimen is large as already shown in Table 3. Increasing input level, δ of L60-k increases quickly and finally it exceeds δ of B60-k. This means that difference of vertical load influences directly to value horizontal displacement when specimen has large deformation.

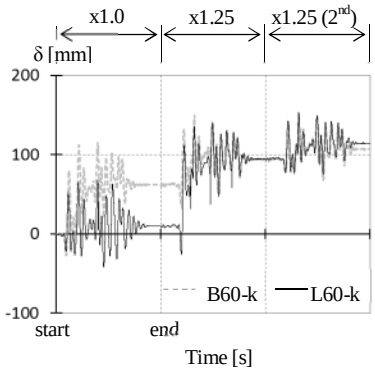


Figure 16 Comparison between B60-k and L60-k

5. SAMMARY

A new test method of shaking table system with reduced-model due to reproduce collapse behavior of buildings is proposed in this paper. Using the new method, a series of dynamic test is conducted. The important findings are follows;

1. Results of the shaking table test matches response analysis of single degree freedom model.
2. Collapse behavior by P-△ effect is able to reproduce in shaking table test with small-scale model inputting earthquake record along the real axis of time.
3. Shaking table test is able to conducted with portable parts and general experimental apparatus

On the other hand, some problems to execute test was happened. These problems are follows;

1. Deformation of some specimen was limited because wire lope and jigs are touched each other during the excitation. At last, the specimen was finished without collapsing perfectly.
2. Some specimen did not collapse because their stiffness element was not able to follow the large deformation of specimen.

The new test method will reproduce more accurate behavior of models up to collapse by improving some operative problems such as above.

Acknowledgements:

This work was supported by JSPS Grants-in-Aid for Challenging Exploratory Research, Grant Number 23656337.

References:

Shimada, Y., Suita, K., Yamada, S., Matsuoka, Y., Tada, M., Ohsaki, M., Kasai, K. (2010), "Collapse Behavior on Shaking Table Test －Dynamic Collapse Test of Full-Scale 4-story Steel Building Part-3－," *J. Struct, Constr, Eng.*, AIJ, **74**(653), 1351-1360.

Ohsaki, Y. (1994), "A New Introduction on Spectrum Analysis of Earthquake Ground Motion," *Kajima Institute Publishing Co., Ltd.*

Shibata, A. (2001), "Dynamic Analysis of Earthquake Resistant Structures," *Morikita Publishing Co., Ltd.*

10CUEE CONFERENCE PROCEEDINGS
10th International Conference on Urban Earthquake Engineering
March 1-2, 2013, Tokyo Institute of Technology, Tokyo, Japan

NUMERICAL ANALYSIS ON PLASTIC DEFORMATION CAPACITY OF STEEL BEAM UNDER VERIOUS LOADING HISTORIES

Satoshi Yamada[1], Yu Jiao[2], and Shoich Kishiki[3]

1) Associate Professor, Structural Engineering Research Center, Tokyo Institute of Technology, Japan
2) Assistant Professor, Dept. of Architecture, Tokyo University of Science, Japan Chile
3) Lecturer, Dept. of Architecture, Osaka Institute of Technology, Japan
naniwa@serc.titech.ac.jp, yujiao@rs.tus.ac.jp, kishiki@archi.oit.ac.jp

Abstract: Ductile fracture occurs when the steel beam reaches its ultimate plastic deformation capacity. In order to evaluate the plastic deformation capacity of beam determined by ductile fracture, it is necessary to clarify the plastic strain capacity of the beam-end flange. In this paper, the in-plane beam analysis was conducted to achieve the strain history at the fracture zone. A hysteresis model of the structural steel effective in evaluating material damage was introduced into this analysis. Moreover, loss of beam section due to the weld access holes and the local out-of-plane bending of the tube wall on the RHS column were taken into account to the analytical model. The analytical method was proved by comparing the analytical results to the experimental results from a database. The plastic strain capacity of beam-end flange till ductile fracture was evaluated by studying the analytical flange strain histories.

1. INTRODUCTION

In the 1994 Northridge earthquake and the 1995 Kobe earthquake that occurred one year later, a great deal of steel beam damage due to brittle fracture was observed. After that, many efforts have been made to prevent the brittle fracture mostly due to the lack of ductility and poor weld. However, even though the brittle fracture can be avoided during earthquakes; there is still a possibility of the flange ductile fracture, which is often observed at the beam-end. Especially in the WF composite beam connected to RHS column that is commonly used in Japan, ductile fracture occurs due to the decrease of the joint efficiency and the strain concentration on the flange.

Ductile fracture occurs when the beam reaches its ultimate plastic deformation capacity. The plastic deformation capacity of steel beams has been discussed for decades. Almost all the research work related to the evaluation of the beam's ultimate plastic deformation capacity bases on the results of steel beam tests. (Suita et.al, 1998, Jiao et.al, 2011, etc.) For different sizes of steel beam made of different types of steel, subjected to distinct earthquake effects, in order to obtain accurate evaluation results, the above mentioned beam tests must consider as many parameters as possible. The parameters of the tests should include at least the material's yield strength/ratio, the beam's moment gradient, as well as loading history. Consequently, a huge number of beams need to be tested, which is hardly reasonable. Therefore, it is necessary to find a method that can evaluate the plastic deformation capacity of the steel beams with different parameters.

In this paper, a new in-plane beam analysis method was proposed to achieve the strain history at the fracture zone. A hysteresis model of the structural steel effective in evaluating material damage was introduced into this analysis. Moreover, loss of beam section due to the weld access holes and the local out-of-plane bending of the tube wall on the RHS column were taken into account to the analytical model. The analysis is proved to be valid by comparing the analytical results to the experimental results from an experimental database. The stress-strain histories at the beam-end flanges till fracture were obtained through the analysis. By studying the strain capacity of both the skeleton curves and Bauschinger parts that were derived from the stress-strain histories, the plastic strain capacity of beam-end flange till ductile fracture was evaluated using the same evaluation method of the plastic strain capacity of the structural steel under axial strain histories

2. ANALITICAL METHOD

2.1 Assumptions

The in-plane analysis of the ideal cantilever wide-flange beams subjected to cyclic loading histories was conducted under the following assumptions:
1) The assumption of the plane section.
2) The deformation due to shear force is considered to be always elastic.
3) There is no out-of-plane deformation of the beam.
4) The beam reaches its maximum load without local buckling.

2.2 Basic algorithm

The algorithm of this analysis is based on the monotonic in-plane analy (Yamada, M. et. al. 1966). The basic idea is to obtain the moment-curvature relation (M-φ) of a certain beam section through the internal force balance under the assumption of the plane section. Additionally, the load-deformation relation (M-θ) of the beam can be derived by integrating the moment-curvature relation along the beam span. This analytic method is known to be sufficiently accurate before the beam reaches its maximum strength.

2.3 Material hysteresis model

A material hysteresis model that is effective in material damage evaluation is very important for the cyclic beam analysis in this study. A multi-linear hysteresis model of structural steel considering Bauschinger effects based on the monotonic true stress-strain relation (Yamada, S. et. al. 2002) was employed in this analysis. The hysteresis loops are made up of the skeleton curves and the Bauschinger parts. The skeleton curves are picked up from the coupon tests results (converted into the true stress-strain relation). Each fragment of the Bauschinger part is simplified as a bi-linear curve, with the requirement that the bi-linear curve dissipates approximately same amount of plastic energy as the Bauschinger part does.

2.4 Modeling of the decrease of joint efficiency

The joint efficiency of the beam web at the beam-to-column connection γ_w is defined in Equation (1) .

$$\gamma_w = \frac{{}_jM_{wu}}{M_{wu}} \tag{1}$$

where ${}_jM_{wu}$ is the maximum moment of the beam web at the connection considering the loss of the beam section and local bending of the column tube wall, $M_{wu} = \sigma_{wu} \cdot Z_{wp}$ is the ideal maximum moment of the beam web at the connection, σ_{wu} is the tensile strength of the beam web, and Z_{wp} is the plastic section modulus of the full section beam web. The calculation method of γ_w (Equations (1)) is suggested in the Japanese "Recommendation for design of connections in steel structures" (AIJ 2006).

$${}_jM_{wu} = m \cdot Z_{wpe} \cdot \sigma_{wy} \tag{2}$$

where σ_{wy} is the yield stress of the beam web, $Z_{wpe} = \frac{1}{4}(H - 2t_f - 2S_r)^2 \cdot t_w$ is the plastic section modulus of the beam web considering the loss of cross section, and m is the normalized bending strength of the beam web at the beam-to-column connection $m = \frac{{}_jM_{wu}}{M_{wp}}$, where M_{wp} is the full plastic moment of the beam web considering the loss of section due to the weld access holes. Here, m is controlled by the size of the column, beam, and the weld access holes as well as the yield strengths of the column and beam. In design, it is possible to approximate m as follows: for the RHS columns, $m = \min\left\{1,\ 4\frac{t_c}{d_j}\sqrt{\frac{b_j \cdot \sigma_{cy}}{t_w \cdot \sigma_{wy}}}\right\}$, where σ_{cy} is the yield stress of the column, H is the beam height, t_f is the thickness of the beam flange, S_r is the loss of cross section in the beam height dimension (usually the length of the weld access hole along the beam height), t_w is the thickness of the beam web, t_c is the thickness of the RHS column, d_j is the inner distance of two diaphragms, $b_j = B_c - 2t_c$ is the width of the yield area on the RHS column obtained from the yield line theory, and B_c is the width of the RHS column. In this paper, only the most commonly used steel beams with weld access holes are discussed.

In the recent monotonic beam analysis (Suzuki et.al 1999), a part of the beam web (the isosceles right triangle ABC in Figure 4) close to the column face was set to be ineffective in transferring the bending stress from the column. So that the ultimate moment (when the stress at each point of the web section equals to the ultimate strength of beam web σ_{wu}) of rest of the web cross section would be the same as ${}_jM_{wu}$ mentioned previously. h_r is the length of the ineffective area in the web along the beam height, which can be expressed in Equation (3).

$$h_r = \sqrt{1 - \frac{m \cdot \sigma_{wy}}{\sigma_{wu}}} \cdot (H - 2 \cdot t_f - 2 \cdot S_r) \tag{3}$$

Nevertheless, this method didn't consider the loss of section due to weld access holes. With the effect of the weld access holes, the ineffective area of the web should be the pentagone ADCEB. Furthermore, two rectangles at the location of the weld access holes, with the length of each side equals to S_r and the length of the weld access hole along the beam span respectively, should also be set to be ineffective in carrying the bending stress. Figure 1 shows three ineffective parts of the beam close to the column face in the analysis. Note here, shear force is carried by the net beam section without weld access holes.

Moreover, comparing with the beam flange, the strength of the diaphragms and the full-penetrated weld area is considered to be much higher. In the cyclic in-plane beam analysis, these parts were assumed to be always elastic.

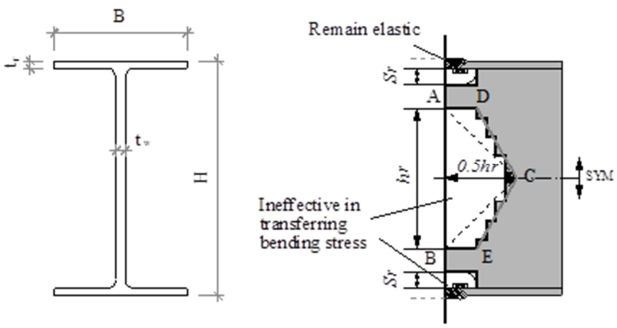


Figure 1. The ineffective area of the beam web

3. VERIFICATION OF THE IN-PLANE BEAM ANALYSIS

3.1 Experiment of steel beams subjected to various cyclic loading histories

In order to verify the analytical method introduced in Section 2, total 13 T-type beam-column subassemblies were tested under four different loading histories. (Jiao et.al (2011), Kobayashi (2005), Okada et.al (2003) and Yamada, S. et.al (2011)) Test set-up is shown in Figure 2. In the tset, load-deformation relationships and local strain histories of the flange surface close to the toe of the weld access hole were collected. The beam was shop welded onto the column via through-diaphragms with the improved type of weld access holes and solid end tab in accordance with Japanese Standard Specification JASS 6. In order to prevent local buckling, stiffeners were welded to the beams near the column faces and the loading points.

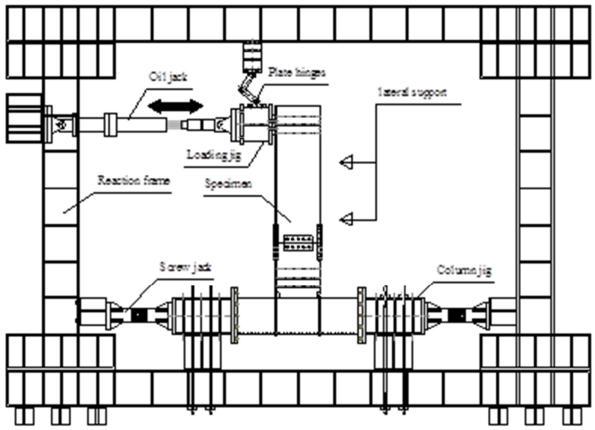


Figure 2 Tset set-up

3.2 Comparison of the experimental and analytical results

The in-plane analysis of all the steel beams specimens in the database was conducted. Figure 3 shows the example of the comparison of analytical and the experimental results of the load-deformation relations of some specimens. Two specimens from each series of the cyclic loading beam test were listed as examples. Good correspondences between the experimental and analytical results can be found from these graphs. The measurements of the plastic strain gauges on each flange are compared with the nominal analytical strain history results at the same position, shown in Figure 4. The experimental strain value of certain flange is the average value of the gauges attached on the flange.

The analytical strain histories of the beam flange match the experimental strain histories well before fracture occurred. When it comes closer to the fracture points, although relatively larger disagreement can be seen from the graph, it is still within the range of tolerable range. The disagreement observed might because of the soar of the local strain due to the sudden strain concentration at the fracture area on the flange. In addition, there is also a possibility of the existence of the measurement error from the plastic strain gauges after many loading cycles in large strain regions. Summing up the above verification, the cyclic in-plane beam analysis is effective in simulating the overall beam behavior (load-deformation relation) and local material behavior (strain history) during the loading procedure till fracture.

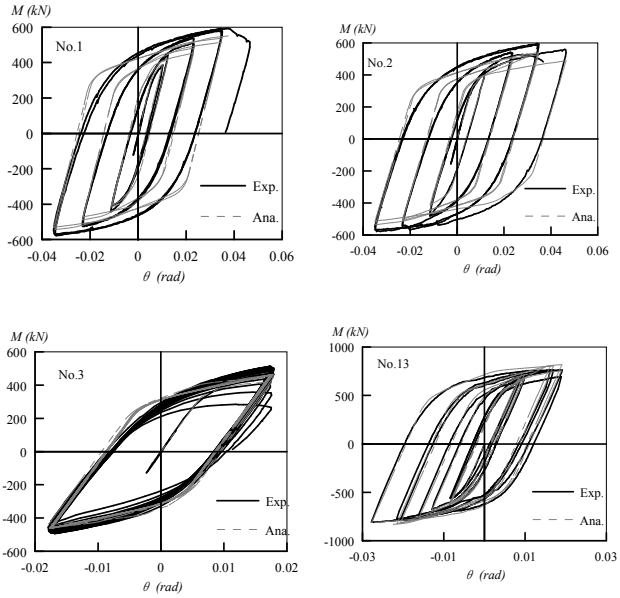


Figure 3 Comparison of the analytical and experimental results ; load-deformation relations

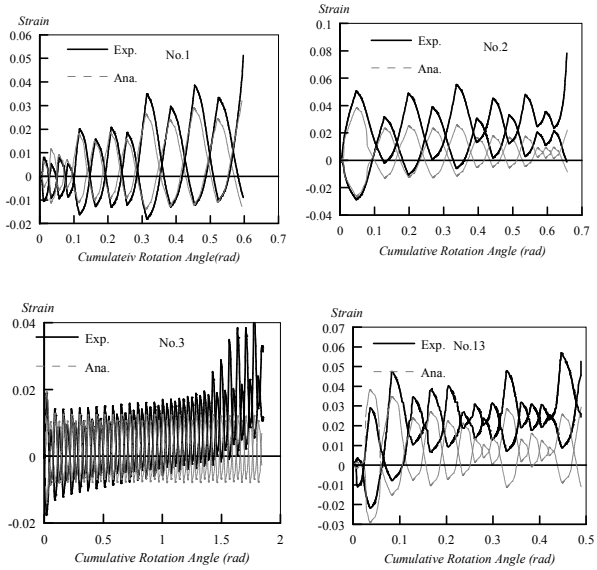


Figure 4 Comparison of the analytical and experimental results ; Strain histories

4. EVALUATION OF THE PLASTIC DEFORMATION CAPACITY OF STEEL BEAMS SUFFERING DUCTILE FRACTURE

The average surface stress-strain histories of the section at the toe of the weld access hole can be obtained from the analyses. The cumulative strain capacity of the beam flange is evaluated based on the average flange surface strain histories of the section at toe of the weld access hole through the same evaluation method of the strain capacity of structural steel mentioned (Jiao et.al, 2010) The fracture condition of steel beam-end flange subjected to random cyclic loadings is proposed in this section.

Refer to the evaluation method of the plastic strain capacity of steel material introduced in the reference (Jiao et.al, 2010), the cumulative plastic strain ratio ($\eta_S^+, \eta_S^-, \eta_B^+, \eta_B^-$) at the toe of the weld access hole on the fractured flange of each specimen was output from the analyses. Where $\eta_S^+, \eta_S^-, \eta_B^+, \eta_B^-$ are the cumulative plastic strain ratio defined as the cumulative plastic strain of both tension and compression side in the skeleton curve and Bauschinger part ($_t\varepsilon_S^+, _t\varepsilon_S^-, _t\varepsilon_B^+, _t\varepsilon_B^-$) divided by yield strain $_t\varepsilon_y$ (Equations (4)-(7)). The total plastic deformation capacity was the summation of that obtained from each part of the hysteresis loops, which can be written as $\eta_T = \eta_S^+ + \eta_S^- + \eta_B^+ + \eta_B^-$.

$$\eta_S^+ = {}_t\varepsilon_S^+ / {}_t\varepsilon_y \quad (4)$$

$$\eta_S^- = {}_t\varepsilon_S^- / {}_t\varepsilon_y \quad (5)$$

$$\eta_B^+ = {}_t\varepsilon_B^+ / {}_t\varepsilon_y \quad (6)$$

$$\eta_B^- = {}_t\varepsilon_B^- / {}_t\varepsilon_y \quad (7)$$

Here, all the values were normalized by dividing the cumulative plastic strain ratio of material test η_0, in order to eliminate the effect of different materials and steel lots.

The growing processes of η_S^+ / η_0 and η_T / η_0 of all the specimens in the database are plotted in Figure 3. The points in Figure 5 show the fracture points of the beam specimens from the database. The cumulative plastic strain ratio η_S^+ / η_0 and η_T / η_0 of the beam-end flange also shows a linear relation at the fracture point. Equation (8) expresses the linear relation. Ductile fracture of the beam flange occurs when the cumulative plastic strain ratio at the critical area satisfies this equation. Note here, since η_S^+ / η_0 is always less than η_T / η_0, the scope of Equation (8) ends when it hits the monotonic growing processes line, where $\eta_S^+ / \eta_0 = \eta_T / \eta_0$.

$$\eta_T / \eta_0 = 7 \cdot (1 - \eta_S^+ / \eta_0) - 0.5 \quad (8)$$
$$(0.22 < \eta_S^+ / \eta_0 \le 0.8125)$$

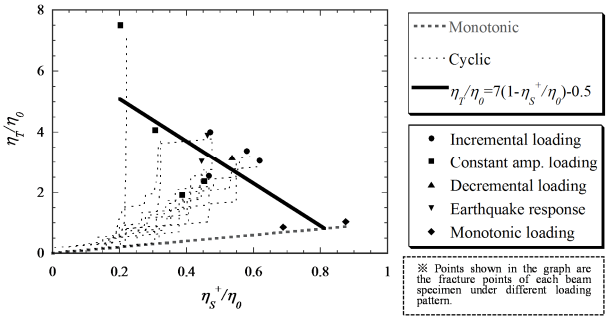


Figure 5 Growing processes of η_S^+ / η_0 and η_T / η_0

5. CONCLUSIONS

The plastic deformation capacity of the structural components till ductile fracture plays a significant role in seismic design because it is one of the indexes of structural performance. In this paper, the fracture condition of the steel beam flange was discussed by studying the average flange surface stress-strain history of the beam section at the toe of the weld access hole. The in-plane analyses of the steel beams subjected to cyclic loading histories were conducted to obtain the above mentioned average stress-strain history. A hysteresis model of the structural steel considering Bauschinger effect, which is effective in evaluating material damage, was introduced into this analysis. Moreover, the analytical model takes into account the decrease of the joint efficiency, which directly affects the strain capacity of the beam flange. By comparing the analytical load-deformation relation as well as the local strain histories to the experimental results from a database, the analytical simulation was proved to be authentic.

The plastic strain capacity of beam flange till ductile fracture was evaluated using the evaluation method. This method focuses on the relation between the cumulative plastic strain ratio of both the skeleton curves and the Bauschinger parts derived from the average beam-end flange stress-strain histories obtained in the in-plane analysis. At the fracture zone of the beam flange, there is a linear relation between the ultimate normalized cumulative plastic strain ratio of the skeleton curve on the tension side (η_S^+ / η_0) and the total normalized cumulative plastic strain ratio (η_T / η_0). Ductile fracture of the beam flange occurs when the cumulative plastic strain ratio at the critical area satisfies Equation (8).

References:

Architectural Institute of Japan (2006) Recommendation for design of connections in steel structures (In Japanese).

Architectural Institute of Japan (1996) Japanese architectural standard specification JASS 6, steel work (In Japanese).

Jiao Y., Yamada S., and Kishiki S. (2010) Plastic deformation capacity of structural steel under various axial strain histories. 8th International Conference on Urban Earthquake Engineering. Tokyo, Japan: 935-40.

Jiao Y., Yamada S., Kishiki S., and Shimada Y. (2011), "Evaluation of plastic energy dissipation capacity of steel beams suffering

ductile fracture under various loading histories", DOI:10.1002 /eqe.1103.

Kobayashi A. (2005) "Evaluation of ultimate energy dissipation capacity of steel under cyclic loading" (In Japanese). Master Thesis submitted to Tokyo Institute of Technology; 2005.

Okada K, Matsumoto Y, Yamada S. (2003), "Evaluation of effect of joint efficiency at beam-to-column connection on ductility capacity of steel beams" (In Japanese). Journal of Structural and Construction Engineering, Transactions of AIJ; No 568: 131-8.

Suita K., and Tada M. "Full-scale Tests to Determine Plastic Rotation Capacity of Steel Wide-flange Beams Connected with Square Tube Columns" Proceedings on Welded Construction in Seismic Areas, International Conference on Welded Constructions in Seismic Areas, 289-301.

Suzuki T, Ishii T, Morita K, and Takanashi K. (1999) "Experimental study on fracture behavior of welded beam-to-column joint with defects" (In Japanese). Steel construction engineering; Vol 6, No 23:149-64.

Yamada M, Sakae K, Tadokoro T, Shirakawa K. (1966), "Elasto-plastic bending deformation of wide flange beam-columns under axial compression, Part I: Bending moment-curvature and bending moment-deflection relations under static loading" (In Japanese). Journal of structural and construction engineering, Transactions of the AIJ ; No 127: 8-14.

Yamada S, Imaeda T, and Okada K. (2002), "Simple hysteresis model of structural steel considering the Bauschinger effect" (In Japanese). Journal of structural and construction engineering. Transactions of AIJ ; No 559, 225-32.

Yamada S., Jiao Y. and Kishiki S., (2011) "Cyclic Loading Test on Steel Beam under Various Loading Histories "(in Japanese), Proc. of annual meeting, JAEE, 286-287

10CUEE CONFERENCE PROCEEDINGS
10th International Conference on Urban Earthquake Engineering
March 1-2, 2013, Tokyo Institute of Technology, Tokyo, Japan

EFFECTS OF CORE PLATES LOCAL BUCKLING FOR CUMULATIVE DEFORMATION CAPACITY OF BUCKLING RESTRAINED BRACES

Ryota Matsui[1] and Toru Takeuchi[2]

1) Assistant Professor, Architecture and Building Engineering Dept., Tokyo Institute of Technology, Japan
2) Professor, Architecture and Building Engineering Dept., Tokyo Institute of Technology, Japan
matsui.r.aa@m.titech.ac.jp, ttoru@arch.titech.ac.jp

Abstract: Buckling restrained braces (BRBs) are widely used in the world as seismic resistant and seismic energy dissipation devices. As an energy dissipation brace, one key limiting state of BRBs is governed by cumulative deformation capacity until core-plate fracture. Such capacity will always be less than that of the steel material employed. The view expressed in this paper is that the mechanism decreasing cumulative deformation capacity in the BRB is attributable to local buckling of the core plate, which leads to non-uniform strain distribution of the core plate in a longitudinal direction. This decrease in the cumulative deformation capacity of the BRB can be explained by applying the fatigue performance formula for the relevant steel material to the strain encountered at the local zone of the core plate. A ratio that compares degree of strain concentration at this localized zone with the total normalized deformation is proposed as determining the strain at the core plate local zone relative to total normalized deformation. In addition, the effect of the exponential value of the fatigue performance formula on methods for predicting cumulative deformation capacity of the BRB is investigated.

1. INTRODUCTION

Buckling restrained braces (BRBs) are widely used as seismic resistant and energy dissipation devices. As an energy dissipation brace, one key limiting state of BRBs is determined by cumulative deformation capacity until the core plate fractures. The BRB's capacity for stable dissipation of energy when its restraint conditions are satisfied allows for absorption of seismic energy. This absorption eventually leads to fracture of the BRB. Since BRBs are generally designed to avoid fracture during seismic events, determining cumulative capacity for energy dissipation proves crucial in evaluating performance and in assessing any needed replacement.

Several researchers have confirmed that the core plate of the BRB undergoes a high-mode buckling deformation that leads to non-uniform strain distribution. In particular, Takeuchi and Hajjar, et al., (2010) studied such high-mode buckling of the core plate in BRBs.

Cumulative deformation capacity of the BRB itself is most generally evaluated directly, using the Manson–Coffin fatigue formula to resolve fatigue performance in BRBs. However, cumulative deformation capacity should be evaluated initially by applying the fatigue performance formula to the strain concentration zone in the steel material of the core plate itself.

In this paper, the mechanism that decreases cumulative deformation capacity of the BRB— other than steel material specifications— is sought in examination of local buckling of the core plate. This buckling leads to non-uniform strain distribution of the core plate in a longitudinal direction. This, in turn, causes a plastic strain concentration in the localized zone. Decrease in the cumulative deformation capacity of the BRB is accounted for by applying the fatigue performance formula for steel material to the strain at the local zone. A ratio comparing strain concentration degree at the local zone with the total normalized deformation is proposed to differentiate strain at the local zone from the total normalized deformation. Finally, the cumulative deformation capacity of the BRB is evaluated using the local zone strain already calculated from the total normalized deformation.

In addition, the effect of the exponential value of the fatigue performance formula on the methods for predicting cumulative deformation capacity of the BRB was investigated.

2. FATIGUE FORMULA FOR BRB

From various past experiments on BRBs, Takeuchi and Ida, et al., (2008) proposed the following low-cycle fatigue formula for the BRB as Eq. (1):

$$\Delta\varepsilon_n = 0.5 \cdot N_f^{-0.14} + 54.0 \cdot N_f^{-0.71} \quad (1)$$

Here, $\Delta\varepsilon_n$ is the normalized deformation amplitude, and N_f is the fracture cycle number. In addition, the results of Takeuchi and Shirabe, et al., (2006) have been employed in

Eq. (1) to obtain Eq. (2.2) for a fracture cycle number of less than 20.

$$N_f = \left(1 - \frac{3\Delta\varepsilon_n}{70}\right) \cdot \left(\frac{\Delta\varepsilon_n^{-1.41}}{3.63\times10^{-3}}\right) + 0.75 \qquad (2)$$

This modification expresses a partial concentration of plastic strain in the core plate at ultra-low fatigue failure zones, where stress exceeds maximum value and the tangent modulus becomes negative. The fatigue formula for a BRB derived jointly from Eqs. (1/ 2) is consistent with results based on the experimental data from Nakamura and Takeuchi, et al., (2000), as shown in Figure 1. In this figure, the fatigue performance of the BRB will be less than the fatigue performance of the steel material determined on the basis of the normalized deformation amplitudes given by Eq. (3)

$$\begin{cases} \Delta\varepsilon_n = 0.74N_f^{-0.11} + 35.0N_f^{-0.47} & (\mathrm{SS400}) \\ \Delta\varepsilon_n = 0.47N_f^{-0.087} + 33.0N_f^{-0.48} & (\mathrm{LY100}) \\ \Delta\varepsilon_n = 0.88N_f^{-0.14} + 72.0N_f^{-0.55} & (\mathrm{LY225}) \end{cases} \qquad (3)$$

3. STRAIN CONCENTRATION AT CORE PLATES

Takeuchi and Suzuki, et al., (2006) have proposed an index of strain-concentration-ratio for ordinary circular tube braces, whereby the local strain at the point of plastic strain concentration is divided by the normalized deformation. The strain concentration ratio is defined by individual specification of each brace. This index enables one to estimate local plastic strain without significant calculation, such as arise from use of the finite element method. Brace fracture is then simply defined by the point at which local strain value becomes equivalent to the fatigue formula for the steel material. Therefore, this method efficiently assesses brace fracture using a macro-model of the braces in question. In this paper, the authors have attempted to evaluate BRB fracture using a similar method.

In our study, the BRB is constituted by a plane steel core plate restrained by a mortar filled steel tube, as shown in Table 1 and in Figures 2 and 3. The mechanical property of SN400 is assumed to be same as that of SS400. Hypothetically, the core plate exhibits a high-mode local buckling deformation continuously within the clearance between the core plate and the restrainer s under cyclic loading. In such case, the local buckling deformation y is calculated from the half amplitude of the local buckling wave l_p as Eq. (4).

$$\begin{cases} y = s\sin\left(\pi x / l_p\right) \\ s = s_0 + 0.5\nu_p\varepsilon_{ntm}t_c \end{cases} \qquad (4)$$

Here, ε_{ntm} is the maximum value of normalized tensile deformation, and s_0 is the initial value of the clearance between core plate and restrainer. Although local buckling occurs both in- and out-of-plane, only the latter is considered

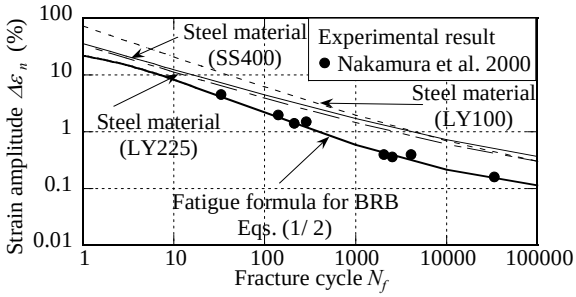


Figure 1 Low-cycle Fatigue Capacity for BRBs and Steel Material

Table 1 Mechanical Properties of BRBs

Specimen	Steel	t_c (mm)	B_c (mm)	$\Delta\varepsilon_n$ (%)	N_f	Input strain amplitude
400-200	SN400B (SS400)	25	100	2	176	Constant (Nakamura et al. 2000)
400-150				1.5	140	
400-040				0.4	211	
100-150	LY100			1.5	287	
100-040				0.4	2041	
235-150	LY225	28		4.5	33	
235-016				0.16	2520	
-	SS400	12	50	3.2	19	Random (Takeuchi et al. 2010)

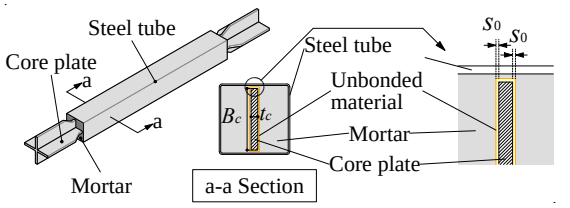


Figure 2 BRB Composition

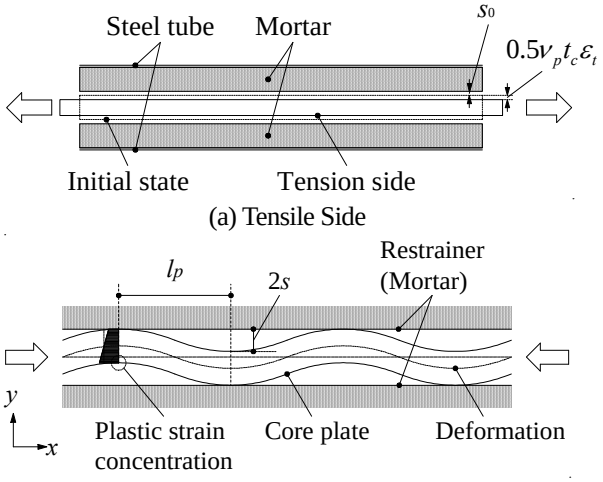


Figure 3 Core Plate Deformation

initially. The half amplitude of the local buckling wave l_p is calculated as Eq. (5),

$$l_p = \pi t_c \sqrt{E_t / 3\sigma_{cy}} / 2 \tag{5}$$

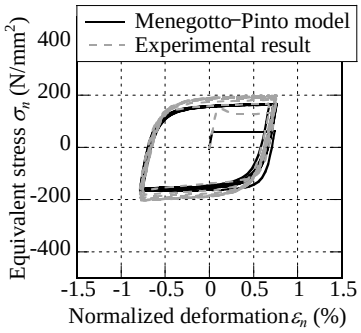
where t_c represents thickness of the core plate, σ_{cy} yield stress of the core plate, and E_t the tangent modulus of the steel material. The stress–strain hysteresis curve can be modeled by the modified Menegotto–Pinto model, as proposed by Yamazaki and Kasai, et al., (2006). The hysteresis curve calculated using the Menegotto–Pinto model is consistent with the experimental results obtained by Nakamura and Takeuchi, et al., (2000) as demonstrated in Figure 4. Here, ε_n is the normalized deformation, while σ_n is the equivalent stress calculated by dividing axial force by initial sectional area. The amplitude of the normalized deformation $\Delta\varepsilon_n$ is defined as Eq. (6), as shown in Figure 5.

$$\Delta\varepsilon_n = \varepsilon_{ntm} - \varepsilon_n \tag{6}$$

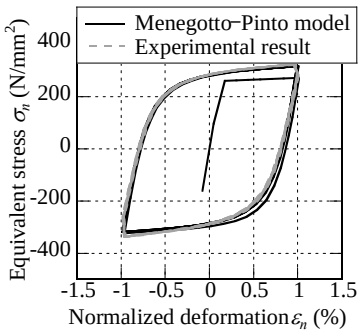
The tangent modulus E_t is directly calculated using the proposed Menegotto–Pinto model. Here, for ease, the tangent modulus is approximated by the normalized deformation function as Eq. (7), illustrated in Figure 6.

$$E_t = \begin{cases} \begin{cases} -3.68\times10^5\,\Delta\varepsilon_n + E(\mathrm{SS400}) \\ -1.12\times10^5\,\Delta\varepsilon_n + E(\mathrm{LY100}) \quad \left(0 \le \Delta\varepsilon_n \le 2\varepsilon_y\right) \\ -4.84\times10^5\,\Delta\varepsilon_n + E(\mathrm{LY225}) \end{cases} \\ \begin{cases} 6.45\times10^3\,\Delta\varepsilon_n^{-2.04} + E(\mathrm{SS400}) \\ 1.27\times10^3\,\Delta\varepsilon_n^{-1.84} + E(\mathrm{LY100}) \quad \left(2\varepsilon_y \le \Delta\varepsilon_n\right) \\ 1.93\times10^3\,\Delta\varepsilon_n^{-2.65} + E(\mathrm{LY225}) \end{cases} \end{cases} \tag{7}$$

The local buckling deformation gives the bending strain ε_b as in Eq. (8).



(a) 100-150 Specimen



(b) 400-200 Specimen

Figure 4 Menegotto-Pinto Model

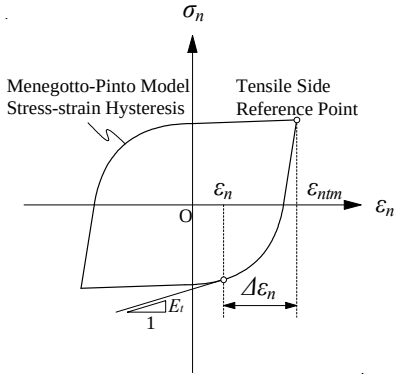
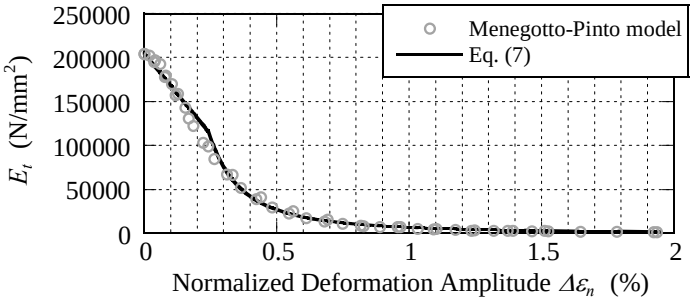
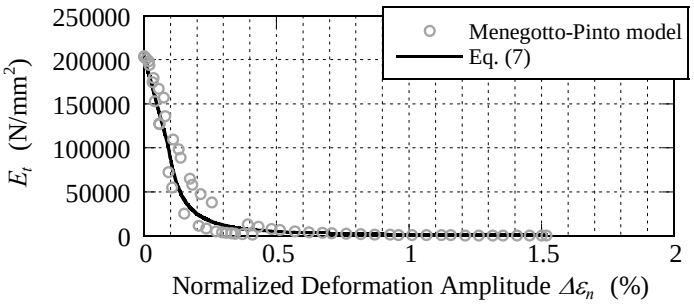


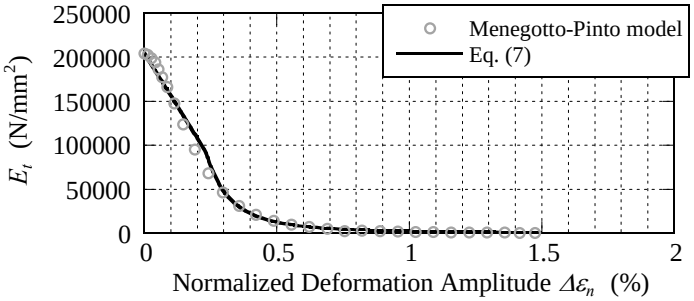
Figure 5 Normalized Deformation



(a) SS400



(b) LY100



(c) LY225

Figure 6 Tangent Modulus of Core Plate

$$\varepsilon_b = t_c/2\left(\pi/l_p\right)^2 s = 6s\sigma_{cy}/E_t t_c \tag{8}$$

The geometrical deformation ε_g is additional to the normalized deformation ε_n as in Eq. (9).

$$\varepsilon_g = 1/4\left(\pi s/l_p\right)^2 = 3s^2\sigma_{cy}/E_t t_c^2 \tag{9}$$

The local strain amplitude $\Delta\varepsilon_h$ at the point at which the most concentrated plastic strain occurs in the core plate is calculated using Eq. (10), and strain concentration ratio is α_c as defined by Eq. (11).

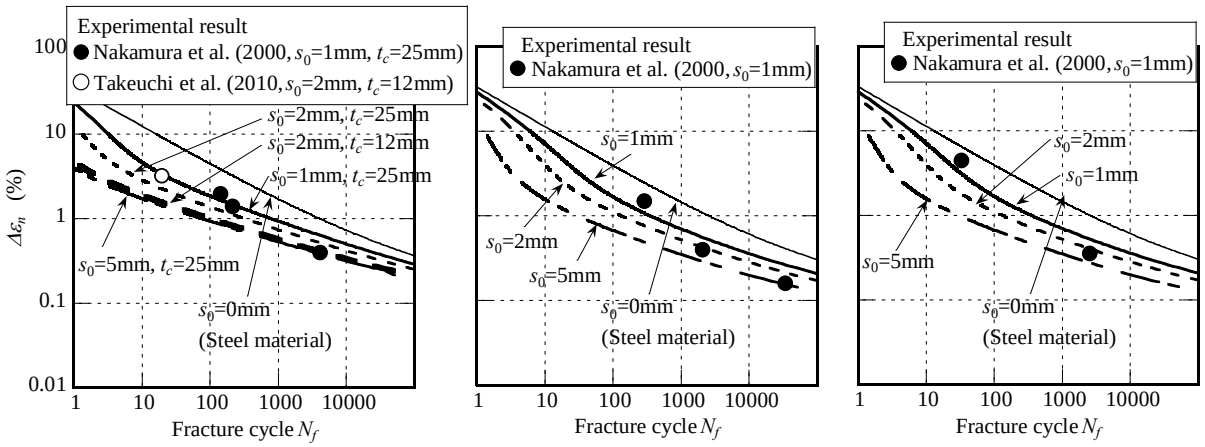
$$\Delta\varepsilon_h = \Delta\varepsilon_n + \varepsilon_b - \varepsilon_g \tag{10}$$

$$\alpha_c = \frac{\Delta\varepsilon_h}{\Delta\varepsilon_n} = \frac{\Delta\varepsilon_n + \varepsilon_b - \varepsilon_g}{\Delta\varepsilon_n} \tag{11}$$

Local in-plane strain may also be calculated using Eqs. (6) ~ (10) by substituting the thickness of the core plate t_c for the width of the core plate B_c. The local in-plane strain is generally one eighth (1/8) the local strain out-of-plane. Moreover, maximum strain positions do not necessarily coincide in- and out-of-plane. Therefore, the effect of in-plane local buckling generally does not significantly affect cumulative deformation capacity of a BRB, so that out-of-plane strain is considered as predominant overall.

4. EVALUATION OF CUMULTAIVE DEFORMATION CAPACITY

A BRB fracture can be established as the point at which local strain— calculated from normalized deformation ε_n and multiplied by strain concentration ratio α_c— is consistent with the fatigue formula given in Eq. (3). Using this evaluation method, the BRB fatigue formula may be assessed as shown in Figure 7. The plots in this figure show experimental results derived from Nakamura and Takeuchi, et al., (2000) and Takeuchi and Ohyama, et al., (2010). This fatigue formula is by and large consistent with experimental results. Here, strain amplitude derived from experimental results using random amplitudes is assessed by the rain-flow method as the average plastic strain amplitude, and cumulative plastic strain is the sum of all plastic strains. The initial clearance between the core plate and the restrainer s_0 is set at 1 mm in Nakamura and Takeuchi, et al., (2000) and at 2 mm in Takeuchi and Ohyama, et al., (2010). Figure 7 demonstrates that performance given by the BRB fatigue formula decreases as the clearance s between core plate and restrainer increases. Therefore, the strain-concentration-ratio



(a) SS400 (b) LY100 (c) LY225

Figure 7 BRB Fatigue Formulas Based on Eqs.

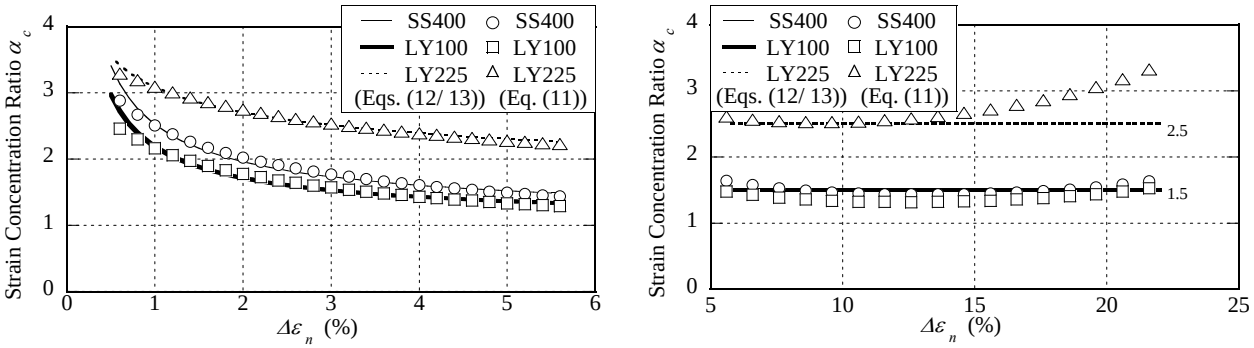


Figure 8 Strain Coefficient Ratio

α_c of a BRB may be described as a function of clearance s. For example, the strain-concentration-ratio α_c is approximated as in Eqs. (12/ 13) by the least squares method, as shown in Figure 8, where ε_y is the yield strain and $\Delta\varepsilon_{low}$ the strain amplitude, when the fracture cycle number is 20.

$$\alpha_c = \frac{\Delta\varepsilon_h}{\Delta\varepsilon_n} = \begin{cases} 1 & \left(\Delta\varepsilon_n \le 2\varepsilon_y\right) \\ 1+25\dfrac{s}{t_c} f\left(\Delta\varepsilon_n\right) & \left(2\varepsilon_y \le \Delta\varepsilon_n \le \Delta\varepsilon_{low}\right) \\ 1+25\dfrac{s}{t_c}\beta & \left(\Delta\varepsilon_{low} \le \Delta\varepsilon_n\right) \end{cases} \quad (12)$$

$$\begin{cases} f\left(\Delta\varepsilon_n\right) = \begin{cases} 1.90\Delta\varepsilon_n^{-0.62} & (\text{SS400}) \\ 1.51\Delta\varepsilon_n^{-0.64} & (\text{LY100}) \\ 2.82\Delta\varepsilon_n^{-0.35} & (\text{LY225}) \end{cases} \\ \beta = \begin{cases} 0.5 & (\text{SS400}) \\ 0.5 & (\text{LY100}) \\ 1.5 & (\text{LY225}) \end{cases} \end{cases} \quad (13)$$

In Figure 9, Eqs. (12/ 13) are compared with behaviour of restrainers, which is generally consistent with our test results.

5. DAMAGE INDEX ASSESSMENT

The fatigue evaluation of BRBs was originally based on constant stress amplitudes. Conversely, the amplitude of the response of each member subjected to seismic input is random. In such a case, stress amplitude distribution is generally determined by the rain-flow method.

As an approach to applying the fatigue formula under random amplitude, as in Eq. (3), Miner (1945) defined a fatigue condition based on Eq. (14). Here, as soon as the cumulative damage factor of individual amplitude reaches 1.0, the element is considered as exhibiting fatigue failure.

$$D = \sum_{i=1}^{m} D_i = \sum_{i=1}^{m} \frac{n_i}{N_{fi}} \quad (14)$$

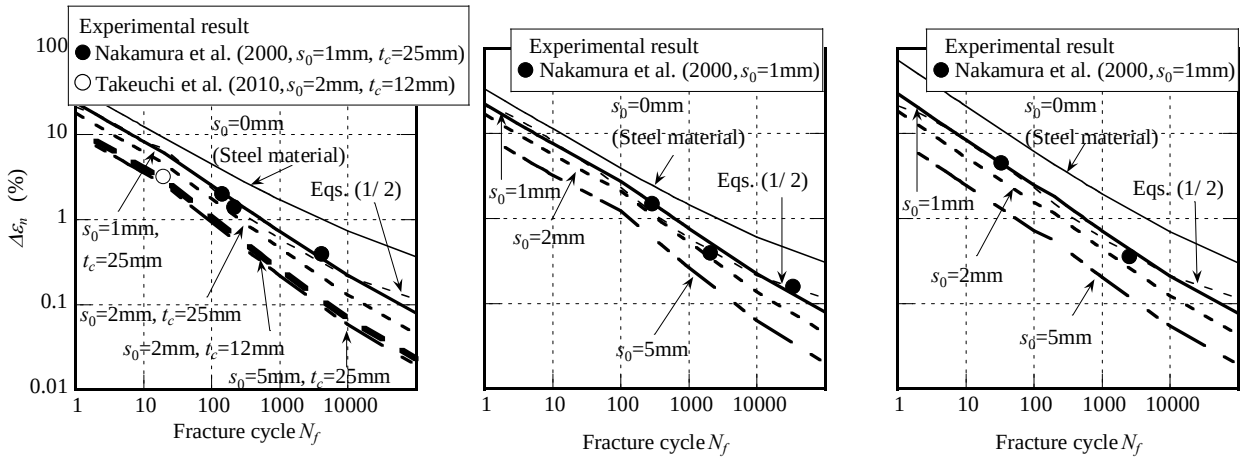
Here, D is the damage factor, n_i the number of cycles for the strain amplitude, and N_{fi} the number of failure cycles for a given strain amplitude. Additionally, Takeuchi and Ida, et al., (2008) proposed a method whereby average plastic strain amplitude is applied to fatigue failure conditions, as performed in evaluation in the previous section. In this section, the difference between Miner's rule and average plastic strain amplitude is discussed. The number of fracture cycles is defined for average plastic strain amplitude by Eq. (15).

$$\overline{N_f} = \left(\frac{\overline{\Delta\varepsilon_p}}{C_2}\right)^{-\frac{1}{m_2}} \quad (15)$$

Here, $\overline{\Delta\varepsilon_p}$ is the average plastic strain amplitude, and C_2 and m_2 are exponential values of the fatigue formula within the range of the plastic region. Cumulative plastic strain is calculated as in Eq. (16).

$$\sum \overline{\Delta\varepsilon_p} = 2\cdot\overline{N_f}\cdot\overline{\Delta\varepsilon_p} = \frac{2\cdot\overline{\Delta\varepsilon_p}^{\frac{m_2-1}{m_2}}}{C_2^{-m_2}} \quad (16)$$

Conversely, cumulative plastic strain calculation by applying Miner's rule is shown as Eq. (17)



(a) SS400 (b) LY100 (c) LY225

Figure 9 BRB Fatigue Formulas Based on Eqs.

$$\begin{cases} \sum \overline{\Delta\varepsilon_p} = 2\sum_{i=1}^{m} n_i \Delta\varepsilon_p \\ \sum_{i=1}^{m} \dfrac{n_i}{N_{fi}} = 1 \end{cases} \tag{17}$$

When the exponential value m_2 = 1.0, Eq. (16) will be identical to Eq. (17), with both evaluations perfectly consistent. Thus, the difference between evaluations must rely on the exponential value m_2.

To investigate the influence of the exponential value m_2, seismic response analysis results obtained by Takeuchi and Miyazaki (2006) were used. The analysis model was a 15-story, rigid BRB frame. For seismic-wave input, BCJ-L2, El Centro NS, Hachinohe EW, Taft EW, and JMA Kobe NS were applied. Maximum velocities for these seismic wave inputs were normalized at 75 cm/s. The ratio of the stiffness of the frame to that of the BRB was 1.0. BRB core plate material was LY225.

Figure 10 displays damage factors calculated using Miner's rule with average plastic strain amplitude; Figure 11 shows their ratios, indicating that damage factors increase as the exponential value m_2 decreases from 1.0. From Eq. (1) we see the exponential value m_2 is 0.71, and the damage factor calculated using Miner's rule is approximately 1.2 times that calculated using average plastic strain amplitude. Takeuchi and Ida (2008) reported that the damage factor calculated using average plastic strain amplitude affords a degree of accuracy better than that calculated by Miner's rule— and easier to evaluate, as it does not require individual amplitudes. To obtain the results of this study, the present authors have taken average plastic strain amplitude as an index for evaluating cumulative deformation capacities of BRBs under the strain of random amplitudes in preference to applying Miner's method.

6. CONCLUSIONS

In this paper, the cumulative deformation capacity of BRBs is assessed using steel materials fatigue formula and mechanical models. In addition, evaluation of damage factors regarding such material under random amplitudes through seismic response analysis is discussed. Conclusions are here summarized in the following statements:

1) Strain-concentration-ratios of BRBs may be attributable to a mechanism that reveals high-mode local buckling as it occurs in the clearance between core plate and restrainer.
2) The fatigue formula for a BRB evaluated from strain-concentration-ratio shows the clearance affecting the cumulative deformation capacity of a BRB, which in turn explains the test results.
3) The damage factors for steel materials calculated by Miner's rule slightly increases from those calculated using average plastic strain amplitude, as the exponential value of the fatigue formula decreases from 1.0.

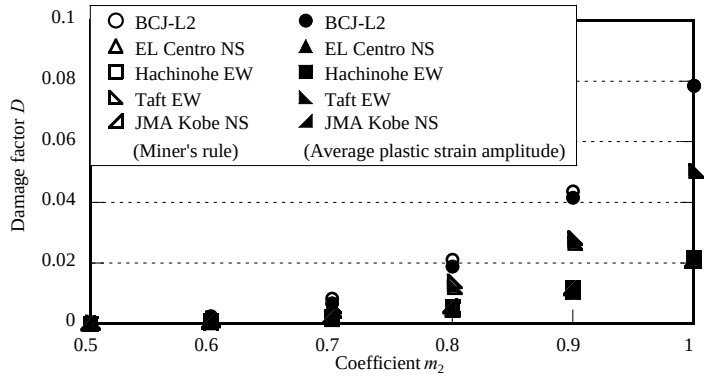


Figure 10 Differences in Evaluation by Miner's Rule Evaluation Using Average Plastic Strain Amplitude

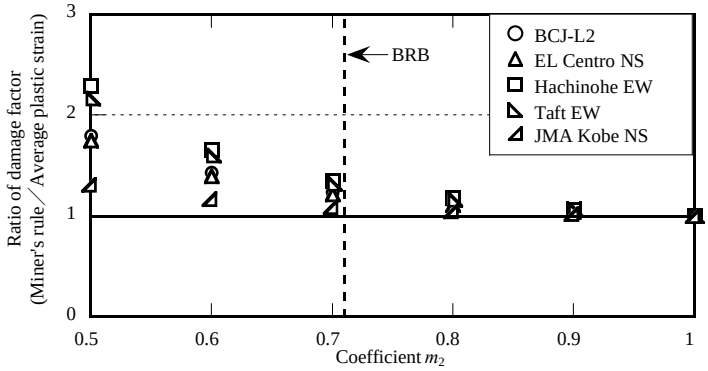


Figure 11 Ratio of Damage Factor

References:

Miner, M. A. (1945) "Cumulative Damage in Fatigue," *Journal of Applied Mechanics*, **12**, A159-A164.

Saeki E, Sugisawa M, Yamaguchi T, Mochizuki H, and Wada A. (1995) "A study on low cycle fatigue characteristics of low yield strength steel," *Journal of Structural and Constructional Engineering*, Architectural Institute of Japan, **472**(6), 139-147, (in Japanese).

Shimokawa, H., Morino, S., Kamiya, M., Ito, S., Kawaguchi, J., Kamura, H. and Hirota, M. (1998)"Elasto Plastic Behavior of Flat-Bar Brace Stiffened by Square Steel Tube (Part 7)," *Summaries of technical papers of the Annual Meeting of the Architectural Institute of Japan*, **C-1, Structures III**, "Timber structures, steel structures, and steel reinforced concrete structures", 843-844.

Nakamura, H., Takeuchi, T., Maeda, Y., Nakata, Y., Sasaki, T., Iwata, M., and Wada, A. (2000) "Fatigue Properties of Practical Scale Unbonded Braces," *Nippon Steel Technical Report*, Nippon Steel Corporation, **81**, 51-57.

Takeuchi, T., Shirabe, H., Yamada, S., Kishiki, S., Suzuki, K., Saeki, E., and Wada, A. (2006) "Cumulative Deformation Capacity and Damage Evaluation for Elasto-plastic Dampers at Beam Ends", *Journal of Structural and Constructional Engineering*, Architectural Institue of Japan, **600**, 115-122. (in Japanese)

Takeuchi, T. and Miyazaki, K. (2006) "Estimation of Cumulative Deformation Capacity for Buckling Restrained Braces Placed in Frames ", *Journal of Structural and Constructional Engineering*, Architectural Institue of Japan, **603**, 155-162

Yamazaki, H., Kasai, K., Ono, Y., Kaneko, H., and Sadasue, K. (2006) "Curved Hysteresis Model of Structural Steel under Cyclic Loading (Part 3),", *Summaries of technical papers of the Annual Meeting Architectural Institute of Japan*. **C-1**, **Structures III**, "Timber structures, steel structures, steel reinforced concrete structures", 935-936 (in Japanese)

Takeuchi, T., Suzuki, K., Matsui, R. and Ogawa, T. (2006) "Cumulative Cyclic Deformation Capacity of Tubular Braces with Local Buckling", *Journal of Structural and Constructional Engineering*, Architectural Institue of Japan, **608**, 143-150 (in Japanese)

Takeuchi, T., Ida, M., Yamada, S., and Suzuki, K. (2008) A. "Estimation of Cumulative Deformation Capacity of Buckling Restrained Braces", *Journal of Structural Engineering*, ASCE, **134(5)**, 822-831

Koetaka, Y., Kinoshita, T., Inoue, K. and Iitani, K. (2008) "Criteria of Buckling-Restrained Braces to Prevent Out-of-Plane Buckling", *14th World Conference on Earthquake Engineering*, Paper No. 05-05-0121

Takeuchi, T., Hajjar, J. F., Matsui, R., Nishimoto, K. and Aiken, I. D. (2010) "Local buckling restraint condition for core plate in buckling restrained braces", *Journal of Constructional Steel Research*, Elsevier, **66(2)**, 139-149

Midorikawa, M., Sasaki, D., Asari, T., Murai, M. and Iwata, M. (2010) "Experimental Study on Buckling Restrained Braces Using Steel Mortar Planks (Effects of the clearance between core plate and restraining member on compressive strength and estimation of the number of buckling mode related to compressive strength)", *Journal of Structural and Constructional Engineering*, Architectural Institute of Japan, **75(653)**, 1361-1368 (in Japanese)

Takeuchi, T., Ohyama, T., and Ishihara, T. (2010) "Cumulative Cyclic Deformation Capacity of High Strength Steel Frames with Energy Dissipation Braces (Part 1)", *Journal of Structural and Constructional Engineering*, Architectural Institute of Japan, **75(653)**, 1671-1679 (in Japanese)

10CUEE CONFERENCE PROCEEDINGS
10th International Conference on Urban Earthquake Engineering
March 1-2, 2013, Tokyo Institute of Technology, Tokyo, Japan

PREDICTIVE EQUATIONS FOR MODELING CYCLIC BUCKLING AND FRACTURE OF STEEL BRACES

Dimitrios G. Lignos[1], and Emre Karamanci[2]

1) Assistant Professor, Dept. of Civil Engineering and Applied Mechanics, McGill University, Canada
2) Graduate Student, Dept. of Civil Engineering and Applied Mechanics, McGill University, Canada
dimitrios.lignos@mcgill.ca, emre.karamanci@mail.mcgill.ca

Abstract: This paper discusses the development of empirical formulations for modeling the post-buckling behavior and fracture of three main steel brace shapes (HSS, round HSS and W-shapes). These formulations are based on extensive calibrations of a state-of-the-art fiber-based steel brace model. The calibration process is based on an optimization scheme that utilized several hundreds of monotonic and cyclic tests on steel braces that have been conducted worldwide during the last 40 years and have been assembled into a steel brace database. The utilization and importance of the predictive formulations is demonstrated through a case study of a 2-story special concentrically braced frame (SCBF). Its seismic performance is assessed through collapse due to P-Delta effects accelerated by structural component deterioration due to cyclic loading. Emphasis is placed on the reserved capacity of the SCBF once its steel braces fracture and structural damage is concentrated in local stories. This is particularly important in the case of major aftershocks once the primary lateral resisting system of SCBFs is severally damaged.

1. INTRODUCTION

Performance-Based Earthquake Engineering (PBEE) necessitates the use of advanced simulation models to compute engineering demand parameters of frame buildings subjected to earthquakes. The input parameters of such models need to be calibrated with large sets of experimental data for reliable computed dynamic response predictions. In the case of steel braced frames, the need for a comprehensive set of data that will allow to realistically model the post-buckling behaviour and fracture due to low cycle fatigue of various shapes of steel braces is evident.

Tremblay (2002) and Lee and Bruneau (2005) compiled a partial dataset of 76 and 66 specimens, respectively. However, these datasets were employed (1) to assess the expected post-buckling compressive resistance of steel braces at different compression ductility levels; (2) to quantify the extent of hysteretic energy dissipation achieved by braces in compression and (3) to develop regression equations that estimate the out-of-plane rotation of rectangular Hollow Structural Section (HSS) braces to fracture. None of these datasets was employed for the development of modelling parameters that control post-buckling behaviour and fracture initiation due to low cycle fatigue. More recently, Hsiao et al. (2012b) compiled a dataset of 44 rectangular HSS sections. They developed a strain-based analytical model that is able to simulate the buckling capacity and post-buckling response of Special Concentrically Braced Frames (SCBFs). However, to the best of our knowledge, there is no information for round HSS and W-shape steel braces.

This paper discusses the development of predictive equations for comprehensive modelling of post-buckling behaviour and fracture due to low cycle fatigue of HSS, round HSS and W-shape steel braces that are commonly used in modern steel construction of CBFs designed in highly seismic regions. These equations are developed based on several hundreds of monotonic and cyclic tests on steel braces that were conducted as part of 24 different experimental programs in Japan, U.S., Canada and Europe that are briefly summarized herein. The utilization of these relationships is demonstrated through a case study of a 2-story SCBF designed in urban California. The reserved capacity of the SCBF is quantified once the steel braces fracture through incremental dynamic analysis from the onset of damage to collapse.

2. FIBER-BASED INELASTIC BRACE MODEL

The inelastic brace model developed by Uriz (2005) is employed herein in order to develop modeling guidelines for simulating the post-buckling behaviour and fracture of steel braces. This model is employed in the OpenSees simulation platform (McKenna 1997). In brief, the brace component model, which is shown in Figure 1, is divided into eight segments in order to represent well the local strains and stresses of a steel brace. The brace cross section is discretized into fibres (see Figure 1). Depending on the cross

section, a different discretization process is employed. A uniaxial stress-strain formulation is assigned to each one of the fibre elements. This formulation is described with the Menegotto-Pinto model (see Figure 1). Global buckling is captured with an initial camber, which is assigned at the mid-length of the steel brace (see Figure 1). Based on a sensitivity study with a number of different steel brace shapes, an initial camber of 0.1% of the brace length was found to adequately capture the flexural buckling local of a brace regardless its shape. This agrees with earlier studies by Uriz (2005). The out-of-plane flexibility and bending strength of the gusset plates is simulated with the zero-length spring, whose hysteretic behaviour is controlled with the proposed model by Hsiao et al. (2012a). Note that the modeling approach discussed herein is only applicable for steel braces that fail at their mid-length due to inelastic buckling and fracture due to low cycle fatigue at the same location. Steel braces that fail at their end locations due to premature net section fracture are not covered as part of this investigation.

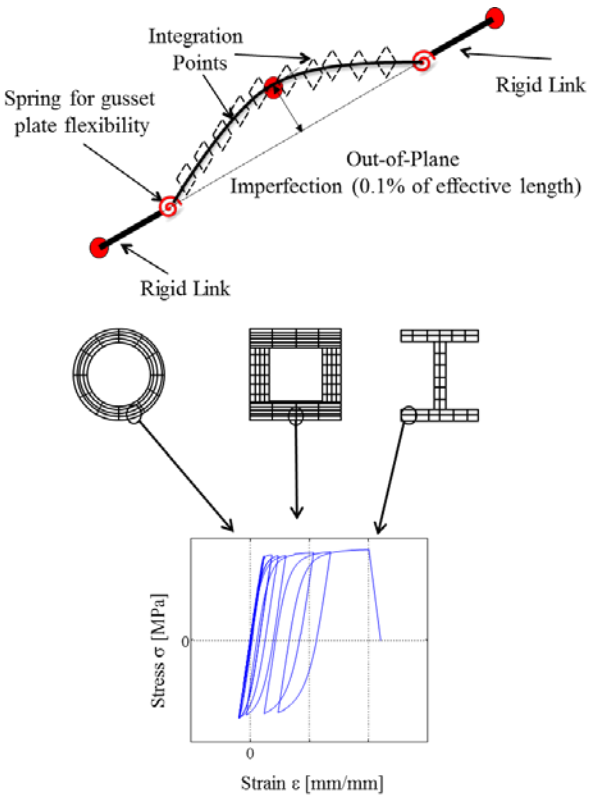


Figure 1 Description of the steel brace component model

Fracture due to low cycle fatigue is simulated with the Fatigue material model (Uriz 2005), which is available in the OpenSees simulation platform. This model is based on a linear strain accumulation rule based on a Coffin-Manson relationship (Manson, 1965) in the logarithmic domain:

$$\varepsilon_i = \varepsilon_0 (N_f)^m \quad (1)$$

In this equation, ε_0 is a material parameter that indicates the strain amplitude ε_i at which one complete cycle of an undamaged material will cause fracture. The coefficient m is a material parameter that relates the sensitivity of the total strain amplitude of the material to the number of cycles to fracture N_f. Fracture is initiated according to a modified rain-flow-counting rule based on Miner's rule that was developed by Uriz (2005). The modeling approach is summarized in Karamanci and Lignos (2012) and in Lignos et al. (2012).

3. STEEL BRACE DATABASE FOR INELASTIC MODEL CALIBRATION

The calibration process of the inelastic model discussed in Section 2 is facilitated with the utilization of a steel brace database that includes 317 steel braces of different geometries, materials and testing procedures. A total of 158 HSS, 65 W-shape, 55 round HSS, 37 angle and channel sections and 2 T sections are included in the database. These braces have been fabricated from 14 different material grades that are used in the U.S., Canada, Japan and Europe. Figure 2 shows the normalized buckling load versus slenderness based on the measured yield stress of each steel brace (noted λ_m) for the four classes of steel braces per CSA-S16-09 (2009) compactness criteria. The slenderness parameter λ_m as defined in the equation:

$$\lambda_m = \frac{kL}{r}\sqrt{\frac{F_{y,m}}{\pi^2 E}} \quad (2)$$

In this equation, k is the effective length factor, L is the centerline length of the brace, r is the radius of gyration of the steel brace cross section in the plane of buckling, E is the modulus of elasticity and $F_{y,m}$ is the measured or expected yield stress of the steel material. From this figure, the majority of the steel braces are distributed well within the design buckling loads by CSA-S16-09 (2009). Extensive details regarding the steel brace database are summarized in Karamanci and Lignos (2012).

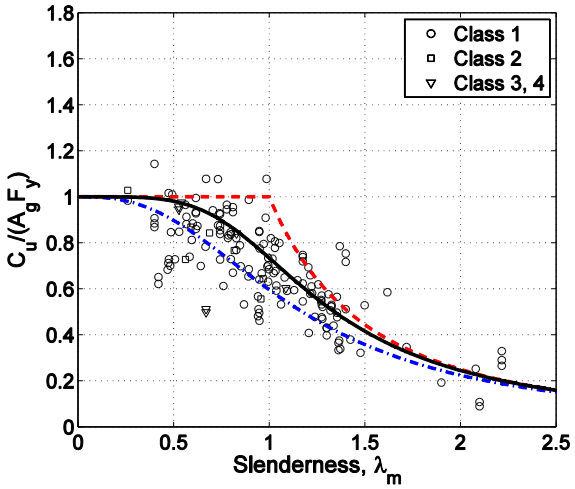


Figure 2 Normalized buckling load versus slenderness based on measured yield category by ductility classes

3.1 Optimization-Based Calibration Process

The input parameters of the hysteretic response of the inelastic model discussed in Section 2 is calibrated with the experimental data that was assembled as part of the steel brace database discussed in this section.

Several considerations were employed for the qualification of steel braces to be used as part of the calibration process of the inelastic steel brace model. Emphasis is placed on steel braces that experience fracture due to low cycle fatigue at their mid-span, where a plastic hinge occurs. Steel braces that experience net section failures are not part of this investigation. Another consideration is related with the brace slenderness ratio, *kL/r*. In particular, steel braces that fail the slenderness limit for axially loaded members, $kL/r < 200$ (see AISC-360-10 2010, CISC 2010) are not considered as part of the calibration process. An optimization scheme was developed to calibrate the input parameters of the inelastic steel brace model discussed in Section 2. To facilitate this process, an interactive interface was developed in MATLAB programming language. This interface was linked with the OpenSees simulation platform (McKenna 1997). In order to calibrate the two parameters ε_o and m of Eq. (1) that control the fatigue life of a steel brace, the Mesh Adaptive Search Algorithm was employed since the objective function (see Eq. 3) is non-differentiable:

$$H(\varepsilon_o, m) = \sqrt{\sum_{i=1}^{N}\left[F_{\exp.}(\delta_i) - F_{simul.}(\delta_i)\right]^2} \tag{3}$$

From the above equation, the objective function H is the square root of the sum of the squares of the differences between the simulated $F_{simul.}$ and experimentally measured $F_{exp.}$ axial force of the brace for each axial displacement δ_i (total of N points) of the testing loading protocol. Specific details regarding the optimization algorithm and its constraints are summarized in Karamanci and Lignos (2012). Figure 3 shows a successful calibration using this optimization scheme. Note that the parameter m can be treated as constant and equal to -0.3. This assumption agrees with earlier findings by Ballio and Castigliori (1995).

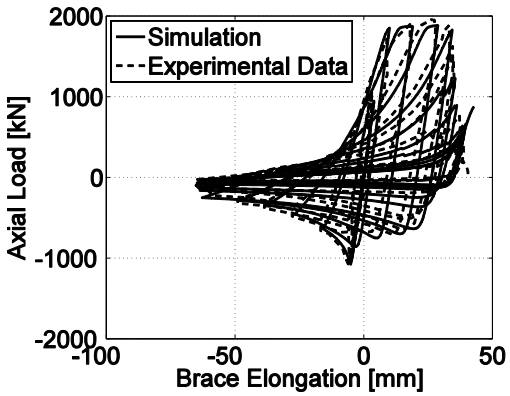


Figure 3 Sample calibrated rectangular HSS steel braces (data from Haddad et al. 2004)

4. MULTIVARIATE REGRESSION FORMULAS TO MODEL FRACTURE OF STEEL BRACES

This section summarizes predictive equations for cyclic buckling and fracture of the three main steel braces (HSS, round HSS and W-shapes). The parameter ε_0 that controls fracture is estimated based on multivariate regression analysis (Chatterjee et al. 2000). The global and local slenderness ratios and the material yield stress F_y are found to have an effect on the fracture life of a steel brace.

4.1 Rectangular HSS Braces

A power-law fitting model was found to best describe the dataset of rectangular HSS braces. For this dataset the predictive equation for ε_o based on a 95% confidence bound is:

$$\varepsilon_0 = 0.291\left(\frac{kL}{r}\right)^{-0.484}\left(\frac{w}{t}\right)^{-0.613}\left(\frac{E}{F_y}\right)^{0.3} \tag{4}$$

In Eq. (4), the expected yield stress of the steel brace F_y is normalized with respect to the Young's modulus E. The predictor w/t is the slenderness ratio of the HSS cross section as defined per AISC-360-10 (2010). Equation (4) is obtained for the following range of predictive parameters:

- $27 \leq kL/r \leq 85$
- $4.20 \leq w/t \leq 30.40$
- $223 \leq F_y \leq 532$ MPa

The coefficient of determination R^2 and the standard error of the mean of the regression of the statistical sample of the HSS braces is 0.493 and 0.249, respectively. These values indicate a relatively good match between the predicted and calibrated ε_o values for rectangular HSS braces. This is also confirmed from Figure 4 that shows the predicted versus calibrated ε_o values for the HSS dataset.

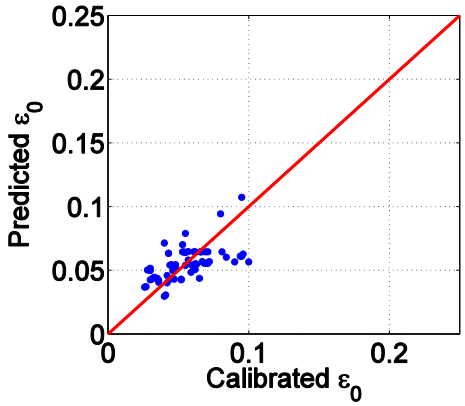


Figure 4 Predicted versus calibrated εo values for HSS braces using Equation (4)

4.2 Round HSS Braces

This section summarizes the proposed recommendations for

modelling the post-buckling behaviour and fracture due to low-cycle fatigue of round HSS braces. Similarly with HSS braces, the *kL/r*, *D/t*, where *D* is the outer diameter of the round cross section of the brace, *t* is its through thickness and F_y parameters are the ones that mostly affect the fracture life of round HSS braces. The predictive equation for the parameter ε_o of round HSS braces based on a 95% confidence bound is:

$$\varepsilon_0 = 0.748\left(\frac{kL}{r}\right)^{-0.399}\left(\frac{D}{t}\right)^{-0.628}\left(\frac{E}{F_y}\right)^{0.2} \quad (5)$$

Equation (5) is obtained for the following range of predictive parameters:

- $29 \leq kL/r \leq 128$
- $12.75 \leq D/t \leq 39.91$
- $326 \leq F_y \leq 521\ MPa$

Figure 5 shows the predicted versus calibrated ε_o values for the subset of round HSS steel braces. This figure indicates that Eq. (5) reliably predicts the parameter that controls fracture due to low cycle fatigue for round HSS braces. The coefficient of determination R^2 of Eq. (5) is $R^2 = 0.636$ and the standard error is 0.146. Note that the exponential coefficients of the predictive parameters in Eq. (5) suggest that the local slenderness term, *D/t*, is the most dominant parameter affecting ε_o of round HSS braces. This agrees with earlier findings by Fell et al. (2009).

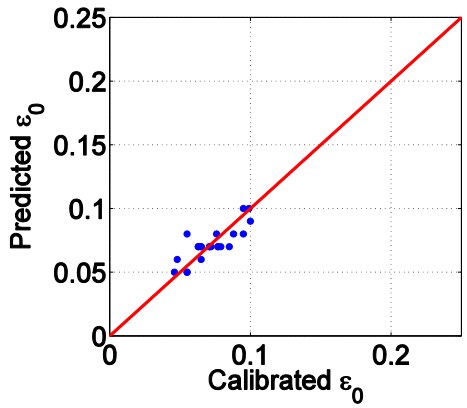


Figure 5 Predicted versus calibrated εo values for round HSS braces using Equation (5)

4.3 W-Shape Braces

In the case of W-shape braces, the parameters *kL/r*, $b_f/2t_f$, h/t_w, and F_y are found to influence the fracture life of W-shape braces the most. For the dataset of W-shape braaces the predictive equation for ε_o based on a 95% confidence bound is:

$$\varepsilon_0 = 0.0391\left(\frac{kL}{r}\right)^{-0.234}\left(\frac{b_f}{2t_f}\right)^{-0.169}\left(\frac{h}{t_w}\right)^{-0.065}\left(\frac{E}{F_y}\right)^{0.351} \quad (6)$$

Equation (6) is obtained for the following range of predictors:

- $39 \leq kL/r \leq 153$
- $4.19 \leq b_f/2t_f \leq 10.20$
- $7.99 \leq h/t_w \leq 49.40$
- $284 \leq F_y \leq 414$ MPa

The local slenderness ratios $b_f/2t_f$ and h/t_w are defined based on the AISC-360-10 (2010) seismic provisions. Figure 6 shows the predicted versus the calibrated εo values for the W-shape braces. This plot indicates that Eq. (6) can be reliably used for predicting the cyclic buckling and fracture of W-shape steel braces. Note that the same equation considers the influence of the web local slenderness on the fracture life of a W-shape brace. However, the flange local slenderness has a stronger influence on ε_0 compared to h/t_w since it is expected that the local instabilities will first be triggered at the flange of the W-shape. The coefficient of determination and the standard error of Eq. (6) for the dataset of the W-shape braces is 0.592 and 0.161, respectively.

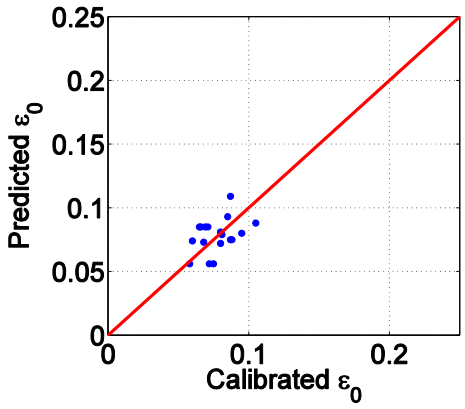


Figure 6 Predicted versus calibrated εo values for W-shape braces using Equation (6)

5. CASE STUDY

The predictive equations discussed in Section 4 for various types of steel braces are utilized in order to conduct a post-fracture evaluation of a 2-story steel braced frame and in particular to quantify its collapse capacity when it is subjected to a set of ground motion records. The one-bay, two-story Special Concentric Braced Frame (SCBF) is designed and built in accordance with the AISC Seismic Design Provisions (AISC 1997) and the Load and Resistance Factor Design (LFRD) (AISC 1993) as discussed in Uriz (2005). Figure 7 shows the basic dimensions of the prototype CBF. Its total height is 5.8 meters (19ft) and its bay width is 6.1 meters (20ft). The first story of the SCBF is 3.0 meters (10ft) tall and the upper story is 2.8 meters (9ft) tall suggesting that the frame is a nearly full-scale representation of the prototype design (Uriz 2005). A chevron configuration bracing system employing square

HSS braces of ASTM A500 GR.B steel is used as the lateral load resisting system. The beams and columns of the frame are W-shape members of ASTM 992 and ASTM 572 Grade 50 steel, respectively. Connection details are designed based on AISC (1993, 1997) provisions. The gusset plate connections are determined using the uniform force method (AISC 1993) and designed to allow for a fold line formation equal to twice the thickness of the gusset plate. The steel braces are reinforced with steel plates in the gusset plate connection region in order to prevent premature fractures at the reduced net section. Uriz (2005) tested quasi-statically the 2-story SCBF through complete failure using the AISC symmetric loading protocol. The next section summarizes the basic modeling approach that was employed for all the structural components of the 2-story SCBF in order to assess its collapse capacity.

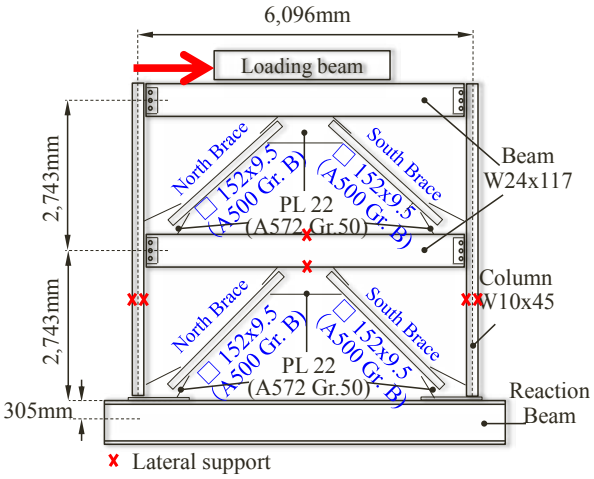


Figure 7 Geometry and member sizes of the 2-story SCBF

5.1 Analytical Model of the Special Concentrically Braced Frame

A 2-dimensional (2-D) analytical model is built in OpenSees (McKenna 1997) in order to simulate the seismic performance of the 2-story SCBF, which is shown in Figure 7. Strength and stiffness deterioration of various structural components of the SCBF is considered as part of its 2-D numerical model. In particular, the steel columns and beams are modeled with elastic elements with concentrated plasticity springs at their ends. These springs utilize the bilinear modified Ibarra-Medina-Krawinkler (IMK) deterioration model (Ibarra et al. 2005, Lignos and Krawinkler 2011). The deterioration parameters that determine the behaviour of these springs are determined based on multivariate regression equations developed by Lignos and Krawinkler (2011). These equations have been adopted by ATC-72 (ATC/PEER 2010) modelling guidelines for tall buildings.

The gusset plate beam-to-column shear connections of the test frame are modeled with the pinching version of the modified IMK model, which was implemented in OpenSees for this purpose (Lignos and Krawinkler, 2012). The properties of these springs are calibrated based on experimental data from cyclic static tests of typical composite shear tab connections from Liu and Astaneh (2000). More recent experimental data on the cyclic behaviour of gusset plate beam-to-column shear connections have become available by Stoakes and Fahnestock (2011). This experimental data can also serve for the same purpose. Figure 8 displays an example of the hysteretic moment-rotation behaviour of the modified IMK model with pinching hysteretic response that can represent each of the aforementioned cases.

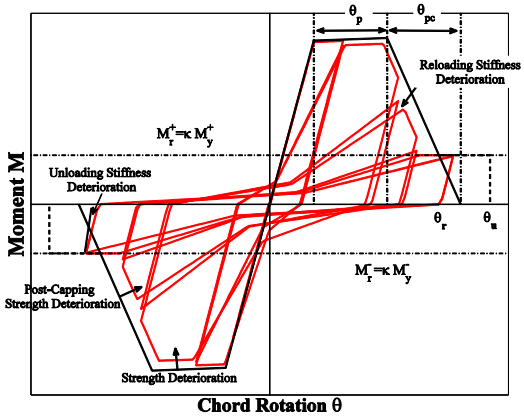


Figure 8 Typical hysteretic behavior of the modified IMK model with pinching hysteretic response

The modified IMK model is able to capture the deterioration in strength, post-capping strength, unloading stiffness and reloading stiffness based on a parameter Λ that defines the reference energy dissipation capacity of a gusset plate beam-to-column connection. More information about the modified IMK model can be found in Karamanci and Lignos (2012).

The out-of-plane flexibility and flexural strength of the gusset plates are modeled with concentrated plasticity springs that are placed between the physical ends of the braces and the rigid offsets that represent the rest of the gusset plates. These springs utilize the Menegotto-Pinto material model. The flexural stiffness and strength of these springs is determined with the proposed relationships by Hsiao et al. (2012a).

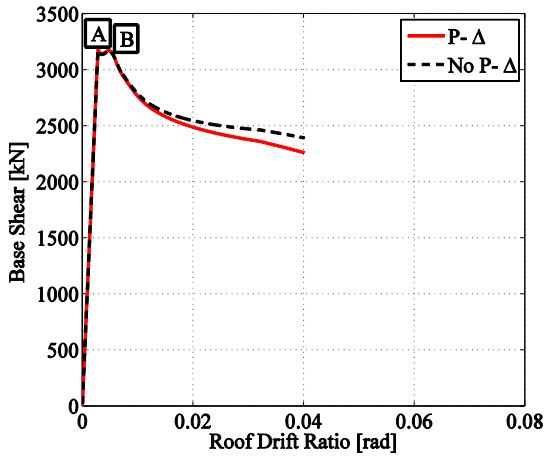
The steel braces are modeled with the approach discussed in Section 4.1. The parameter ε_0 that is used to model fracture due to low-cycle fatigue is determined based on the multivariate regression Eq. (4). The determined fracture parameters ε_0 and m used for all the steel braces are 0.064 and -0.3, respectively, given their kL/r and w/t ratios and their measured yield stress.

5.2 Pushover Analysis

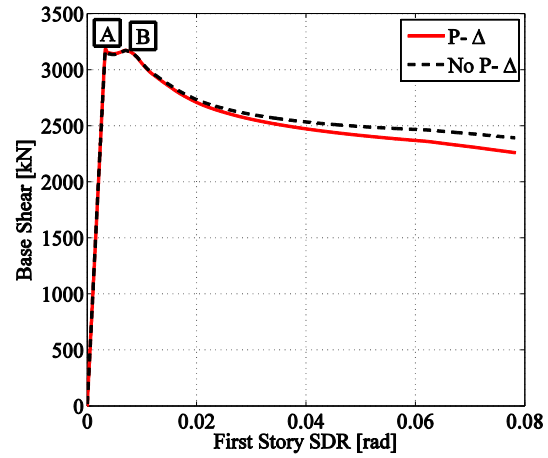
A pushover analysis is conducted with the 2-story SCBF, assuming a first mode lateral load pattern as determined by the equivalent lateral force procedure (IBC, 2003). P-Δ effects are considered in the analysis with a presence of a fictitious leaning column. Due to similitude, 1000kN per

story was assumed to represent the gravity and seismic loading that this frame carries.

Figure 9a shows the pushover curve in terms of base shear versus roof drift ratio (defined as the roof displacement normalized by the total height of the test frame). Figure 9b shows the base shear versus first story drift ratio. From these figures it is concluded that a first story collapse mechanism forms since the plastic deformation is concentrated at the first story of the SCBF. In these figures, point A represents the point that global buckling of the south lower story brace occurs. Point B represents the formation of plastic hinges at the top and bottom of the first story columns. The upper story beam, columns and braces remained elastic during the pushover analysis. In Figures 9a and 9b we have also superimposed the same results without the consideration of P-Δ effects. A comparison of the two curves (noted as P-Δ and No P-Δ) shows that the strength deterioration of the structural components of the test frame is significant compared to the geometric effects that are associated with the vertical load applied to the 2-story SCBF.



(a)



(b)

Figure 9 Pushover analysis of the 2-story SCBF based on a first mode lateral load pattern; (a) Base shear versus roof drift ratio; (b) base shear versus first story SDR

5.3 Collapse Assessment

In this section, a collapse assessment of the 2-story SCBF is conducted through Incremental Dynamic Analysis (IDA: Vamvatsikos and Cornell, 2002). A set of 40 ground motions, compiled by Medina and Krawinkler (2003) is used for this purpose. These ground motions represent ordinary records with a Magnitude $6.5 < M < 6.9$ and a distance $13 < R < 40$km from the rapture zone. The 5% damped spectral acceleration at the first mode period of the test frame $S_a(T_1,5\%)$ is used as an Intensity Measure (*IM*) to scale incrementally the 40 ground motions. In order to conduct the nonlinear response analysis a $\zeta=2\%$ Rayleigh damping approximation at the first and second mode of the 2-story SCBF is used to simulate viscous damping. The first and second modes of the 2-story CBF frame are 0.30sec, and 0.1sec, respectively. The Rayleigh damping matrix is formed based on the tangent (current) stiffness of the structural components of the 2-story SCBF in order to avoid issues related with artificial damping forces as discussed in Karamanci and Lignos (2012).

A time-variant integrator has been developed and implemented in the OpenSees simulation platform that guarantees numerical convergence of the equations of motion particularly at large deformations. The numerical stability of this integrator and its reliability to compute the response history of frame structures through collapse has been validated with recent small and full-scale collapse experiments (Lignos et al. 2011, 2012b, Suita et al. 2008). Dynamic collapse due to sidesway instability is traced once a story or a number of stories displaces sufficiently and the second order shear due to P-Delta effects accelerated by component deterioration fully offsets the first order story shear force of the 2-story SCBF. This implies that dynamic collapse due to sidesway instability should be traced base on a combination of criteria that associate large story deformations and story shear forces. This is consistent with recent shake table collapse experiments (Lignos et al. 2011, 2012b, Suita et al. 2008). Figure 10 shows an example of such definition. The results have been computed based on the scaled intensity of the fault normal record from the Canoga Park station during the Northridge 1994 earthquake. The scaled intensity of this ground motion represents a Maximum Considered Earthquake (MCE) in urban California for 0.3seconds with 2% probability of exceedence in 50 years. Figure 10a shows the first and second story drift ratio histories of the SCBF during the ground motion. This figure suggests that a first story collapse mechanism forms in the 2-story SCBF since the lateral deformations at the same story become excessive. Figure 10b shows the base shear versus first story drift ratio SDR_1 of the same frame. From this figure, once the steel braces fracture, the framing action solely contributes to the lateral resistance of the 2-story SCBF. When the first story deformations become excessive the 2-story SCBF collapses. The collapse point is the one associated with zero base shear force (see Figure 10b).

Figure 10c shows the hysteretic response of the two steel braces of the first story of the SCBF. From this figure,

both braces fracture and once they lose their tensile load carrying capacity their axial resistance remains at zero for the rest of the dynamic response of the 2-story SCBF. Note that the upper story steel braces remained elastic throughout the entire nonlinear response of the 2-story SCBF.

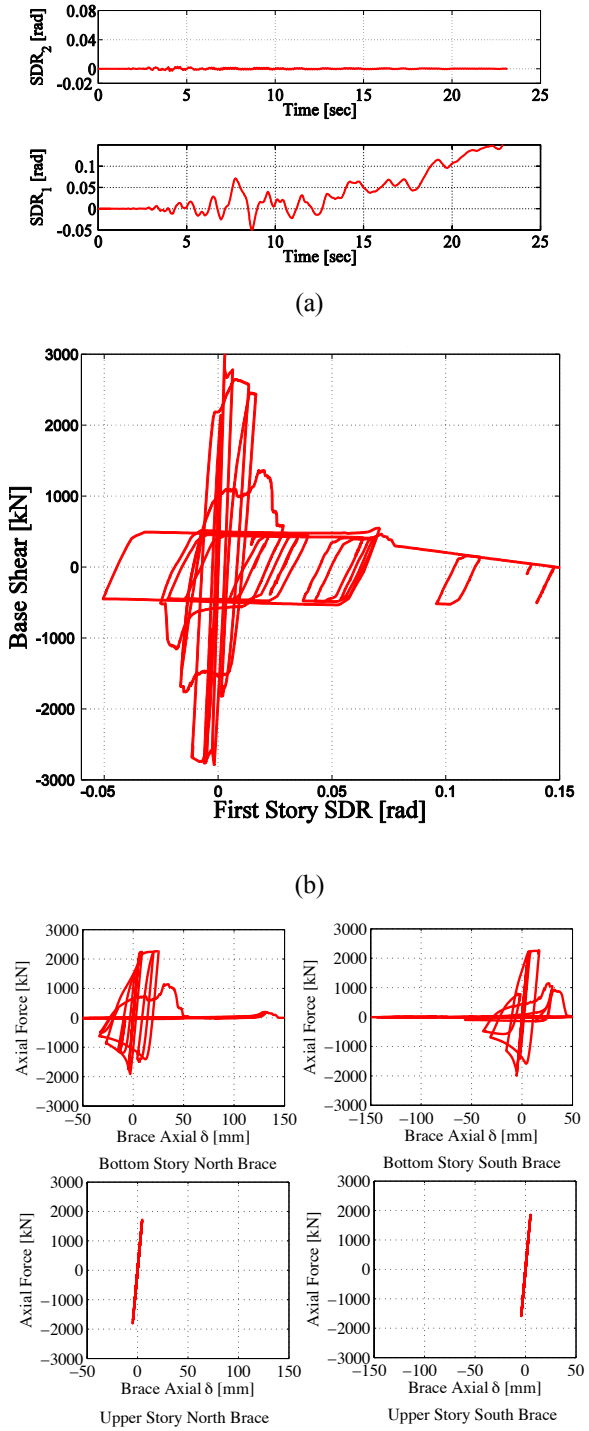


Figure 10 Nonlinear dynamic analysis of the 2-story SCBF for a scaled intensity of the Canoga Park record from the Northridge 1994 earthquake; (a) story drift ratio histories; (b) base shear versus first story drift ratio; (c) steel brace hysteretic response

Figure 11a shows the incremental dynamic analysis results for the 2-story SCBF in terms of IM versus maximum story drift ratios (SDRs). Once each one of these curves becomes flat, dynamic instability of the 2-story SCBF occurs. The collapse assessment of the 2-story SCBF in a probabilistic basis is seen through the collapse fragility curves as suggested by Ibarra et al. (2002). Figure 11b shows the collapse fragility curve of the 2-story SCBF. From this curve, the median collapse capacity of this frame is 1.17g and the logarithmic standard deviation of the 40 collapse intensities is 0.43.

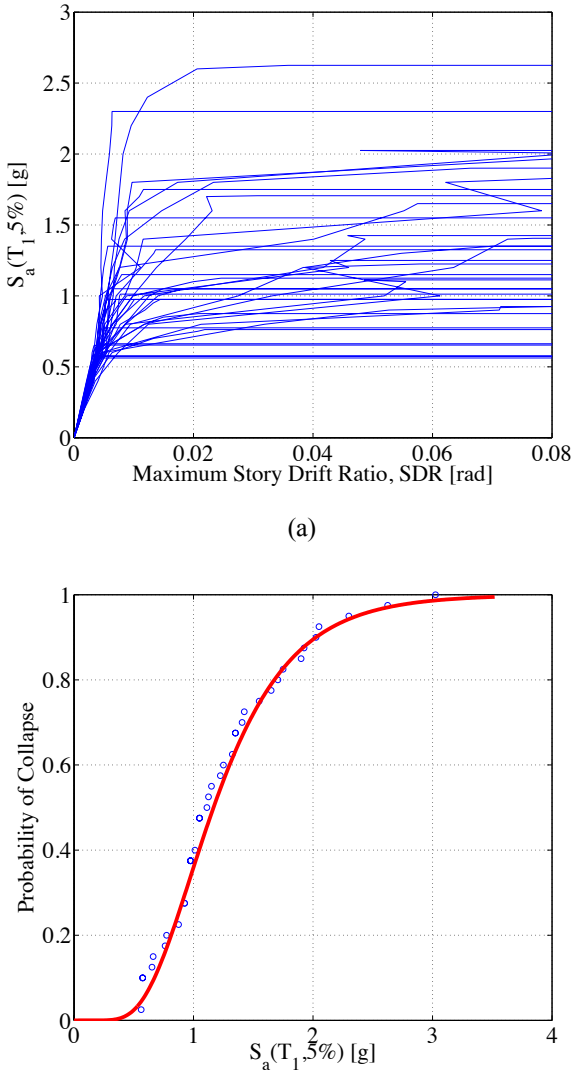


Figure 11 IDA curves and collapse fragility curve of the 2-story SCBF

6. CONCLUSIONS

This paper discusses the development of predictive equations for modeling the inelastic cyclic buckling and fracture of rectangular Hollow Square Steel (HSS) braces,

round HSS and W-shape braces. These cross sections are typically used in the modern steel construction of Concentrically Braced Frames (CBFs). These relationships are based on extensive calibrations of the hysteretic response of a state-of-the-art steel brace model with available experimental data from steel braces that have been assembled into a recently developed steel brace database. The effectiveness of the proposed relationships is demonstrated through a case study of a 2-story special concentrically braced frame (SCBF) designed in urban California. A 2-Dimensional (2-D) representation of the 2-story SCBF is built in the OpenSees simulation platform. Component deterioration of various components including steel braces, gusset plate beam-to-column connections, beams and columns is explicitly considered as part of 2-D the numerical model. The following findings from the present study are summarized as follows:

- The effect of global slenderness ratio *kL/r* on the fracture life of HSS and round HSS steel braces diminishes once these braces buckle globally and local buckling forms at their mid-span.
- The effect of local slenderness ratio of the individual cross sections is found to be the most critical parameter to control the fracture life of a steel brace regardless of its structural shape.
- W-shape braces are more resilient against fracture than round HSS. Rectangular HSS steel braces have the lowest fracture life compared to the other two steel brace shapes that were examined.
- Once steel braces fracture, the primary lateral resistance of a steel brace is attributed to its framing action only. However, once strength deterioration of steel columns of CBFs occurs, dynamic collapse due to sidesway occurs.
- Dynamic collapse of CBFs should be traced based on a combination of criteria that associate large story drift deformations and story shears at these deformations.

In the author's opinion, reliable collapse assessment of steel braced frames is a difficult task due to various failure mechanisms that may occur in such frames. However, the present study is a step towards the quantification of the reserved capacity of modern concentrically braced frames once their steel braces fracture during severe ground shaking.

Acknowledgements:

This study is based on work supported by the National Science and Engineering Research Council of Canada (NSERC) under the Discovery Grant Program. Partial funding was provided by the McGill University Summer Undergraduate Research in Engineering (S.U.R.E) program to support Mr. Gabriel Martin, who contributed to the development of the steel brace database, which is briefly discussed in this paper. This support is gratefully acknowledged. The authors would like to sincerely thank Prof. Ben Fell (Sacramento State), Dr. Patzi Uriz (Exponent Failure Analysis) and Prof. Steven Mahin (University of California at Berkeley) for their willingness to share their experimental data in order to assemble part of the steel brace database discussed in the paper. Any opinions, findings, and conclusions or recommendations expressed in this paper are those of the authors and do not necessarily reflect the views of sponsors.

References:

AISC (1993), "Load and Resistance Factor Design LRFD," American Institute of Steel Construction AISC, Chicago, Illinois.

AISC (1997), "Seismic Provisions for Structural Steel Buildings," American Institute of Steel Construction AISC, Chicago, Illinois.

AISC (2010), "Specification for Structural Steel Buildings," ANSI/AISC 360-10, American Institute of Steel Construction AISC, Chicago, Illinois.

Ballio, G., and Castiglioni, C. A. (1995), "A Unified Approach for the Design of Steel Structures Under Low and/or High Cycle Fatigue," *Journal of Constructional Steel Research*, Elsevier, **34**(1), 75-101.

Chatterjee, S., Hadi, A. S., Price, B. (2000), "Regression Analysis by Example," 3rd Edition, John Wiley and Sons Inc., New York, NY.

CISC (2010), "Handbook of Steel Construction," Canadian Institute of Steel Construction, 10th Edition, Toronto, ON.

CSA (2009), "CAN/CSA-S16-09 Limit States Design of Steel Structures," Canadian Standard Association, Rexdale, ON.

Fell, B. V., Kanvinde, A. M., Deierlein, G. G., and Myers, A. T. (2009), "Experimental Investigation of Inelastic Cyclic Buckling and Fracture of Steel Braces," *Journal of Structural Engineering*, American Society of Civil Engineers, **135**(1), 19-32.

Haddad, M. A. (2004), "Design of Concentrically Braced Steel Frames for Earthquakes," *Ph.D. Thesis*, Department of Civil Engineering, University of Calgary, Calgary, AB.

Hsiao, P. C., Lehman, D. E., and Roeder, C. W. (2012a), "Improved Analytical Model for Special Concentrically Braced Frames," *Journal of Constructional Steel Research*, Elsevier, 73, 80-84.

Hsiao, P. C., Lehman, D. E., and Roeder, C. W. (2012b), "A Model to Simulate Special Concentrically Braced Frames Beyond Fracture," *Earthquake Engineering & Structural Dynamics,* EESD, doi: 10.1002/eqe.2202 (in press).

Ibarra, L. F., Medina, R., and Krawinkler, H. (2002), "Collapse Assessment of Deteriorating SDOF Systems," *Proceedings 12th European Conference on Earthquake Engineering*, London, U.K.

Ibarra, L. F., Medina R., and Krawinkler, H., (2005), "Hysteretic Models that Incorporate Strength and Stiffness Deterioration," *Earthquake Engineering & Structural Dynamics*, EESD, **34**(12), 1489-1511.

IBC, (2003), "International Building Code," International Code Council (ICC), Falls Church, VA.

Karamanci, E., and Lignos, D. G. (2012), "Collapse Assessment and Performance-Based Evaluation Techniques for Concentrically Braced Frames Designed in Seismic Regions," *M.Eng. Thesis*, Department of Civil Engineering and Applied Mechanics, McGill University, Montreal, Quebec, Canada.

Lee, K., and Bruneau, M. (2005), "Energy Dissipation of Compression Members in Concentrically Braced Frames: Review of Experimental Data," *Journal of Structural Engineering,* American Society of Civil Engineers, **131**(4), 552-559.

Lignos, D. G., and Krawinkler, H. (2011), "Deterioration Modeling of Steel Components in Support of Collapse Prediction of Steel Moment Frames Under Earthquake Loading," *Journal of Structural Engineering*, American Society of Civil Engineers, **137**(11), 1291-1302.

Lignos, D. G., Krawinkler, H., and Whittaker, A. S. (2011), "Prediction and Validation of Sidesway Collapse of Two Scale Models of a 4-Story Steel Moment Frame," *Earthquake*

Engineering & Structural Dynamics, EESD, **40**(7), 807-825.

Lignos, D. G., Karamanci, E., Martin, G. (2012a), "A Steel Database for Modeling Post-Buckling Behavior and Fracture of Concentrically Braced Frames under Earthquakes," *Proceedings of the 15th World Conference of Earthquake Engineering,* (15WCEE), Lisboa, Portugal, Paper No. 4366.

Lignos, D. G., Hikino, T., Matsuoka, Y., Nakashima, M. (2012b). "Collapse Assessment of Steel Moment Frames Based on E-Defense Full-Scale Shake Table Collapse Tests," *Journal of Structural Engineering,* American Society of Civil Engineers, doi: 10.1061/(ASCE)ST.1943-541X.0000608 (in press).

Liu, J., and Astaneh-Asl, A. (2000), "Cyclic Testing of Simple Connections Including the Effects of Slab," *Journal of Structural Engineering,* American Society of Civil Engineers, **126**(1), 32-39.

Manson, S. S. (1965), "Fatigue: A Complex Subject - Some Simple Approximations," *Experimental Mechanics*, **5**(7), 193-226.

McKenna, F. (1997), "Object Oriented Finite Element Programming Frameworks for Analysis, Algorithms and Parallel Computing," *Ph.D. Dissertation*, University of California at Berkeley, Berkeley, CA.

Medina, R. A., and Krawinkler, H. (2003), "Seismic Demands for Non-Deteriorating Structures and Their Dependence on Ground Motions," *Report No. 144*, John. A. Blume Earthquake Engineering Research Center, Stanford University, Stanford, CA.

PEER/ATC, (2010). "Modeling and Acceptance Criteria for Seismic Design and Analysis of Tall Buildings," *Rep. PEER/ATC-72-1*, prepared by the Applied Technology Council in cooperation with the Pacific Earthquake Engineering Research Center, Redwood City, CA.

Stoakes, C. D., and Fahnestock, L. A. (2011), "Cyclic Flexural Testing of Concentrically Braced Frame Beam-Column Connections," *Journal of Structural Engineering,* American Society of Civil Engineers, **137**(7), 739-747.

Suita, K., Yamada, S., Tada, M., Kasai, K., Matsuoka, Y., and Shimada, Y. (2008), "Collapse Experiment on 4-story Steel Moment Frame: Part 2 Detail of Collapse Behavior," *Proceedings of the 14th World Conference on Earthquake Engineering (14WCEE),* Beijing, China.

Tremblay, R. (2002), "Inelastic Seismic Response of Steel Bracing Members," *Journal of Constructional Steel Research*, Elsevier, 58, 665-701.

Uriz, P. (2005), "Towards Earthquake Resistant Design of Concentrically Braced Steel Structures," *Ph.D. Dissertation*, Department of Civil and Environmental Engineering, University of California, Berkeley, CA.

Vamvastikos, D., and Cornell, C. A. (2002), "Incremental Dynamic Analysis," *Earthquake Engineering & Structural Dynamics*, EESD, **31**(4), 491-514.

10CUEE CONFERENCE PROCEEDINGS
10th International Conference on Urban Earthquake Engineering
March 1-2, 2013, Tokyo Institute of Technology, Tokyo, Japan

IMPROVEMENT IN SSWS DESIGN AND STUDY ON THE PERFORMANCE OF STEEL FRAME-SSWS SYSTEM

Yiyi CHEN[1)], Ke KE[2)]

1) Professor, State Key Laboratory of Disaster Reduction for Civil Engineering, Tongji University, China
2) Ph.D Candidate, State Key Laboratory of Disaster Reduction for Civil Engineering, Tongji University, China
yiyichen@tongji.edu.cn, 1987keke@tongji.edu.cn

Abstract: Steel shear wall with slits (SSWS) is an efficient structural component equipped both loading-resistant capacity and energy dissipating ability. Recently the study of the design details and the design procedure for using the component as an effective energy consumption device in the steel frames subject to seismic load is reported. In the previous laboratory tests on full scale SSWS and other large scale steel shear wall, the slippage of bolt connection and accompanied noise were noticed. Based on observation and analysis, rational method is proposed to evaluate the shear force and its distribution on bolt connection linking SSWS and frame beams, and proper arrangement of bolt is suggested. Furthermore, the influence of axial stress on the thin SSWS is carefully studied. By the criteria to keep the horizontal ultimate strength of SSWS, the limitation for axial stress ratio is determined. Two assemblages of SSWS together with its surrounding frames were tested under cyclically horizontal load and constant vertical load to check the validity of the proposal. The test results show that the presence of finite vertical load does not affect the performance of SSWS, and the synergistic effect for frame and SSWS is quite noticeable. Finally, the design rules are put forward to guarantee that the yielding of SSWS precedes the yielding of frame members. A quantitative method in calculating energy dissipation capacity is proposed. And a practical design approach considering yielding sequence and energy dissipation are also addressed and discussed.

1. INTRODUCTION

Steel shear wall with slits (SSWS), which is designated to resist seismic load, is observed significantly functional in seismic design and retrofit of structures for its stable response as well as noteworthy features in engineering practice (Hitaka and Matsui 2003).

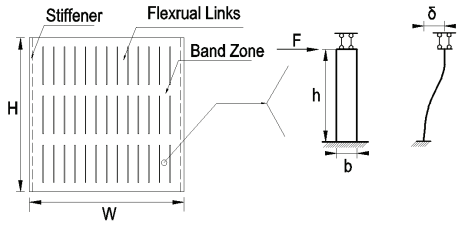


Figure 1 Configuration of SSWS

Observations in the previous laboratory tests on full scale SSWS and other large scale steel shear wall (Chen Y.Y. et al 2009) indicate that the slippage of bolt connection might impose adverse impact on performance of the component, leading to undesirable failure mode ultimately. As for its behavior in structural system, critical issues concerning the influence of axial stress induced by gravity load and the performance of the global system combining with frame are needed to be investigated. Moreover, past designs were generally carried out based on elastic theory, which might not incorporate the function as energy dissipative device into procedure. Moreover, the actual response and performance in inelastic range is still unclear if not considered directly.

In this research, two assemblages of SSWS together with its surrounding frames were experimentally investigated under a combination of cyclically horizontal load and constant vertical load. To eliminate the undesirable bolts slippage in connection area, a proper arrangement of bolt was proposed and applied into tested specimens. The detailed results of tests and corresponding numerical analysis incorporating the evaluation of vertical load and bolts force distribution are reported herein to validate the proposal. Observations regarding the synergistic effect of system is also addressed and discussed.

Further, to achieve a more rational design of system incorporating inelastic behavior, the yielding sequence of different components and energy concept are employed. Calculation method in dealing with plastic energy dissipation of SSWS is addressed. A practical design procedure considering energy dissipation and yielding sequence are also presented and discussed.

2. EXPERIMENTAL PROGRAM

2.1 Test specimens

Practically, SSWS is generally installed in frames with bolted connection. In this study, the full scale tests based on

two specimens incorporating SSWS and surrounding frame components were conducted to simulate the behavior of different subassemblies in system, and different boundary constraints were considered during test procedure. Specifically, the specimen FSSWS1 was intended to simulate the subassemblies when the SSWS were located in the same bay from the bottom floor to the above floor while the specimen FSSWS2 corresponded to cases where SSWS were not arranged continually in vertical direction considering the flexibility of beam (Figure 2). The frame was composed of H shaped beam and cold-formed square tubular column with nominal yield stress of 345MPa while SSWS was constructed with steel plate with nominal yield stress of 235MPa. The dimension and detail of specimens were determined based on practical structure, given in Figure 3 and Table 1.

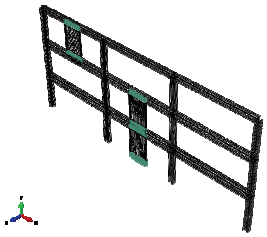
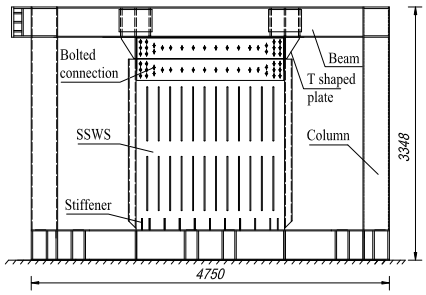


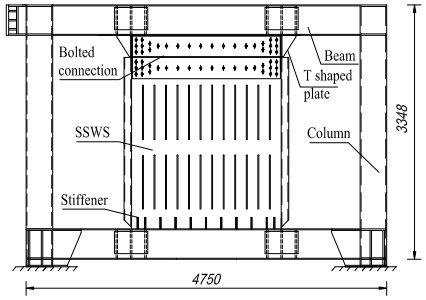
Figure 2 Steel frame-SSWS system

Table 1 Dimension and boundary condition of specimens

Specimen	Beam	Column	Boundary condition
FSSWS1	H400×200×8×13	350×12	Fixed
FSSWS2	H400×200×8×13	350×12	Partially fixed



(a) Specimen FSSWS1



(b) Specimen FSSWS2

Figure 3 Configuration and detail of specimens

The SSWS in two specimens were designed with the same parameters (plate thickness 12mm), and detailed information is illustrated in Figure 4.

In dealing with the undesirable early slippage of bolts observed in past research, an improved detail of bolt arrangement was proposed and applied to specimens, as illustrated in Figure 5. It is believed reasonable to introduce this modified arrangement to eliminate the potential slippage due to non-uniform force distribution in connection area, and the detailed analysis concerning the bolt force is presented in following parts.

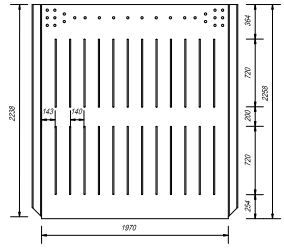


Figure 4 Dimension of SSWS

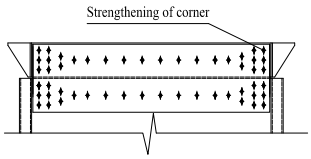
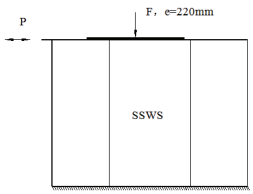


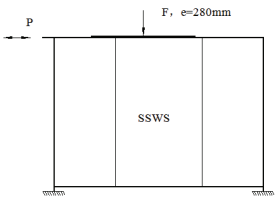
Figure 5 detail of proposed arrangement of bolts

2.2 Test setup and loading procedure

A constant vertical load was applied on SSWS during test since the SSWS can bear a proportion of gravity load in building structure. In this study, the vertical load was determined as 350kN and 650kN for specimen FSSWS1 and FSSWS2, respectively (a value of 300kN was close to the accumulated live load on the bottom floor of a 30-story building according to current Chinese codes). During the test procedure, the constant vertical load was firstly applied to specimens, and lateral cyclic load was subsequently incorporated. The loading diagram and test setup are illustrated in Figure 6 and Figure 7.



(a) Specimen FSSWS1



(b) Specimen FSSWS2

Figure 6 Loading diagram for specimens

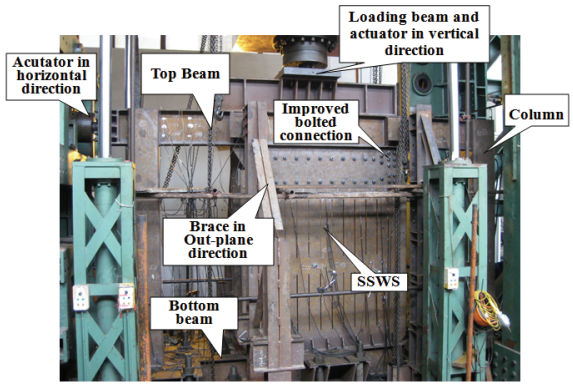


Figure 7 Test setup

3. TEST RESULTS AND ANALYSIS

3.1 Overview

With the load increasing, the specimens began to develop plasticity with a favorable sequence. The SSWS firstly yielded and dissipated energy. In the subsequent stage, the beam and column also developed inelasticity and dissipated energy. During the loading process, the distortional buckling of flexural links and out-plane deformation of panel occurred when plastic deformation was sufficiently large, as shown in Figure 8. The fractures initiated at end of slits were also noticed at large drift, as observed in related studies (Hitaka and Matsui 2003;Gotes and Liu 2010).

It should be noted that even though the out-plane deformation occurred, the global response was still relatively stable in spite of stiffness degradation in SSWS, as the frame was also significantly functional in inelastic range. This was reflected by cyclic curves presented next. Essentially, the synergistic effect was dependent on the property of the structure behaving as a dual system in which SSWS and frame both can provide considerable energy dissipation capacity. And the application of a dual system can lead to a more flexible adjustment of stiffness allocation as well energy dissipation distribution, which is addressed in a practical design approach in this study.

Further, during the load cycles, no observations regarding the slippage of bolted connection was captured, for no obvious deformation of bolts and holes observed, as indicated in Figure 9.This implies the effectiveness of proposed arrangement of bolt connection stated above.



(a) FSSWS1 (b) FSSWS2

Figure 8 Out-plane deformation of specimens



Figure 9 No obvious deformation of hole and bolts(after test)

3.2 Analysis of bolt force in connection

Slippage of bolts in connection was observed in past full scale tests in SSWS, which inevitably employed the undesirable failure mode of the system. Essentially, this was mainly induced by the non-uniform distribution of internal force induced by both overturning moment and shear force when the SSWS was subjected to a large lateral loads, as conceptually illustrated in Figure 10. It reveals that a conventional consideration of a uniform bolts arrangement might increase the risk of connection failure, especially in both ends of connection plate, which had been demonstrated in past full scale tests (Chen Y.Y. et al 2009). In this study, a non-uniform distribution of strain intensity in connection area was also observed, demonstrating the necessity of proposed modified bolts arrangement.

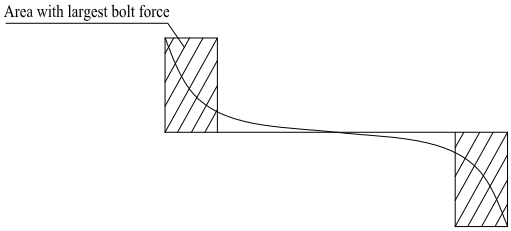


Figure 10 Conceptual illustration of bolt force distribution

On the other hand, numerical analysis was also conducted to investigate the bolt force distribution in this research. The vertical internal forces distribution(Y direction in Figure 11) corresponding to different lateral load levels in connector which was intended to simulate bolts are plotted in Figure 12, where *F* denotes the bolt force in vertical direction .

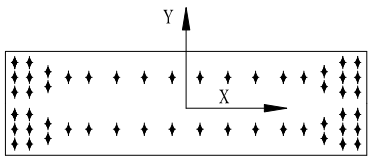
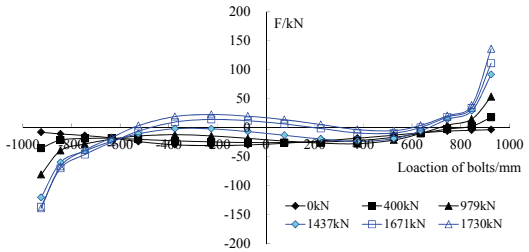
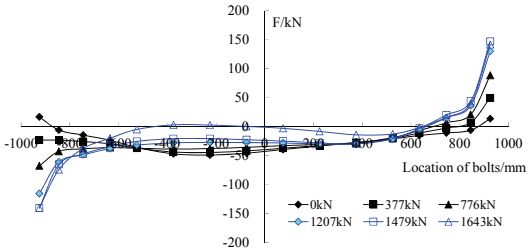


Figure 11 Bolts arrangement in cover plate in connection



(a) FSSWS1



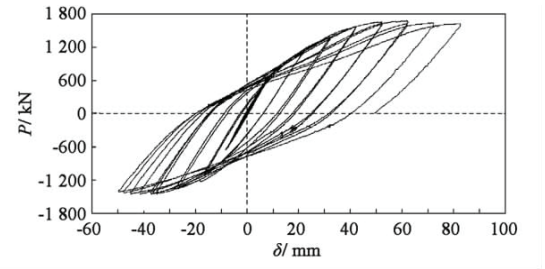
(b) FSSWS2

Figure 12 Vertical internal force in bolts

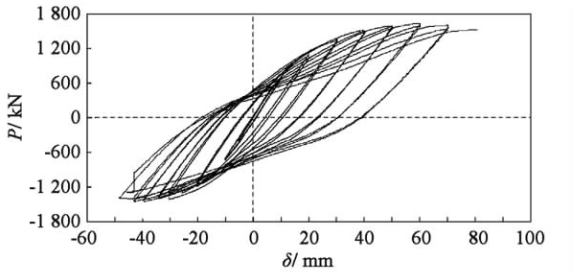
As can been seen, when the lateral load was relatively small, the corresponding bolts force in vertical direction was not significant. Nevertheless, the bolts force at both ends grew sharply as the lateral load increased, which essentially reveals the adverse effect induced by overturning moment, demonstrating the rationality of proposed bolts arrangement.

3.3 Hysteretic behavior

The global load-deformation curves of FSSWS1 and FSSWS2 are shown in Figure 13, where δ denotes the relative lateral displacement between top beam and bottom beam of specimens, and P denotes the total lateral force applied on specimens. Compared with related research (Hitaka and Matsui 2003; Chen Y.Y. et al 2009;Gotes and Liu 2010) concentrating on the behavior of panel only, the test results exhibit a more stable response of system for no obvious pinching and strength degradation observed. The results radically reveal that the assemblages of SSWS and surrounding frame components are significantly functional in resisting the seismic load. On the other hand, the corresponding load-displacement curves of SSWS in each specimen can also be captured with equilibrium relationship, which are plotted in Figure 14, where P_w denotes the lateral load taken by SSWS.

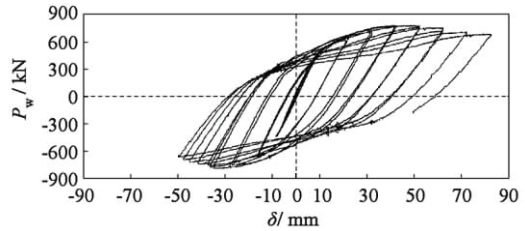


(a) FSSWS1

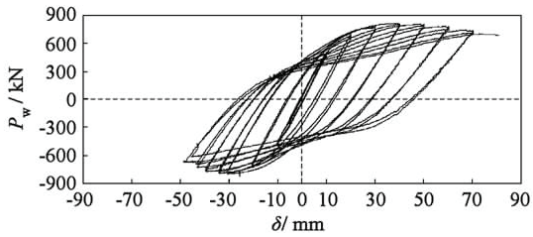


(b) FSSWS2

Figure 13 Load-displacement curves of specimens



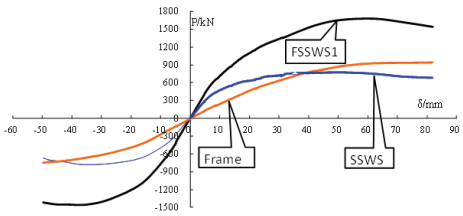
(a) SSWS in FSSWS1



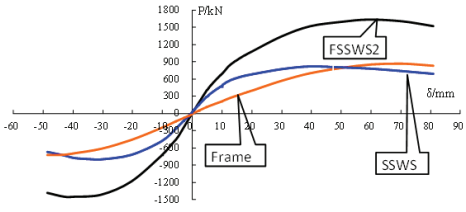
(b) SSWS in FSSWS2

Figure 14 Load-displacement curves of SSWS in specimens

Further, the skeleton curves of specimens are illustrated in Figure 15. It essentially reveals the synergistic effect of the structure working as a dual system. In the elastic range, both SSWS and frame provided lateral stiffness to resist lateral loads and SSWS played a predominant role in this stage for relatively larger stiffness. As the SSWS experienced the degradation of stiffness in inelastic range, the contribution of frame became more significant. This synergistic effect was reflected by the stable response in test. In the perspective of energy dissipation, the system exhibited a favorable behavior that different parts might contribute to energy absorption with a favorable sequence. This desirable sequence divided the global performance of system into certain states, making the design more reasonable for considering the concept of damage control and resilience. Moreover, although different boundary conditions were considered in specimens, there were not obvious differences in performance observed or reflected in results curves, indicating the flexibility of allocation of SSWS in system practically.



(a) FSSWS1

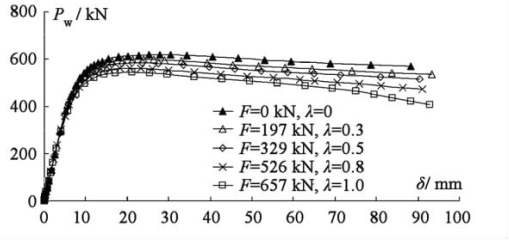


(b) FSSWS2

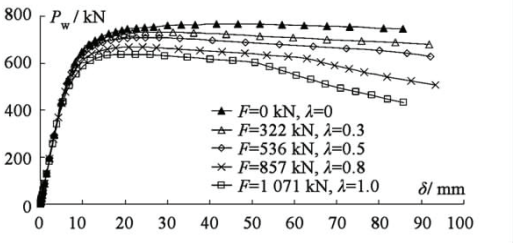
Figure 15 Skeleton curves of specimens

3.4 The influence of axial force in SSWS

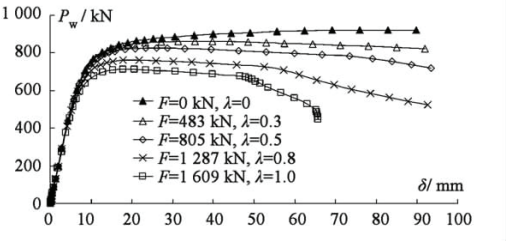
Although a constant axial load was applied in specimens, there was no significantly adverse effect observed. To evaluate the influence induced by axial stress, numerical analysis was also conducted. Specifically, based on the model of SSWS in specimens, the axial stress was introduced as a parameter, defined with a ratio of axial load to corresponding buckling load ($\lambda=F/F_{cr}$).Pushover analysis were carried out with variation of plate thickness and λ. The results are illustrated in Figure 16, indicating that the axial load in SSWS might induce reduction in strength. Nevertheless, this reduction is believed not significant as only approximation of 10% in strength was observed at a stage with λ of 0.5. It is pointed out the aforementioned analysis did not incorporate the noticeable synergistic effect of system as the frame will also bear a proportion of vertical load practically, and it is thought conservative to define λ as 0.5 as a threshold of axial load in engineering practice.



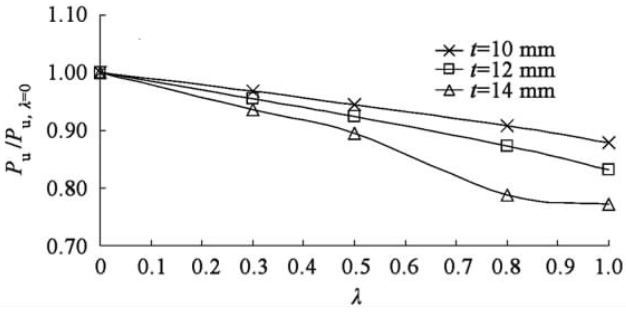
(a) t=10mm



(b) t=12mm



(c) t=14mm



(d) Load capacity ratio versus axial load ratio

Figure 16 Influence of axial load in SSWS

4. DESIGN METHOD

4.1 The yielding sequence

Practically, when a frame-SSWS system is subjected to lateral loads, it is expected that the SSWS yield earlier than the frame components as energy dissipative devices, which can also reflects the concept of damage control design (J.J. Connor. et al 1999).With a preselected yielding sequence ensured, the system will exhibit a more reasonable performance, as the damage can be constrained in SSWS, making the whole system essentially operational by replacing the panels after earthquakes. Accordingly, a critical issue lies within the practical approach to achieve the expected sequence. Conceptually, the behavior of system might be reflected by the idealized illustration given in Figure 17.

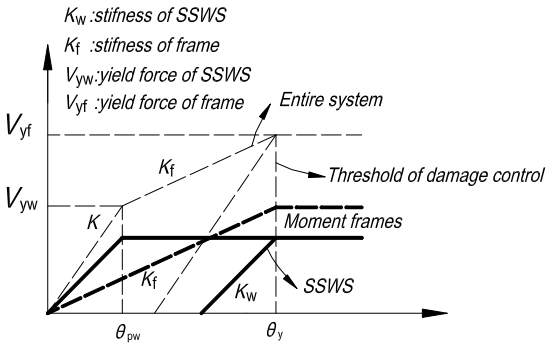


Figure 17 Idealized behavior of frame-SSWS system

Accordingly, the yielding sequence can be determined given by Eq.(1),

$$\frac{V_{yw}}{K_w} < \alpha \frac{V_{yf}}{K_f} \qquad (1)$$

in which α is defined as an index to control the yielding sequence. The yielding sequence can be explicitly designed by adjusting the strength and stiffness of SSWS and frame, as SSWS with relatively larger stiffness and lower strength tends to yield earlier.

4.2 Application of energy concept in SSWS

SSWS can be viewed as an excellent energy dissipative device when subjected to lateral loads. Accordingly, the plastic energy dissipation can be determined with plastic theory (Ke K. and Chen Y.Y. 2012), the plastic energy absorbed by panel can be determined by Eq.(2).

$$E_{pw} = \left(\frac{n\Delta}{h} - \frac{nmf_y h}{3Eb}\right)\frac{f_y b^2 t}{2} \qquad (2)$$

In Eq.(2), E_{pw} = plastic energy dissipation of SSWS; n=number of links in a row; m =number of rows in wall; Δ= total lateral displacement of the wall; f_y=yield stress; E =Young's modulus and t= thickness of plate. Eq.(2) can be used to measure the plastic energy dissipation under certain drift of SSWS. It also reveals that the energy dissipation capacity can be adjusted with geometric parameters of slits in SSWS as well as the material property quantitatively, which is believed a significant index in design procedure. An

optimized design can be achieved combining the adjustment of strength and stiffness (Hitaka and Matsui 2003).

4.3 Design procedure considering energy dissipation

As the energy dissipation capacity can be determined, a practical approach is constructed in designing the system and is illustrated in the flow chart given by Figure 18.

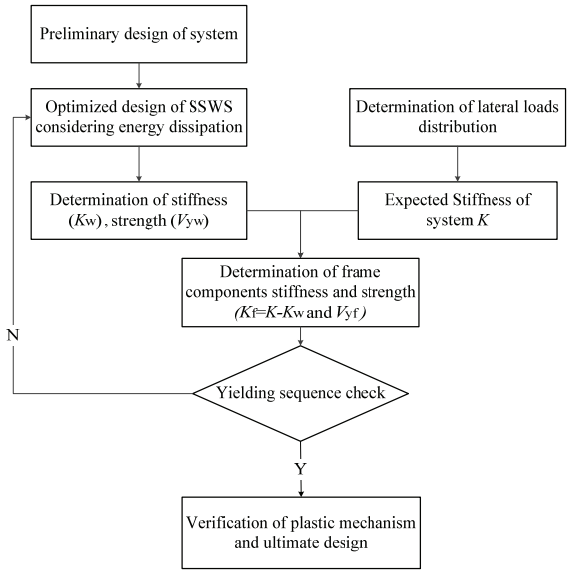


Figure 18 Design procedure considering energy dissipation

More specifically, the design procedure is based on optimization of energy dissipation capacity of SSWS given in Eq. (2). This motive is thought to be rational viewing the SSWS as the predominant energy dissipative devices in earthquakes. A sequence design is also involved as a criterion in procedure with aforementioned derivation. In essence, the target of proposed design is to concentrate damage reflected by plastic energy into replaceable SSWS by adjusting the stiffness and strength of different components in the system. Considering that the frame-SSWS will behave as an integrated system that all components will bear the service loads as well as seismic loads, the application of energy concept and an explicit concern of yielding sequence can effectively take the inelastic behavior into consideration, which is thought to be more reasonable compared with conventional value-based (force or displacement) design methodology.

5. CONCLUSIONS

Full scale laboratory test on two assemblages of SSWS with surrounding frame components were performed. Critical issues concerning the slippage of bolts in connection area, the influence of SSWS allocation and the effect of axial stress in SSWS were carefully studied experimentally and numerically.

Test results indicate that the proposed arrangement of bolts can effectively eliminate the undesirable slippage under large drift observed in past research, which was also validated by numerical analysis.

In order to investigate the performance of SSWS in frame system, specimens were tested with different boundary constraints. Since no significant differences in behavior were observed, it is believed that the discontinuous arrangement of SSWS in structure may not impose an adverse effect on system, providing much flexibility in engineering practice.

During test procedure, a constant vertical load was applied to specimens to simulate the vertical load in structural system, while no obvious adverse effect induced by axial stress was observed. Parametric study was carried out subsequently to evaluate the influence of vertical load. Although the existence of axial stress will lead to reduction in strength as indicated by analysis, it is believed the effect is not significant when the axial load is not large. Accordingly, a value of 0.5 is recommended as limitation of axial load ratio ($\lambda=F/F_{cr}$). When the axial stress is in this range, its effect might be minor and can be neglected in practice.

Over all, two specimens behaved with desirable performance during load cycles, which is believed contributed by the synergistic effect as SSWS and frame worked as a dual system. Based on test results, the design method is also studied with application of energy concept and damage control design philosophy. A practical design procedure incorporating yielding sequence control and energy dissipation optimization are addressed and discussed.

Acknowledgements:

This research is supported by National Science Foundation of China (Grant No.51038008).

References

Hitaka, T. and Matsui, C. (2003)," Experimental study on steel shear wall with slits." *Journal of Structural Engineering*, American Society of Civil Engineers, **129**(5),586-595.

Choi, I.R. and Park, H.G. (2008)," Ductility and energy dissipation capacity of shear-dominated steel plate walls," *Journal of Structural Engineering*, American Society of Civil Engineers, **134**(9),1495-1507.

Choi, I.R. and Park, H.G. (2009)," Steel Plate Shear Walls with Various Infill Plate Designs," *Journal of Structural Engineering*, American Society of Civil Engineers, **135**(7), 785-796.

Jiang, L., Chen, Y.Y. and Wang, W.H. (2009)," Experimental study Ⅰ on full size steel plate shear wall with slits under low-frequent cyclic loads," *Journal of Building Structures*, **30**(5),57-64.(in Chinese)

Cortes, G. and Liu, J. (2011)," Experimental evaluation of steel slit panel-frames for seismic resistance," *Journal of Constructional Steel Research* ,**67**(3), 181-191.

Chen, Y.Y., Ning, Y.Q. and Jiang, L. (2012)," Experimental study on Seismic behavior of frame-steel plate shear wall with slits," *Journal of Building Structures*, **33**(7),133-139. (in Chinese)

Ke, K., and Chen, Y.Y. (2012),"Design Method of Steel Plate Shear Wall with Slits Considering Energy Dissipation," *Proceedings of the 15th World Conference on Earthquake Engineering*, Paper No. 570.

Connor, J.J., Wada, A., Iwata, M. and Huang, Y.H. (1997)," Damage-controlled structures. Preliminary design methodology for seismically active regions," *Journal of Structural Engineering*, American Society of Civil Engineers, **123**(4), 423-431.

10CUEE CONFERENCE PROCEEDINGS
10th International Conference on Urban Earthquake Engineering
March 1-2, 2013, Tokyo Institute of Technology, Tokyo, Japan

EXPERIMENTAL STUDY ON BUCKLING-RESTRAINED STEEL PLATE SHEAR WALLS WITH DIFFERENT ASPECT RATIOS

Y. Lu[1], G.Q. Li[2], H.J. Jin[3], X.L. Liu[4], and F.F. Sun[1]

1) Associate Professor, State Key Laboratory of Disaster Reduction in Civil Engineering, Tongji University, China
2) Professor, State Key Laboratory of Disaster Reduction in Civil Engineering, Tongji University, China
3) Ph.D Candidate, College of Civil engineering, Tongji University, China
4) Master student, College of Civil engineering, Tongji University, China
luyet@tongji.edu.cn, gqli@tongji.edu.cn, benny_7096@hotmail.com

Abstract: Two types of I-shape buckling-restrained steel plate shear walls are introduced, which are characterized by large aspect ratio and small aspect ratio. Thus, 5 series of large-aspect-ratio specimens with 1/3 scale and 3 small ones but with full scale are tested both monotonically and cyclically, in order to make a thorough investigation into their seismic performance such as energy-absorbing capacity and deformability, and so on. The test results indicate that the I-shape buckling-restrained steel plate shear wall with large aspect ratio is capable of dissipating earthquake energy stably and efficiently, judging from its almost spindle-shape hysteretic curves, as well as excellent deformability. Meanwhile, the small-aspect-ratio one also proves to be an ideal structural member, which exhibits even fatter hysteretic curves when the buckling restrainer is upgraded from the reinforced concrete panels to the stiffened steel cases. Apparently, the buckling restrainer is the key parameter deciding the seismic performance. Finally, the theoretical model for both walls is put forward, from which the yielding strength and initial stiffness can be predicted precisely to a large extent. And he theoretical model agrees with the test results to a satisfactory degree.
Keywords: Buckling-restrained, aspect ratio, seismic performance

1. INTRODUCTION

For the past four decades, steel plate shear walls (SPSWs) have been widely used as lateral resisting members in tall buildings. However, the premature buckling under lateral forces proves to be detrimental to the capability of energy dissipating and serviceability to a large degree, when subjected to medium-strong earthquakes. Thus, buckling restrainers are applied to improve its seismic performance by preventing the buckling, after considering that simply thickening the steel plate is not economical at all.

Apparently, the larger flexural stiffness of buckling restrainers, the higher efficiency of restraining, and the better performance. Currently, commonly used form of restrainers is reinforced concrete panel (RC panel), which shows larger flexural stiffness, compared to the steel stiffeners.

In 1995, a steel plate shear wall, composed of a steel plate stiffened with RC panels at both sides, was first introduced[1]. The steel plate is connected to the reinforced concrete with bolts that play an important role in preventing the buckling of the steel plate, which resists lateral forces between the stories by yielding in shear. However, cracks and buckling are also developed in the RC panels at the same time. And due to the failure of the RC panels, the hysteretic curve exhibits obvious pinching problem, as shown in Figure 1. Following experimental investigations, conducted by Astaneh-Asl A. (2004)[2], Y.L. Guo(2005)[3], K.C. Tsai (2006)[4] and G.Q. Li(2007)[5] have also indicated that, although the RC panel is capable of providing buckling restraining to a certain amount of degree, it's still prone to fracture significantly, due to the brittleness of concrete. And the hysteretic curve is also not fat enough to absorb earthquake energy as much as possible.

Besides, in most cases, the aspect ratio of buckling-restrained steel plate shear walls (BRSWs) that have been studied both experimentally and theoretically is small, that is to say, the width of the steel plate is no smaller than the height and the shearing deformation far outweighs the flexural one. However, in some cases the construction space left for the wall is so limited that only a large-aspect-ratio one is suited. And sometimes the required steel plate is so thin that it is even unavailable.

Therefore, BRSW with large aspect ratio is investigated, for the first time, both experimentally and theoretically. Meanwhile, knowing that RC panels of common rectangular-shape BRSW tend to fracture at the corners, due to the severe stress concentration, the steel plate is then I shaped to function in a more ductile way by shifting the high-stress zone from the corners to the inside, as shown in Figure 2.

Finally, more efficient buckling restrainers, modified reinforced concrete panels and stiffened steel cases, are put

forward and experimentally studied in this article.

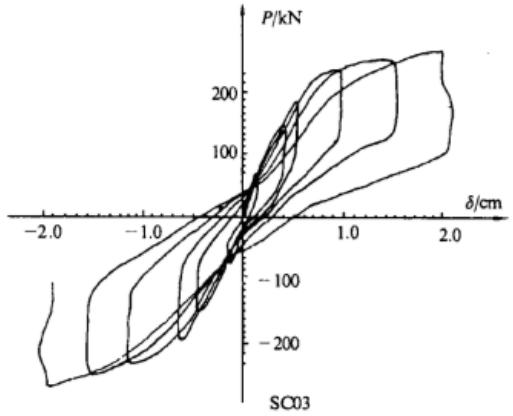


Figure 1. Hysteretic curve of lateral displacement and force

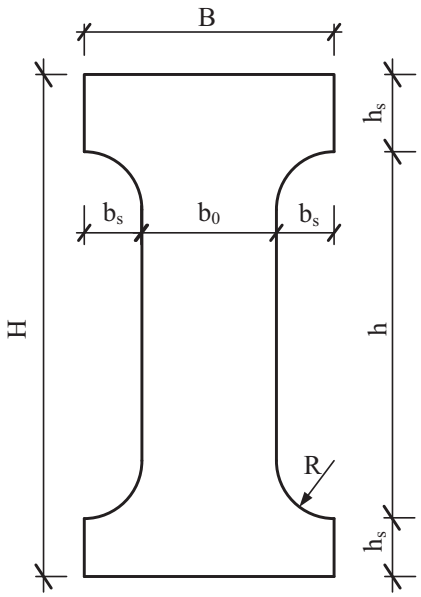


Figure 2. I-shape steel plate

2. TESTS ON LARGE-ASPECT-RATIO WALLS

2.1 Experimental specimens

Four series of BRSWs with different aspect ratios, from 2:1 to 4:1, have been designed, along with one control group, SPSWs with aspect ratio of 3:1. And all above-mentioned specimens are in a scale of 1/3, due to the limitation of the laboratory.

All the steel plates are 3.5mm in thickness and 900mm in height, made from structural steel Q235 that is widely used in China, the nominal yielding strength of which is 235MPa and 308MPa from the coupon tests. The detailed dimensions of the steel plate are summarized in Table 1, in which IC signifies BRSW and I signifies SPSW, as well as that -1 denotes monotonically loading and -2 means cyclically loading.

Besides, the buckling restrainers also adopt RC panels, 35mm thick with two-layer reinforcement, the volumetric ratio of which is 0.25%. And the both-side RC panels connect to inside steel plate through plain bolts. These bolt holes are designed slotted eyes, with a horizontal distance of 60mm, which allows the steel plate and the RC panels to inter-slip to a drift ratio of 1/30, back and forth.

Table 1. The detailed dimensions of the steel plate

series	specimen	H/B	H/b_0	h/b_0	R(mm)
1	I-180-1	3	5	3	70
	I-180-2				
2	IC-280A-1	2	3	2	80
	IC-280A-2				
3	IC-280B-1	2	3	2	80
	IC-280B-1				
4	IC-180-1	3	5	3	70
	IC-180-2				
5	IC-140-1	3	6	4	80
	IC-140-2				

2.2 Setups

In order to fully focus on the hysteretic performance of the BRSW and also to reuse the loading frame, the hinge frame is thus applied, as shown in Figure 3, in which the lower beam is anchored to the ground and the BRSW is high-strength bolted to the upper and lower beams through so-called fin plates. The actuators, loading capacity of which is 20 tons, are located at each side of the frame. And the out-of-plane supports at both sides ensure that the frame keeps functioning in plane.

The story drift ratio of the frame is measured as the key parameter, and the out-of-plane displacement of upper beam and specimen is also monitored as auxiliaries.



Figure 3. The hinge frame

2.3 Loading protocol

In the monotonic loading, the target drift ratio is 5%. And in the cyclic loading, the protocol is based on displacement control and elaborated in Figure 4.

Meanwhile, at the time that there is an obvious inflection point in the lateral force-displacement curve，the state of initial yielding is assumed to be reached. And when the strength deteriorates to a degree of 15%, it is assumed

that the BRSW is not able to carry loads any more.

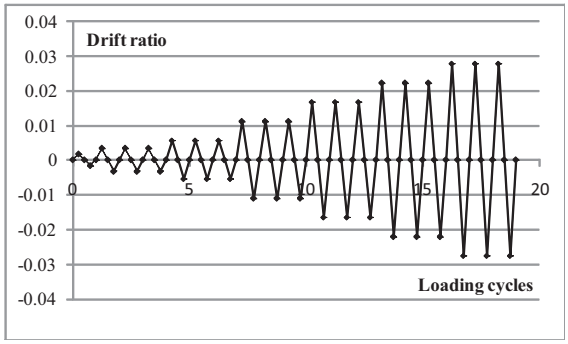


Figure 4. Cyclic loading protocol

3. RESULTS OF LARGE-ASPECT-RATIO WALLS

3.1 Overview

I-180 (SPSWs)

There is no surprise to see that both SPSWs have buckled at the very beginning of the loading since the critical shear buckling strength is significantly smaller than the yielding strength. And the location of buckling is all around the reduced sections, as shown in Figure 5 and Figure 6. The ultimate out-of-plane displacement is up to almost 35mm.

Both monotonic and cyclic curves, along with each FEM curve, are shown in Figure 7 and Figure 8, from which typical pinching problem, due to the buckling, can be observed.



Figure 5. Buckling of the monotonically loaded specimen



Figure 6. Buckling of the cyclically loaded specimen

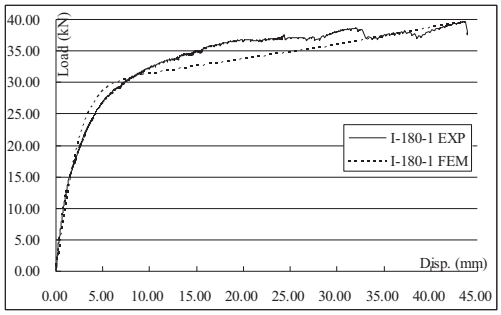


Figure 7. The monotonic curves of I-180-1

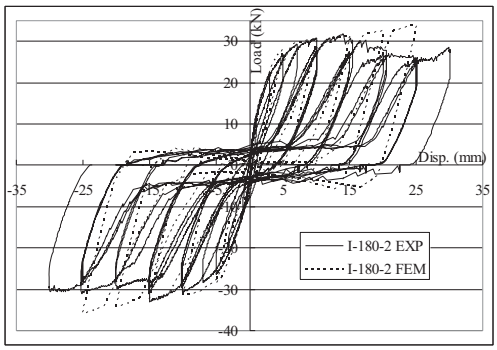


Figure 8. The cyclic curves of I-180-2

IC-280A and IC-280B

Thanks to the RC panels, the maximum out-of-plane displacement of these BRSWs is only 4mm. And no significant cracks develop, except for a few micro cracks that are mainly result from the tightening of bolts before loading, as shown in Figure 9 and Figure 10.

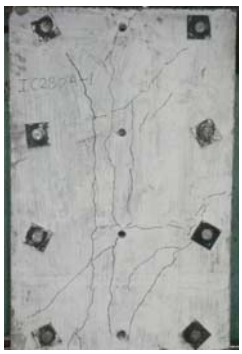


Figure 9. The cracks of the RC panel before loading



Figure 10. The cracks of the RC panel after loading

And although no observable buckling is seen from outer appearance during the loading, the hysteretic curves do have shown the pinching, as exhibited in Figure 11, as well as the monotonic curves shown in Figure 12, which is very much believed that there is an un-ignorable gap between the steel plate and the RC panels.

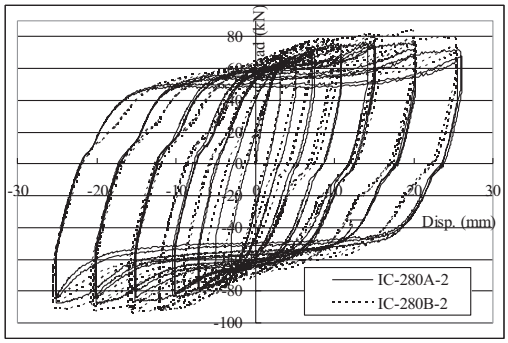


Figure 11. The hysteretic curves of IC-280

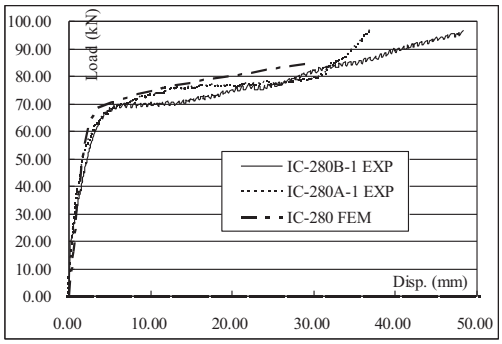


Figure 12. The monotonic curves of IC-280

IC-180

Similar to the IC-280, there is no significant crack observed after loading, except some cracks because of the tightening before the test. And several diagonal cracks between bolts have developed with the loading, as shown in Figure 13. However, the hysteretic curve, shown in Figure 14, still pinches apparently. The monotonic curve along with the FEM curve is also presented in Figure 15.



Figure 13. The diagonal cracks between the bolts

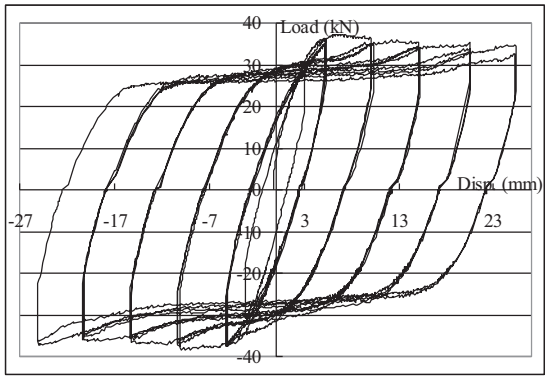


Figure 14. The hysteretic curve of IC-180-2

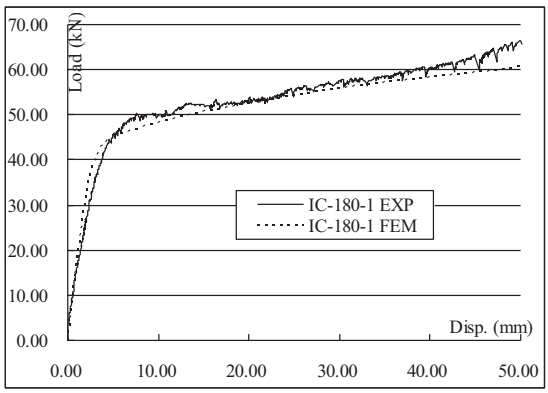


Figure 15. The monotonic curve of IC-180-1

IC-140

The failure of the RC panels in IC-140 is even minor, compared to the above specimens, as shown in Figure 16. The hysteretic curve is thus fatter than previous specimens, as shown in Figure 17, which is most likely due to the fact that narrower width of the steel plate enhances the critical shear buckling strength and lower the demands on the buckling restrainer.

The monotonically loaded curve of IC-140-1 is plotted in Figure 18 below.



Figure 16. RC panel of IC-140 after loading

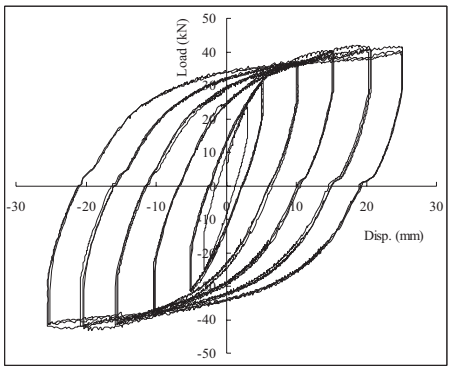


Figure 17. The hysteretic curve of IC-140-2

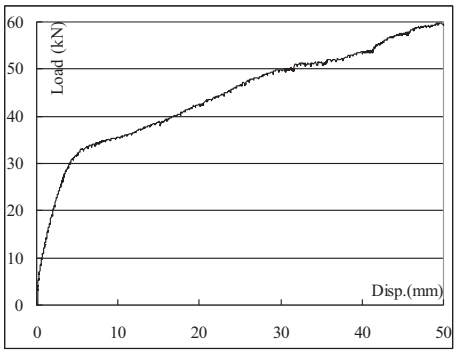


Figure 18. The monotonic curve of IC-140-1

3.2 The energy-dissipating coefficient

The energy-dissipating capability can be defined by the amount of energy, which is just equivalent to the area of the hysteretic loop. And to make it easier, the dimensionless parameter, energy-dissipating coefficient defined by the Figure 19 and Eq. (1), is introduced.

Therefore, the calculated energy-dissipating coefficient of above-mentioned specimens is listed in Table 2. Ordinarily, the hysteretic loop with a spindle shape has a coefficient of 3, more or less.

From Table 2, it can be seen that the BRSWs with large aspect ratio do have absorbed a great deal of energy, since the coefficient is almost 3.

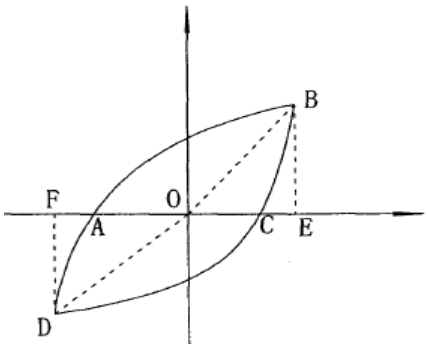


Figure 19. The definition of energy-dissipating coefficient

$$E = \frac{S_{ABCD}}{S_{OBE} + S_{ODE}} \quad (1)$$

Table 2. The energy-dissipating coefficient

Drift ratio	1/300	1/150	1/100	1/60	1/50	1/40
I-180-2	0.5	0.6	0.7	0.8	0.9	0.8
IC-280A-2	1.4	1.9	2.5	2.5	2.5	2.5
IC-280B-2	1.1	1.6	2.3	2.3	2.4	2.4
IC-180-2	1.2	1.6	2.4	2.7	2.8	2.8
IC-140-2	1.3	1.5	2.1	2.2	2.5	2.6

3.3 The cumulated plastic deformation

Similarly, the deformability can be evaluated by the ratio of cumulated plastic deformation to the yielding displacement, which is denoted as CPD in short. Therefore, CPD of those specimens are listed in Table 3, from which it is concluded that the maximum CPD have already exceeded 200 to a large extent and certainly meet the demands.

Table 3. The CPD

Drift ratio	1/300	1/150	1/100	1/60	1/50	1/40
I-180-2	4	16	52	111	195	303
IC-280A-2	7	26	76	156	269	412
IC-280B-2	9	31	89	181	308	470
I-180-2	4	19	61	130	227	361
IC-140-2	3	12	43	96	172	285

4. TESTS ON SMALL-ASPECT-RATIO WALLS

4.1 Experimental specimens

3 full-scale BRSWs (IC-1600, ISC-1600-1 and ISC-1600-2) with small aspect ratio of around 0.6 have been tested cyclically, in which the steel plates are 30mm, 25mm and 25mm thick respectively, and made of three parts that are welded together, as shown in Figure 21. The upper and lower parts are made from Q345 and the middle BLY225, aims to take advantage of the ductility of low-yield point steel. And the nominal yielding strength of BLY225 steel is 225MPa and 213MPa from the coupon tests.

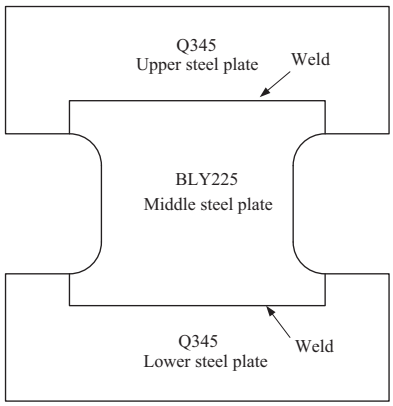


Figure 21. The three-part steel plate

Besides, RC panels are improved with extra built-in channel steels and used in IC-1600, as sketched in Figure 22. Stiffened steel case is used as buckling restrainer in ISC-1600-1, while a certain amount of concrete is casted in the stiffened steel case of ISC-1600-2, as shown in Figure 23 - Figure 25.

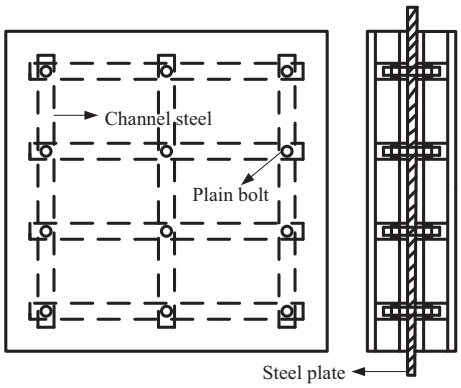


Figure 22. RC panel with built-in channel steels

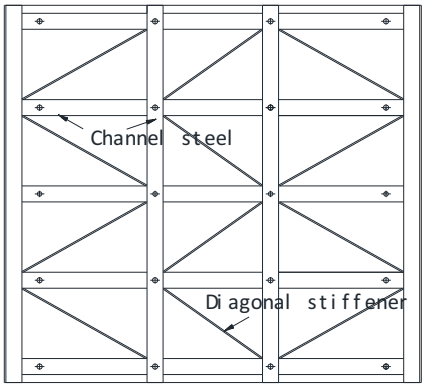


Figure 23. The plan of the stiffened steel case (ISC-1600-1)

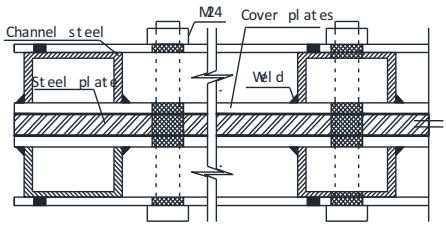


Figure 24. The section plan of the stiffened steel case

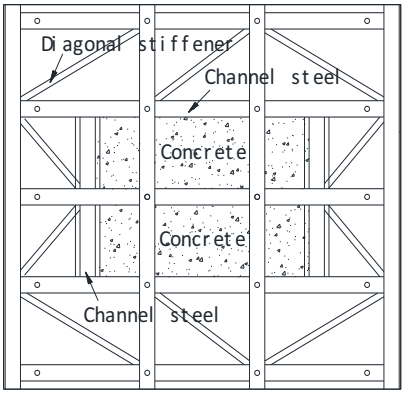


Figure 25. The plan of the stiffened steel case (ISC-1600-2)

4.2 Setups

Similar to previous setups, still a hinge frame but with full scale，as shown in Figure 26. The similar measurements are also presented in Figure 26.



Figure 26. The hinge frame

4.3 Loading protocol

Certainly, following tests also adopt displacement control principle and exactly same criterion to previous. The detailed protocol is plotted in Figure 27.

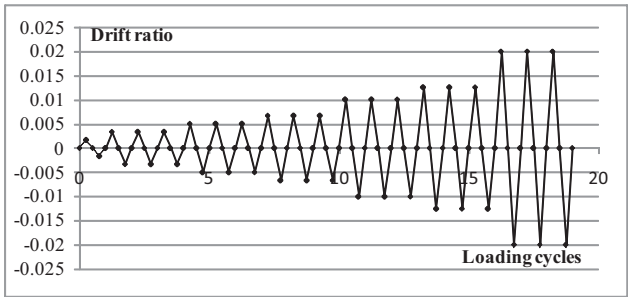


Figure 27. The loading protocol

5. RESULTS OF SMALL-ASPECT-RATIO WALLS

5.1 Overview

IC-1600-1

No significant cracks occur until the drift ratio exceeds 1/100, which is blamed to inadequate reinforcement. Before that, the buckling restraining, provided by the RC panels, is adequate, judging from the fact that there is no obvious pinching in hysteretic curve, as indicated in Figure 28.

After first cycle of 1/80 drift ratio, the out-of-plane displacement of the specimen is up to 10mm, and after the second cycle of 1/80, the RC panels have already fractured severely because of the buckling, as shown in Figure 29 and Figure 30.

ISC-1600-1

Still, nothing can be observed from outside, due to the

large flexural stiffness of stiffened steel case. However, through the gap between the steel cases, buckling of the inner steel plate is noticed, when the drift ratio reaches 1/100, as shown in Figure 31. Therefore, a micro pinching occurs in the hysteretic curve, as plotted in Figure 32.

Finally, the maximum drift ratio achieves 1/50, when further loading degrades the strength to a degree of more than 15%. And after removing the both-side steel cases, the buckling shape of the steel plate is clearly presented, as shown in Figure 33. So does the local failure of steel case shown in Figure 34.

ISC-1600-2

There is nothing significant noticed during the test, when specimen ISC-1600-2 is finally loaded to target drift ratio of 1/50. Much milder local failure occurs, thanks to the strengthened steel case by concrete, as shown in Figure 35. Therefore, a spindle-shape hysteretic curve is obtained, as shown in Figure 36.

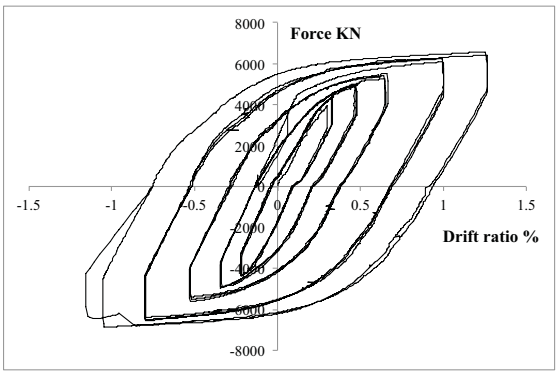


Figure 28. The hysteretic curve of IC-1600-1



Figure 29. Fracture of RC panels



Figure 30. Buckling of inner steel plate



Figure 31. Buckling of inner steel plate (1/100)

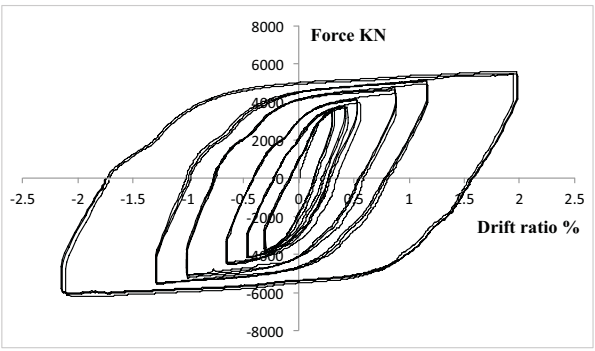


Figure 32. The hysteretic curve of ISC-1600-1



Figure 33. The buckling of inner steel plate after test



Figure 34. The local failure of stiffened steel case



Figure 35. The local failure of the steel case

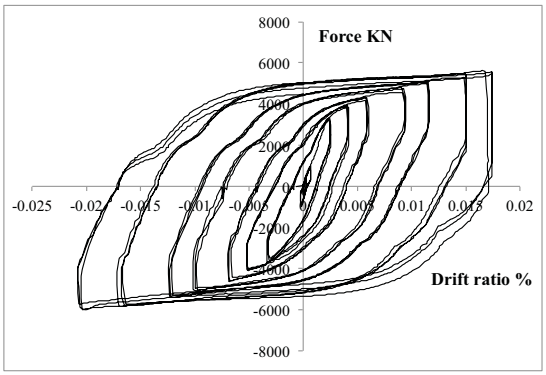


Figure 36. The hysteretic curve of ISC-1600-2

5.5 The energy-dissipating coefficient

The calculated energy-dissipating coefficient is listed in Table 4, from which it is concluded that RC panels with built-in channel steels and stiffened steel cases can provide even stronger buckling restraining, compared to the ordinary RC panels, since the maximum coefficient has already exceeds 3 in specimen ISC-1600-2. And the steel case strengthened by concrete provides the strongest restraining.

Table 4. The energy-dissipating coefficient

Drift ratio	1/300	1/200	1/150	1/100	1/80	1/50
IC-1600-2	1.0	1.6	2.0	2.3	2.8	\
ISC-1600-1	1.6	1.9	2.1	2.4	2.4	2.7
ISC-1600-2	1.4	2.1	2.8	2.9	3.2	2.9

5.6 The cumulated plastic deformation

And without suspense, the deformability of these specimens also meet the demands, since the maximum cumulated plastic deformation exceeds 200 times of yielding displacement, as indicated in Table 5.

Table 5. The CPD

Drift ratio	1/300	1/200	1/150	1/100	1/80	1/50
IC-1600-2	5	16	34	64	90	\
ISC-1600-1	15	41	80	138	219	352
ISC-1600-2	12	36	67	120	189	304

6. THEORETICAL MODEL

6.1 Yielding strength

Similar to the rectangular steel plate, the yielding line of I-shape steel plate is around reduced section. Therefore, a parametric study on the location of yielding line has been conducted, as shown in Figure 37. And the analysis indicates that this location is directly influenced by H, h_s and b_s, which have been defined in Figure 38. The distance between the yielding line and the centerline of steel plate is thus obtained by Eq.(2).

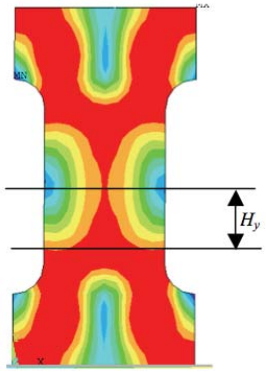


Figure 37. The yielding line of I-shape steel plate

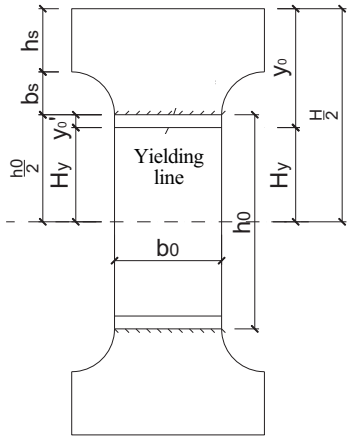


Figure 38. The dimension of I-shape steel plate

$$H_y = 0.88(\frac{H}{2} - h_s - b_s) \quad (2)$$

After confirming the position of yielding line, the yielding strength Q_y of I-shape BRSW with different aspect ratios can be predicted by Eq.(3) - Eq.(5), in which M_p is the yielding moment and Q_p is the yielding shear force.

$$Q_y = \frac{M_p Q_p}{\sqrt{Q_p^2 H_y^2 + M_p^2}} \quad (3)$$

$$M_p = \frac{t b_0 f_y}{4} \quad (4)$$

$$Q_p = \frac{t b_0 f_y}{\sqrt{3}} \quad (5)$$

6.2 Initial stiffness

Numerically, I-shape wall is equivalent to rectangular wall. Therefore, initial stiffness of I-shape BRSW can be obtained by introducing an equivalent width of steel plate, which is expressed in Eq.(6). After series of numerical study and parametric analysis, the magnification factor β_b can be gotten by Eq.(7), approximately. Besides, given h_s and b_s that don't outreach the range below, as expressed in Eq.(8), Eq.(6) is able to predict the yielding strength precisely to a satisfactory degree.

$$K = \frac{Et}{2.6\frac{H}{\beta_b b_0} + (\frac{H}{\beta_b b_0})^3} \quad (6)$$

$$\beta_b = 1.05(\frac{4(h_s + b_s)b_s - \pi b_s^2}{Hb_0} + 1) \quad for\ \frac{H}{B} \geq 1$$
$$\beta_b = 0.96(\frac{4(h_s + b_s)b_s - \pi b_s^2}{Hb_0} + 1) \quad for\ \frac{H}{B} < 1 \quad (7)$$

$$0.10B \leq b_s \leq 0.30B, \quad 0.10H \leq h_s \leq 0.22H \quad (8)$$

6.3 Verification by tests

Based on given equations, the yielding strength and initial stiffness of all above-mentioned specimens are obtained, as summarized in Table 6 below, compared with the test results. And from the comparison, it is concluded that the theoretical model can predict the yielding strength (Q_y) and initial stiffness (K) to a satisfactory degree.

Table 6. Comparison of Q_y and K between theoretical and test results

	Q_y(KN)			K (KN/mm)		
	Theory	test	Error %	Theory	test	Error %
IC-280A	68.3	70.3	-2.9	35.4	36.4	-2.8
IC-280B		67.0	1.9		39.0	-9.3
IC-180	30.6	46.6	-34.4	15.9	16.4	-3.2
IC-140	19.1	34.1	-44.0	10.2	12.8	-20.4
IC-1600-1	4812	4705	2.3	1213	603	101.2
ISC-1600-1	4010	4004	0.2	1010	1001	0.9
ISC-1600-2	3980	4100	-2.9	983	837	17.4

7. CONCLUSIONS

5 series of BRSWs with large aspect ratio and 3 BRSWs with small aspect ratio have been experimentally studied, in which the large aspect ratio ones are buckling restrained by ordinary reinforcement concrete panels. One of the small aspect ratio BRSWs is buckling restrained by reinforcement concrete panels with built-in channel steels, while the others use stiffened steel cases. The test results indicate that BRSWs with either large or small aspect ratio exhibit excellent capability of energy dissipating, as supreme as deformability, judging from the obtained energy dissipating coefficient and the cumulated plastic deformation.

Besides, corresponding theoretical models, which are used for calculating the yielding strength and initial stiffness are put forward and also verified by previous test results. Above all, the equations are capable of predicting the yielding strength and initial stiffness to a satisfactory degree.

Acknowledgements:

The authors acknowledge support from the National Key Technology R&D Program of China (NO. 2012BAJ13B02).

References:

G.Q. Li and X.G. Zhang. (1995), "Experimental study on the hysteretic behavior of concrete-incased steel plate shear walls" *Journal of Industry buildings*, **25**(6), 32-35.

Zhao. Q and Astaneh-Asl A. (2004). "Cyclic behavior of traditional and an innovative composite shear wall" *Journal of structural engineering*, **130**(2), 271-284.

Y.L. Guo and Q.L. Dong. (2005). "Static Behavior of Buckling-Restrained Steel Plate Shear Walls" *Tall Buildings From Engineering to Sustainability*. World Scientific, **6**(8), 666-670.

K.C. Tsai, C.H. Lin, Y.C. Lin, W.D. Hsieh and Qu B. (2006) "Sub-structural Hybrid Tests of A Full Scale 2-story Steel Plate Shear Wall" *Technical Report NCREE-06-017*, National Center for Research on Earthquake Engineering, Taipei, Taiwan.

H. Gao and G.Q. Li "Experimental and theoretical study on composite steel plate shear walls" [D]. Shanghai: Tongji University.

10CUEE CONFERENCE PROCEEDINGS
10th International Conference on Urban Earthquake Engineering
March 1-2, 2013, Tokyo Institute of Technology, Tokyo, Japan

STATIC TEST AND NUMERICAL ANALYSIS OF COMPOSITE CONCRETE STEEL-PLATE SHEAR WALLS WITH BINDING BARS

Zhou Deyuan[1)2)], Zhu Limeng[2)], and Zhou Ying[1)2)]

1) Professor, State Key Laboratory of Disaster Reduction in Civil Engineering, Tongji University, Shanghai, China
2) Research Institute of Structural Engineering and Disaster Reduction, College of Civil Engineering, Tongji University, Shanghai, China
dyzhou@tongji.edu.cn, zlm5075270@163.com, yingzhou@tongji.edu.cn

Abstract: Composite concrete steel-plate shear walls with binding bars are composed of a slender rectangular steel plate box infilled with concrete and connected by binding bars using bolt connection. In this paper, cyclic testing and numerical analysis were performed on three composite walls whose aspect ratios are 1.5 to investigate their seismic behavior. These specimens are designed with different spacing of binding bars. The failure modes and deformation performance were observed. Valuable results were evaluated including the hysteretic curves, bearing capacity and skeleton curves. Numerical analysis was performed to analyze the effects of different axial compression ratios and spacing of binding bars. The results indicate that bolt connection is feasible between two steel plates. The seismic performance of bolted double steel plates-concrete filled composite shear walls is well and the seismic performance was enhanced effectively by increasing the number of binding bars especially when axial compression ratio is high.

1. INTRODUCTION

Composite concrete steel-plate shear walls with binding bars (SCS walls), defined herein as concrete-filled slender steel box walls with binding bars connecting the two long-side plates (Figure 1.), are characterized by high strength and significant deformation ductility for compressive and shear loading due to the composite action of steel plates and concrete. The SCS wall can serve as both a structural unit and a prefabricated construction system. If the SCS wall can be applied to the super tall or tall buildings, the cross section of the structural element could be largely decreased, which would save much space and beautify the architecture. The existence of the steel plates replaces the building template, which facilitates the energy conservation and environmental protection.

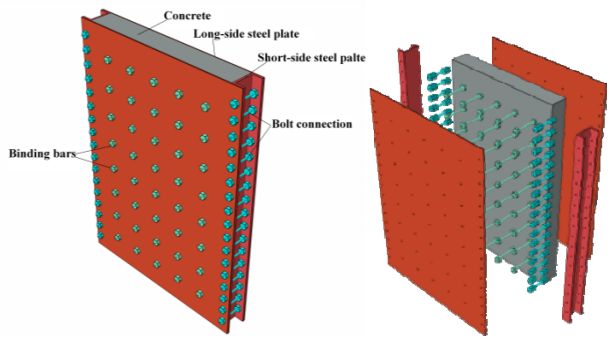


Figure 1 Composite concrete-steel plate shear walls with binding bars

Many researchers have carried out experimental and analytical study and found that this kind of composite wall is characterized by high strength and ductility.

Wright *et al*. (1995) conducted some pilot studies on the composite concrete and steel plate walling system and found that the steel sheeting provides similar characteristics to conventional framework for concrete casting. Three 1/4 scale specimens of SCS walls were built to take cyclic shear loading test by Emori K. (2002). The shear test exhibited high strength and significant ductility of SCS walls. Wielded connection was used between the insert plates and the long-side steel plate, which would result in the deficiency of the steel plates and be difficult to be applied to the engineering. Anwar *et al*. (2004) presented the studies of the in-plane shear behavior of such walls and it was found that the walls could provide high shear resistance if adequate boundary connections between sheeting and concrete were ensured. Tae-Sung *et al*. (2009) took in-plane cyclic loading test of double skin composite walls. Nie *et al*. (2011) conducted the cyclic loading tests on low shear-span ratio composite walls. Mydin *et al*. (2011) have finished some tests to study the structural behaviour of composite concrete and steel plate shear walls under axial compression. The test results have shown that the seismic performance of such composite shear walls was much better than the conventional shear walls.

In this study, cyclic lateral loading tests were conducted on three specimens of SCS walls to investigate its seismic performance. The wielded connection was normally used to connect two steel plates, but bolt connection was used between the long-side steel plate and short-side steel plate in the test which was different from existing research. The

feasibility of the bolt connection between the steel plates was tested, and the influence of the spacing of binding bars on the buckling behavior of steel plates was investigated.

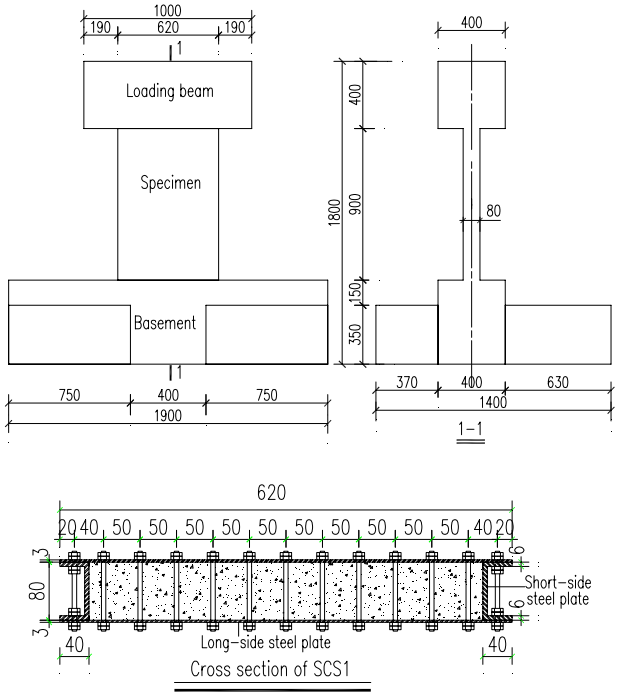
2. EXPERIMENTAL PROGRAM

2.1 SPECIMEN DESIGN AND FABRICATION

Three specimens of SCS walls were designed (Table 1) and quasi-static cyclic loading test was conducted in Tongji University (Figure 2 and Figure 3). The cross section of the specimens is 86mm×620mm and the detail is show in Figure 2. The aspect ratio of these three specimens is 1.5. The concrete strength grade is C30 and Q235 steel is used for steel plates. The yield stress of the binding bars is 400MP. Diameter of the binding bars is 6mm, thickness of short-side steel plates is 6mm, thickness of long-side steel plates is 3mm and thickness of core concrete is 80mm. Bolt connection was used between the long-side steel plate and short-side steel plate, which also could prevent buckling of the wing of shot-side steel plate.

Table 1 Parameters of specimens

NO.	Cross section (mm)	Spacing of binding bars (mm)	Axial compression ratio
SCS1	620×86	50	0.3
SCS2	620×86	100	0.3
SCS3	620×86	150	0.3



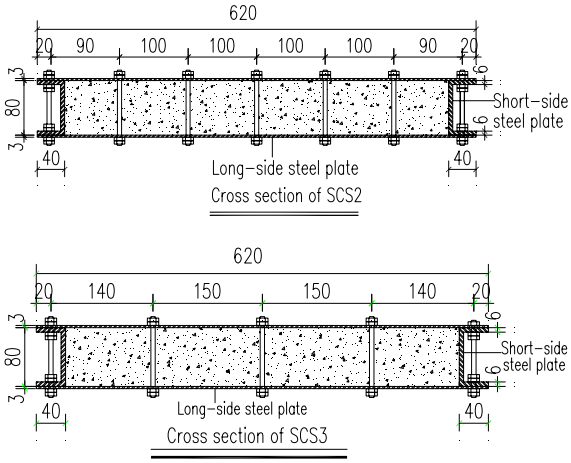


Figure 2 Cross section and detailing of composite concrete and steel plate shear walls with binding bars

Two ends of the specimen are embedded into the reinforced concrete loading beam and basement.

The axial compression ratio is a very important parameter which can affect the ductility of the SCS walls and it is calculated by Equation 1.

$$n = \frac{N}{f_c A_c + f_y A_s} \tag{1}$$

where n=axial compression ratio, N=the axial force, f_c=the uni-axial compressive strength of concrete, f_y=the yield stress of the steel plate, A_c=the cross section area of the core concrete, and A_s=the cross section area of the steel.

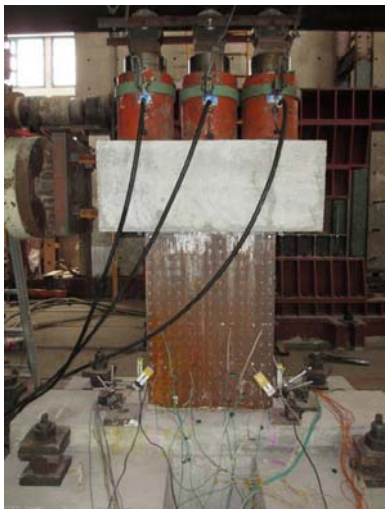


Figure 3 Test setup and specimen SCS1

2.2 EXPERIMENTAL PHENOMENA

In the tests, the axial loads remained unchanged and the gradually increasing positive and negative lateral loads were repeatedly applied so as to subject specimens to both bending and shear forces simulating the behavior of SCS walls under earthquakes. The load actuator was hinged together with the loading beam, therefore, the forces on the roots of specimens are the largest.

The failure positions were focused on their roots. The

loading process could be divided into three stages: pre-yielding stage (from beginning to yielding point on the load-displacement envelope curve), plastic stage (from yielding point to the peak point) and failure stage.

2.2.1 SPECIMEN SCS1

The binding bar spacing of specimen SCS1 is 50mm. The hysteretic force-displacement curve of SCS1 is plotted in Figure 4. The performance of SCS1 in three stages are described as follows.

(1) Pre-yielding stage

The specimen yielded when the lateral force reached 318.5KN (-307.6KN) at the drift ratio of 1/131 (-1/134). During this process, some voice could be heard because of the crack of the concrete and the friction between the concrete and steel plate. There was no evident phenomenon on the steel plates or binding bars and the state of the specimen was well.

(2) Plastic stage

When the lateral force reached the peak value 383.1KN (-364.9KN) at the drift ratio of 1/64 (-1/56) , elastic buckling deformation took place in the bolt connection area of the long-side steel plate in the root on the edge, where a small gap was opening and closing continuously with the increasing repeatedly lateral load. The buckling did not develop to the central part of the root.

(3) Failure stage

When the lateral load is reduced to 85 percent of the peak value at the drift ratio of 1/36 (-1/34), the specimen was considered to come to failure. The convex buckling area of the long-side steel plates developed gradually from the edge to the central part of the specimen and the deformation of long-side steel plates on both sides were almost symmetrical. The lateral load was reduced slowly before the fracture of the bolt connection. With the increasing of lateral displacement, five bolt connections were broken, the lateral force was largely reduced, the long-side and short-side steel plates was toned and the core concrete was crushed as shown in Figure 5.

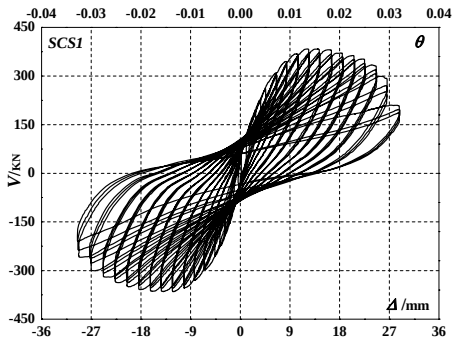


Figure.4 The hysteretic force-displacement curves of SCS1



Figure 5 Fracture of long-side and short side steel plates of specimen SCS1

2.2.2 SPECIMEN SCS2

The binding bar spacing of specimen SCS2 is 100 mm. The hysteretic force-displacement curve of SCS2 is plotted in Figure 6. The performance of SCS2 in three stages are described as follows.

(1) Pre-yielding stage

The specimen yielded when the lateral force reached 306.8KN (-271.9KN) at the drift ratio of 1/162 (-1/170). During this process, some voice could be heard because of the crack of the concrete and the friction between the concrete and steel plate. There was no evident phenomenon on the steel plates or binding bars and the state of the specimen was well.

(2) Plastic stage

When the lateral force reached the peak value 372.0KN (-325.7KN) at the drift ratio of 1/80 (-1/68) , elastic buckling deformation took place in the bolt connection area of the long-side steel plate in the root on the edge, where a small gap was opening and closing continuously with the increasing repeatedly lateral load. The buckling did not develop to the central part of the root but the buckling area is larger than that of SCS1.

(3) Failure stage

When the lateral load is reduced to 85 percent of the peak value at the drift ratio of 1/56 (-1/54), the specimen came to failure. The convex buckling area of the long-side steel plates developed symmetrically and gradually from the edge to the central part of the specimen. With the increasing of lateral displacement, fifteen bolt connections was broken continuously, the lateral force was largely reduced, the local buckling of long-side and short-side steel plates took place , the core concrete was crushed on the whole cross section and one vertical and several diagonal cracks appeared on the core concrete as shown in Figure 7.

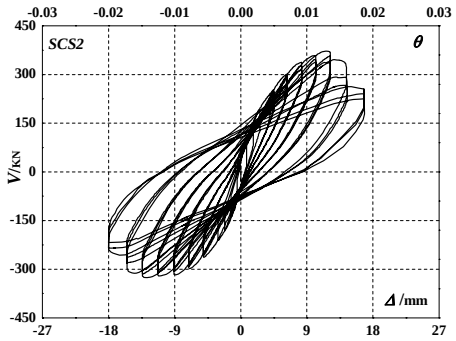


Figure.6 The hysteretic force-displacement curves of SCS2



Figure.7 Buckling of long-side and short side steel plates and crush of concrete of specimen SCS2

2.2.3 SPECIMEN SCS3

The binding bar spacing of specimen SCS3 is 150 mm. The hysteretic force-displacement curve of SCS3 is plotted in Figure 8. The performance of SCS3 in three stages are described as follows.

(1) Pre-yielding stage

The specimen yielded when the lateral force reached 253.2KN (-271.9KN) at the drift ratio of 1/206 (-1/192). During this process, some voice could be heard because of the crack of the concrete and the friction between the concrete and steel plate. There was no evident phenomenon on the steel plates or binding bars and the state of the specimen was well.

(2) Plastic stage

When the lateral force reached the peak value 305.5KN (-293.5KN) at the drift ratio of 1/105 (-1/90) , elastic buckling deformation took place in the bolt connection area of the long-side steel plate in the root on the edge, where a small gap was opening and closing continuously with the increasing repeatedly lateral load. The buckling also took place in the central part of the root.

(3) Failure stage

When the lateral load is reduced to 85 percent of the peak value at the drift ratio of 1/69 (-1/66), the specimen came to failure. The convex buckling area of the long-side steel plates developed asymmetrically and gradually on the edge and the central part of the specimen. With the increasing of lateral displacement, nineteen bolt connections were broken continuously, the lateral force was largely reduced, the local buckling of long-side plates took place, the core concrete was crushed on the whole cross section and two cross inclined cracks appeared on the core concrete as shown in Figure 9. But no large deformation or local buckling of the short-side steel plate took place when the specimen came to failure. The binding bar spacing of SCS3 is too large to prevent convex buckling of long-side steel plate effectively and the buckling of long-side steel plate took place before yielding of the steel, which made its ultimate capacity largely decreased.

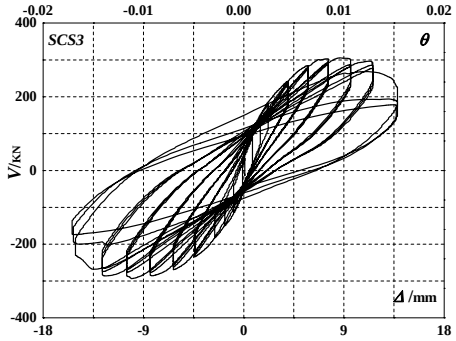


Figure 8 The hysteretic force-displacement curves of SCS3



Figure 9 Buckling of long-side steel plates and crush of concrete of specimen SCS3

2.2 EXPERIMENTAL RESULTS ANALYSIS

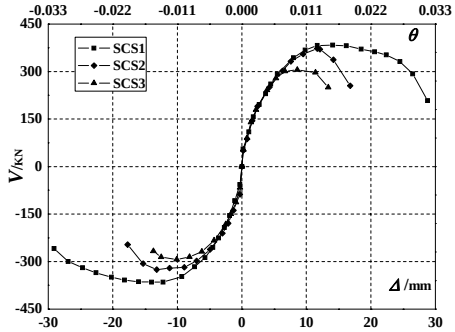


Figure 10 Comparison of load-displacement envelope curves of three specimens

Figure 10 shows the comparison of load-displacement envelope curves of three specimens under different drift ratios. When the drift ratio was less than 1/200 in the yielding stage, there was no evident difference on the

envelope curves of specimens. But the binding bar spacing has an obvious influence on the ultimate capacity and ductility of SCS walls. Specimens with different binding bar spacing exhibited different ultimate capacity: the smaller the binding bars spacing, the greater the ultimate capacity (V_u) and the drift ratio (θ_u) at ultimate strength as shown in Figure 10.

Table 1 shows the typical values of the specimens. The ultimate capacity of SCS1 is 2.85% greater than that of SCS2 in compression direction and 11.74% greater than that of SCS2 in tension direction. The ultimate capacity of SCS2 is 21.76% greater than that of SCS3 in compression direction and 3.63% greater than that of SCS3 in tension direction. The ductility of the specimens was evaluated by the displacement ductility coefficient μ, which is evaluated as $\mu = \theta_d/\theta_y$. With the decrease of binding bar spacing, the ductility of the specimen was obviously improved especially when the binding bar spacing was reduced from 100mm to 50mm. The displacement ductility coefficient of SCS1 is 27.2% greater than that of SCS2 in compression direction and 22.7% greater than that of SCS2 in tension direction.

Table.1 The typical values of lateral force and displacement

NO.	Yield		Peak		Failure		Ductility
	V_y (KN)	θ_y (rad)	V_u (KN)	θ_u (rad)	V_d (KN)	θ_d (rad)	μ θ_d/θ_y
SCS1	318.5	1/131	383.1	1/64	325.6	1/36	3.65
	-307.6	-1/134	-364.9	-1/56	-309.3	-1/34	3.89
SCS2	306.8	1/162	372.0	1/80	316.2	1/56	2.87
	-271.9	-1/170	-325.7	-1/68	-276.8	-1/54	3.17
SCS3	253.2	1/206	305.5	1/105	259.7	1/69	2.99
	-239.0	-1/192	-293.5	-1/90	-267.1	-1/66	2.92

\+ SCS wall in compression

– SCS wall in tension

3. NUMERICAL ANALYSIS

3.1 FINITE ELEMENT MODEL

A finite element model of SCS wall was built in software ABAQUS to simulate its seismic behavior (Figure.11).

Shell element S4 was used to simulate the behavior of the long-side steel plate including its buckling behavior. Truss model was applied to the binding bars and continuum element was applied to concrete and short-side steel plate.

The elastic modulus of loading beam and the basement is set the same as steel. The ends of concrete and steel plates are embedded into the beam and basement to simulate the boundary condition. The binding bars are embedded into the concrete and tied to the long-side steel plates. A surface-to-surface contact was defined between the steel and concrete. The penalty method that permits some relative motion of the surfaces when they should be sticking was selected to simulate the tangential and normal behavior between the concrete and steel. The friction coefficient was taken as 0.6 (Rabbat and Russell,1985).

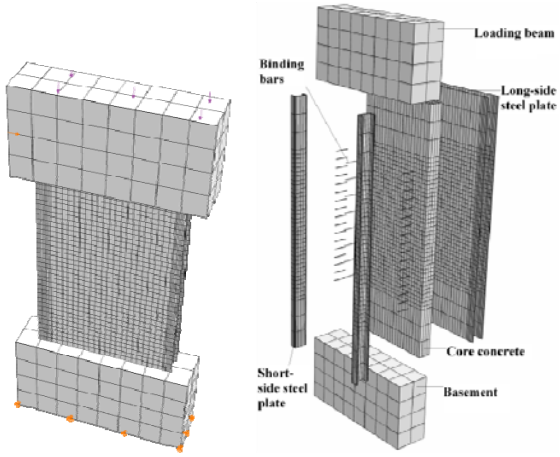


Figure.11 Finite element model

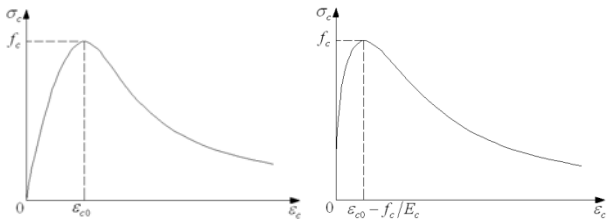
The model of the steel and concrete used in the FEM analysis are as follows:

(1) The damaged plasticity model (Table 2) (Chen, X., &Zhou, D.Y., 2009.) was used for concrete. The failure surface of it was shown in Figure.14. The dilation angle of the concrete was 30^0. The uniaxial compressive stress-strain curve of concrete (Eq. 2) proposed by Guo, Z.H. (1991) was used in analysis as shown in Figure.12. The ascending part of the tensile stress-strain curve of the concrete was linear and the descending part of it was proposed by Guo Z.H. (1991) (Eq.3) as shown in Figure.13.

$$\left.\begin{aligned} y &= \alpha_a x + (3-2\alpha_a)x^2 + (\alpha_a - 2)x^3, (0 \le x \le 1) \\ y &= x/[\alpha_d (x-1)^2 + x],\ (x > 1) \end{aligned}\right\} \quad (2)$$

where $x = \varepsilon_c/\varepsilon_{c0}$, $y = \sigma_c/f_c$, $\varepsilon_{c0} = (700 + 172\sqrt{f_c}) \times 10^{-6}$, $\alpha_a = 2.4 - 0.0125 f_c$, $\alpha_d = 0.157 f_c^{0.785} - 0.905$.

f_c is the uni-axial compressive strength of the concrete, ε_{c0} is the peak compressive strain of the concrete, α_a、α_d are the parameters of the stress-strain curve.

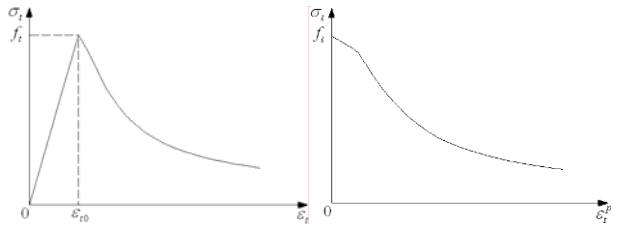


(a) Stress-strain curve (b) Stress-plastic strain curve

Figure.12 Uniaxial compressive stress-strain curves of concrete

$$\left.\begin{aligned} y &= x, \qquad (0 \le x \le 1) \\ y &= x/[\alpha_t (x-1)^{1.7} + x],\ (x > 1) \end{aligned}\right\} \quad (3)$$

Where, $x = \varepsilon_t/\varepsilon_{t0}$, $y = \sigma_t/f_t$, $\varepsilon_{t0} = 65 \times 10^{-6} f_t^{0.54}$, $\alpha_t = 0.312 f_t^2$, f_t is the tensile strength of the concrete, ε_{t0} is the peak tensile strain, α_t is a parameters of the tensile stress-strain curve.



(a)Stress-whole strain curve (b) Stress-plastic strain curve

Figure.13 Uniaxial tensile stress-strain curves of concrete

Table 2 Damaged Plasticity Model

Yielding function		Plastic potential function
$\sigma_1 \le 0$	$f = q - 3\alpha p + \gamma\sigma_1 - (1-\alpha)\sigma_c = 0$	$g = q - p\tan\psi$
$\sigma_1 > 0$	$f = q - 3\alpha p + \beta\sigma_1 - (1-\alpha)\sigma_c = 0$	

Where, $q = \sqrt{\left((\sigma_1-\sigma_2)^2+(\sigma_2-\sigma_3)^2+(\sigma_3-\sigma_1)^2\right)/2}$, $p = -(\sigma_1+\sigma_2+\sigma_3)/3$, $\cos\theta = (-2\sigma_1+\sigma_2+\sigma_3)/2q$. α 、 β 、 γ are material parameters. ψ is the dilation angle.

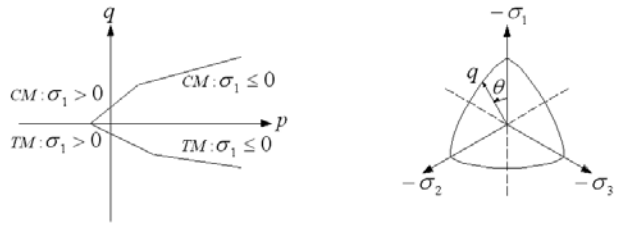
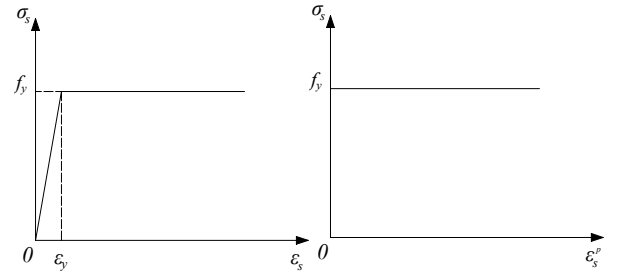


Fig.14 The failure surface of damaged plasticity model

(2) The constitution rule for steel was based on the plasticity theory with the Von Mises (1928) yielding condition. The stress-strain relationship for the steel box and insert plate were simply assumed as bi-linear models as shown in Figure.15.

The strain hardening effect was not considered in this model. The elastic modulus of steel before yielding is 200,000N/mm^2 and the elastic modulus of steel after yielding is 0N/mm^2 as shown in Figure.15. The dilatancy effect of concrete cause the bulging of the steel plate which could cause the buckling of the steel plate.



(a) Stress-whole strain curve (b) Stress-plastic strain curve

Figure.15 Uniaxial compressive stress-strain curves of steel

3.2 RESULTS ANANALYSIS

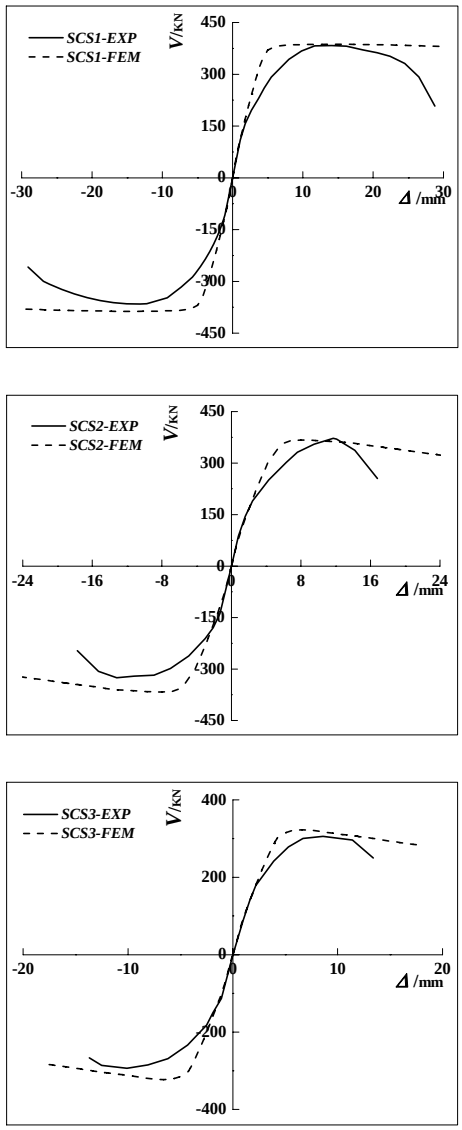


Figure.16 Comparison of load-displacement envelope curves between the FEM and experimental results

The calculated load-displacement curve of SCS1, SCS2 and SCS3 are shown in Figure. 16. The negative curve is drawn anti-symmetrically by the positive curve. The computed load-displacement envelope curves are in close agreement with those obtained by the tests of three specimens up to the yielding strength. During the plastic process, from yielding point to the peak point on the curve, the computed lateral stiffness is much larger than that obtained by the tests of three specimens. The FEM could not take into account of the damages during the cyclic loading tests. Therefore, the stiffness degradation of test results is much faster than that of computed results. During the failure stage, the strength degradation of the test results is more evident than that of computed results. When the bolt connections were coming into fracture in the tests, the strength began to degrade rapidly but it could not be simulated exactly in the numerical analysis. The computed ultimate capacities ($V_{u,FEM}$) of SCS1 and SCS2 are in close agreement with the experimental ones which are obtained by

the average value of peak loads ($V_{u,EXP}$) on the positive and negative curves as shown in Table 3. The computed ultimate capacities ($V_{u,FEM}$) of SCS3 is in good agreement with the experimental one ($V_{u,EXP}$) which is obtained by the average value of peak loads ($V_{u,EXP}$) on the positive and negative curves as shown in Table 3. This finite element model is acceptable to simulate the behavior of SCS walls and some parameter analysis was made as follows on the basis of this finite element model.

Table 3. Comparison of ultimate capacities between the test results and computed results

NO.	Test results $V_{u,EXP}$ *(KN)*	Computed results $V_{u,FEM}$ *(KN)*	$V_{u,FEM}/V_{u,EXP}$
SCS1	374.00	382.54	1.03
SCS2	348.85	367.20	1.05
SCS3	299.51	339.90	1.13

Figure.17 shows the influence of binding bar spacing on the ultimate capacity and a comparison was made between the experimental and analytical results. The computed ultimate capacities are little greater than the experimental ones and the computed ultimate capacity is decreasing with the decrease of binding bar spacing which is consistent with the experimental results. The decreasing of binding bar spacing can both weaken the confining effect of core concrete and reduce the buckling stress of the steel plate.

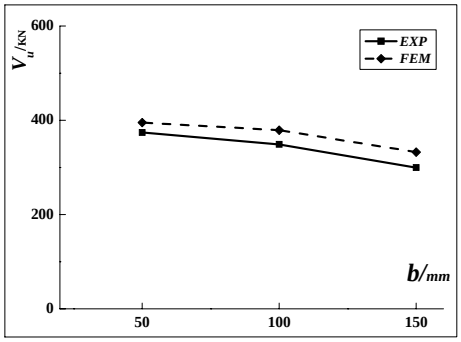


Figure.17 Comparison of influence of spacing of binding bar on the ultimate capacity

In order to study the influence of axial compression ratio to the ultimate capacity of SCS walls, six models (*SCS1-n*) were analyzed according to SCS1, six models (*SCS2-n*) were analyzed according to SCS2 and six models (*SCS3-n*) were analyzed according to SCS3. The axial compression ratio was changed from 0.1 to 0.6 accordingly. Figure.18 represents the ultimate capacity-axial compression ratio curves with different binding bar spacing.

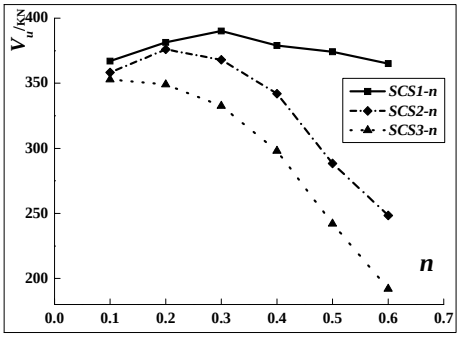


Figure.18 The ultimate capacity-axial compression ratio curves

It can be seen from curve *SCS1-n* in Figure 18 that the ultimate capacity increased when the axial compression ratio changed from 0.1 to 0.3 and decreased when the axial compression ratio changed from 0.3 to 0.6. The maximum value of ultimate capacity of SCS1-n models is obtained when the axial compression ratio is 0.3. The maximum value of ultimate capacity of SCS2-n models is obtained when the axial compression ratio is 0.2. For the models SCS3-n the ultimate capacity decreased with the change of axial compression ratio from 0.1 to 0.6. It can be concluded that with the increasing of binding bar spacing, the adverse effect of axial compression ratio on the ultimate capacity is greatly increased.

4. CONCLUSIONS

Three specimens of SCS walls were tested experimentally under cyclic loading condition and three models of each SCS walls with different axial compression ratios were selected and analyzed using the finite element method allowing nonlinear behavior for the material. Based on the test observations and analysis of the data, the following conclusions were obtained.

(1) The seismic performance of composite concrete and steel plate shear walls with binding bars is very well. Its ultimate bearing capacity and ductility are both great.
(2) The bolt connection between the long-side steel plate and the short-side steel plate is feasible. If the bolt connection is strengthened to avoid its fracture, the ductility would be highly improved.
(3) The decrease of spacing of binding bars has an evident effect on the ductility and the shear capacity. When the binding bar spacing is 50mm, the effect of axial compression ratio on the ultimate capacity is not evident and the ultimate capacity comes to maximum value at the axial compression ratio of 0.3.
(4) The stiffness degradation speed of the SCS wall with small binding bar spacing is slower, indicating that the behavior of this structure is correspondingly more stable and therefore more favorable for seismic resistance.

Acknowledgements:

The authors acknowledge support from Ministry of Science and Technology of China (SLDRCE09-D-03) and National Natural Science Foundation of China (51178333).

References:

Anwar Hossain KM, Wright H D. (2004) "Experimental and theoretical behaviour of composite walling under in-plane shear," *Journal of Constructional Steel Research*, **60** (1): 59-83.

Chen,X.,and Zhou D.Y.(2009), "Comparison among axial behaviors of rectangular CFT tube columns by adopting five material models". *Journal of Building Structures*, **30**(3):120-125. (in Chinese).

Emori K.(2002) "Compressive and shear strength of concrete filled steel box wall," *Steel Structures*, **68** (2) : 29-40.

Guo, Z.H.andWang, C.Z. (1991). "Investigation of strength and failure criterion of concrete under multi-axial stresses". *China Civil Engineering Journal*, **24** (3): 1-14.(in Chinese).

Mohammed A. Mousa and Nasim U. (2011) "Global buckling of composite structural insulated wall panels," *Materials and Design*, **32**(2):766-772.

Mydin, MAO and Wang YC. (2011) "Structural performance of lightweight steel-foamed concrete–steel composite walling system under compression," *Thin-Walled Structures* , **49**(1):66-76.

Nie Jianguo, Bu Fanmin, Fan Jiansheng. (2011) "Experimental research on seismic behavior of low shear-span ratio composite shear wall with double steel plates and infill concrete," *Journal of Building Structures*, **32**(1) : 74-81. (in Chinese)

Tae-Sung E. Hong-Gun P. and Cheol-Ho L. *et al.* (2009) "Behavior of Double Skin Composite Wall Subjected to In-Plane Cyclic Loading," *Journal of Structural Engineering*, 1**35**(10):1239-1249.

Wright H D and Gallocher S.C. (1995), "The behavior of composite walling under construction and service loading," *Journal of Constructional Steel Research*, **35** (3): 257-273.

10CUEE CONFERENCE PROCEEDINGS
10th International Conference on Urban Earthquake Engineering
March 1-2, 2013, Tokyo Institute of Technology, Tokyo, Japan

BEHAVIOR OF STEEL TUBE-DOUBLE STEEL PLATE-CONCRETE COMPOSITE WALLS SUBJECTED TO AXIAL FORCE AND CYCLIC LOADING

Xiaodong Ji[1], Feiming Jiang[2], Jiaru Qian[3]

1) Associate Professor, Department of Civil Engineering, Tsinghua University, China
2) Graduate student, Department of Civil Engineering, Tsinghua University, China
3) Professor, Department of Civil Engineering, Tsinghua University, China
jixd@mail.tsinghua.edu.cn, jiangfeiming@163.com, qianjr@mail.tsinghua.edu.cn

Abstract: The "steel tube-double steel plate-concrete composite wall" consists of concrete filled steel tubular (CFST) boundary elements and a double "skin" composite web where two steel plates are connected by tie bolts with space between them filled with concrete. In this paper, the behavior of the composite walls was examined through experiments in which five slender rectangular wall specimens were subjected to axial forces and lateral cyclic loading. The specimens failed in local buckling of the steel tubes and plates, fracture of the steel tubes, and concrete crushing at the wall base. The extent of the CFST boundary element was found to significantly affect the wall's deformation capacity. The area ratio of steel plates had a minimal effect on the deformation capacity of the slender walls. The addition of circular steel tubes embedded in the CFST boundary elements obviously increased the strength of the walls. When the CFST boundary element's extent was 0.2 times the wall's sectional depth and the axial force ratio was no more than 0.25, the walls had an ultimate drift ratio of around 0.03. Design formulas used to calculate the flexure strength of the walls were proposed, and the prediction had good agreement with the test results.

1. INTRODUCTION

The use of composite structural members that combine the advantages of two constructional materials, steel and concrete, has gained popularity. A variety of steel-concrete composite walls have been developed. These composite walls can be classified into three categories. The first category consists of steel panels combined with concrete walls, for instance, the single skin composite wall (Zhao and Abolhassan 2004) and the double skin composite wall (Emori 2002, Hossain and Wright 2004, Eom et al. 2009). The second category comprises of steel frame boundary and infilled RC walls (for example, Tong et al, 2005, Liao et al. 2009). The third category are the so-called steel reinforced concrete (SRC) walls which include additional steel (or steel tubes) embedded at the wall boundary elements (for example Wallace et al. 2000, Qian et al. 2012). Extensive studies, including both experimental testing and numerical simulation, have indicated that these composite walls are characterized by a combination of good strength, stiffness and deformation capacity properties, exhibiting an excellent seismic performance.

This paper proposes an innovative composite wall, named "the steel tube-double steel plate-concrete composite wall", which is particularly well suited for use in high-rise buildings in regions of high seismicity. Fig.1 shows a sketch of typical cross-section of the rectangular composite wall. Rectangular steel tubes act compositely with infilled concrete to form the concrete-filled steel tubes (CFSTs), serving as the wall boundary elements. Additional circular steel tubes could be embedded at the CFST boundary elements for further enhancement of the earthquake-resistant capacity of the wall. Double steel plates, as the skins of wall web, are connected by tie bolts, with the space between them filled with concrete. The CFST boundary elements primarily resist the bending moment exerted on the wall, while the double steel plates, together with the filled concrete, primarily resist the shear force exerted on the wall. The steel tubes and plates are used as the formwork for the concrete filler, enabling rapid construction of the walls. The filled concrete prevents early buckling of the steel tubes and plates, whereas the confinement provided by the steel tubes increases the strength and ductility of the filled concrete. Therefore, such a cross-sectional arrangement of the composite wall is expected to enhance the wall's seismic performance.

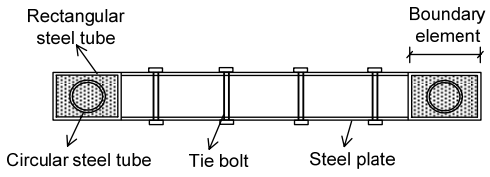


Figure 1. Sketch of cross-section of steel tube-double steel plate-concrete composite wall

The objective of this paper is to examine the seismic behavior of the proposed composite walls through a series of quasi-static tests of rectangular wall specimens. The first section introduces the experimental program in detail. The second section presents the test results, including the failure mode, lateral load-carrying, deformation and energy dissipation capacities of the walls. The third section proposes simplified formulas used to evaluate the wall's flexural

strength, and calibrates them through comparisons with the test results.

2. EXPERIMENTAL PROGRAM

2.1 Test Specimens

2.1.1 Specimen Design

A total of five test specimens, labeled SW1 to SW5, were tested. The specimens were designed to represent the lower stories of structural walls in high-rise buildings, and were fabricated at approximately 1/6 scale to accommodate the capacity of the loading facility. All specimens had the same overall geometry, as shown in Fig. 2. The wall was 2600 mm tall, and had a rectangular cross-section with a depth of 1100 mm and a thickness of 140 mm. The aspect ratio (i.e., height-to-width ratio) of the wall was about 2.5, ensuring a flexure-dominated deformation mode. A RC foundation beam with a cross-section of 750 mm by 600 mm was cast together with the wall, through which the specimen was securely clamped to the reaction floor. A RC top beam with a cross-section of 300 mm by 300 mm was cast as well, through which the vertical and horizontal loads were applied to the wall.

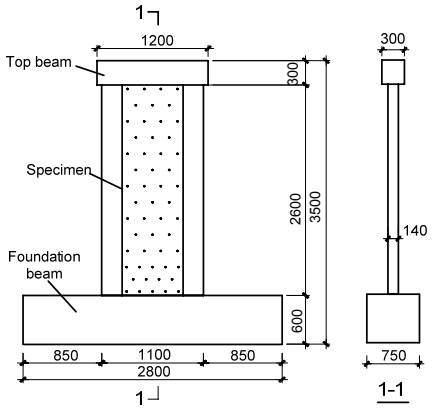


Figure 2. Elevation view of wall specimens (Unit: mm)

Fig. 3 shows the sectional dimensions and details of the wall specimens. The specimens were designed to satisfy the "strong shear and weak bending" mechanism, and the test results showed that all specimens failed in a flexural mode. Three variables were considered for design of the specimens: (1) the extent of the CFST boundary element, (2) presence or absence of embedded circular steel tubes at the CFST boundary elements, and (3) the area ratios of the steel tubes and of the steel plates. The extent of the CFST boundary element of Specimen SW1 was equal to the cross-sectional thickness of the wall. For Specimens SW2 through SW5, the extent of the CFST boundary element was designated to be 0.2 times the wall's cross-sectional depth, according to the provision for RC walls stipulated by the Chinese Code for Seismic Design of Buildings (GB 50011-2010). Circular steel tubes were embedded at the CFST boundary elements for Specimens SW1 through SW4, whereas no additional circular tubes were placed in Specimen SW5. The area ratios of the steel tubes and of the steel plates varied for different specimens by changing the thickness of steel tubes and plates. Details on this variable are described later in Subsection 2.2.2.

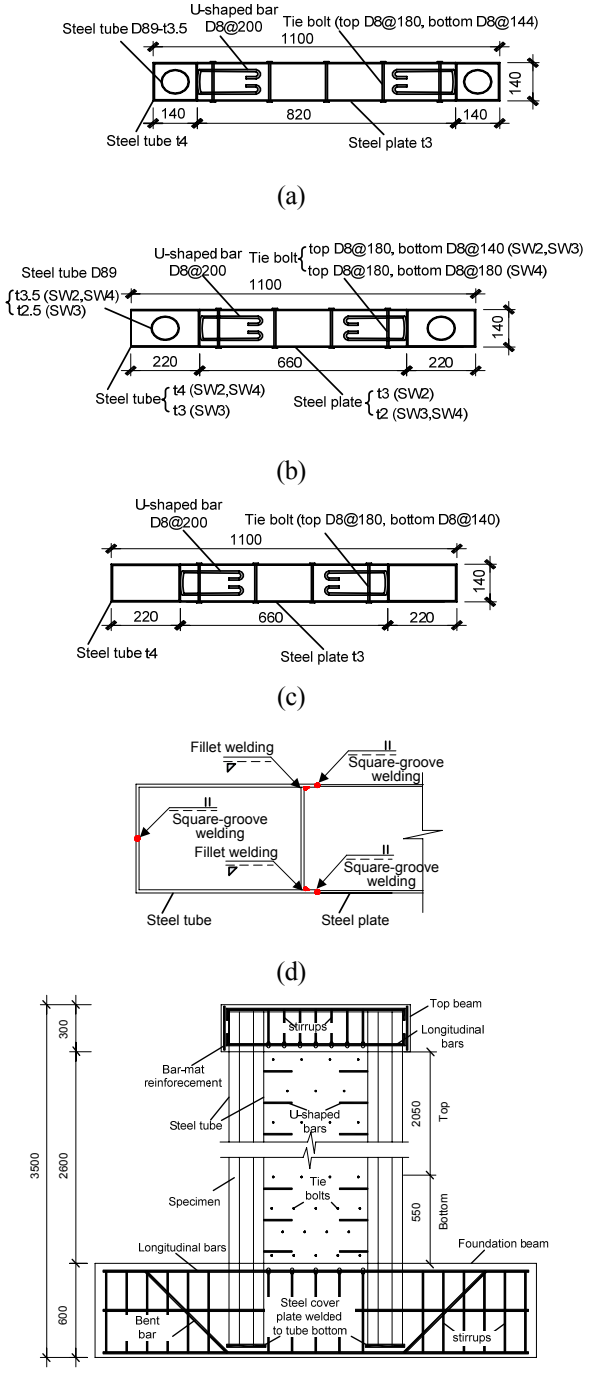


Figure 3. Section dimensions and details (Unit: mm): (a) SW1, (b) SW2 through SW4, (c) SW5, (d) Welding details of steel tubes and steel plates, and (e) Elevation drawing of steel tubes and reinforcement for SW2

The rectangular steel tubes were fabricated by connecting cold-formed thin plates with full penetration square-groove welds and with fillet welds, as shown in Fig. 3(d). The rectangular steel tubes and steel plates were

connected by full penetration square-groove welding. D8 (Diameter = 8mm) U-shaped bars, which were welded to the rectangular steel tubes and extended into the web concrete, were used to ensure the shear transfer between the CFST boundary elements and wall web concrete. The U-shaped bars extended 180 mm to the web concrete, and had a vertical spacing of 200 mm. Double steel plates were fastened to each other by D8 (Diameter = 8 mm) high strength bolts. The vertical and horizontal spacings of tie bolts were 200 and 180 mm, respectively, and the ratio of the bolt spacing to steel plate thickness varied from 60 to 90 for different specimens. Note that the region from the base of the wall up to a height equal to 0.5 times the cross-sectional depth of the wall was supposed to form a plastic hinge and to experience significant inelastic deformation. Therefore, the spacing of tie bolts in this region was reduced to 140 to 150 mm and the ratio of the bolt spacing to steel plate thickness was around 45 to 70.

Fig. 3(e) shows an elevation drawing of the steel tube and reinforcement for Specimen SW2. The steel tubes and plates were extended into the RC foundation and top beams to achieve full anchorage. The anchorage depth of the rectangular steel tubes within the foundation beam was no less than 2.5 times the tube's sectional depth. In addition, a steel cover plate was welded at the tube bottom and three rows of rebars were welded along the tube perimeter as ribs, which also contributed to secure anchorage. Reinforcing details of the foundation and top beams were designed to ensure that the beams were damage free during testing.

2.1.2 Material Properties

The concrete used in the specimens had a strength grade of C40 (nominal cubic compressive strength $f_{cu,d}$ = 40 MPa, and design value of axial compressive strength $f_{c,d}$ = 19.1 MPa). Specimens SW1 and SW4 were cast with a batch of concrete, and Specimens SW2, SW3 and SW5 with another batch of concrete. Actual cubic compressive strength $f_{cu,t}$ of the concrete was tested on cubes of 150 mm size and the results are shown in Table 1(a). Note that the actual value (referred to as "test value" hereinafter) of axial compressive strength of concrete $f_{c,t}$ was taken as 0.76 $f_{cu,t}$ according to Chinese Code for Design of Concrete Structures (GB50010-2010).

Steel tubes and plates were fabricated from Grade Q235 steel (nominal yield strength f_y = 235 MPa, and design value of yield strength $f_{y,d}$ = 215 MPa). The U-shaped bars were plain steel bars, and their strength grade was HPB235 (f_y = 235 MPa). D8 tie bolts had a strength grade of 8.8 (nominal ultimate strength f_u = 800 MPa, and the ratio f_y/f_u = 0.8). The material properties of steel were measured by coupon tests, and the test values of yield and ultimate strengths $f_{y,t}$ and $f_{u,t}$ are shown in Table 1(b).

Table 1(a) Material properties for concrete

Specimen No.	cubic compressive strength, $f_{cu,t}$ (MPa)	Axial compressive strength, $f_{c,t}$ (MPa)
SW1, SW4	44.0	33.4
SW2, SW3 & SW5	40.8	31.0

Table 1(b) Material properties for steel

Nominal thickness (mm)	Measured thickness (mm)	Yield strength, $f_{y,t}$ (MPa)	Ultimate strength, $f_{u,t}$ (MPa)
2.0	1.83	332.4	440.7
2.5	2.38	345.7	393.2
3.0	2.94	322.1	433.5
3.5	3.12	383.7	461.3
4.0	3.73	298.6	443.6
8.0 (bolt diameter)	7.63 (bolt diameter)	788.3	914.0

2.2 Test variables

Besides the extent of the CFST boundary element, and presence or absence of circular steel tubes at the CFST boundary elements, the major test variables were the axial force ratio applied to the wall, and the area ratios of the steel tubes and of the steel plates.

2.2.1 Axial Force Ratio

The axial force is one of the critical concerns for the design of a ductile structural wall. An increase of the axial force ratio increases the depth of the compression zone of the wall section and consequently decreases the ductility of the wall. For the steel tube-double steel plate-concrete composite wall, the axial force ratio is defined as follows:

$$n_d = \frac{N_d}{f_{c,d}\left(A - \sum\left(A_a + A_p\right)\right) + \sum\left(f_{a,d}A_a + f_{p,d}A_p\right)} \quad (1a)$$

$$n_t = \frac{N_t}{f_{c,t}\left(A - \sum\left(A_a + A_p\right)\right) + \sum\left(f_{a,t}A_a + f_{p,t}A_p\right)} \quad (1b)$$

in which, n denotes the axial force ratio; N denotes the axial load applied on the specimen; f_c denotes the axial compressive strength of the wall concrete; f_a and f_p denote the yield strengths of steel tubes and steel plates, respectively; A denotes the gross cross-sectional area of the wall; A_a and A_p denote the gross cross-sectional areas of steel tubes and steel plates, respectively; and subscripts d and t represent the values of design and test, respectively. According to GB50011-2010, the load factor (i.e., the ratio of the design value of the axial load to the actual value) was 1.2. The material strength reduction factor (i.e., the ratio of the design value of material strength to the corresponding test value) was also considered. Allowing for both the load factor and material strength reduction factor, the design value of the axial force ratio was approximately 1.9 times the corresponding test value. It is notable that, under the same axial compressive load, the axial force ratio of the composite wall is 35%~40% lower than the corresponding RC wall with the same sectional geometry, due to the increase in the axial load-carrying capacity provided by the steel tubes and plates. It is beneficial to reduce the wall thickness if it is governed by the limit of axial force ratio in design.

Table 2 shows the axial compressive loads applied to the specimens and the corresponding axial force ratios. Specimens SW1 and SW2 had the similar axial force ratios,

with a design value of 0.45 to 0.49 and a test value of around 0.25. Specimens SW3 through SW5 had the similar axial force ratios with the design value of 0.36 to 0.39 and the test value of 0.20.

Table 2 Axial force ratio of specimens

Specimen No.	N (kN)	n_d	n_t
SW1	2061	0.49	0.25
SW2	1908	0.45	0.24
SW3	1431	0.38	0.20
SW4	1546	0.39	0.20
SW5	1431	0.36	0.20

2.2.2 Area Ratios of Steel Tubes and of Steel Plates

Steel tubes and steel plates for the composite walls are analogous to the reinforcing bars for the RC walls. Accordingly, the area ratios of the steel tubes and of the steel plates are critical factors for design of the composite walls. The area ratio of the steel tubes is defined as the ratio of the cross-sectional area of the steel tubes to that of the CFST boundary element. The area ratio of the steel plates is defined as the ratio of the cross-sectional area of the steel plates to that of the wall web. Table 3 lists the area ratios of the steel tubes and of the steel plates for the specimens. The area ratio of the rectangular steel tubes for Specimens SW2, SW4, and SW5 was 0.085, larger than the ratio of 0.068 for Specimen SW3. The area ratio of the steel plates for Specimens SW1, SW2 and SW5 was 0.042, larger than the ratio of 0.026 for Specimens SW3 and SW4.

The confinement index of CFSTs is used to quantify the extent of confining of the infilled concrete by the steel tubes. The confinement index combines the area and strength ratios of the steel tubes and the infilled concrete, given by:

$$\theta = \frac{f_a A_a}{f_c A_c} \tag{2}$$

in which, θ denotes the confinement index; f_a and f_c denote the yield strength of the steel tubes and the axial compressive strength of the infilled concrete, respectively; A_a and A_c denote the cross-sectional areas of the steel tube and infilled concrete, respectively. The CFST confinement indices for the test specimens are listed in Table 3 as well.

Table 3 Parameters of steel tubes and plates

Specimen No.	Rectangular steel tube			Circular steel tube			Steel plate
	B/t	ρ	θ	D/t	ρ	θ	ρ
SW1	37.5	0.104	1.0	28.5	0.043	1.8	0.042
SW2	59.0	0.085	0.9	28.5	0.027	1.9	0.042
SW3	74.8	0.068	0.8	37.4	0.021	1.3	0.026
SW4	59.0	0.085	0.8	28.5	0.027	1.8	0.026
SW5	59.0	0.085	0.9		——		0.042

Note: 1) θ represents the confinement index of CFSTs.
2) ρ represents the area ratios of the steel tubes and of the steel plates.
3) B/t represents the depth-to-thickness ratio of rectangular steel tubes, where B denotes the sectional depth of the rectangular tube; and D/t denotes the diameter-to-thickness ratio of circular steel tubes.

2.3 Test setup, loading program and instrumentation

Fig. 4 shows the test setup, where the specimen was placed in a load frame. The foundation beam was clamped to the reaction floor. The top beam was clamped to two hydraulic actuators, one in the horizontal direction and another in the vertical direction. A rigid steel beam was placed between the specimen's top beam and vertical actuators to distribute the vertical load uniformly on the wall section. The vertical actuator could move freely in the horizontal plane to accommodate the lateral displacement of the specimen. A pair of steel beams, which were clamped to the load frame and connected to the wall through rollers, were used to provide the out-of-plane restraint to the wall specimen. A vertical load was applied to the specimen initially and was maintained constantly for the duration of the test. Afterwards, cyclic lateral loads were applied quasi-statically by the actuator mounted horizontally to the reaction wall. The horizontal loading point (i.e., the mid-point of the top beam) was 2750 mm above the base of the wall. The shear span ratio for the wall specimens was 2.5.

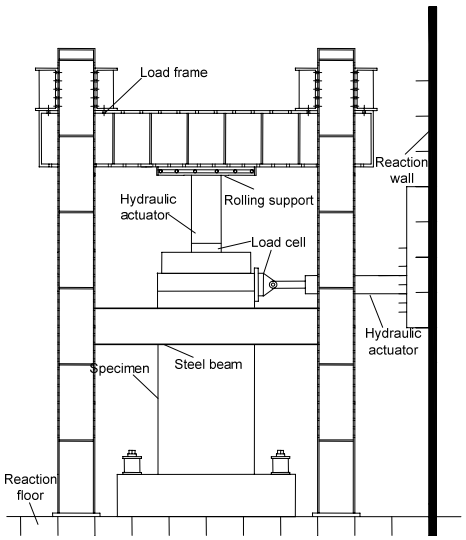


Figure 4. Test setup

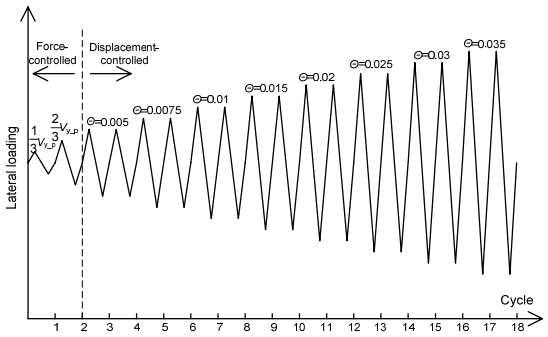


Figure 5. Loading history

Fig. 5 shows the history of lateral cyclic loading for the tests. Before the specimen yielded, the lateral loading was

force-controlled and one cycle was performed at each force level. Two levels were considered in this phase, which were 1/3 and 2/3 the predicted yield load of the specimen $V_{y,p}$. The loading was changed to displacement controlled after the specimen yielded. The lateral displacement of the wall top was monitored by the linear variable differential transformer (LVDT) 1#, as shown in Fig. 6. The displacement was expressed in terms of the drift ratio θ, which was defined as the ratio of the lateral displacement over the height of LVDT 1# relative to the base of the wall (i.e. 2550 mm). The lateral drift ratios increased in the sequence of 0.005, 0.0075, 0.01, 0.015, 0.02, 0.025, 0.03, and 0.035, and two cycles were repeated at each drift level. In each loading cycle, a push was exerted first, followed by a pull, where the push was defined as the positive loading and the pull as the negative loading. The test was terminated when the specimen completely failed due to steel fracture and concrete crushing developing at the base of the wall. Except for Specimen SW1 that failed at 0.03 drift, all other specimens failed at 0.035 drift.

Instrumentation was used to measure the loads, displacements and strains of the specimens. Load cells measured the vertical and lateral loads applied to the specimen. The LVDTs measured the global and local deformations of the specimen. Fig. 6 shows the locations of the LVDTs mounted on the specimen. Four LVDTs (i.e., LVDTs 1# through 4#) measured the lateral displacements at 650 mm intervals along the height of the wall. Two pairs of crossed LVDTs (i.e., LVDTs 5# through 8#) measured the shear deformation of the wall. Three LVDTs (i.e., LVDTs 9# through 11#) were mounted on the foundation beam to monitor any horizontal slip of the foundation beam along the reaction floor and any rocking of foundation beam during the loading. Seven LVDTs (i.e., LVDTs 12# through 18#) were mounted at the base of the wall to measure the local deformation from which the average vertical strains could be estimated. In addition, strain gauges were installed to measure the vertical, horizontal and shear strains of the steel tubes and plates. The gauges were located 20 mm and 500 mm above the base of the wall, as indicated by Sections A and B shown in Fig. 6. The strains of the two tie bolts at the base of the wall were also measured. The measurements were recorded automatically by a computer data acquisition system.

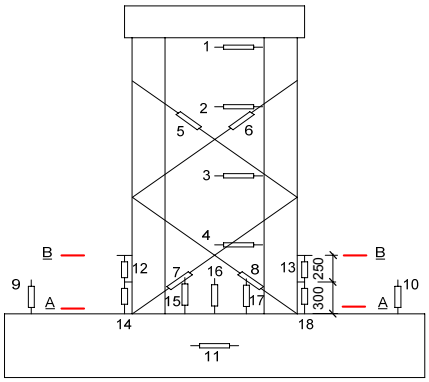


Figure 6. Specimen instrumentation

3. EXPERIMENTAL PROGRAM

3.1 Damage and Failure Mode

The wall specimens experienced similar damage patterns, which included local buckling of steel tubes and steel plates, fracture of steel tubes, and compressive crushing of concrete at the base of the wall. The damage process could be characterized by three stages: the elastic stage, damage developing stage, and failure stage. The damage observed at each stage is summarized as follows.

Elastic stage: This stage began from the onset of testing up to the instant when the lateral drift ratio reached 0.005. The specimens remained nearly elastic in this stage. None of local buckling of steel was observed. The strain measurements indicated that the steel tubes and plates did not yield, except that the steel at two farthest edges of the base of the wall yielded slightly.

Damage developing stage: This stage started from the 0.005 drift to the peak load of the specimens. The rectangular steel tubes sustained slight local buckling at the base of the wall when the drift ratio increased from 0.005 to 0.0075. The local buckling of steel tubes became noticeable upon further loading. The steel plates experienced local buckling at 0.015 drift. The specimens reached their peak loads when the drift ratio increased to approximately 0.02.

Failure stage: This stage began at the peak load and continued to the complete failure of the specimens. At further cycles after the peak load, the existing buckling of steel tubes and steel plates was significantly extended and aggravated, and new buckling occurred. The buckling was located in the region from the base of the wall up to a height equal to 0.5 times the sectional depth of the wall. For Specimen SW1 and SW4, vertical fracture developed along the weld of the compressive rectangular steel tubes at 0.025 drift. For Specimen SW2, SW3 and SW5, the vertical weld fracture occurred at 0.03 drift. The vertical weld fracture in steel tubes was caused by several cycles of large plastic transverse strains induced by the lateral expansion of infilled concrete in compression. Note that the weld quality of the thin steels was not high, which could accelerate the fracture. At further cycles, the steel tube in tension experienced tensile fracture of steel and the fracture was gradually extended in horizontal. Concrete crushing was observed at the base of the wall. Ultimately, the local buckling of the steel tubes interfered with the buckling of the steel plates. The wall specimens lost their vertical load-carrying capacity and suffered a complete failure. Fig. 7 shows photographs of Specimen SW4 post testing. A photograph of the details of a CFST boundary element after the test is shown in Fig. 8, where the buckling of steel tube, vertical weld fracture, horizontal steel fracture, and concrete crushing are annotated.



Figure 7. Photograph of Specimen SW4 after test

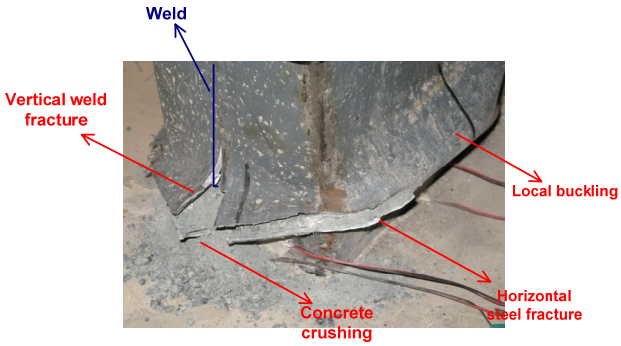
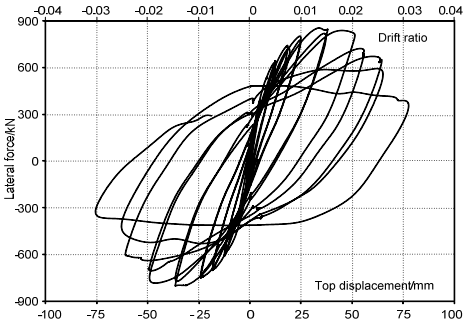


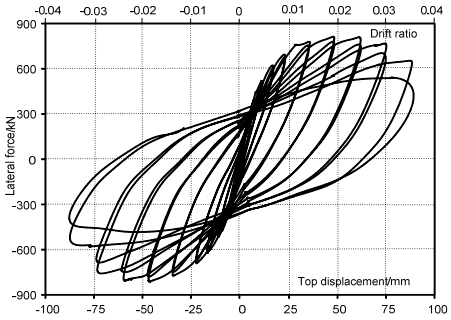
Figure 8. Photograph of CFST boundary element of Specimen SW4 at end of test

3.2 Force-Displacement Relationship

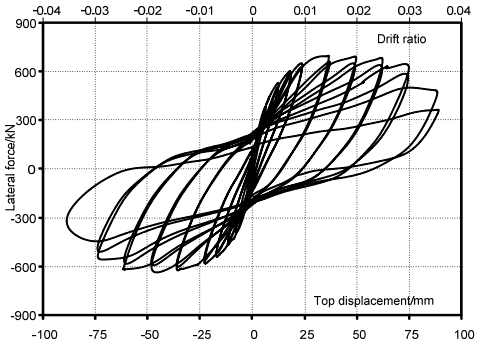
Fig.9 shows the measured lateral force versus top displacement relationships for the specimens. The hysteresis loops of all specimens were plump and not significantly pinched, showing the characteristics of the flexural failure mode. When the loading and unloading within a drift ratio less than 0.005, the hysteretic curves cycled almost linearly with minimal residual displacement. When the drift ratio exceeded 0.005, the loading stiffness clearly decreased and the strength steadily increased. Residual displacement was observed in unloading. After the peak load, the hysteresis curves showed slightly pinching effects, and the residual deformation became more noticeable. The strength of the composite walls dropped slowly, showing an excellent deformation capacity, except for Specimen SW1 that exhibited rapid strength degradation.



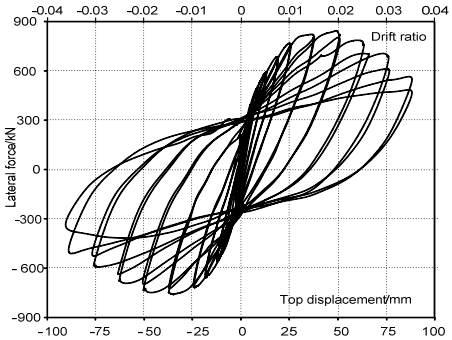
(a)



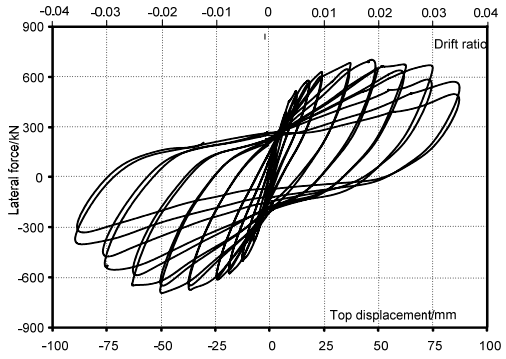
(b)



(c)



(d)



(e)

Figure 9. Hysteresis loops of lateral force versus top displacement relationships of specimens: (a) SW1, (b) SW2, (c) SW3, (d) SW4, and (e) SW5

The top displacement shown in Fig. 9 included the deformations induced both by flexure and by shear. The shear deformations were determined using measurements from the LVDTs placed diagonally from 0 to 1100 mm (i.e., DLVTs 7# and 8#) and from 1100 to 2200 mm (i.e., DLVTs 5# and 6#), as shown in Fig. 6. It is noted that the inelastic shear deformations were limited to the bottom 1100 mm of the wall and that the measurements between 1100 and 2200 mm were essentially elastic. Therefore, the shear deformations between 2200 and 2550 mm were assumed to be proportional to those measured between 1100 and 2200 mm. Fig. 10 shows the estimated shear deformations compared with the total deformations for Specimen SW2. As expected, the shear deformations were relatively small compared with flexure deformations, and they accounted for no more than 20% of the total deformations.

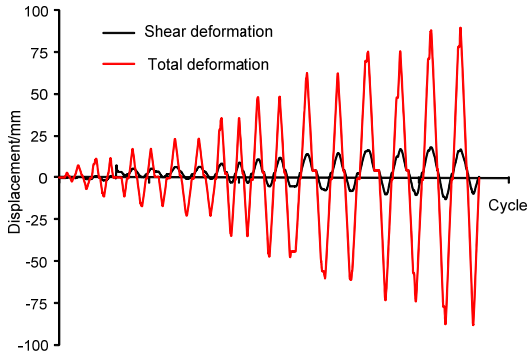


Figure 10. Shear deformations versus total deformation for Specimen SW2

Fig.11 shows the envelope curves of the lateral force versus displacement relationships. All specimens had nearly identical initial stiffness. The difference of the lateral load-carrying capacity and deformation capacity for the specimens will be described later.

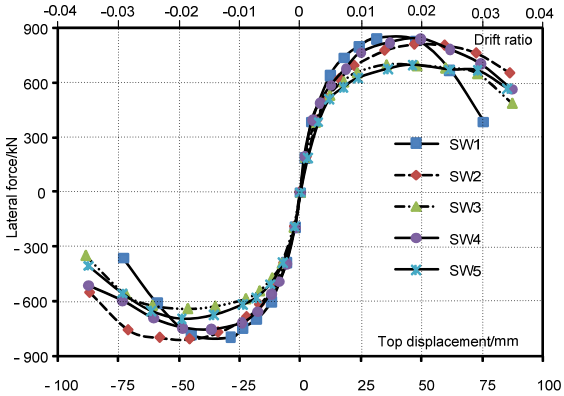


Figure 11. Envelope curves of lateral force versus top displacement of specimens

3.3 Lateral Load-Carrying Capacity

Table 4 shows the measured yield load $V_{y,m}$ and peak load $V_{p,m}$ of the specimens. Note that the values shown in Table 4 were calculated using the average values of the loads measured in the push and pull directions. The yield load point was determined by using the method proposed by Park et al. (1982). The yield loads were approximately 0.75 times the peak loads. Specimens SW1 and SW2 had similar peak loads, indicating that the extent of the CFST boundary element had minimal influence on the lateral load-carrying capacity of the composite walls. The peak load of Specimen SW4 was 20.0% higher than Specimen SW3, indicating that an increase in the area ratio of steel tubes increased the lateral load-carrying capacity of the composite walls. The comparison between Specimens SW4 and SW5 indicates that the presence of circular CFSTs at the boundary elements increased the yield load, and enhanced the peak load by 16.2%.

Table 4 Lateral load-carrying capacity of specimens

Specimen No.	Test results		Evaluated Peak load $V_{p,e}$ (kN)	$V_{p,m}/V_{p,e}$
	Yield load $V_{y,m}$ (kN)	Peak load $V_{p,m}$ (kN)		
SW1	669	814	839	0.97
SW2	614	809	810	1.00
SW3	509	669	630	1.06
SW4	597	799	778	1.03
SW5	532	698	633	1.10

3.4 Deformation Capacity

Table 5 shows the yield displacement Δ_y, ultimate displacement Δ_u, ultimate drift ratio θ_u, and displacement ductility ratio μ_Δ of the specimens. The yield displacement Δ_y was the displacement at the yield load $V_{y,m}$. The ultimate displacement Δ_u was defined as the post-peak displacement at the instance when the lateral load decreased to 85% of the peak load. The ultimate drift ratio was calculated as $\theta_u = \Delta_u / H$, where H was the height of the LVDT 1# relative to the wall base. The displacement ductility ratio was defined as $\mu_\Delta = \Delta_u / \Delta_y$. Note that the values shown in Table 5 were

calculated using the average values of the displacements measured in the push and pull directions.

Table 5 Deformation capacity of specimens

Specimen No.	Yield disp. Δ_y (mm)	Ultimate disp. Δ_u (mm)	Ultimate drift ratio θ_u	Disp. ductility ratio μ_Δ
SW1	13.72	56.12	0.022	4.09
SW2	16.26	79.16	0.031	4.87
SW3	12.45	75.58	0.030	6.07
SW4	13.81	69.84	0.027	5.06
SW5	13.88	75.53	0.030	5.44

Table 5 indicates the following four observations. (1) The ultimate drift ratio of Specimen SW1 was 0.022, much smaller than the ultimate drift ratio of 0.031 for Specimen SW2. It thus indicates that the extent of the CFST boundary element had significant effects on the deformation capacity of the composite walls. (2) The nearly identical ultimate drift ratios for Specimen SW3 through SW5 indicates that the area ratio of steel plates and addition of embedded circular steel tubes had a minimal effect on the wall's deformation capacity. (3) The ultimate displacements for Specimens SW2 through SW5 were similar, whereas the yield displacement of Specimen SW2 was larger than those of Specimens SW3 through SW5. Therefore, an increasing axial force ratio increased the yield displacement and decreased the ductility ratio of the composite walls. (4) When the CFST boundary element's extent was 0.2 times the wall's sectional depth and the test axial force ratio was 0.20 to 0.25, the wall specimens had a yield drift ratio of over 0.005 and an ultimate drift ratio of approximately 0.03.

3.5 Energy Dissipation Capacity

Fig.12 shows the cumulative energy dissipation curves for the specimens. The energy dissipated in each loading cycle is equal to the area enclosed by the corresponding hysteresis loop. The cumulative energy dissipated by Specimen SW1 was 28.6% lower than that of Specimen SW2, because the former had a smaller deformation capacity than the latter. Although the deformation capacity was similar, Specimens SW2 and SW4 showed a larger accumulative energy dissipation capacity than Specimens SW3 and SW5, because the former possessed greater strength than the latter.

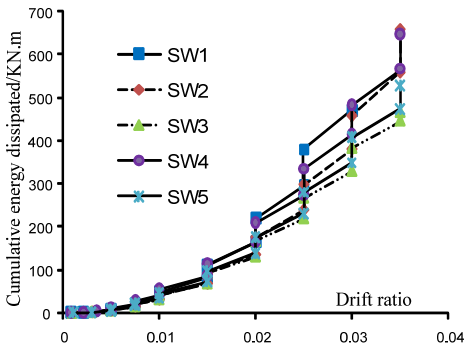


Figure 12. Energy dissipation curves for specimens

4. STRENGTH CAPACITY EVALUATION

Since the specimens displayed a flexure-dominated behavior, the lateral load-carrying capacity could be estimated from the flexure strength at the wall base section. The following assumptions were made in assessing flexural strength. (1) Initially plane sections remained plane after bending. (2) The compressive strength of unconfined concrete f_c was used for the wall concrete, except for the concrete filled in the circular steel tubes for which the strength increased significantly due to the confinement effect. Note that the confinement effect of rectangular steel tubes can not increase the strength of filled concrete, but improve its ductility (Sakino et al. 2004). Tensile strength of concrete was ignored. (3) The internal compressive force of concrete was calculated by using the equivalent rectangular stress block of average stress αf_c and the extent of βx from the extreme compression fiber, where x denotes the neutral axis depth and α and β are two parameters of the equivalent stress block. (5) Steel tubes in two edges yielded in tensile and in compression, respectively. The ultimate strength of steel was used, given the significantly hysteretic strain hardening that developed in the steel tubes. (6) Full plastic stress developed at the steel plates. Considering the relatively small plastic strain developed in steel plates, the yield strength of steel was used and the strain hardening effect was ignored. Fig. 13 illustrates the mechanism for simplified evaluation of the flexure strength of the wall section.

According to the force and moment equilibrium with respect to the wall's centroid, the follow equations were established:

$$N = N_c + N_{CFST} + \left(A_{p,c} - A_{p,t}\right) f_p - A_a^c f_a^c \qquad (3\text{-a})$$

$$M_p = N_c d_c + A_a^r f_a^r \left(h_w - l_c\right) + 0.5\left(N_{CFST} + A_a^c f_a^c\right)\left(h_w - l_c\right) + 0.5A_{p,c} f_p \left(h_w - x - l_c\right) + 0.5A_{p,t} f_p \left(x - l_c\right) \qquad (3\text{-b})$$

where N denotes the axial load applied on the wall; M_p denotes the flexural strength at the wall bottom section under the axial compressive load N; N_c denotes the compression reaction forces provided by the concrete excluding the concrete filled in the circular steel tubes; N_{CFST} denotes the reaction force provided by the circular CFST; $A_{p,c}$ and $A_{p,t}$ denote the gross cross-sectional areas of steel plates in compression and in tension, respectively; A_a^r and A_a^c denote the cross-sectional areas of the rectangular steel tube and the circular tube, respectively, at one boundary element; f_a^r, f_a^c and f_p denote the strengths of rectangular steel tube, circular steel tube and steel plate, respectively; f_c denotes the axial compressive strength of concrete; h_w denotes the depth of the wall section; l_c denotes the extent of the CFST boundary element; d_c denotes the distance between the centroid of the internal compressive force of concrete N_c and the centroid of the wall section; and x denotes the neutral axis depth.

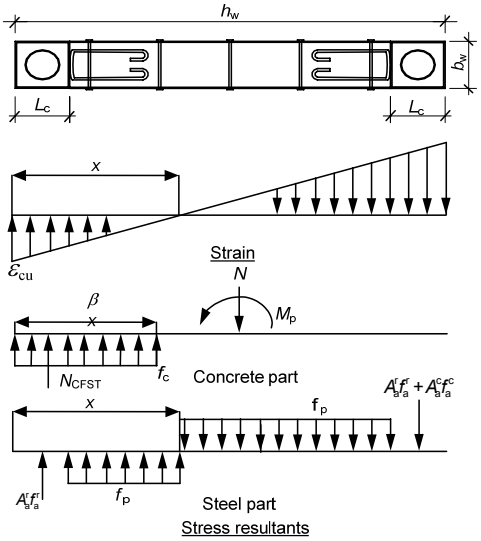


Figure 13. Flexure strength evaluation of wall section

The internal compressive force of concrete was calculated using the equivalent rectangular stress block, given by

$$N_c = \alpha f_c \left(\beta x b_w - A_{CFST} \right) \tag{4}$$

in which, A_{CFST} represents the gross cross-sectional area of the circular CFST; b_w denotes the thickness of the wall section. The value for α factor is taken to be 1.0 for the concrete of which the cubic compressive strength is not higher than C50, and the value of β factor is taken to be 0.85 for the walls (GB 50010-2010).

The compressive force of the circular CFST, N_{CFST}, was calculated by Eq. (5) which took into account the increase of concrete strength due to the confinement provided by the circular steel tube (Specification CECS 28: 1990).

$$N_{CFST} = f_{cor} A_{cor} \left(1 + 1.8\theta \right) \tag{5}$$

in which, f_{cor} and A_{cor} denote the axial compressive strength and cross-sectional area of the concrete filled in the circular steel tube, respectively; and θ denotes the confinement index of the circular CFST.

The flexure strength at the wall bottom section, M_p, was assessed by substituting Eqs. (4) and (5) into Eq. (3) and solving these equations. The lateral load-carrying capacity of the wall was then calculated. Table 4 shows the values of $V_{p,e}$ for the specimens and the comparison with the measured peak lateral load $V_{p,m}$ in the tests. The evaluated results for the composite walls are in good agreement with the test results, with errors no greater than 10%.

5. CONCLUSIONS

This paper proposed an innovative composite wall, named the steel tube-double steel plate-concrete composite wall. A series of quasi-static tests were carried out to examine the seismic behavior of slender composite walls. Major findings and conclusions obtained from this study are summarized as follows:

(1) The slender composite wall specimens failed in a flexural mode, characterized by the buckling of steel tubes and steel plates, fracture of steel tubes, and compressive crushing of concrete at the base of the wall.

(2) The extent of the CFST boundary element significantly affected the seismic behavior of the rectangular composite walls. An increase in the extent of the CFST boundary element increased the wall's deformation and energy dissipation capacities.

(3) The area ratio of steel plates showed a minimal effect on the deformation capacity of the slender composite walls that failed in a flexural mode.

(4) The addition of circular steel tubes embedded in the CFST boundary elements led to an increase in the lateral load-carrying capacity of the composite walls, but it did not increase the wall's deformation capacity.

(5) When the CFST boundary element's extent was 0.2 times the wall's sectional depth and the test axial force ratio applied to the wall was no more than 0.25, the wall specimens showed excellent deformation capacity, with a yield drift ratio of over 0.005 and an ultimate drift ratio of around 0.03.

(6) Simplified formulas were developed to evaluate the lateral load-carrying capacity of the composite walls. The evaluated results for the composite walls showed errors less than 10% when compared with the corresponding test results.

Acknowledgements:
The work presented in this paper was sponsored by the National Natural Science Foundation of China (Grant No. 51008173 and No. 51261120377), and by Tsinghua University Initiative Scientific Research Program (Grants No. 2012THZ02-1 and No. 2010THZ02-1). The writers wish to express their sincere gratitude to the sponsors.

References:

CECS (1990), "Specification of Design and Construction of Concrete-Filled Steel Tubular Structures (CECS 28: 1990)," China Planning Press (in Chinese).

CMC (2010), "Code for Design of Concrete Structures (GB 50010-2010)," China Architecture & Building Press (in Chinese).

CMC (2010), "Code for Seismic Design of Buildings (GB 50011-2010)," China Architecture & Building Press (in Chinese).

Emori, K. (2002), "Compressive and Shear Strength of Concrete Filled Steel Box Wall," *Steel Structures*, **68**(2), 29-40.

Eom, T.S., Park, H.G., Lee, C.H., Kim, J.H., and Chang, I.H. (2009), "Behavior of Double Skin Composite Wall Subjected to In-Plane Cyclic Loading," *Journal of Structural Engineering (ASCE)*, **135**(10), 1239-1249.

Hossain, K.M.A., and Wright, H.D. (2004), "Experimental and theoretical Behaviour of Double Skin Composite Walls under In-Plane Shear," *Journal of Constructional Steel Research*, **60**(1), 59-83.

Liao, F.Y., Han, L.H., Tao, Z. (2009), "Seismic Behaviour of Circular CFST Columns and RC Shear Wall Mixed Structures: Experiment," *Journal of Constructional Steel Research*, **65**(8-9), 1582-1596.

Park, R., Priestley, M.J.N., and Gill, W.D. (1982), "Ductility of Square-Confined Concrete Columns," *Journal of the Structural Division (ASCE)*, **108**(4): 929-950.

Qian, J., Jiang, Z., and Ji, X. (2012) "Behavior of Steel

Tube-Reinforced Concrete Composite Walls Subjected to High Axial Force and Cyclic Loading," *Engineering Structures*, **36**(3), 173-184.

Sakino, K., Nakahara, H., Morino, S., and Nishiyama, I. (2004), "Behavior of Centrally Loaded Concrete-Filled Steel Tube Short Column," *Journal of Structural Engineering (ASCE)*, **130**(2), 180-188.

Tong, X.D., Hajjar, J.F., Schultz, A.E., and Shield, C.K. (2005), "Cyclic Behavior of Steel Frame Structures with Composite Reinforced Concrete Infill Walls and Partially-Restrained Connections," *Journal of Constructional Steel Research*, **61**(4), 531-552.

Wallace, J.W., Orakcal, K., Cherlin, M.E., and Sayre, B.L. (2000), "Lateral-Load Behavior of Shear Walls with Structural Steel Boundary Columns," *Proceedings of Sixth ASCCS Conference on Composite and Hybrid Structures*, Los Angeles, USA: 801-808.

Zhao, Q.H. and Abolhassan, A.A. (2004), "Cyclic Behavior of Traditional and Innovative Composite Shear Wall," *Journal of Structural Engineering (ASCE)*, **130**(2), 271-285.

10CUEE CONFERENCE PROCEEDINGS
10th International Conference on Urban Earthquake Engineering
March 1-2, 2013, Tokyo Institute of Technology, Tokyo, Japan

VIBRATION TESTS ON SINGLE LAYER LATTICE DOMES SUBJECTED TO HORIZONTAL BI-DIRECTIONAL EARTHQUAKE MOTIONS

Tomohiko Kumagai [1], Takunori Ozawa [2], Toru Takeuchi [3], and Toshiyuki Ogawa [3]

1) Assistant Professor, Department of Architecture and Building Engineering, Tokyo Institute of Technology, Japan
2) Structural Engineer, Structural Engineering Department, Nikken Sekkei Ltd, Tokyo, Japan
3) Professor, Department of Architecture and Building Engineering, Tokyo Institute of Technology, Japan
kuma@arch.titech.ac.jp, ozawa.takunori@nikken.co.jp, ttoru@arch.titech.ac.jp, togawa@arch.titech.ac.jp

Abstract: There are many studies for seismic response behavior of lattice domes. Static seismic loads in consideration with vertical responses subjected to horizontal seismic waves are proposed in recent years. However, there are few studies dealing with actual response behavior of lattice domes by vibration tests. The seismic response behavior subjected to multi-directional input is not particularly investigated. Therefore, this paper is intended as an investigation of elastic seismic response behavior of single layer lattice domes subjected to horizontal bi-directional inputs by vibrational tests using small-scale models. In examination, the effects of phase difference between input waves and ratios of natural period of substructure to that of roof structure on response behavior are made clear. In addition, the evaluation methods for response accelerations those are adjusted to responses under horizontal bi-directional inputs are proposed.

1. INTRODUCTION

The lattice domes are used for the roofs of a gymnasium, an exhibition hall and so on. These structures are also used for evacuation facility and disaster prevention base in a time of disaster such as an earthquake or a typhoon. Therefore, it is hoped that these structures have sufficient earthquake performance for resisting large earthquake motions. For that purpose, there are many studies for seismic response behavior of lattice domes ((Kato and Mukaiyama 1996, Ogawa et al. 2003). Static seismic loads in consideration with vertical responses subjected to horizontal seismic waves are proposed in recent years (Takeuchi et al. 2004, Takeuchi et al. 2007). However, there are few studies dealing with actual response behavior of lattice domes by vibration tests (Maeda et al. 1999). The seismic response behavior subjected to multi-directional input is not particularly investigated. Therefore, this paper is intended as an investigation of elastic seismic response behavior of single layer lattice domes subjected to horizontal bi-directional inputs by vibrational tests using small scale models. In examination, the effects of phase difference between input waves and ratios of natural period of substructure to that of roof structure on response behavior are made clear. In addition, the evaluation methods for response accelerations those are adjusted to responses under horizontal bi-directional inputs are proposed.

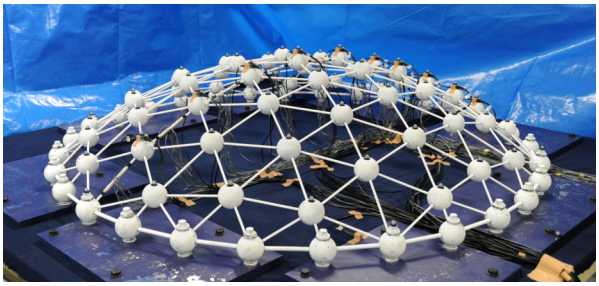


Photo 1 Experimental Model

2. OUTLINES OF VIBRATION TESTS ON SINGLE LAYER LATTICE DOME

The experimental model is the single layer lattice dome as shown in Photo 1 and Fig.1. The model consists of the ball joint system. The nodes of ball joint are steel balls with ϕ 63.5mm. The members of dome are acrylic resin (PMMA) round bar with ϕ 6.0mm. The steel balls and round bars are

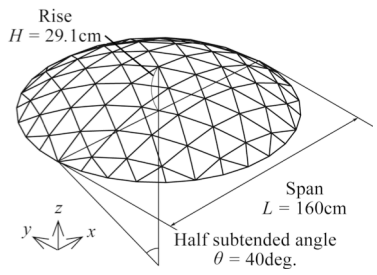


Figure 1 Shape of Single Layer Lattice Dome

Table 1 Results of Tension Test for Members and Bending Tests for Joints

Material (Diameter ϕ(mm))	Young's modulus E [N/mm^2]	Yield stress σ [N/mm^2]	Stiffness of rotational spring K_B [Nm/rad]	Dimensionless spring constant κ
PMMA(6.0)	4200	53.9	58.4	46.5

joined with the epoxy resin adhesives. For the boundary condition, the nodes of boundary of dome are pin supported by using the spherical washers. Table 1 shows the results of tension tests for members and bending tests for joints. The bending tests for joints are carried out as a simple beam test under concentrated loading.

Table 2 shows the parameters for experiments. The input directions of input waves are the uni-direction in NS direction, the uni-direction in EW direction and the bi-direction in NS and EW directions. The ratios R_T of the natural period of equivalent single mass system T_{eq} to the predominant natural period of dome structure T_R are adjusted to 0, 1 and 1.2. The names of models are defined as R_T =(the natural period ratio R_T), for example R_T=1 model. The parameter for bi-directional input is the phase differences between inputs in NS direction and EW direction. The phase differences are dealt with as the time differences, these time differences are represented by putting the time base of input wave in EW direction forward $-T_R/4 \sim +T_R/4$ ($T_R/8$ intervals). The input waves are are sine waves and JMA Kobe NS & EW (1995) which is an observed earthquake motion. At R_T=1, 1.2 models, the response accelerations of equivalent single mass system with period $T_{eq} = T_R$, $1.2T_R$ subjected to earthquake motions are used for input earthquake motion for vibration tests. The maximum accelerations of input earthquake motions A_{gmax} are standardized to be 300 cm/s^2 for R_T=0, 100 cm/s^2 for R_T=1, 1.2. The period of sine waves are set based on the natural period of dome structure T_R. The shaking table with bi-axis shaking systems of permanent magnet type (San-Esu Co., Ltd.) is used for the vibration tests.

Table 2 Parameters for Experiments

Input direction	Uni-directional input (NS direction) Uni-directional input (EW direction) Bi-directional input (NS & EW directions)
Natural period ratio R_T	0, 1, 1.2
Time differences between inputs for NS direction and EW direction	$-T_R/4$, $-T_R/8$ 0, $+T_R/8$, $+T_R/4$

At the design of experimental model, the law of similarity shown by following equations (1)~(4) (Matsuoka et al. 2006) are used.

$$T_m = \frac{1}{\lambda}\sqrt{\frac{\mu}{\rho}}T_p \quad (1)$$

$$\sigma_m = \frac{1}{\rho\alpha\lambda}\sigma_p \quad (2)$$

$$\varepsilon_m = \frac{\mu}{\rho\alpha\lambda}\varepsilon_p \quad (3)$$

$$\delta_m = \frac{\mu}{\rho\alpha\lambda^2}\delta_p \quad (4)$$

Table 3 shows the scale ratio of scale model to full-scale structure.

The supposed full-scale model is the single layer lattice dome with span of 70 m and natural period of 0.34 sec. The time axes of earthquake motions are shortened in one-ninth (1/9) by following the law of similarity. The positions for measurements are shown in Fig.2. The responses of dome structure are measured with the accelerometers, the motion capture systems (MC) and the strain gauges. The response accelerations in x, y and z directions are measured with the accelerometers and obtained by differentiating the measured displacements by MC twice with respect to time t. The out-of-plane and in-plane strains of ends of members are measured with the strain gauges. The absolute displacements of shaking table are measured with the laser displacement sensors.

Table 3 Parameters for Experiments

	Scale ratio	
Dimension	$1/\lambda=L_m/L_p$	1/44
Weight per unit volume	$1/\rho=\rho_m/\rho_p$	1/2.0
Young's modulus	$1/\mu=E_m/E_p$	1/49
Acceleration	$1/\alpha=\alpha_m/\alpha_p$	1/1.0
Stress	σ_m/σ_p	1/88
Strain	$\varepsilon_m/\varepsilon_p$	1/1.8
Deformation	δ_m/δ_p	1/79
Period	T_m/T_p	1/8.9

*Subscripts m and p represent the scale model and the full-scale model respectively.

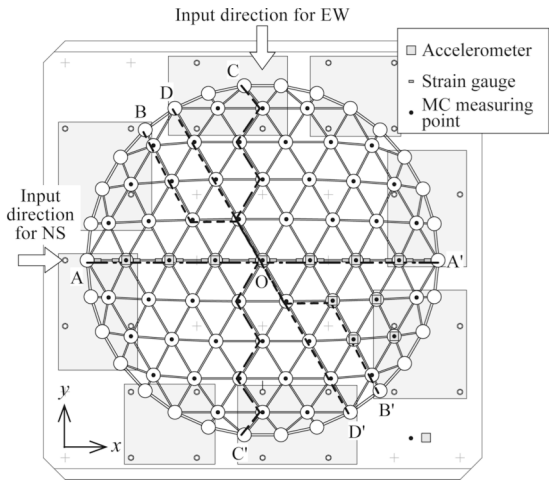


Figure 2 Positions for Measurements

3. VIBRATIONAL CHARACTERISTICS OF SINGLE LAYER LATTICE DOME

The eigenmodes of dome structure are measured by inputting sweep waves and sine waves. The natural periods are obtained from the predominant periods at Fourier spectra of the responses under sweeping sine waves. The mode order is determined by the length of period of mode. The shapes of eigenmode are obtained by inputting the sine wave with natural period of each mode.

Fig.3 shows the time history of strain of end of member and the damping factors at each amplitude ratio in free vibration. The damping factors are calculated from the amplitude ratios of strains in free vibration. The amplitude dependence occurs in the relationships between the damping factor and the amplitude of strain.

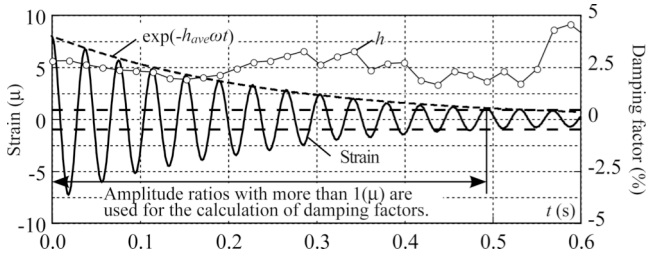


Figure 3 Time History of Strain of End of Member and Damping Factors at Each Amplitude Ratio in Free Vibration

Fig.4 shows the natural vibrational characteristics of dome structure. In the figures, the shapes of eigenmode, the natural periods, the damping factors, the phase differences between the nodes are indicated. The shapes of eigenmodes with maximum amplitude at all nodes are shown in figures because the phase differences are observed. The angles of phase differences are shown based on the phase of input wave. The lengths of straight line in figures represent the amplitudes. The amplitude ratios for calculating the damping factors are the average of amplitude ratios of strains with more than 1 μ. The damping factors in y direction are larger than those in x direction. The shapes of modes are close to the shapes with antisymmetrical 1 wave in any modes. However, the local deformations are observed at the shapes of higher order modes. The angles of phase differences between the nodes placed in symmetry about node O are about 180 deg. (opposite phase) in x direction. On the other hand, those are 140 ~ 270 deg. in y direction. In addition, the angles of phase differences between the nodes adjoining each other are small in x direction. The phases of these nodes are almost in coordinate phase. On the other hand, in y direction, the phase differences of these nodes are observed.

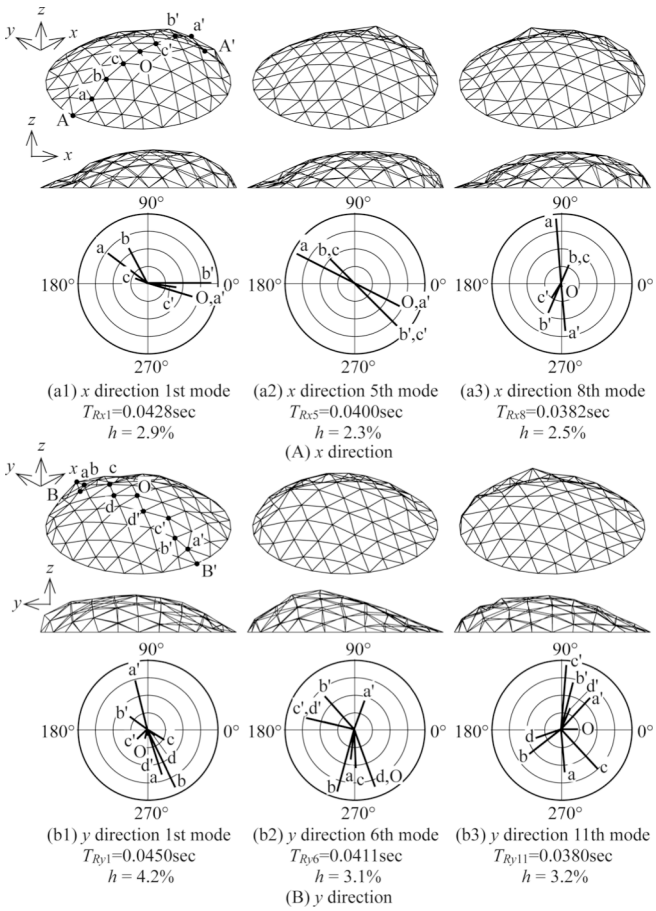


Figure 4 Natural Vibrational Characteristics of Dome Structure

Fig. 5 shows the vertical response magnification factors at node with maximum response of dome structure subjected to sine wave with natural period of each mode. There are a lot of predominant modes in narrow periodic band around 0.038 sec regardless of input direction. The average of periods of predominant modes in x and y directions are adopted as the period of dome structure T_R. In this experiments, the period T_R is 0.0381 sec which is the average of 8th mode in x direction and 11th mode in y direction.

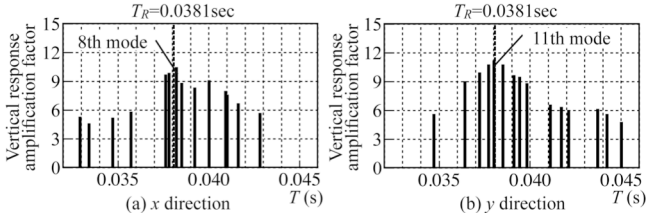


Figure 5 Vertical Response Magnification Factors at Node with Maximum Response Subjected to Sine Wave with Natural Period of Each Mode

4. SEISMIC RESPONSE BEHAVIOR OF SINGLE LAYER LATTICE DOME

4.1 Comparisons between Response Behavior under Uni-directional Input and that under Bi-directional Input

In this section, the response behavior under uni-directional input is compared with that under bi-directional input. The maximum vertical response acceleration magnification factors on line DOD' under sine waves with phase differences $T_p = +T_R/8, +T_R/4$ are shown in Fig.6. The distributions of maximum vertical response acceleration magnification factors on entire dome roof under sine wave with phase difference $T_p = +T_R/8$ are shown in Fig.7. The distributions of response magnification factors under bi-directional input obtained as the sum of time

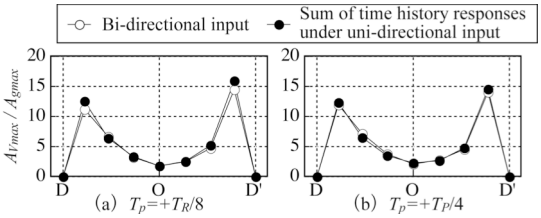


Figure 6 Maximum Vertical Response Acceleration Magnification Factors (line DOD', Sine Waves with Phase Differences $T_p = +T_R/8, +T_R/4$)

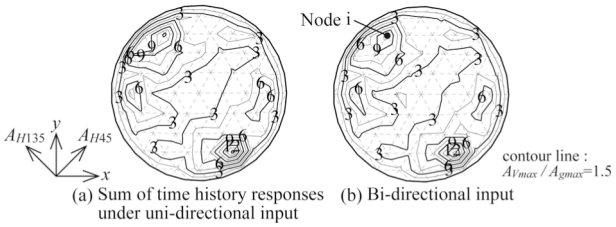


Figure 7 Distributions of Maximum Vertical Response Acceleration Magnification Factors (Sine Wave with Phase Difference $T_p = +T_R/8$)

history responses under uni-directional input are indicated in these figures. The response magnification factors are the response accelerations divided by the maximum input acceleration A_{gmax}. The distributions obtained as the sum of responses under uni-directional input are in agreement with the distributions under bi-directional input. However, the response magnification factors obtained as the sum of responses under uni-directional input disagree slightly with the distributions under bi-directional input at nodes with large responses. Fig.8 shows the time history horizontal response accelerations at node i those are decomposed in the directions A_{H135} and A_{H45} (shown in Fig.7). The horizontal responses under bi-directional input are smaller than the sum of responses under uni-directional input regardless of the direction of response. That is to say that the responses under bi-directional input are smaller than the sum of responses under uni-directional input regardless of the magnitude and direction of input acceleration vector of bi-directional input.

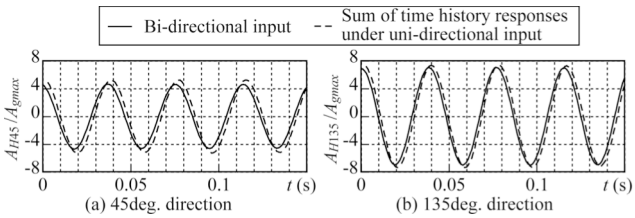


Figure 8 Time History Horizontal Response Accelerations at Node i (Decomposition in the directions A_{H135} and A_{H45}, Sine Wave with Phase Difference $T_p = +T_R/8$))

4.2 Effects of Natural Period Ratio on Response Behavior

In this section, the effects of the natural period ratio R_T on seismic response behavior of single layer lattice dome are examined. Fig.9 shows the maximum vertical response acceleration magnification factors on lines AOA'~ COC' under bi-directional input of JMA Kobe. The angle of phase difference shown in figures is about 90 deg. that the locus of input acceleration is a circular locus. The response magnification factors of R_T=1 are largest, those of R_T=0 are smallest. The shapes of distribution are the shape with large response at the periphery of dome at R_T=1, on the other hand, the shape with long wavelength at R_T=1.2. The distribution shape of R_T=1.2 is similar to the shape of 1st mode in x direction. Fig.10 shows the Fourier spectra for vertical response accelerations at nodes with maximum responses

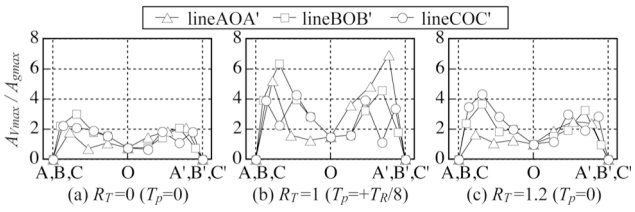


Figure 9 Maximum Vertical Response Acceleration Magnification Factors for Each R_T (lines AOA'~ COC', Bi-directional Input of JMA Kobe)

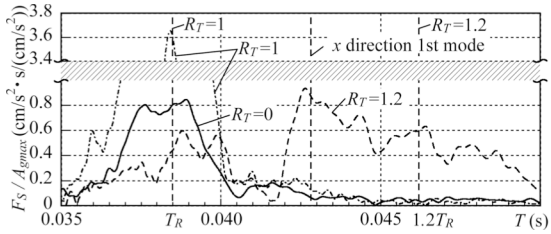


Figure 10 Fourier Spectra for Vertical Response Accelerations at Nodes with Maximum Responses for Each R_T (Bi-directional Input of JMA Kobe)

for each natural period ratio. The Fourier spectra are divided by the maximum input acceleration. The spectrum levels of R_T=1.2 are larger at 1.2T_R (the period of input wave) and the period of 1st mode in x direction. The spectrum of R_T=1 has peak value only at T_R, that of R_T=0 is large in the range of vicinity of T_R.

4.3 Effects of Phase Difference between Input Seismic Waves of Bi-directional Input on Response Behavior

The distributions of maximum vertical response acceleration magnification factors on entire dome roof under seismic waves with phase differences T_p = -T_R/8, 0, +T_R/8 are shown in Fig.11. The responses of R_T=1 model are indicated in figures. The loci of input accelerations for each T_p are shown in the upper right of each figure. The large responses occur at a lot of nodes at $T_p = +T_R/8$ that the locus of input acceleration is a circular locus. On the other hand at $T_p = -T_R/8$ that the locus of input acceleration is a linear locus, the large responses occur only at a few nodes. From the above, it follows that the distribution and the nodes with larger response vary according to the phase difference T_p.

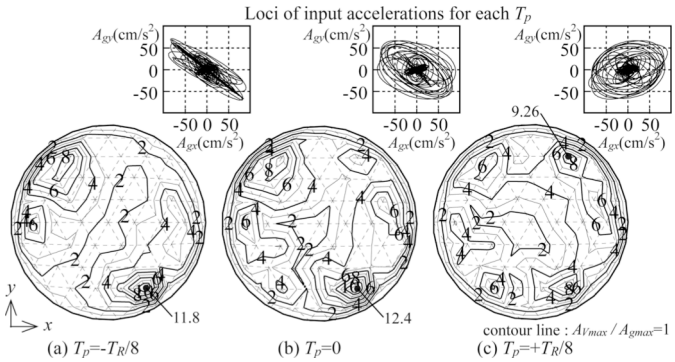


Figure 11 Distributions of Maximum Vertical Response Acceleration Magnification Factors for Each T_p (R_T=1, Bi-directional Input of JMA Kobe)

5. PROPOSITION OF RESPONSE ACCELERATION EVALUATION METHOD ADAPTED TO HORIZONTAL BI-DIRECTIONAL EARTHQUAKE MOTION

In this chapter, the response acceleration evaluation method adapted to the horizontal bi-directional earthquake motion is proposed.

First, the response accelerations under bi-directional input are estimated by adding the time history responses under uni-directional input in NS and EW directions. The input seismic wave is JMA Kobe. The comparisons between the maximum responses of estimated results and those of experimental values under bi-directional input are shown in Fig.12. Although a few differences are observed, the maximum responses of estimated results agree with the responses under bi-directional input, as mentioned in section 4.1.

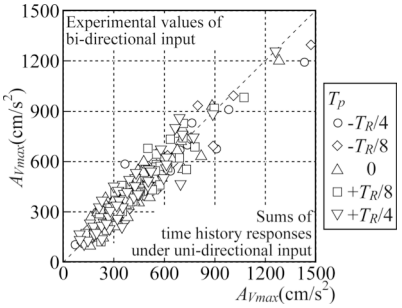


Figure 12 Comparisons between Maximum Responses of Sum of Time History Responses under Uni-directional Input and Those of Experimental Values under Bi-directional Input (R_I=1, JMA Kobe)

Next, the response accelerations under bi-directional input are calculated by square root of sum of squares (SRSS) of the maximum response accelerations under uni-directional input in NS and EW directions. Fig.13 shows the comparisons between the calculated maximum responses and the maximum responses of experimental values under bi-directional input. The calculated results are in approximate agreement with the maximum responses under bi-directional input. However, the nodes whose calculated results are disagreement with the results under bi-directional input are found.

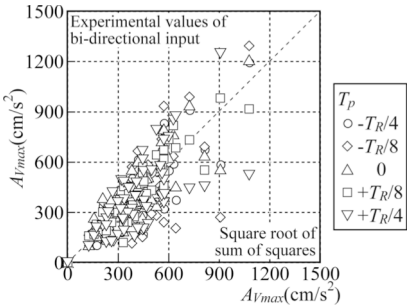


Figure 13 Comparisons between Square Root of Sum of Squares (SRSS) of Maximum Response Accelerations under Uni-directional Input in NS and EW directions and Maximum Responses of Experimental Values under Bi-directional Input (R_I=1, JMA Kobe)

Finally, the reconstructions of the instantaneous distributions when the maximum response accelerations occur are attempted by using the two vibration modes. The response accelerations of top of column for substructure are able to treat as the sine wave with specific period. Therefore it is supposed that the input waves to dome roof are represented as the periodic functions (equations (5) and (6)).

$$A_{NS}(t)=A_{NS}\sin(2\pi ft) \tag{5}$$

$$A_{EW}(t)=A_{EW}\sin(2\pi ft+\theta) \tag{6}$$

where A_{NS} and A_{EW} are the maximum accelerations of input waves, θ is the angles of phase differences between inputs in NS direction and EW direction.

it is supposed that the maximum response accelerations occur by the input accelerations at the time t' when the Euclidean norm of input acceleration comes to the maximum value, then the response acceleration for each node of dome roof under bi-directional input is evaluated by equation (7).

$$A_{2i}=\frac{A_{NS}(t')\cdot amp_{xi}\cdot Sa_{earthNS}+A_{EW}(t')\cdot amp_{yi}\cdot Sa_{earthEW}}{Sa_{sine}} \tag{7}$$

where amp_{xi} and amp_{yi} are the amplification factor for each node of the mode which appears in accordance with the period with input wave, Sa_{earth} and Sa_{sine} are the values of acceleration response spectra of input seismic wave and sine wave respectively.

Fig.14 shows the shapes of modes used for the evaluation and the distributions of response acceleration calculated by evaluation method and by vibration test under bi-directional input. Fig.15 shows the comparisons between the response accelerations obtained by evaluation method

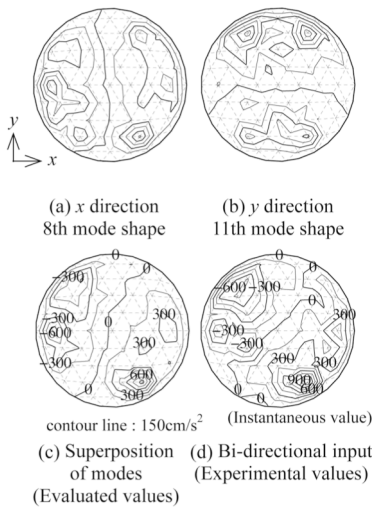


Figure 14 Shapes of Modes Used for Evaluation and Distributions of Response Acceleration Calculated by Evaluation Method and by Vibration Test under Bi-directional Input (R_I=1, T_p=0, JMA Kobe)

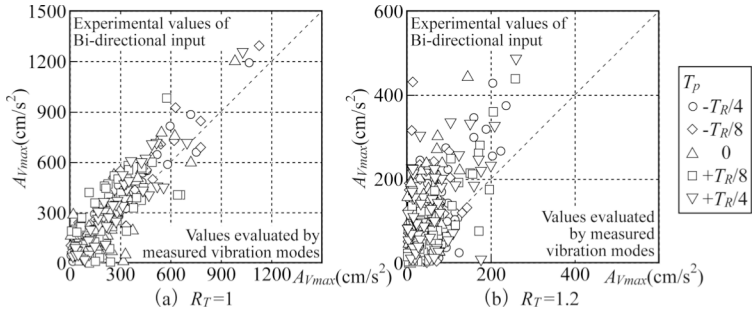


Figure 15 Comparisons between Response Accelerations Obtained by Evaluation Method Which Uses Two Vibration Modes and Those by Vibration Tests under Bi-directional Input (JMA Kobe)

and those by vibration tests under bi-directional input. At R_T=1 model the evaluated results are in approximate agreement with the response accelerations by vibration tests under bi-directional input. However, at R_T=1.2 model the response accelerations by vibration tests are larger than the evaluated results. It is for this reason that the plural modes excite at R_T=1.2 model as shown in Fig.10.

6. CONCLUSIONS

It is concluded as follows, from the above results.

1) At the single layer lattice dome with a lot of vibrational modes in narrow periodic band when the natural period of substructure (equivalent single mass system) is equal to that of predominant mode of roof structure (natural period ratio R_T=1), the response magnification factor becomes large.
2) The phase difference between input waves of horizontal bi-directional input affects the distributions of maximum response accelerations and the node at which the maximum response occurs.
3) The distribution of maximum response accelerations under bi-directional input estimated by adding the time history responses under uni-directional input agrees with the distribution of maximum response accelerations under bi-directional input.
4) When the natural period ratio R_T is 1, the distribution of response accelerations under bi-directional input evaluated by using the two vibration modes is in approximate agreement with the distribution of response accelerations under bi-directional input at the time when the maximum response acceleration occurs.

Acknowledgements:

The present paper was supported in part by a grant from Grant-in-Aid for Young Scientists (B) (Research No.21760427) by Japan Society for the Promotion of Science (JSPS). The experiments in this paper are carried out using the facility by JSPS the 21st Century COE Program "Evolution of Urban Earthquake Engineering".

References:

Kato, S. and Mukaiyama, Y. (1996), "Dynamic Behaviour of Low-rise Single Layered Domes Subjected to Earthquake Motions," Jour. of Structural and Construction Engineering (Transaction of AIJ), No.488, 87-96. (In Japanese)

Ogawa, T., Nakagawa, M. and Kumagai, T. (2003), "Earthquake Response Analysis of Single Layer Lattice Domes with Response Spectrum Analysis," Jour. of Structural Engineering, Vol.49B, 291-296. (In Japanese)

Takeuchi, T., Ogawa, T., Nakagawa, M. and Kumagai, T. (2004), "Response Evaluation of Medium-Span Lattice Domes with Substructures Using Response Spectrum Analysis," Shell and Spatial Structures from Models to Realization, IASS2004 symposium, Montpellier, TP076 (CD-ROM 1-8)

Takeuchi, T., Ogawa, T. and Kumagai, T. (2007), "Seismic Response Evaluation of Lattice Shell Roofs using Amplification Factors," Journal of the International Association for Shell and Spatial Structures, Vol. 48 n. 3, n. 160, 197-210.

Maeda, S., Watanabe, K., Hiyama, Y and Takashima, H. (1999), "Buckling Behavior of Ball Jointed Single Layer Reticular Domes Using Aluminum Alloys : Part3. Free vibration tests," *Summaries of Technical Papers of Annual Meeting Architectural Institute of Japan*, Vol.**B**, 947-948. (In Japanese)

Matsuoka, Y., Takeuchi, T., Kasai, K and Midorikawa, M. (2006), "About the Test-bed for Experiments on Innovative Systems Vol. 2 : E-Defense Experimental Projects for Steel Buildings - Part 5," *Summaries of Technical Papers of Annual Meeting Architectural Institute of Japan*, Vol.**C**, 705-706. (In Japanese)

10CUEE CONFERENCE PROCEEDINGS
10th International Conference on Urban Earthquake Engineering
March 1-2, 2013, Tokyo Institute of Technology, Tokyo, Japan

DAMAGE DETECTION FOR STEEL STRUCTURES USING THE HILBERT-HUANG TRANSFORM APPROACH

Wen-Ko Hsu[1)], Dung-Jiang Chiou[1)]

1) Research Center for Hazard Mitigation and Prevention, National Central University, Jhung-li, Taoyuan County, Taiwan, R.O.C.

Abstract: The objective of this study is to examine the relationship between structural damage and sensitivity indices using the Hilbert-Huang transform (HHT) method. Two damage detection indices are proposed: the ratio of bandwidth (RB), and the ratio of effective stiffness (RES). The nonlinear four bays multiple degree of freedom models with various predominant frequencies are constructed using the SAP2000 program. Adjusted PGA earthquake data (Japan 311, Chi-Chi 921) are used as the excitations. Next, the damage detection indices obtained using the HHT and the fast Fourier transform (FFT) methods are evaluated based on the acceleration responses of the structures to earthquakes. Simulation results indicate that, the column of the 1st floor is the first yielding position and the RB value is changed when the RES<90% in all cases. Moreover, the RB value of the 1st floor changes more sensitive than those from the top floor. In addition, when the structural response is nonlinear (i.e., RES<100%), the RB and the RES curves indicate the incremental change in the HHT spectra. However, the same phenomenon can be found from FFT spectra only when the stiffness reduction is large enough. Therefore, the RB estimated from the smoothed HHT spectra is an effective and sensitive index for detecting structural damage.

1. INTRODUCTION

Structural health monitoring (SHM) has received considerable attention recently in structural engineering. While SHM attempts to detect structural damage in buildings, various approaches have been developed for detecting damage based on various methods (Sun et al. 2002, Lei et al. 2003, Rucka et al. 2006, Ren et al. 2008, Nair et al. 2009 and Akanshu et al. 2010).

It has been proposed in several previous studies that the empirical mode decomposition (EMD) and Hilbert–Huang transform (HHT) methods can be used for nonstationary and nonlinear time series analysis (Huang et al., 1998, 1999). This method has also been extensively adopted for the detection of structural damage. Based on EMD and HHT, Yang et al. (2003a) proposed a linear least-square fit procedure to identify the natural frequency and damping ratio from the instantaneous amplitude and phase angle for each modal response. Frequently, all eigenvalues and eigenvectors of linear structures are found to be complex (Yang et al. 2003b). The HHT based method has been extended further to identify general linear structures with complex modes using the free vibration response data polluted by noise. Although structural damage information is generally extracted from the measured data, recorded acceleration data in the damage location normally have a discontinuity relationship when the damage event occurs. Huang et al. (1998, 1999) showed the feasibility of using EMD and HHT to decompose a signal in the time-frequency domain more precisely than wavelet analysis can. Consequently, two methods were proposed based on EMD and HHT for detecting structural damage (Yang et al. 2004). The first method extracts damage spikes due to a sudden change of structural stiffness from the measured data. The damage time instant and damage locations can then be detected. The second method can detect the damage time instant and determine the natural frequencies and damping ratios of the structure before and after damage. These two proposed methods are then applied to a benchmark problem. According to those results, the proposed methods can detect damage and evaluate related structures efficiently.

However, the mode mixing problem often occurs with the HHT method when intermittency is involved in the data. A new ensemble empirical mode decomposition (EEMD) method (Wu and Huang 2004) was proposed to overcome the intermittence phenomenon. The latest new HHT ensemble skills method has been utilized to analyze the Tai-power Building's strong-motion station records from 1994-2006 (Su et al. 2008). According to those results, the acceleration relations between the basement and the 27th story (top) are not proportional, even when the building maintains elasticity. The relationship between structural damage and the sensitivity indices is obtained using the HHT method (Chiang et al. 2011). Three sensitivity indices are proposed: the ratio of rotation (RR), the ratio of shifting value (SV) and the ratio of bandwidth (RB). Simulation results indicate that the RB obtained from the HHT spectra displays a trend of incremental change with an increasing RR, making it an effective and sensitive index for detecting structural damage. Next, a damage index, the ratio of bandwidth (RB) is used to demonstrate the effectiveness from real steel models for detecting structural damage

(Chiou et al. 2011). Results indicate that, when the response of the structure is in the elastic region, the RB value only slightly changes in both the HHT and the fast Fourier transform (FFT) spectra. Additionally, RB values estimated from the HHT spectra vs. the PGA values change incrementally when the structure response is nonlinear i.e., member yielding occurs, but not in the RB curve from the FFT spectra.

Tang (et al. 2011) proposed a different damage detection index, the ratio of equivalent damping ratio (RED). It is evaluated using the FFT and HHT methods for analysis of the shaking table test data obtained from the benchmark models. The results show that the RED estimated from the smoothed HHT spectra is an effective and sensitive index for detecting structural damage. Furthermore, the changes in RED present more sensitivity at the top floor than other floors. The proposed RED strategy will be used to establish an on-line health monitoring scheme for detecting structural damage in steel structures right after the occurrence of ground motion. Atul (et al. 2011) propose an improved HHT combined with wavelet packet decomposition for diagnosis of damage in structures. Numerical simulation studies have been conducted by solving a bridge girder as a numerical example to validate the proposed time series analysis based damage diagnostic method. Results present the combined wavelet packet and EMD based sifting process can successfully decompose a signal into components with simple frequency content.

Referring to the results of Chiang (et al. 2011) and Tang (et al. 2011), the single bay MDOF models are constructed to obtain the acceleration spectra based on the HHT and FFT methods during earthquakes. In fact, a multiple bays model can be found easily in a real structure. Whether the damage detection index, RB (or RED) proposed by Chiang (et al. 2011) keeping provide the sensitivity of damage detection in a complex structure or not, the objective of this study is to discuss the relationship between RB and the change of ratio of effective stiffness, RES for four bays steel structure subjected to earthquakes. First, the three, five and ten story four bays steel models are established using the SAP2000 program. Two types time history earthquake data (Japan 311, Chi-Chi 921) are adopted as the excitations. Next, the rotational stiffness of columns of these structures is then simulated using Wen's model (Wen 1976). The nonlinear time history analysis is used to generate the acceleration data from models. Then the damage indices, RB and RES can be obtained from HHT and FFT spectra separately based on the acceleration responses of the structures to earthquakes. Additionally, Tang (et al. 2011) shows the trend of RB in top floor is more sensitive than other floors while the nonlinearity is happened to a structure. In this study, the change of RB in the first yielding floor will be discussed with the top floor deeply to demonstrate the RB of roof provides more sensitivity than other floors.

2. Hilbert -Huang Transformation (HHT)

The HHT, developed by Huang et al. (Huang *et al*. 1998, 1999), consists of a two step-empirical mode decomposition (EMD) and the Hilbert spectral analysis (HSA). The principles and procedures for the HHT method are briefly summarized in this section. Detailed information can be found in the quoted references (Huang *et al*. 1998, 1999).

The EMD method involves the extraction of the IMFs from a given time series.Once all IMFs are sifted from a given signal $x(t)$, it can be expressed as follows:

$$x(t)=\sum_{i=1}^{n} c_i(t)+r_n(t) \tag{1}$$

where n is the total number of the IMFs, and $r_n(t)$ denotes the final residue which represents the DC component containing the overall trend of $x(t)$. The $c_i(t)$ are almost orthogonal to each other and have nearly zero means.

For an arbitrary time series $X(t)$, the Hilbert transformation, $Y(t)$, is defined as follows:

$$Y(t)=\frac{1}{\pi} P\int_{-\infty}^{\infty}\frac{X(t')}{t-t'}dt' \tag{2}$$

where P indicates the Cauchy principal value.
With this definition, $X(t)$ and $Y(t)$ can be combined to form the analytical signal $Z(t)$

$$Z(t)=X(t)+iY(t)=a(t)e^{i\theta(t)} \tag{3}$$

where

$$a(t)=\left[X^2(t)+Y^2(t)\right]^{1/2}$$

$$\theta(t)=\arctan\left(\frac{Y(t)}{X(t)}\right).$$

From the polar coordinate expression in Eq. (3), the instantaneous frequency can be defined as

$$\omega(t)=\frac{d\theta(t)}{dt}. \tag{4}$$

Applying the Hilbert transform to the IMFs components of $X(t)$ in Eq. (3), the data $X(t)$ can be written as follows:

$$X(t)=\Re\sum_{j=1}^{n} a_j(t)e^{i\int\omega_j(t)dt} \tag{5}$$

where R is the real part of the value.

Similar to the Fourier amplitude spectrum, the Hilbert amplitude spectrum $H(\omega,t)$ is the time-frequency distribution of the amplitude. The marginal spectrum $h(\omega)$ is a measure of the total amplitude (or energy) contribution from each frequency value. It represents the accumulated amplitude over the entire data span in a probabilistic sense. The marginal spectrum is obtained by the integration of the Hilbert spectrum over the time duration T:

$$h(\omega)=\int_0^T H(\omega,t)dt. \tag{6}$$

3. Sensitivity of damage detection

3.1 Damage detection index

Structural damage is usually represented by the natural frequency and the damping ratio of the structure changes

when any structural member is damaged due to strong ground motion. The most obvious of these indexes is the change in the equivalent damping ratio of the structure before and after damage by earthquakes. Furthermore, a damage detection index, the ratio of an equivalent damping ratio RED, has been derived by Tang et al. (Tang et al. 2011). The procedures of the derivation are briefly summarized as follows:

As is well known, the half-power bandwidth (Chopra 2001) is related to the equivalent damping ratio of an SDOF structure. Then the definition of the ratio of bandwidth RB can be expressed as follows:

$$RB = \frac{f'2 - f'1}{f2 - f1} \tag{7}$$

where the bandwidth ($f2 - f1$) or ($f'2 - f'1$) denotes the half-power bandwidth, as estimated from the acceleration frequency response curve Ra, as shown in Figure 1.

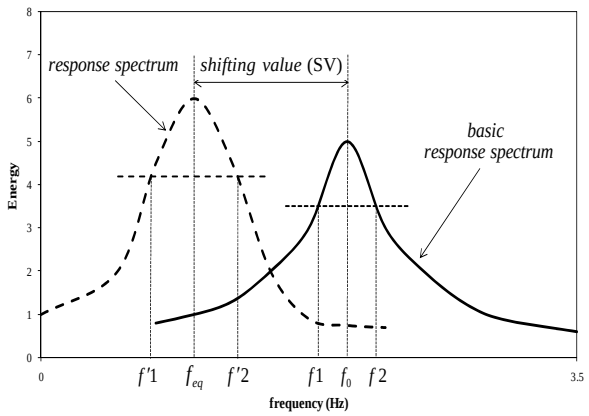


Figure 1 Definition of the ratio of bandwidth (RB) and definition of the ratio of equivalent damping ratio (RED) (Tang et al. 2011)

Besides, the change of stiffness to a member can be observed when the structure is in nonlinear region. Figure 2 shows the hysteresis of a column during a strong ground motion. The change of stiffness can be expressed to a new damage detection index, the ratio of effective stiffness, RES. The derivation of RES is shown as follow:

$$K_{eff} = \min\left(\frac{M_{\max}}{R_{\max}}, \frac{M_{\min}}{R_{\min}}\right) \tag{11}$$

$$RES(\%) = \frac{K_{eff}}{K_0} \tag{12}$$

In which, the K_{eff} can be calculated from a hysteresis taking the minimum positive stiffness or negative stiffness to the structure during an excitation. Then the RES can be evaluated from K_{eff} to K_0. Hence, if RES=100%, the structure remains in the elastic region. However, if RES<100%, the nonlinear behavior of the structure exists and is revealed in the acceleration responses.

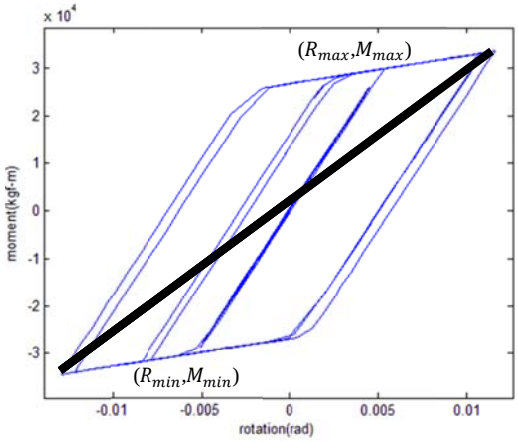


Figure 2 Definition of the ratio of effective stiffness (RES)

3.2 Sensitivity of detecting damage to MDOF models

Figure 3 presents four bays three and ten story steel models generated by the SAP2000 program. The length of one bay is 3 m and the height of one story is 4 m.

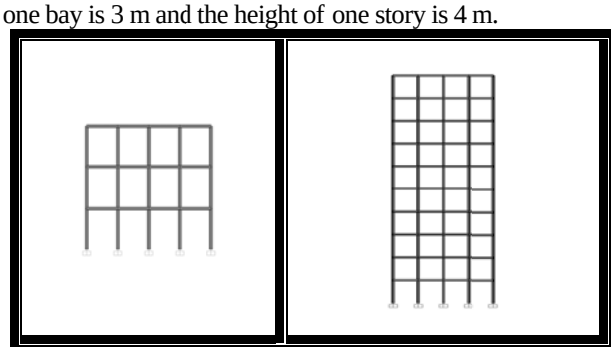


Figure 3 Four bays MDOF steel structures with two types

Table1 lists the member section and the modal frequency of these models. The rotational stiffness of columns of these structures is then simulated using Wen's model (Wen 1976). Furthermore, the Japan 311 (MYG010, IWT026, TCG009) and Chi-Chi (TCU138, CHY008, ILA061) earthquakes are adopted as the excitations. The time history records are shown in Figure 4.

Table 1 Modal frequency and frame section of the structures

		Three-story	Ten-story
Section	Beam	W12X22	W12X22
	Column	W18X35	W18X35
Modal frequency (Hz)	f_1	3.4	1.0
	f_2	11.2	3.4
	f_3	20.2	5.8

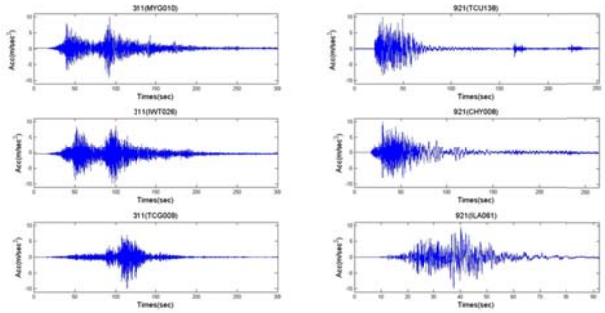


Figure 4 Time history records of Japan 311 and Chi-Chi 921 earthquakes

Next, the acceleration responses of the floor for each case are evaluated after inputting the adjusted Japan 311 and Chi-Chi 921 earthquake excitations (PGA = 0.1, 0.2, 0.3, 0.4, 0.5, 0.6, 0.8 and1.0g). In which, for example, if the first yielding point is occurred at PGA=0.2g, the increment of PGA value changes to 0.02g (0.2g, 0.22g, 0.24g,…, 0.3g). Then the change of RES and RB can be observed more clearly before and after yielding of the structure. There are 18 response cases (three models and six earthquakes) used to evaluate the damage indices. The sensitivity indices RB and RES are computed from the acceleration response data using the HHT and FFT methods. Given the difficulty in estimating the bandwidth based on the original structural response spectrum, the moving average method with span 3 (Chou 1975) is used to smooth the spectrum to evaluate the indices.

A portion of the above results are summarized in Figures 5 and 6.The acceleration response spectra (PGA=0.1g, 0.6g, 0.8g and 1.0g) for three-story models from first and top floor using the FFT and HHT methods respectively are shown in Figure 5 and 6. Both the change of bandwidth in the predominant frequency cannot be observed clearly at 1F and 3F from FFT spectra in the 311 (TCG009) cases as shown in Figure 5. Opposite to the FFT spectra, the change of bandwidth can be seen obviously when the responses of three-story structure before and after first column yielding occurred from HHT spectra as shown in Figure 6.

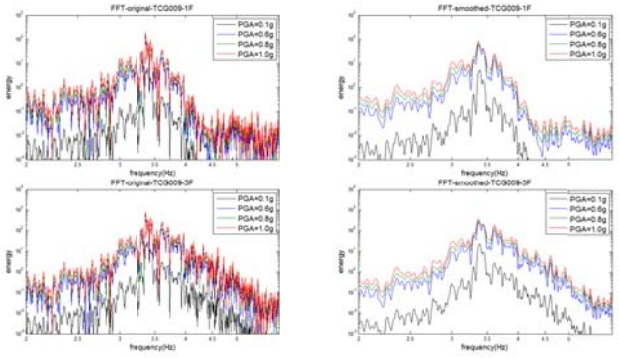


Figure 5 Acceleration response spectra obtained using FFT for three -story cases (TCG009)

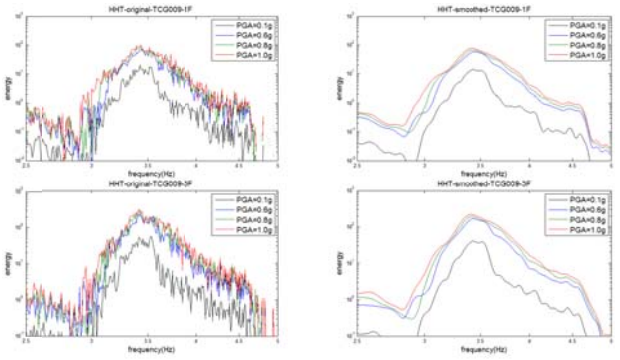


Figure 6 Acceleration response spectra obtained using HHT for three -story cases (TCG009)

Figure 7-10 display the results of RB with RES for three type structures in all cases from FFT and HHT spectra. In which, the change of RB with RES are summarized in Figure 7 and 9 based on FFT spectra. For example, the maximum value of RB is 1.0703 when the RES=93.78% in the TCU138 (3F) case as shown in Figure7. Then the RB decreases with a decreasing RES, when the RES=56.54%, the RB reduces to 1.0535. Next, for ILA061 (1F) case, the RB almost retain around 1.0 when the RES=100%~72%. The change of RB can be observed when the RES<61.74% as shown in Figure7. That is to say, in the FFT spectra, RB occasionally increases with decreasing RES, and occasionally decreases with RES. The same phenomena also can be seen in ten-story cases. Besides in the MYG010 and TCU138 cases, the RB almost has no change with RES as shown in Figure 9. Therefore, no steady trend of change is found for the RB vs. RES when analyzed with the FFT method.

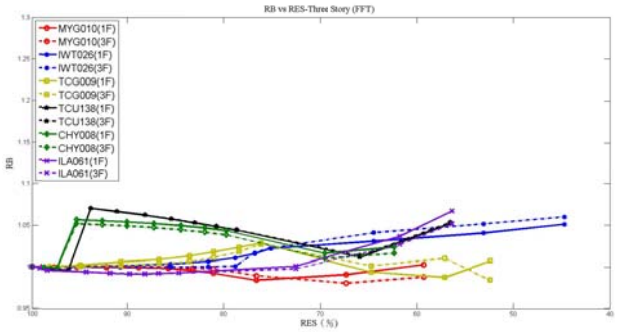
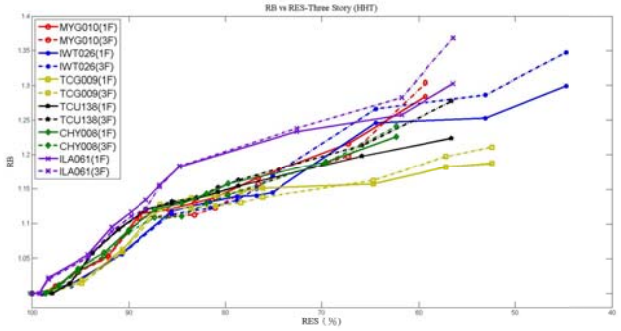
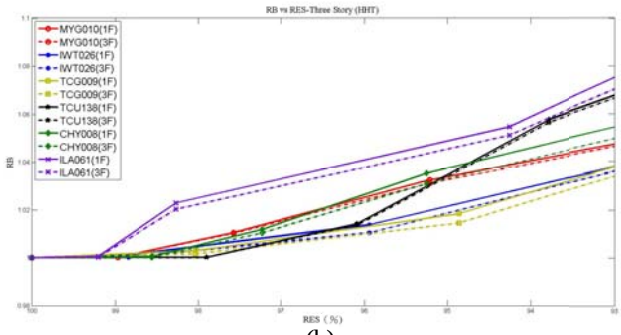


Figure 7 Results of RB vs. RES using FFT for all cases (three-story)



(a)



(b)

Figure 8 Results of (a) overall (b) zoom-in RB vs. RES using HHT for all cases (three-story)

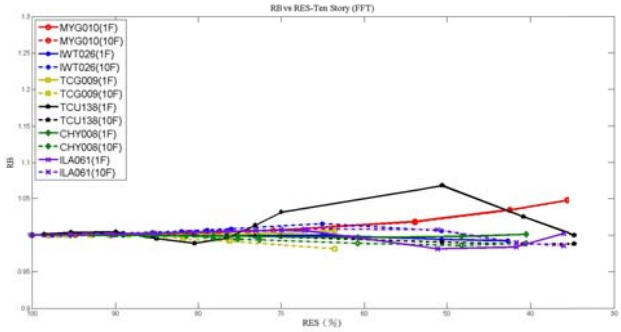
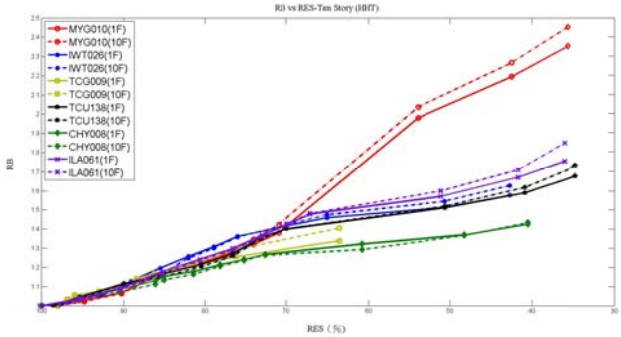
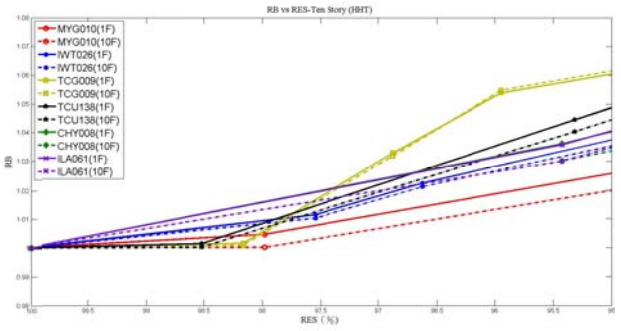


Figure 9 Results of RB vs. RES using FFT for all cases (ten-story)



(a)



(b)

Figure 10 Results of (a) overall (b) zoom-in RB vs. RES using HHT for all cases (ten-story)

Figure 8 and 10 indicate the analyzed results from HHT spectra. The positive trend of RB vs. RES can be found clearly for three-story model in all cases as shown in Figure 8(a). For example, the change of RB can be observed (RB=1.0229 at 1F; RB=1.0203 at 3F) when the first column yielding occurred (RES=98.27%) in ILA061 case. Moreover the change of RB at 1F shows more sensitive than that at 3F in the initial yielding stage of three-story model as shown in Figure 8(b). Next the RB increases with a decreasing RES both at 1F and 3F. When the RES<84.68%, the RB of 3F begins to larger than the RB at 1F. And the maximum of RB is 1.3683 at 3F when the RES reduces to 56.37% as shown in Figure 8(a). It means that the change of RB at 1F shows higher sensitivity while the yielding of column just occurred. As the degree of damage goes on, the change of RB at 3F presents the highest sensitivity in detecting structural damage.

The similar analyzed results also can be obtained from ten-story cases as shown in Figure 10. When the 1F column begins to yield (RES<100%), the change of RB at 1F is larger than those at 10F as shown in Figure 10(b). With the damage increasing, the incremental of RB at 10F is greater than RB at 1F as shown in Figure 10(a). For instance, when the RES=94.81%, the RB= 1.0271 at 1F but the RB=1.0211 at 10F in MYG010 case. Then the RES decreases with increasing structural damage, when the RES reduces to 35.59%, the RB increases to 2.3542 at 1F and the RB reaches to 2.4732 at 10F. Therefore, the change of RB at first yielding floor presents more sensitive than top floor. But when the damage grows up, the RB at top floor still shows the highest sensitivity for damage detection of a structure.

3. CONCLUSIONS

This study proposes the RB and RES as the damage detection indices to detect the structural damage of the steel structure to strong ground motions. Two type four bays MDOF steel models are constructed to subject the adjusted PGA Japan 311 and Chi-Chi 921 earthquakes. The acceleration response spectra evaluated from the first yielding floor and roof are using HHT and FFT methods respectively.

The simulation results indicate that the change of RB can be seen clearly when the RES<90% in all cases from HHT spectra. Moreover, the RB at first yielding floor changes more sensitive than those at roof when the response of a

structure is in initial yielding stage (RES<100%) from HHT spectra. With the nonlinear hysteresis grows up, the RB increases with a decreasing RES can be observed clearly especially the incremental change in RB at roof shows the highest sensitivity to detect the structural damage. Opposite to the results of HHT, the sensitive damage detection phenomena cannot be obtained from FFT spectra. The change of RB can be observed while the reduction of RES is large enough. However, there is no steady relationship between RB and RES from FFT spectra. Therefore, the damage detection index RB evaluated from HHT spectra presents more sensitive than FFT spectra. Moreover, the first yielding floor can be detected precisely and the structural damage can be observed in the top floor using damage detection index, RB from the HHT spectra.

Acknowledgements:

The authors would like to thank Dr Norden E. Huang, Director of the Adaptive Data Analysis Research Center at the National Central University, for his invaluable introduction to the HHT method and encouragement and advice for this study. The authors would like to thank the National Science Council of the Republic of China, Taiwan, for their financial support of this research under contract no. NSC 101-2221-E-008-077.

References:

Akanshu Sharma, G.R. Reddy, Rolf Eligehausen, K.K. Vaze, A.K. Ghosh and H.S. Kushwaha (2010), "Experiments on reinforced concrete beam-column joints under cyclic loads and evaluating their response by nonlinear static pushover analysis," STRUCTURAL ENGINEERING AND MECHANICS, 35(1), pp.99-117.

Chiang W.L., Chiou D.J., Chen C.W., Tang J.P., Hsu W.K. and Liu T.Y. (2011), "Detecting the sensitivity of structural damage based on the Hilbert-Huang transform approach," Engineering Computations, 27(7), pp.799-818.

Chiou D.J., Hsu W.K., Chen C.W., Hsieh C.M., Tang J.P. and Chiang W.L. (2011), "Applications of Hilbert-Huang transform to structural damage detection," Structural Engineering and Mechanics, 39(1), pp. 1-20.

Chopra Anil K. (2001), "Earthquake Dynamics of Structures: Theory and Applications to Earthquake Engineering," Second Edition , pp.83.

Chou Ya lun (1975), "Statistical Analysis," 2d ed. New York: Holt Rinehart and Winston, pp. 562–565.

Huang N E., Shen Z., Long S. R., Wu M. C., Shih H. H., Zheng Q., Yen N. C., Tung C. C. and Liu .H. H. (1998), "The Empirical Mode Decomposition and the Hilbert Spectrum for Nonlinear and Non-stationary Time Series Analysis," Proc. R. Sec.115London A, The Royal Society, pp.903-995.

Huang N. E., Shen Z. and Long S. R. (1999), "A new view of nonlinear water waves: The Hilbert spectrum," Annu. Rev. Fluid Mech. 31, pp.417–457.

Lei Y., Kiremidjian A. S., Nair K. K., Lynch J. P., Law K. H., Kenny T. W., Carryer Ed and Kottapalli A. (2003), "Statistical Damage Detection Using Time Series Analysis on a Structural Health Monitoring Benchmark Problem," in Proceedings of the 9th International Conference on Applications of Statistics and Probability in Civil Engineering, San Francisco, CA, USA, July, pp.6-9.

Nair K. Krishnan and Kiremidjian Anne S. (2009), "Derivation of a Damage Sensitive Feature Using the Haar Wavelet Transform," Applied Mechanics 76, 061015, pp.1-9.

Ren Wei-Xin and Sun Zeng-Shou (2008), "Structural damage identification by using wavelet entropy," Engineering Structures 30, pp.2840–2849.

Rucka M. and Wilde K. (2006), "Application of continuous wavelet transform in vibration based damage detection method for beams and plates," Sound and Vibration, 297, pp.536–550.

Su S. C., Huang N. E. and Wen K. L. (2008), "A new spectral representation of strong motion earthquake data: Hilbert spectral analysis of Taipower building station, 1994~2006," Proc.,5th Int. Conf. on Urban Earthquake Engineering, (Tokyo, Japan).

Sun Z. and Chang C.C. (2002), "Structural damage assessment based on wavelet packet transform," J Struct Engng, 128(10), pp.1354–61.

Tang J. P., Chiou D. J., Chen C. W., Chiang W. L., Hsu W. K., Chen C. Y. and Liu T. Y. (2011), "A case study of damage detection in benchmark buildings using a Hilbert-Huang Transform-based method" Journal of Vibration and Control, 17(4), pp.623-636

Wen Y. K. (1976), "Method for random vibration of hysteretic system," Journal of Engineering Mechanics – ASCE, 102(2), pp. 249-63.

Wu Z. and Huang N. E. (2004), "Ensemble Empirical Mode Decomposition: a noise-assisted data analysis method," Centre for Ocean-Land-Atmosphere Studies, Tech. Rep, 173.

Yang, J. N., Lei Y., Pan S., and Huang, N. (2003a), "Identification of linear structures based on Hilbert-Huang transform. Part I: Normal modes," Earthquake Eng. Struct. Dyn., 32 (9), pp.1443–1467.

Yang, J. N., Lei Y., Pan S., and Huang N. (2003b), "Identification of linear structures based on Hilbert-Huang transform. Part II: Complex modes," Earthquake Eng. Struct. Dyn., 32 (10), pp.1533–1554.

Yang J. N, Lei Y., Lin S. and Huang N. (2004), "Hilbert–Huang based approach for structural damage detection," Eng. Mech-ASCE, 130(1), pp.85–95.

10CUEE CONFERENCE PROCEEDINGS
10th International Conference on Urban Earthquake Engineering
March 1-2, 2013, Tokyo Institute of Technology, Tokyo, Japan

MEMBER DAMAGES OF HIGH-RISE BUILDING STRUCTURES UNDER SEVERE EARTHQUAKES: EFFECT OF MEMBER DETERIORATION

Yongtao Bai[1)], Akihiko Kawano[2)], and Shintaro Matsuo[3)]

1) PhD Candidate, Department of Architecture, Kyushu University, Japan
2) Professor, Department of Architecture, Kyushu University, Japan
3) Assistant Professor, Department of Architecture, Kyushu University, Japan
bai@kyudai.jp, kawano@arch.kyushu-u.ac.jp, matsuo@arch.kyushu-u.ac.jp

Abstract: Probability of severe ground motions generate potential seismic safety problem on various existent high-rise steel and concrete filled steel tubular (CFT) buildings, due to the effects of local-failure of steel and CFT members on the seismic damages have not been clearly included in current performance-based seismic design. The global seismic-resistant capacity of high-rise buildings may be significantly affected by the local-failure of structural members. In this study, deterioration behavior after local buckling of steel and CFT members is incorporated in the incremental dynamic analysis (IDA) of existent high-rise S and corresponding CFT buildings (based on equivalent horizontal stiffness) with various levels of member deterioration. Performance-based earthquake damages of these high-rise building models are analytically investigated and compared in terms of the ductility response and cumulative hysteretic energy of the beam and column members in the planar weak-beam frame models of high-rise steel and CFT buildings. Analytical results show that the effect of member deterioration significantly amplified the member damages of high-rise buildings to various extent based on deterioration parameters. High-rise CFT buildings incorporating member deterioration demonstrates higher collapse margin than that of the corresponding high-rise steel building.

1. INTRODUCTION

Great east Japan earthquake (AIJ 2011) has manifested enormous power to destroy infrastructures and human life. Furthermore, very high probability of extreme ocean-ridge earthquakes also exists in the future (e.g. 30 years). Furthermore, since the seismic risk of long-period ground motions associated with long duration on the structures with long 'first mode' natural period (e.g., high-rise building) has been focused by researchers during the Tokachi earthquake (2003), the seismic damages and energy-dissipating capacity of such building structures become more important for the assessment of the seismic safety of varied existent high-rise buildings. Energy dissipation has been treated as an indicator for the seismic performance of building structures, since Housner (1956) suggested an energy-based design approach. Thereafter, Akiyama et al. (1985) proposed the relation between energy dissipating capacity of structure and its corresponding demand by using an indicator of cumulative plastic deformation.

In this study, we especially concentrate on the member damages of the existent high-rise steel and CFT buildings based on the indexes of the ductility ratios and the cumulative plastic deformation of beam and column members. Moreover, due to the strength and stiffness deteriorations of steel and CFT members under cyclic loading has significantly influences on the failure mechanism of such members, the effect of member deterioration on the member damages of above buildings structures is also comparatively evaluated. The deterioration margin and collapse margin of various deteriorating model are also quantified and compared with non-deteriorating model.

2. MEMBER DETERIORATION

2.1 Steel members

Accurate stress-strain models for rectangular steel tube and H-shaped steel members associated with strength deterioration caused by local-buckling, Bauschinger effect, and unloading stiffness deterioration, as shown in Figure 1, are developed on the basis of Menegotto-Pinto model (1973), in order to be capable of capturing the effect of member deterioration on the seismic damages and collapse-resistant capacity of high-rise steel and CFT buildings. Formulae to define the parameters (as shown in Figure 1) in deteriorating model for various steel members and the corresponding preliminary studies on the calibration of deteriorating stress-strain models of steel and concrete have been conducted by Bai et al. (2012).

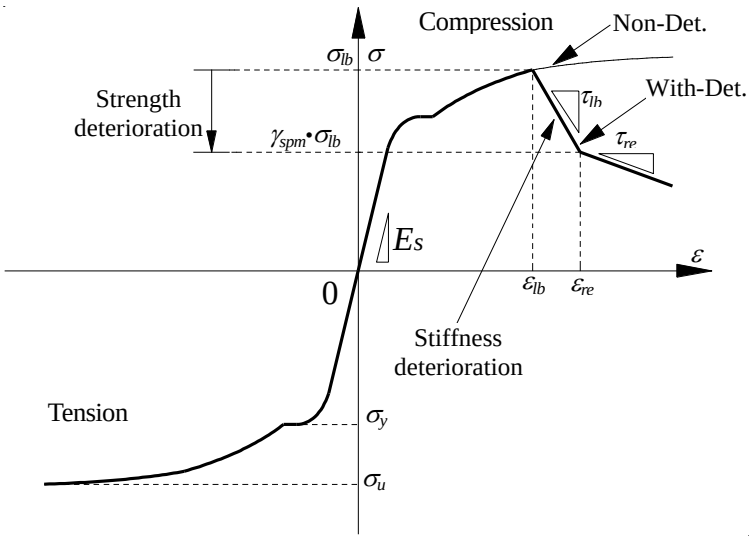


Figure 1 Deteriorating stress-strain model for steel members

2.2 Confined Concrete

Confining effect on the strength and deformability of the in-filled concrete in square CFT section is considered by utilizing Sakino-Sun model (1995), as shown in Figure 2. Flat curve after peak-point is analogous to non-deterioration situation, and on the other hand, the post-peak deterioration is considered by capturing the inflexion point of the Sakino-Sun model to maintain equilibrium in deterioration and residual branches.

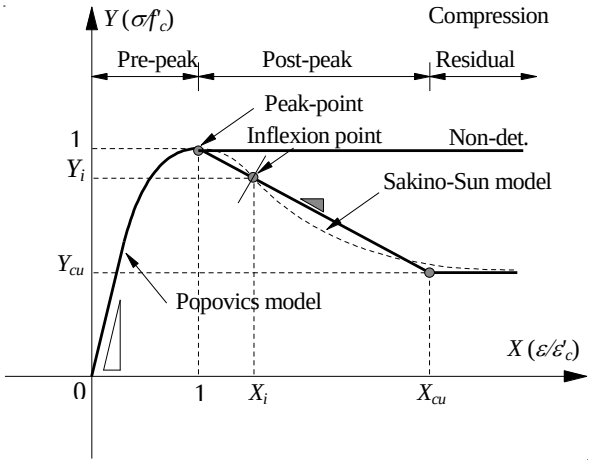


Figure 2 Deteriorating model of confined concrete

In order to respectively predict the deterioration gradient and residual strength of the confined concrete, we specifically simplified the deterioration branch (post-peak branch and residual branch) into bi-linear relation, as shown in Figure 2, where, according to the reference (Bai et al. 2012) the ultimate point (X_{cu}, Y_{cu}) between post-peak branch and residual branch is defined by

$$\begin{cases} X_{cu} = \dfrac{\varepsilon_{cu}'}{\varepsilon_{cc}'} = 1.96\left(\dfrac{V}{W}\right)^{0.88} + 4.77 \\ Y_{cu} = \dfrac{\sigma_{cu}'}{f_{cc}'} = \lim\limits_{X\to\infty} \dfrac{VX + (W-1)X^2}{1 + (V-2)X + WX^2} = 1 - \dfrac{1}{W} \end{cases} \quad (1)$$

Moreover, both deteriorating stress-strain models for steel members (H-shaped steel, square HST and CFT) and the confined concrete in square CFT members have been calibrated by Bai et al. (2012), based on extensive database of such structural members.

3. VARIOUS HIGH-RISE BUILDINGS

3.1 Square HST and CFT columns

Based on the various statistical databases (AIJ 2007) on the existent high-rise steel and CFT buildings, increasing cases of high-rise CFT building necessitate the assessment on their seismic safety under severe seismic excitations. Furthermore, in order to compare and quantify the collapse margin of high-rise CFT buildings to analogical high-rise steel buildings, only the square HST column in high-rise steel building models are replaced by the square CFT column based on equivalent horizontal stiffness K [$(12EI)/l^3$]. As shown in Figure 3, the equivalent square CFT column which is analogous to square HST column, can make the tubular section be more compact by keeping the same width-thickness ratio (B/t) than associated HST column, or safe the steel material by reducing the thickness of steel tube.

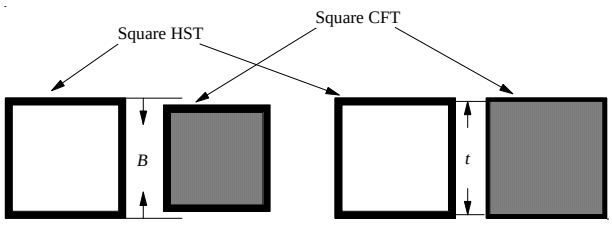


Figure 3 Equivalent square CFT and HST column

As mentioned above, both of the above advantages show different deterioration features for CFT column due to the local-buckling of steel tube and confining effect to in-filled concrete are overtly affected by B/t of tube, as discussed in Section 2. Therefore, we respectively employ the compact CFT column and uncompact CFT column in

high-rise CFT building models, in order to be analogous to FA_c-FA_b model and FB_c-FB_b high-rise steel building models (ASCCS Bai et al. 2012). Figure 4 shows the different criterion (FA, FB) of width-thickness ratios of square HST columns (MLIT 2007) and CFT columns (AIJ 2008).

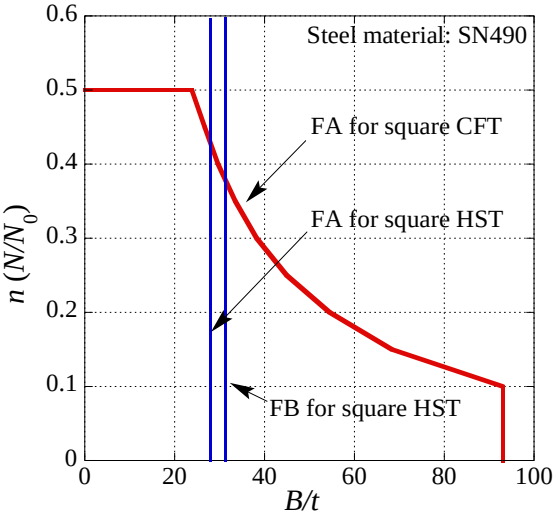


Figure 4 Dependence of *B/t* and *n* (N/N_0) on the ranks of square HST and CFT columns

3.2 High-rise steel and CFT buildings

According to the assessment on the structural system, member, and material in existent high-rise buildings (AIJ 2007), for the existent high-rise steel and CFT buildings, moment-resistant frame structures with H-shaped steel girder and square HST or CFT columns were preferred during 1980~1990 in Japan. Thus, various existent high-rise steel and CFT buildings [i.e., 20, 30 and 40 story levels (denoted as 20S, 30S and 40S), compactness ranks of columns and beams (denoted as FA_c-FA_b, FB_c-FB_b for high-rise steel buildings, and FA_c-FA_b, FA'_c-FB_b for high-rise CFT buildings)] with planar moment-frame models are seismic designed by current building standard. The component section, elevation and plan views of the planar models are shown in Figure 5.

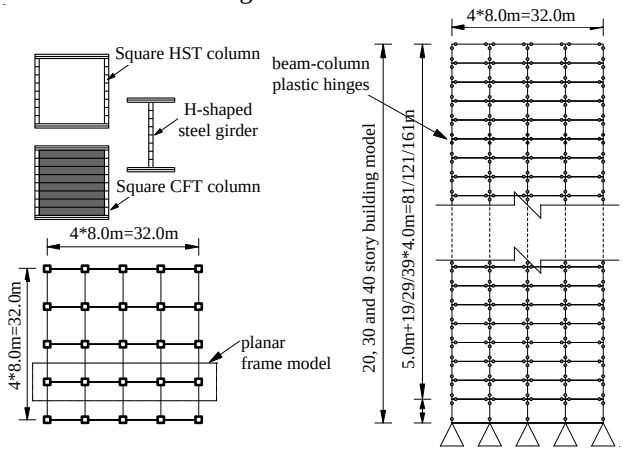


Figure 5 Component section, Plane and elevation views of high-rise building models

4. EARTHQUAKE WAVES

With respect to the seismic excitations on structures, peak ground velocity (i.e., PGV) likely to have higher correlation as an intensity measure with the performance parameters (e.g., maximum and residual drift, ductility and hysteresis energy) of high-rise building structures with long natural period. Thus, in order to simulate large earthquake excitations on high-rise building and also try to relatively eliminate the record-to-record uncertainty, analogous typical artificial-waves (i.e., Art-Hachi, BCJ-L2, JSCA-Kobe and Yokohama) for seismic design are picked, as shown in Table 6. The maximum and cumulative member damages of various high-rise buildings under high-level intensity earthquakes are assessed on the basis of incremental dynamic analyses [IDA (Vamvatsikos and Cornell 2002)] controlled by the incremental factors ϕ from elastic to collapse, based on the PGV of each artificial waves.

Table 1 Details of artificial earthquake waves

Ground motion	PGA (gal)	PGV (kine)	Duration (sec)
Art-Hachi	466.7	64.0	163.8
BCJ-L2	355.7	80.4	120.0
JSCA-Kobe	469.5	58.7	60.0
Yokohama	350.2	62.0	80.0

Moreover, according to the pseudo velocity response spectrum of such artificial earthquake waves as illustrated in the Figure 6, nearly flat velocity excitations of such waves is observed on long 'first-mode' natural periods high-rise building models.

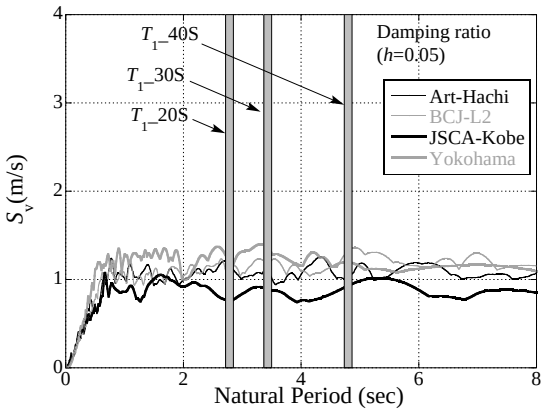


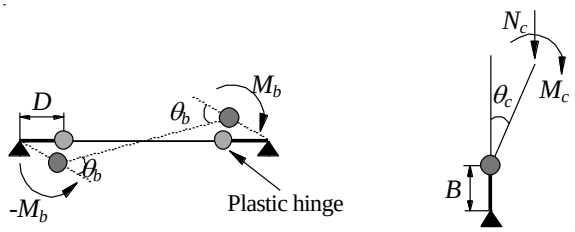
Figure 6 Pseudo velocity response spectrum of artificial earthquake waves

4. PLASTIC DAMAGES

4.1 Plastic hinge mechanism

The plastic-hinge rotation at the inside beam and column members in high-rise steel buildings are also initiated. Plastic-hinge rotation is an index for evaluating the plastic-deformation capacity of local regions (Wakabayashi, 1986). Local buckling and damage of steel members can be examined by normalized rotation of steel member, i.e., ductility ratio. As introduced in Section 2, the strength and stiffness deterioration of various steel and CFT members caused by local buckling under cyclic loading is expected to

show significant impact on the nonlinear dynamic responses of such steel members (Bai et al. 2012). Thus, more widely the plastic-hinges and more severe the ductility ratios are correspondingly induced at the endings of beam member and column-base of the weak-beam high-rise buildings. Figure 7 shows the definition of the ductility ratio of girder and column-base in high-rise steel and CFT buildings.



(a) Girder (b) Column-base

Figure 7 Plastic hinge rotations for beam and column

Thus, the effect of the member deterioration on the local-responses (i.e. component responses) of the critical regions (i.e., plastic hinges) in existent high-rise buildings are focused, in order to reveal how much the member damages of such buildings structures has been initiated. For the high-rise building structures under time-history earthquake excitations (time-history analysis), maximum ductility ratios (μ_b, μ_c) of H-shaped steel girder and square HST/CFT column-bases at bottom story are feasible to be treated as the damage index calculated by

$$\begin{cases} \text{Max.}\mu_b = \dfrac{\max(\theta_b)}{\theta_y} \\ \text{Max.}\mu_c = \dfrac{\max(\theta_c)}{\theta_y} \end{cases} \tag{2}$$

where, $\max(\theta_b)$ and $\max(\theta_c)$ are the maximum responses of plastic-hinge rotation at beam and column base, θ_y is the rotation at yield point of beam/column members that is calculated by $\theta_y=(M_y/K)$, K (=6EI/l) is the flexural stiffness of beam/column members, M_y (=$Z\times F_y$) is bending moment capacity at yield point, Z (=I/(D/2)) is section modulus, F_y is yield strength of steel material.

For the high-rise steel and CFT buildings designed by weak-beam moment-resistant frame, beam and column-base plastic-hinge mechanism of high-rise steel building is assumed (in Figure 8). In particular, plastic-hinge at the column base of the bottom-story of high-rise building could modify the side-sway of high-rise buildings and the phenomenon of deformation concentration can be observed at lower-story (Uetani 1996). Therefore, we respectively compare the ductility ratios of beam and column-base between deteriorating and non-deteriorating models.

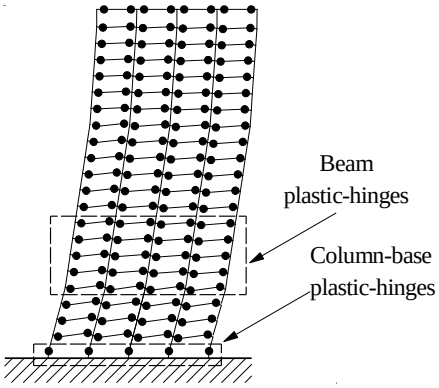
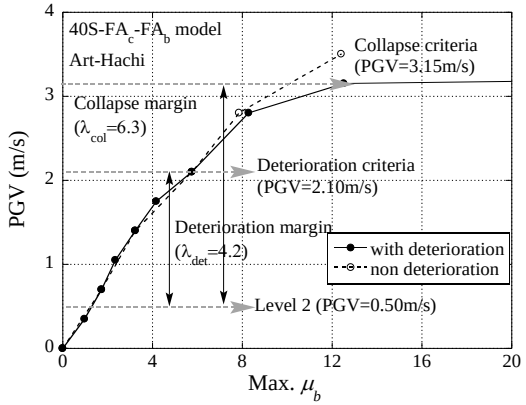


Figure 8 Plastic-hinge mechanism of high-rise steel building

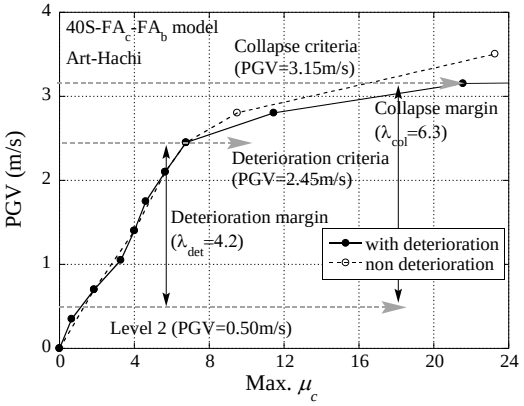
4.2 Incremental ductility ratios

In order to capture the criterion of the effect of member deterioration on ductility ratios of high-rise buildings, the maximum ductility ratios of the deteriorating and non-deteriorating building models (i.e., high-rise steel and CFT building) under incremental dynamic loadings (e.g., Art-Hachi) are compared, as shown in Figures 9~10. Meanwhile, indexes for indicating the deterioration margin and collapse margin of the corresponding high-rise buildings comparing to the intensity measure of level 2 (PGV=0.50m/s) are separately proposed as follows

$$\begin{cases} \lambda_{col} = \dfrac{PGV_{col}}{PGV_{level\,2}} \\ \lambda_{det} = \dfrac{PGV_{det}}{PGV_{level\,2}} \end{cases} \tag{3}$$

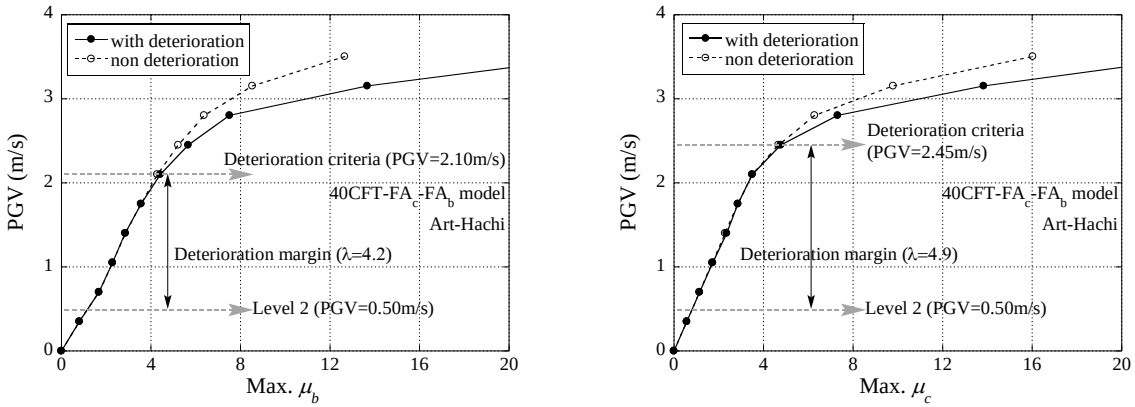


(a) Maximum ductility ratio of beam members



(b) Maximum ductility ratio of column members

Figure 9 Dependence of member deterioration on ductility ratios of high-rise steel building



(a) Maximum ductility ratio of beam members (b) Maximum ductility ratio of column members

Figure 9 Dependence of member deterioration on ductility ratios of high-rise CFT building

As observed in Figures 9~10, effect of member deteriorations gradually shows extensive influence on the maximum ductility ratios of each corresponding members (i.e., girder and column) of various high-rise buildings (steel and CFT structure). Some relationships can be observed as follows.

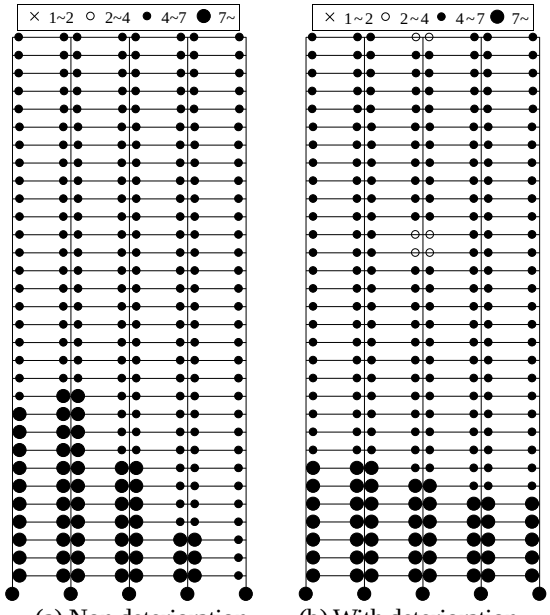
(a) With respect to the relationship between the maximum ductility ratios of the deteriorating and the corresponding non-deteriorating steel models, in Figure 9, Even though the effect of deterioration on the ductility ratios of beam and square HST column base is simultaneously initiated at the incremental factor of ϕ=3.0, which indicates the same deterioration margin (λ_{det}=4.2), seismic-resistant capacity of such building to significantly deteriorates since then and collapse is induced eventually. Collapse margin λ_{col}=6.3 is correspondingly derived for this Low-det. High-rise steel building.

(b) Likewise, for the effect of member deterioration on maximum ductility factors of high-rise CFT buildings, as shown in Figure 10, effect of member deterioration on ductility ratios of beam and column-base is initially captured at the incremental factor of ϕ=3.0 and ϕ=3.5, the reason why column-base deterioration emerges later than that of beam deterioration is that weak-beam mechanism makes beam firstly yield. However, the sway collapse of such Low-det. High-rise CFT building has not been observed, no matter for deteriorating model and non-deteriorating model. This indicates that λ_{col} is larger than 7.0.

(c) Based on the viewpoint of seismic-redundancy of structures, deterioration margin and collapse margin on the basis of intensity measures (PGV) of earthquake are assessed. Within the range of incremental factor ($\phi \leq 5.0$), collapse of high-rise steel buildings is induced, while is not feasible to high-rise CFT buildings. Furthermore, for the deterioration margins of steel and CFT models, various ductility redundancies of column-based are also captured, due to the various deteriorations of square HST and CFT columns, e.g., λ_{det} of the square CFT column-base of associated high-rise CFT building models is 4.9 [shown in Figure 10 (b)], but λ_{det} of the square HST column-base of associated high-rise steel building models is 4.2 [shown in Figure 9 (b)].

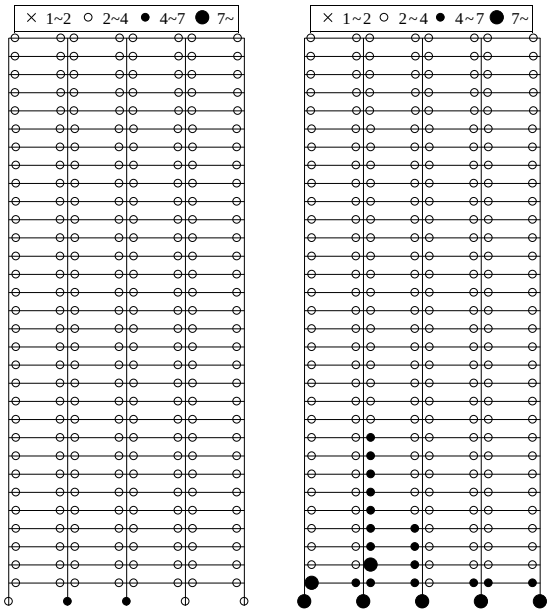
4.2 Collapse mechanism

Conventionally, the plastic collapse criterion of steel member and frame are considered by the occurrence of plastic-hinge, based on the elastic-perfectly plastic assumption. While, in this study, as mentioned in Section 2, we think the local-buckling of steel members is the criteria of member's failure (collapse), and the collapse of frame is subsequently considered to be occurred by extensive local-failure of members at critical regions (e.g., endings of beam and column-based). Thus, member damages based on the ductility ratios of beam and column-based in the weak-beam frame are expected to indicate the collapse mechanism of corresponding high-rise buildings. We specifically show the collapse mechanism of existent high-rise steel buildings with Low-det. and High-det. levels (i.e., 40S-FA$_c$-FA$_b$ and 40S-FB$_c$-FB$_b$ model). Figures 11~12 respectively show the ductility ratios of low-det. and high-det. high-rise steel buildings, at the time that collapse is induced in deteriorating model under Art-Hachi wave.



(a) Non deterioration (b) With deterioration

Figure 11 Collapse of low-det. high-rise steel building



(a) Non deterioration (b) With deterioration

Figure 12 Collapse of high-det. high-rise steel building

As shown in Figure 11, it is obvious that the low-det. model (40S-FA_c-FA_b) shows ductile behavior to resist collapse being occurred (Art-Hachi, ϕ=5.0), even though extensively severe member damages are both observed in deteriorating and non-deteriorating models. Furthermore, as shown in Figure 13, relatively large μ_b (≤15) can still not generate collapse, but sudden increasing ductility ratios at lower-story of high-rise building make it collapse.

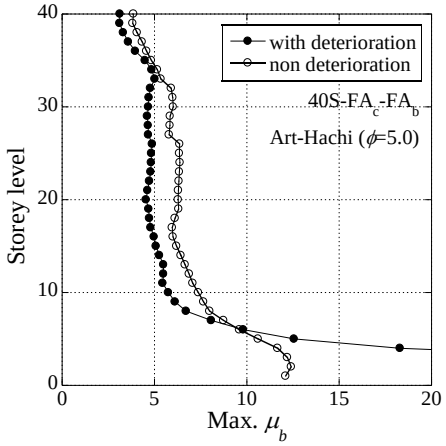


Figure 13 Collapse of high-det. high-rise steel building

Contrarily, the corresponding high-det. high-rise building model (40S-FB_c-FB_b) demonstrates non-ductile behavior to resist collapse occurring (Art-Hachi, ϕ=2.0), as shown in Figure 12. In particular, extremely large ductility factor μ_c of the square HST column-base caused by the column deterioration is the key reason to make the building structure collapse at bottom story.

5. CUMULATIV PLASTIC DAMAGES

Kato and Akiyama (1975) have proposed a hypothesis in which the term cumulative plastic deformation is introduced. The cumulative plastic deformation (η) implies the dissipated energy that is obtained from the hysteretic loops of the members (E_h) divided by energy product of the full-plastic moment (M_p) and corresponding yield rotation (θ'_y) of the members in high-rise buildings Thus, for the cumulative plastic deformations of each model under incremental dynamic loading, the maximum η of beam and column can be calculated by

$$\eta_{b,c} = \frac{\max.E_h(\tau)}{E_e} = \frac{\max.E_h(\tau)}{{}_{b,c}M_p \times {}_{b,c}\theta'_y} \qquad (4)$$

where E_h is hysteretic energy dissipation of beam and column components, M_p is the full-plastic moment of beam and column components, θ'_y is the rotation corresponding to M_p with elastic modulus.

5.1 Steel and CFT deteriorations

In addition to ductility ratio (μ), cumulative plastic deformation (η) is also capable of representing the member damages of various high-rise building based on hysteretic energy dissipation. Although the ultimate energy-dissipating capacity (E_e) of various ranks (FA, FB) of steel and CFT components is slightly different, as shown in Fig. 14, if the effect of member deterioration after peak-point show considerable influence on collapse-resistant capacity of such high-rise buildings is still not clearly. Thus, in order to quantify the effect of member deterioration (local-buckling) on the energy-dissipating capacity of high-rise steel and CFT building models (low-det. and high-det.) under severe earthquake excitation, the time history responses of the maximum η of each building model are calculated and demonstrated in Figures. 15~16.

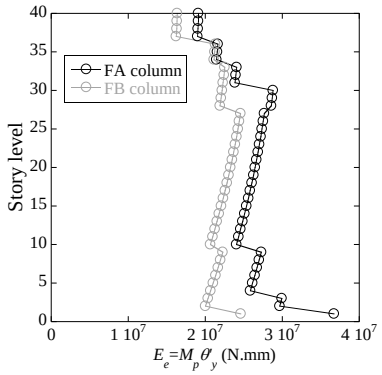
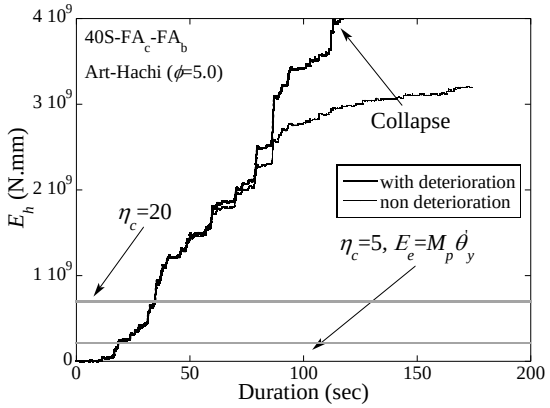


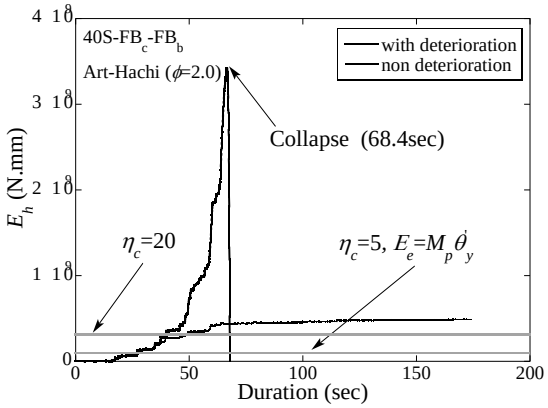
Figure 14 Energy-dissipating capacities of various square HST columns with FA and FB of *B/t* ranks

Due to different collapse mechanisms of various high-rise building models is induced, as mentioned in Section 4.2, we correspondingly compare the maximum η between deteriorating and non-deteriorating models, and between square HST and CFT columns as well.

(a) According to the comparison between the low-det. steel and CFT models, as shown in Figures 15~16 (a), although difference between the maximum η cumulation of non-deteriorating steel and CFT models are hardly observed, degrading of energy-dissipating capacity of the steel model

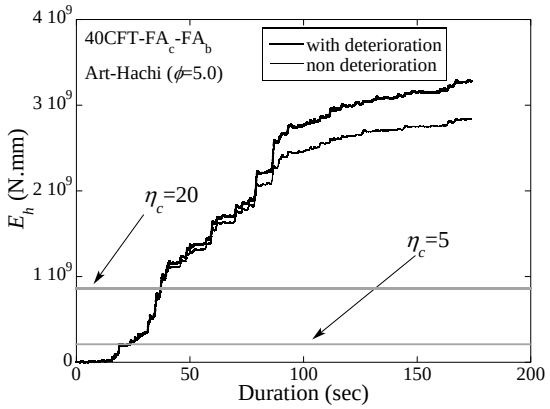


(a) Low-det. 40S-FA_c-FA_b model

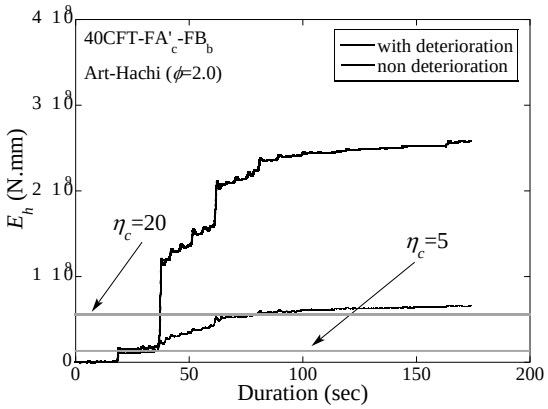


(b) High-det. 40S-FB_c-FB_b model

Figure 15 Maximum Hysteretic energy at the largest energy-dissipated element of high-rise steel building model



(a) Low-det. 40S-FA_c-FA_b model



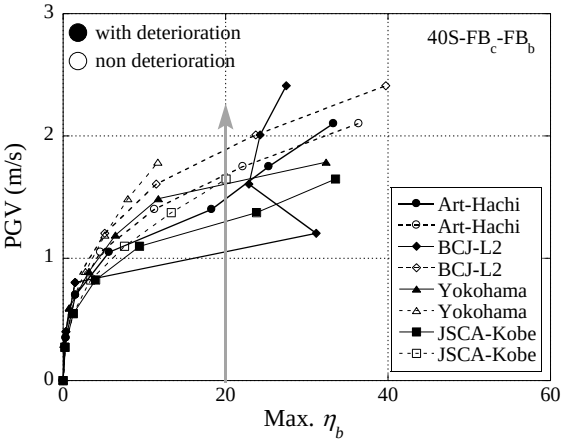
(b) High-det. 40S-FB_c-FB_b model

Figure 15 Maximum Hysteretic energy at the largest energy-dissipated element of high-rise CFT building model

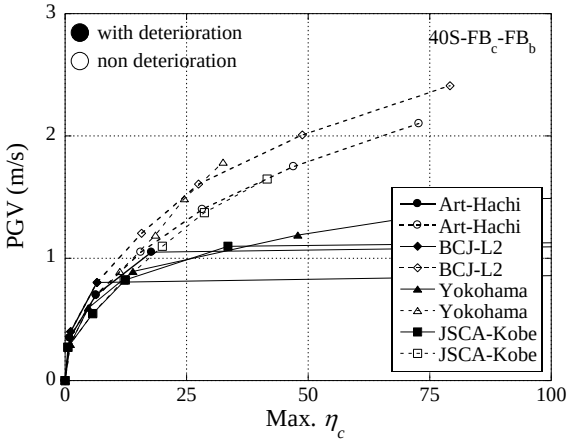
due to the member deterioration is gradually larger than that of CFT building model. In addition, it is noted that extremely large h has been cumulated in both deteriorating and non-deteriorating models under severe earthquake (e.g., Art-Hachi, ϕ=5.0).

(b) On the other hand, for the high-det. steel and CFT building models, as shown in Figures 15~16 (b), ignoring the member deterioration would overestimate the energy-dissipating capacity of steel model compared with CFT model, and non-ductile collapse of steel model is captured at the duration of 68.4sec of Art-Hachi wave (ϕ=2.0).

In addition, to be analogous to the incremental dynamic responses of ductility ratios as shown in Section 4, the maximum η of beam (max. η_b) and column (max. η_c) members of high-det. high-rise steel building model (40S-FB_c-FB_b) are also compared between deteriorating and non-deteriorating consideration, as shown in Figure 17.



(a) Max. η_b of beam component



(b) Max. η_c of column component

Figure 17 Incremental responses of maximum cumulative plastic deflection of beams and columns:

As shown in Figure 17, firstly, various earthquake waves induced similar incremental responses of the maximum h of beam and column, but the aleatory uncertainty caused by earthquakes is still not avoided due to the various energy inputting of each wave. Besides, the amplified effect of member deterioration on the max. η_b of beam component is significantly different from that of column (max. η_c) from the initial range of deterioration is observed. In particular, energy-dissipating capacity of beam members deteriorates stably, and in the case of BCJ-L2 waves [as shown in Figure 17 (a)], the strengthening of energy-dissipating capacity of beam is even observed, which is owing to the extreme softening (collapse) of column, as shown in Figure 18 (b). In contrast, maximum h of column is suddenly increased from initial deterioration to final collapse. This process is mainly because that the developing of column deterioration produces more cycles and larger hysteresis loops under incremental earthquake excitations.

3. CONCLUSIONS

On the basis of above works addressed on ductility and energy dissipation of the members of high-rise steel and CFT buildings, the effects of member deterioration on the member damage and collapse mechanisms were quantified and discussed above.

The effect of member deterioration is initiated at the lower-story portion of high-rise steel and CFT building, and extended upward. The plastic-hinge rotations produced at beam and column-base is significantly amplified by member deterioration, and the occurring of various collapse mechanisms (ductile and non-ductile) of high-rise steel buildings with deterioration can be captured. Furthermore, deterioration margin and collapse margin based on ductility and energy are completely different, but the unified processes of the deterioration and collapse producing of beam and column members are analogical between ductility and energy. Even though the high-rise CFT buildings has the identical horizontal stiffness with that of high-rise steel building, collapse margin of high-rise CFT building is obviously larger than corresponding steel building.

Acknowledgements:

The authors acknowledge support from the Grants-in-Aid for Scientific Research (B) No. 23360245 (Principal Investigator: Professor Uetani, Setsunan University). Besides, authors are grateful for the invaluable advices and helps from Prof. Araki (Kyoto University), graduate students Shoichi Egashira and Masayuki Fujii.

References:

Akiyama, H. (1985), Earthquake-resistant limit-state design for buildings, University of Tokyo Press.

Architectural Institute of Japan (2007), "Structural Response and Performance for Long-Period Ground Motions," Architectural Institute of Japan (AIJ).

Architectural Institute of Japan (2008), "Recommendations for Design and Construction of Concrete Filled Steel Tubular Structures," Architectural Institute of Japan (AIJ).

Bai, Y., Kawano, A., Odawara, K., Matsuo, S. (2012), "Constitutive Models for Hollow Steel Tubes and Concrete Filled Steel Tubes Considering the Strength Deterioration," J. Struct. Constr. Eng., AIJ, 77(677), 1141-1150.

Housner, G. W. (1956), "Limit design of structures to resist earthquakes", First World Conference on Earthquake Engineering, Berkeley, California.

Menegotto, M., Pinto, P. E (1973), "Method of Analysis for Cyclically Loaded R. C. Frames Including Changes in Geometry and Non-elastic Behaviour of Elements under Combined Normal Force and Bending," IABSE Congress Reports of the Working Commission, Band 13.

Ministry of Land, Infrastructure, Transport and Tourism (2007), "Building Standards Act," MLIT.

Uetani, K., Tagawa, H. (1996), "Deformation Concentration Phenomena in the Process of Dynamic Collapse of Weak-Beam-Type Frames," Journal of Structural and Construction Engineering, **483**(5), 51-60.

Vamvatsikos, D., Cornell, C. A. (2002), "Incremental Dynamic Analysis," Earthquake Engng Struct. Dyn., **31**, 491-514.

Wakabayashi, M. (1986), "Design of Earthquake-Resistant Buildings," Mcgraw-Hill Inc.

10CUEE CONFERENCE PROCEEDINGS
10th International Conference on Urban Earthquake Engineering
March 1-2, 2013, Tokyo Institute of Technology, Tokyo, Japan

STUDY ON COLUMN BEHAVIOR IN A FULL-SCALE STEEL BUILDING SUBJECTED TO STRONG GROUND MOTIONS ON SHAKING TABLE

Tran Tuan Nam[1], and Kazuhiko Kasai[2]

1) Graduate Student, Department of Built Environment, Tokyo Institute of Technology, Japan
2) Professor, Structural Engineering Research Center, Tokyo Institute of Technology, Japan
tuanam.t.aa@m.titech.ac.jp, kasai@serc.titech.ac.jp

Abstract: A full-scale four-story steel building specimen was experimented on the E-Defense shake-table in 2007, inputting various scales of ground motion until collapse. To extend the discussion on the building specimen performance in the experiment, this study addresses the deterioration of column shear strength resulting in the base shear strength degradation and finally the collapse of the whole building. Degradation of column strength is defined as the state when the displacement of the building still increases but column shear capacity cannot increase any further and drops down, induced by plastification and local buckling of column wall at both ends. From this point of view, the sequence of deterioration is detected and clarified for each column. Then, the study specifies timing ranges of deterioration of story shear strength before the building settles down on the supporting table due to collapse. The study also finds out the difference of degradation behavior among each column during the excitation loading due to the corresponding position of columns on the building plan.

1. INTRODUCTION

In September 2007, a full-scale four-story steel building was experimented to collapse on the E-Defense which is the world's largest three-dimensional shake-table located in Miki City, Hyogo Prefecture, Japan. The ground acceleration histories recorded at the JR Takatori station during the 1995 Hyogo-ken Nanbu earthquake were used as the input for the shake-table experiments under various scales. Experimental result shows that collapse occurred under the 100% Takatori motion, due to local buckling leading to deterioration of columns in the base story.

Elastic and elastoplastic behavior of the building specimen in the experiment was studied and presented in several papers by Suita et al (2009), Yamada et al (2009) and Shimada et al (2010). Collapse mechanism is also discussed; however, detailed behavior of each column in accordance with global behavior of the building was not indicated in details. To give further comprehension about the building specimen performance in the test, this study addresses the deterioration of column shear strength resulting in the base shear capacity degradation and finally the collapse of the whole building. Interaction of column axial force and biaxial bending moment capacity is observed in the response of the building, especially under strong shaking. The study also investigates behavior of column base and its influence on column bending deformation, which takes also an important part in global behavior of the building specimen.

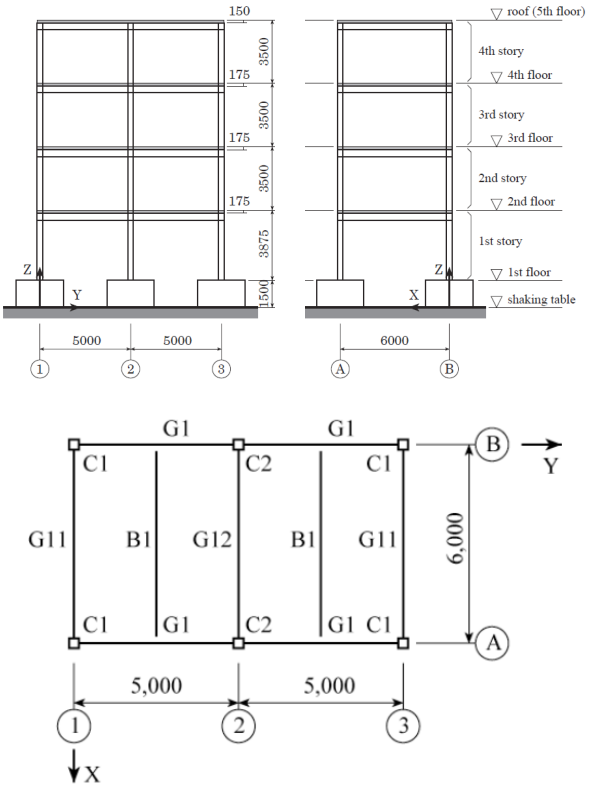


Figure 1 Building Specimen

Table 1 Sections and Materials of the Steel Frame

	Beam (SN400B)			Column (BCR295)
Story	G1	G11	G12	C1,C2
4	H-346×174×6×9	H-346×174×6×9	H-346×174×6×9	RHS-300×9
3	H-350×175×7×11	H-350×175×7×11	H-350×175×9×14	RHS-300×9
2	H-396×199×7×11	H-400×200×8×13	H-400×200×8×13	RHS-300×9
1	H-400×200×8×13	H-400×200×8×13	H-390×200×10×16	RHS-300×9

2. GENERAL INFORMATION

2.1 Building specimen

The building specimen is a full-scale four-story steel moment frame with concrete slabs and autoclaved aerated concrete panels for exterior walls. The plan dimension is 6×10 m, and the total height from the upper surface of stiff foundation to the roof is about 14 m (Fig. 1). Wide-flange sections are used for beams and hollow square sections are used for columns. Steel material type is SN400B and BCR295 for beams and columns, respectively. Section shapes are given in Table 1.

The building specimen is subjected to the input Takatori ground acceleration histories under various scales. Up to 20% Takatori ground motion, the building behaves almost elastically. Then, along with gradually increased scale factors, yielding is observed more obviously in the building behavior, especially in Y-axis. This paper mainly discusses about the two strongest shaking cases, including 60% and 100% Takatori motion when column deterioration occurs.

2.2 Sign convention

All kinds of forces and deformation mentioned in this paper follow sign convention as fully displayed in Fig. 2. Rotational vector is supposed to follow the right-hand screw rule; however, there is only one exception that the sign of rotational vector about X-axis (related to θ_X, M_X) is defined oppositely so as to be consistent with the sign of translational vector causing rotation about this axis. It is also noted that story drift angle is symbolized by r_X and r_Y for X & Y-dir, respectively.

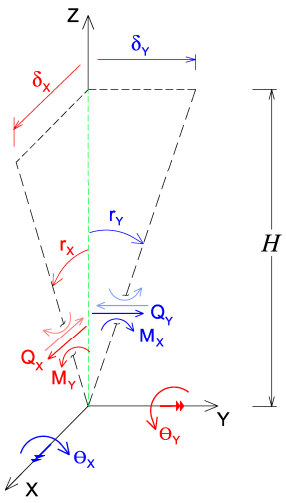
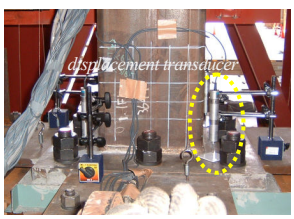


Figure 2 Sign Convention



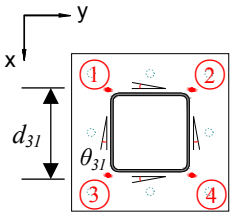


Figure 3 Measurement of Base-Plate Deformation

2.3 Measurement information

Details of general measurement devices (for recording member forces, building displacement, etc.) and processing method for experimental output data are fully described in the publication by Suita et al (2009). This paper gives further information about the measurement of column base-plate deformation. The column is fixed to the stiff foundation by eight anchor bolts M36 (ABR490) through a 50 mm thick base-plate (600×600 mm) welded to column bottom end.

Base-plate displacement of each column is recorded at four places close to column corners, as can be seen in Fig. 3. Upward displacement is defined positive sign. Base-plate rotation angle on each side of column wall is computed using Eq. (1) in which, u_i, u_j - uplift displacement of two conjunctive points i & j, d_{ij} - distance between points i & j. Average rotation angle of two parallel sides is assumed base-plate deformation angle with respect to that side.

$$\theta_{ij} = \frac{u_i - u_j}{d_{ij}} \quad (1)$$

3. 60% TAKATORI LOAD CASE

3.1 Column behavior

Subjected to 60% Takatori ground motion which is 1.5 times larger than the Japanese Level-2 design earthquake (i.e. peak ground velocity at 0.75 m/s), the building performed inelastic behavior. Significant yielding occurs at around 6 s

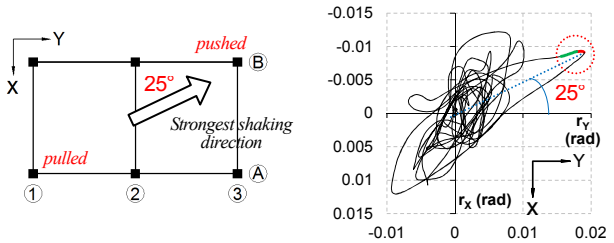
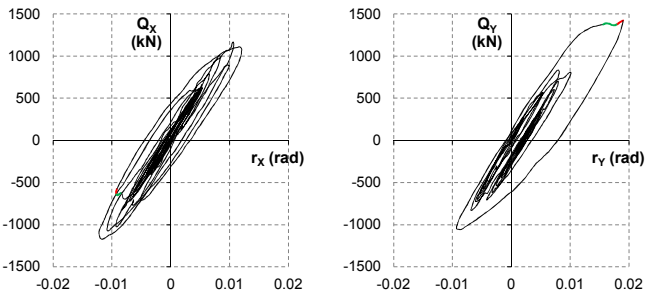


Figure 4 Base Story Drift Orbit (60% Takatori)



(a) X-dir. (b) Y-dir.

Figure 5 Base Shear vs. Base Story Drift (60% Takatori)

elapsed from the excitation start. At that moment, the base story drift reaches to r_Y = 0.019 rad and r_X = 0.009 rad (as highlighted in Fig. 4). Basically, the building moves in 45° diagonal direction and is subjected to balance biaxial bending. However, due to severe yielding in Y-dir rather than X-dir. (displayed by base shear hysteresis curves in Fig. 5), the farthest translational orientation angle of the building at 6.05 s is about 25° with respect to Y-axis.

It is noteworthy that during the time when yielding happens (5.93~6.05 s), hysteresis curve of base shear Q_Y has a little strange performance with a sudden pinching after yielding, exactly occurring from 6.00 s to 6.05 s. Such behavior is also found in column shear hysteresis curves, as can be seen in Fig. 6 for typical columns A1 & B3 at two opposite corners. This phenomenon can be explained due to the interaction of column axial force. Fig. 7-a superposes typical column shear history (Q_Y - primary axis) with story drift history (r_Y - secondary axis). Up to 5.99 s, absolute column axial force (N - primary axis) shown in Fig. 7-b is still increasing in accordance with story drift; however suddenly turns down from 6.00 s and later on, resulting in higher moment capacity of column section. It is the reason why column shear increases after yielding as shown in Fig. 6. On the other hand, it should be noted that upper stories do pull back the base story which is still moving further away during this time, stopping the development of column seismic axial force. Time-history of overturning moment induced by upper stories (M_{OVT-X} - secondary axis) shown in Fig. 7-b proves this situation. In summary, those all interactions are thought to be a reasonable interpretation for pinching behavior in the base shear hysteresis curve.

3.2 Influence of column base rigidity on column bending behavior

Detailed uplift displacement [unit: *mm*] and rotation angle of base-plates at 6.05 s for all columns are given in Fig. 8. It should be noted the building is pulled in corner A1 and pushed in corner B3 at this moment (as can be seen in Fig. 4). Therefore, a gradual increase of base-plate uplift and inclination is identified starting from the corner B3 through to A1, clearly shown in Fig. 8. Base-plate rotation angle $\theta_{X\text{-}BASE}$ of A1 & B3 is selected to plot for comparison in Fig. 9-a, indicating that the separation of column base-plate occurs more significantly in A1 than B3.

Consequently, the rigidity of column base A1 becomes smaller than that of column B3 at the opposite corner. It can hence be deemed that the actual bending deformation of column end B3 must be larger than A1 at 6.05 s. This fact is proved in Fig. 9-b which apparently displays the resultant moment $M_{X\text{-}BOT}$ developed at the bottom-end of column B3 much larger than that of column A1 during the yielding time. In the meantime, column top-end moments $M_{X\text{-}TOP}$ of A1 & B3 are almost equal (Fig. 9-c), stating that the different shear behavior between each column does not come from column top but from the different base-plate fixity behavior during the excitation loading. In other words, different loosening of each base-plate during seismic excitation causes different biaxial bending response of each corresponding column.

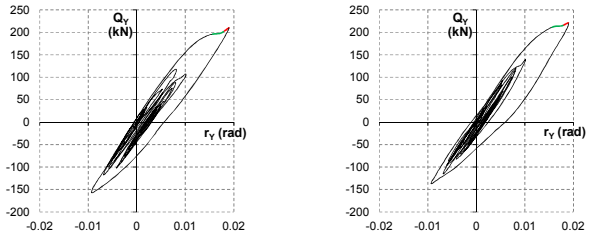


Figure 6 Column Shear Hysteresis Curve (60% Takatori, base story)

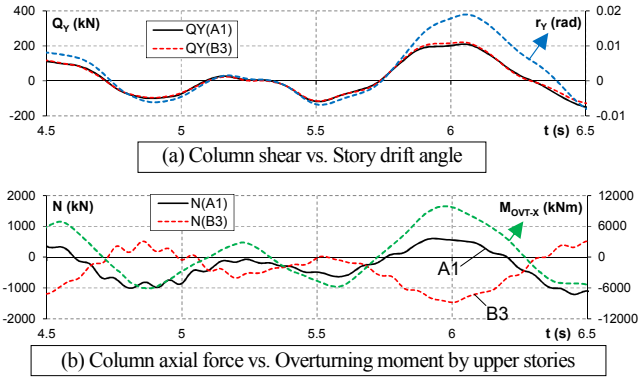


Figure 7 Time-History Curves of Columns and Building (60% Takatori, base story)

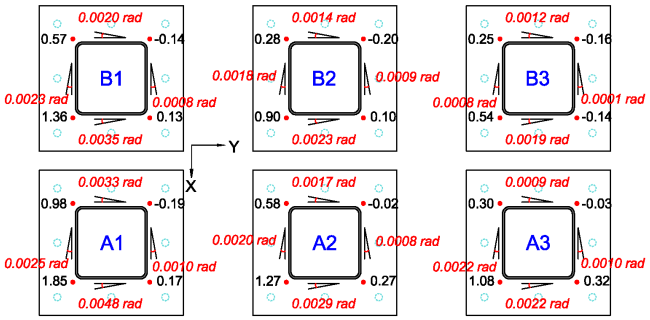


Figure 8 Base-Plate Deformation (60% Takatori, at 6.05 s)

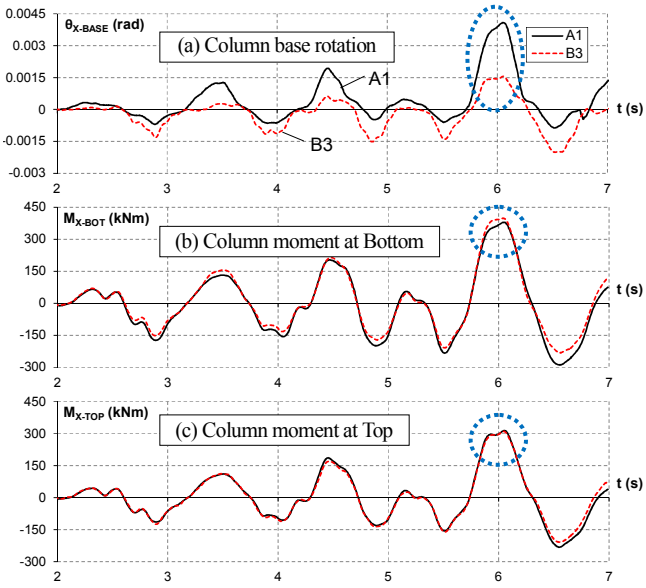


Figure 9 Column Behavior Comparison (60% Takatori)

4. 100% TAKATORI LOAD CASE

4.1 Shear strength deterioration

Before advancing into details, this section summarizes timing ranges of column shear deterioration in the 100% Takatori case. Degradation of column shear is defined as the state when the displacement of the building still increases but column shear capacity cannot increase any further and falls down. From this point of view, the building behaves elastically during the first three seconds elapsed from the start of 100% Takatori excitation. Nonlinear behavior was only observed after 3.00 s. Histories of column shear forces superposed with those of base story drift angle (given in Fig. 10-a for X-dir. & 10-b for Y-dir., where column shear curves represented by colored lines are respect to primary axis, and story drift represented by heavy dashed line is respect to secondary axis) indicate four specific timing ranges of column deterioration before collapse, namely as follows:

① 3.26~3.55 s; ② 3.76~4.05 s;
③ 4.48~4.66 s; ④ 5.68~6.22 s.

4.2 Stages of column shear strength deterioration

The first degradation of column strength (denoted by range ① in Fig. 10) occurs at 3.32 s to column B2 in X-dir. even the story drift angle is not very large (r_X = -0.006 rad) at that time. Column B3 deteriorates right after that at 3.37 s. Other columns still maintain capacity in X-dir. during this duration. However, all columns perform deterioration in Y-dir., starting from columns B2 & B3 at 3.42 s, then to columns B1, A1, A2 and A3 at 3.44 s. Story drift angle in Y-dir. at this level is approximately 0.01 rad. Especially, column B2 gets degradation again at 3.54 s and 3.85 s.

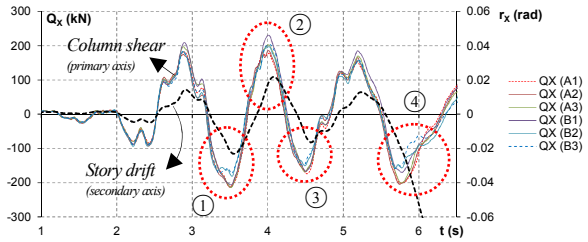
The second deterioration of column strength (denoted by range ② in Fig. 10) can be deemed to start at 3.85 s where columns B1, B2 & B3 deteriorate in both X-dir. and Y-dir. On the other hand, columns A1, A2 & A3 begin degradation in X-dir. at 3.92 s.

The third degradation of column strength (denoted by range ③ in Fig. 10) takes place at 4.50 s where columns B2 & B3 perform significant deterioration of about 20% capacity in both X-dir. and Y-dir. No further deterioration is observed for other columns during this range.

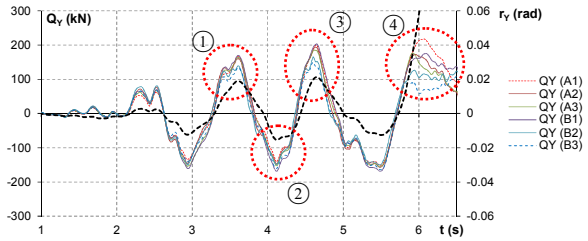
The forth and also the most severe deterioration of column strength (denoted by range ④ in Fig. 10) that leads to the overall collapse mechanism of the building starts from 5.68 s. Damage to columns occurs earlier in X-dir. than in Y-dir. From 5.68 s and later on, story drift angle r_X = -0.012 rad and keeps increasing whilst column shear forces Q_X start decaying. Out of columns B2 & B3 degraded already from previous stages, column A2 deteriorates at 5.73 s, then column A1 & A3 at 5.75 s, and finally degradation of column B1 takes place at 5.78 s.

After that, when story drift r_Y overpasses 0.01 rad, column shear forces in Y-dir. start deterioration. At 5.79 s, column B3 decays earliest and most significant where almost 50% shear capacity is lost. Column B2 degrades mostly at the same time with column B3 but still remains larger capacity of about 65% peak column strength. Then, column B1 deteriorates at 5.85 s, column A3 at 5.91 s, and column A2 at 5.95 s. Story drift angle r_Y corresponding to those moments is 0.018, 0.031 and 0.042 rad, respectively. Deterioration of those columns is about 10-15% shear capacity. Finally, the strongest column A1, which is under tension, keeps up strength the best and only starts decaying until 6.08 s when the story drift r_Y is equal to 0.082 rad.

After all, the building reaches to peak displacement in X-dir. at 6.22 s and then turns back, but still keeps up moving forward in Y-dir. until the building touches the supporting table and surrounding fence. Discussion on this final duration is to be presented in the upcoming section. Deterioration sequence of column shear behavior in both X and Y-dir. is summarized in Table 2.



(a) X-dir.



(b) Y-dir.

Figure 10 Time-History of Column Shear vs. Story Drift

Table 2 Deterioration Sequence of Column Shear Behavior

Range	t (s)	Q_x	Q_y
①	3.32	B2 starts deterioration	
	3.37	B3 starts deterioration	
	3.42		B2, B3 start deterioration
	3.44		B1, A1, A2, A3 start deterioration
	3.54		B2 deteriorates again
②	3.85	B2, B3 deteriorate	
	3.92	A1, A2 deteriorate	
③	4.50	B2, B3 deteriorate	B2, B3 deteriorate
	4.60		B2, B3 deteriorate again
④	5.68	B2, B3 deteriorate	
	5.73	A2 deteriorates	
	5.75	A1, A3 deteriorate	
	5.78	B1 deteriorates	
	5.79		B3 deteriorates
	5.81		B2 deteriorates
	5.85		B1 deteriorates
	5.91		A3 deteriorates
	5.95		A2 deteriorates
	6.08		A1 deteriorates

4.3 Deterioration sequence of column capacity

As presented in the previous section, the building experiences the most vulnerable time starting from 5.79 s elapsed from the start of 100% Takatori excitation. Fig. 11 plotting the base story drift orbit shows the significant yielding and Segment A-B-C (elapsed from 5.74 s to 6.22 s) is selected to discuss. During this segment timing, some important instants should be noted, such as (A) 5.74 s starting at story drift $r_Y = 0$ while $r_X = -0.02$ rad; (B) 5.93 s when the column seismic axial force reaches to peak value and then turns back due to resistant movement of upper stories; and (C) 6.22 s when the building reaches to peak r_X and then unloading in X-axis happens. Total collapse finally takes place a little moment after that.

Subject to 100% Takatori ground motion, the building specimen has the same yielding translational direction (about 30° diagonal with respect to Y-axis) as in case of 60% Takatori. The study again explores behavior of two typical columns A1 & B3 like the aforementioned 60% load case. In this diagonal direction, timing from 5.74 s to 6.22 s, column A1 is subject to largest seismic tension whilst column B3 has the most significant seismic compression. It is one of reasons why deterioration of column moment B3 is more severe than A1 (as displayed in Fig. 12). $M_{Y\text{-}BOT}$ of column A1 starts decaying from point A (5.74 s) but at that time $M_{Y\text{-}BOT}$ of column B3 has deteriorated already. Advancing to point B (5.93 s), column B3 has $M_{Y\text{-}BOT} = -87$ kNm while column A1 has $M_{Y\text{-}BOT} = -216$ kNm. Column B3 suffers the most resistance loss of about 50% capacity and becomes damaged first. As a result, loss of bending moment capacity leads to deterioration of column shear.

Comparative behavior of column shear (typically Q_Y) is selected for plotting in Fig. 13-a. It can be realized that due to the position of each column over the building plan, deterioration sequence of column shear is varied. Starting from point A (5.74 s), the building moves forward in Y-dir. Compression keeps up developed in column B3. On the contrary, tension is increasing in column A1. However, up to point B (5.93 s), column axial forces all of sudden turn back although base story displacement is still growing up (as shown by column axial force history in Fig. 13-b, with respect to primary axis). It is because of the resistant displacement of upper stories helping pull back the base story. Overturning moment induced by those upper stories (shown in Fig. 13-b, with respect to secondary axis) clarifies this situation.

Correlation between bending moment behavior at column bottom-end and top-end is investigated by exploring the changing trend of inflection point position (see Figs. 13-c & d for column A1 & B3, respectively). Effective length of the 1st story column (defined as the height from the column base to the center line of girder) is 3500 mm. Before the vulnerable time, inflection point is still stable at around the middle of column effective height. But when the column bottom-end deteriorates capacity and yields, the column top-end still remains capacity and works better. Therefore, the inflection point is shifted down significantly. Column bottom-end is deemed to get damaged earlier than top-end.

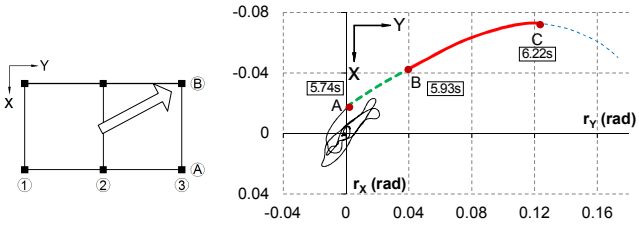
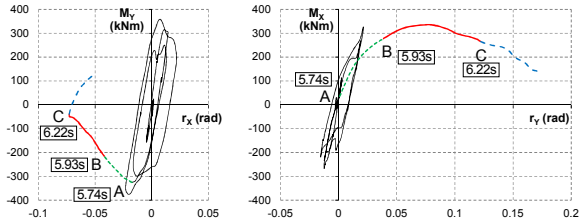
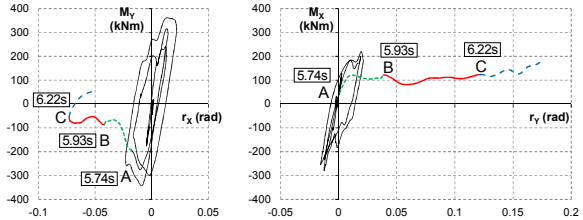


Figure 11 Base Story Drift Orbit (100% Takatori)

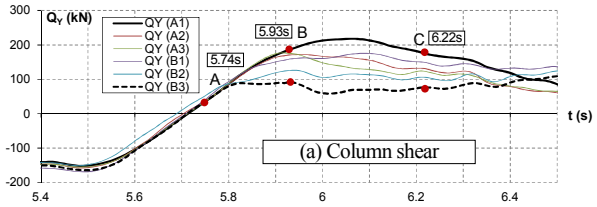


(a) Column bottom moment vs. Story drift (Column A1)

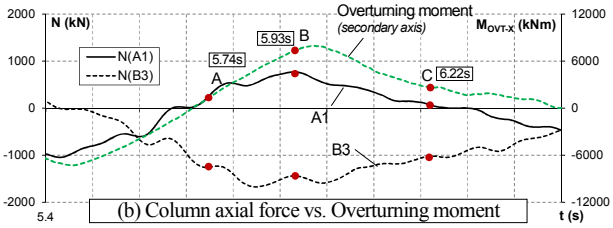


(b) Column bottom moment vs. Story drift (Column B3)

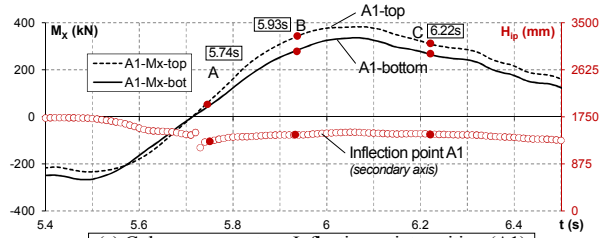
Figure 12 Column Moment Hysteresis (100% Takatori)



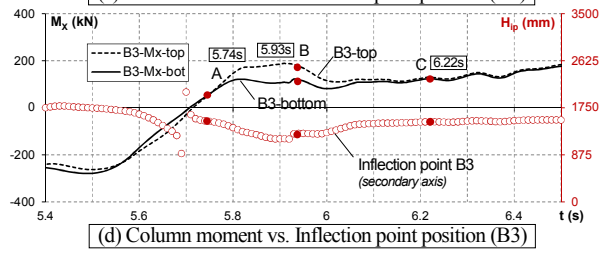
(a) Column shear



(b) Column axial force vs. Overturning moment



(c) Column moment vs. Inflection point position (A1)



(d) Column moment vs. Inflection point position (B3)

Figure 13 Time-History Curves (100% Takatori)

To summarize the situation, Fig. 14 plots the extracted base story drift orbit measured in the collapse test with segment A-B-C-D (5.74 ~6.50 s). Drift orbit of the upper 2nd story is also plotted in this figure, showing that unloading happens to upper stories after point B (5.93 s) while the frame in the base story is still yielding and moving forward because of losing resistance. Unloading in X-axis might have started from this point of time. But the base story keeps up displacement along this way until point C (6.22 s).

In addition, to easily follow column behavior during the vulnerable time, Fig. 15 shows the integrated graphs for column forces (N, Q & M), tracing the same column top-end translational orbit with segment A-B-C-D given in Fig. 14. Column axial force diagram is shown uppermost. Plotted in the middle are column shear vectors Q_X & Q_Y. Resultant bending moment vectors M_Y & M_X at column bottom-end are plotted lowermost. Values of force vectors corresponding to each important point are indicated in the figure. The spline connecting vectors in series gives a relative diagram depicting behavior trend of column forces in accordance with the building displacement history.

Biaxial moment vector M_{XY} defined as the addition of partial moment vectors M_X and M_Y is adopted to evaluate moment capacity of columns. M-N (moment – axial force) interaction rule is visible in Fig. 15. During the pre-collapse time, moment capacity of column A1 becomes much larger than that of column B3 because the absolute axial force developed in A1 is smaller than in B3. On the other hand, local buckling occurring significantly in column B3 additionally reduces column strength, which means the column subjected to both compression and biaxial bending tends to be damaged by local buckling earlier than being subjected to pure biaxial bending only.

5. CONCLUSIONS

This study gives further investigation on the building specimen performance in the collapse test, addressing the column strength deterioration. Some concluding remarks can be stated as followings:

(1) The interaction of column axial force on bending moment capacity was observed in the test. The changing of column axial force during the seismic loading results in the changing of biaxial bending moment capacity of the cross section. As a result, column shear capacity might deteriorate.

(2) Interaction of column axial force is also found in mechanism of local buckling. The column subjected to both compression and biaxial bending tends to be damaged by local buckling earlier than being subjected to pure biaxial bending only.

(3) Discrepancy of degradation behavior among each column during the seismic loading due to the different position of columns on the building plan is also clarified in the study. On the other hand, loosening behavior of each base-plate during seismic excitation also comes from column position distribution, which slightly takes part in reducing rigidity of column base, resulting in different bending response of each relevant column.

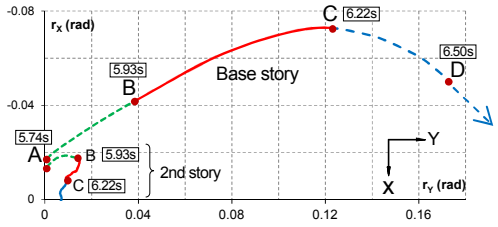


Figure 14 Extracted Story Drift Angle Orbit (100% Takatori, 5.74 ~ 6.50 s)

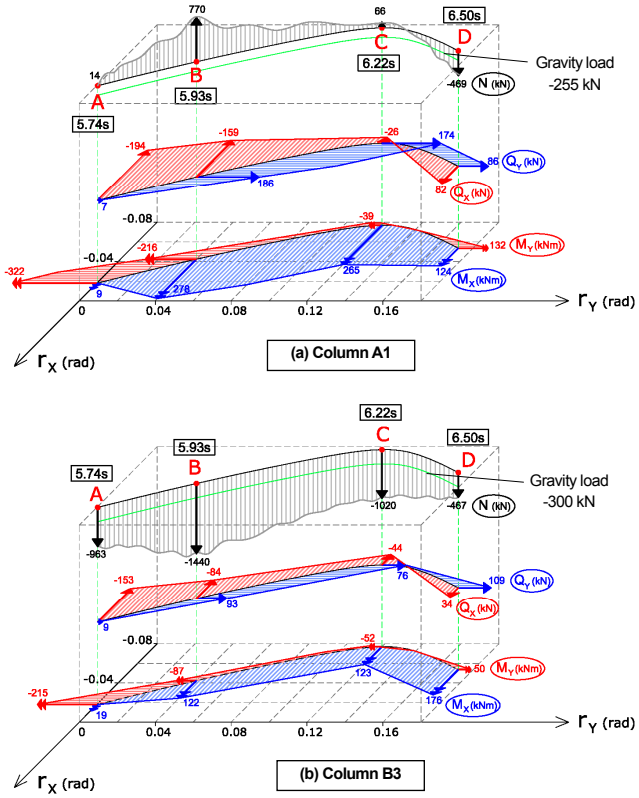


Figure 15 Integrated Graphs Describing Column Response (100% Takatori, 5.74 ~ 6.50 s)

Acknowledgements:

The authors acknowledge Dr. Bruce F. Maison (California, USA), Prof. Satoshi Yamada (TIT, Japan) and Prof. Motohide Tada (Osaka University, Japan) for their enthusiastic technical supports.

References:

Shimada, Y., Suita, K., Yamada, S., Matsuoka, Y., Tada, M., and Kasai, K. (2010) Collapse Behavior on Shaking Table Test – Complete Collapse Test of Full-Scale 4-Story Steel Building Part 3, *Journal of Structural and Construction Engineering, Transactions of AIJ*, Vol.75, No.653, pp.1351-1360 (in Japanese).

Suita, K., Y., Matsuoka, Yamada, S., Shimada, Y., Tada, M., and Kasai, K. (2009) Experimental Procedure and Elastic Response Characteristics of Shaking Table Test – Complete Collapse Test of Full-Scale 4-Story Steel Building Part 1, *Journal of Structural and Construction Engineering, Transactions of AIJ*, Vol.74, No.635, pp.157-166 (in Japanese).

Yamada, S., Suita, K., Matsuoka, Y., and Shimada, Y. (2009) Elasto-Plastic Responses and Process Leading to a Collapse Mechanism – Complete Collapse Test of Full-Scale 4-Story Steel Building Part 2, *Journal of Structural and Construction Engineering, Transactions of AIJ*, Vol.74, No.644, pp.1851-1859 (in Japanese).

10CUEE CONFERENCE PROCEEDINGS
10th International Conference on Urban Earthquake Engineering
March 1-2, 2013, Tokyo Institute of Technology, Tokyo, Japan

CYCLIC LOADING TEST ON RHS COLUMNS UNDER BI-DIRECTIONAL HORIZONTAL FORCES

Takanori Ishida[1], Yuko Shimada[2], and Satoshi Yamada[3]

1) Graduate Student, Tokyo Institute of Technology, Japan
2) Assistant Professor, Faculty of Engineering, Chiba University, Chile
3) Associate Professor, Structural Engineering Research Center, Tokyo Institute of Technology, Japan
ishida.t.ae@m.titech.ac.jp, yshimada@faculty.chiba-u.jp, naniwa@serc.titech.ac.jp

Abstract: Columns are subjected to bi-axial bending moment, since buildings behave 3-dimensionally under seismic excitations. However, only few researches on post local buckling and deterioration behavior of RHS columns under bi-directional horizontal forces have been reported. In this study, at first, the simple horizontal loading protocol was proposed based on the investigation of random horizontal displacement orbits obtained by elasto-plastic response analyses of multi-story steel frames subjected to bi-directional horizontal ground motions. After that, using the simple loading protocol, a series of tests on RHS columns subjected to bi-directional horizontal cyclic loading and constant axial force were conducted. The experimental results were compared with the analytical results using multiple shear spring (MSS) model.

1. INTRODUCTION

In Japan, Rectangular Hollow Section (RHS) steel tubes are generally used as columns for steel buildings. Columns are subjected to bi-axial bending moment that because buildings behave 3-dimensionally under seismic excitations. In order to evaluate the seismic resistance of steel building structures, it is important to clarify the bi-axial bending behavior of RHS-columns including deterioration range governed by local buckling. However, only few researches on post local buckling and deterioration behavior of RHS columns under bi-directional horizontal forces have been reported.

In this study, to investigate the hysteresis of RHS columns including post local buckling and deterioration range under bi-axial bending moments, a series of tests on RHS columns subjected to bi-directional horizontal cyclic loading and constant axial force were conducted. In addition, the experimental results were compared with the analytical results using multiple shear spring (MSS) model.

2. CYCLIC LOADING TEST ON RHS COLUMNS UNDER BI-DIRECTIONAL HORIZONTAL FORCES

2.1 Test Specimen

The test specimen consist of RHS column; □-200×9 (BCR295, Width-to-thickness ratio: 22.2, length: 1734mm) and steel plates welded to both ends of RHS-column to connect to the loading frame, as shown in Figure 1. Tensile coupon test of the flat part of RHS column was conducted using JIS-1A testing sample and the result is shown in Figure 2.

2.2 Horizontal Loading Protocol

The simple horizontal loading protocol was proposed based on the investigation of random horizontal displacement orbits obtained by elasto-plastic response analyses of multi-story steel frames subjected to bi-directional horizontal ground motions. The configuration of the horizontal loading protocol is shown in Figure 3 (1). The horizontal loading protocol was configured as follows,

1. The basic shape of the horizontal loading protocol consists of three ellipses. The angle of shifting major axis of each ellipse was set to -30 deg., 0 deg., +30 deg. from the main axis direction of the horizontal loading protocol and frequency of loading was 1 to 2 to 1.
2. The ellipticity of each ellipse was set to 0.3.
3. A displacement-controlled cyclic loading was applied with increasing the length of major axis of an ellipse. Displacement amplitude was increased by $2\theta_{pc0}$. Where, θ_{pc0} is the elastic column rotation corresponding to the full plastic moment with axial force of the column under uni-axial bending M_{pc0}.
4. The rotational direction was constant.

The outline of the loading order is shown in Figure3 (2). The four loading steps make one set. Displacement amplitude was increased after finishing the one set. The four loading steps that make one set are as follows (At the first set, step 0 is added to one set),

Step 0: At the first set, loading from the original point O along the main axis direction of the horizontal loading protocol toward the point A. (Point A is the intersection of the ellipse of 0 degree).

Step 1: Loading clockwise along the ellipse of 0 degree from the point A. After go around along the ellipse of 0 degree, continuously loading to the point B (Point B is the intersection that can transition smoothly to the ellipse of +30 degree).

Step 2: Loading clockwise along the ellipse of +30 degree from the point B. After go around along the ellipse of +30 degree, continuously loading to the point C (Point C is the intersection that can transition smoothly to the ellipse of 0 degree).

Step 3: Loading clockwise along the ellipse of 0 degree from the point C. After go around along the ellipse of 0 degree, continuously loading to the point D (Point D is the intersection that can transition smoothly to the ellipse of -30 degree).

Step 4: Loading clockwise along the ellipse of -30 degree from the point D. After go around along the ellipse of -30 degree, continuously loading to the point E (Point E is the intersection that can transition smoothly to the ellipse of 0 degree of the next set).

After finishing the first set, cyclic loading was applied by repeat the step 1-4.

2.3 Parameters

The test parameters were main axis direction of the horizontal loading protocol and axial force ratio. The main axis direction of the horizontal loading protocol was set to 0 or 45 degree from principal axis of the column cross-section. Constant axial force was applied to the specimen and axial force ratio was set to 0.2 or 0.4 for each of the main axis direction. The list of test parameters is shown in Table 1.

2.4 Test Setup

The test specimen was placed in the loading frame, as

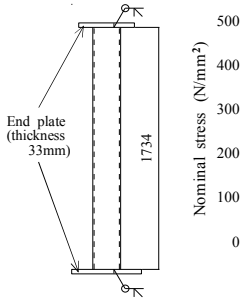


Figure 1 Test Specimen

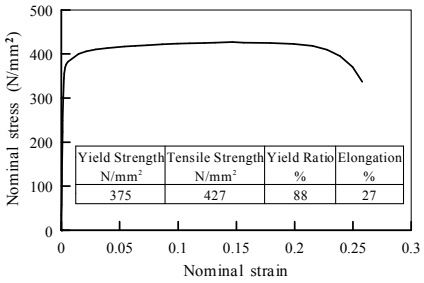
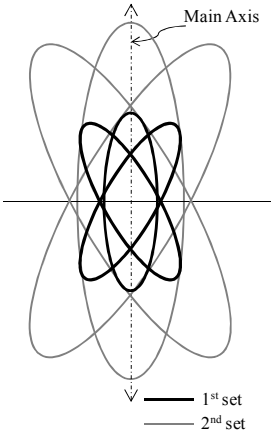


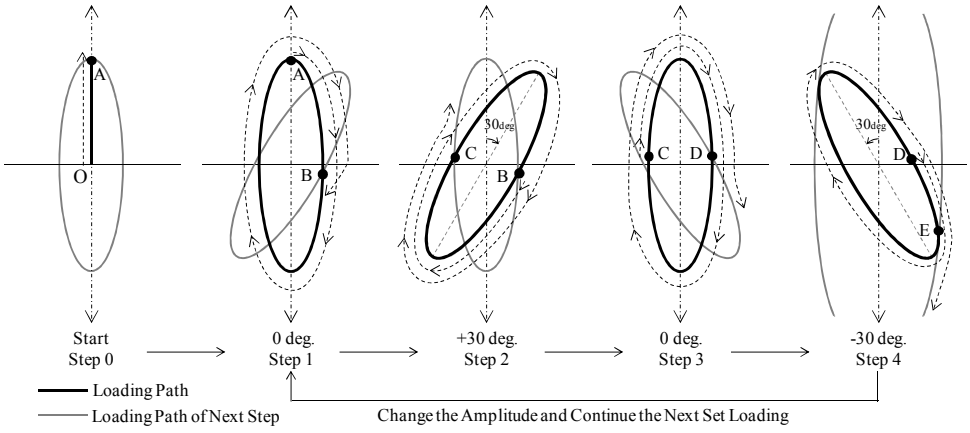
Figure 2 Coupon Test Result

Table 1 List of Test Parameters

Specimen Name	CB00_0.2_22	CB00_0.4_22	CB45_0.2_22	CB45_0.4_22
Axial Force Ratio	0.2	0.4	0.2	0.4
Horizontal Loading Protocol	Main Axis of Loading Protocol; Main Axis Direction 0 deg		Main Axis of Loading Protocol; Main Axis Direction 45 deg	

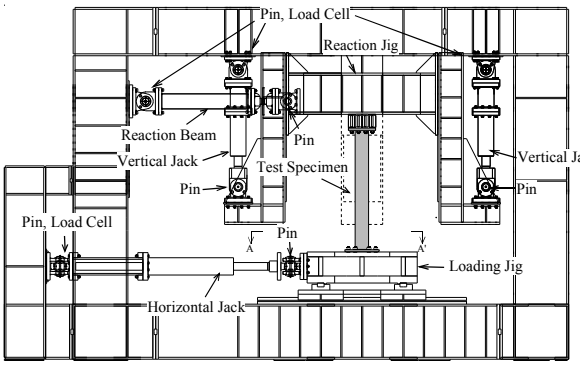


(1) Configuration

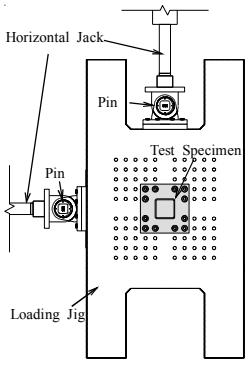


(2) Loading Order

Figure 3 Horizontal Loading Protocol



(1)Elevation



(2)A-A' Section

Figure 4 Test Setup

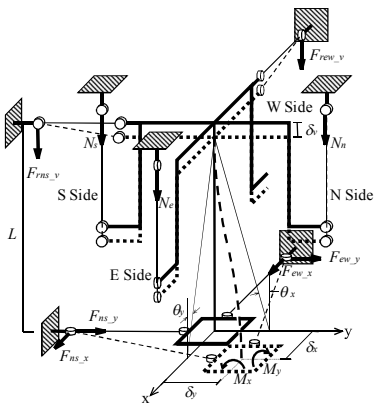


Figure 5 Measurement System

shown in Figure 4 (1), (2). Both ends of the column were fixed on the reaction jig and the horizontal loading jig. The specimen was subjected to a horizontal force by the two horizontal jacks through the horizontal loading jig. Constant axial force was applied by three vertical jacks through the reaction jig. To load under the condition of anti-symmetric bending moment, the reaction jig was kept horizontally. Instrumentation was placed to monitor loads and deformation of the specimen. Displacement transducers monitored the deformation of the specimen and test jig. Strain gauges were attached to the column in order to confirm if the inflection point located at mid height of the column. The rotation angle of the column, axial force and bending moment, assuming an anti-symmetric distribution bending moment along the column height, were calculated by Equation (1) -(7) (Figure 5).

$$Q_x = F_{ew_x} + F_{ns_x} \quad (1)$$

$$Q_y = F_{ns_y} + F_{ew_y} \quad (2)$$

$$N = N_n + N_s + N_e + F_{rns_v} + F_{rew_v} \quad (3)$$

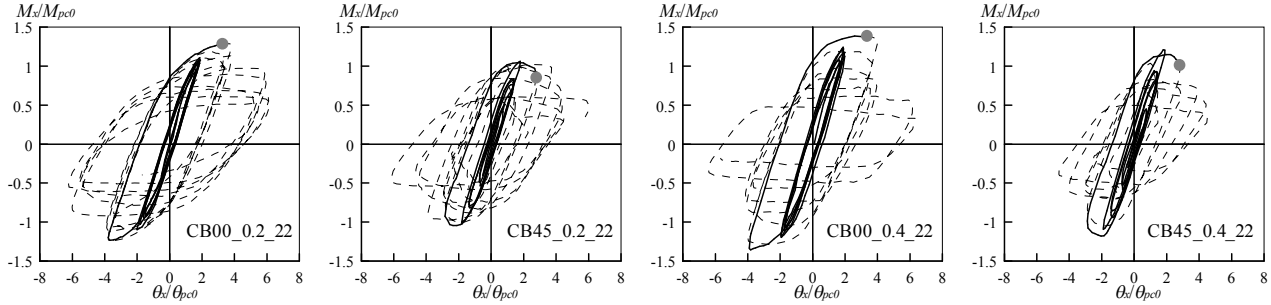
$$M_x = Q_y(L - \delta_v)/2 + N \cdot \delta_y/2 \quad (4)$$

$$M_y = Q_x(L - \delta_v)/2 + N \cdot \delta_x/2 \quad (5)$$

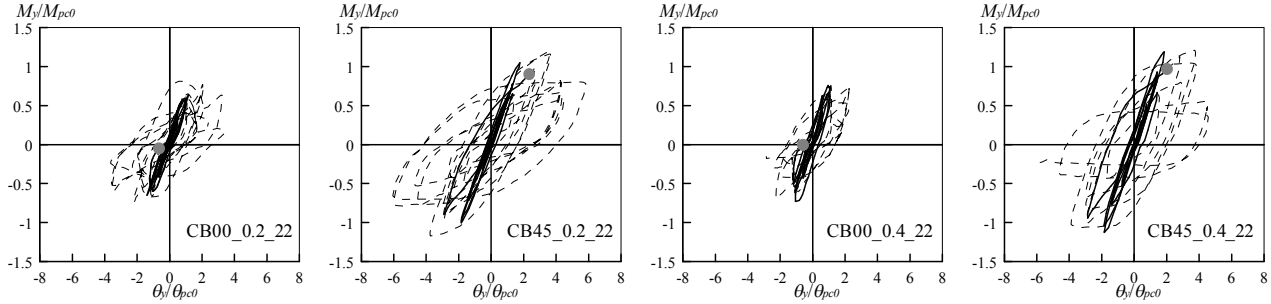
$$\theta_x = \tan^{-1}\{\delta_y/(L - \delta_v)\} \quad (6)$$

$$\theta_y = \tan^{-1}\{\delta_x/(L - \delta_v)\} \quad (7)$$

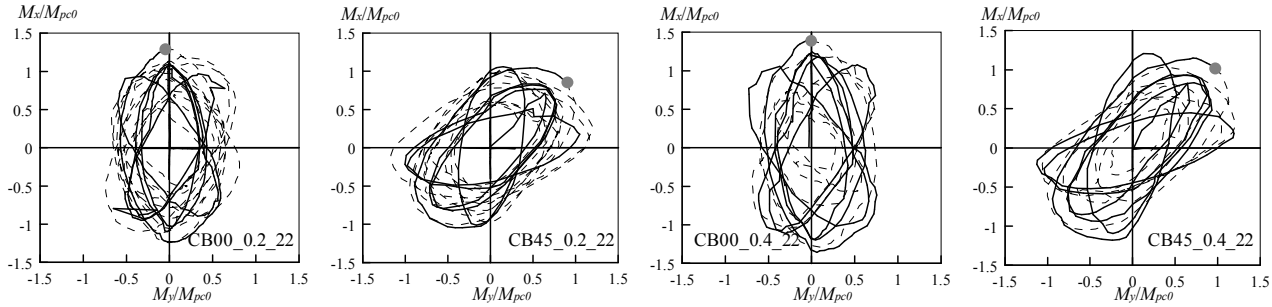
Where,



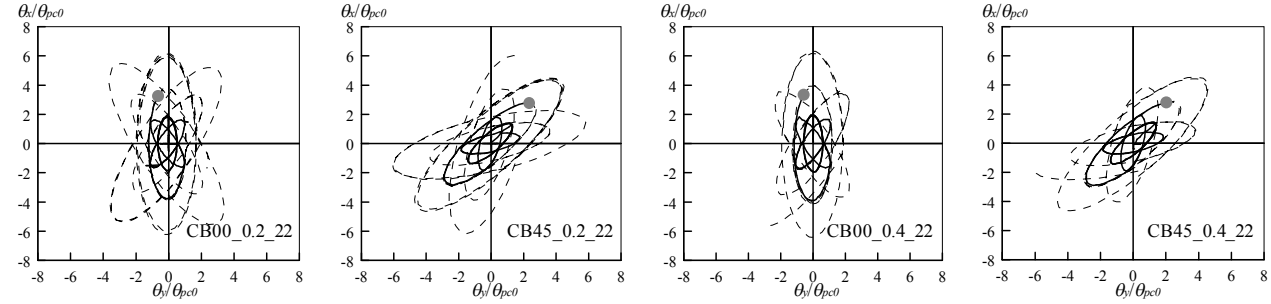
(1) x Axis Moment- Rotation Relationships



(2) y Axis Moment- Rotation Relationships



(3) Load Orbits



(4) Displacement Orbits

Figure 6 Test Results

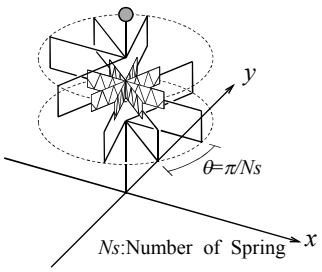
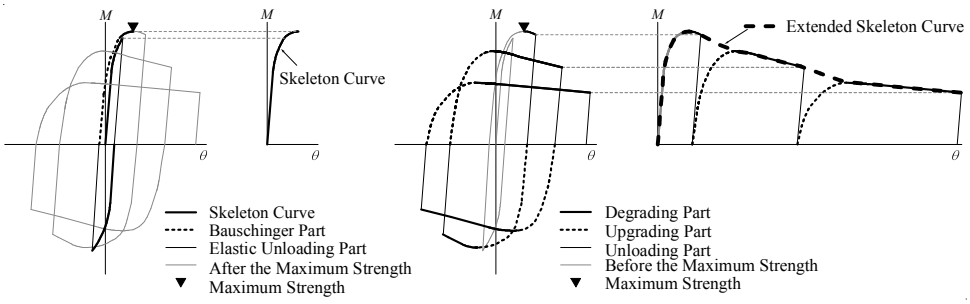


Figure 7 MSS Model



(1)Before the Maximum Strength (2)After the Maximum Strength

Figure 8 Decomposition of Hysteresis Curve and Skeleton Curve, Extended Skeleton Curve

L	: column length
δ_x	: x axis direction story drift
δ_y	: y axis direction story drift
δ_v	: vertical deformation
θ_x	: x axis rotation angle of the column
θ_y	: y axis rotation angle of the column
F_{ns_x}	: x axis direction external force applied by NS direction horizontal jack
F_{ns_y}	: y axis direction external force applied by NS direction horizontal jack
F_{ew_x}	: x axis direction external force applied by EW direction horizontal jack
F_{ew_y}	: y axis direction external force applied by EW direction horizontal jack
Q_x	: x axis direction shear force
Q_y	: y axis direction shear force
N_n	: vertical direction external force applied by N side vertical jack
N_s	: vertical direction external force applied by S side vertical jack
N_e	: vertical direction external force applied by E side vertical jack
F_{rns_v}	: vertical direction external force applied by NS direction reaction beam
F_{rew_v}	: vertical direction external force applied by EW direction reaction beam
N	: axial force
M_x	: x axis moment applied to the column end
M_y	: y axis moment applied to the column end

2.5 Test Results

The maximum strength of all specimens was governed by local buckling. Loading was continued either until the specimen completely lost their axial force supporting capacity or until before local buckling wave comes in contact with the jig. All specimens were observed that the inflection point located close to mid height of the column by strain gauges. Figure 6 (1)-(4) show the x axis and y axis moment-rotation relationships, the load orbits, and the displacement orbits for all specimens that were normalized M_{pc0} and θ_{pc0}. In these figures, ● plot shows the maximum resultant moment of x axis and y axis $\sqrt{M_x^2 + M_y^2}$. Solid line shows the behavior till the maximum resultant moment. Broken line shows the behavior after reaching the maximum resultant moment.

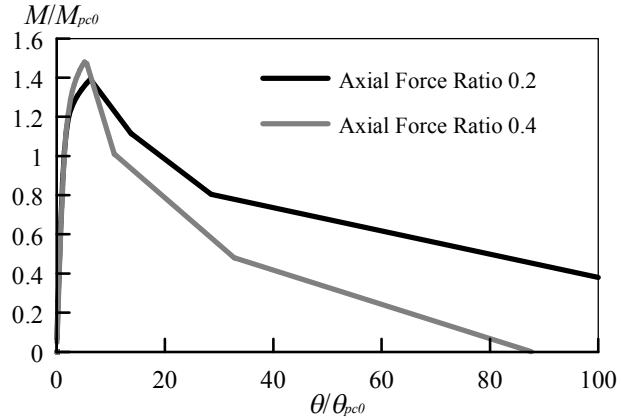


Figure 9 Calculated Load-Deformation Relationships under Monotonic Loading

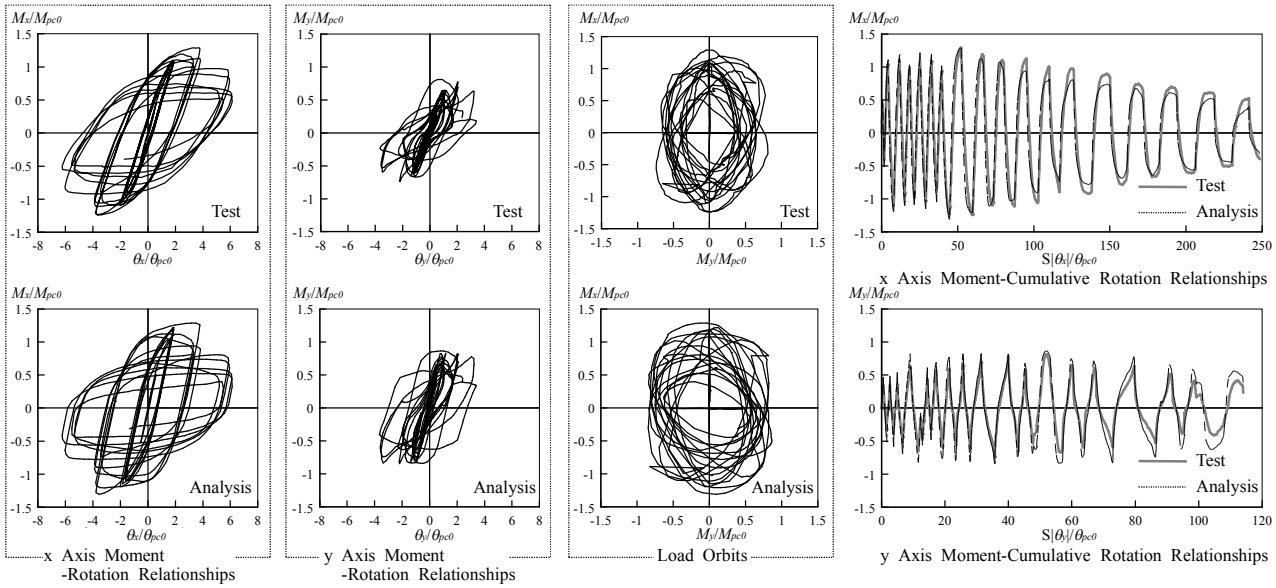
As observed from the displacement orbits, in the second set that set the length of major axis of an ellipse to $4\theta_{pc0}$, all specimens reached the maximum resultant moment on the step 1. In comparison of the maximum resultant moment of specimens which were set the main axis direction to 0 or 45 degree, in case of axial force ratio 0.2, specimen CB00_0.2_22 was $1.29M_{pc0}$, specimen CB45_0.2_22 was $1.24M_{pc0}$, in case of axial force ratio 0.4, specimen CB00_0.4_22 was $1.39M_{pc0}$, specimen CB45_0.4_22 was $1.41M_{pc0}$, hence, the maximum resultant moment of 0 degree and 45 degree were almost same.

3. ANALYSIS OF RHS COLUMNS SUBJECTED TO BI-DIRECTIONAL HORIZONTAL FORCES USING MSS MODEL

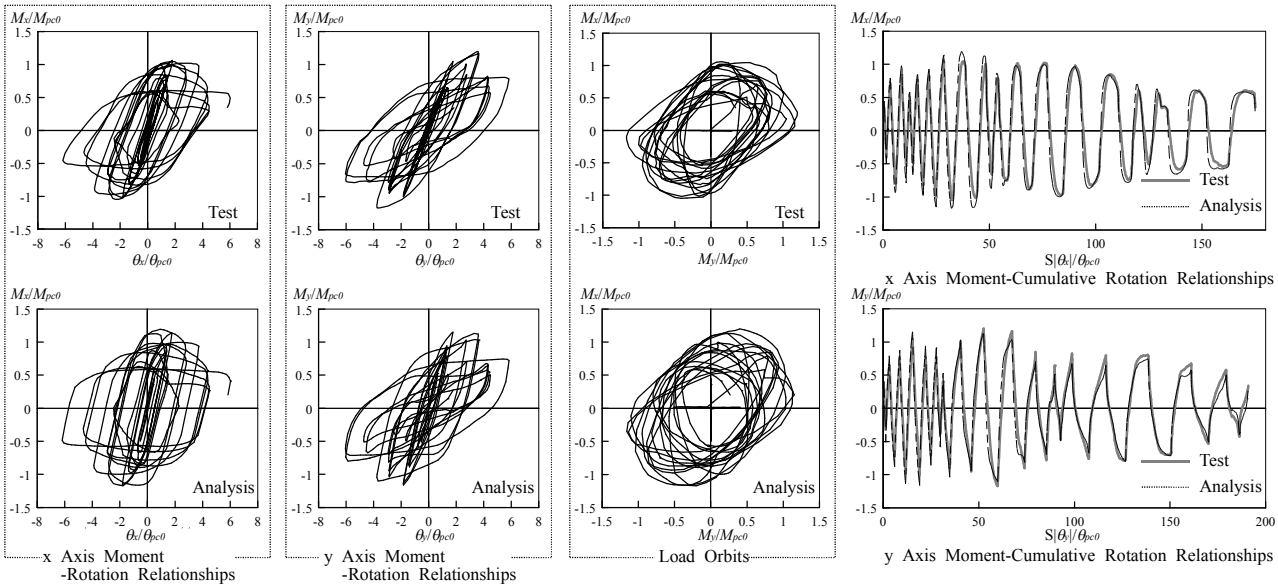
3.1 Analytical Model

In this study, MSS (Multiple Shear Spring) model shown in Figure 7 was used. In the MSS model, the bi-directional horizontal behavior is expressed by the equal shear springs which placed at an equal angle. The reason to use this model is that RHS columns have small directionality of the structural characteristics.

Before the maximum strength, the hysteresis model used in this analysis consists with the skeleton curve which corresponds to the load-deformation relationship under monotonic loading, Bauschinger part, and elastic unloading



(1)CB00_0.2_22



(2)CB45_0.2_22

Figure 10 Comparison between Experimental and Analytical Results

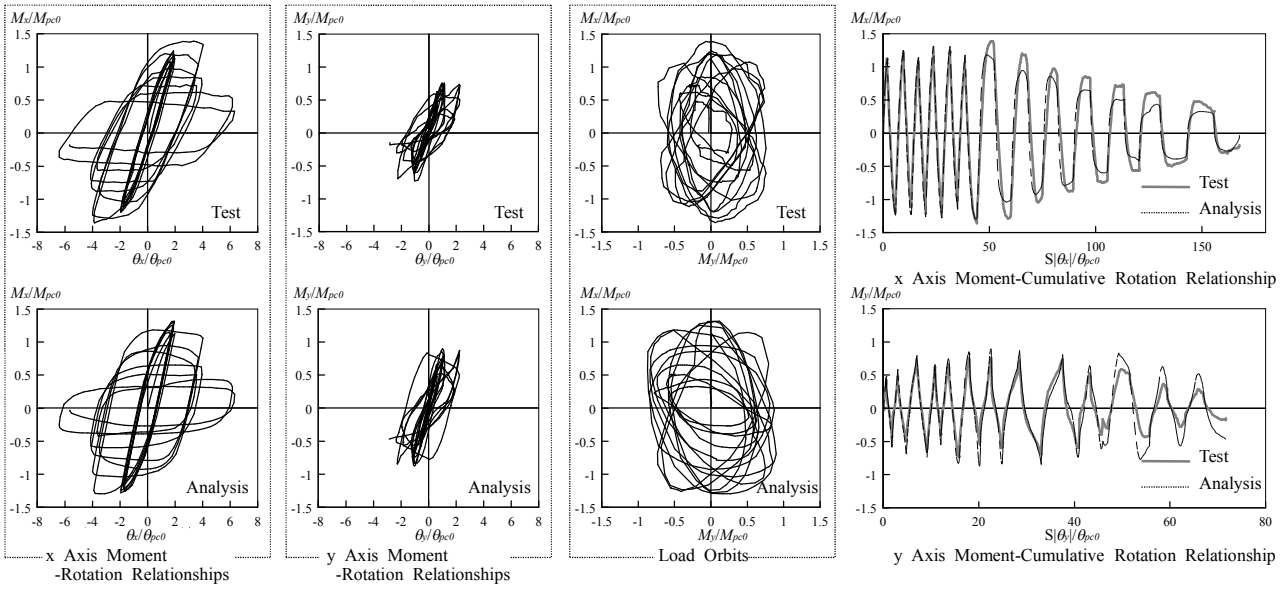
part, as shown in Figure 8 (1). After the maximum strength, the hysteresis model consists with the degrading part which corresponds to the extended skeleton curve, the upgrading part, and unloading part, as shown in Figure 8 (2). Among them, the extended skeleton curve approximately corresponds to the load-deformation relationship including deterioration range under monotonic loading. Using the calculated load-deformation relationship of RHS column under monotonic loading including deterioration behavior governed by local buckling, as shown in figure 9, the extended skeleton curve was modeled. In the analysis, the extended skeleton curve was divided into the element springs in the MSS model. By consideration of accuracy, the number of shear springs was set to 16.

As the Bauschinger part, Akiyama and Takahashi's model was applied. As the upgrading part, the bilinear model proposed by Yamada et al. was applied.

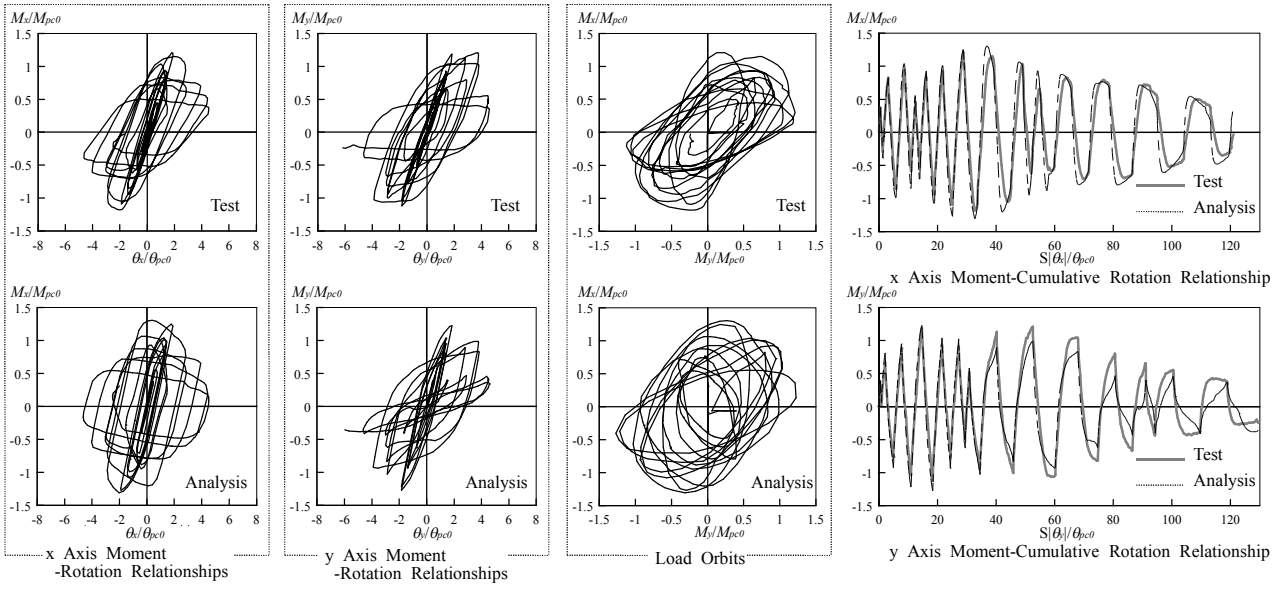
3.2 Comparison Between Experimental and Analytical Results

Figure 10 (1)-(4) show the x axis and y axis moment-rotation relationships, the load orbits, and the x axis and y axis the moment-cumulative rotation relationships for all experimental and analytical results that were normalized M_{pc0} and θ_{pc0}.

Regarding the x axis and y axis moment-rotation relationships of all specimens, although the errors of unloading stiffness were observed in deterioration range that because degrading of unloading stiffness is ignored in this hysteresis model, overall, the analytical results including deterioration range agreed the experimental results. Moreover, the analytical model also is able to trace the load orbits. On the basis of these investigations, it can be concluded that the analytical model using the MSS model



(3)CB00_0.4_22



(4)CB45_0.4_22

Figure 10 Comparison between Experimental and Analytical Results (Cont.)

closely approximated the hysteresis of RHS columns including the deterioration range under bi-directional horizontal forces and constant axial force.

4. CONCLUSIONS

To investigate the hysteresis of RHS columns including post local buckling and deterioration range under bi-axial bending moments, a series of tests on RHS columns subjected to bi-directional horizontal cyclic loading and constant axial force were conducted using the simple horizontal loading protocol. The test parameters were main axis direction of the horizontal loading protocol and axial force ratio. The maximum strength of each specimen was governed by local buckling. In comparison of the maximum resultant moment $\sqrt{Mx^2 + My^2}$ of specimens which were set the main axis direction to 0 or 45 degree, the maximum resultant moment of 0 degree and 45 degree were almost same.

In addition, the experimental results were compared with the analytical results using MSS model. The analytical model using the MSS model closely approximated the hysteresis of RHS columns including the deterioration range under bi-directional horizontal forces and constant axial force.

References:

Chen, Y., Ohi, K. and Takanashi, K. (1993), "The Inelastic Behavior of Square-Box Steel Beam-Columns Subject to Tri-Directional Varying Loads," *Journal of Structural and Construction Engineering*, AIJ, No. 447, 139-148. (in Japanese)

Yamada, S., Ishida, T. and Shimada, Y., (2013), "Cyclic Loading

Tests on RHS Columns under Bi-Directional Horizontal Forces", *Journal of Structural and Construction Engineering*, AIJ, No. 683, 203-212. (in Japanese)

Wada, A. and Hirose, K., (1989), "Elasto-Plastic Dynamic Behaviors of the Building Frames Subjected to Bi-Directional Earthquake Motion", *Journal of Structural and Construction Engineering*, AIJ, No. 399, 37-47. (in Japanese)

Yamada, S., Ishida, T. and Shimada, Y., (2012), "Hysteresis Model of RHS Columns in the Deteriorating Range Governed by Local Buckling", *Journal of Structural and Construction Engineering*, AIJ, No. 674, 627-636. (in Japanese)

Yamada, S., Akiyama, H. and Kuwamura, H., (1993), "Post-Buckling and Deteriorating Behavior of Box-Section Steel Members", *Journal of Structural and Construction Engineering*, AIJ, No. 444, 135-143. (in Japanese)

Akiyama, H. and Takahashi, M., (1990), "Influence of Bauschinger Effect on Seismic Resistance of Steel Structures", *Journal of Structural and Construction Engineering*, AIJ, No. 418, 49-57. (in Japanese)

Chiu, J., Yamada, S., Kuwamura, H. and Akiyama, H., (1992), "A Research on the Ability of Cold Forming Box-Shaped Steel Members", *Summaries of Technical Papers of Annual Meeting*, AIJ, 1275-1276. (in Japanese)

10CUEE CONFERENCE PROCEEDINGS
10th International Conference on Urban Earthquake Engineering
March 1-2, 2013, Tokyo Institute of Technology, Tokyo, Japan

Test on Eccentric Beam-to-RHS Column Connections

Norihito Miki[1], Yu Jiao[2], Satoshi Yamada[3], Shoichi Kishiki[4] and Takashi Hasegawa[5]

1) Graduate Student, Tokyo Institute of Technology, Japan
2) Assistant Professor, School of Engineering, Tokyo University of science, Japan
3) Associate Professor, Structural Engineering Research Center, Tokyo Institute of Technology, Japan
4) Lecturer, Dept. of Architecture, Osaka Institute of Technology, Japan
5) Building Research Institute, Japan
miki.n.ac@m.titech.ac.jp, yujiao@rs.tus.ac.jp, yamada.s.ad@m.titech.ac.jp, kishiki@archi.oit.ac.jp, hase@kenken.go.jp

Abstract: In multistory steel structures, for it is convenient to attach the external wall, the edge of the beam is aligned with the face of the column. This is called an eccentric beam-to-column connection. In case of such connection type, the panel zone is also subjected to torsion. Therefore, the outside panel will take a larger amount of shear force than the inside panel, hence it will yield before the inside panel. Further on, because of the eccentricity, the strain in the beam flange may be asymmetric, which leads to early fracture of the beam. However, since the beam web is connected to the column skin plate near the outside panel, the resistance of the web might increase. Experimental tests were conducted to investigate the behavior of the eccentric beam-to-column connections under cyclic loading.

1. INTRODUCTION

Usually, in the exterior frames of a multistory steel structure, the edge of the beam is aligned with the column face, because it is convenient to attach the nonstructural walls.

Such a connection is called eccentric beam-to-column connection because the longitudinal axis of the beam is shifted to the exterior with respect to the center of the column. Therefore because of this eccentricity, the strain distribution in the beam flange is asymmetric, which might lead to early fracture in this region.

In addition, since the beam web is connected to the column skin plate in the region of the outside panel, the joint efficiency of the web might increase. Another phenomenon that has to be accounted for in eccentric beam-to-column connections is the torsion that occurs in the panel zone, (Tanaka et al. 1999). This may be due to the fact that the outside panel is acted upon by larger shear forces than the inside one, hence it will probably yield earlier than the inside panel. In order to closely investigate the behavior of eccentric beam to column connections, a set of tests was conducted.

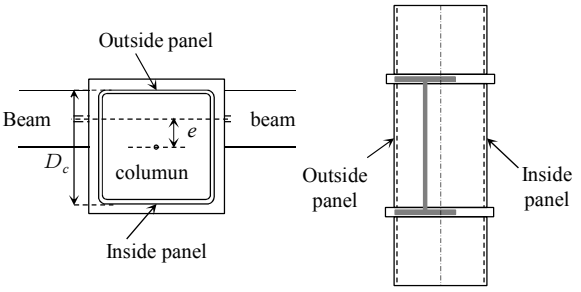


Figure 1 Eccentric beam to column connection

Table 1 Properties of Specimens

Specimen	column	Beam	Panel	Eccentricity	Element which first yields
C-200-12	□-300×300×12	RH-500×200×10×16	□-300×300×12	0	Beam
E-200-12				0.167	
C-200-9			□-300×300×9	0	Panel
E-200-9				0.167	
C-150-9		RH-500×150×10×16		0	Beam
E-150-9				0.25	

C : Ordinary Connection
E : Eccentric Connection
E-150-9
Panel Thickness (mm)
Beam Width (mm)

2. TEST PROGRAM

2.1 Specimens and Parameters

In the present experiments, 6 specimens were tested as listed in Table1.Each specimen consists of two members: a rectangular hollow section column (RHS column) and an H-shaped beam. In order to achieve a smooth stress flow from the flange of the beam to the column, two steel plates are welded to the RHS column as shown in figure 2. The parameters of the present test are the thickness of the panel and the eccentricity ratio of the beam (Table 1). The latter is defined as: e/D_c.

2.2 Test Setup

In figure 3, the test setup is shown. The beam is set on the vertical direction and the column on the horizontal one. Loading is applied at the free end of the beam.

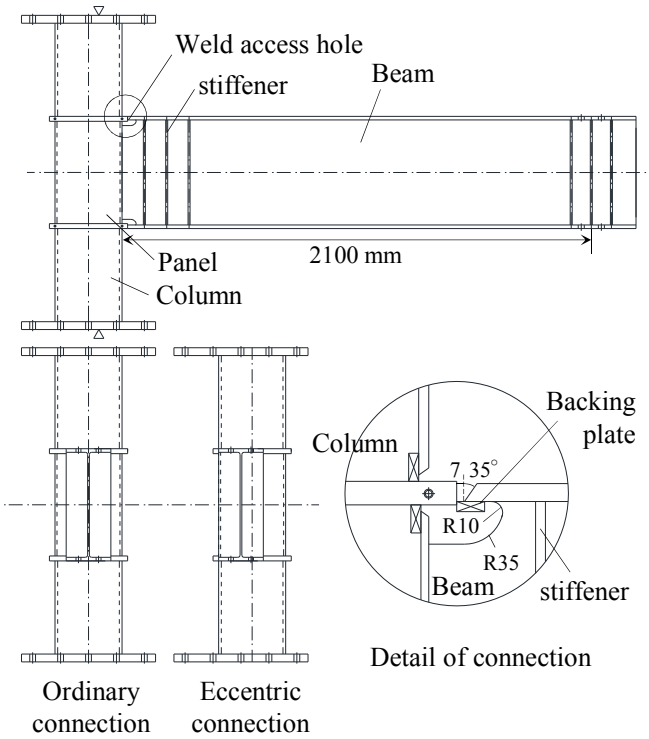


Figure 2 Test Specimen

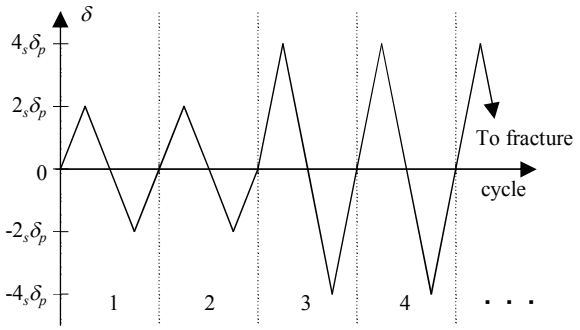


Figure 4 Loading History

2.3. Loading History

Displacement controlled cyclic loading is applied at the free end of the beam in the horizontal direction. The loading history of this test consists of incremental displacement amplitude with intervals of $2_s\delta_p$ as shown in figure4, (Japan Iron and Steel Federation 2002). $_s\delta_p$ represents the elastic deformation of beam to column connection when in the element that yields first the full plastic strength is reached ($_s\delta_p$=20 mm). Moreover, because of the restrictions of the loading system, the displacement amplitude after 3 cycles is set to $4_s\delta_p$ until the fracture of the beam.

2.4. Measurement System

In this experimental study, $_bM$, $_b\theta$, $_pM$, and $_p\gamma$ are defined as follows: $_bM$ = bending moment of beam; $_b\theta$ = rotation of beam; $_pM$ = moment of panel; and $_p\gamma$ = shear deformation of panel.

Figure 5 shows how the displacements and shear force are measured. $_bM$, $_b\theta$, $_pM$, and $_p\gamma$ are calculated using these measurement data (Eq.(1) to (7)) .

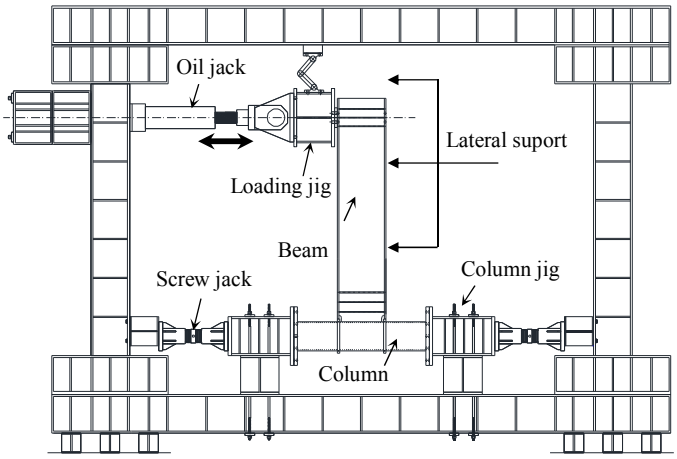


Figure 3 Test Setup

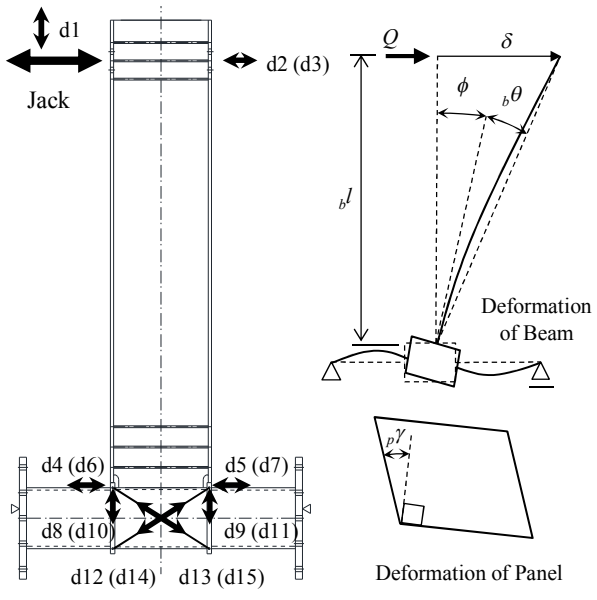


Figure 5 Measurement System

$$ {}_bM = Q \cdot l_b \tag{1}$$

where Q = horizontal load of oil jack ; and l_b = length of beam.

$$ {}_b\theta = \frac{\delta}{l_b} - \phi \tag{2}$$

$$ \delta = -\frac{\mathrm{d2}+\mathrm{d3}}{2} - \frac{\mathrm{d4}-\mathrm{d5}+\mathrm{d6}-\mathrm{d7}}{4} \tag{3}$$

$$ \phi = \left(\frac{1}{2}+\frac{e}{D_c}\right)\frac{(\mathrm{d9}-\mathrm{d8})}{h_b} + \left(\frac{1}{2}-\frac{e}{D_c}\right)\frac{(\mathrm{d11}-\mathrm{d10})}{h_b} \tag{4}$$

where δ = displacement at load application point ; ϕ = rotation angle in the connection ; and h_b = distance between centers of the beam flanges.

$$ {}_pM = {}_bM - Q \cdot \frac{L_b}{L_c} \cdot h_b \tag{5}$$

where L_b = distance between load application point and the center of the panel ; and L_c = length of the column.

$$ {}_p\gamma_{ex} = \frac{\sqrt{h_b^{\,2}+h_c^{\,2}}}{2 \cdot h_b \cdot h_c} \cdot (\mathrm{d13}-\mathrm{d12}) \tag{6}$$

$$ {}_p\gamma_{in} = \frac{\sqrt{h_b^{\,2}+h_c^{\,2}}}{2 \cdot h_b \cdot h_c} \cdot (\mathrm{d15}-\mathrm{d14}) \tag{7}$$

where h_c = distance between centers of the column flanges.

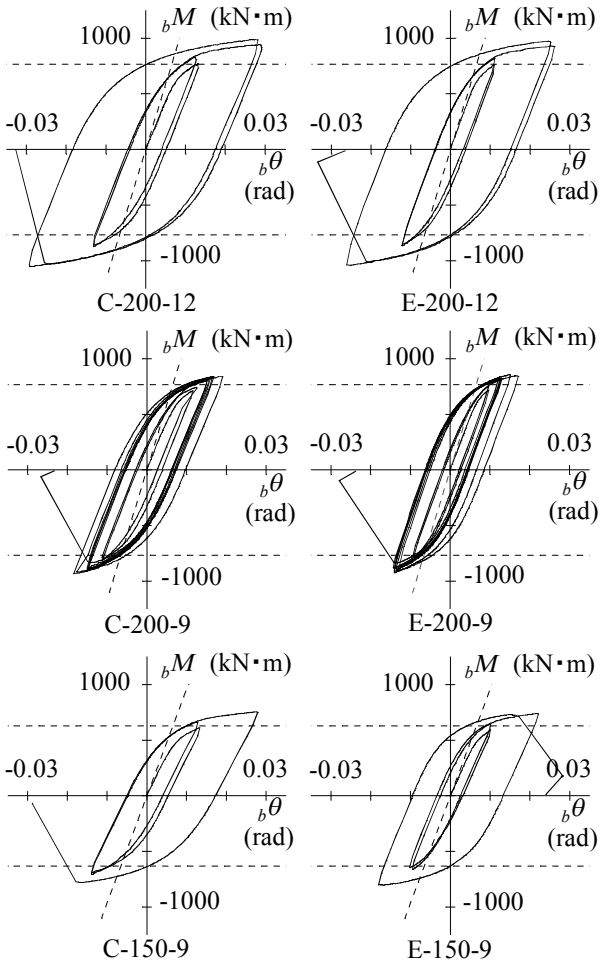


Figure 6 Behavior of beam

3. TEST RESULTS

3.1 Moment-Rotation Relationships of the Beam

In figure 6 one can observe the hysteretic behavior of the beam. Full plastic moments and the calculated value of elastic stiffness are also shown in this figure. All six specimens have fractured in the beam flange.

The influence of the eccentricity of the eccentricity on the plastic energy dissipation was investigated. In figure 7, the hysteretic behavior of the beam under cyclic loading can be decomposed into skeleton curve, Bauschinger part and an elastic unloading part. The energy dissipation of a steel beam serves as the sum of the energy dissipation in skeleton curve and Bauschinger part, and is defined as in Eq.(8).

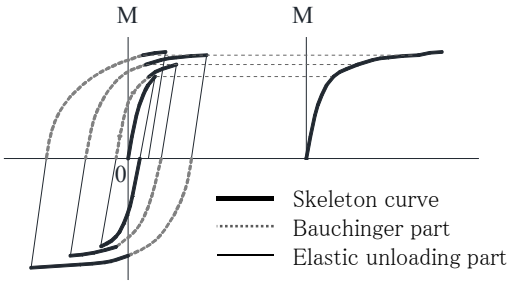


Figure 7 Skeleton Curve

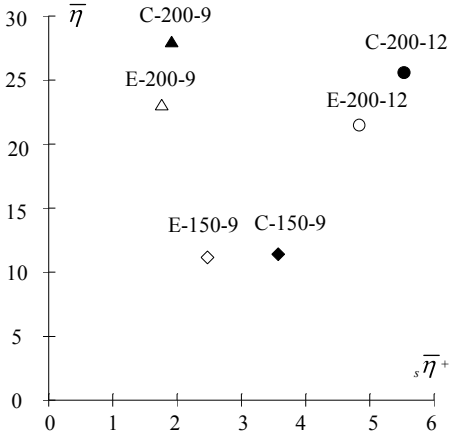


Figure8 Plastic deformation capacity of beam

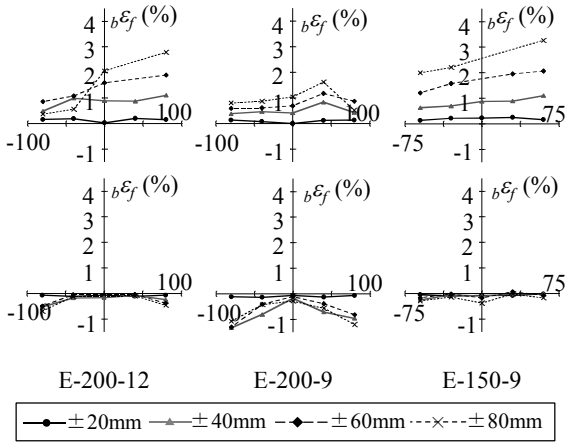


Figure 9 Strain distribution of the beam flange

$$W_P = W_S + W_B \quad (8)$$

W_P, W_S, and W_B are defined as follows: W_P = dissipated energy of beam; W_S = dissipated energy of skeleton curve; and W_B = dissipated energy of Bauschinger part.

In this study, these dissipated energies are normalized by the unit plastic energy dissipation obtaining the equivalent cumulative plastic deformation ratio: $\overline{\eta}$

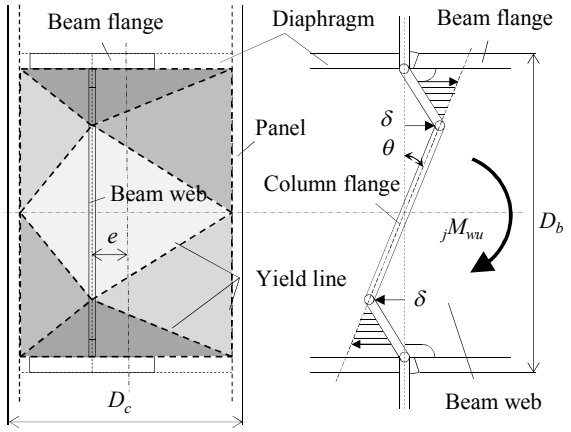
$$\overline{\eta} = {}_S\overline{\eta} + {}_B\overline{\eta} \quad (9)$$

$$\overline{\eta} = \frac{W_p}{M_p \cdot \theta_p} \quad (10)$$

$${}_S\overline{\eta} = \frac{W_S}{M_p \cdot \theta_p} \quad (11)$$

$${}_B\overline{\eta} = \frac{W_B}{M_p \cdot \theta_p} \quad (12)$$

In figure 8, the plastic deformation capacity of the beam is shown. On the vertical axis is the equivalent cumulative plastic deformation ratio of beam. On the horizontal axis is the one of the skeleton curve. The plastic energy dissipation of the hysteresis curve of eccentric connection is smaller than one of ordinary connection. In addition, for the connections in which the panel is designed to yield first, deformation of the beam is rather small because the one of the panel increases. Hence the number of cycles until the beam fractures also increases, which leads to larger energy dissipation capacity than for the connections in which the beam yields first.



(a) Yield line on column face (b)Yield field of beam web

Figure 10 Collapse Mechanisms of Beam Web

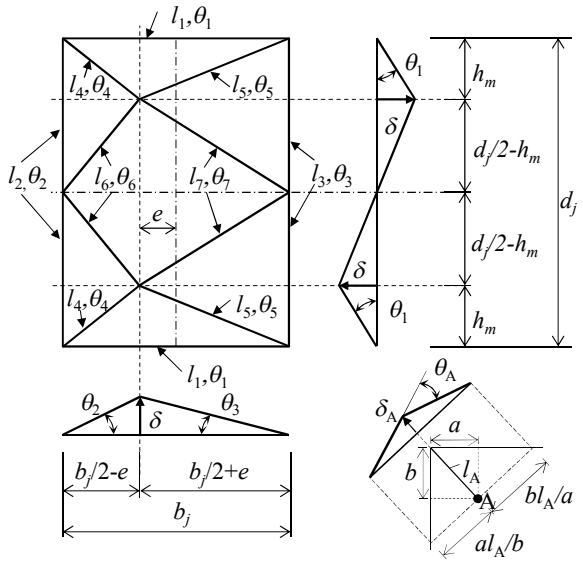


Figure 11 Plastic Rotation of Yield Line

3.1 The joint efficiency of the Beam Web

The joint efficiency of the web increases due to the fact that the beam web is connected to the column skin plate near the outside panel. In order to assess the influence of the joint efficiency of the eccentric beam web, both experimental and theoretical approaches are used, (Matsumoto et al. 1999).

In figure 10, the theoretical one is calculated from the collapse mechanisms for such web connections, (Suita K. and Tanaka T 2000).

Internal work - deformation of column skin plate

In figure 11, internal work of deformation of column skin plate is

$$E_c = 2M_0 \sum_{n=1}^{7} l_n\theta_n = \frac{-4h_m^2 b_j d_j - h_m b_j^3 + 2h_m b_j d_j^2 + 4h_m b_j e^2 + b_j^3 d_j - 4b_j d_j e^2}{h_m(b_j - 2e)(b_j + 2e)(d_j - 2h_m)} {}_c t_f^2 \, {}_c F_{fy} \delta \quad (13)$$

where δ= displacement at the point where the deformation of column skin plate is maximum ; l_n = length of the yield line(n=1~7) ; θ_n = rotation of the yield line (n=1~7); ${}_cF_{fy}$ = yield strength of column ; ${}_ct_f$= thickness of column ; and M_0 = full plastic moment of each length (M_0=${}_ct_f^2 {}_cF_{fy}$/4).

Internal work -deformation of beam web

In figure 10(b), the yield field is assumed in the beam web. Plastic deformation of the beam web at the upper and lower ends is

$$\delta_w = \frac{d_j(h_m - S_r)2}{(d_j - 2h_m)h_m}\delta \quad (14)$$

Internal work of deformation of beam web is

$$E_b = 2\frac{\delta_w(h_m - S_r)}{2} {}_b t_w \, {}_b F_{wy} = \frac{d_j(h_m - S_r)^2}{(d_j - 2h_m)h_m} {}_b t_w \, {}_b F_{wy}\delta \quad (15)$$

where ${}_bF_{wy}$ = yielding strength of beam web ; and ${}_bt_w$ = thickness of beam web. The formula of the principle of virtual work may be thought of as

$${}_jM_{wu}\theta = E_c + E_b \quad (16)$$

Further on, knowing that the angle θ can be expressed as shown in Eq.(17), and by replacing Eq.(13), (14) into Eq.(16), it result that ${}_jM_{wu}$ can be computed using Eq.(18).

$$\theta = \frac{2\delta}{d_j - 2h_m} \quad (17)$$

$$ {}_jM_{wu} = \frac{-4h_m{}^2 b_j d_j - h_m b_j{}^3 + 2h_m b_j d_j{}^2 + 4h_m b_j e^2 + b_j{}^3 d_j - 4b_j d_j e^2}{2h_m (b_j - 2e)(b_j + 2e)} {}_ct_f{}^2 {}_cF_{fy} + \frac{d_j (h_m - S_r)^2}{2h_m} {}_bt_w \cdot {}_bF_{wy} \quad (18) $$

The minimum value of h_w is found by applying Eq.(19). By doing so, the yielding strength ${}_cF_{fy}$ will become the ultimate strength ${}_cF_{fy}$ and h_w will result as shown in Eq.(20).

$$ \frac{\partial {}_jM_{wu}}{\partial h_m} = 0 \quad (19) $$

$$ h_m = \sqrt{\frac{{}_bt_w {}_bF_{wy} S_r{}^2 + b_j {}_ct_f{}^2 {}_cF_{cfy}}{{}_bt_w {}_bF_{wy} - 4{}_ct_f{}^2 {}_cF_{fy} b_j / (b_j{}^2 - 4e^2)}} \quad (20) $$

Next, by replacing Eq.(20) into Eq.(18), ${}_jM_{wu}$ is found to be Eq.(21).

$$ {}_jM_{wu} = \gamma_w \cdot {}_bM_{wp} \quad (21) $$

The joint efficiency of the beam web is defined as: γ_w

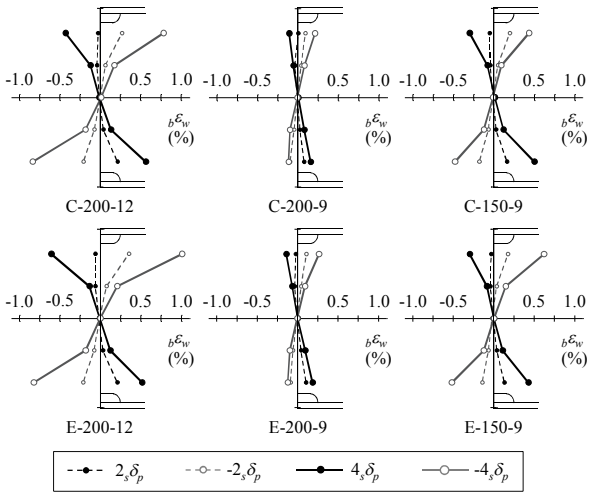


Figure 12 Strain Distribution of Beam Web

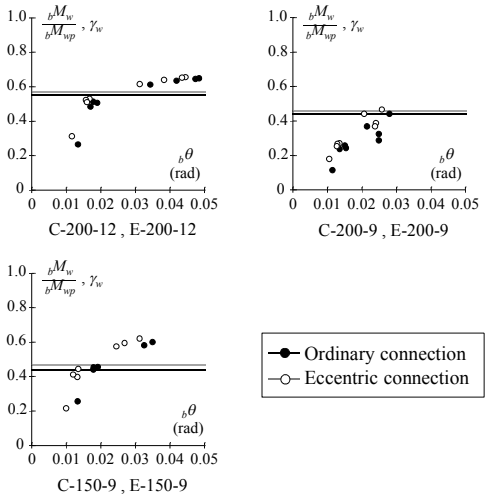


Figure 13 Joint Efficiency of the Beam Web

The experimental value of the joint efficiency of the web is calculated from the strain distribution (Figure 12) and coupon test result.

In figure 13 the joint efficiency for the ultimate state of the beam web is shown. On the vertical axis is the joint efficiency of beam web. On the horizontal axis is the deformation of beam.

In both experimental and theoretical results, the joint efficiency of the beam web in eccentric connection is slightly larger than that of ordinary connection. Hence one can say that the influence of the eccentricity on the joint efficiency is small.

4. MOMENT-ROTATION RELATIONSHIPS OF THE PANEL ZONE

Figure 14 shows the force-deformation relationships for the panel. Full plastic strengths and the calculated value of elastic stiffness as also shown in this figure. ${}_pM$, ${}_p\gamma$, ${}_p\gamma_i$, and ${}_p\gamma_o$ are defined follows: ${}_pM$ = panel moment; ${}_p\gamma$ = shear deformation of panel; ${}_p\gamma_i$ = shear deformation of inside panel; and ${}_p\gamma_o$ = shear deformation of outside panel.

Figure 15 shows the skeleton curves for the panel of eccentric connections. On the vertical axis is the moment of each inside and outside panels based on the moment assignment ratio in the elastic region. The horizontal axis represents the deformation of the panel. After yielding (white point), the deformation of the outside panel increases. In addition, for ordinary connections, the deformation of the panel before its yielding is also considerable. However, when the sum of the moments of the inside and outside panels reaches the yielding strength, the outside panel in the eccentric connections has larger deformations than the one in ordinary connection. On the other hand, the deformation of

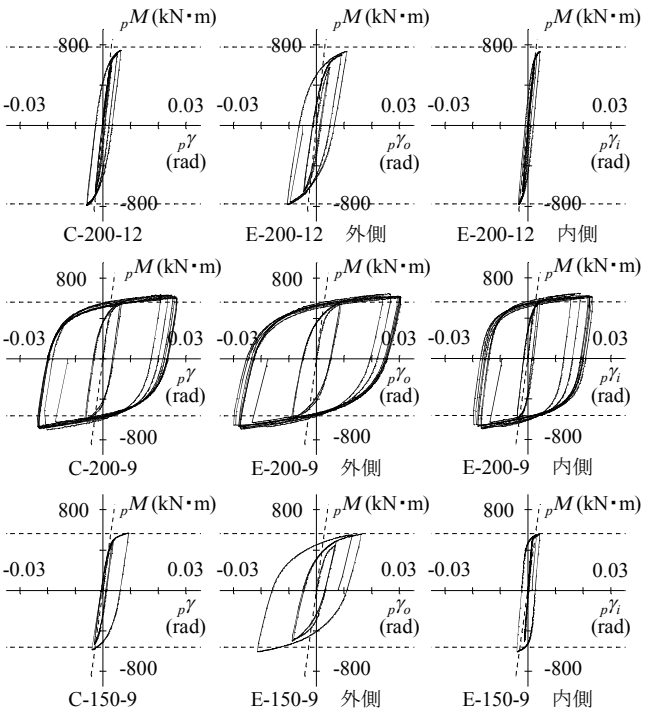


Figure 14 Behavior of Panel Zone

inside panel stops at the beginning of the plastic incursion zone.

5. ENERGY DISSIPATION OF THE BEAM TO COLUMN CONNECTION

Figure 16 shows the energy dissipation of the beam to column connection. One can notice that even though the energy dissipation of beam in eccentric connection is smaller than that in ordinary connection, the difference is not so large. For the connections in which the panel is designed to yield first, deformation of the beam is rather small because the one of the panel increases. Hence the number of cycles until the beam fractures also increases, which leads to larger energy dissipation capacity than for the connections in which the beam yields first. This can be noticed in Figure 16 where the energy dissipation of the panel for both panel yielding type and beam yielding type is shown. The panel yielding type has energy dissipation 3.2 times and 3.3 times larger than the beam yielding type. Moreover, for the specimen with large eccentricity, the energy dissipation increased by 1.2 times due to the eccentricity.

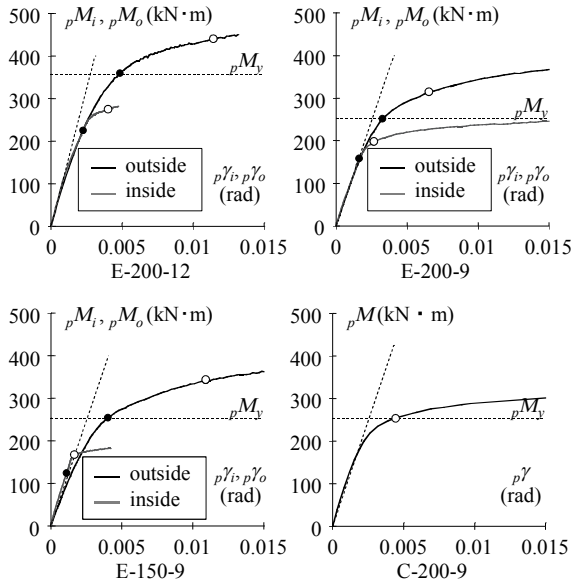


Figure 15 Skeleton curves for the panel of eccentric connection

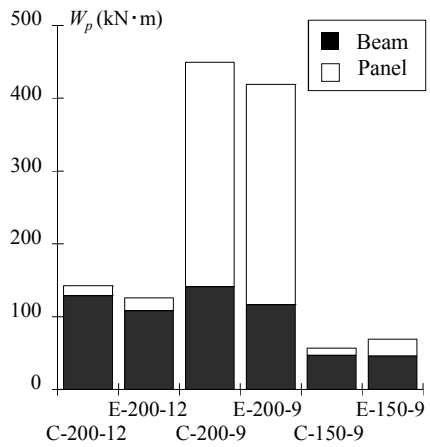


Figure 16 Energy dissipation of the beam to column connections

6. CONCLUSIONS

The main purpose of the present study was to investigate the influence of the beam eccentricity on the plastic deformation capacity of the eccentric beam to column connections under cyclic loading. This has been achieved by conducting a set of tests and then comparing the experimental data with the theoretical results in terms of joint efficiency, strains etc.

Based on these results, it can be concluded that for eccentric connections, the joint efficiency of the beam web for the ultimate states is slightly larger than that corresponding to centric connections. This leads to an increase in the stiffness of the beam. In addition, due to the fact that the strain distribution in the beam flanges is asymmetric, the plastic deformation capacity of an eccentric connection slightly decreases.

Another important conclusion is that the behavior of the outer panel at yielding can be predicted by applying the moment assignment ratio in elastic range.

In the end, it can be concluded that the presence of the eccentricity can be accounted for by using appropriate computation methods and does not represent a major problem in structural safety.

References:

Tanaka T., Tabuchi M., Tanaka T. and Nanba H., (1999), "A study on joint panel in RHS column to beam eccentric connection -part 1. Preliminary investigation-", *Summaries of Technical Papers of Annual Meeting,* AIJ, 551-552. (in Japanese)

An Independent Administrative Agency, Japan Iron and Steel Federation (2002), "Testing Methods of the Evaluation of Structural Performance for the Steel Structures" (in Japanese)

Matsumoto Y., Akiyama H. and Yamada S., (1999), "Relation between Deformation Capacity of Beam at Steel Beam-to-Column Connection and Joint Efficiency" *Journal of Structural and Construction Engineering*, AIJ, No523, 117-124. (in Japanese)

Suita K. and Tanaka T., (2000), "Flexural Strength of Beam Web to Square Tube Column Joint" *Steel Construction Engineering*, JSSC, No26, 51-58. (in Japanese)

10CUEE CONFERENCE PROCEEDINGS
10th International Conference on Urban Earthquake Engineering
March 1-2, 2013, Tokyo Institute of Technology, Tokyo, Japan

EVALUATION OF THE COMPOSITE BEAM STRESS SUBJECTED TO BENDING AND AXIAL FORCE

Yoriyuki MATSUDA[1], Kazuhiko KASAI[2]

1) Graduate student, Graduate school of Tokyo Institute of Technology, Japan
2) Professor, Structural Engineering Research Center, Tokyo Institute of Technology, Japan
matsuda.y.ag@m.titech.ac.jp, kasai@serc.titech.ac.jp

Abstract: The composite beam cross section does not remain plane due to the slip that occurs at the interface of the slab and the steel beam. For this reason, it is difficult to evaluate how the load is distributed to slab and steel beam. In addition, the column portion in contact with the concrete can deform due to low rigidity and cause the slip in the vicinity, but the influence of this behavior on the composite beam has not been discussed. Moreover, it is necessary to consider large axial force produced by damper reaction force for a composite beam in the frame of the passively controlled structure which uses a damper to a structure to reduce a seismic response.

1.1 RESEARCH BACKGROUND

The beam of a steel structure is designed as a composite beam that is concrete slab and steel beam are united by a stud connector. Its cross section does not remain plane due to the slip that occurs at the interface of the slab and the steel beam. For this reason, it is difficult to evaluate how the load is distributed to slab and steel beam (Internal force). Furthermore, osculating plane of column and concrete slab is judged with fixed end, but there is possibility of bending deformation out of plane of column flange and estrangement of column and concrete slab, and it is not argued whether it is proper (Figure 1) .

In addition, in frame of the passively controlled structure which uses a damper to a structure to reduce a seismic response, to evaluate internal force is still more difficult by existence of gusset plate and by bending moment by story drift and axial force by damper act on frame (Figure 2).

1.2 RESEARCH METHODS

This research suggests formula and easy analysis method to get internal force about composite beam that bending moment and axial force act.

This research suggests formula and easy analysis method that can reproduce the effect of the slip and the change of boundary condition in fixed end that are the element to affect composite beam behavior.

2. THE INFLUENCE THAT A SLIP GIVES TO BEHAVIOR OF THE COMPOSITE BEAMS

Resistance for the slip (slip rigidity) is one of the important elements to influence behavior of composite beam, and this size affects strain distribution in case external force acts on the composite beam. As an example, strain

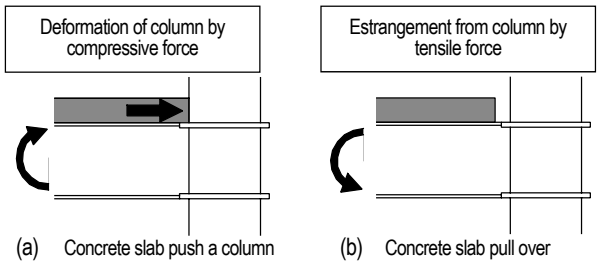


Figure 1 Boundary condition of concrete slab on column contact point

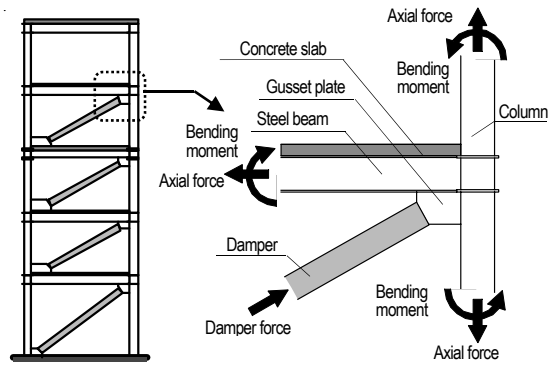


Figure 2 Stress which acts on passively controlled buildings

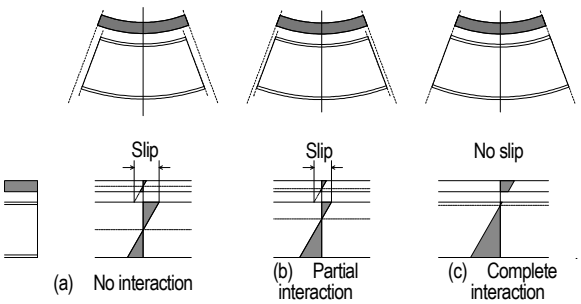


Figure 3 Composite beam deformation and strain distribution

distribution in the case of composite beam subjected to shear force and axial force shown in Figure 3.

When slip rigidity is zero, there is no interaction between the concrete slab and the steel beam. For this case, there are two neutral axes. They are at the center of gravity of the concrete slab and the steel beam. The slip occurs by a difference of strain which arises in bottom of concrete slab and top of steel beam (Figure 3a). When the slip rigidity increases, two neutral axes approaches, and slip decreases (Figure 3b). When the slip rigidity is large enough, the slip does not occur and remain plane (Figure 3c).

3. COMPOSITE BEAMS SUMMARY

This research examines the cantilever composite beam shown in Figure 4 and Figure 5. Shear force and axial force act on the center of gravity of the steel beam of the free end. Positive bending moment acts on composite beam by positive shear force and tensile force acts on composite beam by positive axial force.

Where, y_c is distance of each the center of gravity of steel beam and concrete slab, E_s is Young's modulus, A_s is cross-sectional area of steel beam, I_s is moment inertia of steel beam. Cross section and geometrical moment inertia of concrete express it in A_c/n and I_c/n with n (ratio of Young's modulus of steel beam and concrete). k_0 is rigidity of column, k is slip rigidity. In addition, Cross section and geometrical moment inertia of concrete do not consider a part of ditch.

4. ANALYSIS OUTLINE

The analysis model of composite beam is shown in figure 6. It's had advanced member, which column flange plate bending deformation on concrete slab end. Analysis were carried out on cantilever composite beam subjected to a axial force and shear force. The analysis assumption follows:

1) The models consisted of beam element, truss element and rigid element. A beam, shear connector and column flange plate is beam element part. A concrete slab is truss part. Which beam and shear connector linked by rigid element. Moreover, beam curvature and concrete slab curvature share the same rotation on each section.
2) All elements were in elastic region.
3) Beam node, slab node pitch and shear connect arrangement pitch was 16.5mm.
4) Axial and shear force were acting free end of steel section centroid.
5) Each element set up was centroid of each member.

5. FORMULA IN CASE OF SHEAR FORCE ACTS ON THE COMPOSITE BEAMS

Inter force equilibrium and deformation under pure bending force from shear force are shown in Figure 7. In this case, internal force is 3 ingredients of the axial force which acts on concrete slab and steel beam, the bending moment which

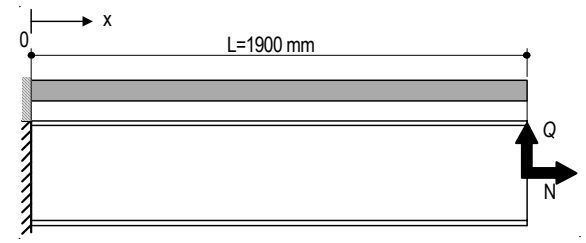


Figure 4 Cantilever composite beam

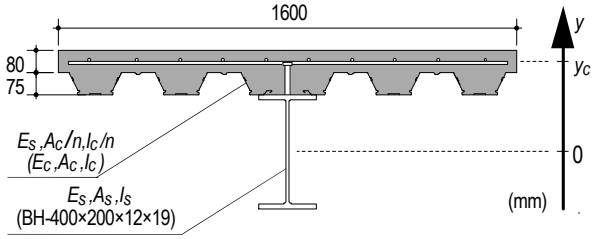


Figure 5 Detail and geometrical rules of composite beam

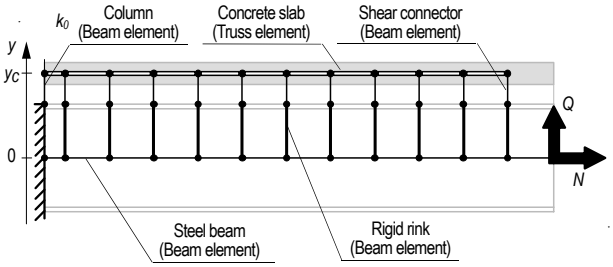


Figure 6 Analysis model of composite beam

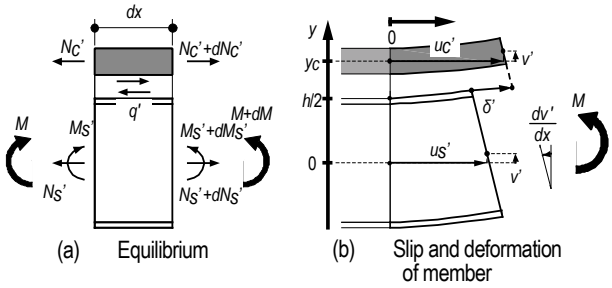


Figure 7 Inter force equilibrium and deformation under pure bending force from shear force

acts on steel beam and expresses it in N_c', N_s', M_s'. Inter force equilibrium is obtained from Equ. (1a-c). Slip is obtained from Equ. (1d).

$$0 = N_s' + N_c' \ , \ M = M_s' - N_c' y_c$$

$$-\frac{dN_s'}{dx} = \frac{dN_c'}{dx} = q' = k\delta' \ , \ \delta' = u_c' - u_s' + \frac{dv'}{dx} y_c \quad \text{(1a-d)}$$

The differential equation about axial force which acts on concrete slab can be obtained from Equ. (2a).

$$\frac{d^2 N_c'}{dx^2} - C N_c' = \frac{k y_c}{\sum EI} QL - \frac{k y_c}{\sum EI} Qx$$

$$C = k \frac{\overline{EI}}{\overline{EA} \sum EI} \ , \ \sum EI = E_s I_s + E_s \frac{I_c}{n}$$

$$\frac{1}{\overline{EA}} = \frac{1}{E_s A_s} + \frac{1}{E_s A_c / n} \ , \ \overline{EI} = \sum EI + \overline{EA} y_c^{\,2} \quad \text{(2a-e)}$$

A general solution and the boundary condition of Equ (2a) is as follows.

$$N_c'(x) = A'\cosh\left(\sqrt{C}x\right) + B'\sinh\left(\sqrt{C}x\right) + \frac{\overline{EA}}{EI} y_c Q\left(x - L\right) \tag{3}$$

$$N_c'(0) = N_{c0}', N_c'(L) = 0, \frac{dN_c''(0)}{dx} = \frac{k}{k_0} N_{c0}' \quad \text{(4a-e)}$$

Than the above, N_c' can be obtained from Equ. (5).

$$N_c'(x) = \left[\frac{\left\{\sinh\left(\sqrt{C}L\right)\cosh\left(\sqrt{C}x\right) - \cosh\left(\sqrt{C}L\right)\sinh\left(\sqrt{C}x\right)\right\}}{\sqrt{C}\cosh\left(\sqrt{C}L\right) + k/k_0 \sinh\left(\sqrt{C}L\right)} \right.$$

$$\left. \cdot\left(1 + L\cdot k/k_0\right) - L + x \right] \frac{\overline{EA}}{EI} y_c Q \tag{5}$$

6. FORMULA IN CASE OF AXIAL FORCE ACTS ON THE COMPOSITE BEAMS

6.1 FOR AXIAL FORCE ACTING ON THE CENTROID OF THE BEAM

Since axial force of external force is acting on the centroid of the steel beam, it is divided into axial force and bending moment which axial force causes (Figure 8). Where, e is distance of each the centroid of steel beam and composite beam.

Inter force equilibrium and deformation under pure axial force are shown in Figure 9. In this case, internal force is 2 ingredients of the axial force which acts on concrete slab and steel beam and expresses it in N_c", N_s". Balance of force is obtained from Equ. (6ab). Slip is obtained from Equ. (6c).

$$N = N_s'' + N_c'' \quad , \quad \frac{dN_s''}{dx} = -\frac{dN_c''}{dx} = q'' = k\delta''$$

$$\delta'' = u_s'' - u_c'' \tag{6a-c}$$

The differential equation about axial force which acts on concrete slab can be obtained from Equ. (7a).

$$\frac{d^2 N_c''}{dx^2} - D N_c'' = -\frac{k}{E_s A_s} N \quad , \quad D = \frac{k}{\overline{EA}} \tag{7ab}$$

A general solution and the boundary condition of Equ (7a) is as follows.

$$N_c''(x) = A''\cosh\left(\sqrt{D}x\right) + B''\sinh\left(\sqrt{D}x\right) + \frac{A_c/n}{A_s + A_c/n} N \tag{8}$$

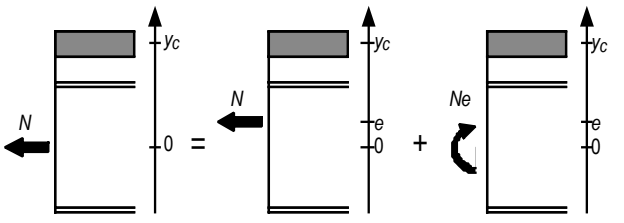
$$N_c''(0) = N_{c0}'', N_c''(L) = 0, \frac{dN_c''(0)}{dx} = \frac{k}{k_0} N_{c0}'' \quad \text{(9a-c)}$$

Than the above, N_c"can be obtained from Equ (8) and (9a-c).

$$N_c''(x) = \frac{A_c/n}{A_s + A_c/n} N \left[1 - \frac{\cosh\left(\sqrt{D}x\right)}{\cosh\left(\sqrt{D}L\right)} \right.$$

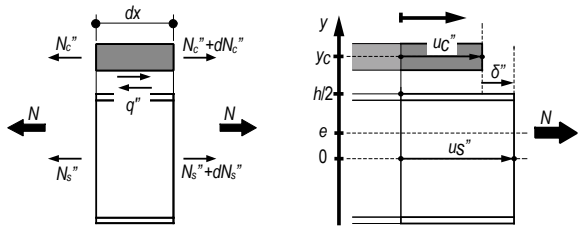
$$- \frac{k\left\{\sinh\left(\sqrt{D}L\right) - \tanh\left(\sqrt{D}L\right)\right\}\cosh\left(\sqrt{D}x\right)}{\sqrt{D}\left\{k_0\cosh\left(\sqrt{D}L\right) + \sqrt{\overline{EA}k}\sinh\left(\sqrt{D}L\right)\right\}}$$

$$\left. + \left\{\cosh\left(\sqrt{D}L\right) - 1\right\}\sinh\left(\sqrt{D}x\right) \right] \tag{10}$$



(a) External axial force (b) pure axial force from external axial force (c) pure bending moment from external axial force

Figure 8 Disassembly of axial force



(a) Equilibrium (b) Slip and deformation

Figure 9 Inter force equilibrium and deformation under pure axial force

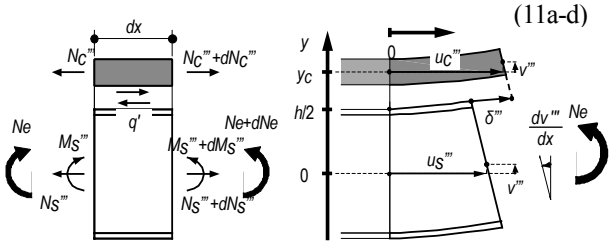
6.2 FOR THE BENDING BY THE AXIAL FORCE

Inter force equilibrium and deformation under pure bending moment from axial force are shown in Figure 10. In this case, internal force is 3 ingredients of the axial force which acts on concrete slab and steel beam, the bending moment which acts on steel beam and expresses it in N_c"', N_s"', M_s"'. Balance of force is obtained from Equ. (11a-c). Slip is obtained from Equ. (11d).

$$0 = N_s''' + N_c''' \ , \ Ne = M_s''' - N_c''' y_c$$

$$-\frac{dN_s'''}{dx} = \frac{dN_c'''}{dx} = q''' = k\delta''' \ , \ \delta''' = u_c''' - u_s''' + \frac{dv'''}{dx} y_c$$

(11a-d)



(a) Equilibrium (b) Slip and deformation

Figure 10 Inter force equilibrium and deformation under pure bending force from axial force

e can be obtained from N_c", N_s" and balance of the moment in the centroid of composite beam (Figure11).

$$e = \frac{N_c''}{N} y_c \tag{12}$$

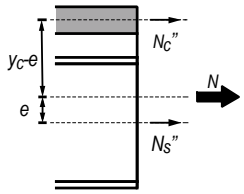


Figure 11 Distance of each section and composite beam

The differential equation about axial force which acts on concrete slab can be obtained from Equ. (13).

$$\frac{d^2 N_c'''}{dx^2} - C N_c''' = \frac{k y_c^{\,2}}{\sum EI}\left\{ A''\cosh\left(\sqrt{D}x\right) + B''\sinh\left(\sqrt{D}x\right) + \frac{A_c/n}{A_c/n + A_s} N \right\} \tag{13}$$

A general solution and the boundary condition of Equ (13) is as follows.

$$N_c'''(x) = A'''\cosh\left(\sqrt{C}x\right) + B'''\sinh\left(\sqrt{C}x\right) + \frac{k y_c^{\,2}}{\sum EI}\frac{1}{D-C}\left\{ A''\cosh\left(\sqrt{D}x\right) + B''\sinh\left(\sqrt{D}x\right)\right\} + \frac{\overline{EA}}{\overline{EI}} y_c^{\,2}\frac{A_c/n}{A_c/n + A_s} N \tag{14}$$

$$N_c'''(0) = N_{c0}''', N_c'''(L) = 0, \frac{dN_c'''(0)}{dx} = \frac{k}{k_0} N_{c0}''' \tag{15a-c}$$

Than the above, N_c''' can be obtained from Equ. (14) and (15a-c). Where, this formula leaves it out, because an expression is long.

7. THE TOTAL OF EACH INGREDIENT

Internal force in case of shear force and axial force act on centroid of steel beam is a total of internal force by three components. Where, N_c is the axial force which acts on concrete slab, N_s is the axial force which acts on steel beam, M_s is the bending moment which acts on steel beam. N_c, N_s, M_s and equilibrium are as follows.

$$N_c = N_c' + N_c'' + N_c''' \quad , \quad N_s = N_s' + N_s'' + N_s'''$$
$$M_s = M_s' + M_s'''$$
$$N = N_c + N_s \quad , \quad M = M_s - N_c\left(y_c - y_s\right) \tag{16a-e}$$

8. RESULTS & DISCUSSION

Comparison of analysis and formula in case of $k_0=\infty$ or $k_0=0$ are shown in Figure 12 and Figure 13. The external force assumes that shear force is 60kN and axial force is 360kN. This external force is the experiment that assumed that steel damper attached frame to shown in Reference 3, and axial force is bigger than shear force because steel damper is elasticity.

A difference of Analysis and formula is less than 1% at the maximum and shows good correspondence. In addition, axial force of external force is relatively big, but S has a big influence on internal force. In other words positive and negative of initial force is decided by shear force.

In the case of k=0, it may be said that tensile force is near to a condition acting on concrete slab. Likewise, In the case

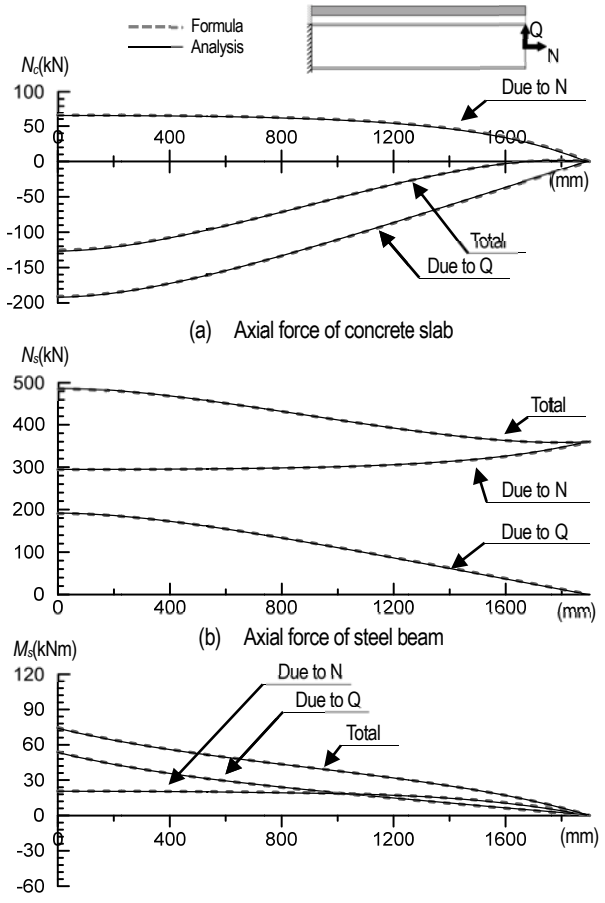


Figure 12 Force distribution subjected to shear force Q and axial force N ($k_0=\infty$)

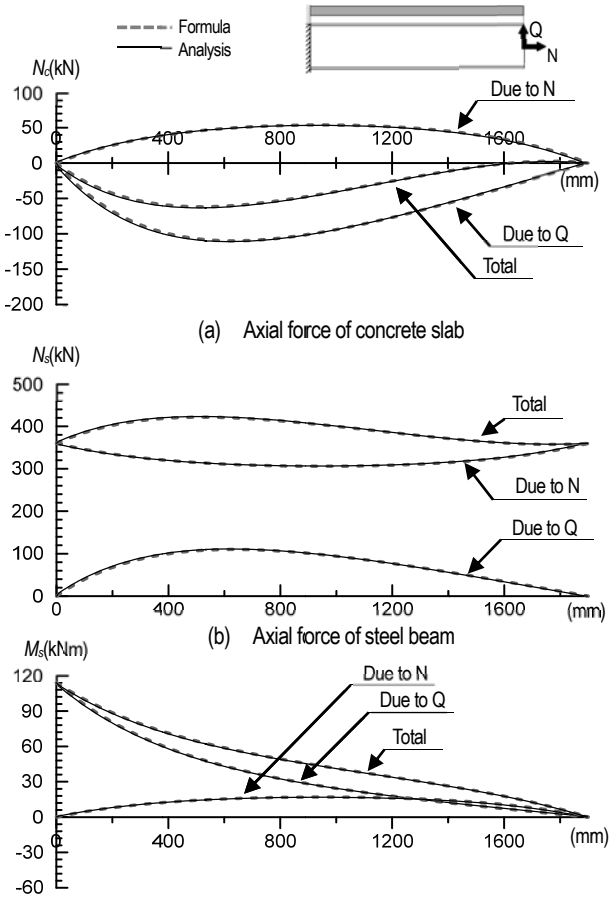


Figure 13 Force distribution subjected to shear force Q and axial force N ($k_0=0$)

of k=∞, it may be said that compressive force is near to a condition acting on concrete slab. In the case of k_0=0 has smaller 34% N_c and bigger 32% M_s than k_0=∞. In other words concrete slab becomes safe, but steel beam becomes dangerous. This shows that it is reduction of a composition effect.

When positive shear acts on composite beam, concrete slab bears compressive force, and concrete slab bears tensile force when positive axial force acts on composite beam. In other words, N_c decreases to a case of a positive and negative of shear force and axial force are same, and increases to a case of both are different.

9. WITH GUSSET PLATE

The cantilever composite beam with gusset plate shown in Figure 14 and Figure 15 is examined. The gray line of Figure 14 is the specification of the gusset plate of the specimen shown in the Reference 3. In this research, cutout portion of the gusset plate and the existence of the stiffener do not consider. A_{sg} is cross-sectional area of gusset plate, A_{s2} is cross-sectional area of the steel beam part which gusset attaches, I_{sg} is moment inertia of gusset plate, I_{s2} is moment inertia of the steel beam part which gusset attaches. y_s is centroid position of the steel beam part which gusset attaches.

Analysis model in consideration of gusset plate shown in Figure 16. In addition to the above-mentioned assumption, change of the center of gravity position of steel beam by gusset plate is connected by rigid rink.

About the formula, internal force in the case of gusset plate attaches steel beam demands the section that gusset plate attaches and the section that it does not attaches individually and gets it by agreeing on a border of both. In addition, the formula in consideration of deformation of column is not produced.

Comparison of analysis and formula in case of k_0=∞ is shown in Figure 17, analysis in case of k_0=0 is shown in Figure 18.

The ratio that concrete slab contributes to cross-section area and geometrical moment of inertia of composite beam decreases in the cross-section that gusset attaches steel beam. For this reason the absolute value of N_c becomes smaller than the cross-section that gusset does not attach steel beam. In addition, the absolute value of N_s which matches with it by horizontal force becomes small, too. On the other hand, M_s usually becomes big when moment inertia of steel beam becomes big. However, in the section that the gusset plate attaches, M_s becomes small because distance of each center of gravity of steel beam and slab becomes big by gusset plate.

Next, a difference of an effect by presence of gusset plate is considered. In composite beam which attached gusset plate, about the whole beam, N_c and N_s decrease and M_s is increasing. It is thought that an effect produced this in internal force of the whole beam because internal force in the sectional border where gusset plate attaches varies with gusset plate as having mentioned above.

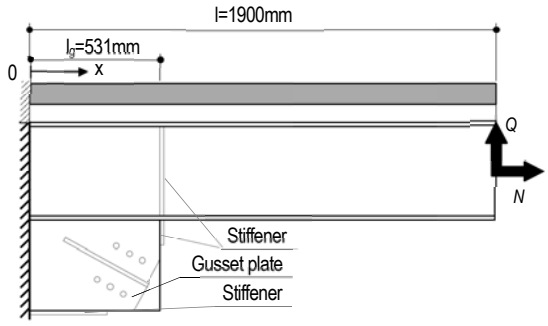


Figure 14 Cantilever composite beam with gusset plate

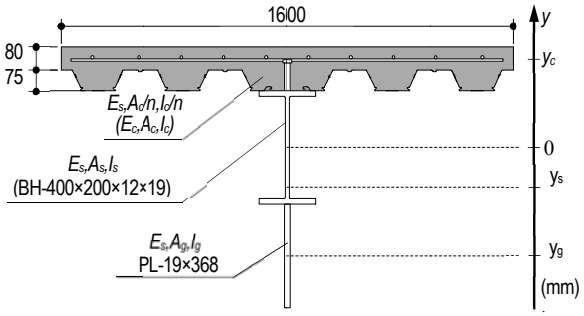


Figure 15 Detail and geometrical rules of composite beam with gusset plate

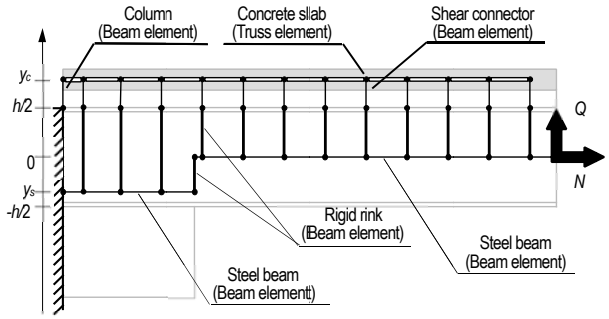


Figure 16 Analysis model of composite beam with gusset plate

From Figure 17 and Figure 18, in the case of k_0=0 has smaller 20% N_c than k_0=∞. Since contribution for composite beam of concrete slab decreased by gusset plate, the decline by k_0 is smaller than a case without gusset plate.

10. CONCLUSION

Analysis model and formula were proposed about internal force of composite beam that shear force and axial force act on, and consideration was performed from the result of analysis model and formula about the influence which deformation of column and gusset plate have. The following conclusions were obtained.

1) There are few differences of internal force provided from analysis model and formula.
2) By transformation of column, absolute value of N_c and N_s become small, and M_s becomes big. In addition, flexural rigidity becomes small, and deformation of column is equal to a decline of a composition effect.
3) In the case of gusset plate attaches the steel beam, N_c and N_s become small and M_s becomes large, and the influence that deformation of column gives to a

composition effect becomes small.

REFERENCES

Newmark,M.N.et.al. : Test and analysis of composite beams with incomplete interaction , Proc. Of the Society of Experimental Analysis, Vol.9,no.1, 1951

S.Kishiki.et.al. : Consideration of composite effects on elasto-plastic behavior of panel-zone, Architectural Institute of Japan. Vol. 74, No. 644, 1841-1849 (in Japanese)

Y.Matsuda.et.al. : Behavior of incomplete composite beam subjected to bending and axial Force. Summaries of Technical Papers of Annual Meeting, Architectural Institute of Japan, 2012.9

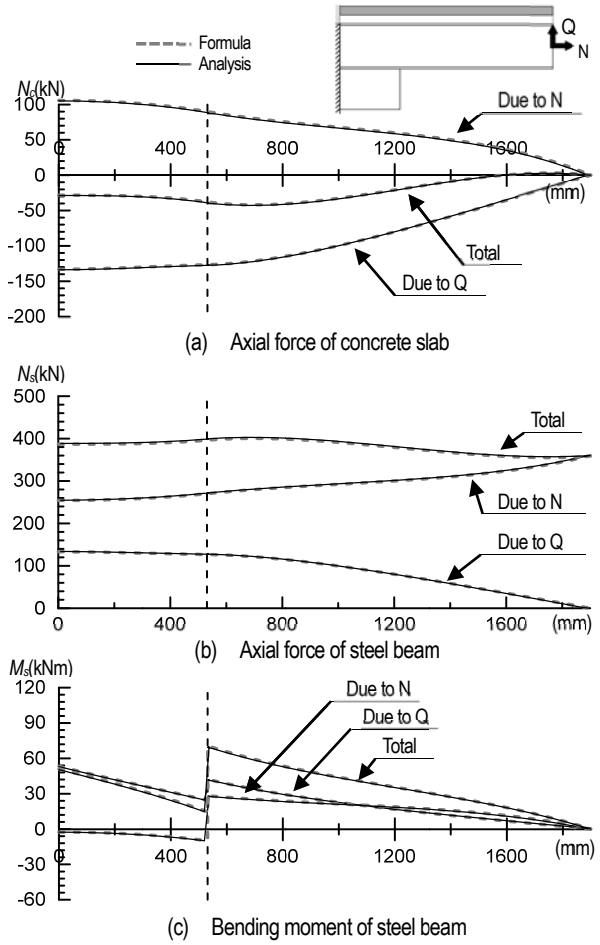


Figure 17 Force distribution subjected to shear force Q and axial force N (with gusset plate, $k_0=\infty$)

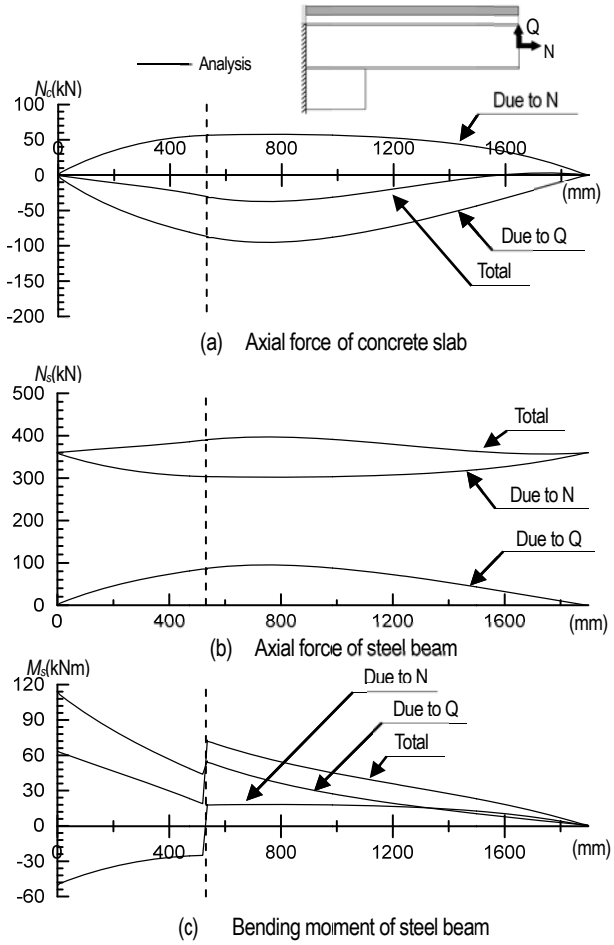


Figure 18 Force distribution subjected to shear force Q and axial force N (with gusset plate,$k_0=0$)

10CUEE CONFERENCE PROCEEDINGS
10th International Conference on Urban Earthquake Engineering
March 1-2, 2013, Tokyo Institute of Technology, Tokyo, Japan

EFFECT OF COLUMN BASE BEHAVIOR ON SEISMIC PERFORMANCE OF MULTI-STORY STEEL MOMENT RESISTING FRAMES

Yao Cui[1], Satoshi Yamada[2]

1) Associate Professor, School of Civil Engineering, Faculty of Infrastructure Engineering, Dalian University of Technology, China
2) Professor, Structural Engineering Research Center, Tokyo Institute of Technology, Japan
cuiyao@dlut.edu.cn, naniwa@serc.titech.ac.jp

Abstract: Column base is one of the most important element of steel structures. It is important to investigate the effect of column bases on the ultimate earthquake resistance of steel frames. In this paper, a series of inelastic response analysis of multi-story steel frames with exposed type column bases, especially weak anchor bolt type column bases, were carried out. From the analytical results, following conclusions were obtained. The intensity of the damage concentration at the structural element of the 1st story in the frames with exposed column bases were much less than that of the frames with pin type column bases and the frames with fixed column bases. Ultimate earthquake resistance of the frames with exposed type column bases were similar to that of the frames with pin type column bases. If columns of the frames were ductile, ultimate earthquake resistance of the frames with exposed type column bases were similar to or a little better than that of the frames with fixed column base. If columns of the frames were not ductile, ultimate earthquake resistance of the frames with exposed type column bases were much better than that of the frames with fixed column bases.

1. INTRODUCTION

In steel moment-resisting frames, the column base plays a very significant function to transmit active loading from the soil to the structure and return inertia forces from the structure back to the ground. The failure of column bases will result in the collapse of structure, regardless if the beam-to-column connections behave in a ductile manner. Extensive researches have been conducted on the behavior of the column bases. However, few studies have been conducted to investigate the seismic response of the frame by considering the column base behavior. Exposed column base is commonly used in multi-story steel moment frames in Japan. And the column base is recommended to be designed as the anchor-yield type, which showed the slip behavior of the hysteresis curves.

In this paper, a typical 4-story steel frame was chosen as a prototype frame to investigate the effect of the hysteresis behavior of column base on the whole frame behavior. The strength deterioration of columns caused by local buckling and slip behavior of exposed column bases caused by elongation of anchor bolts are considered in this study.

2. PROTOTYPE FRAME

To help understand the effects of column bases on seismic safety and response, numerical simulations were carried out on a four-story, four-bay moment-resisting steel frame, which was introduced as a design example in Reference (JSSC, 2009). The prototype frame is designed according to the current Japanese specifications and practices (post 1995 Kobe earthquake). The prototype frame is five spans and four stories with a uniform story height of 3.5 m, as shown in Fig. 1. SN400B and BCR 295 steel are used for beams and columns, respectively. The seismically effective weight of the analyzed frame is 609 kN, 605kN, 598 kN, and 762 kN for the first floors and the roof. The wide flange beams with 500 mm in depth, 200 mm in width, 10 mm of flange thickness, and 16 mm of web thickness were used. And columns were square hollow sections of 350 mm in width and 19 mm in thickness. The information of beams and columns are listed in Table 1. The full plastic moment ratio between beam and column ($M_{p,c}/M_{b,c}$) is 1.82. To get the larger response of column, the ratio ($M_{p,c}/M_{b,c}$) was reduced by 75% intentionally. Therefore, in the analyzed frame the full plastic moment of column ($M_{p,c}$) is 766 kNm in the analysis. The fundamental period of the frame is 0.59 s.

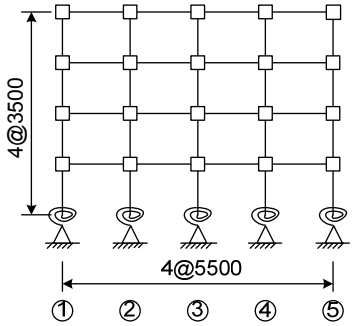


Fig. 1 Prototype frame (unit: mm)

Table 1 Component properties of prototype frame

	Section	Material	M_p (kNm)
Beam	H-500x200x10x16	SN 400B	560
Column	□-350x350x19	BCR 295	1021

3. ANALYSIS MODEL

Beams and columns in the analytical models employed in this study are represented by elastic elements with point plastic hinges at the ends. The point hinges are represented by rotational springs, whose properties are intended to represent all inelastic moment-rotation characteristics of flexural components (concentrated plasticity model). The hysteresis models of members used in this study are based on the experimental results. The hysteresis model could reproduce the strength deterioration caused by local buckling in the column and the slip behavior of the exposed column base. The hysteresis models of each component are introduced in details as follows.

Rayleigh damping ratio was assumed to be 2% for the first and second mode. P-Delta effects were considered in the numerical simulation.

3.1 Column

Past investigations have clarified that the load-displacement curve of steel members subjected to cyclic loading can be decomposed into the skeleton part, the Bauschinger part and the elastically unloaded part as shown in Fig. 2 (Kato et.al. 1968). The skeleton part is formed for each direction of loading connecting sequentially the inelastic part in each cycle of the M-θ curve (i.e., connecting the solid bold lines in Fig. 2(a)). The rest of the curve is composed of the elastically unloaded part and the softened part due to Bauschinger effect. The unloaded part keeps the initial elastic stiffness. The skeleton part is equivalent to the load-deflection relationship under monotonic loading (Kato et.al. 1968). And the hysteresis model of the Bauschinger part proposed by Akiyama (1990) is used to transfer the load-deflection curve under monotonic loading to the required hysteresis curves under various loading history.

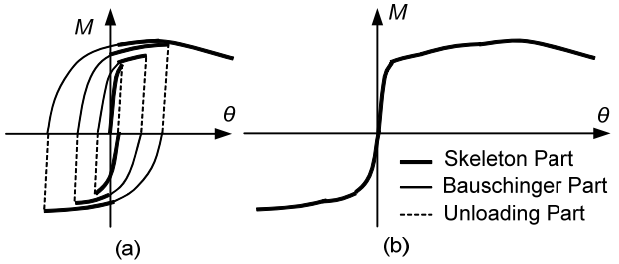


Fig. 2 Example of decomposition of a cyclic curve: (a) decomposition of a cyclic curve; (b) skeleton part

The load-deflection relationship of steel members under monotonic loading is able to be analyzed including the deterioration behavior governed by local buckling (Yamada et.al. 1995). As shown in Fig. 3, tetra-linear model (Yamada et.al. 1995) is used as the skeleton curve for the hysteresis model of the column. Therefore, the different strength deterioration caused by the different width thickness ratio could be considered in this model.

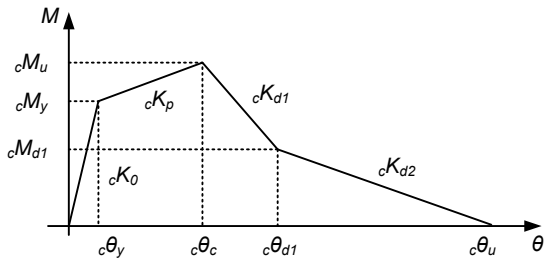


Fig. 3 Modeled Skeleton curve of column

Examples of the calculated load-deflection relationship of members are shown in Fig. 4. It is notable that the strength deterioration could be reasonably traced by the tetra-liner model proposed by Yamada (1995).

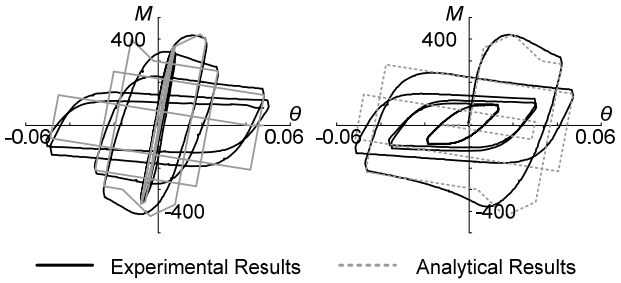


Fig. 4 Comparison of the experimental and analytical results of column hysteresis curve

3.2 Column Base

Exposed column bases have been popularly used for low-to medium-rise structures because of better constructability and low cost. In Japan, the yielding is allowed for the column bases (anchor bolts) under large earthquakes, if "ductile anchor bolts" are to be used (AIJ 2006, BCJ 2001). A "ductile" anchor bolt is defined by the yield ratio of the steel. The yield ratio of a ductile anchor bolt is no more than 0.75 (0.65 for some special anchor bolts). These values are determined so that the yield strength of the anchor bolt's shank exceeds the ultimate strength of its thread section. The column base connections with such anchor bolts posses the plastic rotation capacity of more than 0.03 rad. Yielding of base plates is not favored. The exposed column base exhibits slip behavior of hysteresis curves due to the elongation of anchor bolts under cyclic loading as observed in Fig. 5(a) (Cui et. al. 2009).

A numerical model as shown in Fig. 5(b) is used to reproduce the hysteresis behavior of the exposed column base. In this model, ${}_{cb}M_n$, ${}_{cb}M_y$, and ${}_{cb}K$ are the resisting moment to the axial force, yield moment of column base, and stiffness of column base, respectively. The detached moment ${}_{cb}M_n$ is affected by the axial force. The yield moment ${}_{cb}M_y$ and initial stiffness ${}_{cb}K$ of column base are controlled by the material and geometrical properties of anchor bolts and base plate (AIJ, 2006). Strain hardening

with 2% was considered to represent the strain hardening of the anchor bolts.

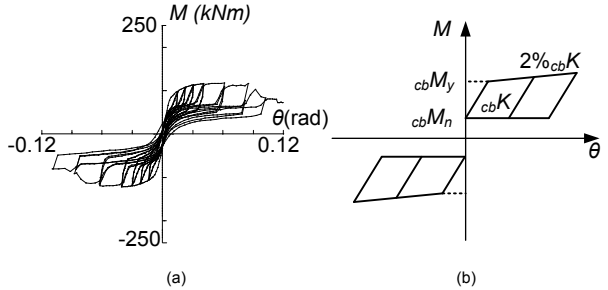


Fig. 5 (a) Hysteresis curve of column base; (b) Hysteresis model of column base

3.3 Beam and Panel Zone

Bilinear model was used for the skeleton curve of the hysteresis curve of beam and panel zone. The strain hardening of the beam and panel zone was 4% and 2%, respesctively. Composite slab action and the contributions of the gravity system to lateral strength and stiffness are not considered.

4. OVERVIEW OF ANALYTICAL STUDY

4.1 Parameters

The parameters of the analysis are the stiffness ratio between column base and column ($_{cb}K/_cK_0$), post-buckling behavior of column, and failure region (bottom end of column or column base). The analytical models are listed in Table 2.

Table 2 List of analytical models

Specimen name	$_{cb}K/_cK_0$	Width thickness ratio	Failure region
C-F	∞	25/43	C
C/B-2.0	2.0	25/43	C/B
C/B-1.0	1.0	25/43	C/B
C/B-0.5	0.5	25/43	C/B
C-P	0	25/43	C

*C— failure concentrated at the bottom end of the column
B – failure concentrated at the column base

In addition to the frame with pinned and fixed column base, three frames with partially restrained column bases were modeled. The stiffness ratio between column base and column varied from infinity (fixed, F), 2.0, 1.0, 0.5, 0.0 (pinned, P).

Two type width thickness ratios were used. The skeleton curve of the column with the two width thickness ratios is shown in Fig. 6. According to BCJ (2008), the column with width thickness ratio of 25 is cataloged as FA rank which is a ductile member, while the column with width thickness ratio of 43 is cataloged into FC rank as a non-ductile member. As illustrated in Fig. 6, the strength of the column with the width thickness ratio of 43 deteriorated sharply compared with another column.

The frames with partially restrained column bases were adopted to investigate the effect of failure region on the seismic behavior of frames.

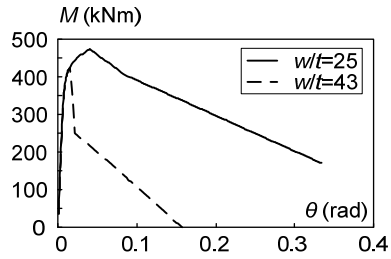


Fig. 6 Moment-rotation curves of column with different width thickness ratio

4.2 Ground Motion

Four ground motions were used. There are Hachinohe (t=36s), Kobe (t=0.84s), Elecentro (t=1.98s), and Takatori (t=0.61s) wave. Figure 7 shows the acceleration spectrum of the four ground motion waves with the damping ratio of 2%.The prototype frame was designed to resist level-2 input ground motion (PGV=500 mm/s). To get the extreme deformation of the frame, the input ground motion was scaled till the frame lose its resistance. For the frame failed at the bottom of column, the frame is assumed to lose its resistance when the 1st story column resistance is reduced to 80% maximum resistance. For the frame failed at the column base, the frame is assmued to lose its resistance when the column base rotation is larger than 0.03 rad.

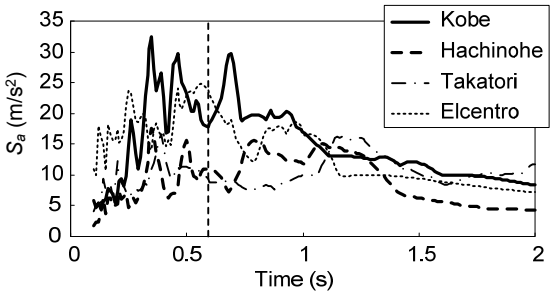


Fig. 7 Response Spectra

5. ANALYSIS RESULTS

5.1 Response Shear Force and Story Drift at Design Level

As shown in Fig.8, the large story drift angle occurred at the 1st story. When the column base is pin connected, the drift angle of the 1st story is larger than 3%, which indicated the collapse of the frame. When the S_a of input ground motion is relatively small (Hachinohe and Takatori, see Fig. 8), the peak story drift and shear force of each story are nearly the same regardless of the stiffness ratio of the column base and column ($_{cb}K/_cK_0$) and the failure region. When the S_a of input ground motion is relatively large (Kobe and ElCentro, see Fig. 8), the frame with the smaller column base stiffness ($_{cb}K/_cK_0$=0.5) show the larger peak story drift of each story. The effect of the post-buckling behavior of the column on the story drift is not significant.

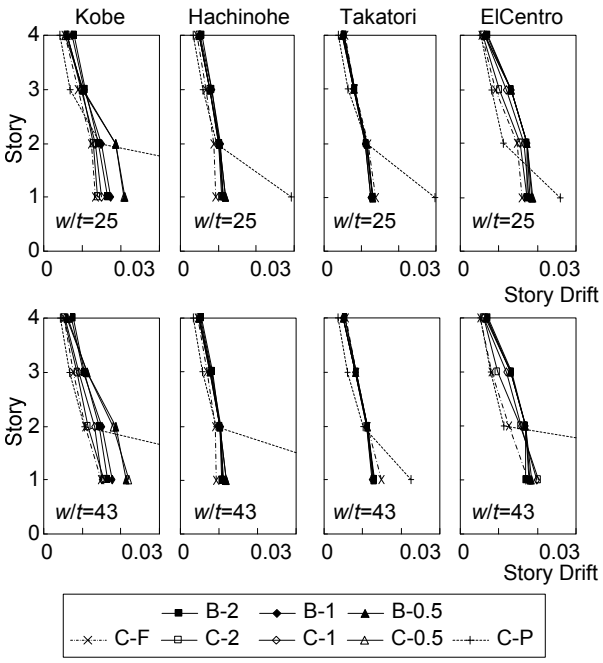


Fig. 8 Absolute peak drift angle

5.2 Response Hysteresis Curves of Story and Components

The response of the frame under level 3 (PGV=750 mm/s) Kobe ground motion is dicussed in this section. Figure 9 shows the response of the story shear force-story dirft relationship of the 1st story. There is no strength deterioration observed in the story shear force-drift angle relationship when the column has good post-buckling behavior with fixed column base connection. However, the same frame with fixed column base connection has severe strength deterioration and stiffness reduction if the column does not have the ability to resist the local buckling (larger width thickness ratio). Once the column base connection changed from fixed connection to pin connection, the damage on the 1st story became significantly. As shown in Fig. 9, the 1st story showed large permanent displacement and lose the resistance completely when the column width thickness ratio is 25 and 43, respectively.

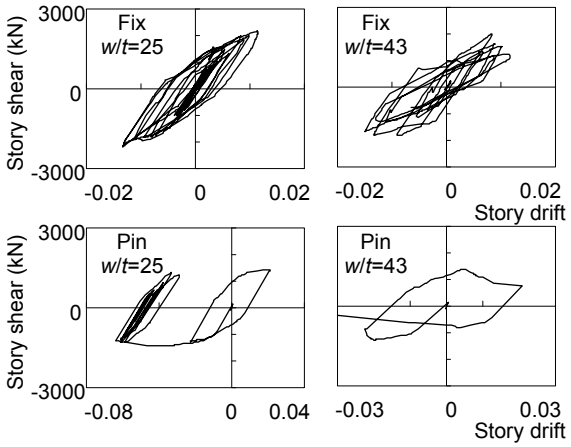


Fig. 9 1st story shear force-story drift relationship

Figure 10 shows the response hysteresis curves of the beam, bottom end of column, column base, and 1st story of the frame with exposed column base. It is noted that the damage concentrated in the 1st story when the frame with pin connection column base is released by using exposed column base, as shown in Fig. 10 (a). With the exposed

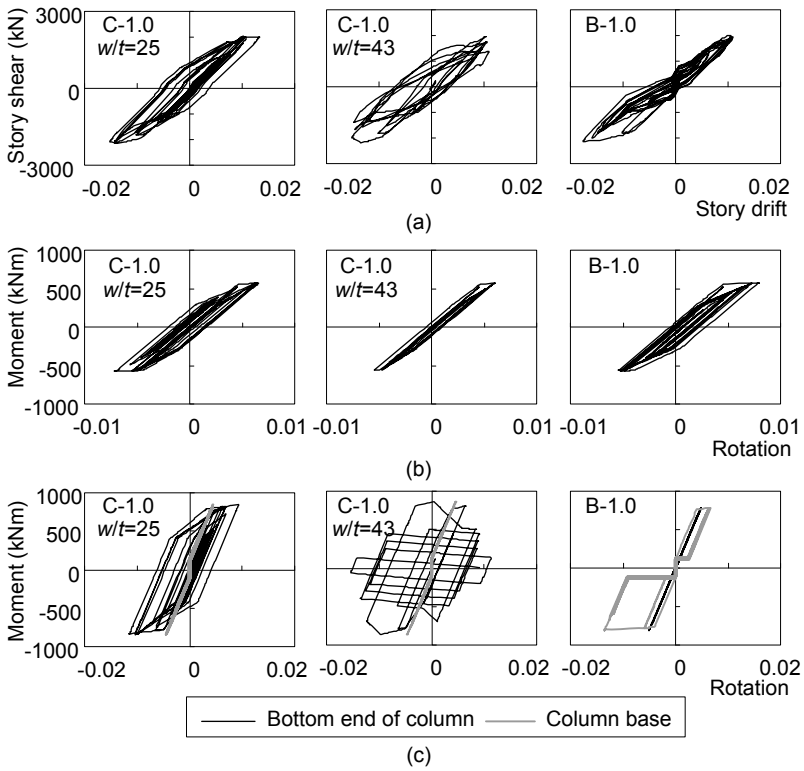


Fig. 10 Response hysteresis curves: (a) 1st story; (b) 1st story beam; (c) bottom end of 1st story column and column base

column base, the response of the frame is governed by the post-buckling behavior of the column, if the failure occurred at the bottom end of the 1st story column instead of the column base. As shown in Fig. 10 (c), the column with smaller width thickness ratio (w/t=25) showed fat hysteresis curve. On the contrary, the strength deteriorated signifcantly when the column width thickness ratio was increased to 43.

When the failure occured at the column base, the response of frame is regardless of the width thickness ratio of the column. As shown in Fig. 10 (a), the hysteresis curve of the 1st story is more pinch than the other two. It is because of the slip behavior of the column base (Fig. 10 (c)). Moreover, because the column did not lose its resistance capacity, the beam on the 1st floor could contribute more to transfer the force from 1st story column to the 2nd story column, as shown in Fig. 10 (b).

5.3 Relationship between the input ground motion and the 1st story column/column base ration

Figure 11 showed the relation between the level of input ground motion and the deformation of 1st story column/column base. The vertical axis represents the level of input ground motion. In Fig. 11 (a) and (b), the horizontal axis is the cumulative plastic rotation of the column end for the frame failed at the bottome end of column. The dot line indicated the plastic rotation of the column when the strength reduced to 80% of the maximum strength for the column with width thickness ratio of 25 and 43, respectively. And the horizontal axis is the column base rotation in Fig. 11(c). The dot line indicated the ultimate rotaion of the column base required by AIJ (2006).

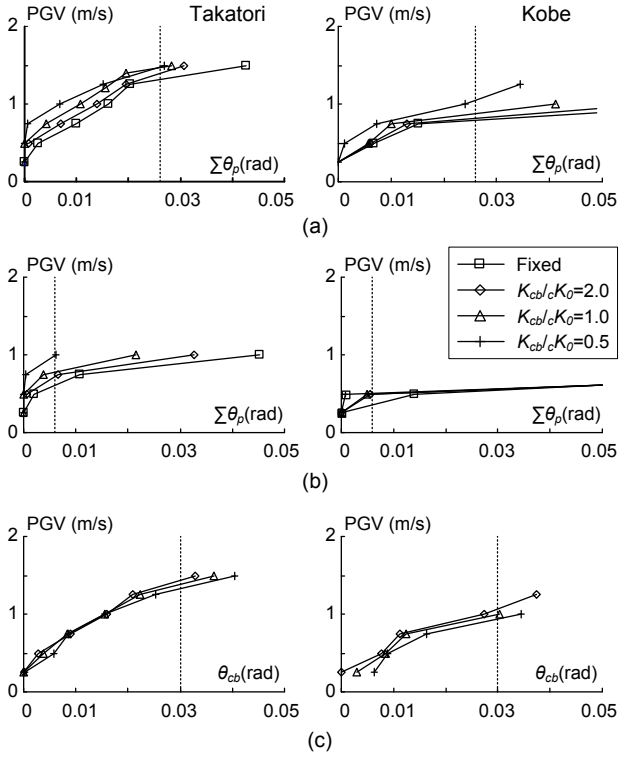


Fig. 11 Relation between input ground motion level and the cumulative plastic rotation of 1st story column or column base: (a) frame failed at the bottom of column, w/t=25; (b) frame failed at the bottom of column, w/t=43; (c) frame failed at the column base

As illustrated in Fig. 11 (a) and (b), the contribution of the column base rotation could increase the sesmic behavior of the frame if the frame was designed to fail at the bottom end of the column. Compard with the the frame failed at the bottom end of the column, the frame failed at the column base could resist larger level of input ground motion, as shown in Fig. 11(c).

5.4 Distribution of Accumulated Plastic Energy Absorption

As indicated in Fig. 8, the damage was concentrated in the 1st story. The dissipated energy in the 1st story is adopted in this section to discuss the effect of the column base behavior. The energy dissipation of the frame at the ultimate state is discussed in this section. Figure 12 shows the proportion of the energy dissipated by each component to the energy dissipated by the whole frame.

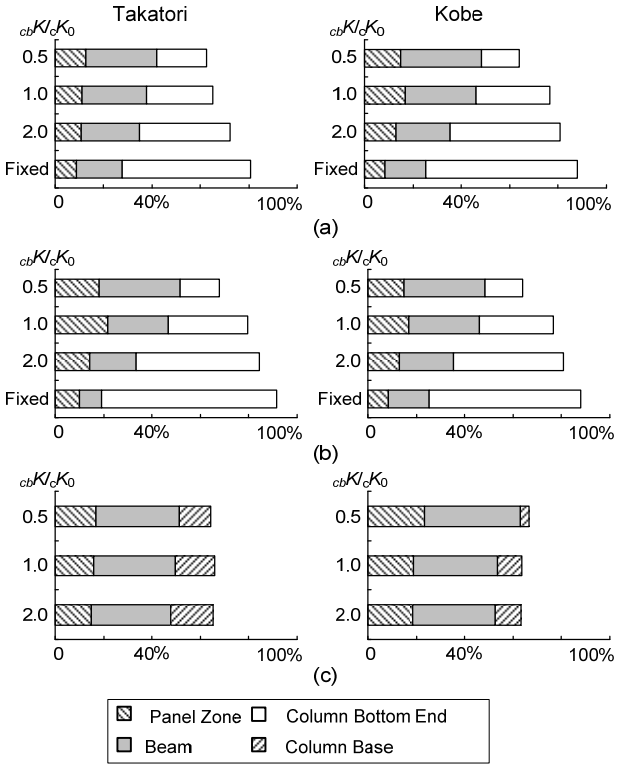


Fig. 12 Energy dissipation proportion of the 1st story: (a) frame failed at the bottom of column, w/t=25; (b) frame failed at the bottom of column, w/t=43; (c) frame failed at the column base

It is notable that the damage at the bottom of the 1st story column controls the frame behavior when the column base is completely fixed ($_{cb}K/_cK_0=\infty$). When the frame failed at the bottom end of the column, the energy dissipation proportion of each component is shown in Fig. 12 (a) and (b). The energy dissipated by the column was increased as $_{cb}K/_cK_0$ increased. Meanwhile, the energy dissipated by other components, such as panel zone and beam, was reduced as

$_{cb}K/_cK_0$ increased. If the column is non-ductile members (w/t=43), the dissipated energy of the frame is mainly contributed by the 1st story column. It might cause the sway failure of the frame, which is unfavorable.

When the frame failed at the column base instead of the bottom end of column, the frame response are the same with different width thickness ratio of the column. It is because that the damage was concentrated at the anchor bolts of the column base connection and the damage on the column was thereby reduced. As shown in Fig. 12, the energy was mainly dissipated by the panel zone and beam, which could be intentionally designed to dissipate more energy in practice. Same as observed when the frame failed at the bottom end of the column, the energy dissipated by the column base was increased as $_{cb}K/_cK_0$ increased. However, compared with the energy dissipated by the other components, the energy dissipated by the column base is relatively small.

6. CONCLUSIONS

Seismic analysis of frame was conducted. The effects of column post-buckling and slip behavior of column base were considered.

1. The intensity of the damage concentration at the structural element of the 1st story in the frames with exposed type column bases were much less than that of the frames with pin type column bases.

2. The seismic performance of the frame with fixed column base connection is affected by the post-buckling behavior of the column.

3. Using exposed column base, the damage could be distributed evenly in the frame. And the collapse caused by the non-ductile column could be avoided.

4. Absorbed energy by the exposed column base is fairly small.

Acknowledgements:

The first author acknowledges the great support from the Center for Urban Earthquake Engineering (CUEE) in Tokyo Institute of Technology during the stay in Tokyo Institute of Technology as a postdoctoral research fellow.

References:

Japanese Society of Steel Construction (JSSC) (2009), "Fundamentals of Steel Structure Design (4th Edition)," Gihodoshuppan, Tokyo.(in Japanese).

Kato, B. and Akiyama, H. (1968), "The Ultimate Strength of the Steel Beam-Column (Part 4)," *Trans. of AIJ*, 151, 15-20.

Yamada, S. Akiyama, H. and Kuwamura, H. (1993), "Post-buckling and Deteriorating Behavior of Box-section Steel Members," *Journal of Struct. Constr. Engng*, AIJ, 444, 135-143.

Akiyama, H. and Takahashi, M.(1990), "Influence of Bauschinger Effect on Seismic Resistance of Steel Structures," *Trans. of AIJ*. 418, 49-57.

Yamada, S. and Akiyama, H. (1995), "Deteriorating Behavior of Steel Members in Post-Buckling Range," *Structural Stability and Design* (Proc. of ICSSD'95 at Sydney), 169-174.

Cui, Y. Nagae, T. and Nakashima, M. (2009), "Hysteretic Behavior and Strength Capacity of Shallowly Embedded Steel Column Bases," *Journal of Structural Engineering* (ASCE), **135**(10):1231-1238.

Architectural Institute of Japan (AIJ). Recommendations for Design of Connections in Steel Structures, Tokyo, 2006. (in Japanese).

Building Center of Japan (BCJ). Commentary on Structural Design Standard and Techniques, Tokyo, 2001. (in Japanese).

Building Center of Japan (BCJ). Manual of Design and Construction of Cold Formed Hollow Section Steel Tube, Tokyo, 2008. (in Japanese).

10CUEE CONFERENCE PROCEEDINGS
10th International Conference on Urban Earthquake Engineering
March 1-2, 2013, Tokyo Institute of Technology, Tokyo, Japan

EVALUATION OF THE RESPONSE MODIFICATION COEFFICIENT INCLUDING COLLAPSE ASSESSMENT OF SCBFS

Po-Chien Hsiao[1], Dawn E. Lehman[2], and Charles W. Roeder[3]

1) Ph.D.: Department of Civil Engineering, University of Washington, Seattle, WA, USA
2) Associate Professor: Department of Civil Engineering, University of Washington, Seattle, WA, USA
3) Professor: Department of Civil Engineering, University of Washington, Seattle, WA, USA
pchsiao@uw.edu, delehman@uw.edu, croeder@uw.edu

Abstract: Special concentrically braced frames (SCBFs) are commonly used for seismic design of buildings. Their large elastic stiffness and strength efficiently sustains the seismic demands during smaller, more frequent earthquakes. During large, infrequent earthquakes, SCBFs exhibit highly nonlinear behavior due to brace buckling and yielding and the inelastic behavior induced by secondary deformation of the framing system. These response modes reduce the system demands relative to an elastic system without supplemental damping using a response modification coefficient, commonly termed the *R* factor. More recently, procedures put forth in FEMAP695 have been made to quantify the R factor through a formalized procedure that accounts for collapse potential. The primary objective of the research in this paper was to evaluate the approach for SCBFs. An improved model for SCBFs that permits simulation of brace fracture was used to conduct response history analyses. A series of 3-, 9- and 20-story SCBFs were designed and evaluated. Initially, the FEMAP695 method was conducted to estimate collapse and the corresponding R factor. An alternate procedure for scaling the multiple acceleration records to the seismic design hazard was also evaluated. The results show significant variation between the two methods. Of the three variations building studied, the large vulnerability was identified for the 3-story building. To achieve a consistent margin of safety against collapse, a significantly lower *R* factor is required for the low-rise SCBFs (3-story), while the mid-rise and high-rise SCBFs (9- and 20-story) may continue to use the current value of 6.

1. INTRODUCTION

Special concentrically braced frames (SCBFs) are commonly used as the primary lateral-load resisting system in buildings. These frames have beams, columns and braces concentrically joined at work points. In the design office, the system is initially designed as a vertical truss system, and the initial lateral stiffness and resistance of the frame is provided through the axial response of all members (beams, columns and braces). Conventional design uses reduced seismic loads. In larger, less frequent earthquakes, inelastic action in the brace is expected. This inelastic behavior is primarily governed by the severe buckling, post-buckling and tensile yield deformations of the brace; secondary yield mechanisms may occur in the gusset plate connection, beams and columns.

To assure that the system can achieve these large inelastic deformations without premature failure, current AISC SCBF design requires capacity design of the beams, columns and connections to meet the tensile and compressive capacity of the brace (AISC 2005a). Local and global slenderness limits are applied to the brace to assure that the brace can sustain multiple large drift cycles.

Currently there are few design restrictions on or understanding of the gusset plate, which leads to considerable variation in the gusset plate connections designed for SCBF systems. Prior research has shown that different gusset plate designs influence the seismic performance of the braced frame and that poorly designed gusset plates can severely decrease the drift capacity of an SCBF (Lehman and Roeder 2008). These findings have led to a new, balanced design procedure that provides a method for consistent gusset plate design and increasing the ductility of the braced frame system beyond that achievable with the current AISC SCBF seismic design criteria (Roeder et al. 2011a, Lumpkin et al. 2012) including a new elliptical clearance model (Lehman and Roeder 2008).

The method was developed and supported by a coordinated experimental and analytical research program on SCBF systems. In all, more than 30 single-story, single-bay frames were tested and analyzed (Johnson 2005, Herman 2006, Kotulka 2007, Powell 2010). A multi-story experimental program, including 3 two- and three-story frames (Roeder et al. 2011b, Lumpkin et al. 2012), was also conducted to investigate application of the design recommendations developed from the single-story research, to validate a design method for midspan gusset plate connections, and to evaluate the distribution of inelastic deformation between different stories.

Design of SCBFs depends on several seismic performance factors (SPFs). In particular, the response modification coefficient (*R* factor), which is used to reduce

the elastic seismic design loads to those used for member design, significantly influences the design and, therefore, would be expected to influence the performance of SCBFs. *R* factors were originally derived in an ATC-3-06 report (1978), with the historic values determined from engineering judgment and qualitative comparisons with the known response capabilities of a relatively few, well-understood seismic-force-resisting systems. In general, these *R* values were also related to the R_w values used in the Uniform Building Code for allowable strength seismic design. In the most recent provisions, the National Earthquake Hazards Reduction Program (NEHRP) Recommended Provisions for Seismic Regulations for New Buildings and Other Structures (FEMA 450) provided the *R* factors for more than 75 different seismic-force-resisting systems including SCBFs. However, the *R* values were somewhat arbitrarily assigned without appropriate verification of their seismic response characteristics. It has become clear that a more rational assessment of the *R* value is needed for all seismic resisting systems, including SCBFs.

In modern design, large, nonlinear inelastic deformations are expected during large seismic loads and the system must be detailed to sustain these demands. However, the seismic design forces must be large enough to result in sufficient strength and stiffness to meet the elastic demands in lesser events. The seismic design forces are determined by reducing the expected elastic seismic forces by the *R* value.

An analytical study was undertaken to evaluate the seismic performance and R values for SCBF systems. SCBF systems were designed based using newly proposed seismic design procedures (Lumpkin et al. 2012), and then nonlinear dynamic analysis were performed using practical, validated models as described below. The improved models of SCBFs combined with ATC-58 fragility curves allow accurate prediction of all performance limit states, such as no repair, possible brace replacement, brace fracture, and potential collapse, in the performance evaluations.

The impact of the R value was studied by evaluating the full seismic performance, including collapse. A series of SCBF buildings were designed using a range of R values. The building designs were assessed with two methods. The first method used the FEMA P695 incremental dynamic analysis (IDA) procedure (2008) to estimate collapse potential and to propose R values that consistently achieved the collapse prevention performance limit state. The second method included a suite of 20 acceleration records for the 10% and 2% in 50 year seismic hazards that were scaled to the seismic hazard level for the building site, and the predicted system performance was used to propose appropriate *R* factors of SCBF structural systems.

2. DESIGN OF THE MODEL BUILDINGS

A series of 3-, 9- and 20-story idealized SCBF buildings were designed using the equivalent lateral force procedure. The buildings were based on the model buildings in the SAC Steel project, adopting the basic floor plan, story height, and gravity loads (FEMA 355C). Appropriate modifications were made to translate the buildings to SCBFs. Figure 1 shows the typical elevations and floor plans of the different buildings considered here.

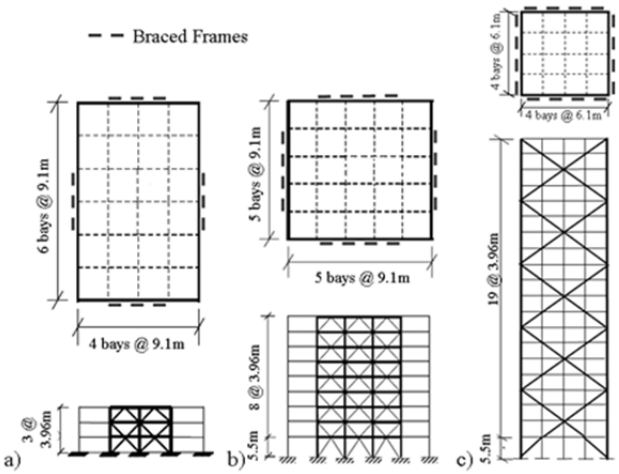


Figure 1. Elevations and Floor Plans of (a) 3-, (b) 9- and (c) 20-story Buildings.

A primary study parameter was the impact of variation in the *R* value. Several different *R* values were evaluated, and include: (1) *R* of 3, 4, 5, and 6 for the 3-story buildings, (2) *R* of 3, 6, 7 and 8 for the 9-story buildings, and (3) *R* of 3, 4, 6, and 8 for the 20-story buildings. Current codes employed an *R* value of 6 for SCBF systems.

The buildings were designed using the NEHRP recommended provisions (FEMA 450). All of the buildings were designed for a location in Seattle, WA, using a Seismic Design Category D with soil Site Class C. The 3-story buildings had 4-by-6 bays with identical story height, while the 9- and 20-story buildings have 5-by-5 and 4-by-4 bays, respectively and with a taller bottom story to reflect typical midrise construction, as shown in Fig. 1. The 20-story frame exceeds the height limit of 48.8m (160 feet) for steel SCBF as per NEHRP (FEMA 450), and the design requires peer review which was not considered by this study. Therefore, the designed 20-story buildings might be different in practice. However, it should be noted that this research used larger seismic design forces than the minimum required by the specification, and it is unlikely that the seismic performance of the buildings will be better than that predicted here.

The braced bays were situated along the perimeter of the buildings in a symmetric plan configuration using a multi-level X-bracing configuration, as illustrated in the figure. Table 1 summarizes the total gravity loads for individual floors and the roof (lighter loads were applied to the roof) for each building configuration. The buildings were designed to meet the NEHRP design spectrum using the United States Geological Survey's (USGS) mapped spectral acceleration values at 2% in 50 years hazard level for the location of Seattle (updated in 2008). All buildings are designed with equivalent lateral force procedures. The 20-story buildings would ordinarily be designed using the response spectrum procedure. The equivalent lateral force method was used to permit direct comparison of all building

heights. However, response spectra analyses were performed, and they showed that the equivalent static analysis resulted in larger member design forces and different distribution of forces over the frame than the response spectrum method. The following values were used: S_S (mapped spectral acceleration parameter at short periods) of 1.4g and S1 (mapped spectral acceleration parameter at a period of one second) of 0.53g. The site class effect was included and the damped spectra were adjusted to 2% of critical damping by the applying β_S and β_1 factors of 0.8. The resulting design spectral acceleration parameters were S_{DS} of 1.17g and S_{D1} of 0.57g. The buildings were considered to be general office buildings, and an occupancy importance factor, I, of 1.0 was used. The redundancy factor of 1.0 was used for all model buildings; while higher value of the redundancy factor would lead to heavier braces and stiffer structures, and would potentially increase the seismic design forces for load combinations including gravity load.

Table 1. Design Parameters and Periods

Model Buildings	R	Gravity Loads (kN)		C_S	T (sec.)	T_1 (sec.)
		Floor	Roof			
3-Story	3	9379	9011	0.390	0.31	0.34
	4			0.293		0.36
	5			0.234		0.37
	6			0.195		0.38
9-Story	3	9721	9317	0.258	0.73	0.69
	6			0.129		0.84
	7			0.111		0.88
	8			0.097		0.94
20-Story	3	2952	2610	0.144	1.31	1.49
	4			0.108		1.66
	6			0.072		1.85
	8			0.054		2.01

In the design of the 3-, 9- and 20-story buildings, the braces were all rectangular Hollow Structural Sections (HSS) and satisfied the AISC seismic compactness criteria (AISC 2005b). The gusset plate connections were rectangular and designed using two different methods to compare current and the proposed balanced design procedure (Roeder et al. 2011a). All of the beam-to-column connections of the frames were designed as welded-flange welded-web connections. Framing members were designed to develop the expected capacity of the braces. Table 1 shows the seismic response coefficient, C_S, design periods, T, and the fundamental periods obtained from modal analysis, T_1, for all the model buildings.

3. SYSTEM MODELING INCLUDING EFFECT OF GRAVITY FRAMES

To assess the seismic performance of SCBFs and the R value in a rational manner, comprehensive nonlinear dynamic analysis models are required. These models must include every yield mechanism and failure mode that impacts the seismic response of the frame and must be capable of simulating the response beyond initial fracture. These modeling requirements have been met for CBFs and proposed in prior studies. Detailed information on the modeling techniques used is provided in the following references (Hsiao et al. 2012a, 2012b).

All of the braced frame systems of the buildings in the study were modeled using the proposed simulation model of SCBFs, which consisted of the proposed spring models of gusset plate connection, rigid links and line-elements (Hsiao et al. 2012a), and the brace-fracture model (Hsiao et al. 2012b) to enable accurate simulation of the SCBF systems to well beyond brace fracture.

The gravity loads and second order effect (P-delta) effects were included in the simulation by employing a leaning column connected to the frame by rigid links, as illustrated in Fig. 2. When this secondary resistance was included, nonlinear springs simulating the combined rotational strength and stiffness of gravity beam-column connections were placed between the rigid link and the leaning column. Half of the building gravity loads at each floor level were supported by the leaning column, since each building model used two seismic frames in each direction to resist the lateral loads, as shown in Fig. 1.

The properties of the nonlinear spring were based upon Liu's model (2004) of shear-plate connections with composite slabs, and the springs were simulated using the Pinching4 material model in OpenSees. Each spring element had the number of the gravity bays within a half building, modeled using the total moment strength of all of the contributing single shear-plate connections (for example a multiplier of 12 was used for the 3-story model buildings to simulate the contribution of half of the total number of gravity connections). The rigid beams used in the gravity frame model were supported by rollers, which were slaved to the nodes at the middle of the frame in the lateral direction at each level.

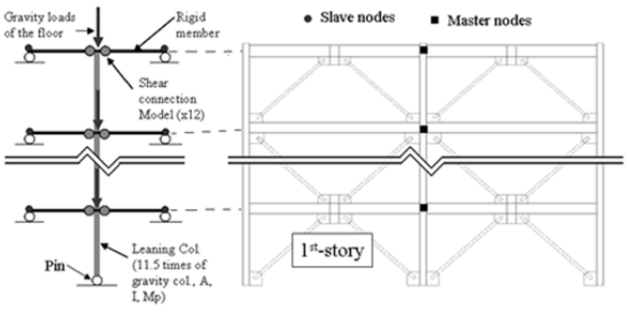


Figure 2. Illustration of the Simulation of P-delta Effect and the Lateral-load Resisting Contribution of Gravity Frames

The base of the leaning column was pinned. Wide-flange sections W10x49 and W12x65 were selected for the gravity columns of the 3- and 9-story buildings throughout the height, respectively. The gravity columns of the 20-story buildings varied: the smallest wide flange section was a W8x31 and the largest wide-flange section was a W14x90. To represent the initial axial and bending stiffness and strength of the gravity columns, a particular

cross section of the leaning column was adopted with a cross-sectional area, moment of inertia and plastic moment capacity equal to the total of the gravity columns in half the building (for example 11.5 columns total for the 3-story model buildings). The resulting models led to that the slenderness of the leaning column for the 3-story buildings was much lower than that for the 9- and 20-story buildings, while that of 20-story buildings was slightly larger than 9-story buildings. However, based on the analytical predictions, this variation did not have a great impact on the results.

To simulate the earthquake characteristics of the ground motions in Seattle, the SAC ground motion record sets assembled for Seattle (each set consists of 20 acceleration records) (FEMA 355C, Somerville 1997) were used in this investigation. All of the ground motions were applied using a time step of 0.005 sec. To represent the different seismic hazards, the records were appropriately scaled using the fundamental period of the structure and the periods resulting from the probable damage states. The details and the consequences of the scaling procedure are described below, in the section on multi-performance level evaluation.

4. COLLAPSE ASSESSMENT USING FEMA P695 METHODOLOGY

The FEMA P695 Incremental Dynamic Analysis (IDA) method was used to estimate collapse potential, as related to the R factors and the four idealized buildings. The following provides an overview of the methodology and its application to this research project. Further information is found in the reference report (ATC-63).

In the IDA and P695 methodology, considered buildings are grouped into "archetypes" that are expected to have similar performance characteristics. Archetype structures should be designed with a selected range of structural geometry and design parameters including structural configurations, seismic design categories, fundamental periods, etc. These archetypes were assembled into "performance groups" reflecting major changes in structural behaviors within the archetype design space. Given the archetype performance group development, nonlinear models are developed and nonlinear analysis and performance evaluation of the system are completed.

The FEMA P695 analysis method for evaluation of collapse potential was used in the research. Figure 3 illustrates the relations between the important design parameters used in the methodology. The figure shows three important design states. The elastic response is based on the assumption that 100% of the effective seismic weight of the structure, W, participates in fundamental mode of the system with a period of T1. The second is that the ratio of the mean spectra acceleration corresponding to the Maximum Considered Earthquake (MCE), SMT, to the seismic response coefficient, C_S (V/W, the ratio of the design base shear and the weight of the structure) is defined as 1.5 times of the R value. The third and final design concept is that the median spectral acceleration at collapse initiation is $\hat{S}_{CT}$, which is predicted using the IDA method.

The primary objective of the method is to evaluate the collapse potential of an archetype for a given R value. This evaluation compares the computed Adjusted Collapse Margin Ratio with the Acceptable Collapse Margin Ratio, which is based on the Collapse Margin Ratio. The following paragraphs briefly quantify each.

The Collapse Margin Ratio (CMR) is defined as the ratio of the median 5%-damped spectral acceleration of the collapse level ground motions, ŜCT, to the SMT at the fundamental period of the structure, T_1, of the MCE seismic hazard for the site. This ratio is shown in Fig. 3. The IDA procedure is used to determine $\hat{S}_{CT}$.

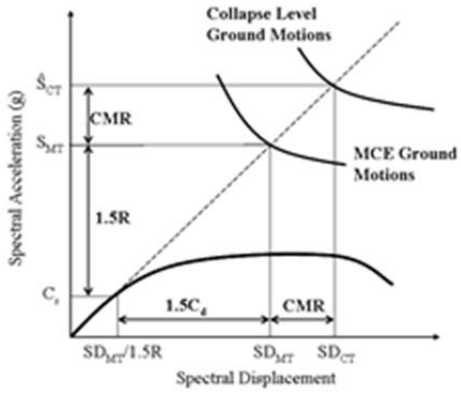


Figure 3. Illustration of the R Factor as Defined by the FEMA P695 Methodology (FEMA P695)

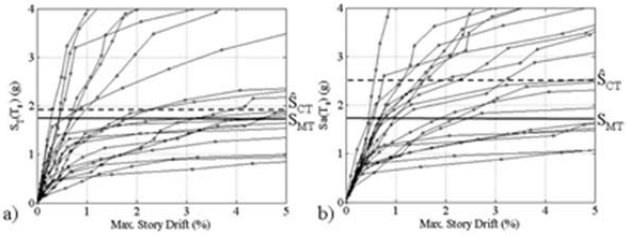


Figure 4. IDA Results for the 3-story Building (R=6) using (a) M1 and (b) M2 Scaling Methods with Collapse Story Drift Capacity of 5% Radians.

The method accounts for the frequency content (spectral shape) of the ground motions, and a consistent set of ground motion variation parameters is defined for different sites, hazard levels and structural periods (Baker and Comell 2006), where $\hat{S}_{CT}$ is determined using the forty-four selected acceleration records which satisfy the ground motion selection criteria. To account for statistical variation in the records, the CMR is multiplied by a simplified Spectral Shape Factor (SSF) to obtain the Adjusted Collapse Margin Ratio (ACMR). The SSF values are specified in the report, and depend on the structural period and the building ductility capacity.

Finally, the archetype is evaluated by comparing the

calculated ACMR to an acceptable ACMR which was specified according to the uncertainty factors of structural system, including the quality of design requirements, test data, numerical modeling, and a prescribed set of ground motions. By the FEMA P695 procedure, the acceptable AMCR should reflect conditional probability of collapse of 20% for individual archetype (AMCR20%). The ACMR of an individual archetype needed to be greater than the corresponding acceptable AMCR to pass the trial. If the determined ACMR was less than the Acceptable ACMR, the R value of the performance group does not meet the performance requirements of collapse prevention.

The 3- and 20-story buildings were evaluated using the FEMA P695 IDA procedure with design spectral acceleration, S_{DS}, of 1.17g, which is slightly greater than the value of 1.0g suggested by the methodology. For the research, the SAC ground motion set for 2% in 50-year seismic hazard in Seattle was used in place of the 44 ground motion records provided by the methodology. Originally, the SAC ground motion records had been scaled to fit the USGS mapped spectral acceleration values at multiple period points (FEMA 355C). For this research, all of the SAC acceleration records were scaled back to original ground motion records prior to the IDA process by simply dividing the SAC records by their scaling factors, which were from 0.94 to 10.04 with a median of 2.34, used for scaling the SAC ground motions given in the SAC report. The original records were subsequently increased until collapse was predicted for each record following the IDA process.

Two methods for scaling the intensity of ground motions were investigated. The first method, designated Method M1, collectively increased the entire set of ground motion records upon the median spectral acceleration of the record set at the fundamental period, so-called Record Set Intensity (RSI), $S_T(T)$, rather than using different intensities for each record. Using this method, the records were scaled as a group in proportional amounts, and the value of $\hat{S}_{CT}$ was defined as the RSI of the group when 50% of the records predicted failure.

The second method, designated Method M2, scaled each record individually, using different intensities for each record at the design period of T, Sa(T). Using this method, $\hat{S}_{CT}$ was defined as median at the period T1 of the response spectra that resulted in predicted collapse by the IDA procedure (FEMA 355F). Figures 4a and b shows the resulting IDA curves using the methods M1 and M2, respectively. It is apparent that scaling the ground motions in different ways significantly changed the distribution of the resulting IDA curves, which results in different CMRs for the same set of ground motions.

In an actual building, collapse will depend on the resistance of the gravity frame as well as the residual resistance of the braced frames. Braced frames dramatically lose most of their resistance and sustain increasing story drift after prediction of the brace fracture. In many IDA evaluations, the collapse prediction is based on flattening of the IDA responses curves, such as those shown in Fig. 4. The results show that some brace fracture curves flatten at relatively low spectral accelerations while others do not flatten at all. This is partly caused by the irregular characteristics of acceleration response spectra and the large increases or decreases that may occur with modest changes in period.

In this research, to account for these and other uncertainties, a potential collapse limit state corresponding to 5% drift was selected for two reasons. First, the nonlinear analyses were deemed to have sufficient accuracy to approximately 5% story drift. Second, experimentation indicates that most beam-column connections and columns do not retain sufficient resistance beyond this drift level. Tests, including SCBF gusset plate connections, indicate that they retain their basic moment resisting connection integrity well beyond brace fracture, but this integrity cannot be assured for drift levels larger than 5% (Lehman and Roeder 2008). This limiting story drift capacity was used to determine $\hat{S}_{CT}$. In Figs. 4a and b, $\hat{S}_{CT}$ was determined when the analyses for 10 out of 20 ground motions (50%) had a story drift greater than 5%.

The results shown in Fig. 4 were compared with the acceptable ACMR20% values in FEMA P695 to evaluate the collapse resistance of each system, as shown in Table 2. The P695 method requires an estimate of the system ductility and the structural fundamental period to determine the acceptable ACMR20%. Based on the prior experimental results (Lumpkin et al. 2012, Johnson 2005, Herman 2006, Kotulka 2007, Powell 2010), SCBF usually buckled around story drift of 0.3% and fractured brace around story drift of 2.5%, which led to the story-drift ductility of 8.3. The corresponding SSF values, required to scale to CMR to determine the ACMR, were 1.4 and 1.65 for 3- and 20-story buildings, respectively. (These values are for structures having the ductility greater than 8). An acceptable ACMR20% of 1.73 was determined, in which the 3-story and 20-story buildings were regarded as an archetype and the quality ratings for design requirements, test data, and numerical modeling were all quantified as "B-Good". The resulting total uncertainty factor was 0.65.

Table 2 summarizes the parameters and the results of the evaluations for the 3- and 20-story buildings with design R values of 6 and 3. As expected, decreasing the R-factor increases the CMR for all systems studied.

However, the results are not consistent between the two methods. Using method M1 (as defined in FEMA P695), both of the system designed using an R-factor of 3 "passes" the evaluation criteria, while the values of ACMR for the 20-story buildings were smaller than those for 3-story buildings. This result suggests that SCBF systems meeting current design will fail. In contrast, using scaling method M2, only the 20-story building designed with R=6 fails to meet the acceptable ACMR20%. The M1 scaling method suggested that R factor of 3 is appropriate for both of 3-story and 20-story buildings. The M2 scaling method suggest that R factor of 6 is appropriate for 3-story SCBFs, while an R value of 3 is needed for 20-story SCBFs. These contrasting results suggest significant ambiguity with the proposed method.

Finally, the analysis for both scaling methods M1 and M2 predicted greater potential for collapse with the 20-story SCBF than for the 3-story SCBF. These results are contrary to findings from prior earthquakes and other studies, in which low rise SCBFs have been deemed more vulnerable (Chen and Mahin 2010).

Table 2. Summary of Evaluations of the 3- and 20-story Buildings Using FEMA P695 IDA Procedure

Scaling Methods	M1 [$S_T(T)$]				M2 [Sa(T)]			
Model Buildings	3-Story		20-Story		3-Story		20-Story	
R Factors	6	3	6	3	6	3	6	3
S_{MT} (g)	1.76	1.76	0.65	0.65	1.76	1.76	0.65	0.65
$\hat{S}_{CT}$ (g)	1.88	2.8	0.55	0.82	2.5	3.35	0.65	0.93
CMR	1.07	1.60	0.85	1.26	1.42	1.91	1.00	1.43
SSF	1.4	1.4	1.65	1.65	1.4	1.4	1.65	1.65
ACMR	1.50	2.23	1.39	2.08	1.99	2.67	1.65	2.36
Accep. ACMR20%	1.73	1.73	1.73	1.73	1.73	1.73	1.73	1.73
Pass/Fail	Fail	Pass	Fail	Pass	Pass	Pass	Fail	Pass

5. MULTI-PERFORMANCE LEVEL EVALUATION PROCEDURE

The results of the P695 analyses revealed ambiguities in the method. To study these further and potentially eliminate them, an alternate evaluation approach for SCBFs was investigated. This procedure directly scaled each ground motions to the seismic hazard for the site (M2) with enhancements described below. In addition to investigating the collapse limit state, the resulting multiple damage limit states of the SCBFs were examined and considered. Therefore, the range of system performance limit states was evaluated (e.g., brace buckling, fracture) for each acceleration record and was then considered in the evaluation of the R factors, as opposed to only the collapse potential. Again, potential collapse of the structure was assumed if any floor level of the structural system developed a 5% story drift.

The 20 SAC Seattle ground motions were scaled to the 2/50 hazard level (MCE level). In addition, the seismic performance at the 10/50 hazard level was evaluated, using SAC 10% in 50 year records for Seattle (FEMA 355C). The target spectra for each hazard level followed the NEHRP recommended provisions (FEMA 450) using the corresponding USGS mapped spectral acceleration values representative of different hazard levels, 10/50 and 2/50. Without the reduction of 2/3, the 2/50 target spectrum is 1.5 times of the design spectrum, while the 10/50 target spectrum is slightly smaller than the design spectrum, as shown in Fig. 5a.

In addition to the 3- and 20-story SCBFs idealized buildings, an idealized 9-story SCBFs was investigated. A larger number of R values were evaluated for each system.

The evaluation of the P695 procedure revealed ambiguities associated with scaling ground motions and results that contradict the normal expected performance of the SCBF system (Chen and Mahin 2010, AIJ 1995). The research team considered various scaling approaches that have been used to evaluate the seismic performance of structures. Prior studies have scaled records using a single period, multiple periods, or a period range (FEMA 355C). Multi-period scaling was deemed important for SCBFs because SCBFs are initially stiff and significant shifts in structural period are expected beyond brace buckling and again beyond brace fracture. Therefore, an approach of scaling the ground motions to match the design response spectra prior to and beyond the brace fracture was used.

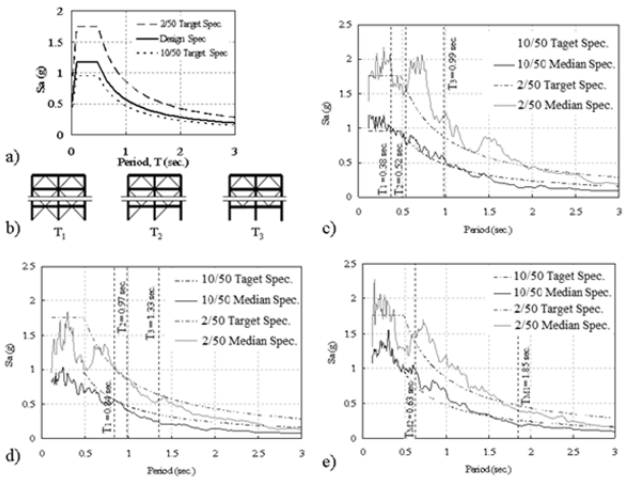


Figure 5. (a) Adopted Target and the Design Spectra at Seattle; (b) Illustrations of the Corresponding Frames for the Three Periods, T_1, T_2 and T_3; (c) the Scaled Median Acceleration Spectra and The Corresponding Target Spectra for the 3-, (d) 9- and (e) 20-story SCBF Buildings.

This conclusion was substantiated by a preliminary study. All of the idealized buildings were analyzed using earthquake records scaled to the first mode only. These analyses demonstrated that significant brace damage (buckling, yielding, and eventually fracture) was sustained by the 3 and 9-story building models, but much more limited brace damage in the 20-story building models. Conversely, the 20-story building models exhibited significant higher mode effects, and these higher modes must be including in the scaling procedure.

As a result two different scaling approaches were used. For the structures primarily governed by the fundamental mode prior to damage, i.e. the 3- and 9-story buildings, the following approach was used. For the 10/50 target spectrum, minimal nonlinearity was observed from the preliminary analysis and those ground motions were scaled to meet the 10/50 target spectrum using only the first (fundamental) period (T_1) of the structure. (Each ground motion was scaled independently and for the structure, that is the number of stories plus *R* factor, of interest.)

The analyses indicated structural damage occurred at the 2/50-hazard level, typically in the form of brace fracture at the critical story. Therefore multi-period scaling was used,

including the fundamental period (T_1) and two additional periods for the more severe damage states of the structure. The second period of interest (T_2) corresponded to loss of braces in one-direction. The third period of interest (T_3) corresponded to loss of all braces at the critical story were used. These two states are illustrated in Fig. 5b. The dynamic analyses indicated that the critical story was the bottom story for the 3- and 9-story building models.

Using this method, the following expressions of scaling factor, f10/50 and f2/50, were developed to scale each ground motions for each hazard level.

$$f_{10/50} = \frac{Sa_{1,t}}{Sa_{1,g}} \tag{1}$$

$$f_{2/50} = \frac{Sa_{1,t}}{Sa_{1,g}} w_1 + \frac{Sa_{2,t}}{Sa_{2,g}} w_2 + \frac{Sa_{3,t}}{Sa_{3,g}} w_3 \tag{2}$$

The expression is a weighted function of the spectra accelerations at the periods of interest. In the expression, $Sa_{i,t}$ is the target elastic spectral (acceleration) values corresponding to each T_i period as described previously (i =1 to 3), $Sa_{i,g}$ is the spectral (acceleration) value of the ground motion at the period T_i, and wi is the weight for the T_i period points. The weights were 0.55, 0.35 and 0.1 for T_1, T_2 and T_3, respectively. Using this scaling approach, the median scaled acceleration spectra at 10/50 and 2/50 hazard levels shown in Figs. 5c and d were developed comparing with the corresponding target spectra for the 3- and 9-story SCBF buildings, respectively. The values of three periods, T_1 to T_3, are indicated in the figures. The plots show that the median scaled (acceleration) spectra matches the target spectra on average between T_1 and T_3 period points, which is the region of primary variation in the period.

The preliminary analysis of the 20-story building models indicated significant contributions of the second mode in top and bottom stories with the first mode governing the response of the remainder of the building. To include the second mode effects, a modified scaling approach was adopted to scale the ground motions for use in the 20-story building analysis, basing the scaling function on the first two modal periods for both of the hazard levels. Note that because significant damage was not observed in high-rise building, the larger periods resulting from brace damage were not included as they had been in the 3- and 9-story scaling methods. The resulting expression, given in Eq. 3, was used to scale the ground motions for both of the 10/50 and 2/50 events.

$$f_{m,10/50} \; and \; f_{m,2/50} = \frac{Sa_{m2,t}}{Sa_{m2,g}} w_{m2} + \frac{Sa_{m1,t}}{Sa_{m1,g}} w_{m1} \tag{3}$$

In the expression, $Sa_{mi,t}$ is the target design elastic spectral acceleration value for the ith modal period (i=1 and 2), $Sa_{mi,g}$ is the spectral acceleration value of the ground motions at the ith modal period. For the second expression, weights of w_{m2} =0.6 and w_{m1} =0.4 were used. Figure 5e shows the median scaled acceleration spectra for 10/50 and 2/50 hazard levels and the corresponding target spectra for the 20-story SCBF building. The values of the first two mode periods, T_{M1} and T_{M2}, used for scaling were indicated in the figure.

A single set of the scaled ground motion records were used for the analyses, which were scaled based upon the computed periods of the 3-, 9- and 20-story buildings. In all cases, the computed periods for the buildings designed using an *R* value of 6 were used for the other *R*-value building design with the assumption that variation of the periods due to different *R* factors had a minor effect of the scaled ground motions.

The scaled 2% and 10% in 50 year (2/50 and 10/50) ground motions were used for the performance evaluation of SCBFs, which varied with building height. Figures 6a, b and c show the average Maximum Story Drifts (MSD) computed for the 3-, 9- and 20-story SCBFs for the 10/50 and 2/50 hazard levels, respectively. As noted in the figures, a range of *R* values were studied, and included *R*=3 and 6 for the 3-story building models, and *R*=3, 6, and 8 for the 9-and 20-story building models.

The deformation concentrated in the bottom story for the 3- and 9-story frames, which always occurred after brace fracture at that story. The results show that the 3-story SCBFs designed with *R*=6 had much more severe deformation and damage than the 9- and 20-story SCBF building models designed using the same response modification factor. In the 10/50 events, the average MSDs vary between 0.3% and 0.5%, and brace fracture was not predicted. During the 2/50 earthquakes, brace fracture initiated between drifts of 1.5% to 2%. As mentioned previously, brace fracture resulted in severe concentration of deformation. The average MSDs varied from 1% to 3% for the 3-story buildings for *R* values of 3 to 6, while the MSDs varied from 1% to 2% radian for 9-story buildings with *R* values of 3 to 8. These results show that brace fractures occurred in the 3-story building models, with a lesser number for 9-story building models.

The response of the 20-story building models differed significantly from the 3-story and 9-story building models in two ways. First the upper stories sustained some of the largest deformations. Response to the 2/50 ground motions indicates concentration of story drift and inelastic deformation occurred in both the bottom and upper stories due to the brace fracture. Further, the distribution of deformation along the height of the building depends on the R values used in the frame design. Finally, the resulting peak MSDs, which varied between 1.0 to 1.3%, indicated minimal brace fracture in these structures. These results suggest an increase in structural performance with building height, which is contrary to the results from the P695 methodology discussed earlier.

The average maximum story drift distributions shown in Fig. 6 provide interesting and valuable information, but they do not specifically quantify performance. The analytical models used to simulate SCBFs, discussed in the prior section, are capable of predicting both the global seismic behavior as well as the local performance including brace buckling capacity, out-of-plane brace displacement and the onset of brace fracture. This model allows more

comprehensive evaluation of the system performance at all performance levels.

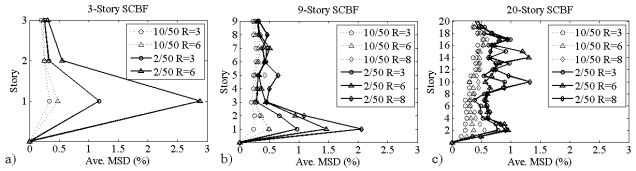


Figure 6. Seismic Responses of (a) the 3-story, (b) 9-story and (c) 20-story Buildings with Various R Factors at 10/50 and 2/50 Hazard Levels.

Several performance limit states were considered here including: 1) brace buckling, 2) possible replacement of the brace, 3) brace fracture, and 4) potential collapse of the building. The brace buckling (and yielding) and fracture behaviors were computed directly. Requirements for possible replacement of the brace was defined as: (1) the maximum out-of-plane displacement of the braces exceeded three times the brace depth or (2) prediction of brace fracture. These damage states are based upon definitions developed in a prior study on fragility curves of CBFs [24]. The same story drift limit of 5% was adopted as the potential collapse criteria, because experiments show that braced frames have considerable inelastic deformation capacity after brace fracture due to the gusset plate connections. Therefore basing collapse solely on brace fracture is unduly conservative. Experiments also show that these connections are unlikely to be reliable at drifts greater than 5%. The authors have greater confidence in the predicted damage states with this alternate evaluation procedure than with the IDA procedure, because the damage states are based upon experimental observation rather than an unverified analytical procedure.

All analytical responses were assembled to determine the occurrence probability of the four performance limit states. Figures 7a, b and c show the probabilities of those damage limit states for the 3-, 9- and 20-story buildings for each of the studied R factors at the 2/50 hazard level (MCE level), respectively.

As expected significant reductions in *R* factors effectively reduced the probabilities of all damage limit states beyond the brace buckling for all story-height buildings. Clearly brace buckling will occur in the 2%-in-50 year event, even for very low *R* values. Yet the results show that it is not the *R* factor alone to impact system performance. Clearly the number of stories impacts performance, with the 20-story building sustaining significantly less damage than the 3-story building for a given *R* factor. The reduced damage of the 20-story building might partially results from the use of equivalent lateral force procedure in design. These results suggest that a smaller *R* factor may be needed for consistent performance of all SCBF buildings. This clearly contradicts the prediction from the P695 IDA evaluation.

Figure 8 shows similar damage level comparisons for the 10/50 hazard level. Figure 5a shows that the 10/50 hazard level is very close to the design spectrum (2/3 of the MCE). Results show that the probability of brace buckling was high, but little additional damage was predicted regardless of the *R* value.

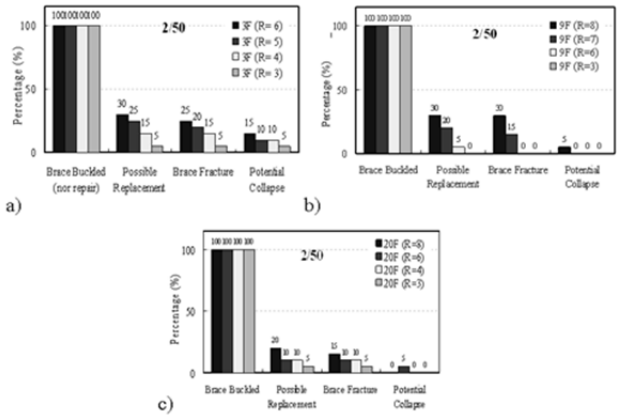


Figure 7. Probability of Damage at the 2/50 Hazard Level with Various R Values (a) 3-story SCBF, (b) 9-story SCBF, and (c) 20-story SCBFs.

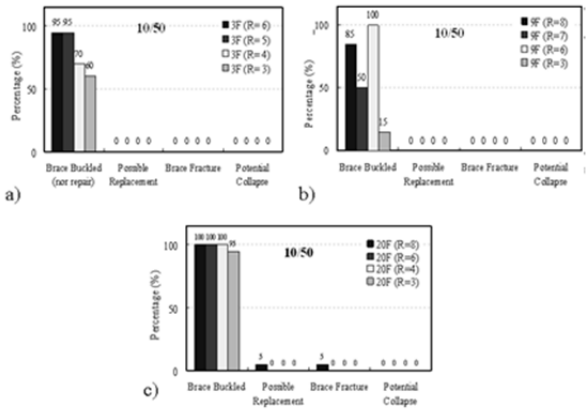


Figure 8. Probability of Damage at the 10/50 Hazard Level with Various R Values (a) 3-story SCBF, (b) 9-story SCBF, and (c) 20-story SCBFs.

6. COMPARISON OF THE RESULTS USING THE PROPOSED AND FEMA P695 PROCEDURES

Comparison of the FEMA P695 methodology with the alternate method described here raises several major concerns about accuracy and reliability of the FEMA P695 procedure for evaluation of braced frames. In particular:

1) The probability of the potential collapse estimated by the P695 methodology was significantly higher for the 20-story building models than for the 3-story building models. In stark contrast, the alternate analysis procedure clearly showed that the 3 story frames had much larger story drift demands with increased structural damage and brace fracture (for the hazard level corresponding to the 2% in 50 year event). The later finding is consistent with findings from earthquake reconnaissance (AIJ 1995).

2) The FEMA P695 procedure would suggest that a relatively smaller *R* value is required for the 20-story (high-rise) buildings comparing with 3-story building. This

is clearly different than the large body of existing knowledge of earthquake engineering (Chen and Mahin 2010, AIJ 1995) in direct opposition to the alternate analysis performed here.

3) The FEMA P695 procedure is sensitive to the scaling methods used in IDA evaluation as shown by the different results achieved from scaling methods M1 and M2 in Table 2. This sensitivity increases the ambiguity of the method.

The results show that of the two evaluation methods, the proposed evaluation procedure is more reliable, for two reasons. First, the FEMA P695 focuses on an imperfect collapse assessment, which is difficult to validate. The alternate method evaluates validated multiple limit states to captures a wide range of performance states that are 1) documented by experimental observations, 2) important to the building owner and occupants, and 3) ignored by the P695 method.

Second, the alternate method provides a rational mechanism for scaling the earthquake ground motions to meet both the seismic hazard level and expected structural performance. Higher mode effects are considered in the evaluation of the high-rise buildings; effects of structural damage on the dynamic response are incorporated as appropriate.

Both methods used a modeling approach, which employed the most accurate modeling of braced frame behavior used to date, since the models were validated to simulate the full range of behaviors and damage states, including brace fracture, observed in experiments. This final point emphasizes the primary limitation with the P695 procedure. Focusing solely on the stability or toppling aspects of collapse does not provide a reliable method to provide consistent performance among building archetypes. Collapse prediction is a highly uncertain response mechanism, difficult to fully simulate in a nonlinear dynamic response analysis, and its validate is not possible with the current experimentation. The P695 procedure extends this uncertain prediction with statistical predictions that imply great accuracy and reliability of the prediction. Engineers and building owners are more concerned by the probability of brace fracture, reparability of the structure, and other structural performance states that impact building performance. The alternate procedure provides a mechanism to estimate structural performance for SCBF systems and provide a consistent level of performance using the *R* value method.

7. CONCLUSIONS

To investigate of the impact of and appropriate values for *R* factors of SCBF systems, 3-, 9- and 20-story SCBF buildings, which were designed based on the equivalent lateral force procedure with various *R* factors, were evaluated by nonlinear dynamic analysis. All of the buildings were idealized multi-story structures designed for the seismic hazards of Seattle, Washington. The buildings in the study were designed to account for the lower damping of steel structures (2%-damping) by amplifying the design base shear by 1.25 (=1/0.8) which is not required in NEHRP (2003), but 2% damping is closer to that typically measured in steel buildings. As a result, the resulting design *R* values with the consideration of this amplification, as adopted in the study, would be 0.8 times those obtained with the normal 5% damped spectrum. Two methods were used to evaluate the appropriate *R* factor values as well as their impact on the seismic performance and design parameters for SCBFs. Initially the P695 methodology was used. Finally, an alternative performance-based method was developed and used to evaluate the SCBF models.

The ground motions selected for analysis were from two bins, including the 2% in 50 year and 10% in 50 year Seattle SAC ground motions. Both methods used state-of-the-art line-element modeling which were experimentally validated. The modeling approach was also used to accurately predict the yielding and buckling behavior of the brace, the post-buckling behavior of the systems, the onset of brace fracture, and the post-fracture behavior of the system.

The research was carried out by first evaluating a pair of 3- and 20-story SCBFs designed with *R* factors of 3 and 6 using the methodology of FEMA P695 (ATC-63). These results were compared with the alternative evaluation process, which used an appropriate scaling method of ground motions to meet the higher mode and performance of a range of SCBF archetypes, including a series of SCBF buildings (3-, 9- and 20-story).

The results were compared with the P695 evaluate results to determine appropriate design parameters, R-factor, for SCBFs. The conclusions of the modeling requirements, ground motion scaling procedures, effectiveness of the P695 procedure and the proposed procedure follow.

The contribution of gravity frames to the lateral resistance had considerable impact on and reduces the seismic responses for the low-rise buildings (3-story buildings) and needs to be considered in the performance evaluation. For mid-rise and high-rise buildings (9- and 20-story buildings in the study), the effect of the gravity frame is relatively small.

The evaluation of SCBFs using the FEMA P695 methodology with the IDA procedure to assess collapse potential led to uncertainty of estimating the R factors. This uncertainty results from the variations of the resulting IDA curves by different scaling approaches of ground motions as well as the difficulty in predicting collapse.

In the alternate performance evaluation procedure, the proposed scaling method effectively reflects the characteristics of the structural systems to best represent the ground motion intensity at certain hazard levels. For first-mode-governed structures, such as the low- and mid-rise buildings, the proposed scaling method provided a reasonable fit of the ground motion response spectra to the design response spectra for the variation of structural periods due to brace fracture. For the taller buildings, which are mainly governed by the second mode, the scaling method assures the ground motion response spectra reasonably

matching the design response spectra at the first two mode structural periods.

Seismic performance evaluation and particularly collapse entails many variability and uncertainties. The alternative evaluation procedure is much better able to address these uncertainties and provide a better picture of SCBF performance than the FEMA P695 method.

By using the accurate analytical models including fracture prediction and proper scaling approach of ground motion records, the seismic performance of the SCBFs can be assessed at multiple damage levels for multiple hazard levels. This fulfills the objectives of performance based earthquake engineering and provides a mechanism for a more consistent design among building archetypes. Solely focusing on collapse does not fulfill this objective or provide this consistency.

The analytical results show that the appropriate R factors actually varied with the number of stories. The results suggest that if consistent safety against collapse is to be achieved, low-rise SCBFs (3-story) require smaller R value for low-rise buildings. An R factor of 3 is suggested. The results showed acceptable results for the mid-rise and high-rise SCBF buildings (9- and 20-story) designed with an R-value of 6.

Acknowledgements:
This research was funded by the National Science Foundation under grants CMS-0619161, NEESR-SG International Hybrid Simulation of Tomorrow's Braced Frames. Supplemental funding was provided by AISC. Advice and guidance was provided by Stephen Mahin, Keh-Chyuan Tsai, Tom Schlafly (AISC), Tim Fraser, Walterio Lopez (Rutherford and Chekene), Larry Muir (CIVES) and Rafael Sabelli (Walter P. Moore). The advice and financial support of these individuals and institutions is greatly appreciated.

References:

AISC. (2005a). "Manual of Steel Construction, Load and Resistance Factor Design", 3rd Edition, *American Institute of Steel Construction*, Chicago, IL.

Lehman, D.E., Roeder, C.W. (2008) "Improved seismic design of concentrically braced frames and gusset plate connections." *ASCE*

Roeder, C.W., Lumpkin, E.J., and Lehman, D.E. (2011a) "Balanced Design Procedure for Special Concentrically Braced Frame Connections." Elsevier, *Journal of Constructional Steel Research*, Vol 67, No. 11, pgs 1760-72.

Lumpkin, E.J., Hsiao, P-C, Roeder, C.W., Lehman, D.E., Tsai, C-Y, Wu, A-C, Wei, C-Y, Tsai, K-C (2012). "Investigation of the Seismic Response of Multi-Story Braced Frames." *Journal of Constructional Steel Research*; Vol 77, pgs 130-144.

Johnson, S. (2005). "Improved seismic performance of special concentrically braced frames." MS thesis, University. of Washington, Seattle.

Herman, D. (2006). "Further improvements on and understanding of SCBF systems." MS thesis, University of Washington, Seattle.

Kotulka, B.A. (2007). "Analysis for a design guide on gusset plates used in special concentrically braced frames." MS thesis, University of Washington, Seattle.

Powell, J.A. (2010). "Evaluation of special concentrically braced frames for improved seismic performance and constructability." MS thesis, University of Washington, Seattle.

Roeder, C.W., Lehman, D.E., Clark, K, Powell, J., Yoo, J-H, Tsai, K-C, Lin, C-H, and Wei, C-Y (2011b) "Influence of Gusset Plate Connection and Braces on the Seismic Performance of X-Braced Frames." *Earthquake Engineering and Structural Dynamics*, Vol 40, No. 4, pgs 355-74.

ATC-3-06 report. (1978) "Tentative Provisions for the Development of Seismic Regulations for Buildings." *ATC*.

FEMA. 450 (2004a) "NEHRP Recommended Provisions for Seismic Regulations for New Buildings and Other Structures." FEMA 450-1/2003 Edition, Part 1: Provisions, *Federal Emergency Management Agency*, Washington, D.C.

FEMA. P695 (2008) "Quantification of Building Seismic Performance Factors FEMA P695 ATC-63 Project Report." *Federal Emergency Management Agency*, Washington, D.C.

FEMA 355C (2000) "State of the Art Report on Systems Performance of Steel Moment Frames Subject to Earthquake Ground Shaking." *Federal Emergency Management Agency*, Washington, D.C.

AISC. (2005b) "Seismic Provisions for Structural Steel Buildings." ANSI/AISC Standard 341-05, American Institute of Steel Construction, Chicago, IL.

Hsiao, P-C, Lehman, D.E., Roeder, C.W. (2012a) "Improved Analytical Model for Special Concentrically Braced Frames." *Journal of Constructional Steel Research*, Vol.73, pp.80-94.

Hsiao, P-C, Lehman, D.E., Roeder, C.W. (2012b) "A Model to Simulate Special Concentrically Braced Frames Beyond Brace Fracture." *Earthquake Engineering and Structural Dynamics*; DOI: 10.1002/eqe.2202.

Liu, J., Astaneh-Asl, A. (2004) "Moment-Rotation Parameters for Composite Shear Tab Connections." *Journal of structural engineering, ASCE*, Sep. 2004; Vol.130, No. 9.

Somerville, P., Smith, N., Punyamurthula, S., and Sun, J. (1997) "Development of Ground Motion Time Histories for Phase 2 of the FEMA/SAC Steel Project." SAC Background Document, Report No. SAC/BD-97/04.

Baker, J.W. and Cornell, C.A. (2006) "Spectral shape, epsilon and record selection." *Earthquake Engineering. & Structural Dynamics*, 34(10), 1193-1217.

FEMA 355F (2000) "State of Art Report on Performance Prediction and Evaluation of Steel Moment-Frame Buildings" *Federal Emergency Management Agency*, Washington, D.C.

Chen, C-H, and Mahin, S. (2010) "Seismic Collapse Performance of Concentrically Steel Braced Frames" Proceedings of the Structures Congress and 19th Analysis and Computation Specialty Conference, Orlando, Florida.

AIJ (1995) "Preliminary Reconnaissance Report of the 1995 Hyogoken-Nanbu Earthquake." Architectural Institute of Japan.

ATC-58 (2009) "Fragility Curves for Concentrically Braced Steel Frames with Buckling Braces" Applied Technology Council.

10CUEE CONFERENCE PROCEEDINGS
10th International Conference on Urban Earthquake Engineering
March 1-2, 2013, Tokyo Institute of Technology, Tokyo, Japan

SEISMIC DESIGN AND TEST OF BUCKLING-RESTRAINED BRACE CONNECTIONS TENTH INTERNATIONAL CONFERENCE ON URBAN EARTHQUAKE ENGINEERING

Pao-Chun Lin[1], Keh-Chyuan Tsai[2], An-Chien Wu[1], and Ming-Chieh Chuang[1]

1) Assistant Researcher, National Center for Research on Earthquake Engineering (NCREE), Taipei, Taiwan
2) Professor, Dept. of Civil Engineering, National Taiwan University (NTU), Taipei, Taiwan
r97521211@ntu.edu.tw, kctsai@ntu.edu.tw, acwu@ncree.narl.org.tw, mcchuang@ncree.narl.org.tw

Abstract: The gusset plates in a steel braced frame can be subjected to the forces not only from the brace but also from the effects of the frame actions. In this study, several finite element models are constructed to analyze the gusset to beam and column interface forces. It is found that the frame actions affect the gusset interface force distributions significantly. A simplified strut model to represent the gusset plate is adopted to evaluate the frame action forces. In addition, the Generalized Uniform Force Method (GUFM) is adopted as it provides more freedom for designers to configure the gusset plate shapes than using the traditional Uniform Force Method (UFM). In this paper, a performance based design method is proposed. The gusset interface force demands take into account the combined effect of the brace maximum axial force capacity and the peak beam shear possibly developed in the frame. The specimen design and key results of a series of full-scale 3-story buckling-restrained braced frame (BRBF) hybrid tests are discussed. The gusset interface cracks observed at the inter-story drift greater than 0.03 radians can be well predicted by using the proposed design method. The BRBF tests and analyses confirm that the proposed design method is quite reasonable. The paper concludes with the recommendations for the seismic design of gusset plate.

1. INTRODUCTION

The buckling-restrained brace (BRB) can be viewed as a high-efficiency energy dissipation device as it can dissipate the earthquake energy through its development of the full yield strength in both tension and compression in the BRB steel core (Watanabe et al. 1988). The gusset plates which connect the two BRB ends to the frame must be properly designed so that they can sustain the maximum axial force capacities induced from the BRBs. The UFM (Thornton 1984) has been widely adopted for the gusset designs for steel braced frames as it provides a straightforward design procedure to obtain an economical and admissible force distribution (AISC 2010). In addition, when the BRBF is deformed, the beam-to-column joint would either open or close. Thus, the corner gusset plate in the BRBF is required to sustain not only the BRB axial force but also additional forces resulted from the frame action. Several studies have reported that the gusset to beam or column interface fractures (Uriz et al. 2004) and the gusset plate ruptures (Kaneko et. al 2008) in large-scale steel braced frame tests. It is found that the frame action forces could create large force demands on the gusset plate. However, these force demands were often ignored in the design procedures commonly adopted by the practitioners. A research on the rib-reinforced steel moment connection has investigated the frame action forces on the reinforcing ribs by using an equivalent strut to represent the ribs (Lee 2002). Several researches on the force demands on the gusset plate resulted from braces and frame action effects have also been studied on the corner gusset connections (Kaneko et al. 2008, Chou et al. 2012). The frame action effects on the gusset interfaces can be calculated by using the aforementioned equivalent strut model. The gusset interface force results from BRB axial forces can be derived by either the UFM or the GUFM (Muir 2008). In this study, the GUFM is adopted for the gusset plate design which could allow the designers to configure the gusset shape more freely. A simple seismic performance design procedure for BRBF gusset plates is developed by incorporating the GUFM and the frame action forces computed from the equivalent strut model. The normal and shear stress distributions on the gusset interfaces induced from the BRB and frame actions are discussed in detail by using the finite element analysis. In this paper, the performance design considers the BRB's maximum axial force capacity and the maximum beam shear due to the frame action. Results of a series of a full-scale 3-story BRBF hybrid and cyclic loading tests are evaluated using finite element analyses. The gusset interface welding fractures, occurred prior to the BRB failure when the inter-story drifts exceeded 0.03 radians, are analyzed in detail. The test and finite element analysis results confirm that the proposed design method can satisfactorily predict the force demands on the gusset interfaces.

2. COMMON DESIGN METHODS FOR BRBF GUSSET PLATE

2.1 Generalized uniform force method

The UFM (Thornton 1984) has been widely adopted for the design of gusset plates in the concentrically braced frames (CBFs) and buckling restrained braced frames (BRBFs). It has been included in the AISC Manual of Steel Construction (AISC 2010) as it provides a straight-forward procedure to compute the forces on the gusset interfaces. For the BRBF gusset plate design, the BRB's maximum axial force capacity P_{max} is used as the force demand for the gusset plate. It can be computed as follows (AISC 2010):

$$P_{max} = \beta \times R_y \times \omega_y \times \sigma_y \times A_c \quad (1)$$

where A_c and σ_y are the cross section area and yield stress of the BRB steel core material. ω_y and R_y are the material strain hardening and overstrength factors. β is the compression strength adjustment factor. As illustrated in Figure 1a, the force components on the gusset to beam and column interfaces resulted from P_{max} can be calculated as follows:

$$V_{gc} = P_{max} \times \beta_g / r \quad (2)$$

$$H_{gc} = P_{max} \times e_c / r \quad (3)$$

$$V_{gb} = P_{max} \times e_b / r \quad (4)$$

$$H_{gb} = P_{max} \times \alpha_g / r \quad (5)$$

$$r = \sqrt{\left(e_b + \beta_g\right)^2 + \left(e_c + \alpha_g\right)^2} \quad (6)$$

$$\tan\varphi = \left(e_b + \beta_g\right) / \left(e_c + \alpha_g\right) \quad (7)$$

where φ is the inclination angle of the brace. According to the UFM, the gusset interface forces must be computed by using the gusset length and height ($2\alpha_g$ and $2\beta_g$). During the design, either the gusset length or the height must be determined first, and then the second undetermined dimension can be computed from the geometric relation of Eq. (7). Therefore, the gusset plate shapes can often be irregular or undesirable when the brace inclination angle or beam-to-column depth ratio is too large or too small. An alternative design method, the GUFM has been proposed (Muir 2008) for alleviating this issue. The GUFM allows the designers to have more freedom in choosing the dimensions of the gusset plate. As shown in Figure 1b, the GUFM assumes that the force directions on the gusset interfaces and the brace force pass through the same "Gusset control point" to achieve the moment equilibrium. The gusset to beam interface force passes through the intersection of the beam center line and column surface (Beam control point). Using the force equilibrium requirements for the gusset plate, beam, and column free bodies, the gusset interface forces can be computed as follows: (Muir 2008)

$$H_{uc} = \frac{P_{max} e_c \sin\varphi}{e_b + \beta_U} \quad (8)$$

$$V_{ub} = P_{max}\left[\frac{e_b\left[\left(e_b + \beta_U\right)\cos\varphi - e_c \sin\varphi\right]}{\alpha_U\left(e_b + \beta_U\right)}\right] \quad (9)$$

$$H_{ub} = P_{max}\cos\varphi - H_{uc} \quad (10)$$

$$V_{uc} = P_{max}\sin\varphi - V_{ub} \quad (11)$$

The detailed procedure of applying the GUFM will be given later. If the gusset length and height satisfy Eq. (7), the gusset interface forces would be identical computed from using either the UFM or the GUFM. The result of using the UFM is only one of the possible applications of the GUFM. Two gusset design examples using the UFM and GUFM are demonstrated. As shown in Figure 2a, the example frame is a one-story one-bay BRBF with top and bottom beams (594×302×14×23mm), two columns of 500mm deep, and a BRB with a maximum axial force capacity of 8800kN. The story height is 4m and the bay width is 7m. The gusset plate thickness is 38mm of SN490B steel (nominal yield stress is 325MPa). A BRB using the end-slotted connection (Lin et al. 2012) is adopted. The required welding length of the BRB joint section on the gusset plate is 420mm. A 75mm clearance (Figure 2a) is arranged between the BRB and the beam top surface. Figures 2b and 2c show the design results using the UFM and GUFM respectively. The horizontal gusset lengths (L_h) can be the same but the vertical gusset length (L_v) is shorter when the UFM is used because of the ration constraint of the gusset length and height given by Eq. (7). As a result, when the UFM is used, the gusset free edges may not be able to maintain vertical or horizontal due to the geometric configuration requirements. However, when the GUFM is adopted, the gusset plate free edges could be configured as horizontal, vertical, or any other slopes as desired. Figure 2c shows the results of using the GUFM to design the gusset plate with a vertical and a horizontal edge. This example clearly demonstrate that when the GUFM is used, the designer could more practically configure the gusset shape to meet the constructional space demands and still obtain desirable force distributions on the gusset interfaces than applying the UFM.

2.2 Frame action effects

As shown in Figure 3, the gusset plate in the braced frame are subjected to additional tension or compression forces P_{FA} due to the opening and the closure of the corner adjacent to the beam-to-column joint when the frame deforms. As shown in Figure 3a, the beam-to-column joint is opened when the BRB is compressed. In this case, the gusset plate is subjected to the compression due to the BRB compression force $P_{max,c}$, and subjected to a tension force $P_{FA,t}$ due to the opening of the beam-to-column. Likewise (Figure 3b), when the beam-to-column joint is closed, the BRB is in tension. The gusset plate is subjected to the tension force from the BRB tension $P_{max,t}$. In this case, the gusset is subjected to a compression $P_{FA,c}$ due to the closure of the beam-to-column joint. An equivalent strut model was developed to represent the reinforcing ribs in the welded moment connections (Lee 2002). As shown in Figure 4, the

two ends of the equivalent strut are located at the points of 0.6 times of the gusset length and height ($0.6L_h$ and $0.6L_v$) from the column and beam surfaces, respectively. The width of the strut can be assumed the same as the gusset plate thickness (t_g), and the depth is assumed equal to half of the strut length ($L_g/2$) (Kaneko et al. 2008). According to the study (Lee 2002), the closure or opening of the beam-to-column joint is accompanied by the presence of a beam shear. The gusset interface forces due to the frame actions can be computed from the equivalent strut axial force. When the strong column weak condition exits, the maximum force in the equivalent strut can be computed from the maximum beam shear V_{beam} as shown in Figure 4. The maximum beam shear can be conservatively estimated from assuming the beam plastic hinges have formed adjacent to the gusset tip and column face (Figures 3a and 3b). In addition, by using the force equilibrium of the strut and the compatibility condition that the strut elongation is identical to the beam flexural deformation, the horizontal (S) and vertical (N) force components (Figure 4) of the strut axial force can be computed as follows (Lee 2002):

$$S = \frac{d_b L_h V_{beam}\left(0.3L - 0.18L_h\right)}{4I_b/t_g + d_b L_h\left(0.3d_b + 0.18L_v\right)} \tag{12}$$

$$N = \frac{d_b L_v V_{beam}\left(0.3L - 0.18L_h\right)}{4I_b/t_g + d_b L_h\left(0.3d_b + 0.18L_v\right)} \tag{13}$$

$$V_{beam} = \frac{2R_{y,b}M_{p,beam}}{L - L_h} \le V_{p,beam} \tag{14}$$

where $M_{p,beam}$ is the beam flexural capacity and L is the beam clear span. The overstrength factor of the beam material ($R_{y,b}$) is considered. However, the beam shear V_{beam} need not to exceed the beam nominal shear strength ($V_{p,beam}$) (AISC 2010).

2.3 Combination of BRB axial forces and frame action effects

The corner gusset plate is subjected to the forces from both the BRB axial force and frame actions when the frame deforms. This combined force effect has been studied by researchers (Kaneko et al. 2008, Chou et al. 2012). In this study, the gusset plate design considers the ultimate state that the beam reaches maximum shear V_{beam} (Eq. (14)) and the BRB develops the maximum compression force $P_{\max}$ (Eq. (1)). The ideal capacity design of the gusset is to keep the gusset intact before BRB fails.

For the design of gusset plates, the first step is to select the gusset initial length (L_h) and height (L_v) considering the beam, column depths, and the sizes of BRB end joint to meet the welding or bolting requirement. Then the gusset interface force demands resulted from BRB axial force and the frame action can be computed by using the GUFM (Eqs. (8) to (11)) and the equivalent strut model (Eqs. (12) to (14)), respectively. Figures 5a shows the gusset interface forces when the BRB is in compression and beam-to-column joint opens. Figure 5b shows the BRB in tension with the closure of the beam-to-column joint. It can be found on both the beam and column interfaces, the shear force components result from the BRB and frame effects are always in the same direction. On the contrary, the normal forces on the interfaces due the two different effects are always in the opposite directions. Thus, the total force demands on the gusset interfaces can be computed by combining the BRB and frame actions together as follows:

$$H_c = S - H_{uc} \tag{15}$$

$$V_c = N + V_{uc} \tag{16}$$

$$H_b = S + H_{ub} \tag{17}$$

$$V_b = N - V_{ub} \tag{18}$$

where V_b and H_c are the normal force demands on the gusset to beam and column interfaces respectively. The H_b and V_c are the shear force demands on the gusset to beam and column interfaces respectively. Other design limit stated for the gusset should be considered including the yielding and buckling strength of the Whitmore area (Whitmore 1952, Thornton 1984) on the gusset plate must sustain the maximum BRB maximum axial force $P_{\max}$. The thickness of the gusset plate t_g and the BRB end-to-gusset plate welding length must designed to prevent the block shear failure (AISC 2010). In addition, the gusset plate is required to check other limit states including the von Mises yield criteria, tensile, and shear ruptures at the gusset interfaces. All these will be illustrated in the following sections. When the check of any of these aforementioned limit states is not satisfactory, the gusset plate shape or thickness is required to be reconfigured until all the limit states are qualified. In order to investigate the effectiveness of the proposed gusset plate design procedures and to gain insight into the stress distributions in the gusset interfaces, the results of the tests and finite element analyses of a full-scale 3-story BRBF are investigated.

3. ANALYTICAL INVESTIGATION USING FINITE ELEMENT METHODS

3.1 The 3-story full-scale BRBF hybrid tests

A full-scale 3-story BRBF specimen measuring 6.0m wide and 9.27m tall was tested using hybrid and cyclic loading procedures (Lin et al. 2012). Six BRBs with the same strength were installed in the frame specimen (Figures 6a and 6b). This test was to examine the newly developed BRB types and the performance of the gusset connections. The LA03 ground accelerations (Figure 7) with a peak ground acceleration of 530 gal were applied to the specimen twice. The maximum inter-story drifts are 0.0283, 0.0293, and 0.0095 radians for the first to the third stories respectively. The BRB axial forces reached the maximum axial force of 603kN in the first and second story. In the first hybrid test, all the gusset plates worked well without failure except the south BRB in the first story bulged out locally (Lin et al. 2012). Before the second test, only the gusset plates and two BRBs in the 1st story were replaced. The

second hybrid test adopted the same ground accelerations but the direction was reversed. A 20mm long weld crack was observed at the second story north top gusset to column interface after the peak inter-story 0.0327 radians was reached. This crack did not propagate until the end of the test. At the end of the second hybrid test, none of the BRBs was found failed except the gusset welding crack noted above. Test results showed that the cracks did not influence the BRBF strength notably. After the second hybrid test, the cyclic increasing roof displacements were applied without straightening the BRBF or repairing the weld crack in the specimen. During the cyclic loading test, the first story south bottom gusset-to-base plate interface weld fractured up to a length of 140mm (Figure 8a) while the inter-story drift reached 0.0320 radians. At the end of the test, the aforementioned weld crack in the second story north gusset extent to 85mm long at the end of the cyclic loading test (Figure 8b). The 2nd story gusset interface welding fracture has been investigated using finite element analyses. The analysis results and the design review for the gusset plate will be presented in the following sections.

3.2 Finite element analyses of the 3-story BRBF specimen

In order to investigate the gusset force distributions on the beam and column interfaces, three finite element models were constructed and analyzed by using ABAQUS (2010) program. The dimensions of the analytical models are identical to those in the 3-story BRBF specimen described above. The first model (FEM_C, C stands for combined) is for analyzing the 2nd story gusset plate under the combined effects of BRB and frame actions. The FEM_B and the FEM_F, models are for analyzing the gusset plate under the BRB axial force and frame action, respectively. Only part of the 2nd and 3rd stories is considered, the FEM_C is constructed as shown in Figures 6a, 9, and 10a. The simplified analytical model contains half of the middle beam segment which ranges from the middle Point C to the beam-to-column connection. The column ranges from the lower beam-to-column connection (Point A) to the mid-height of the 3rd story (Point B). The BRBs of the 2nd and the 3rd story and the lower beam are represented by using truss elements in order to consider axial forces only. A rigid link is introduced from Points E to B in the mid-height of the 3rd story to maintain the brace angles. The middle beam, column, and the gusset plates including the BRB end joint segments are represented by using 3D solid elements. The bilinear material model with a yield stress of 390MPa obtained from the coupon tests (Lin et al. 2012, Lumpkin et al. 2012) is adopted. The post yield stiffness is assumed 1% of Young's modulus. The reference axes and boundary conditions for the Points A to E are described in Figure 9. The forces and the deformations of the structural model are constrained in the yz plane. As illustrated in Figure 9, the y-axis displacements at Points D and E are imposed considering the maximum experimental displacements at these reference points when the inter-story drifts reached 0.035 and 0.0089 radians for the 2nd and 3rd stories, respectively. The contents of the FEM_B and FEM_F are similar to the FEM_C except the truss elements and the boundary conditions were modified. For the FEM_B (Figure 10b), the lower beam and the link were removed. In this case, the boundary conditions as shown in Figure 9 set Points A, B and C as hinges without any translation. Impose displacements on Points D and E will induce axial forces in the truss elements representing the BRBs. Likewise, for the FEM_F (Figure 10c), the truss elements for BRBs were removed and the same displacements stated above were applied at the beam ends (Points D and E) to get the gusset interface forces resulted from the frame action. In this manner, the gusset plate is subjected to the opening effects of the beam-to-column joint.

Tables 1 to 3 show the gusset interface forces compare the results of using Eqs. (8) to (18) and finite element analyses. Comparing the GUFM with the finite element analytical results caused by BRB force, Table 1 shows that the shear force component on each interface is underestimated and the normal force is overestimated. Table 2 compares the gusset interface forces caused by the frame action effects only. Compared with the finite element analytical results, the force components computed from the equivalent strut are only slightly underestimated. It is evident in Tables 1 to 2 that the interface forces resulted from the BRBs' axial force are relatively small compared with the frame action effects. It appears that more than half of the contribution of the gusset interface forces came from the frame action forces. Table 3 compares the gusset interface forces under the combined effects. All the combined interface force components calculated by using the proposed method (Eqs. (15) to (18)) are lower than the finite element analysis results. This seems reasonable as high stresses concentrated at the gusset tips cannot be included in the GUFM procedures or equivalent strut model.

Figure 11 shows the analytical normal, shear, and von Mises stress distributions along the gusset interfaces computed from finite element analyses. It can be found that when only the BRB force acts on the gusset plate, the normal stresses (Figure 11a) distribute uniformly along both the beam and column interfaces. However, the shear stresses (Figure 11b) distribute in a triangular pattern with the maximum value developed at the beam-to-column corner, and the minimum value almost equal to zero at the gusset two tips. In addition, when only the frame action occurs, both the normal and shear stresses distribute triangularly (Figure 11b) along the two interfaces with the maximum value at the gusset tips and the minimum value at the beam-to-column corner. Figure 11c shows the von Mises stress distributions considering the BRB and frame actions separately or combined. Although the frame action effect results in a high von Mises stress at the two gusset tips, the von Mises stress is also very high at the beam-to-column corner due to the high shear stress from the BRB action. The interface von Mises stresses under the combined effects are higher than the effect only from the BRB or the frame action. From Figures 11a and 11b, it appears that the normal and shear stresses under the BRB and frame actions can be

assumed to distribute linearly (triangularly or uniformly) as shown in Figures 12a and 12b. Table 4 and Figure 12c show the combined shear and normal stresses after distributing the shear and normal forces triangularly or uniformly on the gusset interfaces. In Table 4, the peak von Mises stresses at the two interfaces computed from the FEM_C analysis and the proposed procedures using the linearized stress distributions are also compared. It appears that the results of using these linearization procedures can predict these peak von Mises stresses satisfactorily. Therefore, the aforementioned linearization techniques are adopted to compute the peak stress demands for the design of the gusset plate. The detailed design procedures are presented in the following sections.

4. LIMIT STATES AND DESIGN PROCEDURES FOR GUSSET CONNECTIONS

4.1 Limit states of gusset plate seismic design

As shown in Figure 12, the normal and shear stresses can be assumed uniformly and triangularly distribute along the gusset interfaces. Therefore, based on the finite element analytical results, it appears that the stresses can be computed by using linear functions of positions at the gusset interfaces. The normal (σ_{GUFM}) and shear (τ_{GUFM}) stresses induced by the BRB axial force only are represented for the beam and column interfaces Figure 12a as:

$$\sigma_{GUFM,b}(x)=\frac{V_{ub}}{L_h t_g} \text{ and } \tau_{GUFM,b}(x)=\frac{2H_{ub}}{L_h t_g}\left(1-\frac{x}{L_h}\right) \quad (19)$$

$$\sigma_{GUFM,c}(y)=\frac{H_{uc}}{L_v t_g} \text{ and } \tau_{GUFM,c}(y)=\frac{2V_{uc}}{L_v t_g}\left(1-\frac{y}{L_v}\right) \quad (20)$$

where the subscript b and c represent the beam and column interfaces respectively. The x and y represent the distances from the beam-to-column corner to the points on the beam and column interfaces as shown in Figure 12. In addition, the triangularly distributed normal (σ_{FA}) and shear (τ_{FA}) stresses resulted from the frame action (Figure 12b) on the beam and column interfaces are represented using similar subscribes b and c as:

$$\sigma_{FA,b}(x)=\frac{2N}{L_h^2 t_g}x \text{ and } \tau_{FA,b}(x)=\frac{2S}{L_h^2 t_g}x \quad (21)$$

$$\sigma_{FA,c}(y)=\frac{2S}{L_v^2 t_g}y \text{ and } \tau_{FA,c}(y)=\frac{2N}{L_v^2 t_g}y \quad (22)$$

Thus, the interface normal (σ) and shear (τ) stresses under the combined effects (Figure 12c) can be expressed as:

$$\sigma_b(x)=\sigma_{FA,b}(x)-\sigma_{GUFM,b}(x), \quad 0\le x\le L_h \quad (23)$$

$$\tau_b(x)=\tau_{GUFM,b}(x)+\tau_{FA,b}(x), \quad 0\le x\le L_h \quad (24)$$

$$\sigma_c(y)=\sigma_{FA,c}(y)-\sigma_{GUFM,c}(y), \quad 0\le y\le L_v \quad (25)$$

$$\tau_c(y)=\tau_{GUFM,c}(y)+\tau_{FA,c}(y), \quad 0\le y\le L_v \quad (26)$$

The maximum stresses on the gusset interfaces for a properly designed gusset plate should satisfy the following requirements:

(1) Von Mises yield criteria

The maximum von Mises stresses are computed to combine the normal and shear stress demands on the two gusset interfaces. If the $\sigma_{y,g}$ is the yield stress of the gusset plate material, the limit on the demand-to-capacity-ratios (DCRs) of the von Mises stresses can be calculated as:

$$DCR_{m,b}=\max\left[\sqrt{\sigma_b(x)^2+3\left[\tau_b(x)\right]^2}\Big/\phi\sigma_{y,g}\right]\le 1.0 \quad (27)$$

$$DCR_{m,c}=\max\left[\sqrt{\sigma_c(y)^2+3\left[\tau_c(y)\right]^2}\Big/\phi\sigma_{y,g}\right]\le 1.0 \quad (28)$$

Without considering the possible material overstrength of the gusset plate, a strength reduction factor ϕ=1.0 in Eq. (27) and 28 has been considered in order to avoid a too conservative design.

(2) Tensile and shear rupture

The gusset must sustain the maximum normal and shear forces to avoid tensile and shear rupture failures of the plate (AISC 2010). According to Figure 12, the peak normal stresses are located at the two gusset tips where the tensile rupture failure is most likely to occur. Thus, using a strength reduction factor ϕ= 0.75, the DCR limit to prevent the tensile rupture on each gusset interface is:

$$DCR_{t,b}=\max\left[\sigma_b(x)/\phi\sigma_{u,g}\right]\le 1.0 \quad (29)$$

$$DCR_{t,c}=\max\left[\sigma_c(y)/\phi\sigma_{u,g}\right]\le 1.0 \quad (30)$$

The DCR limit to prevent the shear rupture on each gusset interface is:

$$DCR_{s,b}=\max\left[\tau_b(x)/\phi\tau_{u,g}\right]\le 1.0 \quad (31)$$

$$DCR_{s,c}=\max\left[\tau_c(x)/\phi\tau_{u,g}\right]\le 1.0 \quad (32)$$

where $\sigma_{u,g}$ and $\tau_{u,g}$ (equals to $0.6\sigma_{u,g}$) are the tensile and shear strengths of the gusset plate material.

4.2 Evaluations of the 3-story BRBF hybrid and cyclic loading test results

During the 3-story BRBF tests mentioned previously, the 2nd story gusset to column interface welding fracture was found during the second hybrid test. Another welding fracture was found on the 1st story gusset to base plate interface at the end of the cyclic loading test. Compare Table 1 with Table 2, it can be found that the results of using both the finite element analysis and the aforementioned design procedures show that more than half gusset interface forces is contributed from the frame action effects. This is because

the BRB force demands were relative small (P_{max}=603kN), and the beam size is significant to result in a rather high force demands on the gusset interfaces from the frame action (S=608kN and N=422kN). Figures 13 and 14 show the calculated stress distributions on the 2nd and 1st story gusset interfaces by using the aforementioned design procedures (Eqs. (19) to (26)). Compare Figure 13 with the finite element analytical results shown in Figure 11, both figures show that the peak normal and von Mises stresses concentrate at the gusset tips. Even though the stress distributions obtained from the finite element and simplified analyses are not exactly the same, however, the trends of the stress variation along the gusset interfaces are similar. Table 4 compares the maximum normal, shear, and von Mises stresses on the 2nd story gusset interfaces by using finite element analyses and the proposed design procedures. The peak stresses occur at the gusset tips on both beam and column interface. The peak von Mises stresses computed from the proposed design procedures and the finite element analysis are similar. However, the maximum normal and shear stresses computed from using the proposed design procedures are smaller than the finite element analysis results. This should be reasonable as bi-linear material model has been used in the finite element models, and the frame action in the finite element model results in a high strain and stress concentrations at the gusset tips. It should be noted that. Table 5 shows all the aforementioned limit state checks using Eqs. (27) to (32) for the two gusset plates failed during these tests. For the 1st story gusset, the highest DCR (1.51) is the von Mises stress on the gusset to base plate interface ($DCR_{m,b}$) where the crack was found at the end of the test. And the tension rupture $DCR_{t,b}$ of 1.13 also suggests that the gusset plate bottom edge may rupture. It appears that inadequate gusset thickness is responsible for the gusset fracture near the column base. For the 2nd story gusset, the highest DCR is the von Mises stress on the gusset to column interface ($DCR_{m,c}$=1.22) where the crack was found during the second hybrid test. The high DCR on the beam interface ($DCR_{m,b}$ of 1.03) also suggests that the gusset to beam interface may fail under the large inter-story drifts. Compare the higher $DCR_{m,b}$ of 1.51 in the 1st story than the $DCR_{m,c}$ of 1.22 in the 2nd story (1.22), it may help to explain that the 1st story gusset to base plate interface welding crack occurred rather suddenly and the crack length was more than 55% of the total welding length. However, the 2nd story gusset to column interface welding crack occurred at the gusset tip first in the second hybrid test, and then grew gradually during the cyclic loading test. At the end of the cyclic loading test, the crack length was 34% of the entire welding length of the 2nd story gusset to column interface. Although the maximum DCR in the 1st story gusset is as large as 1.51, the 1st story gusset to base plate weld crack did not occur only until the cyclic loading test. Furthermore, the maximum DCR in the 2nd story gusset is 1.22, however, the gusset interface weld crack was not found until the second hybrid test. Both of the two gussets sustained at least a complete hybrid test with maximum inter-story drift exceeding 0.03 radians. Therefore, these tests confirmed that the proposed design procedure would lead to a conservative and acceptable design.

5. CONCLUSION

Based on these tests and analyses, conclusions can be drawn as follows:

1. In this paper, the gusset interface forces resulted from BRB and frame actions are combined to compute the force demands for gusset plate seismic design.
2. The GUFM is adopted in the gusset plate design procedure as it provides more freedoms for designers to configure the gusset plate shape. The gusset interface forces computed from using GUFM well agree with the finite element analysis results.
3. The gusset interface forces demands result from the frame action effects can be computed from an equivalent strut model. The peak axial force in the strut can be estimated from a beam shear force corresponding to the beam plastic hinge forms at the gusset tip. The BRBF tests and the finite element analyses show that the equivalent strut models can satisfactorily estimate the peak frame action forces on the gusset plate.
4. Based on the finite element analysis results, when the BRB force acts on the gusset plate alone, the normal stress distributions can be assumed uniform along the gusset interfaces. The shear stress distributions can be assume triangular with the peak stresses at the beam to column corner and zero stress at the gusset tips.
5. When the frame action occurs on the gusset plate alone, both normal and shear stress distributions can be assumed triangular with the peak stresses developed at the gusset tips and zero stress at the beam-to-column corner.
6. When the BRB and the frame actions are combined, the calculated stress distributions and the finite element analysis results are similar. The peak von Mises stresses at the gusset interfaces can be well predicted using the proposed procedures.
7. The design limit states of the gusset plate interfaces include von Mises yield stress criteria, tensile, and shear rupture. Based on the BRBF design review and test results, even though the DCRs of the 2nd and 1st story gussets are greater than 1.0, these two gusset plates sustained at least a complete hybrid test with a peak inter-story drift more than 0.03 radian. This suggests that the proposed design procedure could lead to a conservative and acceptable gusset plate design.

References:

Watanabe, A., Hitomi, Y., Saeki, E., Wada, A., and Fujimoto, M. (1988), "Properties of Brace Encased in Buckling-restraining Concrete and Steel Tube," *Proceedings of the 9th World Conference on Earthquake Engineering*, **4,** 719-724.

Thornton, W.A. (1984), "Bracing Connections for Heavy Construction," *Engineering Journal*, AISC, **21**(3), 139-148.

AISC (2010), "Steel Construction Manual," American Institute of Steel Construction, Inc., Chicago, Illinois.

Uriz, P. and Mahin, S.A. (2004), "Seismic Performance Assessment of Concentrically Braced Steel Frames," *Proceedings of the 13th World Conference on Earthquake Engineering*.

Kaneko, K., Kasai, K., Motoyui, S., Sueoka, T., Azuma, Y., and Ooki, Y. (2008), "Analysis of Beam-Column-Gusset Components in 5-Story Value-Added Frame," *Proceedings of the 14th world conference on Earthquake Engineering*.

Lee, C.H. (2002), "Seismic Design of Rib-Reinforced Steel Moment Connections Based on Equivalent Strut Model," *Journal of Structural Engineering*, 1121-1129.

Chou, C.C., Liu, C.H., and Pham, D.H. (2012), "Steel Buckling-Restrained Braced Frames with Single and Dual Corner Gusset Connections: Seismic Tests and Analysis," *Earthquake Engineering and Structural Dynamics*, **41**(7), 1137-1156.

Muir, L.S. (2008), "Design Compact Gussets with the Uniform Force Method," *Engineering Journal*, AISC, 1st quarter.

Whitmore, R.E. (1952), "Experimental Investigation of Stress in Gusset Plate," University of Tennessee Engineering Experiment Station Bulletin No. 16, May.

Lin, P.C., Tsai, K.C., Wang, K.J., Yu, Y.J., Wei, C.Y., Wu, A.C., Tsai, C.Y., Lin, C.H., Chen, J.C., Schellenberg, A.H., Mahin, S.A. and Roeder, C.W. (2012), "Seismic Design and Hybrid Tests of A Full-scale Three-story Buckling-restrained Braced Frame Using Welded End Connections and Thin Profile," *Earthquake Engineering and Structural Dynamics*, **41**(5), 1001-1020.

Lumpkin, E.J., Hsiao, P.C., Roeder, C.W., Lehman, D.E., Tsai, C.Y., Wu A.C., Wei, C.Y., and Tsai, K.C. (2012), "Investigation of Seismic Performance of Three-story Special Concentrically Braced Frames," *Journal of Constructional Steel Research*, **77**, 131-144.

Table 1 Comparison of the Gusset Interface Forces Caused by BRB Axial Force (kN)

	H_{ub}	V_{ub}	H_{uc}	V_{uc}
FEM	316	263	97	180
GUFM	231	344	183	96

Table 2 Comparison of the Gusset Interface Forces Caused by Frame Action Force (kN)

	S		*N*	
	column	beam	column	beam
FEM	725	725	464	461
equivalent strut	608	608	422	422

Table 3 Comparison of the Gusset Interface Forces Under the Combined Effect (kN)

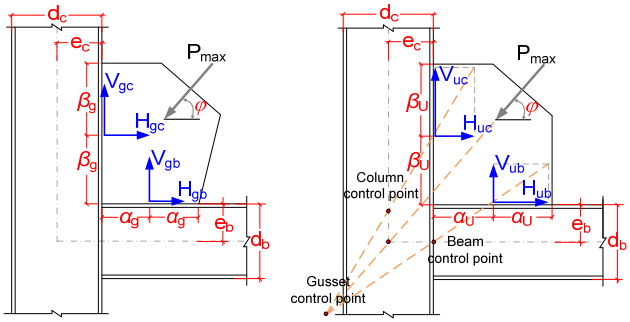
	H_b	V_b	H_c	V_c
FEM	943	169	539	615
GUFM + equivalent strut	838	78	425	518

Table 4 Maximum Stresses Computed from the Proposed Design Procedures and Finite Element Analysis (GPa)

	column interface			beam interface		
	normal	shear	von Mises	normal	shear	von Mises
FEM	0.433	0.147	0.411	0.325	0.127	0.355
GUFM + equivalent strut	0.275	0.225	0.477	0.092	0.225	0.401

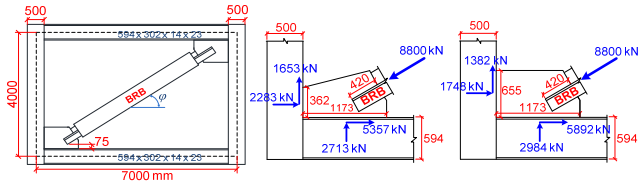
Table 5 DCRs of the 1st and 2nd Story Gussets in the 3-story BRBF Specimen

story	column interface			beam interface		
	$DCR_{m,c}$	$DCR_{t,c}$	$DCR_{s,c}$	$DCR_{m,b}$	$DCR_{t,b}$	$DCR_{s,b}$
1st	1.03	0.42	0.97	1.51	1.13	0.97
2nd	1.22	0.71	0.96	1.03	0.34	0.96



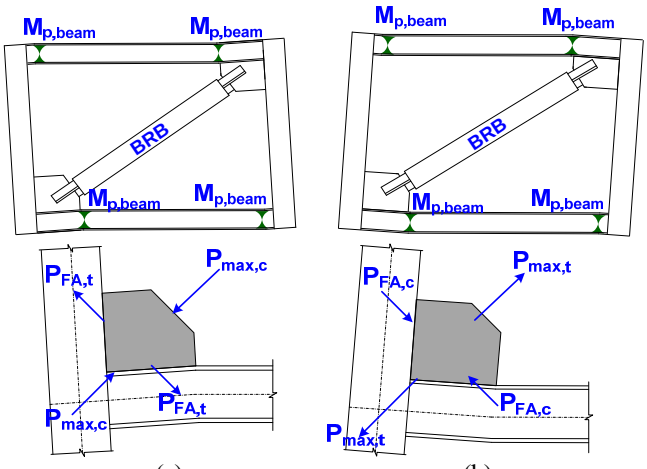
(a) (b)

Figure 1 The Force Distribution on Gusset Interfaces Computed from Using (a) the UFM and (b) the GUFM



(a) (b) (c)

Figure 2 (a) The BRBF of the Design Example and the Gusset Plate Design by Using (a) the UFM and (b) GUFM



(a) (b)

Figure 3 The Forces Acting on Gusset Plate Under the Frame Action Effect when (a) the BRB is Compressed with Beam-to-column Joint Opens and (b) the BRB is Tensioned with Beam-to-column Joint Closes

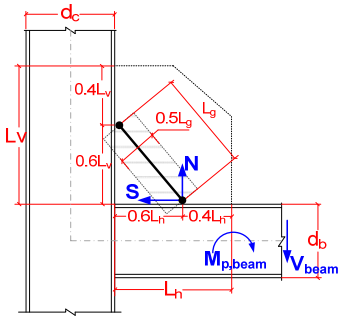


Figure 4 The Equivalent Strut Model for the Frame Action Effect and the Locations of the Beam Plastic Hinges

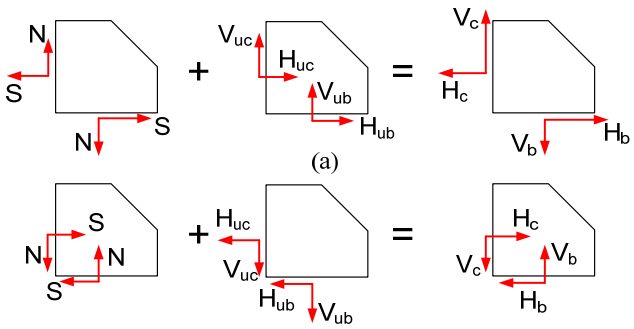


Figure 5 Combining the BRB and Frame Action Forces when (a) the Beam-to-column Joint Opens with the BRB in Compression, and (b) the Beam-to-column Joint Closes with the BRB in Tension

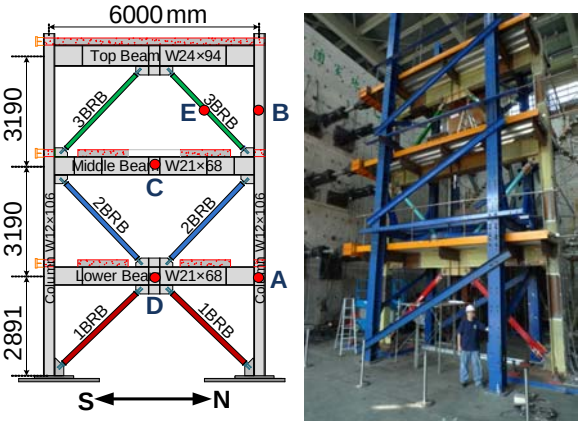


Figure 6 (a) The BRBF Elevation and (b) the Test Setup

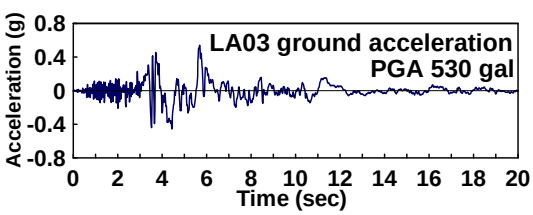


Figure 7 The Input Ground Acceleration History of the BRBF Hybrid Tests

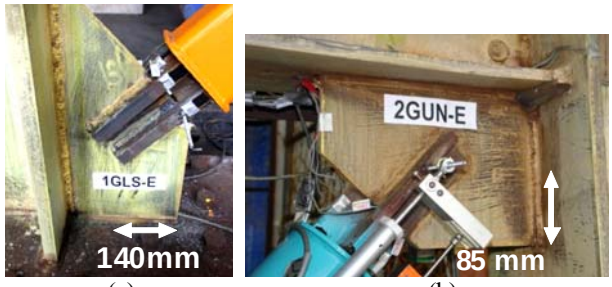


Figure 8 The Welding Fractures (a) in the 1st Story Lower Gusset and (b) the 2nd Story Upper Gusset

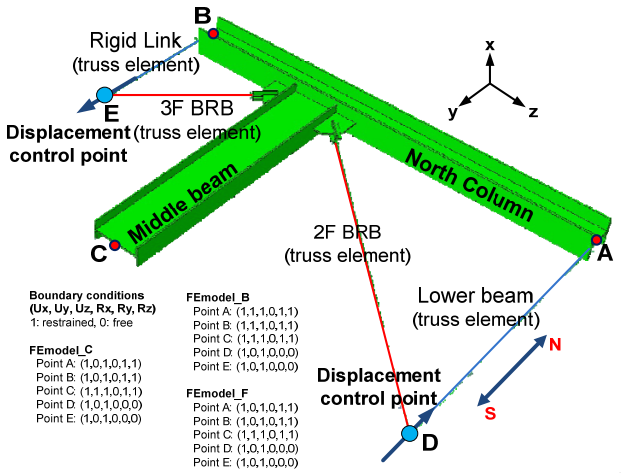


Figure 9 The Finite Element Model for Analysis of the 2nd Story Gusset Plate in the 3-story BRBF Specimen

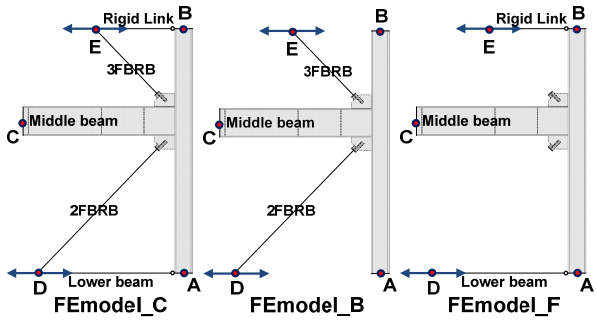


Figure 10 The Schematics of the Models (a) FEM_C, (b) FEM_B, and (c) FEM_F

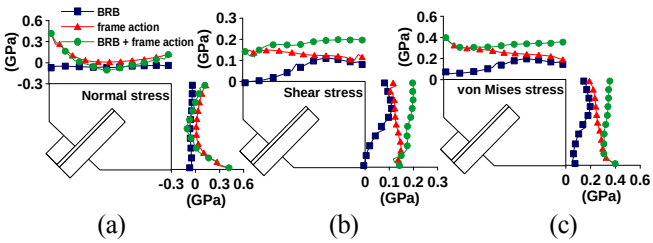
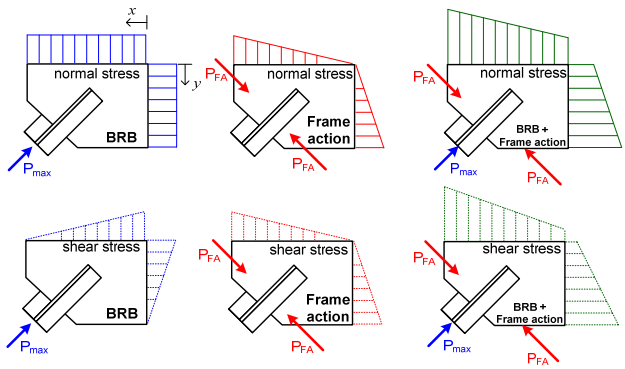
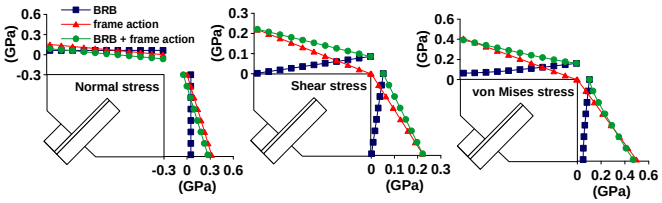


Figure 11 (a) The normal, (b) Shear, and (c) von Mises Stress Distributions Along the Gusset Interfaces Observed in the Finite Element Analyses



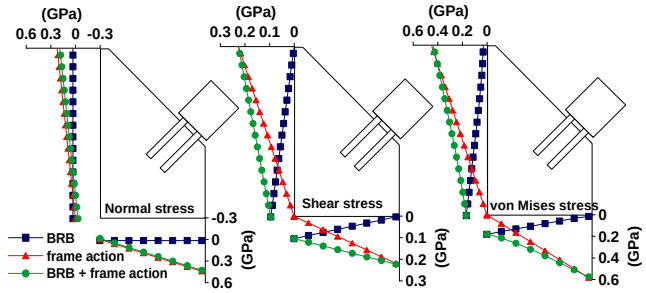
(a) (b) (c)

Figure 12 The Normal and Shear Stress Distributions on the Gusset Interfaces Under (a) BRB Axial Force only, (b) Frame Action Effect Only, and (c) the Combined Effects



(a) (b) (c)

Figure 13 The (a) Normal, (b) Shear, and (c) von Mises Stresses of the 2nd Story Gusset Interfaces Computed from the Proposed Method



(a) (b) (c)

Figure 14 The (a) Normal, (b) Shear, and (c) von Mises Stresses of the 1st story Gusset Interface Computed from the Proposed Method

10CUEE CONFERENCE PROCEEDINGS
10th International Conference on Urban Earthquake Engineering
March 1-2, 2013, Tokyo Institute of Technology, Tokyo, Japan

CYCLIC LOADING TESTS OF SINGLE ANGLE BRACE FOCUSING ON OUT-OF-PLANE STIFFNESS OF GUSSET PLATE

Hayato Asada[1], Tsuyoshi Tanaka[2], Hidenori Tanaka[3]

1) Assistant Professor, Dept. of Architecture, Kobe University, Japan
2) Professor, Dept. of Architecture, Kobe University, Japan
3) Undergraduate, Dept. of Architecture, Kobe University, Japan
asada@people.kobe-u.ac.jp, tanaka@arch.kobe-u.ac.jp,

Abstract: This paper presents experimental study on effect of out-of-plane stiffness of gusset plate on seismic performance of single angle brace with slenderness ratio of more than 100. Cyclic loading tests were performed with nine test specimens that have various gusset plate connection details. Test results shows AIJ design provision overestimated connection strength when braces connected to gusset plate with low out-of-plane stiffness; achievement of minimum requirements of strength ratio of connection strength to brace strength according to AIJ design provisions by considering effect of out-of-plane stiffness of gusset plate on connection strength results in improvement of deformation capacity of brace

1. INTRODUCTION

In recent earthquake, many conventional steel brace suffering the failure of their connections has been reported (Krawinkler, 1994, AIJ Kinki-branch 1996, AIJ, 2012). One of the conventional braces, single angle braces with large slenderness ratio of more than 100 are commonly used in low-rise conventional braced frame buildings such as factories and gymnasiums in Japan. These types of braces generally are connected to beam and column of frame thorough gusset plate with low out-of-plane stiffness, since they does not expect to resist the compression force. And also brace are connected to gusset plate thorough bolted connection. In the case of single angle braces, out-of-plane bending moment resulting from eccentricity of brace acts on their connection. Therefore, when the out-of-plane stiffness of gusset plate connection is small, severe out-of-plane deformation occurs at connection not only in compression but also in tension as shown in Figure 1. It is concerned that these out-of-deformation deformations induced by lack of out-of-stiffness lead to the decrease in tensile strength of connection since local strain concentration occurs around first bolt due to the secondary bending moment. As a result, brace connection would be failed at net section of brace prior to exert expected sufficient deformation capacity of brace. In this study cyclic loading tests were conducted to discuss the effects of out-of-plane stiffness of gusset plate connection on seismic performance of single angle brace.

2. TEST PROGRAM

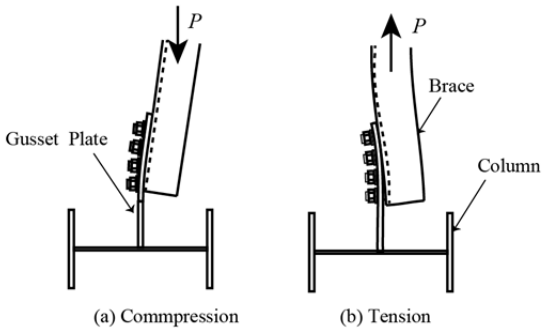


Fig.1 Out-of-plane Deformation of Gusset Plate

2.1 Test Specimen

Configuration of test specimen is shown in Figure 2.the test specimen is taken from the conventional low-rise braced frame building. the test Specimens consist of L steel brace with equal leg. whose slenderness ratio was 140, and gusset plate connection. The dimension of braces was 75mm(width and depth)×6mm (thickness) fabricated of SS400. Braces were connected to one side of gusset-plates with high strength bolts. List of specimens are shown in Table 1 Experimental parameters were connection details which includes the number of bolts(connection length), thickness of plate, with or without side stiffeners and geometric offset of last bolt l_o as illustrated in Figure 3 to alter the out-of-plane stiffness of gusset plate connection.

2.2 Calculated Strength

All of test specimens were designed in accordance with Japanese "Recommendations for Design of

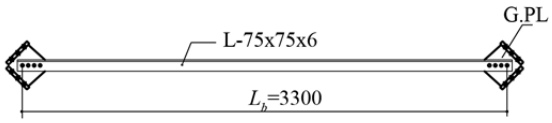


Fig. 2 Configuration of Test Specimen (L-4-6)

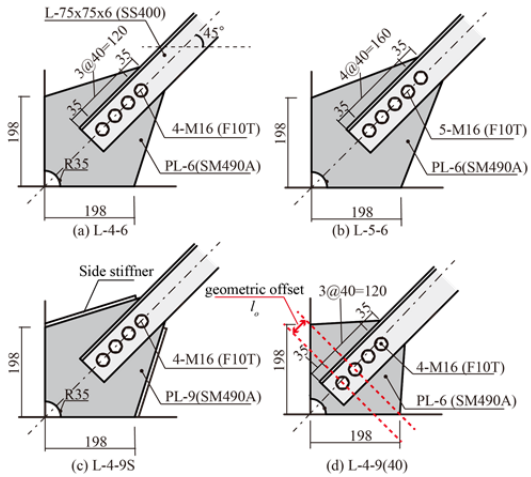


Fig. 3 Connection Details

Table 1 List of Test Specimen

Specimen	the number of bolts n	Geometric offset l_o[mm]	thckness of gusset plate t_g[mm]
L-4-6	4	40	6
L-4-9	4	40	9
L-4-12	4	40	12
L-4-9S	4	40	9 (with side stiffner)
L-4-9(40)	4	-40	9
L-5-6	5	40	6
L-5-9	5	40	9
L-5-12	5	40	12
L-5-9S	5	40	9 (with side stiffner)

Table 2 Calculated Strength

Brace	n	N_y [kN]	${}_jN_u$ [kN]	ξ
L-75×75×6	4	257	259	1.01
	5		274	1.07

Note: n :Number of bolts, N_y : yield Strength of gross section of brace; ${}_jN_u$: Connection capacity determined by nets section fracture

Table 3 Average Measured Material Properties

Member	Steel grade	F_y [N/mm^2]	F_u [N/mm^2]	Y.R. [%]	E.L. [%]
Brace	SS400	314	448	70	37
PL-6*		365	520	70	37
PL-9*	SM490A	390	553	70	39
PL-12*		409	551	74	43

Note: * used for gusset plate

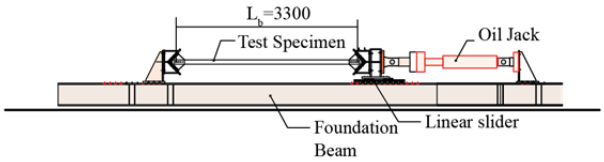
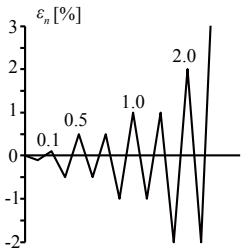


Fig. 4 Test Setup



3.3mm(0.1%) :1cycle
16.5mm(0.5%):2cycle
33.0mm(1.0%):2cycle
66.0mm(2.0%):2cycle
After cyclic loading, push-over loading in positive(in tension) was conducted

Fig. 5 Loading Protocol

Connections in Steel Structure" (AIJ, 2012). The calculated strengths of test specimens are summarized in Table 2. The strengths of connection and brace were calculated using the average measured cross-section dimensions and the measured material properties obtained from the coupon tests summarized in Table 3. The maximum connection strengths of all of specimens were determined by net section fracture regardless of thickness of plate and other connection details. In the case of specimens with five bolts, the ratio of maximum connection strength (N_u) to yield strength of brace (${}_bN_y$) ξ was 1.07. this values satisfied that of minimum requirement ξ_{req} (=1.05) to assure sufficient plastic deformation capacity of brace. On the other hand, ${}_jN_u$ / ${}_bN_y$ of the specimens with four bolts, ξ was 1.01. which was dissatisfied minimum requirement ξ_{req}. it is indicated that the specimens with four bolts would fail by forming net section failure at connection prior to exert plastic deformation capacity of brace.

2.3 Setup and Loading Protocol

Figure 4 shows setup of test specimen. Gusset plate connections were connected to rigid jig to neglect beam and column deformations on out-of-plane behavior of brace. Axial load was applied to specimen by oil jack. Tests were conducted by displacement control using average strain of L_b which was length between last bolt hole of one side connection and that of other side connection described in Figure 4. Figure 5 shows loading protocol. The amplitudes of applied average strain were 0.1, 0.5, 1 and 2%. After cyclic loading, monotonic loading in tension was conducted until specimen was failed, when specimen did not fail during cyclic loading. Longitudinal displacements and out-of-plane displacements as well as applied load were measured by using LVDTs and load cell embedded in oil jack respectively. Strain gauges were attached at brace net section and gusset plate.

3. TEST RESULTS AND DISCUSSIONS

3.1 Overview of Test Results

All of specimens were failed by forming of net section

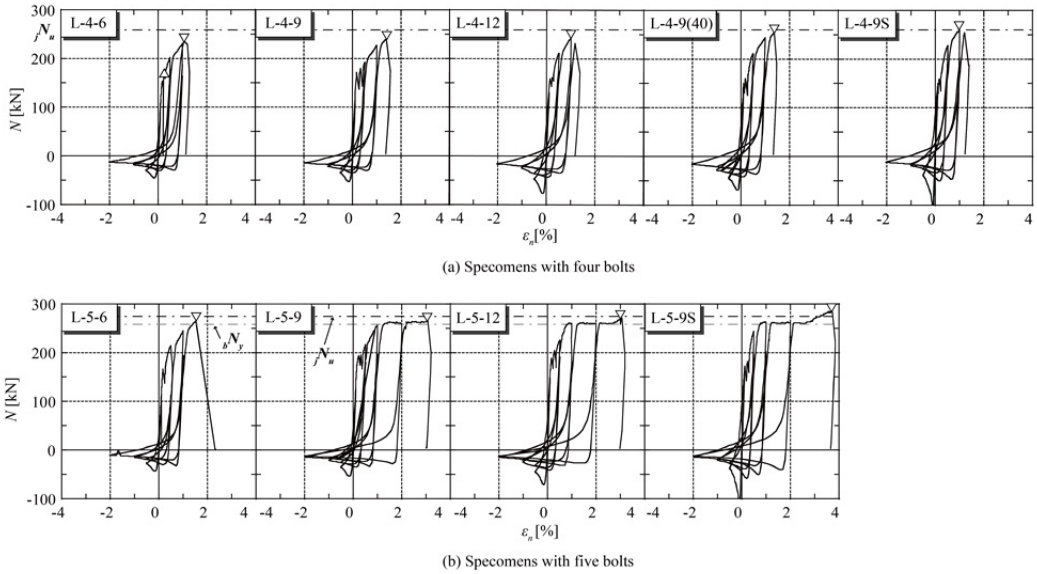


Photo 1 Net section Fracture Occurred around First bolt



(a) Compression (b) Tension

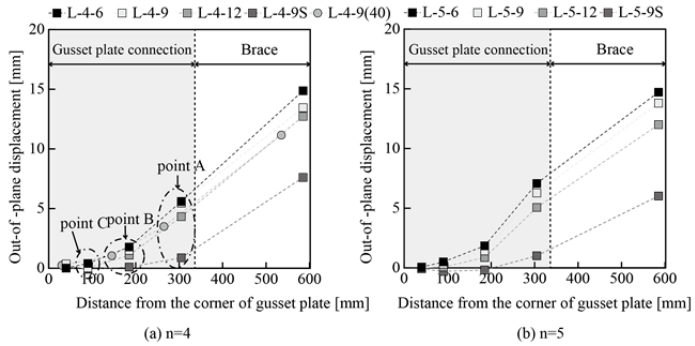
Photo 2 Out-of-plane Deformation Observed in L-4-6



(a) Specomens with four bolts

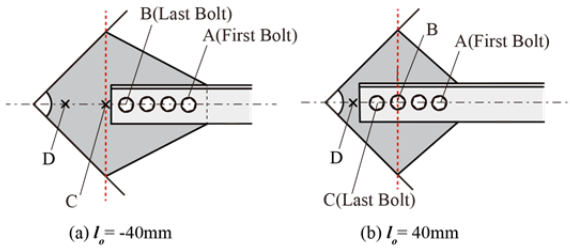
(b) Specomens with five bolts

Fig. 6 Axial Load Versus Axial Strain



(a) n=4 (b) n=5

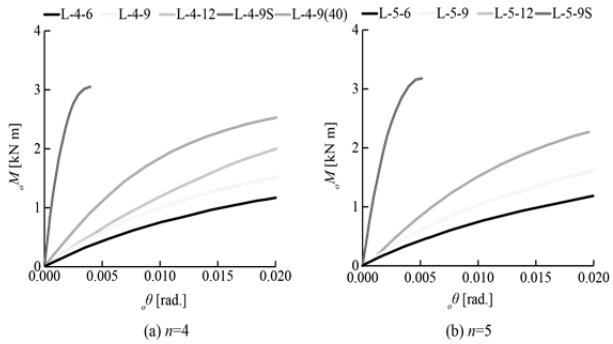
Fig. 7 Out-of-plane Displacements around Connections



(a) l_o = -40mm (b) l_o = 40mm

Fig. 8 Measurement Points of Connections

failure as shown in Photo 1. Extensive out-of-plane deformations as shown in Photo 2were observed in specimens with thin gusset plate not only in tension but also in compression. Axial load versus axial strain of the brace are shown in Figure 6. Calculated value of connection strength determined by net section fracture is also plotted as dashed line. Specimens with 4 bolts were failed prior to axial strain reaches to 2%. At this time, significant plastic deformation along the braces could not be observed . On the other hand, specimens with 5 bolts which have larger strength compared with specimen with 4 bolts could not be failed during cyclic loading except specimen L-5-6 with gusset plate of 6 mm. Finally, specimen with 5 bolts except L-5-6 showed large deformation capacity exceed 4% which



(a) n=4 (b) n=5

Fig. 9 Relations between Out-of plane Moment and Rotation

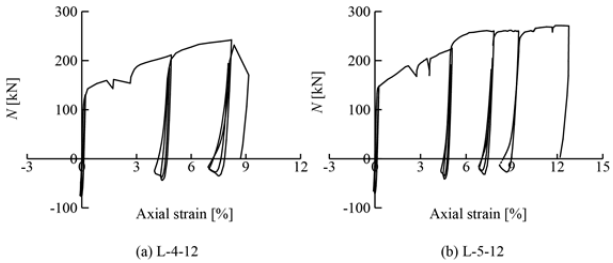


Fig. 10 Load-Local Strain Measured at Net Section Curves

corresponds to approximately more than 5% story drifts in -X-steel braced frame. However, L-5-6 was failed before it reach 2% as is the case with specimens with four bolts.

3.2 Out-of-plane Behavior of Connections

Out-of-plane displacements observed in first compressive loading are shown in Figure 7. Out-of plane displacements were measured at the points described in Figure 8. In the case of specimens with geometric offset of last bolt hole in direction toward the center of brace of 40mm, out-of-plane deformation were occurred starting from point at the intersection of the line connecting with corner of welding with brace axis as shown in Figure 2. In specimens with geometric offset in direction toward the corner of gusset plate, out-of-plane deformation was occurred starting from last bolt. Based on these results, relations between out-of plane bending moment and rotation was obtained as shown in Figure 9. It is confirmed that out-of-plane stiffness of gusset plate connection were increased not only by increasing thickness of plate and geometric offset toward the corner of gusset plate. Especially, by attaching side stiffener, out-of-plane stiffness of connection increased approximately eight times of non-stiffener connection.

3.3 Axial Strains at Net Section

Relations between axial load and axial strain measured at the point beneath the first bolt hole were shown in Figure 10. Axial strains occurred under compression force was not significant. Consequently, Axial strains increases monotonically in tensile direction. It can be concluded that out-of-plane deformation due to the compression force did not lead to significant damage to net section for this test.

Figure 11 shows that axial strains occurred at net section in L-4-6 and L-4-12, when axial force was 50kN (Braces including connection remain elastic) Calculated values which were calculated by considering out-of plane stiffness of gusset plate is also plotted in Figure 9(c). In these figure, distance from edge of web was reset by transforming net section as shown in Figure 9(a). When brace remain elastic, axial strains observed in L-4-6 were slightly larger than that of L-4-12. The calculated values include gusset plate contribution had good correspondence with measured value for both L-4-6 and L-4-12. On the other hand, calculated value ignore the out-of-plane stiffness of gusset plate connection, significantly overestimate the test results

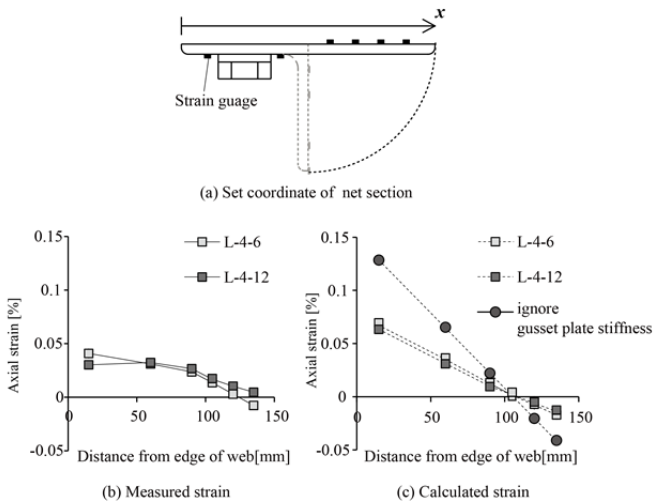


Fig. 11 Axial Strains Measured at Net Section (N=100kN)

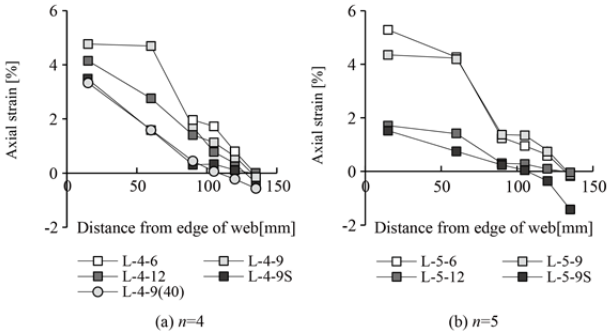


Fig. 12 Axial Strains Measured at Net Section (N=200kN)

This results indicated that gusset plate contribute to the out-of-plane resistance of connection subjected to eccentrically tension loading. Figure 12 shows that strain distribution in net section when it reach 200kN. In plastic region, strain concentration occurred at fracture point, was significant. Magnitude of the strain concentration was increased by out-of-plane stiffness of the gusset plate was reduced. It appears that the decrease of strength capacity was caused by these strain concentration along the web.

3.4 Effect of Out-of-plane Stiffness on Strength and Deformation Capacity

Figure 13 shows measured maximum strength divided by estimated yield strength. These values are plotted as a function of restraint factor k_r defined by following equations In this figure, previous experimental data (Asada, 2012) were also plotted.

$$k_r = \frac{k_{rb}}{k_{ro}} \tag{1}$$

$$k_{ro} = \frac{2EI_b}{l_b} \tag{2}$$

where, k_{ro} : out-of-plane stiffness of connections obtained from test results, I_b: moment inertia of brace, l_b: buckling length of brace As shown in this plots, connection strength

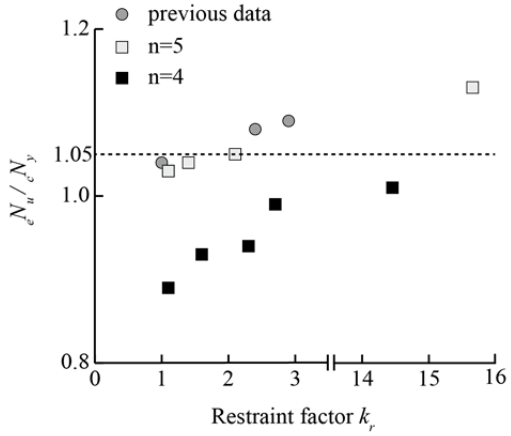


Fig. 13 Relation of Strength Capacity and Restraint Factor

increased as the out of plane stiffness of gusset plate connection get higher in the range of 1.0 to 2.0 of k_r. On the other hand, out-of-plane stiffness had small effect on connection strength when k_r exceed 2.0. Based on these results, plastic deformation capacity is discussed here. Figure 14 shows Relation between deformation capacity represents as ductility factor and cumulative plastic deformation ratio given by following equations, and the ratio of maximum strength to yield strength ξ*.

$$\mu = \frac{\delta_u}{\delta_y} \tag{3}$$

$$\eta = \frac{W_p}{P_y \cdot \delta_y} \tag{4}$$

where, δ_u : axial deformation of brace at maximum strength, δ_y : axial yield deformation based on calculated yield strength of brace, P_y: calculated yield strength of brace. Deformation capacity was also improved by increase of connection strength provided by means of increase of out-of-plane-stiffness. It should be noted that deformation capacity was dramatically improved when ξ * was more than 1.05 which corresponds to minimum requirement of AIJ design provision.

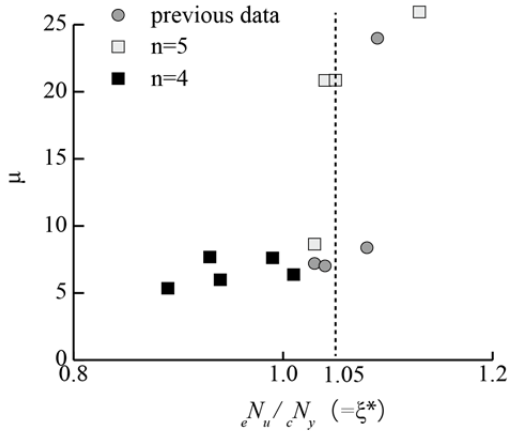
3. CONCLUSIONS

This paper presents the results of cyclic loading tests of single angle brace with large slenderness ratio focusing on the out-of-plane stiffness of gusset plate. Test results were summarized as follows;

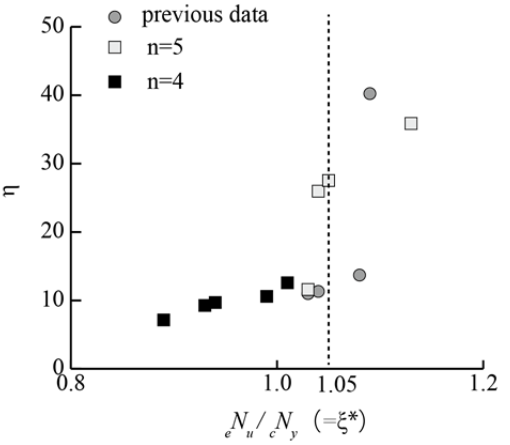
Out-of-plane stiffness of gusset plate had effects on strength when failure mode was determined by net section failure.

AIJ design provision overestimated the maximum strengths of specimens with low out-of plane stiffness because magnitude of local strain concentration at fracture point was increased by decrease of gusset plate stiffness

Connection strength capacity was improved by increase



(a) Ductility factor



(b) Cumulative plastic deformation ratio

Fig. 14 Relation of Deformation Capacity and Strength

of out-of-plane stiffness of gusset plate. As a result, deformation capacity of brace was also improved.

Acknowledgements:
This work was supported by JSPS KAKENHI Grant-in-Aid for Young Scientists (B). This work was partly supported by the Japan Iron and Steel Federation.

References:

Krawinkler, H. et al,(1994) Northridge earthquake of January 17, reconnaissance report, Volume 2 -- steel buildings, Earthquake Spectra, 11, Suppl. C, EERI, Jan. 1996, pp 25-47.

AIJ Steel Committee of Kinki Branch, (1995), "Reconnaissance report on damage to steel building structures observed from the 1995 Hyogoken-Nanbu (Hanshin/Awaji) earthquake".

AIJ, (2012) "Preliminary Reconnaissance Report of the 2011 TohokuCchiho Taiheiyo-Oki Earthquake (Geotechnical, Geological and Earthquake Engineering)", Springner

AIJ. (2012), "Recommendations for Design of Connections in Steel Structure" (in Japanese)

Asada, H. and Tanaka,T. (2012), "Effects of out-of-plane stiffness of gusset plate on elasto-plastic behavior of tension-only brace," *proc.of the 9th annual meeting of Japan Association for Earthquake Engineering*, 168-169.

10CUEE CONFERENCE PROCEEDINGS
10th International Conference on Urban Earthquake Engineering
March 1-2, 2013, Tokyo Institute of Technology, Tokyo, Japan

CYCLIC LOADING TESTS OF STEEL SLIT-DAMPERS WITH VARIOUS SHAPES

Yu Jiao[1], Yukako Katsuyama[2], and Mamoru Kohno[3]

1) Assistant Professor, Department of Architecture, Tokyo University of Science, Japan
2) Master student, Department of Architecture, Tokyo University of Science, Japan
3) Professor, Department of Architecture, Tokyo University of Science, Japan
yujiao@rs.tus.ac.jp, katsu.5230@gmail.com, kohno@rs.kagu.tus.ac.jp

Abstract: Slit-dampers are one of the frequently used dampers with many advantages, such as light-weight, easily replaceable, low-cost, and stable hysteresis characteristics. By changing the damper shapes, slit-dampers can be set at different locations in the structures. Most of the current research about slit-dampers focuses on the low-cycle fatigue behavior of dampers with certain shapes. However there is no universal evaluation method of the low-cycle fatigue behavior of slit-dampers with various shapes. As a result, there are no available design guidelines for slit-dampers. The main purpose of this study is to quantitatively evaluate the low-cycle fatigue behavior of slit-dampers with different shapes. In this paper, the first step of this study, cyclic loading tests of slit-dampers with various shapes are reported. Eight series of different shaped slit-damper specimens (flexural yielding type) are made of SN400B steel, which is one of the most common used structural steel in Japan. Constant amplitude cyclic loadings are applied to the specimens in order to obtain the fatigue curve. The effects of each shape parameter on the low-cycle fatigue behavior are evaluated through the tests results.

1. INTRODUCTION

Passive control structural systems with seismic dampers have achieved significant progresses in recent decades (for example: Roeder et al., 1977, Uang et al., 2004). In this type structural system, dampers dissipate most of the earthquake induced energy to minimize damage to the parent structures (Wada et al., 1998). The energy dissipation of dampers can be achieved by different mechanisms: friction, plastification of metals, deformation of viscoelastic solid or liquid, etc. In particular, one of the most popular dampers is the hysteretic dampers usually made of metallic materials. Generally, during moderately severe earthquakes these dampers act as stiff members which reduce structural deformations, while during very severe earthquakes hysteretic dampers dissipate the earthquake input energy (Skinner et al., 1975).

There are many kinds of hysteretic dampers such as steel triangular plate dampers TADAS (Tsai et al., 1993), buckling restrained braces (for example: Maeda et al., 1998), honeycomb dampers (Kobori et al., 1992) and steel slit-dampers (Wada et al., 1997). Among them, steel slit-dampers are known to have stable and large energy dissipation capacity. This kind of dampers is fabricated by simply cutting slits on steel plates, leaving a number of strips in between (Figure 1). All slits are rounded at their ends to reduce stress concentration. High tension bolts are set at the end of the plates to connect the dampers to the parent structures. Each strip behaves as a fixed-ended beam and deform in double curvature. Plastic hinges formed at the end of the strips to dissipate energy under deformation. This kind of device is light-weighted and can be easily set and replaced at various locations in the structures where necessary. By changing the shape of the damper, its stiffness, strength, and energy dissipation capacity can be adjusted to different levels to meet the need of structural design. Moreover, steel slit-dampers are sensitive to small deformation too. Therefore, they are not only effective under large deformation due to major earthquakes. Under long duration earthquake with relatively small deformation amplitude, slit-dampers are also helpful in restraining structural shaking.

Research has been done related to the dampers low cycle fatigue behavior and hysteretic characteristics. Cyclic loading tests were performed; the results demonstrated stable hysteretic behavior and adequate energy dissipation capacity (Chan et al., 2008, etc.). In (Wada et al., 1997) real time speed tests were carried out, which showed that loading speed does not seem to affect the damper's hysteretic characteristics significantly. However, in most of the current research work, only slit-dampers with very limited geometries were studied, while "shape" is one of the most important variables in the design of slit-dampers as well as the structures with slit-dampers inside. As a result, there is no practical design guideline for structures with slit-dampers

which makes it difficult to use this type of device.

For the purpose of building up the design guideline for slit-dampers, it is necessary to clarify how geometric shapes affect the energy dissipation capacity and hysteretic characteristics of slit-dampers. In this paper, preliminary experimental study of slit-dampers of various shapes was carried out. Basic information of the influence of geometries on the behavior of slit-dampers is obtained from the tests.

2. CYCLIC LOADING TESTS OF SLIT-DAMPERS

2.1 Specimen Information

Four different types of slit-damper specimens were loaded in the cyclic loading tests. For each specimen type, 3 specimens were prepared for the tests under different loading histories. All specimens were flexural yielding members where bending moment is the main reason that causes yielding of the dampers.

Figure 1 and Table 1 show the basic information of the specimens. Specimen SLD_1 was taken as the basic model in the tests, while specimens SLD_2~SLD_8 were designed by changing one or several of the shape parameters from specimen No.1. The main parameters in this study include: radius at the end of the slits (R), depth of the strips (B), number of the strips (N), thickness of the damper plate (T), and length of parallel sections of the strips (H). In phase I tests, specimens SLD_1~SLD_4 were loaded till their ultimate states, which will be reported in this paper.

Blast furnace steel plate (SN400B) is used to fabricate the specimens. SN400B steel is one of the structural steel that is commonly used in Japan in recent years in steel buildings. The yield strength is 300MPa while the ultimate strength is 428MPa according to the coupon tests (T=16mm). Figure 2 shows the stress-strain relationship of the material (T=16mm) obtained from coupon tests using JIS-1A test pieces.

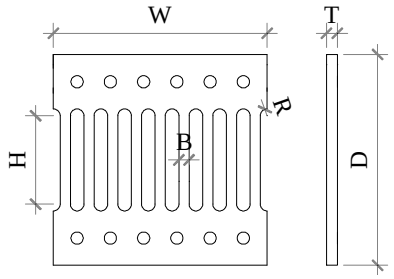


Figure 1 Shape parameters of slit-damper specimens

2.2 Test Setup

Figure 3 shows the test setup details. The specimen was connected to L shape jigs at top and bottom parts through M16 high tension bolts to form the fixed connections. The lower L shape jigs were set up through the reaction jig, with the latter fastened onto the reaction frame to offer horizontal and vertical support. A loading jig connecting the upper L shape jigs and the oil jack (maximum load capacity of 200KN) which was installed horizontally on the reaction frame composed the loading system. Moreover, lateral supports (stiffening systems) consisting of 4 truss members were set at both sides of the specimen to avoid out-of-plane deformation of the whole system. At the same time, this stiffening system was capable to deform following the trail of the specimen under horizontal loading, in other words, to keep the loading jig horizontal during the tests.

2.3 Measuring System

Deformation

Four displacement transducers (LVDT) were set up to measure the shear deformation (δ) of the specimens, which is defined in Eq. (1). Locations of these transducers are shown in Figure 4.

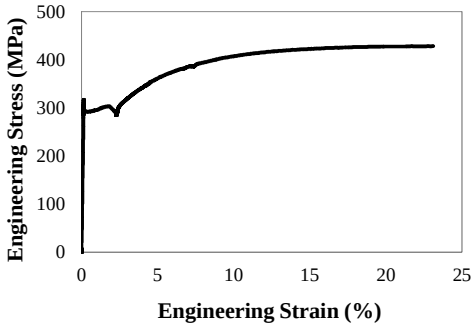


Figure 2 Coupon tests results (T=16mm) (JIS-1A)

Table 1 Details of the slit-damper specimens

	SLD_1	SLD_2	SLD_3	SLD_4	SLD_5	SLD_6	SLD_7	SLD_8
D (mm)	310	310	310	310	250	250	310	310
W (mm)	315	405	360	455	315	360	315	225
T (mm)	16	16	16	16	16	16	22	22
H (mm)	130	120	130	130	70	70	130	140
B (mm)	15	15	20	15	15	20	15	15
R (mm)	10	15	10	10	10	10	10	5
N	9	9	9	13	9	9	9	9

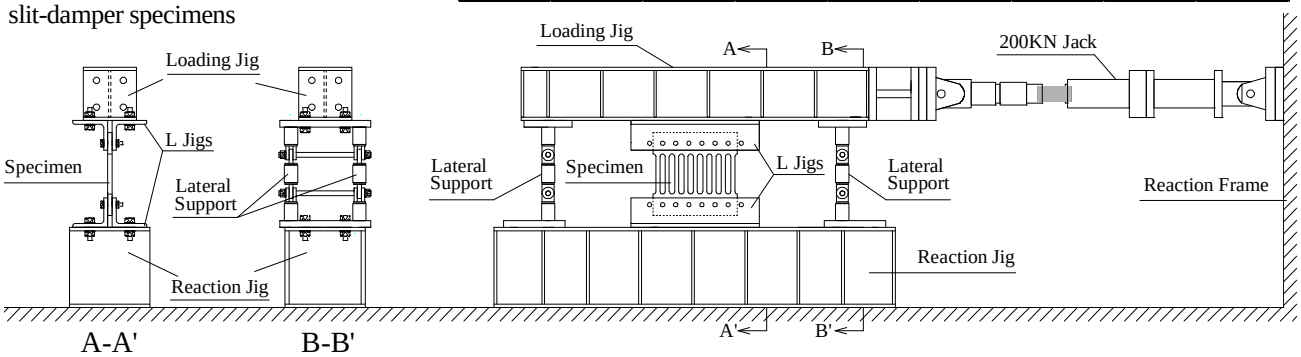


Figure 3 Setup details of the experiments

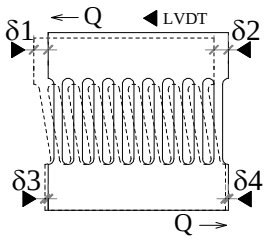


Figure 4 Deformation measuring system

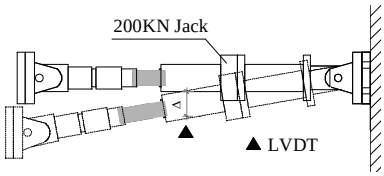


Figure 5 LVDT records the rotation of oil jack

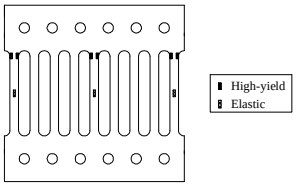


Figure 6 Strain gauge arrangements

$$\delta = \frac{(|\delta_1| + |\delta_2|) - (|\delta_3| + |\delta_4|)}{2} \quad (1)$$

where δ1 and δ2 are the deformation recorded at the top (left & right) of the damper specimens; and δ3 and δ4 are the deformation recorded at the bottom (left & right) of the specimens.

Load

Shear force is recorded through the built-in load cell in the oil jack. Notice that in order to obtain the horizontal force applied to the damper; one displacement transducer (LVDT) was set to record the rotation of oil jack's loading end (Figure 5).

Strain

Figure 6 shows the strain gauge arrangements. High-yield strain gauges, which work effectively under large strain, were attached to the ends of the parallel sections in both sides and the middle strips where significant strain concentration is expected to occur. Elastic strain gauges were attached at the center of the above mentioned strips (front and back sides) to track the axial force in the specimen.

2.4 Loading Histories

The loading history is another variable of this experiment. In order to estimate the fatigue behavior of the slit-dampers, for each type of damper specimen (three specimens), three deformation-controlled cyclic loading histories with different constant amplitudes were employed. The amplitudes were set as $\pm 8mm$, $\pm 24mm$, and $\pm 40mm$.

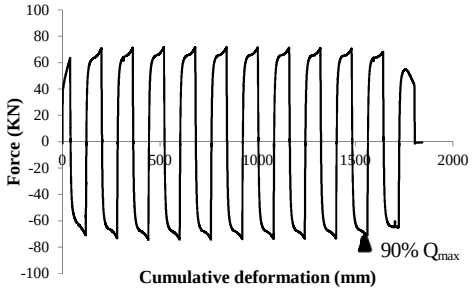


Figure 7 Force history of SLD_1 till fracture

Table 2 Experimental results till the ultimate states

Specimen	SLD_1			SLD_2			SLD_3			SLD_4		
Amp. (mm)	40	24	8	40	24	8	40	24	8	40	24	8
Number	11	26.5	184	10	20	147	7	15	119.5	8.5	22.5	153.5
η	1763	2097	3220	1537	1800	2961	1356	1500	2193	1243	1671	2489

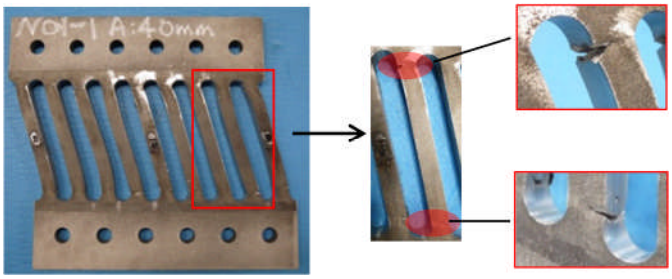


Figure 8 Ductile failure/cracks of SLD_1

3. EXPERIMENTAL RESULTS

3.1 Force-deformation Relationships

Each specimen was loaded till fracture during the tests. As an example, the force history during loading till fracture of SLD_1 is shown Figure 7. It is observed that the maximum force of each cycle decreased rapidly after it dropped below 90% of the maximum value during the whole loading procedure. Therefore, the ultimate states of the slit-dampers were defined to be the point when the maximum force of a certain cycle dropped below 90% of the maximum value. The numbers of loading cycles till the ultimate states of the specimens are listed in Table 2.

Ductile cracks initiated at the end of the parallel sections of each strip close to the rounded toes of the slits during the loading of all specimens. In the wake of loading, those cracks propagated wider and longer, which led to the decrease of the load carrying capacity of the dampers. Figure 8 shows the failure of specimen SLD_1 and its ductile cracks.

The force-deformation relationships from SLD_2 and SLD_3 are shown in Figure 9 as examples, with the 90% maximum force points pointed out. For each type of specimen, the experimental results under 3 different loading histories are shown. The graphs in Figure 9 indicate stable hysteresis loops of all specimens till the ultimate states of the dampers, which are likely to be simplified as bi-linear hysteretic models. The yield point and maximum force of SLD_3 are larger than those of SLD_2 due to large strip

depths.

3.2 Fatigue behavior

In order to investigate the fatigue characteristics of slit-dampers with different shapes, the experiment results are plotted into the log-log graph (Figure 10). The X-axis is the number of loading cycles till ultimate state, and the Y-axis is the full amplitude of each loading history (Manson-Coffin relations) (Manson, 1954, and Coffin et al., 1954). The ultimate number of loading cycles decreases while the deformation amplitude increases. For each type of specimens, linear relations can be found between the plots. However, for the specimens of different geometries, different Manson-Coffin relations are observed. The trend lines of the specimens approximately parallel with each other in this experiment. The steel material all comes from the same lot is considered to be the reason.

The plastic deformation capacity (energy dissipation capacity) of slit-dampers is evaluated by studying the cumulative plastic deformation ratio (η) of the specimen. η is defined as follows (Eq.(2))

$$\eta = \frac{W_p}{Q_p \cdot \delta_p} \tag{2}$$

where W_p is the plastic energy dissipation of the steel slit-damper; where Q_P is the experimental full-plastic shear force of slit-damper, and δ_p is the experimental elastic slit-damper rotation corresponding to Q_P. The values of η are also shown in Table 2. Figure 11 is the comparison of energy dissipation capacity of specimens SLD_1 to SLD_4 in terms of the cumulative plastic deformation ratio. The energy dissipation gets smaller when raising the deformation amplitude.

From Figure 10 and Figure 11, basic information of how shape factors influence the fatigue behavior of steel slit-dampers is obtained.

When the total length of the strip (including the rounded ends) remains unchanged, larger R results in shorter parallel sections of the strips. Being loaded to the same deformation amplitudes, SLD_2 (R=15mm) reached failure earlier than SLD_1 (R=10mm). At the same time, the energy dissipation capacity of SLD_2 is also smaller than that of SLD_1. Strain concentration due to the changing of R seems to be the minor influencing factor in this case.

Specimens with larger depth of the strips (SLD_3) reached failure earlier than the ones with smaller depth of strips (SLD_1) under same loading amplitude and dissipate smaller amount of energy; because the fiber at the edges of the fat strips deforms harder than that of the thin strips.

Slit-dampers with more strips (SLD_4) show worse fatigue behaviors compared to the ones with fewer strips (SLD_1). A part of reason might be the slight slope of the

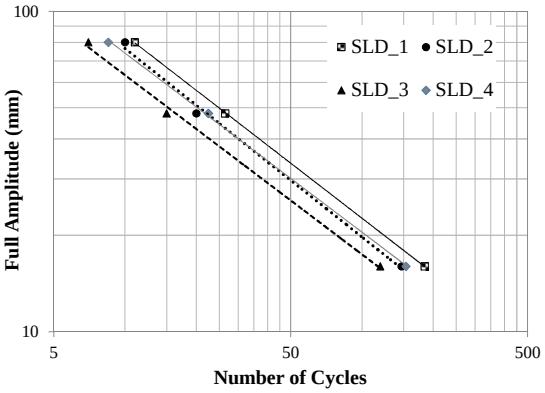


Figure 10 Fatigue life (S-N curve)

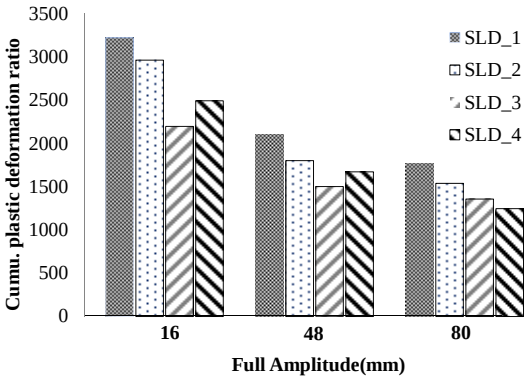


Figure 11 Comparison of energy dissipation capacity

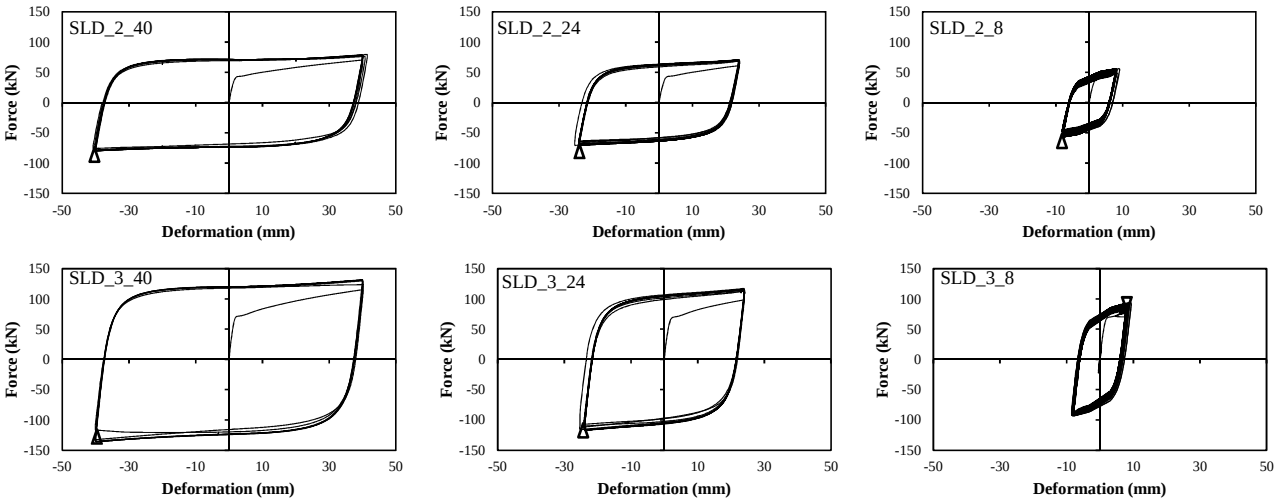


Figure 9 Force-deformation relationships of SLD_2 and SLD_3

loading jig during the tests. The slit-dampers with more strips are wider, which make them more sensitive to the axial force caused by the slight slope of the loading jigs. This phenomenon may also happen at certain locations in real buildings where slit-dampers are installed.

3.3 Local Strain States

To each specimen, 6 high-yield strain gauges were attached to the end of the strips. As an example, the strain histories (first three cycles) at the end of one of the strips' parallel sections from SLD_2 are shown in Figure 12. Under the deformation amplitude of 40mm, the strain recorded in the first loading cycle reached out to 10%, which damaged the strain gauge easily. Therefore, only the data under the amplitude of 24mm and 8mm are shown. The strain under larger loading amplitude grew significantly during the tests, which also showed quick increasing in each cycle. The whole strain histories shifted to the tension side during loading due to the residual strain after plastification.

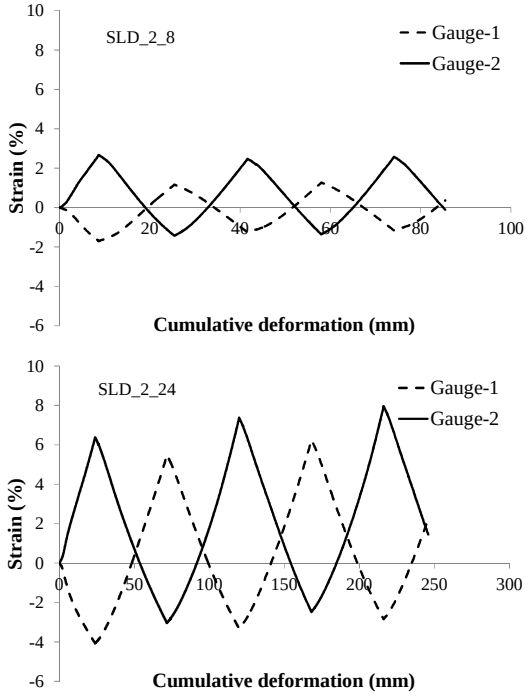


Figure 12 Strain histories of SLD_2 at the end of the strips

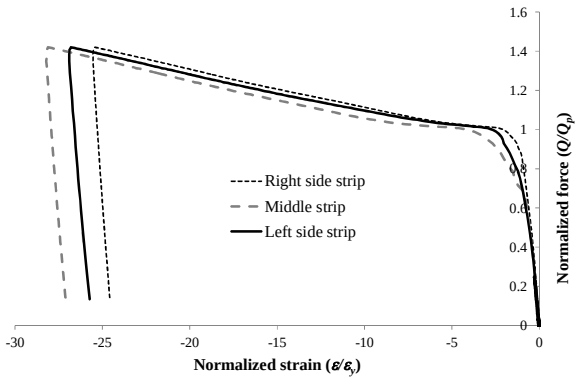


Figure 13 Normalized strain of SLD_1_24mm(1st half cycle)

Figure 13 shows the strain measured through the high-yield strain gauges in the first half loading cycle of specimen SLD_1, with the deformation amplitude of 24mm. The recorded strain is normalized by yield strain when the Y-axis shows the force normalized by the experimental yield force of SLD_1. The strain histories of the right, middle, as well as the left strips in SLD_1 are highly close to each other, which confirm that loading is uniformly distributed between the strips in the slit-damper.

4. CONCLUSIONS

Steel slit-damper is one type of hysteretic dampers that has lots of advantages. In this paper, basic information about the influence of geometries on the behavior of slit-dampers was obtained through cyclic loading tests.

In the future, more experiments are to be carried out to enrich the variables. Together with some numerical analyses, the ultimate objective is to quantitatively evaluate the plastic energy dissipation capacity of steel slit-damper of various shapes under random loading histories.

References:

Roeder, C.W., and Popov, E.P. (1977), "Inelastic Behavior of Eccentrically Braced Steel Frames Under Cyclic Loadings". *Report No. UCB/EERC-77/18*, Earthquake Engineering Research Center, College of Engineering, University of California Berkeley, Berkeley, CA.

Uang, C.U, Nakashima, M., and Tsai K.C. (2004), "Research and Application of Buckling-Restrained Braced Frames," *Steel Structures* 4(2004) 301-313.

Wada, A., Shimitsu, K., Kawaai, H., Iwata, M., and Abe, T. (1998), "Damage Control Design of Building," Maruzen Inc.

Skinner R.I., Kelly J.M., and Keine A.J.(1975), "Hysteretic Dampers for Earthquake-resistant Structures," *Earthquake Engineering and Structural Dynamics*, Vol.3, pp. 287-296.

Tsai K.C., Chen H.W., Hong C.P., and Su Y.F.(1993), "Design of Steel Triangular Plate Energy Absorbers for Seismic - Resistant Construction," *Earthquake Spectra*, Vol. 9, No. 3, pp. 505-528

Maeda Y., Nakata Y., Iwata M., and Wada A.(1998), "Fatigue Properties of Axial-yield Type Hysteresis Dampers (In Japanese)," *Journal of Structural and Construction Engineering*, AIJ, No503, pp. 109-115

Kobori T., Miura Y., Fukusawa E., Yamada T., Arita T., Takenake Y., et al.(1992), "Development and Application of Hysteresis Steel Dampers," *Proceedings of 11th World Conference on Earthquake Engineering*. pp. 2341–6.

Wada A., Huang Y.H., Yamada T., Ono Y., et al. (1997) "Actual Size and Real Time Speed Tests for Hysteretic Steel Damper," *Proceedings of STESSA'97*, pp. 778–785.

Chan R.W.K., and Albermani F. (2008) "Experimental study of steel slit damper for passive energy dissipation," *Engineering Structures*, 30, pp. 1058–1066.

Manson S.S.(1954), Behavior of materials under conditions of thermal stress, NASA TND, 2933

Coffin L.F. JR., Schenectady N.Y. (1954), A study of the effect of cyclic thermal stresses on a ductile metal, Transactions of the ASME,pp.931-950

10CUEE CONFERENCE PROCEEDINGS
10th International Conference on Urban Earthquake Engineering
March 1-2, 2013, Tokyo Institute of Technology, Tokyo, Japan

3-D DYNAMIC ANALYSIS OF BRIDGES IN ULTIMATE STATES UNDER EARTHQUAKES

Tzu-Ying Lee[1], Kun-Jun Chung[2], and Yi-Wen Chen[2]

1) Associate Professor, Department of Civil Engineering, National Central University, Taiwan
2) Student, Department of Civil Engineering, National Central University, Taiwan
tylee@ncu.edu.tw, 100322016@cc.ncu.edu.tw, always0429@hotmail.com

Abstract: This study is aimed to analyze the ultimate situation of bridges under extreme earthquakes in 3-D space. Since the Vector Form Intrinsic Finite Element (VFIFE) has the superior in managing the engineering problems with material nonlinearity, discontinuity, large deformation, large displacement and arbitrary rigid body motions of deformable bodies, it is selected to be the analysis method in this study. The analysis methods for sliding of structures and fracture of elements are developed to predict the failure process of the bridges in 3-D space. Through numerical simulation of an bridge with a three-span-continuous deck and unseating prevention devices, the ultimate state is demonstrated. The results confirm that the VFIFE is a powerful computation method to simulate the failure behavior of bearings, columns as well as unseating prevention devices and to predict the collapse situation of bridges.

1. INTRODUCTION

In the past extreme earthquakes, such as Kobe earthquake and Chi-Chi earthquake, a number of bridges suffered damage with unseating of the superstructures. Isolated bridges have been extensively used to mitigate the induced seismic forces by a shift of natural period. However, the trade-off is that the deck displacement becomes excessively large when subjected to a ground motion with large intensity or unexpected characteristics. Such a large displacement may increase the hazard of the unseating of decks. Therefore, unseating prevention devices are important for isolated bridges in particular (Kawashima and shoji 2000). Lately, modern bridge seismic design has been developed toward the seismic performance design on whole bridges as well as their elements. Understanding of the performance of the components of bridges, such as bearings, unseating prevention devices, columns, under extreme condition shall be favorable to determine the goal of performance. In this paper, a new nonlinear structural dynamic analysis method is used to simulate the dynamic behavior of the isolated bridges with unseating prevention devices under extreme earthquakes.

The Vector Form Intrinsic Finite Element (VFIFE), a new computational method developed by Ting et al. (2004), is adopted in this study because the VFIFE has the superior in managing the engineering problems with material nonlinearity, discontinuity, large deformation, large displacement and arbitrary rigid body motions of deformable bodies. To simulate the extreme situation of bridges in 3-D space, the analysis methods for sliding of structures and fracture of elements are developed in this study. Numerical simulation of a practical bridge with unseating prevention devices is conducted to predict the failure process. The results present the design concept of the fracture sequence of the structural components. Due to the insufficient strength of the unseating prevention devices, the unseating of decks occurs under an ultimate condition.

2. VECTOR FORM INTRINSIC FINITE ELEMENT

The Vector Form Intrinsic Finite Element has been developed based on theory of physics to simulate failure responses of structural systems due to applied loads. The first step in the VFIFE analysis is to construct a discrete model for a continuous structure by using a lumped-mass idealization. It is noted that all lumped masses are connected by deformable elements without mass. Then applying Newton's Second Law of Motion, the equations of motion are assembled at each mass for all degrees of freedoms. Assume that a structural system consists of a finite number of particles. A particle designated as α has a diagonal mass matrix $\mathbf{M}^{\alpha}$ and a displacement vector $\mathbf{d}^{\alpha}(t)$ at time t. The equations of motion for particle α are written as

$$\mathbf{M}^{\alpha}\ddot{\mathbf{d}}^{\alpha}(t) = \mathbf{P}^{\alpha}(t) - \mathbf{f}^{\alpha}(t) \tag{1}$$

where $\mathbf{P}^{\alpha}$ are the applied forces or equivalent forces acting on this particle; $\mathbf{f}^{\alpha}$ are the total resistance forces or internal resultant forces exerted by all the elements connecting with this particle.

Note that each element without mass in the VFIFE is assumed to be in static equilibrium. Observed from Eq. (1), it is not necessary to assemble the global stiffness matrix for structures with multiple degrees of freedom in the VFIFE analysis. A matrix algebraic operation for the entire system is

waived. Instead, each equation of motion for each particle, Eq. (1), can be individually solved. Since the failure progress of structures involves changes in material properties and structural configuration, discrete time domain analysis is used to solve the equations of motion. The central difference method, an explicit time integration method, is adopted to solve the equations of motion, Eq. (1).

Compared to the traditional finite elements, the feature of the VFIFE is that element internal forces are calculated by deformations of elements through subtracting rigid body motion from total displacements. Therefore, a set of deformation coordinates are defined for each element in each time increment. The VFIFE is capable of dealing with large displacements, deformations and rigid body motion simultaneously.

3. SIMULATION OF ULTIMATE STATES

Bridges may undergo highly nonlinear behavior even structural failure when subjected to strong earthquakes with ground dislocation. In the past large earthquakes, a number of bridges suffered deck unseating, which is high nonlinearity along with rigid body motion. To simulate the collapse mechanism of bridges, the failure mechanism of major bridge components should be taken into account.

The failure components may be high-damping-rubber isolators, unseating prevention devices and plastic hinges of decks and columns. Firstly, isolators are idealized as a bilinear model. Assume that the bearings fracture as the resistance force reaches rupture strength. Once the isolator ruptures, there is no resistance shear force between the superstructure and column other than the friction force in the interface. When the relative displacement between superstructure and column exceeds the unseating prevention length, the superstructure will lose the supporting force provided by the column and then fall down from the column due to the gravity force.

The failure of isolators represents a typical failure mechanism completing material linear and nonlinear hysteretic behavior, fracture, and sliding of structures. The writers have developed the nonlinear elements in VFIFE in the previous study. This paper herein introduces the analytical methods for sliding structures and fracture of elements in VFIFE (Lee et al. 2009, 2010).

3.1 Elements with a Gap or a Hook

Whenever deck unseating failure occurs, local cracking or crushing due to pounding between superstructures can be observed in the sites. To simulate the pounding effect, the pounding force during collision is generally modeled by impact elements. The simplest impact element first developed by Kawashima and Penzien (1979) is a linear elastic spring model simulated by an element with a gap.

The unseating prevention devices are generally with non-working length before they are triggered to function. There are two categories of the unseating prevention devices, compression and tension. The compression device, such as a stopper, is idealized as an element with a gap, whereas the tension device is idealized as an element with a hook. The elements with a gap or a hook in the VIFIFE have been developed for studying the effectiveness of unseating prevention devices. (Lee et al., 2009, 2010)

3.2 Sliding of Structures

After a bearing ruptures, the interface between the superstructure and the column turns to a sliding surface if the relative displacement between the superstructure and the cap beam of column is still within the unseating prevention length. The motion on the sliding surface can be separated into stick and slip phases. When the friction force is smaller than the maximum static friction force, there is no relative motion in the interface, i.e. in stick phase. Once the friction force overcomes the maximum static friction force, relative movement starts in the interface and the friction force converts to dynamic friction force, i.e. in slip phase. In this study, assume that the maximum static friction force is equal to the dynamic friction force, and the dynamic friction coefficient remains constant during sliding.

In the calculation process of the VFIFE, the material properties and structural configuration are assumed to be unchangeable in each time increment. Therefore, the interface should be in either stick phase or slip phase during each incremental time. Before solving the response at next time step $i+1$, the condition at the interface must be determined. In this study shear-balance procedure, which was proposed by Wang et al. (2001) for analyzing sliding structures by state-space approach, is used to determine which phase the interface is in.

The first step is to calculate the friction force in the interface on assumption of stick phase. It is noted that the relative displacement is null in stick phase. The interface is in stick phase if the calculated friction force is less than the dynamic friction force while it is in slip phase if the calculated friction force is equal or larger than the dynamic friction force.

Figure 1 illustrates the motion of the superstructure with mass $\mathbf{M}^p$ and the column with $\mathbf{M}^b$ at time step i and $i+1$. The equations of motion for the two masses in numerical integration equations are

$$\hat{\mathbf{K}}^p \mathbf{d}_{i+1}^p = \hat{\mathbf{P}}_i^p - \mathbf{f}_{Fi} \tag{2}$$

$$\hat{\mathbf{K}}^b \mathbf{d}_{i+1}^b = \hat{\mathbf{P}}_i^b + \mathbf{f}_{Fi} \tag{3}$$

where $\hat{\mathbf{K}}^p, \hat{\mathbf{P}}_i^p$ are the effective stiffness and force, respectively; $\mathbf{f}_{Fi}$ is designated the friction force in the interface. If the interface is in stick phase, the relative displacement $\mathbf{u}_i = \mathbf{d}_i^p - \mathbf{d}_i^b$ between the superstructure and the column at time step i is the same as the relative displacement $\mathbf{u}_{i+1} = \mathbf{d}_{i+1}^p - \mathbf{d}_{i+1}^b$ at time step $i+1$.

$$\mathbf{d}_{i+1}^p - \mathbf{d}_{i+1}^b = \mathbf{d}_i^p - \mathbf{d}_i^b \tag{4}$$

Rearranging and substituting Eqs. (2) and (3) into Eq. (4), the calculated friction force $\mathbf{f}_{Fi}$ is obtained as

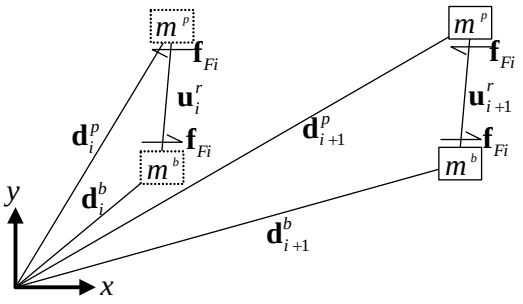


Figure 1 The motion of the superstructure and the column

$$\tilde{\mathbf{f}}_{Fi} = \frac{\hat{\mathbf{K}}^b \hat{\mathbf{P}}_i^p - \hat{\mathbf{K}}^p \hat{\mathbf{P}}_i^b - \hat{\mathbf{K}}^p \hat{\mathbf{K}}^b \left(\mathbf{u}_i^p - \mathbf{u}_i^b \right)}{\hat{\mathbf{K}}^p + \hat{\mathbf{K}}^b} \tag{5}$$

If the calculated friction force $\tilde{\mathbf{f}}_{Fi}$ is less than the dynamic friction force, the assumption of stick phase is correct and the calculated friction force can be used in the next time increment, i.e. $\mathbf{f}_{Fi} = \tilde{\mathbf{f}}_{Fi}$. Otherwise, the interface is in slip phase. The friction force $\mathbf{f}_{Fi}$ must be substituted by dynamic friction force μN, i.e. $\mathbf{f}_{Fi} = \mu N$. The above can be summarized as

$$\begin{cases} \mathbf{f}_{Fi} = \mu N & \text{if } \tilde{\mathbf{f}}_{Fi} \geq \mu N, \text{ slip phase} \\ \mathbf{f}_{Fi} = \tilde{\mathbf{f}}_{Fi} & \text{if } \tilde{\mathbf{f}}_{Fi} < \mu N, \text{ stick phase} \end{cases} \tag{6}$$

3.3 Fracture of Elements

The design principle of isolated bridges is the appropriate utilization of isolators and dampers to shift the main periods of vibration and increase the energy-dissipation capacity of the structures. High-damping-rubber bearings are commonly utilized and can be idealized by a bilinear model. In addition, it has been shown in the past study that the columns of isolated bridges may exhibit nonlinear behavior under extreme earthquakes (Lee and Kawashima 2007). The bilinear model can also be used to idealize reinforced concrete columns and steel columns. It must be carefully managed in constructing the bilinear element of the VFIFE for the loading, unloading and reloading paths. The unseating prevention devices are designed to provide the function against unseating. The unseating prevention devices are generally with non-working length before they are triggered to function. Therefore they are idealized as elements with a hook or/and a gap.

All properties and configuration of elements are assumed to be unchangeable in each time interval $t_i \leq t \leq t_{i+1}$ in the VFIFE. The internal forces are calculated based on the element properties and configuration at the initial time t_i. The deformation coordinates of elements are redefined at the beginning of each time step. Therefore, once an element undergoes nonlinear or discontinuous behavior, all changes are reflected at the beginning of next time step. In this study, the aforementioned elements are considered failure components. Assume that an element fractures as its deformation reaches rupture deformation. At the beginning of each time step it is checked where the element failures or not. Once the element meets the fracture condition, the element and its restoring forces are released from the system.

4. NUMERICAL SIMULATION

A three-span isolated bridge with total length of 3@40 m = 120 m and a width of 12 m, which is supported by two reinforced concrete columns with a height of 12.2 m in each and two abutments, as shown in Figure 2(a), is designed based on the Japan highway bridge design codes. In addition, a three-span bridge with hinge and roller bearings shown in Figure 2(b) is also analyzed to study the failure mechanism. The columns are idealized as a perfect elastoplastic model with a fracture ductility of 21.5 shown in Fig. 3(a). The isolators are idealized as a bilinear elastoplastic model with a fracture shear strain of 500% by general material experiment, as shown in Fig. 3(b). However, in Eastern Japan Great

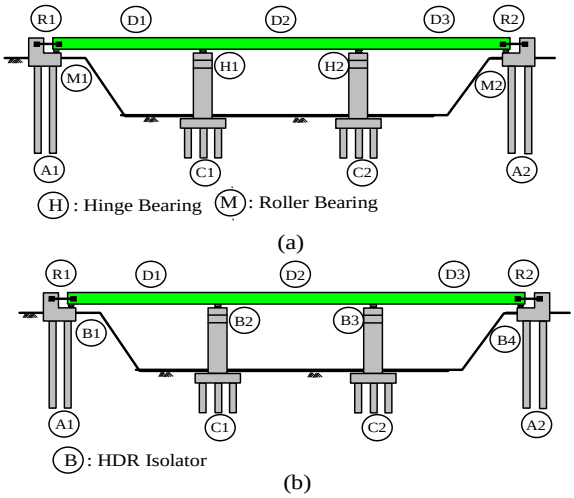


Figure 2 Three-span continuous bridge with unseating prevention devices (a) ridge bearings (b) isolator bearings

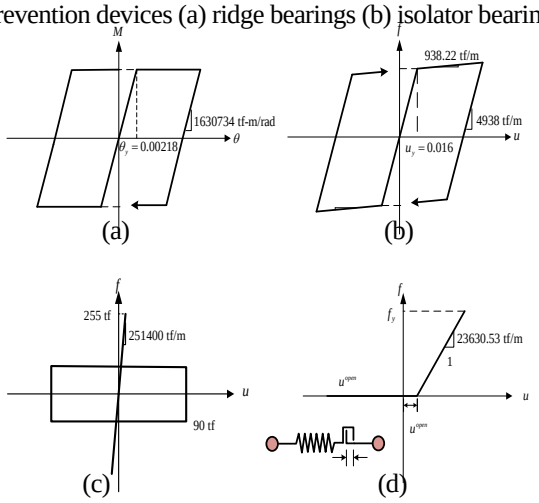


Figure 3 Material properties (a) column (b) isolator (c) hinge bearing (d) steel tendon

Earthquake, isolators failed at the shear strain smaller than 500%. In this study, the dynamic behaviors of bridge with different fracture shear strains of isolators are compared. The hinge bearings and roller bearing are idealized as a linear model with a fracture shear of 168 tf and a friction model, respectively, as shown in Figure 3(c). After hinge bearings rupture, the dynamic friction coefficient at the interface is assumed to be 0.15. The dynamic friction coefficient of roller bearings is assumed to be 0.1.

Steel tendons are installed at each expansion joint as the unseating prevention devices. The tendons are simulated by a tension element with a yielding force of 85.74 tf, an ultimate force of 94.96 tf and a hook of 40 cm shown in Figure 3(d). The pounding effect of two adjacent decks is also considered by using an element with a gap of 28 cm. The unseating prevention length at each column and abutment is 96 cm. In simulation, the bridges are subjected to near-field ground motions recorded at JR Takatori and JMA station, in the 1995 Kobe, Japan earthquake and 1999 Chi-Chi, Taiwan earthquake. The ground acceleration is amplified from 100% to 300% at an increment of 10%.

Through numerical simulation of bridges, the ultimate states are demonstrated and compared. It is interesting to observe that the isolated bridge with 500% of fracture shear strain suffers unseating of the superstructure severer than that with 300% of fracture shear strain. Figure 4 depicts the failure procedure of the bridge with hinge and roller bearings and 0.3 of friction coefficient under 160% of the Chi-Chi earthquake. Figure 5 shows the failure procedure of the isolated bridge with 500% of fracture shear strain and 0.15 of friction coefficient under 220% of JR Takatori ground motion. The first characters H, M, B, C, D and R of the notions denote the hinge bearings, roller bearings, isolators, column, deck and tendon, respectively. It is noted that all the collapse is attributed to column failure because the fracture shear force of the isolators is larger than the fracture force of the columns, in particular, for the isolated bridge with 500% of fracture shear strain. The results show that lager fracture shear strain does not increase the safety of the studied bridges.

5. CONCLUSIONS

Since the VFIFE has the advantages in managing the engineering problems with material nonlinearity, discontinuity, large deformation, large displacement, arbitrary rigid body motions of deformable bodies and even fracture and collapse, it is adopted in this study to predict the ultimate states of bridges under extreme earthquakes in 3-D space. The isolated bridges with different fracture shear strain are analyzed under ground motion amplified from 100% to 300%. The numerical 3-D simulation successfully predicts the failure process of the bridges under extreme earthquakes. The results show that lager fracture shear strain of bearings does not increase the safety of the studied bridges. Also, the results confirm that the VFIFE is a powerful computation method to simulate the failure mechanism of devices and structural elements in 3-D space.

References:

Kawashima, K. and G. Shoji, (2000), Effect of restraints to mitigate pounding between adjacent decks Subjected to a strong ground motion, 12th World Conference on Earthquake Engineering.

Kawashima, K. and Penzien, J. (1979), "Theoretical and experimental dynamic behavior of a curved model bridge structure," *Earthquake Engineering and Structural Dynamics*, **7**, 129-145.

Lee, T.-Y. and K. Kawashima, (2007), Semiactive control of nonlinear isolated bridges with time delay, Journal of Structural Engineering, ASCE 133, 235-241.

Lee, T.Y., Chen, P.H. and Wang, R.Z. (2009), "Dynamic analysis of bridges in the ultimate state under earthquakes," *Sixth International Conference on Urban Earthquake Engineering*, Tokyo, Japan, March 3-4.

Lee, T.Y., Wong, P.L. and Wang, R.Z. (2010), "Dynamic behavior of seismic-excited bridges in ultimate states," *Proc. of 9th U.S. National and 10th Canadian Conference on Earthquake Engineering*, Toronto, Canada, July 25-29.

Ting, E. C., Shih, C. and Wang Y. K. (2004), "Fundamentals of a vector form intrinsic finite element: Part I. basic procedure and a plane frame element," *Journal of Mechanics*, **20**, 113-122.

Wang Y.P., Liao W. H. and Lee, C.L. (2001), "A state-space approach for dynamic analysis of sliding structures," *Engineering Structures*, **23**, 790-801.

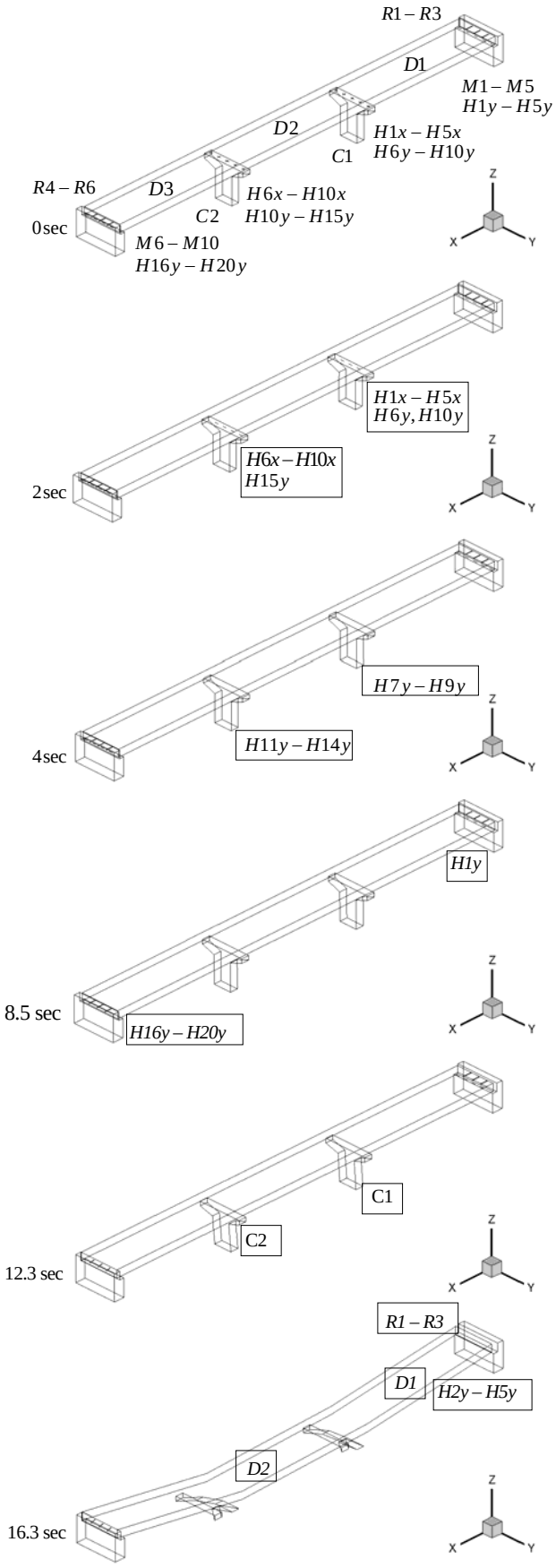


Figure 4 Rigid bearing bridge with 0.3 of dynamic friction coefficient under 160% of Chi-Chi ground motion

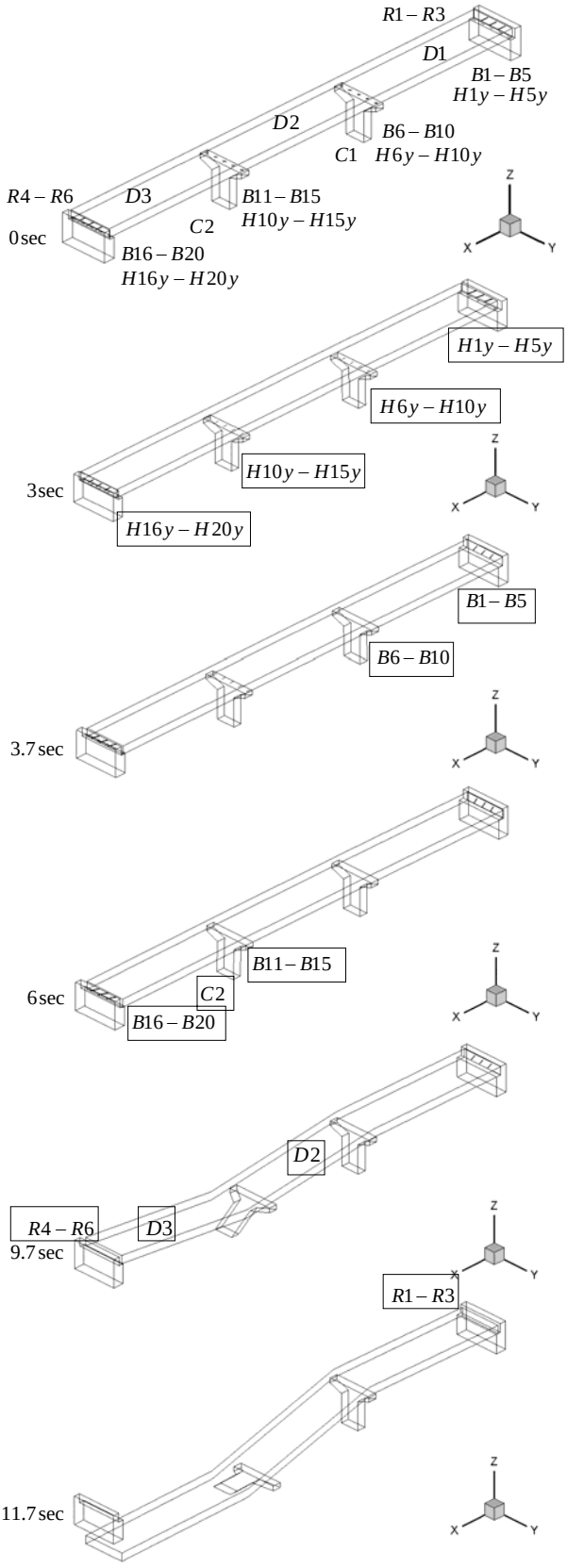


Figure 5 Isolated bridge with 500% of fracture shear strain and 0.15 of dynamic friction coefficient under 220% JR Takatori ground motion

10CUEE CONFERENCE PROCEEDINGS
10th International Conference on Urban Earthquake Engineering
March 1-2, 2013, Tokyo Institute of Technology, Tokyo, Japan

FIBER MODEL ANALYSES OF STEEL BRIDGE CIRCULAR COLUMNS CONSIDERING LOCAL BUCKLING

Koji Kinoshita[1)]

1) Assistant Professor, Dept. of Civil Engineering, Gifu University, Japan

Abstract: One of the most concerned problems for analytical estimation of ultimate strength and ductility of steel bridge columns is the consideration of local buckling. Fiber model analysis method is considered as the most practical analysis method that considers the effects of local buckling in the stress-strain curves. In addition, stress-strain curves with softening behavior to include local buckling were proposed by several researchers. However, accuracy of those models is still relatively low. As a consequence, most bridge designs have been done using fiber model analysis method without consideration of local buckling. In order to improve the analytical response estimation of steel bridge columns, a fiber model analysis method considering local buckling is proposed in this study. In this method, multi fiber elements were used to model the local buckling length to simulate local buckling deformation. The proposed method shows good results not only for estimating peak strength but also post-peak strength compared to previous experimental results. However, improvements can be made to increase the accuracy of the deformation modes.

1. INTRODUCTION

Consideration of local buckling on analytical estimation of ultimate strength and ductility of steel bridge columns is one of the important lessons learned from severe bridge damage in past earthquakes (Figure 1). This local buckling was found in many different forms including variations from different column sections.

In general, fiber model analysis is used for seismic evaluation of steel bridge columns. For steel bridge columns with the consideration of local buckling, there are modeling techniques that include local buckling effects in the stress-strain curves of the plastic hinge zone, where local buckling is occurred.

Although the modeling techniques are not new and many suggestions have been made by previous studies (Ishizawa and Iura, 2005), a common assumption in the analysis of steel bridge columns using fiber model is to ignore the local buckling. The Japanese Standard Specification for Seismic Design of Steel and Composite Structures (JSCE, 2008) permits these structures to be evaluated using the average strain of the plastic hinge zone as an alternative to evaluation peak strength without consideration of local buckling. However, Kakiuchi et al. (2009) concluded that this approach cannot capture the actual behavior and would result to overly conservative evaluation.

The common assumption may be based on two major reasons. First, some of the suggested models do not have hard evidence that they can capture actual behavior because of lack of agreement with experimental results, and second, there are many different forms of local buckling as

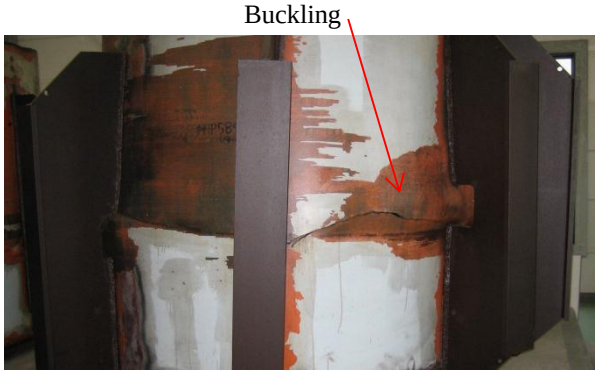


Figure 1 Damaged Steel Bridge Circular Column, Kobe Earthquake, 1995

mentioned above. It is therefore necessary to develop new modeling techniques that can provide not only a better representation for local buckling, but also have good agreement with experimental results.

A recent study on a fiber modeling technique to estimate local buckling of longitudinal bars in RC columns was reported by Ichikawa et al. (2010). The study aimed to directly capture non-linear deformation of local buckling by using fiber elements to model longitudinal bars individually. The study shows a possibility of further extension of the fiber modeling technique. However, there has been no further study to develop fiber modeling technique for steel bridge columns.

The main objective of this study is to propose a fiber model analysis method considering local buckling of steel bridge circular columns. In this method, multi fiber elements are used to model the local buckling length, where the

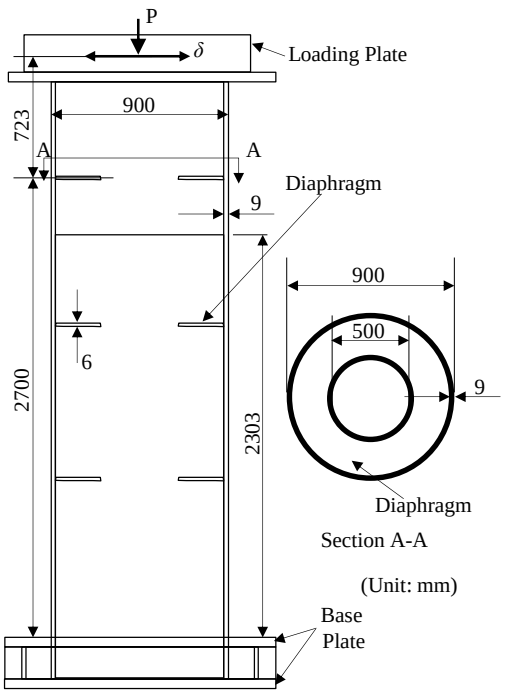


Figure 2 Steel Bridge Circular Column Model (PWRI, 1999)

Table 1 Properties of the Column Model

	Experimental Model
Steel Grade	SS400
Height h (m)	3.423
Thickness t (mm)	9
Diameter D (mm)	900
λ	0.268
R_t	0.123
H_0 (kN)	400.82
δ_y (mm)	10.5
$P/\sigma_y A$	0.199

plastic hinge zone is, to simulate local buckling deformation. This concept is different from previous studies that consider effects of local buckling in the stress-strain curves of the plastic hinge zone. This paper discusses analysis results using the proposed method compared to the previous experimental work.

2. OVERVIEW OF PREVIOUS STEEL BRIDGE CIRCULAR COLUMNS EXPERIMENT (PWRI, 1999)

The geometry and section properties of the steel bridge circular column used in the analyses are shown in Figure 1 and summarized in Table 1. This experimental work was carried out by PWRI (1999).The column was 900mm in diameter with 9mm thickness. The boundary conditions were:

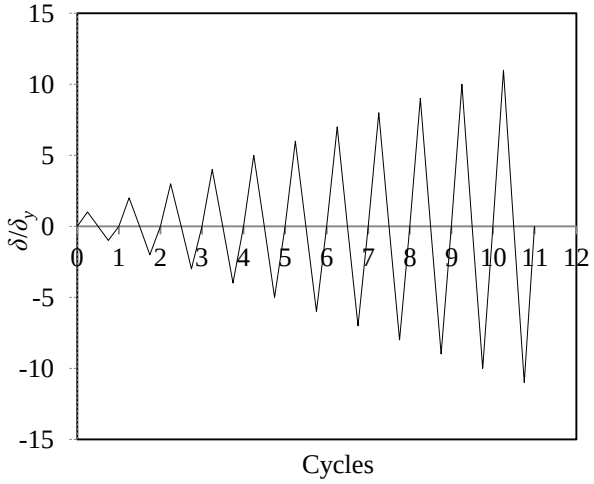


Figure 3 Displacement Controlled Testing Protocol

a) fixed column base that was fixed by high tension bolts or pre-stressed steel bars. The base was built-up sections consisting of thick steel plates, and hence was assumed to be rigid.
b) pin connection between the top of the column and loading jacks of each direction.

A displacement-controlled testing on the horizontal direction with a constant axial load was conducted with the loading history, shown in Figure 3, applied to the column. The ratio of the axial force, P, to the value of the yield strength of steel plate, σ_y, multiplied by the section area, A, was approximately 20%. The slenderness parameter, $\bar{\lambda}$, the radius thickness parameter, R_t, the yield horizontal strength, H_0, and the yield horizontal displacement, δ_y, in Table 1 are given as follows:

$$\bar{\lambda} = \frac{2h}{\pi\sqrt{I/A}}\sqrt{\frac{\sigma_y}{E_s}} \quad (1)$$

$$R_t = \frac{R}{t}\frac{\sigma_y}{E_s}\sqrt{3(1-\nu_s^2)} \quad (2)$$

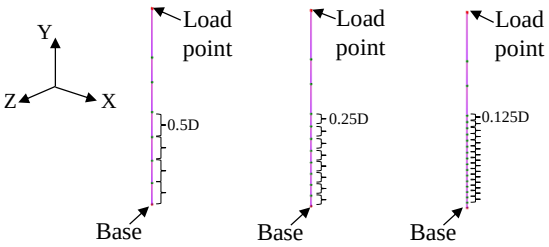
$$H_0 = (\sigma_y - P/A)Z/h \quad (3)$$

$$\delta_y = H_0 h^3/3EI \quad (4)$$

The experiment showed that the peak-strength was about 553kN, and local buckling occurred at the bottom plastic hinge zone of the column, which is known as "elephant foot bulge".

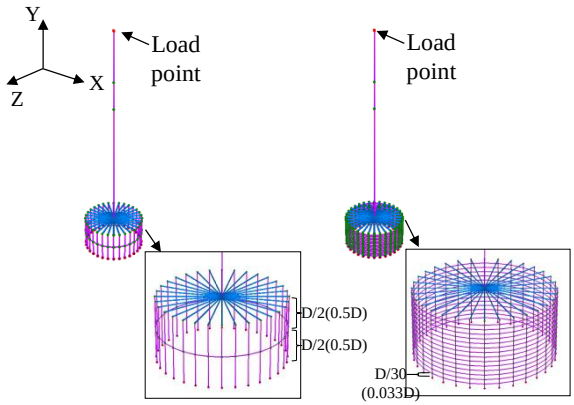
3. FIBER MODELING OF STEEL BRIDGE CIRCULAR COLUMNS

In general, the circular column is modeled as a single fiber element that has fine fiber division in the section (Figure 4). However, the local out-of-plane deformation cannot be obtained from single fiber element, because each fiber division calculates only the axial deformation. In the circular column, local out-of-plane bending deformation is created due to local buckling. Because of this, this modeling does not give results for out-of-plane deformation such as local buckling.



(a) 0.5D (b) 0.25D (c) 0.125D

Figure 4 Single Fiber Model



(a) D/2 (b) D/30

Figure 5 Proposed Fiber Model

Previous studies tried to consider softening for post-peak behavior in order to assume local buckling in the stress-strain curve of steel plates. However, as mentioned above, this approach may not be able to capture the actual behavior of every steel bridge column because of lack of agreement with experimental results. Moreover, additional calculations based on experimental tests or finite elements analyses are required to consider more accurate stress-strain curve. In fact, some of calculations are complicated.

In the proposed model (Figure 5), the plastic-hinge zone is modeled as multi fiber elements while the general region is modeled as single fiber elements. The out-of-plane bending deformation can be captured directly. Thus, the proposed model takes advantage of the modeling technique that does not need any additional calculations.

A bi-linear stress-strain curve with post yield stiffness, which is assumed as 1% of the Young's Modulus of steel plate, was used to model the steel plates. The yield strength of steel plate, σ_y, is assumed as 308N/mm2, which corresponds to the experimental tests.

4. EFFECT OF MODELING

Different analysis results from the single fiber model case and multi fiber model cases are presented in terms of strength and deformation. The effect of modeling was determined by comparing with the experimental results as the baseline. In addition, the results are also compared with

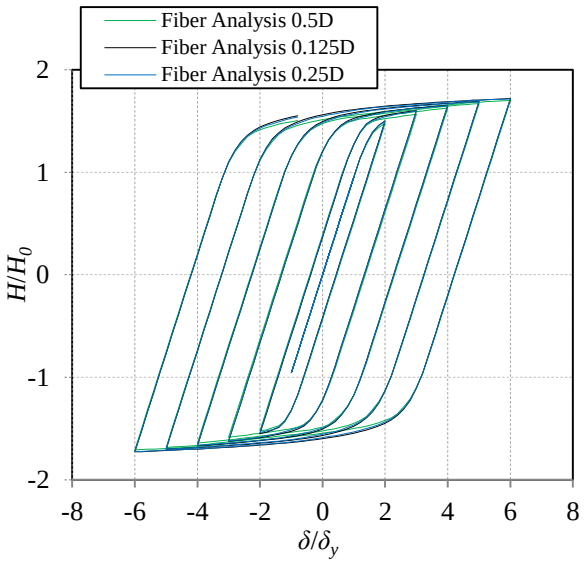


Figure 6 Effect of Element Division on Single Fiber Model

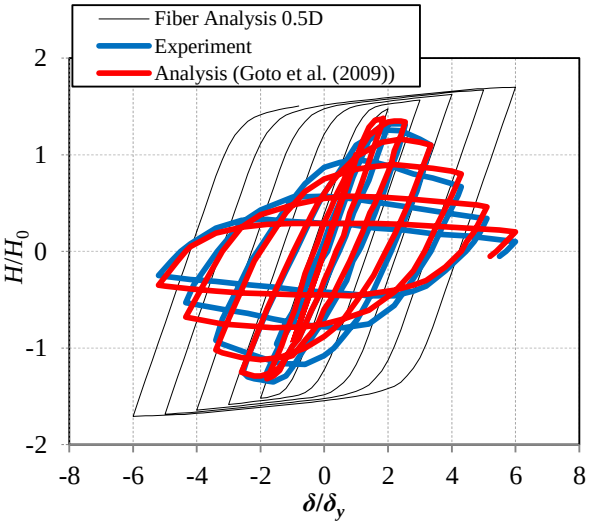


Figure 7 Comparison of Relationship between H/H_0 and δ/δ_y in Experiment and Single Fiber Analysis

the previous analysis results by Goto et al., (2011) that used finite element model.

4.1 Strength

Figures 6 to 9 show the relationship between load and displacement at the loading point. Figure 6 indicates that the effect of element division (see Figures 4(a), (b), (c)) on the single fiber model is not significant. As shown in Figure 7, the discrepancy in this relationship is observed. The single fiber model overestimates not only the peak strength, but also post-peak strength. The peak strength obtained from the single fiber model can be about 1.5 times greater than in the peak strengthfrom the experimental results. This is due to the use of the bi-linear stress-strain curve in the steel plates without consideration of local buckling, which stiffens the plastic hinge zone causing it to allow more load to be carried. This overestimation can have a significant effect during seismic performance evaluation.

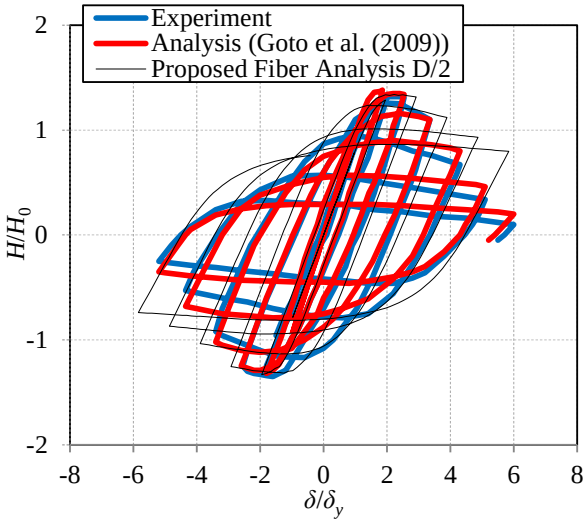


Figure 8 Comparison of Relationship between H/H_0 and δ/δ_y in Experiment and Proposed Fiber Analysis

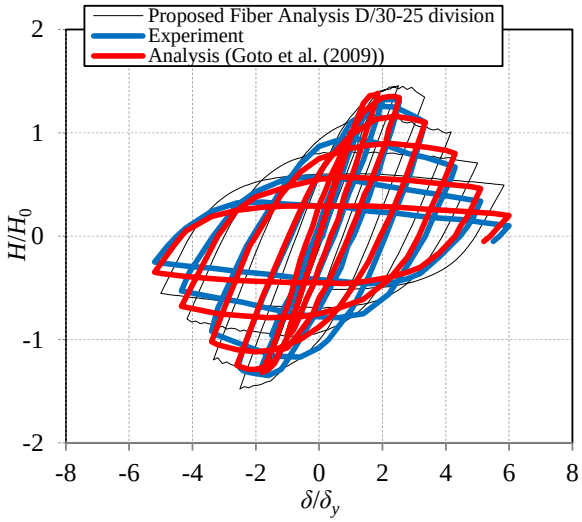


Figure 9 Comparison of Relationship between H/H_0 and δ/δ_y in Experiment and Proposed Fiber Analysis with Fine Element Division in Axial Direction

On the other hand, as shown in Figure 8, the proposed multi-fiber model estimates well the peak strength, and slightly overestimates the post-peak strength, but agrees well with the experimental results compared to the single fiber model. A slight overestimation of the post-peak strength is due to the use of rough fiber element division on the plastic hinge zone. As a follow up, a parametric study has been conducted to study the sensitivity of the division of the fiber elements used on the plastic hinge zone to the results. More specifically, the division of the fiber elements in the axial direction is investigated as shown in Figures 5(a), (b). The division in the circumferential direction is kept the same while the division in the axial direction is varied. Goto et al. (2011) also reported that the FEM analysis using shell elements is excellent in estimating the response of steel bridge frame piers with the circular columns subjected to cyclic loading when a small element division or fine mesh is

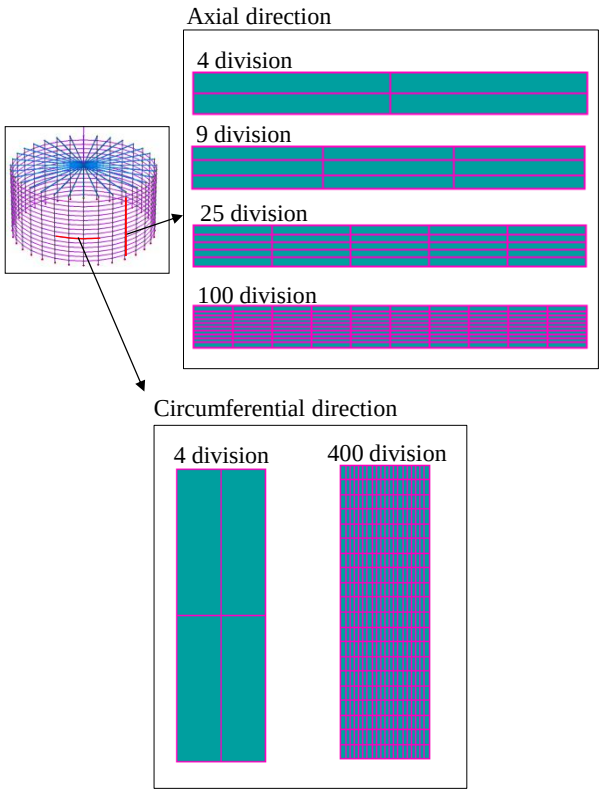


Figure 10 Division of Fiber Section in both the Axial Direction and the Circumferential Direction

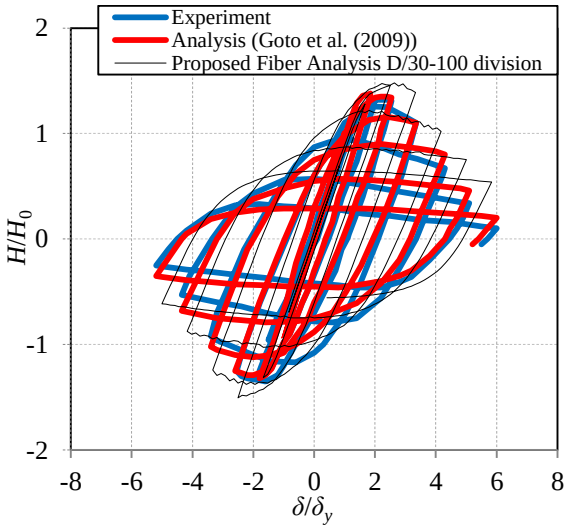


Figure 11 Comparison of Relationship between H/H_0 and δ/δ_y in Experiment and Proposed Fiber Analysis (with 100 Division of Fiber Section)

utilized. Yamaguchi et al. (2005) indicated that the element division on the plastic hinge zone in the axial direction should be less than D/30 and the aspect ratio of the shell element length in the axial direction to the circumferential direction should be less than 1/3 to accurately capture the peak strength when an error of less than 10% is desired. In this study the element division of the plastic hinge zone in the axial direction is under D/30, and the aspect ratio of the length in the axial direction to the circumferential direction

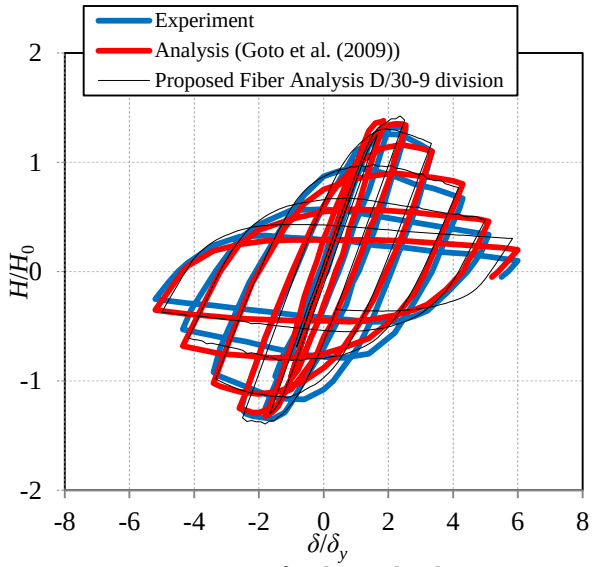


Figure 12 Comparison of Relationship between H/H_0 and δ/δ_y in Experiment and Proposed Fiber Analysis (with 9 Division of Fiber Section)

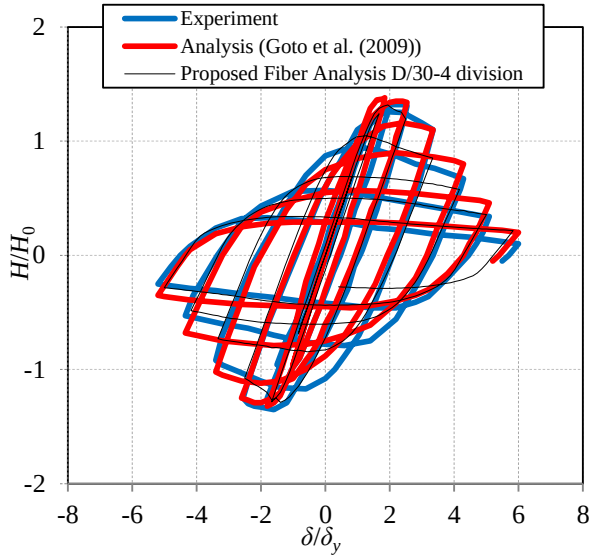


Figure 13 Comparison of Relationship between H/H_0 and δ/δ_y in Experiment and Proposed Fiber Analysis (with 4 Division of Fiber Section)

in the plastic hinge zone is less than 1/3 (see Figure 5(b)). Figure 9 shows that as the element division in the axial direction increases, the post-peak strength decreases and becomes closer to the experiment, but not for the entire history. Therefore, an additional analysis is performed to determine the effect of division of fiber section on the post-peak strength. The division of fiber section was varied from 4-, 9-, 25-, to 100-division as shown in Figure 10. Figures 11to 13 show that as the division of fiber section in the axial direction decreases, the accuracy of the estimated response in terms of peak strength and post-peak strength improves. Thus, it can be concluded that the division of fiber section in the axial direction has significant effect on the post-peak strength. Similarly, the division of the fiber section

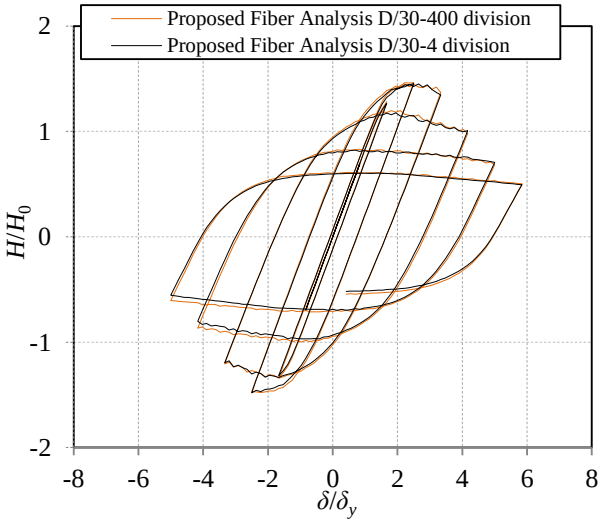


Figure 14 Effect of Division of the Fiber Section in Circumferential Direction

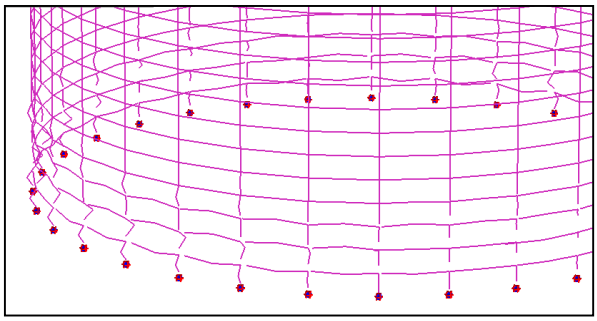


Figure 15 Deformation at Plastic Hinge Zone

in the circumferential direction is investigated. As shown in Figure 14, both the peak strength and post-peak strength are similar regardless of the division of the fiber section in the circumferential direction. Therefore, it can be argued that the proposed method, with adequate division of both fiber element and fiber section in the axial direction, gives good results in estimating not only the peak strength, but also the post peak strength.

4.2 Out-of-Plane Bending Deformation

Figure 15 shows the out-of-plane bending deformation of the plastic hinge zone obtained from the proposed method. As shown, out-of-plane bending deformation due to local bucking occurs in the proposed model. The multi-fiber elements in the plastic hinge zone allow this deformation mode. However, it is also observed that there is a difference in the deformation mode at the plastic hinge zone if compared to the experiment. The proposed model tends to deform toward the inside of the column as opposed to the real deformation observed in experiment. This suggests that some improvements can be made to the modeling of the plastic hinge zone, although estimations of the peak strength and the post-peak strength are good as described in Section **3.1**.

5. CONCLUSIONS

Fiber model analysis techniques used in the analysis of steel bridge circular columns have been discussed in this paper. The effect of modeling on strength was determined by comparing results from single fiber model with multi fiber model proposed in this study. It is shown that peak strength and post-peak strength of the proposed model are comparable to those of the previous experimental work. However, single fiber model is shown to be prone of large error.

The effect of proposed modeling on out-of-plane bending deformation is determined by comparing the deformation from analysis results using the proposed model to the previous experimental results. It is shown that proposed model can be improved to better capture the out-of-plane bending deformation in the plastic hinge zone, where the local buckling occurred.

References:

Ishizawa, T. and Iura, M. (2005), "Analysis of Tubular Steel Bridge Piers," *Earthquake Engineering and Structural Dynamics*, **34**, pp. 985-1004.

Kodama, N. and Yoda, T. (2003), "Dynamic Response Analysis of Box Section Steel Frames Considering Local Buckling," *Journal of Structural Mechanics and Earthquake Engineering*, Japan Society of Civil Engineers, **731/I-63**, pp. 169-184. (In Japanese)

Japan Society of Civil Engineers (JSCE). (2008), "The Japanese Standard Specification for Seismic Design of Steel and Composite structures," JSCE. (In Japanese)

Kakiuchi, T., Kasai, A., Inagaki, S., Fujiwara, Y. and Usami, T. (2009), "Seismic Performance Evaluation of Steel Continuous Bridges with Rigid Superstructure-pier connections," *Journal of Structural Engineering*, Japan Society of Civil Engineers, **55A**, pp. 564-572. (In Japanese)

Ichikawa, S., Sasaki, T., and Kawashima, K. (2010), "Analytical Idealization of Local Buckling of Longitudinal Bars for Analyzing the Seismic Performance of RC Columns," *Proc. 13th Japan Earthquake Engineering Symposium*, Japan Association for Earthquake Engineering, **13**, pp. 3247-3254.

PWRI. (1999), "Summary of the Cooperation Research on the Seismic Limit State Design of Highway Bridge Piers," PWRI. (In Japanese)

Goto, Y., Kumar, P., G. and Kawanishi, N. (2009), "FEM Analysis for Hysteretic Behavior of CFT Bridge Piers Considering Interaction between Steel Tube and Infilled Concrete," *Doboku Gakkai Ronbunshuu A*, Japan Society of Civil Engineers, **65**(2), pp. 564-572. (In Japanese)

Yamaguchi, E., Oniki, K., Nagamatsu, H., and Nannno, Y. (2005), "On finite element mesh in nonlinear analysis of a steel circular-section bridge pier," *Journal of Structural Engineering*, Japan Society of Civil Engineers, **51A**, pp. 1781-1787. (In Japanese)

10CUEE CONFERENCE PROCEEDINGS
10th International Conference on Urban Earthquake Engineering
March 1-2, 2013, Tokyo Institute of Technology, Tokyo, Japan

DEVELOPMENT OF AN ANOMALIES DETECTION METHOD BASED ON NONLINEARITY EXPRESSION

Eiichi Sasaki[1)], Nguyen Khac Thanh[2)]

1) Associate Professor, Department of Civil Engineering, Tokyo Institute of Technology, Japan
2) Graduate Student, Department of Civil Engineering, Tokyo Institute of Technology, Japan

Abstract: Real-time evaluation of structural anomalies has long been a challenging subject for structural monitoring systems (SHM). As a new approach to this problem, a method namely Nonlinearity Index is developed to evaluate nonlinearity expression in the relationship between inputs and outputs during real-time behavior of structures. In case anomalies occur in structures, nonlinearity level in input-output relationship is expected to changes abruptly. In this study, the proposed method is demonstrated on seismic simulation data to verify its accuracy and to obtain the characteristics of nonlinearity at the times of failure events. Then its applicability to experimental data is discussed. Results show strong relationship between changes in nonlinearity expression and times and locations when anomalies occur.

1. INTRODUCTION

During their service lives, civil and industrial structures are prone to anomaly/damage. Those damages can be gradual such as fatigue, corrosion or extreme such as earthquakes, blasts. For the sake of safety, especially in the case of earthquake, it is urgent to monitor the health of structures. The development of SHM system has received significant attention in recent years due to its broad applications to civil, mechanical, and aerospace structures. However, ability to real-timely detect anomalies in the structures is still one of the biggest challenging issues for structural health monitoring (SHM) systems. Besides limits in data storage, linearization-based evaluation method is the biggest drawback. For instance, system parameters governing its behavior are estimated from measured data using linear model, whereas actual structures usually behave nonlinear.

Many approaches have been proposed in order to evaluate nonlinearity of the structures. The vibration-based approach is promising because it is nondestructive and the vibration signal of a structure is easily measurable using properly deployed sensors.

In this research, a new method of evaluating nonlinearity, Nonlinearity Index, is developed. It is computed directly from measured data (acceleration, velocity, etc) without linearization. Discussions on the potentiality of using NI in SHM systems are included by demonstrating the proposed Index on simulated and experimental data.

2. DEVELOPMENT OF NONLINEARITY INDEX

It is common knowledge that structural damages modify the dynamical behavior of structures, which can be explored by evaluating the Frequency Response Function (FRF). According to K.Worden and Tomlinson G.R (2001), FRF is estimated as ratio of auto and cross spectral density. In many previous research (Chanpheng T., Sasaki E. et.al 2009, Simon M. and Tomlinson G.R. 1984), whole-length input and output data are used in estimation. However in the case of civil structures, generally, system vibration caused by input only lasts a certain amount of time and dies out afterward due to system attenuation. Thus in this research, data are divided into a certain amount of time (time interval) and FRF is estimated using data in that period to improve accuracy. The size of time interval depends on attenuation property of structures. Moreover, since changes in the structures due to anomalies are instantaneous events, overlap is employed to monitor these. The process of FRF estimation is illustrated in Figure 1.

To evaluate the level of nonlinearity present in FRF, Hilbert transform is often employed. The main characteristic is that FRF of any linear system remain intact under Hilbert transform. In other words, any change in FRF under Hilbert transform suggests anomalies present in the system.

$$FRF'(\omega) = -\frac{1}{\pi i}\int_{-\infty}^{\infty}\frac{FRF(\Omega)}{\Omega-\omega}d\Omega \quad (1)$$

However, implementation of numerical Hilbert transform is not straightforward as due to pole at $\omega=\Omega$ and data truncation. Depend on research purpose and characteristic of data using, many calculation algorithms have been proposed, most commonly Kramers-Kronig (K.Worden and Tomlinson G.R 2001, Tomlinson G.R. 1987) and Matlab hilbert. However, these two methods still leave

numerical errors in the transformed FRF, thus not appropriate to use in evaluating level of nonlinearity. In this research, a new algorithm is proposed with reference of K.Worden and Tomlinson G.R (2001) and proved by test data to have the best result in accuracy and calculation time. Using the characteristic of Hilbert transform, nonlinearity is defined as

$$N = \int_{\omega_2}^{\omega_1} \left| FRF'(\omega) - FRF(\omega) \right| d\omega \qquad (2)$$

$[\omega_1 \ \omega_2]$ is the frequency range where FRF is estimated. Nonlinearity is averaged as Nonlinearity Index (NI) by number of estimated FRF in one time interval $n(\omega)$ to mitigate the effect of time interval's size. $n(\omega)$ can be directly computed from sampling rate and the size of time interval. NI at each time t_i is computed as NI_i. By overlapping time interval as described above, NI is obtained as a function of time, thus make it possible for real-time detection.

$$NI_i = \frac{\int_{\omega_2}^{\omega_1} \left| FRF'(\omega) - FRF(\omega) \right| d\omega}{n(\omega)} \qquad (3)$$

$$n(\omega) = \frac{rF_S}{2} + 1 \qquad (4)$$

Generally, nonlinearity can exist from the beginning (for instance, geometry-wise nonlinear) or newly introduced by anomalies occurring in the system. The former remains constant as long as the system is healthy, therefore by tracking nonlinearity over time, anomalies can be detected.

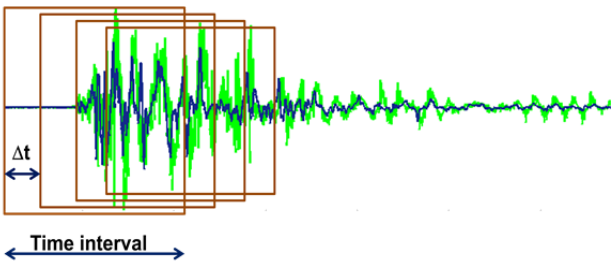


Figure 1 Time interval and overlap

3. METHOD VERIFICATION BY SIMULATING EARTHQUAKE DAMAGE ON A TRUSS BRIDGE

3.1 Simulation Conditions

Simulated model is closely based on the Tokyo Gate Bridge, a large truss bridge of total 2.9 km and 10 spans. This bridge includes three parts, two PC parts (rigid frame) and one steel part (truss). Along with distinguished design in geometry, behavior of this bridge is considered complicated and is an appropriate target of SHM systems. For complex structures like this, conventional linearization approach is not effective in detecting anomalies. Therefore, this bridge is chose in order to verify the proposed NI.

Overall model is shown in Figure 2. Boundary conditions are modified as following to serve the simulation purpose. Simulated model has four bearings, fixed (N1, N4) and moveable (N2, N3) at the main section. As shown in Figure 3, bearings N2 and N3 move along in the bridge's longitudinal and transverse directions by friction of coefficient 0.15 between vertical and horizontal forces. Meanwhile, bearings N1 and N4 are designed as fixed bearings which operate in the same way with N2 and N3 in the longitudinal direction. In the transverse direction, however, a side-block as illustrate in Figure 4 is set up. This side-block allows the bearing to move within 0.01m and fails if contact force reaches 20000kN. In the vertical direction, all bearing is assumed to be fixed.

Apart from two types of nonlinearity above, all material is modeled according to nonlinear constitutive law in order to simulate structure damage caused by material yielding.

Ground motion (acceleration) in 3 directions recorded at JR Takatori station in 1995 Kobe Earthquake with amplitude timed 1.5 is used as input and placed at all pier bottoms. The amplification factor 1.5 is used to assure the bearing failure and bridge collapse to be simulated.

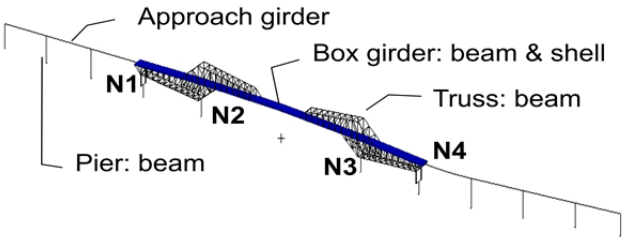


Figure 2 Model overview

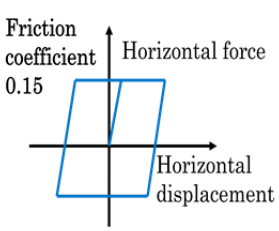


Figure 3 Friction

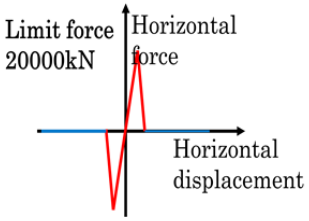


Figure 4 Side-block

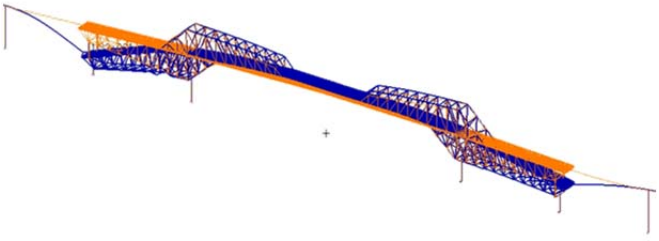


Figure 5 Collapse at left side

Figure 6 Sensor locations

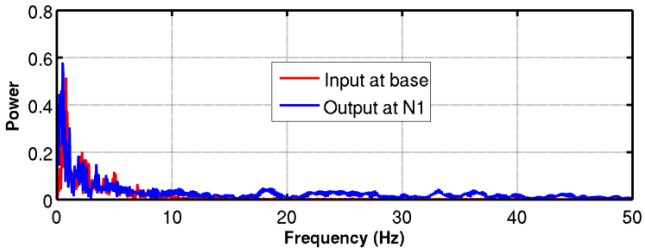


Figure 7 Frequency decomposition

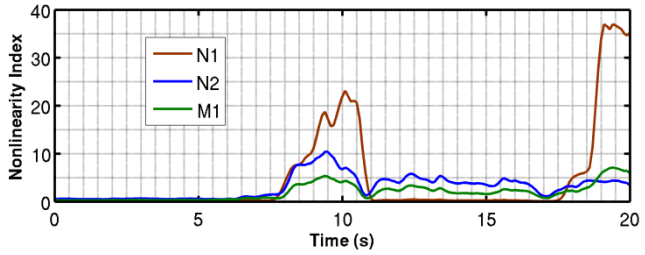


Figure 8 NI between input and bearing N1, N2,M1

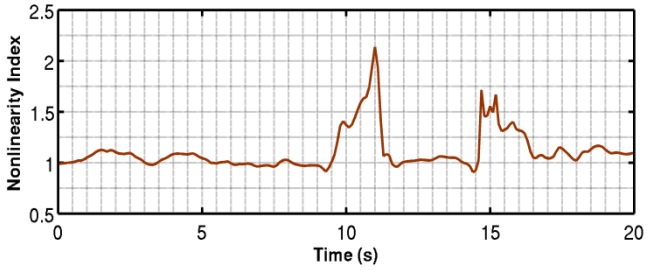


Figure 9 NI between trusses M2 and M3

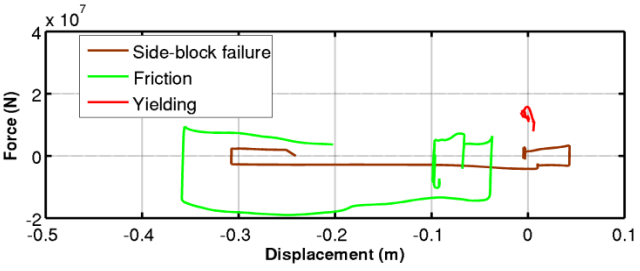


Figure 10 Energy comparison

3.2 Failure

Side-block failures occur at bearing N1 and N4 at 7.5s. After that N1 and N4 lost bearing function while N2 and N3 continue to operate due to friction. Bridge collapses at 17.5s at the side of bearing N1 by gravity of super structures as in Figure 5. Buckling in truss members are observed at the span between N1 and N2 because of this collapse.

3.3 Result evaluation

NI has three components corresponding to input and output (acceleration). However overall result suggests that all components yield similar tendency in term of detecting anomalies, NI in bridge's longitudinal direction is presented here. Figure 6 illustrates locations of sensors used in following evaluation. Frequency range is set as [0 50Hz] based on Figure 7.

Two peaks in NI of bearing N1 in Figure 8 indicate the times of side-block failure and collapse respectively. The first peak is also observed in NI of N2 and M1, which suggests side-block failure in bearing N1 to have impact on whole N1-N2 span. However, after side-block failure, bearing N1 loses bearing function; therefore there is no longer link in movement between N1 and N2. That is why there is no second peak in NI of bearing N2.

Meanwhile, NI of bearing N2 from 11-20s is higher than initial level which proves that friction movement of bearing N2 also causes nonlinearity in the system.

As for material yielding, with same method, yielding times 9s and 14s cannot be clearly observed in NI of M1 due to impact from N1 failures. However, this problem can be overcome by examining NI between two neighbor trusses M2 and M3 as in Figure 9, which also yields at 9s and 11s.

Behavior of NI can be explained assuming nonlinearity expression as a method of energy dissipation which is large (bearing failure) compared to small (local truss yielding). To confirm these assumptions, simulated result about energy dissipation of 3 failure types (side-block N1, friction N2, material yielding M1) is shown in Figure 10. Clearly, energy dissipation by side-block failure or friction is significantly larger than that of material yielding as expected.

4. APPLICABILITY TO MEASURED DATA ON A FOUR-STORY STEEL CONTRUCTED BUILDING COLLAPSE EXPERIMENT

This experiment is conducted to simulate the total collapse under strong earthquakes of a four-story steel constructed building (Figure 11). With Takatori motion as input, loading is divided into 20%, 40%, 60%, and 100% loading. The building collapses at 1F when loading is 100%. NI component in North-South direction (strongest input direction) is presented. Based on Figure 12, frequency range is set as [0 15Hz].

Figure 13 shows the NI between 1F and base according to loading. Clearly, despite input acceleration increases from 20%~60%, level of NI remains constant, which means no major anomaly occurs in the building. Also it is clear that NI is independent to level of input or output. Meanwhile, NI changes abruptly when input acceleration reaches 100%. This agrees with experiment's outcome, where 1F collapses under 100% loading. Even in 100% loading, NI remains constant till 15s despite increase in acceleration. NI starts to rise in 15-20s even with level of acceleration is smaller than previous period. Strain gauge data confirms various yielding in from 15s to 18s while peak at 20s corresponds with total collapse of 1F.

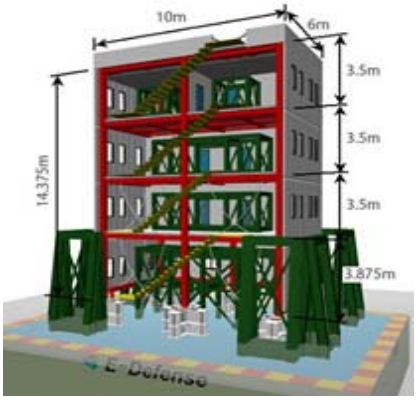


Figure 11 Experiment overview

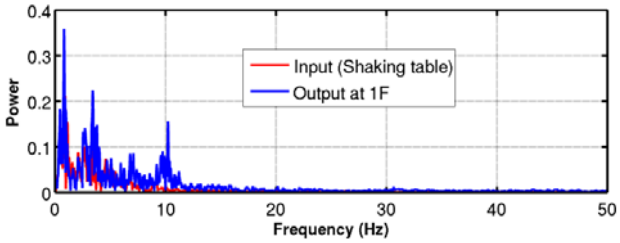


Figure 12 Frequency decomposition

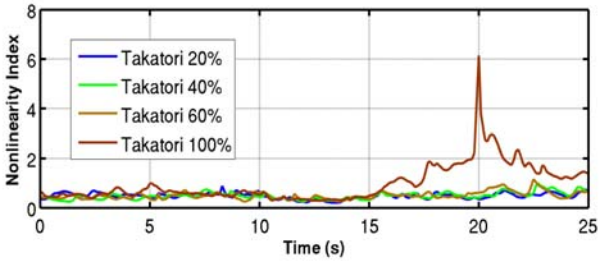


Figure 13 NI between input and 1F

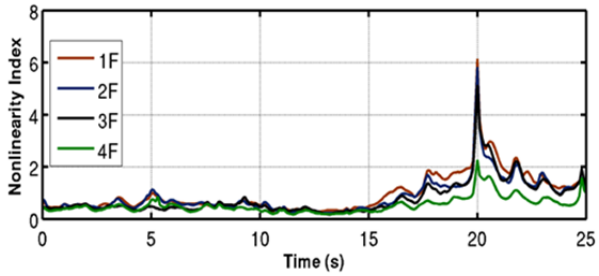


Figure 14 NI between input and 1F

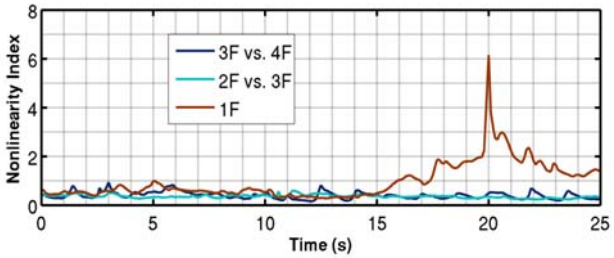


Figure 15 NI between input and 1F

Above results confirm that NI can successfully detect anomalies real-timely and is more sensitive toward anomalies than raw acceleration data.

Figure 14 shows NI for other floors with 100% loading. NI rises in all floors, which seems to be against actual experimental result where upper floors remain undamaged. To see whether those changes in NI come from impact of collapse in 1F or anomalies in upper floors themselves, Figure 15 examines NI between floors. Obviously, level of NI at each output-output is noticeably smaller than failure level, and almost constant, therefore no anomaly detected in upper floors.

5. CONCLUSIONS

By using new method in FRF estimation and numerical Hilbert transform, nonlinearity present in the behavior of the systems is successfully evaluated in order to capture instantaneous changes in the systems. It is demonstrated by simulated and experimental data that NI changes abruptly when anomalies occur in the structures. Since NI is independent of either input or output, it is more sensitive to anomalies than raw data themselves.

References:

Worden K. and Tomlinson G.R. (2001) "Nonlinearity in structural dynamics – Detection, Identification and Modelling" Taylor & Francis.

Chanpheng T., Sasaki E. et.al (2009) "A method for vibration-based health monitoring using nonlinearity measurement," *Journal of Structural Engineering*, Vol.55A.

Simon M. and Tomlinson G.R. (1984) "Use of the Hilbert transform in modal analysis of linear and non-linear structures," *Journal of Sound and Vibration*, **96**(4), 421-436.

Tomlinson G.R. (1987) "Developments in the use of the Hilbert transform for detecting and quantifying non-linearity associated with frequency response functions" *Mechanical Systems and Signal Processing* **1**(2) 151-171.

E-defense experiment: total collapse of a four-story steel constructed building.

10CUEE CONFERENCE PROCEEDINGS
10th International Conference on Urban Earthquake Engineering
March 1-2, 2013, Tokyo Institute of Technology, Tokyo, Japan

INVESTIGATION OF THE EFFECTS OF MODEL COMPLEXITY ON THE PREDICTED SEISMIC RESPONSE OF BRIDGE PILE FOUNDATIONS

Roshanak Omrani[1], Bahareh Mobasher[2], Farzin Zareian[3] , and Ertugrul Taciroglu[4]

1) Postdoctoral Research Associate, Dept. of Civil and Environmental Engineering, University of California, Los Angeles
2) Graduate Student Research Associate, Dept. of Civil and Environmental Engineering, University of California, Irvine
3) Associate Professor, Dept. of Civil and Environmental Engineering, University of California, Irvine
4) Associate Professor, Dept. of Civil and Environmental Engineering, University of California, Los Angeles

romrani@ucla.edu, bmobashe@uci.edu, zareian@uci.edu, etacir@ucla.edu

Abstract: This paper summarizes our investigation in comparing the performance of a computationally efficient reduced-order model of soil-foundation system of a bridge column, and a high-fidelity three dimensional finite element model. Performance assessment is evaluated at the level of Engineering Demand Parameters, and comparisons are made between the deformation histories of the piles. The study focuses on the interaction between the piles and the surrounding soil media during strong seismic excitations. The high computational cost and the complexity of the full model render finite element models impractical for routine engineering tasks. Consequently, reduced models, which employ the theory of beam on nonlinear Winkler foundations, have become attractive predictive tools in engineering practice. Macroelement models are used for representing the near-field soil-pile interaction effects, including nonlinear soil response, gapping effects, skin friction, as well as far-field radiation damping. Effects of the pile head fixity conditions and properties of the soil strata on the results of the aforementioned models are investigated through parametric sensitivity studies.

1. INTRODUCTION

The existing seismic design guidelines ignore the effects of soil-foundation-structure interaction on the seismic response of ordinary bridges by prescribing either fixed or flexible supports at the boundaries of the bridge superstructure (SDC, 2010; Aviram et al., 2008). Although elimination of soil-foundation system from the numerical model simplifies the analysis and design tasks, it leads to increased uncertainties. The current state of practice compensates for the reduced level of certainty by adopting larger margins of safety, which in turn lead to uneconomical designs. On the other hand, detailed finite element models are aimed to reduce the epistemic uncertainties by integrating elements of superstructure, foundation, and soil into the analysis (Elgamal et al., 2008; Zhang et al., 2003; Jeremic et al., 2002). Nonetheless, tuning the relatively large number of model parameters in order to generate meaningful results is not always a feasible task. Furthermore, the high cost associated with the intensive computational effort is often prohibitive of the adoption of high-fidelity models for routine engineering tasks. As an intermediate alternative, Performance-Based Earthquake Engineering (PBEE) methodologies aim to incorporate the actual nonlinear behavior and energy dissipation characteristics of the soil-foundation system into reduced-order models. As such, they can provide an enhanced understanding of the actual capacities of the bridge at affordable computational costs. However, prior to employing such reduced-order models in everyday engineering practice, their robustness and advantage over existing guidelines needs to be rigorously verified against the output of high-fidelity models and/or experimental data (Dryden and Fenves, 2009; Shin, 2007).

In this study, the outputs of a reduced-order and a three-dimensional finite element model in predicting the Engineering Demand Parameters imposed by seismic excitations on a single pile embedded in homogeneous soil are compared. Brief descriptions of the reduced-order and the finite element models are provided and the key features of each model are emphasized prior to demonstrating the simulation results. The Open System for Earthquake Engineering Simulation (OpenSees) (McKenna, 1997; McKenna and Fenves, 2001) has been used for creating the aforementioned numerical models and for carrying out the nonlinear analysis tasks of the current study. OpenSees is considered a suitable platform for performing PBEE related studies, particularly due to the relatively large number of nonlinear constitutive models as well as solution techniques for nonlinear problems which have been incorporated into its framework since its initial development.

2. MODELING DETAILS

2.1 Modeling the Vertical Propagation of Seismic Waves

Opposite to building structures, which are subjected to uniform strong motion excitation through the base, embedded pile foundations are directly excited by the ground motion at all degrees of freedom. Consequently, the assumption of uniform excitation may not be appropriate in case of significant variation of the ground motion in the vertical direction.

In order to address the spatial variability of the input motion, the dynamic analysis of an embedded pile needs to be performed in two steps. First, a site response analysis is carried out in order to simulate the far-field ground motion and determine if the seismic waves are altered as they propagate in the vertical direction. This is done through the dynamic analysis of a soil column that represents the far field soil domain. In order to achieve the shear-type behavior of soil, four-node plane-strain elements with 2 translational degrees of freedom per node are used and shear-type boundary conditions are imposed on the lateral sides of the representative soil column. Since only the variation of seismic shear waves in the vertical direction is of interest, the Poisson's ratio is set to zero. Therefore, no acceleration is incurred in the vertical direction, i.e., no horizontal propagation of seismic waves occurs and a single element in the horizontal direction would suffice. However, the number of elements in the vertical direction should be chosen such that the characteristics of the propagating waves can be adequately captured. It is often recommended that the element dimension be 1/8 to 1/10 of the wave length, which can be decided from the shear wave velocity and the maximum frequency content of the ground motion. The former depends on the soil shear modulus and density of soil while the latter can be considered not to exceed 25 Hz for most strong motion records. Plane-strain assumption restricts the out-of-plane deformations and mimics the infiniteness of the soil domain in the direction normal to the planes where shear deformations happen. UC San Diego soil models, which are already available in OpenSees, have been used to incorporate nested yield surfaces with elastoplastic constitutive relations for the deviatoric part of the stress and strain tensors. Namely, Pressure Independent Multi Yield Surface (PIMY) and Pressure Dependent Multi Yield Surface (PDMY) material models were used for modeling clay and sand, respectively.

The nodes at the bottom of the soil column are fully and partially restrained in the vertical and horizontal directions, respectively. The partial fixity is achieved by attaching a viscous dashpot to one of the bottom nodes. The dashpot represents the energy absorbing properties of the domain beneath the column of soil, hence, its coefficient is defined in terms of the shear wave velocity and the density of the underlying soil/bedrock. The incoming seismic waves are modeled as a velocity proportional equivalent nodal force at the base of the soil column. The wave and stress field equations which lead to the aforementioned modeling procedure are based on the work done by Lysmer and Kuhlemeyer (1969) for characterizing "absorbing/transmitting boundaries" as described in details by Zhange et al. (2003).

As suggested by the developers of the nonlinear soil models described earlier, in order to develop confinement pressures a gravity analysis under the self weight of soil—while the material is forced to exhibit linear behavior—needs to be completed prior to any seismic analysis. The shear-type boundary conditions on the lateral boundaries provide the necessary constraints for generating the confining pressures. Afterwards, the linearity restriction can be removed for the subsequent gravity and seismic analyses under confining pressures.

In addition to the material nonlinearity, which is the main mechanism for energy dissipation within the plastic range, energy dissipation within the small strain range of deformation is introduced with Rayleigh damping, with Rayleigh coefficients calculated based on a 2% damping ratio corresponding to 0.2 and 20 Hz frequencies. Nodal response (displacement and velocity) along the height of the soil column are recorded to be later used as the input motion for the seismic analysis of the embedded pile.

Excluding the pile from the site response analysis ensures that the far-field effects are isolated from the pile inertia. It is possible to produce similar results by increasing the size of soil domain and integrating the pile and far-field soil in the same model. However, the undesirable increase in the amount of computational efforts—due to the increased number of soil elements—renders this approach disadvantageous.

A source code for performing 1D nonlinear site response analysis in pressure independent material (e.g., clay) is available through OpenSees website. The code was adapted to the current study by amending additional material models.

2.1 Reduced-Order Pile Model (ROM)

The theory of beam on nonlinear Winkler foundation is used for the dynamic analysis of pile. It is essentially assumed that the passive resistance of soil can be modeled with a series of discrete nonlinear springs known as *p-y* springs. The backbone curve of each *p-y* spring is a function of the depth below the surface and is defined due to the relationships recommended by the American Petroleum Institute (API 2000) for clay (Matlock, 1970; Rees and Cox, 1975) and sand (O'Neill and Murchinson 1983). Similarly, skin friction effects are modeled with a series of tangential nonlinear springs referred to as *t-z* springs. A single nonlinear spring (*q-z* spring) at the tip of the pile models end bearing. The present study does not take into account the deteriorative effects of cyclic loading—as described by API recommendations— on the lateral load bearing capacity of soil.

Particular assemblages of the abovementioned nonlinear springs and a number of physical and semi-physical components can incorporate additional

near-field soil-pile interaction effects—such as gapping, drag, and radiation damping—and are referred to as macroelements (Taciroglu et al., 2006; Boulanger et al., 1999). The macroelement described in the work by Boulanger et al. (1999), hereinafter referred to as the *p-y* macroelment, is available in OpenSees and has been adopted for the current study.

The pile is discretized into 15 beam-column elements with three translational and three rotational degrees of freedom per node). Lateral and vertical support is provided by two sets of orthogonal *p-y* macroelement at each node as well as *t-z* springs at the intermediate nodes and a *q-z* spring at the bottom node. The nodal displacement histories form site response analyses of the horizontal component of a strong motion event are applied at the free ends of one set of the orthogonal *p-y* macroelements. It should be noted that no coupling exists between the two orthogonal directions. In other words, the pile response to a component of the ground motion in each direction at a time is identical to its response when the two components are applied simultaneously. However, the ultimate objective of the reduced-order modeling approach is to incorporate the model into three dimensional analyses of bridge structures. Thus, it is essential to develop the model in a manner such that it can lend itself to concurrent application of orthogonal input motions.

2.2 Three-Dimensional Finite Element Model (FEM)

The near field soil is modeled as a 10×10×18 m tub. Eight-node brick elements with 3 translational degrees of freedom per node are used for discretizing the soil domain. The soil domain consists of a total of 5340 brick elements. The side length of the individual elements does not exceed 1 m. The volume of the pile is accounted for as a cylindrical void of 0.6m in diameter. The pile is discretized into 15 beam-column elements at the centerline of the cylindrical void. The translation degrees of freedom of the pile nodes are constrained to the adjacent soil nodes with rigid links. The commercial software GiD (Diaz and Amat 1999) was utilized for the mesh generation. The finite element mesh of the soil tub and the pile-soil connectivity are illustrated in Figures 1 and 2. PIMY and PDMY material models (described in section 2.1) are assigned to the soil elements.

Lysmer_Kuhlemeyer boundary elements (1969) are attached along the base and the lateral planes of the soil tub to mimic the energy dissipation characteristics of the semi-infinite soil domain surrounding the tub. The tub is restrained against vertical motion. The input motion is modeled as equivalent nodal forces applied at the base and the sides of the tube normal in the direction of the ground motion. The nodal forces at each height are proportional to the ground motion velocity, which was obtained from the 1D site response analysis described in section 2.1. In order to generate confinement pressures, a gravity analysis precedes the dynamic analysis (similar to the procedure described in section 2.1.)

3. CASE STUDIES

3.1 Site Response Analysis

The current study addresses the case of a single pile

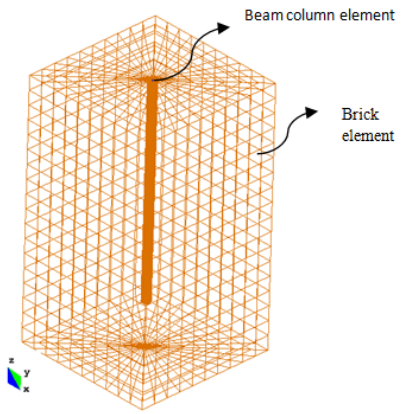


Figure 1. Three Dimensional Finite Element Mesh

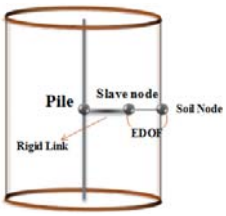


Figure 2. Pile Soil Rigid Connections

embedded in a homogeneous layer of soil subjected to the (unidirectional) horizontal component of 1989 Loma Prieta Earthquake (PEER Strong Motion Database, 2000) recorded at Gilroy No.2 station (Figure 3). The ROM was analyzed using the full history of the ground motion. Due to the high computational burden, the analysis of the FEM was carried out using only the strong motion duration (i.e., portion of the ground motion record which corresponds to 5% to 95% of the arias intensity as marked in Figure 3). In order to decide whether truncating the beginning part of the ground motion has significant effects on the analysis results, the analysis for the pile in the stiff clay was repeated using the first 9 seconds of the full ground motion record. Three types of soil materials including soft and stiff clay, as well as loose sand have been considered. The effects of ground water are excluded from the current study. Tables 1 and 2 list the major properties of the three types of soil material used in this study, where ρ, G, c, S_u and ϕ denote mass density, shear modulus, cohesion, undrained shear strength, and friction angel, respectively. The rest of parameters required for defining the PIMY and PDMY material models are chosen based on recommended values available through OpenSees website. The dimension of the soil elements were set to 0.5 m—which was decided according to the most critical case,

i.e., the soft clay material which possesses the smallest shear wave velocity amongst the three materials— in both vertical and horizontal directions.

Table 1. Material Properties for Clay

Material	ρ (ton/m^3)	G (kPa)	c (kPa)	S_u (kPa)
Soft Clay	1.3	1.3×10^4	18	20
Stiff Clay	1.8	1.5×10^5	75	80

Table 2. Material Properties for Sand

Material	ρ (ton/m^3)	G (kPa)	ϕ (degrees)
Loose Sand	1.7	5.5×10^4	29

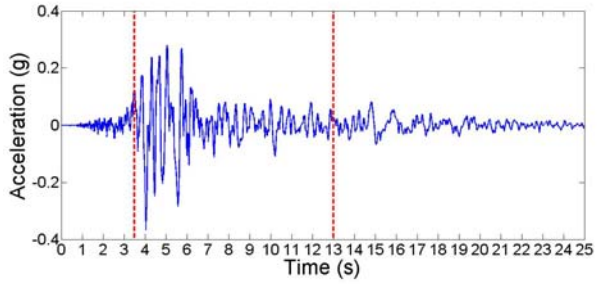


Figure 3. 1980 Loma Prieta Ground Acceleration

The displacement response histories of soil at the pile tip and head elevations due to the site response analysis of a 40 m soil column resting on dense rock are shown in Figure 4. It is observed that the variation of ground motion is more prominent in cohesionless soil (sand) compared to cohesive soil (clay). Qualitative comparison of the displacement records implies that the overall trend of the response history in soft clay slightly deviates from the trends observed for the rest of materials.

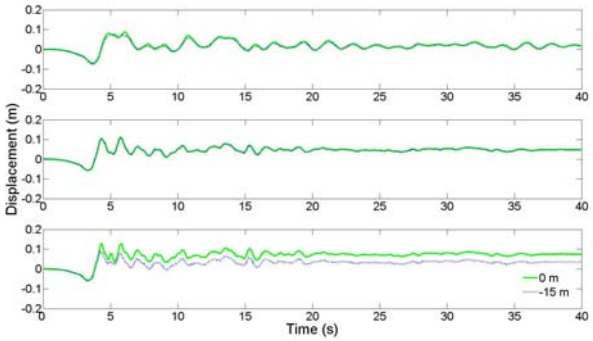


Figure 4. Vertical Variation of Ground Motion in (a) Soft Clay, (b) Stiff Clay, and (c) Loose Sand

It is evident from the stress-strain curves—shown at several representative depths (Figure 5) for soft clay—that the material nonlinearity is mostly concentrated in the lower 10 m of the soil column. Therefore, the 40 m height for the soil column in the site response analysis is an appropriate choice as long as the embedded length of pile falls outside the region of the soil which is highly affected by the boundary conditions at the bottom of the soil column.

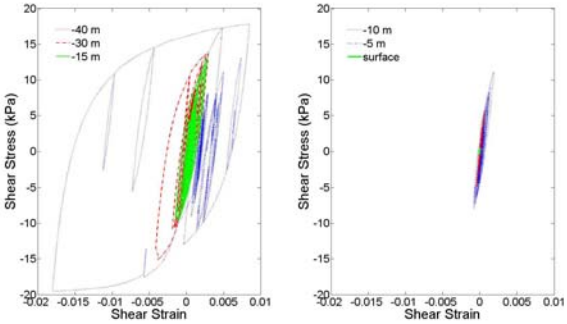


Figure 5. Stress-Strain Curves of Soft Soil

In order to investigate the effect of material nonlinearity on the outcome of site response analysis, the analysis was repeated for soft clay assuming linear elastic relationship for both deviatoric and volumetric parts of the stress and strain tensors during the dynamic analysis, which is initiated from a confined state of material. As illustrated in Figure 6, the upper layers of soil exhibit oscillatory displacement response with peak magnitudes almost twice the peak values observed for the nonlinear clay. The site response analysis results for the nonlinear soil materials are used, henceforth, for the rest of this study.

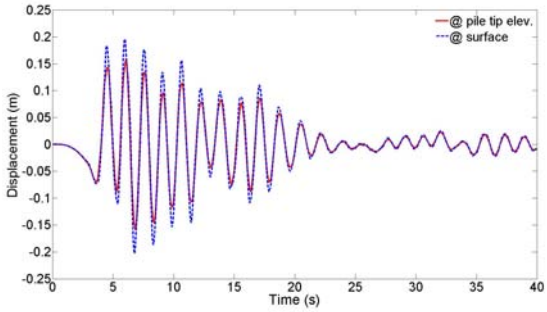


Figure 6. Site Response Analysis Results of Soft Clay using Linear Elastic Material Model

3.2 Pile Response

The pile is fully embedded with an embedded length of 15 meters and a diameter of 0.6 m. A linear elastic material with Young's modulus value, E_c, of 28 MPa and Poisson's ratio, ν, of 0.2 is used for modeling the pile. The pile is restrained against lateral and vertical displacement at top, i.e., pinned-head (PH) condition. Furthermore, all nodes are restrained against torsion. In order to investigate the effect of head fixity on the dynamic response, the analysis was repeated with fixed-head (FH) condition for the pile

embedded in stiff clay. In reality, various degrees of rotational fixity can be achieved, depending on the inertia of pile cap as well as the development length of pile rebars in the pile cap. The degree of restraint against rotation also depends on the number of piles and location of a pile in the bent. We assumed moment of inertial in the longitudinal direction of a bridge is significantly larger than moment of inertia in the transverse direction, thus, a higher degree of fixity is provided against rotation about an axis parallel to the transverse direction of the bridge. Therefore, both pinned and fixed boundary conditions are idealized representations of the actual boundary conditions.

The lateral deformation of pile at four representative depths for the four cases are presented in Figures 7 through 10. As shown in the time history plots, the ROM generates smaller displacements for the PH pile in soft and stiff clay compared to the FEM. The results from the ROM reports spatial variation of displacement along the height of the PH pile in loose sand and FH pile in stiff clay. In general, the pile exhibited smaller displacements in the soft clay material. The effect of neglecting the early portion of the ground motion on the output of the FEM was examined by repeating the analysis for the PH pile in stiff clay. Excluding the beginning portion of the specimen ground motion has resulted in a baseline drift (bias) in the displacement time history at all depths (Figure 11). The most extreme deformed shapes generated by ROM and FEM for all cases are compared side-by-side in Figure 12.

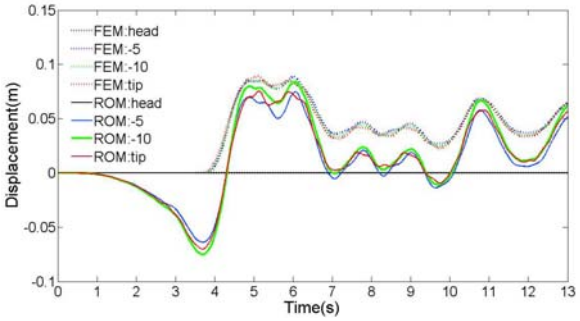


Figure 7. Response History of PH Pile in Soft Clay

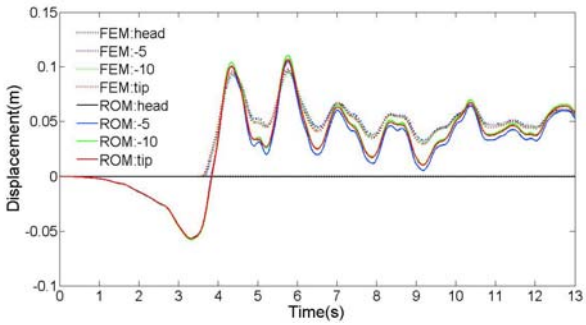


Figure 8. Response History of PH Pile in Stiff Clay

The maximum bending moment demands and their locations are listed in Table 3. The results from the ROM and FEM are in good agreement for the case of loose sand. However, the maximum bending moments generated by the ROM are 25% of the moment obtained through FEM for PH pile embedded in soft clay. This ratio is increased to about 45% for the case of FH pile in stiff clay. Including the first part of the ground motion in the FEM analysis yields 16% reduction in the maximum demand inserted on the pile in stiff clay. The maximum bending moment for the FH pile is incurred at top of the pile. In general, the location of the maximum demand under the PH condition is 2-3 m below the surface in FEM. This location moves further down to 3-4 m below the surface in the ROM. The difference in the location of the maximum moment is also evident from the location of the maximum curvature of the deformed pile profiles displayed in Figure 12 .

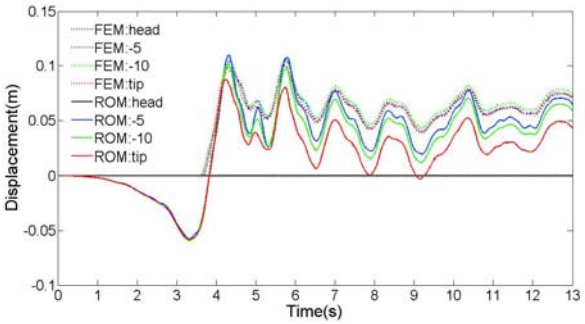


Figure 9. Response History of PH Pile in Loose Sand

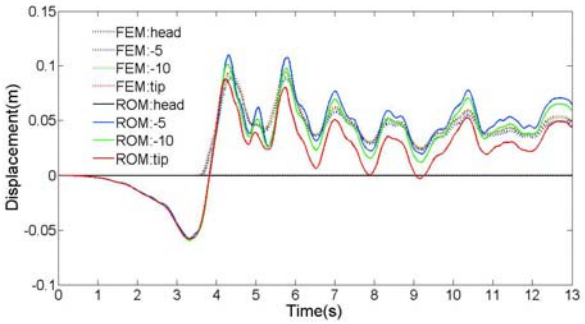


Figure 10. Response History of FH Pile in Stiff Clay

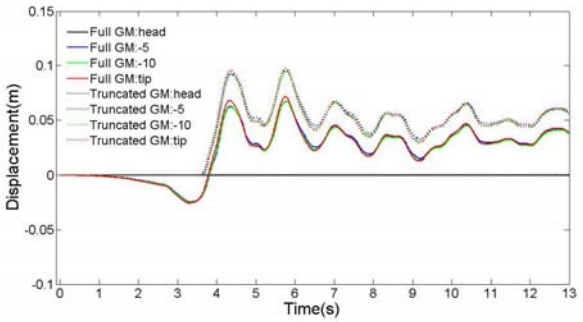


Figure 11. Effect of Neglecting The Early Portion of Ground Motion on the FEM Response of PH Pile in Stiff Clay

As expected, the fixed head condition imposes large bending moment demand on the top. However, the influence

of the fixed head condition on the internal moment becomes less significant in sections away from the top.

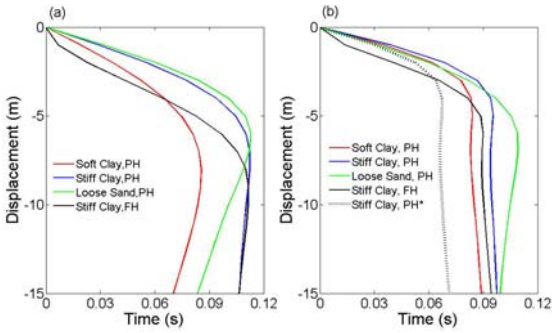


Figure 12. Extreme Deformed Shapes from (a) ROM, and (b) FEM

Table 3. Maximum Internal Moments

Case	M (kN.m)	M (kN.m)
Soft Clay (PH)	588 (@-4)	2322(@-2)
Stiff Clay (PH)	1081 (@-3)	2474/2074*(@-2)
Loose Sand(PH)	1328 (@-4)	1486 (@-3)
Siff Clay (FH)	2874 (@0)	6433 (@0)

* The first part of ground motion included in the analysis.

4. CONCLUSIONS

The results of employing a reduced-order and a finite element model for the seismic analysis of an elastic pile which is embedded in homogeneous soil are investigated. The effects of soil properties and head fixity on the displacement response history and internal bending moments of the pile are examined. The results indicate that the two modeling approaches yield comparable results for both displacement and bending moment in case of pinned-head pile embedded in loose sand. The two models also generate similar displacement response histories for the pile in clay material. However, significant discrepancies are observed in the bending moment demands predicted by the two models in case of both soft and stiff clay. An investigation of the effect of the arriving portion of the ground motion on the results of FEM revealed their influential effects on the displacement response. Addressing the effects of pile inelastic behavior as well as bidirectional excitations can provide directions for future studies.

Acknowledgements:

This study is based on work supported by the California Department of Transportation (Caltrans) under Award No. 65A0454. This financial support is gratefully acknowledged. Any opinions, findings, and conclusions or recommendations expressed in this paper are those of the authors and do not necessarily reflect the views of sponsors.

References:

American Petroleum Institute (API) (2000), "Recommended Practice for Planning, Designing and Constructing Fixed Offshore Platforms-Working Stress Design," 21st Ed., *API RP 2A-WSD* , Washington, D.C.

Aviram, A., Mackie, K.R., and Stojadinovic, B., (2008), "Guidelines for Nonlinear Analysis of Bridge Structures in California," *PEER Report* No. 2008/03, Pacific Earthquake Engineering Research Center, University of California, Berkeley.

Boulanger R.W., Curras C. J., Kutter B.L, Wilson D.W., and Abghari A. (1999), "Seismic soil-pile-structure interaction experiments and analysis," *Journal of Geotechnical and Geoenvironmental Engineering*, **125**(9), 750-759, 1999.

Caltrans SDC (2010), *Caltrans Seismic Design Criteria, Version 1.6*, California Department of Transportation, Sacramento, California.

Diaz, N.D., and Amat, P.S., (2010), *GiD the Personal Pre/Postprocessor User's Manual, version 10.0*, CIMNE, Barcelona, Spain, (http://gid.cimne.upc.es).

Dryden, G. M. (2009), "The Integration of Experimental and Simulation Data in the Study of Reinforced Concrete Bridge Systems including Soil-Foundation-Structure Interaction," Doctoral Dissertation, University of California.

Elgamal, A., Yan, L., Yang, Z., and Conte, J.P. (2008), "Three-Dimensional Seismic Response of Humboldt Bay Bridge-Foundation-Ground System," *Journal of Structural Engineering*, **134**(7), 1165-1176.

Jeremic, B., Guanzhou, J., Preisig, M., and Tafazzoli, N. (2002), "Time domain simulation of soil-foundation-structure interaction in non-uniform soils," *Earthquake Engineering & Structural Dynamics*, **38**(5), 699-718.

Lysmer, J., and R.L. Kuhlemeyer (1969), "Finite Dynamic Model for Infinite Media," *Journal of the Engineering Mechanics Division, ASCE*, **95**(EM4), 859-877.

Matlock H. (1970), "Correlations for Design of Laterally Loaded Piles in Soft Clay," *Proceeding of 2nd Annual Offshore Technology Conference*, OTC 1204.

O'Neill, M.W. and Murchison, J.M. (1983), "An Evaluation of p-y Relationships in Sands," *Report PRAC 82-41-1* prepared for the American Petroleum Institute.

Pacific Earthquake Engineering Research Center (PEER) (2000), PEER Strong Motion Database (http://peer.berkeley.edu/smcat), Regents of the University of California.

Reese, L. C. and Cox, W. R. (1975), "Field Testing and Analysis of Laterally Loaded Piles in Stiff Clay," *Proceedings of 5th Annual Offshore Technology Conference*, OTC 2312.

Shin, H. (2007), "Numerical Modeling of a Bridge System & its Application for Performance-Based Earthquake Engineering," Doctoral Dissertation, University of Washington.

Taciroglu, E., Rha C., and Wallace, J.W. (2006), "A Robust Macroelement Model for Soil-Pile Interaction under Cyclic Loads," *Journal of Geotechnical and Geoenvironmental Engineering*, **132**(10), 1304-1314.

Zhang, Y., Yang, Z., Bielak, J., Conte J. P., and Elgamal, A. (2003), "Treatment of Seismic Input and Boundary Conditions in Nonlinear Seismic Analysis of a Bridge Ground System," *Proceedings of 16th ASCE Engineering Mechanics Conference*, Seattle, WA.

10CUEE CONFERENCE PROCEEDINGS
10th International Conference on Urban Earthquake Engineering
March 1-2, 2013, Tokyo Institute of Technology, Tokyo, Japan

ANALYTICAL INVESTIGATION ON THE EFFECT OF NUMBER OF VEHICLES ON THE SEISMIC RESPONSE OF A HORIZONTALLY CURVED BRIDGE MODEL

Hartanto Wibowo[1], Danielle M. Sanford[1], Ian G. Buckle[2], and David H. Sanders[3]

1) Graduate Research Assistant
2) Foundation Professor and Director of Center for Civil Engineering Earthquake Research
3) Professor
Department of Civil and Environmental Engineering, University of Nevada, Reno, USA
hwibowo@unr.edu, igbuckle@unr.edu, sanders@unr.edu

Abstract: Although it is clear that live load provides additional gravity load and dynamic force effects due to its sprung nature, the significance of these effects on the seismic response of a bridge still remains unclear. Therefore, implications of live load on the seismic response of a bridge need to be understood especially since traffic congestion has become a new normal in most major cities in the world. The main objective of this study is to investigate and obtain insight into the effect of vehicle-bridge interaction during earthquakes. The study consists of experimental and analytical work. An experimental test program was conducted that includes multiple shake table testing of a 2/5-scale model of a three-span horizontally curved steel girder bridge loaded with a series of six representative trucks. From the experimental data, a numerical model has been validated to be used in the analytical study. This model has also been used to study the effect of number of vehicles placed along the length of the bridge model. It is shown that the maximum column displacements vary in the range of approximately 15% when the number of vehicles is varied from one to six and that adverse behavior occurs with fewer vehicles.

1. INTRODUCTION

Although earthquake reconnaissance reports have shown that live load is present during earthquake events, design procedures for earthquake-resistant bridges in most countries do not require the simultaneous presence of live load and earthquake load to be considered. This decision is based on two major assumptions. First, it is unlikely that the full design live load will be on the bridge at the time of the design earthquake, and second, the seismic response of a bridge is dominated by its dead load and live load inertial effects are negligible by comparison. However for bridges in urban and metropolitan areas where congestion is a frequent occurrence, some fraction of the design live load (usually taken as 50%) is now recommended to be included with the dead load when computing gravity load effects (AASHTO, 2012). But this recommendation applies only to gravity load effects and not to inertial effects.

The omission of inertial effects in design is the result of a prevailing attitude that the suspension system of a heavy vehicle acts in a manner similar to a tuned mass damper and reduces the motion in the bridge. It is therefore believed to be conservative to ignore these effects. But in fact little is understood about the dynamic interaction between heavy vehicles and bridge systems during strong shaking and there is no hard evidence that the tuned mass damper model is universally applicable. It is equally possible that the added weight increases the inertial loads in the bridge and the corresponding displacements and forces.

An experimental shake table study was carried out in the Large-Scale Structures Laboratory at University of Nevada, Reno to obtain insights on the vehicle-structure interaction during earthquake shakings. Although the experimental study was useful to calibrate and validate the numerical model, this only represents one case of the problem. There are still possibilities for various different cases that may occur. Therefore, a set of analytical parameter studies were devised. In this paper, the effect of the number of vehicles present on the bridge is presented.

2. LITERATURE REVIEW

Currently, very little research has been conducted to resolve the live load issue. Previous work has shown that live load can either have a beneficial or an adverse effect on the structure during earthquake shaking. However, there are still uncertainties about the reason why this is so and there has been no large-scale experimental work to investigate the effects of live load on the seismic response of bridges prior to this experiment.

An earlier study by Sugiyama *et al.* (1990) used a single degree-of-freedom vehicle system that can model rolling in the transverse direction and pitching in the longitudinal

direction, but the properties are not given. The bridge was idealized as a nine-mass system with transverse and rotation inertia connected by linear springs and damper elements. A vibration test is reported on an existing steel girder bridge with and without trucks in the longitudinal and transverse directions to verify the results. In the test, two large trucks were parked facing the same direction on a portion of an existing off ramp whose girders were vibrated with an electro-hydraulic exciter. The bridge was tested with the vehicles empty and loaded to various capacities. The results show that the dynamic effect of the vehicle is more dominant in the transverse direction and the vehicle tends to reduce the response of the bridge. They also mentioned that as the exciting force level increases, the effects of nonlinearity become more apparent since the dynamic characteristics of the vehicle itself are nonlinear. These results are corroborated by Kameda *et al.* (1992) who used a 5 degree-of-freedom model in their study. These authors state that the vehicle tends to increase the bridge response when the vehicle is in the in-phase mode with the bridge and decrease the bridge response when it is in the out-of-phase mode. Moreover, they also concluded that the ratio of the fundamental frequencies of the bridge and the vehicle plays an important role for the response of the bridge.

Furthermore, another study of seismic response of a bridge with live load was done by Kawatani *et al.* (2007). They analyzed the seismic response of a steel plate girder bridge under vehicle loadings during earthquakes. The vehicles were modeled with 12 degree-of-freedom that took sway, yaw, bounce, pitch, and roll into account. The observations from the numerical analysis showed that heavy vehicles acting as a dynamic system can reduce the seismic response of bridges under a ground motion with low frequency characteristics, but the vehicles have the opposite effect and slightly amplify the seismic response of the bridge under high frequency ground motions.

Kawashima *et al.* (1994) and Otsuka *et al.* (1999) performed a series of study to determine the effect of live load on a bridge when combined with seismic load. The study modeled a two-span simply supported girder bridge with a mix of ordinary cars, modeled as additional dead load, and large trucks, each modeled with 5 degree-of-freedom. The bridge was only analyzed in the transverse direction because it was estimated that the deck response would be significantly affected by the rolling of the large trucks. The studies found that the displacement response of the girders increased by 10% when the live load was included; ductility demand at the bottom of the column also increased by 10% with live load on the bridge. This study concluded that this was not enough of an effect to be significant and safety factors can be modified to take this effect into account if they are not already sufficient enough. It was also concluded that the increase in response was due to the increase of weight, however, the effect of the large trucks was not just to increase the dead weight, and they also behaved as a mass damper.

Scott (2010) developed a simplified modeling approach for dynamic analyses to account for combined live load and seismic load. It is shown that for short-span bridges, the displacement responses are mainly due to the fundamental bridge mode. In addition, for long-span bridges, vehicle speed has small influence on the displacement and acceleration responses of the bridge.

A recent study on the effects of live load a highway bridge under moderate earthquake in the horizontal and vertical directions was reported by Kim *et al.* (2011). The study concluded that the seismic responses of the bridge are amplified when the vehicle is considered as merely additional gravity load or mass and the amplification is dependent on the relationship between the fundamental frequency of the bridge and the response spectra of the ground motion. However, when the vehicle is considered as dynamic or mass-spring-damper system, which is more realistic, the dynamic effect of the vehicle is greater than its gravity load addition effect and thus it reduces the seismic response. In addition, the study also showed that the effect of moving vehicle as compared to stationary vehicle is negligible. Therefore, it is sufficient to model the vehicle as stationary for this purpose.

The presence of multiple vehicles on a bridge can be seen as a series of mass damper placed on a structure. Therefore, the effects of vehicles on the bridge may be observed as if multiple mass dampers, not necessarily tuned, on a structure. Some articles have discussed the effects of multiple tuned mass dampers (MTMD) on structure (Xu and Igusa, 1992; Abé and Fujino, 1994; Park and Reed, 2001). The results show that MTMD system is slightly more effective in reducing the seismic demand since it operates in a broader range of frequency. Another possibility to explain the effect of vehicles on the bridge is that the suspension system behaves as passive nonlinear energy sinks. The concept of nonlinear energy sinks (NES) is similar to a tuned mass damper but the stiffness of the secondary system is nonlinear which makes it become load dependent but can dissipate the energy more efficiently. This has been shown to reduce the demand in the structure subjected to seismic loading (Wierschem *et al.*, 2011; Wierschem *et al.*, 2012). The nonlinear nature of the vehicle suspension system can be thought as NES in this sense.

3. OVERVIEW OF BRIDGE MODEL AND REPRESENTATIVE VEHICLE IN EXPERIMENT

A three-span, curved bridge model was tested on the NEES Shake Table Array in the Large-Scale Structures Laboratory at University of Nevada, Reno. This 0.4-scale model has a steel plate girder superstructure, single-column reinforced concrete substructures, and seat-type abutments, as shown in Figure 1. Overall dimensions of the bridge model are shown in Table 1 below.

The bridge model has a total length of 145 ft [44.196 m], a total width of 12 ft [3.658 m], and subtended angle of 104° as shown in Figures 1 and 2. Each bent has a single circular column. The column height is 7 ft - 8 in [2.337 m] with a diameter of 24 in [0.61 m]. The superstructure is a

three-span, three-girder steel bridge with concrete deck. The detail of the superstructure and the column can be seen in Figure 2. The superstructure is supported by fixed (rotation-only) pot bearings at the bent locations and sliding bearings at the abutments. Moreover, shear keys are provided at the abutments to restrain movement in the radial direction during small amplitude earthquakes, but are designed to fail at higher events to protect the abutment foundations against damage.



Figure 1 Wide-Angle Lens View of the Bridge Model with Vehicles in the Large-Scale Structures Laboratory

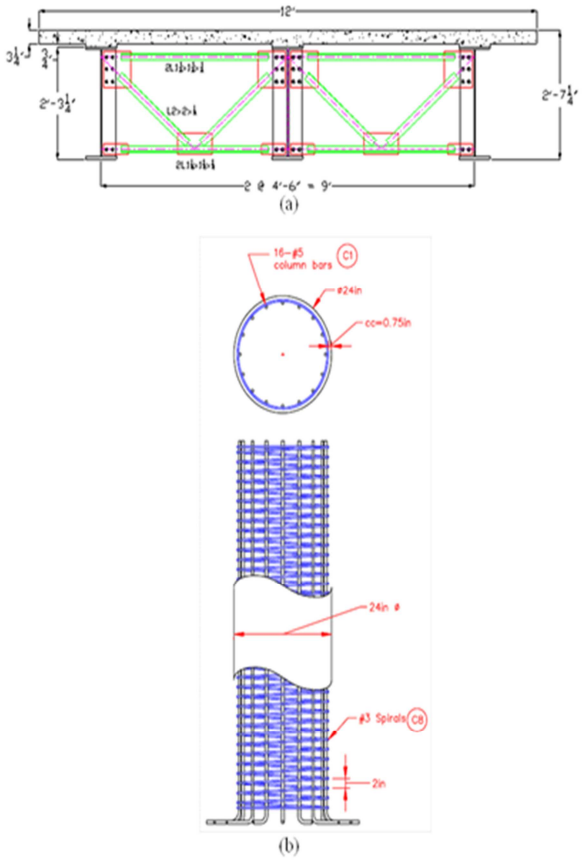


Figure 2 Typical (a) Superstructure and (b) Column Details

Table 1 Summary of Bridge Geometry

Parameter	Prototype	Model
Total Length	362.5'-0"	145'-0"
Span Lengths	105'-0", 152'-6", 105'-0"	42'-0", 61'-0", 42'-0"
Radius at Centerline	200'-0"	80'-0"
Subtended Angle	104° (1.8 rad)	104° (1.8 rad)
Total Width	30'-0"	12'-0"
Girder Spacing	11'-3"	4'-6"
Total Superstructure Depth	6'-6⅛"	2'-7¼"
Column Height	19'-2"	7'-8"
Column Diameter	5'-0"	2'-0"

The prototype bridge was designed for a site in Seismic Zone 3 (AASHTO, 2012) with a 1,000-year spectral acceleration at 1.0 second (S1) of 0.4 g. Under this Design Earthquake (DE), the bridge is expected to be damaged but not collapse. The record selected as the input motion for the experimental studies was the Sylmar record from the 1994 Northridge Earthquake near Los Angeles, scaled to have the same spectral acceleration at 1.0 second. A scale factor of 0.475 was therefore applied to both the NS and EW time histories of ground acceleration from this station.

The starting point for selection of the test vehicle was the H-20 truck, which is a two-axle vehicle weighing 40 kip [178 kN] (8 kip [35.6 kN] on the front axle and 32 kip [142.4 kN] on the rear axle) with a 14 ft [4.267 m] wheel base. For a 0.4-scale model, the model truck would have a wheel base of 5.6 ft [1.707 m], a width of 2.4 ft [0.732 m], and weigh 6.4 kip [28.48 kN]. Since such a vehicle would most likely have to be custom-built and thus not economically feasible, the decision was made to select from commercially available vehicles. The closest vehicle to match the modeling requirements and constraints of the experimental setup was found to be the Ford F-250. The overall dimensions and weight ratings of this vehicle are presented in Table 2. If six vehicles were placed on the bridge, the mass ratio was found to be approximately 20%. Although the similitude requirements are not fully satisfied, the dynamic properties of the chosen vehicle can produce similar effects to those of the target vehicle.

Table 2 Ford F-250 Dimensions and Weight Ratings

Parameter	Value
Overall Length	247 in [6.274 m]
Overall Width	68 in [1.727 m]
Overall Height	80 in [2.032 m]
Wheel Base Length	156 in [3.962 m]
Ground Clearance	7.9 in [0.201 m]
Curb Weight	6.7 kip [29.815 kN]
Gross Vehicle Weight Rating	10 kip [44.500 kN]
Max. Allowable Payload	2.3 kip [10.235 kN]

4. OVERVIEW OF NUMERICAL MODEL IN ANALYSIS

In the finite element model developed for SAP2000, the superstructure is modeled with shell elements, the substructure with frame elements, and column plastic hinges with fiber elements. The abutment towers used in the experiment are also included in the model as shown in Figure 3 below.

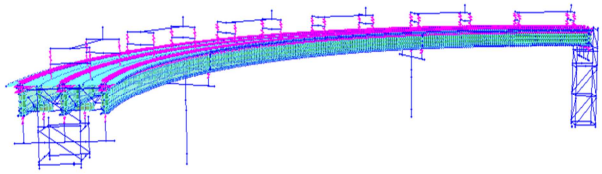


Figure 3 Finite Element Model of Bridge with Vehicles

Two different boundary conditions were modeled to represent the sacrificial shear keys at the abutments in their intact and failed states, as follows:

1. Intact shear keys located in the inner bay of the abutment cross frames allowing tangential movement but restraining radial displacement, i.e. tangentially free, radially restrained condition (TFRR).
2. Failed shear keys that provided no restraint at the abutments in any direction, i.e., free condition (Free).

In addition, no vertical restraint was imposed at the abutments which were therefore free to uplift as necessary. Pinned bearings were assigned to each girder over the bents, which allowed rotation about any axis but restrained displacement in both horizontal and vertical directions.

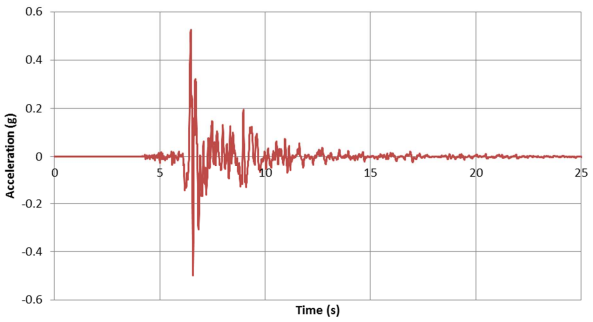
In the numerical model, the vehicle is modeled as a 16 degree-of-freedom, mass-spring-damper system, as shown in Figure 3. The mass is distributed in the suspension and axle levels and each spring or damper represents the stiffness or damping at suspension or axle/tire levels. This model is an expansion of the vehicle model that was used by Kim *et al.* (2005). The properties of the vehicle were obtained from single truck experiments carried out previously on one of the shake tables at the University of Nevada, Reno. The results of these experiments gave stiffness and damping values in the vertical, transverse, and longitudinal directions both for an empty and fully loaded vehicle. Table 3 summarizes the properties of the fully loaded vehicle, which is used in the numerical model.

5. EARTHQUAKE INPUT MOTION

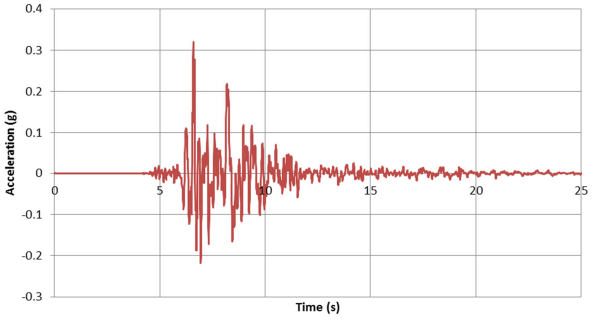
As previously mentioned, the bridge model was subjected to Sylmar record of the 1994 Northridge Earthquake scaled accordingly to match the design spectrum at the period of 1 s. The acceleration histories used as the input motion for the analytical study were the average of the table accelerations in the longitudinal and transverse directions, as measured in the laboratory. The observed accelerations for each table were found to be within reasonable agreement with each other and all four tables were deemed to be moving synchronously. Averaging to obtain input motions for the analytical studies was therefore considered appropriate. In addition, filtering and base-line correction were also applied to obtain the final input acceleration histories. These are shown for the longitudinal and transverse directions of the 100% design earthquake (DE) run in Figures 4a and 4b, respectively.

Table 3 Fully Loaded Vehicle Dynamic Properties

	Direction	Suspension Level			Tire Level		
		Stiffness (kip/in)	Damping (kip.s/in)	Damping Ratio (%)	Stiffness (kip/in)	Damping (kip.s/in)	Damping Ratio (%)
Front	Vertical	0.459	0.037	25.92	3.48	0.000	0.00
	Transverse	1000	0.000	0.00	1.73	0.000	0.00
	Longitudinal	1000	0.000	0.00	0.56	0.000	0.00
Rear	Vertical	0.718	0.041	19.89	3.48	0.000	0.00
	Transverse	1000	0.000	0.00	1.73	0.000	0.00
	Longitudinal	1000	0.000	0.00	0.56	0.000	0.00



(a)



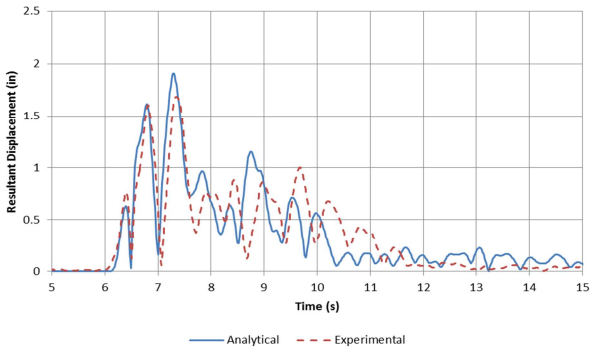
(b)

Figure 4 Input Acceleration Histories in (a) Longitudinal and (b) Transverse Directions for 100% DE Run

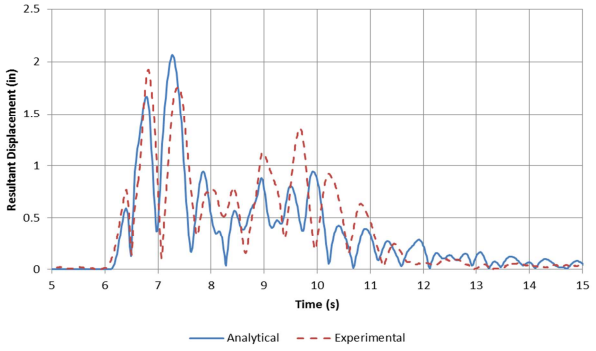
6. NUMERICAL MODEL VALIDATION

Analysis results for the 100% DE are presented below. For this earthquake, the boundary conditions at the abutments were taken to be 'free' since the shear keys failed during the 75% DE run for the experiment without live load, and during the 100% DE run for the case with live load. During the course of the experiment, it was observed that live load had a beneficial effect on the seismic response of the bridge model and that column damage was less with live load than without. In order to represent the different levels of inelasticity in the column with and without live load, different EI modifiers were used in the numerical model for these two cases. For 100% DE, the modifier with and without live load was taken to be 60% and 30% respectively.

Figures 5a and 5b show comparisons between the analytical and experimental results for resultant displacement histories under 100% DE for the north and south columns, respectively. It is seen that the analytical results for peak values have good agreement in magnitude to the experimental results. The agreement later in the record is not as favorable and indicates further refinements to the bridge and vehicle models can be done. Nonetheless, the numerical model developed can provide good estimation of the peak displacement as a measure of the seismic demand in the structure.



(a)



(b)

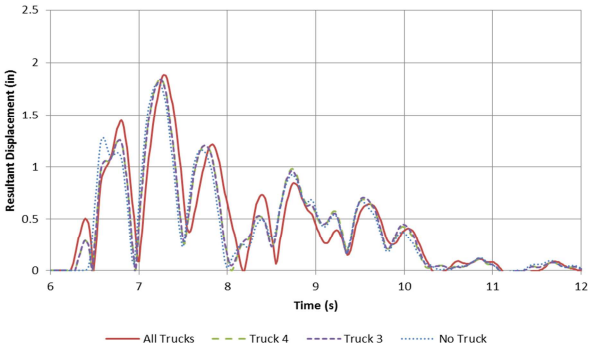
Figure 5 Analytical and Experimental (a) North and (b) South Column Resultant Displacement Histories Comparison under 100% DE

Some of the results from the experimental study suggested that live load gave beneficial effects for this particular bridge model and earthquake excitation (Wibowo *et al.*, 2012). The presence of live load was shown to impede the cracks or damage in the columns and reduce the movement of the structure. These could be due to the vehicles acted as multiple mass dampers and/or the vehicle suspension acted as nonlinear energy sinks, as mentioned earlier, besides some experimental differences between the experiment cases with and without live load.

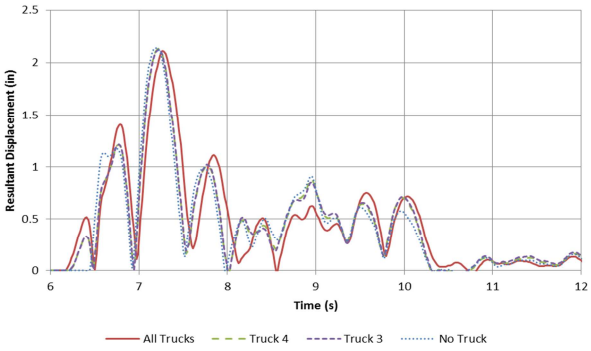
7. PARAMETER STUDY RESULTS

As previously mentioned, this parameter study tries to investigate the effect of varying the number of vehicles on the deck to the seismic response of the bridge. The trucks are numbered 1 through 6 starting from the north end of the bridge. The displacement histories obtained analytically from several cases are presented herein.

Two cases of one vehicle present were analyzed. One is only Truck 3 and another is only Truck 4 present. Figures 6a and 6b show the resultant displacement histories at the top of north and south bents during 100% DE. It is observed that when only one vehicle is present, the displacement of the north column is slightly reduced while the displacement of the south column is slightly increased compared to when all six trucks are present.

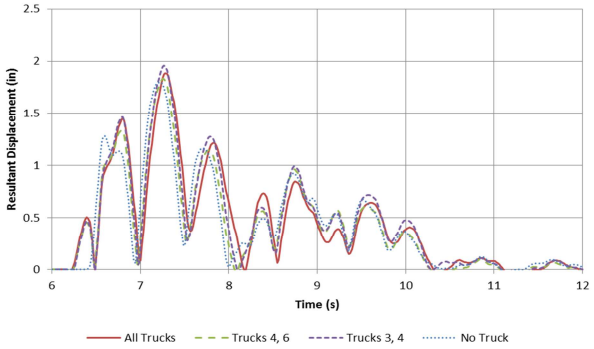


(a)

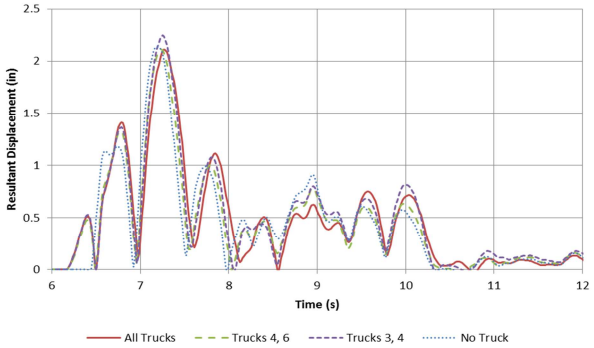


(b)

Figure 6 (a) North and (b) South Column Resultant Displacement Histories for One-Vehicle Case

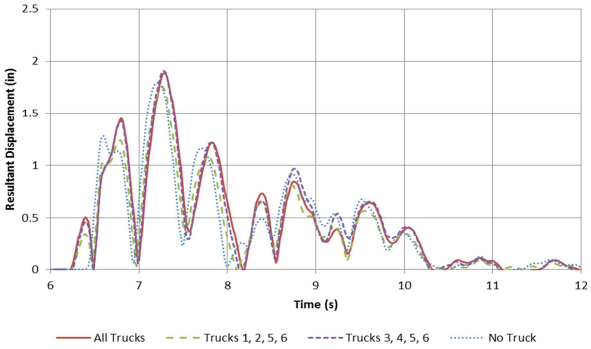


(a)

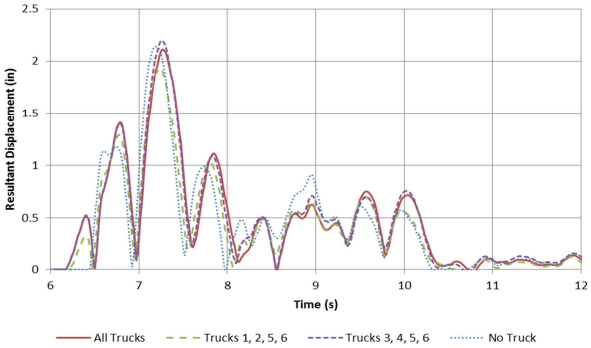


(b)

Figure 7 (a) North and (b) South Column Resultant Displacement Histories for Two-Vehicle Case

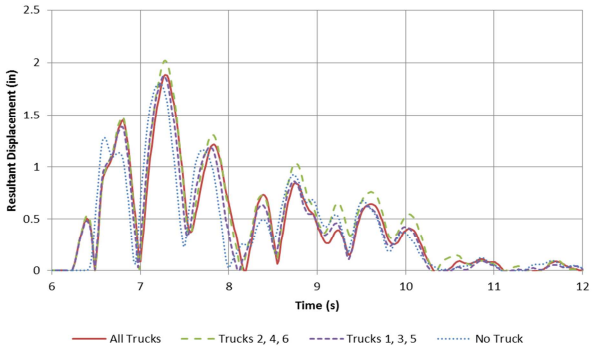


(a)

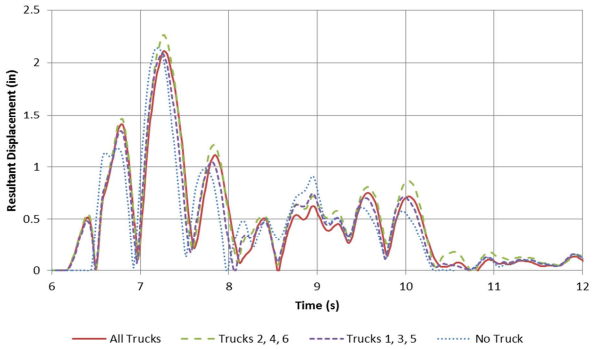


(b)

Figure 9 (a) North and (b) South Column Resultant Displacement Histories for Four-Vehicle Case

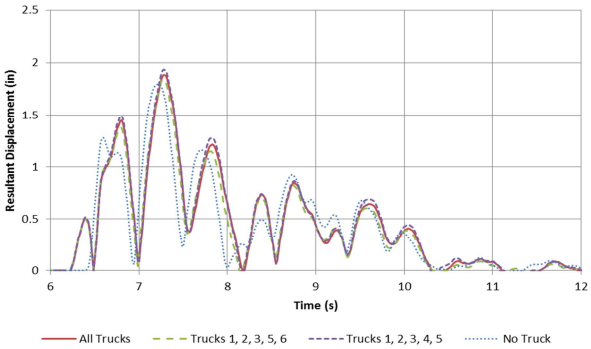


(a)

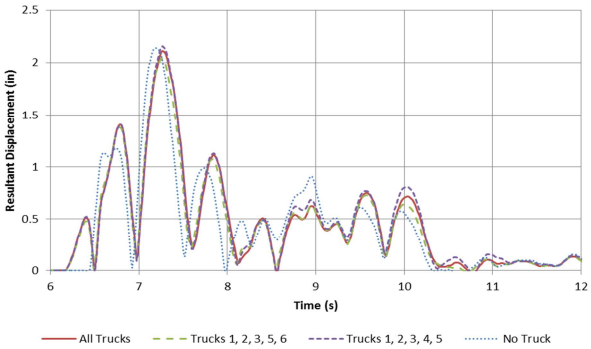


(b)

Figure 8 (a) North and (b) South Column Resultant Displacement Histories for Three-Vehicle Case



(a)



(b)

Figure 10 (a) North and (b) South Column Resultant Displacement Histories for Five-Vehicle Case

For two vehicles present, two cases are presented. One case is when Trucks 4 and 6 are present and another when Trucks 3 and 4 are present. The resultant displacement histories for these cases are presented in Figure 7. Trucks 3 and 4 are the ones closest to the center span of the bridge. When two vehicles are placed on the middle, the resultant displacement demand is increased compared to when all six trucks are present. However, the opposite observation is true when only Trucks 4 and 6 are present, which in this case the resultant displacement demand is decreased.

When comparing two cases of three vehicles present, which are Trucks 1, 3, 5 and Trucks 2, 4, 6 cases, it is shown that the latter case gives the greatest maximum resultant displacement demand of all cases. The maximum resultant displacements were found to be 2.02 in [5.13 cm] and 2.26 in [5.74 cm] for the north and south bents, respectively. The resultant displacement histories at the top north and south bents for these cases are shown in Figure 8.

While the greatest maximum resultant displacement was found in the case where three vehicles are present, the least maximum resultant displacement was found in the case where four vehicles are present. As depicted in Figure 9, the least maximum bent displacements were obtained when Trucks 1, 2, 5, and 6 are present, which were found to be 1.75 in [4.45 cm] for north bent and 1.93 in [4.90 cm] for south bent. Trucks 1 and 2 are located on the north end of the bridge while Trucks 5 and 6 are located on the south end of the bridge. Moreover, when four vehicles were grouped on one side of the bridge such as the case when Trucks 3, 4, 5, and 6 are present, the displacement of the columns is very close to the case when all six trucks are present.

Table 4 Comparison of Maximum Displacements from Various Cases

Truck(s)	Mass Ratio	Max. Disp. (in)		Disp. Ratio	
		North Bent	South Bent	North Bent	South Bent
3	0.031	1.842	2.127	0.976	1.007
4		1.853	2.135	0.982	1.011
3,4	0.063	1.957	2.245	1.037	1.063
4,6		1.833	2.112	0.972	1.000
1,3,5	0.094	1.873	2.088	0.993	0.988
2,4,6		2.021	2.263	1.071	1.071
1,2,5,6	0.125	1.754	1.929	1.930	0.913
3,4,5,6		1.907	2.200	1.011	1.041
1,2,3,5,6	0.157	1.842	2.038	0.976	0.965
1,2,3,4,5		1.939	2.158	1.028	1.021
1,2,3,4,5,6	0.188	1.887	2.112	1.000	1.000

The resultant displacement histories from cases where five vehicles are present are shown in Figure 10. Similarly, two cases were investigated. One is when Trucks 1, 2, 3, 4, and 5 are present and another is when Trucks 1, 2, 3, 5, and 6 are present. From these two cases, the displacement of the columns was found to have little difference than the case when all six trucks are present.

Table 4 presents the comparison of the maximum resultant displacements at the top of north and south bents obtained from various different cases. The mass ratio is the ratio of the mass of the vehicle(s) to the total mass of the structure and it ranges from 3.1% to 18.8%. The displacement ratio is the ratio of maximum displacement of a particular case to the maximum displacement when all trucks are present.

From the results presented, it is shown that the maximum displacement varies in the range of approximately 15% when the number of vehicles is changed from one, two, three, four, five, and six. Moreover, this shows that the presence of live load alters the dynamic behavior of the structure and the problem is not merely an additional gravity load. For cases of the same mass ratio, the seismic response of the structure can be different depending on the placement of the vehicles.

8. CONCLUDING REMARKS

From the data presented in this paper, several observations can be made:

1. The developed numerical model has been validated and is shown to have good agreements with the experiment results.
2. The beneficial effects observed in the experiment results could be due to multiple mass dampers and nonlinear energy sinks effects.
3. The change in the maximum displacement demand at the top of the bents ranges up to approximately 15% when the number of vehicles is varied from one to six.

In addition, more parameter studies are currently ongoing to better understand the behavior of vehicle-bridge interaction during earthquakes and to obtain the limits of when live load gives beneficial and adverse effects.

Conversion Table:

From	To	Multiply by
in	mm	25.4
ft	mm	304.8
kip	kN	4.45

Acknowledgements:

This project was funded by California Department of Transportation (Caltrans) under contract number 59A0695 and the Federal Highway Administration (FHWA) under contract number DTFH61-07-C-00031: Improving the Seismic Resilience of the Federal Aid Highway System. The Caltrans Program Manager was Dr. Allaoua Kartoum and the FHWA Contracting Officer's Technical Representative was Dr. Wen-huei (Phillip) Yen. The Principal Investigator was Dr. Ian Buckle and the co-investigators included Drs. Ahmad Itani, Manos Maragakis, Gökhan Pekcan, and David Sanders. The project manager was Kelly Doyle. A number of graduate students have worked on this project including Nathan Harrison, Ebrahim Hormozaki, Michael Levi, Eric Monzon, Ahmad Saad, Chunli Wei, and Joseph Wieser. In addition, Dr. Arash

Esmaili Zaghi (Post-doctoral Scholar) and Moustafa Al-Ani (Visiting Researcher) have also provided valuable assistance with the project. The authors would also like to acknowledge the National Science Foundation for the use of NEES Shake Table Array at the University of Nevada, Reno under a Shared-Use Agreement with NEEScomm at Purdue University.

References:

AASHTO. (2012). "AASHTO LRFD Bridge Design Specifications, Customary U.S. Units, 6th Edition," Washington, DC: AASHTO.

Abé, M. and Fujino, Y. (1994). "Dynamic Characterization of Multiple Tuned Mass Dampers and Some Design Formulas.," *Earthquake Engineering and Structural Dynamics*, **23**(8), pp. 813-835.

Kameda, H., Murono, Y., Maekawa, Y., and Sasaki, N. (1992). "Dynamic Structure-Vehicle Interaction for Seismic Load Evaluation of Highway Bridges," *Proceedings of the Tenth World Conference on Earthquake Engineering*, Madrid, Spain, July 19-24, pp. 4861-4866.

Kawashima, K., Unjoh, S., and Mukai, H. (1994). "Research on Live Load Effect to Earthquake Response of Bridges (Part 1)," PWRI Research Report No. 3316, 59 pp. (In Japanese)

Kawatani, M., Kim, C. W., and Yasui, K. (2007). "Seismic Response of a Highway Bridge under Traffic Loadings," *Proceedings of Pacific Structural Steel Conference 2007: Steel Structures in Natural Hazards*, Wairakei, New Zealand, March 13-16, pp.183-188.

Kim, C. W., Kawatani, M., and Kim, K. B. (2005). "Three-Dimensional Dynamic Analysis for Bridge-Vehicle Interaction with Roadway Roughness," *Computers and Structures*, **83**(19-20), pp. 1627-1645.

Kim, C. W., Kawatani, M., Konaka, S., and Kitaura, R. (2011). "Seismic Responses of a Highway Viaduct Considering Vehicles of Design Live Load as Dynamic System during Moderate Earthquakes," *Structure and Infrastructure Engineering*, **7**(7-8), pp. 523-534.

Otsuka, H., Unjoh, S., and Mukai, H. (1999). "Research on Live Load Effect to Earthquake Response of Bridges (Part 2)," PWRI Research Report No. 3355, 40 pp. (In Japanese)

Park, J. and Reed, D. (2001). "Analysis of Uniformly and Linearly Distributed Mass Dampers under Harmonic and Earthquake Excitation," *Engineering Structures*, **23**(7), pp. 802-814.

Scott, M. H. (2010). "Combined Seismic Plus Live Load Analysis of Highway Bridges," Report OTREC-RR-09-261. Portland: Oregon Transportation Research and Education Consortium.

Sugiyama, I., Kameda, H., Sasaki, N., and Kawakita, S. (1990). "Dynamic Structure-Vehicle Interaction of Highway Bridges and Its Implication to Seismic Design," *Proceedings of the 6th U.S.-Japan Bridge Engineering Workshop*, Lake Tahoe, NV, May 7-8, pp. 379-392.

Wibowo, H., Sanford, D. M., Buckle, I. G., and Sanders, D. H. (2012). Effects of Live Load on Seismic Response of Bridges: A Preliminary Study. *Civil Engineering Dimension*, **14**(3), pp. 166-172.

Wierschem, N. E., Spencer, Jr., B. F., Bergman, L. A., and Valakis, A. F. (2011). "Numerical Study of Nonlinear Energy Sinks for Seismic Response Reduction," *Proceedings of the 6th International Workshop on Advanced Smart Materials and Smart Structures Technology (ANCRiSST 2011)*, Dalian, China, July 25-26, 9 pp.

Wierschem, N. E., Quinn, D. D., Hubbard, S. A., Al-Shudeifat, M. A., McFarland, D. M., Luo, J., Fahnestock, L. A., Spencer, Jr., B. F., Vakakis, A. F., and Bergman, L. A. (2012). "Passive Damping Enhancement of a Two-Degree-of-Freedom System through a Strongly Nonlinear Two-Degree-of-Freedom Attachment," *Journal of Sound and Vibration*, **331**(25), pp. 5393-5407.

Xu, K. and Igusa, T. (1992). "Dynamic Characteristics of Multiple Substructures with Closely Spaced Frequencies," *Earthquake Engineering and Structural Dynamics*, **21**(12), pp. 1059-1070.

10CUEE CONFERENCE PROCEEDINGS
10th International Conference on Urban Earthquake Engineering
March 1-2, 2013, Tokyo Institute of Technology, Tokyo, Japan

INVESTIGATION OF THE RESISTANCE OF OLDER STEEL BRIDGE BEARINGS UNDER BIDIRECTIONAL SEISMIC LOADING

Xiaohu Fan[1] and Jason McCormick[2]

1) Graduate Research Assistant, Dept. of Civil and Environmental Engineering, University of Michigan, Ann Arbor, MI USA
2) Assistant Professor, Dept. of Civil and Environmental Engineering, University of Michigan, Ann Arbor, MI USA
xhfan@umich.edu, jpmccorm@umich.edu

Abstract: As highway bridges approach their design life, concerns of the influence of aging on their seismic performance increase. In particular, a large number of highway bridges still utilize steel bearings that have been shown to be susceptible to failure in the past. This paper presents the results from a numerical study used to investigate the lateral response of a typical highway bridge with steel bearings under various ground motions. Previous finite element results and theoretical findings are used to develop hysteretic models of the bearing behavior in each orthogonal direction considering the effects of corrosion and axial load level. Nonlinear time history analyses are conducted for a suite of bidirectional ground motions and the longitudinal and transverse displacements are compared to allowable displacement levels representing potential failure modes. The results provide information on expected maximum lateral displacements in bridges with steel bearings and potential need for retrofit or rehabilitation.

1. BACKGROUND

Failures of highway bridges during past seismic events have been associated with the use of steel bridge bearings. Many older bridges, particularly those located in the Central and Eastern United States, continue to use steel bearings as a mechanism for transferring load from the superstructure to the substructure while also accommodating displacements and rotations caused by thermal changes and vehicular motion. The continued use of older steel bearings combined with moderate to high seismic regions in the Central and Eastern United States (i.e. New Madrid Seismic Zone and Charleston South Carolina Seismic Zone) result in the potential for bridge damage, loss of evacuation routes, and economic impact from an earthquake (Nielson and DesRoches 2008). Given the vital role highway bridges play in transportation networks, there is increased concern regarding seismic performance given their deteriorated in-situ condition (Padgett and DesRoches 2008).

Steel bearings are assemblages of steel components in various geometric forms that utilize rolling and sliding mechanisms between steel surfaces to permit small translations and rotations (Chen and Duan 2003). These bearings often can regain their original positions after small perturbations due to the restoring mechanism associated with their geometric form. However, these bearings are not designed to accommodate large displacements and rotations that can result from a seismic event and knowledge of their behavior under earthquake loads, even in a pristine condition, is limited.

Lack of routine maintenance, such as regular painting and lubricating of the contact surfaces can lead to severe corrosion in steel bearings. Corrosion can result in material loss, section reduction, and decreased stiffness of steel components (Kayser and Nowak 1989). As a result, corrosion can significantly alter the mechanical mechanisms that steel bearings depend on to function properly. Also, debris and corrosion products can accumulate between contact surfaces causing locking of the bearing and interfering with the rolling and sliding mechanism. Locking can then lead to unanticipated and unfavorable lateral forces in the bearing. It has been observed that locking has caused unseating of spans and toppling of the steel bearings due to excessive lateral forces even under only vehicular braking action (Splitstone et al. 2010).

In a seismic event, highway bridges are subjected to large loads and have demonstrated poor performance in the past (Bruneau et al. 1996; Housner and Thiel 1995; and Mitchell et al. 1995). A variety of failure modes for steel bearings has been observed during past earthquakes such as lateral instability, bearing connection fracture, steel component fracture (i.e. keeper plate and stopper), and strength failure (i.e. anchorage failure). Common highway bridge failures owing to failure of steel bearings during an earthquake include damaged piers, unseated or collapsed spans, localized buckling of steel girders, and rupture of end diaphragms.

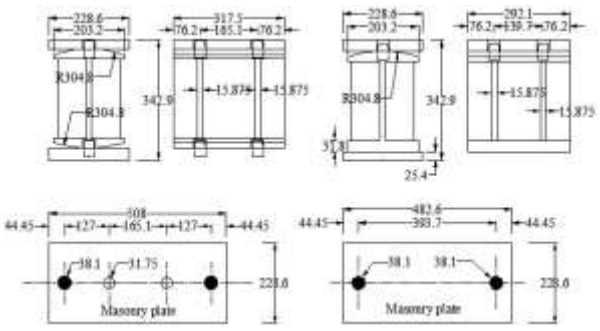
Past studies of the seismic response of steel bridge bearings and their influence on the performance of bridges under earthquakes are limited due to a multitude

of reasons. The most obvious reason is that in regions of frequent seismic activity, most highway bridges have been upgraded or retrofitted with elastomeric or other types of seismic bearings. In addition due to the secondary role they play, steel bearings are often overlooked in the seismic research of bridges (Mander et al. 1996). Yet, an accurate account of the seismic behavior of steel bearings is crucial in assessing the true seismic performance of an in-situ bridge, particularly one that has deteriorated significantly due to corrosion.

In this study a set of hysteretic models is proposed for steel bridge bearings based on the results of a previous finite element study of the cyclic behavior of corroded steel bridge bearings (Fan and McCormick 2011; Fan and McCormick 2012). The hysteretic models are implemented in a model of a simply supported bridge to investigate the maximum lateral displacements of steel bearings under a suite of ground motions. Aging effects are also examined by looking into the influence of friction on the overall seismic response of the bridge. The influence of the superstructure weight on the lateral response of the bridge also is studied.

2. HYSTERETIC MODELS OF STEEL BEARINGS

The lateral response of steel bearings in the two orthogonal directions, longitudinal and transverse, is of concern. A previous finite element study (Fan and McCormick 2012) simulated both the longitudinal and transverse behavior for two prevalent rocker (expansion) and bolster (fixed) bearing types (Figure 1). The rocker bearing, also known as an expansion bearing, permits both longitudinal translation and rotation about the transverse axis while the bolster bearing, also known as a fixed bearing, only accommodates rotation about the transverse axis. From the finite element results, the hysteretic models are created using a combination of existing material models (e.g. Steel01, ElasticPPGap, and Hysteretic) in the Open System for Earthquake Engineering Simulation (OpenSEES 2012).



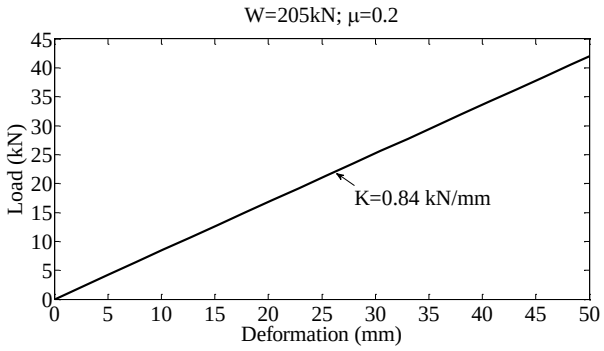
(a) Rocker Bearing (b) Bolster Bearing

Figure 1 Configuration and Dimensions (mm) of the Bearings

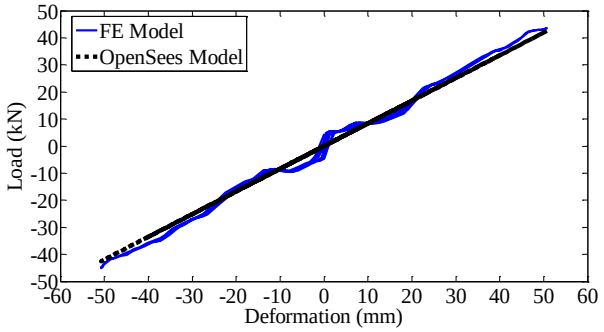
2.1 Rocker bearing models

The results of the finite element study show that the rocker bearing exhibits a constant longitudinal stiffness. A theoretical derivation by Fan and McCormick (2012) reached the same conclusion and determined that this behavior was associated with the rolling mechanism along the rocker bearing's cylindrical contact surface. As a result of this constant longitudinal stiffness, the load-displacement relationship in the longitudinal direction displays a linear behavior that can be mathematically described by Eq. (1). This behavior is captured well using the elastic material model available in the OpenSEES (Figure 2). However, the linear behavior is only applicable until the displacement capacity of the bearing is reached. For the rocker bearing considered in this study, a displacement capacity of 64 mm is assumed. Previous studies also revealed that the rolling mechanism of the rocker bearing is influenced by the axial load and geometry of the rocker body, not by the sliding friction coefficient (Fan and McCormick 2012). This finding suggests that section reduction due to corrosion can influence a rocker bearings longitudinal response.

$$H = W\frac{2R-h}{h^2}u \qquad (1)$$



(a) Model Based on FEM Findings

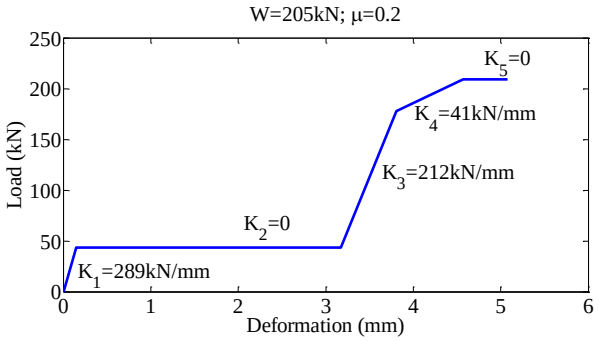


(b) Validation of the Proposed Model

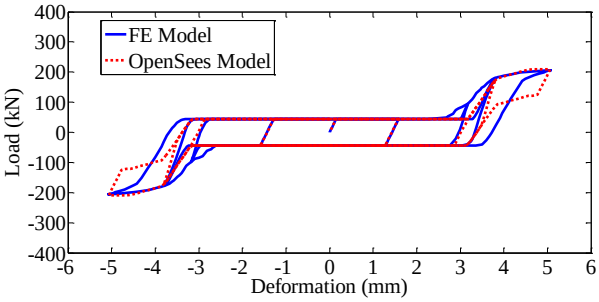
Figure 2 Longitudinal Model for the Rocker Bearing

In the transverse direction, the rocker bearing is designed to be rigid under service loads, such as thermal action and vehicular forces. However, the rocker bearing

is predisposed to experience instability under large lateral forces due to the nature of the rocker bearing assemblage. The previous finite element study indicates a limited sliding behavior and then instability as lateral displacements or loads increase (Fan and McCormick 2012). The sliding behavior is attributed to the gap between holes in the masonry plate and sole plate and the pintles in the bearing body that prevent lateral translation at the top and bottom rocker bearing contact surfaces. A slight elongation of the sliding plateau is observed in the finite element study from the accumulation of plastic shear deformation in the pintles. The load-deformation behavior under transverse loading captures both the observed sliding and the loss of stiffness with continued displacement (Figure 3). The OpenSEES model captures the observed behavior from the finite model well, but cannot account for the increase in the sliding plateau due to plastic deformation of the pintles and shows some small differences in the unloading behavior. However, these differences are minor. Toppling of the rocker bearing is not explicitly accounted for, but is assumed to occur when the transverse displacement reaches 5 mm.



(a) Model Based on FEM Findings

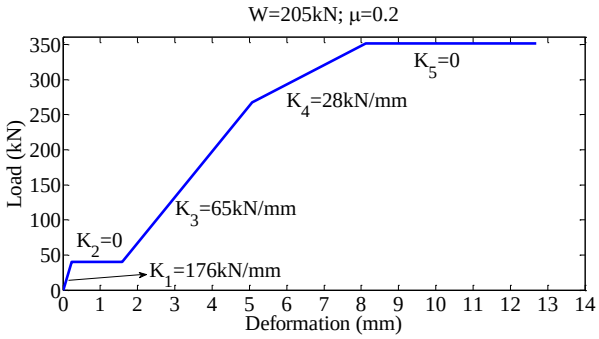


(b) Validation of the Proposed Model

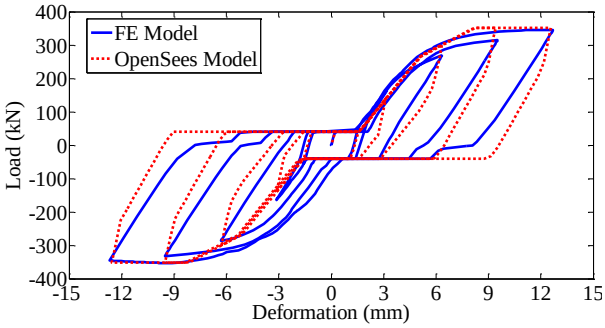
Figure 3 Transverse Model for the Rocker Bearing

2.2 Bolster bearing models

The behavior of the bolster bearing is highly nonlinear in both the longitudinal and transverse directions. This nonlinear behavior depends on the transfer of load through contact, friction, and anchorage elements. From the finite element study, it is found that the bolster bearing has a larger displacement capacity in the longitudinal direction as compared to the transverse direction. This displacement capacity is due to the fact that under longitudinal displacement the bearing bends about its weak axis and the anchor rods provide only a single line of resistance at the centroid of the bearing. Conversely under transverse displacements, bending occurs about the strong axis of the bearing body and the two anchor rods form a couple moment to resist overturning leading to a much stiffer response. The overall behavior in both directions consists of an initial elastic response until the friction coefficient is overcome causing rigid sliding. Once the available sliding distance associated with the oversize of the pintles holes is overcome, a hardening response is observed until loss of stiffness and failure. The adopted hysteretic models in OpenSEES shows similar behavior in the two orthogonal directions while accounting for the difference in the stiffness as illustrated in Figure 4 and 5.



(a) Model Based on FEM Findings



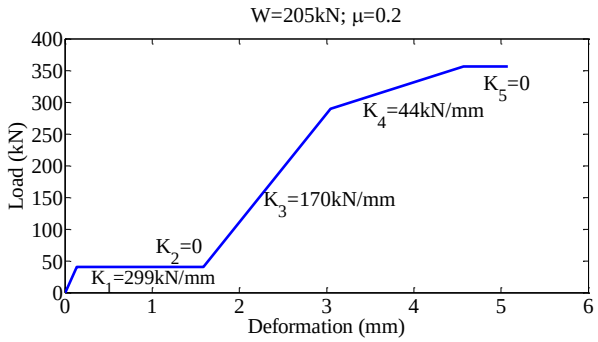
(b) Validation of the Proposed Model

Figure 4 Longitudinal Model for the Bolster Bearing

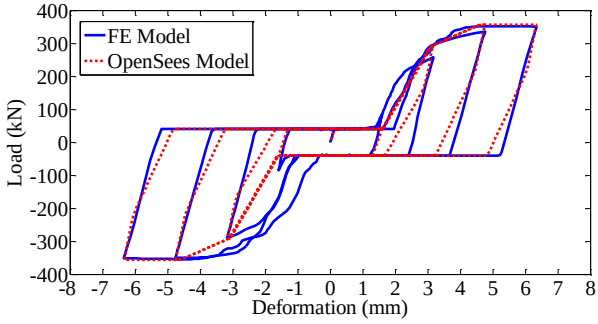
The rigid sliding portion at the initial loading stage in the model for both the longitudinal and transverse behavior is a result of the clearance that exists between the pintle hole and the pintle. Rocking and prying dominate the deformation mode of the bolster bearing and dictate the failure pattern as illustrated by the hardening portion in the OpenSEES models. Degradation of the bearing after reaching its ultimate strength is not explicitly addressed in the current models. Instead, a failure criterion is defined using allowable displacements. For the longitudinal behavior of the considered bolster bearings, the allowable displacement is assumed to be 13 mm, while 6.4 mm is used for the transverse behavior.

As shown in Figures 4 and 5, the proposed OpenSEES models for the bolster bearing agree well with

the finite element results with only minor differences at certain loading and unloading regions. The examples shown in the figures for the bearing models are all derived for an axial load of 205 kN and a friction coefficient of 0.2. Considering different bridge configurations and various corrosion levels, both the axial load and friction behavior are subject to change. Nevertheless, similar procedures are applied to generate and update the current bearing models to account for these differences based on the finite element study by Fan and McCormick (2012).



(a) Model Based on FEM Findings



(b) Validation of the Proposed Model

Figure 5 Transverse Model for the Bolster Bearing

3. MODEL DESCRIPTION

3.1 Bridge Model

The rocker and bolster bearings modeled in this study are based on those from a typical steel girder highway bridge found in the Central and Eastern United States. These bearings are similar to other steel bearings used throughout the world and function based on similar mechanisms to accommodate thermal expansion and vehicular loads. The highway bridge has four continuous spans of varying lengths and a composite superstructure consisting of concrete slabs and wide-flange steel girders. As a result of the configuration of the bridge, the steel bearings that support the outside girders sustain different axial loads than those supporting the interior girders. However to simplify the study, a simply supported single span bridge resembling the main span of the highway bridge is modeled. One pair of rocker and bolster bearings is located at each end of the span, respectively. The simply supported bridge has a net span of 17.83 m and a width of 9.14 m. The weight of the superstructure accounts for both the concrete slab and two steel girders.

To better understand the potential behavior of the bearings under varying earthquake loads and deteriorated conditions, several assumptions are made in modeling the bridge. First, the bridge superstructure is idealized as rigid with mass being assigned to the center of the block. Also, the interaction between the abutment and the superstructure is ignored for the purpose of investigating the maximum displacement of the bridge under earthquake loads. Third, the bearings on each end of the span are lumped together such that the rigid superstructure is supported at the four corners. A detailed illustration of the bridge model is provided in Fig. 6.

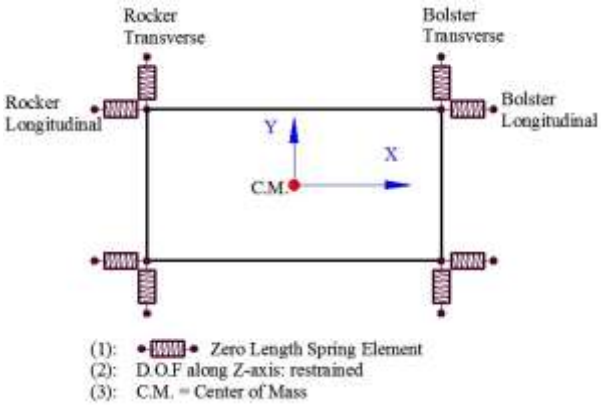


Figure 6 Schematic of the Bridge Model

3.2 Ground Motion Information

Since the bearings being considered are typically found in the Central and Eastern United States, ten pairs of ground motion accelerations representing a 2% probability of exceedance in 50 years for the Boston, MA area are used to evaluate the behavior. Each pair of ground motions has two orthogonal components, one normal to the fault and another parallel to the fault. For all nonlinear time history analyses, the normal component is applied along the longitudinal direction of the bridge while the parallel component is applied in the transverse direction allowing the effects of bi-directional motion to be evaluated. A detailed description of the ground motions is provided in Table 1 while the response spectra for the set of ground motions are shown in Fig. 7. Figure 7 suggests that the ground motions in each orthogonal direction have almost identical response spectrum. The mean peak pseudo acceleration occurs at a period of roughly 0.12 seconds for both components. The normal component produces a mean peak pseudo acceleration of approximately 0.13g while the parallel component has a mean peak pseudo acceleration of 0.11g. This suggests that the ground motion set is insensitive to directivity effects.

Table 1 Ground Motion Data, 2% Exceedance in 50 Years

EQ	Description	Magnitude	Distance (km)	PGA (g's)
bo21	fn simulation, foot wall	6.5	30	0.32
bo22	fp simulation, foot wall	6.5	30	0.36
bo23	fn simulation, foot wall	6.5	30	0.34
bo24	fp simulation, foot wall	6.5	30	0.24
bo25	fn simulation, foot wall	6.5	30	0.29
bo26	fp simulation, foot wall	6.5	30	0.31
bo27	fn Nahanni, 1985 Station 1	6.9	9.6	0.25
bo28	fp Nahanni, 1985 Station 1	6.9	9.6	0.24
bo29	fn Nahanni, 1985 Station 2	6.9	6.1	0.17
bo30	fp Nahanni, 1985 Station 2	6.9	6.1	0.21
bo31	fn Nahanni, 1985 Station 3	6.9	18	0.38
bo32	fp Nahanni, 1985 Station 3	6.9	18	0.39
bo33	fn Saguenay, 1988	5.9	96	0.57
bo34	fp Saguenay, 1988	5.9	96	0.78
bo35	fn Saguenay, 1988	5.9	98	1.50
bo36	fp Saguenay, 1988	5.9	98	0.71
bo37	fn Saguenay, 1988	5.9	118	0.52
bo38	fp Saguenay, 1988	5.9	118	0.65
bo39	fn Saguenay, 1988	5.9	132	0.51
bo40	fp Saguenay, 1988	5.9	132	0.78

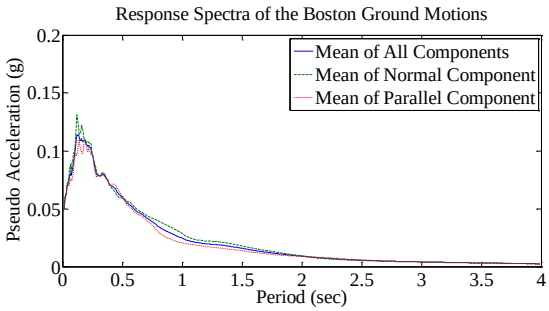


Figure 7 Mean Response Spectra of the Ground Motion Data Pairs with 5% Damping

4. INVESTIGATION OF BEARING DISPLACEMENTS UNDER SEISMIC LOADS

To consider the behavior of the overall bridge structure under seismic loads, the lateral displacements of the bearings in the longitudinal and transverse directions are evaluated through nonlinear time history analyses using OpenSEES. The developed models for the bearing behavior in the longitudinal and transverse directions are applied to the zero length spring elements shown in Figure 6. In evaluating the behavior of the bearings, the assumed displacement capacities are taken into account by noting those ground motions that cause lateral or transverse displacements that exceed these limits suggesting potential failure of the bearings.

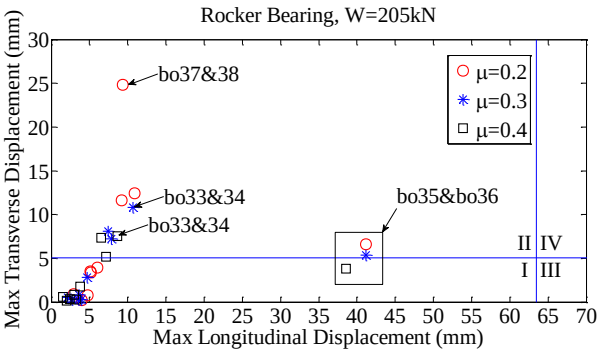
The effect of aging and deterioration of the bearings also is investigated by considering changes in the friction behavior at the contact interfaces where sliding and rolling occur. In addition, the effect of different axial loads on the bearings is taken as another parameter since the axial load level sustained by the bearings also affects the frictional force generated at the sliding interfaces in the bearings. The findings provide a better understanding of how aging affects the performance of the steel bearings and overall bridge under seismic loads. This method can then be used to better assess potential threats to in-situ bridges and aid in the development of cost effective strategies to ensure the continued safety of older steel girder bridges relying on steel bearings in seismic regions.

4.1 Effect of Friction Coefficient

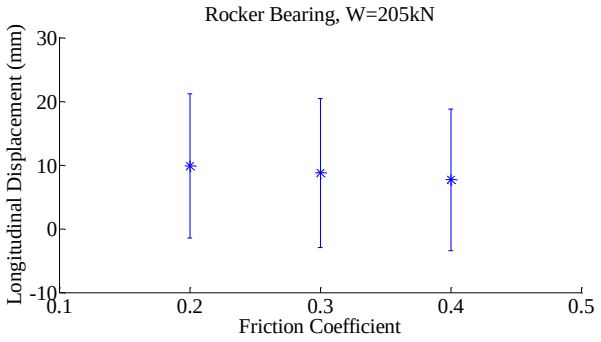
Figures 8 and 9 provide details on the effect that the friction coefficient has on the seismic response of the bridge in terms of the longitudinal and transverse bearing displacements. The bearing models are derived as discussed in Section 2 using the finite element analyses considering friction coefficients of 0.2, 0.3, and 0.4 (Fan and McCormick 2012). Since bidirectional ground motion pairs are applied simultaneously through the nonlinear time history analysis, displacement interaction diagrams are created for both the rocker and bolster bearing to provide a means of better understanding the bidirectional response under seismic loads.

The displacement interaction diagram is divided into four zones based on the assumed allowable displacements in the two orthogonal loading directions. If the displacement pair falls within Zone I, then the bearing under consideration functions well under the input ground motion pair. When the displacement pair is in Zone II, the considered bearing fails in the transverse direction due to instability for the rocker bearing or due to excessive displacement of the bolster bearing. If the displacement pair falls within Zone III, the failure is due to large displacements in the longitudinal direction. Zone IV is where the displacement capacity of the bearing is surpassed in both the longitudinal and transverse directions.

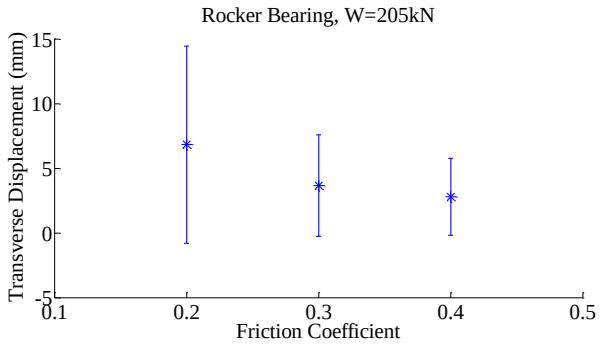
Figure 8(a) shows a clear trend in the displacement of the rocker bearing with respect to the friction coefficient. As the friction coefficient increases from 0.2 to 0.4, the maximum transverse displacement decreases from 25 mm to 7.5 mm for all considered ground motions, while the maximum longitudinal displacement remains at approximately 41 mm for all levels of the friction coefficient. The ground motion pair that results in the maximum transverse displacement varies for the different levels of friction coefficient. The responsible ground motion pair changes from bo37&38 to bo33&34 as the friction coefficient is increased from 0.2 and 0.3 to 0.4. However, the maximum longitudinal displacement for all three friction coefficient levels is caused by the same ground motion pair, bo35&36. This pair has the largest PGA of 1.5g for the normal component that is applied in the longitudinal direction of the bridge.



(a) Interaction of Longitudinal and Transverse Displacements



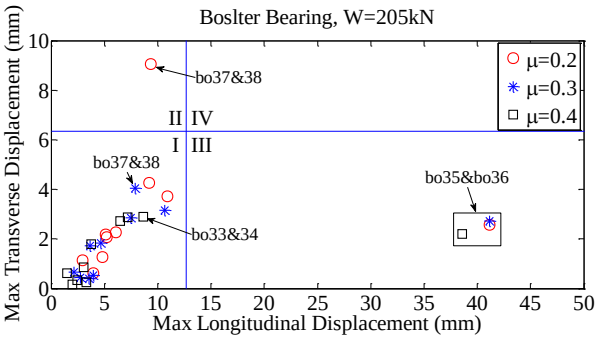
(b) Longitudinal Displacement, Mean ± 1σ



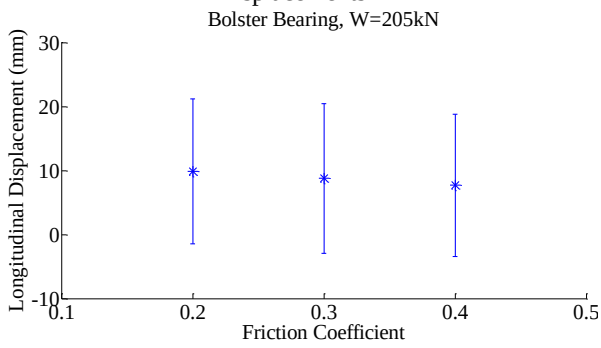
(c) Transverse Displacement, Mean ± 1σ

Figure 8 Effect of Friction on the Displacement Response of the Rocker Bearing under Seismic Loads

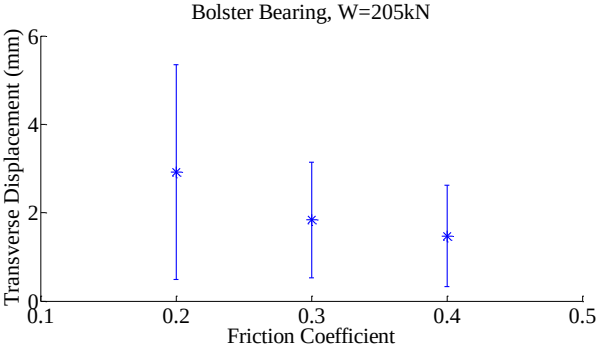
The displacement pairs for all ground motions fall within Zone I and II. This finding indicates that the rocker bearing has adequate displacement capacity in the longitudinal direction and failure is more likely to occur due to instability in the transverse direction. As a result, rehabilitation and retrofit techniques should focus on the transverse response of rocker bearings. Figures 8(b) and (c) also clearly shows that the longitudinal displacement of the rocker bearing is negligibly affected by changes in the friction coefficient, which is due to the fact that rolling is the dominant deformation mode, not sliding. However, the transverse displacement is influenced by the value of the friction coefficient showing more dispersed and larger displacements for lower friction coefficients suggesting that aging will have a greater effect on the transverse response of rocker bearings.



(a) Interaction of Longitudinal and Transverse Displacements



(b) Longitudinal Displacement, Mean ± 1σ



(c) Transverse Displacement, Mean ± 1σ

Figure 9 Effect of Friction on the Displacement Response of the Bolster Bearing under Seismic Loads

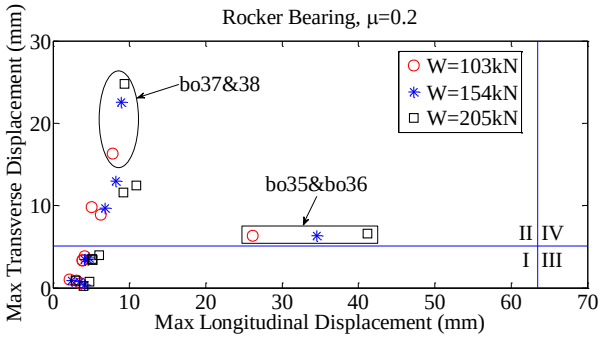
For the bolster bearing, Figure 9(a) shows that an increase in the friction coefficient from 0.2 to 0.4 leads to a decrease from 9 mm to 2.9 mm in the maximum transverse displacement. Conversely, insignificant decreases are observed for the maximum longitudinal displacement as the friction coefficient increases. Additionally, the maximum transverse displacement is caused by two different ground motion pairs depending on the friction coefficient (bo33&34 and bo37&38), while the maximum longitudinal displacement for all friction coefficient values is caused by the same ground motion pair (bo35&36). Unlike the rocker bearing, the analysis of the bolster bearing shows potential failure in both the transverse and longitudinal directions with displacement pairs found in Zone I, II, and III.

Figure 9(b) and (c) reveal a decreasing trend for the mean maximum displacement for both the longitudinal and transverse directions as the friction coefficient increases. This trend is less obvious for the longitudinal response. The transverse response also has a more dispersed displacement distribution at lower friction coefficient values compared to the longitudinal response. These findings suggest that aging may have a greater effect on the response of fixed bearings and that retrofit and rehabilitation methods need to consider both the transverse and longitudinal response.

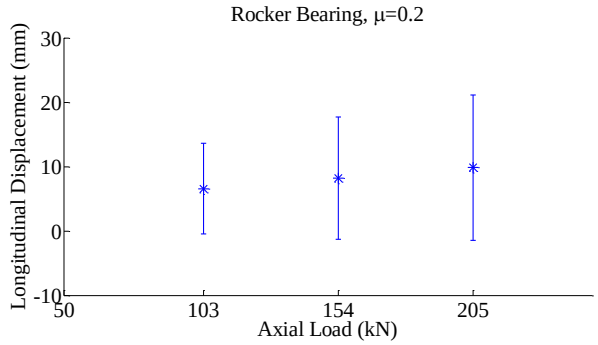
A close examination of Figures 8 and 9 reveals that the longitudinal responses for the rocker and bolster bearing are of similar magnitudes for each ground motion pair. On the contrary, the transverse responses for the rocker and bolster bearing have significant discrepancies in displacement magnitudes under the same ground motion pair with the rocker bearing showing approximately three times larger displacements. This observation suggests a twisting of the bridge about the vertical (Z-axis) axis caused by the bidirectional motion and different stiffness of the bolster and rocker bearing in the transverse and longitudinal directions, respectively. The lower magnitude in displacement for the bolster bearing is a result of its higher transverse stiffness than that of the rocker bearing.

4.2 Effect of Axial Load

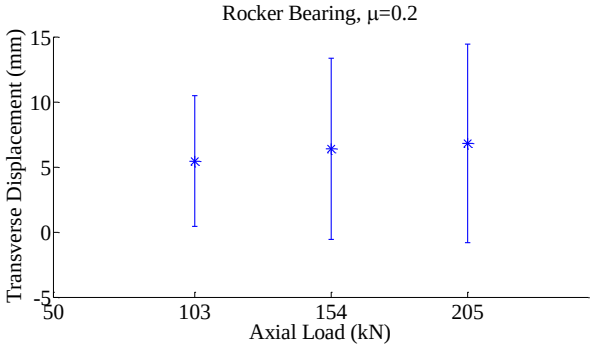
The effect that the axial load level sustained by the bearings has on the seismic response of the bridge under bi-directional earthquake loads also is investigated to account for different bridge configurations and span lengths. Figures 10 and 11 provide the findings considering three common levels of axial load in an individual bearing: 103 kN, 154 kN, and 205 kN. The behavior of the bearings at these axial load levels is achieved by varying the overall mass of the bridge segment considered in the OpenSEES model and modifying the parameters of the bearing model to represent the behavior found through the previous finite element analysis of the rocker and bolster bearings under the specified axial loads (103 kN, 154 kN, 205 kN) with a constant friction coefficient of 0.2 (Fan and McCormick 2012).



(a) Interaction of Longitudinal and Transverse Displacements



(b) Longitudinal Displacement, Mean ± 1σ

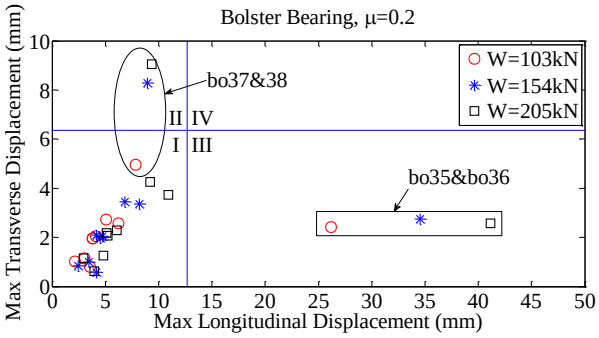


(c) Transverse Displacement, Mean ± 1σ

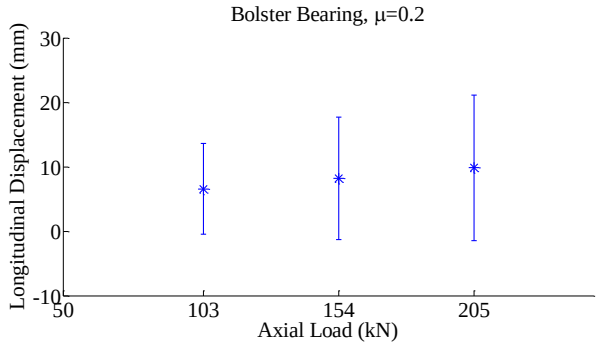
Figure 10 Effect of Axial Load on the Displacement Response of the Rocker Bearing under Seismic Loads

Figure 10(a) shows that for the maximum longitudinal and transverse displacements of the rocker bearing are dependent on the axial load level or mass of the bridge. The maximum longitudinal displacement increases from 26 mm to 35 mm to 41 mm as the axial load is increased from 103 kN to 154 kN to 205 kN, respectively. The ground motion pair, bo35&bo36, causes the largest longitudinal displacement for the three considered axial load levels. The maximum transverse displacement increases from 16 mm to 22 mm to 25 mm as the axial load level is raised from 103 kN to 154 kN to 205 kN, respectively. Again, a single ground motion pair, bo37&38, causes the maximum transverse displacement for all of the axial load levels. However, it is a different ground motion pair than that causing the maximum

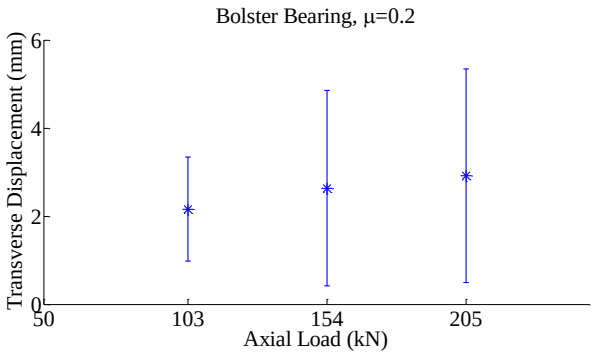
longitudinal displacement. This finding is different than the behavior observed when varying the friction coefficient where different ground motion pairs resulted in the maximum displacements for the different friction levels. These findings are consistent with basic structural dynamics since larger axial loads on the bearings indicate a heavier superstructure and thus greater inertial forces under the same ground motion input resulting in greater displacements in the bearings. In addition, all of the displacement pairs are located in Zone I and II, suggesting that the rocker bearings are more susceptible to failure in the transverse direction. Figure 10(b) and (c) shows a similar trend for the longitudinal and transverse displacements. At higher axial loads the maximum displacements for all ground motion pairs is more dispersed and has a larger mean value.



(a) Interaction of Longitudinal and Transverse Displacements



(b) Longitudinal Displacement, Mean ± 1σ



(c) Transverse Displacement, Mean ± 1σ

Figure 11 Effect of Axial Load on the Displacement Response of the Bolster Bearing under Seismic Loads

Fig. 11 provides the response of the bolster bearing under the considered suite of bidirectional ground motions. As the axial load level increases both the longitudinal and transverse displacements increase. The maximum longitudinal displacement increases from 26 mm to 35 mm to 41 mm and the transverse displacement increases from 5 mm to 8 mm to 9 mm when the axial load increases from 103 kN to 154 kN to 205 kN. The responsible ground motion pairs causing the maximum longitudinal and transverse displacement are bo35&36 and bo37&38 under all three axial load levels, respectively. As a result of the limited displacement capacity of the bolster bearing in both loading directions, the displacement pairs are scattered throughout Zone I, II, and III indicating that the bolster bearing has potential to fail in either the longitudinal or transverse direction given the considered suite of ground motions. Fig. 11(b) and (c) reveal that a higher axial load level generates a more dispersed distribution of maximum displacements with a larger mean value for both the longitudinal and transverse responses of the bridge.

A comparison of the data points between Figures 10(a) and 11(a) suggests that under the same ground motion pair, the longitudinal displacement in the rocker bearing is the same as that in the bolster bearing, while the transverse displacement differs. This again suggests that twisting of the rigid bridge deck about a vertical axis is occurring due to the difference in the stiffness of the two bearing types in the transverse direction.

5. CONCLUSIONS

To assess the seismic performance of older highway bridges utilizing steel bearings, credible models for the behavior of steel bearings under both the longitudinal and transverse displacements are needed. Due to the fact that steel bearings are designed solely for gravity loads and are susceptible to corrosion, their effect on the seismic response of highway bridges is of concern. In this study, a set of hysteretic models are developed for two types of steel bearings, rocker and bolster bearings, considering the influence of the friction coefficient and axial load. The friction coefficient is considered to account for potential deterioration of the steel bearing components as a result of corrosion over time. The axial load effect also is investigated to account for the influence of the bridge mass on the initial stiffness, sliding resistance, and critical load for instability. These hysteretic models are incorporated into a simply supported bridge model in OpenSEES to examine its response under a suite of ground motions through nonlinear time history analyses. The maximum longitudinal and transverse displacements are used to determine the influence of the various parameters on the response of the bridge. Allowable displacements are defined for the bearings based on potential failure modes in each orthogonal direction.

The results suggest that larger friction coefficients

can lead to a reduction in the maximum displacement sustained in the transverse loading direction for the rocker bearing and in the two orthogonal loading directions for the bolster bearing. Larger friction coefficients also lead to a less dispersed distribution of maximum displacements and smaller maximum displacements for the suite of ground motions considered. The effect of the friction coefficient is rather limited for the longitudinal response of the rocker bearing.

The findings with respect to the axial load level show that an increase in axial load leads to greater displacements for both the rocker and bolster bearing in the longitudinal and transverse loading directions. Additionally, larger dispersions in the distribution of the maximum displacements are observed for higher axial loads.

For the suite of ground motions, the observed failure modes for the rocker bearing are due to transverse displacement of the bearing. The rocker bearing shows adequate displacement capacity in the longitudinal direction. Moreover, the bolster bearing exhibits possible failure in both the longitudinal and transverse direction due to excessive displacement. This finding suggests that retrofit and rehabilitation of bridges utilizing steel bearings should focus on minimizing displacements in the transverse direction and strengthening bolster bearings in both orthogonal directions.

The conclusions reached in this study are based on a simplified and idealized bridge model for a simply supported single span bridge neglecting the interaction between the abutment and the deck. However, the findings give a general understanding of the influence of aging and bidirectional motion on the response of bridges utilizing typical steel bearings. The overall finding suggests that the presence of steel bearings can lead to damage under moderate ground motions and either retrofit or replacement of steel bearings is suggested for highway bridges in regions of low to moderate seismicity.

Acknowledgements:

The authors would like to acknowledge the in-kind support of the Illinois Department of Transportation for donation of the physical bearings being considered in this study and documentation in regards to the bridge from which they were salvaged. The opinions and findings presented are those of the authors and do not necessarily represent those of any sponsors.

References:

Bruneau, M., Wilson, J.C., and Tremblay, R. (1996), "Performance of Steel Bridges during the 1995 Hyogo-ken Nanbu (Kobe, Japan) Earthquake," *Canadian Journal of Civil Engineering*, **23**,678-713.

Chen, W-F. and Duan, L. (2003), Bridge Engineering: Substructure Design, CRC Press, Boca Raton, Florida, USA.

Fan, X. and McCormick, J. (2011), "Finite Element Analysis of the Cyclic Behavior of Corroded Bridge Bearings," *The 2011World Congress on Advances in Structural Engineering and Mechanics*, Seoul, Korea.

Fan, X. and McCormick, J. (2012), "Seismic Performance Evaluation of Corroded Steel Bridge Bearings," *The 15th World Conference on Earthquake Engineering*, Lisbon, Portugal.

Housner, G.W. and Thiel, C.C. (1995), "The Continuing Challenge: Report on the Performance of State Bridges in the Northridge Earthquake," *Earthquake Spectra*, **11**(4), 607-636.

Kayser, J.R., and Nowak, A.S. (1989), "Capacity Loss due to Corrosion in Steel Girder Bridges," *Journal of Structural Engineering*, American Society of Civil Engineers, **115**(3), 1525-1537.

Mander, J.B., Kim, D-K., Chen, S.S., and Premus, G.J. (1996), "Response of Steel Bridge Bearings to Reversed Cyclic Loading," Technical Report NCEER-96-0014, National Center for Earthquake Engineering Research.

Mitchell, D., Bruneau, M., Williams, M., Anderson, D., Saatcioglu, M., and Sexsmith, R. (1995), "Performance of Bridges in the 1994 Northridge Earthquake," *Canadian Journal of Civil Engineering*, **22**,415-427.

Nielson, B. and DesRoches, R. (2008), "Seismic Fragility Curves for Typical Highway Bridge Classes in the Central and Southeastern United States," *Earthquake Spectra*, **23**(3), 615-633.

Open System for Earthquake Engineering Simulation (2012), OpenSEES 2.4.0, http://opensees.berkeley.edu/index.php

Padgett, J.E. and DesRoches, R. (2008), "Three-dimensional Nonlinear Seismic Performance Evaluation of Retrofit Measures for Typical Steel Girder Bridges," *Engineering Structures*, **30**(7), 1869-1878.

Splitstone, D.E., Stonecheck, S.A., Dodson, R.L., and Fuller, J.A. (2010), "Birmingham Bridge Emergency Repairs: Micropile Foundation Retrofit," *GeoFlorida 2010: Advances in Analysis, Modeling, and Design*, Florida, USA.

10CUEE CONFERENCE PROCEEDINGS
10th International Conference on Urban Earthquake Engineering
March 1-2, 2013, Tokyo Institute of Technology, Tokyo, Japan

PRECAST CONCRETE BRIDGE COLUMNS MADE WITH UNBONDED PRE-TENSIONING AND HYBRID FIBER REINFORCED CONCRETE FOR IMPROVED SEISMIC RESISTANCE

Olafur S. Haraldsson [1], Gunnsteinn Finnsson[1], Phillip M. Davis[2], Marc O. Eberhard[3], and John F. Stanton[3]

1) Graduate Research Assistant, Department of Civil and Environmental Engineering, University of Washington, USA
2) Design Engineer, Degenkolb Engineers, Portland, OR, USA
3) Professor, Department of Civil and Environmental Engineering, University of Washington, USA
olafurh@u.washington.edu, finnsson@u.washington.edu, eberhard@u.washington.edu, stanton@u.washington.edu

Abstract: This paper describes the development and testing of a new pre-tensioned bridge bent system that includes 1) precast components to reduce construction time, 2) unbonded pre-tensioned strands in the columns to minimize post-earthquake residual displacements, and 3) Hybrid Fiber Reinforced Concrete (HyFRC) located in the plastic-hinge regions to reduce spalling, and delay bar buckling and bar fracture.

Quasi-static, cyclic tests were conducted previously on two subassemblies that represented a column-to-footing connection and a beam-to-column connection. Those specimens contained conventional concrete in the plastic hinge region. Those tests showed that bents built with this technology would likely re-center better than conventional bents, but the columns experienced bar buckling and bar fracture at lower drift ratios than observed in previously tested RC specimens without the pre-tensioning. To address this concern, the system was modified to include HyFRC shells in the plastic-hinge regions. The performance of this modified system was then first investigated with a series of shake-table tests on a single column. That testing showed that the specimen was able to re-center up to a peak drift ratio of 5.5%. It also showed that the HyFRC shell delayed spalling, bar buckling, and bar fracture. To allow direct comparison, under identical conditions, of specimens with and without the HyFRC shell, quasi-static test of the new system was conducted in December 2012.

1. INTRODUCTION

Reinforced concrete bridge construction techniques in seismic regions have changed little since the mid-1970s, when ductile details were first introduced. Nearly all bridge bents (intermediate supports) in seismic regions are now constructed of cast-in-place reinforced concrete using those ductile details. Such bridges have served well in the past, but to meet current design expectations, they need to be improved in three main areas: 1) speed of construction, 2) seismic resilience and 3) durability.

New structural systems and construction methods are needed to make improvements in these three areas. One approach for reducing construction-related delays is to precast structural elements off-site and then assemble them rapidly once they arrive on site. Post-earthquake residual displacements can be reduced by prestressing the precast bridge columns. The prestressing is designed to bring the system to its original plumb position when lateral load is removed. Durability of the system can be enhanced by the selection of high-performance materials to improve the system structural performance and minimize corrosion. Precasting also has other benefits, such as improved worker safety and higher construction quality.

This paper describes a new unbonded, pre-tensioned precast bent system developed to meet the current design expectations. Different connection systems are used at the column-to-foundation and at the cap beam-to-column interfaces, because the conditions at each location have unique constraints and opportunities. Both connections are pre-tensioned. The connections were tested quasi-statically for seismic performance using conventional concrete in the plastic hinge region. In June 2012, an improved pre-tensioned system with Hybrid Fiber Reinforced Concrete (HyFRC), in the plastic hinge region, was tested on the shake table at the Richmond Field Station Earthquake Simulation Laboratory of the University of California at Berkeley. A quasi-static version of the improved system is being tested in December 2012.

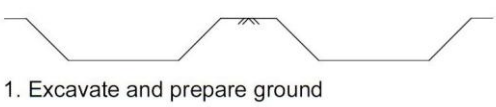
2. PRE-TENSIONED BRIDGE BENT SYSTEM

2.1 System Overview

The new system is an outgrowth of concept development and experimental research on a fully precast bent system at the University of Washington (Stueck et al. 2007, 2009, Pang et al. 2008, 2010, Cohagen et al. 2008, and Haraldsson et al. 2012a, 2012b).

Figure 1 shows the construction sequence for the new pre-tensioned bent system. Once the footing has been

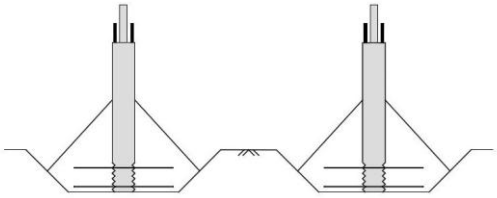
excavated (Step 1), top and bottom reinforcement is placed (Step 2). The precast pre-tensioned column is then brought to site, plumbed, leveled and braced (Step 3). The footing can then be cast-in-place (Step 4). Alternatively, the precast column can be plumbed and leveled before the footing reinforcement is placed. The final step is to connect the column to the cap-beam (Step 5). In comparison with conventional cast-in-place system, the primary advantage of this system is that a footing and a column can be built in little more time than is needed to cast the footing alone. A main time-saving factor in the bent construction is the presence of the precast cap-beam (Marsh et al. 2011, Weinert 2011). By precasting the cap-beam, time needed to complete various tasks, such as shoring, rebar placement, casting and curing, are relieved.



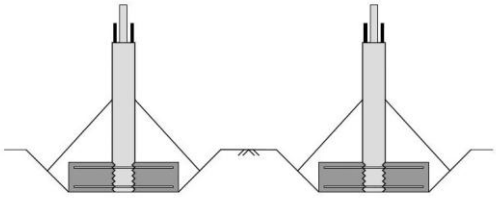
1. Excavate and prepare ground



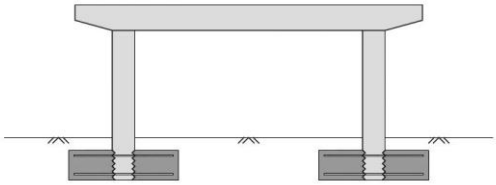
2. Place Rebars (and formwork)



3. Position and brace precast column



4. Cast footing



5. Position precast cross-beam and grout projecting column segment and bars

Figure 1. Construction Sequence

The pre-tensioned bent system concept is shown in Figure 2.

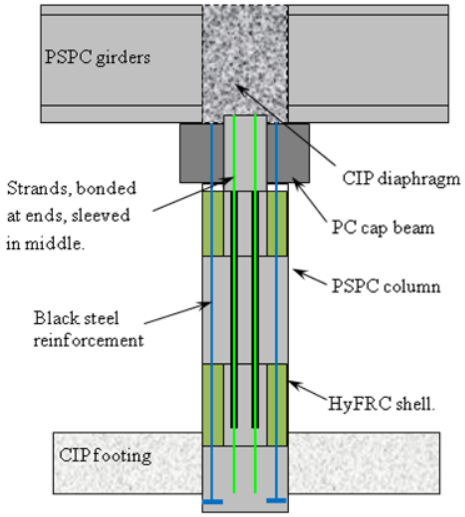


Figure 2. Pre-Tensioned Bridge Bent System

In this system, bridge elements are precast off-site and assembled rapidly on-site. To facilitate rapid construction, the precast column is connected to a cast-in-place spread footing with a "socket" connection (Haraldsson et al. 2012a, 2012b). At the top, the column is connected to a precast cap-beam using a modified grouted bar connection (Davis et al. 2012a, 2012b). The connection concepts are described further in subsections 2.2 and 2.3.

To increase resilience and durability, the column is precast with pre-tensioning that is bonded within the connections and unbonded within the clear height of the bent. The prestressing strands are designed to remain elastic to a specific drift target, and they are intended to bring the bent system back to its original plumb position following an earthquake. The purpose of debonding the strands over the clear height of the column is to distribute strains during the earthquake. To dissipate energy, bonded mild reinforcement crossed the crack planes located at the beam-to-column and column-to-foundation interfaces. In order to delay spalling and buckling of the longitudinal bars, plastic hinge regions were made more ductile with prefabricated elements made of Hybrid Fiber Reinforced Concrete (HyFRC) composite material (Kumar et al. 2011). For fabrication reasons, those elements were cast in the form of cylindrical pipes that were subsequently filled with conventional concrete.

2.2 Column-to-Footing Connection: Socket Connection

The system uses a socket connection to connect the precast column to the cast-in-place spread footing (Haraldsson et al. 2012a, 2012b).

The construction process for this connection is simple, as shown in Figure 1. The location of the footing is excavated, and the precast column is brought in, plumbed and braced. Then, the footing reinforcement is put in place and the concrete is cast around the column. Alternatively, the footing reinforcement could be placed before the column is set.

The precast column has an intentionally roughened exterior surface where it is to be embedded in the cast-in-place footing. The column bars are terminated with mechanical anchors instead of being bent out into the spread footing to facilitate handling and to improve the flow of internal forces. The prestressing strands are bonded within the embedded portion of the column.

2.3 Colum-to-Cap Beam Connection: Grouted Bar Connection

At the top of the column, the socket connection concept could not be used easily with a precast beam. Thus, a new connection was developed, based on the concept of grouted bars, to incorporate bonded prestressing strands as well. It can be seen in Figure 3.

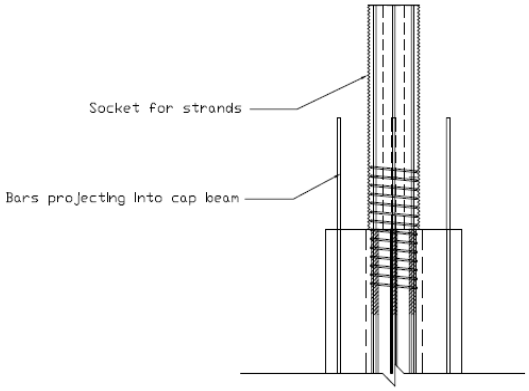


Figure 3. Hybrid Grouted Bar Socket Connection

The grouted bar connection was a modification of the one developed by Pang et al. (2008, 2010). In Pang's connection, large bars extend from the column and are grouted into matching ducts in the cap beam. Their large diameter means that few are needed, so large ducts can be used and fit-up is easy. In the modified version, a central section of column with a reduced diameter extends beyond the body of the column and is grouted into a large central duct. This section contains the prestressing strands and allows the bonding to be completed within the depth of the cap-beam, thereby maximizing the unbonded length of strand. The shoulder on the column provides a temporary erection support for the cap-beam. Mild reinforcement is also connected as in Pang's system and provides energy dissipation by cyclic yielding under seismic loading.

2.4 Constructability

The parent system of the pre-tensioned system (i.e., the non-prestressed precast bent system) was recently deployed in Washington State as part of the construction of a bridge over Interstate-5 (Khaleghi et al. 2012). The bridge had two spans, tall abutments on the ends and a center pier of four columns. Even though the columns were light enough to be lifted in one pick, the columns were fabricated in several pieces to verify the constructability of a segmental version of the system for future applications.

The precast columns were connected to the cast-in-place spread footings using the socket connection. No major problems were encountered and alignment was relatively straight forward (Haraldsson et al. 2012b). At the top, the precast columns were connected to the precast cap-beam using a Large-bar connection (Pang et al. 2008, 2012). The cap-beam was in two segments because of weight constraints. The placement of each cap-beam segment was a quick operation and it took less than 30 minutes per segment.

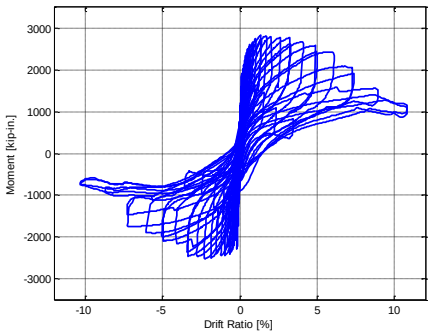
The pre-tensioned bent system relies essentially on same connections as the precast bent system. Thus, it is expected that the system is both easily and rapidly assembled together on site. The prestressing and fabrication of the HyFRC are performed simultaneously in the precast plant and so are taken off the critical path.

3. QUASI-STATIC TESTS

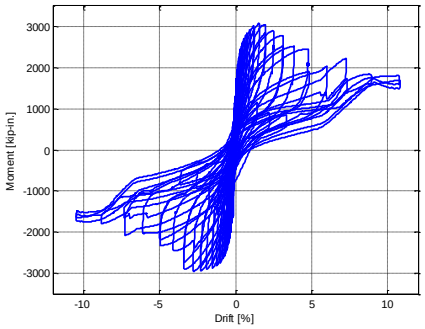
Davis et al. (2012a, 2012b) report the details of the experimental program and the measured response of a pre-tensioned column-to-cap beam and a column-to-spread footing connection using conventional concrete in the plastic hinge region.

Two 42% scale cantilever subassemblies were tested at the University of Washington Structural Laboratory. The specimens had columns that were 508-mm (20-in.) in diameter (representing 1.22-m [4-ft] diameter prototype column) and 1.52-m (60-in.) high, resulting in a span-to-depth ratio of 3.0. Both test columns had the same octagonal cross section with a 508-mm (20-in.) diameter from flat face to flat face. The number and configuration of bonded reinforcing bars and unbonded strand was identical for both columns. Six D-13 (No. 4) bars were used in a circular pattern with a 438-mm (17.25-in.) diameter and six 10-mm (0.375-in.) diameter epoxy-coated strands were used in a circular pattern in the column center. Each strand was jacked to a stress of 1241 MPa (180 ksi) and after taking into account all losses, the resulting strand stress was estimated to be 1124 MPa (163 ksi), providing the system a total prestressing force of 369 kN (83 kips).

Under cyclic load, both specimens hinged above the connection region and had nearly identical force-displacement curves and damage progression, as shown in Figure 4. They showed good re-centering capability (less than 1% drift residual after being cycled to 10% drift), but spalling and bar buckling were initiated at drift ratios lower than those typically achieved in non-prestressed specimens (e.g., Pang et al. 2008, 2010, and Haraldsson et al. 2012a, 2012b). Even though they experienced early damage, both specimens maintained 80% of their peak lateral strengths up to a drift ratio of 5%.



a) Column-to-Footing Connection



b) Column-to-Bap Beam Connection

Figure 4. Moment-Drift Ratio Response for a) Bottom Connection and b) Top Connection

To delay bar buckling and fracture, the system was modified by including Hybrid Fiber Reinforced Concrete (HyFRC) in the plastic hinge region. HyFRC has been shown to exhibit superior durability and cracking resistance (Yi and Ostertag 2004, Grupp et al. 2007, Ostertag et al. 2007, and Jen et al. 2011). At the time of writing (December 2012), an identical column-to-footing specimen with HyFRC shell in the plastic hinge region is being tested (Finnsson 2012).

4. SHAKE-TABLE TEST OF ISOLATED COLUMN

In June 2012, shake-table tests were performed at the Richmond Field Station Earthquake Simulation Laboratory of the University of California, Berkeley to evaluate the damage susceptibility and re-centering capability of new resilient columns. The following discussion describes the unbonded, pre-tensioned precast column using HyFRC in the plastic hinge regions. A reference column (a typical Caltrans design) for the new designs is scheduled to be tested in late December 2012.

4.1 Connection Specimen

A cantilever unbonded, pre-tensioned precast column was designed and fabricated for the shake-table test. The full-scale prototype was assumed to be a 1.2-m (4-ft) diameter column. The specimen represented the column-to-foundation connection at a 33% scale with an aspect ratio of 6.0.

Figure 5 shows the details of the scaled test specimen. The final design resulted in eight D-13 (No. 4) bars (A_s = 1.6 in^2, ρ_l = 0.75%) and eight 10-mm (3/8-in.) diameter prestressing strands (A_p = 439 mm^2 [0.68 in^2], ρ_p = 0.32%). Epoxy-coated strands were used to improve bond and minimize corrosion. Each strand was jacked to a stress of 1117 MPa (162 ksi) that resulted in an effective stress of 986 MPa (143 ksi), thus providing a total prestressing force of 431 kN (97 kips). The strands were designed to have first yield at 3.0% drift. The transverse reinforcement consisted of 4-gauge spiral at 32-mm pitch (ρ_s = 0.88%). The column cross-section was octagonal to facilitate fabrication. The HyFRC shell height in the plastic hinge region was 711 mm (28 in.) with a wall thickness of 71 mm (2.8 in.). The shell extended 102 mm (4 in.) into the spread footing to avoid cold joint opening at the column-to-foundation interface, therefore leaving a length of 1.5 times the column diameter extending up the column.

4.2 Experimental Setup

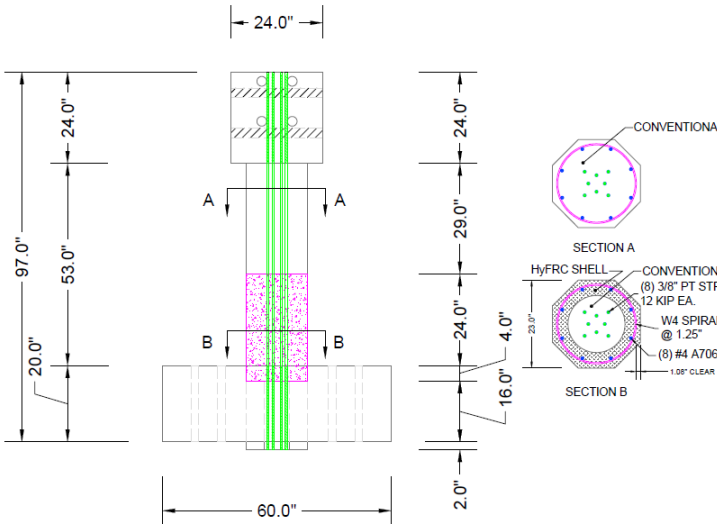


Figure 5. Scaled Colum-to-Foundation Connection

Figure 6 shows the test setup. The specimen was placed on the shake table, leveled with shims and post-tensioned to the top of underlying tri-axial load cells. On top of the column were three mass blocks (each of size 3.048 m [120 in.] x 3.048 m [120 in.] x 0.356 m [14 in.]) that provided approximately 240 kN (54 kips) dead load. To support the mass blocks on top of the column, steel brackets were post-tensioned to the top of the column (via a "load stub") in two orthogonal directions.

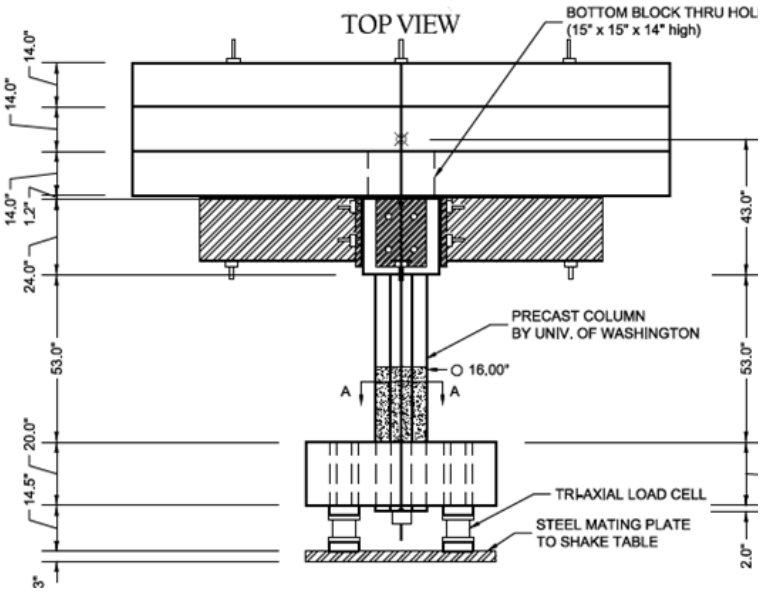


Figure 6. Experimental Test Setup

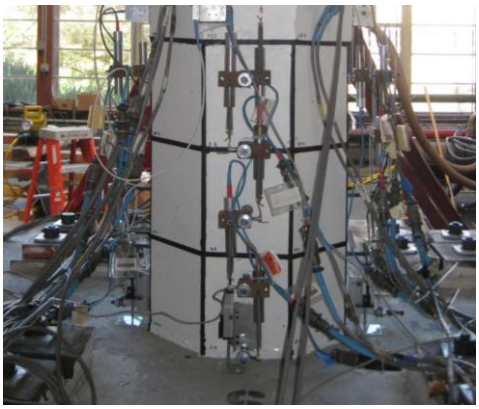


Figure 7. Column at the Start of the Test Program

4.3 Testing Protocol

The test protocol consisted of eight ground motions, applied in order of ascending intensity. The ground motions were selected on the basis of how they displaced the reference column in a nonlinear time-history analysis. Table 1 summarizes target drifts and ductility demands for the reference column. Before each earthquake test, low-amplitude white noise tests were performed to detect any change in natural period and damping as damage accumulated. Table 1 shows that the intensity level was increased in six stages. The first level was intended to keep the specimens below first yield, while the other levels would push the specimens beyond yield.

Table 1. Target Drift and Ductility Demand for the Reference column

EQ No.	EQ. Name	Drift Ratio (%)	Ductility Demand (-)
1	Coalinga, 1983	< 0.47	-
2	Imperial Valley, 1979	2.1	2.0
3	Morgan Hill, 1984	2.1	2.0
4	Northridge, 1994	4.2	4.0
5	Northridge, 1994	4.2	4.0
6	Northridge, 1994	6.3	6.0
7	Kobe, Japan 1995	8.4	8.0
8	Kobe, Japan 1995	10.5	10.0

4.4 Damage Progression

Figure 7 shows the pre-tensioned test specimen prior to the shake table tests.

During the shake-table testing, the table was not set down for inspection after every ground motion. The table was first set down after Earthquake 2 (2.1% target drift). The column was plumb and hairline cracks (<0.1 mm) were found in the bottom 406 mm (16 in.) of the column.

The column was next inspected after Earthquake 4 (4.2% target drift). The column re-centered back to its original plumb position. Cracks propagated around the column but very little cracking occurred higher than 406 mm (16 in.) above the interface. The largest residual crack measured 0.76 mm (0.03 in.) approximately 203 mm (8 in.) above the interface. Noticeable spalling was observed after Earthquake 4 (4.2% target drift). No separation between the column and the spread footing was noticed. In Earthquake 5 (4.2% target drift) new spalling occurred 102 mm (4 in.) above the interface on the whole north side of the column (north, northwest, northeast). A level placed on the column showed that the column was still re-centering to its original position, confirming visual observation.

Cracking and spalling became more pronounced after Earthquake 6 (6.3% target drift). A very visible dominant crack formed 102 mm (4 in.) above the interface, and was seen opening and closing during the whole test. The column continued to be plumb when it was at rest. After Earthquake 7 (8.3% target drift), the column appeared to have residual drift. For the first time a hairline crack was noticed at the cold joint (located 610 mm [24 in.] above the interface) between the HyFRC shell and the conventional concrete. Earthquake 8 (10.4% target drift) was the last record that the column was subjected to. During the shaking, two fracture sounds were heard. A spiral fracture became visible through spalling crack (the spalling was held together by the steel fibers) on the north face of the column approximately 152

mm (6 in.) above the interface. The other fractured spiral or longitudinal bar could not be located. Bar buckling was observed 203 mm (8 in.) above the interface on the northeast face of the column. Spalling increased around the perimeter of the column but was held in by the steel and plastic fibers in the HyFRC shell. Residual drift was apparent. Figure 8 shows the specimen after the test program.



Figure 8. Column at the End of the Testing

4.5 Column Drift Response

The specimen was subjected to all eight ground motions without failing. Table 2 summarizes peak drifts and residual drifts measured in any direction. The table shows the column re-centered almost perfectly through Earthquake 6 (6.3% target drift), as found by the visual observations. The column had been expected to re-center perfectly when displaced less than 3.0% peak drift, because up to that displacement the strand stress remained below yield, as shown by the strand strain gages (first yield detected in Earthquake 4). Nevertheless, the column continued to re-center past first yield.

Table 2. Column Drift Response Results

EQ No.	Ref. Col Target Drift Ratio (%)	Pre-T Col. Meas. Drift Ratio (%)	Pre-T Col. Res. Drift Ratio (%)
1	< 0.47	0.4	0.00
2	2.1	1.7	0.06
3	2.1	2.1	0.01
4	4.2	4.0	0.13
5	4.2	5.2	0.19
6	6.3	5.5	0.06
7	8.4	8.7	1.07
8	10.5	5.9	0.52

5. SUMMARY

This paper presents a new bridge bent system that is rapidly constructible and provides excellent seismic performance. The rapid construction features are achieved by precasting the elements and by using innovative connections and erection procedures. The superior seismic performance is obtained through the use of unbonded prestressing in the column.

The constructability of the new system has been demonstrated. The new system is an outgrowth from an already developed non-prestressed precast bridge bent system that has been implemented in a bridge construction in Washington State. At the bottom, a precast column is connected to a cast-in-place foundation using a socket connection. At the top, the precast column in connected to a precast cap-beam using a modified grouted bar connection. The seismic performance has been tested in three stages.

In the first stage, quasi-static tests were conducted on two, 42% scale sub-assemblies that used conventional concrete in the plastic hinge region, and represented the system's bottom and top connections. The specimens behaved almost identically and maintained 80% of their peak lateral strength up to a drift ratio of 5%. Furthermore, they showed the system is able to re-center to its original plumb position (1% residual drift after being displaced to 10% peak drift). However, initial spalling, bar buckling and bar fracture were observed at a lower drifts than observed in previously in non-prestressed specimens (Davis et al. 2012a, 2012b).

The system was improved by including Hybrid Fiber Reinforced Concrete (HyFRC) in the plastic hinge region. The HyFRC composite is expected to delay premature spalling, bar buckling and bar fracture (Kumar et al. 2011). In the second stage, completed in July 2012, a 33% scaled shake-table test was conducted on a column that contained HyFRC in the plastic hinge region. The column was subjected to eight different earthquakes with six different intensity levels. During shake table testing, the column was seen to rock about a crack 4-5 in. above the column-to-footing interface. The column showed a excellent re-centering through the first six earthquakes (no residual drift up to 5.5% peak drift, and 1% residual drift after the extreme peak drift of 8.7%).

In the third stage, in December 2012, quasi-static testing was conducted on the system with HyFRC in the plastic hinge region to permit direct comparison, under identical loading conditions, the effect of the HyFRC on the system. Ideally this step would have been conducted before the shake table testing, but the schedule was controlled by the availability of test facilities.

6. CONCLUSIONS

The following conclusions were drawn from the study:

- Response of both quasi-static test specimens and shake table test specimens were controlled by column properties. Essentially no damage occurred in the connection region.

- In the first stage, the unloading curves of quasi-static tests specimens (with conventional concrete in the plastic hinge region) showed that pre-tensioned specimens are likely to re-center, and have lower residual drifts (specimens returned to 1% residual after being displaced laterally to a drift ratio of 10%), than previously tested non-prestressed specimens (Pang et al. 2008, 2010, Haraldsson et al. 2012a, 2012b). In the second stage, the measured response of the shake table specimens showed that re-centers after being displaced laterally up to 5.5% drift. At that time, prestressing strands had already yielded, as intended.
- The pre-tensioned quasi-static tests suffered spalling and bar buckling at a lower drift ratios than did in previously tested non-prestressed specimens. The pre-tensioned system was modified by including Hybrid Fiber Reinforced Concrete (HyFRC) in the plastic hinge region and tested first in series of shake table tests in the UC Berkeley Earthquake Simulation Laboratory. Currently (December 2012), the effect of the HyFRC on the plastic hinge region is being evaluated through a direct quasi-static test comparison.
- The presence of prestressing in the column is not expected to affect the constructability of the connections. The system relies essentially on the same connection as its parent system that is already developed and implemented in practice (i.e., precast bent system).

Acknowledgements:

Funding for this research was provided by the Pacific Earthquake Engineering Research (PEER) Center, by TransNow and by the Valle Foundation of the University of Washington. The findings and conclusions contained herein are those of the authors alone.

The quasi-static tests were conducted at the University of Washington with the help of students Po-Chien Hsiao, Travis Thonstad, Max Stephens, Francesca Renouard, Kevin Tsuchida**,** Spencer Livermore, Jacob Meader and Hung Viet Tran, Will Trono, Gabriel Jen, Professor Donald Janssen and Laboratory Manager Vince Chaijaroen. The shake table tests were conducted by the staff of the UC Berkeley Earthquake Simulator Laboratory, under the leadership of Dr. Matt Schoettler, with additional help from students Will Trono, Gabriele Guerrini, Gabriel Jen and Yosuke Ishihara. The support of all of them is gratefully acknowledged.

References:

"*AASHTO Guide Specifications for LRFD Seismic Design"* (2009). AASHTO, Washington DC.

Building Seismic Safety Council for FEMA. (2004) *"NEHRP Recommended Provisions for Seismic Regulations and forNew Buildings and Other Structures (FEMA 450) 2003 Edition,"* Washington D.C.

Caltrans (2006). *"Seismic Design Criteria Version 1.4".* Caltrans, Sacramento, CA.

Cohagen, L.S., Pang, J.B.K., Eberhard, M.O., and Stanton, J. F. (2008). " A Precast Concrete Bridge Bent Designed to Re-center after an Earthquake." *Washington State Department of Transportation Report No. WA-RD 684.3*, Washington State Department of Transportation, Washington, 2008.

Davis, P.M., Janes, T.M., Eberhard, M.O., and Stanton, J.F., (2012a). "Unbonded Pre-Tensioned Columns for Bridges in Seismic Regions," *Pacific Earthquake Engineering Research Center Report PEER-2012*, 147 pp. (submitted)

Davis, Phillip M., Janes, Todd M., Stanton, John F., Eberhard, Marc O., and Haraldsson, O.S. (2012b). "Unbonded Pre-tensioned Columns for Accelerated Bridge Construction in Seismic Regions," to *Journal of Bridge Engineering, ASCE* (submitted November 2012).

Grupp, J., C.P. Ostertag, T. Devine, (2007). "Effect of Steel Microfibers on Corrosion of Steel Reinforcing Bars." *Cement and Concrete Research*, Vol. 37, pp. 1115-1126.

Haraldsson, O.S., Janes, T.M., Eberhard, M.O., and Stanton, J.F. (2012a). "Laboratory Tests of Column-to-Footing Socket Connections." U.S. Department of Transportation, Federal Highway Administration, Washington, DC.

Haraldsson, O.S., Janes, T.M., Eberhard, M.O., and Stanton, J.F. (2012b). "Seismic Resistance of Socket Connection between Footing and Precast Column." *Journal of Bridge Engineering.* 10.1061/(ASCE)BE.1943-5592.0000413 (12 December 2012)

Jen, G., Trono, W., Ostertag, C.P. (2011). Design and Properties of Self compacted Hybrid Fiber reinforced composites, *CCC Journal*, (submitted).

Khaleghi, B., Schultz, E., Seguirant, S., Marsh, L., Haraldsson, O., Eberhard, M., and Stanton, J. (2012). "Accelerated Bridge Construction in Washington State -- From Research to Practice", *PCI Journal*, Autumn, pp. 34-49 (PCI's Cover Story).

Kumar, P., Jen, G., Trono, W., Lallemant, D., Panagiotou, M., & Ostertag, C.P. (2011). Self Compacting Hybrid Fiber Reinforced Concrete Composites for Bridge Columns. Pacific Earthquake Engineering Research Center; PEER report 2011/106.

Marsh, L.M., Wernli, M., Garrett, B.E., Stanton, J.F., Eberhard, M.O., and Weinert, M.D. (2011). NCHRP Report 698: "Application of Accelerated Bridge Construction Connections in Moderate-to-High Seismic Regions." Transportation Research Board, Washington, D.C.

Nakaki, S., Stanton, J., Sritharan, S. (1999). *"Overview of the PRESSS Five Story Precast Test Building,"* PCI Journal, V.44 No. 2, March-April 1999, pp 26-39.

Osanai, Y., Watanabe, F. and Okamoto, S., (1996). "Stress Transfer Mechanism of Socket Base Connections with Precast Concrete Columns". *ACI Structural Journal*, ACI, Chicago. IL. May-June, pp. 266-276.

Pang, J.B.K., Steuck, K., Cohagen, L., Stanton, J.F., Eberhard, M.O. (2008). "Rapidly Constructable Large-Bar Precast Bridge-Bent Seismic Connection." *Washington State Department of Transportation Report No. WA-RD 684.2*, Washington State Transportation Center.

Pang, J.B.K., Eberhard M.O., and Stanton, J.F. (2010). "Large-Bar Connection for Precast Bridge Bents in Seismic Regions." *Journal of Bridge Engineering, ASCE*, May-June, pp. 231-239.

Precast and Prestressed Concrete Institute (2004). "*PCI Design Handbook*". 6th ed. Chicago, IL.

Steuck, K., Pang, J., Stanton, J. and Eberhard, M. (2007) *"Anchorage of Large Bars in Grouted Ducts,"* Washington State Transportation Center Report WA-RD 684.1, Seattle, WA.

Steuck, K., Stanton, J.F. and Eberhard, M.O., "Anchorage of Large-Diameter Reinforcing Bars in Ducts," *ACI Structural Journal*, July-August 2009, pp 506-513.

Weinert, M.D. (2011). "Substructure Connections for Accelerated Bridge Construction in Seismic Regions". MSCE thesis. University of Washington, Seattle, WA, 239 p.

Yi, C.K. and C.P. Ostertag, (2004), Mechanical Approach in Mitigating Alkali Silica Reaction, *Cement and Concrete Research*, Vol. 35, pp. 67-75.

CONFERENCE PROCEEDINGS
10th International Conference on Urban Earthquake Engineering
March 1-2, 2013, Tokyo Institute of Technology, Tokyo, Japan

Performance-Based Seismic Retrofit of Soft-Story Light-Frame Wood Buildings

John W. van de Lindt[1], Pouria Bahmani[2], Mikhail Gershfeld[3], Xiaoyun Shao[4], Weichiang Pang[5], Michael D. Symans[6], Gary Mochizuki[7]

1)George T. Abell Professor in Infrastructure, Civil and Env. Engineering, Colorado State University, Fort Collins, Colorado, USA.
2) Ph.D. Student, Civil and Env. Engineering, Colorado State University, Fort Collins, Colorado, USA.
3) Professional Practice Professor, Civil Engineering, California State University, Pomona, California, USA.
4) Assistant Professor, Civil and Environmental Engineering, Western Michigan University, Michigan, USA.
5) Assistant Professor, Glenn Department of Civil Engineering, Clemson University, Clemson, South Carolina, USA.
6) Associate Professor, Rensselaer Polytechnic Institute, Troy, New York, USA.
7) Principal, Structural Solutions, Walnut Creek, California, USA
jwv@engr.colostate.edu , pouria.bahmani@colostate.edu , mgershfeld@csupomona.edu , xiaoyun.shao@wmich.edu , wpang@clemson.edu
symans@rpi.edu , gary@structsol.com

Abstract: The NEES-Soft Project, whose full title is "Seismic Risk Reduction for Soft-Story Woodframe buildings," is a five-university, multi-industry, NSF-funded project that has the objectives of (1) enabling performance-based seismic retrofit (PBSR) for at-risk soft-story woodframe buildings; and (2) experimentally validating the U.S. Federal Emergency Management Agency (FEMA) P-807 retrofit methodology. This paper focuses on the development, refinement, and future full-scale experimental validation of the Performance Based Seismic Retrofit (PBSR) methodology, which is an extension of the Direct Displacement Design (DDD) applied during the NEESWood project, but with the ability to include torsion which is often present in these soft-story structures. The PBSR approach decouples the translational and torsional response and allows the analyst to decide what portion of the allowable target story drift may be due to torsion with the remainder of the allowable target drift coming from translation. This illustrative example of a four-story building retrofit includes design of a steel cantilevered columns retrofit option, initial validationo of PBSR approach using nonlinear time history analysis, and shake table testing program at U.C. San Diego. A variety of retrofits will be considered in the testing but only one retrofit approach (steel cantilevered columns) is presented in this paper. Nonlinear time history analysis provides initial validation of the PBSR approach and plans for shake table testing at U.C. San Diego for the four-story building are discussed .

1. INTRODUCTION

The NEES-Soft Project, whose full title is "Seismic Risk Reduction for Soft-Story Woodframe buildings," is a five-university, multi-industry, NSF-funded project that has the objectives of (1) enabling performance-based seismic retrofit (PBSR) for at-risk soft-story woodframe buildings; and (2) experimentally validating the U.S. Federal Emergency Management Agency (FEMA) P-807 retrofit procedure. A soft-story building is a building that has one or more stories with significantly less stiffness (and strength) than the stories above or below. This condition usually occurs at the bottom story of a multi-story building and is often the result of large openings that are used for main building entrances or parking garages. Figure 1 shows a typical soft-story building in San Francisco, California. It is estimated that there are thousands of these buildings in San Francisco alone and many more throughout California and the United States. These buildings were generally built before 1970 and many as early as the 1920's, which means that they used construction practices not considered acceptable by today's codified standards. For example, many of these buildings do not have wood structural panels but rather rely on plaster on wood lathe, horizontal wood siding made up of dimension lumber planks, and diagonal bracing for shear resistance. These archaic assemblies require significant wall lengths in order to supply the necessary lateral capacity. The wall lengths available for soft-story buildings are, in general, too short at the bottom story, thereby resulting in a soft-story. The soft-story condition is exacerbated by the poor performance of these archaic assemblies, making it difficult to retrofit in many cases. In addition, as the buildings have undergone remodeling over the years, more and either additional layers of what are considered non-structural finishes by today's engineering standards have been added, or some portions of the assemblies replaced further complicating the analysis and retrofit of these buildings.

In order to better understand the seismic behavior of soft-story woodframe buildings, the NEES-Soft project

consists of numerous tasks ranging from numerical analysis and model development, hybrid testing, and full-scale shake table tests for validation of the methods developed within the project. This paper focuses on (1) the performance-based seismic retrofit (PBSR) approach with application to a four-story apartment building; and (2) explanation of the shake table test program at NEES@UCSD wherein the same four-story building will be tested.



Figure 1. Example of a soft-story woodframe building in San Francisco, California (Photo: M. Gershfeld)

2. PERFORMANCE-BASED SEISMIC RETROFIT

Displacement-based design was originally proposed by Priestley (1998) and later modified by Filiatrault and Folz (2002) for wood structures. Pang and Rosowsky (2009) proposed the direct displacement design (DDD) method by employing modal analysis of the structure and used the code-specified acceleration response spectral values in order to calculate the displacement at each story. Later, Pang et al. (2009) proposed a simplified procedure for applying the DDD method by modeling the structure with an equivalent single degree of freedom system and Wang et al. (2010) further refined the procedure.

The current DDD methodology (Pang et al., 2009) determines the required lateral stiffnesses over the height of the building such that the building meets the target displacement. This method serves as the basis for a direct displacement retrofit (DDR) procedure and can be used to retrofit symmetric buildings (i.e., no torsional moment due to seismic force) or irregular buildings that after retrofit would have negligible asymmetry (eliminating torsion by reducing the in-plane eccentricity) (Bahmani and van de Lindt, 2012). The proposed Performance-Based Seismic Retrofit (PBSR) in this study can be used to retrofit existing buildings such that all stories meet the performance criteria (not necessarily meeting the exact target drift because of the constraints formed by the existing design) and it can be used to retrofit buildings that are weak (and soft) in both translation and rotation.

In the PBSR approach being developed in the NEES-Soft Project, the DDD method is employed to design the retrofits such that the building meets the performance criteria communicated by the owner or stakeholders for different seismic hazard levels. The first step is identifying the target story drift and corresponding seismic intensity at which that drift is not to be exceeded for the specific building; then, in the second step, the DDD method is employed to determine the distribution of lateral and torsional stiffness for each story such that the target performance requirements (story drifts limits) are satisfied 50% of the time (i.e., a non-exceedance probability of 50%).

3. DIRECT DISPLACEMENT RETROFIT (DDR)

The DDR method proposed in this paper can be used to design buildings with horizontal irregularities (torsionally unbalanced) by distributing the stiffness of the structure vertically, along its height, and horizontally, in the plane of each story, such that the target displacement of each horizontal line of the resistance can be achieved under a specific seismic intensity, taking into account the nonlinear behavior of the structure. In order to simplify the DDR procedure, the structure can be modeled as a single degree of freedom (SDOF) system. Figure 2 presents an equivalent SDOF system for an N-story building. It can be seen that the total displacement measured at the center of mass of the story is a summation of displacement due to translation ($\Delta^{Tns.}$) and displacement due to torsion ($\Delta^{Tor.}$). The superscripts "*Tns.*" and "*Tor.*" are corresponding to translational and torsional displacements, respectively. The effective mass (W_{eff}) and lateral force distribution factors (C_v) can be calculated based on the approach used in Pang et al. (2009). The fundamental translational period of the building can be obtained from the displacement response spectrum that is developed based on the design spectral acceleration maps (ASCE7, 2010) and should be modified to take into account the effect of equivalent damping in the system as shown in Figure 3.

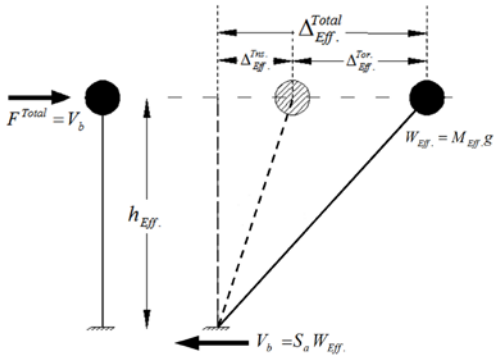


Figure 2. Equivalent SDOF model of multi-story building

Having the fundamental period of the building, the effective lateral stiffness, and consequently the distribution of the stiffness for lateral load resisting system at each story, can be obtained. The last step is locating the lateral load resisting systems (i.e., shearwalls or other retrofit assemblies in woodframe buildings) such that the design satisfies the initial assumption that is made regarding the contribution of torsion to the total displacement.

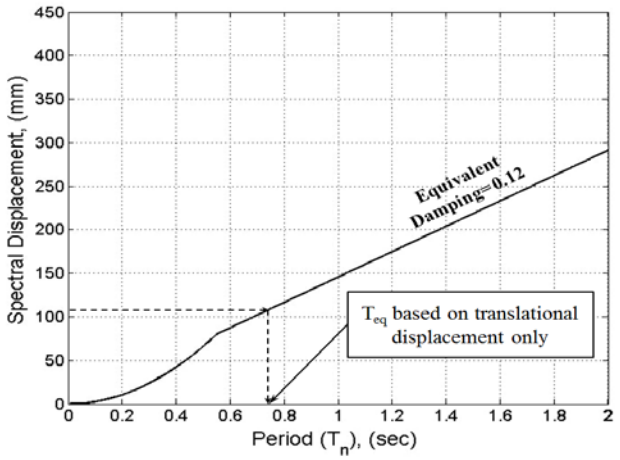


Figure 3. Displacement response spectrum

Retrofit Techniques

In this study, steel cantilever columns were used to retrofit the first story (soft story) and standard wood shearwalls with different nail patterns were used to retrofit the upper stories. The required lateral stiffness of each story was calculated based on the DDR method and using the secant stiffness of standard wood shearwalls and steel cantilever columns at the target displacement of the retrofit design (assuming that all walls along a common wall line experience the same displacement). For the steel frame, the initial stiffness of each column is given by (using DDR method):

$$K_{\sec ant} = \frac{(1-r)\Delta_Y + r\,\Delta_{T\arg et}}{\Delta_{T\arg et}} K_{in.} \quad (1)$$

where, $K_{in.}$ is the initial stiffness of a cantilevered column and r is the ratio of the secondary stiffness to the initial stiffness in a bilinear spring model. Δ_y is the lateral displacement associated with the yield strength (F_y) of at which point the initial stiffness reduces to secondary stiffness. Having the stiffness of each column, the initial stiffness of the frame can be calculated and the best cantilevered column design can be selected by using the lateral stiffness of two-column inverted moment frames with infinitely rigid beam (Equation 2). In this study, the grade beam was considered much stiffer than the columns and thus the columns were treated as inverted moment frames (IMF). The initial stiffness of each IMF is given by:

$$K_{in.} = \frac{6EI_c}{L_c^3} \quad (2)$$

where, I_c is the second moment of inertia of each column about its strong axis and L_c is the height of the frame. The secant stiffness corresponding to target drifts of 0.5% to 4% for 11.9 mm think OSB wood shearwall connected to framing member by 10d common nails is tabulated in Table 1.

Table 1. Secant stiffness for standard wood shearwall

		Secant Stiffness, K_s (kN/mm per m)				
		Wall Drift				
	Edge/Field Nail Spacing (mm)	0.50%	1.0%	2.0%	3.0%	4.0%
Standard Wood Shearwall	51/304	1.570	1.100	0.657	0.385	0.244
	76/304	1.214	0.786	0.448	0.256	0.159
	102/304	0.955	0.611	0.340	0.194	0.121
	152/304	0.684	0.422	0.231	0.132	0.082

4. FOUR-STORY FULL-SCALE SHAKE TABLE TESTING

A four-story woodframe building with a footprint of 11.6 m × 7.3 m (38 ft × 24 ft) and total height of 9.8 m (32 ft) was designed based on the proposed DDD method for nonlinear structures and its response was verified using the SAP2000© software. A solid model of the building is presented in Figure 4.

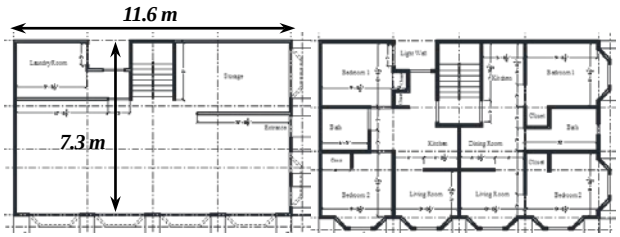


Figure 4. Solid model of soft-story woodframed building to be tested at NEES@UCSD.

Figure 5 presents the ground and typical floor plans of the building. At ground level (level 1), the building has four parking bays, a laundry room, and storage space; Levels 2-4 consist of two 2-bedroom apartments per story. The bold lines represent the lateral load resisting elements (i.e., wood shearwalls in this case) at each story. It should be noted that the ground floor has fewer shearwalls than the upper stories and their horizontal distribution at ground floor is highly

unsymmetrical which makes the building vertically and horizontally irregular. Figure 6 presents the CDF of peak story drifts when the building is subjected to a suite of 22 earthquakes along its long direction scaled for San Francisco, which verifies that the first story is, in fact, soft and weak and would collapse at a spectral acceleration well below MCE. In fact, there is a 98% probability that a 2% story drift will be exceeded. If 7% story drift is taken as a conservative collapse estimate, there is approximately a 70% probability of collapse for the un-retrofitted building at MCE level. Furthermore, the configurations of shearwalls in both ground and upper floors are not symmetric about the center of mass of the building; hence, the building was classified as an unsymmetric structure with severe torsion.

The eccentricity ratios in x- and y-directions at the ground floor are e_x/L_x = 27.8% and e_y/L_y = 34%, respectively. The in-plane eccentricity ratios in x- and y-directions at the upper stories are e_x/L_x = 12.9% and e_y/L_y = 18.2%, respectively. It should be noted that the location of centers of rigidity were calculated assuming that the relative stiffness ratio of all shearwalls remain constant during the analysis. Hysteretic models for horizontal wood siding and gypsum wall board were used to model exterior and interior walls for the non-retrofitted building. The results from a multi-record analysis shows that the building is weak in both translation and torsion, hence structural retrofit is required.



a) Ground floor plan b) Typical floor plan

Figure 5. Floor plans for the four-story building

Using the proposed DDR procedure, the building was retrofitted such that it would perform well during MCE level earthquakes in the San Francisco area, specifically to satisfy the desired performance criteria which is represented here as not exceeding a 2% story drift for half of the MCE level earthquake motions. In order to determine the contribution of torsion to the total displacement, the effective (i.e., equivalent) eccentricity of the building in the y-direction was calculated and divided by the width of the floor (i.e, L_y). The result was that, for all stories, 20% of the total displacement was due to rotation and the remainder was due to translation. Therefore, the building was designed for 80% of the target drift (i.e., 1.6%) and was checked to ensure that each story has enough torsional stiffness to limit the torsional displacement to 20% of the target drift (i.e., 0.4%). The equivalent damping ratio for all wood shearwalls was assumed to be 12% (i.e., 80% of 15% damping ratio proposed by Filiatrault and Folz, 2002). The fundamental period of the equivalent SDOF system was determined using response spectra for 12% damping and consequently the spatial distribution of lateral load resisting elements at each floor was calculated. A distributed load of 2.4 kN/m^2 (50 psf) was assigned to all floors and 1.9 kN/m^2 (40 psf) to the roof. Table 2 presents the design parameters and the distribution of the lateral and torsional stiffnesses of the building calculated based on the proposed DDR procedure. It can be seen that the torsional stiffness at all stories is greater than the required torsional stiffness which limits torsional displacements to be less than $\Delta^{Tor.}$. Ten inverted steel columns where used at the first story to retrofit the building. 11.9 (15/32") think wood shearwalls with nail patterns of 76/304 mm (3"/12"), 102/304 mm (4"/12") and 152/304 mm (6"/12") were used to retrofit the 2nd, 3rd and 4th stories, respectively. Each upper story needed about 14.6 m (48 ft.) of wood shearwall except the 4th story which required only 8.5 m (28 ft.) of wood shearwall.

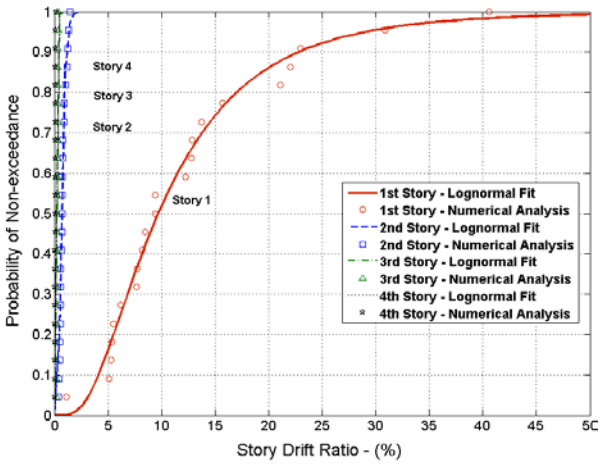


Figure 6. CDF of the peak drifts of the un-retrofitted four-story woodframe apartment building

Table 2. Summary of DDR method with torsion

Building Location	Story No.	Weight, KN (Kips)	Eccentricity X-Dir. (%)	Eccentricity Y-Dir. (%)	Target Drift $\Delta^{Trs.}$ (%)	Target Drift $\Delta^{Tor.}$ (%)	$C_{v,i}^{Total}$	Effective Height, m (ft)	Available Lateral Stiffness X-Dir. kN/mm (Kip/in)	Available Lateral Stiffness Y-Dir. kN/mm (Kip/in)	Required Lateral Stiffness X & Y, kN/mm (Kip/in)	Retrofit Lateral Stiffness X-Dir. kN/mm (Kip/in)	Retrofit Lateral Stiffness Y-Dir. kN/mm (Kip/in)	$K_{Avail.}^{Tor.} > K_{Req.}^{Tor.}$
San Francisco	1	222 (50)	27.8	34.0	1.6	0.4	0.11	7.10 (23.3)	1.13 (6.35)	0.86 (4.81)	13.2 (74.1)	12.07 (67.8)	12.34 (69.3	OK
	2	222 (50)	12.9	18.2	1.6	0.4	0.22				11.8 (66.0)	10.14 (56.7)	10.18 (56.9)	OK
	3	222 (50)	12.9	18.2	1.6	0.4	0.33		1.66 (9.31)	1.62 (9.08)	8.90 (49.9)	7.24 (40.6)	7.28 (40.8)	OK
	4	178 (40)	12.9	18.2	1.6	0.4	0.35				4.60 (25.8)	2.94 (16.5)	2.98 (16.7)	OK

Verification Using Non-linear Time History Analysis

The four-story building was modeled using the SAP2000© software and a detailed finite element time-history analysis was conducted to verify the performance of the building subjected to 22 far field earthquake records (FEMA P695, 2009) scaled to a seismic intensity corresponding to MCE level in San Francisco, California. The fundamental period of the building and the corresponding spectral acceleration were T_n = 0.45 seconds and S_a = 1.5g (5% damped), respectively. It should be noted that the effective period is a

combination of the first torsional and translational mode shapes of the building.

Figure 7 presents the rank-ordered peak story drifts from time history analysis, providing the probability of exceedance versus story drift of the building under the 22 far-field earthquakes scaled to 1.5g spectral acceleration. It can be seen that the story drift ratio corresponding to 50% probability of non-exceedance at the third story is 2.04% which is very close to the target drift of 2.00% giving only 2.0% error. The inter-story drift ratios at the 1st, 2nd, and 4th stories are all less than 2.00% which meets the desired performance criteria.

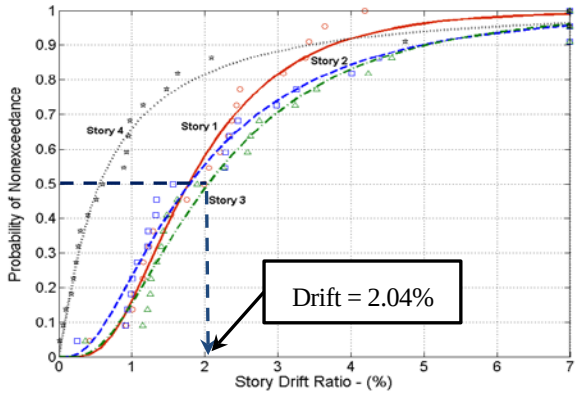


Figure 7. Probability of non-exeedance of 2% inter-story drift under 22 far-field earthquakes scaled to MCE level earthquake in San Francisco, California.

5. SUMMARY AND CONCLUSIONS

This paper provided a brief introduction to the NEES-Soft Project and focused on the performance-based seismic retrofit procedure entitled Direct Displacement Retrofit (DDR). This procedure is based on previously developed DDD methods. The four-story woodframe apartment building scheduled to be tested on the outdoor shake table at NEES@UCSD in the summer of 2013 was introduced and used to highlight the DDR procedure proposed in this paper. This building is a soft-story multi-family residential building that will be retrofitted using four different techniques as part of the test program. Numerical analysis of the steel cantilevered column retrofit was described in this paper. The DDR procedure appears to work well for buildings with extreme vertical and horizontal irregularities, making it a general enough to be used for woodframe systems and even other systems.

Acknowledgements:

This material is based upon work supported by the National Science Foundation under Grant No. CMMI-1041631 (NEES Research) and NEES Operations. Any opinions, findings, and conclusions or recommendations expressed in this material are those of the investigators and do not necessarily reflect the views of the National Science Foundation. The authors kindly acknowledge the senior personnel of the NEES-Soft project: David V. Rosowsky at Rensselaer Polytechnic Institute, Andre Filiatrault at University at Buffalo, Shiling Pei at South Dakota State University, Douglas Rammer at U.S. Forest Products Lab., David Mar at Tipping Mar, and Charles Chadwell at Cal-Poly; the other graduate students participating on the project: Ershad Ziaei (CU), Chelsea Griffith (WMU), Jingjing Tian (RPI), and Robert McDougal (CPP); and the practitioner advisory committee: Laurence Kornfield, Steve Pryor, Tom Van Dorpe, Doug Thompson, Kelly Cobeen, Janiele Maffei, Doug Taylor, and Rose Grant.

References:

Applied Technology Council (2011). "ATC 71-1: Guidelines for Cost-Effective Seismic Retrofit of Weak-Story Wood-Frame Buildings," Draft version dated Jan. 21, 2011.

ASCE (2010). "Minimum Design Loads for Buildings and other Structures." American Society of Civil Engineering; *Structural Engineering Institute 7-10*, Reston, VA.

Bahmani, P., and van de Lindt, J. W. (2012). "Numerical modeling of soft-story woodframe retrofit techniques for design." *Proc. of Structures Congress 2012*, ASCE, 1755-1766.

Federal Emergency Management Agency (2012). "Seismic Evaluation and retrofit of Multi-Unit Wood-frame Buildings With Weak First Stories., FEMA P-807, Washington D.C.

Filiatrault A. and Folz B. (2002). "Performance-based seismic design of wood framed buildings," *ASCE Journal of Structural Engineering*, 128(1): 39-47.

Folz, B. and Filiatrault, A. (2001)."Cyclic Analysis of Wood Shear Walls." *ASCE Journal of Structural Engineering*, Vol. 127(4), 433-441.

Pang, W.C., and Rosowsky, D.V. (2009). "Direct Displacement Procedure for Performance-based Seismic Design of Mid-rise Woodframe Structures," Earthquake Spectra, 25(3), 583–605.

Pang, W.C., Rosowsky, D. V., van de Lindt, J.W., and Pei, S. (2009), "Simplified Direct Displacement Design of Six-story NEESWood Capstone Building and Pre-Test Seismic Performance Assessment." NEESWood Report NW-05.

Pang. W., and Shirazi, S. M. H., (2012). "A Co-rotational model for cyclic analysis of light-frame wood shear walls." *ASCE Journal of Structural Engineering, NEES Special Issue*.

Priestley, M.J.N. (1998). "Displacement-based approaches to rational limit states design of new structures." Keynote Address, *Proceedings of the 11th European Conference on Earthquake Engineering*, Paris, France, 1998.

Shao, X., Reinhorn, A.M., Sivaselvan, M.V. (2011). "Real Time Hybrid Simulation Using Shake Tables and Dynamic Actuators." Journal of Structural Engineering, 137 (7), 748-760.

Wang, Y., Rosowsky, D. V., Pang W. C. (2010). "Performance-Based Procedure for Direct Displacement Design of Engineered Wood-Frame Structures." *ASCE Journal of Structural Engineering*, Vol. 136(8), 978-988.

10CUEE CONFERENCE PROCEEDINGS
10th International Conference on Urban Earthquake Engineering
March 1-2, 2013, Tokyo Institute of Technology, Tokyo, Japan

PERFORMANCE-BASED SEISMIC DESIGN FOR WOOD HOUSES USING EQUIVALENT LINEARIZATION METHOD

Hiroshi Isoda[1)] and Shu Nagaoka[2)]

1) Professor, Department of Architecture, Faculty of Engineering, Shinshu University, Japan
2) Graduate Student, Department of Architecture, Faculty of Engineering, Shinshu University, Japan
hisoda@shinshu-u.ac.jp, 11ta327b@shinshu-u

Abstract: Performance-based seismic design is a developing design methodology in the modern seismic design and research community and has already been applied to the building standard law and enforcement in Japan. However, the application to wood houses, which represents the vast majority of the residential building stock, is still under early stage of development, mainly due to a lack of understanding of the dynamic response.
This paper discusses the application of performance-based seismic design to wood houses through an equivalent linearization method. In the first part of the paper, the fundamentals of the equivalent linearization for wood houses are outlined. Thereafter, a description of the system parameters required for its application is descried. For the purpose of evaluating these parameters for wood houses, non-linear time history analyses for predicting the response and evaluating the energy dissipation of wood houses under from moderate to severe earthquakes are presented. As the result of numerical studies, equivalent period of non-linear system and equivalent viscous damping with pinching behavior are summarized. As application examples, peak displacements are compared with the displacement calculated from both non-linear time history analysis and proposed equivalent linearization method.

1. INTRODUCTION

The building code of Japan has been changed from current prescriptive and the traditional force-based design into performance-based approach in 2000 in order to newly compile a highly flexible Building Standard Law of Japan (The Build Center of Japan 2004). Several key papers laid the foundation for the standard and code development of performance-based seismic design (PBSD) including in timber-based building .

In that decade, PBSD has been developed all over the world. As for the timber-based structure in the late 1990's and early 2000's, the CUREE-Caltech Woodframe Project in the U.S. focusing on the improvement of woodframe codes and standards through a detailed and robust experimental, numerical and documentation effort to examine current practices in the design and construction of woodframe buildings has been started. Several useful papers laid the foundation for the development of PBSD in the project. The NEESWOOD project which has started since 2006 sought to develop a performance-based seismic design philosophy for mid-rise woodframe buildings through an extensive siries of numerical simulations and full-scale system-level experiments (Filiatrault et al, 2010; van de Lindt et al, 2010) as well as numerical modeling (Christovasilis, 2010; Pei and van de Lindt, 2010). .

This paper discusses the application of performance-based seismic design to wood houses through an equivalent linearization method. In the first part of the paper, the fundamentals of the equivalent linearization for this study are outlined. Thereafter, a description of the system parameters such as an equivalent elastic period and damping required for its application is descried. For the purpose of evaluating these parameters for wood houses, non-linear time history analyses for predicting the response and evaluating the energy dissipation of wood houses under from moderate to severe earthquakes are presented. As the result of numerical studies, equivalent period of non-linear system and equivalent viscous damping with pinching behavior are summarized. As application examples, peak displacements are compared with what calculated from both non-linear time history analysis and proposed equivalent linearization method.

2. FUNDAMENTAL OF DISPLACEMENT-BASED DESIGN PROCEDURE

2.1 Key Equation for Target Displacement

Since interstory drift is a key parameter for the control of damage and collapse in timber-based structure, it is rational to examine a procedure wherein displacements are considered at the beginning of the seismic design process. The fundamental components of this procedure, known as the direct-displacement method (Priestley 1993) are discussed. In Japan, mainly for steel construction including in the structure with dampers, some equations to evaluate

equivalent stiffness and equivalent viscous damping at a target drift have been proposed (Nakashima 1999). A following equation (Kasai 2003) is now discussing in this paper.

$$S_d(T_e, h_{eq}) = \frac{T_e}{2\pi}\overline{S_{pv}}(T_0 - T_e) \times D_h(h_{eq}) \quad (1)$$

Where T_e=equivalent elastic period of the structure at the target displacement S_d, $\overline{S_{pv}}$=the average of pseudo velocity from T_o to T_e and D_h=damping reduction factor. $D_h = \sqrt{(1+25h_0)/(1+25h_{eq})}$

In this equation, T_o which is given from initial stiffness and effective mass is a key parameter but it is difficult to evaluate the initial stiffness in a timber-based structure because the load-displacement response of the structure is highly nonlinear behavior under monotonic and cyclic loading. In this study, T_o-T_e is replaced to T_{eff} which is calculated only from a peak target displacement as shown in Eq. (2). The heq in Eq. (1) which is an average of ductility factors in each cyclic loading is also replaced to an equivalent viscous damping calculated from a peak target displacement.

$$S_d(T_e, h_{eq}) = \frac{T_{eff}}{2\pi}\overline{S_{pv}}(T_{eff}) \times D_h(h_{eq}) \quad (2)$$

2.2 Determination of Effective Elastic Period, T_{eff}

The effective elastic period, T_{eff} is regarded as the elastic period obtained from the energy spectrum in nonlinear time history analysis. The detail is shown below.

STEP 1: response velocity and response acceleration is computed by nonlinear time history analysis. Total energy input is calculated from Eq. (3).

$$E_a = \int_0^{T_d} \dot{x} \cdot \ddot{y}\, dt \quad (3)$$

STEP2: equivalent velocity, V_{Ea} obtained from Eq. (4) is calculated.

$$V_{Ea} = \sqrt{\frac{E_a}{2m}} \quad (4)$$

STEP 3: time history analysis for elastic system is conducted and V_{Ea}-T spectrum is drown.

STEP 4 : T_e is calculated from effective seismic mass, m and equivalent lateral stiffness which is a tangent stiffness, k_e of a peak displacement as shown in Eq. (5).

$$T_e = 2\pi\sqrt{\frac{m}{k_e}} \quad (5)$$

STEP 5: effective elastic period T_{eff} is determined from following equation and parameters, A and B, in the equation is defined as the factors to correspond to V_{Ea}-T spectrum.

$$T_{eff} = A \cdot \left(1 + \frac{1-A}{(T_e \cdot 10)^B}\right) \cdot T_e \quad (6)$$

2.3 Determination of Equivalent Viscous Damping

In order to capture the energy dissipation characteristics of the structure at the target displacement an equivalent viscous damping ratio must be determined. For this purpose, several damping database has been established for the selected structural system from the global hysteretic behavior of the structure. During earthquake the structure behave in unstable amplitude. The story drift of the structure depends on not only the performance of the structure but also the phase and strength of the ground motions. That means equivalent viscous damping obtained from regular scheduled cyclic loading test and the testing protocol (Krawinkler et al. 2000) modeled from time history analysis does not express the energy dissipation correctly.

In this study, four equations of equivalent viscous damping were used:

$$hs = \frac{-\int_0^t \ddot{y}_0 \dot{y}\, dt}{2\omega_e \int_0^t \dot{y}^2\, dt} \quad (6)$$

$$ht = \frac{1}{2\pi} \cdot \frac{\Delta W}{W} \times 0.8 \quad (7)$$

$$h = 0.2\left(1 - 1\Big/\sqrt{\frac{\Delta_{\max}}{\Delta_y}}\right) + 0.05 \quad (8)$$

$$hp = 1/30 \cdot \Delta + 0.05 \ : \ 0 < \Delta \le 3$$

$$hp = 0.15 \ : \ 3 < \Delta \quad (9)$$

Where $\ddot{y}_0$ = ground acceleration, $\ddot{y}$ =response acceleration and ω_e = angular frequency at the tangent angle of a peak displacement

hs from Eq. (6) which is called "substitute damping" is the damping computed from non-linear time history analysis. *ht* is the damping calculated from ΔW which is energy dissipated per cycle at the target displacement Δ and W which is $ke \cdot \Delta^2$ under cyclic loading test. *h* in the Eq. (8) is the damping factor defined in the performance-based seismic code in Japan. Δ_y is the yield displacement of the structure. Then *hp* is the damping proposed by the result of the analytical study (Filiatrault 2003) and the damping was reduced in 80% as well as *ht*.

3. TIME HISTORY ANALYSIS

A series of nonlinear time history analyses were performed to determine effective elastic period, T_{eff} and to calculate substitute damping.

3.1 Histeresis Model and Seismic Mass

The EPHM model (Pnag, 2007) modified by the

authors to correspond to Japanese post-beam wood house (Hitomi and Isoda 2010) as shown in figure 1 was used in the nonlinear time history analysis. The parameters shown in Table 1 in the hysteresis model are defined by the result of shaking table test for the two story structure which has minimum requirement of the Japanese building standard law. Seismic mass is the effective mass of the two-degree of freedom system.

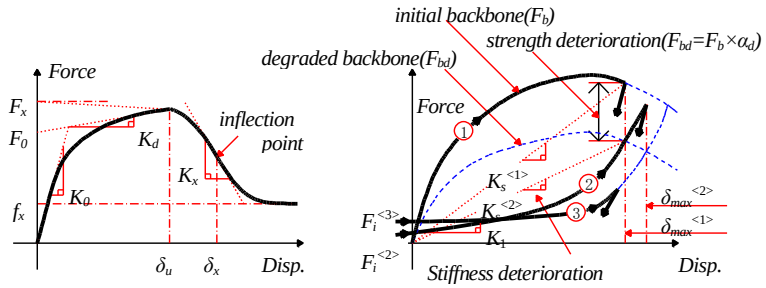


Figure 1 Modified EPHM model

Table 1 Parameters for time history analysis

K_0	K_d	F_0	D_x	K_x	F_x	f_x	K_{fi}	$K_{\lambda u}$	$\lambda_{\lambda u}$	$X_{\lambda u}$	γ_u	γ_1	M
32.7	1.0	37.2	15.0	-1.6	50.9	16.2	-0.2	0.08	-0.003	3.7	0.1	0.5	82.9

Table 2 Earthquake records in this study

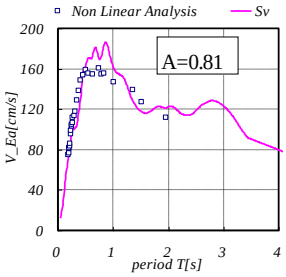
No.	Name of Earthquake		*PGA* [cm/sec^2]	Scale factor 50[cm/sec]	Duration time [sec]	Parameters	
						A	B
1	Imperial Valley 1940	El Centro NS	341.70	1.35	33.60	0.81	0.88
2		El Centro EW	210.10	1.09	44.42	0.96	0.13
3	Kern Country 1952	Taft N021E	152.70	2.88	42.08	1.00	0.10
4		Taft N111E	175.90	2.84	41.14	0.79	0.39
5	Tokachi-oki 1968	Hachinohe NS	239.65	1.45	38.86	0.82	0.38
6		Hachinohe EW	180.23	1.32	38.76	0.78	0.32
7	Kobe 1995	JMA Kobe NS	804.90	0.62	14.18	1.00	0.10
8		JMA Kobe EW	586.54	0.67	14.58	0.90	1.00
9		JR Takatori NS	599.18	0.39	19.97	0.77	0.43
10		JR Takatori EW	603.21	0.41	18.33	0.88	0.26
11	Iran 1978	Tabas N074E	819.09	0.51	22.14	0.99	1.00
12		Tabas N344E	834.73	0.41	23.46	0.84	0.10
13	Northridge 1994	Newhall NS	577.98	0.52	12.74	0.98	1.00
14		Newhall EW	571.37	0.67	14.12	0.93	0.91
15		Sylmar NS	826.44	0.39	10.98	0.96	1.00
16		Sylmar EW	592.40	0.64	15.68	0.98	1.00
17	Chichi (Taiwan) 1999	TCU065 NS	590.72	0.64	38.15	1.00	0.26
18		TCU065 EW	797.54	0.40	37.06	0.64	0.44
19		TCU068 NS	452.47	0.19	23.56	0.57	0.10
20		TCU068 EW	554.65	0.28	24.37	0.77	0.27
21		TCU074 NS	341.89	1.22	35.06	0.82	0.35
22		TCU074 EW	585.29	0.68	28.55	0.78	0.37
23	Kocaeli (Turkey) 1999	Ypt NS	342.01	0.80	20.72	0.71	0.17
24		Ypt EW	262.31	0.76	22.00	0.83	0.36
25		Sakarya	386.90	0.63	18.90	0.93	0.27
26	Artifical wave	BCJ_L1	207.33	1.60	45.32	0.90	0.22
27		BCJ_L2	355.66	0.69	93.02	0.90	0.16
28		BSL	591.92	0.56	14.49	0.92	0.60
29		Medium soil condition	540.87	0.72	94.05	0.88	0.20
30	Niigata Chuetsu 2004	JMA OjiyaNS	779.24	0.75	33.60	0.93	0.29
31	Noto 2007	K-net Anamizu	781.96	0.52	27.32	0.93	0.19

3.2 Ground Motions

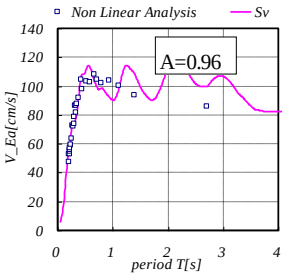
Table 2 presents the characteristic of the 31 earthquake records in this study. These records are scaled in the maximum velocity of 50cm/sec. The duration time of the earthquake is from 1% to 99% in the squared cumulative acceleration.

3.3 Definition of the parameters

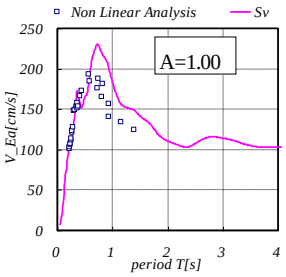
Figure 2 show the comparison of effective elastic period with energy spectrum. The variable parameter of this study is the seismic mass. The mass was divided from 0.5 to 3.0. The parameter A in Eq. (6) is shown in the figure and summarized in table 2. Note that upper limit of A is 1.00. The energy input for the structural system can be expressed by the effective elastic period although availability appears to be inconsistent. The averages of the 31 earthquake records in parameter A and B are 0.87 and 0.43, respectively.



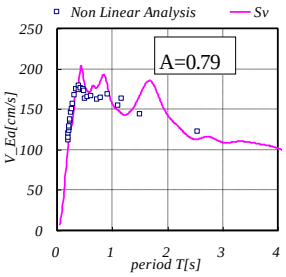
1) No.1



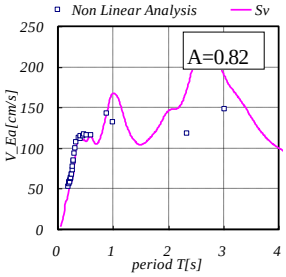
2) No.2



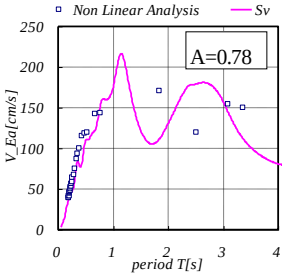
3) No.3



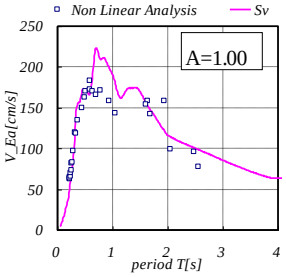
4) No.4



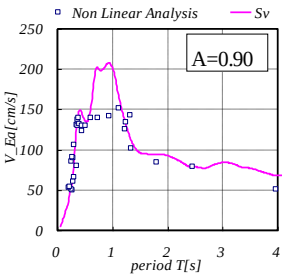
5) No.5



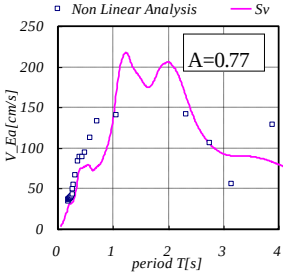
6) No.6



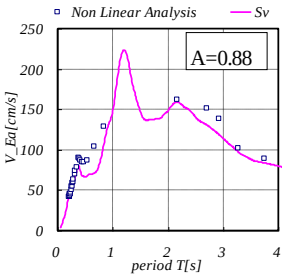
7) No.7



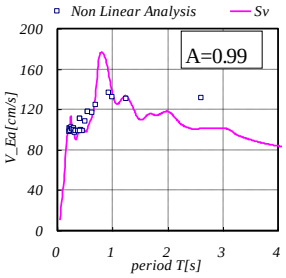
8) No.8



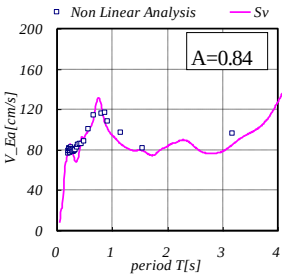
9) No.9



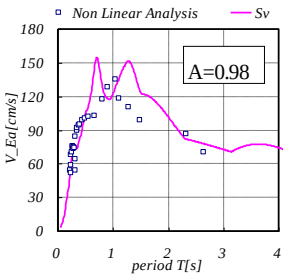
10) No.10



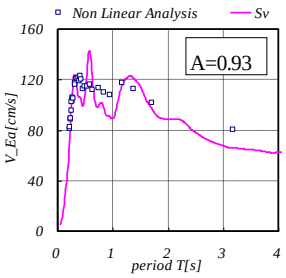
11) No.11



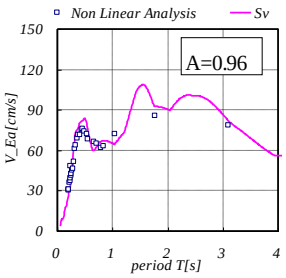
12) No.12



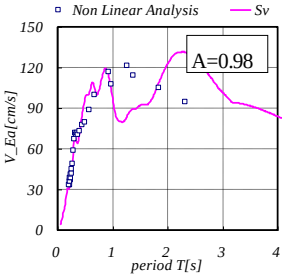
13) No.13



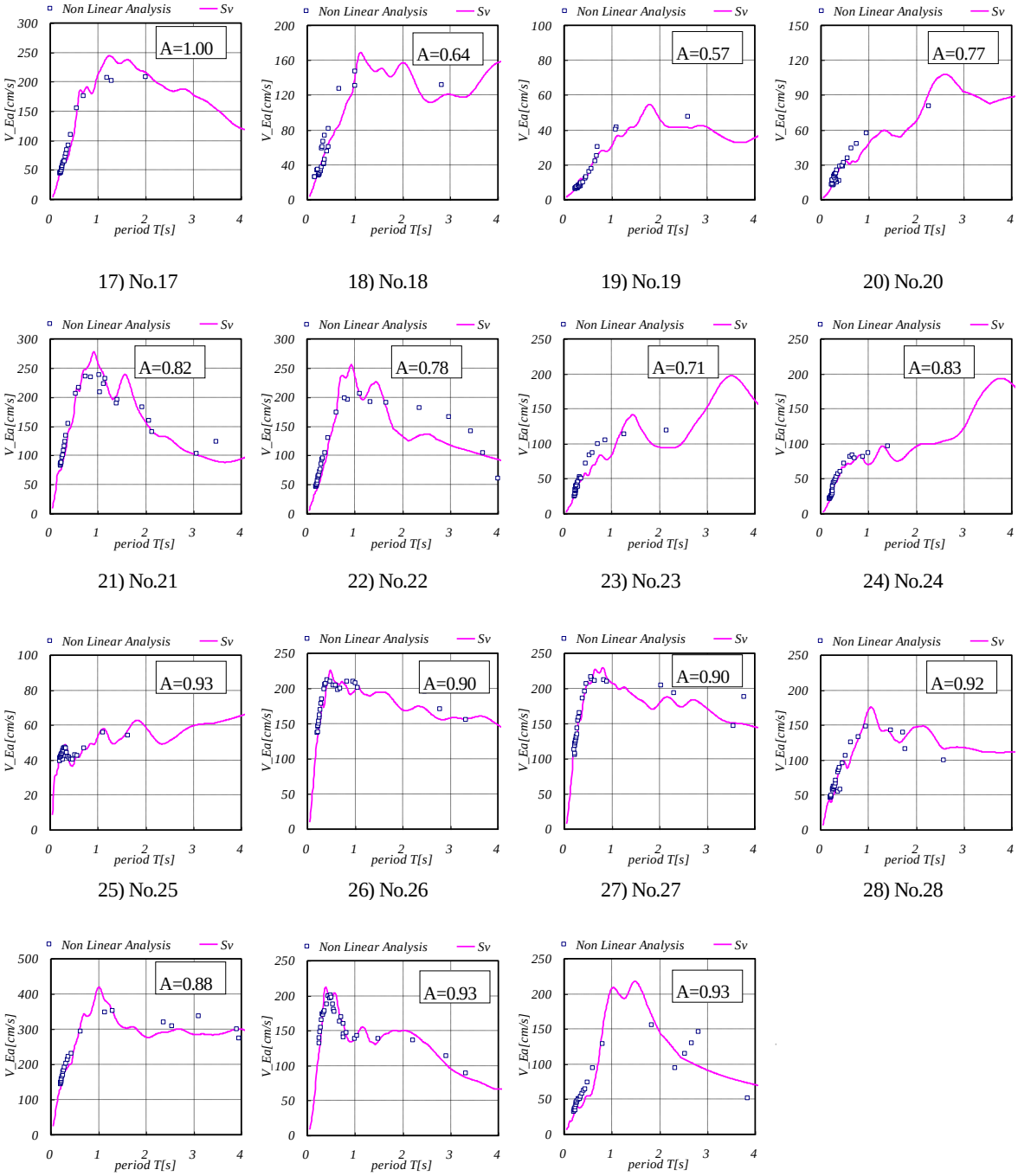
14) No.14



15) No.15



16) No.16



17) No.17 18) No.18 19) No.19 20) No.20

21) No.21 22) No.22 23) No.23 24) No.24

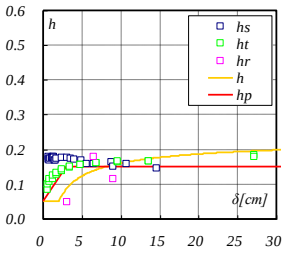
25) No.25 26) No.26 27) No.27 28) No.28

29) No.29 30) No.30 31) No.31

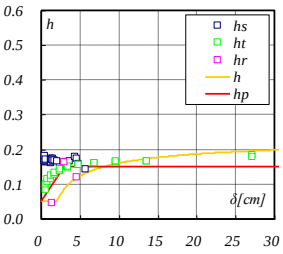
Figure 2 Distributions of effective elastic period in energy spectrum

The distributions obtained from damping factor are shown in Figure 3. Note that seismic mass is the variable parameter for calculating *hs* and *hr* is the damping factor which gives the same peak displacement as time history analysis. At the calculation of *hr* the parameter of seismic mass in table 1 is divided in 0.7, 1.0 and 1.5. *ht* is also calculated from the shear wall test for plywood sheathing panel against simple step-up cyclic loading.

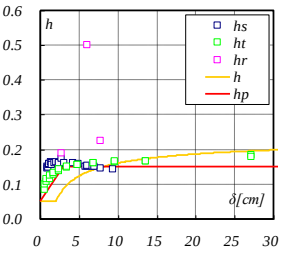
The damping of *ht*, *h* and *hp* remains almost constant for a given amplitude beside *hs* and *hr*. *hr* giving the actual peak displacement varies. It means that damping factor giving actual displacement can't express as the normal equation.



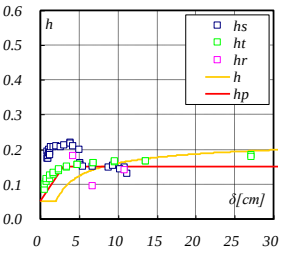
1) No.1



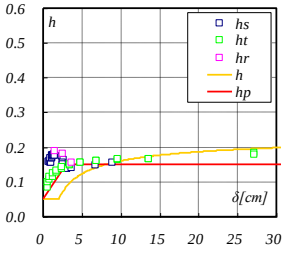
2) No.2



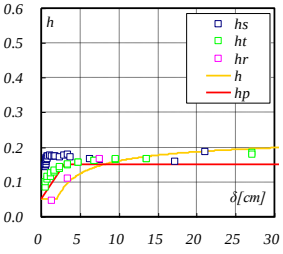
3) No.3



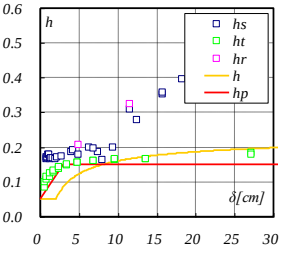
4) No.4



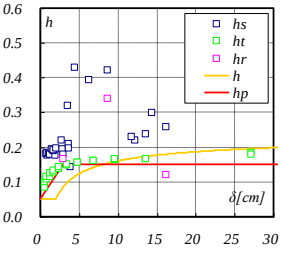
5) No.5



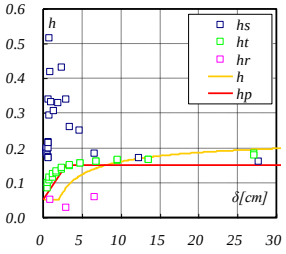
6) No.6



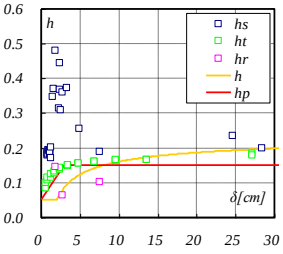
7) No.7



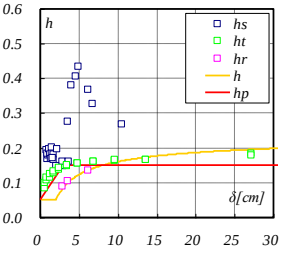
8) No.8



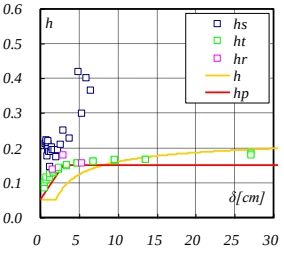
9) No.9



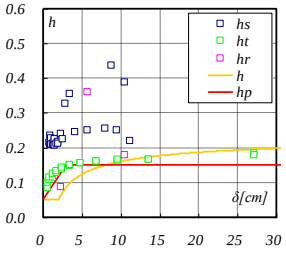
10) No.10



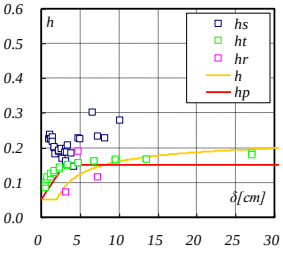
11) No.11



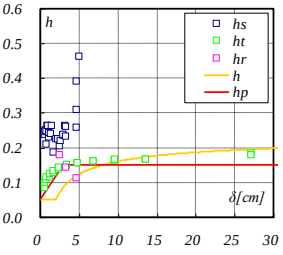
12) No.12



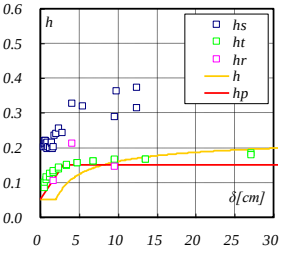
13) No.13



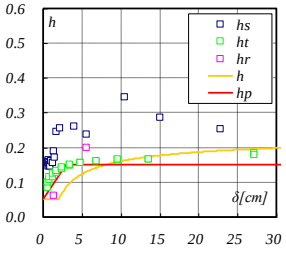
14) No.14



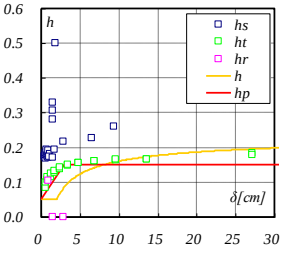
15) No.15



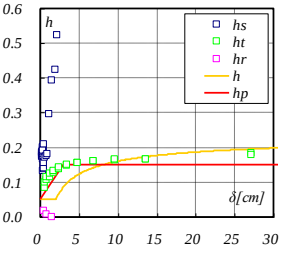
16) No.16



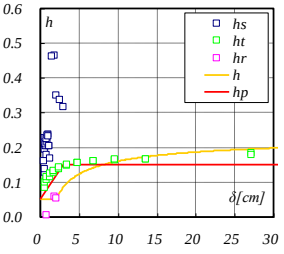
17) No.17



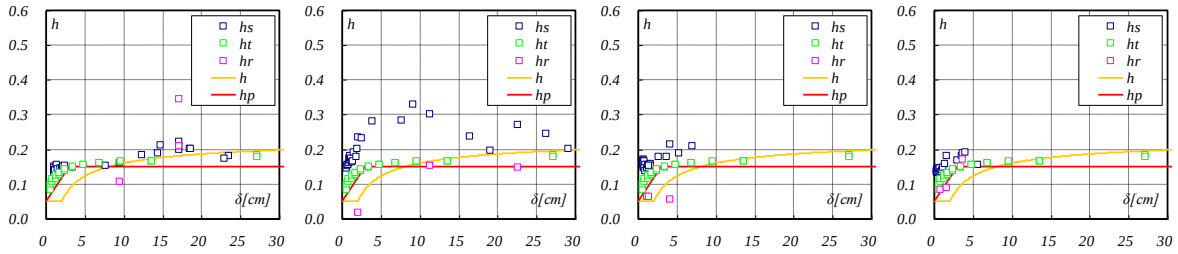
18) No.18



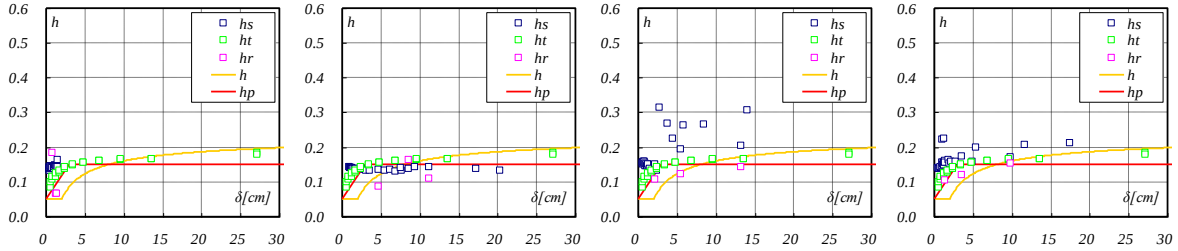
19) No.19



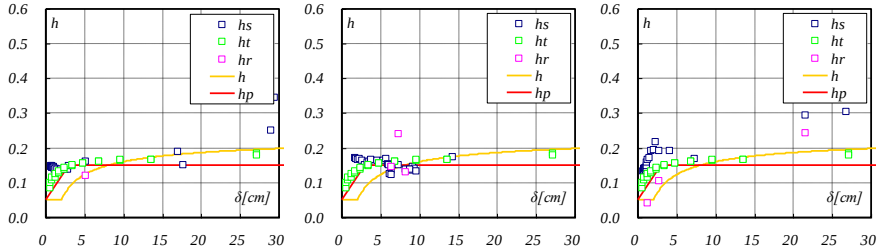
20) No.20



21) No.21 22) No.22 23) No.23 24) No.24



25) No.25 26) No.26 27) No.27 28) No.28



29) No.29 30) No.30 31) No.31

Figure 3 Distribution of damping factor

4. VALIDATION OF EQUIVALENT LINEAR MODEL

Figure 4 presents the comparisons of the peak displacement obtained from several equivalent linear models (ELM) and nonlinear time history analysis (NLTHA). Note that analyses are produced the combination of the system which has seismic mass of division of 0.7, 1.0 and 1.5 and 31 earthquake records. Total number of analyses is 93 cases. The parameters in Eq. (6) were used 0.87 and 0.43, respectively. Figure 5 shows the result coming from the conventional method calculated from Eq. (1) and figure 6 also shows the result of equivalent period T_e. The result from proposed effective elastic periods, T_{eff} in Eq.(6) .and constant damping expressed of h_p=15%i is equal to or more correct than that of the past method.

3. CONCLUSIONS

An outline of framework of the performance-based seismic design of timber-based structure and a validation of the peak displacement computed from proposed effective elastic period and several values of damping were describe in this paper. The peak displacement used the effective elastic period expressed only in a target displacement is equal or more accurate to the displacement used the past procedure. Although the equivalent damping depends on variety of waves and target displacement and isn't able to express to equation correctly, the constant damping factor of 15% gives almost agreement in displacement.

The numerical results confirmed the validity of this proposed direct-displacement based design procedure.

References:

The Building Center of Japan (2004), "The Building Standard Law of Japan", 613-626.

Filiatrault, A, Christovasilis, I.P, Wantikorkul, A. and J.W. van de Lindt. (2010), "Experimental Seismic Response of a Full-Scale Light-Frame Wood Building," *ASCE Journal of Structural Engineering*, 136(3): 246-254

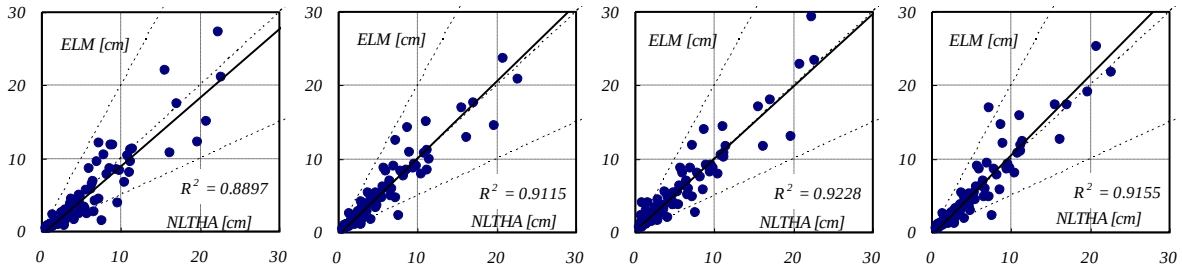
Van de Lindt, J.W., S.Pei, S.E. Pryor, S.E., Shimizu, H. and Isoda H. (2010), "Experimental Seismic Response of a Full-Scale Six-Story Light-frame Wood Building," *ASCE Journal of Structural Engineering*, 136(10): 1262-1272

Christovasilis, I.P and Filiatrault, A. (2010), "Two-Dimensional Seismic Analysis of Multi-Story Light-Frame Wood Buildings," *9th US National & 10th Canadian Conference on Earthquake Engineering: Reaching Beyond Borders*, Toronto, Canada, Paper No.69, 10 p.

Pei, S. and van de Lindt, J.W. (2010), "Seismic Numerical Modeling of a Six-story Light-frame Wood Building," *Journal of Earthquake Engineering and Structural Dynamics*, 38: 1631-1647

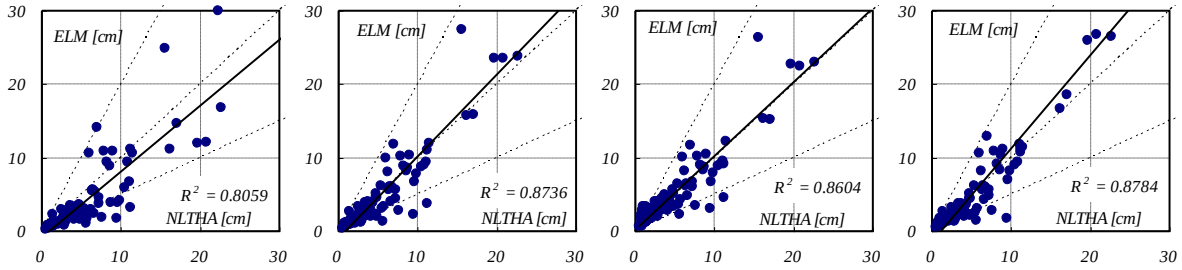
Priestley, M. J. N. (1993), "Myths and fallacies in earthquake engineering – conflicts between design and reality," *Bull. New*

Zealand national Sec. for Earthquake Eng., 26(3), 329-341
Nakashima, M. and Inaoka, S. (1999), "Ductility Demanded of Members in Steel Moment Frames Sustaining Beam-Hinging Mechanism," *Transactions of the AIJ*, 903-904
Kasai, K., Ito, H., Watanabe, A. (2003), "Peak Response Prediction Rule for a SDOF Elasto-plastic System Based on Equivalent Linearization Technique," *AIJ Journal of Structural Engineering*, 53-62
Krawinkler, H., Parisi, F., Ibarra, L., Ayoub, A., and Medina, R. (2000). "Development of a testing protocol for wood frame structures," *CUREE Publication* No. W-02, Richmond, Calif.
Filiatrault, A., Isoda, H. and Folz, B. (2003) "Hysteretic Damping of Wood Framed Buildings," *Engineering Structures*, (25), 461-471
Pang, W.C., Rosowsky, D.V., Pei, S. and van de Lindt J.W. (2007), "Evolutionary Parameter Hysteretic Model for Wood Shear Walls," *ASCE Journal of Structural Engineering*, 133(8), 1118-1129
Hitomi, Y., Isoda, H. and Kawai, N. (2009) "Hysteresis Model of Wood Shear Wall Considering of Large Displacement and Deterioration of Cyclic Load," *AIJ Journal of Structural Engineering*, 2299-2306



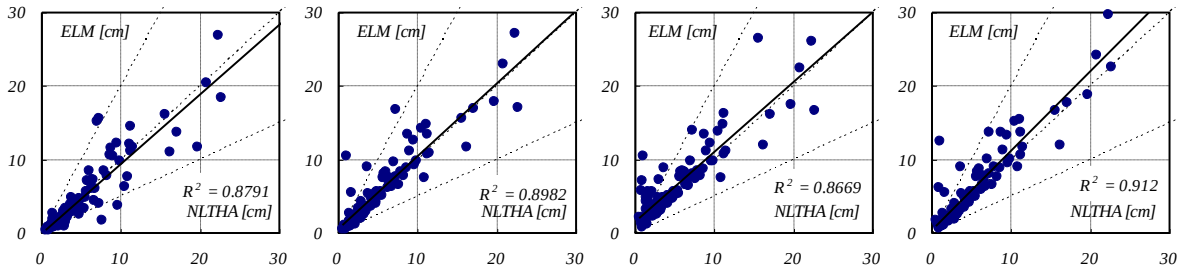
a) *hs* b) *ht* c) *h* d) *hp*

Figure 4 Validation of result (T_{eff})



a) *hs* b) *ht* c) *h* d) *hp*

Figure 5 Validation of result (T_o-T_e)



a) *hs* b) *ht* c) *h* d) *hp*

Figure 6 Validation of result (T_e)

10CUEE CONFERENCE PROCEEDINGS
10th International Conference on Urban Earthquake Engineering
March 1-2, 2013, Tokyo Institute of Technology, Tokyo, Japan

COLLAPSING ANALYSIS OF SHAKE TABLE TESTS OF THREE STORY POST-AND-BEAM WOOD HOUSES

Takafumi Nakagawa[1], Tatsuya Miyake[2], Hiroshi Isoda[3], Naohito Kawai[5] and Takahiro Tsuchimoto[4]

1) Senior Research Engineer, Building Research Institute, Japan
2) President, Nihon System Sekkei Architects & Engineers, Japan
3) Professor, Department of Engineering, Shinshu University, Japan
4) Professor, Faculty of Architecture, Kogakuin University, Japan
5) Head, National Institute for Land and Infrastructure Management, MLIT, Japan
nakagawa@kenken.go.jp, miyake@nittem.co.jp, hisoda@shinshu-u.ac.jp,
kawai-nk@cc.kogakuin.ac.jp, tsuchimoto-t92ta@nilim.go.jp

Abstract: In our previous reports, we executed the collapsing tests of three story post-and-beam wood houses by the shake table (E-Defense, NIED) and the three dimensional numerical analysis. The result of the numerical analysis based on the static element tests of seismic components of the specimens roughly agreed with experimental results. But at the detailed points, analysis model didn't correspond well with the test results and calibrated input parameters were not explained completely. In this paper, we modified the input parameters of numerical models by the result of the dynamic element tests of seismic components, and tried to trace the collapsing process at shake table tests.

1. INTRODUCTION

In our previous reports (Tsuchimoto 2010, Miyake 2010), we executed the collapsing tests of four post-and-beam wood houses by the shake table (E-Defense, NIED) and the three dimensional numerical analysis models of the specimens were verified. The two of the specimens (No.1 and No.2) have the same amount of shear walls, but the specification of the column end joints was different. The specimen No.2 didn't have sufficient tensile capacity of column end joint and No.1 have enough tensile capacity. At the shake table tests, the shear walls of No.1 failed and collapsed without no breakage of the column end joint, but the column end joints of the specimen No.2 were pull out at early stage and survive by the rocking behaviour of whole structure.

In the current seismic design method of Japanese post-and-beam wood houses, it is not considered that the column end joints are pulled out before the shear walls yield, so it is impossible to explain these shake table results. But it is necessary for further structural design to explain the ultimate collapsing behaviour like these shake table specimens.

In this paper, we executed the additional shear tests of shear walls that were seismic components of shake table specimens and the tensile tests of metal fasteners of the specimens. The displacement waves observed at the shake table test were used for the loading schedule of these element tests. The both dynamic and static loadings were carried out.

By these test results, we improved our numerical models and carried out the response analysis for shake table tests. The several variations of load displacement relationships for the springs of numerical models were used for numerical analysis. The numerical analysis uses one of these spring parameters agreed well with shake table result.

2. SHAKE TABLE TESTS

2.1 Outline of specimens

Table 1 shows specifications of shake table specimens. Four types of specimens were used for the tests. In this study, No.1 and No.2 is the target specimens for our numerical analysis. Figure 1 shows the picture of specimens No.1 and No.2. The both specimens are real-size three story wood house by post-and-beam construction. The main seismic element is bracing shear walls, gypsum board wall, and siding panel sheathed wall. The shake table tests were carried out at the E-Defence (National institute of earth science and disaster prevention) in Kobe prefecture. The two of the specimens (No.1 and No.2) have the same amount of shear walls, but the specification of the column end joints was different. The specimen No.2 didn't have sufficient tensile capacity of column end joint and No.1 have enough tensile capacity.

The column end joints of No.1 are designed to have enough tensile capacity if its shear walls reach their allowable shear force. But the column end joints of No.2 are designed to

have tensile capacity for the lateral load that is demanded at the building standard.

Figure 2, 3 shows the configuration of seismic elements All of the columns and beams were made from Glue-Lam. Cross section of columns is 105 x 105 (mm). Cross section of beams is 105 (mm) in width, 180-240 (mm) in depth. Shear walls were composed with brace, gypsum board and siding board. Braces were made from LVL with cross section of 45 x 90 (mm). The gypsum boards were set on the structural frame with screw nails as the substrate of interior walls. The siding boards were set on the structural frame with nails as the exterior walls.

The hardware for reinforcement of the column-end joints were selected from common hardware appearing on the market. 'P06' and 'P10' in Figure 2, 3 are L-shaped metal plate, 'H15', 'H20' and 'H25' are the hold-down hardware. All of the hardware was set on the structural frame with the screw nails. The allowable tensile force of 'P06' and 'P10' are 6.2 (kN) and 19.4 (kN). of 'H15', 'H20' and 'H25' are 15 (kN), 20 (kN) and 25 (kN) for each.

The horizontal plane of structure was composed with the plywood boards with the thickness of 28 (mm) which were set on the structural frame with the nails.

2.2 Input ground motion

Input seismic motion was the artificial seismic motion with acceleration spectrum which suited to the response spectrum of 2nd class of soil ruled in building standard as shown in Figure 4. The duration of the seismic motion is 20 (sec) as shown in Figure 5, The intensity of the seismic motion is approximately equal to it of the large earthquake with the return period of 400 year in Japan. The seismic motion was input to one direction of the shake table shown in Figure 1. This input wave is called "BSL" in this paper.

Table 1 Specifications of shake table specimens

Specimen	Shear walls and diaphram	Column end joints
No.1	1.25 times larger shear wall capacity than building standard requirement	adequately designed
No.2	1.25 times larger shear wall capacity than building standard requirement	inadequately designed
No.3	minimum shear wall capacity for building standard requirement and weaker floor diaphram	adequately designed
No.4	minimum shear wall capacity for building standard requirement	adequately designed



Figure 1 The photograph of shake table specimens

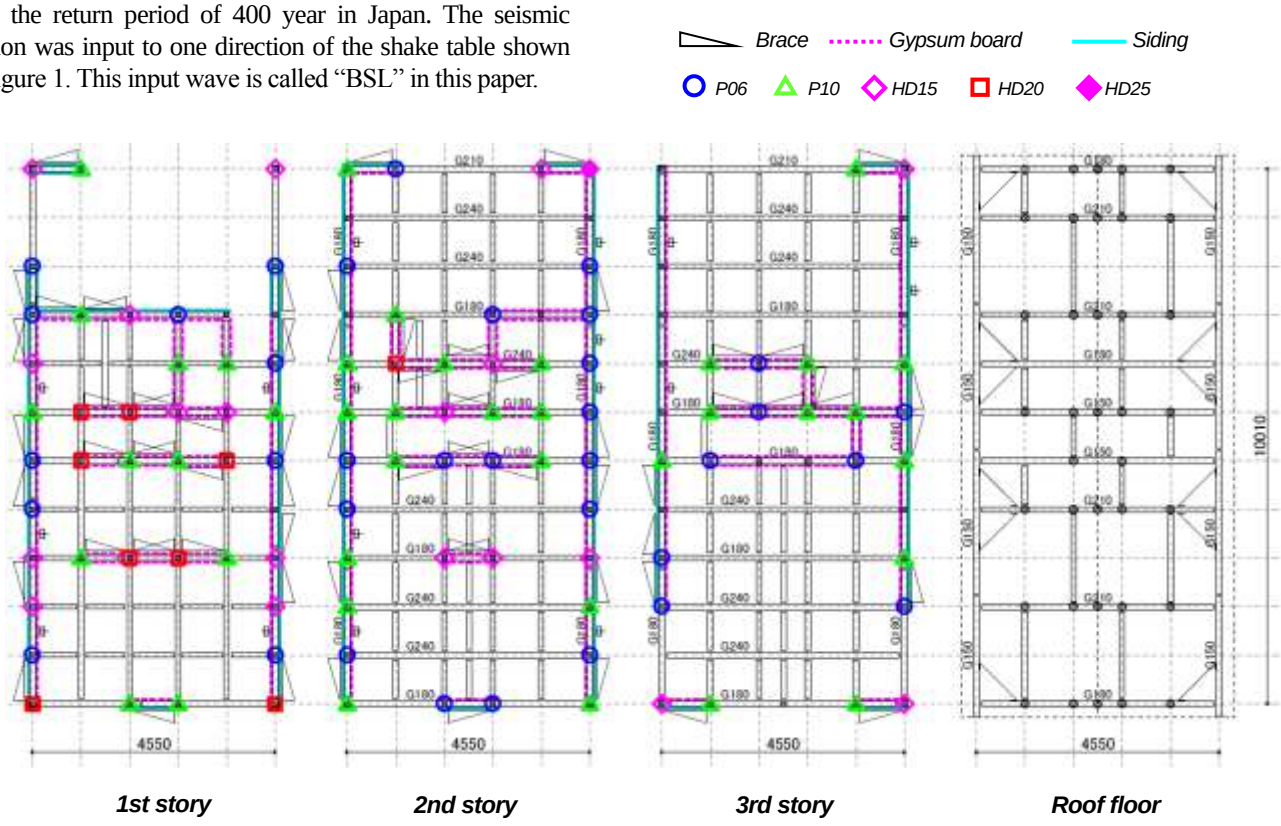


Figure 2 Configuration of shear wall and specification of column end joints at specimen No.1

2.2 Test results

At the BSL 90% level input, the maximum story drift angle of both models was approximately 1/100 (rad). There was no damage except slight cracks of the gypsum boards at the corner of the openings. The relation of the story shear and the story drift was almost linear.

At the BSL 160% level input, the story drift angle in 1st story of specimen No.1 reached 1/5 (rad) at 9.0 (sec) from the start of the seismic motion. Thereafter the story drift was kept 1/5 or less for approximately 6 (sec). Lastly, No.1 collapsed to the minus direction. On specimen No. 2, the mass of the joints of column base in 1st story fractured until 5.0 (sec) from the start of the seismic motion. All column base in 1st story in X0 axis lifted to 150 (mm) or more at 5.0 (sec) from the start of the seismic motion. Then the column bases didn't return to the original position, i.e. to the sill, but they reposed on the steel frame which was used for fixation of the model to the shake table. Thereafter, they slid in Y-direction like base-isolated building, Model 2 escaped from collapse.

Table 2 Maximum story drift of first floor (unit: mm)

Specimen	BSL input level			
	90%	112.50%	150%	160%
No.1	27.6 (1/102)	–	–	Collapse
No.2	26.2 (1/107)	–	–	426 (1/5.4)
No.3	–	99.7 (1/28)	336 (1/8.3)	–
No.4	–	61.1 (1/46)	349 (1/8.0)	–

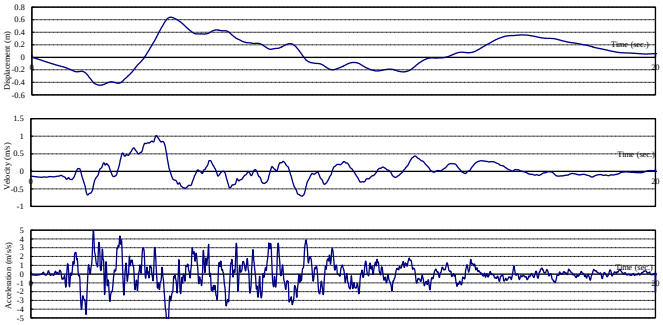


Figure 4 Input ground motion of shake table test.

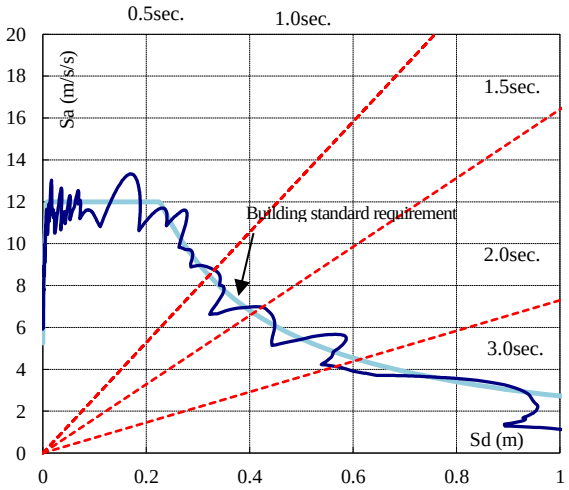


Figure 5: Response spectrum of Input ground motion

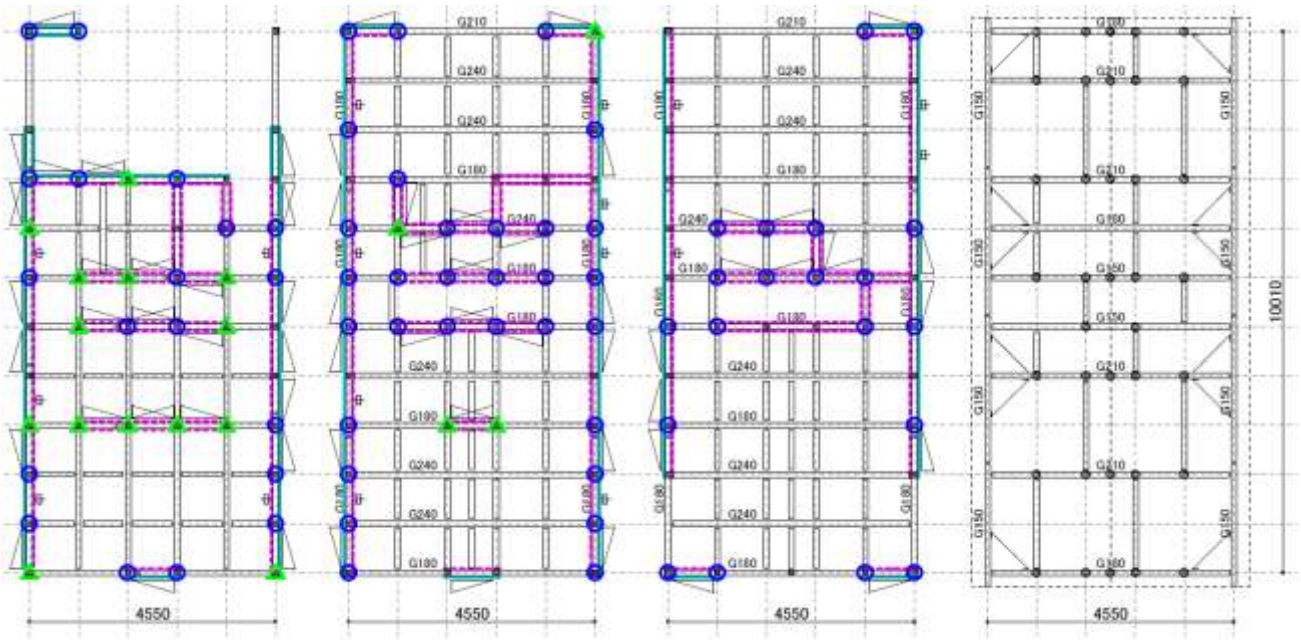


Figure 3 Configuration of shear wall and specification of column end joints at specimen No.2

3. DYNAMIC AND STATIC ELEMENT TESTS

3.1 Outline of elements tests

The dynamic and static element tests of shear wall and metal fasteners were carried out to confirm dynamic behaviour of seismic components. Table 3, Table 4 and Figure 6 shows the outline of specimens. The configuration of the dynamic shear wall tests was shown in figure 7. In shear wall tests, the story shear deformation of the first story of the specimen No.1 is input to the beam of the element test specimen by the actuator. At the dynamic tests, the velocity of the actuator is controlled to fit to that of story shear observed at shake table test at BSL 160% input. In the joint tensile tests, the uplift displacement of column end joint is input to the column of the element test specimens.

3.2 Test Result

Figure 8 and Figure 9 shows the load displacement curves of shear wall tests, and joint tensile tests. At the shear tests of shear walls, the difference between dynamic loading and static loading was very small. At the tensile tests of metal fasteners, tensile forces of dynamic tests were larger than that of static loading.

Table 3 Load displacement curves of shear wall tests

試験体記号	Brace	Exterior	Interior	Number	
				Dynamic	Static
F	-	-	-	3	3
G2	-	Gypsum Board	Gypsum Board	3	3
B2-G2	Double	Gypsum Board	Gypsum Board	3	3
B2-S-G	Double	Siding	Siding	3	3

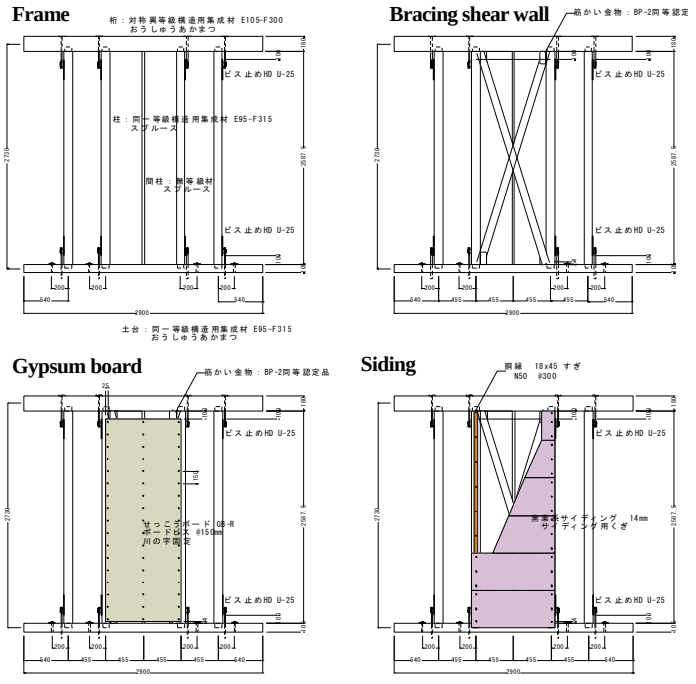


Figure 6 Configuration of element tests specimens

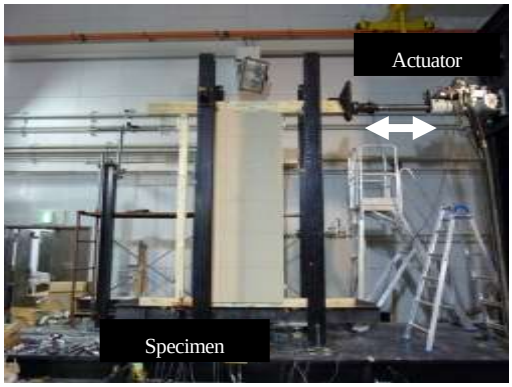


Figure 7 Configuration of test equipment

Table 4 Load displacement curves of joint tensile tests

Specimen	Metal fastener	Allowable tensile force	Number	
			Dynamic	Static
P06	Screw type	6.2kN	3	3
P10	Screw type	10.4kN	3	3
HD15	Hold down	15.6kN	3	3
HD20	Hold down	10.9kN	3	3
HD25	Hold down	28.7kN	3	3

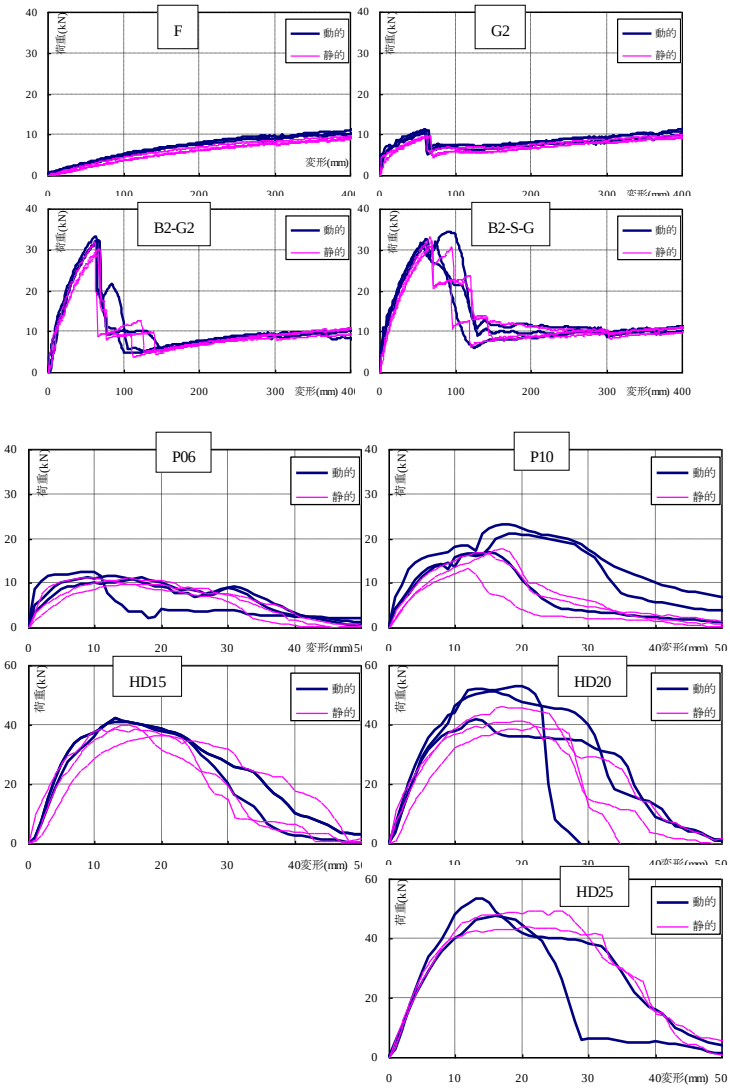


Figure 9 Tensile load and displacement curves of tensile tests of joints

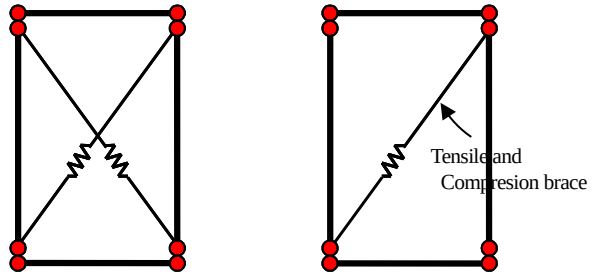
4. Numerical analysis

In our analysis, we used the three dimension frame analysis using the software "wallstat" that was developed at Building Research Institute. The fundamental analysis theory of wallstat is based on Distinct Element Method (DEM). A detailed explanation of DEM and our theory was given in our previous papers(Nakagawa 2008). DEM is a non-continuum analysing method, so the large deformation analysis of the fracture developing processes is possible.

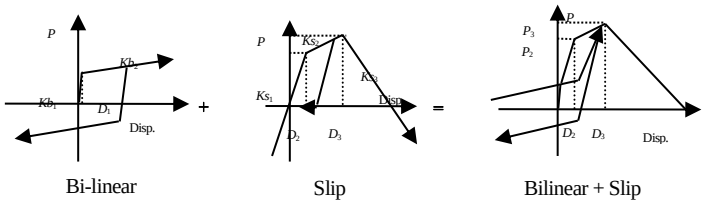
4.1 Outline of numerical models

The analysis models used here were depicted in Figure 10. The plan of this analysis model was based on the specimen used in the shake table test. The wood frames of numerical models were modelled by beam element as indicated in figure10 (a). The moment of beam elements starts to fall once the maximum bending moment has been exceeded, with transformation into a pinned state occurring at the point in time when 0 is reached, at which point the member is adjudged to have been broken. Vertical shear walls are modelled by the replacement of braces in truss elements as indicated in figure 11(a). Hysteric characteristics are expressed according to the bi-linear + slip-type models indicated in figure 11(c). Parameters designate bi-linear and slip skeleton curves. Bracing shear walls are modelled by the positioning of two compression and tensile truss elements for each brace, as indicated in figure 11(b). As with shear wall springs, bracing spring hysteric characteristics are expressed according to the bi-linear + slip-type l models.

As indicated in figure12, joints are modelled using the rotational spring + elasto-plastic spring (for strong shearing). Hysteric characteristics of the compression / tensile elasto-plastic spring are set as per the one side elastic + one side slip-type.



(a) gypsum board, siding wall (b)bracing shear wall



(c) Hysteretic rules for shear wall elements

Figure 11 Modelling of shear walls

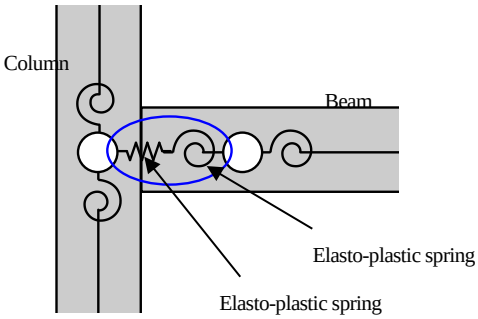
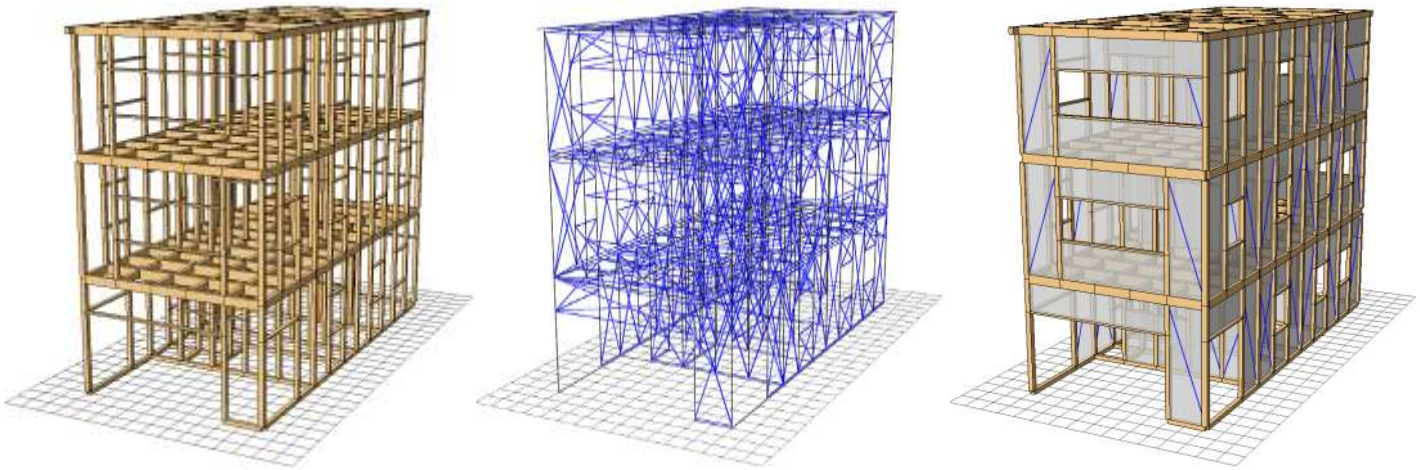


Figure 12 Modelling of joint springs for metal fasteners



(a)Wood frames (b)Shear walls and floor diaphragms (c)Whole image of numerical model

Figure 10 Outline of numerical models

4.2 Spring parameters used in numerical models

The parameters of the connections were defined according to the specifications of the target specimen, and the corresponding load-displacement relationships in figure 13 were selected for each connection respectively.

The shear wall parameters of analytical models were also selected at figure 14 according to the specifications of the target specimen. In the figure13 and figure 14, each line means the following definition.

Dynamic: The skeleton curve defined according to the dynamic loading tests in the section 3.
Static: The skeleton curve defined according to the static loading tests in the section 3.
Pre-analysis: The skeleton curve used in preliminary analysis in our previous paper (Miyake 2010).
Post-analysis: The skeleton curve defined in this paper.

In figure 15, moment frame effect means the moment resistance due to the rotation of the column end and top joint defined by the loading test at section 2. It was modelled by moment spring at numerical model.

two types. “Gypsum board” means the bracing shear walls which buckling is prevented by the gypsum board. “Siding” means the bracing shear walls which buckling is prevented by the exterior siding.

The mass of the analysis model was equalized with the actual weight of the target specimen measured by the load cell of the crane before the shaking table test. The equilibrium weight of the second floor was 103kN, and the weight of the third floor was 104kN, and the weight of the third floor was 61.2kN. The weight was distributed to the element of each floor in the analysis model.

All lateral elements against the horizontal forces in the shaking table specimen were modelled in the analytical model. The roof structure was not modelled, but accounted for as seismic weight. The damping coefficients were defined to be 2.0%. We used the instantaneous stiffness proportional damping. The damping coefficients were assumed to be zero, when the instantaneous stiffness became negative as a matter of analytic convenience.

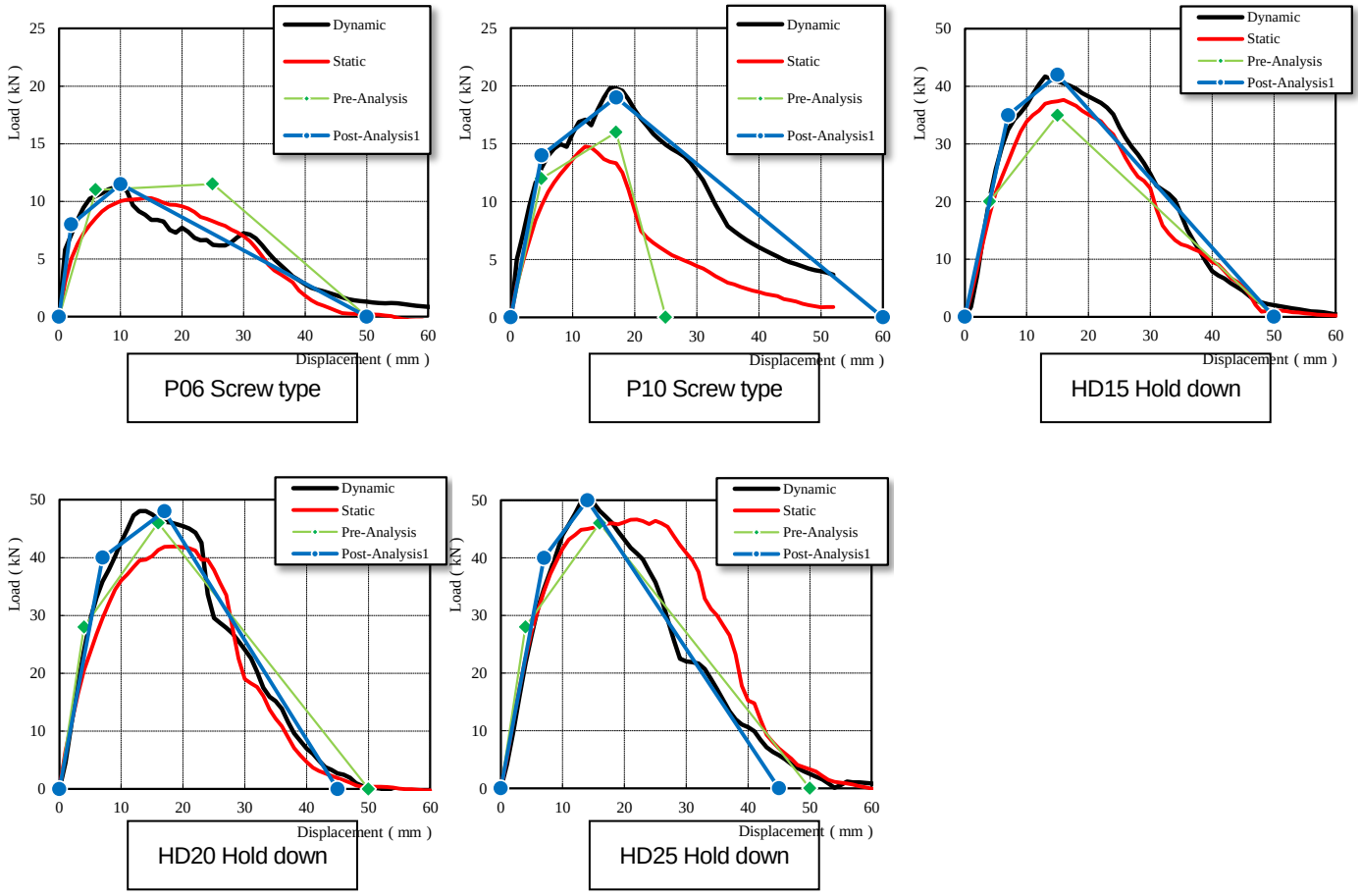


Figure 14 Skeleton curves of joint springs for metal fasteners used in numerical analysis

Skeleton curves of double bracing shear walls have

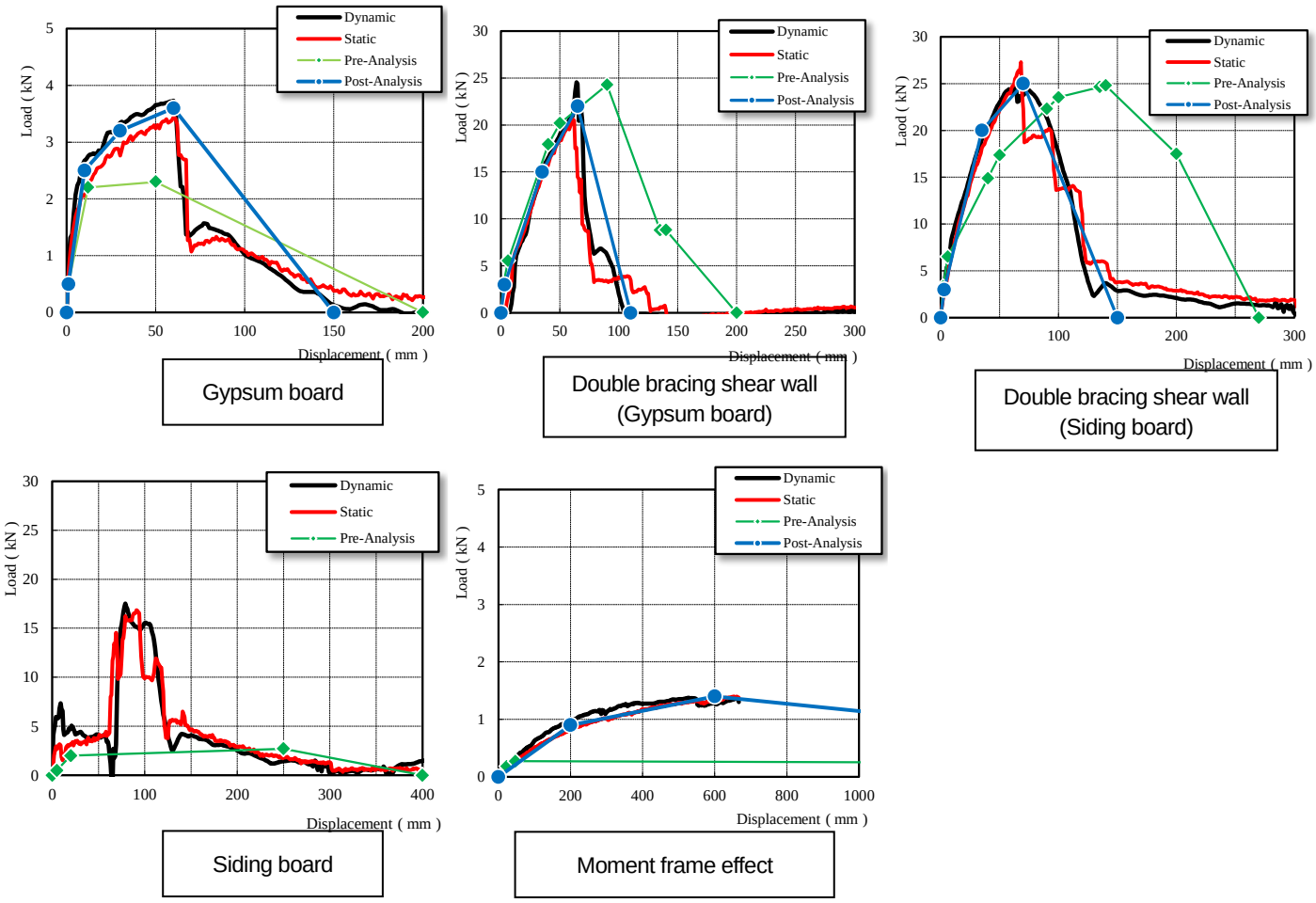


Figure 15 Skeleton curves of shear walls used in numerical analysis

4.3. Conditons of numerical analysis

Table 5 shows the conditions of parameters for numerical analysis. In this paper, model A, model B and model C parameter sets were calculated to trace the results of shake table tests. The truss spring of shear walls were defined as post-analysis and pre-analysis skeleton curves. The moment springs of moment frame for the column end of P06 and P10 were defined 70% of post-analysis, because moment frame effect of figure15 was the experimental result of HD25.

4.4. Result and discussion

Table 6 shows the results of numerical analysis for each model. In the model A, both No.1 and No.2 collapsed. In the model B, both No.1 and No.2 didn't collapse. In the model C, No.1 collapsed and No.2 didn't collapsed.

Figure 16 shows the time history of story drift of each story of each model. Figure 17 shows the load displacement curves of first story of each model. Figure 18 shows the movie snapshot for analytical results of Model C. The rocking behaviour of No.2 was simulated in calculation. The numerical analysis uses Model C agreed well with shake table result in terms of the collapsing behaviour of No.1 and rocking behaviour of No.2.

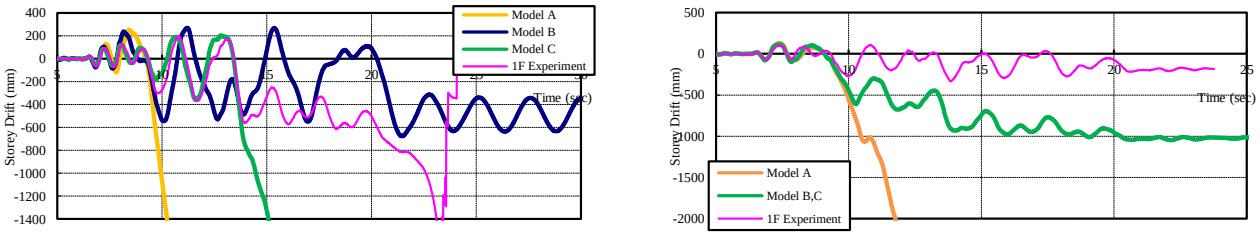
It was found that the skeleton curves for moment frame effect were sensitive to the ultimate behaviour of numerical models

Table 5 Calculation condition of numerical models

Model	Shear wall spring	Joint spring	Moment frame spring of P06, P10	Moment frame spring of HD15, HD20
A	Post-Analysis	Post-Analysis	70% of Post-Analysis	100% of Post-Analysis
B	Pre-Analysis	Post-Analysis	70% of Post-Analysis	100% of Post-Analysis
C	Pre-Analysis	Post-Analysis	70% of Post-Analysis	90% of Post-Analysis

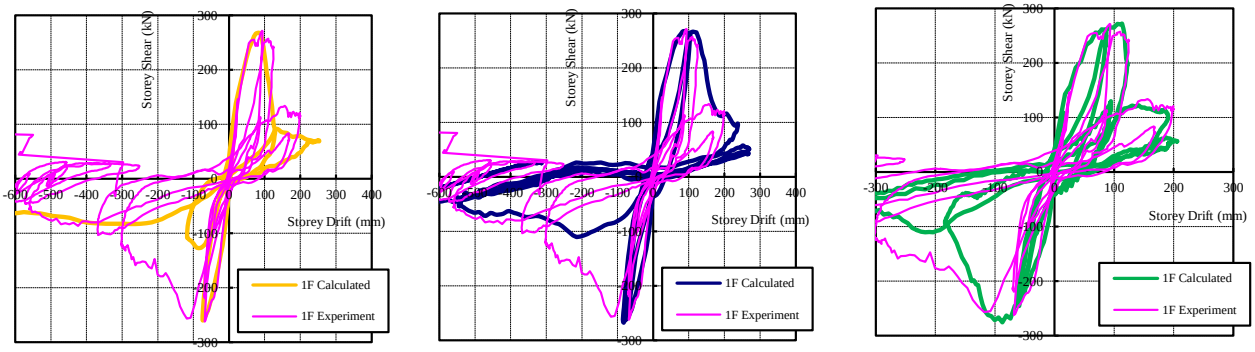
Table 6 Maximum story drift at first story

Model		Maximum story drift (mm)
A	No.1	Collapsed
	No.2	Collapsed
B	No.1	-676
	No.2	-1048
C	No.1	Collapsed
	No.2	-1048
Experiment	No.1	Collapsed
	No.2	-426

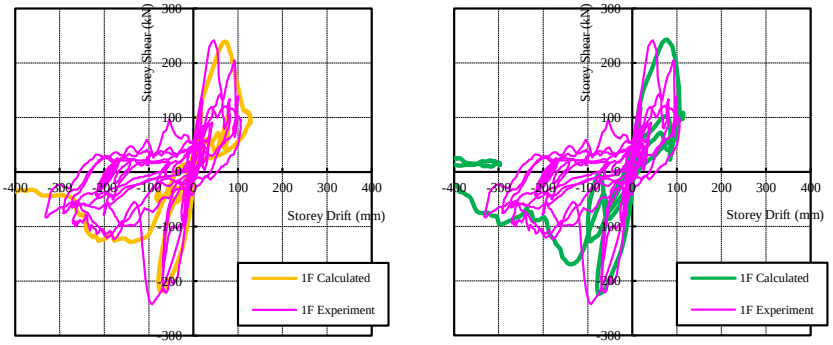


(a) No.1 (b) No.2

Figure 16 Story drift at first story



Model A (No.1) Model B (No.1) Model C (No.1)



Model A (No.2) Model B,C (No.2)

Figure 17 Load displacement relationships at first story



Figure 18 Movie snapshot of numerical analysis(model C) and shake table test

5. CONCLUSION

In this paper, we executed the additional shear tests of shear walls that were seismic components of shake table specimens and the tensile tests of metal fasteners of the specimens. By these test results, we improved our numerical models and carried out the response analysis for shake table tests. The several variations of load displacement relationships for the springs of numerical models were used for numerical analysis. The numerical analysis uses one of these spring parameters agreed well with shake table result in terms of the collapsing behaviour of No.1 and rocking behaviour of No.2.

Acknowledgements:
These shaking table tests were carried out by the project, "the grant to strengthen a technical base to realize the long-life quality houses", which financially supported by the Ministry of Land, Infrastructure, Transport, and Tourism.

References:

Tsuchimoto T et al.:(2010) Effect of horizontal diaphragm and column-end Joints on ultimate seismic performance of fullsized 3-story wood houses on shaking table. 10th World Conference on Timber Engineering, Italy

Miyake T. et al.: (2010) Dependence of Ultimate Seismic Performance on Specifications of Column-end Joints in 3-story Wood Houses. 10th World Conference on Timber Engineering, Italy

Nakagawa T., Kawai N., Tsuchimoto T., Ohta M.(2008) Collapsing Process Simulations of Wooden Houses by the Extended Distinct Element Method, 10th World Conference on Timber Structures, Miyazaki, p.282

10CUEE CONFERENCE PROCEEDINGS
10th International Conference on Urban Earthquake Engineering
March 1-2, 2013, Tokyo Institute of Technology, Tokyo, Japan

ULTIMATE EARTHQUAKE RESISTANCE OF TORSIONALLY COUPLED STRUCTURE HAVING DUCTILE TIMBER SHEAR WALLS

Yoshihiro Yamazaki[1], Hiroyasu Sakata[2], and Kazuhiko Kasai[2]

1) Assistant Professor, Structural Engineering Research Center, Tokyo Institute of Technology, Japan
2) Professor, Structural Engineering Research Center, Tokyo Institute of Technology, Japan
yamazaki.y.ai@m.titech.ac.jp, sakata.h.aa@m.titech.ac.jp, kasai@serc.titech.ac.jp

Abstract: Horizontal displacement mode including torsion in ultimate state is clearly related to strength balance of each frame while elastic torsional vibration is characterized by stiffness balance. Therefore, this paper presents horizontal displacement mode prediction method especially focusing on timber structure having large strength eccentricity. The method is simpler than conventional ones because mechanism in ultimate state and corresponding external force distribution are assumed. The method also considers variability of response due to earthquake characteristics. The accuracy of the evaluation method is demonstrated via numerous time history analyses and shaking table test.

1. INTRODUCTION

Unbalanced distribution of shear walls leads to stiffness and strength eccentricity and results in torsional vibration. It is not desirable from a point of view of seismic resistance because of concentration of damage on particular shear wall. Such damages of timber houses were often observed in the past severe earthquakes in Japan.

As for elastic structure, horizontal displacement mode including torsion can be easily evaluated, and the method is well-established. However, evaluation methods covering inelastic structure are usually complicated and demanding non-linear pushover analysis (Hoshi et al. 2007, Fuji 2004). To apply these methods to timber houses is likely to difficult because of the huge number of them. In other words, easier solution considering non-linearity is desperately needed.

2. PRECONDITION

2.1 Conventional method and Problem

Performance based seismic design method is based on non-linear pushover analysis. As mentioned above, it is not suitable for timber houses. Similar solutions based on equivalent linearization method also require a lot of effort such as convergence calculation. Therefore, final goal of this research is to propose new method based on limit analysis, which takes less effort compared to equivalent linearization method.

In Japan, Eccentric ratio (See Equation(3c)) is used to check eccentricity between center of mass and center of elastic stiffness. The value must be less than 0.3 for timber structures and 0.15 for the other structures. This method may be reasonable for allowable stress design. However, the problem is that this confirmation is extended to ultimate state regardless of ignoring non-linearity. In addition, eccentric ratio does not consider mass distribution. Therefore, the new method we will propose should solve these problems.

2.2 Ultimate State and Mechanism

If there are not any eccentricity of mass, stiffness and strength, torsion will not occur. Then, skeleton curve of story equals to that of summation of each wall. Therefore, ultimate deformation of system is the same as that of shear wall, and evaluation is quite simple. However, if torsion occurs, deformations of each shear wall are not the same. How to define "ultimate state" is one of the problems.

In the beginning, the following two conditions are set.

i) Shear wall arrangement in one direction is eccentric. Structure is subjected to earthquake input motion along the direction.
ii) When maximum deformation of shear wall which is the most deformed reaches its ultimate deformation, the system is "Ultimate State".
iii) When system becomes ultimate state, all shear walls along earthquake motion are plastic and all shear walls perpendicular to earthquake motion are elastic.

Condition iii) is about mechanism of structure and expects that ultimate strength of story equals to that of summation of each shear wall.

3. ANALYTICAL MODEL

3.1 Considering Model

As shown in Figure 1, one-story wall structure is

considered, whose vibration analysis model is shown in right figure. x-directional shear walls are unbalanced, while y-directional shear walls are symmetry. x-directional earthquake motion is assumed. Floor diaphragm is infinitely rigid. The dimension of floor is $0.67L$ in x-direction and L in y-direction, respectively.

There are two shear walls in each direction; "Weak Wall" in x-direction, "Strong Wall" in x-direction and two "Transverse Walls" in y-direction, respectively.

Force-deformation curve of shear wall is approximated by elasto-perfectly plastic model. F_{xi} and δ_{xvi} are ultimate strength and yield deformation of i-th x-directional shear wall. Similarly, F_{yi} and δ_{yvi} of i-th y-directional shear wall are also defined. Ultimate deformations of each shear wall are all δ_u.

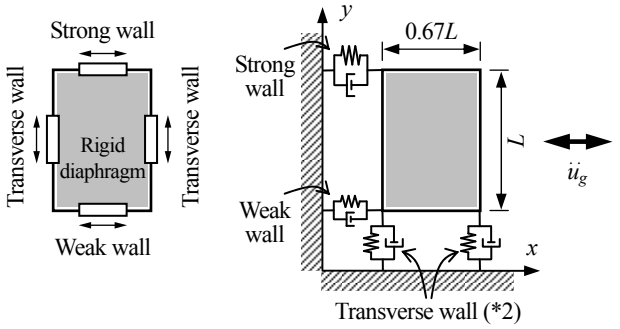
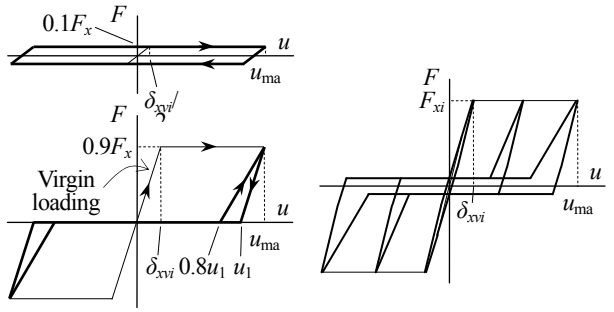


Figure 1 Considering Wall Structure and its Vibration Analysis Model

3.2 Hysteresis Model

Bi-linear + slip model is used as hysteresis model of timber shear walls (Isoda et al. 2007). In order to approach its envelope curve to elasto-perfectly plastic model, parameters are set as shown in Figure 2. Second stiffness ratio of bi-linear model is 0.001, and that of slip model is 0.02, respectively.



(a) Bi-linear Element (Upper) and Slip Element (Lower) (b) Bi-linear + Slip Element

Figure 2 Hysteresis Model

3.3 Parameters and Input Earthquake Motion

The most important parameter is strength balance between weak wall and strong wall. It is represented by strength eccentricity e_{fy}. Non-dimensional strength eccentric ratio $\bar{e}_{fy}$ is mainly used for discussion.

$$e_{fy} = \sum F_{xi} y_i \Big/ \sum F_{xi} \quad , \quad \bar{e}_{fy} = e_{fy} / r_m \quad , \quad r_m = \sqrt{I/m} \qquad \text{(1a-c)}$$

Where, m = mass, I = moment of inertia and r_m = radius of gyration, respectively. For comparison, stiffness eccentric ratio $\bar{e}_{ky}$ and eccentric ratio R_{ex} are shown as follows.

$$e_{ky} = \sum k_{xi} y_i \Big/ \sum k_{xi} \quad , \quad \bar{e}_{ky} = e_{ky} / r_m \qquad \text{(2a,b)}$$

$$K_x = \sum k_{xi} \quad , \quad K_\theta = \sum (k_{xi} y_i^2 + k_{yi} x_i^2)$$

$$R_e = \frac{e_{ky}}{\sqrt{(K_\theta / K_x)^2 - e_{ky}^2}} \qquad \text{(3a-c)}$$

Where, k_{xi} and k_{yi} are initial stiffness of i-th x- and y-directional shear wall, respectively. They are calculated as F_{xi}/δ_{xvi} and F_{yi}/δ_{yvi}. x_i and y_i are coordinate of i-th shear wall, and the origin is set at center of mass. Eccentric ratio R_e is defined in Building Standard Law of Japan. It must be less than 0.3 for timber structures and 0.15 for the other structures, respectively.

In this study, $\bar{e}_{fy}$ will be changed from 0.1 to 0.77. Ultimate deformation of shear wall is 91mm, which means corresponding deformation angle is 1/30rad when the height of shear wall is 2730mm. The following three cases of yield deformations are considered.

Case1 : Yield deformations of all walls are 22.8mm (1/120rad)
Case2 : Yield deformations of weak wall is 30.3mm (1/90rad), strong wall is 18.2mm (1/150rad) and transverse wall is 22..8mm(1/120rad)
Case3 : Yield deformations of weak wall is 18.2mm (1/150rad), strong wall is 30.3mm (1/90rad) and transverse wall is 22..8mm(1/120rad)

In case1, stiffness is proportional to strength. However, in case2 and case3, stiffness is not proportional to strength (Table 1).

In all cases, base shear coefficient is set to be 0.38. If torsion of the system is fixed, elastic natural period is 0.49 second, and 5% viscous damping proportional to initial stiffness is added. Mass is assumed to be equally distributed in the floor.

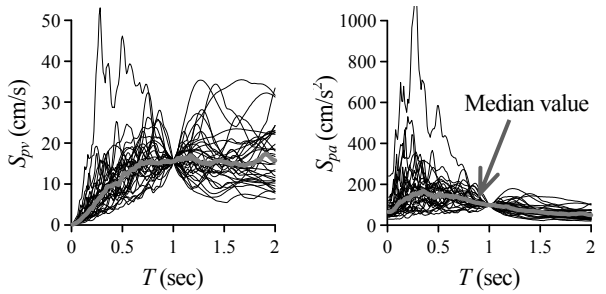
33 earthquake motions are used. 31 motions are Japanese and world real earthquakes, and 2 motions are artificial ones provided by Building Center of Japan (Kasai et al. 2003). Their response spectra are shown in Figure 3. In Figure 3, each spectrum is scaled to S_{pa} = 98cm/s^2 in T = 1 sec. In analysis, scale factor is, however, decided through a trial and error process so that structure just reaches ultimate state.

4. PREDICTION OF ULTIMATE DISPLACEMENT MODE

Prediction method of ultimate displacement mode including torsion is presented. The important thing is to assume mechanism and external force distribution as shown

Table 1 List of Analysis Cases

	Yield deformation (angle)			Yield Force			Strength balance	Stiffness balance	Eccentric ratio
	Weak mm (rad)	**Strong** mm (rad)	**Transverse** mm (rad)	**Weak** kN	**Strong** kN	**Transverse** kN	$\bar{e}_{fy}$ —	$\bar{e}_{ky}$ —	R_{ex} —
Case 1	22.8 (1/120)	22.8 (1/120)	22.8 (1/120)	14 → 7	16 → 23	15	0.1 → 0.77	0.1 → 0.77	0.06 → 0.5
Case 2	30.3 (1/90)	18.2 (1/150)					0.1 → 0.77	0.45 → 1	0.27 → 0.72
Case 3	18.2 (1/150)	30.3 (1/90)					0.1 → 0.77	-0.27 → 0.47	-0.16 → 0.28



(a) Pseudo Velocity (b) Pseudo Acceleration

Figure 3 Response Spectra of 33 Earthquakes (5% damping, Scaled to S_{pa} = 98cm/s^2 in T = 1 sec)

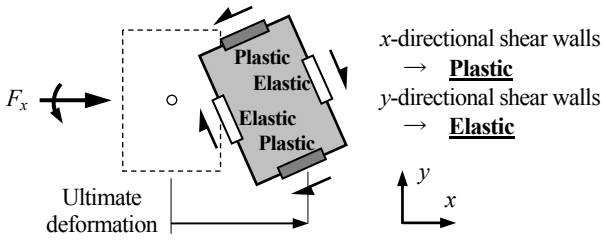


Figure 4 Assumed Mechanism and External Force Distribution

in Figure 4. It achieves easy solution without complicated calculation. In addition, variability of response due to earthquake will be considered using unique method.

4.1 Theory

In ultimate state, story shear force F_x and moment M are expressed as follows.

$$F_x = \sum F_{xi} = F_{x0} \quad , \qquad M = -F_{x0} e_{fy} + K_\theta^{(y)} \theta \tag{4a,b}$$

$$K_\theta^{(y)} = \sum k_{yi} x_i^2 \tag{5}$$

Where, θ = rotation of floor, F_{x0} = summation of ultimate strength of x-directional shear walls or ultimate strength of story. $K_\theta^{(y)}$ = rotational stiffness around center of mass contributed by y-directional shear walls.

Equation(4) also means external force distribution $\mathbf{f_{u1}}$. Therefore, we can define ultimate 1st. mode $\boldsymbol{\phi}_{\mathbf{u1}}$ and assume the following relationship using mass matrix $\mathbf{m}$.

$$\mathbf{f_{u1}} = \{F_{x0} \; M\}^{\mathrm{T}} \quad , \qquad \boldsymbol{\phi}_{\mathbf{u1}} = \{\phi_{u11} \; \phi_{u21}\}^{\mathrm{T}} \tag{6a,b}$$

$$\omega_{u1}{}^2 \mathbf{m} \boldsymbol{\phi}_{\mathbf{u1}} = \mathbf{f_{u1}} \, , \qquad \mathbf{m} = \begin{bmatrix} m & 0 \\ 0 & I \end{bmatrix} \tag{7a,b}$$

Equation(7a) means equilibrium of system having natural circular frequency ω_{u1} and displacement mode $\boldsymbol{\phi}_{\mathbf{u1}}$ in steady state. It is similar to eigen equation of elastic system. From Equation(7a), we can obtain $\boldsymbol{\phi}_{\mathbf{u1}}$ as follows.

$$\boldsymbol{\phi}_{\mathbf{u1}} = \frac{1}{\omega_{u1}^2} \mathbf{m}^{-1} \mathbf{f_{u1}} = \frac{1}{\omega_{u1}^2} \frac{1}{mI} \begin{Bmatrix} IF_{x0} \\ m\left(-F_{x0} e_{fy} + K_\theta^{(y)} \theta\right) \end{Bmatrix} \tag{8}$$

First line of $\boldsymbol{\phi}_{\mathbf{u1}}$ shows translational displacement of center of mass, and second line shows rotation. Here, we focus on the ratio of rotation to translation ϕ_{u21}/ϕ_{u11}.

$$\frac{\phi_{u21}}{\phi_{u11}} = \frac{-F_{x0} e_{fy} + K_\theta^{(y)} \theta}{F_{x0} r_m^2} \tag{9}$$

Since Equation(9) includes θ, it can be rewritten using u_x = translational displacement of center of mass in ultimate state and $\theta = u_x \phi_{u21}/\phi_{u11}$.

$$\frac{\phi_{u21}}{\phi_{u11}} = \frac{F_{x0} e_{fy}}{K_\theta^{(y)} u_x - F_{x0} r_m^2} \tag{10}$$

In this research, we should pay attention to ultimate state when deformation of the wall the most apart form center of strength reaches ultimate deformation δ_u. Therefore, the following relationship is achieved.

$$u_x (1 + l_y \phi_{u21} / \phi_{u11}) = \delta_u \tag{11}$$

Where, l_y = y-directional distance between center of mass and shear wall in ultimate state. By substituting Equation(11) into (10), we can obtain second degree equation of u_x, and it is expressed as follows.

$$u_x = \max\left(u_{x0}, \frac{\delta_u + \delta_{xv,s}}{2}\right) \tag{12a,b}$$

$$u_{x0} = \frac{F_{x0}(r_m^2 - e_{fy} l_y) + K_\theta^{(y)} \delta_u + \sqrt{\left[F_{x0}(r_m^2 - e_{fy} l_y) + K_\theta^{(y)} \delta_u\right]^2 - 4 K_\theta^{(y)} F_{x0} r_m^2 \delta_u}}{2 K_\theta^{(y)}}$$

Where, $\delta_{xy,s}$ = yield deformation of strong wall. Second part of right member in Equation(12a) ($\delta_u + \delta_{xy,s}$)/2 means lower limit of u_x promising assumed mechanism.

By substituting Equation(12a) into (10), we can obtain maximum displacement vector $\mathbf{u_{max}}$ as follows.

$$\mathbf{u_{max}} = \begin{Bmatrix} u_x \\ u_x(\phi_{u21}/\phi_{u11}) \end{Bmatrix} \tag{13}$$

4.2 Variability of Earthquake Response

In order to simulate arbitrary displacement mode of 2DOF, two independent vectors are needed. Although ultimate 1st. mode is likely to be dominant mode, another mode is required to simulate variability of earthquake response.

At first, an example of strong non-linear response is shown in Figure 5(a). This is an orbit of lateral force F_x and moment M obtained from time history analysis. The hysteresis is like a ellipse, and its slope appears to be simulated by external force vector $\mathbf{f_{u1}}$. It is also found that orthogonal vector to $\mathbf{f_{u1}}$ seems to affect variability of response. Therefore, established method to simulate variability of earthquake force is applied to this problem (Matsumori et al. 2004).

As shown in Figure 6, ultimate 2nd. mode $\boldsymbol{\phi}_{\mathbf{u2}}$ is defined as it is orthogonal to $\boldsymbol{\phi}_{\mathbf{u1}}$ through mass matrix.

$$\boldsymbol{\phi}_{\mathbf{u2}} = \{\phi_{u12}\ \phi_{u22}\}^{\mathbf{T}}, \qquad \boldsymbol{\phi}_{\mathbf{u1}}{}^{\mathbf{T}}\mathbf{m}\boldsymbol{\phi}_{\mathbf{u2}} = \boldsymbol{\phi}_{\mathbf{u2}}{}^{\mathbf{T}}\mathbf{m}\boldsymbol{\phi}_{\mathbf{u1}} = \mathbf{0} \tag{14a,b}$$

$$\mathbf{f_{u2}} = \left\{(-F_{x0}e_{fy} + K_\theta^{(y)}\theta)/r_m \quad -F_{x0}r_m\right\}^{\mathbf{T}} \tag{15}$$

$$\boldsymbol{\phi}_{\mathbf{u2}} = \frac{1}{\omega_{u2}^2}\mathbf{m}^{-1}\mathbf{f_{u2}} = \frac{1}{\omega_{u2}^2}\frac{1}{mr_m}\begin{Bmatrix} -F_{x0}e_{fy} + K_\theta^{(y)}\theta \\ -F_{x0} \end{Bmatrix} \tag{16}$$

By assuming $\boldsymbol{\phi}_{\mathbf{u1}}$ and $\boldsymbol{\phi}_{\mathbf{u2}}$ are a couple of eigen vectors, we can obtain participation function $\beta_{u1}\boldsymbol{\phi}_{\mathbf{u1}} = \{\beta_{u1}\phi_{u11}\ \beta_{u1}\phi_{u21}\}^{\mathbf{T}}$, $\beta_{u2}\boldsymbol{\phi}_{\mathbf{u2}} = \{\beta_{u2}\phi_{u12}\ \beta_{u1}\phi_{u22}\}^{\mathbf{T}}$ as follows.

$$\begin{aligned} \beta_{u1}\boldsymbol{\phi}_{\mathbf{u1}} &= \boldsymbol{\phi}_{\mathbf{u1}}{}^{\mathbf{T}}\mathbf{m}\{\mathbf{1}\}/\boldsymbol{\phi}_{\mathbf{u1}}{}^{\mathbf{T}}\mathbf{m}\boldsymbol{\phi}_{\mathbf{u1}} \\ \beta_{u2}\boldsymbol{\phi}_{\mathbf{u2}} &= \boldsymbol{\phi}_{\mathbf{u2}}{}^{\mathbf{T}}\mathbf{m}\{\mathbf{1}\}/\boldsymbol{\phi}_{\mathbf{u2}}{}^{\mathbf{T}}\mathbf{m}\boldsymbol{\phi}_{\mathbf{u2}} \end{aligned} \tag{17a,b}$$

$$\beta_{u1}\phi_{u11} = \frac{1}{1+r_m^2(\phi_{u21}/\phi_{u11})^2}, \quad \beta_{u1}\phi_{u21} = \frac{\phi_{u21}/\phi_{u11}}{1+r_m^2(\phi_{u21}/\phi_{u11})^2}$$

$$\beta_{u2}\phi_{u12} = \frac{1}{1+r_m^2(\phi_{u22}/\phi_{u12})^2} = 1-\beta_{u1}\phi_{u11}, \quad \beta_{u2}\phi_{u22} = \frac{\phi_{u22}/\phi_{u12}}{1+r_m^2(\phi_{u22}/\phi_{u12})^2} = -\beta_{u1}\phi_{u21} \tag{18a-d}$$

Where, $\{\mathbf{1}\} = \{1\ 0\}^{\mathbf{T}}$. By combining $\beta_{u1}\boldsymbol{\phi}_{\mathbf{u1}}$ with $\beta_{u2}\boldsymbol{\phi}_{\mathbf{u2}}$, the following two modes are newly defined.

$$\boldsymbol{\phi}_{\mathbf{u}}{}^{(+)} = \begin{Bmatrix} \beta_{u1}\phi_{u11} + \alpha\beta_{u2}\phi_{u12} \\ \beta_{u1}\phi_{u21} + \alpha\beta_{u2}\phi_{u22} \end{Bmatrix}, \quad \boldsymbol{\phi}_{\mathbf{u}}{}^{(-)} = \begin{Bmatrix} \beta_{u1}\phi_{u11} - \alpha\beta_{u2}\phi_{u12} \\ \beta_{u1}\phi_{u21} - \alpha\beta_{u2}\phi_{u22} \end{Bmatrix} \tag{19a,b}$$

$\boldsymbol{\phi}_{\mathbf{u}}{}^{(+)}$ = ultimate sum mode and $\boldsymbol{\phi}_{\mathbf{u}}{}^{(-)}$ = ultimate difference mode, respectively. α is combine ratio of $\beta_{u1}\boldsymbol{\phi}_{\mathbf{u1}}$ and $\beta_{u2}\boldsymbol{\phi}_{\mathbf{u2}}$, which is originally defined as the ratio of their acceleration spectra. These two modes represent the smallest and the largest torsion situations, respectively. In this research, Equations(19) are simplified by assuming $\alpha = 1$.

$$\boldsymbol{\phi}_{\mathbf{u}}{}^{(+)} = \begin{Bmatrix} 1 \\ 0 \end{Bmatrix}, \qquad \boldsymbol{\phi}_{\mathbf{u}}{}^{(-)} = \begin{Bmatrix} 2\beta_{u1}\phi_{u11} - 1 \\ 2\beta_{u1}\phi_{u21} \end{Bmatrix} \tag{20a,b}$$

Finally, we can obtain maximum displacement vector $\mathbf{u}_{\mathbf{max}}^{(+)}$ and $\mathbf{u}_{\mathbf{max}}^{(-)}$ corresponding to $\boldsymbol{\phi}_{\mathbf{u}}{}^{(+)}$ and $\boldsymbol{\phi}_{\mathbf{u}}{}^{(-)}$ as follows.

$$\mathbf{u}_{\mathbf{max}}^{(+)} = \begin{Bmatrix} \delta_u \\ 0 \end{Bmatrix}$$

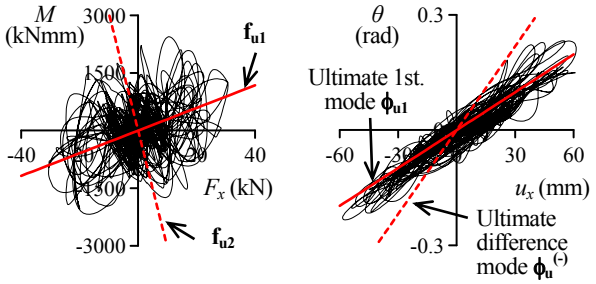
$$\mathbf{u}_{\mathbf{max}}^{(-)} = \frac{\delta_u}{1 + l_y(2\beta_{u1}\phi_{u21})/(2\beta_{u1}\phi_{u11} - 1)}\begin{Bmatrix} 1 \\ \dfrac{2\beta_{u1}\phi_{u21}}{2\beta_{u1}\phi_{u11} - 1} \end{Bmatrix} \tag{21a,b}$$

Figure 5(b) shows an orbit of translation u_x and rotation θ. The slope of the hysteresis is roughly expressed by $\boldsymbol{\phi}_{\mathbf{u1}}$, and increase of θ at large u_x is simulated by $\boldsymbol{\phi}_{\mathbf{u}}{}^{(-)}$.

For comparison, 1st. mode shape and 2nd. mode shape in elastic state are shown below.

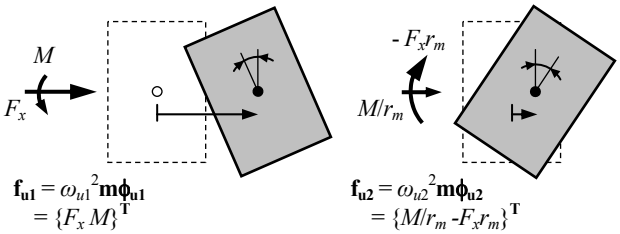
$$\omega_i^2 = \frac{IK_x + mK_\theta \mp \sqrt{(IK_x + mK_\theta)^2 - 4mI(K_xK_\theta - K_x^2e_{ky}^2)}}{2mI}$$

$$\boldsymbol{\phi}_{\mathbf{ei}} = \begin{Bmatrix} 1 \\ \dfrac{1-\omega_i^2/\omega_x^2}{e_{ky}} \end{Bmatrix}, \qquad \omega_x = \sqrt{\frac{K_x}{m}} \tag{22a-c}$$



(a) Lateral Force and Moment (b) Translation and Rotation

Figure 5 Orbits of (a) External Forces and (b) Displacement ($\bar{e}_{fy} = 0.48$, BCJ-L2 Wave)



(a) Ultimate 1st. Mode (b) Ultimate 2nd. Mode

Figure 6 Assumed Vibration Mode in Ultimate State

4.3 Relationship between Strength Eccentric Ratio and Ultimate Displacement Mode

In this section, new indexes, *Torsion Ratios* Δ_1, $\Delta^{(+)}$ and $\Delta^{(-)}$ are defined. They are the ratio of increase displacement at floor edge due to torsion to translational displacement, and are defined with respect to ultimate modes ($\boldsymbol{\phi}_{\mathbf{u1}}$, $\boldsymbol{\phi}_{\mathbf{u}}{}^{(+)}$ and

$\phi_u^{(-)}$) as shown in Figure 7(a).

Although we assume *x*-directional shear walls are plastic and *y*-directional shear walls are elastic, it may not be satisfied if torsion is too large. Therefore, torsion ratios are defined as follows.

$$\Delta_1 = \min\left(\frac{\phi_{u21}}{\phi_{u11}} l_y \,,\ \frac{\delta_u - \delta_{xv,s}}{\delta_u + \delta_{xv,s}}\right)$$
$$\Delta^{(+)} = 0 \qquad \text{(23a-c)}$$
$$\Delta^{(-)} = \min\left(\frac{2\beta_{u1}\phi_{u21}}{2\beta_{u1}\phi_{u11} - 1} l_y \,,\ \frac{\delta_u - \delta_{xv,s}}{\delta_u + \delta_{xv,s}}\right)$$

$(\delta_u - \delta_{xv,s})$ / $(\delta_u + \delta_{xv,s})$ is torsion ratio when displacement of weak wall is δ_u and that of strong wall is $\delta_{xv,s}$, which is upper limit of torsion ratio.

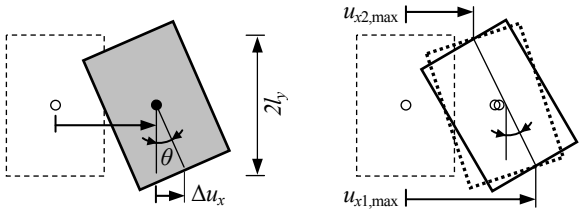
If we obtain torsion ratio by time history analysis, maximum deformations of weak wall and strong wall do not occur at the same time. Since we are interested in distribution of maximum deformations of weak wall and strong wall, torsion ratio from time history analysis is defined as follows.

$$\Delta_{ana} = \frac{u_{x1,\max} - u_{x2,\max}}{u_{x1,\max} + u_{x2,\max}} \qquad (24)$$

Where, $u_{x1,\max}$, $u_{x2,\max}$ = maximum deformation of weak wall and strong wall obtained from time history analysis as shown in Figure 7(b).

Relationship between strength eccentric ratio $\bar{e}_{fy}$ and torsion ratio are shown in Figure 8. White plots are results of analyses, and black plots are their averaged values. Figure 8(a) is comparison between analytical results and predicted results with proposed method while Figure 8(b) shows predicted results with conventional method using elastic mode.

At first, the following tendency is confirmed. Three cases show similar relations between $\bar{e}_{fy}$ and Δ_{ana}. In other words, Δ_{ana} is close related to strength balance rather than stiffness balance. Δ_{ana} is proportionally increased until $\bar{e}_{fy}$ = 0.5, and its slope becomes loose at large $\bar{e}_{fy}$. That is why torsion ratio is limited to $(\delta_u - \delta_{xv,s})$ / $(\delta_u + \delta_{xv,s})$ in Equation(23). The upper limit of torsion ratio can simulate the tendency of analytical results.



u_x : Translational displacement
θl_y : Additional translational displacement due to torsion
$\Delta = \theta l_y / u_x$

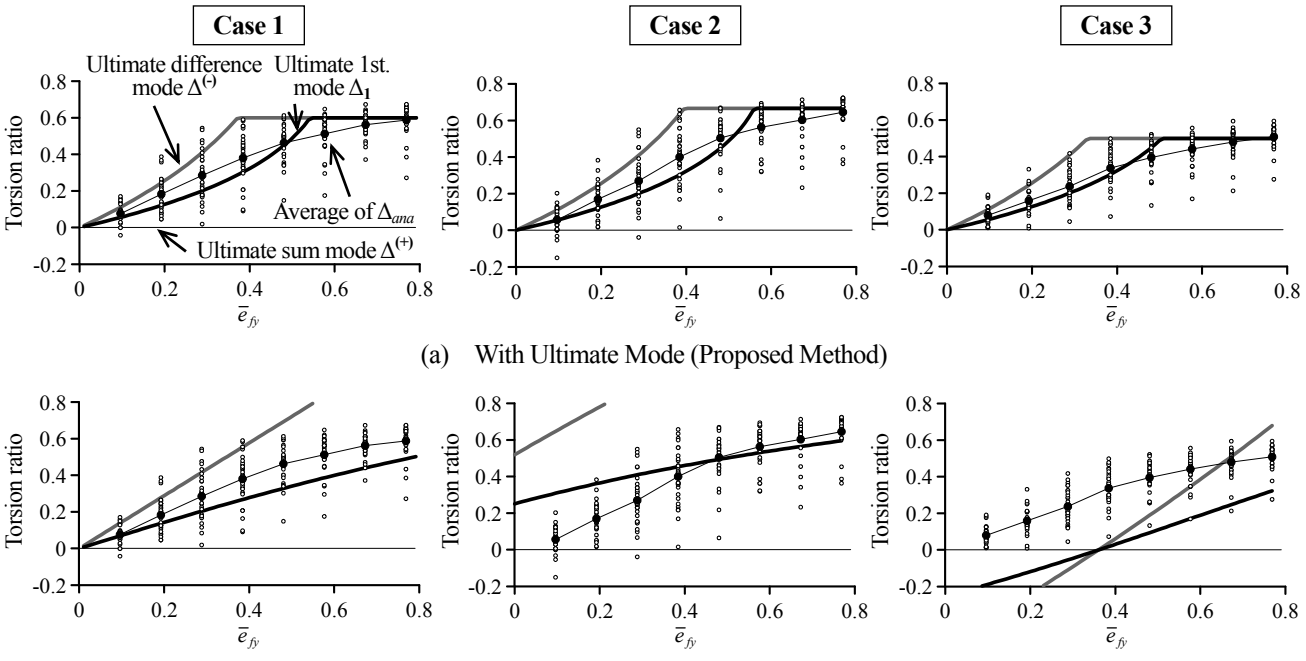
$u_{x1,\max}$: Max. deform. of weak wall
$u_{x2,\max}$: Max. deform. of strong wall
$\Delta_{ana} = (u_{x1,\max} - u_{x2,\max}) / (u_{x1,\max} + u_{x2,\max})$

(a) Prediction Method (b) Time History Analysis

Figure 7 Definition of Torsion Ratio

4.4 Verification of Accuracy

Accuracy of prediction method is mentioned here. Predicted results using ultimate 1st. mode (bold black line) approximately trace average of analytical results. In addition, predicted results using ultimate difference mode (gray black line) and ultimate sum mode (black line) approximately show maximum and minimum curves of analytical results.



(a) With Ultimate Mode (Proposed Method)

(b) With Elastic Mode (Conventional Method)

Figure 8 Comparison of Torsion Ratio Obtained from Time History Analysis and Prediction Method
White circle: Analytical results of 33 waves Δ_{ana}, Black circle: Average of analyses, Bold lines: Prediction Δ_1, $\Delta^{(+)}$, $\Delta^{(-)}$

In contrast, predicted results using elastic mode can not simulate analytical results except for case1 when stiffness is proportional to strength.

5. APPLICATION TO SHAKE TABLE TEST OF TIMBER STRUCTURE

Ultimate displacement prediction method proposed in the former chapter is applied to shake table test of timber structure (Yamazaki et al. 2010).

5.1 Outline of test

Specimen is shown in Figure 9. It is single story timber shear wall structure having eccentric wall arrangement. One-directional input motion is applied by shake table.

Figure 10 shows force-deformation relation of each shear wall subjected to full scaled JMA Kobe motion 1995. Weak wall (hanging wall) has long elastic range compared to strong wall due to elastic flexure of column. Therefore, stiffness is not proportional to strength such as case3.

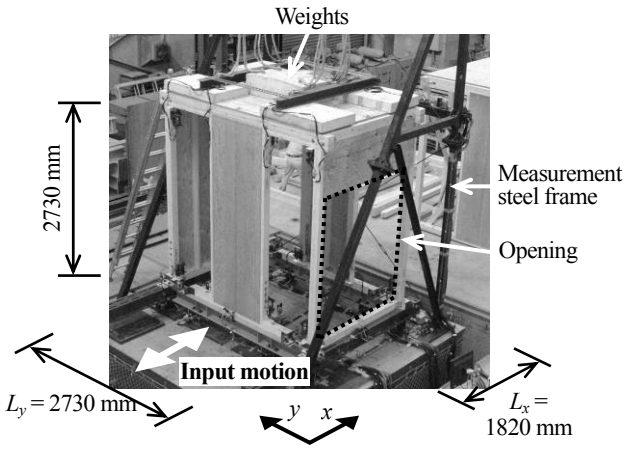


Figure 9 Setup of Specimen[21)]

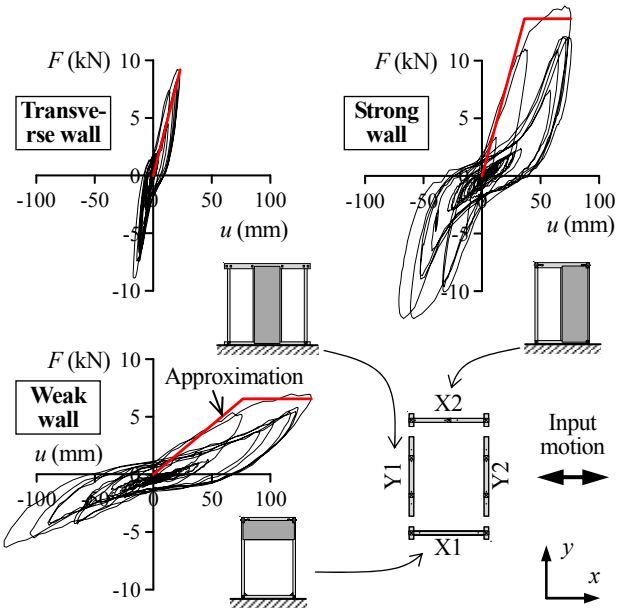


Figure 10 Force-Deformation Relation of Each Shear wall Subjected to Full Scale JMA Kobe Wave

5.2 Shear Wall Model

In Figure 10, elasto-perfectly plastic approximations of weak wall and strong wall, and elastic stiffness of transverse wall are superposed. Properties of each shear walls are summarized in Table 2. Using these values, we can obtain stiffness eccentricity e_{ky} = 859mm and strength eccentricity e_{fy} = 480mm, respectively.

5.3 Prediction of Ultimate Displacement Mode

Maximum displacement modes obtained from shake table and prediction method are compared in Figure 11 and Table 3. Ultimate 1st. mode, ultimate difference mode and elastic 1st. mode are used. Ultimate 1st. mode is the closest to test result, and ultimate difference mode and elastic 1st. mode predicts larger torsion. This is likely due to the difference between stiffness eccentricity and strength eccentricity.

Table 2 Properties of Each Shear Wall

	Stiffness kN/mm	Strength kN	Yield deform. mm	Ult. deform. mm
Weak	0.086	6.54	76.5	135.0
Strong	0.376	13.64	36.3	75.9
Transverse	0.400	—	—	—

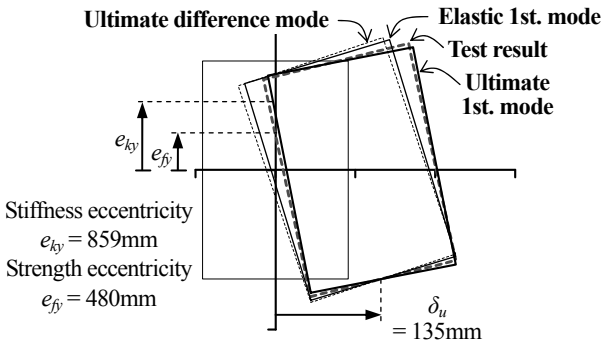


Figure 11 Maximum Displacement Mode

Table 3 Prediction of Maximum Displacement

	Test result mm	Ult. 1st. mm	Ult. diff. mm	Elast. 1st. mm
Weak	135.0			
Strong	75.9	81.5	43.9	52.1
Transverse	22.6	17.8	36.7	31.9

6. CONCLUSIONS

In this paper, the following findings are obtained.

1) Ultimate displacement mode is close related to strength balance of each shear wall rather than stiffness balance.
2) Dominant response in ultimate state can be simulated by ultimate 1st. mode, which is obtained by assuming mechanism and external force distribution.
3) Variability of earthquake response can be simulated using ultimate 2nd. mode orthogonal to ultimate 1st. mode.

4) Ultimate displacement prediction method can be applied to shake table test of timber structure.

References:

MURAKAMI, M., and INAYAMA, M. (2000) "Flexible Horizontal Diaphragm Effect on Seismic Torsional Resistance System with Ductile Walls (in Japanese)", *Journal of structural and construction engineering*. Architectural Institute of Japan, **530**, pp.93-98

ISODA, H., and KAWAI, N. (2007) "Hysteresis Model of Walls on Japanese Conventional Construction : Study on seismic behavior of wooden construction (in Japanese)", *Journal of structural and construction engineering*. Architectural Institute of Japan, **616**, pp.157-163

KASAI, K., ITO, H., and WATANABE, A. (2003) "Peak Response Prediction Rule for A SDOF Elasto-Plastic System Based on Equivalent Linearization Technique (in Japanese)", *Journal of structural and construction engineering*. Architectural Institute of Japan, **571**, pp.53-62

MATSUMORI, T., OTANI, S., SHIOHARA, H., and KABEYASAWA, T. (2004) "Estimation of Seismic Demands for R/C Frame Structures : Procedure to estimate the demand distribution using nonlinear push-over analyses (in Japanese)", *Journal of structural and construction engineering*. Architectural Institute of Japan, **576**, pp.119-123

YAMAZAKI, Y. (1981) "Inelastic Torsional Response of Structures Subjected to Earthquake Ground Motions (in Japanese)", *Transactions of the Architectural Institute of Japan*. Architectural Institute of Japan, **310**, pp.61-69

YAMAZAKI, Y., KASAI, K., SAKATA, H., and OOKI, Y. (2010) "Torsional seismic response control by viscoelastic damper for three-dimensional wood-frame structure with stiffness eccentricity (in Japanese)", *Journal of structural and construction engineering*. Architectural Institute of Japan, 75**(576)**, pp.1691-1700

10CUEE CONFERENCE PROCEEDINGS
10th International Conference on Urban Earthquake Engineering
March 1-2, 2013, Tokyo Institute of Technology, Tokyo, Japan

SEISMIC RESPONSE ANALYSIS OF TIMBER STRUCTURE WITH PASSIVE CONTROL SYSTEM USING SIMPLIFIED SPRING MODEL

Kazuhiro Matsuda[1], Kazuhiko Kasai [2], and Hiroyasu Sakata[3]

1) Assistant Professor, Structural Engineering Research Center, Tokyo Institute of Technology, Japan
2) Professor and Director, Structural Engineering Research Center, Tokyo Institute of Technology, Japan
3) Professor, Structural Engineering Research Center, Tokyo Institute of Technology, Japan
matsuda@serc.titech.ac.jp, kasai@serc.titech.ac.jp, hsakata@serc.titech.ac.jp

Abstract: In order to mitigate the damage of timber houses against large earthquake, the writers developed so-called shear-link-type passive control systems having either velocity- or deformation- dependent dampers. A number of full-scale tests were conducted including from static tests of the member joints to shaking table tests of the 2-story timber frames. The dynamic characteristics of the specimens were examined, and the effectiveness of the passive control system was validated. In the next stage of this research, in order to propose the evaluation method and design method for the passive control systems, analytical study must be conducted for validations covering much wide range of applications.

This paper proposes a modeling method of simplified spring model for 1-story timber structures having energy dissipation walls which have either velocity- or deformation- dependant damper. The principal feature of this method is that it could be composed of iterated calculation of linear elasticity model so that the timber structure having energy dissipation walls are analyzed by common software. In this paper, story drift, story shear force, and the behavior of damper could be duplicated by the simplified model. The accuracy of the model will be verified through comparisons with detailed frame model.

1. INTRODUCTION

It is said that approximately 10 million wooden houses are insufficient for earthquake resistant in Japan, and those houses need to be reinforced immediately. Moreover, to design new wooden houses to be resistant to earthquakes, it is important to investigate rational methods applying the passive control scheme to wooden houses. In order to mitigate the earthquake response and damage of wooden houses, an energy dissipation wall was developed (Kasai and Sakata et al. 2005, Appendix 1) and a lot of experimental studies using the wall were carried out, such as dynamic cyclic loading tests of the energy dissipation walls (Matsuda et al. 2008), shaking table tests of 1-story and 2-story wooden frames (Sakata et al. 2007 and Matsuda et al. 2007), and so on. In addition, analytical studies also need to be carried out to develop more effective energy dissipation wall and to propose the design method. Accurate, framed analytical models for the wooden energy dissipation wall with damper and plywood shear wall were proposed (Matsuda et al. 2011 and 2012).

There are some design methods to apply the passive control scheme to wooden houses, and one of them is seismic response analysis. Although it is rare for seismic response analysis to be adopted to small wooden houses, considering the seismic response analysis of wooden houses leads to increasing options of design and research. It is desirable for wooden house model to be composed of simple models which are able to be used by generalized software. Therefore this paper proposes a simplified seismic response analysis for passively controlled wooden frame. And through comparison with a detailed frame model, accuracy verification of the simplified seismic response analysis will be discussed.

2. CONTRACTING METHOD TO SYMPLIFIED SPRING MODEL

In order to carry out the simplified seismic response analysis, degrees of freedom of the energy dissipation wall are reduced to two. The model is composed three springs, pseudo-brace, pseudo-frame and pseudo-damper (see Fig. 1). Where pseudo-brace, pseudo-frame are linear elastic springs which have stiffness K_{bs} and K_{fs}. Every damper is classified roughly into two kinds, deformation-dependent damper and velocity-dependent damper. The hysteresis of velocity-dependent damper is modeled by linear stiffness K_{ds} and viscous coefficient C_{ds} (so-called ellipse shape). The hysteresis of deformation-dependent damper is modeled by linear stiffness K_{d1s}, second stiffness ratio p_s, yield strength F_{dys} (so-called parallelogram shape, Appendix 2).

In order to create the simplified spring model, the evaluation method (Kasai et al. 2006 and 2011) could be

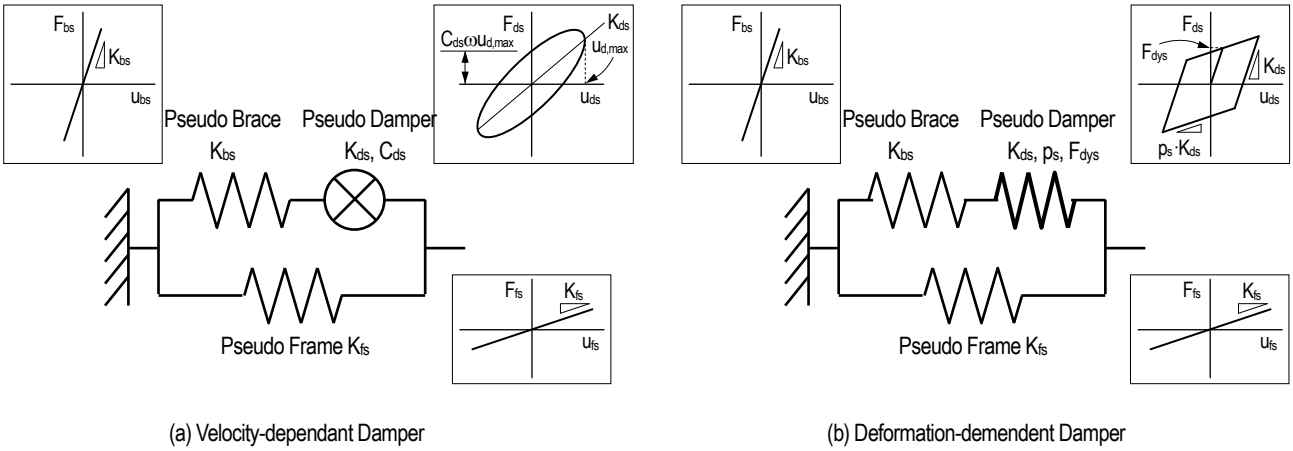


Fig. 1 Simplified Spring Model of Energy Dissipation Wall

applied. It's called "State-NR estimation". This estimation method reduces the degree of freedom of the energy dissipation wall to two by conducting twice the static analysis of the frame without dampers. As indicated Fig.2, one is State-N whose damper part is free (No-Damper), the other is State-R whose damper part is rigid absolutely (Rigid-Damper). The hysteresis of the energy dissipation wall whose damper information (hysteretic performance and quantity) had been given preliminarily could be estimated by using the two analytical results. By using this method, the performance of the energy dissipation wall for changing damper kind and/or damper quantity could be estimated properly. The simplified spring model is extremely useful for efficient time history analysis, and it also provides a new and important tool to evaluate the control effectiveness of different systems on a common scale.

Incidentally, the spring specification would be changed in each deformation since this paper is focused on timber structure which has nonlinear property. In the case of velocity-dependent damper, the spring specification also would be changed in assumed frequency.

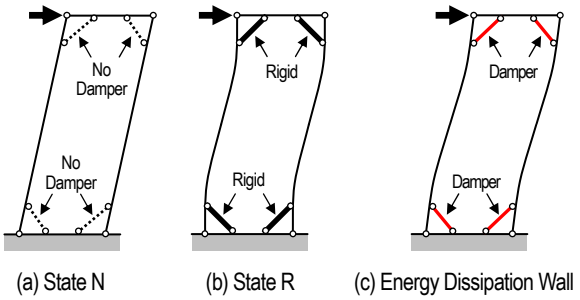


Fig. 2 Image of State-NR

3. SEISMIC RESPONSE ANALYSIS METHOD BY USING SIMPLIFIED SPRING MODEL

The relationship between system force and system deformation could be obtain for each deformation by using State-NR estimation, however seismic response analysis of

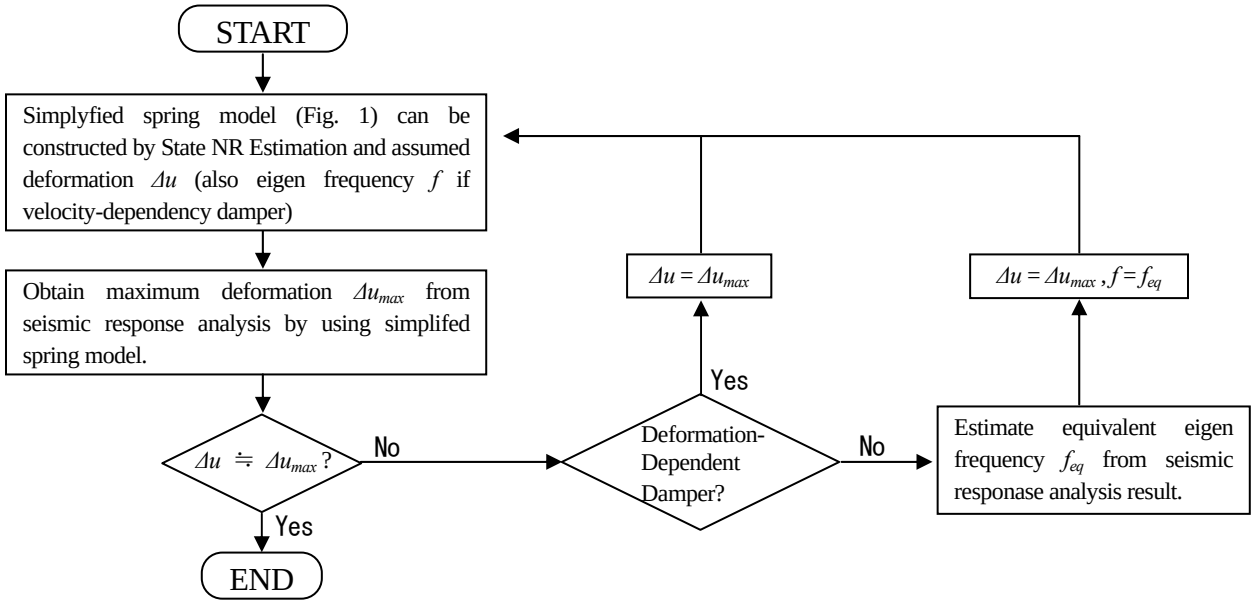


Fig. 3 Flowchart of seismic response analysis by simplified response analysis

nonlinear system is not able to be carried out since yet, since the spring specification is not equal in each deformation. Therefore, convergent calculation will be carried out in keeping with the flowchart of Fig. 3.

At first, deformation Δu is assumed, then seismic response analysis of simplified spring model is carried out by using the specification of the assumed deformation. Secondary, maximum deformation $\Delta u_{\max}$ is obtained from the previous analysis, then seismic response analysis of simplified spring model is carried out again by using the specification of the new deformation $\Delta u_{\max}$. This iteration continues until the variation of $\Delta u_{\max}$ becomes small. In the case of using velocity-dependent damper, eigen frequency f is also assumed at first. And then, eigen frequency is also included in the iteration by estimating from the seismic response analysis.

In this report, the tolerance of the convergent calculation was set to 1% variation. The first assumed Δu was set to story shear angle 1/120rad., incidentally it had been confirmed that the convergent solution became same result even if the first assumed Δu was whichever 1/480rad. and 1/30ard. The equivalent eigen frequency was derived from the equivalent stiffness which was derived from least-squares method of the relationships between system force and system deformation.

4. ACCURACY VERIFICATION

In order to confirm the accuracy of proposed seismic response analysis in chapter 3, the comparison of detailed frame model and simplified spring model will be discussed. A simplified spring model will be created by using a detailed frame model (Matsuda et al. 2011) whose accuracy is verified through comparison with shake table test. After that, comparison of seismic response analysis between detailed frame model and simplified spring model will be discussed.

4.1 Outline of Detailed Frame Model

An accurate, framed analytical model for the wooden energy dissipation wall with damper was proposed (Matsuda et al. 2011). The framed analytical model was constructed by using many kinds of nonlinear springs whose properties are derived from the test results of the joint (see Fig. 4). The joint spring between column and horizontal member consists of three types of spring, axial, rotational and shear spring. The damper is arranged at the point between the intersection of the braces and the steel plate. The frame model was able to duplicate not only global behavior but also local behavior with a high degree of accuracy in many tests of 1-story timber structure.

In this paper, viscoelastic damper is used as the velocity-dependent damper, and the viscoelastic element was proposed by Kasai et al. (2002). Basically following equations are used in viscoelastic element.

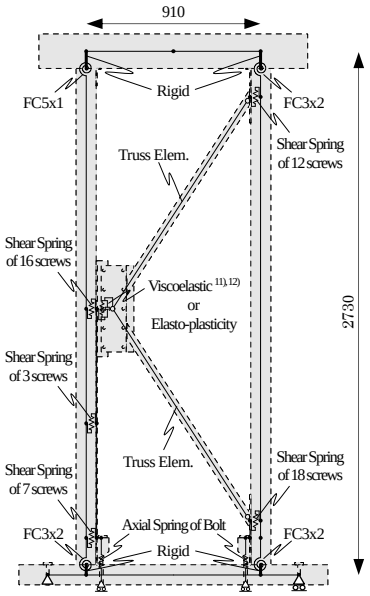


Fig. 4 Detail of Frame Model

$$\tau(t) + aD^{\alpha}\tau(t) = G\,[\gamma(t) + bD^{\alpha}\gamma(t)] \quad (1)$$

$$a = a_{ref}\lambda^{\alpha} \quad , \quad b = b_{ref}\lambda^{\alpha} \quad (2a,b)$$

$$\lambda = \exp[-p_1(\theta - \theta_{ref})/(p_2 + \theta - \theta_{ref})] \quad (3)$$

Where D^{α} is operator of fractional derivative, α is order of fractional derivative. a, b and G are parameter to depend on frequency, a_{ref} and b_{ref} are parameter to depend on temperature. In this paper, effect due to temperature raise of viscoelastic material is not considered in order to make the study simple.

In this paper, steel damper is used as the deformation-dependent damper, and improved Menegotto-Pinto model element which was proposed by Kasai et al. (2001, 2002) is used as steel damper. The improved Menegotto-Pinto model is able to duplicate the stress-strain relationship for steel material such as strain hardening, Bauschinger effect and hardening/softening effect due to repeated deformation.

4.2 Preparation of Simplified Spring Model

Fig. 5 indicates the comparison between detailed frame model and simplified spring model by State-NR estimation estimation. As for both velocity- and dependent-damper, system- and damper-hysteresis, the two curves are corresponding each other with high accuracy.

4.3 Outline of Seismic Response Ayalysis

Accuracy verification of seismic response analysis will be discussed by using the 1-Story timber frame which was modeled as the specimen of the shake table test. It was confirmed that the frame model was able to duplicate not only global behavior but also local behavior with a high degree of accuracy in many tests of 1-story timber structure. The structural part of shake table test specimen is same as Section 4.2 frame basically. In addition, mass totally 3.64ton is allocated in the beam. The damping ratio is

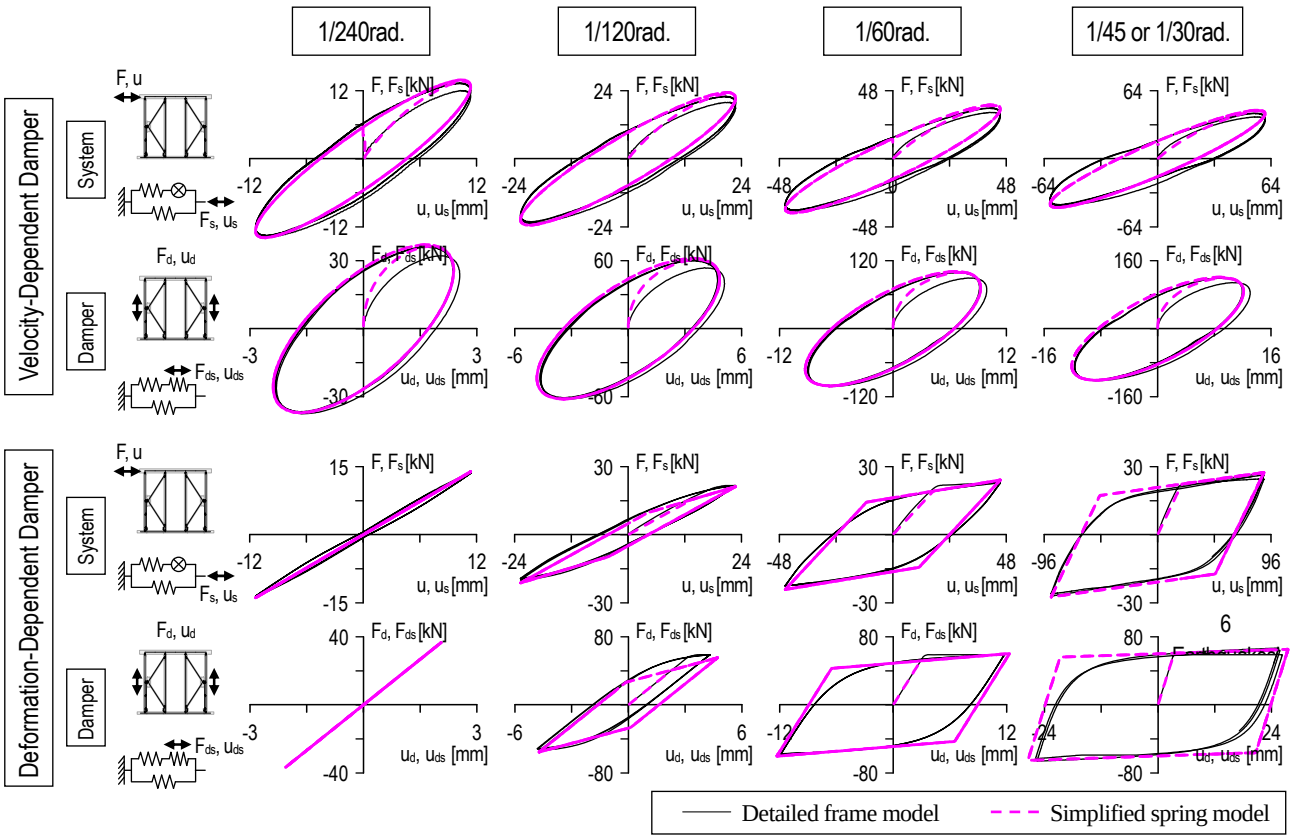


Fig. 5 Comparison between detailed frame model and simplified spring model by State-NR estimation

0.5% in both simplified spring model and detailed frame model. A seismic response analysis software, PC-ANSR, was used.

For time-history analysis, 6 artificial earthquakes are considered. These artificial earthquakes, which are scaled to Level 2, have similar spectrum characteristics. Fig. 6 shows the pseudo acceleration spectra of there earthquake (5% damping ratio).

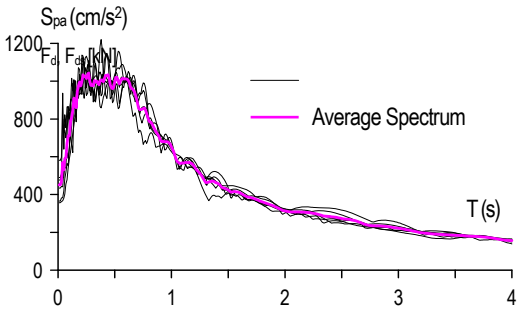


Fig. 6 Spectra of Artificial Earthquake (h = 0.05)

4.4 Results of Accuracy Verification

Comparison between detailed frame model and simplified spring model by State-NR estimation is indicated in Fig. 7. In the case of velocity-dependent damper, simplified spring model and detailed frame model are corresponding each other in both time history and force-deformation relationships.

In the case of deformation-dependent damper, linear stiffness Kd1s, second stiffness ratio ps and yield strength Fdys are basically corresponding each other in force-deformation relationships. However residual deformation and amplitude under vibration are not corresponding. The reason is that the effect of hysteresis damping due to frame yielding is not considered to pseudo-brace and pseudo-frame.

Table 1 lists summary of seismic response analysis. While there is difference in deformation range between velocity- and dependent-damper, the maximum deformation is corresponding between detailed frame model and simplified spring model in all case. Therefore it's confirmed that the simplified spring model is able to duplicate the maximum response deformation. The maximum response acceleration of simplified spring model is about 10% higher than that of detailed frame model. That's why the equivalent stiffness of simplified spring model is higher than that of detailed frame model a little, and effect of hysteresis damping due to frame yielding is not included in pseudo-brace and pseudo-frame of simplified spring model. Even if 1.5 times earthquakes are used, same tendency was obtained.

In this report, the tolerance of the convergent calculation was set to small value, 1% variation, however average number of iteration was 3.3 times. 2 times iteration approximately made the solution convergent. If design purpose is supposed to check whether maximum deformation is smaller than target deformation, it is only necessity to use specification of the target deformation to analyze.

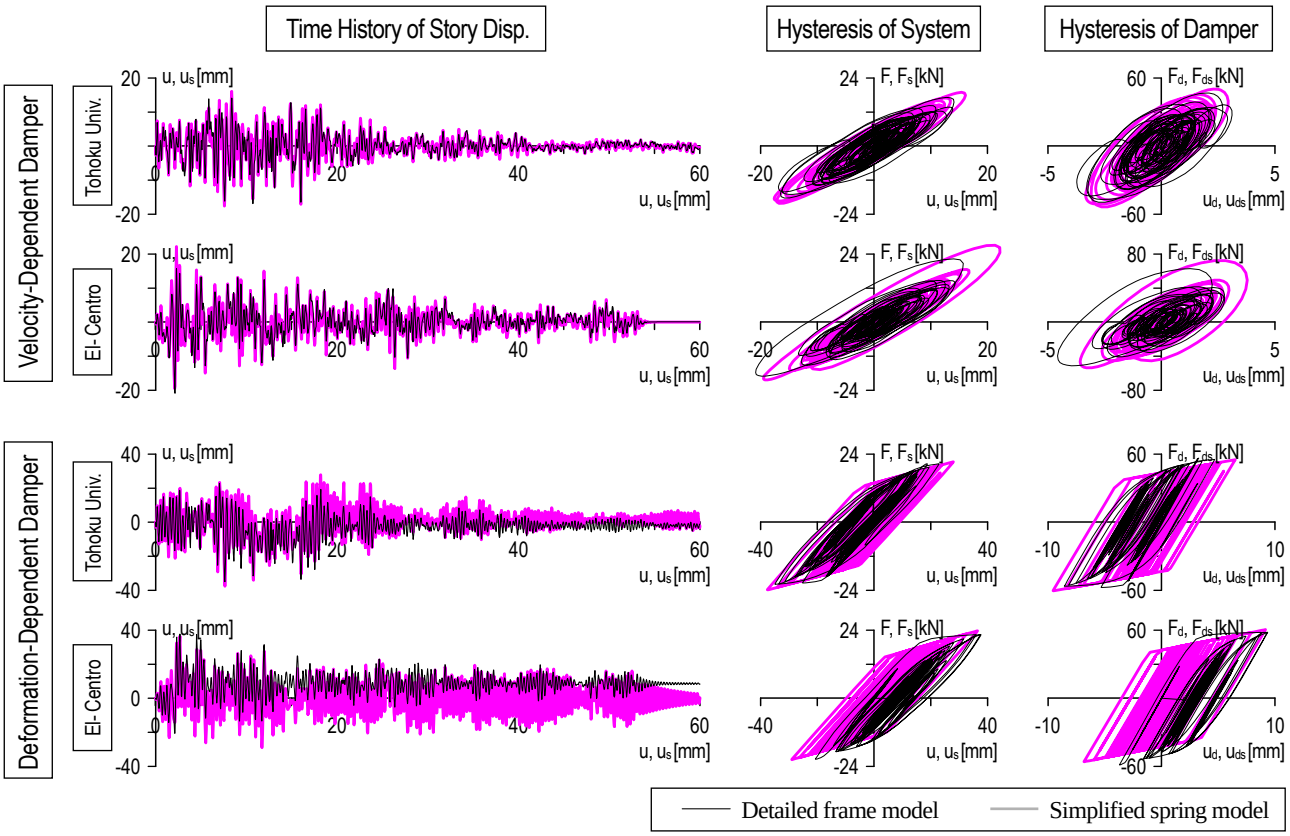


Fig. 7 Comparison between detailed frame model and simplified spring model by State-NR estimation

Table 1 Summary of comparison between detailed frame model and simplified spring model by State NR estimation

	Velocity-Dependent Damper							Deformation-Dependent Damper						
	Maximum Deform.			Maximum Acc.			Number of Iteration	Maximum Deform.			Maximum Acc.			Number of Iteration
	Detailed Frame Model (a)	Simplified Spring Model (b)	Ratio (b/a)	Detailed Frame Model (c)	Simplified Spring Model (d)	Ratio (d/c)		Detailed Frame Model (e)	Simplified Spring Model (f)	Ratio (f/e)	Detailed Frame Model (g)	Simplified Spring Model (h)	Ratio (h/g)	
	mm	mm	-	cm/s^2	cm/s^2	-	-	mm	mm	-	cm/s^2	cm/s^2	-	-
BCJ-L2	17.9	17.6	0.98	508	560	1.10	4	35.3	33.4	0.95	606	639	1.05	3
El-Centro	20.9	22.2	1.06	613	745	1.21	3	37.7	36.5	0.97	616	653	1.06	5
Hachinohe	16.2	15.7	0.97	464	537	1.16	3	32.9	35.6	1.08	613	648	1.06	3
JMA-Kobe	20.2	20.5	1.02	578	650	1.12	3	40.7	45.0	1.11	616	663	1.08	4
Tohoku Univ.	16.9	17.6	1.04	503	555	1.10	4	35.0	37.6	1.08	601	656	1.09	3
Taft	17.7	15.5	0.88	472	509	1.08	3	29.0	29.6	1.02	596	621	1.04	2
Average	18.3	18.2	0.99	523	593	1.13	3.3	35.1	36.3	1.03	608	646	1.06	3.3

5. CONCLUSION

A method to analyze timber frame with passive control scheme by using simplified spring model was proposed. Through the comparison with detailed frame model, the accuracy was confirmed. Major findings are;

- The hysteresis of velocity-dependent damper was modeled to linear viscoelastic element (ellipse shape) and the hysteresis of deformation-dependent damper was modeled to bilinear element (parallelogram shape) in order to be able to use generalized structural analysis software. Pseudo-brace and pseudo-frame which frame specification was summarized in were modeled to linear elastic springs.
- It was confirmed that the simplified spring model is able to duplicate the maximum response deformation of the detailed frame model. In the case of deformation-dependent damper, the accuracy of residual deformation should be improved.

References:

Kasai, K., Sakata, H., Wada, A. and Miyashita, T. (2005): "Dynamic Behavior of a Wood Frame with Shear Link Passive Control Mechanism Involving K-brace", Journal of Structural and Construction Engineering, No.598, pp.51-60 (In Japanese)

Matsuda, K., Sakata, H., Kasai, K. and Ooki, Y. (2008): "Experimental Study on Dynamic Response of Wooden Frames with Passive Control", Journal of Structural Engineering, Vol.54B, pp.149-156 (In Japanese)
Sakata, H., Kasai, K., Wada, A., Midorikawa, M., Ooki, Y., Nakagawa, T. and Matsuda, K. (2007): "Shaking Table Tests of Wood Frames with Velocity-Dependent Dampers", Journal of Structural and Construction Engineering, No.615, pp.161-168 (In Japanese)
Matsuda, K., Kasai, K., Sakata, H., Ooki, Y. and Wada, A. (2007): "Shaking Table Tests of Two-Story Frames with Passive Control System", Proceedings of 4th International Conference on Urban Earthquake Engineering, Center on Urban Earthquake Engineering, pp.369-374, Yokohama, JAPAN
Matsuda, K., Kasai, K. and Sakata, H. (2011): Earthquake Response Analysis of Timber Structure with Passive Control Scheme by Detailed Frame Model, 8th International Conference on Urban Earthquake Engineering, pp.1167-1173, Tokyo, Japan, 2011.3
Kasai, K. and Iwasaki, K. (2006): "Reduced Expression for Various Passive Control Systems and Conversion to Shear Spring Model", Journal of Structural and Construction Engineering, No.605, pp.37-46 (In Japanese)
Kasai, K., Yamazaki, Y., Ooki, Y. and Sakata, H. (2011): "Dynamic Behavior and Simplified Modeling Method for a Timber Frame with Knee Brace Dampers", Journal of Structural and Construction Engineering, No.664, pp.1109-1118 (In Japanese)
Kasai, K. and Tokoro, K. (2002): "Constitutive Rule for Viscoelastic Materials Considering Temperature Frequency, and Strain Sensitivities, part 2 Nonlinear Model Based on Temperature-Rise, Strain and Strain-Rate", Journal of Structural and Construction Engineering, No.561, pp.55-63 (In Japanese)
Kasai, K., Yamazaki, H., Kozawa, H., Kaneko, H., Sadasue, K. and Ono, Y. (2008): "Curved Hysteresis Model of Structural Steel under Cyclic Loading, part 7, 8", Summary of Technical papers of Annual meeting of AIJ, C-1, 907-910 (In Japanese)

Appendix 1: Outline of Energy Dissipation Wall

The feature of K-brace passive control wall is shown below (Fig. A1). When the wall deforms by horizontal force, there is vertical deformation between the brace and the steel plate and the damper is inserted in the place. The wall is classified in to a series of so-called shear link type. In order to reduce the effect of the column's bending, the edge of the brace is fixed near the joint of the column and horizontal member. There are many advantages because the contents of the wall are able to fit in inside of frames. For example it is possible to fix without an attachment of other walls. K-brace is screwed on wooden frames by a lot of screws because of high safety factor.

A stub tenon, L-type metal and bolt (hold-down metal) are allocated in the joint of the column and horizontal member. The square steel pipe is fillet-welded to steel plate B and C (Fig. A1(c)). Energy absorption capacity is increased as much as possible by allocating the bolt closer to the column, and integrating the steel plate C into the hold-down metal.

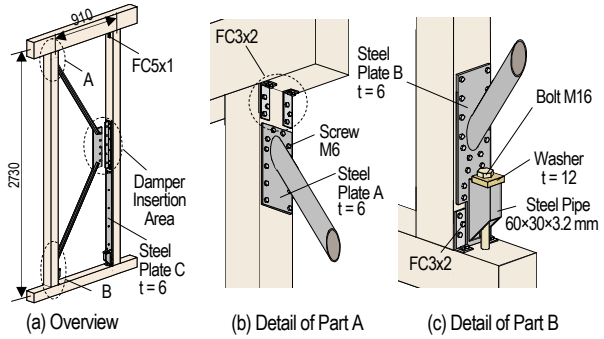


Fig. A1 Detail of Energy Dissipation Wall

Appendix 2: Modelization of Steel Damper

Hysteresis of steel damper is modeled by following step from 1) to 4). Fig. A2 indicates the example of modelization of steel damper.

Step 1) K_{d1+} is obtained from least-square method by using unloading area of the first quadrant (see Fig. A3). Likewise, K_{d1-} is obtained from least-square method by using unloading area of the third quadrant and initial stiffness K_{d1} is obtained as the average K_{d1+} and K_{d1-}.

Step 2) K_{d2+} is obtained from least-square method by using loading area of the first quadrant (see Fig. A3). Likewise, K_{d2-} is obtained from least-square method by using loading area of the third quadrant and second stiffness K_{d2} is obtained as the average K_{d2+} and K_{d2-}.

Step 3) Maximum deformation of positive and negative side are $u_{d\max+}$ and $u_{d\max-}$. $F_{d\max+}$, $F_{d\max-}$ are obtained from force at maximum deformation of positive and negative side. Maximum deformation $u_{d\max}$ and maximum force $F_{d\max}$ are obtained from the average of their two values.

Step 4) Yielding strength F_{dy} and second stiffness ratio p are obtained from following equations.

$$F_{dy} = \frac{F_{d\max} - p \cdot u_{d\max} \cdot K_{d1}}{1-p}, \quad p = \frac{K_{d2}}{K_{d1}} \qquad \text{(A1)}$$

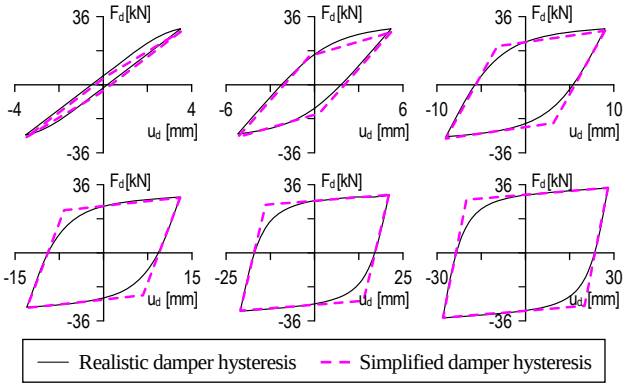


Fig. A2 Example of bilinear model

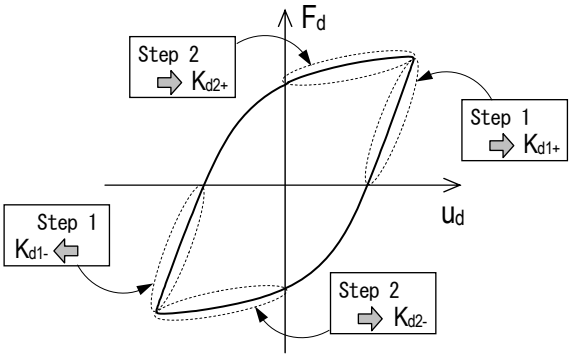


Fig. A3 Range of used data

10CUEE CONFERENCE PROCEEDINGS
10th International Conference on Urban Earthquake Engineering
March 1-2, 2013, Tokyo Institute of Technology, Tokyo, Japan

FLEXURAL PERFORMANCE OF JAPANESE TRADITIONAL MORTISE - TENON JOINT WITH SPLIT WEDGE

Hiroyasu Sakata [1], Yoshihiro Yamazaki [2], Takuya Noguchi[3], and Yoshimitsu Ohashi [4]

1) Professor, Structural Engineering Research Center, Tokyo Institute of Technology, Japan
2) Assistant Professor, Structural Engineering Research Center, Tokyo Institute of Technology, Japan
3) Graduate Student, Department of Built Environment, Tokyo Institute of Technology, Japan
4) Professor, Department of Architecture, Tokyo City University, Japan
sakata.h.aa@m.titech.ac.jp, yamazaki.y.ai@m.titech.ac.jp, noguchi.t.ad@m.titech.ac.jp, ohashi-y@tcu.ac.jp

Abstract: In this paper, moment resisting behavior of mortise-tenon joint with split wedge is examined. Flexural-shear tests for split wedge joint are conducted. Seventy-two specimens are tested, and their parameters are dimension of post, beam, tenon, notch line and wedge and tree species of members. The effect of prestressing due to wedge is also discussed. Evaluation method of moment resisting performance of split wedge joint is proposed using simplified mechanical model. It is based on the result of embedment test of wooden materials. The key techniques of the model are how to determine the location of rotation center and consideration of prestressing due to wedge. In addition, closed-form equation to evaluate moment-rotation relation of joint is also proposed.

1. INTRODUCTION

Mortise-tenon joint is one of the most typical connections of Japanese traditional wooden structure. In order to resist tensile force, wooden dowel is often used. We reported tensile tests and flexural-shear tests of mortise-tenon joint with dowel (Sakata et al. 2012). In addition, evaluation method of moment-rotation relation was proposed.

In this paper, we focused on split wedge joints, which are effective to increase initial stiffness because of prestressing due to wedge. Experimental reports on structural performance of split wedge joints are few, and its design rule is not proposed so far. Therefore, we tried to extend the evaluation method to wedge joint.

Seventy two of flexural-shear tests are carried out, and moment-rotation relation, maximum moment and failure patterns are compared. After that, evaluation method of flexural performance is proposed. The analysis model considers compatibility of deformation and equilibrium of force at the joint section and also the effect of initial stress caused by wedge. However, non-linear simultaneous equation has to be solved to determine rotation center of joint. Therefore, detailed analysis and simplified analysis are presented. Simplified approach gives closed-form solution of moment-rotation relation of joint.

2. FLEXURAL-SHEAR TEST

2.1 Outline

Specimens are shown in Figure 1. Post and beam are connected each other with mortise and tenon. Two notches are preliminary made, and wedges are inserted to the notches.

List of specimens is shown in Table 1. Their parameters are dimension of tenon, post, beam and wedge and tree species of members. Six specimens per one specification were tested. Material properties are shown in Table 2. Specimen name is determined in the following manner.

Example 120-30-CC
(1) (2) (3)

(1) Depth of beam h_b
(2) Thickness of tenon b_t
(3) Tree species of post and beam
(C=Cedar, H=Hinoki cypress)

Setup of flexural-shear tests is shown in Figure 2. Post was fixed to steel foundation beam with anchor bolts. Lateral force was applied to loading point of beam by actuator. Let γ be drift angle of beam, and it is calculated using following equation.

$$\gamma = \left(\frac{\delta_1 + \delta_2}{2} - \frac{\delta_3 + \delta_4}{2} \right) / L \quad (1)$$

Where, δ_1, δ_2 = lateral displacement of loading point, and δ_3, δ_4 = those of post. L is vertical distance between center axis of post and loading point, which was set 700 mm.

Loading schedule was controlled by γ, and static reverse cyclic loading was applied as shown in Figure 3. In

Table 1 List of Specimens

Unit:mm

No.	Name	Post		Beam		Wedge			Tenon						Mortise				No. of Speci-mens
		Tree species	Section $b_c \times h_c$	Tree species	Section $b_b \times h_b$	Tree species	Dimension $l_w \times t_w \times b_w$	Angle θ_w (rad.)	Length l_t	Width h_t	Thick-ness b_t	Notch l_{ts}	Notch h_{ts}	Notch angle θ_s (rad.)	Width(1) w_b	Width(2) w_s	Depth l_s	Angle θ_m (rad.)	
1	120-30-CC	Cedar	120×120	Cedar	120×120	Oak	125×15×30	0.120	150	90	30	110	15	0.136	105	90	50	0.107	6
2	120-30-CH	Cedar		Cedar															
3	120-30-HH	Hinoki		Hinoki															
4	120-36-CC	Cedar	120×120	Cedar	120×120		125×15×36	0.120	150	90	36	110	15	0.136	105	90	50	0.107	6
5	120-36-CH	Cedar		Cedar															
6	120-36-HH	Hinoki		Hinoki															
7	150-36-CC	Cedar	150×150	Cedar	150×150		145×18×36	0.124	180	120	36	125	18	0.144	140	120	60	0.111	6
8	150-36-CH	Cedar		Cedar															
9	150-36-HH	Hinoki		Hinoki															
10	180-36-CC	Cedar	180×180	Cedar	180×180		160×20×36	0.125	210	150	36	150	20	0.133	175	150	70	0.114	6
11	180-36-CH	Cedar		Cedar															
12	180-36-HH	Hinoki		Hinoki															

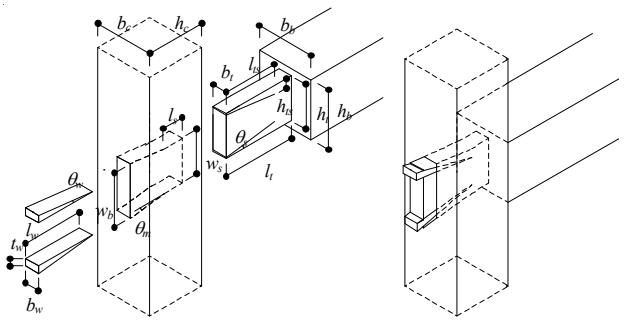


Figure 1 Dimension of Split Wedge Joint

Table 2 Material Properties of Timber

	Moisture content (%)	Specific gravity	Young's modulus (kN/mm^2)	Modulus of rupture σ_b (N/mm^2)
Cedar	10.17	0.41	6.51	42.87
Hinoki cypress	9.38	0.51	8.84	60.01

* Young's modulus and modulus of rupture were identified by three-point bending test

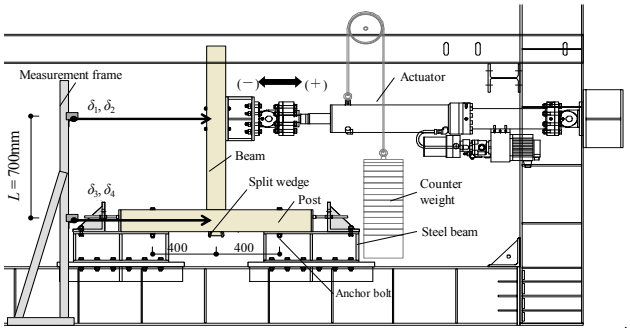


Figure 2 Setup of Flexural-Shear Test

addition, relative rotation angle, uplift and shear sliding between post and beam were also measured.

2.2 Result and Discussion

Let M and θ be moment and relative rotation angle at critical section, respectively, which are shown in Figure 4. An example of M-θ hysteresis of joint is shown in Figure 5.

2.2.1 M-θ relation and failure mode

High initial stiffness was observed due to prestressing of wedge. After that, slope of M-θ relation was quite decreased. Bending failure of tenon was usually observed. As shown in Picture 1, out side of notch might get broken at first, and then moment drastically decreased due to failure of middle of tenon. Deformation of wedges was not observed. Eighteen of seventy two specimens were not broken until 1/7.5rad.

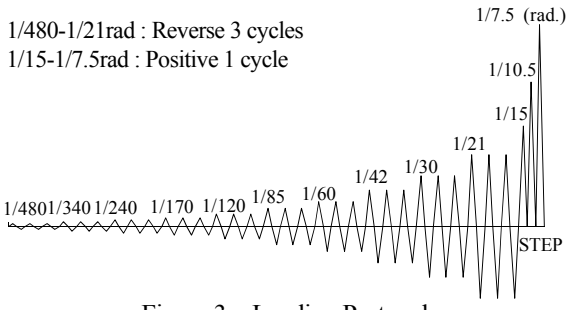


Figure 3 Loading Protocol

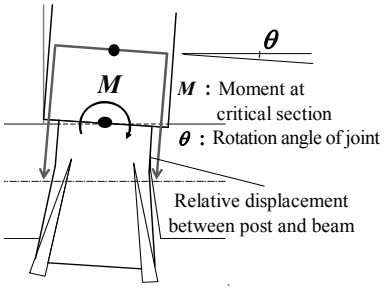
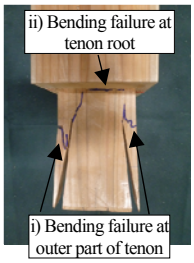


Figure 4 Definition of M and θ



Picture 1 Failure Pattern

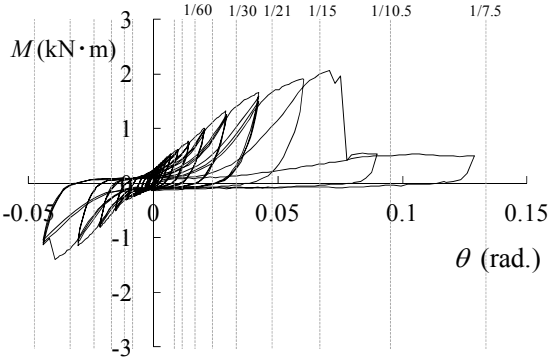


Figure 5 M-θ Hysteresis of 120-30-CC

2.2.2 Comparison of envelope curve

Envelope curves of 120-30-CC, CH and HH are shown in Figure 6(a), (b), (c), respectively. Average and standard deviation curves of six specimens are superposed.

Variation of M-θ curve in six specimens was small in the range of small θ. Rotation angle at occurrence of failure , however, were widely varied.

Maximum moment M_{max} seem to be located between $Z\sigma_s$ and $Z_0\sigma_s$. These are also superposed in the figure with lateral dash lines. Here, σ_s = modulus of rupture of tenon

identified by three-point bending test, Z = section modulus of whole section and Z_0 = that of partial section. Partial section means section from notch to notch (See Figure 6).

In addition, considering accuracy of mortise and tenon dimension, small gap between mortise and tenon might exist. This is why some envelope curves have slip in small θ.

2.2.3 Comparison of M_{max} and θ_{Mmax}

Figures 7, 8 and Table 3 show comparison of M_{max} and θ_{Mmax}. Here, θ_{Mmax} means rotation angle at $M = M_{max}$. The larger the dimension of tenon is, the larger M_{max} and θ_{Mmax} seem to be. M_{max} of CH and HH are larger than those of CC while θ_{Mmax} are not so different regardless of tree species. This means tree species of tenon has much effect on M_{max}.

3. MODELING OF FLEXURAL-SHEAR RESISTANCE

3.1 Mechanical model

Figure 9 shows equilibrium condition of joint. External forces consist of axial force N, shear force Q and moment M, and following four kinds of internal forces are considered.

F_{c1}, F_{c2} and F_{c3} are local compression forces of tenon. F_{c4} shows local compression force of post. F_{fc1}, F_{fc2} and F_{fc3} are friction forces between tenon and mortise. F_{fc4} is friction force between beam and post.

The followings are assumed in order to construct mechanical model.

1) Tenon is enough rigid except for local embedment perpendicular to the grain. Wedges are infinitely rigid.
2) Tenon rotates around rotation center determined by x_n and y_n.
3) Initial stress angle is geometrically calculated using dimension of tenon, mortise and wedge.

3.2 Local Embedment of Timber Perpendicular to the Grain

The authors have conducted rotational compression test of timber perpendicular to the grain as shown in Figure 10 (Sakata et al. 2002). We found evaluation method of moment-rotation relation using properties of parallel

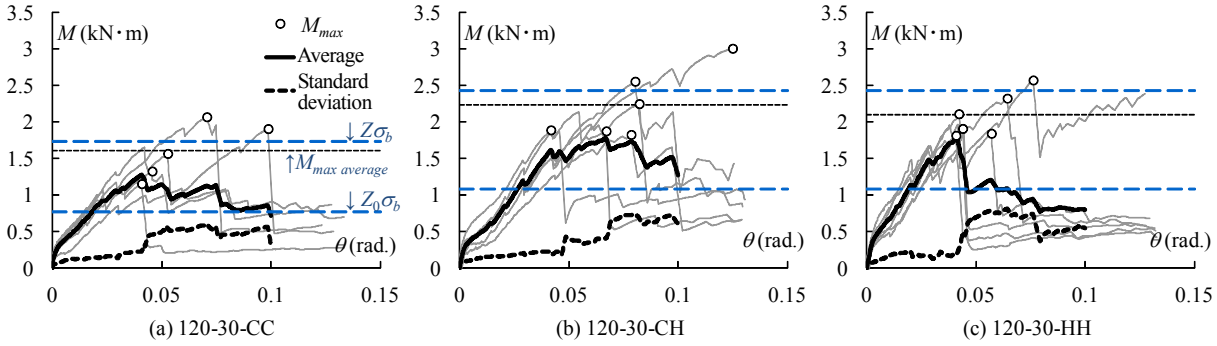


Figure 6 Envelope curve of M-θ Relation (120-30)

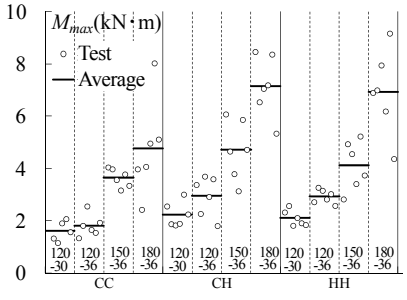


Figure 7 Comparison of M_{max}

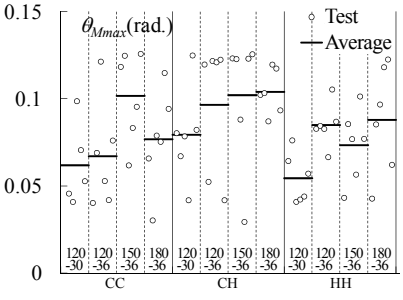


Figure 8 Comparison of θ_{Mmax}

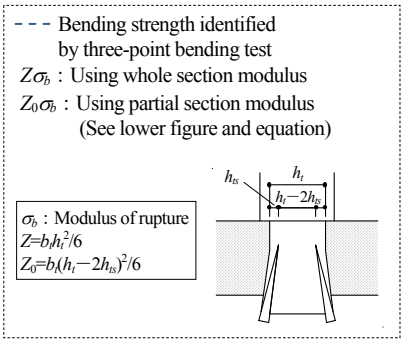


Table 3 List of Test Results

No.	120-30						120-36						150-36						180-36					
	CC		CH		HH		CC		CH		HH		CC		CH		HH		CC		CH		HH	
	M_{max} (kN・m)	θ_{Mmax} (rad.)	M_{max} (kN・m)	θ_{Mmax} (rad.)	M_{max} (kN・m)	θ_{Mmax} (rad.)	M_{max} (kN・m)	θ_{Mmax} (rad.)	M_{max} (kN・m)	θ_{Mmax} (rad.)	M_{max} (kN・m)	θ_{Mmax} (rad.)	M_{max} (kN・m)	θ_{Mmax} (rad.)	M_{max} (kN・m)	θ_{Mmax} (rad.)	M_{max} (kN・m)	θ_{Mmax} (rad.)	M_{max} (kN・m)	θ_{Mmax} (rad.)	M_{max} (kN・m)	θ_{Mmax} (rad.)	M_{max} (kN・m)	θ_{Mmax} (rad.)
1	*	*	2.55	0.08	2.32	0.06	1.34	0.04	3.38	0.12	2.72	0.08	4.04	0.12	6.07	0.12	2.82	0.04	3.97	0.07	8.47	0.10	6.90	0.04
2	1.33	0.05	1.87	0.07	2.57	0.08	1.81	0.07	2.27	0.05	3.27	0.08	3.97	0.12	4.65	0.12	4.93	0.09	2.42	0.03	6.54	0.10	7.00	0.09
3	1.15	0.04	1.83	0.08	1.81	0.04	2.55	0.12	3.70	0.12	3.15	0.08	3.56	0.06	3.79	0.09	4.56	0.08	4.07	0.08	7.06	0.09	7.95	0.10
4	1.91	0.10	1.89	0.04	2.11	0.04	1.66	0.05	2.92	0.12	2.82	0.07	3.16	0.08	3.13	0.03	3.41	0.06	4.96	0.08	7.19	0.12	6.19	0.12
5	2.07	0.07	3.00	0.13	1.91	0.04	1.54	0.04	3.60	0.12	3.03	0.11	3.78	0.10	5.87	0.12	5.23	0.10	8.03	0.11	8.37	0.12	9.17	0.12
6	1.57	0.05	2.25	0.08	1.84	0.06	1.93	0.08	1.80	0.04	2.57	0.09	3.34	0.13	4.72	0.13	3.74	0.08	5.11	0.09	5.34	0.09	4.37	0.06
	1.60	0.06	2.23	0.08	2.09	0.05	1.80	0.07	2.94	0.10	2.93	0.08	3.64	0.10	4.71	0.10	4.11	0.07	4.76	0.08	7.16	0.10	6.93	0.09
	0.21	0.34	0.19	0.31	0.13	0.24	0.21	0.41	0.24	0.36	0.08	0.13	0.09	0.23	0.22	0.34	0.21	0.26	0.36	0.34	0.15	0.11	0.21	0.32

Average (Upper), Coefficient of variation (Lower)

compression perpendicular to the grain. It consists of the following three steps.

Step1 : Bi-linear approximation of stress-strain curve of parallel compression perpendicular to the grain

Parallel compression tests perpendicular to the grain were carried out, and stress-strain curves were obtained. They were approximated by bi-linear model in the manner we proposed (Sakata et al. 2006), and their elastic Young's modulus E_{10}, plastic Young's modulus E_{20} and yield stress σ_{y0} were obtained. Maximum, average and minimum values of E_{10}, E_{20} and σ_{y0} are shown in Table 4.

Step2 : Conversion rule of parallel compression to rotational partial compression (Table 5)

In our previous research, stress-strain relation of parallel compression and edge stress-edge strain relation of rotational compression were compared. The results are shown in Table 6. We found that yield stress of rotational compression were about 1.5 times of σ_{y0}. Elastic Young's modulus and plastic Young's modulus seemed not to be changed.

In addition, rotational partial compression tests were also conducted. Specimen of partial compression had surplus timber along x-direction as shown in Table 5. Apparent edge stress-edge strain curves were obtained. The effects of surplus length are summarized in Figure 11 and Figure 12. If the surplus length is larger than contact length, elastic and plastic Young's modulus seems to be about 1.75 times of E_{10} and E_{20}, respectively, while yield stress is about 2.625 (= 1.5 × 1.75) times of σ_{y0}.

Step3 : Consideration of strain distribution

Although we assumed triangle strain distribution as shown in Figure 13(a), actual strain distribution on surplus timber is quite complicated. Inayama and Tanahashi used exponential function to model the distribution. However, our objective is to simulate the effect of surplus length shown in Figure 11, and we try to use simpler model, half length triangle distribution. This assumption gives easier solution, and matches tendency of test results by using properties of rotational compression without surplus timber. Therefore, we can obtain moment-rotation relation from strain distribution shown in Figure 13(b) using elastic Young's modulus $E_1 = E_{10}$, plastic Young's modulus $E_2 = E_{20}$, and yield stress $\sigma_s = 1.5\sigma_{s0}$, respectively.

3.3 Initial Stress Caused by Wedge

Kitamori has proposed evaluation method of initial stress of wedged Nuki joint (Kitamori et al. 2003). In this paper, the method is applied to split wedge joint.

Initial stress angle could be geometrically calculated using dimension of tenon, mortise and wedge (Table 1), and corresponding forces were assumed to occur as shown in Figure 14. Table 7 shows mortise angle θ_m, wedge angle θ_w and initial stress angle θ_0 of each specimen. θ_0 is defined as θ_w-θ_m from geometrical relationship.

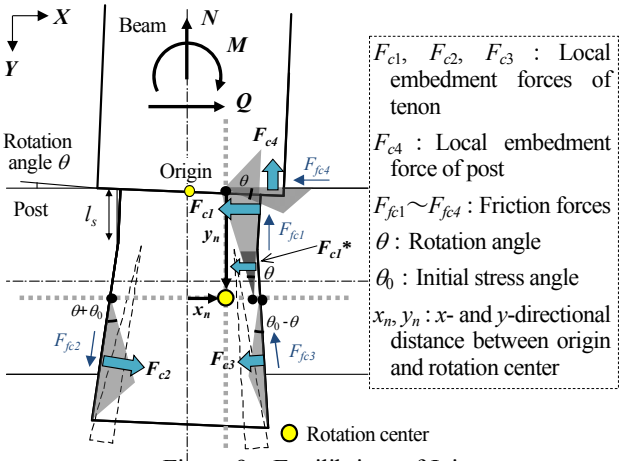


Figure 9 Equilibrium of Joint

Table 4 Result of Parallel Compression Test of Timber

Tree species		Elastic Young's modulus E_{10} (N/mm^2)	Plastic Young's modulus E_{20} (N/mm^2)	Yield stress σ_y (N/mm^2)
Cedar	Maximum	370.7	10.1	3.7
	Average	275.9	5.6	3.4
	Minimum	192.8	1.9	3.0
Hinoki cypress	Maximum	553.0	11.6	6.8
	Average	436.6	8.9	4.7
	Minimum	391.8	5.5	4.1

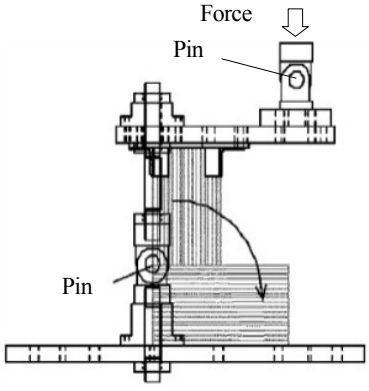


Figure 10 Rotational Compression Test of Timber (2002 Sakata et al.)

Table 5 Evaluation Method of Local Embedment

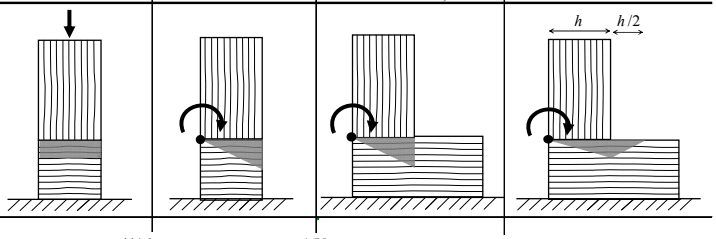
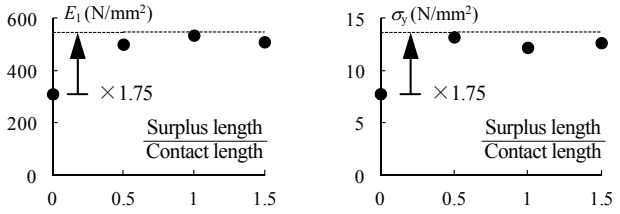
Model	Parallel compression	Rotational compression	Rotational partial compression (Apparent strain distribution)	Rotational partial compression (Modified strain distribution)
				
Elastic Young's modulus E_1	E_{10}	×1.0 → E_{10}	×1.75 → $1.75E_{10}$	×(1/1.75) → E_{10}
Plastic Young's modulus E_2	E_{20}	×1.0 → E_{20}	×1.75 → $1.75E_{20}$	×(1/1.75) → E_{20}
Yield stress σ_y	σ_{y0}	×1.5 → $1.5\sigma_{y0}$	×1.75 → $2.625\sigma_{y0}$	×(1/1.75) → $1.5\sigma_{y0}$

Table 6 Comparison of Yield Stress of Parallel/Rotational Compression of Timber Perpendicular to the Grain

Width (mm)	Depth (mm)	Yield stress σ_y (N/mm^2)		Rot./Par.
		Parallel comp.	Rotational comp.	
50	50	3.81	6.52	1.71
200	100	5.17	7.61	1.47
100	150	3.86	6.09	1.58
150	200	4.12	5.93	1.44



(a) Elastic Young's Modulus (b) Yield Stress

Figure 11 The Effect of Surplus Length

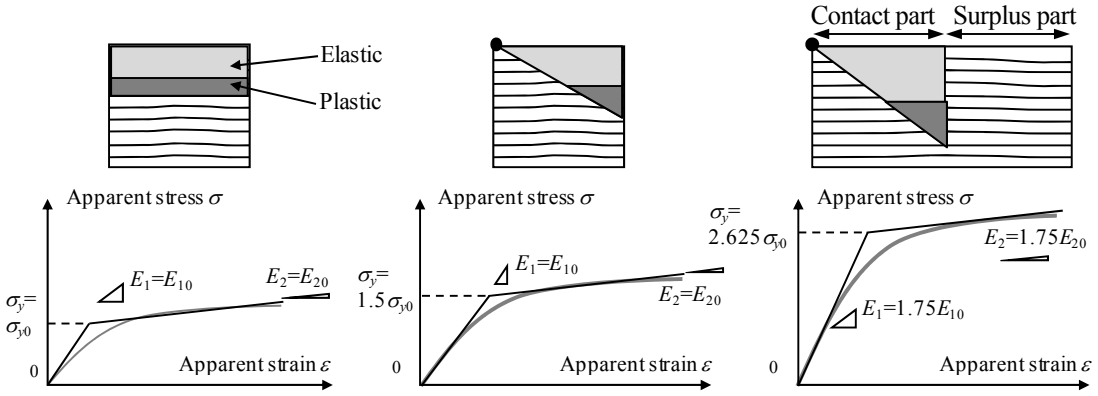
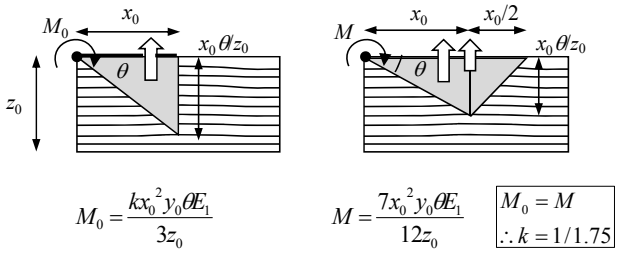


Figure 12 Distribution of Strain and σ-ε Relation

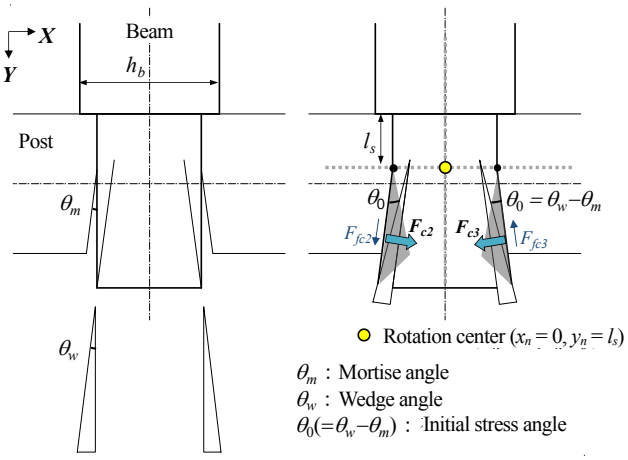


(a) Rotational Compression (b) The effect of Surplus Length

Figure 13 Evaluation of Rotational Compression Considering the Effect of Surplus Length

Table 7 List of Initial Stress Angle

Name		Mortise angle θ_m (rad.)	Wedge angle θ_w (rad.)	Initial stress angle $\theta_0 (=\theta_w - \theta_m)$ (rad.)
120-30	CC	0.1067	0.1194	0.0127
	CH			
	HH			
120-36	CC	0.1067	0.1194	0.0127
	CH			
	HH			
150-36	CC	0.1107	0.1235	0.0128
	CH			
	HH			
180-36	CC	0.1132	0.1244	0.0112
	CH			
	HH			



(a) Before Wedged (b) After Wedged ($\theta = 0$)

Figure 14 Evaluation of Initial stress

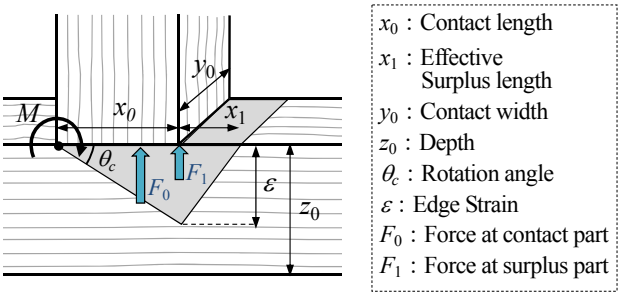


Figure 15 Definition of Local Embedment

3.4 Formulation of Local Embedment of Timber

Based on findings of section 3.2, local embedment forces F_{c1}-F_{c4} and corresponding moment M_{c1}-M_{c4} can be mathematically obtained using geometric parameters (tenon length, width and thickness and so on) and material properties (Young's modulus and yield stress).

As shown in Figure 15, formulation of local embedment force F (= F_0 + F_1) and corresponding moment M are expressed using generalized parameters : contact length x_0, effective surplus length x_1, contact width y_0, depth

z_0, rotation angle θ_c and material properties E_1, E_2 and ε_y (= σ_y/E_1).

$$\varepsilon = \frac{x_0 \theta_c}{z_0} \tag{2}$$

$$F = F_0 + F_1 \tag{3}$$

$$F_0 = F_{0e} \quad (\varepsilon \le \varepsilon_y) \qquad = F_{0p} \quad (\varepsilon > \varepsilon_y) \qquad F_{0e} = \frac{1}{2} x_0 y_0 \varepsilon E_1$$

$$F_{0p} = F_{0e}\left\{1 - \left(1 - \frac{E_2}{E_1}\right)\left(\frac{\varepsilon - \varepsilon_y}{\varepsilon}\right)^2\right\} \tag{4a-c}$$

$$F_1 = F_{1e} \quad (\varepsilon \le \varepsilon_y) \qquad = F_{1p} \quad (\varepsilon > \varepsilon_y) \qquad F_{1e} = \frac{1}{2} x_1 y_0 \varepsilon E_1$$

$$F_{1p} = F_{1e}\left\{1 - \left(1 - \frac{E_2}{E_1}\right)\left(\frac{\varepsilon - \varepsilon_y}{\varepsilon}\right)^2\right\} \tag{5a-c}$$

$$M = M_0 + M_1 \tag{6}$$

$$M_0 = M_{0e} \quad (\varepsilon \le \varepsilon_y) \qquad = M_{0p} \quad (\varepsilon > \varepsilon_y) \qquad M_{0e} = \frac{2}{3} x_0 F_{0e}$$

$$M_{0p} = M_{0e}\left\{1 - \frac{3}{2}\left(1 - \frac{E_2}{E_1}\right)\left(\frac{2\varepsilon + \varepsilon_y}{3\varepsilon}\right)\left(\frac{\varepsilon - \varepsilon_y}{\varepsilon}\right)^2\right\} \tag{7a-c}$$

$$M_1 = M_{1e} \quad (\varepsilon \le \varepsilon_y) \qquad = M_{1p} \quad (\varepsilon > \varepsilon_y) \qquad M_{1e} = x_0 F_{1e}$$

$$M_{1p} = M_{1e}\left\{1 - \left(1 - \frac{E_2}{E_1}\right)\left(\frac{\varepsilon - \varepsilon_y}{\varepsilon}\right)^2\right\} \tag{8a-c}$$

Where, ε = edge strain of triangle distribution, F_0, M_0 = contribution of contact part to local embedment force/moment, F_1, M_1 = contribution of surplus part, respectively. Indexes "*e*" and "*p*" mean elastic ($\varepsilon \le \varepsilon_y$) and plastic ($\varepsilon > \varepsilon_y$), respectively. List of generalized parameters (x_0, x_1, y_0, z_0 and θ_c) for calculation of F_{c1}-F_{c4} and M_{c1}-M_{c4} is shown in Table 8. Note that "*" means virtual force on non-contact surface. For example, F_{c1}* should be subtracted from F_{c1} as shown in Figure 9.

Table 8 Generalized Parameters of Local Embedment (Detailed Analysis)

Force, Moment	Contact length x_0	Surplus length x_1	Contact width y_0	Depth z_0	Rotation angle θ_c
F_{c1}, M_{c1}	y_n	$\frac{1}{2} y_n$	b_t	h_t	θ
F_{c1}*, M_{c1}*	$y_n - l_s$	0			
F_{c2}, M_{c2}	$\frac{h_c - y_n}{\cos\theta_m}$	$l_t - l_s - \frac{h_c - l_s}{\cos\theta_m}$			$\theta + \theta_0$
F_{c2}*, M_{c2}*	$\frac{l_s - y_n}{\cos\theta_m}$	0			
F_{c3}, M_{c3}	$\frac{h_c - y_n}{\cos\theta_m}$	$l_t - l_s - \frac{h_c - l_s}{\cos\theta_m}$			$\max.\{\theta_0 - \theta, 0\}$
F_{c3}*, M_{c3}*	$\frac{l_s - y_n}{\cos\theta_m}$	0			
F_{c4}, M_{c4}	$\frac{h_b}{2} - x_n$	$\frac{1}{2}\left(\frac{h_b}{2} - x_n\right)$	b_c	h_c	θ
F_{c4}*, M_{c4}*	$\frac{h_t}{2} - x_n$	0	b_t		

3.5 Friction Force

Friction forces F_{fc1}-F_{fc4} can be modeled on Coulomb's friction, and F_{c1}-F_{c4} are their corresponding normal forces. Moments derived from F_{fc1}-F_{fc4} are calculated as follows.

$$M_{fc1} = \left(\frac{h_t}{2} - x_n\right) \cdot \mu F_{c1}$$

$$M_{fc2} = \left(x_n + \frac{h_t}{2}\right) / \cos\theta_m \cdot \mu F_{c2}$$

$$M_{fc3} = \left(x_n - \frac{h_t}{2}\right) / \cos\theta_m \cdot \mu F_{c3}$$

$$M_{fc4} = y_n \cdot \mu F_{c4} \tag{9a-d}$$

Where, μ = coefficient of friction. In order to take into account variability of test result, both coefficient of dynamic friction and static friction are used. As for dynamic friction, $\mu = 0.17$ is used for CC, $\mu = 0.22$ for HH, and $\mu = 0.2$ for CH, respectively. As for static friction, $\mu = 0.54$ is used regardless of tree species by referring to Wood Industry Handbook.

3.6 Equilibrium of Force

Equilibrium of force in *x*- and *y*-direction and moment around rotation center is expressed as follows.

$$\sum X : -F_{c1} + F_{c2}\cos\theta_m - F_{c3}\cos\theta_m - F_{fc2}\sin\theta_m + F_{fc3}\sin\theta_m - F_{fc4} + Q = 0$$

$$\sum Y : -F_{c2}\sin\theta_m - F_{c3}\sin\theta_m + F_{c4} + F_{fc1} - F_{fc2}\cos\theta_m + F_{fc3}\cos\theta_m - N = 0 \tag{10a-c}$$

$$\sum M : M_{c1} + M_{c2} - M_{c3} + M_{c4} + M_{fc1} + M_{fc2} + M_{fc3} + M_{fc4} - Q\left\{\left(L - \frac{h_c}{2}\right) + y_n\right\} - N x_n = 0$$

If θ is given, above equations are non-linear simultaneous equations of three variables : x_n, y_n and Q. In chapter 4, convergence calculation is used to determine the unknown parameters and solve the equations. On the other hand, in chapter 5, rotation center (x_n, y_n) is assumed instead of conducting convergence calculation. Therefore, we can obtain closed-form solution.

4. DETAILED ANALYSIS

4.1 Outline

At first, arbitrary θ is applied, and three equations of equilibrium are solved, which requires convergence calculation. After that, θ is gradually increased. Above calculation leads to getting M-θ relation of joint. This procedure is named "detailed analysis".

4.2 Comparison between Test Results and Analytical Results

Accuracy of detailed analysis is confirmed. Figure 16 shows comparisons between test results and analytical results of M-θ relation. In order to take into account

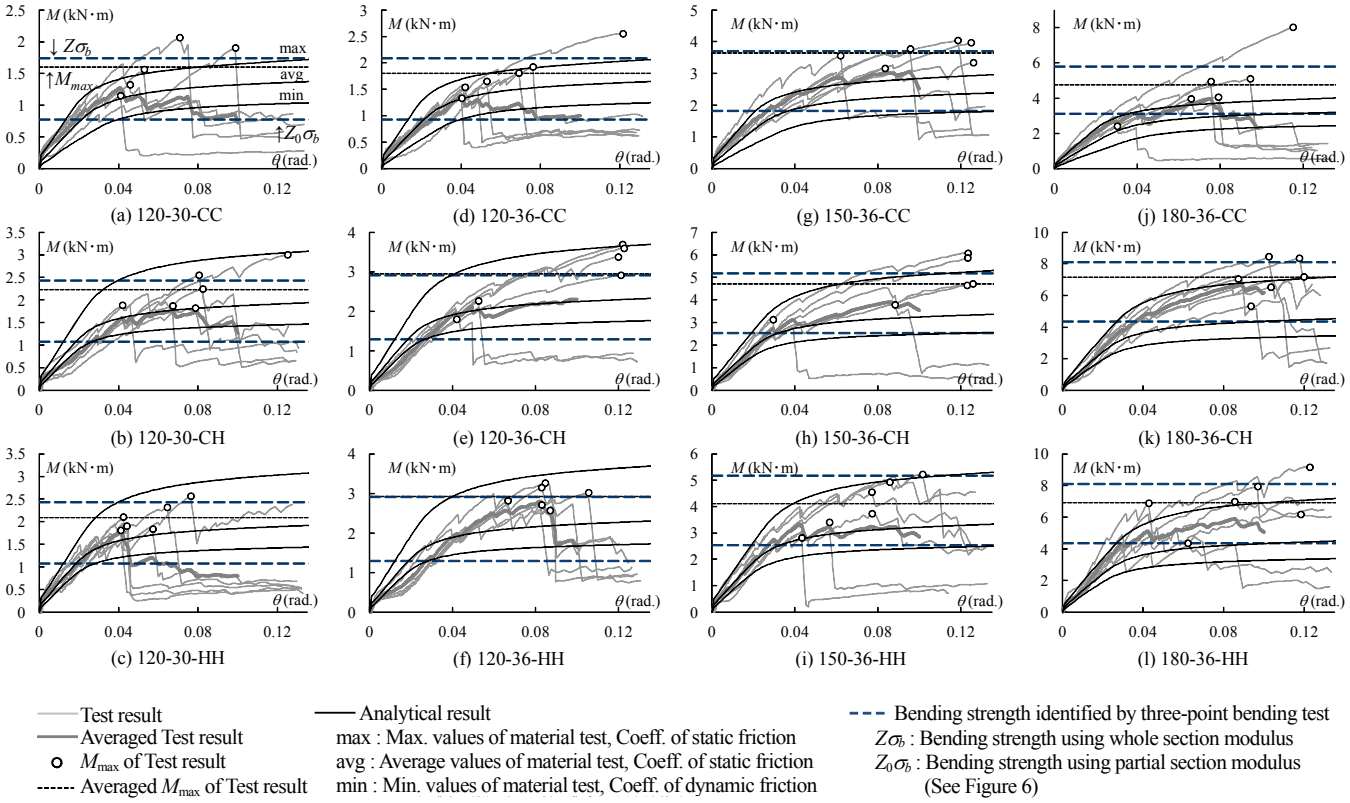
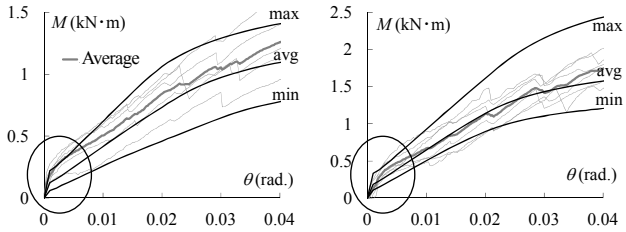
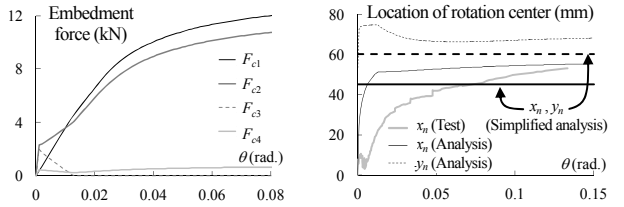


Figure 16 Comparison between Test Results and Detailed Analysis Results



(a) 120-30-CC (b) 120-30-HH

Figure 17 The Effect of Initial Stress



(a) Local Embedment Forces (b) Location of Rotation Center

Figure 18 Local Behavior (120-30-CC-avg)

variability of test result, three cases of analysis were conducted. Result of "max" is using maximum value of material test (Table 4) and coefficient of static friction. Result of "min" is using minimum value of material test and coefficient of dynamic friction. In addition, result of "avg" is using average value of material tests and average coefficient of dynamic and static friction.

avg curve seems to give good agreement with average curve of test result. In addition, test results appear to range from max curve to min curve of analysis. Therefore, variability of test results is also evaluated. Failure points are likely to range from $Z\sigma_b$ to $Z_0\sigma_b$. Figure 17 shows close-up of M-θ relation at small θ. High initial stiffness due to prestressing of wedge is also simulated.

5. SIMPLIFIED ANALYSIS

5.1 Assumption

In this chapter, rotation center x_n and y_n are determined by assuming simpler mechanical model, which means two of three unknown variables are obtained already. Therefore, Q and corresponding moment is expressed by closed-form. In addition, we set particular events to calculate M-θ relation, and M-θ curve from the event to the next event is approximated by linear relation. In this way, multi-linear M-θ curve is obtained.

As shown in Figure 18(a), F_{c1} and F_{c2} are dominant forces, and their amplitudes are nearly the same. This is why $x_n = h_f/2$ and $y_n = h_c/2$ can be assumed. Figure 18(b) shows location of rotation center identified by experiment and detailed/simplified analysis. Although simplified analysis is not able to take into account a change of rotation center according to θ, experimental and two analytical results show close values at large θ.

5.2 Formulation

Generalized parameters of local embedment for simplified model are summarized in Table 9. We can

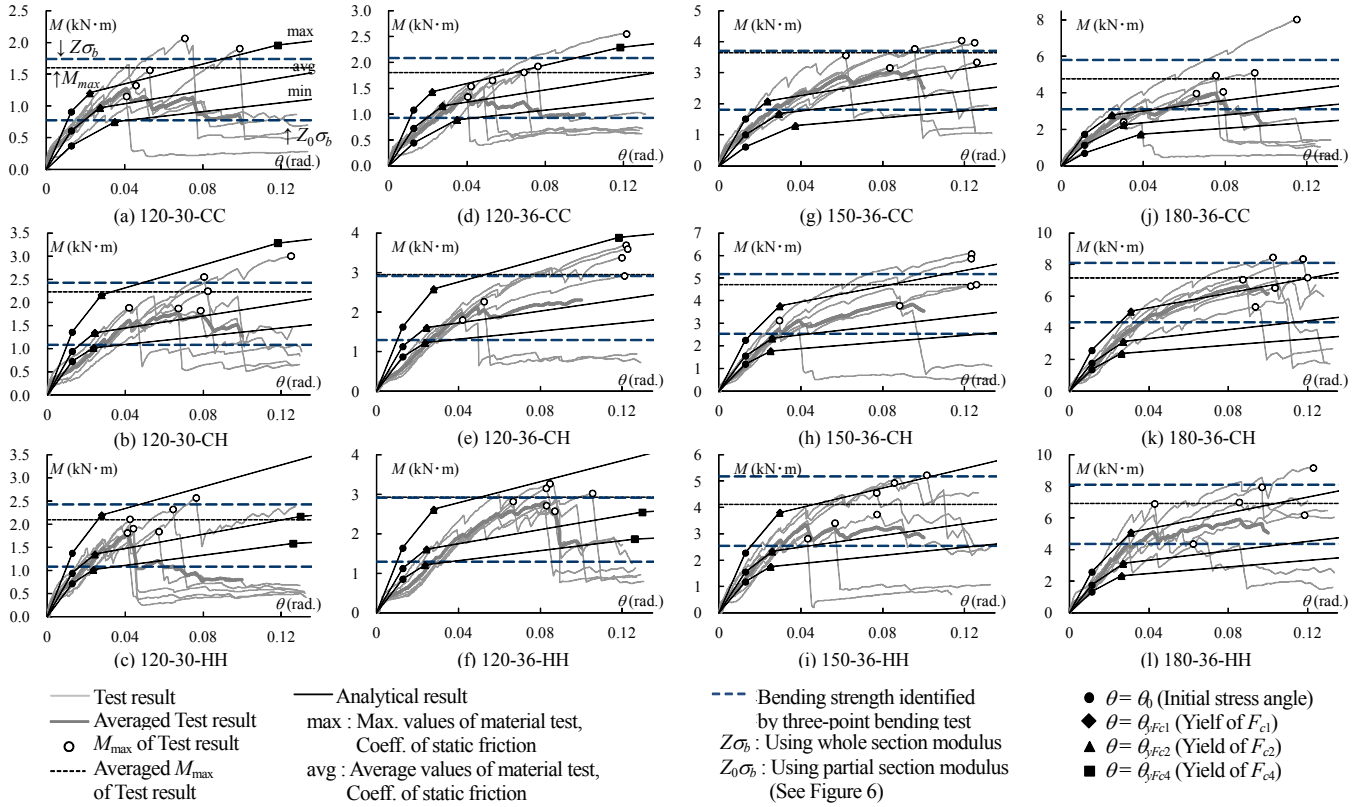


Figure 19 Comparison between Test Results and Simplified Analysis Results

Table 9 Generalized Parameters of Local Embedment (Simplified Analysis)

Force, Moment	Contact length x_0	Surplus length x_1	Contact width y_0	Depth z_0	Rotation angle θ_c
F_{c1}, M_{c1}	$\frac{h_c}{2}$	$\frac{h_c}{4}$	b_t	h_t	θ
F_{c1}^*, M_{c1}^*	$\frac{h_c}{2} - l_s$	0			
F_{c2}, M_{c2}	$\frac{h_c}{2\cos\theta_m}$	$l_t - l_s - \frac{h_c - l_s}{\cos\theta_m}$			$\theta + \theta_0$
F_{c4}, M_{c4}	$\frac{h_b - h_t}{2}$	$\frac{h_b - h_t}{4}$	b_c	h_c	θ

calculate all forces and moments without any convergence calculation. Moment at critical section is calculated as follows.

$$M = \left(M_{c1} + M_{c2} + M_{c4} + M_{fc2} + M_{fc4}\right)\frac{L - h_c/2}{L} \qquad (11)$$

5.3 Comparison between Test Results and Analytical Results

Accuracy of simplified analysis is confirmed. Figure 19 shows comparisons between test results and analytical results of M-θ relation. Analysis curve is broken at $\theta = \theta_0$, θ_{Fc1}, θ_{Fc2} and θ_{Fc4}. At $\theta = \theta_0$, prestressing of wedge at location of F_{c3} goes off (Figure 9). At $\theta = \theta_{Fci}$, local embedment force F_{ci} yields.

Simplified analysis seems to give similar tendency to detailed analysis. In other words, its mechanical model is reasonable to simulate moment-rotation relation with less effort.

6. CONCLUSIONS

In this paper, flexural-shear tests of mortise-tenon joint with split wedge were conducted, and its structural performance was shown. After that, evaluation method of M-θ relation was proposed. Its applicability was also shown. Analytical results gave close agreement with test results until the failure point.

References:

SUZUKI, Y., MAENO, M., SAITO, S., KITAHARA, A., GOTOU, M., SUDA, T, and OHSHITA, T. (2003) "Full-Scale Dynamic and Static Tests of Traditional Wooden Frame [in Japanese]", *Journal of structural and construction engineering*. Architectural Institute of Japan, **574**, pp.135-142

OHASHI, Y., MATONO, H., NAKAGAWA, T., MAEKAWA, H., KAWAI, N., and MATSUDOME, S. "Lateral Loading Tests of Wooden Houses with Traditional Details : Part 1 Outline of Lateral Loading Tests [in Japanese]" *Summaries of technical papers of Annual Meeting Architectural Institute of Japan*. **C-1**, pp.579-580,

SATO, H., MATSUDA, M., FUJITA, K., KOSHIHARA, M., and SAKAMOTO, I. (2006) "Study on the Structural Performance of Traditional Timber House Based on On-site Loading Test : Lateral Loading Test of A Farmhouse in Yamaguchi Prefecture [in Japanese]" *Journal of structural and construction engineering*. Architectural Institute of Japan, **602**, pp.187-194

SAKATA, H., YAMAZAKI, Y., UDAGAWA, H., and OHASHI, Y. (2012) "Experimental Study on Flexural-shear Behavior of Mortise-tenon Joint with Dowel [in Japanese]" *Journal of*

structural and construction engineering. Architectural Institute of Japan, **671**, pp.45-54

SOMA, T., INAYAMA, M., INOUE, M., OBAYASHI, H., and ANDO, N. (2007) "Study on Relationship between Load and Deformation on WARI-KUSABI Joint : Part I: Pull-out Resistant Mechanism of WARI-KUSABI Joint [in Japanese]" *Summaries of technical papers of Annual Meeting Architectural Institute of Japan*. **C-1**, pp.77-78

KITAMORI, A., KATO, Y., KATAOKA, Y., KOMATSU, K. (2003), "Proposal for a Mechanical Model of Beam-Column "Nuki" Joints in Traditional Timber Structures [in Japanese]", *Journal of the Japan Wood Research Society*, **Vol.49**, pp.179-186

MATSUBARA, Y., DU, Z., SAKATA, H., WADA, A., ITO, H., and KATAOKA, R. (2002) "Experimental Study on the Behavior of Rotational Embedment between Douglas Fir Glulams [in Japanese]", *Summaries of technical papers of Annual Meeting Architectural Institute of Japan*. **C-1**, pp.27-28

SAKAGUCHI, Y., SAKATA, H., NAKATA, K., NAKANO, T., ITO, H., KATAOKA, R. (2006) "Experimental Study on Mechanical Behavior of Timber Semi-Rigid Joint using Hanger with Drift Pins : Part2. M-θ Estimation Method [in Japanese]", *Summaries of technical papers of Annual Meeting Architectural Institute of Japan*. **C-1**, pp.127-128

INAYAMA, M. (1991) "A Theory and Application of Local Embedment of Timber Perpendicular to the Grain [in Japanese]" *Doctor thesis of the University of Tokyo*

TANAHASHI, H., and SUZUKI, Y. (2011) "Characteristics of Elasto-plastic Rotational Embedment of Traditional Wooden Joints and Formulation of Crosspiece Joints [in Japanese]" *Journal of structural and construction engineering*. Architectural Institute of Japan, **667**, pp.1675-1684

FORESTRY AND FOREST PRODUCTS RESEARCH INSTITUTE (2004), Wood Industry Handbook, *Maruzen*, **Vol.4**, pp.128-129

ARCHITECTURAL INSTITUTE OF JAPAN (2009), Design Manual for Engineered Timber Joints, pp.203-204

10CUEE CONFERENCE PROCEEDINGS
10th International Conference on Urban Earthquake Engineering
March 1-2, 2013, Tokyo Institute of Technology, Tokyo, Japan

NEW DAMAGE AVOIDANCE CONNECTION FOR MULTI-STORY TIMBER-STEEL HYBRID MOMENT FRAME BUILDINGS

Mamoon Jamil[1)], Pierre Quenneville[2)], and Charles Clifton[3)]

1) Doctoral Student, Faculty of Civil and Environmental Engineering, the University of Auckland, New Zealand
2) Professor, Faculty of Civil and Environmental Engineering, the University of Auckland, New Zealand
3) Associate Professor, Faculty of Civil and Environmental Engineering, the University of Auckland, New Zealand
mjam057@aucklanduni.ac.nz, p.quenneville@auckland.ac.nz, c.clifton@auckland.ac.nz

Abstract: Conventional buildings systems can sustain heavy uneconomical to repair damage in a major earthquake. There is a lack of damage avoidance moment resisting systems in timber. A new damage avoidance system with gravity rocking and friction damping is under development. Both beams and columns are continuous through the joint in the hybrid timber-steel frame. Damage to the seismic frame and floor slab is minimized as a result. Tests at 1:20 scale have shown damage avoidance and full self-centering as expected. A simplified SAP2000 model has been developed which models the first large displacement cycles well but loses accuracy in later large displacement cycles.

1. INTRODUCTION

Major earthquakes in recent decades have resulted not only in unfortunate loss of life, but also extensive damage to infrastructure. Aseismic design is improving and the number of fatalities is gradually decreasing in developed nations. The performance threshold is being raised and damage reduction is now commonly a performance target in addition to providing for life-safety.

Capacity design principles direct inelastic action to dedicated zones in the structural system. In conventional systems, these dedicated ductile zones protect the rest of the structural system from inelastic demand and damage but sustain damage themselves. The goal of the system presented here is to minimize damage to the structural frame, floor slab and also non-structural elements. A timber-steel hybrid system is used to make best use of material properties; however, the main principles involved are largely independent of material.

2. EXISTING SYSTEMS

Energy dissipaters or dampers are often used to dissipate earthquake energy, reduce building drift and thus reduce damage. They can be added to conventional structural systems or be incorporated into advanced damage avoidance systems which are capable of large inelastic deformation without damage. Some damage avoidance moment frame systems of particular interest are described briefly here. More reading can be found in (Jamil, Quenneville et al. 2012).

The Sliding Hinge Joint (SHJ) shown in Figure 1 is a semi-rigid connection with the beam top flange effectively pinned to the column, web bolts for vertical shear transfer and a slotted bolted friction slider at the bottom flange. The SHJ remains rigid under serviceability level loads but rotates with friction sliding at the bottom flange under ultimate limit state or higher earthquake load. After the strong motion stops, the connection becomes rigid again. It has a tendency to self-center as the earthquake motion gradually stops but does not reliably fully self-center. There is also some loss of friction slider bolt tension force and hence connection strength. The addition of a ring spring (Ringfeder Gmbh 2008) for added self-centering has been investigated (Khoo, Clifton et al. 2011) but cost is an issue.

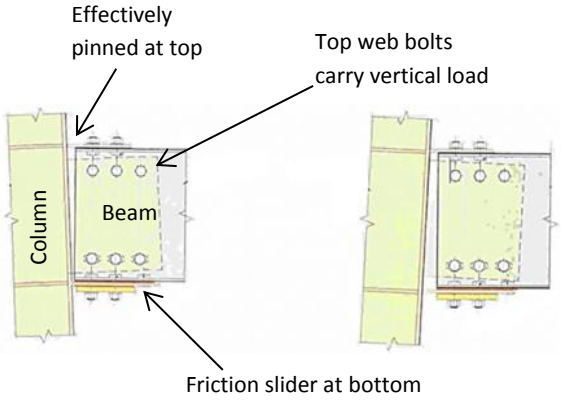


Figure 1 The Sliding Hinge Joint – copied from (Clifton 2005)

Post-tensioned connection technology was originally developed for pre-cast concrete construction under the PRE-cast Seismic Structural System (PRESSS) research program in the 1990s and is being adapted to steel and timber. The concept is illustrated in Figure 2. Un-bonded tendons clamp the joint together to provide moment strength and self-centering. Mild steel or other dampers may be added. It is difficult to use this system with timber because the post-tension force causes creep shrinkage in the timber over time. This causes a reduction in post-tension force and thus a reduction in connection strength.

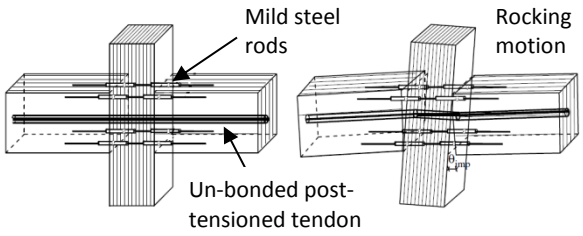


Figure 2 Post-tensioned timber moment connection – copied from (Buchanan, Deam et al. 2008)

Gravity rocking Greek and Roman masonry temples have a similar mechanism to post-tensioned systems except that the columns are non-continuous and beams may be continuous. Furthermore, normal force at the joint interface is provided by gravity instead of post-tensioned tendons. Figure 3 shows some sliding of column drum sections in addition to rocking. Japanese wood temples or pagodas have a less explicit rocking and sliding mechanism but still show structural period elongation with increased displacement (Hanazato, Minowa et al. 2010). Comparison of a typical Greek temple connection with a Japanese pagoda connection is shown in Figure 4. If columns are non-continuous, these systems are prone to soft-story formation. The new system presented here therefore has continuous columns.

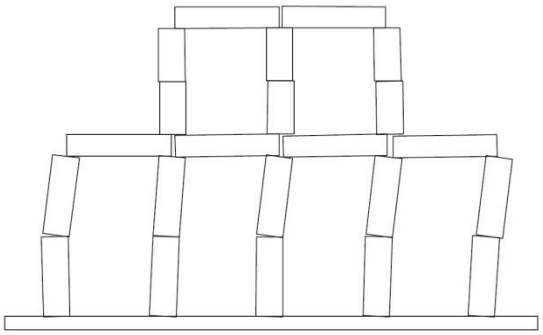


Figure 3 Gravity rocking and friction sliding in ancient Greek/Roman temples – copied from (Papaloizou and Komodromos 2011)

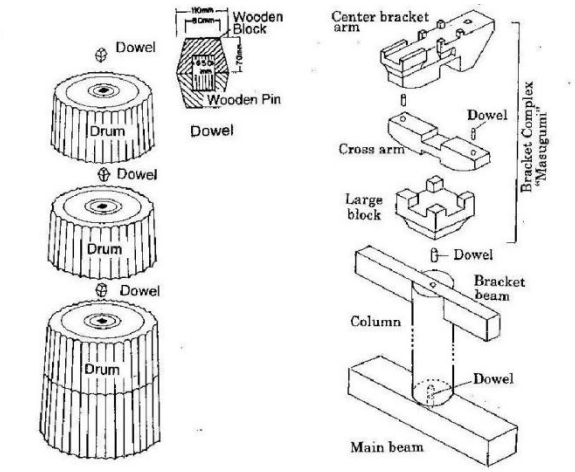


Figure 4 Comparison of connection used in Greek masonry temples with that in Japanese wood temples – copied from (Hanazato, Minowa et al. 2010)

3. NEW DAMAGE AVOIDANCE SYSTEM

3.1 Target Minimum Performance

Table 1 Minimum performance target for new system

Limit State (return period)	Mode of operation	Condition of structure	Drift residual/ peak
SLS (25 years)	Elastic	As new	0.0% / ~ 0.33%
ULS (500 years)	Inelastic connection rotation. Timber members to remain elastic	Close to as new. No wood crushing or strength/stiffness degradation. Minimal non-structural damage including partitions and floor slab	~ 0.2% / 2.5%
MCE (2500 years)	Large inelastic connection rotation. Some inelastic action may occur in the wood	Any damage economically reparable. Possible damage to non-structural elements. Structural collapse reliably avoided	No strict limit. ~ 4 to 5% expected

3.2 Connection detail

The new connection combines gravity rocking and friction damping. The concept was developed through several iterations and work is still in progress. Some detail of the development process can be found in (Jamil, Quenneville et al. 2012). A steel column / LVL beam hybrid option was chosen because the column is relatively heavily loaded with combined bending and axial actions. Furthermore, a steel column simplifies the

connection and also has a smaller foot-print. The overall connection and assembly steps are shown in Figure 5.

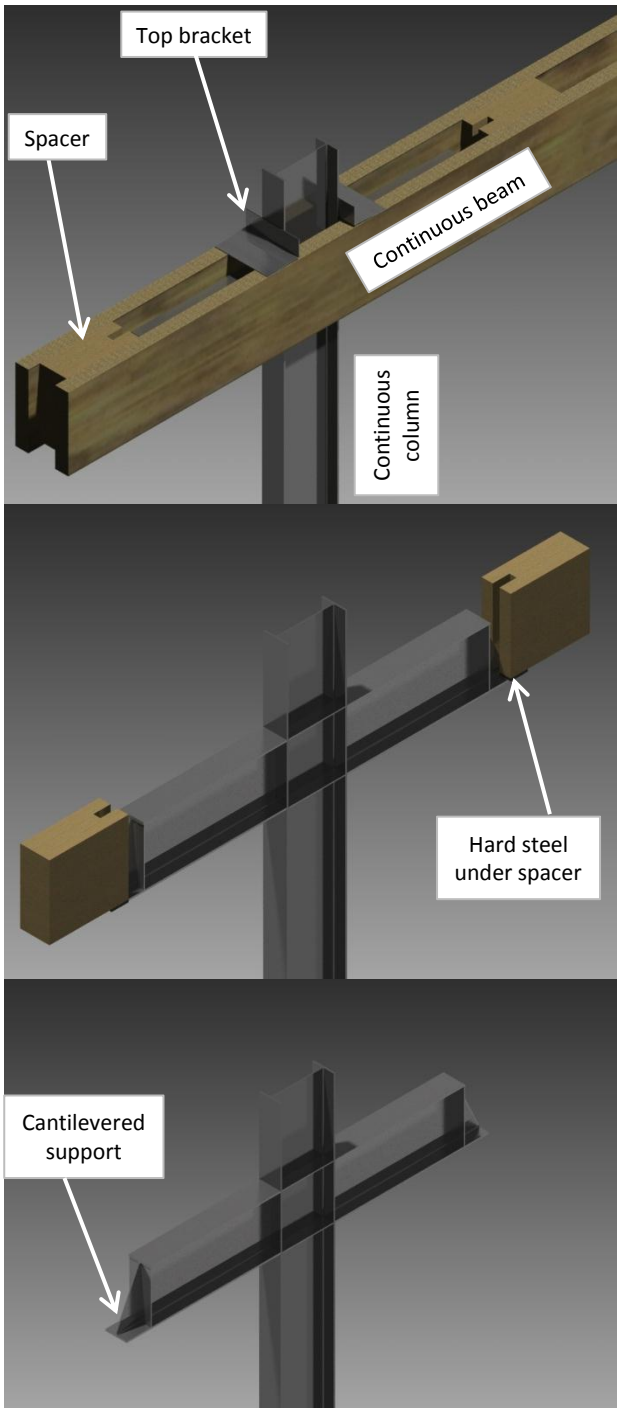


Figure 5 New connection. (top): Overall connection; (middle): construction step 2 and; (bottom): construction step 1

There are four main features: (1) gravity rocking on cantilever supports; (2) friction damping due to sliding between underside of armored spacer and cantilevered support; (3) brackets on top which restrain the beam horizontally to the column but allow the beam to uplift and (4) beam and column both continuous through the joint. One way to assemble the joint is to: (1) fabricate the column with cantilevered supports; (2) hold the spacers in place on cantilevered supports; (3) screw the two halves of the beam into the spacers; and (4) install the two top brackets.

3.3 Connection mechanics

Figure 6 shows how the connection develops moment resistance. The principal source of resistance is the gravity load carried by the joint acting at an eccentricity to the column center line. The brackets on top are bent so that the beam is restrained horizontally to the column face but can uplift upon rocking at the connection. Because the beam is restrained horizontally at the top, the bottom of the beam must slide in order for the connection to rotate. A friction force equal to the coefficient of friction, μ, multiplied by the gravity load on the joint is generated. This acts through a lever arm approximately equal to the beam depth and thus adds to moment resistance. The bracket on top has a small vertical resistance force which acts through a lever arm from the support point to the opposite column face. The other bracket has a lower moment resistance which is ignored here. Table 2 presents moment resistance calculation for an example case. Note that the calculation method is based on principles of mechanics and take no account of possible unforeseen effects.

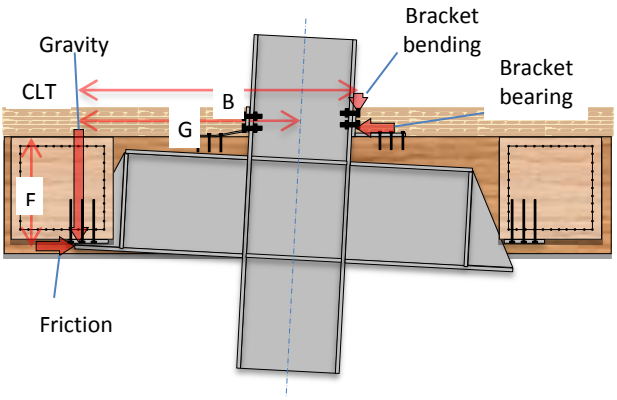


Figure 6 Connection at 50 mrad (5%) rotation. Forces are as acting onto the column

Table 2 – Example joint moment resistance calculations

	Force (kN)	Lever arm (m)	Moment (kNm)
Gravity	200 Inner column, perimeter frame, 10 m grid, 4.0 kPa	1.0 (Support point to column centre line)	200
Friction	200×0.48=70 μ=0.48	0.7	96
Top Bracket yielding	40 (depends on bracket size)	1.5+0.7/2=1.15 (support to opposite column face)	74
Total			370

4 1:20 SCALE SHAKE TABLE TESTS

4.1 Test Model

A 1:20 scale, 1 by 2 bay, 3-storey model was built following scaling similitude laws. As shown in Figure 7, Laminated Veneer Lumber was used for both the columns and beams. The test was done before switching to the steel column option. Frame members are designed to remain elastic therefore the column material has little influence on the global behavior of the model.

A length scale factor of 1:20 was used whereas acceleration and material Young's modulus were left unchanged. This resulted in a time scale factor of 1:4.47. The model was about 1000 mm long, 500 mm wide and 600 mm high overall. The total mass was about 500 kg. All connections used in the model were identical and a close up is shown in Figure 8. More detail on the model can be found in (Jamil, Quenneville et al. 2012).



Figure 7 1:20 scale model on shake table. The side frames (circled red) are not part of the model; they restrict the model to in-plane movement

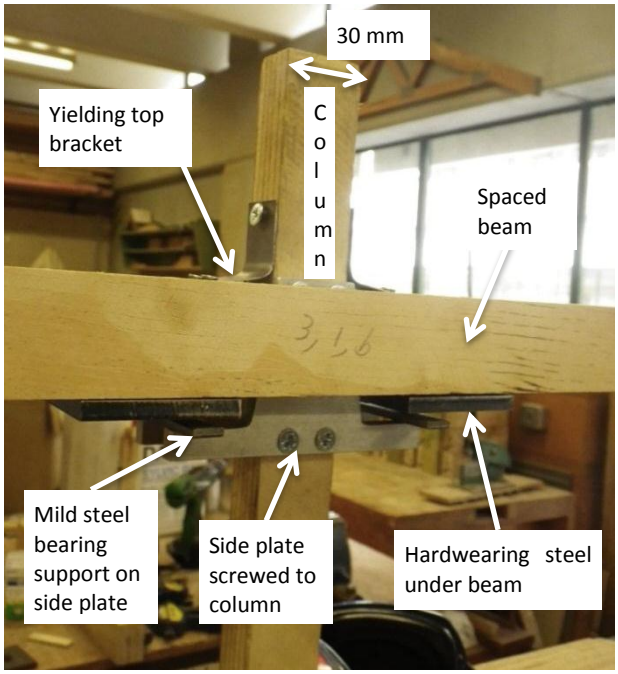


Figure 8 Connection in 1:20 scale model building

4.2 Test Results

Snap back tests were done by pulling the top of the model and releasing. Free vibration decay after releasing from a pull of 40 mm at the top is shown in Figure 9. The model returned to its original position in about two cycles showing high damping and re-centering.

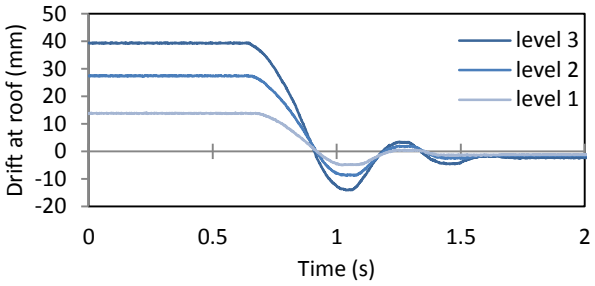


Figure 9 Free vibration decay with top floor pulled to 40 mm and released

Top floor displacement for the 1940 El-Centro earthquake displacement scaled to 0.1, 0.2 and 0.3× is plotted in Figure 10. According to similitude scaling laws, a displacement or length scale factor of 1/20 or 0.05 should have been applied. However, a stronger earthquake was used to excite the model well into the non-linear range. After about 20 earthquake tests which forced the model to a drift of over 5%, no visible damage or degradation in performance was found except minor loosening of some screws.

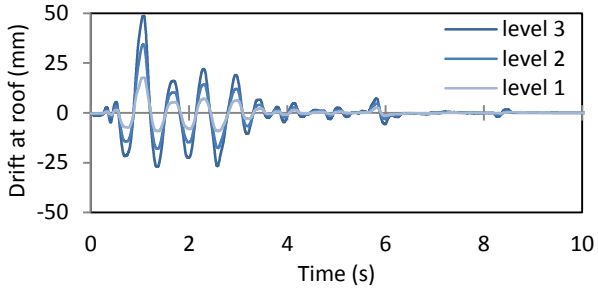


Figure 10 Top floor displacement of 1:20 scale model for scaled El-Centro 1940 earthquake

5 1:20 SCALE SAP2000 ROTATIONAL SPRING MODEL

5.1 Model setup

The SAP2000 model was setup to be the same size as the scaled down test model. A single frame was modeled as shown in Figure 11. The laminated veneer lumber (LVL) was modeled as isotropic and the material characteristic value for Young's Modulus were assumed. A uniformly distributed load was assigned to each level to match the load and self-weight of the physical model. Unprocessed shake table acceleration recorded with an accelerometer from the earthquake test reported in the previous section was used as input.

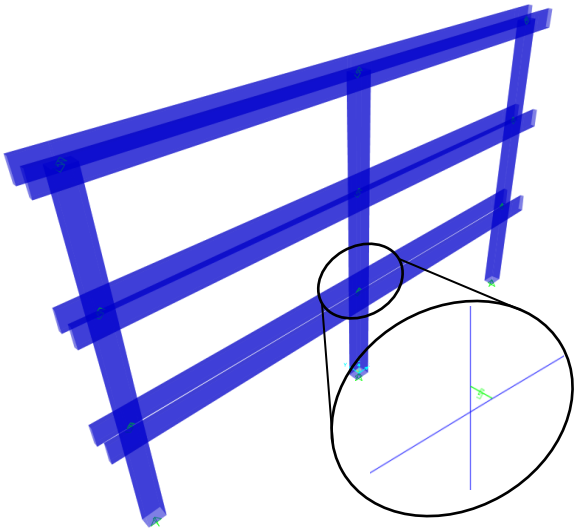


Figure 11 Overall 1:20 scale model in SAP2000. Note that line elements were used in the model but an extruded 3-D view is shown here. Close-up shows node location and rotational spring connection to nodes

Line elements were used with rotational springs at the joint. Nodes were placed at a small offset of 1mm from where the beam crosses over the column. The beam and column are not linked at the intersection but are only connected through the rotation springs. Four rotational springs were used at each joint. Spring moment-rotation curves from the shake table test described above are shown in Figure 12. A multi-linear elastic link element definition was used to represent moment due to gravity load acting at an eccentricity to the column. Multi-linear plastic link elements were used for friction damping and the two top brackets. A post-yield stiffness of 3% of the pre-yield stiffness was assumed for the brackets. A pre-yield stiffness was specified for when the bracket spring rotation exceeded the physical bracket uplift gap. This level of rotation was not reached in the simulation as can be seen in Figure 12 (c) and (d). Rotational spring strengths were calculated based on the same principles as in Section 3.3. An estimate joint elastic stiffness had to be assumed because of the difficulty in measuring the actual stiffness of the joint in the small scale model. A connection rotation of 0.01 radians to initiation of rocking and friction at the joint was specified in the SAP2000 model. Geometry and material properties were used to calculate the yield rotation of each mild steel top bracket.

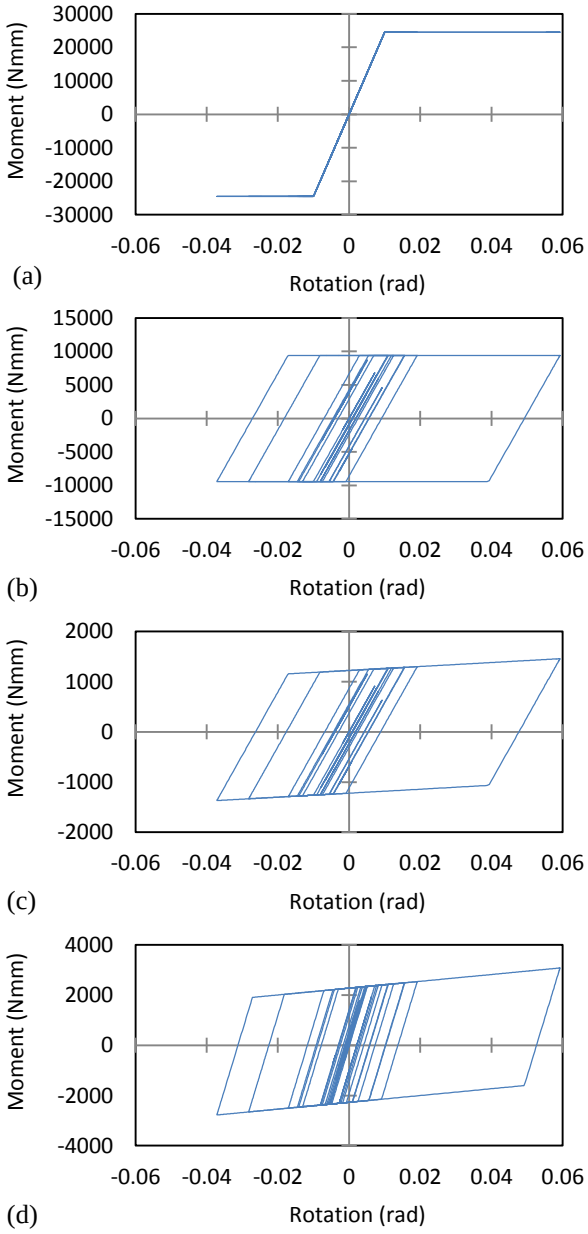


Figure 12 Moment rotation of each spring at the middle first level beam column joint of the 1:20 scale SAP2000 model subjected to the scaled 1940 El-Centro earthquake: (a) Gravity load at eccentricity to column; (b) Friction; (c) Top bracket A; and (d) Top bracket B.

5.2 Analysis method and assumptions

Hilber-Hughes-Taylor direction integration with alpha set to zero, which is the same as the Newmark method, with a maximum time step of 0.001 s was used to solve the model. A non-linear analysis with consideration of P-Delta and large displacement effects was used. First and second mode periods of vibration of 0.4 s and 0.07 s respectively were found using Ritz modal analysis. A Rayleigh proportional equivalent viscous damping of 2% was specified at these two natural periods.

A 2-D single frame model was used in SAP2000 and motion was limited to the in-plane direction. A purely pinned column base was assumed. Vertical inertia effect from uplift of the floor was not considered in the simplified rotational spring model.

5.3 Comparison of test result and SAP2000 model

Figure 13 shows the roof drift time history from the shake table test and that from the SAP2000 model. The first large motion pulse is well represented by the SAP model but drift in later cycles is under-predicted. In-accuracy of recorded shake table acceleration which was used as input for the SAP model and assumptions stated earlier are thought to be a major cause of this discrepancy.

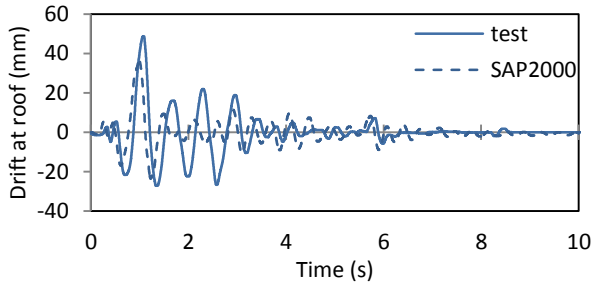


Figure 13 Drift of 1:20 scale model at top level subjected to scaled 1940 El-Centro earthquake: Test result compared with SAP2000 model

6 PLANNED WORK

Further tests on the 1:20 scale model and shake table tests on a 1:4 scale model are planned. A more sophisticated numerical model which models the actual rocking effect with contact elements is under development. The final expected outcome is a design procedure for implementing the new connection in practice.

7 CONCLUSIONS

A novel damage avoidance moment connection with gravity rocking and friction damping is under development. The system avoids post-tensioning which can cause creep issues and strength loss in the long-term when used with timber. Early 1:20 small scale testing has shown damage avoidance performance as expected with full self-centering and high damping. A simplified numerical model of the scaled physical model predicted peak drift satisfactorily but under predicted later large drift cycles. Work is underway on a more sophisticated numerical model which should capture vertical inertia effects and joint elastic stiffness. The final aim is to develop the new connection for use in low to medium rise multi-story timber-steel hybrid buildings in medium to high seismic zones.

Acknowledgements:

The authors would like to thank the New Zealand Ministry of Primary Industries for funding this research. The input of staff and colleagues at all stages of this work is also greatly appreciated.

References:

Buchanan, A., Deam, B., et al. (2008), "Multi-storey prestressed timber buildings in New Zealand," *Structural Engineering International*, **18**(2), 166-173.

Clifton, G. C. (2005), "Semi-rigid joints for moment-resisting steel framed seismic-resisting systems," Dept of Civil and Environmental Engineering, The University of Auckland. PhD.

Hanazato, T., Minowa, C., et al. (2010), "Seismic and wind performance of five-storied Pagoda of timber heritage structure," *Advanced Materials Research*, **133-134**, 79-95.

Jamil, M., Quenneville, P., et al. (2012), "Low-damage moment resisting timber multi-storey buildings," *World Conference on Timber Engineering*, *Auckland, New Zealand*.

Jamil, M., Quenneville, P., et al. (2012), "New low damage timber frame solution for multi-storey office type buildings," *SESOC Conference*, *Auckland, New Zealand*. Paper 21.

Khoo, H. H., Clifton, G. C., et al. (2011), "Development of the self-centering Sliding Hinge Joint," *Proceedings of the Ninth Pacific Conference on Earthquake Engineering*, *Auckland, New Zealand*.

Papaloizou, L. and Komodromos, P. (2011), "Investigating the seismic response of ancient multi-drum colonnades with two rows of columns using an object-oriented designed software," *Advances in Engineering Software*, **44**, 136-149.

Ringfeder Gmbh (2008), "Damping technology." Krefeld, Germany.

10CUEE CONFERENCE PROCEEDINGS
10th International Conference on Urban Earthquake Engineering
March 1-2, 2013, Tokyo Institute of Technology, Tokyo, Japan

BASIC STUDY ON TORSIONAL BEHAVIOUR OF TWO-STORY TIMBER HOUSES WITH ECCENTRICITY

Kento Suzuki[1)], Hiroyasu Sakata[2)], and Yoshihiro Yamazaki[3)]

1) JSPS Research Fellow, Department of Built Environment, Tokyo Institute of Technology, Japan
2) Professor, Structural Engineering Research Center, Tokyo Institute of Technology, Japan
3) Assistant Professor, Structural Engineering Research Center, Tokyo Institute of Technology, Japan
suzuki.k.bq@m.titech.ac.jp, hsakata@serc.titech.ac.jp, yamazaki.y.ai@m.titech.ac.jp

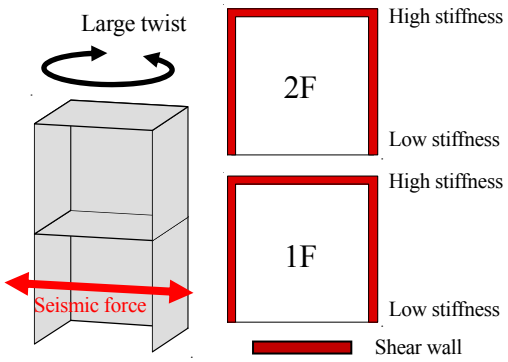
Abstract: This paper focuses on torsional behaviour of two-story timber house with eccentricity. The Japanese current design standard doesn't consider dynamic effect and torsional interaction. Therefore the rotational component of the external force is not properly evaluated. In this study, torsional behaviour of two-story timber house having rigid floor diaphragm is verified by seismic response analyses. As a result, we found that torsional deformation occurred even in the story without eccentricity, if the other story had eccentricity. When two story's eccentricities were same direction, torsional deformation increased. When two story's eccentricities were opposite direction, torsional deformation decreased. It was revealed that the transition of torsional behaviour caused by yielding of walls could be evaluated using modal shape of the equivalent linear structure.

1. INTRODUCTION

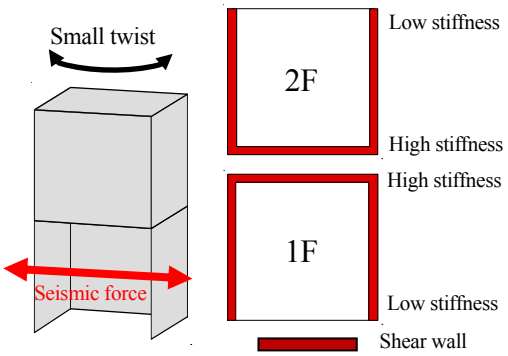
The seismic performance of timber houses in Japan has been improved especially after the 1995 Kobe earthquake. However, there are many timber houses with large opening on the south face or with opening facing to the road for garage. Such houses are likely to have unsymmetrical plan of shear walls. So these houses tend to separate the center of mass from the center of stiffness. On the other hand, most timber houses without large opening also have eccentricity. So houses without eccentricity are few.

Because of these concerns, many studies about eccentricity have been carried out. But most of them targeted on single-story buildings. In addition, the Japanese seismic design method for eccentricity is based on the rigid floor assumption and assumes the equivalent seismic force was proportional to the floor mass. Furthermore, it considers the balance of walls on each floor individually. So this method does not give enough consideration to the dynamic effect and ignores the influence of the torsional motion of a story to the other stories.

In Japan, there are many two-story and three-story timber houses. Previous studies showed that torsional behaviour of a story of a two-story unsymmetrical house can affect other stories and discussed the need to clarify the mechanism of torsional behaviour of multi-story buildings (Fig.1). Knowing the exact torsional behaviour of buildings will give valuable information not only to improve the seismic performance but also to better plan dampers for the mitigation of torsional motions.



(a) Sequential Eccentricity



(b) Reversal Eccentricity

Figure 1 Sequential and Reversal Eccentricity

2. SHEAR WALL TESTS

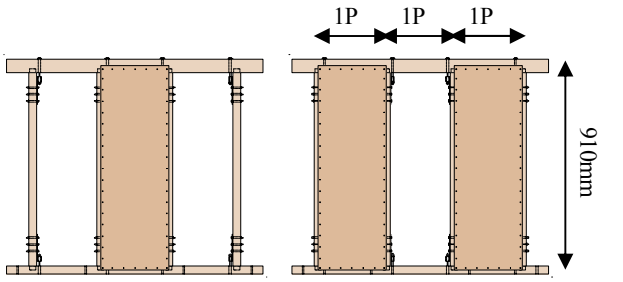
2.1 Outline

Fig.2 shows specimens and Table.1 shows

specifications of elements. Specimens scaled full scale shear wall 1/3 times larger (1P=303mm). Column capitals and column bases manufactured stub tenon. In addition, column capitals and column bases were attached to the HD. Fig.3 shows set up of shear wall tests. Test was performed in accordance with 2nd references. Tests using specimens of the same specification were carried out 3 times.

2.2 Result

Fig.4 shows the relationship between shear force (Q) and the apparent shear deformation angle (θ). θ is calculated by the Eq.1. First, the failure characteristics are shown below. When θ becomes approximately 1/150rad, nail head began to lean. When θ becomes approximately 1/100rad, pull - out of nails began to be observed and nail head began to be sunk to the plywood. These destructions proceeded to approximately 1/75rad. Peeling of plywood began about a 1/50rad. Nail was completely pull - out and punching out occurred at the corner of the plywood leading up to 1/15rad. Through all the tests, most of the fracture mode was pull - out of nails. Cracking and torn off of plywood and breakage of the nail did not occurred. Next, the relationship between hysteresis and the fracture mode is shown. When nail head began to lean, stiffness was reduced gradually. Around the lifting of the plywood was observed, shear walls reached a maximum strength. After reaching the maximum strength, because the lifting of the plywood had become more pronounced, the load was reduced. In addition, specimens



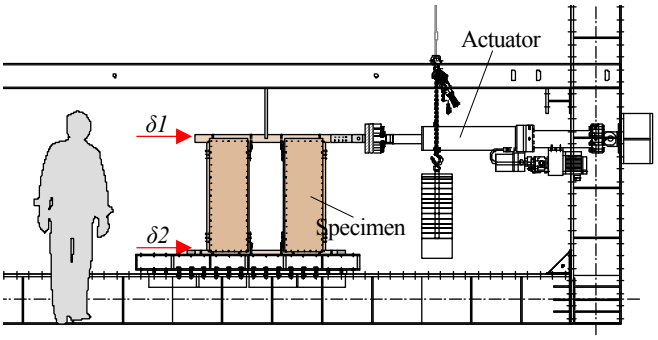
(a) Soft Specimen (b) Basic Specimen

(c) Hard Specimen (d) Long Span Specimen

Figure 2 Specimens of Shear Wall Tests

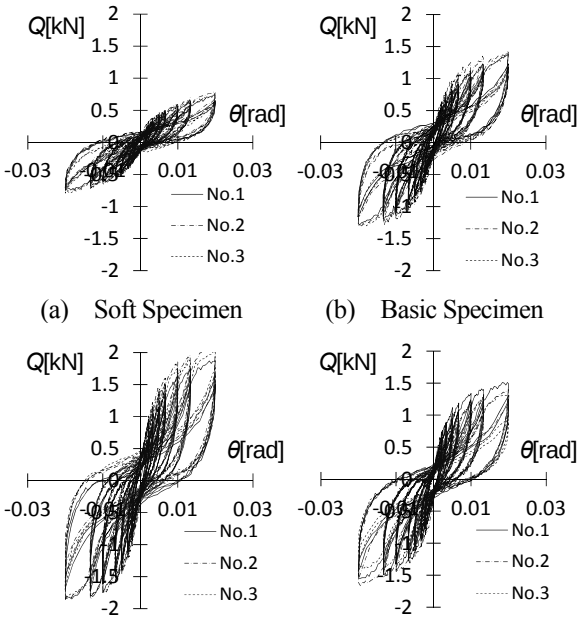
Table 1 Specifications of Elements

Frame				
Tree Species(Laminated Timber)	Grade	Cross-Section of The Foundation B×D [mm]	Cross-Section of The Column B×D [mm]	Cross-Section of The Beam B×D [mm]
Column: Spruce	E95-F315	35×35	35×35	35×60
Beam: Pinus sylvestris	E105-F300			
Foundation: Pinus sylvestris				
Plywood		Nail		
Tree Species	Thickness t [mm]	Type of Nail		Nail Pitch [mm]
Lauan Plywood	3	L16×d0.9		@50



$\theta=(\delta 1-\delta 2)/910$[rad]…(1)

Figure 3 Set Up (ex. Basic specimen)



(a) Soft Specimen (b) Basic Specimen

(c) Hard Specimen (d) Long Span Specimen

Figure 4 Results of Shear Wall Tests (Q-θ)

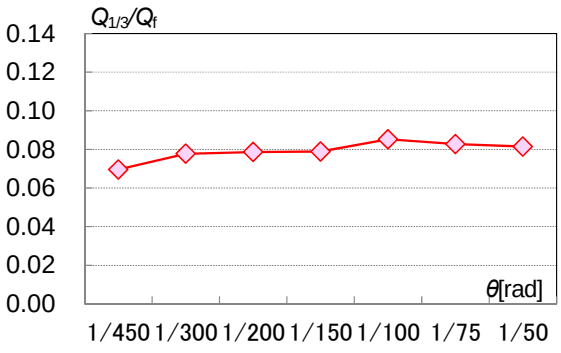


Figure 5 The Comparison of Shear Force of Each Deformation Angle ($Q_{1/3}/Q_f$)

structure. These characteristics are slip behaviour, pinching that were used in study had peculiar characteristics of timber behaviour and strength degradation due to cyclic loading. In other words, hysteresis and the fracture mode were similar to that of a typical full scale shear wall.

3. ANALYSIS STUDY USING 3D FRAME MODEL

3.1 Analysis Objects

Analysis objects were 1/3 scale multi-story timber houses (Fig.6). Fig.7 shows floor plans of each model. In this study, 5 type models that had difference alignment of shear walls were provided. ±00±00 model has not eccentricity. ±00+44 model has eccentricity in only 1st story. +44±00 model has eccentricity in only 2nd story. +44+44 model and +44-44 model have eccentricity in 1st and 2nd story. Position of center of rigidity of the layers of +44+44 model (hereinafter called Sequential Eccentricity model) is in the same direction for the position of the center of gravity. On the other hand, position of center of rigidity of the layers of +44-44 model (hereinafter called Reversal Eccentricity model) is in the different direction for the position of the center of gravity. There are two parameters. One parameter is the ratio ($k2/k1$) of 2F story stiffness ($k2$) for 1F story stiffness ($k1$). In this study, $k2/k1$ assumed it $k2/k1$=0.8,0.6. When $k2/k1$ was changed, $k1$ was not changed but $k2$ was changed. The other is the ratio ($m2/m1$) of 2F story's mass ($m2$) for 1F story's mass ($m1$). In this study, $m2/m1$ assumed it $m2/m1$=0.9,0.6. When $m2/m1$ was changed, total mass ($m1+m2$) was not changed. Total mass assumed it 360kg in reference to 3rd and 4th references.

3.2 Analysis Model

Analysis objects were modeled by 3D frame model (Fig.8) and shear walls were modeled by brace substitution method (Fig.9). The hysteresis model of brace was W.Stewart model. Axial springs which modeled tensile performance of the joint were placed in column capitals and column bases. Mass points were arranged on the each floor so that did not change the value of the rotational inertia (I) that was calculated when mass were placed evenly on the floor. Damping model was the proportional model of initial stiffness. Damping constant was 2%.Input motion was set to unidirectional shaking (direction X). The time axis of seismic waves was shortened to times due to the reduction of the model (the mass ratio of full scale model to 1/3 scale model was 0.111 and stiffness ratio was 0.225). The input earthquake waves were 3 types JMA-KOBE waves and BCJ-LEVEL2 (hereinafter called BCJ-L2) wave. Maximum acceleration of 2 types JMA-KOBE waves was standardized. 1st type JMA-KOBE wave's acceleration was 0.2G (hereinafter called KOBE_0.2G), 2nd type JMA-KOBE wave's acceleration was 0.6G (hereinafter called KOBE_0.6G), and 3rd JMA-KOBE wave was original wave (hereinafter called KOBE_Ori).

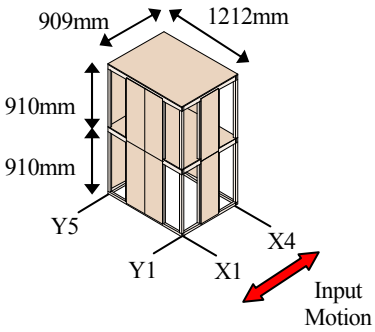


Figure 6 Analysis Objects

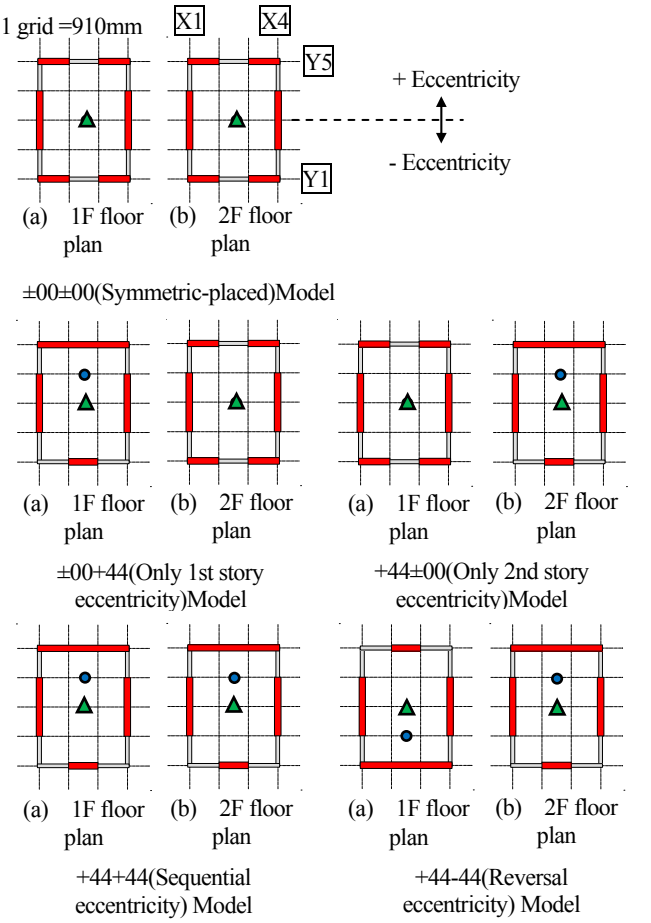


Figure 7 Floor Plans of Each Model

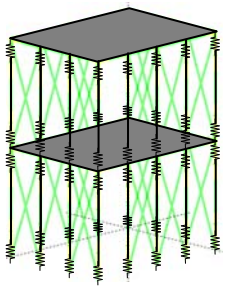


Figure 8 3D Frame Model of Specimen

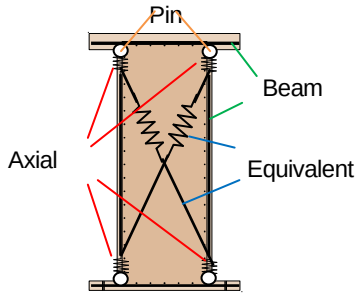


Figure 9 Frame Model of Shear Wall

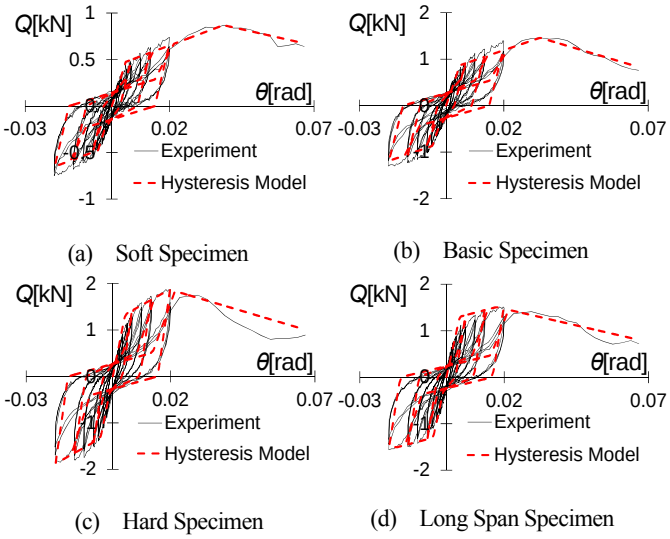


Figure 10 The Hysteresis Model of Each Wall

3.3 Result

In this paper, describes only the case of $k2/k1$=0.8 and $m2/m1$=0.9. Fig.11 shows the maximum displacement of each wall when the displacement of the center of mass of each story was maximum. Fig.12 shows the response rate of twist ($\Delta u/u_{c.m.}$). $\Delta u/u_{c.m.}$ is the ratio of the displacement that the incremental displacement caused by the torsional (Δu) for the displacement of the center of mass ($u_{c.m.}$). $\Delta u/u_{c.m.}$ means the degree of twist. Though the 1F of +44±00 model and the 2F of ±00+44 model had not eccentricity, torsional deformation occurred on the both stories. So this result shows that the existence of torsional interaction. First, make a comparison between the models for $\Delta u/u_{c.m.}$. Focus the models which have eccentricity in both stories. $\Delta u/u_{c.m.}$ of reversal eccentricity model is smaller than $\Delta u/u_{c.m.}$ of sequential eccentricity model. The reason for these results is shown below. Because 1st and 2nd stories of Sequential Eccentricity model (+44+44) twisted in the same direction, torsional deformation of Sequential Eccentricity model was got a helping hand.

On the other hand, because 1st and 2nd stories of Reversal Eccentricity model (+44-44) twisted in the opposite direction, torsional deformation of Reversal Eccentricity model was became suppressed. Next, consider the transition of the $\Delta u/u_{c.m.}$. The larger $u_{c.m.}$, $\Delta u/u_{c.m.}$ was increased once. When $u_{c.m.}$ was increased further, $\Delta u/u_{c.m.}$ was decreased. This phenomenon was considered to be due to changes in the characteristic mode shapes of each story which were caused by the damage of shear walls.

Fig.14 shows the change of characteristic mode shape which was caused by the damage of shear walls if the walls yielded in order of low stiffness wall, high stiffness wall, and orthogonal wall (Pattern1).

First, when the low stiffness walls yield, spring radius is decreased. So twist component of the mode shape is increased. Next, when the high stiffness walls yield, spring radius is increased. So twist component of the mode shape is decreased. Finally, when the orthogonal walls yield, spring radius returns to the initial state. So twist component of the mode shape returns to the initial state too.

Fig.16 shows the change of characteristic mode shape which was caused by the damage of shear walls if the walls yielded in order of low stiffness wall, orthogonal wall and high stiffness wall (Pattern2). As well, in this study, all yield patterns was (Pattern1). Then changes in the value of the characteristic mode shape and $\Delta u/u_{c.m.}$ were similar. In other words, the impact of the change of characteristic mode shape on the torsional behaviour of house with eccentricity is great.

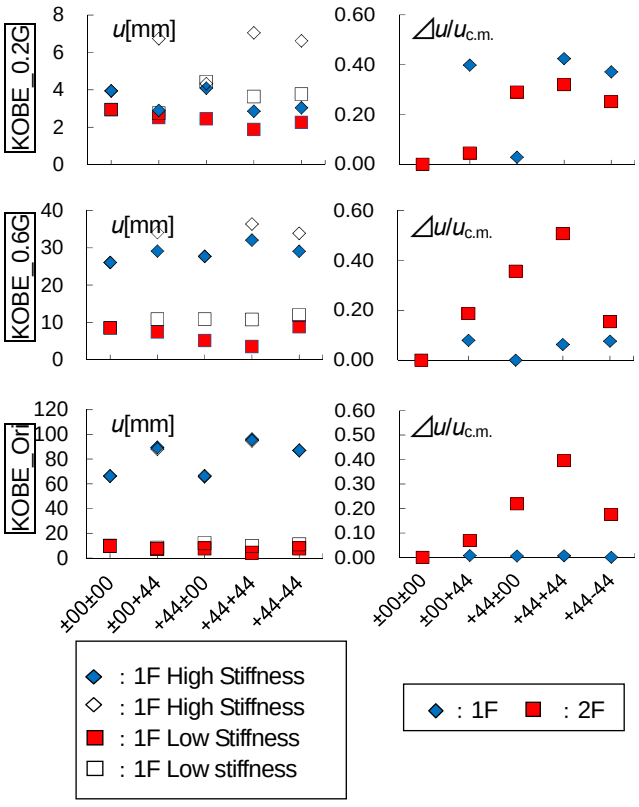


Figure 11 The Maximum Displacement of Each Wall

Figure 12 The Response Rate of Twist

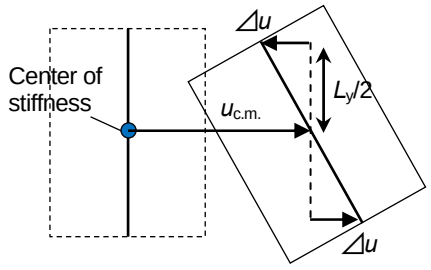


Figure 13 The Response Rate of Twist ($\angle u/u_{c.m.}$)

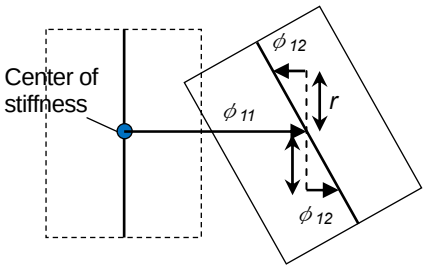


Figure 14 The Characteristic Mode Shapes of Each Story

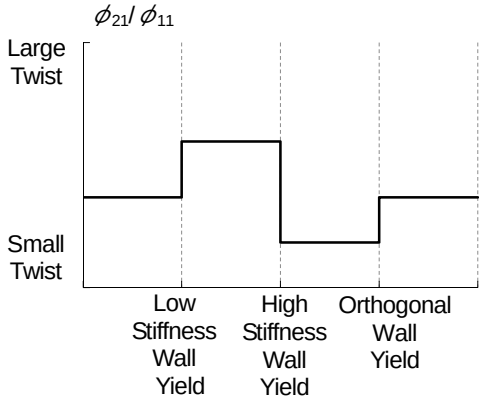


Figure 15 The Change of Characteristic Mode Shape (Pattern1)

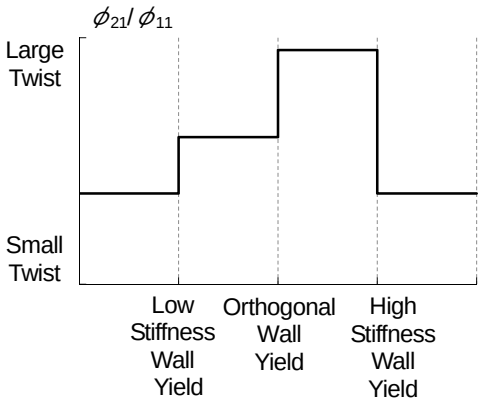


Figure 16 The Change of Characteristic Mode Shape (Pattern2)

5. CONCLUSIONS

In this study, element tests and dynamic analysis using 1/3 scale model. Seismic behaviour of multi-story timber houses with eccentricity was understood. The dynamic tests using 1/3 scale specimens are in execution now.

References:

Kenji Miyazawa, Shinji Hikita, Kento Suzuki and Yasutaka Irie: Three Dimensional Static and Dynamic Eccentricity of Multi-story Wooden Houses. 11th World Conference on Timber Engineering. pages 1037-1040, Italy, 2010

The Foundation of Japan Housing & Wood Technology Center: Allowable stress design of Wooden Houses,pp.565-574, 2008

Sakata H., Kasai k., Ooki Y. and Matsuda K. : Experimental study on dynamic behaviour of passive control system applied for conventional post-and-beam two-story wooden house using shaking table, Journal of structural and construction engineering Transactions of AIJ, 73(631), pp. 1607-1615, 2008.9.

Emori I., Saitou K., Sekimoto K.: Theory and Application of Model Tests, Gihodo Shuppan Co., Ltd.

W.Stewart : The seismic design of plywood sheathed shear walls, Ph.D. Thesis, University of Canterbury

Yamazaki Y.: Inelastic torsional response of structures subjected to earthquake ground motions, Journal of structural and construction engineering Transactions of AIJ, (310), pp. 61-69, 1981.12.

10CUEE CONFERENCE PROCEEDINGS
10th International Conference on Urban Earthquake Engineering
March 1-2, 2013, Tokyo Institute of Technology, Tokyo, Japan

EXPERIMENTAL STUDY ON TIMBER FRAMED MASONRY STRUCTURES

Andreea Duţu [1], Hiroyasu Sakata [2] and Yoshihiro Yamazaki [3]

1) Postdoctoral fellow, Center for Urban Earthquake Engineering, Tokyo Institute of Technology, Japan
2) Professor, Structural Engineering Research Center, Tokyo Institute of Technology, Japan
3) Assistant Professor, Structural Engineering Research Center, Tokyo Institute of Technology, Japan
dutu.a.aa@m.titech.ac.jp, sakata.h.aa@m.titech.ac.jp, yamazaki.y.ai@m.titech.ac.jp

Abstract: Since so far there is no design standard or published method that can be used to analytically evaluate the capacity of timber framed masonry buildings, an experimental study was developed having the objective to assess the mechanical behaviour of these structures.
Assessment of timber framed masonry structure's behaviour when subjected to lateral forces also involves the evaluation of each component material's contribution. The complexity of structure is given by the masonry panels and the interaction between masonry and timber frame.
The present paper presents the results of the experimental campaign developed on both component materials (first part) and timber framed masonry panels (second part). Based on the first part an evaluation of the timber framed masonry wall was made according to Japanese and Romanian design standard and was compared with the results obtained in the second part.

1. INTRODUCTION

Timber framed masonry buildings represent a special type of structure that can be found in both countries with and without seismicity. In some countries they are special for their beautiful architecture and in others for their seismic resistance, too. The structural system that consists in timber beams and columns, filled with masonry may be left visible (Figure 1) for aesthetical reasons or covered with finishing (Figure 2).



Figure 1 Timber framed masonry house in Romania



Figure 2 Timber framed masonry house in Portugal

They are spread in Europe, but they also exist in Haiti, India, and other countries in the world. For some of these countries they represent valuable heritage, but even though, the studies about them are quite scarce. The seismic design codes do not provide information on how to evaluate the behaviour of these structures when subjected to lateral loads.

2. OBJECTIVE OF STUDY

Giving these buildings' heritage value, within the Center of Urban Earthquake Engineering of Tokyo Institute of Technology, a research project was developed having as objective the efficiency analysis of a retrofitting method, using aramid fiber sheets in different layouts for timber framed masonry panels. This strengthening method aims to increase the strength, stiffness and ductility of the compound. One of the main advantages of this solution is that the intervention is low invasive, this being an important issue when retrofitting heritage buildings.

Nevertheless, in order to evaluate the retrofitting solution's efficiency, first the evaluation of non-retrofitted structure is needed. For this reason, the present paper aims to analytically evaluate the strength and the stiffness of timber framed masonry panels, and compare the results with the ones from the experimental study. Both European and Japanese design standards are used. The evaluation is especially difficult, as there is no dedicated evaluation method for this structural system. The component parts (timber, masonry) are evaluated separately.

3. DESCRIPTION OF THE STUDIED TIMBER FRAMED MASONRY PANEL

For reasons of space, capacity and economy, only a part of the structure has been chosen to be studied, namely a representative part of the wall (the frontais), taken as a reference structure the Portuguese pombaline building.

The pombaline (pombalino) building is a structure no more than four storeys high, with arcades at ground floor

level and with wood framed masonry walls (frontais) which, together with the floors' timber beams, form a cage (gaiola) (Figure 4, a) and constitute the resistant structure. They were named after the Marquis of Pombal, the man who ordered their construction after the 1755 earthquake that destroyed Lisbon, because he wanted buildings to have a seismic resistant structure (Dutu et al., 2012).

The pombaline buildings have a unique structure: external structural masonry walls; internal timber-masonry structural walls (Figure 3), and internal dividing walls.

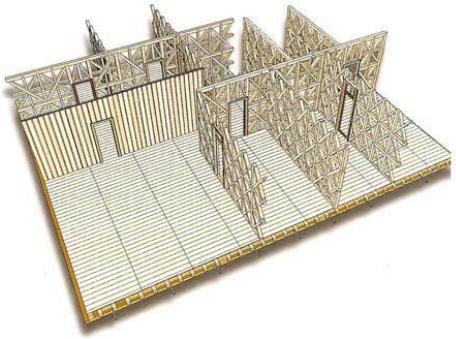


Figure 3 Pombaline building internal structural wall (Appleton J., 2003)

The specimens were chosen to have the layout in the Figure 4, without the diagonals, due to the difficulty to execute the masonry infill. Moreover, the layout without masonry it is used in other countries' timber framed masonry buildings, and the study is thought to be even more valuable, as it concerns more countries. The connections between the timber elements are cross-halving type, reinforced with screw nails.

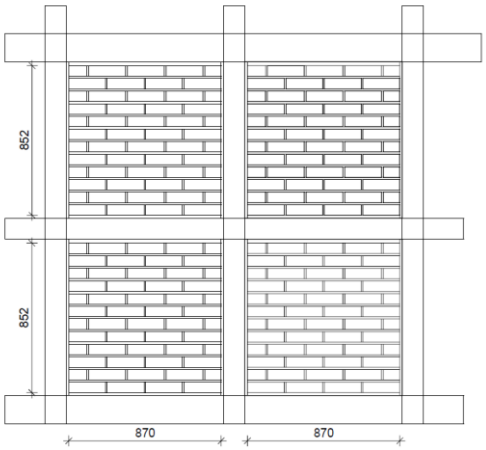


Figure 4 Timber framed masonry wall

Thus, the system is composed of the timber frame and the masonry panels, and considering the philosophy of the capacity design described by Paulay and Priestley as a chain that is as strong as its weakest link, the panels is assumed to be as strong as the shear strength of masonry or the compressive strength perpendicular to the grain of timber. So, if the masonry panels are strong, the timber may be locally crushed by compression or, if the masonry is weaker than the timber, it may present shear failure, but the timber frame would still be able to carry lateral loads, until the failure of one of its elements or joints.

The principle of this system is to have weak masonry, to fail before the timber frame, and thus, to dissipate energy through sliding of the bricks in the joints, where mortar has first failed.

4. MATERIALS TESTS

4.1 Masonry prisms

The complexity of the system is given mainly by the masonry's behavior, which is difficult to evaluate considering the fact that it consists of two different materials, mortar and bricks. Even the simple compression tests on masonry prisms showed a different behavior for each specimen, i. e. first crack occurred at the bottom or at the top brick, depending on the specimen. The elasticity modulus was also difficult to evaluate, because the results are very different between them. However, the values were calculated similar to concrete, as the 1/3 of the ratio between the maximum strength, σ, and its corresponding strain, ε (Table 1).

Table 1 Values of elasticity modulus for masonry, determined through compressive strength test on masonry prisms

No. of specimen	Young's modulus [GPa]	Compressive strength [MPa]
1	0,88	13,2
2	0,99	12,16
3	2,54	10,9
4	2,69	24,95
5	1,02	15,57
6	3,97	12,14
Average	2,01	14,82

The deformation was measured with 4 pi displacement transducers as shown in Figure 5, the total strain value being the average of the 4 values divided to the gage length.



Figure 5 Test setup of masonry prism for strain measuring

4.2 Mortar

The mortar recipe is according to Portuguese timber framed masonry buildings, 1:2:6 (cement:lime:sand). The water/(cement+lime) ratio is 1.75/2.

Uniaxial compressive and split tests were performed on mortar specimens with 50 mm diameter and 100 mm height, according to Japanese standard (JIS). Test results are shown in Table 2, respectively Table 3.

Table 2. Mortar properties after compressive tests

No. of specimen	Failure force [kN]	Strength [MPa]
1	9,2	6,87
2	11.58	8,65
3	8,77	6,55
4	0,832	6,22
5 (1st wallet)	18,8	14,05
6 (2nd wallet)	10,83	8,09
7 (3rd wallet)	7,23	5,4
8 (1st wallet)	13,16	9,83
Average		**8,21**

Table 3. Mortar properties after split tests

No. of specimen	Failure force [kN]	Tension strength [MPa]
1	5,2	0,69
2	6,28	0,84
3	5,47	0,73
4	7,77	1,04
Average	**6,18**	**0,82**

Mortar in timber framed masonry buildings is meant to be weak, as through its cracking before the bricks, bricks slide in the joints, thus more energy is dissipated.

To be mentioned that for compression tests on mortar, the 5 to 8 specimens were tested at 66, respectively 63 days after executing them and they were taken from the mortar used to build the diagonal compression test specimens, that will be discussed later in this paper.

4.3 Bricks

Compressive tests were also conducted on bricks, and the tests results are presented in Table 4. In Japan three types of burned clay bricks can be found, and according to their compressive strength given by the producer they are: 14,71, 19,61, and respectively, 29,42 MPa. Two types were selected to be tested, the 14,71 and 29,42 MPa.

For economical reasons the 29,42 MPa brick type was selected for further experimental studies.

Table 4. Compressive tests on two types of bricks

No. of specimen	Type [MPa]	Compressive strength [MPa]	Average strength [MPa]
1	14,71	38,4	41,26
2		36,8	
3		42,8	
4		42,4	
5		41,2	
6		46,0	
7	29,42	36	44,95
8		70,1	
9		38,9	
10		34,8	

4.4 Masonry wallets

Diagonal compression tests on unreinforced masonry specimens were also performed. Such "indirect" tests were preferred over "direct" shear-compression tests because of their limited cost and duration of setup preparation, and ability to provide valuable estimates of mechanical properties used in analytical models (Calvi G.M., 1996).

The diagonal compression test is the standard method in some international codes such as FEMA 356. In this paper, the results of the tests are considered according to ASTM E 519-07. This research test method is used for the purpose of evaluating the effects of variables such as type of masonry unit, mortar and workmanship, thus a smaller specimen was used. The dimensions of the specimens were chosen according to the tests conducted on timber framed masonry panels, namely to the masonry panels within the frame (Figure 4).

Thus, masonry specimens with 100x870x852 mm in size were tested. The masonry was made of burned clay bricks with dimensions 100x60x210 mm and mortar joints with 12 mm thickness (Figure 6). Diagonal compression tests were carried out on 3 specimens, built with the same characteristics.

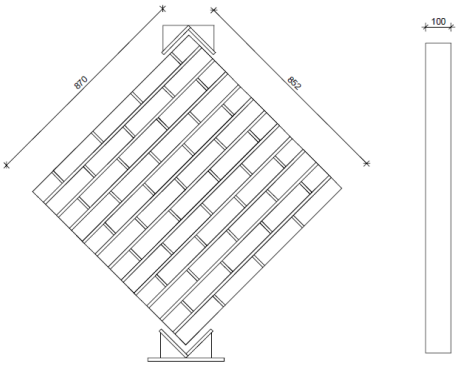


Figure 6 Dimensions of specimens

Two of the specimens suffered shear sliding involving both bed and head joints in a stepwise way (Figure 7 and Figure 9). Bed joint sliding typically produces higher energy dissipation. Specimen 2 suffered a diagonal cracking

involving both mortar joints and masonry units (Figure 8).

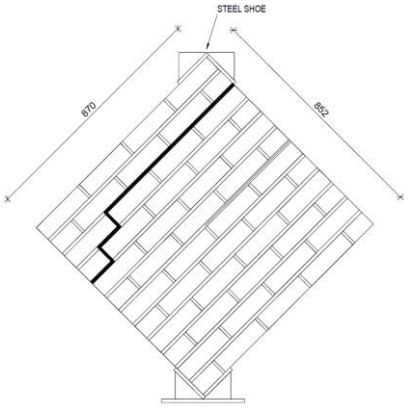


Figure 7 Specimen 1 (M1) failure mode

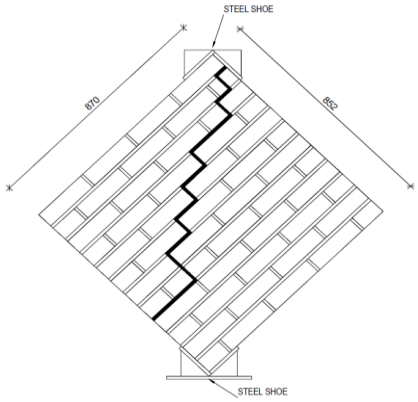


Figure 8 Specimen 2 (M2) failure mode

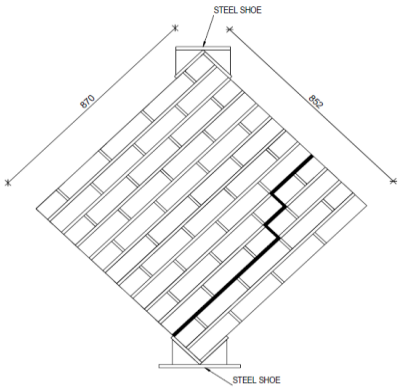


Figure 9 Specimen 3 (M3) failure mode

In ASTM E 519-07, a shear stress state at zero confining is assumed at the centre of the specimen, resulting in a shear stress equal to both tensile and compressive principal stresses. Diagonal cracking is then assumed to be caused by the attainment of masonry tensile strength f_t, which is equal to shear strength at zero confining stress τ_0. Based on displacement readings on both specimen sides, axial strains along a single direction were derived as average displacement readings divided by the gage length. The test setup is shown in Figure 10.



Figure 10 Position of displacement transducers

The stress – strain curves are shown in Figure 11 and Figure 12. The stress was calculated as the force divided by the cross sectional area.

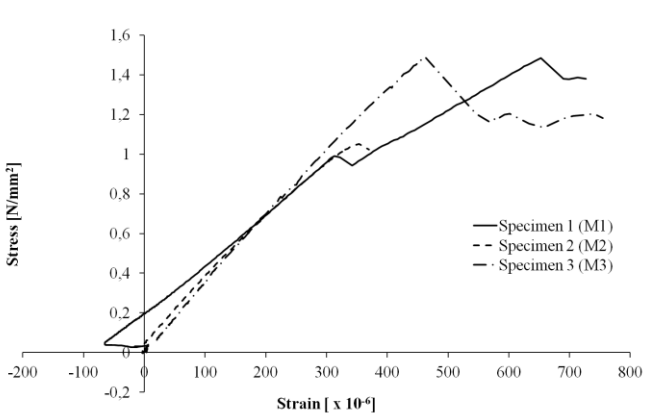


Figure 11 Stress – strain curves for compression

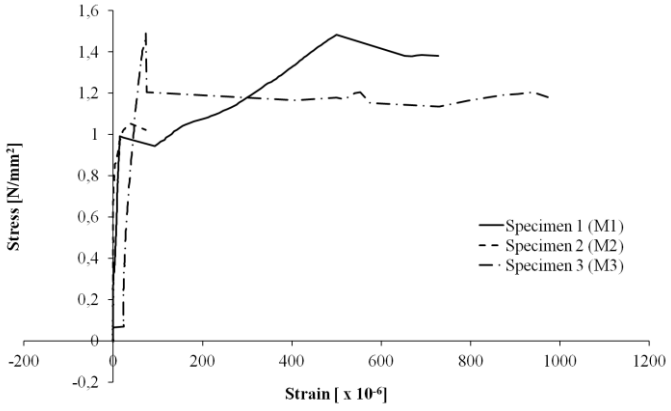


Figure 12 Stress – strain curves for tension

It can be seen that the specimens which failed through joint sliding showed higher shear strength than the one that failed through diagonal cracking.

As mentioned before, for timber framed masonry structures, mortar is weak, this being the principle of this

structural type. So the failure should occur due to mortar cracking in the joints and thus causing bricks to slide, as the assumed behaviour of the panel within the studied structure type. It can be observed that for specimens 1 and 3, the failure mode was similar to the assumed one.

Relevant parameters are shown in Table 5 where: P is the failure force; A_n is the area calculated according to ASTM E 519-07, meaning the cross-sectional area of the panel; σ_o is the shear stress; γ is the shear strain; ν is the Poisson's ratio; G is the shear modulus; and μ is the shear strain ductility as $\mu = \gamma_u / \gamma_{max,}$ were γ_u is the shear strain corresponding to the ultimate stress and γ_{max} is the shear strain corresponding to the maximum stress.

Table 5. Parameters determined according to ASTM E 519-07

Sp	P [kN]	A_n [mm^2]	σ_0 [N/mm^2]	$\gamma_{1/3}$ [x10^{-6}]	ν	$G_{1/3}$ [N/mm^2]	μ
1	129	86100	1,05	72	0,76	4896	1,11
2	91		0,75	60	0,11	416	1,05
3	128		1,05	124	0,15	2812	1,63
Av	116		0,95	85,3	0,33	2708	1,26

5. EVALUATION OF MASONRY PANEL

According to the P100-3:2008, the Romanian seismic design code for evaluation of existing buildings, the shear force associated to failure due to eccentric compression of an unreinforced masonry wall subjected to the design axial force, N_d, is calculated with:

$$V_{f1} = \frac{N_d}{c_p \lambda_p}(1 - 1{,}15\upsilon_d) \quad (1)$$

Where:

$\lambda_p = \frac{H_p}{l_w}$ is the shape factor of masonry

H_p = the height of the wall

l_w = length of the wall

c_p = coefficient depending on the support conditions of the wall (we consider $c_p = 1$, as being fixed on all edges)

$\sigma_0 = \frac{N_d}{t l_w}$ the medium compressive unit effort corresponding to the design axial force

t = width of the wall

$$\upsilon_d = \frac{\sigma_0}{f_d} \quad (2)$$

f_d = design compressive strength, determined from experimental testing on bricks = 3,51N/mm^2

The capacity of the unreinforced masonry wall in shear is given by

$$V_{f2} = \min(V_{f21}, V_{f22}) \quad (3)$$

The shear capacity according to the sliding shear mechanism:

$$V_{f21} = f_{vd} D' t \quad (4)$$

Where:

D' = the length of the compressed area in the wall

f_{vd} = design mortar joint slippage strength,

$$f_{vd} = \frac{f_{vm}}{\gamma_M CF} \quad (5)$$

$$f_{vm} = 1{,}3 f_{vk} \quad (6)$$

$$f_{vk} = f_{vk0} + 0{,}4\,\sigma_d \text{ (Eurocode 6)} \quad (7)$$

Where:

f_{vm} = shear strength of joint slippage mechanism

f_{vk} = characteristic failure strength

f_{vk0} = 0,2 N/mm^2 (according to CR6:2006)

The shear capacity according to the diagonal tension crack mechanism:

$$V_{f22} = \frac{t l_w f_{td}}{b}\sqrt{1 + \frac{\sigma_0}{f_{td}}} \quad (8)$$

b = coefficient having values $1{,}0 \le b = \lambda_p \le 1{,}5$

f_{td} = design tensile strength of masonry.

Thus, for the studied masonry panel, failure occurs due to flexure, as:

$$V_{f1} = 23{,}92 < V_{f21} = \mathbf{24{,}61\ kN,}$$

but since the tests aimed to simulate a pure shear stress state, only two failure type were considered, diagonal tension crack and sliding shear. Thus, the tests showed two shear sliding mechanisms involving both bed and head joints in a stepwise way, and the other one diagonal cracking involving both mortar joints and masonry units, as expected.

The evaluated shear strength according to the diagonal tension crack mechanism was:

$$V_{f22} = \mathbf{38{,}88\ kN}$$

The results interpretation according to (Tomazevic, 2000) and (Sheppard P., 1980) showed:

$$\sigma_0 = 0{,}83\frac{P}{A} = 1{,}10 \text{ N/mm}^2 \quad (9)$$

$$\tau_0 = \frac{\sigma_0}{0{,}98} = 0{,}84\frac{P}{A} = 1{,}12 \text{ N/mm}^2 \quad (10)$$

$$\sigma_t = -\frac{\sigma_0}{2} + \sqrt{\left(\frac{\sigma_0}{2}\right)^2 + (b\tau)^2} = 0{,}67 \text{ N/mm}^2 \quad (11)$$

$$H_{s,w} = A_w \cdot \tau = A_w \frac{\sigma_t}{b}\sqrt{\frac{\sigma_0}{\sigma_t} + 1} = \mathbf{96{,}67\ kN} \quad (12)$$

Where σ_0 is the axial compressive strength of masonry, τ_0 is the shear strength of masonry, the aspect ratio is h/d=0,98, σ_t the tensile strength of the specimen, τ is the shear strength of the specimen and $H_{s,w}$ is the lateral resistance of the plane masonry specimen.

The values above were calculated with the medium P, the force measured by the load cell of the testing machine when the failure occurred.

6. EVALUATION OF THE TIMBER FRAME

To evaluate the shear strength of the timber frame, the timber design standard issued by the Japan Housing and Wood Technology Center was used.

Thus,

$$P_a = \min(P_y, P_{150}) \quad (13)$$

$$P_{150} = K\left(\frac{1}{150} - \frac{R_0}{4}\right) \quad (14)$$

$$R_0 = \{\psi(\gamma_A - \gamma_B) + \frac{\mu}{b} \quad (15)$$

R_0 is considered 0,0095 as in the example given in the standard.

$$P_y = \frac{u \cdot v \cdot \Delta M_y}{H} \quad (16)$$

With

$$\Delta M_y = \frac{21 \cdot b^2 \cdot h \cdot F_{cv}}{55 \cdot \sqrt{1+\frac{8b}{3nh}}} \quad (17)$$

Stiffness of timber frame is calculated with the following equation:

$$k = \frac{1}{\frac{1}{K_f}+\frac{1}{K_j}+\frac{R_0}{P_y}} \quad (18)$$

$$K_f = \frac{12EI \cdot u^2 \cdot v^2}{H(uL+vH)} \quad (19)$$

$$K_j = \frac{u \cdot v \cdot k_R}{H} \quad (20)$$

$$k_R = \frac{7}{400} b^2 hE \quad (21)$$

$$I = \frac{\frac{h}{2} b^3}{12} \quad (22)$$

Where:

P_a = timber frame design shear strength

P_y = yielding strength

P_{150} = corresponding shear strength at 1/150 rad displacement

u = the number of horizontal timber elements

v = the number of vertical timber elements

ΔM_y = rotational moment of the timber elements' joint

H = the wall's height

K = the wall's stiffness

R_0 = initial deformation angle determined by initial slippage

F_{cv} = the local perpendicular to the grain compression strength of timber element having surrounding elements

h = element's cross section height

b = element's cross section width

n = coefficient taking into account compression of surrounding elements (we have considered as being 5, corresponding to the wood type)

E = Young's modulus perpendicular to the grain

I = inertial moment

L = the length of the wall

K_R = rotational stiffness of one joint

Ψ = the shrink ratio of dried wood

γ_a = moisture content of timber at the moment of building the wall

γ_b = moisture content of timber after the timber is dried

μ = working coefficient (when cut with machine or manual).

Considering F_{cv} = 0,78 kN/cm^2 according to (AIJ, Standard for structural design of timber structures, 2006) and Young's modulus of timber according to the data given by the company that provided the timber, the equations 13 to 22 are applied for the present study.

The number of horizontal, respectively, vertical elements is considered u=v=3.

The results are shown in Table 6.

Table 6. Analytical evaluation of timber frame

Case	K_f [kN/rad]	K_j [kN/rad]	K [kN/rad]	P_y [kN]	P_{150} [kN]
u=v=3	2878,93	1125,95	556,30	16,90	2,38

7. QUASI-STATIC CYCLIC TESTING ON TIMBER FRAMED MASONRY PANEL

For the cyclic test the deformation controlled CUREE-Caltech standard (CUREE) protocol was used (Figure 13). It was specifically developed for woodframe shearwall testing and is based on the hysteretic response of woodframe structures (Gatto K., 2003). The ASTM E 2126-02a standard includes the CUREE protocol as one of the loading options (Krawinkler H., 2009).

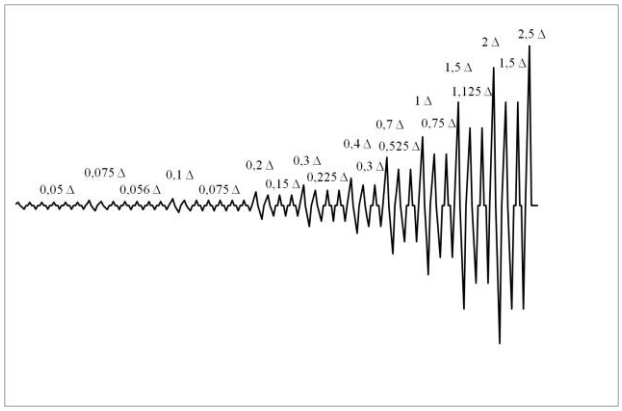


Figure 13 CUREE loading protocol

As the input deformation the shear angle, δ, was used to cancel the rocking and thus to observe the pure shear capacity of the wall, being calculated with the following equation:

$$\delta = \frac{D_1+D_2}{2} - \frac{D_3+D_4}{2} \quad (23)$$

Where D_1, D_2, D_3, D_4 are the measured displacements, as in Figure 14.

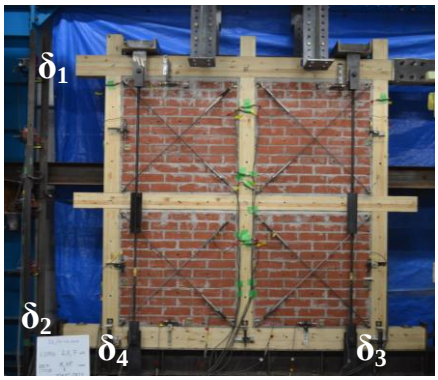


Figure 14 Parameters used to calculate δ

The hysteretic behaviour of the timber framed masonry panel (S2) is represented in terms of lateral force and lateral displacement at the top of the specimen with respect to the

height (drift) and shows an important stiffness and ductility of the system (Figure 15). The failure occurred at 5,3% drift, due to tension in the upper horizontal beam and in the same time shear in the right column (Figure 16).

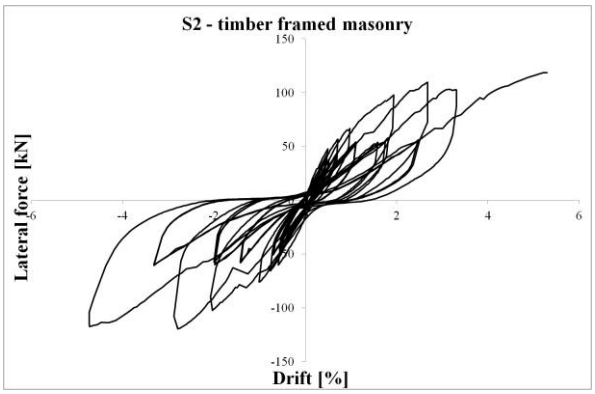


Figure 15. Lateral force – drift diagram of S2

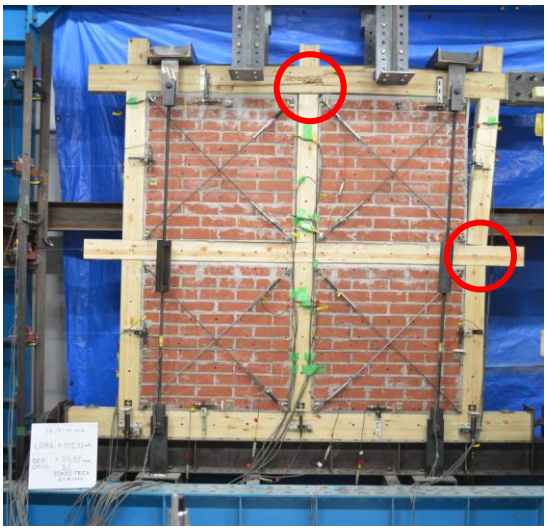


Figure 16. Failure mode of S2

Stiffness decreased direct proportional with each cycle and being strongly influenced by the reversed cycle degradation (Figure 17).

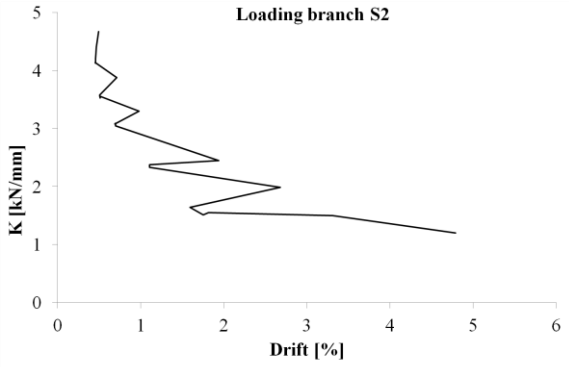


Figure 17. Stiffness degradation on the loading branch for S2

Masonry panels separated from the timber frames since first cycle.

Although the masonry failed at 1,93 % drift, at 97 kN lateral force, the masonry panels continued to ensure the system's stiffness and to dissipate energy until the timber frame's failure. The cracks of the masonry panels started appearing from the bottom and continued, with every new cycle, layer after layer, towards the top.

The upper masonry panels did not show any cracks, but near to the failure, at 4,7 %drift, the left one showed out of plane behaviour.

The middle timber joint showed important damages from 0,7 % drift and was strongly subjected to shear force, resulting in compression perpendicular to the grain of timber elements, by the masonry.

8. QUASI-STATIC CYCLIC TESTING ON TIMBER FRAME

The timber frame specimen (S1) was tested using the same loading protocol (CUREE) and the same values of the shear angle as input deformation.

The dimensions of the specimen were identical with the ones of the frame within S2 and the purpose of this test was to observe the contribution of the masonry infill.

The hysteretic behaviour (Figure 18) shows a reduced stiffness, a high ductility and important slippage in the timber connections.

The rotation angle in the connections was similar to the shear angle, this meaning that the connections are very flexible and not allowing the timber elements to bend.

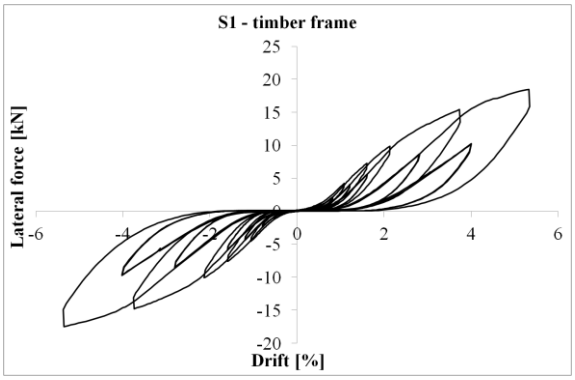


Figure 18. Lateral force – drift diagram of S1

After 5,33% drift, due to reaching the maximum stroke of the jack used to introduce the lateral force, a monotonic loading was performed until 9,4% drift.

The specimen did not show a failure mode, but the upper timber beam cracked starting from the middle connection (Figure 19).



Figure 19 Deformation of S1 at 9,4 % drift

The stiffness increased with every cycle until 2,14 % drift (Figure 20).

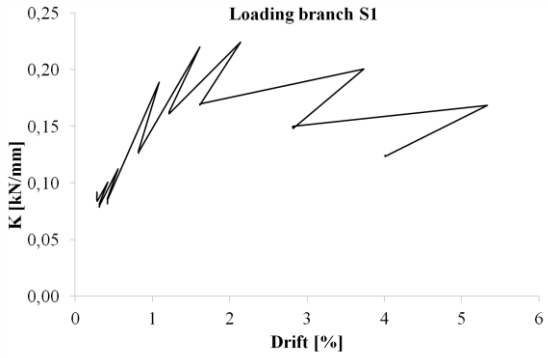


Figure 20 Stiffness degradation on the loading branch for S1

9. DISCUSSION

Comparison of S1 with S2 shows that the masonry infill has very important influence, as it determines the strength of the system.

Basically for S2, the observed principle of the system is that the masonry carries, besides the vertical forces, also lateral forces even if it presents important cracks. Considering the ratio between the ultimate displacement and the yielding displacement, a ductility factor 2,03 was determined.

Since in S1 no significant bending of the timber elements was observed, for S2 the bending was very clear for all the timber elements, except the bottom beam.

In terms of energy dissipation, S2 shows a significant higher total value, 37,69 kNm, than in case of S1, that showed a total value of 2,94 kNm. The energy dissipation, ΔW, was calculated as the area of the hysteretic curve for each specimen. In Figure 21 is shown the energy dissipation of S1 and S2 in every cycle, highlighting the initial ones.

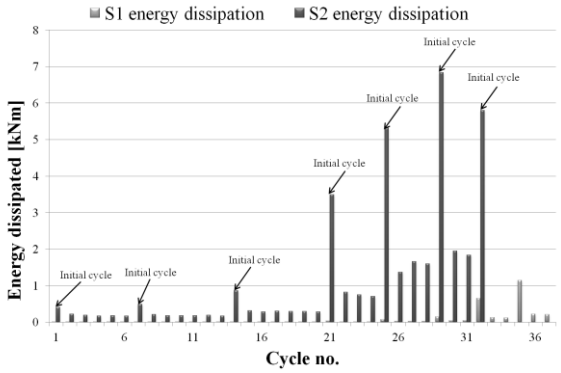


Figure 21 Energy dissipation of S1 and S2

Equivalent damping ratio h_e of system was also calculated using the formula:

$$h_e = \frac{1}{4\pi} \cdot \frac{\Delta W}{W} \quad (24)$$

Where ΔW is the total dissipated energy by the specimen under cyclic loading and W is the energy dissipated in the cycle corresponding to peak value of the force, for all cycles. The values are presented in Table 7.

Table 7. Equivalent damping ratios of all specimens according to each considered loading cycle

Cycle no.	h_e S1 [%]	h_e S2 [%]	Cycle no.	h_e S1 [%]	h_e S2 [%]
1	0,005	0,546	**20**	0,009	0,374
2	0,004	0,299	**21**	0,110	4,722
3	0,004	0,249	**22**	0,038	1,112
4	0,004	0,231	**23**	0,036	1,006
5	0,004	0,234	**24**	0,035	0,958
6	0,004	0,227	**25**	0,287	7,181
7	0,010	0,660	**26**	0,086	1,849
8	0,005	0,277	**27**	0,083	2,239
9	0,005	0,246	**28**	0,081	2,156
10	0,005	0,244	**29**	0,544	9,239
11	0,005	0,243	**30**	0,155	2,639
12	0,005	0,249	**31**	0,149	2,482
13	0,005	0,233	**32**	2,426	7,828
14	0,018	1,157	**33**	0,468	
15	0,009	0,428	**34**	0,437	
16	0,009	0,383	**35**	4,214	
17	0,009	0,406	**36**	0,833	
18	0,008	0,397	**37**	0,764	
19	0,009	0,388			

Thus, the masonry infill also produces a significant increase in damping of the timber framed masonry system.

The behavior of masonry wallets in diagonal compression tests were further compared with the behavior of masonry panels within S2 subjected to cycling loading.

Within the cyclic test it was observed that at 1, 93% drift, corresponding to a value of 97 kN for the lateral force, the bottom right masonry panel failed first due to bed joint sliding. This failure mode was also seen as predominant in the diagonal compression tests.

Moreover, according to the diagonal compression test results interpretation using (Tomazevic, 2000) and (Sheppard P., 1980) equations, the lateral resistance of the plane masonry specimen was 96,67 kN, similar to the observed failure in S2.

In Figure 22 the results of both types of tests are compared in terms of compression stress – strain relationship, highlighting the corresponding stress value for the 97 kN lateral force.

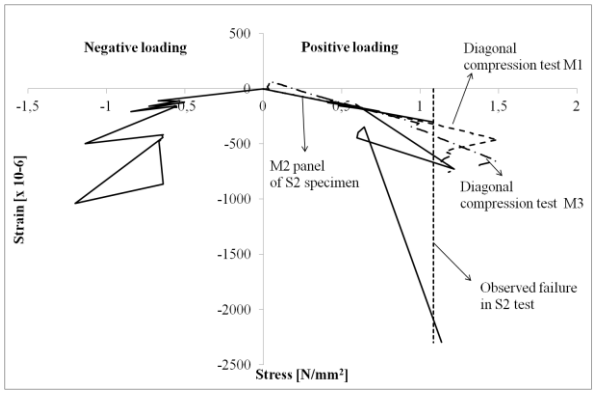


Figure 22 Comparison of Compression Stress – Strain diagrams of S2 and masonry wallets M1 and M3

Comparison of timber frame analytical evaluation with experimental results is shown in Figure 23 in terms of lateral force – lateral displacement at the top of the specimen with respect to the height (drift).

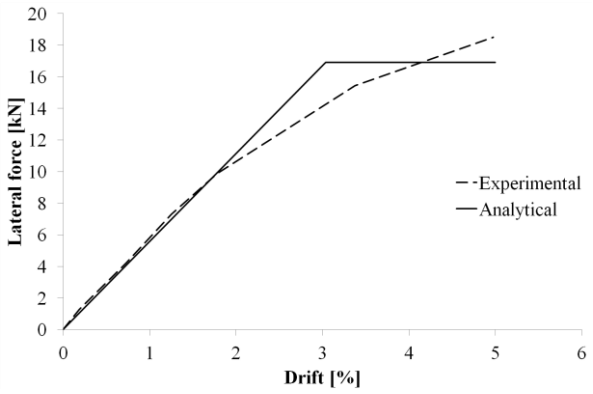


Figure 23 Comparison of analytical evaluation with experimental results for S1

The results are very similar in terms of stiffness.

However, the yielding point is difficult to be precisely determined in timber walls, where the behaviour is determined by local compression.

10. CONCLUSIONS

Present experimental study confirms the good in plane behaviour of the timber framed masonry system. It showed a significant deformation capacity and important stiffness and strength.

It is clear that the masonry infill determines the strength and stiffness of the system, while the timber frame is responsible for the high ductility.

The main purpose of the materials and diagonal compression tests was to evaluate the capacity of the masonry panel within the timber framed masonry walls, even though the boundary conditions are not the same as the actual situation, and compare the results with the ones from timber framed masonry panel test.

In timber framed masonry structures, mortar is weak, this being the principle of this structural type. So the failure of the masonry infill occurs due to mortar cracking in the joints and thus causing bricks to slide. The results of the tests confirmed this principle, the predominant failure mode in diagonal compression was bed joint sliding and the cyclic test on timber framed masonry panel also presented this type of failure of the masonry panels.

Comparing the analytical evaluation results for masonry, according to P100-3:2008 with the (Tomazevic, 2000) and (Sheppard P., 1980) equations, the latter value is almost four times higher.

Also, when further comparing the diagonal compression tests with the masonry panels within S2, it was observed that at 1, 93% drift, corresponding to a value of 97 kN for the lateral force, the bottom right masonry panel failed first due to bed joint sliding. Thus, besides confirming the failure mode shown in previous tests, it also confirmed that the use of (Tomazevic, 2000) and (Sheppard P., 1980) equations was appropriate.

The purpose of the timber frame test was to observe the contribution of the masonry infill in terms of stiffness, but it was difficult to also compare in other terms the behaviour of the two specimens as, the presence of masonry completely changes the stress state in the timber frame.

The timber frame test showed very similar results with the analytical evaluation, this indicating that the equations given in the timber design standard are also appropriate for this case.

Although the overall behaviour of timber framed masonry panel studied was good for in plane forces, the out-of-plane behaviour still needs to be considered, as even when subjected to in plane forces, the upper right masonry panel showed out of plane displacement.

The timber framed masonry structure's behaviour described in this paper corresponds to the specimen made with new materials, i.e. new timber, new bricks and new screw nails. All these materials may have higher strength than the ones used in the real situation, thus future research will also focus on retrofitting solutions to avoid out of plane behaviour and to increase capacity of timber framed masonry structures when subjected to strong motions.

Acknowledgements:

The authors acknowledge support from the Japan Ministry of Education, Culture, Sport, Science, and Technology (MEXT) for establishing the Center for Urban Earthquake Engineering (CUEE) in Tokyo Institute of Technology. This support makes possible the forthcoming international conference, as well as international joint research projects and exchange programs with overseas universities.

References:

Augenti N, Parisi F, Acconcia E (2012). MADA: online experimental database for mechanical modelling of existing masonry assemblages. Proc., 15th World Conference on Earthquake Engineering, Lisbon, Portugal (CD-ROM).

ASTM E 519-07 "Standard test method for diagonal tension (shear) in masonry assemblages"

Calvi G.M., Kingsley G.R. and Magenes G., "Testing of masonry structures for seismic assessment", Earthquake spectra, Volume 12, No. 1, February 1996

Sathiparan N., Mayorca P., Nesheli K.N., Guragain. R., Meguro K., "Experimental study on in-plane and out-of-plane behaviour of masonry wallettes retrofitted by PP-band meshes", Seisan-Kenkyu, 56/6/2005, p. 530-533

Chiostrini S., Galano L. And Vignoli A., „On the determination of strength of ancient masonry walls via experimental tests**",** 12WCEE 2000

P100-3:2008 „ Romanian seismic design code for evaluation of existing buildings"

Tomazevic, 2000 „Earthquake-resistant design of masonry buildings" Series on innovation in structures and construction – Vol.1, Imperial College London

Sheppard P., Tercelj S., „The effect of repair and strengthening methods for masonry walls", 7WCEE Istanbul, Turkey, 1980

Shahzada K., Goto T., „Improvement of masonry structures against seismic force", 3rd National Conference on Retrofitting of Iran by Engr., 2008

CR 6:2006 "Romanian design code for masonry structures"

Japan Housing and Wood Technology Center (2004) "The timber design standard", February

Sakata H., Yamazaki Y., Ohashi Y., "A study on Moment Resisting Behavior of Mortise-Tenon Joint Dowel or Split wedge", 15th World Conference of Earthquake Engineering, Lisbon, 2012

Standard for structural design of timber structures, AIJ, 2006

Gatto K., Uang C.-M., „Effects of Loading Protocol on the Cyclic Response of Woodframe Shearwalls", Journal Of Structural Engineering © Asce , October 2003

Krawinkler H., „Loading Histories For Cyclic Tests In Support Of Performance Assessment Of Structural Components", 3rd International Conference on Advances in Experimental Structural Engineering, 2009, San Francisco

Appleton, J.; *Reabilitação de Edifícios Antigos – Patologias e tecnologias de intervenção* (in portuguese), Editure Orion, 1st edition, Amadora, 2003

10CUEE CONFERENCE PROCEEDINGS
10th International Conference on Urban Earthquake Engineering
March 1-2, 2013, Tokyo Institute of Technology, Tokyo, Japan

POST-EARTHQUAKE INVESTIGATION AND SEISMIC EVALUATION OF A DAMAGED RC BUILDING IN VAN, TURKEY

Viorel Popa[1], Radu Vacareanu[2] and Faruk Karadogan[3]

1) Lecturer, Reinforced Concrete Department, Technical University of Civil Engineering, Romania
2) Professor, Reinforced Concrete Department, Technical University of Civil Engineering, Romania
3) Professor, Civil Engineering Department, Istanbul Technical University, Turkey
vpopa@utcb.ro, radu.vacareanu@utcb.ro, karadogan@itu.edu.tr

Abstract: A post-earthquake investigation team observed a large building stock still standing but listed for demolition in the city of Van, eastern Turkey, half a year after two strong earthquakes hit the region in 2011. The focus point of this investigation was to observe structural and non-structural damage for several engineered reinforced concrete or masonry buildings and to apply and compare Turkish and Romanian procedures for post-earthquake investigation and seismic evaluation. This paper presents the observed damage and the seismic evaluation for a relatively new multi-storey residential building and the comparison between the damage observed and analytic damage state. The structural system of the building consists of RC frames and shear walls. The non-structural infill partitions made out of hollow bricks sustained severe damage. At the time of the inspection the building was evacuated and listed for demolition. A detailed structural analysis was carried out to understand the seismic response and the observed damage state. The results of the seismic investigation are presented in this paper together with some comments about the effectiveness of the post-earthquake quick inspection methods. The post-earthquake investigation team has been dispatched to Van with the support of the UNESCO - IPRED Platform.

1. INTRODUCTION

In June 2012 an investigation mission was dispatched to the city of Van strongly affected by two earthquakes in the fall of 2011, Van-Ercis, October 23, 2011, Mw=7.1 and Van-Edremit, November 09, 2011, Mw=5.6 (METU/EERC, 2011). The epicentral distances from Van downtown are 40km and 10km, respectively. Academic staff and professional engineers from Turkey and Romania participated in this mission organized with the support of the UNESCO IPRED Platform.

More than 30000 buildings were heavily damaged or collapsed after the earthquakes (EERI, 2012). A large part of the vulnerable building stock in Van consists of multistory (5-8 story) reinforced concrete frame or shear wall structures with brittle masonry infill partition walls. At the time of the mission the debris of the collapsed buildings were removed from the city. Many evacuated buildings listed for demolition still standing were observed. Most of these buildings sustained severe structural and nonstructural damage. For many buildings the nonstructural damage of exterior masonry walls was obvious from the outside.

Two identical RC residential buildings (A and B) with seven stories were investigated. This paper refers to the most damaged one, i.e. building B (Figure 1). Both buildings were designed and built in 2005. The structural system consists of cast in place reinforced concrete shear walls and frames (Figure 2). In the transversal direction the lateral resisting structure consists mainly of shear walls. Five shear walls were identified. In the longitudinal direction only two shear walls were identified so the RC frames represent an important part of the lateral resisting structure.

The structural system presents vertical regularity. No sudden changes in stiffness or strength of the structural elements occur over the building height. The transversal sections of shear walls, columns and beams are similar at each floor.

The shear walls location within the structure suggest that the building is likely to experience a strong torsional response. In the transversal direction the lever arm of the forces in shear walls to resists the building torsional moment is a merely 7,60m. In the longitudinal direction the existing shear walls are collinear so no lever arm of the shear forces in the RC walls can be considered for the torsional strength and stiffness. This particular layout of the shear walls is determined by the architectural constraints. The building has relatively large windows on each facade regularly placed in each bay and at each storey. No full masonry infills are placed in the outer frames.

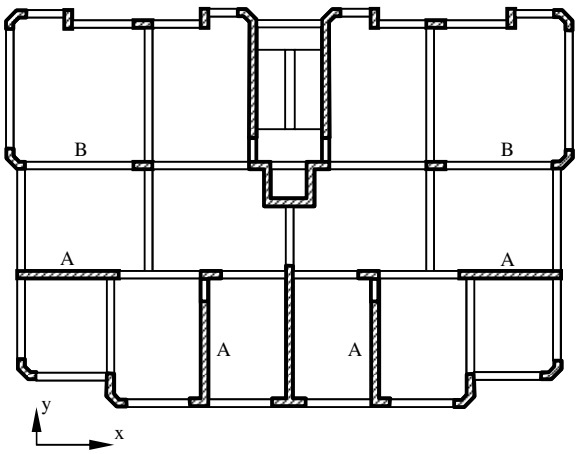
The RC frames consist of rather stiff beams with height of 60cm and widths of 25 or 30cm. Most of the columns have rectangular sections of 30x60cm or 30x80cm usually aligned with the *x-x* axis of the building (longitudinal) to compensate for the reduced number of shear walls.

Relatively stiff frames were obtained in this direction. Most of the beams intersection points correspond to a column or wall end. Only two transversal beams are supported at one end by two longitudinal beams. Outer frames present beam offsets of 50...150cm from one bay to another. This unfavorable layout of the beams is caused by architectural constraints regarding the aspects of the facades. These beams are supported on thin columns that connect the beams end. The effectiveness of such layout upon the strength and stiffness of the outer frame is questionable.

A 12cm continuous slab is supported by the beams. Given the layout of the slab a rigid diaphragm assumption can be made. For many of the multistory RC buildings built in recent years in Van, infill joist system was used for the floor structural system. This resulted in shallow beams of 30-35cm not suitable for earthquake resisting frames.



Figure 1 Main façade of building B



A: Shear walls introduced during construction B: Original position of the shear walls in *x-x* direction

Figure 2 General layout of the structural system

The foundation system consists of foundation beams that connect the shear walls and columns under the basement. The basement is used also for apartments so windows are placed on the perimeter just above the ground level. No change in the vertical structural system was noticed at this level. Given the relatively weak foundation beams in comparison with the supported shear walls, uplift and even plastic hinging of the foundation beams might be expected.

Important changes in the layout of the shear walls as in blueprints of the building were observed. Shear walls in the longitudinal (*x-x*) direction were moved from one axis to another. Their web length was reduced from 6.55m to 4.55 while the width was preserved. In the transversal direction two additional shear walls were placed increasing the shear strength in the transversal direction and improving the torsional stiffness of the building as the two walls are located at 7.60m apart from each other.

Reinforcement details for beams and columns as given in the design drawings generally meet the requirements of both Turkish and European seismic codes (TERDC 2007, EN 1998-1). The columns have continuous longitudinal reinforcement from bottom to top with reinforcement ratio of around 1%. The beams have continuous reinforcement at both sides. Longitudinal reinforcement ratios ranging roughly from 0,5% to 1% could be observed.

Closed stirrups with hoops bended at 135º are used; 8mm diameter stirrups spaced at 160m or 180mm are usually provided for beams. Spacing of the stirrups in the critical regions of the beams does not meet the requirements of EN1998-1 for high ductility class.

In some elements, curtailment of the top bars in beams at the limits of the critical regions at beams ends indicates that the plastic hinges might appear closer to the middle of the beam.

At interior supports, anchorage of the bottom reinforcements is not obtained by bending the bar inside the beam-column joint. Instead, the straight bottom bars pass through the interior joints being cut in the plastic regions of the adjacent beam. Otherwise, development length of more than 40 bar diameters were used for the anchorage of the longitudinal rebars.

Masonry infills are built according to the construction practice in the region using hollow clay units. The width of the masonry panels is 30cm for exterior walls and 15cm for interior walls. Double layer masonry panels with thermal insulation in the middle have been used for exterior panels. Usually, no concrete ties were used to confine the masonry near windows or doors or to prevent out of plane failure for the large interior masonry panels. Apparently, no steel anchor ties were provided to connect the panels to the adjacent beams and columns.

2. OBSERVED DAMAGE

The analyzed buildings were inspected by IPRED mission in June 2012. At the time of the inspection both buildings were evacuated and listed for demolition. This

decision was made based on the rapid assessment performed immediately after the earthquakes. According to the owner, the buildings sustained limited damage after the first earthquake (October, 23) and was evacuated. The buildings suffered most of the existing damage during the second earthquake (November, 11).

For building A no major damage could be observed from the outside. Building B sustained more severe damage as reported in the following.

Most of the outer masonry panels and parapets below the windows at the lower stories were damaged. Most of the interior masonry panels at the first three stories sustained severe damage beyond reparability. Replacement of these panels is necessary for future use of the building. Full or partial collapse of some masonry panels parallel to the *x-x* direction at the first floor was observed (Figure 3, a). These masonry infills replaced the RC shear walls that were moved to the adjacent bay.

Damage to the nonstructural masonry panels with no corner bonding can be noticed in Figure 3, b. Two perpendicular panels connected using just polyurethane foam inserted in the vertical separation joint detached from each other with a vertical crack. The panel oriented in the *x-x* direction of the building crashed at the bottom corner.

Overturning of an exterior leaf of a double layer masonry panel can be observed in Figure 3, c. No connectors between the leaves were noticed on the site; In the same figure the shear crack developed in the captive column between the basement windows can be observed.

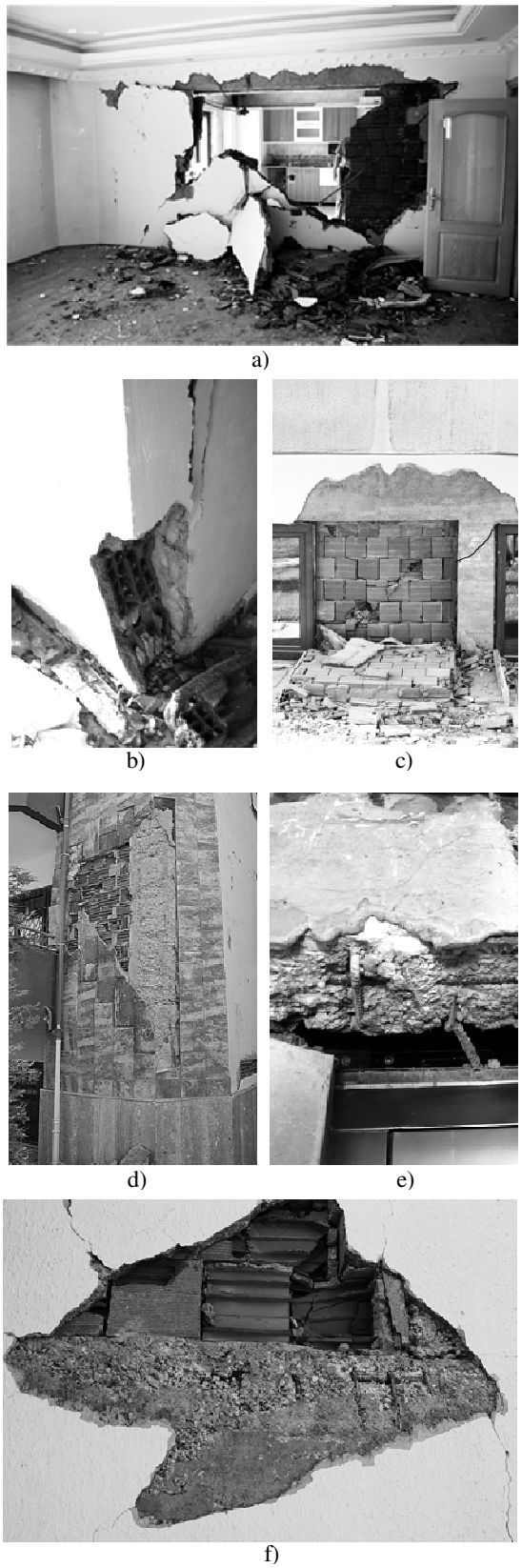
No major structural damage has been noticed. Shear and flexural cracks occurred in the critical regions of the beams. Inclined shear cracks occurred in beams due to the interaction with the masonry infills as well.

Inclined shear cracks were observed in the columns and shear walls. The largest crack width measured in the shear walls was 0,3mm. Thinner cracks could be observed in the L shaped columns on the building perimeter.

Despite the shallow structural damage the site inspection revealed the low quality of structural concrete. Removal of the finishing layers exposed the members' concrete surfaces (Figure 3, d). In some members even the steel reinforcements were exposed as can be seen in the case of the coupling beam that connect the two wings of the shear walls around the elevator shelf (Figure 3, e). Ready mix concrete for building construction is available in Van area since 5-7 years ago (EERI, 2012). Inspection showed that the construction quality of the RC structure was rather poor. The low concrete quality is further illustrated in Figure 3, f. Improper water/cement ratio, improper combination of gravel sorts, segregation, lack of vibration, and concrete settlements under steel rebars can be noticed.

Samples of the concrete extracted from the columns and shear walls revealed a very low compressive strength of 6-7MPa for B building and 12MPa for A building.

No severe settlement could be observed around the building perimeter or at the basement floor. An uplift of the building of 3cm from the sidewalk level was measured at one corner of the building.



a) b) c) d) e) f)

Figure 3: Observed damage

3. STRUCTURAL ANALYSIS

3.1 Analytical model

Structural analysis was performed using ETABS (CSI, 1995). Static nonlinear analysis (pushover) is used to investigate the structural response in the nonlinear range. The main objective of the structural analysis was to determine the lateral yielding force and, consequently, the displacement demand.

A 3D computer model which accounts for the nonlinear response of the structural system is developed. Beams and columns are modeled using frame elements. Shear walls having length of the transversal section smaller than 1,5m (including) are modeled using frame elements. Shear walls having length of the transversal section larger than 1,5m are modeled using shell elements.

Within the boundaries of the columns sections the longitudinal and the transversal beams are considered rigid. If the transversal beam axis, the longitudinal beam axis and the column axis did not intersect in a single point a stiff beam link is considered to model the connection. The equivalent "elastic" stiffness is taken equal to half of the gross stiffness for each structural member.

Foundation beams are supported on springs with homogenous elastic behavior in vertical direction. The translation of the foundations in *x-x* and *y-y* direction is restrained. No other external restraints are applied.

Horizontal rigid diaphragms are considered at each level.

Gravity loads, other than the dead weight of the structure, are applied as uniform load on the slabs at each floor. An equivalent uniform load of 12.8 kN/m^2 is obtained for the entire building.

Nonlinear M3 hinges are introduced at the end of each beam. Nonlinear P-M2-M3 hinges are introduced at the bottom of each column, directly above the foundation beams. Nonlinear P hinges are introduced at the boundary columns of shear walls. Nonlinear P hinges are used to simulate the yielding of the vertical reinforcement in the web of the shear walls, as well (Figure 4).

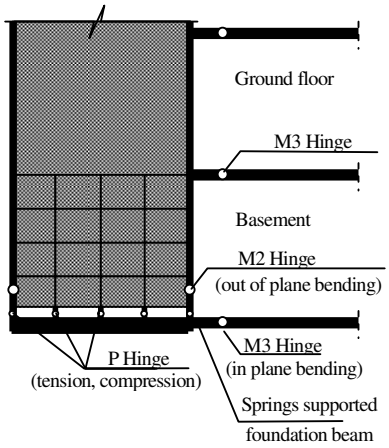


Figure 4: Modeling assumptions

Pushover analysis is performed in both *x-x* and *y-y* direction. Two lateral load distribution patterns are considered for each direction: uniform (mass proportional) and triangular (acceleration proportional).

3.2 Masonry infills

Regarding the contribution of the masonry infills to the lateral strength and stiffness of the building the following comments are made:

- Interior masonry panels are just 15cm thick.
- Double layer masonry panels with a glass wool layer in the middle are used for exterior walls. No connectors could be observed between the masonry layers.
- All masonry panels are made using hollow masonry units. These are multi-cell clay blocks with large rectangular holes, with the holes oriented in the horizontal direction. The vertical interior walls of the bricks have out of plane defects that significantly reduce their strength and stiffness for diagonal stresses in the vertical plane (Figure 5).
- Most of the exterior masonry panels have large openings for windows. Most of the interior infill panels have door openings usually located at one end. The formation of the compression diagonal is prevented as the small lateral drifts are usually accommodated by the door opening.

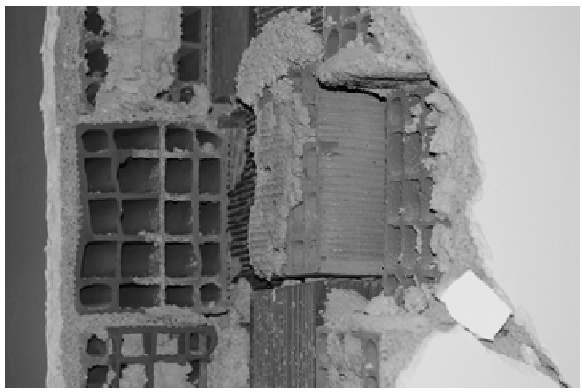


Figure 5: Typical masonry work in the building

All these comments suggest that the contribution of the infill masonry panels upon the lateral strength and stiffness of the building is questionable. As the main objective of the structural analysis was to determine the peak lateral drift demand using the capacity spectrum method, the contribution of the masonry infills is not accounted for directly. A sensitivity study to account for the influence of the masonry infills by changing the lateral stiffness of the structure to the dynamic response of the building is performed using time-history linear analysis. Further studies will be performed to account for this contribution using time-history nonlinear analysis.

3.1 Push-over analysis

The modal analysis of the building revealed a strong torsional response. The modal participating mass ratios are listed in Table 1.

The second and the third vibration modes are considered to determine the seismic demand for the equivalent lateral load method in the Turkish Earthquake Standard (TERDC, 2007). The required lateral seismic coefficient in the longitudinal direction results:

$$C^x = \frac{A(T)}{R} = \frac{A_0\, I\, S(T)}{R} = 0.108 \qquad (1)$$

considering an effective ground acceleration coefficient A_0=0.3, a spectrum coeficient S(T)=1.42, an importance factor I=1 and a reduction factor R=4. For the transversal direction S(T)=1.80 and C^y=0.135.

Based on the simplified representations of the force-displacement capacity curves as presented in Figure 7, the normalized yield strength of the structure in x and y directions can be estimated:

$$R_y^x = \frac{F_y^x}{W} = \frac{8700}{39000} = 0.22 \qquad (2)$$

$$R_y^y = \frac{F_y^y}{W} = \frac{12000}{39000} = 0.31 \qquad (3)$$

The calculated values of the R_y are larger than the required lateral seismic coefficient. Resulted values of the overstregth factors are 2.03 in the longitudinal direction and 2.30 in the transversal direction, considering the characteristic steel strength. To account for a partial safety coeficient γ_S=1.15 for the steel strength, lower-bound values of the lateral overstregth of 1.77 and 2.00 are obtained.

The Capacity Spectrum Method (ATC 40, 1996) is used to determine displacement demand for the structure. Two levels of the effective ground acceleration are considered:

- 0.25g, corresponding to the recorded earthquake of November 11, 2011, Van Merkez Station, E-W direction
- 0.4g, corresponding to the design acceleration of the updated version of the Turkish Earthquake Standard. This value was selected for Van region after the earthquakes of 2011.

Considering a control period of the acceleration response spectrum of 0.4s the following coefficients results: C_a=C_v=0.25 for a_g=0.25g and C_a=C_v=0.4 for a_g=0.4g.

The performance points determined using capacity spectrum method are presented in Figures 8...11. For the effective ground acceleration of 0,25g peak lateral displacements of 46mm in *x-x* direction and 36mm in *y-y* direction are determined. These values correspond to maximum lateral drifts in the longitudinal direction of approximately 0.25% at the first story. Such values of the lateral drift suggest an essentially elastic response of the structure. The same comment is valid noticing the location of the performance points in Figures 9 and 11.

For the design acceleration of 0.4g peak lateral displacements of 74mm and 56mm are determined for the longitudinal and transversal direction of the building. Even under the design earthquake limited structural incursion in nonlinear range are expected.

These relatively low values of the lateral displacement demand can be explained by the short control period of the acceleration response spectrum for the building site and the relatively high lateral strength of the building. Regarding the strength of the building, a lateral overstrength factor of 2,0 corresponding to a reduction factor R=4 suggest that limited nonlinear behavior is expected.

Table 1: Modal participation mass ratios

Mode	Period	Participating mass ratios		
		UX	UY	RZ
	(s)	%	%	%
1	0.91	21.1	0	58.3
2	0.77	57.2	0	21.7
3	0.61	0	78.1	0

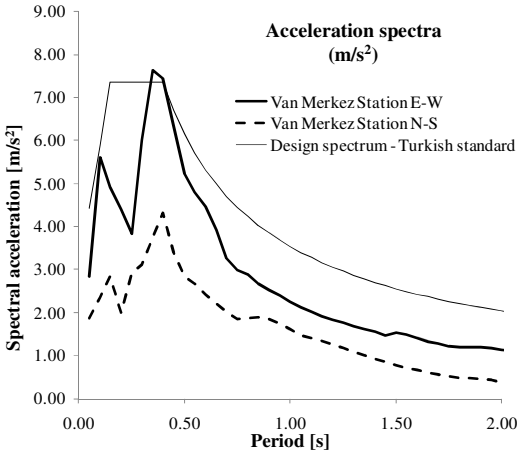


Figure 6 Absolute acceleration response spectra

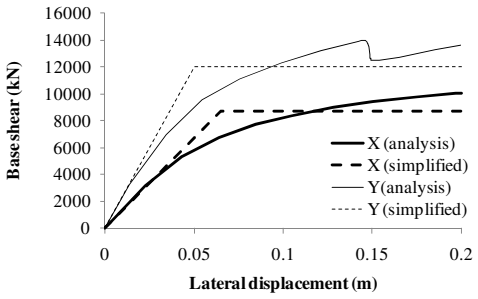


Figure 7 Pushover results: force-displacement curve

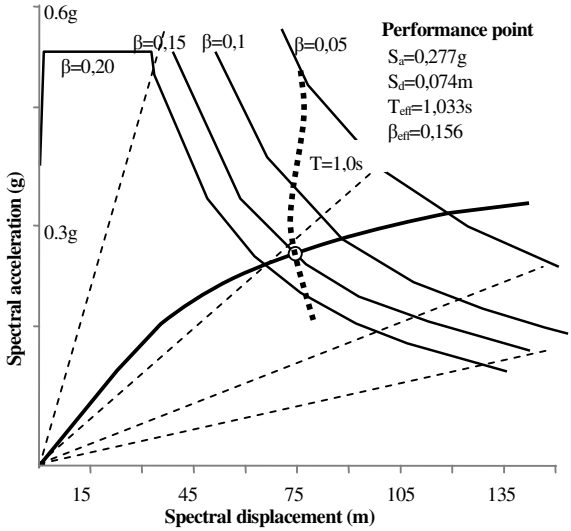


Figure 8: Capacity spectrum method: C_A=0,40, *x-x* direction

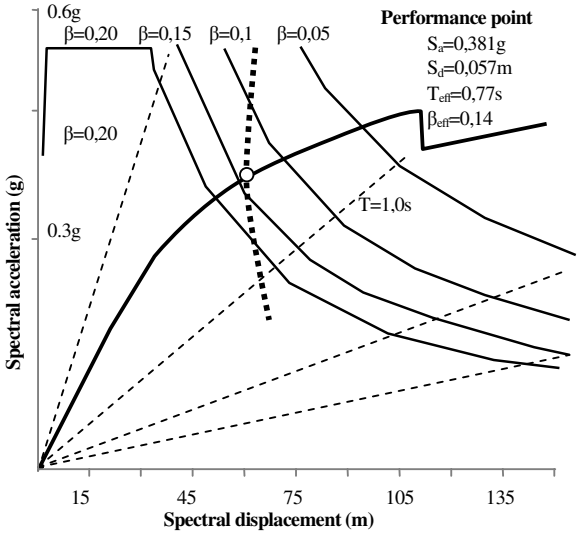


Figure 10: Capacity spectrum method: C_A=0,40, *y-y* direction

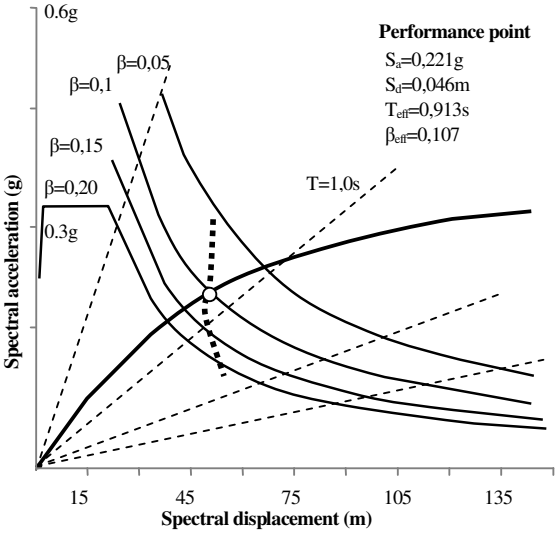


Figure 9: Capacity spectrum method: C_A=0,25, *x-x* direction

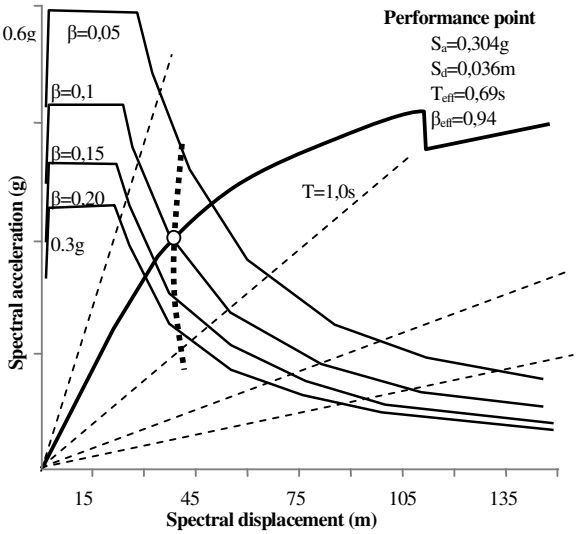


Figure 11: Capacity spectrum method: C_A=0,25, *y-y* direction

3.4 Linear time-history analysis

To determine the amplification of the lateral displacement caused by the structural torsional response, linear time-history analysis is performed. The low lateral displacement demand determined using capacity spectrum method suggested that time-history considering a linear response of the building represents a suitable method of analysis. Unscaled ground motions recorded in Van Merkez station on November 11, 2011, on N-S and E-W direction are simultaneously used in the analysis. E-W component was considered in the longitudinal direction of the building while N-S was considered in the transversal direction.

This is consistent with the real location of the building as the longitudinal façade is roughly aligned with E-W direction. The Van Merkez seismic station is located in the Van downtown at around 1.5 km from the building site.

The inelastic displacement response spectra for E-W component of the recorded ground motion showed that for any single degree of freedom system with relatively high lateral strength the inelastic displacements is roughly equal to the displacements of the elastic system with same vibration period. This is consistent with the Newmark rule for relatively flexible systems. This remark makes the results obtained using the linear time-history analysis more credible.

A damping ratio of 5% is considered in the analysis.

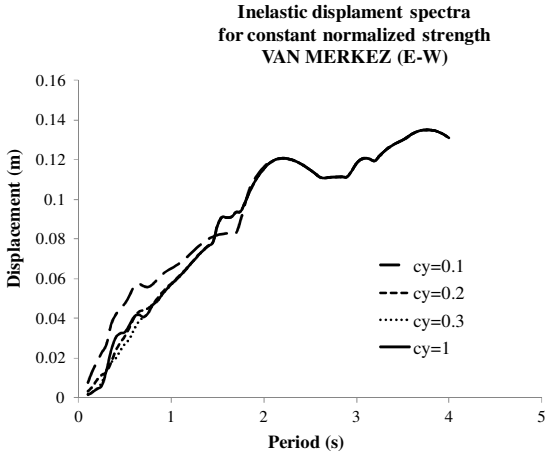


Figure 12: Inelastic design spectra

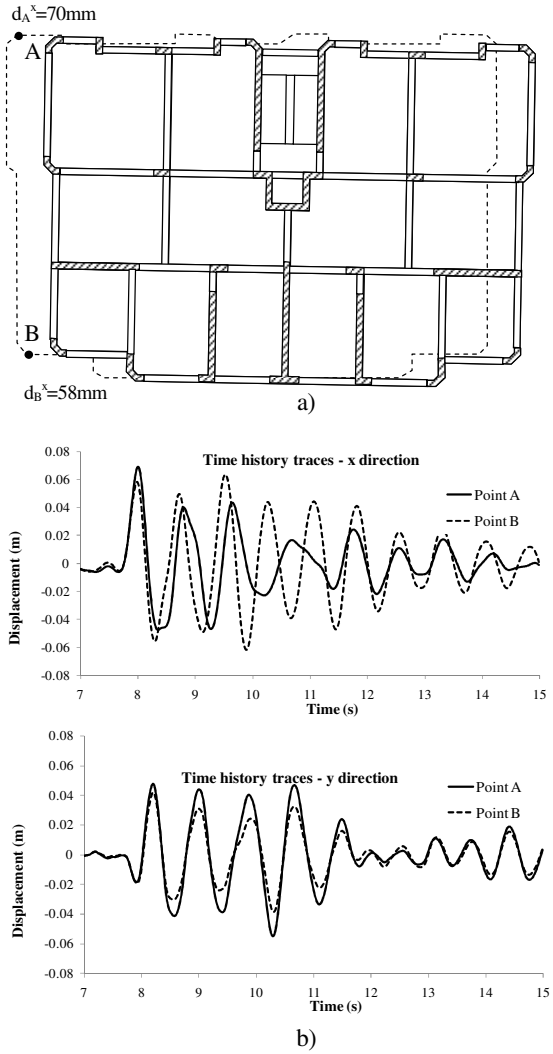


Figure 13: Amplification of the lateral displacement caused by torsion and time history traces at the roof level

The time history analysis revealed that the building might experience a relatively strong torsional response. Only the inherent torsion caused by the eccentricity between the center of mass and center of rigidity is considered in the analysis. Accidental torsion is not accounted for. Peak displacements in the longitudinal direction at roof level vary from 58mm to 70mm on the building perimeter (Figure 13, a). This represents a 10% amplification of the perimeter displacements in comparison with the displacement calculated in the center of mass. This amplification increases in the following cycles but the absolute value of the displacement decreases (Figure 13, b).

An additional time history analysis carried out using the unscaled El Centro ground motion record showed that at the time step when the peak lateral displacement at the roof level of 10,3cm was reached in the main façade in the rear façade the displacement was close to 0. That means that the maximum lateral displacement on the building perimeter is twice as large as the displacement in the center of mass. This analysis clearly shows the torsional sensitivity of the structure. Interaction with the nonstructural infilled masonry walls can further increase this torsional instability.

Time history analysis confirmed the low values of the lateral displacement obtained using the capacity spectrum method. For the Van Merkez station record, maximum base shear forces of 8000kN and 6900kN were determined in the longitudinal and transversal direction. This proves that the structural response was essential elastic behavior with limited incursions in the nonlinear range.

The lateral stiffness of the structure is difficult to be precisely assessed due to the scattered and uncertain quality of the concrete and interaction with the masonry infills. The dynamic characteristics of the building are related to the lateral stiffness and directly influence the displacement demand. In this respect, a sensitivity analysis was carried out. The variation of the peak displacement demand at the roof level is determined for different values of the vibration period of the building in the longitudinal direction. The concrete modulus of elasticity was varied from 5000Mpa to 22500Mpa to determine a variation of the vibration period from 1,43s to 0,68s. The calculated peak displacement increased with the vibration period (Figure 14) as revealed by the displacement spectrum as well. This shows that a change in the lateral stiffness of the structure is not likely to significantly modify the conclusions of this analysis. Such variation of the lateral stiffness might occur the masonry infills are accounted for or the assumed concrete modulus of elasticity is reduced.

A similar sensitivity study was performed to determine the variation of the peak displacement demand with the stiffness of the linear springs that vertically supports the foundation beams. The results presented in Figure 15 showed that the stiffness of the support springs have little influence on the calculated peak displacement demands at roof level.

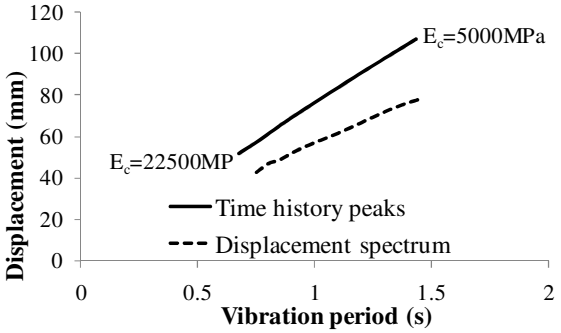


Figure 14: The variation of the peak displacement with the vibration period of the structure

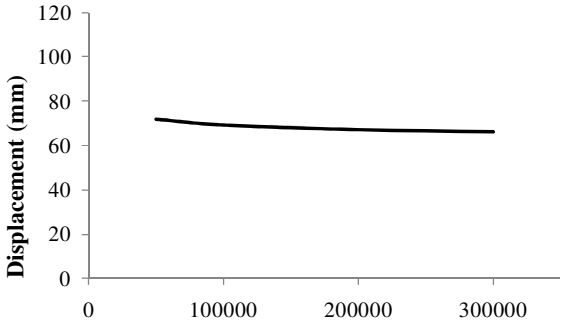


Figure 15: The variation of the peak displacement with the stiffness of the support springs

4. RETROFITTING SOLUTION

The structural analysis proved that the buildings have suitable lateral strength and deformation capacity. Retrofitting of the buildings for future use is feasible. Some retrofitting solutions are presented in this paragraph but other options can be considered as well.

Retrofitting work should address mainly the lateral stiffness of the building and its torsional sensitivity. The lateral stiffness should be increased especially in the longitudinal direction. The masonry panels severely damaged aligned with x-x direction (position B in Figure 2) shall be replaced at all stories with structural infills such as RC panels or steel braces. These panels shall be connected with the outer RC frame using post-installed anchor bolts.

Solid units masonry infills can be an option if adequate strength can be obtained but special attention should be paid to possible shear failure of the adjacent concrete members. The connection of the infills with the outer frame is weak so most of the shear force is supported through the bracing action of the masonry. Since several shear cracks were noticed in beams and columns due to the interaction with the existing weak masonry infills it is questionable if the use of stronger infills represents a reliable option.

If two effective shear resisting elements are created, parallel to the existing shear walls in x-x direction, the torsional sensitivity of the building is reduced.

Retrofitting work shall be preceded by repairing of the existing structural members. Resin injection of the wider cracks might be necessary. Such cracks were noticed especially in some beams at the first three stories.

To obtain a ductile response of the building it is necessary to prevent the local brittle failure modes. These include the shear failure of the captive columns on the basement perimeter. Their shear strength can be increased by steel jacketing. Another option is to replace some of the exterior masonry walls with RC panels properly connected to the existing frame.

Furthermore, in order to reduce the building mass it is recommended to replace the existing damaged partition walls with light and deformable partitions. Plasterboard panels represent a relatively cheap solution for interior partitions. Special care should be taken to prevent the occurrence of soft story type of failures. If a masonry infill is replaced in the ground floor it should be replaced in the upper stories as well.

The proposed retrofitting works can be done using construction materials locally available and require moderate skills of the workers. Engineer supervision is mandatory.

4. CONCLUSIONS

The IPRED post-earthquake investigation mission was dispatched to Van in June 2012, six month after two severe earthquakes hit the region. Ten engineered reinforced concrete and masonry buildings were investigated to observe the damage and to check the applicability of the rapid assessment techniques. Subsequently, detailed structural analyses were carried out for some of these buildings to evaluate their seismic vulnerability.

The results obtained for two of these buildings are reported in this paper. The structural system consists of reinforced concrete shear walls and moment resisting frames. Infilled masonry walls made out of hollow, multi-cell, clay units were used for exterior walls and interior partitions.

At the time of the inspection both buildings were evacuated and listed for demolition.

Nonstructural masonry walls were severely damaged at the first three stories of the building. Some of these walls partially collapsed. Most of the masonry infills had multiple diagonal cracks in both directions. Limited structural damage consisting mainly in shear cracks in beams, columns and shear walls was observed.

A very low concrete quality was observed, especially in one of the buildings. A low quality of the masonry works could be observed as well. During the construction the design prescriptions were not followed as some shear walls were erected in different positions. However this did not affected strongly the general structural layout.

The structural design solution meets most of the

requirements of current advanced seismic design codes. The main shortcoming refers to the torsional sensitivity of the structure and the details for local ductility.

The structural analysis showed that building have enough strength according to the provision of the Turkish earthquake standard at the time of construction. Lateral overstrength factors of around 2,0 were determined. After the earthquake the design acceleration was increased with 25% but the lateral strength of the buildings is still enough.

The lateral displacement demand are relatively low with peak lateral drifts of around 0,5%. These include the amplification caused by the torsional response observed using linear time history analysis.

The structural analysis proved that the buildings have suitable lateral strength and deformation capacity. Retrofitting of the buildings for future use is feasible.

The rapid assessment of these buildings failed to converge to this rather positive conclusion. Nevertheless, the results of the rapid assessment are justified by the low quality of concrete and the noncompliance with the blueprints of the design.

Quality of the construction works represents the main reason for the damage suffered by this building during the earthquakes. The structural works presented major deficiencies opposite to the relatively good quality of the finishing's. Special attention should be paid to the quality of the retrofitting works as it strongly influences their effectiveness.

The post-earthquakes investigation techniques applied worldwide proved to be not always successful because they did not incorporate parameters regarding the local construction techniques, materials, social and economic climate and the expectations of the residents at risk. The lack of methodologies adapted to the regional constraints might lead to overwhelming social problems and misguided decisions of the engineers. Further developing of credible, reliable custom made post-earthquake investigation techniques incorporating parameters regarding the local construction techniques, materials, social and economic climate and the expectations of the residents at risk such as to alleviate the social and economic impact and to improve the decision of engineers is desirable.

Acknowledgements:

The authors gratefully acknowledge the support of UNESCO – IPRED platform for financing the post-earthquake investigation mission. The support of local engineers/authorities and local people for the profound and heartfelt hospitality and kindness in very harsh times is also acknowledged.

References:

Earthquake engineering research institute (2012), Special earthquake report, The Mw 7.1 Erciş-Van, Turkey Earthquake of October 23, 2011

Ministry of Publicworks & Settlement, (2007). Turkish Earthquake Resistant Design Code - TERDC, Ankara, Turkey.

Applied Technology Council, (1996). Seismic Evaluation and Retrofit of Concrete Buildings, Report No. ATC-40, Redwood City, CA-USA.

European Committee for Standardization (2005). European Standard EN 1998-1:2005 Eurocode 8: Design of structures for earthquake resistance. Part 1: General rules, Seismic action and rules for buildings, Brussels, Belgium

Middle East Technical University, Earthquake Engineering Research Center (2011), The 23 October 2011 Mw 7.2 Van earthquake seismic and structural damage field observations (in Turkish), Report METU/EERC 2011-04

Middle East Technical University, Earthquake Engineering Research Center, 2011b. Processed Mainshock Accelerometric Recordings of the 23 October 2011 Van Earthquake, Report METU/EERC 2011-02"

10CUEE CONFERENCE PROCEEDINGS
10th International Conference on Urban Earthquake Engineering
March 1-2, 2013, Tokyo Institute of Technology, Tokyo, Japan

PERFORMANCE OF SANDWICH COLUMNS UNDER ECCENTRIC CYCLIC LOAD

H.-L. Hsu [1] and C.-Y. Zhan [2]

1) Professor, Dept. of Civil Engineering, National Central University, Taiwan
2) M.S., formerly Graduate Student, Dept. of Civil Engineering, National Central University, Taiwan
hhsu@ncu.edu.tw

Abstract: This paper investigated the performance of sandwich columns subject to eccentric cyclic load. A series of cyclic loading tests were conducted to evaluate the flexural-torsional response of the members. It was found from the tests that the member strength decreased when the magnitude of torsion was increased. It was further observed from the tests that the member strength was higher for sandwich column with larger sectional void ratio. However, the member's energy dissipation capacity was decreased when the member's sectional void ratio was increased. Therefore, it is recommended that composite member with adequate sectional void ratio be adopted should higher member performance be expected. Finally, a simplified expression for the strength interaction was proposed for engineering references.

1. INTRODUCTION

Composite members, such as concrete-filled tubes, possess high strength and significant ductility, thus are suitable structural forms for earthquake-resistant purposes (Kitada 1998). However, for structures subject to extreme loads, the dimensions and the weight of the structures might increase dramatically that reduces the efficiency of the design. In order to improve the design efficiency, a modified structural form, namely sandwich column, was proposed in this study. The sandwich columns were composed of double steel tubes and in-filled concrete between the double tubes. The advantages of adopting sandwich included higher strength and lower structural weight, compared with the concrete-filled tubes with similar dimensions.

For sandwich columns subject to earthquakes, combined loads coupled with torsion due to load eccentricity are usually observed. It has been indicated in several investigations (Han et al. 2009, Tao et al. 2004, Uenaka et al. 2008) that the presence of torsion will significantly affect the flexural strength of the member. Therefore, the structural performance of sandwich columns under combined loading coupled with torsion must be evaluated so that structural safety can be assured. This paper focused on the experimental investigation of sandwich column performance under combined bending and torsion. A series of combined loading tests were conducted to evaluate the member strength under combined loads. Energy dissipation of members was evaluated to correlate the relationship between member performance and sectional compositions.

2. EXPERIMENTAL PROGRAM

2.1 Specimen Details

Sixteen composite members, including 12 sandwich columns and 4 concrete-filled tubes, were fabricated for testing. The sandwich columns were composed of double steel tubes with concrete filled in-between. All specimens were composed of identical outer tubes and the sandwich members were fabricated with inner tubes of various dimensions. The sandwich columns were distinguished by the various inner tubes that used to form the hollow composite sections. Figure 1 shows the dimensions and sectional details of the specimens. The yield stress of the steel tubes was 300 MPa. Concrete strength was 48 MPa, determined from cylinder test after 28-day curing. The details of the specimens are listed in Table 1. The effective height of all specimens was 1650 mm. The diameter and thickness of the outer tube were 318.5 mm and 6 mm, respectively, that resulted in a diameter-to-thickness ratio (D_o / t_o) of 53. Three inner tubes with diameter-to-thickness ratios (D_i / t_i) equaling to 31, 36, and 42, were used for the sandwich columns. They were labeled series B, C, and D, respectively. The normalized member weights of sandwich columns with respect to that of the concrete-filled tube, ranged from 0.91to 0.79, as listed in Table 1.

2.2 Test Setup

The specimens were tested under constant axial load and cyclically eccentric load. Each specimen was rigidly fastened to a pair of stiffened platforms at the member bottom. A stiffened loading beam was attached to the top of the specimen so that the combined loads could be applied. Constant axial load was generated using a hydraulic jack acting on a stiffened reaction beam. The eccentric load was generated by a servo-controlled actuator through a series of increasing displacement commands. The servo-controlled actuator was attached to the loading beam with three eccentricities (e), 0 mm, 460 mm, and 920 mm, respectively, so that various combinations of bending and torsion could be

generated. Parameters considered in the tests included the sectional void ratio (η) and the eccentric ratio of loading (χ). Table 1 listed the specimen details and the loading arrangements. The test setup and the loading history were shown in Figures 2 and 3, respectively.

3. EXPERIMENTAL RESULTS

3.1 Failure Modes

The failure mode of members subject to bending was governed by the alternating local buckling and tensile fracturing of the outer tube, as shown in Figure 4. It should be noted that, for all specimens, the local buckling of outer tubes occurred at the inelastic stages. Once the tube reached the buckling state, alternating elongation of the steel tube was observed. Strength deterioration was observed when the drift of the member increased. For members subject to combined bending and torsion, failure was governed by the coupled action of the flexural stress and the torsion-induced stress. Inclined deformation on the steel tube was observed during the test. The angle of the inclined deformation increased when the ratio between torsion and bending increased. Figure 5 showed the flexural-torsional failures of sandwich columns subject to various load combinations.

3.2 Member Strength

Figures 6 and 7 showed the typical hysteretic loops of composite members subject to various combined loading. It could be observed from the figure that the strength of sandwich columns was higher than that of the concrete-filled tube. Strength enhancements for the sandwich columns over the corresponding concrete-filled tube ranged from 11% to 23%. Further enhancement in strength for the sandwich columns was achieved when the structural weight was considered. The further strength enhancement was 22% to 56%, respectively. It was found from the test result comparisons that the ultimate strength of the sandwich members increased when the members' sectional void ratios increased. However, higher strength deterioration was also exhibited in such members, thus indicating the necessity to optimize the sectional compositions should higher seismic performance in sandwich column design be desired.

3.3 Strength Interaction

In order to evaluate the member's performance under combined bending and torsion, the achievable strength of member was compared. It could be found from the tests that the member strength decreased when the magnitude of eccentricity increased. Figure 8 shows the relationship between the strength deterioration and the applied load eccentricity. It can be further observed from the normalized strength of sandwich columns with various sectional compositions that the relationship, as shown in Figure 9, could be approximated by a linear expression as shown below:

$$\frac{M}{M_{u0}} = 1 - 0.228\left(\frac{e}{h}\right) \tag{1}$$

This expression provides a simple yet effective estimation of the member strength under combined loads, and can be used for engineering design purpose.

3.4 Energy Dissipation

Figure 10 shows the relationship between the cumulative energy and the member strength. The energy dissipation was evaluated by the areas of the hysteretic loops. In order to define the member performance, the member's energy dissipation was compared at the state when member strength dropped to 95% of the member's ultimate strength. Figure 11 compared the energy dissipation of members with various sectional compositions. It could be found from the comparison that the strength of sandwich columns was larger than the corresponding concrete-filled tube. It was also observed from further comparison that the energy dissipation capacity of sandwich column decreased when the sectional void ratio of the member increased. Therefore, it is recommended that composite member with adequate sectional void ratio be adopted should higher member performance be expected.

4. CONCLUSIONS

This study investigated the performance of sandwich columns subject to various combinations of torsion and bending. A series of cyclic loading tests were conducted to evaluate the flexural-torsional response of the member. It is justified from the tests that the sandwich columns possessed significant strength and energy dissipation capacity. It was found from the tests that the member strength decreased when the magnitude of torsion was increased. It was further observed from the tests that the member strength was higher for sandwich column with larger sectional void ratio. However, the member's energy dissipation capacity was decreased when the member's sectional void ratio was increased. Therefore, it is recommended that composite member with adequate sectional void ratio be adopted should higher member performance be expected. Finally, a simplified expression for the strength interaction was proposed for engineering references.

References:

Han, L. H., Huang, H., and Zhao, X. L. (2009). "Analytical behavior of concrete-filled double skin steel tubular (CFDST) beam-columns under cyclic loading." *Thin-walled structures*, 47(6-7), 668-680.

Kitada, T. (1998). "Ultimate strength and ductility of state-of-art concrete-filled steel bridge piers in Japan." *Engineering structures*, 20(4-6), 347-354.

Tao, Z., Han, L. H., and Zhao, X. L. (2004). "Behaviour of

concrete-filled double skin (CHS inner and CHS outer) steel tubular stub columns and beam-columns." *Journal of constructional steel research*, 60(8), 1129-1158.

Uenaka, K., Kitoh, H., and Sonoda, K. (2008). "Concrete filled double skin tubular members subjected to bending." *Steel and composite structures*. 8(4), 297-312.

Table 1 Descriptions of Specimens (unit: mm).

Section	Label	Outer tube (mm)		Inner tube (mm)		η	χ
		D_o	t_o	D_i	t_i		
	M-A	318.5	6	0	0	0	0
	SE-A	318.5	6	0	0	0	0.25
	LE-A	318.5	6	0	0	0	0.50
	T-A	318.5	6	0	0	0	-
	M-B	318.5	6	139.8	4.5	0.17	0
	SE-B	318.5	6	139.8	4.5	0.17	0.25
	LE-B	318.5	6	139.8	4.5	0.17	0.50
	T-B	318.5	6	139.8	4.5	0.17	-
	M-C	318.5	6	165.2	4.5	0.24	0
	SE-C	318.5	6	165.2	4.5	0.24	0.25
	LE-C	318.5	6	165.2	4.5	0.24	0.50
	T-C	318.5	6	165.2	4.5	0.24	-
	M-D	318.5	6	190.7	4.5	0.33	0
	SE-D	318.5	6	190.7	4.5	0.33	0.25
	LE-D	318.5	6	190.7	4.5	0.33	0.50
	T-D	318.5	6	190.7	4.5	0.33	-

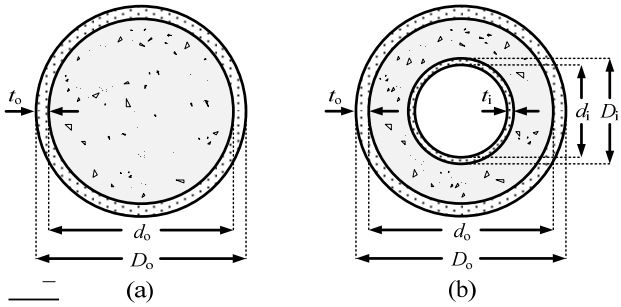


Figure 1 Details of Specimens: (a) Concrete-filled Tube; (b)Sandwich Columns

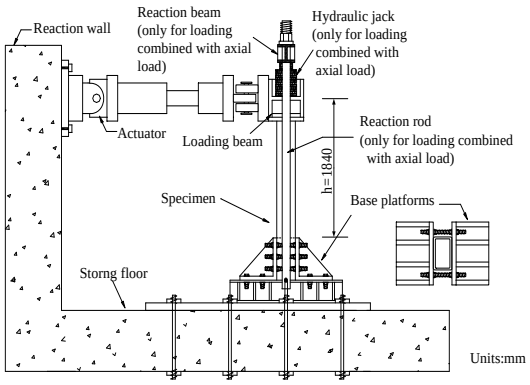


Figure 2 Test Setup

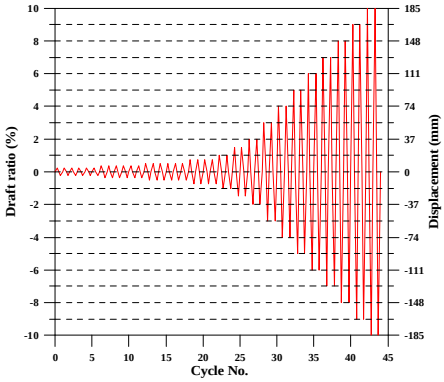
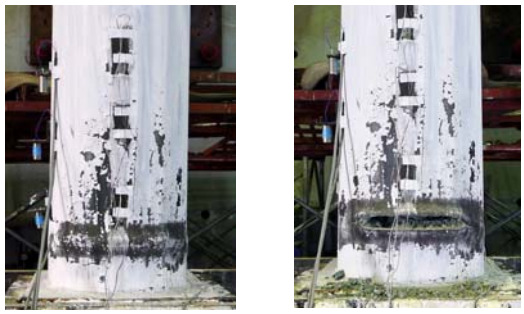


Figure 3 Loading History.



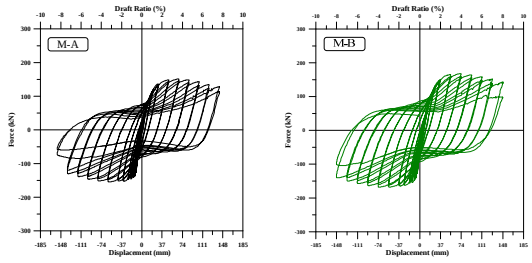
(a) (b)

Figure 4 Failure Modes of Sandwich Columns Subject to Bending: (a) Local Buckling; (b) Tensile Fracturing.



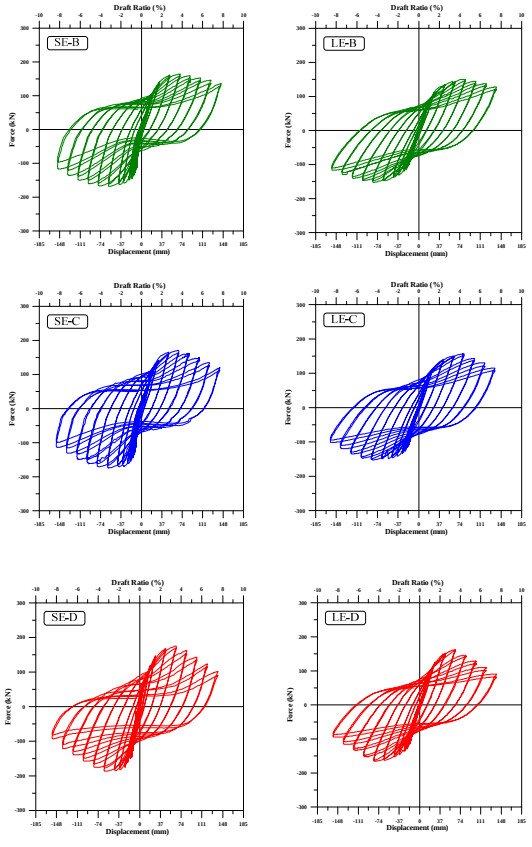
(a) (b)

Figure 5 Failure Modes of Sandwich Columns Subject to Combined Loading: (a) Smaller Eccentricity; (b) Larger Eccentricity.



(a) (b)

Figure 6 Typical Hysteretic Behavior of Composite Members: (a) Concrete-filled Tube; (b) Sandwich Column.



(a) (b)

Figure 7 Responses of Sandwich Columns Subject to Combined Loading: (a) Smaller Eccentricity; (b) Larger Eccentricity.

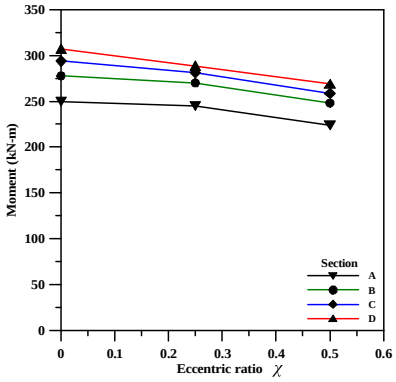


Figure 8 Relationship Between Strength Deterioration and Eccentric Ratio

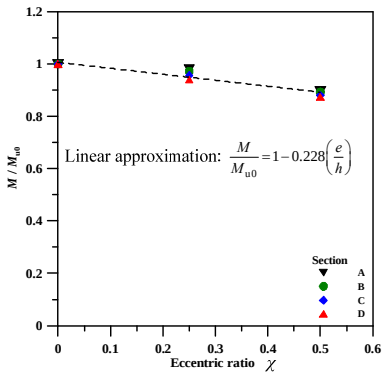
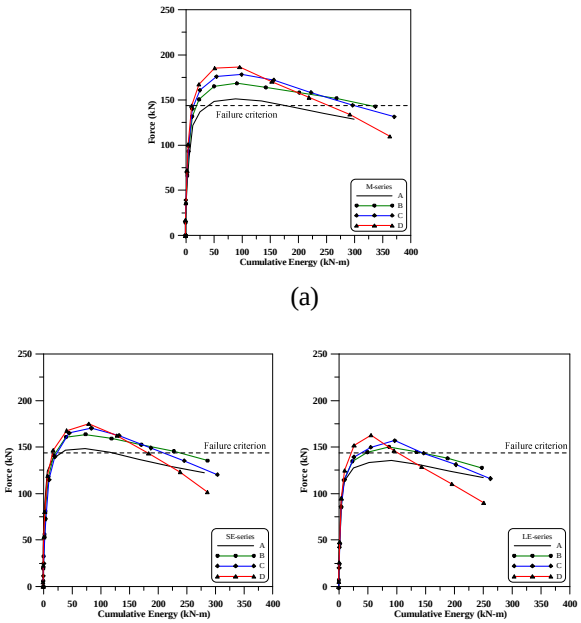


Figure 9 Strength Interaction for Sandwich Columns



(a)

(b) (c)

Figure 10 Relationships Between the Cumulative Energy and the Member Strength: (a) M-series; (b) SE-series; (c) LE-series.

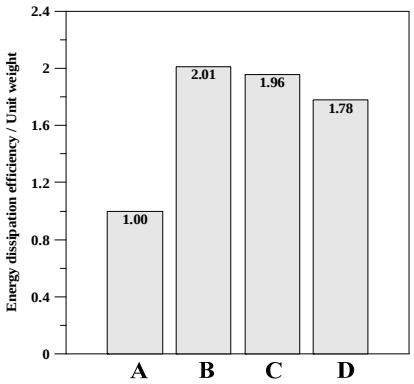


Figure 11 Comparison of Energy Dissipation Efficiency.

10CUEE CONFERENCE PROCEEDINGS
10th International Conference on Urban Earthquake Engineering
March 1-2, 2013, Tokyo Institute of Technology, Tokyo, Japan

URBAN SEISMIC RESPONSE SENSITIVITY OF ADJACENT BUILDINGS

H. B. Mason[1], W. S. White[2], and M. H. Scott[3]

1) Assistant Professor, School of Civil and Construction Engineering, Oregon State University, USA
2) Graduate Research Assistant, School of Civil and Construction Engineering, Oregon State University, USA
3) Associate Professor, School of Civil and Construction Engineering, Oregon State University, USA
ben.mason@oregonstate.edu, whitew@onid.orst.edu, michael.scott@oregonstate.edu

Abstract: In urban areas, structures interact with each other through the surrounding soil. This phenomenon is referred to as structure-soil-structure interaction (SSSI). Theoretical, numerical and experimental work has shown that SSSI effects can be important for certain types of structure pairs. To date, however, few parametric studies have been performed to elicit specific SSSI effects. In this paper, parametric studies involving soil-foundation-structure modeling properties are conducted using the direct differentiation method to understand which modeling properties, if any, control the interaction between structure pairs. Steel, moment-resisting frames are considered. The structural response is examined in terms of roof displacement. Preliminary results show that SSSI effects are minimal for the adjacent steel, moment-resisting frames investigated.

1. INTRODUCTION

Within a city block in densely populated urban areas there are different types of structures (i.e., different height, different building materials, etc.), which is exhibited in Figure 1. During an earthquake, the adjacent structures within the city block will interact with each other through the soil. This phenomenon, whereby adjacent structures interact through the soil, is generally referred to as structure-soil-structure interaction (SSSI). SSSI effects are not well understood by earthquake engineers. Accordingly, earthquake engineers must work to understand which scenarios lead to detrimental, beneficial and/or neutral SSSI effects. The purpose of this paper is to present some analyses that progress our understanding of SSSI effects.

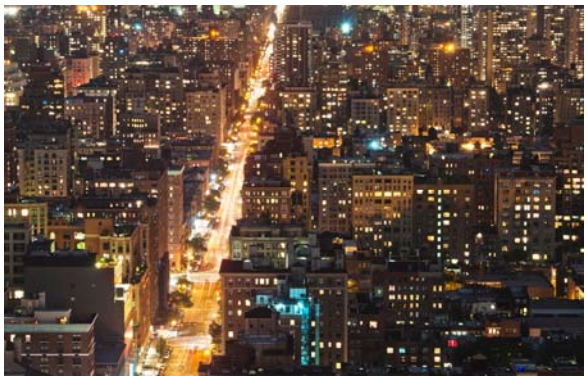


Figure 1. The Upper West Side of New York City, which shows the complex building arrangements (city blocks) of an urban area (photo courtesy of Ben Leshchinsky).

Steel, moment-resisting frame structures are considered herein. Parametric studies are undertaken to understand which modeling parameters control the interaction between adjacent pairs of frame structures. The parametric studies are performed using the direct differentiation method (DDM), which is a very efficient method for performing many parametric analyses. The results are presented for only one earthquake motion. In future efforts, a suite of 100 earthquake motions will be used for the parametric studies.

A short literature review is first presented, which frames the subsequent methodology and results sections. The focus of this paper is on the methodology section. For brevity, the results of only one pair of adjacent structures will be presented. Future publications by the authors, including the second author's M.S. thesis (released June 2013), will include more results and findings. It should be stated up front that pounding (i.e., adjacent buildings hitting one another during an earthquake) was not considered during any of the analyses presented in this paper.

2. LITERATURE REVIEW

2.1 Structure-soil-structure interaction

During an earthquake, seismic waves from a source eventually reach the ground surface. In urban areas, the waves interact with the foundations of buildings. In turn, the waves travel through the foundations and into the supported superstructure. The superstructure vibrates, and the vibrational energy propagates downwards into the foundation and eventually into the surrounding soil. These complex interactions encapsulate the phenomenon of

soil-foundation-structure interaction (SFSI) or soil-structure interaction (SSI). The impedance contrast between the various system subcomponent materials (i.e., soil to foundation to superstructure) as well as the vibrational characteristics of the system subcomponents, makes SFSI a complex phenomenon. However, SFSI effects have been investigated for many years, as reported by Kausel (2010), and earthquake engineers and scientists have developed a good understanding of these effects for individual buildings.

SSSI is a phenomenon related to SFSI. As noted, SSSI effects are not well understood; however, they have been shown to be significant for various soil-foundation-structure (SFS) systems (e.g., Luco and Contesse 1973; Lee and Wesley 1973; Wong and Trifunac 1975; Mason 2011). Menglin et al. (2011) contains a literature survey of SSSI research.

Incorporating SSSI effects into engineering design is a novel concept, and to the authors' knowledge, is currently not widely considered outside the nuclear industry (the results from nuclear industry research are usually either classified and/or proprietary). Theoretical studies from the 1970s exist (e.g., Luco and Contesse 1973; Lee and Wesley 1973; Wong and Trifunac 1975). These theoretical studies focus on solutions to governing partial differential equations. To make the solutions tractable, a number of simplifying, and often unrealistic assumptions are made. These researchers have generally focused on understanding the displacement response of two adjacent rigid shear walls using a plane strain assumption. Some numerical SSSI studies, which rely on using finite-element, finite-difference, or boundary-element methods, have been developed since the 1970s (e.g., Qian and Beskos 1995; Mulliken and Karabalis 1998; Padron et al. 2009). The first two references were only concerned with the response of two adjacent, shallowly-embedded footings, and the third reference was concerned with the response of advanced structures founded on pile foundations. More recently, researchers have performed centrifuge experiments to investigate SSSI effects (e.g., Mason 2011; Mason et al. 2013; Trombetta et al. 2013).

2.2 Direct differentiation method

Exhaustive parametric analyses are usually employed to answer outstanding earthquake engineering questions. This strategy is time consuming. The direct differentiation method (DDM) is a more efficient alternative. In the DDM, model parameters are identified and the gradient of time history response is computed with respect to each parameter. Considering a nonlinear dynamic analysis, the sensitivity of a nodal response is calculated by solving the following system equation, which is obtained by differentiation of the equation of motion with respect to a model parameter, θ:

$$\tilde{\mathbf{k}}_T \frac{\partial \mathbf{u}}{\partial \theta} = -\frac{\partial \mathbf{m}}{\partial \theta}\left[\ddot{\mathbf{u}} + \iota \ddot{u}_g(t)\right] - \frac{\partial \mathbf{c}}{\partial \theta}\dot{\mathbf{u}} - \left.\frac{\partial \mathbf{p}_r}{\partial \theta}\right|_{\mathbf{u},\dot{\mathbf{u}}} \quad (1)$$

where $\tilde{\mathbf{k}}_T$ is the effective stiffness matrix, $\mathbf{u}$ is the lateral nodal displacement vector, $\mathbf{m}$ is the mass matrix, $\ddot{\mathbf{u}}$ is the lateral nodal acceleration vector, ι is the influence vector, $\ddot{u}_g(t)$ is the acceleration-time series of the ground, $\mathbf{c}$ is the damping matrix, $\dot{\mathbf{u}}$ is the lateral nodal velocity vector, and $\mathbf{p}_r$ is the static resisting force vector (Franchin 2004; Kleiber et al. 1997).

The DDM is performed using OpenSees (the Open System for Earthquake Engineering Simulation; McKenna et al. 2000). OpenSees provides a nonlinear finite element framework in which SSSI problems can be modeled efficiently. In addition, OpenSees is fully equipped for computing nonlinear dynamic response sensitivity by the DDM (Scott and Haukaas 2008).

3. METHODOLOGY

3.1 Soil-foundation model

Figure 2 shows a schematic of a soil-foundation model. As shown in the figure, the flexibility of the soil-foundation interface is modeled by a series of translational springs. The stiffness values of these translational springs were determined using formulas and charts in Gazetas (1991), and the values were checked based on guidance in Wolf (1985). In addition, the "structure-soil-structure" link is also modeled as a translational spring in this initial work. Calibrating and validating this newly defined structure-soil-structure spring will be one of the contributions of this ongoing work. Simplified values of the spring coefficient are chosen, which are based on the work of Mulliken and Karabalis (1997) and Qian and Beskos (1995). The translational springs are modeled in OpenSees using "zero length elements," which allows the user to define a stiffness between two nodes. In future work, complex springs, which also include damping (as shown in Figure 2), will be used to model the soil-foundation interface (i.e., Winkler springs; Allotey and Naggar 2007).

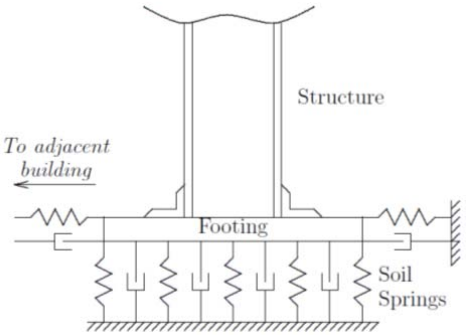


Figure 2. The soil-foundation model represented as a series of springs and dashpots.

Reasonable assumptions for the shear modulus and Poisson's ratio of the soil, as well as the geometry of the foundations, were made to estimate the stiffness of the soil springs. In this paper, the underlying soil was assumed to be a dense sand with shear modulus of about 35 MPa and

Poisson's ratio of about 0.33 (Budhu 2011). All moment-resisting frame structures were assumed to have square spread footings at the base of each column resting on the surface of the soil. Adjacent footings were assumed to be immediately adjacent. The 4-story structure shown in Figure 3 was assumed to have a footing width of 1.8 meters, and the 8-story structure shown in Figure 4 was assumed to have a footing width of 2.4 meters.

3.2 Moment-resisting frame model

The models used for moment-resisting frame structures were largely based on a previously developed proof of concept model; accordingly, the models presented in this paper are not based on an established structure. The models presented herein have wide-flange sections and are either four or eight stories tall. Shallower W12x or W14x shapes were used for the columns and deeper W21x or W24x sections were used for the beams. All steel sections were assumed to have a modulus of elasticity, *E*, of 207 GPa. The steel section models, in combination with the force-based beam-columns, allow for non-linear analysis of the structural model. Building models of 3.0-m story height and 3.7-m base width were constructed for each combination of 4-story and 8-story buildings. A typical floor mass of 89 kN was divided in half and placed at the nodes of each floor on either side of the structure. The depth of the columns, was user-defined and was found suitable to be varied in order to determine the sensitivity to building stiffness. Although the models presented herein were not based on established designs, the authors were careful to choose realistic geometric and material properties.

In the first iteration of the analyses, the structures were initially fixed at the far ends and allowed to translate laterally at the near end, where the structure-soil-structure spring was placed. Figure 3 is an example of this model for the 4-story by 4-story system. Using this model, it was found that buildings with the same number of floors and identical floor masses translated in harmony, resulting in zero sensitivity to the structure-soil-structure spring stiffness. For analysis of these systems, the Secondary structure was assigned a mass equal to three-quarters that of the Primary structure. The Primary and Secondary nomenclature is adopted for convenience.

After further consideration, the first iteration model was thought to be too restrictive, because a structure is not usually constrained against lateral motion at one of its foundations. The only restraint against lateral motion is applied by the rigidity of the foundation and the underlying soil. As a result, the lateral constraint was removed from the far end of the Secondary structure and soil springs were placed at each of the column bases to reflect the actual behavior of structures placed on a flexible soil medium. The far end of the Primary structure was left fixed with the knowledge that the displacements experienced by both structures would be relative to the far end of the Primary structure. The improved structure-soil interface model is depicted for the 8-story by 4-story system in Figure 4.

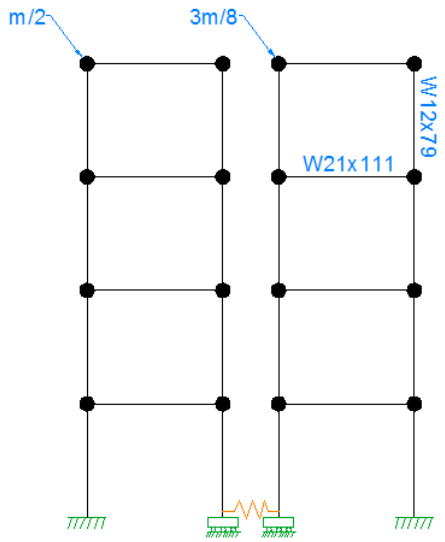


Figure 3. Four-by-Four system with lateral constraint on far end of Secondary structure. Each floor mass (m) is divided in half and placed at either end of the floor.

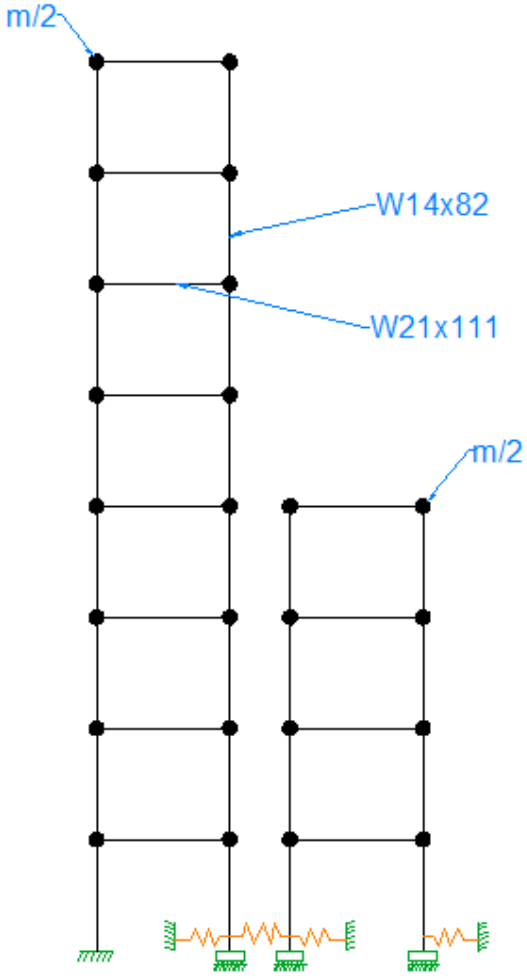


Figure 4. Eight-by-four system with column bases restrained by structure-soil springs.

4. RESULTS

To date, the structural models previously described have only been subjected to the north-south component of the earthquake motion recorded at the El Centro station during the 1940 Imperial Valley, California. Figure 5 shows the roof displacement response of both the Primary and Secondary structures throughout the duration of the motion. The configuration of the Primary and Secondary structures for this analysis is identical to that shown in Figure 4, with an 8-story building adjacent to a 4-story building. The floor mass used was 89 kN.

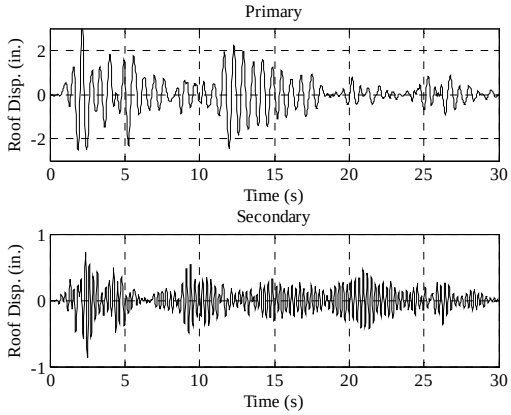


Figure 5. Roof displacement response time series of both Primary and Secondary structures subject to the 1940 El Centro earthquake motion.

In addition to the mean displacement response, sensitivities to structural stiffness, structure-soil-structure spring, and floor mass are calculated and compared to the mean values. Figure 6 shows the mean roof displacement response, *u*, and the responses when the story stiffness of the Primary structure is increased or decreased by 10 percent, from t = 2 s to t = 6 s. Likewise, Figure 7 shows the roof displacement responses when the mass of the 7th floor of the Primary structure is varied by 10 percent.

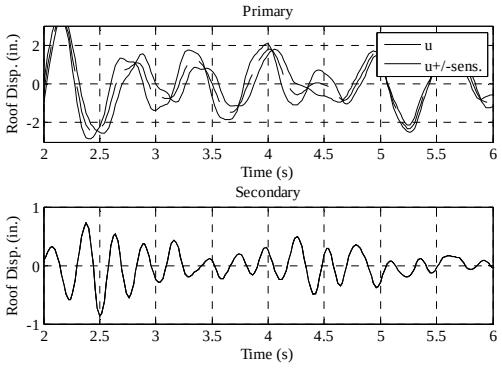


Figure 6. Roof displacement response with sensitivity to the story stiffness of the Primary structure.

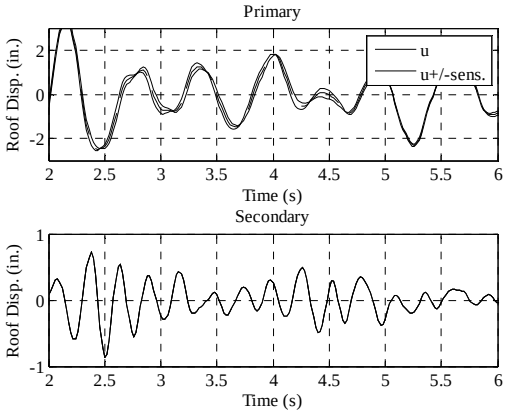


Figure 7. Roof displacement response with sensitivity to the 7th floor mass of the Primary structure.

Based on the presented analyses, the sensitivity of the roof displacement response of the Secondary building to changes in the Primary structural properties and soil parameters appears to be minimal. As expected, the response of the Primary building was sensitive to changes in its own story stiffness and floor mass. However, the response of the Secondary structure, even with 10-percent changes in design parameter values, remained almost identical. This result implies that there is negligible interaction between the two building models through the structure-soil-structure spring. Even as the response of the Primary structure changes with changes in the design parameters, the response of the Secondary structure remains constant.

5. CONCLUSIONS

The DDM has been found to be an efficient method for analyzing the response sensitivity related to SSSI effects. This method allows 100s of analyses to be performed within the OpenSees framework. With tools such as batch processing, and parallel computing, many analyses can be performed efficiently.

For the specific case of an 8-story by 4-story building system subject to the 1940 Imperial Valley earthquake motion, the response of the Secondary structure is not particularly sensitive to changes in the model parameters of the Primary structure. The roof displacement response of the Secondary structure was practically unchanged with 10 percent changes in both the story stiffness and floor mass of the Primary structure. These results suggest that structure-soil-structure interaction is not significant in this particular case and may not be significant in other steel frame buildings. It should be noted that these results are contingent upon the stiffness of the structure-soil-structure spring; however, preliminary analyses shows that SSSI effects are minimal for this case when the stiffness of the structure-soil-structure spring varies between reasonable values.

The lack of structure-soil-structure interaction seen in the particular case presented in this paper is likely

attributable to one of three causes: (1) the employed earthquake motion did not elicit significant response in either structure; (2) the model of simple, horizontal springs is not sufficient to model SSSI effects; and (3) steel, moment-resisting frame structures are sufficiently flexible to prevent SSSI effects that might occur in more rigid structures (Luco & Contesse 1973).

The methodology and results shown in this paper represent a very initial effort of ongoing work. Future contributions of this work will include: (1) more guidance for modeling the structure-soil-structure spring; (2) more advanced spring models (i.e., Winkler springs) to account for the damping and flexibility of the interfaces; (3) inclusion of more DDM results to investigate the design optimization and reliability of adjacent structures in urban areas; (4) an examination of more earthquake motions; and (5) a finite element model of the soil with a proper constitutive model. In closing, it must be noted that finding that SSSI effects are potentially unimportant for a given scenario is still an important finding. Future efforts will try to find scenarios where SSSI effects are detrimental; however, finding scenarios where SSSI effects are beneficial or neutral is also valuable for earthquake engineers.

Acknowledgements:

The authors acknowledge support from the Oregon State University College of Engineering and travel support from the Pacific Earthquake Engineering Research (PEER) Center.

References:

Allotey, N. and Naggar, M. H. E. (2007). An investigation into the Winkler modeling of the cyclic response of rigid footings, *Soil Dynamics and Earthquake Engineering* 28, 44-57.

Budhu, M. (2011) *Soil Mechanics and Foundations*, 3rd edition, John Wiley & Sons.

Franchin, P. (2004). Reliability of uncertain inelastic structures under earthquake excitation, *Journal of Engineering Mechanics* 130(2), 180-191.

Gazetas, G. (1991). Foundation vibrations, In *Foundation Engineering Handbook*, 2nd edition, Fang, H. Y., editor, Van Nostrand Reinhold. 553-593.

Kausel, E. (2010). Early history of soil-structure interaction, *Soil Dynamics and Earthquake Engineering* 30(9), 822-832.

Kleiber, M., Antunez, H., Hien, T. D., and Kowalczyk, P. (1997). *Parameter Sensitivity in Nonlinear Mechanics*. John Wiley & Sons.

Lee, T. H., and Wesley, D. A. (1973). Soil-structure interaction of nuclear reactor structures considering through-soil coupling between adjacent structures, *Nuclear Engineering and Design* 24(3), 374-387.

Luco, J. E., and Contesse, L. (1973). Dynamic structure-soil-structure interaction, *Bulletin of the Seismological Society of America* 63(4), 1289-1303.

Mason, H. B. (2011). *Seismic Performance Assessment in Dense Urban Environments*. Ph.D. thesis, University of California, Berkeley, CA.

Mason, H. B., Trombetta, N. W., Bray, J. D., Chen, Z., Hutchinson, T. C., and Kutter, B. L. (2013). Soil-foundation-structure interaction of shallowly embedded footings supporting inelastic frame structures, *Soil Dynamics and Earthquake Engineering*. Accepted for publication.

McKenna, F., Fenves, G. L., and Scott, M. H. (2000). *Open System for Earthquake Engineering Simulation*. University of California, Berkeley, CA. http://opensees.berkeley.edu.

Menglin, L. Huaifeng, C., Xi, C., and Yongmei, Z. (2011). Structure-soil-structure interaction: Literature review, *Soil Dynamics and Earthquake Engineering* 31, 1724-1731.

Mulliken, J. S., and Karabalis, D. L. (1998). Discrete model for dynamic through-the-soil coupling of 3-D foundations and structures, *Earthquake Engineering and Structural Dynamics* 27(7), 687-710.

Padron, L. A., Aznarez, J. J., and Maeso, O. (2009). Dynamic structure-soil-structure interaction between nearby piled buildings under seismic excitation by BEM-FEM model, *Soil Dynamics and Earthquake Engineering* 29(6), 1084-1096.

Qian, J., and Beskos, D. E. (1995). Dynamic interaction between 3-D rigid surface foundations and comparison with the ATC-3 provisions, *Earthquake Engineering and Structural Dynamics* 24(3), 419-437.

Scott, M. H., and Haukaas, T. (2008). Software framework for parameter updating and finite-element response sensitivity analysis, *Journal of Computing in Civil Engineering* 22(5), 281-291.

Stewart, J. P., Fenves, G. L., and Seed, R. B. (1999). Seismic soil-structure interaction in buildings. I: Analytical methods, *Journal of Geotechnical and Geoenvironmental Engineering* 125(1), 26-37.

Trombetta, N. W., Mason, H. B., Chen, Z., Hutchinson, T. C., Bray, J. D., and Kutter, B. L. (2013). Nonlinear dynamic foundation and frame structure response observed in geotechnical centrifuge experiments, *Soil Dynamics and Earthquake Engineering*. Accepted for publication.

Wolf, J. P. (1985). *Dynamic soil-structure interaction*. Prentice Hall.

Wong, H. L. and Trifunac, M. D. (1975). Two-dimensional, antiplane, building-soil-building interaction for two or more buildings and for incident plane SH waves, *Bulletin of the Seismological Society of America* 65(6), 1863-1885.

10CUEE CONFERENCE PROCEEDINGS
10th International Conference on Urban Earthquake Engineering
March 1-2, 2013, Tokyo Institute of Technology, Tokyo, Japan

DAMAGE ASSESSMENT OF BUILDINGS. CASE STUDY OF AN EDUCATIONAL BUILDING

Claudiu-Sorin Dragomir[1), 2)]

1) Senior Researcher, Laboratory of Seismic Risk Assessment and Action in Constructions, National Institute for Building, Development and Urban, NIRD URBAN-INCERC, Bucharest, Romania
2) Lecturer, Department of Environmental, Faculty of Land Reclamation and Environmental Engineering, U.S.A.M.V. Bucharest, Romania
dragomircs@incerc2004.ro, claudiu.dragomir@fifim.ro

Abstract: Due to the time evolution of the design provisions, in Romania there are buildings that were designed decades ago, after the less stringent provisions. Thus, when the earthquake is produced there are many cases where the buildings are badly damaged. Some buildings were rehabilitated, but most of them maintained the original appearance. In addition to the historical or heritage value they reflect the conception and economic power of their time. According to the modern approach of the post-seismic investigation the damage building assessment should be clearly foreseen and properly planned in order to obtain dynamic parameters for the analysis. In this context, determining the fundamental period of building oscillation and comparison with the original data is a first comprehensive method for assessing the variation of rigidity building due to the earthquake. The paper is emphasis the need for extensive seismic instrumentation of national interest buildings so that information on the behavior of structural categories is available in a limited time from the occurrence of an earthquake. All the aforementioned ideas are illustrated through a study case of an educational building.

1. INTRODUCTION

In Romania, Vrancea earthquakes occur every few decades, and approximately 60% of territory is affected by them. There are buildings that were designed decades ago, after the less stringent provisions. Thus, when the earthquake occurs there are many cases where buildings are badly damaged.

The university centres shelter large concentrations of young intellectuals which in the near future are assumed to take over most the society duties. Besides education, in universities are carried out scientific research activities for the modern technology of society. For that reason, seismic protective measures of the university buildings according to the new requirements are necessary as well as drawing up some assistance strategies and interventions for emergency situations similar with those already existing in the technologically advanced countries. The priority for the university centres is to respect the clause 1.1.2 of the Romanian Code P100-1:2006 which provides avoiding of human loss, maintenance of the activities and limitation of damages.

Currently, there are no specific programs for university building inspection to verify the compliance with new requirements of safety standards and no organized programs in emergency areas such as in countries like U.S.A. and Japan. For this reason the paper tries to present a method for assessing the vulnerability of university buildings through a case study for the building that houses the Faculty of Land Reclamation and Environmental Engineering in Bucharest.

2. MODERN CONCEPT FOR POST-SEISMIC ASSESMENT OF BUILDINGS

The experimental model presented in the case study was conducted in 1990-1991 in the seismic Hall of INCERC Bucharest, in view of full-scale tests.

The construction is based on a modular square grid 3.90 x 3.90 m and a floor height of 2.75 m, consisting of two openings and two bays, which comprises a single structural wall.

At the intersection of axes, constant cross-section poles are placed, 500 x 500 mm, covering the entire height of the building. Pillars are prefabricated for two-story height, with a non-concrete portion in the middle of 350 mm, which includes reinforcement of strips of plate. Full-scale tests were conducted as follows (Vlaicu, 1999):

- The first step of testing the experimental system was to load the tare weight and more concrete weights.
- In 1995 took place the first test with lateral loading forces, using presses, while in 1996 post-elastic horizontal loads were applied, in 8 cycles (incremental loads).
- In 1997 the experimental model testing was resumed, aiming at the evaluation of the behavior to breaking stress.

To simulate the behavior of a future earthquake damaged building, the following steps were followed:

- Determination of the own vibration periods by

microseism measurements and their processing;

- Modeling a spatial structure identical to that found in seismic Hall; noting that the model was created with five levels unlike the existing one that had four levels (being tested at the top- -floor - terrace to simulate the loading of an extra floor).

- The time-history analysis to determine the structure response spectrum using accelerograms recorded in the earthquakes in from the '77, '86 and '90.

Following the above steps, microseism measurements were made on the experimental model, following two sensor placement schemes presented in Fig. 2. Measurements were made both by applying shocks in the center of the 2nd floor and the microseism movement from the site.

Microseism measurement results obtained in the case of the full-scale experimental model, with GF+3 floors are presented in Table 1. These values of own periods of vibration are determined from the Fourier spectrums. Processing the records made at this stage of cracking of the model are presented in Fig. 4 (Dragomir et al. 2012).



Figure 1 Full scale experimental model



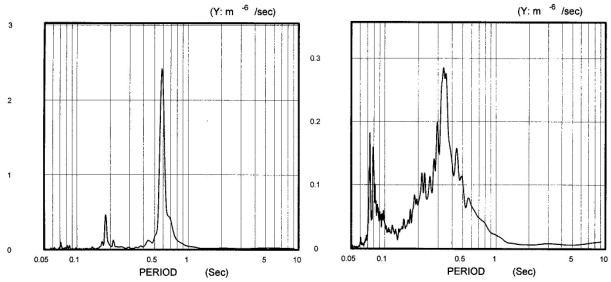
Figure 2 GEODAS 12-USB, 12-channel seismic station, Buttan Service, Japonia

Table 1 Dynamic characteristics of the experimental model in the present state of cracking

Equipment / Program used	$T_{dir.\,x}$ (s)	$T_{dir.\,y}$ (s)
GEODAS 12-USB, Buttan Service, Japonia /Microwave tremor observation	0.60	0.32



Figure 3 Sensor placement on experimental model at natural scale

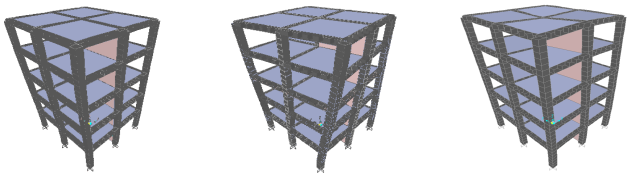


a) x direction b) y direction

Figure 4 The response spectrums obtained by processing the microseism records

For structural calculation, the following material characteristics were used:

- Concrete features: elastic modulus E=22.500 MPa, the weight per volume unit ρ_W=23 kN/m^3.
- Steel features: elasticity modulus E=199.900 MPa, the weight per volume unit ρ_W=77 kN/m^3.



T_1=0,64s z-x plane

T_2=0,49s x-y plane

T_3=0,34s y-z plane

Figure 5 Own modes of vibration. System dynamic characteristics

Note: reinforced concrete diaphragm is arranged by the structural model *y* direction.

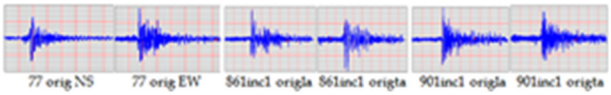


Figure 6 Accelerograms used in the time-history analysis

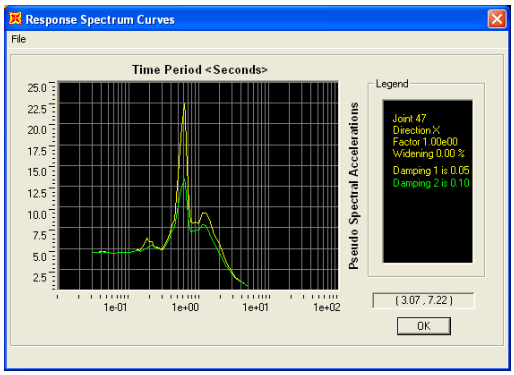


Figure 7 The response spectrum obtained at the top level of the structure for the accelerogram recorded on the N-S direction in the '77 earthquake, applied to *x* direction

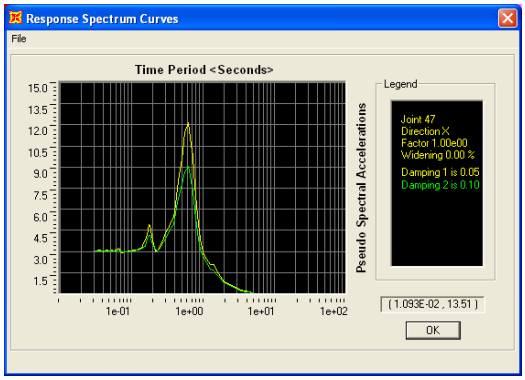


Figure 8 The response spectrum obtained at the top level of the structure for the accelerogram recorded on the longitudinal direction in the '86 earthquake, applied to *x* direction

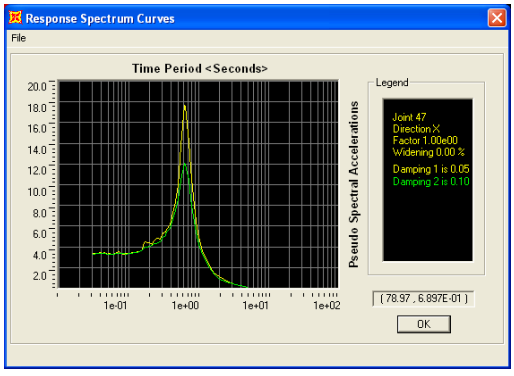


Figure 9 The response spectrum obtained at the top level of the structure for the accelerogram recorded on the longitudinal direction in the '90 earthquake, applied to *x* direction

The linear modal time-history analysis provides the results as graphs and comprises, for the structural system studied, the movement and acceleration variations versus time, in a node at the top level and at the level 1.

Regarding the movements, the results are shown in Fig. 10 and Fig. 11.

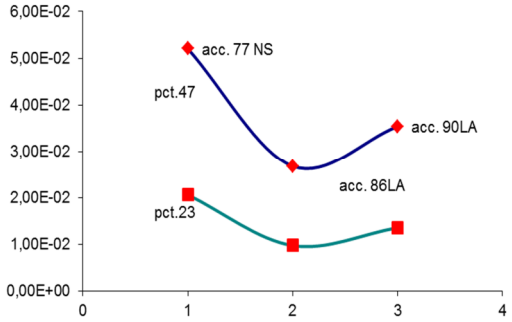


Figure 10 Maximum values of movements in the x direction, corresponding to nodes 47 and 23 at different earthquakes ('77, '86 and '90)

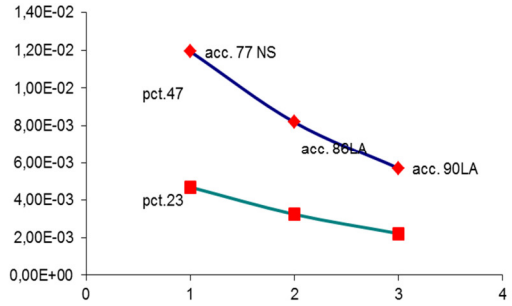


Figure 11 Maximum values of movements in the y direction, corresponding to nodes 47 and 23 at different earthquakes ('77, '86 and '90)

In terms of accelerations, the results are shown in Fig. 12 and Fig. 13.

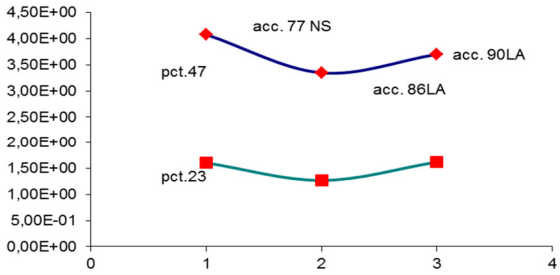


Figure 12 Maximum values of accelerations in the *y* direction, corresponding to nodes 47 and 23 at different earthquakes ('77, '86 and '90)

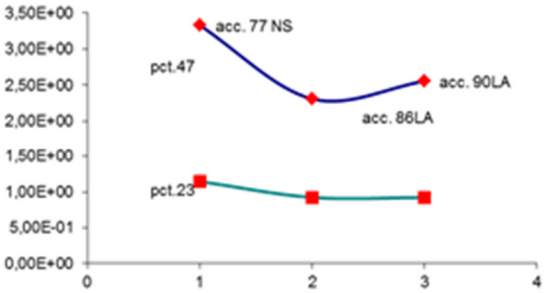


Figure 13 Maximum values of accelerations in the *x* direction, corresponding to nodes 47 and 23 at different earthquakes ('77, '86 and '90)

3. SOLUTIONS TO STRENGTHEN THE MASONRY PANELS IN RC FRAMES STRUCTURES

To highlight the efficiency of carbon fiber reinforcement, the full-scale attempts made in the INCERC Bucharest laboratories are presented. The masonry panels presented are made of ceramic blocks with vertical hollows.

3.1 Strengthening with carbon fiber strips

The basic concept of the experiments was to use a standardized test - the diagonal test – on the same specimens of masonry in two situations: in the initial state, masonry made according to usual procedures and after applying a reinforcement with carbon fiber plates attached to specific adhesives (Dragomir, 2009).

The results indicated that the tested systems are effective, with the clarifications that it is also advisable to apply the strips on the diagonal of the panels in two directions close to the main efforts, so that the strips work on stretching. In this case, it would be reasonable to recalculate the size and arrangement of the strips used, for cost optimization.



Figure 14 Making specimens, by applying the carbon fiber plates

Since parametric testing was done in one direction, in static stress, monotone increasing, while the real seismic application is dynamic in nature, it is necessary to extend the research, to highlight the differences in behavior. It is advisable to symmetrically apply the strips on both sides of the specimens, as consolidation on only one side can cause failure by bending in a direction normal to the sample plane, at forces below the original test. The application process can be done on masonry with superior resistance characteristics, thus ensuring the entry into work and working together between the two materials during the stress application, avoiding crushing masonry in the nodes areas. From this point of view, because in practical applications two diagonal strips are applied, at higher levels of alternating stress, it is possible that masonry work stop of the corners of the frame may occur successively, where the grip is redundant, the rest of the strip remaining as active zone, on the long direction, but with some contribution of the strips from the other direction. These considerations should be taken into account in determining the actual size of the strips area of contact with the masonry, in relation to the computing area. If anchoring the strips to concrete slabs on the contour, some of these effects may be compensated, the strips may work efficiently throughout the whole stress application. Additional tests are needed to clarify the concrete behavior particularities and the strips adherence to concrete in the node zone.

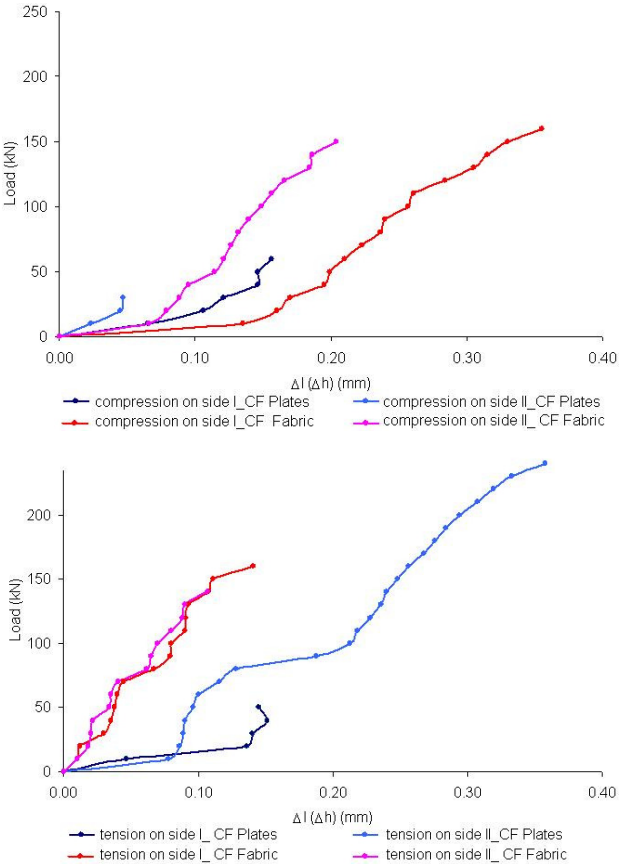


Figure 15 Relationship between effort - relative compression / relative elongation corresponding for two of the samples tested

3.2 Strengthening masonry panels with carbon fiber fabric

The aim of the trials carried out at INCERC was to test for bending four models of masonry made of ceramic blocks, with the same plan dimensions 1.50 x 1.00 m, but with different thickness: 2 models with 30 cm thickness (M30) and 2 models with 38 cm thickness, M38 (Dragomir et al. 2009).

Attempts have been made at various stages, as follows:

- In the first stage two models of simple masonry (different thickness) were tested;

- In the second stage the other two models were tested, but this time they were consolidated on the side with fabric from reinforced carbon fiber. The test results of the two

stages will be presented in comparison to highlight the effectiveness of consolidation.

The two models tested in the second stage were consolidated on the side with carbon fiber fabric. To apply this fabric, a bicomponent Epoxy resin was used.

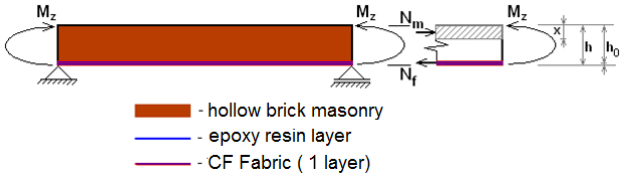


Figure 16 Analysis scheme of rectangular sections under bending stress

To emphasize the need to strengthen with a larger or smaller number of carbon fiber fabric layers, the model with 30 cm thickness was coated with two layers of fabric overlapping on a width of 20 cm, while the model with 38 cm thickness was coated on the side with only one layer. In Fig. 16, a calculus scheme to determine the required reinforcement area at stretched fiber.

The balance equations obtained on the basis of scheme emphasized in Fig. 16 are:

$$M_z = N_m h_m \quad (1)$$

$$N_f = N_m \quad (2)$$

where

$$N_f = A_f f_f; \quad N_m = bxf_m \quad (3)$$

N_f is tensile stress into carbon fiber fabric layer;
N_m is compression stress into hollow brick masonry.

From this equations was resulted the height of the compressed zone (neutral axis position), as follow

$$x = \frac{A_f f_f}{bf_m} \quad (4)$$

From Eq. 1 was obtained a second degree equation,. The accepted solution for this equation is:

$$A_f = \frac{bh_0 f_m}{f_f}\left(1 - \sqrt{1 - \frac{2M_z}{bh_0^2 f_m}}\right) \quad (5)$$

where A_f = area of the carbon fiber fabric.

In Fig. 18 and Fig. 19, the force-arrow diagrams are shown in comparison, with the two versions of the M30 model: unconsolidated and consolidated.



Figure 17 The M30 model after failure

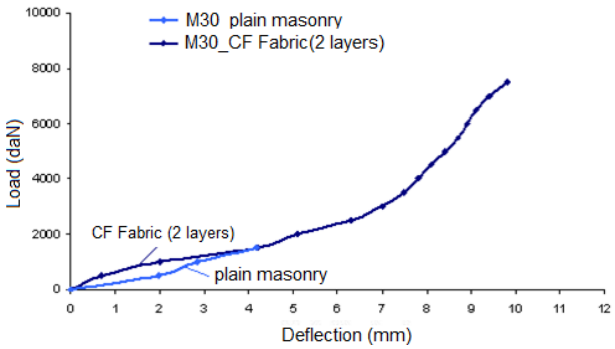


Figure 18 Force-arrow diagram for the M30 masonry model (30 cm thick)

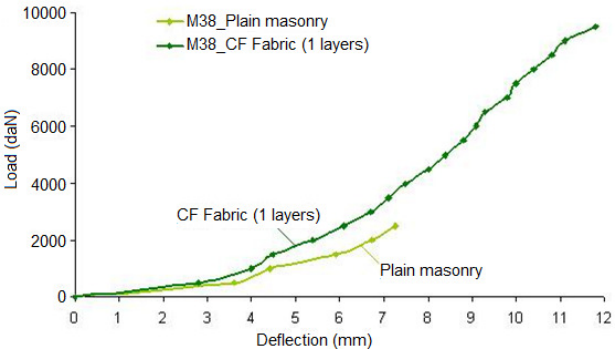


Figure 19 Force-arrow diagram for the M38 masonry model (38 cm thick)

Comments:

- Results demonstrate the efficiency obtained for the application of layers of carbon fiber fabric on the model stretched fiber.
- After the failures of the two modules, was found that the masonry failed, as expected, because it exceeded the compressive resistance on the compressed side.
- Under the conditions of these tests, the contribution to the rigidity conferred by the blocks size was greater than the contribution given by applying a double number of layers of carbon fiber fabric;
- Because the failure point doesn't appear in the zone of

the stretched fiber, where for fabric is applied, but in the compressed side with simple masonry, a single layer of fabric is enough, because the advantage of an increased number of layers may not be exploited.

4. CASE STUDY OF AN EDUCATIONAL BUILDING

The method for assessing the vulnerability of university buildings is illustrated through the case study of the Faculty of Land Reclamation and Environmental Engineering (F.L.R.E.E.) in Bucharest.

The F.L.R.E.E. building has resistance structure of reinforced concrete frames designed in the '70s, according to the Code P13-70 (see Fig. 20).



Figure 20 The F.L.R.E.E. building from Bucharest

Although the height is low (H = 20.33 m) and the shape in plane is regular, the earthquake of 4 March 1977 have caused damage, especially to non-structural elements due to insufficient stiffness for the protection of subdivision elements.

In Figure 21 is shown the time evolution of part A's own periods of Faculty of Land Reclamation and Environmental Engineering in Bucharest, with records made available by INCERC Bucharest between 1986-1998.

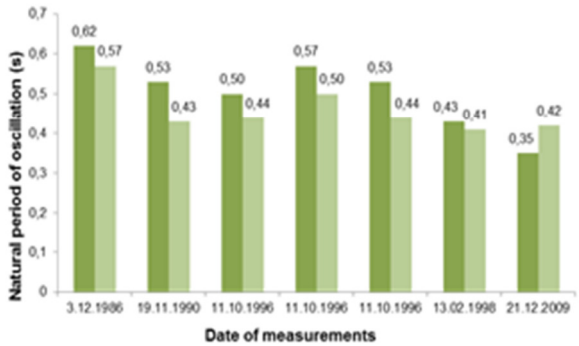


Figure 21 Time evolution of own periods of part A of F.L.R.E.E.

By determining the dynamic characteristics of part A of the Faculty of Land Reclamation and Environmental Engineering, from December 2009, and then in 2012, it was found that the period of oscillation of the building was reduced by approximately 19% compared to values determined in 1998.

The recordings made after the entry into force of the new design code P100-1: 2006 are presented. Recordings were made on the 4th floor of part A of building F.L.R.E.E.

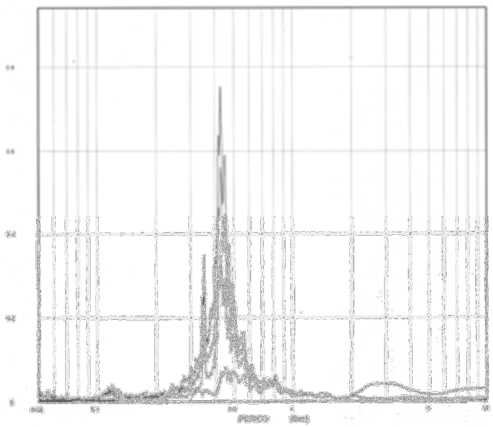


Figure 22 Fourier Spectra obtained from processing of recorded data

It is estimated that this reduction is due to the collaboration processes of the various parts of old and the new structure and to earthquake of magnitude Mw = 6.0, which took place on October 27, 2004, in Vrancea seismic zone, which may contributed to structural transfer efforts from the four concrete caissons to the structure.

Following the changes made in the composition of the building, either to the structural or non-structural elements, through the interventions to strengthen the building from damage caused by earthquake or other causes, the building suffered significant changes both in terms of both mass and own periods.

All those three types of calculation for that comparative study was performed (initial structure before the 1977 earthquake; structure after consolidation in 1986; structure after consolidation in 1996) are shown in Figure 23.

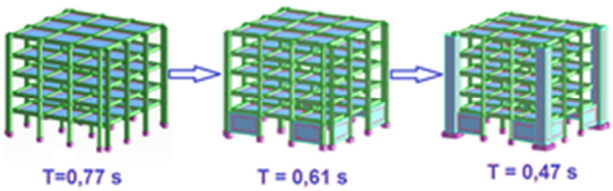


Figure 23 Oscillation periods of FLREE determined by dynamic analysis

From the image shown in Fig. 23, it can be seen that the two consolidations have brought an decreases in the period of fundamental mode of oscillation (39% compared to initial version). This demonstrates the effectiveness of interventions to strengthen applied throughout the period of

life of the structure, but they have become inadequate because of changes occurring over time with the introduction of new design codes.

Basically, the building interventions to strengthen were designed to increase the rigidity of structure that is obtained by increasing the size of structural elements and/or adding other structural elements.

However, while reducing their periods of oscillation for the T…Tc of the spectrum (Tc is in this case under the Code P100-1/2006 equal with 1.6s) not reduces the design forces due to the covering adoption of a constant value (landing) for spectral acceleration in this area, removal of the resonance conditions T = Tc is a goal of always watching.

Based on the results of the presented structural calculations, can be made the following comments:

- In any of the situations, permissible value of the relative displacement at the service limit state has not been exceeded and the allowable amount of relative displacement at ultimate limit state has been exceeded in a single statement in the version I of calculation; this would have contributed to serious damage to the building in the earthquake of 1977 (according to the P100-1/2006, the value of $SLU_{r\,ad}$ = 0.025 h and $SLS_{r\,ad}$, = 0.008h).
- After the first consolidation, the relative displacement was decreased by 38% and after the second by 40% compared to the previous consolidation, representing 63% compared to the relative displacement in the initial situation. In this way, the structure fulfills the conditions imposed by the current seismic design code, code P100-1/2006 from the point of view of the relative displacement.

Although, despite the increased rigidity of the building after the building interventions, the bending and twisting ratio remained less than 1.5, which means that the danger of coupling between the three modes of oscillation remained.

Thus, the results of calculation in ROBOT program were validated through the dynamic parameters of the structure, i.e. the periods and the frequencies determined by measurements.

In comparison calculation were taken into account the two structural assumptions: 1. the parts were separated by virtual seismic joints, and, 2. the parts were linked together without seismic gaps. These assumptions were applied to both rigid and elastic soil.

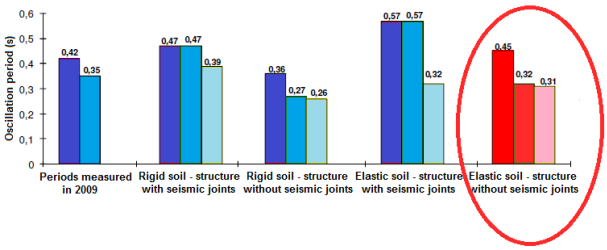


Figure 24 Oscillation periods of the first three modes obtained from analysis performed in the 4 assumptions compared with recently measured oscillation periods

From the point of view of their periods of oscillation, the comparative analysis shows (Fig. 24) that the real behavior of the structure corresponds to the elastic structure hypothesis (there is a ground-structure interaction) without seismic joints, which is the real situation at this moment (Dragomir and Calin, 2011).

In Figure 25 are shown the periods measured by INCERC for some specimens of the existing buildings of reinforced concrete frame made in Bucharest in different periods.

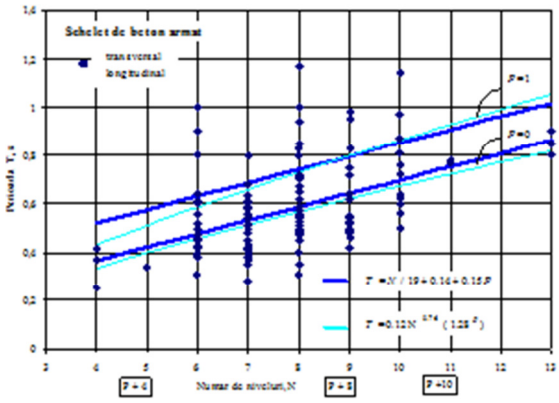


Figure 25 Periods measured by INCERC for RC structures

Two regression models (other than those presented in previous sections): linear and nonlinear (UBC format, Eurocode) are sized. The exponent of 0.76 determined for the reinforced concrete frame structures is closed to value 0.75 specified in UBC and Eurocode8.

Based on the formulas established by INCERC, the value of the period of vibration of the fundamental mode, obtained by temporary seismic instrumentation is:

$$T = 0.12N^{0.76} => T = 0.41s \qquad (6)$$

5. CONCLUSION

The concept of investigating the performance of a building proposes the validation of calculations with a program dedicated to structural analysis using instrumental data processing techniques.

The tests made on masonry panels confirmed the usefulness of using composite materials. Tests proved that it is possible a successive strengthening of clay blocks with plates and fabrics and avoiding demolition of cladding when structure is not damaged. Application to existing buildings is feasible, although some cost-benefit analysis must be done.

Based on the results obtained on site with throught temporar seismic instrumentation, a structural model with identical dynamic characteristics can be modeled and thus the behavior of the existing structure to strong earthquakes in Romania can be studied.

It can say that in this way one can predict how certain structures that have experienced earthquakes in the last century will respond to future earthquakes.

Acknowledgements:
The author thanks the staff of the National Seismic Network for Constructions of the I.N.C.D. URBAN-INCERC for the contribution to the temporary seismic instrumentation.

References:

Dragomir, C.S., Dobre, D., Croicu, N.C., Georgescu, E.S. (2012),"Integrated investigation of building performance", Architecture Urbanism Construction Magazine, vol.3, nr. 4, Bucharest.

Dragomir, C.S., Calin, M.C. (2011), "Dynamic Response Parameters and Damage Assessment of Educational Building located in Earthquake Prone Area", 15 World Conference for Earthquake Engineering, Lisbon, paper 1940.

Dragomir, C.S., Matei C., Dobre D., Georgescu E.S. (2009), "Behaviour of structural masonry envelope element under extreme actions", Construcţii Magazine, INCERC, Nr. 2, 9-16, ISSN 1221-2709. http://www.getcited.org/pub/103470720.

Dragomir, C.S. (2009), "Comparative study on the protection of masonry buildings to seismic actions", AICPS Bulletin, no. 2-3, 12-22, Bucharest, ISSN 1454-928X, Code CNCSIS 316.

Vlaicu G., (1999), "Contributions to the improvement of seismic design methods of the mixed structures with prefabricated diaphragms and reinforced concrete frames", *PhD Thesys.* Technical University of Civil Engineering of Bucharest.

10CUEE CONFERENCE PROCEEDINGS
10th International Conference on Urban Earthquake Engineering
March 1-2, 2013, Tokyo Institute of Technology, Tokyo, Japan

DAMPING CHARACTERISTICS OF STEEL PLATE CONCRETE WALL BASED ON THE CYCLIC LOAD TEST

Sung Gook Cho[1], Dookie Kim[2], Gihwan So[3] and Woong Ki Park[3]

1) Director, R&D center JACEKOREA Company, Incheon, Korea
2) Professor, Dept. of Civil Engineering, Kunsan University of Korea, Kunsan, Korea.
3) Researcher, R&D center JACEKOREA Company, Incheon, Korea
sgcho@jacekorea.com, kim2kie@chol.com, ghso@jacekorea.com, wkpark@jacekorea.com

Abstract: The modularized construction method applying SC (steel plate concrete) structure as the measure to reduce the construction period of nuclear power plants (NPP) has been developed. SC structure applied to the nuclear power plants requires a seismic design and thus the dynamic properties of SC structures need to be decided for accurate designing. The damping ratio of dynamic properties is an important design parameter governing the seismic response of structures. This paper has compared the damping ratios of SC structures suggested in the design criteria and the regulatory guide. To identify the damping ratio of SC shear walls, SC wall specimens without shear reinforcement were manufactured and cyclic loading tests and vibration tests were conducted. During the tests, SC walls exerted large ductility while its load increased due to the confining effect by the steel plates and the damping ratio increased continuously to the moment of failure. The experimental results showed that the damping ratio of SC walls increased by about 6-20% depending on the amplitude of the load.

1. INTRODUCTION

The SC structures arrange steel plates on both sides and/or single side of walls to replace the reinforced steel bars of RC structures and places concrete inside. In other words, SC structure complements the concrete tensile strength and flexural strength by installing the steel plates instead of the reinforcement steel bars used in the previous RC structures and performs a role as a formwork, which shortens the construction period and ensures the systematic quality management. Recently, the major countries with nuclear power plants try to apply SC structures to the safety structures of nuclear power plant. Thus, there is a need to analyze the dynamic behaviors of the composite structure and study the mechanical properties of that. SC structure has been recently developed, thus the research history is rather short and there is a lack of studies to secure the structural safety. To apply the SC structures to nuclear power plant structures, the studies on dynamic characteristics and seismic performance as well as the characteristics of stiffness due to the composite action between the steel plate and concrete are additionally required. The studies on SC structures are conducted mainly in Japan and the research results started being published since the early 2000s. Japan Electric Association has announced the steel plate concrete seismic design provisions in 2008. Kashiwa nuclear power plant has constructed a solid waste incinerator building as a demonstration building by applying SC structure and conducted a research on the dynamic characteristics of the building through vibration tests. Some research cases that performed a load analysis on this building and analyzed the in-plane behavior due to the composite action of SC structure have been reported.

The studies on the behavioral characteristics of SC structures conducted in Korea include the static experimental researches on the ductility of concrete and steel composite columns; an analytical research on compressive strength and failure mode according to width-thickness ratio; an experimental research on the lateral load performance of wall and the strength characteristics by producing non-reinforced steel concrete specimen. As a research that used an analytical method, a research to develop equivalent plate element model of SC structure was conducted. The researches on the dynamic characteristics of SC structures have seldom been conducted in Korea. Lee, Seung Joon et al, in his study, has suggested the damping ratio for SC structure seismic design by analyzing the results of a free vibration analysis, yet has analyzed the damping ratio in the stress state lower than the yield stress level of structures. In the seismic design of nuclear power plants, the damping ratio is defined at the level of the yield stress level of structures and 1/2 of the damping ratio of the yield stress. This study has organized the damping ratio regulations applied to NPP structures and compared them in order to analyze the damping characteristics of the dynamic characteristics of SC structure; furthermore performed transverse cyclic load tests and vibration tests using impact hammers after manufacturing SC shear wall specimen

without shear reinforcement. The acceleration signals measured from experiments and load-displacement curves were analyzed and the natural frequency and damping ratio of the target specimen were analyzed. The values of the damping ratio of SC structure identified by experiments were compared with the values suggested in the design regulations.

2. Damping Ratio of Structures

2.1 Methods to Determine Damping Ratio

Damping ratio refers to a phenomenon of energy loss and the response reduction in structures due to natural resistance, and is divided into material damping and friction damping. Material damping is refers to the damping due to the relation between the molecules that comprise the materials of structures, and friction damping refers to the damping at the joints of structures due to the structural members and the friction between components. Damping is one of the variables influencing the dynamic behaviors of structures significantly and is expressed in the equation of motion representing the dynamic system,

$$\ddot{u} + 2\xi\omega_n\dot{u}(t) + \omega_n^2 u(t) = f(t) \qquad (1)$$

Where, u is the displacement of the structure, ξ is damping ratio, ω_n is natural frequency, f(t) is external load.

The damping of structures is difficult to measure and the cause of its occurrence is uncertain. The report of the U.S. Nuclear Regulatory Commission (NUREG/CR-6011) suggests the ways to obtain the vibration response of the structure and calculate the damping ratio from that. The experimental methods to measure the damping of structures are divided into a forced vibration method and a free vibration method. Damping ratio of structures can be identified in several ways. National Center for Earthquake Engineering Research (NCEER) in the US introduces the ways to determine the damping ratio of concrete frame specimens: a way using a transfer function, a way using the half-power bandwidth, and a way to determine the damping ratio by using logarithmic decrement. Furthermore, to obtain the damping ratio in the state of huge load inducing the yield stress in structures, ways to measure the force-displacement hysteresis curve through a harmonic motion experiment and determine the equivalent viscous damping from the area of the hysteresis curve are used..

2.2 Techniques to Extract the Damping Ratio of Measurement Signals

(1) Half-Power Bandwidth Method

Even if the characteristics of the load is unknown, it is possible to calculate the damping ratio from the results of a forced vibration test by using half-power bandwidth. As known well, this method determines the damping ratio as shown in equation (2) by using the values of the left and right frequency corresponding to the $1/\sqrt{2}$ of the value corresponding to the top of the dynamic amplification factor curve.

$$\boldsymbol{\xi = \frac{\beta_b - \beta_a}{2}} \qquad (\mathbf{2})$$

(2) A Method Using Logarithmic Decrement

This method estimates the damping ratio from the time history displacement records in the system vibrating freely. Logarithmic decrement represents the reduction rate of the amplitude after the one period of free vibration. ξ value of the exponential equation in the graph represents the value of the damping ratio of the structure.

To calculate the damping ratio, the logarithmic decrement after n periods can be expressed in the following equation.

$$\delta = \frac{1}{n}\ln\left(\frac{u_1}{u_{n+1}}\right) = 2\pi\xi\frac{2}{\sqrt{1-\xi^2}} \qquad (3)$$

where, u, in the first displacement amplitude of free vibration curve, and u_{n+1} is the u_{n+1}–th amplitude.

When the amplitude decreases by half, the period of ($u_1 / u_{n+1} = 2$) can be expressed in equation (4).

$$n = \ln 2\frac{\sqrt{1-\xi^2}}{2\pi\xi} \qquad (4)$$

The period of half-bandwidth can be calculated by using above equation, which will calculate the damping ratio.

(3) Polynomial Regression Analysis

Equation (1) can be expressed in the following transfer function, after the extension with multi-degree freedom and Laplace transformation

$$\{X(s)\} = [H(s)]\{F(s)\} \qquad (5)$$

Where s is Laplace variable; [H(s)] is transfer function matrix, {X(s)} is the Laplace transform of displacement, {F(s)} is the Laplace transform matrix of load, The following transfer function matrix can be deployed in the form of a fraction partial fraction part.

When the evaluation of transfer function is made along the vibration contraction in s-plane, the frequency response function is obtained. Thus, by substituting $s = i\omega$, the frequency response function $H(i\omega)$ is generated.

$$H_k(i\omega) = \frac{r_k}{(i\omega - p_k)} + \frac{r_k^*}{(i\omega - p_k^*)} \qquad (6)$$

When polynomial curve fitting technique is applied for the regression analysis of transfer function, the transfer function can be developed as shown in equation (7)

$$H_k(i\omega) = \frac{r2_k\sigma_k + r1_k\omega_k + ir2_k^{\omega}}{\sigma_k^2 + \omega_k^2 - \omega + 2i\sigma_k^{\omega}} + A0 + A1(i\omega) + A2(-\omega^2) \quad (7)$$

where $\omega_k, \sigma_k, r_k = r1_k + i2r_k$ represent kth mode natural frequency, mode attenuation value and the dynamic characteristic values obtained as a result of the regression analysis as complex residue number, respectively. And A0, A1, A2 are the constants of the rest functions obtained in the course of calculation.

(4) Equivalent Viscous Damping

Damping has the feature that dissipates energy. Thus, by using this feature, it is possible to estimate the damping. By assuming that the dissipation energy (E_D) per one period, the area of the general hysteresis curve obtained by vibration tests by harmonic load is equivalent to the area of an ellipse in hysteresis loop representing the dissipation energy by equivalent viscous damping, the equivalent viscous damping can be obtained.

The dissipation energy per one period E_D can be obtained in the following equation.

$$E_D = \pi c_{eq}\omega_d A^2 = \pi\left(2m\xi_{eq}\omega_e\right)\omega_d A^2 = 2\pi\xi_{eq}\beta kA^2 \quad (8)$$

Here, c_{eq} is equivalent viscous damping, ξ_{eq} is equivalent viscous damping ratio, ω_d is damping natural frequency, ω_e is forcing frequency, β is vibration ratio($= \omega_e/\omega_d$).

When substituting static strain energy (E_{S0}) in the above equation, the equivalent viscous damping ratio at resonance (β = 1) can be calculated as shown in the following equation

$$\xi_{eq} = \frac{1}{4\pi\beta}\frac{E_D}{E_{S0}}\Big|_{\beta=1} = \frac{1}{4\pi}\frac{E_D}{E_{S0}} \quad (9)$$

$$\text{Where } E_{S0} = \frac{1}{2}kA^2 \quad (10)$$

2.2 Regulations on the Damping Ratio of SC Structure

Damping ratio of Korean NNPs follows the regulatory standards published by the U.S. Nuclear Regulatory Commission (USNRC). The damping ratios applied to NNP are defined after being classified into Operating-Basis Earthquake (OBE) and Safe-Shutdown Earthquake (SSE) and also being classified depending the types of structures in use. Korea's KEPIC-SNG suggests the damping ratio in the design of SC structures on the basis of the results of the recent studies; Japan's JEAC-4618 also suggests the damping ratio in the design of SC structures. However, the United States Nuclear Regulatory Commission do not suggests the damping ration of SC structures until now and thus the damping ratio between reinforced steel concrete (RC) and pre-stressed SC structures were compared.

As shown in Table 1, regarding the RC structures in the regulatory standards of the United States and Korean power industry technical standards, the damping ratio is decided at 7% and 4% in case of SSE standard and OBE standard, respectively. Furthermore they suggest that the damping ration can be decided by estimating the dissipation energy by viscous damping in cases other than the structures suggested. Korea's KEPIC SN nuclear structure and SNG steel plate concrete structure define the damping ratio of RC structure as 4% equivalent to the damping ratio suggested by the United States Nuclear Regulatory Commission in OBE standards and 6% which is smaller than RC structures by 1% in RC standard. Seismic design provisions of steel plate concrete structure issued by the Standards Committee of the Japan Electric Association (JEAC 4618-2009) defines the damping ration of RC structure as 5% equivalent to steel concrete. It is because they regard the damping ratio of SC structure to be equivalent to RC structure based upon concrete damping mechanism.

Table 1. damping ratio of each code

code	type	SSE	OBE
USNRC (KEPIC STB)	RC	7%	4%
	PSC	5%	3%
KEPIC-SNG	SC	6%	4%
JEAC-4618	SC	5%	

3. Damping Ratio Estimation Tests

In this study, in order to investigate the damping ratio of SC structure, simple unreinforced SC wall specimens were manufactured and then vibration tests and cyclic loading tests were conducted. The transfer function obtained through shock hammer vibration tests was analyzed by polynomial curve fitting method and then the natural frequency and damping ratio of specimens were calculated. In addition, the dissipation energy by period in cyclic loading was calculated from force-displacement curve obtained through cyclic loading tests and then the damping ratio was determined.

3.1 SC Wall Specimens

The specification of the specimens used in the tests is shown in Figure 1. The size of specimen is 1100mm x 400mm x 150mm (Height x Length x Thickness).

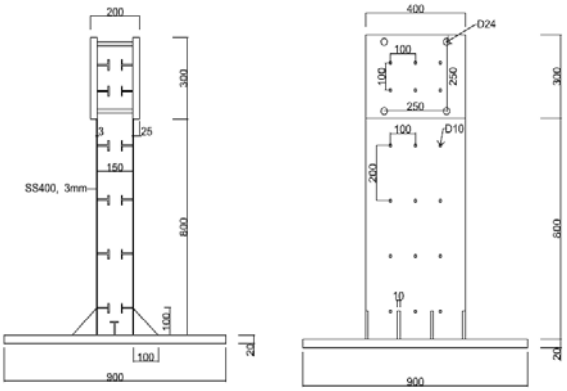


Fig. 1. size of specimens

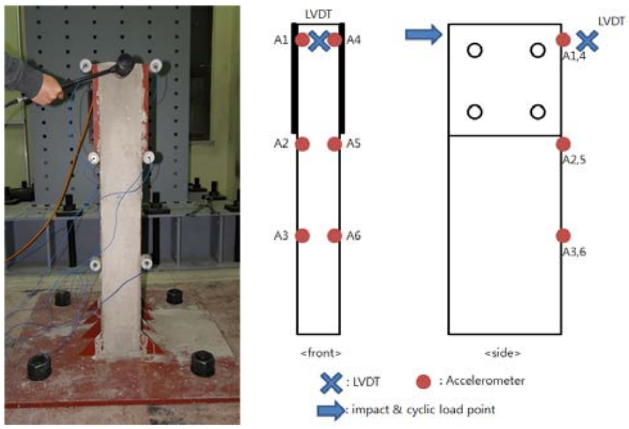


Fig. 2. Impact hammer test and measuring points

The specimen with 2 steel plates with studs is designed compositely at compressive strength of 35MPa and concrete was placed. The material of the steel plate attached to the specimen is SS400 steel plate with 3mm thickness. As for studs, 6 lines were welded to both steel plates in the length direction (3 lines each along to the height of wall). 20mm thick steel plate are attached on the bottom of the specimen to fix the specimen and 3 studs attached to the base plate connect the plate to the walls. To the bottom of walls, 4 ribs are welded on the left and right side for the reinforcement. The size of the studs used in the specimen is 8mm x 45mm (diameter x length). On the top of the specimen, 25 mm steel plates are reinforced on both sides of the walls to add the mass and fix an actuator, considering the dynamic characteristics of wall. The name of each specimen is decided as shown in Table 2.

Table 2. names of specimens

	Specimen 1	Specimen 2	Specimen 3
name	SXC1	SXC2	SXC3

3.2 Impact Hammer Test

To analyze the vibration characteristics of the SC walls and examine the damping ratio at low levels of stress, a vibration test was conducted by using impact hammer. The specimen was the same as that used in cyclic load tests and tightly fixed to mass foundation, and a test was conducted as shown in Fig.2. impact hammer used in the test was DYTRAN's Model 5802A with the head weight of 1.36kg (3 lb) and 6 x PCB PIEZOTRONICS's 1-axis accelerometer (PCB 393B04) were used to measure the acceleration response. OROS's FFT Analyzer was used to analyze the signal. In the impact test, 6 acceleration measuring devices were attached to the specimen on the left and right of specimen (bottom, middle, top). And then, the average acceleration response transfer function signal was recorded after striking the top-center of specimen in the back.

3.3 Cyclic load Test

Cyclic load was performed in the direction of specimen's length. The loading equipment used in the test was hydraulic servo loading equipment with the capacity of 500KN. The specimen was fixed tightly on mass foundation and abutment test walls by using bolts. Fig 3 exhibits the diagram of the experimental apparatus and the test scenes.

Load was applied on the wall through displacement control as shown in the graph in Figure 4 and the displacement was increased gradually up to about 110mm. The loading was repeated in the forward and backward direction. To measure the displacement of the target specimen, 2 LVDTs were additionally installed on the specimen on both sides and whether there was the displacement of the specimen in to the sides was monitored

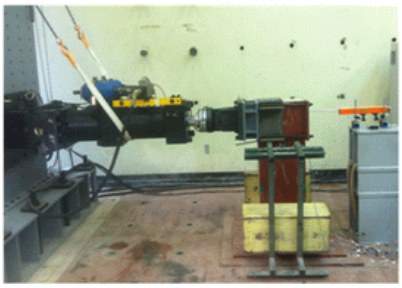


Fig. 3. cyclic load test apparatus

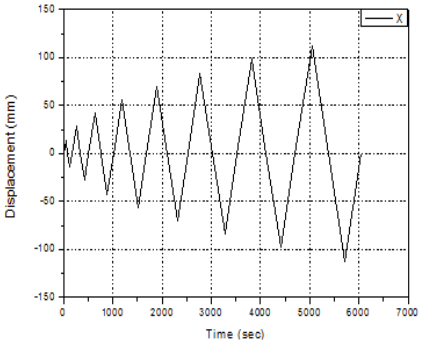


Fig. 4. input load of cyclic load test

3.4 Test Results

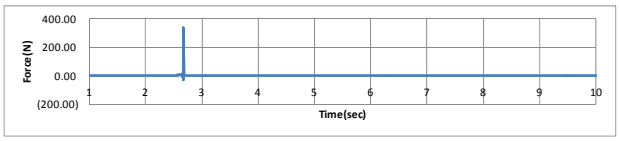
(1) Impact Hammer Test

The acceleration time history measured through impact hammer test was converted into response acceleration transfer function for loading load and expressed in Figure 5 and 6. As shown in Figure 7, the vibration characteristics of SC wall specimens can be identified by using a polynomial curve fitting method. The damping ratio and natural frequency of each specimen is summarized in Table 3.

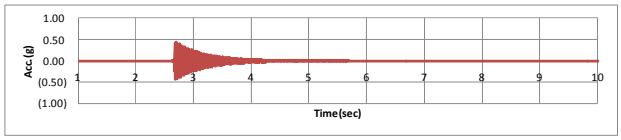
The results of test showed there is a difference of natural frequency even though the specimens have the same shape and weight. It is likely because the degree of the attachment of concrete and steel plate inside the specimens varies depending on specimen due to the effect of dry contraction. As a result of the analysis of damping ration, every specimen had about 1% the damping ratio. This damping ratio is low in low-stress state and thus it will rise in real earthquake vibration.

Table 3.impact hammer test result

	SXC1	SXC2	SXC3
natural freq.(Hz)	43.5	45.1	46.5
damping ratio(%)	0.72	0.80	0.95



(a) impact force



(b) Acc. Response

Fig. 5. time history response

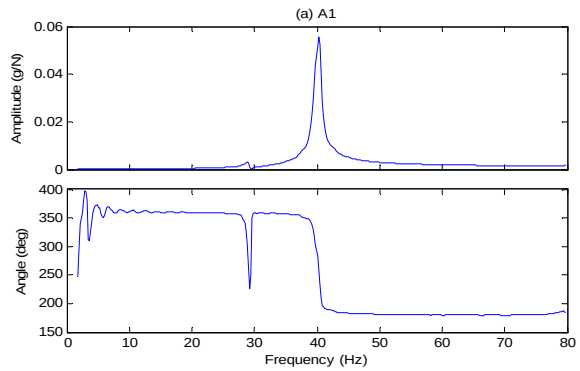


Fig. 6. transfer function of SXC1 top location

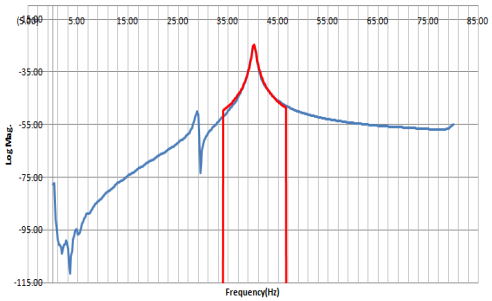


Fig. 7. Polynomial Curve Fitting

(2) Cyclic Load Test

The load-displacement hysteresis curve of each specimen by cyclic load tests is shown in Fig 8.

As a result of cyclic loading tests of SC wall specimens, the average of the forward maximum load was 130.4kN; the average displacement was about 46mm; the average of the backward maximum load was 118.8kN; the average displacement was 45mm. Damping ratios shown in Table.5 were identified from the each cyclic loop of Fig. 8. The results from analyzing the damping ratio demonstrate that the size of ellipse increases and the damping ratio increases from 6% to about 20% as the cycle of loading load increases. In the first cycle, 60kN, about 50% of the maximum specimen load, is loaded and the damping ratio at this moment is about 6%. After the 3rd cycle, the load is greater than yield strength and ductile fracture occurs during this interval. After the 3rd cycle, loading load gradually decreases, whereas the damping ratio continues to increase gradually. It is because the internal concrete cracks increase and the binding force continue to increase due to the steel plate arranged on both sides and as a result the internal friction forces increase, which results in a continued increase of damping ratio.

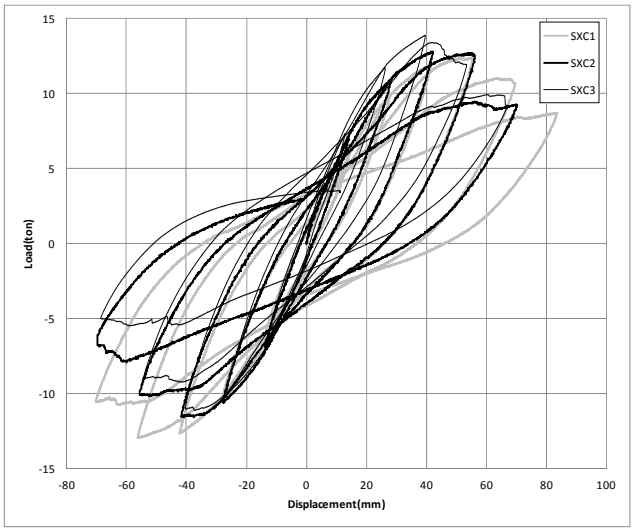


Fig. 8. load-displacement hysteresis curve

Table 4. result of cyclic load test

	forward		backward	
	Max. load(kN)	Max. disp.(mm)	Max. load(kN)	Max. disp.(mm)
SXC1	124.4	55	129.9	56
SXC2	128.1	42	115.5	42
SXC3	138.8	40	111.2	37
Avg.	130.4	46	1188	45

Table 5. damping ratios of each cycle

Cycle	Damping Ratio(%)		
	SXC 1	SXC 2	SXC 3
1	6.95	6.14	6.5
2	9.64	10.51	10.46
3	13.29	14.46	14.16
4	16.85	17.75	19.02
5	20.43	20.92	19.84
6	20.95	-	-

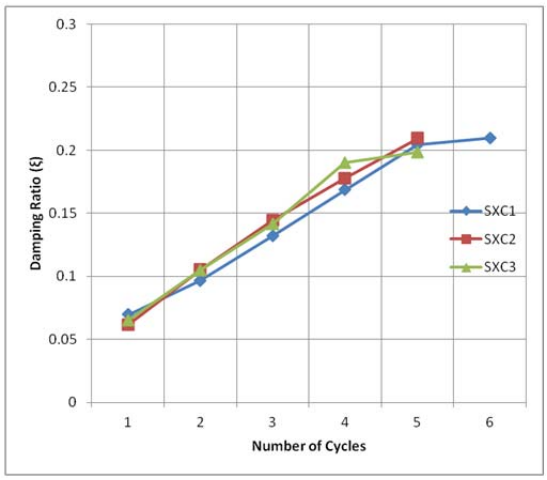


Fig. 9. Damping ratio changes of each cycle

4. CONCLUSIONS

To find out the damping ratio which is one of the dynamic characteristics of the SC structure wall, specimens were manufactured and static and dynamic tests were conducted. The test results are as follows:

1) As a result of cyclic loading tests, the damping ratio of SC structure specimen was about 7% when the steel plates yielded. Furthermore, there is a large ductility capacity in the length direction after the concrete yields due to the composite action between concrete and steel plates, and a binding force occurs in both steel plates installed outside the concrete due to the attributes of SC structure. Due to this, the frictional effect increases due to an increase of binding force as the cracks of internal concrete increases, which results in an increase of damping ratio as tests progress and loading load increases.

2) Seismic design code on steel plates in Korea prescribes the damping ratio as SSE 6%, explaining SC structure incurs less cracks than RC structure. However, as a result of the test, it is not possible to check the cracks that occur inside due to effect of steel plates and the damping ratio rather increases due to the binding force of the steel plates installed outside. Thus, there is a need to conduct further studies and tests to suggest reasonable damping ratio regulations.

3) As the dynamic characteristics through impact tests, the values vary depending on specimen. It is because the bonding between steel plate and concrete varies depending on specimen due to the curing condition.

4) As a result of vibration tests using impact hammers, very small damping ratio was calculated compared to the cyclic loading test using a hydraulic loading device. It is because the compliance energy of vibration tests using impact hammers is relatively smaller than the compliance energy using a hydraulic loading device. Thus, a large scale vibration test like a shaking table test is considered to be needed to evaluate the damping ratio of structure.

Acknowledgements:

This work was supported by the Nuclear Innovation Program of the Korea Institute of Energy Technology Evaluation and Planning (KETEP) grant funded by the Korea government Ministry of Knowledge Economy (No. 20101620100230). The authors would like to express their appreciation for the financial support.

References:

Masahiko Ozaki, Shodo Akita, Nobuyuki Niwa, Ippei Matsuo, and S. Usami (2001), "Study on Steel Plate Reinforced Concrete Bearing Wall for Nuclear Power Plants Part1; Shear and Bending Loading Tests of SC Walls", *SMiRT 16 Conference, Washington, DC, USA*, paper H01/1554.

Shodo Akita, Masahiko Ozaki, Nobuyuki Niwa, Ippei Matsuo, and K. Hara (2001), "Study on Steel Plate Reinforced Concrete Bearing Wall for Nuclear Power Plants Part2; Analytical Method to Evalute Response of SC Walls", *SMiRT 16 Conference, Washington, DC, USA*, paper H01/1555.

Masahiko Ozakia, Shodo Akitab, Hiroshi Osugac, Tatsuo Nakayamad, and Naoyuki Adachic (2004), "Study on Steel Plate Reinforced Concrete Panels Subjected to Cyclic In-Plane Shear", *J. Nuclear Engineering and Design*, 228, 225-244.

Japan Electric Association Code (2009), "Seismic design of steel plate concrete technical regulations", JEAC 4618-2009.

Ali Niousha, Yukio Naito, Eiji Miyasaka, Shoji Uchiyama (2007), "Dynamic Characteristics of a SC Building in Kashiwazaki NPP site using Vibration Test – Part 1: Data analysis and system identification", Transactions, *SMiRT 19, Toronto*, Paper #K09/2.

Eiji Miyasaka, et al(2007)., "Dynamic Characteristics of a SC Building in Kashiwazaki NPP site using Vibration Test – Par 2:

Simulation Analysis", Transactions, *SMiRT 19, Toronto*, Paper #K09/4.
Ari Danay (2012), " Response of steel-concrete composite panels to in-plane loading", *Nuclear Engineering and Design*, **242**, 52-62.
Song, J.Y., Kwon, Y. B., and Kim, S. K. (2001), "A Study of the Ductility of Concrete-Filled Composite Columns under Cyclic Loading", *Journal of Earthquake Engineering Society of Korea*, **5**(6), 11-19. (in Korean).
Han, H. S., Choi, B. J., and Han, K. G. (2011), "Compression Behavior of steel Plate-Concrete Structures with the Width-to-Thickness Ratio", *Journal of Korean Society of Steel Construction*,**23**(2), 299-236. (in Korean).
Cho, S. G., So, G. H., Kim, D. K., and Kwon, M. H.(2012), "Experimental Investigation of the Lateral Load Capacity and Strength Characteristics of a Steel Plate Concrete(SC) Shear Wall", *Journal of Earthquake Engineering Society of Korea*, **16**(5), 23-32. (in Korean).
So, G. H., and Cho, S. G. (2011), "Investigation of Dynamic Characteristics of SC Wall Structures by Different Modeling Techniques", *KSCE Conference & Civil Expo 2011, Songdo, Incheon, Korea*, 427-430. (in Korean).
Lee, S. J., and Kim, W. K.(2010), "Damping Ratios for Seismic Design of SC Structures", *Journal of Korean Society of Steel Construction*, **22**(5), 487-496. (in Korean).
Mario Paz (2004), "Structural Dynamics", Kluwer Academic Publishers, fifth edition, 153-154.
U.S. Nuclear Regulatory Commission (2006), "Recommendation for Revision of Seismic Damping Values in Regulatory Guide 1.61"
J.M. Bracci, A.M. Reinhorn and J.B. Mander (1992), "Seismic Resistance of Reinforced Concrete Frame Structures Design Only for Gravity Loads, Part I – Desing and Properties of a One-Third Scale Model Structure", National Center for Earthquake Engineering Research, Technical Report NCEER-92-0027.
Kim, D. K.(2009), "Dynamics of Structures." , Goomibooks, second edition.(in Korean).
STAR Modal Operation Manual (1996), Spectral Dynamics Inc.
U.S. Nuclear Regulatory Commission (2007), Damping Values for Seismic Design Of Nuclear Power Plants, 2007
EQE Engineering Consultants (1993), "Review of Structure Damping Values for Elastic Seismic Analysis of Nuclear Power Plants"
Korea Electric Association (2010), "KEPIC-SNG Steel Plate Concrete Structure" Korea Electric Power Industry Code.(in Korea)

10CUEE CONFERENCE PROCEEDINGS
10th International Conference on Urban Earthquake Engineering
March 1-2, 2013, Tokyo Institute of Technology, Tokyo, Japan

LATERAL FORCE RESISTANCE CHARACTERISTICS OF STEEL PLATE CONCRETE WALL BASED ON THE PUSH-OVER TEST

Sung Gook Cho[1], Dookie Kim[2], Woong Ki Park[3] and Gi Hwan So[3]

1) Director, Research & Development Center, JACEKOREA Company, Korea
2) Professor, Department of Civil Engineering, Kunsan University, Korea
3) Researcher, Research & Development Center, JACEKOREA Company, Korea
sgcho@jacekorea.com, kim2kie@kunsan.ac.kr, wkpark@jacekorea.com, ghso@jacekorea.com

Abstract: In this study, lateral force resistance capacity and failure mode of steel plate concrete (SC) wall element were evaluated based on the static push-over tests. Seismic capacity and stiffness characteristics of unstiffened SC shear walls under lateral force were investigated from the test result. Failure modes, sectional strength, and stiffness characteristics of SC structures under lateral loads were investigated by analyzing the experimental results. One of the main failure of unstiffened SC shear walls were found to be the type of bending shear failure due to the debonding of steel plate at the concrete interface. In addition, finite element model of the specimen was also created and nonlinearly analyzed for the static load. The failure modes of the SC wall due to the lateral force were analyzed and compared with those identified by the test. The initial stiffness and displacement due to the lateral load which were analyzed by the finite element model were in good agreement with the experimental results. Overall patterns of structural behavior identified by analysis showed very similar to those obtained from the test.

1. INTRODUCTION

Nuclear power plant (NPP) is formed of reinforced concrete buildings with shear walls for seismic resistance effectively. Steel plate Concrete (SC) structure is the alternative to Reinforced Concrete (RC) structure of NPP. The researches on SC structures for the modularization of nuclear power plants have been performed recently in Korea. In order to design the SC element to be rational, its structural behavior should be clearly investigated.

Unlike general industrial facilities, to adopt SC member to the safety-related major structures, various research on structural behavior and mechanical characteristics is required. To date, experimental research on SC type has been actively performed. However, research results on the development of analytical model, which can apply in the design practice, and the prediction technique of performance are uncommon.

Research (Chen, 1999; Mello et al., 2008) using finite element analyses (FEA) on composite action between concrete and steel plate has been trying for a lone time. To date, it is increasingly becoming the development trend owing to the improvement of analytical program. Chaudhary et al. (2011) studied, for bridge structures, the behavior characteristics considered the nonlinearity of each material on composite structures composed of concrete and steel plate. Based on these fundamental researches, the study (Ahmer et al., 2011) on the effectiveness of SC walls after comparing RC and SC shear walls was carried out. However, they are not only research qualified practically based on the actual test results but also the comparison research between FEAs based on the theory.

In this paper, to qualify the practicality of a static analytical technique for applying to the practice, FEA for targeting the test results of RC shear walls were performed. The reliability of static analytical technique for the length direction of walls was qualified and mechanical behaviors were predicted by comparing stiffness and failure modes with test results.

2. STATIC PUSH-OVER TEST

This study was performed based on Cho et al.'s (2012) published in recent year. All data including the spec of specimens were referenced from the research (Cho et al., 2012).

To confirm the mechanical behavior of SC shear walls, a total of three specimens were fabricated and the monotonic increasing load (Figure 1) were applied. Concrete design strength is 35MPa. SS400 having a thickness of 3mm was used and 36 numbers of studs was installed in the steel plate. And, concrete was placed inside the steel plates. All tested specimens were 150 mm x 400 mm rectangular sections and the height was 1100 mm as shown in Figure 2. To anchor the static loading device, the steel plate having the holes was welded to the upper part of the specimen. Lateral direction loading tests were carried out using a hydraulic universal

testing machine (UTM) with a capacity of 500 kN.

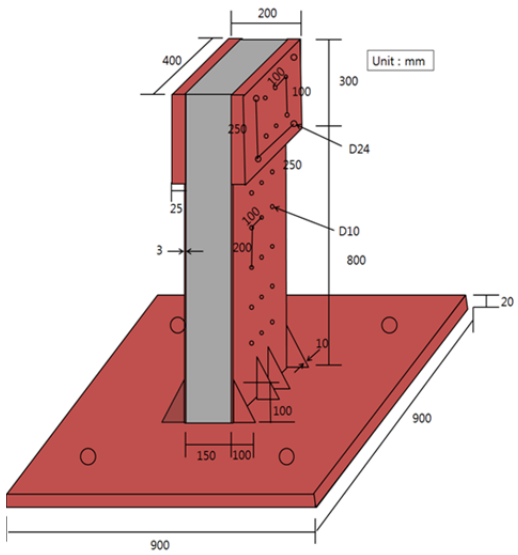


Figure 1. Specification of specimen

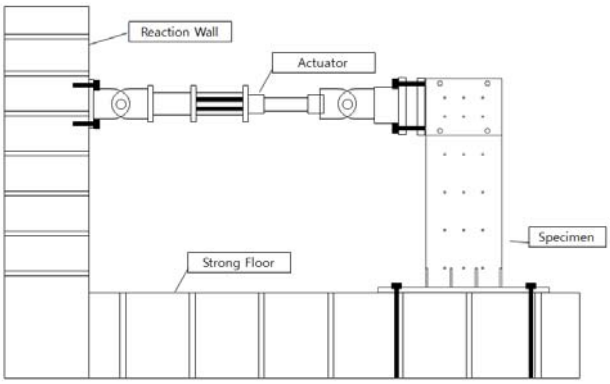


Figure 2. Test set-up

To measure the strain distribution of specimens, eight three-axial steel strain gauges (for example, ST21) and four concrete gauges (for example, CON1) were attached in the tensile and compressive surfaces of the steel and concrete. Linear variable differential transducers (LVDTs) were installed at the opposite side center of point applying the force and two sides of each specimen to clarify the existence of torsion. Overall view of test set-up and details of attachment locations of LVDTs and strain gages are shown in Figure 3.

Monotonically increasing loads on the specimens put the pressure on slowly increasing the lateral displacement loading was displacement-controlled. Lateral load tests were performed for each specimens the longitudinal direction, the name of the longitude direction of the wall specimen SXP1, SXP2 and SXP3 as were classified.

The average maximum load on the specimen is about 115.25kN, when the average displacement reached of about 66mm. As shown in Figure 4 was compared of the load-displacement graph of each specimen.

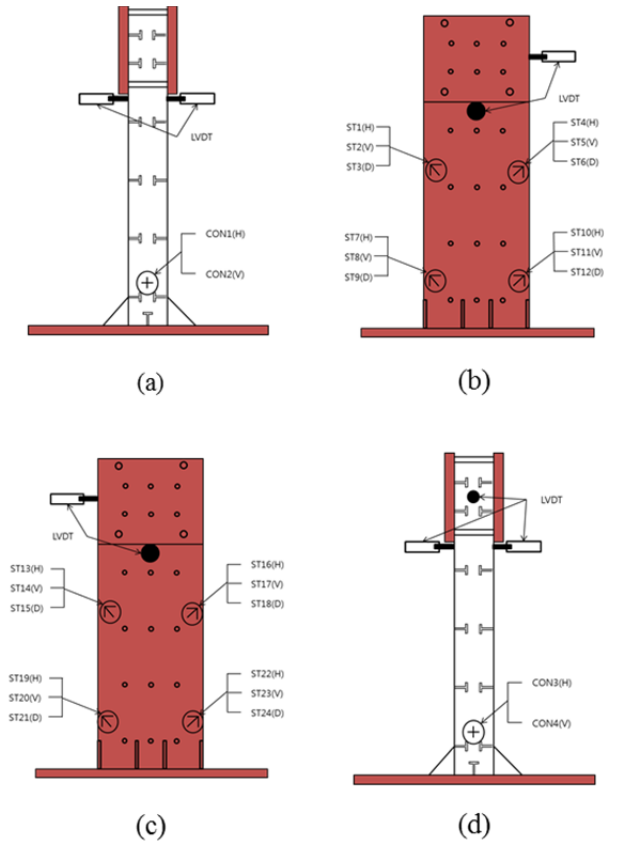


Figure 3. Detail drawings of LVDT & strain gage point at (a) front (b) left (c) right (d) back

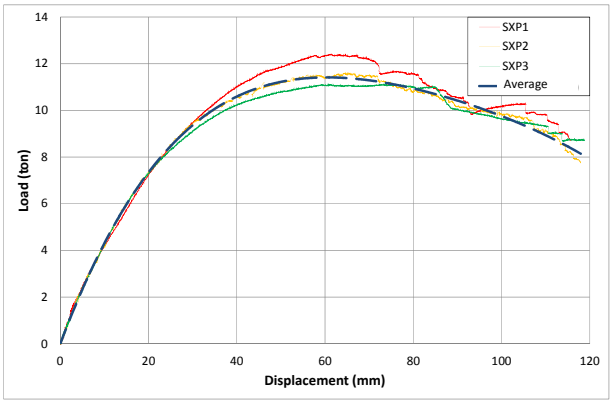


Figure 4. Load-displacement curve obtained result of test

3. FINITE ELEMENT ANALYSIS

To predict the behavior of SC walls, finite element analyses (FEA) was performed using the actual size and materials of specimens from ahead performed research (Cho et al., 2012). For the analyses, the universal structure analysis program (ABAQUS Ver. 6.10 (2011)) was used. Steel plate, concrete, and studs were considered to be perfectly bonded. The load was applied to the center of upper part of the specimen using the displacement control. 3-dimensional nonlinear static-analyses considering the

nonlinear behavior between concrete and steel plate were performed and the relationships between load and displacement and crack patterns of concrete were evaluated.

3.1 Modeling

As shown in Figure 5, target structures were modeled using 3-dimensional finite elements (solid elements of Mesh Tools of ABAQUS) based on the real size considering the nonlinear behavior of the concrete. Compressive strength of concrete was 35 MPa and yield strength of steel plate was 400 MPa. To prevent the shear locking phenomenon, which does not present the shear deformation of solid elements, the reduced integration technique was applied. As the boundary condition, the lower part of bottom plate of the steel plate was fixed.

As the model applied to the concrete solid element, concrete damaged plasticity model to confirm the failure behavior in concrete of the compressive and tensile stage was used. This model is an appropriate model to predict the damage behavior of concrete and contains the characteristics of tensile hardening, compressive softening, stiffness damage, and plastic expansion under the restrained compression condition.

As the constitutive model applied to three-dimensional element of the steel plate, Von Mises plasticity model was used considering the non-linearity of the steel plate. Drucker-Prager plasticity model is an appropriate one for materials showing the volumetric plastic strain such as concrete. On the other hand, Von Mises plasticity model is a proper one for ductile materials showing the plastic incompressibility like metal and steel plate.

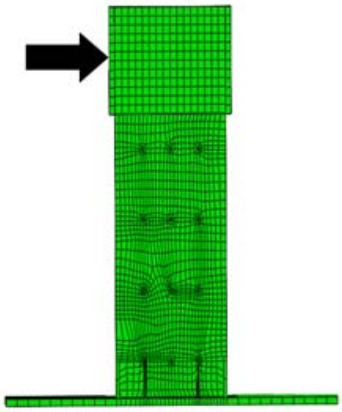


Figure 5. Load point of specimen

3.2 Analysis Method

Pushover analysis was conducted by applying displacement load on the top as shown in Figure. 5. Pushover analysis is effective in identifying the behaviors and limit state of structures after the yield, by considering the material nonlinear characteristics can establish the target performance of structures and accomplish that. Pushover analysis calculates load-displacement relation curves, by gradually applying the pre-set static load to the performance point that can be expected in structures. It is possible to compare the performance of specimens by comparing the calculated load-displacement curves. Thus, pushover analysis aims to identify the vulnerability of specimens by analyzing the behaviors of specimens and identifying the stress distribution of steel plates.

4. ANALYSIS OF RESULTS

Actual specimens are modeled into an analytical program in actual scale and a pushover analysis was conducted by applying displacement load to the top-center. After the analysis, concrete crack distribution and steel stress distribution of specimens were confirmed and load-displacement and failure mode between tests and analysis were compared.

4.1 Stress of Specimens

Results of Stress distribution acting on the steel plate of the specimen are shown in Figure 6. Displacement increase concentrates the stress of specimens on the mid-bottom and the consequential flexural crack and shear crack progress from the front to the rear. The cracks are concentrated on the mid-bottom of the front of concrete. Due to the failure of concrete because of these cracks, the analysis stopped even though the steel plates did not yield. V-shaped failure occurred on the bottom in the rear. It is likely because the concentration of stress on the bottom in the rear incurs V-shaped failure.

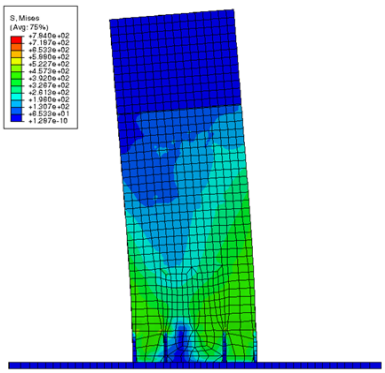
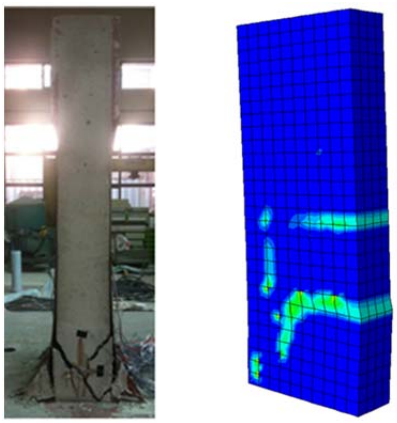


Figure 6. Stress distribution of specimen

4.2 Failure Mode of Specimen

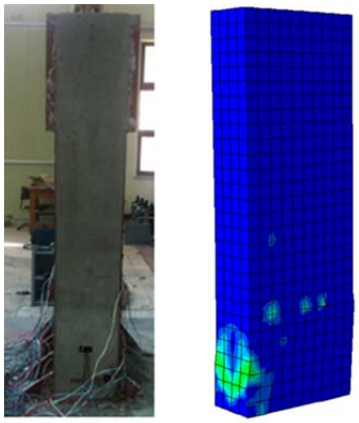
Figure 7 & 8 shows the comparisons of failure patterns between experiments and analyses for length direction of the wall. There is a little difference because the failure mechanism was changed. Namely, due to studs and reinforcement attached to the bottom of side and foundation, the stress concentration in the tension part compared to that of analyses excessively occurred. In addition, the reinforcement was failed and concrete went overall on. Finally, it can be concluded that the failure of concrete of was controlled by the tension. Figure 9 & 10 shows the buckling phenomenon of steel plates obtained from experiments and analyses. As the displacement increases, the junction between steel plate and concrete in the front and rear parts of the specimen was separated and, accordingly,

the buckling phenomenon was happened. It shows the similar pattern with experimental results.



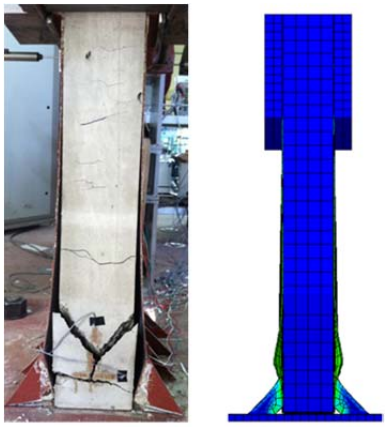
(a) (b)

Figure 7. Comparison of Failure of (a) test and (b) analysis on front.



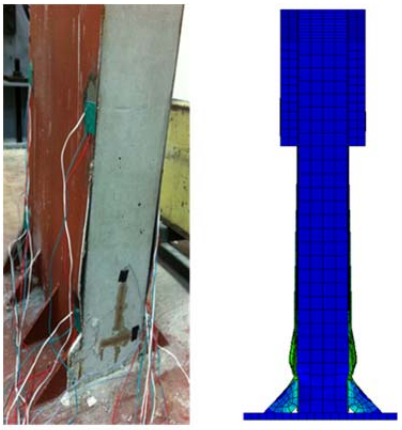
(a) (b)

Figure 8. Comparison of failure of (a) test and (b) analysis on back.



(a) (b)

Figure 9. Comparison of buckling of (a) test and (b) analysis on front.



(a) (b)

Figure 10. Comparison of buckling of (a) test and (b) analysis on back

4.3 Load-Displacement Curve

Figure 11 shows the displacement in accordance with the experimental and analytical load. In experimental and analytical results, the initial rigidity and displacement agree with each other and behavioral modes are very similar to each other. ABAQUS curve in Figure 11 represents the specimens modeled by attaching stiffener and abacus-x/o stiffener curve represent the specimens without stiffener.

The specimens except SXP3 have the similar results strength to that of the specimens without stiffener and the results strength was smaller than the specimens with stiffener. With respect to the results of the specimens with stiffener, the strength increased more than the tests due to the effect of the attachment between steel plates and concrete and the assumptions applied to weld model of stiffener attached to the floor. Thus, it was expected that more accurate modeling of welding zone of stiffener and steel pate-concrete modeling would lead to the improvement of analysis results.

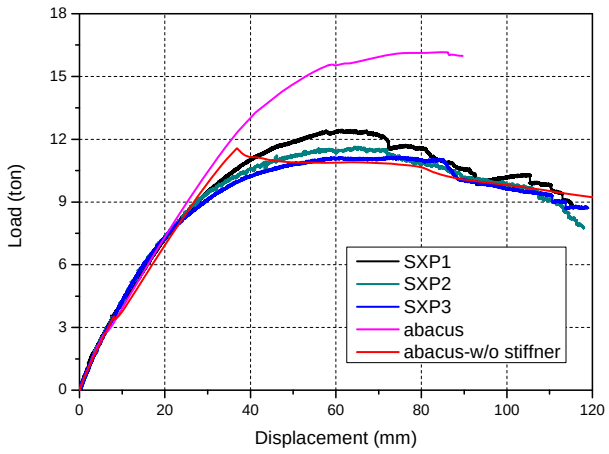


Figure 11. Comparison of load-displacement by test and analysis

5. CONCLUSIONS

In this study, to predict the behavior of SC shear wall structure accurately, by analysis SC shear wall specimens were manufactured and a lateral load test on specimens was conducted. In addition, a finite element analysis was conducted by modeling the specimens in real scale. The stress distribution, failure mode, buckling modes and load-displacement curve of specimens and the safety test results and analysis results of SC structure were compared. The following conclusions have been reached.

(1) As a result of the comparison between test results and analysis results regarding SC shear walls, it is known that the results of nonlinear analysis of stress, failure mode and buckling mode by three-dimensional elements depicts the actual behaviors of specimens accurately.

(2) As a result of the analysis of load-displacement by tests and analysis, the displacement and initial strength appear relatively similar to each other. Furthermore the result of the comparison of load-displacement curves show similar results in tests and analysis when specimens yield, which indicates that a finite element analysis of SC shear walls in fact depicts the actual behaviors well.

(3) In case of finite element analysis, the presence of reinforcement materials changes the strength interpretation. Thus, more accurate depiction of the attachment between concrete and stiffener and welding zone modeling is expected to produce more accurate analysis results.

(4) The attachment between steel plates and concrete in SC structure relies on studs and the gap between studs and the length of studs influence the behavioral characteristics of SC walls, which require careful attention. The reliability of the behavioral analysis of SC structure is expected to improve though further studies on the gap between studs and the length of studs.

Acknowledgements:

This research was supported by the Nuclear Innovation Program (No. 20101620100230) of the Korea Institute of Energy Technology Evaluation and Planning (KETEP) grant funded by the Korea Ministry of Knowledge Economy (MKE), the authors would like to express their appreciation for the financial support.

References:

Chen, Y. (1999), "Finite element analysis for walking vibration problems for composite precast building floors using ADINA: modeling, simulation, and comparison," *Computer & Structures*, **72**(1), 109-126.

Mello, A. V. D., Silva, J. G. S., Vellasco, P. C. G. S., Andrade, S. A. L., and Lima, L. R. O. (2008), "Modal analysis of orthotropic composite floors slabs with profiled steel decks," *Latin American Journal of Solids and Structures*, Vol. 5, pp. 47-73.

Sandeep Chaudhary, Ahmer Ali, Dookie Kim, Sung Gook Cho. (2011), "SEISMIC ANALYSIS OF STEEL CONCRETE COMPOSITE WALLS OF NUCLEAR POWER PLANT STRUCTURES," 21st International Conference on Structural Mechanics in Reactor Technology (SMiRT 21), 6-11 November, 2011, New Delhi, India, Paper 499.

Ahmer Ali, Sung Gook Cho, Dookie Kim, Jintao Cui. (2011), "Numerical Study on Cyclic Behavior of I-shaped Composite SC Shear Walls for Nuclear Power Plants", Proceedings of KSCE Conference, Korean Society of Civil Engineering, 2255-2258.

Cho, Sung Gook, So, Gi Hwan, Kim, Doo Kie & Kwon, Min Ho. (2012), "Experimental Investigation on Lateral Load Capacity and Strength Characteristics of Steel Plate Concrete(SC) Shear Wall", Journal of the Earthquake Engineering Society of Korea, EESK, 16(5), 23-32.

ABAQUS, Dassault Systems Simulia Corp. (2011), "Abaqus Analysis User's Manual", Version 6.10.

10CUEE CONFERENCE PROCEEDINGS
10th International Conference on Urban Earthquake Engineering
March 1-2, 2013, Tokyo Institute of Technology, Tokyo, Japan

EFFECT OF RC TIE-COLUMNS ON CONFINED BRICK PANELS SUBJECTED TO IN-PLANE ALTERNED LOADING

Abdelkrim Bourzam[1)], Toshikazu Ikemoto[2)], Saiji Fukada[2)] and Masakatsu Miyajima[3)]

1) Assoc. Professor, Univ. of Scs and Technology USTHB- Faculty of Civil Engr., Algiers, Algeria
2) Assoc. Professor, Department of Civil Engineering, Kanazawa University, Japan
3) Professor, Department of Civil Engineering, Kanazawa University, Japan
bourzam@gmail.com, tikemoto@t.kanazawa-u.ac.jp, miyajima@t.kanazawa-u.ac.jp

Abstract: The approach as proposed in this paper is based on predicting the diagonal cracking strength, considered as the shear capacity of the brick panel and an amount of shear coming from the tie-columns due to dowel mechanism. In this type of structural members, tie-columns are used mainly to provide post-cracking deformation capacity by maintaining the integrity of the masonry after diagonal cracking.
Two analytical models (linear and non linear) are used to compute the dowel action coming from longitudinal reinforcements. To access the influence of the two models an experimental study is carried out on a half scale confined brick wall. The general applicability of the proposed approach regarding the maximum lateral resistance was confirmed by a good correlation between experimental data and calculated values which obeys to the linear model.
Keywords: Confined masonry, brick wall, tie-columns, dowel action, lateral resistance.

1. INTRODUCTION

During earthquakes, when, the drift storey of confined masonry wall becomes large, tension in tie-columns' reinforcement dominates on both directions of imposed lateral displacements. At such level, the cracked masonry panel pushes the tie-column sideward inducing tension in the reinforcing bars. In other words, the RC confining elements prevent the collapse of the masonry and cause additional compression stress in the vertical and horizontal directions; hence a certain amount of additional shear can be transmitted by dowel action of the vertical bars. This mechanism occurs mainly at wall corners.

2. ANALYTICAL DEVELOPMENT

The dowel effect (Dowel action) in RC column and/or RC tie-column is a very complex phenomenon involving the shear resistance of longitudinal bars and their interaction with stirrups and concrete see Figure.1-a.

The problem can be reduced to a pure calculation of strength of materials, where, the flexion of longitudinal steel bars, the compression of the concrete surrounds them and tensions created by stirrups are considered together, see Figure.1-a and Figure.1-b.

The vertical tie-columns significantly improve the ductility of masonry walls, but have a little effect on the lateral shear resistance (≈20%, Umek 1971), then, it is more economic to reduce the web reinforcement ratio in tie-columns by increasing S_t the distance between two successive stirrups. S_t is usually considered equal to (3/4)*t* (Yoshimura *et al.,* 1996) or simply to "*t*" (Yoshimura *et al.*, 1996 & Goto *et al.*,1993), where "*t*" is the width of the tie-columns. It is also known that the shear cracks in the RC tie columns occurs at the four corners of the wall inclined by an approximate angle $\alpha = 45^{o}$ (Pillai and Kirk, 1988).

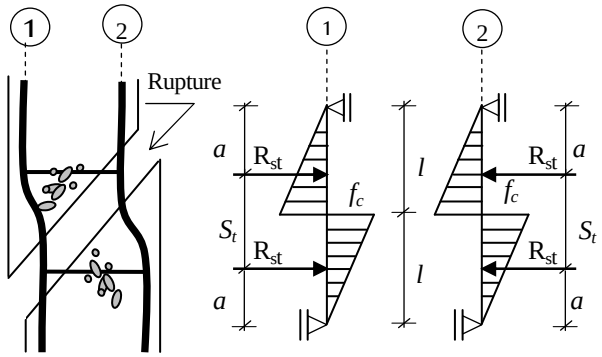
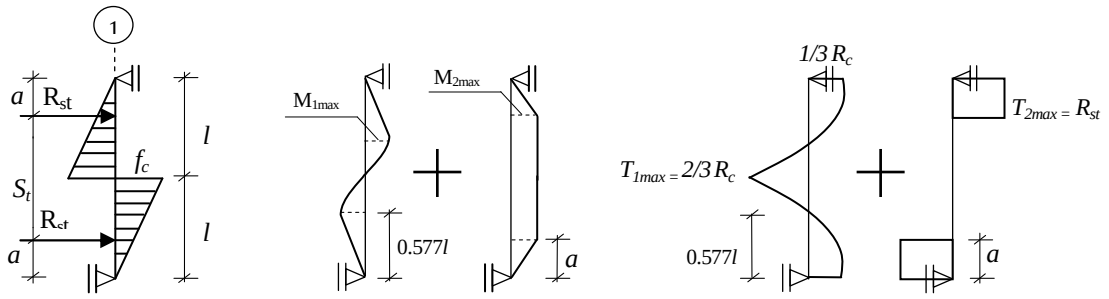


Figure 1-a Reactions on main bars which causes the dowel effect

According to the above reasoning, the shear crack would cross 1 or 2 stirrups at maximum (the stirrups are supposed positioned symmetrically from the inflection point of the bars presenting dowel action). The appropriate presentation of the dowel action phenomenon is clearly shown by the Figure1-a. This will result in moment and shear force distributions of the form shown in Figure1-b.



1) Flexural moment diagrams 2) Shear diagrams

Figure1-b Flexural and shear diagrams resulting from the dowel-action model

From the bending moment equilibrium:

$$M_{\max} = \frac{0.256}{f_c \phi} R_c^2 + \frac{2R_{st}}{f_c \phi} R_c - \frac{R_{st} S_t}{2} \qquad (1)$$

Where,
M_{max} = maximum external moment on the main bar.
$R_c = f_c \phi l /2$ = reaction of the concrete on the main bar.
f_c = compressive strength of concrete
ϕ = the main bar diameter
$R_{st} = f_{yt} A_{st}$ = reaction of the stirrup on the main bar.
(f_{yt} and A_{st} are the yield stress of stirrup and its section, respectively).
S_t= distance between two successive stirrups.

The internal moment in the main (longitudinal) bar is equal to:

$$M_{\max,b\,e} = z_e\ f_y = \frac{\pi \phi^3}{32} f_y \quad \text{for linear case} \qquad (2\text{-a})$$

$$M_{\max,b\,p} = z_p\ f_y = \frac{\phi^3}{6} f_y \quad \text{for nonlinear case} \qquad (2\text{-b})$$

$M_{max,b,e}$ and $M_{max,b,p}$ = maximum internal moment in the main bar for both cases linear and nonlinear, respectively. .
f_y = yield stress of the main bar.
Z_e and Z_p = Plastic and elastic section modulus, respectively (Figure 2)
f_y = yield stress of the main bar.
Equalizing the Eqs. (2-a) and (2-b) consecutively to the Eq. (1) gives:

$$\frac{0.256}{f_c \phi} R_c^2 + \frac{2 f_{yt} A_{st}}{f_c \phi} R_c - \frac{16 f_{yt} A_{st} S_t + \pi \phi^3 f_y}{32} = 0$$

for linear model (3-a)

$$\frac{0.256}{f_c \phi} R_c^2 + \frac{2 f_{yt} A_{st}}{f_c \phi} R_c - \frac{3 f_{yt} A_{st} S_t + \phi^3 f_y}{6} = 0$$

for nonlinear model (3-b)

After solving Eqs. (3-a) and (3-b) i.e (determination of the value of R_c), the maximum value of shear resistance due to the dowel action of one single bar is obtained by the superposition of shear force diagrams shown in Figure1-b, where:

$$T_{\max,b} = \max\left(\tfrac{2}{3} R_c, \tfrac{1}{3} R_c + R_{st}\right) \qquad (4)$$

$T_{max,b}$ = The maximum value of shear resistance due to the dowel action of one single bar on the dowel length 2l

Taking into account that, $R_c = f_c \phi\, l /2$, the value of the dowel length 2l is then deduced.

In case $2l \leq S_t$ (stirrups positioned outside of the dowel length), the stirrups will not contribute to the shear resistance due to dowel mechanism ($R_{st} = f_{yt} A_{st} = 0$), however, only the effect of concrete would be considered and the reaction of the concrete R_c will be recalculated consequently.

The shear resistance H_{cf} of 2n vertical bars, which represents the total lateral resistance induced by the tie-columns, is equal to:

$$H_{cf} = \sum_{i=1}^{2n} T_{\max,bi} \qquad (5)$$

n = the total number of longitudinal bars in each tie-column.

As a result, the maximum shear or lateral resistance of a confined masonry wall H_{wall} is then:

$$H_{wall} = H_m + H_{cf} \qquad (6)$$

Where;

1- Failure of the wall by diagonal splitting:

$$H_m = A_m \frac{f_{t1}}{b} \sqrt{\frac{\sigma_V}{f_{t1}} + 1} \quad \text{if} \quad \sigma_V \leq 0.5 \text{ MPa} \qquad (7.a)$$

(Bourzam et. al, 2008)

$$H_m = \frac{A_m}{b\left(1+\frac{f_{t2}}{f_m}\right)}\sqrt{f_{t2}^2+\sigma_V f_{t2}\left(1-\frac{f_{t2}}{f_m}\right)-\sigma_V^2\frac{f_{t2}}{f_m}}$$

if $\sigma_V > 0.5$ MPa (7.b)

2- Mortar-joint separation in stairs shape along the strut of the wall:

$$H_m = A_m(\tau_0 + \mu\sigma_V) \quad (8)$$

Where,

H_m = the shear resistance (lateral resistance) of masonry panel.

σ_V = the average compression stress on the brick panel due to vertical (axial) load V.

b= the shear stress distribution factor depends of the height to length ratio h/l of the brick panel (b= 1 for $h/l \le 1$, $b = h/l$ for $1< h/l <1.5$ and b=1.5 for $h/l \ge 1.5$) (Tomaževič, 1999).

A_m = the horizontal cross-section area of the masonry panel.

f_{t1} and f_{t2} = tensile strengths of masonry, where:

$f_{t1}=0.519P_d/A$ the average masonry tensile strength, obtained by diagonal compression test as specified by ASTM C1391) (P_d and A are the maximum diagonal compressive load and the test panel section, respectively).

$f_{t2} = 0.5187\, f_m \frac{P_d}{\left(f_m A - 1.683 P_d\right)}$ obtained by Mohr's failure theory (Yokel, 1976 and Sucuoglu, 1991).

f_m = the masonry compressive strength obtained by testing stack bonded prisms of five bricks according to the specifications of LUMB1, (1994).

τ_0 = the shear strength at zero pre-compression.

μ = the friction coefficient in mortar-brick interface.

The Coulomb failure mode (refer to Eq. (8)) is then valid for lower axial stresses σ_V or low quality of mortar joints. In case of lower axial loading, it is recommended to calculate the brick panel resistance H_m by both Eqs. (7-b) and (8) where the greater value of H_m will be considered in the rest of calculations.

3. EXPERIMENTS AND RESULTS

The test specimen is a 1/2 scale of a common confined masonry bearing wall with h/l ratio equal to 1.5 surrounded by RC tie-columns.

The panel of the wall is composite of Japanese solid clay brick units with 210x100x60 mm of nominal dimensions. The bricks are laid with plain cement mortar, with a joint thickness of 10 mm.

The surrounding frame which serves to confine the brick panel is made by reinforced concrete. Mechanical characteristics of used materials, details of dimension, arrangement of reinforcement and member sections are summarized in Table 1 and Figure 3.

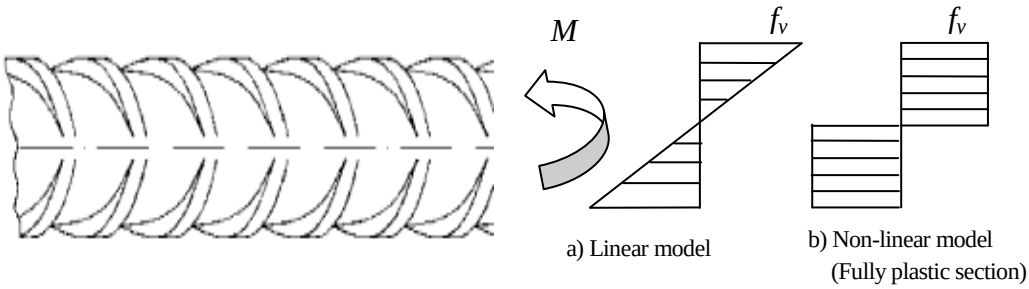


Figure 2 Internal repartition of stresses of main bars due to bending moment of linear and non linear models

The confined wall was tested in the laboratory of structural members of Kanazawa University by the loading system as shown in Fig.ure 4. The constant vertical load to simulate the dead load was represented by the weight of the top RC gravity beam which offered an axial stress of 0.1MPa.

The specimen was subjected to a quasi-static horizontal cyclic loading applied to the center of the top-beam by the mean of a horizontal hydraulic jack. The specimen was designed as a cantilever vertical structural element. The lateral displacement at the top of the wall was measured by two transducers of LVDT type.

Increasing the drift angle (displacement) gradually from 1/5000 the maximum resisting force of specimen was attained

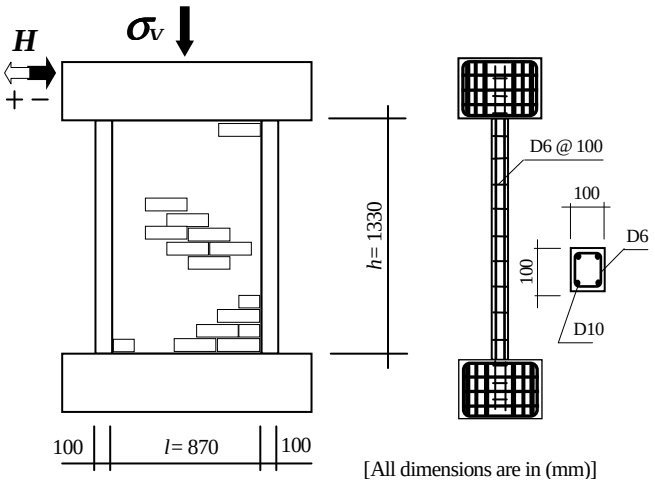


Figure 3 Test specimen

Table1. Material properties

Property		Exp. value
Brick compression strength (MPa)	f_b	60
Mortar compression strength (MPa)	f_{mor}	27
Concrete compression strength (MPa)	f_c	18
Diameter of longitudinal steel bars (mm)	ϕ	10
Diameter of steel bars forming the stirrups (mm)	ϕ_t	6
Distance between two successive stirrups (mm)	S_t	100
Yielding stress in longitudinal steel bars (MPa)	f_y	325
Yielding stress in stirrups (MPa)	f_{yt}	400
Masonry compression strength (MPa)	f'_m	21
Masonry tensile strength (MPa)	f'_{t1}	1.52
Modulus of elasticity of masonry (MPa)	E_m	11833
Shear modulus of masonry (MPa)	G_m	3120
Modulus of elasticity of concrete (MPa)	E_c	27000
Shear modulus of concrete (MPa)	G_c	11441

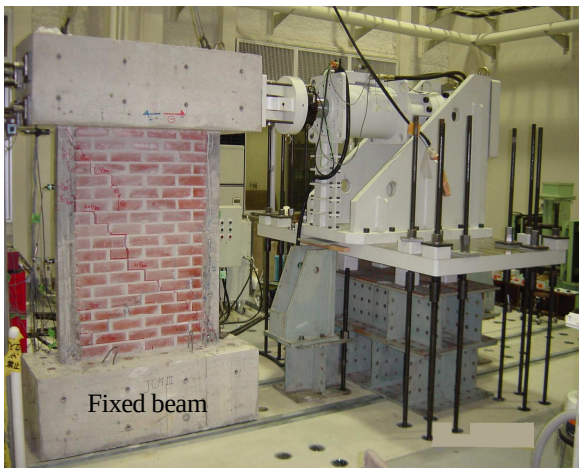


Figure 4 Loading system.

Table 2 Experimental and theoretical lateral resistances of the wall

		Linear model		
$H_{wall\ Exp}$* (kN)	H_m (kN)	H_{cf} (kN)	$H_{wall}= H_m+H_{cf}$ (kN)	$(H_{wall}- H_{wall\ Exp.})/H_{wall\ Exp.}$ %
52.35	40.47	24.91	65.38	24.90
		Non linear model		
		32.45	72.92	39.29

* Experimental value

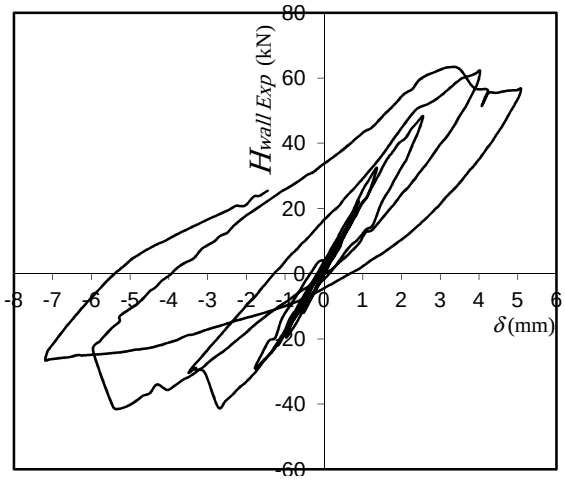


Figure 5 Lateral load-displacement hysteresis loops.

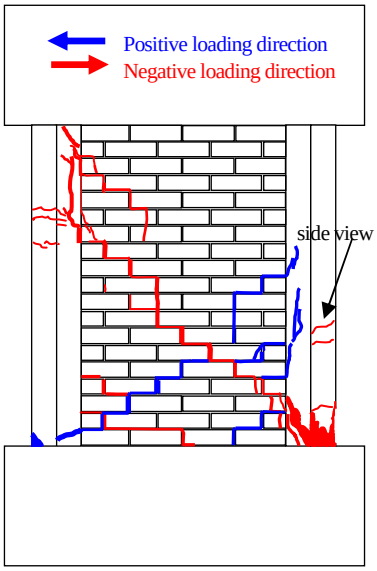


Figure 6 Final crack pattern of the wall.

4. CONCLUSIONS

It is concluded in the case of the linear model the contribution of tie-columns to the total shear capacity represents an average value of 38.1%. This ratio is greater when the non-linear model is adopted (44.5%). According to Umek (1971) almost 20% of the total resistance is attributed to both confinements, which means the linear model is more representative.

In the other hand, the analysis of the correlation of the theoretical predictions to the experimental values have shown that the linear model overestimates the real shear resistance (experimental value) by only 24.90% but the nonlinear model pushes this value to 32.45%.

In conclusion, in this type of structural member, confinements or tie columns do not acquire the possibility to be plastically hinged. The linear model is then the best representative.

Acknowledgements:

The authors acknowledge support from the Japan Ministry of Education, Culture, Sport, Science, and Technology (MEXT) for establishing the Center for Urban Earthquake Engineering (CUEE) in Tokyo Institute of Technology. This support makes possible the forthcoming international conference, as well as international joint research projects and exchange programs with overseas universities.

References:

Umek, A. (1971),"Comparaison between unreinforced, confined and horizontally reinforced masonry walls," *Civil Engrg. J.,Vol. 20 (Society of Civil Engineers, Ljubljana)*, 241-248.

Yoshimura, K., Kikuchi, K., Okamoto, T. and Sanchez, T, (1996), "Effect of vertical and horizontal wall reinforcement on seismic behavior of confined masonry walls," *Proc. of 11th World Conf. Earthquake Engrg.* (11thWCEE), CD-ROM, No. 191.

Goto, T., Mizuno, H., Iiba, M. and Kato, H.,(1993), "Cyclic loading tests of confined masonry walls," *Research report, B.R.I*, Tsukuba, Japan, March.

Pillai, S.U. and Kirk, D.W., (1988), "Reinforced concrete design," Canadian Cataloguing in Publication Data, 2nd ed.

Yokel, F. Y., and Fattal, S, G. (1976),"Failure hypothesis for masonry shear walls,"*J. Struct. Div.*, ASCE, 102(3), 515-532.

Sucuoglu, H. and McNiven, H. D. (1991),"Seismic shear capacity of reinforced masonry piers," *J. Struct. Engrg.*Vol. 117, No 7, 2166-2186.

Tomasevic, M. and Klemenc, I. (1997),"Seismic behaviour of confined masonry walls,"*Earthquake Engrg. Struct. Dynamics*,Vol. 26, 1059-1071.

Bourzam, A., Goto, T. and Miyajima, M. (2008), "Shear capacity prediction of confined masonry walls subjected to cyclic lateral loading,"*JSCE Journal of Structural and Earthquake Engineering, (Doboku Gakkai Ronbunshuu A)*, Vol. 64, No. 4, 2008, 692-704.

Turnsek, V. and Cacovic, F. (1971), "Some experimental results on the strength of brick masonry walls," *Proc.2nd int. brick masonry conf.*, Stoke-on-Trent, 149-156.

Priestley, M.J.N. and Bridgeman, D.O. (1974), "Seismic resistance of brick masonry walls," *Bull. of the New Zealand Nat. Soc.* for *Earthquake Engrg.* 7 (4) (New Zealand National Society for Earthquake Engineering, Wellington),167-187.

Rilem. Technical recommendations for the testing and use of constructions materials (1994), "LUMB1, Compressive strength of small walls and prisms".

Chiostrini, S., Galano, L. and Vignoli, A.(2000), "On the determination of strength of ancient masonry walls via experimental test," *Proc. of 12th World Conf. Earthquake Engrg.*, CD-ROM.

Tomaževič, M. (1999), "Earthquake-resistant Design of Masonry Buildings, (Innovation in Structures and Construction," *Vol. (I), Imperial college press.*

10CUEE CONFERENCE PROCEEDINGS
10th International Conference on Urban Earthquake Engineering
March 1-2, 2013, Tokyo Institute of Technology, Tokyo, Japan

SHEAR DESIGN OF STRUCTURAL WALLS

John W. Wallace[1], Chris Segura[2], and Thien Tran[3]

1) Professor, Civil Engineering, University of California, Los Angeles, United States of America
2) PhD Student, Civil Engineering, University of California, Los Angeles, United States of America
3) Post Doctoral Reseacher, Civil Engineering, University of California, Los Angeles, United States of America
wallacej@ucla.edu, christopherlsegura@gmail.com, thientran@ucla.edu

Abstract: The Los Angeles Tall Buildings Structural Design Council and PEER Tall Buildings Initiative performance-based design guidelines for shear design of structural walls are reviewed. Provisions in the two documents are identical, except for the recommended capacity reduction factor ϕ, which is 1.0 for the LATBSDC document and 0.75 for the PEER document. Shear wall failure modes, test results, ACI 318-11 code provisions, and modeling approaches are reviewed to assess the current design approaches and to propose changes.

1. INTRODUCTION

Performance-based design of tall buildings is commonly based on the comparison of analysis demands and capacities for at least two hazard levels, service-level earthquake (SLE) and maximum considered earthquake (MCE). Service-level analysis is typically accomplished using a linear model of the building and a site-specific response spectrum analysis for a 43-year return period earthquake (50% probability of being exceeded in 30 years), although use of a nonlinear analysis is generally permitted. Three dimensional, nonlinear models of the building system are developed and subjected to seven or more pairs of earthquake records at the building base for the MCE analysis; MCE ground motions are defined in Chapter 21 of ASCE 7-05.

Acceptance criteria for various response parameters, including demand-to-capacity ratios for force-controlled components, plastic rotations and strain demands for deformation-controlled components, and story and residual drift limits are used as a basis to judge whether a building design complies with the expectation that the building performance will be equal to or better than the performance of a building meeting prescriptive code requirement (ASCE 7-05, Section 12.2.2). Consensus documents such as the Los Angeles Tall Buildings Seismic Design Council Guidelines (LATBSDC, 2011) and the PEER Tall Buildings Initiative Guidelines (Peer TBI, 2010) include example acceptance criteria for both SLE and MCE analyses. In the following paragraphs, example acceptance criteria for MCE are briefly reviewed.

Global Acceptance Criteria: Global acceptance criteria include story drift and residual drift are commonly expressed as (LATBSDC, 2011, Section 3.5.4.2; PEER TBI, 2010, Section 8.7):

$$\begin{aligned} \bar{\theta}_{max,\ transient} &\le 3.0\% \quad & \bar{\theta}_{max,\ transient,\ residual} &\le 1.0\% \\ \theta_{max,\ transient} &\le 4.5\% \quad & \theta_{max,\ transient,\ residual} &\le 1.5\% \end{aligned} \tag{1}$$

Where $\bar{\theta}$ is the mean of the maximum absolute values obtained from seven or more pairs of earthquake records applied to the building and θ is the maximum absolute value obtained for a single pair of earthquake records applied to the building.

Deformation-controlled Acceptance Criteria: Criteria for deformation-controlled components are typically take the form of:

$$\begin{aligned} \bar{\theta}_{plasitc,\ max,\ transient} &\le \theta_{limit} \\ \bar{\varepsilon}_{max,\ transient} &\le \varepsilon_{limit} \end{aligned} \tag{2}$$

where $\bar{\theta}$ and $\bar{\varepsilon}$ are the mean of the maximum absolute values of plastic rotation and total axial strain obtained from seven or more pairs of earthquake records applied to the building and θ_{limit} and ε_{limit} are a limiting values of plastic rotation and axial strain. Limiting values of rotation and demand are determined using available test data and judgment, e.g., as included in ASCE 41-06 (2013) for reinforced concrete columns, beams, and slender structural walls. The value of limiting concrete compressive strain depends on how the strain value is obtained (e.g., as an average value over a height that is selected to be approximately equal to the plastic hinge length), and how modeling uncertainty is treated (e.g., the potential bias in the model strain value). Commonly used values are in the range of: $\bar{\varepsilon}_{max,\ t} \le 0.05$ and $\bar{\varepsilon}_{max,\ c} \le -0.015$.

Force-controlled Acceptance Criteria: Acceptance criteria for force-controlled components can be represented as:

$$(1+\beta)\bar{F}_u \le \phi F_{n,e} \quad (3)$$

where β accounts for uncertainty in the maximum mean force demand $\bar{F}_u$, and strength reduction factor ϕ accounts for uncertainty in nominal strength for expected material properties $F_{n,e}$. Nominal strengths are typically computed using ACI 318-11 provisions. Values for β and ϕ depend on the whether the element is a "critical" on "non-critical". The LATBSDC and PEER TBI Guidelines define critical actions as those "*in which the failure mode poses severe consequences to the structural stability under gravity and/or lateral loads*". Ideally, the β-value could be determined directly from the variation in the maximum values obtained from the analysis results; however, because it is common to use only seven (and certainly less than 15) pairs of earthquake ground acceleration histories applied at the base of the building, little confidence can be placed on the computed values of the mean and standard deviation. Studies (PEER, TBI, 2010) have shown that the true coefficient of variation in force-controlled actions due to record-to-record variability is on the order of 0.4; therefore, both the LATBSDC and PEER TBI Guidelines recommend using β = 0.5. The slightly higher value (0.5 vs 0.4) is used to account for modeling uncertainties and uncertainty in the mean value. The LATBSDC (2011) and PEER TBI (2010) Guidelines are effectively identical, except for the recommended value of ϕ; with the LATBSDC Guidelines (2011) recommend ϕ = 1.0, whereas the PEER TBI Guidelines (2010) recommend using the ϕ-value from ACI 318. For wall shear design, the ACI 318 ϕ-value for shear is 0.75; therefore, shear design of a structural wall according to PEER TBI will be 1.0/0.75 = 1.33 times thicker than the LATBSDC designed wall. For the relatively thick walls required for tall buildings, e.g., 1m to 1.33m thick, a 33% increase in wall thickness is significant.

Given the difference in the ϕ-values for the LATBSDC and PEER TBI Guidelines, and the significant impact this difference has on wall design, a study is undertaken to review shear design of structural walls using a reliability-based approach.

2. SHEAR DESIGN OF STRUCTUAL WALLS

2.1 Strength Design Requirements

Code based shear design of structural walls is based on satisfying:

$$\phi V_n \ge V_u \quad (4a)$$

Where V_n is calculated using the ACI 318-11 nominal shear strength equation:

$$V_n = A_{cv}\left[\alpha_c \lambda \sqrt{f_c'} + \rho_t f_y\right] \le A_{cv}\left[0.67\sqrt{f_c'}MPa\right] \quad (4b)$$

Where f_c' is specified compressive strength of concrete, f_y is specified yield strength of reinforcement, A_{cv} is gross area of concrete section bounded by web thickness and length of section in the direction of shear force considered, α_c is coefficient defining the relative contribution of concrete strength to nominal wall shear strength, and ρ_t is ratio of area of distributed transverse reinforcement to gross concrete area perpendicular to that reinforcement. Coefficient α_c is 3.0 for $h_w/l_w \le 1.5$, is 2.0 for $h_w/l_w \ge 2.0$, and varies linearly between 3.0 and 2.0 for h_w/l_w between 1.5 and 2.0. ACI 318-11 also limits the maximum shear stress on any one wall to $v_n \le 0.83\sqrt{f_c'}MPa$ and the average shear stress on all walls providing lateral force resistance to $v_n \le 0.67\sqrt{f_c'}MPa$. Shear demand V_u is determined using ASCE 7-05 provisions using either the equivalent lateral force procedure (Section 12.8), modal response spectrum analysis (Section 12.9), or seismic response history procedures (Chapter 16).

The ACI 318-11 Equation for V_n is a relatively simple expression and does not include factors that are known to have an impact on shear strength, such as axial load and the quantity of boundary transverse reinforcement. However, until more comprehensive relations are developed and validated, use of the current ACI 318 equation, which has remained effectively unchanged since it was introduced in ACI 318-83, is common (LATBSDC, 2011; PEER TBI, 2010). As is common with code equations used to determine nominal strength for design of new buildings, the ACI 318 wall shear strength equation tends to produce a low estimate of the actual shear strength to ensure a low probability of wall shear failure in the Design (Basis) Earthquake. For design of new buildings using prescriptive design approaches, nominal material properties are used and code specified strength reduction factors are applied, i.e., $\phi = 0.75$.

As noted in the introduction, for performance-based seismic (or non-prescriptive) design, the LATBSDC (2011) and PEER TBI (2010) documents use Equation (3), which is a slightly modified form of Equation (4a) to account for use of a response history analysis procedure. Equation (3) is restated here as:

$$\phi \bar{F}_{n,e} \ge \gamma \bar{F}_u \quad (5)$$

where γ accounts for uncertainty in the maximum mean force demand $\bar{F}_u$, and strength reduction factor ϕ accounts for uncertainty in mean nominal strength for expected material properties $\bar{F}_{n,e}$.

Equation (5) is used as a basis to apply reliability-based design approach to assess shear design of structural walls. The objective is to evaluate the probability of shear failure given distributions and uncertainties in demand and capacity, and to determine if it exceeds a limiting value, taken as 10% for MCE demands.

2.2 Wall Failure Modes, Capacities, and Demands

Reliability-based design requires a review of shear wall behavior (failure modes), wall capacities, both force and deformation using available test data, and wall demands determined from response history analysis. Each of these topics is reviewed in the following subsections.

(a) Wall behavior: Three structural wall failure modes, similar to those proposed for columns by Elwood and Moehle (2008), are depicted in Fig. 1; (a) shear, (b) flexure-shear, and (c) flexure. Flexural failures are typically characterized by concrete crushing followed by buckling of boundary vertical reinforcement and eventual fracture of boundary vertical reinforcement. Shear failures, in the absence of sliding shear failures, are typically characterized by either diagonal tension failure or crushing of concrete along diagonal compressive struts within the wall web (or web crushing). For flexure-shear failure, as nonlinear flexural deformation (ductility) increases, flexural and bond crack widths grow and the expectation is that shear resistance will degrade, leading to shear failure. Flexural-shear failures are likely to look like flexural failures, i.e., concrete crushing followed by buckling of boundary vertical reinforcement and/or diagonal tension failures (Tran, 2012). For both flexure and flexure-shear failures, the compressed boundary region may buckle in - or out-of-plane depending on the ratio of wall thickness to concrete side cover, axial load, and shear demand (Tran and Wallace, 2012).

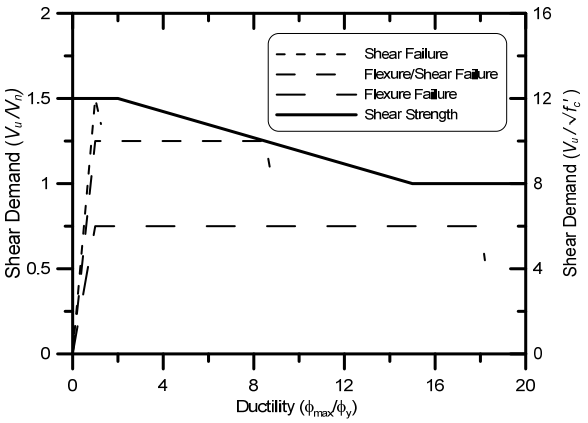


Figure 1 Wall Shear Behavior: (a) Shear, (b) Flexure-shear, (c) Flexure

(b) Wall Capacity (Test Data): Test data for relatively slender, well-detailed, walls were compiled to assess the relationship shown in Fig. 1. For this study, well-detailed walls were defined as walls with area of boundary transverse reinforcement at least equal to one-half of that required by ACI 318-11 and ratio of vertical hoop/crosstie spacing to vertical boundary bar diameter (s/d_{bl}) less than 8 (ACI 318-11, 21.9.6.4 limits this ratio to 6). Failure modes for each test also are characterized based on information reported in the literature. Plastic rotation θ_{pl} and curvature ductility $\mu_\phi = \phi_u/\phi_y$ for each test were calculated using the following relation (e.g., see Wallace, 1994):

$$\delta_u = \delta_y + \theta_{pl}\left(h_w - l_p/2\right) = \delta_y + l_p\left(\phi_u - \phi_y\right)\left(h_w - l_p/2\right) \quad (6)$$

where δ_u is the lateral displacement at significant strength loss, δ_y is the yield displacement, ϕ_u is the ultimate curvature, ϕ_y is the yield curvature, h_w is the wall height, and l_p is the plastic hinge length. Values for δ_u, δ_y, and ϕ_y are determine directly from test data; plastic hinge length for the well-detailed walls was taken as one-half the wall length $(l_w/2)$.

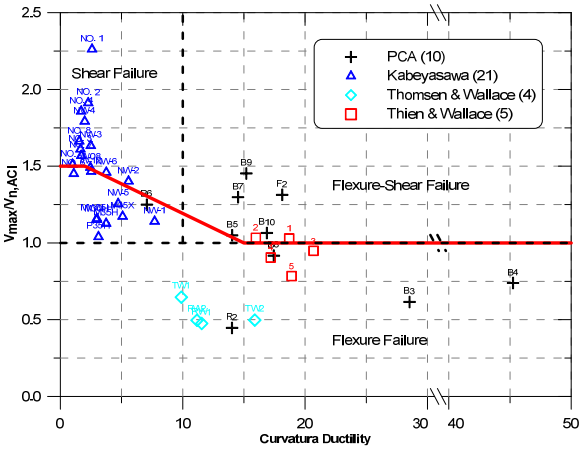
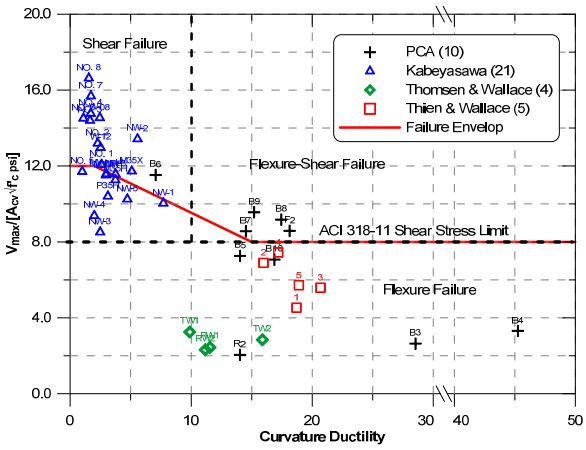


Fig. 2(a) Wall curvature ductility versus $V_{u,test,max}/V_n$

Fig. 2(b) Wall curvature ductility versus $V_{u,test,max}/\sqrt{f'_c}$



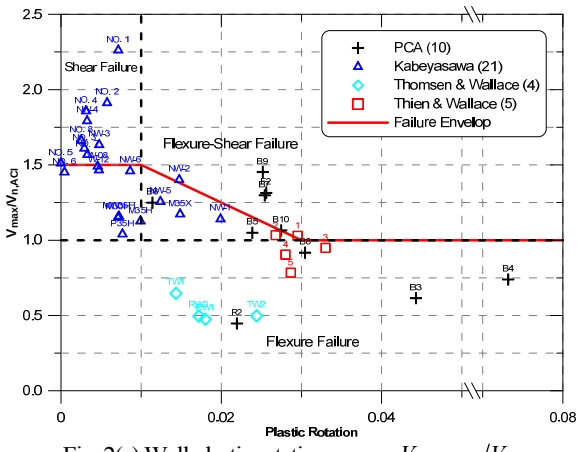


Fig. 2(c) Wall plastic rotation versus $V_{u,test,max}/V_n$

Results for the test database are presented in Fig. 2, with V_{max} is the maximum shear measured in the test. For the 22 test specimens with $\mu_\phi = \phi_u/\phi_y < 10$, the following observations are noted from Fig. 2(a): (a) mean value and

coefficient of variation of V_{max}/V_n are 1.47 and 0.21, (b) mean value and coefficient of variation of μ_ϕ are 3.2 and 1.8, and (c) majority of data points below the shear strength trend line were for walls with barbell cross sections subjected to biaxial loading which failed due to web crushing. For the 11 test specimens with $V_{max}/V_n \le 1.0$ and $\mu_\phi = \phi_u/\phi_y \ge 10$ all failures except B6 were characterized as "flexure". Test specimens in the transition region (flexure-shear failures) with $V_{max}/V_n > 1.0$ consist primarily of barbell-shaped wall cross-sections designed according to ACI 318-95 or earlier codes in which web-crushing failures were observed (e.g., B5-B9, F2). Such walls typically have substantial flexural overstrength, resulting in higher wall web shear demands than were used for design (Wallace and Orakcal, 2002). Current US construction practice is to use rectangular (versus barbell) wall cross sections and for ACI 318-99 and later versions, code provisions were changed to reduce flexural overstrength and thus the potential for web crushing failures.

Test results are presented in a slightly modified format in Figures 2(b) and 2(c), with vertical axis is normalized shear stress $V_{max}\Big/\left(A_{cv}\sqrt{f_c'}\right)$ for Fig. 2(b) and plastic rotation θ_{pl} on the horizontal axis for Fig. 2(c). Trends observed for Fig. 2(b) are similar to Fig. 2(a), with shear failures observed for walls with demands substantially above the ACI 318-11 limiting shear stress of $V_{max}\Big/\left(A_{cv}\sqrt{f_c'}\right) = 0.67$ and flexure failures displaying modest to large curvature ductility μ_ϕ for demands less than the ACI limiting shear stress. Results presented in Fig. 1(c) indicate modest plastic rotation θ_{pl} capacity even for walls with shear failure and plastic rotation capacities of 0.02 to 0.03 for most walls with flexure failure. Top drift ratios at yield for wall tests with $1.5 \le h_w/l_w \le 3.0$ were typically 0.005 to 0.01, resulting in roof drift ratios at significant strength loss of 0.025 to 0.035; larger roof drift ratios are likely for more slender walls in very tall buildings.

Test parameters and results for walls with shear failure are examined more closely to evaluate their relevance to current US practice for tall buildings. Since shear strength is not impacted significantly by the detailing provided at wall boundaries, the restriction that the wall boundary be "well-detailed" is relaxed; the database used here is the same as that used by Wallace (1998) and includes 37 wall tests. Ratios of the test measured maximum shear V_{max} to the computed ACI 318-11 strength V_n using equation (4b) and plotted versus $\rho_t f_y / f_c'$. Mean test shear strength is $1.57\,V_n$ with a coefficient of variation of only 0.20. Results presented in Fig. 3 reveal that ACI 318-11 Equation (21-6), Equation (4b) in this paper, significantly underestimates wall shear strength, with a slight trend for less conservatism as the ratio of $\rho_t f_y / f_c'$ increases from 0.02 to 0.16.

The test results presented in Fig. 3 include tests with quantities of web reinforcement that significantly exceed that required by ACI 318-11, i.e., the value of $\rho_t f_y / f_c'$ exceeds the value required to reach the ACI 318-11 limiting shear stress of $V_n \le A_{cv}\left[8\sqrt{f_c'}\,psi\right]$. To assess the potential bias in the mean and COV associated with including these data, the test results were sorted to into bins with $V_n \le 1.1\left[0.67\sqrt{f_c'}\,MPa\right]A_{cv}$ and $V_n > 1.1\left[0.67\sqrt{f_c'}\,MPa\right]A_{cv}$. Mean and COV for the entire database and the two bins, along with information on concrete strength, are given in Table 1 and indicate no significant bias.

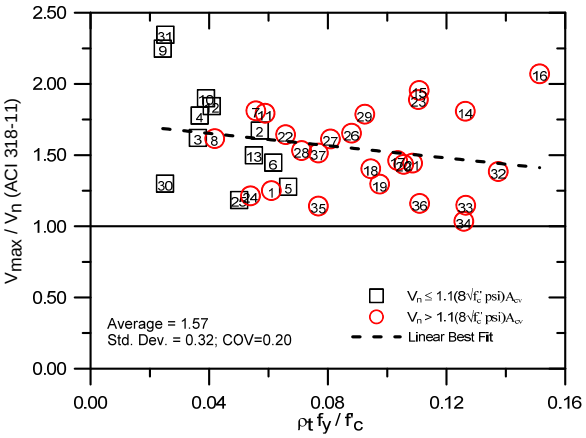


Figure 3 Wall tests with shear failure – $V_{test}/V_{n,ACI}$ Wall shear strength versus $\rho_t f_y / f_c'$

Table 1 Wall Shear and Concrete Strength

Database	Tests	$V_{test,max}/V_n$		f_c'	
	#	Mean μ	COV σ	Mean μ	COV σ
All	37	1.57	0.20	11.05	0.23
$V_n \le 1.1\left[0.67\sqrt{f_c'}\right]A_{cv}$	12	1.68	0.22	10.81	0.21
$V_n > 1.1\left[0.67\sqrt{f_c'}\right]A_{cv}$	25	1.52	0.19	11.27	0.24

It is noted that the mean values of concrete compressive strength and reinforcement yield strength for the 37 tests were $\mu_{concrete} = 1.1 f_c'$ and $\mu_{steel} = 1.05 f_y$. Mean and coefficient of variation reported by Nowak et al (2008) for concrete compressive strengths of 8 to 10 ksi (55.2 to 69.0 MPa) in the range of 1.1 to 1.16 and 0.09 to 0.12, whereas values for reinforcement reported by Bournonville et al (2004) for #7 to #10 bars (22.2mm to 32.3mm diameter bars) are about 1.12 to 1.14 and 0.02 to 0.03.

(c) Nonlinear Wall Modeling for Response History Analysis and Wall Shear Demands: Common practice is to model axial-bending behavior independent of shear behavior using beam-column fiber (BC-Fiber) elements with concrete and rebar fibers with defined uniaxial material relations. Use of BC-Fiber models is attractive because: (1) element yield moment and bending stiffness automatically vary with level of axial load, (2) element overstrength depends directly on element demands and defined material relations, (3) migration of the neutral axis along the wall cross-section during loading and unloading varies with applied P-M, (4) wall axial growth or shortening are captured, and as a consequence of (1) through (4), (5) interactions with connecting elements (e.g., beams and slabs), both in the

plane of the wall and perpendicular to the wall, are captured. Nonlinear shear behavior is typically modeled using multi-linear segment backbone relation defined by shear strength associated with inclined cracking, yielding, and degrading strengths (e.g., ASCE 41 backbone relations).

As noted in the introduction, values for $\gamma = (1 + \beta_{tot})$ and ϕ depend on the whether the element is a "critical" on "non-critical". Studies (PEER TBI, 2010) have shown that the true coefficient of variation in force-controlled actions due to record-to-record variability is on the order of 0.4; therefore, both the LATBSDC and PEER TBI Guidelines recommend using γ = 1.5. The slightly higher value (1.5 vs 1.4) is used to account for modeling uncertainties and uncertainty in the mean value.

The PEER TBI notes that: "*The use of use of 1.3σ, where σ is the standard deviation obtained from Maximum Considered Earthquake response analysis is permitted for specific cases, such as beam shear in a moment-resisting frame, where localized or global mechanisms may limit the force value to a rather stable maximum value and inflation to 1.5 times the mean value may be too large. This would not, in general, apply to shear in structural walls*". The last sentence is included despite the fact that nonlinear modeling of axial-bending behavior over the entire wall height, nonlinear modeling of coupling beams, and nonlinear modeling of outrigger slabs (if they are included in the model) provide a fuse to limit wall shear demands (Salas, 2008). Additional studies are needed to assess wall shear dispersion for tall buildings utilizing structural walls for lateral-force resistance (i.e., core wall buildings) using appropriate sets of ground motion records; until additional information is available, continued use of *1.5σ* on force-critical elements is likely to continue. The appropriate multiplier on capacity, ϕ, is examined using a reliability-based analysis is the following section.

2.3 Reliability-Based Design

A framework is developed for reliability-based assessment of structural wall failure based on Equation (5) using Monte Carlo Simulation. The objective of this preliminary study, given a mean demand multiplier of $\gamma \bar{F}_u = (1 + \beta)\bar{F}_u$, what is the appropriate multiplier ϕ on mean capacity $\bar{F}_n$ mean ($\phi \bar{F}_n$) to limit collapse probability to an acceptable level (90% reliability against collapse) under MCE demands. For this preliminary study, all random variables associated with capacity and demands are assumed to be normally distributed (it is noted a Beta-distribution is more appropriate for reinforcement).

Wall shear strength is based on ACI 318-11 requirements, i.e., using Equation (4b). Assuming negligible variability in cross-section properties (i.e. A_{cv} and ρ_t constant), mean overstrength associated with the 37 shear-controlled tests are:

$$\begin{aligned} \mu_{vn} &= V_{\max,test}/V_n = 1.73 \qquad \beta_{vn} = 0.22 \\ \mu_{vne} &= V_{\max,test}/V_{ne} = 1.57 \qquad \beta_{vne} = 0.20 \end{aligned} \tag{7}$$

Where μ_n and μ_n are the mean values for nominal and expected material properties, respectively, and β_{vn} and β_{vne} are the coefficients of variation (cov). For the 37 tests, expected material properties were approximately $f'_{ce} = 1.10 f'_c$ and $f_{ye} = 1.05 f_y$; therefore, the mean values are related by:

$$\mu_{vn} = \left(\sqrt{1.1}\right)(1.05)(\mu_{vne}) \tag{8}$$

The square root on the concrete term is because wall nominal shear strength (V_n) according to ACI 318-11 is related to $\sqrt{f'_c}$. The dispersion values of 0.20 and 0.22 for expected and nominal properties, respectively, is relatively low for brittle failure modes of reinforced concrete members; therefore, for this preliminary study, dispersion values β_{vn} and βvne are assumed to be 0.3. Examination of a larger test database is needed to resolve this issue for typical materials used for tall buildings.

As discussed previously, for collapse assessment, shear demands in PEER TBI and LATBSDC are taken as:

$$(1 + \beta)\bar{F}_u = 1.5\bar{F}_u \tag{9}$$

With the design objective of:

$$\phi V_n \geq 1.5\bar{F}_u \tag{10}$$

Therefore, for the purpose of this reliability study, demand is defined as:

$$\bar{F}_u = \frac{\phi V_n}{1.5} \quad and \quad \bar{F}_{ue} = \frac{\phi V_{ne}}{1.5} \tag{11}$$

Nominal material properties are used to define $\bar{F}_u$ and expected (mean) material properties are used to define $\bar{F}_{ue}$.

For capacity, mean values and dispersion are described by Equation (7), with expected concrete and steel strengths treated as random variables. Given these distributions, the reliability analysis assesses the following relation using Monte Carlo Simulation:

$$Reliability = P\left[V_{\max} \geq \bar{F}_u\right] \tag{11}$$

Monte Carlo Simulation is used to predict the reliability. By determining an adequate distribution for each of the random variables that make up the capacity and demand as described above, random sampling may be performed over an acceptable number of iterations to obtain dependable results. Dependable results are determined by convergence of a solution as the number of iterations is increased.

2.4 Application: Shear Reliability Assessment

Reliability analysis is performed on the following rectangular wall using the following values: f'_c=8 ksi (55.2 MPa), f_y=60 ksi (414 MPa), ρ_t= 0.011, and A_{cv} = 30" x 360" = 10,800 in^2 (0.76m x 9.14m = 6.97 m^2).

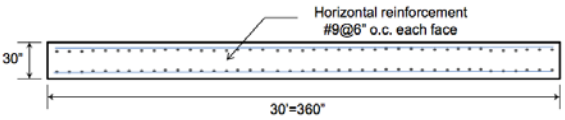


Figure 4 Wall Section for Reliability Analysis (#9@6" or 28.7mm diameter bar @152.4mm)

Reliability results are summarized in Table 2 for various criteria. Values for expected concrete compressive $\left(f_{ce}^{'}=1.13f_{c}^{'}\right)$ and reinforcement yield $\left(f_{ye}=1.13f_{y}\right)$ strengths, along with COV (0.10 and 0.02) are taken based on results presented by Nowak et al (2008) and Bournonville et al (2004), and are slightly higher than reported for the shear-controlled tests. The results presented in Table 2 indicate that reliability exceeding 94% can be achieved for all cases. It is noted that, expected material properties used in the LATBSDC (2011) or PEER TBI Guidelines are higher, i.e., $f_{ce}^{'}=1.3f_{c}^{'}$ and $f_{ye}=1.17f_{y}$. Assuming dispersions (cov) of 0.2 and 0.1 for concrete and steel, respectively, the reliabilities are lower slightly lower for Design Cases II and IV in Table 2. To obtain a reliability factor of 90% for Design Case IV requires use of $\mu_{vne}=V_{\max,test}/V_{ne}=1.35$, which is a low overstrength value Equation (4b).

Table 2 Wall Shear Reliability

	DESIGN CASE			
PARAMETER	I	II	III	IV
CRITERIA	$\phi F_n=1.5\bar{F}_u$	$\phi F_{n,e}=1.5\bar{F}_u$	$\phi F_n=1.5\bar{F}_u$	$\phi F_{n,e}=1.5\bar{F}_u$
f'_c(psi)	8,000	9,040	8,000	9,040
f_y(psi)	60,000	67,800	60,000	67,800
ϕ	0.75	0.75	1.0	1.0
$\bar{F}_u$ (KIPS)	4563	5091	6084	6788
RELIABILITY	98.7	97.7	96.9	94.0
RELIABILITY*	--	97.6	--	93.8

* Based on LATBSDC (2011) and PEER TBI (2010)

3. CONCLUSIONS

The Los Angeles Tall Buildings Structural Design Council and PEER Tall Buildings Initiative performance-based design guidelines for shear design of structural walls are reviewed. Provisions in the two documents are identical, except for the recommended capacity reduction factor ϕ, which is 1.0 for the LATBSDC document and 0.75 for the PEER document. Shear wall failure modes, test results, ACI 318-11 code provisions, and modeling approaches are reviewed to assess the current design approaches and to propose changes. Based on the study, the following conclusions are reached:

- Flexure failures with curvature ductility capacity exceeded approximately 15.0 and plastic rotation capacity exceeding nearly 0.025 were reported for all well-detailed walls with ACI 318-11 $V_n \le 0.67A_{cv}\sqrt{f_c^{'}}$ MPa. Walls not achieving these deformation capacities, the walls tested by Thomsen and Wallace (2004), had approximately one-half the area of boundary transverse reinforcement required by ACI 318-11.
- Thirty-seven wall tests were categorized as shear failures. In all tests, $V_{test,max}/V_{n,ACI}>1.0$, with mean nominal shear strength of $1.57V_{n,ACI}$ and coefficient of variation of 0.20. For all walls, $V_{max,test}>0.67A_{cv}\sqrt{f_c^{'}}$ MPA. Curvature ductility for all tests were less than 10.0 (and generally less than 5.0) and plastic rotation capacities were less than 0.01.
- Tests categorized as flexure-shear failures all had $V_{test,max}/V_{n,ACI}>1.0$. Curvature ductility for these walls was generally between 5.0 and 15.0 and plastic rotations were generally between 0.01 and 0.025.
- Continued use of demands equal to $1.5\bar{F}_u$ is likely until studies are conducted to assess the role of various wall modeling parameters (e.g., component stiffness, reinforcement yield, material overstrength, and redistribution) and ground motion parameters (e.g., number of records used and scaling process). It would appear that use of a lower multiplier on mean demand is appropriate for walls that yield in flexure with shear demands $V_n \le 0.67A_{cv}\sqrt{f_c^{'}}$.
- Material overstrength values should modified to depend on design concrete compressive strength, with expected values of $f_{ce}^{'}=1.2f_{c}^{'}$ for $f_{c}^{'}<6$ ksi (48 MPa) and $f_{ce}^{'}=1.10f_{c}^{'}$ for 6 ksi (48 MPa) $<f_{c}^{'}<12$ ksi (83 MPa).
- Use of $\phi F_{n,e}=1.5\bar{F}_u$, with ϕ=1.0, $f_{ce}^{'}=1.3f_{c}^{'}$, and $f_{ye}=1.17f_{y}$, as recommended by the LATBSDC Guidelines, along with the assumption of normally-distributed random variables, produces the highest probability of failure, but it is still significantly less than 10%. Use of ϕ=0.75 appears excessively conservative.
- Data presented in Figures 2(a) through 2(c) provide valuable information for modeling wall behavior. Efforts are needed continue and expand data sharing to enable rapid progress to mitigate losses in earthquakes.

Acknowledgements:

The authors acknowledge support from the National Science Foundation under Grant NSF CMMI-0825347 in laboratory space renovated with funds provided by the National Science Foundation under Grant No. 0963183, which is an award funded under the American Recovery and Reinvestment Act of 2009 (ARRA). The authors acknowledge Mr. Ronald O. Hamburger and Dr. Ady Aviram of SGH, San Francisco for their contributions related to the reliability study and example. Any opinions, findings, and conclusions expressed in this paper are those of the authors and do not necessarily reflect those of the supporting organization or other people acknowledged herein

References:

American Concrete Institute. (2011). Building Code Requirements for Structural Concrete (ACI 318-11) and Commentary *(ACI 318R-11)*, Farmington Hills, Michigan.

American Society of Civil Engineers. (2005). ASCE7-05: Minimum Design Loads for Buildings and Other Structures, Reston, VA.

American Society of Civil Engineers (2007), "ASCE/SEI Standard 41-06, Seismic Rehabilitation of Existing Buildings," Reston,

VA, 428 pp.
Bournonville M, Dahnke J, Darwin D (2004), "Statistical Analysis of the Mechanical Properties and Weight of Reinforcing Bars," SL Report 04-1, Structural Engineering and Engineering Materials, 198 pp.
Elwood KJ and Moehle JP (2008). "Dynamic collapse analysis for a reinforced concrete frame sustaining shear and axial failures," Earthquake Engineering and Structural Dynamics, V. 37, N. 7, pp. 991-1012.
LATBSDC (2011). An Alternative Procedure for Seismic Analysis and Design of Tall Buildings Located in the Los Angeles Region. Los Angeles Tall Buildings Structural Design Council: Los Angeles, CA, 48 pp.
Nowak AS, Szersen MM, Szeliga EK, Szwed A, and Podhorecki PJ (2008), "Reliability-Based Calibration for Structural Concrete, Phase 3," PCA R&D Serial No. 2849, 115 pp.
Salas MC (2008), Modeling of Tall Reinforced Concrete Wall Buildings, MSCE Thesis, Department of Civil Engineering, University of California, Los Angeles, 96 pp.
TBI (2010). Guidelines for performance-based seismic design of tall buildings. Report PEER-2010/05, Pacific Earthquake Engineering Research Center, University of California, Berkeley, CA, 104 pp.
Thomsen IV, JH and Wallace JW (2004), "Displacement-Based Design of Slender RC Structural Walls – Experimental Verification, J. Struct. Eng., ASCE, Vol. 130, No. 4, pp 618-630.
Wallace JW, Orakcal K. (2002), "ACI 318-99 Provisions for Seismic Design of Structural Walls," ACI Structural Journal, Vol. 99, No. 4, American Concrete Institute, pp. 499-508.
Wallace, JW (1998), "Behavior and Design of High-Strength RC Walls," ACI Structural Journal, SP-176, American Concrete Institute, Farmington Hills, MI, pp. 259-279.
Wallace, JW (1994) "A New Methodology for Seismic Design of Reinforced Concrete Shear Walls," J. Struct. Eng., ASCE, Vol. 120, No. 3, pp.863-884.

10CUEE CONFERENCE PROCEEDINGS
10th International Conference on Urban Earthquake Engineering
March 1-2, 2013, Tokyo Institute of Technology, Tokyo, Japan

STATIC LOADING TEST OF RC SHEAR WALLS WITH MULTI-OPENINGS FAILING IN FLEXURAL MODE

Masato Sakurai[1], Hiroshi Kuramoto[2], and Tomoya Matsui[3]

1) Research Fellow of the Japan Society for the Promotion of Science for Young, Osaka University, Japan
2) Professor, Dept. of Global Architecture, Osaka University, Japan
3) Associate Professor, Dept. of Architecture and Civil Eng., Toyohashi University of Technology, Japan
sakurai_masato@arch.eng.osaka-u.ac.jp, kuramoto@arch.eng.osaka-u.ac.jp, matsui@ace.tut.ac.jp

Abstract: Static loading tests of RC shear walls with diagonally arranged two openings were carried out to grasp the seismic performance. Specimens were designed to be the flexural failure mode and the variable investigated was the opening layouts. In this paper, the experimental results on failure mode, hysteresis characteristic and deformation capacity are compared with the shear failure mode specimens tested by the authors in 2010, which have the same configuration, opening layout and bar arrangement but the different shear-span ratio. As the result, the deformation capacity of RC shear walls with openings arranged adjacent to the boundary column failing in flexure was lower than that failing in shear because the shear failure occurred at bottom of the column adjacent to the opening.

1. INTRODUCTION

In Japan, the shear strength of reinforced concrete (RC) shear walls with openings is estimated by multiplying the strength of the shear walls without opening by a reduction factor based the opening details. However, according to the existing experimental results and the actual damages under real seismic forces, the behavior of RC shear walls with multi-openings is very complex. Especially, the shear strength, hysteresis characteristics, failure mode and deformation capacity of RC shear walls with several opening layouts are more significantly influenced than specified by the simplified methods in the AIJ standard for RC buildings (2010). Moreover, little quantitative evaluation for the seismic performance of the shear walls with multi-openings has been done so far.

The main objective of this study is to propose the quantitative evaluation for RC shear walls with multi-openings. Therefore, static loading tests of RC shear walls were carried out to investigate basic performance under seismic loadings from 2006 to 2009 (Sakurai et al. 2008, Sakurai et al. 2008 and Sakurai et al. 2010). As a result, their seismic performances were clarified when failing in shear. On the other hand, there are few studies on RC shear wall with openings when failing in flexure.

The static loading tests of RC shear walls were carried out to grasp flexural failing behavior. Comparing specimens in 2009, the specimens in 2010 had the same configurations, opening layout and bar arrangement but the different shear span ratios. In this case, the result showed that the specimen without opening had flexural failing behavior. While the specimen with multi-openings failed in shear because its shear strength deteriorated under the influence of openings.

In this paper, the results of static loading tests of RC shear walls with multi-openings designed to have flexural failure mode are described. Then the experimental results on failure mode, hysteresis characteristic and deformation capacity were compared with those of shear walls failing in shear tested in 2010.

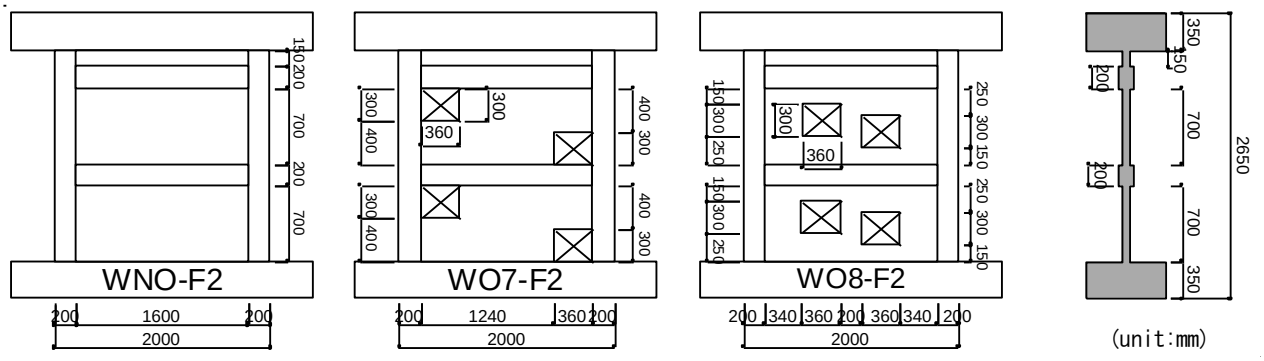


Figure 1 Specimens

2. EXPERIMENTAL PROGRAM

2.1 Specimens

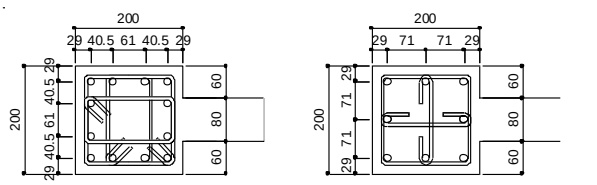
A total of three specimens of RC shear walls without or with opening were tested, which were one-third scale models simulating the lower 2.3 stories of multi-story shear walls in a medium-rise RC building. Details of the section and configuration of specimens are shown in Table 1 and Fig.1. Each specimen was based on previous test by the authors (Sakurai et al. 2008, Sakurai et al. 2008 and Sakurai et al. 2010). Variables investigated were the layout of the openings. Specimen WNO-F2 without opening was the standard specimen and Specimens WO7-F2 and WO8-F2 had two openings located diagonally. As shown in Fig.1, the diagonal openings in Specimen WO7-F2 were located at the boundary column while those in Specimen WO8-F2 were located at the center of the wall. The equivalent perimeters ratios of openings were almost the same for all specimens, i.e. about 0.4.

The experimental results of RC shear walls with multi-openings in 2010 showed shear failing behavior. Therefore, in this test, the number of longitudinal bars as well as their specific yield strength was reduced compared with the specimens tested in 2010 to have flexural failure mode.

The mechanical properties of materials used are listed in Tables 2 and 3.

2.2 Loading Method

The loading apparatus used in this test is shown in Fig.2. The wall specimens were loaded with horizontal shear reversals applied by a manual jack of 1,000kN capacity and a constant axial force of 442kN by two vertical manual jacks of 2,000kN capacity for each. During the testing, an additional moment was also applied to the top of specimens using vertical jacks to keep the prescribed shear-span ratio of 1.80. The loading was conducted by controlling the relative wall drift angle, R, given by the ratio of the height of corresponding to the measuring point of horizontal displacement at the top of the specimen, h, to the horizontal deformation, δ, i.e. R=δ/ h.



Longitudinal bar : 12-D13 (SD390) (p_g=3.8%)
Tie : 2-D6@60 (p_s=0.53%)
Sub-tie : 2-D6@120 (p_w=0.27%)

Longitudinal bar : 8-D13 (SD295A) (p_g=2.5%)
Tie : 2-D6@60 (p_s=0.53%)
Sub-tie : D6@60 (p_w=0.27%)

Figure 2 Sections of Columns

Table 1 Specification of sections

Column	B×D	200×200
	Longitudinal bar	8-D13 (p_g=2.5%)
	Tie	2-D6@60 (p_w=0.53%)
	Sub-tie	D6@60 (p_w=0.27%)
Beam	B×D	150×200
	Longitudinal bar	4-D10(p_t=0.54%)
	Tie	2-D6@100 (p_w=0.42%)
Wall	Thickness	80
	Longitudinal bar	D6@100zigzag (p_s=0.4%)
	Transverse bar	D6@100zigzag (p_s=0.4%)
	Bar around opening	D10 (Longitudinal,Horizontal)

unit: mm, Fc=27MPa, The steel grade of all bars is SD295A.

2.3 Measurement

Displacement transducers were used to measure horizontal displacement of the upper stub, longitudinal deformation of column and deformation of wall panel. The strain of longitudinal and transverse reinforcement of columns and walls were measured by using strain gauges. In addition, the crack widths were measured by using crack scale at the peak of each loading and unloading cycles.

3. EXPREIMENTAL RESULT

3.1 Damage Process and Hysteresis Loop

Cracking patterns of each specimen after the loading cycle of 1/100 rad. are shown in Fig.4. The loading toward the north direction (Fig. 3) is defined as the positive loading while the loading toward the south direction is the negative loading. The shear force versus drift angle relationships of specimens are shown in Fig.5. In this figure, the ultimate flexural strength calculated by Eq. (1) is shown by horizontal line. The results of specimens tested in 2010 failing in shear are also shown to compare in Figs.4 and 5.

$$Q_{mu} = (a_t \cdot \sigma_y \cdot l_w + 0.5a_w \cdot \sigma_{wy} \cdot l_w + 0.5N \cdot l_w) / h_w \quad (1)$$

For each specimen, the initial crack occurred at the wing wall and column in the first story in the loading cycle of 1/800 rad. The flexural cracks increased at the column in

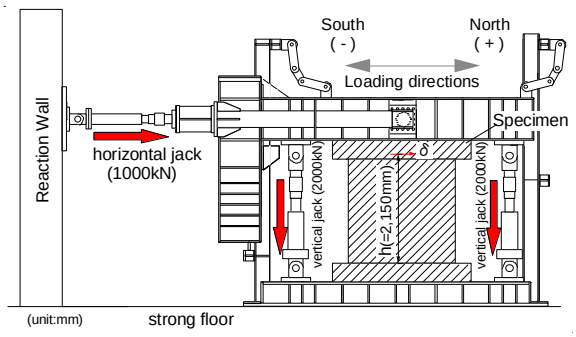


Figure 3 Loading apparatus

Table 2 Properties of steels

Steel bar		Yield strength (MPa)	Young's modulus (GPa)	Ultimate strength (MPa)
D6 (SD295A)	Wall reinforcement, Tie, Stirrup	338	160	384
D10 (SD295A)	Beam reinforcement, Bar around opening	347	185	408
D13 (SD295A)	Column reinforcement	343	199	483

Table 3 Properties of concretes

Concrete		WNO-F2	WO7-F2	WO8-F2
σ_B (MPa)	1st story	27.7	27.2	29.6
	2nd story	25.6	26.5	28.4

the first story in the loading cycle of 1/400 rad., and new cracks occurred in wing wall of the second story. In the loading cycle of 1/200 rad., the cracks propagated throughout the wall and the column and the longitudinal bars of the tensile column were yielded.

In Specimen WNO-F2 without opening, the flexural cracks at middle of the tensile column of the first story were propagated for the loading cycle of 1/100 rad., and the shear cracks at bottom of the compressive column of the first story occurred for loading cycle of 1/67 rad.. Then, the maximum shear force reached 375.5kN at R of 1/50 rad., and -379.5kN at R of -1/50 rad., and shear strength deterioration occurred by failing in shear and buckling of the longitudinal bars at the column in compression for the loading cycle of 1/40 rad.. In Specimen WNO-F tested in 2010, the longitudinal bar at the columns yielded at R of 1/200 rad., and the maximum shear force reached 481.5kN at R of 1/100 rad., and -477.0kN at R of -1/100 rad.. Then, the wall panel at the first story failed in shear and the shear strength deterioration occurred for the loading cycle of 1/67 rad.. Comparing specimen WNO-F, it was suggest that the deformation capacity of Specimen WNO-F2 was enhanced by reducing the amount of the longitudinal bars.

In Specimen WO7-F2 in which diagonal openings were arranged adjacent to the boundary columns, the maximum shear force reached 315kN at R of 1/200 rad., and -349.5kN at R of -1/100 rad.. Then, the flexural cracks at middle height of the tensile column propagated in the first story, and the shear failure occurred at bottom of the north column in compression in the first story. The maximum shear force in

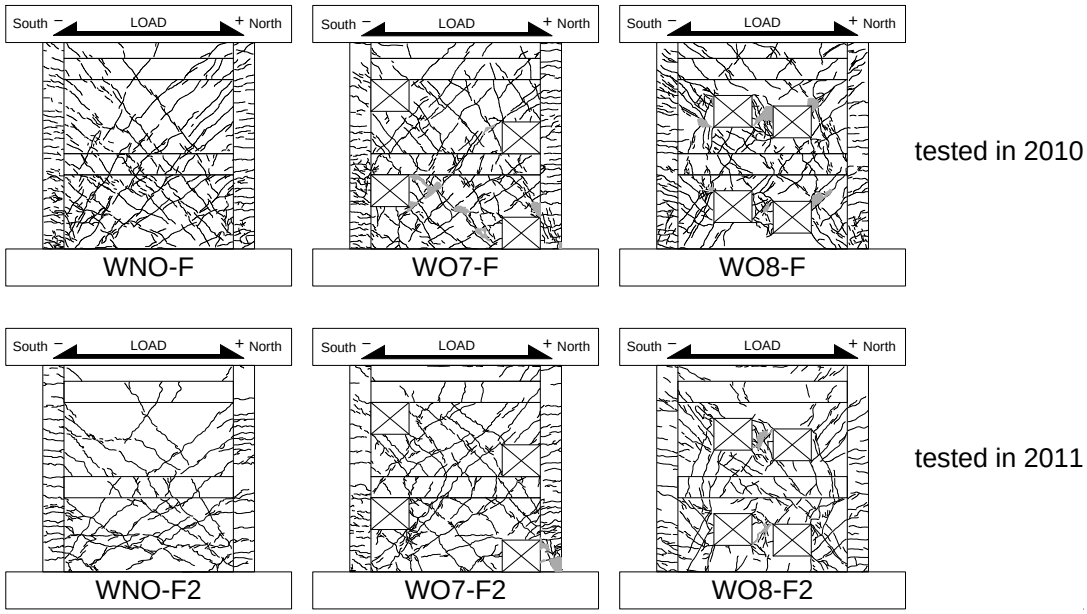


Figure 4 Cracking patterns R of 1/100 rad.

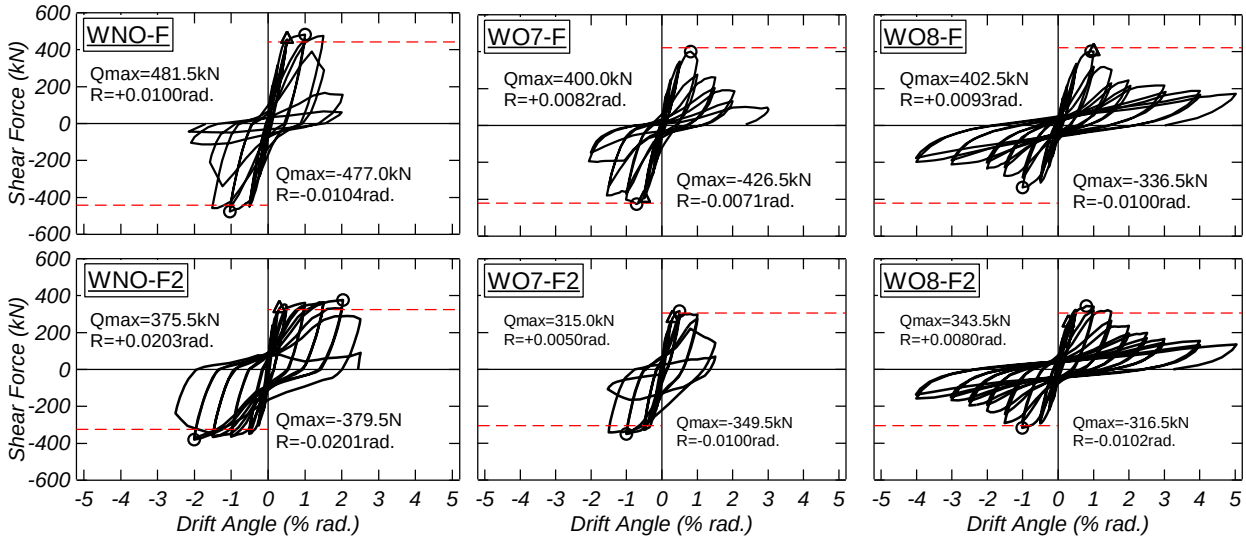


Figure 5 Shear force versus drift angle relationships

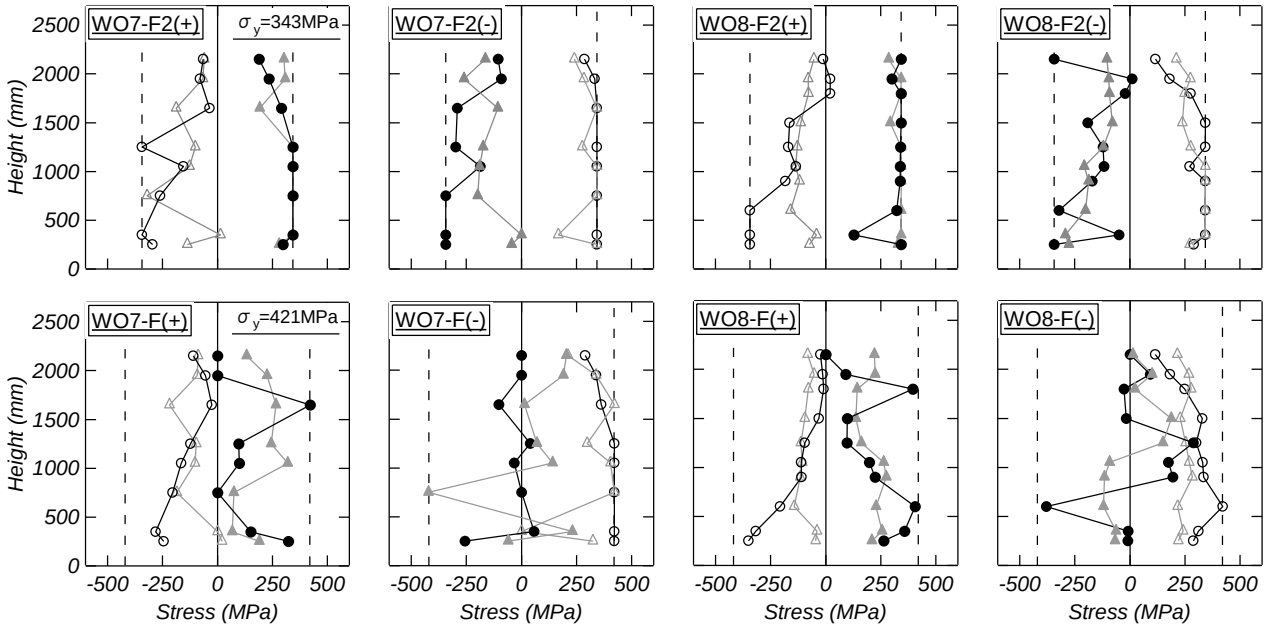


Figure 6 Stress distribution at columns (R=1/200 rad.)

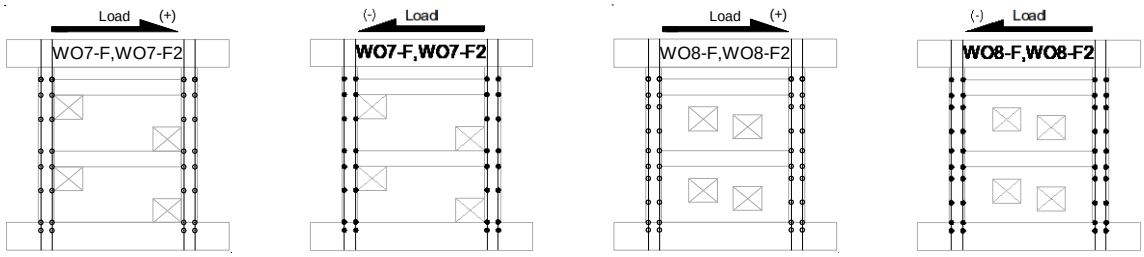


Figure 7 Locations of measuring strain

positive loadings was smaller than that in negative loadings because there was opening arranged adjacent to the bottom of the north column and the transferring stress from top of the wall was not concentrated at bottom of the north column. In the loading cycle of 1/67 rad., compression failure of the central wall panel, and buckling of longitudinal bars at bottom of the north column occurred in the first story were observed. In Specimen WO7-F tested in 2010, shear strength deterioration occurred by failing of concrete around the south side opening. On the other hand, Specimen WO7-F2 showed shear strength deterioration because the buckling of the longitudinal bars at bottom of the north column occurred before compression failure of the concrete at the wall panel.

In Specimen WO8-F2 in which diagonal openings were positioned close to each other, in the loading cycle of 1/200 rad., the failing of concrete at the central panel occurred in the second story, and the maximum shear force reached 343.5kN at R of 1/100 rad., and -316.5kN at R of -1/100 rad.. After the loading cycle of 1/100 rad., the failing of concrete at the central panel and wing walls in the first story. Finally, it was showed that the shear strength of columns maintained about 200kN until R of 1/20 rad. with damages at bottom of the beam in the first story. The failure mode of Specimens WO8-F2 and WO8-F tested in2010 were similar regardless the difference of the amount of longitudinal bars.

3.2 Deformation Capacity

(a) Stress distribution at columns

The stress distribution at each column at the R of ± 1/200 rad. for Specimens WNO-F, WO7-F, WO8-F, WNO-F2, WO7-F2 and WO8-F2 are shown in Fig.6 (plus = tension, minus = compression). The locations of measured stress on the specimens are also shown in Fig.7. On the assumption that the stress - strain relationship of a steel bar is bilinear curves, the stress was calculated using strain measured by the strain gauge.

In Specimens WO7-F and WO8-F tested in 2010, the stress at the south column in tension was small in the first story. However, in Specimens WO7-F2 and WO8-F2, the yielding of longitudinal bars occurred along the whole the first story column.

In addition, in Specimens WO7-F and WO8-F, the stress distributions at the column in compression showed that the stress varied widely whole columns. On the other hand, in Specimens WO7-F2 and WO8-F2, the stress concentrated at bottom of the column, and yielding occurred at the compression side.

As described above, in RC shear wall with openings, regardless the opening arrangement, longitudinal bars in the tensile column yielded in the whole length of the first story, and that in the compressive side at bottom of the column.

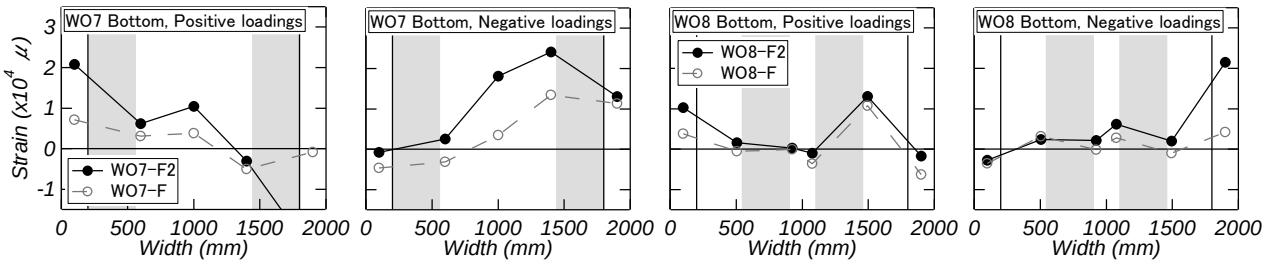


Figure 8 Stain distribution at bottom of walls (R=1/100 rad.)



Figure 9 Locations of measuring displacement (Bottom of walls)

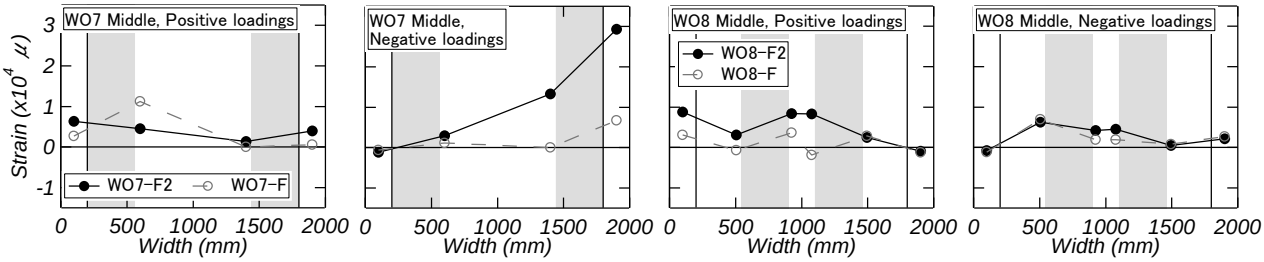


Figure 10 Stain distribution at middle height section of walls (R=1/100 rad.)

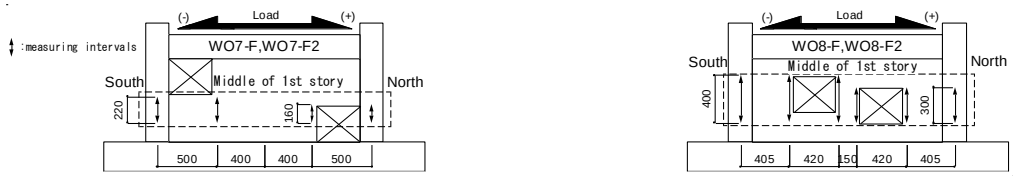


Figure 11 Location of measuring displacement (Middle height of walls)

(b) Strain distribution at bottom and middle height of walls

The strain distributions at the bottom section of walls at the R of ± 1/100 rad. for Specimens WNO-F, WO7-F, WO8-F, WNO-F2, WO7-F2 and WO8-F2 are shown in Fig.8 (plus = tension, minus = compression). Strains calculated using the displacement measured by transducer divided by its measuring intervals. The locations of measured displacement on the specimens are shown in Fig.9.

In Specimen WO7-F2, the strain at bottom of the south column increased in tensile and that of the north column increased in compressive by failing in shear at the north column in the positive loadings.

In Specimen WO8-F2, although the strain at bottom of the north column increased in tensile, the strain distribution at bottom of the wall showed similar tendency of Specimen WO8-F. In the test, the flexural crack in each specimen propagated at bottom of wall as well as middle height of walls in the first story. Then, the following passages describe the strain at middle section of walls.

The strain distributions at the middle height section of walls at the R of ± 1/100 rad. are shown in Fig.10 (plus = tension, minus = compression). The locations of measured displacement on the specimens are shown in Fig.11.

In Specimen WO7-F2, the strain at middle height of the north column and the wall panel increased widely in tension compared with Specimen WO7-F in the positive loadings. This is a reason why the failing in shear at bottom of the north column in tension progressed in the positive loadings, and the flexural cracks at middle height of the north column and the wall panel propagated instead of bottom of the north columns in the negative loadings.

On the other hand, in Specimen WO8-F2, although the strain at middle height of the wall panel slightly increased in tension, the strain distribution of Specimen WO8-F showed similar tendency.

As described above, in Specimen WO7-F2, the deformation at bottom of the north column adjacent to the openings increased early because Specimen WO7-F2 had few amount of steel at the columns compared with Specimen WO7-F. Therefore, the deformation capacity of Specimen WO7-F2 was not enhanced as compared with Specimen WO7-F.

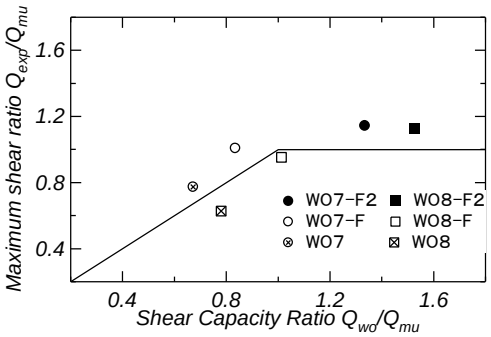


Figure 12 Maximum shear ratio – shear capacity ratio relationship

4. FAILURE MODE ESTIMATION

The shear capacity ratio of calculated flexural strength and shear strength of the specimens are shown in Fig. 12. The calculated flexural strength Q_{mu} is given by Eq. (1) (Japan Building Disaster Prevention Association, 2001) The calculated shear strength, Q_{wo} (Eq. (2), Eq. (3) and Eq. (4)), is proposed by the authors, where Q_{wo} was considered on the basis of shear transferring struts in RC shear wall and can estimate the difference of shear strength depending on the opening arrangement. The shear resisting model proposed by equations Eq. (2), Eq. (3) and Eq. (4) are shown in Fig.13, and the assumptions of boundary columns are also shown in Fig.14.

In Fig.12, the experimental value used for the maximum shear ratio is the absolute value among the positive and negative loading values. The test result of Specimens WO7, WO8 tested in 2010, which have the same configuration, opening layout and bar arrangement but the different shear-span ratio of 1.2 are also shown in Fig.12.

$$Q_{wo} = \sum_{i=1}^{n+1} Q_{wi} \tag{2}$$

$$Q_{wi} = \nu\sigma_B \cdot \cos\theta_i \sin\theta_i \cdot 0.5 l_{p_i} \cdot t_i \tag{3}$$

$$\nu = -0.016\sigma_B - 0.16\frac{M}{QD} + 0.36\frac{N}{bD\sigma_B} + 0.27 p_W + 1.23 \tag{4}$$

where, n: number of openings
σ_B: concrete cylinder strength (MPa)
θ_i: the angle of strut at wall panel
l_{pi}: wall panel length (mm)
t_i: wall panel width (mm)

For the details of the equation, see the reference (Sakurai et al. 2012)

In Fig.12, although the calculated the shear capacity ratio Q_{wo}/Q_{mu} of Specimen WO8-F slightly exceeds 1.0 in the calculation, the failure mode in the test was in shear failure. However, the calculated shear strengths of Specimens WO7-F2 and WO8-F2 which failing in flexure were over 1.3 respectively and it certified that the calculated

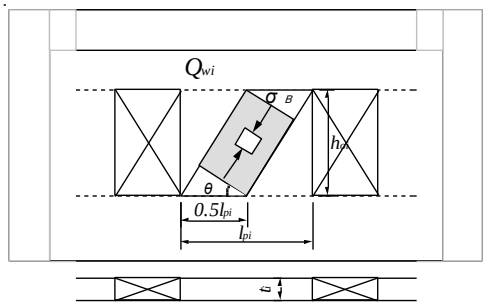


Figure 13 Proposed shear resisting model in wall panels

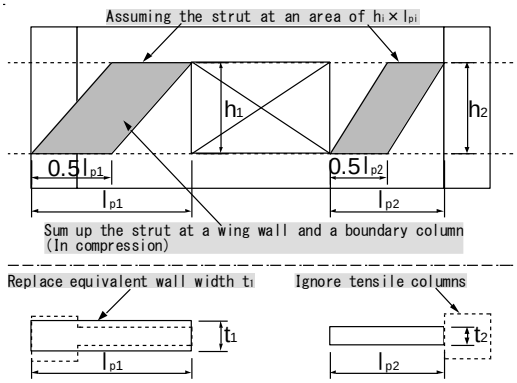


Figure 14 Assumption of boundary columns

shear strength is in accordance with the failure mode in test. In addition, the calculated the shear capacity ratio Q_{wo}/Q_{mu} of Specimens WO7, WO8 and WO7-F which failed in shear were under 0.8, it was showed similar tendency.

As described above, using the shear capacity ratio given by Q_{mu} (Japan Building Disaster Prevention Association, 2001) and Q_{wo} proposed by the authors, the failure mode of RC shear walls with openings can be estimated. However, due to the small number of specimen tested so far, additional tests are necessary for further validation.

5. CONCLUSIONS

In this paper, static loading tests of RC shear walls with multi-openings designed to have flexural failure mode were carried out to grasp the seismic performance. Then the experimental results in terms of failure mode, hysteresis characteristic and deformation capacity were compared with those of shear walls failing in shear tested by the authors in 2010. The following conclusions are obtained.

1) RC shear wall with opening decreased the deformation capacity compared with that without opening regardless the difference of the failure mode.

2) The failure mode and hysteresis loop of RC shear walls in which diagonal openings were positioned close to each other failing in flexure showed similar tendency of that failing in shear.

3) The deformation capacity of RC shear walls with openings arranged adjacent to the boundary column failing in flexure was lower than that failing in shear because the

shear failure occurred at bottom of the column adjacent to the opening.

4) In RC shear walls with openings failing in flexure, the stress distribution at longitudinal bar of the columns showed similar tendency regardless opening arrangement.

5) Using the shear capacity ratio calculated by Q_{mu} and Q_{wo} proposed by authors, it is possible to estimate the failure mode of RC shear walls with openings in case of the static loading test.

Acknowledgements:

This work was supported by Grant-in-Aid for Japan Society for the Promotion of Science (JSPS) Fellows.

References:

Architectural Institute Japan (1999), "AIJ Standards for Structural Calculation of Reinforced Concrete Structures," (In Japanese)

Sakurai. M, Kuramoto, H., T., Matsui, and Akita, T. (2008). Seismic Performance of RC Shear Walls with Multi-openings, *Proseedings of 14th World Conference on Earthquake Engineering*, Paper-ID12-03-0071.

Sakurai, M., T., Matsui, Suzuki, K. and Kuramoto, H. (2008). "Effect of Opening layout on Seismic Performance of RC Shear Walls with Multi-Openings", *Proceedings of the Japan Concrete Institute*, **30**(3), 421-426. (In Japanese)

Sakurai, M., T., Matsui, and Kuramoto, H. (2010). "Effect of Opening Arrangement on Shear Failure Mode of RC Shear Walls with Multi-Openings", P*roceedings of The 12th Taiwan-Korea-Japan Joint Seminar on Earthquake Engineering for Building Structures*, 247-254.

Japan Building Disaster Prevention Association (2001), "Evaluation Standard of Seismic Capacity on Existing RC Building, Japan," (In Japanese)

Sakurai. M, Kuramoto, H. and Matsui, T. (2012). "An Evaluation Method of Shear Strength for RC Shear Walls with Multi-Openings", *Journal of Structural and Construction Engineering, Architectural Institute Japan*, **77**(679), 1445-1453. (In Japanese)

10CUEE CONFERENCE PROCEEDINGS
10th International Conference on Urban Earthquake Engineering
March 1-2, 2013, Tokyo Institute of Technology, Tokyo, Japan

RESIDUAL SEISMIC PERFORMANCE OF SCALED THREE-STORY STEEL FRAMES TESTED ON A SHAKING TABLE USING THE SUBSTITUTE DAMPING MODEL

Miguel A. Diaz[1)], Koichi Kusunoki[2)], and Akira Tasai[3)]

1) PhD. Candidate, Department of Architecture and Building Science, Yokohama National University, Japan
2) Associate Professor, Department of Architecture and Building Science, Yokohama National University, Japan
3) Professor, Department of Architecture and Building Science, Yokohama National University, Japan
miguel.ad17@gmail.com, kusunoki@ynu.ac.jp, tasai@ynu.ac.jp

Abstract: This paper compares the experimental and estimated seismic performance using the results of scaled three-story steel frames tested on a shaking table, excited with artificial and earthquake waveforms, and formulations based on the capacity spectrum method and the substitute damping model, such as the equivalent damping ratio and the response reduction ratio. For each specimen, the elastic and inelastic behavior is reproduced; in the last, the specimen was excited by the mainshock, and then the maximum expected aftershock in order to analyze the residual seismic performance.

1. INTRODUCTION

The collapse of structures, in many cases, is not caused by the mainshock, but it may be caused by the subsequent aftershocks due to the seismic capacity degradation of the building during the mainshock. Entry into a damaged building at earliest is often indispensable for different emergency reasons. Thus the estimation of the seismic performance due to the maximum expected aftershock is very much important in order to determine if the building may or may not survive.

This paper presents an instrument to conduct this estimation; it is based on the capacity spectrum method and the substitute damping model; by means of formulations, such as the equivalent damping ratio and response reduction ratio given for the life-safety limit state. This limit is established for earthquakes motions whose return period is approximately 500 years, as prescribed the Japanese Building Standard Law Enforcement Order.

The equivalent damping and response reduction ratios are prescribed by Notification No. 1457-6 (2000) of Ministry of Land, Infrastructure, Transport and Tourism of Japan (MLIT). They are used to estimate the seismic performance due to the mainshock.

On the other hand, the equation of the equivalent damping ratio for the seismic performance estimation due to aftershock proposed in previous work by Kusunoki et al. (2006) and Diaz et al. (2012) is used in this paper. Additionally, a new equation of the response reduction ratio proposed by Diaz et al. (2012) which holds good for mainshocks and aftershocks is also used.

Thus the seismic performance due to mainshocks and aftershocks from the shaking table tests are compared with the estimated seismic performance using the formulations of equivalent damping and the response reduction ratios. Ten specimens were tested under one artificial waveform and two earthquake waveforms; properties such as period, equivalent damping and response reduction ratios due to mainshocks and aftershocks are analyzed.

2. RESIDUAL SEISMIC PERFORMANCE

2.1 Aftershock assumption

The aftershock is defined as the subsequent shakes after a significant earthquake with a magnitude less than the given earthquake (mainshock).

Generally, a magnitude of the largest aftershock is smaller by 1 than that of the mainshock. The largest aftershock, in many cases, occurs within 3 days after the occurrence of the mainshock in the case of inland earthquake. As for those occurred in sea area, the largest aftershock generally occur within about 10 days (Japan Meteorology Agency).

The energy released by earthquake is proportional to its magnitude. Thus, a rough approximation may suppose that the energy released by the maximum expected aftershock is relatively close to that by the mainshock.

Therefore, if a given earthquake and its subsequent aftershocks are considered as one-long duration earthquake from the beginning of the mainshock toward the end of the maximum expected aftershock; the motion of the maximum expected aftershock can be supposed same as that of the

mainshock, then neglect the inner shakes, because they do not produce larger responses than the maximum expected aftershock.

Using this assumption, the total motion to conduct the residual seismic performance analysis is given by the earthquake inputted twice, mainshock and aftershock, and a gap between both. The duration of this gap is set in the measure that the system vibration converges to zero, as shown in Figure 1.

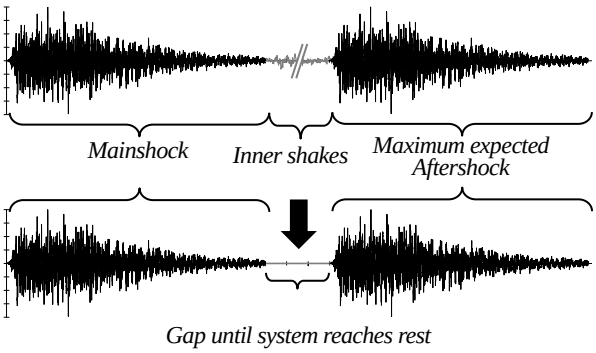


Figure 1 Aftershock assumption

2.2 Equivalent damping ratio

The equivalent damping ratio for yielding structures can be determined by the hysteresis damping in terms of the elastic strain energy of a structure by means of the geometric stiffness method (Jennings, 1968).

Notification No. 1457-6 (2000) prescribes the equivalent damping ratio ${}_mh_{eq-i}$ of a structural member i in Eq. (1) for the life-safety limit state.

$$ {}_mh_{eq-i} = \gamma \cdot (1 - 1/\sqrt{\mu}) \tag{1} $$

The coefficient γ in Eq. (1) is assumed as 0.25 in case of material which constitutes the member, and the joint connected to the adjacent member are rigid; and as 0.20 in cases of members or braced members where the buckling strength is degraded by the compressive forces when seismic forces acts (member exhibits a slip-type characteristic), as prescribed Notification No. 1457-6 (2000).

The coefficient γ in Eq. (1) may hold good for the estimation of the equivalent damping ratio due to mainshocks; otherwise the energy dissipation (or equivalent damping) due to the aftershock is less than or equal to that due to its corresponding mainshock. Therefore, this coefficient can be conveniently reduced in order to obtain larger responses, such as responses during an aftershock, since the response reduction ratio in Eq. (3) is inversely proportional to the equivalent damping ratio in Eq. (1). Thus, the coefficient γ is reduced to 0.12 and 0.08 by an appropriate curve fitting based on a series of nonlinear simulations obtained for systems under aftershocks (Diaz et al., 2012).

Eq. (2) is also prescribed by Notification No. 1457-6 (2000), based on the substitute structural method (Shibata and Sozen, 1976). It estimates the equivalent damping ratio of an equivalent SDOF system as the weighted average respect to the strain energy with a viscous damping ratio of 0.05 for the first-mode at the damaged-initiation limit state, since at this stage the building behavior remains elastic. ${}_mW_i$ is the strain energy dissipated in member i.

$$ h_{eq} = \frac{\sum {}_mh_{eq-i} \cdot {}_mW_i}{\sum {}_mW_i} + 0.05 \tag{2} $$

2.3 Response reduction ratio

The response reduction ratio reduces the elastic spectral response to the inelastic response. Notification No. 1457-6 (2000) also prescribes the response reduction ratio as Eq. (3), which guarantees the life-safety limit state.

$$ F_h = \frac{1.5}{1+10 \cdot h_{eq}} \tag{3} $$

Additionally, previous work by Diaz et al. (2012) proposes a new equation of the response reduction ratio, given by Eq. (4). It is developed solving the equation of motion under the stationary vibration, and then adapting it to the non-stationary vibration, such as earthquake motions, by means of curve fitting to analytical response of a series of nonlinear simulations.

$$ F_h{}^* = \sqrt{\frac{1.1+\alpha \cdot h_{eq}{}^2}{1+(40+\alpha) \cdot h_{eq}{}^2}} \tag{4} $$

The Japanese Building Standard Law Enforcement Order requires that spectral acceleration of a structure at a limit state should be higher than the corresponding acceleration of the reduced demand spectrum using the equivalent damping ratio at the same limit state.

2.4 Seismic performance evaluation

During a damaging earthquake, some buildings may survive, but the subsequent aftershocks may or may not cause the building collapse; that's why, it is desirable to recognize the building state (seismic performance) after a mainshock, and to estimate the seismic performance due to the maximum expected aftershock in order to anticipate if the building may or may not survive, and so safeguard life.

The seismic performance of a building due to a given earthquake motion is examined by comparing the capacity curve and demand spectrum in terms of $S_a - S_d$ relations, as shown in Figure 2. The intersection between the capacity curve and the demand spectrum for an appropriate equivalent damping ratio which represents the inelastic response under the given earthquake, is called the performance point (ATC-40, 1996).

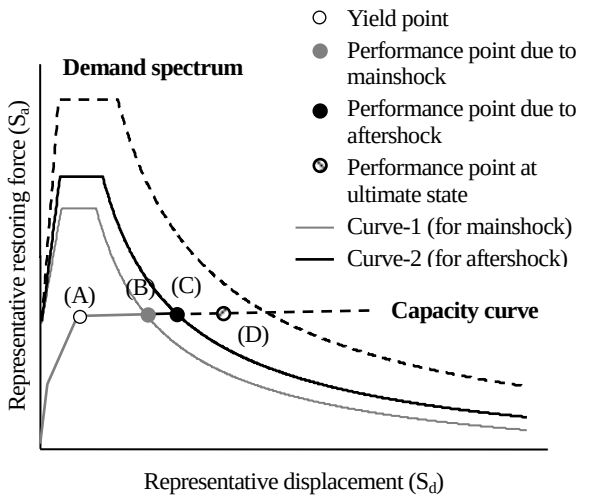


Figure 2 Scheme of the seismic performance evaluation

The concept of the seismic performance evaluation method is represented by the scheme shown in Figure 2. The performance point due to the mainshock is represented by the point (B) on the capacity curve, in this figure; the demand spectrum is reduced by increasing the viscous damping ratio until it intersects the point (B). Thus the reduced demand spectrum is represented as curve-1 in Figure 2, and the converged viscous damping ratio is defined as the equivalent damping ratio for mainshock.

The maximum response during the maximum expected aftershock, represented by the performance point (C) on the capacity curve in Figure 2, is larger than or equal to that during the mainshock, represented by the performance point (B) in the same figure. Thus the equivalent damping ratio for aftershock is less than or equal to that for mainshock, as observed in Figure 2, because the energy dissipation (or equivalent damping) during the maximum expected aftershock is less than or nearly equal to energy dissipation during its corresponding mainshock. Then the demand spectrum is again reduced until it intersects the performance point (C) in Figure 2; the reduced demand spectrum is represented as curve-2 and the converged viscous damping ratio is defined as the equivalent damping ratio for aftershock.

3. SHAKING TABLE TESTS

The experimental tests are based on the assumption described in Section 2.1. The testing program consists in four series of excitation. The first excitation was produced by the white-noise in order to evaluate the dynamic properties. The second excitation was the test using the input motion with small acceleration amplitude to induce an elastic response. The third excitation was the test using large acceleration amplitude, so that the specimen was within the inelastic range (mainshock). And, the fourth excitation was the test using the previous acceleration amplitude (or slightly less) to produce the maximum expected aftershock.

3.1 Tests specimens

The specimen consists in a scaled three-story and one-bay steel plane frames; their members are connected by bolts to a rigid joint, as shown in Figure 3.

The bay width is 1000 mm, the first-story height varies from 805 mm to 1005 mm, and the second and third stories heights are 700 mm. The beams are rectangular bars of 100×6 mm widened at the middle to support the accelerometer on each level. The first-story is constituted by rectangular bars as columns without braces; the second and third stories are braced frames with rectangular bars of 100×6 mm as columns, and circular bars M10 as braces (a pair in each front).

The design of the specimen supposed that the columns of the first-level would be only affected during the tests, due to the soft-story behavior of this structure. The sections of these columns were reduced in 50% at the bottom in order to provide to the specimen a plastic hinge to control the failure mechanism.

Thus, the properties of the specimen depend on the dimensions of first-story columns (thickness and height); the second, third braced frames are preserved for all tests. However, the second and third braced frames are also observed by the measurement system.

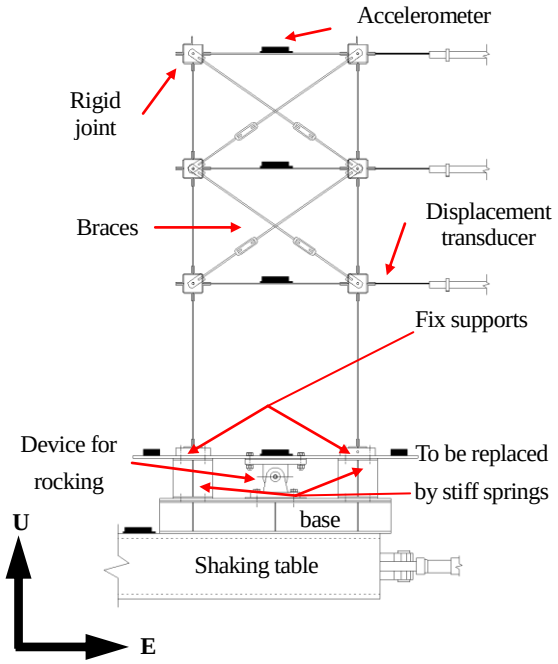


Figure 3 Configuration of specimens

The specimens Frame1a, Frame2a,b and S-F01,02,03 are fixed support; while specimens S-S01,02,03,04 are also fixed support, but the base (ground) includes a small rocking effect due to the adding of stiff springs (K_{spring}=500 N/mm) between supports and base, as shown Figure 3. The initial compressive deformations of springs were 1 mm and 7 mm for S-S01,02 and S-S03,04, respectively. Members of these specimens consisted of SS400 (326 MPa). Table 1 presents characteristics of these specimens.

Table 1 Characteristics of specimens

Specimen	Thickness 1st F column (mm)	Height 1st F (mm)	Total weight (kN)	Natural period (s)	Yield. Disp. (mm)
Frame1 a	4.5	805	1.450	1.03	66
Frame2 a, b	4.5	1005	1.464	1.66	101
S-F 01, 02, 03	6.0	1000	1.485	0.93	71
S-S 01, 02	6.0	1000	1.485	0.99	73
S-S 03, 04	6.0	1000	1.485	0.98	73

The measurement system was given by accelerometers at the base and beams of each level, and displacement transducers connected at each eastern rigid joint, as shown in Figure 3.

3.2 Input waveforms

The input motions to conduct this study were one artificial wave: the WG60, and two earthquake records: the KOBE-NS (Kobe, 1995) and the MYG013 (Tohoku, 2011). The input motions were scaled in order to induce different performance levels on the specimen within elastic and inelastic ranges, both mainshocks and aftershocks. Figure 4 shows the WG60, the KOBE-NS and the MYG013 waveforms.

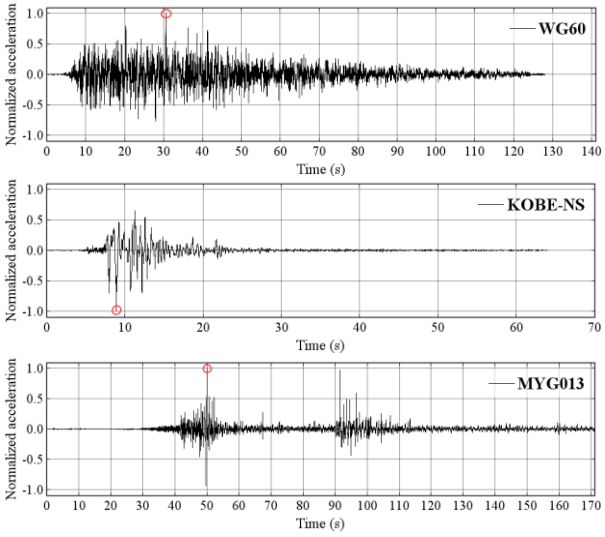
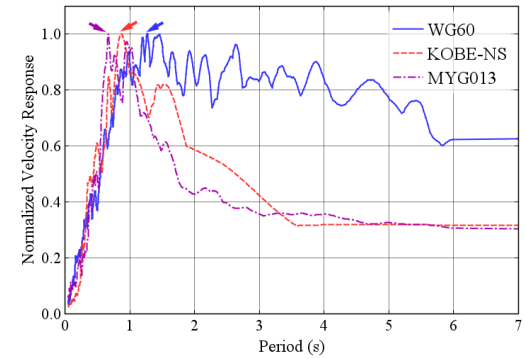
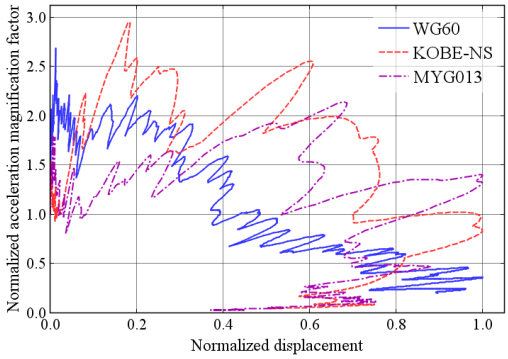


Figure 4 Input waveforms

Figure 5 shows their respective a) normalized velocity response spectra respect to the maximum spectral velocity, and b) normalized response spectra respect to peak ground acceleration (PGA) and maximum spectral displacement. The maximum spectral response with viscous damping ratio of 0.05 was obtained at periods of 1.27 seconds, 0.87 seconds and 0.67 seconds for the WG60, the KOBE-NS and the MYG013 waveforms, respectively (Figure 5a).



a) Velocity response spectra



b) Displacement and acceleration response spectra

Figure 5 Response spectra

3.3 Equivalent SDOF

In order to conduct the residual seismic performance analysis, it is necessary to transform the capacity curve of the specimen in terms of $S_a - S_d$ relations.

The probable value of the maximum response is usually given by the square root of the sum of square (SRSS) of the maximum modal response components. Then the maximum displacement at i-th story and the base shear force can be expressed approximately by Eq. (5) and Eq. (6) (Shibata, 2010), respectively; where ${}_sS_d$, ${}_sS_a$ is the spectral displacement and spectral acceleration for the s-th mode. The base shear force of N-DOF is given by Eq. (7).

$$|\delta_i|_{max} \approx \sqrt{\sum_{S=1}^{N} \left| {}_s\beta \cdot {}_su_i \cdot {}_sS_d \right|^2} \quad (5)$$

$$Q \approx \sqrt{\sum_{S=1}^{N} \{ \sum_{i=1}^{N} m_i \cdot {}_s\beta \cdot {}_su_i \cdot {}_sS_a \}} \quad (6)$$

$$Q = \sum_{i=1}^{N} m_i \cdot (\ddot{x}_i + \ddot{x}_g) \quad (7)$$

Particularly, the specimens can be assumed as 3-DOF systems. Their configuration allows that second and third participation factor can be neglected, and the first-mode distribution can be assumed as the unit $\{ {}_1u \} \approx \{1\}$. Then Eq. (5) is rewritten as Eq. (8) to calculate the spectral acceleration, and Eq. (7) into Eq. (6) is rewritten as Eq. (9) to calculate the spectral displacement.

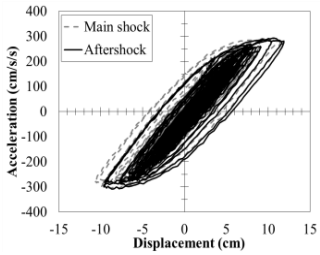
$$ {}_1S_d \approx \frac{|\delta_i|_{max}}{{}_s u_i} \quad (8) $$

$$ {}_1S_a = \frac{\sum_{i=1}^{3} m_i \cdot (\ddot{x}_i + \ddot{x}_g)}{\sum_{i=1}^{3} m_i} \quad (9) $$

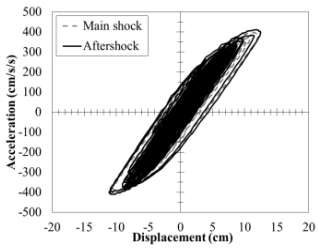
3.4 Tests results

The representative response or spectral response is calculated by Eq. (8) and Eq. (9), using experimental data such as the displacement from transducers and the absolute acceleration from accelerometers on each level. The responses during mainshocks and aftershocks, in terms of $S_a - S_d$ relations, with different maximum acceleration amplitudes of waveforms are plotted in Figure 6, Figure 7 and Figure 8, where g is the acceleration of gravity.

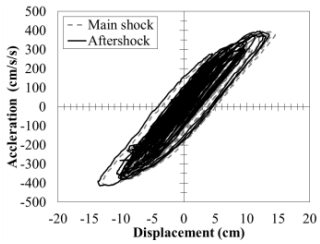
Figure 6 shows the response during the WG60 waveform for four specimens, namely: Frame1a, S-F01, S-S01 and S-S04 with maximum acceleration amplitude of waveform of 0.36g, both mainshock and aftershock.



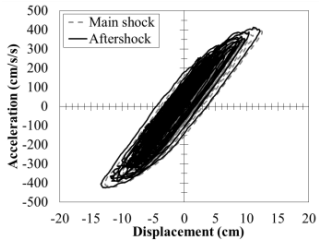
a) Frame1a (0.36g)



b) S-F01 (0.36g)



c) S-S01 (0.36g)

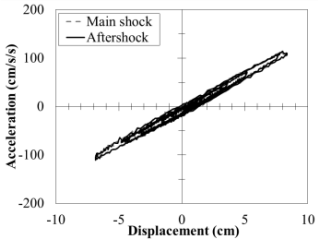


d) S-S04 (0.36g)

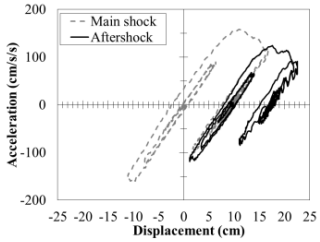
Figure 6 Response during the WG60 waveform

Figure 7 shows the response during the KOBE-NS waveform for five specimens, namely: Frame2a with maximum acceleration amplitude of waveform of 0.17g (mainshock and aftershock), Frame2b with 0.33g for mainshock and 0.25g for aftershock; and S-F02, S-S02 and S-S03 with 0.38g, both mainshock and aftershock.

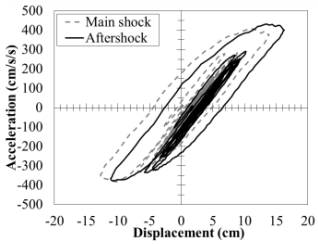
In Figure 7b, a negative slope arose in the representative acceleration; it is because the specimen Frame2b is slender and long-period frame (see Table 1), and suffered the P-Δ effect (its capacity is reduced in front of the gravity effect). The maximum response within the inelastic range was larger than the elastic spectral response with damping ratio of 0.05.



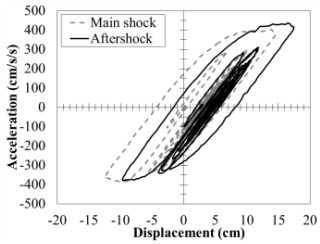
a) Frame2a (0.17g)



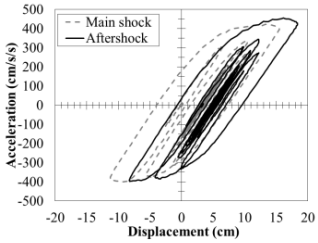
b) Frame2b (0.33g→0.25g)



c) S-S02 (0.38g)



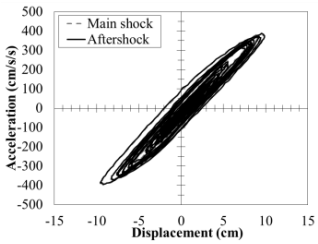
d) S-S03 (0.38g)



e) S-F02 (0.38g)

Figure 7 Response during the KOBE-NS waveform

Figure 8 shows the response during the MYG013 waveform for the specimen S-F03 with maximum acceleration amplitude of waveform of 0.39g, both mainshock and aftershock.



a) S-F03 (0.39g)

Figure 8 Response during the MYG013 waveform

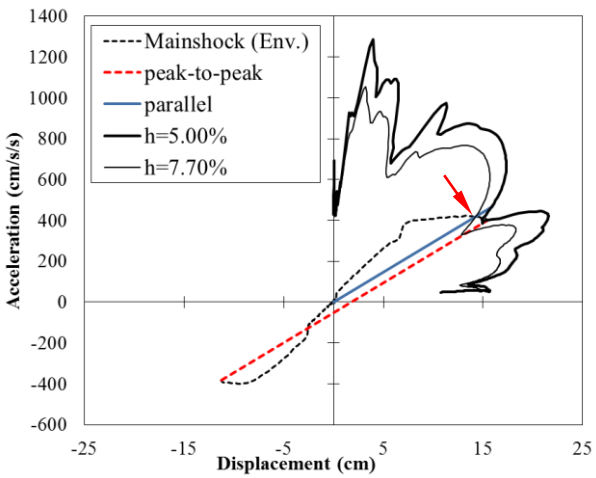
In the previous experimental study (Diaz, Kusunoki and Tasai, 2012), the equivalent damping ratio was estimated using the maximum response amplitude, negative or positive, to estimate the equivalent damping ratio; by increasing the damping ratio until the resulting demand spectrum is intersected with this maximum response amplitude, as described Section 2.4 in Figure 2.

Those results showed that some responses such as those from specimens S-F02, S-S02 and S-S03 were unsafely

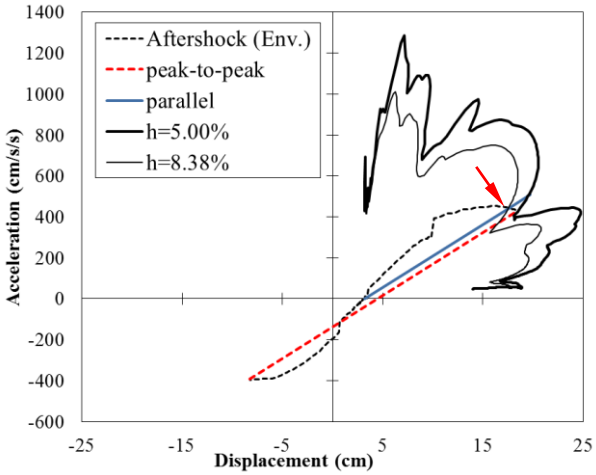
estimated using the formulations of the equivalent damping and response reduction ratios presented in this paper. It is because the fundamental period of these specimens are close to the predominant period of the corresponding input waveform (KOBE-NS). Also, the specimen Frame2b could not be used because it suffered the P-Δ effect and its maximum response amplitude is larger than the elastic spectral response with damping ratio of 0.05.

On the other hand, the equation of equivalent damping ratio given in Eq. (1) is developed by the geometric stiffness method which supposes that the positive and negative amplitudes of the hysteresis loop are equal. Although, as shown in Figure 6a, 6c, 7b, 7c, 7d and 7e, the hysteresis loops are shifted in many cases toward negative or positive direction, and amplitudes (negative and positive) turn out to be quite different; this shifting is intensified during aftershocks, where a residual deformation due to the mainshock may occur.

Thus the energy dissipation, or equivalent damping, is represented much closer to the true value when both amplitudes, negative and positive, are used to estimate an equivalent period (peak-to-peak), and then defining the equivalent amplitude.



a) Response during mainshock



b) Response during aftershock

Figure 9 Estimation of parameters using the equivalent amplitude

An important characteristic is that the envelope of the spectral response during the mainshock maintains the same shape during the aftershock, but moved toward one direction or another, and the residual deformation becomes the new origin. It means the capacity curve preserves the same shape until the structure sustains major damage (large deformation). This phenomenon can be observed in Figure 9, the envelope of the response during mainshock looks like moved toward positive direction during the aftershock, and the new origin is relocated at 3.2 cm.

Therefore, the equivalent damping and response reduction ratios are calculated after defining the equivalent amplitude as the intersection between the line parallel to the resulting line of joining the peak amplitudes (peak-to-peak) which crosses the origin and the negative or positive branch of the envelope of the spectral response (Figure 9a). In case of the response during the aftershock (Figure 9b), the parallel line crosses the new origin (residual deformation).

After defining the equivalent amplitude, the equivalent damping ratio is calculated by reducing the demand curve toward the equivalent amplitude, as describe in Section 2.4. Then the response reduction ratio is calculated as the ratio of the equivalent amplitude to the elastic response. The elastic response corresponds to the intersection between the parallel with the demand spectrum with damping ratio of 0.05, as shown in Figure 9a. In case of aftershocks, the demand spectrum is moved toward the residual deformation as shown in Figure 9b.

4. ANALYSIS OF RESULTS

Figure 10 shows the relation between the ductility factors due to mainshocks and aftershocks, using the absolute maximum displacement (maximum amplitude), and the negative and positive maximum displacement (equivalent amplitude).

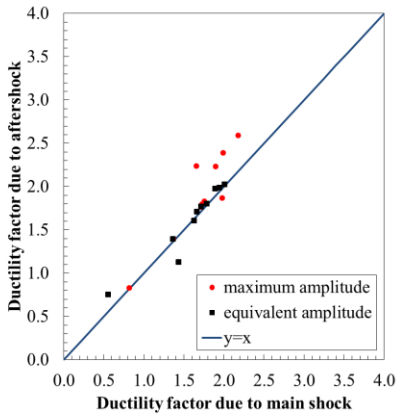


Figure 10 Relation between ductility factors

Table 2, Table 3, Table 4 and Table 5 show the ductility factor (μ), the equivalent damping ratio (h_{eq}) and the response reduction ratio (F_h) obtained from the experimental tests, and the estimated response reduction ratio. In order to

estimate the response reduction ratio, the ductility factor is evaluated into Eq. (2) to estimate the equivalent damping ratio and then it is evaluated into Eq. (3) and Eq. (4), F_h and $F_h{}^*$, respectively.

Table 2 and Table 3 show results due to mainshocks and aftershocks, respectively, using the maximum absolute displacement. As shown in these tables, the equivalent damping and response reduction ratios are not calculated for the specimen Frame-2b, because the inelastic response is much larger than the spectral response with damping ratio of 0.05, both mainshock and aftershock.

Table 2 Results due to mainshock using the maximum absolute amplitude

Specimen	waveform	Experimental			Estimated	
		μ	h_{eq}	F_h	F_h	$F_h{}^*$
Frame-1a	WG60	1.73	16.57%	0.540	0.714	0.874
Frame-2a	KOBE-NS	0.82	5.19%	0.968	1.081	1.018
Frame-2b	KOBE-NS	1.66	-	-	-	-
S-F01	WG60	1.72	11.24%	0.651	0.915	0.974
S-F02	KOBE-NS	2.18	4.42%	1.028	0.879	0.960
S-F03	MYG013	1.37	7.57%	0.770	0.935	0.981
S-S01	WG60	1.98	10.62%	0.672	0.895	0.966
S-S02	KOBE-NS	1.90	6.48%	0.907	0.890	0.964
S-S03	KOBE-NS	1.99	5.57%	0.959	0.882	0.961
S-S04	WG60	1.76	10.91%	0.665	0.897	0.967

Table 3 Results due to aftershock using the maximum absolute amplitude

Specimen	waveform	Experimental			Estimated	
		μ	h_{eq}	F_h	F_h	$F_h{}^*$
Frame-1a	WG60	1.80	16.41%	0.542	0.831	0.939
Frame-2a	KOBE-NS	0.83	4.99%	0.976	1.056	1.013
Frame-2b	KOBE-NS	2.23	-	-	-	-
S-F01	WG60	1.76	10.83%	0.671	0.905	0.970
S-F02	KOBE-NS	2.59	5.19%	1.002	0.858	0.951
S-F03	MYG013	1.39	7.37%	0.778	0.929	0.978
S-S01	WG60	1.87	10.04%	0.699	0.901	0.968
S-S02	KOBE-NS	2.23	5.95%	0.981	0.872	0.957
S-S03	KOBE-NS	2.39	5.60%	0.987	0.855	0.950
S-S04	WG60	1.83	10.07%	0.691	0.884	0.962

Table 4 and Table 5 show results due to mainshocks and aftershocks, respectively, using the equivalent amplitude defined by the positive and negative peak amplitudes (peak-to-peak). Contrasting with the maximum absolute amplitude, the equivalent amplitude allows calculating the equivalent damping and response reduction ratios for the specimen Frame-2b, which suffered P-Δ effect.

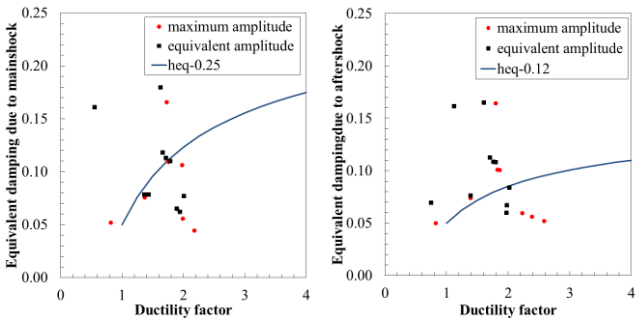
Table 4 Results due to mainshock using the equivalent amplitude

Specimen	waveform	Experimental			Estimated	
		μ	h_{eq}	F_h	F_h	$F_h{}^*$
Frame-1a	WG60	1.63	17.95%	0.525	0.735	0.887
Frame-2a	KOBE-NS	0.56	16.09%	0.639	1.305	1.044
Frame-2b	KOBE-NS	1.44	7.83%	0.885	0.984	0.996
S-F01	WG60	1.66	11.82%	0.642	0.927	0.978
S-F02	KOBE-NS	2.01	7.70%	0.892	0.892	0.965
S-F03	MYG013	1.36	7.83%	0.757	0.939	0.982
S-S01	WG60	1.79	10.99%	0.613	0.909	0.971
S-S02	KOBE-NS	1.89	6.49%	0.912	0.894	0.966
S-S03	KOBE-NS	1.95	6.19%	0.946	0.887	0.963
S-S04	WG60	1.72	11.29%	0.648	0.901	0.968

Table 5 Results due to aftershock using the equivalent amplitude

Specimen	waveform	Experimental			Estimated	
		μ	h_{eq}	F_h	F_h	$F_h{}^*$
Frame-1a	WG60	1.61	16.50%	0.498	0.855	0.950
Frame-2a	KOBE-NS	0.75	6.93%	0.886	1.084	1.019
Frame-2b	KOBE-NS	1.13	16.14%	0.698	0.985	0.996
S-F01	WG60	1.71	11.24%	0.663	0.924	0.977
S-F02	KOBE-NS	2.03	8.38%	0.870	0.890	0.964
S-F03	MYG013	1.39	7.61%	0.772	0.935	0.980
S-S01	WG60	1.80	10.80%	0.644	0.907	0.971
S-S02	KOBE-NS	1.98	5.98%	0.955	0.888	0.963
S-S03	KOBE-NS	1.98	6.70%	0.927	0.882	0.961
S-S04	WG60	1.77	10.84%	0.669	0.896	0.966

Figure 11 shows the relationship between the ductility factor and the equivalent damping ratio from the experimental test using the maximum absolute amplitude and the equivalent amplitude due to a) mainshocks and b) aftershocks.



a) mainshocks b) aftershocks

Figure 11 Estimation of equivalent damping ratio

Results in Figure 11 are compared with the estimated equivalent damping ratio which is defined by the curve heq-0.25 and heq-0.12, for mainshock and aftershock,

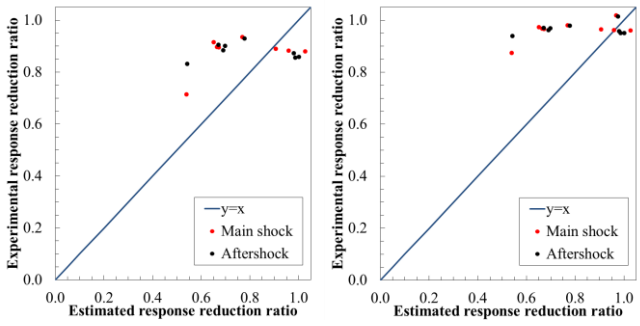
respectively. It corresponds to coefficients γ 0.25 and 0.12 in Eq. (1), because the hysteretic behavior is quiet close to the perfect elasto-plastic bilinear model.

The equivalent damping ratio becomes larger using the equivalent amplitude than using the maximum absolute amplitude, it is observed in Figure 11. It means that the equation of the equivalent damping ratio can be estimated more safely these values using the equivalent amplitude.

In order to compare the experimental and estimated response, the response reduction ratio is calculated from the shaking table tests and formulations. The response is safely estimated when the actual response reduction ratio (experimental) is less than or equal to the estimated response reduction ratio using the formulations presented in this paper, both mainshock and aftershock, whichever is applicable.

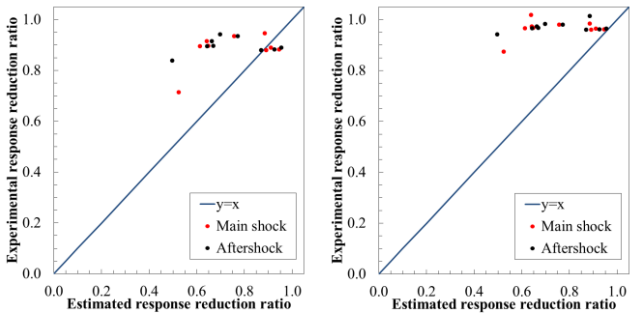
$$F_h^{experimental} \leq F_h^{estimated} \tag{10}$$

The comparison between the estimated response reduction ratio and the experimental response reduction ratio due to mainshocks and aftershocks is presented in Figure 12 and Figure 13, using Eq. (3) and Eq. (4), respectively. These figures show this comparison using a) the maximum absolute amplitude and b) the equivalent amplitude. Here, the response safely estimated are represented by points above the line (y=x).



a) maximum amplitude b) equivalent amplitude

Figure 12 Response reduction ratio by F_h , Eq. (3)



a) maximum amplitude b) equivalent amplitude

Figure 13 Response reduction ratio by $F_h{}^*$, Eq. (4)

5. CONCLUSIONS

From the analysis conducted for the experimental and estimated results, the following conclusion can be drawn:

- Ten scale three-story steel frames were tested on a shaking table, seismic performance is determined from the experimental results and compared with the estimated values.
- The definition of the equivalent amplitude allows calculating responses where the maximum absolute amplitude exceeds the elastic spectral response, even for the specimen which suffered the P-Δ effect.
- The equivalent damping ratio can be more safely estimated when the equivalent amplitude is defined instead of the maximum absolute amplitude.
- The formulations estimated safely the equivalent damping ratio and then the response reduction ratio due to mainshocks and aftershocks using the peak amplitudes to define the equivalent amplitude. The response reduction ratio is more safely estimated using Eq. (4) than Eq. (3).

However, this technique would become safer for the seismic performance estimation if an equation to estimate the shifting displacement is incorporated.

Acknowledgements:

Authors acknowledge Miho Yamashita, Yuichi Hatanaka, Daiki Hinata, and Yuki Hattori for their great contributions during the tests. The installation and maintenance of the measurement system has been supported by Mr. Masayuki Araki, Mr. Takamori Ito and other staffs of aLab Co. Also, the authors would like to express their gratitude to the Japan Science and Technology Agency (JST) through the Science and Technology Research Partnership for Sustainable Development (SATREPS) project "Enhancement of earthquake and tsunami disaster mitigation technology in Peru" for the fellowship during this research.

References:

Ministry of Land, Infrastructure, Transport and Tourism (2000). "Notification No. 1457-6." Technical Standard for Structural Calculation of Response and Limit Strength of Buildings.

Jennings P. (1968). "Equivalent Viscous Damping for Yielding Structures." *Proceedings of ASCE*, Vol.94, No. 1, 103-116.

Kusunoki, K. (2006) "Analytical Study on Estimation of Equivalent Viscous Damping Ratio for aftershock", *Proceedings of the Japan Concrete Institute Proceedings of the Japan Concrete Institute* 28(2), 1057-1062.

Diaz M., Kusunoki K. and Tasai A. (2012). "Analytical Study of Residual Seismic Performance by Estimation of Response Reduction Ratio and Equivalent Damping for Aftershocks." *Proceedings of 15th World Conference on Earthquake Engineering*, Paper ID 1950.

Shibata A. and Sozen M. (1976). "The Substitute Structure Method for Seismic Design in RC." *Proceedings of ASCE, Journal on Structural Division*, Vol. 102, No. 1, 1-18.

ATC-40 (1996). Seismic Evaluation and Retrofit of Concrete Buildings, Report No. SS 96-01, Applied Technology Council.

Shibata A. (2010). "*Dynamic Analysis of Earthquake Resistant Structures*", Tohoku University Press.

Diaz M., Kusunoki K. and Tasai A. (2012). "Experimental Study on Residual Seismic Performance of Scaled Three-Story Steel Frames Tested on a Shaking Table." *Proceedings of International Symposium on Earthquake Engineering*, 349-356.

10CUEE CONFERENCE PROCEEDINGS
10th International Conference on Urban Earthquake Engineering
March 1-2, 2013, Tokyo Institute of Technology, Tokyo, Japan

INVESTIGATION OF DYNAMIC STABILITY ON EFFECT OF RESTORATION FOR AGED CASTLE MASONRY WALL

Yasutaka Noma[1)], Tsuyoshi Nishimura[2)], Hiroyuki Yamamoto[3)], Hiroyoshi Kasa[4)], Tatsuaki Nishigata[5)] and Kazuhiko Nishida[6)]

1) Researcher, Technical Research Institute, Hazama Corporation, Japan
2) Chief Researcher, Technical Research Institute, Hazama Corporation, Japan
3) Section Chief, Department of Civil Design, Hazama Corporation, Japan
4) Division Chief, Department of Environment, Hazama Corporation, Japan
5) Professor, Department of Civil, Environment and Applied System Engineering, Kansai University, Japan
6) Professor Emeritus of Kansai University, Kansai Ground Environmental Research Center, Japan
ynoma@hazama.co.jp, nisimura@ hazama.co.jp, yamamotoh@hazama.co.jp, casa@hazama.co.jp, nisigata@kansai-u.ac.jp, nishida@ks-dositu.or.jp

Abstract: Aging of castle masonry walls in Japan after 400 years since their construction has become problematic. The application of restoration works is examined when bulging phenomena are confirmed. However, methods to evaluate stability before and after repair of aged castle masonry walls have not been established. Hence, the effect of restoration has not been clarified.

The variation of dynamic stability of castle masonry walls before and after restoration was investigated by stability analyses using the distinct element method, which is one of discontinuous analyses, focused on actual repair works. The effect of repair was well represented by the analyses.

1. INTRODUCTION

In Japan, there are a lot of castle masonry walls being of historically and culturally inestimable value. It is important to appropriately maintain these walls because most of the castle ruins are used as historical places and parks where many people visit. Recently, aging of these walls has become problematic in terms of structure stability and functions.

Many restoration works of castle masonry walls have been conducted. It is required to sustain the authenticity of the walls and use traditional materials and techniques in principle for repair works of cultural heritages having historical values.

It is a present condition that the effect of repair works of castle masonry walls cannot be known because it is difficult to evaluate stability of these walls behaving complicatedly as discontinuous structures. Stability analyses by using the distinct element method which is one of discontinuous analyses (Kasa et al. 2007) were conducted to quantitatively evaluate the improvement of stability after restoration works of these walls.

In the present study, quantitative evaluation of stability of castle masonry walls before and after restoration works were conducted by referring to measures of actual restoration works of these walls. The restoration work of Takamatsu castle which is one of examples referred in this investigation is shown in Photo 1.

Dynamic analyses by means of distinct element method were conducted by using models before and after restoration works. The model before the works has the bulging phenomenon. On the other hand, rearrangement of stones, improvement of the thickness of cobble layers and ground, and arrangement of frames were reflected in models after the works.



Photo 1 Restoration work of castle masonry wall in Takamatsu castle

The variation of dynamic stability of structures before and after works was investigated. The effect of reinforcement of the bottom parts of stones by arrangement of frames was especially focused on.

2. MODELING IN ANALYSES

2.1 General restoration work

General castle masonry walls have the recurvate stone arrangement. This arrangement changes to arch shape in the front direction because of earthquakes, weather, and growth of roots of trees. This is called the bulging phenomenon. Restoration works are often conducted when this phenomenon is confirmed.

In general restoration works, castle masonry walls are dismantled to rearrange stones into the original shape. Rearrangement of stones is reconstruction of bulged stone parts into the original gradient of stone parts which is determined by using inclination of existing castle masonry walls or ancient texts such as Goto family texts (Nishida et al. 2003). Improvements of the thickness of the cobble layer and back ground are also conducted in some cases when the thickness of the cobble layer and the strength of the ground are not enough. Lime powder is used in the ground improvement as traditional material.

2.2 Frame in Takamatsu castle

Frame works modeled as one of restoration measures in this investigation were used in the restoration works of castle masonry walls in Takamatsu castle from 2009 to 2011.

Frame works are shown in Figure 1. Pine piles are constructed in front of the bottom stones and stones are filled to constraint the deformation of the bottom stones under water surface in the front direction. This work seems to contribute to the improvement of structural stabilitiy of castle masonry walls (Nishida et al. 2009).

2.3 Outline of castle masonry wall model

Referring to the above, the cross-section of castle masonry walls used in analyses was decided and shown in Figure 2. The cross-section of castle masonry walls before restoration works has a bulging part and the thickness of cobble layers is inconstant in the vertical direction. Rearrangement of stones, uniformalization of the thickness of the cobble layer, improvement of the ground, and the frame were incorporated into the cross-section of walls after works. The height of models of castle masonry walls is from 10 to 15 m. The model after works is not only with rearrangement of stones but also with the frame used in Takamatsu castle as actual works. The effect of reinforcement by the frame is especially investigated in the following analyses.

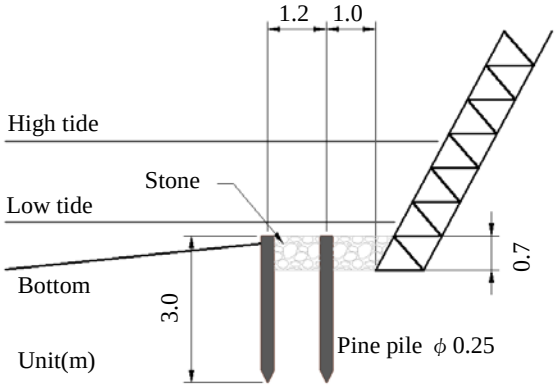


Figure 1 Arrangement of frame (Modified figure of Nishida et al. 2009)

3. INVESTIGATION OF DYNAMIC STABILITY

3.1 Outline of analysis

Analytical cases are shown in Table 1. Case 1 assumes the bulging castle masonry wall before restoration works. Case 2 and 3 consider walls after works and application of measures shown in Table 1 was took into account. The difference between Case 2 and 3 is with or without the frame.

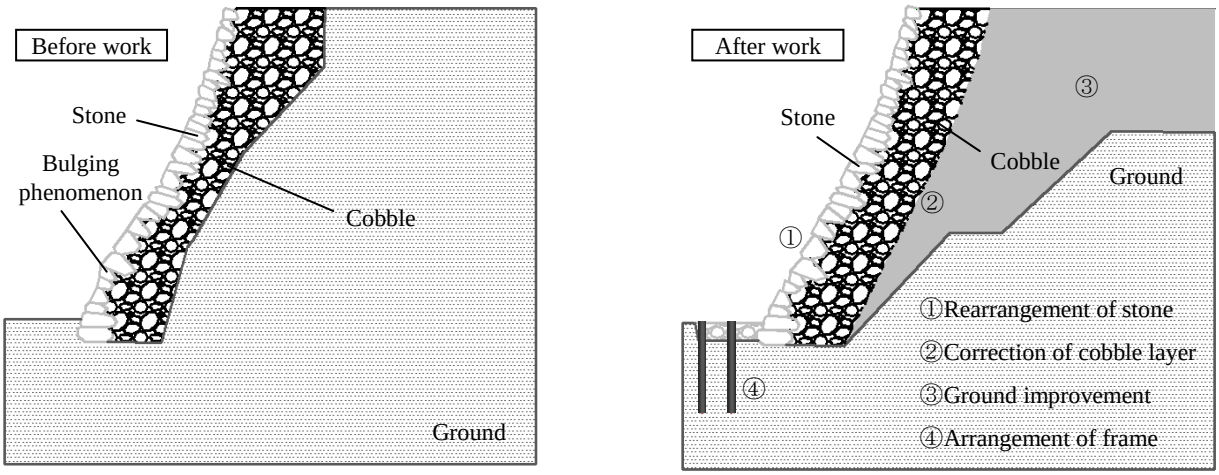


Figure 2 Pattern diagram of cross-section of castle masonry wall before and after restoration work

PFC2D which is one of versatile analysis codes of the granular distinct element method is used in the analyses. Input parameters used in the analyses are shown in Table 2. Each material is modeled as a shape shown in Figure 3 by clumped elements assembled with circular elements. Sizes of stone and cobble elements are decided by sizes of stone (500～1500 mm) and cobble (100～300 mm) of walls in Takamatsu castle. Particle frictions of the ground and the improved ground are calibrated to satisfy ϕ=40° and ϕ=45° respectively (Noma et al. 2011). The particle friction of the stone was determined by using analytical results of shear analyses to satisfy ϕ=25～35° . Input parameters of the frame are the same as the stone because stones are filled inside the frame.

Analytical models after obtaining static stability for each case are shown in Figure 3. The height of models is 14 m from the bottom stone because the height of the castle masonry wall of Takamatsu castle is about 13.5 m. Cross-sections of stones are similar to the shape of actual stones and simplified. The upper line of the ground is modeled as flat and the height is the same as the upper stone. The frame is modeled by considering stones and pine piles (embedded length is 3 m).

Takamatsu castle has experienced several large-scale earthquakes such as Hoei Nankai Earthquake (M8.6) in 1707, Ansei Nankai Earthquake (M8.4) in 1854, Showa Nankai Earthquake (M8.0) in 1946, and Hyogoken Nanbu Earthquake (M7.3) in 1995. 20 times sinusoidal waves whose frequency is 3 Hz and the amplitudes of 400 and 800 Gals are used in dynamic analyses. This frequency is decided by eigenvalue analyses and in-situ inspection of castle masonry walls. These amplitudes are determined by referring the above earthquakes and assuming seismic intensities of about 4 and 6.

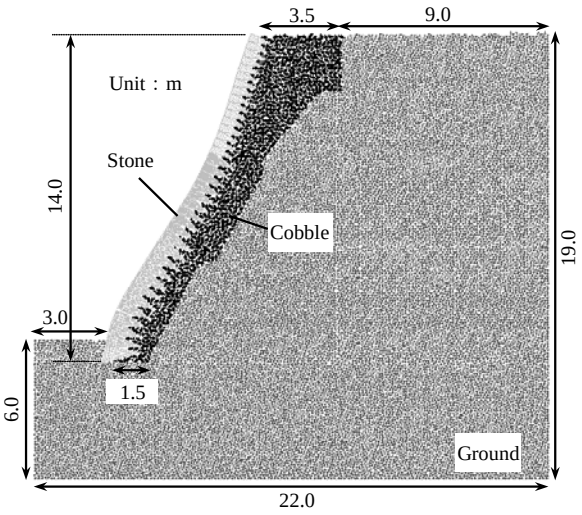
Table 1 Analytical case

Item	Before work	After work	
	Case 1	Case 2	Case 3
Bulging phenomenon	○		
Rearangement of stone		○	○
Correction of cobble layer		○	○
Ground improvement		○	○
Arrangement of frame			○

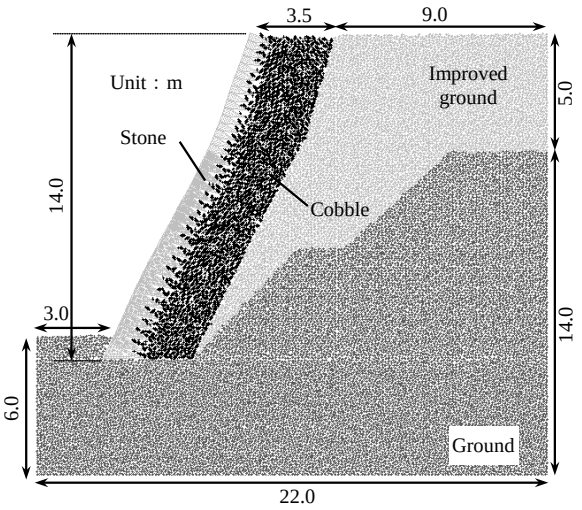
Table 2 Input parameter

Item	Stone	Cobble	Ground	Improved ground
Shape of element	Polygonal clump	Saturnian shape clump		
Maximum diameter (mm)	1000～1500	200～300	150～200	
Density (kg/m^3)	2650			
Normal・tangential spring stiffness (N/m)	1×10^8			
Particle bond (kN)	0			
Particle friction	2.00	0.65	0.66	0.84

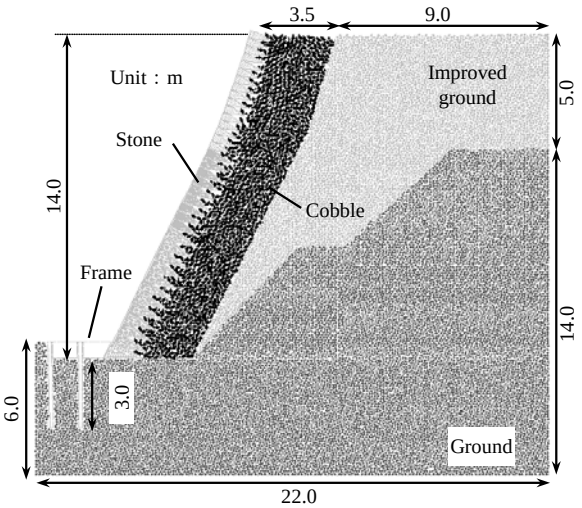
1 s static analyses after dynamic analyses were conducted.



(a) Case 1



(b) Case 2



(c) Case 3

Figure 3 Analytical model

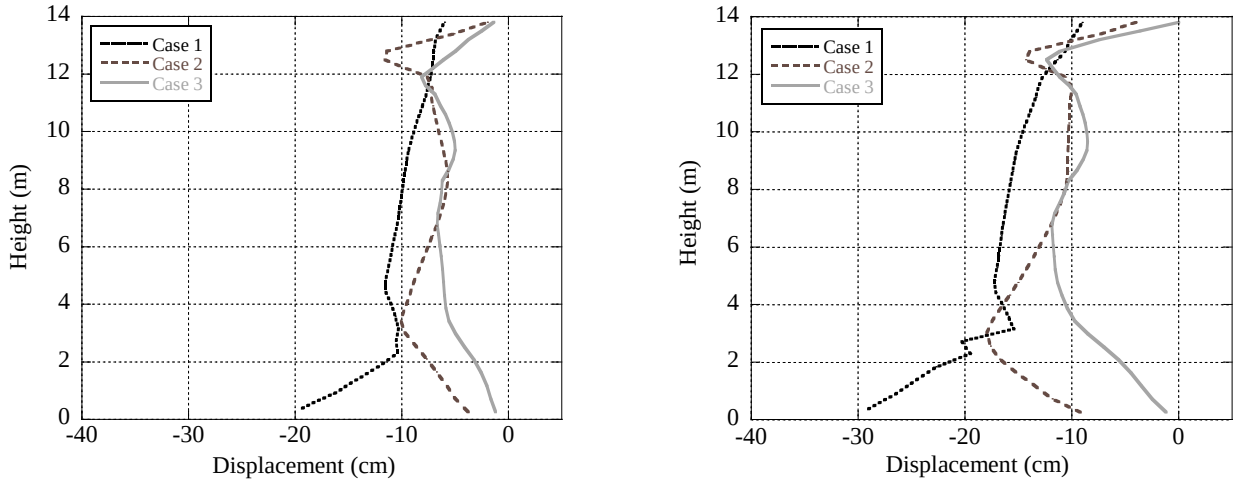
3.2 Analytical result

Displacement distribution of stones at the end of analyses, the relationship between time and displacement of stones showing the maximum displacement and deformation diagrams are shown in Figure 4, 5, 6 and 7. Displacements in the front direction of walls show negative values.

Maximum displacement of about 18 cm is confirmed at the bottom stone of Case 1 in the dynamic analytical result with amplitude of 400 Gals. However, Maximum displacements of about 8～12 cm are confirmed near the upper stone of Case 2 and 3. Maximum displacement of about 28 cm is confirmed in Case 1 in the dynamic analytical result with amplitude of 800 Gals. However, maximum displacements of about 18 cm in Case 2 and about 13 cm in Case 3 are confirmed. From these results, it is confirmed that dynamic stability is improved by conducting repair works. Especially, deformation of stones near the bottom stone becomes smaller by using the frame.

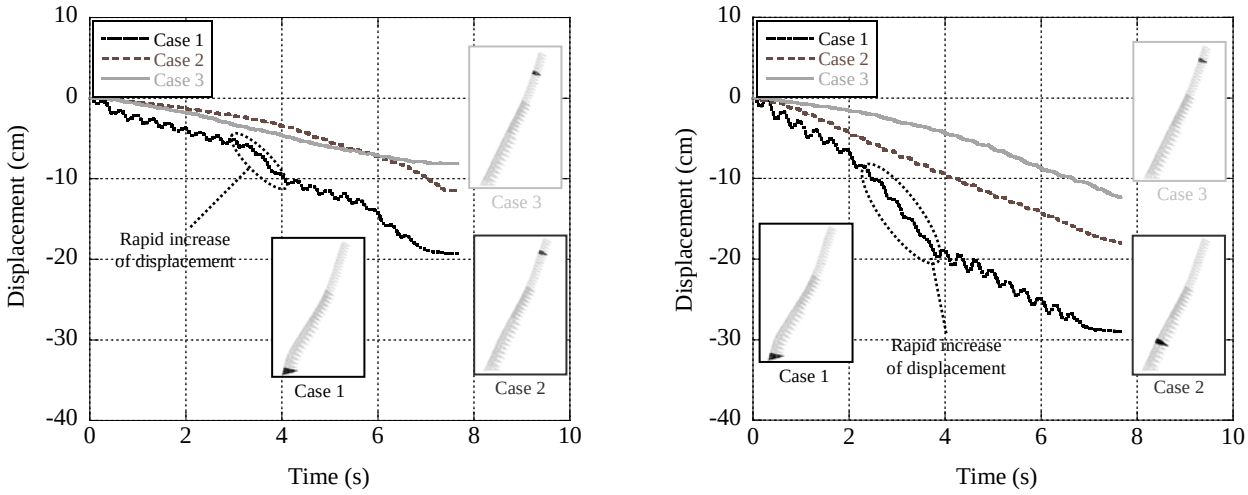
Rapid increase in displacement of stones can be confirmed in analytical results with amplitude of both 400 and 800 Gals in Case 1 as shown in Figure 5. This shows the deformation changed from continuous behavior to discontinuous behavior and is progressive. On the other hand, time histories of displacement do not change in Case 2 and 3, and continuous behavior can be confirmed from these cases.

The above results can also be confirmed in Figure 6 and 7. Slips of stones near the bottom stone and irreversible behavior as a discontinuous structure can be observed and displacements of stones become large in Case 1. In Case 2, bulging phenomenon and changes from continuous behavior to discontinuous behavior can be confirmed. However, performance of a continuous structure is sustained because only small deformation near the upper stones and no bulging phenomenon are observed in Case 3.



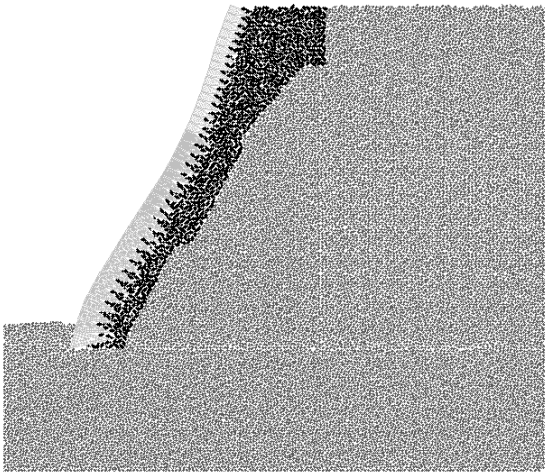
(a) 400 Gals (b) 800 Gals

Figure 4 Displacement distribution of stone after analyses

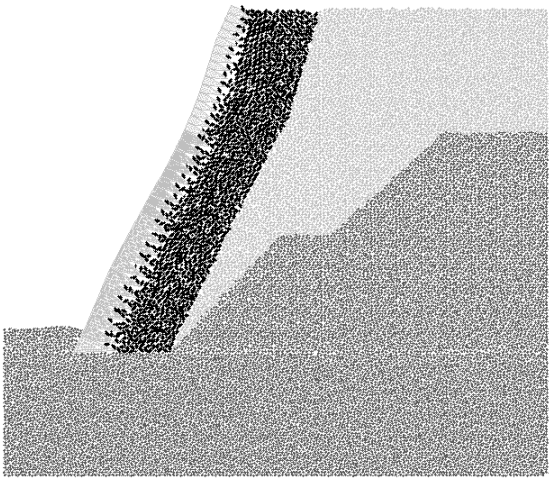


(a) 400 Gals (b) 800 Gals

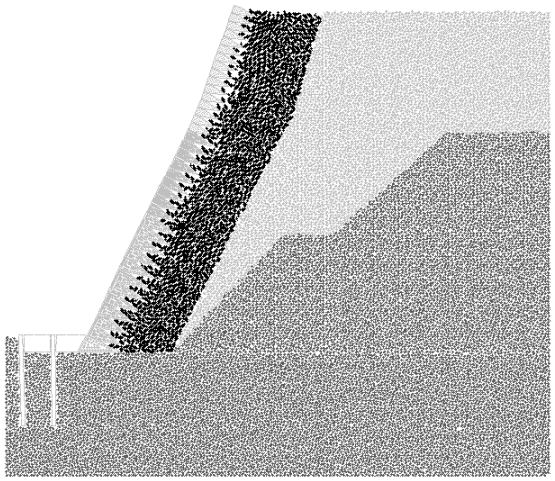
Figure 5 Time history of displacement of stone showing maximum displacement after analyses



(a) Case 1

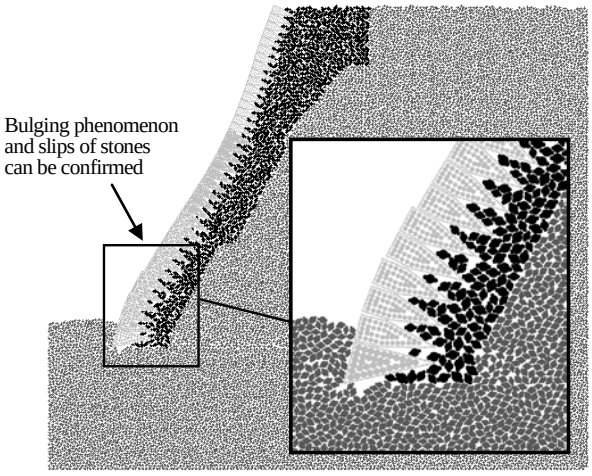


(b) Case 2

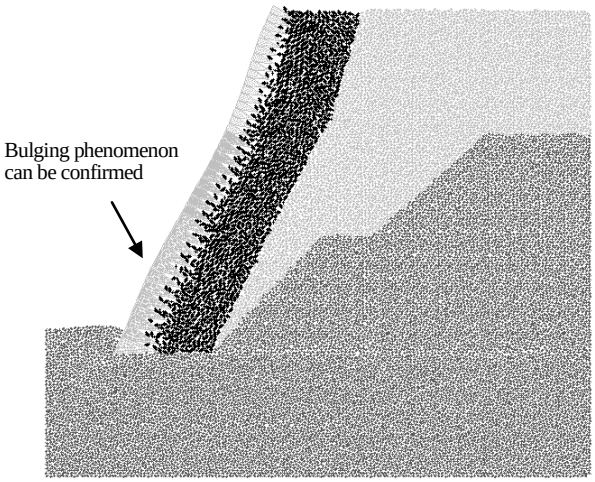


(c) Case 3

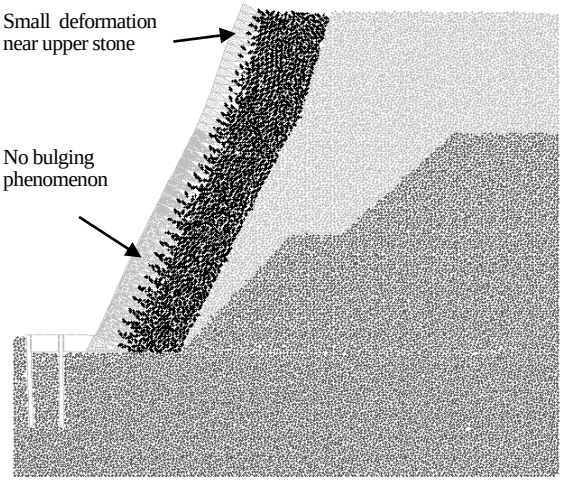
Figure 6 Deformation diagram of analytical model after analyses (400 Gals)



(a) Case 1



(b) Case 2



(c) Case 3

Figure 7 Deformation diagram of analytical model after analyses (800 Gals)

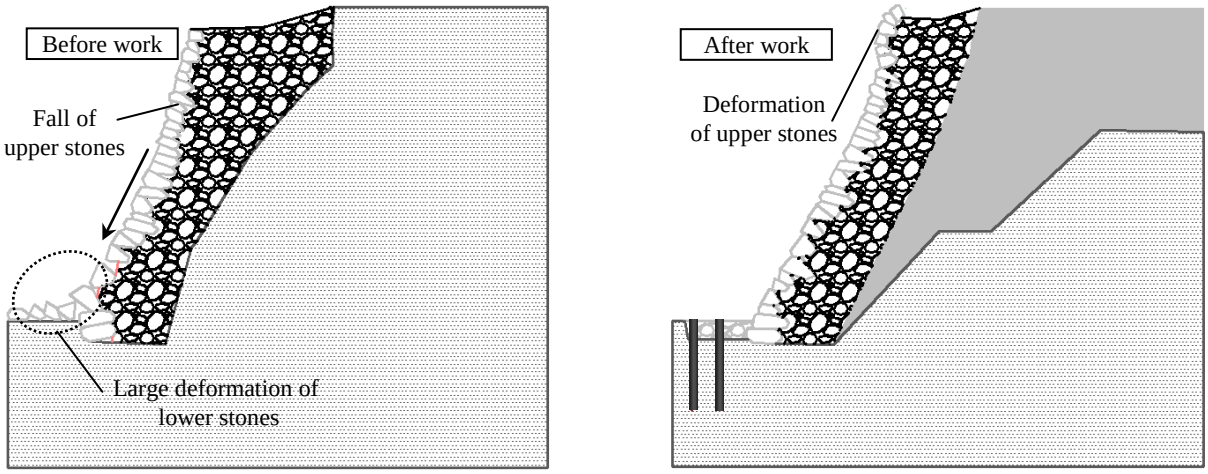


Figure 8 Pattern diagram of dynamic stability of castle masonry wall before and after restoration work

3.3 Evaluation of dynamic stability

Pattern diagrams related to dynamic stability of castle masonry walls before and after restoration works assumed from analytical results of this study are shown in Figure 8. Slips of lower stones in the front direction are confirmed in dynamic analyses in bulging castle masonry walls before works. This indicates that the collapse of castle masonry walls is caused by the movement of lower stones in the front direction and fall of upper stones in earthquakes. On the other hand, only small deformations are observed in dynamic analyses in castle masonry walls after works. It can be considered that the effect of earthquakes is moderated and seismic resistance is improved by the restoration works.

4. CONCLUSIONS

Dynamic stabilities of castle masonry walls before and after restoration works are evaluated for a model of aged walls and restoration works in Takamatsu castle by using the distinct element method in this study. As a result, it is indicated that displacement of stones become smaller by conducting repair works. Especially, it is considered that frames arranged in front of the bottom stone contribute to the improvement of seismic performance from analytical results.

Acknowledgements:

The authors acknowledge information support such as frame works from the educational committee of Takamatsu City.

References:

Kasa, H., Nishida, K., Nishigata, T., Morimoto, H., Awatani, Y., and Yamamoto, H. (2007), "A Study on Stability Analysis of Castle Masonry Walls by Using the Distinct Element Method," *Journal of Civil History Research*, Japan Society of Civil Engineers, **27**, 45-51.

Nishida, K., Nishigata, T., Tamano, T., and Morimoto, H. (2003) , "A Numerical Study on Cross Sectional Shape in Design Procedure of Castle Masonry Walls," *Proceedings of JSCE*, Japan Society of Civil Engineers, **750**, 89-98.

Nishida, K., Oshima, K., Tamano, T., Kanaoka, M., Kitazono, K., Yamanaka, M., and Shiraishi, Ken. (2009), "Mechanical investigations and preservation methods at dismantling the tower platform of Takamatsu-Castle," *Journal of Civil History Research*, Japan Society of Civil Engineers, **29**, 235-242.

Noma, Y., Nishimura, T., Yamamoto, H., Kasa, H., and Nishigata, T. (2011) , "A Discussion on Parameter Setup of Cobble and Ground Parts in Stability Analysis of Castle Masonry Wall by Using the Distinct Element Analysis," *Proceedings of JSCE annual conference*, Japan Society of Civil Engineers, **66**, 323-324.

10CUEE CONFERENCE PROCEEDINGS
10th International Conference on Urban Earthquake Engineering
March 1-2, 2013, Tokyo Institute of Technology, Tokyo, Japan

SEISMIC BEHAVIOR OF OTTOMAN EMPIRE CLASSICAL PERIOD STONE MASONRY WALLS

Cem Demir[1)], Emre Dogu[2)], Medine Ispir[3)], and Alper Ilki[4)]

1) Post-Doctoral Researcher at Akita Prefectural University, Japan and Research Associate at Istanbul Technical University, Turkey
2) Civil Engineer (MSc), Nodus Engineering and Consult. Ltd., Istanbul, Turkey
3) Researcher (PhD), Civil Engineering Faculty, Structural and EQ Engineering Lab., Istanbul Technical University, Turkey
4) Professor, Civil Engineering Faculty, Structural and EQ Engineering Lab., Istanbul Technical University, Turkey
demirce@itu.edu.tr, emreast@gmail.com, medispir@gmail.com, ailki@itu.edu.tr

Abstract: A large number of the historical structures in Turkey are under high seismic risks. Since the knowledge on the traditional masonry walls and masonry constituents of the historical structures in Turkey is scarce, particularly from the structural engineering perspective, this study intends to enlarge the experimental data concerning the behavior of the Ottoman period multi-leaf stone masonry walls under cyclic in-plane loads that represent the seismic effects. For this purpose, four stone masonry walls, representative of the investigated wall typology, were constructed with similar materials and construction techniques. A well-known local limestone (Küfeki limestone), widely used in ancient structures in Istanbul, was utilized during the construction of the wall members with dry joints. The Küfeki units were interconnected to each other via metal cramps as also done in the past practice. The main parameter of the tests was the level of pre-compression stress that was kept constant during the lateral cyclic loading. The experimental study provided data on the failure mode, lateral load capacity and load-displacement response of the investigated walls and showed the influence of pre-compression stress level on these characteristics.

1. INTRODUCTION

Most of the historical structures in Turkey are under high seismic risk since the overall seismicity of the region is considerably high. Particularly, in and around the old imperial city of Istanbul, where numerous monumental structures from the Roman, Byzantine and Ottoman periods exist, this risk is even more solid. Although a number of studies on seismic behavior of stone masonry walls exist in the engineering literature (such as Lorenço et al. 2005, Corradi et al. 2008, Vasconcelos and Lourenço 2009 and Galasco et al. 2010), the knowledge on the traditional masonry walls and masonry constituents of the historical structures in Turkey is scarce. Consequently, new experimental and analytical studies are needed for development of well-established assessment and intervention procedures. This study intends to enlarge the experimental data concerning the behavior of the Ottoman period multi-leaf stone masonry walls under cyclic in-plane loads that represent the seismic effects.

In order to achieve this purpose, the mechanical characteristics of multi-leaf stone masonry walls of classical era Ottoman Imperial structures are investigated through an experimental campaign carried out at the Structural and Earthquake Engineering Laboratory of Istanbul Technical University Civil Engineering Faculty. A prototype wall, representative of the investigated walls is designed, scaled down and wall specimens produced accordingly are subjected to combined vertical and in-plane lateral forces. Two typical structures from Ottoman period, Edirnekapı Mihrimah Sultan (16^{th} century) and Fatih (initial construction 15^{th} century, reconstructed in 18^{th} century) Mosques, and their multi-leaf walls can be seen in Figure 1.



Figure 1 Ottoman period structures in Istanbul and their multi-leaf stone masonry walls

2. EXPERIMENTAL STUDY

2.1 Experimental Program

The experimental study carried out on multi-leaf stone masonry that represent the walls used in the Ottoman Period multi-leaf walls in and around the Istanbul city were subjected to in-plane quasi-static displacement cycles. The main parameter of the study was the level of vertical stress level acting on the walls. The shear compression tests aimed to obtain failure modes and lateral force-displacement hysteresis loops that can be used to evaluate a number of parameters such as ductility, energy dissipation and stiffness variation. Please note that more details of this study can be found in Demir (2012).

2.2 Specimen Characteristics

A survey of the existing literature and site observations on the main aspects of the historical masonry walls of Ottoman period structures reveal that it is generally typical for monumental structures in and around Istanbul to have thick ashlar external leaves made of limestone (local Küfeki stone) that cover the inner rubble masonry core. Limestone blocks are generally connected to each other via metal cramps (and in some cases with pins), which are fixed to the stone units with molten lead, in case no mortar is used between the units. The inner rubble masonry mainly consists of lime based mortar mixed with stone and brick pieces. Illustration of a typical three-leaf wall can be seen in Figure 2.

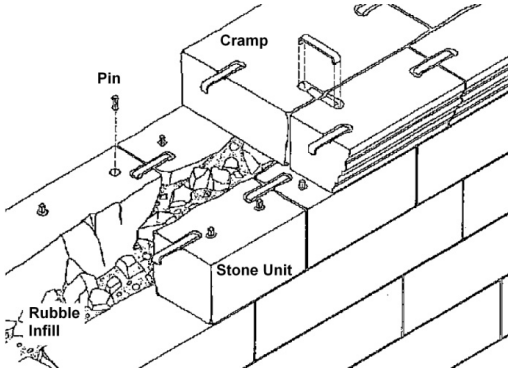


Figure 2 Typical wall configuration (modified from Tanyeli, 1990)

Considering the actual dimensions of walls and stone units together with the capabilities of the available testing facilities of Istanbul Technical University Structural and Earthquake Engineering Laboratory, an approximate scale factor of 1/3 was preferred that led to wallet dimensions of 1.20×1.20×0.30 m in length, height and thickness, respectively (as seen in Figure 3). Width of each leaf along the thickness of the wall was about 100 mm, however, at alternating stone courses the units of the external leaves were protruding into the rubble core for about 30 mm from both side, leaving a clear core thickness of 40 mm.

During the construction of the specimens, in order to replicate the main characteristics of the multi-leaf walls in the heritage structures around Istanbul, special attention was paid to apply similar materials and techniques. For this purpose, prior to the laying of the stone units, holes and channels required for the attachment of the cramps were prepared on the top surfaces of machine sawn limestone blocks. The Küfeki stone blocks were obtained from a quarry near Istanbul and sawn into desired dimensions. After laying and leveling the first course of stone units, U-shaped cramps were inserted into their slots. In the next step, lead melt in a pot was poured into the cramp slots, fixing them to the adjacent stone units as seen in Figure 4. After laying two rows of stone units of external leaves, rubble masonry was used to fill the gap between them. The rubble masonry was prepared by using the Albaria Struttura ready-mix mortar (from BASF Construction Chemicals) and irregular stone pieces obtained by crushing Küfeki stone blocks. Since the compressive strength of the ready-mix mortar was relatively high (approximately 20 MPa at 28 days), after a number of trials, sand and water was added to the ready-mix mortar to achieve a mortar compressive strength in the order of 5 MPa to replicate the actual mortar quality for the examined type historical structures more realistically. Steps described above were repeated until a height of 1200 mm was achieved. Construction steps indicated above can be seen in Figure 4.

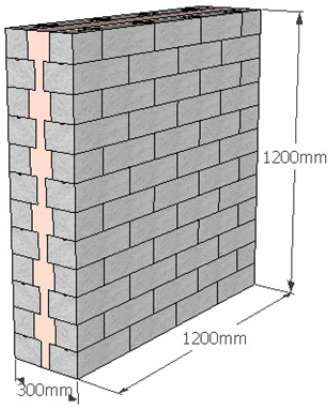


Figure 3 Dimensions of the tested walls



Figure 4 Construction of the specimens

During the application of lateral displacement cycles, normal stress level was kept constant as one of the following values: 0.25, 0.50, 0.75 and 1.00 MPa. Since it was the main parameter of the study, the names of the constructed walls were designated with respect to the targeted normal stress level of each specimen. Accordingly; M-25-C wall was tested under 0.25 MPa normal stress level; while M-50-C, M-75-C and M-100-C specimens were tested under 0.50, 0.75 and 1.00 MPa normal stresses, respectively. These stress levels were decided by considering the results of structural analyses available in literature for Ottoman period structures with multi-leaf walls and they represent normal stresses at different elevations of a structure.

2.3 Material Characteristics

Several material tests were also undertaken for defining the mechanical characteristics of materials used for construction of the shear compression test specimens. This stage of the experimental campaign included tests such as compression and modulus of rupture tests on Küfeki stone units; compression and splitting tests on rubble masonry standard cylinders; tension tests on steel material used for production of cramps; and initial shear tests on ashlar masonry dry joints. By utilizing these material tests, mechanical characteristics such as compressive strength, Young's modulus, tensile strength, friction coefficient, and stress-strain diagrams of the constituent materials were obtained. Accordingly, the mean compressive strength of the Küfeki stone material was 18 MPa (with a coefficient of variation of 29.6%) and mean modulus of rupture was 3.2 MPa. The rubble masonry material, that was formed by a mortar matrix and randomly distributed stone pieces placed without compaction had a mean compressive strength of 3.3 MPa at 28 days that dropped to 1.7 MPa at 180 days. Tensile strength of rubble masonry obtained from cylinder splitting tests was around 0.3 MPa at 28 and 90 days. The yielding stress of the mild steel used for the cramps was 250 MPa while the tensile strength was about 350 MPa. Finally, the friction coefficient of dry joints formed between the units of the ashlar external leaves was obtained as 0.76. It should be noted that more information on material characteristics can be found in Demir and Ilki (2013)

2.4 Test Setup and Loading Pattern

The in-plane lateral displacement cycles and the constant vertical load were applied to the walls by using the test setup shown in Figure 5. Test rig and the reaction frame were strictly fixed to the 1.20 m thick strong floor (reaction slab) of the laboratory via post-tensioned rods. Two 20 mm thick steel plates, stiffened with steel ribs, were used to restrict the horizontal sliding at the support level (first course) of the walls. Specimens were carefully positioned and aligned between these reaction plates that were located at both ends of the walls.

Lateral force required for displacement cycles was exerted by a ±990 kN force and 400 mm displacement capacity TDG actuator that was fixed to a reaction frame. A 600 kN capacity hydraulic jack pressurized by an electric pump was used for acting the vertical load. This hydraulic jack was coupled with a 1000 kN capacity loadcell for monitoring and keeping of the vertical load at the desired vertical load level. Both the hydraulic jack and the loadcell were placed between the test rig, which supplied a closed reaction frame for applying the vertical force, and a stiff steel beam. The in-plane translation of the upper end of the walls was eased by using steel cylinders placed between a steel encased reinforced concrete bond beam resting on the top surface of the specimen and the stiff steel beam. In addition to distributing the vertical load, the bond beam was also used for attachment of the lateral actuator. Although the measurements did not indicate a noticeable out-of-plane translation, as an additional precaution, walls were supported by two steel beams and wheels attached to them.

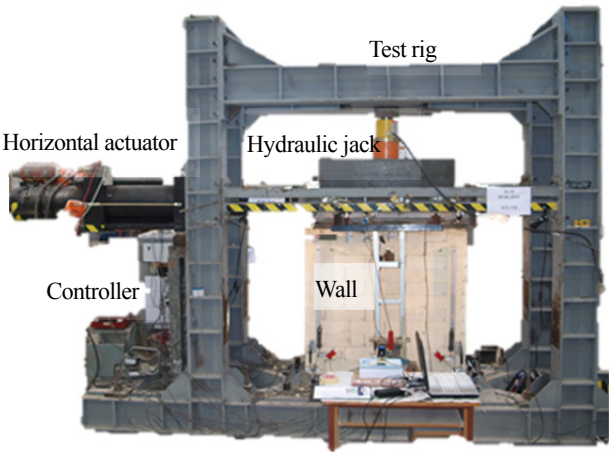


Figure 5 Test setup of the shear compression tests

The displacements, deformations and loads were measured by using different types of sensors. A total of 43 data collection channels; 35 linear variable differential transformers (LVDTs), two loadcells and six strain gauges; were installed on each shear compression test specimen. Data collected from all sensors were transferred to the computer by a TML TDS 302 Data Logger.

Loading of the walls was performed at two steps. At the first step, the axial load was applied until the desired pre-compression stress level (0.25, 0.50, 0.75 or 1.00 MPa) and then unloaded. These loading and unloading cycles were repeated for three times. Simultaneously data was collected from all sensors, so that variation of deformations under axial loading and unloading cycles could be recorded.

After completing the first step, all sensor channels were initialized and the axial load was increased to the targeted load level for the last time and lateral loading started. During the tests, axial force acting on the walls was carefully monitored and necessary adjustments were made to keep it at the desired value.

In all tests, reversed cyclic in-plane loading was applied under displacement control. All lateral displacement cycles targeted prescribed drift ratios, which progressively increased in amplitude: 0.05, 0.10, 0.25, 0.50, 0.75, 1.00, 1.25, 1.50 and 2.00%. Certain cycles near the peak load and in the post-peak region (0.5, 1.0 and 2.0%) were applied for

three times while the rest of the cycles were applied only once. The loading of the walls continued until peak load dropped in both directions at least by 20% or extensive damage occurred with an indication of loss of stability. Please note that a schematic representation of the applied loading pattern can be seen in Figure 6.

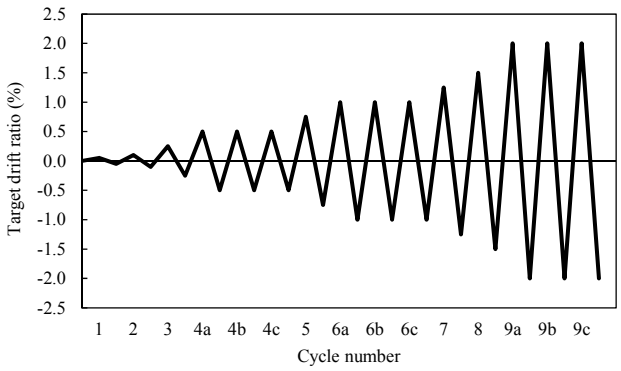


Figure 6 Loading pattern

3. RESULTS OF SHEAR COMPRESSION TESTS

3.1 Evolution of Damage and Failure Modes

All specimens exhibited failure types mainly dominated by the shear effects. However, depending on the level of axial stress level, differences in the behavior of the walls could be observed during the tests. For instance, bending effects as well as sliding of stone units were also observed, particularly for walls with relatively lower axial stress levels, whereas shear and compression effects were more dominant for walls with higher pre-compression loads. The damage distributions of M-25-C, M-50-C, M-75-C and M-100-C walls, observed during the shear compression tests and photographs taken after the tests can be seen in Figure 7.

The damage evolution generally started with vertical cracks passing through the stone units. These vertical cracks were mainly concentrated in the compression zones. Except the M-100-C specimen (with the highest level of axial stress considered in this study), horizontal flexural cracks appeared on rubble masonry between the initial stone courses at the lower halves of the specimens. Since the dry bed joints had zero tensile strength in the vertical direction, only the tensile strength of the rubble masonry resisted the tensile stresses at the tension side of the neutral axis.

Further increase of the lateral displacement caused formation of shear cracks along the diagonals of the walls. As also seen in Figure 7, due to the low tensile strength of the lime stone used in the specimen production and the restraining effects of the cramps interconnecting the head joints of adjacent units, these cracks were crossing the stone units rather than the head joints. The first diagonal cracks generally appeared near the 0.50% drift ratio.

Majority of the vertical and diagonal cracks crossing the stone units were generally, either at mid-length of the units or near the anchorage sockets of the cramps. Due to the existence of the cramps, that were transferring tension forces from one unit to adjacent one at singular points, diagonal cracks were wide spread across the wall faces. It should be noted that, number of cracks was higher in the case of specimens with relatively higher axial stresses, but crack widths were relatively smaller.

After opening of the wide spread diagonal cracks and failure of some of the cramp anchors (due to cracking of stone units), the concentrated compressive stresses around the toes caused crushing of these zones. In M-25-C and M-50-C walls, where the vertical compression stress levels were rather small, sliding at some of the stone courses were also observed.

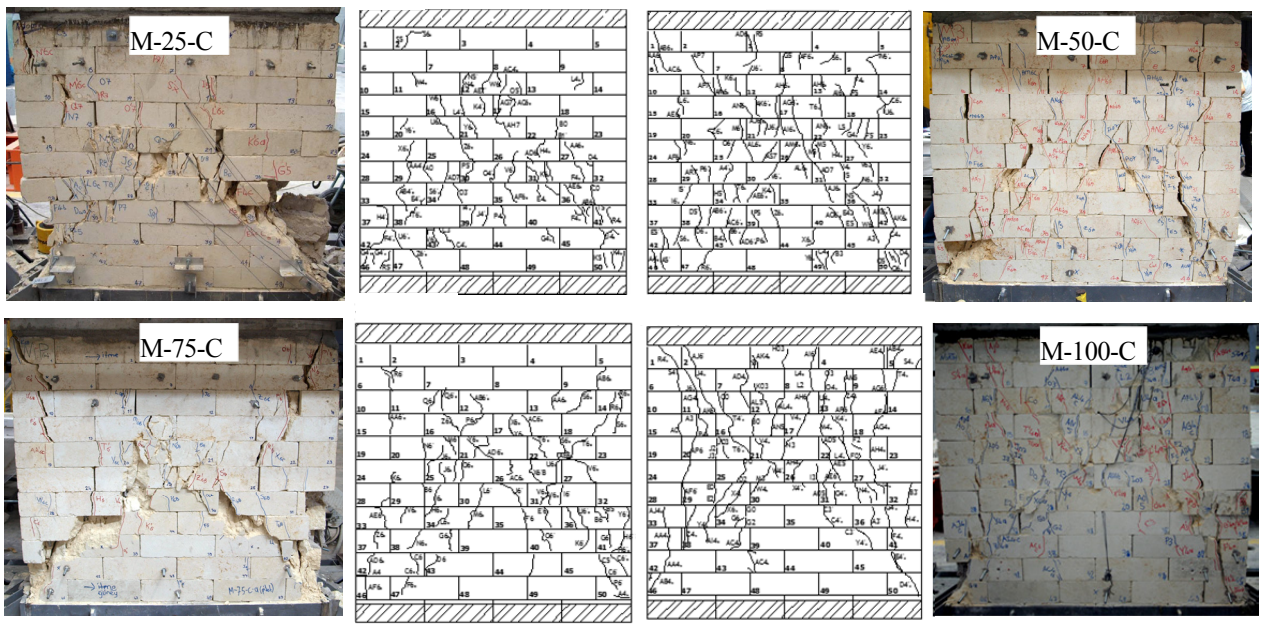


Figure 7 Damage patterns of tested walls

3.2 Test Results

Typical lateral load-displacement diagrams of specimens subjected to the lowest and highest constant normal stresses (0.25 and 1.0 MPa) are presented in Figure 8. Data points corresponding to first flexural cracking ($H_{f,cr}$), first diagonal cracking ($H_{dia,cr}$), maximum lateral resistance (H_{max}), 20% strength loss ($H_{0.8max}$) and ultimate displacement ($H_{d,max}$), are also marked in the same figure. The upper horizontal axes of these diagrams indicate the drift ratio values that correspond to displacement values of the lower horizontal axes.

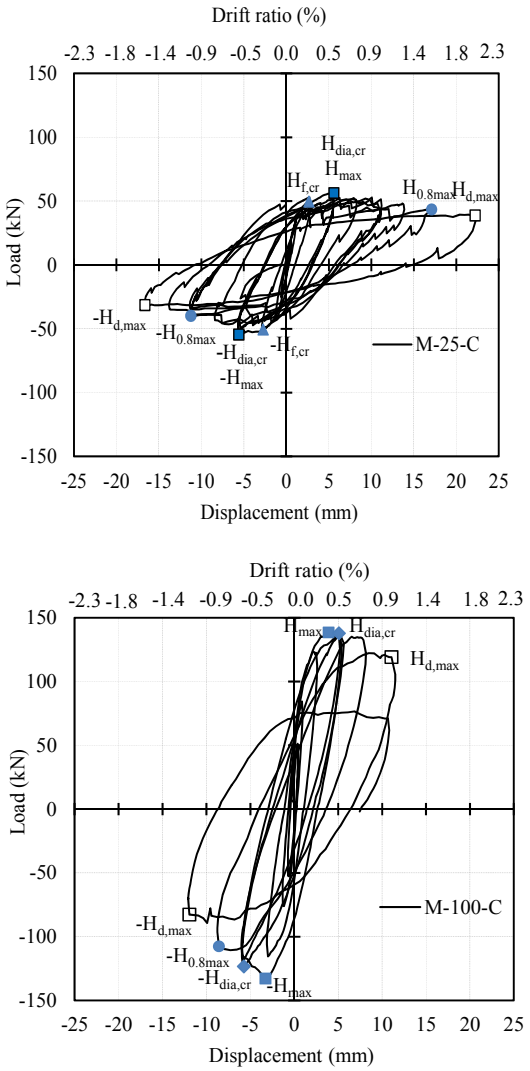


Figure 8 Lateral load-displacement diagrams for M-25-C and M-100-C walls

From the lateral load-displacement hysteresis diagrams, it can be observed that, at small displacement levels (i.e. at target drift ratios less than 0.50%) the walls exhibited elastic behavior and showed negligible residual displacement upon the reversal of the applied horizontal load. With the increase in the achieved lateral displacement, the walls exhibited a highly nonlinear response with significant residual displacements after each load reversal, which is typical for shear-controlled behavior of masonry walls. With the substantial loss in the horizontal load capacity and due to formation of extensive damage, the specimens reached their ultimate stages.

It should be noted that the tests were resumed until formation of extensive damage (namely, $H_{d,max}$ point), which could cause safety problems during the implementation of the tests. However, in order to define a uniform failure condition, during the interpretation of experimental results of this study, the ultimate state will be assumed as the critical state that corresponds to 20% strength degradation ($H_{0.8max}$ point on the hysteresis diagrams). Assumption of 20% strength loss for ultimate state has also been made by other researchers such as Magenes and Calvi (1997) and Frumento et al. (2009). Envelope curves derived from the hysteresis diagrams by considering this ultimate state definition are presented in Figure 9 for the pushing direction.

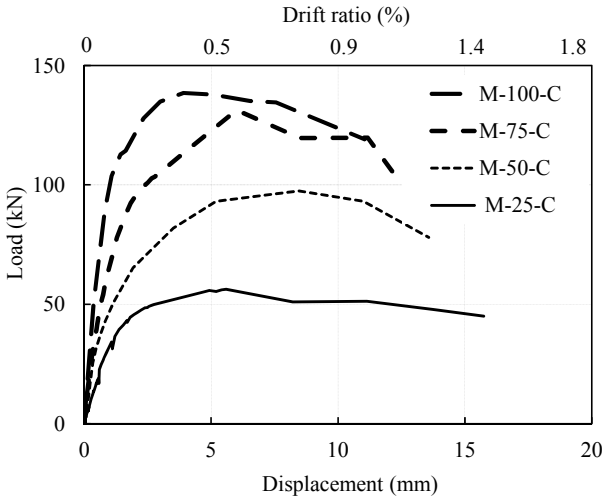


Figure 9 Envelope curves for the pushing direction

Comparison of lateral load-displacement envelope curves clearly shows that the variation of the pre-compression stress level has remarkable effect on the behavior. When submitted to low and moderate axial compression stresses, as in the case of M-25-C and M-50-C walls, larger displacement capacities can be achieved with lower lateral strengths. On the other hand, walls with higher axial pre-compression stresses (walls M-75-C and M-100-C) may reach higher lateral force capacities with less displacement capacities.

Tested walls reach their maximum resistance values (H_{max}) between 0.30 and 0.70% drift ratios (DR_{Hmax}). Assumed ultimate state, which corresponds to 20% strength loss ($H_{0.8max}$), is generally achieved between 0.80 and 1.50% drift ratios. Drift ratios corresponding to 20% strength loss ($DR_{0.8max}$) tend to decrease with the increase of the pre-compression stress level.

Shear strength (τ) is a key mechanical parameter for evaluation of the stress states in masonry walls. By using the test data, the variation of the shear capacity with respect to the pre-compression stress level (σ) can be visualized as shown in Figure 10. An analogy with the Coulomb criterion points to a global friction coefficient of 0.3 and adhesion strength of 0.09 MPa as seen in Equation 1. It should be

noted that the obtained global shear coefficient is smaller than the 0.4 and 0.5 values provided by the Eurocode 6 (CEN (2005)) and Turkish Seismic Design Code (2007) documents, respectively.

$$\tau = 0.09 + 0.3\sigma \quad (1)$$

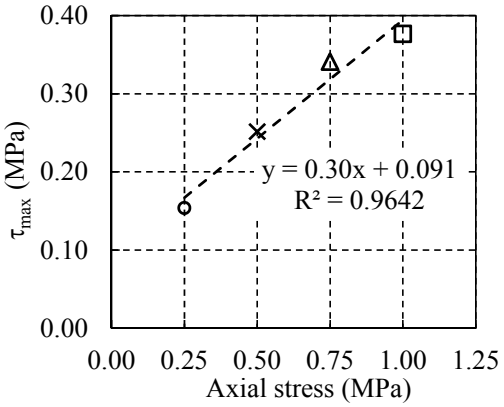


Figure 10 Variation of shear strength with pre-compression stress level

In Figure 11, variation of secant stiffness (K) with respect to displacement at peak values of each cycle (d_i) is presented for pushing direction of the M-25-C, M-50-C, M-75-C and M-100-C walls, for which the sole test parameter is the level of the pre-compression level. As it can be observed from this diagram, an increase in the axial stress level leads to remarkably higher secant stiffness values. However, the difference in stiffness parameter diminishes remarkably, as soon as the first significant cracks occur in the walls (before reaching drift ratio of 5%). Moreover, stiffness values of all investigated walls tend to approximate to very small values especially after formation of the diagonal cracks.

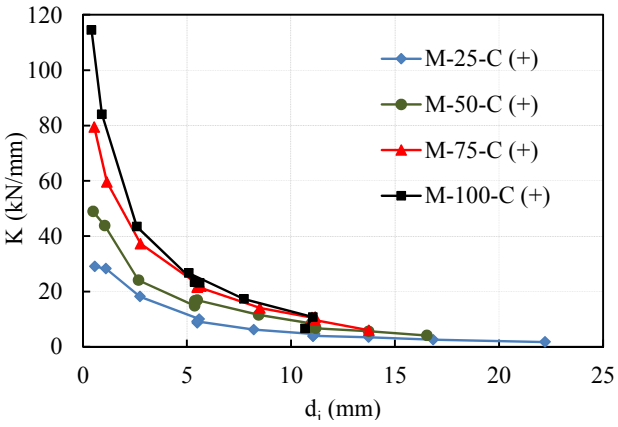


Figure 11 Variation of secant stiffness

4. CONCLUSIONS

An experimental study is carried out for investigating the in-plane seismic behavior of multi-leaf stone masonry walls observed in the Ottoman period structures. For this purpose, four multi-leaf masonry walls with ashlar external leaves and rubble masonry core were constructed and tested. The following conclusions can be drawn from the cyclic shear compression tests performed for four different normal stress levels:

- Although all shear compression test specimens clearly exhibited a shear-dominated behavior, bending effects were also observed particularly for walls with relatively lower axial stress levels.
- Due to the existence of the cramps, that were transferring tension forces from one unit to adjacent one, diagonal cracks were wide spread across the wall faces.
- The obtained hysteresis loops showed that the walls exhibited a highly nonlinear response with significant residual displacements after each load reversal.
- Shear strengths of the walls were directly proportional with the pre-compression stress level while the displacement capacities were inversely proportional.
- Increase in the axial stress level led to higher initial secant stiffness values.
- Stiffness values of tested walls approximated to each other particularly after formation of the diagonal cracks.

Acknowledgements:
This study is financially supported by the Istanbul Technical University Research Fund (Project No 33037). Support provided by the BASF-Turkey, Rozak Demir, Erk Construction, Er-Pa Metal Barshan Mining and Kesan Sac Companies are highly acknowledged. The authors would like to express their appreciation to Prof.Dr. Zekai Celep, Prof.Dr. Fatma İlknur Kolay, Prof.Dr. Nahit Kumbasar, Prof.Dr. Mehmet Ali Taşdemir, Prof.Dr. Hüseyin Çimenoğlu, Assist.Prof.Dr. Gülsün Tanyeli and Assist.Prof.Dr. Ihsan Engin Bal. The authors are also thankful to Dr. Çağlar Göksu Akkaya, Mustafa Cömert and Hanife Korkmaz for their assistance.

References:

CEN EN-1996-1-1 (2005), "EN-1996-1-1 Eurocode 6: Design of Masonry Structures – Part 1 – Common Rules for Reinforced and Unreinforced Masonry Structures," European Committee for Standardization.

Corradi, M., Tedeschi, C., Binda, L. and Borri, A. (2008), "Experimental Evaluation of Shear and Compression Strength of Masonry Wall Before and After Reinforcement: Deep Repointing," *Construction and Building Materials*, **22**(4), 463-472.

Demir, C. (2012), "Seismic Behaviour of Historical Stone Masonry Multi-Leaf Walls," *PhD Thesis*, Istanbul Technical University, Turkey.

Demir, C. and Ilki, A. (2013), "Characterization of the Materials Used in the Multi-Leaf Masonry Walls of Monumental Structures in Istanbul, Turkey," *Construction and Building Materials (to be submitted)*.

Frumento, S., Magenes, G., Morandi, P. and Calvi, G.M. (2009), "Interpretation of Experimental Shear Tests on Clay Brick Masonry Walls and Evaluation of q-Factors for Seismic Design," *Eucentre Research Report 2009/02*, IUSS Press, Pavia.

Galasco, A., Magenes., G., Penna, P. and Da Pare, M. (2010), "In-plane Cyclic Shear Tests of Undressed Double Leaf Stone Masonry Panels," *Proc. 14th European Conference on Earthquake Engineering*, Ohrid, Macedonia, 20 August-3 September (CD-ROM).

Lourenço, P.B., Oliveira, D.V., Roca, P. and Orduña, A. (2005), "Dry Stack Joint Stone Masonry Walls Subjected to In-Plane Combined Loading," *J. Struct. Eng.*, **131**(11), 1665–1673.

Magenes, G. and Calvi, G.M. (1997), "In-Plane Seismic Response of Brick Masonry Walls," *Earthq. Eng. and Struct. Dyn.*, **26**,

1091-1112.
Tanyeli, G. (1990), "Osmanlı Mimarlığında Demirin Strüktürel Kullanımı (15.-18. yüzyıl) (in Turkish)," PhD Thesis, Istanbul Technical University, Istanbul, Turkey.
Turkish Seismic Design Code (2007), "Deprem Bölgelerinde Yapılacak Binalar Hakkında Yönetmelik (in Turkish)," Türk Standardları Enstitüsü, Ankara.
Vasconcelos, G.F.M. and Lourenço, P.B. (2009), "In-Plane Experimental Behavior of Stone Masonry Walls under Cyclic Loading," *J. Struct. Eng.*, **135**(10), 1269-1277.

10CUEE CONFERENCE PROCEEDINGS
10th International Conference on Urban Earthquake Engineering
March 1-2, 2013, Tokyo Institute of Technology, Tokyo, Japan

STRESS STRAIN CHARACTERISTICS OF POLYPROPYLENE BAND (PP-BAND) AND FIBER REINFORCED POLYMER (FRP) COMPOSITE RETROFITTED MASONRY WALL SYSTEMS

Saleem Muhammad Umair[1], Muneyoshi Numada[2], and Kimiro Meguro[3]

1) PhD Candidate, Department of Civil Engineering, The University of Tokyo, Japan
2) Research Associate, ICUS, Institute of Industrial Science, The University of Tokyo, Japan
3) Professor/Director, ICUS, Institute of Industrial Science, The University of Tokyo, Japan

mumair@iis.u-tokyo.ac.jp, numa@iis.u-tokyo.ac.jp, meguro@iis.u-tokyo.ac.jp

Abstract: Seismic retrofitting of unreinforced masonry structures in earthquake prone areas using cost effective and high performance materials is one of recent challenges which have attracted the attentions of many researchers worldwide. In this study, stress strain characteristics of FRP and FRP+PP-band retrofitted masonry wallets are studied under diagonal compression test. This study helps to quantify the amount of strain transferred from brick surface to the FRP. FRP can increase initial shear strength but exhibits a brittle failure. In spite of high cost and brittle failure, high tensile strength of FRP has made it a popular material. While PP-band retrofitted method do not affect initial shear strength but significantly increases the deformation and energy dissipation capacities of masonry structure at rate of very low cost. Whereas the FRP+PP-band composite, increases not only the initial strength but also deformation and energy dissipation capacities of masonry wall system. Diagonal compression test is carried out on a non-retrofitted, PP-band retrofitted, FRP retrofitted and one FRP+PP-band retrofitted masonry wallet. 45^{o} strain rosettes are applied on FRP and FRP+PP-band retrofitted masonry wallet on brick and FRP surface in order to evaluate the complete state of normal and shear strains and stresses.

1. INTRODUCTION

Masonry is worldwide famous material because of its local availability and minimum cost of construction. Masonry contributes a biggest number of houses in world building inventory. In the past, masonry structures were rarely designed for seismic loadings. Some of the recent earthquakes in Bam Iran, 2003, Kashmir Pakistan, 2005 and Wenchuan China, 2008 have exposed the vulnerability of masonry structures against earthquakes. In earthquake prone regions of developing countries, most of the existing masonry structures are still at high level of risks. Many different researchers have proposed different retrofitting and strengthening methods each method has its own advantages and disadvantages. Adding steel or concrete frames, applying thick and strong pilasters, shotcreting and applying ferrocement to the wall surface are some of the retrofitting methods. Most of these methods are time consuming, add mass and reduces clear spacing [J.M. Gilstrap et al., 1998]. FRP retrofitting has also become popular in the last two decades. Initially, FRP was used for concrete and later on its application was further increased on masonry structures. Figure 1 shows some of the experiments conducted by different researchers in order to determine the in plane behavior of FRP for different FRP retrofitting procedures. FRP application was easy; fast and also do not require skilled labor. Different researchers tried different application procedures and found that FRP can significantly increase the initial shear strength but the final failure of masonry was highly brittle. FRP has overcome the problem of difficult application procedures with less retrofitting time but at the rate of very high retrofitting cost. In this regard Kimiro Meguro and Paola Mayorca have developed a new PP-band retrofitting method [Meguro and Mayorca, 2003]. PP-band retrofitting method uses polypropylene band. It is very cheap and locally available material. Because of its local applicability, easy applicability and social acceptability, PP-band retrofitting method is one of the cheapest retrofitting techniques. PP-band retrofitting technique has been used for retrofitting of masonry and non-engineered houses in Indonesia, Nepal and in some parts of Pakistan. Figure 2 shows the application of PP-band over a masonry house in Kashmir, Pakistan after 2005 Kashmir Earthquake. FRP can increase the initial strength but it is a brittle and costly material. But, PP- band cannot increase the strength but can hold the wall system for a much bigger ground motion without collapse. PP-band hold the masonry wall system and give deformation capacity and energy

dissipation capacity to the masonry wall system [Meguro et al., 2008].

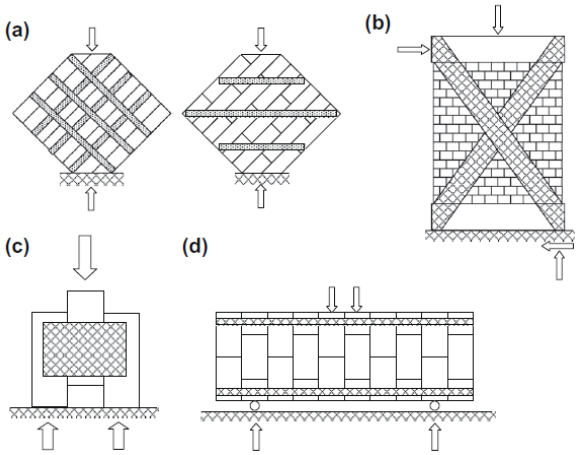


Figure 1 Different in-plane tests configurations utilized to investigate the in-plane response of reinforced wallets and specimens ((a) Valluzzi et al. (b) ElGawady et al, (c) Eshani and Saadatmanesh , (d) Triantafillou, P. Roca et al.)



Figure 2 Field Application of PP-band retrofitting technique to a sample masonry house in Kashmir, 2005

2. RESEARCH OBJECTIVES

In current research, stress strain characteristics of a new proposed composite retrofitting material are assessed. This composite material consists of Glass Fiber Reinforced polymer and PP-band. For efficient utilization of FRP and PP-band, both of these materials are applied in a specific way to the masonry structure. For most of the researchers, it is always the point of concern to transfer the maximum amount of strain from the brick to the FRP for better utilization of FRP strength. In this study, four types of masonry wallets are tested. Out of four types, one is non-retrofitted (URM), one is PP-band retrofitted and one is FRP+PP-band retrofitted masonry wallet. In case of FRP and FRP+PP-band retrofitted masonry wallet, a 45^{o} degree strain rosette is used to measure the strains on FRP and brick surface. In order to plot the stress strain curves of all types of masonry wallets a diagonal compression test is carried on all type of masonry wallets.

3. EXPERIMENTAL PROGRAM

3.1 Materials

Masonry materials are selected based upon the masonry construction in most of the developing countries. In order to construct the wallets at 1-4 scale, specially made clay burnt bricks of 75mm x 50mm x 38mm bricks are used. Bricks were soaked in water before construction of masonry wallet. Bricks were laid in cement lime mortar with weight mixed proportion (140g: 1110g: 2800g) of cement, lime and sand respectively. Mortar mixed is selected to replicate the decayed mortar conditions used in most parts of developing countries. Compression test is carried out on bricks and 50mm x50mm x 50mm mortar cubes according to ASTM C-67 and ASTM C-109. Bricks have shown an average compressive strength of 26.10 MPa. Whereas average compressive strength of mortar cubes is 1.16 MPa. Shear test, bond test and compression test is also carried out on masonry prisms. These masonry prisms were made using 5mm mortar thickness between the bricks. Brick triplets were made to measure the shear strength of mortar. The average shear strength of brick triplets was found to be 0.20 MPa. Biaxial type of GFRP is used with a fabric thickness of 0.5mm. Dimensions of PP-band are 6mm x 0.3mm. In order to determine the properties or GFRP and PP-band, tension test are carried out on one GFRP and 3 PP-band samples. Figure 3 shows the stress strain curve of PP-band and GFRP. GFRP has shown a very high tensile strength of 490 MPa with a failure strain of 2.7%. On the other hand, PP-band has shown relatively low tensile strength with an average value of 245 MPa but PP-band has shown a fairly long deformation capacity and has reached to a failure strain of 12.3%. E-250 epoxy bond is used to apply the GFRP over the surface of masonry wallet. Whereas PP-band is applied with the help of out of plane connectors provided at certain locations.

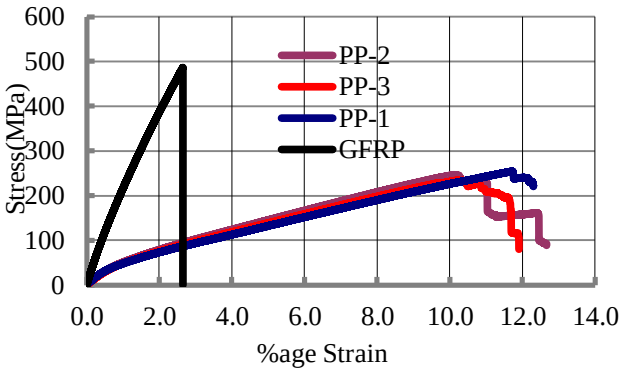


Figure 3 Stress strain curves of Glass Fiber Reinforced Polymers FRP and Polypropylene band

3.2 Experimental Setup

In current research, four types of masonry wallets are tested, one is non-retrofitted (URM), one is PP-band retrofitted, one is GFRP retrofitted and one GFRP+PP-band retrofitted wallet. All wallets were constructed using same constituent material and cured for 28 days before testing under same environmental conditions. Figure 4 shows the details of GFRP+PP-band retrofitted masonry wallet. All wallets have dimensions of 290mm x 280mm x 50mm.

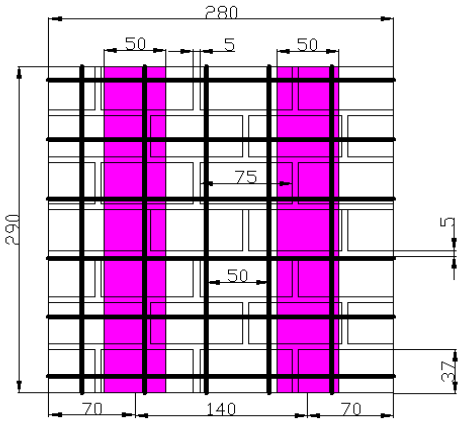


Figure 4 Details of GFRP+PP-band retrofitted masonry wallet

Wallet is tested under a static displacement control system. Response of wallet is measured in term of load and vertical displacement (ΔV) and horizontal displacement (ΔH). For displacement response measurement, two different type of test setup are used. High power lasers are used to measure the in plane horizontal deformation for URM and PP-band retrofitted masonry wallets. In case of FRP and FRP+PP-band retrofitted masonry wallet case two LDTV displacement transducers with 500×10-6/mm sensitivity are used. Six strain gauges are also used on each GFRP and GFRP+PP-band retrofitted wallet. Strain gauges at an angle of 45^{o} from each other are pasted using CN bond after application of PS bond over the brick surface whereas 3 strain gauges are directly applied over the GFRP surface using CN bond after rubbing the GFRP surface using a sand paper. In all masonry wallets, initial loading rate is kept equal to 0.15KN/mm up to the initial failure. In case of PP-band retrofitted and GFRP+PP-band retrofitted masonry wallets a loading rate of 1.00mm/min is used. PP-band is connected at 40mm from each corner of wallet. PP-band and FRP is applied on both faces of masonry wallet.

Shear stress and shear strain developed can be computed by the following equation (1) and (2).

$$v = \frac{P\cos\alpha}{((L+W)/2)t} \quad (1)$$

$$\gamma = \frac{(\Delta H+\Delta V)}{\sqrt{L^2+W^2}} \quad (2)$$

Where P = load applied, α = angle between the load and wallet top surface, L = length of wallet, W = height of wall, t = thickness of wall, ΔV = vertical deformation and ΔH = horizontal deformation.

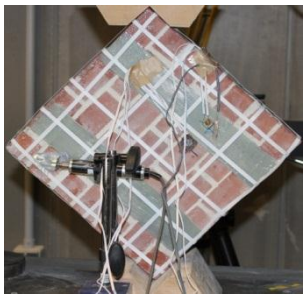


Figure 5 Experimental setup of a GFRP+PP-band retrofitted masonry wallet.

4. RESULTS AND DISCUSSION

4.1 Stress Strain Curve of Non-Retrofitted Masonry Wallet

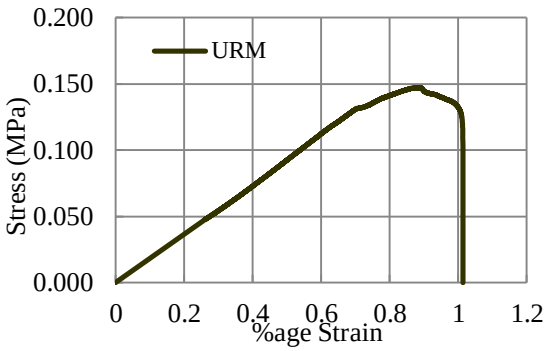


Figure 6 Stress strain curves of non-retrofitted masonry wallet

Figure 6 shows the stress strain curve of URM masonry wallet. Wallet has shown a peak stress of 0.144 MPa at a failure strain of almost 1%. URM wallet has shown a fairly linear behavior up to 0.6% strain. Failure of masonry wallet is shown in Figure 7.

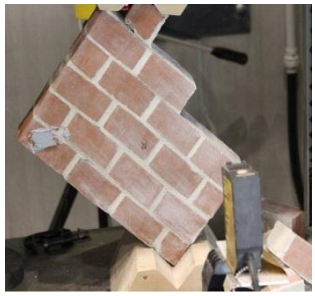


Figure 7 Failure Pattern of non-retrofitted masonry wallet

4.2 Stress Strain Curve of PP-band Retrofitted Masonry Wallet

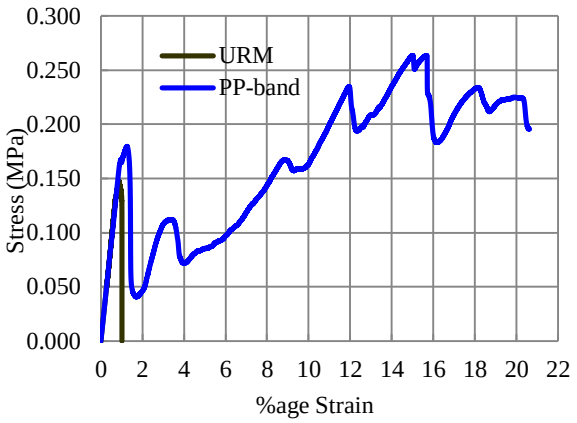


Figure 8 Stress strain curves of non-retrofitted and PP-band masonry wallet

Stress strain curve of URM and PP-band retrofitted masonry wallets are shown in Figure 8. URM and PP-band retrofitted masonry wallet has shown similar initial stiffness and peak load. In case of PP-band retrofitted masonry wallet, after the initial peak wallet again start taking load due to holding and confining effect provided by the PP-band. After the %age strain of 10, the wallet has shown a stress value which is greater than the initial peak strength of URM. PP-band retrofitted has shown a very high %age strain which indicates a very high ductility and deformation capacity of masonry wallet. Failure pattern of masonry wallet is shown in Figure 9.

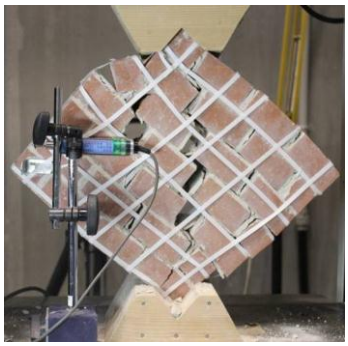


Figure 9 Failure Pattern of PP-band retrofitted masonry wallet

4.3 Stress Strain Curve of GFRP Retrofitted Masonry Wallet

Figure 10 shows the stress strain curve of URM, PP-band retrofitted and GFRP retrofitted masonry wallet. GFRP has increase the initial shear strength of URM and PP-band retrofitted masonry wallet from 0.17 MPa to 0.81MPa. But, failure strain of GFRP retrofitted masonry wallet was found to be only 4%. Final failure of GFRP retrofitted wallet was also brittle and failure was initiated due to debonding of GFRP from the wallet surface. Figure 11 shows the failure of masonry wallet due to detachment of GFRP from the wallet surface.

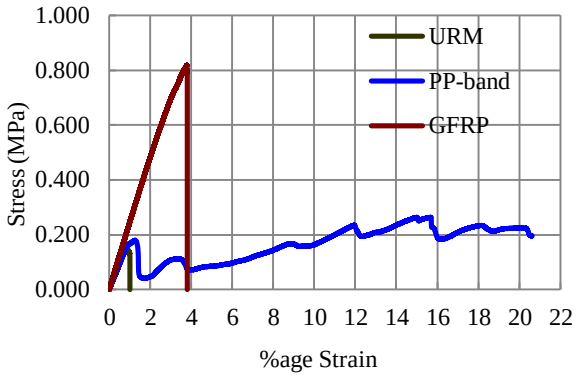


Figure 10 Stress strain curves of non-retrofitted, PP-band retrofitted and GFRP retrofitted masonry wallet

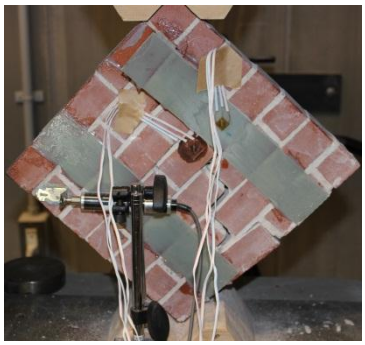


Figure 11 Failure Pattern of GFRP retrofitted masonry wallet

4.4 Stress Strain Curve of GFRP+PP-band Retrofitted Masonry Wallet

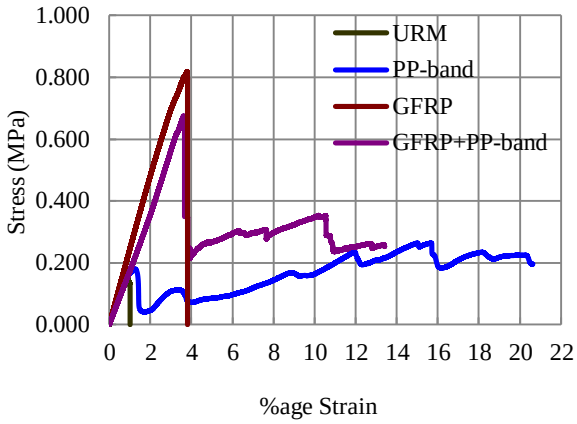


Figure 12 Stress strain curves of non-retrofitted, PP-band retrofitted, GFRP and GFRP+PP-band retrofitted masonry wallet

Stress strain curve of URM, PP-band retrofitted, GFRP retrofitted and GFRP+PP-band retrofitted masonry wallets are shown in Figure 12. GFRP+PP-band retrofitted masonry wallet has not only increased the initial strength as that of GFRP retrofitted masonry wallet but also the ductility and %age strain as that of PP-band retrofitted masonry wallet. Final failure of masonry wallet has also become gradual and ductile. In addition to, application of GFRP+PP-band has also increased the residual strength of masonry wallet. Figure 13 shows the failure mechanism of GFRP+PP-band retrofitted masonry wallet.

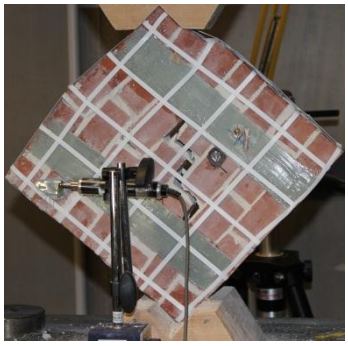


Figure 13 Failure Pattern of GFRP+PP-band retrofitted masonry wallet

5. CONCLUSIONS

Current study provides a very simple and clear stress strain analysis of different retrofitting methods. Each method has its strong points and weak points but proposed GFRP+PP-band composite retrofitting techniques is one the cost efficient and high performance composite retrofitting method which can be used for seismic retrofitting of masonry structures. GFRP is a cheapest type of FRP as compared to Carbon Fiber reinforced polymer and Aramid Fiber Reinforced Polymer. On the other hand PP-band is also one of the cheapest retrofitting materials. As a result, GFRP+PP-band composite is cost effective material which can increase the initial strength, ductility, deformation capacity and energy dissipation capacity. Failure of GFRP and GFRP+PP-band of wallets was started due to debonding of GFRP from the brick surface which motivates to use a strong epoxy agent rather than a strong FRP.

References:

Gilstrap J.M. and Dolan C.W. (1998). "Out of Plane Bending of FRP Reinforced Masonry Walls," *Journal of Composite Science and Technology* 58, 1277-1284.

Paola Mayorca and Kimiro Meguro. (2003). "Proposal of a New Economic Retrofitting Method for Masonry Structures," *Proceedings of the 27th JSCE Symposium of Earthquake Engineering*. CD ROM.

K. Meguro, P. Mayorca, N. Sathiparan. (2008). "Shaking Table Test Timber Masonry House Models Retrofitted with PP-band Meshes," *Proceedings of the Seventh International Symposium on New Technologies for Urban Safety of Mega Cities in Asia, Beijing, China,* CD-ROM.

Valluzzi MR. Tinazzi D. Modena C. (2002). "Shear Behavior of Masonry Panels Strengthened with FRP Laminates," *Constr Build Mater*, 16, 409–416.

ElGawady M. Lestuzzi P. Badoux M. (2005). "In-plane Response of URM Walls Upgraded with FRP" *J Compos Constr,* 9(6), 524–535.

Eshani MR. Saadatmanesh H. (1997). "Shear Behavior of URM Retrofitted with FRP Overlays," *J Compos Constr*, 1(1), 17–25.

Triantafillou TC. (1998). "Strengthening of Masonry Laminates using Epoxi-bonded FRP Laminates," *J Compos Constr*; 2(2), 96–104.

P. Roca and G. Araiza. (2010). "Shear Response of Brick Masonry Small Assemblages Strengthened with Bonded FRP Laminates for in-plane Reinforcement," *Construction and Building Materials,* 24, 1372–1384.

10CUEE CONFERENCE PROCEEDINGS
10th International Conference on Urban Earthquake Engineering
March 1-2, 2013, Tokyo Institute of Technology, Tokyo, Japan

AN EXPERIMENTAL STUDY OF NONLINEAR SHORT-PERIOD STRUCTURES WITH UPLIFT UNDER NEAR-FAULT PULSE MOTIONS

Yuanzhi Chen[1)], Tam Larkin[2)], and Nawawi Chouw[3)]

1) PhD student, Department of Civil and Environmental Engineering, University of Auckland, New Zealand
2) Senior lecture, Department of Civil and Environmental Engineering, University of Auckland, New Zealand
3) Associate professor, Department of Civil and Environmental Engineering, University of Auckland, New Zealand
yche521@aucklanduni.ac.nz, t.larkin@auckland.ac.nz, n.chouw@auckland.ac.nz

Abstract: Near-fault earthquake motion usually contains early arriving, large velocity pulses when forward directivity is present. These velocity pulses may greatly increase the strength demand on structures. To include the effect of near-fault motion the New Zealand design standard NZS 1170.5 introduce a spectral amplification factor for structures with periods longer than 1.5 s, but neglect this effect on short period structures. Previous research has shown that structural uplift can reduce the development of plastic hinges in structures. However, very few experimental studies of structural uplift including near-fault effects are contained in the literature; nearly all studies are numerical analyses. In this paper shake table tests of a multi-story building are presented and discussed. Two support conditions, i.e. fixed at the base and with uplift permitted on a rigid platform, are considered. To simulate possible damage to the moment-resistant frames artificial plastic hinges are constructed. Pulse motions were chosen from the recent series of Christchurch earthquakes. Structural response under a selected motion and a simulated motion from NZS 1170.5 is compared to reveal the effect of near-fault forward directivity related pulses. The influence of a velocity pulse on plastic hinge development, the maximum displacements of floors and maximum bending moments of columns are discussed.

1. INTRODUCTION

Urban areas have developed rapidly in seismically active zones worldwide since last century. Only in recent decades it has been noticed that the characteristics of ground motions in the vicinity of a fault are different from those of far-fault motions (Chopra and Chintanapakdee, 2001). Near-fault ground motion sometimes contains long-duration, low acceleration pulses. Forward directivity effects that occur in the near-fault region can be particularly damaging at sites lying in the direction of advancement of fault rupture from the hypocenter. The propagation of rupture towards a site, at a large shear wave velocity, causes most of the seismic energy from the rupture to arrive in a single large pulse of motion at the beginning of the record. To numerically describe these pulses the term incremental velocity has been used. This is defined as the area under the acceleration pulse (Anderson and Bertero, 1987). The long duration pulses that induce intensive incremental velocity can lead to unfavorable seismic performance of structures (Hall et al., 1995, Anderson and Bertero, 1987).

The study of near-fault ground motions has been difficult to carry out due to only a small number of near-fault ground motions being recorded. The damaging characteristics of near-fault ground motions are only apparent in moderate to large earthquakes, and these events occur relatively infrequently. The sparse spatial coverage of recording stations has also been a reason for the limited number of ground motions recorded close to fault rupture. After the 1994 Northridge and 1995 Kobe earthquakes, which occurred near large centers of population with more dense station coverage, more near-fault strong motions have been recorded. Somerville (1997) identified the characteristics of near-fault ground motions with forward directivity, especially the large spectral displacements in the strike-normal direction at long periods. Somerville et al. (1997) also suggested a simple model for near-fault design spectra to accommodate the effects of near-fault ground motions. This model has been adopted to derivate the near-fault spectral amplification factor in the New Zealand design standard NZS1170.5 (2004). However, the design standard NZS1170.5 applies no spectral modification factor to structures with a period less than 1.5 s. Somerville et al. (1997) also highlighted that the near-fault pulse could have significant effects on non-linear systems. To investigate this further a short-period structure with possible plastic hinge development during response has been utilized in this experimental study.

In the 2011 Christchurch earthquakes, a series of ground motions were recorded near a blind fault lying within 6 km of the city center. The characteristics of near-fault ground motion are able to be observed in some of these records. A very large amount of structural damage was reported. The performance of a 36 m high industrial

chimney at the Air New Zealand Engineering Base at the Christchurch airport (18 km away from the epicenter) during the February 17 main event is worthy of investigation. This chimney is one of the early structures that was designed to uplift under strong earthquake motion (Sharpe and Skinner, 1983). The design was carried out to avoid the difficulty of detailing the ductile region and the potential permanent deformation after shaking. Although the chimney was subjected to strong ground motions, no structural damage has been observed (Chouw and McCue, 2012). The superstructure was protected from seismic moment and shear by the redistribution of loads caused by lift-off.

The benefit of structural uplift was first recognized by Housner (1963) where the good performance of several elevated water tanks in the 1960 Chile earthquake was reported. He also initiated the study of structural uplift using a rectangular rigid and free standing block. This work established that earthquake energy can be dissipated via rocking. Huckelbridge and Clough (1978) were the pioneers of physical investigations of structural uplift when they tested a nine story steel frame with uplift using a shake table. They found that significant uplift to the structure would occur during a moderate, credible earthquake. The results also confirmed that a design including a planned uplift capability would provide a structure with a higher possibility of surviving a strong earthquake. About the same time Priestly et al. (1978) carried out shake table tests on a single degree of freedom model. Based on the results they suggested the first design approach to rocking structures. This design approach has been adopted by the FEMA 356 Guidelines (FEMA356, 2000). Recently, Hung et al. (2011) performed pseudo-dynamic and cyclic loading tests on bridge piers with and without plastic hinge. The uplift benefit of reducing ductility demand was confirmed.

However, research of structural uplift so far has infrequently considered the difference of response induced by near-fault and far-fault earthquakes. In Housner's work on rocking in 1963 it was stated that overturning of a block also depends on the incremental velocity and not merely on the peak ground acceleration, but this important concept received little attention. A procedure to estimate the level of a pulse-type ground motion that is needed to overturn a rectangular rigid block was provided by Makris and Roussos (2000). Hung et al. (2011) described experiments that focused on rocking and compared the effect of artificial earthquake accelerations generated from a design code with real ground motion records from a near-fault site. Results showed that the near-fault earthquake with high velocity impulses produced higher displacement demand at the deck level of a rocking pier.

In this paper the effect of near-fault pulse ground motions on structural displacements, bending moment and plastic hinge development is discussed. Shake table tests of a scaled six story building with a fundamental period less than 1 s are presented. Artificial plastic hinges were constructed to simulate the possible structural damage during the earthquake. The response of structure is compared for two different support conditions, 1) fixed at the base and 2) on a rigid base but with uplift permitted. In order to highlight the effect of near-fault ground motion, the model was subjected to a ground motion selected from the February 2011 Christchurch earthquake and a simulated motion shaped according to NZS 1170.5.

2. EXPERIMENTAL INVESTIGATION

2.1 Model design

A six-story office building was considered as the prototype structure. The building has a 3 m floor height, 48 m^2 floor areas and a 6 m × 6 m spread footing. The columns of the top three levels were 310UC118 and the columns of the bottom three levels were 310UC158. The size of the beams was 410UB53.7 throughout the entire structure. The beam and column arrangement is explained in Figure 1(a). A 170 mm thick reinforced concrete slab was placed on each floor. In Figure 1(b) the general view of the prototype and the coordinate system is shown. Excitations were applied in the x direction. The lateral stiffness in the direction of excitation for the top and bottom three levels was 3.21E7 N/m and 4.44E7 N/m, respectively. According to the NZS 1170.5 (2004) for earthquake actions, the seismic masses were 24 tones for the roof and 29 tones for each floor. The natural periods of the 1st to 6th modes are 0.680, 0.245, 0.151, 0.116, 0.101 and 0.087 s, respectively.

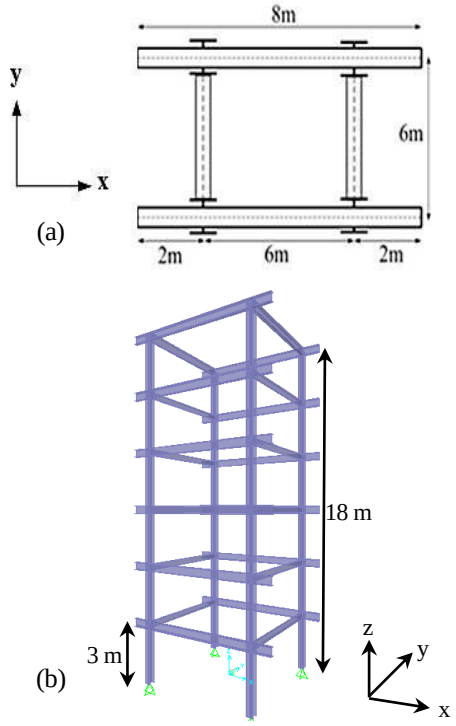


Figure 1 Prototype structure: (a) Beam and column arrangement and (b) general view

The experimental model was scaled to fit the capacity of the shake table. The scaling is based on the model and the prototype obeying the law of similitude. To achieve this similarity, dimensional analysis based on Buckingham π theorem (Buckingham, 1914) was performed. The three

basic dimensions: mass *M*, length *L* and time *T* in the dynamics of scale model were considered. All other dimensions of the selected physical parameters were then derived based on these three basic dimensions as displayed in Table 1. In numerous shake table tests with scaled structures the Cauchy number and Froude number are usually considered. The Cauchy number is the ratio between inertial and elastic restoring forces, and the Froude number is the ratio between inertial and gravitational forces. In Qin et al. (2012) experiments using a modified Cauchy number were adopted. The following dimensionless groups based on the new modified Cauchy Number are given in equation 1.

$$\pi_1 = t * \sqrt{\frac{a}{l}} \text{ and } \pi_2 = \frac{E*l^2}{m*a} \quad (1)$$

where *t, a, l, m, k* and *E* are defined in Table 1.

By equating these dimensionless groups when applied to the prototype and the model, the scale factors of all physical quantities considered were determined (Table 1). The model was scaled down 15 times. PVC was used to construct the columns (E_{PVC} = 2.5 GPa and E_{steel} = 200 GPa), and aluminium angle sections were selected to simulate the rigid beams. The lateral stiffness of the prototype was scaled in the excitation direction only. A scale factor of two was used for time. After applying the scale factor for time the fundamental period of the model is 0.340 s.

Table 1 Scale factors of parameters

Parameters	Symbols	Dimensions	Scale Factors
Length	*l*	L	15
Mass	*m*	M	4800
Time	*t*	T	2
Acceleration	*a*	LT^{-2}	3.75
Stiffness	*k*	MT^{-2}	1200
Young's Modulus	E	$ML^{-1}T^{-2}$	80

2.2 Artificial plastic hinges

Because of the difficulty of scaling the yielding moment of structural members in small-scale laboratory tests, artificial plastic hinges were constructed (Figure 2). These hinges are located at the supports and beam-column joints. The moment capacity of each artificial hinge was set using a torque wrench. A torque of 5 Nm was applied to all the hinges. Analysis of experimental test results for overturning moment showed that initiation of plastic rotational slippage occurred when the overturning moment was 140 Nm. A torque of 20 Nm was found to be sufficient to prevent any plastic hinge developing when the objective was to perform elastic analyses.

Once the bending moment reaches the capacity of a hinge, rotational sliding will occur. Thus, the structure becomes nonlinear and structural damage is able to be simulated. To ensure the repeatability of the artificial hinge performance, Teflon washers were placed as shown in Figure 2. Since the moment capacity of the artificial plastic hinge along the height of the building was the same, a beam-sway mechanism was represented.

2.3 Test setup

Two support conditions were considered in this project. The structure was fixed at the base to replicate the support assumption in most conventional design. To reveal the effect of structural uplift, the same structure was placed free standing on a rigid platform. Sand paper was attached to the top of the rigid base and the bottom of the foundation to increase the friction between the footing and base surfaces. Thus, sliding during uplift could be minimized. The other quantities measured include the acceleration and lateral displacement on each floor, the vertical displacements during uplift and the bending moment at the base of each column.

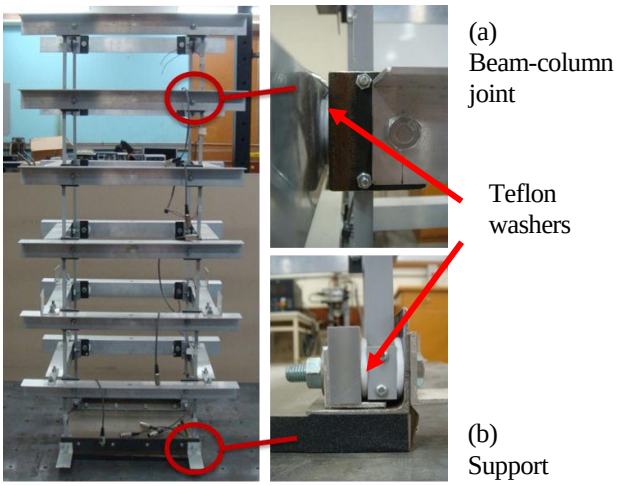


Figure 2 Model artificial plastic hinges

3. GROUND MOTIONS

The near-fault pulse ground motions were selected from records of 45 stations recorded in the February 2011 Christchurch earthquake. In order to identify the near-fault characteristics of the ground motions, a classification scheme modified from the work of Hayden et al. (2012) has been applied. The near-fault ground motions utilized were recorded within 30 km of the epicenter, with the largest peak to peak velocity (PPV) occurring over less than 2.5 significant cycles which have amplitudes larger than 25% of the PPV. These ground motions were than scaled to a very severe level using the highest hazard factor of NZS1170.5 (0.6) and a return period of 1000 years. In this paper, the structural response using the S88E component recorded in Christchurch Resthaven (denoted as REHS), scaled in the manner described, is presented. This station is 8 km from the source and on a site with a classification of class D (deep or soft soil site). The scaled time history is displayed in Figure 3(a).

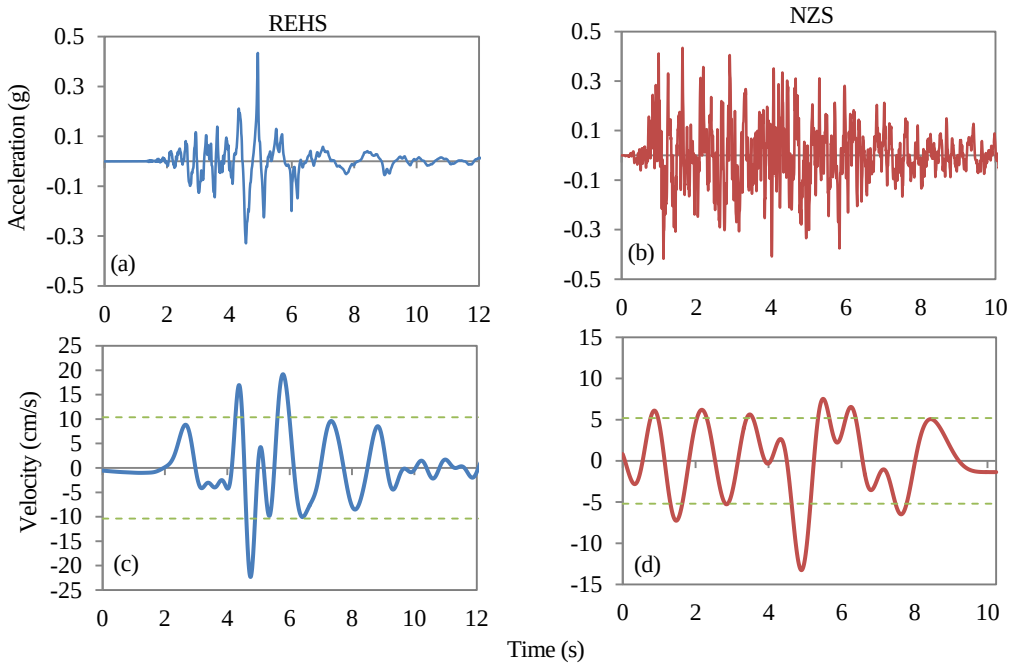


Figure 3 Scaled acceleration and velocity time histories of REHS ((a), (c)) and NZS ((b), (d)) ground motions

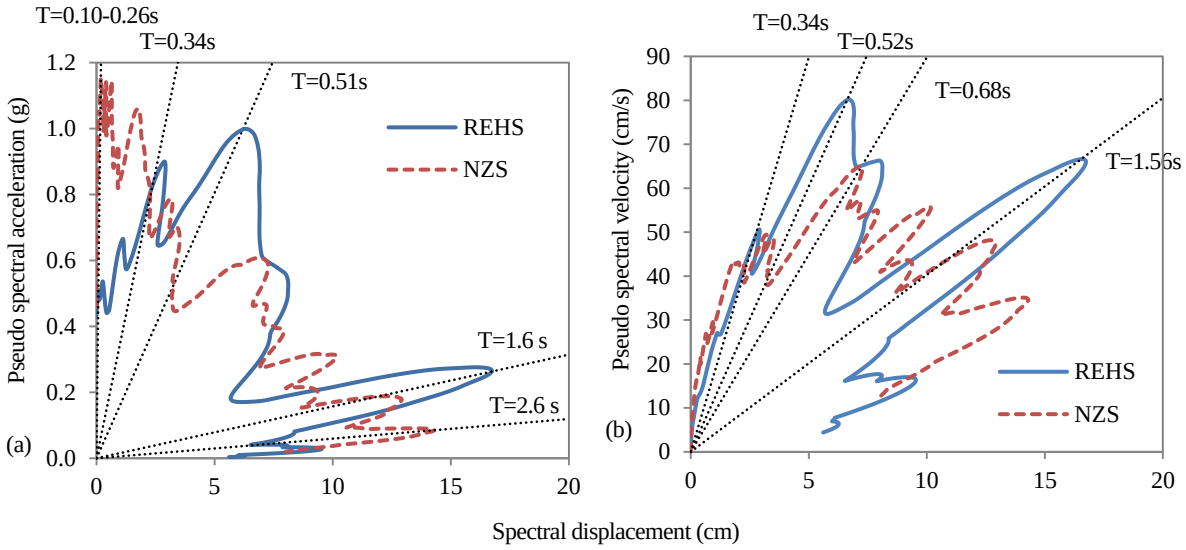


Figure 4 Scaled elastic spectral displacement, pseudo spectral acceleration and pseudo spectral velocity of REHS and NZS ground motions

A simulated ground motion based on NZS1170.5 (2004) design spectra for a class D site was used as a comparison to reveal the effect of velocity pulses. The simulated ground motion has the characteristic of far-field ground motion which is not affected by forward directivity. To simulate this ground motion, base rock excitations were filtered from white noise and the site effect was computed based on wave propagation theory (Bi and Hao, 2011). Since in conventional seismic design, peak ground acceleration is generally considered to be the main governing parameter, the simulated ground motion (denoted as NZS) was scaled to yield a peak ground acceleration (PGA) of 0.43 g, the same as the modified recorded REHS ground motion (Figure 3(b)).

The spectral displacement, pseudo spectral velocity and pseudo spectral acceleration (5% damping) of the two scaled ground motions are shown in Figure 4. The predominant period of the NZS motion lies between 0.1 to 0.26 s (0.05 to 0.28 s, scaled from NZS1170.5), while that of the REHS motion is 0.51 s (Figure 4(a)). The response of long period structures are more pronounced when they are subjected to a near-fault earthquake. The peak spectral acceleration of NZS motion (1.15 g) is 15% larger than that of the REHS motion. The spectral values for both ground motion at the fundamental period (T = 0.34 s) of the model are coincidentally the same.

The greatest spectral displacement of 16.7 cm is observed at a period of 1.6 s in the REHS ground motion, while peak spectral displacement of 14.3 cm is shown at a period of 2.6 s in the NZS motion. The periods 1.6 s and 2.6 s are the periods of the velocity pulses of the REHS and NZS ground motions, respectively. A corner period that is equal to one third of the pulse period was used to filter the velocity time history for each ground motion with a low-pass Butterworth filter. The filtered velocities of two ground motions are shown in Figure 3(c) and (d). PPVs of 41.5 cm/s and 20.8 cm/s are shown in the REHS and NZS ground motion, respectively. The stronger velocity effects of REHS ground motion can also be seen in the pseudo spectral velocity-spectral displacement plot (Figure 4(b)). Indicators of 25% of PPVs are illustrated using dash lines in Figure 3(c) and (d). There are one and an half significant velocity cycles of REHS motion, while the NZS motion contains four cycles. In near-fault motions with forward directivity effects, seismic energy is concentrated in one or two strong velocity cycles (Hayden et al., 2012).

4. RESULTS AND DISCUSSION

4.1 Plastic hinge development

In order to reveal the effect of velocity pulses on the plastic hinge development in structures, the bending moments at the base of the column near the support is plotted against the flexural displacement of the first floor in Figure 5. The values of residual deformation are shown on the top right corners of all the plots in Figure 5. The response of the structure fixed at the base is illustrated in Figures 5 (a) and (b). A larger maximum flexural displacement (8.5 mm) is measured when the structure is subjected to REHS ground motion. This deformation is 52% larger than the response under the NZS motion.

As displayed in the velocity time history of the REHS motion (Figure 3(c)), the first strong velocity pulse arrives at 4.4 s, followed by another pulse in the opposite direction and the last strong pulse is evident at 5.8 s. In Figure 5 (a), the first strong velocity pulse induces a dislocation of 7.9 mm in the positive direction. The first floor is almost pulled back to the origin due to the following pulse in the opposite direction. As a result of the third pulse, the first floor has an offset of 7.6 mm. A residual deformation of 5.3 mm was ascertained after the shaking. However, there is no obvious pulse dependent deformation of the structure under the NZS ground motion (Figure 5(b)). In the case of NZS ground motion, a residual deformation of 1.6 mm is resulted from the accumulation of small increments.

Severe damage of the plastic hinge, perhaps even structural collapse, is likely to occur under near-fault ground motion at the moment a strong velocity pulse strikes. Since a large amount of energy is stored in this pulse, to achieve the same ductility factor a higher strength of column plastic hinge would be required when the near-fault pulse ground motion is considered.

The responses of the structure with freedom to uplift and plastic hinge development are shown in Figures 5(c) and 5(d). The maximum flexural displacement of the structure with uplift (8.8 mm) is slightly less than that of structure

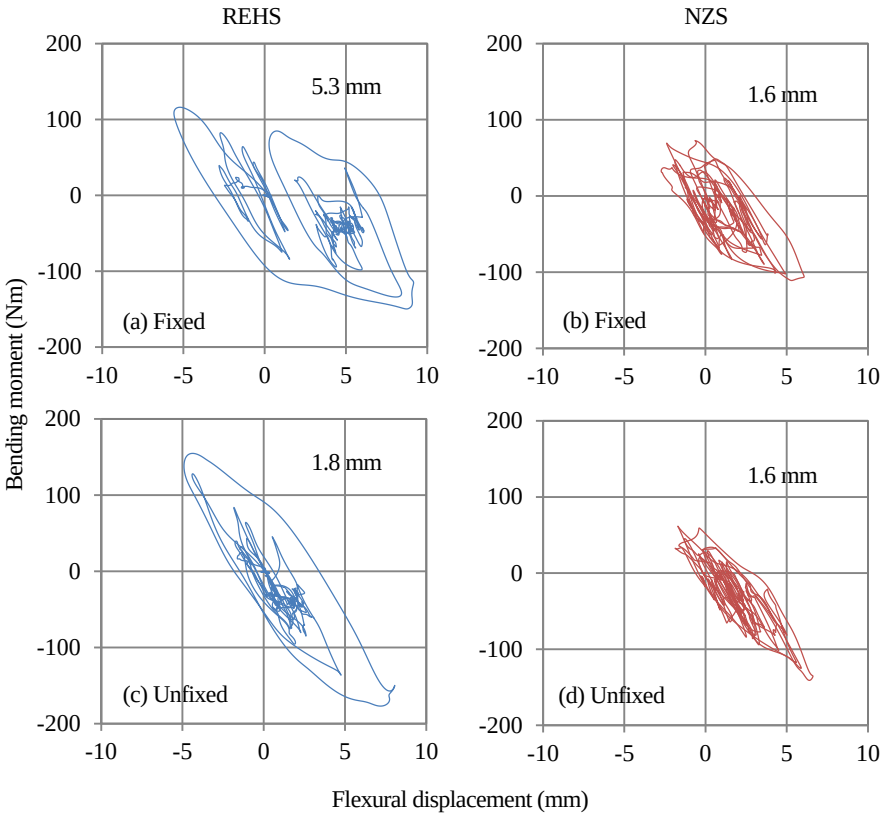


Figure 5 Bending moment at the base of column near the support and flexural displacement of first floor of the model (a) (b) fixed at the base and (c) (d) with uplift under both ground motions

fixed at the base (9.2 mm) in the case of REHS ground motion. However, the maximum flexural displacement of the structure free at the base is 0.5 mm larger than that of structure fixed at the base under NZS motion.

It is illustrated in Figure 5(c) that structural uplift has a large influence on the residual displacement in the case of near-fault ground motion containing large velocity pulses (i.e. the REHS case). The first velocity pulse leads to a similar deformation in both the free to uplift and the fixed base case. The subsequent pulse in the opposite direction lifts the structure and shifts the center of gravity in the negative direction. Thus a displacement of -5 mm is recorded. The last velocity pulse pushes the structure back to its original position. At the end of the excitation the residual displacement is 1.8 mm which is only one third of the fixed base case using the REHS motion containing velocity pulses. However, the effect of uplift on the structural response under the NZS ground motion is not significant, because no strong velocity pulse occurs when using this motion. The result confirms that the structure is more likely to uplift when it is subjected to near-fault motion containing velocity pulses.

4.2 Predominant periods

The predominant periods of the structures, of different cases, are summarized in Figure 6. The predominant period is where the maximum Fourier amplitude, calculated from recorded accelerations on the top of the structure, takes place. Using the motion REHS when the structure remains elastic a large predominant period of 0.75 s is obtained. This predominant period is the same as the rocking period of the structure with a foundation rotation of approximately 0.04 rad. Thus most of the lateral displacement arises from the base rotation rather than the flexural displacement.

In the case of the fixed base structures the predominant period of the structure does not change when nonlinearity is included under REHS ground motion. This predominant period is the same as the fundamental period of the elastic and fixed-base structure (0.34 s). When the structure is subjected to near-fault pulse motion, damage occurs at the moment the intense velocity pulse takes place.

However, the periods are lengthened from 0.34 s to 0.39 s in the case of NZS ground motion. Small increments of plastic deformation as a result of the artificial plastic hinges not being an ideal elasto-plastic system occur throughout the whole simulated excitation, since there is no intense velocity pulse.

4.3 Maximum lateral displacements of floors

The change of lateral displacements along the height of the building is displayed in Figure 7. Comparing the response of the linear structure under REHS and NZS ground motion, the lateral displacement of each floor is greater in case of the pulse ground excitation. Since the response to NZS ground motion is more pronounced for periods shorter than the structural fundamental period (0.34 s), as indicated in Figure 4(a), the higher modes of the structure are more readily excited. The contribution of the higher modes can reduce the maximum displacement of each floor.

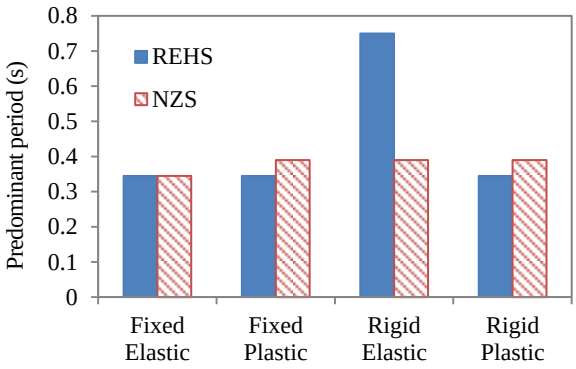


Figure 6 The predominant periods of the structures under different conditions

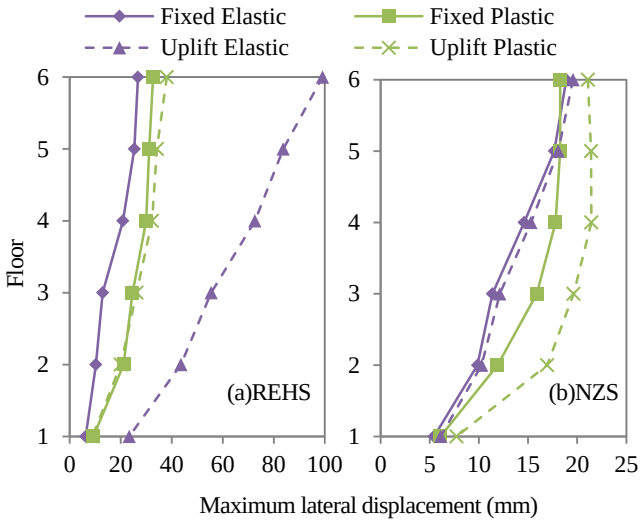


Figure 7 The maximum lateral displacement of each floor

The lateral displacements of structures with uplift are larger than those of structures fixed at the base as shown in Figure 7. When the structure without plastic hinge development is subjected to REHS ground motion, the maximum displacement at the top of the structure with uplift (99.1 mm) is 3.7 times that of the fixed base case (26.8 mm). However, the increase of displacement (3.7%) due to uplift is small in the case of NZS ground motion. The lateral displacement from footing uplift is substantially greater in the REHS case, as the overturning of a structure is related to the incremental velocity. This increase of displacement under REHS motion is greatly reduced to 16.3% when the structure deforms plastically. The coupling effect of plastic hinge development and structural uplift depends on both the yielding capacity of the plastic hinges and the resistance moment of overturning due to structural self-weight. Further investigation is required to understand the interaction of structural nonlinear behavior and footing uplift in near-source earthquakes.

4.4 Maximum bending moment of columns

The bending moment at the end of each column was evaluated using strain gauges. Figure 8 shows the maximum

bending moment developed by the structure under different conditions. Except for the case when large foundation rotation is present, both structural uplift and plastic hinge development can reduce the strength demand of columns. Comparing the response of structure under REHS and NZS ground motions, greater bending moments are developed during near-fault pulse excitation. Generally speaking, the effects of near-fault ground motion with forward directivity are significantly stronger at the base of building than at the top. For example, the bending moment of column on the fifth floor of structure with plastic hinges developed and footing uplift under REHS motion is 59% larger than that of structure under NZS motion. However, the value of bending moment near the supports is 1.1 times larger.

When plastic hinges are developed, the bending moment at the end of column on the second floor could be less than that on the third floor. Although same torque has been applied on each hinge, the yielding capacities of beam-column joint hinge and support hinge are different due to the variation of friction between different fabrication materials. As indicated in Figure 2, the beam-column joint hinge involves frictional contact between the Teflon and metal, while the support hinge has Teflon-PVC contact on one side and Teflon-metal on the other. Therefore, the effect of plasticization of the second floor beam-column hinge on bending moment is more obvious comparing to the other locations.

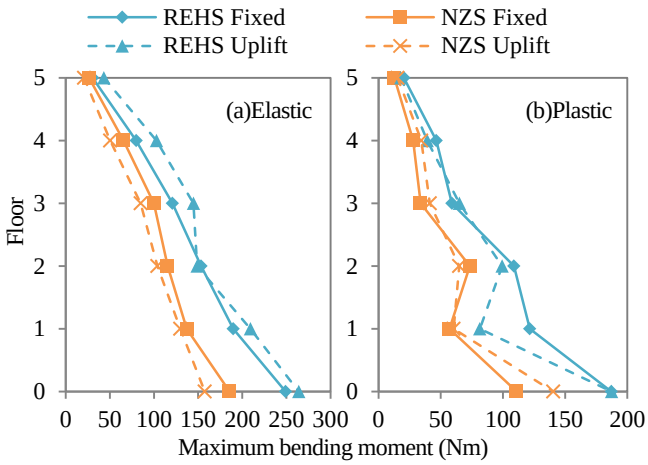


Figure 8 The maximum bending moment of column on each floor

5. CONCLUSIONS

In this work, shake table tests on a small scale six story building with a fundamental period of 0.68 s were performed to investigate the effect of near-fault pulse motion on the performance of structures with foundation uplift and plastic hinge development. The artificial plastic hinges are able to control the moment capacities of bean-column joints as well as the supports and were constructed to simulate the damage to the structure under strong seismic motions. Scaled near-fault ground motions recorded in the 2011 Christchurch earthquake containing intense velocity pulses were utilized. A simulated ground motion based on the site class D spectrum from NZS 1170.5 (scaled to the same PGA as the Christchurch motion) was also applied to reveal the effects of the characteristics of near-fault ground motion.

The responses of structures with and without plastic hinge development incorporating different support conditions, i.e. fixed at the base and with uplift on a rigid base, were studied. The study reveals that:

- The velocity pulses of near-fault ground motion can induce large rotations of plastic hinges almost instantaneously and may lead to large residual deformation.
- Structural uplift reduces the residual deformation of a structure subjected to near-fault ground motion with forward directivity effect.
- Near-fault pulse ground motion can induce larger lateral displacements compared to simulated ground motion broadly shaped to agree with a design code ground motion (far-field motion). The strength demand on plastic hinges of the structure will be underestimated when following conventional design procedures.
- Larger bending moments of the structural members will be induced by near-fault pulse ground motion compared with far-field motion.
- The effect of near-fault ground motion with forward directivity characteristics on a structure with a short period is likely to be significant. This effect is currently neglected in the design standard NZS1170.5 (2004). Where possible time history analyses with consideration of pulse type ground motion is recommended for important short period structures to avoid poor performance during near-fault forward directivity seismic motions.

Acknowledgements

The authors would like to thank the Ministry of Business, Innovation and Employment for the support of this research.

References:

Anderson, J. C. and Bertero, V. V. (1987), "Uncertainties in Establishing Design Earthquakes," *Journal of Strucutral Engineering*, **113,** 1709-1724.

Bi, K. and Hao, H. (2011), "Modelling and Simulation of Spatially Varying Earthquake Ground Motions at Sites with Varying Conditions," *Probabilistic Engineering Mechanics*.

Buckingham, E. (1914), "Illustrations of the Use of Dimensional Analysis," *On Physically Similar Systems, Physics Review,* **4,** 354-377.

Chopra, A. and Chintanapakdee, C. (2001), "Comparing Response of SDOF Systems to Near-fault and Far-fault Earthquake Motions in the Context of Spectral Regions," *Earthquake Engineering and Structural Dynamics*, **30,** 1769-1789.

Chouw, N. and McCue, K. (2012), "An Upliftable Structure in the 2010-2012 Canterbury Earthquake Swarm," *AEES Newsletter September 2012*.

FEMA356 (2000), "Prestandard and Commentary for the Seismic Rehabilitation of buildings," America: American society of

civil engineers for the federal emergency management agency.

Hall, J., Heaton, T., Halling, M. and Wald, D. (1995), "Near-source Ground Motions and Its Effects on Flexible Buildings," *Earthquake Spectra,* **11,** 569-605.

Hayden, C. P., Bray, J. D., Abrahamson, N. and Acevedo-Cavrera, A. L. (2012), "Selection of Near-fault Pulse Motions for Use in Design," *15th World Conference of Earthquake Engineering.* Paper No. 3752

Housner, G. W. (1963), "Behavior of Inverted Pendulum Structures during Eathquakes," *Bulletin of the Seismological Society of America,* **53,** 403-417.

Huckelbridge, A. A. and Clough, R. W. (1978), "Seismic Response of Uplifting Building Frame," *Journal of Structural Division,* **104,** 1211-1229.

Hung, H.-H., Liu, K.-Y., Ho, T.-H. and Chang, K.-C. (2011), "An Experimental Study on the Rocking Response of Bridge Piers with Spread Footing Foundation," *Earthquake Engineering and Structural Dynamics,* **40,** 749-769.

Makris, N. and Roussos, Y. S. (2000), "Rocking Response of Rigid Blocks under Near-source Ground Motions," *Geotechnique,* **50,** 243-262.

NZS1170.5 (2004), "Structural Design Actions. Part 5: Earthquake Action,*"* Standard New Zealand.

Qin, X., Chen, Y. and Chouw, N. (2012), "Effect of Uplift and Soil Nonlinearity on Plastic Hinge Development and Induced Vibrations in Structures," *Journal of Advances of Structural Engineering*.

Sharpe, R. D. and Skinner, R. I. (1983), "The Seismic Design of an Industrial Chimney with Rocking Base," *Bulletin of the New Zealand Society for Earthquake Engineering,* **16,** 98-106.

Somerville, P. (1997), "The Characteristics and Quantification of Near-fault Ground Motion," California: National Center for Earthquake Engineering Research.

Somerville, P., Smith, N., Graves, R. and Abrahamson, N. (1997), "Modification of Empirical Strong Ground Motion Attenuation Relations to Include the Amplitude and Duration Effects of Rupture Directivity," *Seismological Research Letters*, **68,** 199-222.

10CUEE CONFERENCE PROCEEDINGS
10th International Conference on Urban Earthquake Engineering
March 1-2, 2013, Tokyo Institute of Technology, Tokyo, Japan

CONTROLLED SOFT STORY MECHANISM AS A SEISMIC PROTECTION SYSTEM

Hossein Agha Beigi[1], Timothy Sullivan[2], Constantin Christopoulos[3] and Gian Michele Calvi[4]

1) PhD Student, Department of Civil Engineering, University of Toronto, Toronto, Canada
2) Assistant Professor, Department of Civil Engineering and Architecture, University of Pavia, Pavia, Italy
3) Professor, University of Toronto, Department of Civil Engineering, Toronto, Canada
4) Professor, IUSS Pavia, Pavia, Italy

hossein.ashabeigi@mail.utoronto.ca, timothy.sullivan@unipv.it, c.christopoulos@utoronto.ca, gm.calvi @ iusspavia.it

Abstract: A new viewpoint to buildings with open ground storey is roposed. The potential benefits of soft storey mechanisms in existing buildings are numerically investigated. Response parameters from different case studies with and without soft-storey mechanisms are compared. The study initially considered two different infill configurations: the first with full masonry infill and the second with an open ground storey with full masonry infill above the first floor. Results of incremental dynamic analyses indicate that structures with uniform infill are less likely to collapse. However, the responses in isolated floors above the first floor are considerably improved for soft storey cases, provided that the large displacement demands at the soft storey are controlled properly. Then it is recognized that the need to retrofit structures with partial infill depends on the seismic hazard and acceptable risk. Loss estimation also demonstrates that the expected reduction of cost to non-structural components in isolated floors is a great advantage of buildings with soft-first storey.

1. INTRODUCTION

Earthquake surveys have shown that soft storey buildings, also called pilotis structures, are one the most vulnerable structures and their behaviour has been recognized as one of the most undesirable mechanisms among the structural and earthquake engineering society. For example, serious damages or collapse of first floor structural elements are reported in the 1971 San Fernando (M_w=6.6) and 1978 Miyagi-ken Oki (M_s=7.7) earthquakes. As a result, soft story structures were thoroughly studied and design procedures and recommendations were developed to prevent column side-sway mechanisms . Most of these studies emphasized that the column elements at the soft floor reach their ultimate capacity at considerably lower levels of intensity than mechanisms that involve distributed deformation demands over the height of the buildings.

2. CLASSIFICATION OF SOFT STOREY BUILDINGS

Based on current code definition, buildings are classified as having a "soft storey" if that level is less than 70% as stiff as the floor immediately above it, or less than 80% as stiff as the average stiffness of the three floors above it. In the other hand, general classification is to say that a soft-storey building is one in which deformations are expected to concentrate in a single “soft” storey. The most common types of existing building based on soft storey behaviour are called as: a) Discontinuous structural walls or infills, b) Strong beam- Weak column in frame type, c) Discontinuous load path, d)Walls in large openings at base.

Structures with discontinuous walls or infills are the most common type of existing soft storey buildings. Typical damage to buildings with this type of soft storey is shown in Figure 1.a, where a two-storey building is suffered significant lateral displacement at the ground floor level during the 1972 Managua Earthquake. In Figure 1.b. a five-storey residential reinforced concrete building is shown, which had been collapsed in Izmit, Turkey earthquake in 1999. Figure 1.c shows partial collapse due to Northridge earthquake occurred in Kaiser Permanente health institution in the form of pancaking of a weak second story, which was possible due to the weak column- strong beam mechanism. Finally, a well-known example of discontinuous structural wall is the Olive View Hospital, which had been badly damaged in the 1972 San Fernando earthquake, as shown in Figure 1.d.

Even though current design practice aims to avoid the occurrence of soft-storey mechanisms, there are a large number of older existing buildings that are expected to develop soft-storeys. Engineers must therefore decide when retrofit is required for such structures and what the best retrofit strategy is. This paper examines the effect of different structural characteristics on the seismic response of structures with soft storey mechanisms. Some initial case study structures are taken as benchmark buildings and incremental non-linear time history analyses are repeated by varying some key parameters including P-Delta effects of the first storey columns. Then, the effect of some key characteristics on the strength and deformation capacity of

the columns is investigated. The last part of the paper compares the losses in an open ground storey building to the full infill building, and consequently, the potential benefits of the soft storey scenario in loss estimation is explored. Finally, in light of all the results obtained, a potentially advantageous retrofit strategy for soft-storey structures is introduced.



Figure 1**.** Typical damage due to soft storey buildings, (a) Discontinuous Infill, Managua,1971 (b) Discontinuous Infill, Izmit 1999 (c) Discontinuous load path, Imperial Valley, 1979 (d) Strong-beam-weak column, San Fernando, 1972

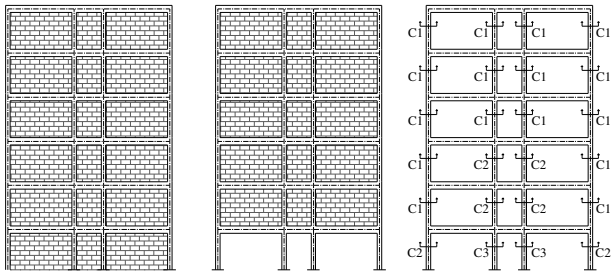
2. DESCRIPTION OF CASE STUDIES

The six storey three bay concrete frame structure shown in Figure 2 is studied in this paper for two different distributions of masonry infills. In the first scenario, it is assumed that masonry infills are distributed over all storeys uniformly, while in the next step and for considering soft storey effects, it is assumed that masonry infills are omitted at the ground storey. The frame configurations are taken from . These frames are representative of typical buildings designed during the 1950s to the 1970s. Accordingly, structural elements were designed only for gravity loads without following any capacity design rules for seismic protection.

Time history analyses are carried out using ten recorded horizontal accelerograms selected as part of the DISTEEL project . The record set consists of 10 records that are scaled to be compatible with Eurocode 8 spectrum for soil type C and a corner period T_d = 8s. The acceleration and displacement response spectra of the selected records are shown in Figure 3. As it can be seen from this figure, the records show a good fit with the EC8 design displacement spectrum (shown for a peak ground acceleration (PGA) on rock of 0.4g) but they drop below the design acceleration spectrum in the low period range (T< 1s).

2.1 Modeling Approach

A two-dimensional non-linear Giberson beam element (refer Carr, 2006) is used for modelling the beams and columns. To this end, a plastic hinge is concentrated at the two ends of each element. RUAUMOKO contains several types of moment-curvature hysteretic rules for definition of plastic hinges in the elements and joints. Among them, the Takeda hysteresis rule is selected, where unloading and reloading stiffness reduces as a function of ductility. The model is used in order to obtain the unloading stiffness. Due to the fact that the structure is designed for gravity loads only, the hysteretic shape should be defined so that relatively low levels of energy dissipation occur, assuming relatively high axial load ratios and therefore relatively pinched hysteretic response.



(Variant1) (Variant2) (Variant 3)

Figure 2. Six-storey concrete frame, variant 1) full infill uniform distribution, variant 2) Partial infill disconnected in the first floor, 3)Bare Frame

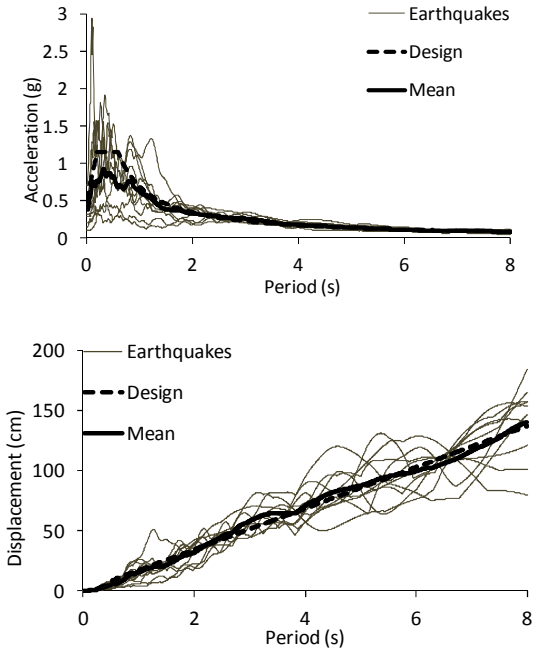


Figure 3. Acceleration and displacement Response Spectra for the selected records sets

A widely used approach is adopted for the modelling of masonry infills, based on the use of axial springs acting as equivalent compression diagonal struts. The stiffness of the equivalent diagonal strut is evaluated according to the model modified as proposed by . Moreover, four modes of failure are considered in order to evaluate the strength of the masonry infills: compression at the centre of the panel, compression of corners, sliding shear failures, and diagonal tension. cyclic behaviour of infill panels is modelled using the hysteresis rule proposed by Crisafulli (1997). This model takes into account the non-linear response of masonry in compression, including contact effects in the cracked material (pinching) and small cycle hysteresis. Based on this model, stiffness degradation due to shortening of the contact length between the frame and the panel is also considered. It should be noted that the dispersion of mechanical properties of masonry with respect to the mean values increases uncertainty of the infills characteristics and affects the global response of the structure.

In order to model joint behaviour, springs are inserted at beam-column locations using the approach proposed by Trowland (2003). The cyclic behaviour of the joint rotational springs has been defined using a hysteretic rule available in the RUAUMOKO program and specifically proposed to describe the characteristics of the joint response. In particular, the adopted hysteretic loop is able to describe the typical "pinching" effect due to the slippage of plain round reinforcing bars through the joint panel zone and to the opening and closing of diagonal shear cracks in the joint region.

2.1. Analytical Results

Response parameters of interest such as peak inter storey drift, peak acceleration and residual drift will be plotted versus the intensity of the ground motions. In order to estimate the mean response of all ground motions the geometric mean value (defined as per) as per Equation 3.1 is adopted.

Figure 4 shows the responses obtained from the nonlinear Incremental Dynamic Analysis (IDA) for the full infill and partial infill variants. In Figure 4.a the maximum of peak inter-storey drift in the full infill case, the maximum of peak inter-storey drift in the partial infill case, and the maximum of peak inter-storey drift above the first floors of the partial infill case (called isolated floors) are plotted separately.

The maximum of peak inter-storey drift in the partial infill case occurs in the open ground floor, and thus is indicated as the first floor in this figure. It can be seen that the inter-storey drift of the isolated floors is reduced significantly. However, as the intensity level is increased, the level of isolation is increased. The maximum drift ratio in the first floor of the partial infill case at the intensity level of 0.6g is double what it is for the full infill case, while the average drift in the upper floors are less than 0.3.

The peak floor acceleration of the full and partial infill variants are plotted in Figure 4.b. The peak floor accelerations are close to each other at the lower intensity level. This is explained by examining the acceleration response spectra that are shown in Figure 3. The elastic period of the full and partial infill frames is 0.78 and 0.32 sec respectively, and it can be seen that both these periods correspond to the short period spectral plateau. However, for high intensity levels, the period elongation of the soft storey case (partial infill) is higher than that of the full infill case, which results in lower acceleration demands for the whole structure. The reduction in peak floor accelerations in the soft storey frame could have a significant effect on the damage sustained by non-structural components and building contents.

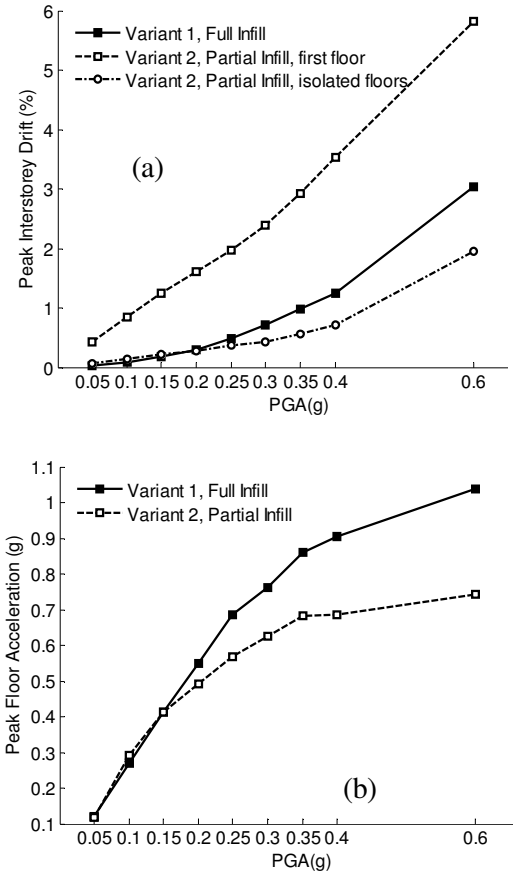


Figure 4. Comparison of peak inter-storey drift and floor acceleration obtained from IDA for two variants of full and partial infill

3 INFLUENCE OF P-DELTA EFFECTS ON SOFT STOREY RESPONSE

This section presents the results of numerical analyses of the six-storey frame with and without the inclusion of P-Δ effects. To this end, incremental time-history analyses of the structure with full and partial infills are carried out when large displacements are considered in the nonlinear deformation capacity of the structure. These results are

compared with the results obtained using small displacement analyses. Figure 5 shows the structural responses with and without considering P-Δ.

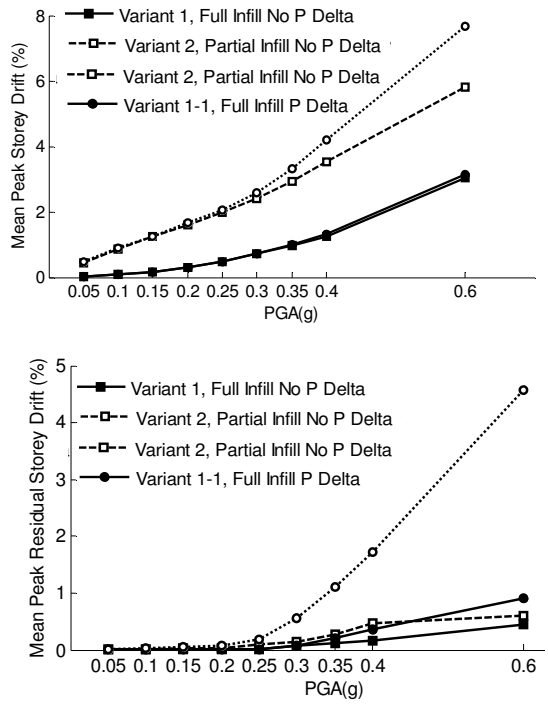


Figure 5. Influence of P-Delta effects on peak and residual drift variants

For the structure with full infill, considering P-Δ effects does not cause any difference in responses. On the other hand, the impact of P-Δ effects is more obvious for the soft storey case, where infills are not present in the ground floor. However, the difference between system response with and without P-Δ effects are not significant at low levels of intensity, and this is probably a reflection of the low stability indices for this structure. The drift ratios for the partial infill case at the hazard level of 0.6g are, respectively, 7.5% and 5.9% with and without P-Δ effects. On the other hand, the effect of P-Δ on residual drift is much more sensitive to the increasing level of intensity. It can be seen that the residual drift at a PGA of 0.6g is less than 1% without P-Δ effects, while P-Δ effects amplify this value by a factor of approximately 5.

4. INFLUENCE OF COLUMN CHARACTERISTICS ON SOFT-STOREY CAPACITY

Another aspect that to consider in this study is the impact of different column response characteristics on the frame capacity. To this end, cyclic analyses are conducted for the columns, considering different section depths, different axial load ratios and different reinforcement ratios in order to identify the likely strength and deformation capacity of the columns. Parameters γ, ρ and CF are axial force ratio, longitudinal reinforcement ratio, and confinement factor, respectively, defined as:

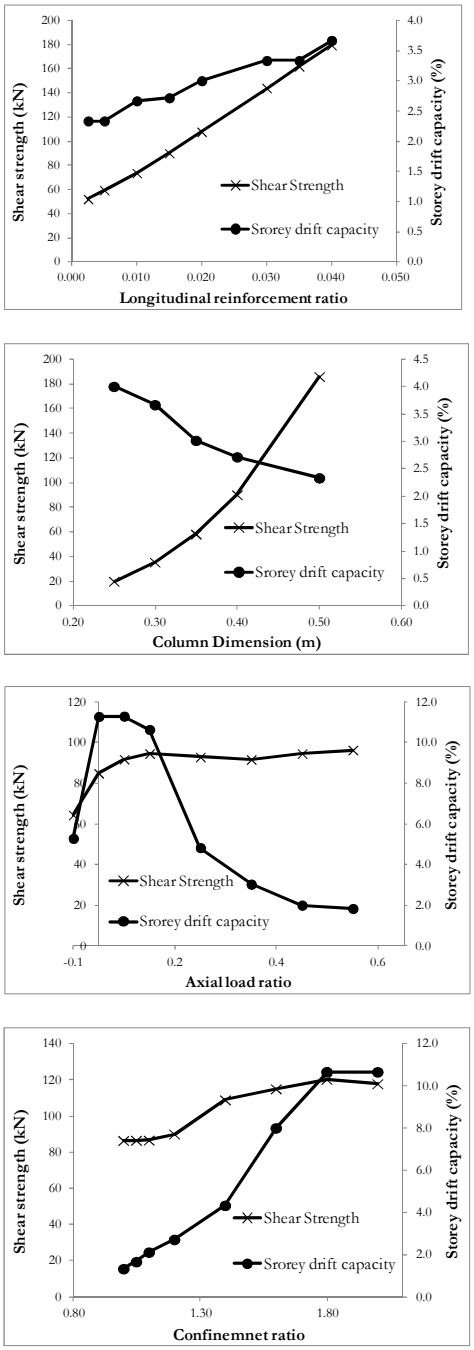


Figure 6. Comparison of key characteristics on column hysteresis response

$$\gamma = \frac{N}{A_g f_{cc}}, \quad , \quad \rho = \frac{A_{st}}{A_g} \quad , \quad \mathrm{CF} = \frac{f_c'}{f_{cc}}, \tag{1}$$

Where, N is the axial load, A_{st} is the total area of longitudinal reinforcement, Ag is gross section area, and f'_c and f'_{cc} are respectively the unconfined and confined

concrete compressive strength. For this study, wherever one parameter is changed, other parameters are kept constant.

Numerical models were developed and analyzed in Seismo-Struct for all geometrical and loading characteristics. The model is adopted in order to define constitutive relations for the concrete in compression. All piers are modelled by a single force-based element along the column height. The model of is applied for the longitudinal reinforcement. Additionally, a co-rotational formulation is used to account for geometrical nonlinear effects. Cyclic loading is implemented through lateral displacement control of the top end of the each column.

5. DISCUSSION OF RESULTS

This work began by comparing the behaviour of two RC frame buildings (variant 1 and variant 2 of Figure 2) that differed only by the fact that one had masonry infill from the first floor upwards whereas the other had masonry infill over its full height. Results of incremental dynamic analyses tend to indicate that the full masonry infill case could sustain much larger ground motion intensities when considering the collapse limit state. This might encourage structural engineers faced with the task of retrofitting the partial infill building to consider adding infills to the ground storey to render the structure similar to variant 1. While this option may help in reducing the probability of collapse, it would not necessarily reduce the damage and losses expected in the building for low to moderate earthquake intensities. This is partly because the floor accelerations for the infill case are likely to be higher than in the partial infill case but in addition, it is well known that damage to infill masonry occurs at much lower levels of drift than traditional RC frame structures. In addition, the open ground storey scenario would have a lower probability of reaching a partial-collapse limit state associated with masonry failure out-of-plane.

In addition to the points made above, it is recognised that the decision to retrofit a structure or not should be made within a risk assessment framework in which the probability of different levels of seismic intensity is considered along with the probable losses for each intensity level. With this in mind, it was decided that the effect of different structural characteristics on the seismic vulnerability of RC frame structures with soft storey mechanisms should be examined in more detail. As such, sections 3 has examined the influence of P-delta effects on the drift and acceleration demands of the open-ground-storey structure, whereas Section 4 examined how column dimensions, reinforcement contents and axial loads could affect deformation capacity.

The results in Figure 5 indicate that if the gravity load system could be de-coupled from the lateral load resisting system this could help reduce the likely deformation demands, which tend to be amplified by P-delta effects. In addition, it was demonstrated in Figure 6 that if the axial load ratios on column sections could be reduced their deformation capacities could be significantly increased. One potentially effective and innovative means of retrofitting a structure with an open-ground storey could therefore be to introduce a series of gravity columns at the ground level, as shown in Figure 7 that slide with the first storey. By doing this, P-delta effects would be minimised. In addition, by jacking the gravity column system into position, the axial loads on existing columns could also be reduced, thus greatly increasing their deformation capacity, without significantly affecting their lateral strength and potential for energy dissipation. Given the potential benefits of this retrofit scheme, this possibility is currently exploring as part of an undergoing research project. Detailing of the proposed system is not presented here as it is out of the scope of this paper.

It should be noted that with this retrofit strategy, the first floor deformations can be significantly increased, and thus damage is considerable in this floor, which is different from the traditional goals of base isolation where damage is avoided in most structural elements. In the next section, the expected repair cost to the existing open ground storey and the full infill case are compared together, and then the effect of the proposed retrofit strategy on the expected loss of the soft storey case is investigated.

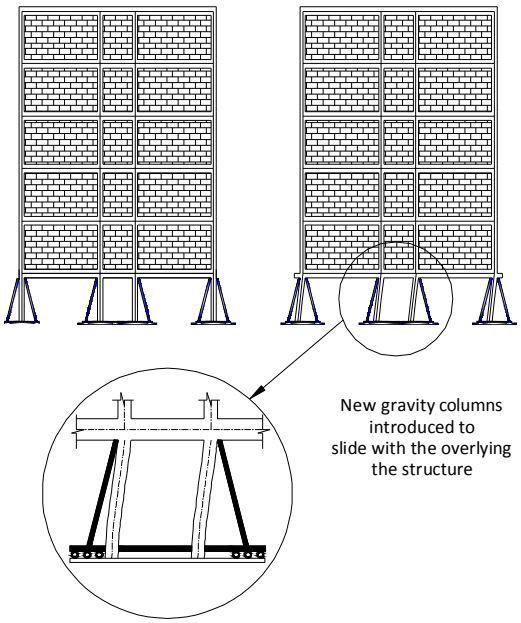


Figure 7. Possible means of de-coupling gravidity loads from lateral loads in a soft storey building

6. DAMAGE ANALYSIS AND LOSS ESTIMATION

Economic issues play an important role in the performance based design and assessment of buildings. It is stipulated that, provided that collapse does not occur and retrofit is possible, the total losses in buildings in which damage is concentrated in the first floor would be less than the case where it is distributed over all floors. However, this

could be sensitive to the performance level of the building and hazard intensities. For conventional buildings, where damage is distributed almost uniformly in all of the floors, non-structural components in the upper floors could be damaged even for low or moderate intensities. As non-structural costs are usually much higher than structural costs, this can result in high repair costs.

On the other hand, and for the case of soft storeys, the isolated floor can reduce the response in the storeys above, by sacrificing itself with higher levels of damage. In this case, even if the damage to the structural components in the first floor is significantly greater, as they cost less than non-structural elements, one can infer that the total damage will be decreased (provided that repair is possible) when compared to conventional methods to retrofit. The advantages of this response would be more beneficial as the number of storeys increases. This is studied quantitatively in this section by comparing the expected losses for the different variants.

It should be noted that the storey loss is obtained for the uniform pattern of component distribution over the building height. However, if the non-structural elements are distributed differently along the height, which is the case for soft storey buildings, their portion in the first floor is considerably changed. For the case of open ground storeys, where parking or stores are located at the first floor, the portion of the non-structural components in the first level may be considerably less than the other typical floors.

Figure 8 illustrates how the ratio of non-structural components in the first floor can affect the total cost of the building. As such, the total expected loss conditional on no collapse of the building is obtained by the summation of the components through the height of the building. To this end, different weights are assigned for the ratio of non-structural to structural elements in the first level, starting from zero (meaning that there is no structural component in the first level) to 1.6 (means that the value of the NS components at the first level are expensive, being 60% more than the typical levels). It should be noted that the total amount through the building height is kept constant, e.g. If the ratio in the first level is halved, it is increased by 10% in the rest of the five stories. The results obtained for the whole range of NS component ratios at the first level are compared to the full infill case in Figure 16a. From this graph, it can be seen that the NS distribution in the first level can highly change the total cost.

As a result, the main conclusion is that soft storey buildings could perform better than "no soft-storey" buildings depending on the intensity level and the contribution of non-structural elements to the total losses. For this case study, one can infer that for moderate intensity levels (0.25g-0.3g), and for a NS ratio of 0.5-0.6, the existing soft storey building (without any retrofit since the maximum expected drift in the first floor is 2.2% and the residual drift is around 0.5%) would perform better than the "no soft-storey" case. For very low intensity levels, the soft storey case has greater losses, since the first floor does not isolate the upper storeys for the very low intensity levels. To explain this, one can refer to the acceleration spectra in Figure 3. The elastic period of the partial infill case is T= 0.78 sand this period has higher acceleration demands than the full infill case with T= 0.32s, for the accelerograms used. However, for higher intensity levels, the period elongation in addition to inherent hysteretic damping of the soft storey is quicker, which decreases the acceleration demands at higher intensity levels. The acceleration demand can also be seen in Figure 4 where the peak floor acceleration for the soft storey case is higher than the full infill case for intensity values of 0.05 to 0.1g.

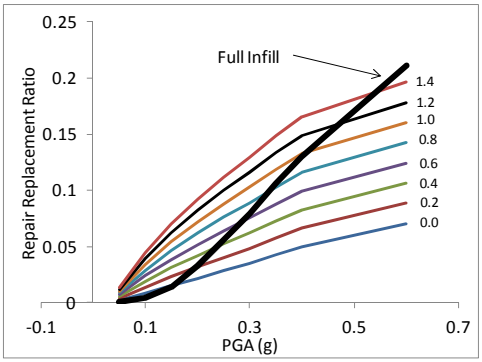


Figure 8. Effect of non-structural component distribution through the height of the building on the expected loss conditioned of open ground storey

Figure 9 shows the total cost for the three variants of full infill, partial infill, and the case where the proposed retrofit strategy is applied. It should be noted that it his plot, the collapse condition is considered in the loss estimation and in the event of collapse, a full replacement cost factor of 1.0 is assumed. However, it is assumed that by applying the conceptual retrofit strategy, the collapse is always prevented. It can be seen that the loss for the traditional soft storey case the costs increase rapidly compared to the full infill case. On the other hand, the effect of applying the proposed retrofit strategy on the soft storey case is significant. As a result, it can be argued that if the collapse of the soft storey case by applying P-delta mitigation strategy is prevented, the loss for the open ground storey case is significantly reduced. Furthermore, and as it can be seen from the figure, the total expected loss in the rerofitted soft storey building is less than the full infill case for a high range of the intensity levels.

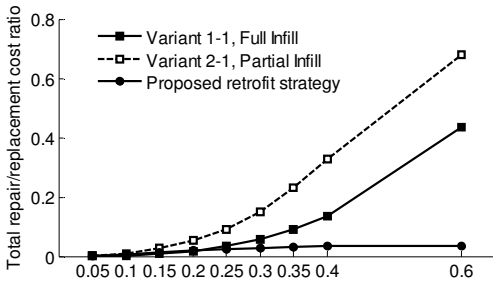


Figure 9. Total expected repair cost ratio for variants partial

infill, full infill, and the partial infill with collapse mitigation

7. CONCLUSIONS

The potential advantages of buildings with open ground storeys were discussed. It was observed that higher mode effects are less important in the global dynamic behaviour of the partial infill case. The incremental non-linear time history analysis results illustrated that peak floor accelerations in partial infill case are less than the full infill case, which can reduce damage to non-structural elements. In addition, the peak and residual inter storey drift at storeys above the open ground floor is highly decreased. However, the potential of collapse of the partial infill case is increased as the intensity level is increased, reflecting the observations made in past earthquakes.

The implications of the analysis findings were discussed in relation to potential retrofit schemes. A novel retrofit scheme was proposed in which sliding gravity columns are introduced to reduce the impact of P-delta effects on displacement demands and to increase the deformation capacity of existing columns. Based on that, an axial ratio, which has the largest improvement on the deformation capacity, is found, and applied to the case study. A comparison of the response parameters for each floor shows that if the first floor can be designed to respond in a stable manner, the upper floors can be isolated to remain without or with low levels of damage.

Damage analysis and loss estimation of the two variants with and without soft first storeys indicate that repair costs for the isolated floors is considerably reduced for the soft storey variant. It was shown that the distribution of the value of non-structural elements on the total loss of the open ground storey buildings is significant. For soft storey buildings where non-structural elements at the ground storey have low value, the expected loss is low and can be less than the full infill case. This conclusion is based on the condition that the structure does not collapse, which is attained by the proposed conceptual retrofit strategy. Based on these results, the main conclusion is that permitting a building to behave as a soft first storey, could be more efficient than preventing it. However, parameters like architecture, downtime, and performance should be considered in the final retrofit decisions.

Acknowledgements:
The authors gratefully acknowledge Guido Magenes and Mario Galli for providing background data and analytical models of the case study structure. In addition, the support offered by the ROSE programme at the UME School, IUSS Pavia as well as the Italian national 2010-2013 RELUIS project.

References:

Bertero. "Seismic Behavior of R/C Wall Structw Syst." *Journal of Structural Engineering* 110, no. 8 (1984): 1803-21.

Bertero, V.V. "Illustrated Introduction to Earthquake Engineering Principles." Berkeley: University of California, 1997.

Bertoldi, S.H., Decanini, L.D. and Gavarini,. "Telai Tamponati Soggetti Ad Azione Sismica, Un Modello Semplificato: Confronto Sperimentale E Numerico." *ANIDIS* 2 (1993): 815-24,.

Blakeborough, A., and et al. "The Northridge California Earthquake of 17 Jan 1994." London: ISE, 1994.

CEN. "Eurocode 8: Design of Structures for Earthquake Resistance -Part 1: General Rules, Seismic Actions and Rules for Buildings." Brussels, Belgium.: Comité Européen de Normalisation, 2004.

Emori, K., and W. C. Schonbrich. "Analysis of Reinforced Concrete Framewall Structures for Strong Motion Earthquakes." In *Civil Engineering Studies, Structural Research Series, N434*. University of Illinois, Urbana, Illinois, USA, 1978.

Esteva, L. "Nonlinear Seismic Response of Soft-First-Storey Buildings Subjected to Narrow Band Accelerograms." *Earthquake Spectra* 8, no. 3 (1992): 373-89.

FEMA310. "Handbook for the Seismic Evaluation of Buildings." 1998.

Filippou, F.C., V.V. Bertero, and E.P. Popov. "Effects of Bond Deterioration on Hysteretic Behavior of Reinforced Concrete Joints." edited by Earthquake Engineering Research Centre. Report UCB/EERC-83/19, University of California, Berkeley, USA., 1983.

Galli. "Evaluation of the Seismic Response of Existing R.C. Frame Building with Masonry Infills." IUSS, 2006.

Mahin, S. A., Vitelmo V. Bertero, Anil K. Chopra, and Robert G. Collins. "Response of the Olive View Hospital Main Building During the San Fernando Earthquake." Berkeley, California: University of California, 1976.

Maley, T.J., R. Roldán, A. Lago, and T.J. Sullivan. "Effects of Response Spectrum Shape on the Response of Steel Frame and Frame-Wall Structures." Pavia, Italy, 2012.

Mander, J.B., M.J.N. Priestley, and R. Park. "Theoretical Stress-Strain Model for Confined Concrete." *Journal of Structural Engineering, ASCE* 114, no. 8 (1988): 804-1826.

Naeim, F. ed. *The Seismic Design Handbook*. Van Nostrand Reinhold, 1989.

Otani, S. . "A Computer Program for Inelastic Response of R/C Frames to Earthquakes." Civil Engineering Studies, Univ. Of Illinois at Urbana-Champaign, 1974.

Ramirez, Carlos Marcelo, and Eduardo Miranda. "Building-Specific Loss Estimation Methods & Tools for Simplified Performance-Based Earthquake Engineering." Stanford University, 2009.

A Computer Program for Processing Strong Motion Data. Retrieved from http://www.seismosoft.com.

Shome, Nilesh. "Probablistic Seismic Demand Analysis of Nonlinear Structures." Stanford University, 1999.

Stafford, Smith. "A Method of Analysis for Infilled Frames." *Proceedings of the institution of civil engineers* 44 (1969): 31-48.

Vukazich, S. M., G. Selvaduray, and J. Tran. "Conducting a Soft First-Story Multifamily Dwelling Survey: An Example Using Santa Clara County, California." [In English]. *Earthquake Spectra* 22, no. 4 (Nov 2006): 1063-79.

10CUEE CONFERENCE PROCEEDINGS
10th International Conference on Urban Earthquake Engineering
March 1-2, 2013, Tokyo Institute of Technology, Tokyo, Japan

TWO DIRECTIONAL SEISMIC RESPONSE EVALUATION OF BUILDINGS WHICH DO NOT HAVE WELL-REGULATED PLANE SHAPES

Yoshina Takahashi[1)], Hisato Hotta[2)]

1) Graduate Student, Dept. of Arch. and Bldg. Engrg., Tokyo Institute of Technology, Tokyo, Japan
2) Associate Professor, Dept. of Arch. and Bldg. Engrg., Tokyo Institute of Technology, Tokyo, Japan
takahashi.y.az@m.titech.ac.jp,

Abstract: When seismic response analyses of buildings are conducted, habitually it is not considered the case that the buildings do not have well-regulated plane shapes, of which principal elastic axis is not perpendicular to the yield surface. And also, habitually it is not considered that seismic motions are input in two directions of principal elastic axes. The objective of this study is to examine the validity of seismic response evaluation by current equivalent linearizing method and the possibility that the seismic response through two directional input exceeds the one through one directional input. We conducted time history response analyses inputting in one direction and in two directions using one mass bidirectional vibration model. It is concluded that seismic responses appear in the direction differs from input direction of principal elastic axis by yielding when the principal elastic axis is not perpendicular to the yield surface, and that the maximum response displacement which is obtained through two directional input often exceeds the one which is obtained through one directional input.

1. INTRODUCTION

Considering seismic response of buildings, it is habitually premised that plastic deformation occurs in direction in which seismic motion is input. That means it's regarded that buildings have well-regulated plane shapes, and principal elastic axes are perpendicular to yield surface. For instance, equivalent linearizing method used for seismic response evaluation also considers only a principal elastic axis. However, buildings do not always have well-regulated plane shapes, and the principal elastic axis and the yield surface often do not cross at right angles. The problem is whether seismic response can be evaluated by current equivalent linearizing method when the principal elastic axes are not perpendicular to the yield surface. Meanwhile, seismic motion input is two directional in fact, but going seismic response evaluation considers only a direction of principal elastic axes. It is required to investigate whether the seismic response through two directional input exceeds the response through one directional input. In this paper, we examine the validity of seismic response evaluation by current equivalent linearizing method and possibility that the seismic response through two directional input exceeds the one through one directional input, using one mass bidirectional vibration model.

2. OUTLINE OF ANALYSIS

2.1 Establishment of Vibration Model

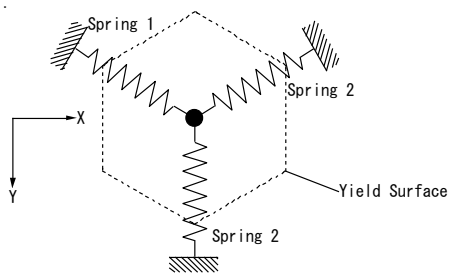


Figure 1 Vibration Model

Figure 1 shows the vibration model. It is composed of one mass point and three springs which have bilinear-type elasto-plastic restoring force characteristics. The yield surface is considered the boundary where two springs yield, and is shown as dashed line in Figure 1. The yield resistances of three springs are set to be equivalent, and the shape of the yield surface is hexagon as shown. The ratio of yield resistance of a spring to the mass is set to 0.32.

Stiffness matrix of this vibration model is given by following equation.

$$[K] = \begin{bmatrix} \frac{3}{4}(k_1 + k_2) & \frac{\sqrt{3}}{4}(k_1 - k_2) \\ \frac{\sqrt{3}}{4}(k_1 - k_2) & \frac{1}{4}(k_1 + k_2 + 4k_3) \end{bmatrix} \quad (1)$$

Where k_1, k_2 and k_3 indicate the stiffness of springs 1, 2 and 3 shown in Figure 1. We solved the generalized eigenvalue problem. The determinant to be solved is given

by following equation.

$$|[K] - \omega^2[M]| = 0 \tag{2}$$

The fundamental circular frequencies are obtained from Eq. (2), and Ax and Ay which provide the eigenvector are calculated. Ax and Ay give the directions of principal elastic axes in X-Y coordinate system. We defined *a* and *b* as shown in the following equation.

$$a = k_1/k_3 \tag{3}$$

$$b = k_2/k_3 \tag{4}$$

The following equation gives the ratio of Ay to Ax.

$$\frac{A_y}{A_x} = \frac{-(a+b-2) \pm 2\sqrt{a^2+b^2+1-ab-b-a}}{\sqrt{3}(a-b)} \tag{5}$$

T_1 and T_2, which indicate the primary natural period and the secondary natural period, are calculated from the fundamental circular frequencies. The ratio of primary natural period to secondary natural period is shown in the following equation.

$$\frac{T_1}{T_2} = \sqrt{\frac{(a+b+1)-\sqrt{a^2+b^2+1-ab-b-a}}{(a+b+1)+\sqrt{a^2+b^2+1-ab-b-a}}} \tag{6}$$

Equations (1) and (2) indicate that it is possible to vary the principal elastic axes and the ratio of natural periods by coordinate the stiffness of three springs. When the ratio of natural periods is equal to 1.0, the stiffness of the three springs is equivalent.

2.2 Behavior of Vibration Model

Time history response analyses are conducted by seismic motion of Kobe. The north-south motion and east-west motion of Kobe were reconstituted to two seismic motions. One of them is in direction in which maximum acceleration from the origin appears, and the other one is in direction which is at right angles to the other. And they were multiply by coefficients so as to provide appropriate ductility factors. The time histories of acceleration of seismic motion of Kobe and acceleration response spectrum are shown in Figure 2.

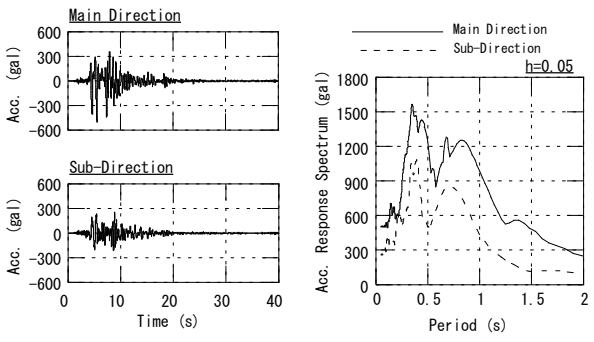


Figure 2 Seismic Motion of Kobe

Newmark-β method made use of numerical integration for dynamic response analysis of equation of motion. The β is equal to one-fourth.

We defined the direction which is input the seismic motion having maximum acceleration as "main direction" and the direction which is input the other seismic motion as "sub-direction". We also defined the ratio of the natural period in main direction to the natural period in sub-direction as "T_x", and set the natural period in main direction 0.5 seconds uniformly. The angle between the direction which is perpendicular to the main direction and yield surface is defined as "crossing angle". Figure 3 illustrates the results when T_x is set to 1.0, the crossing angle is zero degree, and seismic motion is input only in main direction. It contains graphs of time history response of restoring force and displacement in main direction, relation between restoring force and displacement in main direction, and orbits of restoring force and displacement in plane system. It is indicated that behavior doesn't appear in the direction other than the main direction. Figure 4 gives the relation between restoring force and displacement of springs 1 and 2. The behavior does not appear in spring 3 because the main direction is set in the direction which is at right angles to the direction of spring 3. Naturally, the behavior of springs 1 and 2 is symmetrical about a point.

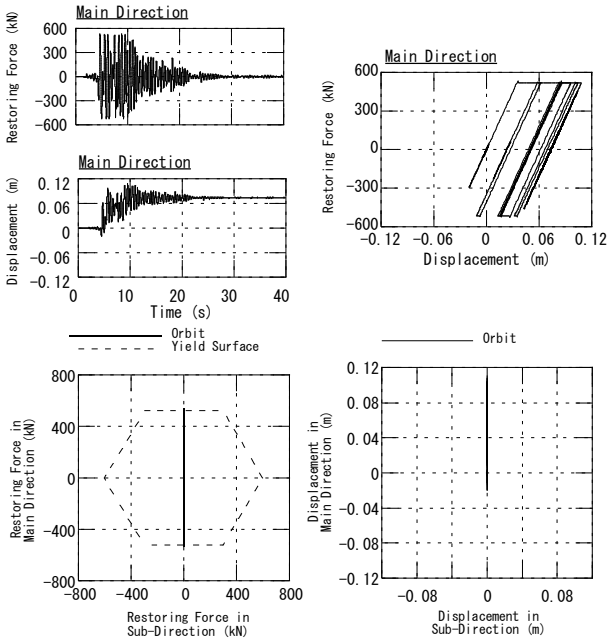


Figure 3 Behavior of Vibration Model When The Crossing Angle Is Zero Degree Inputting in One Direction

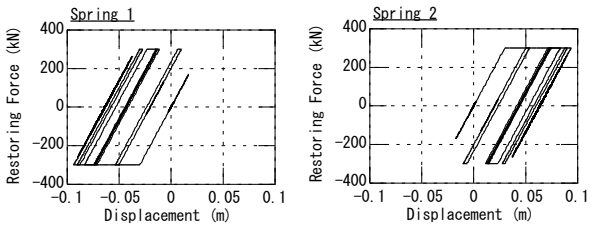


Figure 4 Relation between Restoring Force and Displacement of Spring 1 and 2

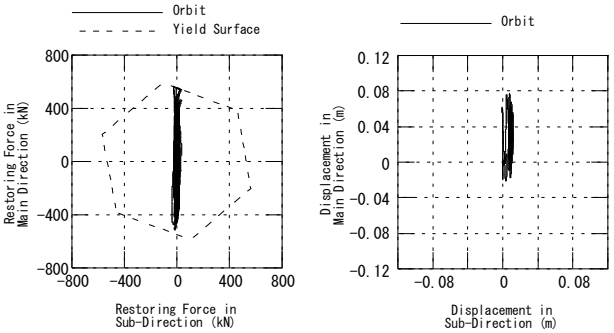


Figure 5 Orbits of Restoring Force and Displacement When The Crossing Angle Is 20 Degrees Inputting in One Direction

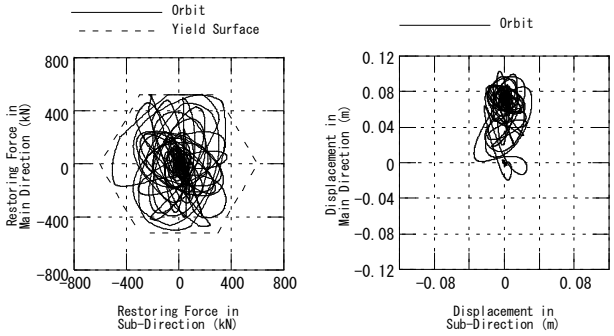


Figure 6 Orbits of Restoring Force and Displacement When The Crossing Angle Is Zero Degree Inputting in Two Directions

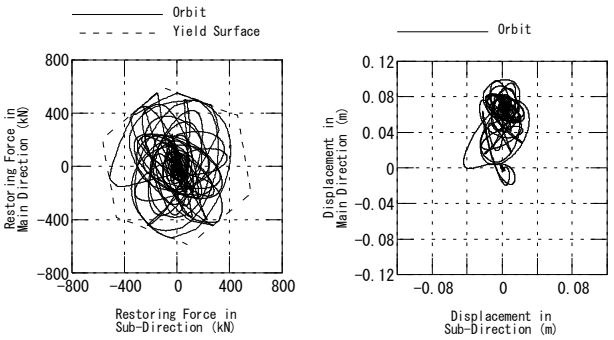


Figure 7 Orbits of Restoring Force and Displacement When The Crossing Angle Is 20 Degrees Inputting in Two Directions

Figure 5 gives the orbits of restoring force and displacement in plane system when the crossing angle is 20 degrees and seismic motion is input only in main direction. In spite of being input only in one direction of principal elastic axes, restoring force and displacement appear in the other direction by yielding.

Figure 6 gives the orbits of restoring force and displacement when the crossing angle is zero degree and seismic motion is input in main direction and sub-direction, and Figure 7 gives the orbits when the crossing angle is 20 degrees and seismic motion is input in two directions. When the crossing angle is zero degree, it is shown that the maximum response displacement in the main direction through which seismic motion is input only in main direction doesn't much differ from the one in the main direction through which seismic motion is input in two directions in Figures 3 and 6. In contrast, when the crossing angle is 20 degrees, the maximum response displacement in the main direction through which seismic motion is input only in main direction is smaller than the one when seismic motion is input in two directions, as illustrated in Figures 5 and 7.

3. PARAMETRIC EXAMINATION

3.1 Parameters

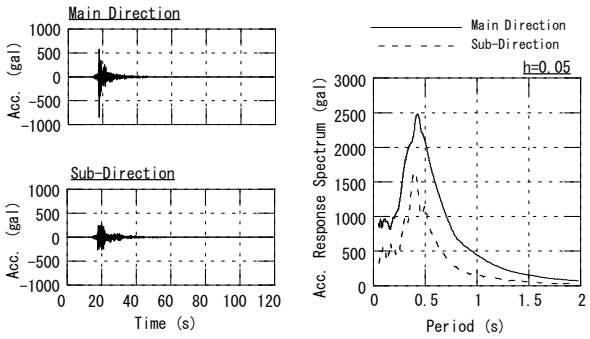


Figure 8 Seismic Motion of Ojiya

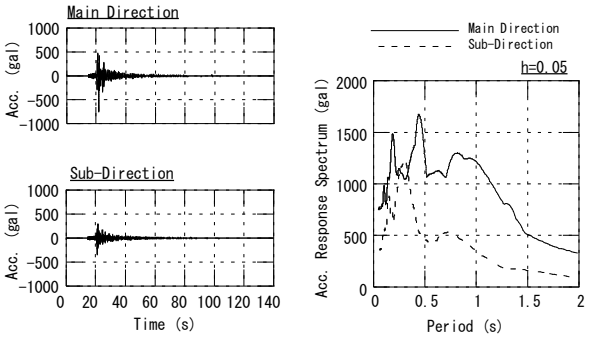


Figure 9 Seismic Motion of Yokaichiba

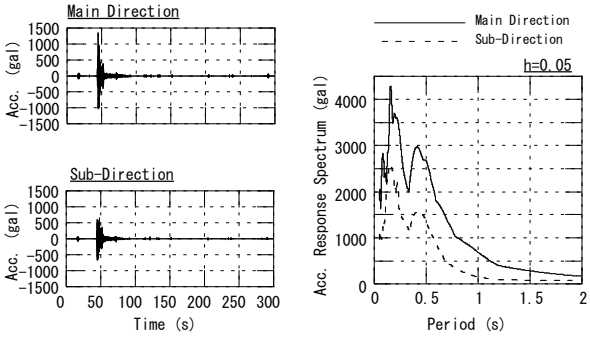


Figure 10 Seismic Motion of Takahagi

We used another three seismic motions for analysis. Seismic motions of Ojiya, Yokaichiba and Takahagi were quoted from K-net (Japanese strong-motion seismograph network). Their north-south motion and east-west motion

were reconstituted to two seismic motions to be input in the main direction and the sub-direction, and they were multiply by coefficients so as to provide appropriate ductility factors in the same way as Kobe. The time histories of acceleration and the acceleration response spectrum of the seismic motions of Ojiya, Yokaichiba and Takahagi are shown in Figures 8, 9 and 10.

The time history response analyses were conducted with four seismic motions. The natural period in main direction was set to 0.5 seconds uniformly. We set T_x 0.8, 1.0 and 1.2, and the crossing angles at intervals of five degrees from zero to 30 degrees. The vibration model was input only in the main direction and in two directions of the main and sub-direction.

3.2 Results and Discussion

Figure 11 shows the maximum of response displacements when the seismic motions are input in one direction and in two directions. The graphs are arranged by the seismic motions and the ratio of natural periods. Vertical axis gives displacement, and horizontal axis gives crossing angle.

The maximum response displacements for SDOF model which has restoring force characteristics of vibration model in the main direction are also shown in Figure 11, as the case the principal elastic axis of the analytical model is perpendicular to yield surface. Additionally, estimated values by equivalent linearizing method are shown in Figure 11. These values by equivalent linearizing method are supposed to be estimated low in some degree. The absorbed energy through one cycle of hysteresis loop which is used for calculation of equivalent linearizing method needs to be reduced because the vibration model does not always perform steady motion, but the absorbed energy is not reduced in these analyses.

Comparing the maximum response displacements by one directional input and the one from the analytical model, some difference can be identified, but it is not so large. The difference appears when the main direction is not at right angles to the yield surface. The difference does not appear when the crossing angle is 30 degrees because there is a singular point where the three springs yield on the principal elastic axis input. It seems whether the difference appears or not depends on the seismic motions and the ratio of natural periods, but what causes the difference was not able to be clarified.

The maximum response displacements by two directional input and the one from the analytical model are compared. The values by two directional input greatly exceed the values from the analytical model when the

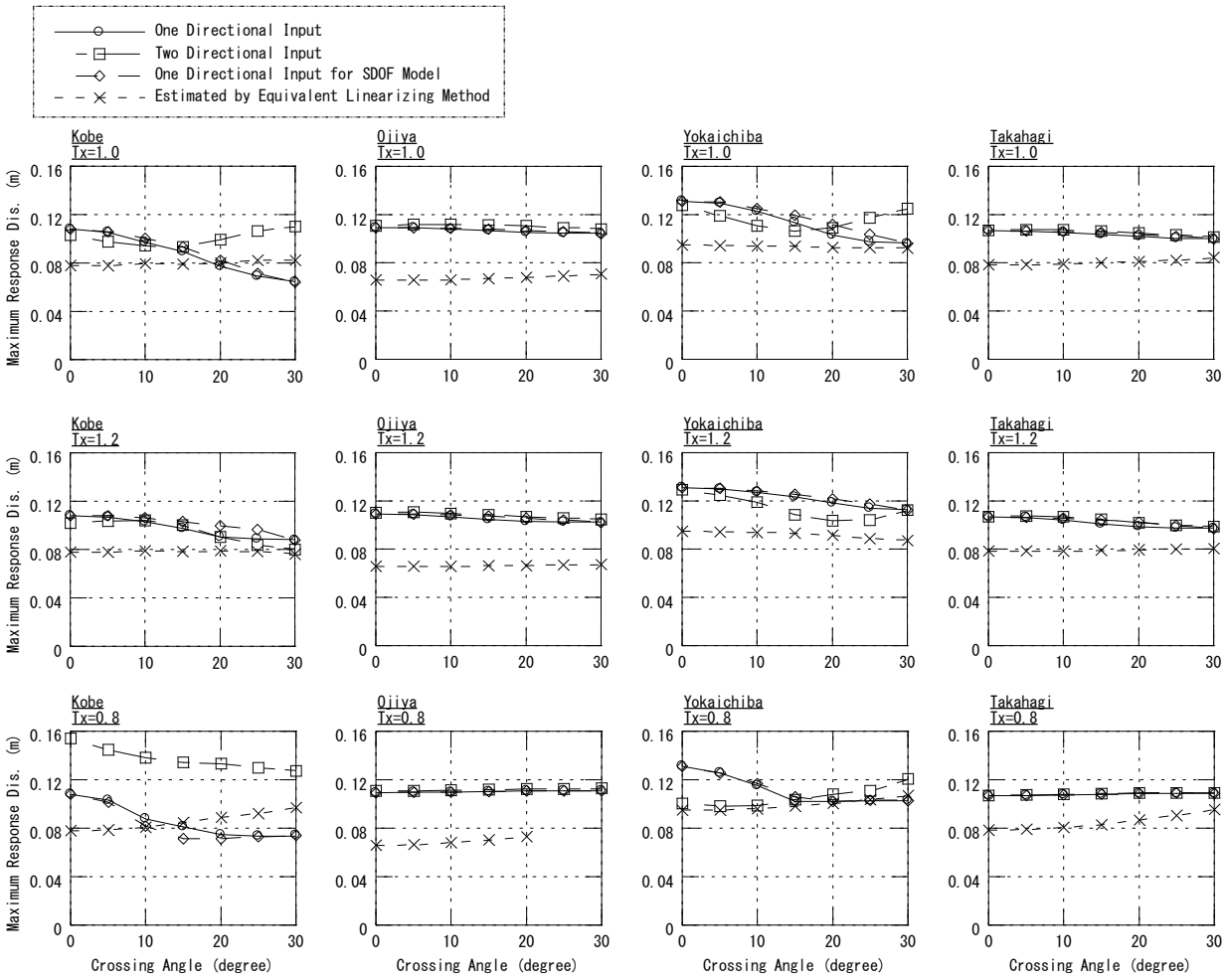


Figure 11 Comparison of Analytic Values

inputting seismic motion is Kobe or Yokaichiba and T_x is 1.0 and 0.8. We found it often happens that the seismic response displacements through two directional input greatly exceed the values through one directional input.

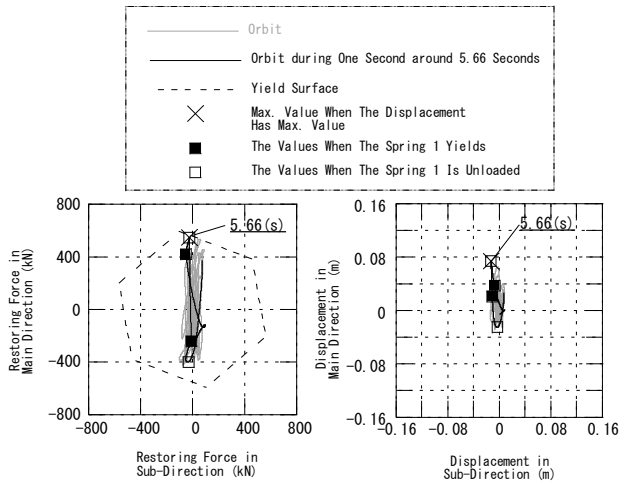


Figure 12 Detailed Analysis Results through One Directional Input

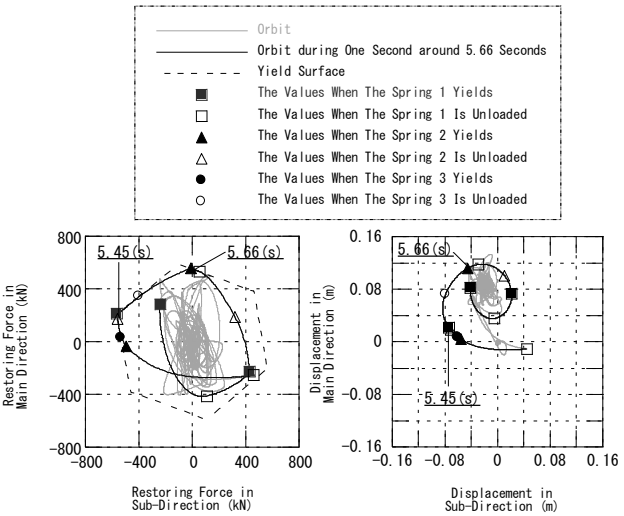


Figure 13 Detailed Analysis Results through Two Directional Input

The case of which input seismic motion is that of Kobe, crossing angle is 20 degrees, and T_x is 0.8 was investigated in more detail, as shown in Figures 12 and 13, in order to clarify differences of events when the response displacements through two directional input greatly exceed the values through one directional input. Figure 12 gives orbits of restoring force and displacement in plane system through one directional input, and Figure 13 illustrates the orbits through two directional input. The maximum response displacement through one directional input appears at 5.66 seconds as shown in Figure 12. The orbits during one second around 5.66 seconds (i.e. from 5.16 seconds to 6.16 seconds) and points which illustrate yielding and unloading of springs are also given in Figures 12 and 13.

In the case of one directional input, it is found that yielding and unloading of springs occur almost on the principal elastic axis of main direction as given in Figure 12. Meanwhile, as shown in Figure 13, some yielding and unloading occur around 5.45 seconds on the part of yield surface which does not cross the principal elastic axis of main direction, and it can be seen that that yielding is a reason of the differences of response displacements.

4. CONCLUSION

Time history response analyses were carried out inputting seismic motions in one direction of principal elastic axis and in two directions of principal elastic axes, varying crossing angles. The following results were obtained:

(1) When the principal elastic axis is not perpendicular to the yield surface and seismic motions are input in one direction of the principal elastic axes, restoring force and displacement appear in the direction which differs from inputting direction by yielding.
(2) There were some difference between the maximum response displacements when the principal elastic axis is not perpendicular to the yield surface and the ones when the principal elastic axis is at right angles to the yield surface.
(3) The maximum response displacements which is obtained through two directional input often exceed greatly the ones which are obtained through one directional input. Considering elastic-plastic seismic response of buildings, two directional input should be taken into account.

It is future issue to find the cause for which the maximum response displacements through two directional input exceeds the ones through one directional input.

References:

Osaki, Y. (1994), "A New Guide to Spectral Analysis of Seismic Motions," Kajima Institute Publishing Co., Ltd.

10CUEE CONFERENCE PROCEEDINGS
10th International Conference on Urban Earthquake Engineering
March 1-2, 2013, Tokyo Institute of Technology, Tokyo, Japan

3-DIMENSIONAL FEM ANALYSIS OF SHIELD TUNNEL AND ITS APPLICATION ON REBOUND ESTIMATION

Yang Shen[1)], Kiwamu Tsuno[2)], Takashi Nakayama[3)], Sohichi Hirose[4)]

1) Doctoral Student, Dept. of Mechanical and Environmental Informatics, Tokyo Institute of Technology, Japan
2) Doctor, Structures Technology Division, Railway Technical Research Institute, Japan
3) Structures Technology Division, Railway Technical Research Institute, Japan
4) Professor, Dept. of Mechanical and Environmental Informatics, Tokyo Institute of Technology, Japan
shen.y.aa@m.titech.ac.jp, tsuno@rtri.or.jp, nakayama@rtri.or.jp, shirose@cv.titech.ac.jp

Abstract: Shield tunneling has become one of the main approaches of large length tunnel construction in recent decades. However, the analysis technique of shield tunnel widely used among consulting engineers by now is still based on 2-D beam-spring model, which is hardly to be able to describe the contact mechanism of the interfaces between segments and rings. 3-D FEM analysis was always considered to be time consuming, therefore, was only adopted in local analysis, e.g. tunnel joints or connections to underground stations. With the demand of complicated underground environment analysis for shield tunnel, full-length 3-D FEM analysis is required more than ever. This paper presents a full-length shield tunnel 3-D FEM model with solid elements. In this model, both spring connection and interface contact between segments and rings are considered; the edge of each segment is treated as a strengthen part on elastic property; the nodes on the outer surface are connected with ground springs as boundary conditions. To keep computation accuracy, displacement under the same load is compared with another shell element model, and good agreement is reached. As an application, the rebound effect after earth remove due to the construction above an existing tunnel has been estimated.

1. INTRODUCTION

With the vast demand of city underground transportation system and expressway system covering large area, a lot of shield tunnels have been constructed, as one of the main approaches to construct large length tunnels in urban areas. Through decades' practice, large amount of techniques and field experiences have been accumulated, however, conventional 2-Dimensional beam-spring model is still mainly utilized to design the shield tunnels in Japan. The beam-spring model is convenient and has been contributed to obtain comparatively good results corresponding to the cross-sectional behavior of shield tunnels, but, it is hardly to be able to describe the contact mechanism of the interfaces between segments and rings, which may affect their longitudinal behavior. Therefore, it is necessary to develop the analysis method with 3-Dimensional FEM to investigate the long-term behavior of shield tunnels. However, 3-Dimensional FEM analysis was always considered to be time consuming, therefore, was only adopted in local analysis, e.g. tunnel joints or connections to underground stations (Lee 2009).

The development of computation technology has pushed the analysis technique forward. Several novel 3-Dimensional FEM models of shield tunnel have been proposed, among them, the full-length shell model developed by (Tsuno et al. 2012) is an effective tool for shield tunnel design and has been applied in engineering analysis. But due to the property of shell element it uses, this model cannot describe the surface connection between segments well. Another model (Tajima et al. 2004) tried to describe the interface connection using solid elements, but not yet been implemented to the full-length tunnel. Although the longitudinal behavior of shield tunnels was investigated with a full-length 3-Dimensional FEM model with solid elements (Wang et al. 2012), it can be said that analytical method with 3-Dimensional FEM in consideration of the connections between segments has not been established.

In this study, a full-length 3-Dimensional FEM model of shield tunnel with solid elements is presented, in which all the connections between segments will be considered, including the surface contact and spring connection. Through this model, a new full-length analyze approach for shield tunnel can be proposed.

2. 3-D SOLID FEM MODEL

2.1 Objective

The complication of shield tunnel engineering requires a numerical analysis method that can describe the tunnel components, including segments, joints, bolts, etc. and their connections as much close to the real engineering situation. However, due to the limitation of computation capability, the previous numerical analyze approaches are mostly based on

2-Dimensional method. 3-Dimensional FEM analysis was always considered to be time consuming. This limitation is about to be changed, at least moderated through the development of computation technology in recent years. The PC with multi-CPU and the parallel computing FEM technique can be easily afforded and applied by consulting company and institution now, which is an elementary platform for 3-Dimensional FEM analysis of shield tunnel. Under this background, 3-Dimensional FEM analysis is gradually applied in the simulation of shield tunnel, especially on the mechanism research of joints between segments and rings (Teachavorasinskun and Chub 2010), whereas the 3-Dimensional full-length shield tunnel simulation considering all the connection conditions is still rare to be seen.

In order to give a precise and trustable numerical analyze approach for shield tunnel engineering, e.g. design, construction, maintenance, monitoring, a full-length 3-Dimensional solid FEM model has been proposed in this study. In this model, both spring connection and interface contact between segments and rings are considered; the edge of each segment is treated as a strengthen part on elastic property; the nodes on the outer surface are connected with ground springs as boundary conditions. A 3D 8-node linear isoparametric element is used to simulate the concrete segment; nonlinear spring element is used to simulate the bolt connection between segments and rings, and the ground support; hard surface contact is considered for the interface contact between segments and rings. Abaqus v6.11 has been utilized as the FEM solver.

2.2 Details of The Model

A completed shield tunnel consists of thousands of segments, which are made of concrete or steel. In annular, several pieces of segments combine each other as a ring. In axial, two rings of segments connect together with a certain angle difference, then these two rings form a unit, repeatedly installed along the tunnel route. The connection mechanism of those segments is extremely important to analyze the whole tunnel structure, however, not yet to be understood so well.

In practical, in annular, between each two segments, there will be 2 joints of tension bolt as connection, and in axial, between each two rings, there will be numbers of joints of tension bolt evenly distributed on the circle. Usually attentions can be easily drawn by those joint-type connections, especially for the segmental joints, numbers of experimental studies have been conducted, to understand the mechanical performance of those segmental tension bolts (Koyama et al. 1994). In simulation, those joint-type tension bolt connections can be substituted by spring elements in FEM analysis, whose elastic constant can be partial-nonlinear, fitting the experimental data as much as possible. The longitudinal tension bolt connection performance is not clearly known due to the difficulty in ring-ring loading test. Another connection, which is hard to quantify and easily to be neglected, is the surface contact on each interface between two segments or two rings. Because of the existence of tooth-like concrete concave-convex on the edge of the segments, the friction on the interfaces may affect the mechanical behavior of shied tunnels. The effect of this surface-type connection also needs to be considered in this model.

Figure 1 shows the detail of connection simulation in this model. Figure 1 (a) and (b) are the surface contact between segments and rings respectively. The contact type is called “Hard contact”, which implies that only when the surfaces are in contact, namely, the clearance between them is zero, the contact pressure can be transmitted, otherwise, if the surfaces separate, then no pressure can be delivered. This “Hard contact” can be well applied in both static and dynamic analysis. Friction can also be considered on the interface. In this model, the element faces on the edges of the segments are set to be pairs of surface contact, including 7 pairs on each ring and 1 circle-shape pair between two rings, with “Hard contact” as normal behavior for pressure transmission and friction coefficient 0.6 as tangential behavior for concave-convex grip.

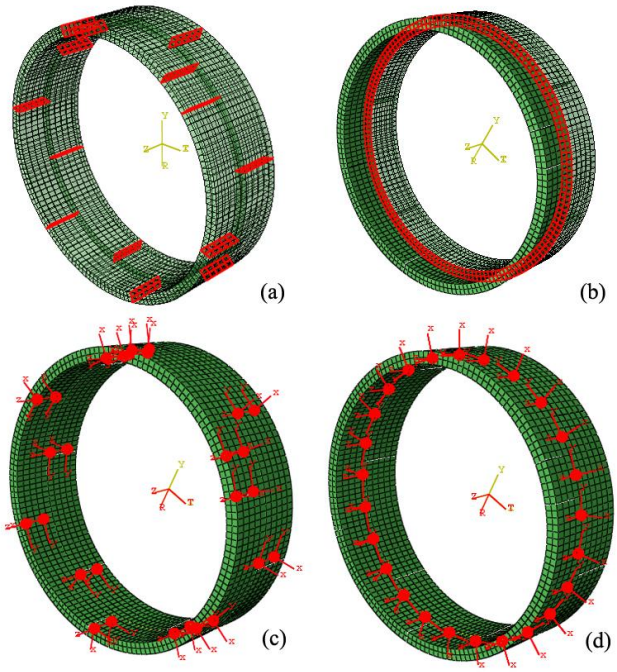


Figure 1 Surface Contact and Springs between Segments and Rings: (a) Surface Contact between Segments, (b) Surface Contact between Rings, (c) Springs between Segments, (d) Springs between Rings.

Figure 1 (c) and (d) are the spring connections between segments and rings respectively. Those springs are approximation of tension bolt on the interfaces. According to the knowledge about the tension bolt from experiments, 4 types of springs are set between segments: namely, radial, annular, axial, and rotational springs, while 3 types of springs are set between rings: namely, radial, annular, and axial springs. Springs’ amount and position setting is based on the design example (Railway Technical Research Institute, 2001).

Besides of the springs on the interfaces, 2 types (radial and axial) of ground springs will be set on each node on the outer surface of the tunnel, and the spring constant is evenly distributed.

For the 2-ring unit, which will be utilized in validity confirmation later, the number of elements is 10535. For the 50-ring full-length model, which will be utilized in rebound estimation, the number of elements is 293783.

3. VALIDITY AND MODEL MODIFICATION

Before this model being applied in any engineering computation, it needs to be examined with its validity. As the compared model, a 3-Dimensional FEM model with shell elements has been checked on validity by comparing the results obtained by beam-spring model (Tsuno et al. 2012). Then, the results of model with solid elements will be compared with those of shell elements model, which adds spring elements as the connections between segments, without considering surface contact on the interfaces.

The validity work will be carried out simultaneously with the process of parameter modification. The spring constants and friction coefficients on the interface are the parameters under modified. Another important factor is the material elastic property on the edge part of every segment. A special edge part is designed in this model, as Figure 2 shows. For these edge part elements, the Young's modules can be higher than the inner part, which is a simplification of the high strength design in practical treatment. In the process of parameter modification, those edge part elements' elastic property will be adjusted.

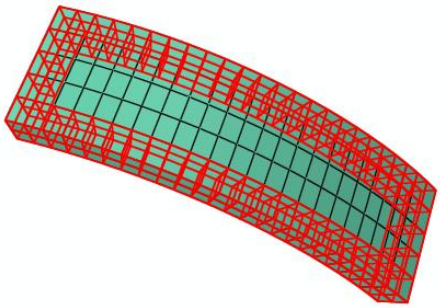


Figure 2 Edge Part Element with Different Parameter

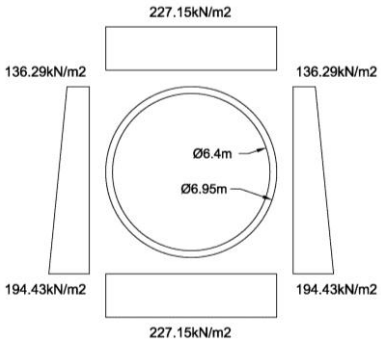


Figure 3 Earth Pressure Load on 2-ring Model

An earth pressure load (Figure 3), is applied on both solid and shell model. Figure 4 shows the result of u_2 component. After model parameter modification, the two FEM models get a good agreement on u_2 component, with a difference of 2.6%. Besides of the displacement, the solid model gives more information on edges and joints, which shows a capability of local detail analysis.

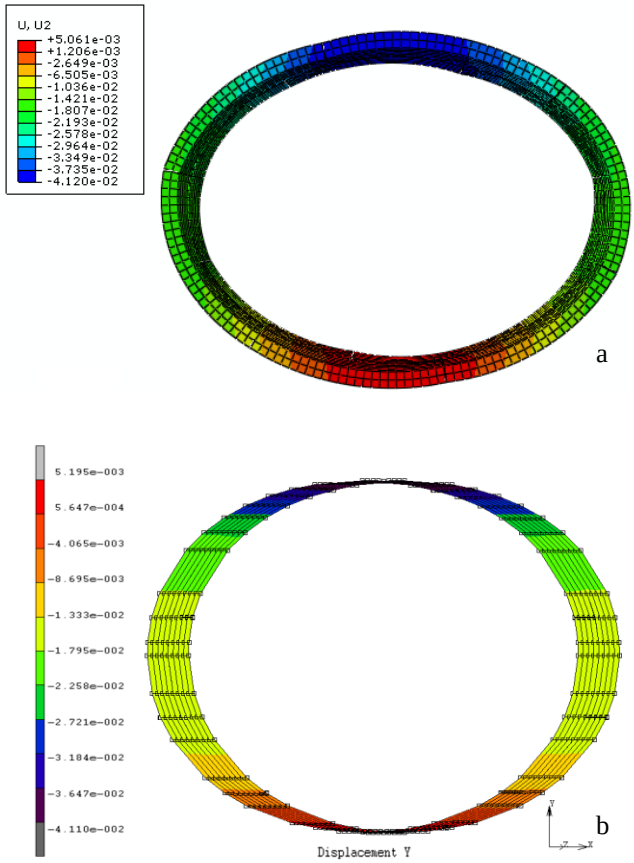


Figure 4 Displacement Comparison between Solid Model and Shell Model: (a) u_2 Solid Model, (b) u_2 Shell Model

4. SIMULATION OF CONNECTION

To look into the performance of those connections, including the surface contact and springs between segments and rings, and to find out how they work properly and how much they can affect the results, several cases of different damaged conditions (remove surface contact or spring somewhere) will be analyzed.

4.1 Effect of Surface Contact

Table 1 Damaged Cases when Surface Contact is Removed

Connect Type	with all contact (health)	without all contact	without ring contact	without segmental contact
Lateral Extension (mm)	5.90	11.6	5.91	10.8
Vertical Contraction (mm)	5.22	14.5	5.22	13.5
Damage Coeff. 1	1.00	1.97	1.00	1.83
Damage Coeff. 2	1.00	2.77	1.00	2.59

The first damaged condition is that surface contact in somewhere is removed, while all the spring connections are kept. 4 cases are considered: 1) with all surface contact, namely, health; 2) all the surface contact has been removed; 3) only the surface contact between rings is removed; 4) only the surface contact between segments is removed.

Two deformation value, lateral extension and vertical contraction, are used here as damage index. All cases are under the same earth pressure load. The results are shown in Table 1, where the Damage Coeff. 1&2 are the ratio of each case's lateral extension/vertical contraction compared to those of first case (health case) respectively. A larger value the Damge Coeff. 1&2 is, a severer damaged condition it represents. From Table 1 we can see that removing all the surface contact will bring a serious damaged condition. It will amplify the lateral extension for 2 times and vertical contraction for nearly 3 times as before. However, only removing the surface contact between rings seems will not affect too much. But if no segmental contact is considered, then the damaged level is almost the same with the one when they all gone.

From this table, we find that the surface contact between segments (annular) plays a much more important role compared to those between rings (longitudinal), under a symmetric and axial-even loading. The surface contact on the interfaces of every two segments supports the tunnel structure to withstand the vertical and lateral (in-plane) earth pressure with large percentage. Without it, the tunnel will deform more. On the other hand, the surface contact between rings cannot contribute too much even though the friction has been considered.

4.2 Effect of Segmental Spring

When the surface contact between segments is considered, most of the earth pressure load will be resisted by the surface contact, not the segmental springs. Only if all the contact is removed, left the spring type connection only, the function of those spring elements shows.

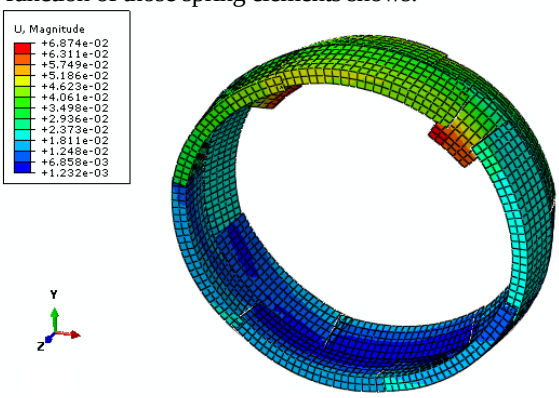


Figure 5 Deformation when Surface Contact and Segmental Spring are both removed

Figure 5 is the deformed shape of a 2-ring unit when both the surface contact and segmental springs have been removed. Without segmental springs, more local damage occurs, correspondingly with more rotational deformation, compared to the case with only no surface contact, which is generally a global deformation. Through analyzing more cases, among the 4 types of segmental springs, the annular and radial direction springs give most contribution to resist the earth pressure load, compared to the annular and rotational type.

4.3 Connection between Rings

In order to see the connection effect between rings, an offset loading needs to be applied. In this loading type, only one ring is loaded, lacking loading on another ring. Then, large shear force will occur on the interface between two rings, which will be resisted by the connection (surface contact and spring) between them.

Figure 6 shows the deformation of the 2-ring unit under this offset loading, without springs between them but with surface contact between them. Apparently, one ring keeps almost undeformed, while another deforms a lot. The connection between them almost failed when springs been removed, though the surface contact still there. This case has confirmed again that on the interface between two rings, the dominant connection is the spring element, not the surface contact. The surface contact may resist the axial load, but to the in-plane load, it cannot help much.

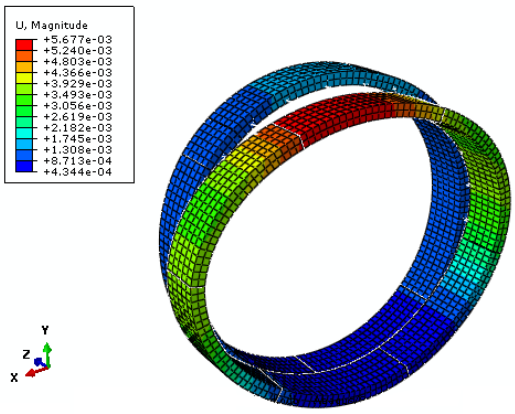


Figure 6 Deformation under Offset Loading without Springs between Rings but with Surface Contact between Rings

5. REBOUND ESTIMATION

This full-length 3-Dimensional solid FEM shield tunnel model can be applied in various engineering analyses. This chapter shows the application of this model in rebound effect estimation of shield tunnel.

5.1 Problem Statement

The rebound effect is the secondary upward deflection of shield tunnel caused by the removal of the covering earth above the tunnel, as shown in Figure 7. Usually this situation occurs when some new construction is developed above an existing tunnel. The removal of the earth pressure above will bring an unbalance in local area on the tunnel. The uplifting force below will cause a notable deflection on a short length of the tunnel. If the volume of the removed earth is large, some serious situation may happen.

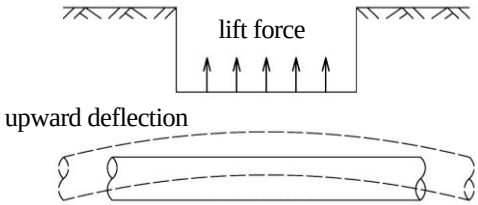


Figure 7 Rebound Effect due to Earth Removal

Since the impact of the rebound effect poses problem, it is necessary to estimate this effect according to soil properties, and the amount and depth of removed soil. Some empirical equations have been deduced based on monitoring or measurement after rebound (Okada et al. 2004).

With a field earth property assumption, the full-length model can soundly simulate the process of rebound, and give an estimation of final rebound value. In the following example, various cases of earth removal and the respective rebound effect will be calculated.

5.2 Results

The length of shield tunnel under consideration is 50m. In the middle 10m part, some volume of earth is removed. The condition of calculation is determined based on the site information (Railway Technical Research Institute 2007). The whole length of shield tunnel is assumed been built under 30m depth's earth, from which the elastic constant of ground spring can be set. Figure 8 shows one case of the rebound deformations. The inner-diameter of the tunnel is 6.4m, and the maximum rebound value in the center top is approximately 0.1m.

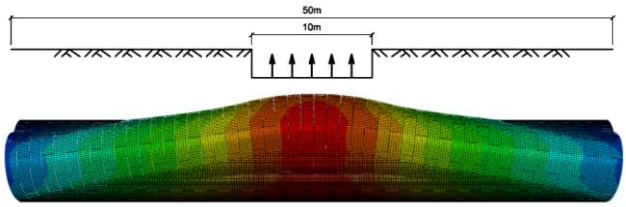


Figure 8 Simulation of Rebound Effect

After calculate 8 cases of different removed earth pressure from 57kN/m^2 to 413kN/m^2, the relationship between rebound values and removed earth pressure can be described by polynomial fitting.

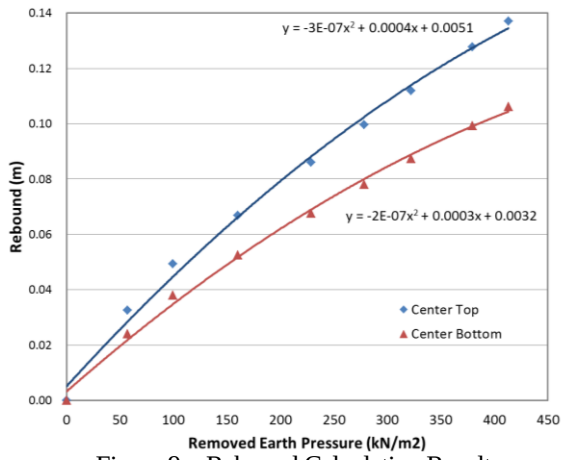


Figure 9 Rebound Calculation Results

Figure 9 shows the rebound value on center top and center bottom of the tunnel and their polynomial fitting. An approximate linear relation can be found between rebound and removed earth pressure, but small nonlinear also shows. More earth been removed, more rebound occurs, and more difference between top and bottom shows, which is due to the increasing vertical extension. Here we can see that the full-length solid model can successfully calculate the rebound effect with an earth environment assumption. In actual situation, this assumption can be substituted by soil investigation data and construction information. With this full-length FEM model, the estimation of rebound effect is feasible, and it is more accurate then empirical approach.

6. CONCLUSIONS

A 3-Dimensional full-length solid FEM model of shield tunnel has been developed. Different connection types between segments and rings have been considered. Through damage simulation, the performance of each connection type has been found, that is, on interface between segments in the circular direction, the surface contact will resist the in-plane load mostly; on interface between rings in the longitudinal direction, the spring element is much more effective than surface contact. Although the results are obtained by the calculation under some assumptions, they may be able to give advice to design and analysis work of shield tunnel. In the end, an application of this model has been shown, and a method of rebound estimation has been proposed.

Acknowledgements:

The authors acknowledge the support from the Tunnel Engineering Laboratory of Railway Technical Research Institute (RTRI). This support makes possible the research been completed.

References:

Lee, J.S. (2009), "An Application of Three-dimensional Analysis around A Tunnel Portal under Construction," *Tunnelling and Underground Space Technology*, **24**, 731-738.

Tsuno, K., Nakayama, T. and Kimata, H. (2012), "Basic Research on Analytical Method of Shield Tunnel in The Longitudinal Direction," *Proceedings of GeoKanto2012*, (in Japanese).

Tajima, H., Kishida, M., Fukai, N., and Saito, M. (2004), "Study on Shield Tunnel Construction Loads using a Three-dimensional FEM Model," *Proceedings of Tunnel Engineering*, **14**, 353-360 (in Japanese).

Wang, F., Huang, H., Soga, K., Li, Z., and Tsuno, K. (2012), "Deformation Analysis of a Tunnel with Concrete Segmental Lining Subjected to Ground Surface Loading using Novel Joint Model," *Proceedings of ITA World Tunnel Congress*, **38**.

Teachavorasinskun, S. and Chub-uppakarn, T. (2010), "Influence of Segmental Joints on Tunnel Lining," *Tunnelling and Underground Space Technology*, **25**, 490-494.

Koyama, Y., Matsumoto, Y. and Inaghaki, T. (1994), "Study on Shield Design Model Based on Shield Segment Loading Tests," *Proceedings of tunnel Engineering*, **4**, 187-192 (in Japanese).

Railway Technical Research Institute (2001), "Manual of Design Standard for Railway Shield Tunnels," 7-35 (in Japanese).

Okada, H., Nakamura, M., Kasai, Y., Kurihara, M., and Yamamoto, M. (2004), "Prediction for Behavior of Ground Heave and Existing Tunnel due to Open Cut," *JSCE*, **763**(63), 53-69.

Railway Technical Research Institute (2007), "Manual for Countermeasures of Urban Railway Structures against Adjacent Construction," 232-233 (in Japanese).

10CUEE CONFERENCE PROCEEDINGS
10th International Conference on Urban Earthquake Engineering
March 1-2, 2013, Tokyo Institute of Technology, Tokyo, Japan

CYCLIC TESTING OF ALUMINUM ALLOY CORE BUCKLING RESTRAINED BRACES (BRBS)

Cigdem Karatas[1] and Oguz C. Celik[2]

1) Ph. D. Candidate, Institute of Science and Technology, Istanbul Technical University, Istanbul, Turkey
2) Professor, Division of Theory of Structures, Faculty of Architecture, Istanbul Technical University, Istanbul, Turkey
cigdem.karatas@hotmail.com, celikoguz@itu.edu.tr

Abstract: Aluminum alloy BRBs could be preferable in new buildings or bridges where severe corrosion effects are expected. BRBs can also be used in existing steel or reinforced concrete frames for seismic retrofit purposes to achieve the required strength, stiffness, and ductility. To the best knowledge of the authors, aluminum alloy core and outer tube BRBs having specific details developed in this study are designed, produced, and cyclically tested for the first time in this area. Two aluminum alloy, almost full-scale BRB specimens (TURKBRACE BRB-AC1 and TURKBRACE BRB-AC3) use rectangular plates as the core material made of A5083-H111. The core is surrounded by an aluminum square tube infilled with a high strength grout as the buckling restraining system. Both bolted (weld-free) and welded end connections are used. Experimental results show that, cumulative energy dissipation can be significantly increased when weld-free BRBs are tested. The fabricated BRBs achieved the desired behavior while no global buckling occurred under inelastic displacement cycles. Compared to steel core BRBs, relatively symmetrical hysteretic curves are obtained in aluminum alloy core BRBs. As a result, aluminum alloy core BRBs with special details developed herein showed promise for use in new buildings/bridges or as a retrofitting technique in buildings/bridges that lack strength, stiffness, and ductility.

1. INTRODUCTION

Since steel moment frames did not show the expected performance during the 1994 Northridge and the 1995 Kobe earthquakes, new effective solutions which could reduce the destructive effects of earthquakes have been sought. Structural dampers of various types which dissipate seismic energy have beneficial results in this sense. Buckling Restrained Braces (BRBs), being a sort of mechanical damper, display a balanced hysteretic behavior by axial yielding under reversed cyclic tension and compression forces during major earthquakes. BRBs can be used in existing steel or reinforced concrete (RC) frames for seismic retrofit purposes to achieve the required strength, stiffness, and ductility. Implementation of BRBs in new building and bridge projects is increasing.

Experimental and numerical studies have been conducted to promote the application different types of BRBs. For example, Sabelli et al. (2003) analytically investigated the seismic response of BRB frames (BRBFs) considering a number of important parameters, such as ground motion characteristics and the structural configuration. Fahnestock et al. (2003) addressed global ductility demands of BRBFs and local ductility demands of BRBs by nonlinear time-history analyses, which were compared with BRBF Recommended Provisions. Later, numerical and experimental simulations of a large-scale BRBF were given by Fahnestock et al. (2007a, 2007b). Besides, a series of pseudodynamic tests of a full-scale, three-story, three-bay BRBFs using concrete-filled tube columns was performed by Tsai et al (2008a, 2008b). Takeuchi et al. (2008, 2012) proposed a simple method for predicting the cumulative deformation capacity and energy absorption capacities of BRBs under random amplitudes. Three real substructures (parts of an existing RC building upgraded by means of several metal-based innovative techniques including BRBs) are tested to calibrate numerical models by Mazzolani (2008). Usami et al. (2008) studied buckling prevention condition with a series of well-controlled experiments. Vargas and Bruneau (2009a, 2009b) proposed an alternative design approach for systems with metallic fuses. An experimental work was also conducted on a three-story frame designed with BRBs to verify the proposed design procedure. A series of performance tests and analyses are carried out by Usami et al. (2009) to clarify the requirements of high-performance BRBs for the damage controlled seismic design of steel bridges. Celik and Bruneau (2009, 2011) analytically investigated the best geometrical layout to maximize the dissipated hysteretic energy in ductile diaphragms with BRBs end diaphragms in straight and skewed steel bridges. Component tests were conducted by Zhao et al. (2012) to address the effect of brace end rotation on the global buckling behavior of pin-connected BRBs with end collars. To increase the efficiency of BRBFs, a novel connection where the gusset is only connected to the beam and is offset

from the column face is proposed and tested in a three-story frame under quasi-static loading by Berman and Bruneau (2009). Palazzo et al. (2009) and Tsai et al. (2012) proposed new types and configurations for steel BRBs. All of these researches have sped up the application of steel BRBs in building and bridge engineering. Mostly, the concepts of BRBs published or applied for patents are essentially similar and the BRB's core brace member is mostly manufactured of steel owing to its great hysteretic performance.

Aluminum is being used increasingly in a variety of structural engineering applications due to its superior characteristics such as low density, high strength-to-weight ratio, good corrosion-resistant, durability, recyclability properties, high strength similar to steel and excellent formability (e.g., extrusion). These characteristics are of particular significance in the design of lightweight and transportable BRBs, for which ease and speed of construction, low maintenance, and long service life are important considerations. When compared to steel core BRBs, aluminum alloy core BRBs are expected to dissipate seismic energy through stable, relatively symmetrical compression-tension inelastic cycles. These considerations motivated the research presented in this paper that was addressed to study a special and unique aluminum alloy BRB, to be used for the aim of improving traditional steel BRB durability in corrosive environments.

Aluminum alloy core BRB is a relatively recent development in the field of BRB technology. Limited studies are present for the development of aluminum alloy core BRBs. For example, a series of low-cycle fatigue tests were conducted by Usami et al. (2012) to address the performance of the all-aluminum alloy BRB which has an aluminum core is separated by the restraining member by a small gap without mortar. Several experiments on welded and bolt-assembled aluminum alloy BRBs are performed. Extruded aluminum alloy BRBs were produced and tested to address their low-cycle fatigue performance and to evaluate the effect of stoppers which were used to prevent the slip-off movement of the restraining members (Wang et al. 2013).

To the best knowledge of the authors, two aluminum alloy core and outer tube BRBs (TURKBRACE BRB-AC1 and TURKBRACE BRB-AC3) having the same yield strength and simple end connection details developed in this study are designed, produced, and cyclically tested for the first time in this area as an alternative to commercially available BRB types in the U.S.A. and Japan (Karatas and Celik 2011, 2012, Karatas 2012). Examining the possible superiority of aluminum alloy BRBs that are developed herein is considered to be of importance in terms of earthquake engineering research and design applications. Reversed cyclic quasi-static loading tests were carried out in the Structural and Earthquake Engineering Laboratory (STEEL) at the Technical University of Istanbul. An unique strain-gauge placement configuration is also suggested and tested in order to measure strains and yield strength of the aluminum alloy core as precisely as possible. A displacement loading protocol proposed by the Seismic Provisions for Structural Steel Buildings, AISC-341 (2010) was used for all BRB tests. Details of the test set-up, details of specimens, cyclic testing of specimens, experimental observations, and conclusions are summarized.

2. EXPERIMENTAL PROGRAM

2.1 Test Set-up

A versatile test set-up composed of a steel L frame was previously constructed for cyclic testing of classical braces and was designed to accommodate different bracing sizes and lengths (Fig. 1, Haydaroglu at al. 2011). Using high safety factors, the test set-up was designed to remain elastic under the maximum actuator force. The steel grade used for testing set-up was S275JR. Loads were applied by a computer-controlled MTS hydraulic actuator, capable of producing up to 250kN horizontal loading. Displacement capacity of the actuator is ±300mm. Displacement-controlled testing was carried out via LVDTs mounted on the column face at the same height with the actuator. All specimens were designed well less than the capacity of the actuator. The specimens were tested a 38-degree diagonal bracing configuration with the steel foundation beam.

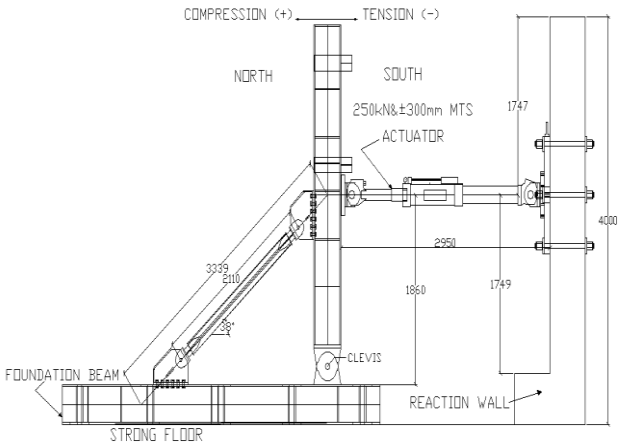


Figure 1 Test Set-up for specimens

2.2 Material Characteristics

In order to exactly determine the mechanical properties of aluminum alloy core materials from which the BRBs were produced, numerous tensile test specimens (coupons) were prepared in prototype samples according to the recommended standard (ASTM-E8/E8M-09, 2009). There are two types of aluminum alloys, A5083-H111 (nonheat-treated) and A6061-T6 (heat-treated and then artificially aged), used to manufacture the BRB's specimens considered in this work. 5xxx series aluminum alloy (namely A5083-H111 and is produced by adding magnesium, resulting in strong, corrosion resistant, and high welding strength alloy) is used one of the two BRBs. The second BRB was a 6xxx series aluminum alloy (namely A6061-T6 and contains magnesium and silicon and has a

good corrosion resistance and strength). Silicon provides excellent fluidity, so these alloys are well suited to intricate castings (Kissell and Ferry 2002).

Stress-strain relations of two tensile coupon test specimens, used in production of aluminum alloy core BRBs, are shown in Figure 2. Post-yield strain-gauges (namely TML-YFLA-10-3L with a gauge factor of 2.1) were used to determine the exact values of the yielding points, ultimate strength and strains as well as and the modulus of elasticity of the material.

The average coupon test results of the specimens are listed in Table 1. The yield strength of the BRB core coupons was calculated using a 0.2% yield strain offset, since aluminum alloy had no definite yield plateau. $F_{ysc}^{0.2}$ is the 0.2% yield strength/stress, ε_0 is the strain equal to $0.8\varepsilon_y^{0.2}$ for A5083-H111 and $0.9\varepsilon_y^{0.2}$ for A6061-T6, F_{ysc}^{0} is the strength/stress corresponding to the strain ε_0, F_u is the ultimate tensile strength, ε_u is the total tensile strain at fracture. The Poisson's ratio was obtained as ν=0.32~0.33. Prior to testing, these material data were used in static pushover analyses of the specimens conducted using SAP2000 v14 (CSI 2009) to predict the load-displacement curves of the specimens.

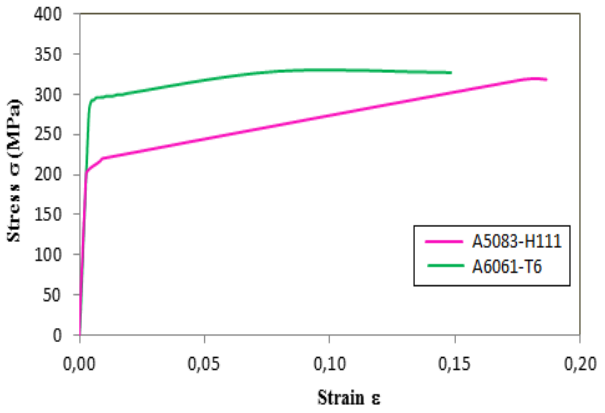


Figure 2 Stress-strain curves from the coupon tests

As per the results to be obtained from coupon test, the production was initiated by revising the structural calculations. Material test results contain valuable information on choosing the material classes to be used in designing the aluminum alloy BRBs. Failure mode of the welded aluminum alloy BRB (the core material is made of A6061-T6) is obviously affected by the ribs' welding under variable strain amplitudes. Although A6061-T6 aluminum alloy has notably higher yield stress than A5083-H111, another type of aluminum alloy core BRB (the core material is made of A5083-H111) was developed and tested.

Welding significantly reduces the strength of artificially aged aluminum alloys like A6061-T6 which has a tensile strength about 40% less than portions of the material not affected by welding. Aluminum alloy tubes of specimens are made of A6060-T66 hollow structural section.

Compression tests of the infill material revealed that the specified 7-day and 28-day mortar strength were 52.34MPa and 64.06MPa, respectively.

Steel bolts used are fully-tensioned, high-strength A490grade (10.9) in gussets-to-BRB and gussets-to-L frame connections. A manuel torque wrench was used to assure the minimum AISC specified slip-critical connection bolt pretension.

Table 1 Average material properties of aluminum alloys

Aluminum Alloy Series	E (GPa)	$F_{ysc}^{0.2}$ (MPa)	F_{ysc}^{0} (MPa)	$\varepsilon_y^{0.2}$ (%)	ε_0 (%)	F_u (MPa)	ε_u (%)
A5083-H111 (BRB-AC1)	73	182	145.6	0.27	0.22	314	17.5
5083-H111 (BRB-AC3)	73	177	141.6	0.27	0.22	318	20.0
A6061-T6	71	292	262.8	0.49	0.44	327	13.1

A5183 (ϕ=1.2mm) was used in all aluminum alloy welding process (AWSD1.2/D1.2M, 2008) as a special aluminum alloy solid MIG wire containing 5% Magnesium and 0.75% Manganese for improved weld strength and resistance to water.

Specially designed gusset-plates were used for the BRBs to avoid out-of-plane buckling. In order to have mobility for the replacement of BRBs, gusset-plates were designed as removable elements bolted to the test set-up. Rib stiffeners were added to gusset-plates to improve local and out-of-plane buckling capacity at the connection points. Higher safety factors were used in the design of gussets and all welds to achieve the desired ductile behavior of BRBs.

2.3 Details of Specimens

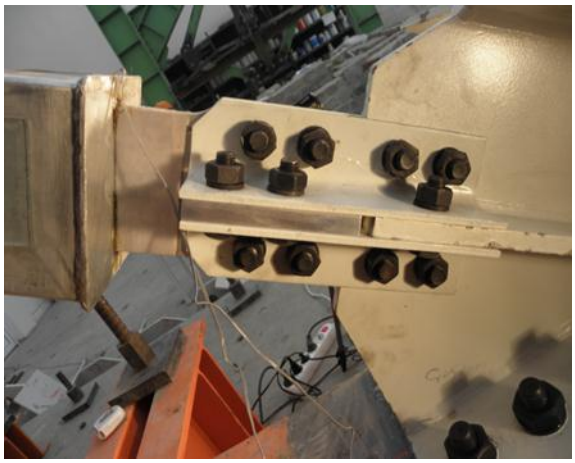
As an alternative to the existing BRBs, produced firstly under the patents of various firms in the U.S.A and Japan, two BRBs (TURKBRACE BRB-AC1 and TURKBRACE BRB-AC3) with aluminum alloy core and outer tube having the same yield strength, and simple edge details were designed, fabricated, and tested.

Aluminum alloy BRBs were designed to achieve the same yield strength for a better comparison of their cyclic performances. General views from the end connection of BRBs are given in Figure 3.

The geometrical parameters are summarized in Table 2. The length and width of the yielding portion of the brace are denoted by L_{ysc} and b_{ysc}, respectively. And likewise, L_{con} and b_{con}, are the length and width of the connection portion. The transition zone has a length of L_{tr} and a width of b_{tr}. The thickness of the cores is denoted by t.



(a)



(b)

Figure 3 General view from the end connection of BRBs (a)TURKBRACE BRB-AC1: Welded end connections, (b)TURKKBRACE BRB-AC3: Bolt-assembled (weld-free) cruciform end connections

Table 2 General geometrical parameters of the cores

Specimens	L_{ysc} (mm)	b_{ysc} (mm)	t (mm)	L_{con} (mm)	b_{con} (mm)	L_{tr} (mm)	b_{tr} (mm)
TURKBRACE BRB-AC1	1278	35	15	184	165	315	115
TURKBRACE BRB-AC3	1195	40		140	137	258	115

Two specimens have been produced according to the described details given below:

Almost full-scale BRBs specimens use rectangular plates (15mmx35mm for TURKBRACE BRB-AC1 and 15mmx40mm for TURKBRACE BRB-AC3) as the core material of A5083-H111 nonheat-treated aluminum alloy, which mostly expands at the ends to form a cruciform section. Both bolted (weld-free) and welded end connections are used to compare their performance under cyclic loading. Cross-sectional areas of the BRBs were selected based on the possible smallest core. For specimens, longer core yielding lengths were used (67% of the total braces length, $L_{ysc} \leq 1410$mm). The total lengths of BRBs are limited to 2275mm. Hole diameter for aluminum alloy connection plates is limited to no more than 0.7mm larger than the nominal steel bolt diameter.

The core is surrounded by an aluminum square tube infilled with a high strength non-shrink grout as the buckling restraining system. It is clear that the restraining member of the BRBs does not intend to withstand any axial force. For the cases when the yield load of the core exceeds the buckling load of the outer tube, brace fails in a global buckling mode. P_e/P_{ysc}, ratio of the Euler buckling load of the outer tube (P_e) to the yield load of the core (P_{ysc}), has to be checked as a criterion to guarantee the yielding of the core material. Watanabe et al. (1988) suggested that this ratio P_e/P_{ysc} should be over 1.5. Contributions of the mortar and the core to the buckling resistance of the brace have been neglected. Higher ratios of 12.7 and 14.2 were used in this work for TURKBRACE BRB-AC1 and TURKBRACE BRB-AC3, respectively.

An unbonding material is adopted for the interface of aluminum alloy core and high strength mortar. It is required to prevent excessive shear stress transfer, since it would reduce the longitudinal stress in the core thus impairing the energy dissipation. Also, this interface involves some clearance between the core and the mortar to allow the Poisson expansion of the core during compression. When the unbonding material is too thin, the thickness does not tolerate the expansion in the plate thickness direction of the core caused by its axial deformation; on the other hand, when the unbonding material so thick, local buckling of the core is possible. The problems mentioned above are solved in this study by using the unbonding material having a thickness at least 0.5 to 10% of the core plate thickness and width.

A key issue of the design is to ensure a proper sliding between the core and mortar to avoid relevant shear stress transfer. In the proposed BRBs, the sliding is ensured by a three-layer interface: the aluminum alloy core coated with polytetrafluoroethylene, lubricated with rubber grease, and wrapped with air bubbles. The purpose of the air bubbles is to provide shear flexibility, to guarantee an even sliding surface and to allow the transversal expansion of the core when compressed.

Aiming at improving the out-of-plane stiffness of the core in the unrestrained segment, cruciform section at both ends of the core is expanded by welding the same thickness plates. However, cyclic performance of this type of aluminum alloy BRBs was not satisfactory mainly due to the adverse effect of welding. Therefore, another type of aluminum alloy BRB (TURKBRACE BRB-AC3) was developed with multi-bolted end connections (Figure 4). The difference between two kinds of aluminum alloy BRBs is

that four steel angle members are bolt-assembled around the core to prevent weak axis buckling of the core in the unrestrained region and avoid the cyclic fatigue performance degradation caused by welding of the rib stiffeners.


(a)

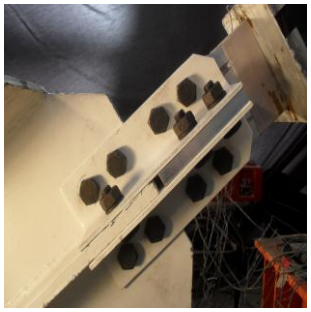

(b)

Figure 4 Bolted end connection (a) General view, (b) Side view

According to AISC-341 (2010), the axial yield strength of the BRBs, P_{ysc}, shall be determined as Eq. (1):

$$P_{ysc} = \beta\omega R_y F_{ysc} A_{sc} \quad (1)$$

where β and ω are the compression and strain-hardening adjustment factors, respectively, R_y is the ratio of the expected yield stress to the specified minimum yield stress, F_{ysc} is the specified actual yield stress of the core as determined from the coupon test, and A_{sc} is the net area of the core. The strain-hardening adjustment factor, ω, is calculated as the ratio of the maximum tension force (T_{max}) measured from the qualification tests to the yield force, P_{ysc}, of the test specimen. The compression strength adjustment factor, β, is calculated as ratio of the maximum compression force (P_{max}) to the maximum tension force of the test specimen. Value of β, at the point of maximum deformation, was obtained from previous studies (e.g., Meritt et al. 2003, and Lopez and Sabelli, 2004) as 1.15. Values of ω for TURKBRACE BRB-AC1 and TURKBRACE BRB-AC3 were determined, according to the strain-hardening properties of coupons, as 1.73 and 1.81, respectively. R_y was taken as 1.1 from Table I-6-1 from AISC-341 (2010).

Maximum displacement ductility of brace, μ_{max} was calculated as ratio of the maximum plastic displacement, Δ_u, to the yield displacement, Δ_{by}, and assumed as 7.5 for aluminum alloy BRBs.

Further details regarding the specimens can be found in Karatas and Celik (2012), and Karatas (2012).

2.4 Instrumentation

Instrumentation for the experimental part has been designed to measure global response of the steel test set-up and local performance of aluminum alloy BRBs. Seismic response of the column, foundation beam, and BRBs was obtained from strain gauges and LVTDs installed at critical points. In total, 21 strain-gauges were installed on TURKBRACE BRB-AC1, TURKBRACE BRB-AC3, and testing set-up. To monitor the internal forces and to verify that the loading frame remained elastic, a few gauges were used at the critical sections. Outer tubes were instrumented by 12 strain-gauges on the each side of the tube at the midpoint of the each side. The LVDT and strain-gauge layout was identical for both specimens (Figure 5). LVDT-T1E and LVDT-T1W were mounted to measure lateral drift of the frame. Several LVDTs were used to monitor accidental movement of the frame with respect to strong floor (e.g. at the mid-point of the column, on gusset plates, and on the foundation beam). The applied load was measured by a load cell installed in the actuator.

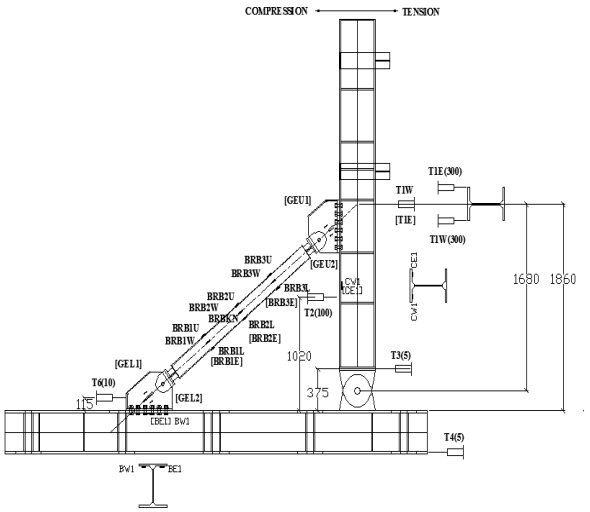


Figure 5 Instrumentation for TURKBRACE BRBs

2.5 Cyclic Testing

To characterize the hysteretic behavior of aluminum alloy BRBs and to develop bilinear analytical models, both BRBs were cyclically tested per the loading protocol proposed in AISC-341 (2010). The experiments are designed to reach the goals while accounting for the time, budget, and availability.

Quasi-static reversed cyclic testing in subassemblage configuration was carried out for each BRB based on the acceptance criteria given in AISC-341 (2010) loading protocol. Although additional cycles to satisfy the Office of Statewide Health Planning and Development (OSHPD) requirement for cumulative inelastic deformation are proposed, aluminum alloy BRBs did not arrive at the last cycles. Top horizontal displacement is related to the brace axial displacement and was taken as the displacement control parameter. Loading protocol used for the specimens and the vertical line normalized with respect to first axial yielding deformation of BRB, $\Delta_{by,}$ are depicted in Figure 6.

The calculation Δ_{by} was based on the deformation expected over the length L_1, which is the pin-to-pin distance of the core plate. Δ_{by} is estimated by Eq. (2).

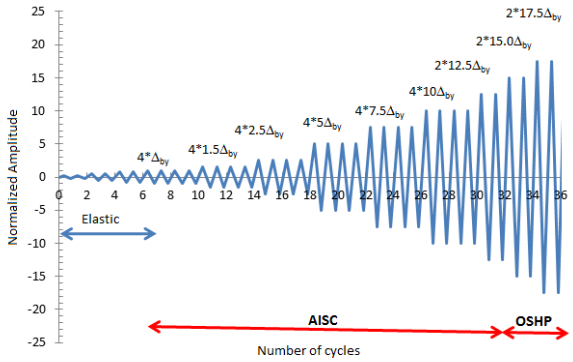


Figure 6 Test protocol normalized with respect to Δ_{by}

$$\Delta_{by} = \frac{P_{ysc} L_{ysc}}{EA_{sc}} + \frac{P_{ysc}\left[\dfrac{L_1 - L_{ysc}}{2}\right]}{EA_{tr}} \qquad (2)$$

Here, A_{tr} and E are the area of transition zone and modulus of elasticity for aluminum alloy BRB, respectively. Also, elastic deformation of the aluminum alloy core plate outside the yielding length on the each end of the core is included. The brace deformation at the design story drift, Δ_{bm}, was taken as $5\Delta_{by}$ as proposed by AISC-341 (2010). Also, it was proposed that the design story drift shall not be taken as less than 0.01 times the story height ($\Delta_{bm}/h>0.01$).

In the present study, the following loading sequence for the elastic cycles was applied to the specimens, where the deformation is the axial deformation of the aluminum alloy core plate:

(1) 2 cycles of the loading at the elastic deformation corresponding to $1/4\Delta_{by}$,
(2) 2 cycles of the loading at the elastic deformation corresponding to $2/4\Delta_{by}$,
(3) 2 cycles of the loading at the elastic deformation corresponding to $3/4\Delta_{by}$

Table 3 presents the details of loading sequence for the inelastic range cycles according to the proposed provision. Shaded rows were not used for aluminum alloy BRBs.

Table 3 Loading protocol for the inelastic cycles

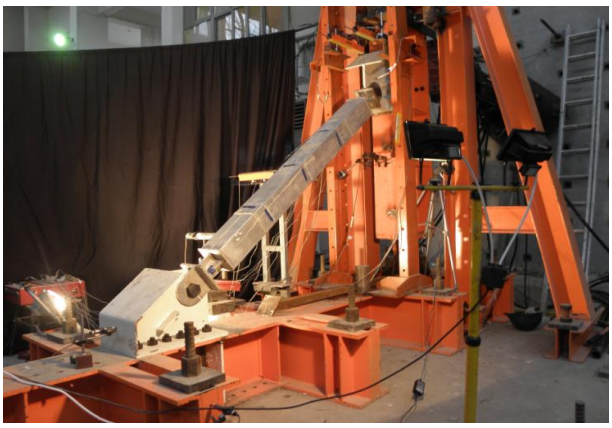
Cycles	Axial Displacement	η Cum. Inelastic Displacement	Estimated Axial Displacement (mm)	
			TURKBRACE BRB-AC1	TURKBRACE BRB-AC3
4	$1.0\Delta_{by}$	$0\Delta_{by}$	2.68	2.58
4	$1.5\Delta_{by}$	$4\Delta_{by}$	4.02	3.87
4	$2.5\Delta_{by}$	$16\Delta_{by}$	6.70	6.45
4	$5.0\Delta_{by}$	$48\Delta_{by}$	13.40	12.90
4	**$7.5\Delta_{by}$**	**$100\Delta_{by}$**	**20.10**	**19.35**
4	$10\Delta_{by}$	$172\Delta_{by}$	26.80	25.80
2	$12.5\Delta_{by}$	$218\Delta_{by}$	33.50	32.25
2	$15\Delta_{by}$	$274\Delta_{by}$	40.20	38.70

Testing was terminated at $7.5\Delta_{by}$ displacement level since the brace fractured. Yield values of forces and displacements were analytically estimated by static pushover analyses using SAP2000 (2009), and were used to initially control the tests. However, the experimentally obtained values were used as test control parameters beyond the elastic range. These were determined at the onset of visible nonlinearity in the force-displacement curve, or by using the strain-gauge data that were obtained in the mid-section of core.

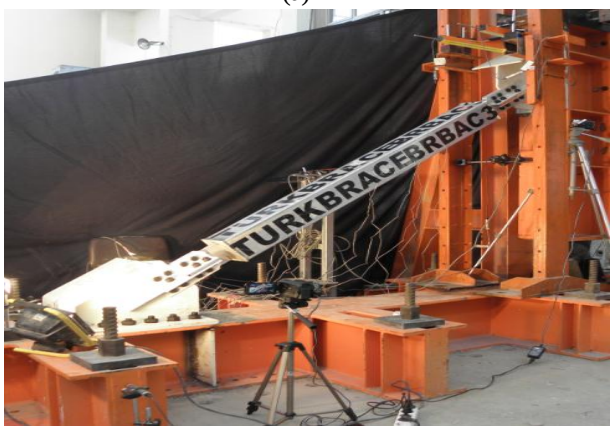
Figure 7 shows aluminum alloy BRBs installed in the test set-up and ready for testing. Two gusset-plates are placed at the both ends to ensure a proper anchoring to the test set-up.

For both specimens, load was firstly applied to have a lateral load producing tension in the brace. Both tests were performed until the brace fractured. The loading sequence for the static test was performed by deformation-controlled. Loading was applied slowly due to the limited actuator speed and the need to closely monitor the behavior of specimens.

Using experimental hysteresis, some behavioral characteristics of specimens such as the maximum strength in tension and compression cycles, η cumulative inelastic deformation, E_h cumulative hysteretic energy dissipation, and ξ_{effb} hysteretic damping values are summarized and compared in the next section.



(a)

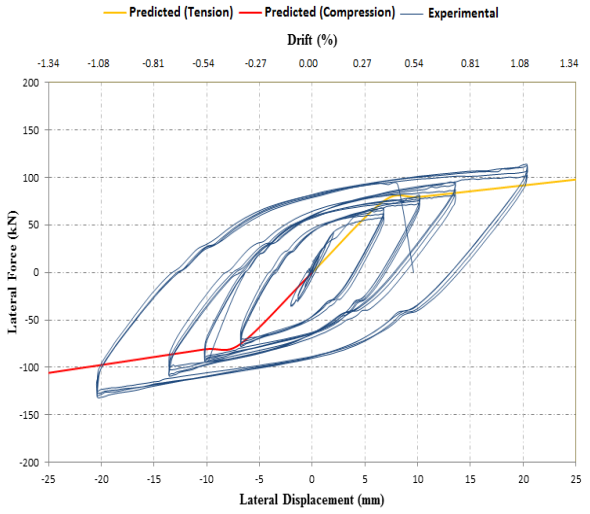


(b)

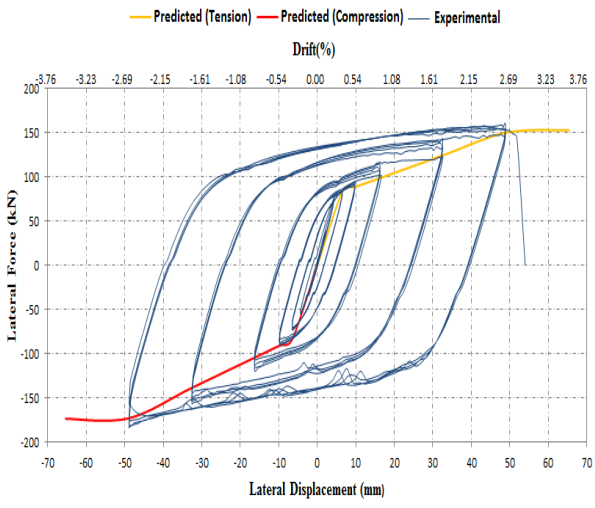
Figure 7 Overall view from the specimens prior to testing (a) TURKBRACE BRB-AC1 (b) TURKBRACE BRB-AC3

3. EXPERIMENTAL OBSERVATIONS

TURKBRACE BRB-AC3 performed well under the Standard Loading Protocol while a premature failure in TURKBRACE BRB-AC1 was experienced as the aluminum welds had an adverse effect on the failure mode. Up to core fracture, no fracture in welds, brace instability or no brace-to-end connection failures were observed in TURKBRACE BRB-AC3. Experimental horizontal force-horizontal displacement hysteretic curves representing the cyclic behavior and predicted pushover curves for specimens are given in Figure 8. Theoretical pushover curves are obtained using the axial plastic hinge properties proposed by FEMA 356 (2000). Plots showing the applied lateral load versus brace lateral displacement show stable, repeatable behavior with positive incremental stiffness. It was observed that elastic parts of hysteretic curves of the specimens obtained as a result of experimental study were similar and close to the curves obtained with coupon test results.



(a)



(b)

Figure 8 Experimental hysteretic curves and predicted pushover curves for specimens (a) TURKBRACE BRB-AC1, (b) TURKBRACE BRB-AC3.

The force amplitude decreases after first cycles at each displacement step but tends to stabilize quite fast. This is possibly due to a progressive detachment between the core and mortar. Estimation of experimental success ratio in terms of yield strength and initial stiffness were over 90%. Experimental force-displacement hysteretic loops for the BRBs reveal that no slip between the aluminum alloy BRBs and gusset-plates occurred. Obtained peak values of Δ_{by}, ω, β, maximum strength in tension (T_{max}), maximum strength in compression (P_{max}), and drifts are summarized and tabulated in Table 4 and Table 5 for TURKBRACE BRB-AC1 and for TURKBRACE BRB-AC3, respectively. Shaded rows show the yield displacement cycles.

Table 4 Peak response quantities and behavioral characteristics of TURKBRACE BRB-AC1

Δ_{by} (mm)	T_{max} (kN)	P_{max} (kN)	β	ω	Drift (%)
±1.69	24.60	-22.00	0.89	0.37	0.09
±3.40	44.00	-40.00	0.91	0.66	0.18
±5.10	59.50	-59.50	1.00	0.89	0.27
±6.80	**63.26**	**-74.51**	**1.18**	**1.00**	**0.37**
±10.19	77.51	-90.73	1.17	1.23	0.55
±13.59	89.31	-104.32	1.17	1.41	0.73
±20.39	108.97	-127.95	1.17	1.72	1.10

Table 5 Peak response quantities and behavioral characteristics of TURKBRACE BRB-AC3

Δ_{by} (mm)	T_{max} (kN)	P_{max} (kN)	β	ω	Drift (%)
±1.63	21.00	-20.00	0.95	0.25	0.09
±3.26	41.00	-32.00	0.78	0.49	0.18
±4.89	59.50	-54.50	0.92	0.70	0.26
±6.52	**84.50**	**-71.25**	**0.84**	**1.00**	**0.35**
±9.78	92.50	-87.50	0.95	1.09	0.53
±16.30	108.75	-113.75	1.05	1.29	0.88
±32.60	132.50	-149.25	1.13	1.57	1.75
±48.90	153.25	-174.00	1.14	1.81	2.63

Among the aluminum alloy BRBs, the highest tension adjustment factor at the maximum displacement level was obtained as ω=1.81 in TURKBRACE BRB-AC3. Also, the reached maximum tension and compression capacities are +153.25kN and -174.00kN, respectively. For TURKBRACE BRB-AC1, the reached maximum tension and compression capacities are +108.97kN and -127.95kN, respectively. Out-of-plane displacement of mid-span of TURKBRACE BRB-AC3's outer tube was measured between -2.82mm~+0.44mm. These values prove that out-of-plane

buckling was effectively prevented during the tests.

Out-of-plane displacement of mid-span of TURKBRACE BRB-AC1's outer tube was measured between -1.48mm~+1.24mm. For all inelastic cycles, in both specimens, the ratio of maximum compression force to the maximum tension force (i.e. β) did not exceed 1.3 for the specimens.

4. DISSIPATED HYSTERETIC ENERGY and EQUIVALENT DAMPING RATIOS

For any cycle, total area under the experimentally obtained hysteretic curve gives the dissipated energy through inelastic behavior. Since the cumulative energy dissipation is a useful measure of the seismic efficiency of a structural system, these values were calculated, and the variation of cumulative energy dissipation with cumulative number of cycles is plotted in Figure 9 as comparison for aluminum alloy BRBs having various end connection details.

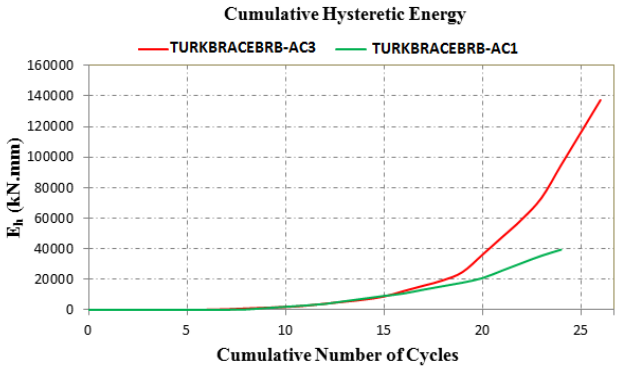


Figure 9 Comparison of cumulative energy dissipation

Numerical values of the cumulative hysteretic energy E_h and cumulative inelastic deformation η achieved by each specimen are summarized in Table 6.

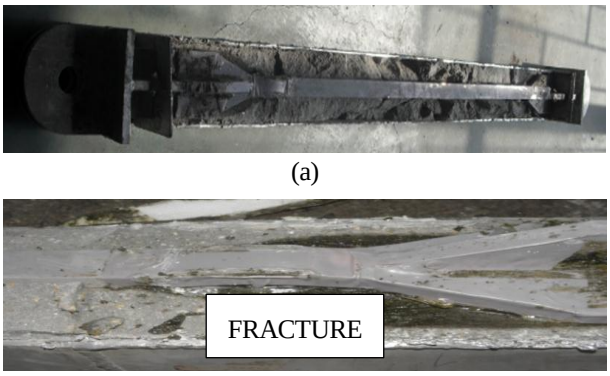
Table 6 Hysteretic energy and cumulative inelastic deformation

Specimens	Cumulative Inelastic Deformation η	Hysteretic Energy E_h (kN.mm)
TURKBRACE BRB-AC1	$48\Delta_{by}$	39,443.33
TURKBRACE BRB-AC3	$100\Delta_{by}$	137,301.40

Note that TURKBRACE BRB-AC1 core plate fractured at the transition zone from the yielding section to the cruciform section (elastic part) mainly due to the presence of heat affected zone (HAZ). η, maximum value of cumulative inelastic deformation was obtained to be $100\Delta_{by}$ in TURKBRACE BRB-AC3. Note that AISC-341 (2010) requires the braces to achieve a cumulative inelastic axial deformation of at least $200\Delta_{by}$ before failure during BRB component testing. However, for an experimental testing method as followed in this study, cumulative inelastic deformation of $200\Delta_{by}$ is not required. The most common method for defining equivalent damping ratio is to equate the energy dissipated in a cycle of the braces (Chopra, 2001). The computed values of equivalent damping ratios, ξ_{effb}, were obtained between 8.29%~32.56% for TURKBRACE BRB-AC1, and 8.10%~42.85% for TURKBRACE BRB-AC3. Maximum value of ξ_{effb} is taken as a representative value of equivalent damping. The maximum values were obtained at 0.55% and 2.63% drift ratios for BRB-AC1 and for BRB-AC3, respectively. Since ξ_{effb}, is greater than 15% for both specimens, the tested aluminum alloy BRBs can be classified as Energy Dissipating Devices (EDD) as per EN 15129 D.1 (2010).

5. DAMAGE DETECTION

Both specimens were disassembled by cutting them in half longitudinally and removing the fractured aluminum alloy core after failure. TURKBRACE BRB-AC3 fractured in the middle of yielding zone (Figure 10 and Figure 11).



(a)

(b)

Figure 10 Disassemble of TURKBRACE BRB-AC1 (a) General view (b) Fracture around the Heat-Effected-Zone (HAZ)



(a)

(b)

Figure 11 Disassemble of TURKBRACE BRB-AC3 (a) General view (b) Visible residual plastic deformation and typical buckling waves

The elastic transition zones at both ends of the aluminum alloy cores showed no damage or impairment; therefore it was safe to conclude that these parts remained elastic during the tests. No cracks or damage was apparent on the surface of the mortar that shall be separated from aluminum alloy core by the air gap. This leads to the conclusion that the mortar casing was not carrying axial loads, thus it was effectively decoupled from aluminum alloy cores. Typical buckling waves are shown in Figure 11a,b.

6. CONCLUSIONS

Two energy dissipative aluminum alloy BRBs having the same yield strength and simple edge details have been designed fabricated and cyclically tested. All experiments were conducted to failure of BRBs.

Based on the test results presented herein, the following conclusions and observations can be drawn from this work:

- TURKBRACE BRB-AC3 with bolted end connection details, performed well under the Standard Loading Protocol, and no premature fracture, brace instability or brace end connection failures were observed. However, TURKBRACE BRB-AC1 with welded end connection details experienced a lower fracture life mainly due to the heat affected zone (HAZ).
- Both tests showed that, in general, the devices performed properly, without relevant shear stress transfer to the casing and with stable hysteretic behavior.
- Plots showing the applied load versus lateral displacement revealed stable, repeatable behavior with positive incremental stiffness.
- For all displacement cycles greater than the yield deformation, Δ_{by}, the maximum tension and compression force were not less than the nominal brace yield force, P_{ysc}.
- For all inelastic displacement cycles, the ratio of the maximum compression force to the maximum tension force did not exceed 1.3 in aluminum braces (i.e. $\beta<1.3$).
- Experimental results show that, cumulative energy dissipation of aluminum alloy core BRBs can be significantly increased when weld-free BRBs are used in design.
- BRBs with high corrosion resistance requested by the industry were manufactured with aluminum alloy BRBs within the scope of this study.
- Compared to steel core BRBs, relatively symmetrical hysteretic curves are obtained in aluminum alloy core BRBs.

As a result, aluminum alloy core BRBs showed promise for use in new buildings/bridges or as a retrofitting technique in buildings/bridges that lack strength, stiffness, and ductility.

Acknowledgments:

This research was supported in part by the Scientific and Technological Research Council of Turkey (TUBITAK) and the Istanbul Technical University Research Projects Unit (ITU-BAP). Steel gusset plates and bolts were produced by CIMTAS. Aluminum alloy outer tubes were provided by FENIS. Teflon bands were provided by FIBERFLON. Technical assistance from the staff at Istanbul Technical University, Structural and Earthquake Engineering Laboratory (ITU-STEEL) and Bogazici University, Civil Engineering Department, Structures Laboratory are gratefully acknowledged and appreciated. However, any opinions, findings, conclusions, and recommendations presented in this paper are those of the authors and do not necessarily reflect the views of the supports.

References:

AISC (2010), "ANSI/AISC 341-10 Seismic Provisions for Structural Steel Buildings," *American Institute of Steel Construction*, Inc., Chicago.

ASTM E8/E8M-09 (2009), Standard Test Methods for Tension Testing of Metallic Material, ASTM International, 100 Barr-Harbor Drive, PO Box C700, Wast Conshohocken, PA 19428-2959.

Berman, J. and Bruneau, M. (2009), "Cyclic Testing of a Buckling Restrained Braced Frame with Unconstrained Gusset Connections," *ASCE Journal of Structural Engineering*, Vol.135, No.12, pp.1499-1510.

Celik, O. C. and Bruneau, M. (2009), "Seismic Behavior of Bidirectional-Resistant ductile end diaphragms with Buckling Restrained Braces in Straight Steel Bridges," *Engineering Structures Journal*, Vol.31, Issue 2, February, pp.380-393.

Celik, O. C. and Bruneau, M. (2011), "Skewed Slab-on-Girder Steel Bridge Superstructures with Bidirectional-Ductile End Diaphragms," *Journal of Bridge Engineering, ASCE*, Vol.16, No.2, March, pp.207-218.

Chopra, A. K. (2001), "Dynamics of Structures, Theory and Applications of Earthquake Engineering," *2nd Edition, Prentice-Hall*, Chapter 3, Response to harmonic and periodic excitations.

EN 15129 (2010), "Anti-seismic devices," *European Committee for Standardization* (CEN/TC 340).

Fahnestock, L.A., Sause, R., Ricles, J. M. and Lu, L.W. (2003), "Ductility Demands on Buckling Restrained Braced Frames under Earthquake Loading," *Earthquake Engineering and Engineering Vibration*, 2(2), pp.255–268.

Fahnestock, L. A., Ricles, J. M. and Sause, R. (2007a), "Experimental Evaluation of a Large Scale Buckling Restrained Braced Frame," *Journal of Structural Engineering* (ASCE), 133(9): 1205–1214.

Fahnestock, L. A., Sause, R. and Ricles, J. M. (2007b), "Seismic Response and Performance of Buckling Restrained Braced Frames," *Journal of Structural Engineering* (ASCE)," 133(9), pp.1195–1204.

FEMA-356 (2000), "Pre-standard and Commentary for the Seismic Rehabilitation of Buildings," *Prepared by SAC Joint Venture for the Federal Emergency Management Agency*, Washington, DC.

Haydaroglu, C., Taskin, K. and Celik, O. C. (2011), "Ductility Enhancement of Round HSS Braces Using CFRP Sheet Wraps," EUROSTEEL 2011, August 31- September 2, Budapest, Hungary.

Karatas, C. and Celik, O. C. (2011), "Design and Fabrication of Aluminum Alloy Core Buckling Restrained Braces (BRBs)," *Proceedings of the 4th Steel Structures Symposium*, Turkish Chamber of Civil Engineers (TMMOB), October 8-9-10, Istanbul, Turkey.

Karatas, C. and Celik, O. C. (2012), "Experimental and Numerical Investigation of Hysteretic Behaviors of Buckling Restrained Braces (BRBs) having Steel and Aluminum Alloy Cores," *Technical Report, No.110M779, TUBITAK-MAG*, Ankara, Turkey.

Karatas, C. (2012), "Design, Fabrication, and Cyclic Behavior of Steel and Aluminum Alloy Core Buckling Restrained Braces (BRBs)," *PhD Thesis*, Istanbul Technical University, Istanbul, Turkey.

Kissell, J. R. and Ferry, R. L. (2002), Aluminum Structures, JOHN WILLEY&SONS, INC., Second Edition, New York, ISNB 0-471-01965-8.

Lopez, W. A. and Sabelli, R. (2004), "Seismic Design of Steel Buckling-restrained Braced Frames," *Steel Tips, Structural Steel Education Council Technical Information & Product Service*, July.

Mazzolani, F. M. (2008), "Innovative Metal Systems for Seismic Upgrading of RC Structures," *Journal of Constructional Steel Research* , 64(7–8), pp.882–895.

Meritt, S., Uang, C. M. and Benzoni, G. (2003), "Subassemblage Testing of Star Seismic Buckling Restrained Braces," Technical Report No. TR-2003/04, *Department of Structural Engineering*, University of California, San Diego.

Palazzo, G., Lopez-Almansa, F., Cahis, X. and Crisafulli, F. (2009), "A Low-tech dissipative Buckling Restrained Brace," Design, Analysis, Production and Testing," *Engineering Structures*, Vol.31, pp.2152-2161.

Sabelli, R., Mahin, S. and Chang, C. (2003), "Seismic Demands on Steel Braced Frame Buildings with Buckling Restrained Braces,".*Engineering Structures,* 25(5), pp.655–666.

SAP2000 v14 (2009) Structural Analysis Program, *Computers and Structures Inc.*

Structural Welding Code-Aluminum (2008), ANSI/AWS D1.2/D1.2M:2008, *American Welding Society*, Miami.

Takeuchi, T, ASCE, A. M., Ida, M., Yamada, S. and Suzuki, K. (2008), "Estimation of Cumulative Deformation Capacity of Buckling Restrained Braces," *Journal of Structural Engineering*, Vol.134, No.5,May 1, pp.822-831.

Takeuchi, T., Matsui, R., Tada, T. and Nishimoto, K. (2012), "Out-of-plane Stability of Buckling Restrained Braces Including Their Connections," *15th World Conference on Earthquake Engineering*, 24-28 September, Lisbon, Portugal.

Tsai, K. C. and Hsiao, P. C. (2008a), "Pseudo Dynamic Test of a Full Scale CFT/BRB Frame—Part II: Seismic Performance of Buckling Restrained Braces and Connections," *Earthquake Engineering and Structural Dynamics*, 37(7), pp.1099–1115.

Tsai, K. C., Hsiao,, P. C., Wang, K. J., Weng, Y. T., Lin, M. L., Lin, K. C., Chen, C. H., Lai, J. W. and Lin, S. L. (2008b), "Pseudo Dynamic Tests of a Full Scale CFT/BRB frame-Part I: Specimen Design, Experiment and Analysis," *Earthquake Engineering and Structural Dynamics*, 37(7), pp.1081–1098.

Tsai, C. S., Su, H. C. and Chiang, T. C. (2012), "Huge Scale Tests of All-Steel Multi-curve Buckling Restrained Braces," *15th World Conference on Earthquake Engineering*, 24-28 September, Lisbon, Portugal.

Usami, T., Ge, H. and Kasai, K. (2008), "Overall Buckling Prevention Condition of Buckling-Restrained Braces as a Structural Control Damper," *Proc. the 14th World Conference on Earthquake Engineering*, Beijing, China.

Usami, T., Ge, H. and Luo, X.Q. (2009), "Experimental and Analytical Study on High-Performance Buckling Restrained Brace Dampers for Bridge Engineering," *3rd International Conference on Advances in Experimental Structural Engineering*, October 15-16, San Francisco.

Usami, T., Wang, C. L. and Funayama, J. (2012), "Developing High-performance Aluminum Alloy Buckling-restrained Braces Based on Series of Low-cycle Fatigue Tests," *Earthquake Engineering and Structural Dynamics*, Vol.41, pp.643-661.

Vargas, R. E. and Bruneau, M. (2009a), "Experimental Response and Design of Buildings with Metallic Structural Fuses.II," *Journal of Structural Engineering*, ASCE, April 2009/395, Vol.135, No.4, pp.394-403.

Vargas, R. E. and Bruneau, M. (2009b), " Analytical Response and Design of Buildings with Metallic Structural Fuses. I," *Journal of Structural Engineering*, ASCE, April 2009/387, Vol.135, No.4,pp.386-393.

Wang, C. L.,Usami, T., Funayama, J. and Imase, F. (2013), "Low-cycle Fatigue Testing of Extruded Aluminum Alloy Buckling-restrained Braces," Engineering Structures, Vol.46, pp.294-301.

Watanabe, A., Hitomi, Y., Saeki, E., Wada, A. and Fujimoto, M. (1988), "Properties of Brace Encased in Buckling-Restraining Concrete and Steel Tube," Proceedings of 9th World Conference on Earthquake Engineering, Tokyo-Kyoto, Japan.

Zhao, J., Wu, B. and Ou, J. (2012), "Effect of the Brace End Rotation on the Global Buckling Behavior of Pin-Connected Buckling-Restrained Braces with end Collars," *Engineering Structures*, Vol.40, pp.240-253.

10CUEE CONFERENCE PROCEEDINGS
10th International Conference on Urban Earthquake Engineering
March 1-2, 2013, Tokyo Institute of Technology, Tokyo, Japan

SENSITIVITY ANALYSES OF VARIATIONS ON SEISMIC RESPONSE VIA VISCOUS DAMPER PLACEMENT IN PLANAR BUILDING STRUCTURES

Ersin Aydin[1], Baki Ozturk[2], and Deniz Guney[3]

1) Assistant Professor, Department of Civil Engineering, Nigde University, Nigde, Turkey
2) Associate Professor, Department of Civil Engineering, Nigde University, Nigde,Turkey
3) Assistant Professor, Department of Architecture, Yildiz Technical University, Istanbul, Turkey
eaydin@nigde.edu.tr, bakiozturk@nigde.edu.tr, deguney@yildiz.edu.tr

Abstract: In this study, without using any optimization method, two main structural models that are five-storey and ten-storey planar building models with 43 different damper distribution sub-models are firstly constructed; and later analyzed to understand the suitable damper designs in terms of some structural response parameters such as story displacements, inter-storey drifts and storey absolute accelerations. El Centro earthquake acceleration record is used for time history analyses. Total damper capacity that is the sum of damping coefficient of the added dampers is chosen for each one of the main structural models. Then, a damper whose damping coefficient presents total damper capacity is passed through each storey level. In other damper designs, the total damper capacity is divided by the damper number, and more than one damper is placed on each storey sequentially and is passed on the height of the structure. The results of analyses point out that proper damper distribution relatively changes in terms of different response parameters. Suitable damper designs determined according to any performance parameter from the time history analyses are verified by sensitivity analyses. Sensitivity information is analytically derived based on transfer functions. The effects of distribution of the added dampers on performance functions are investigated by using sensitivity analysis.

1. INTRODUCTION

Since the exact nature of the external forces such as earthquake, wind and impact excitations that affect structures is unknown, structural control systems such as passive, active and semi-active systems have been developed to protect the civil engineering structures from dynamic vibrations. Passive energy dissipation devices have been used to absorb dynamic external effects in new structures or for the rehabilitation of old structures. Passive energy devices are inserted in the bare structures to improve damping, stiffness and strength. All such control systems are commonly used in practical applications in addition to designs using classical structural design methods. In recent years, various studies have investigated the proper placement of different types of control devices in order to obtain the best distribution by minimization or maximization of the defined structural responses.

A fluid viscous damper is one of the commonly known passive dampers. Fluid viscous devices that use a cylindrical piston immersed in a viscous fluid are extensively used in aerospace and military applications and more recently have been adapted for building applications as shown in Figure 1 [1].

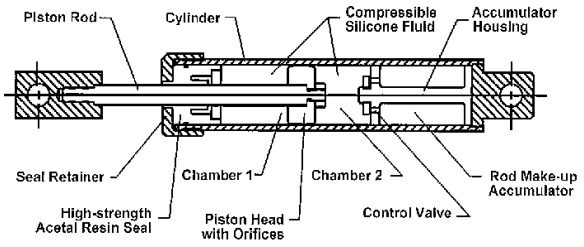


Figure 1. Taylor devices fluid damper [1]

The primary characteristics of these devices for structural applications are the linear viscous response achieved over a broad frequency range, insensitivity to temperature and compactness in comparison to the stroke and output force. The damper absorbs energy through movement of the piston in the highly viscous fluid. If the fluid is purely viscous, then the output force of the damper is directly proportional to the velocity of the piston. When this type of passive dampers began to be used in buildings, it was essential to ascertain the appropriate location

and number of dampers within the structure. However, there are a limited number of studies about damper allocation in structures.

The results of reducing the seismic response of multi-storey shear type buildings with first storey damping were presented by an optimization study [2]. The flexibility of the structure actually affects the optimal damping of the system and suitable objective functions were proposed for high buildings. Ashour and Hanson [3] conducted an interesting study on the optimal placement of visco-elastic dampers in relation to seismic excitation. An evaluation of the effect of added visco-elastic dampers on reducing the earthquake response of multi-storey steel frame structures was presented by Zhang and Soong [4].The seismic responses of simple building structures were examined in a study carried out by Hahn and Sathiavageeswaran [5] to assess the effects of different distributions and magnitudes of the damping derived from added visco-elastic dampers. A simple optimal design procedure was proposed by which the dimension and number of visco-elastic dampers could be determined and the results of the proposed method were also supported by experimental measurements [6]. An algorithm was introduced to find the optimum sets of storey stiffness coefficients and damping coefficients of dampers of an elastic planar shear building with viscous dampers [7]. Some of the optimal damper procedures based on active control theories were investigated to determine damper allocations [8], [9], [10], [11], [12] and [13]. Takewaki [14] devised an efficient method based on minimizing the sum of the amplitudes of the transfer functions of inter-storey drifts evaluated for the undamped fundamental natural frequency of a structural system together with a constraint on the sum of the damping coefficient of the dampers to obtain the optimal damper placement. A control strategy of seismic response of multi-storey building frames using optimally placed visco-elastic dampers was investigated using spectral analysis for narrow and broad band stationary random ground motions [15]. An efficient procedure, a steepest direction search algorithm, was devised to find the optimal damper distribution in a three dimensional shear building model [16]. A procedure for obtaining the optimal stiffness and damping distributions based upon the optimality criteria was presented by Takewaki [17]. An optimal damper placement method was proposed to minimize the dynamic compliance of a planar building frame [18]. An optimization approach based on a genetic algorithm was developed to find the optimal size and location of dissipation devices [19]. The proposed simplified sequential search algorithm (SSSA) for the optimization of damper configurations was simple and practical [20]. A simultaneous optimization procedure was presented to install both visco-elastic dampers and supporting braces in a structure [21]. Lavan and Levy [22] investigated a method for the optimal design of added viscous damping for an ensemble of realistic ground motion records and a constraint on an energy based global damage index for regular as well as irregular yielding shear frames. Cimellaro [23] defined top absolute acceleration as an objective function to find optimal damper placement and compared this with other methods. For planar building frames, a new objective function as base shear force based transfer functions was defined and the optimal damper location and size were determined [24].

To obtain an optimal solution of the damper distribution, we should define an objective function dependent on the structural response. An optimal solution upon damper placement relatively changes by the choice of objective function [23], [24]. There are some relevant investigations in the literature. To understand the effect of distribution of dampers, in the first step, it needs to be known which damper placement mitigates which response of the structures.

This study will help to understand the effects of viscous damper (VD) distribution in mitigating dynamic response of building structures due to seismic excitation. It needs to be pointed out how many and/or where the dampers should be supplemented. This study doesn't use any optimization method. In this study, without using any optimization method, two main structural models that are five stories and ten stories planar buildings, and 43 damper distribution sub-models are constructed and analyzed to understand the best suitable damper design in terms of some structural response parameters such as top displacement, inter-story drifts and top absolute acceleration. For each one of main structural model, a total damper capacity that is the sum of damping coefficient of the added dampers is chosen. Then, a damper whose damping coefficient presents total damper capacity is passed on each story level. In other damper designs, the total damper capacity is divided by the damper number and more than one damper is placed on each story sequentially and is passed on the height of the structure. In addition to time history analysis, the sensitivity analyses are performed for different damper placement according to the different structural response. The results of the time history analyses are compared with the sensitivity analyses for each model. The first order sensitivities are derived based on transfer functions for top displacement, inter-storey drifts and top absolute acceleration. It can be seen that the sensitivities of damper placement on structural response give us useful information for proper damper design among different damper placing options.

2. PLANAR BUILDING STRUCTURE WITH DAMPERS

The N-storey planar building frame as shown in Figure 2 is used to design the placement of the added dampers. In the case of no added dampers, the equation of motion for the model structure subjected to horizontal acceleration at fixed base is as follows:

$$\boldsymbol{M\ddot{u}(t) + C\dot{u}(t) + Ku(t) = -Mr\ddot{u}_g(t)} \quad (1)$$

where $\boldsymbol{u(t), \dot{u}(t), \ddot{u}(t)}$ represents displacement, velocity

and acceleration vector of the structural model, ***M***, ***C***, ***K*** represents the mass matrix, stiffness matrix and the structural damping matrix of the frame. ***r*** is the influence vector in terms of the direction of the base acceleration, $\ddot{u}_g(t)$ is the horizontal acceleration of ground motion. Let $\boldsymbol{U}(\omega)$ and $\ddot{U}_g(\omega)$ denote the Fourier Transform of $\boldsymbol{u}(t)$and $\ddot{u}_g(t)$, respectively. Eq. (1) is transformed to the following form using the Fourier transform:

$$(\boldsymbol{K} + i\omega\boldsymbol{C} - \omega^2\boldsymbol{M})\boldsymbol{U}(\omega) = -\boldsymbol{M}\boldsymbol{r}\ddot{U}_g(\omega) \tag{2}$$

Let ωdenote the circular frequency of excitation, i is $\sqrt{-1}$. If the added dampers are included in the equation of motion, the Fourier transform of the equation of motion converts to:

$$(\boldsymbol{K} + i\omega(\boldsymbol{C} + \boldsymbol{C}_{ad}) - \omega^2\boldsymbol{M})\boldsymbol{U}_{ad}(\omega) = -\boldsymbol{M}\boldsymbol{r}\ddot{U}_g(\omega) \tag{3}$$

where $\boldsymbol{C}_{ad}$is the added damping matrix which covers the design parameters, and $\boldsymbol{U}_{ad}(\omega)$ represents the Fourier transform of the displacement vector with added dampers. A new quantity defined by Takewaki [18] can be written as:

$$\hat{\boldsymbol{U}}(\omega) = \frac{\boldsymbol{U}_{ad}(\omega)}{\ddot{U}_g(\omega)} \tag{4}$$

If ω is taken as ω_1, the ground motion will have a harmonic excitation frequency which equals the fundamental natural frequency of the structure. Using Eq. (4), Eq. (3) can be rewritten as:

$$\boldsymbol{A}\hat{\boldsymbol{U}}(\omega_1) = -\boldsymbol{M}\boldsymbol{r} \tag{5}$$

Let $\hat{\boldsymbol{U}}(\omega_1)$ denote the transfer function vector of the displacements evaluated at the fundamental natural frequency of the structure and the matrix $\boldsymbol{A}$ which also includes the design variables ($c_1, c_2, \ldots, c_N$,), is presented as follows:

$$\boldsymbol{A} = \boldsymbol{K} + i\omega_1(\boldsymbol{C} + \boldsymbol{C}_{ad}) - \omega_1^2\boldsymbol{M} \tag{6}$$

where ***K***, ***M*** and ***C*** are prescribed. The construction of the added damping matrix ($\boldsymbol{C}_{ad}$) is the major objective of this study. Eq. (5) can be rewritten as:

$$\hat{\boldsymbol{U}}(\omega_1) = -\boldsymbol{A}^{-1}\boldsymbol{M}\boldsymbol{r} \tag{7}$$

The transfer function of the displacements has been derived by Takewaki [18]. The transfer function vector of the absolute acceleration at the fundamental natural frequency of the structure has been presented by Cimellaro [23] to find the placement of the optimal visco-elastic dampers as follows:

$$\hat{\ddot{\boldsymbol{U}}}(\omega_1) = -\boldsymbol{M}^{-1}(\boldsymbol{K} + i\omega_1\boldsymbol{C})\boldsymbol{U}(\omega_1) \tag{8}$$

The transfer function of inter-storey drifts at the first undamped natural frequency can be written as:

$$\boldsymbol{\delta}(\omega_1) = \boldsymbol{T}\hat{\boldsymbol{U}}(\omega_1) \tag{9}$$

where ***T*** is the transformation matrix that converts the displacements to the relative displacements [18].

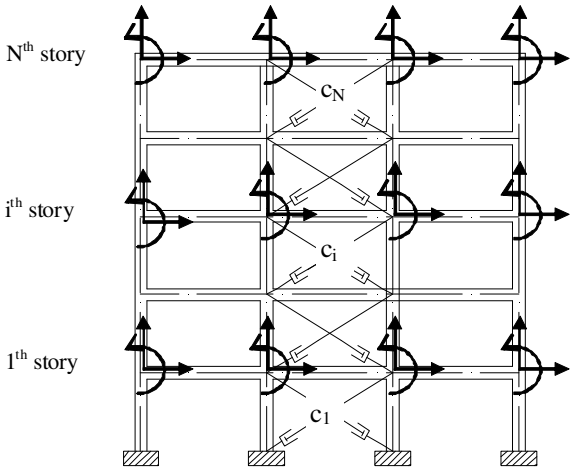


Figure 2. N-storey planar steel building with local coordinate systems

2.1 First Order Sensitivities of Structural Responses

If Eq. (5) is differentiated with respect to c_i as given below:

$$\frac{\partial \boldsymbol{A}}{\partial c_j}\hat{\boldsymbol{U}} + \boldsymbol{A}\frac{\partial \hat{\boldsymbol{U}}}{\partial c_j} = \boldsymbol{0} \qquad (j=1\ldots,N) \tag{10}$$

The first order sensitivity of $\hat{\boldsymbol{U}}$ is written as:

$$\frac{\partial \hat{\boldsymbol{U}}}{\partial c_j} = -\boldsymbol{A}^{-1}\frac{\partial \boldsymbol{A}}{\partial c_j}\hat{\boldsymbol{U}} \tag{11}$$

Eq. (10) and Eq. (11) have been derived by Takewaki [18]. The first order sensitivity of the transfer function vector of inter-storey drift multiplied by **T** is written as follows:

$$\frac{\partial \boldsymbol{\delta}}{\partial c_j} = -\boldsymbol{T}\boldsymbol{A}^{-1}\frac{\partial \boldsymbol{A}}{\partial c_j}\hat{\boldsymbol{U}} \tag{12}$$

The first order derivatives of the absolute accelerations

$\hat{\boldsymbol{U}}(\omega_1)$ at the first undamped natural circular frequency have been derived by a partial differential of Eq. (8) [23] as follows:

$$\frac{\partial \hat{U}}{\partial c_j} = -\boldsymbol{A}^{-1}\frac{\partial \boldsymbol{A}}{\partial c_j}\omega_1 \boldsymbol{U}(\omega_1) \tag{13}$$

The quantities of $\hat{U}_i$, δ_i and $\ddot{\hat{U}}_i$, which are given in Eqs. (7), (8) and (9) can be written as:

$$\hat{U}_i = Re[\hat{U}_i] + Im[\hat{U}_i] \tag{14}$$

$$\delta_i = Re[\delta_i] + Im[\delta_i] \tag{15}$$

$$\ddot{\hat{U}}_i = Re\left[\ddot{\hat{U}}_i\right] + Im\left[\ddot{\hat{U}}_i\right] \tag{16}$$

where $\hat{U}_i$, δ_i, and $\ddot{\hat{U}}_i$ are the transfer function values of the i^{th} storey displacement, i^{th} inter-storey drift and i^{th} storey absolute acceleration respectively in complex form. The first order sensitivities of the quantities $\hat{U}_i$, δ_i and $\ddot{\hat{U}}_i$, in Eqs. (11), (12) and (13) can be expressed as:

$$\frac{\partial \hat{U}_i}{\partial c_j} - Re\left[\frac{\partial \hat{U}_i}{\partial c_j}\right] + Im\left[\frac{\partial \hat{U}_i}{\partial c_j}\right] \tag{17}$$

$$\frac{\partial \delta_i}{\partial c_j} = Re\left[\frac{\partial \delta_i}{\partial c_j}\right] + Im\left[\frac{\partial \delta_i}{\partial c_j}\right] \tag{18}$$

$$\frac{\partial \ddot{\hat{U}}_i}{\partial c_j} = Re\left[\frac{\partial \ddot{\hat{U}}_i}{\partial c_j}\right] + Im\left[\frac{\partial \ddot{\hat{U}}_i}{\partial c_j}\right] \tag{19}$$

The absolute value of $\hat{U}_i$, δ_i and $\ddot{\hat{U}}_i$ can be written as:

$$\left|\hat{U}_i\right| = \sqrt{(Re[\hat{U}_i])^2 + (Im[\hat{U}_i])^2} \tag{20}$$

$$|\delta_i| = \sqrt{(Re[\delta_i])^2 + (Im[\delta_i])^2} \tag{21}$$

$$\left|\ddot{\hat{U}}_i\right| = \sqrt{(Re[\ddot{\hat{U}}_i])^2 + (Im[\ddot{\hat{U}}_i])^2} \tag{22}$$

If $\left|\hat{U}_i\right|$, $|\delta_i|$, and $\left|\ddot{\hat{U}}_i\right|$ are differentiated with respect to the j^{th} damping coefficient c_j, the first order sensitivity of the absolute value of transfer function amplitude of the i^{th} displacement [18], the i^{th} inter-storey drift [18] and the i^{th} absolute acceleration [23] are found as:

$$\frac{\partial\left|\hat{U}_i\right|}{\partial c_j} = \frac{1}{\left|\hat{U}_i\right|}\left\{Re\left[\hat{U}_i\right]\left(Re\left[\frac{\partial \hat{U}_i}{\partial c_j}\right]\right) + Im\left[\hat{U}_i\right]\left(Im\left[\frac{\partial \hat{U}_i}{\partial c_j}\right]\right)\right\} \tag{23}$$

$$\frac{\partial|\delta_i|}{\partial c_j} = \frac{1}{|\delta_i|}\left\{Re[\delta_i]\left(Re\left[\frac{\partial \delta_i}{\partial c_j}\right]\right) + Im[\delta_i]\left(Im\left[\frac{\partial \delta_i}{\partial c_j}\right]\right)\right\} \tag{24}$$

$$\frac{\partial\left|\ddot{\hat{U}}_i\right|}{\partial c_j} = \frac{1}{\left|\ddot{\hat{U}}_i\right|}\left\{Re\left[\ddot{\hat{U}}_i\right]\left(Re\left[\frac{\partial \ddot{\hat{U}}_i}{\partial c_j}\right]\right) + Im\left[\ddot{\hat{U}}_i\right]\left(Im\left[\frac{\partial \ddot{\hat{U}}_i}{\partial c_j}\right]\right)\right\} \tag{25}$$

2.2 Numerical Examples

To illustrate the effect of damper placement on planar steel building structures, two models which are 5-storey and 10-storey planar building structures are considered as shown Figure 3. The height of each storey is 4m, the span of each bay is 8m., Young modulus is $2.0*10^{11}$ N/m^2 in columns and beams. Shear deformation of members is neglected. Only bending deformation in beams, both bending and axial deformations in columns are considered. The critical damping ratio of steel structures is ξ=0.02 in the lowest undamped natural circular frequency. A lumped mass of 51'200 kg is placed on every interior node and a lumped mass of 25'600 kg is placed on every exterior node. Every interior node is assumed to possess a mass moment of inertia of $5.46*10^5$ kg.m^2, and every exterior node is assumed to possess a mass moment of inertia of $1.71*10^5$ kg.m^2. Structural member properties are shown in Table 1.

Table 1. Member properties of buildings

Models	Storey No	Beams		Columns	
		A(m^2) (10^{-4})	I(m^4) (10^{-5})	A(m^2) (10^{-4})	I(m^4) (10^{-5})
5-Storey	1st-2nd	756	383	756	383
	3rd-4th	683	353	683	353
	5th	365	205	365	305
10-Storey	1st-4th	756	383	756	383
	5th-7th	683	353	683	353
	8th-10th	365	205	365	305

The sums of damping coefficients of the dampers are chosen such as in Table 2. Total damping coefficients of the added dampers for each one of the models are equal to the values as shown in Table 2.

Table 2. Total damper capacity for the main models

Main Models	The sum of the damping coefficients of the added dampers (Ns/m)
5-Storey	$1.47*10^7$
10-Storey	$2.94*10^7$

It is possible to calculate the damping coefficient for a storey according to Eq. (26) given as below:

$$c = \frac{Total \quad Damper \quad Capacity}{Damper \quad Number} \tag{26}$$

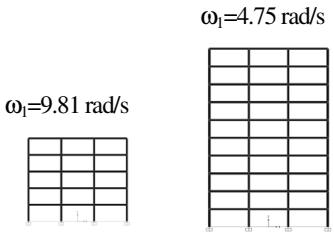


Figure 3. 5-storey and 10-storey model planar building frames

Initially, a damper is placed on the first storey. A damper whose damping coefficient presents the total damping capacity is moved on to the fifth storey level afterwards for the five storey building model. Then, multi damper placement models shown in Figure 4 are investigated. For 5-storey model structures as shown in Figure 4, time history analysis is performed by using El Centro (NS) ground motion record.

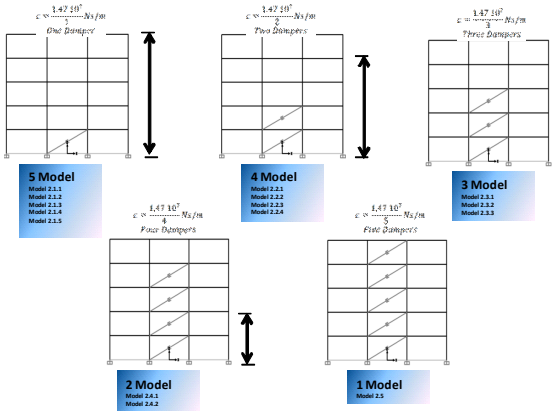


Figure 4. Sub models for 5-storey main planar building model

Figure 5 presents both the maximum story displacement profiles in top lines of the figures and the first order sensitivities of top displacement in the lower line. The sign of the sensitivities are changed by multiplying negative sign. It can be seen from these sensitivity figures that the sensitivities of top displacement according to the damping coefficients c_i of the 2nd and the 3rd stories are larger than the others in the case for without dampers. The best design in terms of both top displacement response and the sensitivities of the transfer function of top displacement is the model 2.2.2 (Dampers are uniformly placed to 2nd and 3rd storeys). It is observed that dampers should be distributed to the storeys where the inter-storey drifts are larger than in other storeys.

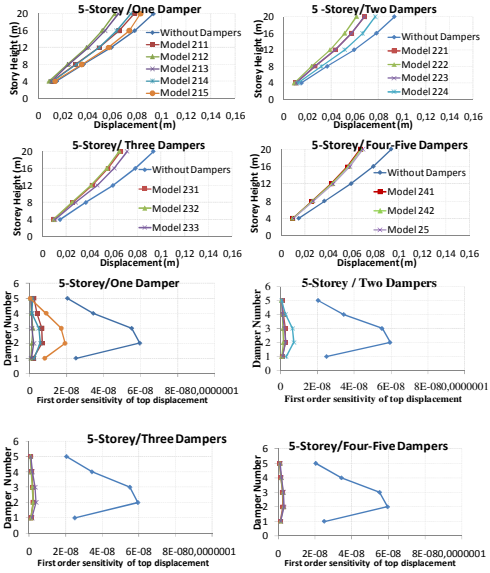


Figure 5. Storey displacement profiles and sensitivities of the top displacement according to the dampers for 5-storey planar building models

The best convergence among the damper designs also satisfy for the model 2.2.2 as shown in Figure 5. The maximum inter-story drift response and sensitivities of the first three inter-story drifts are plotted in Figures 6(a) and 6(b). For one damper case, the best design in terms of any inter-storey drift is either placement of a damper to that storey or placement of a damper to its neighboring storey.

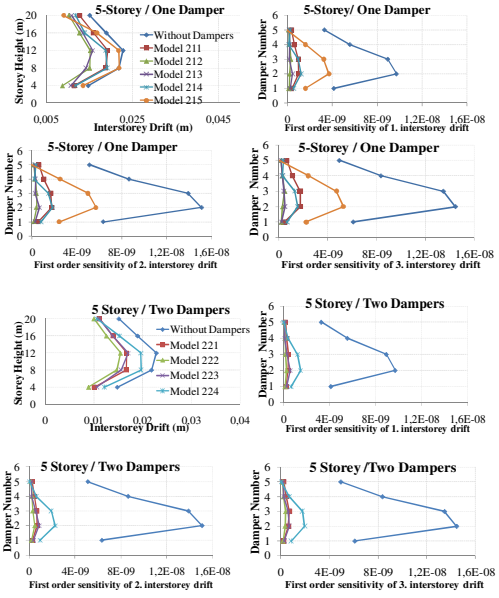


Figure 6(a). Interstorey drift profiles and sensitivities of the interstorey drifts according to the dampers for 5-storey planar building models

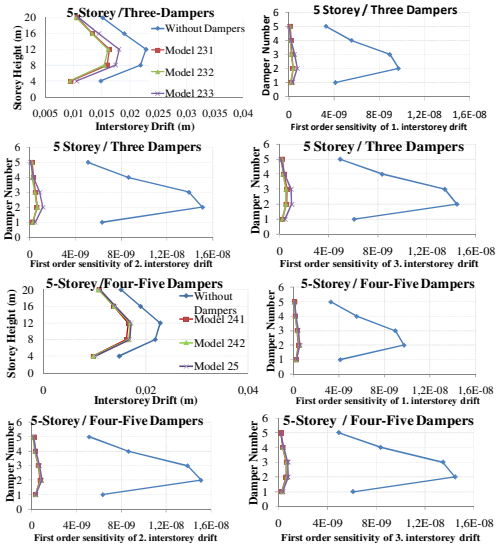


Figure 6(b). Interstorey drift profiles and sensitivities of the interstorey drifts according to the dampers for 5-storey planar building models

The best damper design in terms of top acceleration is the model 2.2.2 (Dampers are placed to 2nd and 3rd storeys). Figure 7 presents top absolute acceleration under El Centro earthquake ground motion and sensitivities of the acceleration. These sensitivity figures give us some information such that the 2nd and 3rd storeys are sensitive storeys in terms of damper placement.

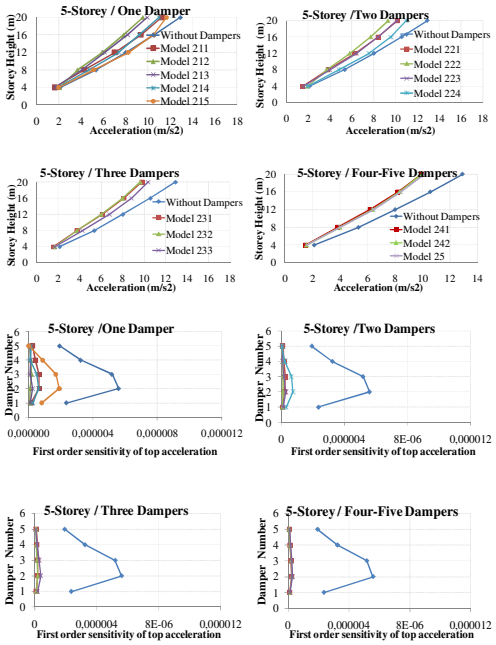


Figure 7. Storey absolute acceleration profiles and sensitivities of the top acceleration according to the dampers for 5-storey planar building models

The second main model is chosen as 10-storey planar building shown in Figure 3. The sub-damper placement models are constructed as given in Figure 8.

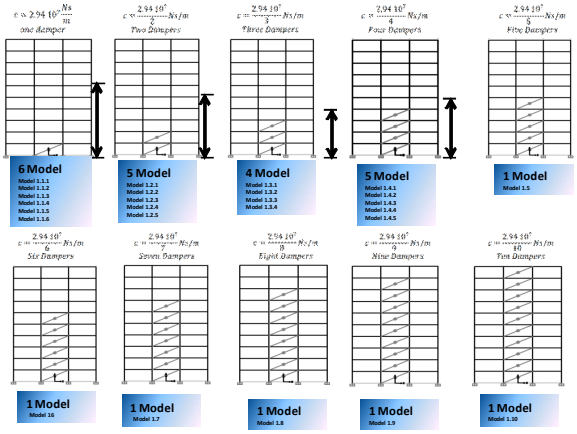


Figure 8. Sub models for 10-storey main planar building model

The results of earthquake analyses denote that the model 1.9 (Dampers are placed to the first nine storeys) and the model 2.2.1 (Dampers are placed to the 2nd and 3rd storeys) are better damper designs in terms of top displacement as shown in Figure 9.

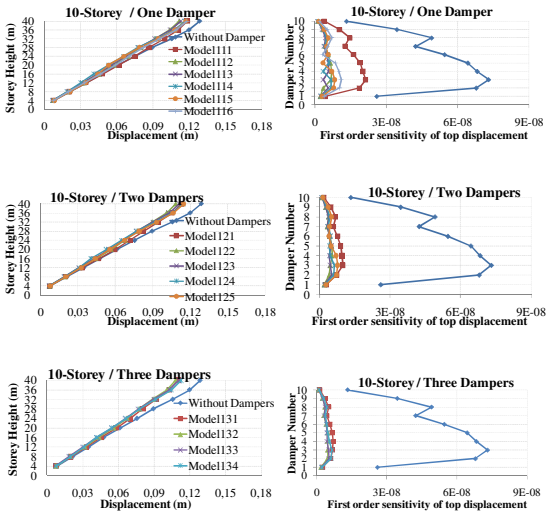


Figure 9. Storey displacement profiles and sensitivities of the top displacement according to the dampers for 10-storey planar building models

Dampers must be distributed to either the first nine storeys or to 2nd and 3rd storeys where the inter-storey drifts are large. If the dampers are placed to only 2nd and 3rd storeys, this damper design is preferred in terms of both good response and economical respect. As can be shown in Figures 9 and 10, the second and third storeys are sensitive storeys for placement of dampers.

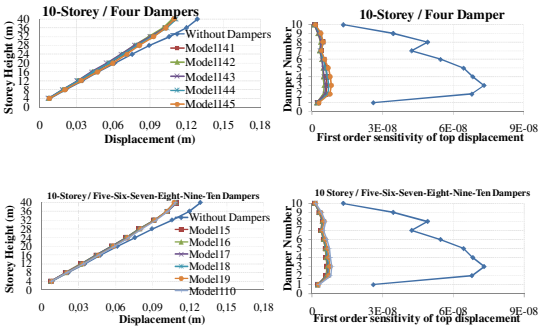


Figure 10. Storey displacement profiles and sensitivities of the top displacement according to the dampers for 10-storey planar building models

Figures 11(a) and 11(b) present the inter-storey drifts under El Centro earthquake and the inter-storey sensitivities for the first three inter-storey drifts. If a damper is placed on a storey, this damper design doesn't give us a good performance. This situation reveals the discontinuity in between sequential interstorey drifts, so it is not desirable. The second, third and fourth storeys are also sensitive storeys for placement of dampers. The amplitudes of sensitivities are also large in these storeys.

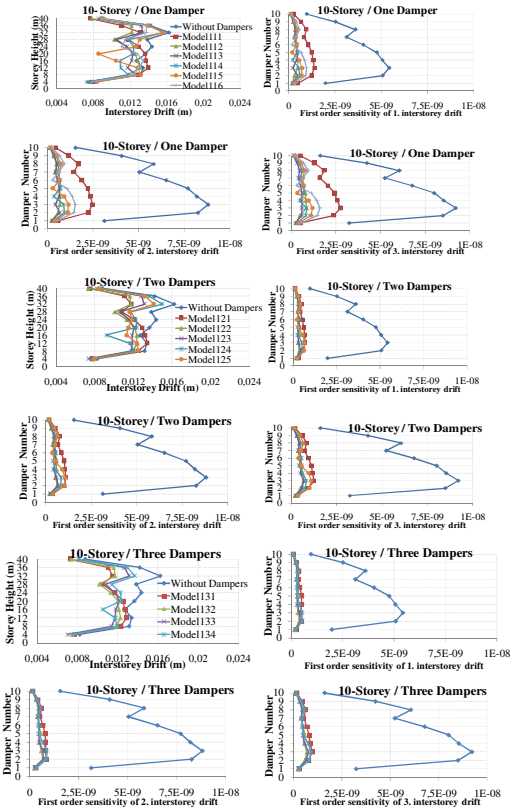


Figure 11(a). Interstorey drift profiles and sensitivities of the interstorey drifts according to the dampers for 10-storey planar building models

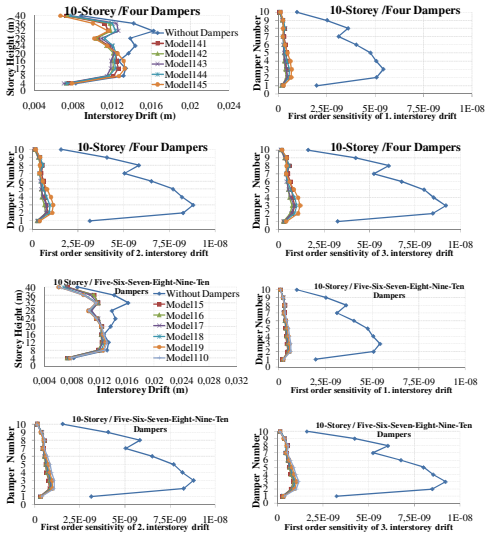


Figure 11(b). Interstorey drift profiles and sensitivities of the interstorey drifts according to the dampers for 10-storey planar building models

The absolute acceleration obtained from earthquake analyses and the top absolute sensitivities are plotted in Figures 12(a) and 12(b), respectively. The best design in terms of top acceleration is the model 1.10 (Dampers are placed to all storeys).

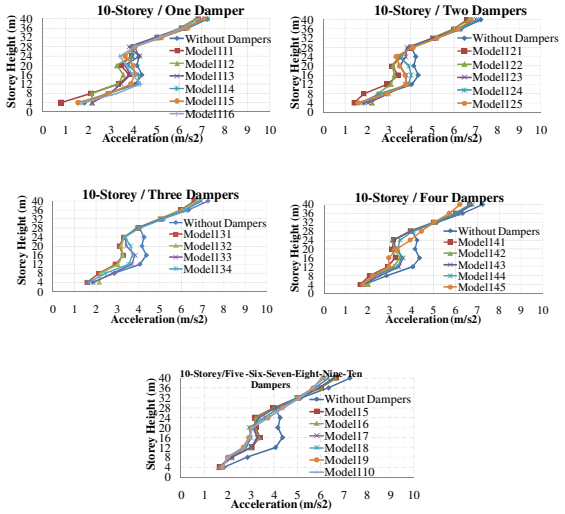


Figure 12(a). Storey absolute acceleration profiles according to the dampers for 10-storey planar building models

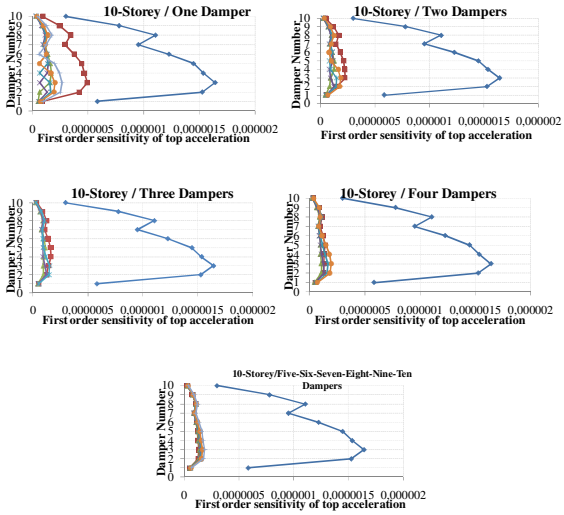


Figure 12(b). First order sensitivities of the top acceleration according to the dampers for 10-storey planar building models

For 5-storey building, the best design is the same both in terms of top displacement, top absolute acceleration and inter-storey drift values. For both of the two main models, the best design for top displacement occurs upon placement of dampers at storeys with high levels of inter-story drift. In the 5-storey building, the best design in terms of top displacement is the model 2.2.2 (Dampers are placed to 2nd and 3rd storeys). It is observed that dampers should be distributed to the storeys where the inter-storey drifts are larger compared to other storeys (The best damper design reduces the top displacement by 35 %.).

The best design in terms of any inter-storey drift is either placement of a damper to that storey or placement of a damper to its neighboring storey (Damper design reduces the inter-storey drifts by 33% to 40%). The best design in terms of top acceleration is the model 2.2.2 as in the case of top displacement (Dampers are placed to 2nd and 3rd storeys and top acceleration reduces by 28%).

In the 10 storey building, the best design in terms of top displacement is the model 1.9 (Dampers are placed to the first nine storeys and reduce the top displacement response by 20%). The model 2.2.1 (Dampers are placed to 2nd and 3rd storeys.) gives close solution to the solution of the best design. Dampers must be distributed to either the first nine storeys or to 2nd and 3rd storeys where the inter-storey drifts are large. The best design in terms of inter-storey drift is either placement of a damper to that storey or placement of a damper to its neighbor storey (Inter-storey drift response reduces by 15% to 28%). The best design in terms of top acceleration is the model 1.10 (Dampers are placed to all storeys and top acceleration is reduced by 17%)

3. CONCLUSIONS

This study investigates the effects of different damper placements on the different structural response parameters. In addition to time history analyses, sensitivity analyses are also performed to understand the effects of different damper distributions. The numerical results give us some information about damper placement as follows: 1) The potential locations for damper placements are some sensitive storeys where the inter-storey drifts are large. 2) One damper placement is not effective; even though it reduces the inter-storey drift of the storey it is located. 3) In the 5-storey building model, the best damper design brings on the best decrease in both top displacement and top absolute acceleration. 4) The increase in the building height causes the change on the damper designs for different response parameters. 5) If there are different damper distribution designs to select, the sensitivity analyses give beneficial information for proper damper allocation.

References:

Constantinou, M.C., Symans M.D. Experimental and analytical investigation of seismic response of structures with supplemental fluid viscous dampers. Report No NCEER-92-0032 National Center for Earthquake Engineering Research, Buffalo, New York, 1992.

Constantinou M.C., Tadjbakhsh I.G. Optimum design of a first storey damping. Computer&Structures 1983; 17(2):305-10.

Ashour S.A., Hanson R.D. Elastic response of buildings with supp. damping. Report UMCE 1987; 87-1.

Zhang R.H., Soong T.T., Mahmoodi P. Seismic response of steel frame structures with added viscoelastic dampers. Earthquake Engineering & Structural Dynamics 1989; 18:389-96.

Hahn G.D., Sathiavageeswara KR. Effects of added-damper distribution on the seismic response of building. Computer and Structures 1992; 43(5): 941-50.

Zhang R.H., Soong T.T. Seismic design of visco–elastic dampers for structural applications. Journal of Structural Engineering ASCE 1992; 118(5):1375-92.

Tsuji M., Nakamura T. Optimum viscous dampers for stiffness design of shear buildings. The Structural Design of Tall Buildings 1996; 5:217-34.

Hwang J.S., Min K.W., Hong S.M. Optimal design of passive viscoelastic dampers having active control effect for building structures. Trans. Korean Soc. Noise Vib. Eng. 1995; KSNVE 5(2):225-34.

Gluck N., Reinhorn A.M., Gluck J., Levy R. Design of supplemental dampers for control of structure. Journal of Structural Eng. ASCE 1996; 122 (12):1394-9.

Agrawal A.K., Yang J.N. Optimal placement of passive dampers on buildings using combinatorial optimization. Journal of Intelligent Material Systems and Structures 2000; 10(12):997-1014.

Agrawal A.K., Yang J.N. Design passive energy dissipation systems based on LQR methods. Journal of Intelligent Material Systems and Structures 2000; 10(20):933-44.

Loh C.H., Lin P.Y., Chung N.H. Design of dampers for structures based on optimal control theory. Earthquake Engineering & Structural Dynamics 2000; 29:1307-23.

Yang J.N., Lin S.,.Kim J.H., Agraval A.K. Optimal design of passive energy dissipation systems based on H∞ and H2 performances. Earthquake Engineering & Structural Dynamics 2002; 31: 921-36.

Takewaki I. Optimal damper placement for minimum transfer functions. Earthquake Engineering & Structural Dynamics 1997; 26:1113-24.

Shukla A.K., Datta T.K. Optimal use of viscoelastic dampers in building frames for seismic force. Journal of Structural Engineering 1999; 125(4):401-409.

Takewaki I. Non-monotonic optimal damper placement via steepest direction search.Earthquake Engineering & Structural Dynamics 1999; 28:655-70.

Takewaki I. Displacement-acceleration control via stiffness-damping collaboration. Earthquake Engineering & Structural Dynamics 1999; 28:1567-85.

Takewaki I. Optimum damper placement for planar building frames using transfer functions. Structural and Multidisciplinary Optimization 2000; 20, 280-7.

Singh M.P., Moreschi L.M. Optimal placement of dampers for passive response control. Earthquake Engineering & Structural Dynamics 2002; 31:955-76.
Lopez Garcia D., Soong T.T. Efficiency of a simple approach to damper allocation in MDOF structures. Journal of Structural Control 2002; 9:19-30.
Park J.H., Kim J., Min K.W. Optimal design of added viscoelastic dampers and supporting braces. Earthquake Engineering & Structural Dynamics 2004; 33:465-84.
Lavan O., Levy R. Optimal design of supplemental viscous dampers for irregular shear frames in the presence of the yielding. Earthquake Engineering & Structural Dynamics 2005; 34: 889-907.
Cimellaro GP. Simultaneous stiffness-damping optimization of structures with respect to acceleration displacement and base shear. Engineering Structures 2007; 29:2853-70.
Aydin E., Boduroglu M.H., Guney D. Optimal damper distribution for seismic rehabilitation of planar building structures. Engineering Structures 2007; 29:176-85.

10CUEE CONFERENCE PROCEEDINGS
10th International Conference on Urban Earthquake Engineering
March 1-2, 2013, Tokyo Institute of Technology, Tokyo, Japan

GENERALIZED OPTIMAL LOCATIONS OF VISCOUS DAMPERS IN TWO-WAY ASYMMETRICAL BUILDINGS

Jui-Liang Lin[1)], Manh-Tien Bui [2)], and Keh-Chyuan Tsai [3)]

1) Associate Researcher, National Center for Research on Earthquake Engineering, Taiwan
2) Song Da Construction and Investment joint stock company, Ha Noi, Vietnam
3) Professor, Department of Civil Engineering, National Taiwan University, Taiwan
jllin@ncree.narl.org.tw, bumatite@yahoo.com, kctsai@ntu.edu.tw

Abstract: This paper proposes a simple approach to the generalized optimal locations of linear viscous dampers in elastic two-way asymmetrical buildings under bi-directional ground excitations. The control target used in this optimization process is to maximize the average dissipation rate of the overall strain energy of the two-way asymmetrical building under the ground excitation of two bi-directional unit impulses. The proposed control target, referred to as the smeared damping ratio, is an intrinsic property of the building system. Two advantages of the proposed approach are appealing to engineering practice. First, the proposed approach does not require a complicated optimization algorithm. Second, due to the employment of an intrinsic property rather than a certain response parameter as the target performance index, the optimal damper locations resulting from the proposed approach are generalized, which are independent on the characteristics of input ground motions.

1. INTRODUCTION

Finding an effective method of placing viscous dampers in a building is a common issue in earthquake engineering practice. This issue may be considered from the viewpoint of optimal damper placement, with the constraint of either a given number of added dampers or a specified structural peak response. While investigating this issue, research into the literature found many published works that significantly contributed to this topic (Zhang and Soong 1992, Wu et al. 1997, Takewaki 1997, Agrawal and Yang 1999, Chen and Wu 2001, Lopez-Garcia 2001, Lopez-Garcia and Soong 2002, Singh and Moreschi 2002, Wongprasert and Symans 2004, Liu et al. 2005, Lavan and Levy 2006a, Lavan and Levy 2006b, Levy and Lavan 2006, Garcia et al. 2007, Levy and Lavan 2009, Aguirre et al. 2012). In much of these literatures, researchers usually first constructed the optimization problem in a formal mathematical format, and subsequently proposed suitable optimization procedures, *e.g.*, a sequential optimization procedure, heuristic search, a gradient-based approach or a genetic algorithm, to solve it. Liu et al. (2005) classified the previous studies into four categories, *i.e.*, parametric studies, analytical optimization, evolutionary approaches, and heuristic approaches, and carried out extensive literature reviews of these four categories. The efficiency and effectiveness of these powerful optimization procedures were validated by adopting different performance indices and considering various ground excitations. The performance indices were usually structural response parameters, such as inter-story drifts, absolute floor accelerations, *etc*. Liu et al. (2005) pointed out that the optimal damper configuration might be different if the performance index is selected differently.

Originating from the sequential search algorithm (Zhang and Soong 1992), Lopez-Garcia and Soong (Lopez-Garcia 2001, Lopez-Garcia and Soong 2002) proposed the simplified sequential search algorithm (SSSA), which appears to be the simplest way of optimizing the damper locations developed thus far. In the SSSA, the designer sequentially adds one damper at the location with the greatest engineering demand, which is determined by performing a response history analysis of the building with the previously added dampers. Obviously, the optimal placement of dampers resulting from the SSSA depends on the applied seismic ground motions. Takewaki (1997) proposed optimizing the damper placement by minimizing the sum of the amplitudes of the transfer functions of the inter-story drifts evaluated at the undamped fundamental natural frequency. Because the transfer functions are structural dynamic properties irrespective of the characteristics of input ground motions, the optimal damper placement resulting from Takewaki's approach (1997) was independent of the input ground motions. These works highlight the fact that an approach optimizing the damper locations without using complicated optimization theories and without depending on the seismic ground motion is attractive to engineering practice.

Due to architectural and commercial constraints, asymmetric-plan buildings are common among building

structures. Compared with symmetrical buildings, optimizing the damper placement in two-way asymmetrical buildings is more difficult, not only because of their complicated seismic responses, but also because of their various control targets and bi-directional ground excitations. The possible control targets for two-way asymmetrical buildings could be the response parameters at the four edges of the floor planes, or one rotational and two translational types of response parameters at the center of mass (CM). The response parameters may be inter-story drift, inter-story velocity, absolute floor acceleration, roof displacement, base shear, *etc*. As Liu et al. (2005) pointed out, even under the exertion of an ensemble of seismic ground accelerations or a white-noise ground motion, selecting a different response parameter as the control target is very likely to lead to a different optimal damper placement. Although response parameters are direct measures of the seismic performances of structures, differing optimal damper placements are usually an undesired engineering solution for building owners.

The aim of this research is to provide a simple approach to the generalized optimal locations of viscous dampers in two-way asymmetrical buildings. No complicated optimization algorithms or mathematical models will be adopted in this approach. For generalized optimal damper locations, an intrinsic property of the overall building system will be selected as the control target. Thus, the outcome of optimizing the damper locations will be independent of the response states of the building systems subjected to varied seismic ground motion inputs.

2. THE ENERGY-BASED APPROACH

2.1 The control target used in the proposed approach

It is useful to consider that there are some elastic oscillators with springs and dashpots. The only difference between these oscillators is the arrangement of their dashpots. The task is to find out which dashpot arrangement is the most effective at reducing the oscillators' vibrations. A very intuitive and simple way to do this is to excite these oscillators and then find out which oscillator reaches a stationary state first. This implies that the dissipation rate of the elastic strain energy is the generalized criterion for judging the effectiveness of the dashpot arrangement. Furthermore, to be shown later in this section, the dissipation rate of the elastic strain energy is correlated with the damping ratio, which is an intrinsic property of the building system. Thus, this study proposes to use the dissipation rate of the elastic strain energy, rather than a certain response parameter, as the control target for achieving the generalized optimal damper placement. In addition, due to the employment of an intrinsic property of the building system as the control target, the generalized optimal damper locations resulting from the proposed approach do not depend on the characteristics of input ground motions. Figure 1a shows the strain energy history of an elastic multistory two-way asymmetrical building subjected to a pair of unit impulses applied in the *x*- and *z*-horizontal directions, respectively. Figure 1a indicates that the dissipation rate of the elastic strain energy reflects the decrease of the peaks of the strain energy history.

When a single-degree-of-freedom (SDOF) oscillator is subjected to a unit impulse, its displacement response is the well-known unit impulse response function, denoted by $h(t)$:

$$h(t) = \frac{1}{m\omega_D} e^{-\xi\omega t} \sin(\omega_D t) \tag{1}$$

where m, ω, and ξ are the mass, vibration frequency, and damping ratio of the SDOF oscillator, respectively, and $\omega_D = \omega\sqrt{1-\xi^2}$. The unit impulse response function is the inverse Fourier transform of the frequency response function, which is a general dynamic property of the oscillator independent of the characteristics of the input excitations. The strain energy of the SDOF oscillator, denoted by E_S, is:

$$E_S(t) = \frac{1}{2} k h(t)^2 = \frac{1}{2m\left(1-\xi^2\right)} e^{-2\xi\omega t} \sin^2(\omega_D t) \tag{2}$$

where k is the stiffness of the SDOF oscillator. Thus, the damping ratio ξ of the SDOF oscillator can be approximated from Eq. 2 as:

$$\xi \approx \frac{\xi}{\sqrt{1-\xi^2}} = \frac{1}{4\pi} \ln\left(\frac{E_S(t)}{E_S\left(t + \frac{2\pi}{\omega_D}\right)} \right) \tag{3}$$

For a multi-degree-of-freedom (MDOF) building, the input seismic energy is the sum of the kinetic energy, the damping energy, and the absorbed energy. The absorbed energy, computed as the integration of the restoring force with respect to the displacement, is the sum of the energy dissipated by yielding and the elastic strain energy of the system (Chopra 2007). It is clear that the absorbed energy of an elastic MDOF building is only the elastic strain energy, E_S, and can be computed as $(\mathbf{Ku})^T \mathbf{u}/2$, where $\mathbf{K}$ and $\mathbf{u}$ are the stiffness matrix and the displacement vector of the MDOF building, respectively. Nevertheless, the damping ratio of a multi-degree-of-freedom oscillator computed from Eq. 3 depends on which cycle of the strain energy history is considered. This is because the higher modes' vibration, usually accompanied by larger modal damping ratios, diminishes faster than the lower vibration modes. It is clear that the influence of an impulse on the structural responses decreases with elapsed time. Thus, for a multistory asymmetrical building, the first and third peak values of the elastic strain energy history (marked in Fig. 1a), which represent the two peaks that occurred in the same direction during the first cycle of vibration, are used in Eq. 3. In addition, in order to consider the two-way asymmetrical buildings under the excitation of bi-directional ground motions, the two loading cases shown in Fig. 1b are used to excite the multistory buildings. The first case is a pair of in-phase impulses applied as the ground accelerations in the two horizontal directions, respectively. The second case is a pair of 180°-out-of-phase impulses applied as the ground

accelerations in the two horizontal directions, respectively. It is assumed that the probabilities of occurrence of in-phase and 180°-out-of-phase impulses in the two orthogonal components of historical seismic ground motion records are equal. Thus, the index of the dissipation rate of the elastic strain energy, denoted by I_E, for an asymmetrical building is defined as follows:

$$I_E = \frac{1}{2}\left(\frac{\xi_1}{\sqrt{1-\xi_1^2}} + \frac{\xi_2}{\sqrt{1-\xi_2^2}} \right) \approx \frac{\xi_1 + \xi_2}{2} \qquad (4)$$

where ξ_1 and ξ_2 are the damping ratios computed from Eq. 3 for the building under the exertion of the first and second loading cases, respectively. Furthermore, for each loading case, $E_s(t)$ and $E_s(t+2\pi/\omega_D)$ shown in Eq. 3 represent the first and third peak values of the strain energy history of the building. As the I_E value increases, the damping system becomes more effective at dissipating energy. Thus, the control target used in the proposed approach for the generalized optimal damper placement in the asymmetrical buildings is to maximize the value of I_E. It is worth noting that the I_E index can be considered as the smeared damping ratio of an asymmetrical building with supplemental damping. The smeared damping ratio reflects the combined effects of the overall supplemental damping parameters on the suppression of the vibration of two-way asymmetrical buildings under bi-directional ground excitations.

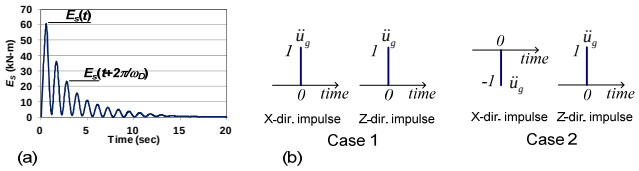


Figure 1 (a) The strain energy history of an elastic multistory two-way asymmetrical building subjected to a bi-directional unit impulse, and (b) the two applied loading cases.

2.2 Design procedures of the proposed approach

In engineering practice, the number and capacity of added dampers are usually limited by budgetary and commercial manufacturing constraints. Therefore, this study assumed that the number of added viscous dampers, denoted by *ND*, and the damping coefficient of each damper are known. The design procedures using the proposed control target are as follows:

Step 1: Confirm the possible damper locations in the multistory two-way asymmetrical building. The number of these locations is denoted by *NL*.

Step 2: Set $j = 1$.

Step 3: Place the jth damper at the ith possible location in the multistory asymmetrical building with $j - 1$ previously added dampers. Because there are *NL* possible locations for placing the jth damper, *i.e.*, $i = 1$ to *NL*, this results in *NL* buildings with different locations of the jth damper. Perform the elastic response history analyses to each of these *NL* buildings using the two loading cases shown in Fig. 1b as the ground excitations.

Step 4: Compute the *NL* values of the index I_E, denoted by $I_{E,ij}$, where $i = 1$ to *NL*. The subscript ij indicates that the index value corresponds to the jth damper at the ith location.

Step 5: Find the jth damper's optimal location, in which the corresponding index value is the maximum among $I_{E,ij}$, where $i = 1$ to *NL*. Add the jth damper to the building at this obtained optimal location.

Step 6: Set $j = j + 1$. If j is larger than *ND*, then stop the design procedure. Otherwise, repeat Steps 3 to 6.

Note that if only one added damper is permitted for each possible location, then the number of remaining possible locations is $NL - j + 1$ rather than *NL*, after $j - 1$ dampers have already been added. In such a case, the *NL* shown in Steps 3 to 5 should be replaced with $NL - j + 1$. Obviously, the design procedures of the proposed approach are very similar to those of the SSSA (Lopez-Garcia 2001, Lopez-Garcia and Soong 2002), which is straightforward and practical. It is worth noting that if a white noise input, a harmonic input of desired frequency, or an impulsive input is desired, then the SSSA can also easily adopt these as inputs. Thus, the key difference between the SSSA and the proposed approach is the control target. In this study, the proposed control target, which is an intrinsic property of the building system irrespective of the building's response states and the characteristics of the input ground motions, leads to the generalized optimal damper placement. The generalized optimal damper placement maximizes the efficiency of the supplemental damping system, *i.e.*, the building with this damper configuration can rapidly dissipate the strain energy and return to the stationary state.

3. NUMERICAL VALIDATIONS

Figure 2 shows the floor plan and the elevation of the two nine-story example buildings, which is a variation of the symmetrical building located in Los Angeles used in the SAC steel research project (Krawinkler 2000). Each floor was simulated as a rigid diaphragm with a lumped mass located at the CM. The center of rigidity (CR) was the geometric center. Details of the member sizes, materials, masses, and so forth can be found in the associated report (Krawinkler 2000). The z-directional span length of the original symmetrical building was reduced from 9144 mm to 6096 mm. In addition, the CM is intentionally located away from the geometric center, resulting in the 20% and 15% eccentricity ratios in the x- and z-directions, respectively. Figure 2 indicates that the flexible side (FS) and the stiff side (SS) in the x-direction are Frame 6 and Frame 1, respectively. The FS and the SS in the z-direction are Frame F and Frame A, respectively. The only difference between these two example buildings is the mass moment of inertia of each story, which is equal to 1 and 2.5 times the values of the original symmetrical building. The x- and z-directional frequency ratios of the example buildings, denoted by $\Omega_{\theta x}$ and $\Omega_{\theta z}$, are defined as the ratios of the rotational frequency

to the *x*- and *z*-translational frequencies of the corresponding symmetrical building, respectively. The building with the same mass moment of inertia as the original symmetrical building is designated Building TS, whose values of $\Omega_{\theta x}$ and $\Omega_{\theta z}$ are equal to 1.55 and 1.43, respectively. Another example building is designated Building TF, whose values of $\Omega_{\theta x}$ and $\Omega_{\theta z}$ are equal to 0.98 and 0.90, respectively. Thus, it is obvious that Building TS was torsionally-stiff in the *x*- and *z*-directions. Building TF was approximately torsionally-similarly-stiff and torsionally-flexible in the *x*- and *z*-directions, respectively. Rayleigh damping with a 2% damping ratio for the first and the second vibration modes was assumed to represent the inherent damping.

In order to validate the effectiveness of the proposed approach, elastic response history analyses using historical ground motion records were carried out on the example buildings with added dampers. Five pairs of historical ground motion records were selected for these analyses. The selected ground motion records were designated as LA21 to LA30 in the SAC steel research project for the buildings located in Los Angeles (Krawinkler 2000). Each pair of selected ground motion records has two orthogonal components. The two orthogonal components were interchanged for application along the *x*- and *z*-directions, respectively. In addition, the *x*-directional component was varied by multiplying plus and minus one. Therefore, this study applied a total of 20 pairs of ground motion records to each example building.

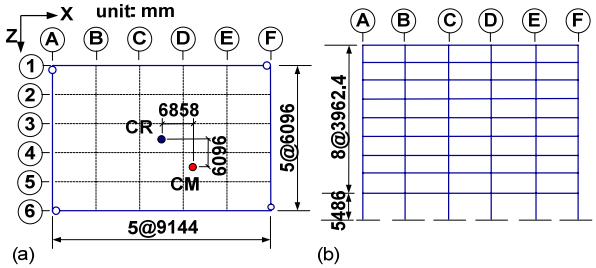


Figure 2 (a) The floor plan and (b) the elevation of Buildings TS and TF.

There were ten linear viscous dampers with a damping coefficient equal to 5×10^4 kN×sec/m to be diagonally installed in each example building. Because each floor was simulated as a rigid diaphragm, there were 36 possible locations for adding dampers. In the numerical validations, it was assumed that the optimal damper location could not be repeated, *i.e.*, there was only one damper at each optimal damper location.

For the purpose of comparison, the optimal damper locations were also designed based on the SSSA approach. The control target used in the SSSA approach was the peak inter-story velocity, which is the same as that used by Lopez-Garcia (2001). Based on the literature (Lopez-Garcia 2001), to decide the *n*th damper's optimal location, perform the elastic response history analysis to the building with the *n-1* previously added dampers using a selected pair of ground motions. Then, the *n*th damper was added to the building at the location where the peak inter-story velocity was the maximum among those in the *x*- and *z*-directions. Nevertheless, all of the aforementioned 20 pairs of ground motions should be considered in these numerical examples. It is clear that under different ground excitations, the peak inter-story velocities are likely to vary, *i.e.*, the optimal damper locations under different applied ground motions may be changed (Lopez-Garcia and Soong 2002, Aguirre *et al*. 2012). Thus, in order to decide the *n*th damper's optimal location, 20 elastic response history analyses using these 20 pairs of ground motions were carried out to the building with the *n-1* previously added dampers. Under the excitation of each pair of ground motion, the priority sequence for the *n*th damper's location is based on the peak inter-story velocities in descending order, that is, the location where the peak inter-story velocity was the highest in the x- and z-directions would be assigned the first priority location. With these 20 elastic response history analyses, the *n*th damper's optimal location is where the maximum first priority occurrences were observed. In case the maximum first priority occurrences were observed at more than one location, the number of second priority occurrences at these specific locations was further compared to decide the optimal damper location, and so forth. For example, when placing the *n*th damper, the highest number of first priority occurrences for the building under the 20 applied pairs of ground motions is six, which occurred at only one location, A. Unquestionably, location A is the *n*th damper's optimal location. Nevertheless, when placing the *n*th damper, the highest number of first priority occurrences for the building under the 20 applied pairs of ground motions is four, which occurred at two locations, A and B. That is, four first priority events occurred each at locations A and B. The remaining 12 first priority events occurred at other locations. The number of second priority occurrences at locations A and B under the 20 pairs of applied ground motions were one and three, respectively. In this case, location B was chosen as the optimal location for the *n*th damper because there was a higher occurrence of second priority events at this location when compared with location A. The approach discussed above allows a set of applied ground motions to be considered and is herein named the modified SSSA approach.

Figures 3a and 3b show the optimal damper locations of the ten viscous dampers in Building TS resulting from the proposed approach, denoted as GOLD, and the modified SSSA approach, respectively. The designation GOLD of the proposed approach stands for the generalized optimal locations of dampers. Figures 4a and 4b show the optimal damper locations of the ten viscous dampers in Building TF resulting from the GOLD and the modified SSSA approach, respectively. Figures 3 and 4 show that most of the dampers were located in the lower half of the buildings by using the GOLD. On the contrary, most of the dampers were located in the upper half of the buildings when using the modified SSSA approach. Furthermore, most of the dampers were located on the FS in both directions for Building TS

regardless of the adopted approaches (Fig. 3). Nevertheless, Fig. 4 shows that the dampers were more uniformly placed on the four sides of the floor plan for Building TF when compared with Building TS. The observations made from Figs. 3 and 4 indicate that the peak inter-story velocity and the strain energy demands on the FS of Building TS were significantly larger than on the SS of this torsionally-stiff building. Nevertheless, for the torsionally-flexible Building TF, the peak inter-story velocity and the strain energy demands were somewhat evenly distributed on the SS and the FS.

Table 1 shows the values of the index I_E when different numbers of dampers were added to the two buildings by using the GOLD. As a reminder, the index I_E represents the smeared damping ratio (including the inherent damping). Thus, Table 3 indicates that the smeared damping ratios were 0.210 and 0.155 for Buildings TS and TF, respectively, when all the ten dampers were added by using the GOLD. This indicates that adding the ten dampers benefitted the torsionally-stiff Building TS more than the torsionally-flexible Building TF.

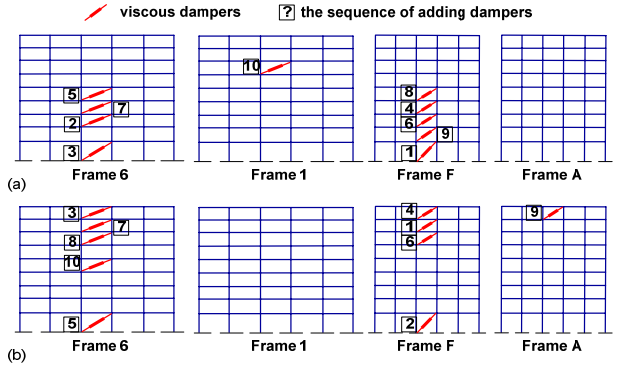


Figure 3 The optimal damper locations of the ten viscous dampers in Building TS resulting from (a) the GOLD and (b) the modified SSSA approach.

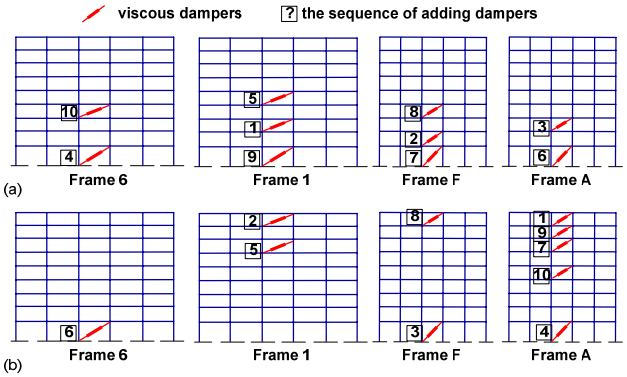


Figure 4 The optimal damper locations of the ten viscous dampers in Building TF resulting from (a) the GOLD and (b) the modified SSSA approach.

Table 1 The values of the index I_E (%) for different numbers of added dampers placed by using the GOLD.

bldg	The accumulative number of the added dampers									
	1	2	3	4	5	6	7	8	9	10
TS	4.3	6.3	7.8	9.7	11.3	13.2	14.9	17.9	19.2	21.0
TF	5.5	6.2	7.2	8.1	9.2	10.1	11.6	12.8	13.7	15.5

Figures 5 to 8 compare the seismic responses of Buildings TS and TF with the ten dampers resulting from the GOLD with those resulting from the modified SSSA approach. For the purpose of convenience, the modified SSSA approach is simply denoted as SSSA in these figures. Figure 5 shows the strain energy history of Buildings TS and TF with and without the ten dampers under the exertion of the two cases of ground unit impulses (Fig. 1b). It is apparent in Fig. 5 that Buildings TS and TF with the ten dampers located using the GOLD reached a stationary state faster than the two buildings with the dampers placed using the modified SSSA approach. In other words, the arrangements of the ten dampers in Buildings TS and TF obtained by using the GOLD were more effective at dissipating the strain energy than those obtained by using the modified SSSA approach.

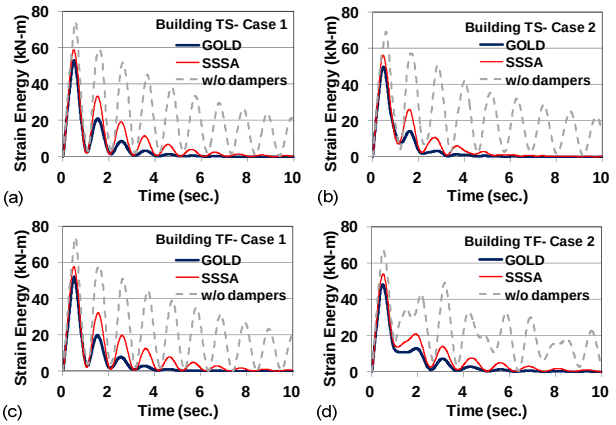


Figure 5 The strain energy histories of Building TS under loading (a) case 1 and (b) case 2, and of Building TF under loading (c) case 1 and (d) case 2.

Figures 6 to 8 show the peak story displacements at the CM, the peak story displacements and the peak story drifts on the four floor sides, respectively. Note that the abscissa values shown in Figs. 6 to 8 are the average of the 20 peak values obtained by applying the 20 pairs of ground motions to the buildings. Almost all of the average peak story displacements at the CM, including the two translations and one rotation, obtained using the GOLD were less than those obtained using the modified SSSA approach (Fig. 6). Almost all of the average peak story displacements on the sides of the floor plan obtained using the GOLD were significantly less than those obtained using the modified SSSA approach, with the exception of the *z*-directional SS (Fig. 7). Figure 8 shows that the average peak story drifts on the four floor sides obtained using the GOLD were more uniformly distributed along the building height than those obtained using the modified SSSA approach. Furthermore, the average peak story drifts from the first to the sixth stories were more significantly reduced using the GOLD than the

modified SSSA approach, except in the *z*-directional SS (Fig. 8). On the contrary, the average peak story drifts from the seventh to the ninth stories resulting from the modified SSSA approach were less than those resulting from the GOLD. This is reasonable because the layout of the added dampers using the modified SSSA approach concentrated on the upper stories (Figs. 3b and 4b). After all, Figs. 5 to 8 clearly indicate that the ten damper locations in the two example buildings obtained from the GOLD were more effective than those obtained from the modified SSSA approach.

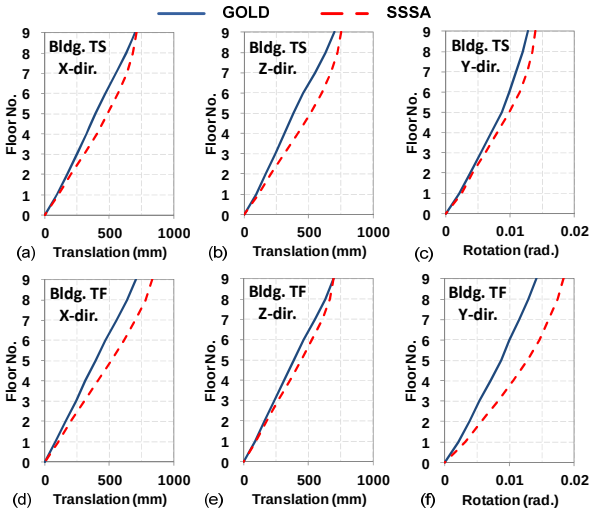


Figure 6 The average peak story translations in (a) the *x*-direction and (b) the *z*-direction, and (c) the average peak story rotation at the CM of Building TS. The average peak story translations in (d) the *x*-direction and (e) the *z*-direction, and (f) the average peak story rotation at the CM of Building TF.

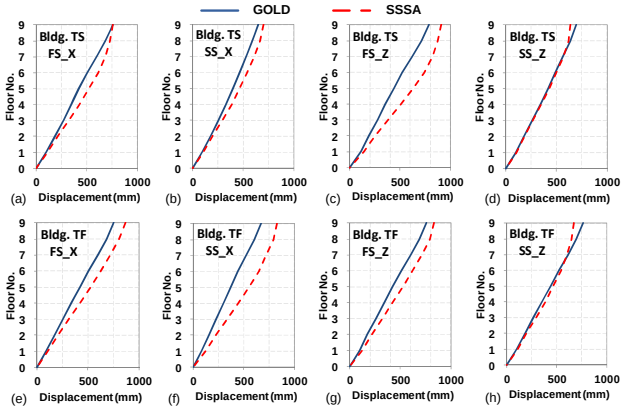


Figure 7 The average peak story displacements on (a) the FS and (b) the SS in the *x*-direction, and on (c) the FS and (d) the SS in the *z*-direction of Building TS. The average peak story displacements on (e) the FS and (f) the SS in the *x*-direction, and on (g) the FS and (h) the SS in the *z*-direction of Building TF.

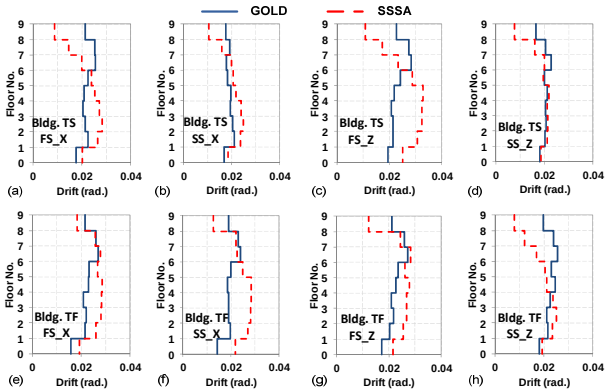


Figure 8 The average peak story drifts on (a) the FS and (b) the SS in the *x*-direction, and on (c) the FS and (d) the SS in the *z*-direction of Building TS. The average peak story drifts on (e) the FS and (f) the SS in the *x*-direction, and on (g) the FS and (h) the SS in the *z*-direction of Building TF.

4. CONCLUSIONS

This study demonstrated a satisfactory approach to the generalized optimal locations of viscous dampers by maximizing the dissipation rate of the overall strain energy of two-way asymmetrical buildings under the excitation of the two pairs of unit impulses. The defined dissipation rate of the overall strain energy used in this study is referred to as the smeared damping ratio, which is an intrinsic characteristic of the building system rather than any seismic response of the building system. In the numerical validations, the proposed approach ensured that the strain energy of the two example buildings was dissipated as fast as possible, which simultaneously resulted in several satisfactory seismic performances. These seismic performances included the displacements at the CM, the story drifts, and displacements at the four edges of the floor planes. In addition, the optimized damper configuration obtained by using the proposed approach is generalized, *i.e.*, not aimed at any specific set of seismic ground motions. This proposed approach is straightforward and suitable for engineering practice.

References:

Aguirre, J.J., Almazan, J.L. and Paul, C.J. (2012), "Optimal control of linear and nonlinear asymmetric structures by means of passive energy dampers," *Earthquake Engineering and Structural Dynamics*, DOI:10.1002/eqe.2211.

Agrawal, A.K. and Yang, J.N. (1999), "Optimal placement of passive dampers on seismic and wind-excited buildings using combinatorial optimization," *Journal of Intelligent Material Systems and Structures*, **10**(12), 997-1014.

Chen, G. and Wu, J. (2001), "Optimal placement of multiple tuned mass dampers for seismic structures," *Journal of Structural Engineering*, **127**(9), 1054-1062.

Chopra, A.K. (2007), "Dynamics of Structures: Theory and Applications to Earthquake Engineering," Prentice-Hall: New Jersey.

Lopez-Garcia, D. (2001), "A simple method for the design of optimal damper configurations in MDOF structures," *Earthquake Spectra*, **17**, 387-398.

Lopez-Garcia, D. and Soong, T.T. (2002), "Efficiency of a simple approach to damper allocation in MDOF structures," *Journal of structural control*, **9**, 19-30.
Garcia, M., de la Llera J.C. and Almazan J.L. (2007), "Torsional balance of plan asymmetric structures with viscoelastic dampers," *Engineering Structures*, **29** (6), 914-932.
Krawinkler H. (2000), "State of the art report on systems performance of steel moment frames subject to earthquake ground shaking," *Report No. FEMA-355C*, SAC Joint Venture.
Lavan, O. and Levy R. (2006a), "Optimal design of supplemental viscous dampers for linear framed structures," *Earthquake Engineering and Structural Dynamics*, **35**, 337-356.
Lavan, O. and Levy R. (2006b), "Optimal peripheral drift control of 3D irregular framed structures using supplemental viscous dampers," *Journal of Earthquake Engineering*, **10**, 903-923.
Levy, R., and Lavan, O. (2006), "Fully stressed design of passive controllers in framed structures for seismic loadings," *Structural and Multidisciplinary Optimization*, **32**(6), 485-498.
Levy, R. and Lavan, O. (2009), "Quantitative comparison of optimization approaches for the design of supplemental damping in earthquake engineering practice," *Journal of Structural Engineering*, ASCE, **135**, 321-325.
Liu, W., Tong, M. and Lee, G.C. (2005), "Optimization methodology for damper configuration based on building performance indices," *Journal of Structural Engineering* (ASCE), **131**(11), 1746-1756.
Singh, M.P. and Moreschi, L.M. (2002), "Optimal placement of dampers for passive response control," *Earthquake Engineering and Structural Dynamics*, **31**, 955-976.
Takewaki, I. (1997), "Optimal damper placement for minimum transfer functions," *Earthquake Engineering and Structural Dynamics*, **26**, 1113-1124.
Whittle, J.K., Williams, M.S., Karavasilis, T.L. and Blakeborough, A. (2012), "A comparison of viscous damper placement methods for improving seismic building design," *Journal of Earthquake Engineering*, **16**, 540-560.
Wongprasert, N. and Symans, M.D. (2004), "Application of a genetic algorithm for optimal damper distribution within the nonlinear seismic benchmark building," *Journal of Engineering Mechanics*, ASCE, **130**, 401-406.
Wu, B., Ou, J.P. and Soong, T.T. (1997), "Optimal placement of energy dissipation devices for three-dimensional structures," *Engineering Structures*, **19**, 113-125.
Zhang R.H. and Soong, T.T. (1992), "Seismic design of viscoelastic dampers for structural applications," *Journal of Structural Engineering*, ASCE, **118**, 1375-1392.

10CUEE CONFERENCE PROCEEDINGS
10th International Conference on Urban Earthquake Engineering
March 1-2, 2013, Tokyo Institute of Technology, Tokyo, Japan

USE OF THREE KINDS OF DAMPERS FOR A STEEL TALL BUILDING SHAKEN BY 2011 EAST JAPAN EARTHQUAKE--CHINA-JAPAN COOPERATION PROGRAM (PART 1)

Xilin Lu[1], Kazuhiko Kasai[2], Ying Zhou[3], Dagen Weng[1], Kun Ding[4], Shunming Gong[5], Yue Jiang[5], Tetsuo Yamashita[6]

1) Professor, State Key Laboratory of Disaster Reduction in Civil Engineering, Tongji University, Shanghai, China
2) Professor, Structural Engineering Research Center, Tokyo Institute of Technology, Japan
3) Associate Professor, State Key Laboratory of Disaster Reduction in Civil Engineering, Tongji University, Shanghai, China
4) PhD candidate, College of Civil Engineering, Tongji University, Shanghai, China
5) Graduate student, College of Civil Engineering, Tongji University, Shanghai, China
6) Associate Professor, Kogakuin University, Japan
lxlst@tongji.edu.cn, kasai@serc.titech.ac.jp, yingzhou@tongji.edu.cn, wdg@tongji.edu.cn, dingkun22@163.com, gshm1989@163.com, 13564004903@126.com, dt13182@ns.kogakuin.ac.jp

Abstract: A 29-story steel frame building in Kogakuin University was strongly shaken during the Great East Japan Earthquake, March 11, 2011. To study the feasible retrofitting schemes for the building in the future, Buckling-Restrained Braces (BRBs), Viscoelastic Dampers (VEDs) and Viscous Dampers (VDs), which are increasingly popular in Japan and China, are selected to study the energy dissipation effect of various dampers. About half of the steel braces in the building are replaced by BRBs, VEDs and VDs, respectively, and the location of those three types of dampers are identical. Nonlinear time history analysis is performed under the valuable base excitation recorded during the earthquake. The seismic performance of this building without dampers, with BRBs, VEDs and VDs are investigated respectively. It is concluded that the seismic effect of two velocity-dependent dampers, i.e. VEDs and VDs, behave better than BRBs. Further research will be performed on the optimization of the number and location of the dampers.

1. INTRODUCTION

This study is part of the Strategic China-Japan Cooperative Program on "Science and Technology (S&T) for Environmental Conservation and Construction of a Society with Less Environmental Burden". The research field of the program is "Evaluation and Mitigation of Environment Impacts of Earthquake and Typhoon Disaster on Urban Area and Infrastructures". The principal investigators of the China and Japan teams are Xilin Lu, (Tongji University) and Kazuhiko Kasai (Tokyo Institute of Technology).

This paper focuses on the application of energy dissipation devices on a tall steel building experienced the Great East Japan Earthquake, March 11, 2011. About half of existing building bracings are replaced by three kinds of dampers, including Buckling-Restrained Braces (BRBs), Viscoelastic Dampers (VEDs) and Viscous Dampers (VDs). The seismic performance of this building without dampers, with BRBs, VEDs and VDs are investigated.

The companion paper (Kasai *et al*., 2013) discusses an alternative design, where existing bracings are retained and dampers placed at half number of building stories, aiming at minimum alterations with good seismic performance.

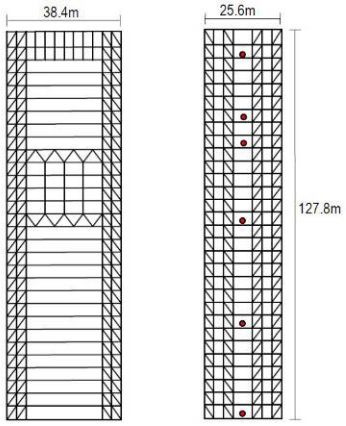
2. DESCRIPTION OF THE 29-STORY STEEL BUILDING

The building is a 29-story steel braced frame constructed in 1989. It is a school building of Kogakuin University, located in Shinjuku ward of central Tokyo. Figure 1 shows the elevation and plan layout of the building as well as locations of sensors instrumented.

At 14:46 on March 11, 2011, a 9-magnitude earthquake occurred off Sanriku coast of Japan and the 29-story steel building was strongly shaken. The sensors instrumented in the building recorded the valuable data of accelerations.

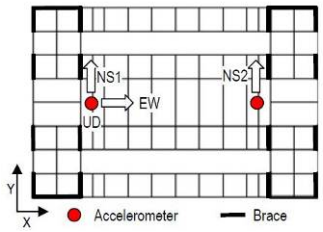
According to the report of the recorded data (Kasai *et al*., 2012), the peak accelerations in *X* and *Y* directions were 92 and 97 cm/s^2 at the first floor, and 235 and 316 cm/s^2 at the top floor, respectively. The average drift angle (i.e., top floor displacement divided by the height) is 1/350. The vibration periods for the first three modes are 2.96s, 1.00s, and 0.52s for *X* direction, and 3.10s, 0.94s, and 0.47s for *Y* direction, respectively. The corresponding damping ratios are 1.7%, 1.8%, and 3.4% for *X* direction, and 2.1%, 1.6%, and 3.4% for *Y* direction.

Figure 2 shows the time history curves of acceleration recorded at the first floor, which are used as actual ground input in the following analysis of the paper.



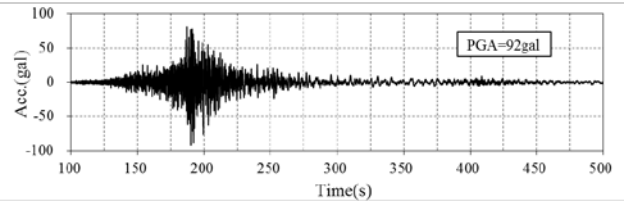
X direction *Y* direction

(a) Elevation of the building

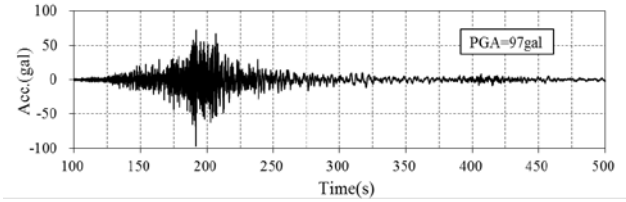


(b) Typical plan layout of the building

Figure 1 Elevation and plan layout of the building



(a) *X* direction



(b) *Y* direction

Fig. 2 Time history curves of acceleration at the first floor

3. VERIFICATION OF THE STRUCTURAL MODEL

The finite element modeling is carried out using ETABS software. The dynamic properties and floor accelerations are firstly compared between analytical model and actual structure to verify the analytical model used in the paper.

3.1 Comparison of Dynamic Properties

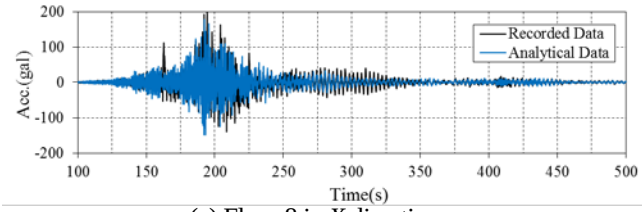
The dynamic property of the analytical model is obtained by performing modal analysis, and the actual structure's dynamic property has been obtained through small-amplitude vibration test (Hisada *et al.*, 2011). The comparison of dynamic property is shown in Table 1, which shows that the structural periods are very close.

Table1 Comparison of dynamic property between the analytical model and actual structure

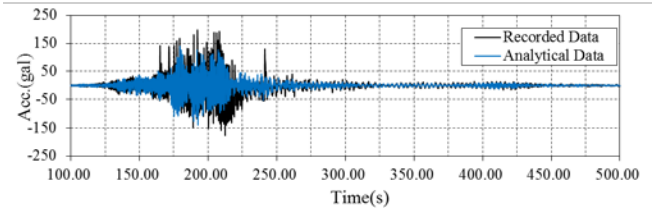
Mode	Period (sec)		Error
	Analytical Model	Actual Structure	
1	3.076 (*Y*)	3.10 (*Y*)	-0.8%
2	3.032 (*X*)	2.96 (*X*)	2.4%
3	2.358 (*Torsion*)	-	-
4	1.039 (*X*)	1.00 (*X*)	3.9%
5	0.978 (*Y*)	0.94 (*Y*)	4.0%
6	0.788 (*Torsion*)	-	-
7	0.558 (*X*)	0.52 (*X*)	7.3%
8	0.504 (*Y*)	0.47 (*Y*)	7.2%
9	0.446 (*Torsion*)	-	-

3.2 Comparison of Floor Accelerations

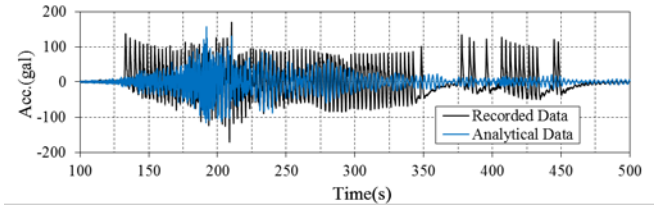
The sensors were instrumented on Floor 1, 8, 16, 22, 24 and 29, and they recorded the accelerations of those floors. The accelerations recorded on Floor 1 are input into the structural model and the analytical accelerations are thus obtained and compared as shown in Figure 3. It can be seen that the accelerations agree quite well except the one in *X* direction on 16th Floor, which would be considered as fault record.



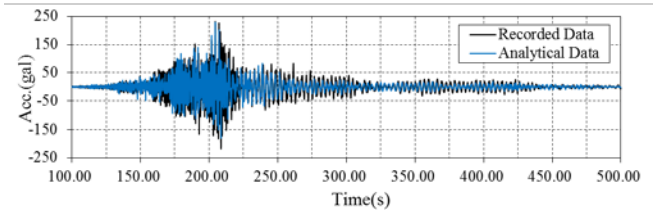
(a) Floor 8 in *X* direction



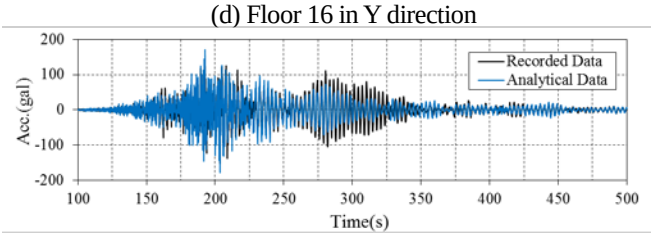
(b) Floor 8 in *Y* direction



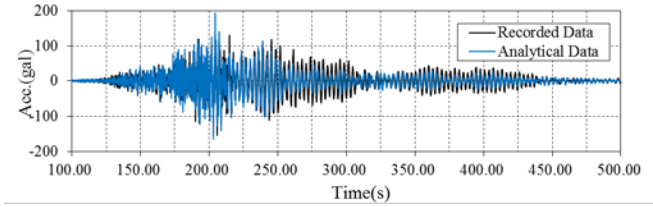
(c) Floor 16 in *X* direction



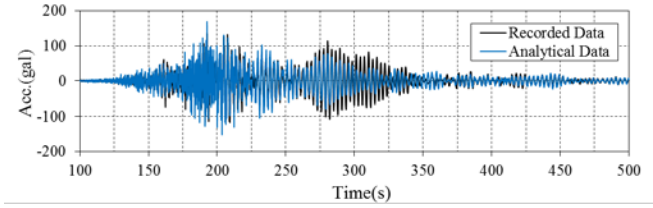
(d) Floor 16 in Y direction



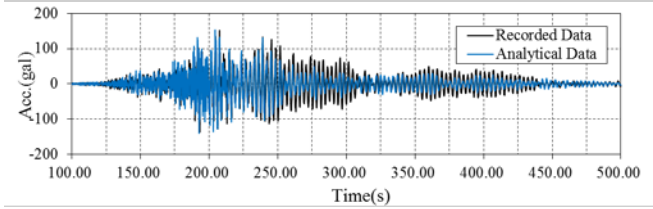
(e) Floor 22 in *X* direction



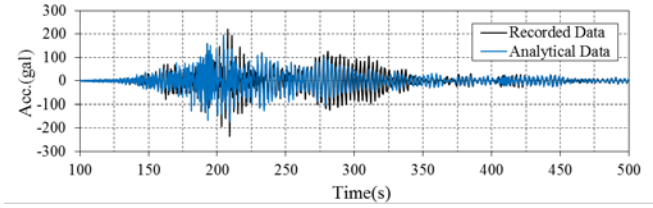
(f) Floor 22 in *Y* direction



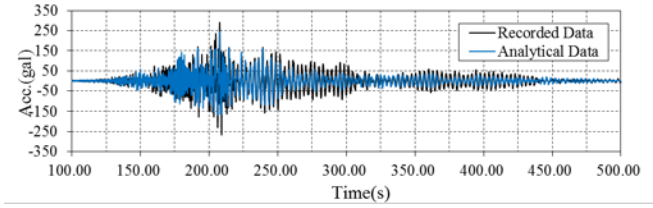
(g) Floor 24 in *X* direction



(h) Floor 24 in *Y* direction



(i) Floor 29 in *X* direction



(j) Floor 29 in *Y* direction

Fig. 3 Comparisons of time-history accelerations between the analytical model and actual structure

4. DAMPER DESIGN AND SEISMIC ANALYSIS

As described above, the original structural model without damper (ND) is established and bi-directional time history analysis is performed. Three other structural models are established too, they are structures with BRBs, VEDs and VDs replacing some braces of original structure respectively.

4.1 Location and Parameters of Dampers

The original structure has 240 braces in *X* direction and 460 braces in *Y* direction. About half of the steel braces are replaced by BRBs, VEDs and VDs, respectively, at the location shown in Figure 4. So the number and location of those three types of dampers are identical. In each structure with dampers, there are 120 dampers employed in *X* direction and 224 dampers employed in *Y* direction.

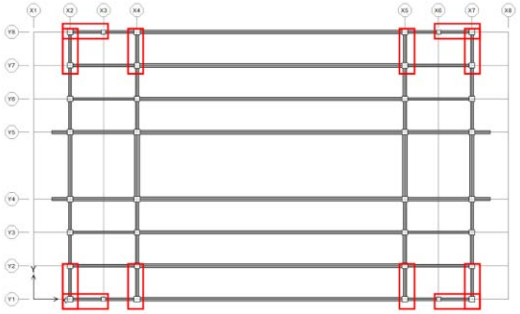


Fig. 4 Location of the dampers

The parameters of the BRBs are designed according to the axial stiffness of the replaced steel braces. As listed in Table 2, the designed damping forces are from 400kN to 800kN, and the average damping force is about 500kN. Wen model (Wen, 1976) is used for the simulation of the BRBs in ETABS program. The yield displacement of the BRBs is supposed to be 1.5mm, and the other parameters of the BRBs are listed in the Table 3, where K is the initial stiffness, F is the yield force, r is post yield stiffness ratio, exp is the yielding exponent.

The parameters of the VEDs are designed for a yield force of 500kN. The hysteretic behavior of viscoelastic damper is simulated by parallel connection of Wen and Maxwell models (Wen, 1976; Malvern, 1969) in ETABS program. Nonlinear parameters of Wen and Maxwell models are listed in Table 4. The physical meaning of the parametric symbols of Wen model is the same as Table 3, while in the Maxwell model K_d is stiffness, C is damping coefficient, and α is damping exponent. And the effective stiffness K_e of a VED is 60kN/mm.

Table 2 Distribution of the BRBs

Floor	BRBs		
	X-direction (axis Y1,Y8)	Y-direction (axis X2,X7)	Y-direction (axis X4,X5)
30	4×400 kN	-	-
29	4×400 kN	-	-
28	4×400 kN	4×400 kN	4×400 kN
27	4×400 kN	4×400 kN	4×400 kN
26	4×400 kN	4×400 kN	4×400 kN

25	4×400 kN	4×400 kN	4×400 kN
24	4×400 kN	4×400 kN	4×400 kN
23	4×400 kN	4×400 kN	4×400 kN
22	4×400 kN	4×400 kN	4×400 kN
21	4×400 kN	4×400 kN	4×400 kN
20	4×500 kN	4×400 kN	4×400 kN
19	4×500 kN	4×400 kN	4×400 kN
18	4×500 kN	4×400 kN	4×400 kN
17	4×500 kN	4×400 kN	4×400 kN
16	4×600 kN	4×400 kN	4×400 kN
15	4×600 kN	4×400 kN	4×500 kN
14	4×600 kN	4×400 kN	4×500 kN
13	4×700 kN	4×400 kN	4×500 kN
12	4×700 kN	4×400 kN	4×500 kN
11	4×700 kN	4×400 kN	4×500 kN
10	4×700 kN	4×400 kN	4×500 kN
9	4×700 kN	4×500 kN	4×600 kN
8	4×700 kN	4×500 kN	4×600 kN
7	4×700 kN	4×500 kN	4×600 kN
6	4×700 kN	4×500 kN	4×600 kN
5	4×700 kN	4×500 kN	4×600 kN
4	4×800 kN	4×500 kN	4×600 kN
3	4×800 kN	4×500 kN	4×600 kN
2	4×800 kN	4×600 kN	4×600 kN
1	4×800 kN	4×600 kN	4×600 kN

Table 3 Parameters of BRBs

Designed Damping Force(kN)	BRB			
	K(kN/mm)	*F*(kN)	*r*	*exp*
400	267	400	0.01	10
500	333	500	0.01	10
600	400	600	0.01	10
700	467	700	0.01	10
800	533	800	0.01	10

The parameters of the VDs are designed according to an actual maximum damping force of 500kN. The Maxwell model (Malvern, 1969; Lu *et al*., 2011; Lu *et al*., 2012) is used for the simulation of the viscous dampers in ETABS program. Because of the low velocity of the structure, the value of damping exponent should be low. When the structure is in low velocity, the dampers can rapidly generate force. Nonlinear parameters of viscous dampers are listed in the Table 5, where the physical meaning of the parametric symbols of Maxwell model is the same with Table 4. And the effective stiffness K_e of a VD is 20kN/mm.

Table 4 Parameters of VEDs

Model	Parameters			
Wen	*K*(kN/mm)	*F*(kN)	*r*	*exp*
	420	500	0.09	0.5

Maxwell	K_d(kN/mm)	C(kN/(mm/s)$^\alpha$)	α	
	30	0.2	0.2	

Table 5 Parameters of VDs

Model	Parameters		
Maxwell	K_d(kN/mm)	C(kN/(mm/s)$^\alpha$)	α
	280	500	0.1

4.2 Dynamic Properties of the Structures

The comparison of the first nine periods of the original structure and the structure with BRBs, VEDs and VDs are shown in Table 6. All periods of the structures with dampers are longer than that of the original structure, because the stiffness provided by dampers is lower than the replaced steel braces. The periods of structure with BRBs is the shortest and that of structure with VDs is the longest, because the BRBs provide the biggest stiffness and the VDs provide the smallest stiffness.

Table 6 Dynamic properties of the structures

Mode	Period(sec)(Mode shapes)			
	ND	BRB	VED	VD
1	3.076(*Y*)	3.096(*Y*)	3.310(*X*)	3.375(*X*)
2	3.032(*X*)	3.057(*X*)	3.239(*Y*)	3.294(*Y*)
3	2.358(*T*)	2.383(*T*)	2.564(*T*)	2.626(*T*)
4	1.039(*X*)	1.048(*X*)	1.101(*X*)	1.117(*X*)
5	0.978(*Y*)	0.988(*Y*)	1.053(*Y*)	1.075(*Y*)
6	0.788(*T*)	0.799(*T*)	0.864(*T*)	0.885(*T*)
7	0.558(*X*)	0.565(*X*)	0.619(*X*)	0.631(*X*)
8	0.504(*Y*)	0.511(*Y*)	0.550(*Y*)	0.564(*Y*)
9	0.446(*T*)	0.454(*T*)	0.501(*T*)	0.514(*T*)

4.3 Input Time-history Records

The accelerations recorded by sensors instrumented on the first floor (Figure 2) are input into the structural models with dampers. Figure 5 shows corresponding response spectra in *X* and *Y* directions with 2% damping ratio.

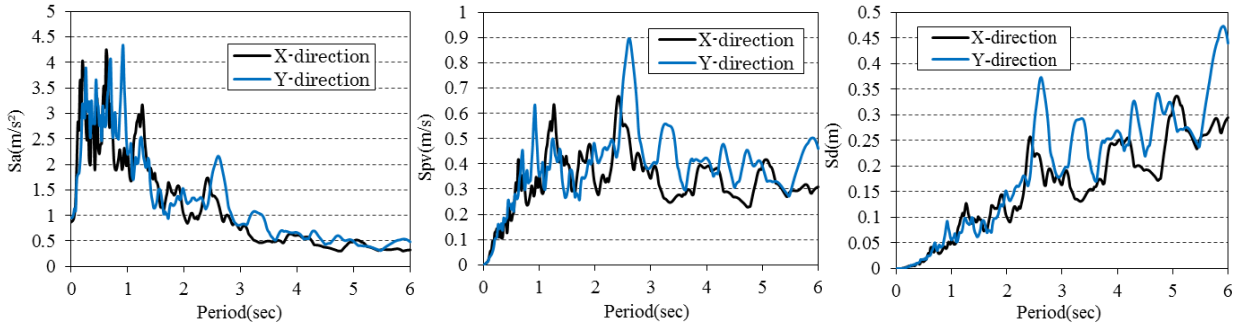
4.4 Seismic Responses of the Structures

The comparison of maximum seismic responses of structures is shown in Table 7 and pictured in Figure 6~8.

From Table 7, it can be seen that all three kinds of dampers have good energy dissipation effect under the recorded base excitations. The two velocity-dependent dampers (VEDs and VDs) have similar energy-dissipating effect and both are better than the displacement-dependent dampers (BRBs).

The comparison of the inter-story drifts is shown in Figure 6. After half of the steel braces being replaced by BRBs, VEDs and VDs, the maximum inter-story drift of the structure decrease from 1/328 to 1/374 (BRB), 1/508 (VED) and 1/539 (VD) in *X* direction and from 1/241 to 1/276 (BRB), 1/320 (VED) and 1/346 (VD) in *Y* direction.

The distribution of the story displacement along the height is shown in Figure 7. It can be seen that the reduction of global displacement is more efficient in *X* direction that *Y* direction.



(a) Acceleration spectra (b) Pseudo-velocity spectra (c) Displacement spectra

Fig. 5 Response spectra of the input time-history records in *X* and *Y* directions

Table 7 Comparison of maximum responses of structures

Parameter	Direction	No Damper	With BRBs (Reduction percentage)	With VEDs (Reduction percentage)	With VDs (Reduction percentage)
Inter-story Drift	*X*	1/328	1/374 (-12%)	1/508 (-35%)	1/539 (-39%)
	Y	1/241	1/276 (-13%)	1/320 (-25%)	1/346 (-30%)
Story Displacement(mm)	*X*	256	226 (-12%)	160 (-37%)	182 (-29%)
	Y	314	301 (-4%)	287 (-9%)	282 (-10%)
Story Shear Force(kN)	*X*	1.76×10^4	1.38×10^4 (-22%)	1.21×10^4 (-31%)	1.10×10^4 (-37%)
	Y	2.16×10^4	1.70×10^4 (-22%)	1.61×10^4 (-25%)	1.53×10^4 (-29%)

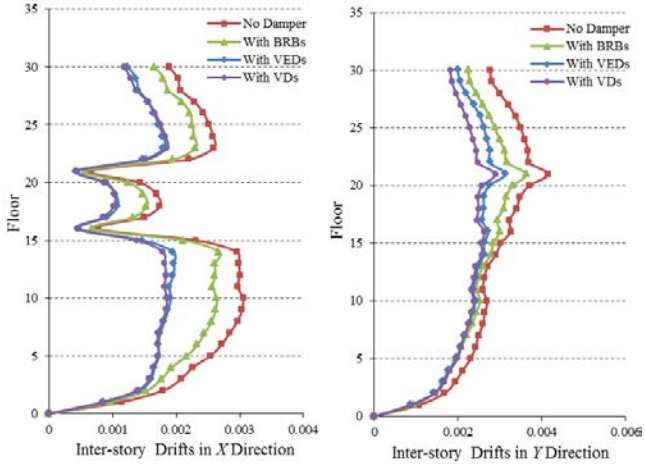


Fig. 6 Comparison of the inter-story drifts

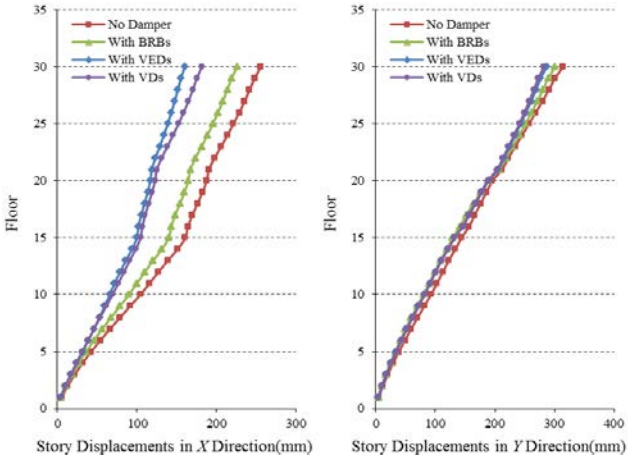


Fig. 7 Comparison of the story displacements

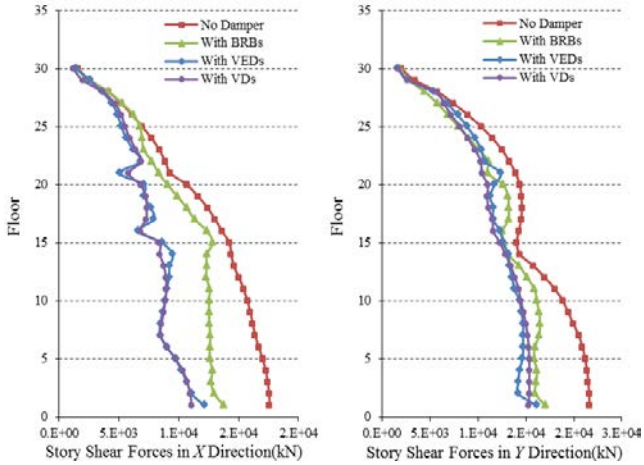


Fig. 8 Comparison of the story shear forces

The comparison of the story shear forces is shown in Figure 8. All dampers have similar effect on shear forces in *Y* direction, while in *X* direction VED and VD has better energy dissipation than BRB.

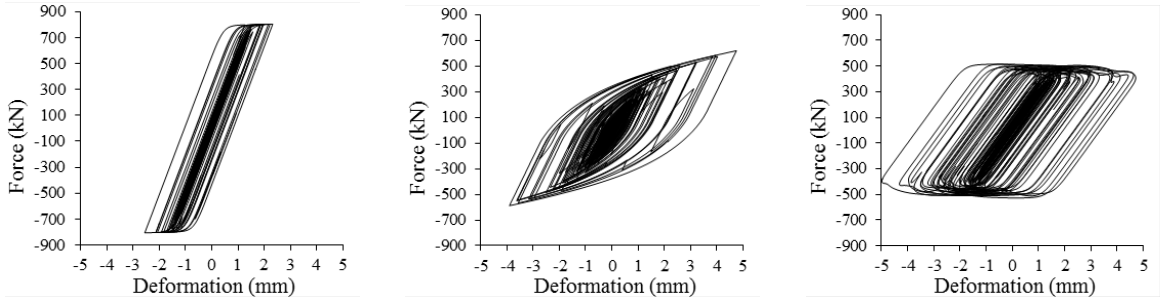
From the comparisons above, we can see that structure with VEDs and structure with VDs have similar control effect, and structures with VDs is slightly better than that with VEDs from the perspective of the maximum seismic responses. They have excellent structural performances and remarkable energy-dissipation capacity which is much better than structure with BRBs. In addition to the difference of energy-dissipation capacity, the earthquake energy input to the structure is not exactly the same due to the different stiffness of the structures which should be taken into account.

4.5 Hysteretic Curves and Energy Time-history Curves

The force-deformation hysteretic curves of a BRB, VED, and VD damper are shown in Figure 9, which has a maximum force of 806kN, 619kN and 515kN, respectively. The maximum deformation of three types of dampers is 2.55mm, 4.75mm and 4.98mm. The full shapes of the hysteretic curves indicate that a large amount of energy input by the earthquake is dissipated by dampers.

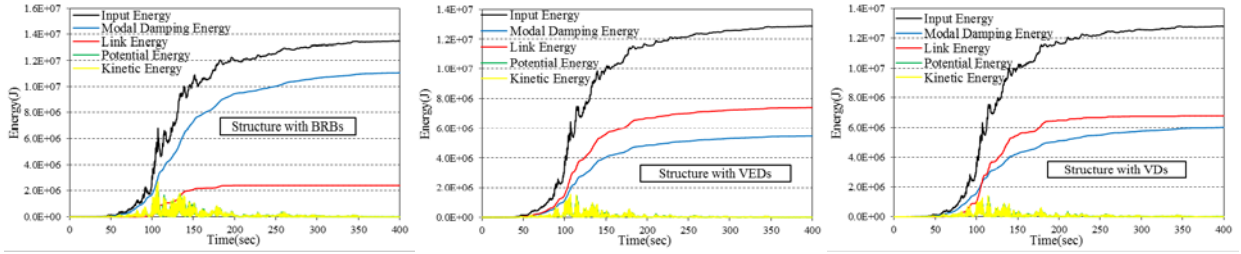
The control effect in *Y* direction is not as good as that in *X* direction, the most likely cause is that the earthquake load will increase along with the extension of period as described in Figure 5.

As shown in Figure 10, the energy curves express the variation of the earthquake input energy, the energy dissipated by dampers, model damping energy, kinetic energy and potential energy with the times. About 18.3%, 56.5% and 53.1% input energy is dissipated by BRBs, VEDs, and VDs, respectively. This result indicates the energy dissipation capacity of those three types of dampers, structures with VEDs dissipate most seismic energy, followed by structures with VDs and BRBs, and this can explain why structures with VEDs and VDs have better control effect than structure with BRBs.



(a) BRB (b) VED (c) VD

Fig. 9 Force-deformation hysteretic curves of three types of dampers



(a) Structure with BRBs (b) Structure with VEDs (c) Structure with VDs

Fig. 10 Energy time-history curves of structures with dampers

5. FURTHER ANALYSIS UNDER INCREASED PEAK GROUND ACCELERATIONS

In order to investigate the energy dissipation effect of those three kinds of dampers under various peak ground accelerations (PGA), the PGA of the original recorded accelerations are scaled to 0.2g and 0.4g respectively and are input into those four models for nonlinear time history analyses.

5.1 Under a PGA of 0.2g

When the PGA of the input accelerations is 0.2g, the comparison of the inter-story drifts and story shear forces of the structures are shown in Figure 11 and 12, and the maximum seismic responses of structures are compared in Table 8.

From the comparisons above, we can see that the control effect of structure with VDs is obviously better than that of structure with VEDs and BRBs on inter-story drifts, and structures with VEDs is better than structures with

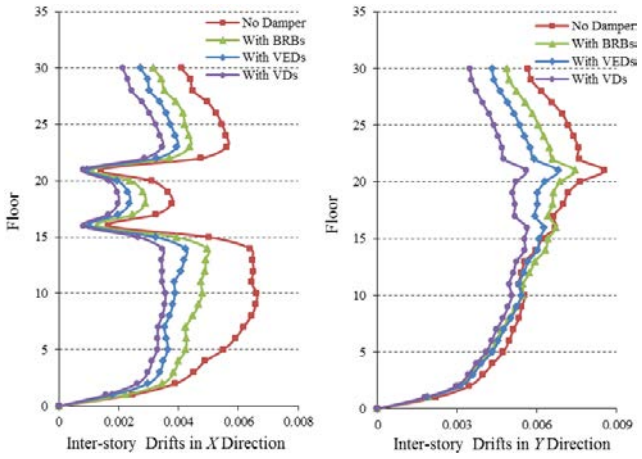


Fig. 11 Comparison of the inter-story drifts (0.2g)

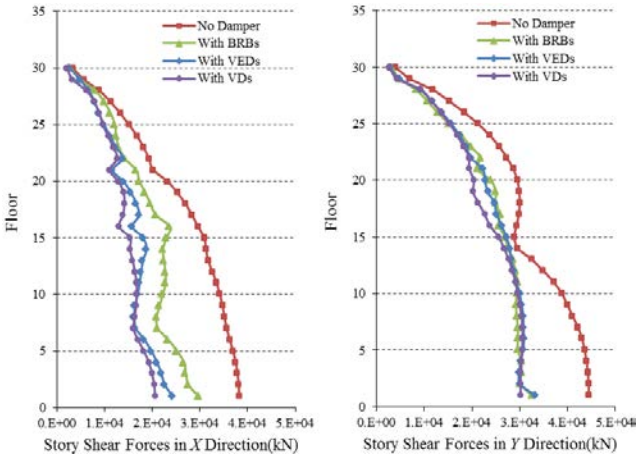


Fig. 12 Comparison of the story shear forces (0.2g)

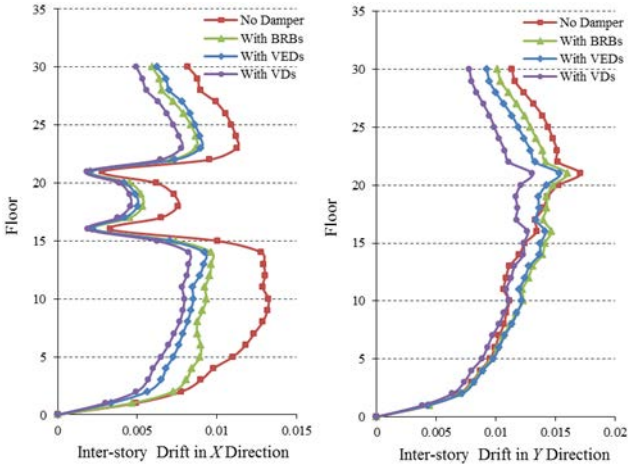


Fig. 13 Comparison of the inter-story drifts (0.4g)

BRBs. All dampers have similar effect on shear forces in *Y* direction, while in *X* direction VED and VD has better control effect than BRB.

In this case, about 30.3%, 55.7% and 65.0% input energy is dissipated by BRBs, VEDs, and VDs, respectively. This indicates the energy dissipation capacity of BRB and VD will improve under increased peak ground accelerations, and the increase of BRB is more obvious.

5.2 Under a PGA of 0.4g

When the PGA of the input accelerations is 0.4g, similar comparison is made in Figure 13~14 and Table 9. It can be seen that the distinction of the control effect of those three kinds of dampers reduces with the increase in PGA, and the control effect on inter-story drifts decreases while that on shear forces increases. The structure with VDs also shows better control effect than structures with VEDs and BRBs.

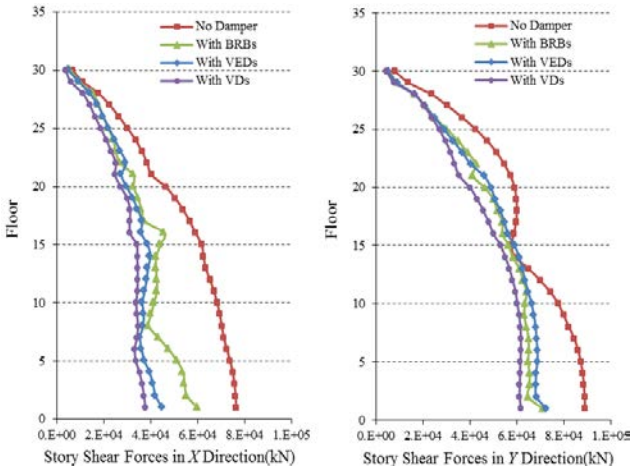


Fig. 14 Comparison of the story shear forces (0.4g)

In this case, about 30.6%, 49.7% and 65.0% input energy is dissipated by BRBs, VEDs, and VDs, respectively. The result indicates that the energy dissipation capacity of VED will decrease with the increase in PGA.

Table 8 Comparison of maximum responses of structures when the PGA is 0.2g

Parameter	Direction	No Damper	With BRBs (Reduction percentage)	With VEDs (Reduction percentage)	With VDs (Reduction percentage)
Inter-story Drift	X	1/151	1/201 (-25%)	1/236 (-36%)	1/281 (-46%)
	Y	1/117	1/134 (-13%)	1/147 (-20%)	1/178 (-34%)
Story Shear Force(kN)	X	3.82×10^4	2.97×10^4 (-22%)	2.43×10^4 (-36%)	2.05×10^4 (-46%)
	Y	4.45×10^4	3.26×10^4 (-27%)	3.32×10^4 (-25%)	3.02×10^4 (-32%)

Table 9 Comparison of maximum responses of structures when the PGA is 0.4g

Parameter	Direction	No Damper	With BRBs (Reduction percentage)	With VEDs (Reduction percentage)	With VDs (Reduction percentage)
Inter-story Drift	X	1/76	1/103 (-26%)	1/108 (-30%)	1/121 (-37%)
	Y	1/59	1/63 (-6%)	1/65 (-9%)	1/77 (-23%)
Story Shear Force(kN)	X	7.64×104	5.99×10^4 (-22%)	4.49×10^4 (-41%)	3.76×10^4 (-50%)
	Y	8.90×104	7.09×10^4 (-20%)	7.25×10^4 (-19%)	6.18×10^4 (-31%)

6. CONCLUSIONS

A 29-story steel building which has been strongly shaken during the Great East Japan Earthquake was introduced, and the structural model was established and verified by the valuable acceleration recorded during the quake. Three other structural models are also established, in which about half of the steel braces are replaced by buckling-restrained braces, viscoelastic dampers and viscous dampers, respectively. Modal analyses and dynamic time-history analyses of four structural models were conducted. Comparisons of dynamic properties, inter-story drifts, story displacements, and story shear forces of those four structures are carried out.

Through the comparison, we can come to the conclusion that structure with VEDs and structure with VDs have similar control effect, and structure with VDs is slightly better than that with VEDs from the perspective of the maximum seismic responses. They have excellent structural performances and remarkable energy-dissipation capacity which is much better than structure with BRBs.

The control effect of all structures with dampers in *Y* direction is not as good as that in *X* direction, the most likely cause is that the earthquake load will increase along with the extension of period as described by the seismic response spectra of the input time-history records.

In the further study, the PGA of the original recorded accelerations are scaled to 0.2g and 0.4g respectively and are input into those four structural models for nonlinear dynamic time-history analyses. The results indicate that the energy dissipation capacity of BRB and VD will improve while that of VED will reduce under increased peak ground accelerations. The structure with VDs continued to show better control effect than structures with VEDs and BRBs.

Although there are some differences in energy dissipation principle and mechanical properties and the control effects are dissimilar, all the three types of dampers show good damping effect and evidently can be used to achieve the expected energy-dissipation objectives if designed and distributed properly. Further research will be performed on the optimization of the number and location of dampers.

Acknowledgements:

This study is part of the Strategic Chinese-Japanese Cooperative Program on "Science and Technology (S&T) for Environmental Conservation and Construction of a Society with Less Environmental Burden". The research field of the program is "Evaluation and Mitigation of Environment Impacts of Earthquake and Typhoon Disaster on Urban Area and Infrastructures". The principal investigators of the China and Japan teams, respectively, are Xilin Lu, Tongji University, and Kazuhiko Kasai, Tokyo Institute of Technology. The writers acknowledge financial support provided by the National Natural Science Foundation of China (NSFC, grant No.51021140006, 51078274) and Japan Science and Technology Agency (JST).

References:

Kasai, K., Lu, X., Pu, W, Yamashita, T., Arakawa, Y., and Zhou, Y. (2013), "Effective Retrofit Strategy Using Dampers for a Steel Tall Building Shaken by 2011 East Japan Eartheuake – China-Japan Cooperation Program," 10th International Conference on Urban Earthquake Eangineering (10CUEE), March 1-2, 2013, Tokyo, Japan.

Kasai, K., Pu, W.C., and Wada A., (2012), "Responses of Tall Buildings in Tokyo during the 2011 Great East Japan Earthquake," *Keynote Paper, STESSA 2012 (Behaviour of Steel Structures in Seismic Areas)*, January 9 - 11, 2012, Santiago, Chile.

Hisada, Y., Kubo, T., and Yamashita, T. (2011), Shaking and Damage of the Shinjuku Campus Building and Shinjuku Campus, Report from Kougakuin University.

Malvern, L.E. (1969), "Introduction to the Mechanics of a Continuous Medium," *Prentice-Hall, Inc.*, Library of Congress Catalog Card No. 69-13712 (USA).

Lu, X.L., Kasai, K., Weng, D.G., *et al*. (2011), "China-Japan (NSFC-JST) Research on Use of Dampers for Repair of RC Building Damaged During 2008 Wenchuan Earthquake Part 1: Analytical Simulation Based on Full-Scale Damper Tests", Proceedings of the 8th International Conference on Urban Earthquake Engineering, March 7-8, 2011, Tokyo, Japan.

Lu, X.L., Ding, K., Weng, D.G., *et al*. (2012), " Comparative Study on Seismic Behavior of RC Frame Structure Using Viscous Dampers, Steel Dampers and Viscoelastic Dampers", Proceedings of the 15th World Conference on Earthquake Engineering, September 24-28, Potugal.

Wen, Y.K. (1976), "Method for Random Vibration of Hysteretic Systems," *Journal of the Engineering Mechanics Division*, 102 (EM2), 249-263.

Chang, K.C., Lai, M.L., Soong, T.T., Hao, D.S., Yeh, Y.C. (1993), "Seismic Behavior and Design Guidelines for Steel Frame Structures with Added Viscoelastic Damper," *NCEER* 93-009.

10CUEE CONFERENCE PROCEEDINGS
10th International Conference on Urban Earthquake Engineering
March 1-2, 2013, Tokyo Institute of Technology, Tokyo, Japan

EFFECTIVE RETROFIT USING DAMPERS FOR A STEEL TALL BUILDING SHAKEN BY 2011 EAST JAPAN EARTHQUAKE -- CHINA-JAPAN COOPERATION PROGRAM (PART 2)

Kazuhiko Kasai[1], Xilin Lu[2], Wuchuan Pu[3], Tetsuo Yamashita[4], Yousuke Arakawa[5], and Ying Zhou[6]

1) Professor and Director, Structural Engineering Research Center, Tokyo Institute of Technology, Japan
2) Professor, State Key Laboratory of Disaster Reduction in Civil Engineering, Tongji University, Shanghai, China
3) Associate Professor, Department of Civil Engineering, Wuhan University of Technology, Wuhan, China
4) Associate Professor, Kogakuin University, Japan
5) Graduate Student, Kogakuin University, Japan
6) Associate Professor, State Key Laboratory of Disaster Reduction in Civil Engineering, Tongji University, Shanghai, China
kasai@serc.titech.ac.jp, lxlst@tongji.edu.cn, puwuchuan@gmail.com,dt13182@ns.kogakuin.ac.jp, dm12005@ns.kogakuin.ac.jp, yingzhou@tongji.edu.cn

Abstract: A monitored 29-story steel frame building in Tokyo was strongly shaken during the Great East Japan Earthquake, March 11, 2011. By using its base acceleration records, the companion paper Part 1 explored effectiveness of seismic retrofit, hypothetically replacing about half of the existing steel braces with dampers at almost every story. Three cases using the buckling-restrained braces, viscoelastic dampers, and nonlinear viscous dampers were studied. The present paper as Part 2 considers an alternative retrofit scheme by adding oil dampers to half number of stories without removing the existing steel braces, in an attempt to minimize alterations of the building. A method to select appropriate locations to attach dampers to maximize control effect is proposed. It considers a special shear beam model to characterize the building with considerably reduced degrees of freedom. Excellent control performance of the building using the method is demonstrated. The accuracy of the shear beam model, in spite of complex deformation mode of the building, is also shown by comparing its global and local responses to those of a 3D member-to-member model.

1. INTRODUCTION

1.1 Strategic China-Japan Cooperative Program

This study is part of the Strategic China-Japan Cooperative Program on "Science and Technology (S&T) for Environmental Conservation and Construction of a Society with Less Environmental Burden". The research field of the program is "Evaluation and Mitigation of Environment Impacts of Earthquake and Typhoon Disaster on Urban Area and Infrastructures". The principal investigators of the China and Japan teams are Xilin Lu, (Tongji University) and Kazuhiko Kasai (Tokyo Institute of Technology), respectively.

1.2 First Phase - RC Building Repair with Dampers

In the first phase of this study, key issues related to repair of RC buildings using dampers were discussed (Lu *et al.* 2011, Kasai *et al.* 2011), by considering existing Chinese 7-story RC building damaged due to the 2008 Wenchuan Earthquake. Actual repair work performed, detailed full-scale damper tests, and hypothetical repair and analysis using the damper test results were discussed (Lu *et al.* 2011). A comprehensive design method was also proposed to determine the required capacity of viscous damper and its story-by-story distribution for RC building structure whose hysteresis is of a stiffness-degrading type. The design method was used for the existing 7-story RC building, and its accuracy demonstrated by time history analyses (Kasai et al. 2011).

1.3 Second Phase - Tall Building Retrofit with Dampers

As the second phase, key issues related to seismic retrofit of a tall building by using dampers are being discussed. The companion paper (Part 1) focused on a Japanese tall steel building that experienced the 2011 Great East Japan Earthquake (Lu *et al*., 2013). The building is instrumented and response records during the earthquake are also considered in the study. About half of existing building bracings are replaced by three kinds of dampers, buckling-restrained braces, viscoelastic dampers and viscous dampers. Seismic performance of the building with or without dampers were investigated (Lu *et al*., 2013).

This paper (Part 2) discusses an alternative design, where existing bracings are retained and dampers placed at

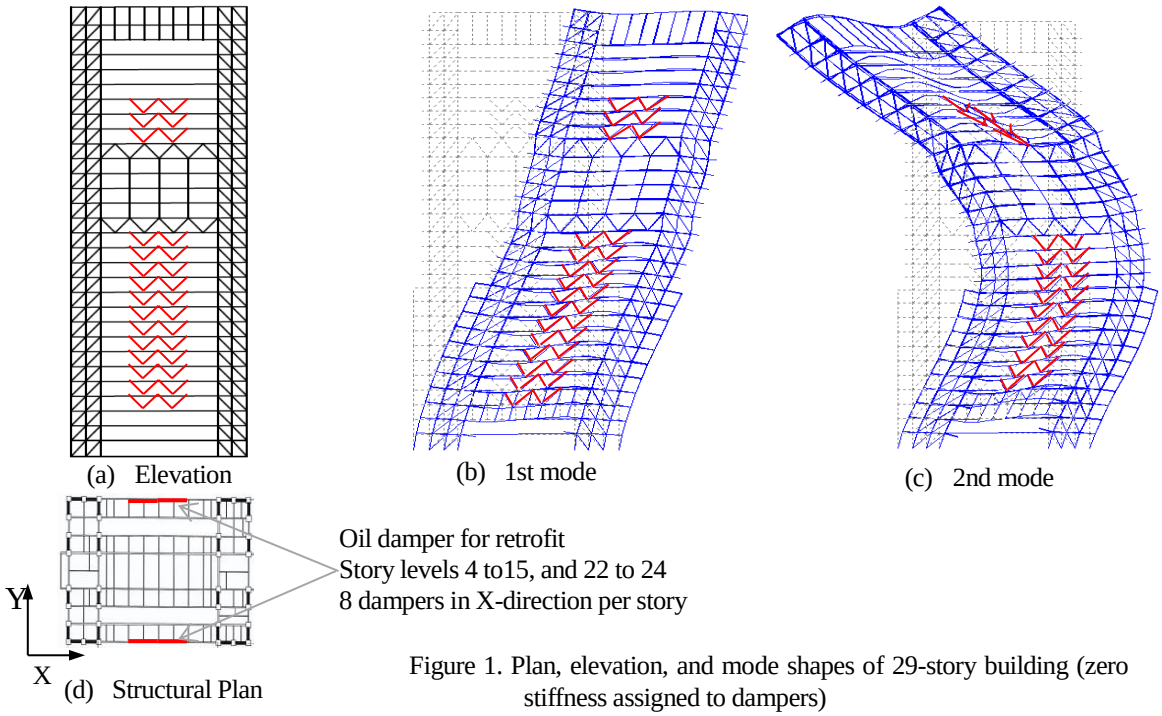


Figure 1. Plan, elevation, and mode shapes of 29-story building (zero stiffness assigned to dampers)

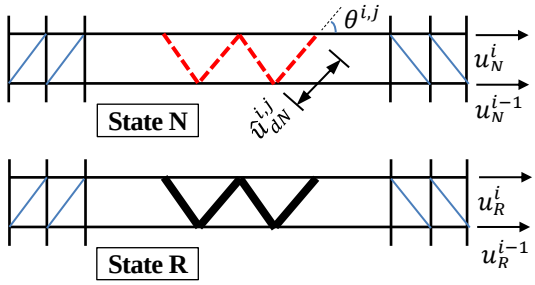
half number of building stories, aiming at minimum alterations with good seismic performance. A method to select appropriate locations to attach dampers to maximize control effect is proposed. It considers a special shear beam model to characterize the building with considerably reduced degrees of freedom. Excellent control performance of the building using the method is demonstrated. The accuracy of the shear beam model, in spite of complex deformation mode of the building, is also shown by comparing its global and local responses to those of a 3D member-to-member model.

2. SELECTION OF LOCATIONS FOR DAMPER INSTALLATION

Passive control effectiveness depends on properties of both damper and frame. In this study, the effects of frame properties are discussed by isolating those of dampers, and the contents in this section are applicable to any dampers. Effects of oil damper properties will be considered in the next section.

2.1 Initial Selections of Damper Locations

Fig. 1 shows the elevation and plan of the 29-story building (Hisada *et al.* 2012, 2013, Kasai *et al.* 2012, Lu *et al.* 2013). The dampers are assumed to be at story levels 1 to 15, and 22 to 24, respectively. The story levels as well as plan locations were selected by examining vibration modes of the 3D frame (member-to-member) model without dampers: by drawing dampers at the hypothetical locations in the undamped building (Figs. 1a to 1c), the locations assuring large axial deformations of the dampers are selected. This initial selection is checked and improved by the writers' method explained below:



$$K_N^i = \frac{Q^i}{u_N^i - u_N^{i-1}} \qquad K_R^i = \frac{Q^i}{u_R^i - u_R^{i-1}}$$

$$\alpha_N^{i,j} = \frac{\hat{u}_{dN}^{i,j}}{\cos\theta^{i,j}(u_N^i - u_N^{i-1})} \qquad \alpha_N^i = \frac{1}{8}\sum_{j=1}^{8}\alpha_N^{i,j}$$

Figure 2. Frame parameters K_N^i, K_R^i, and α_N^i, indicating control effectiveness

2.2 Frame Parameters Indicating Control Effectiveness

As shown in Fig. 2, inclined brace-type dampers are considered for the frame model. Each inclined member includes not only the damper but also brace and connections, and will be called as an "added component" that is oriented to directly connect the lower and upper beams in Fig. 2.

We define State *N* (no damper) and State *R* (rigid damper) where the added component has no stiffness and infinite stiffness in its stroke direction, respectively. Elastic static analyses are conducted for the two states of the frame model by applying lateral forces. From State *N* and *R* displacements u_N^i, u_N^{i-1} and u_R^i, u_R^{i-1}, and shear force Q_i at story levels *i* and *i*-1, story stiffnesses K_N^i and K_R^i are estimated as follows:

$$K_N^i = Q^i / (u_N^i - u_N^{i-1}) \quad , K_R^i = Q^i / (u_R^i - u_R^{i-1}) \quad \text{(1a,b)}$$

where K_R^i should be larger than K_N^i. Larger K_R^i means

Table 1. Calculation of frame parameters and shear beam parameters (unit: kN and mm).

Story i	W^i(kN)	h^i(mm)	L^{ij}(mm)	$\cos\theta^{i,j}$	$K_N^i(=K_f^i)$ (kN/mm)	K_R^i (kN/mm)	K_{tr}^i (kN/mm)	K_{tr}^i/K_f^i	α_N^i	C_d^i (kN·s/mm)	K_d^i (kN/mm)	K_b^i (kN/mm)	$K_{b,eq}^i$ (kN/mm)
30	6218	5220	3200	0.523	170	221	51	0.300					
29	5402	4020	3200	0.623	325	421	96	0.295					
28	10407	3920	3200	0.632	488	624	137	0.280					
27	8415	3920	3200	0.632	563	721	159	0.282					
26	8423	3920	3200	0.632	634	817	183	0.288					
25	8434	3920	3200	0.632	704	976	272	0.387					
24	8450	3920	3200	0.632	767	1349	582	0.759	1.420	242.0	2775	7832	453
23	8451	3920	3200	0.632	832	1727	895	1.075	1.409	238.0	2730	7704	620
22	7366	3920	3200	0.632	1059	2627	1568	1.481	1.485	264.6	3034	8564	922
21	9669	5470	3200	0.505	3055	2961	-94	-0.031					
20	12640	4220	3200	0.604	1546	1825	278	0.180					
19	8981	4220	3200	0.604	1340	1634	294	0.219					
18	9005	4220	3200	0.604	1376	1688	311	0.226					
17	9042	4220	3200	0.604	1871	2210	338	0.181					
16	11114	5120	3200	0.530	3832	4054	222	0.058					
15	14129	4320	3200	0.595	1398	3036	1638	1.172	1.150	140.6	1613	4087	678
14	9681	4320	3200	0.595	1154	2567	1413	1.224	1.494	237.3	2721	6897	820
13	8933	3920	3200	0.632	1322	2829	1506	1.139	1.513	274.7	3150	8891	914
12	8363	3920	3200	0.632	1366	2908	1542	1.129	1.531	281.1	3224	9098	936
11	8771	3920	3200	0.632	1427	3017	1590	1.114	1.543	285.7	3276	9247	959
10	8505	4320	3200	0.595	1293	2691	1398	1.081	1.535	250.3	2870	7274	832
9	8862	4320	3200	0.595	1331	2737	1406	1.056	1.541	252.6	2896	7340	838
8	8874	4320	3200	0.595	1389	2816	1426	1.026	1.545	253.8	2910	7376	847
7	8926	4320	3200	0.595	1475	2930	1455	0.986	1.550	255.3	2927	7419	859
6	8981	4320	3200	0.595	1569	3090	1521	0.970	1.545	253.7	2909	7373	880
5	8663	4320	3200	0.595	1721	3401	1681	0.977	1.559	258.2	2961	7503	938
4	9130	4320	3200	0.595	1946	3147	1201	0.618	1.552	128.0	1468	3721	561
3	6956	4320	3200	0.595	2167	2831	664	0.307					
2	8820	4320	3200	0.595	2506	2968	463	0.185					
1	6232	4620	3200	0.569	3509	3887	377	0.107					

Notes: Each span for damper L^{ij}=3200mm is common for all story level and dampers. Brace cosine angle $\cos\theta^{i,j}$ is common for j=1 to 8. Viscosity coefficient $\hat{C}_d^{i,j}$=37.5 kN·s/mm, post-relief viscosity ratio p=0.03, relief load $\hat{F}_d^{i,j}$=1200 kN, damper internal oil stiffness $\hat{K}_d^{i,j}$=430 kN/mm, and they are common for j=1 to 8. Brace cross section = circular tube 318.5x17.4 (=16459 mm^2), and typically $\hat{K}_b^{i,j}$ was estimated as diagonal length $\sqrt{(L^{ij})^2+(h^i)^2}$ minus rigid end zone length 800 mm and damper length 1480 mm.

more possibility for the added component to attract forces and make the control more effective.

For State *N*, axial deformation of the added component located at story level i and location j is defined as $\hat{u}_{aN}^{i,j}$. In order to indicate horizontal component of maximum possible deformation of the added component, we define deformability ratio $\alpha_N^{i,j}$ as follows:

$$\alpha_N^{i,j}=(\hat{u}_{aN}^{i,j}/\cos\theta^{i,j})/(u_N^i-u_N^{i-1}) \quad (2)$$

where $\cos\theta^{i,j}$ coverts axial deformation of each added component to horizontal direction. Larger $\alpha_N^{i,j}$ suggests good possibility of larger deformation and energy dissipation of the added component.

2.3 Control Effectiveness for 29-Story Building

For the 29-story building, the magnitudes of the three key parameters K_N^i, K_R^i, and $\alpha_N^{i,j}$ are indicated in Table 1. The K_R^i indicates maximum possible value of increased stiffness, and should be much larger than K_N^i for an ideal structure. For the 29-story frame, the K_R^i at the story with the added components is much lower, varying from 1.6 to 2.2 times K_N^i, as Fig. 3 shows. This is because, in spite of the rigid added component, the frame displaces due to flexural deformations of the girder connected to the added components, column flexural deformations, and column axial deformations causing overall chord drift. These deformations will reduce damper deformations and are detrimental to control.

However, it can be shown from the design theory of various dampers that $K_R^i \approx 2K_N^i$ is still acceptable for good passive control (e.g., Kasai, Ito, and Ogura 2008). Moreover, the value is found to be still much larger than when selecting other story levels or locations.

Noted also that $\alpha_N^{i,j}$ values at the selected locations are very large and well exceeding 1.0 as understood from Fig. 1b. In a typical diagonal brace-type damper, the value is usually close to but less than 1.0, and in a typical knee-brace type, it is usually less than 0.3. The present location took advantage of the double curvature deformation mode of the main girder to amplify $\alpha_N^{i,j}$, after confirming adequacy of

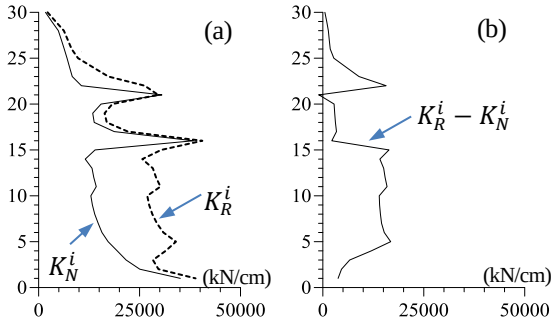


Figure 3. Plots of (a) K_N^i, K_R^i and (b) $K_R^i - K_N^i$

bending stiffness and strength of the girder, good control effectiveness was expected.

After the appropriate story levels and locations for the damper are determined, damper properties must be carefully chosen by maintaining good balance of stiffness with the frames. But due to time limitation, the present study crudely set damper sizes equally at every location, and did not necessarily assured the best performance. Nevertheless, significant improvement of building behavior will be noted later.

3. SHEAR BEAM MODEL

Based the frame model discussed above, a simple analytical model can be developed for time consuming dynamic analysis. The shear beam model is also suitable to understanding of passive control effect, by clearly expressing roles of damper, its support members, and frame, respectively.

3.1 Shear Beam Modeling for Frame Portion

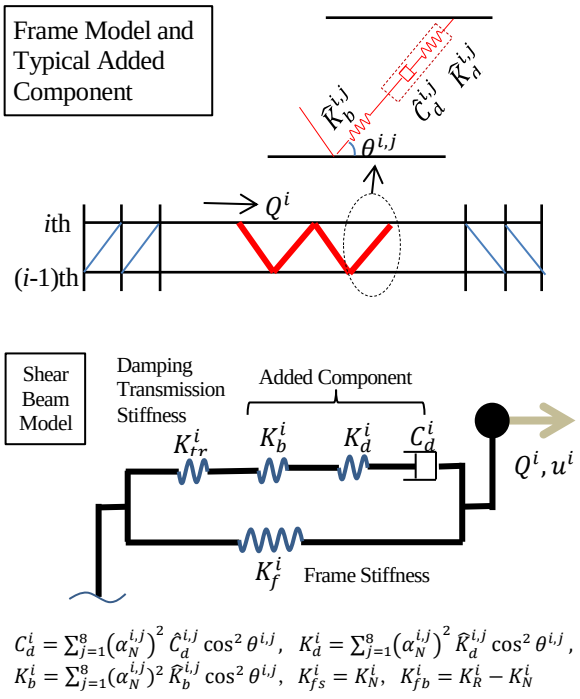
Based on States *N* and *R* analyses of the frame model (Eq. 1), a shear beam model is created. The method is shown in Fig. 4. The K^i_N obtained from the frame (Eq. 1a) is equal to the frame stiffness K^i_f. In order to express the aforementioned deformations detrimental to control, the maximum possible added stiffness discussed earlier will be named now as "damping transmission stiffness" K^i_{tr}, and is included in the shear beam model *i.e.*,

$$K^i_f = K^i_N, \quad K^i_{tr} = K^i_R - K^i_N \qquad (3a,b)$$

where larger K^i_{tr} will transmit and distribute the localized damping of the added component to the overall structure.

3.2 Shear Beam Modeling for Added Components

Each added component of the frame model consists of three elements, bilinear viscous element of viscosity coefficients $\hat{C}_d^{i,j}$ and $p\hat{C}_d^{i,j}$ one of which is selected according to the damper force relative to the relief load $\hat{F}_{dy}^{i,j}$ (Fig. 5 right); damper internal elastic element $\hat{K}_d^{i,j}$ and; brace-connection element of stiffness $\hat{K}_b^{i,j}$ in axial



$C_d^i = \sum_{j=1}^{8} (\alpha_N^{i,j})^2 \hat{C}_d^{i,j} \cos^2\theta^{i,j}$, $K_d^i = \sum_{j=1}^{8} (\alpha_N^{i,j})^2 \hat{K}_d^{i,j} \cos^2\theta^{i,j}$,
$K_b^i = \sum_{j=1}^{8} (\alpha_N^{i,j})^2 \hat{K}_b^{i,j} \cos^2\theta^{i,j}$, $K_{fs}^i = K_N^i$, $K_{fb}^i = K_R^i - K_N^i$

Figure 4. Conversions Form 3D Frame Model to Shear Beam Model

direction, respecively (Fig. 5). For the shear beam model, the properties are converted to C_d^i, K_d^i, K_b^i, and F_{dy}^i as follows (Kasai and Iwasaki 2006) :

$$C_d^i = \sum_{j=1}^{8} (\alpha_N^{i,j})^2 \hat{C}_d^{i,j} \cos^2\theta^{i,j}$$

$$K_d^i = \sum_{j=1}^{8} (\alpha_N^{i,j})^2 \hat{K}_d^{i,j} \cos^2\theta^{i,j}$$

$$K_b^i = \sum_{j=1}^{8} (\alpha_N^{i,j})^2 \hat{K}_b^{i,j} \cos^2\theta^{i,j}$$

$$F_{dy}^i = \sum_{j=1}^{8} \alpha_N^{i,j} \hat{F}_{dy}^{i,j} \cos\theta^{i,j} \qquad (4a\text{-}d)$$

where $\cos\theta^{i,j}$ converts the axial property into that of horizontal direction, and $\alpha_N^{i,j}$ converts the frame model property to the shear beam property (Kasai and Iwasaki 2006, Ishii and Kasai 2010).

Eqs. 4 are based on the theoretical and exact relationship between the frame model and shear beam of a single story building (Kasai and Iwasaki 2006). They also provide good approximation for multistory models (Ishii and Kasai 2010).

3.3 Response Conversion between Shear Beam Model and Frame Model

Note also that the responses of thus-formulated shear beam model can be converted to represent responses of the frame model. First, the global displacements, velocities, and accelerations of the former are equal to those of the latter. Second, the local deformation and velocity of the damper

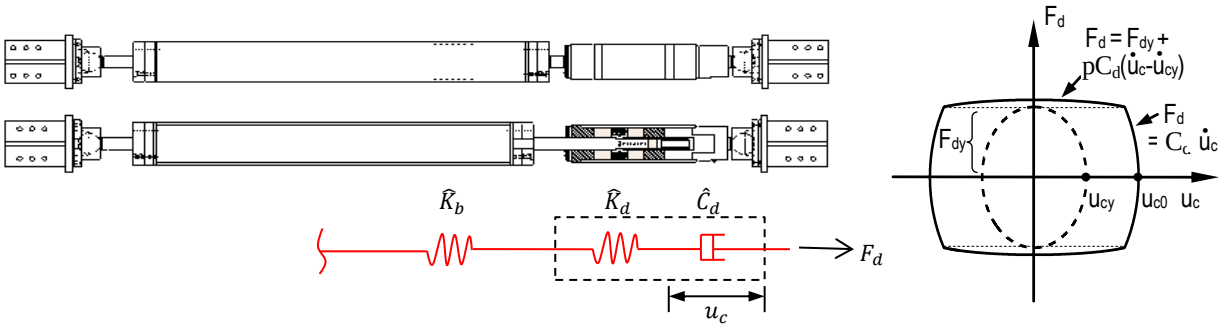


Figure 5. Bilinear oil damper and Maxwell model

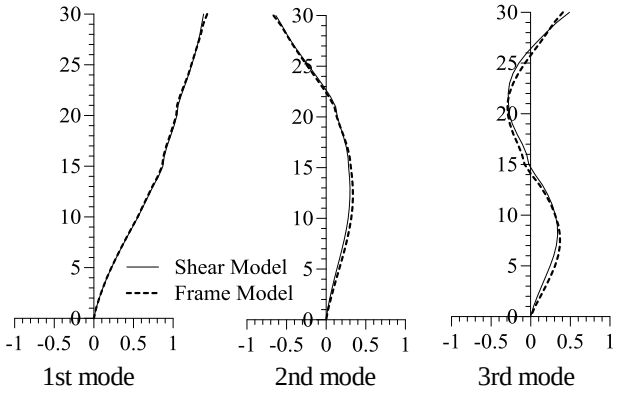


Figure 6. Comparison of modes between 3D Frame Model and Shear Beam Model

Table 2. Comparison of vibration periods and damping ratios between 3D Frame Model and Shear Beam Model

Model	T_1(s)	T_2(s)	T_3(s)	h_1	h_2	h_3
3D Frame	2.958	1.031	0.547	0.0147	0.0151	0.0235
Shear Beam	2.958	1.112	0.678	0.0147	0.0146	0.0198

Note: Rayleigh damping is used, of which 1st mode of X-dir. and 3rd mode of Y-dir. are set to be 0.015 and 0.025, respectively.

and other elements of the shear beam model are converted to those of the frame model by multiplying them with $\alpha_N^{i,j}\cos\theta^{i,j}$, respectively. Third, their local forces are converted similarly using $1/(\alpha_N^{i,j}\cos\theta^{i,j})$.

3.4 Shear Beam Model of 29-Story Building

For the 29-story building, the magnitudes of the shear beam parameters K_f^i, K_{tr}^i, C_d^i, K_d^i, K_b^i, and F_{dy}^i are indicated in Table 1. Note also that K_{tr}^i is small but not necessarily zero at the story without added components. This is because the deformation pattern there at Sate R is somewhat altered from that in Sate N. After some numerical experiments of validations, it was decided to use the value of K_R^i instead of K_f^i where added component is absent.

For simplicity, the stiffnesses K_{tr}^i, K_d^i, and K_b^i are reduced to an "equivalent brace stiffness" $K_{b,eq}^i$ as follows:

$$\frac{1}{K_{b,eq}^i} = \frac{1}{K_{tr}^i} + \frac{1}{K_b^i} + \frac{1}{K_d^i} \qquad (5)$$

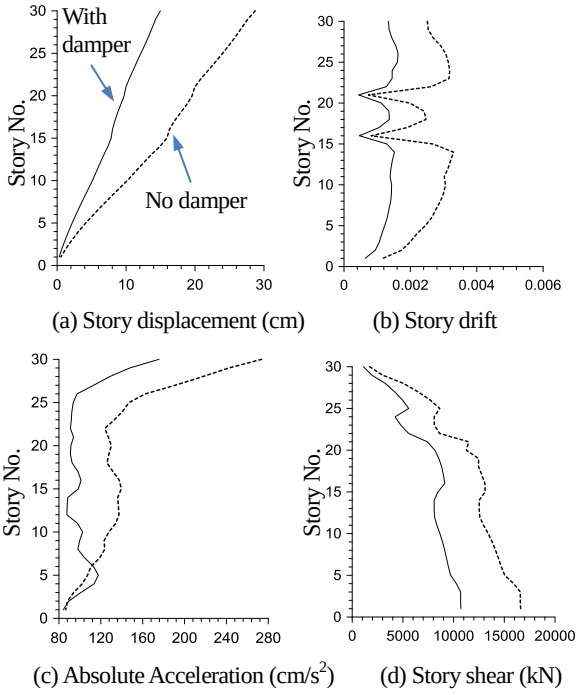


Figure 7. Comparison of maximum response of structures with and without dampers (PGA=92cm/s^2)

4. ANALYSES WITH OR WITHOUT DAMPERS

4.1 Frame Model Analysis and Retrofit Validations

Fig. 6 shows the 3D frame model mode shapes, and Table 2 indicates vibration periods and damping ratios for the 1st to the 3rd modes in X-direction. Rayleigh damping is used and set to satisfy damping ratio of 0.015 for the 1st mode of X-direction and 0.025 for the 3rd mode in Y-direction, respectively. Because of belt trusses in some stories, some abrupt change in the mode shapes occurs over the height (see also Fig. 3). For retrofit of the building with the oil dampers in X-direction, the damper properties (Figs. 4 and 5) are summarized at the footnote of Table 1.

The frame model is subjected to the recorded X-direction motion of PGA 92 cm/s^2. As will be shown, this level of shaking did not activate the relief valve, and the damper behaved linearly. Fig. 7 contrasts the responses between damped and undamped cases, where the response reduction by dampers is apparent, the maximum drift angles

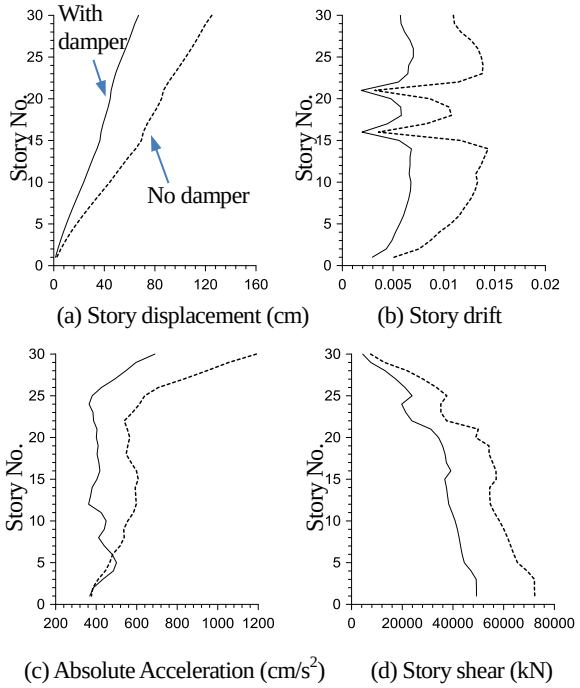


Figure 8. Comparison of maximum response of structures with and without dampers (PGA=400cm/s^2)

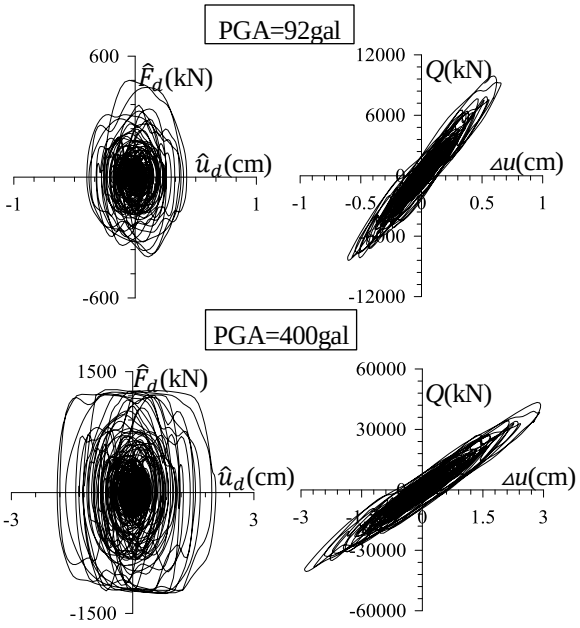


Figure 9. Hysteresis of damper subjected to different PGA

of the damped case and undamped case are 0.0015 and 0.0032 rad, accelerations are 180 and 270 cm/s^2, and base shear forces are 10715 kN and 16608 kN, respectively, indicating drift, accelerations, and base shear are reduced to 0.47, 0.67, and 0.64 times, respectively, by using the oil dampers.

Note also the reduction is more profound than the retrofit scheme in Part 1 where the most significant reduction of

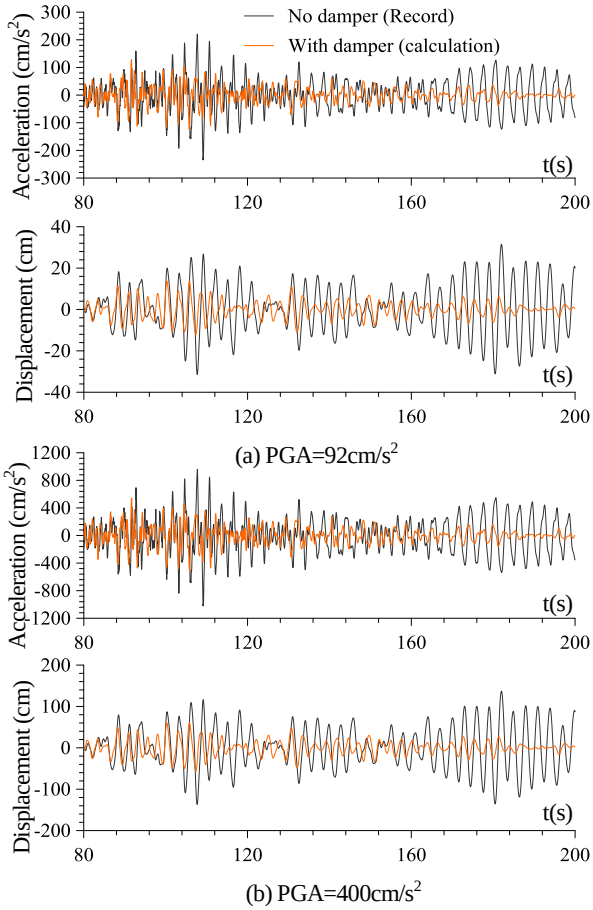


Figure 10. Comparison of response history between structures with and without dampers

drift angle and base shears were 0.61 and 0.63 times, over the three different kinds of dampers used.

The earthquake is amplified to PGA 400cm/s^2. The relief valve was active, and the damper behaved bi-linearly. Fig. 8 contrasts the responses between damped and undamped cases, where the latter is only 4.35 times scaled response from analysis using PGA 92 cm/s^2, since linear behavior is assumed for the undamped case. The maximum drift angles of the damped case and undamped case are 0.0069 and 0.0144 rad, accelerations are 689 and 1,190 cm/s^2, and base shear forces are 49276 kN and 72280 kN, respectively, indicating drift, accelerations, and base shear are reduced to 0.48, 0.58, and 0.68 times, respectively, by using the oil dampers.

Note also the reduction is more profound than the retrofit scheme in Part 1 where the most significant reduction of drift angle and base shears were 0.63 and 0.50 times, over the three different kinds of dampers used.

Fig. 9 shows the difference in hysteresis of the dampers with or without relief mechanism between the two distinct PGA values. Fig. 10 shows the response histories between the damped and undamped cases. The damped case does not only reduce the peak responses but also significantly reduces

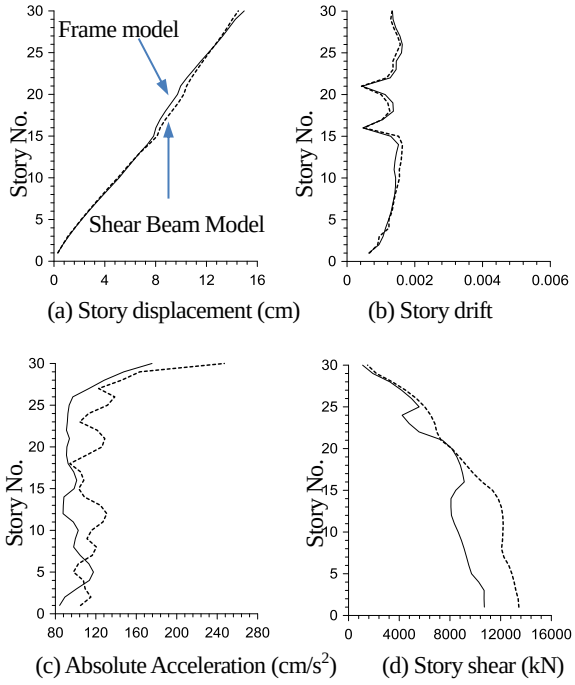


Figure 11. Comparison of maximum response between shear beam model and frame model (PGA=92cm/s^2)

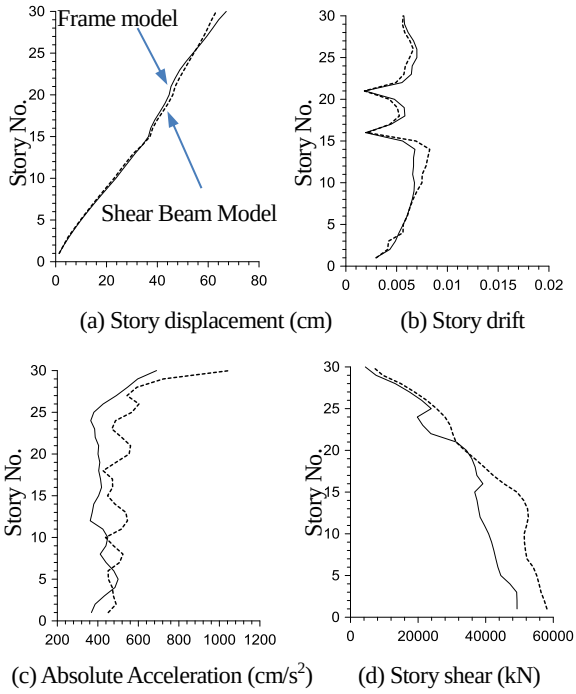


Figure 12. Comparison of maximum response between shear beam model and frame model (PGA=400cm/s^2)

the number of strong cycles as well as root mean square response of the building, which should be beneficial to reduce fatigue of building elements as well as fear of human-being.

4.2 Shear Beam Model Analysis

Fig. 11 shows the comparison of maximum story displacement, story drift, acceleration and story shear between shear beam model and 3D frame model. The displacement and story drift of two models agrees very well. However, the accuracy of acceleration and consequently the story shear are not as good as that of story drift. Figure 12 shows the same 4 kinds of maximum responses for 3D frame model and shear beam model with amplified PGA of 400 cm/s^2. They show the similar comparison results as in Fig.11, and good agreement of story drift is obtained. These results indicate that shear beam model obtained based on the previously described conversion rules is very useful to simulate the structures with added dampers. Through the proposed method, the damper quantity can be theoretically and effectively determined. The shear beam model produce good accuracy with frame model, it can be used to substitute frame model in earthquake response analysis, especially in preliminary design. On the other hand, there is still a little large difference in acceleration response, so further studies such as contribution of modes are also required to improve its accuracy.

5. CONCLUSIONS

The present paper (Part 2) together with the companion paper (Part 1) discussed seismic retrofit methodology using dampers for tall buildings, by considering an example Japanese 29-story steel building that experienced the 2011 Great East Japan Earthquake. The building is instrumented and its acceleration responses during the earthquake were recorded.

The companion paper considered replacement of half number of existing bracings by dampers, and three damper types are considered (Lu et al., 2013). The present paper discusses an alternative design, where existing bracings are retained, and dampers placed elsewhere at half number of building stories, aiming at minimum alterations with good seismic performance. Summary and conclusions are as follows:

(1) The present paper has identified parameters that can indicate effectiveness of passive control based on the frame static stiffness and orientation of dampers therein.

(2) The parameters were used to find suitable story levels and locations for the dampers, after which bilinear oil dampers are selected as an example.

(3) Time history analyses of the 3D frame model with oil dampers are conducted, and considerable improvement of seismic performance is demonstrated in comparison with the analysis and records of the original undamped building.

(4) The parameters identified to characterize the frame and evaluate control effectiveness can also be used to formulate a shear beam model that considerably reduces the degrees of freedom of the frame mode. Reasonable accuracy of the shear model is demonstrated by time history analyses.

Acknowledgements:

This study is part of the Strategic Chinese-Japanese Cooperative Program on "Science and Technology (S&T) for Environmental Conservation and Construction of a Society with Less Environmental Burden". The research field of the program is "Evaluation and Mitigation of Environment Impacts of Earthquake and Typhoon Disaster on Urban Area and Infrastructures". The principal investigators of the China and Japan teams, respectively, are Xilin Lu, Tongji University, and Kazuhiko Kasai, Tokyo Institute of Technology. The writers acknowledge financial support provided by the National Natural Science Foundation of China (NSFC, grant No.51021140006, 51078274) and Japan Science and Technology Agency (JST).

REFERENCES:

Hisada, Y., Yamashita, T., Murakami, M., Kubo T., and Arata, T. Shindo, J., and Aizawa, K. (2012), "Seismic Response and Damage of High-Rise Buildings in Tokyo, Japan, during the 2011 Tohoku Earthquake, Proceedings of the 15th World Conference on Earthquake Engineering, September 24-28, Potugal.

Hisada, Y., Kubo, T., and Yamashita, T. (2011), Shaking and Damage of the Shinjuku Campus Building and Shinjuku Campus, Report from Kougakuin University.

Ishii M. and Kasai K. (2010), "Shear Spring Model for Time History Analysis of Multi-story Passive Control Buildings", J. Structural and Construction Eng., Trans. AIJ, No.647, pp.103-112, Jan. (in Japanese)

Kasai, K., Lu, X., Pu, W., Weng, D., Zhou, Y., and Wada, A. (2011), "China-Japan (NSFC-JST) Research on Use of Dampers for Repair of RC Building Damaged During 2008 Wenchuan Earthquake. Part II : Design Method for RC Building Repair Using Dampers", Proceedings, 8CUEE, Tokyo Institute of Technology, March 7-8, 2011, Tokyo, Japan.

Kasai, K., Pu, W.C., and Wada A., (2012), "Responses of Tall Buildings in Tokyo during the 2011 Great East Japan Earthquake," Keynote Paper, STESSA 2012 (Behaviour of Steel Structures in Seismic Areas), January 9 - 11, 2012, Santiago, Chile.

Kasai, K. Ito, H., and Ogura, T., (2008), "Passive Control Design Method Based on Tuning of Equivalent Stiffness of Bilinear Oil Damper", J. Structural and Construction Eng., Trans. AIJ, No.630, 1281-1288, Aug. (in Japanese)

Kasai, K., and Iwasaki, K. (2006), "Reduced Expression for Various Passive Control Systems and Coversion to a Shear Spring Model", J. Structural and Construction Eng., Trans. AIJ, No.605, pp.37-46, July (in Japanese).

Lu. X., Kasai, K., Zhou Y., Weng D., Ding, K., Gong S., Jiang, Y, and Yamashita, T. (2013), "Use of Three Kinds of Dampers for a Steel Building Shaken by 2011 East Japan Earthquake -- China-Japan Cooperation Program," 10th International Conference on Urban Earthquake Eangineering (10CUEE), March 1-2, 2013, Tokyo, Japan.

Lu, X.L., Ding, K., Weng, D.G., et al. (2012), " Comparative Study on Seismic Behavior of RC Frame Structure Using Viscous Dampers, Steel Dampers and Viscoelastic Dampers", Proceedings of the 15th World Conference on Earthquake Engineering, September 24-28, Potugal.

Lu, X.L., Kasai, K., Weng, D.G., Pu, W., Zhou, Y., and Wada, A. (2011), "China-Japan (NSFC-JST) Research on Use of Dampers for Repair of RC Building Damaged During 2008 Wenchuan Earthquake. Part I : Analytical Simulation Based on Full-Scale Damper Tests," Proceedings of the 8th International Conference on Urban Earthquake Engineering 8CUEE), March 7-8, 2011, Tokyo, Japan.

Wen, Y.K. (1976), "Method for Random Vibration of Hysteretic Systems," Journal of the Engineering Mechanics Division, 102 (EM2), 249-263.

10CUEE CONFERENCE PROCEEDINGS
10th International Conference on Urban Earthquake Engineering
March 1-2, 2013, Tokyo Institute of Technology, Tokyo, Japan

BLIND SIMULATION OF FULL SCALE FREE VIBRATION TESTS ON A THREE STORY BASE ISOLATED BUILDING

Giuseppe Oliveto[1)], Anastasia Athanasiou[2)], and Mario Granata[3)]

1) Professor, Dept. of Civil and Environmental Engineering, University of Catania, Italy
2) PhD Student, Dept. of Civil and Environmental Engineering, University of Catania, Italy
3) Executive Director, S.A.P. Studio Engineering , Catania, Italy
goliveto@dica.unict.it, athanasiou@dica.unict.it, granata@sapstudio.com

Abstract: A building in the town of Augusta in eastern Sicily has recently been constructed using a hybrid base isolation system composed of 16 High Damping Rubber Bearings and 20 Low Friction Sliding Bearings. The building has three stories above the isolation plane and one story beneath it. Laboratory tests on the bearings have been performed by the manufacturers and the results have been used for the definition of a suitable model for the prediction of the behavior of the building under dynamic excitations. In order to make sure that the performance of the installed bearings will reflect the behavior exhibited during the laboratory tests, full scale dynamic tests are planned to be performed on the building by statically imposing a displacement and then suddenly releasing it. The purpose of these experiments, which pose several challenges, is to ascertain several characteristics of the isolation system of the building. The basic challenge is represented by the fact that the building is finished and that therefore no sort of damage can be accepted. The main objective of the simulation is to determine the maximum imposed displacement which causes no non-structural damage to the building. Other objectives include the prediction of the residual displacement after each test, the simulation of the re-centering process after each test, and the prediction of the real and of the apparent static friction force during each test. The blind simulations will serve as guidance in the preparation of the tests.

1. INTRODUCTION

A base isolated building has been recently designed and constructed in the Sicilian town of Augusta using the new Italian technical regulations, D.M. 14/01/2008 (NTC08). It is a reinforced concrete building composed of a story below the ground level, two stories above the ground level and a penthouse on the top, Figure 1.

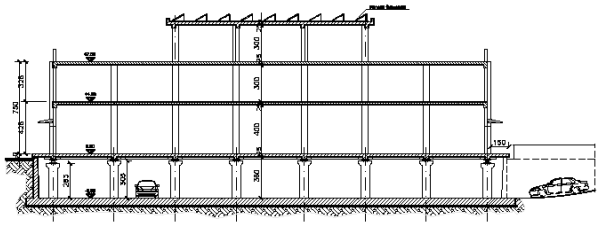


Figure 1 Longitudinal Cross-Section of the Building

The isolation plane runs along the top of the pillars of the basement story slightly above the ground level. The new Italian technical regulations, issued at the beginning of 2008, conclude a phase of evolution of the Italian construction code during which two intermediate documents have been issued in the same decade, O.P.C.M 3274 (2003) and D.M. 14/09/2005. The innovations introduced by the new code essentially consist of a point by point definition of the seismic input, a first attempt to a performance based engineering design and the inclusion of specific chapters dedicated to seismic isolation and supplemental energy dissipation. One of the aims of the present work is to illustrate through a case study the implications of the new code on the structural design of base-isolated buildings. In the Italian tradition all buildings need an independent certification before they are accepted for use. In the present code the certification authority is in charge of deciding whether special tests are needed on a building for the dynamic characterization of the isolation system. The main purpose of the present paper is to carry out a blind simulation of free vibration tests to be performed on the building considered. The simulations of the tests are meant to predict the dynamic behavior of the building so that the tests can be performed effectively and safely.

2. THE AUGUSTA BUILDING

The Augusta building considered was planned and constructed for commercial use. It has a rectangular shape with a length of 35.70 m, a width of 16.00 m and a maximum height above the ground of 10.50 m. The basement story has a free height of 3.60 m. A picture of the part of the building above the ground is shown in Figure 2.

The hybrid seismic isolation system consists of 16 High Damping Rubber Bearings (HDRB) and 20 Low Friction Sliding Bearings (LFSB). The design characteristics of the isolators are specified in Table 1, while the plan distribution is shown in Figure 3.



Figure 2 Picture of the Augusta Building above the Isolation Surface

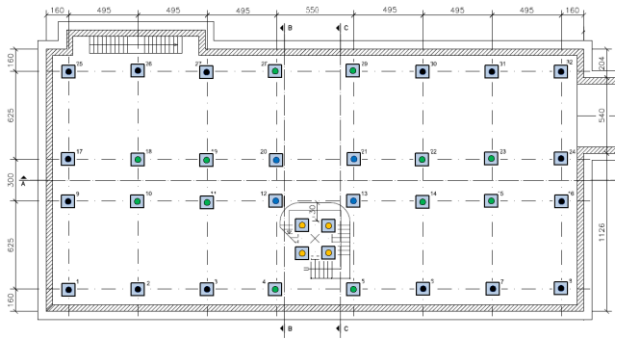


Figure 3 Plan Distribution of the Isolators

Table 1 Technical Requirements for Seismic Isolators

	HDRB : High Damping Rubber Bearings Vertical load in seismic condition 1000 KN Damping ratio at γ=1 ξ=15% Secant horizontal stiffness at γ=1 K_e = 1.00 *kN/mm* Vertical stiffness K_v>800 K_e Horizontal displacement at γ=2 d_c = 300 *mm*

	LFSB : Low Friction Sliding Bearings	
	Load (*kN*)	Displacement (*mm*)
	2000	300
	1500	300
	250	300

3. THE ITALIAN SEISMIC CODE

3.1 Seismic Input

According to NTC08 the seismic input is defined in terms of the geographical coordinates at the building site. For the Augusta building these are Longitude 15.2135° E and Latitude 37.2508° N. The seismic input at the site also depends on the limit state considered for the building. The Italian technical regulations consider two serviceability and two ultimate limit states. The two serviceability limit states are denoted respectively as Operational (SLO) and Damage (SLD) limit states. The two ultimate limit states are the Life safety (SLV) and the Collapse prevention (SLC) limit states. For each limit state and a reference life of the building, a probability for the seismic action to be exceeded is provided, as shown in Table 2.

Table 2 Probability P_{Vr} for the Seismic Action to be exceeded during the reference life V_R

Limit states		P_{Vr}
Service limit states	SLO	81%
	SLD	63%
Ultimate limit states	SLV	10%
	SLC	5%

The reference life V_R of the building is obtained by multiplying the nominal life V_N by a usage coefficient C_U depending on the class of importance of the building. The Italian technical regulations consider four usage classes shown in Table 3.

Table 3 Values of the Usage Coefficient C_U

Usage Class	I	II	III	IV
C_U	0.7	1.0	1.5	2.0

The owner of the building at hand chose the usage class III. This class includes buildings whose seismic resistance is important in view of the consequences associated with a collapse. Among these are schools, assembly halls, cultural institutions etc. The nominal life V_N of various types of constructions is specified by Italian technical regulations as shown in Table 4.

Table 4 Nominal Life for Various Construction Types

	Construction type	Nominal life V_N (years)
1	Provisional structures, temporary structures, structures in the construction phase.	≤ 10
2	Standard structures, bridges, infrastructures and dams of normal importance	≥ 50
3	Large structures, bridges, infrastructures and dams of large size and strategic importance	≥ 100

The building considered belongs to the second construction type of the classification above and its nominal life was chosen to be V_N=50 years. The reference life for the Augusta building is therefore $V_R = C_U \cdot V_N = 1.5 \cdot 50$ years =75years. The building reference life V_R is used for the calculation of the return period T_R, for each of the limit states specified in Table 2, through the following formula:

$$T_R = -\frac{V_R}{\ln(1 - P_{V_R})} \qquad (1)$$

For the four limit states specified in Table 2 the return periods are given in Table 5.

Table 5 Return Periods for the Augusta building

	SLO	SLD	SLV	SLC
T_R(years)	45	75	712	1462

In the Italian technical regulations the response spectrum as a function of the return period is given in terms of three parameters that for the case considered take the values provided in Table 6. The three parameters specified in Table 6 for the building considered and for each of the limit states are the maximum ground acceleration a_g, the maximum amplification of the horizontal spectral acceleration F_o and the separation period T_c^* between the acceleration and velocity sensitive regions of the response spectrum for firm soil.

Table 6 Response Spectrum Parameters for the Augusta Building (V_R=75 years, Long. 15.2135° E, Lat. 37.2508° N)

	SLO	SLD	SLV	SLC
a_g/g	0.057	0.076	0.286	0.408
F_o	2.512	2.493	2.314	2.348
T_c^* (s)	0.267	0.289	0.447	0.499

The characteristic periods of the response spectrum are defined in terms of the period T_c^* and of an additional parameter C_c depending on the soil properties as follows:

$$T_C = C_C \cdot T_C^*; \quad T_B = \frac{T_C}{3}; \quad T_D = \frac{4a_g}{g} + 1.6 \tag{2}$$

The soil classification of the Italian technical regulations complies with the Eurocode 8 standards and defines subsoil classes A, B, C, D and E. The building considered is on a site of class B and the parameter C_C takes the expression $C_C = 1.10 \cdot (T_c^*)^{-0.20}$. In order to be able to define the spectral acceleration an additional parameter is required in the characterization of the soil and topographical conditions. This parameter is given by the expression $S=S_S \cdot S_T$. For a soil of class B the subsoil coefficient S_S is provided by the formula:

$$1.00 \le S_S = 1.40 - 0.40 F_0 \frac{4a_g}{g} \le 1.20 \tag{3}$$

The topographical coefficient S_T for the site at hand is equal to 1.0 (flat topography). The elastic design spectrum is finally given in terms of pseudo spectral acceleration as follows:

$$\begin{aligned}
&S_e(T) = a_g \cdot S \cdot \eta \cdot F_o \cdot \left[\frac{T}{T_B} + \frac{1}{\eta \cdot F_o} \left(1 - \frac{T}{T_B} \right) \right], && 0 \le T \le T_B \\
&S_e(T) = a_g \cdot S \cdot \eta \cdot F_o, && T_B \le T \le T_C \\
&S_e(T) = a_g \cdot S \cdot \eta \cdot F_o \cdot \left(\frac{T_C}{T} \right), && T_C \le T \le T_D \\
&S_e(T) = a_g \cdot S \cdot \eta \cdot F_o \cdot \left(\frac{T_C T_D}{T^2} \right), && T_D \le T
\end{aligned} \tag{4}$$

The parameter η in Equations (4) accounts for damping and is defined by the following formula:

$$\eta = \sqrt{10/(5+\xi)} \tag{5}$$

where ξ is given in percentage and depends on the type of materials, soil, and structure.

3.2 Design Spectrum for Base Isolated Buildings

For ordinary structures the design spectrum is obtained from the elastic spectrum provided by Equations (4) by replacing the damping parameter η with the reciprocal of the strength reduction factor q, that is $\eta=q^{-1}$. This factor depends on materials and construction types and is specified in a particular section of the code. For base-isolated structures the code states that the substructure and the superstructure must be designed to behave elastically. For reinforced concrete structures this implies a strength reduction factor $q=1.5$.

This spectrum is further modified in the period range $T \ge 0.80 T_{is}$, T_{is} being the fundamental period of the base-isolated building. In this range the parameter η takes the value corresponding to the damping ratio of the isolation system, Equation (5). The parameters required for the full definition of the response spectra of the various limit states are given in Table 7, calculated according to the formulae previously specified.

Table 7 Spectral Parameters for the Augusta Building

Limit State	S	T_C (s)	T_B (s)	T_D (s)
SLO	1.200	0.382	0.127	1.828
SLD	1.200	0.407	0.136	1.904
SLV	1.135	0.578	0.193	2.744
SLC	1.017	0.631	0.210	3.232

As shown in the following section 3.3, the fundamental period of the Augusta building is T_{is}= 2.38*s*. The design spectra for the building are shown in Figure 4. The evident jump in spectral values in Figure 4 is needed to account for the different response behavior between the isolation and the structural modes.

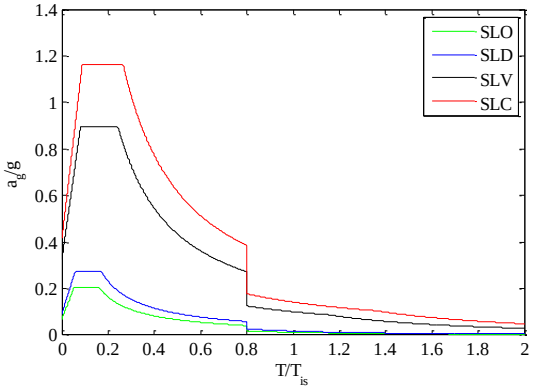


Figure 4 Elastic Spectra for the Augusta Building

3.3 Preliminary Design

The Italian seismic code for base isolated buildings requires that the isolation period (fundamental period of the base isolated building) be in the range $3T_{bf} \leq T_{is} \leq 3s$, T_{bf} being the period of the same structure on fixed base. This period may be calculated using the empirical formula $T_{bf}=C \cdot H^{0.75}$, where C is a coefficient depending on the type of construction and H is the height of the building expressed in meters, provided that it is less than 40*m*. For reinforced concrete framed buildings C=0.075 and so for the Augusta building it follows that

$$T_{bf}=0.075 \cdot (10.5)^{0.75}=0.44\ s$$

Therefore the seismic code suggests that the isolation period for the Augusta building be in the range $1.32s \leq T_{is} \leq 3s$. The actual isolation period is then a compromise between the value selected by the designer and the availability of commercial isolation bearings with the required stiffness. In the case at hand a reasonable period was T_{is}=2.40*s*. The required horizontal stiffness for the isolation system is therefore provided by the formula

$$K_{esi} = \frac{4\pi^2 \mathrm{M}}{\mathrm{T}_{is}^2} \qquad (6)$$

where M is the mass of the building above the isolation plane. For the case at hand, where M=2400 *tons*, the required overall stiffness is 16.45 *kN/mm*. The designer, in view of the plan presented in Figure 3, decided for the distribution of elastomeric bearings shown in Figure 5.

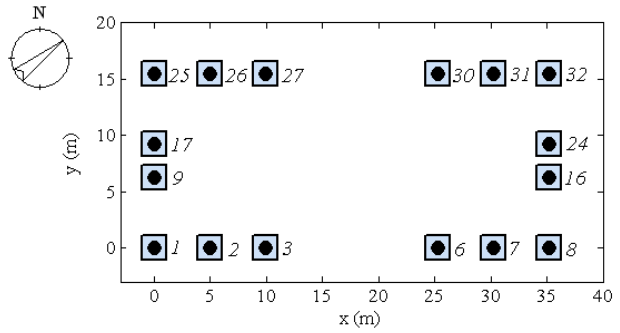


Figure 5 Distribution of High Damping Rubber Bearings for the Augusta Building.

The Italian manufactures of High Damping Rubber Bearings (HDRB) provide catalogs of bearings for maximum displacements in the range of 100 *mm* to 400 *mm*, assuring damping ratios of 0.10 or 0.15 at a shear strain of γ=1, FIP Industriale SpA (2006). The damping ratio decreases of about 12% the nominal value when the shear strain reaches γ=2.

The displacement at the collapse prevention limit state can be calculated by the following formula:

$$d_{dc} = \left(\frac{\mathrm{T}_{is}}{2\pi} \right)^2 S_e^{SLC} \left(\mathrm{T}_{is}, \xi_{esi} \right) \qquad (7)$$

If a damping ratio ξ_{esi} = 0.15 is used and large strains are assumed at the collapse prevention limit state, then introducing the reduced damping ratio $\xi_{esi,min}$ = 0.132 in Equation (7) leads to the following value for the displacement:

$$d_{dc}(2.40,0.132)=272mm$$

For economic reasons related to device testing, the HDRB where chosen of the same size. Therefore the required horizontal stiffness for the HDRB is 16.45/16 *kN/mm* = 1.03*kN/mm*. In the catalog provided by the manufacturer the isolator with the nearest horizontal stiffness is the type SI-N500/150 which has the geometrical and mechanical characteristics shown in Table 8.

Table 8 Characteristics of Isolator SI-N500/150

Characteristic	*Value*	*Units*
External diameter of isolator	500	*mm*
Diameter of internal steel shims	480	*mm*
Thickness of steel shims	3	*mm*
Number of rubber layers	25	
Thickness of a single rubber layer	6	*mm*
Total thickness of the rubber	150	*mm*
Primary shape factor S_1	20	
Secondary shape factor S_2	3.2	
Total height with cover plates	312	*mm*
Seismic vertical load capacity	1200	*kN*
Maximum horizontal displacement	300	*mm*
Vertical stiffness K_V	1016	*kN/mm*
Horizontal stiffness K_e	1.05	*kN/mm*
Equivalent viscous damping ξ_e at shear deformation γ=1	15	%

The total horizontal stiffness of the isolation system is therefore K_{esi} =16.8 *kN/mm* and the isolation period turns out to be T_{is}=2.38*s*. The displacement evaluated according to Equation (7) is

$$d_{dc}(2.38,0.132) = 269\ mm$$

3.4 Modeling Base Isolated Structures

The superstructure and the substructure are modeled as linear elastic systems. The isolation system can be modeled, according to its mechanical characteristics, as a linear viscous-elastic system or as a system with non-linear constitutive behavior. The vertical deformability of the isolators must be accounted for when the ratio of the vertical stiffness of the isolation system K_v to the equivalent horizontal stiffness K_{esi} is less than 800. If a linear model is adopted, then the equivalent stiffness must be referred to the total design displacement at the considered limit state, for each isolation device belonging to the isolation system. The energy dissipated by the isolation system must be expressed in terms of a viscous equivalent damping ratio ξ_{esi} evaluated with reference to vibration cycles within the interval of the natural frequencies of the isolation modes. For

the higher structural modes the damping ratios of the complete model must be those of the superstructure on fixed base. When the equivalent stiffness and/or damping ratio depend significantly on the design displacement, an iterative procedure must be applied.

The behavior of the isolation system can be modeled as linear equivalent if the following conditions are satisfied:

a) The equivalent stiffness of the isolation system is at least equal to 50% of the secant stiffness for cycles with displacement amplitude equal to 20% of the reference displacement.
b) The equivalent linear damping ratio of the isolation system must be less than 30%.
c) The load-displacement characteristics of the isolation system do not vary more than 10% due to variations in the strain velocity in a range of $\pm 30\%$ about the design value, and to the vertical loads in the design variability range.
d) The increase of the restoring force in the isolation system, for displacements between $0.5d_{dc}$ and d_{dc}, is not less than 2.5% of the total gravity load above the isolation system.

If a non-linear model is adopted, the constitutive law for the individual isolation devices must adequately describe their behavior in the strain and velocity ranges that occur during seismic action. The model considered must also provide a correct estimate of the energy dissipated during the earthquake motion.

3.5 Linear Static Analysis

The linear static analysis can be applied to base-isolated structures if some basic requirements are satisfied. The most important are the following:

a) The isolation system can be modeled as an equivalent linear viscous system.
b) The period of the isolated structure is in the range $3T_{bf} \le T_{is} \le 3\ s$.
c) The vertical stiffness K_V of the isolation system is not smaller than 800 times the equivalent horizontal stiffness of the isolation system K_{esi}.
d) The period of the isolation system in the vertical direction must be smaller than 0.1 *s*.
e) No isolator must be in tension under the combined seismic and gravity action.
f) The structural configuration must be regular in plan.
g) The height of the building must be less than 20 *m* and the number of stories less than 6.
h) The period of the substructure must not be larger than 0.05 *s*.
i) The maximum plan dimension of the structure cannot be larger than 50 *m*.
j) In each principal direction, the eccentricity of the center of mass with respect to the center of rigidity of the isolation system cannot be larger than 3% the size of the structure in the direction transversal to the considered one.

If the above conditions are satisfied, the total force to be applied to the isolation system is given by the formula

$$F = M \cdot S_e(T_{is}, \xi_{esi}) \tag{8}$$

where $S_e\ T_{is}, \xi_{esi}$ is the spectral acceleration specified by Equation (4).

The displacement of the center of rigidity due to the seismic action d_{dc} must be calculated through the formula

$$d_{dc} = \frac{M \cdot S_e(T_{is}, \xi_{esi})}{K_{esi,\min}} \tag{9}$$

where $K_{esi,min}$ is the minimum equivalent stiffness considering variability of the mechanical properties of the isolation system due to various factors such as strain amplitude, manufacturing and material uncertainties, maximum strain velocity, amplitude of gravity forces acting simultaneously to the seismic action, temperature, aging, etc.

The horizontal forces to be applied at each story of the superstructure must be calculated for each horizontal direction by using the following expression:

$$f_j = m_j \cdot S_e(T_{is}, \xi_{esi}) \tag{10}$$

where m_j is the mass of story *j*.

Torsional effects of the superstructure on individual isolation devices may be accounted for by amplifying in each direction the displacements and forces given above by the following factors δ_{xi} and δ_{yi}:

$$\delta_{xi} = 1 + \frac{e_{tot,y}}{r_y^2} y_i; \quad \delta_{yi} = 1 + \frac{e_{tot,x}}{r_x^2} x_i \tag{11}$$

where (x_i, y_i) are the coordinates of the isolation device considered with respect to the center of rigidity; $e_{tot,x}$ and $e_{tot,y}$ are the total eccentricities (permanent + accidental) in the direction *x* and *y* respectively; r_x and r_y are the components in the *x* and *y* directions of the radius of gyration of the isolation system:

$$r_x^2 = \frac{\sum_i \left(x_i^2 K_{yi} + y_i^2 K_{xi} \right)}{\sum_i K_{yi}}; \quad r_y^2 = \frac{\sum_i \left(x_i^2 K_{yi} + y_i^2 K_{xi} \right)}{\sum_i K_{xi}} \tag{12}$$

In Equations (12) K_{xi} and K_{yi} are the stiffness of the isolation device "*i*" in the directions *x* and *y* respectively.

3.6 Linear Dynamic Analysis

Linear dynamic analysis is admitted for base-isolated structures when the behavior of the isolation system can be modeled as elastic. For the complete system composed of the substructure, the isolation system and the superstructure a linear elastic behavior is assumed. The model must include the substructure any time the isolation system is not right above the foundation. Modal decomposition and response

spectrum analysis can be performed or step-by-step integration of` the equations of motion, possibly after modal decoupling. When the substructure is included in the model, a sufficient number of modes must be considered in the analysis to account for a significant part of its mass.

The two horizontal components of the seismic action must be considered as acting simultaneously, using prescribed combination rules. The vertical component of the ground motion must be accounted for any time the ratio of the vertical to the horizontal stiffness of the isolation system is $K_v/K_{esi} < 800$. In such cases a number of vertical modes have to be considered in the analysis to excite vertically a significant part of the system mass.

When the step-by-step integration of the equations of motion is performed, the correct value of the equivalent viscous damping ratio can be introduced directly in the modal equations, if modal decoupling is used, or by providing the appropriate damping matrix if integration is performed on the coupled system.

NTC08 totally ignores the fact that the equations of motion for base-isolated structures are not classically damped and that modal decoupling is only possible if complex modes are used. No information is provided on whether to use complex modes or to neglect modal coupling. However it is reasonable to assume that approximate modal uncoupling is suggested by neglecting the coupling terms.

3.7 Safety Checks

Serviceability Limit States. Safety checks are prescribed with reference to both the serviceability limit states and the ultimate limit states. Of the two serviceability limit states, only the Damage Limit State (SLD) is considered. For the superstructure it is required that the story drifts be less than 2/3 of the bound prescribed for fixed base structures in the SLD limit state. For reinforced concrete structures such bound is 0.005 for in-fills rigidly connected to the structural members and 0.01 for in-fills designed in such a way that they are not damaged by structural drifts.

The isolation devices must not undergo damage that compromises their correct functioning under service conditions. These conditions are considered to be satisfied and the checks omitted if the requirements for the Life Safety Limit State (SLV) are satisfied. In the case of systems with non-linear behavior, residual displacements at the end of an SLD earthquake must be compatible with the functionality of the construction. Under an SLD earthquake, all connections, whether between the isolated structure and the ground or between isolated and non-isolated parts of the structure, must be able to absorb relative displacements with no damage or usage limitations.

Ultimate Limit States

Life Safety Limit State. For the Life Safety Limit State (SLV) the substructure and the superstructure must be verified with the same material safety factors γ_m used for non-isolated structures. If the substructure is included in the analysis, the structural elements of the substructure must be verified with respect to the stress resultants obtained directly from the analysis. If not they must be verified with respect to the forces transmitted by the isolation system combined with the stress resultants due to the accelerations directly applied by the ground motion to the substructure. When the substructure can be considered as rigid (natural period less than 0.05*s*) the inertia forces applied to the substructure may be taken equal to the mass multiplied by the ground acceleration. The combination of the stress resultants can be carried out using the SRSS rule.

The strength of the structural members of the superstructure can be verified by considering the effects of the seismic action divided by q=1.5 combined with the other actions using the combination rules specified for non-isolated structures.

In the conditions of maximum stress, the parts of any device that are not directly involved in the dissipation of energy must remain elastic in conformity with the standards for the constituent materials and a safety factor of at least 1.5.

For constructions of usage class IV (maximum seismic protection) structural and non-structural connections between the isolated structure and the ground or non-isolated parts of the structure, particularly those concerning equipment, must absorb the relative displacements deriving from the analysis with no damage.

Collapse Prevention Limit State. The isolation devices must be able to avoid ruptures when undergoing the displacements d_2 evaluated for an earthquake having a probability of being exceeded equal to that expected for the Limit State of Collapse Prevention (SLC). In the case of systems with non-linear behavior the maximum displacement must be calculated by adding that due to the considered seismic action and the largest between the residual displacement at the SLD and the displacement corresponding to the vanishing of the restoring force along the unloading branch starting from the maximum displacement at SLD.

In all constructions, the gas connections and the connections of any dangerous equipment crossing the separation joints must be designed to allow the relative displacement of the isolated superstructure with the same safety factor adopted for the isolation system.

3.8 Acceptance Tests for Elastomeric Bearings

NTC08 prescribe qualification and acceptance tests for elastomeric bearings. The qualification tests are more detailed and severe than acceptance tests and shall not be considered herein. The requirements of the acceptance tests will be briefly described because the results of these tests will be used in the following.

The acceptance tests on the isolation devices are performed with the same methodology used for the qualification tests. The devices are considered acceptable whenever they satisfy the requirements specified below and the static shear modulus G does not differ more than $\pm 10\%$ from the value obtained from the qualification tests.

a) The external geometry must satisfy the prescriptions of the standards on bearing devices. For isolators taller than 100 *mm* the height

tolerance is 6 *mm*.

b) Evaluation of the static vertical stiffness between 30% and 100% of the vertical load V.

c) Evaluation of the static shear modulus G, or alternatively, of the dynamic shear modulus G_{din}, by the same methodology adopted for the qualification tests. Whenever possible, it is preferable to evaluate the dynamic shear modulus G_{din} because it reduces uncertainties on the control of the real dynamic behavior of the device.

d) Evaluation of the effectiveness of the steel-rubber adhesion by the same methodology used for the qualification tests but adopting the value corresponding to the displacement d_2 for the strain γ.

The acceptance tests must be performed on at least 20% of the devices and in any case on not less than 4 and not more than the total number of the devices to be used on site.

4. MODELING LABORATORY TESTS

Two series of acceptance tests were performed by the manufacturer on the isolators used in the Augusta building, one for the rubber bearings and another for the sliding bearings.

4.1 Rubber Bearings

Vertical Stiffness. In conformity with the acceptance tests specified by NTC08, four elastomeric bearings were tested for the evaluation of the vertical stiffness. The values of the vertical stiffness obtained were (1167, 1316, 1566, 1299) *kN/mm*, FIP Industriale SpA (2009-a). Since the design requirements were $K_v > 800K_e$ = 840 *kN/mm*, the acceptance tests for the vertical stiffness are amply satisfied.

Static Horizontal Stiffness. Again four elastomeric bearings were tested for the evaluation of the static shear modulus G. The testing facility allows for the testing of two isolators in parallel and therefore the results are the average properties of the couple of isolators considered. The cyclic tests were performed at a peak shear strain $\gamma = 1$ providing at the third cycle the stress-strain curve shown in Figure 6.

The static shear modulus was evaluated by the manufacturer from the curve in Figure 6 according to EN 1337-3 (2005) and resulted equal to 0.48*MPa*. Such value is in fact a tangent shear modulus but the manufacturer also calculated a secant shear modulus at $\gamma = 1$ equal to 0.65*MPa*. A bilinear identification of the stress-strain curve shown in Figure 6 led to the parameters k_o, k_1, Q for the device, (Naeim and Kelly 1999).

For the second couple of isolators (IT752E, IT753E) the measured static shear modulus was 0.51*MPa*, the secant static shear modulus at $\gamma = 1$ was 0.69*MPa*, while the identified parameters for the bearings were k_o = 3521 *N/mm*, k_1 = 708 *N/mm*, Q = 28 *kN*.

Dynamic Horizontal Stiffness. Four elastomeric bearings were tested for the evaluation of the dynamic shear modulus G_{din}. For each couple of isolators five sinusoidal cycles with peak strain $\gamma = 1$ were applied at a frequency of

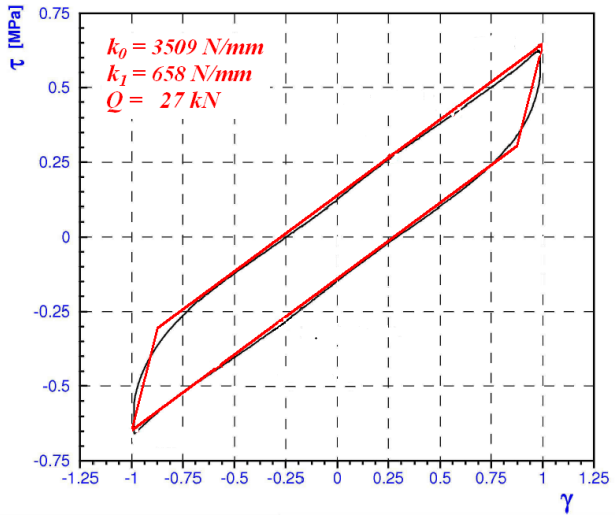


Figure 6 Third Cycle Static Stress-Strain Curve for Isolators IT421E and IT404E

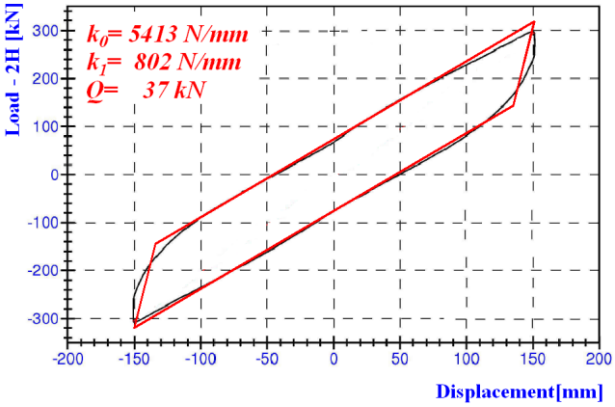


Figure 7 Third Cycle Load-Displacements Curve for Isolators IT421E and IT404E

0.5 *Hz*. The load-displacement curve obtained for the third cycle is shown in Figure 7. From the load-displacement curve in Figure 7 the manufacturer evaluated the secant stiffness K_e = 1.0 *kN/mm* at $\gamma = 1$ and the energy dissipated in the cycle W_d = 21097 *J*. From the above values the dynamic shear modulus G_{din}=0.77 *MPa* and the damping ratio ξ_e = 14.8% were derived. From the test performed on the second couple of isolators (IT752E, IT753E) the following parameters were evaluated: K_e =1.05 *kN/mm*, W_d = 22588 *J*, G_{din} = 0.81 *MPa*, ξ_e = 15%.

The bilinear identification of the isolation bearings led to the following sets of parameters: (k_o = 5413 *N/mm*, k_1= 802 *N/mm*, Q= 37 *kN*) for isolators IT421E and IT404E and (k_o=6199 *N/mm*, k_1= 847 *N/mm*, Q = 40 *kN*) for isolators IT752E and IT753E.

Adhesion Tests. The adhesion acceptance tests mentioned at point d) of section 3.8 were performed in couples on all isolators. A typical test result is shown in Figure 8.

In principle the adhesion test on only four isolators would have been sufficient for the acceptance of the total supply of sixteen SI-N500/150 elastomeric isolators.

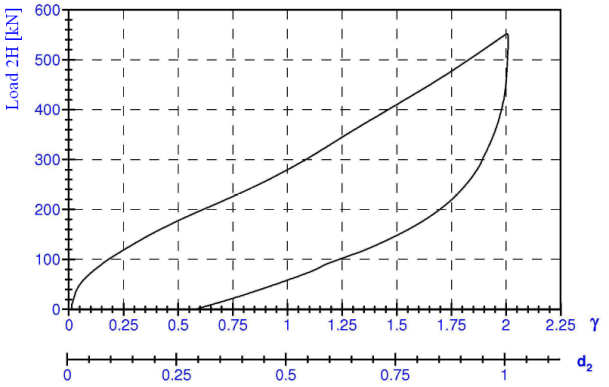


Figure 8 Load-Displacement Curve for Isolators IT421-404 during Adhesion Test at displacement d_2=300*mm*

However, the adhesion acceptance test on a previous batch of isolators failed and therefore every isolator of the new batch was tested for adhesion by autonomous decision of the manufacturer.

4.2 Sliding Bearings

One couple of each of the three types of sliding bearings used in the Augusta building has been tested simultaneously for the evaluation of the friction coefficient, FIP Industriale SpA (2009-b). The tests were performed at a velocity of 4 *mm/s* and at 0.5 V_{max}, 0.75 V_{max} and V_{max}, where V_{max} is the maximum vertical load. The results are shown in Figure 9.

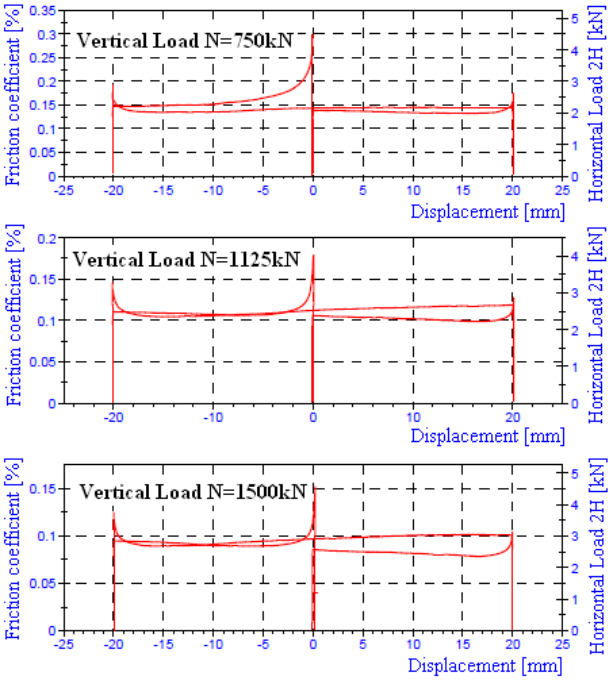


Figure 9 Friction Coefficient for the Sliding Isolators VM 150/600/600 at 0.5 V_{max}, 0.75 V_{max} and V_{max} maximum vertical load

The start-up friction coefficient for the isolators considered varies from a maximum of 0.3% when the vertical load is 0.5 V_{max} to a minimum of 0.15% under V_{max}. The dynamic friction coefficient ranges from a maximum of 0.15% to a minimum 0.09%. Such exceptionally low values of the friction coefficient are due to the lubrication of the PTFE and, in the case of the dynamic friction coefficient, to the very low testing velocity.

5. DISPLACEMENTS ESTIMATES

NTC08 prescribes the evaluation of displacements by means of an iterative procedure when the stiffness and/or the damping ratio of the isolation system depend significantly on the design displacement. By using the two bilinear models derived from the laboratory tests, the suggested iterative procedure leads to the results shown in Table 9. The corresponding displacements, calculated using the linear equivalent model suggested by NTC08, are shown in Table 10.

Table 9 Displacements of the Center of Rigidity of the Isolation System for Four Different Earthquake Levels based on two Bilinear Models

Model 1	*Q (kN)*	*k_0 (N/mm)*	*k_1 (N/mm)*	*D_y (mm)*
	37	5413	802	8.02
	SLO	SLD	SLV	SLC
T(s)	1.29	1.47	2.46	2.56
ξ (%)	20	26	11	7
D (mm)	13	19	209	354
γ (%)	9	13	140	236
Model 2	*Q (kN)*	*k_0 (N/mm)*	*k_1 (N/mm)*	*D_y (mm)*
	40	6199	847	7.47
	SLO	*SLD*	*SLV*	*SLC*
T(s)	1.21	1.39	2.38	2.48
ξ (%)	20	27	12	8
D (mm)	12	18	198	336
γ (%)	8	12	132	224

Table 10 Displacements of the Center of Rigidity of the Isolation System calculated using an Equivalent Linear Model suggested by NTC08

NTC 08	*SLO*	*SLD*	*SLV*	*SLC*
T(s)	2.38	2.38	2.38	2.38
ξ (%)	15	15	15	15
D (mm)	21	31	181	257
γ (%)	14	21	121	171

The linear equivalent model suggested by the Italian code NTC08 underestimates the displacements at the limit states SLV and SLC, while it overestimates the displacements at the limit states SLO and SLD. The discrepancies are due to the fact that the damping ratio and the stiffness of the isolation system are considered constant and equal to the values established at the shear strain amplitude $\gamma = 1$. Better results are obtained if the equivalent secant stiffness K_e and the equivalent damping ratio ξ_e are

Table 11 Modified Linear Equivalent Model for the calculation of the System Displacements at various Limit States

NTC 08	SLO	SLD	SLV	SLC
T(s)	2.38	2.38	2.38	2.38
ξ (%)	12	12	12	12
D (mm)	23	34	197	279
γ (%)	15	22	131	186

calibrated at the displacement of the system under the SLV earthquake. In this case the results shown in Table 11 are obtained.

By comparing the results of Table 9 with those of Table 11 it may be seen that the displacements under the SLV earthquake are very close to each other. As it may have been expected the displacement under the SLC earthquake is still underestimated and those under the SLO and SLD earthquakes are overestimated. However, the underestimation under the SLC earthquake might not be a serious matter because the bilinear model may be unreliable under such an earthquake. In fact the tangent stiffness is expected to increase under large shear strains and this is not accounted for by the bilinear model. The overestimation of the SLD displacement is balanced in part by the underestimation of the stiffness and in part by a code prescription which requires the drift at the SLD to be less than two thirds of the value accepted for fixed base structures. No verification is required by the code for the SLO earthquake.

6. SIMULATION OF FREE VIBRATION TESTS

For the simulation of the free vibration tests to be performed on the Augusta building in the near future, the formulation presented by (Oliveto et al. 2012) is being used. The main parameters required for the analysis are the three parameters defining the behavior of the HDRB Q, k_0, k_1, and the friction coefficient for the characterization of the sliding bearings. Ideally, the parameters for the characterization of the HDRB could be specified for each isolator and the same applies for the friction coefficient of the sliding isolators. However, as shown in Table 9, only average data are available for two couples of HDRB. If the average values from the two sets were to be taken, the properties would be the average taken over four samples out of sixteen. Since no other data is available, the average properties chosen from Table 9 are used for simulation purposes, that is Q= *38.5 kN*, k_0= *5806 N/mm*, k_1= *824.5 N/mm*. The friction coefficients provided by the manufacturer for the LFSB were evaluated at very low testing velocities and appear to be too low for working conditions applications. For this reason the information obtained by identification of the Solarino Buildings isolation system is used, (Oliveto et al. 2010). The average friction coefficient from those tests was μ *=0.8 %*. The values of the vertical load for the evaluation of the friction force in the expected test conditions were taken as follows: 750 *kN*, 900 *kN*, 25 *kN* in the order of load bearing capacity of each type of sliding isolator.

6.1 Choice of Initial Test Displacements

The Augusta building shown in Figure 2 is architecturally finished and therefore no structural or non-structural damage must be produced by the tests planned. The internal and external partition walls have been designed and constructed with a fixed connection to the structural members. The Italian code NTC08 prescribes a drift limit of 0.5% to ensure that no non-structural damage can occur when the in-fills are rigidly connected to the structure. The purpose of the present analysis is to evaluate the maximum initial displacement that can be imposed to the building so that the drift limit is not exceeded during the phase of free vibration following the sudden release of the force used to impose the displacement. For safety reasons several tests will be performed under increasing initial displacement. Apart from the need to avoid damage, two other factors limit the maximum displacement that can be applied. One is related to the capacity of the available equipment in terms of force, stroke and strength of the contrast wall. The other is connected to the validity of the bilinear model which is expected to fail at large strain amplitudes. Therefore a suitable test protocol is given in Table 12.

Table12 Initial Strain and Displacement for Planned Tests

Strain amplitude γ(%)	Initial Displacement (mm)
20	30
50	75
80	120
100	150
120	*180*
140	*210*

6.2 Effects of the Friction Coefficient on Test Response

The friction coefficient is a main uncertainty in the evaluation of the test response because of the discrepancies between the results of the available laboratory tests, obtained under very low testing velocities and displacement amplitude, and the results deriving from full scale dynamic identification tests. For this reason a test has been simulated using different friction coefficients ranging from 0.2% to 1%. The results of the simulation are shown in Figure 10 in terms of displacement and in Figure 11 in terms of velocity.

The main effects of an increasing friction coefficient appear to be a reduction of the duration of motion and an increase of the residual displacement. When the largest friction coefficient is considered the system comes to rest after only 2 cycles, while when the lowest friction coefficient is used the motion of the system stops after 6 cycles. However, it should be noticed that only two cycles of motion involve energy dissipation in the HDRB. In the remaining cycles, according to the bilinear model, the behavior is purely elastic. The full scale dynamic tests to be performed on the Augusta building in the near future should provide a realistic value of the friction coefficient under seismic conditions.

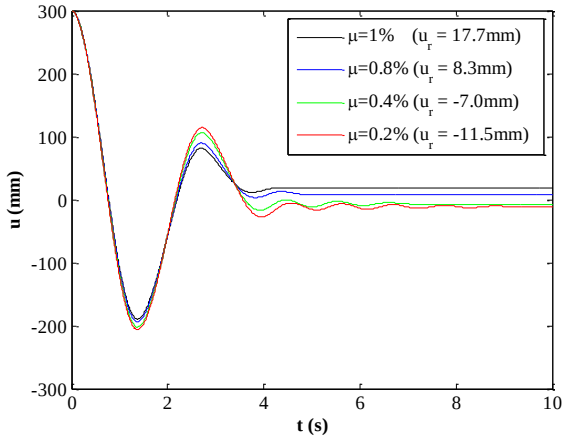


Figure 10 Displacement Response as a function of the Friction Coefficient

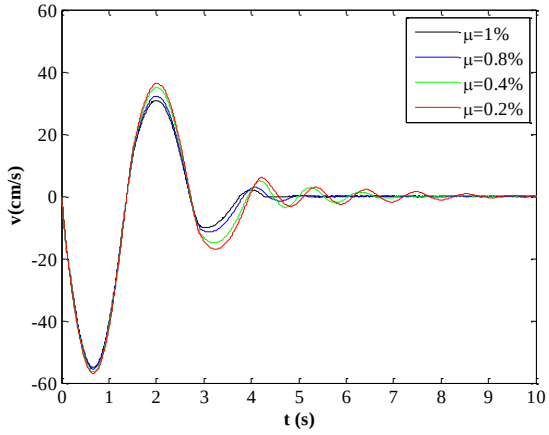


Figure 11 Velocity Response as a function of the Friction Coefficient

6.3 Application of Initial Displacement

The planning of free vibration tests under imposed initial displacements requires the evaluation of the static load needed to apply the considered displacement. The load-displacement curve for the Augusta building shown in Figure 12 has been evaluated using a bilinear model for the HDRB with the properties derived by the static laboratory tests described in section 4.1, namely k_0= 3515 *N/mm*, k_1= 683 *N/mm*, *Q*=28*kN*. For the friction coefficient the value μ=0.8% has been used.

The value of the friction force which must be overcome for the building to start moving has been evaluated as 111 *kN*, using the friction coefficient μ = 0.8%. Whether this value is realistic or not will be assessed when the tests are performed. The experience gained with the tests on the Solarino building shows that the considered value of the friction coefficient may be underestimated in static conditions. However, as the building starts to move the friction coefficient is expected to shift from the static value to the dynamic one. Therefore the use of the dynamic coefficient will underestimate the static friction force but might provide a good estimate of the force required to apply the considered displacement. The table in Figure 12 provides the force

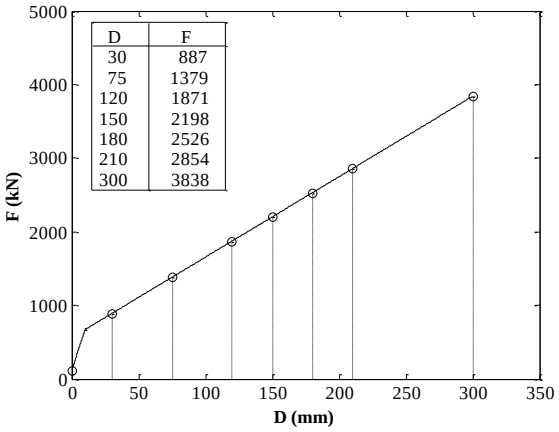


Figure 12 Static Load Displacement Curve for the Augusta Base Isolation System

required to apply a given displacement and is essential for the planning of the tests. The same push and quick release device used in the Solarino tests will be used for the Augusta building. A description of the device and of the preliminary results of the tests on the Solarino building has been given by Oliveto et al. (2004).

6.4 Effect of Initial Displacement on System Response

The amplitude of the initial displacement can considerably affect the response of the system as the results of Figure 13 show for the case when no mass eccentricity is considered. Response histories can be easily obtained also in terms of velocity, acceleration and of any other response parameter. Some typical response parameters are shown in Table 13.

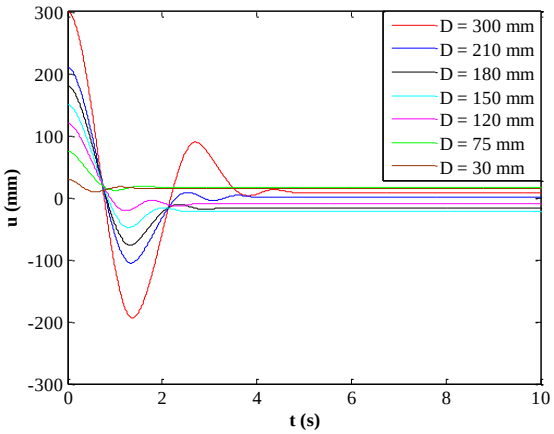


Figure 13 Free Vibration Response of the Isolation System as a function of the Imposed Initial Displacement

As expected the peak values of velocity and acceleration increase as the initial displacement increases. The initial period (T_1) and the time required for the motion to stop (t_r) are also increasing functions of the initial displacement. The residual displacement (u_r) does not show a characteristic pattern. The largest value (u_r = 21.2 *mm*) is obtained with an initial displacement *D* = 150 *mm* and the

Table13 Variation of System Response Parameters with Displacement Amplitude in the Absence of Mass Eccentricity

D (*mm*)	*peak v* (*cm/s*)	*peak a* (*gal*)	T_1 (*s*)	u_r (*mm*)	t_r (*s*)
30	5.7	33.8	1.115	14.6	1.650
75	9.6	56.3	1.550	16.6	2.080
120	16.9	78.7	1.780	-9.1	2.850
150	22.9	93.7	2.035	-21.2	3.090
180	29.3	108.7	2.355	-16.0	3.420
210	35.7	123.7	2.540	0.3	4.130
300	55.5	168.6	2.710	8.3	4.950

smallest (u_r = 0.3 *mm*) is obtained for an initial displacement of D = 210 *mm*.

When the accidental eccentricity is considered as prescribed in D.M. 14/01/2008, the displacement response of the corner isolator 32 in the longitudinal and transverse directions are those of Figure 14 and Figure 15. If the scale used in Figure 14 were to be used in Figure 15 the transverse displacement would be barely noticeable. Therefore the response of the system to the experiments is expected mainly in the longitudinal direction.

Peak velocities and accelerations at corner isolators are given in Table 14 for different levels of imposed initial displacement. The increase in peak velocity due to considering the accidental mass eccentricity is barely noticeable, while the increase in peak acceleration is on average about 6%. The fundamental period seems to be little affected by the presence of the accidental eccentricity, the maximum amplification being less than 1%. The residual displacement appears to increase everywhere because of the effect of the mass eccentricity. The variation of the time required for the motion to stop seems to occur randomly.

Table14 Variation of System Response Parameters with Displacement Amplitude in the Presence of Mass Eccentricity

D (*mm*)	*peak v* (*cm/s*)	*peak a* (*gal*)	T_1 (*s*)	u_r (*mm*)	t_r (*s*)
30	5.7	35.9	1.120	14.8	1.685
75	9.6	59.8	1.550	17.9	2.080
120	17.0	83.6	1.790	10.0	2.890
150	23.0	99.5	2.045	21.2	3.075
180	29.3	115.4	2.370	19.0	3.430
210	35.8	131.3	2.550	3.0	4.190
300	55.7	179.0	2.720	9.3	4.915

6.5 Story Drifts

It is recognized in the international literature that structural and nonstructural damage in a building is related to story drifts. The Italian code NTC08 prescribes that for RC structures with in-fills rigidly connected to the structural members, story drifts at the damage limit state should not

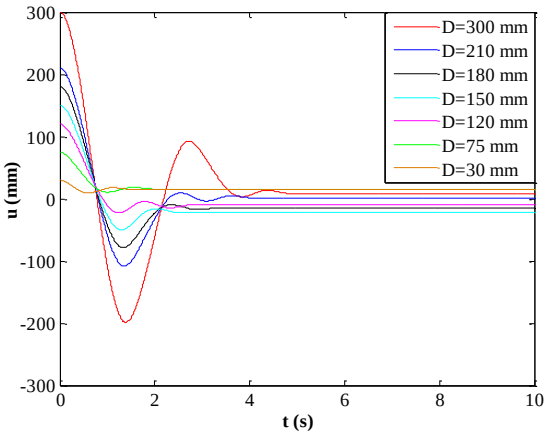


Figure 14 Free Vibration Displacement Response of Isolator 32 in the Longitudinal Direction as a function of the Imposed Initial Displacement

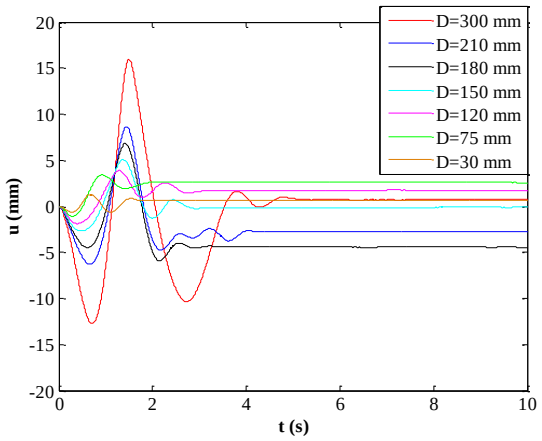


Figure 15 Free Vibration Displacement Response of Isolator 32 in the Transverse Direction as a function of the Imposed Initial Displacement

exceed 5‰. During the tests planned for the Augusta building the story drift should be comfortably smaller than the damage limit. The aim of this subsection is to evaluate the story drifts arising from the test conditions and to check that they do not exceed the stated limit. The procedure used for this evaluation starts from the following equation of motion for the base-isolated structure.

$$\mathbf{M}\ddot{\mathbf{u}} + \mathbf{C}\dot{\mathbf{u}} + \mathbf{K}\mathbf{u} + \mathbf{F} = \mathbf{0} \tag{13}$$

where

$$\mathbf{u} = \begin{bmatrix} \mathbf{u}_S \\ \mathbf{u}_B \end{bmatrix}, \mathbf{M} = \begin{bmatrix} \mathbf{M}_{SS} & \mathbf{0} \\ \mathbf{0} & \mathbf{M}_{BB} \end{bmatrix}, \mathbf{C} = \begin{bmatrix} \mathbf{C}_{SS} & \mathbf{C}_{SB} \\ \mathbf{C}_{BS} & \mathbf{C}_{BB} \end{bmatrix},$$

$$\mathbf{K} = \begin{bmatrix} \mathbf{K}_{SS} & \mathbf{K}_{SB} \\ \mathbf{K}_{BS} & \mathbf{K}_{BB} \end{bmatrix}, \mathbf{F} = \begin{bmatrix} \mathbf{0} \\ \mathbf{F}_B \end{bmatrix}$$

The matrices **M, C** and **K** in Equation (13) refer to the superstructure, while $\mathbf{F_B}$ is the vector of the restoring forces provided by the isolators. The partitioned form of the above matrices is used to separate the degrees of freedom of the superstructure from those shared with the base isolation system. Therefore vector **F** is a known function of time evaluated by considering the superstructure as rigid (Oliveto et al. 2012). The results shown in subsection 6.4 were obtained by such a method and the sub-vector $\mathbf{F_B}$ is a bi-product of that analysis. The damping matrix has been calculated by assuming a 2% modal damping ratio for all the superstructure modes. The response of the superstructure is shown in Figures 16, 17 and 18 in terms of displacements, velocities and accelerations. From Figure 16 it may be seen that displacements at the various floors are barely distinguishable. The high frequency components, which provide a significant contribution to velocity and acceleration, determine significant variations of these response parameters from floor to floor. The peak acceleration on the top floor appears to be significantly larger than that at lower floors.

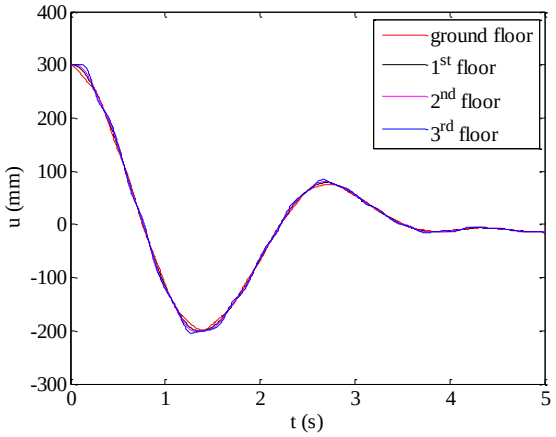


Figure 16 Predicted Floor Displacement Response for the Augusta Building under D = 300 *mm*

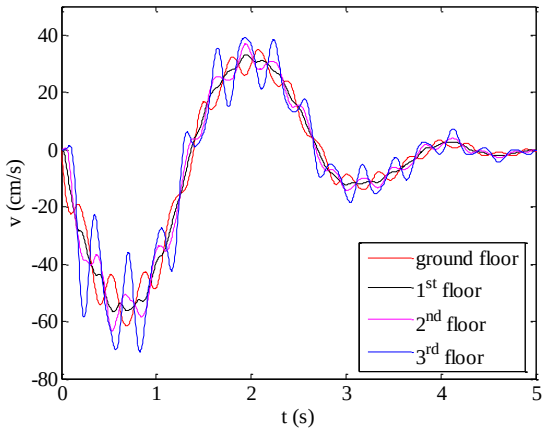


Figure 17 Predicted Floor Velocity Response for the Augusta Building under D = 300 *mm*

The story drifts are shown in Figure 19 and, although the displacement imposed to the isolation system reaches the

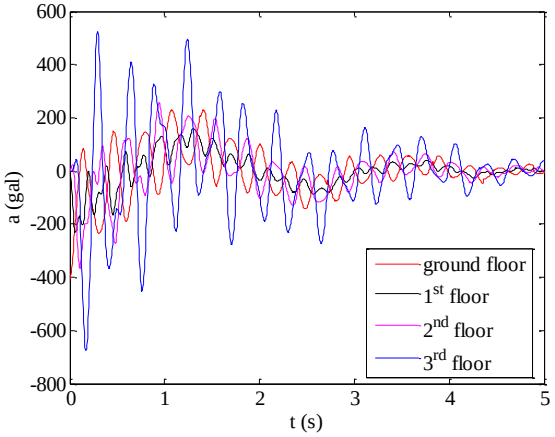


Figure 18 Predicted Floor Acceleration Response for the Augusta Building under D = 300 *mm*

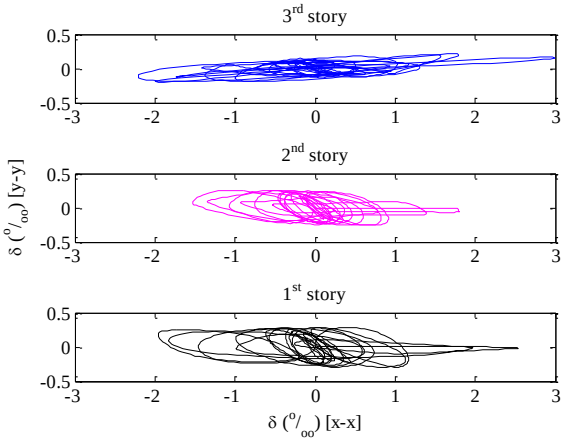


Figure 19 Predicted Story Drifts for the Augusta Building under D = 300 *mm*

maximum guaranteed by the manufacturer for the Collapse Limit State (SLC), the maximum drift does not exceed the limit value for the Damage Limit State (SLD). The variation of peak velocity and peak acceleration at the various floors, as a function of the amplitude of the imposed initial displacement, is shown in Table 15.

Table15 Variation of System Response Parameters with Displacement Amplitude in the Absence of Mass Eccentricity

D (mm)	*peak v (cm/s)*			*peak a (gal)*		
	Floor			*Floor*		
	1	*2*	*3*	*1*	*2*	*3*
30	6.2	7.7	11.8	46.6	73.2	135.7
75	10.4	12.7	19.6	77.5	121.8	225.8
120	18.4	22.2	27.4	108.5	170.5	316.0
150	24.7	29.1	33.1	129.2	202.9	376.1
180	31.0	36.0	40.2	149.8	235.4	436.2
210	37.4	42.8	47.5	170.4	267.8	496.3
300	56.7	63.4	70.6	232.4	365.1	676.8

Table16 Variation of the Maximum Story Drifts [‰] with Displacement Amplitude

D (mm)	*Mass eccentricity neglected*			*Mass eccentricity considered*		
	Story			*Story*		
	1	*2*	*3*	*1*	*2*	*3*
30	0.51	0.36	0.66	0.52	0.37	0.66
75	0.85	0.60	1.10	0.86	0.61	1.09
120	1.19	0.85	1.54	1.20	0.86	1.53
150	1.41	1.01	1.83	1.43	1.02	1.82
180	1.64	1.17	2.13	1.65	1.18	2.12
210	1.87	1.33	2.42	1.88	1.34	2.41
300	2.54	1.81	3.30	2.57	1.83	3.28

As expected peak velocity and acceleration increase as the amplitude of the imposed displacement increases and they are generally higher at the top floor. The maximum story drift is shown in Table 16 as a function of the imposed initial displacement for the case when accidental mass eccentricity is neglected and for the case when it is considered. Again the story drifts increase as the amplitude of the imposed initial displacement increases. The effect of the accidental eccentricity is that of increasing the maximum drift at the first and second stories and decreasing it at the top story. It is important to notice that the maximum story drift is always well within the limit of the SLD. Therefore the story drifts will not be a limiting factor in the definition of the maximum imposed displacement during the tests on the building.

7. CONCLUSIONS

This work has considered the Italian construction code NTC08 with reference to seismically isolated buildings through a case study. The code prescribes the seismic actions by providing response spectra for four different limit states on a point by point basis. The spectral ordinates have different characteristics for isolation modes and for structural modes. Provided that some specific conditions are satisfied, linear static analysis and/or linear dynamic analysis can be used for design purposes. Linear analysis, either static or dynamic, seems to be based on viscous equivalent properties of the base isolation system obtained from tests at a shear strain $\gamma = 1$. The behavior of the base isolation system at the ultimate limit states SLV and SLC involves values of the shear strain well above $\gamma = 1$ and the Italian manufacturers of elastomeric bearings guarantee the integrity of the elastomeric isolators up to a maximum shear strain $\gamma = 2$. The analysis of the seismic response at the ultimate limit states SLV and SLC should therefore converge to results where the corresponding shear strain should be $\gamma \leq 2$. This can be easily achieved if the base isolation system is treated as an equivalent linear system with the properties calibrated at a shear strain $\gamma = 1$. However it would seem more appropriate to calibrate the equivalent linear system at the shear strain competing to each of the limit states considered. In order to do this the designer should have at his disposal not only the results of the acceptance tests, but also the results of the qualification tests on the isolation bearings. In fact these are performed at different levels of shear strain up to the maximum value for which the isolation device is guaranteed. At the present time it does not appear that such tests are available to the designer.

The code seems to imply that if the stated conditions for linear analysis, whether static or dynamic, are not fulfilled by the isolation system, the designer should opt for a non-linear analysis. However, as far as models are concerned, no guidance is offered and these are left to the responsibility of the designer.

Typical results of acceptance tests performed on samples of the batch of isolators used for the Augusta building have been discussed in this paper. Based on these results a bilinear model has been developed for the elastomeric bearings and a Coulomb friction model has been calibrated for the sliding isolators. The two models have been combined and used for the simulation of free vibration tests to be performed on the building under imposed initial displacements. Some basic facts necessary for the planning of the tests have been established. Among these are the evaluation of the forces needed to apply each initial displacement, the duration of the successive phase of free motion, the residual displacements at the end of the motion, periods and number of cycles of free vibration. Other response parameters that have been evaluated are peak floor velocities and accelerations in test conditions.

One particularly relevant issue involved in performing a dynamic test on a finished building is that of avoiding structural and non-structural damage. International building codes define the limit state that separates undamaged and damaged states of a building in terms of the value of the story drift. For this reason the story drifts have been evaluated for various imposed initial displacements in the absence and in the presence of accidental mass eccentricity.

Even for the largest displacement considered, corresponding to the integrity limit for the isolators, the story drifts remain well below the value stated by NTC08 for the SLD. Therefore it is believed that the maximum applicable displacement depends more on the available equipment in terms of maximum force and/or stroke rather than on the necessity of avoiding damage.

The results of the tests planned for the near future will provide a means of assessing the reliability of the predictions presented. Anyway, this study allows the performance of the tests with a sufficient degree of reliance.

Acknowledgements:

The authors acknowledge support from the Japan Ministry of Education, Culture, Sport, Science, and Technology (MEXT) for establishing the Center for Urban Earthquake Engineering (CUEE) in Tokyo Institute of Technology. This support makes possible the forthcoming international conference, as well as international joint research projects and exchange programs with overseas universities.

References:

D.M. 14/01/2008, "Norme Tecniche per le Costruzioni," *G.U.R.I. n° 29 del 4 Febbraio 2008 – Suppl. Ord. N° 30.*

O.P.C.M. 3274, " Primi elementi in materia di criteri generali per la classificazione sismica del territorio nazionale e di normative tecniche per le costruzioni in zona sismica," Norme Tecniche per le Costruzioni," *G.U.R.I. n° 72 del 8Maggio 2003 – Suppl. Ord. N° 105.*

D.M. 14/09/2005, "Norme Tecniche per le Costruzioni," *G.U.R.I. n° 222 del 23Settembre 2005 – Suppl. Ord. N° 159.*

Eurocode 8 , "Design of structures for earthquake resistance- Part 1: General rules, seismic actions and rules for buildings," *European Committee for Standardization –December 2004*

FIP Industriale SpA (2006), "Elastomeric isolators - Series SI," – www.fip-group.it/fip_ind_eng/prodotti.html

FIP Industriale SpA (2009-a) , "Isolatori Sismici in elastomero armato SI-N 500/150 -Prove di accettazione,"VP 44/09.

EN 1337-3 (2005), " Structural bearings –Part 3: Elastomeric bearings," *European Committee for Standardization –March 2005*

Naeim, F. and Kelly, J.M. (1999), "Design of Seismic Isolated Structures, " *John Wiley & Sons, Inc*. New York

FIP Industriale SpA (2009-b), "Isolatori a scorrimento Augusta-Prove di accettazione,"VP 48/09.

Oliveto, N.D., Athanasiou, A. and Oliveto, G. (2012), "Mixed Lagrangian formulation for dynamic and earthquake response of 2D hybrid base isolation systems," *Joint conference proceedings: 9th International Conference on Urban Earthquake Engineering / 4th Asia Conference on Earthquake Engineering, Tokyo Institute of Technology,* Japan, 1373–1382.

Oliveto, N.D., Scalia, G. and Oliveto, G. (2010), "Time Domain Identification of Hybrid Base Isolation Systems using Free Vibration Tests," *Earthquake Engineering and Structural Dynamics*, **39**(9),1015–1038.

Oliveto, G., Granata, M., Buda, G. and Sciacca, P. (2004), "Preliminary Results from Full-Scale Free Vibration Tests on a Four Storey Reinforced Concrete Building after Seismic Rehabilitation by Base Isolation", *JSSI 10th Anniversary Symposium on Performance of Response Controlled Buildings* ,Yokohama, Japan.

10CUEE CONFERENCE PROCEEDINGS
10th International Conference on Urban Earthquake Engineering
March 1-2, 2013, Tokyo Institute of Technology, Tokyo, Japan

POUNDING IN THREE DIMENSIONAL BASE ISOLATED BUILDINGS

Armin Masroor[1)] and Gilberto Mosqueda[2)]

1) Graduate Student, Dept. of Civil, Structural, and Environmental Engineering, State University of New York, Buffalo, USA
2) Associate Professor, Dept. of Structural Engineering, University of California, San Diego, USA
am249@buffalo.edu, gmosqueda@ucsd.edu

Abstract: Base isolated buildings subjected to extreme earthquakes can exceed their design displacements and impact against the surrounding moat wall. To better understand the consequences of impact on the superstructure, experimental simulations of a base isolated structure with simulated moat walls were conducted on a shaking table. Based on experimental observations and impact theory, an impact element considering moat wall compliance was proposed and shown to accurately capture impact forces. In this paper, the impact model is extended to 3-D structures and the response of 3-story moment and braced frame prototype models is examined considering impact to a surrounding moat wall at the base level by implementing the proposed impact element to finite element models of the buildings. The effect of pounding to moat wall in both prototype buildings were investigated by comparing the superstructure response with and without the presence of the moat wall. These studies provide critical information for the design of base isolated buildings, particularly the moat wall clearance and its potential effect on the superstructure response.

1. INTRODUCTION

A typical base isolated basement design requires a space in which the building is free to move sideways without contacting the surrounding structure. This space is commonly referred to as the "moat". Structural design codes such as ASCE 7-05 (ASCE 2005) specify the minimum moat wall distance equal to the expected displacement of the isolation system under the maximum considered earthquake (MCE) while the superstructure is designed for design basis earthquake (DBE). Despite the cautious regulation for moat wall gap distance, pounding of base isolated building to moat wall has been reported in previous earthquakes. Current design specifications may not adequately account for the large forces generated during impact in base isolated buildings.

The base-isolated Fire Command and Control (FCC) building in Los Angeles experienced pounding to its moat wall during the 1994 Northridge earthquake (EERI 1995). Post-earthquake evaluations showed that the base isolated FCC building performed well, except for impact, which increased structural shear, and drift demands (Nagarajaiah and Sun 2001). In the more recent 2011 Christchurch earthquake, post-earthquake investigations revealed pounding of the only base isolated building in that region to moat wall resulting in damage to sacrificial non-structural components at the seismic gaps (Gavin and Nigbor 2012).

Komodromos et al. (2007) conducted a series of parametric studies to investigate the influence of potential poundings of seismically isolated buildings with adjacent structures on the effectiveness of seismic isolation. The numerical simulations demonstrated that poundings may substantially increase floor accelerations, especially at the base floor where impacts occur. The effects of seismic pounding on the structural performance of a base-isolated reinforced concrete (RC) building are investigated by Pant and Wijeyewickrema (2012). In particular, seismic pounding of a typical four-story base-isolated RC building with retaining walls at the base and with a four-story fixed-base RC building is examined. Three-dimensional finite element analyses are carried out considering material and geometric nonlinearities. It is found that the performance of the base-isolated building is substantially influenced by the pounding.

Masroor and Mosqueda (2012a) investigated experimentally the behavior of base isolated buildings during contact with different types of moat wall. The test setup consists of a quarter scale three-story frame isolated at the base with friction pendulum bearings and various moat wall models. The moat wall was modeled as either a rigid steel stopper or concrete walls of various thicknesses with soil backfill. Test results indicate that the contact forces are largely dependent on the gap distance, impact velocity and wall flexibility and, in extreme cases, pounding can induce yielding in the superstructure. They proposed a simplified impact element considering moat wall flexibility based on impact theory and observations during experimental simulations (Masroor and Mosqueda 2012b). It was demonstrated that numerical simulations using the proposed impact element can capture the dominant characteristics of the contact force observed in experiments of base isolated buildings impacting various moat wall configurations.

In this paper, the impact model proposed by authors (Masroor and Mosqueda 2012b) is extended to 3-D structures for improved modeling of limit states in base isolated structures. Two moment frame and two braced frame base isolated structures designed by professional engineers are examined. The effects of pounding to moat wall in these prototype buildings were investigated by comparing the superstructure response with and without the presence of the moat wall.

2. PROTOTYPE BUILDINGS

As part of the NEES TIPS project (Ryan et al. 2008), a series of conventional and base-isolated buildings were professionally designed by Forell/Elsesser Engineers Inc. and adapted here for use in the experimental and numerical studies on structural pounding. The 3-story base isolated building models include a base isolated Intermediate Moment Resistant Frame (IMRF), and a base isolated Ordinary Concentric Braced Frame (OCBF). These buildings were designed for occupancy category II and importance factor I = 1.0 according to ASCE 7-05. These office buildings were designed by the Equivalent Lateral Force Method to meet the requirements of 2006 International Building Code, ASCE 7-05, and AISC 341-05. The buildings were designed for a Los Angeles, California, location (34.50 N, 118.2 W) on stiff soil (site class D with reference shear wave velocity of 180 to 360 m/s). The mapped spectral accelerations for this location are S_S = 2.2 g for short periods and S_1 = 0.74 g for a 1-s period.

The model layout is 6 by 4 bays with 30 ft. width in both directions for both frames. The height of each story is equal to 15 ft. Lateral resistance is provided by two 5-bay perimeter moment frames in the X-direction and two 3-bay perimeter and two 2-bay interior moment frames in the Y-direction in the IMRF model. The exterior brace system shown in Figure 1 was used for the OCBF model. Both base isolated IMRF and OCBF models were designed for the same hazard level and location although the IMRF model was designed for response modification factor of R=1.67 and the OCBF model was designed for R=1. A higher R for IMRF model resulted in a more flexible superstructure in comparison with the OCBF. The superstructure first mode period for the IMRF and OCBF models are 1.4 and 0.4 sec.

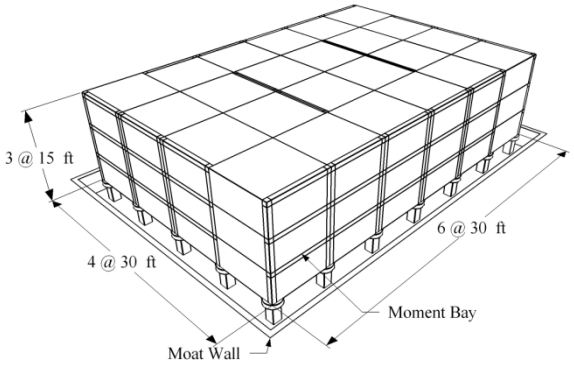
Table 1 summarizes the design parameters for the isolation system. These parameters are comparable for both the IMRF and OCBF since the total weight of the two systems are very close (~7200 kips). In this table, T_D and T_M are effective isolation periods at DBE and MCE level, D_M and D_{TM} are the maximum displacement and total maximum displacement of the isolation system calculated from Equations 17.5-3 and 17.5-6 in ASCE7-10:

$$D_M = \frac{gS_{M1}T_M}{4\pi^2 B_M},\ D_{TM} = D_M\left[1 + y\frac{12e}{b^2+d^2}\right] \qquad (1)$$

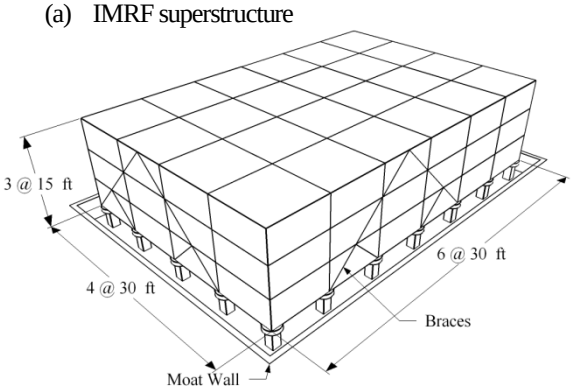
where B_M is a coefficient that modifies from 5% damping spectrum to a desired damping (Table 17.5-1 in ASCE7-10), S_{M1} is 1-s spectral acceleration for MCE events, e is the actual eccentricity plus accidental eccentricity taken as 5 percent of the longest plan dimension of the structure perpendicular to the direction of force under consideration, and b and d are the shortest and longest plan dimension of the structure, respectively. The minimum moat wall gap distance required by ASCE 7-10 equals to D_{TM} (approximately 760 mm or 30 in. for these models).

Table 1 Design parameters for isolation systems

Isolator Properties	DBE Event	MCE Event
Effective period (s)	$T_D = 2.77$	$T_M = 3.1$
Effective Damping (%)	$\beta_D = 24.2$	$\beta_M = 15.8$
Isolator Displacement (in)	$D_D = 12.7$	$D_M = 24.3$
Total Displacement (in)	$D_{TD} = 15.3$	$D_{TM} = 29.4$



(a) IMRF superstructure



(b) OCBF superstructure

Figure 1 Prototype base isolated IMRF and OCBF

3. ISOLATED BUILDINGS WITH MOAT WALL

3.1 Superstructure and Isolator Model

Detailed 3D numerical models of the IMRF and OCBF buildings were developed in OpenSees (Erduran et al. 2011; Sayani et al. 2011). Equivalent mass and rotational inertia were lumped at the center of mass (master node) at each level which is shifted by 5% of the longest plan dimension in both directions to account for accidental torsion. Slab action was accounted for through a rigid diaphragm constraint. Energy dissipation was added to the superstructure using

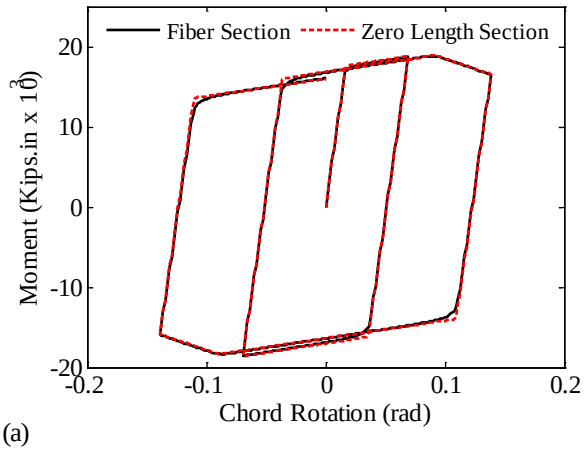
tangent stiffness proportional damping calibrated to give 2.5% damping at its respective first mode frequencies.

All columns and moment-resisting beams were modeled using force-based nonlinear beam-column elements that combine finite length "plastic hinge" regions at the element ends with an interior elastic region. Modeling structural behavior through collapse requires, to the extent possible, numerical models that directly simulate all significant deterioration modes contributing to collapse behavior such as stiffness, strength, and inelastic deformation simulation in structural component models. For this purpose, the steel stress-strain and moment-curvature relationships for all the elements were modified to include strength and stiffness degradation using Modified Ibarra Krawinkler (MIK) deterioration model (Lignos and Krawinkler 2011). Lignos and Krawinkler (2011) tested a large number of beam section under cyclic loading and proposed equations to calculate the degradation parameters for different beam section. They proposed these parameters for moment-chord rotation behavior for each section. Assigning moment-curvature relationships for beam elements in which axial force plays insignificant role is adequately reasonable. Unlike beam elements, column section experienced a large axial force especially under large deformations. For this reason, fiber sections were selected to property account for the effects of axial load on moment strength of the columns.

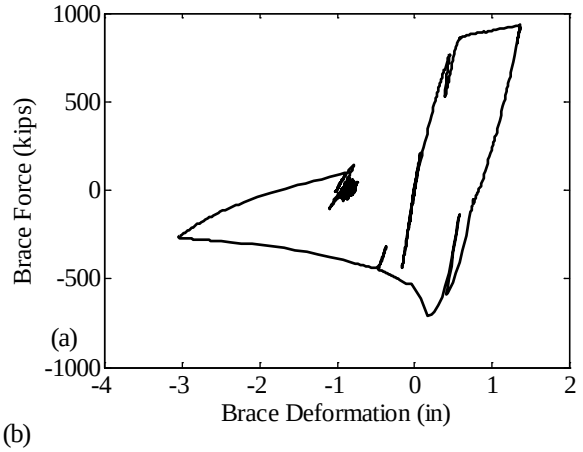
In order to consider the effects of strength degradation for column sections, the following procedure was conducted to modify the MIK model proposed by Lignos and Krawinkler (2011) for stress-strain relationship. First, moment-rotation response of each column section was developed using parameters proposed by Lignos and Krawinkler (2011) and assigning these values to a zero length section for a cyclic pushover. Then, a fiber section for the same column geometry was generated with the MIK model assigned to each fiber element as stress-strain behavior. The required parameters for the fiber section using MIK model was calibrated based on comparing these two responses for a given displacement history. Figure 2(a) compares the zero length section response with fiber section element for moment frame column section in the first floor of the IMRF model.

In the OCBF model, multiple nonlinear beam–column elements were strung together to physically simulate the inelastic buckling behavior in braces (Uriz et al. 2008). A single brace using two force-based nonlinear beam–column elements with fiber sections and three numerical integration points along the length of the element was selected. An initial camber of 0.1% of the brace length was applied at the brace midpoint to initiate buckling. The resultant simulated cyclic force–deformation of a representative brace is shown in Figure 2(b).

In both models, isolators were modeled independently, one beneath each column, using a combination of elements to realize a composite force deformation in each direction that could represent either elastomeric or friction pendulum devices. An elastic column element and an elastic-perfectly plastic spring were assembled in parallel to obtain the composite bilinear lateral force-deformation behavior. The compressive stiffness of the isolators was computed assuming a vertical frequency of 10 Hz. Since typical bearings have no or low resistance to tension, the tensile stiffness was assumed to be 1% of the value of the compressive stiffness.



(a)

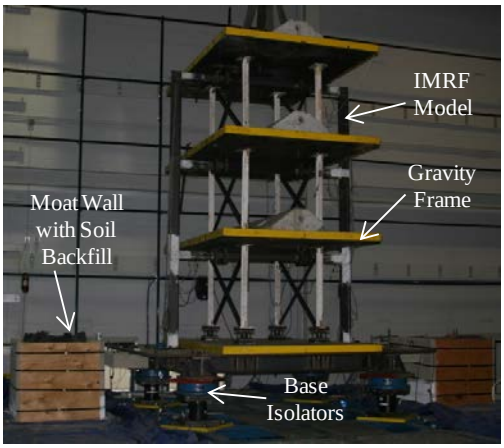


(b)

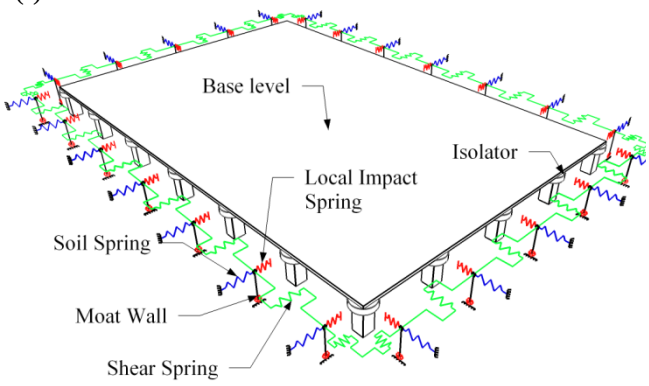
Figure 2 (a) Cyclic behavior of column section at the first floor of the IMRF model (W 14x176), (b) A representative brace force-deformation of OCBF model.

3.2 Moat Wall Model and Experimental Verification

In order to consider the potential and effects of pounding in a time history analysis of base isolated buildings under ground motion, a comprehensive study was conducted by Masroor and Mosqueda (2012b) leading to propose an impact element based on impact theory and verifications with experimental simulations. It is demonstrated that numerical simulations using the proposed impact element can capture the dominant characteristics of the contact force observed in experiments. The experimental program consisted of shake table testing of a quarter-scale model representative of the IMRF model using the NEES equipment site at the University at Buffalo. The principal objective of these experiments was to generate experimental data for base isolated building pounding against a moat wall, specifically the impact force and the superstructure response. Figure 3(a) shows the shake table test setup. In this



(a)



(b)

Figure 3 (a) Shake table test setup, (b) Proposed impact element implemented at base level of the prototype model.

experiment, different types of moat walls were installed at various gap distances relative to base level of isolated model and different ground motions were applied to capture the variation in response with moat wall stiffness and impact velocity.

Based on nonlinear dynamic response of moat walls with soil back fill and verification with experimental results, an impact element for moat walls was proposed. This element is implemented in finite element modeling of the base isolated buildings at the base level (Figure 3(b)). The contact force is dependent on impact velocity, geometry and material properties at the contact surface, as well as the global dynamic flexibility characteristic of the moat wall. This moat wall model includes both local deformation and global vibration aspects of structural impact. The local aspect of impact consist of local material deformation or indentation and can be implemented using a Hertz damped element (Muthukumar and DesRoches 2006) at the contact location. The global vibration aspects of impact results from deformations of the moat wall and soil backfill excited by a dynamic impact force. To simulate nonlinearity in the concrete moat wall and soil back fill due to the pushing impact force, a single beam element is combined with a nonlinear spring in series. The single beam element simulates vibration response of the moat wall representing a certain wall width. The height of the beam element can be set to the height of the wall and a rotational spring is assumed at the base of the beam to capture the post-elastic behavior due to the formation of a plastic hinge.

A hyperbolic force-displacement (HFD) relationship was developed by Shamsabadi et al. (2007) to simulate the mobilized passive pressure behind the abutment back wall in bridges. The HFD tool is found to be a good fit with many experimental test data and all curves calculated by the log-spiral hyperbolic (LSH) model. This model was used here to simulate the response of soil back fill by assuming a nonlinear spring connected to top of the moat wall beam element.

The proposed moat wall model consists of moat wall nonlinear beam element, a Hertz damped local spring in front and HFD soil spring behind to capture the impact forces between a point at the base level of the superstructure and a point on the moat wall with specific length and fixed boundary condition at the bottom. This element can be replicated at a given distance to represent continuous walls along the base level of the superstructure. Figure 3(b) shows the simulated moat wall model using this element. The spacing between these moat wall elements could be set to the bay span of the superstructure to align the end of column elements with moat wall elements. These single moat wall elements should be connected using interactional elements to represent continues moat wall behavior. The behavior of these internal elements was defined here based on finite element analysis.

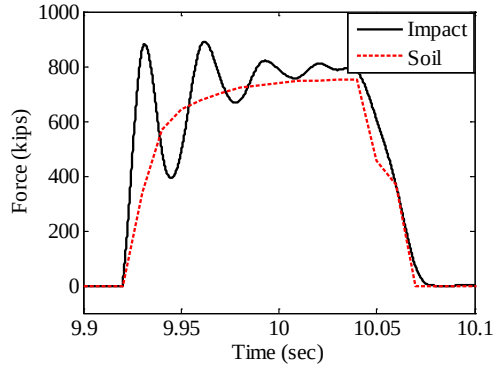
The shape of the impact force generated due to pounding to the base level at one corner impact element and also displacement in this moat wall node is shown in Figure 4 The total impact force is a combination of dynamic oscillation in the moat wall element and force generated in soil backfill. Residual deformation shown in this figure verifies plastic deformation in the moat wall and soil backfill, which is a source of damping for the impact force.

4. EFFECT OF POUNDING ON RESPONSE OF BASE ISOLATED MODELS

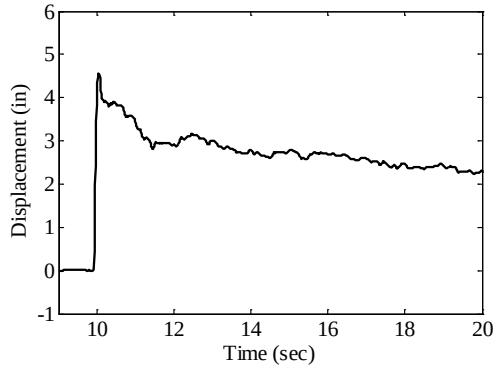
The performance of the two prototype base isolated models was examined under 20 ground motions from the NEES TIPS project with and without moat walls. All the ground motions were scaled to MCE level for the period range of 0 to 3 sec. Two horizontal components of each ground motion were applied on the frame simultaneously. The moat wall gap distance was set to 30 in, which is approximately equal to D_{TM} specified by ASCE (2005) based on a static design procedure.

Figure 5 shows the maximum base level corner node displacement in X and Y directions for each ground motion for both frames for the case that there is no moat wall. The reference gap distance from ASCE 7-05 is shown by the dashed line (30 in.). It can be seen that only 8 ground motions induce corner node displacements larger than 30 in. in the IMRF model while 11 ground motions induce corner displacement more than the specified gap distance in the OCBF frame. Higher participation of the first mode of the IMRF model resulted in reducing maximum base level

displacement demand in comparison with equivalent single degree analysis. Stiff behavior of the OCBF model leads to larger displacement at base level resulting in stronger pounding to moat walls.



(a)



(b)

Figure 4 Corner impact element (a)force and (b)displacement

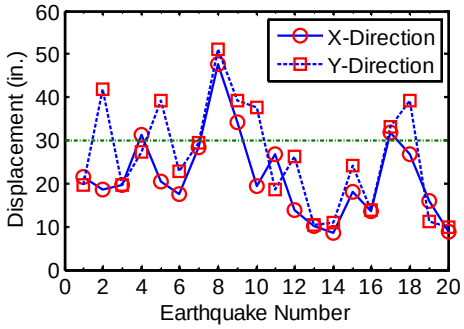
Installing the moat wall at 30 in. gap distance (equal to D_{TM} for both models) resulted in pounding of base level to moat walls in 8 and 11 ground motion for IMRF and OCBF models. The average impact force generated is equal to 2000 and 3300 kips for ground motions inducing pounding in IMRF and OCBF, respectively.

Seismic response, when sampled over many motions, are widely accepted to follow a lognormal statistical distribution. As such, the median and dispersion of the lognormal data, defined as

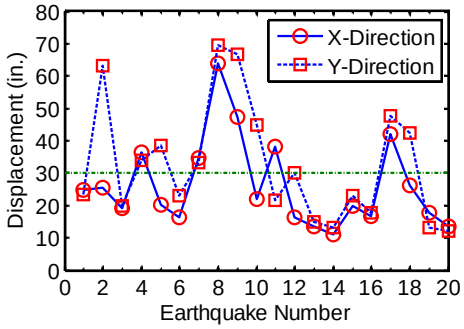
$$\mu = exp\left[\frac{\sum_{i=1}^{n} \ln x_i}{n}\right], \quad \zeta = \left[\frac{\sum_{i=1}^{n} (\ln x_i - \ln \mu)^2}{n-1}\right]^{1/2} \qquad (2)$$

are generally used to describe the central tendencies and variability of the response quantities for different ground motion sets. The median plus one standard deviation, or 84 percentile values, were computed as $\mu.\exp(\zeta)$.

Median and 84% of story drift ratio (SDR) and acceleration for both IMRF and OCBF models are shown in Figure 6 and Figure 7. Story drift ratio was evaluated as the maximum drift among the four corners of the building while the maximum vector summation acceleration for the master node in each floor was used. These parameters are compared for the two cases with and without moat wall to show the effect of pounding.

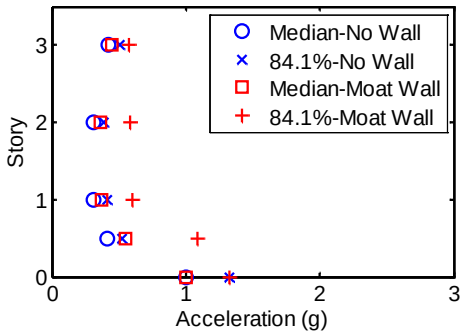


(a)

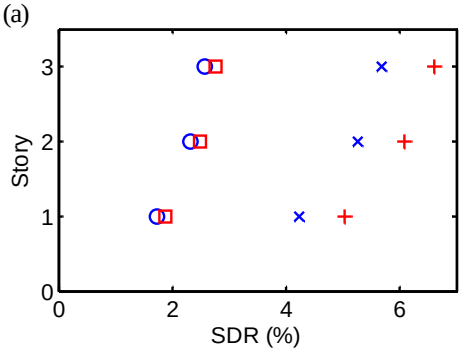


(b)

Figure 5 Base level corner node displacement for (a) IMRF model and (b) OCBF model without moat wall



(a)

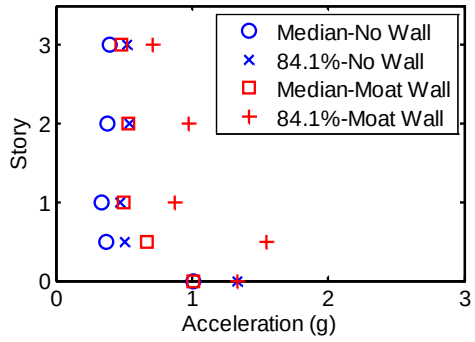


(b)

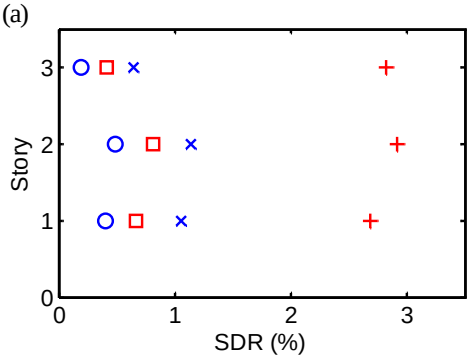
Figure 6 Median and 84% of (a) Acceleration (b) SDR for IMRF

Both frames show that the median floor accelerations are held within about 0.5g without moat walls although median PGA is on the order of 1g. Pounding to moat walls increases the acceleration in all levels especially in lower levels. The median floor acceleration does not show

significant increase although 84% value shows 200% increase in base level and approximately 80% increase in floor levels. The average value remains the same because of the fact that in many ground motions no pounding occurs but the 84% value increases substantially since the ground motions pounding to moat wall contribute a significant deviation from the average.



(a)



(b)

Figure 7 Median and 84% of (a) Acceleration (b) SDR for OCBF.

Large median and 84% SDR in IMRF model for the case without moat wall verifies the effects of the flexible superstructure. Unlike the IMRF model, OCBF model shows very stiff behavior. The median SDR value is on the order of 0.5 to 0.9% with smaller dispersion. Pounding to moat walls increases SDR in all levels especially in upper floors. The effect of pounding on median SDR is more clear for OCBF model because of the fact that 11 out of 20 ground motions induce pounding to moat walls in OCBF model while 8 out of 20 ground motions pound in the IMRF model. The flexible superstructure of the IMRF model leads to large SDR even in cases without moat walls. When the moat walls are added, the SDR increases only slightly, but as a percentage it is less significant compared to the OCBF. A larger increase in SDR response for the OCBF frame is obtained that is likely due to the larger number of ground motions inducing pounding, stiffer and non-ductile superstructure frame. Stiff superstructure in OCBF frame also results in larger displacement demand at the base level inducing stronger pounding to moat walls in comparison to the IMRF model.

As expected, larger dispersions are obtained in both acceleration and SDR for the cases with pounding in comparison with the case without moat walls. This shows that the response of the models worsens for the case of pounding to moat walls, inducing sudden increased accelerations and drifts.

5. CONCLUSIONS

The response of 3-story IMRF and OCBF prototype models were examined considering impact to a surrounding moat wall at the base level by implementing the proposed impact element to finite element models of the buildings. The effect of pounding to moat wall in both prototype buildings were investigated by comparing the superstructure response with and without the presence of the moat wall under 20 ground motions from the NEES TIPS project scaled to MCE ground motions. Response of the minimally code-compliant IMRF based isolated structure without considering pounding to moat walls does not perform satisfactorily at for MCE events. Large story drift ratio and yielding occurs in the building at this level of shaking. Pounding to moat walls worsen this situation for the IMRF model. A more robust design is necessary for this model to improve its performance in a rare earthquake. One suggestion in this regard could be designing a stiffer superstructure which leads to larger period shifting by considering the base isolation system or decreasing R factor to design for higher base shear. Although the response of the isolated OCBF is better compared with the IMRF for the case without moat walls, wherein the median demands for story drifts are substantially lower than those of the IMRF, pounding to moat walls makes a significant change in this behavior resulting in large median SDR with huge dispersions. Brace buckling and significant inelastic response were observed in all the motions inducing pounding to moat walls. It can be concluded that pounding to moat walls worsens the response of both frames in terms of both acceleration and SDR, although this effect is worse for stiff OCBF frame.

Acknowldedgements:

This work is part of the NEES TIPS project supported by the National Science Foundation (NSF) under Grants No. CMMI-0724208 and CMMI-1113275. The authors are grateful to Drs. Keri Ryan (PI), Stephen Mahin, (CO-PI) for their input into the test program.

References:

American Society of Civil Engineers (ASCE). (2005). Minimum Design Loads for Buildings And Other Structures. SEI/ASCE 7-05.

Earthquake Engineering Research Institute (EERI) (1995). "Northridge Earthquake Reconnaissance Report." Earthquake Engineering Research Institute.

Erduran, E., N. D. Dao and K. L. Ryan (2011). "Comparative response assessment of minimally compliant low-rise conventional and base-isolated steel frames." *Earthquake Engineering & Structural Dynamics* **40**(10): 1123-1141.Doi 10.1002/Eqe.1078.

Gavin, H. P. and R. L. Nigbor (2012). Performance of the Base-Isolated Christchurch Women's Hospital in the September 4, 2010, Darfield Earthquake and the February 22, 2011, Christchurch Earthquake. 20th Analysis and Computation

Specialty Conference**:** 554-563.
Komodromos, P., P. C. Polycarpou, L. Papaloizou and M. C. Phocas (2007). "Response of seismically isolated buildings considering poundings." *Earthquake Engineering & Structural Dynamics* **36**(12): 1605-1622.10.1002/eqe.692.
Lignos, D. G. and H. Krawinkler (2011). "Deterioration Modeling of Steel Components in Support of Collapse Prediction of Steel Moment Frames under Earthquake Loading." *Journal of Structural Engineering* **137**(11): 1291-1302
Masroor, A. and G. Mosqueda (2012a). "Experimental simulation of base-isolated buildings pounding against moat wall and effects on superstructure response." *Earthquake Engineering & Structural Dynamics*.10.1002/eqe.2177.
Masroor, A. and G. Mosqueda (2012b). "Impact model for simulation of base isolated buildings impacting flexible moat walls." *Earthquake Engineering & Structural Dynamics*.10.1002/eqe.2210.
Muthukumar, S. and R. DesRoches (2006). "A Hertz contact model with non-linear damping for pounding simulation." *Earthquake Engineering & Structural Dynamics* **35**(7): 811-828.Doi 10.1002/Eqe.557.
Nagarajaiah, S. and X. H. Sun (2001). "Base-isolated FCC building: Impact response in Northridge earthquake." *Journal of Structural Engineering (ASCE)* **127**(9): 1063-1075
Pant, D. R. and A. C. Wijeyewickrema (2012). "Structural performance of a base-isolated reinforced concrete building subjected to seismic pounding." *Earthquake Engineering & Structural Dynamics* **41**(12): 1709-1716.10.1002/eqe.2158.
Ryan, K. L., S. A. Mahin and G. Mosqueda (2008). Introduction to NEES TIPS: Tools for Isolation and Protective Systems. Structures Congress 2008**:** 1-16.
Sayani, P. J., E. Erduran and K. L. Ryan (2011). "Comparative response assessment of minimally compliant low-rise base-isolated and conventional steel moment-resisting frame buildings." *Journal of Structural Engineering* **137**(10): 1118-1131.10.1061/(asce)st.1943-541x.0000358.
Shamsabadi, A., K. M. Rollins and M. Kapuskar (2007). "Nonlinear soil-abutment-bridge structure interaction for seismic performance-based design." *Journal of Geotechnical and Geoenvironmental Engineering* **133**(6): 707-720.Doi 10.1061/(Asce)1090-0241(2007)133:6(707).
Uriz, P., F. C. Filippou and S. A. Mahin (2008). "Model for cyclic inelastic buckling of steel braces." *Journal of Structural Engineering-Asce* **134**(4): 619-628.Doi 10.1061/(Asce)0733-9445(2008)134:4(619).

10CUEE CONFERENCE PROCEEDINGS
10th International Conference on Urban Earthquake Engineering
March 1-2, 2013, Tokyo Institute of Technology, Tokyo, Japan

SELECTION OF APPROPRIATE VISCOUS DAMPING MODEL FOR NONLINEAR TIME-HISTORY ANALYSIS OF BASE-ISOLATED REINFORCED CONCRETE BUILDINGS

Deepak R. Pant[1)] and Anil C. Wijeyewickrema[2)]

1) Graduate Student, Department of Civil and Environmental Engineering, Tokyo Institute of Technology, Japan
2) Associate Professor, Department of Civil and Environmental Engineering, Tokyo Institute of Technology, Japan
pant.d.aa@m.titech.ac.jp, wijeyewickrema.a.aa@m.titech.ac.jp

Abstract: The effects of modeling viscous damping on the response of seismically isolated reinforced concrete buildings subjected to earthquake ground motions, are investigated. The test results of a reduced-scale three-story building previously tested on a shaking table are compared with three-dimensional finite element simulation results. The study is focused on nonlinear direct-integration time-history analysis, where many different approaches of modeling viscous damping, developed within the framework of Rayleigh damping are considered. It is found that the damping ratio as well as the approach used to model damping has significant effects on the response. It is shown that stiffness-proportional damping, where the coefficient multiplying the stiffness matrix is calculated from the frequency of the base-isolated building with the post-elastic stiffness of the isolation system, provides reasonable estimates of the peak response indicators, in addition to being able to capture the frequency content of the response very well.

1. INTRODUCTION

Modeling energy dissipation in structures is a challenging task, adding complexity to nonlinear time-history analysis of structures. The major source of energy dissipation due to inelastic material behavior can be modeled with reasonable accuracy using material models based on experiments. Other sources of energy dissipation such as (a) foundation damping due to soil nonlinearity and radiation of seismic waves and (b) damping in the structure including non-structural elements, are usually modeled using linear viscous damping. In base-isolated buildings, it is logical to prescribe viscous damping separately for the isolation system and the superstructure, where the use of viscous damping in the isolation system can be avoided by using hysteretic models of bearings to account for all the energy dissipation. On the other hand, the application of viscous damping to the superstructure alone can be done using various approaches within the Rayleigh damping framework, where damping matrix $\mathbf{c}$ is given as,

$$\mathbf{c} = a_0\mathbf{m} + a_1\mathbf{k}, \tag{1}$$

where $\mathbf{m}$ is the mass matrix, $\mathbf{k}$ is the stiffness matrix, and a_0 and a_1 are the damping coefficients. The damping ratio for the n^{th} mode of a structure ξ_n is defined as,

$$\xi_n = \frac{a_o}{2\omega_n} + \frac{a_1\omega_n}{2}, \tag{2}$$

where ω_n is the frequency of the n^{th} mode. The coefficients a_0 and a_1 are determined assuming the same damping ratio ξ for two selected modes as,

$$a_0 = \xi\frac{2\omega_i\omega_j}{\omega_i + \omega_j}, \qquad a_1 = \xi\frac{2}{\omega_i + \omega_j}, \tag{3}$$

where ω_i and ω_j are the frequencies of mode *i* and mode *j*, respectively. The two modes *i* and *j* are chosen to ensure nearly the same amount of damping for all the modes significantly contributing to the response of the structure. Typically, ω_i is selected to be the frequency of the first mode and ω_j corresponds to a higher mode. Mass-proportional damping where $\mathbf{c} = a_0\mathbf{m}$ and $a_0 = 2\xi\omega_i$; and stiffness-proportional damping where $\mathbf{c} = a_1\mathbf{k}$ and $a_1 = 2\xi/\omega_i$, can be viewed as special cases of Rayleigh damping.

Because of the potential problems associated with the use of Rayleigh-type damping, several studies have been carried out concerning the analysis of *fixed-base buildings* (Priestley and Grant 2005, Hall 2006, Smyrou et al. 2011, and Erduran 2012). These studies highlight the undesirable effects of improper use of Rayleigh-type damping in time-history analysis of inelastic structures. Various suggestions have been proposed to avoid problems, which include the use of the tangent inelastic properties of the system instead of the initial elastic properties and imposing bounds on the damping forces. Nonetheless, there is no consensus among researchers regarding the best approach to

model viscous damping, due to uncertainties associated with quantification of energy dissipation. While the issue of modelling viscous damping has been explored extensively for fixed-base buildings, it is only recently that the base-isolated buildings have been considered (see Hall 2006 and Ryan and Polanco 2008). Hall (2006) studied the effects of mass-proportional damping and stiffness-proportional damping using a rigid superstructure model. Ryan and Polanco (2008) recommended the application of stiffness-proportional damping instead of Rayleigh damping to the superstructure of the building but their study was based on two-dimensional models of the buildings assuming linear elastic behavior of the superstructure. Stiffness-proportional damping was also used by Pant and Wijeyewickrema (2012) to evaluate the performance of a base-isolated reinforced concrete (RC) building subjected to seismic pounding using three-dimensional nonlinear finite element (FE) models. However, the effects of modeling viscous damping on the structural response of the building were not discussed in that study. Therefore, a systematic study investigating the effects of modeling viscous damping on the important response indicators of base-isolated buildings such as floor displacements, floor accelerations and story shear forces, using rigorous three-dimensional FE models, is needed. In addition, none of these previous studies have compared numerical analysis results with the results from experiments or instrumented buildings.

In the present study, the consequences of modeling viscous damping in time-history analysis of base-isolated RC buildings by using various approaches based on the Rayleigh damping framework, are investigated. Existing shaking table test results of a three-story base-isolated building, where the superstructure was shaken strongly but did not undergo significant inelastic excursions, are compared with the numerical analysis results to arrive at the appropriate technique for modeling viscous damping. In these numerical simulations, energy dissipation due to inelastic material behavior of the superstructure was simulated using well-established material models, while the viscous damping was applied to the superstructure using many different approaches. All the energy dissipation in the isolation system was explicitly modeled using bilinear hysteretic models of bearings.

2. BENCHMARK BUILDING AND MODELING

2.1 Benchmark Building and Shaking Table Tests

The base-isolated benchmark building used to compare numerical simulation results is a 0.4 scale model of a three-story two-bay by one-bay RC structure built in Japan (Fig. 1) and reported by Clark et al. (1997). To maintain proper scaling, packets of lead billets were tied down to each slab and the total weight of the model was 400 kN. Three phases of shaking table tests were carried out following initial system identification tests including the static pull-back tests. However, due to improper calibration of loadcells during the first static pull-back test, localized cracking was observed especially in first-floor beam-column joints (Clark et al. 1997). Despite this shortcoming, this test was chosen as a benchmark for the present study; because this represents the only experiment conducted on a code-compliant multi-story base-isolated RC framed-building with a fairly well-documented report. In the first phase of the shaking table tests, the structure was braced in the transverse direction as well as the longitudinal direction to enable comparison of various isolation systems by avoiding damage to the superstructure. Design-level 1 and design-level 2 earthquake excitations, according to Japanese practice were used as input in this stage. In the second phase of the tests, the model was braced only in the transverse direction and the two design-level earthquakes were run again, followed by very high-intensity motions intended to cause damage to the structure. In the final phase, the model was repaired and moderate-intensity motions were applied. It is noted that in all the tests, the earthquake excitation was only in the longitudinal direction. This study focuses on the second phase of the tests where design-level earthquakes were used. In this phase, identical 176 mm diameter high damping rubber bearings with twenty 2.2 mm thick rubber layers alternating with 1 mm thick steel shims were used under each of the six column bases.

Design-level 2 tests are considered in the present study. In these tests, recordings of the 1940 El Centro, 1968 Tokachi-oki, and 1979 Miyagiken-oki earthquakes were run at an intensity corresponding to the full-scale peak velocity of 50 cm/sec (corresponding to the design-level 2 earthquake) and are referred to as ELC-50, HACH-50, and MIYA-50, respectively. One additional excitation that represented the design forces typically specified by the US codes was also used in these tests. The excitation referred to as ELC-S1, is a synthetic record generated from the 1940 El Centro earthquake recording. The sequence of excitation was in the following order: ELC-S1, ELC-50, HACH-50, and MIYA-50.

2.2 Modeling of Structural Elements

A three-dimensional FE model of the building was developed in OpenSees (2012). Beams and columns were modeled using force-based, Euler-Bernoulli fiber beam-column elements that account for the spread of inelasticity along the length of the element. For concrete the modified Kent and Park model (Park et al. 1982) was used in compression and an initial linear elastic branch together with a linear softening branch up to zero stress was used in tension. The model proposed by Yassin (1994) was used to account for concrete damage and hysteresis. For reinforcing steel, the constitutive model of Menegotto and Pinto (1973), which includes strain hardening and the Bauschinger effect, was used. In this study, the strain-hardening ratio is taken as 1%. Bearings were modeled using elastomeric bearing elements with a bilinear hysteretic model used to represent the lateral force-deformation relationship of each element and to simulate all the energy dissipation in the isolation system. The parameters of the bilinear hysteretic model for each

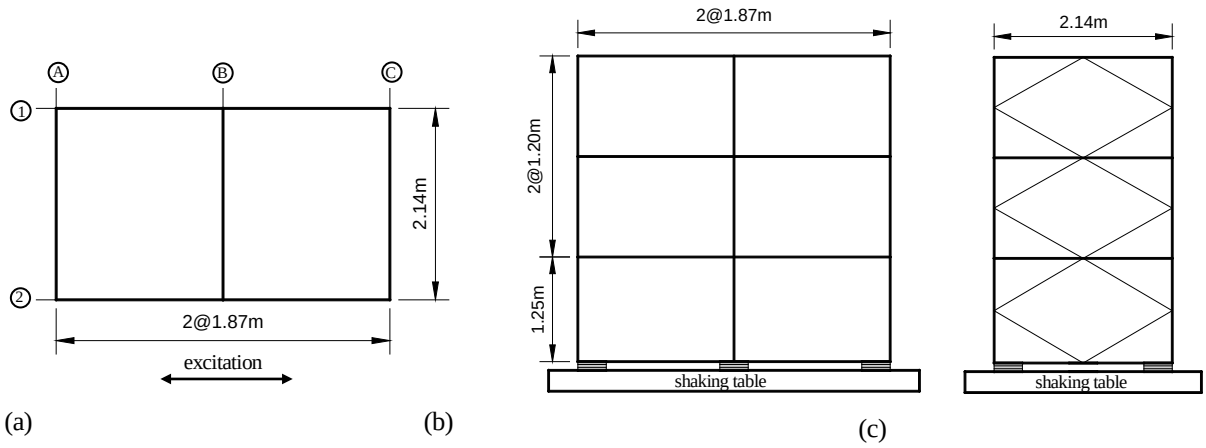


Fig. 1. Geometry of the three-story building tested on shaking table: (a) plan; (b) elevation along longitudinal direction; and (c) elevation along transverse direction (note that no braces were used along grid line B).

element as determined from the component test results of a bearing that was similar to the ones used in the building, are initial stiffness $K_1 = 1{,}167.5$ kN/m, post-elastic stiffness $K_2 = 300$ kN/m, and yield force $F_y = 3.94$ kN. The vertical force-deformation relationship of each element was simulated using a linear elastic compression-only spring with a stiffness $K_v = 338{,}000$ kN/m. The standard horizontal characteristic test of the bearing at 100% shear strain level and an axial load of 78.5 kN was reproduced quite well using these properties as shown in Fig. 2.

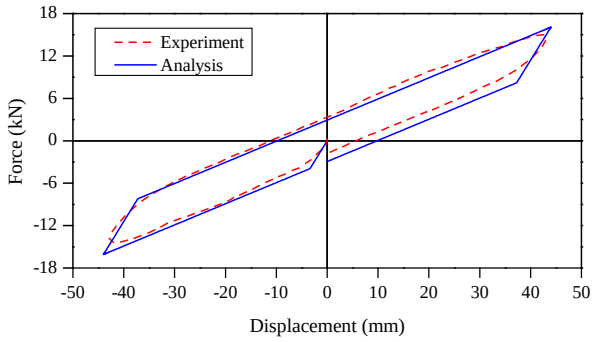


Fig. 2. Hysteretic loop of the bearing for one cycle of displacement at 100% shear strain level. Experimental curve is reproduced after Clark et al. (1997).

2.3 Modeling of Viscous Damping

Viscous damping was applied only to the superstructure of the building using many different approaches of computing the damping matrix $\mathbf{c}$ that cover a wide range of options available in many existing FE programs (Table 1). The relevant frequencies as obtained from modal analyses are also shown in Table 1. Since the modal damping values could not be estimated reasonably well during the test (Clark et al. 1997), numerical simulations were performed using damping ratio $\xi = 1\%$, 2%, 3%, 4%, and 5%. This also enables the investigation of the effects of damping ratio on the analysis results. The approaches considered here depend on:

(1) Damping type: Rayleigh, mass-proportional or stiffness-proportional damping.
(2) Damping coefficients a_0, a_1: The damping coefficients a_0 and a_1 are constant throughout the analysis (based on the initial stiffness) or updated in each analysis step (based on the tangent stiffness).
(3) Basis for computing a_0, a_1: Modes of deformation chosen and the structural model considered for modal analysis to calculate frequencies necessary for the evaluation of damping coefficients.
(4) Stiffness matrix: Initial or tangent stiffness matrix used in Eq. (1).

The approaches are categorized in 7 groups as shown in Table 1.

3. COMPARISON OF SHAKING TABLE TEST AND NUMERICAL ANALYSIS RESULTS

Nonlinear direct-integration time-history analysis of the building was carried out using OpenSees (2012) for a single continuous sequence of concatenated records ELC-S1, ELC-50, HACH-50, and MIYA-50 using the 28 approaches of modeling viscous damping. The $P-\Delta$ effect for the superstructure as well as the isolation system was included in the analysis to consider geometric nonlinearity effects. Numerical analysis results only for the strongest (i.e., MIYA-50) excitation are discussed in this paper, for brevity. The selected response indicators are relative floor displacements, absolute floor accelerations, and story shear forces. To enable the comparison of various approaches of modeling damping, the error E_n of the peak value of the response indicator representing displacement, acceleration or shear force at n^{th} story was calculated as,

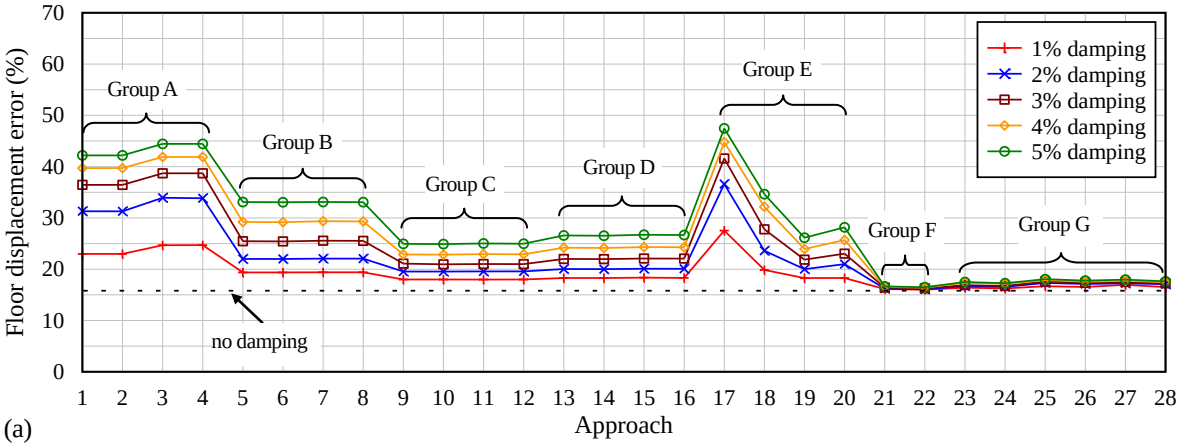
Table 1. Different approaches of modeling viscous damping considered in this study.

Approach	Group	Damping	Damping coefficients a_0, a_1	Basis for computing a_0, a_1		Stiffness matrix	ω_i (rad/s)	ω_j (rad/s)
				Modes i, j	Structural model			
1	A	Rayleigh	Constant	1, 3	SS	Initial	37.14	66.62
2	A	Rayleigh	Constant	1, 3	SS	Tangent	37.14	66.62
3	A	Rayleigh	Constant	1, 4	SS	Initial	37.14	130.62
4	A	Rayleigh	Constant	1, 4	SS	Tangent	37.14	130.62
5	B	Rayleigh	Constant	1, 3	BIB-I	Initial	12.61	60.18
6	B	Rayleigh	Constant	1, 3	BIB-I	Tangent	12.61	60.18
7	B	Rayleigh	Constant	1, 4	BIB-I	Initial	12.61	64.03
8	B	Rayleigh	Constant	1, 4	BIB-I	Tangent	12.61	64.03
9	C	Rayleigh	Constant	1, 3	BIB-P	Initial	6.58	58.58
10	C	Rayleigh	Constant	1, 3	BIB-P	Tangent	6.58	58.58
11	C	Rayleigh	Constant	1, 4	BIB-P	Initial	6.58	64.03
12	C	Rayleigh	Constant	1, 4	BIB-P	Tangent	6.58	64.03
13	D	Rayleigh	Updated	1, 3	BIB	Initial	—	—
14	D	Rayleigh	Updated	1, 3	BIB	Tangent	—	—
15	D	Rayleigh	Updated	1, 4	BIB	Initial	—	—
16	D	Rayleigh	Updated	1, 4	BIB	Tangent	—	—
17	E	Mass prop.	Constant	1	SS	—	37.14	—
18	E	Mass prop.	Constant	1	BIB-I	—	12.61	—
19	E	Mass prop.	Constant	1	BIB-P	—	6.58	
20	E	Mass prop.	Updated	1	BIB	—	—	—
21	F	Stiffness prop.	Constant	1	SS	Initial	37.14	—
22	F	Stiffness prop.	Constant	1	SS	Tangent	37.14	—
23	G	Stiffness prop.	Constant	1	BIB-I	Initial	12.61	—
24	G	Stiffness prop.	Constant	1	BIB-I	Tangent	12.61	—
25	G	Stiffness prop.	Constant	1	BIB-P	Initial	6.58	
26	G	Stiffness prop.	Constant	1	BIB-P	Tangent	6.58	
27	G	Stiffness prop.	Updated	1	BIB	Initial	—	—
28	G	Stiffness prop.	Updated	1	BIB	Tangent	—	—

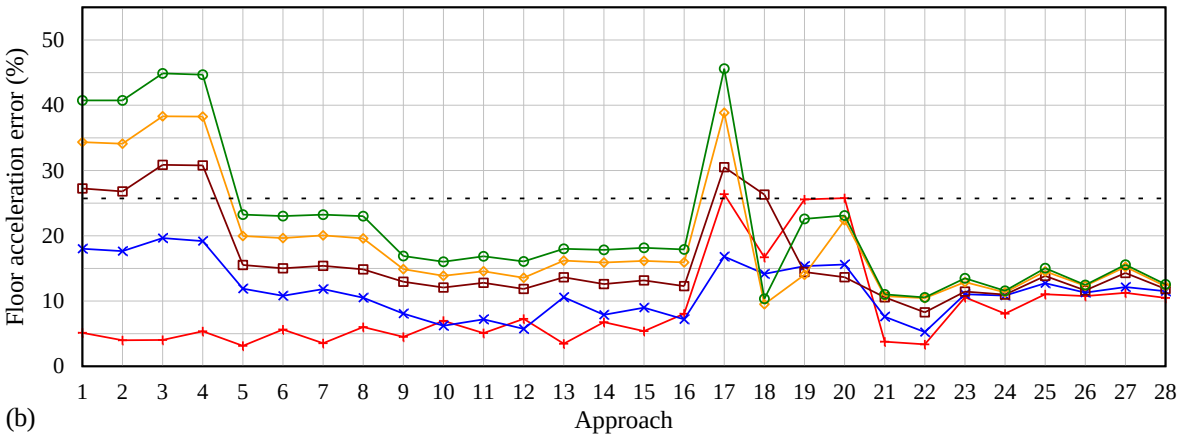
$$E_n = \left| \frac{N_n - T_n}{T_n} \right|, \qquad n = 0 \text{ (base)}, 1, 2, 3 \text{ (roof)}, \quad (4)$$

where N_n and T_n are the peak values of numerical analysis and test results, respectively of the response indicator at n^{th} story. Maximum of E_n values at all the stories for various damping ratios and approaches of modeling viscous damping are shown in Fig. 3 for the MIYA-50 excitation. Maximum errors when the viscous damping was not considered in the analysis are also shown for comparison purposes.

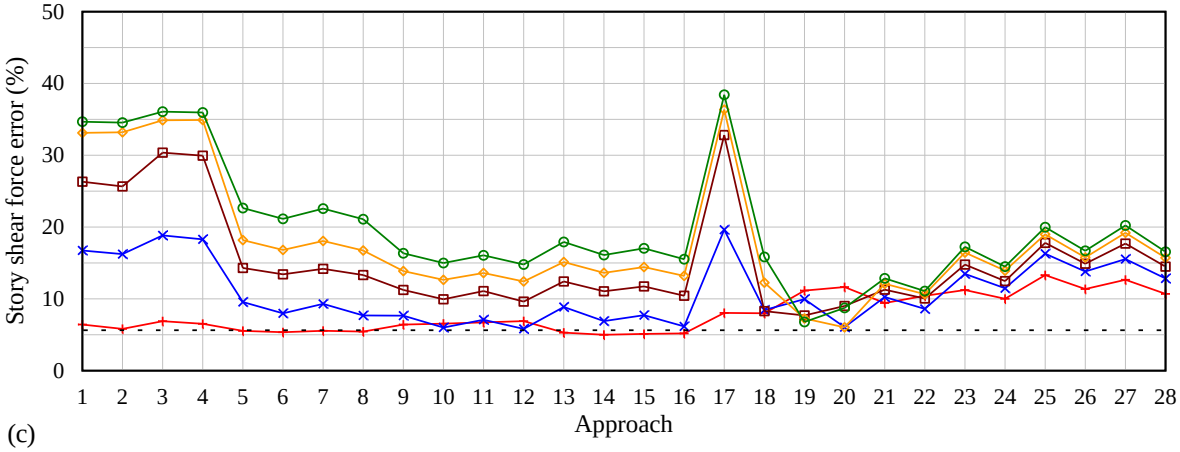
It is clearly seen from Fig. 3 that errors for a particular damping ratio using various approaches within any group other than Group E, do not show significant differences for all the response indicators. This implies that the choice of (a) higher mode (mode 3 or mode 4) frequency and (b) stiffness matrix (initial or tangent), in the application of viscous damping has negligible influence on the response indicators. The choice of stiffness matrix does not have a significant influence because stiffness-proportional damping constitutes a very small fraction of viscous damping, compared with mass-proportional damping. In addition, the fact that the stiffness of the superstructure is not changed significantly during the excitations also implies that the choice of stiffness matrix in the application of damping has negligible influence. This is different from fixed-base or base-isolated structures subjected to strong ground motions which result in significant stiffness degradation. The errors



(a)



(b)



(c)

Fig. 3. Maximum errors in peak values of response indicators for all the stories for the MIYA-50 excitation: (a) relative floor displacement; (b) absolute floor acceleration; and (c) story shear force. The dashed line indicates the maximum error when viscous damping was not considered.

for a particular damping ratio using the approaches within Group E are significantly different. In addition, the error trends with respect to damping ratio are changed for Approaches 18–20 compared with other approaches. Although the related results are not shown here for brevity, it was found from the numerical analysis results that Approaches 18–20 underestimate the floor displacement response but overestimate the floor acceleration and story shear force responses for almost all the damping ratios. The floor displacement response using Approaches 18–20 were found to be slightly smaller than the corresponding Rayleigh damping counterparts, while the floor accelerations and story shear forces were significantly larger for all the damping ratios. This is because mass-proportional damping, which can be visualized as dampers connecting each mass to an external support, does not correspond to a realistic physical phenomenon. Therefore, the application of only mass-proportional damping is not desirable. Here it is noted that although the mass-proportional damping dominates, the errors obtained using only the mass-proportional damping part of Approaches 1–16, are not the same errors when only mass-proportional damping is considered in Approaches 17–20, as the damping coefficient a_0 is computed using different equations. For example, for $\omega_1 = 37.14$ rad/s and $\omega_3 = 66.62$ rad/s ($\omega_4 = 130.62$ rad/s), $a_0 = 47.7\xi$ ($a_0 = 57.8\xi$) for the mass-proportional part of Rayleigh damping and $a_0 = 74.3\xi$ for only mass-proportional damping. Therefore, the damping coefficient for only mass-proportional damping is larger than that for the mass-proportional part of Rayleigh damping, which essentially results in higher degree of damping. Similar results were observed by Erduran (2012) for fixed-base steel buildings.

Another important observation from the results is that for the floor displacements, smallest errors occur when viscous damping was neglected in the model (Fig. 3(a)). However, Fig. 3(b) and (c) suggests that neglecting such damping may lead to higher errors in terms of the floor accelerations and story shear forces. In certain scenarios, viscous damping is also desirable by analysis programs for purposes of numerical stability. In addition, the higher error due to a particular approach of modeling damping, results mainly because of the inclusion of higher degree of damping.

It is observed that the errors using the updated damping coefficients a_0 and a_1 are smaller compared with using constant a_0 and a_1, and the differences are more obvious for higher damping ratios. For example, consider the errors using approaches in Group B (constant a_0 and a_1) and Group D (updated a_0 and a_1), where in the latter group the errors are smaller (Fig. 3). It is interesting to consider the results obtained using the approaches in Group C, where damping coefficients were computed based on the modal analysis of the base-isolated building with post-elastic stiffness of the isolation system. The errors using the approaches in Group C are either smaller than or comparable with the errors in Group D for all the damping ratios (Fig. 3). In addition, the analysis time with the approaches in Group C was found to be about one fourth of the analysis time using approaches in Group D, where damping coefficients were updated in each analysis step. Therefore, approaches in Group C are more attractive from the view point of computational cost than approaches in Group D.

The analysis results in terms of peak response indicators clearly indicate that it is preferable to use 1% damping. Although there is no unique best approach suitable for all situations, the following two methods yield the least errors:

Method 1: Group C type damping, i.e., Rayleigh damping, with the damping coefficients a_0 and a_1 computed from the frequencies of the base-isolated building with the post-elastic stiffness of the isolation system. However, with this type of damping, the errors depend greatly on the selected damping ratio ξ (Fig. 3).

Method 2: Group F or Group G type damping, i.e., stiffness-proportional damping. With this type of damping, the errors do not vary significantly with the selected damping ratio ξ, compared with Group C type damping, indicating less uncertainty in the predicated response with the choice of ξ (Fig. 3).

To further understand the differences in response indicators using various approaches, and to investigate the ability of an approach in capturing the frequency content of the response, *acceleration time histories* and *response spectra* for all floors corresponding to MIYA-50 excitation were examined for the approaches in all the groups. Here, only roof acceleration time histories and roof response spectra for approaches in Groups C, F, and G, which lead to least simulation errors in terms of peak response indicators, are discussed in detail. Similar results were obtained for the other floors. The absolute roof acceleration time histories for the MIYA-50 excitation are shown in Fig. 4, while the roof response spectra evaluated for secondary systems with damping ratio $\xi_{sub} = 1\%$ attached to the roof are plotted in Fig. 5. Figure 4(a) shows that when viscous damping is not considered in the analysis, the acceleration response is characterized by spurious high-frequency content, which is also manifested as an unrealistic peak appearing at about 8 Hz in the response spectra shown in Fig. 5. Approach 9 (Group C) and Approach 21 (Group F) with 1% damping, which resulted in relatively smaller errors in the peak response indicators (Fig. 3), do not capture the frequency content of the response well as seen in Fig. 4(b) and (c), which is also indicated in Fig. 5(a) by a peak at about 8 Hz in the response spectrum that is not present in the test results. It was found that the use of 5% damping with Approach 9 suppresses the presence of unrealistic high-frequency content as seen in Figs. 4(f) and 5(b) but was shown to be resulting in higher errors in the peak response indicators (Fig. 3). Although the corresponding time history is not shown here for brevity, similar observations were also made for the Approach 21 with 5% damping. Furthermore, it was noted that Approach 9 (Approach 21) at a particular damping ratio produces the results nearly identical to those produced by Approaches 10–12 (Approach 22). Roof accelerations using Approaches 23 and 25 (Group G) with 1% damping match with the test results in terms of frequency content reasonably well as shown in Figs.

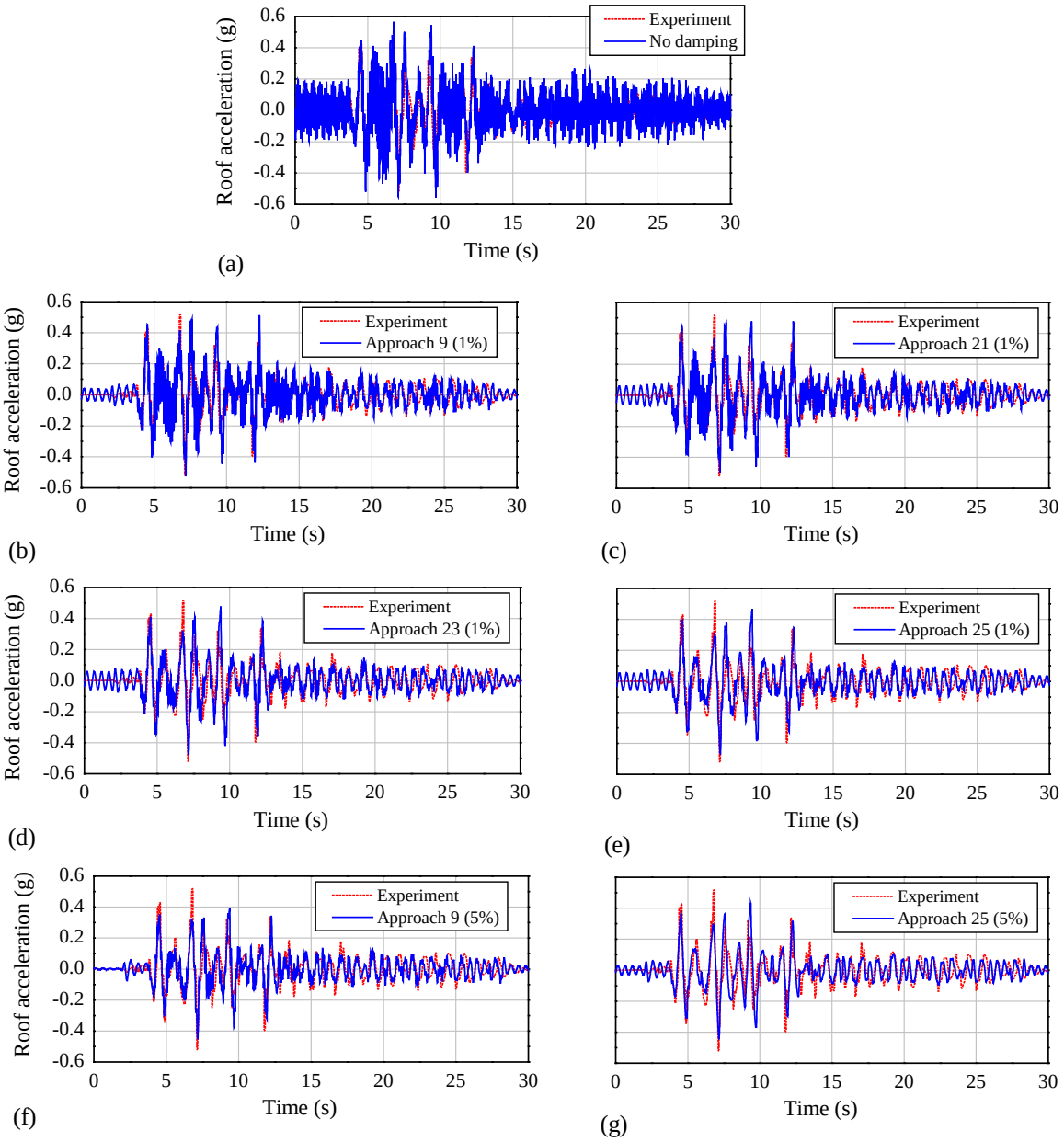


Fig. 4. Absolute roof acceleration time histories for MIYA-50 excitation: (a) no damping; (b)–(e) 1% damping; and (f)–(g) 5% damping. Experimental curve is reproduced after Clark et al. (1997).

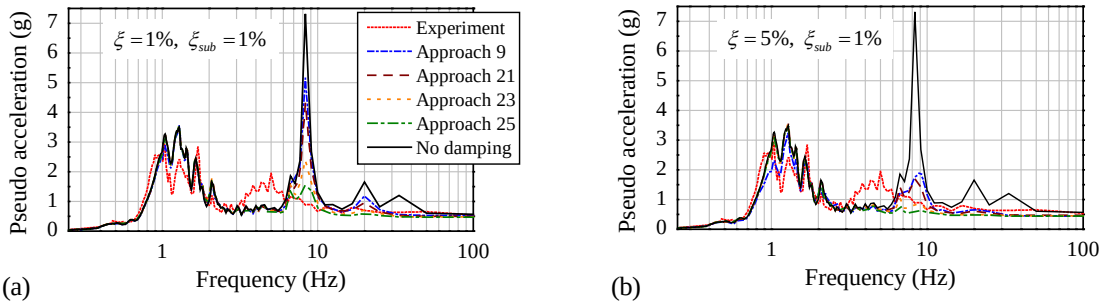


Fig. 5. Roof acceleration response spectra for the MIYA-50 excitation for different damping ratios of the structure: (a) $\xi = 1\%$ and (b) $\xi = 5\%$. The damping ratio for the secondary systems $\xi_{sub} = 1\%$. Experimental curve is reproduced after Clark et al. (1997).

4(d), 4(e), and 5(a). In the high-frequency range, results of Approach 25 are closer to the test results. It is noted that the errors in peak response indicators using Approaches 23 and 25 are not necessarily the smallest but are still smaller than the errors using many of the other approaches (Fig. 3). Since the errors in peak response indicators were not found to be much different between Approaches 23 and 25, it is preferable to use Approach 25. Figure 4(e) and (g) shows that there is a slight difference between the results for $\xi = 1\%$ and $\xi = 5\%$ with Approach 25 but close examination of Fig. 5 suggests the use of 1% damping, because 5% damping causes excessive suppression of the high-frequency response, particularly in the frequency range of 7–9 Hz. Although the corresponding results are not shown, the response histories obtained using Approach 23 (Approach 25) at a particular damping ratio were identical to those obtained using Approach 24 (Approaches 26–28).

In summary, it can be said that Approaches 25–28 with 1% damping provide reasonable estimates of the peak response indicators in addition to being able to capture the frequency content of the response very well. Furthermore, considering the higher computational cost associated with Approaches 27 and 28, it is preferable to use either Approach 25 or Approach 26. It is also important to note that the stiffness-proportional damping in contrast to the Rayleigh damping is effective in suppressing the spurious high-frequency content of the response without affecting its low-frequency content (Fig. 5). However, a large amount of stiffness-proportional damping may lead to undesirable suppression of the high-frequency content of the response.

4. CONCLUDING REMARKS

The consequences of modeling viscous damping in base-isolated RC buildings using different approaches were investigated, by evaluating the response of a three-story building previously tested on a shaking table. The results of nonlinear direct-integration time-history analysis, where Rayleigh-type damping is used, have led to the following conclusions and recommendations:

(1) Application of Rayleigh damping where the damping coefficients a_0 and a_1 are calculated from the frequencies of the superstructure for a fixed-base condition (Group A) and mass-proportional damping (Group E) should be avoided, as these approaches could produce large errors in response predictions.

(2) Rayleigh damping where damping coefficients a_0 and a_1 are calculated from the frequencies of the base-isolated building with the post-elastic stiffness of the isolation system (Group C), at $\xi = 1\%$ results in relatively lower simulation errors in peak response indicators but does not capture the frequency content of the response well. Stiffness-proportional damping where the damping coefficient a_1 is computed from the frequency of the base-isolated building with the post-elastic stiffness of the isolation system (Group G), at $\xi = 1\%$ is found to be better compared with the other approaches investigated in this study, as it provides reasonable estimates of the peak response indicators, in addition to being able to capture the frequency content of the response very well.

(3) Updating damping coefficients in each analysis step is computationally demanding and does not provide substantially improved results compared with the results when damping coefficients computed based on the post-elastic stiffness of the isolation system are considered.

Acknowledgements:

The first author is pleased to acknowledge a Monbukagakusho (Ministry of Education, Culture, Sports, Science and Technology, Japan) scholarship for graduate students. Financial support from Center for Urban Earthquake Engineering (CUEE), Tokyo Institute of Technology is gratefully acknowledged.

References:

Clark, P.W., Aiken, I.D., and Kelly, J.M. (1997), "Experimental studies of the ultimate behavior of seismically-isolated structures", *Technical Report*, *UCB/EERC-97/18*, Earthquake Engineering Research Center, University of California, Berkeley, CA.

Erduran, E. (2012), "Evaluation of Rayleigh damping and its influence on engineering demand parameter estimates", *Earthquake Engineering and Structural Dynamics*, **41**(14)**,** 1905-1919.

Hall, J.F. (2006), "Problems encountered from the use (or misuse) of Rayleigh damping", *Earthquake Engineering and Structural Dynamics*, **35**(5)**,** 525-545.

Menegotto, M. and Pinto, P. (1973), "Methods of analysis for cyclically loaded R/C frames", *Symposium of Resistance and Ultimate Deformability of Structure Acted by Well Defined Repeated Load*, Lisbon, Portugal.

Open system for earthquake engineering simulation (OpenSees) (2012), Computer Program, University of California, Berkeley, CA.

Pant, D.R. and Wijeyewickrema, A.C. (2012), "Structural performance of a base-isolated reinforced concrete building subjected to seismic pounding", *Earthquake Engineering and Structural Dynamics*, **41**(12)**,** 1709-1716.

Park, R., Priestley, M.J.N., and Gill, W.D. (1982), "Ductility of square-confined concrete columns", *Journal of Structural Engineering (ASCE)*, **108**(4)**,** 929-950.

Priestley, M.J.N. and Grant, D.N. (2005), "Viscous Damping in Seismic Design and Analysis", *Journal of Earthquake Engineering*, **9**(S2)**,** 229-255.

Ryan, K.L. and Polanco, J. (2008), "Problems with Rayleigh damping in base-isolated buildings", *Journal of Structural Engineering (ASCE)*, **134**(11)**,** 1780-1784.

Smyrou, E., Priestley, M.J.N., and Carr, A.J. (2011), "Modelling of elastic damping in nonlinear time-history analyses of cantilever RC walls", *Bulletin of Earthquake Engineering*, **9**(5)**,** 1559-1578.

Yassin, M.H.M. (1994), "Nonlinear analysis of prestressed concrte structures under monotonic and cyclic loads", *Ph.D. Dissertation*, University of California, Berkeley, CA.

10CUEE CONFERENCE PROCEEDINGS
10th International Conference on Urban Earthquake Engineering
March 1-2, 2013, Tokyo Institute of Technology, Tokyo, Japan

SIMULATION AND SENSITIVITY OF THE CRITICAL LOAD BEHAVIOR OF ELASTOMERIC SEISMIC ISOLATION BEARINGS

Xing Han[1], and Gordon P. Warn[2]

1) Doctoral Candidate, Dept. of Civil and Environmental Engineering, The Pennsylvania State University, United States
2) Assistant Professor, Dept. of Civil and Environmental Engineering, The Pennsylvania State University, United States
xinghan@psu.edu, gpw1@psu.edu

Abstract: Elastomeric bearings are typically used for seismic isolation of buildings, bridges and structures. Assessment of individual bearing stability is an important consideration for the design of seismic isolation systems composed of elastomeric bearings. In this study, critical load behavior of one elastomeric bearing was simulated using both a detailed three-dimensional (3D) finite element (FE) modeling and using an existing two-spring based analytical model. From a comparison of result, the simple analytical model showed similar simulation capability to the detailed 3D FE model. A global variance-based sensitivity technique was applied to the analytical model whereby the sensitivity of the simulated critical displacements to variations in four independent model parameters was determined. The results of the sensitivity analysis demonstrate that the simulation of critical displacement is sensitive to the shear modulus and the rotational spring parameter for large vertical load that are 0.6 to 0.9 times the critical load at zero lateral displacement. For small vertical loads, those less than 0.6 times the critical load at zero lateral displacement, the critical displacement is most sensitive to values of the rotational spring parameter.

1. INTRODUCTION

Elastomeric bearings are widely used for the seismic isolation of buildings, bridges and other important structures. A typical elastomeric seismic isolation bearing consists of a number of rubber layers (natural or synthetic) bonded to intermediate steel shim plates. The total thickness of rubber provides the low horizontal stiffness required to shift the structure's fundamental period into the long period range (e.g. 2.5s to 4s) whereas the spacing of the intermediate steel shim plates directly affects the vertical stiffness and critical load capacity of the bearing for a given bonded rubber area and shear modulus. An important consideration for the design of isolation systems composed of elastomeric bearings is stability of the isolation system and the individual bearings under service (laterally undeformed configuration) and seismic loading (laterally deformed configuration).

When an elastomeric bearing is subjected to simultaneous vertical compressive load, P, and increasing lateral displacement, u, the shear force might pass through a maximum value at which point the tangential stiffness is zero. This point is the point of neutral equilibrium that is considered the stability limit of the bearing and characterized by the critical lateral displacement, u_{cr}, and corresponding vertical load referred to herein as the critical load, P_{cr}.

In practice, the critical load capacity of the bearing in the laterally undeformed configuration, P_{cro}, is estimated based upon theoretical work of Haringx (1948, 1949a, 1949b) for rubber rods that accounts for shear deformations assuming geometric and material linearity. The critical load in the laterally undeformed configuration is calculated according to:

$$P_{cro} = \frac{\sqrt{(GA_s)^2 + 4P_E GA_s} - GA_s}{2} \quad (1)$$

where GA_s = effective shear rigidity and P_E = Euler buckling load (Kelly 1997).Though not codified, the reduced area (RA) method (Buckle and Liu 1994) is the generally accepted procedure for estimating critical loads in the lateral deformed configuration. Using this RA method, the critical load at a given lateral displacement is estimated by multiplying P_{cro} (Eq. 1) by a ratio of areas as:

$$P_{cr} = \left(\frac{A_r}{A_b}\right) P_{cro} \quad (2)$$

where A_r is the overlapping area between the top-bonded and bottom-bonded elastomer area at a given lateral displacement, u. Buckle et al. (2002) showed the RA method conservatively estimated critical loads for elastomeric bearings with shape factors ranging from 1.67 to 5 though the RA method did not capture well the general trends observed in the experimental data.

The primary objective of this study was to investigate the capability of a two-spring based analytical model (Iizuka 2000) for simulating the critical load behavior of elastomeric bearings. The specific objectives of the work presented in this paper were: (i) use the analytical model to simulate the critical load behavior of an elastomeric bearing and to compare the analytical results to those obtained from

detailed three-dimensional (3D) finite element (FE) modeling; and (ii) to perform a global variance-based sensitivity analysis on the output of the analytical model to identify the parameter(s) controlling the simulation of the critical displacement. Furthermore, the results of the global sensitivity analysis might identify model parameters to which the simulated critical displacement is insensitive, thus enabling model simplifications for practical implementation and simulation of critical loads for the analysis and design of elastomeric isolation systems.

2. FINITE ELEMENT MODEL

Past research (Warn and Whittaker 2006) suggests 3D Finite Element (FE) modeling is able to simulate the vertical force-displacement and vertical stiffness response of elastomeric bearings in both the laterally undeformed and laterally deformed configurations with reasonable accuracy. The bearing (details presented in Fig. 1) utilized by Warn and Whittaker (2006) is modeled in this study using 3D FE analysis. The general purpose finite element software package ABAQUS (DSSC 2010) is used to develop the FE model and to simulate the critical load behavior of the elastomeric bearing. A mesh sensitivity analysis was performed on different meshes of the bearing model to determine the converged mesh. Fig. 2a shows a rendering of the converged mesh for the FE model. In an effort to minimize the computation demand the symmetry of the bearings and loading is exploited so that only half of the bearing needed to be modeled However, nodes which are located on the "cut" surface of the bearings were constrained against lateral translation to prevent bulging of the rubber layers that would be restrained by the other half of the bearing(shown in Fig. 2a).Boundary conditions are used to simulate the restrain that would be provided by structural framing above and below the bearings in which the bottom end plate is fixed in all degrees of freedom and the top end plate is fixed against rotation yet allowed to translate freely in the horizontal and vertical directions.

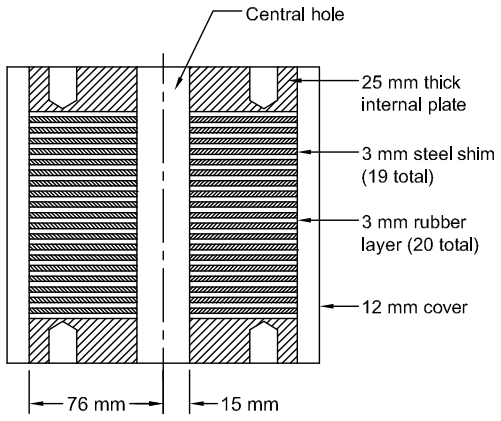
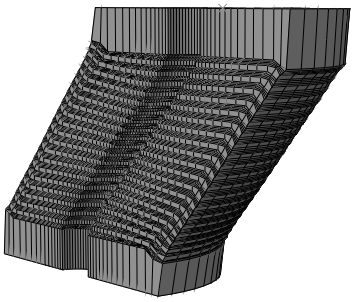
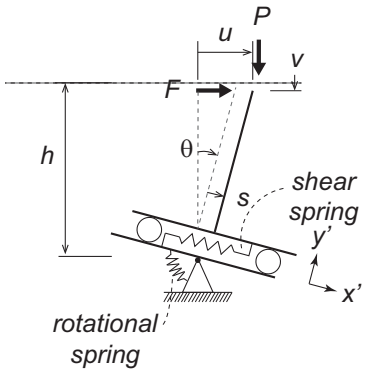


Figure 1 Details of elastomeric bearing specimen



(a) FE model



(b) Two-spring model

Figure 2 Models used for simulating critical loads of elastomeric bearings

The rubber components in the bearing, i.e. rubber layers and cover are modeled using 8-node solid elements (C3D8H) with first order hybrid formulation. The C3D8H element is able to specify the pressure and displacement fields independently to prevent volumetric locking due to the nearly incompressible material behavior of rubber (Poisson's ratio, $\nu \approx 0.5$). The steel shim plates and end plates were also modeled using C3D8H element also to prevent volumetric locking during plastic flow. The Neo-Hookean constitutive model is selected since both the model parameters have a direct relationship with the engineering properties, specifically, the shear modulus, G and bulk modulus, κ. The Neo-Hookean model assumes that the material is hyper elastic, isotropic, and incompressible or nearly incompressible if a value of the bulk modulus is specified. The strain energy potential for the Neo-Hookean model is defined as:

$$U = C_{10}(\bar{I}_1 - 3) + \frac{1}{D_1}(J^{el} - 1)^2 \tag{3}$$

where U is the volumetric strain energy; C_{10} is equal to $G/2$; D_1 is equal to $2/\kappa$; $\bar{I}_1$ is the first strain invariant of the Cauchy–Green deformation tensor; and J^{el} is the elastic volume ratio. The shear modulus G, used in the FE study is the effective shear modulus at 100% shear strain determined from characterization tests performed on the bearing (Warn an Whittaker 2006). The effective shear modulus G at 100% shear strain is reported to be 0.84 MPa (120psi) that results in a C_{10} value of 0.42 MPa. Although the exact value of bulk modulus was not determined from their tests, Warn and Whittaker (2006) showed that the FE solution is insensitive

to the bulk modulus over a range of 20% of the assumed 2,000 MPa (290,000 psi) value. Therefore the bulk modulus is assumed to be 2,000 MPa. The steel material is modeled as a plastic isotropic material with v = 0.3, elastic Young's modulus E = 200 GPa (29,000 ksi) and yield strength σ_y = 448 MPa (65 ksi).The strain hardening ratio was assumed to be 2% for the steel.

3. ANALYTICAL MODEL

The analytical models for simulating the critical load behavior of elastomeric bearings considered in this study is from Iizuka (2000) and based on the two-spring model (TSM) introduced by Koh and Kelly (1988).The two-spring model (see Fig. 2b) consists of a shear spring and a rotational spring that are connected through rigid elements and frictionless rollers. The height of the model from the applied load at the top of the rigid tee to the hinge is h. Under simultaneously vertical force, P, and shear force, F, the top of the model translates with a lateral displacement, u, and height reduction, v (see Fig. 2b). The global deformation (u and v) are the result of local deformations, s, and θ, in the shear and rotational springs, respectively, due to the internal shear spring force, Q_s, and internal rotational spring moment, M. Considering equilibrium and compatibility of the two-spring model in the deformed configuration (see Fig. 2b), the following equations are derived:

$$u = s\cos\theta + h\sin\theta \tag{4}$$

$$v = s\sin\theta + h(1-\cos\theta) \tag{5}$$

$$M = Pu + F(h-v) \tag{6}$$

$$Q_s = P\sin\theta + F\cos\theta \tag{7}$$

Specifying linear properties for the shear, K_s, and rotational, K_θ, springs, Koh and Kelly (1988) demonstrated the two-spring model was able to simulate the reduction in initial horizontal stiffness, increased mechanical damping, and reduction in height, v, with increasing vertical load, P. From the two-spring model, the initial shear spring stiffness, K_{so}, is calculated according to:

$$K_{so} = \frac{GA_b}{T_r} \tag{8}$$

where T_r= total rubber thickness; A_b and G as previously defined. The initial rotational spring stiffness, $K_{\theta o}$, calculated according to:

$$K_{\theta o} = \frac{\pi^2 E_b I}{T_r} \tag{9}$$

where E_b = bending modulus of an individual rubber layer; and I = moment of inertia of bonded rubber area.

Iizuka (2000) proposed a nonlinear model, based on the two-spring model, for the purpose of predicting the shear force response at large shear strains for a range of vertical loads. The model proposed by Iizuka uses semi-empirical nonlinear relationships for the shear and rotational springs. The relationship for the rotational spring is based, in part, on the yield moment, M_y, and ultimate moment, M_u, for an individual rubber layer. Details for the yield and ultimate moment calculations are provided in Iizuka (2000). The tangential rotational stiffness in the elastic range ($dM/d\theta$) is given as:

$$\frac{dM}{d\theta} = K_{\theta o} \quad \left(\theta \le \theta_y\right) \tag{10}$$

where $K_{\theta o}$ is calculated according to Eq. (9) and θ_y = yield rotational angle calculated according to:

$$\theta_y = \frac{M_y}{K_{\theta o}} = \frac{2Z\left(\sigma - \sigma_y\right)}{K_{\theta o}} \tag{11}$$

where Z = elastic section modulus of bonded rubber area; σ = nominal stress ($\sigma = P/A$); and σ_y = tensile yield stress of rubber (assumed to be equal to $3G$ (Gent 2001)). For rotations beyond yield, i.e. $\theta \ge \theta_y$, $dM/d\theta$ is assumed to be:

$$\frac{dM}{d\theta} = \frac{K_{\theta o}}{\left[1 + \frac{r}{3}\left(\frac{\theta}{\theta_y} - 1\right)\right]^{\frac{1+r}{r}}} \quad \left(\theta > \theta_y\right) \tag{12}$$

where r = a dimensionless parameter. Iizuka reported values for r ranging from 1.2 to 3.5 determined empirically from characterization tests performed on elastomeric bearings.

Iizuka proposed the following relationship for the tangential stiffness of the shear spring:

$$\frac{dQ_s}{ds} = \left[1 + s_1\left(1 + s_2\right)\left(\frac{s}{T_r}\right)^{s_2}\right] K_{so} \tag{13}$$

where s_1 and s_2 = dimensionless parameters. Similar to r, s_1 and s_2 are empirical parameters determined from the results of characterization testing. Iizuka specified values for s_1 ranging from 0.0068 to 0.01 and a value of 3 for s_2.

Iizuka's model requires an incremental form of the two-spring equilibrium and compatibility equations presented in Eqs. (4) through (7) be solved using a stepwise procedure. The incremental equilibrium and compatibility equations are:

$$\begin{Bmatrix} {}_i(\Delta\theta) \\ {}_i(\Delta s) \\ {}_i(\Delta v) \\ {}_i(\Delta F) \end{Bmatrix} = \left[K\right]^{-1} \times \begin{Bmatrix} 0 \\ 1 \\ P \\ 0 \end{Bmatrix} \times \Delta u \tag{14}$$

where incremental force and deformation quantities ${}_i(\Delta\theta)$, ${}_i(\Delta s)$, ${}_i(\Delta v)$ and ${}_i(\Delta F)$are obtained for step i from Eq. (14) for a specified vertical force, P, incremental lateral displacement, Δu, and the matrix $[K]$ is defined by:

$$\left[K\right] = \begin{bmatrix} h\sin{}_i\theta + {}_i s\cos{}_i\theta & \sin{}_i\theta & -1 & 0 \\ h\cos{}_i\theta - {}_i s\sin{}_i\theta & \cos{}_i\theta & 0 & 0 \\ {}_i\left(\frac{dM}{d\theta}\right) & 0 & {}_i F & {}_i v - h \\ P\cos{}_i\theta - {}_i F\sin{}_i\theta & {}_i\left(\frac{dQ_s}{ds}\right) & 0 & \cos{}_i\theta \end{bmatrix} \tag{15}$$

The incremental response quantities obtained from the solution of Eq. (14) are added to those from the current step to obtain response values for the subsequent (i+1)th step. Linear spring properties are assumed for the first step and the initial response quantities determined using Eqs. (4)

through (7) to avoid an ill-conditioned matrix for solving Eq. (14) (Iizuka 2000).

The analysis is terminated when the height reduction v is larger than the total rubber thickness T_r. The shear force response, $F(u)$ is obtained from the solution for a specified vertical load P. The critical displacement u_{cr} is determined by numerically differentiating the shear force- lateral displacement response from which the displacement where the tangential stiffness equals zero is determined, i.e. $dF/du = 0$. The stepwise solution procedure is repeated for several values of P to obtain a series of critical points (i.e. P_{cr} and u_{cr}) used to develop a "stability" curve.

4. GLOBAL SENSITIVITY ANALYSIS

Sensitivity analysis quantifies how variability in a given model output, $y = f(x_1, x_2 \ldots x_k)$, can be attributed to variability in model factors $x_1, x_2, \ldots, x_k$ (Saltelli et al.2004). Sobol' method (Sobol'1993), a global, variance-based, sensitivity analysis technique is used in this study to identify model factor (e.g. parameters, variables, and initial conditions) to which the model output (i.e. u_{cr}) is most sensitive.

Sobol' sensitivity analysis method (Saltelli et al.2008) is unique among the sensitivity methods in that it decomposes a models output variance $V(y)$ into the relative contributions from individual factors and factor interactions through numerical integration in a Monte Carlo framework. The term factor is used as an umbrella term including model parameters (those that do not vary with time) and variables. Assuming the factors are statistically independent, the model's output variance can be expressed as:

$$V(y) = \sum_i V_i + \sum_i \sum_{j>i} V_{ij} + \ldots + V_{12\ldots k} \tag{16}$$

where k = number of factors (e.g. parameters); y = distribution of model output; $V(y)$ = total model output variance; V_i = output variance due to the ith parameter; V_{ij} = output variance due to interaction of factors x_i and x_j; $V_{12\ldots k}$ = output variance due to higher order interactions. A given parameter's sensitivity is quantified by a ratio of variance contributing to the total (i.e. due to all parameters) output variance, resulting in an index value ranging from 0 to 1. The "First order" Sobol' sensitivity index used in this study reflects the effect of the ith parameter alone and is defined as:

$$S_i = \frac{V_i}{V(y)} \tag{17}$$

The "total" Sobol' sensitivity index, also used in this study, reflects the effect of the ith parameter alone plus interactions of the ith parameter with all other parameters and is defined as:

$$S_{Ti} = 1 - \frac{V_{\sim i}}{V(y)} \tag{18}$$

where $V_{\sim i}$ =the average variance from all factors but f_i. The total order index S_{Ti} is the sum of the interactions index and the first order index S_i.

5. RESULT AND DISCUSSION

5.1 FE model validation

Prior to the critical load simulation of elastomeric bearing (shown in Fig. 1), a comparison between the experimentally obtained vertical force displacement response and that from the FE analysis is performed to partially validate the capability of the FE model to simulate bearing behavior. Figure 3 shows the comparison between experimental and FE force-displacement response. From the comparison, the FE model captures well the vertical stiffness behavior of elastomeric bearings. The relative error between the vertical stiffness from the FE simulation and experimental data is within 10% where the vertical stiffness was calculated as the secant slope between minimum and maximum force values. Based on the comparison of the vertical force-displacement response, it was judged that the FE model is sufficiently able to capture the mechanic behavior of elastomeric bearings. The FE model was then used to simulate the critical load behavior of elastomeric bearings.

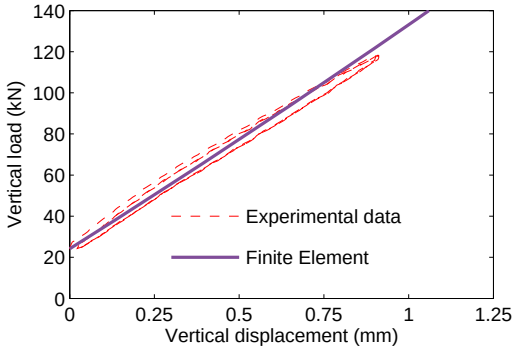


Figure 3 Vertical stiffness comparison between experimental data and FE analysis

5.2 Critical load simulation

Both the detailed FE model and Iizuka analytical model were used to simulate the critical load behavior of the elastomeric bearing shown in Fig. 1. The purpose is to assess the capability of the simple analytical model (Iizuka model) to simulate critical load behavior by comparison to the more detailed and computationally intensive FE model.

A series of FE analyses were performed whereby the model was subjected to vertical compressive load P ranging then sheared to a target lateral displacement. This analysis was repeated for vertical compressive loads ranging from 0 to 356 kN. The results of these FE analyses are presented in Fig. 4. The plots presented in Fig. 4 show the effect of axial load on the force–displacement response: specifically, as the axial load increases, the initial stiffness, maximum shear force attained and critical displacements decrease. The critical displacements (i.e. point of zero horizontal stiffness) and corresponding vertical load from the force-displacement results taken as the critical points and are plotted in Fig. 5.

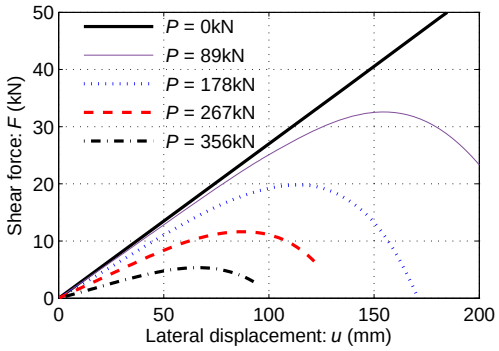


Figure 4 Shear force-lateral displacement relationship for elastomeric bearing

Critical loads simulation results (u_{cr}, P_{cr}) obtained using Iizuka model are also shown in Fig. 5 along with those obtained from the analyses of the detailed FE model. However, values for parameters r, s_1 and s_2 had to be assumed in lieu of characterization data for each of these bearings. Based on values provided in Iizuka (2000), s_1 ands_2 were assumed to be $s_1 = 0.01$ and $s_2 = 3$, respectively. Values of the parameter r reported in Iizuka (2000) ranged from 1.2, 1.5 and 3.5. With no guidance provided by Iizuka for determination of the value of the r parameter, an average value of 2 was used for the analytical simulations.

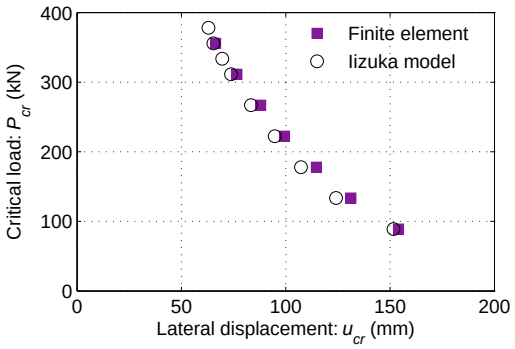


Figure 5 Critical load simulation comparison between FE model and Iizuka model

Critical loads simulated from the FE model and Iizuka model presented in Fig. 5 show a similar trend of reducing critical load values with increasing lateral displacement, which was also found in previous experimental testing (Buckle and Liu 1993, 1994). From the result presented in Fig. 5, the simulation capability of Iizuka's simple analytical model agrees well with the more detailed and computationally demanding 3D FE model over a wide range of lateral displacement. The relative difference between the analytical and FE critical load values at particular lateral displacement range between 2 and 8% with the FE values assumed as the true value in the relative error calculation. Based on these results, Iizuka model is capable to simulate the critical load behavior of this elastomeric bearing.

5.3 Global sensitivity analysis

Sobol' method was used to compute sensitivity indices for the four independent Iizuka model parameters, specifically G, r, s_1 and s_2, to identify the relative importance of the individual parameters in the simulation of the critical displacement, u_{cr}. The sensitivity analysis was performed on an ensemble of u_{cr} values generated for various levels of vertical load, P. Table 1 presents the range of values considered in the sensitivity analysis for the four model parameters (i.e. G, r, s_1 and s_2). Each parameter was assumed to be uniformly distributed over the ranges presented in Table 1. The range of values for parameters r, s_1 and s_2 were kept as broad as possible while avoiding non-physical combinations leading to nonrealistic predictions, noting $s_1 = 0$ was considered in the parameter range.

Table 1 Varied parameter and parameter ranges used for global sensitivity analysis

Type	Symbol	Unit	Range
Material	G	MPa	0.77-0.87
Model	r	n.a.	0.5–6
	s_1	n.a.	0–0.01
	s_2	n.a.	0–5

Total indices (individual contribution plus interactions) and first order indices (individual) computed using the properties of the bearing shown in Fig. 1 are presented in Figs. 6. Figure 6 includes four bar graphs, one for each parameter, with total and first order sensitivity indices plotted for vertical load values P normalized by the corresponding P_{cro} (calculated by Eq. 1) ranging from 0.3 to 0.9. The total and first order indices for parameters s_1 and s_2 are near zero, indicating variability in these parameters has no impact on the critical displacement value simulated by the Iizuka model over the range of vertical load values considered. By considering $s_1 = 0$ and $s_2 = 0$ in the parameter range, these results demonstrate the relationship assumed for the shear spring (i.e. linear vs. nonlinear) has no effect on the predicted critical displacement Therefore, the Iizuka model could be simplified by assuming linear spring properties.

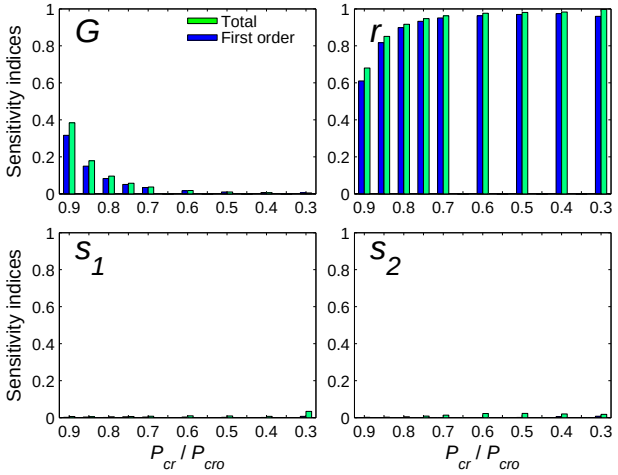


Figure 6 Sensitivity indices for elastomeric bearings

The results presented in Figs. 6 show that both total and

first order indices for the shear modulus, G, decrease as P_{cr}/P_{cro} decreases. This result suggests variation in the shear modulus only has an appreciable impact on the u_{cr} value when P_{cr} is a significant percentage (70 to 90%) of P_{cro}. There is a difference between the total and first order indices for G when P_{cr}/P_{cro} is large. This suggests there is interaction between G and r for large P_{cr}/P_{cro}. Sensitivity indices for parameter r show that as P_{cr}/P_{cro} decreases, both first and total order indices increase approaching a value of nearly 1 for P_{cr}/P_{cro} equal to or less than 0.6.

6. CONCLUSION

The critical load behavior of one bearing (see Fig. 1) was simulated using FE analysis of a detailed 3D model and an existing analytical model. A comparison of the simulated critical displacement values showed the values obtained from the simple Iizuka model compare well with those from the significantly more detailed and computationally demanding finite element model. This result suggests the Iizuka model could be an efficient and accurate method of simulating the critical load behavior of elastomeric bearings.

A global variance-based sensitivity analysis was performed on the Iizuka model output whereby the sensitivity of the u_{cr} simulation to variability in four independent model parameters, specifically, G, r, s_1 and s_2 was determined. The results of the sensitivity analysis demonstrated that the simulated u_{cr} value is sensitive to the shear modulus G and the rotational spring parameter r for vertical loads that are a large percentage (e.g. 60 to 90%) of P_{cro}. As the vertical load decreases, the sensitivity of the u_{cr} value to the G diminishes and the rotational parameter r becomes the controlling parameter. Additionally, the results of sensitivity analysis demonstrated that the u_{cr} prediction is insensitive to the value of the shear spring parameters (i.e. s_1 and s_2) even when values of zero are considered. It can be concluded then that the form of the shear spring (linear versus nonlinear) has no appreciable impact on the critical load values simulated using the Iizuka model.

Acknowledgements:

The authors gratefully acknowledge the support provided by the National Science Foundation through award number CMMI-1031362. Any opinions, findings and recommendations expressed in this paper are those of the authors and do not necessarily reflect the views of the funding institutions.

References:

Buckle, I.G., and Liu, H. (1993). "Stability of elastomeric seismic isolation systems."*Proc.*, *Seminar on Seismic Isolation*, *Passive Energy Dissipation, and Control*, Applied Technology Council, Redwood City, Calif., 293–305.

Buckle, I.G., and Liu, H. (1994). "Experimental Determination of Critical Loads of Elastomeric Isolators at High Shear Strain." *NCEER Bulletin*, 8(3), 1–5.

DSSC (2010). ABAQUS/CAE User's Manual: Version 6.10. Dassault Systèmes Simulia Corp., Providence, RI.

Gent, A. N. (2001). *Engineering with rubber*: *How to design rubber components*, 2nd Ed., Hanser, Munich.

Haringx, J. A. (1948). "On highly compressible helical springs and rubber rods and their application for vibration-free mountings. I." *Philips Res Rep*., 3, 401–449.

Haringx, J. A. (1949a). "On highly compressible helical springs and rubber rods and their application for vibration-free mountings. II." *Philips Res Rep*., 4, 49–80.

Haringx, J. A. (1949b). "On highly compressible helical springs and rubber rods and their application for vibration-free mountings. III." *Philips Res Rep*., 4, 206–220.

Iizuka, M. (2000). "A macroscopic model for predicting large-deformation behaviors of laminated rubber bearings." *Eng*. *Struct*., 22(4), 323–334.

Kelly, J. M. (1997). *Earthquake Resistant Design with Rubber*, 2nd Ed., Springer, London.

Koh, C. G., and Kelly, J. M. (1988)."A simple mechanical model for elastomeric bearings used in base isolation." *Int*. *J*. *Mech*. *Sci*., 30(12), 933–943.

Saltelli, A., Tarantola, S., Campolongo, F., and Ratto, M. (2004). *Sensitivity Analysis in Practice: A guide to assessing scientific models*, Wiley, Hoboken, NJ.

Saltelli, A., Ratto, M., Andres, T., Campolongo, T., Cariboni, J., Gatelli, D., Saisana, M., and Tarantola, S. (2008). *Global sensitivity analysis: the primer*, Wiley, Hoboken, NJ.

Simlab (2011).Software package for uncertainty and sensitivity analysis. Joint Research Centre of the European Commission. Downloadable for free at:http://simlab.jrc.ec.europa.eu.

Sobol', I. M. (2001). "Global sensitivity indices for nonlinear mathematical models and their Monte Carlo estimates." *Mathematics and Computers in Simulation*, 55(1-3), 271–280.

Warn, G. P. and Whittaker, A.S. (2006). "*A Study of the Coupled Horizontal-Vertical Behavior of Elastomeric and Lead-Rubber Seismic Isolation Bearings*." Report No. MCEER-06-0011, Multidisciplinary Center for Earthquake Engineering Research, Buffalo, NY

10 CUEE CONFERENCE PROCEEDINGS
10th International Conference on Urban Earthquake Engineering
March 1-2, 2013, Tokyo Institute of Technology, Tokyo, Japan

DESIGN FOR UNIFORM RISK TO STANDARDIZED NUCLEAR POWER PLANTS USING SEISMIC ISOLATION

Troy A. Morgan[1] and Brian M. McDonald[2]

1) Senior Engineer, Exponent Inc., New York, NY
2) Principal Engineer, Exponent Inc., Menlo Park, CA
tmorgan@exponent.com, bmcdonald@exponent.com

Abstract: The design of structures, systems and components of nuclear power plants (NPPs) in the United States is moving toward a risk-informed performance-based approach. Seismic risk is an important concern for NPPs due to the extremely rare levels of shaking that must be considered in design. In response to events at Fukushima Dai-ichi following the Great Eastern Japan Earthquake, renewed attention has been focused on the mitigation of seismic risk to NPPs. The goal of this paper is the introduction of a practical strategy for the design of seismic isolation systems for standardized NPPs who's structural and non-structural components have been certified to a particular level of seismic demand. Such a design may be considered a template of a standard NPP to be deployed in multiple geographic regions, all having varying levels of seismic hazard, fault mechanisms, soil types, etc. Whereas a conventionally-built standard NPP would be expected to have varying seismic reliability for each seismic hazard environment in which it is built, the introduction of a properly-tuned seismic isolation layer can modify the seismic effects such that the target performance objectives are met regardless of the original design basis. This paper presents a practical method to target bilinear isolation system properties (strength and stiffness) given a standard NPP design and a set of seismic hazard curves for a specific site and soil type. This method has the potential to simplify the design of new NPPs located worldwide, while providing the high level of reliability against failure that is required of such crucial facilities.

1. INTRODUCTION

The goal of this paper is the development of a practical strategy for the design of seismic isolation systems for standardized nuclear power plants (NPPs.) In this context, "standardized" refers to an NPP who's structural and non-structural components have been certified to a particular level of seismic demand. Such a design may be considered a template of a standard NPP to be deployed in multiple geographic regions, all having varying levels of seismic hazard, fault mechanisms, soil types, etc. Whereas a conventionally-built standard NPP would be expected to have varying seismic reliability for each seismic hazard environment in which it is built, the introduction of a properly-tuned seismic isolation layer can modify the seismic effects such that the target performance objectives are met regardless of the original design basis of the superstructure and associated components. This idea has been investigated for small modular reactors by Blandford et al [2009.] The deployment of numerous small-scale, standard NPPs throughout the US is an attractive way to increase and distribute nuclear energy output with higher safety and less expense [The Economist, 2009.]

In this study, the standard NPP has been designed as a conventional structure at a site with very low seismicity, representing a practical minimum for seismic certification of the plants structures, systems, and components (SSCs.) Such an NPP could be constructed in any region with very low exposure to seismic hazard, and the structural system and non-structural components and contents could be identical for each NPP. The structural system, once designed to the original very low seismic criteria, has quantifiable force-deformation characteristics which may be adopted from the pushover curve and transformed into fragility curves for performance states applicable to NPPs. The non-structural systems, including electrical, mechanical, and plumbing equipment, and the associated distribution systems, would also be subjected to some floor response spectrum based on the initial design criteria. Once the structural and non-structural systems have been certified to the level of seismic demand, this design basis is used in the optimization of isolation systems considering a broad classification of seismic hazard, from the lowest to the most severe found in the US. The isolation systems considered in this study are assumed to be bilinear with supplemental dampers, and are applicable to either spherical sliding bearings or lead rubber bearings. However, the conceptual framework is easily extensible to other devices should they be considered.

Unless otherwise indicated, design of NPP structures,

systems, and contents (SSCs) in this paper is based on the provisions and underlying philosophy described in ASCE 43-05 [2005.]

2. SEISMIC RESISTANCE OF STRUCTURAL SYSTEMS

The standard design of an NPP in this study is based on one constructed in a region of very low seismicity. The site is arbitrarily chosen as Houston, TX, since it is among the least active seismic regions in the US. Applying the provisions of ASCE 43-05 [2005], the design base shear for a structure at this site would be 0.21 *g*, assuming a rock site and stiff containment structure with a natural period around 0.25 sec. This base shear corresponds to an annual return period of 10,000 years, plus a modification to achieve uniform risk of failure. ASCE 43-05 also provides estimates of structural system over-strength based on the random strength having a 98% exceedance probability relative to the design strength, and an assumed dispersion of 0.35. This leads to an over-strength factor of 2.05. Assuming the NPP structure is reinforced concrete, a reasonable estimate of the pushover curve for our standard NPP is shown below in Figure 1. This pushover curve may be thought of as the seismic certification of the structure, since it is a measure of seismic resistance, and depends only on the structural geometry and detailing, and not on the assumed hazard environment.

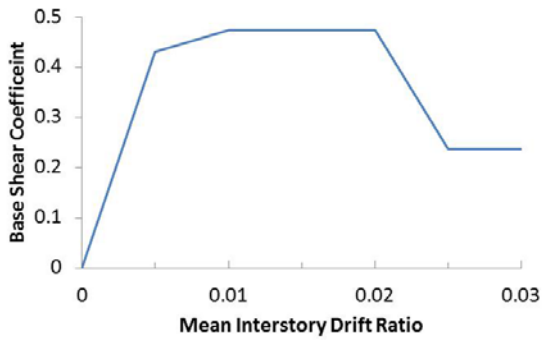


Figure 1. Assumed pushover curve for the standard NPP structure

3. SEISMIC CERTIFICATION OF EQUIPMENT

The seismic certification of an equipment unit establishes the ability of that unit to withstand a particular intensity of seismic shaking and perform its function immediately following that shaking. Recognizing that earthquake shaking produces a broadband excitation, the intensity is generally represented not by a single parameter or even acceleration history, but by an acceleration response spectrum (ARS). This ARS is a demand imposed on an equipment unit by an earthquake, and is a function of many parameters: structural system supporting the equipment, earthquake magnitude, site-to-source distance, soil type, etc. The resistance of an equipment unit must also be described in terms of a spectrum, since harmonic shaking at a fixed frequency may not cause a failure, whereas the same or lower amplitude shaking at a different frequency may cause a failure due to the dynamic response of the internal components of the unit. To address this, equipment manufacturers develop what is known as the Required Response Spectrum (RRS) to describe the maximum amplitude of shaking across a range of frequencies the unit may experience while remaining functional. The ability of the equipment to function is established by testing, and if the tested response spectrum envelopes the RRS for the frequency range of interest, the equipment units are considered to be seismically certified for that RRS. Further information about the seismic certification of electrical equipment can be found in Wilkie et al [2009.]

Given the standard NPP structure, the in-structure floor spectra may be computed for a specific level of seismic hazard. To generate a spectrum, a set of spectrum-compatible ground motions was selected and scaled to the original Houston, TX site. The mean in-structure floor spectrum was then computed at the roof level based on response history analysis (RHA.) The roof is the location with highest acceleration demand. A generic spectrum was then generated based on the assumed peak roof acceleration from static analysis, and an amplification factor of 5 for peak roof spectral acceleration. The peak of the spectrum is based on the natural period of the standard NPP structure = 0.25 sec. The generic spectrum is compared with that obtained from RHA in Figure 2. The generic spectrum is denoted the required response spectrum (RRS) since this spectrum forms the basis of seismic certification testing for all nonstructural systems and components.

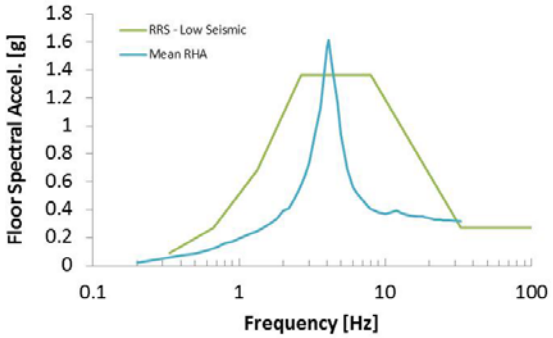


Figure 2. Comparison of mean floor spectrum from RHA with generic RRS for the standard NPP.

4. APPLICATION OF SEISMIC ISOLATION TO STANDARD NPP DESIGN

With the seismic resistance of the standard NPP structural and non-structural components defined, we apply seismic isolation technology to this standard design and enhance its performance capabilities so it may be

constructed in any part of the US, regardless of the seismic hazard environment. To motive this study, three sites have been selected to represent large, moderate, and low levels of seismic hazard. These sites are located, respectively, in Los Angeles CA, St. Louis MO, and Boston MA, each with firm soil site conditions (shear wave velocity between 200 m/s and 400 m/s). The seismic hazard curves for each of these sites, assuming rock sites, are shown in Figure 3, where the intensity measure is taken to be the spectral acceleration at a period of 1-sec (commonly denoted S_{a1}.) This is an appropriate measure for isolated structures, where the period range is generally in the constant-velocity region.

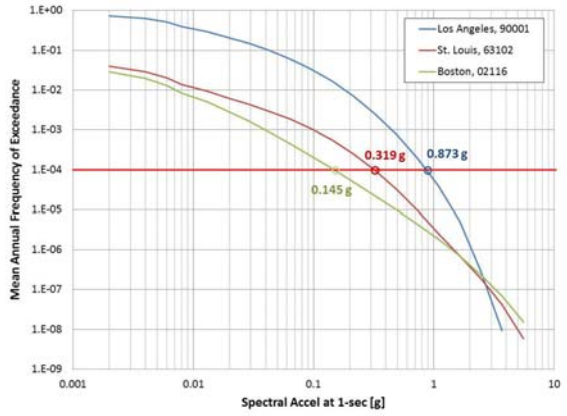


Figure 3. Comparison of seismic hazard curves for S_{a1} used in this study, including demand at MAFE = $1x10^{-4}$.

In selecting the basic properties of the target isolation system, the adequate performance of the structure and non-structural components must be targeted. First considering the structure, the primary design parameter is the base shear demand. By limiting the design base shear of the isolated NPP to that of the standard NPP described in Section 2, elastic behavior of both structures with the equivalent level of confidence is achieved. The basic procedure for this is to develop the constant velocity region of the design spectrum based on the 10,000 yr return period earthquake as

$$S_a = \frac{S_{a1}}{T_I B} \quad (1)$$

Where S_{a1} is the spectral acceleration at 1-sec with an MAFE = 1 x 10^{-4}, T_I is the isolation period, and B is a damping-based spectral reduction factor which can be taken as $B = 2.4\zeta^{0.3}$ (ζ is the critical damping ratio of the isolation system.) By setting Eq. (1) equal to the design base shear coefficient 0.21 g for the standard NPP above, some combination of isolation period and damping can be determined. In the protection of nonstructural components, it is generally advised to use lower-damping isolators (Yang et al, 2010.)

To facilitate comparison of in-structure floor spectra with the RRS for equipment, some generic in-structure spectrum must be developed based on the intensity of shaking at the floor levels of the isolated NPP. Since isolated structures may be treated as a single-degree-of-freedom system, this study considers a single representation of demand for all locations above the isolation layer. This assumption is valid for stiff superstructures having an isolation system with a substantial period separation (say fixed-to-isolated period ratio = 4.) The estimated in-structure ARS is based on the peak floor acceleration and an amplification factor to reach the peak spectral acceleration. This amplification factor depends on the hysteretic properties of the bearings, but can be as large as 4.5 (Yang et al, 2009.) For simplicity, a conservative amplification factor of 4.0 was adopted here, and nonlinear RHA supports its use over a range of isolator types.

The isolator properties are selected so that Eq. (1) is satisfied (for structural performance) and such that the in-structure demand ARS exceeds the RRS for all frequencies between 1 Hz and 35 Hz. A comparison of the ARS for the three sites with the RRS for the standard NPP is shown in Figure 4. A summary of isolator properties which provides the standard NPP with suitable performance for each of the three sites is given in Table 1. These properties are easily achievable in practice with either elastomeric or spherical sliding bearings.

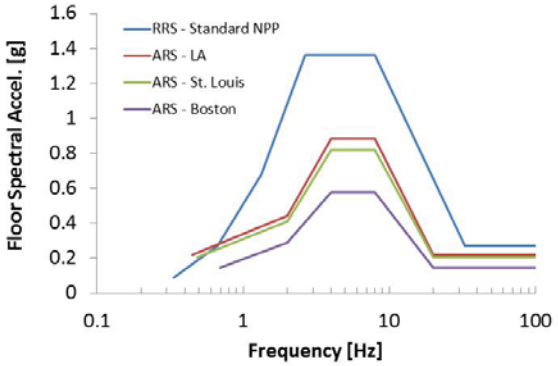


Figure 4. Comparison of floor acceleration response spectra (ARS) for three sites with the required response spectrum (RRS) for the standard NPP.

Table 1. Isolation system period, damping, and displacement demand for each of the three selected sites.

Site	T_b	ζ_b	Δ_b
LA	4.0 s	20%	34.6"
St. Louis	2.0 s	15%	8.04"
Boston	1.5 s	10%	3.19"

5. CONCLUSIONS

This paper concludes with practical method to target bilinear isolation system properties (stiffness and damping) given a standard NPP design and a set of seismic hazard curves for a specific site and soil type. The standard NPP was designed as a conventional structure assuming a site with very low seismicity. A procedure for developing optimal strength and stiffness of the isolators was presented starting with the seismic hazard environment and soil type, certified design strength of standard NPP, and required response spectra (RRS) for nonstructural components. This method therefore incorporates the performance both structural- and non-structural systems, and uses nonlinear response history analysis to validate the procedure presented. This design approach has the potential to simplify the design of new NPPs located in all parts of the US and around the world, while providing the high level of reliability required for such crucial facilities.

REFERENCES:

ASCE/SEI 43-05, Seismic Design Criteria for Structures, Systems, and Components in Nuclear Facilities, American Society of Civil Engineers, 2005.

Wilkie E, Paul FM, Ahmed MA, and Glen NM, Seismic White Paper SA12501SE, Eaton Corporation, August 2009.

Blandford, E., Keldrauk, E., Laufer, M., Mieler, M., Wei, J., Stojadinovic, B., and Peterson, P.F. (2009). Advanced seismic base isolation for modular reactors. Report No. UCBTH-09-004, University of California, Berkeley, CA.

Yang TY, Konstantinidis D, Kelly JM. The Influence of Isolator Hysteresis on Equipment Performance in Seismic Isolated Buildings. EERI Spectra, **26**(1), pp. 275–293, February 2010.

The Economist Technology Quarterly, Mini nuclear reactors: Thinking small.
http://www.economist.com/node/17647651

10CUEE CONFERENCE PROCEEDINGS
10th International Conference on Urban Earthquake Engineering
March 1-2, 2013, Tokyo Institute of Technology, Tokyo, Japan

IDENTIFICATION OF MASS ECCENTRICITIES FROM SEISMIC RESPONSE OF THREE DIMENSIONAL BUILDINGS

Roshanak Omrani[1], Ralph E. Hudson[2], and Ertugrul Taciroglu[3]

1) Postdoctoral Research Associate, Dept. of Civil and Environmental Engineering, University of California, Los Angeles
2) Research Scientist, Dept. of Electrical Engineering, University of California, Los Angeles
3) Associate Professor, Dept. of Civil and Environmental Engineering, University of California, Los Angeles
romrani@ucla.edu, ralph@ucla.edu, etacir@ucla.edu

Abstract: We propose an algorithm for identification of mass-eccentricities in a one-story framed building from its nonlinear response to moderate seismic excitations. Most time-domain system identification techniques assume the mass of the structure to be a known parameter, which can be determined from the structural and architectural drawings with reasonable accuracy. However, in the presence of torsional motion, mass eccentricities are needed in addition to the lateral mass of the structure in order to characterize the mass matrix. Often, high uncertainties associated with the spatial distribution of mass complicate the determination of mass eccentricities. The proposed algorithm adopts the well-known Bouc-Wen model to represent the nonlinear force-displacement relationships in the lateral load resisting elements of the structure. Subsequently, Unscented Kalman Filtering is employed to carry out a sequential state and parameter estimation by using the lateral and torsional accelerations of the structure as the observed response quantities. The identified state/parameter vector includes the deformation and the internal force of individual lateral load resisting elements, Bouc-Wen parameters, and mass eccentricities.

1. INTRODUCTION

System identification techniques have become conventional tools for assessing the state of health of civil structures either on a permanent basis during the service life of a structure, or after extreme events. In addition to structural health monitoring purposes, these methods can be utilized to identify the actual—versus the expected—behavior of structural systems during seismic events so that predictive response models can be validated or calibrated. Enhanced understanding of the inelastic response of structural systems and characterization of their deformation and energy dissipation capacities can be utilized towards the improvement of performance-based seismic assessment methodologies.

Most methods concentrate on response characteristics that exhibit variations within different regimes of response (e.g., restoring forces), or structural properties whose values are altered from a baseline value, typically due to extreme damage scenarios (e.g., stiffness). Consequently, identification of mass properties, which are generally presumed to remain constant over the service life of a structure and throughout damaging events, has received less attention. Nonetheless, model updating and most of the time-domain identification methods require reasonable estimates of structural mass and its distribution.

The most common approach encountered in the current literature for identification of structural mass properties is the calibration of these properties via model updating techniques, such that the output of the model matches the measured response of the structure (Yu et al., 2006; Ventura et al., 2001). Another conventional approach employs the definition of impulse response function to identify lumped masses associated with discrete degrees of freedom. This is achieved by using the vibration history induced by impulsive forces applied at the location of the lumped masses (Masri 1982). A publication by Ruge (1992) describes a state-space technique, which extracts the stiffness matrix of the system from the eigenvalue problem associated with the state-space representation of the system. This is done by imposing conditions that correspond to a static response. Having the stiffness matrix, the mass matrix is deduced from the eigenvalue problem under the dynamic conditions. Angeles-Cervantes and Alvarez-Icaza (2011) propose a least-squares-based method for identifying the products of the inverse of mass matrix with both stiffness and damping matrices and approximating the center of torsion of shear-type buildings. If the mass of the structure is given, then the stiffness and damping matrices can be extracted from the identified matrix products. Zhou et al. (2012) propose a method, which utilizes the forced vibration testing results of a continuous structure, before and after addition of a known mass, to identify the unknown mass of the structure.

The present paper elaborates on extending the previous work (Omrani et al. 2012) in developing an algorithm for identifying nonlinear response of torsionally coupled buildings from their seismic response. The new extension identifies the floor's mass eccentricities and moment of

inertia—which were previously considered as given—along with the nonlinear force-deformation history of the lateral-load-resisting elements of the building. The identification of the aforementioned quantities allows the characterization of the distribution of the mass, which usually cannot be decided accurately from the structural drawings. The current approach does not estimate the value of lateral mass. However, the lateral mass can be evaluated with reasonable accuracy from the structural and architectural drawings. Furthermore, it is possible to identify the *extent* of nonlinearity and the *shape* of the hysteretic force-deformation loop of each lateral-load-resisting element, even without a precise knowledge of the lateral mass, by assuming a unit value.

2. METHODOLOGY

2.1 State-Space Formulation

The general form of the second order differential equation which governs the response of a system to support excitation is given in Equation (1),

$$\mathbf{M}\ddot{\mathbf{U}} + \mathbf{f}\left(\mathbf{U}, \dot{\mathbf{U}}\right) = -\mathbf{M}\ddot{\mathbf{U}}_{\mathbf{g}} \tag{1}$$

Matrix **M** is the global mass matrix and **U** is the (relative to support) displacement vector, where $\dot{\mathbf{U}}$ and $\ddot{\mathbf{U}}$ denote the first and second derivatives of **U** with respect to time, respectively. Vector **f** contains the nonlinear restoring (resisting) forces. In case of a viscously damped linear system, **f** reduces to a linear combination of relative displacement and velocity terms. Vector $\ddot{\mathbf{U}}_g$ contains the support accelerations.

Assuming that the total mass can be lumped at the roof level in a one-story shear-type building with a rigid roof slab, three degrees of freedom (two translational and one torsional) would suffice for characterizing the motion of the building, i.e.,

$$\mathbf{U} = \begin{bmatrix} u_x & u_y & u_q \end{bmatrix}^{\mathrm{T}} \tag{2}$$

Under the aforementioned assumptions the mass matrix will assume the following form,

$$\mathbf{M} = \begin{bmatrix} m & 0 & -me_y \\ 0 & m & me_x \\ -me_y & me_x & I_O \end{bmatrix} \tag{3}$$

where m is the lateral mass of the building, e_x and e_y are the orthogonal distances between the center of mass and the origin of the Cartesian coordinate system with respect to which the equations of motion are defined, and I_o is the mass moment of inertia with respect to the same origin.

The elements of the resisting force vector, **f**, are the resultants of the resisting forces which are developed in all lateral-load-resisting elements of the structure. It can be reasonably assumed that the contribution of the gravity load bearing elements—such as beams or columns that are not integrated into a moment resisting frame or a shear wall—to the overall lateral-load-bearing capacity of the structure is negligible compared to the capacity provided by moment resisting frames and/or shear walls, henceforth referred to as Lateral Load Resisting Systems (LLRSs). Hence, if the structural system consists of a total of r LLRSs, q of which are aligned with the x and the rest with the y directions, **f**, will acquire the following form,

$$f = \begin{bmatrix} \sum_{j=1}^{q} z_j & \sum_{j=q+1}^{r} z_j & -\sum_{j=1}^{q} z_j y_j + \sum_{j=q+1}^{r} z_j x_j \end{bmatrix}^{\mathrm{T}} \tag{4}$$

in which ζ_j denotes the restoring force in the j^{th} LLRS, and y_j's and x_j's correspond to the normal distance from the origin, to the vertical planes where the LLRS is aligned.

The well-known Bouc-Wen model (Bouc 1971, Wen 1976) has been adopted for parameterizing the nonlinear force-deformation relationship in the LLRSs, i.e., the restoring force in each LLRS is related to the deformation, u, and velocity, $\dot{u}$, at the top of the system relative to its base through a first-order differential equation,

$$\dot{z}_j = k_j \dot{u}_j - b_j \left|\dot{u}_j\right| \left|z_j\right|^{n-1} z_j - g_j \dot{u}_j \left|z_j\right|^{n} + c_j \ddot{u}_j \tag{5}$$

The relationship defined by Equation (5) is a semi-physical constitutive law, as the coefficients of the first and the last terms (i.e., k and c) correspond to the initial stiffness and the viscous damping coefficient. However, the rest of the parameters that appear in the formula do not have any physical attributes.

The aforementioned parameterization of the restoring forces is used to develop the state-space representation of the equation of motion by assigning the restoring forces and the displacements of LLRSs, and roof velocity relative to the base as the state variables. The state vector is further extended to include the unknown parameters of the system, as well as the mass eccentricities and moment of inertia. As such,

$$\mathbf{X} = \begin{bmatrix} k_1 & \cdots & k_r & b_1 & \cdots & b_r & g_1 & \cdots & g_r \\ a_1 & \cdots & a_r & c_1 & \cdots & c_r & \dot{u}_x & \dot{u}_y & \dot{u}_q \\ u_1 & \cdots & u_2 & z_1 & \cdots & z_r & e_x & e_y & \bar{I} \end{bmatrix}^{\mathrm{T}} \tag{6}$$

where $\bar{I}$ is the moment of inertia normalized by the lateral mass, i.e.,

$$\bar{I} = \frac{I_o}{m} \tag{7}$$

The state-space equation would follow as,

$$\dot{\mathbf{X}} = \left[\begin{array}{cccccccccc} 0_{1\times 5r} & \ddot{u}_x & \ddot{u}_y & \ddot{u}_q & & & & & & \\ & & & & \dot{u}_1 & \cdots & \dot{u}_r & \dot{z}_1 & \cdots & \dot{z}_r \end{array} \quad 0_{1\times 3} \right]^{\mathrm{T}}. \tag{8}$$

The state variables including model parameters need to be tied to the observed response of the system through an observation equation in order to be able to utilize an extended state estimation filter for their identification. Accelerometers are the most common type of measurement instruments that are used for the vibration monitoring of building structures. Therefore, an appropriate formulation for the observation equation should devise a relationship between the state variables/parameters and the recorded acceleration of the building. This can be achieved through the reconfiguration of Equation (1) as follows,

$$-\left(\ddot{\mathbf{U}}_{\mathbf{g}} + \ddot{\mathbf{U}}\right) = \mathbf{M}^{-1}\mathbf{f}\left(\mathbf{U}, \dot{\mathbf{U}}\right) \tag{9}$$

The vector on the left-hand-side of Equation (9) corresponds to the total acceleration of roof and consists of two lateral, (a_x and a_y) and one torsional (a_θ) components of acceleration. The product on the right-hand-side can be fully characterized in terms of the unknown state variables and parameters. Thus,

$$-\begin{bmatrix} a_x \\ a_y \\ a_q \end{bmatrix} = \frac{1}{m\left(\bar{I} - e_x^2 - e_y^2\right)} \begin{bmatrix} \bar{I} - e_x^2 & -e_x e_y & e_y \\ -e_x e_y & \bar{I} - e_y^2 & e_x \\ e_y & e_x & 1 \end{bmatrix} \times \begin{bmatrix} \sum_{j=1}^{q} z_j & \sum_{j=q+1}^{r} z_j & -\sum_{j=1}^{q} z_j y_j + \sum_{j=q+1}^{r} z_j x_j \end{bmatrix}^{\mathrm{T}} \tag{10}$$

Subsequently, the elements of the state vector can be approximated recursively through a pair of prediction and correction steps as the dynamic system evolves in time. The values of the elements of the state vector are predicted due to the adopted model of the system (Equations 5 and 8). The predicted quantities are then corrected based on the measured response of the system, which, as mentioned earlier, is related to the state variables through the observation equation (Equation 10). Unscented Kalman filtering algorithm (Julier and Uhlmann, 1997; Cao, 2008), which is an extension of the well-established Kalman filtering for the state-estimation of nonlinear dynamic systems, has been employed in the present study. Details of the Kalman filtering algorithm and the formulation of predictor-corrector equations are omitted here for brevity, and may be found, for example, in Speyer and Chung (2008).

Although the lateral mass of the structure, m, is appearing in the right-hand-side of the observation equation, it was not included in the state vector (Equation (6)). Theoretically, Equation (10) implies that m can also be estimated along with the eccentricities and moment of inertia. However, as discussed in the authors' previous work on an earlier version of the algorithm (Omrani et al. 2012), the scales of the physical and non-physical parameters of the Bouc-Wen model are significantly different. The scale difference leads to singularity problems in the matrices that are involved in the correction step. In order to circumvent the numerical issues due to the parameters' scales, the restoring forces are normalized by the lateral mass. This does not affect the estimates of the story velocities and the deformations of the LLRSs. However, the identified restoring forces needs to be scaled by the lateral mass, m, after the filtering is complete, if the actual magnitudes of the restoring forces are desired in addition to the shape of the hysteretic force-deformation response. This would exclude the lateral mass from the identification process. The revised form of the observation equation would follow as,

$$-\begin{bmatrix} a_x \\ a_y \\ a_q \end{bmatrix} = \frac{1}{\bar{I} - e_x^2 - e_y^2} \begin{bmatrix} \bar{I} - e_x^2 & -e_x e_y & e_y \\ -e_x e_y & \bar{I} - e_y^2 & e_x \\ e_y & e_x & 1 \end{bmatrix} \times \begin{bmatrix} \sum_{j=1}^{q} \tilde{z}_j & \sum_{j=q+1}^{r} \tilde{z}_j & -\sum_{j=1}^{q} \tilde{z}_j y_j + \sum_{j=q+1}^{r} \tilde{z}_j x_j \end{bmatrix}^{\mathrm{T}} \tag{11}$$

in which $\tilde{\zeta}_j$ is the restoring force, ζ_j, normalized by the lateral mass, m. The mass-normalization procedure alters the scale of the model parameters as follows,

$$\tilde{k} = \frac{k}{m} \quad , \quad \tilde{c} = \frac{c}{m} \quad , \quad \tilde{b} = m^{n-1} b \quad , \quad \tilde{g} = m^{n-1} g \tag{12}$$

3. NUMERICAL EXAMPLE

The simulated response of a one-story building to the 1989 Loma Prieta earthquake (PEER 2012) has been used to investigate the performance of the proposed method. The dimension of the building is 40 m in the east-west and 20 m in the north-south direction. Two LLRSs are aligned with the east-west direction and are located 10 m to the north and 6 m to the south of the floor's center of geometry. Two other LLRSs are aligned with the north-south direction, 15 m to the east and 20 m to the west of the center of geometry.

The robustness of the algorithm is assessed through a Monte Carlo analysis. For that purpose lateral mass, m, and Bouc-Wen parameters—except for the exponent n, which was fixed at 2 for all simulations—were drawn from random number generators with uniform distributions between -10% and +10% of the nominal values listed in Table 1. The normalized nominal values are shown in Table 2 to better

clarify the effect of normalization on the scaling properties of the model parameters. The coordinates of the center of mass was also perturbed about the geometric center of the floor by selecting the eccentricities, e_x and e_y, randomly from uniform distributions over -l/4 and l/4, where l is the dimension of the floor in each direction. Subsequently half of the mass of the structure was modeled as uniformly distributed over the ceiling slab. The other half was modeled as a concentrated mass at the (e_x, e_y) coordinates. In addition to the structural properties, the incident angle of the ground motion was extracted from a uniform distribution between 0° and 90° (with respect to the east-west direction). Acceleration records from 25 simulations were polluted with realizations of a 5×10^{-4} g root-mean-square Gaussian white-noise process in order to account for instrument (measurement) noise. The same realizations were used to model the measurement noise in all 25 simulations. Table 3 contains the a priori mean (μ_0) and variance (σ_0^2) values, which were adopted to initialize the filter. The initial values for parameters β and γ are set to zero. This is analogous to presuming the system to be linear. In order to incorporate the high level of uncertainty associated with the abovementioned a priori values for β and γ, arbitrarily large a priori variances have been assigned to them. No a prior information is assumed regarding the mass distribution, i.e., the eccentricities are initialized as zero and the moment of inertia is taken as $1/12\,(l_x^{\,2}+l_x^{\,2})$, which corresponds to a uniform mass distribution.

Table 1 Nominal Values of Model Parameters

m (kg)	k (N/m)	c (N/m/s)	β	γ
6×10^6	8×10^7	3.5×10^5	3.5×10^{-5}	7.0×10^{-5}

Table 2 Normalized Values of Model Parameters

m	k	c	β	γ
1	133.33	0.5833	21	50

Table 3 A Priori Mean and Variance Values

	k	c	β	γ	n	e_x, e_y	$\bar{I}$
μ_0	10^3	10	0	0	4	0	1.66×10^2
σ_0^2	10^6	10^2	10^3	10^3	1	4×10^2, 10^2	2.77×10^4

Except for 2 cases out of the 25 simulations, the identified and simulated force-displacement loops show fair agreement. Figures 1 and 2 illustrate representative best- and worst-case scenarios.

The distribution of relative estimation errors for the normalized physical and nonphysical parameters (100 samples per each), as well as eccentricities and normalized mass moment of inertia (25 samples per each) are demonstrated in Figures 3 through 5. The samples corresponding to the two worst-case scenarios (8 samples per each model parameter and 2 samples per each mass property) are marked with asterisks in the figures.

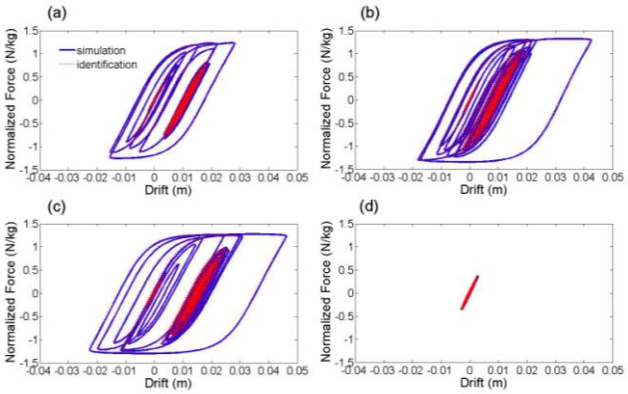


Figure 1 Representative Best-Case Scenario (a) North LLRS, (b) East LLRS, (c) South LLRS, and (d) West LLRS

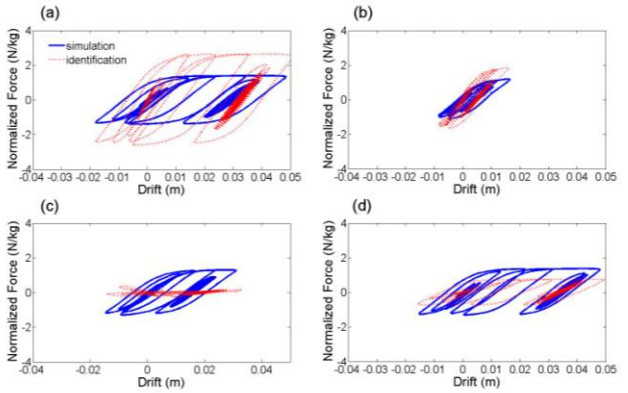


Figure 2 Representative Worst-Case Scenario (a) North LLRS, (b) East LLRS, (c) South LLRS, and (d) West LLRS

It is evident from the error distributions that large errors associate with the non-physical Bouc-Wen parameters (i.e., β, γ, and n) alone do not necessarily lead to the divergence of the identified hysteretic loops from the actual ones. On the other hand, large deviations in the estimated values of physical parameters k and c from the actual values always lead to inferior identification results for the force-deformation loops.

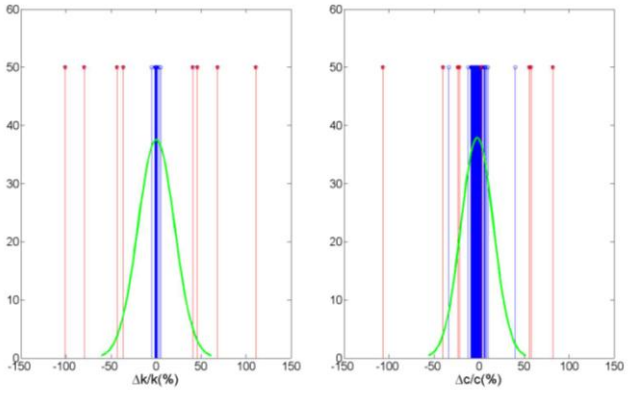


Figure 3 Distribution of Estimation Error for Parameters k and c

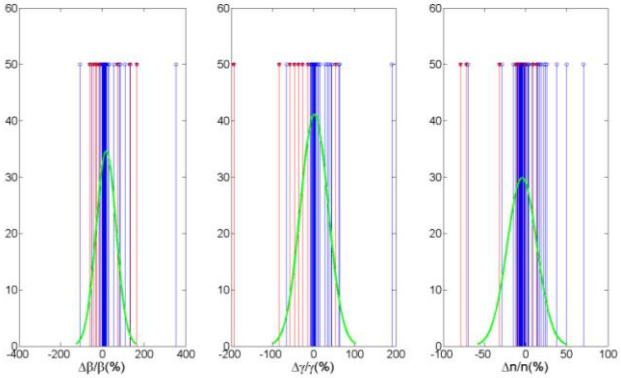


Figure 4 Distribution of Estimation Error for Parameters β, γ, and n

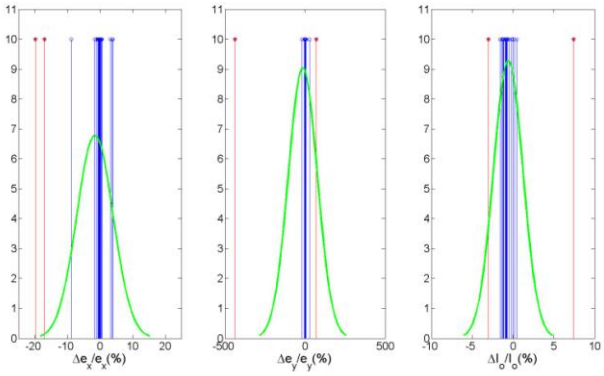


Figure 5 Distribution of Estimation Error for Mass Eccentricities and Moment of Inertia

Figures 6 and 7 display plots of the estimated versus the actual values of model parameters, eccentricities, and moment of inertia. These plots can be used to study the dispersion of the abovementioned parameters about the line of unit slope. Except for a few outliers, the data points are well aligned with the unit-slope line. However, the estimated values for parameter β seem to be biased.

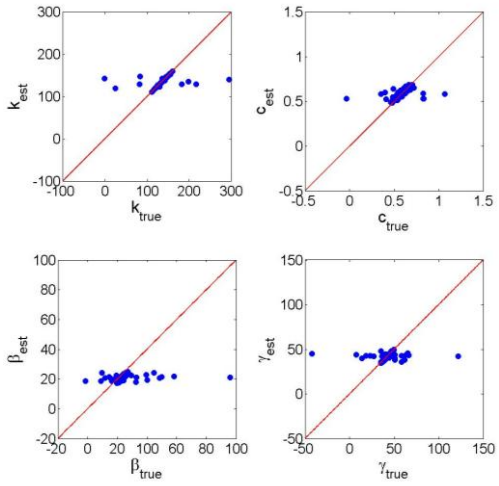


Figure 6 Dispersion of Identified Bouc-Wen Parameters

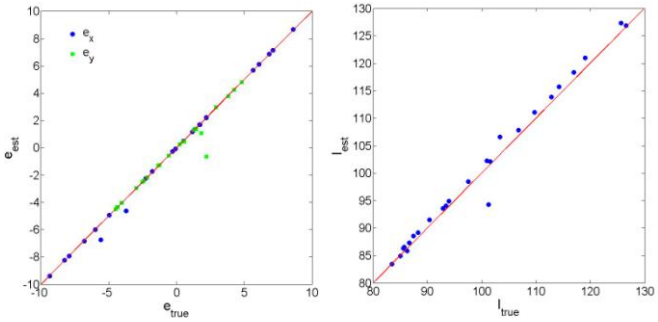


Figure 7 Dispersion of Identified Eccentricities and Moment of Inertia

The importance of including the unknown mass eccentricities and moment of inertia in the identification process was investigated by running the filter while the eccentricities and moment of inertia were frozen to their initial values. This is achieved by assigning very small initial variances to those parameters. Figure 8 implies that parallel identification of the distribution of mass of the structures is inevitable in order to achieve reasonable estimates of the hysteretic force-deformation loops.

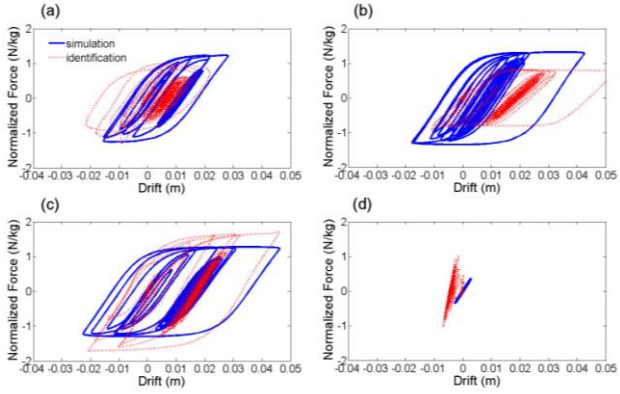


Figure 8 Effect of Excluding Unknown Eccentricities and Moment of Inertia from the Identification Scheme

3. CONCLUSIONS

An algorithm for identifying mass eccentricities and normalized moment of inertia is developed. The algorithm is an extension of a previous method, which identifies the nonlinear response of individual moment resisting frames and/or shear walls that contribute to the overall resistance of a one-story shear building against lateral loads. The capability and robustness of the algorithm is demonstrated through Monte Carlo analysis of the simulated responses of a one-story torsionally-coupled shear-type building. The identified force-displacement loops exhibit very good agreement with the simulation response in most cases. It is observed that large estimation errors in the parameters that have physical attributes lead to poor estimation of the hysteretic loops. An investigation of the specific

combinations of mass eccentricities and incident angle of ground motion that have resulted in poor performance of the method can be a topic of future studies. Numerical convergence issues are prohibitive of identifying the value of lateral mass. Improvement of this aspect of the algorithm can also be an area for further investigations.

References:

Angeles-Cervantes, J.M., and Alvarez-Icaza, L. (2011), "Identification of Seismically Excited Buildings with Two Orthogonal Horizontal Components," *Journal of Vibration and Control*, **17**(6), 881-901.

Bouc, R. (1971), "Modele Mathematique d'Hysteresis," *Acustica*, **21**, 16-25.

Cao, Y. (2008), "Learning the Unscented Kalman Filter: An Implementation of Unscented Kalman Filter for Nonlinear State Estimation," MATLAB Central: An open exchange for the MATLAB and Simulink user community, http://www.mathworks.com/matlabcentral.

Julier, S.J., and Uhlmann, J.K. (1997), "New Extension of the Kalman Filter to Nonlinear Systems," *Proceedings of AeroSense'97 International Society for Optics and Photonics*, 182-193.

Masri, S.F., Bekey, G.A., Sassi, H., and. Caughey, T.K. (1982), "Non-Parametric Identification of a Class of Nonlinear Multi-Degree Dynamic Systems," *Earthquake Engineering and Structural Dynamics*, **10**(1),1–30.

Omrani, R., Hudson, R.E. and Taciroglu, E. "Parametric Identification of Non-Degrading Hysteresis in a Laterally-Torsionally Coupled Building using an Unscented Kalman Filter," *ASCE Journal of Engineering Mechanics* (in print, doi: 10.1061/(ASCE)EM.1943-7889.0000498).

Pacific Earthquake Engineering Research Center (PEER) (2000), PEER Strong Motion Database (http://peer.berkeley.edu/smcat), Regents of the University of California.

Ruge, P. (1992), "Mass identification from lambdamatrices in structural dynamics," *Acta mechanica*, **95**(1), 157-166.

Speyer, J.L. and Chung, W.H. (2008). "Stochastic Processes, Estimation, and Control," Society for Industrial and Applied Mathematics (SIAM).

Venture, C.E., Brincker, R., Dascotte, E., and Andersen, P. (2001), "FEM Updating of the Heritage Court Building Structure," *Proceedings of IMAC-XIX: A Conference on Structural Dynamics*, **1**, 324-330.

Wen, Y.K. (1976), "Method for Random Vibration of Hysteretic Systems," *Journal of Engineering Mechanics*, **102**(2), 246-263.

Yu, E., Wallace, J.W. and Taciroglu, E. (2007), "Parameter Identification of Framed Structures using an Improved Finite Element Model-Updating Method. Part I: Formulation and Verification," *Earthquake Engineering & Structural Dynamics*, **36**(5),619-639.

Zhou, K., Tang, J., and Christenson, R. (2012), "Rapid Identification of Structural Properties based on Mass Response Method," *Proceedings of SPIE* , Paper No. 834703.

10CUEE CONFERENCE PROCEEDINGS
10th International Conference on Urban Earthquake Engineering
March 1-2, 2013, Tokyo Institute of Technology, Tokyo, Japan

THE BEHAVIOR OF RC ROCKING WALL-FRAME BUILDINGS UNDER PULSE-LIKE GROUND MOTIONS

H.A.D Samith Buddika[1] and Anil C. Wijeyewickrema[2]

1) Graduate Student, Department of Civil Engineering, Tokyo Institute of Technology, Japan
2) Associate Professor, Department of Civil Engineering, Tokyo Institute of Technology, Japan
samithbuddika.h.aa@m.titech.ac.jp, wijeyewickrema.a.aa@m.titech.ac.jp

Abstract: The development of new structural systems which suffer no or minor damage following a severe event was a key interest of researchers during the past few decades. Self-centering walls with alternative dissipation mechanisms were among the next generation candidates for a damage avoidance design of structures while being cost effective. However, the applications of such rocking wall systems are limited in practice due to the lack of experimental and analytical evidences. Therefore, in this study the dynamic characteristics of a four-story RC rocking wall-frame was evaluated under near-fault pulse-like and far-field ground motions considering both design and risk-targeted maximum considered earthquake levels. For that purpose, a three dimensional finite element model of the prototype structure was developed using OpenSees. The rocking wall system was designed as a retrofitting solution for existing RC frame structures, but equally suitable for use in new buildings. The wall was designed to confirm to the requirements in ACI ITG-5.2-2009. The energy dissipation of walls has been introduced through unbonded mild steel bars located at the base. The rocking wall-frame system undergoes only moderate damage. Moreover, negligible residual drifts proved the superiority of the systems with self-centering ability. Hence, repairs are more likely to be feasible following a severe event.

1. INTRODUCTION

The rocking motion of structures to mitigate earthquake induced damage to buildings was first investigate by Housner (1963). Rocking response of massive concrete blocks studied by Aslam et al. (1980) identified that rocking can be further improved against overturning by anchoring to the ground by prestress tendons or allow it to slide by reducing the coefficient of friction. However, the energy dissipation capacities of such systems were negligible. Stone et al. (1995) tested hybrid systems which combines the mild steel bars to dissipate energy and unbonded post-tensioned bars to provide sufficient flexural resistance. Kurama et al. (1998) introduce a seismic design methodology for unbonded post-tensioned precast walls and subsequently developed a numerical modeling procedure to simulate the lateral load behavior of rocking walls (Kurama 1999).

While earlier studies were focused only on the wall behavior, many recent studies have been conducted on the interaction between wall and frame system (Lu 2005, Marriott et al. 2008 and Nagae et al. 2011). Lu (2005) showed the benefits of incorporating the three dimensional effect in the analysis of wall-frame structures allowed to rock on their foundation. However, the rocking walls used by Lu (2005) did not possess the self-centering ability. Marriott et al. (2008) tested precast, post-tensioned walls with alternative dissipation solutions for existing frame structures. Nagae et al. (2011) simultaneously tested a four-story RC wall-frame building and RC precast rocking wall-frame building on the E-Defense shaking table in Japan under three dimensional ground motions. However, the results of the shaking table test are still subject to further investigations. On the other hand, no previous numerical studies have been focused on RC rocking wall-frame buildings designed according to contemporary design guidelines. Since, only hand full of evidence for RC rocking wall-frames are available, further investigations are required to build the confidence among Engineers prior to implement such rocking wall-frame structures in practice.

In this study, a rocking wall system was designed as a retrofitting solution to the existing four-story RC frame structure, but equally suitable for use in new buildings. The rocking wall was designed using ASCE 7 (2010), ACI 318 (2011) and ACI ITG-5.2 (2009). A three dimensional finite element model created using OpenSees (2011) was analyzed under two sets of ground motions namely, near-fault pulse-like and far-field considering both design earthquake (DE) and risk-targeted maximum considered earthquake (MCE_R) levels. The performance of the rocking wall-frame system was evaluated by comparing the building drift demands with the performance levels specified in the documents such as ASCE 41 (2006) and Elnashai and Sarno (2008).

2. BUILDING DESCRIPTION

The plan view of the prototype structure is shown in Fig. 1. The typical story height is 3.6 m. The lateral load resistance of the building in the X- direction is provided by the two rocking walls and Y- direction is provided by the special moment resistance frame system. The design short period and 1.0 s spectral accelerations were $S_{DS} = 0.921g$ and $S_{D1} = 0.488g$ respectively. When designing the rocking DE and MCE_R levels were considered. The design strength of the concrete was 28 N/mm^2 chosen to satisfy the minimum requirements given in ACI ITG-5.2 (2009). The unit weight of concrete was 22.76 kN/m^3. The yield strengths of the main steel reinforcement and tie bars were taken as 420 and 280 MPa respectively (ASTM A 615-2003). The floor live load and roof live load are 4.79 kN/m^2 and 0.96 kN/m^2 respectively. The typical column size is 400 mm × 400 mm. The typical floor beam size is 550 mm × 300 mm and roof beam size is 350 mm × 300 mm. The wall size is 5000 × 300 mm in plan. The slab thickness is 200 mm.

The performance objective for the rocking wall-frame was set to be 1.0% transient drift under DE level which is corresponding to a moderate joint damage. The joints are likely to suffer some strength degradation but repair should be possible. Furthermore, a transient drift of 1.5% was established under MCE_R level which would result in an extensive damage to the exterior joints while maintaining the gravity load carrying capacity of the joints, and hence the frame (Marriott et al. 2008).

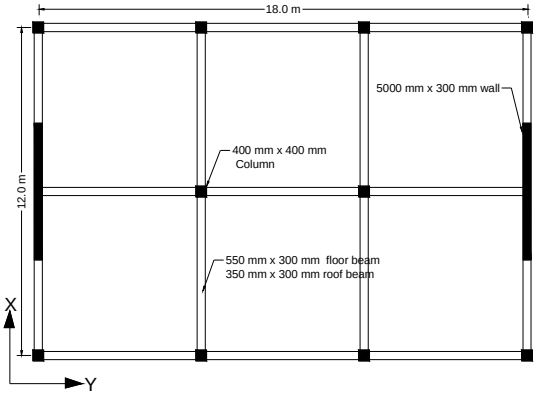


Fig. 1. Plan view of the prototype building.

3. ROCKING WALL DESIGN

The design loads for the rocking walls were calculated using ASCE 7 (2010). The walls were conservatively analyzed as an isolated lateral load bearing system. The lateral load capacity of the existing frame system is not considered. When designing, the ACI ITG-5.2 (2009), specific guidelines for the design of special unbonded post-tensioned precast shear walls and ACI 318 (2011) were followed. A more details about the calculation procedure can be found in Smith and Kurama (2012). The wall height (h_w) and length (l_w) was 14.4 m and 5.0 m respectively (resulting in an aspect ratio of 2.88). The wall design was carried under two different drift limits: (1) Design drift limit (Δ_{wd}) according to ASCE 7 (2010) considering as a fixed base wall (2) Validation drift limit (Δ_{wm}) from Equation 1 according to ACI ITG-5.2 (2009). The linear elastic drift was calculated by assuming a cracked flexural stiffness of $I_{cr} = 0.5I_{gross}$ and a shear area of $A_{sh} = 0.8A_{gross}$. When calculating design level drift a displacement amplification factor of $C_d = 5.0$ was used. The calculated drift limits were $\Delta_{wd} = 0.362\%$ and $\Delta_{wm} = 2.84\%$.

$$0.90 \le 0.8\left[h_w / l_w\right] + 0.5 \le 3.0 \qquad (1)$$

The proportioning of the amount of mild steel bars and post-tensioned bars were done in order dissipate sufficient amount of energy at the base of rocking wall while ensuring the re-centering of the system. The unbonded mild steel bars were designed to resist about 38% of the total base moment of the wall. The details of the rocking wall near the base are shown in Fig. 2.

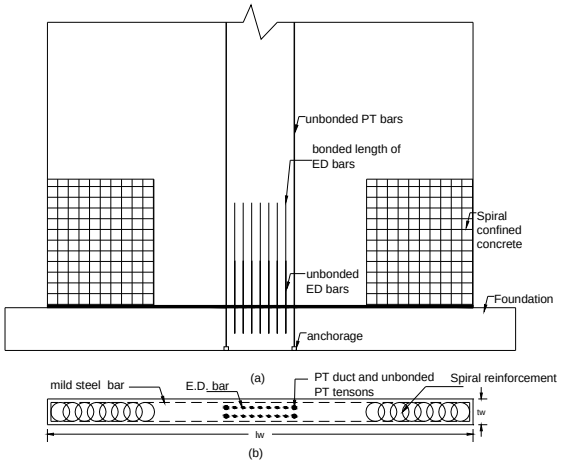


Fig. 2. Details of the rocking wall near the base: (a) Elevation (b) Plan view.

3.1 Modeling of the Post-Tensioned Rocking Wall

The analytical modeling procedure described in this paper is developed based on the DRAIN – 2DX model proposed by Brian et al. (2011). More details of the modeling procedure can be found Kurama et al. (1999). In this study OpenSees (2011) was used to simulate the rocking wall behavior with some minor modifications to the original model. In OpenSees model, a large numbers of displacement-based beam column elements were used at the base of the wall. The rest of the wall was modeled with force-based beam column elements. The gap opening of the rocking wall was simulated by setting a zero tensile strength and zero stiffness of the wall concrete over a critical height (H_{cr}) of the wall. The H_{cr} was taken as the confined concrete thickness of the wall as specified by Brian and

Kurama (2012). Confinement reinforcement details were not modeled along the region of H_{cr}. The unbonded mild steel bars were modeled using truss elements on the outside of the wall to have a uniform strain along the length of the element (Brian et al. 2011). The truss elements were considered to be fixed at the foundation level and kinetically constrained to the corresponding fiber element nodes of the wall at the top. The post-tensioned bars were modeled with co-rotational truss elements with initial strain material models available in OpenSees. The use of co-rotational truss elements with initial strain material model did not consider the secondary effect as the real system behavior. At the top of the rocking wall, the wall degree of freedoms (both translation and rotation) and tendon degree of freedoms were make equal by kinetic constrains. At other floor levels, only the lateral movements (vertical and rotational movement are free) of the post-tension tendons were kinetically constrained to the corresponding fiber element node of the wall to simulate the unbonded behavior of tendons.

4. MODELING OF THE ROCKING WALL-FRAME BUILDING.

A three dimensional model of the rocking wall-frame structure was developed with OpenSees (2011) by considering both material and geometric nonlinearities. The Nonlinear Beam Column elements were used to model the beams and columns. The concrete and steel material models are chosen to be Concrete02 and Steel02, respectively. The constitutive behavior of concrete modeled using the modified Kent and Park model (Kent 1971). For reinforcing steel, the constitutive model of Menegotto and Pinto (1973) is used.

The modeling of rocking walls was done as explained in Section 3.1. The initial post-tension stress was 60% of the yield stress limit (F_y .= 1686 MPa). A frame element with high flexural and axial rigidity was used at each floor level to represent the width of the wall (Fig. 3). The restraining effect of the slab was modeled with the truss elements with higher axial rigidity instead of rigidDiaphragm command available in OpenSees (Vesna 2011). The plastic mechanism of the structure is shown in Fig. 4.

Nonlinear time history analyses of the structure were carried out where the system of equations are solved using Newmark method with β = 0.5 and γ = 0.25 along with modified Newton-Raphson technique. Stiffness proportional damping was used with coefficients calculated based on 1st fundamental frequency with a 5% damping ratio. The fundamental period of the building was T= 0.626 s .

5. GROUND MOTION SELECTION AND MATCHING

Response of the rocking wall-frame structure were evaluated under two sets of ground motions (10 per each) namely, near-fault pulse-like and far-field (Table 1). The ground motion records were obtained from PEER NGA Ground Motion data base (PEER 2012). The wavelet analysis algorithm developed by Baker (2007) was used to identify the pulse-like characteristics of ground motion records. The seed ground motions were linearly scaled in such a way that the average value of the 5% damped response spectra for the suite of ground motions is not less than the design response spectrum (Figs. 5 and 6) in the period range of $0.2T$ to $1.5T$. The scaling factors for DE level were in the range of $0.7-1.7$ and MCE_R level were in the range of $1.0-2.6$. The DE level was taken as 2/3 MCE_R.

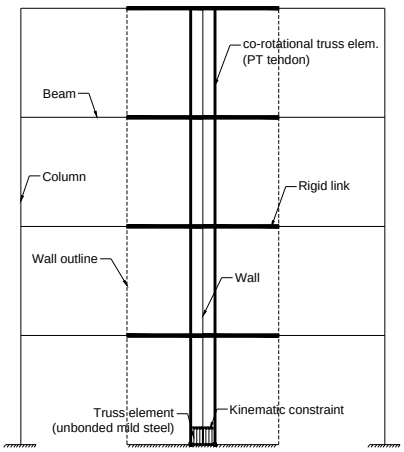


Fig. 3. Elevation of the rocking wall-frame model.

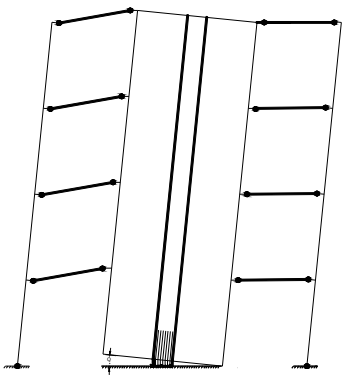


Fig. 4. Expected plastic mechanism of the rocking wall-frame structure.

Table 1. The seed ground motion records used in the analysis.

EQ.No	NGA. Seq. No	Event	Year	M_w	Station	PGA (g)	PGV (cm/s.)
Near-Fault Pulse-Like Record Set							
1	181	Imperial Vally-06	1979	6.5	EI Centro Array # 06	0.44	111.9
2	182	Imperial Vally-06	1979	6.5	EI Centro Array # 07	0.46	108.9
3	292	Irpinia, Italy-01	1980	6.9	Sturno	0.31	45.5
4	723	Superstition Hill-02	1987	6.5	Parachute Test Site	0.42	106.8
5	802	Loma Prieta	1989	6.9	Saratoga - Aloha	0.38	55.6
6	821	Erzican, Turkey	1992	6.7	Erzincan	0.49	95.5
7	828	Cape Mendocino	1992	7	Petrolia	0.63	82.1
8	879	Landers	1992	7.3	Lucerne	0.79	140.3
9	1063	Northridge-01	1994	6.7	Rinaldi Receving Sta	0.87	167.3
10	1086	Northridge-01	1994	6.7	Sylmar - Olive View	0.73	122.8
Far-Field Record Set							
11	169	Imperial Vally	1979	6.5	Delta	0.35	33
12	174	Imperial Vally	1979	6.5	EI Centro Array # 11	0.38	42
13	721	Superstition Hills	1987	6.5	EI Centro Imp. Co.	0.36	46
14	725	Superstition Hills	1987	6.5	Poe Road (temp)	0.45	36
15	752	Loma Prieta	1989	6.9	Capitola	0.53	35
16	767	Loma Prieta	1989	6.9	Gilroy Array # 3	0.56	45
17	900	Landers	1992	7.3	Yermo Fire Station	0.24	52
18	1116	Kobe, Japan	1995	6.9	Shin-Osaka	0.24	38
19	1158	Kocaeli, Turkey	1999	7.5	Duzce	0.36	59
20	1602	Duzce, Turkey	1999	7.1	Bolu	0.82	62

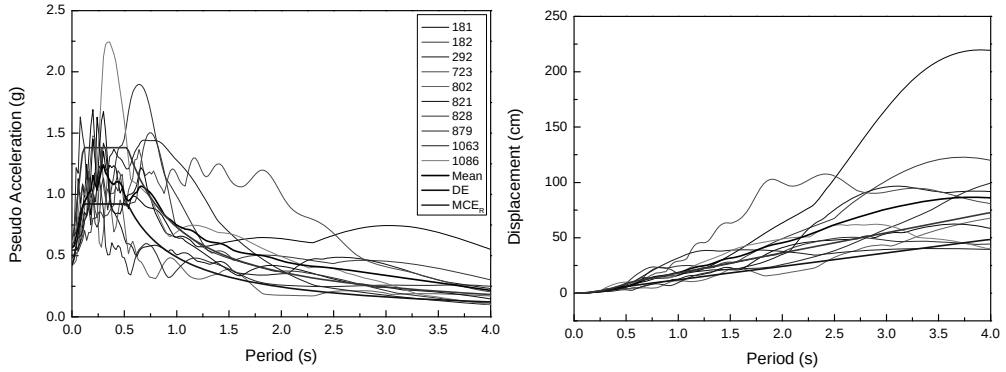


Fig. 5. 5%-damped response spectra for near-fault pulse-like ground motion set: (a) Pseudo Acceleration (b) Displacement.

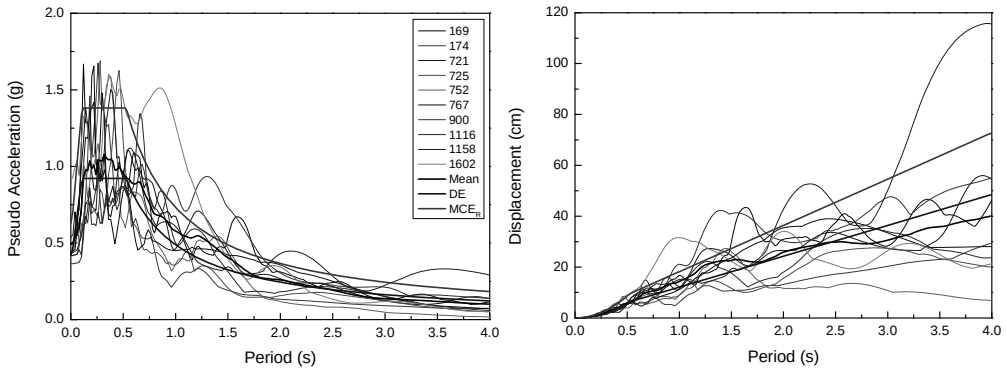


Fig. 6. 5%-damped response spectra for far-field ground motion set: (a) Pseudo Acceleration (b) Displacement.

6. RESULTS AND DISCUSSIONS

The maximum inter-story drifts results for the near-fault ground motion suite under MCE_R level is shown in Fig. 7. The inter-story drifts showed a uniform variation over the height of the building. Hence, prove the advantage of having such wall elements to eliminate the soft-story mechanism in frame structures to enhance the seismic resistance. It is important to highlight that a minimum damage to the rocking wall was ensured during the design phase by providing spiral reinforcement at base of the wall (Fig. 2). Due to the gap opening behavior at the base of the rocking wall, the damage to the rocking wall-frame structure is mainly concentrated at monolithically cast joints (Fig. 4). Therefore, the inter-story drifts indicate the degree of damage to the beams, columns and their connections only.

The maximum residual drift observed was 0.4% (Fig. 8) which is well below the 1.0% residual drift limit required for life safety according to ASCE 41 (2006). In all other cases the residual deformations were negligible. This proves the superior performance of systems with self-centering walls. The maximum 1st story drifts results found during the analysis are shown in Figs. 9 and 10 respectively.

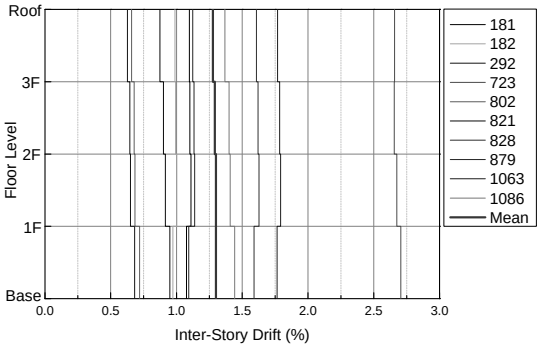


Fig. 7. Typical inter-story drift variation of the rocking wall-frame building under near-fault MCE_R level.

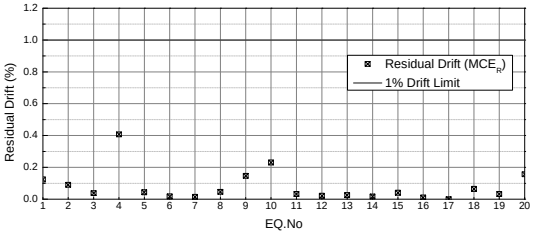


Fig. 8. The resulting residual drifts for MCE_R level ground motions.

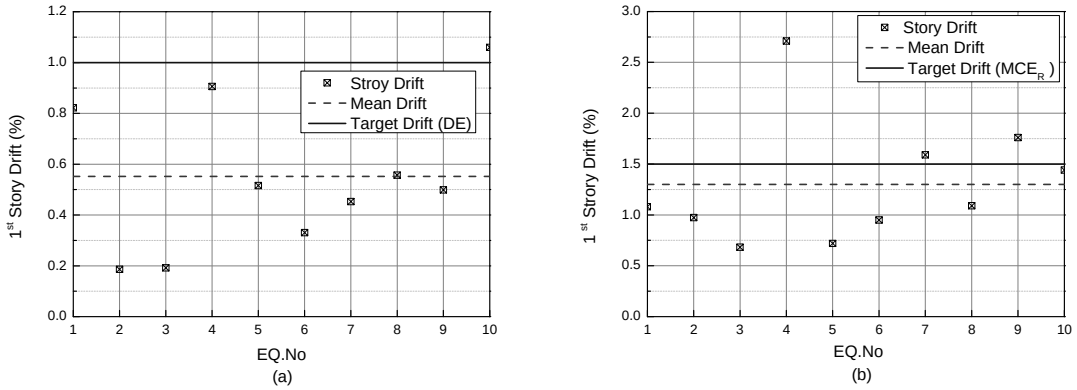


Fig. 9. Comparison of 1st story drift results for near-fault pulse-like ground motion set: (a) DE Level (b) MCE_R Level.

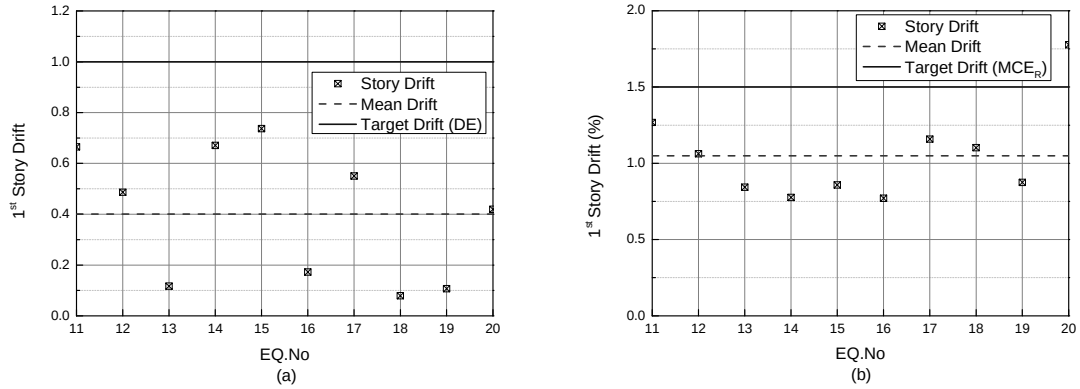


Fig. 10. Comparison of 1st story drift results for far-field ground motion set: (a) DE Level (b) MCE_R Level.

For DE level, the mean 1st story drifts for near-fault (Fig. 11a) and far-field (Fig. 12a) ground motions were 0.55% and 0.40% respectively. The story drift of 0.55% is corresponding to moderate type of damage to the building (Elnashai and Sarno 2008). However, the expected damage is unlikely to be considerable. Under far-field ground motions only a non-structural type damages to the building was expected. The resulting mean drifts were well below the limiting inter-story drift requirement of 1.0% **.**

Under MCE_R level, the resulting mean 1st story drifts were 1.29% and 1.04% for near-fault (Fig. 11b) and far-field (Fig. 12b) ground motions respectively. Both the drift limits are corresponding to moderate type of damage to the building. Hence, the load carrying capacity of the exterior joints can be maintained to prevent local collapse. Therefore, the structure is more likely to undergo repair together with negligible residual deformation of the building. In other words, the rocking wall-frame structure developed in this study showed superior performance against both near-fault pulse-like and far-field ground motions.

In order to have a better understanding about the performance of the rocking wall itself, the roof drift results obtained during the analysis was compared with the design drift limits for the rocking wall. The roof drift results for near-fault and far-field ground motions are shown in Figs. 11 and 12 respectively.

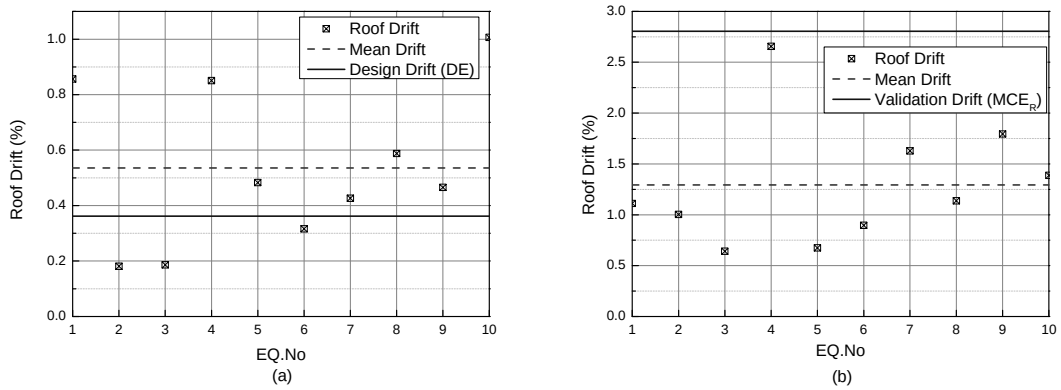


Fig. 11. Comparison of roof drift results for near-fault pulse-like ground motion set: (a) DE Level (b) MCE_R Level.

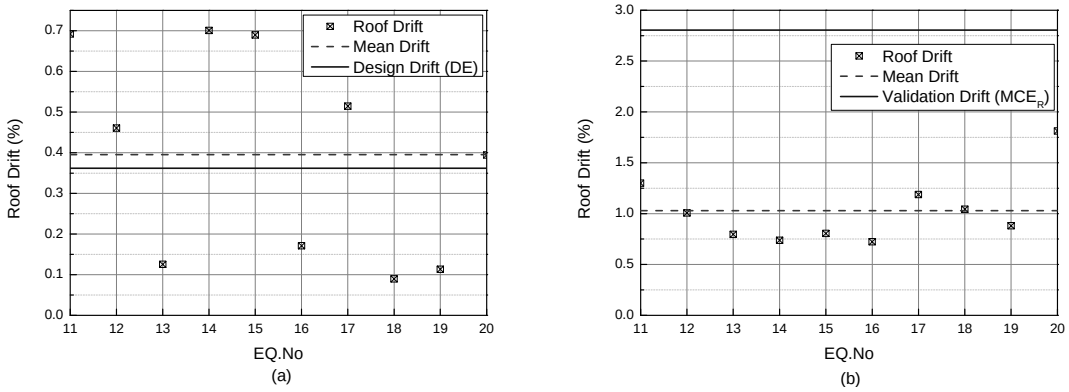


Fig. 12. Comparison of roof drift results for far-field ground motion set: (a) DE Level (b) MCE_R Level.

Under DE level, for near-fault ground motion set the mean roof drift was found to be approximately 150% of the design drift level (Fig. 11a). Such variations can be as a result of gap opening behavior due to the large seismic demand induced by the pulse-like characteristics of ground motions (which did not considered while calculating the DE level drift). For far-field ground motions the variation was only about 9% (Fig. 12a). However, a large variation of the roof drift response was found.

For MCE_R level, the mean drift was found to be less than 50% of the validation drift limit for both near-fault and far-field ground motions. Hence, the post-tension tendons were remained essentially elastic while no fractures in unbonded mild steel bars.

7. SUMMARY AND CONCLUSIONS

A RC rocking wall-frame system was successfully developed as a retrofitting solution to an existing four-story frame structure, but equally suitable for use in new buildings. Moreover, a fiber based model to simulate the lateral load behavior of rocking walls under both static and dynamic loading conditions were developed with OpenSees (2011).

The rocking walls were designed according to the according to ACI ITG-5.2 (2009). A three dimensional finite element model developed with OpenSees (2011) was analyzed under two sets of ground motions namely, near-fault pulse-like and far-field (under both DE and MCE_R levels). The results obtained were compared with limiting drifts to investigate the performance of the structural system. The findings of this study can be summarized as bellow.

The introduction of rocking walls resulted in a uniform inter-story drift variation over the height of the building. As a result of that, no soft-story mechanism was observed. In general near-fault pulse-like ground motions resulted in a larger drift response of the building compared to far-field set (37.5% for DE level and 24% for MCE_R level). Other than that, large scattering of the data was observed.

Under DE level near-fault pulse-like ground motions, moderate damage to the frame systems was expected. However, the expected damage is likely to be minor. In contrast, under DE level far-field ground motions, only non-structural damage was expected. However, the mean story drifts results were well below the 1.0% target performance drift level of the building under DE level.

Under MCE_R, moderate damage to the building under both near-fault and far-field ground motions were expected. However, the mean story drifts were under the 1.5% target performance drift level of the building. Moreover, the residual deformation was negligible. Therefore, the load carrying capacity of the exterior joints can be maintained to prevent local collapse.

The DE level roof drifts were found to be under estimate by the current design procedure for pulse-like ground motions. Therefore, it is highly recommended to carry out dynamic analysis of rocking walls under specific ground motion suites to estimate the design drift limits due to the uncertainties of results observed during the present study.

In general, the rocking wall-frame structure investigated in this study showed superior performance against the both near-fault pulse-like and far-field ground motions. Therefore, such structural systems with self-centering rocking walls can be utilized as a cost effective solution to retrofit existing frame structures or to design new structures.

REFERENCES

ACI 318 (2011), *Building code requirements for structural concrete* and *commentary*, American Concrete Institute, Farmington Hills, MI.

ACI ITG-5.2 (2009), *Requirements for Design of a Special Unbonded Post-Tensioned Precast Shear Wall Satisfying ACI ITG-5.1 and Commentary*, ACI Innovation Task Group 5, Farmington Hills, MI.

ASCE 41 (2006), *Seismic Rehabilitation of Existing Buildings*, American Society of Civil Engineers, Reston, VA.

ASCE 7 (2010), *Minimum Design Loads for Buildings and Other Structures*, American Society of Civil Engineers, Reston, VA.

Aslam, M., Goddon, W. G., and Scalise, D. T. (1980), ''Earthquake rocking response of rigid bodies''. *Journal of Structural Division, American Society of Civil Engineers*, **106**(2), 377–392.

ASTM A 615 (2003), *Standard Specification for Deformed and Plain Billet-Steel Bars for Concrete Reinforcement*. American Concrete Institute, Farmington Hills, MI.

Baker, J. W. (2007), "Quantitative Classification of Near-Fault Ground Motions Using Wavelet Analysis". *Bulletin of Seismological Society of America*, **97**(05), 1486-1500.

Elnashai, S. and Sarno, L. D. (2008), "Fundamentals of Earthquake Engineering". John Wiley and Sons Ltd, United Kingdom.

Housner, G. W. (1963), ''The behavior of inverted pendulum structures during earthquake". *Bulletin of the Seismological Society of America*, **53**(2), 403–417.

Kent, D. C. and Park, R. (1971). "Flexural member with confined concrete". *Journal of Structural Division, Proceedings of the American Society of Civil Engineers*, **97** (ST7), 1969-1990.

Kurama, Y. C., Sause, R., Pessiki, S., Lu, L. W., and EI-Sheikh, M. (1998), "Seismic design and response evaluation of unbounded post-tensioned precast concrete walls". *Precast Seismic Structural Systems (PRESSS) Rep. No. 98/03*, Lehigh University.

Kurama, Y. C., Sause. R., Pessiki, S., and Lu, L. W. (1999), "Lateral Load Behavior and Seismic Design of Unbonded Post-Tensioned Precast Concrete Walls". *ACI Structural Journal*, **96**(4), 622-632.

Lu, Y. (2005), "Inelastic behavior of RC wall-frame with a rocking wall and its analysis incorporating 3-D effect". *Structural Design of Tall and Special Buildings*, **14**: 15–35.

Menegotto, M. and Pinto, P. (1973). "Methods of analysis for cyclically loaded R/C frames", *Proceedings of the Symposium of Resistance and Ultimate Deformability of Structure Acted by Well Defined Repeated Load*, IABSE, Lisbon, Portugal.

Open System for earthquake engineering simulation (OpenSees) (2011), Pacific Earthquake Engineering Research Center, University of California, Berkeley, http://opensees.berkeley.edu/.

Nagae, T., Tahara, K., Matsumori, T., Shiohara, H., Kabeyasawa, T., Kono, S., Nishiyama, M., Wallace, J., Ghannoum, W., Moehle, J., Sause, R., Keller, W., Tuna, Z., "Design and Instrumentation of the 2010 E-Defense Four-Story Reinforced Concrete and Post-Tensioned Concrete Buildings". *Technical Report PEER 2011/104*, Pacific Earthquake Engineering Research Center, University of California, Berkeley.

PEER (2012), Pacific Earthquake Engineering Research Center: PEER Ground Motion Database (Beta), http://peer.berkeley.edu/peer_ground_motion_database.

Smith, B. J., Kurama, Y. C. and McGinnis, M. J. (2011), "Design and Measured Behavior of a Hybrid Precast Concrete Wall Specimen for Seismic Regions". *Journal of Structural Engineering*, **137**(10), 1052-1062.

Smith, B. J. and Kurama, Y. C. (2012), " Seismic Design Guidelines for Special Hybrid Precast Concrete Shear Walls". *Structural Engineering Research Report NDSE-2012-02*, University of Notre Dame.

Stone, W. C., Cheok, G. S. and Stanton, J. F. (1995), "Performance of Hybrid Moment-Resisting Precast Beam-Column Concrete Connections Subjected to Cyclic Loading". *ACI Structural Journal*, **91**(2), 229-249.

Vesna, T. (2011), "Modeling Diaphragms in 2D Models with Linear and Nonlinear Elements". University of California, Berkeley. http://opensees.berkeley.edu/wiki/.

10CUEE CONFERENCE PROCEEDINGS
10th International Conference on Urban Earthquake Engineering
March 1-2, 2013, Tokyo Institute of Technology, Tokyo, Japan

MODAL IDENTIFICATION OF OUTPUT-ONLY STRUCTURES UNDER AMBIENT VIBRATION

Weixing Shi[1], Xi Chen[2], and Jin Wang[3]

1) Professor, Research Institute of Structural Engineering and Disaster Reduction, Tongji University, P. R. China
2) Doctoral Student, Research Institute of Structural Engineering and Disaster Reduction, Tongji University, P. R. China
3) Engineer, China Resources Land (Shenyang) Co., Ltd, P. R. China
swxtgk@tongji.edu.cn, chencici214@hotmail.com, wangjin111@126.com

Abstract: In this paper, five output-only modal identification techniques are systematically investigated, which can be categorized as frequency domain, time domain, and time-frequency domain approaches. A numerical three-story frame model is firstly utilized for the application of the five techniques to show the identification performance of these techniques under different situations, such as seismic excitation, closely spaced modes, noise effect, and local damage. Secondly, these modal identification approaches have been applied to identify the modal information of a high-rise building in Shanghai with measurements under microtremors. The accuracy and efficiency of these techniques are then investigated. Finally, an integrated algorithm is proposed to improve the in situ modal identification of the output-only structures under microtremors.

1. INTRODUCTION

Performance of a civil engineering structure subjected to seismic, wind and other dynamic loads depends upon its modal properties such as natural frequencies, damping ratios and mode shapes. A good knowledge of the dynamic properties would pave the way to dynamic analysis, structural health monitoring, updating finite-element models, detecting structural modification, and so on. The modal parameter information is usually obtained by means of artificial excitation or ambient vibration tests using modal identification techniques. For civil engineering structures, cases exist where it is rather difficult to apply an artificial force. Thus, ambient vibration test is the better candidate, insofar as it constitutes an efficient, easy and inexpensive way to understand the dynamic behavior without causing any harm to the structure. The excitation of ambient vibration test is natural form (i.e., wind, traffic, or waves) which cannot be controlled or measured, hence the name "unknown input" and the need for special processing to obtain the modal parameters.

Recently the extension of modal identification methods to ambient vibration cases, in which an input cannot be measured, has received considerable attention in civil engineering community. The operational modal identification methods including frequency domain, time domain, and time-frequency domain approaches. Individual output-only modal analysis methods are discussed in many papers (Clough and Penzien 1995; Brincker et al. 2001a; Ibrahim 1977b; Shi et al. 2012); unfortunately, hardly any studies have pursued an overview or comparison of the state-of-the-art modal identification algorithms. In response of this, five output-only modal identification methods are investigated and compared in this study including Peak-Picking with Half-Power Bandwidth (PP-HPBW), Enhanced Frequency Domain Decomposition (EFDD) method in the frequency-domain; Single Station Time Domain (SSTD) technique, Covariance driven Stochastic Subspace Identification (SSI-COV) in the time-domain; Hilbert-Huang Transform (HHT) in frequency-time domain.

The performance of the five modal identification techniques under different situations (i.e., white noise or seismic excitation, closely spaced modes, noise effect, and local damage) was firstly presented by applying to a numerical three-story frame model in this paper. Then, the acceleration time series recorded during the ambient vibration test of a high-rise building in Shanghai were processed with these algorithms. Finally, it proposed an integrated algorithm to improve the in situ modal identification of the output-only structures under microtremors.

2. MODAL IDENTIFICATION ALGORITHMS

2.1 Peak-Picking method with Half-Power Bandwidth method (PP-HPBW)

The Peak-Picking (PP) method is a traditional frequency domain method using output-only data and already applied to the modal identification of engineering structures. It stems from the fact that the frequency response function (FRF) of a given system will peak at the modal frequencies of the system. For instance (Andersen et al. 1999; Peeters and Roeck 2001), the method is described in details. With the broadband white noise assumption, the Fourier power spectrum of the response data can be considered as

equal to the FRF of the structure at that sensor location. The modal frequencies are identified through the power spectrums from every experimental measurement. The corresponding damping ratios can be estimated with half-power bandwidth method, defined as:

$$\xi_i = \frac{B_i}{2 f_i} \tag{1}$$

where B_i is the half-power bandwidth of the spectral peak corresponding to ith-order modal frequency f_i.

2.2 Enhanced Frequency Domain Decomposition (EFDD) method

The enhanced frequency domain decomposition (EFDD) technique which was developed by Brincker et al. (2001c) is an extension of the Peak-Picking (PP) method and keeps the important features of user-friendliness. With the assumption that the input is a white noise, the structure is slightly damped, and the modal forms of the coupled modes are orthogonal, the results of the EFDD are exact.

In the EFDD identification, the first step is to estimate the power spectral density (PSD) matrix. The estimate of the output PSD $\hat{G}_{yy}(j\omega)$ known at discrete frequencies $\omega = \omega_i$ is then decomposed by taking the SVD of the matrix

$$\hat{G}_{yy}(j\omega) = U_i S_i U_i^H \tag{2}$$

where the matrix $U_i = [u_{i1}, u_{i2}, ..., u_{im}]$ is a unitary matrix of singular vectors u_{ij}; and S_i is a diagonal matrix of scalar singular value s_{ij}. Near a peak in the PSD function corresponding to a given mode in the spectrum, this mode or a possible close mode will be dominating. From the piece of the SDOF density function obtained around the peak of the PSD, the natural frequency and the damping ratio can be obtained.

2.3 Single Station Time Domain (SSTD) method

The SSTD method is a variant of the Ibrahim Time Domain (ITD) technique. In the standard ITD method (Ibrahim and Mikulcik 1973; Ibrahim and Mikulcik 1976; Ibrahim and Mikulcik 1977a), at least 2N response locations need to be measured to identify a model of order N. In the SSTD method (Zaghlool 1980), the identification can be conducted based on the response at a unique location, considered for different time intervals. The correlation functions between measured responses to random excitation can be written as

$$x(k\Delta t) = x_k = \sum_{r=1}^{2N} a_r e^{s_r k\Delta t} \tag{3}$$

where x_k is the discrete correlation function at kth discrete time, a_r is a constant associated with rth mode and s_r is the rth complex frequency defined as

$$s_r = -\xi_r \omega_r + i\omega_r \sqrt{1-\xi_r^2} \tag{4}$$

Writing Eq. (3) for different shifted starting time samples, gives

$$\begin{bmatrix} x_1 & x_2 & \cdots & x_L \\ x_2 & x_3 & \cdots & x_{L+1} \\ \vdots & \vdots & \ddots & \vdots \\ x_{2N} & x_{2N+1} & \cdots & x_{L+2N-1} \end{bmatrix} = \begin{bmatrix} a_1 & a_2 & \cdots & a_{2N} \\ a_1 e^{s_1 \Delta t} & a_2 e^{s_2 \Delta t} & \cdots & a_{2N} e^{s_{2N} \Delta t} \\ \vdots & \vdots & \ddots & \vdots \\ a_1 e^{s_1 (2N-1)\Delta t} & a_2 e^{s_2 (2N-1)\Delta t} & \cdots & a_{2N} e^{s_{2N} (2N-1)\Delta t} \end{bmatrix} \cdot \begin{bmatrix} e^{s_1 t_1} & e^{s_1 t_2} & \cdots & e^{s_1 t_L} \\ e^{s_2 t_1} & e^{s_2 t_2} & \cdots & e^{s_2 t_L} \\ \vdots & \vdots & \ddots & \vdots \\ e^{s_{2N} t_1} & e^{s_{2N} t_2} & \cdots & e^{s_{2N} t_L} \end{bmatrix} \tag{5}$$

where $t_k = k\Delta t$, N is the total number of modes considered for the identification and L is the number of correlation values per row. The modal order N is usually not known a priori but it is a general practice to compute poles at different modal orders and at last correct poles and number of modes are chosen from convergence of poles in the stabilization diagram.

In symbolic form, Eq. (5) can be written as

$$\underset{(2N\times L)}{\mathbf{X}} = \underset{(2N\times 2N)}{\mathbf{A}} \underset{(2N\times L)}{\mathbf{\Lambda}} \tag{6}$$

A similar equation can be written by shifting all the discrete response values by as Δt follows

$$\begin{bmatrix} x_2 & x_3 & \cdots & x_{L+1} \\ x_3 & x_4 & \cdots & x_{L+2} \\ \vdots & \vdots & \ddots & \vdots \\ x_{2N+1} & x_{2N+2} & \cdots & x_{L+2N} \end{bmatrix} = \begin{bmatrix} a_1 e^{s_1 \Delta t} & a_2 e^{s_2 \Delta t} & \cdots & a_{2N} e^{s_{2N} \Delta t} \\ a_1 e^{s_1 2\Delta t} & a_2 e^{s_2 2\Delta t} & \cdots & a_{2N} e^{s_{2N} 2\Delta t} \\ \vdots & \vdots & \ddots & \vdots \\ a_1 e^{s_1 2N\Delta t} & a_2 e^{s_2 2N\Delta t} & \cdots & a_{2N} e^{s_{2N} 2N\Delta t} \end{bmatrix} \cdot \begin{bmatrix} e^{s_1 t_1} & e^{s_1 t_2} & \cdots & e^{s_1 t_L} \\ e^{s_2 t_1} & e^{s_2 t_2} & \cdots & e^{s_2 t_L} \\ \vdots & \vdots & \ddots & \vdots \\ e^{s_{2N} t_1} & e^{s_{2N} t_2} & \cdots & e^{s_{2N} t_L} \end{bmatrix} \tag{7}$$

$$\underset{(2N\times L)}{\widehat{\mathbf{X}}} = \underset{(2N\times 2N)}{\widehat{\mathbf{A}}}\,\underset{(2N\times L)}{\mathbf{\Lambda}} \tag{8}$$

Now let us define a system **matrix S** so that

$$\underset{(2N\times 2N)}{\mathbf{S}}\,\underset{(2N\times 2N)}{\mathbf{A}} = \underset{(2N\times 2N)}{\hat{\mathbf{A}}} \tag{9}$$

Pre-multiplying Eq. (6) by **S and** taking account of Eq. (9)

$$\underset{(2N\times 2N)}{\mathbf{S}}\,\underset{(2N\times L)}{\mathbf{X}} = \underset{(2N\times 2N)}{\mathbf{S}}\,\underset{(2N\times 2N)}{\mathbf{A}}\,\underset{(2N\times L)}{\mathbf{\Lambda}} = \underset{(2N\times 2N)}{\widehat{\mathbf{A}}}\,\underset{(2N\times L)}{\mathbf{\Lambda}} \tag{10}$$

Taking account of Eq. (8)

$$\underset{(2N\times 2N)}{\mathbf{S}}\,\underset{(2N\times L)}{\mathbf{X}} = \underset{(2N\times L)}{\widehat{\mathbf{X}}} \tag{11}$$

The system matrix **S** can thus be computed as a least square solution of Eq. (11) (taking $L > 2N$).

Finally the eigenvalues are deduced from S be observing that Eq. (9) can be decomposed as

$$\mathbf{S}\begin{Bmatrix} a_r e^{s_r 0\Delta t} \\ \vdots \\ a_r e^{s_r (2N-1)\Delta t} \end{Bmatrix} = \begin{Bmatrix} a_r e^{s_r 0\Delta t} \\ \vdots \\ a_r e^{s_r (2N-1)\Delta t} \end{Bmatrix} e^{s_r \Delta t}, r = 1, 2, \cdots, 2N \tag{12}$$

and therefore

$$\left\{\mathbf{S} - e^{s_r \Delta t}\right\}\begin{Bmatrix} a_r e^{s_r 0\Delta t} \\ \vdots \\ a_r e^{s_r (2N-1)\Delta t} \end{Bmatrix} = \mathbf{0} \tag{13}$$

Eq. (13) is a standard eigenvalue problem, from which s_r can be found. Modal frequencies and damping ratios can be computed from the values of s_r.

2.4 Covariance driven Stochastic Subspace Identification (SSI-COV) method

It is well known that the stochastic subspace model of a linear time-invariant structure at the *k*th time step with the white noise assumption is defined as

$$\begin{aligned} x_{k+1} &= Ax_k + w_k \\ y_k &= Cx_k + v_k \end{aligned} \tag{14}$$

where x is the state vector, A is the state matrix, C is the real output influence matrix, w_k,v_k are white noise terms representing process noise and measurement noise together with the unknown inputs, and y is the output vector.

The Covariance driven Stochastic Subspace identification technique is a two-step data-analysis method. The first step involves making projection of certain subspaces generated from the input/output observations to estimate the state vector (x) of the system by linear algebra tools such as QR decomposition and singular value decomposition (SVD). The second step retrieves the system matrices A and C from the estimated states based on a linear least-squares solution. It is proven that the output covariances Λ_i can be decomposed as

$$\Lambda_i = CA^{i-1}G \tag{15}$$

where G is the next state-output covariance matrix and is defined as

$$G = E\left[x_{k+1} y_k^T\right] \tag{16}$$

Hereto, a block Toeplitz matrix $T_{i,i}$ is formed that consists of covariances

$$\begin{aligned} T_{i,i} &= \begin{pmatrix} \Lambda_i & \Lambda_{i-1} & \cdots & \Lambda_1 \\ \Lambda_{i+1} & \Lambda_i & \cdots & \Lambda_2 \\ \vdots & \vdots & \ddots & \vdots \\ \Lambda_{2i-1} & \Lambda_{2i-2} & \cdots & \Lambda_i \end{pmatrix} \\ &= \begin{pmatrix} C \\ CA \\ \vdots \\ CA^{i-1} \end{pmatrix}\begin{pmatrix} A^{i-1}G & \cdots & AG & G \end{pmatrix} = O_i \Gamma_i \end{aligned} \tag{17}$$

where matrix O_i is the extended observability matrix and Γ_i is the reversed extended stochastic controllability matrix. By computing the SVD of $T_{i,i}$ and splitting the SVD in two parts, A, C, G is finally estimated. The complex eigenvalues (λ) and eigenvectors (Ψ) of the damped system can be calculated from the system matrix A, according to

$$A = \Psi \Lambda \Psi^{-1} \tag{18}$$

It is then straightforward to determine the modal parameters (natural frequencies, damping ratios and mode shapes) as (Alvin and Park 1994; Safak 1991)

$$f_i = \frac{|\lambda_i|}{2\pi} \tag{19}$$

$$\xi_i = \frac{\mathrm{Re}(\lambda_i)}{2\pi f_i} \tag{20}$$

$$\phi_i = \left|C\Psi_i\right| \cdot sign\left[\mathrm{Re}\left(C\Psi_i\right)\right] \tag{21}$$

for the *i*th mode where $\mathrm{Re}(\cdot)$ and $sign[\cdot]$ denote the real part and the algebraic sign of $\cdot$.

In order to obtain a good model for modal analysis applications, a construction of the stabilization diagram, by identifying a whole set of models with different orders, is an efficient idea (Bodeux and Golinval 2001).

2.5 Hilbert-Huang transform (HHT) method

The HHT method is a two-step data-analysis method (Huang et al. 1998). The first step is the empirical mode decomposition (EMD) by which a complicated time history can be turned into a series of intrinsic mode functions (IMFs) that admit well-behaved Hilbert transforms. The second step of the HHT method is implemented by performing the Hilbert transform (HT) to each IMF component (Xu et al. 2003). With Hilbert transform, an analytic signal $z(t)$ for a real-valued function $y(t)$ can be defined as

$$z(t) = y(t) + i\tilde{y}(t) = A(t)\cdot e^{-i\theta(t)} \tag{22}$$

$$\tilde{y}(t) = H\left[y(t)\right] = \int_{-\infty}^{\infty} \frac{y(u)}{\pi(t-u)} du \tag{23}$$

where $\tilde{y}(t)$ is the Hilbert transform of $y(t)$, i is the imaginary unit, $A(t)$ and $\theta(t)$ are the amplitude and instantaneous phase angle of $y(t)$, respectively. The instantaneous frequency $\omega(t)$ is thus the time derivative of $\theta(t)$. The definition equations of $A(t)$, $\theta(t)$, $\omega(t)$ and are shown as follow

$$A(t) = \left[y^2(t) + \tilde{y}^2(t)\right]^{(1/2)} \tag{24}$$

$$\theta(t) = \tan^{-1}\left[\frac{\tilde{y}(t)}{y(t)}\right] \tag{25}$$

$$\omega(t) = \frac{d\theta(t)}{dt} \tag{26}$$

For a linear Single-Degree-of-Freedom (SDOF) system under impulsive loading, the free vibration response function of the system is

$$v(t) = A_0 \sin\left(\omega_d t\right) e^{-\xi\omega_0 t}, t \geq 0 \tag{27}$$

where ω_0 is the natural circular frequency, ξ is the damping ratio, ω_d is the damped natural circular frequency and A_0 is a constant depending on the intensity of impulsive loading and the mass and frequency of the system. By applying the Hilbert transform method, the signal $z(t)$ for $v(t)$ can thus be obtained using Eq. (22)

$$z(t) = v(t) + i\tilde{v}(t) = A(t)\cdot e^{-i\theta(t)} \tag{28}$$

For a special case in which ξ is small and ω_0 is large, the amplitude $A(t)$ and the phase angle $\theta(t)$ for the SDOF system can be obtained as follow (Yang and Lei 1999)

$$A(t) = A_0 e^{-\xi\omega_0 t} \tag{29}$$

$$\theta(t) = \omega_d t - \frac{\pi}{2} \tag{30}$$

By introducing the logarithmic and differential operators to Eqs. (29) and (30), respectively, one obtains

$$\ln A(t) = -\xi\omega_0 t + \ln A_0 \tag{31}$$

$$\omega(t) = \frac{d\theta(t)}{dt} = \omega_d \tag{32}$$

Therefore, the damped natural circular frequency ω_d can be identified from instantaneous frequency $\omega(t)$ by Eq. (32). With the identified ω_d and the slope $-\xi\omega_0$ of the straight line of the decaying amplitude $A(t)$ in a semi-logarithmic scale, the damping ratio can be identified from the function $\omega_d = \omega_0 (1 - \xi^2)^{1/2}$. It should be noted that the Random Decrement technique (RDT) is performed on the target IMF to derive the free vibration response $v(t)$ before the Hilbert transform.

3. COMPARISONS UNDER DIFFERENT SITUATIONS

3.1 Numerical Model

In this section, a three-story concrete frame finite element model (FEM) with damping ratio of 4% is established using ANSYS (see Figure 1) to investigate the identification performance of the aforementioned modal identification approaches. The FEM is excited by white noise or seismic excitation in two translational directions, and then the acceleration responses at the centre of the third floor are recorded in both directions with an acquisition frequency of 50 Hz in order to identify the natural frequencies and damping ratios of the structure.

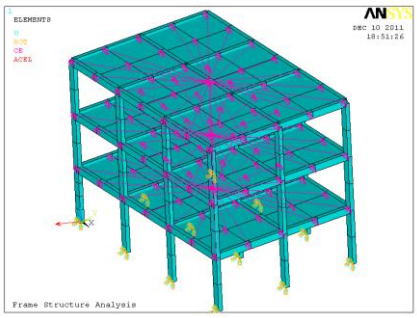


Figure 1 The finite element model.

3.2 White Noise Input

Ambient vibrations commonly have a multiple input

nature and wide band frequency content, and it is assumed to be a stationary zero-mean Gaussian white noise in the application of the output-only modal identification techniques. Thus, the FEM is firstly calculated under stationary white noise input which last for 12 minutes and the acceleration responses at the centre of the third floor are recorded for data processing like that in the field test. The estimates of the first four modes obtained by the five methods are characterized in Figure 2 and quantified in Table 1. It shows that the estimated modal frequencies and damping ratios are approximately identical with the theoretical values calculated directly from the FEM, especially for the first two modes. And the identified damping ratios do not show the same agreement as the modal frequencies. A satisfactory correspondence can be seen to be better for the method in time-frequency domain and in time domain than for that in frequency domain in the evaluation of damping ratios. There is a general accepted opinion that the spectral damping is generally overestimated and can have significant uncertainty in light of variance errors. There must be at least four spectral lines in the half-power bandwidth of each mode for limit bias errors (Bendat and Piersal 1993). Since it is recommended that the length of FFT should be 1024×2^{n} if the interested modal frequency is in the range of ($f_{nst}/2^{n+1}$~ $f_{nst}/2^{n}$, where f_{nst} is the Nyquist frequency of the test), the segment length utilizes 2048 in the PP method. It presents that the accuracy of PP-HPBW method and EFDD technique are similar with each other. Employing the stabilization diagram in SSI method, the structural modes can be distinguished from superfluous modes which improve its identification performance. The Random Decrement technique (RDT) plays an important role in ensuring the accuracy of the HHT method by providing the free vibration modal response. The applied modal identification methods need more or less user interaction to try to improve the estimate results, and they sensitize to the selection of the parameter in data processing.

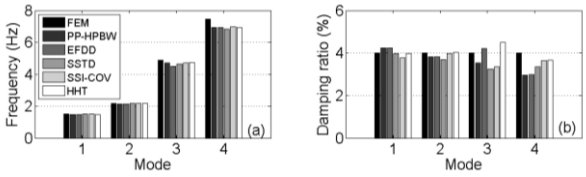


Figure 2 Comparison of the identified modal information under white noise input: (a) modal frequency; (b) damping ratio.

Table 1 The frequencies and damping ratios of the FE model under white noise input.

Method	f_1(Hz)	f_2(Hz)	f_3(Hz)	f_4(Hz)	ξ_1(%)	ξ_2(%)	ξ_3(%)	ξ_4(%)
FEM	1.50	2.16	4.88	7.45	4.00	4.00	4.00	4.00
PP-HPBW	1.49	2.15	4.71	6.93	4.25	3.81	3.54	2.97
EFDD	1.49	2.15	4.51	6.93	4.25	3.81	4.22	2.98
SSTD	1.50	2.16	4.65	6.85	3.99	3.68	3.24	3.34
SSI-COV	1.50	2.16	4.73	6.98	3.77	3.98	3.34	3.63
HHT	1.49	2.17	4.76	6.93	3.97	4.03	4.51	3.66

3.3 Noise Effect

In real field test, noise caused by environment or experimental instruments is inevitable which may affect the identified result. Signal-to-noise ratio (SNR) is a measure used in science and engineering that compares the level of a desired signal to the level of background noise. It is defined as

$$SNR_{dB} = 10\log_{10}\left(\frac{P_{signal}}{P_{noise}}\right) = 20\log_{10}\left(\frac{A_{signal}}{A_{noise}}\right) \qquad (33)$$

where P_{signal} is the signal power, P_{noise} is the noise power, A_{signal} is the signal amplitude and A_{noise} is the noise amplitude.

In this section, acceleration series with SNR equal to 0.1 are utilized by adding a white noise to the acceleration records in Section 3.2. The estimates are essentially the same as that in Section 3.2. Since the adding noise is white noise of which the energy is well-distributed, it is not difficult to identify the real mode. However, the noise would be more complicated in practice.

3.4 Local Damage

It is demonstrated that natural frequencies are sensitive indicators of structural integrity which can be used as a diagnostic parameter in structural assessment (Salawu 1997). This offers the possibility of using data from dynamic testing to detect damage. The stiffness of the three side columns at the first floor in the modified FEM is 40% lower than that in the FEM in Section 3.2. The stiffness reduction can be regarded as local damage in the primary structure. The first four modal frequencies of the modified FEM are estimated from the white noise induced responses at the same location with that in Section 3.2 by using the five algorithms. The identified frequencies are listed in Table 2 and the rates of frequency reduction based on the primary model in Section 3.2 are reported in the same table as well. The rate of frequency reduction is defined as

$$\delta f_i = \frac{f_{i,p} - f_{i,d}}{f_{i,p}} \times 100\% \qquad (34)$$

where $f_{i,p}$ is the ith modal frequency of the primary FE model, $f_{i,d}$ is the ith modal frequency of the model with local damage. The damage is well-estimated in the first two modes for all the adapted methods. Generally, the identification techniques in time domain are better performed than these in frequency domain.

Table 2 The frequencies of the FE model with local damage and the rates of frequency reduction.

Method	f_1(Hz)	f_2(Hz)	f_3(Hz)	f_4(Hz)	δf_1(%)	δf_2(%)	δf_3(%)	δf_4(%)
FEM	1.47	2.13	4.80	6.95	2.00	1.39	1.64	6.71
PP-HPBW	1.46	2.12	4.54	6.79	2.01	1.40	3.61	2.02
EFDD	1.46	2.10	4.64	6.93	2.01	2.33	-2.88	0.00
SSTD	1.47	2.13	4.60	6.74	2.00	1.39	1.08	1.61
SSI-COV	1.47	2.12	4.68	6.90	2.00	1.85	1.06	1.15
HHT	1.46	2.13	4.67	7.08	2.01	1.84	1.89	-2.16

Table 3 The frequencies and damping ratios of the FE model with the property of closely spaced modes.

Method	f_1(Hz)	f_2(Hz)	f_3(Hz)	f_4(Hz)	ξ_1(%)	ξ_2(%)	ξ_3(%)	ξ_4(%)
FEM	2.35	2.42	8.49	8.67	4.00	4.00	4.00	4.00
PP-HPBW	2.34	2.42	7.84	7.93	4.03	3.95	3.42	3.22
EFDD	2.37	2.42	7.86	7.93	4.19	4.44	3.38	3.25
SSTD	2.34	2.41	8.13	/	3.95	3.33	2.01	/
SSI-COV	2.32	2.38	7.80	7.92	4.44	3.64	3.65	3.32
HHT	2.35	2.39	7.92	7.93	4.15	3.79	3.52	1.83

3.5 Closely Spaced Modes

The finite element model is then modified to possess the characteristic of closely spaced modes and calculated to obtain the theoretical modal frequencies (see Table 3). The same stationary white noise is used as the input to the finite element model for the acquisition of acceleration responses as well. The identification procedure furnished the values of the dynamic properties reported in Table 3 and Figure 3. The PP-HPBW method, EFDD method, SSI method and HHT method reveal a good performance in close modes identification. However, a modal missing appears in the result of ITD technique.

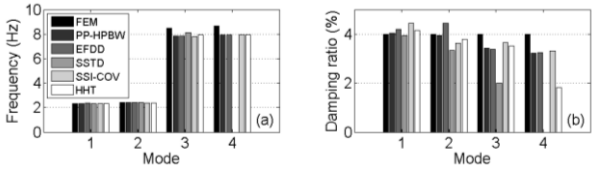


Figure 3 Comparison of the performance in closely spaced modes identification: (a) modal frequency; (b) damping ratio.

3.6 Seismic Excitation

The assumption of stationary white noise input may be a little tough for practical use. This section introduces a non-stationary excitation – El Centro earthquake motion records as an input to explore the evaluation of structural parameters. The FE model utilized here is the same as the one in Section 3.2. The identification procedure furnished the values of the parameters reported in Table 4 and Figure 4. Limited modal parameters (only the first two modes) are obtained because of the narrow band characteristic of seismic excitation. It is observed that the estimated frequencies are similar with that under white noise input, showing a very good fitting with the calculated values. However, the damping ratios are not well-estimated except the HHT method. Since the EMD is based on the local characteristic time scale of the data, the HHT algorithm is applicable to non-stationary processes.

Table 4 the frequencies and damping ratios for the FEM under El Centro seismic excitation.

Method	f_1(Hz)	f_2(Hz)	ξ_1(%)	ξ_2(%)
FEM	1.50	2.16	4.00	4.00
PP-HPBW	1.46	2.15	5.76	5.04
EFDD	1.46	2.15	5.80	5.05
SSTD	1.47	2.15	1.52	1.04
SSI-COV	1.48	2.22	2.56	4.01
HHT	1.47	2.21	3.99	3.50

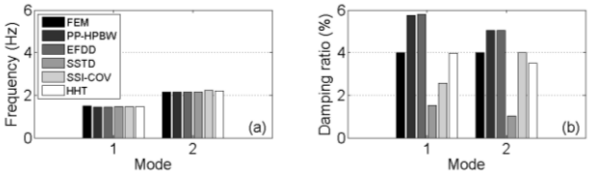


Figure 4 Comparison of the identified modal information under El Centro seismic excitation: (a) modal frequency; (b) damping ratio.

4. AMBIENT VIBRATION TEST AND DATA PROCESSING

4.1 Field Test

A field test of Tongji United Plaza Block B was took place. It is an office high-rise building located in Shanghai, China. The height of 23-storey building (one basement floor and 22 ground floors) is 99 m above ground (see Figure 5). The lateral force resistant system of the structure is a combined system of concrete core wall – steel frame.



Figure 5 General view of Tongji United Plaza Block B.

The field test was performed on the 22th floor (22F) of the building to record the acceleration responses in two translational directions. In order to record the accurate low frequency behaviors of the structure, the acceleration responses were sampled at a rate of 10 Hz. The acquisition time of the measurement was about 30 minutes. A dynamic response range of piezoelectric accelerometers used in this test is from 0.05 Hz to 500 Hz, the measurement capacity range is 0.1 g, and the sensibility is 10^{-5} g.

4.2 Data Processing

The acceleration records passed the augmented Dickey-Fuller unit root test after detrending, which confirm the stationary property of the *in situ* measurements. The density of probability of the ambient vibration responses is hypothesized as a Gaussian distribution, indicating that the structure is subjected to a broadband white noise excitation. To perform a Gaussian distribution test, the dynamic records were first normalized by their mean and standard deviation values, and then the K-S test was used for determining whether the records contained the hypothesized cumulative distribution function. It was verified that the records passed the test.

The data are then processed by the five modal identification approaches, respectively. The results are listed in Table 5 and presented in Figure 6 as well. The PP-HPBW method and HHT technique, as shown in Table 5, miss to identify the second mode which can be regarded as a closely spaced mode. A very good agreement can be observed in frequency evaluation that increase the confidence on the obtain results. The damping ratios extracted using the frequency domain methods are larger than that obtained by the other methods for the probability of overestimate.

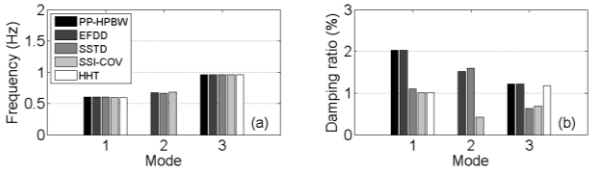


Figure 6 Identified modal information of Tongji United Plaza Block B: (a) modal frequency; (b) damping ratio.

Table 5 The identified frequencies and damping ratios of Tongji United Plaza Block B.

Method	f_1 (Hz)	f_2 (Hz)	f_3 (Hz)	ξ_1 (%)	ξ_2 (%)	ξ_3 (%)
PP-HPBW	0.6055	/	0.9651	2.03	/	1.22
EFDD	0.6055	0.6738	0.9647	2.03	1.52	1.22
SSTD	0.6003	0.6676	0.9613	1.10	1.60	0.63
SSI-COV	0.5990	0.6811	0.9610	1.01	0.42	0.68
HHT	0.5986	/	0.9588	1.01	/	1.18

5. DISCUSSION

Based on the performance of the five state-of-the-art modal identification approaches both in numerical model and full-scale building, there is not any perfect method in application. Therefore, an integrated method is proposed to improve the data processing by taking the advantages of all the techniques. It is firstly to have a quick estimation of frequency and damping ratio by using PP-HPBW method and EFDD method which ensure to identify the closely spaced modes. Then, the empirical mode decomposition (EMD) is applied to turn a complicated time history into a series of intrinsic mode functions (IMFs) and the selection of IMFs is based on the information obtained by the frequency domain approaches. Finally, except performing the Hilbert transform to each IMF component, it can be processed by SSI-COV technique or SSTD technique which abandon the superfluous modes by using stabilization diagram. In addition, the traditional SSTD method, SSI-COV method and HHT method can be used as references. Nonetheless, this integrated method is very time-consuming. It is revealed

that the frequency domain approaches are more suitable for real-time modal identification.

6. CONCLUSION

This paper reviewed five different output-only modal identification methods and the performance of these methods have been compared and discussed both in numerical simulated test and full-scale field test. The five algorithms can be categorized as frequency domain (PP-HPBW method and EFDD method), time domain (SSTD method and SSI-COV method), and time-frequency domain (HHT method) approaches.

The comparison reveals that all the techniques give reasonable estimates of the natural frequencies. The time domain and frequency-time domain approaches return more stable estimates of the damping ratios, while the frequency domain approaches seem to be overestimate. However, the frequency domain algorithms are simpler and faster. Therefore, there is not a perfect method with both advantages of accuracy and efficiency. The integrated method proposed in this paper can be applied to improve the modal identification of a structure under ambient vibration.

References:

Alvin, K.F. and Park, K.C. (1994), "Second-order structural identification procedure via state-space-based system identification," AIAA Jouranl, 32(2), 397-406.

Andersen, P., Brincker, R., Peeter, B. and Roeck, G.D. (1999), "Comparison of system identification methods using ambient bridge test data," Proceedings of 17th International Modal Analysis Conference, Society for Experimental Mechanics, 3727, 1035-1041.

Bendat, J.S. and Piersal, A.G. (1993), "Engineering applications of correlation and spectral analysis," 2nd Ed., Wiley, New York.

Bodeux, J.B. and Golinval, J.C. (2001a), "Application of ARMAV models to the identification and damage detection of mechanical and civil engineering structures," Smart Materials and Structures, 10, 479-489.

Brincker, R., Zhang, L. and Andersen, P. (2001b), "Modal identification of output-only systems using frequency domain decomposition," Smart Materials and Structures, 10, 441-445.

Brincker, R., Ventura, C. and Andersen, P. (2001c), "Damping estimation by frequency domain decomposition," Proceedings of IMAC, Kissimmee, USA, 698-703.

Clough, R.W. and Penzien, J. (1995), "Dynamics of structures," Computers &Structures Inc.

Huang, N.E., Shen, Z., Long, S.R., Wu, M.C., Shih, H.H., Zheng, Q. and et al. (1998), "The empirical mode decomposition and the Hilbert spectrum for nonlinear and non-stationary time seies analysis," Proceedings of the Royal Society of London, Series A: Mathematical, Physical and Engineering Sciences, 454(1971), 903-995.

Ibrahim, S.R. and Mikulcik, E.C. (1973), "A time domain vibration test technique," The Shock and Vibration Bulletin, 43(4), 21-37.

Ibrahim, S.R. and Mikulcik, E.C. (1976), "The experimental determination of vibration parameters from time responses," The Shock and Vibration Bulletin, 46(5), 187-196.

Ibrahim, S.R. and Mikulcik, E.C. (1977a), "A method for direct identification of vibration parameters from the free response," The Shock and Vibration Bulletin, 47(4), 183-198.

Ibrahim, S.R. (1977b), "Random decrement technique for modal identification of structures," Journal of Spacecraft and Rockets, 14(11), 696-698.

Peeters, B. and Roeck, G.D. (2001), "Stochastic system identification for operational modal analysis: A review," Journal of Dynamic Systems, Measurement, and Control, 123, 659-667.

Safak, E. (1991), "Identification of linear structures using discrete-time filters," Journal of Structural Engneering, 117, 3064-3085.

Salawu, O.S. (1997), "Detection of structural damage through changes in frequency: a review," Engineering Structures, 19(9), 718-723.

Shi, W., Shan, J. and Lu, X. (2012), "Modal identification of Shanghai World Financial Center both from free and ambient vibration response," Engineering Structure, 36, 14-26.

Xu, Y., Chen, S. and Zhang, R. (2003), "Modal identification of Di Wang Building under Typhoon York using the Hilbert-Huang transform method," The Structural Design of Tall and Special Buildings, 12(1), 21-47.

Yang, J. and Lei, Y. (1999), "Identification of natural frequencies and damping ratios of linear structures via Hilbert transform and empirical mode decomposition," Proccedings of the international conference on intelligent systems and control, Anaheim, CA: IASTED/Acta Press, 310-315.

Zaghlool, S.A. (1980), "Single station time-domain (SSTD) vibration testing technique: theory and application," Journal of Sound and Vibration, 72(2), 205-234.

10CUEE CONFERENCE PROCEEDINGS
10th International Conference on Urban Earthquake Engineering
March 1-2, 2013, Tokyo Institute of Technology, Tokyo, Japan

ACTIVE VIBRATION CONTROL TESTS OF ARCH STRUCTURES USING ACCELERATION FEEDBACK

Ken'ichi Minowa[1], Tomohiko Kumagai[2], and Toshiyuki Ogawa[3]

1) Graduate Student, Department of Architecture and Building Engineering, Tokyo Institute of Technology, Japan
2) Assist. Professor, Department of Architecture and Building Engineering, Tokyo Institute of Technology, Japan
3) Professor, Department of Architecture and Building Engineering, Tokyo Institute of Technology, Japan
minowa.k.aa@m.titech.ac.jp, kuma@arch.titech.ac.jp, togawa@arch.titech.ac.jp

Abstract: The present paper discusses the active vibration control of arch structures. In previous paper discussing the active vibration control tests, it is successful to reduce the seismic response. However, this control by displacement feedback is impractical in point of the sensors. Therefore, this paper deals with the active vibration control on the Optimal control theory with Kalman filter so that the acceleration feedback control using accelerometers as a sensor should be possible. First, we explain the control algorithm with Kalman filter. Next, for demonstration, the active vibration control tests of the arch structures are carried out. As a result, the response to sine waves reduces by up to 70 % and that to seismic wave reduces by up to 20 %.

1. INTRODUCTION

In recent year, the number of building structures equipped with response control mechanisms increases for the sake of its safety. Especially in spatial structures, the safety demands are higher, for these are the places to attract customers and for disaster refuge. But we suffered some damage such as the fall of roof members also from the 2011 Great East Japan Earthquake. Thus the provision for earthquake disasters is not sufficient and the response control is the prime task. It is considered that an active response control is applied to the spatial structures as one method of response control. In high-rise buildings, a large number of studies are made on the active vibration control, for example the studies by Tsuji et al. (1995), Nishitani et al. (1996), and Haramoto et al. (2000). But only a few studies have so far been made at the active response control of spatial structures, for example the study by Shingu et al. (1990), in comparison with the studies of the passive response control by Xue et al. (2001), and Yoshinaka et al. (2010). In comparison with the passive vibration control, the active vibration control is able to reduce the responses more and characterized by the vibration control in no relations at the period of ground motion.

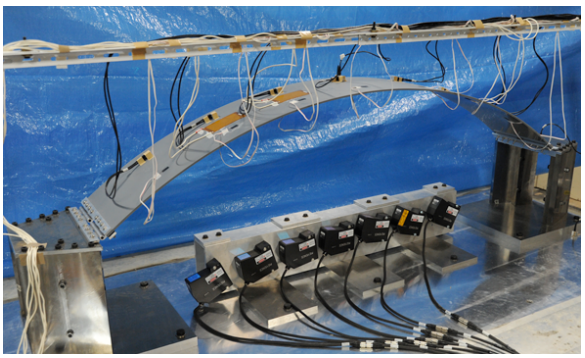


Figure 1 Picture of Vibration Control Test of Arch Structures

Because of this, we have studied the active vibration control of arch structures in previous works by Minowa et al. (2010, 2011, and 2012). In references by Minowa et al. (2011 and 2012), the active vibration control tests of arch structure models with piezoelectric films and a digital signal processor (DSP) are carried out (Fig.1). As a result, the control by displacement feedback was effective but the control by acceleration feedback was ineffective. However, the control by displacement feedback is impractical in point of the sensors. Therefore, this study deals with the acceleration feedback control with Kalman filter in order to improve the effects of acceleration feedback control. In this study, the demonstration tests of active vibration control of arch structures using accelerometers are carried out.

2. ACTIVE VIBRATION CONTROL TESTS OF ARCH STRUCTURES

2.1 Experimental Outline

For actual proof of the active vibration control with the modal control, we carry out the active vibration control tests. Specimens are the same arch structures as references by Minowa (2011 and 2012) (Fig.1). The shape properties are

Table 1 Shape Properties

Arch Structure	
Span L_x [mm]	1500
Width L_y [mm]	250
Rise H [mm]	236
Curvature Radius R [mm]	1308
Subtended Half-angle θ [deg.]	35

Table 2 Material Properties

Material	Acrylic Resin
Thickness t [mm]	5.18
Young's Modulus E [N/mm^2]	3.10×10^3
Tensile Strength σ_b [N/mm^2]	61.8
Fracture Strain ε_b [%]	3.8

shown in Table 1 and the material properties are shown in Table 2. The thicknesses t is about 5 mm so that the 1st natural periods T_1 is about 0.2 s.

Figure 2 shows experimental mechanism. The responses of arch structure are measured with laser displacement sensors, accelerometers and strain gages. An input direction of earthquake motion is the horizontal direction. Input waves are sine waves with 1st natural period T_1 and BCJ-L1 (artificial earthquake motion of the Building Center of Japan). The maximum accelerations A_g of sine waves are 20 cm/s^2 and those of seismic waves are normalized to 100 cm/s^2. In case of Ra0.2 model's tests, the time bases of seismic waves are halved as the natural period of arch structure becomes relatively long against the seismic waves.

For control, a digital signal processor (DSP), piezoelectric films, and accelerometers are used. The piezoelectric films generate force in direct proportion voltage. In this paper, the voltage amplifier limits the voltage for control force to plus or minus 600 V.

Here, names of control models are defined as Ra (1st natural period) - (control type) - (kind of weighting coefficient matrix **Q**). Where, the control type expresses the control positions as shown in Table 3.

2.2 Vibration Characteristics of Arch Structure

The vibration characteristics of arch structure are grasped by inputting sweep waves. Table 4 shows measured vibration characteristics. The 1st natural period T_1 of Ra0.2 model is 0.175 s. Antisymmetrical 2 waves mode and antisymmetrical 4 waves mode are observed and called 1st mode and 3rd mode. Every damping ration is about 10 %.

3. CONTROL SYSTEM AND ALGORITHM

Figure 3 shows detail of control system on this study. First, the accelerometers at the points 3 and 7 measure the accelerations. Then, DPS calculates control input **u**. In DSP, a band-pass filter eliminates noise from the observation data.

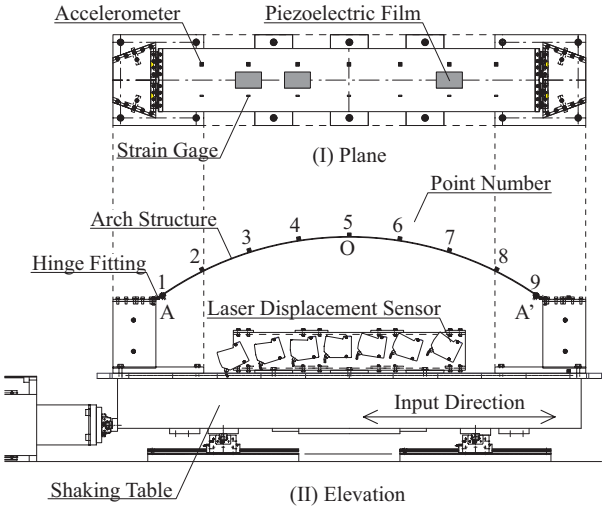


Figure 2 Experimental Mechanism

Table 3 Control Positions

Control Type	Point Number		
	3	4	7
1M1	O	-	-
1M3	-	O	-
2M1	O	-	O

Table 4 Vibration Characteristics

Ra0.2 Model	1st Mode	3rd Mode
Natural Period T [s]	0.175	0.0372
Damping Ratio h [%]	8.1	11.5
Effective Mass Ratio [%]	31.5	5.1

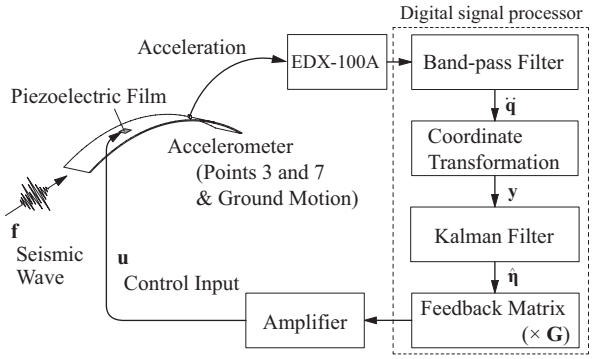


Figure 3 Detail of Control System

And a coordinate transformation of the observation date is carried out. Moreover, Kalman filter is used. Then, the feedback matrix **G** determines the control input **u**. Also, detailed accounts of these theories are given below. Finally, the piezoelectric film generates the control force.

MATLAB 7.10.0 and Simulink ver.7.5 are used for the design for the control system.

3.1 Reduction of Degree-of-Freedom of Model

In this study, a reduction of the degree-of-freedom of controlled model is carried out in order to easy the hardship of control system design and decrease the delay time. First, the equation of motion expresses controlled structures, as follow:

$$\mathbf{M}\ddot{\mathbf{q}} + \mathbf{C}\dot{\mathbf{q}} + \mathbf{K}\mathbf{q} = \mathbf{F}\mathbf{f} + \mathbf{U}\mathbf{u} \tag{1}$$

Where **M** is a mass matrix, **C** is a damping matrix and **K** is a stiffness matrix. **q** is a relative displacement vector, **f** is a disturbance vector and **u** is a control input vector. And **U** and **F** are coefficient matrices expressing positions where the forces are added.

Next, the overall coordinate is transformed into the modal coordinate by the modal matrix **Φ**, as follow:

$$\mathbf{M}_m\ddot{\boldsymbol{\xi}} + \mathbf{C}_m\dot{\boldsymbol{\xi}} + \mathbf{K}_m\boldsymbol{\xi} = \mathbf{F}_m\mathbf{f} + \mathbf{U}_m\mathbf{u} \tag{2}$$

$$\mathbf{M}_m = \boldsymbol{\Phi}^T\mathbf{M}\boldsymbol{\Phi} \quad \mathbf{C}_m = \boldsymbol{\Phi}^T\mathbf{C}\boldsymbol{\Phi} \quad \mathbf{K}_m = \boldsymbol{\Phi}^T\mathbf{K}\boldsymbol{\Phi}$$
$$\mathbf{F}_m = \boldsymbol{\Phi}^T\mathbf{F} \quad \mathbf{U}_m = \boldsymbol{\Phi}^T\mathbf{U} \tag{3}$$

Where ξ is a displacement vector on the modal coordinate. Index *m* expresses the modal coordinate.

Then, some modes are truncated based on the generalized orthogonality of eigenmodes. As a result, it is important to reduce measure points for the feedback control.

In this study, for the reduction of degree-of-freedom, the models approximate 1st ~ 4th modes those are the dominant modes and these periphery modes. The measure points are the points 3 and 7 those are in the vicinity of antinode of 1st mode.

3.2 Application of Optimal Control Theory

A controller to compute control forces is designed on the Optimum control theory. In order to use the Optimal control theory, the equation of motion, Eq.(2), is transformed into the state equation, as follow:

$$\dot{\boldsymbol{\eta}} = \mathbf{A}\boldsymbol{\eta} + \mathbf{B}\mathbf{u} + \mathbf{E}\mathbf{f} \tag{4}$$

$$\boldsymbol{\eta} = \begin{Bmatrix} \dot{\boldsymbol{\xi}} \\ \boldsymbol{\xi} \end{Bmatrix} \quad \mathbf{A} = \begin{bmatrix} -\mathbf{M}_m^{-1}\mathbf{C}_m & -\mathbf{M}_m^{-1}\mathbf{K}_m \\ \mathbf{I} & \mathbf{O} \end{bmatrix}$$
$$\mathbf{B} = \begin{bmatrix} \mathbf{M}_m^{-1}\mathbf{U}_m \\ \mathbf{O} \end{bmatrix} \quad \mathbf{E} = \begin{bmatrix} \mathbf{M}_m^{-1}\mathbf{F}_m \\ \mathbf{O} \end{bmatrix} \tag{5}$$

The control input vector **u**, the amount of feedback, is calculated from the feedback matrix **G**. The feedback matrix **G** is determined so that a linear quadratic evaluation function *J* is minimized, as follows:

$$J = \int_0^\infty \left\{ \boldsymbol{\eta}^T\mathbf{Q}\boldsymbol{\eta} + \mathbf{u}^T\mathbf{R}\mathbf{u} \right\} dt \tag{6}$$

Where **η** is a state vector in the modal coordinate. **Q** and **R** are weighting coefficient matrices those keep a balance between reduction effects of the responses and the quantity of control input. The weighting coefficient matrix **R** is calculated so that the responses with control become *r* times compared with those without control as shown in previous work by Minowa et al. (2010).

In this study, the weighting coefficient matrix $\mathbf{Q}_1$ is the unit matrix. In the case of $\mathbf{Q}_2$, the weighting is put on the only 1st mode and improvement in stability is attempted.

3.3 Application of Kalman Filter

This study tries the vibration control using accelerometer. In reference by Minowa et al. (2012), the suboptimal theory is used for the realization of acceleration feedback control. However, that control method is ineffective. The reason is thought that a phase of control force is not considered on the suboptimal theory. Therefore, this study uses Kalman filter as an observer as shown in the work by Kalman (1960). The observer is a mechanism that estimates all states from the observed variable when it is difficult to observe all the states.

Kalman filter is a method to estimate state vector $\hat{\boldsymbol{\eta}}$ form output vector **y** in case system noise **f** (i.e. the disturbance vector) and measurement noise **v** are a white noise. The above is expressed to the equation, as follow:

$$\dot{\hat{\boldsymbol{\eta}}} = \mathbf{A}\hat{\boldsymbol{\eta}} + \mathbf{B}\mathbf{u} + \mathbf{K}_\mathbf{f}\left(\mathbf{y} - \mathbf{H}\hat{\boldsymbol{\eta}}\right) \tag{7}$$

Where $\mathbf{K}_\mathbf{f}$ is Kalman gain and **H** is a matrix shown the relation between the output vector **y** and the state vector $\hat{\boldsymbol{\eta}}$, as follow:

$$\mathbf{y} = \mathbf{H}\hat{\boldsymbol{\eta}} + \mathbf{v} \tag{8}$$

Then, the Kalman gain $\mathbf{K}_\mathbf{f}$ is expressed, as follow:

$$\mathbf{K}_\mathbf{f} = \mathbf{X}\mathbf{H}^T\mathbf{V}^{-1} \tag{9}$$

Where **V** is a covariance matrix of measurement noise **v**. And **X** is obtained as the solution of Riccati matrix equation, as follow:

$$\mathbf{A}\mathbf{X} + \mathbf{X}\mathbf{A}^T - \mathbf{X}\mathbf{H}^T\mathbf{V}^{-1}\mathbf{H}\mathbf{X} + \mathbf{E}\mathbf{W}\mathbf{E}^T = \mathbf{O} \tag{10}$$

Where **W** is a covariance matrix of system noise **f**.

As seem above, the covariance matrices **V** and **W** are set for the design of Kalman filter. In this study, the covariance matrix of system noise **W** is calculated from BCJ-L1 normalized to 100 cm/s^2. And the covariance matrix of measurement noise **V** is calculated form the observation data, the output vector **y**, in the absence of the disturbance vector **f**.

Also, in this study, the output vector **y** and the matrix **H** are expressed on the relationship between Eq.(2) and Eq.(8), as follow:

$$\mathbf{y} = \ddot{\boldsymbol{\xi}} - \mathbf{M}_m^{-1}\mathbf{F}_m\mathbf{f} \tag{11}$$

$$\mathbf{H} = -\mathbf{M}_m^{-1}\left(\begin{bmatrix} \mathbf{C}_m & \mathbf{K}_m \end{bmatrix} + \mathbf{U}_m\mathbf{G}\right) \tag{12}$$

3.4 Control Properties

The band-pass filter (BPF) is used to eliminate noise from the observation data. The BPF consists of a low-pass filter and a high-pass filter as shown in the work by Minowa et al. (2011). Figure 4 shows the property of BPF. In this study, cutoff frequencies ω_{lc} and ω_{hc} are 162.5 rad/s and 31.13 rad/s, respectively.

Table 5 shows the delay time. The ratios of delay time to 1st natural period d/T_1 are 11.5 %. In comparison with reference by Minowa et al. (2012), the delay time d/T_1 increases because of the calculation on Kalman filter. However, we showed that the response reduction is possible when the delay time d/T_1 is less than 12 % in reference by Minowa et al. (2012). Thus it is possible to suppress the delay time d/T_1 of the control using Kalman filter within 12 %.

4. RESULTS OF ACTIVE VIBRATION CONTROL TESTS

In the following results, the responses are shown in the relative coordinate to the shaking table. The maximum response displacement and acceleration are normalized with the maximum input displacement D_g and acceleration A_g. The maximum member force is normalized with N_b or M_b. Where, N_b is the axial force with the fracture strength and M_b is the moment with the edge stress reaching the tensile strength σ_b. Moreover, r = 1.0 shows the condition that control does not exist.

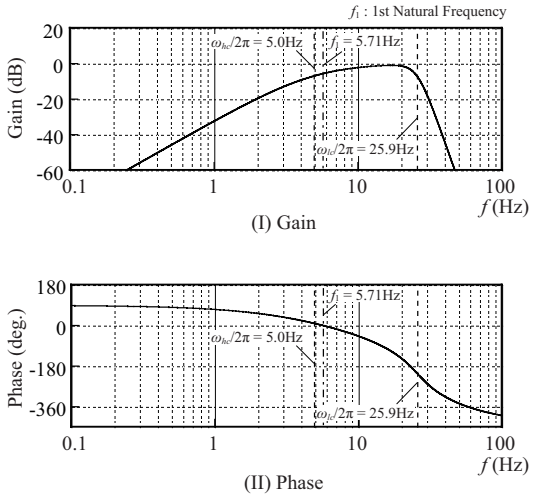


Figure 4 Property of Band-pass Filter

4.1 Comparison with Past study about Control Effect

Figure 5 shows the results of the active vibration control tests. Where, ratio of response displacement d_n^c/d_n^{uc}, on the left axis, is defined as the value of the maximum displacement with control d_n^c divided by that without control d_n^{uc} at the points 3 and 7. The point 3 and 7 are in the vicinity of antinode of the dominant mode, which is the first antisymmetrical mode. The response reduces on every

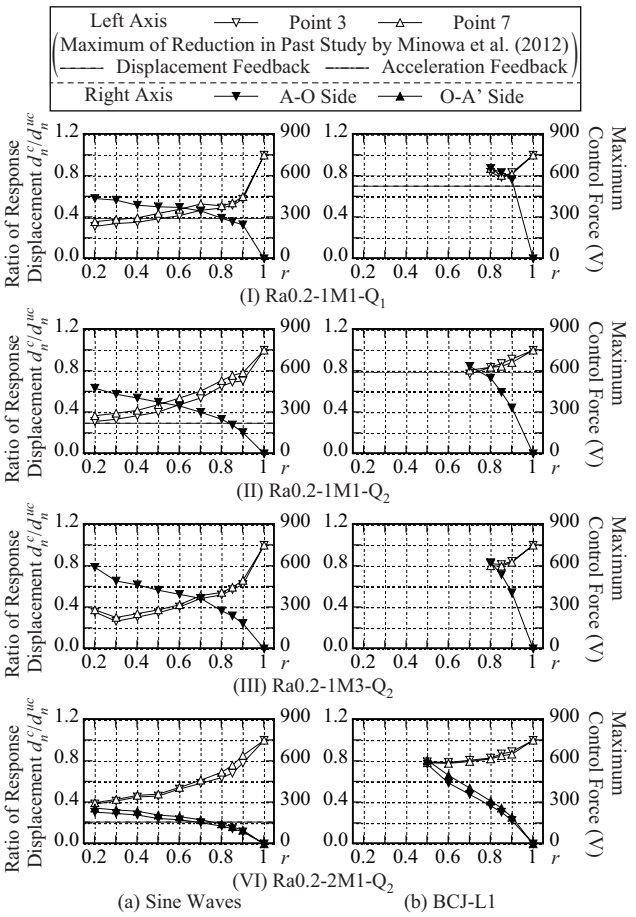


Figure 5 Results of Active Vibration Control Tests of Arch Structure

Table 5 Delay Time

Ra0.2 Model	1M	2M
Data Processing Time at EDX-100A d_1 [ms]	2.9	2.9
Calculating Time at DSP d_2 [ms]	13.7	13.8
Delay Time at Piezoelectric Film d_3 [ms]	3.5	3.5
Total Delay Time $d = d_1 + d_2 + d_3$ [ms]	20.1	20.2
Ratio to 1st Natural Period d/T_1 [%]	11.5	11.5

model. The response to sine waves reduces by up to 70 % and that to seismic wave reduces by up to 20 %. In reference by Minowa et al. (2012), in the case of displacement feedback control, the response to sine waves reduces by up to 80 % and that to seismic wave reduces by up to 40 %. And, in the case of acceleration feedback control, the response to sine waves reduces by up to 40 % and that to seismic wave reduces by up to 20 %. The latest results are better than the results of acceleration feedback control in reference by Minowa et al. (2012) but worse than the results of displacement feedback control in the reference above. Although it is difficult to get the higher effects than the displacement feedback control because of the use of observer, it is thought to be possible to acquire an effect equivalent to it. This means there is still room for improvement in the acceleration feedback control.

4.2 Analyses of Control Results

In this section, we analyze the results of Ra0.2-2M1-Q_2 model. This control model is characterized by the large response reduction.

Figure 6 shows the distributions of maximum response displacement. Although the response of the center point 5 increases, the responses of the other points decrease. The distribution shapes do not vary regardless of presence of control force. As mentioned in references by Minowa et al. (2010 and 2012), the response reduction to BCJ-L1 is smaller than that to sine waves in the case of same r.

Figure 7 shows the distributions of maximum response acceleration. In reference by Minowa et al. (2012), the reduction of response acceleration is smaller than that of response displacement. However, in this study, the reduction of response acceleration is large and approaches that of response displacement. The reason is that the BPF eliminates the high frequency area of the control force through narrowing its range. In this way, the setting of BPF affects the control results. How decisions on the setting of BPF are made will be an issue to be addressed in the future.

Figure 8 shows the distributions of maximum member force and the maximum control force. The axial force reduces except for the control positions, the points 3 and 7. The bending moment reduces at all the points. For the sake of control, the required control force is about equal to the member force without control.

Figure 9 shows the time history responses to sine waves. In the response displacement, the response reduction is shown. The period of vibration does not vary despite the control. The phase of bending moment with control progresses by a half of the vibration period compared with that without control, as r is small. The phase of axial force is the same as that of control force.

Figure 10 shows the Fourier amplitude spectra of response displacement at the point 3. In the vicinity of 1st natural period T_1, the Fourier amplitude spectrum to BCJ-L1 reduces like the Fourier amplitude spectrum to sine waves. However, the Fourier amplitude spectrum to BCJ-L1 increases in the vicinity of about 0.147 s. Figure 11 shows the ratio of Fourier amplitude spectrum of response displacement at these periods. Where, F_s^{uc} is a value of Fourier amplitude spectrum without control and F_s^c is a value of Fourier amplitude spectrum with control. At the 1st natural period T_1, the reduction of Fourier amplitude spectrum to BCJ-L1 is the same as that to sine waves. When r is 0.5, the Fourier amplitude spectrum at T_1 decreases by about 50 %. However, at 0.147 s, the Fourier amplitude

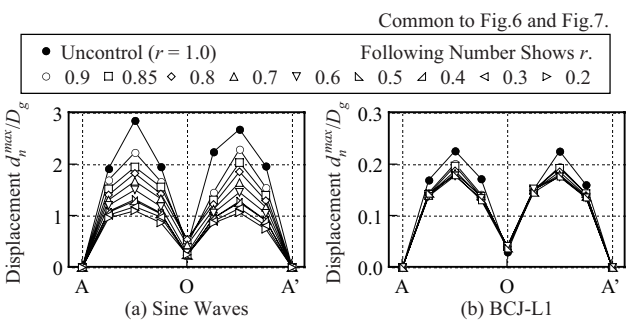


Figure 6 Distributions of Maximum Response Displacement (Ra0.2-2M1-Q_2, Normal Direction)

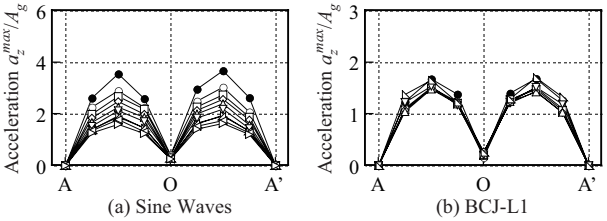


Figure 7 Distributions of Maximum Response Acceleration (Ra0.2-2M1-Q_2, Vertical Direction)

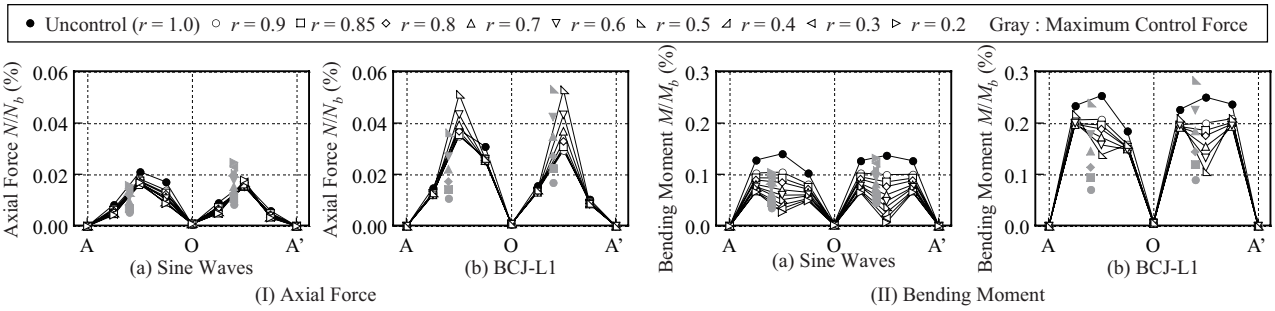


Figure 8 Distributions of Maximum Member Force and Maximum Control Force (Ra0.2-2M1-Q_2)

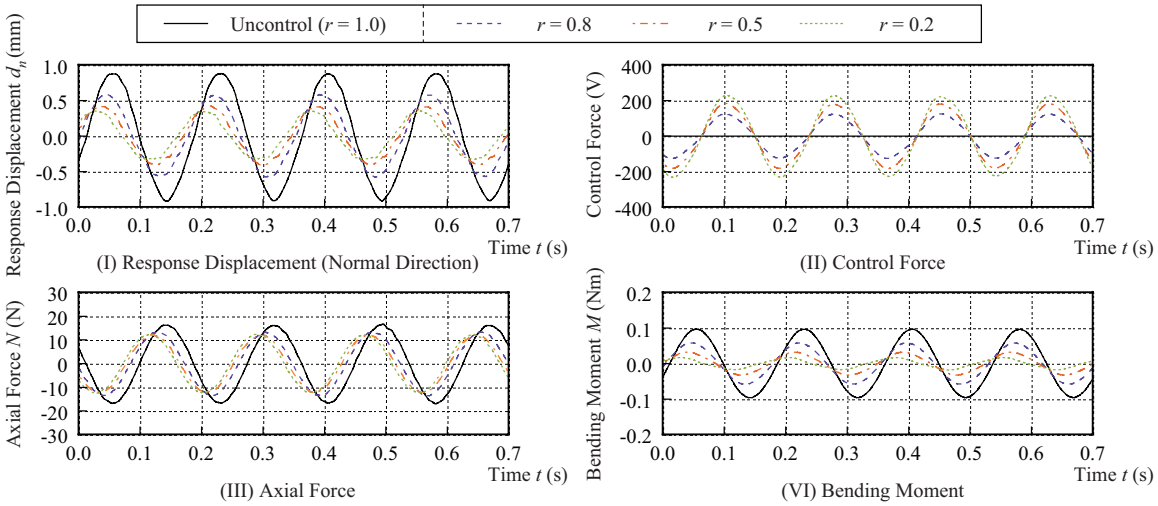


Figure 9 Time History Responses (Ra0.2-2M1-Q_2, Point 3, Sine Waves)

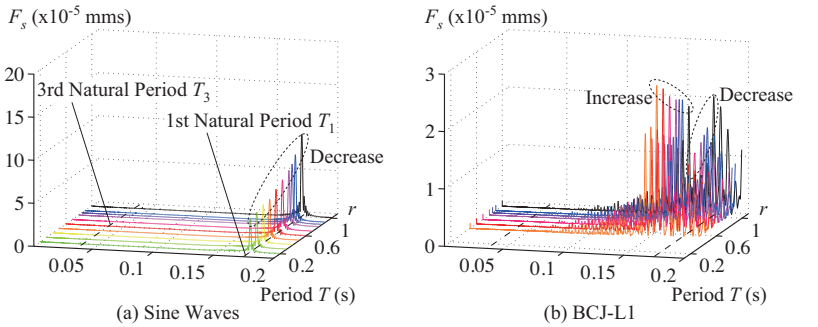


Figure 10 Fourier Amplitude Spectra of Response Displacement (Ra0.2-2M1-Q_2, Point 3)

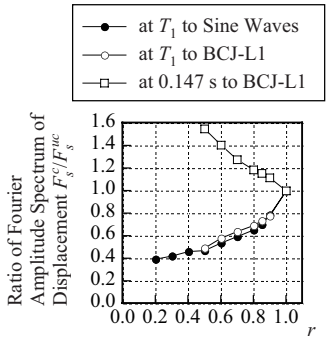


Figure 11 Ratio of Fourier Amplitude Spectrum of Response Displacement (Ra0.2-2M1-Q_2, Point 3)

spectrum to BCJ-L1 increases by about 60 %, when r is 0.5. Also, at the reference by Minowa et al. (2012), such an increase is not seen. In other words, this increase is the main reason that the response reduction to earthquake motion is smaller. The reason for this increase is that the control phase on this period deviates from the phase of response velocity because the setting of BPF is narrow, in addition to the long delay time. As mentioned above, how decisions on the setting of BPF are made will be an issue to be addressed in the future.

5. CONCLUSIONS

This study discussed the active vibration control on the Optimal control theory with Kalman filter for the acceleration feedback control. The vibration control tests of arch structure model are carried out. It is concluded as follows, from the above results.

1) In the experiment, the response to sine waves reduces by up to 70 % and that to seismic wave reduces by up to 20 %.
2) The response reductions are larger than the results of acceleration feedback control in reference by Minowa et al. (2012). However, the response reductions are smaller than the results of displacement feedback control in the reference above.

Acknowledgements:

The present paper was supported in part by a grant from Grant-in-Aid for Scientific Research (B) (Research No.22360223) by Japan Society for the Promotion of Science (JSPS).

References:

Tsuji, H., Itoh, H., Ogasawara, Y., and Mitsuta, S. (1995), "Vibration Control by Optimal Trajectory with Feedback System: Suppression of Residual Vibration," *JSME International Journal*, **38-C**(4), 663-669.

Nishitani, A., Nitta, Y., and Yamada, N. (1996), "Variable Gain-based Structural Control Considering The Limit of AMD Movement," *Proceedings of The 35th IEEE*, **1**, 185-190.

Haramoto, H., Seto, K., and Koike, Y. (2000), "Active Vibration Control of Triple Flexible Structures Arranged in Parallel," *JSME International Journal*, **43-C**(3), 712-718.

Shingu, K., Kawanishi, T., and Harumoto, M. (1990), "A Study on Active Control of A Conical Shell Subjected to Seismic Forces," *Proc. IASS 1990*, 33-42.

Xue, S., Qin, L., Yamada, M., Otani, S., Nagasawa, K., and Higuchi, H. (2001), "Vertical Vibration Control for Large Space

Arch Subject to Horizontal Earthquake Wave," *Proc. IASS 2001*, 1-8. (CD-ROM : TP123.)
Yoshinaka, S., Taniguchi, Y., and Nakatani, M. (2010), "Vibration Control Using Tuned Mass Dampers with Initial Displacement for Spatial Structures," *Proc. IASS 2010*, 1869-1881. (CD-ROM)
Minowa, K., Kumagai, T., and Ogawa, T. (2010), "Seismic Response Controls of Arch Structures on Optimal Control Theory, " *Proc. IASS 2010*, 1814-1824. (CD-ROM)
Minowa, K., Kumagai, T., and Ogawa, T. (2011), "Vibration Control Tests of Arch Structures with Piezoelectric Films," *Proc. IABSE-IASS 2011*, 1-7. (CD-ROM : Ref. No.0402.)
Minowa, K., Kumagai, T., and Ogawa, T. (2012), "Active Vibration Control of Arch Structures Using Modal Control Method," *Summaries of Technical Papers of Annual Meeting AIJ 2012*, **B-1**, 765-768. (In Japanese)
Kalman, R.E. (1960) "A New Approach to Linear Filtering and Prediction Problems," *Transactions of the ASME - Journal of Basic Engineering*, **82**(D), 35-45.

10CUEE CONFERENCE PROCEEDINGS
10th International Conference on Urban Earthquake Engineering
March 1-2, 2013, Tokyo Institute of Technology, Tokyo, Japan

SEISMIC RESPONSE AND PERFORMANCE OF FIXED BASE AND BASE ISOLATED STRUCTURES CONSIDERING CONTINUED FUNCTIONALITY DAMAGE STATE

Sarun Chimamphant[1)], Kazuhiko Kasai[2)]

1) Graduate Student, Tokyo Institute of Technology, Japan
2) Professor, Structural Engineering Research Center, Tokyo Institute of Technology, Japan

Abstract: In this paper, the seismic performance of fixed base and base isolated structures are investigated. MDOF linear response history analysis is utilized to investigate the seismic responses of these fixed base and base isolated structures. Fixed base structures with different superstructure damping ratios and damping mechanisms are investigated. Also base isolated structures with several combinations of isolation period and superstructure period are examined and compared with the response of the fixed base structures. How well the isolation system added to the fixed base structure improves the overall structural responses of drift ratios and floor accelerations is observed. Floor response spectrum analysis is conducted on these structures to examine the influences of the superstructure damping ratio, superstructure damping mechanism, and the isolation period of the isolated structure on the floor spectrum. Furthermore, to study the performance of these structures considering continued functionality, the PEER Performance Based Earthquake Engineering (PBEE) methodology is adopted. A continued functionality *CF* performance state is obtained from the fragility functions for nonstructural components. In this study, the *CF* performance state of nonstructural partition walls and suspended ceilings are adopted to determine the seismic performance of the structures. The performance of these structures, in term of return period *TR*, is observed and compared.

1. INTRODUCTION

Base isolation of structures is usually characterized by a low frequency of the fundamental mode which corresponds to low pseudo-acceleration spectral values for the possible earthquake excitations. This leads to a significant reduction of the forces experienced by the superstructure. However, this reduction of forces is achieved on the expense of displacement being concentrated at the isolation level. To reduce the base displacement, isolation damping is usually added by inserting devices with energy dissipation capacity. Additional isolation damping results in the significant reduction of the base displacement. However, it could cause higher forces and accelerations attributed to high damping and also render the drift distribution along the superstructure.

Nevertheless, base isolation system has gained large attention by researchers from around the world and also popularity among practice engineers. Therefore, in order to properly observe how well the added isolation improves the overall performance of the structure, several fixed base structures are investigated in comparison with those isolated structures. In addition, the performance of these fixed base and base isolated structures are also investigated following the PEER Performance Based Earthquake Engineering.

2. ANALYTICAL MODEL

The analytical model for a generic MDOF system is represented in this study by a shear model. An example model representing a 3-story fixed base and base isolated structures are shown in Figures 1(a) and 2(a). The superstructure is assumed to have an inverted triangular mode shape as shown in Figures 1(b) and 2(b). The mass in each floor is assumed to be equal, $m_b = m_1 = m_2 = \ldots = m_n$.

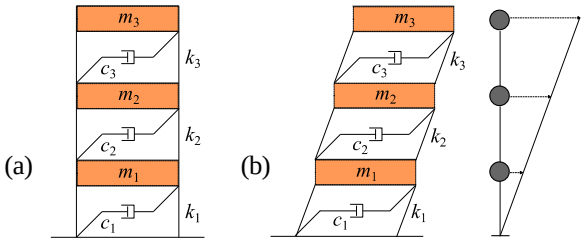


Figure 1 Fixed Base Structure Model:
(a) Shear Model (b) Mode Shape

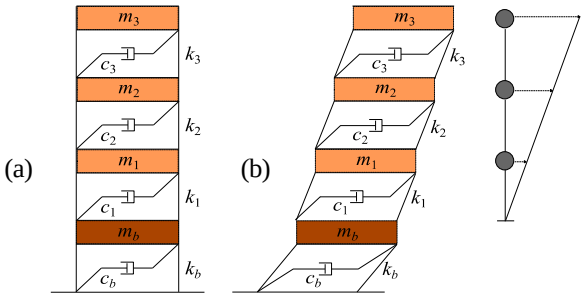
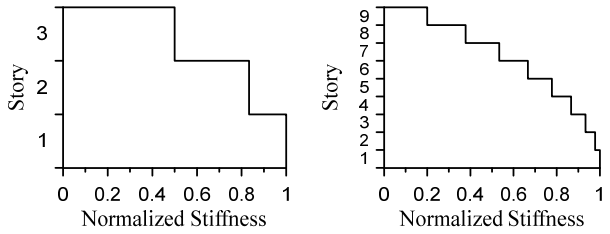


Figure 2 Base Isolated Structure Model:
(a) Shear Model (b) Mode Shape

For the fixed base structures, superstructure period T_s is assumed to be $0.1N_s$ where N_s is the number of stories. In order to control the superstructures to have the periods T_s, the stiffnesses, k_1, k_2, …, k_n distribution along the superstructure is obtained by solving simultaneous equations in Equation 1, where ϕ is the mode shape vector of the superstructure that is $\{1 \;\; 2 \;\; \ldots \;\; N_s\}^T$. The normalized stiffness distribution is shown in Figure 3(a) and 3(b) for 3- and 9-story structures. The superstructure is assumed to behave linearly throughout the excitation of the ground acceleration.

$$\left(\underset{N_s \times N_s}{\tilde{k}} - \frac{4\pi^2}{T_s^2} \underset{N_s \times N_s}{\tilde{m}} \right) \underset{N_s \times 1}{\tilde{\phi}} = \underset{N_s \times 1}{\tilde{0}} \qquad (1)$$



(a) (b)

Figure 3 Normalized Stiffness Distribution: (a) 3-story and (b) 9-story structures

Two types of superstructure damping of the fixed base structures are studied which are (1) stiffness proportional damping matrix $(\underset{\sim}{c} = \beta \underset{\sim}{k})$ and (2) Rayleigh damping matrix $(\underset{\sim}{c} = \alpha \underset{\sim}{m} + \beta \underset{\sim}{k})$

For the base isolated structures, an additional flexible floor is added at the bottom of the fixed base structure. The isolation period T_b and isolation damping ratio ζ_b are defined with the assumption that the superstructure is infinitely rigid. A linear viscous base isolation system is considered. Therefore, the isolation stiffness k_b and the isolation dashpot c_b can be obtained from Equation 2. Due to high demand concentration at the isolation level, the demands induced on the superstructure are reduced largely. Therefore, the superstructure damping for the base isolated structure is considered only 2% and is proportional to the stiffness matrix of the superstructure $(\underset{\sim}{c} = \beta \underset{\sim}{k})$.

$$k_b = \frac{4\pi^2}{T_b^2}\left(m_b + \sum_{j=1}^{N_s} m_j \right), \;\; c_b = \frac{4\pi\zeta_b}{T_b}\left(m_b + \sum_{j=1}^{N_s} m_j \right) \qquad (2)$$

Masses in all floors are assumed equal to one, story heights are equal in all stories and are assumed to be equal to 350 cm. Twenty ground accelerations from Los Angeles SAC suite of ground accelerations for a 2% in 50 years seismic hazard (LA21–LA40) are used in this study. Figure 4 shows the response spectra plots with 5% damping ratio for these ground accelerations.

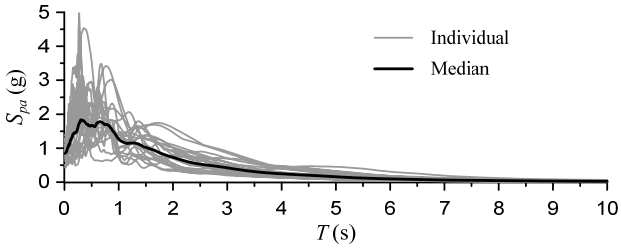


Figure 4 Pseudo Spectral Acceleration of LA21 – LA40 Ground Accelerations

3. CASE STUDIES

By using the previously defined analytical model, a parametric study is conducted. For the fixed base structures, several combinations of (1) superstructure damping ratio ζ_s and (2) number of stories N_s are investigated as listed below.

(1) ζ_s = { $0.2(\beta \underset{\sim}{k})$, $0.5(\beta \underset{\sim}{k})$, $0.5(\alpha \underset{\sim}{m} + \beta \underset{\sim}{k})$ }
(2) N_s = { 3, 9, 20 } stories

Although such small damping ratio ζ_s of $2\%(\beta \underset{\sim}{k})$ is not realistic, it is also investigated in order to compare the responses with the base isolated structures which have ζ_s of 2%, and also to compare, among the fixed base structures as well, the effects of damping ratio and damping mechanism on the response demand and distribution along the height of the superstructure. For Rayleigh damping mechanism, the first two modes are specified with the selected damping ratio.

For the base isolated structures, a variety of (1) base isolation period T_b and (2) number of stories N_s (above the isolation, excluding the isolation floor) with isolation damping ratio ζ_b of 10% are investigated as listed below.

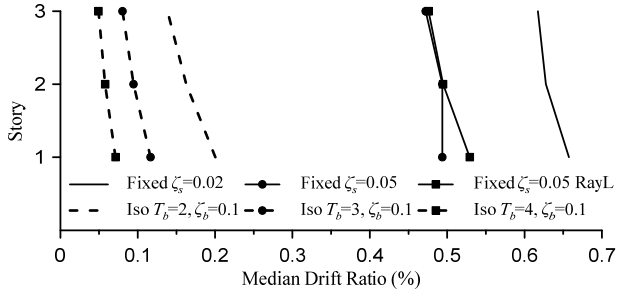
(1) T_b = { 2.0, 3.0, 4.0 } seconds
(2) N_s = { 3, 9, 20 } stories

These fixed base and base isolated structures are subjected to the 20 ground motions previously defined. The responses are described as median values with an assumption that these responses are lognormally distributed. Therefore, the medians and dispersions are calculated for each structure by Equations 3 and 4 respectively,

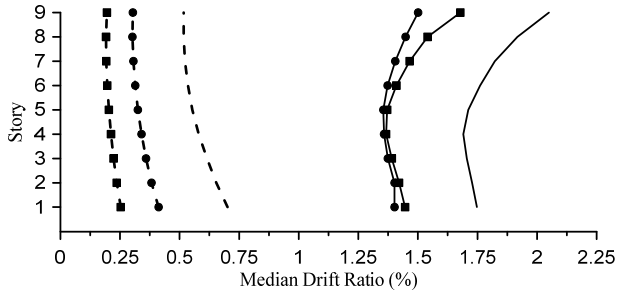
$$x_m = \exp\left(\frac{1}{M} \sum_{i=1}^{M} \ln r_i \right) \qquad (3)$$

$$\beta = \sqrt{\frac{1}{M-1} \sum_{i=1}^{M} \ln\left(r_i / x_m \right)^2} \qquad (4)$$

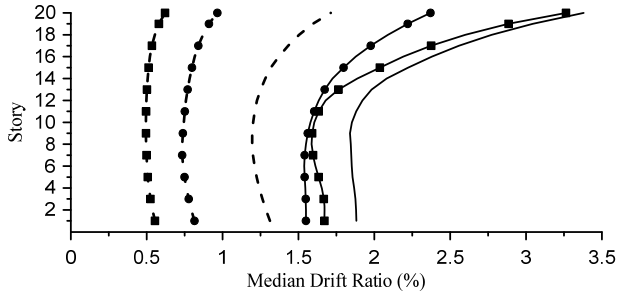
where x_m is median, β is dispersion, M is number of ground accelerations, and r_i is unique response for each ground motion.



(a) 3-Story Structures

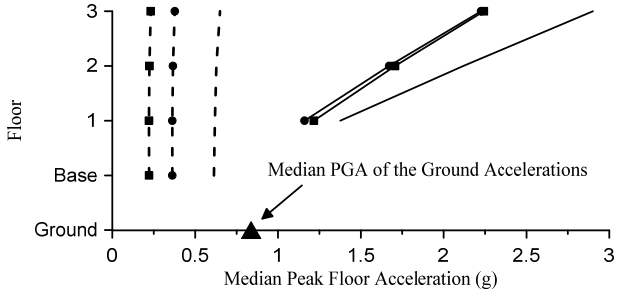


(b) 9-Story Structures

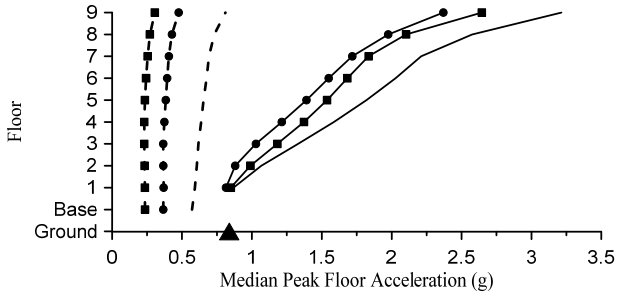


(c) 20-Story Structures

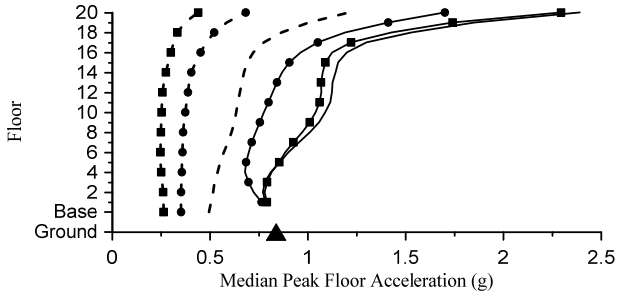
Figure 5 Median Drift Ratios for (a) 3-Story, (b) 9-Story, and (c) 20-Story Fixed Base and Base Isolated Structures



(a) 3-Story Structures



(b) 9-Story Structures



(c) 20-Story Structures

Figure 6 Median Peak Floor Accelerations for (a) 3-Story, (b) 9-Story, and (c) 20-Story Fixed Base and Base Isolated Structures

4. ANALYSIS RESULTS

It is necessary to study the natural behaviors of these fixed base and base isolated structures. Hence, these structures are subjected to the real unscaled ground accelerations (LA21–LA40). Median drift ratios and median peak absolute accelerations are used to describe the response. Median drift ratios for 3-, 9-, and 20-story structures are shown in Figure 5(a), 5(b), and 5(c), respectively. Median absolute peak floor accelerations for 3-, 9-, and 20-story structures are shown in Figures 6(a), 6(b), and 6(c), respectively. The comparisons of these structures are described in subsequent sections.

4.1 Comparison among the Fixed Base Structures

Since all fixed base structures have linear elastic behavior, there is no other source of damping, such as hysteretic damping, involved. Only the influence of the inherent structure damping is considered. From Figures 5 and 6, solid lines, for less superstructure damping cases, ζ_s = 2%, the responses are observed to be always higher, while cases of ζ_s = 5% (stiffness proportional) and 5% (Rayleigh), the responses are slightly different. For 3-story structures, drift and peak acceleration demands show almost the same, this is due to short and stiff nature of the structure. However, for taller structures, 9- and 20-story structures, slightly larger difference start to appear. When the structure is very tall, 20-story structure, the responses of 5% Rayleigh damping structures, seem to get closer to the response of 2% superstructure damping structures. This is because when the structures are very tall, 2nd mode, 3rd mode or even higher mode response may become dominant. And higher mode damping ratios for the Rayleigh damping case seems to be much lower than the stiffness proportional damping case, ζ_s = 5%, but closer to the 2% case as clearly shown in Table 1.

Table 1 Modal Damping Ratios of 20-Story Fixed Base Structures

Mode	Modal Damping Ratio		
	Stiffness Proportional Case		Rayleigh Case
	ζ_s = 2%	ζ_s = 5%	ζ_s = 5%
1	0.020	0.050	0.050
2	0.049	0.122	0.050
3	0.077	0.194	0.065
4	0.106	0.265	0.083
5	0.134	0.335	0.103

4.2 Comparison among the Base Isolated Structures

From Figures 5 and 6, dashed lines, it can be clearly observed that an increase of base isolation period T_b reduces both the drift and acceleration demands in superstructures of both stiff and flexible buildings. This is unsurprising because an increase of the base isolation period T_b is a reduction in the isolation stiffness resulting in concentration of drift demand in the base isolation level. More details of the effects of other properties influencing the response of the base isolated structures are described in the previous work by the authors (Chimamphant et al. 2012)

4.3 Comparison between the Fixed Base and Base Isolated Structures

Figures 5 and 6 reveal that adding the isolation system to the fixed base structure reduces the demands significantly. Comparison of the drift demands between the fixed base (ζ_s = 5% Rayleigh) and base isolated (T_b = 2 sec, ζ_s = 10%) structures show that the drift demands are reduced to around 30-50% at the top story as shown in Figure 5. However, in tall buildings, 9- and 20-story structures, the drift demands become concentrated in the upper stories more severely than the base isolated structures.

Comparison of the peak floor accelerations between the fixed base and base isolated structures also exhibit the reduction of the acceleration demands on the superstructures as shown in Figure 6. The results show similarly with the drift demands that the accelerations get severely concentrated in the upper stories. The difference is that the acceleration demand is slightly more steadily increasing along the height of the superstructure, unlike the drift demands that they tend to jump to rapid concentration at the upper stories.

In short buildings, the response could be reduced even more if the isolation system is more flexible by increasing the isolation period T_b as shown clearly in both Figures 5 and 6. This indicates that adding isolation system could always reduce the drift and acceleration responses on the superstructure.

5. FLOOR RESPONSE SPECTRA

In order to observe how the floor response spectra (FRS) are influenced by the structures having a variety of properties, floor response spectra with 2% damping ratio are conducted by using the absolute floor acceleration at the top floor of the structures. Figures 7 and 8 show the floor response spectra of the fixed base and base isolated structures, respectively. These floor response spectra represent the median values of the floor response spectra from all the ground accelerations. Median value is used to represent the value at the 50 percentile. Also it is easier to observe the peak at the natural periods and the smooth plateau at the other periods.

5.1 FRS of the Fixed Base Structures

The effects of the superstructure damping ratio and damping mechanism on the floor response spectra can be observed shown in Figure 7. Increasing the superstructure damping ratio from 2%$(\beta\underset{\sim}{k})$ to 5%$(\beta\underset{\sim}{k})$ results in rather uniform reduction in the floor response spectra as shown consistently in Figure 7(a), 7(b), and 7(c). However, alteration of the damping mechanism from stiffness proportional to Rayleigh results in the differences shown in the same Figure. As previously shown in Table 1, the 1st mode damping ratio for the 5% Rayleigh damping case is the same as the 5%$(\beta\underset{\sim}{k})$ case, which results in rather same pseudo spectral accelerations at the 1st mode period. However, the 2nd mode damping ratio for the 5% Rayleigh damping case is very close to the 2nd mode damping ratio of the 2% $(\beta\underset{\sim}{k})$ case. Therefore, the pseudo spectral acceleration at the 2nd mode period is shifted upwards close to what is observed for the 2%$(\beta\underset{\sim}{k})$ case.

5.2 FRS of the Base Isolated Structures

The effects of the base isolation periods T_b are observed and shown in Figure 8. It is obvious that not only is the natural period shifted, but also the reduction of the pseudo acceleration is significant. This is clear why increasing the isolation period T_b always improves the performance or reduces the demands induced on the superstructure.

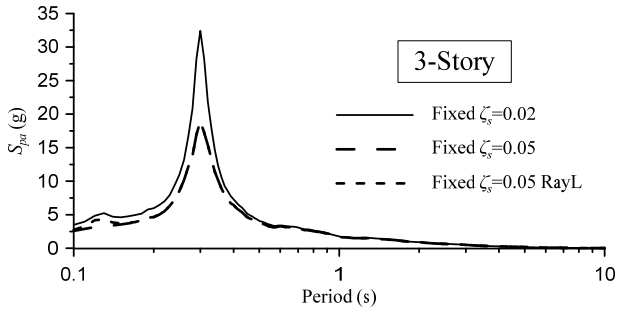
5.3 Comparison between the FRS of the Fixed Base and Base Isolated Structures

Examining the results described in Figures 7 and 8, comparison between the fixed base structures with ζ_s = 0.05 (Rayleigh) and the base isolated structures with T_b = 2 and ζ_b = 0.1 in both Figures show clearly that the maximum acceleration reduces almost around 10 times at the 1st mode natural period for the 3-story structures, and reduces smaller for 9- and 20-story structures shown in Figures 7 and 8. The reduction is smaller in taller structures because the isolation period T_b of 2 seconds is getting close to the superstructure T_s of 0.9 and 2 seconds for the 9- and 20-story fixed base structures, resulting in merely slight improvement. The improvement is usually higher since the isolation period T_b should always be much higher than the superstructure period T_s. Despite the slight improvement, this serves as a proof that adding a flexible isolated floor always improves the superstructure resting on it.

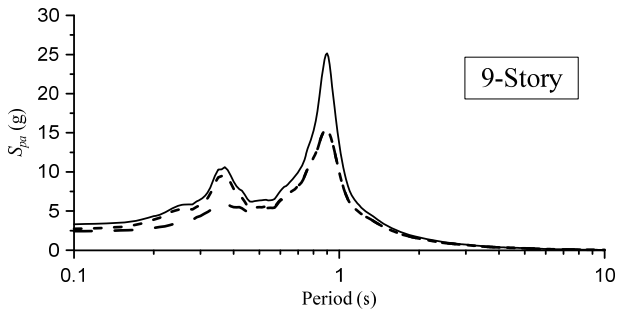
6. PERFORMANCE EVALUATION METHOD

6.1 Performance Based Earthquake Engineering

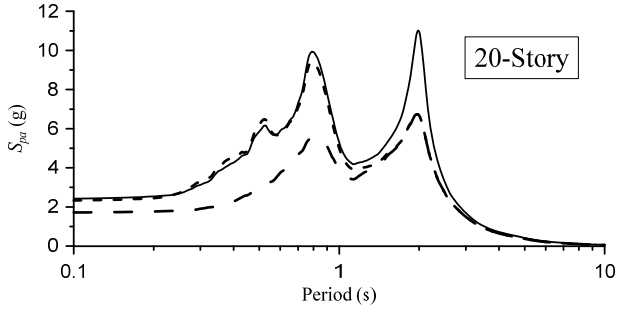
To determine the performance of the fixed base and base isolated structures considering the continued functionality (*CF*) damage state by using the drift ratios and the accelerations at the ceiling's period as the engineering demand parameters (*EDP*), the PEER Performance Based Earthquake Engineering (PBEE) methodology is adopted.



(a) 3-Story Fixed Base Structures (Top Floor)

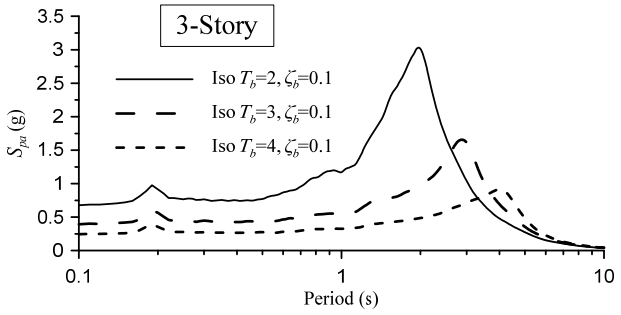


(b) 9-Story Fixed Base Structures (Top Floor)

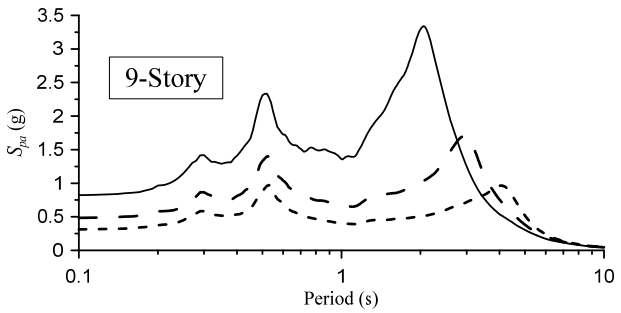


(c) 20-Story Fixed Base Structures (Top Floor)

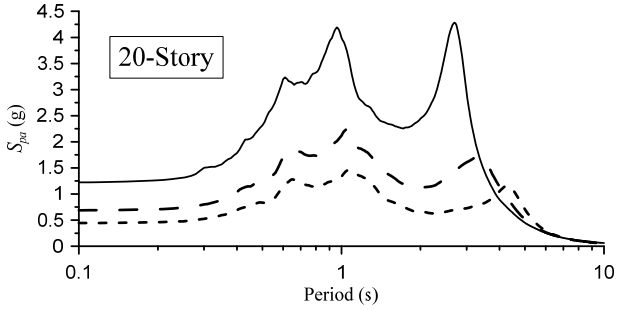
Figure 7 Top Floor Response Spectra for (a) 3-Story, (b) 9-Story, and (c) 20-Story Fixed Base Structures



(a) 3-Story Base Isolated Structures (Top Floor)



(b) 9-Story Base Isolated Structures (Top Floor)



(c) 20-Story Base Isolated Structures (Top Floor)

Figure 8 Top Floor Response Spectra for (a) 3-Story, (b) 9-Story, and (c) 20-Story Base Isolated Structures

In this framework, seismic hazard analysis, structural analysis, and damage analysis are used concurrently. The hazard analysis is used to define the seismic intensity at a specific location and mean annual exceedance frequency of interest. Structural analysis is conducted by linear response history analysis using a suite of scaled ground acceleration records to obtain story drifts at multiple levels of seismic intensity. Damage analysis, obtained from experimental data and damage observations of partition walls and suspended ceilings, describes the likelihood of exceeding continued functionality (*CF*) as a function of seismic demand.

The complete equation for calculating λ_{CF}, the annual probability that a fixed base or base isolated structure exceeds the continued functionality of partition walls (or other drift-sensitive components), is shown in Equation 5.

$$\lambda_{CF} = \sum_{k=1}^{n} \left\{ \begin{array}{l} P\left[dm > CF \,|\, \delta = \delta_k\right] \cdot \\ \sum_{j=1}^{m} \left\{ P\left[\delta = \delta_k \,|\, S_a = \overline{S}_{a,j}\right] P\left[S_a = \overline{S}_{a,j}\right] \right\} \end{array} \right\} \quad (5)$$

$P\left[dm > CF \,|\, \delta = \delta_k\right]$ is the probability of damage state exceeding continued functionality state for a specific drift ratio and is determined from the damage fragility curve.

$P\left[\delta = \delta_k \,|\, S_a = \overline{S}_{a,j}\right]$ is the probability that a specific drift occurs for a specific ground motion intensity level and is determined from drift distribution at each intensity level.

$P\left[S_a = \overline{S}_{a,j}\right]$ is the annual probability that a specific seismic intensity level is observed at a specific site and is obtained directly from hazard curve corresponding to a specific site location and natural period of interest.

6.2 Definition of Continued Functionality

Continued functionality is the performance state in which a building remains usable without interruption after

an earthquake. Hence, the damage that triggers this continued functionality state is very slight, corresponding to small values of drift ratio and floor acceleration.

7. FRAGILITY FUNCTIONS

In this study, the performance based on continued functionality (*CF*) damage state of partition walls and suspended ceilings, which serve as general representations of drift sensitive and acceleration sensitive components, respectively.

7.1 Fragility of Drift Sensitive Components

To represent drift sensitive components, fragility functions for partition walls are selected. Experiments on light gauge steel studded gypsum partition walls have been conducted recently at the University of Buffalo to assess their seismic fragility (Filiatrault et al. 2010). Fifty partition wall specimens, corresponding to 22 different wall configurations, were constructed following standard construction techniques. The fragility functions reported in their study is adopted here. The damage description corresponding to *CF* is "slight damage to partition walls." For this damage state, the median drift ratio and dispersion are 0.35% and 0.56, respectively.

7.2 Fragility of Acceleration Sensitive Components

To represent acceleration sensitive components, fragility functions for suspended ceilings are selected. From recent work by the authors (Motoyui et al. 2011), fragility of Japanese ceiling systems is obtained through Monte Carlo analysis using 2D finite element analysis and assumed statistical variation of the strength of connections from experimental testing. The period of the ceiling T_{ceiling} is 0.32 second. The fragility function describing "failure of ceiling" reported in their study is used. The median acceleration and dispersion are 0.505g and 0.046, respectively.

8. SEISMIC HAZARD CURVE

The last component needed in order to determine the performance is the seismic hazard curve for a site. This hazard curve can be obtained for a specific site location and a natural period of interest based on some attenuation model. In this study, the site is assumed to be located in downtown Los Angeles area, where the latitude and longitude used to specify the location are 34 and -118, respectively. The hazard curve is then obtained using the attenuation model by Campbell and Bozorgnia (2008) with V_{S30} = 760 m/s representing the boundary between B and C soil types, as defined in ASCE 7 (2005).

9. PERFORMANCE EVALUATION RESULTS

In order to obtain the performance, three components are needed as described previously which are (1) the probability of damage state exceeding continued functionality state, (2) the probability that a specific drift occurs for a specific ground motion intensity level, and (3) the annual probability that a specific seismic intensity level is observed at a specific site. These components are used concurrently as shown in Equation 5. The value obtained from this Equation is the mean annual frequency of exceeding the continued functionality damage state λ_{CF}. The expected return period *TR* can be calculated by taking the reciprocal of λ_{CF} ($TR = 1/\lambda_{CF}$). Figures 9 and 10 show the performances in terms of return periods *TR* for the fixed base structures based on the continued functionality damage state of partition walls and suspended ceilings, respectively. Figures 11 and 12 show the performances in terms of return periods *TR* for the base isolated structures based on the continued functionality damage state of partition walls and suspended ceilings, respectively. Note that TR_{drift} means the expected return period *TR* considering drift-sensitive components and TR_{acc} means the expected return period *TR* considering acceleration-sensitive components.

9.1 Performance of the Fixed Base Structures

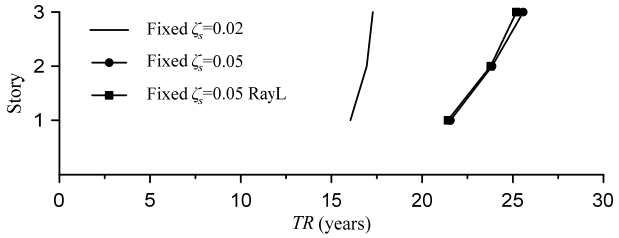
Examining the results described in Figure 9, the performance in terms of return period TR_{drift} (years) in each story corresponds well to the drift demands described previously in Figure 5. Higher drift demands result in poorer performance, whereas lower drift demands result in better performance. All results show that the expected return period TR_{drift}, Figure 9, are lower than 30 years. The TR_{drift} in the top story of the 20-story fixed base structure could be as low as 7 years, meaning that there is very high chance that the walls will need to be fixed or replaced during the expected return period of 7 years.

From Figure 10, the performances TR_{acc} in the 3-story cases are the same. This is because of the nature of short buildings; the accelerations induced on the structure are almost same in all cases when the ground accelerations are scaled to the same level. However, in taller buildings, the differences in the TR_{acc} start to appear, since damping ratio and damping mechanism start to take part more in the response.

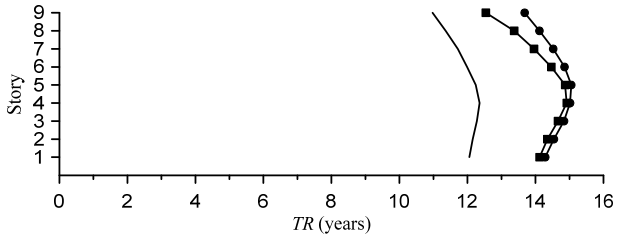
The fixed base structures are assumed to be linearly elastic and have no other supplemental dampers to absorb energy. Therefore, the performance observed here could be served as a generic performance observation where it could be improved and worsened if the structure implements additional control system or experiences severe nonlinearity.

9.2 Performance of the Base Isolated Structures

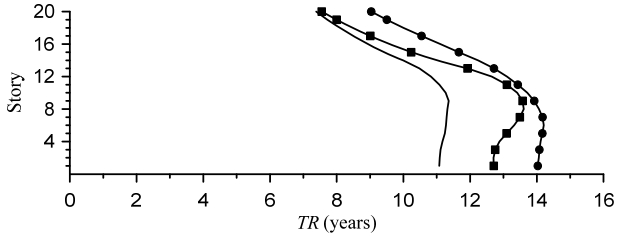
Similar to the performance observed in the fixed base structures, the results described in Figure 11 also correspond well to the drift demands described previously in Figure 5. Observing the expected return period TR_{drift} for 3-, 9-, and 20-story isolated structures, it is seen clearly that the return periods in short buildings are significantly higher than tall buildings. This indicates that, considering drift-sensitive components, isolation systems work well for short buildings.



(a) 3-Story Fixed Base Structures

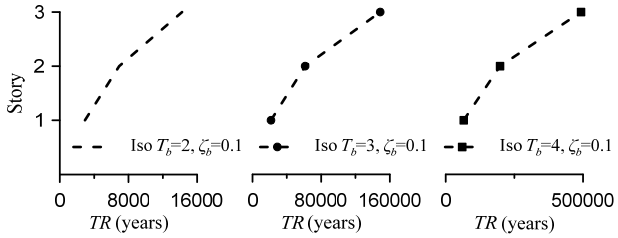


(b) 9-Story Fixed Base Structures

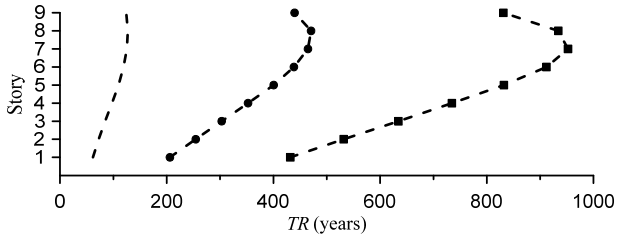


(c) 20-Story Fixed Base Structures

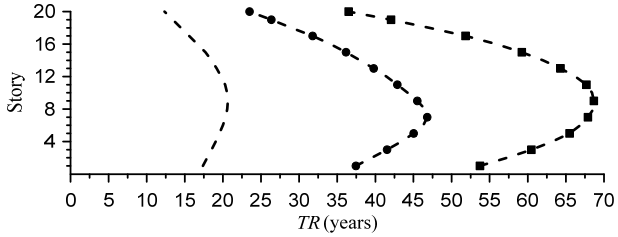
Figure 9 Performance in Return Period (years) Based on the Continued Functionality Damage State of Partition Walls



(a) 3-Story Base Isolated Structures

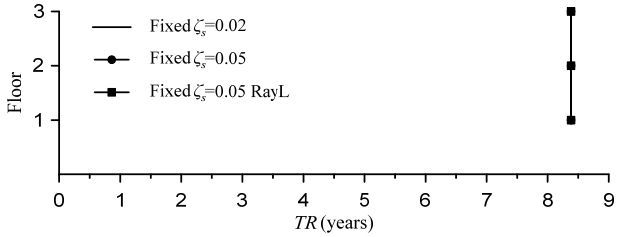


(b) 9-Story Base Isolated Structures

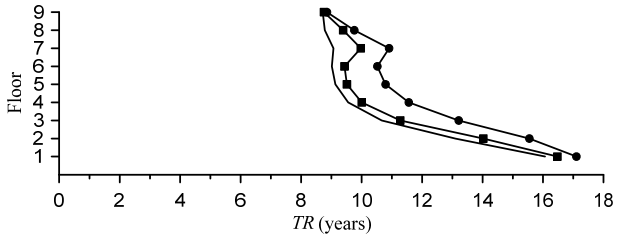


(c) 20-Story Base Isolated Structures

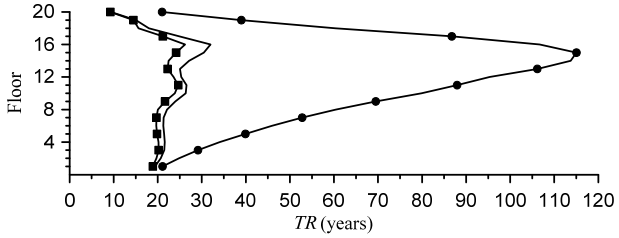
Figure 11 Performance in Return Period (years) Based on the Continued Functionality Damage State of Partition Walls



(a) 3-Story Fixed Base Structures

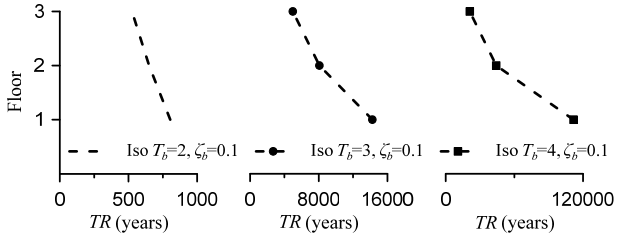


(b) 9-Story Fixed Base Structures

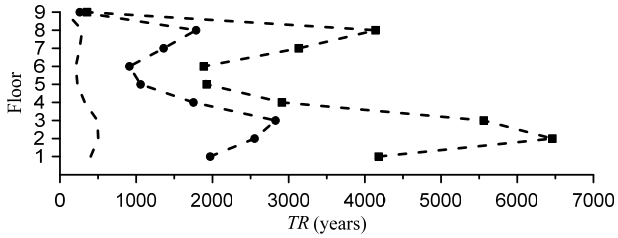


(c) 20-Story Fixed Base Structures

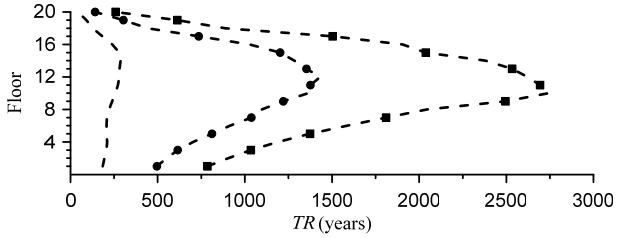
Figure 10 Performance in Return Period (years) Based on the Continued Functionality Damage State of Suspended Ceilings



(a) 3-Story Base Isolated Structures



(b) 9-Story Base Isolated Structures



(c) 20-Story Base Isolated Structures

Figure 12 Performance in Return Period (years) Based on the Continued Functionality Damage State of Suspended Ceilings

However, for tall buildings, the expected return period TR_{acc} could be as low as around 10 years at the top story of 20-story base isolated structures, meaning that there is a high chance that some partition walls need to be fixed or replaced over the life of the building, resulting in interruption of the usage of this story due to wall repair or replacement. The performance is always improved as well as the isolation period T_b increases.

Examining the results in Figures 12, the expected return period TR_{acc} in each floor does not correspond well to the acceleration demands described earlier in Figure 6. This is because the performance calculated is based on the peak acceleration at the period of the ceiling, T_{ceiling} = 0.32 sec as defined in Section 7.2, not the peak floor acceleration as shown in Figure 6. The improvement when increasing the isolation period T_b is more pronounced in short buildings, 3-story isolated structures. In tall buildings, the improvement can still be obviously observed. Also in tall buildings, higher mode response contribution could play an important role in the total response. Therefore, the expected return periods TR could become irregular as shown in the 9-story isolated structures, Figure 12(b), where in the middle floors, the return periods decrease significantly. This is because the 3rd mode period of this 9-story isolated structure, which is 0.296 second, falls in the proximity of the ceiling's period. More detail has been described by the authors (Chimamphant et al. 2012).

9.3 Comparison between the Performance of the Fixed Base and Base Isolated Structures

Examining the results described in Figures 9 to 12, the results confirm that the isolation system helps improve the fixed base structures significantly. The comparison between the 3-story fixed base structure with ζ_s = 5% Rayleigh damping and the 3-story isolated structure with T_b = 2 sec and ζ_b = 10%, shows that the expected return periods TR_{drift} increase from around a few ten years to several thousand years, which is around a thousand times as shown in Figures 9(a) and 11(a). The expected return periods TR_{acc} also show similarly that the improvement is around a hundred times as shown in Figures 10(a) and 12(a). It is obvious that the expected periods increase even more significantly, if the isolation period T_b increases.

For 9-story cases, the improvement still exists, however, less significantly as can be seen between Figures 9(b) and 11(b) for the TR_{drift} and Figures 10(b) and 12(b) for the TR_{acc}.

For 20-story cases, the improvement is rather small. It is interesting to see that adding an isolated floor with T_b = 2 seconds actually improves the expected return periods TR_{acc} only a few years. This might actually be expected since the isolation period T_b is equal to the superstructure period T_s. Therefore, by adding more flexibility to the isolation story, the performance can be gained as shown in Figure 11(c). On the other hand, the TR_{acc} always exhibits improvement as seen in Figures 10(c) and 12(c). This is again because the performance is considered at the ceiling's period. As long as none of the natural modes of the structure falls close to the ceiling's period, the performance should be improved.

10. CONCLUSIONS

This research focuses on the comparison of the responses and performances between fixed base structures and base isolated structures in order to clearly observe how well an isolation system can contribute to a fixed base structure in terms of the response demands, drift ratios and peak floor accelerations, and the performance, return periods. By adopting the PEER PBEE methodology, the mean annual frequency of exceeding the continued functionality damage state is obtained, leading to the expected return period *TR*.

In the fixed base structures, reducing the superstructure damping ζ_s increases the demands on the superstructure accordingly. However, when the mechanism changes from stiffness proportional damping to Rayleigh damping, the demands appear differently, due to different modal damping ratios in higher modes. This becomes obvious in tall buildings because in tall buildings higher mode responses start to contribute to the total response. These can be observed clearly in the FRS shown in Figure 7. For base isolated structures, the performance can always be improved by adding the flexibility to the isolation story as shown clearly in Figures 11 and 12

All the results described indicate that isolation system could always improve the overall performance of the superstructure resting on it, if the selection of the base isolation properties is properly made. In summary, it is possible to conclude that isolation system is significantly beneficial to short buildings, while also exhibiting moderate improvement on taller buildings

References:

Moehle, J. and Deierlein, G. (2004), "A Framework Methodology for Performance-Based Earthquake Engineering," *Proceedings of the 13th World Conference on Earthquake Engineering*, Vancouver, Canada

Retamales, R., Davies, R., Mosqueda, G., Filiatrault, A. (2010), "Experimental Seismic Fragility Assessment of Light Gauge Steel Studded Gypsum Partition Walls," Toronto, Canada.

Motoyui, S., Sato, Y., Macrae, G.A., Dhakal, R.P. (2011), "Ceiling Fragility of Japanese Ceiling Systems," *Proceedings of the 9th Pacific Conference on Earthquake Engineering*, Auckland, New Zealand

Campbell, K.W. and Bozorgnia, Y. (2008), "NGA ground motion model for the geometric mean horizontal component of PGA, PGV, PGD and 5% damped linear elastic response spectra for periods ranging from 0.01 to 10 s," *Earthquake Spectra* 24, 139–171.

Chopra, A. K., "Dynamics of Structures: Theory and Applications to Earthquake Engineering," *Prentice-Hall*, Upper Saddle River, NJ, 2007.

Vamvatsikos, D., Cornell, C.A. (2001), "Incremental Dynamic Analysis," *Earthquake Engineering & Structural Dynamics*, J. Wiley & Sons, v. 31, pp. 491-514.

ASCE 7-05, "Minimum Design Loads for Buildings and Other Structures," *American Society of Civil Engineers*: Reston, VA, 2005

Chimamphant, S., Kasai, K., Morgan, T. (2012), "Continued Functionality Performance for Base Isolated Structures Subjected to Earthquakes", *9th International Conference on Urban Earthquake Engineering and 4th Asia Conference on Engineering Joint Conference*, Tokyo

10CUEE CONFERENCE PROCEEDINGS
10th International Conference on Urban Earthquake Engineering
March 1-2, 2013, Tokyo Institute of Technology, Tokyo, Japan

AN INERTER VIBRATION ISOLATION SYSTEM FOR THE CONTROL OF SEISMICALLY EXCITED STRUCTURES

Irina F. Lazar[1)], David J. Wagg[2)], and Simon A. Neild[3)]

1) PhD Student, Department of Mechanical Engineering, University of Bristol, U.K.
2) Professor, Department of Mechanical Engineering, University of Bristol, U.K.
3) Reader, Department of Mechanical Engineering, University of Bristol, U.K.
Irina.Lazar@bristol.ac.uk, David.Wagg@bristol.ac.uk, Simon.Neild@bristol.ac.uk

Abstract: Despite recent advances in active and semi-active control, the majority of civil engineering structures are still controlled via passive devices. A key limitation of this approach is that classical passive devices are typically only efficient over a narrow frequency band for which they are tuned, while earthquakes display complex frequency content. Therefore, we have developed an improved control system that overcomes this limitation. We proposed the use of the inerter, a device that was initially developed for the high-performance suspension systems of Formula 1 racing cars. This type of device is to be employed in vibration control of single and multiple storeys buildings subjected to earthquake loads. The inerter is designed to replace devices such as tuned mass dampers and its main advantage is that a better isolation level can be achieved with lower physical mass installation. Moreover, the device no longer sits on the building's floor, but is mounted on braces between adjacent storeys. Different configurations are studied in order to find the one offering best performance for a one-storey and a two-storeys building. We show results as the key parameters are varied to study the system performance under a range of operating conditions. Based on this parametric analysis, we propose a series of guidelines for inerter systems tuning.

1. INTRODUCTION

Research in the field of vibration isolation has been carried out since early 1900s. The complexity and dimensions of civil engineering structures make this problem particularly difficult to solve due to high control effort demand and many other associated limitations. Attempts are being made towards the use of active and semi-active control, but practical application of these techniques is still limited. Many state of the art reviews have been conducted in this respect (Soong and Spencer (2002), Soong and Cimellaro (2008), Wagg and Neild (2011)). Active control and its related problems regarding costs, stability and robustness have also been extensively studied (Preumont (2002), Wagg and Neild (2009)). Semi-active control devices seem to be closer to large scale application and they have already been installed on bridges (Dongting Lake Bridge, China – magneto-rheological dampers). Most of the civil structures are still controlled passively via base isolation systems, tuned mass dampers (TMDs) or viscous dampers (Soong and Dargush (1997)).

The aim of this paper is to introduce a new type of control system to be used for unwanted vibration mitigation in civil engineering applications. The systems presented in this paper are passive, but it is our intention to study semi-active systems of the same type. The proposed configurations are based on an inerter device mounted in series and/or parallel with spring and damper elements.

The inerter is a new device that has been proposed by M.C. Smith (2002). This device completes the force-current analogy between mechanical and electrical networks and it is equivalent to the capacitor. The inerter overcomes the limitations present in the mass-capacitor equivalence, its advantage being that it no longer needs to be grounded. Smith defines the ideal inerter as a two terminal device with the property that the force generated is proportional to the relative acceleration between the two nodes. Its constant of proportionality is intuitively named inertance and is measured in kilograms, suggesting its similarity to mass. The force produced by an inerter is given by:

$$F = b(\ddot{x}_i - \ddot{x}_j) \tag{1}$$

where b is the constant inertance and $\ddot{x}_i - \ddot{x}_j$ is the relative acceleration between its nodes.

Initially, the inerter has been used in Formula 1 racing cars suspension systems, under the name of "J-damper", as explained by Chen et al. (2009). Currently, several attempts are being made to widen its field of application. Experimental testing has been conducted for studying several types of inerters and many installation possibilities. Wang et al. (2010) propose the use of a hydraulic inerter. Chen et al. (2009) describe the rack and pinion inerter and the ball and screw inerter. Wang and Chan (2011) propose a vehicle suspension system employing a mechatronic network strut. Papagiorgiou et al. (2009a and 2009b) conduct a

series of experimental tests on several types of inerter devices. Kuznetsov et al. (2010) study the optimisation of inerter-based suspension systems.

Research is carried out towards the practical use of inerters in vehicle suspension systems. Several installation layouts have been studied in order to ensure optimal performance by Scheibe and Smith (2009), Smith and Wang (2004) and Wang and Su (2008a and 2008b). Train suspension systems have been studied by Wang et al. (2009a) and Wang and Liao (2010). Motorcycle steering compensator applications were proposed by Evangelou et al. (2007).

In the field of Civil Engineering, inerters have been proposed for use in buildings suspensions, namely in base isolation systems, by Wang et al. (2007, 2009b). They investigate several suspension layouts for both a one-degree of freedom (DOF) and a two-DOF model.

The novel aspect of this paper is that we intend to go one step further and model the inerters inside the building, ideally on braces situated between adjacent storeys. Therefore, the inerter is no longer used in a suspension system, but in a vibration suppression one.

As explained earlier, the inerter device employed in this paper is passive and therefore it has constant inertance. Depending on the other elements used in the system, this can remain passive (e.g. when springs and viscous dampers are used) or become semi-active (e.g. in the case when magneto-rheological (MR) dampers are present). Zhang et al. (2012) studied a semi-active suspension system employing a passive inerter.

The inerter chosen in this paper is of rack and pinion type and the inertance is a function of the moment of inertia of the flywheel and the flywheel rotation as detailed by Chen et al. (2009). Therefore, the inertance produced depends on the choice of gearing and can be much higher than the physical mass of the device.

Given its equivalence with mass, it is intuitive to compare the inerter-based systems performance with that of tuned mass dampers (TMD). TMDs were introduced by Den Hartog (1940). He proposed the use of a mass-spring system called undamped dynamic vibration absorber. Optionally, a damper can also be introduced. Den Hartog gave a series of guidelines for optimal tuning of TMDs. However, the TMD performance is limited by the amount of mass that needs to be mounted. Generally, this has to be in the range of 1%-10% of the mass on the targeted vibration mode. The inerter overcomes this limitation due to its small physical mass and proves to be very efficient in vibration suppression.

We will test six different layouts employing either an inerter or an additional mass and assess their performance. The systems' parameters will be varied and their influence discussed. We first investigate a one-DOF system and then a two-DOF system. Both types of structure are subjected to seismic excitation. We used an acceleration time history recorded during the Great East Japan Earthquake (Tohoku Earthquake) that took place on the 3rd of March, 2011.

If proved efficient in practice, an inerter-based vibration suppression system could solve the problems associated with TMD installation. Most important, there is no need for significant additional mass installation, the inertance being dependent on the choice of gearing only. Moreover, the overall dimensions of the control system will be much smaller, a fact that is advantageous from architectural point of view and space considerations.

2. ONE-DOF STRUCTURAL SYSTEM

Firstly, a one-DOF structure is proposed for analysis. The uncontrolled system is shown in Figure 1(a). The control is applied via the concentrated force F which depends on the configuration chosen (Figure 1(b)). Six configurations have been proposed, four of them being based on the inerter, Figure 2(a)-(d), and two on additional mass elements, Figure 2(e)-(f).

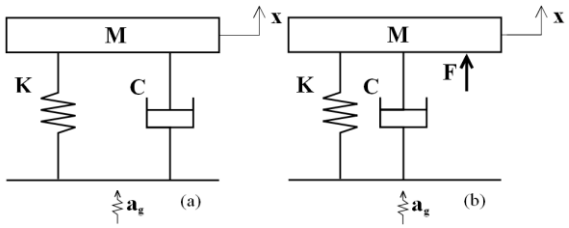


Figure 1 One-DOF structural system (a) uncontrolled and (b) with general control force – Parameters: M=1kNs^2/m; K=1000 kN/m; C= 3.16kNs/m.

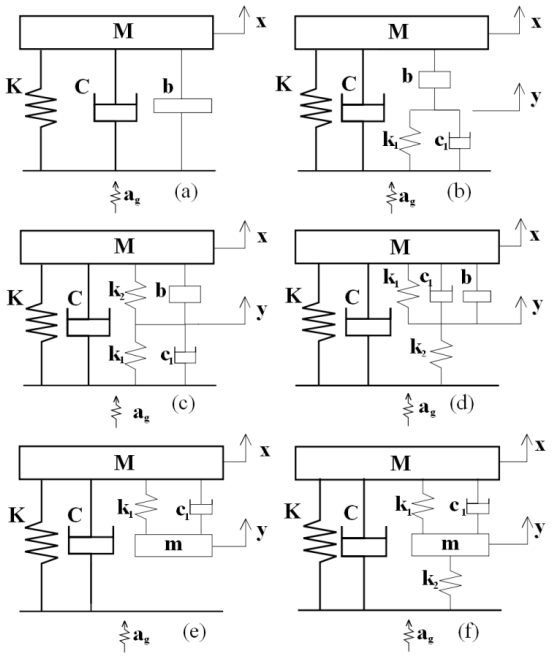


Figure 2 Controlled systems (a) Inerter 1; (b) Inerter 2; (c) Inerter 3; (d) Inerter 4; (e) TMD 1; (f) TMD 2;

The system in Figure 2(e) represents a classical TMD system. For all uncontrolled and controlled systems M, C and K represent the structural mass, damping and stiffness respectively. The structural parameters values have been chosen such that the natural frequency of the uncontrolled system is $\omega_n = 5.03Hz$. This is because the Fourier spectrum of the seismic input used has highest amplitudes at

low frequencies, situated mainly under $6Hz$. Therefore, the structure will be sensitive to the chosen ground-motion record.

The ground acceleration has been conventionally represented as vertical in Figure 2, but the equations of motion remain unchanged regardless its direction.

The equation of motion for the uncontrolled one-DOF system, expressed in physical coordinates is given in Eq. (2). Eq. (3) shows the equation of motion for the controlled systems.

$$M\ddot{x}(t) + C\dot{x}(t) + Kx(t) = -Ma_g(t) \quad (2)$$

$$M\ddot{x}(t) + C\dot{x}(t) + Kx(t) = -Ma_g(t) + F \quad (3)$$

Writing Eq. (2) in the Laplace domain, the displacement response is obtained as:

$$X(s) = \frac{-M}{Ms^2 + Cs + K} A(s) \quad (4)$$

where *X(s)* and *A(s)* are the Laplace transforms of the displacement and ground acceleration, respectively.

The control force can be written as:

$$F(s) = T_{XF} X(s) + T_{AF} A(s) \quad (5)$$

where T_{XF} and T_{AF} are the transfer functions from structural displacement and ground acceleration to the control force, respectively. Therefore, by writing Eq. (3) in the Laplace domain and replacing the control force expression from Eq. (5), the structural displacement is obtained as:

$$X(s) = \frac{-M + T_{AF}}{Ms^2 + Cs + K - T_{XF}} A(s) \quad (6)$$

The displacement response has been calculated by evaluating Eq. (6) for all layouts shown in Figure 2.

2.1 Parameters Tuning

The mass-based systems (Figure 2(e)-(f)) are tuned based on Den Hartog's guidelines for damped vibration absorbers. The expressions of the newly introduced components, *m*, *b*, c_1, k_1 and k_2 are shown in Eq. (7).

$$m = \mu_m M;\ \ b = \mu_b M;\ \ k_1 = k_2 = \frac{\mu}{(1+\mu)^2} K;$$
$$\xi = \sqrt{\frac{3\mu}{8(1+\mu)}};\ \ c_1 = 2\xi \frac{\omega_n}{1+\mu} \mu M;\ \ \mu \in \{\mu_m, \mu_b\} \quad (7)$$

where ξ represents the damping ratio and μ_m and μ_b are the mass ratios for the mass-based and inerter-based systems, respectively.

Given our intention to compare the inerters performance to that of a TMD we will start our analysis by using the same tuning rules. It must be mentioned that this may not be the optimal tuning philosophy. However, the tuning rules have been adapted to base-excited structures according to Soong and Dargush (1997). We have considered that $\mu_m = 0.1$. This is close to the maximum allowable mass ratio in case of regular TMDs. Since the inerters can produce much higher mass ratios compared to their actual mass, we chose $\mu_b = 0.7$. Smith (2002) shows that the ratio between the inertance and the actual inerter mass, can attain values as high as 300, much greater than the one considered in this paper, which is only 7.

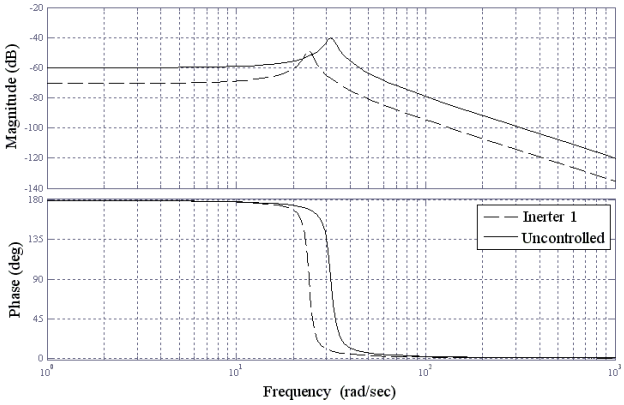


Figure 3 Comparison between Inerter 1 controlled system and the uncontrolled system

2.2 Frequency Domain Performance Analysis

Figures 3-7 show the frequency response of the systems shown in Figure 2, in the form of bode plots, based on the transfer functions described in Eq. (6), evaluated for each of the six layouts. All responses are shown in comparison to the uncontrolled system frequency response.

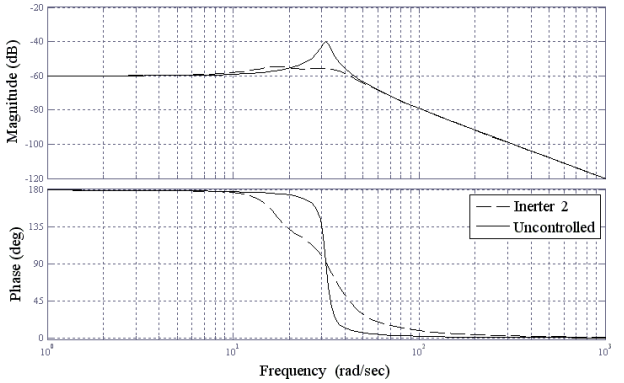


Figure 4 Comparison between Inerter 2 controlled system and the uncontrolled system

Figure 3 shows that the system represented by Inerter 1 shifts the natural frequency of the uncontrolled system to the left and improves its performance significantly for the entire frequency range. Inerter 2 shows promising results as well, the displacement amplitudes are reduced and it can be seen in Figure 4 that the resonant peak is split as in the case when TMDs are used. Inerter 3 creates a new resonant peak at lower frequency, but this is smaller in amplitude than the uncontrolled one.

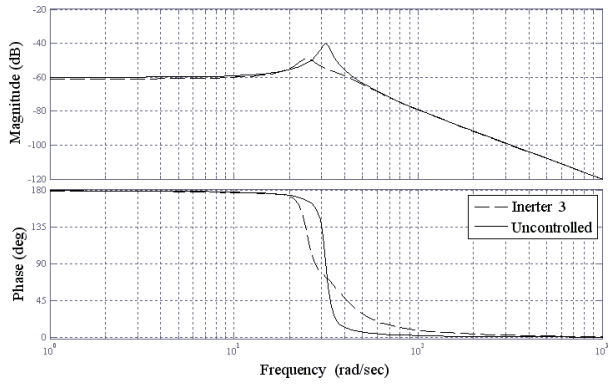


Figure 5 Comparison between Inerter 3 controlled system and the uncontrolled system

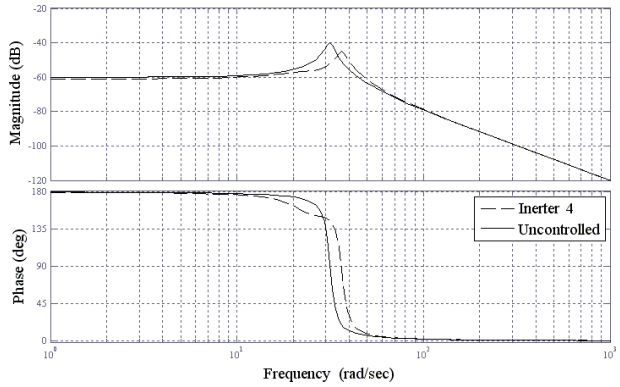


Figure 6 Comparison between Inerter 4 controlled system and the uncontrolled system

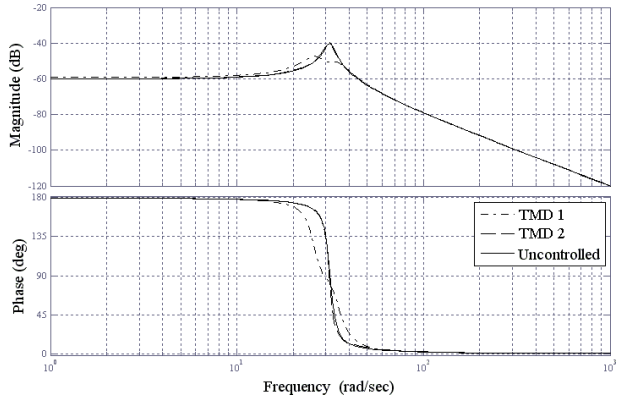


Figure 7 Comparison between TMD 1 and TMD 2 controlled systems and the uncontrolled system

Inerter 4 has a good performance as well, despite some slight overshooting present in the case of high frequency excitation. The same resonant peak split, specific to TMDs, is observed. However, the lower frequency peak has smaller amplitude, due to the presence of a heavily damped pole of the new system. The poles and zeros of all one-DOF systems are given in Tables 1 and 2. As seen from Figure 7, TMD 1 displays the behaviour of a classical TMD system, while TMD 2 proves to have a poor performance, very close to that of the uncontrolled system. Figure 8 shows a comparison between all the inerter based systems, Inerter 1-4.

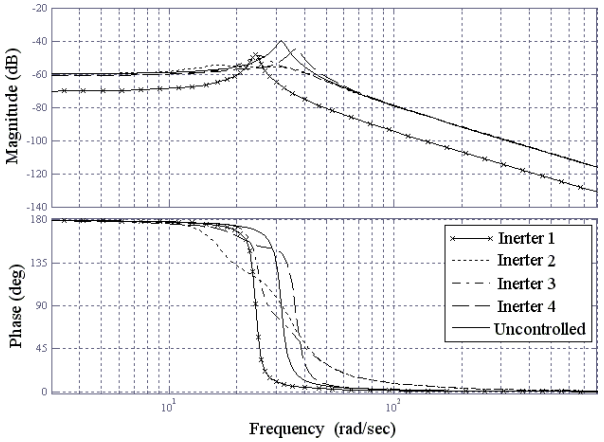


Figure 8 Comparison between the inerter-based systems and the uncontrolled system

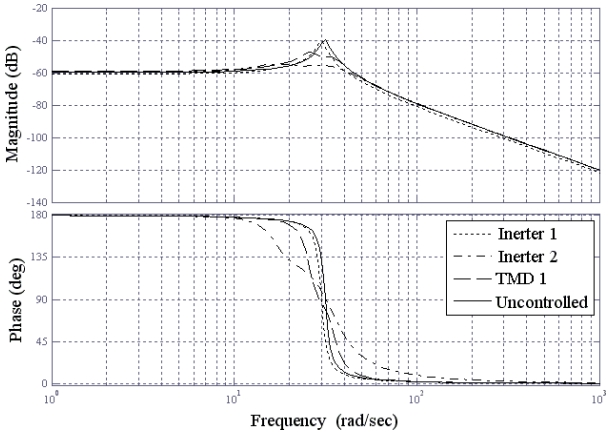


Figure 9 Comparison between Inerters 1, 2, TMD 1 and the uncontrolled system for $\mu_m = \mu_b = 0.1$

Table 1 Poles of the one-DOF systems, of the form x+yj

System	x	y
Uncontrolled	-1.58	±31.58
Inerter 1	-0.90	±24.23
Inerter 2	-9.77	±32.84
	-4.24	±16.64
Inerter 3	-9.42	±49.98
	-4.59	±35.72
Inerter 4	-2.29	±36.56
	-6.60	±23.13
TMD 1	-4.48	±34.39
	-2.94	±26.05
TMD 2	-6.02	±41.45
	-1.40	±31.29

The systems represented by Inerter 1 and Inerter 2 display the best frequency response. In order to underline once again the advantages of the inerter systems over systems implying additional mass installation, Figure 9 shows a comparison between Inerters 1, 2, TMD 1 and the uncontrolled system, for $\mu_m = \mu_b = 0.1$. This is done to show that even in the case of equal mass ratios, the inerter performance is similar

to that of the mass-based systems.

Table 2 Zeros of the one-DOF systems, of the form x+yj

System	x	y
Inerter 2	-7.31	± 17.105
Inerter 3	-7.31	± 25.271
Inerter 4	-7.31	± 25.271
TMD 1	-5.839	± 29.580
TMD 2	-5.839	± 41.249

However, we must keep in mind that much larger mass ratios can be achieved in the case of inerter-based systems. It can be seen that Inerter 2 system still performs better than the classical TMD 1. Inerter 1 system is not as efficient, but this is not a problem since much higher mass ratios can be selected. Given the results shown so far, it can be concluded that the inerter-based systems are a very feasible solution for replacing the classical TMDs.

2.3 Seismic Performance

For this analysis we have chosen an acceleration time history recorded during the Tohoku Earthquake at the Sendai station, on NS direction. The time history is shown in Figure 10.

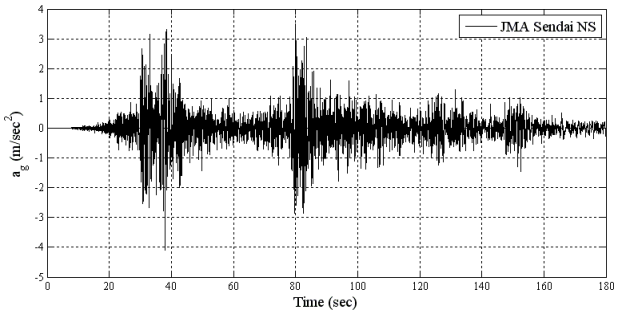


Figure 10 Acceleration time history – Tohoku Earthquake

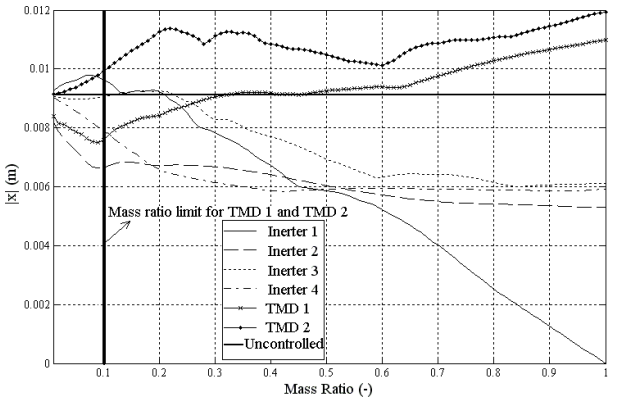


Figure 11 Maximum absolute response variation with mass ratio

Figure 11 shows the variation of the maximum absolute displacement of the structure with the mass ratio. We have chosen $\mu \in [0, 1]$. For $\mu = 0$ the structure is uncontrolled, while for $\mu = 1$ we add 100% more mass/inertance. Such a mass ratio is unrealistic for mass-based systems, but an inerter-based system can easily attain this value. As revealed by Figure 11, Inerter 1 has the best performance. The maximum displacement decreases continuously as the mass ratio becomes higher. As expected, the behaviour of Inerter 2 is similar to that of TMD 1 for mass ratios up to 10% of the total mass. Inerter 2 behaviour improves as the mass ratio is further increased. Inerter 3 becomes efficient for mass ratios $\mu_b > 0.6$. After passing this threshold, its performance is close to Inerter 2 and Inerter 4. TMD 2 has the same limitations regarding the mass ratio as TMD 1. However, its performance is poor.

Figures 12(a)-(c) show the displacement time histories obtained with Inerter 1, Inerter 2, TMD 1 and the uncontrolled system. It can be seen that the systems represented by Inerter 1 and Inerter 2 display improved behaviour, while the TMD 1 response is similar to the uncontrolled one. This proves that the inerter-based systems are more efficient than the classical TMD.

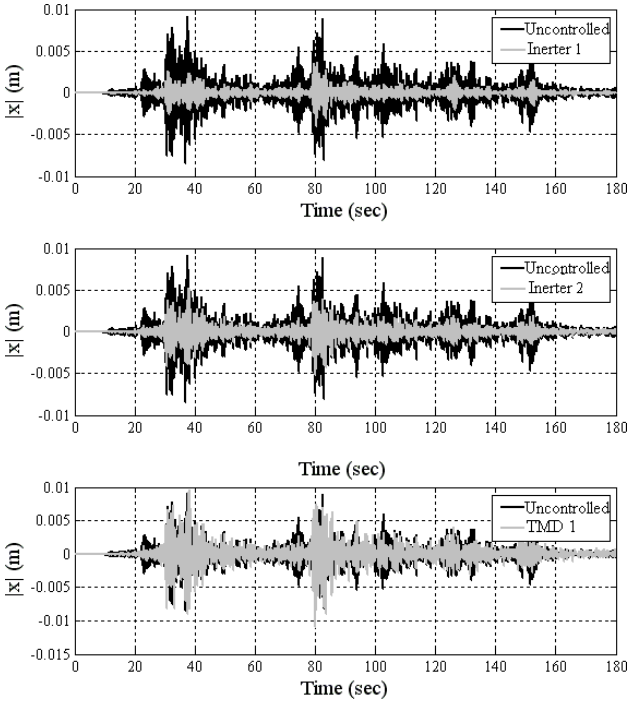


Figure 12 Displacement time histories for Inerter 1, Inerter 2 and TMD 1 compared to the uncontrolled response to the Tohoku Earthquake record ($\mu_b = 0.7$ and $\mu_m = 0.1$)

3. TWO-DOF STRUCTURAL SYSTEM

The two-DOF system chosen and the equivalent controlled system are shown in Figures 13(a) and (b) respectively. The analysis carried out on the one-DOF structure is extended for the system represented by Inerter 2. The classical TMD case (TMD 1) is also kept for reference. The new controlled systems are shown in Figures 14(a)-(b).

The control systems were placed alternatively at the upper and lower floor levels. However, only results pertinent to the upper location are presented in this paper as these systems proved to be more efficient. This result was

expected, since it is known that in order to control the first mode of vibration (the predominant one, with higher participation factor), the control force must act in the point of maximum displacement amplitude in the first vibration mode.

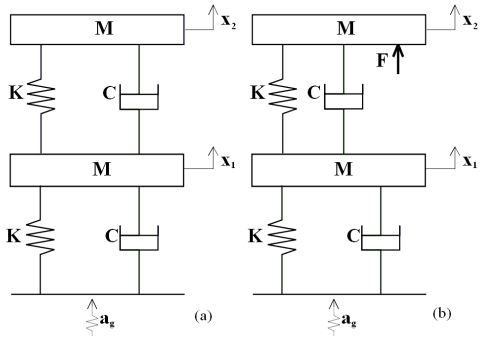


Figure 13 Two-DOF structural system (a) uncontrolled, and (b) with general control force

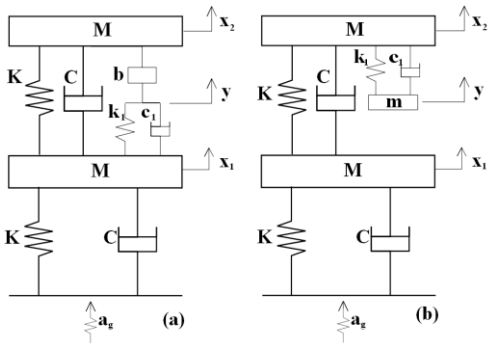


Figure 14 Controlled systems (a) Inerter 2' and (b) TMD 1'

The equations of motion of the uncontrolled and controlled systems can be expressed using Eq. (2) and (3). In this case, *M*, *K* and *C* are matrices, not scalars. They are given in Eq. (8).

$$M = \begin{bmatrix} 1 & 0 \\ 0 & 1 \end{bmatrix} kNs^2/m; \quad K = \begin{bmatrix} 5000 & -2500 \\ -2500 & 2500 \end{bmatrix} kN/m; \quad C = \begin{bmatrix} 6.708 & -2.236 \\ -2.236 & 4.472 \end{bmatrix} kNs/m \tag{8}$$

3.1 Parameters Tuning

The tuning is done following the same principles as in the case of the one-DOF system (Eq. (7)), keeping in mind that we are targeting the first mode of vibration. We have set the mass ratios to be $\mu_m = 0.05$ and $\mu_b = 0.7$.

3.2 Frequency Domain Performance Analysis

Figures 15 and 16 show the frequency response of all the two-DOF systems in the form of bode plots, for each displacement output. The behaviour of the two systems appears to be similar. However, the inerter-based system, Inerter 2', displays a heavily damped pole at low frequency, which isn't present in the case of the mass-based system. TMD 1' generates a split of the original resonant peak, but the resulting poles are similarly damped.

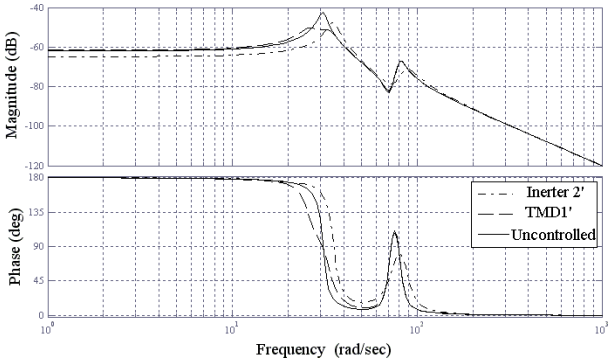


Figure 15 Bode plots for x_1 displacement output

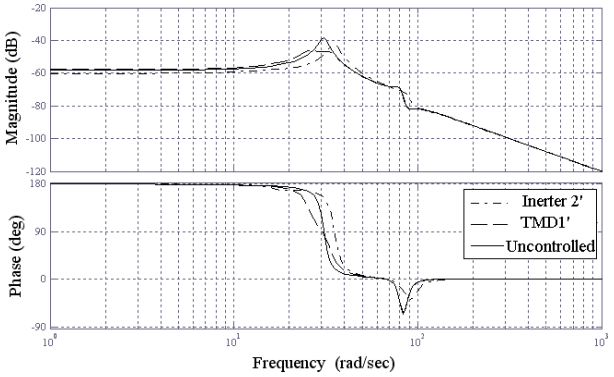


Figure 16 Bode plots for x_2 displacement output

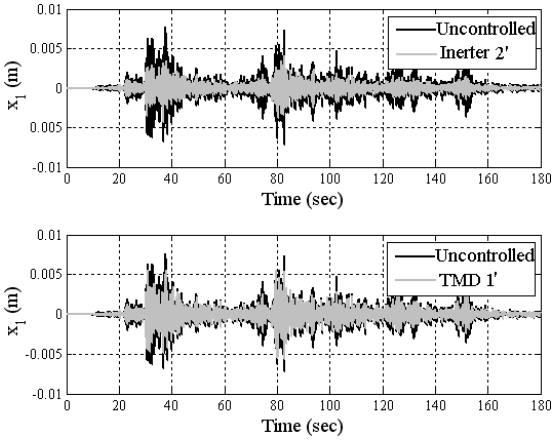


Figure 17 x_1 displacement time history

In both Figures 15 and 16 it can be seen that the inerter-based system displays better behaviour at low frequencies. Although on the upper DOF there appears some amplification in response in the region of the second fundamental frequency, this is not a problem because the response amplitudes are relatively small and it is unlikely for the ground excitation frequency content to be dominated by such high frequencies.

The frequency response of the structures can also be explained by analyzing the poles and zeros locations for each of the two considered outputs. These are not given explicitly.

3.3 Seismic Performance

The structures have been subjected to the same ground

motion as the one-DOF systems (Figure 10). The displacement time histories are shown on each DOF in Figures 17 and 18, respectively. It is visible that the inerter-based system has better results on both degrees of freedom. The structural response is reduced with respect to the uncontrolled system. The TMD 1' system does not bring a significant improvement of the uncontrolled response. Moreover, Figure 19 shows that the mass from system TMD 1' displaces more that the Inerter 2' system. Therefore, it is advantageous to use an inerter-based system which has lower displacement and is lighter, since in some cases the required additional mass may be very large.

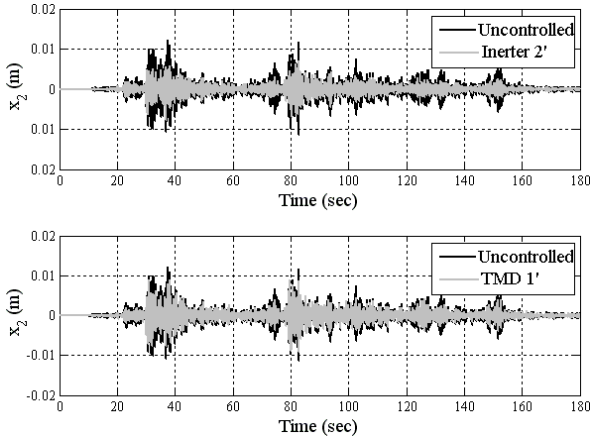


Figure 18 x_2 displacement time history

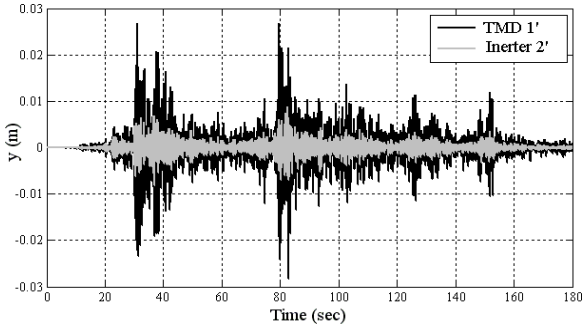


Figure 19 Control system displacement time history (new y -DOF)

4. CONCLUSIONS

This paper introduced a new type of control system to be used for the control of seismically excited structures. The proposed systems are based on a new device, called an inerter that has been successfully installed in high performance car suspension systems, mainly in the Formula 1 industry. We have chosen four design layouts comprising of inerters mounted in series and/or parallel with springs and dampers. The performance of the newly introduced device has been compared with that of two reference mass-based systems, a classical TMD and a TMD having an extra spring component. All systems have been subjected to a seismic record from the Tohoku Earthquake.

We have firstly considered a one-DOF structural system. Given the mass-capacitor equivalence and the obvious similarities between a mass element and an inerter, the tuning of the inerter-based systems was done using the well know TMD tuning rules, adapted for base-excited structures. We have evaluated the influence of each of the six layouts on the frequency response of the system. Since inerters can display very high mass ratios with respect to their actual mass, we have initially chosen $\mu_b = 0.7$, which is still a small mass ratio for an inerter device, and $\mu_m = 0.1$, the latter being considered the maximum TMD mass ratio. Results revealed that the best performing inerter-based systems are Inerter 1 and Inerter 2. A more in depth analysis has been carried out on these systems and their performance has been compared to that of the traditional TMD 1 system. We have shown that even for equal mass ratios $\mu_m = \mu_b = 0.1$, the inerter-based systems have better performance. Moreover, in the case when an earthquake load is applied, TMD 1 creates a dangerous new low resonant frequency, which is prone to being excited by the seismic action. Hence, the TMD controlled system doesn't change the performance of the uncontrolled system significantly. The inerter-based systems improve the uncontrolled system response.

We have also presented results for a two-DOF system. In this case we have only analyzed the behaviour of one of the best performing systems in the one-DOF case, Inerter 2'. This has been compared with the response obtained using a classical TMD located at the top of the structure (TMD 1'). It has been shown that the inerter-based system has better frequency response. Moreover, the structural displacements were improved when the structure was subjected to the Tohoku Earthquake record. The inerter-based control ensemble has smaller displacement than the TMD. Therefore the inerter-based system has a good performance in the case of two-DOF structures, superior to that of a classical TMD.

The inerter represents a promising feasible solution for the control of seismically excited structures. In future work, we will evaluate the performance of inerters that are mounted in series and/or parallel with semi-active devices, such as MR dampers. Another promising research direction is represented by the introduction of variable inertance devices (e.g. by using a clutch). Moreover, the inerter-based systems have smaller overall displacement and represent a good solution for problems related to installation, costs, space and aesthetics.

Acknowledgements:
Irina F. Lazar is funded by a University of Bristol Studentship.

References:

Soong, T.T., and Spencer B.F. Jr. (2002), "Supplemental Energy Dissipation: State-of-the-Art and State-of-the-Practice", *Journal of Engineering Structures*, **24**, 243-259.

Soong, T.T., and Cimellaro G.P. (2009), "Future Directions in Structural Control", *Journal of Structural Health Monitoring*, **16**, 7-16.

Wagg, D,J., and Neild S.A. (2011), "A Review on Nonlinear Structural Control Techniques", *Proceedings of the Institution of Mechanical Engineers*, **225**(C4), 759-770.

Preumont, A. (2011), "Vibration Control of Active Structures,"

Springer Verlag.
Wagg, D.J. and Neild, S.A. (2009), "Nonlinear Vibration with Control," John Wiley & Sons.
Soong, T.T. and Dargush, G.F. (1997), "Passive Energy Dissipation Systems in Structural Engineering," John Wiley & Sons.
Smith, M.C., (2002), "Synthesis of Mechanical Networks: The Inerter," *IEEE Transactions on Automatic Control*, **47**(10), 1648-1662.
Chen M.Z.Q, Papageorgiu F., Sheibe F., Wang F. and Smith M.C., (2009), "The Missing Mechanical Circuit", *IEEE Circuits and Systems Magazine*, **1531-636X**, 10-26.
Wang , F-C., Hong M-F., and Lin, T-C. (2010), "Designing and Testing a Hydraulic Inerter", *Proceedings of the Institution of Mechanical Engineers Part C: Journal of Mechanical Engineering Science*, **225**, 66-72.
Wang, F-C., and Chan H-A. (2011), "Vehicle Suspensions with a Mechatronic Network Strut", *International Journal of Vehicle Mechanics and Mobility*,, **49**(5), 811-831.
Papageorgiu C., and Smith M.C., (2009a), "Laboratory Experimental Testing of Inerters", 44th *IEEE Conference on Decision and Control* .
Papageorgiu C., Houghton N.E. and Smith M.C., (2009b), "Experimental Testing and Analysis of Inerters", *Journal of Dynamic Systems, Measurement and Control*, **131** .
Kuznetsov, A., Mammadov, M., and Sultan, I. and Hajilarov E. (2010), "Optimization of Improved Suspension System with Inerter Device of the Quarter-Car Model in Vibration Analysis," *Arch Applied Mechanics*, **81**, 1427-1437
Sheibe, F., and Smith MC. (2009), "Analytical Solutions for Optimal Ride Comfort and Tire Grip for Passive Vechicle Susspension", *Journal of Vehicle System Dynamics*, **47**(10), 1229-1252.
Smith, MC., and Wang F-C. (2004), "Performance Benefits in Passive Vehicle Suspensions Employing Inerters", *Journal of Vehicle System Dynamics*, **42**(4), 235-257.
Wang, F-C., and Su W-J. (2008a), "Impact on Inerter Nonlinearities on Vehicle Suspension Control", *International Journal of Vechicle Mechanics and Mobility*, **46**(7), 575-595.
Wang, F-C., and Su W-J. (2008b), "Inerter Nonlinearities and the Impact on Suspension Control", *Proceedings of the American Control Conference* , Seattle, Washington, USA
Wang, F-C., Liao M-K., Liao B-H., Su W-J. and Chan H-A. (2009a), "The Performance Improvements of Train Suspension Systems with Mechanical Networks Employing Inerters", *International Journal of Vehicle Mechanics and Mobility*, **47**(7), 805-830.
Wang, F-C., and Liao M-K., (2010), "The Lateral Performance of Train Suspension Systems Employing Inerters", *International Journal of Vehicle Mechanics and Mobility*, **48**(5), 619-643.
Evangelou, S., Limebeer D.J.N., Sharp R.S., and Smith M.C., (2007), "Mechanical Steering Compensators for High-Performance Motorcycles", *Transactions Of the ASME*, **74**, 332-346.
Wang , F-C., Chen, C.-W., Liao M-K. and Hong M-F., (2007), "Performance Analyses of Buildings Suspension Control with Inerters," *Proceedings of the 46 IEEE Conference on Decision and Control*, New Orleans, LA, USA
Wang , F-C., Hong M-F., and Chen, C.-W. (2009b), "Building Suspensions with Inerters," *Proceedings of IMech Vol. 224 Part C: Journal of Mechanical Engineering Science.*
Zhang, X-J., Achmadian M., and Guo, K-H. (2012), "On the Benefits of Semi-Active Suspensions with Inerters," *Journal of Shock and Vibration*, **19**, 257-272.
Den Hartog, J.P. (1940), "Mechanical Vibrations," McGraw Hill.

10CUEE CONFERENCE PROCEEDINGS
10th International Conference on Urban Earthquake Engineering
March 1-2, 2013, Tokyo Institute of Technology, Tokyo, Japan

SEISMIC POUNDING OF BASE-ISOLATED BUILDINGS UNDER BIDIRECTIONAL EXCITATION

Deepak R. Pant[1] and Anil C. Wijeyewickrema[2]

1) Graduate Student, Department of Civil and Environmental Engineering, Tokyo Institute of Technology, Japan
2) Associate Professor, Department of Civil and Environmental Engineering, Tokyo Institute of Technology, Japan
pant.d.aa@m.titech.ac.jp, wijeyewickrema.a.aa@m.titech.ac.jp

Abstract: The effects of seismic pounding on the response of a four-story base-isolated reinforced concrete (RC) building subjected to bidirectional excitation are investigated. Three-dimensional nonlinear finite element analyses are carried out, where a new contact element capable of simulating pounding including friction, is utilized. Performance of the building is evaluated separately for the subsets of far-fault non-pulse-like ground motions and near-fault pulse-like ground motions, which are scaled to represent two levels of shaking viz. the design earthquake (DE) level and the risk-targeted maximum considered earthquake (MCE_R) level. Nonlinear time-history analyses are carried out considering lower bound as well as upper bound properties of isolators. It is found that if pounding is avoided, performance of the building is satisfactory under DE-level motions and MCE_R-level far-fault motions, while unacceptably large demands are imposed by MCE_R-level near-fault motions. Seismic pounding under MCE_R-level near-fault motions is found to be detrimental, where the effect of pounding is mostly concentrated at the first story.

1. INTRODUCTION

Seismic pounding of base-isolated buildings with adjacent structures is likely under near-fault ground motions containing long-period pulses. Several previous studies have been carried out to investigate the effects of seismic pounding on base-isolated buildings. (Hall et al. 1995, FEMA 2009, Matsagar and Jangid 2010, Polycarpou and Komodromos 2010, Pant and Wijeyewickrema 2012, and Masroor and Mosqueda 2012). Previous studies indicate that the response of base-isolated buildings can be substantially influenced by seismic pounding. However, except the work by Matsagar and Jangid (2010), other studies on seismic pounding of base-isolated buildings have been carried out considering only one component of horizontal excitation. Matsagar and Jangid (2010) investigated seismic pounding of a single-story structure under bidirectional horizontal excitation by neglecting friction, using a shear-building idealization, and considering linear elastic behavior of the superstructure.

The effect of bidirectional horizontal excitation on base-isolated buildings is an important issue and has been mostly studied in the past without considering seismic pounding (see for example Jangid and Kelly 2001, Tena-Colunga and Pérez -Osornio 2006, Ozdemir and Constantinou 2010, and Erduran et al. 2011). While most of these previous studies focused on the response of the isolation system by adopting rigid or linear elastic models for the superstructure, the study by Erduran et al. (2011) focused on the multi-level seismic response of a *steel* superstructure through three-dimensional models considering nonlinear behavior of the superstructure as well as the isolation system. Multi-level seismic response evaluation is important in performance-based earthquake engineering. In addition, two levels of excitations are explicitly considered for the design of seismically isolated buildings, where the superstructure is designed for the forces associated with design earthquake (DE) and the isolation system is designed for the effects of risk-targeted maximum considered earthquake (MCE_R) (BSSC 2009 and ASCE 2010). None of the previous studies have investigated multi-level seismic performance of base-isolated *reinforced concrete (RC)* buildings under bidirectional horizontal excitation considering nonlinear behavior of the superstructure as well as the isolation system.

In the present study, the response of a typical four-story base-isolated RC building, under bidirectional excitation is evaluated with the objectives to investigate (i) multi-level seismic performance considering bounding values of isolator properties and (ii) influence of seismic pounding. A three-dimensional finite element (FE) model of the building is created considering material and geometric nonlinearities. A new contact element is developed and utilized to simulate seismic pounding of the building with the retaining wall at the base. A set of 40 pairs of ground motions containing far-fault non-pulse-like motions and near-fault pulse-like motions is considered. Scaled earthquakes are employed to represent both the DE and MCE_R.

2. METHODOLOGY OF SEISMIC POUNDING SIMULATION

In the present study, a previously developed modified Kelvin-Voigt model for pounding without friction (Pant et al. 2010 and Pant and Wijeyewickrema 2012) has been extended based on the models proposed by Zhu et al. (2002) and Guo et al. (2011) to simulate pounding with friction, specifically that of a base-isolated building with the retaining wall at the base. This new model has been used to develop a contact element, which is then implemented in OpenSees (2012). The underlying assumptions for the development of the new element are (i) base slab has in-plane rigidity and (ii) retaining wall behaves rigidly under earthquake ground motions. Due to these assumptions (i) the use of contact elements only at the corner nodes of the base slab becomes adequate and (ii) the contact condition depends only on base displacement. The contact element is used as a zero-length element between the slab corner node i and a fully-restrained fictitious node i'. The response of the element does not depend on the position of node i relative to node i' and the orientation vector of the element is set such that the local x- and y-directions of the element coincide with the normal and tangential directions to the target surface (i.e., the retaining wall), respectively. It is noted that though the focus of the present study is on symmetric structures, this contact element is capable of simulating pounding in asymmetric structures as well. Consider an instance where one corner of the base slab has a potential of pounding with the retaining wall along the positive X-direction as shown in Fig. 1. Note that the expressions presented herein are derived for one contact element, and in base-isolated buildings, a pair of such contact elements is necessary at each corner of the base slab to simulate pounding with the retaining wall in two orthogonal horizontal directions. The impact force in the direction normal to the target surface F_n is given by,

$$F_n = \begin{cases} F_{sn} + F_{dn} & u_X^i > d_g \text{ and } \dot{u}_X^i > 0 \\ F_{sn} & u_X^i > d_g \text{ and } \dot{u}_X^i \le 0 \\ 0 & u_X^i \le d_g \end{cases}, \qquad (1)$$

where F_{sn} and F_{dn} are forces analogous to the spring and dashpot forces, respectively in normal direction, where $|F_{sn}| = k_n |u_X^i - d_g|$ and $|F_{dn}| = c_n |\dot{u}_X^i|$, where k_n is element stiffness in normal direction, u_X^i and $\dot{u}_X^i$ are displacement and velocity, respectively of node i in X-direction, d_g is separation distance between the building and the retaining wall, and damping coefficient in normal direction c_n is expressed as,

$$c_n = \frac{3k_n(1-r_n^2)}{2|\dot{u}_{X0}^i| r_n^2} |u_X^i - d_g|, \qquad (2)$$

where r_n is coefficient of restitution in normal direction and $\dot{u}_{X0}^i$ is velocity of node i in X-direction at the instance of time immediately prior to impact. The impact force in tangential direction F_t is given by,

$$F_t = \begin{cases} F_{st} + F_{dt} & u_X^i > d_g,\ |F_t| \le \mu_s |F_n| \\ F_f & u_X^i > d_g,\ |F_t| > \mu_s |F_n| \\ 0 & u_X^i \le d_g \end{cases}, \qquad (3)$$

where F_{st}, F_{dt}, and F_f are forces analogous to the spring, dashpot, and frictional forces, respectively in tangential direction, where $|F_{st}| = k_t |u_Y^i - u_{Y0}^i|$, $|F_{dt}| = c_t |\dot{u}_Y^i|$, and $|F_f| = \mu_k |F_n|$, where k_t is element stiffness in tangential direction, u_Y^i and $\dot{u}_Y^i$ are displacement and velocity, respectively of node i in Y-direction, u_{Y0}^i is displacement of node i in Y-direction at the instance of time immediately prior to impact, μ_s and μ_k are coefficients of static and kinetic friction, respectively, and c_t is damping coefficient in tangential direction. It is customary to assume that the expression for c_t follows the same pattern as that of c_n (see Zhu et al. 2002 and Guo et al. 2011) and is given as,

$$c_t = \frac{3k_t(1-r_t^2)}{2|\dot{u}_{Y0}^i| r_t^2} |u_Y^i - u_{Y0}^i|, \qquad (4)$$

where r_t is coefficient of restitution in tangential direction and $\dot{u}_{Y0}^i$ is velocity of node i in Y-direction at the instance of time immediately prior to impact. Sign convention for the forces analogous to the spring, dashpot, and frictional forces (if applicable) is such that they are always negative (i.e., compressive forces) in the normal direction, while they could be positive or negative in the tangential direction depending on the orientation of the contact element in the tangential direction as well as the movement of the node i with respect to the point of first impact on the retaining wall.

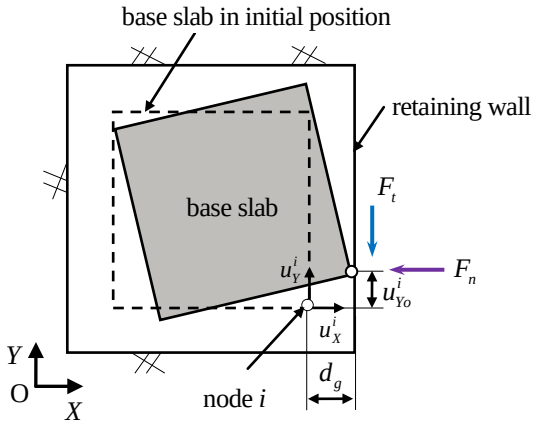


Fig. 1. Illustration of impact between base slab and retaining wall.

3. BUILDING DESCRIPTION AND DESIGN

A four-story, three-bay by three-bay base-isolated RC moment-frame building was chosen as a typical building (Fig. 2). The retaining wall extends from ground level up to the base level of the building. The bay width of the building in both directions is 6.0 m. The story height of the building is 4.0 m, except for the first story which is 4.5 m high. The building was designed by the ELF procedure, following the provisions of 2012 International Building Code (ICC 2012), ASCE 7-10 (ASCE 2010), and ACI 318-11 (ACI 2011). The building was assumed to be located on a stiff soil site (site class D) and was intended to be used as an office building (risk category II). The mapped MCE_R spectral response acceleration parameters are $S_s = 1.609g$ and $S_1 = 0.593g$ at short periods and 1 s period, respectively. The compressive strength of concrete is 28 MPa, and the yield strengths of main steel reinforcement bars and ties are 420 MPa and 300 MPa, respectively. Dead load consists of member self-weight, and 7.6 kN/m and 6.8 kN/m loads due to partitions and external cladding on base beams and upper floor beams, respectively. Live loads on floor and roof slabs were assumed to be 4.8 kPa and 1.0 kPa, respectively. Total seismic weight of the building $W = 21{,}809$ kN.

A lead rubber bearing (LRB) isolation system was designed for the building where typical bounding values of isolation system parameters shown in Table 1 were considered (Constantinou et al. 1999, Naeim and Kelly 1999, and Pavlou 2005). Identical 650 mm diameter circular bearings having a lead core of 113 mm diameter were provided under each of the sixteen column bases. Each bearing consists of forty seven 5 mm thick rubber layers alternating with 2 mm thick steel shims. Based on lower bound properties of isolators, for the isolation system at DE (MCE_R) effective period $T_D = 2.24$ s ($T_M = 2.53$ s), effective damping $\beta_D = 27.2\%$ ($\beta_M = 18.8\%$), isolator displacement $D_D = 201$ mm ($D_M = 383$ mm), and total displacement $D_{TD} = 231$ mm ($D_{TM} = 440$ mm).

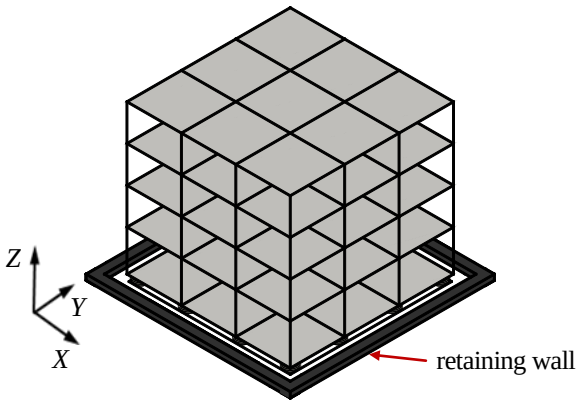


Fig. 2. The four-story building considered in the present study.

Table 1. Bounding values of the parameters for the isolation system.

	Lower bound	Upper bound
Rubber shear modulus G (MPa)	0.44	0.6
Lead stiffening factor f_L	0.95	1.05
Lead yield stress σ_{YL} (MPa)	10	12

4. NUMERICAL MODELING

Three-dimensional FE modeling was carried out using OpenSees (2012). Beams and columns were modeled using force-based, Euler-Bernoulli fiber beam-column elements that account for the spread of inelasticity along the length of the element. A section discretized into unconfined concrete, confined concrete, and steel fibers is located at each integration point in the element. In this study five Gauss-Lobatto integration points were taken per element. Uniaxial material models with nonlinear constitutive relationship were assigned to the fibers. The section response is derived through the integration of uniaxial responses of the fibers. For concrete, the modified Kent and Park model (Park et al. 1982) was used in compression and an initial linear elastic branch together with a linear softening branch up to zero stress was used in tension. The model of Yassin (1994) was used to account for concrete damage and hysteresis. For reinforcing steel, the constitutive model of Menegotto and Pinto (1973), with a strain-hardening ratio of 1% was used. In this study 2% stiffness-proportional damping, where the damping coefficient was calculated from the fixed-base frequency of the superstructure, was applied to the superstructure. In-plane stiffness of slabs was accounted for by using rigid truss elements connecting two ends of each beam element and opposite corners of each slab of every bay, while out-of-plane stiffness was neglected.

Lead rubber bearings were modeled using elastomeric bearing elements. A coupled plasticity model, with a circular yield surface is used for bidirectional lateral response of these elements (Huang 2002). Parameters of the coupled plasticity model are based on a bilinear force-deformation relationship. Here, for the lower bound properties (upper bound properties), initial stiffness $K_1 =$ 5,945.5 kN/m (8,858.7 kN/m), yield force $F_y =$ 111.4 kN (133.7 kN) and $\alpha = K_2/K_1 =$ 0.1, where K_2 is the post-elastic stiffness.

A pair of the new contact elements (see Section 2) was used at each corner of the base slab to simulate pounding with the retaining wall in two orthogonal horizontal directions. The parameters of each contact element computed based on previous studies (Zhu et al. 2002, Guo et al. 2011, and Pant and Wijeyewickrema 2012) are $k_n = k_t = 2{,}500$ MN/m, $r_n = r_t = 0.65$, $\mu_s = 0.5$, and $\mu_k = 0.4$.

5. SELECTION AND SCALING OF GROUND MOTIONS

Two subsets of earthquake ground motions were taken from the Pacific Earthquake Engineering Research Center database (PEER 2011) viz. subset 1 containing 20 pairs of far-fault non-pulse-like motions (Table 2) and subset 2 containing 20 pairs of near-fault pulse-like motions (Table 3). The ground motions had been rotated to fault-normal (FN) and fault-parallel (FP) components. Pulse-like nature of a ground motion was identified using the method proposed by Baker (2007).

Selection and scaling was accomplished using the interactive web interface of the PEER database (PEER 2011), where the ground motion pairs with geometric mean spectrum of two horizontal components that are most similar in shape to the target spectrum in the desired period range are selected and subsequently linear amplitude scaled. The ground motions were first selected and scaled to the MCE_R level such that the mean of the 5%-damped geometric mean spectrum of two components of ground motion pairs closely matches the 5%-damped target spectrum in the period range of 0.75 s to 5 s, which covers the recommended range of $0.5T_D$ to $1.25T_M$ by ASCE 7-10 (ASCE 2010). The acceleration time-histories of records scaled to represent MCE_R were then multiplied by $2/3$ to obtain the records representing DE.

6. ANALYSIS RESULTS

Nonlinear time-history analyses were carried out first by assuming that a sufficient separation distance d_g is available between the building and the retaining wall such that pounding does not occur, and then by setting the separation distance d_g equal to the total maximum displacement of the isolation system $D_{TM} = 440$ mm, to investigate the effects of seismic pounding. Fault-normal (FN) and fault-parallel (FP) components of ground motions correspond to X-direction and Y-direction, respectively. The numerical models with lower bound and upper bound properties of isolators are referred to as lower bound model and upper bound model, respectively.

Peak response indicators are presented as the mean values from time-history analysis for all the ground motions in each subset of ground motions. Superstructure response is discussed in terms of mean values of peak inter-story drift ratio, peak column curvature ductility, peak normalized story shear force, and peak absolute floor acceleration. The story shear force was normalized by the seismic weight W. Peak inter-story drift ratio is presented for both X- and Y-directions. Since mean values of X-direction response indicators were found to be larger than those of Y-direction, column curvature ductility and normalized story shear forces are presented only for the X-direction. Floor accelerations are presented as resultant of the demands in two orthogonal directions. In this study, peak inter-story drift ratios in the ranges of 0.2–0.5%, 0.5–1.5%, and 1.5–3% correspond to damage of drift-sensitive nonstructural components, moderate structural damage, and severe structural damage, respectively (Elnashai and Sarno 2008). Peak inter-story drift ratios greater than 3% can be assumed to correspond to a collapsed story.

Table 2. *Far-fault* ground motions scaled to represent MCE_R.

EQ No.	Event	Year	Station	M_W	Scale factor
1	Tabas, Iran	1978	Dayhook	7.4	3.8
2	Imperial Valley	1979	Delta	6.5	2.4
3	Imperial Valley	1979	Array #12	6.5	4.0
4	Superstition Hills	1987	Westmorland	6.5	2.8
5	Superstition Hills	1987	Wildlife Liquef. Array	6.5	2.2
6	Loma Prieta	1989	Dumbarton Bridge	6.9	3.9
7	Loma Prieta	1989	Hollister	6.9	1.8
8	Loma Prieta	1989	Hollister DA	6.9	2.4
9	Chi-Chi, Taiwan	1999	TCU116	7.6	2.0
10	Landers	1992	Amboy	7.3	4.0
11	Landers	1992	San Bernardino	7.3	4.0
12	Kobe, Japan	1995	OSAJ	6.9	4.0
13	Kocaeli, Turkey	1999	Bursa Tofas	7.5	4.0
14	Chi-Chi, Taiwan	1999	CHY015	7.6	3.0
15	Chi-Chi, Taiwan	1999	CHY029	7.6	2.4
16	Chi-Chi, Taiwan	1999	CHY046	7.6	3.6
17	Chi-Chi, Taiwan	1999	CHY088	7.6	4.0
18	Hector Mine	1999	Amboy	7.1	3.1
19	Hector Mine	1999	Indio	7.1	4.0
20	Hector Mine	1999	Mecca	7.1	4.0

Table 3. *Near-fault* ground motions scaled to represent MCE_R.

EQ No.	Event	Year	Station	M_W	Scale factor
1	Imperial Valley	1979	Array #4	6.5	1.7
2	Imperial Valley	1979	Array #7	6.5	1.3
3	Imperial Valley	1979	Array #8	6.5	2.0
4	Imperial Valley	1979	El Centro DA	6.5	1.9
5	Loma Prieta	1989	LGPC	6.9	1.0
6	Loma Prieta	1989	Saratoga	6.9	2.2
7	Erzican, Turkey	1992	Erzincan	6.7	1.4
8	Cape Mendocino	1992	Cape Mendocino	7.0	1.9
9	Cape Mendocino	1992	Petrolia	7.0	1.6
10	Northridge	1994	JFPG	6.7	1.3
11	Northridge	1994	LA Dam	6.7	1.6
12	Northridge	1994	Newhall	6.7	1.2
13	Northridge	1994	Rinaldi	6.7	1.1
14	Kocaeli, Turkey	1999	Yarimca	7.5	1.4
15	Chi-Chi, Taiwan	1999	TCU049	7.6	2.5
16	Chi-Chi, Taiwan	1999	TCU053	7.6	3.2
17	Chi-Chi, Taiwan	1999	TCU065	7.6	0.8
18	Chi-Chi, Taiwan	1999	TCU076	7.6	1.8
19	Duzce, Turkey	1999	Duzce	7.1	1.3
20	Denali, Alaska	2002	TAPS PS #10	7.9	1.1

6.1 Superstructure Response without Considering Pounding

When pounding was not considered in the analysis, under DE-level ground motions, as expected, the superstructure response is governed by the upper bound model, where larger forces are transmitted to the superstructure compared with the lower bound model (Fig. 3). Under DE-level far-fault motions, the peak inter-story drift ratio is very small and reaches a maximum value of 0.25% at the second story in X-direction, indicating no structural damage to the building (Fig. 3(a) and (b)). Column curvature ductilities are less than one indicating that yielding of columns does not occur in any story (Fig. 3(c)). Maximum superstructure base shear force is about $0.15W$, which is half of the base shear capacity of $0.3W$, predicted based on the pushover analysis (Fig. 3(d)). Maximum floor acceleration is $0.42g$ at the roof level (Fig. 3(e)), which is slightly higher than the limit of $0.35g$ often exercised in the design of seismically isolated buildings. Under DE-level near-fault motions maximum drift is 0.36% in X-direction and column curvature ductilities and superstructure base shear force remain small (Fig. 3(f)–(i)). Effect of near-fault motions is more pronounced in lower stories. Furthermore, peak roof-level acceleration under near-fault motions is nearly the same as that under far-fault motions (Fig. 3(j)).

Under MCE_R-level ground motions the superstructure response is also governed by the upper bound model, similar to the case of DE-level ground motions (Fig. 4). For MCE_R-level far-fault motions, the peak inter-story drift ratio is 0.57%, the maximum at the first story which then gradually reduces at upper stories (Fig. 4(a) and (b)). This indicates some moderate structural damage to the building at the first story. Compatible with the drift is the peak column curvature ductility which is 2.3 at the first story and remains less than one at upper stories (Fig. 4(c)). Superstructure base shear force is much less than the capacity (Fig. 4(d)). Maximum floor acceleration is $0.5g$ at the roof level (Fig. 4(e)). Peak inter-story drift ratio under MCE_R-level near-fault motions is 2.4% at the first story, 0.59% at the second story, and then gradually reduces at upper stories (Fig. 4(f) and (g)). The demand at the first story is unacceptably large and shows 321% larger drift compared with the drift under corresponding far-fault motions. Column curvature ductility also indicates extensive yielding of columns in the first story and some minor yielding in the second story, while upper story columns remain elastic (Fig. 4(h)). Superstructure base shear force reaches a value of $0.26W$ but is still less than the capacity (Fig. 4(i)). The maximum floor acceleration which is observed at the roof level is the same as that observed under far-fault motions (Fig. 4(j)).

6.2 Superstructure Response Considering Pounding

When the retaining wall is located at a separation distance $d_g = D_{TM}$, DE-level far-fault motions do not induce pounding, while only 2 of the DE-level near-fault motions induce pounding. Therefore, the effect of pounding on all the superstructure response indicators, except the floor accelerations was found to be negligible for DE-level motions. Under MCE_R-level far-fault motions, inter-story drift ratios using lower bound model are slightly increased due to pounding but are still less than the drifts using upper bound model which are negligibly influenced due to pounding (Fig. 5(a)). Drift response predictions

using lower and upper bound models have become very close compared with the no-pounding case (Fig. 5(a) and (b)). Similar is the case for column curvature ductilities and story shear forces (Fig. 5(c) and (d)). This also highlights the benefits of conducting a bounding analysis, where even neglecting the pounding could provide conservative estimates of drifts, ductilities, and shear forces. However, this is not true for floor accelerations, which show a maximum value of 2.3*g* at the base level using lower bound model, which is much larger than that obtained using upper bound model and marks a substantial increase due to pounding (Fig. 5(e)).

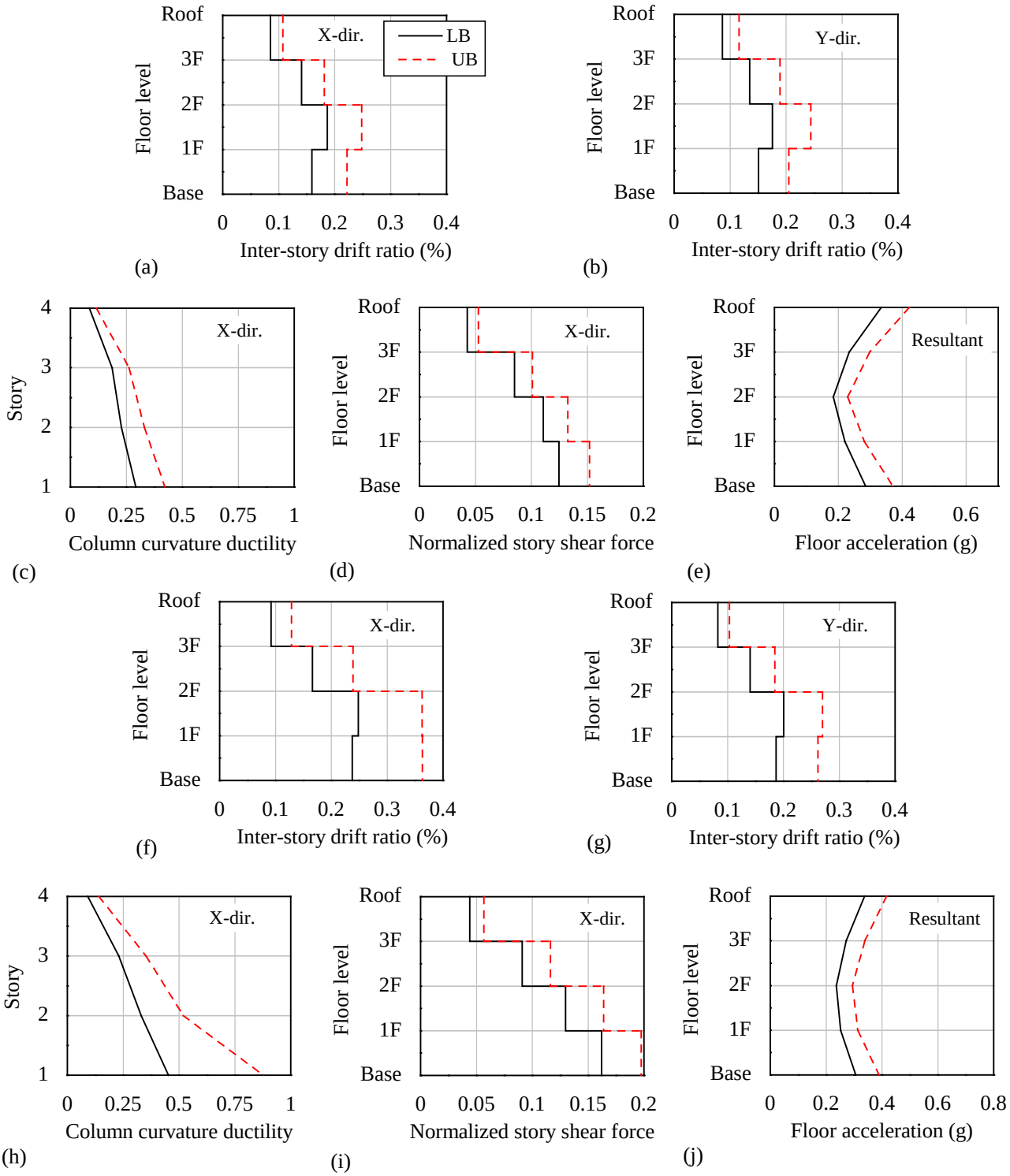


Fig. 3. Mean values of superstructure response indicators for DE-level ground motions without considering pounding: (a)–(e) far-fault and (f)–(j) near-fault.

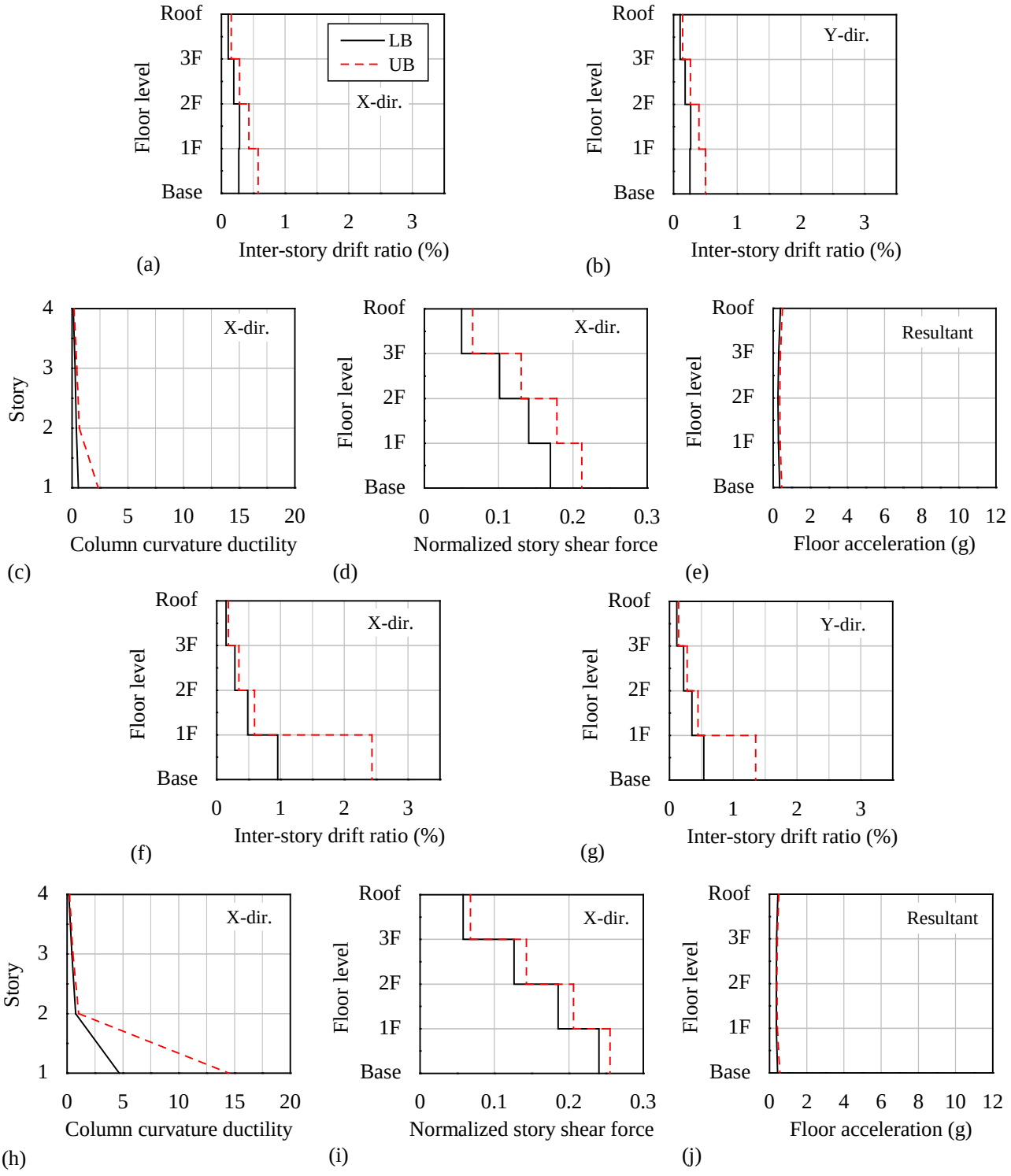


Fig. 4. Mean values of superstructure response indicators for MCE_R-level ground motions without considering pounding: (a)–(e) far-fault and (f)–(j) near-fault.

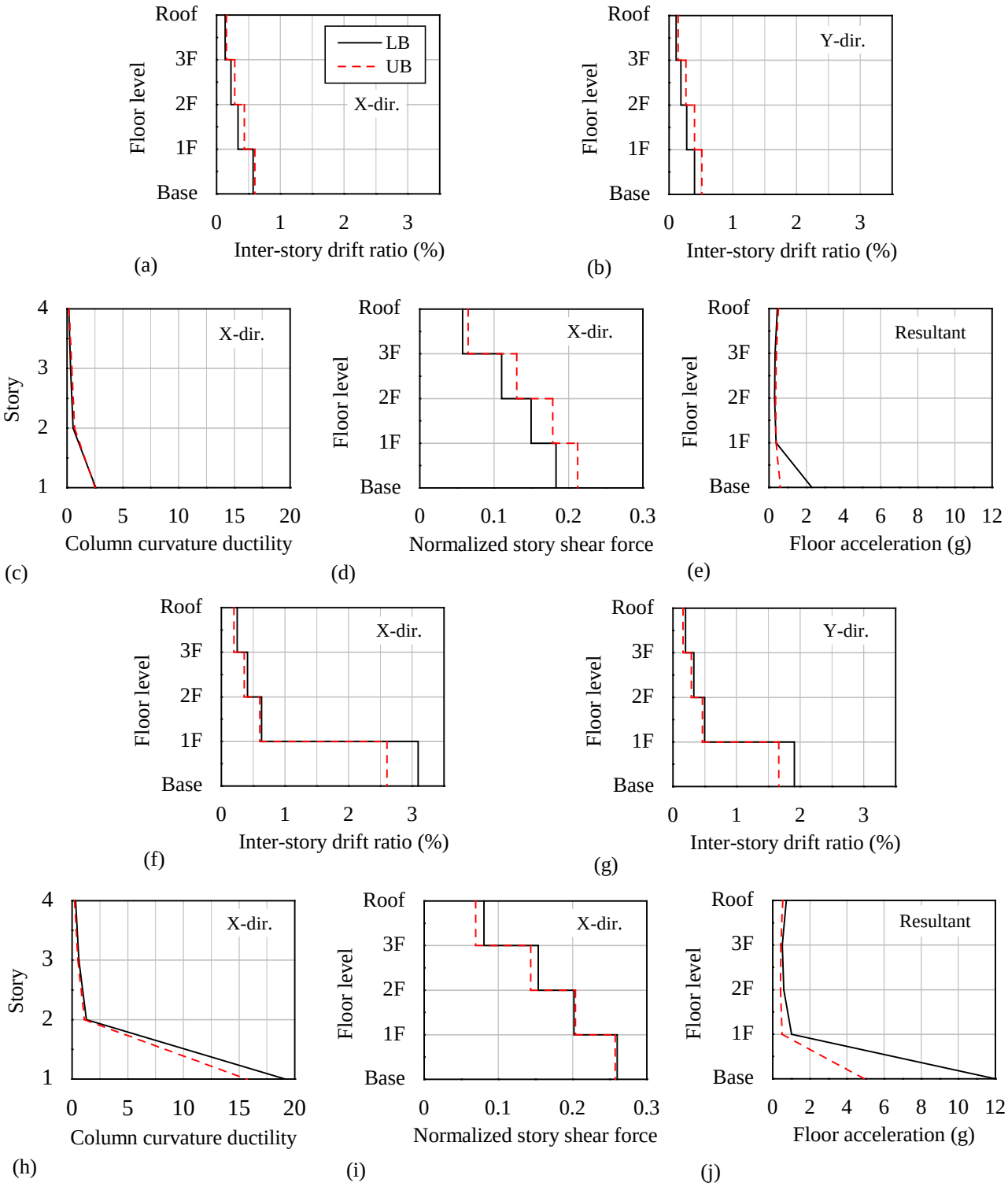


Fig. 5. Mean values of superstructure response indicators for MCE_R-level ground motions considering pounding at $d_g = D_{TM}$: (a)–(e) far-fault and (f)–(j) near-fault.

Significant influence of pounding is observed under MCE_R-level near-fault motions. Considering lower bound model, the inter-story drift ratio at the first story in X-direction has increased from 0.96% to 3.1% (Fig. 5(f)) due to pounding, indicating remarkable three-fold increase. As expected, the drift demands using upper bound model are not much influenced due to pounding and in contrast to all the previous cases, the lower bound model governs the drift response (Fig. 5(f) and (g)). While building suffered severe structural damage when pounding was not considered, the drift ratio greater than 3% indicates imminent collapse of the first story due to pounding. Furthermore, extremely large column curvature ductilities at the first story are also observed with a maximum value of 19 (Fig. 5(h)). Story shear forces are also increased due to pounding but the increase is not as severe as the increase in drifts, and the superstructure base shear force is below the capacity of $0.3\,W$ (Fig. 5(i)). This indicates that the predominant mode of failure due to pounding is flexural. Dramatic increase only in the base-level acceleration is observed due to pounding, where a maximum value of $12g$ is resulted (Fig. 5(j)).

7. CONCLUDING REMARKS

Seismic performance of a typical four-story base-isolated RC building was investigated under bidirectional far-fault and near-fault ground motions scaled to represent DE and MCE_R. Seismic pounding of the building with the retaining wall at the base was simulated using a newly developed special purpose contact element. Bounding values of isolator properties were considered in the nonlinear time-history analyses. The main conclusions based on the mean values of response indicators are as follows:

(1) Floor accelerations, which affect the building contents and nonstructural components, remain relatively low when pounding is not considered but may increase dramatically due to pounding.

(2) Regardless of whether pounding is considered or not, structural damage to the building does not occur under DE-level far-fault as well as near-fault motions, while some moderate structural damage is observed under MCE_R-level far-fault motions. This reveals the satisfactory performance of the base-isolated building, where superstructure remains essentially elastic under DE-level motions and some minor yielding occurs under MCE_R-level far-fault motions. However, the building experiences severe structural damage under MCE_R-level near-fault motions when pounding is not considered while pounding with the retaining wall at a separation distance equal to the total maximum displacement D_{TM} of the isolation system, initiates collapse. The predominant mode of structural failure when pounding is considered or not, is flexural and shear failure does not occur.

(3) The adverse effects of pounding are mostly concentrated in the immediate vicinity of impact i.e., at the first story.

(4) The superstructure response of the building is entirely governed by the upper bound properties of isolators when pounding is not considered. Considering pounding increases the dependence of the superstructure response on the lower bound properties of isolators, where in some instances the response is entirely governed by these properties.

Acknowledgements:

The first author is pleased to acknowledge a Monbukagakusho (Ministry of Education, Culture, Sports, Science and Technology, Japan) scholarship for graduate students. Financial support from Center for Urban Earthquake Engineering (CUEE), Tokyo Institute of Technology is gratefully acknowledged.

References:

American Concrete Institute (ACI) (2011), *Building Code Requirements for Structural Concrete, ACI 318-11*, Farmington Hills, MI.

American Society of Civil Engineers (ASCE) (2010), *Minimum Design Loads for Buildings and Other Structures, ASCE 7-10*, Reston, VA.

Baker, J.W. (2007), "Quantitative classification of near-fault ground motions using wavelet analysis", *Bulletin of the Seismological Society of America*, **97**(5)**,** 1486-1501.

Building Seismic Safety Council (BSSC) (2009), *NEHRP Recommended Seismic Provisions for New Buildings and Other Structures, FEMA-P750*, Washington, DC.

Constantinou, M.C., Tsopelas, P., Kasalanati, A., and Wolff, E.D. (1999), "Property modification factors for seismic isolation bearings", *Technical Report MCEER-99-0012*, University at Buffalo, State University of New York, NY.

Elnashai, A.S. and Sarno, L.D. (2008), "Fundamentals of Earthquake Engineering", Wiley: United Kingdom.

Erduran, E., Dao, N.D., and Ryan, K.L. (2011), "Comparative response assessment of minimally compliant low-rise conventional and base-isolated steel frames", *Earthquake Engineering and Structural Dynamics*, **40**(10)**,** 1123-1141.

Federal Emergency Management Agency (FEMA) (2009), *Quantification of Building Seismic Performance Factors, FEMA P695*, Washington, DC.

Guo, A., Li, Z., and Li, H. (2011), "Point-to-surface pounding of highway bridges with deck rotation subjected to bi-directional earthquake excitations", *Journal of Earthquake Engineering*, **15**(2)**,** 274-302.

Hall, J.F., Heaton, T.H., Halling, M.W., and Wald, D.J. (1995), "Near-source ground motion and its effects on flexible buildings", *Earthquake Spectra*, **11**(4)**,** 569-605.

Huang, W.H. (2002), "Bi-directional testing, modeling and system response of seismically isolated bridges", *Ph.D. Dissertation*, University of California, Berkeley, CA.

International Code Council (ICC) (2012), *International Building Code*, Country Club Hills, IL.

Jangid, R. and Kelly, J. (2001), "Base isolation for near-fault motions", *Earthquake Engineering and Structural Dynamics*, **30**(5)**,** 691-707.

Masroor, A. and Mosqueda, G. (2012), "Experimental simulation of base-isolated buildings pounding against moat wall and effects on superstructure response", *Earthquake Engineering and Structural Dynamics*, **41**(14)**,** 2093-2109.

Matsagar, V. and Jangid, R. (2010), "Impact response of torsionally coupled base-isolated structures", *Journal of Vibration and Control*, **16**(11)**,** 1623-1649.

Menegotto, M. and Pinto, P. (1973), "Methods of analysis for cyclically loaded R/C frames", *Symposium of Resistance and Ultimate Deformability of Structure Acted by Well Defined Repeated Load*, Lisbon, Portugal.

Naeim, F. and Kelly, J.M. (1999), "Design of Seismic Isolated Structures", Wiley: New York, NY.

Open system for earthquake engineering simulation (OpenSees) (2012), Computer Program, University of California, Berkeley, CA.

Ozdemir, G. and Constantinou, M.C. (2010), "Evaluation of equivalent lateral force procedure in estimating seismic isolator displacements", *Soil Dynamics and Earthquake Engineering*, **30**(10)**,** 1036-1042.

Pant, D.R. and Wijeyewickrema, A.C. (2012), "Structural performance of a base-isolated reinforced concrete building subjected to seismic pounding", *Earthquake Engineering and Structural Dynamics*, **41**(12)**,** 1709-1716.

Pant, D.R., Wijeyewickrema, A.C., and Ohmachi, T. (2010), "Three dimensional nonlinear analysis of seismic pounding between multi-story reinforced concrete buildings", *Seventh International Conference on Urban Earthquake Engineering (7CUEE) and Fifth International Conference on Earthquake Engineering (5ICEE)*, Tokyo, Japan, 1829-1840.

Park, R., Priestley, M.J.N., and Gill, W.D. (1982), "Ductility of square-confined concrete columns", *Journal of Structural Engineering (ASCE)*, **108**(4)**,** 929-950.

Pavlou, E.A. (2005), "Performance of primary and secondary systems in buildings with seismic protective systems", *Ph.D. Dissertation*, University at Buffalo, State University of New York, NY.

PEER (2011), Pacific Earthquake Engineering Research Center: Ground Motion Database-Beta Version.

Polycarpou, P.C. and Komodromos, P. (2010), "On poundings of a seismically isolated building with adjacent structures during strong earthquakes", *Earthquake Engineering and Structural Dynamics*, **39**(8)**,** 933-940.

Tena-Colunga, A. and Pérez -Osornio, M.A. (2006), "Design displacements for base isolators considering bidirectional seismic effects", *Earthquake Spectra*, **22**(3)**,** 803-825.

Yassin, M.H.M. (1994), "Nonlinear analysis of prestressed concrte structures under monotonic and cyclic loads", *Ph.D. Dissertation*, University of California, Berkeley, CA.

Zhu, P., Abe, M., and Fujino, Y. (2002), "Modelling three-dimensional non-linear seismic performance of elevated bridges with emphasis on pounding of girders", *Earthquake Engineering and Structural Dynamics*, **31**(11)**,** 1891-1913.

10CUEE CONFERENCE PROCEEDINGS
10th International Conference on Urban Earthquake Engineering
March 1-2, 2013, Tokyo Institute of Technology, Tokyo, Japan

REAL-TIME HYBRID TESTING OF A SMART BASE ISOLATION SYSTEM EMPLOYING A MAGNETORHEOLOGICAL DAMPER

Pei-Ching Chen[1], Keh-Chyuan Tsai[2], and Pei-Yang Lin[3]

1) Ph.D. Candidate, Department of Civil Engineering, National Taiwan University, Taiwan
2) Professor, Department of Civil Engineering, National Taiwan University, Taiwan
3) Researcher, National Center for Research on Earthquake Engineering, Taiwan
d96521014@ntu.edu.tw, kctsai@ntu.edu.tw, pylin@ncree.narl.org.tw

Abstract: A smart base isolation system is composed of conventional low-damping isolators and controllable damping devices such as magnetorheological (MR) dampers. The controllable damping devices provide additional damping to the structure and reduce the base drift without the accompanying acceleration increases if appropriate control algorithms for the dampers are adopted. In this paper, real-time hybrid testing of a smart base isolation system has been conducted. It is a base-isolated where the superstructure and the low-damping base isolator are numerically simulated and the MR damper is physically tested. The control voltage is computed by using a linear-quadratic controller or a fuzzy-logic controller and converted to a corresponding current sent to the MR damper. Meanwhile, the target displacement obtained from the step-by-step integration of the numerical substructure is imposed on the MR damper in a real-time manner. An adaptive phase-lead compensator is implemented to compensate the actuator delay and increase the accuracy of the test. Experimental results demonstrate the effectiveness of the smart base isolation system as well as the accuracy of each test which is investigated by the root mean square error and the tracking indicator. .

1. INTRODUCTION

A smart base isolation system is composed of conventional low-damping elastomeric bearings and controllable damping devices such as magnetorheological (MR) dampers (Ramallo et al. 2002). Compared with the passive damping devices, a smart base isolation system can reduce base drifts without the accompanying acceleration. Several control methodologies have been studied and implemented for the smart base isolation system such as sliding-mode control, clipped-optimal control, and fuzzy control. (Yang et al. 1996; Symans and Kelly 1999; Spencer et al. 2000).

Real-time hybrid testing, combining numerical simulation with experimental testing, provides an efficient method to evaluate the dynamic responses of rate-dependent structural systems subjected to earthquake excitation. During a real-time hybrid test, the target displacement is obtained using a step-by-step integration scheme and applied on the test specimen through servo-hydraulic actuators. The restoring force is measured from the test specimen and fed back to the integration algorithm to calculate the target displacement for the next time step. Real-time hybrid testing provides an alternative way to evaluate the seismic responses of structures subjected to earthquake ground motions. However, it is very challenging because there is a small but significant enough time delay between the command and the achieved displacements due to the dynamics of the servo-hydraulic systems (Dyke et al. 1995; Zhao et al. 2003). This time delay is often referred as actuator delay, which produces a negative damping effect and adds energy into a hybrid test (Horiuchi et al. 1999).

Various compensation methods have been developed and proposed to minimize the effects of actuator delay for real-time testing. Horiuchi et al. proposed two compensation schemes based on polynomial extrapolation and linear acceleration assumptions. Nakashima and Masaoka made use of interpolation schemes to refine the time stepping. Zhao et al. used a first-order phase-lead compensator to improve the tracking performance of a real-time hybrid test. Chen and Ricles simplified the dynamics of the servo-hydraulic as a first-order discrete transfer function and then performed the inverse compensation. Phillips and Spencer developed a model-based feedforward feedback control framework to achieve more accurate real-time hybrid testing. Chen and Tsai proposed an adaptive phase-lead compensator (PLC) which is formulated by using weighted linear extrapolation and the inverse model principle. The stability of the PLC is guaranteed as long as the selected weightings locate in the derived stable regions. In addition, the gradient adaptive law with instantaneous cost function is adopted to estimate the actuator delay online.

In this paper, real-time hybrid testing of a smart base isolation system has been conducted. The numerical model contains the superstructure, low-damping base isolator, and MR damper control algorithm. The hysteresis response of

the MR damper is identified and verified first. Then a linear-quadratic (LQ) controller and a fuzzy-logic controller (FLC) are designed for computing the control voltage which is sent to the physically tested MR damper in a real-time manner. The adaptive PLC, proposed by Chen and Tsai, is adopted to compensate the actuator delay to increase the accuracy during the test. The efficacy and feasibility of the compensation strategy for servo-hydraulic system and the controller for the MR damper are examined through several analytical simulations. Finally, the overall task is validated by conducting real-time hybrid tests of a smart base isolation system using a dynamic servo-hydraulic actuator. The performance of a real-time hybrid testing is evaluated by introducing the root mean square (RMS) error and the tracking indicator (TI) proposed by Mercan and Ricles.

2. SYSTEM IDENTIFICATION

An online identification proposed by Chassiakos et al. is used to identify the hysteresis response of the MR damper. It introduces a linear parameterized estimator to represent the Bouc-Wen model and then separates the responses and model parameters. The restoring force $F_{MR}(t)$ of MR damper simulated by using the Bouc-Wen model can be expressed as:

$$F_{MR}(t) = C(V)\dot{x}(t) + \upsilon(t)$$
$$\dot{\upsilon}(t) = A\dot{x}(t) + \beta\left|\dot{x}(t)\right|\left|\upsilon(t)\right|^{n-1}\upsilon(t) + \gamma\dot{x}(t)\left|\upsilon(t)\right|^{n} \quad (1)$$

where υ(t) is a hysteretic parameter that follows the differential equation in Eq. (1). A, β, γ and n are parameters that determine the scale, general shape, and smoothness of the hysteretic loop. The hysteretic model is parameterized linearly with respect to the coefficients A, β, and γ, but nonlinearly with respect to the power n. It is noted that most of the test facilities in the lab are running in digital form. The system identification experiments were conducted in discrete time with a sampling time Δt (50ms in the study). As a result, a discrete-time modified model considering the contribution of the power n to the response is adopted:

$$\upsilon[k+1] = \upsilon[k] + \Delta tA\dot{x}[k] + \Delta t\sum_{n=1}^{N}\kappa_n\left\{\beta\left|\dot{x}[k]\right|\left|\upsilon[k]\right|^{n-1}\upsilon[k] + \gamma\dot{x}[k]\left|\upsilon[k]\right|^{n}\right\} \quad (2)$$

where κ_n is the coefficient corresponding to the power of n. By separating the unknown parameters from the known signals, the parametric model of the estimator is constructed:

$$\tilde{\upsilon}[k+1] = \upsilon[k] + \theta_0[k+1]\dot{x}[k] + \sum_{n=1}^{N}\left\{\theta_{2n-1}[k+1]\left|\dot{x}[k]\right|\left|\upsilon[k]\right|^{n-1}\upsilon[k] + \theta_{2n}[k+1]\dot{x}[k]\left|\upsilon[k]\right|^{n}\right\}$$
$$= \upsilon[k] + \Phi^{T}[k]\Theta[k+1] \quad (3)$$

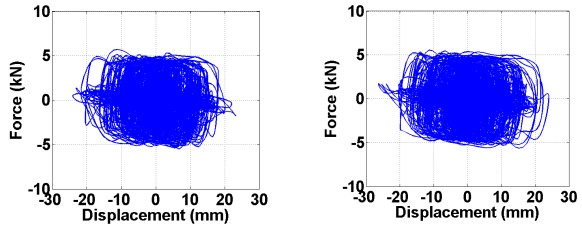
where N is a large enough integer and the coefficients θi [k], i=0,…2N are estimates at time step k of the corresponding coefficients from Eq. (2). The vector Φ[k] contains the known signals measured from the identification tests, and Θ[k+1] is a vector of the parameters estimated at time step k+1. Based on Eq. (3), the parameters of the MR damper can be identified. The detail of the identification method and application can be referred to Lin et al.

The MR damper employed in this study is made at the National Center for Research on Earthquake Engineering (NCREE) in Taiwan in 2005. Its maximum generated force and stroke are ±7kN and ±150mm, respectively. Three different approaches of performance tests have been conducted: (a) Sinusoidal displacement excitation with constant voltage input. Different excitation frequencies, strokes, and command voltages are tested; (b) Random displacement and constant voltage input. Different stroke levels and frequency contents of random excitations are tested with different constant command voltages; and (c) Random displacement and random voltage input. Both the displacement and command voltage are random. Each performance test was conducted for 120 seconds. It is noted that one set of model parameters can only represent the MR damper response under a specific command voltage. As a result, the nonlinear regression is used to get the model function corresponding to different command voltages. The Matlab function lsqcurvefit is used to solve nonlinear curve-fitting problems in least-squares sense. Finally, the identified Bouc-Wen model takes the form:

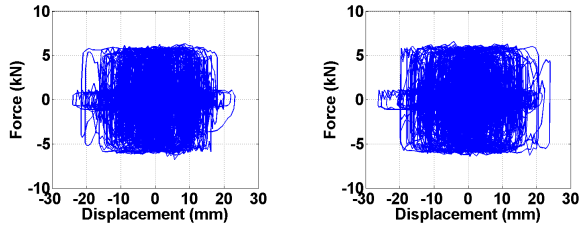
$$\tilde{F}_{MR}[k] = C(V[k])\dot{x}[k] + \upsilon[k]$$
$$\upsilon[k+1] = \upsilon[k] + \sum_{n=1}^{N}\theta_n(V[k])\phi_n[k]\Delta t \quad (4)$$

where θ_n is the identified parameters with respect to the power of n. The parameter $\tilde{F}_{MR}[k]$ is the identified generated force of the MR damper at the time step k. It is a function of control voltage V at each time step. The signal ϕ_n can be measured from the identification tests.

Two more performance tests are conducted to validate the mathematical model. The two input excitations are generated with a series of random displacements and random control voltage inputs for the MR damper in 60 seconds. The peak stroke for each test is 22mm with a frequency contents from 0.1Hz to 5Hz. The control voltages vary from 0V to 1.2V. Figure 1(a) and 1(b) show the hysteresis loops of the MR damper in the two performance tests and the identified Bouc-Wen model for the MR damper, respectively. It demonstrates that the identified model can predict the damper force fairly well. In addition, this mathematical model is approved to be stable in the two cases of performance tests. Figure 2(a) and 2(b) illustrate the time histories of the MR damper force from the identified model and measured from the two identification tests from 50 to 60 seconds. It appears that the global behavior of the MR damper can be captured by the numerical model. However, the force computed form the MR damper model is larger than the measured force from the test. The peak force of the numerical model is 20% larger than that of the test. It indicates that the seismic response of a smart base isolation system may not be accurately evaluated through numerical simulation. As a result, real-time hybrid testing becomes a necessity for investigating the behavior of a smart base isolation system.

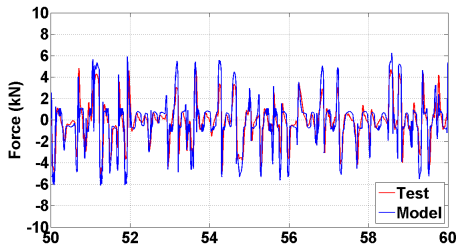


(a)

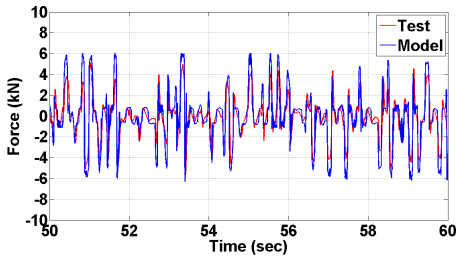


(b)

Figure 1 Hysteresis loops of the MR damper with random displacement and random voltage (a) experimental results (b) simulation results



(a)



(b)

Figure 2 Time histories of the MR damper force (a) test1 (b) test2

3. STRUCTURE MODEL

Consider a base-isolated building as shown in Figure 3, where the superstructure is modeled as a single degree-of-freedom (SDOF) system representing the one-story residential house. The mass, damping coefficient and the stiffness of the base isolation and the superstructure are mb, cb, kb and ms, cs, ks, respectively. The structural parameters of the SDOF fixed-base and 2DOF isolated structure models are given in Table 1. It is known that the linear behavior of low-damping rubber bearings can extend to shear strains above 100% and even 150%. Therefore, the isolation layer is modeled as a combination of linear stiffness and viscous damping with a fundamental period of 2.5 s period and a 2% of damping ratio. It is assumed that the nonlinear response of the superstructure can be neglected due to the moderate application of the base isolation system. In addition, the maximum generated force of the MR damper in the lab is 7kN. Therefore, the total mass of the base-isolated building is assumed to be 7000 N-s^2/m. In other words, the MR damper is assumed to be able to provide shear force up to 10% gravity force of the building.

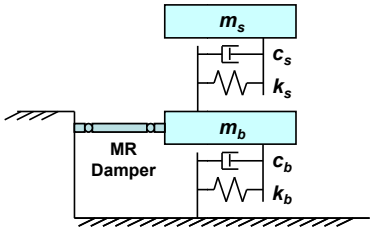


Figure 3 2DOF model of a smart structure adopted in the study

Table 1 Structural properties of the smart structure

Mass (N-s^2/m)	Damping Coefficient (N-s/m)	Stiffness (N/m)
Isolation Parameters		
3000	720	44600
Structure Parameters		
4000	3350	1754600

4. CONTROLLER FOR THE MR DAMPER

Various active control algorithms have been used to oppose earthquake excitations in numerical and experimental studies such as linear-quadratic regulator, modal control, and sliding mode control. In this paper, the state output-feedback linear-quadratic (LQ) control algorithm, and the fuzzy-logic control (FLC) algorithm are adopted.

4.1 Linear-quadratic Control

The equations of motion of the base-isolated system may be expressed as:

$$\mathbf{M}\ddot{\mathbf{u}}(t) + \mathbf{C}\dot{\mathbf{u}}(t) + \mathbf{K}\mathbf{u}(t) = \mathbf{\Lambda}F_{MR}(t) - \mathbf{M}\mathbf{l}\ddot{u}_g(t) \quad (5)$$

where $\mathbf{\Lambda}$ gives the position of the MR damper force; $\mathbf{l}$ is a vector whose elements are all unity; u_g is the ground displacement. The mass, damping, and stiffness matrices are represented as **M**, **C**, and **K**.

The state-space form of the equation of motion is given by:

$$\dot{\mathbf{x}}(t) = \mathbf{A}\mathbf{x}(t) + \mathbf{B}F_{MR}(t) + \mathbf{E}\ddot{u}_g(t) \quad (6)$$

where the system matrix **A**, the control force distributed matrix **B**, and the disturbance location matrix **E** are:

$$\mathbf{A}=\begin{bmatrix}\mathbf{0} & \mathbf{I}\\ -\mathbf{M}^{-1}\mathbf{K} & -\mathbf{M}^{-1}\mathbf{C}\end{bmatrix};\quad \mathbf{B}=\begin{bmatrix}\mathbf{0}\\ \mathbf{M}^{-1}\mathbf{\Lambda}\end{bmatrix};\quad \mathbf{E}=\begin{bmatrix}\mathbf{0}\\ -\mathbf{I}\end{bmatrix} \tag{7}$$

In this study, the MR damper is installed between the isolation layer and the ground as shown in Figure 3; therefore, $\mathbf{\Lambda}=[1\ \ 0]^T$. The system parameters of the superstructure are: m_s=3000 N-s^2/m, c_s=720 N-s/m, and k_s=44600 N/m. Also, the system parameters of the isolation layer are: m_b=4000 N-s^2/m, c_b=3350 N-s/m, and k_b=1754600 N/m. The associated structural period and the damping ratio of the superstructure and the isolation layer are: T_s=0.3 sec, ζ_s=2% , and T_b=2.5 sec , ζ_b=2%, respectively. The regulated output vector $\mathbf{y_r}$ used for designing the linear-quadratic controller takes the form:

$$\mathbf{y}_\mathbf{r}(t)=\mathbf{C}_\mathbf{r}\mathbf{x}(t)+\mathbf{D}_\mathbf{r}F_{MR}(t) \tag{8}$$

The vector $\mathbf{y_r}$ includes the inter-story drifts and absolute floor accelerations. The matrices $\mathbf{C_r}$ and $\mathbf{D_r}$ are:

$$\mathbf{C}_\mathbf{r}=\begin{bmatrix}1 & 0 & 0 & 0\\ -1 & 1 & 0 & 0\\ -\mathbf{M}^{-1}\mathbf{K} & & -\mathbf{M}^{-1}\mathbf{C} & \end{bmatrix};\quad \mathbf{D}_\mathbf{r}=\begin{bmatrix}\mathbf{0}\\ \mathbf{M}^{-1}\mathbf{\Lambda}\end{bmatrix} \tag{9}$$

The state-feedback control force is obtained by minimizing the quadratic cost function:

$$J=\int_0^\infty\left(\mathbf{y}_\mathbf{r}^T\mathbf{Q}\mathbf{y}_\mathbf{r}+F_C{}^T R F_C\right)dt \tag{10}$$

where $\mathbf{Q}$ and $\mathbf{R}$ are the state weighting matrix and the control cost, respectively. The parameter F_C is the state feedback control force of the MR damper. By solving the Ricatti equation and the state feedback gain $\mathbf{K_g}$ is obtained. Finally, the control force for the MR damper, F_C = - $\mathbf{K_g}$ $\mathbf{x}$ is obtained.

The idealized optimal control force, F_C = - $\mathbf{K_g}$ $\mathbf{x}$, is imposed on the base-isolated building by a semi-active MR damper. As a result, it is necessary to convert the optimal control force to equivalent control voltage (CV) for the MR damper. As the MR damper is a nonlinear device, the calculation of the inverse model (input: response and damper force/output: control voltage) is difficult. As a result, the clipped optimal control (Lin et al. 2005) is used to calculate the suitable control voltage at each time step. With the Bouc-Wen model of the MR damper, the damper force in each voltage level can be calculated. Thus, the closest damper force is obtained by comparing to the calculated optimal control force. Similarly, the control voltage at time each time step can also be found.

4.2 Fuzzy-logic Control

In addition to the linear-quadratic control algorithm, a fuzzy logic control (FLC) method is also studied in this paper. Fuzzy-logic theory, introduced by Zadeh in 1965, has been extensively applied on complex control problems. FLC is a type of intelligent language control and adopts manual control rules established by engineering intuition and experience. It provides a simple and robust nonlinear control strategy and can be accommodated to the uncertainties and un-modeled dynamics of the MR damper.

Fuzzy-logic operations consist of three steps: fuzzification, fuzzy inference and defuzzification. In the fuzzification module, crisp values are converted into fuzzy sets and degrees of membership. A membership function defines how each point in the input space is mapped to a membership value between 0 and 1. The fuzzy inference consists of the linguistic IF–THEN rules, which connect the mapping relationship between the input and output. The defuzzification, the opposite of fuzzification, converts the output of the inference rules back to a crisp control signal.

In this study, the control targets are: (1) to control the displacement of the isolation layer when it is under large deformation; (2) when the deformation of the isolator is small, do not apply any force on it; (3) to limit the control voltage up to 1.2V; and (4) to reduce the inter-story drift and absolute acceleration of the superstructure. It is noted that the fuzzy rule base in this study is proposed by engineering experience without optimization. Some optimal approaches for FLC such as genetic algorithm or neural network are not discussed.

The displacement and the velocity of the base isolation are used as the control inputs for the FLC. The output of the FLC is the control voltage for the MR damper. In this paper, the triangular membership functions are used for all variables. The membership functions are obtained through trial and error in numerical simulation. The parameter CV represents the control voltage for the MR damper. The fuzzy rule base is shown in Table 2 where NL, NM, NS, ZR, PS, PM, and PL represent negative large, negative medium, negative small, zero, positive small, positive medium, and positive large, respectively. Mamdani's method is used for fuzzy inference due to its simple structure of 'min-max' operations. For defuzzification, the center of area method is adopted. The surface of the fuzzy rule base is illustrated in Figure 4.

Table 2 The fuzzy rule base in the study

CV		x_b				
		NL	NS	ZR	PS	PL
$\dot{x}_b$	NL	PL	PM	ZR	ZR	ZR
	NS	PM	PS	ZR	ZR	ZR
	ZR	PS	ZR	ZR	ZR	NS
	PS	ZR	ZR	ZR	NS	NM
	PL	ZR	ZR	ZR	NM	NL

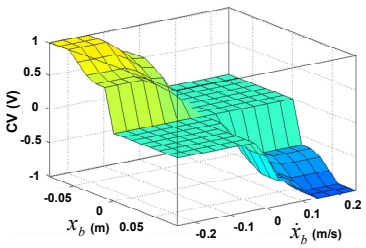


Figure 4 The rule surface of the proposed FLC

5. ADAPTIVE PHASE-LEAD COMPENSATOR

Various compensation methods have been developed and proposed to achieve more accurate strucutral responses of real-time hybrid testing. Most of the compensation methods require a prior knowledge of the servo-hydraulic system. Therefore, system identification of the servo-hydraulic system needs to be conducted to obtain the system dynamics before performing a real-time hybrid test. In addition, these compensation methods are mostly based on a fixed identified system parameter, for example, the actuator delay, to complete the design of the compensation. However, it has been shown that the actuator delay would vary during a hybrid test due to the nonlinear structural responses (Darby et al.). The transfer function of a servo-hydraulic system would also change due to the nonlinearity of the test component such as a MR damper (Phillips and Spencer 2012). It appears that the system parameters would not be fixed during a real-time hybrid test. As a result, a parameter estimator is necessary to detect the system parameters online to further improve the accuracy of the real-time hybrid testing.

Chen and Tsai have introduced the adaptive control theory to propose an adaptive phase-lead compensator (PLC) for the servo-hydraulic system. The discrete transfer function of the PLC is formulated by using weighted linear extrapolation and the inverse model principle. It has also been proved stable as long as the selected weightings locate in the derived stable regions. The only one parameter, delay constant, is obtained online by the delay estimator which adopts the gradient adaptive law formed in the format of parametric model. The stability and parameter convergence have been strongly supported by mathematics. The discrete PLC, C(z), takes the form:

$$C(z)=\frac{\left[W_1+(W_1+W_2+1)\alpha\right]z^2+\left[W_2-(W_1+W_2+1)\alpha\right]z+1}{W_1z^2+W_2z+1} \quad (11)$$

where z is a complex number in the z domain and α is the delay constant which is an integer greater than 0. The variables W_1 and W_2 are the weightings. The stable regions for the weightings are shown in Figure 5. By selecting different pairs of weightings, the PLC could be more accommodating to different compensation demands.

In order to evaluate the effects of different weightings for the PLC, frequency response analyses of four pairs of weightings located in the stable regions are carried out: (1)PLC1 with large W_1 and W_2 values ($W_1 = W_2 = 10000$); (2) PLC2 with large W_1 and small W_2 values($W_1 = 10000$ and $W_2 = 0.01$); (3) PLC3 with intermediate W_1 and W_2 values ($W_1 = 3$ and $W_2 = 2$); and (4) PLC4 with extremely small W_1 and W_2 values ($W_1 = 0.0001$ and $W_2 = 0.025$). Generally, the servo-hydraulic system is viewed as a first-order dominant system (Zhao et al. 2003). Magnitude reduction and response delay are expected for a first-order transfer function. Figure 6 shows the Bode diagram of the four PLCs applied on a servo-hydraulic system simulated as a first-order transfer function with a roll-off frequency of 11Hz. It is found that PLC4 under-compensates the magnitude but over-compensates the phase. On the other hand, PLC3 performs the best among the four PLCs because the magnitude is less amplified and the phase lag is close to zero. In addition, the weightings for PLC3 are more reasonable because they are close to each other. As a result, PLC3 is adopted for delay compensation in the study.

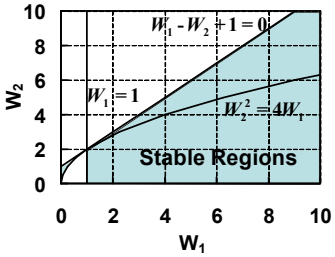


Figure 5 Stable regions of W_1 and W_2

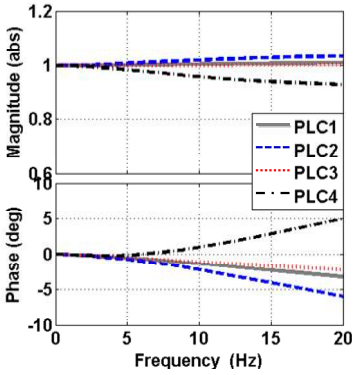


Figure 6 Frequency responses of the compensated servo-hydraulic systems

6. EXPERIMENTAL STUDIES

6.1 Test Setup

The schematic of the 2DOF smart structure shown in Figure 3 can be divided into two parts: (1) the experimental substructure, consisting of the semi-active MR damper, and (2) the numerical model, consisting of the stiffness, damping and mass terms of the superstructure and the isolation layer with a lightly-damped base isolator. The experimental test setup is shown in Figure 7. The MR damper is pin-connected to a 250kN dynamic servo-hydraulic actuator

at one end by a high strength bolt while the other end is connected to a reaction support fixed to a stiff frame.

The test facility can be divided into two major components: (1) the MTS GT digital controller, and (2) the dSPACE system. The dSPACE system is adopted in the test because it supports a large number of D/A and A/D input/output channels. It provides solutions for automotive engineering and industrial control throughout the integration of the control desk and Matlab/Simulink. The control desk is used to compute and collect the signals of a test system with a friendly graphical-user-interface. The layout of the test facilities is shown in Figure 8. The adaptive phase-lead compensator and control algorithms for the MR damper are programmed and compiled in a host computer with the Matlab/Simulink. With Real-Time Workshop and C complier, executable codes can be created and linked to the dSPACE which runs in real time. Signals generated by the dSPACE are passed to the GT controller (command displacement) and the MR damper (control voltage) in analog form through the cables. The measured signals including the displacement and force of the MR damper are sent back to the GT controller and conditioned. After that, the measured signals are sent from the GT controller to the dSPACE to compute the command displacement and control voltage in the next time step. By using these advanced experimental control facilities, complex hybrid simulation test could be conducted in real time. The GT controller is a well-tuned proportional-integral controller and forms a closed-loop system together with the servo-hydraulic system. All the tests are conducted with a sampling rate of 200Hz. The response of the MR damper is related to the velocity which is obtained by directly differentiating the measured displacement in the test. As a result, a second-order digital low-pass filter is used to cut off the measurement noise above 30Hz. The magnitude of the signal passed by the filter is 30% reduced at the frequency of 30Hz. The block diagram of the real-time hybrid testing is illustrated in Figure 9, where x_c and x_m are the command and measured displacements, respectively.

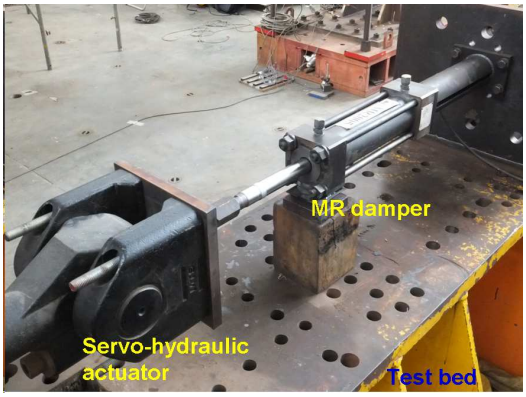


Figure 7 Test setup

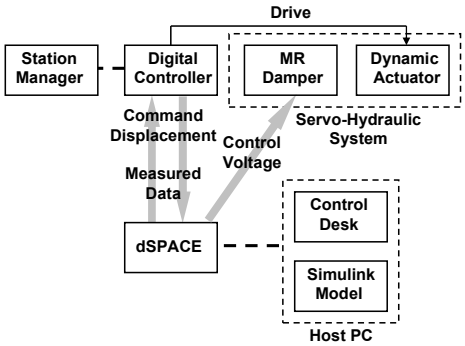


Figure 8 Hardware layouts for the 2DOF base-isolated building test

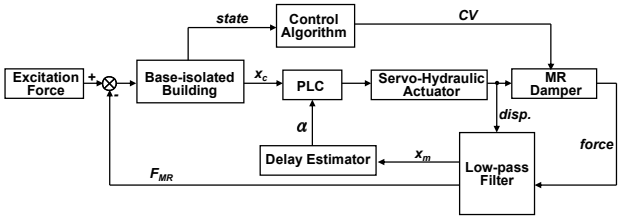


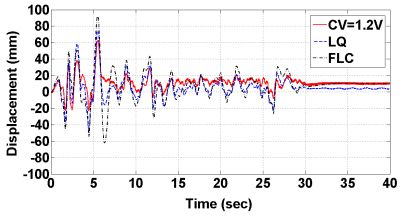
Figure 9 Block diagram of the real-time hybrid testing in this study

6.2 Experimental Results

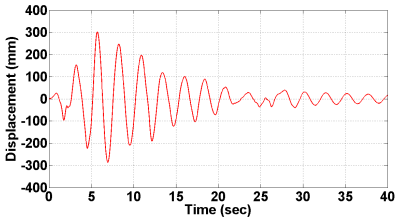
Three control algorithms are adopted for the MR damper: case (1) a constant voltage of 1.2V, which can be viewed as a passive damper; case (2) the MR damper is driven by using the linear-quadratic (LQ) control algorithm; and case (3) the MR damper is driven by using fuzzy logic control (FLC) algorithm. The feedback control gain vector $\mathbf{K_g}$= [368045 -307514 47750 -16262] is obtained by solving the Ricatti equation. The adaptive gain for the delay estimator is set 100 to prevent it from oscillation.

It is noted that the force capacity and peak stroke of the MR damper are 7kN and ±150mm, respectively. If the peak displacement of any test is larger than 150mm, the servo-hydraulic actuator could break the MR damper. Therefore, numerical simulation has been conducted to evaluate the potential peak displacement imposed on the MR damper under different levels of earthquake ground accelerations. From the analytical simulation results, two records of earthquakes are adopted: the 1940 El Centro Earthquake and the 1999 Chi-chi Earthquake and the peak ground accelerations (PGA) are normalized to 0.33g and 0.20g, respectively. It is worth noted that the record of the 1999 Chi-chi earthquake, TCU068EW, was measured at a near-source location. According to the previous research results, base-isolated buildings are vulnerable to strong near-fault impulsive ground motions (Hall et al. 1995). On the other hand, smart dampers have been shown to provide a superior base isolation system for near-source excitations. As a result, special concerns to the efficacy of base isolation system subjected to near-fault ground acceleration have been raised in this study.

For the smart base isolation system subjected to the 0.33g 1940 El Centro Earthquake, the displacement time histories of the isolation layer for each case are shown in Figure 10(a). It appears that case (1) performs the best among the three cases because the control voltage for case (1) is kept 1.2V, which is the maximum control voltage for the MR damper. The displacements of the isolation layer for all the three cases are significantly reduced due to the MR damper compared with the uncontrolled building as shown in Figure 10(b). Figure 11(a) and 11(b) show the time histories of the relative displacement and the absolute acceleration of the superstructure in each case. Both case (2) and (3) have smaller relative displacements and absolute accelerations compared with case (1). It demonstrates that the semi-active controlled damper can effectively reduce the relative displacement and absolute acceleration of the superstructure as well as the displacement of the isolation layer.

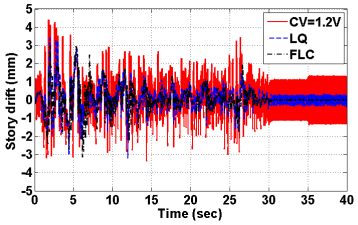


(a)

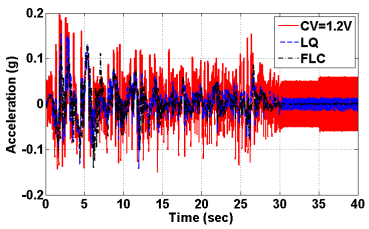


(b)

Figure 10 Displacement time histories of the isolation layer (0.33g El Centro): (a) controlled, (b) uncontrolled



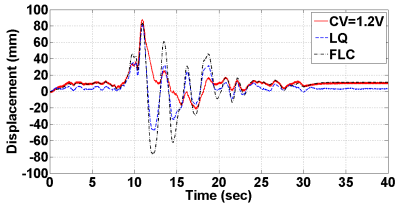
(a)



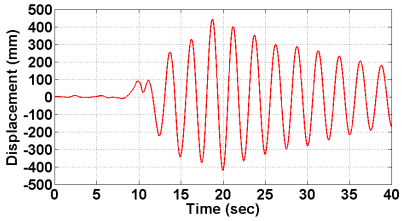
(b)

Figure 11 Time histories of the superstructure (0.33g El Centro): (a) story drift, (b) absolute acceleration

For the smart base isolation system subjected to the 0.20g near-fault Chi-chi Earthquake, The state feedback control gains and the fuzzy rule base remain unchanged. However, as mentioned in the system identification section, the force measured from the MR damper is smaller than that obtained from the numerical simulation. As a result, the displacement of the isolation layer in the validation test is larger than that in the simulation. If the peak displacement of any test is larger than 150mm, the servo-hydraulic actuator could break the MR damper. The peak displacement in case (3) is larger than 140mm, the limit of safety for the MR damper. Therefore, the PGA of the near-fault Chi-chi Earthquake is reduced to 0.15g for the experimental studies. The displacement time histories of the isolation layer in each case and the uncontrolled building are shown in Figure 12(a) and 12(b), respectively. Again, case (1) performs the best among the three cases. The time histories of the relative displacement and the absolute acceleration of the superstructure in each case are shown in Figure 13(a) and 13(b). It appears that case (2) and (3) have smaller relative displacements and absolute accelerations compared with case (1). Summarily, the advantages of a smart base isolation system (reducing base drifts without the accompanying acceleration increases) has been observed and demonstrated through real-time hybrid tests.



(a)



(b)

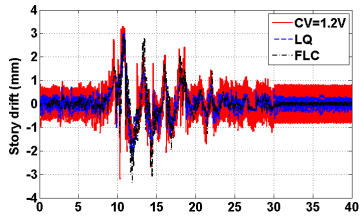
Figure 12 Displacement time histories of the isolation layer (0.15g near-fault Chi-chi): (a) controlled, (b) uncontrolled

6.3 Tracking Performance

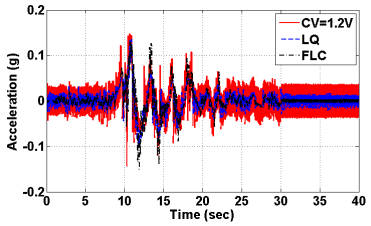
The tracking performance of a real-time hybrid test depends on the difference between the computed command and the measured displacements. For simplicity, the root mean square (RMS) error is mostly used as an index of the tracking performance. The RMS error is defined as:

$$RMS_{error}(\%) = \sqrt{\frac{\sum_{k=1}^{N}\left(x_c[k]-x_m[k]\right)^2}{\sum_{k=1}^{N}x_c[k]^2}} \times 100\% \quad (12)$$

where $x_c[k]$ and $x_m[k]$ are the command and measured displacements at the step k, respectively. Good tracking performance is indicated by a low RMS error between the command and measured displacements. Table 3 shows the RMS errors of each test. It appears that all the RMS errors are within 6% indicating that the adaptive PLC compensates the servo-hydraulic system fairly well. It is noted that the passive-on case has larger RMS error than the other two semi-active cases subjected to the two different earthquake ground accelerations. This is because in the passive-on case, little oscillation was observed when the response is small. Before the test was conducted, a small but significant enough restoring force (about 0.5kN) was measured from the MR damper under the maximum input voltage 1.2V. This small measured force was larger than the restoring force provided by the stiffness term. The equation of motion could not be in equilibrium; as a result, the structural system was oscillated until the earthquake ground acceleration became relatively significant. However, the oscillation was not observed in the two semi-active cases because the control voltage varied from time to time. Even though, the RMS error for the passive-on case is still good enough.



(a)



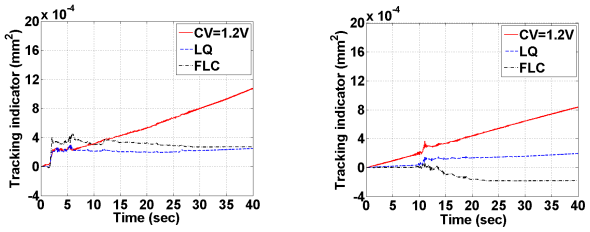
(b)

Figure 13 Time histories of the superstructure (0.15g near-fault Chi-chi): (a) story drift, (b) absolute acceleration

The tracking performance can be also evaluated by introducing the so-called tracking indicator (TI) proposed by Mercan and Ricles in 2007. The initial values for the enclosed and complementary areas are set as zero. A positive slope of TI corresponds to a lagged actuator response, meaning that negative damping is introduced into the real-time hybrid testing. On the other hand, a negative slope of TI represents a leading actuator response, indicating that artificial damping is added into the test. In addition, a zero slope of TI demonstrates a perfect tracking, i.e., the measured and command displacements are identical. Figure 14 shows the tracking indicators of the displacement for each test. It shows that the responses of the constant voltage case are mostly lagged, while the other two cases perform much better. It is also because the MR damper was oscillated when the displacements were small in the constant voltage case. The high-frequency oscillation leads to significant tracking errors during the test and result in worse TI values. Even though, all the TI values are considered acceptable because they are close to zero. A good tracking performance of the proposed PLC is then demonstrated.

Table 3 Tracking performance for each test in terms of RMS error

Earthquake Record	Controller for the MR damper	RMS_{error} (%)
El Centro (0.33g)	Passive-on	5.97
	LQ	4.84
	FLC	4.07
Chi-chi near-fault (0.15g)	Passive-on	4.55
	LQ	3.22
	FLC	2.36



(a) (b)

Figure 14 Displacement tracking indicator for each case: (a) 0.33g El Centro, (b) 0.15g near-fault Chi-chi

7. CONCLUSIONS

The efficacy of a combination of low-damping elastomeric bearings and controllable MR dampers, namely smart base isolation system, has been evaluated using real-time hybrid testing methodology. The numerical model contains the superstructure, low-damping base isolator, and MR damper control algorithm. The control voltage computed by the control algorithm is sent to the MR damper which is physically tested in a real-time manner. An adaptive phase-lead compensator (PLC) is adopted to compensate the actuator delay to increase the accuracy during the test. The main observation and contribution of the study are summarized below:

(1) A series of identification tests of the MR damper have been performed to calibrate the nonlinear Bouc-Wen model of the MR damper. However, it is shown that the numerical model could not be perfectly represented the physical MR damper in terms of maximum generated force. The response of a smart base-isolation structure could not be clearly investigated through numerical

simulation. As a result, real-time hybrid testing is considered an alternative and necessary approach to evaluate the behavior of a smart base-isolation structure.

(2) The PLC is proved to successfully compensate the time delay and magnitude reduction due to the servo-hydraulic actuator and the low-pass filter. The frequency response analyses with different selected weightings provide the design flexibility of the PLC. Experimental studies demonstrate the delay estimate of the PLC converges to a constant within limited time duration. It indicates the adaptive PLC can be applied on a nonlinear test system as the servo-hydraulic actuator with the MR damper in the study.

(3) The MR damper is demonstrated to provide additional damping to the structure and reduce base drifts without the accompanying acceleration increases if appropriate control algorithms for the dampers are adopted. Experimental results indicate that the linear-quadratic control and the fuzzy logic control algorithms can be effectively reduce the relative displacement and absolute acceleration of the superstructure compared with the constant voltage case.

(4) The accuracy of the real-time hybrid test is evaluated by the tracking performance in terms of the root mean square error (RMS) and the tracking indicator (TI). The RMS error for each test is under 6%, showing that the test results are fairly enough to investigate the behavior of the smart base-isolation system. In addition, the TI time history for each test demonstrates the PLC can well-compensate the phase lag induced by the servo-hydraulic system as well as the low-pass filter.

Acknowledgements:

The tests were conducted at the National Center for Research of Earthquake Engineering (NCREE) in Taiwan. The authors would like to thank the technicians from NCREE for their assistance in test setup. In addition, the works carried out by Mr. Li-Hao Chen on the system identification tests of the MR damper was also acknowledged.

References:

Ramallo, J.C., Johnson, E.A. and Spencer, B.F. (2002), "Smart Base Isolation Systems," *Journal of Engineering Mechanic*, **128**(10): 1088-1099.

Yang, J.N., Wu, J.C., Reinhorn, A.M. and Riley, M. (1996), "Control of Sliding-isolated Buildings using Sliding-mode Control," *Journal of Structural Engineering*, **122**(2):179-186.

Symans, M.D. and Kelly, S.W. (1999), "Fuzzy Logic Control of Bridge Structures using Intelligent Semi-active Seismic Isolation," *Earthquake Engineering and Structural Dynamics*, **28**(1): 37-60.

Spencer, B.F., Johnson, E.A. and Ramallo, J.C. (2000), "Smart Isolation for Seismic Control," *Japan Society Mechanical Engineering International Journal* ,**43**(3): 704-711.

Dyke, S.J., Spencer, B.F., Quast, P. and Sain, M.K. (1995), "Role of Control-structure Interaction in Protective System Design," *Journal of Engineering Mechanics*, **121**(2): 322-338.

Zhao, J., French, C., Shield, C. and Posbergh, T. (2003), "Considerations for The Development of Real-time Dynamic Testing using Servo-hydraulic Actuation," *Earthquake Engineering and Structural Dynamics,* **32**(11):1773-1794.

Horiuchi, T., Inoue, M., Konno, T. and Namita, Y. (1999), "Real-time Hybrid Experimental System with Actuator Delay Compensation and Its Application to A Piping System with Energy Absorber," *Earthquake Engineering and Structural Dynamics*, **28**(10):1121-1141.

Nakashima, M. and Masaoka, N. (1999)," Real-time On-line Test for MDOF Systems," *Earthquake Engineering and Structural Dynamics*, **28**(4): 393-420.

Chen, C. (2007), "Development and Numerical Simulation of Hybrid Effective Force Testing Method," Ph.D. Dissertation, Department of Civil and Environmental Engineering, Lehigh University, Bethlehem, PA.

Phillips, B.M. (2012), "Model-based Feedforward-feedback Control for Real-time Hybrid Simulation of Large-scale Structures," Ph.D. Dissertation, Department of Civil and Environmental Engineering, University of Illinois at Urbana Champaign, Champaign, IL.

Chen, P.C. and Tsai, K.C. (2013), "Dual Compensation Strategy for Real-time Hybrid Testing," *Earthquake Engineering and Structural Dynamics*, **42**(1): 1-23.

Mercan, O. and Ricles, J.M. (2007), "Stability and Accuracy Analysis of Outer Loop Dynamics in Real-time Pseudodynamic Testing of SDOF Systems," *Earthquake Engineering and Structural Dynamics*, **36**(11):1523-1543.

Chassiakos, A.G., Masri, S.F., Smyth, A.W. and Caughey, T.K. (1998), "On-line Identification of Hysteretic Systems," *Transactions of the ASME* , **65**: 194-203.

Wen, Y.K. (1976), "Method for Random Vibration of Hysteretic Systems," *Journal of Engineering Mechanics*, **102**(2): 249-263.

Lin, P.Y., Chung, L.L. and Loh, C.H. (2005), " Semiactive Control of Building Structures with Semiactive Tuned Mass Damper," *Computer-Aided Civil and Infrastructure Engineering*, **20**: 35-51.

Zadeh, L.A. (1965), "Fuzzy Sets," *Information and Control*, **8**: 338-353.

Darby, A.P., Williams, M.S. and Blakeborough, A. (2002), "Stability Delay Compensation for Real-time Substructure Testing," *Journal of Engineering Mechanics*, **128** (12):1276-1284.

Hall, J.F. and Holmes, W.T. (1994), "Northridge Earthquake of January 17, 1994 Reconnaissance Report," *Earthquake Spectra*, **11** (1), Supplement C.

10CUEE CONFERENCE PROCEEDINGS
10th International Conference on Urban Earthquake Engineering
March 1-2, 2013, Tokyo Institute of Technology, Tokyo, Japan

STUDY ON IMPLEMENTATION OF REMOTE BUILDING DAMAGE ASSESSMENT SYSTEM DURING LARGE SCALE EARTHQUAKE DISASTER

Makoto FUJIU[1], Miho OHARA[2] and Kimiro MEGURO[3]

1) Ph.D. Candidate, Department of Interdisciplinary Information Studies, The University of Tokyo, Japan
2) Associate Professor, Interfaculty Initiative in Information Studies, The University of Tokyo, Japan
3) Professor, Interfaculty Initiative in Information Studies, The University of Tokyo, Japan
fujiu@iis.u-tokyo.ac.jp, ohara@iis.u-tokyo.ac.jp, meguro@iis.u-tokyo.ac.jp

Abstract: This paper proposed the new system for building damage assessment using photos of damaged house taken by residents or volunteer fire corps in damaged area. Specialists outside the damaged confirm these photos on the website and assess their damage levels. All the data used for building damage assessment is managed with GIS database on the management server located outside the damaged area under cloud condition. This kind of digital management system can contribute to enhance the accuracy and efficiency of the procedures for issuing the Victim Certificates for residents. In this paper, the total system for supporting building damage assessment was designed and its prototype system was developed. The system for uploading the photos of damaged houses was developed as mobile communication service. The remote system for specialists to assess the damage level was developed as web service.

1. INTRODUCTION

In Japan, several big earthquakes are expected to occur in the near future. A lot of structural damages due to these earthquakes will cause enormous needs for building damage assessment. Building damage assessment is necessary for governments to issue the Victim Certificates for residents who suffered housing damages. However, current number of human recourses who are trained with the procedure of building damage assessment is not enough. It is necessary to develop the new system which can correspond to next large-scale earthquake disaster. The guidelines of general procedure for inspecting building damage and evaluating loss due to disasters were published by the Cabinet Office in 1968, 2001 and 2009. However, in past disasters, various problems of building damage assessment have been pointed out such as inaccurate inspection, difficulty in quick inspection and lack of human recourses with sufficient skill of assessment.

New remote system for building damage assessment using IT system was proposed and prototype system was developed. These systems have some features that can solve some problems pointed out by past building damage assessments and execute building damage assessment quickly after a large scale earthquake disaster. This proposed system has two sub-systems. First one is photo uploading system used in damaged area. Second one is assessment system for supporting experts such as registered architects and experienced workers outside the damaged area. But authors only develop the prototype system, and do not evaluate the effectiveness of developed system. In this research, authors conducted operation test for some local government staffs to evaluate the effectiveness of developed systems.

2. CONCEPT OF NEW REMOTE SYSTEM FOR BUILDING DAMAGE ASSESSMENT

As a new system for achieving all the solutions for the problems reported at the past building damage assessments, we proposed a new remote system for supporting building damage assessments during large-scale earthquake disaster. The concept of the system is illustrated in figure 1.

The total system consists of two sub-systems. The first one is photo upload system in damaged area. Photos of a damaged house are taken by residents or volunteer fire corps in damaged area and those data is uploaded to the server. The second one is remote assessment system for specialists. Specialists located outside the damaged area confirm these photos through the website, and assess their damage levels and area.

All the data used for building damage assessment is managed with GIS database on the management server located outside the damaged area under cloud condition. This kind of digital management system can contribute to enhance the accuracy and efficiency of the procedures for issuing the Victim Certificates for residents.

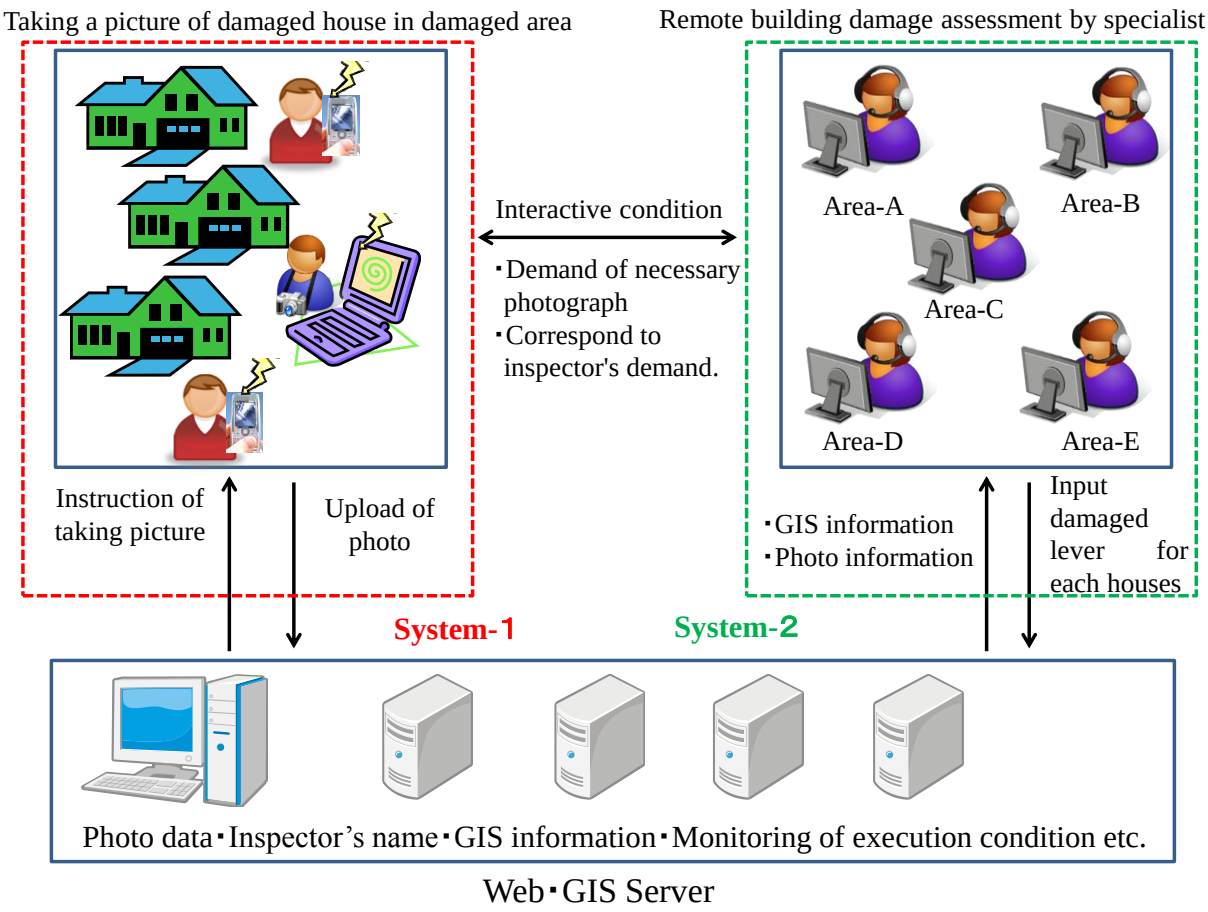


Figure 1: Concept of remote building damage assessment system

3. DEVELOPMENT OF REMOTE BUILDING DAMAGE ASSESSMENT SYSTEM

3.1 Development of photo upload system in damaged area

Here, prototype of "Photo upload system in damaged area" was developed. Photos of a damaged house are taken by residents or volunteer fire corps in damaged area and those data is uploaded to the server. This system was developed by Android as the mobile phone operating system which is installed in almost all the smart phones except iPhone. Photo upload application is installed to each Android smart phone by inspectors who are residents or volunteer fire corps in damaged area.

Flow of photo upload system is as follows. Firstly, residents or volunteer fire corps as inspectors input the basic information such as GPS information, address and owner name. Secondary, they upload some photos such as overview of damaged house, incline of damaged house and damaged point of roofs, walls and fundamentals. Finally, they confirm the input data and some photos.

Method of completing for photo upload in damaged area using upload application is as follows. Inspectors take some damaged house photos which are full views of a damaged house (north side, east side, south side and west side) and closeup views of damaged points. They select some photos for upload in each factors page, and fill in the comments about damage level and location of a house etc. Inspectors should take pictures of damaged house concerning three factors: externals, inclination and building element (roof, exterior wall and foundation). Furthermore, they have to relate closeup views of damaged points to full views using touch screen functions. The prototype system of photo upload system was developed based on the data of totally damaged houses due to the 2011 off the Pacific coast of Tohoku Earthquake.

After taking some pictures, inspectors need to upload them to an exclusive server in cloud condition using upload application. Using this application makes it easier to select and upload photos which are taken by inspector in damaged area. The reason is that smart phone has touch screen functions which are tap, drag, flick and pinch out/in operations.

3.2 Development of remote assessment system for specialists

Here, prototype of "remote assessment system of

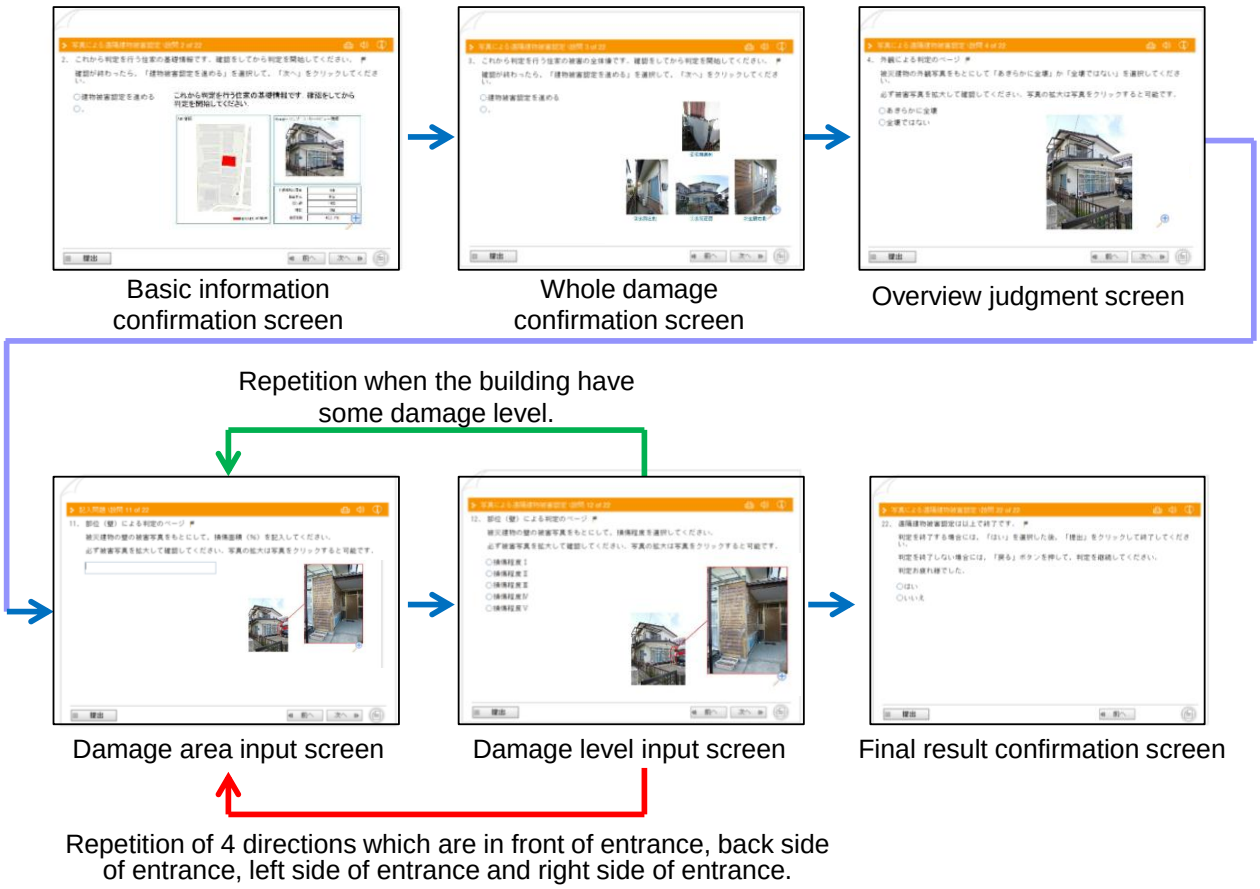


Figure 2: Remote building damage assessment system

photos of damaged houses was developed as shown in figure 2. Specialists outside the damaged area confirm these photos on the website and assess their damage levels. All the data used for building damage assessment is managed with GIS database on the management server located outside the damaged area under cloud condition.

Flow of remote assessment system is as follows. Firstly, specialists who are registered architects and experienced workers outside the damaged area confirm the basic information such as shape of damaged house, location and seismic level on the web system and overview all the photos of a damaged house. Secondary, they assess the damage level and area using some photos such as overview of damaged house, incline of damaged house and damaged point of roofs, walls and fundamentals. Finally, specialists confirm the input data and some photos. Then result of first assessment is passed to the next specialist to carry out double check.

Figure 2 shows the prototype system of the system for primary inspection. These systems were developed based on the data of moderate damaged houses due to the 2011 off the Pacific coast of Tohoku Earthquake. Total damage level of a house is decided based on damage levels of three factors: externals, inclination and building element. Assessment for one damaged house should be conducted by two or three specialists to double-check the result and keep accuracy, fairness and objectivity.

They can see close-up photos if necessary. They evaluate the photos and decide its damage level and damage area as shown in figures 2. Specialists select the damage level and area from pull down choice set in each factor page. In addition, they can request additional photos for accurate assessment to inspectors in damaged area through the each assessment page. In final page, fill in the special or caution comments of assessed damaged house and pass to the next specialist. When the assessment ends here, Victim Certificates for resident is issued from local government.

4. EVALUATION OF EFFECT OF REMOTE BUILDING DAMAGE ASSESSMENT SYSTEM

4.1 Condition of Operation test

Authors conducted operation test for twenty local government staffs which experienced building damage assessment due to the the 2011 off the Pacific coast of Tohoku Earthquake, and they belong to Yokohama city and Sendai city as shown in figure 3.

The date of operation test is 26 and 27 April in Yokohama city, and 15th May in Sendai city. Duration of operation time is about two hours. Contents of operation test are explanation of building damage assessment, developed



Figure 3: Operation test in Yokohama city

Table 2: Condition of operation test

Scenario	Damage Level	Test Conditions
1	Major damage	Easy to assess for all test persons
2	Major damage	Easy to assess for all test persons
3	Major–moderate damage	Difficult to assess for experienced person
4	Moderate damage	Easy to assess for all test persons
5	Moderate damage	Difficult to assess for experienced person
6	Minor damage	Easy to assess for all test persons
7	Minor damage	Difficult to assess for experienced person



Scenario 4



Scenario 5

Figure 4: Example of damage photo for remote assessment system

system and questionnaire survey for developed system. After the explanation of that, operation test was started by author using developed system. When the operation test finished, test staffs answer the questionnaire survey regarding usability and feasibility of developed system.

Table 1 shows condition of operation test. Operation test has four damage patterns and two cases respectively (except major-moderate damage). Totally seven scenarios of operation test are examined by operation test staffs. Damage patters of operation test are major damage, major-moderate damage, moderate damage and minor damage, and two scenarios are easy to assess and difficult to assess for experienced person. Operation test adopt local government staffs which have experienced to carry out the building damage assessment during the 2011 off the Pacific coast of Tohoku Earthquake. Figure 4 shows example of damage photo for remote assessment system due to the 2011 off the Pacific coast of Tohoku Earthquake which are moderate damaged houses. Scenario 4 is moderate damaged house which is easy to assess for all test persons, and scenario 5 is also moderate damaged house which is difficult to assess for experienced person.

4.2 Result of Operation test

Figure 5 shows result of final damage level using developed remote building damage assessment. As a result of operation test, scenario 1 and 2 are all operation staffs assess correct damage level. On the other hand, scenario 3,4,5,6 and 7 does not assess completely. East to assess for all test persons cases are high correct answer ratio which is about 80%. But, correct ratio of difficult to assess for experienced person cases is lower than another case.

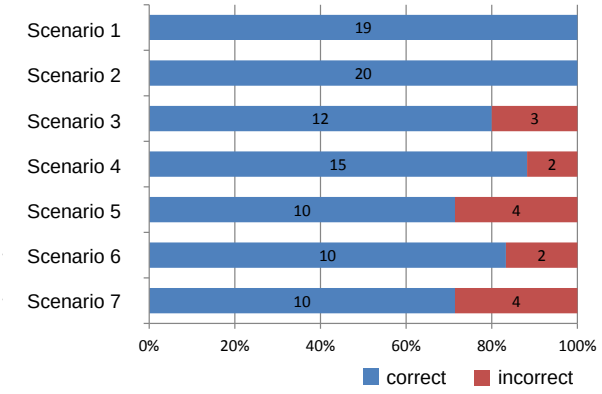


Figure 5: Result of final damage level

Figure 6 shows result of judgment of damage level which is scenario 7. Scenario 7 is difficult to assess for experienced person case. Scenario 7 has three walls which locate left side of entrance and back side of entrance. Red circle in the graph indicate correct judgment. As a result of operation test, about 70% of test staffs can assess correct damage level of wall. But, about 30% of test staffs do not assess the damage level correctly because of small cracks cannot find.

Figure 7 shows result of judgment of damage area which is scenario 7. Scenario 7 is difficult to assess for experienced person case. Scenario 7 has three walls which locate left side of entrance and back side of entrance. Red circle in the graph indicate correct judgment. As a result of operation test, wall 1 and wall 2 is assessed larger damaged area than correct damaged area, but wall 3 is assessed smaller than correct damaged area. The reason of that result as follows. Test staffs cannot evaluate correct damaged area because of small cracks. Damaged area is difficult to assess using photos for test persons. As a result of two reasons, it is necessary to install the easy calculation system using area mesh, and procedures which can assess the damage level using example of damage.

Figure 8 shows result of questionnaire survey regarding usability and feasibility. This system has many advantages than present procedures. Especially, "reducing inspection time" and "Result of inspection is managed by digital data." is high evaluated point by test staffs thorough the questionnaire survey. As a result of discussion as test staffs, developed system is very useful to carry out the primary inspection.

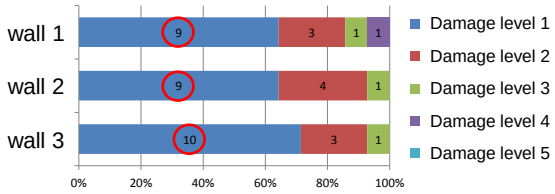


Figure 6: Result of assessment of damage level (wall inspection)

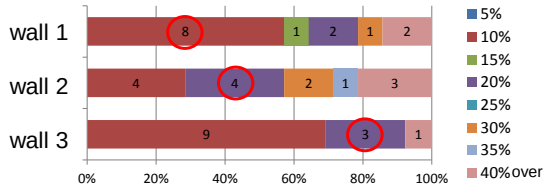


Figure 7: Result of assessment of damaged area (wall inspection)

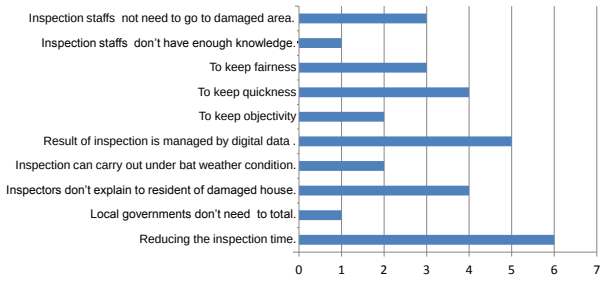


Figure 8: Result of questionnaire survey regarding usability and feasibility

5. Conclusions

In Japan, several big earthquakes are expected to occur in the near future. It is necessary to develop the new system which can be corresponds to next large-scale earthquake disaster. In this research, new remote assessment system for building damage assessment was developed and conducted operation test.

The prototype system of remote building damage assessment system was developed based on the data of damaged houses due to the 2011 off the Pacific coast of Tohoku Earthquake, and conducted operation test for local government staffs which experienced building damage assessment. As a result of operation test and questionnaire survey, it become clear that building damage suffered from earthquake can assess using developed system and this system has many advantage point than present procedures.

In the future, we plan to conduct the operation simulation using developed system for Tokyo metropolitan inland earthquake, and examine its effectiveness and quickness.

REFERENCES

Murao, O., Yamazaki, F., 1999, Comparison of Building Damage Evaluation by Local Governments after the 1995 hyogoken-nanbu earthquake, Journal of Architecture Planning and Environmental Engineering, No.515, pp.187-194

Shigekawa, K., Tanaka, S., Horie, K., Hayashi, H., 2005, Some Regulational Issues on Building Damage Assessment –A Case Study of Niigata-ken Chuetsu Earthquake- , Journal of social Safety Science No.7, pp.133-140

Horie, K., Shigekawa, K., Maki, N., Tanaka, S., Hayashi, H., 2005, Application of Damage Assessment Training (DATS) to Ojiya City following 2004 Niigata-ken Chuetsu Earthquake –Through a Disaster Response Support Activity for Issuing Victim Certificate- , Journal of social Safety Science No.7, pp.123-132

Yoshitomi, N., Hayashi, H., Urakawa, G., Shigekawa, K., Tanaka, S., Horie, K., Matsuoka, K., 2005, The Development of a Damage Certificate Issuing Support System –A new disaster response database schema created for the Niigata Chuetsu Earthquake- , Journal of social Safety Science No.7, pp.141-150

Tanaka, S., 2008, A Study on the Building Damage Assessment Processes for the 2007 Niigata Chuetsu Oki Earthquake Disaster : Kashiwazaki Case Study , Proceedings of social Safety Science No.22, pp.35-38

Fujiu, M., Ohara, M., Meguro, K., 2011, Development of remote system for supporting building damage assessment during large-scale earthquake disaster, Proceedings of the Eighth International Symposium on New Technologies for Urban Safety of Mega Cities in Asia, Chiang Mai, Thailand, CD-ROM

Fujiu, M., Ohara, M., Meguro, K., 2012, Development of remote system for supporting building damage assessment during large-scale earthquake disaster, Proceedings of 9th International Conference on Urban Earthquake Engineering, CD-ROM

Fujiu, M., Ohara, M., Meguro, K., 2012, Development of remote building damage assessment system during large-scale earthquake disaster, Proceedings of the 15th World Conference on Earthquake Engineering, CD-ROM, Lisbon, Portugal

10CUEE CONFERENCE PROCEEDINGS
10th International Conference on Urban Earthquake Engineering
March 1-2, 2013, Tokyo Institute of Technology, Tokyo, Japan

A PRELIMINARY STUDY ON THE IDENTIFICATION OF SEISMIC ISOLATION SYSTEMS FROM EARTHQUAKE RECORDS

Giuseppe Oliveto[1)], Anastasia Athanasiou[1)], Mineo Takayama[2)]and Keiko Morita[2)]

1) Department of Civil and Environmental Engineering, University of Catania, Italy
2)Faculty of Engineering ,Fukuoka University, Japan
goliveto@dica.unict.it,athanasiou@dica.unict.it,mineot@fukuoka-u.ac.jp, keikomt@fukuoka-u.ac.jp

Abstract: This work is an attempt to the dynamic identification of base isolation systems from earthquake response records. A very simple base isolation system is considered, composed of only four lead rubber bearings at the four corners of a building in the city of Kushiro in northern Japan. The acceleration of the building, recorded during the 2003 Tokachi-oki earthquake, is used for the identification. The identification procedure is based on the minimization of the distance between the acceleration of the building measured during the earthquake and the simulated one obtained by using a model presented at CUEE-12. A state-of-the art optimization algorithm (CMA-ES), based on the adaptation of the covariance matrix of a multivariate Gaussian probability distribution, is used to guide the identification process. The model parameters, obtained by identification from three laboratory tests performed in 1996 and in 2004, are used as a reference for the definition of the search space where the system parameters are expected to be. The optimal solution is given in probabilistic terms, namely the average value, standard deviation and coefficient of variation of the system parameters. The work is completed with a critical analysis of the minimal system response required to obtain a realistic prediction of the system parameters for the model considered.

1. INTRODUCTION

The design of seismic isolation systems is usually based on static and/or dynamic laboratory tests performed on individual isolation devices and on suitable models derived from such tests. A model widely used for the simulation of the dynamic response of a wide class of isolation devices, including various types of elastomeric bearings, lead core elastomeric bearings and friction pendulum bearings is the so-called bi-linear spring model, (Naeim and Kelly 1999). Such a model, in parallel with a Coulomb type model for sliding bearings, has been used for the identification of hybrid base isolation systems composed of High Damping Rubber Bearings (HDRB) and Low Friction Sliding Bearings (LFSB) from full scale free vibration tests performed on a base-isolated building, (Oliveto et al. 2004), (Oliveto et al. 2010). The full scale tests are justified by the fact that laboratory tests are usually performed on a limited number of isolation devices, while a full scale test involves the whole isolation system and engages the isolators as they are installed in the construction with possible manufacturing and placing defects. Therefore full-scale tests allow for the assessment of the overall isolation system as it really is. If the test is performed soon after the construction is completed, it could play the role of a certification test that qualifies the isolation system and the building to which it belongs. If it is performed several years after the installation of the isolation system it may be used to assess the present state of the system and to gather some information on the aging process. Free vibration tests on base-isolated buildings have usually been performed by applying a static displacement to the part of the structure above the isolation system and then suddenly removing the force used to apply the initial displacement. The collaborative work by the designer, the constructor, the certifying authority and the owner is required to perform such tests and usually they result in well-conceived and executed experiments. In all known tests, the buildings and the isolation systems were symmetrical, with negligible mass eccentricity or none. This leads to a 1D motion of the superstructure relative to the substructure. For this reason the mechanical models for the identification of the isolation system were 1 Degree of Freedom (1DOF) systems. In spite of the high non-linearity of Hybrid Base Isolation Systems (HBIS) it was possible to provide an analytical solution for the response of such systems under free vibration conditions, (Oliveto et al. 2010), (Athanasiou and Oliveto 2011). The analytical solution made the simulation of the free vibration tests very simple and the identification of the HBIS from such tests very effective. The main ingredients that led to such effectiveness were the analytical solution and the limited number of system parameters to be identified. The least squares method was successfully used for the identification of the isolation system of the Solarino building, (Oliveto et al. 2010). In that case system parameters were identified along with the imposed initial displacement. Subsequent developments allowed for considerable improvements in the simulation of the response of HBIS and in their dynamic identification. A first improvement derived from the extension of the analytical solution from free vibration to forced vibration and earthquake motion,

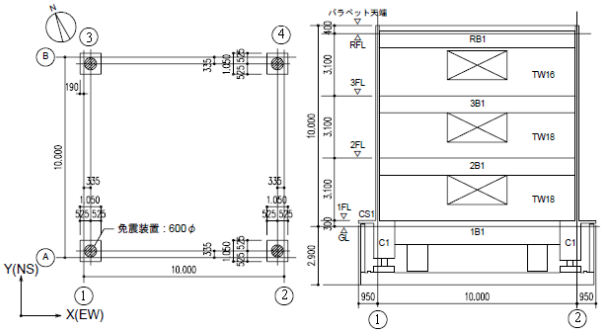
(Athanasiou et al. 2011-a, Oliveto et al. 2012-a). A second improvement came from the application of state-of-the-art methods of system identification imported from computer science, (Athanasiou et al. 2011-b). The extension of the analytical solution to the case of earthquake excitation is a simple derivation based on the assumption that the ground acceleration is linear within a time step. The analytical solution is evaluated within each time step using the initial conditions at the beginning of the step and therefore assuring continuity for all the loading history. The interaction with researchers in the computer science field led to the testing of several evolutionary algorithms on a basic identification problem, denoted " The Toy Problem", specifically designed for base isolation systems. Of all the tested algorithms, the most effective one, by several orders of magnitude, was the CMA-ES, (Athanasiou et al. 2011-b). This algorithm has been successfully used thereafter in all of our subsequent identifications, (Athanasiou et al. 2013) and (Oliveto et al. 2012-b). The analytical solution, although effective, is limited to symmetrical systems under symmetrical excitation. For this reason a numerical solution based on a Mixed Lagrangian Formulation (MLF) was originally developed for 1DOF systems, (Athanasiou et al. 2011-c), and subsequently extended to 3DOF systems, (Oliveto et al. 2012-c). The original development was extremely useful as it allowed checking the numerical solution against the available analytical solution. The extension to the 3DOF systems allowed overcoming the limitations of the previous formulation by including 2D ground motion excitations and considering non-symmetrical systems with mass eccentricities. The mathematical formulation, along with some numerical applications may be found in the previously quoted work (Oliveto et al. 2012-c). The object of the present work is to use the numerical formulation for 3DOF base isolation systems in the identification of the mechanical properties of such systems, using their recorded response to actual earthquakes. The work is exploratory in nature and is meant to identify all the difficulties that may be involved in the pursuit of the stated goal. In principle each isolator can have different properties and it may be interesting to identify the properties of all isolators as independent quantities so that eventually defective or damaged isolators can be singled out. However, this goal may be overambitious because when many isolators are being used, the number of system parameters to be identified can easily become very large and the identification task can become prohibitive. The problem can be easily simplified, or reduced in size, if classes of isolators are assumed to have the same properties. This way the properties of classes of isolators are sought rather than those of individual isolators. However, even in a simplified form, the problem is still daunting because the inverse solution of a highly non-linear problem is being sought. Even for linear systems it is well known that inverse problems do not have a unique solution, meaning that several systems can produce the same record data on which the identification is being based. However, a good identification algorithm can produce several of the possible solutions and with suitable bounds and engineering judgment the real solution can often be found. In the present paper, the ideas that have been briefly exposed shall be illustrated by several trials of parameter identification on a simple base-isolated building with a simple base isolation system.

2. PREVIOUS STUDIES ON THE BUILDING CONSIDERED

The building considered, which belongs to the Manboku Construction Company, is an office building located in the city of Kushiro. It has three stories above the ground for a total height of 9.6 m. A view of the building is given in Figure 1 while a plan and a cross-section are shown in Figure 2 and Figure 3.



Figure 1 Photograph of the exterior of the building



Figures 2 and 3 Plan and cross-section of the building

The fundamental periods of the fixed base building are 0.095 s in the X direction and 0.105 s in the Y direction. The isolation system is composed of four identical Lead Rubber Bearings (LRB) centered at the corners of a 10mx10m square. The bearings have a diameter of 600 mm and the total thickness of the rubber is 200 mm with a secant shear modulus G=0.39 N/mm^2 at γ=1. The equivalent periods of the isolated building at γ=1 are 2.396 s in the X direction and 2.397 s in the Y direction. The building was erected in 1996 and was hit by the Tokachi-oki Earthquake in 2003. The response of the building to the earthquake has been studied by Suzuki et al. (2004), who have reported the motions recorded at the basement level below the isolation system, at the first floor and on the roof. These show a considerable reduction of the peak acceleration above the isolation plane; in the X direction the reduction factor is 0.8 for both the first

floor and the roof, while in the Y direction it is 0.47 for the first floor and 0.51 for the roof. An orbit tracer device installed at a certain location of the isolation plane of the building shows the trace of the relative horizontal displacement at that location with a maximum displacement of about 300 mm in the X direction. The authors also show a comparison between the 5% damping response spectrum for the horizontal ground motion recorded by a K-net station at a distance of 2.2 km from the building and that for the motion recorded in the basement of the building. As compared to the motion recorded by the K-net station, the motion recorded in the basement of the building shows a significant spectral amplification in the range of periods of interest for base-isolated buildings. The second part of the study, authored by Kaneko et al. (2004), concerns the simulation of the response of the building and the comparison between the simulated and the measured responses. The first comparison is in terms of the orbit of the relative motion. Although the amplitude and the general direction of motion are evaluated with sufficient accuracy, the simulated and recorded paths do not exactly match. The authors provide estimates of the peak acceleration at the first floor and on the roof that are somewhat lower than the measured ones. Of great interest to the mentioned work are three static cyclic tests performed on one of the isolation bearings. The bearing was originally tested in 1996, and in 2004 it was removed from the building and tested in the two perpendicular directions along which the earthquake acceleration had been measured, that is the two principal directions of the building. The authors note how the properties of the bearing changed in the eight years between the tests. The increase in secant stiffness k_d at γ=1 appears to be negligible in the Y direction and only about 2% in the X direction; this seems to point out that the small change in stiffness may be due more to strain hardening induced by the seismic action than to aging. The yield strength instead shows an increase of about 5% in the X direction and about 7% in the Y direction. By integration of the recorded acceleration the authors obtain the following peak velocity and displacement components: v_x=872mm/s, v_y=490mm/s, u_x=304mm, u_y=152mm. The orbit calculated by integration of the recorded acceleration is in good agreement with the recorded one. Of considerable interest are the graphs of the restoring force in the isolators versus the relative displacement. The graphs are given separately for the X and Y direction and a comparison between recorded and simulated responses is provided. The simulated response appears to be based on a bilinear model while for the experimental response the restoring force is most likely derived by equilibrium based on an estimated mass and the recorded acceleration. Moreover, the displacement is derived by double integration of the recorded acceleration. The matching between simulated and experimental responses appears to be reasonably good. The authors also provide an estimate of how the secant stiffness and the yield strength of the isolators vary with the shear strain amplitude. The stiffness and the strength at a shear strain γ=100% are taken as reference points and the variations at shear strains of γ=50% and γ=150% are provided. A 20% increase in the secant horizontal stiffness is shown at γ=50% and a decrease slightly larger than 10% is shown at γ=150%. In terms of yield strength the behavior is inverted; a slight decrease is seen at γ=50% while a slight increase seems to occur at γ=150%. Anyway, the decrease and the increase are significantly less than 10%. The authors finally present an estimate of the energy dissipated by the isolation system for the X and Y direction respectively. The experimental and simulated estimates are in good agreement for the Y direction while in the X direction the results from the simulation appear to underestimate the experimental ones. Finally a cross-section of the removed isolator shows no apparent damage caused by the earthquake.

3. IDENTIFICATION OBJECTIVES

The building described in the previous section is taken as a case study to investigate the level of information that can be gathered from the use of suitable models and structural identification techniques on base isolation systems, given the structural response to actual earthquakes. The building considered and its isolation system are a perfect fit in serving the purpose of this work since the isolation system is composed of only four identical isolators. This considerably simplifies the mechanical model and reduces to a bare minimum the number of parameters to be identified. In principle the four isolators that compose the isolation system are different entities with different properties depending on material characteristics, manufacturing process, installing tolerances, possible damage due to external agents, and so on. As it was shown in the previous section, the building is very stiff and, as far as the isolation system is concerned, it is quite reasonable to consider the superstructure as a rigid body. The negligible difference between the acceleration records at the first floor and on the roof appears to corroborate this hypothesis. Therefore a simple model for the description of the behavior of the isolation system may be one that considers the superstructure as a rigid body. Moreover if the substructure can also be considered as rigid, then the model only needs to include 6 degrees of freedom. However, the seismic isolators are very stiff in the vertical direction so that the relative vertical displacement between the substructure and the superstructure can be neglected and negligible are also the two rocking motions about any two perpendicular horizontal axes through the isolation plane. Therefore the mechanical model can be further simplified to include only 3 degrees of freedom, i.e. the two components of the horizontal displacement and the rotation about a vertical axis. Even though the number of degrees of freedom is reduced to a bare minimum, the problem can still be highly redundant due to a large number of isolation devices, which could also be of different types and sizes. Based on a Mixed Lagrangian Formulation, a robust algorithm for the numerical evaluation of the dynamic response of HBIS was proposed at 9th CUEE and 4th ACEE by Oliveto et al. (2012-c). This algorithm will be used, along with a state of

the art system identification strategy, in the attempt of identifying the properties of the isolation system of the considered building, from its response to the 2003 Tokachi-oki Earthquake. The system identification algorithm to be used is the Covariance Matrix Adaptation – Evolution Strategy and a tutorial can be found on-line, (Hansen 2011). The readers that are interested in a comparison between the considered algorithm and competing ones are referred to (Hansen 2006). To set the stage for the identification problem one should first have clear how the identification algorithm works. The algorithm considers a population of feasible systems, where the parameters of each system are generated by using a multivariate Gaussian distribution. Using our mechanical model, the response to the given earthquake is generated for each member of the population, i.e. for each system belonging to the population. The simulated response is then compared to the measured one and the distance between the two is evaluated. This distance is the identification error, which in computer science jargon is called fitness of the individual (i.e. system). All the λ members of the population are ranked according to their fitness and only the best $\mu<\lambda$ are retained. The covariance matrix of the Gaussian distribution is then updated by taking into account the retained μ members of the population and a new generation of λ individuals is created. These are ranked again according to their fitness and the worse $(\lambda-\mu)$ are discarded. The procedure is terminated either when the distance between simulated and experimental response becomes very small or when the number of iterations (generations) exceeds a given limit. Below is a brief description of the identification method introducing aspects of the problem that will motivate the numerical applications presented later. First a set of parameters is generated, defining one of the λ individuals of the population; with this set of parameters a model is constructed and the earthquake response is simulated. This simulation requires a computation time that depends on the size of the system considered. For the time being we can assume that the size of the system is a function of the number of isolators and therefore, the larger is the number of isolators, the larger is the computation time required to produce a system response. At each iteration of the identification procedure, λ of such system responses need to be generated, one for each member of the population. Therefore, since a large number of iterations could be performed before convergence is achieved, it seems clear that large computation times could be involved and that the procedure could benefit from parallel processing. For instance at each iteration, λ different processors could be used simultaneously to evaluate the λ system responses. The CMA-ES software already has parallel processing as an option but this feature has not been exploited within the present work. The size of the population λ depends on the number of parameters needed to be identified. Generally the larger the number of parameters to be identified and the larger is the size of the population required for an effective identification. Moreover, the larger the required size of the population and the larger is the computation time necessary for an identification run. Therefore, if we have good reasons to believe that each isolator in a set of isolators has the same properties as all the others, for that set we can reduce the number of parameters to be identified to those of a single member of the set. This results in a huge saving of computation time making the identification objective more achievable. If however there is evidence that the properties of one or more isolators in a given set may be different because of defective manufacture, installation or exposure, then it may be necessary to consider independent parameters for those isolators or for the whole set, according to whether they are recognizable or not. In that case the computational effort will be much larger but the identified parameters will in the end lead to a more reliable model. The number of parameters to be identified therefore depends on the objectives of the identification and is largely problem dependent. Another aspect of the identification problem that will also guide the applications is related to the fact that an inverse problem can admit more than one solution, i.e. different systems can produce the same response. In such cases any additional knowledge can guide the user to choose the physically consistent solution and to abandon those that are not physically significant. In a way, the more we know about a system, the higher is the probability that we can identify the true parameters. However, there is a minimum amount of information that is required for the true solution to be included among all the possible ones. We shall show, by means of an artificially constructed problem, how a better approximation to a known solution can be achieved, when a minimum amount of information is available, and how worse the approximation can be when the available information drops below that minimum.

4. MODEL PARAMETER IDENTIFICATION FROM LABORATORY TESTS

In order to define a search domain within which the system parameters are expected to be found, it is useful to estimate average values of the system parameters and typical scatters about these average values. To this purpose, static and/or dynamic laboratory tests performed on individual isolators belonging to the class used in the building may be particularly useful. For the building considered, three cyclic tests performed under static conditions at a strain amplitude γ=1 are available in the literature, Kaneko et al. (2004). A set of parameters for a bilinear model were evaluated from each of these tests using the CMA-ES evolution strategy and the fitness function (error function) defined below:

$$e^2 = \left(\frac{A-A^e}{A^e}\right)^2 + \left(\frac{I_{xx}-I^e_{xx}}{I^e_{xx}}\right)^2 + \left(\frac{I_{yy}-I^e_{yy}}{I^e_{yy}}\right)^2 + \left(\frac{I_{xy}-I^e_{xy}}{I^e_{xy}}\right)^2 \quad (1)$$

where $A^e, I^e_{xx}, I^e_{yy}, I^e_{xy}$ are the area and second moments of area of the experimental restoring force-displacement curve, and $A, I_{xx}, I_{yy}, I_{xy}$ are the corresponding quantities from the

model. The minimum value attained by Equation (1) provides an optimal set of parameters for each test. A comparison between experimental and identified curves for the test performed in 1996 is shown in Figure 4, while the three sets of identified parameters from the three available tests are shown in Table 1. A comparison between the results from the 1996 and 2004 tests shows that aging results in a 5% increase of the hardening stiffness k_1, a 10% increase of yield strength Q and a 13% reduction in the initial stiffness k_0. A comparison between the results from the two tests performed in 2004 provides hints of anisotropic behavior, possibly due to large strains induced by the 2003 earthquake.

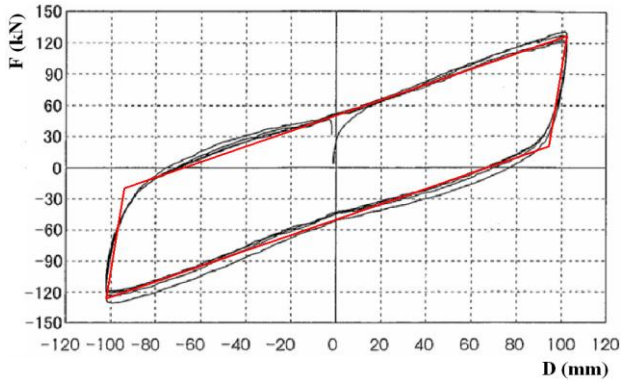


Figure 4 Experimental and identified curves for the test performed in 1996

Table 1 Identified bilinear curve parameters from the provided laboratory tests

Test	*Q (kN)*	k_0 *(N/mm)*	k_1 *(N/mm)*
1996	50	13569	755
2004 X	55	10443	788
2004 Y	55	13043	800

5. MODEL PARAMETER IDENTIFICATION FROM EARTHQUAKE RESPONSE RECORDS

When trying to identify the system parameters, it is useful to define a search space within which realistic values of the unknown parameters may be found. This can be achieved by defining lower and upper bounds for each system parameter. Starting point in this case are the results from the static laboratory tests performed in 1996 and 2004. The lower bounds for each parameter are tentatively set to 80% of their lowest value obtained from the laboratory tests, while the upper bounds are set to 140% of their largest value obtained from the same tests. For the system mass the same criterion is applied starting from a reference mass of 575 tons. The lower bound for the damping ratio is set to zero while the upper bound is set to 5%. The resulting search space is given in Table 2.

5.1 Isolators with identical properties

In this first identification application it is assumed that the four isolators all have the same properties. The identification of the system parameters is based on the

Table 2 Search space for the real problem

	Lower bound	*Upper bound*
m (ton)	460	716
k_0 *(N/mm)*	8354	18996
k_1*(N/mm)*	604	1119
Q (kN)	40	77
ζ *(%)*	0	5

minimization of the distance between the recorded and simulated responses of the building to the earthquake. Available are the horizontal input motion in terms of acceleration components measured at the basement of the building below the isolation surface, and the response of the roof and first floor of the building, just above the isolation system. Because the model used for the identification considers the superstructure as a rigid body, the simulated acceleration is compared to the average of the accelerations measured on the first floor and on the roof. The fitness of the solution, or error function, is defined as follows:

$$e^2 = \frac{\left[a_x - a_x^e, a_x - a_x^e\right]}{\left[a_y^e, a_y^e\right]} + \frac{\left[a_y - a_y^e, a_y - a_y^e\right]}{\left[a_y^e, a_y^e\right]} \quad (2)$$

where a_x, a_y, a_x^e, a_y^e are the acceleration components obtained from the numerical simulation and the earthquake response records. The inner product in Eq. (2) is defined as follows:

$$[a,b] = \sum_{i=1}^{N} a_i b_i = \sum_{i=1}^{N} a(t_i) b(t_i) \quad (3)$$

A first run of the CMA-ES led to a solution with an identification error e^2 = 0.0823 or 8.23%. However, two of the identified parameters were at their bounds. The mass, at 716 tons, was at the upper bound, while the initial stiffness k_0, at 8338 N/mm, was slightly below the lower bound. For this reason the search space was enlarged as shown in Table 3. This way the identified parameters are all well within the chosen bounds. It's worth observing that the initial stiffness k_0 is much lower than the values obtained from the identification of the static laboratory tests. This can be explained by the fact that the tests were performed at a much lower strain level than that experienced during the earthquake. On the other hand, the yielding stiffness k_1 is much larger than the one obtained from the static laboratory tests in 1996 and 2004. This can be explained by the fact that the tangent stiffness is generally larger in dynamic conditions than in static ones. The yield strength parameter Q was in all runs somewhat smaller than that obtained from the static laboratory tests; again this result can be attributed to the much larger strains experienced under the earthquake than in the laboratory. The identified mass was in all runs 16 to 36% greater than the reference value. Finally the

Table 3 Identified system in run 1 and new search space

	Identified	*Lower bound*	*Upper bound*
m (ton)	716.0	460	800
k_0 *(N/mm)*	8338.3	6000	18996
k_1*(N/mm)*	1102.3	604	1200
Q (kN)	44.4	40	77
ζ *(%)*	4.1	0	5

identified value of the structural damping resulted in a minimum value of 4.11% and a maximum value of 4.63%.

The quality of each solution is measured by the error function which, as shown in Table 4, is minimum in run 4 and maximum in run 1. Table 4 provides also information about the number of iterations in each run and also the iteration at which the minimum error was obtained. It should be noticed that 8 system response simulations are required at each iteration. The fittest 4 are then used to update the mean and the covariance matrix of the multivariate Gaussian distribution used to select the members of the next generation. Table 4 also includes the iteration at which the best fitness or least error was achieved.

Table 4 Performance of each identification run

	Run 1	*Run 2*	*Run 3*	*Run 4*
Iterations	86	122	100	72
Minimum error	0.0823 (iter.84)	0.0814 (iter.120)	0.0815 (iter.92)	0.0809 (iter.69)

The comparison between simulated and recorded accelerations is shown in Figures 5 and 6. Figure 5 (a) and 5 (b) show the NS and EW components of the first floor accelerations, while the NS and EW components of the roof accelerations are shown in Figure 6(a) 6 (b). Although the comparisons refer to the solution of best fitness, i.e. e^2 = 0.0809, almost the same plots are obtained for the other runs since the order of magnitude of the fitness is the same in all cases.

In order to appreciate the difference between the solutions produced in various runs some histories of selected response parameters are shown in the following. In Figure 7 the history of the yield force is shown in different colors for the four runs. It is obvious that the vertical lines between positive and negative yield loads correspond to phases of elastic behavior. The differences among the various solutions can be appreciated in terms of amplitude of the yield load. The histories of the restoring force in each isolator are shown in Figure 8 (a) and 8 (b) for the NS and EW directions respectively. The major differences among the solutions appear to be in terms of stiffness and peak force rather than of peak displacement. Finally the orbit of the relative motion of the isolation system is shown in Figure 9. It is worth noticing that the differences among the solutions barely emerge in the orbits. A statistical interpretation of the results may be worth considering, especially for cases in which the number of runs should assume a statistical significance. The solutions for each of the four runs are

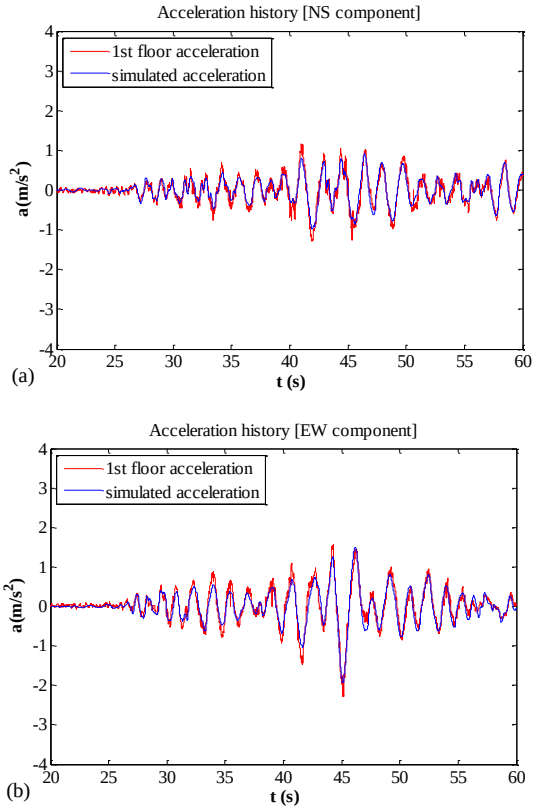


Figure 5 Simulated and recorded 1st floor acceleration history, (a) NS, and (b) EW component

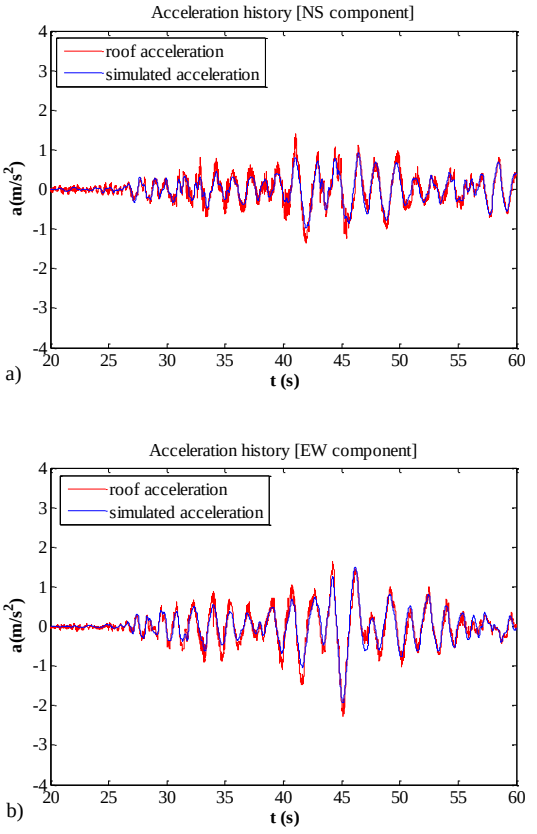


Figure 6 Simulated and recorded roof acceleration history, (a) NS, and (b) EW component

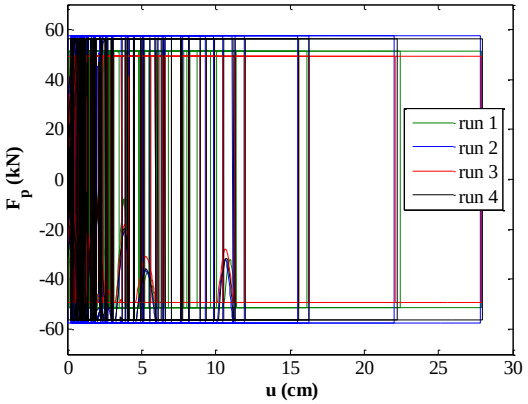


Figure 7 History of the yield force for all runs

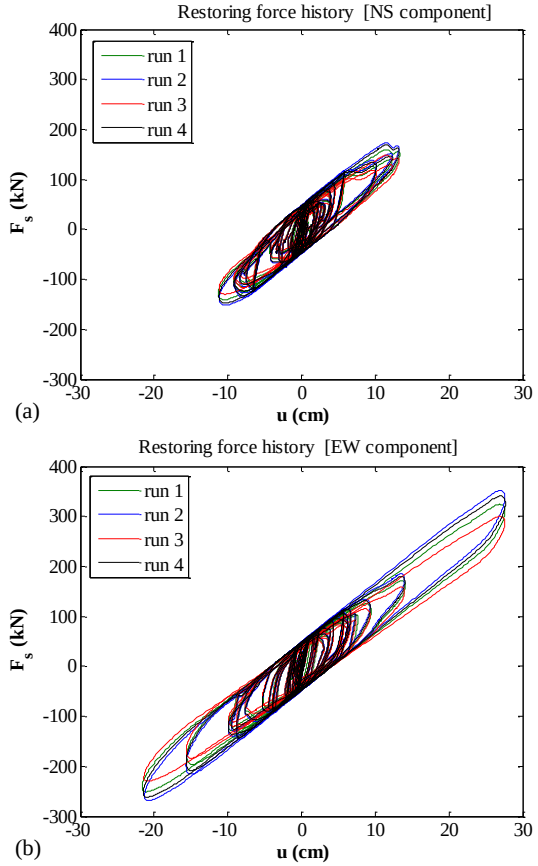


Figure 8 History of the restoring force of each isolator for all runs, (a) NS, and (b) EW component

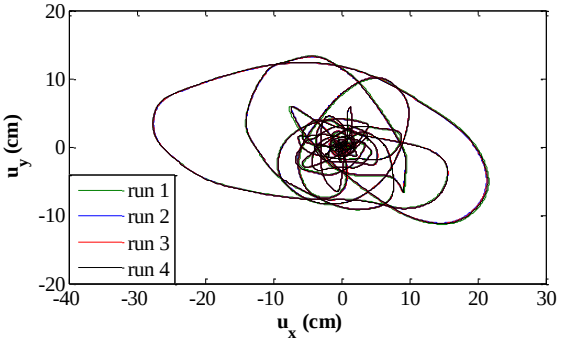


Figure 9 Orbit of the relative motion of the isolation system for all runs

shown in Table 5, while their average, standard deviation and coefficient of variation are shown in Table 6. For the initial stiffness only the coefficient of variation is almost 10%, while for all the other identified parameters it is in the range 5%-7%. It is reasonable to believe that for a large number of runs the coefficient of variation could become considerably smaller and the solution may be given a probabilistic structure.

Table 5 Identified systems for each of the four runs

	Run 1	*Run 2*	*Run 3*	*Run 4*
m (ton)	716.0	782.5	665.7	755.5
k_0 *(N/mm)*	8338.3	7674.9	6526.4	7558.1
k_1*(N/mm)*	1102.3	1194.7	1018.2	1153.8
Q (kN)	44.4	48.5	41.6	47.6
ζ *(%)*	4.1	4.6	4.6	4.5

Table 6 Average, standard deviation and coefficient of variation for the identified parameters of all runs

	average	*st. deviation*	*c.o.v. (%)*
m (ton)	729.9	50.8	7.0
k_0 *(N/mm)*	7524.4	748.8	10.0
k_1*(N/mm)*	1117.3	76.1	6.8
Q (kN)	45.6	3.2	7.0
ζ *(%)*	4.5	0.2	5.3

5.2 Isolators with different properties

The manufacturing process of component materials and of the isolators themselves can hardly assure the identity of the mechanical properties of the isolators even when they are designed to be the same. Installing imperfections and damage during service can also contribute to the diversification of the mechanical properties from one unit to another. If each isolator has to be considered has having independent properties, the number of parameters to be identified can easily become quite large and the identification problem can become unmanageable. For the problem at hand, where there are three mechanical parameters to be identified for each isolator, the number of unknown parameters increases from 3 to 12. The computational time becomes exceedingly long and several computers may have to be committed to this single task. Preliminary runs have shown that a good match between simulated and recorded accelerations can be obtained by considering widely different values of the mechanical properties among the isolators. However the physical conditions did not point to such large diversification. This rose doubts about the well-posedness of the problem and whether the available data is sufficient to obtaining a realistic solution. In order to provide some insight in the problem a fictitious system with known properties was generated as follows. The isolators were numbered from 1 to 4, as shown in Figure 2, and given properties estimated from the 1994 test (isolator 1), the 2004 test in the X direction (isolator 2), the 2004 test in the Y direction (isolator 3) and the average value from the three previous estimates (isolator 4). The mass of the system was assumed as provided by the designer

and damping was set to 1%. The data specified above are shown in the second column of Table 7. In the third and fourth column of the same table the lower and upper bounds are shown, established on the base of a normal distribution with a 80% probability of the parameters being within the bounds. The bounds for the system mass were established by using a standard deviation equal to 10% of the mean, while the bounds for the damping ratio were arbitrarily chosen as 0 and 5%.

Table 7 Data and search space for the constructed problem

	Data	*Lower bound*	*Upper bound*
m (ton)	511.2	446	577
k_0 *(N/mm)*	11431 10395 9563 10463	7649	13276
k_1*(N/mm)*	746 769 733 749	693	816
Q (kN)	50 55 56 54	47	60
ζ (%)	1	0	5

5.3 Minimum requirements for measured response

It has already been mentioned that dynamic identification is equivalent to the solution of an inverse problem whereby several systems can provide the same solution; therefore the solution of an inverse problem is generally not unique and only engineering judgment can help to select a physically acceptable solution among several ones that are mathematically feasible. Heuristically it may be thought that the more information is available, the closer one can get to the actual solution. However, one may enquire what is the minimal information required to obtain acceptable identification results. We argue that with a model like ours, characterized by three degrees of freedom, at least three independent acceleration components are required for the identification to converge to a physically acceptable solution. To verify this assumption a system simulation was run under the considered earthquake and the three independent acceleration components shown in Figure 10 (a) were calculated. These were assumed as the recorded system response under the earthquake and used for system identification. For comparison the two acceleration components at the center of mass, Figure 10 (b), were also calculated to be used as an alternative system identification. If our assumption is valid, the identification obtained by using the data of Figure 10 (a) should provide better results than the identification obtained by using the data acquired according to Figure 10 (b).

5.4 Results and comments

All together 7 runs were performed, 5 of which referring to the system response described in Figure 10 (a)

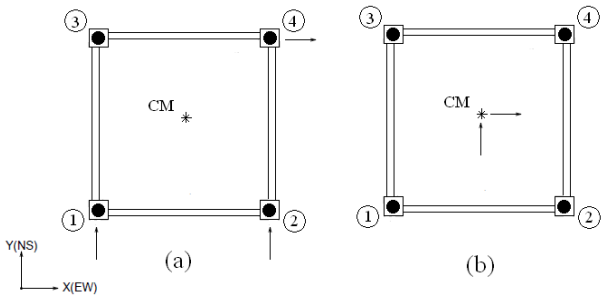


Figure 10 System identification using (a) 3, and (b) 2 acceleration components

and 2 concerned with the system response sketched in Figure 10 (b). The results of runs 1,2,3,4,6 are shown in Table 8 in terms of errors of the identified parameters. Before commenting on the errors it is worth mentioning some general features. On the first row of the table, besides the number characterizing the run, the total population λ is shown along with the number μ of the fittest members retained as parents for the next generation. It may be worth noticing how the results of section 5.1 were obtained with the couple (μ,λ)=(4,8), while in the present application two different settings have been used: (μ,λ)=(5,11) which is the default setting for CMA-ES and (μ,λ)=(11,22), used in an attempt to get closer to the real solution. The use of a larger population results in a much larger number of fitness (error) evaluations and in the exploration of a larger area of the search space. By looking at the last row of Table 8, where the best fitness obtained in each run is shown along with the iteration in which that fitness was obtained, it may be observed that the best fitness was obtained with the larger population. In general we may expect that the best results should be those in run 6, where the smallest fitness (error) is obtained, followed by those in run 3. However, a large population does not always lead to better results because the worst fitness is obtained in run 4, which is characterized by a large population. The next worst solution is obtained in run 2 where the default population was used. A very important point that needs to be emphasized is that the best fitness or minimum error results also in the least error for the system parameters, as may be seen from the row above the last where the average of the absolute value of the error on all the identified parameters is shown. It is true that the average of the absolute errors for run 3 is smaller than that for run 6, but the difference in fitness is very small in the two cases. Another point worth noticing is that the error on individual parameters can be positive or negative, that is the value of the parameter can be approached from above or from below. Although the best fitness value would indicate that run 6 provides the best solution, the error on each parameter and the average of the absolute value of the errors tells us that run 3 is the one providing the best approximation to the real solution. However, in a real situation we would know the best fitness but not the error on the individual parameters. The results of runs 5 and 7, obtained from only two acceleration components of the response, are shown in Table

Table 8 Error (%) on identified parameters when 3 components of acceleration are used in the identification

Run	*1*	*2*	*3*	*4*	*6*
(μ,λ)	*(5,11)*	*(5,11)*	*(11,22)*	*(11,22)*	*(11,22)*
m	-1.56	4.93	-0.11	-0.85	-0.53
k_0	-1.65	7.31	-0.07	-13.48	-0.77
	-1.33	3.30	-0.15	7.81	-0.22
	-1.60	2.90	-0.17	10.50	-0.24
	-1.58	9.53	-0.07	-6.91	-0.79
k_1	-1.99	5.86	-0.76	-2.05	2.56
	-1.27	3.92	0.54	-0.31	-3.53
	-1.29	4.42	0.63	-1.35	-3.73
	-1.91	5.25	-0.82	-0.12	2.60
Q	-1.74	7.48	-0.21	6.29	-1.02
	-1.15	2.59	-0.05	-6.35	-0.05
	-1.28	2.55	0.00	-8.20	-0.08
	-1.87	7.06	-0.13	4.82	-1.06
ζ	0.00	-1.70	0.05	3.10	-0.05
Mean |error|	1.44	4.91	0.27	5.15	1.23
Fitness	8.87 $*10^{-7}$	4.19 $*10^{-4}$	1.71 $*10^{-7}$	4.94 $*10^{-4}$	1.64 $*10^{-7}$
(iter)	(142)	(198)	(143)	(129)	(159)

Table 9 Error (%) on identified parameters when 2 components of acceleration are used in the identification

Run	*5*	*7*
(μ,λ)	*(5,11)*	*(5,11)*
m	5.37	-2.06
k_0	-8.18	-2.81
	16.09	-9.40
	2.36	19.68
	15.88	-14.02
k_1	7.97	-4.96
	6.04	-0.80
	4.22	-2.78
	2.41	0.39
Q	10.89	0.92
	-7.11	-3.59
	5.95	0.31
	11.90	-6.40
ζ	-1.15	0.55
Mean|error|	7.54	4.90
Fitness(iter)	$4.02*10^{-4}$(117)	$3.49*10^{-4}$(203)

9. In these cases only the default population was used and the fitness obtained is comparable to the worse results of the previous case, i.e. in the order of 10^{-4}. The mean value of the absolute error on the individual parameters is also comparable to the worse results of the previous case. In general one would be tempted to conclude that better results are obtained by using three independent acceleration components of the response rather than just two. However, the comparison is unfair for two reasons. Only two runs are considered in the second case against five in the first, and a larger population is used in three out of five runs in the first case against none out of two runs in the second. At this point the results should be considered inconclusive until a fair comparison can be made by using the same number of runs and the same population size in both cases.

6. CONCLUSIONS

The dynamic identification of base isolation systems from earthquake response acceleration records has been considered. A mathematical model based on a Mixed Lagrangian Formulation presented at CUEE_12 has been used as the theoretical basis for the prediction of the dynamic response of the system. The model parameters are the basic unknowns of the identification procedure, which is based on the optimal match between the response recorded during the earthquake and the simulated response by means of the mechanical model. While it may be easy to simulate the response of a given system and to find a measure of the distance between recorded and simulated response, it may be difficult to guide the process of generating a new system that provides a better match than previous ones and eventually converge to the actual or optimal system. This task is performed by a state-of-the-art algorithm denoted "Covariance Matrix Adaptation – Evolution Strategy" or simply CMA-ES. Although the identification has been carried out for a very simple base isolation system composed of only four identical isolators, the exercise has given rise to a series of problems that need to be solved if the dynamic identification of such systems is to be of any use in practice. The first problem is in terms of computational time. The simulation of the response of a single isolation system to a given earthquake motion takes a given time depending on the complexity of the system. However, the identification process requires the simulation of the response of a large number of base isolation systems, and therefore the computational time can easily become very large, even for the simple system considered in this work. This problem can be handled by parallel computing by which a number of processors can be used at the same time to perform different tasks of the same problem. The CMA-ES algorithm is already predisposed for parallel applications but this capability was not exploited in the present study. A second problem concerns the possibility of solutions characterized by unrealistic system parameters but a very good match between recorded and simulated response. Understanding why these situations arise and how to handle them is an obvious and interesting problem. An answer lies in the very nature of the identification problem which, being an inverse problem, can admit multiple solutions. A possible barrier to unsuitable system parameters may be devised by defining suitable search spaces where physically admissible system parameters can be found. The barrier is obviously provided by the boundary of the search space. In the applications of the present work the construction of the search space was aided by the identification of laboratory tests performed on the isolators constituting the isolation system considered. Another problem is given by the possible incompleteness of the measured data. In order to define without ambiguity the

configuration of the system considered, which is modeled as a three degrees of freedom system, three independent kinematic response parameters (displacements, velocities or accelerations) are needed; if we only have two of them we do not have a unique configuration and a multiplicity of systems could produce the same response. An experiment has been carried out within this study to verify whether the assumption is correct or defective; the results are so far inconclusive but the direction to pursue in order to obtain a clear answer seems well defined. In conclusion it can be said that one identification run is not sufficient to provide reliable results, even when the problems outlined above have been handled with care. Several runs are generally necessary which at best can all provide the same results, but in general do not. The solution is therefore provided in probabilistic terms with a mean vector of system parameters, the standard deviation and the coefficient of variation. The smaller is the standard deviation and the associated coefficient of variation, the more accurate is the solution obtained. For the case considered, the elastic stiffness k_0 evaluated from system identification is considerably lower than the one obtained from laboratory tests. The yield strength parameter Q is also considerably smaller than the value obtained from laboratory tests. In both cases the discrepancy can be attributed to the considerably different strain level in the two cases (much larger under the earthquake than during the laboratory tests). The post yielding stiffness k_1 obtained from system identification is much larger than that identified from laboratory tests. The discrepancy is justified by the fact that dynamic tests always provide larger values of this parameter than static tests do.

Acknowledgements:

The authors are grateful to Manboku Construction Company Ltd for allowing the use of the building earthquake records and to Kajima Corporation for providing data on the building design and post-earthquake analysis.

References:

Naeim, F. and Kelly, J.M. (1999), "Design of Seismic Isolated Structures, from Theory to Practice," John Wiley & Sons Inc.

Oliveto, G., Granata, M., Buda, G. and Sciacca, P. (2004), "Preliminary Results from Full-Scale Free Vibration Tests on a Four Storey Reinforced Concrete Building after Seismic Rehabilitation by Base Isolation," *JSSI 10th Anniversary Symposium on Performance of Response Controlled Buildings* ,Yokohama, Japan.

Oliveto, N.D., Scalia, G. and Oliveto, G. (2010), "Time Domain Identification of Hybrid Base Isolation Systems using Free Vibration Tests," *Earthquake Engineering and Structural Dynamics*, **39**(9),1015–1038.

Athanasiou, A. and Oliveto, G. (2011), "Modelling Hybrid Base Isolation Systems for Free Vibration Simulations," *8CUEE conference proceedings: 8th International Conference on Urban Earthquake Engineering. Center for Urban Earthquake Engineering, Tokyo Institute of Technology,* Japan, 1293–1302.

Athanasiou, A., Oliveto, G. and Oliveto, N. D. (2011-a), "Modelling Hybrid Base Isolation Systems for Earthquake Response Simulations", *Proceedings Conference of Italian Association of Earthquake Engineering, (ANIDIS 11)*, Bari, Italy.

Oliveto, G., Athanasiou, A. and Oliveto, N.D. (2012-a), "Analytical Earthquake Response of 1D Hybrid Base Isolation Systems," *Soil Dynamics and Earthquake Engineering*, **43**, 1-15.

Athanasiou, A., De Felice, M., Oliveto, G. and Oliveto, P.S. (2011-b), "Evolutionary Algorithms for the Identification of Structural Systems in Earthquake Engineering," Proceedings of *ECTA 2011: International Conference on Evolutionary Computation Theory and Applications*, Paris, France, 52–62.

Athanasiou, A., De Felice, M., Oliveto, G. and Oliveto, P.S. (2013), "Dynamical Modeling and Parameter Identification of Seismic Isolation Systems by Evolution Strategies," *Studies in Computational Intelligence*, Springer-Verlag. (to appear).

Oliveto, G., Markou, A. and Athanasiou, A. (2012-b). "Recent Advances in Dynamic Identification and Response Simulation of Hybrid Base Isolation Systems," *Proceedings of 15thWCEE 2012: 15thWorld Conference on Earthquake Engineering*, Lisbon, Portugal.

Oliveto, G., Oliveto, N. D. and Athanasiou, A. (2011-c), "Mixed Lagrangian Formulation versus Exact Solution in the Dynamic and Earthquake Response of Hybrid Base Isolation Systems", *Proceedings Conference of Italian Association of Theoretical and Applied Mechanics*, (AIMETA 11), Bologna, Italy.

Oliveto, N.D., Athanasiou, A. and Oliveto, G. (2012-c), "Mixed Lagrangian Formulation for Dynamic and Earthquake Response of 2D Hybrid Base Isolation Systems," *Joint conference proceedings: 9th International Conference on Urban Earthquake Engineering/4thAsia Conference on Earthquake Engineering, Tokyo Institute of Technology,* Japan, 1373–1382.

Suzuki, Y., Takashi, U., Saito, Y.and Takenaka, H. (2004), Behaviors of a Base-Isolated Building in Kushiro City for the Tokachi-oki Earthquake in 2003: Part 1. Earthquake Observation Records, *In: Summaries of technical papers of Annual Meeting Architectural Institute of Japan. B-2, Structures II, Structural dynamics nuclear power plants Architectural Institute of Japan 2004 (20040731)*, paper no.21140, 279-280[in Japanese].

Kaneko, S., Suzuki, Y., Takashi, U., Takenaka, Y., and Kawaguchi, S. (2004),Behaviors of a Base-Isolated Building in Kushiro City For the Tokachi-oki Earthquake in 2003 : Part 2. Examination of the Soundness of Lead Rubber Bearing, *In: Summaries of technical papers of Annual Meeting Architectural Institute of Japan. B-2, Structures II, Structural dynamics nuclear power plants Architectural Institute of Japan 2004 (20040731)*,paper no.21141, 281-282 [in Japanese].

Hansen, N. (2011), "The CMA Evolution Strategy: A Tutorial," online: http://www.lri.fr/~hansen/cmatutorial.pdf, 1-34.

Hansen, N. (2006), "The CMA Evolution Strategy: a Comparing Review," *In: J. Lozano, P. Larranaga, I. Inza, E. Bengoetxea (Eds.), Towards a New Evolutionary Computation, Advances on Estimation of Distribution Algorithms*, Springer, 75-102.

10CUEE CONFERENCE PROCEEDINGS
10th International Conference on Urban Earthquake Engineering
March 1-2, 2013, Tokyo Institute of Technology, Tokyo, Japan

EXPERIMENTAL STUDY ON U-SHAPED STEEL DAMPERS UNDER 2D RANDOM LOADING HISTORIES

Diana Ene[1)], Yu Jiao[2)], Shoichi Kishiki[3)], Satoshi Yamada[4)]
Yoshinao Konishi[5)], Norihisa Kawamura[5)], Masao Terashima[5)],

1) Graduate student, Dept. of Environmental Science and Technology, Tokyo Institute of Technology, Japan
2) Assistant Professor, Dept. of Architecture, Tokyo University of Science, Japan
3) Lecturer, Dept. of Architecture, Osaka Institute of Technology, Japan
4) Associate Professor, Structural Engineering Research Center, Tokyo Institute of Technology, Japan
5) Nippon Steel and Sumikin Engineering CO., LTD., Tokyo, Japan
ene.d.ab@m.titech.ac.jp, yujiao@rs.tus.ac.jp, kishiki@archi.oit.ac.jp, yamada.s.ad@m.titech.ac.jp
konishi.yoshinao@eng.nssmc.com, kawamura.norihisa@eng.nssmc.com, terashima.masao@eng.nssmc.com

Abstract: In the past few decades, the concept of "base-isolation" has been adopted as a practical strategy for earthquake-resistant design. Many base-isolated structures use 2 types of devices: one with high compressive strength and low lateral stiffness (e.g. rubber bearings) and the other with high energy dissipation capacity (e.g. U-dampers). U-shaped steel dampers are a relatively new system, therefore the previous research involves only the basic behavior under 1D dynamic loading test (Kishiki 2008) and 2D static loading test with circular and elliptical patterns (Takayama 2012). These studies proposed a fatigue evaluation curve using the cumulative damage index D_2 and the index for torsion-induced reduction of the cyclic deformation capacity J_f. The present study focuses on assessing the behavior under 2D random loading histories and establishing whether the results agree with the previously proposed relationship. This objective was achieved by conducting 2 sets of experimental tests: (1) 2D dynamic random loading test (UCSD) and (2) 2D static random loading test (Tokyo Tech). The results show the following: (1) all the specimens fracture after meeting the minimum requirements given by the D_2-J_f relationship; (2) Tokyo Tech test results agree with those from UCSD test, which proves that loading speed has negligible effect on the U-dampers' hysteresis curves.

1. INTRODUCTION

The present study focuses on the fatigue behavior of U-dampers as energy dissipating elements during a seismic event. The main goal of the present paper is to assess whether the fatigue evaluation curve D_2-J_f defined in (Takayama 2012) can be applied to estimate the damage induced by a two-dimensional seismic excitation. In order to do that, the first step was to establish a set of realistic loading histories (named "orbits") by conducting appropriate response analysis as described in (Ene 2012). Using these orbits, two sets of experimental tests were performed as summarized in **Table 3**. In the following, the obtained results are explained and compared to each other.

2. FATIGUE EVALUATION CURVE

The algorithm and formulae for computing the damage index D_2 and J_f index are described in (Takayama 2012) and summarized below.

The first step for the computation of D_2 induced by a 2D orbit is to compute the damage index of the dampers on X (**Eq. (1a)**) and the one of those on Y direction (**Eq. (1b)**) by using Miner's rule. This is done by summing up the damage at 0º and 90º for each direction. The total damage index D_2 will be the maximum value (**Eq. (2)**).

$$D_{2_X} = \sum_i \frac{1}{N^{0^\circ}_{fX,i}} + \sum_i \frac{1}{N^{90^\circ}_{fY,i}} \tag{1a}$$

$$D_{2_Y} = \sum_i \frac{1}{N^{0^\circ}_{fY,i}} + \sum_i \frac{1}{N^{90^\circ}_{fX,i}} \tag{1b}$$

$$D_2 = \max(D_{2_X}, D_{2_Y}) \tag{2}$$

where:
D_{2_X} – damage index for dampers parallel to X axis;
D_{2_Y} – damage index for dampers parallel to Y axis;
$N^{0^\circ}_{fX,i}$ – number of cycles to fracture for amplitude A_i selected when applying the displacement on X (for dampers parallel to X);
$N^{90^\circ}_{fY,i}$ – number of cycles to fracture for amplitude A_i selected when applying the displacement on Y (for dampers parallel to X);
D_2 – total damage index.

$$J_f = \sum_{i=1}^{n} \left(\gamma_i \cdot \gamma_{i+1} \cdot \frac{\gamma_i + \gamma_{i+1}}{2} \cdot \left| \Delta\varphi_i \right| \right) \qquad (3)$$

where:

$\gamma_i = \frac{R_i}{H}$ is the ratio between the radius at step "i" and the height of the damper element (**Figure 1**);

$\Delta\varphi_i$ infinitesimal angle between 2 consecutive steps

n total number of steps in the input orbit.

Using these 2 indices, the fatigue evaluation curve is defined as:

$$D_2 = \begin{cases} 1 & \text{if } J_f \le 15 \\ 1.6 - 0.04 \cdot J_f & \text{if } 15 < J_f \le 30 \\ 0.4 & \text{if } 30 < J_f \end{cases} \qquad (4)$$

3. SETUP

The basic concept of the setup is the same for both tests: specimen is loaded by inducing at its bottom part a given displacement history – dynamically for UCSD test, statically for Tokyo Tech test – while its upper part is kept fixed.

The setup for the static loading test is shown in **Figure 2**. The moving table is acted upon by two orthogonal horizontal jacks that control the input orbit. The reaction block keeps the upper part of the specimen fixed and prevents it from tilting.

3. PARAMETERS OF ANALYSIS AND ANALYTICAL RESULTS

The target parameter for both dynamic and static test is the input orbit. The set of orbits has been established by conducting 2D response analysis on a single mass system with 2 degrees of freedom and bilinear behavior (Figure **5**). The response of the system is determined by using Multiple Shear Spring model (MSS) (**Figure 4**). Using this analytical model and the fatigue evaluation curve, preliminary analysis was conducted for El Centro, Hachinohe, JMA Sendai and Kobe records. By looking at the results shown in **Figure 6**, one can easily notice that the damage produced by the original records is very small. That is why a maximum displacement limit of 400mm was set, in accordance to typical design criteria for base-isolated structures in Japan. Thus, each seismic record has been assessed a suitable amplification factor in order to reach this value. Moreover, since the limit capacity of the actuators in the UCSD facility is 8m of cumulative displacement, some of the records had to be trimmed or divided into two parts.

As input data, 21 seismic records were used and, function of the value of the damage index D_2 and of the shape of the orbit, 14 of them were selected to be conducted in the dynamic test (**Table 3**) (Ene 2012).

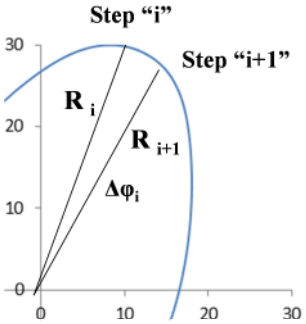


Figure 1 Computation of J_f and γ

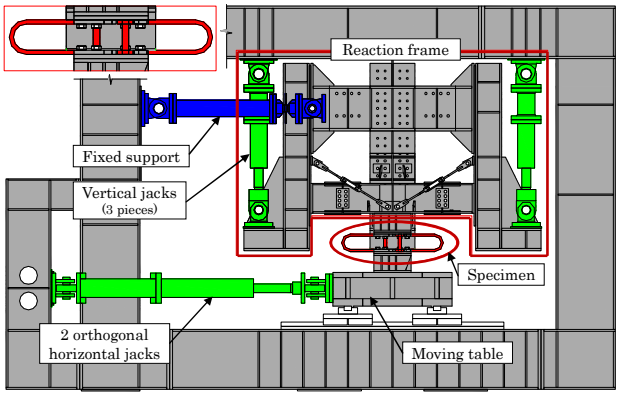


Figure 2 Setup plan (static loading test)

Table 1 Geometric characteristics of U-dampers

Type	L_t [mm]	L_f [mm]	H [mm]	w [mm]	t [mm]	Q_y^{exp} [kN]
U40	610	415.5	231	60	28	133
U50	872	601.5	335	85	40	270

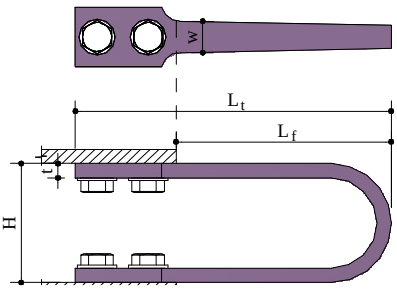


Figure 3 Geometric characteristics of U-dampers

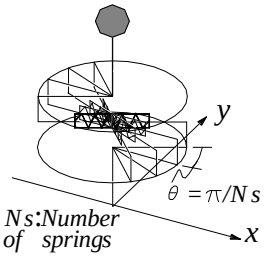


Figure 4 MSS model

4. LOADING HISTORIES AND RESULTS OF THE DYNAMIC LOADING TEST

The specimens used in UCSD test consist of 4 units of 4 U50 and 2 units of 8 U50 (**Table 3**). The geometric characteristics of U40 and U50 elements are given in Table **1**.

According to Miner's rule, a specimen fractures when the damage index D_2 reaches 1.0. By looking at the values of the damage indices listed in **Table 2**, one can understand that it takes several earthquakes to reach the fracture of a specimen. Hence, a sequence of seismic events is required in order to load one specimen up to fracture. This will be called a "loading protocol".

The 14 orbits obtained by conducting response analysis are organized into 4 loading protocols. Theoretically, one loading protocol ends when it intersects the fatigue evaluation curve because that is considered to be the point where the specimen reaches fracture. However, in practice, the specimens proved to be able to take a larger number of cycles. The objectives of the loading protocols as well as the main observations during the test are listed in **Table 3**. The obtained results show that, with the exception of unit UD4 which was able to resist considerably longer than expected, all the data points are situated on the conservative side, relatively close to the fatigue evaluation curve. The latter represents, thus, the lower bound of the data set, therefore it can be stated that the proposed fatigue evaluation curve is suitable to estimate the amount of damage induced by seismic excitation.

5. LOADING HISTORIES AND RESULTS OF THE STATIC LOADING TEST

The specimens for the static loading test consist of 4 units of 4 U40 (**Table 3**). Since the size of the U-damper elements in this test (U40) is different from the one used in the dynamic loading test (U50), in order to be able to compare the two sets of results, the orbits were scaled down with factor r:

$$r = \frac{H_{U40}}{H_{U50}} \cdot d_{\max} \qquad (5)$$

where: H_{U40}, H_{U50} heights of U40, U50
$d_{\max}$ maximum displacement in UCSD test (400mm).

Because loading random orbits using Tokyo Tech's facilities is time-consuming and difficult to conduct, the number of data points for each input orbit has been reduced and part of the small amplitude cycles was disregarded. The orbits obtained after applying this and **Eq. (5)** are further on referred to as "simplified orbits". The loading protocols for the static loading test are summarized in **Table 3**, and are, generally, the same with the ones used in UCSD test.

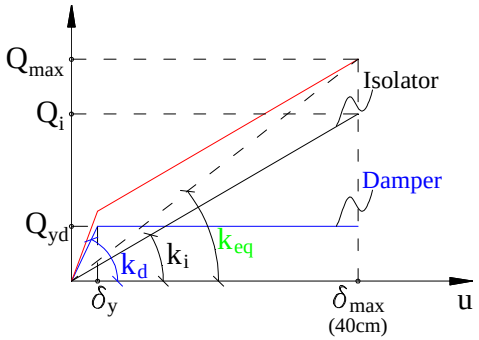


Figure 5 Behavior of the analytical model

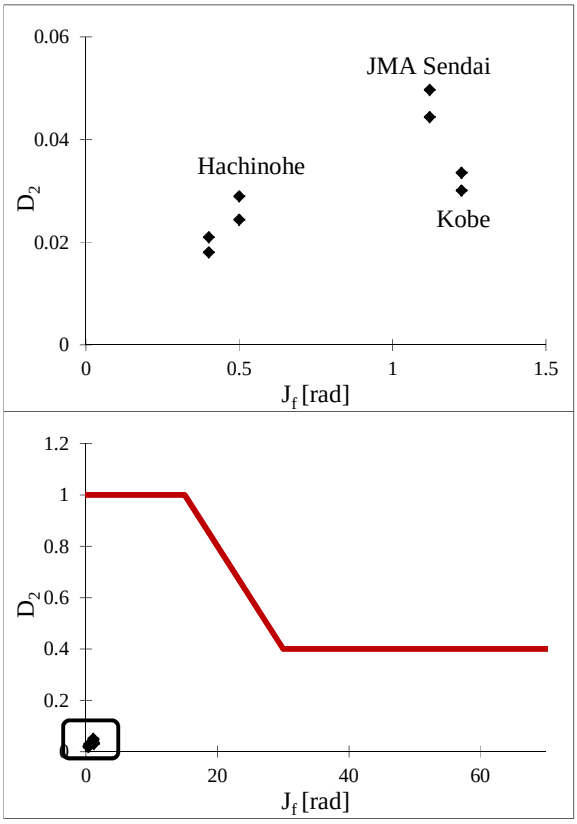


Figure 6 Results of the preliminary analysis

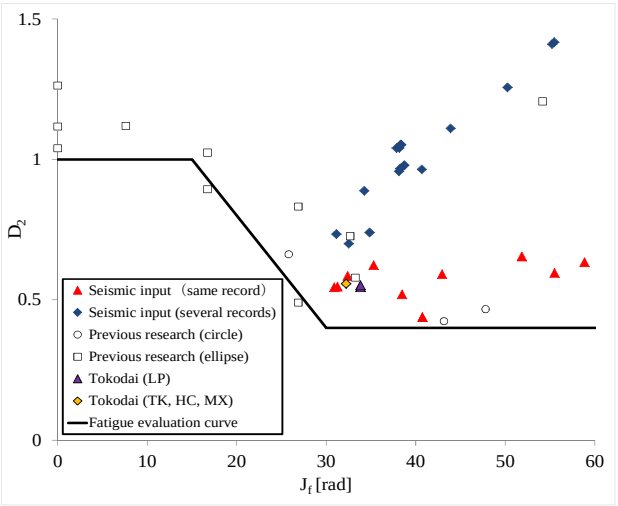


Figure 7 Fatigue evaluation curve and fracture points

5. COMPARISON BETWEEN THE TWO SETS OF RESULTS

As stated above, the main objective of the present study is to investigate the hysteresis behavior and the deformation capacity of U-dampers under 2D random loading histories. Hence, the most representative results are the force-deformation relationships for each specimen.

In order to be able to compare the hysteresis curves from the two sets of tests one needs to take into consideration the fact that different damper sizes have been used. This is done by calibrating the data in the static test as it follows:

a. Displacement is multiplied with scale factor s_{f1} :

$$s_{f1} = \frac{h_{U50}}{h_{U40}} = 1.450 \qquad (6)$$

b. Force is multiplied with scale factor s_{f2}:

$$s_{f2} = \frac{Q_{y_U50}}{Q_{y_U40}} = 2.030 \qquad (7)$$

where Q_{y_U50} is the yileding force of U50 damper size found in UCSD test

Q_{y_U40} is the yileding force of U40 damper size found in Tokyo Tech test

In Figure **8** are plotted the results obtained by applying **Eq. (6)** and **(7)** to the data in the static test against the original data in the dynamic test, both for the first set of (Takatori, Hachinohe, Mexico). In Figure **9** the same data types are plotted for the units loaded with Loma Prieta input orbit. Based on these graphics, one can state that the shape of the hysteresis curves in UCSD test agrees well with that in Tokyo Tech test. The slightly larger differences in Figure **9** are more noticeable because the simplified version of Loma Prieta orbit neglects a considerable part of the small amplitude cycles in the dynamic orbit in order to reduce the difficulty and the loading time during the test.

Overall, the results show that the loading speed has negligible effect on the force-deformation relationships for U-dampers.

5. CONCLUSIONS

The results of the two tests can be summarized in the following conclusions:

1) The relationship between the damage index D_2 and fracture index J_f (Takayama 2012) provides a conservative and sufficiently accurate estimation for the damage induced by earthquake excitation.
2) The force-deformation curves for the dynamic and static tests have almost the same shape which proves that the loading speed has negligible effect on the fatigue behavior of U-dampers.

Table 2 Analyzed seismic records and values of the D_2

No.	Seismic record		Earthquake	Ampl. factor	D_2 (U50)
	Full name	Short			
1	Takatori	TK	Kobe '95	0.65	0.06
2	Osaka NP	NP		2.20	0.10
3	Hachinohe	HC	Tokachi-oki '68	1.90	0.06
4	Yarimca	YP	Kochaeli '99	0.57	0.04
5	TCU078	CA	Chichi '99	2.60	0.06
6	TCU129	CB		1.35	0.06
7	JMA Sendai	JS	Tohoku 2011	1.55	0.06
8	Ishinomaki Hos.	IH[1]		-	0.02
		IH[2]			0.04
9	K-net Iwaki	IK		1.25	0.04
10	K-net Fukushima	FS[1]		3.80	0.05
		FS[2]			0.05
11	NewHall	NH	Northridge '94	0.85	0.04
12	Olive View	SO		0.80	0.04
13	Agnews Hospital	LP	Loma Prieta '89	2.60	0.09
14	Mexico	MX	Victoria '80	2.39	0.06

References:

Kishiki, S., Ohkawara, Y., Yamada, S. and Wada, A. (2008). "Experimental Evaluation of Cyclic Deformation Capacity of U-shaped Steel Dampers for Base-Isolated Structures"; AIJ, vol.73, No. 624, 333-340, Feb. 2008;

Yoshikawa, H., Takayama, D., Ene, D., Kishiki, S., Yamada, S., Konishi, Y., Kawamura, N., Terashima, M. (2012). "Experimental Study on Characteristics of U-Shaped Damper under Two Directional Horizontal Loading", part 1: "Bi Axial Loading Test of U-damper"; AIJ, No. 21170, 339-340;

Takayama, D., Ene, D., Kishiki, S., Yamada, S., Konishi, Y., Kawamura, N., Terashima, M. (2012). "Experimental Study on Characteristics of U-Shaped Damper under Two Directional Horizontal Loading", part 2: "Evaluation of Low Cycle Fatigue under Bi Axial External Force"; AIJ, No. 21171, 341-342;

Ene, D., Kishiki, Takayama, D., S., Yamada, S., Konishi, Y., Kawamura, N., Terashima, M. (2012). "Experimental Study on Characteristics of U-Shaped Damper under Two Directional Horizontal Loading", part 3: "Experimental Plan of U-shaped Damper under Random Loading Histories"; AIJ, No. 21172, 343-344.

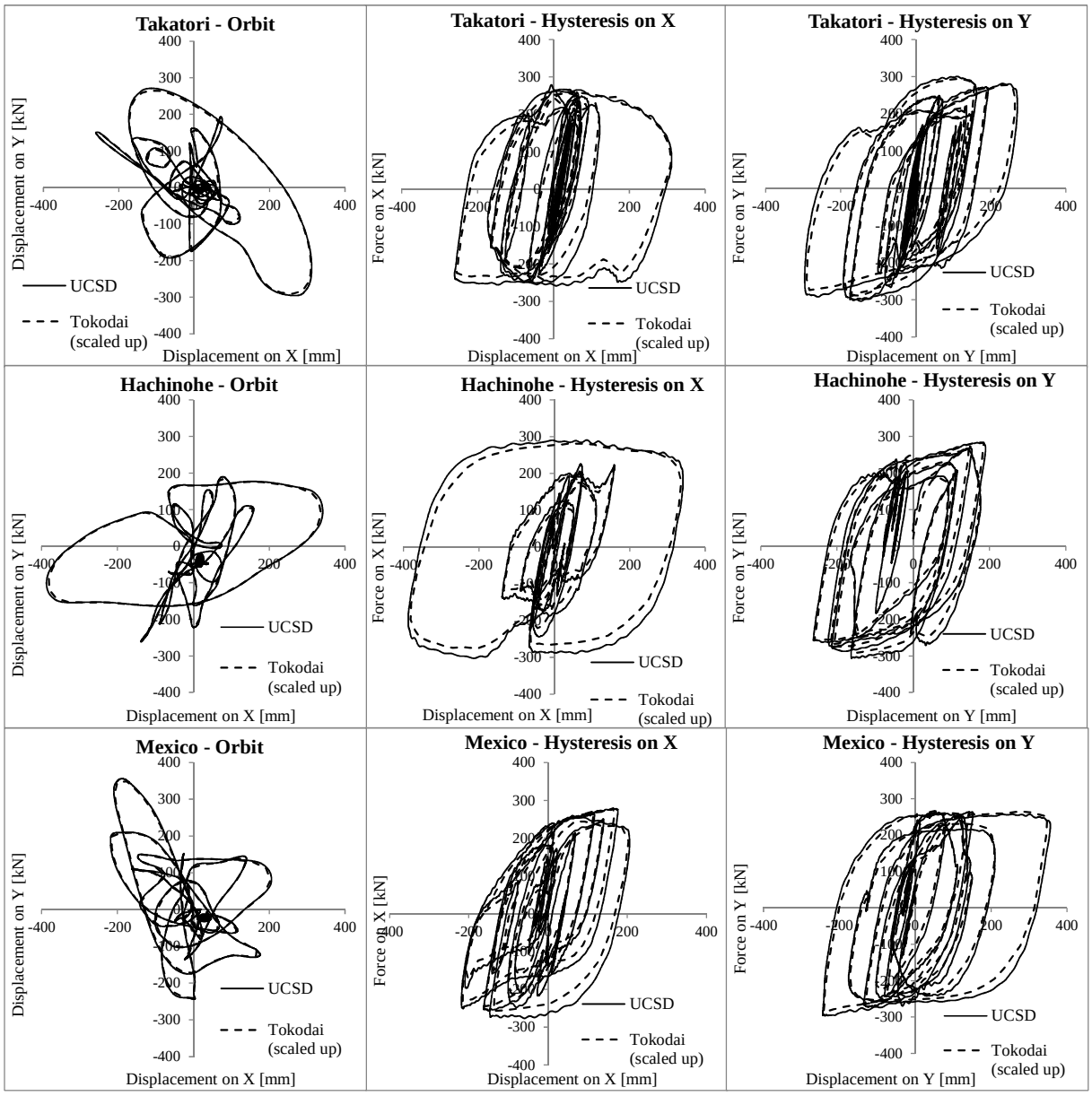


Figure 8 Comparison between the dynamic test (UCSD) and static test (Tokodai) – 1st set of (TK, HC, MX)

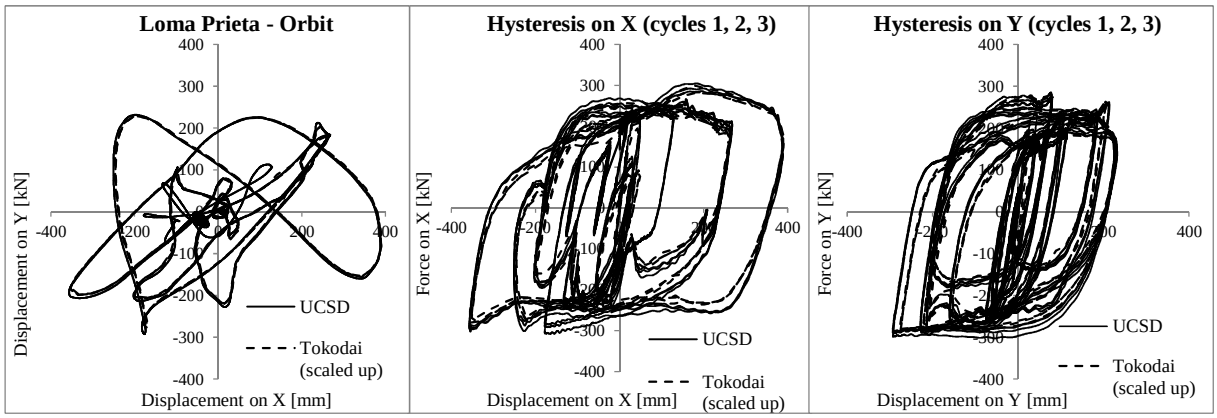


Figure 9 Comparison between dynamic test (UCSD) and static test (Tokodai) – Loma Prieta (cycles 1, 2 and 3)

Table 3 Loading protocols for each test

Test	Unit	Element Type	Input Orbits	Objective of the Loading Protocol	Observations
UCSD: Dynamic	UD1	4U50	***LP1:*** (TK→HC→ MX)x5	Evaluate the fatigue behavior when subjected to repeated changes in the direction of the max. displacement	X-1, Y -1 fractured during MX4, X-2 during TK5, Y -2 in MX5;
	UD2		***LP2:*** LPx7	Evaluate the fatigue behavior when subjected to a strong seismic motion	Y-1, Y -2 fractured during LP6, X-1, X-2 during LP7;
	UD3		***LP3:*** JSx8→YPx2	Evaluate the fatigue behavior at minimum slope	Slight contact with the jigs during JS8; when loading YP, deformation starts to reverse; X -1 fractured during YP2, X -2 & Y -1 in YP3, Y-2 in YP4;
	UD4		***LP4:*** IH→SO→NH →CA→NP→MX→ CB→IK→FS→LP, (NP→LP)x4	Evaluate the fatigue behavior when subjected to various seismic records	Little damage after the designed loading protocol; Y-1 fractured in NP4, Y -2 in LP5, X-1 & X-2 in NP5;
	UD5	8U50	***LP1:*** (TK→HC→ MX)x4	Same as for unit UD1	X-1 fractured during MX4, the rest of 7 U -dampers fractured during TK5;
	UD6		***LP3:*** JSx5→YPx12	Same as for unit UD2	1st contact during JS5 => switch to YP; X -1 fractured during YP9, Y -1 in YP10, Y-2 in YP11, X-2 in YP12; 2nd contact during YP12 => stopped loading;
Tokyo Tech: Static	US1	4U40	***LP1-s**:*** (TK→HC →MX)→LPx5	Compare with unit UD1	X-1 fractured during LP5;
	US2		***LP2-s***: LPx7	Compare with unit UD2	X-1 & Y -1 fractured during LP7.

* Simplified orbits

** X-1, X-2 are the dampers placed parallel to X direction, Y-1, Y-2 are the ones placed parallel to Y axis.

10CUEE CONFERENCE PROCEEDINGS
10th International Conference on Urban Earthquake Engineering
March 1-2, 2013, Tokyo Institute of Technology, Tokyo, Japan

INFLUENCE OF UNBONDING MATERIAL ON LOW-CYCLE FATIGUE PERFOMANCE OF BUCKLING-RESTRAINED BRACES

Chun-Lin Wang, Quan Chen, Tao Li, and Shao-Ping Meng

Key Laboratory of Concrete and Prestressed Concrete Structures of the Ministry of Education, Southeast University, Nanjing, China
chunlin@seu.edu.cn; quanchenseu@gmail.com; litaojinling@126.com; msp1960@vip.sina.com

Abstract: This paper presents component tests of two all-steel buckling-restrained braces (BRBs) to examine the effect of unbonding materials on their low-cycle fatigue performance. The axial loading history consisted of the variable strain amplitude and the constant strain amplitude. Test results showed that the BRB with the unbonding material has a better low-cycle fatigue capacity than the BRB without the unbonding material. Unbonding materials can reduce the friction coefficient between the core brace member (BM) and the restraining members (RMs). The gradually stripping of oxygen films of the BM and the RMs increases the friction coefficient and the unbonding material can also prevent the core brace from wear. The friction between the BM and the RMs causes the concentration and accumulation of negative plastic deformations in the middle region and positive plastic deformations in the end region. The accumulation of plastic deformations is significant, when the friction is large enough.

1. INTRODUCTION

Buckling-restrained braces (BRBs) are one of the structural components with excellent hysteretic behavior, which have found widespread applications in the US, Japan, Taiwan and elsewhere (Uang *et al.*, 2004; Tsai *et al.*, 2004). Wakabayashi *et al.* (1973) developed a pioneering system with a flat steel plate sandwiched between a pair of precast reinforced concrete panels, and a layer of epoxy resin and silicon resin was covered over the steel plate to reduce the friction between the steel plate and the concrete panels. Watanabe *et al.* (1988) conducted tests on BRBs with the core members coated with the concrete encased in a steel tube, using vinyl/mastic tape to permit the transverse expansion due to the effect of Poisson's ratio and to avoid the adhesion between the steel core and the restraining concrete. Until now, some possible unbonding materials (e.g. epoxy resin, silicon resin, vinyl tapes, etc.) have been widely employed (Black *et al.*, 2002; Tsai *et al.*, 2004). Especially, Tsai *et al.* (2004) tested ten BRBs with the different unbonding materials and found that a 2-mm thick silicon rubber sheet has the least axial load difference for the proposed BRB.

However, pouring and curing of the concrete rise the manufacturing costs of BRBs. As an alternative, all-steel BRBs have been developed (Tsai *et al.*, 2004; Trembly *et al.*, 2006; Usami *et al.*, 2008, Chou and Chen, 2010). Iwata (2004) studied all-steel BRBs without the unbonding materials and found they finally fractured as a result of the continued progress of the plastic deformation. Tremblay *et al.* (2006) compared the performance of the conventional BRBs with all-steel BRBs without the unbonding material. The results indicated that it is necessary to minimize the friction and satisfy the uniform strain demand in the brace core. Recently, in the experiment presented in the literature (Chou and Chen, 2010), a small air gap, replacing the unbonding material, was used between the brace member and the steel restraining tubes. Test results showed the small air gap does not affect the cyclic behavior of the proposed BRB.

It is obvious that additional experiments are needed to further investigate the necessity of the unbonding materials. In this paper, two BRB specimens with the same dimensions are employed to estimate the effect of the unbonding material on the low-cycle fatigue performance of the all-steel BRB. Their difference is one specimen with the unbonding material, a type of butyl rubber, and another without the unbonding material, instead of a small air gap.

2. TEST PROGRAM

2.1 Specimens

As shown in Figure 1, the employed BRB consists of a steel plate brace member (BM), a pair of steel restraining members (RMs) and a pair of steel fillers. The end ribs are welded on the steel plate to increase the out-of-plane stiffness of the end region. The stopper is set by enlarging the width of the brace member at the center. Specimen A-2.0, has a 1-mm thick air gap, and specimen U-2.0 employed the unbonding material, a 1-mm thick butyl rubber, on four sides of the BM.

Figure 2 gives the nominal geometric dimensions of the BM and Table 1 lists some corresponding measured geometric dimensions. As shown in Figure 3, the BM is inserted between a pair of RMs connected by the

high-strength bolts through two filler members. The out-of-plane and in-plane gaps d and d_0, respectively, are between the BM and the RMs or filler members. Table 2 provides the actual values of the gap widths.

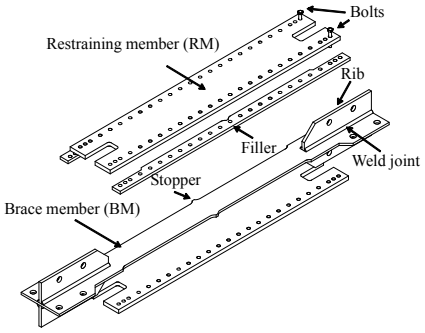


Figure 1 Assemblage of BRB

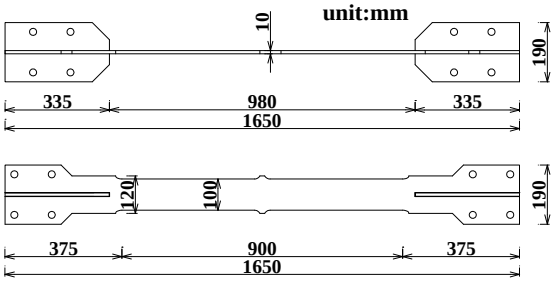


Figure 2 Dimensions of BM

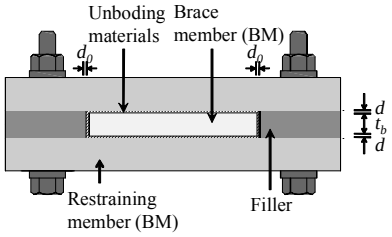


Figure 3 Cross-section Details

Table 1. Geometric Dimensions of BM

Specimen	b_b(mm)	t_b(mm)	Unbonding material
A-2.0	100.12	9.83	No
U-2.0	100.04	9.77	Yes

Note: b_b and t_b are the width and the thickness of BM.

Table 2. Values of Gap Width

Specimen	Actual gap width (mm)	
	Out-of-plane d	In-plane d_0
A-2.0	0.94	0.97
U-2.0	0.97	1.01

2.2 Test Setup and Loading Pattern

The specimen was vertically mounted on the Material Test System (MTS) by high-strength bolts. A hydraulic actuator with a loading capacity of 1000 kN and with a displacement capacity of +/-75mm was used for the cyclic loading, which was displacement-controlled via a linear variable displacement transducer mounted on the actuator.

As show in Figure 4, the test programs consisted of two phases, including the variable strain amplitude (VSA) loading and the constant strain amplitude (CSA) loading. At the beginning, four cycles with the strain amplitude of $0.75\varepsilon_y$ were adopted to measure the initial axial stiffness of the specimens within the elastic stage. Subsequently, the loading was imposed at the target brace strain amplitude (the yielding segment deformation δ divided by its length L_b) of 0.5, 1.0, 1.5, 2.0, 2.5 and 3.0% (two cycles at each strain level). The second phase was the CSA loading with the constant strain amplitude of 2.0%.

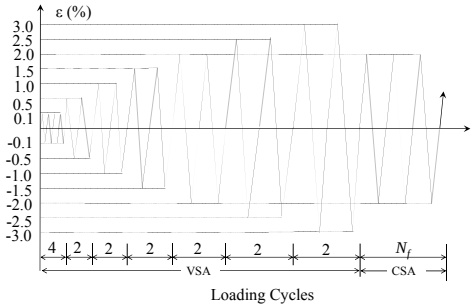


Figure 4. Strain-controlled loading pattern

3. TEST RESULTS

3.1 Hysteretic Curves

The stress-strain relations of the two specimens are presented in Figures 5 and 6. They exhibit stable behavior without any signs of degradation until the 45th and the 53rd cycles of the CSA loading, respectively. It can be concluded from the different failure cycle numbers that specimen U-2.0 has a better low-cycle fatigue properties due to the existence of the unbonding material.

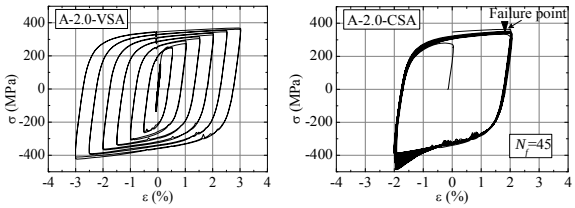


Figure 5 Stress-strain curve of A-2.0

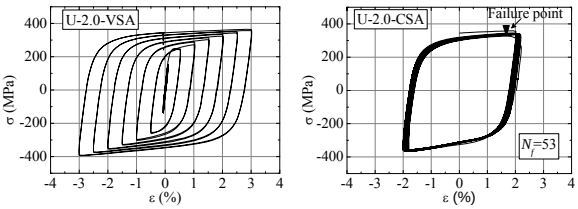


Figure 6 Stress-strain curve of U-2.0

It can be seen in Figure 5 that the tension behavior and compression behavior of specimen A-2.0 are severely asymmetry. The maximum compressive force of BRBs is generally greater than the tensile force, due to the friction and the Poisson's effect (Tsai *et al.*, 2004). The axial load difference Γ is defined as:

$$\Gamma = \frac{P_{\max} - T_{\max}}{T_{\max}} \quad (1)$$

where P_{max} and T_{max} are the maximum compressive and tensile brace forces at a same absolute axial deformation level.

Figure 7 provides the Γ values of the two specimens except for the first cycle of the two phases, which are significantly influenced by strain-hardening effect. During the VSA loading, the Γ values of the two specimens both increase as the strain becomes larger. It is because that the friction between the BM and the RMs increases as the normal contact force between the BM and the RMs enlarges. However, the Γ values of specimen A-2.0 increase more rapidly than those of specimen U-2.0. It can be concluded that the unbonding material can reduce the friction coefficient between the BM and the RMs. When it comes to the CSA, The Γ values of Specimen U-2.0 remain steady. However, the Γ values of Specimen A-2.0 increase much higher with the load imposing on it. The maximum Γ value of Specimen A-2.0 before fracture is 42.7%, which is exceeding the recommended value of 30% (AISC, 2010). The excessive Γ value could bring the unbalanced force to structures under earthquake.

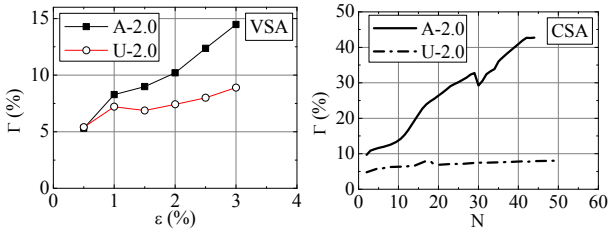


Figure 7 Axial loading difference under cyclic loading

It can be inferred that the friction between the BM and RMs of specimen A-2.0 gradually increases, even though the strain retains constant. As shown in Figure 8, the polishing of the surface and the absence of surface oxygen films were observed after the test in the BM of specimen A-2.0. The removal of the surface oxygen films from the brace member could amplify the coefficient of kinetic friction for several times, due to the greater molecular interaction and adhesion between the surface of the BM and the RMs, as discussed in the literature (Bowden amd Hunghes, 1939). The stripping of surface oxygen films in specimen A-2.0 was gradually happened due to the friction between the BM and the RMs, while this phenomenon was not found in specimen U-2.0 which is protected and lubricated by unbonding materials. So, without polishing and wear, the friction between the BM and RMs will not increase rapidly during the CSV loading. Unbonding materials can limit the Γ value of all-steel BRBs in an acceptable level. In addition, unbonding materials can prevent the BM from wear, which allows all-steel BRBs to suffer three strong earthquakes without severe damage and replacement (Usami *et al.*, 2007).

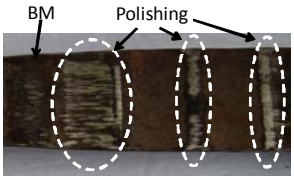


Figure 8 The absence of oxygen films after the test

3.2 Failure Mode

The failure modes of the two specimens are presented in Figures 9 and 10. These figures show that the brace's failure was induced by the crack initiating from the weld toes of the ribs. Reduction of the section area was found at the center of the brace member of specimen A-2.0 and there is not the same phenomenon in specimen U-2.0. Besides, a few subtle cracks were found near the stopper in specimen U-2.0.

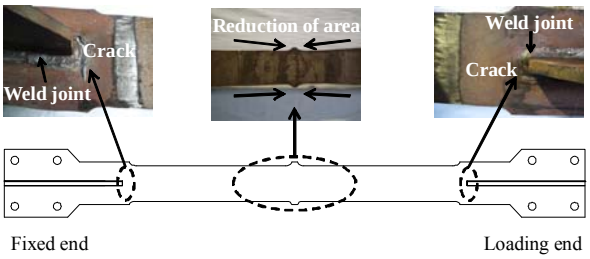


Figure 9 Failure mode of A-2.0

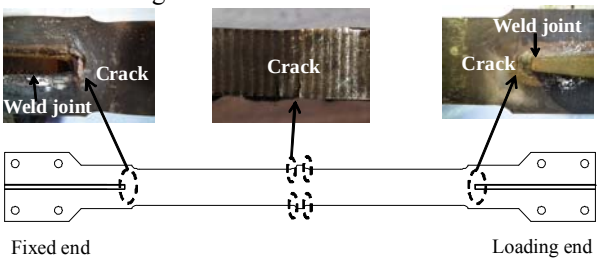


Figure 10 Failure mode of U-2.0

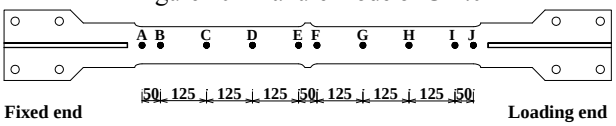


Figure 11 The locations of measured points in specific brace regions

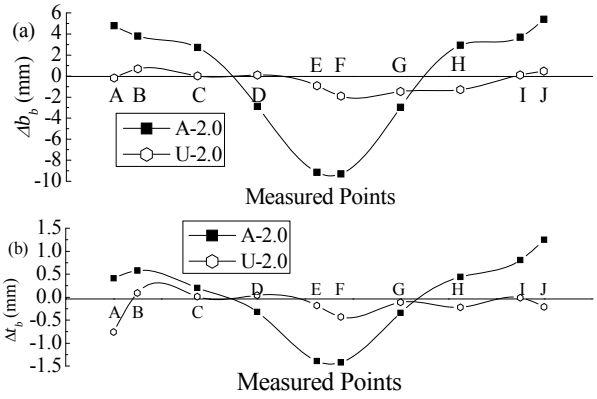


Figure 12 The brace residual transverse deformations of the two specimens (a) in the direction of the width; (b) in the direction of the thickness

After tests, the brace members were examined and residual transverse dimensions were measured along the brace yielding segment (points A-J in Figure 11). The fabrication errors of the brace member are controlled within 0.2mm for the width and 0.05mm for the thickness, so the initial average width (b_b) and thickness (t_b) of the brace member are used to calculate the brace residual transverse deformations. The brace residual transverse deformations are showed in Figure 12.

These observations indicate that, in specimen A-2.0, the middle region of the yielding segment shrunk and the end region of the yielding segment expanded obviously after the test, while the residual deformations of specimen U-2.0 are irregular and relatively small. The reason for the residual deformations in specimen A-2.0 could be the large friction between the BM and the RMs. Figure 13 shows the friction between the BM and the RMs under compression in the influence of the stopper. Then the axial force in the end region of the yielding segment F_e and the axial force at the middle region of the yielding segment F_m can be calculated as:

Under compression:

$$F_e=P \quad (2)$$

$$F_m=P-f_p \quad (3)$$

Where P is the axial force imposed on the specimen by the actuator under compression; f_p is the friction force between the BM and the RMs under compression.

Under compression, F_e is larger than F_m due to friction, so the section of the end region of the yielding segment expanded much more than that of the middle region of the yielding segment. And when it came to tension, the stress of the middle region of the yielding segment is higher than that of the end region due to the smaller section area. As a consequence, the middle region of the yielding segment developed more residual transverse deformation in tension.

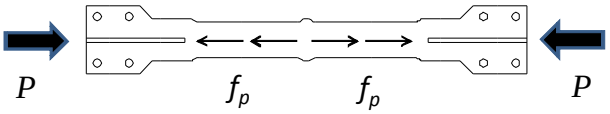


Figure 13 The friction between the BM and the RMs under compression

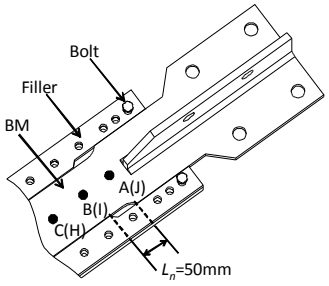


Figure 14 Details of the assemblage in the end region

What's more, in specimen A-2.0, the brace residual transverse deformations in the width direction of the measured points A, B, C, H, I and J exceeded the constrained dimension, which is twice the in plane gap width d_0 (0.97mm). As shown in Figure 14, points A and J lie in the in-plane unrestrained region (L_n), so the two sections can expand freely under compression. However, if the width of the restrained region (points B, C, H and I) expands more than twice the in plane gap width d_0, the BM would squeeze into the RMs. If the squeezing force is large enough, the filler will move aside slightly, allowing larger expansion of the section of points B, C, H and I. The squeezing force could intense the phenomenon that F_e is larger than F_m, encouraging more pronounced concentration and accumulation of negative and positive plastic deformations in specific brace regions. The concentration deformations in the end region of the yielding segment also enlarge the squeezing force, which forms a vicious circle. The squeezing force not only contributes to the residual deformation of all-steel BRBs, but also enlarges the axial load different. Lager in-plane width is needed to avoid the squeezing force. However, the comparable tests showed that unbonding materials can avoid the squeezing force and decrease the demands of the in-plane gap width.

4. CONCLUSIONS

Component tests of two BRB specimens was performed to examine the effect of unbonding materials on their low-cycle fatigue performance. The main results are summarized as follows:

(1) Test results showed that the BRB with the unbonding material has a better low-cycle fatigue capacity than the BRB without the unbonding material.

(2) Unbonding materials can reduce the friction coefficient between the BM and the RMs. The test of specimen A-2.0 show that the gradually stripping of oxygen films of the BM and the RMs increases the friction coefficient and the unbonding material can also prevent the BM from wear.

(3) The friction between BM and the RMs causes the concentration and accumulation of negative plastic deformations in the middle region and positive plastic deformations in the end region. The accumulation of plastic deformations is significant, when the friction is large enough.

(4) The in-plane squeezing force occurred between the BM and the fillers of the BRB without the unbonding material because of the excessive plastic deformation in the end region, which contributes to the large axial loading difference. The test of specimen U-2.0 showed that the unbonding material can avoid the squeezing force and decrease the in-plane gap width demand.

Acknowledgements:

The authors would like to acknowledge financial supports from the National Natural Science Foundation of China (51008077, 51278105) and the Priority Academic Program Development of Jiangsu Higher Education Institutions. Grateful acknowledgments are given to Professors Tsutomu Usami and Hanbin Ge at Meijo University for their suggestions for relevant research.

References:

AISC (2010). Seismic Provisions for Structural Steel Buildings. Chicago, Illinois.

Bowden, F.P. and Hunghes, T.P. (1939), "The Friction of Clean Metals and the Influence of Adsorbed Gases. The Temperature Coefficient of Friction", *Proceedings of the Royal Society A*. 263-279.

Black, C.J., Makris, N., and Aiken, I.D. (2002), "Component Testing, Stability Analysis and Characterization of Buckling-Restrained Unbonded Braces", Pacific Earthquake Engineering Research Center, University of California, Berkeley.

Chou, C.C. and Chen, S.Y. (2010), "Subassemblage Tests and Finite Element Analyses of Sandwiched Buckling-Restrained Braces", *Engineering Structures*. 32(8), 2108-2121.

Iwata, M. (2004), "Applications-Design of Buckling Restrained Braces in Japan", *13th World Conference on Earthquake Engineering*, Vancouver, B.C., Canada.

Usami, T. (2007), "Developing High-Performance Damage Control Seismic Dampers", *10th symposium on ductile design method for bridges (Special Lecture)*, JSCE, 11-22. (in Japanese)

Usami, T., Ge, H.B., and Kasai, A. (2008), "Overall Buckling Prevention Condition of Buckling-Restrained Braces as a Structural Control Damper", *14th World Conference on Earthquake Engineering*. Beijing, China.

Uang, C.M., Nakashima, M., and Tsai, K.C. (2004), "Research and Application of Buckling Restrained Braced Frames", *International Journal Steel Structure*. 4(4), 301-313.

Wakabayashi, M., Nakamura, T., Katagihara, A., Yogoyama, H., and Morisono, T. (1973), "Experimental Study on the Elastoplastic Behavior of Braces Enclosed by Pre-cast Concrete Panels under Horizontal Cyclic Loading - Parts 1 & 2", *Summaries of technical papers of annual meeting: Kinki Branch of Architectural Institute of Japan*. 121–128.

Watanabe, A., Hitomi, Y., Saeki, E., Wada, A., and Fujimoto, M. (1988), "Properties of Brace Encased in Buckling-Restraining Concrete and Steel Tube", *9th World Conference on Earthquake Engineering*. Tokyo-Kyoto, Japan. 719-724.

Tsai, K.C., Lai, J.W., Hwang, Y.C., Lin, S.L., and Weng, C.H. (2004), "Research and Application of Double-core Buckling Restrained Braces in Taiwan", *13th World Conference on Earthquake Engineering*. Vancouver, B.C., Canada.

Tremblay, R., Bolduc, P., Neville, R., and DeVall, R. (2006), "Seismic Testing and Performance of Buckling-Restrained Bracing Systems", *Canadian Journal of Civil Engineering*. 33(2), 183-198.

10CUEE CONFERENCE PROCEEDINGS
10th International Conference on Urban Earthquake Engineering
March 1-2, 2013, Tokyo Institute of Technology, Tokyo, Japan

A NEW RESTRAINING SYSTEM FOR BUCKLING-RESTRAINED BRACES

Quan Chen Tao Li Chun-Lin Wang Shao-Ping Meng

Key Laboratory of Concrete and Prestressed Concrete Structures of the Ministry of Education, Southeast University, Nanjing China
quanchenseu@gmail.com; litaojinling@126.com; chunlin@seu.edu.cn; msp1960@vip.sina.com

Abstract: A new restraining system for Buckling-Restrained Brace (BRB) has been proposed in this paper. Its feature is that the steel plate core is partially sandwiched by the restraining system. The corresponding advantages include increasing the stiffness of the restraining system, enhancing the design flexibility and decreasing the self-weight of the brace. In order to investigate this new partial restraining mechanism, a relatively simple restraining system made of the multilayer steel plates, is presented. Component tests are conducted on three BRB specimens under the uniaxial quasi-static cyclic loading. Test results reveal that this type of BRB with proper details exhibits a stable cyclic behavior and cumulative inelastic ductility capacity, so it can serve as the effective hysteretic damper. Moreover, the failure mechanism is experimentally verified by investigating the ratio of the unrestrained width to the thickness of the core plate as an important design parameter. At last, some suggestions for the design of this BRB are summarized based on the experimental results and they are considered helpful to develop the similar BRBs.

1. INTRODUCTION

Buckling-restrained braces (BRBs), which exhibit stable and predictable hysteretic behavior both in tension and compression, are an attractive alternative to conventional steel braces. To ensure the performance of BRBs under earthquake loading, the AISC Seismic Provisions for Structural Steel Buildings (2010) recommend each tested brace to achieve ductility corresponding to 2.0 times the design story drift and a cumulative inelastic axial ductility capacity of 200 times the yield displacement. Component tests of BRBs have been conducted by numerous researchers (Black, *et al.*, 2002, Merritt, *et al.*, 2003, Wang, *et al.*, 2012). As shown in Table 1, the maximum and cumulative ductility requirements in these tests can be easily achieved, which are defined as (Fahnestock, *et al.*, 2007)

$$\mu_{max} = \frac{\Delta_{max}}{\Delta_{by}} = 2\frac{\Delta_{bm}}{\Delta_{by}} \approx 1.8C_d \tag{1}$$

$$\mu_c = \frac{\sum \Delta_i}{\Delta_{by}} \tag{2}$$

Where Δ_{max} is the brace maximum deformation, Δ_{by} is the brace yield deformation; Δ_{bm} is the brace deformation corresponding to design story drift; C_d is the displacement amplification factor; Δ_i is the brace inelastic deformation. What's more, previous large-scale tests of BRBFs developed failure modes that did not permit BRB ductility capacity to be fully utilized (Lin, *et al.*, 2011).

When BRBs are applied to bridge structures or large-span frame structures, the deflection dramatically grows and the construction becomes rather difficult. Therefore, the development of lightweight BRBs is essential. Moreover, lightweight BRBs have the potential to allow manual transport, lifting and connection of braces to the existing structures. In the past few years, several types of lightweight BRBs have been proposed to achieve weight savings against mortar-filled steel tubes. Tests of the BRB composed of an H-shaped core element and an external tube (Ju, *et al.*, 2009) show that global flexural buckling is the main failure mode. Another new type of aluminum alloy BRBs is proposed and its low-cycle fatigue performance has proved to be well in the experiment (Usami, *et al.*, 2012, Wang, *et al.*, 2013). What's more, Ultra-Lightweight BRBs (composed of BRBs, structural aluminum seismic dissipaters and FRP) is designed (Tinker and Dusicka 2012), reducing the weight by 59% to 76% of conventional BRBs.

Since conventional BRBs demonstrate much greater ductility capacity than needed, it is cost-efficient to develop lightweight BRBs by reducing the materials used in the restraining system with limited impact to the ductility capacity. Based on this idea, a new type of BRB as one example has been given in this paper, as shown in Figure 1. The new restraining system comprises four small steel tubes, a pair of steel fillers and a few connecting plates. The proposed restraining system can provide sufficient stiffness against the overall and local buckling of the BRBs with fewer materials.

In order to investigate this new partial restraining mechanism, this paper gives a relatively simple type of BRB made of the multilayer steel plates, which is convenient for manufacture. Tests of three BRB specimens with different

ratios of the unrestrained width to the thickness of the core plate are conducted to estimate the performance of the new restraining system.

Table 1 Ductility Capacity for BRB Component Tests

Reference	Designation	μ_{max}	μ_c
Black *et al.* (2002)	99-1	20	324
	00-11	15	1045
	00-12	15	538
Merritt *et al.* (2003)	1	15	900
	2	15	600
	4	15	1100
	5	15	1300
	6	15	800
Wang *et al.* (2012)	FT-2.0	15.4	2277
	FT-3.0	23.1	1169
	FT-3.5	26.9	908
	FT-3(6)	23.1	969
AISC(2010) Requirements	-	14.4	200

Note: the test data are selected from the three references when the specimens are tested with a maximum ductility more than 14.4. The ductility requirements of the AISC Seismic Provisions (2010) are based on a response modification coefficient of 8.

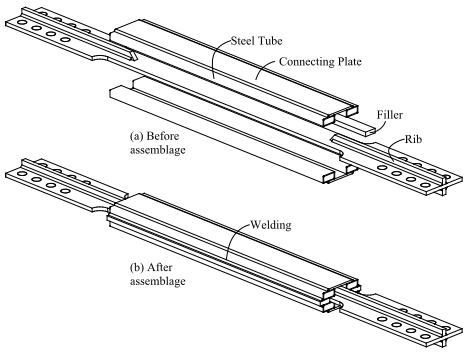


Figure 1 Configurations of the new type of BRB

2. TEST PROGRAM

2.1 Specimens

As shown in Figure 2, the employed all-steel BRB consists of a steel core plate, a pair of steel outer restraining plates, four steel inner restraining plates and a pair of steel fillers. End ribs are welded on the steel brace core to increase the out-of-plane stiffness of the end region. A stopper is set in the center by enlarging the width of the brace core.

The cross-section of the BRB is shown in Figure 3. The core plate is inserted between a pair of outer restraining plates and four steel inner restraining plates connected by the high-strength bolts through two filler plates. The unrestrained width of the core plate (b_u) is shown in Figure 3, which is an important factor for this type of BRB. Figure 4 gives the nominal geometric dimensions of the core plate and Table 2 lists some corresponding measured geometric dimensions. The three specimens have different values of b_u, which is illustrated in Table 2 along with the values of b_u/t.

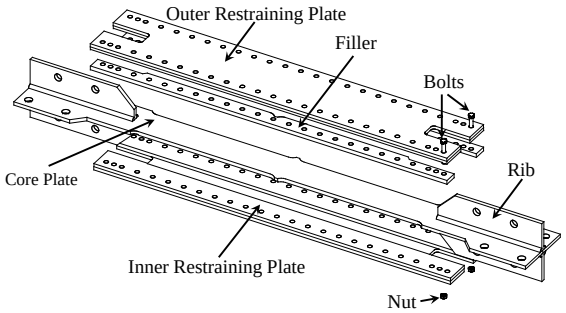


Figure 2 Assemblage of the BRB

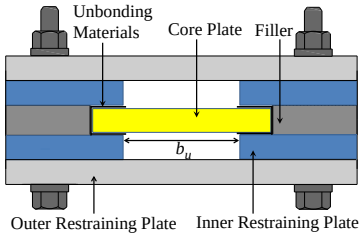


Figure 3 Cross-Sectional Details

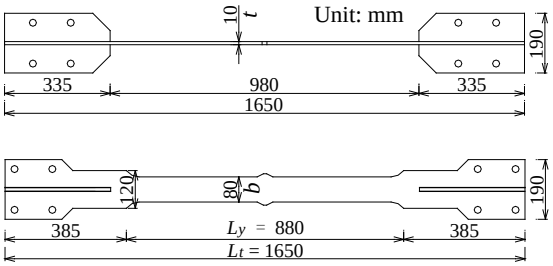


Figure 4 Dimensions of the Core Plate

Table 2 Geometric Dimensions of the Core Plate

Specimen	L_y (mm)	t (mm)	b (mm)	b_u (mm)	b_u/t
P1	879.5	9.68	79.81	0.00	0.00
P2	879.5	9.71	79.90	49.66	5.11
P3	879.5	9.72	79.80	69.94	7.19

Note: L_y is the length of yielding segment of the core plate; t and b are the thickness and the width of the core plate; b_u is the unrestrained width of the core plate.

2.2 Test Setup and Loading Pattern

The specimen is vertically mounted on the Material Test System (MTS) by high-strength bolts. A hydraulic actuator, with a loading capacity of 1000 kN and a displacement capacity of +/-75mm, is used for the cyclic loading, which is displacement-controlled via a linear variable displacement transducer mounted on the actuator.

As show in Figure 5, the test programs consisted of four main phases, including three identical variable strain amplitude (VSA) loadings and one constant strain amplitude (CSA) loading. Before the four main phases, four cycles with the strain amplitude (the yielding segment deformation δ divided by its length l_y) of $0.75\varepsilon_y$ are adopted to measure the initial axial stiffness of the specimens within the elastic

stage. Subsequently, the three VSA loadings are imposed at the target brace strain amplitude of 0.5%, 1.0%, 1.5%, 2.0%, 2.5% and 3.0% (three cycles at 0.5%, two cycles at the other strain levels). The fourth phase is the CSA loading with the constant strain amplitude of 2.0%. The three continuous VSA loadings are designated as VSA1, VSA2 and VSA3 hereinafter, respectively.

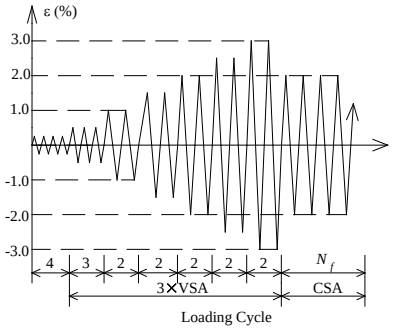


Figure 5 Strain-Controlled Loading Pattern

3. TEST RESULTS

3.1 Hysteretic Curves

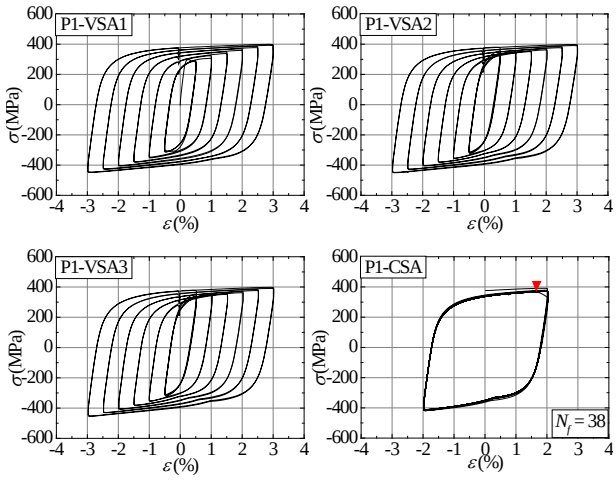


Figure 6 Stress-strain curve of Specimen P1

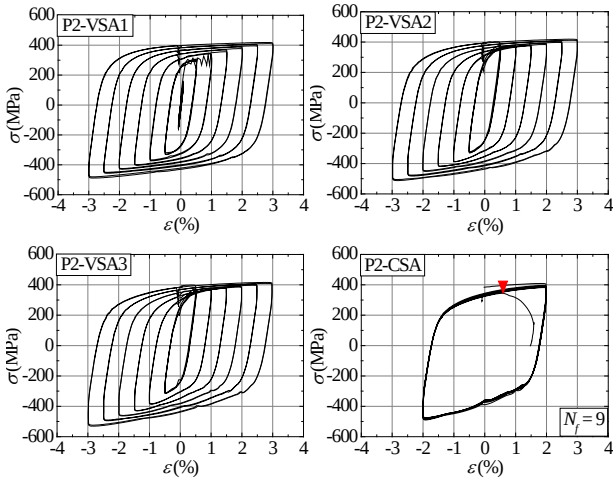


Figure 7 Stress-strain curve of Specimen P2

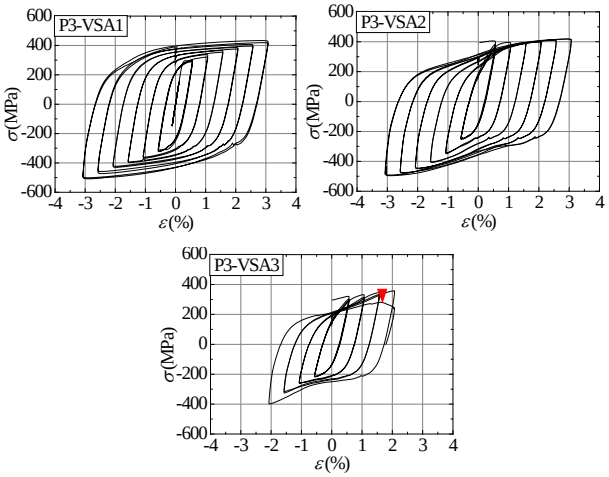


Figure 8 Stress-Strain Curve of Specimen P3

The stress-strain relationships of the three specimens are presented in Figures 6, 7 and 8. Specimen P1 and Specimen P2 exhibit stable behavior without any signs of degradation until the 39th and the 10th cycles of the CSA loading, respectively. Specimen P3 witnesses its failure at the second cycle of 2.0% during VSA3 loading.

3.2 Failure Mode

The failure modes of the three specimens are presented in Figures 9, 10 and 11. The fracture of specimen P1 is induced by the main crack initiating in the middle of the core plate besides the stopper. Other subtle cracks are also found in this region, where there is a stress concentration caused by the change of section and the great friction force applied by the restraining plates. Similarly, the main crack of specimen P2 is also in this region. What's different is that obvious out-of plane waves are found in the unrestrained region of specimen P2, especially in the end region of the core plate.

However, the out-of-plane waves of specimen P3 are so significant that the wave peak touches the outer restraining plates, as shown in Figure 11. Unlike the other two specimens, the main crack of specimen P3 initiates in the wave valley near both the loading end and the fixed end. The out-of-plane deformation will induce great bending strain in the wave valley, which contributes to the strain concentration in the core plate (Wang *et al.*, 2012). Therefore, specimen P3 fractured before the other two specimens. According to the test results, employing a b_u/t less than 5.1 can avoid excessive out-of-plane deformation and strain concentration in the core plate.

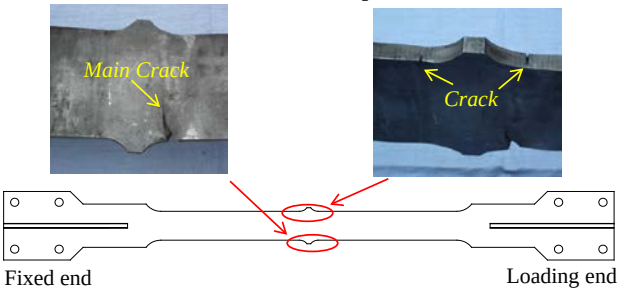


Figure 9 Failure Mode of Specimen P1

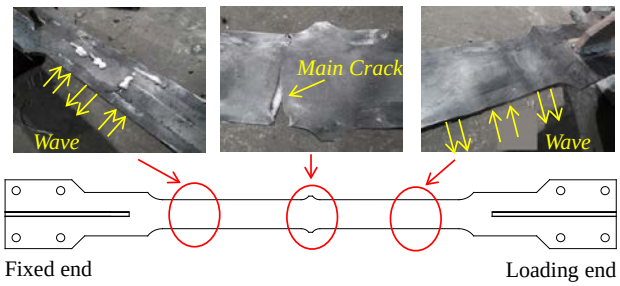


Figure 10 Failure Mode of Specimen P2

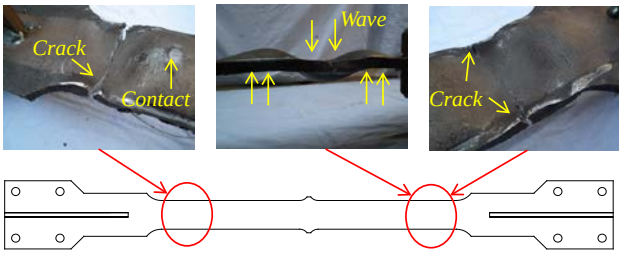


Figure 11 Failure Mode of Specimen P3

4. RESULT DISCUSSION

4.1 Compression strength adjustment factor

The compression strength adjustment factor is defined as (AISC, 2010)

$$\beta = T_{max} / P_{max} \quad (3)$$

Where T_{max} and P_{max} are the maximum tensile brace force and the maximum compressive brace force at an axial deformation level, respectively. The compression strength adjustment factors of all specimens (for the last cycle of each deformation level) during the three VSA loadings are presented in Figure 12. The β values of all the three specimens increase with the level of strain amplitude during each VSA loading.

During VSA1 loading, the β values of the three specimens remain stable at about 1.10 before the strain amplitude reaches 2.5%. Then the β values of specimen P2 and specimen P3 become greater than the β value of specimen P1 at large strain amplitudes, especially at 2.5% and 3.0%. This phenomenon is caused by the great friction force between the core plate and the inner restraining plates at large strain in Specimen P2 and P3. After test, gridding is found at the core plate of specimen P2 and specimen P3, which is illustrated in Figure 13. The great contact force in a small region of the core plate induces the gridding in spite of the protection of the unbonding materials, increasing the friction force between the core plate and the inner restraining plates. Nevertheless, the β values of the three specimens during the three VSA loadings are smaller than the limiting value of 1.3 in the AISC Seismic Provisions (2010).

It is noted that the β value of specimen P3 at 0.5% during VSA2 and VSA3 loadings lies below the β values of the other two specimens. The reason can be illustrated from the maximum compressive brace force (for the last cycle of each deformation level) during the three VSA loadings, which is plotted in Figure 14. The P_{max} values of specimen P1 and P2 at 0.5% during the three VSA loadings almost remain the same level (240kN-250kN), while the P_{max} value of specimen P3 drops to under 200kN at 0.5% during VSA2 and VSA3 loadings.

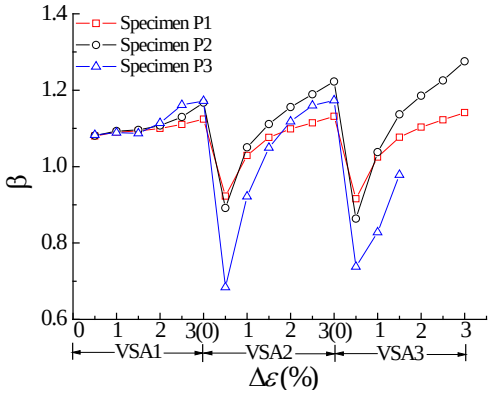
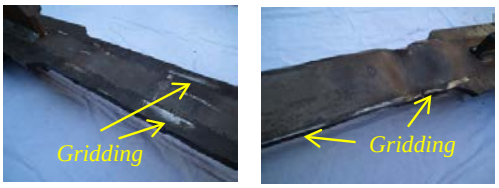


Figure 12 Compression Strength Adjustment Factor



(a) Specimen P2 (b) Specimen P3

Figure 13 Gridding of the brace plate

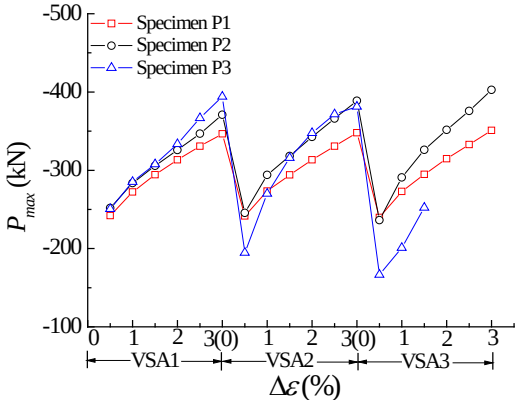


Figure 14 Maximum compressive brace force

4.2 Energy Dissipation and Ductility Capacity

The relationships between the hysteretic energy and cumulative deformation of the three specimens are shown in Figure 15. Specimen P1 has a great hysteretic energy of 1218 kN.m before fracture, while the value of specimen P2 and specimen P3 are only 760 kN.m and 437 kÑ.m, respectively. It is obvious that the low-cycle fatigue properties of the three specimens decrease with the growth of b_u/t. The hysteretic energy of specimen P2 is greater than that of specimen P1 at the same cumulative deformation, for the maximum compressive brace force of specimen P2 is larger at the same deformation level. In addition, the energy dissipation capacity of specimen P3 decreases slightly when the cumulative deformation reaches 1.7m.

All the three specimens reach a maximum ductility

capacity (μ_{max}) of 20.3, exceeding the requirement value (14.4) by the AISC Seismic Provisions (2010) for a response modification coefficient of 8. The cumulative ductility capacities (μ_c) of the three specimens are presented in Figure 16, which are 3489, 2068 and 1256, respectively. It is noted that though the μ_c values of specimen P2 and specimen P3 are much smaller than the value of specimen P1, they are significantly higher than that (200) required by the AISC Seismic Provisions (2010) for uniaxial testing.

4.3 Equivalent Viscous Damping

Equivalent viscous damping (ζ_{eq}) is an important factor for nonlinear analysis of structures, which is also an indicator to evaluate the plump degree of the hysteretic curves. Based on the hysteretic curves of the specimen, equivalent viscous damping of the BRBs can be calculated (Clough and Penzien, 1993) as

$$\zeta_{eq} = \frac{E_d}{4\pi(A_{AOB} + A_{COD})/2} \quad (4)$$

Where E_d is the energy dissipation per cycle; A_{AOB} and A_{COD} are the areas of the triangles, as shown in Figure 16.

The results during the three VSA loadings (for the last cycle of each deformation level) are plotted in Figure 17. The ζ_{eq} value of specimen P1 at the same deformation level remains stable during the three VSA loadings, while the ζ_{eq} value of specimen P2 at the same deformation level degrades gradually with the loading history. The degradation of ζ_{eq} value is more significant for specimen P3, which is coincident with the plump degree of the of the strain-stress curves in Figure 8.

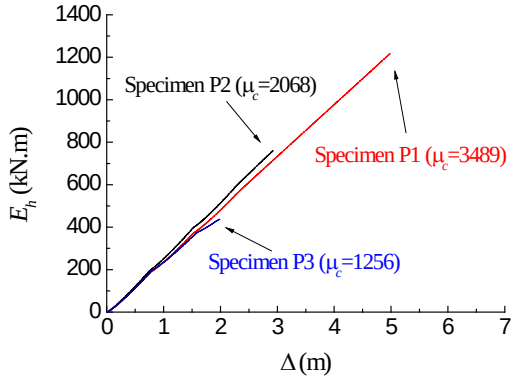


Figure 15 Hysteretic Energy (E_h) *vs* Cumulative Deformation (Δ)

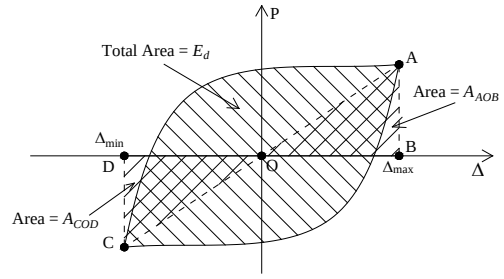


Figure 16 Model for the Calculation of the Effective Viscous Damping

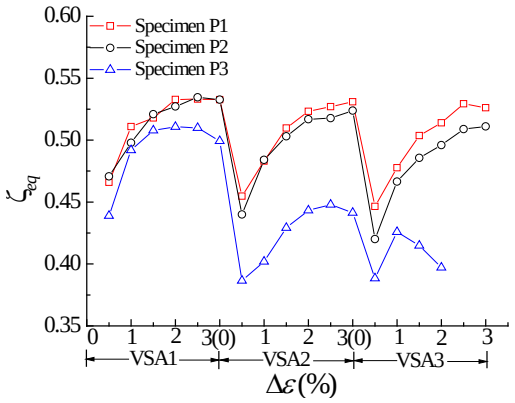


Figure 17 Equivalent Viscous Damping

5. CONCLUSIONS

Component tests of three BRB specimens are performed to investigate the performance of the new partial restraining mechanism. The main results are summarized as follows:

(1) The out-of-plane deformation of the BRB in the unrestrained region increases with the growth of b_u/t, which will eventually degrade the low fatigue properties of the BRB. Tests shows that employing a b_u/t less than 5.1 can avoid excessive out-of-plane deformation and strain concentration in the core plate. Nevertheless, the cumulative ductility capacities of the three specimens are sufficient for the requirements in the AISC Seismic Provisions (2010).

(2) Compared with conventional BRBs, the proposed BRBs have a greater compression strength adjustment factor, which is caused by the large contact force between the core plate and the inner restraining plates. In spite of that, the value is smaller than the limiting value of 1.3 in the AISC Seismic Provisions (2010).

(3) Equivalent viscous damping for the proposed BRBs decreases with the loading history and the increase of b_u/t.

Acknowledgements:

The authors would like to acknowledge financial supports from the Priority Academic Program Development of Jiangsu Higher Education Institutions, the National Natural Science Foundation of China (51008077, 51278105) and the Qinglan Project. Grateful acknowledgments are given to Professors Tsutomu Usami and Hanbin Ge at Meijo University for their suggestions for relevant research.

References:

AISC (2010), "Seismic Provisions for Structural Steel Buildings," Chicago, Illinois.

Black, C.J., Makris, N. and Aiken, I.D. (2002), "Component Testing, Stability Analysis and Characterization of Buckling-Restrained Unbonded Braces," Pacific Earthquake Engineering Research Center, University of California, Berkeley.

Merritt, S., Uang, C.M. and Benzoni, G. (2003), "Subassemblage Testing of Star Seismic Buckling-Restrained Braces," Structural Systems Research Project, Univ. of California at San Diego, San

Diego.
Wang, C.-L., Usami, T. and Funayama, J. (2012), "Improving Low-Cycle Fatigue Performance of High-Performance Buckling-Restrained Braces by Toe-finished Method," *Journal of Earthquake Engineering*, **16**(8), 1248-1268.
Fahnestock, L.A., Ricles, J.M. and Sause, R.. (2007), "Experimental Evaluation of a Large-Scale Buckling-Restrained Braced Frame," *Structural Engineering*, American Society of Civil Engineers, **133**(9), 1205-1214.
Lin, P.-C., Tsai, K.-C., Wang, K.-J., Yu, Y.-J., Wei, C.-Y., Wu, A.-C., Tsai, C.-Y., Lin, C.-H., Chen, J.-C., Schellenberg, A.H., Mahin, S.A. and Roeder, C.W. (2011), "Seismic Design and Hybrid Tests of a Full-Scale Three-Story Buckling-Restrained Braced Frame Using Welded End Connections and Thin Profile," *Earthquake Engineering and Structural Dynamics*, Published online.
Ju, Y.-K., Kim, M.-H., Kim, J. and Kim, S.-D. (2009), "Component Tests of Buckling-Restrained Braces with Unconstrained Length," *Engineering Structures*, **31**(2), 507-516.
Usami, T., Wang, C.-L. and Funayama, J. (2012), "Developing High-Performance Aluminum Alloy Buckling-Restrained Braces Based on Series of Low-Cycle Fatigue Tests," *Earthquake Engineering and Structural Dynamics*, **41**(4), 643-661.
Wang, C.-L., Usami, T., Funayama, J. and Imase, F. (2013), "Low-cycle Fatigue Testing of Extruded Aluminum Alloy Buckling-Restrained Braces," *Engineering Structures*, **46**, 294-301.
Tinker, J. and Dusicka, P. (2012), "Challenges in Designing Ultra-Lightweight Buckling Restrained Brace," *Proceedings of the 7th International Conference on Behaviour of Steel Structures in Seismic Areas*, Paper No.569-575.
Clough, R.W. and Penzien, J. (1993), "Dynamics of Structures," 2nd ed., McGraw-Hill.

10CUEE CONFERENCE PROCEEDINGS
10th International Conference on Urban Earthquake Engineering
March 1-2, 2013, Tokyo Institute of Technology, Tokyo, Japan

BEHAVIOUR AND DESIGN OF AN ALL-STEEL SELF-CENTERING BUCKLING-RESTRAINED BRACE

Peng Zeng[1)], Quan Chen[1)], Chun-Lin Wang[1)], Tsutomu Usami[2)], and Shao-Ping Meng[1)]

[1]*Key Laboratory of Concrete and Prestressed Concrete Structures of the Ministry of Education, Southeast University, Nanjing, China*
[2]*Department of Civil Engineering, Meijo University, Tempaku-ku, Nagoya, Japan*
ranbow.zp@qq.com; quanchenseu@gmail.com; chunlin@seu.edu.cn; usamit@meijo-u.ac.jp; msp1960@vip.sina.com

Abstract: A new self-centering energy-dissipative brace is developed based on the all-steel buckling-restrained brace to control maximum and residual drift of frame structures subjected to several earthquakes. This energy-dissipative brace employs the steel prestressing tendons as the self-centering system. Therefore, it is called the all-steel self-centering buckling-restrained brace in this paper. To overcome this limitation of the elastic deformation of the prestressing tendons, an enhanced-elongation dual-tendon system has been designed. Theoretical study shows that this dual-tendon system allows for self-centering response over two times the range achieved with the original self-centering system with the prestressing tendons. Furthermore, when the initial prestressing force is larger than the given value, the performance of the self-centering buckling-restrained brace can be achieved. Based on the discussion, one possible realization of this system, which combines the merits of both self-centering devices and buckling-restrained braces, is presented. Numerical results show that if the length of the yielding segment of the steel core is decreased, the performance of the self-centering BRB is improved.

1. INTRODUCTION

To meet the performance-based design philosophy for the seismic design of structures, residual drift of structures should be diminished as much as it can be. Conventional buckling-restrained braces (BRBs) can dissipate energy via yielding of the steel core, but their residual deformations cannot be ignored due to the severe impacts on post-earthquake operation of structures. In some cases, it is much more expensive to repair the structure than to rebuild it due to too large residual deformation and drift. Then in recent years new types of braces aiming at controlling residual deformation and drift have been put forward, which utilized the prestressing tendons to press or pull back the braces so as to diminish the residual deformations of braces and dissipate seismic energy in the meantime. These braces with self-centering property demonstrate a flag-shaped hysteretic response. It means that they dissipate energy well and meanwhile deminish residual drifts of structures perfectly. One of the key points for designing these braces is that the tendons must be prestressed enough and keep in elastic state all over the working process. Otherwise the prestressed force will disappear progressively and self-centering aim cannot be achieved. So large enough elastic strength, elastic strain capacity and stiffness are essential requirements for choosing tendons. Previous studies have successfully adopted aramid polymer fibers (Chistopoulos *et al.* 2008) and E-glass fibers (CHOU *et al.* 2012) as prestressing tendons to press back the original friction energy dissipating braces, proposing new types of braces namely self-centering energy dissipating braces (SCEDs). Results of those studies show that SCEDs can evidently reduce seismic force in the base and the residual drift of the structures in comparison with those installing traditional steel braces in the same positions. However, despite of enough elastic deformation capacity, fibers are difficult to be anchored to the braces and the expenses of anchorages and fibers are relatively high, which extensively affect the applications of those SCEDs to the practical engineering. On the other hand, Zhu *et al.* (2008) exploited super-elastic shape memory alloys (SMAs) as prestressing tendons into SCED braces, and Miller *et al.* (2012) combined SMAs with BRB to develop a new kind of brace called self-centering buckling-restrained brace (SCBRB) for the first time. The two braces above can undergo much larger deformations due to SMAs' super-elasticity, but that SMAs are quite susceptible to temperature variation and their prices are usually much higher than other building materials brings about the same problem as fibers for application to practical engineering. Considering those facts mentioned above, Lu *et al.* (2012) developed a new kind of SCBRB with steel prestressing tendons as the prestressing system. But the braces' deformation capacity is confined in a small scope due to the limitation of elastic strain capacity of the steel prestressing tendons.

In the present paper, a new self-centering buckling-restrained brace with an enhanced-elongation dual-tendon system is developed on the base of the abovementioned

researches and the experimental studies on BRBs that our research group has done. The steel prestressing tendons are chosen as the self-centering system for their relatively high elastic strength, enough stiffness and easy anchoring, along with one realistic superiority for their acceptable expense. Because the components of this SCBRB are all steel materials, it is called the all-steel self-centering buckling-restrained brace in this paper. According to the material experiment, the extreme elastic elongation of prestressing steel tendons is about 0.80%, from which point unloading residual strain is less than 0.02%. To extend SCBRB's extreme elongation capacity, dual-tendons are installed in parallel, actually connected in series by a floating intermediate steel member at working. This paper will first describe the characterization of conventional SCBRBs, then the mechanism of an enhanced-elongation dual-tendon self-centering system and the configuration of this dual-tendon SCBRBs. Finally, a numeral parameter study is conducted on the dual-tendon SCBRBs to evaluate the performance under a cyclic loading.

2. MECHANICS OF SCBRB

2.1 Component Characterization

A conventional SCBRB is commonly composed of two components: a BRB and a self-centering system. The hysteretic response of BRB is shown in Figure 1, which is obtained in experiments of our research group on BRBs. From the hysteretic response, one conclusion can be drawn that BRB demonstrate excellent energy dissipation property and its restoring force model for numeral simulation can be depicted in Figure 2.

The self-centering system's composing elements are mainly prestressing tendons which provide re-centering force and steel tubes or plates passing on inner force. In fact, all the self-centering systems with different tendons such as fibers, SMA rods or wires and steel prestressing tendons can be explained by the same schematic diagram as illustrated in Figure 3. Because tendons need to be prestressed during assembly, the self-centering system will get some compressive deformation before uploading external load as shown in Figure 3(a). The compressive formation u_{ys} can be defined as follows:

$$u_{ys} = \frac{F_0}{K_1 + K_2} \tag{1}$$

Where F_0 is the prestressing force for the system and K_1, K_2 are the two elements' axial stiffness respectively. In most cases, u_{ys} is relatively small for the elements are usually steel tubes with relatively large stiffness. The allover loading process is divided into two stages with a turning point that is when the system's deformation gets back to zero under the external load F_{ys} as shown in Figure 3(b), which can be defined as follows:

$$F_{ys} = \left(K_1 + K_2 + K_s\right) \times u_{ys} \tag{2}$$

Where K_s is the tendon's stiffness. Once the system's deformation returns to zero, the two elements begin to move relative to each other, leaving a gap between them and the tendons kept on elongating. This results in the system's stiffness changing from K_1+K_2+K_s to the tendon's stiffness K_s. When the system is in compression, the same case happens as in tension.

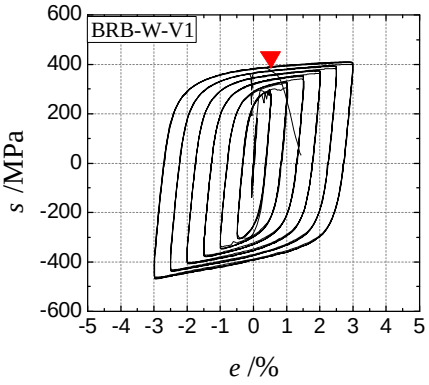


Figure 1 Hysteretic response of BRB specimen

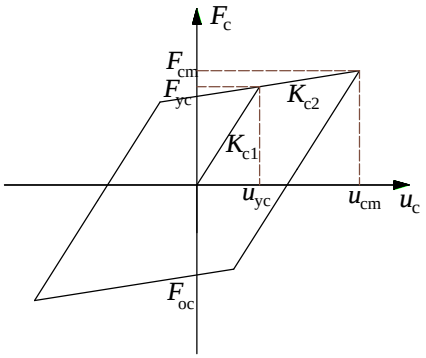


Figure 2 Restoring Force Model of BRB

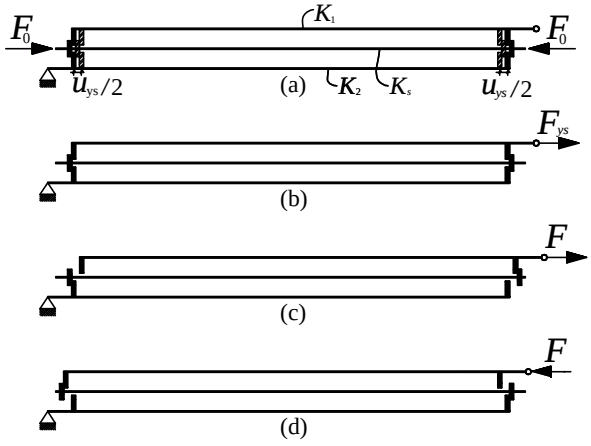


Figure 3 Sketch of Self-Centering System

On the other hand, because K_1+K_2+K_s is greater than K_1+K_2, the turning point external force F_{ys} is reasonably greater than the prestressed force F_0, which will be exploited in latter formula derivation in this paper. When the elements of the self-centering system begin to move relatively, the system's stiffness gets changed like the system got yielded at the point (u_{ys}, F_{ys}). No matter the system is in tension or in compression, this behavior is symmetric. So the restoring force model of self-centering system can be illustrated as Figure 4, where u_m is the maximum elastic deformation of

the self-centering system. And u_m is decided by the elastic deformation capability of prestressing tendons. Besides, there is one fact that the post-yielding stiffness of the system during compression is the stiffness of the two elements and tendons in series. It is a bit different from K_s in tension for the load transferring route on the elements is not the same as that in tension. But as the stiffness of the two elements is relatively quite large, the post-yielding stiffness in compression is almost equivalent to K_s. This will explain the tiny difference of the SCBRBs' numerical response in compression and tension. Figure 5 shows the stress-strain relation of the prestressing tendon employed in this paper. The largest elastic deformation of the prestressing tendon is about 0.8%.

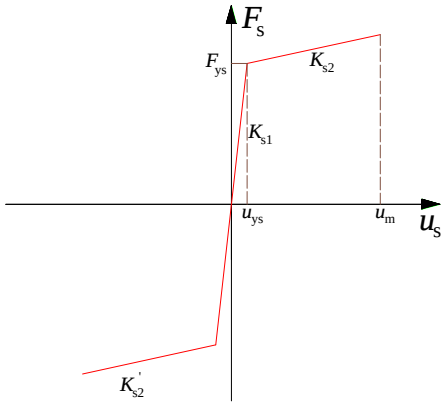


Figure 4 Restoring Force Model of Self-Centering System

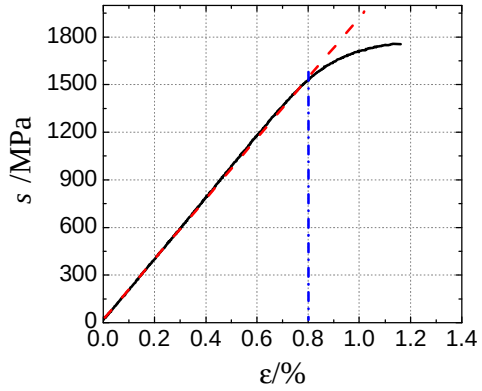
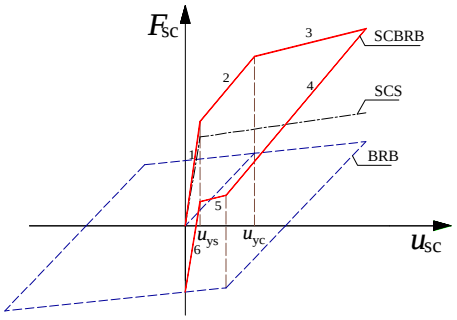


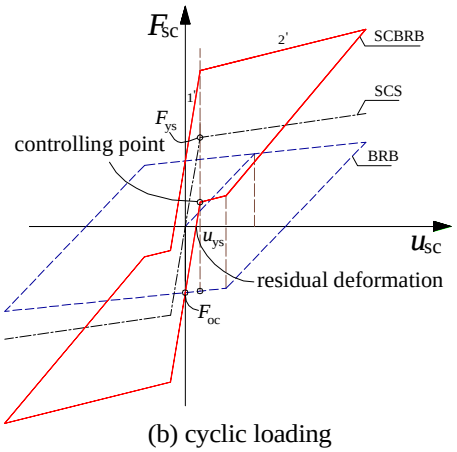
Figure 5 Stress-Strain Relation of Prestressing Tendon

2.2 SCBRB Mechanics

A SCBRB is realized when installing a self-centering system in parallel with a BRB. As the self-centering system and BRB is configured to bear external load jointly any time, the restoring force model of SCBRB is the superposition of them and can be divided into two stages due to the different states that BRB gets during first loading and cyclic loading(see Figure 6). When it is on the first loading procedure, the restoring force curve of SCBRB(see in Figure 6(a)) is composed of three fold lines with two turning points: self-centering system's yielding(u_{ys}, F_{ys}) and BRB's yielding (u_{yc}, F_{yc}); If on the cyclic loading procedure, its stiffness will change only once from the superposition of self-centering system's pre-yielding stiffness and BRB's post-yielding stiffness to that of both components' post-yielding stiffness(as shown in Figure 6(b)). As for unloading stage, the SCBRB's stiffness is just the same superposition of the two components.



(a) first loading



(b) cyclic loading

Figure 6 Restoring Force Model of Self-Centering BRB

Because of the restoring force that self-centering system provides, SCBRB demonstrates a flag-shaped hysteric response with much smaller residual deformation and identical energy dissipating capability as the original BRB. To guarantee this self-centering performance, the controlling point in Figure 6(b) is a key factor for designing the SCBRBs: if the controlling point is greater than zero, the residual deformation will be smaller than u_{ys}, which should be quite a small data due to the relatively large stiffness of elements in self-centering system. Now that the residual deformation is less than u_{ys}, it is convinced that self-centering aim has been achieved for the SCBRB. So in order to keep the controlling point greater than zero, F_{ys} should be greater than F_{oc}. On the other hand, F_{ys} is greater than F_0, so if F_0 is kept greater than F_{oc}, the brace will get re-centered. In other words, when the initial prestressing force is larger than the given value based on the BRB core, the performance of the SCBRB can be achieved.

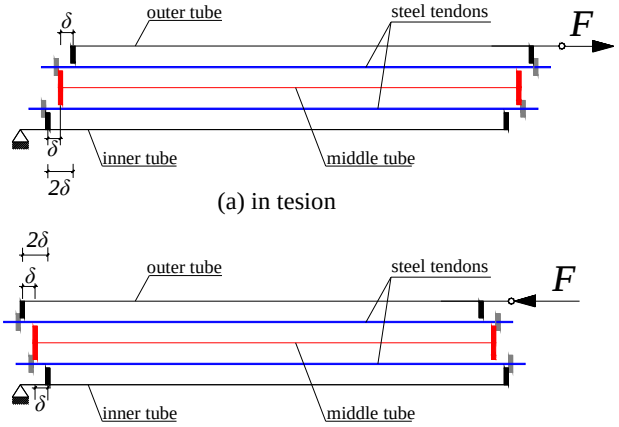
Based on the analysis above, the tendons in self-centering systems should get large enough elastic strength and modulus of elasticity to press or pull back the BRB core, and enough elastic deformation capacity to satisfy the braces' deformation requirement. Besides, the initial prestressing force of the tendons shouldn't be too large. Otherwise the tendons would be short of elastic deformation capability and get into plastic state due to over-tension. And

consequently, self-centering performance would not be achieved due to the loss of prestressing force in tendons.

3. DESIGN OF DOUAL-TENDON SELF-CENTERING SYSTEM

3.1 Dual-Tendon Self-Centering System

The steel prestressing tendon is in some way a good option as prestressing tendons in SCBRBs for its stable performance such as large enough yielding strength and modulus of elasticity, also for relatively more feasible anchoring. But its elastic deformation capability is only about 0.8% (as shown in Figure 5), setting a severe limitation to the SCBRB's deformation capability. To solve the abovementioned problem, this paper introduces a dual-tendon self-centering system to enhance the elongation of SCBRB with steel prestressing tendons. For the convenience to describe the design and configuration of the dual-tendon SCBRB, this paper will emphasize on a dual-tendon SCBRB with four steel prestressing tendons installed in series (two tendons in each set).



(a) in tesion

(b) in compression

Figure 7 Self-Centering System with Double Tendons

The dual-tendon self-centering system consists of three types of elements: three tubes (outer tube, middle tube and inner tube), two sets of steel prestressing tendons, two pairs of anchorages. As illustrated in Figure 7, one pair of anchor plates is sized to interact with the inner and middle tubes, while the other pair with the middle and outer tubes; the middle tube is not connected with any other elements but clamped by the anchor plates to a "floating" state and its role is to pass on inner force and make the two sets of tendons work in series. The one set of tendons elongates δ under external load, and then the dual-tendon self-centering system deforms 2δ, extending the system's deformation capability successfully.

3.2 SCBRB Configurations

Based on the dual-tendon self-centering system, a dual-tendon SCBRB with four steel prestressing tendons is developed in our research group. Its schematic assembly is illustrated in Figure 8. The inner tube and middle tube take an innovative role of not only passing on inner force but also restraining the BRB core from buckling. The BRB core is welded to inner tube on one end and bolted to the outer tube on the other end, with no abutting to the middle tube via interspaces and slots on the elements. Besides, the outer tube can protect the bolts on middle tube and the left-hand and right-hand joint members are the positions to connect to frame structures.

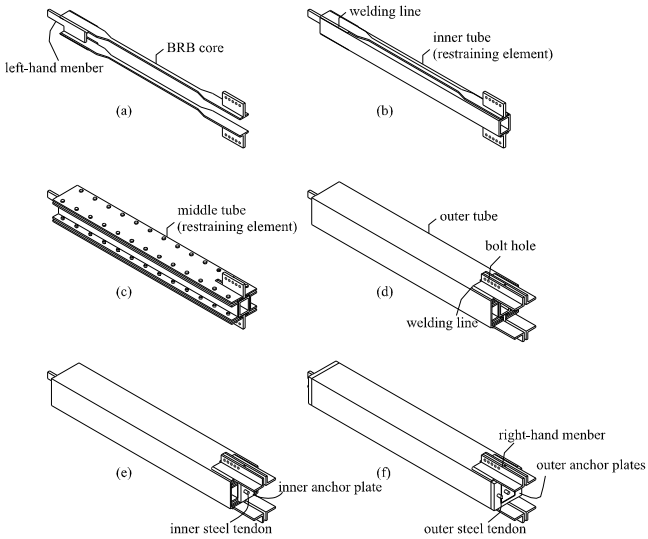


Figure 8 Configurations of All-Steel Self-Centering BRB

4. NUMERAL SIMULATION OF DOUAL-TENDON SCBRB

4.1 Numeral Model

A numeral model was created using OpenSees to simulate the SCBRB illustrated in the Figure 8. For a SCBRB, the design strength is defined as the summation of the BRB steel core yielding force and the initial prestressing force in the tendons. The SCBRBs simulated in this paper are designed with design strength of 200kN according to the abovementioned concept. Actually, the design strength should be in accordance with practical frame structures, but in order to testify the SCBRB's performance first, the design strength is supposed temporarily.

The schematic diagram of the model is shown in Figure 9.This numeral mode uses a nonlinear beam column element for the BRB core and loading ends, an elastic truss element for the three tubes. Because the steel tendon is not tensed out of its elastic stress all over the loading procedure, it is also modeled using an elastic truss element and the initial strain is imposed to it as pretension force. An elastic no-tension material truss element is exploited to represent the anchor plates for the fact that the anchor plates would be separated from the tubes in tension but get abutted during compression. As for the connection between BRB steel core and the inner and outer tubes, equaldolf command is used for them. And it is the same with the relationship between the two sets of steel tendons and the anchor plates. All material properties used in this model are based on results from experimental tests by our research group.

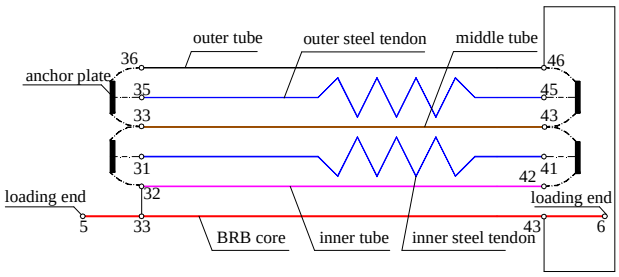
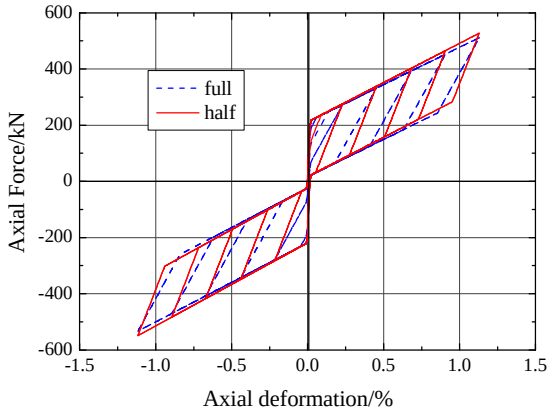


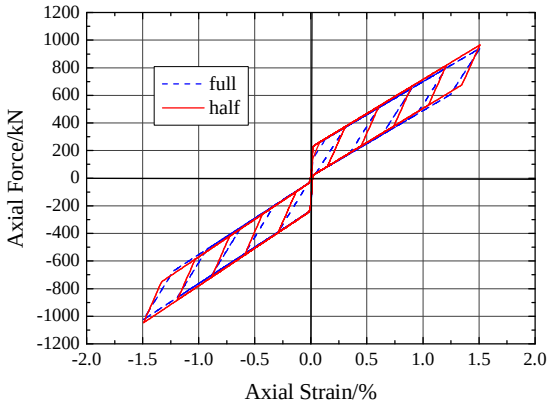
Figure 9 Opensees numerical model

4.2 Numeral Simulation Results

According to the analysis on self-centering system on section 2.2, the initial strain imposed to the two sets of steel tendons should be 0.227%. Since the extreme elastic strain of steel tendons is 0.8%, this dual-tendon SCBRB (with four steel tendons) can achieve an elongation of 1.15% (as shown in Figure 10(a)).



(a) Dual-tendon SCBRB with 2 steel tendons



(b) Dual-tendon SCBRB with 4 steel tendons

Figure 10 Numerical results

On the other hand, if installing four more steel tendons which means two sets of four steel tendons in series, the required initial strain would decrease to 0.113% and the dual-tendon SCBRB can achieve the elongation of 1.49% (as shown in Figure 10(b)). Both the dual-tendon SCBRBs display a full self-centering response. What's more, the length of the yielding segment of the steel core is changed as a parameter. The result is that the SCBRB with steel cores whose yielding segment is half of the brace's length dissipate energy better than that with yielding segment full of the brace's length. As for the extreme force of dual-tendon SCBRB, it is 570kN for the four-tendon brace and 1066kN for the eight-tendon brace. They are in accordance with the extreme force 551kN and 1050kN calculated by using the actual stiffness of each element.

5. CONCLUSIONS

In order to control maximum and residual drift of frame structures subjected to several earthquakes, an enhanced-elongation dual-tendon all steel SCBRB has been developed in this paper. The configuration and numeral simulation of this all-steel dual-tendon SCBRB is illustrated, with the following conclusions: (1) the dual-tendon self-centering system allows the SCBRB to deform twice the range achieved with the original self-centering system with the prestressing tendons, which can generally meet the requirement of traditional frame structures; (2) the key point of designing the SCBRB is to guarantee the initial prestressing force greater than the fixed value based on the steel core. (3) reducing the length of the yielding segment of the steel core can improve a SCBRB's energy-dissipating performance.

Acknowledgements:

This work was supported by the Priority Academic Program Development of Jiangsu Higher Education Institutions and the National Natural Science Foundation of China (51008077, 51208095) and was partially supported by JSPS KAKENHI Grant Number 23656292.

References:

Christopoulos, C., Tremblay, R., Kim, HJ. And Lacerte, M. (2008), "Self-centering energy dissipative bracing system for the seismic resistance of structures: development and validation," *Journal of Structural Engineering*, ASCE, 134: 96-107.

Chou, C-C. and Chen, Y-C. (2012), "Development and seismic performance of steel dual-core self-centering braces," *The 15th World Conference on Earthquake Engineering*, Paper No. 1648.

Zhu, S. and Zhang, Y. (2008), "Seismic analysis of concentrically braced frame systems with self-centering friction damping braces," *Journal of Structural Engineering*, ASCE, 134: 121-131.

Miller, DJ., Fahnestock, LA. And Eatherton, MR. (2012), "Development and experimental validation of a nickel–titanium shape memory alloy self-centering buckling-restrained brace," *Engineering Structures*, 2012, 40: 288-298.

Lu Liu, Bin Wu, Wei Li and Jun-Xian Zhao. (2012), "Cyclic tests of novel self-centering buckling-restrained brace," *Journal of Southeast University(Natural Science Edition)*, 2012, 42(3): 536-541 (in Chinese).

Bo Huang, Quan Chen, Tao Li, Chun-Lin Wang and JingWu. (2012), "Low-cycle fatigue test of buckling-restrained braces made of Q235 steel," China Civil Engineering Journal, 2012 (in review, in Chinese).

10CUEE CONFERENCE PROCEEDINGS
10th International Conference on Urban Earthquake Engineering
March 1-2, 2013, Tokyo Institute of Technology, Tokyo, Japan

DEVELOPMENT OF RING-SHAPED STEEL PLATE SHEAR WALLS THAT RESIST BUCKLING FOR IMPROVED SEISMIC PERFORMANCE

Matthew R. Eatherton[1], Natalia Egorova[2], and Abhilasha Maurya[2]

1) Assistant Professor, Dept. of Civil and Environmental Engineering, Virginia Tech, U.S.A.
2) Graduate Research Assistant, Dept. of Civil and Environmental Engineering, Virginia Tech, U.S.A.

Abstract: A new type of steel plate shear wall has been devised which resists out-of-plane buckling without requiring stiffeners. The ring-shaped steel plate shear wall (RS-SPSW) includes a web plate that is cut with a pattern of holes leaving ring-shaped portions of steel connected by diagonal links. The ring shape resists out-of-plane buckling through the mechanics of how a circular ring deforms into an ellipse. It has been shown that the ring's compression diagonal will shorten a similar amount as the tension diagonal elongates, essentially eliminating the slack in the direction perpendicular to the tension field. Because of the unique features of the ring's mode of distortion, the load-deformation response of the resulting RS-SPSW system can exhibit full hysteretic behavior and possess greatly improved stiffness relative to thin unstiffened SPSW. Furthermore, through the introduction of more design variables associated with the geometry of the rings, it is possible to separately tune the strength, stiffness, and ductility of the RS-SPSW system. The RS-SPSW has been validated through testing on small panels, approximately 1 m x 1 m.

1. INTRODUCTION AND MOTIVATION

Steel plate shear walls (SPSW) have been used in numerous buildings as the primary seismic force resisting system for a variety of reasons ranging from reduced cost as compared to concrete shear walls, speed of construction, efficient use of slender wall elements, and minimal architectural wall thickness. As such, SPSW are an important option for seismic load resisting system.

The approach to SPSW design in Japan is inherently different than the form of SPSW used in the United States and Canada. Japanese SPSW as well as pre-1980's SPSW in the United States are designed so that the web plate does not buckle under shear loading (e.g. ENR 1978, Troy and Richard 1979). To prevent buckling, the web plates are stiffened at intermediate points across a shear panel as shown in Figure 1. The web plate undergoes shear yielding without buckling, resulting in substantial energy dissipation and primarily axial forces in the beams and columns.

Conversely, the fact that web plates have post-buckling capacity has been applied in plate girder design for decades (Basler 1961, Porter 1975). Upon buckling, a diagonal tension field develops in the plate, which, along with the boundary members, creates a truss-like system that can resist significant shear. Starting in the 1980's, steel plate shear walls that utilize tension field action were investigated (Thorburn et al. 1983; Timler and Kulak 1983; Tromposch and Kulak 1987). Since these systems allow thinner plates and do not require stiffeners, they can be cheaper, and thus have become more popular than their stiffened counterparts in the United States and Canada. A typical unstiffened steel plate shear wall is shown in Figure 2.

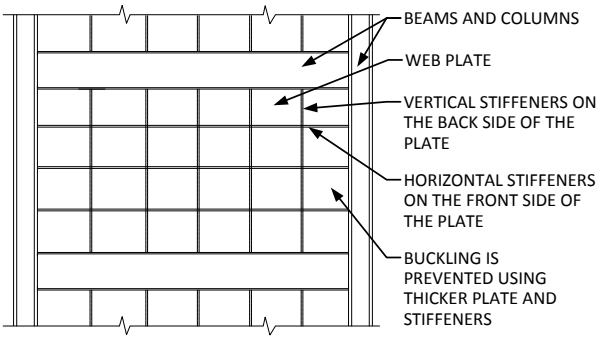


Figure 1 –Stiffened Steel Plate Shear Wall Used in Japan

Unstiffened steel plate shear walls consist of a web plate bounded at the sides by columns, also referred to as vertical boundary elements (VBE), and at the floor levels by beams, also referred to as horizontal boundary elements (HBE). The alternate nomenclature for beams and columns emphasizes the boundary element's role of resisting the tension field developed in the plate.

There are several challenges associated with unstiffened SPSW. The system is inherently challenged by the rivalry between the web plate and the boundary members. The web plate develops incredible strength in tension field action, but does so after buckling at a relatively small lateral load. In the design process, there is a desire to increase plate thickness to limit buckling and increase stiffness. However,

the boundary elements which are subjected to large inward acting forces associated with anchoring the tension field are required to be larger than an equivalent concentrically braced frame to elastically resist the combined axial forces and moments. It is desirable therefore to decrease the plate thickness to minimize the required boundary element sizes. The results of this balancing act are web plates that can be as thin as 1.3 mm and exceptionally large boundary element sizes.

Because of early buckling, SPSW web plates act like tension-only bracing with highly pinched hysteretic behavior, low stiffness, and limited energy dissipation. Current unstiffened SPSW are therefore designed in conjunction with moment connections which often requires even larger column sections and additional connection costs. In short, current unstiffened SPSW design suffers from inherent challenges associated with the buckling behavior that results in low stiffness, low energy dissipation, large boundary elements to resist the tension field, and costly moment connections.

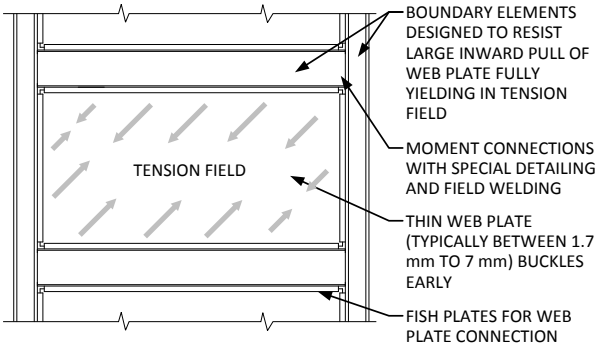


Figure 2 –Un-Stiffened Steel Plate Shear Wall Typical in Canada and the United States

A ring-shaped steel plate shear wall (RS-SPSW) has been devised which is capable of resisting buckling and producing the full hysteretic behavior of stiffened SPSW without requiring stiffeners. The concept for the RS-SPSW is developed in this paper including description of the deformation mode which resists buckling and analytical expressions for strength derived based on plastic mechanism analyses. Experimental tests are then described which are used to verify the expected behavior of the RS-SPSW as well as shed light on the two possible buckling modes and how to prevent them.

2. CONCEPT OF THE RING-SHAPED SPSW

The RS-SPSW consists of a SPSW in which the steel web plate is cut with a pattern of holes leaving ring-shaped portions of steel connected by diagonal links as shown in Figure 3. The ring shape resists out of plane buckling through the mechanics of how a circular ring deforms into an ellipse.

It will be demonstrated in the following paragraphs that the ring's compression diagonal will shorten a similar amount as the tension diagonal is elongating, essentially pulling the plate tight in the direction transverse to the tension, thus resisting the tendency for the plate to buckle. Because of the unique features of the ring's mode of distortion, the load-deformation behavior of the resulting RS-SPSW system can exhibit full hysteretic behavior. Reduced buckling also leads to greatly improved stiffness. Furthermore, through the introduction of more design variables associated with the geometry of the rings, it is possible to separately tune the strength, stiffness, and ductility of the RS-SPSW system. Effectively, the RS-SPSW system is a method for reducing the cost of the SPSW while improving the performance and design flexibility of a steel plate shear wall by strategically removing portions of the web plate.

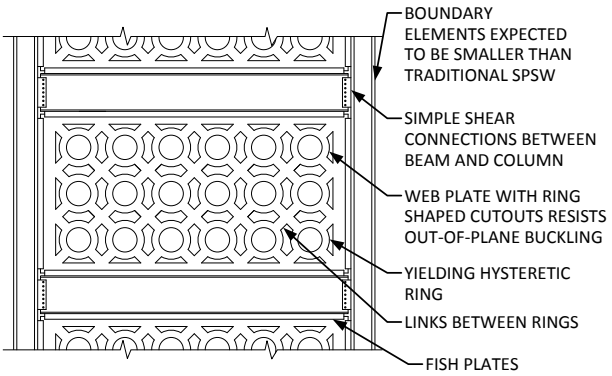


Figure 3 – Ring-Shaped Steel Plate Shear Wall (RS-SPSW)

The ring shape is the critical feature in resisting out-of-plane buckling. Consider one ring from the RS-SPSW panel and the equivalent portion of solid plate from a conventional SPSW panel as shown in Figure 4. As shear is applied to the wall, a diagonal tension is developed in both the ring and the solid plate. The amount of deformation along the tension diagonal is denoted by δ_1 in Figure 4. If the amount of shortening transverse to the tension direction is defined as δ_2, the relationship between δ_1 and δ_2 can be derived for the ring assuming that the perimeter stays constant. The approximate perimeter of an ellipse, $L_{per\text{-}ellipse}$, is given in Eq. (1) where R is the radius of the original circle. The perimeter of the original ring is given by Eq. (2), and when the two perimeters are set equal, the resulting relationship between δ_1 and δ_2 is found to be Eq. (3).

The relationship given by Eq. (3) is labeled as Ring in Figure 4c for an arbitrary value of the radius, R. Because the shortening in the transverse direction is equal to or greater than the elongation in the tension direction, the slack in the transverse direction is removed. That is, the material in the compression diagonal will shorten a similar amount as the tension diagonal is elongating, essentially pulling the plate taught in the transverse direction, thus resisting the tendency for the plate to buckle.

$$L_{per-ellipse} = 2\pi\sqrt{\frac{\left(R+\delta_1\right)^2+\left(R-\delta_2\right)^2}{2}} \quad (1)$$

$$L_{per-circle} = 2\pi R \quad (2)$$

$$\delta_2 = R - \frac{1}{2}\sqrt{4R^2 - 4\delta_1^2 - 8R\delta_1} \quad (3)$$

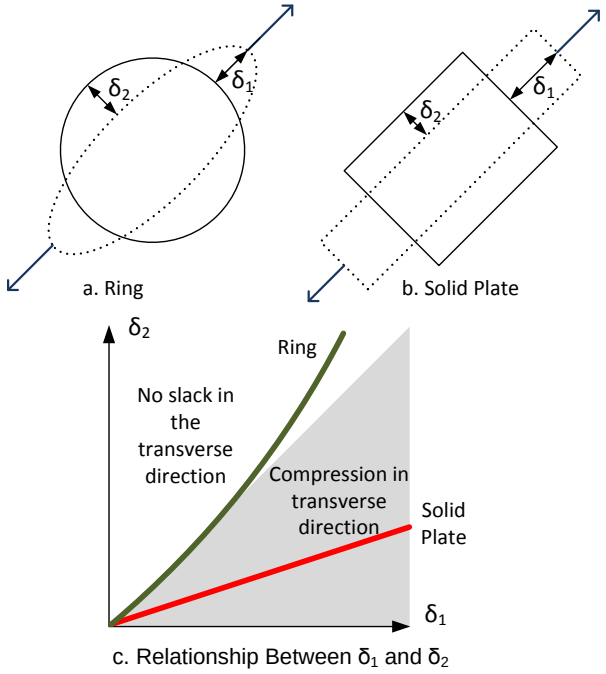


Figure 4 – Mechanics of Ring-Shaped Shear Wall Concept Demonstrating RS-SPSW Resistance to Buckling

The solid plate, on the other hand, experiences transverse shortening approximately equal to the longitudinal elongation multiplied by the Poisson's ratio. For steel, the Poisson's ratio is about 0.3 so the transverse shortening of the plate, δ_2, is approximately 30% of the elongation in the tension direction, δ_1, although this relationship may change when plasticity occurs. For an idealized SPSW panel deformed in pure shear (assuming rigid boundary elements and pinned connections), the elongation in the tension diagonal will equal the shortening of the compression diagonal. However, since the shortening of the solid plate material in the transverse direction is just a fraction of the elongation in the longitudinal direction, there is excess material in the transverse direction leading to buckling of the solid plate.

Preliminary analytical expressions for strength have been derived using plastic mechanism analysis (e.g. Bruneau et al 2011). Interaction between axial forces and flexure were neglected because the effects were generally found to be small (Maurya 2012). The first mechanism considered (shown in Figure 5b), assumes four plastic hinges will form at the intersection of the ring centerline and the centerline of the links connecting the rings. However, since the links have a discrete width, the plastic hinges are forced to occur at the edges of the link as shown in Mechanism 2 (Figure 5c).

The shear loads (horizontal component of the diagonal force) associated with Mechanism 1 (Q_1) and Mechanism 2 (Q_2) were derived in Maurya (2012) and are given by Eq. (5) and Eq. (6) respectively. Both equations are based on the geometry of the ring shown in Figure 5a including the centerline radius, R, the ring width, w_c, the link width, w_L, and the plate thickness, t. The plastic moment capacity, M_p, is given by Eq. (4) as a function of the plate yield strength, F_y. The shear capacity of a solid unstiffened steel plate shear wall, Q_{solid}, as derived in multiple references (e.g. Sabelli and Bruneau 2006), is provided in Eq. (7), and is a function of the web plate clear width, L_{cf}, and the tension field angle, α.

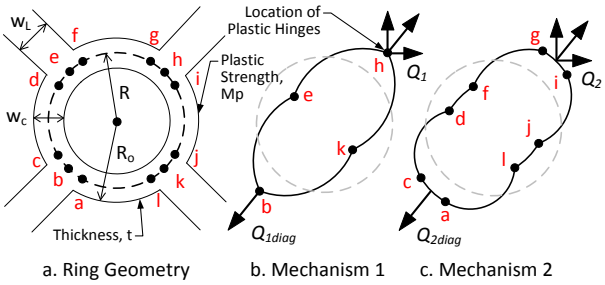


Figure 5 – Plastic Mechanism Analysis to Determine Shear Yield Capacity of the RS-SPSW

$$M_p = \frac{w_c^2 t}{4} F_y \quad (4)$$

$$Q_1 = \frac{2\sqrt{2}M_p}{R} \quad (5)$$

$$Q_2 = \frac{2\sqrt{2}M_p}{R - \frac{w_L}{2}} \quad (6)$$

$$Q_{Solid} = 0.5 F_y t L_{cf} \sin(2\alpha) \quad (7)$$

3. DESIGN OF THE EXPERIMENTAL STUDY

A series of experiments are being conducted at the Thomas M. Murray Structural Engineering Laboratory at Virginia Tech in the United States to validate the RS-SPSW concept, investigate the cyclic hysteretic behavior of these panels, verify strength predictions, and study the buckling modes associated with these plate configurations. The tests are performed on plates that are approximately one meter on each side. This size plate is adequate to investigate the behavior of full scale ring units.

3.1 Test Setup

The test setup shown in Figure 6 is designed to apply shear deformations to a steel plate. The free end shown on the left of Figure 6 is moved up and down using an MTS 243.60 actuator with a force capacity of 650 kN and 1015 kN in tension and compression respectively. The fixed end, shown on the right of Figure 6, is anchored to the strong floor. The web plate is sandwiched between angles on all four edges. The horizontal angles are attached to the vertical elements using 50 mm diameter steel pins. The horizontal angles therefore act as pinned struts that hold a constant distance between the pins creating an arc motion of the free side. Out-of-plane lateral bracing is provided for the actuator and at the middle of the W12x26 free end vertical element. The out-of-plane rotational stiffness of the fixed end reaction frame was considered adequate to restrain out-of-plane motion.

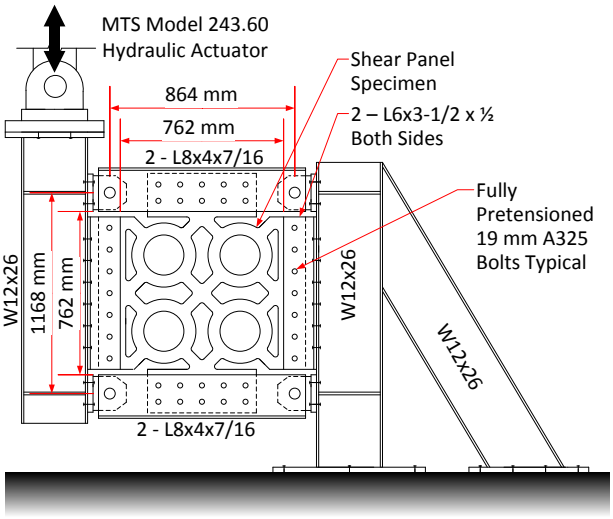


Figure 6 – Test Setup for Panel Shear Experiments

The instrumentation plan is shown schematically in Figure 7 as overlaid on a photograph of the test setup. The built-in actuator LVDT with 508 mm range was used to control the test. The ATC-24 loading protocol was utilized assuming a yield drift equal to 0.5% shear deformation over the 864 mm pin to pin distance. After testing specimen 1, the displacement protocol was amplified for all subsequent specimens by a factor of 1.3 to partially account for elastic deformations in the reaction frames.

A load cell with 1015 kN capacity was attached in line with the actuator. Four string potentiometers were used to measure the in-plane displacements of the test setup. String potentiometer 1 shown in Figure 7 measured the vertical displacement of the frame free end. Differences between the measurements of string potentiometer 1 and the actuator LVDT are due to elastic deformations of the actuator reaction frame. String potentiometers 2, 3, and 4 are used to compute the shear deformations of the web plate. Differences between the computed shear deformation and the displacement measured using string potentiometer 1 are due to deformations in the boundary elements, their connections, and fixed end reaction frame.

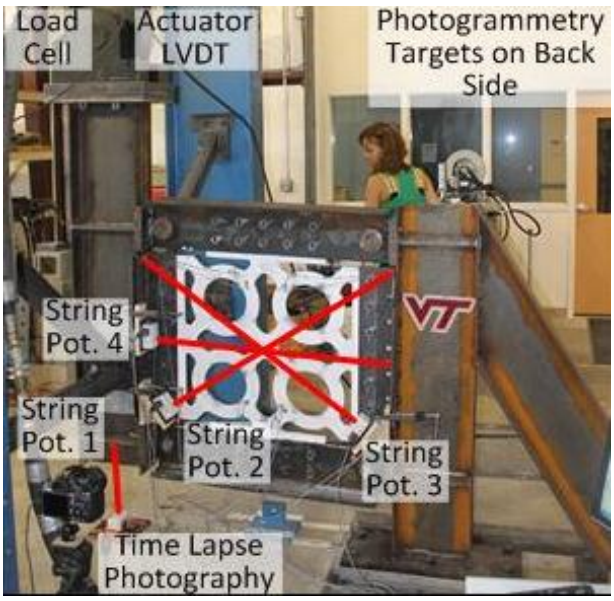


Figure 7 – Photograph of Test Setup with Instrumentation Plan Shown

Photogrammetry was used to track the out-of-plane displacement of the web plates. Data from photogrammetry is being used to understand the buckling modes of the RS-SPSW, identify the onset of buckling, and quantify the magnitudes of out-of-plane displacements. The photogrammetry targets are placed around the inside and outside perimeter of the rings and along the edges of the links connecting the rings. The photogrammetry process is conducted before the beginning of the test and at four times during the test. The photogrammetry targets are shown below in Figure 9, but the results are not discussed in detail in this paper.

3.2 Specimen Design and Fabrication

The test matrix is given in Table 1. The definitions of the outer ring radius, R_o, ring width, w_c, link width, w_L, and plate thickness, t, are shown in Figure 5a. Three nondimensional slenderness parameters are also given in Table 1. The ring slenderness as given by R_o/t and w_c/t are related to lateral torsional buckling of individual legs of the ring. Conversely, the global slenderness of the web plate as given by the ratio of the clear distance between panel supports (a=762 mm) to the panel thickness, t, is related to global shear buckling.

The test matrix was designed to separately study the effect of ring slenderness and global panel slenderness. Specimens 1, 3, and 4 have varying ring slenderness (R_o/t and w_c/t) and are thus intended to investigate the lateral torsional buckling of the ring legs. An unstiffened solid panel is tested for comparison that has significantly higher global panel slenderness to produce the same design shear

capacity. Specimens 1 through 4 are designed to have nominally the same shear capacity to isolate the differences in hysteretic behavior. Future tests will also vary panel slenderness (a/t) and will vary the ring width, w_c, for a fixed ring radius, R_o.

Table 1 – Test Matrix

	t (mm)	R_o (mm)	w_c (mm)	w_L (mm)	R_o / t	a / t	w_c / t
1	13	150	56	56	12	60	4.4
2	2	Solid Plate				400	--
3	13	300	112	112	24	60	8.8
4	13	100	37	37	8	60	2.9
Future Tests:							
5	6	150	46	56	24	120	7.2
6	6	150	56	56	24	120	8.8
7	10	100	37	37	10	80	3.9
8	6	100	37	37	16	120	5.9

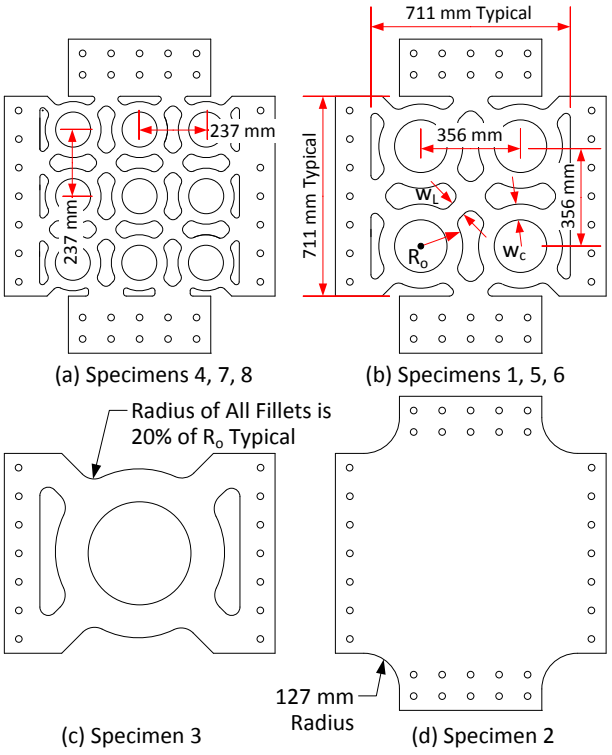


Figure 8 – Geometry of Test Specimens

The panels are shown graphically in Figure 8. The outside ring diameters vary from 100 mm to 300 mm and represent full scale rings that might be used in actual buildings. At the intersection of any two edges (e.g. the intersection of the outer perimeter of the ring and the link), the surface is rounded with a fillet that has a radius equal to 20% of the outside ring radius, R_o. This fillet radius was determined by finite element modeling to reduce the likelihood of fracture (Maurya 2012).

The ring shapes were made using water jet cutting with the highest quality setting. A photograph of the cut edge is shown in Figure 9. Cutting of the web plates to produce the RS-SPSW can be conducted using automated tools operated by computer numerical control (CNC) machines which are common in many fabrication and machine shops. Similarly, many machine shops have capabilities for water jet cutting or laser cutting. As an example, a machine shops near Virginia Tech has the ability to water jet cut sheets of steel as large as 12' x 20' at reasonable cost.



Figure 9 – Close-Up Photograph of Smooth Cut Surface Obtained Using Water Jet Cutting (Photogrammetry Targets Also Shown)

3.3 Material Behavior

Three tension coupons were conducted on the same material used for each plate thickness. All plate of a given thickness was obtained from the same heat (same batch of material). A representative plot of stress versus strain is provided in Figure 10 for both the 13 mm thick steel plate and the 2 mm thick steel plate. The measured yield stress was 331 MPa (48.0 ksi) for the 13 mm thick steel plate and 294 MPa (42.6 ksi) for the 2 mm thick steel sheet.

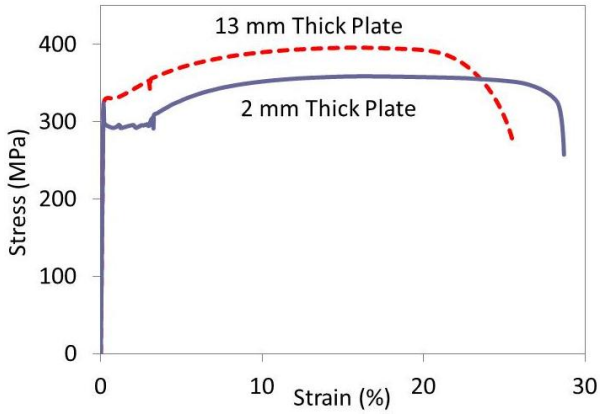


Figure 10 – Representative Material Behavior

4. EXPERIMENTAL RESULTS

The results from the first four specimens are discussed starting with the solid panel and then progressing from the largest ring diameter to the smallest ring diameter. None of the RS-SPSW panels experienced any fractures. The solid panel test did experience tearing and was stopped after the fracture propagated through a large section of the plate. The RS-SPSW tests were ended when there was either a significant loss of load carrying capacity (specimen 3) or when the test setup experienced damage (specimens 1 and 4).

The cyclic shear load-deformation behavior of the solid plate (specimen 2) is shown in Figure 11. The solid plate specimen with no stiffeners represents conventional SPSW construction in the U.S. with the exception of excluding moment connections between the beams and columns. As expected, the very thin web plate buckled at small shear load and a tension field developed as shown in Figure 16a. The corresponding hysteretic behavior was highly pinched as the plate acted in a manner similar to tension-only bracing producing little resistance during load reversal. The energy dissipated during the 4% drift cycle was computed, E_d, and found to be 44% of the energy that would be dissipated by an equivalent elastic perfectly plastic system, E_{EPP}. The comparison is shown graphically in the inset diagram of Figure 11 and tabulated in Table 2. The test was stopped after significant tearing developed in the web plate as shown in Figure 12.

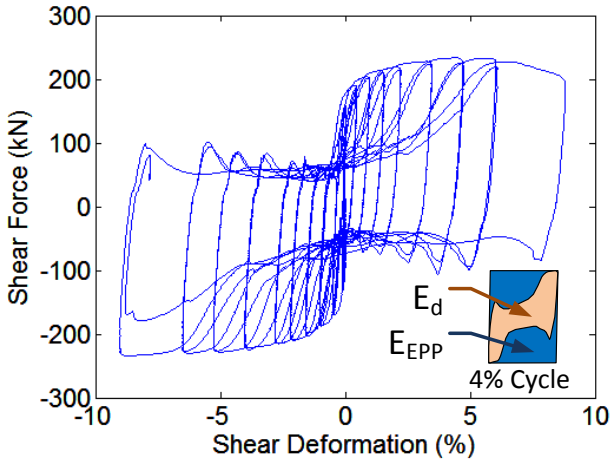


Figure 11 – Hysteretic Behavior of Solid Panel (Specimen 2)



Figure 12 – Tears in the Solid Plate (Specimen 2)

The hysteretic behavior of specimen 3 is shown in Figure 13. This specimen consisted of one large ring with large ring slenderness (R_o/t and w_c/t). The ring experienced lateral torsional buckling of the top and bottom legs of the ring as shown in Figure 16c. The lateral torsional buckling caused considerable deterioration in the strength and energy dissipation capability. The resulting hysteretic behavior was pinched leading to an energy dissipation ratio (E_d / E_{EPP}) of 0.33 for the 4% drift cycle which was 25% less than that of the solid plate.

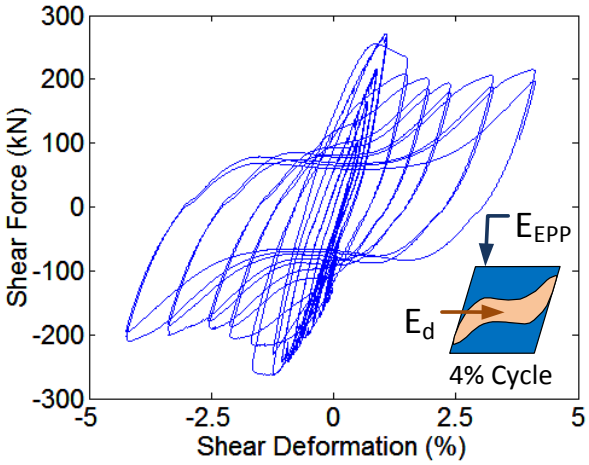


Figure 13 – Hysteretic Behavior of Panel Undergoing Lateral Torsional Buckling (Specimen 3)

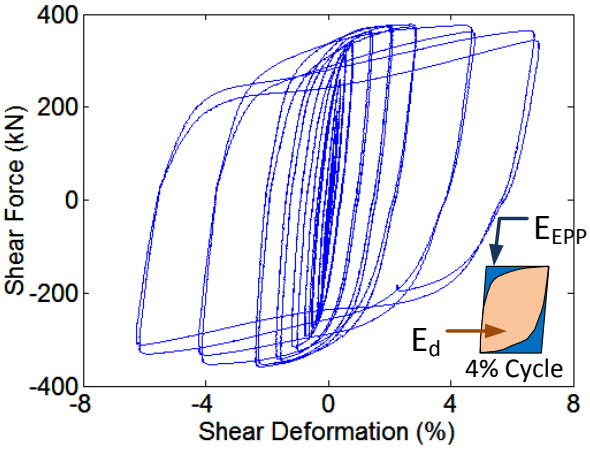


Figure 14 – Hysteretic Behavior Panel Undergoing Minimal Buckling (Specimen 1)

As the ring slenderness, represented by the nondimensional ratios R_o/t and w_c/t, were reduced, the propensity for lateral torsional buckling was reduced. Figure 14 shows behavior of specimen 1 which did not experience buckling until the second cycle at 4% drift. This amount of buckling might be acceptable in a practical design since the web plate might only buckle under extreme earthquake motions and even then, the energy dissipation and strength are only mildly affected. As shown graphically in the inset of Figure 14 and tabulated in Table 2,

the energy dissipation is approximately twice that of the solid plate or the RS-SPSW with high ring slenderness that experienced significant ring leg lateral torsional buckling.

If the ring slenderness is reduced further, buckling can be completely prevented as shown in Figure 15 and figure 16b for specimen 4. The energy dissipation ratio increased 9% as compared to specimen 1. The resulting full hysteretic behavior is similar to systems in which buckling is restrained and provides nearly the maximum amount of hysteretic energy dissipation possible.

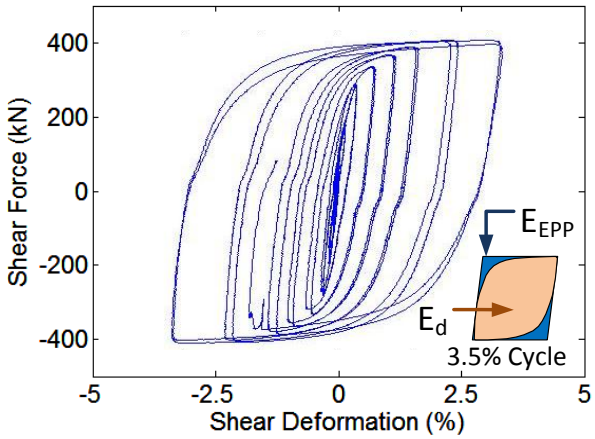


Figure 15 – Hysteretic Behavior of Panel That Experiences No Buckling (Specimen 4)

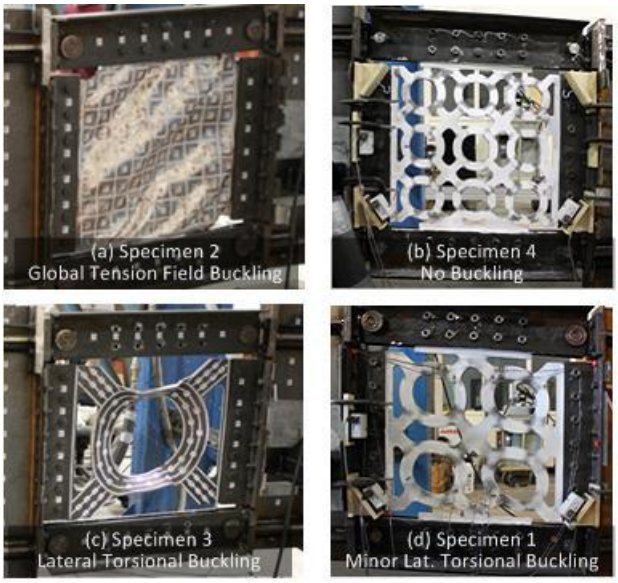


Figure 16 – Photographs of Specimens Demonstrating Buckling Modes

Additional results are provided in Table 2. The measured shear yield force, V_y, was computed as the approximate load at which significant nonlinearity began occurring. The measured ultimate shear strength, V_u, was the maximum shear force recorded during the test. Also presented in Table 2 are the computed shear capacity using plastic mechanism 1 (Q_1) and plastic mechanism 2 (Q_2), the ratio of ultimate strength to yield strength, and the energy dissipation ratio. As described previously, the energy dissipation ratio is computed for the 4% drift cycle as the ratio of the measured dissipated hysteretic energy, E_d, to the hysteretic energy that would be absorbed by an equivalent elastic perfectly plastic system, E_{EPP}.

Table 2 shows that the analytical solution for the RS-SPSW shear capacity can be quite conservative underestimating the capacity by approximately 60%. Further work is being conducted to evaluate whether the boundary conditions in the plate are causing a higher energy plastic mechanism to form. On the other hand, the shear capacity of the solid plate specimen was fairly well predicted by the calculated capacity, Q_{solid}, assuming a tension field angle of α=45°.

The effects of preventing buckling are twofold. First it is evident that the energy dissipation ratio goes up significantly. Secondly, the overstrength of the web plate given by the ratio V_u/V_y increased as buckling was prevented. For the configuration in which buckling was fully prevented, the ultimate strength was 28% greater than the yield strength.

Table 2 – Summary of Test Results

	V_y (kN)	Q_1 (kN)	Q_2 (kN)	V_u (kN)	$\frac{V_u}{V_y}$	$\frac{E_d}{E_{EPP}}$
1	320	154	200	377	1.18	0.79
2	200	Q_{solid} = 220		233	1.17	0.44
3	272	154	200	272	1.00	0.33
4	320	153	199	410	1.28	0.86

5. DISCUSSION AND CONCLUSIONS

Although ongoing work is being conducted to further study the ring shaped steel plate shear wall system, several preliminary observations and conclusions can be made based on the work presented herein.

1. The RS-SPSW system can be designed to prevent buckling without using any stiffeners. This was demonstrated experimentally with a specimen that produced large stiffness and energy dissipation.
2. The added geometric parameters in the RS-SPSW system allow the strength, stiffness, and ductility to be separately tuned to a particular building's needs.
3. RS-SPSW have the potential to reduce cost of SPSW and provide enhanced seismic performance. The reduction in cost compared to stiffened steel plate shear walls would come with the elimination of stiffeners and associated welds. The potential cost savings compared to unstiffened SPSW may be due to elimination of moment connections and resulting reduction in boundary elements sizes.
4. Two distinct buckling modes have been identified associated with RS-SPSW. The global shear

buckling experienced by the solid plate specimen can occur in RS-SPSW for large values of the global panel slenderness. Lateral torsional buckling of ring legs was investigated in the experiments presented herein and found to be related to the ring slenderness.

5. It is expected that both buckling modes can be predicted and prevented based on slenderness parameters. Equations for shear buckling of a solid plate will be examined in future work to determine if they adequately predict global shear buckling of the RS-SPSW panels. Future work will also help develop methods to predict lateral torsional buckling of the ring legs based on ring slenderness.
6. Analytical solutions for shear capacity of RS-SPSW plates were found to be conservative. Further work is being conducted to investigate alternate plastic mechanisms with more constrained boundary conditions.

Acknowledgements:

The authors gratefully acknowledge support from the American Institute of Steel Construction through the Milek Faculty Fellowship Program and Virginia Tech. Thanks to Michael Wood, Adam Phillips, and Chris Galitz for their contributions to this work.

References:

Basler, K. (1962) "Strength of Plate Girders in Shear", Journal of the Structural Division, ASCE, Vol. 87, No. ST7.

Bruneau, M., Uang, C.-M., and Sabelli, R. (2011) Ductile Design of Steel Structures, Published by McGraw Hill (Great focus on ductile steel systems)

ENR (1978) "Quake-proof hospital has battleship-like walls", Engineering News Record, Sept. 21, 1978, pp. 62-63.

Maurya, A. (2012) Computational Simulation and Analytical Development of Buckling Resistant Steel Plate Shear Wall (BR-SPSW), M.S. Thesis, Virginia Tech

Porter, D.M., Rockey, K.C. and Evans, H.R. (1975) "The collapse behavior of plate girders loaded in shear", The Structural Engineer, London England, Vol. 53, No. 8.

Sabelli, R. and Bruneau, M. (2006) Steel Design Guide 20 – Steel Plate Shear Walls, Published by the American Institute of Steel Construction.

Thorburn, L. Jane, Kulak, G.L. and Montgomery, C.J. (1983) Analysis of Steel Plate Shear Walls, Structural Engineering Report No. 107, Department of Civil Engineering – University of Alberta at Edmonton.

Timler, P.A., and Kulak, G.L. (1983) Experimental Study of Steel Plate Shear Walls, Structural Engineering Report No. 114, Department of Civil Engineering, University of Alberta, Edmonton, Alberta, Canada.

Tromposch, E.W. and Kulak, G.L. (1987) Cyclic and Static Behaviour of Thin Panel Steel Plate Shear Walls, Structural Engineering Report No. 145, Department of Civil Engineering, University of Alberta, Edmonton, Alberta, Canada.

Troy, R.G. and Richard, R.M. (1979) "Steel plate shear walls resist lateral load, cut costs", Civil Engineering, ASCE Feb. 1979.

10CUEE CONFERENCE PROCEEDINGS
10th International Conference on Urban Earthquake Engineering
March 1-2, 2013, Tokyo Institute of Technology, Tokyo, Japan

SEISMIC RESPONSE OF RECENTERING PRECAST COMPOSITE CONCRETE-DUAL-SHELL-STEEL COLUMNS

Gabriele Guerrini[1] and José I. Restrepo[2]

1) Graduate Student Researcher, Dept. of Structural Engineering, University of California - San Diego, La Jolla, California, USA
2) Professor, Dept. of Structural Engineering, University of California - San Diego, La Jolla, California, USA
gguerrin@ucsd.edu, jrestrepo@ucsd.edu

Abstract: An innovative bridge pier technology for application in seismic regions is under development at the University of California, San Diego, in collaboration with the Pacific Earthquake Engineering Research (PEER) Center. The proposed solution combines a precast composite concrete-steel hollow-core column with recentering behavior and supplemental energy dissipation.
The precast hollow-core column consists of two concentric cylindrical steel shells, with concrete sandwiched in between. The shells act as permanent formwork, the outer one substituting traditional reinforcing cage and providing concrete confinement, the inner one preventing concrete implosion. These features are aimed to improve constructability and to reduce on-site construction burdens.
Large inelastic rotations can be accommodated at the end joints with minimal structural damage: gaps are allowed to open in tension at these locations and to close upon load reversal. Post-tensioned longitudinal bars induce recentering behavior together with gravity forces; rubber pads, in series with these bars at their anchorages, protect bars from yielding. Specifically designed steel devices provide energy dissipation by axial yielding. High-performance mortar and headed reinforcement are used to prevent mortar-joint premature crushing.
Outcomes from dynamic shake-table tests conducted at the PEER-UC Berkeley laboratories, as well as from numerical simulations performed in OpenSees, are summarized herein.

1. INTRODUCTION

Current provisions for seismic design of bridges (Caltrans, 2010; AASHTO, 2012) allow columns to respond beyond the elastic limit and to be damaged under the design earthquake, provided that collapse is prevented. Inelastic behavior is localized within flexural plastic-hinge regions at the bottom and/or top of the columns. These regions may experience some structural damage which may lead to temporary closure of the bridge to the public. However, the consequences could be critical if associated with the interruption of an important road path: obstruction of rescue and recovery operations, and economical losses related to business interruption and displacement of people and goods (Palermo et al., 2008).

While the notion of structural damage is accepted in design, resilient communities expect bridges to survive a moderately strong earthquake with little or no disturbance to traffic: this implies that partial or total bridge closures are tolerated with uneasiness, particularly in heavily congested urban areas. As a consequence, research efforts have been prompted into advanced technologies that reduce residual damage to the main structural elements, and encompass recentering properties which allow the structural system to return to its original position after an earthquake. Moreover, these innovative solutions need to be economically viable when compared to existing technologies (Guerrini et al., 2011).

This paper describes the main outcomes of an experimental and analytical work on a post-tensioned self-centering precast concrete dual-shell steel column, which is an enhancement to the earlier research described in Restrepo et al. (2011) and Guerrini et al. (2012). Use of precast members, replacement of traditional time-consuming reinforcing cages with steel pipes, and adoption of lighter hollow cross-sections are aimed to improve constructability and to reduce on-site burdens. In parallel, the combination of unbonded post-tensioned joint connections with specific energy dissipating devices ensure seismic resilience, in the form of recentering capability, facilitation of structural fuse repair, and minimization of damage to the main structural elements. As a consequence, traffic impacts, environmental disruptions, and life-cycle costs can be reduced.

2. SYSTEM DESCRIPTION

The precast bridge column described here consists of two concentric cylindrical steel shells (*dual-shell* technology) running for its entire height. High-performance concrete is sandwiched in between the shells and longitudinal reinforcement is detailed only between the

column ends and the footing or bent cap (Fig. 1(*a*)). The outer shell acts as permanent formwork, providing also longitudinal and transverse reinforcement, as it works in composite action with the concrete. The inner shell provides permanent formwork too, reducing unnecessary weight and making the technology suitable for prefabrication and rapid erection. It also prevents concrete implosion under large compressive strains which may develop upon gap opening, and delays buckling of energy dissipating dowels which are embedded in the concrete.

Large inelastic rotations can be sustained at the column-footing and column-cap beam joints with minimal structural damage. These rotations are accommodated within the connections themselves, through the formation of gaps at the member interfaces (Fig. 1(*b*)): gaps are allowed to open in tension under severe lateral displacement demand, and to practically close at the end of the excitation. Recentering/rocking capability is provided by gravity forces and unbounded, threaded post-tensioning (PT) bars, designed to remain elastic. The bolted PT bar anchorages at the bent cap and foundation allow for eventual bar replacement, should corrosion or other types of damage be a concern.

Energy dissipation takes place through axial yielding of internal dowels (Restrepo et al., 2007; Restrepo et al., 2011), as shown in Figure 1(*b*), preventing the main structural members from experiencing significant damage. Under strong-intensity earthquake excitation only these devices may undergo multiple cycles within the inelastic range, with possible need of replacement, but the structure is expected to remain functional overall. To transfer tension between the internal dowels and the outer shell, circumferential weld beads are provided on the internal surface of the outer shell, only near its ends (Gebman et al., 2006; Restrepo et al., 2011).

The resulting lateral force-displacement response shows flag-shaped loops as illustrated in Fig. 1(*c*).

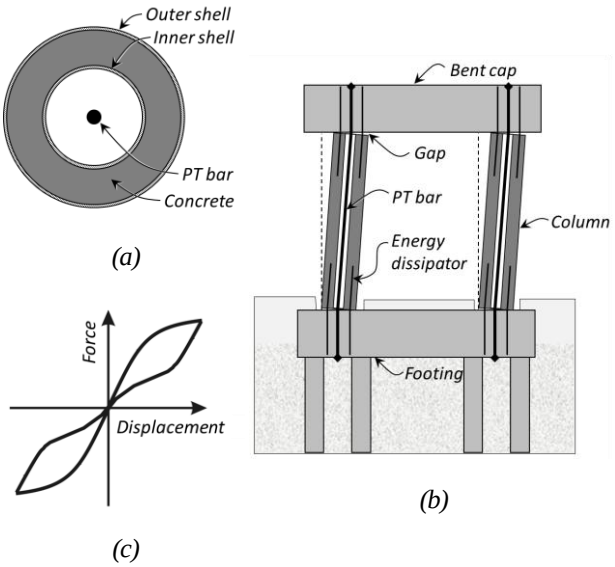


Figure 1 – Sketches of the proposed system: *(a)* column typical cross-section; *(b)* bent components and rocking kinematics; *(c)* flag-shaped hysteretic response.

3. SHAKE TABLE EXPERIMENT

3.1 Test Specimen

A dual-shell column specimen was built at a 1-to-3 scale at the UC San Diego Powell Structural Engineering Laboratories, and tested on the shake table at the PEER-UC Berkeley Laboratories. It was loaded in a cantilever configuration, with fixed base and an inertial mass applied at the top, as shown in Figure 2. The column had an overall diameter of 0.41 m (16 in.) and a height of 1.32 m (52 in.); the total cantilever span from the base to the center of mass was 2.44 m (96 in.). Column, footing, and loading stub were precast separately, and then connected through grouted dowels and a post-tensioning rod. Three inertial mass blocks were subsequently attached to the loading stub.

The column outer shell had a diameter D_O = 0.41 m (16 in.) and a thickness t_O = 6.4 mm (0.25 in.), that is D_O / t_O = 64. The inner shell had a diameter D_I = 0.25 m (10 in.) and a thickness t_I = 3.2 mm (0.125 in.), that is D_I / t_I = 80. Details are shown in Figure 3. The shells were obtained by folding and welding plates made of Grade 50 A572 steel. In practice, the inner shell would be a corrugated drainage pipe (Restrepo et al., 2011). High-performance, normal-weight concrete was used to cast column, footing, and load stub. The specified concrete compressive strength at 56 days was 62 MPa (9.0 ksi), the ones measured at 28 days, 56 days, and 101 days (day of test) were 60 MPa (8.7 ksi), 66 MPa (9.6 ksi) and 70 MPa (10.2 ksi), respectively.

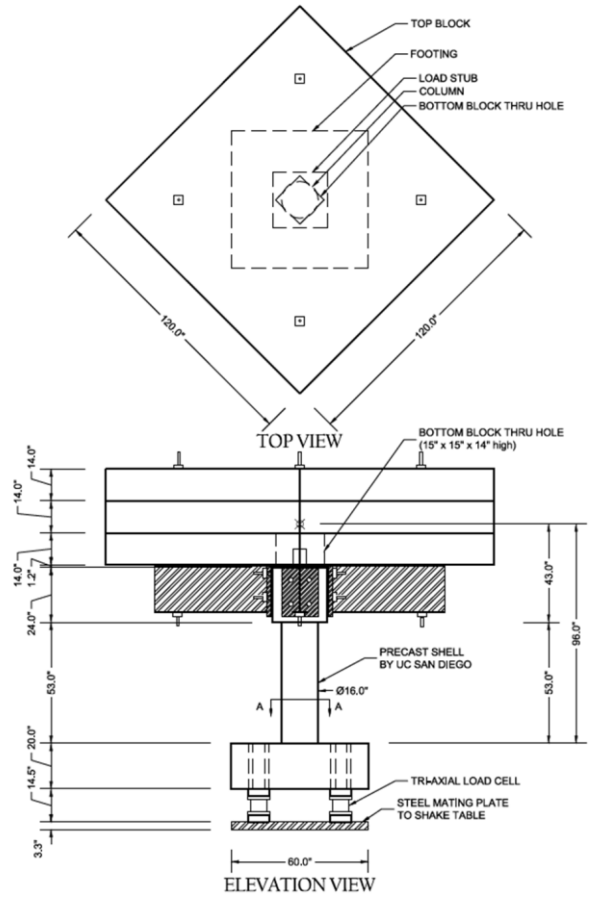


Figure 2 – Test setup and dimensions.

Eight 50.8-mm (2-in.) diameter, 0.48-m (19-in) long, corrugated metal ducts were embedded in the concrete for the installation of the internal energy dissipating dowels at the column bottom (Fig. 3 and 4*(a)*). Eight similar ducts, only 0.38-m (15-in.) long, were placed at the top for grouting the loading stub dowels (Fig. 3 and 5*(a)*). Four circumferential 9.5-mm (3/8-in.) weld beads on the internal surface of the outer shell provided tensile stress transfer between the dowels and the shell at each end.

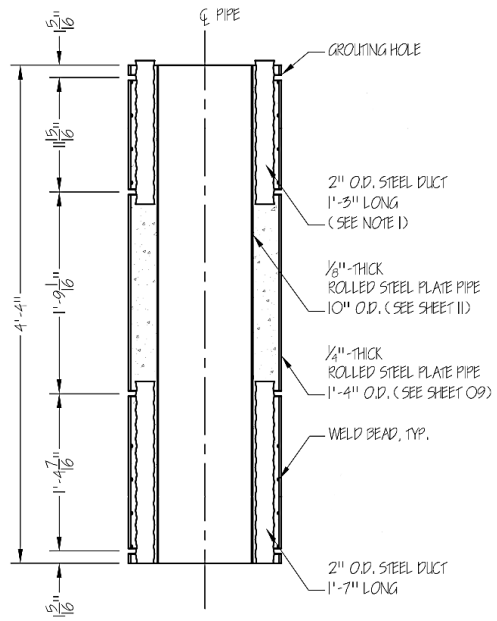


Figure 3 – Column vertical section.



(a) *(b)*

Figure 4 – *(a)* Column base section, with visible metal ducts for dowels and bar heads. *(b)* Footing surface, with visible stainless-steel dowels and bar heads.



(a) *(b)*

Figure 5 – *(a)* Column top section, with visible metal ducts for dowels, post-tensioning threaded bar, and load-stub dowels during stub positioning. *(b)* Post-tensioning bar top anchorage, with polyurethane pad (yellow).

A 19-mm (0.75-in.) thick mortar bed was cast between the column and the footing, to compensate for expected in-situ construction tolerances. Upon rocking, large compressive strains may arise on the mortar; eventually, mortar crushing would cause loss of PT and loss of recentering capacity. Thus, a high-performance mix was used, with the addition of polypropylene fibers in the proportion of 0.035% by weight to increase the mortar toughness. Moreover, the mortar was scraped from underneath the outer shell, to prevent the shell from causing premature crushing under direct compression transfer, a problem noted in earlier experiments (Restrepo et al., 2011). Strengths of 104 MPa (15.1 ksi) and 120 MPa (17.5 ksi) were obtained at 28 and 73 days (day of test), respectively. Eight headed bars were embedded in the column and eight in the footing, with their heads matching at the interface (Fig. 4), to help the mortar transferring compression (Belleri et al., 2013). The upper joint between the column and the load stub, not critical because of the lower bending moment at this location, was realized with the same mortar but without headed bars. All interface surfaces were roughened to improve shear friction. Bond breaker was applied to the surface of the footing, to allow separation from the mortar bed and opening of the gap.

The unit was equipped with eight internal dowels at the column-footing joint, acting as internal energy dissipators (Fig. 4*(b)*). 316LN Grade 75 stainless steel #3 bars were used for this purpose, wrapped with duct-tape wrapping for 152 mm (6 in.) across the interface to destroy the bond within this length. Material testing provided a yield stress of 862 MPa (125 ksi), ultimate strength of 986 MPa (143 ksi), and ultimate strain of 10%. The dowels were tied together with the footing cage and, after the column had been placed on the footing, they were grouted within the column ducts. Similarly, eight dowels were provided to connect the load stub to the column (Fig. 5*(a)*); however, A706 Grade 60 steel reinforcing bars without duct-tape wrapping were used as no yielding was anticipated.

Post-tensioning was provided by a single 44.5-mm (1-3/4 in.) diameter, A722 Grade 150 steel threaded bar (Fig. 5*(a)*). The total effective post-tensioning force was 438 kN (98.5 kips) after losses. The bar ran within the column hollow core, and was screwed into an anchorage device prearranged in the footing, allowing for bar replacement.

Additional bar deformability was provided by placing in series with the post-tensioning bar a polyurethane pad, between the top anchorage plates and the load stub (Fig. 5*(b)*). With this configuration the tensile deformation demand on the bar, due to gap opening, can be partially converted into compressive deformation of the pad, preventing the bar from yielding and avoiding loss of PT and recentering capacity. A disc consisting of 90 Shore-A hardness polyurethane, with a thickness of 47.6 mm (1-7/8 in.), a diameter of 190.5 mm (7.5 in.), and a central hole with a diameter of 57 mm (2-1/4 in.) to accommodate the PT bar, was used for this scope. It had stiffness equal to 1.75×10^5 kN/m (1000 kip/in) when tested at ambient temperature and at a rate of 0.5 kips/sec.

3.2 Test Protocol

The column was subjected to three-dimensional shake-table excitation. The top block provided a translational mass of 2.4×10^4 kg (53 kips), a mass moment of inertia of 2.05 kg-m^2 (6.99×10^4 kip-in^2), and an axial load of 236 kN (53 kips).

A series of 8 ground-motion records from historical events was selected and scaled, based on the displacement demand imposed on a conventional reinforced-concrete column, designed according to Caltrans' Seismic Design Criteria (Caltrans, 2010), carrying the same mass block. The chosen records and the applied scale factors (SF) are summarized in Table 1. EQ1 was selected to maintain the column response within the elastic range. EQ2 and EQ3 represented frequent events with low ductility demands. EQ4 and EQ5 were chosen as design-level excitation. EQ6, EQ7, and EQ8 were intended to bring the conventional reinforced-concrete column to near-collapse conditions. EQ9 was a repeat of EQ5. Free-vibration tests were run at the beginning of the experiment, and white-noise tests were performed between the historical records to assess the dynamic properties of the system.

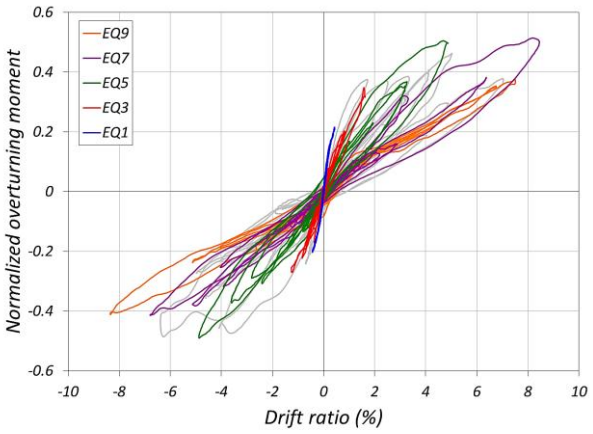
Table 1 – Selected ground motion records and scale factors.

EQ	Event	Date	Station	SF
1	Coalinga	1983/05/09	Harris Ranch – Hdqtrs (temp)	2.50
2	Imp. Valley	1979/10/15	EC Meloland Overpass FF	0.80
3	Morgan Hill	1984/04/24	Coyote Lake Dam (SW abut)	0.70
4	Northridge	1994/01/17	Rinaldi Receiving Station	0.56
5	Northridge	1994/01/17	Sylmar – Olive View Med FF	-0.80
6	Northridge	1994/01/17	Rinaldi Receiving Station	0.90
7	Kobe	1995/01/16	Takatori	0.77
8	Kobe	1995/01/16	Takatori	-0.90
9	Northridge	1994/01/17	Sylmar – Olive View Med FF	-0.80

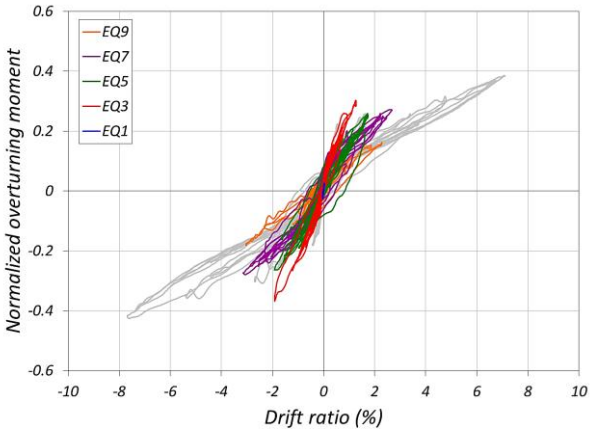
3.3 Test Results

Figures 6*(a)* and 6*(b)* show the hysteretic overturning moment-drift ratio response in the two lateral directions: lateral displacements at the center of mass have been normalized by the height of the center of mass above the column base, and thus, expressed as drift ratios; overturning moments have been normalized by the product of the mass weight times the height of the center of mass above the column base. For drift ratios larger than 0.3%, it was observed that the base joint rotation was contributing to more than 90% of the lateral displacement: for this reason, drift ratios and joint rotations practically coincided. Figure 6*(c)* illustrates the maximum and the residual drift ratio obtained during each run.

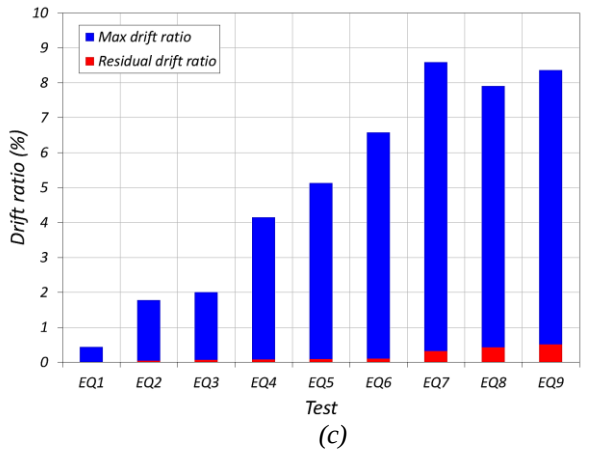
At the end of EQ4 the mortar bed was flaking off without crushing. During EQ5 crushing initiated superficially on the north-east and south-west sides, and after EQ8 it extended all the way around the mortar bed (Fig. 7*(a)*). However, only the outermost 25-mm (1-in.) wide ring of mortar was damaged, while the inner portion remained sound. Energy dissipators started fracturing under EQ6 test (6.6% maximum drift ratio), when one dowel fractured on the north-east side. Subsequently, three dowels were heard fracturing during EQ7 and other two during EQ8.



(a)



(b)



(c)

Figure 6 – Test results: overturning moment- drift ratio response in the longitudinal *(a)* and transverse *(b)* directions; *(c)* maximum and residual drift ratios.



(a) *(b)*

Figure 7 – Damage observed at the end of the test: *(a)* mortar bed superficial crushing; *(b)* stainless-steel dowel buckling and fracture.

After the test, when the column was disassembled from the footing, it was observed that all dowels had buckled and fractured (Fig. 7*(b)*). However, no or negligible permanent deformations of the column concrete and of the steel shells were detected. Some post-tensioning losses were recorded during the test, probably due to mortar damage; at the end of the test they accounted for less than 30% of the initial force (after lock-off and creep losses). Recentering capacity was maintained throughout the test, with residual drift ratios always smaller than 0.6% (Fig. 6*(c)*).

4. NUMERICAL MODELING

4.1 Model Description

A three-dimensional numerical model of the test was developed and validated with the experimental results. For this purpose the software OpenSees (Mazzoni et al., 2007; McKenna et al., 2010), developed by the Pacific Earthquake Engineering Research Center (PEER), was used. Details can be found in Guerrini (2013).

The column was modeled with two elastic frame elements in series, connected to the mortar bed at the base and to the mass block at the top; the intermediate node was necessary for linking the energy dissipating dowels. The stiffness of the lower column element was based on the hollow concrete section only, as the outer shell does not transfer directly compression at the interface (contact with the mortar is avoided) and tension is resisted by the dowels at that level. For the upper segment the transformed section was considered, accounting for the outer steel shell too. According to ACI (2008) the concrete elastic modulus was taken as $E_c = 57 \cdot \sqrt{1000 \cdot f'_c}$ (ksi), were f'_c (ksi) is the concrete compressive strength on the day of testing, while for the steel shell $E_s = 200$ GPa (29000 ksi) was used. A node was defined at the center of mass of the top block to assign masses and vertical forces; since the deformations of the loading stub and mass block are expected to be negligible, this node was linked to the top of the column with a rigid element.

Multiple non-linear truss elements (Taylor, 1977; Vulcano et al., 1987; Carr, 2008) represented the mortar bed between column and footing; their length was set equal to the actual mortar thickness, i.e. 19 mm (0.75 in.). *Concrete01* non-linear material model was applied to these elements; this concrete-specific rule assumes zero tensile strength, consistently with gap opening. Peak compressive stress and strain, and ultimate stress and strain need to be input; a parabola connects the origin to the peak point, and a straight line goes from the peak to the ultimate point; for strains larger than the ultimate one, stresses drop to zero. The initial tangent elastic modulus is automatically derived by fitting a parabola through the origin, being its vertex the peak point. Peak stress and strain of 128 MPa (18.5 ksi) and 0.4%, respectively, were obtained from Mander's model for confined concrete (Mander et al., 1988), assuming a low confinement efficiency coefficient equal to 0.1. The ultimate strain was set to 16%, with a residual stress of 6.9 MPa (1 ksi). Strains in the stress-strain relationship were amplified by the ratio of the theoretical neutral axis depth, taken equal to 63.5 mm (2.5 in.), to the actual thickness of the mortar bed; by doing this, the spread of inelastic behavior within the column concrete, assumed to extend uniformly for a length equal to the neutral axis depth (Restrepo et al., 2007), was approximately taken into account.

The post-tensioning bar was modeled as a non-linear truss element, fixed at the base and connected to the top node of the column. *Steel02* material hysteretic rule (Filippou et al., 1983), based on Giuffré-Menegotto-Pinto model, was assigned to it. An initial stress of 259 MPa (37.5 ksi) was set to represent the effective prestress after losses. An equivalent initial tangent elastic modulus and an equivalent bilinear factor were calculated, accounting for the stiffness of the urethane pad in series with the bar. The yield stress was set equal to 827 MPa (120 ksi). Curvature parameters $R_0 = 18$, $c_{R1} = 0.925$, and $c_{R2} = 0.15$ were chosen, while no isotropic hardening was introduced.

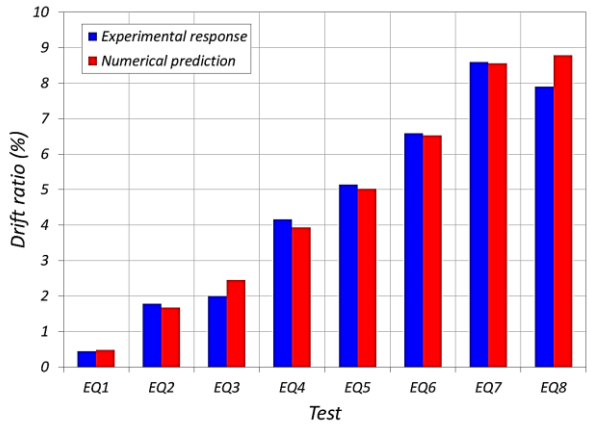
The energy-dissipating dowel bars were represented by non-linear frame elements; the lower ends were fixed to the footing, and the upper ends were connected to the column intermediate node by rigid links. *Steel02* non-linear material model (Filippou et al., 1983) was assigned also to the dissipators. Geometry and material properties reflected the actual ones. However, the yield stress was set equal to 917 MPa (133 ksi) to better match the experimental monotonic stress-strain relationship of the stainless steel. Curvature parameters $R_0 = 18$, $c_{R1} = 0.925$, and $c_{R2} = 0.15$ were chosen, while no isotropic hardening was introduced.

The analysis was performed in two stages: first, the vertical load was applied and held constant; then the time-history analyses were run sequentially, keeping track of the cumulated residual displacements. The Newton-Raphson algorithm was chosen to solve the nonlinear residual equation, and the Newmark method was selected to integrate the equation of motion. Rayleigh damping was used; the contribution of the rigid links was excluded from the stiffness-proportional term, which was based on the initial stiffness. Damping ratios of 1% were assigned to the first two modes (translational in the longitudinal and transverse directions). The analysis was performed under the hypothesis of large displacements, or corotational geometric transformation in OpenSees language.

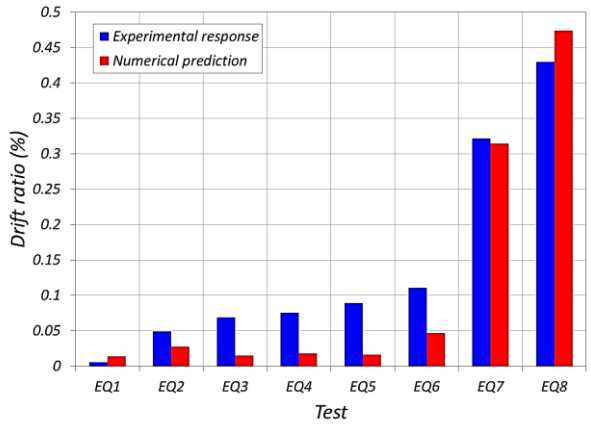
4.2 Numerical Results

When analyzing the quasi-static cyclic tests of similar recentering dual-shell columns, modeled according to the same strategy, Guerrini et al. (2012) found good agreement between the experimental and numerical results, in terms of force-displacement relationship, cumulative energy dissipated, strain histories of the post-tensioning bars, and hysteretic axial strain-stress response of energy dissipators, up to 5% drift ratio.

The numerical model was here used to predict the maximum and residual drift ratios under the given set of ground motions, with the feedback records from the bare shake table as inputs. Simulations were run up to EQ8, as the ninth run was added to observe the behavior of the damaged specimen under a design-level ground motion. The comparison between predicted and measured drift ratios is shown in Figure 8. Good agreement can be found between the maximum drift ratios, while relative discrepancy is observed on the residual drift ratios when they are in the order of 0.1% or less (EQ1 to EQ6). However, being these quantities very small, the absolute error appears negligible, especially considering that residual drift ratios of 0.3% or larger (EQ7 and EQ8) are accurately predicted.



(a)



(b)

Figure 8 – Comparison between numerical prediction and experimental response: *(a)* maximum drift ratios and *(b)* residual drift ratios.

5. CONCLUSIONS

This paper discussed the experimental performance and numerical modeling of a composite concrete-dual steel shell bridge column technology. This column can be specifically designed for damage minimization at the design earthquake and to display a self-centering response. This technology, ideal for prefabrication, simplifies and accelerates bridge construction, as the outer shell makes the reinforcing cage obsolete, and the inner shell removes unnecessary concrete volume.

The use of a metallic-aggregate mortar bed incorporating polypropylene fibers, in combination with headed bars at the column-footing interface, delayed the mortar from crushing, and allowed this unit to display excellent performance up to 8.6% drift ratio without losing recentering capacity. The polyurethane pad in series with the post-tensioning bar proved to be effective in preventing bar yielding, and consequent losses of prestress and of recentering behavior. Fracture of the energy dissipating dowels occurred at a drift ratio of 6.6%.

The test was simulated in OpenSees environment. An accurate representation of the response was obtained in terms of maximum and residual drift ratio demands up to the final stages of testing.

Acknowledgements:

Funding for this project, provided by the Pacific earthquake Engineering Research Center (PEER) and by the California Department of Transportation (Caltrans), is gratefully acknowledged. The precious coordination work of Dr. Matthew Schoettler and the contribution of Dr. Vesna Terzic (PEER) are also thankfully recognized. The collaboration with Prof. Mark Eberhard and Prof. John Stanton (Univ. of Washington), Prof. Marios Panagiotou and Prof. Claudia Ostertag (UC Berkeley), and with the students Olafur Haraldsson (Univ. of Washington) and William Trono (UC Berkeley) is duly acknowledged. The assistance of the technical staff of the Charles Lee Powell Structural Engineering Laboratories at the University of California, San Diego, and of the PEER Center Laboratory at the University of California, Berkeley – Richmond Field Station, is gratefully recognized. The industry support by Hill Brothers Chemical Co., Salit Specialty Rebar, Headed Reinforcement Corp., and BASF-The Chemical Company is also thankfully acknowledged.

References:

AASHTO (2012). "AASHTO LRFD Bridge Design Specifications, 6th Edition". American Association of State Highway and Transportation Officials, Washington, DC.

ACI (2008). "Building Code Requirements for Structural Concrete and Commentary". *ACI 318-08*, American Concrete Institute, Farmington Hills, MI.

Belleri, A., Schoettler, M.J., Restrepo, J.I., and Fleischman, R.B. (2013). "Dynamic Behavior of Rocking and Hybrid Cantilever Walls in a Precast Concrete Building". *ACI Structural Journal*, accepted for publication January 2013.

Caltrans (2010). "Seismic Design Criteria". California Dept. of Transportation, Sacramento, CA.

Carr, A.J. (2008). "Ruaumoko Manual". Department of Civil Engineering, University of Canterbury, Christchurch, New Zealand.

Filippou, F.C., Popov, E.P., and Bertero, V.V (1983). "Effects of

Bond Deterioration on Hysteretic Behavior of Reinforced Concrete Joints". *Report No. UCB/EERC-83/19*, Earthquake Enigneering Research Center, University of California at Berkeley, Berkeley, CA.

Gebman, M., Ashford, S., and Restrepo, J.I. (2006). "Axial Force Transfer Mechanisms within Cast-In-Steel-Shell Piles". *Report No. SSRP-94/10*, Department of Structural Engineering, University of California at San Diego, La Jolla, CA.

Guerrini, G., and Restrepo, J.I., (2011). "Advanced Precast Concrete Dual-Shell Steel Columns". *Proceedings of the 8th International Conference on Urban Earthquake Engineering*. Paper No. 08-144, Tokyo, Japan.

Guerrini, G., Massari, M., Vervelidis, A., and Restrepo, J.I., (2012). "Self-Centering Precast Concrete Dual-Shell Steel Columns". *Proceedings of the 15th World Conference on Earthquake Engineering*. Paper No. 2552, Lisbon, Portugal.

Guerrini, G. (2013, in preparation). "Advanced Self-Centering Precast Concrete Dual-Shell Steel Columns". *Ph.D. Thesis*, Department of Structural Engineering, University of California at San Diego, La Jolla, CA.

Mander, J.B., Priestley, M.J.N., and Park., R. (1988). "Theoretical Stress-Strain Model for Confined Concrete". *ASCE Journal of Structural Engineering*. **114:8**, 1804-1826.

Mazzoni, S., McKenna, F., Scott, M.H., Fenves, G.L. et al. (2007), "Opensees Command Language Manual". Pacific Earthquake Engineering Research Center, Berkeley, CA.

McKenna, F., Scott, M.H., and Fenves, G.L. (2010). "Nonlinear Finite Element Analysis Software Architecture Using Object Composition". *ASCE Journal of Computing in Civil Engineering*. **24:1**, 95-107.

Palermo, A. and Pampanin, S. (2008). "Enhanced Seismic Performance of Hybrid Bridge Systems: Comparison with Traditional Monolithic Solutions". *Journal of Earthquake Engineering*. **12:8**, 1267-1295.

Restrepo, J.I. and Rahman, A. (2007). "Seismic Performance of Self-Centering Structural Walls Incorporating Energy Dissipators". *ASCE Journal of Structural Engineering*. **133:11**, 1560-1570.

Restrepo, J.I., Tobolski, M.J., and Matsumoto, E.E. (2011). "Development of a Precast Bent Cap System for Seismic Regions". *NCHRP Report 681*.

Taylor, R.G. (1977). "The Nonlinear Seismic Response of Tall Shear Wall Structures". *Ph.D. Thesis*, Department of Civil Engineering, University of Canterbury, Christchurch, New Zealand.

Vulcano, A. and Bertero, V.V. (1987). "Analytical Models for Predicting the Lateral Response of RC Shear Walls: Evaluation of Their Reliability". *Report No. UCB/EERC-87/19*, Earthquake Enigneering Research Center, University of California at Berkeley, Berkeley, CA.

10CUEE CONFERENCE PROCEEDINGS
10th International Conference on Urban Earthquake Engineering
March 1-2, 2013, Tokyo Institute of Technology, Tokyo, Japan

SEISMIC RESPONSE OF A ROCKING, POST-TENSIONED HYFRC BRIDGE COLUMN

William Trono[1], Gabriel Jen[1], Claudia Ostertag[2], and Marios Panagiotou[3]

1) PhD Candidate, Dept. of Civil and Environmental Engineering, University of California, Berkeley, CA
2) Professor, Dept. of Civil and Environmental Engineering, University of California, Berkeley, CA
3) Asst. Professor, Dept. of Civil and Environmental Engineering, University of California, Berkeley, CA
will.trono@berkeley.edu, gjen@berkeley.edu, ostertag@ce.berkeley.edu, panagiotou@berkeley.edu

Abstract: Conventional reinforced concrete bridge columns in high seismic regions are designed to be ductile during earthquakes; however, column damage and residual drift can cause bridges to remain out of service for extended periods during replacement or repair. In this study, a rocking post-tensioned HyFRC bridge column was designed to limit damage and residual drifts and was tested dynamically under earthquake excitation. The column utilized post-tensioned strands, hybrid fiber reinforced concrete (HyFRC), and a combination of unbonded and headed longitudinal reinforcement. HyFRC with a total of 1.5% micro and macro fibers by volume and headed steel reinforcement at a ratio of 1.5% (discontinuous at the foundation) were used in the precast end region to improve the behavior of the rocking interface under high compressive forces. The 1/3 scale cantilevered bridge column was subjected to a sequence of nine scaled ground motion records of increasing intensity chosen to produce specific ductility demands in a conventionally designed reference specimen. The column exhibited excellent re-centering capability and light damage in the HyFRC end region, reaching a drift of 8.0% with an accumulated residual drift of less than 0.4%. Compressive damage was controlled in the end region by the HyFRC and the headed reinforcement.

1. INTRODUCTION

Reinforced concrete bridge columns in seismic regions are designed to be ductile by forming plastic hinges to accommodate inelastic deformations during earthquakes. Code requirements are intended to prevent collapse of bridges under design seismic hazards; however, damage in column plastic hinge regions can cause bridges to be out of service during column repair or replacement (CalTrans 2010). Residual column drift ratios (drifts) are expected following earthquakes if concrete and reinforcing bars incur severe inelastic damage in the plastic hinge.

In this study, a bridge column was designed with an objective of reducing or eliminating residual drifts after earthquakes. This objective was satisfied by several unique design details. First, the column was designed to rock about the foundation to avoid plastic hinge formation by unbonding the flexural reinforcement near the column-foundation interface. Second, fully unbonded, post-tensioned steel strands provided axial pre-compression and overturning resistance. Finally, hybrid fiber reinforced concrete (HyFRC) and headed reinforcing bars (rebar) that terminated at the column-foundation interface were employed to reduce compressive damage during rocking.

The rocking, post-tensioned (RPT) HyFRC bridge column was subjected to dynamic excitation in three directions on the Pacific Earthquake Engineering Research Center's (PEER) Earthquake Simulator in Richmond, CA. Eleven scaled earthquake ground motion records were applied.

A reference column with conventional design details and equivalent geometry and inertial mass was tested using the same ground motion sequence for comparison. During the seventh motion, the reference column reached a drift of 10.8% but had a residual drift of 6.8% and testing was halted. The RPT HyFRC column reached a drift of 8.0% during the same motion but had a residual drift of less than 0.4%.

2. BACKGROUND

The equations of motion for slender, inverted pendulum-type structures (structures that can rock freely about their base) were first introduced by Housner (1963) who recognized their tendency to maintain stability during strong ground shaking. Since then, numerous experimental and analytical studies have verified rocking as an effective means of accommodating inelastic displacement demands in reinforced concrete structures during earthquakes. Rocking systems that utilize unbonded post-tensioning (PT) can have re-centering hysteretic response upon unloading and various methods have been employed to add hysteretic energy

dissipation to such systems in addition to re-centering.

2.1 Columns with Unbonded Post-tensioning and Bonded or Unbonded Mild Steel Reinforcing Bars

Many researchers have investigated the use of unbonded post-tensioning in concrete beam and column assemblages to provide re-centering hysteretic behavior (Mander and Cheng 1997, Cheng 2008). Often these assemblages consisted of precast concrete segments connected by post-tensioned strands (Hewes and Priestly 2002, ElGawady et. al. 2010, Billington and Yoon 2004). In all cases, overturning resistance was provided by the elastic response of the unbonded post-tensioned strands and caused origin-oriented hysteretic behavior upon unloading.

Several analytical studies have investigated the performance of bridge columns built with a combination of mild steel longitudinal reinforcement and unbonded post-tensioning which can provide both hysteretic energy dissipation and column re-centering (Kwan and Billington 2003, Sakai and Mahin 2004). Columns with higher proportions of unbonded post-tensioning showed a greater tendency to re-center but often caused crushing of concrete earlier due to higher compressive stresses. Columns with higher proportions of mild steel reinforcement showed more hysteretic energy dissipation.

Billington and Yoon (2004) showed that a ductile fiber reinforced cement-based composite (DFRCC), a class of high performance fiber reinforced cementitious composites (HPFRCC) that exhibits strain hardening behavior in uniaxial tension, provided more energy dissipation in such systems than normal concrete and maintained its integrity considerably better under high compressive loads. Even with modest transverse reinforcement, the DFRCC did not spall.

Jeong et. al. (2008) tested columns with unbonded mild steel reinforcement and unbonded post-tensioning and found that unbonding the mild steel resulted in a shorter plastic hinge region and lower strains in the bars.

2.2 Columns with Hybrid Fiber Reinforced Concrete

This study considers a column designed to rock containing a combination of unbonded post-tensioning strands and unbonded mild steel reinforcing bars. In addition, the column incorporates hybrid fiber reinforced concrete (HyFRC), a class of tensile strain hardening HPFRCC containing both steel macrofibers and polymer microfibers at a fiber volume fraction of 0.015, in the end region. This material was initially developed for lightly reinforced bridge approach slabs with a performance criterion of maintaining strain compatibility with mild steel reinforcement through the tensile yield strain of steel of 0.2% (Blunt and Ostertag 2009). The material was optimized to have self-compacting properties in the fresh state (SC-HyFRC) to ease placement in densely reinforced structures (Jen et. al. 2012).

Cyclic testing of columns built with HyFRC and unbonded longitudinal reinforcement with no post-tensioning showed less spalling and compressive damage compared to conventionally designed columns with twice the transverse reinforcement under the same drift demands (Panagiotou et. al. 2012, Kumar et. al. 2011). Furthermore, small-scale tests revealed greater post-peak compressive strength and stability in confined HyFRC compared to equally confined normal concrete (Trono et. al. 2011). HyFRC is utilized in this column to improve energy dissipation and compressive damage resistance in the end region where large compressive forces are expected.

2.3 Headed Reinforcement Terminating at the Column-Foundation Interface

In addition to using HyFRC, a second detail which differentiates this column design from previous tests on columns with unbonded post-tensioning and unbonded mild steel reinforcement is the inclusion of headed compression-only reinforcing bars which terminated at the column-foundation interface. The 51x51x13 mm steel plate heads reinforce and confine the HyFRC at the column-foundation interface. Holden et. al. (2003) used a similar design in a precast pre-stressed concrete wall, lining the base of the wall with a steel plate and adding additional plates to the extreme ends of the wall at the base. Belleri et. al. (2013) used headed bars which terminated at the foundation of a rocking wall for the same purpose. To the authors' knowledge, this type of detailing has not been tested in post-tensioned columns, although another column in this test bed had similar detailing (Restrepo and Guerrini 2012).

3. TEST PROGRAM

The RPT HyFRC column was tested as part of PEER's Damage Resistant Re-centering Bridge Columns test bed, a collaborative project from three universities consisting of three different advanced bridge column specimens as well as a reference column with conventional design details for comparison. All four columns had equivalent inertial mass and geometry and were subjected to the same sequence of scaled earthquake ground motion records. This paper focuses on the experimental response of the RPT HyFRC column and draws comparisons with the response of the reference specimen.

3.1 RPT HyFRC Column Design Objectives

There were three specific objectives in the design of the RPT HyFRC column: (1) Minimize or eliminate the likelihood of residual column drifts for imposed drift demands up to 7%, (2) Limit inelastic compression damage at the rocking interface, and (3) Ensure that the post-tensioning remains elastic and prevent fracture of the continuous reinforcement at 7% drift.

To reach these objectives, the proportion of unbonded rebar to axial load (from post-tensioning and inertial mass) was optimized to encourage column re-centering and achieve the target lateral strength. HyFRC and headed reinforcement that terminated at the rocking interface were employed to control inelastic compressive damage at the rocking toe. In addition, the post-tensioning was designed to remain elastic up to column drifts of 7%, and the continuous

longitudinal steel was unbonded over a length sufficient to prevent fracture at 7% drift. Preliminary column design and analysis was conducted using an analytical model built in OpenSEES, but details of the model are not included herein.

3.2 Description of Test Specimens

Details of the RPT HyFRC column and the reference column are shown in Figure 1 and Figure 2, respectively. The design of flexural reinforcement and post-tensioning in the rocking column was chosen to achieve approximately the same lateral strength and stiffness as the reference column. The length scale factor for both specimens was 3.

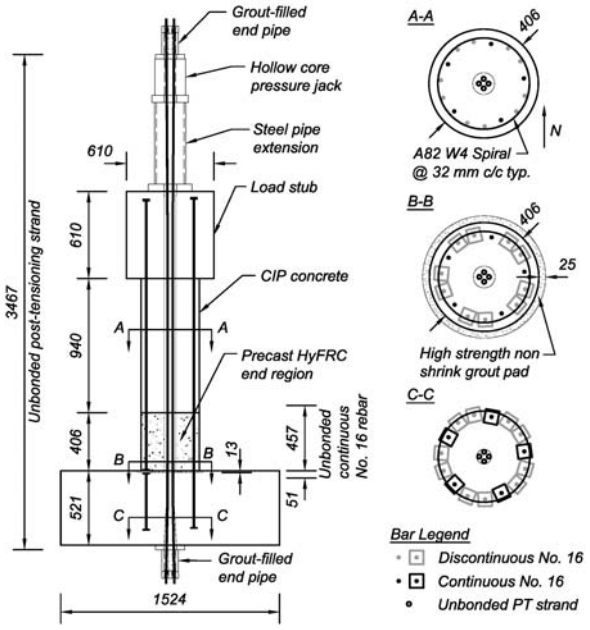


Figure 1 Rocking Post-tensioned HyFRC Column Elevation and Cross Sections

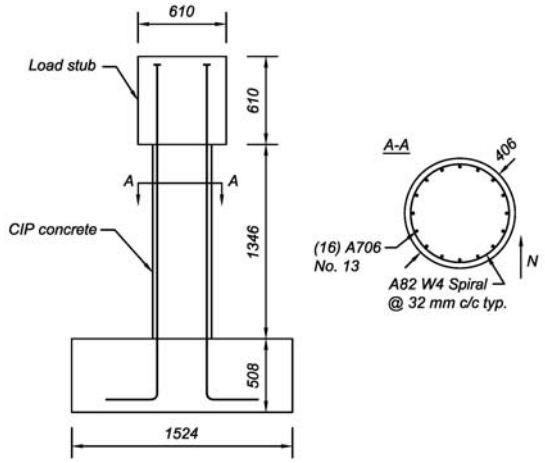


Figure 2 Reference Column Elevation and Cross Section

The RPT HyFRC column contained 15 ASTM A706 Grade 420 No. 16 bars longitudinally. Five of these bars continued from the column into the foundation and were unbonded over the length shown using tightly wrapped duct tape coated with lithium grease. The remaining ten bars terminated at the column-foundation interface with 51x51x13 mm steel heads and were fully bonded to the concrete. Four 15.2 mm dia. ASTM A416 Grade 1860 seven wire strands ran through a corrugated metal duct in the center of the column and were unbonded between their anchorages. As shown in Figure 1, a steel pipe was used to increase the unbonded length of the PT to reduce the chance of yielding the strands (in an actual bridge, the PT could be anchored within the superstructure). The longitudinal steel effective in flexure consisted of the five unbonded No. 16 bars and the four PT strands for a total effective volumetric ratio of $\rho_{l,eff}$ = 1.2%. The volumetric ratio of the discontinuous headed bars terminating at the column-foundation interface was 1.5%. Transverse shear and confinement reinforcement was provided by an ASTM A82 W4 steel spiral (5.7 mm dia.) at 32 mm spacing, for a volumetric ratio of ρ_s = 0.9%. The spiral was discontinuous between the base of the column and the foundation.

The end region was precast with HyFRC and installed onto a wet-set grout pad on the top of the foundation (see Figure 1). The precast element contained ten discontinuous No. 16 headed bars as well as PVC and corrugated metal ducts for the continuous No. 16 bars and PT strands, respectively. No. 16 double-headed bars were also cast in the foundation in the same pattern as the discontinuous bars in the precast end region and terminated at the top of a 13 mm recession in the top of the foundation. These bars acted to distribute the compression from the column above into the foundation (with the high strength grout pad between).

Installation of the precast piece consisted of feeding the five continuous No. 16 bars (which were embedded in the foundation) through the PVC ducts in the precast piece, pouring the wet high strength non-shrink grout into the recession in the top of the foundation, and finally lowering the piece onto the wet grout pad, allowing it to rest on 10 mm shims while the grout cured. Grout was then poured into the void space in the PVC ducts to provide buckling resistance to the unbonded bars.

The remainder of the column was cast in place with normal concrete. Six days prior to testing, the four PT strands were stressed individually to 48% of their yield strength for a total PT force of 455 kN. The end wedge anchor plates fit into specially fabricated steel pipe sections which were filled with grout to a depth of 10 strand diameters (152 mm) after stressing in order to eliminate stress concentrations at the wedge anchors that could lead to premature strand failure. Weld beads on the inside surface of the pipe allowed any increase in strand tensile force during testing to develop in the grout away from the anchorage.

The reference column (Figure 2) was designed with a longitudinal volumetric steel ratio of ρ_l = 1.6% consisting of 16 ASTM A706 Grade 420 No. 13 bars. Transverse reinforcement was continuous into the foundation and consisted of the same A82 W4 smooth steel spiral at the same spacing as the RPT HyFRC column for a spiral volumetric ratio of ρ_s = 0.9%.

3.3 Specimen Material Properties

The HyFRC used in the precast end region of the RPT HyFRC column contained hooked-end steel fibers at 1.3% by volume with a length of 30 mm, a diameter of 0.55 mm, and a yield strength of 1100 MPa. It also contained polyvinyl alcohol (PVA) fibers at 0.2% by volume with a length of 8 mm, a diameter of 0.04 mm, and a yield strength of 1600 MPa. Two chemical admixtures, superplasticizer (SP) and viscosity modifying admixture (VMA), were used to improve the workability of the fresh mix. The material proportions of HyFRC are given in Table 1.

Table 1 HyFRC Material Mix Proportions

kg per cubic meter				*fiber volume %*	
Water	Cement[a]	Fly Ash[b]	Gravel[c]	Steel	PVA
219	*413*	*136*	*418*	*1.3*	*0.2*
Sand[d]	SP	VMA			
1044	*2.3*	*5.6*			

[a]ASTM C150 Type II; [b]ASTM C618 Type C; [c]pea gravel, 9.5 mm MSA; [d]coarse sand, FM = 3.2

The compressive strengths, f_c', of the normal cast-in-place concrete used for the columns and the foundations, the HyFRC, and the high strength non-shrink grout pad are given in Table 2. Concrete and HyFRC compressive strengths were averaged from three 152x304 mm cylinders, while high strength grout strengths were averaged from five 51x51x51 mm cubes.

Table 2 Compressive Strength of Column Materials

	Sampled f_c' (MPa)			
Specimen	*Column*	*Found.*	*HyFRC*	*Grout*
RPT HyFRC	34.5	55.5	44.6[b]	63.8
Reference	22.6[a]	34.7	-	-

[a] 18% lower than design f_c' = 27.6 MPa
[b] average strain at f_c' equal to 0.35%

The A706 No. 16 reinforcing bars used in the RPT HyFRC specimen had an average tested yield strength of 481 MPa and an ultimate strength of 658 MPa. Their tensile stress-strain response is shown in Figure 3(a). The A416 strands had an average tested yield strength of 1704 MPa and a breaking strength of 1874 MPa as shown in Figure 3(b). Finally, the A706 No. 13 bars used in the reference column had an average tested yield strength of 433 MPa and an ultimate strength of 651 MPa as shown in Figure 3(c). In all three cases, strain was measured over 51 mm, stress was calculated assuming nominal cross sectional area, and three coupons of each material were tested. Figure 3(d) shows the stress-strain response of the A82 W4 spiral (after straightening a circularly-deformed sample).

3.4 Test Configuration and Instrumentation

The same test setup was used on the shaking table for both the RPT HyFRC column and the reference column and is shown in Figure 4. Inertial mass was applied in the form of three 3048x3048x356 mm reinforced concrete plates. Wide flange steel cantilevered beams were fixed to the column load stub and the mass plates were fixed to the wide flange steel beams using post-tensioned bars. The total inertial mass applied to the columns was approximately 24500 kg (for a gravity load of 240 kN), and the center of mass was found to be 2438 mm above the top of the foundation. The axial load ratios for RPT HyFRC and reference columns, defined as the gravity load divided by $f_c'A_g$, where f_c' was the tested compressive strength of the column's normal concrete and A_g the gross cross sectional area, were 5.4% and 8.2%, respectively.

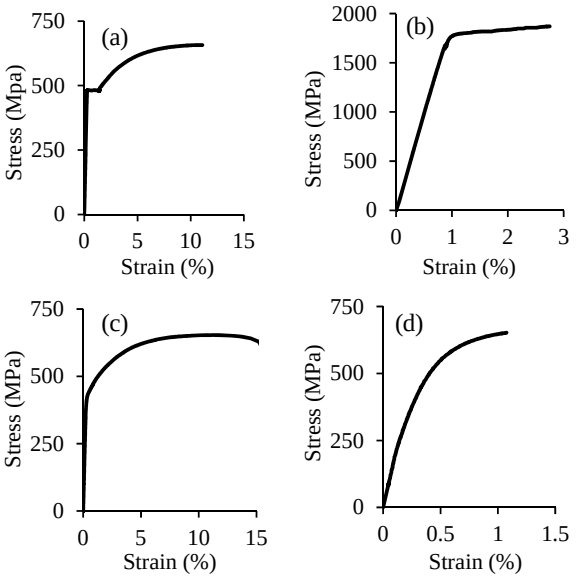


Figure 3 Tensile Stress-Strain Response of (a) A706 No. 16 bars, (b) A416 PT Strand, (c) A706 No. 13 bars, and (d) A82 W4 spiral

Instrumentation for the RPT HyFRC column consisted of five load cells, 30 displacement transducers, and 41 strain gages. Four load cells, 32 displacement transducers, and 54 strain gages were used for the reference column. Thirty-five accelerometers and 21 wire potentiometers were used for both columns. All instruments were sampled at 200 Hz.

Each of the column foundations was fixed upon four tri-axial load cells that measured shear force in two directions and axial force (see Figure 4). The RPT HyFRC column also had a fifth load cell in the form of a hollow core pressure jack (with a pressure transducer) in series with the post-tensioning to measure the PT force during testing.

In both tests, accelerometers were fixed to the foundation, column, and mass plates in both the horizontal and vertical directions at multiple locations. Displacement transducers were fixed to rods embedded in the columns on four sides at discrete heights to estimate the curvature profiles during testing. Seven groups of three wire potentiometers tracked the 3-D displacement at seven points on the specimen—three on the foundation and four on the

mass plates. These displacements were used to resolve three translations and three rotations at the center of mass using the procedure presented in Vithani and Gupta (2002).

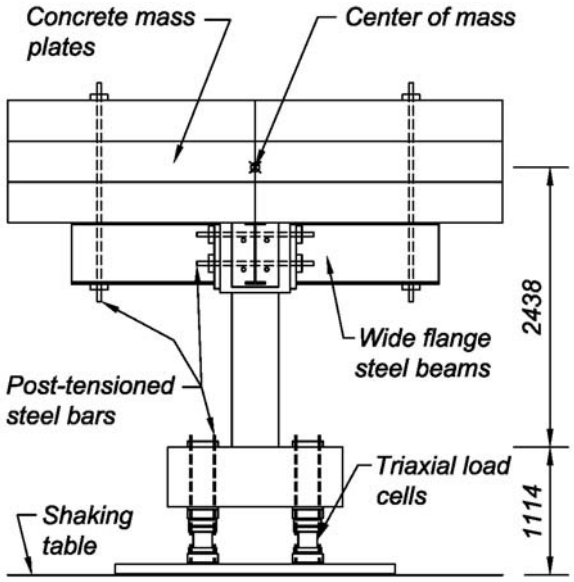


Figure 4 Shaking Table Test Setup

3.5 Shaking Table Test Sequence

A sequence of nine scaled earthquake ground motion records, each with North-South (NS), West-East (WE), and vertical direction components, was chosen by the research group for testing of the RPT HyFRC column, the reference column, and the other columns of the Damage Resistant Re-centering Bridge Columns test bed. Details of each record are given in Table 3. Priority was given to records that satisfied the following criteria: (1) They imposed similar displacements in all test bed columns over the fundamental period range 0.4 to 0.7 seconds, (2) They contained velocity pulses likely to cause large column drifts, and (3) They were generated by strike-slip fault mechanisms.

Time was scaled by $L^{-1/2}$ in order to maintain a scale factor of unity for induced accelerations (the length scale factor, L, was 3). Acceleration values (3 components) were also scaled by a constant for each signal so as to impose specific displacement ductility targets, μ, in the reference column (see Table 3) and comparable peak drifts in all test bed columns. The design level earthquakes were selected to impose a target displacement ductility of 4 (EQ4 and EQ5) to be consistent with the maximum design demand for single column bridge bents according to Caltrans SDC (2010). Some motions were filtered to remove displacement pulses that exceeded the shaking table's limits. Testing of the reference column was stopped after EQ7 due to substantial residual column drift. The RPT HyFRC column was subjected to two additional unplanned ground motions after the first nine since damage and residual drifts had been well controlled during the initial test sequence. Details of these motions are also included in Table 3.

White noise tests (table motions consisting of randomly generated, tri-directional, small-amplitude displacements) were run before each earthquake test for both columns to induce column vibration and evaluate the natural period as damage developed. Prior to the start of any dynamic testing, free vibration tests were performed on both columns by applying a static lateral load and quickly releasing it.

Table 3 Details of Earthquake Tests

Test	Earthquake[a] *Station*	Accel. SF	Target μ (ref. col.)
EQ1	Coalinga 1983/05/09 02:49 *46T07 Harris Ranch - Hdqtrs*	2.50	elastic
EQ2	Imperial Valley - 06 1979 *EC Meloland Overpass FF*	0.80	2
EQ3	Morgan Hill, 1984 *Coyote Lake Dam (SW Abut)*	0.70	2
EQ4[b]	Northridge - 01 1994 *Rinaldi Receiving Station*	0.56	4
EQ5[b]	Northridge - 01 1994 *Sylmar - Olive View Med FF*	-0.80	4
EQ6	Northridge - 01 1994 *Rinaldi Receiving Station*	0.90	6
EQ7	Kobe, Japan, 1995 *Takatori*	0.77	8
EQ8	Kobe, Japan, 1995 *Takatori*	-0.90	9.6
EQ9	Northridge - 01 1994 *Sylmar - Olive View Med FF*	-0.80	4
EQ10	Kobe, Japan, 1995 *Takatori*	0.90	-
EQ11	Northridge - 01 1994 *Rinaldi Receiving Station*	1.17	-

[a] *from PEER Ground Motion Database (2000, 2012)*
[b] *Design level earthquake*

4. TEST RESULTS

Dynamic testing confirmed that the RPT HyFRC column achieved its primary objective of minimizing residual column drifts compared to a conventionally designed column. The post-tensioned strands remained elastic and provided enough overturning resistance to re-center the column throughout testing, while the combination of headed compression-only reinforcement and HyFRC in the precast end region limited inelastic compressive damage. Fracture of the continuous unbonded reinforcement was delayed until the eleventh earthquake test when two bars fractured.

4.1 Measured Peak and Residual Column Drifts

Table 4 shows the peak drifts of the RPT HyFRC and reference specimens measured during testing as well as the

residual drifts measured at the end of each test. Figure 5 shows the same data side by side for the first seven EQ tests which were run on both columns. As shown, the RPT HyFRC column showed near perfect re-centering after the first five earthquake tests with residual drifts under 0.1%, even after reaching 4.3% drift during EQ4 and 6.2% drift during EQ5. During EQ7, the RPT HyFRC column reached a drift of 8.0%, but the residual drift remained less than 0.4%. During EQ11, when the column reached 8.8% drift, two unbonded bars fractured but the residual drift was still only 0.9%. Figure 6(a) shows the RPT HyFRC column after EQ11 at the end of testing.

The reference column developed a residual drift of 0.9% after the first five earthquakes, reaching a peak drift of 3.7% during EQ4 and 5.8% during EQ5 (the design level events). Further testing resulted in increased residual drifts in the reference column; EQ6 caused a drift of 6.1% and increased the residual to 1.6%, while EQ7 induced the largest drift of 10.8% which left a residual of 6.8%. Figure 6(b) shows the reference column after EQ7.

Table 4 Measured Peak and Residual Column Drifts

Test	RPT HyFRC Drift[a] (%) peak	residual	Reference Drift[a] (%) peak	residual
EQ1	0.5	0.0	0.4	0.0
EQ2	2.1	0.1	3.5	0.4
EQ3	2.1	0.1	1.5	0.4
EQ4	4.3	0.1	3.7	0.3
EQ5	6.2	0.1	5.8	0.9
EQ6	5.0	0.2	6.1	1.6
EQ7	8.0	0.4	10.8	6.8
EQ8	6.8	0.4	-	-
EQ9	7.2	0.6	-	-
EQ10	7.2	0.6	-	-
EQ11	8.8	0.9	-	-

[a]*Resultant value in NS, WE directions*

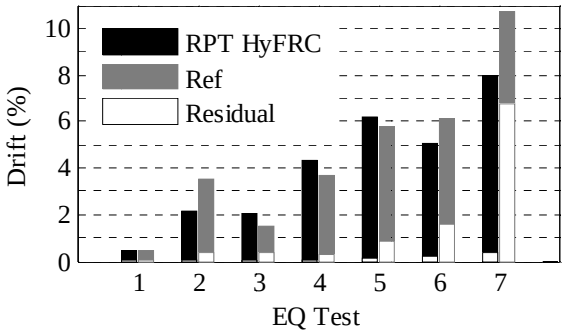


Figure 5 Peak and Residual Drift Comparison of the RPT HyFRC and Reference Column through EQ7

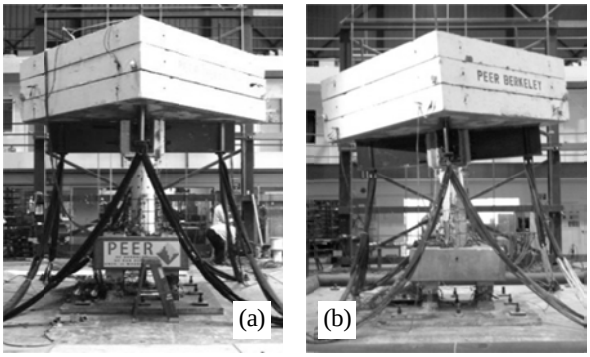


Figure 6 East Elevation after Testing, (a) RPT HyFRC Column at 0.9% Residual Drift after EQ11, (b) Reference Column at 6.8% Residual Drift after EQ7

4.2 Measured Base Rotation and Rocking Behavior

The RPT HyFRC column was designed to rock about its foundation in order to avoid damage caused by formation of a plastic hinge. Inelastic lateral drifts were accommodated by uplift of the column at the interface with the foundation rather than distributed tensile cracking. This mechanism was verified by comparing the measured base rotations to the lateral drift at the center of mass. Uplift from the foundation was measured by displacement transducers mounted to the column at heights of 52, 64, 67, and 49 mm above the foundation on the N, E, S, and W column faces, respectively. Base rotations, θ_b, in the N-S and W-E directions were calculated as the difference in opposite displacement transducer measurements divided by the horizontal distance between the transducers.

Figures 7(a) and 7(b) show the calculated base rotation plotted against drift of the center of mass in the N-S direction for EQ4 and EQ7 where the column reached peak drifts of 4.3% and 8.0%, respectively. The rocking mechanism is clearly illustrated by the fact that the inelastic column drifts are accommodated almost completely by rotation at the base.

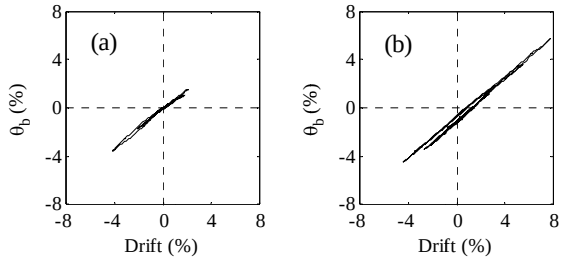


Figure 7 Measured Base Rotation vs. Drift in the NS Direction (N positive) for (a) EQ4 and (b) EQ7

4.3 Measured Overturning Moment vs. Drift Behavior

The hysteretic overturning moment vs. drift response in the N-S direction is shown in Figures 8(a), 8(b), and 8(c) for EQ4, EQ5, and EQ7, respectively. The figures on the left show the response of the reference column, while the figures on the right show the response of the RPT HyFRC column.

The overturning moment was calculated from load cell axial force measurements, corrected for the inertia of the foundation, and normalized by the weight of the inertial mass times the center of mass height.

As shown in Figure 8, the lateral strength of both columns was approximately equal, with inelastic response developing at an overturning moment of approximately 0.3WH. The response shown during EQ4 in Figure 8(a) clearly illustrates the re-centering effect in the RPT HyFRC column (right) as compared to the reference column (left); the reference column unloads and has a residual drift while the RPT HyFRC column unloads through the origin.

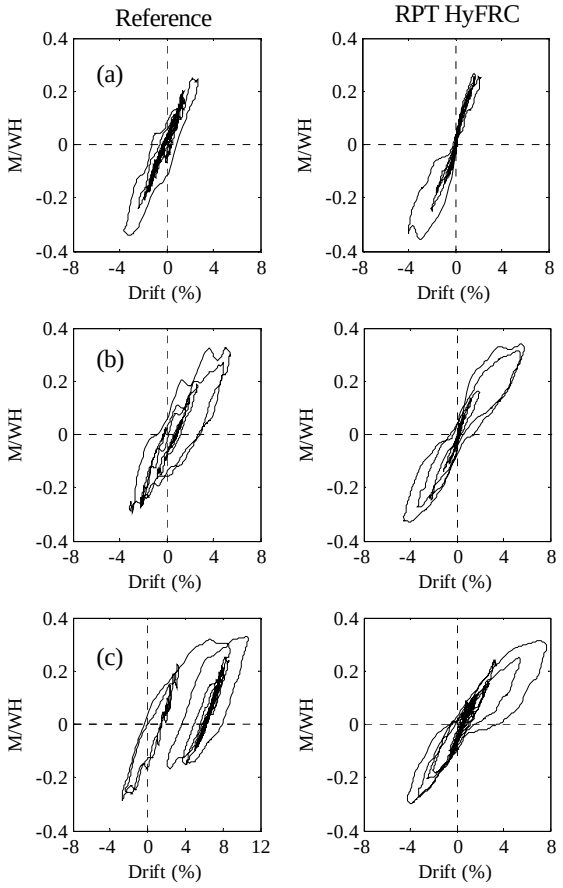


Figure 8 Measured Overturning Moment vs. Drift in the NS Direction for (a) EQ4, (b) EQ5, and (c) EQ7

During EQ5, the reference column reached a peak drift of 5.8% and developed more damage as evidenced by the wider hysteretic loop in the left side of Figure 8(b). In the right side of Figure 8(b), the response of the RPT HyFRC column continues to tend toward the origin upon unloading with only small drifts at zero overturning moment.

Finally, during EQ7, the reference column saw a peak drift of 10.8% and developed a significant residual drift as shown in the left side of Figure 8(c). The hysteretic loop of the RPT HyFRC column widened slightly during EQ7, but the column still re-centered upon unloading as shown in the right side of Figure 8(c).

4.4 Measured Load in the PT Strands

Prior to EQ1, the initial PT load in the RPT HyFRC column was 455 kN (48% yield). By the start of the final test, EQ11, the PT load had only decreased to 432 kN (45% yield) for an accumulated loss of only 5% of the initial load through the duration of all prior tests. The axial force provided by the PT was in addition to the 240 kN inertial mass from the concrete plates. The maximum PT force measured during all tests was 589 kN (62% of yield) which occurred during EQ7. Although there was a slight loss of PT force due to shortening of the column, the strands remained elastic through the duration of testing.

4.5 Measured Peak Tensile and Compressive Strains in the Reinforcing Bars of the RPT HyFRC Column

Table 5 shows the peak compressive strain, ε_c, and tensile strain, ε_t, as measured by strain gages fixed to bars B7 and U1, respectively, during each test. The location of these bars in the RPT HyFRC column cross section is given in Figure 9. The gage on bar B7 was fixed to the bar facing inward at a height 37 mm above the top of the foundation, while the gage on bar U1 was fixed to the bar facing outward at a height 76 mm above the foundation. Table 5 also shows the measured peak drift in the N direction during each EQ test. Drifts in the N direction caused tension in the unbonded bar U1 and compression in the discontinuous headed bar B7.

Table 5 Measured Peak Strains in Bars B7 and U1

Test	Peak Drift N-dir (%)	Peak ε_c Bar B7 (%)	Peak ε_t Bar U1 (%)
EQ1	0.5	-0.05	0.08
EQ2	2.1	-0.11	1.80
EQ3	1.7	-0.16	1.66
EQ4	2.2	-0.13	1.97
EQ5	5.9	-1.79	3.28
EQ6	4.5	-1.92	2.74
EQ7	7.8	-3.14	3.37
EQ8	6.6	-3.64	2.87
EQ9	7.1	-4.04	3.62
EQ10	6.9	-4.10	-
EQ11	8.0	-4.49	-

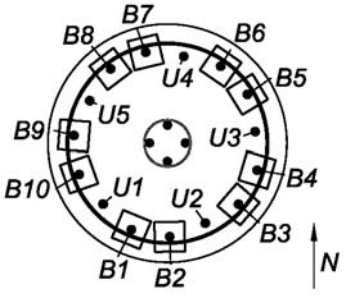


Figure 9 Reinforcing Bar Designations

As shown in Table 5, strains in the unbonded bar U1 were well-controlled by the unbonding of the bar from the surrounding concrete. As the column rocked and reached drifts of 5.9%, 7.8%, and 7.1% in the N direction during EQ5, EQ7, and EQ9, respectively, the measured peak tensile strain in bar U1 remained under 4%. The imposed drift during these tests was accommodated by uplift at the foundation (see Figure 7) and the low strain measurements in Bar U1 confirm that the uplift was distributed as strain over the unbonded length.

The discontinuous headed bars relieved the compressive forces imposed on the precast HyFRC during rocking as evidenced by the high recorded compressive strains in Table 5. Bar B7 yielded in compression, reaching a strain of -1.79%, when the column reached a peak drift of 5.9% in the N direction during EQ5. After yielding, inelastic compressive strains continued to increase during all subsequent tests. Strain gages on the other discontinuous bars B1, B3, B5, and B9 recorded peak compressive strains (over all tests) of 2.4%, 5.7%, 6.0%, and 2.0% but showed no evidence of buckling, and the spiral remained intact through the duration of testing.

4.6 Observed RPT HyFRC Column Damage

As shown by the measured test data, damage to the precast end region of the RPT HyFRC column was limited during testing; the PT strands remained elastic, the unbonded bars avoided fracture during the first ten EQ tests, and the precast end region maintained its integrity with no evidence of bar buckling or spiral fracture and only minor spalling.

The crack at the rocking plane first opened during EQ1 but was only captured in real-time by video cameras mounted on the foundation and was not apparent after the column re-centered. During EQ2, the crack at the rocking plane opened further and inspection showed light compressive scaling/cracking of the HyFRC and grout pad on the NE face of the column as shown in Figure 10(a) approximately 25 mm above the foundation. This cracking progressed slightly after EQ3, as shown in Figure 10(b).

The gap opening at the rocking interface opened significantly during EQ4 and EQ5 as shown in photos of the NE and SE faces of the column in Figure 10(c) and 10(d), respectively. These photos are taken from video of the response when the specimen was at 4.3% drift in the S direction for EQ4 and 6.2% drift in the N direction for EQ5, but in both cases the gap closed and the column re-centered. Figure 10(c) shows that some vertical splitting cracks initiated during EQ3, branching off the compressive cracks on the NE face. Figure 10(d) shows additional compressive cracking on the SE face at a height of approximately 64 mm above the foundation after EQ4.

The HyFRC remained intact with little to no spalling as shown on the four faces of the column in Figure 11(a) through 11(d) after the column reached 8.0% drift in the N direction during EQ7. Vertical splitting cracks that had initiated in prior tests propagated upward but did not extend higher than 200 mm above the foundation. Slight outward bulging of the column base was observed, yet neither spiral fracture nor bar buckling were evident on any face.

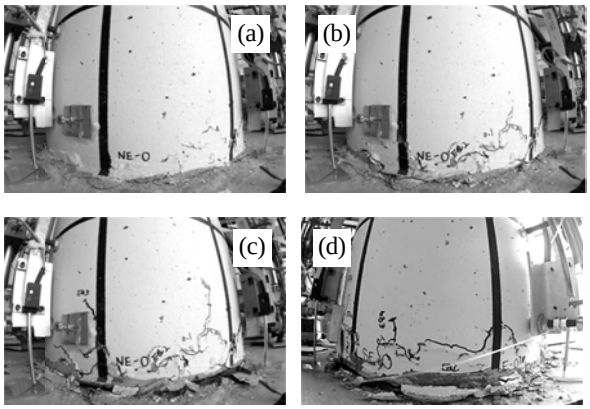


Figure 10 Damage to the Precast HyFRC End Region, (a) NE face after EQ2, (b) NE face after EQ 3, (c) NE face at 4.3% peak drift during EQ4, and (d) SE face at 6.2% peak drift during EQ 5

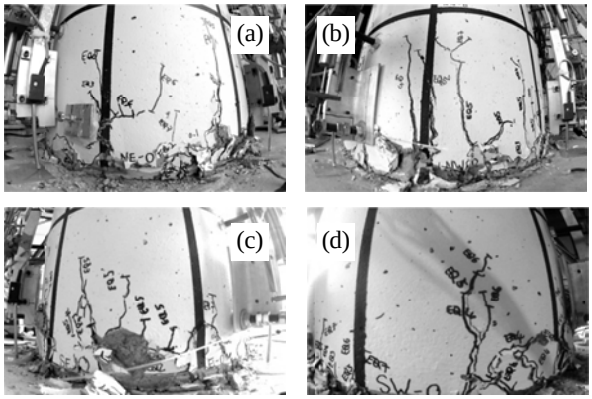


Figure 11 Damage to the Precast HyFRC End Region after EQ7, (a) NE face, (b) NW face, (c) SE face, and (d) SE face

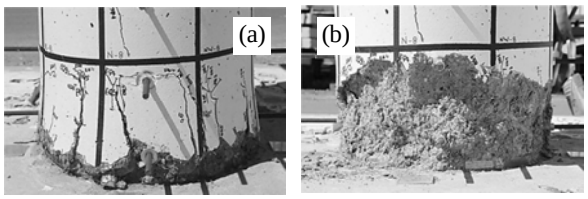


Figure 12 Final RPT HyFRC Damage State, N face (a) before and (b) after damaged HyFRC was removed

Fracture of the unbonded longitudinal bars was delayed until EQ11 when bars U1 and U4 fractured. Even after EQ11, the column residual drift was less than 1%. Figure 12(a) shows the damage state of the N face of the column at the end of testing after instrumentation had been removed. The HyFRC material did not spall from the column face during testing due to the fibers' ability to hold the material together even after splitting and compression cracks had formed. Following testing, damaged HyFRC was removed from the column face manually with a hammer and chisel as shown in Figure 12(b). After the material was removed, it was evident that damage was limited to cover HyFRC below

a height of 200 mm above the foundation and did not penetrate into the HyFRC core confined by the spiral.

4.7 Observed Reference Column Damage

The reference column accommodated the imposed drifts by distributed flexural cracking and eventual plastic hinge formation as imposed drifts increased.

Flexural cracks at spacings between 50 and 125 mm formed up to a height of approximately 600 mm above the foundation after EQ2 when the column reached 3.5% drift and are shown on the NE and NW faces of the column in Figures 13(a) and 13(b), respectively. After EQ6, compression damage in the form of vertical splitting cracks and spalling had extended to a height of 400 mm above the foundation on the SW face of the column as shown in Figure 13(c), and the column had a residual drift of 1.6% in the S direction. Following EQ7, spalling and compressive damage on the S face were substantial as shown in Figure 13(d).

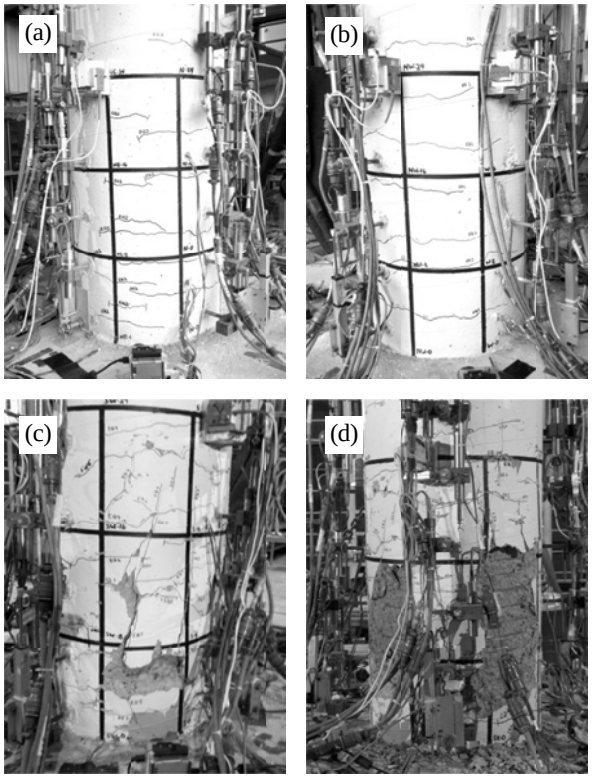


Figure 13 Damage to the Reference Column, (a) NE face after EQ2, (b) NW face after EQ2, (c) SE face after EQ6, and (d) S face after EQ7

5. SUMMARY

This test investigated the dynamic response of a 1/3 scale, rocking, post-tensioned HyFRC bridge column subjected to dynamic loading from scaled earthquake acceleration time history records (three components) on the shaking table. The column was designed to: (1) Minimize or eliminate the likelihood of residual column drifts for design level seismic drift demands up to 7%, (2) Limit inelastic compression damage at the rocking interface, and (3) Ensure that the post-tensioning remains elastic and prevent fracture of the continuous reinforcement at 7% drift.

The RPT HyFRC column consisted of a precast HyFRC end region up to a height of one column diameter (406 mm) containing headed reinforcing bars discontinuous at the column-foundation interface at a volumetric ratio of 1.5% and unbonded continuous reinforcing bars and post-tensioning strands at a volumetric ratio of $\rho_{l,eff}$ = 1.2%. The remainder of the column was cast with normal concrete. Smooth steel wire was used as shear and confinement reinforcement at a volumetric ratio of ρ_s = 0.9%. A reference column having similar geometry, lateral strength, and inertial mass, was also subjected to the same acceleration time histories as the RPT HyFRC column. This column had a volumetric ratio of longitudinal steel of ρ_l = 1.6% and contained the same A82 steel spiral at the same ratio as the RPT HyFRC column.

The test setup was identical in the two tests; accelerometers, linear potentiometers, displacement transducers, and strain gages measured column acceleration, displacement, and strain during testing. Reaction forces were measured with load cells fixed below the rigid foundation.

Seven earthquake tests with increasing ductility targets (in the reference column) were applied to both columns, and the RPT HyFRC column was also subjected to four additional tests.

5.1 Reduction in Residual Column Drifts

Similar peak drifts were imposed in the two columns by the EQ4, EQ5, and EQ6 (less than 20% difference) which targeted μ equal to four, four, and six, respectively, in the reference column. The RPT HyFRC column reached peak drifts of 4.3%, 6.2%, and 5.0% during these tests, but experienced residual drifts of only 0.1%, 0.1%, and 0.2%. The reference column reached peak drifts of 3.7%, 5.8%, and 6.1% during the same tests with residual drifts of 0.3%, 0.9%, and 1.6%. During EQ7, the reference column reached a peak drift of 10.8% due to the large residual of 1.6% after EQ6; following EQ7, the residual drift increased to 6.8%. The RPT HyFRC column showed residual drifts of less than 1% through the duration of testing, reaching peak drifts of 8.0%, 6.8%, 7.2%, 7.2%, and 8.8% with residuals of 0.4%, 0.4%, 0.6%, 0.6%, and 0.9% during EQ7 through EQ11.

5.2 Compressive Damage in the RPT HyFRC Column

The combination of discontinuous headed reinforcing bars and HyFRC in the precast end region prevented major compression damage which aided in preventing residual column drifts caused by damage at the rocking interface.

Measured peak strains over all tests in the discontinuous headed bars reached between 2% and 6% in compression yet buckling was not observed in any test. Spalling of the HyFRC in the precast end region was prevented. Some compressive cracks developed in early tests (Figure 10) on both sides of the column less than 75 mm above the top of the foundation; these cracks slowly propagated vertically as

splitting cracks as testing continued (Figure 11). Post-test inspection showed damage to the HyFRC was limited to the cover material (Figure 12). The spiral did not fracture, although compressive strains in the core material (as measured by strain gages on the headed bars) reached over 6%.

5.3 Behavior of the Unbonded Bars and PT Strands

Fracture of the unbonded bars was prevented for the first ten EQ tests; during EQ11, bars U1 and U4 fractured, likely due to low-cycle fatigue from prior tests. Prior to EQ11 the measured strain in bar U1 remained below 4% as uplift induced strains were spread over the unbonded length.

Losses in the initial PT force were less than 5% over the duration of testing and the force remained well below the expected yield load during testing.

6. CONCLUSIONS

The measured and observed experimental response of the RPT HyFRC column confirmed that the three main design objectives were successfully achieved. Several key observations were drawn from evaluation of the test:

i. Imposed drifts were successfully accommodated by rocking about the column-foundation interface rather than plastic hinge formation.

ii. The overturning resistance provided by the combination of unbonded PT strands and unbonded continuous reinforcing bars encouraged column re-centering behavior, even after yielding the unbonded bars. Residual drifts were significantly lower in the RPT HyFRC column compared to the reference column.

iii. The headed bars helped relieved compression in the HyFRC end region; significant inelastic yielding in compression was observed but buckling was prevented.

iv. Spalling was prevented by the HyFRC and most cracking was limited to below 200 mm from the top of the foundation. Damage to HyFRC was mostly restricted to the cover material.

Acknowledgements:

This project was funded by the Pacific Earthquake Engineering Research Center. The authors would like to acknowledge Bekaert, Headed Reinforcement Corporation, and Dywidag Systems International for their generous donations of material and equipment for this test series. Special thanks to the engineers and staff at the PEER Earthquake Simulator Laboratory for their advice and assistance during specimen construction and testing as well as to Drs. Matthew Schoettler and Vesna Terzic for managing the PEER Damage Resistant Re-centering Bridge Columns test series.

References:

Belleri, A., Schoettler, M. J., Restrepo, J. I., and Fleischman, R. B. (2013), "Dynamic Behavior of Rocking and Hybrid Cantilever Walls in a Precast Concrete Building," *ACI Structural Journal*, American Concrete Institute, accepted for publication Jan. 2013.

Billington, S. L. and Yoon, J. K. (2004), "Cyclic Response of Unbonded Posttensioned Precast Columns with Ductile Fiber-Reinforced Concrete," *Journal of Bridge Engineering*, American Society of Civil Engineers, **9**(4), 353-363.

Blunt, J. and Ostertag, C. P. (2009), "Deflection Hardening and Workability of Hybrid Fiber Composites," *ACI Materials Journal*, American Concrete Institute, **106**(3), 265-272.

California Department of Transportation (2006), "Caltrans Seismic Design Criteria Version 1.6," Sacramento, CA.

Cheng, C. T. (2008), "Shaking table tests of a self-centering designed bridge substructure," *Engineering Structures*, Elsevier, **30**, 3426-3433.

ElGawady, M., Booker, A. J., and Dawood, H. M. (2010), "Seismic Behavior of Posttensioned Concrete-Filled Fiber Tubes," *Journal of Composites for Construction*, American Society of Civil Engineers, **14**(5), 616-628.

Hewes, J. T. and Priestley, M. J. (2002), "Seismic Design and Performance of Precast Concrete Segmental Bridge Columns," *Report No. SSRP-2001/25*, University of California, San Diego.

Holden, T., Restrepo, J., and Mander, J. (2003), "Seismic Performance of Precast Reinforced and Prestressed Concrete Walls," *Journal of Structural Engineering*, American Society of Civil Engineers, **129**(3), 286-296.

Housner, G. W. (1963), "The Behavior of Inverted Pendulum Structures During Earthquakes," *Bulletin of the Seismological Society of America*, **53**(2), 403-417.

Jen, G., Trono, W., and Ostertag, C. P. (2012), "Self-consolidating HyFRC: Processing,, Properties and Applications," to be submitted.

Jeong, H. I., Sakai, J., and Mahin, S. A. (2008), "Shaking Table Tests and Numerical Investigation of Self-Centering Reinforced Concrete Bridge Columns," *PEER Report 2008/06*, Pacific Earthquake Engineering Research Center, Berkeley, CA.

Kwan, W. P. and Billington, S. L. (2003), "Unbonded Posttensioned Concrete Bridge Piers. I: Monotonic and Cyclic Analyses," *Journal of Bridge Engineering*, American Society of Civil Engineering, **8**(2), 92-101.

Kwan, W. P. and Billington, S. L. (2003), "Unbonded Posttensioned Concrete Bridge Piers. II: Seismic Analyses," *Journal of Bridge Engineering*, American Society of Civil Engineering, **8**(2), 102-111.

Kumar, P., Jen, G., Trono, W., Panagiotou, M., and Ostertag, C. P. (2011), "Self Compacting Hybrid Fiber Reinforced Composites for Bridge Columns," *PEER Report 2011/106*, Pacific Earthquake Engineering Research Center, Berkeley, CA.

Mander, J. B. and Cheng, C. T. (1997), "Seismic design of bridge piers based on damage avoidance design," *NCEER 97-0014*, National Center for Earthquake Engineering Research, Buffalo, NY.

Panagiotou, M., Kumar, P., Jen, G., Trono, W., and Ostertag, C. P. (2012), "Experimental Response of Hybrid Fiber Reinforced Concrete Bridge Columns with Novel Detailing of the Longitudinal Reinforcement," to be submitted.

Restrepo, J., and Guerrini, G. (2012). Personal Communication.

Sakai, J. and Mahin, S. A. (2004), "Analytical Investigations of New Methods for Reducing Residual Displacements of Reinforced Concrete Bridge Columns," *PEER Report 2004/02*, Pacific Earthquake Engineering Research Center, Berkeley, CA.

Trono, W., Jen, G., Moreno, D. M., Billington, S. L., and Ostertag, C. P. (2011), "Confinement and Tension Stiffening Effects in High Performance Self-consolidated Hybrid Fiber Reinforced Concrete Composites," *Proceedings, Sixth International Workshop on High Performance Fiber Reinforced Cement Composites*, Rilem, 245-252.

Vithani, A. R. and Gupta, K. C. (2002), "Estimation of Object Kinematics from Point Data," *Proceedings of DETC'02*, American Society of Mechanical Engineers, Montreal, Canada.

10CUEE CONFERENCE PROCEEDINGS
10th International Conference on Urban Earthquake Engineering
March 1-2, 2013, Tokyo Institute of Technology, Tokyo, Japan

HYBRID TESTING OF A FOUR-SPAN CURVED BRIDGE

Chia-Ming Chang[1)], Thomas M. Frankie[2)], Pedro F. Silva[3)], David H. Sanders[4)], Daniel A. Kuchma[5)], and Billie F. Spencer, Jr.[6)]

1) Postdoctoral Research Associate, NEES Laboratory, University of Illinois, USA
2) Ph.D. candidate, Department of Civil and Environmental Engineering, University of Illinois, USA
3) Associate Professor, Department of Civil and Environmental Engineering, George Washington University, USA
4) Professor, Department of Civil and Environmental Engineering, University of Nevada, Reno, USA
5) Associate Professor, Department of Civil and Environmental Engineering, University of Illinois, USA
6) Professor, Department of Civil and Environmental Engineering, University of Illinois, USA
chang37@illinois.edu, frankie2@illinois.edu, silvap@gwu.edu, sanders@unr.edu, kuchma@illinois.edu, bfs@illinois.edu

Abstract: Performance of a four-span curved bridge under multi-directional earthquake loading is investigated through system-level hybrid simulation conducted at the Network for Earthquake Engineering Simulation Laboratory of the University of Illinois. One small-scale and two large-scale piers are tested experimentally using Loading and Boundary Condition Boxes, while a computational model of the bridge deck is concurrently simulated. Due to geometrical asymmetry and combined actions, each pier undergoes six degrees-of-freedom (DOF) motion. The full curved bridge system is tested pseudo-dynamically under an earthquake record at four performance-based scaling levels. To facilitate this hybrid simulation test, a framework is established with respect to communication, coordinate transformation and scaling, data acquisition system. Due to the fact that connections among the specimens, loading boxes and reaction wall may introduce deformations caused by finite stiffness at the fixtures, a high-precision positioning control scheme is developed to compensate for the displacement errors that would otherwise be imposed on the bridge piers. Extensive traditional and advanced non-contact instruments are employed to monitor local and global structural behavior. Using a post-processing toolbox developed in-house, the structural responses of the piers and system-level bridge responses are obtained and represented graphically. Finally, this hybrid test is successfully conducted with the sophisticated control algorithm and dense arrays of advanced instrumentation.

1. INTRODUCTION

Seismic performance assessment of structures is essentially challenging to earthquake engineering. One of major methods to examine seismic performance is structural testing. To date, the common experimenting methods are shaking table, quasi-static, pseudo-dynamic (hybrid simulation), and real-time hybrid simulation testing. Due to limited hydraulic payload, shaking table testing usually requires a scaled model for structural evaluation and may eventually misrepresent structural behavior. Through a slow-loading scheme, quasi-static testing employs predetermined inputs to examine structural performance based on either displacement or force control without considering entire structural systems. Hybrid simulation combines numerical models, time-step integration technique, and experimental specimens to assess structures. Real-time hybrid simulation is an advanced technology for the slow-rate hybrid simulation, but the required hydraulic power for real-time testing is substantially huge with respect to full-scale testing. For understanding structural dynamics, hybrid simulation is nowadays the most available method to investigate seismic performance of large- or full-scale structures through multi-dimensional loadings.

Structural behavior of bridges is quite complicated. Piers in a bridge are usually subjected to combinations of actions and deformations under spatially-complex earthquake ground motions. The combinations contain the features of structural configurations and the interaction between input and response characteristics. As impacted by the combined actions and loadings, the bridge piers may result in large deformations and substantial damages. To understand the effects of the combined actions and loadings, further experimental evaluation over an entire bridge is of need (Silva et al. 2009, Arias-Acosta and Sanders 2010).

To evaluate the combined actions on bridge piers, the full loading and boundary conditions should be considered. In the George E. Brown Network for Earthquake Engineering Simulation (NEES), the Multi-Axial Full-scale Sub-Structuring Testing and Simulation (MUST-SIM) facility at the University of Illinois at Urbana-Champaign (UIUC) has a unique 6DOF loading platform featuring a state-of-the-art, six-actuator, self-reaction loading system, namely the Load and Boundary Condition Box (LBCB) (Nakata et al. 2007). By combining strong wall and floor, one loading point of LBCBs enables applications of

displacement or force at each DOF, resulting in multiple loading points over different LBCBs. A series of LBCBs offer an opportunity to test various components of a structure at the same time. This feature also benefits the hybrid simulation for the assessment of the system-level responses in a structure such as a bridge.

A hybrid simulation framework has been developed for the MUST-SIM facility at the University of Illinois (Kwon and Elnashai 2007). This framework, named UI-SimCor, facilitates the hybrid testing at UIUC to integrate a number of finite element (FE) tools (e.g., ZEUS-NL by Elnashai et al. 2002 and OpenSees by McKenna and Fenves 2011) and realizes the distributed hybrid testing to communicate in different protocols. With the advanced testing capability, this framework can control up to total 18 DOF displacements or forces using the large-scale facility in the MUST-SIM laboratory. Moreover, this framework is flexible to incorporate the three $1/5^{th}$-scale LBCBs with multi-scale specimens in hybrid testing.

Utilizing LBCBs in hybrid simulation, large reaction forces on the reaction wall can cause ineligible deformations and subsequently introduce displacement errors being imposed to the specimens. These displacement errors are essentially critical for the experimental components and numerical integration in hybrid simulation. As indicated in Shing and Mahin (1987) and Shing and Mahin (1990), these deformations between the LBCBs and strong wall would propagate errors throughout the test and affect spurious energy to the structure. To avoid the incorrect displacements being imposed to the specimens, a displacement correcting scheme should be accompanied in controlling LBCBs.

Prior to large-scale testing, small-scale approaches give a preview of the hybrid simulation test and validate functionality of all details in the hybrid simulation framework. Due to economic considerations, large-scale hybrid simulation may only have a one-time chance to fulfill; however, the inexpensive small-scale testing offers an alternative way to verify all features in terms of software and communication first (Holub 2009). In addition, limitations in hardware (e.g., the actuator strokes, resolutions, and control schemes) can be discovered in advance. With the efforts involved in small-scale testing, a successful large-scale hybrid simulation test is foreseeable.

Dense instrumentation definitely helps researchers to explore structural performance during a hybrid simulation test and to process data afterwards. One of the key instruments in the MUST-SIM facility is the non-contact measurement machine, namely K-Series DMM from Nikon Metrology (2012) (the former name is the Krypton system). This machine can detect three-dimensional (3D) displacements on specimens as long as the LED targets are attached to them. Due to the capability of this machine, the detailed behavior of structures can be investigated by adequate data analysis. The high-resolution displacement measurements obtained from this machine can be converted into strain maps over the specimen dimension. For localizing the specific portions, the 3D displacements in a certain region can be transformed into 6DOF motions. During a hybrid simulation test, the curvature can be calculated by multiple LED displacements and then illustrate the moment hysteresis performance online. These methods featuring the non-contact instrumentation interpret the measurements closer to the numerical analysis.

In this study, seismic performance of a four-span curved bridge is evaluated via hybrid simulation under multi-directional earthquake loading. This experiment is carried out by the MUST-SIM facility in the Network for Earthquake Engineering Simulation Laboratory at the University of Illinois. Three physical concrete piers are tested using the Loading and Boundary Condition Boxes, while the bridge deck is computationally modeled and concurrently simulated. To realize this hybrid simulation test, a hybrid simulation framework is established in terms of software, hardware, and communication protocols. For advancing the hybrid simulation in the MUST-SIM NEES site, two additional components are recently developed to enhance the framework. A 6DOF high-precision positioning control scheme is built to achieve accurate displacements on the specimens. A post-processing toolbox is also developed to further investigate the structural responses of the piers and system-level bridge responses based on the non-contact instrumentation. Prior to the large-scale hybrid simulation test, a small-scale approach is employed to validate the hybrid simulation framework. With the completed framework, the curved bridge is successfully evaluated using three LBCBs in hybrid simulation. The associated results obtained from dense arrays of advanced instrumentation are also discussed in this study.

2. HYBRID SIMULATION FRAMEWORK

The MUST-SIM facility utilizes 6DOF LBCBs to fulfill hybrid simulation tests for complex structural systems. A hybrid simulation framework was initiated by Nakata et al. (2007) and Kwon and Elnashai (2007). To further improve the quality of hybrid simulation tests, a number of functions were continuously developed and added into this framework by researchers until now. Figure 1 highlights the current hybrid simulation used for the MUST-SIM NEES facility. This section reviews the existing components as well as provides the details of the recently developed components in this framework.

2.1 Loading and Boundary Condition Boxes

The Loading and Boundary Condition Box (LBCB) consists of six actuators that create 6DOF movements on the loading platform. Each actuator can produce 1,101 kN (216 kips) in tension and 1,383 kN (328 kips) in compression. In terms of the 6DOF displacement capacity, each LBCB can generate ±250mm (10 in), ±125mm (5 in), ±125 mm (5 in) in the *x*-, *y*-, *z*- directions and ±16°, ±11.8°, ±16° in the roll, pitch, yaw directions. Moreover, the maximum force capacity is 1,921/2,918 kN (432/656 kips), 960/1,459 kN

(216/328 kips), 2,882/4,377 kN (648/984 kips) in the *x*-, *y*-, *z*- directions, where both numbers indicate the tension and compression capacity, respectively. The moment capacity is 862 kN-m (636 kip-ft), 1152 kN-m (850 kips-ft), 862 kN-m (636 kip-ft) in the roll, pitch, yaw directions.

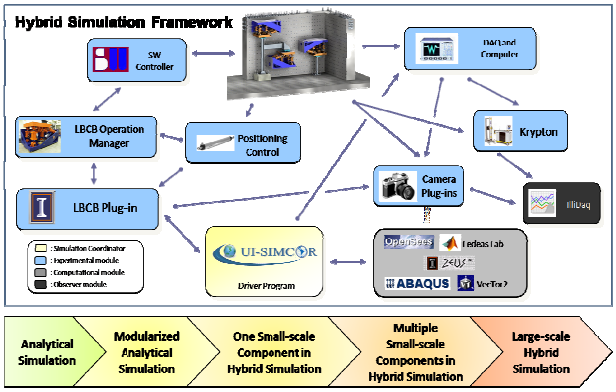


Figure 1 Illustration of The Current Hybrid Simulation Framework

2.2 Shore Western Controller

The Shore Western (SW) Controller is to control all six actuators in LBCB (Shore Western Manufacturing 2012). The control scheme used in the controller is the proportional-integral-derivative (P.I.D.) loop under the displacement feedback. Each actuator is controlled by an independent P.I.D. loop, and these actuators are rated to generate relatively slow movements. Furthermore, the controller also serves as a data acquisition (DAQ) system to output the signals from the displacement transducers and load cells.

2.3 Operation Manager

The operation manager (OM) is an agent to convert the commands from the Cartesian space to the actuator space. Owing to the orientation of the actuators in LBCBs, every command sent in the Cartesian Space will move all six actuators simultaneously. To attain high accuracy in displacements, OM acquires the readings from and sends the commands to the Shore Western Controller with a high sampling rate (Nakata et al. 2007).

OM moves LBCBs under the displacement control. For the multi-DOF displacement commands, OM can send the signals directly to the SW controller. Additionally, OM employs a mixed-mode control scheme to command forces, and these forces are converted into displacements based on the current specimen stiffness or maximum displacement increments with respect to force changes. Each DOF can only be specified with a displacement or force command at a time, while mixed displacement and force commands can be concurrently applied to multiple DOFs.

OM can also impose displacements about the control point in the specimen coordinates. The control point is defined as the loading point of interest to users. At the point, the specimen will displace identically to the loading protocol. Furthermore, OM contains a transformation matrix that maps the displacements of specimens into LBCBs. Thus, the loading axes will be aligned with the specimen coordinates. All these features ensure displacements being correctly imposed to the specimens during tests.

2.4 LBCB Plug-in

The LBCB Plug-in is an interface that implements users-defined functions in a test and communicates data to other modules. This interface can preprocess the loading protocol in accordance to the received responses from the specimen. For instance, the force commands can be calculated by the corresponding displacements obtained from the previous step. The interface also provides a coordinate transformation to alter the axes that corresponds to the finite element model in hybrid simulation. Moreover, the LBCB Plug-in handles all triggers for the modules that are directly associated with the loading protocol, e.g., DAQ, non-contact instrumentation machines, and camera plug-ins.

2.5 UI-SIMCOR

The Multi-site Substructure Pseudo-dynamic Simulation Coordinator (UI-SimCor) is a hybrid simulation coordinator, developed in the MUST-SIM NEES site at UIUC (Kwon et al. 2007). The core of this coordinator is to communicate the components between the specimens and modularized FE solvers (e.g., ZEUS-NL and OpenSees) and to calculate dynamic response based on the integration scheme. To launch a hybrid simulation test through UI-SimCor, the initial stiffness matrices are first established among all experimental and computational components. As LBCBs are capable of applying the gravity forces, the static loading can be added to the entire system before (pseudo-) dynamic testing. These static loading will generate the corresponding displacements from the predetermined stiffness and eventually achieve the target forces. Note that UI-SimCor is not specific to LBCBs and is implementable in the majority of hybrid simulation facilities. Given the mass and damping matrices, the dynamic testing by UI-SimCor will impose displacements to the specimens, sense the achieved displacements and forces, obtain the restoring forces from both experimental and computational components, and then execute next step. In fact, UI-SimCor bridges the experimental specimens into the structural FE model by the integration scheme.

Owing to the limited hydraulic power and laboratory space, hybrid simulation tests may face a scaling issue. UI-SimCor accounts for the scaling factors with respect to the specimen dimensions and forces, resulting in four types of scaling parameters: 1) translational displacements, 2) rotational displacements, 3) translational forces, and 4) moments. In the scaling parameters, the unit conversion is also considered and can fit the unit systems used in both FE tools and experimental facility. Therefore, UI-Simcor can conduct multi-scale responses in distributed hybrid simulation.

2.6 Miscellaneous Modules

The MUST-SIM facility is also known for dense instrumentation in structural testing. The data acquisition

software, named IlliDaq, is a platform that handles all the measurements together. The system can support multi-hundred channels, and the measurement types range from strain gauges, displacement transducers, inclinometers, load cells, and etc. As LBCBs are currently capable of slow-movement tests, these measurements are stored in a step-wise format. In addition, this DAQ platform can also display the results during a test (multiple windows over several screens) and derive the calculated responses based on the predetermined equations such as the curvatures computed by steel strain gauges. To secure all measurements, this platform can upload data to the web repository. All these functions in the DAQ platform provide a flexible environment to explore the behavior of structures.

To visualize the structural responses, the MUST-SIM facility employs a number of digital single-lens reflex (DSLR) cameras. These still pictures taken from the DSLR cameras are triggered and synchronized to the loading steps by the Camera Plug-in. The Camera Plug-in triggers cameras after LBCB accomplishes executing a step. These pictures can be consequently merged together to make a video with respect to the loading history. These visualized data provides an additional option to reinvestigate tests.

The Krypton Plug-in is a part of IlliDaq that acquires the non-contact instrumentation measurements and sends the step-wise data back to the DAQ platform. As mentioned earlier, the Krypton system runs on an independent machine. Thus, the Krypton Plug-in transforms the data format and subsequently synchronizes the data sets with IlliDaq. The data obtained from the Krypton system will then have the same step stamps on measurements.

2.7 High-precision Positioning Control Scheme

Due to finite stiffness and large reaction forces, the fixture between the reaction (strong) wall and LBCBs may induce small elastic deformations or slight slippages. These small movements can cause substantial errors to specimens in terms of forces. To compensate these movements, a high-precision positioning control scheme is developed and added to the hybrid simulation framework. In this control scheme, a 6DOF displacement monitoring strategy is to employ six or more displacement transducers for detecting the actual 6DOF displacements, while a deformation correction method is to introduce the additional movements for achieving the target displacements. Utilizing these two features, the displacements can be accurately achieved.

Figure 2 demonstrates the proposed monitoring strategy for 6DOF displacements. Six displacement transducers (using LVDTs as an example) are instrumented between the specimen and reaction wall. The setup is assumed to be in a rigid-body motion throughout a test. All free-pin locations of LVDTs are directly connected to the top of the specimen, while the fixed-pin locations of LVDTs are supported by solid brackets and connected to the reaction wall. To be fully aware of all 6DOF displacements, the LVDT locations are recommended to follow the proposed configuration, i.e., one LVDT in the first axis, two LVDTs in the second axis, and three LVDTs in the third axis. Note that these LVDTs could be skewed. Then, the three axes in the Cartesian space are defined in accordance to the specimen space in which the sensor space is equivalent to the specimen space. Therefore, the conversion from the Cartesian space to the sensor space is written by

$$\mathbf{x}_{i,\text{new}}^{\text{free}} = \mathbf{T}_1\mathbf{T}_2\mathbf{T}_3\mathbf{x}_{i,\text{original}}^{\text{free}} + \begin{bmatrix} x^{\text{cp}} \\ y^{\text{cp}} \\ z^{\text{cp}} \end{bmatrix} \qquad (1)$$

$$d_i = \left\|\mathbf{x}_{i,\text{new}}^{\text{free}} - \mathbf{x}_i^{\text{fixed}}\right\| - \left\|\mathbf{x}_{i,\text{original}}^{\text{free}} - \mathbf{x}_i^{\text{fixed}}\right\|$$

where

$$\mathbf{T}_1 = \begin{bmatrix} 1 & 0 & 0 \\ 0 & \cos\left(\theta_x^{\text{cp}}\right) & -\sin\left(\theta_x^{\text{cp}}\right) \\ 0 & \sin\left(\theta_x^{\text{cp}}\right) & \cos\left(\theta_x^{\text{cp}}\right) \end{bmatrix}, \mathbf{T}_2 = \begin{bmatrix} \cos\left(\theta_y^{\text{cp}}\right) & 0 & \sin\left(\theta_y^{\text{cp}}\right) \\ 0 & 1 & 0 \\ -\sin\left(\theta_y^{\text{cp}}\right) & 0 & \cos\left(\theta_y^{\text{cp}}\right) \end{bmatrix},$$

$$\mathbf{T}_3 = \begin{bmatrix} \cos\left(\theta_z^{\text{cp}}\right) & -\sin\left(\theta_z^{\text{cp}}\right) & 0 \\ \sin\left(\theta_z^{\text{cp}}\right) & \cos\left(\theta_z^{\text{cp}}\right) & 0 \\ 0 & 0 & 1 \end{bmatrix}$$

$\mathbf{x}^{\text{cp}} = \begin{bmatrix} x^{\text{cp}} & y^{\text{cp}} & z^{\text{cp}} & \theta_x^{\text{cp}} & \theta_y^{\text{cp}} & \theta_z^{\text{cp}} \end{bmatrix}^T$ is a given displacement vector in the 6 DOFs at the control point; $\mathbf{x}_{i,\text{original}}^{\text{free}}$ and $\mathbf{x}_i^{\text{fixed}}$ are respectively the initial free-pin and fixed-pin coordinates of the i-th LVDT; $\mathbf{x}_{i,\text{new}}^{\text{free}}$ is the updated free-pin coordinates of the i-th LVDT; d_i is the differential displacement of the i-th LVDT after the specimen moved. This conversion is straightforward; however, the inverse conversion from the sensor space to the Cartesian space is a highly nonlinear problem requiring a nonlinear solver to obtain the displacements at the control point. To prevent a convergent issue, a number of constraints can be added and given by

$$\left\|\mathbf{x}_{i,\text{new}}^{\text{free}} - \mathbf{x}_{j,\text{new}}^{\text{free}}\right\| = \left\|\mathbf{x}_{i,\text{original}}^{\text{free}} - \mathbf{x}_{j,\text{original}}^{\text{free}}\right\|, \; i, j = 1 \sim n \qquad (2)$$

where n is the number of LVDTs used. Because all free pins travel in the rigid-body motion, the distance from one pin to another is constant. Based on the configuration in Figure 1, the total number of the constraints is 15. To solve the nonlinear problem, the Newton Raphson method or commercial toolbox such as the Matlab optimization toolbox (Matlab 2012) can be used.

Elastic deformation is defined as the slight movement at the reaction fixtures of hydraulic actuators or the slippage between the loading surfaces and specimen. As the movement is introduced, the internal displacement transducers of hydraulic actuators cannot impose consistent displacements to a specimen. As a result, the measured displacements from hydraulic actuators are no longer correct, even though the readings have presented to achieve the target displacements. To account for the deformations, an online iterative process should be performed in order to eliminate the unexpected displacements. Using the solution of the combined Eqs. (1-2), the current displacement of a specimen is therefore available. The command for actuators

or LBCB boxes is then adjusted and given by

$$\mathbf{x}_{l,k+1}^{\text{cmd}} = \mathbf{x}_{l,k}^{\text{cmd}} + \left(\mathbf{x}_{l}^{\text{target}} - \mathbf{x}_{l,k}^{\text{cp}}\right) \tag{3}$$

where $\mathbf{x}_{l,k}^{\text{cmd}}$ and $\mathbf{x}_{l,k+1}^{\text{cmd}}$ represent the commands at the iterative k-th and (k+1)-th correction steps in the l-th time step; $\mathbf{x}_{l}^{\text{target}}$ and $\mathbf{x}_{l,k}^{\text{cp}}$ indicate the target displacement and current position at the control point. This process often needs more than one correction steps within a time step. The process will be accomplished until a predefined tolerance is met and given by

$$\begin{aligned} &\left|y_{l}^{\text{target}} - y_{l,k}^{\text{cp}}\right| \le m, \\ &y \in \mathbf{x} = \left\{x \quad y \quad z \quad \theta_x \quad \theta_y \quad \theta_z\right\}, \\ &m \in \left\{\delta_x \quad \delta_y \quad \delta_z \quad \delta_{\theta_x} \quad \delta_{\theta_y} \quad \delta_{\theta_z}\right\} \end{aligned} \tag{4}$$

where δ indicates the tolerance in terms of DOFs. In Eq. (4), each controlled DOF must satisfy the condition. To avoid the overshooting behavior, Eq. (3) may consider a correction factor to lower the correction amount in a correction step. Even though the displacement error satisfies the tolerance, a small amount of errors still exists. A preliminary adjustment, which is the deviation between the achieved and target displacements in the last time step, is then used to compensate prior to introducing correction steps. By combining these two features, a complete correction procedure is presented by

$$\begin{aligned} \mathbf{x}_{l,0}^{\text{cmd}} &= \mathbf{x}_{l}^{\text{target}} + \alpha\left(\mathbf{x}_{l-1}^{\text{target}} - \mathbf{x}_{l-1}^{\text{cp}}\right), \ \alpha = 0 \text{ or } 1 \\ \mathbf{x}_{l,k+1}^{\text{cmd}} &= \mathbf{x}_{l,k}^{\text{cmd}} + \beta\left(\mathbf{x}_{l}^{\text{target}} - \mathbf{x}_{l,k}^{\text{cp}}\right), \ \beta = 0 \sim 1 \end{aligned} \tag{5}$$

where α and β could be manually adjusted at each time step.

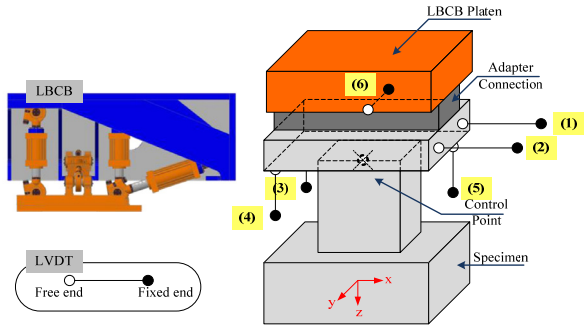


Figure 2 Illustration of 6DOF Displacement Monitoring Configuration

2.8 Post-processing Toolbox

For advancing the use of the Krypton measurements, the data processing methods in this framework comprise the estimation of three types of strains, 6DOF displacements, and curvatures over the structural dimensions. For strains, the normal and shear types are calculated with respect to the coordinates of the testing structure. The 6DOF displacements are generated from a group of LEDs with respect to a specific cross section. The curvatures are approximated from the vertical deformations of LEDs in a line and then computed over the axial loading direction. The followings provide the derivations for each method.

As the Krypton measurements provide 2D or 3D LED positions, plane strains can be calculated from these data. First, the strain calculation needs to accompany a uniform grid of LEDs aligned with the loading direction. For example, LEDs should be attached to a building column or bridge pier with an uniform spaced grid of which two directions are parallel and perpendicular to the structural axis (see Figure 3-a). Each square from four LEDs forms a number of elements derived from interpolating the measured positions into fine meshes, as shown in Figure 3-b. The nodes in these fine meshes are then derived from a quadratic form and given by

$$\begin{cases} x_{ij} = \left[(1-m)(1-n) \quad m(1-n) \quad mn \quad (1-m)n\right]\left[x_1 \quad x_2 \quad x_3 \quad x_4\right]^T \\ y_{ij} = \left[(1-n)(1-m) \quad m(1-n) \quad mn \quad (1-m)n\right]\left[y_1 \quad y_2 \quad y_3 \quad y_4\right]^T \end{cases} \tag{6}$$

where m and n range from 0 to 1, and i and j indicate the element number. The number of spacing can be different in the x and y directions. Subsequently, the normal strains in an element are illustrated in Figure 3-c and calculated by

$$\varepsilon_{x,k} = \frac{l_{x,k} - l_{x,0}}{l_{x,0}}, \ \varepsilon_{y,k} = \frac{l_{y,k} - l_{y,0}}{l_{y,0}} \tag{7}$$

where

$$\begin{aligned} l_{x,k}^2 &= \frac{1}{4}\left(x_{ij,k} + x_{i(j+1),k} - x_{(i+1)j,k} - x_{(i+1)(j+1),k}\right)^2 + \\ &\frac{1}{4}\left(y_{ij,k} + y_{i(j+1),k} - y_{(i+1)j,k} - y_{(i+1)(j+1),k}\right)^2 \\ l_{y,k}^2 &= \frac{1}{4}\left(x_{ij,k} + x_{(i+1)j,k} - x_{i(j+1),k} - x_{(i+1)(j+1),k}\right)^2 + \\ &\frac{1}{4}\left(y_{ij,k} + y_{(i+1)j,k} - y_{i(j+1),k} - y_{(i+1)(j+1),k}\right)^2 \end{aligned}$$

k denotes the k-th step of a test, and 0 means the initial step. The shear strain illustrated in Figure 3-d is derived from

$$\begin{aligned} \gamma_{xy,k} = &\frac{x_{ij,k} + x_{(i+1)j,k} + x_{(i+1)(j+1),k} + x_{i(j+1),k}}{4l_{y,0}} + \\ &\frac{y_{ij,k} + y_{(i+1)j,k} + y_{(i+1)(j+1),k} + y_{i(j+1),k}}{4l_{x,0}} - \\ &\frac{x_{ij,0} + x_{(i+1)j,0} + x_{(i+1)(j+1),0} + x_{i(j+1),0}}{4l_{y,0}} - \\ &\frac{y_{ij,0} + y_{(i+1)j,0} + y_{(i+1)(j+1),0} + y_{i(j+1),0}}{4l_{x,0}} \end{aligned} \tag{8}$$

From these two equations, the normal strains, ε_x and ε_y, are respectively formulated along the axial and transverse directions, while the shear strains, γ_{xy}, have a sign convection identical to the coordinates. The calculated strains in Eqs. (7-8) can be interpreted as the strains at the center point of an element or the constant strains in the entire element.

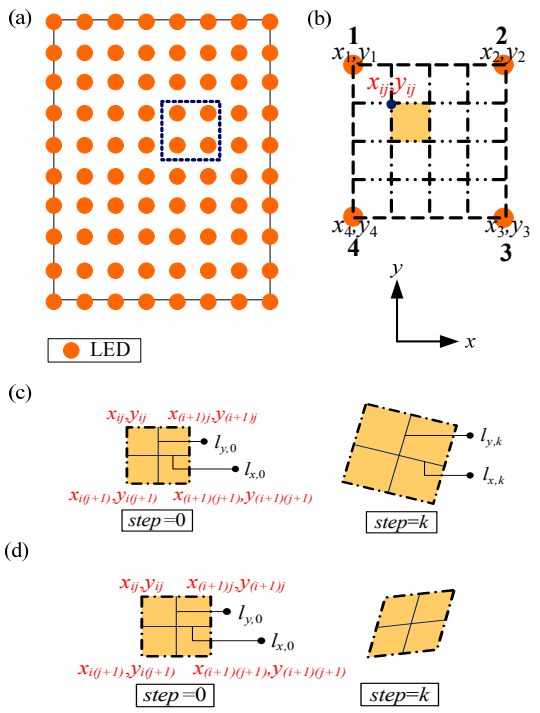


Figure 3 Illustration of Strain Calculation: 1) LED Grid, 2) Interpolation, 3) Normal Strain, and 4) Shear Strain

The Krypton measurements in the static approach only result in LED 3D positions with respect to the user-defined coordinates. With a certain group of LEDs, these position data can be converted into 6DOF displacements that can inform the local behavior of interest. The conversion can be computed by Eq. (1) with an appropriate solver. In this problem, at least three LEDs should be involved in the 6DOF displacement conversion. While this problem only contains six variables as the 6DOF displacements, considering data from only two LEDs may introduce a geometric symmetry, resulting in incorrect rotations. Moreover, the origin in the grouped LEDs can be offset to a point which is different from the one in the coordinates, defined for the entire LEDs. By selecting an appropriate group of LEDs, 6DOF displacements can be generated with respect to the region of this group.

To approximate the real-time curvatures, an approach is proposed based on the absolute LED positions. Assume that four grouped LEDs are attached near the neutral axis, as shown in Figure 4. The curvature can be subsequently estimated by

$$\kappa = \frac{\theta_{12} - \theta_{34}}{h}, \quad \theta_{12} = \frac{y_2 - y_1}{d}, \quad \theta_{34} = \frac{y_3 - y_4}{d} \qquad (9)$$

where κ is the curvature at the center of this four-LED group. In this equation, the rotations are assumed to be constant over the cross section along the perpendicular direction of the neutral axis, e.g., the horizontal direction in Figure 4. As long as h is relatively small, the curvature will be very close to the calculation using the rotations obtained from the 6DOF displacement conversion.

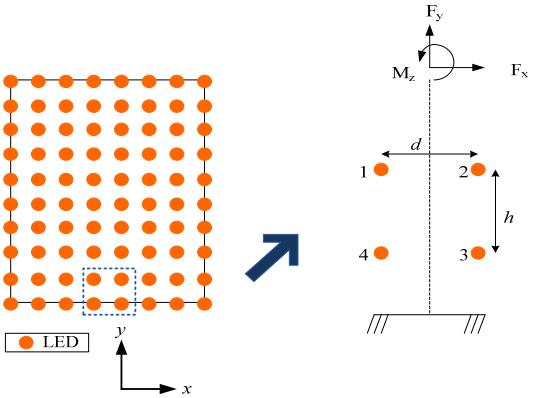


Figure 4 Illustration of Curvature Estimation

2.9 Small-scale Validation

The small-scale validation is to assess the hybrid simulation framework with all newly developed features as well as the existing components using scaled models. This validation process is conducted by different levels of simulation. First, an analytical model of the entire structure is simulated in the FE tool which will be used in the final hybrid test. The modularized analytical simulation is then performed in UI-SimCor so that the integration scheme with the parameters used (e.g., integration time step) can be confirmed. By adding one single experimental small-scale component, the hybrid simulation framework is tested with the communication between UI-SimCor and LBCB Plug-in, coordinate transformation, scaling, and high-precision positioning control scheme. Thus, all the experimental components are employed in the small-scale approach in order to verify the multi-platform communication (e.g. Camera Plug-ins) and hardware limitations (e.g., specimen positions connecting to LBCBs, actuator strokes and forces, and external sensor resolution in terms of the high-precision positioning control scheme). After validating the hybrid simulation framework through a series of simulation tests, a large-scale hybrid simulation test can be implemented.

3. DEVELOPMENT OF A FOUR-SPAN CURVED BRIDGE

Reinforced concrete bridge piers are subjected to a combination of forces and deformations due to spatially complex ground motions, structural or geometry configuration, and the interaction between input and response characteristics. Motivated by the impact of combined actions on piers and overall system response, a four-span curved bridge structure is developed and experimental evaluated using hybrid testing through the unique capabilities of the MUST-SIM facility at UIUC. This bridge test is a part of the Combined Actions on Bridge Earthquake Research (CABER) project, sponsored by National Science Foundation (NSF). Prior to this curved bridge hybrid test, the CABER team has investigated a wide variety of topics associated with the combined actions on

bridge columns. For example, Prakash et al. (2010) explored circular RC columns subjected to axial force, bending, and torsion that interact with shear. Blearbi incorporated the experimental findings of bridge columns to the performance-based evaluation under combined loadings. Xu and Zhang (2012) studied the axial-shear-flexure interaction for the reinforced concrete columns under combined actions. Kim et al. (2011) experimentally investigated a bridge structure subjected to both horizontal and vertical ground motions. Arias-Acosta and Sanders (2010) and Moustafa et al. (2011) employed shaking table testing to study seismic performance of reinforced concrete bridges under bi-directional horizontal excitations. As for this hybrid simulation test, the main objective is to experimentally investigate the four-span curved bridge subjected to bi-directional horizontal ground motions.

The curved bridge is developed based on a seismic design example used by the National Cooperative Highway Research Program (NCHRP) Project 12-49. The prototype bridge is composed of five continuous spans of 30 m (100 ft) each, with four two-pier bents. A box girder on the piers is used to support the superstructure. In this study, some design parameters, addressed in the NCHRP example, are modified. The modification includes reducing from five to four spans and shortening the overall length appropriately, creating non-uniform span lengths, adding curvature to the bridge, and moving to single-pier bents. The resulting geometry was selected via an analytical parametric study to identify a case that generated sufficient torsional response in the piers to investigate higher levels of combined actions.

The overall dimensions of this bridge are presented in Figure 5. The bridge deck is 120 m (400 ft) in total length with a radius of 198 m (660 ft). The cross section of the deck is a box girder with a surface width of 6.6 m (22 ft). Above each pier, the box girder is supported by a 4.8-m (16-ft) cap beam with a cross section of 1.5m (5 ft) x 2.0 m (6.75 ft). The piers are 1.2 m (4 ft) diameter, with 28#10 bars as longitudinal reinforcement, distributed evenly. Transverse reinforcement is a #5 continuous spiral stirrup. The pier lengths are 8.6, 11.3, and 6.8 m (28.5, 37.5, and 22.5ft).

In the experiment, the bridge deck, cap beams, and abutments are modeled analytically using Zeus-NL (Elnashai et al. 2002). The outer two piers are tested at a 1:3 scale, while the inner pier is tested at a 1:20 scale. The 1:3 scale piers are therefore constructed with a 0.4-m (16-in) diameter, and 17#4 longitudinal bars and a #3 spiral at 5-cm (2-in) pitch and 1.9-cm (3/4-in) cover. The resulting heights are 2.9 and 2.3 m (9.5 and 7.5 ft) respectively. Due to the limitation of the laboratory space, the inner pier is down scaled to 1/20th. The resulting dimensions are 57.2-cm (22.5-in) height and 6.1-cm (2.4-in) diameter.

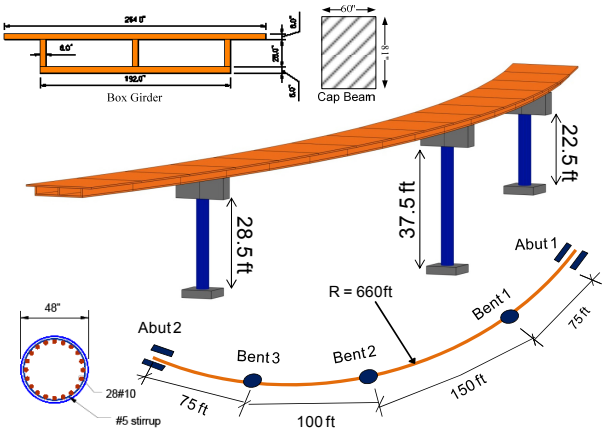


Figure 5 Dimensions of The Curved Bridge

4. HYBRID SIMULATION RESULTS

Circular reinforced concrete piers of a four-span curved bridge are experimentally investigated through large-scale hybrid simulation under bi-directional earthquake loadings. The boundary conditions of the piers are controlled in all six DOFs. The experiment is performed by the MUST-SIM facility at UIUC. In this hybrid test, the bridge structure is composed of one small-scale and two large-scale experimental piers. The curved bridge deck and abutments are modeled analytically in Zeus-NL. This hybrid simulation test is novel because of a) geometric irregularities and varying pier response characteristics, b) multi-directional motions of the applied earthquake record, c) a curved bridge deck and combined actions with torsion, and d) system-level interaction between three experimental piers in two testing facilities with numerical models of deck, restraints, and abutments.

Figure 6 illustrates the experimental setup of this hybrid test. Two large-scale piers representing the outer piers in a bridge are tested by the large-scale LBCBs, while one small-scale pier representing the center pier is tested by the 1/5th-scale LBCB. Extensive instrumentation is employed for the large-scale piers. For example, 170-channel conventional sensors are instrumented including 152 strain gages, 6 string potentiometers, and 12 LVDTs. For the non-contact instrumentation, 200 Krypton LEDs are attached on both large-scale piers. 12 DSLR cameras are placed in different locations in order to capture the pier motions every step. The applied earthquake record is a synthetically generated accelerogram representative of the seismic zone corresponding to Seattle, WA. Four performance levels per 10 seconds are considered and correspond: 1) cracking performance level at 0.08 times of the most credible earthquake (MCE), 2) yielding performance level at 0.30 MCE, 3) design performance level at 1.00 MCE, and 4) failure level at 2.00 MCE, as shown in Figure 7. 100% of this earthquake record is applied to the transverse direction of the bridge, while a 25% scaled version of the record is applied in the longitudinal direction.

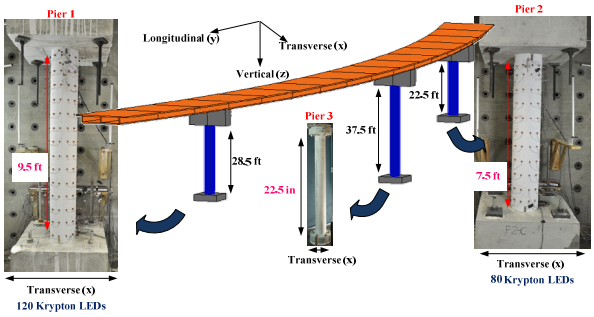


Figure 6 Hybrid Simulation Setup of The Four-span Curved Bridge

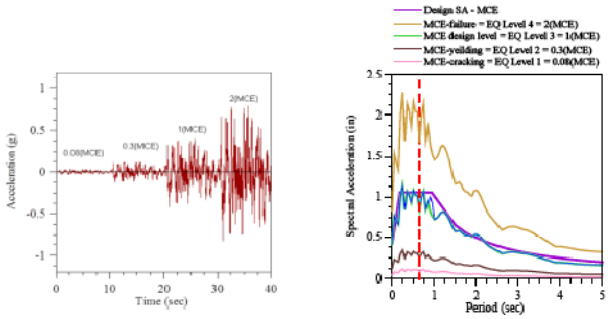


Figure 7 Earthquake Record Used in This Hybrid Test

Figure 8 demonstrates the displacement time histories of the two large-scale piers. The transverse, longitudinal, and vertical directions are denoted as x, y, and z in this figure. The test is ended at 39.72 seconds because the horizontal actuators of the LBCB run out the strokes on the top of the tall pier (the left one in Figure 6). Moreover, the coordinates presented in this figure are in the full scale that corresponds to the analytical model. The maximum drifts of the tall pier reach 5.9% and 1.8% along the transverse and longitudinal directions, while the short pier has 3.3% and 0.6% maximum drifts along the same directions. The maximum transverse rotation and torsion are 3.15° and 1.27° on the tall pier and 2.23° and 0.90° on the short pier. For the center pier, the maximum drifts in the transverse and longitudinal directions are 6.4% and 0.7%, while the maximum transverse rotation and torsion are 3.04° and 1.10°. More results will be documented and published in the near future.

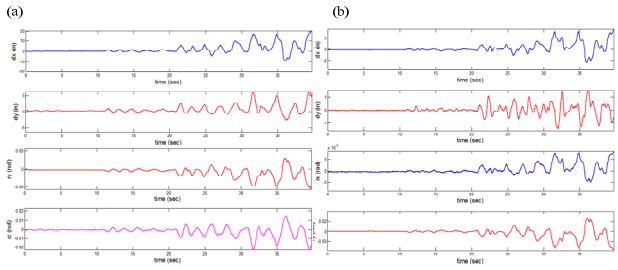


Figure 8 Displacement Responses of The Large-scale Piers: (a) Tall Pier and (b) Short Pier

To demonstrate the high-precision positioning control scheme, the achieved 6DOF displacements are compared to the target ones in the large-scale piers, as shown in Figure 9.

All the units are in the 1/3rd scale (equivalent to the LBCB coordinates). The translational and rotational tolerances are set as 0.127 mm (0.005 in) and 5×10^{-4} radians. The translational tolerances are increased to 0.254 mm (0.01 in) at the time the specimens have large displacements, i.e., during the last 10 seconds of the earthquake record. Due to the 75-cm (30-inch) LVDTs, the moment arms are sufficiently large for monitoring the rotations. The deformation correction is often controlled by the translations, resulting in the consistently small errors for rotations. The results exhibit that the high-precision positioning control scheme produces very accurate displacements to piers. The errors are always within the predetermined tolerances. Consequently, the experimental results are reliable and accurate for this hybrid simulation test.

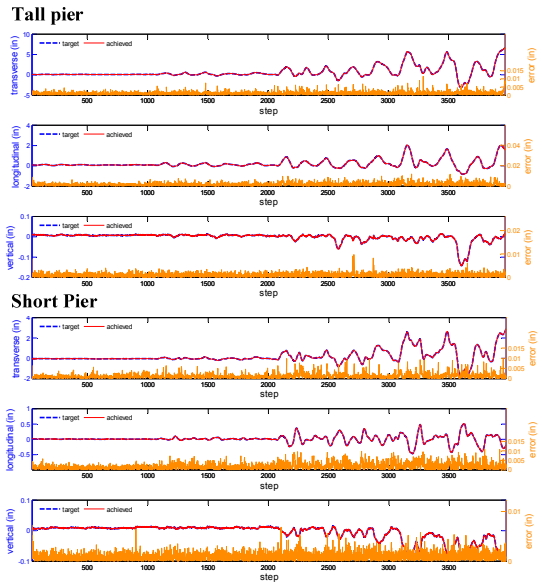


Figure 9 Errors Between Target and Achieved Displacements in Large-scale Piers

In the small-scale validation, the procedures illustrated in Figure 1 are all conducted. The purely analytical modeling is simulated using Zeus-NL. The modularized analytical simulation is performed through UI-SimCor with the Zeus-NL tool in which three piers are modeled linearly. The first small-scale hybrid simulation is carried out with the center pier as the experimental component, while the outer piers are still simulated as linear columns. In this hybrid simulation test, the center pier is scaled to 1/20th that is identical to the large-scale hybrid simulation test. The last test in the small-scale validation is the three-pier small-scale hybrid simulation where the three piers are all scaled to 1/20th. To demonstrate the effectiveness of the small-scale validation, the displacements of the three-pier small-scale hybrid simulation are compared to those of the large-scale test. Figure 10 illustrates the two transverse displacements, transverse rotation, and torsion of the outer tall and center piers. The units are equivalent to the coordinates in the full-scale bridge, and the data shown are the piers subjected to the design performance level at 1.0 MCE (20~30

seconds). This figure shows that the small-scale results are able to inform the response levels in the large-scale test and only small errors are found between two tests. Therefore, the small-scale validation is necessitated for examining the hybrid simulation framework as well as ensuring the feasibility of the large-scale hybrid test.

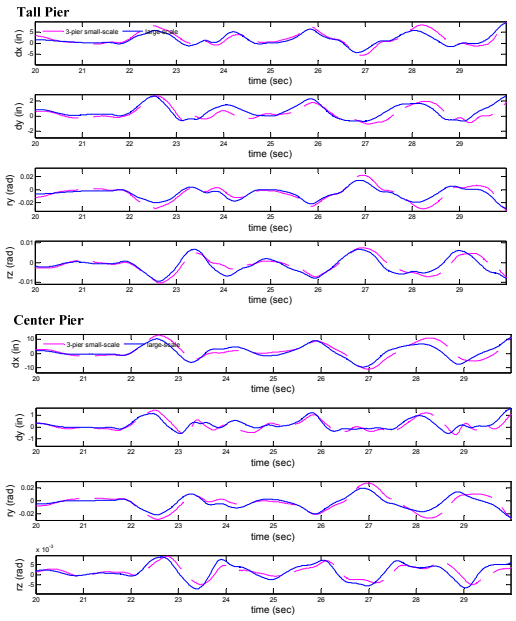


Figure 10 Displacement Responses Between Small-scale and Large-scale Hybrid Simulation Tests

As mentioned earlier, a post-processing toolbox is developed for the non-contact instrumentation measurements. After this hybrid test, the toolbox is also applied to the large-scale piers in order to investigate the detailed behavior. First, strain maps can predict or indicate the cracks of structures during testing. Figure 11 demonstrates vertical strains maps before and after a large crack happens in the tall pier. As can be seen in this figure, the yellow portion indicates the crack position near the bottom of the pier. Because the strains are calculated from the LED positions, the corresponding strains around the crack may overestimate the true surface strain of this concrete pier. However, this strain still gives a good indication of cracks and informs damages in a early time. By inspecting the changes in a strain map, the cracks can be notified in advance if the crack strains are known.

Strain maps also provide a good indication of concrete spalling. In Figure 12, a series of strain maps are compared to the corresponding still pictures. Although these strain maps may overestimate strains near the concrete damages, these strain maps still exhibit an early prediction of concrete spalling. Prior to the occurrence of a peak response, moderate strains are found around the spalling location. With an increase of forces applied at top of the pier, tensile strains in this region are enlarged. When the spalling is visible, the strain map has shown severe damages in an early time. The strains, generated from the LED positions, offer an opportunity to detect damages before they are visibly found.

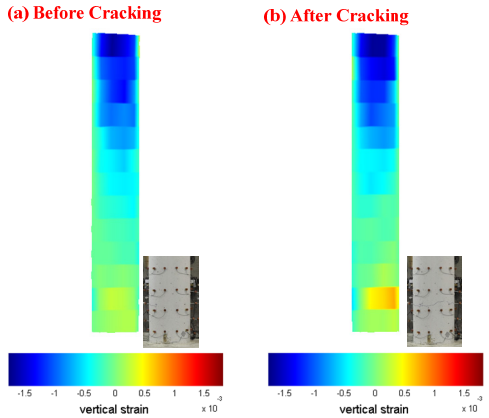


Figure 11 Indication of Cracks: (a) Before Cracking and (b) After Cracking

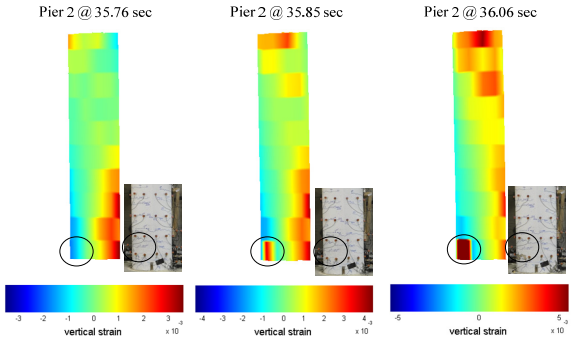


Figure 12 Concrete Spalling Indication from Strain Maps

Structural behavior can be informed from the strain maps. This experiment is conducted by LBCBs which can concurrently impose moments and shear forces at the top of the piers. As shown in Figure 13, the moment distribution along the axial direction of the pier is consistent with the vertical strain map. In this figure, the moment (M_y) imposed at top is positive, while the resulting moment (M_y) at bottom is negative due to the positive shear force (F_x) at top. Obviously, the pier has a double-curvature behavior induced by the complex loadings. Moreover, the positive shear force (F_x) at top, combined with other DOF loadings, results in the shear strain map shown in Figure 13. Because the strain map created in this figure is projected to the *x*-*z* plane, the contribution from the moment (M_x) and force (F_y) is minor. Thus, the most shear strains are induced from the combination of the shear and torsional forces. Additionally, the torsion at top dominates the horizontal strains of the pier, with a combination of the shear force, as shown in Figure 14. The negative torsion at top introduces positive and negative shear strains at the negative and positive *x* direction due to the 3D strains that are projected to the *x*-*z* plane. With the positive shear force at top, the absolute value of the negative strain is greater than the value of the positive strain. Using the strain map, the structural behavior can be easily investigated in comparison with forces.

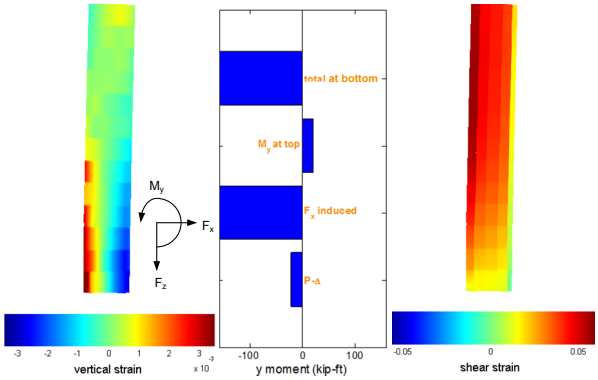


Figure 12 Flexural and Shear Behavior in Strains Compared to Moment Distribution

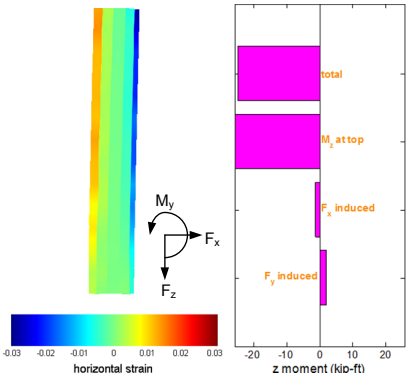


Figure 13 Horizontal Strains As Compared to Torsions

5. CONCLUSIONS

Hybrid testing of a four-span curved bridge structure subjected to bi-directional ground motions was successfully performed by the Multi-Axial Full-scale Sub-Structuring Testing and Simulation facility at the University of Illinois at Urbana-Champaign. In this hybrid simulation test, one small-scale and two large-scale piers were experimentally evaluated using the Loading and Boundary Condition Boxes, while the bridge deck and abutments were computationally modeled in Zeus-NL. Four performance-based levels of an earthquake record were selected to assess the curved bridge. As a result, the performance of all piers and the system-level responses of the bridge were significantly influenced by the 6DOF combined loadings that had been shown in the visualization data.

Prior to the hybrid test, two additional components were developed to complete the hybrid simulation framework. The high-precision positioning control scheme was established to compensate the elastic deformation between the reaction wall and LBCBs, resulting in accurate displacements being imposed to the piers. With the post-processing toolbox, the pier and system-level responses were graphically presented for further investigation on the combined actions of the bridge. Moreover, two small-scale validation tests confirmed all the components in hybrid simulation and enabled the large-scale hybrid test. Finally, the hybrid test of this curved bridge was accomplished by the well-prepared hybrid simulation framework.

Acknowledgements:

The work presented in this paper was supported through a NEESR-SG project (Seismic Simulation and Design of Bridge Columns under Combined Actions and Implications on System Response) funded by the National Science Foundation under Award Number CMMI-0530737. The authors would also like to acknowledge Dr. Oh-Sung Kwon (University of Toronto) and Dr. Adel Abdelnaby (University of Memphis) for their input.

References:

Arias-Acosta, J. and Sanders, D. (2010), "Shake table testing of bridge columns under combined actions," *SEI Structures Congress*, Orlando Florida.

Blearbi, A., Prakash, S., and Silva, P. F. (2010), "Incorporation of decoupled damage index models in the performance-based evaluation of RC circular and square bridge columns under combined loadings," *ACI Special Publication*, SP271-05, 79-102.

Elnashai, A. S., Papanikolaou, V., and Lee, D. (2002), ZEUS NL - A system for inelastic analysis of structures, Mid-America Earthquake Center, University of Illinois at Urbana-Champaign, Urbana, IL.

Holub, C. J. (2009), Interaction of variable axial load and shear effects in RC bridges, Ph.D. disseration, Department of Civil and Environmental Engineering, University of Illinois, Urbana, IL.

Kwon, O. S. and Elnashai, A. S. (2007), Probabilistic seismic assessment of structures, foundation and soil interacting systems, NSEL Report No. NSEL-005, University of Illinois at Urbana-Champaign, Urbana, IL.

Kwon, O. S., Nakata, M., Park, K. S., Elnashai, A. S., Spencer, B. F., Jr. (2007), User manual and examples for UI-SIMCOR v.26, Deparmtne of Civil and Environmental Engineering, University of Illinois at Urbana-Champaign, Urbana, IL.

MATLAB (2012), The Math Works, Inc., Natick, Massachusetts.

McKenna, F. and Fenves, G. L. (2001), The OpenSees command language manual, version 1.2, Pacific Earthquake Engineering Research Center, University of California at Berkeley, Berkeley, CA.

Moustafa, K.F, Sanders, D., Saiid, M.S., and El-Azazy, S. (2011), "Seismic Performance of Reinforced Concrete Bridge Bents," *ACI Structural Journal*, 108(1), 23-33.

Nakata, N., Spencer, B. F., Jr., and Elnashai, A. S. (2007), Mutli-dimensional mixed-mode hybrid simulation control and applications, NSEL Report No. NSEL-005, University of Illinois at Urbana-Champaign, Urbana, IL.

Nikon Metrology NV (2012), Leuven. Http://us.nikonmetrology.com/home.php

Prakash, S., Belarbi, A., and You, Y. M. (2010), "Seismic performance of circular RC columns subjected to axial force, bending, and torsion with low and moderate shear," *Engineering Structures*, 32(1), 46-59.

Shing, P. B. and Mahin, S. A. (1987), "Cumulative experimental errors in pseudodynamic test," *Earthquake Engineering and Structural Dynamics*, 15, 409-424.

Shing, P. B. and Mahin, S. A. (1990), "Experimental error effects in pseudodynamic testing," *ASCE Journal of Engineering Mechanics*, 116(4), 805-821.

Shore Western Manufacturing (2011), Monrovia, CA. http://www./shorewestern.com/

Silva, P. F., Megally, S., and Seible, F. (2009), "Seismic performance of sacrificial exterior shear keys in bridge abutments." *Earthquake Spectra*, 25(3), 643-664.

Xu, S. Y. and Zhang, J. (2012), "Axial-shear-flexure interaction hysteretic model for RC bridge columns under combined actions," *Engineering Structures*, 34(1), 548-563.

10CUEE CONFERENCE PROCEEDINGS
10th International Conference on Urban Earthquake Engineering
March 1-2, 2013, Tokyo Institute of Technology, Tokyo, Japan

NUMERICAL SEISMIC FRAGILITY OF FIRE SPRINKLER PIPING SYSTEMS WITH THREADED JOINTS

Siavash Soroushian[1] , Manos Maragakis[2], Arash E. Zaghi[3], Alicia Echevarria[4], Yuan Tian[5] and Andre Filiatrault[6]

1) PhD Candidate, Civil and Environmental Engineering, University of Nevada, Reno, USA
2) Dean, and Professor, Civil and Environmental Engineering, University of Nevada, Reno, USA
3) Assistant Professor, Department of Civil and Environmental Engineering, University of Connecticut, Storrs, USA
4) Graduate Student, Department of Civil and Environmental Engineering, University of Connecticut, Storrs, USA
5) PhD Candidate, Civil, Structural and Environmental Engineering, State University of New York at Buffalo, USA
6) Professor, Civil, Structural and Environmental Engineering, State University of New York at Buffalo, USA
ssorooshian@unr.edu; maragaki@unr.edu; zaghi@engr.uconn.edu; aechevarria5@live.com; ytian3@buffalo.edu; af36@buffalo.edu;

Abstract: Numerical modeling method was developed for fire sprinkler piping systems and used to generate seismic fragility parameters. The model accounts for inelastic response of threaded joints, braces, hangers, and wire restrainers. The model incorporates a nonlinear hinge model developed for threaded tee joints based on experiments conducted at the University at Buffalo. The hinge model may be adapted to different pipe diameters. This modeling technique was used to simulate the seismic response of the fire sprinkler system of the University of California, San Francisco (UCSF) Hospital using a suite of ninety-six artificially generated tri-axial acceleration. Component fragility parameters were obtained for wire restrainers, pipe hangers, and threaded pipe joints. Three system damage states were defined and a joint probabilistic seismic demand model was utilized to obtain system-level fragility parameters.

1. INTRODUCTION

In recent major earthquakes such as the 2010 Chile earthquake, most of the hospitals in the central south region of Chile were subjected to strong ground motion. A total of sixteen hospitals were inspected after the earthquake (Miranda et al., 2012). Four hospitals were closed due to the loss of functionality, and approximately 75% of function was lost in the remaining twelve (Gupta et al., 2011). The damages to the piping system were mainly associated with pipe hanger failures, failed sprinkler heads due to contact with ceilings elements, leakage of threaded joints, etc. After the great 2011 Tohoku Pacific Earthquake, many structures were inspected. In that earthquake, damage to fire protection systems and plumbing accounted for 10% and 27% of the entire cost of equipment damage, respectively. The damage to the piping adds up to approximately 50% of the total cost with the damage to sprinkler heads second to that. During this earthquake 42% of the damaged piping systems also showed signs of water leakage (Mizutani et al., 2012).

Several experiments have been conducted on piping systems during the last 20 years such as bending tests on sixteen simply supported pipe specimens (Antaki and Guzy, 1998), dynamic tests of twenty pipe specimens (Antaki and Guzy, 1998), shaking table experiments on four hospital piping assemblies (Zaghi et al, 2012), monotonic and cyclic tests on forty-eight pipe tee joints (Tian et. al, 2012a), dynamic analyses of full-scale piping systems (Soroushian et at, 2012a), and dynamic tests of six piping subsystem configurations (Tian,2012).

However, the limited quantitative data collected from past earthquakes and the limitations of system-level experimental studies necessitates reliable system-level numerical tools to allow for a better understanding of the seismic response of piping systems. Also, piping fragility information are yet to be generated to assist the technical community in assessing, managing, and reducing seismic risks.

After the validation of a numerical model for piping systems, a comprehensive fire sprinkler system layout incorporating a variety of commonly used sprinkler piping components was adopted from the medical center building of the University of California, San Francisco (UCSF). Using the OpenSees software (Mazzoni, 2007), the entire three-dimensional piping model was numerical simulated by incorporating approximately nine-hundred inelastic elements for threaded joints, main distribution lines, pipe branches, braces, hangers, wire restrainers, and sprinkler heads. A real-time element removal algorithm was utilized to capture the progression of damage. The numerical model was subjected to a suite of ninety-six artificial tri-axial acceleration histories. The horizontal components of motion

were generated in accordance with the ICC-AC156: Acceptance Criteria for Seismic Certification by Shake-Table Testing of Nonstructural Components acceleration spectra (ICC, 2010), and the ASCE/SEI 7-05 (ASCE, 2005) vertical acceleration spectra were used for generation of the vertical acceleration components.

2. PIPING TEE JOINT TESTS AT THE UNIVERSITY AT BUFFALO

A total of forty-eight tee joints comprised of four different materials, diameters, and joint types were tested at the University at Buffalo NEES site. A diverse database was developed on the cyclic response and damage states of tee joints; however, the main focus of this study was the results of the black iron threaded joint for pipe diameters of 3/4 in., 1 in., 2 in., 4 in., and 6 in. comprising twenty experiments.

The test setup was composed of two pipe runs with a length of L on each side of the tee joint specimen. One end of each segment of the pipe run was attached to the tee joint and the other end was supported using a moment free connection connected to a load cell. One end of a perpendicular pipe segment was attached to the tee joint, and the other end was connected to an actuator which applied a mid-span point load (Figure 1). To capture the leakage during the test, all of the specimens were pressurized with water at 40 psi. The moment demand of each tee joint was calculated by multiplying the force measured by the shear load cells by the distance L. The cord rotation was measured using linear potentiometers attached to each side of the tee joint. Additional details of the test setup are presented in Tian et al. (2012a).

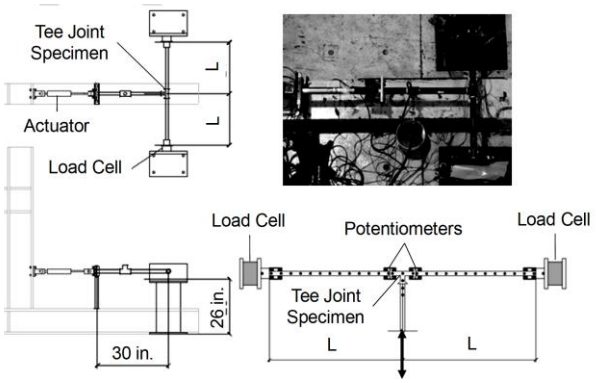


Figure 1 Tee Joint Experimental Set-Up (Tian et al. 2012a).

3. DEVELOPMENT OF AN NUMERICAL MODEL FOR PIPING TEE-JOINTS

The experimental data for tee joints was utilized by the authors to develop an adaptable nonlinear hinge model in OpensSees (Mazzoni, 2007) for the threaded joint of different pipe diameters. The "Pinching4" uniaxial material along with a "zeroLength" element were used to simulate the moment-rotation response of a threaded tee joint connecting two piping nodes (Mazzoni, 2007). The "Pinching4" material enabled the simulation of pinched load-deflection responses accounting for degradations under cyclic loading for different pipe diameters. This material requires the definition of 39 parameters (Figure 2) including the shape of the backbone curve, pinching parameters, damage parameters, etc. A detailed description of these parameters can be found in OpenSees (2012).

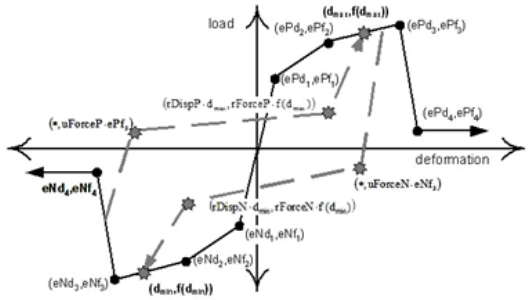


Figure 2 Pinching4 Material Properties (OpenSees, 2012)

3.1 Validation of Numerical Model with Experimental Data for Tee Joint Components

The material model was calibrated using the tee joint moment-rotation hysteresis of all pipe diameters. The moment-rotation hysteresis curve, the value of cumulative hysteresis energy, and moment histories of each pipe were used in the calibration process. The support rotation history was imputed to the model for each of the three varying diameter experiments. Due to the malfunction of some of the potentiometers, the moment-rotation data was not available on both sides of the tee joint for some of the experiments, but at least three moment-rotation data sets were available for each pipe diameter. Figure 3 shows the aforementioned three characteristics of the calibrated model for one of the 3/4" tee joints. The shape of the curve, dissipated energy, and

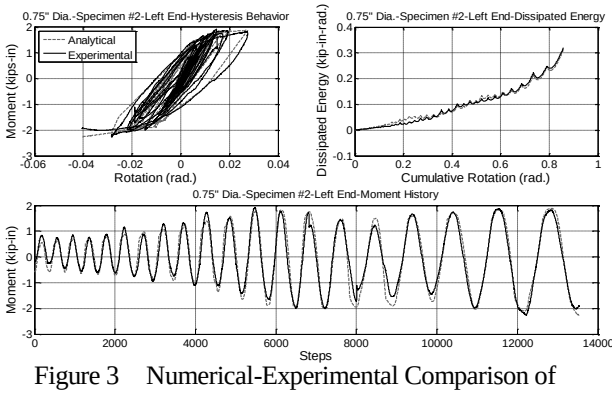


Figure 3 Numerical-Experimental Comparison of Second 3/4" Specimen on Left Side of Tee Joint

the moment magnitudes were considered simultaneously in the calibration process to achieve the best numerical model. After performing a sensitivity analysis on the material parameters, 10 parameters out of 39 parameters were assigned a fixed value independent of the pipe diameter.

The OpenSees "Pinching4" material parameters *gK1* to *gK4*, and *gKLim*, all of which define the unloading stiffness degradation characteristic of the material, were set to the same value as *gK* (Mazzoni, 2007). The "cyclic damage" was used to determine cyclic stiffness and strength degradation, and in all the cases, the *gD* and *gF* material parameters were assumed to be zero. The rest of parameters were used to fit the numerical data to the experimental data. Figure 4 illustrates comparisons of sample numerical and experimental data for four different pipe diameters. Each material parameter has a consistent relationship with the pipe diameter. This allows for the determination of these parameters for other pipe diameters through interpolation.

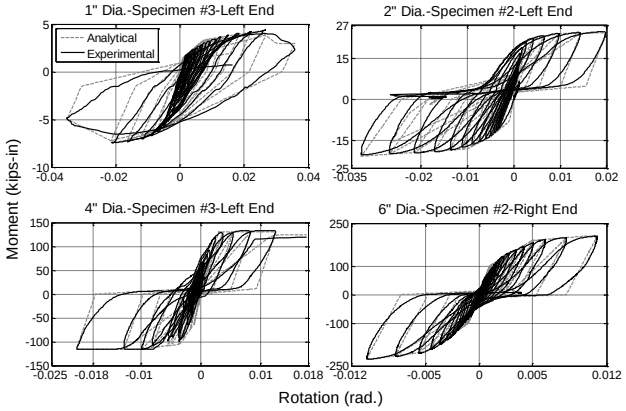


Figure 4 Sample Numerical-Experimental Hysteresis Comparisons of Different Pipe Diameters

Throughout the calibration process, a total of twenty sets of twenty-nine parameters for the "Pinching4" material were optimized based on all available experimental data. Although the results for each set of experiments were quite similar, there were minor discrepancies between the material parameters for the individual experiments of each set. For the future numerical studies of the sprinkler piping systems, one suite of material parameters was selected as the generic parameters for each pipe diameter, called generic model hereafter. To develop this generic model the following assumption were made. 1) A symmetric moment-rotation hysteresis behavior was used, 2) the first point of the backbone curve, ePd_1 (Figure 2), was defined as 0.001 rad. This enabled the use of the average experimental moment values corresponding to 0.001 rad., 3) the rest of the three nonlinear rotation points of the backbone curve of the generic model, ePd_2, ePd_3, ePd_4 (Figure 2), were set to 0.005, 0.01, and 0.023 rad., respectively based on the calibrated backbone curve parameters of each set, 4) a linear interpolation was used to find the moment corresponding to the above mentioned rotations where the moment values at the calibrated backbone curves are unavailable. The average of these moment values for each set were used for ePf_2, ePf_3, and ePf_4 (Figure 2) to define the backbone curve, 5) the average calibrated values were used for the rest of the parameters needed to define the generic hysteresis response. Figure 5 shows the comparison of the generic model with sample experimental data from each set. Table 1 also shows the generic model parameters obtained using the previously mentioned assumptions.

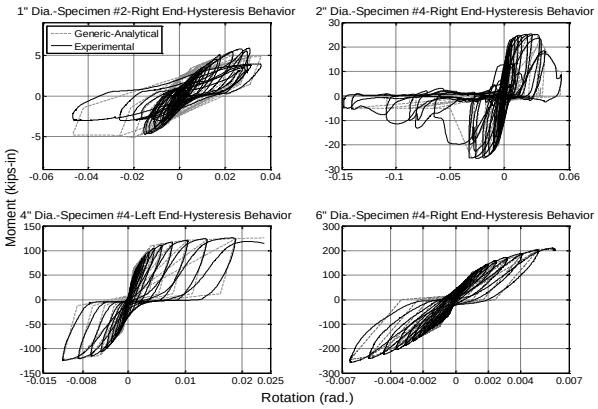


Figure 5 Sample Generic Numerical-Experimental Hysteresis Comparison of Different Pipe Diameters

Based on pipe location and required water pressure, a wide range of pipe diameters is commonly used in sprinkler piping layouts. The test matrix of the University at Buffalo did not include all the pipe diameters that are typically found in a system. Thus, a procedure is proposed to fill this gap in the experimental data and enable estimation of the parameters of the generic hysteresis model for the missing pipe diameters. This methodology is explained in the following steps. First, the parameters of the generic models based on the experimental data were plotted against the pipe

Table1 Generic Pinching4 Calculated Parameters

Pipe Name	e(P-N)f1	e(P-N)f2	e(P-N)f3	e(P-N)f4	rDisp(P-N)	rForce(P-N)	uForce(P-N)	gK(P-N)
TEST SETS								
3/4"	0.47	1.19	2.00	2.36	0.07	0.62	-0.27	0.50
1"	1.50	3.37	4.07	5.08	0.03	0.49	-0.30	0.53
2"	9.75	20.18	22.81	23.43	-0.04	0.15	-0.03	0.58
4"	63.83	114.03	121.51	125.17	0.04	0.08	-0.10	0.34
6"	105.00	224.38	254.38	258.13	0.13	0.07	0.00	0.25
PROPOSED COMPONENTS								
1.25"	1.04	8.24	8.83	9.66	-0.003	0.33	-0.17	0.56
1.5"	2.96	14.30	14.70	15.78	-0.02	0.27	-0.12	0.58
2.5"	20.91	44.54	46.10	48.07	-0.04	0.15	-0.03	0.54
3"	34.15	63.27	66.55	68.91	-0.02	0.12	-0.04	0.48
3.5"	48.78	84.41	90.17	92.88	0.007	0.10	-0.06	0.41
5"	90.24	162.29	180.03	183.59	0.09	0.07	-0.11	0.23

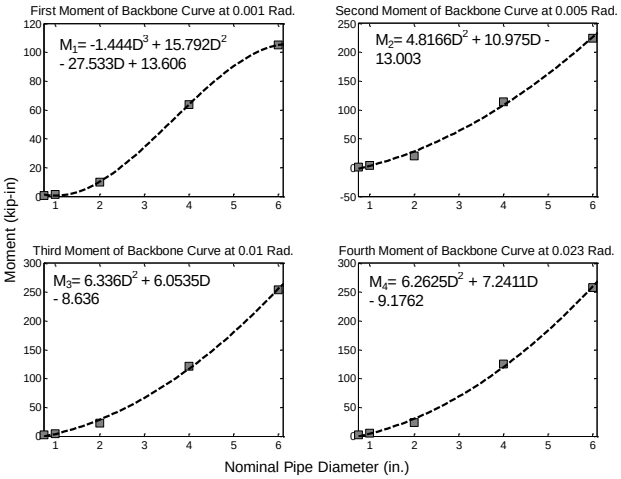


Figure 6 Sample Fitted Curves on Backbone Curve Parameters of the Generic Model

diameter. The values of the moments corresponding to 0.001, 0.005, 0.01, and 0.023 rad. can be plotted against the pipe diameter since these rotations were kept constant for all diameters. Then, the best polynomial curve was fit to the

data for each parameter. Using these algebraic functions of pipe diameter, the modeling parameters were obtained for those pipe diameters that were not tested at the University at Buffalo. Table 1 shows the values of the modeling parameters obtained from this methodology. Figure 6 shows the trends of the modeling parameters for the "Pinching4" material (OpenSees, 2012) with respect to the pipe diameter.

4. FRAGILITY STUDIES

The fragility curves presented herein were obtained from a comprehensive three-dimensional nonlinear model of a typical hospital sprinkler piping system.

4.1 Specifications of Hospital Fire Sprinkler Piping System

The piping system modeled in this study was adopted from the sprinkler system of the University of California (UCSF) Medical Center Building. In this study, a slight modification was implemented on the original system by redesigning the hangers and braces to meet the minimum spacing requirement of NFPA 13: Standard for the Installation of Sprinkler Systems (NFPA, 2011). Also the bracing system was changed from cable bracing to solid sway bracing which is more common in construction. The final system incorporates a variety of commonly used components such as mains runs and branch lines of various diameters, hangers, seismic braces, wire restraints, tee joints, elbow joints, and sprinkler drops and heads. It also contains a sufficiently large quantity of each component which enables a better statistical evaluation of the seismic performance of each component within the system.

The piping system shown in Figure 7 covers an area of approximately 17000 sf. It is 250 ft long and 176 ft wide and has more than 900 threaded joints (649 1-in., 185 1.25-in., 28 1.5-in., 7 2-in., 41 2.5-in, 34 3-in, and 29 4-in diameter joints). A plenum height (the distance between the supporting structural floor and the ceiling system) of 4 ft is used. The piping system is suspended 2.5 ft below the supporting floor, thus the sprinkler drops are1.5-ft long. The sprinkler piping system is connected and braced to the supporting floor with 1-in diameter longitudinal and lateral pipe sway braces (only on main runs), 3/8-in all-threaded hangers, and 12-gauge wire restraints. The sway braces and wire restraints are oriented at 45 degree angles with respect to the plane of the supporting floor.

The piping layout was composed of 4 major areas. Area 1 is composed of main run pipes with total length of 154 ft with diameters varying from 2.5- to 4-in. These pipes feed 23 1.25-in. and 1-in diameter branch lines and 61 sprinkler heads. In Area 2, main run pipes are 97 ft long with 4-in diameter. This pipe supplies the water for 4 1.25-in. and 1-in. branch lines and 15 sprinkler heads. Area 3 integrates 97 ft of 3- and 2.5-in. diameter main runs with 15 branch lines ranging in diameter from 1.5- to 1-in., and a total of 44 sprinkler heads. Area 4 consists of 82 ft of main distribution line varying in diameter from 4- to 2-in. The main distribution line feeds 16 1.5- to 1-in. branch lines. In this area, the main line and branch line supply 47 sprinkler heads.

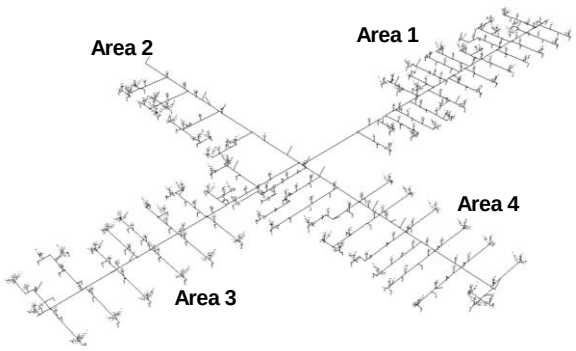


Figure 7 3-D View of UCSF Medical Center Sprinkler Piping System

4.2 Definition of the Numerical Model

The model of the introduced piping subsystem was developed in OpenSees. The pipes including the main runs, branch lines, and sprinkler drops were modeled with "Force-Based Beam-Column" (Mazzoni, 2007) elements with elastic gross section properties of the pipes. The threaded fittings of the branch lines and drop pipes were modeled using one "zeroLength" element on the either end of the pipes. These elements were defined using the nonlinear "Pinching4" material for the rotational degrees of freedom (DOFs) based on the specified characteristics of Table 1, while an elastic material with properties of the pipe cross section were used for the other DOFs. The hangers were modeled using "Force-Based Beam-Column" elements with a fiber-section consisting of the Giuffre-Menegotto-Pinto steel material (CEB, 1996), which is implemented in OpenSess as "Steel02" material. A modulus of elasticity of 29,000 ksi, yield strength of 85 ksi (Goodwin et al., 2007), and hardening slope ratio of 1% were assigned to the hangers. These hangers had pin connection to the pipes. The wire restrainers were modeled using pinned "truss" elements along with a tension only "Elastic-Perfectly Plastic (EPP) Gap" material with the modulus of elasticity of 29,000 ksi and tensile strength of 80 ksi (USG, 2010). The rigid seismic braces were modeled with "Force-Based Beam-Column" elements using elastic section properties of the 1-in. pipe. The connection of the seismic braces was assumed to be rigid at both ends. The schematic of the elements and materials are presented in Figure 8. The mass of the piping system was determined using the wet weight of the pipes. An additional mass of 0.5 lb was used for each sprinkler head. Mass and weight of the system were concentrated at the nodal points. A Rayleigh damping was used for the analysis and 3% damping was assigned to the first and the third modes.

A real time element removal algorithm was incorporated in the analyses to capture the progression of

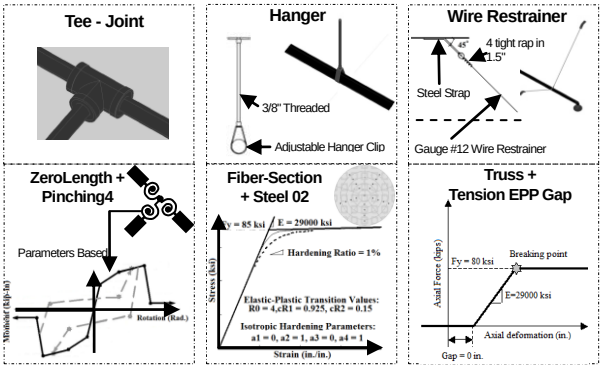


Figure 8 Schematic of the Numerical Models for Main Components

damage to the piping system during seismic excitations. The element removal algorithm enables the model to redistribute the forces after failure occurs in an element using the "remove element" command in OpenSees software (Mazzoni, 2007). This algorithm was set to remove the wire restrainers after reaching their rupture capacity, 0.4 kips from USG (2010). Due to the large spectrum of hanger clip details, the failure force of the pipe hangers was calculated based on the minimum NFPA 13 (NFPA13, 2011) requirements. NFPA 13 mandates that the hangers shall be designed to support five times the weight of the water-filled pipe plus 250 lb at each point of support. The hanger axial forces were calculated after the dead load analysis was concluded. During the response history analyses the program triggered the "remove element" command when the axial force of a hanger reached the five times the recorded axial force plus 250 lb. The first five vibration modes of the model were obtained as 1.22, 1.2, 1.19, 1.17, and 1.16 sec, respectively.

4.3 Generation of the Input Motions

The seismic response of the piping system is evaluated using a suite of 96 synthetic triaxial acceleration which represent floor motions. Input motions were developed by Soroushian et. al, (2012b) using the spectrum-matching procedure. The suites were generated for uniform distribution of SDS values varying from 0.1 g to 3 g and five different height ratios of 0, 0.25, 0.5, 0.75, and 1.0 considering site classes D, E, and F. Acceleration spectra were produced for the horizontal directions following ICC-AC156 (ICC, 2010) parameters while the vertical acceleration response spectrum introduced in ASCE/SEI 7-05 New Chapter 23 (ASCE, 2005) was adopted for the vertical motions.

The statistical distribution of the peak floor accelerations and the median 16th, 84th, and 97th percentile of the 5% damped elastic spectrum for the horizontal and vertical components are presented in Figure 9. The nonlinear numerical model of the UCSF piping system was subjected to the described 96 sets of triaxial motions. The maximum responses of the piping system, including joint rotations, hanger and brace forces, and nodal displacements were recorded.

4.4 Fragility Analysis

The seismic vulnerability of a structural or

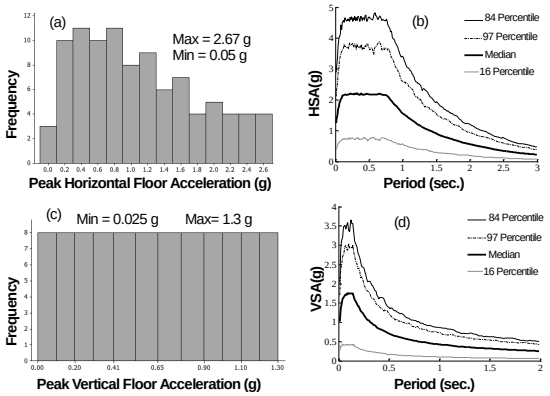


Figure 9 (a) Distribution of Peak Horizontal Floor Acceleration , (b) Horizontal Spectral Floor Acceleration, (c) Distribution of Peak Vertical Floor Acceleration, (d) Vertical Spectral Floor Acceleration (Soroushian et. al., 2012b)

nonstructural component can be graphically represented through the generation of numerical fragility curves. Fragility curves are probabilistic representations of exceeding a capacity or limit state in terms of intensity measures (*IMs*), peak floor acceleration in this case, and engineering demand parameters (*EDPs*) as a measure of piping response. The relationship of the demand, *EDPs*, and floor acceleration, *IMs*, can be approximately represented with the standard normal cumulative distribution function shown in Equation (1) (Nielson and DesRoches, 2007):

$$P(EDP \geq C \mid IM) = \Phi\left(\frac{\ln(S_d / S_c)}{\sqrt{\beta_{EDP|IM}^{\ 2} + \beta_C^{\ 2}}}\right) \qquad (1)$$

Where S_d is the median of the demand estimate as a function of *IM*, S_c is the median estimate of the capacity, $\beta_{d|IM}$ is the logarithmic standard deviation of the demand with respect to the intensity measure, β_c is the logarithmic standard deviation of component capacities, and $\Phi[\cdot]$ is standard normal cumulative distribution.

4.5 Capacity Parameters and Component Demands

The capacities of the pipe hangers and wire restrainers were determined from the median percentage of failed hangers or wire restrainers, θ_{break} , and the logarithmic standard deviation of the rotational capacity, β_C. A constant value of 0.4 was assigned to β_C which is the most frequently used value for this parameter in nonstructural components (ATC 58, 2009). Three damage states (*DS*) were defined for the percentage of failed hangers and wire restrainers. *DS1* represents 5% loss of hangers and 10% loss of restrainers, *DS2* represents 10% loss hangers and 20% loss of restrainers, and *DS3* represents 15% loss of hangers and 30% loss of restrainers. Values of θ_{break} and β_C for the previously defined damage states are presented in Table 2.

The capacity of each pipe diameter was determined from the median rotational threshold corresponding to the first leakage of the joint, θ_{leak} . For the pipe diameters that were tested at the University at Buffalo, θ_{leak} and β_C were borrowed from the work done by Tian et al. (2012a) and are

presented in Table 2. For the rest of pipes, θ_{leak} (rad.) was calculated using Equation (2) (Tian et al., 2012a).

$$\theta_{leak} = \frac{2\bar{s}}{D_0} \quad (2)$$

In this equation $\bar{s}$ is a constant value of 0.019in. for threaded pipe joints and D_0 (in.) is the outside pipe diameter. Table 2 shows that the values of θ_{leak} calculated using Equation (2) correspond very well with the experimentally determined values; therefore, this equation provides a good approximation for the median rotational capacity at first leakage for those pipe diameters that were not previously tested. Also for each pipe diameter in this group, values of β_C were calculated by linear interpolation between two adjacent previously tested diameters.

Table 2 Damage States of Piping Components

Pipe Name	Experiment		Eq. (2)	Interpolation
	θ_{leak}	β_c	θ_{leak}	β_c
TEST SETS				
3/4" Pipe	0.040	0.206	0.037	NA
1" Pipe	0.031	0.146	0.029	NA
2" Pipe	0.014	0.094	0.016	NA
4" Pipe	0.010	0.216	0.009	NA
6" Pipe	0.006	0.204	0.006	NA
PROPOSED COMPONENTS				
1.25" Pipe	NA	NA	0.023	0.133
1.5" Pipe	NA	NA	0.020	0.120
2.5" Pipe	NA	NA	0.013	0.125
3" Pipe	NA	NA	0.011	0.155
3.5" Pipe	NA	NA	0.010	0.186
5" Pipe	NA	NA	0.007	0.210
Component Name	**DS1**	**DS2**	**DS3**	
	θ_{break}	θ_{break}	θ_{break}	β_c
Hangers	5%	10%	15%	0.4
Restrainers	10%	20%	30%	0.4

The response of a piping system can significantly vary due to its geometry. As an example, for the same pipe section, the rotational demands on long (more than 2-ft long) armovers are generally larger than on straight drops (Soroushian et al., 2012a). Therefore, it is necessary to categorize the *EDPs* to better represent the physical damage. To do so, *EDPs* of branch line pipes were categorized based on the pipe diameter and the type of branch line (with or without armovers).

The damage parameters of the piping system were defined as: 1) percentage of failed wire restrainers, 2) percentage of broken hangers, 3) the maximum rotation at the tee armovers and elbow armovers, 4) the maximum rotation at critical joints of the branch lines, and 5) rotation of fittings on the main runs.

Component demands were then considered with respect to the *PFA* of the floor motion that generated the demand. A regression analysis of this data is used to estimate the parameters (S_d and $\beta_{d|IM}$) of the probabilistic seismic demand models using Equation (3, 4) (Cornell et. al., 2002):

$$S_d = aIM^b \quad (3)$$

$$\beta_{d|IM} \cong \sqrt{\frac{\sum_{i=1}^{N}\left(\ln(d_i - \ln(aIM^b))^2\right)}{N-2}} \quad (4)$$

In Equations (3) and (4), S_d and $\beta_{d|IM}$ are the median estimate of the demand and the logarithmic standard deviation of the demand, respectively. The parameter d_i is the peak demand and corresponds to i^{th} floor motion (out of total N motions).

4.6 Component Fragility Curves

After calculating estimated demand and capacity parameters, the fragility curves of different piping components can be obtained from Equation (1). Figure 10 shows the piping component fragility curves using this equation.

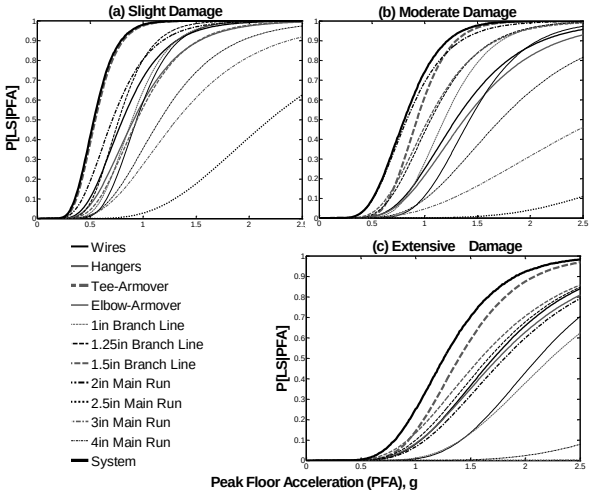


Figure 10 Component fragility curves for piping system

The curves show that the response of tee-armovers is the most dominant component in the vulnerability of piping systems in nearly all damage states. The dominancy of larger diameter branch line pipes (1.5 and 1.25 in.) on overall vulnerability of piping system increases in higher limit states. In higher limit states the pipe hangers start to yield, and more wire restrainers fail. As a result, the branch lines behave like cantilevers, and the demand on these pipe diameters, which usually have only connections to the main

Table 3 Medians and Dispersion Values for Piping Component Fragilities States

Component Name	Slight		Moderate		Extensive	
	Median PFA(g)	Dispersion	Median PFA(g)	Dispersion	Median PFA(g)	Dispersion
ARMOVERS						
Armover-Tee	0.55	0.38	0.93	0.42	1.40	0.53
Armover-Elbow	0.94	0.44	1.43	0.44	2.11	0.45
BRANCH LINES						
1" Pipe	0.89	0.48	1.19	0.49	2.23	0.55
1.25" Pipe	0.77	0.49	1.06	0.54	1.67	0.56
1.5" Pipe	0.94	0.63	1.04	0.62	1.59	0.61
MAIN RUNS						
2" Pipe	0.71	0.96	0.84	0.86	0.94	0.67
2.5" Pipe	2.19	0.61	4.25	0.53	NA*	0.38
3" Pipe	1.32	0.87	2.65	0.88	NA*	0.50
4" Pipe	1.16	0.80	1.73	0.75	4.38	0.55
SUPPORTS						
Hangers	0.91	0.68	1.38	0.68	1.75	0.68
Restrainers	0.81	0.56	1.30	0.56	1.71	0.56

* ESTIMATED MEDIAN VALUES ARE MUCH LARGER THAN CAN BE APPROPRIATELY EXTRAPOLATED FROM REGRESSION ANALYSES

runs, increases. Thus, the general trend is that the demand on the largest and smallest main runs (4in and 2in) is higher. Because these size of pipes are mainly located at the beginning and end of branch lines combined with the existence of solid sway braces, the bending demand at these locations is generally higher than at other locations. Table 3 shows the median and dispersion values for the seismic fragility curves of piping system components.

4.7 System Level Fragility Studies

The assessment of seismic vulnerability for the entire piping system must be made by combining the effects of the various system components. The probability that the piping reaches or goes beyond a particular limit state ($Fail_{system}$) is the union of the probabilities that each of the components will reach that same limit state ($Fail_{component-i}$), as shown in Equation (5) (Nielson and DesRoches, 2007a) :

$$P\left[Fail_{System}\right] = \bigcup_{i=1}^{n} P\left[Fail_{Component-i}\right] \quad (5)$$

4.8 System Limit States

A limit state is a metric that describes the post-earthquake functionality or the level of damage experienced by a component or system subjected to a certain intensity measure. While only a single limit state may exist for certain components within a piping system, multiple limit states can be described for the entire system based on the percentages of component failures. Only one component-level limit state is considered for each of the three components used to develop the piping system fragility curves. These component levels are described as: the break point of the pipe hangers, the break point of the wire restrainers, and leaking threshold at the pipe joints. The leakage limit state, however, is presented as the percentage of the number of the pipe joints for which rotations exceed the leakage threshold. Three system-level limit states corresponding to three increasing levels of system damage were defined to characterize the seismic response of the entire piping system. These limit states were determined based on the percentage of failed hangers and wire restrainers, and the probability that the rotational capacity of the pipe joints would exceed leaking threshold. Brief definitions of each system-level limit state are provided in here.

LIMIT STATE 1: Slight Damage

Limit state 1 (*LS1*) corresponds to loss of 10% of the wire restrainers, loss of 5% if the pipe hangers, and 3% of the pipe joints exceed their leakage rotational capacity.

LIMIT STATE 2: Moderate Damage

Limit state 2 (*LS2*) accounts for loss of 20% of the wire restrainers, 10% of the pipe hangers, and leaked pipe joints exceed 16% of their total number.

LIMIT STATE 3: Extensive Damage

Limit state 3 (*LS3*) is based on more than loss of 30% of the wire restrainers, more than 15% loss of pipe hangers, and 50% leaked pipe joints.

4.9 Joint Probabilistic Seismic Demand Model

A joint probabilistic seismic demand model (*JPSDM*) was used in this study to estimate the piping system level fragility. A *JPSDM* is developed by assessing the demands placed on individual components (marginal distribution) through regression analysis. A covariance matrix is calculated by estimating the correlation coefficients between the demands placed on the various components. Using the capacity parameters and the *JPSDM*, Equation (5) can be evaluated using a Monte Carlo simulation. A Monte Carlo simulation is used to compare some level of correlation realizations between component demands using the *JPSDM* defined by a conditional joint normal distribution in the transformed space and statistically independent component capacities to calculate the probability of system failure. This procedure is applied for each damage state for various levels of IMs.

As previously stated, armovers contribute to the vulnerability of the piping system more than the other components. A simple approach was used to estimate the relative change in the median values of the fragility curves. The median values of the system fragility curves were calculated without considering the armover component demands in the *JPSDMs*. Then the armover component demands were added to the *JPSDMs*, and the percent change in the median value of system fragility curves with and without considering the armovers was calculated. A positive change indicates a less vulnerable piping system. Also the use of over braced main runs may reduce the vulnerability of main runs. To compare the difference between all of the optional configurations, 4 different system level fragility curves were developed, namely, "All"

Table 4 Medians and Dispersions for 4 Different Piping System

System Name	Slight			Moderate			Extensive		
	Median λ	Difference (%)	Dispersion ζ	Median λ	Difference (%)	Dispersion ζ	Median λ	Difference (%)	Dispersion ζ
ALL	0.53	NA	0.31	0.81	NA	0.33	1.26	NA	0.34
w/o Armovers	0.64	20.23	0.35	0.82	1.36	0.37	1.32	5.02	0.36
w/o Main Run	0.54	0.54	0.31	0.88	8.65	0.30	1.27	1.13	0.34
w/o Main Run & Armovers	0.68	27.56	0.32	0.95	17.48	0.34	1.34	6.94	0.37

(considering all the components), "w/o Armovers" (Removing armover demands from *JPSDMs*), "w/o main runs" (Removing main run demands from JPSDMs), and "w/o main runs & Armovers " (Removing both main run and armover demand from *JPSDMs*). Figure 11 shows the piping system fragility curves for the four different cases. Table 4 presents the lognormal parameters (median, λ, and logarithmic standard deviation or dispersion, ζ) that characterize the piping system fragility from regression analysis based on all 4 different cases.

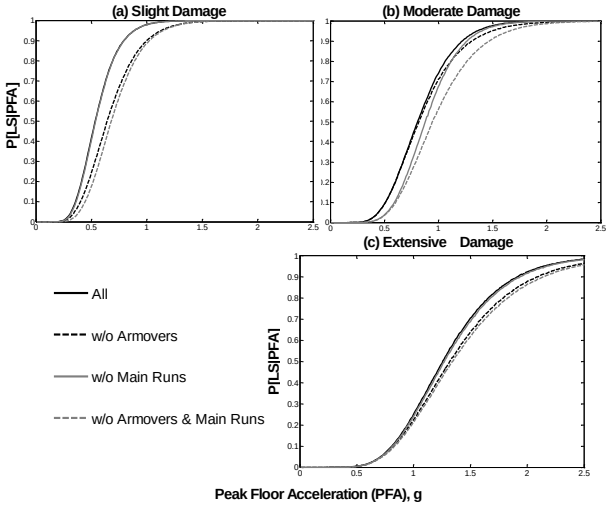


Figure11 System Fragility Curves for Different Piping System Condition

Table 4 shows that armover drops can increase the chance of reaching the slight damage state (which corresponds to the first leaking of the piping system) by 20%. In the other damage states, leaking is not only limited to the armovers. Therefore the probability increased by only 1.4% and 5% for the moderate and extensive damage states, respectively. Using other types of joints or increasing the number of piping braces (to force the main run to move like rigid body instead of bending) will improve the moderate damage state probability by 9%. In the slight damage state the contribution of main run leaking is negligible compare to the contribution from the armovers, so the probability improvement is only 0.5%. When considering progressive damage during an earthquake, the first leaking occurs during the low intensity portion of the ground motion. The presence of the generated hinges created during these lower intensities decreases the demand the rest of the joints experience at higher intensities. As a result, the probability difference at extensive state level is only 1%. In case 4 which is related to the piping system without long armovers and improved main runs, the reduction in probability of the slight, moderate, and extensive limit states is 27%, 18%, and 7%, respectively. Figure 19 shows the piping system fragility curves for the four different cases.

5. SUMMARY AND CONCLUSIONS

In this study a series of nonlinear threaded joint hinges were developed for various pipe diameters based on a previous component experiments. An numerical model was developed and validated using subsystem experimental data. Following the validation of the numerical model, a full fire sprinkler system layout incorporating a variety of common sprinkler piping systems was adopted from the University of California, San Francisco (UCSF) medical center building and was numerically simulated in OpenSees. Seismic fragility curves were generated using this comprehensive three-dimensional model including approximately 900 inelastic members modeling threaded joints, main distribution lines, pipe branches, braces, hangers, wire restrainers, and sprinkler heads subjected to a suite of artificial ground motions. A real time element removal algorithm was incorporated in the analyses to capture the progressive damage of the piping system during seismic excitation. The conclusions made are listed below:

- Among the component fragility curves, long armovers with tee joint connections to the branch lines were the most vulnerable components of the piping system, while long armovers with elbow attachment to the branch lines experienced less damage compared to the other branch line components.
- The dominancy of larger diameter branch line pipes (1.5in and 1.25in.) on overall vulnerability of the piping system increases at higher limit states. This increase can be attributed to the progressive damage during an earthquake. At higher limit states the pipe hangers start to yield, more wire restrainers fail, and as a result, the branch lines will behave as cantilevers. Therefore the demand on these pipe diameters which mainly have connections to main runs, will increase.
- The smallest and largest main run pipe diameters experienced more damage compared to the other pipe diameters. The largest and smallest pipe diameters are generally located at the beginning and end of main run line, respectively. In these locations the rotational demand is higher because of the sway braces required by code.
- The system fragility curves show that the existence of armover drops can increase the chance of reaching the slight damage state (which corresponds to first leaking of piping system) by 20%. At the other damage state levels, the leaking is not only limited to the armovers, therefore, the increase in probability of reaching the moderate and extensive damage is 1.4% and 5%, respectively.
- Using other types of joints (like groove fitting) or increasing the number of piping braces on main runs (to force the main run move like rigid body instead of bending) will decrease the probability of reaching the moderate damage state by 9%.
- When considering progressive damage during an earthquake, the first leaking occurs on a main run pipe during a smaller intensity portion of the motion. The

generated hinges occurring at low intensity levels reduce the demands on the rest of the joints at higher intensity levels. As a result, the probability difference at the extensive damage level is only 1%.

- In a large or poorly detailed piping layout, the piping system might experience leaking at very few locations, but it is highly unlikely that a smaller piping system will reach this rotational demand.
- Piping systems without long armovers and main runs having improved joints or a larger number of braces see reductions in probability of 27%, 18%, and 7% for the slight, moderate, and extensive damage states, respectively.

Acknowledgements:

This material is based upon work supported by the National Science Foundation under Grant No. 0721399. This GC project to study the seismic response of nonstructural systems is under the direction of M. Maragakis from the University of Nevada, Reno and Co-PIs: T. Hutchinson (UCSD), A. Filiatrault (UB), S. French (G. Tech), and B. Reitherman (CUREE). Any opinions, findings, conclusions or recommendations expressed in this document are those of the investigators and do not necessarily reflect the views of the sponsors. The input provided by the Practice Committee of the NEES Nonstructural Project, composed of W. Holmes (Chair), D. Allen, D. Alvarez, and R. Fleming; by the Advisory Board, composed of R. Bachman (Chair), S. Eder, R. Kirchner, E. Miranda, W. Petak, S. Rose and C. Tokas, has been crucial for the completion of this research. The authors are especially grateful to A. Gupta for providing the piping plan.

References:

Antaki, G. and Guzy, D. ,1998. *Seismic testing of grooved and threaded fire protection joints and correlation with NFPA seismic design provisions, ASME Proceedings, Pressure Vessels and Piping Division*, PVP-Vol. 364, Seismic Engineering, 69-75

American Society of Civil Engineers. (2005). ASCE/SEI 7-05, American Society of Civil Engineers

Cornell, A. C., Jalayer, F., Hamburger, R. O., and Foutch, D. A., 2002. *Probabilistic basis for 2000 SAC Federal Emergency Management Agency steel moment frame guidelines, J. Struct. Eng.* 128, 526–532.

Comite Euro-interational du Beton. *RC elements under cyclic loading, state of the art report*. Thomas Telford Publications, London, England, 1996.

Gupta, A., and Ju, B.S., 2011. *Review of existing literature on real-life failures, seismic design guidelines, and experimental tests for piping systems in buildings*. Report, Department of Civil, Construction & Environmental Engineering, North Carolina State University, Raleigh, NC, 30 p.

Goodwin, E., Maragakis, M., Itani, A., and Luo, S., 2005. *Experimental Evaluation of the Seismic Performance of Hospital Piping Subassemblies, Report No. CCEER-05-5*, Center for Civil Engineering Earthquake Research, Department of Civil Engineering, University of Nevada, Reno, NV.

ICC Evaluation Service (2010). *AC 156 Acceptance Criteria for Seismic Certification by Shake Table Testing of Nonstrucutral Components*, ICC Evaluation Service

MathWorks. (2010). *Matlab User Guide*, The MathWorks, Inc

Mazzoni, S., McKenna, F., Scott, M. H., Fenves, G. L., 2007. *OpenSees Command Language Manual*, Berkeley, CA.

Miranda, E., Mosqueda. G., Retamales, R., and Pekcan, G., 2012. *Performance of Nonstructural Components during the February 27, 2010 Chile Earthquake, Earthquake Spectra*, accepted for publication, Earthquake Engineering Research Institute, Oakland, CA.

Mizutani, K., Kim, H., Kikuchihara, M., Nakai, T., Nishino, M., Sunouchi, S., 2012. *The damage of the building equipment under the 2011 Tohoku pacific earthquake, 9th International Conference on Urban Earthquake Engineering & 4th Asia conference on earthquake engineering* , Tokyo Institute of Technology, Tokyo, Japan.

Mosqueda, G., Retamales, R., Filiatrault, A., and Reinhorn, A. M., 2008. *Testing facility for experimental evaluation of nonstructural components under full-scale floor motions, Journal of Structural Design of Tall and Special Buildings*, 18(4), 387–404.

NFPA13., 2011. "*Standard for the Installation of Sprinkler Systems*." National Fire Protection Association, 2010 Edition, Quincy, MA.

Nielson, G. B. and DesRoches, R., 2007a. *Analytical Seismic Fragility Curves for Typical Bridges in the Central and Southeastern United States, Earthquake Spectra*, EERI, 23(3), Oakland, CA, 615-633.

Nielson, G. B. and DesRoches, R., 2007b. *Seismic fragility methodology for highway bridges using a component level approach, Earthquake Eng. Struct. Dyn.* 36, 823–839.

Open System for Earthquake Engineering Simulation (OpenSees) website,2012.: http://www.opensees.berkeley.edu . PEER, Berkeley: University of California

Retamales, R., Mosqueda, G., Filiatrault, A., and Reinhorn, A.M., 2008. *New experimental capabilities and loading protocols for seismic qualification and fragility assessment of nonstructural components, Technical Report MCEER-08-0026, MCEER*, State University of New York at Buffalo, New York.

Retamales, R., Mosqueda, G., Filiatrault, A., and Reinhorn, A.M., 2011. *Testing protocol for experimental seismic qualification of distributed nonstructural systems, Earthquake Spectra*, 27(3):835-856.

SEAOC Seismology Committee. SEAOC Blue Book: *Seismic Design Recommendations*. Sacramento, CA, 2006.

Soroushian, S., Maragakis, M., Ryan, K., Sato, E., Sasaki, T., Okazaki, T., Tedesco, L., Zaghi, E., Mosqueda, G., Alvarez, D., 2012. *Seismic Response of Nonstructural Systems in NEES TIPS/NEES Nonstructural/NIED Collaborative Tests, 9th International Conference on Urban Earthquake Engineering & 4th Asia conference on earthquake engineering*, Tokyo Institute of Technology, Tokyo, Japan.

Soroushian, S., Zaghi, A. E., Maragakis, E. M., Echevarria, A., Tian, Y., Filiatrault, A., 2012b. "*Analytical Seismic Fragility of Fire Sprinkler Piping Systems with Threaded Joints," Earthquake Spectra*, EERI., "Under Review".

Tian, Y., Filiatrault, A., Mosqueda, G., 2012a. *Experimental seismic fragility of pressurized fire suppression sprinkler piping joints, Earthquake Spectra*, In press.

Tian, Y., 2012. *Experimental Seismic Study of Pressurized Fire Suppression Sprinkler Piping System., Doctoral Dissertation*, Department of Civil & Environmental Engineering, State University of New York at Buffalo, Buffalo, NY.

USG Corporation. (2006). Seismic Ceiling Resources Center. http://www.usg.com/rc/technical articles/seismic-technical-guide-hanger-wire-attachment-en-SC2522.pdf

VanMarcke, Dario, Gasparini, A., and Eric, H. (1976). *SIMQKE User's Manual and Documentation*, National Science Foundation.

Zaghi, A. E., Maragakis, E. M., Itani, A., and Goodwin, E. (2012). *Experimental and Analytical Studies of Hospital Piping Subassemblies Subjected to Seismic Loading. Earthquake Spectra*, EERI. 26(1), EERI

10CUEE CONFERENCE PROCEEDINGS
10th International Conference on Urban Earthquake Engineering
March 1-2, 2013, Tokyo Institute of Technology, Tokyo, Japan

CEILING SYSTEMS DESIGN AND INSTALLATION LESSONS FROM THE CANTERBURY EARTHQUAKES

Rajesh P Dhakal[1)], and Gregory MacRae[1)]

1) Associate Professor, Department of Civil and Natural Resources Engineering, University of Canterbury, New Zealand
rajesh.dhakal@canterbury.ac.nz, gregory.macrae@canterbury.ac.nz

Abstract: Damage to ceiling systems resulted in a substantial financial loss to building owners in the Canterbury earthquakes. In some buildings, collapse of ceilings could easily have resulted in severe injury to occupants. This paper summarizes the types of ceiling damage observed in the Canterbury earthquakes, and draws useful lessons from the observed performance of different types of ceiling systems. Existing ceiling manufacturing and installing practices/regulations in New Zealand are critically scrutinized to identify deficiencies, and measures are suggested to improve the practice so that the damage to ceilings and the resulting loss are minimized in future earthquakes.

1. INTRODUCTION

Ceiling systems consist of the ceiling itself, and all the components that may interact with the ceilings. Some common elements interacting with ceilings are partitions, bulk heads, heating, ventilating and air conditioning (HVAC) equipment, electrical equipment, and fire sprinklers. Excessive movement or failure of one of these elements can result in damage to, and/or collapse of, part of a ceiling. Needless to say, utmost care should be taken in installing any of these elements so that the performance of other interacting elements is not adversely affected.

In New Zealand, while there is no restriction on the types of ceiling that may be used in different situations, ceilings in residential dwellings and small ceilings in commercial buildings are commonly constructed with gypsum board. Moderate and large ceilings are more often suspended on a cold-formed steel grid, into which ceiling tiles sit as shown in Figure 1. In these ceilings, the tiles can move a few millimeters in different directions within the grids, so force must be transferred through the grid members, rather than directly between the neighboring tiles. A number of manufacturers provide grid ceilings.

Suspended ceilings are commonly designed to be either fixed to the perimeter walls, or they may be floating. The fixed ceilings are connected to the perimeter walls at least on two sides. When bracing the ceiling off the walls, lateral inertial ceiling forces are taken axially through the tee rails in each direction, to the walls. Axial loads (tension and compression) are at their highest near the walls and at their lowest towards the centre of the room. Each tee rail will be in tension at one end and in compression at the opposite end.

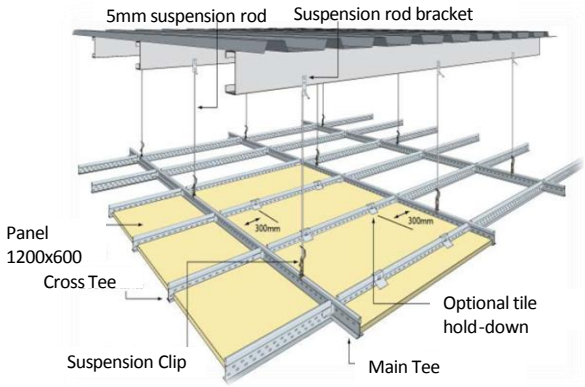


Figure 1. Typical ceiling configuration not showing seismic bracing (based on Rondo, 2009)

On the other hand, floating ceilings are not connected to the wall in any side, but they are braced to the floor or roof above to prevent large movements under service conditions, as well as to transfer horizontal earthquake induced inertia forces. Bracing is normally provided in the form of inclined rods connected to the ceiling grid in one end and the floor at the other end. Typically this system is adopted if tee lengths exceed the maximum length determined for perimeter fixed ceilings.

2. CURRENT DESIGN AND INSTALLATION SPECIFICATIONS FOR CEILINGS IN NZ

Since suspended ceilings are generally developed by companies and are sold as proprietary systems, construction details, element capacities, as well as analysis methods to obtain element demands from global loads are generally provided by companies in their

literature, or through discussion with their engineering staff. Mainly, the following documents are used for ceiling system design and installation in New Zealand:

1. NZS 1170.5:2004 – Structural design actions Part 5- Earthquake Actions Section 8 "Requirements for Parts and Components"
2. AS/NZS 2785:2000 – Suspended Ceilings: Design and Installation
3. NZS 4219:2009 – Seismic performance of engineering systems in a building.

In addition to these three, the following standards used in NZ are also relevant to ceiling design/installation and performance assessments:

- Ministry of Works PW/81/10/1:1985 - Guidelines for the Seismic Design of Public Buildings: Appendix D Suspended Ceilings and Associated Fittings and Fixtures
- AS/NZS 1170.1:2002 - Structural design actions - Permanent, imposed and other actions
- AS/NZS 1530.3:1999 - Methods for fire test on building materials, components and structures - Simultaneous determination of ignitability, flame propagation, heat release and smoke release
- AS 2946:1991 - Suspended ceilings, recessed luminaries and air diffusers – Interface requirements for physical compatibility
- ISO 6308:1980 - Gypsum plasterboard - Specification
- ASTM E1414-11 - Standard test method for airborne sound attenuation between rooms sharing a common ceiling plenum (two room method)

In addition to the abovementioned standards, a number of proprietary guides exist in the industry. As these generally follow loading standards older than NZS 1170.5 and may not necessarily be current, it is the designer's responsibility to ensure that they are current before using these guides. Moreover, information on international practice is also available from groups such as the US Federal Emergency Management Agency (FEMA). Until July 2011, only AS/NZS 1170 was listed as a compliance document to the NZ Building Code as specified by the Department of Building and Housing (DBH). However, in 2011, the DBH also listed NZS 4219:2009 as a compliance document for ceiling (DBH 2011).

Some of the key specifications (related to ceilings) provided in the abovementioned regulatory documents are given below:

2.1 NZS 1170.5:2004

1. All parts of structures including permanent, non-structural components and their connections, and permanent services and equipment supported by structures, shall be designed for the earthquake actions specified in this Section.
2. Buildings parts are divided into seven categories, among which ceilings feature in the following categories:
   - Auditorium ceilings: P.2 (Part representing a hazard to a crowd of greater than 100 people within the building)
   - Light suspended ceilings: P.7 (All other parts)
3. Auditorium ceilings (i.e. category P.2) are designed for ultimate limit state (ULS) whereas suspended ceilings (i.e. category P.7) are designed for serviceability limit state (SLS1).
4. Ceilings directly attached/framed to the structure/walls be designed for ductility 3 or less and a suspended ceiling shall not be designed for ductility greater than 2.

2.2 AS/NZS 2785:2000

1. The aim is to provide a ceiling system that has adequate strength and serviceability, is stable and durable, and satisfies other objectives such as economy and ease of construction.
2. Ceiling systems shall be designed and installed in such a manner that the suspension and frame will remain structurally sound, without maintenance, for a period of 15 years.
3. The following limit states are recommended:
   - Ultimate limit state (for life safety): A ceiling has adequate strength if the probability of failure of the system or components is acceptably low throughout its intended life.
   - Serviceability limit state (for operational continuity and business interruption): A ceiling is serviceable if the probability of loss of serviceability of the system of the components is acceptably low and the ceiling maintains its intended performance level throughout its intended life.
4. The methods to design for the ultimate limit state are given as:
   - The ultimate limit state is reached when the ceiling system or part thereof ruptures, becomes unstable, or loses equilibrium.
   - The member or component shall be proportioned such that the design action effect (calculated for the specified loads/actions and load combinations) is not greater than the design ultimate strength (strength reduction factor times the nominal capacity obtained from the material standard or tests).
   - Ceiling hangers shall be proportioned such that the failure or removal of a single hanger does not trigger a progressive collapse of the ceiling system.
5. The method to design for the serviceability limit state is given as:
   - The total deflection of the ceiling shall take into consideration the deflection of the suspension system, and remain within the specified limits (between L/250 and L/600).

2.3 NZS 4219:2009

1. Suspended ceilings are outside the scope of this standard; only equipments interacting with ceilings are covered by this standard. Where service loads are greater than 3 kg/m^2, the ceiling designer should be advised.
2. Suspended ceilings should be designed and constructed in accordance with AS/NZS 2785.
3. Equipment supported by the ceiling not exceeding 10 kg shall be positively fixed to the suspension system but not supported by the ceiling panels or tiles.
4. Suspended ceilings, equipments in ceiling voids and supported by the ceiling are considered as dead load.
5. Service loads greater than 3 kg/m^2 (0.03 kPa) need special consideration.
6. Equipment with a mass less than 10 kg shall be supported by the grid of the suspended ceiling system. Equipment exceeding 10 kg mass shall be supported independently of the ceiling.
7. Equipment supported independently of the ceiling shall have a clearance of 25 mm all round to allow independent movement between component and the ceiling.
8. Ceiling suspension components (hangers, braces, and so forth) shall be located with specified clearances. A minimum of 50 mm clearance in the vertical and horizontal direction is recommended between restrained components (i.e. ceiling hangers and braces).
9. A minimum clearance of 150 mm in horizontal and 50 mm in vertical direction is recommended between unrestrained components and restrained components.
10. All fixings of hanging luminaries shall be positive, locking type to prevent disengagement.
11. Where luminaries are recessed or surface-mounted on suspended ceilings, they shall be positively clamped to the ceiling suspension systems. Clamping shall be by means of screw and nuts or locking-type clamping devices.

3. ISSUES WITH CURRENT NZ DESIGN PROCEDURES AND PRACTICE FOR CEILINGS

A number of concerns have been expressed by designers, contractors and fabricators on different aspects of the existing ceiling design and installation practice. Some of these concerns are listed below:

3.1 Performance Objectives

- Suspended ceilings are included in the least important category (Category 7 in the recommendations in NZS 1170.5 Clause C8.1) considering the lowest level of design demand (SLS1). The required design level for ceilings may be too low as evidenced by the fact that a number of ceilings were replaced several times in Christchurch during the Canterbury earthquake sequence.
- Life safety threat from ceilings is not fully acknowledged. There were fatalities resulting from ceiling damage in the 2011 Japan earthquake. It is only a good fortune that there was no life loss as a result of the several ceiling collapses in the 2010-2011 Canterbury earthquakes. It seems that ceilings should be designed to have no possibility of causing death/injury during ULS shaking to be consistent with the NZ Building Code.
- If performance objectives become too conservative, this may mean that suspended ceilings will stop being a reasonable design option. This could have a significant adverse effect on the suspended ceiling industry.

3.2 Ceiling Standards

- Some standards are not up-to-date and reference out-of-date standards (e.g. AS/NZS 2815).
- The standards do not emphasize or state specific requirements to ensure good ceiling system performance, such as the gap-size between a floating ceiling and the wall, or how to consider interactions with specific service components.
- Floor acceleration profiles in current standards (NZS1170.5 and NZS4219) are the same up the building height for all building types. In reality, different building types have different accelerations at different heights, so this may result in some conservatism/non-conservatism.

3.3. Assessment of Ceiling Capacity for Design

- Test protocols are available for ceilings. Many of these require shaking table testing, which is too demanding.
- There is no method of relating test protocol results to design.

3.4 Ceiling Design Practice Issues

- No generic information is available on the principles involved in designing ceilings and providing bracing.
- There is a lack of generic design examples, especially regarding lateral bracing.
- Often ceiling systems are designed by engineers who are not the building designers and information necessary for ceiling design is not readily available. This includes the likely accelerations and drifts. It takes time and cost to obtain these parameters from an analysis of the building, and requires knowledge of things such as the soil conditions if the analysis is to be done accurately.
- Ceiling examples are often not checked.
- The documents required by AS/NZS 2785 (Appendix C) for conducting basic design of ceilings (i.e. drawings and documentation on

interaction of the ceiling system and building services) are seldom provided at tender or consent time.

3.5 Installation Issues

- There is a significant amount of poor installation.
- The NZS 4219 recommended minimum clearances between the ceiling and equipment supported independently of ceilings are often not being adhered to in practice.
- Component connection is often inadequate.
- Inappropriate connection of ceilings to suspended services (such as ducts), or a lack of ceiling support being provide around services.
- There is a lack of training opportunity for installers. Hence, many installers have very limited training. No training is required for installation in general.
- While NZS 4219 requires all fixings between hangings of luminaries along with ceiling grid system to be positive (locking type) to prevent disengagement, there are no examples and illustrative sketches provided; thereby leaving room for misinterpretation leading to faulty details.
- Often, there is a lack of inspection.
- Ceiling inspectors are often not trained.

3.6 Political Issues

- Ceiling design is generally considered as an afterthought, rather than as part of the major building contract.
- The tasks of building structure design/construction, service equipment design and placement, partition design/installation and ceiling design/installation are often conducted separately or with little interaction between these groups. Therefore, coordination often does not occur to ensure that each of these parts acts as required.
- Often ceiling design has not been completed at the time of the tender for installation. Also, fees for ceiling design are seldom included in the tender. Responsible contractors, who pay for the ceiling design and pay the building design engineer, therefore have a high contract price. Other installers, who do not perform the full design have lower contract prices and often win the contracts. As a result, the current system discourages rigorous design.
- Anecdotal evidence suggests that the prices for ceilings in Christchurch are some of the lowest in NZ. Also, the quality of installation is correspondingly low.
- Changes to building use or occupancy often result in changes to the building internal layout with movement of partitions and installation of different ceilings. This can result in poor seismic behavior if appropriate precautions are not made.

4. SUMMARY OF CEILING DAMAGE OBSERVED IN CANTERBURY EARTHQUAKES

The damage observed to suspended ceilings described below during the recent Canterbury earthquakes includes that sustained during the September 2010 Darfield earthquake (Dhakal 2010; MacRae et al 2011) as well as the February 22nd and 13th June 2011 Christchurch earthquakes (Dhakal et al 2011). This has been organized by damage type: grid damage; perimeter damage; interaction with other components; grid spreading; and combinations of different damage types.

4.1 Grid Damage

Grid damage results from excessive force on the grid members or connections. This then results in ceiling grid distortion under compression and subsequent buckling of the grid members or failure of the connections while the perimeter connections remain intact. Below are several examples of ceiling grid damage observed in the Canterbury earthquakes.



Figure 2a. Damage resulting from disconnection of cross-tee from the main beam resulting in localized collapse of the grid and loss of tiles (Photos: K Hogg)



Figure 2b. Damage to grid members due to excessive compression force (Photos: K Hogg)



Figure 2c. Damage resulting from main beam splice failure (left) and cross-tee disconnection with main beam (right) (Photos: Hush Interior Ltd)



Figure 2d. Damage resulting from main beam splice connection (left) and buckling of cross-tee connections and main beam splice failure (right) (Photos: K Hogg)

The uniformly distributed mass (in the form of tiles) in a ceiling generates uniformly distributed inertial force, and the accumulated inertial force which causes axial compression in the grid members becomes greater near the supports (i.e. the perimeter) than in the middle (Paganotti et al 2011). In general, the observed compression damage of grid members was hence more severe near the perimeter, whereas failures due to tension and connection fracture did not follow a specific spatial pattern.

4.2 Perimeter Damage

Perimeter damage results from the main tee or cross-tee losing seating on the perimeter angle around the ceiling. Loss of seating can result due to a lack of a rivet to connect the grid member to the angle or failure of the rivet itself. This results in the grid members and tiles dropping from the ceiling. Edge perimeter hanging wires can prevent the member and tiles from falling, however, this can result in the tile and members being forced back into the angle causing damage to the tiles and members; see Figure 3a (right) below.



Figure 3a. Damage caused by disconnection of main beams and cross-tees. Note damage to panels at right which have not dropped from the ceiling but have been forced back into the wall angle causing damage (Photos: Hush Interior Ltd)



Figure 3b. Damage caused by failure of rivet between main beam/cross-tee and wall angle (Photos: Hush Interior Ltd.)

Common current practice is to connect the grid members to the perimeter angle with centre single-size riveting which only connects to the face cap. Such a riveting system was found to be inadequate. In some cases, the inadequate rivets were observed to fail in tension, leaving only the aluminum cap to hold the system together. In other cases, the rivets were also found to have ripped through the steel wall angles and tee rails. Probably, the standards need to provide detail specifications on the number, size and locations of rivets for such perimeter connections.

In one case, during repair after the February earthquake damage, engineered tee connections were provided with an increased number and diameter of rivets. This detail survived the June 13 earthquake and the quakes afterwards. Only the trim suffered a small amount of distortion. A photo of this connection is shown in Figure 3c.



Figure 3c. Perimeter connection with increased number/diameter of rivets (Photo: K Hogg)

4.3 Interaction with other Equipments

Damage to suspended ceilings can result from force transferred from services above the ceiling into the ceiling itself. In a standard installation of a suspended ceiling the hanger wires are placed at 1200 mm centre. However, the presence of services (such as HVAC) above the ceiling can mean this is not possible. As a result suspended ceilings are sometimes partially hung from services within the ceiling (most commonly HVAC ducting and plant). As this plant is rarely secured properly, when it moves it imparts force into the ceiling, causing damage. Additionally, services above the ceiling moving during an earthquake can impact the hanging wires of the suspended ceiling, once again imparting force into the ceiling. Suspended ceilings are not designed to take the additional force from this plant. Grills within the ceiling plane were often observed to have fallen from the ceiling and localized loss of tiles often occurred around the location of these grills. Some instances of ceiling failures resulting from the interaction with the services are shown in the figures that follow.



Figure 4a. Damage caused by interaction with services above the ceiling (Photos: Hush Interiors Ltd.)



Figure 4b. Damage caused by unbraced AC ducts swaying o or causing damage (Photos: R Dhakal, K Hogg)

In some buildings the ducting sizes make it difficult to provide hangers at the required spacing and the service heights provided were too low to provide proper bridging under services. Figure 4c below shows cases like these.



Figure 4c. Damaged ceiling with inadequate service height (Photos: K Hogg)

Interaction with partition walls also caused damage to some ceilings braced to the walls. Some internal walls extend to the floor above and are fixed either directly to the floor or beam or through inclined braces which are required to minimize buckling of slender walls. In some cases the ceiling may also be supported on these internal walls. The braces of these walls are close to the ceiling hangers and other equipment braces and are likely to interact with the system. It was found that the failure of the braces (some of which fell off) could easily have caused significant damage to the ceilings (see Fig 4d left).



Figure 4d. Interaction between internal walls and ceiling (Photos: K Hogg)

In some cases, the partition walls stopped at the ceiling level and were braced by ceilings. Obviously, in such cases the ceiling needs to cater for the wall as well. Glazed partitions fall into this category, and due to small aluminum sections they are difficult to brace. In some buildings, such wall partitions were found to be out of plumb and in one glazed partition, glass jumped out of the top track (see Fig 4d right).

4.4 Grid Spreading

The suspended ceilings discussed in the previous sections are all two-way exposed grid systems. That is, they consist of a two-way grid of inverted 'T' shaped members hung from the ceiling above. The panels are then dropped in and rest on the flanges of the inverted 'T' sections.

The damage shown in the photos below occurred to grids that are different to the two-way type grid discussed in the previous sections of this report. The grids below consist of main beams spanning one way and hung from the structure above. There are typically no transverse runners (except where the ceiling may have been retrofitted with these). The drop-in panels prevent the grids from spreading apart during an earthquake. However, if panels do drop out there are no members to stop the grids moving apart (spreading) and causing further panels to fall from the ceiling. Also, as opposed to the two-way systems discussed above, the panels are not supported on all four edges by the grid system. The panels are instead interlocked, so when one panel falls it leaves the next panel susceptible to falling.



Figure 5. Damage caused by grid spreading causing the panels to fall from the ceiling (Photos: T Abu and Hush Interior Ltd)

4.5 Other Types of Damage

Damage to suspended ceilings can also result from elements that are connected to the ceiling but should be independent of it. Common examples of this are timber or steel framed bulkheads and partitions. Partitions, in particular, should not rely on lateral support during an earthquake from the suspended ceiling. Unless it is considered explicitly in design, this type of construction applies extra force into the ceiling and can result in damage (see Fig 6a for example).

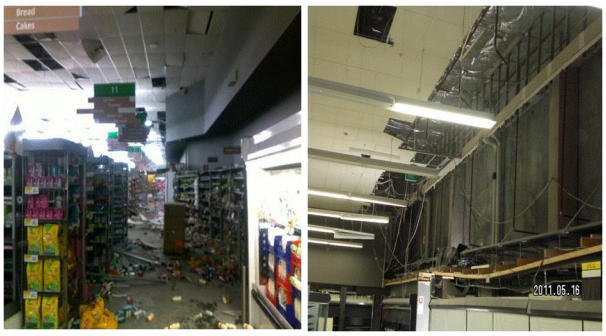


Figure 6a. Damage due to interaction between bulkheads and ceiling (Photos: K Hogg)

In some cases damages were attributable to the interaction between ceilings and bulkheads. Bulkheads hanging from tiled ceilings dropped when the ceiling perimeter detail failed. In a building it was found that during renovation, bulkheads were removed but no bracing was put in place to take the ceiling load. In such cases, the partition loads change during alterations and ceiling line load increases, hence it is advisable to provide bracing to take care of the increased load on ceiling.

The above forms of damage can occur simultaneously during an earthquake causing widespread damage to a single ceiling system. Some examples of this are shown in the figures below.



Figure 6b. Widespread damage of a single ceiling (Photos: R Dhakal, T Abu and Hush Interior Ltd.)

4.6 Summary of Observations

- Compression failure generally occurred closer to the perimeter (than the middle) of two way grids.
- Compression failures were observed to be more severe and more extensive in larger ceilings.
- Ceilings with heavier tiles/panels were observed to undergo more severe damage compared to those of the same size with lighter tiles in the similar shaking region.
- Observed damage in ceilings was very severe in many cases and it was only a coincidence that nobody was killed due to ceiling failure in these earthquakes. As the 2011 Japan earthquake has proved, heavy ceiling tiles falling from several meters can easily be fatal. Even in rooms without heavy tiles, cross members bent down like skewers, causing a major hazard for anyone evacuating the building.
- Interactions with services above the ceilings, partition walls and bulkheads were found to cause many ceiling failures. This was most significant when services/walls were not constrained and interacted with the ceiling.
- Some ceilings were replaced several times during the earthquakes indicating that they were not able to sustain the levels of shaking imposed.
- Poor performance often resulted from poor system installation.

5. RECOMMENDED PRACTICE – DESIGN AND INSTALLATION GUIDANCE FOR CEILING SYSTEMS

A series of brain storming meetings was held between ceiling researchers and practitioners (designers, manufacturers, installers etc) to scrutinize the observed ceiling damage and to come up with immediate measures to improve the performance of ceiling systems in future earthquakes. As a result, the following "recommended practice" guidelines are proposed for ceiling systems, which include the ceiling itself, and all interacting elements:

5.1 Technical recommendations

1. All ceiling systems be designed and installed following appropriate standards.
   - NZS 1170.5:2004: for calculating the seismic demand on ceiling systems
   - NZS 4219:2009: for designing services and their interaction with the ceiling
   - AS/NZS 2785:2000: for designing ceilings
2. While using NZS 1170.5 to determine the design limit state, ceilings shall be placed in the following categories:
   - P.2 – Auditorium ceilings
   - P.3 – Suspended ceilings with one way or two way grid systems
   - P.4 – Suspended ceilings with heavy (more than 10kg) tiles
   - P.7 – All other ceilings
3. If interstorey displacements are not available from the design engineer and they are not computed explicitly, then:
   - the minimum ULS drift ratio demand shall be of 2.5% at all stories
   - the minimum SLS1 drift ratio demand shall be one third of the ULS value above
4. If floor accelerations are not available from the design engineer and they are not computed explicitly, then:

- the minimum ULS acceleration demand shall be 3 times the zone factor, Z, at all levels
- the minimum SLS1 acceleration demand shall be one third of the ULS value above

5. Ceiling connections shall be designed for a ductility of 1.25 for the ULS unless it is shown that another value is satisfactory.
6. Equipment with mass less than 5 kg (per m^2 of ceiling area) may be supported by the grid of the suspended ceiling system, and those exceeding 5 kg mass shall be supported independently of the ceiling. This recommendation overrides the existing statement in Clause 5.13 in NZS 4219:2009.

5.2 Regulatory recommendations

1. If the installer is required to provide the ceiling system design, the following is to be provided by the building design engineer in the tender documents:
   - floor accelerations for SLS and ULS actions.
   - interstorey displacements for SLS and ULS actions.
2. Design and detailing of ceilings and components interacting with ceilings (giving due consideration to the interactions between them) is to be undertaken under the supervision of a Chartered Professional Engineer.
3. Construction of ceilings and services is to be undertaken by a trained and experienced installer.
4. Construction review is to be undertaken by a suitably qualified engineer; preferably the designer.
5. Structural modifications to components interacting with ceiling systems shall consider the implication of the modification to the ceiling.
6. For quality control, the building consent documentation is to define who is responsible for the following design, installation and certification/review processes:
   - Producer Statement 1 (PS1) – Design
   - Producer Statement 3 (PS3) – Construction
   - Producer Statement 4 (PS4) – Construction Review

   If the ceiling is a design and supply item the tender documents shall spell out the requirement for each of these.
7. AS/NZS 2785 needs to be updated in line with the seismic demand stated in NZS 1170.5.
8. Training programmes and qualifications need to be made available for installers.

It is likely that some clients will request buildings and non-structural components, such as ceilings, be designed for greater performance than that associated only with life safety. Also insurance companies may require this in Christchurch and elsewhere as a result of the significant damage resulting from the Canterbury earthquakes. Improved performance may be obtained by designing components greater levels of ground shaking, such as the NZS 1170.5 Maximum Considered Event (MCE) which is defined as being 1.8 times the NZS 1170.5 Ultimate Limit State (ULS) Event. Alternatively, it is possible to design for higher serviceability criteria. In addition, damage may be minimized by using the details recommended below.

6. BEST PRACTICE DETAILING GUIDE FOR CEILINGS

1. Rivets should be placed on the side of a T-section, to go through two, rather than one piece of steel which is the case if they are placed in the middle.

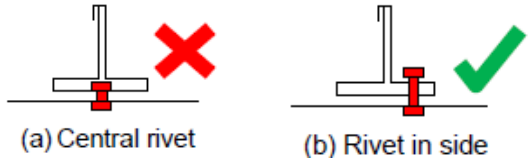


Figure 7a. Locations of rivets in T-rails (Elevation)

2. Rivets be placed with sufficient distance to the end of T-rails so they can develop their full strength.

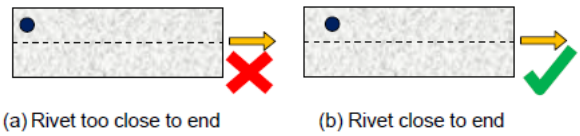
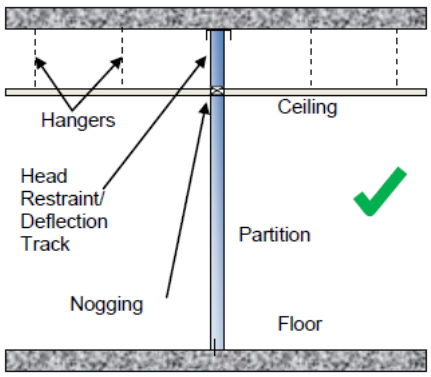


Figure 7b. Locations of rivets in T-rails (Plan)

3. It should be clear whether partitions are bracing the ceiling, ceiling is bracing the partitions, or whether they are independently braced as shown in the Figures below. A head-restraint can be used at the top of the partition. This restrains the partition in the out-of-plane direction. Note that hangers which go to the bottom end of a vertical brace must resist both compression as well as tension, as shown in Figure 7c, in order to prevent large ceiling swinging displacements.
4. Ceilings should be protected from ducts hanging from floor preferably by strongbacks with sufficient space for bridging.
5. Flexible chords should be used for fire sprinklers, or sufficient gaps should be provided in the ceiling so that large forces are not imposed.
6. Lighter tiles should be used rather than heavy tiles as light ceiling systems are likely to sustain less earthquake damage.



(a) Partition Bracing Ceiling

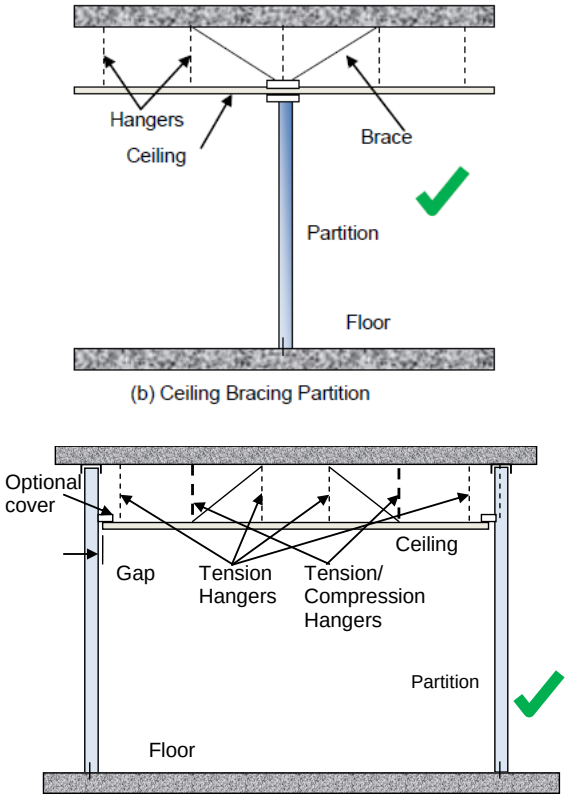


Figure 7c. Some examples of ceilings/partition configurations

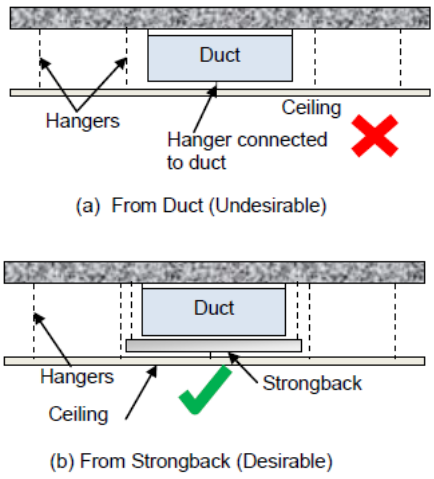


Figure 7d. Suspension of ceiling hangers around ducts

Acknowledgement:

This paper is a summarised version of a report submitted by the authors to the Engineering Advisory Group (EAG) based on the authors' repeated interactions with a number of researchers and practitioners working in NZ in manufacturing, design and installation of ceiling systems. The authors would like to acknowledge their valuable insights which helped prepare this paper.

References:

ASTM International (2011), "ASTM E1414-11 - Standard test method for airborne sound attenuation between rooms sharing a common ceiling plenum," PA, USA.

DBH (2011), "Compliance Document for New Zealand Building Code: B1 Structure," Department of Building and Housing, Wellington, NZ.

Dhakal, R. P. (2010), "Damage to Non-Structural Components and Contents in 2010 Darfield Earthquake," *Bulletin of the New Zealand Society of Earthquake Engineering*, 43(4), 404-411.

Dhakal, R. P., MacRae, G. A., and Hogg, K. (2011), "Performance of ceilings in the February 2011 Christchurch earthquake". *Bulletin of the New Zealand Society of Earthquake Engineering*, 44(4), 377-387.

International Organisation for Standardization (1980), "ISO 6308:1980 - Gypsum plasterboard – Specification," ISO, Geneva, Switzerland.

MacRae, G. A., Hair, J. and Dhakal, R. P. (2011), "Ceiling damage in the 2010 Canterbury earthquake," *Eighth International Conference on Urban Earthquake Engineering* (8CUEE), 6-7 March, Tokyo.

Ministry of Works (1985), "PW/81/10/1: Guidelines for the Seismic Design of Public Buildings: Appendix D Suspended Ceilings and Associated Fittings and Fixtures," MoW, Wellington, NZ.

Paganotti, G., Dhakal, R. P. and MacRae, G. A. (2011), "Development of typical NZ ceiling system seismic fragilities," Paper 116, *Ninth Pacific Conference on Earthquake Engineering* (PCEE), 14-16 April, Auckland.

Rondo Key-Lock (2009), "Concealed Suspended Ceiling Systems," Rondo, Auckland, New Zealand.

Standards Australia (1991), "AS 2946:1991 - Suspended ceilings, recessed luminaires and air diffusers – Interface requirements for physical compatibility," Sydney, Australia.

Standards Australia (1999), "AS/NZS 1530.3:1999 - Methods for fire test on building materials, components and structures - Simultaneous determination of ignitability, flame propagation, heat release and smoke release," Sydney, Australia.

Standards New Zealand (2000), "AS/NZS 2785:2000 Suspended Ceiling – Design and Installation," Wellington, NZ.

Standards New Zealand (2002), "NZS 1170.1:2004 Structural Design Actions Part 1: Permanent, Imposed and Other Actions," Wellington, NZ.

Standards New Zealand (2004), "NZS 1170.5:2004 Structural Design Actions Part 5: Earthquake Actions – New Zealand," Wellington, NZ.

Standards New Zealand (2009), "NZS 4219:2009 Seismic Performance of Engineering Systems in Buildings," Wellington, NZ

10CUEE CONFERENCE PROCEEDINGS
10th International Conference on Urban Earthquake Engineering
March 1-2, 2013, Tokyo Institute of Technology, Tokyo, Japan

THE BEHAVIOR OF CEILING WITH STEEL FURRING DURING EARTHQUAKES

S. Motoyui[1)] and Y. Sato[2)]

1) Professor, Dept. of Built Environment, Tokyo Institute of Technology, Japan
2) Graduate student, Dept. of Built Environment, Tokyo Institute of Technology, Japan
motoyui@enveng.titech.ac.jp, yasuaki.s.aa@m.titech.ac.jp

Abstract: In the Great East Japan Earthquake, many ceilings were damaged in the northern Pacific coast area including the Tokyo area and some people were injured and killed by ceiling failures unfortunately. Furthermore, after the shock, it took a long time to restore ceilings. The fact let us know it was a problem of great urgency to reduce such damage of ceilings from the view point of the business continuity plan. We focus on the Japanese style of ceiling with steel furring. The damage patterns of such ceilings are classified into two categories. One is that ceiling surface falls in a great mass and another is that a part of ceiling board falls in the circumference of ceiling. We show that each pattern of damage is caused with a quite different reason.

1. INTRODUCTION

The significant damage of ceiling had been observed in the recent earthquakes of the 2001 Geiyo earthquake, the 2003 Tokachi-oki earthquake, the 2005 Miyagi-ken-oki earthquake and so on. We had experienced that ceiling failure injured or killed persons during an earthquake and impaired functions of buildings after earthquakes. The similar but much greater scale of ceiling failures occurred at the Great East Japan Earthquake happened on 11th of March, 2011 though we had cautioned about such risk through our research. Many engineers had misunderstood that ceiling failures had been caused by the bad construction and they had not examined their consideration had been true or not. After 3.11, the situation changed completely.

The epicenter of the Great East Japan Earthquake was off the coast of Miyagi prefecture and its magnitude was over 9. A lot of ceilings were damaged at wide area in the northern Pacific coast including the Tokyo area far from the epicenter (Fig.1). Such damages revealed the fact that many existing ceilings might fail under not so great earthquake. After then, the Architecture Institute of Japan or the Ministry of Land, Infrastructure, Transport and Tourism begun to tackle the mission to mitigate ceiling failures. Some committees have been set up to make a draft of the seismic code for ceiling. One of authors participates in such committees.

There are two types of ceiling system as the Japan style and the western (US) style. The Japan style one is more popular than the western style. Regarding the extent of damage, the damage of the Japan style one was much severer than the western one quantitatively and qualitatively. Then we have focused on the Japan style of ceiling. We have studied the

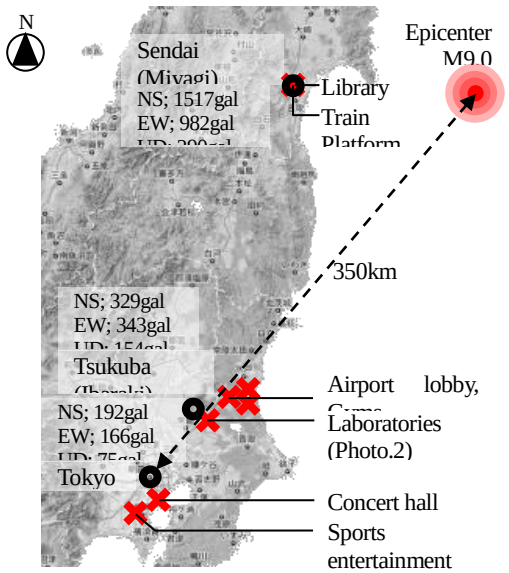


Figure 1 Map of ceiling damages examples by Great East Japan Earthquake

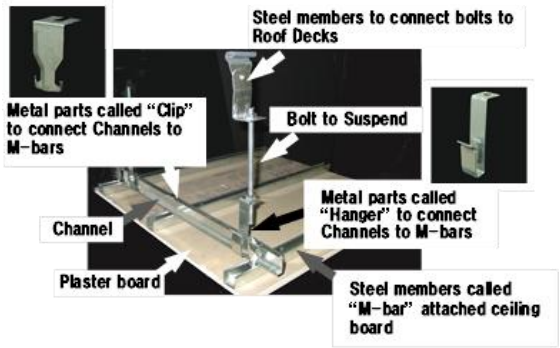


Figure 2 Japan style of ceiling

performance of the ceiling during earthquakes through experimental and numerical results until now. Recently we have found out the reason why ceiling fell down. In Fig.2, the Japan style of ceiling is shown. The Japan style one consists of steel furring and gypsum board. Its standard weight per unit area is approximate 150kN/m2. The Japan style one is heavier than the western one because a urethane board is used in the western style one instead of a gypsum board in Japan. The heavier weight causes severer damage in the Japan style one. The most important feature of the Japan style is the existence of unique metal joint parts which are called "hanger" and "clip" as shown in Fig.2. Though these metal parts have the enough strength to carry the self-weight of ceiling, it is known that they can be easily detached by horizontal force by an earthquake.

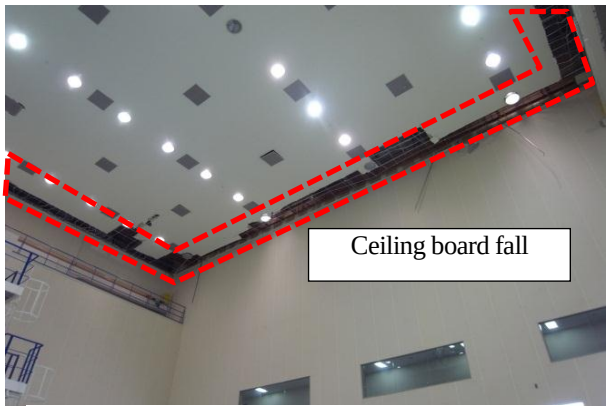
In this paper, we classify the damage patterns of ceiling into two categories. One is that ceiling surface falls in a great mass and another is that a part of ceiling board falls in the circumference of ceiling. We show that each pattern of damage is caused with a quite different reason.

2. Damage Patterns of Ceiling in Earthquakes

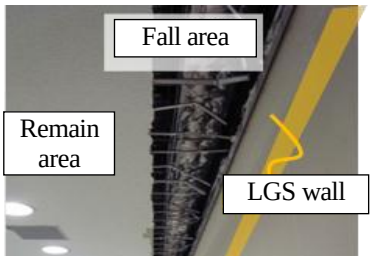
In this section, two typical damage patterns of ceiling are shown. First one is that a part of ceiling board falls in the circumference of ceiling and another is that ceiling surface falls in a great mass. The occasion for each pattern of damage is quite different. The former is caused by the buckling behavior of ceiling surface while the latter is by the detachment behavior of metal joint parts between steel furring. The reason is obvious from the observation of the damage condition. However, the patterns of damage are not always independent each other. In the most tragic ceiling failure, one pattern of damage transitions into another pattern.

The first example in Photo.1 and 2 is the damage of ceiling boards at the laboratories in Tsukuba. The peak of horizontal ground acceleration was recorded 343cm/sec2. As shown in Photo.2, only gypsum boards fell down and steel furring remains original position though it have buckled. At the circumference area of ceiling, the membrane compressive stress is greater than one at other area since an inertia force on the ceiling surface accumulates. Then, the ends of ceiling are easy to suffer damage generally.

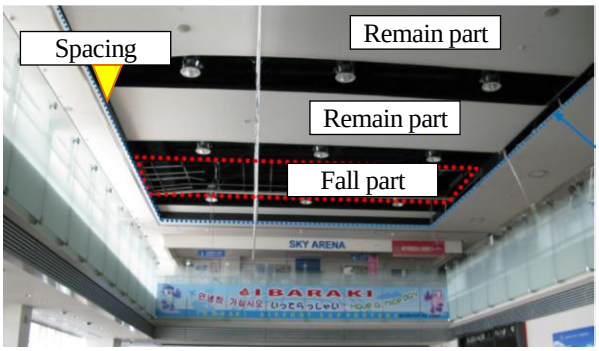
The second in Photo.3 is the ceiling damage at an airport in Ibaraki. In this case, the ceiling fell down in the great mass and both gypsum board and steel furring fell down. This pattern of damage is caused by the detachment of metal joint part called "Clip". Once the detachment of "Clip" occurs, the chain of the detachment can easily happen. As a result, ceiling falls in the great mass. The spacing between ceiling and the surrounding component can be seen. And bracing members are set for ceiling not to swing during



Photograph 1 Pattern 1 of ceiling failure



Photograph 2 Pattern 1 of ceiling failure



Photograph 3 Pattern 2 of ceiling failure



Photograph 4 Ceiling failure by combination of Pattern 1 and 2

an earthquake. The method with the spacing and bracing members are recommended by the Ministry of Land, Infrastructure, Transport and Tourism (ML IT).

The last example in Photo.4 is the ceiling damage at the top floor of an eight-story building in Yokohama. A few persons were injured. The peak of horizontal ground acceleration was recorded 165gal. The roof of the building is formed by truss beams that cover over 34m span. In this case, there were not spacing. The surrounding wall also suffered serious damage. I guess that the ceiling which had lost counterparts fell down.

3. Structural Characteristics of Ceiling Surface under Static Loading

In the previous section, we showed two typical damage of ceiling. We have already published the characteristics of metal joint parts used at the connection between steel furring and the mechanism/process of damage. Then, we focus on the characteristics of ceiling surface. Especially, consider why/how a ceiling surface buckles.

3.1 Compression Test of Ceiling Surface

At first, the compression test of ceiling surface was executed. Fig.3 shows test specimen. The ceiling surface is made of gypsum boards (thickness: 9.5mm) which are attached to M-bars by screws and the steel furring members are suspended with bolts of which outer diameter is 9mm. The spacing of bolts is about 850mm and its length is 1,500mm. As the stress condition on the ceiling surface becomes the uniform uniaxial compression state, the displacement on one edge is controlled by using the H-shaped beam (H-400x400) while another opposite side of edge is fixed by using the same size of H-shaped beam as shown in Photo.5.

Fig.4 shows the relationships between compressive resultant stress and stretch for the respective direction load. The compressive resultant stress means the compressive force by unit length. According to the results, the maximum compressive strength reaches to about 12kN/m. After the maximum strength, the compressive force decreases immediately. The deformation at the post maximum strength shows in Photo.6. It can be understood that both ceiling surface and hanging bolts buckle.

Unfortunately, the compression test was executed only for one test specimen. So, the process to collapse is not obvious through the test result. Is the maximum compressive strength determined by instability of ceiling surface? Of course, it is right but it should be considered why ceiling surface falls into the unstable condition.

3.2 Numerical Analysis for Compression Test of Ceiling Surface

Here, we investigate the unstable behavior of ceiling surface under uniaxial compression force by numerical analysis. To validate a numerical model, we compare the numerical result with the experimental result. See Fig.5 shows the relationship between compressive resultant stress and shortening. The numerical result is close to the

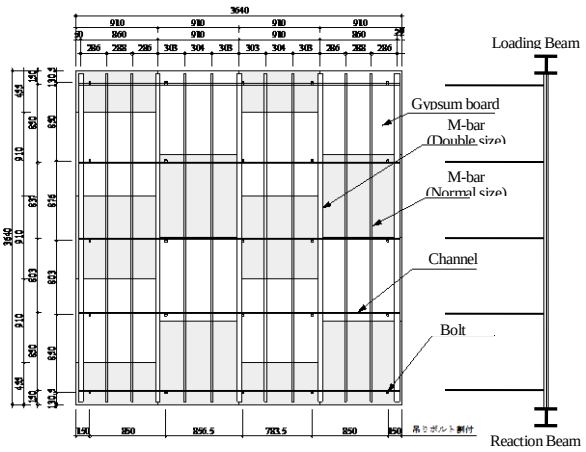


Figure 3 Test specimen



Photograph 5 Loading edge



Figure 4 Compression vs. shortening



Photograph 6 Deformation after peak

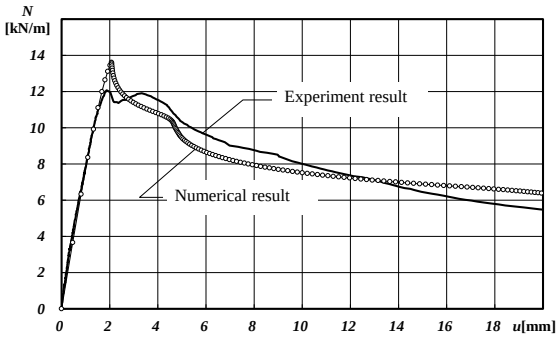


Figure 5 Comparison of numerical and experimental results

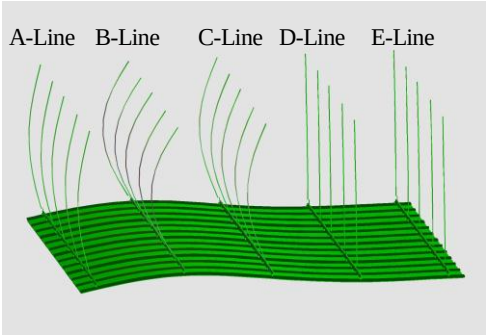


Figure 6 Deformation by numerical

experimental one. And the deformation by numerical analysis also agrees with the observed at the experiment (See Photo.6 and Fig.6). Then, the present numerical model can be considered to be appropriate.

Using the above model, the results obtained by using models with various lengths of bolts are shown in Fig.7. The longer bolts become, the less the compression strengths of ceiling surfaces become. The relationship between compression strength and bolt length is shown in Fig.8. Fig.9 shows the relationship between axial forces on bolts and the shortening of the ceiling surface. By comparing Fig.7 with Fig.9, the maximum compression strengths are determined with the buckling of bolts. Namely, the ceiling surface falls into unstable condition when the bolts buckle. The reason is that the restriction effect of bolts on the out-of-plane deformation of ceiling surface vanishes as soon as bolts buckle. Then, though the longer bolts are sometimes used, a ceiling surface with such bolts is more dangerous than one with the shorter bolts. A lot of engineers think the stress acts on a bolt is tensile and its slenderness ratio is meaningless. However, it is understood that the thought is entirely wrong through the numerical results. The strength of the bolt can be calculated with the formula of Euler's buckling for the pin ended column (Solid line in Fig.10).

The compressive strength of 12kN/m for the bolt length of 1,500mm (See Fig.8) is enough to resist the inertia force by an earthquake. For example, supposing the mass per unit area of ceiling surface [m] and response acceleration on ceiling surface [Sa] are 15kg/m2 and twice of the gravity (2x9.8m/sec2), the limit of ceiling length Llimit can be calculated as following.

$$mL_{limit}S_a < N_{\max}$$

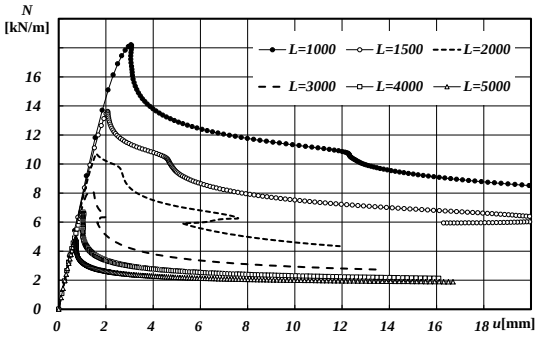


Figure 7 Influence of bolt length

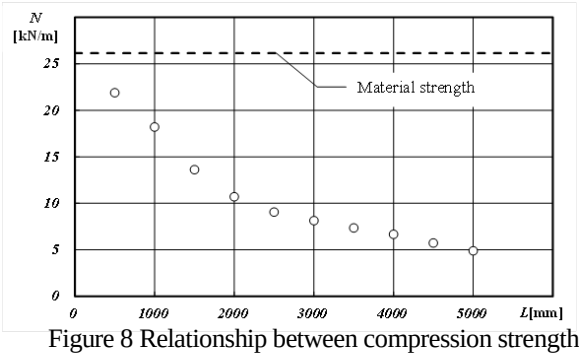


Figure 8 Relationship between compression strength of ceiling surface and bolt length

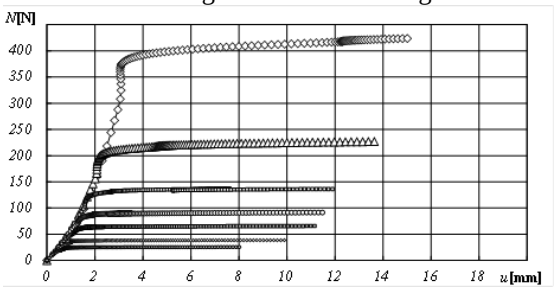


Figure 9 Bolt axial force vs. shortening

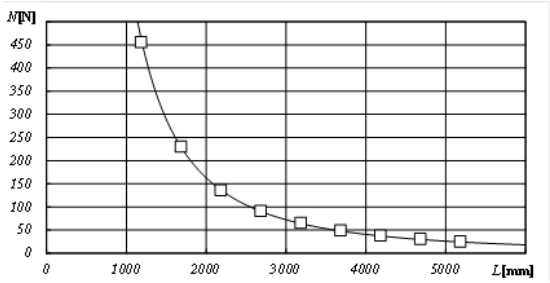


Figure 10 Relationship between bolt axial force and bolt length

$$L_{limit} < \frac{N_{\max}}{mS_a} = \frac{12{,}000^{\mathrm{N/m}}}{15^{\mathrm{kg/m^2}} \times 19.6^{\mathrm{m/sec^2}}} \cong 40\,\mathrm{m} \qquad (1)$$

If this result is true, why the Japan style of ceiling smaller than L_{limit} fell down in earthquakes as shown in Photos.1 and 2? It is thought that the cause of ceiling failure is the impact force generates when ceiling surface collides with a surrounding component like a wall. In this section, the spacing between ceiling surface and the surrounding components is supposed to be zero. But, it is impossible to set the spacing to zero and there is always some unavoidable spacing by the gap of construction actually. So, we

investigate the relationship between the spacing and the impact force in the next section.

3. Impact Force at the End of Ceiling Surface

Now consider the simple model with one mass and two springs as shown in Fig.11 where M is a mass of a ceiling surface and K is a spring constant which represents a surrounding component. It can be considered that the impact force reaches the maximum value when the situation becomes the stationary vibration condition. Readers can understand the fact is right by imaging an old toy called "Clackers". At the time, the mass repeats pounding and leaving behavior alternately. The assumptions that The natural period of ceiling system is assumed to be infinite because the spring constant as a pendulum is much smaller than one of the surrounding component are introduced for the simplicity. It can be led from this assumption that the time in which the mass keeps in contact state is much shorter than the time in which the mass leave the spring. Similarly, the damping effect to the motion of the mass can be neglected during leaving condition. Then the velocity of the mass during leaving is constant. As a result, the period of the stationary vibration state is determined only with the velocity of the mass.

$$T = 4\frac{d}{v} \qquad (2)$$

where T is the period in the stationary condition, d is a spacing and v is a velocity of the mass (See Fig.12). If we can obtain the velocity of the mass, the impact force, F_{impact} can be found by using Eq.(3).

$$F_{impact} = \sqrt{MK}\,v \qquad (3)$$

We make use of the balance of momentum before and after collision. Assuming that the value of K is great, the maximum response displacement is nearly equal to the spacing. Then Eq.(2) can be rewritten in the form;

$$T = 4\frac{u_{\max}}{v_{\max}} \qquad T = 4\frac{S_d(T)}{S_v(T)} \qquad (4.a,b)$$

where S_d and S_v are the values of displacement and velocity response spectra for target input acceleration.

Strictly speaking, the present problem is not a harmonic oscillator problem. Therefore, Eq.(4.a) is a just approximate expression. However, our objective in this paper is that we show the method which engineers can conveniently estimate the approximate intensity of impact force at the collision. From such view point, the expression of the second equation in Eq.(4) is enough. Though by using Eq.(4.b), we can find the period in the stationary condition, Eq.(4.b) is a nonlinear equation. Here, we suggest the convenient method to find the maximum velocity according to Eq.(4.b). Figs.14 and 15 show the displacement response spectrum and the velocity response spectrum for the target input acceleration as shown in Fig.13. From these response spectra, the relationship between the velocity response and displacement response can be obtained as shown in Fig.16.

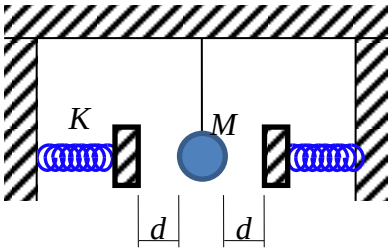


Figure 11 Model

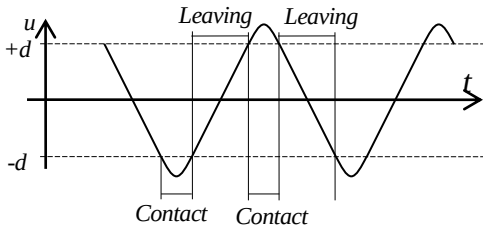


Figure 12 Stationary condition

If the spacing is set to any value, the maximum velocity can be found using Fig.16. For examples, in case that the spacing is 2cm or 10cm, the maximum velocity becomes around 25cm/sec or 62cm/sec respectively. Inserting these values into Eq.(4.b) gives the periods of 0.32sec and 0.65sec. These results are shorter since the displacement response corresponding to these periods is smaller than the spacing. It is inconsistent. Exactly speaking, it is necessary to iteratively process data for eliminating such inconsistence. Therefore, it

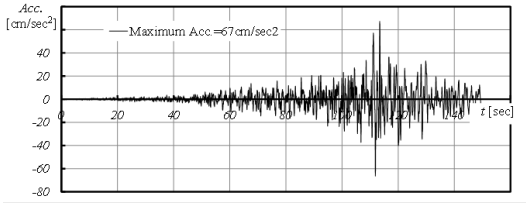


Figure 13 Input acceleration

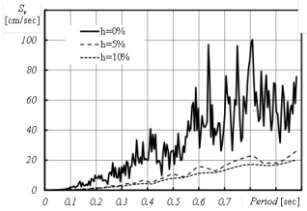


Figure 14 Velocity response spectrum

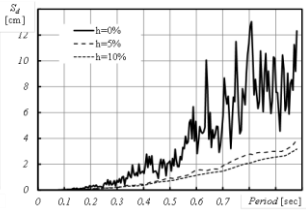


Figure 15 Displacement response spectrum

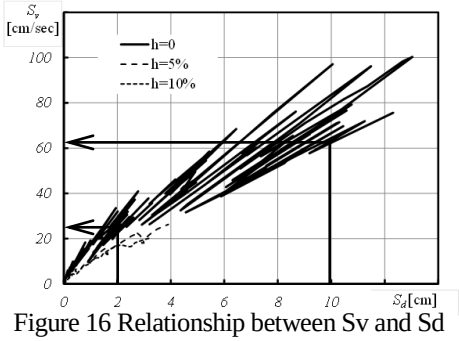


Figure 16 Relationship between Sv and Sd

can be said that the velocities found above, is just approximate. However, it is our objective to suggest the convenient prediction method and the values are adopted. Here, consider the case of M=450kg and K=4,500kN/m. Substituting in Eq.(3) from each value gives impact force;

$$F_{impact} = \sqrt{450 \times 4{,}500{,}000} \times 0.25 = 11.25 \times 10^3 \, N$$

for spacing =2cm (5.a)

$$F_{impact} = \sqrt{450 \times 4{,}500{,}000} \times 0.62 = 27.9 \times 10^3 \, N$$

for spacing=10cm (5.b)

We calculated numerical examples to validate our prediction method. The values of the mass and spring constant are 450kg and 45,000kN/m and the values of spacing are 2cm and 10cm. The damping effect is neglected. Numerical results are shown in Figs.17 and 18. The values of the maximum velocity and impact force are 29.2cm/sec, 13.2kN for spacing of 2cm and 66.8cm/sec, 29.1kN for spacing of 10cm. These values approximately agree with our prediction ones. The present prediction method is useful to estimate the velocity and impact force approximately though the above mentioned inconsistence is involved.

It is noted that the maximum velocity can be determined only by the value of spacing and response spectra of input-acceleration while the impact force can not be calculated by using the value of the system like a mass and spring constant.

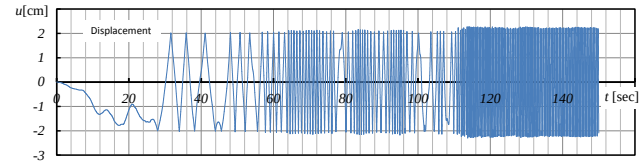
The maximum values of impact forces become much greater in comparison with the ordinary inertia force. For example, in case of the spacing 2cm, the impact force reaches 13.2kN. The value corresponds to around 3G (because the mass is set to 450kg) though the maximum value of input acceleration is not so much. The reason why such great impact force occurs is to make spring constant great and to neglect the damping effect. Therefore, these values should be appropriately evaluated based on the actual situation when engineers consider the reason of ceiling damage. On the other hand, the fact is useful for engineers to consider the seismic design of ceiling. Namely, they should find the suitable stiffness and damping ratio of the surrounding component to degenerate the impact force.

3. CONCLUSIONS

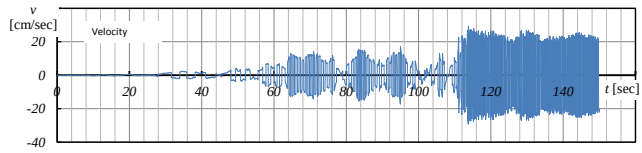
We investigated the behavior of ceiling with steel furring during an earthquake. Especially, we focused on the ceiling without the spacing between ceiling surface and the surrounding component. The obtained results were summarized as followings.

#1. The static compression strength of ceiling surface is enough great to resist the horizontal force in an earthquake except the ceiling suspended with too long bolts.

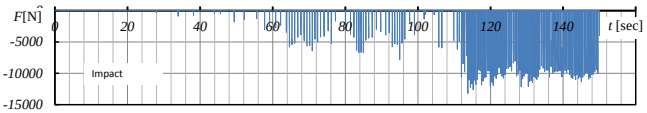
#2. The greater the impact force occurs at the collision of the ceiling surface and the surrounding component becomes, the larger the spacing is. The spacing should be as small as possible or apply any special device like a damper.



Time history of displacement

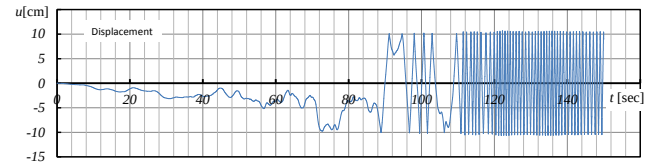


Time history of velocity

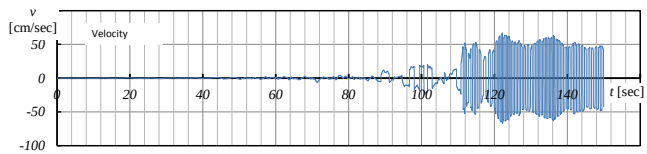


Time history of impact force

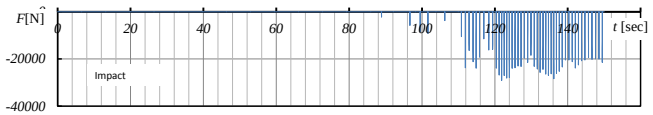
Figure 17 Numerical example spacing=2cm



Time history of displacement



Time history of velocity



Time history of impact force

Figure 18 Numerical example spacing=10cm

Acknowledgements:
This work was supported by JSPS KAKENHI Grant Number 24246094.

References:

Motoyui, S., Sato, Y. and Kawanishi, T., (2010), "Dynamic Characteristics of Japanese Style of Ceiling", *Proceeding of 7th International Conference on Urban Earthquake Engineering*, Tokyo, Japan

Motoyui, S. and Sato, Y., (2011), "Mechanical Characteristics of Metal Joint Parts in Japanese Style of Ceiling", *Proceeding of 8th International Conference on Urban Earthquake Engineering*, Tokyo, Japan

Motoyui, S. Tabuchi, G., Kobayashi, M. and Sato, Y.,(2012), "Ceiling Damage by the Great East Japan Earthquake", *Proceeding of 9th International Conference on Urban Earthquake Engineering*, Tokyo, Japan

10CUEE CONFERENCE PROCEEDINGS
10th International Conference on Urban Earthquake Engineering
March 1-2, 2013, Tokyo Institute of Technology, Tokyo, Japan

SEISMIC CAPACITY IMPROVEMENT OF LIGHTWEIGHT-MORTAR INFILLED STUD WALL SYSTEMS

George C. Yao [1], Wei-Chung Chen [2], and Yi-Chiao Chen [3]

1) *Professor, Department of Architecture, National Cheng Kung University, Tainan, Taiwan*
2) Ph. D. Student, Department of Architecture, National Cheng Kung University, Tainan, Taiwan
3) Master, Department of Architecture, National Cheng Kung University, Tainan, Taiwan
gcyaoncku@gmail.com, jamesjester2000@yahoo.com.tw, nintendo128@hotmail.com

Abstract: Partition walls with light-gauge steel stud, also known as dry-wall, are commonly used in Taiwan since the 1980's. In the past 20 years, there are some modifications by providing lightweight-mortar infill (LIMI) between two surface panels to provide a higher standard for soundproofing and burglary protection. Although LIMI wall is gradually accepted with good response, there are some observed earthquake damages of collapse and flooding caused by water-pipe shear-off. These damage may pose serious consequence that warrant special investigation. This paper summarized a series of full-scale experiment of LIMI walls. Because partition walls are displacement-sensitive elements, two prototypes of LIMI walls were tested separately in plane and out-of-plane cyclically with displacement controlled actuators. Intersection walls in T and L shape were also tested with loading exerted from in-plane direction. Different types of construction details to improve the seismic capacity of LIMI walls were developed to increase the seismic capacity of the prototype LIMI. The test results indicated that the collapse story-drift ratio can be increased from 3% to 5% while the water pipe's rupture story-drift ratio can be increased from 1.5% to 4%.

1. INTRODUCTION

The partition walls in a building are important non-structural components, of which the functions may include partitioning the space, sound-proofing, prevent burglary and securing privacy. In 1980's, the dry-wall (DW) system was first introduced from the USA. This system has the advantages of lightweight structures, ensured quality, and accelerated construction. Due to these advantages, it was commonly used in the construction of commercial, hospital and residential buildings in which the traditional RC and brick partition walls are replaced. However, the DW systems still have problems, such as inadequate strength to hang objects, poor soundproofing, and vulnerable to burglary. To satisfy the needs of the users in Taiwan, the lightweight-mortar infilled stud wall system (LIMI) was developed and Taiwan is distinctive in using this technique.

Although the LIMI system is more appropriate for general living requirements, the seismic behaviors and sturdiness of this system under earthquakes have not been extensively studied. Some post-earthquake survey reports in Taiwan revealed that the building structures could resist small to moderate seismic events without damage, but the LIMI system could have been easily damaged. Damages may include not only the fracture of water pipes to cause flooding in a building, but it may also cause out-of-plane collapse and threaten lives.

This paper aims at the studying on the inter-story drift performances of the LIMI system. The results will be analyzed and discussed for future design specifications in Taiwan.

2. THE LIGHTWEIGHT-MOTAR INFILLED STUD WALL SYSTEM IN TAIWAN

The construction of LIMI system assimilates the grouting formwork of RC walls and is a special technique developed due to the living habits of Taiwanese people. This system is similar to the DW system, since they only differ in interior materials; while the former is filled with lightweight mortar, the latter mainly uses insulation material such as TFRB or FR4.

Figure 1 shows the typical LIMI system in Taiwan. This system consists of horizontally laid out U-shaped tracks and vertical C-shaped studs as its main frames. The U-shaped tracks act as the top and bottom tracks, fixed on the structural components such as slabs or beams with powder-driven nails. The vertical C-shape studs are cut into an appropriate length according to the height of the wall and then are fit snug-tight in the U-shaped tracks. For the LIMI systems, because of the heavy mass of the partition walls

and the pressure during the process of grouting, the stud space are closer with a general distance between each stud ranges from 24-30 cm. If the end studs of the partition walls shown in Figure 2 come into contact with the structural components like columns or walls, they also have to be fixed on the structural components with powder-driven nails, like the U-shaped tracks. After the frame is installed, the surface panels (fiber cement boards) are then fastened to studs as well as the bottom track with tapping screws, whose spacing is 10 cm. There is a 1- cm clearance (see Figure 2) kept between the panels and the structure members. At last, holes were dig on the surface panels and mortar enters from them. The lightweight mortar for grouting is composed of cement, sand and Styrofoam pellets, of which the percentage is 1:2:4.

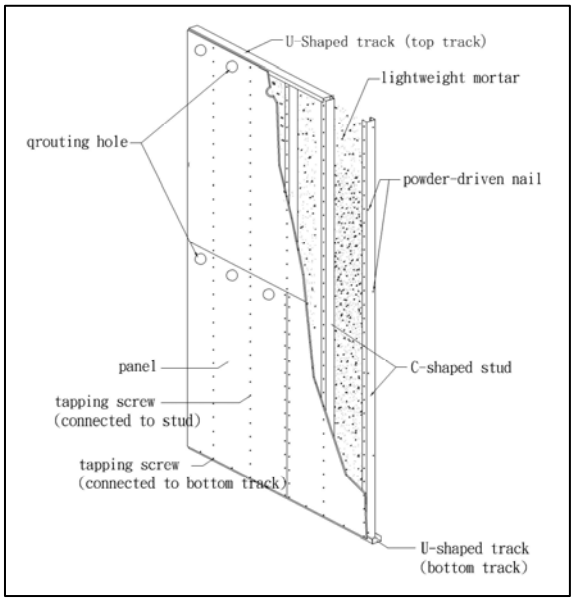


Figure 1 Typical construction of the LIMI system

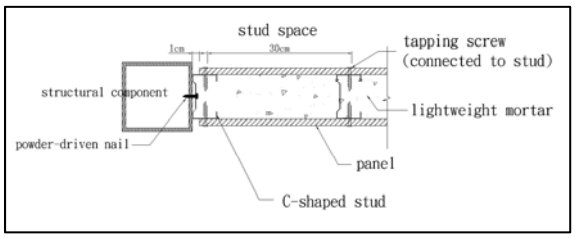


Figure 2 Details of the LIMI system

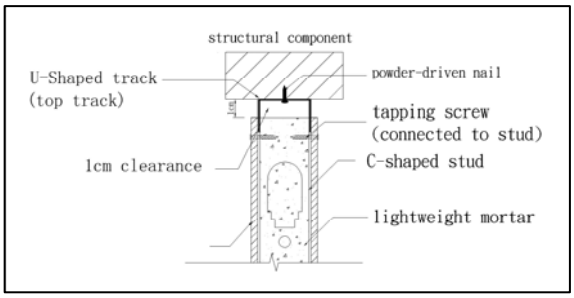


Figure 3 Details of the LIMI system

To prevent the LIMI from carrying vertical dead loads from the upper structures, the studs should not be connected directly with the top track web and the distance between them will be 1-1.5 cm. Similarly, there should be a 1 cm clearance between the mortar and the top track web during grouting (see Figure 3).

The major characteristics of the LIMI system are as follows:

1. Thickness and weight: The thickness of the LIMI system is about 7.5-9 cm. The weight is 60~160kgf/m².
2. Construction: The construction goes fast, and on average a worker per day can accomplish 12 m² of the wall.
3. Fireproofing, moisture-proofing and sound-proofing: The fireproofing capacity can last for 1-2 hours, and the other two functions are satisfied especially the characteristic of sound-proofing is much better than the DW system.
4. Object-hanging: As the walls are solid due to grouting, the characteristic of object-hanging is similar to that of RC walls.
5. Guard against theft: It works better than the DW system and this is one of the reasons why the LIMI system is commonly used in recent years.

3. EXPERIMENTAL PROGRAM

Full-scale specimens of the LIMI system were constructed in this study. Since the partition walls are considered displacement sensitive, the experimental loading steps were displacement controlled by an actuator. The specimens were tested with lateral cyclic loading, and the damage patterns were investigated and recorded during each drift level. This study included two groups of experiments. The first group was to study the seismic performances of the current practice of the LIMI system in Taiwan. The second group experimented on retrofitted tests of partition walls to minimize the possibility of damage during earthquakes.

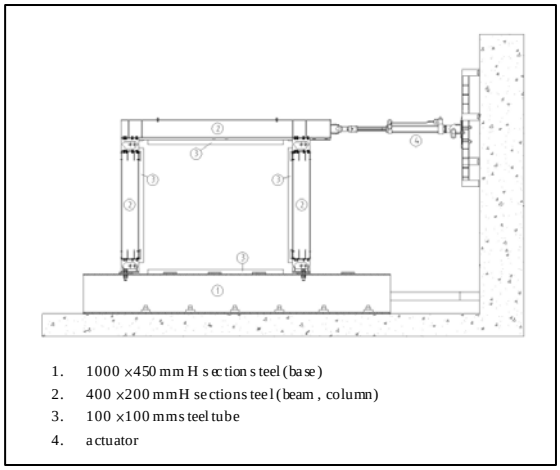


Figure 4 Details of the test frame

A steel test frame shown in Figure 4, composed of one 1000 ×450 mm H section steel (base) and three 400 ×200 mm H section steel, served as beam and column, was built. The joints of the frame were designed as hinges. Inside the frame were 100 ×100 mm steel tubes, which represented the building structures and allowed the specimens to be

constructed on the frame. The actuator was connected to the H section beam, and the cyclic loading was applied from the actuator through the frame to the specimens to simulate the partition walls under earthquakes. The specimens were tested by FEMA-461 experimental program (Figure 5), which provided recommended testing, loading history, and documentation procedures for the investigation of the seismic performance of the partition walls. The actuator was displacement controlled with the velocity of 1.38mm/sec, and 12 different drift levels were tested in sequence (0.15%, 0.21%, 0.29%, 0.41%, 0.57%, 0.8%, 1.1%, 1.5%, 2.1%, 3.0%, 4.0% and 5.0%). The damage conditions were recorded during each level until the specimens damaged seriously or about to overturn.

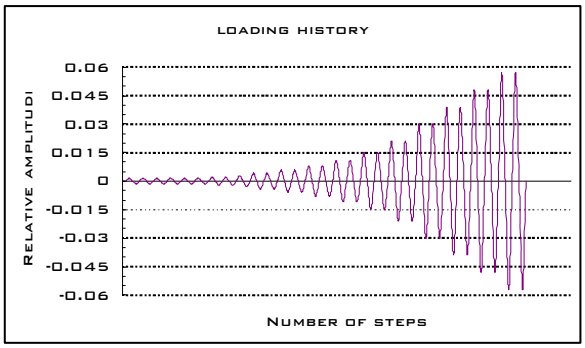


Figure 5 Displacement-controlled loading history

A total of seven specimens (W1, W2, …, W7) were tested in this study. Four single specimens were subjected to the in-plane and out-of-plane loading respectively, and the other 3 specimens were combinations of both in-plane and out-of-plane walls in T and L shape. The out-of-plane specimens were 2720 mm high and 1400 mm long, while the in-plane specimens were 2720 mm high and 3250 mm long. About the L shape and T shape specimens, the out-of-plane walls were 800 ×2720 mm for the former and 1500 ×2720 mm for the latter, and the in-plane walls were 800 ×2250 mm for both. The thickness of the walls was 77 mm including two 6 mm surface panels and the interior mortar. Each specimen had PVC water piping inside.



Figure 6 (a)W1, (b) W2, (c)W3, and (d)W4

Specimens from W1 to W4 followed the typical LIMI system construction practices in Taiwan. Both W1 and W2 were single wall specimens, and W1 specimen was tested out-of plane while W2 was tested in-plane. W3 and W4 specimens were combinations of two perpendicular walls, and the types of W3 and W4 were T shape wall and L shape wall. Figure 6 shows the pictures of the specimens.

W5 and W6 specimens were the comparison groups to W2, which were also subjected to in-plane loading. Details of W5 specimen were almost the same as W2 but adjusted the distance between each powder-driven nail from 60 cm to 30 cm. W6 specimen changed parts of the typical construction especially at the end studs. The end studs in W2 specimen were fastened both to the structural components and the panels; nevertheless, the end studs in W6 were only fastened to the structural components. Additional studs shown in Figure 7 were installed near the end studs and the panels were fastened on them. Between the end stud and the additional stud was filled with TFRB in order to satisfy the fireproofing capacity. In addition, the panels and the bottom track were fixed together in W2 but separated in W6, and the PVC water pipe was wrapped by ceramic fiber carton in W6 specimen. Figure 8 shows the improved construction in W6 specimen.

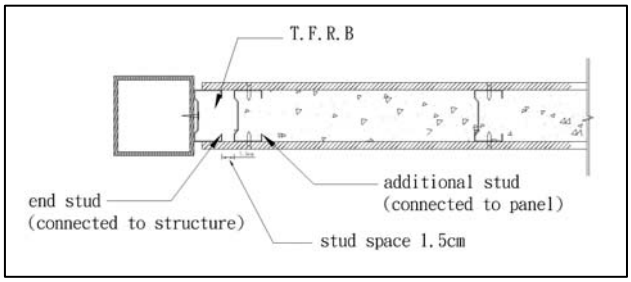


Figure 7 Details of W6 specimen

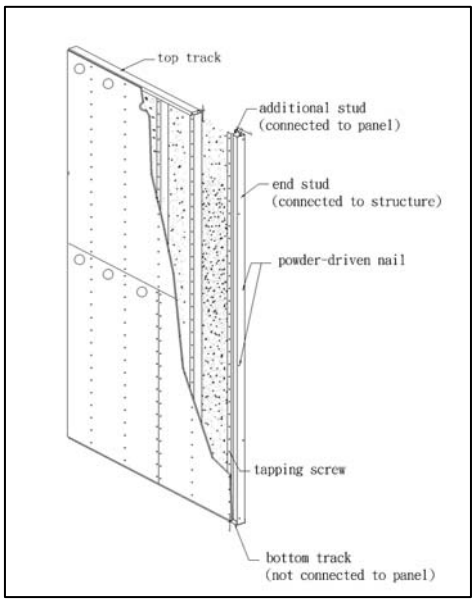


Figure 8 Construction s of W6 specimen

W7 specimen was T shape walls and the construction was similar to W6. In comparison with W3 specimen, who has panels of the in-plane wall directly connected to the out-of-plane wall, a 1cm spacing was left in W7 specimen (see Figure 9).

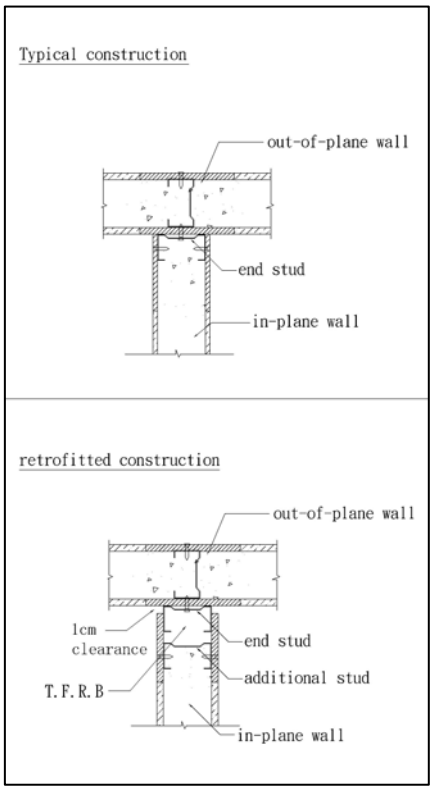


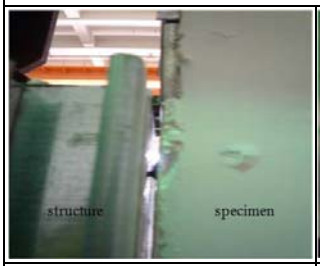
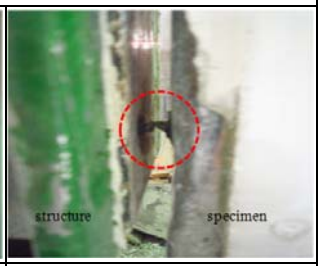
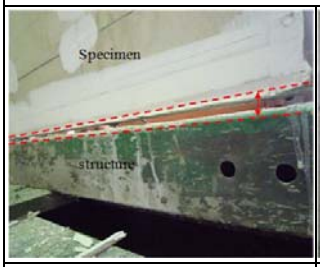
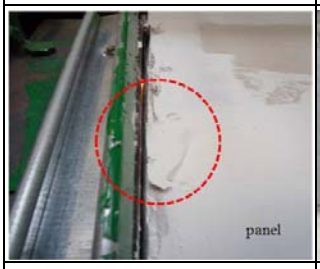
Figure 9 Details of W7 specimen

4. EXPERIMENTAL PROGRAM

Some typical damage patterns of the current LIMI system have been revealed in the first group of the experiments. Failure happened mainly on the end studs, bottom tracks, panels, the water piping and the junction of two walls. Since the end studs were directly fastened to the structures with powder-driven nails, the inter-story drift from the structures was firstly transferred to the interfaces and then to the specimens. Therefore the initial visible damage to the specimens was the separation of the end studs from the structure components. With increasing drift levels, the specimens were uplifted and the bottom tracks were pulled out from the structures. Slight panel damage appeared generally at the top corners and the damage progressed throughout testing. For T and L shape specimens, the connections between two walls were easily damaged and the fracture of the water pipe was observed in all specimens at large drifts. Table 1 lists the typical damage patterns observed from the experiments.

Table 2 shows the earlier stage of different damage patterns in the first group of experiments. From the results, damage to the W1 specimen was very limited and the specimen was almost remained intact. This condition revealed that the out-of-plane loading posed little threat to the partition walls. Compared with W1, obvious and severe damage occurred in the W2 specimen, which was subjected to the in-plane loading. The first failure sign at a drift ratio of 0.8% resulted in separation of the end studs from the structure components. Subsequently, separation zone increased throughout testing and isolated the LIMI from the structures.

Table1 Typical damage patterns

1. End studs failure	
	
Separation between the end studs and the structure components.	Most of the nail heads were pulled out from the end studs and the nails were also damaged.
2. Bottom tracks failure	
	
The specimens were uplifted from the structures.	Some nails were directly pulled out from the structures.
3. Panels failure	4. Water pipe failure
	
Local cracking of the panels.	Shear failure of the water pipe.
5. Junction failure of two walls	
	
Separation at the junction of two walls.	The top track flanges were bended and the out-of-plane walls leaned.

At a drift ratio of 1.5%, separation spread apparently along the interfaces and most of the nail heads were pulled out from the end studs. Other than stud separation, screw embedding was observed at a drift ratio of 1.5%, and the screws were pulled into the fiber cement boards. However, this failure mode was not severe and could be repaired with mud and paint. Failure of the track fasteners occurred only at the bottom. In comparison with the top track, the bottom track was attached to the surface panel but the top track wasn't. While the loading made the specimen rotate and

slide, the powder-driven nails at bottom track were engaged in uplift and shear. The fastener failure appeared to have occurred in two primary modes: the fasteners were threaded through the bottom track and, less frequently, they were tilted. These failure modes were observed at a drift ratio of 1.5%.

Table2 Damage progression of W1, W2, W3 and W4 specimens

Damage pattern	inter-story drift ratio			
End Studs failure	Visible separation appeared between the end studs and the structure components.			
	W1	W2	W3	W4
	none	0.8%	0.8%	0.8%
	Some nail heads were pulled out from the end studs.			
	W1	W2	W3	W4
	none	1.1%	1.1%	1.1%
	Most of the nail heads were pulled out from the end studs and the separation spread apparently.			
	W1	W2	W3	W4
	none	1.5%	1.5%	1.5%
Bottom tracks failure	Visible separation appeared between the bottom tracks and the structure components.			
	W1	W2	W3	W4
	none	1.1%	1.1%	1.1%
	Some fasteners of the bottom tracks were tilted and were threaded through the bottom tracks.			
	W1	W2	W3	W4
	none	1.5%	1.5%	1.5%
	Most of the fasteners were threaded through the bottom tracks and the walls slid.			
	W1	W2	W3	W4
	none	2.1%	2.1%	2.1%
Panels failure	Local cracking of the panels.			
	W1	W2	W3	W4
	none	1.1%	1.5%	1.5%
	Widespread collapse of the panels.			
	W1	W2	W3	W4
	none	2.1%	3.0%	3.0%
Water pipe failure	shear failure of the water pipe.			
	W1	W2	W3	W4
	none	2.1%	2.1%	3.0%
Junction failure	Visible separation appeared at the junction of two walls.			
	W1	W2	W3	W4
	none	none	0.8%	0.8%
	The separation spread widely throughout the junction.			
	W1	W2	W3	W4
	none	none	1.5%	1.5%
	Both the top and the bottom tracks were damaged and the out-of-plane walls started to move.			
	W1	W2	W3	W4
	none	none	1.5%	1.5%
	Severe damage to the top track flanges and the walls leaned seriously.			
	W1	W2	W3	W4
	none	none	3.0%	3.0%

The 1 cm clearance between the panels and the structure components was lost as testing progressed. Subsequently, at large drifts the panels came into contact with the structures and were under compression and shear. The panels sustained localized cracking at the top corners of the walls at a drift ratio of 1.1%, and widespread damage appeared at a drift ratio of 2.1%. At the same drift level, the water piping experienced shear failure.

For W3 and W4 specimens, the damage progression of the in-plane walls resembled that in W2. But another significant failure occurred at the out-of-plane walls. As the specimens were cycled back and forth, the intersection at in-plane and out-of-plane walls was damaged most severely. In addition to the separation appeared at the junction, the top track flanges were bended and no longer restrict the out-of-plane walls. The separation was visible at a drift ratio of 0.8% and was totally separated at a 1.5% drift ratio. At a drift ratio of 3.0%, the out-of-plane walls leaned seriously and the testing stopped in fear of collapse.

Table 3 shows the results of W5 and W6 specimens. An intention of strengthening the shear resistance was applied in W5. From the results, it seemed that increasing the number of powder-driven nails had only small contribution to the water piping. The other damage patterns of W5 were observed at the same drift levels as that of W2. The retrofit construction in W6 specimen intended to reduce the connection between the partition walls and the structure components. The end studs and the bottom tracks fastened to the structures were not attached to the specimen. Despite the end stud flanges were squeezed by the additional studs at a drift ratio of 1.5%, damage to the fasteners was very limited. As the results, the bottom track remained intact and the shear failure of the water piping was finally appeared at a 4.0% inter-story drift ratio. Besides, widespread fall-off of cracked panels occurred at a very large drift ratio of 5%. The testing results of W7 specimens were shown in Table 4. In comparison with the results of W3 specimen, many problems had been improved.

Table3 Damage progression of W2, W5, and W6 specimens

Damage pattern	inter-story drift ratio		
End Studs failure	Visible separation appeared between the end studs and the structure components.		
	W2	W5	W6
	0.8%	0.8%	none
	Some nail heads were pulled out from the end studs.		
	W2	W5	W6
	1.1%	1.1%	none
	Most of the nail heads were pulled out from the end studs and the separation spread apparently.		
	W2	W5	W6
	1.5%	1.5%	none
	The end stud flanges were squeezed by the additional studs		
	W2	W5	W6
	none	none	1.5%
Bottom tracks failure	Visible separation appeared between the bottom tracks and the structure components.		
	W2	W5	W6
	1.1%	1.1%	none
	Some fasteners of the bottom tracks were tilted and were threaded through the bottom tracks.		
	W2	W5	W6
	1.5%	1.5%	none
	Most of the fasteners were threaded through the bottom tracks and the walls slid.		
	W2	W5	W6
	2.1%	2.1%	none
Panels failure	Local cracking of the panels.		
	W2	W5	W6
	1.1%	1.1%	2.1%
	Widespread collapse of the panels.		
	W2	W5	W6
	2.1%	2.1%	5.0%
Water pipe failure	shear failure of the water pipe.		
	W2	W5	W6
	2.1%	3.0%	4.0%

Table4 Damage progression of W3 and W7 specimens

Damage pattern	inter-story drift ratio	
End Studs failure	Visible separation appeared between the end studs and the structure components.	
	W3	W7
	0.8%	none
	Some nail heads were pulled out from the end studs.	
	W3	W7
	1.1%	none
	Most of the nail heads were pulled out from the end studs and the separation spread apparently.	
	W3	W7
	1.5%	none
	The end stud flanges were squeezed by the additional studs	
	W3	W7
	none	1.5%
Bottom tracks failure	Visible separation appeared between the bottom tracks and the structure components.	
	W3	W7
	1.1%	none
	Some fasteners of the bottom tracks were tilted and were threaded through the bottom tracks.	
	W3	W7
	1.5%	none
	Most of the fasteners were threaded through the bottom tracks and the walls slid.	
	W3	W7
	2.1%	none
Panels failure	Local cracking of the panels.	
	W3	W7
	1.5%	2.1%
	Widespread collapse of the panels.	
	W3	W7
	3.0%	4.0%
Water pipe failure	shear failure of the water pipe.	
	W3	W7
	2.1%	4.0%
Junction failure	Visible separation appeared at the junction of two walls.	
	W3	W7
	0.8%	2.1%
	The separation spread widely throughout the junction.	

	W3	W7
	1.5%	2.1%
	Both the top and the bottom tracks were damaged and the out-of-plane walls started to move.	
	W3	W7
	1.5%	2.1%
	Severe damage to the top track flanges and the walls leaned seriously.	
	W3	W7
	3.0%	3.0%

5. CONCLUSION

According to the testing result, the rotational behavior seems to be the major problem of the current LIMI system and causes the fasteners to be pulled out easily. This situation is because of the partition walls are tightly connected to the structural components, therefore the partition walls were damaged easily as soon as the structures deformed. A retrofit construction is applied in this study which reduces the connection between the partition walls and the structural components, and the results have significantly improved with the retrofit details. The retrofit construction has made the partition walls slid rather than rotate and delayed the deformation and the damage of the walls and the water piping against the story-drift. Most important of all, the boundary conditions of the walls remained intact, which efficiently prevents the partition walls from overturning out-of-plane.

Acknowledgements:

This study was supported by the National Science Council, Taiwan, (NSC 100-2625-M-006-004). The authors are grateful to this support.

References:

Lee, T. H., Kato, M., Matsumiya, T., Suita., and Nakashima, M. (2006). "Seismic performace evaluation of non-structural components:Drywall partitions." Earthquake Engineering and Structural Dynamic**36**,367-382.

Restrepo, J.I., and Bersofsky, A. (2010). "Performance characteristics of light gage steel atud partition walls." Thin-Walled Structures**49**,317-324.

Chen J.F. (2000). "Seismic Behaviour Study of Light-gage Partition Walls in Taiwan." Master Thesis, National Cheng Kung University, Tainan, Taiwan

Lu Y.H. (2011). "Deformation And Damage Behavior of Gypsum Partition Wall Under Earthquake Loading." Master Thesis, National Cheng Kung University, Tainan, Taiwan

Federal Emergency Management Agency (FEMA). (2007). "Racking Protocol for Testing of Nonstructural Components fpr the Purpose of Seismic Performance Assessment, " FEMA 461, Washington, D.C.

10CUEE CONFERENCE PROCEEDINGS
10th International Conference on Urban Earthquake Engineering
March 1-2, 2013, Tokyo Institute of Technology, Tokyo, Japan

FUNDAMENTAL STUDY ON SIMPLE EVALUATION METHOD FOR SEISMIC RESISTANCE OF WALL AND FIXED FURNITURE

Yutaka Yokoyama[1], Takeshi Yokoi[2] and Yuki Kawamura[3]

1) Assoc. Prof., Dept. of Architecture and Building Eng., Tokyo Institute of Technology, Dr. Eng.
2) Junior Assoc. Prof., Dept. of Architecture and Building Eng., Tokai University, Dr. Eng.
3) Graduate School, Dept. of Architecture and Building Eng., Tokyo Institute of Technology
yokoyama@arch.titech.ac.jp, tyokoi@keyaki.cc.u-tokai.ac.jp, kawamura.y.ab@m.titech.ac.jp

Abstract: To secure safety when furniture is fixed to wall, seismic resistance should be examined with an entire system which furniture, fixture and wall are combined. And, it should be considered by dynamic experiment. In this research, simple evaluation method for seismic resistance of furniture fixation wall system was established. Eleven kinds of specimen systems those seismic resistance were different from each other were selected. Those systems were constructed on a vibration table, and shaken by some kinds of real seismic waves. Amplitude of the input wave was gradually increased until specimen systems were destroyed, and limit accelerations were recorded. Then, the same specimen systems were shaken by a simple input wave based on the sine wave. This simple input wave could be generated by the simple vibration table, consisted of truck, crank shaft and power machinery. And, a suit combination of frequency and cycle number of the sine wave was discovered which destroyed systems in similar state to real seismic waves. This method of shaking a system by the simple input wave enables to grasp seismic resistance by degree of the limit accelerations. Then, it becomes possible to find out a low-quality system, and to exclude one.

1. INTRODUCTION

Furniture fixation is an important earthquake-proof method. There are a lot of cases of fixing furniture to walls compared with floors or ceilings. Therefore, to secure safety when furniture is fixed to wall, seismic resistance must be examined with an entire system which furniture, fixture and wall are combined. And, it should be considered by dynamic experiment. However, there is no general evaluation method at present, and pull-off strength of fixtures is shown at best.

The seismic resistance of non-structural systems is rarely examined in detail while designing each individual building like structural systems. Besides, furniture and fixtures are ready-made products in most cases, and there is infinity of combinations among furniture, fixture and non-structural element. Therefore, it is impossible to test all combinations by a complex large-scale test method that imitates an actual situation. To put it simply, as for the

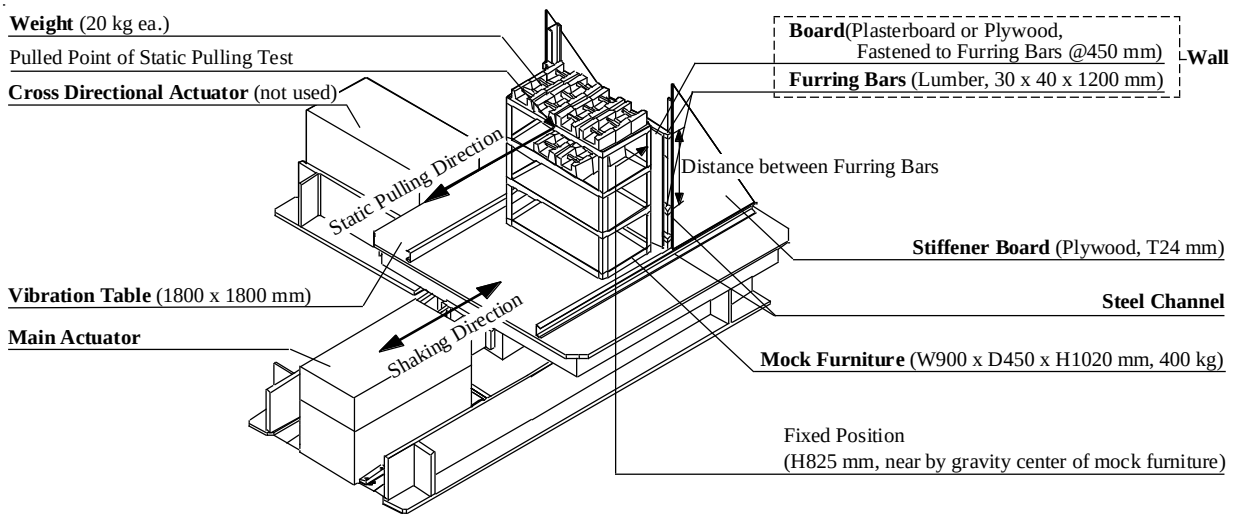


Figure 1 Outline of Specimen on Vibration Table

Table 1 Outline of Specimen

No.	Wall			Fixture	
	Distance between Furring Bars	Board Material (Thickness)	Length and Number of Screws	Length and Number of Screws or Anchors	Position in which Mock Furniture is Fixed to Board
1	300 mm	Plasterboard (12.5 mm)	20 mm x 2	25 mm x 2 (Screws)	On Furring Bar
2	300 mm	Plasterboard (9.5 mm)	20 mm x 2	20 mm x 2 (Screws)	On Furring Bar
3	300 mm	Plasterboard (12.5 mm)	20 mm x 2	20 mm x 2 (Screws)	On Furring Bar
4	600 mm	Plasterboard (9.5 mm)	16 mm x 2	16 mm x 4 (Screws)	Center between Furring Bars
5	600 mm	Plasterboard (9.5 mm)	16 mm x 2	49 mm x 2 (Anchors)	Center between Furring Bars
6	600 mm	Plasterboard (12.5 mm)	20 mm x 2	49 mm x 2 (Anchors)	Center between Furring Bars
7	450 mm	Plasterboard (12.5 mm)	25 mm x 2	49 mm x 4 (Anchors)	Center between Furring Bars
8	300 mm	Plasterboard (9.5 mm)	16 mm x 2	49 mm x 2 (Anchors)	Center between Furring Bars
9	300 mm	Plasterboard (12.5 mm)	20 mm x 2	49 mm x 2 (Anchors)	Center between Furring Bars
10	600 mm	Plywood (9.5 mm)	16 mm x 2	16 mm x 2 (Screws)	Center between Furring Bars
11	600 mm	Plywood (9.5 mm)	16 mm x 2	16 mm x 4 (Screws)	Center between Furring Bars

evaluation of the seismic resistance, it only has to be able to grasp the degree, ranks, or weak points roughly. And it is demanded to be a handy and universal method on practical use.

The purpose of this research is to establish an outline of a simple evaluation method for seismic resistance of furniture fixation wall system. In this thesis, a simple input wave which is essential to this method was examined.

2. SPECIMEN OUTLINE AND EXPERIMENT ITEMS

Figure 1 shows the outline of specimen on vibration table. As shown in the figure, steel channels and stiffener boards (triangle plywood) are fixed on a vibration table. Then, a specimen wall was constructed by lumber furring bars, a plasterboard or plywood and screws fastening the board to furring bars. Finally, mock furniture was fastened to the wall by a specimen fixture (screws or anchors). In this experiment, the horizontal vibration table of CUEE, Tokyo Tech was used.

The mock furniture imitated a bookshelf of ordinary size and shape in offices. A mass is about 400 kg, and a height of gravity center is about 880 mm. These are supposed that documents are fully stored to the bookshelf. The mock furniture is fastened to a specimen wall near the height of gravity center.

By changing distance between furring bars, material and thickness of the board, length and number of screws, stiffness of specimen wall can vary. And by changing length and number of screws or anchors, the position in which the mock furniture is fixed to the board, hardness to pull off resistance of specimen fixture can vary. By such a way, eleven kinds of specimens with a different seismic resistance were set. Table 1 shows the outline of specimens.

Experiment items of these specimens were as follows:

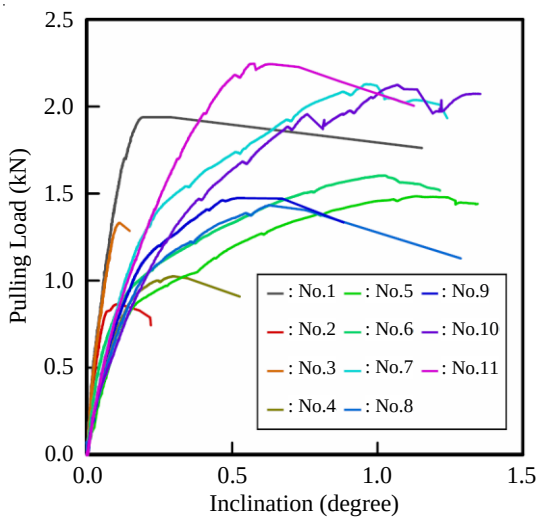


Figure 2 Relation between Pulling Load and Inclination of Mock Furniture

-- Static pulling test
-- Measurement of predominant frequency
-- Vibration test by real seismic waves
-- Vibration test by simple input waves

3. STATIC PULLING TEST

At first, a static pulling test was carried out. At the test, the top of the mock furniture is pulled horizontally as shown in Figure 1, and the load and the inclination of furniture during pulling is measured.

Figure 2 shows the relation between the load and the inclination. In all specimens, the load became maximum when the specimen was completely destroyed. Then, the maximum load was measured as “Destruction Load”, and the inclination at that time was measured as “Destruction

Table 2 Destruction Parts of Each Specimen

No.	Static Pulling Test	Vibration Test by Real Seismic Waves			Vibration Test by Simple Input Waves								
		[Hanshin]	[Hanshin Response]	[Chu-etsu]	[1.5 Hz 3 Cycles]	[1.5 Hz 5 Cycles]	[1.5 Hz 10 Cycles]	[2.0 Hz 3 Cycles]	[2.0 Hz 5 Cycles]	[2.0 Hz 10 Cycles]	[3.0 Hz 3 Cycles]	[3.0 Hz 5 Cycles]	[3.0 Hz 10 Cycles]
1	A	A	A	A	A	A	A	A	A	A	A	A	A
2	A	A	A	A	A	A	A	A	A	A	A	A	A
3	A	A	A	A	A	A	A	A	A	A	A	A	A
4	B	B	B	B	B	B	B	B	B	B	B	B	B
5	B	B	B	B	B	B	B	B	B	B	B	B	B
6	B	B	B	B	B	B	B	B	B	B	B	B	B
7	B, C	C	B	C	B	C	B	B	C	B	C	C	C
8	B	B	B	B	B	B	B	B	B	B	B	B	B
9	B	B	B	B	B	B	B	B	B	B	B	B	B
10	B	C	C	C	C	C	C	C	C	C	C	C	C
11	C	C	C	C	C	C	C	C	C	C	C	C	C

A - C show destruction parts of each specimens:
A: Fixture (Omittion of screws) B: Fixture or Board in vicinity of fixture
C: Board in vicinity of fastened point to furring bar

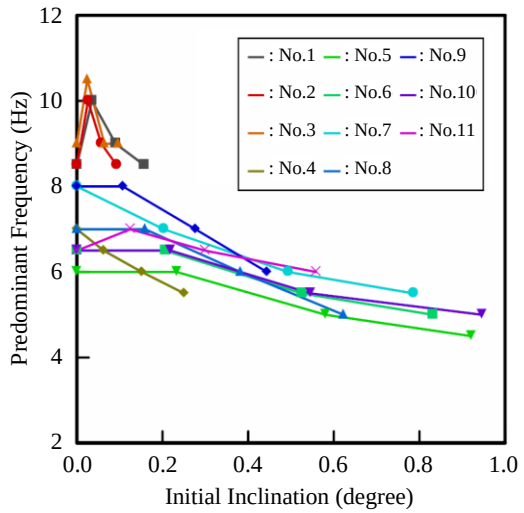


Figure 3 Relation between Predomination Frequency and Initial Inclination of Mock Furniture

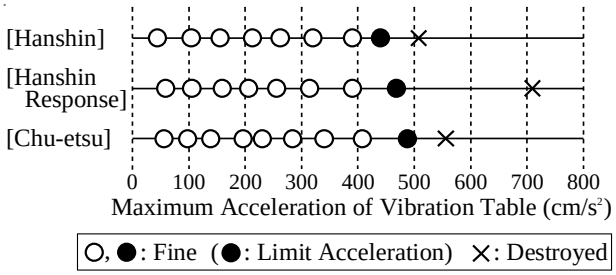


Figure 4 Relation between State of Specimen and Maximum Acceleration (Example of Specimen No. 6 by Shaking Real Seismic Wave)

Inclination". And destruction parts of each specimen were recorded too. The column "Static Pulling Test" of Table 2 shows destruction parts of each specimen in this test.

4. MEASUREMENT OF PREDOMINANT FREQUENCY

Predominant frequencies of each specimen were measured by tapping at the top of the mock furniture with hammer. Additionally, predominant frequencies of pull-apart vibration were also measured. At that time, the top of the mock furniture was pulled till prescribed "Initial Inclination" by all specimens. The initial inclinations were three kinds, 20, 50 and 80 % of destruction inclinations measured in Chapter 3.

Figure 3 shows the relation between predominant frequency and initial inclination. The frequency of zero degrees inclination is the result of hammer tapping. The following is probed from this figure:

-- Predominant frequencies of zero degrees inclination are in the range from 6.0 to 9.0 Hz.
-- When the initial inclination becomes large, predominant frequency varies. The changing tendency differs according to the specimen, and is not uniform.

This result suggests that it is impossible to describe vibration characteristics of the complex furniture fixation wall system as a simple vibration system. In another view, this result also suggests that the resonance is rarely occurred in the system by real seismic waves or simple input waves.

5. VIBRATION TEST BY REAL SEISMIC WAVES

By using the vibration table, vibration test by real seismic waves was carried out, and states of specimen after shaking ("Fine" or "Destroyed") were observed. Input waves

are three real seismic waves as follows:

[Hanshin]: The Great Hanshin earthquake (1995), N-S direction

[Hanshin Response]: Building response wave by [Hanshin], recorded at tenth floor of ten story RC building of which natural frequency is 2.52 Hz and damping ratio is 2 %

[Chu-etsu]: The Chu-etsu earthquake (2004), E-W direction

At first, each specimen was shaken by one input wave of about 50 cm/s^2 in maximum acceleration. Afterwards, the amplitude was increased by 50 cm/s^2 at every test until the specimen was finally destroyed. After the test, the destruction parts of the specimen were recorded. Additionally, behaviors of the specimen during shaking were recorded with video camera. According to this procedure, all specimens were tested by all input waves.

Figure 4 shows the example of the relation between the state of specimen after shaking and the maximum acceleration of vibration table. In this figure, circle symbols mean the state of "Fine", and cross symbol means the state of "Destroyed". Then, the maximum acceleration among "Fine", (shown in black) was recorded as "Limit Acceleration". Additionally, the column "Vibration Test by Real Seismic Waves" of Table 2 shows destruction parts of each specimen in this test.

6. VIBRATION TEST BY SIMPLE INPUT WAVES

The video that recorded the experiment of Chapter 5 was examined in detail. Then, specimen was destroyed in the vicinity to which the amplitude reached in the maximum. In other words, destruction did not advanced gradually while shaking. This discovery suggests that states of specimens are predominantly affected by a few time of the shaking in the vicinity to the maximum amplitude.

As explained above, the concept of the simple input wave based on the sine wave was set as shown in Figure 5.

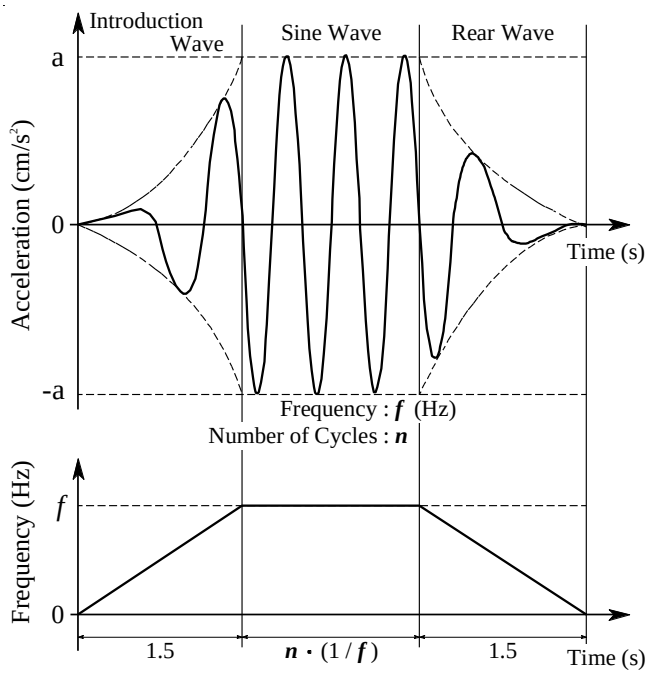


Figure 5 Outline of Simple Input Wave (Example of [2.0 Hz 3 Cycles])

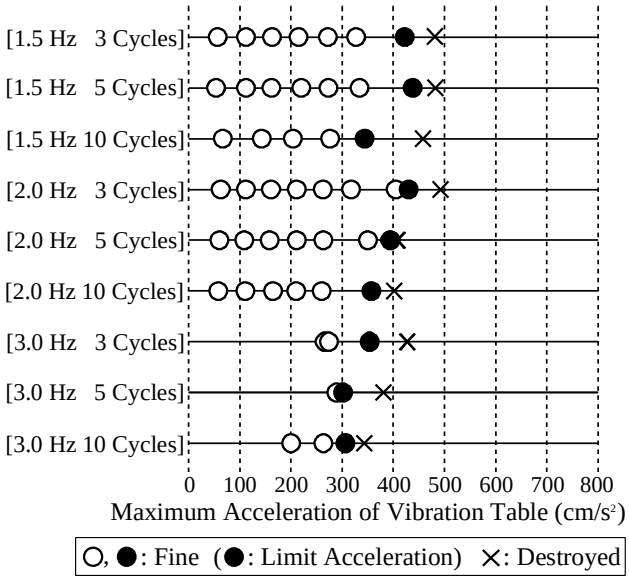


Figure 6 Relation between State of Specimen and Maximum Acceleration (Example of Specimen No. 6 by Shaking Simple Input Wave)

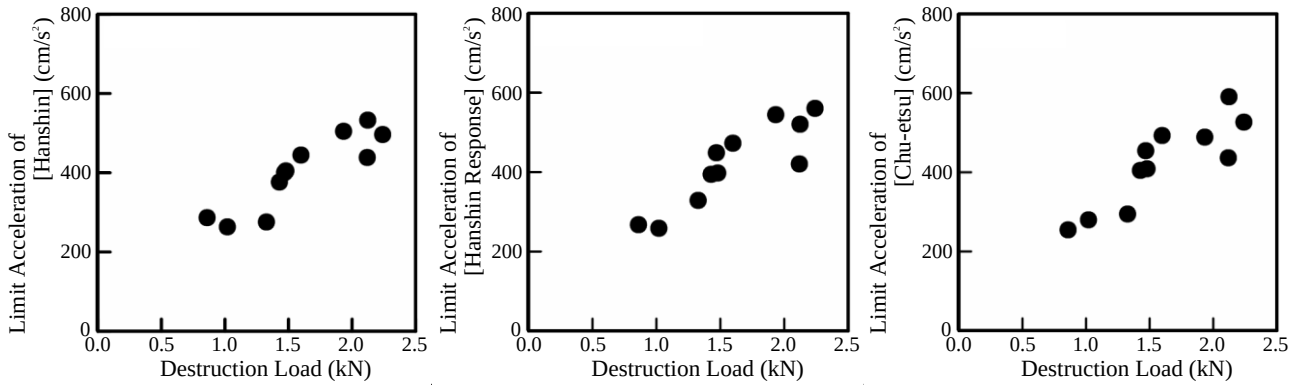


Figure 7 Relation between Limit Acceleration of Vibration Test and Destruction Load of Static Pulling Test

This is a replacement of the maximum amplitude part of real seismic waves. To reduce impacts at the beginning and the ending of shaking, the introduction wave and the rear wave were set. The continuance times of those are 1.5 sec. This input wave was proposed by authors as the simple input wave for evaluating the seismic resistance of furniture fixation free-access floors, and the appropriateness of this wave was confirmed [1].

In this thesis, the applicability of this simple input wave was examined. Specifically, several frequencies and numbers of cycles in the sine wave part were temporarily chosen according to the range of real seismic waves, and specimens were shaken by those combinations. Frequencies "*f*" are three kinds of 1.5, 2.0 and 3.0 Hz. And, numbers of cycles "*n*" are three kinds of 3, 5 and 10. Combined frequencies and cycles, there are nine kinds of input waves.

By using these waves, the same test as Chapter 5 was carried out. Then, limit accelerations and destruction parts of each specimen were recorded.

Figure 6 shows the example of the relation between the state of specimen after shaking and the maximum acceleration of vibration table. Additionally, the column "Vibration Test by Simple Input Waves" of Table 2 shows destruction parts of each specimen in this test.

7. CONSIDERATION

7.1 Comparison of Static Pulling Test to Vibration Test by Real Seismic Waves

Figure 7 shows the relation between limit acceleration of vibration test by real seismic waves (Chapter 5) and destruction load of static pulling test (Chapter 3). When seeing in detail, ranks of some specimens are different. Moreover, according to Table 2, the destruction parts are different in specimen No.10.

As explained above, it is concluded that to grasp ranks or weak points of furniture fixation wall system by static methods might be difficult.

7.2 Effect of Frequency and Number of Cycles of Simple Input Wave

Figure 8 shows some examples of comparison of limit accelerations among simple input waves of different frequency "*f*" (Chapter 6). Ranks of each specimen are almost corresponding. As mentioned Chapter 4, the predominant frequencies of specimens are in the range from 6.0 to 9.0 Hz. Though, in Figure 8, no appearance of resonance is shown. The same result was obtained from the other number of cycles. This result confirms that the resonance is hardly occurred in furniture fixation wall system.

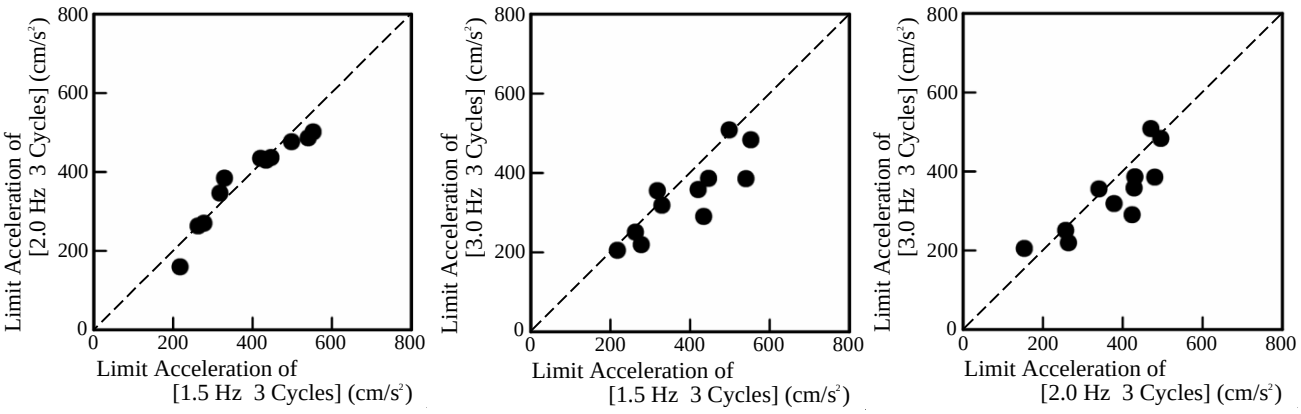


Figure 8 Comparison of Limit Acceleration among Simple Input Waves of Different Frequency (Example of 3 Cycles)

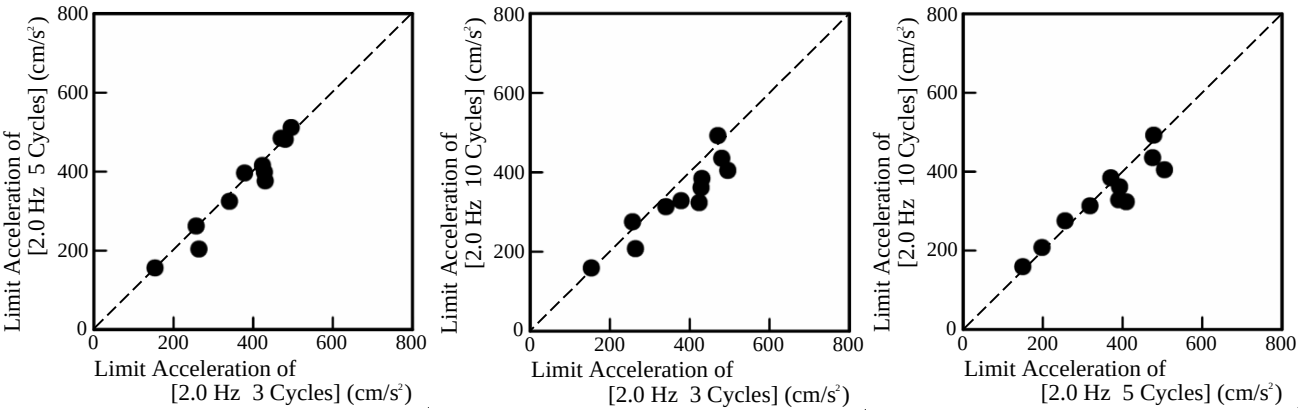


Figure 9 Comparison of Limit Acceleration among Simple Input Waves of Different Number of Cycle (Example of 2.0 Hz)

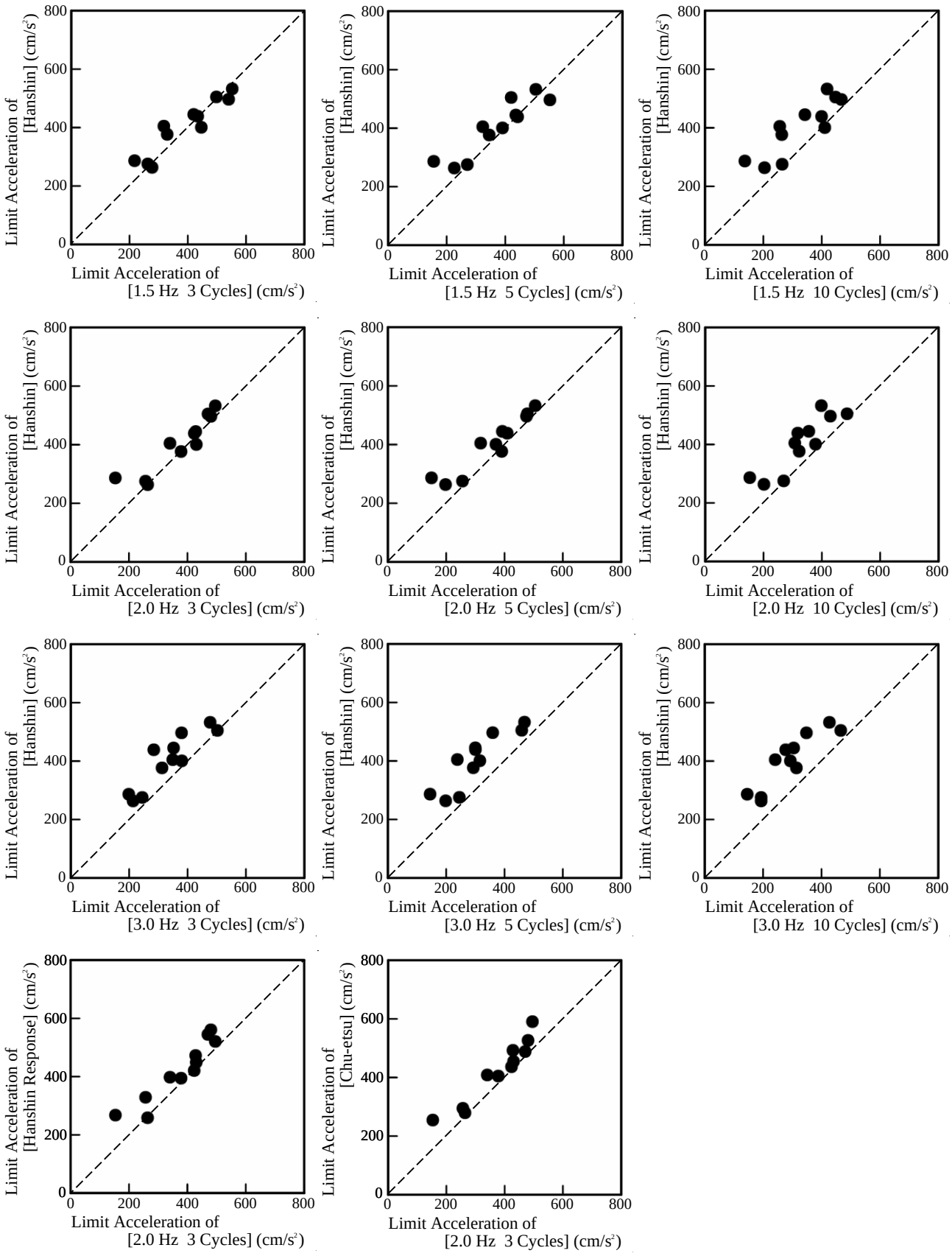


Figure 10 Examples of Comparison of Limit Acceleration between Real Seismic Waves and Simple Input Waves

By the way, limit accelerations of 1.5 Hz and that of 2.0 Hz are similar in each cycle number. But, that of 3.0 Hz is comparatively smaller. Therefore, when the frequency "f" is fixed larger than 3.0 Hz, the limit acceleration might become smaller.

On the other hands, figure 9 shows some examples of comparison of limit accelerations among simple input waves of different number of cycles "n". Ranks of each specimen are almost corresponding. But, when the frequency "f" is 1.5 or 2.0 Hz, limit accelerations of 10 cycles are comparatively smaller than that of 3 and 5 cycles. And when the frequency "f" is 3.0 Hz, limit accelerations of 5 and 10 cycles are comparatively smaller than that of 3 cycles. In other words, the limit acceleration tends to become small gradually as cycle number increases.

7.3 Comparison of Real Seismic Waves to Simple Input Waves

Figure 10 shows examples of comparison of limit accelerations between real seismic waves (Chapter 5) and simple input waves (Chapter 6). As shown in this figure, twenty-seven kinds of combinations (three kinds of real seismic waves and nine kinds of simple input waves) were examined. The following is obtained from this figure:

-- When the frequency "f" is 1.5 or 2.0 Hz and number of cycles "n" is 3 or 5, limit accelerations of simple input waves are similar to those of real seismic waves.
-- When the frequency "f" is 1.5 or 2.0 Hz and number of cycles "n" is 10, limit accelerations of simple input waves are comparatively smaller than those of real seismic waves.
-- When the frequency "f" is 3.0 Hz, limit accelerations of simple input waves are comparatively smaller than those of real seismic waves. This tendency becomes remarkable as cycle number increases.

Moreover, according to Table 2, destruction parts of simple input waves and those of real seismic waves correspond. In other words, weak points of furniture fixation wall systems should be grasped by simple input waves.

As explained above, it is concluded that the simple input wave which main part is the sine wave of 1.5 or 2.0 Hz and 3 or 5 cycles is suit. In this thesis, considering the correspondence with the past research [1] about free-access floor, the simple input wave of 2.0 Hz and 3 cycles will be used as the input wave to evaluate the seismic resistance of furniture fixation wall systems.

8. CONCLUSION

The simple input wave which is essential to establish a simple evaluation method for seismic resistance of furniture fixation wall system was examined. The system consists of complex combinations among furniture, fixture and wall, and it is impossible to grasp ranks or weak points of the system by static methods. Though it was clarified that the simple vibration test based on the sine wave enable to emulate vibration tests by real seismic waves. Considering the correspondence with the past research [1] about free-access floor's seismic resistance, the simple input wave based on 2.0 Hz and 3 cycles of sine wave is set as the appropriate input wave.

The simple vibration table to realize this input wave was already developed by authors [1]. It consists of truck, crank shaft and power machinery. In the future, the simple evaluation method for seismic resistance of entire system will be suggested based on the result of this research.

References:

[1] Yutaka Yokoyama and Takashi Yokoi: Fundamental Study on Evaluation Method for Seismic Resistance of Free-access Floor, Joint Conference of 9th International Conference on Urban Earthquake Engineering / 4th Asia Conference on Earthquake Engineering, pp.1503-1510, 2012. 3

10CUEE CONFERENCE PROCEEDINGS
10th International Conference on Urban Earthquake Engineering
March 1-2, 2013, Tokyo Institute of Technology, Tokyo, Japan

BEHAVIOR ON BUILDING EQUIPMENTS UNDER SEISMIC EXCITATIONS

Kunio Mizutani[1)], Haeyoung Kim[2)], Takuya Nakai[3)], Yasushi Kurokawa[4)] and Takao Kawashima[5)]

1) Professor, Dept. of Architecture, Faculty of Engineering, Tokyo Polytechnic University, Japan
2) GCOE Researcher, Wind Engineering Research Center, Tokyo Polytechnic University, Japan
3) Postgraduate Student, School of Architecture and Wind Engineering, Tokyo Polytechnic University, Japan
4)Group leader ,Structural Design Group, Kajima Corporation, Japan
5)Group leader of technology, Architectural Design Division, Kajima Corporation, Japan
mizutani@arch.t-kougei.ac.jp, haeyoung@arch.t-kougei.ac.jp

Abstract: In the Great East Japan Earthquake in March 2011, the building equipments such as pipe systems, duct, cable rack and ceiling, were damaged a lot while main structural members in building were not damaged. For example, pipes, cable racks and ducts were ruptured in the hanging bolt and fell down. It occurs the building cannot be used over a long period of time. In this study, the behavior of building equipments is investigated by conducting the vibration test to verify the cause of damage. Especially, the damage on sprinkler piping and hanger bolt is investigated by simulating its rupturing mechanism by experiment.

1. INTRODUCTION

In the Great East Japan Earthquake in March 2011, the building equipments such as pipe systems, duct, cable rack and ceiling, were damaged a lot while main structural members in building were not damaged. For example, pipes, cable racks and ducts were ruptured in the hanging bolt and fell down. It occurs the building cannot be used over a long period of time. In this study, the behavior of building equipments is investigated by conducting the vibration test to verify the cause of damage.

2. EXAMPLE OF DAMAGE OF RUPURE ON THE SPRINKLER PIPING AND ITS EXPERIMENTAL SIMULATION

2.1 Outline of example of damage on the sprinkler piping

The amusement center had a lot of damages on building equipment under the Great East Japan Earthquake. It is 8 stories steel structure building. Although there was no serious damage in a building main part, the ceiling of the amusement center on the eighth floor fell extensively. About 80 percent of ceilings fell down and damage was also seen many in equipment such as rupture of sprinkler piping, fall of a fan coil, and fall of an air outlet box. The damage situation of sprinkler piping is shown in Photo. 1.

The sprinkler piping is shown in Fig.1. A 1.4m branch pipe is connected to the main pipe in the vertical direction. Two or four flexible pipes are connected to the branch pipe and sprinkler head is connected to the ceiling. In the investigation after the earthquake, sprinkler piping was



Photo.1 The damage situation of sprinkler piping

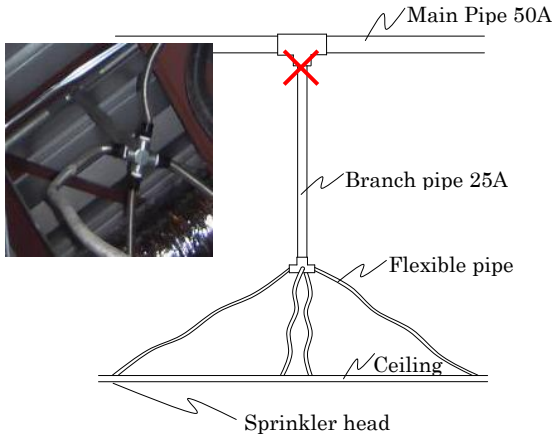


Figure. 1 Branching part of the sprinkler piping

ruptured at eight places among 50 junctions between a main pipe and a branch pipe.

2.2Outline of experiment

The experiment is conducted at the Tokyo Institute of Technology, Suzukake-dai campus in the structural testing laboratory. The carbon steel pipe for ordinary piping 25A is used for the specimen of sprinkler piping (henceforth, SP piping). A thread part is cutting as well as piping with damage. Table 1 shows pipe type used for the experiment.

2.3 Experiment method

An experiment is conducted by using the hydraulic servo fatigue tester(SAGINOMIYA SEISAKUSHO FT-2, maximum loading of 20 kN, henceforth, autograph). The SP piping is set in the shape of cantilever beam. The experiment is carried out by loading to make connection screw part of SP piping rupturing as shown in Photo. 2 and Fig. 2. A screw part of SP piping is examined, where about 5 equal divisions are thrust among ten mountains by the whole screw thread of a taper part as shown in Fig. 3. In addition, the seal tape is wound around the thread part.

2.4 Measurement method and Experiment Case

The stress acting on SP piping is measured with strain gauges on the upper and lower sides of it when the SP piping is loaded in the end part of it by an autograph as shown in Photo.4. In addition, a gap between SP piping and loading part is considered by measuring with the piston type displacement gage. The experimental condition for every case is shown in Table 2.

In Cases from 1-1 to 1-5 (specimen1), the loaded displacement is set as ±3 [mm], and the up-and-down loading is repeated three times. After that, it is carried out until the specimen is ruptured with increasing displacement at 2 [mm] intervals. In Case 2-1 (specimen2), the up-and-down loading displacement is set as ±11 [mm], and it is repeated 20 times. In Case 3-1 (specimen3), the loading displacement is set as 35 [mm] and the experiment is conducted to make the specimen ruptured by 1 time of loading.

Table.1 Pipes used for the experiment

Type	carbon steel pipes (SGP)
Outer diameter[mm]	33.249
Inner diameter[mm]	27.6
Thickness[mm]	3.2
Weight[kg/m]	2.43
Young's modulus[N/mm^2]	205000.0
Screw part	Taper pipe treads
Processing method	Cutting
Diameter of internal thread [mm]	30.291

Table.2 Experiment case

Case	Displacement [mm]	Speed [mm/s]	Numbers of Repetition
1-1	3	0.9	3
1-2	5	0.9	3
1-3	7	0.9	3
1-4	9	0.9	3
1-5	11	0.9	20
2-1	11	0.9	20
3-1	35	0.25	1



Photo.2 Hydraulic servo fatigue tester

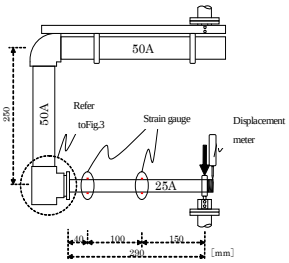


Figure.2 Experiment device

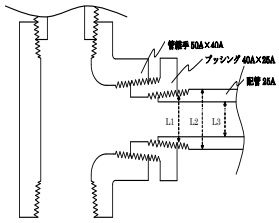


Figure.3 Screw part

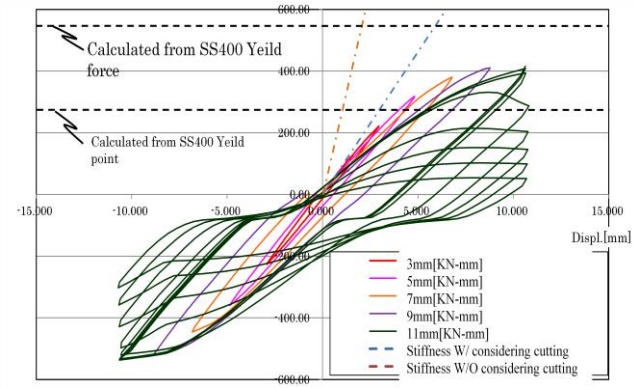


Figure.4 Relation of displacement and moment in Cases from 1-1 to 1-5

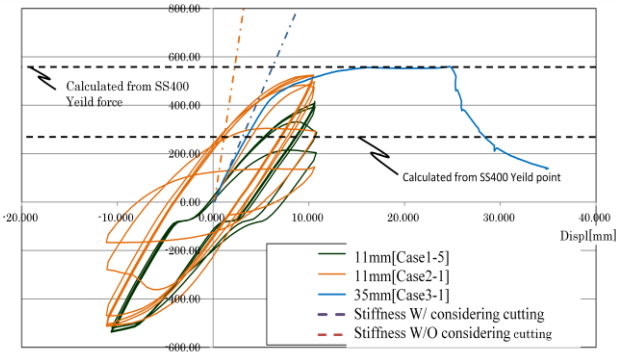
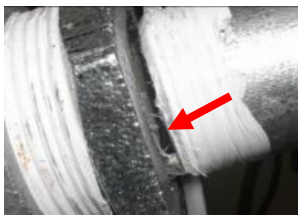


Figure.5 Relation of displacement and moment in Case 1-5, 2-1 and 3-1





(1)outside (2)inside

Photo.3 Connection part of SP piping after loading

2.5 Experiment result

A Relationship between moment(M) of connection part of SP piping and displacement of end part of pipe in Cases from 1-1 to 1-5. is shown in Fig.4. The secondary section moment with considering cutting part is 12,841mm^4 and without consideration, it is 37,110mm^4. Although it is mostly in agreement with the descending slope which the relation between M and displacement calculated in consideration of the cross-sectional deficit by the machined thread of SP piping terminal area in Case 1-1, a descending slope becomes loose and a stiffness of pipe is decreasing as a loading displacement is increasing. Moreover, in case the loading displacement is ±11 [mm], M in the maximum displacement begins to decrease from the 7th loading, and it becomes about 1/4 of the beginning at the 10th loading. As shown in Photo.3, the connection part of SP piping at this time is ruptured and has a crack. The photo.3 shows the inside of a specimen.

The result of Case 2-1 and 3-1 is shown in Fig. 5. The specimen of Case 2-1 is ruptured by the 5.5th loading, although the stiffness at the first time is strong as compared with the specimen of case 1-5.

In Case 3-1, the specimen is ruptured after the M increases up to 560 kN-mm by 25 mm of displacement. From this result, when SP piping is loaded repeatedly, it is ruptured by about 75% of stress where M is about 430kN-mm compared with the stress fractured by one time of loading.

3. EXAMPLE OF DAMAGE OF RUPURE ON THE HANGER BOLT AND ITS EXPERIMENTAL SIMULATION

3.1 Example of damage on the hanger bolt

The damage Case 1 is shown in Fig. 6. A 100 mm hanger bolt which hung a 200A pipe was ruptured at anchor part, and piping fell down in the steel structure factory. The damage Case 2 is shown in Fig.7. A hanging bolt which hung the ceiling concealment package was ruptured at anchor part, and the ceiling board dropped. The damage Case 3 is shown in Fig.8. A hanger bolt which hung the large-sized fan coil unit was ruptured, and the hanger bolt which hung apparatus was also ruptured.

3.2 Investigation of rupture at hanger bolt by shaking table test

In order to simulate the rupture of hanger bolt, the real large shaking table test is conducted as shown in Photo.4. The response under the Great East Japan Earthquake in the fifth floor of 5 stories steel building which exists really is used as a input wave in the experiment as shown in Fig.9-10.

3.3 Experiment result

Table 3 shows experiment results. A 20cm hanger bolt which hung 200A piping is ruptured in 104~105 seconds regardless of existence of vibration stopper.

About apparatus (total enthalpy heat exchanger), two 50cm hanger bolt are ruptured without vibration stopper. In other cases, although a hanger bolt is not ruptured, it is separated from metal fittings of apparatus and the damage is seen in vibration stopper (simplified mold).

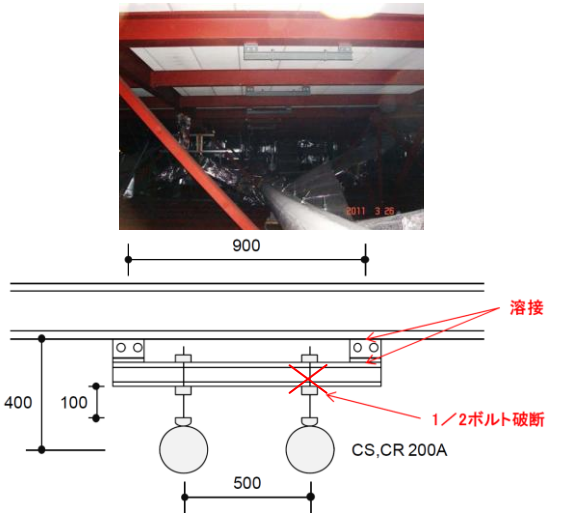


Figure.6 Damage Case 1 on hanger bolt

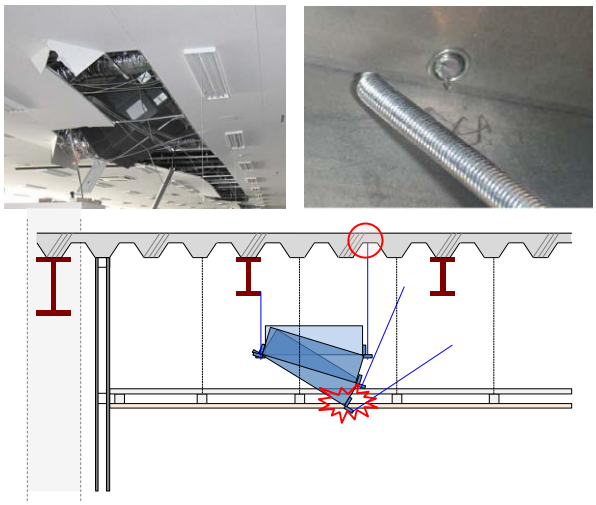


Figure.7 Damage Case 2 on hanger bolt

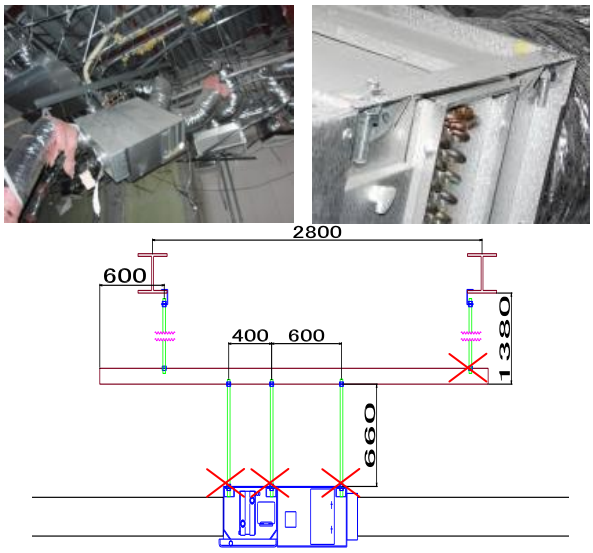


Figure.8 Damage Case 3 on hanger bolt

4. CONCLUSIONS

The behavior of the building equipment under the seismic excitation is conducted by vibration test. Especially, the damage on sprinkler piping and hanger bolt is investigated by simulating its rupturing mechanism by experiment.



Photo.4 Shaking table test

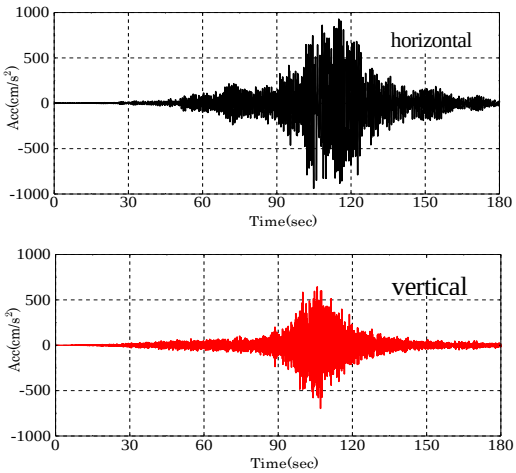


Figure.9 Time history of input acceleration

Table.3 Peak value of input wave

	Acc.(gal)	Vel.(kine)	Dis.(cm)
Horizontal	**939**	97	19
vertical	**696**	19	6

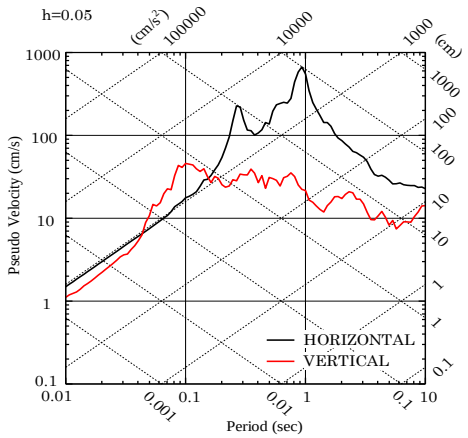


Figure.10 pseudo velocity response spectrum

Acknowledgements:

I wish to express my sincere appreciation to Prof. Motoyui of the Tokyo Institute of Technology and his students for their expert guidance and cooperation.

References:

1) NAKAI Takuya, MIZUTANI Kunio, KIM Haeyoung : Study on the Earthquake Resistance Method for the Building Equipment (Part1)Experimental Study about the Damage Factor of the Piping Equipment System Under the 2011 Tohoku Pacific Earthquake, Summaries of Technical Papers of Annual Meeting, AIJ, 2012.9

Table3. Experiment results

-Piping 200A

Case	Type	Vibration Stopper	Hanging length	Damage state
1	A	O	20cm	Ruptured at full tread at 105 seconds
	B	X		Ruptured at full tread at 104 seconds

-Apparatus (total enthalpy heat exchanger)

Case	Type	Vibration Stopper	Hanging length	Damage state
2	A	External 4	80cm	Separation at 111 seconds
	B	X		No damage on full tread and changing at hanger bolt
3	A	Internal Cross Z	80cm	No falling and
	B	Internal Cross Simple		Separation at metal bar of vibration stopper at 104 seconds and large displacement
4	A	External 4	80cm	The vibration stopper is loose.
	B	X	50cm	Ruptured at full tread at 109 seconds

10CUEE CONFERENCE PROCEEDINGS
10th International Conference on Urban Earthquake Engineering
March 1-2, 2013, Tokyo Institute of Technology, Tokyo, Japan

INFLUENCE OF GROUND MOTION SPECTRAL SHAPE AND DURATION ON SEISMIC COLLAPSE RISK

Reagan Chandramohan[1], Ting Lin[2], Jack W. Baker[3] and Gregory G. Deierlein[4]

1) Graduate Research Assistant, Dept. of Civil and Environmental Engineering, Stanford University, California, USA
2) Post-Doctoral Fellow, Dept. of Civil and Environmental Engineering, Stanford University, California, USA
3) Assistant Professor, Dept. of Civil and Environmental Engineering, Stanford University, California, USA
4) Professor, Dept. of Civil and Environmental Engineering, Stanford University, California, USA
reaganc@stanford.edu, tinglin@stanford.edu, bakerjw@stanford.edu, ggd@stanford.edu

Abstract: The seismic collapse risk of a structure is largely influenced by the intensity and other characteristics of the earthquake ground motions. This study addresses the influence of the shape of the ground motion spectra and the ground motion duration on the structural collapse capacity, as determined by nonlinear response history analysis. The conditional spectrum is proposed as a more realistic characterization of spectral shape, compared to the commonly used uniform hazard spectrum. Ground motion duration is another important characteristic, which is quantified in terms of significant duration. The effects of spectral shape and duration on the estimated collapse capacity of a 5-story steel moment frame are demonstrated. Spectrally equivalent long and short duration record sets are employed to isolate the effects of duration. Preliminary findings indicate that cyclic strength and stiffness deterioration of components and accumulation of drift due to ratcheting can significantly reduce structural collapse capacity under long duration shaking.

1. INTRODUCTION

Calculation of the probability of structural collapse is an integral part of performance-based earthquake engineering. The intensity of ground excitation that causes structural collapse is a random variable, which is often defined by a lognormal cumulative distribution function called the collapse fragility curve – relating ground motion intensity to the probability of collapse. The collapse capacity is a common metric to evaluate the life-safety of buildings and an important component in loss assessment.

The process of estimating the collapse capacity of a structure first involves the creation of a nonlinear numerical model of the structure. Since collapse occurs after the structure has undergone large inelastic deformations, modeling the behavior of structural components at these large inelastic deformations is essential to obtain an accurate estimate of the collapse capacity. This behavior includes the cyclic and in-cycle deterioration of component strength and stiffness (see discussion of cyclic and in-cycle deterioration in FEMA Report 440, 2005).

The next step involves the selection of ground motions at different intensity levels where the characteristics of the chosen ground motions at each intensity level, such as response spectral shape (which acts as a surrogate for frequency content), duration and pulse-like characteristics closely match the characteristics of the ground motions that can be expected at the building site (NIST 2011). Choosing ground motions without ensuring this match in characteristics can lead to erroneous estimates of collapse capacity. This particular study addresses the effects of two of these characteristics: response spectral shape and duration. It is assumed that the expected values of ground motion characteristics for a particular site can be obtained either from seismic hazard curves or from seismic hazard deaggregation.

When different sets of ground motions are chosen at each intensity level, the analysis is called a Multiple Stripe Analysis (Jalayer 2003). On the other hand, where the same set of ground motions is scaled to different intensity levels, the analysis is called an Incremental Dynamic Analysis or IDA (Vamvatsikos and Cornell 2002, 2004). Multiple Stripe Analysis is considered to be more realistic and accurate than IDA since the expected spectral shape and other ground motion characteristics are likely to vary depending on the intensity level. This is in contrast to the linear scaling in the basic IDA procedure, which only addresses the change in ground motion intensity.

Nonlinear dynamic analysis is then conducted using the selected ground motion sets at each intensity level. During each analysis run, the structure is assumed to have collapsed if an unbounded increase in deformations is observed, or if the deformations exceed a rational pre-defined threshold (Haselton and Deierlein 2007). Residual deformations and other damage measures may be considered as an added layer of refinement in the performance assessment. The probability of collapse at each intensity level is then computed as the fraction of ground motions at the intensity level that causes collapse. The collapse fragility curve is then obtained by fitting a lognormal cumulative distribution function through these data points. Naturally, the number of ground motions used at each intensity level influences the accuracy of this estimate.

In this study, the reasons why response spectral shape and duration must be taken into account in ground motion selection are discussed. Finally, the effects of these two parameters on the collapse capacity of a 5-story steel special moment frame are demonstrated.

2. EFFECT OF SPECTRAL SHAPE

While a ground motion's intensity (represented here by $S_a(T_1, 5\%)$, the pseudo spectral acceleration at the 1st mode period and 5% of critical damping) alone is a strong predictor of structural response, it is well known that a structure will respond differently to two different ground motions even if they are scaled to have the same intensity. The reason for this is twofold. First, any multi-degree-of-freedom structure has many modes of vibration with different periods. Therefore, the response of such a structure is related not only to the response spectral ordinate of the ground motion at the fundamental mode period, but also to the ordinates at lower periods corresponding to the higher modes. Secondly, the spectral ordinate at any period is computed assuming linear elastic response, whereas the actual nonlinear response would usually lead to an effective elongation of the natural periods.

Due to the aforementioned reasons, spectral ordinates at periods lower and higher than the fundamental period of a structure influence its dynamic response. This effect of the spectral ordinates at all periods other than the fundamental period is referred to as the spectral shape effect. Statistical studies indicate that if two ground motions have the same $S_a(T_1, 5\%)$, and ground motion #1 has higher spectral ordinates at all other periods than ground motion #2, then ground motion #1 is more likely to result in a lower collapse capacity than ground motion #2 (Baker and Cornell 2008; Haselton et al. 2011).

This effect of spectral shape has large implications on the ground motion selection procedure, or more specifically, the response spectrum that should be used as a target for ground motion selection at each intensity level. As noted previously, the target response spectrum should be representative of the response spectra of ground motions that are expected to be observed at the site. One commonly used target response spectrum is the uniform hazard spectrum, UHS, whose ordinate at each period T is the $S_a(T, 5\%)$ value that has a specified probability of being exceeded each year, defined by the hazard level (hazard levels and spectral intensities being related by the traditional seismic hazard curve). These ordinates are obtained from Probabilistic Seismic Hazard Analysis, $PSHA$ (Kramer 1996; McGuire 2004) conducted at each individual period. As indicated in previous studies, such as Baker and Cornell (2006), traditional $PSHA$ ignores the joint probability of exceedance of a number of spectral ordinates at different periods. Therefore, once the $S_a(T_1, 5\%)$ corresponding to a certain probability of exceedance has been determined, it is conservatively assumed that expected ground motion spectral ordinates at other periods are exceeded with the same probability. Hence, it is conservative to use the UHS as the target response spectrum.

The conditional spectrum has been suggested as an alternative target response spectrum that overcomes the shortcomings of the UHS (Baker and Cornell 2006; Baker 2011; Lin et al. 2012). The conditional spectrum is defined by the conditional mean and standard deviation of the spectral ordinates at all other periods, given a spectral ordinate at a period known as the conditioning period. The conditioning period is often chosen as the 1st mode period of the structure, although other periods could be used. The conditional mean and standard deviation of spectral ordinates are obtained using seismic hazard deaggregation information and regression equations based on statistical observations of correlations between spectral ordinates (Baker and Jayaram 2008). Therefore, given a specified $S_a(T_1, 5\%)$, the conditional spectrum defines the mean and standard deviation of the expected spectral ordinates at all other periods. A procedure has been developed by Jayaram et al. (2011) to select a set of ground motions that match a target mean and standard deviation spectrum. While the conditional spectrum is not without its own challenges, such as the need to define a structure-dependent conditioning period, it provides a much more realistic representation of the seismic hazard than the UHS.

The UHS and conditional mean spectrum at the 2% in 50 year hazard level, for a site in San Francisco, are plotted in Figure 1. A set of 20 ground motions was selected from the PEER NGA West2 database (Ancheta et al. 2012) to match this UHS. Since the shape of the UHS does not change considerably at different intensity levels, this ground motion set was used to conduct an IDA. On the other hand, since the shape of the conditional spectrum changes considerably at different intensity levels, for the Multiple Stripe Analyses different sets of 20 ground motions were chosen to match the conditional spectra for 11 different intensity levels. As described later, collapse analyses using these three alternative ground motion sets were conducted: (1) an *IDA* using a single set matched to the 2% in 50 year UHS, (2) a Multiple Stripe Analysis using 11 different sets, each matched and scaled to the conditional spectra at 11 different intensities, and (3) an IDA using a single set of motions matched to the conditional spectrum at the 2% in 50 year hazard level.

3. EFFECT OF DURATION

After ground motion intensity and spectral shape have been accounted for, it is important to ensure that the durations of the selected set of ground motions match the expected ground motion duration at each intensity level (Bradley 2011). The expected durations could be obtained from seismic hazard deaggregation and a prediction model for duration. The reason duration is expected to influence the predicted collapse capacity is that structural components are known to deteriorate in strength and stiffness under cyclic loading. Therefore the longer the duration of shaking, the larger the number of deformation cycles each component is subjected to, which implies a larger deterioration in strength and stiffness. Moreover, once the

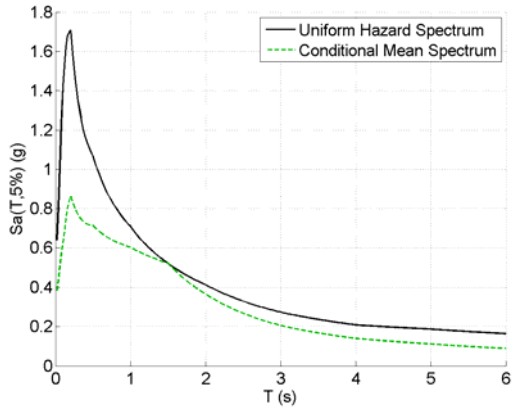


Figure 1: 2% in 50 year uniform hazard spectrum and conditional mean spectrum

structure has suffered inelastic deformations and deteriorated, long duration shaking further hastens sidesway collapse by ratcheting of deformations and drifts. Ratcheting is the phenomenon by which lateral inelastic deformations that occur early in a response history lead to amplified P-Δ moments that hasten subsequent sidesway collapse of the structure under later inelastic excursions in the same direction (Gupta and Krawinkler 2000).

Accurate evaluation of duration effects requires realistic nonlinear numerical models that incorporate in-cycle and cyclic deterioration of strength and stiffness (Ibarra et al. 2005; Lignos and Krawinkler 2011). As demonstrated below using a 5-story steel special moment frame, when included in the model, the combined effects of deterioration and ratcheting under long duration ground motions lead to significantly lower collapse capacities than short duration ground motions of similar intensity and spectral shape. The more ductile a structure and the faster the rate of deterioration, the larger the expected effect of duration of shaking (Ibarra and Krawinkler 2005).

Before the effect of ground motion duration on the predicted collapse capacity of a structure can be quantified, a suitable metric must first be chosen to measure the duration of strong shaking in an accelerogram. The observed correlation between ground motion duration and collapse capacity will largely depend on the chosen duration metric. A number of alternatives exist for defining the duration of an accelerogram (Bommer and Martinez-Pereira 1999). Among these, the following were identified as potential candidates:

- **Bracketed duration** is the time elapsed between the first and last excursions of the accelerogram above a certain acceleration threshold (commonly used thresholds are 0.05g and 0.10g).

- **Significant duration** is the time interval over which a specific percentage of the total energy represented by the integral $\int a^2 dt$ is accumulated, where a represents the ground acceleration. The commonly used ranges are 5% to 95% and 5% to 75% of the calculated energy.

- **Arias Intensity** $= \frac{\pi}{2g}\int_0^{t_{max}} a^2 dt$
  is a measure of the energy contained in an accelerogram, where t_{max} represents the length of the accelerogram. Although not purely a metric of duration, Arias Intensity is considered here since it involves integration over time and is expected to be correlated to the duration of strong shaking.

- **Cumulative Absolute Velocity** $(CAV) = \int_0^{t_{max}} |a| dt$
  is considered for the same reasons as the Arias Intensity above.

- $\boldsymbol{I_D} = \frac{\int_0^{t_{max}} a^2 dt}{PGA \times PGV}$
  is a dimensionless duration metric proposed by Cosenza and Manfredi (1997), with PGA and PGV representing the peak ground acceleration and peak ground velocity respectively.

Each of the metrics defined above were evaluated against the following properties desired in a robust metric of ground motion duration for performance-based structural assessments:

- The duration metric should not be strongly correlated to commonly used intensity measures like pseudo spectral acceleration, since it is proposed that duration be considered *in addition* to intensity and spectral shape. As such, the duration metric should provide new information not quantified by those other measures.
- The duration metric should be unaffected by the process of scaling a ground motion since analysis procedures like IDA that involve ground motion scaling would then require the re-evaluation of ground motion duration at each new intensity level.
- The duration metric should not bias the spectral shape of the chosen ground motions. In other words, long duration ground motions selected on the basis of the duration metric should not have any peculiarities in their spectral shapes.

The comparison of all the selected duration metrics against these criteria is presented in Table 1. As shown, based on the qualitative assessment of the characteristics, significant duration appears to be the most robust measure for duration.

Table 1: Comparison of the selected duration metrics

Desired Properties	**Bracketed duration**	**Significant duration**	**Arias Intensity**	**CAV**	$\boldsymbol{I_D}$
Not strongly correlated to common intensity measures	×	✓	×	×	✓
Unaffected by scaling	×	✓	×	×	✓
Does not bias spectral shape	✓	✓	✓	✓	×

To further evaluate the alternative duration metrics, *IDAs* were conducted on several structures using a set of long and short duration ground motions, where the variation in predicted collapse capacity was plotted against each of the alternative ground motion metrics. It was observed that the 5-95% significant duration, referred to as t_{5-95}, best captured the expected decreasing trend in collapse capacity with duration. Based on this data and the comparison in Table 1, the 5-95% significant duration is considered as the best duration metric to screen ground motions for analysis (Foschaar et al. 2011).

One of the challenges faced in the evaluation of duration in ground motion selection criteria has been the scarcity of long duration ground motions. Such long duration motions are expected to occur in sites where the hazard is dominated by large magnitude subduction zone earthquakes and certain soft soil conditions. The recent 2008 Wenchuan, 2010 Chile and 2011 Tohoku earthquakes have dramatically increased the available inventory of long duration motions. Nevertheless, finding recorded ground motions that both match a target response spectrum and provide a wide distribution of short to long durations remains a challenge.

To demonstrate the effect of ground motion duration on collapse capacity, a long duration record set was created containing ground motions recorded from the 1974 Lima - Peru, 1979 Imperial Valley - USA, 1985 Valparaiso - Chile, 2003 Hokkaido - Japan, 2008 Wenchuan - China, 2010 Maule - Chile, 2010 El Mayor Cucapah - USA and 2010 Tohoku - Japan earthquakes. About 3700 horizontal record pairs were acquired in total from all these events. These were baseline corrected and filtered based on the recommendations of Boore and Bommer (2005) and Boore (2005). To avoid using low intensity and short duration records, record pairs with a mean PGA of both components < 0.1g, mean PGV < 10cm/s or t_{5-95} < 45s were screened out. To prevent a single well-recorded event from dominating the selected record set, a maximum of only 25 record pairs were retained from each event. After the entire screening process, the resulting long duration record set contained 79 two-component record pairs.

A second set of short duration ground motions was selected with a spectral shape that matches that of the long duration record set. For each record in the long duration set, a corresponding short duration record was selected from the PEER NGA West2 database with t_{5-95} < 45s and a closely matching spectral shape. This corresponding set with matching spectral shapes was created so that any difference in the collapse capacities predicted by the two sets could be attributed to the difference in their durations. Figure 2 shows the comparison of the response spectra and time histories of one of the 158 pairs of long and short duration spectrally equivalent records. Figure 3 shows a comparison of the durations (t_{5-95}) of all the ground motions in each set. Both sets of ground motions were then used to conduct individual *IDAs* on the model of a 5-story steel special moment frame.

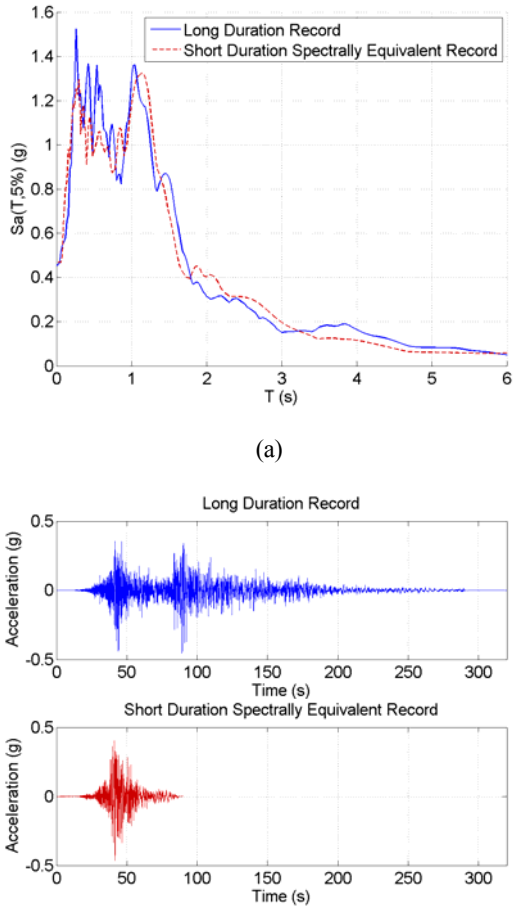


Figure 2: Comparison of (a) response spectra and (b) time series of a long and short duration record pair

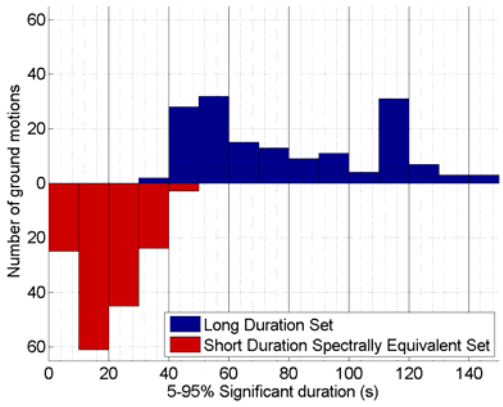


Figure 3: Comparison of the durations (t_{5-95}) of records in the long and short duration spectrally equivalent sets

4. ANALYSIS OF A 5-STORY STEEL SPECIAL MOMENT FRAME

The 2-dimensional numerical model of a 5-story steel special moment frame was created in OpenSees, the Open System for Earthquake Engineering Simulation (McKenna et al. 2006). A schematic of the elevation view of the frame is shown in Figure 4. The lumped plasticity approach was used to model material nonlinearity. The beams and columns were modeled using linear elastic elements. The hysteretic behavior of the panel zones was modeled using a tri-linear backbone curve. Zero-length plastic hinges were located at the two ends of each column and at each RBS cut. The hysteretic behavior of the plastic hinges was modeled using the Modified Ibarra-Medina-Krawinkler bilinear material model that includes a post-capping negative stiffness branch of the backbone curve to capture in-cycle deterioration, as well as an algorithm that cyclically deteriorates strength and stiffness based on the cumulative hysteretic energy dissipated (Ibarra et al. 2005). The contribution of the adjacent gravity system to the destabilizing P-Δ effect was modeled using a pin-ended leaning column. Rayleigh damping of 2.5% was assigned to the linear elastic elements of the frame.

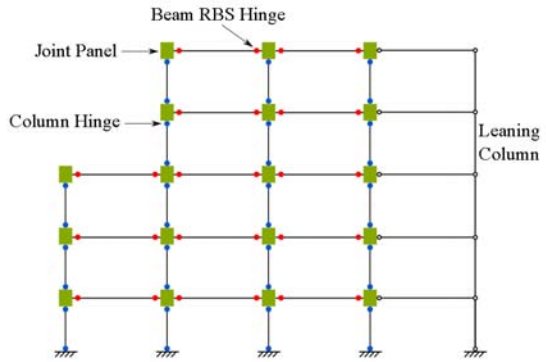


Figure 4: Schematic of the 5-story steel special moment frame model

The fundamental period of the structure was found to be 1.5s. The engineering demand parameter monitored during the nonlinear dynamic analyses was the peak story drift ratio (SDR), defined as the maximum lateral displacement of a story relative to the story below, expressed as a fraction of the corresponding story height, over all the stories and the entire duration of shaking. A peak SDR threshold of 10% was used to indicate structural collapse. The types of analyses performed, the record sets used in each analysis, as well as the collapse capacities computed as $S_a(1.5s, 5\%)$ are summarized in Table 2. The collapse fragility curves estimated from each of the five analyses are plotted in Figure 5.

Comparing the results of analyses #1 and #2, in the context of this example, targeting ground motions to the UHS instead of the conditional spectrum resulted in an under-estimation of the geometric mean collapse capacity by 22%. Comparing the

Table 2: Collapse fragility functions (quantified by geometric mean and lognormal standard deviation) for the example structure, predicted by the 5 analyses

Analysis number	Ground Motion set(s) used	Type of analysis performed	Geometric mean of predicted collapse capacity (g)	Lognormal standard deviation of predicted collapse capacity
1	2% in 50 year UHS matched set	Incremental Dynamic Analysis	0.87	0.30
2	2% in 50 year Conditional spectrum matched set	Incremental Dynamic Analysis	1.11	0.28
3	Conditional spectrum matched set at each intensity level	Multiple Stripe Analysis	1.43	0.40
4	Long duration set	Incremental Dynamic Analysis	0.53	0.42
5	Short duration spectrally equivalent set	Incremental Dynamic Analysis	0.90	0.38

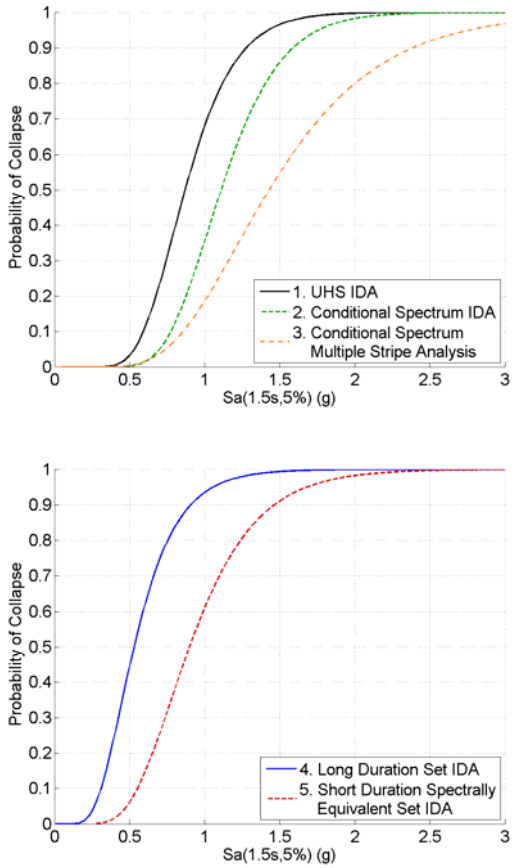


Figure 5: Collapse fragility curves predicted by the 5 analyses

results of analyses #2 and #3, it can be inferred that in the context of this example, conducting IDA instead of Multiple Stripe Analysis resulted in an additional difference of 22% in the geometric mean collapse capacity. Finally, conducting IDA using the UHS instead of the conditional spectrum Multiple Stripe analysis (#1 versus #3) led to an under-estimation of the geometric mean collapse capacity by 39%. These results are consistent with the observations made by Baker and Cornell (2006) that the UHS is a conservative choice for a target spectrum and that the changing spectral shape of the conditional spectrum at different intensity levels should be accounted for by the Multiple Stripe Analysis technique.

The results of analyses #4 and #5 indicate that with spectral shape being controlled for, the use of long duration ground motions reduced the geometric mean collapse capacity by 41%. Figure 6 shows a scatter plot of the collapse capacities predicted by each long and short duration spectrally equivalent record pair. The fact that nearly all the points lie above the 1:1 line indicates that on most occasions, within each record pair, the longer duration record predicts a lower collapse capacity. As shown in Figure 7, the decrease in collapse capacity as a function of ground motion duration (t_{5-95}) is clearly evident.

Figure 8 shows the IDA curves of the two record sets. The IDA curves indicate that the short duration ground motions on average reach a peak SDR of 7.2% before causing collapse. In contrast, the long duration ground motions reach a peak SDR of only 4.3% before collapse. This is believed to suggest that when large inelastic deformations begin to occur in the structure, aided by the resulting deterioration in strength and stiffness, a long duration ground motion is more likely to lead to structural collapse by ratcheting.

Finally, it can be argued that in the absence of a comprehensive description of the site hazard, the result of analysis #3 is expected to be most accurate since it best accounts for the effect of spectral shape. It does however neglect the effect of duration, which is expected to play a secondary role. An analysis that accounts for both spectral shape and duration is expected to produce the most accurate estimate of collapse capacity, but this would require further work to create the necessary framework to select appropriate ground motions that account for spectral shape as well as duration.

5. CONCLUSION

In any performance-based assessment, the chosen ground motions create the link between hazard analysis and demand analysis. Therefore it is critical to ensure that all the characteristics of the chosen ground motions are consistent with the site hazard to produce an accurate estimate of the demands. The effects of ground motion spectral shape and duration are particularly important for evaluating collapse under extreme (rare) ground motions. The 5-story steel special moment frame example illustrates these effects of ground motion spectral shape and duration.

With regard to spectral shape, it was argued and demonstrated that the conditional spectrum is a more accurate choice for a target spectrum than the UHS, which is

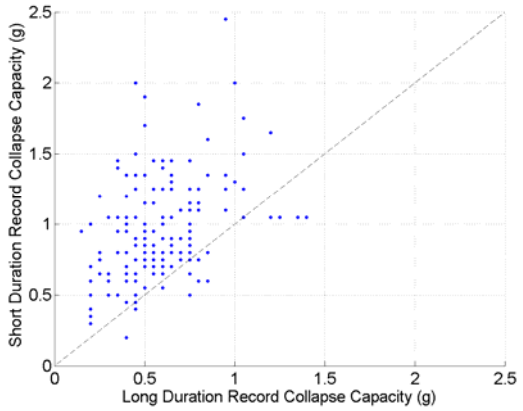
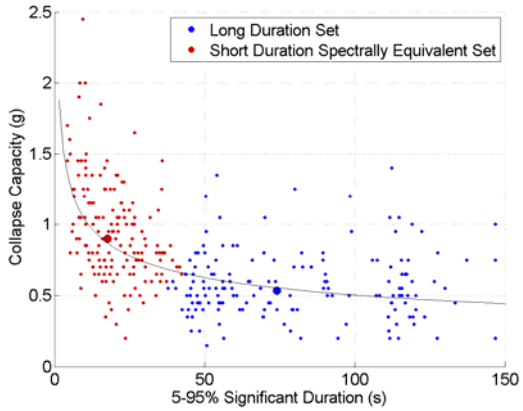
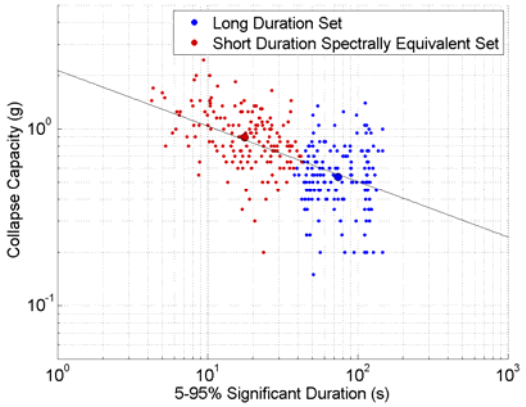


Figure 6: Scatter plot of collapse capacities predicted by long and short duration spectrally equivalent record pairs

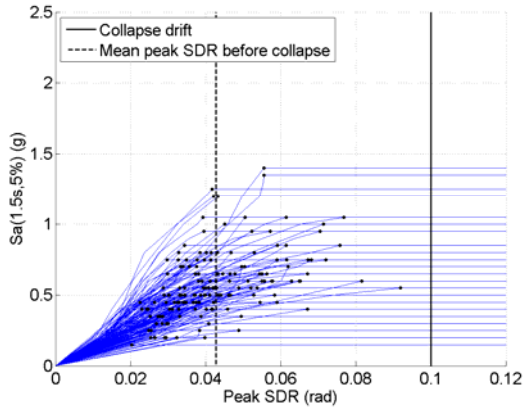


(a)

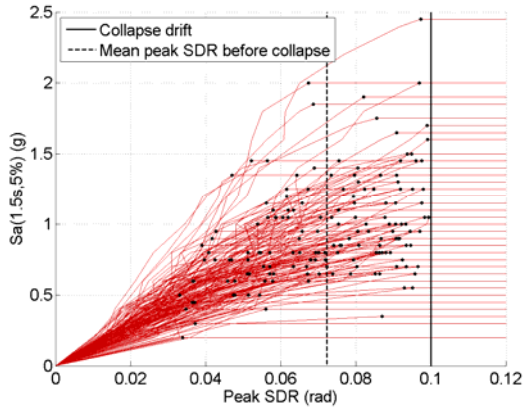


(b)

Figure 7: Collapse capacity versus duration on (a) linear plot (b) log-log plot (larger circles correspond to the geometric mean collapse capacity and geometric mean duration of all records in each set)



(a)



(b)

Figure 8: IDA curves of (a) long duration and (b) spectrally equivalent short duration sets

conservative in nature. With regard to duration, the 5-95% significant duration ($\boldsymbol{t_{5-95}}$) was identified as the duration metric best suited for use within the performance-based framework, where the collapse capacity is conditioned on ground motion intensity. It was also shown that the effect of ground motion duration on predicted collapse capacity could be quantified using spectrally equivalent record sets whose ground motions varied only in duration, represented by t_{5-95}. It should also be emphasized that the detection of ground motion duration effects requires the use of a realistic numerical model that accurately captures component deterioration. It is recognized that a number of previous studies on the effect of ground motion duration on structural damage have produced mixed and inconclusive results (Hancock and Bommer 2006). The reasons for this are believed to be (1) the use of structural models that did not incorporate deterioration, (2) the study of mildly nonlinear rather than collapsing systems, and (3) the use of inefficient duration metrics.

Consideration of both spectral shape and duration requires understanding of the seismic hazard at the site of interest so that ground motions for analysis can be selected to have spectral shapes and durations consistent with those expected at the site. Notably, spectral shape and duration values of ground motions are expected to differ for low-intensity and high-intensity ground motions, even for the same site. Therefore where possible, a different set of ground motions should be chosen at each intensity level to accurately account for these differences. This implies that Multiple Stripe Analysis, rather than IDA, is needed for collapse capacity estimation.

Acknowledgements:

This work was supported by the State of California through the Transportation Systems Research Program of the Pacific Earthquake Engineering Research Center (PEER). Any opinions, findings, and conclusions or recommendations expressed in this material are those of the authors and do not necessarily reflect those of the funding agency.

The authors would like to thank the George E. Brown Jr. Network for Earthquake Engineering Simulation (NEES) for the use of their computing facilities and the prompt help provided, when required.

The Instituto Geofísico del Perú, Departamento de Geofísica, Universidad de Chile, and the National Research Institute for Earth Science and Disaster Prevention (NIED), Japan are also acknowledged for providing the ground motions used in this study.

Finally, the authors would like to thank Wenhao Chen for providing the 5-story structural model used in the example.

References:

Ancheta, T. D., Bozorgnia, Y., Chiou, B., Stewart, J. P., Boore, D. M., Graves, R., Abrahamson, N. A., Campbell, K. W., Idriss, I. M., Youngs, R. R., and Atkinson, G. M. (2012). "PEER NGA-West2 Database : A Database of Ground Motions Recorded in Shallow Crustal Earthquakes in Active Tectonic." *15th World Conference on Earthquake Engineering*, Lisbon, Portugal.

Baker, J. W. (2011). "Conditional Mean Spectrum: Tool for Ground-Motion Selection." *Journal of Structural Engineering*, 137(3), 322–331.

Baker, J. W., and Cornell, C. A. (2006). "Spectral shape, epsilon and record selection." *Earthquake Engineering & Structural Dynamics*, 35(9), 1077–1095.

Baker, J. W., and Cornell, C. A. (2008). "Vector-valued Intensity Measures Incorporating Spectral Shape For Prediction of Structural Response." *Journal of Earthquake Engineering*, Taylor & Francis, 12(4), 534–554.

Baker, J. W., and Jayaram, N. (2008). "Correlation of Spectral Acceleration Values from NGA Ground Motion Models." *Earthquake Spectra*, 24(1), 299–317.

Bommer, J. J., and Martinez-Pereira, A. (1999). "The Effective Duration of Earthquake Strong Motion." *Journal of Earthquake Engineering*, Taylor & Francis, 3(2), 127–172.

Boore, D. M. (2005). "On Pads and Filters: Processing Strong-Motion Data." *Bulletin of the Seismological Society of America*, Seismological Society of America, 95(2), 745–750.

Boore, D. M., and Bommer, J. J. (2005). "Processing of strong-motion accelerograms: needs, options and consequences." *Soil Dynamics and Earthquake Engineering*, 25(2), 93–115.

Bradley, B. A. (2011). "Correlation of Significant Duration with Amplitude and Cumulative Intensity Measures and Its Use in Ground Motion Selection." *Journal of Earthquake Engineering*, 15(6), 809–832.

Cosenza, E., and Manfredi, G. (1997). "The improvement of the seismic-resistant design for existing and new structures using damage criteria." *Seismic Design Methodologies for the Next*

Generation of Codes, H. Krawinkler and P. Fajfar, eds., Balkema, Rotterdam, 119–130.
FEMA (2005). *Improvement of nonlinear static seismic analysis procedures*, FEMA Report 440, Washington, D.C.
Foschaar, J. C., Baker, J. W., and Deierlein, G. G. (2011). "Preliminary Assessment of Ground Motion Duration Effects on Structural Collapse." *15th World Conference on Earthquake Engineering*, Lisbon, Portugal.
Gupta, A., and Krawinkler, H. (2000). "Dynamic P-delta effects for flexible inelastic steel structures." *Journal of Structural Engineering*, 126(1), 145–154.
Hancock, J., and Bommer, J. J. (2006). "A State-of-Knowledge Review of the Influence of Strong-Motion Duration on Structural Damage." *Earthquake Spectra*, 22(3), 827.
Haselton, C. B., Baker, J. W., Liel, A. B., and Deierlein, G. G. (2011). "Accounting for Ground-Motion Spectral Shape Characteristics in Structural Collapse Assessment through an Adjustment for Epsilon." *Journal of Structural Engineering*, American Society of Civil Engineers, 137(3), 332–344.
Haselton, C. B., and Deierlein, G. G. (2007). *Assessing seismic collapse safety of modern reinforced concrete moment frame buildings (PEER 2007/08)*. Pacific Earthquake Engineering Research Center, Berkeley, CA.
Ibarra, L. F., and Krawinkler, H. (2005). *Global Collapse of Frame Structures under Seismic Excitations (PEER 2005/06)*. Pacific Earthquake Engineering Research Center, Berkeley, CA.
Ibarra, L. F., Medina, R. A., and Krawinkler, H. (2005). "Hysteretic models that incorporate strength and stiffness deterioration." *Earthquake Engineering & Structural Dynamics*, 34(12), 1489–1511.
Jalayer, F. (2003). "Direct Probabilistic Seismic Analysis: Implementing Non-Linear Dynamic Assessments." Ph.D. Dissertation, Stanford University.
Jayaram, N., Lin, T., and Baker, J. W. (2011). "A Computationally Efficient Ground-Motion Selection Algorithm for Matching a Target Response Spectrum Mean and Variance." *Earthquake Spectra*, 27(3), 797–815.
Kramer, S. L. (1996). *Geotechnical earthquake engineering*. Prentice Hall, Upper Saddle River, NJ.
Lignos, D. G., and Krawinkler, H. (2011). "Deterioration Modeling of Steel Components in Support of Collapse Prediction of Steel Moment Frames under Earthquake Loading." *Journal of Structural Engineering*, 137(11), 1291–1302.
Lin, T., Harmsen, S. C., Baker, J. W., and Luco, N. (2012). "Conditional Spectrum Computation Incorporating Multiple Causal Earthquakes and Ground Motion Prediction Models." *To appear in Bulletin of the Seismological Society of America*, 103(2a).
McGuire, R. K. (2004). *Seismic hazard and risk analysis*. Earthquake Engineering Research Institute, Oakland, CA.
McKenna, F., Fenves, G. L., and Scott, M. H. (2006). "OpenSees: Open system for earthquake engineering simulation." *Pacific Earthquake Engineering Research Center, University of California, Berkeley, CA., http://opensees. berkeley. edu*.
NIST. (2011). *Selecting and Scaling Earthquake Ground Motions for Performing Response-History Analyses (NIST GCR 11-917-15)*. National Institute of Standards and Technology, Gaithersburg, MD.
Vamvatsikos, D., and Cornell, C. A. (2002). "Incremental dynamic analysis." *Earthquake Engineering & Structural Dynamics*, 31(3), 491–514.
Vamvatsikos, D., and Cornell, C. A. (2004). "Applied Incremental Dynamic Analysis." *Earthquake Spectra*, 20(2), 523–553.

10CUEE CONFERENCE PROCEEDINGS
10th International Conference on Urban Earthquake Engineering (10CUEE)
March 1-2, 2013, Tokyo Institute of Technology, Tokyo, Japan

LOW DAMAGE CONSTRUCTION – SOME SYSTEMS ISSUES

Gregory MacRae

Civil and Natural Resources Engineering, University of Canterbury, Christchurch, New Zealand
gregory.macrae@canterbury.ac.nz

Abstract: This paper describes a number of approaches used to create "low damage" structures. It is shown that a number of low damage techniques and approaches, including post-tensioned beam approaches, rocking structures and others, may result in low-damage elements but not necessarily in low damage building systems. This paper draws on a report provided to and disseminated by the Royal Commission for the Canterbury Earthquakes. It encourages engineers to use "low-damage" technology that will result in low damage building systems.

1. INTRODUCTION

Recent earthquakes have required the demolition of a large number of structures while the life-safety design criteria has been satisfied. As a result there has been a research emphasis and some implementation of *low damage construction* (LDC) techniques. However, these techniques are not all equal, and while some damage may be reduced, other types of damage remain, or may be greater, as a result of different factors affecting the behaviour.

This discussion paper describes a number of LDC techniques and describes them in terms of their ability to actually result in low damage.

Since no structure can withstand an infinitely strong earthquake, it is necessary to firstly describe the performance objectives for LDC. MacRae (2010) proposed that a low damage structure have the performance objectives shown in Figure 1. Here one target level is provided for buildings of all importance levels (or groupings). It is considered that different importance factors provide different probabilities of meeting that performance level. The same effect may be expressed by multiple target performance lines for the same type of structure with the same probability of meeting each one (Buchanan et al., 2011). According to Figure 1, LDC related to the whole building requires that the building be immediately occupiable under Maximum Considered Event (MCE) level (very large) shaking and fully operational under many Design Basis Events (DBE).

The building consists not only of the seismic frame, but also the gravity frame, the slab and the non-structural elements/contents. Any assessment of a building should therefore consider all these effects. Chanchi et al. (2012) have described seismic sustainability of some steel structures in terms of:

- Damage
- Element replaceability
- Slab damage, and
- Structural permanent displacements.

Recently, Lin et al. (2012) have attempted to quantify the effect of earthquake shaking on building contents movement, but the principles developed relate to the damage of other acceleration dependent non-structural elements.

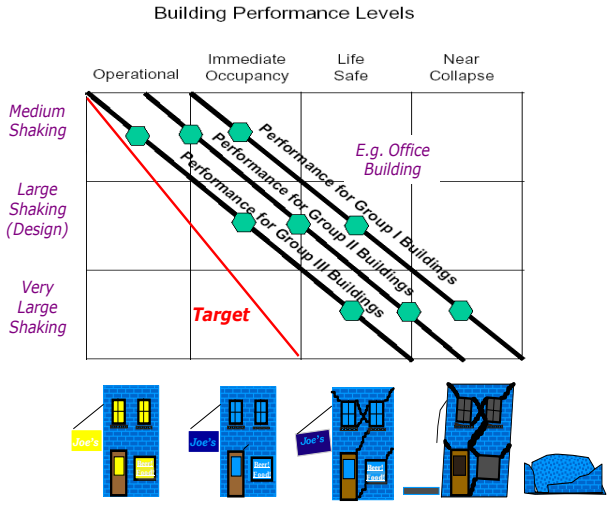


Figure 1. Possible Target Performance Objective for LDC (MacRae, 2010, based on Hamburger, PEER).

2. ELASTICALLY RESPONDING STRUCTURES

Structures designed in zones of low seismicity, or those which use very high strength materials in higher seismic zones, may respond elastically. Elastic response is associated with no damage and no permanent displacements. These structures are generally more expensive than traditional building designs since larger members/connections, and/or higher strength materials may be required. Also, unanchored contents movement is greater than that for yielding structures (Lin et al. 2012).

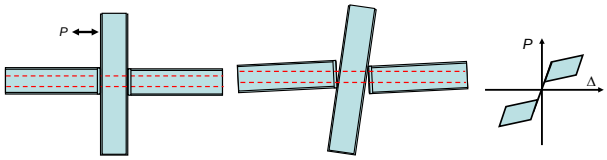
3. BASE-ISOLATED STRUCTURES

Base isolated structures have been designed around the world for many years. They are used extensively in countries like Japan where the cost of an isolated structure may be less

than that for a conventional structure (Wada, 2010). In some western countries, like NZ and the USA, they are currently not popular, possibly as a result of perceived additional initial cost. Also, when base-isolators are placed on soft-soils, the displacements may be greater than on stiff soils, and this may be regarded as another disadvantage of base isolation. In fact, the soft-soil effect is likely to increase the demands of all relatively stiff structures. It seems reasonable to use base isolation on softer soils as long as the isolator displacement demand is less than its capacity. Another benefit of base isolation is that the building structural interstorey drifts and the floor accelerations are generally not large. This means that non-structural elements and contents require less detailing if damage is to be avoided.

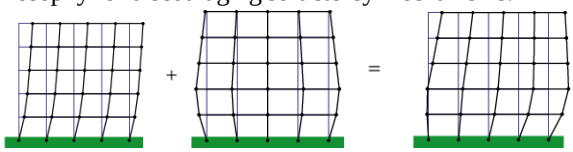
4. BEAM GAPPING SYSTEMS

When a beam is post-tensioned to a column with an unbounded cable, it may undergo significant deformations without damage as the beam end rocks on the column face as shown in Figure 2a&b (Priestley and MacRae, 1996). They "ideal" hysteretic shape is non-linear elastic, unless an energy dissipation device is used and energy is absorbed as shown in Figure 2c.



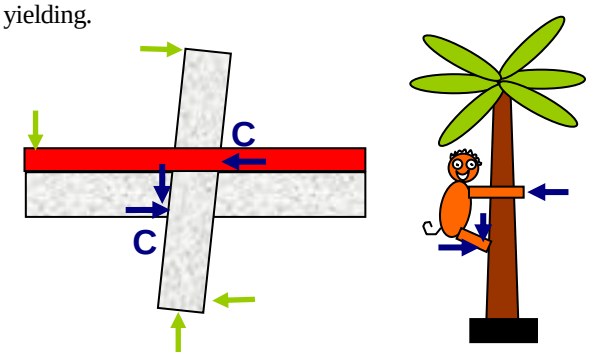
(a) Subassembly (b) Deformed Shape (c) Hysteresis
Figure 2. Post-Tensioned Beam Deformation and Hysteretic Behaviour (MacRae, 2010)

However, the column is part of a frame, and the gapping at the beam ends causes the distance between the column centerlines to move out as shown in a study by Kim et al. (2004). This causes the beams at some levels to be in compression, while at other levels the columns pull away from the beams placing them in tension (MacRae 2010, 2011). This change in axial force modifies the moments applied from the beams to the columns. This effect can only be mitigated if the columns are made to be flexible/weak, which is the opposite of the strong-column weak-beam philosophy for discouraging soft-storey mechanisms.



(a) Conventional (b) Gapping (c) Combined
Figure 3. Gapping Effects (Kim et al., 2004)

Another major issue relates to the building slab. Most buildings have slabs connected to the beams either side of the joint. The slab wraps around the column and under lateral column drifts, the forces resulting from the slab effect alone can be seen in Figure 4. When gapping at the beam ends occurs, the slab must extend (i.e. be damaged). A figure of such damage is shown in Figure 5. This slab damage is not appropriate for LDC. Such slab damage will only occur if the slab is weak. If the slab is strong, then the gap will not open so the desired mechanism will not occur. This may result in other undesirable failure modes such as column yielding.



(a) Subassembly (b) Monkey Idealization
Figure 4. Additional Forces on Column (tree) due to Slab (monkey) Extending around Column

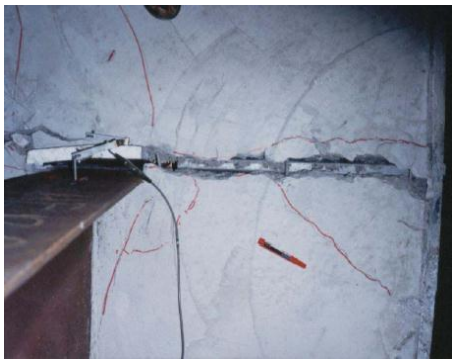


Figure 5. Slab Damage in a Post-Tensioned Beam Subassembly (Clifton, 2005)

Attempts have been made to allow a gapping system work. For example Garlock et al. (2010) proposed connecting the floor diaphragm only to the gravity frame and that the seismic frame transfer forces to the gravity frame through floor-beams bending out-of-plane. This system is very difficult to tune as too low a stiffness of the floor beams results in the seismic frames being isolated from the gravity system, and too high a stiffness results in the gaps not opening. Together with difficulties when considering 3-D response, the approach does not seem practicable as described by MacRae (2010, 2011).

Another approach has been used, and it does work in some cases. This involves connecting the floor slab to only one bay of each seismic frame in each direction, putting a gap around the column, and allowing the beam to slide on the other bays. This has been tested Lin et al. (2009) and used in real construction in Wellington by Dunning-Thornton at the Victoria University campus in 2010. There are still a number of issues with this construction type. Proper analysis of the system is not easy. Also for very tall frames, the column demand issues described in Figure 3 occur. For frames with a large numbers of bays it is not reasonable to transfer all of

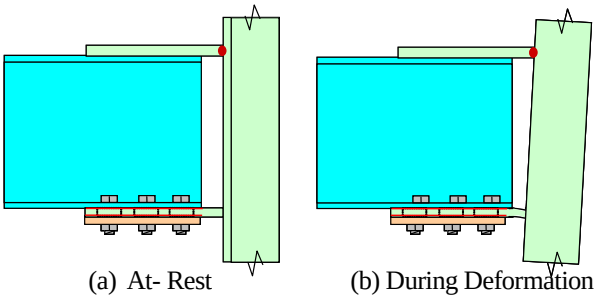
the slab inertia forces through only one bay. However, it is possible to design short buildings with few bays using this technique. Here, special care is required in the analysis and detailing to obtain a "boutique" solution (Buchanan et al. 2011). It is not a general solution for general moment frames.

For the reasons cited above, not a large number of these post-tensioned beam buildings have been constructed. In fact, the NZ Structural Engineering Society (SESOC) does not recommend these systems. It has been stated that they work well in all buildings without floor slabs as long as the extra column demands (as shown in Figure 3) are appropriately considered (Buchanan et al. 2012). While there are some advocates of this system it seems to the author than except for buildings which remain essentially elastic (such as some timber structures), the potential for such systems is limited.

5. NON-TEARING FLOOR SOLUTIONS

Non-tearing methods avoid the beam growth issues which push columns apart. Extensive studies have been conducted on steel structures (E.g. Danner and Clifton, 1995, MacRae et al. 2010) and recent work is being conducted on reinforced concrete structures. Here, the top of the beam is connected to the column. As the column moves over, the gap between the bottom of the beam and the column changes. This is shown in Figure 6 for a friction-type connection. Normally, other components are provided to carry the beam shear force and energy dissipation may occur with a number of different systems/devices including lead dissipaters, and yielding rods.

Since columns are not pushed apart, the floor slab does not tear as it sits on top of the beam. This means that it is easier to understand the behaviour and to perform an appropriate analysis. Since inelasticity occurs in the device/system at the bottom of the beam, the frame is not damaged. Furthermore, it is possible to use devices which have fully self-centering characteristics or with some self-centering properties (E.g. Khoo et al., 2011). Even if these are not used and bolted friction connections are used, then it is possible to unbolt the connection, and straighten the building after a very significant event. If friction connections are used, the bolts can stretch and be replaced. This system (with friction connections) has been implemented in a number of buildings in NZ (MacRae et al., 2010). The same principle can also be used for dissipative braces.



(a) At- Rest (b) During Deformation

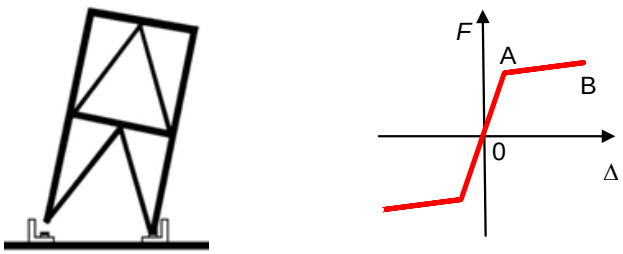
Figure 6. Non-Tearing Slab System (from MacRae 2011)

6. ROCKING SYSTEMS

Rocking structures, deforming like that shown in Figure 7a, have the characteristics that they are stiff and are likely to have low displacements. Since nonlinearity occurs as a result of uplift, it is possible that they should have little, or no, damage. The uplifting elements many be frames (such as concentrically braced frames) or walls (such as a concrete, timber or steel shear walls) and these elements do not need to be designed for large ductility as they are expected to remain essentially elastic. There are no/little tension demands on the foundations, so foundations can be smaller than that used for traditional designs.

If lateral force resistance is provided by gravity forces, elastic post-tensioning, and elastic gravity frame interaction when the rocking frame/wall uplifts, then there is no permanent displacement and the hysteresis loop is that shown in Figure 7b. However, if there is a bilinear, or similar, dissipater used, the system will have a static permanent displacement. That is, the displacement is no longer zero at zero lateral force. Due to dynamic effects, if the dissipater strength is less than the strength at uplift, permanent displacements are likely to be small.

Rocking structures have been built for many years (E.g. the 1981 South Rangitikei Rail Bridge). In addition to gravity forces, rocking frames/walls may use a post-tensioning system. These may be springs holding the base of the frame to the foundation (Gledhill et al., 2007), or post-tensioning cables over the height of the frame (E.g. Deierlein et al., 2009, Sause et al. 2010). The disadvantages of springs is that they may be expensive, while member sizes over the frame height must be increased to carry the post-tensioning forces from cables over the height. It is also possible to avoid post-tensioning and use energy dissipation systems to provide the required uplift resistance.



(a) Frame (Chanchi 2010) (b) Rocking - no dissipaters

Figure 7. Rocking Behaviour of Steel Structure

Issues with rocking frames/walls are described by MacRae and Clifton (2013). These include:

(i) an increase in lateral stiffness at high velocity during unloading which creates extra content movement (Lin et al. 2012). This effect can be addressed with appropriate restraint/anchorage of the contents.

(ii) gravity frame/slab demands due to vertical uplift. These can result in yielding/damage to the gravity frame and the slab and permanent displacements appropriate care is not

taken. Sause et al. (2010) use a separated rocking wall to avoid these issues.

7. OTHER SYSTEMS

A number of other systems which significantly reduce damage are available, including supplemental damping systems. While these can be very effective at reducing both forces and displacements, they are expensive for general buildings and are seldom used. Structures with tuned mass seem to be better suited to reduce wind rather than general earthquake loadings as a result of their narrow frequency response. Active control has still not received universal acceptance as a result of concerns related to cost, effectiveness and reliability. Many LDC systems are available and continue to be developed. How good they are depends on how well they reduce the demands on all elements of the total building system.

8. CONCLUSIONS

In order to make more resilient and sustainable cities, it is necessary to not only ensure life safety, but also to protect the infrastructure so that it can continue to be used after major earthquake shaking. A number of methods of low damage construction have recently been proposed and advocated. This paper shows that not all low damage approaches are equal, and some have more benefits than others. In particular, it is shown that it is not the performance of the device itself, but that within the building system which must be considered if low damage building system performance is desired.

Acknowledgements:
The author also wishes to thank the organizing committee of CUEE for providing the invitation, support and opportunity to present this paper.

References:

Buchanan A. H., Bull D., Dhakal R. P., MacRae G. A., Palermo P., Pampanin S., Base Isolation and Damage-Resistant Technologies for Improved Seismic Performance of Buildings, Report to the Royal Commission for the Canterbury Earthquakes, New Zealand, August 2011. http://canterbury.royalcommission.govt.nz/

Chanchí, J. C., MacRae, G.A., Chase, J.G., Rodgers, G.W., and Clifton, G.C., Methodology for quantifying seismic sustainability of steel framed structures, STESSA Conference, Santiago, Chile, January 2012.

Clifton GC. Semi-Rigid joints for moment resisting steel framed seismic resisting systems. PhD Thesis, Department of Civil and Environmental Engineering, University of Auckland, 2005.

Danner M. and Clifton GC. Development of Moment-Resisting Steel Frames Incorporating Semi-Rigid Elastic Joints: Research Report; HERA, Manukau City, New Zealand, Report R4-87, 1995.

Garlock M. E., Li J., and Vanmarke E. H. 2010. "Floor Diaphragm Design of Steel Self-Centering Moment Frames", STESSA-09, Lehigh, USA, p939-944.

Khoo H-H., Clifton G. C., Butterworth J., C.D. Mathieson C. D. and MacRae G. A., "Development of the Self-Centering Sliding Hinge Joint", Proceedings of the Ninth Pacific Conference on Earthquake Engineering, Building an Earthquake-Resilient Society, 14-16 April, 2011, Auckland, New Zealand. Oral presentation. Paper 106.

Kim J., Stanton J., and MacRae G. A., "Effect of Beam Growth on Reinforced Concrete Frames", Journal of Structural Engineering, ASCE, 130(9), pp. 1333-1342, September 2004.

Lin S-L, MacRae G.A, English R., Yeow T. Z, Dhakal R. P. "Contents sliding response spectra", New Zealand Society of Earthquake Engineering Conference, Christchurch, 13-15 April 2012. Paper 63.

Lin Y. C., Ricles J., Sause R. & Seo C. Y. Experimental assessment of the seismic performance of steel MRF system with beam web friction devices, STESSA, Philadelphia, August 2009. Taylor & Francis Group, London, ISBN 978-0-415-56326-0.

MacRae G. A., 2010. "Some Steel Seismic Research Issues", in Proceedings of the Steel Structures Workshop 2010, Research Directions for Steel Structures, compiled by MacRae G. A. and Clifton G. C., University of Canterbury, 13-14 April.

MacRae G. A., Clifton G. C., Mackinven H., Mago N., Butterworth J. and Pampanin S., The Sliding Hinge Joint Moment Connection, Bulletin of the New Zealand Society for Earthquake Engineering, December 2010.

MacRae G. A., "Damage resistant design of steel structures", "Chapter 7 of Base Isolation and Damage-Resistant Technologies for Improved Seismic Performance of Buildings, by Andrew H. Buchanan, Des Bull, Rajesh Dhakal, Greg MacRae, Alessandro Palermo, Stefano Pampanin , Report to the Royal Commission for the Canterbury Earthquakes, New Zealand, August 2011. http://canterbury.royalcommission.govt.nz/

MacRae G. A. and Clifton G. C. "Rocking Structure Design Considerations", Steel Innovations 2013 Workshop, Christchurch, 21-22 February 2013, Organized by Steel Construction New Zealand.

Priestley M. J. N. and MacRae G. A., "Seismic Tests of Precast Beam-to-Column Joint Subassemblages with Unbonded Tendons", PCI Journal, January-February 1996, pp. 64-80.

Sause R., Ricles J. M., Lin Y-C., Seo C-Y, Roke D., and Chancellor B. Self-Centering Damage-Free Seismic-Resistant Steel Frame Systems, 7th International Conference on Urban Earthquake Engineering & 5th International Conference on Earthquake Engineering Joint Conference March 3-5, 2010, Tokyo, April 2010.

Wada A. (2010). "Changes of Seismic Design after 1995 Kobe Earthquake", in Proceedings of the Steel Structures Workshop 2010, Research Directions for Steel Structures, compiled by MacRae G. A. and Clifton G. C., University of Canterbury, 13-14 April.

10 CUEE CONFERENCE PROCEEDINGS
10th International Conference on Urban Earthquake Engineering
March 1-2, 2013, Tokyo Institute of Technology, Tokyo, Japan

SEISMIC RETROFITTING DESIGN METHOD OF EXISTING RC BUILDINGS WITH BUCKLING RESTRAINED BRACES

Fatih Sutcu[1], Toru Takeuchi[2], and Ryota Matsui[2]

1) Research Associate PhD, Department of Architecture, Istanbul Technical University, Turkey
2) Professor, Graduate School of Engineering, Tokyo Institute of Technology, Japan
3) Assistant Professor, Graduate School of Engineering, Tokyo Institute of Technology, Japan
fatih.sutcu@itu.edu.tr, ttoru@arch.titech.ac.jp, matsui.r.aa@m.titech.ac.jp

Abstract: Existing RC buildings constructed according to relatively older regulations may lack of seismic resistance. Especially, public buildings such as schools or hospitals need to be retrofitted by efficient techniques considering their importance during and also after an earthquake. Buckling Restrained Braces (BRBs), being one of the popular retrofitting tools in recent years, may increase structural strength and at the same time reduce seismic response of a building by absorbing energy. This paper proposes a simplified method for designing the necessary amount of BRB for retrofitting the existing RC buildings. The method is based on equivalent linearization techniques and results are confirmed with non-linear time history analysis using high intensity seismic wave. The results show that, the RC building retrofitted with BRB responds as predicted by the proposed method and the drifts are much smaller than the original building.

1. INTRODUCTION

The catastrophic earthquakes is the past 2 decades resulted in life and economic losses worldwide while the authorities introduced new and comprehensive earthquake resistant building codes and regulations in almost every region. However the existing buildings that are not constructed according to these codes are lacking in seismic resistance as observed during surveys carried out after recent earthquakes. Therefore it is important to retrofit such existing buildings and enhance their seismic performance.

Existing framed structures may be suitably retrofitted by using diagonal braces. However, due to buckling of the brace compression members and material softening, the hysteretic behavior of conventional steel braces is unreliable. Alternatively, buckling-restrained braces (BRBs) being elasto-plastic dampers, may be employed as diagonal braces in seismic retrofitting of steel and RC frames designed for gravity loads only.

Previously several researchers have proposed simplified theories to predict the seismic performance of passive control systems. For such purpose equivalent damping and equivalent period of these systems are proposed by idealizing them as single-degree-of-freedom (SDOF) systems or other equivalent linearization techniques.(Kasai et al. 1998, Takeuchi et al. 2002 and Ichkawa et al. 2002) These studies are using elastic type structures such as steel buildings for the building model.

This paper proposes a simplified method to predict the seismic performance of a non-linear RC building retrofitted by BRB during a major seismic event. Equivalent damping of the retrofitted building is proposed by idealizing it as a linear SDOF system. By extending the SDOF theory, a seismically deficient 5-story RC building is upgraded by BRBs. Extensive multi-degree-of-freedom nonlinear time history analyses are performed for the retrofitted RC building using high intensity earthquake. The retrofitted system responded as predicted by the SOOF theory which showed much smaller drifts than the original RC frame, keeping frame members safe against major earthquakes.

2. EQUIVALENT LINEARIZATION METHOD

Proposed equivalent linearization method is carried out by the following 6 steps.

Step 1: Evaluating structural behavior of the existing building:

The strength of existing building is evaluated by non-linear push-over analysis. Obtained push-over curves are substituted with Takeda degrading tri-linear model. Yielding displacement for each story is assumed to be identical for the simplicity of the method.

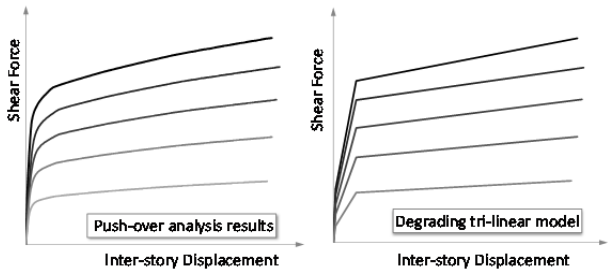


Figure 1.Push-over results and tri-linear degrading model for each story.

The details of degrading tri-linear behavior model of RC frame for each story are shown in Figure 2.

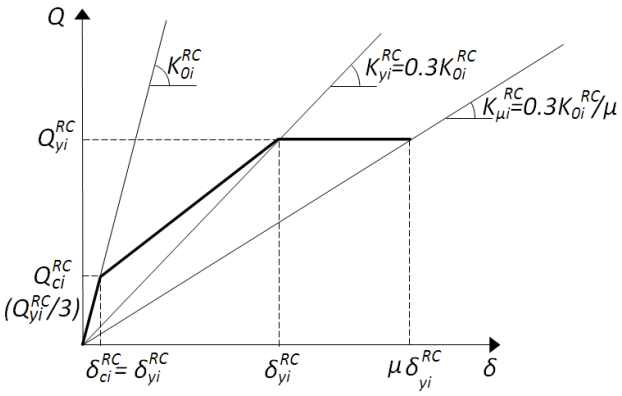


Figure 2.Degrading tri-linear model for i^{th} story of RC frame.

In Figure 2, Q_{yi}^{RC} is the yield shear force; Q_{ci}^{RC} is the crack shear force; δ_{yi}^{RC} is the yield displacement; δ_{ci}^{RC} is the crack displacement; K_{0i}^{RC} is the initial stiffness; K_{yi}^{RC} is the yielding point secant stiffness; $K_{\mu i}^{RC}$ is the post-yielding secant stiffness and μ is the ductility ratio for target displacement, each parameter being defined for an i^{th} story. Although the push-over results shows a hardening effect after yielding, in the BRB design method the post-yielding phase is assumed perfectly plastic.

Step 2: Defining an equivalent SDOF model:

The response prediction of the existing RC building and the evaluation of necessary damping are performed through equivalent linearization. For this purpose an equivalent SDOF model is introduced (Figure 3). In this step the equivalent height and mass of relevant SDOF model is calculated with the following equations.

$$H_{eq}=\frac{\sum_{i=1}^{N} m_i \cdot {}_s u_i \cdot H_i}{\sum_{i=1}^{N} m_i \cdot {}_s u_i},\quad M_{eq}=\frac{\left(\sum_{i=1}^{N} m_i \cdot {}_s u_i\right)^2}{\sum_{i=1}^{N} m_i \cdot {}_s u_i^2} \qquad (1)$$

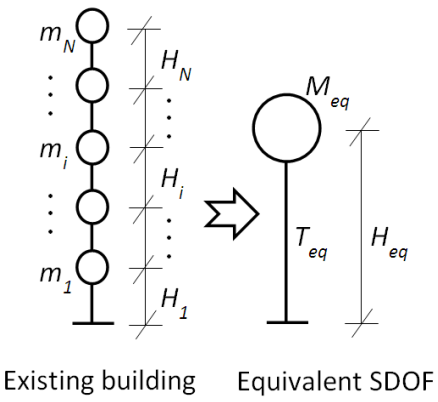


Figure 3.Equivalent SDOF system.

Where m_i , u_i and H_i are the mass, mode vector component and height of i^{th} story, respectively. For obtaining the equivalent period T_{eq}^{RC}, the initial period of the structure T_0 is calculated through eigenvalue analysis and modified for the target displacement. Here, T_{eq}^{RC} represents the equivalent period corresponding to the secant stiffness of target response point. As T_0 is known, equivalent period T_{eq}^{RC} may be evaluated by the following equation.

$$T_{eq}^{RC}=\sqrt{\frac{\mu}{0.3}}T_0 \qquad (2)$$

Using the equivalent period, equivalent stiffness of the SDOF model for target displacement is obtained as follows:

$$K_{\mu}^{RC}=M_{eq}\left(\frac{2\pi}{T_{eq}}\right)^2 \qquad (3)$$

Step 3: Evaluation of existing equivalent damping h_{eq}^{RC}

The equivalent damping of the RC frame h_{eqi}^{RC} for each story is individually calculated with the following equation.

$$h_{eqi}^{RC}=\frac{\Delta W_i^{RC}}{4\pi W_{ei}^{RC}}\cdot 0.8+h_0^{RC}=h_{eq}^{RC} \qquad (4)$$

Where ΔW_i^{RC} is the area of hysteresis loop in one cycle for i^{th} story, W_{ei}^{RC} is the equivalent potential energy of the i^{th} story, h_0^{RC} is the frame damping factor which is assumed to be proportional to the instantaneous tangential stiffness (Figure 4) and 0.8 is the reduction factor for the average loop is smaller than the maximum loop (Kasai et al. 2004). As the yielding displacement of each story was assumed to be identical, same equivalent damping factor is obtained for each story. Therefore the equivalent damping for the overall RC frame h_{eq}^{RC}, which may be obtained by the weighted mean of individual damping factors of each story, is equivalent to that of one story.

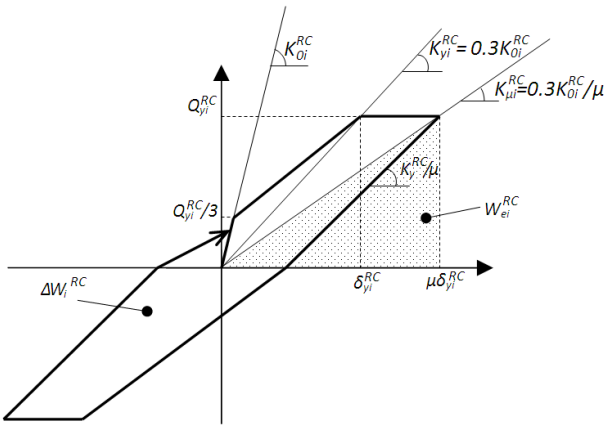


Figure 4. Typical hysteresis loop for RC frame

Step 4.Evaluating the equivalent stiffness of BRB on SDOF model.

Force displacement relation of the BRB is assumed to be elastic-perfectly-plastic and the yielding point drift is approximately 1/830 of story height (H_{eq}/830 for SDOF model). As the BRB is attached to the building through a steel frame, the stiffness of the BRB is evaluated including the effect of the steel frame. The elastic range of the steel frame is beyond the target displacement and depending on actual design experience it is assumed that the steel frame increases the stiffness of BRB 30% approximately (Figure 5). The initial equivalent stiffness of BRB, K_{μ}^{BRB} is evaluated by assuming the amount of maximum shear force supported by BRB, Q_y^{BRB} is equivalent to 30% of the equivalent weight of SDOF model.

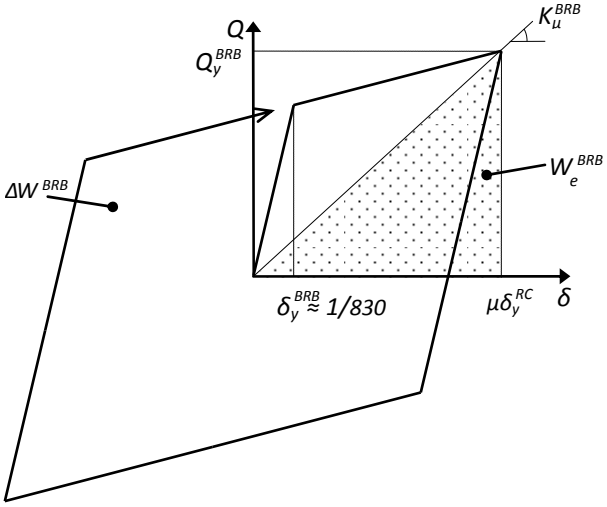


Figure 5. BRB hysteresis loop including steel frame effect.

Step 5: Evaluating the equivalent damping of SDOF model with BRB.

The equivalent damping ratio of SDOF model with BRB, h_{eq}^{Σ} is then evaluated for target displacement with the following equation.

$$h_{eq}^{\Sigma} = \frac{\Delta W^{BRB}}{4\pi W_e^{\Sigma}} \cdot 0.8 + \left(h_{eq}^{RC}\right)\frac{K_{\mu}^{RC}}{K_{\mu}^{\Sigma}} \qquad (5)$$

Where W_e^{Σ} is the equivalent potential energy of the RC frame with BRB, ΔW^{BRB} is the area of BRB hysteresis loop in one cycle, K_{μ}^{Σ} is the equivalent stiffness of the SDOF model with BRB (Figure 6).

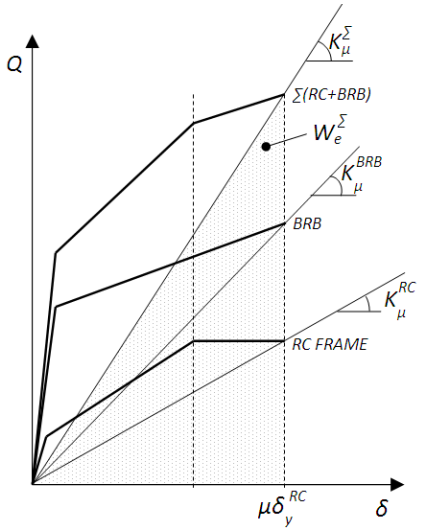


Figure 6. Overall behavior of SDOF model with BRB.

The effect of increased damping on the seismic response is evaluated with the following equation.

$$\delta_{eq}^{\Sigma} = \delta_{eq}^{RC}\frac{T_{eq}^{\Sigma}}{T_{eq}^{RC}} \cdot \sqrt{\frac{1+25h_{eq}^{RC}}{1+25h_{eq}^{\Sigma}}} \qquad (6)$$

In Eq.6 δ_{eq}^{Σ} is the displacement response of the SDOF model with BRB, δ_{eq}^{RC} is the spectral displacement response of the SDOF model and T_{eq}^{Σ} is the equivalent period for the SDOF model with BRB. As clearly seen in the equation, the displacement response of the retrofitted model is reduced by the increased damping and stiffness (therefore reduction of equivalent period). In this step, if the evaluated displacement response does not satisfy the target drift ratios, amount of BRB is adjusted at Step 4 and the method is repeated until satisfactory result is obtained.

Step 6: Evaluating the amount of BRB for each story and validation.

In this step the amount of BRB for each story of the RC building is obtained according to the BRB amount obtained at previous step. As the stiffness ratio of BRB and RC frame is determined for SDOF model ($K_{\mu}^{BRB}/K_{\mu}^{RC}$) the same ratio is used to decide the amount of BRB in the actual building. Instead of K_{μ}^{RC}, $K_{\mu i}^{RC}$ which is obtained by push-over analysis at Step 1 is used.

For validation of the method, the obtained BRB amount is incorporated in each story and time-history analysis with the same seismic wave used for SDOF model is carried out.

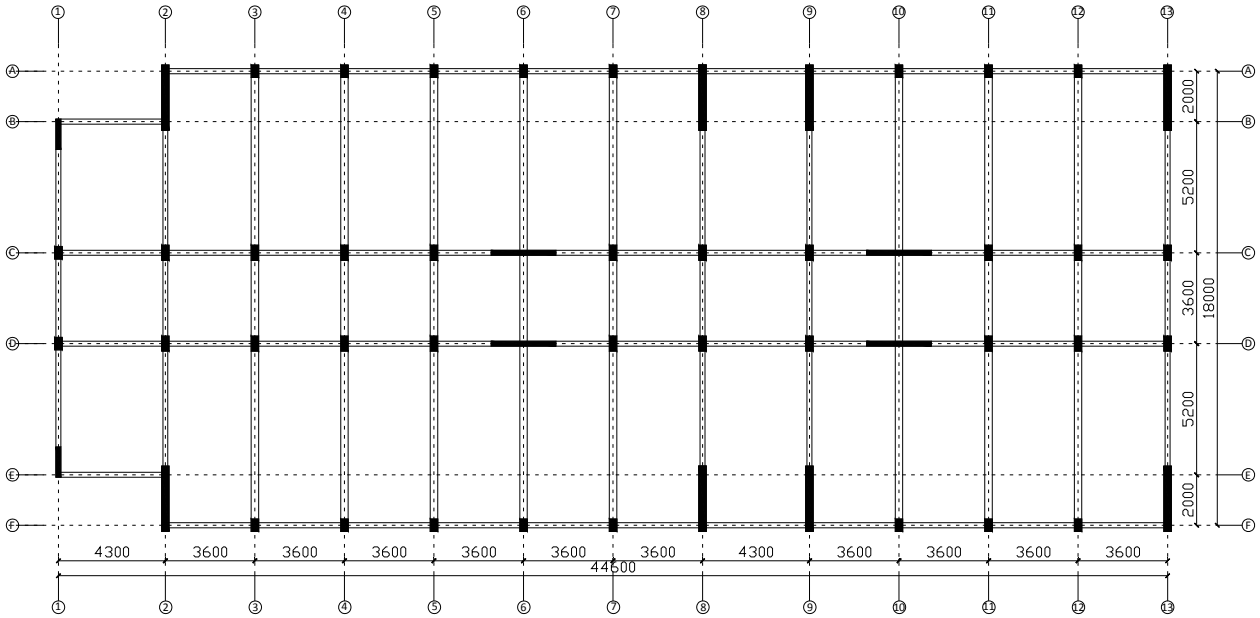


Figure 7 Plan of the RC school building

3. ORIGINAL 5 STORY RC BUILDING AND RESPONSE REDUCTION

A 5-story RC school building in Turkey is used for validation of the method. (Figure 7 and 8) The school building is constructed at 1992 in Istanbul which is a high risk seismic zone. Average concrete compressive strength is 20MPa and structural member section sizes as well as the reinforcement bar amount do not satisfy the current design code. Story height for each story is H_i=3.2m.

In this study the investigation of the building and evaluation of the structural performance before and after BRB retrofitting will be carried out in the longitudinal direction only, which is the weaker direction.



Figure 8. 5-story RC school building in Turkey

The target story drift for this study is 1/150. As for the seismic wave, BCJ-L2 from the Japanese design code is used. The acceleration and displacement response spectrum for BCJ-L2 is given in the following Figures 9 and 10.

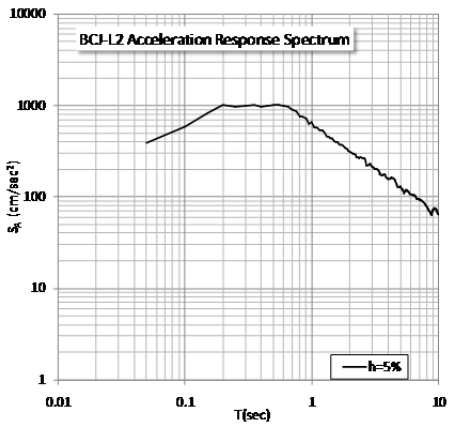


Figure 9. BCJ-L2 Acceleration response spectrum (h=5%)

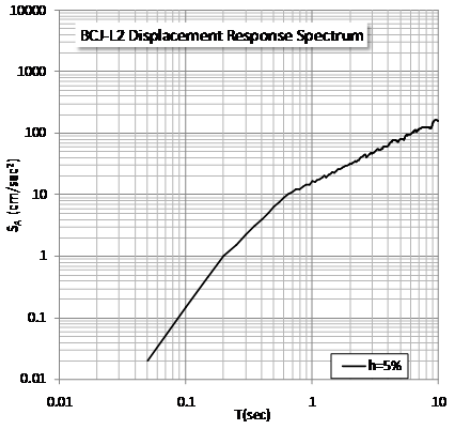


Figure10. BCJ-L2 Displacement response spectrum (h=5%)

By using the proposed BRB design method the amount of BRB to be used is evaluated and time history analysis is carried out for the RC frame with and without BRB. For the time history analysis the same seismic wave, BCJ-L2 is used.

The frame damping factor which is assumed to be proportional to the instantaneous tangential stiffness is taken as h_0^{RC} =0.05. The BRB installation on the RC frame is applied through a steel frame as shown in Fig.11. The steel frame is attached to the RC frame by chemical anchors and shear bolts to transfer sufficient shear force.

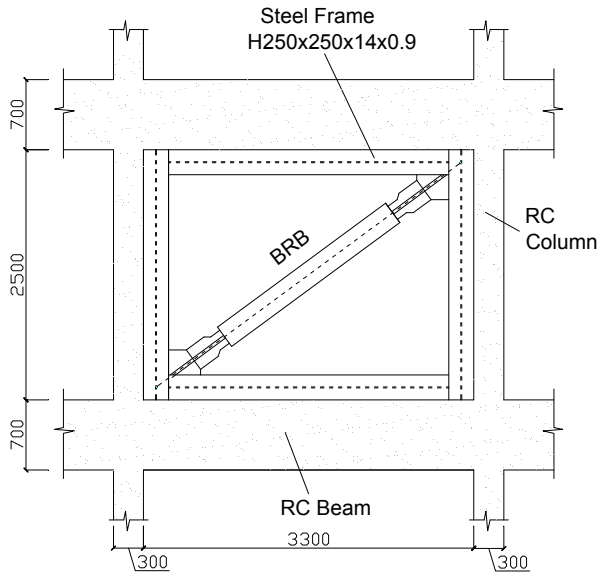


Figure 11. Installation of BRB on the RC frame

The push over analysis results for the sample school building is given in Table 1. As seen on the table, yield displacement values for each story are chosen to be the same for the simplicity of the method.

Table 1. Push-over analysis results for sample building.

	K_{0i}^{RC} (kN/mm)	Q_{ci}^{RC} (kN)	δ_{yi}^{RC} (mm)
5F	377.78	1700	15
4F	644.44	2900	15
3F	866.67	3900	15
2F	1077.78	4850	15
1F	1222.22	5500	15

By eigenvalue analysis the initial period of the structure is calculated to be T_0=0.7sec. while equivalent height and equivalent mass of the structure is calculated by Eq. 1 as H_{eq} =10.5 m and M_{eq} =4433.47 tons respectively. As the target story drift ratio is 1/150, target ductility is μ=1.42 and by using Eq.2 and Eq.3equivalent period and equivalent stiffness of the SDOF model is calculated as T_{eq}=1.54 sec and K_μ^{RC} =73.8 kN/mm, respectively.

In step 3 the equivalent damping of the RC frame is calculated as h_{eq}^{RC} =0.12. By following Step 4 initial equivalent stiffness of BRB is evaluated as K_μ^{BRB} =186.4 kN/mm assuming that the amount of maximum shear force supported by BRB is equivalent to 30% of the equivalent weight of SDOF model. By using the evaluated maximum shear force supported by BRB in Eq.5 the equivalent damping ratio of SDOF model with BRB is evaluated for target displacement as h_{eq}^{Σ} =0.26.

The effect of increased damping on the seismic response is then evaluated by Eq.6 where spectral displacement response of the SDOF RC model is calculated as δ_{eq}^{RC} =18.04cm (≈1/58 story drift). The obtained result is δ_{eq}^{Σ} =6.05cm (≈1/148 story drift) which is satisfactory, therefore initially selected amount of BRB is considered to be effective. In the next stage the ratio of BRB stiffness to the stiffness of RC frame obtained for the equivalent SDOF model ($K_\mu^{BRB} / K_\mu^{RC} = 2.52$) is used to evaluate the amount of BRB for actual RC building.

As for BRB used to retrofit the sample school building, ones with core cross-sectional area A_{core}=55.5cm^2 and yield strength $\sigma_{y\text{-}core}$=225N/mm^2 are selected. The steel frame used to attach the BRB to RC frame is made of H-250.250.14.9 section and the material yield strength is $\sigma_{y\text{-}sf}$=325N/mm^2. The total shear force supported by one set of BRB and steel frame including the application angle to the RC frame is calculated to be Q_y^{BRB} =1230kN.

The number of BRB to be placed on each floor, n_i^{BRB} is calculated depending on the target shear force to be supported by BRBs on each floor by Eq.7 and results are summarized at Table 2.

$$n_i^{BRB} = \frac{K_{\mu i}^{BRB} \cdot \mu \cdot \delta_{yi}^{RC}}{Q_y^{BRB}} \qquad (7)$$

Table 2. Number of BRB to be used on each floor.

	$K_{\mu i}^{RC}$ (kN/mm)	K_μ^{BRB} / K_μ^{RC}	$K_{\mu i}^{RC}$ (kN/mm)	n_i^{BRB}
5F	79.81	2.52	201.58	4
4F	136.15		343.87	6
3F	183.10		462.45	8
2F	227.70		575.10	10
1F	258.22		652.17	12

The maximum inter-story displacement of the original RC frame and the RC frame retrofitted with designed number of BRB is shown in Figure 12. As shown in the figure after the BRB retrofitting the exceeding displacement values of the original RC frame is prevented and target displacement is successfully achieved.

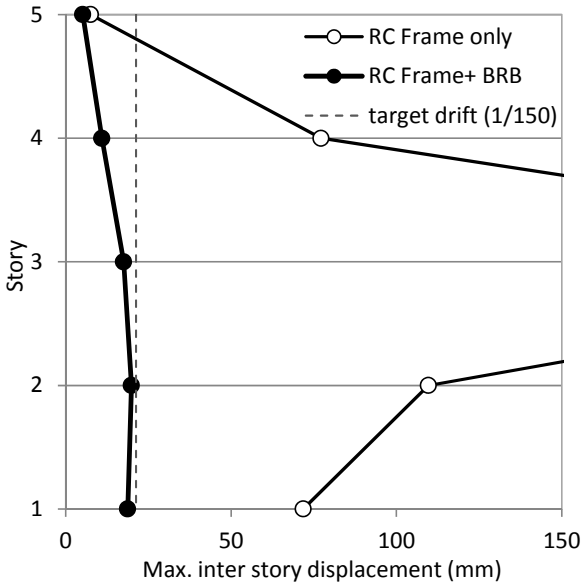


Figure 12. Max. inter-story displacement distribution.

As the steel frame remains elastic within the target drift range this component helps reducing the residual displacement after a severe earthquake motion. The inter-story displacement time-history of the 1st story is shown for the original RC frame and the BRB retrofitted RC frame in Figure 13. As seen in the figure while the original RC frame has significant residual displacement, the retrofitted RC frame has almost no residual displacement after the earthquake.

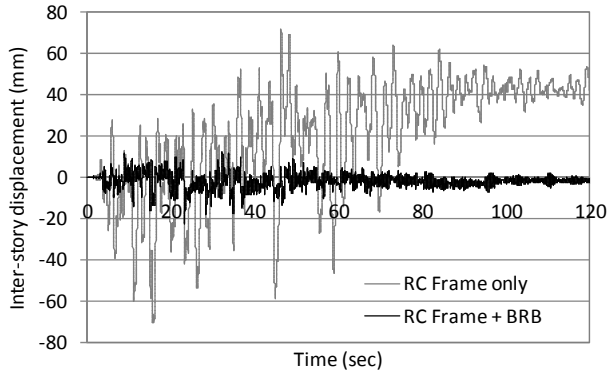


Figure 13. Inter-story displacement time-history (1st story.)

4. CONCLUSIONS

By proposed equivalent linearization method the necessary amount of BRB to retrofit a seismically insufficient RC frame is determined and target drifts are successfully obtained. The results are confirmed by non-linear time history analysis and the accuracy of the proposed method is validated.

Moreover, the residual displacement of the RC frame is significantly reduced after the application of BRB.

References

Kasai K., Fu Y. Watanabe A., (1998), Passive Control Systems for Seismic Damage Mitigation, Journal of Structural Engineering, Vol. 124, No 5, 501-512.

Takeuchi T., Kasai K., Oohara K., Kimura Y., Nakashima H, (2002), Performance Evaluation and Design of Passively Controlled Building Using Equivalent Linearization. SEWC 2002 Conference Proceedings, Yokohama Japan.

Ichikawa Y., Takeuchi T., Morimoto S., Sugiyama M. (2002), Practical Design of High-Rise Structure Using Viscoelastic Dampers and Hysteretic Dampers, SEWC 2002 Conference Proceedings, Yokohama Japan.

Kasai K., Okuma K., (2004) Evaluation Rule and Its Accuracy for Equivalent Period and Damping of Frequency-Dependent Passive Control Systems: Global Damping Model of One-Mass System Having Elastic Frame and Either Viscoelastic or Oil Damper, Journal of Structural and Construction Engineering. Transactions of AIJ, (580), 51-59 (In Japanese)

10CUEE CONFERENCE PROCEEDINGS
10th International Conference on Urban Earthquake Engineering
March 1-2, 2013, Tokyo Institute of Technology, Tokyo, Japan

DETERMINATION OF GROUND SURFACE DEFORMATION TYPE BASED ON FIELD DATA

Naser Amirhesari[1], and Kazuo Tani[2]

1) PhD, Department of Civil Engineering, Yokohama National University, Japan
2) Research Fellow PhD, National Research Institute for Earth Science and Disaster Prevention Hyogo Earthquake Engineering Research Center, Japan
naser-amirhesari-fn@ynu.jp, tani@bousai.go.jp

Abstract: Recent earthquakes have provided lots of examples of ground surface ruptures along the active faults and cause damages to buildings, roads and lifelines. Most of available structural design codes are based on the seismic acceleration during earthquakes while neglecting displacements due to earthquakes. A few design codes are considering the effects of ground surface deformation. Therefore, knowledge of the fault rupture is necessary and some effective design guideline should be developed based on that. The main objective of this study is evolution of ground surface deformation due to earthquake for civil design engineering.
Empirical study shows that ground surface deformations are generally characterized as: discontinuous deformations (raptures) and continuous deformations (deflection). Study shows that ground surface deformation is dependent on some parameters. The important parameters can be categorized in three main categories: source fault (i.e. moment magnitude of earthquake, fault type, slip, dip angle and depth of hypocenter), material type in ground between source fault and ground surface (i.e. incompetent and competent materials) and the type of structures (i.e. importance and shape).
Generally ground surface deformations tend to happen for shallow earthquake with large moment magnitude. Also by increasing thickness of incompetent material, deformation type changes from rupture to deflection.

1. INTRODUCTION

Recent earthquakes have provided lots of examples of ground surface deformations along the active faults and have caused damages to buildings, roads and lifelines. Some examples of earthquakes and damaged caused by ground surface rupture were discussed in following parts:

1.1 1999 Chi-Chi Earthquake

The September 20, 1999 Chi-chi Earthquake with M_w 7.6, happened on the Chelungpu Fault in Taiwan. As shown in Figure1-a, a building was rotated (Dong et al., 2003). This earthquake affected lifeline and infrastructures such as roads and highway. As shown in Figure 2, the Shih-Kang Dam was seriously damaged due to 7 meters vertical displacement in its foundation ground along the Chelungpu Fault (Kelson et al., 2001).

This earthquake also provided examples of deflection on the ground surface. As shown in Figure 3, the structure was stable and safe, however due to ground surface deflection it was necessary to rebuild the structure (Bray, 2009).



Figure 1: Buildings located on the fault and rotated in 1999-Chi-Chi Earthquake: (Dong et al., 2003)

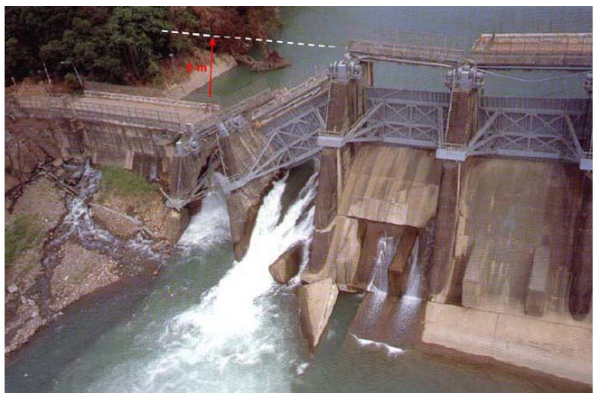


Figure 2: Looking toward the right abutment of Shihkang Dam after 1999 Chi-Chi Earthquake (Kelson et al., 2001)



Figure 3: Continuous deformation in the 1999 Chi-Chi Earthquake (Bray, 2009)

1.2 1999 Kocaeli and Duzce Earthquake

On August 17, 1999 Kocaeli, MW 7.6 earthquake and few days later in November 12, 1999 Duzce M_W 7.3 Earthquake happened along the North Anatoly Fault in Turkey.

Structural damages in some cases were because of unsafe design, poor construction technique and used of non standard materials. Moreover there were some damages caused by ground surface rupture as well. For example as shown in Figure 4, a four-story building collapsed due to ground surface rupture (Lettis et al., 2000)



Figure 4: Four-story building collapsed from surface rupture on right side of photo, west of Golcuk Naval Base (Lettis et al., 2000)

1.3 2002 Denali Earthquake

On November 3, 2002 M_w 7.9 earthquake happened in Denali Fault in Alaska. This particular earthquake was the largest strike-slip earthquake that ever happened in North America in almost 150 years.

The Denali Fault crossed almost all the Alaska as shown in Figure 5. There were no causalities, as there was no human habitation in Alaska. However the Trans-Alaskan Pipeline System (TAPS) across the Denali Fault experienced dislocation of 9 m (Hall et al., 2003). As the pipeline was designed for 11 m displacement; it could survive during this event as shown in Figure 6.

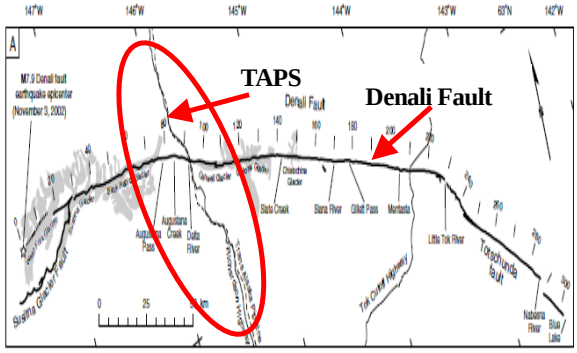


Figure 5: Map of Denali fault and TAPS crossing fault (Haeussler et al., 2004)

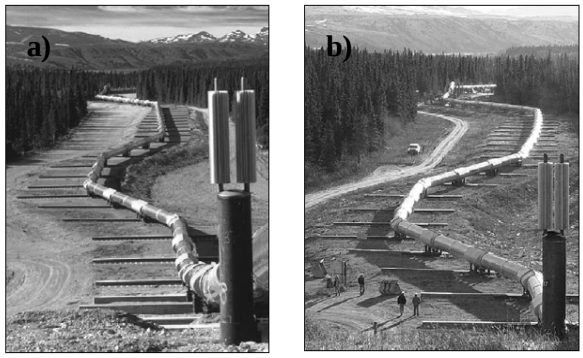


Figure 6: TAPS crossing of Denali Fault before and after earthquake, looking south. Note movement and bowed segment after fault displacement, which acts to compress the pipeline crossing segment: a) before earthquake and b) after earthquake (Hall et al., 2003)

1.4 2007 Niigata-Chuetsu-Oki Earthquake

On July 17, 2007 a M_W 6.8 Niigata-Chuetsu-Oki Earthquake happened in Japan. The epicenter was located 19 km from the site of Kashiwazaki-Kariwa Power Plant. All units in operational automatically shut down safely in response to the earthquake, and there were no significant damages despite large shaking. However there were small displacements of inclination not greater than 1/27,000 (Tani, 2010).

1.5 Ground Surface deformation Type

The ground surface deformations as shown in Figure 7 are generally characterized as:

1- Discontinuous deformations or fault ruptures

2- Continuous deformations or deflection without marked rupture

These examples show that ground surface deformation has great effect on the infrastructures and structures. However in some case such as 2007 Niigata-Chuetsu-Oki Earthquake, due to small value of displacement there is no serious damage related to top ground surface rupture. Therefore the effect of ground surface deformation should

be considered in the civil engineering design. There are some methods to determine the ground surface deformation due to earthquake and the summery of these methods are presented in following section.

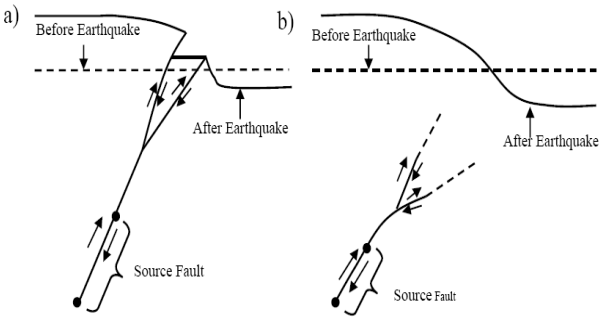


Figure 7: Two types of ground surface deformation:
a) Discontinuous deformation (Fault Rupture) and
b) Continuous deformation (Deflection)

2. CURRENT METHOD

Wells & Coppersmish (1994) defined some empirical relationships by gathered information for several past earthquakes all around world and for all kind of fault type. In their studies, relationship between moment magnitude of earthquake, rupture length, rupture width and surface displacement are discussed. There are some limitations in their studies: They did not consider the oblique fault. They only considered the average lines, and the ignored the upper limit boundary. However average line is not a sufficient guideline for some infrastructure and hence contingency is not enough. It is necessary to know whether the ground surface displacement is horizontal or vertical. However they did not specify the type of surface displacement. Also they did not mention that how to define the possibility of ground surface rupture.

Bray (2009) proposed a mitigation measure for engineered system as shown in Table 1. This system can be used as a guideline for design of structure near active fault based on ground surface rupture hazard. . In this method there are four main sections: land use planning section (avoid area to build structure with potential of ground surface rupture), engineering geology section (specifies location of active fault and estimate the ground surface rupture offset), geotechnical engineering section (some geotechnical techniques to spread the rupture offset) and structural engineering section (some recommendation structural methods to stabilized structure against rupture). However there is no any detail for land use planning section and engineering geology sections. In land use planning section, mentioned that based on Alquits-Priolo Act of 1972 in California, it is recommended that, we should avoid building any structure of human occupancy across the active fault and the safe distance is 50ft (15 m) (Figure 8). There is no reference to specify this number and for all fault type and all types of ground same breadth was proposed. In engineering geology section only some general information about the importance of engineering geology was present and there is no any detail about type of materials and effect of each type on ground surface rupture was presented.

Table 1 Mitigation measures for engineered system (Bray, 2009)

LAND USE PLANNING
Avoid area with the potential for surface fault rupture
ENGINEERING GEOLOGY
Identify and avoid primary faults Establish non-arbitrary setbacks based on fault and ground condition Estimate amount and type of potential fault displacement
GEOTECHICAL ENGINEERING
Construct ductile earth fills to spread out fault displacement Install soil reinforcement Use slip layers to decouple ground movements from foundation Keep the base of all foundation elements at the same elevation Avoid protrusions that would act like cleats to lock the building into ground Place compressible materials adjacent to walls and utilities For dams, use thick, ductile clay cores, thick upstream "crack-stopper" zones, thick downstream filters zone, thick chimney drains, and rockfill zone at the downstream face Increase freeboard, minimize reservoir height, and enlarge crest width Site outlet works and spillway off the fault trace
STRUCTURAL ENGINEERING
Design strong, ductile foundation, such as thickened reinforced mat foundations, waffle slabs, and post-tensioned slabs Do not use piles or piers that tie structure into the ground Design structure to be flexible and with isolation joints Install "catcher bents" or ties for bridge spans that must cross over faults

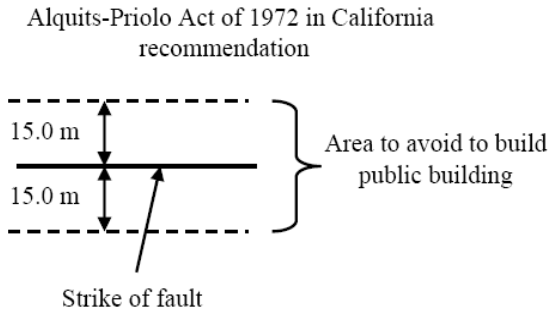


Figure 8: Alquist-Priolo Act of 1972 in California recommendation to avoid to build public structures around the active fault

3. PROBLEM STETMENT

Most of the available structural design codes are based on seismic accelerations or velocity while neglecting displacements during earthquakes. A few design codes are considering the ground surface deformation effects. For example as mentioned before, in California there is recommendation to avoid to build the public structures 15.0 m from the active fault in each side. However this recommendation is general and there is no clear and specific input parameters and Procedure. Therefore, it is necessary to study the ground surface deformation phenomena along the active fault and try to improve the design procedures for civil engineering.

To understand the ground surface deformations due to earthquakes, the important factors should be specified. As shown in Figure 9, there are three main factors as input to determine ground surface deformation:

1- Source fault
2- Ground between source fault and ground surface
3- Surface topography

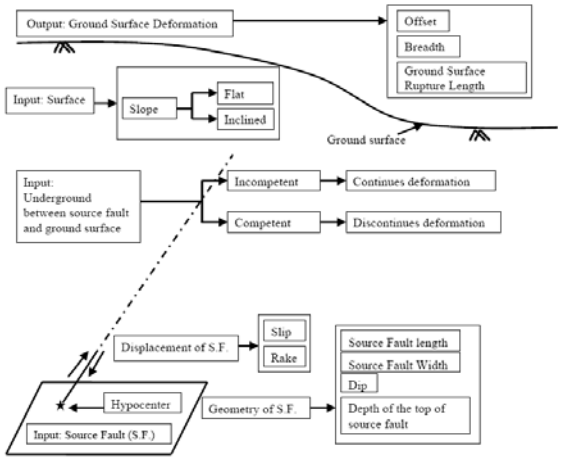


Figure 9: Important input parameters to determine ground surface deformation and list output phenomena of ground surface deformation

Source fault have great influence on ground surface deformation. Source fault has two main sub-factors: geometry and fault displacement. For the geometry, the length, the width, the dip angle of the source fault and the depth of the top of source fault are shown. For the fault displacement, the slip and the rake angle are determined. Source fault also can be specify as point source based on moment magnitude of earthquake and depth of hypocenter.

The other important factor is ground between source fault and ground surface. Generally there are two main sub-factors: "Incompetent material" and "Competent material"

In competent material, deformation occurs in remarkable shear zone. Rupture can be used to identify remarkable shear zone. In incompetent material, deformation happens in non-remarkable shear zone and many small shear zones appear, unlike that in competent material. Deflection can be used to identify non-remarkable shear zone.

Also Surface topography is another parameter which effects the ground surface deformations. Huang & Yen (1997) found that the topographic correction is in the order of five present of fault dislocation.

4. OBJECTIVE OF THIS STUDY

As mentioned ground surface deformation in some earthquakes reached to the ground and caused some damaged. However in some earthquakes, there is no significant ground surface deformation. In cased of ground surface deformation happened, there are two general types of ground surface deformation: rupture and deflection.

The objective of this study is determination of ground surface deformation type due to earthquake for civil design engineering.

5. DETERMINATION OF GROUND SURCFACE DEFORMATION TYPE

Existing literature reviews were conducted to collect information about ground surface deformation for previous earthquakes. The information of field data of ground surface deformation occurred in the past earthquakes was gathered are shown in tables. They are mostly from some data centers such as U.S. Geological Survey (U.S.G.S.), Southern California Earthquake Data Center (SCEDC) and also from some geotechnical journals (i.e. Bulletin of Seismological Society of America, Earthquake Spectra, Engineering Geology, Earth Planets Space and etc.) cited under references. The focus of this study is inland earthquake.

In next step definition of ground surface deformation and earthquake parameters were specified and unreliable data were ignored. The reliable field data was used for analyzed in following parts.

A model should be developed to specify the ground surface deformation type. Ground surface deformation depends on some parameters such as:

1- Moment magnitude of earthquake (M_w).

Mw can be used to show the effect of source fault.

2- Depth of hypocenter (D_h).

The hypocenter is the point within the earth where an earthquake rupture starts. The source fault can be modeled as point source using M_w and D_h.

3- Ground between source fault and ground surface.

There are two types of geological structures, competent material and incompetent material. As shown in Figure 10a, competent material, deformation occurs in remarkable shear zone. Rupture can identify remarkable shear zone. As shown in Figure 10b, incompetent material deformation happens in non-remarkable shear zone and many small shear zones appear, unlike competent material.

Deflection can identify non-remarkable shear zone. As shown in Figure 11, remarkable shear zone (competent material) can be identified as brittle behaviour and non-remarkable shear zone (incompetent material) can be identified as ductile behaviour.

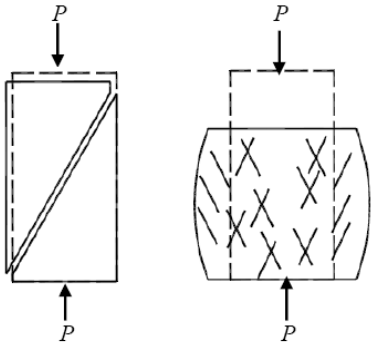


Figure 10: Definition of geological structures for: (a) Competent material, and (b) Incompetent material

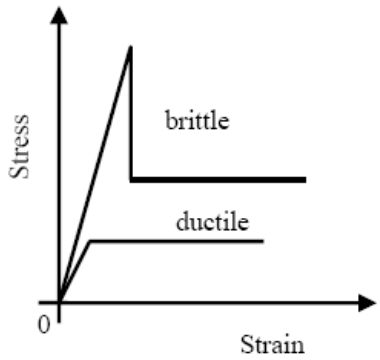


Figure 11: Brittle and ductile behaviour based on stress and strain relationship

The brittle and ductile behaviors can be specified by Young's module (E). As in field applications, velocity of secondary wave, (V_s) can be measured quite easily. Therefore V_s should be used in the model. The relationship between Young module (E) and velocity of secondary wave (V_s) was given in Eq. (1).

$$V_S = \sqrt{\frac{E}{2\rho(1+\upsilon)}} \qquad (1)$$

Where ν is Poisson's ratio and ρ is density. As a general case, the value of V_s was calculated based on E= 42000 MPa, ν= 0.2 and ρ= 2500 kg/m3 (Hoek, 2001). V_s = 800 m/s was specified to determine competent and incompetent material. In some studies, velocity of primary wave (V_p) was used. V_p can be determined from Eq. (2).

Using Eq. (2) and the same values for E, ν and ρ, Vp = 1300 m/s was specified to determine competent and incompetent material.

$$V_P = \sqrt{\frac{E(1-\nu)}{2\rho(1+\upsilon)(1+2\upsilon)}} \qquad (2)$$

If there is no information about shear or primary wave velocity, then the geological classification should be used. Hard rock, metamorphic and igneous, sandstone and shale without intensive fractures were considered as competent material (Table 2). Stiff and soft soils, average and poor rocks and so on were considered as incompetent material (Table 2-1). In case of discrepancy between shear wave velocity, pressure wave velocity and geological classification, shear velocity should be selected as the first priority. Pressure wave velocity should be selected as the second priority.

Table 2 Classification of competent and incompetent material

Material type (Definition)	V_s (m/s)	V_p (m/s)	Classification of ground
Incompetent (Deflection happens)	≤ 800	≤ 1300	Soft soil; Stiff clay and sand soils; Loose to dense sands; Medium to stiff/hard clays; Water-saturated alluvial deposits weak rock; Stiff soil; Deeply weathered and highly fractured bedrock; Soils with more than 20% gravel
Competent (Rupture)	> 800	> 1300	Hard rock; Mostly metamorphic and igneous rock; Fresh conglomerates; Sand stones and shales without intensive fractures

In the step, the data of pervious earthquakes was gathered based on literature reviewed. The source fault was considered as point source and moment magnitude of earthquake and depth of hypocenter was specified for each earthquake. Also the thickness of incompetent material ($H_{InCom.}$) and type of ground surface deformation (i.e. No deformation, Deflection and Rupture) was specified. The data was shown in Table 3.

The relationship between moment magnitude of earthquake (M_w) and hypocenter depth (D_h) was shown in Figure 2-3. As shown in Figure 12 deformation (i.e., rupture or deflection) happened during earthquake with D_h smaller than 20.0 km. For earthquake with D_h higher than 20.0 km there was no remarkable deformation. The upper limit and lower limit to specify the type of deformation were shown in Figure 12b.

Selection between the upper limit and lower limit lines should be done for each area, based on structure type. Structures type can be specified based on their shape and important (Table 4). There are two types of structures based on shape: linear (i.e. pipeline, highway, road, railway) and separate. Structures can also classify based on importance. There are two types of structures based on importance: essential (i.e. infrastructure, government office and etc) and standard (i.e. residual building, local road and etc). In case of essential structure, the contingency should be high. Therefore the upper limit should be used to specify type of

deformation and for standard structure the lower limit can be used.

Table 3 List of field data for ground surface deformation type

Name	*M*w	D_h (km)	H_{InCom} (m)	D.T.	References
1891-Nobi	7.5	7	4	R	Bonilla (1979); Fukuyama et al.(2007)
1906-San Francisco	7.9	8	12	R	Haeussler et al. (2004); Bray &Kelson (2006)
1923-Kanto	7.9	15	N.D.	R	USGS; Wald & Somerville (1995)
1934-Bihar	8	33	N.D.	No. Def.	USGS
1940- Imperial Valley	7.1	9	N.D.	R	SCEDC; Wells & Coppersmith (1994)
1957-Gobi Altay	8.1	10	N.D.	R	USGS; Okal(1976); Bayarsayhan et al. (1996)
1959-Hebgen Lake	7.1	15	N.D.	R	zhang et al.(1999); Bonilla (1979)
1970-Tonghai	7.5	9	N.D.	R	Zhou et al. (1983)
1971-San Francisco	6.6	8.4	N.D.	R	Sirovich et al. (2001); Wells & Coppersmith (1994)
1973-Luhuo	7.5	20	N.D.	R	Zhou et al. (1983)
1976-Tang-Shan	7.8	15	N.D.	R	USGS; Ming (1985)
1976-Guatemala	7.5	5	N.D.	R	Espinosa (1976)
1978-Tabas	7.4	5	N.D.	R	Shoja-taheri & Anderson (1988)
1979-Coyote Lake	5.7	8	N.D.	R	Liu & Helmberger (1983); USGS
1983-Borah Peak	7.3	16	N.D.	R	zhang et al. (1999)
1984-Morgan Hill	6.2	8	N.D.	D	Hartzell & Heaton (1986)
1987-Superstition Hills	6.6	11.2	N.D.	R	Sharp et al. (1989)
1989-Loma Prieta	6.9	18	12	D	Kanamori & Satake (1990)
1990-Manjil-Rodbur	7.3	19	N.D.	R	Berberian et al. (1992); Sarkar et al. (2003)
1991-Uttarkashi	6.8	10	N.D.	D	Cotton et al. (1996)
1992-Landers	7.3	1.1	N.D.	R	Bray (2009)
1994-Northridge	6.7	18.7	200	D	Wald et al. (1996)
1995-Kobe	7.2	16	2,3	R	Wald et al. (1996)
1995- Kobe	7.2	16	89,100	No. Def.	Ide et al. (1996); USGS
1998-Afghanistan-Tajikistan	6.6	33	N.D.	No. Def.	Kanaori, (1997); USGS
1999-Chi-Chi	7.6	7	0	R	USGS
1999- 17 Aug. Kocaeli (Izmit)	7.6	15	0	R	Kelson (2001); USGS
1999- Nov. Duzce	7.3	12.5	0	R	Lettis et al. (2001)
1999-Hector Mine	7.1	0.01	N.D.	R	Lettis et al. (2001)
1999-Ain Temouchent	5.7	8	N.D.	D	SCEDC; Peltzer et al. (2001)
1999-Athens	5.9	10	N.D.	D	Yelles et al.(2004)
2000-Tottori	6	11	N.D.	D	USGS
2001-Kunlunshan	7.8	5	3	R	Peyrat & Olsen (2004)
2001-El Salvador	7.7	60	N.D.	No. Def.	Wei et al. (2008), USGS
2002-Denali	7.9	5	0	R	Haeussler et al. (2004); Phillips et al. (2003)
2002-Hindu Kush Region	7.4	225	N.D.	No. Def.	USGS
2002-Peru-Brazil Border	6.9	535.8	N.D.	No. Def.	USGS
2003-Bam	6.6	8	0	R	Hessami et al. (2005)
2003-Altai	7.3	16	N.D.	R	Lunina et al. (2006)
2003-Miyagi-Ken Hokubu	6.4	12	0	R	Hikima & Koketsu (2004)
2003-Zemmouri	6.8	10	N.D.	D	Mahsas et al. (2008)
2003-South Island of New Zealand	7.2	28	N.D.	No. Def.	USGS
2004-Parkfield	6	8	0	R	Mendoza & Hartzell (2008)
2004-Al Hoceima	6.4	13	N.D.	D	Stich & Mancilla (2005)
2004-Nigita-Chuetsu	6.6	10	13;50; 100; 200; 300; 400	No. Def.	Kamae et al. (2005); Asano & Iwata (2009)
2004-Hindu Kush Region	6.6	191	N.D.	No. Def.	USGS
2005-Kashmir	7.6	11	0	R	Avouac et al. (2006)
2005-West off Fukuoka	6.6	13	60; 225; 250	D	Satoh & kawase (2006)
2005-Tarapaca	7.8	117	N.D.	No. Def.	USGS

2005-Northern Peru	7.5	12	N.D.	No. Def.	USGS
2006-Mozambique	7	11	N.D.	R	Raucoules et al. (2010); USGS
2007-Nigita-Chuetsu-oki	6.6	8	100	D	Raucoules et al. (2010); USGS
2007-Antofagasta	7.7	40	N.D.	No. Def.	USGS
2008-Wechuan	7.9	16	0	R	Lin et al. (2009)

D.T.: Deformation Type; R: Rupture; D: Deflection; No.Def: No Deformation; N.D.: No Data

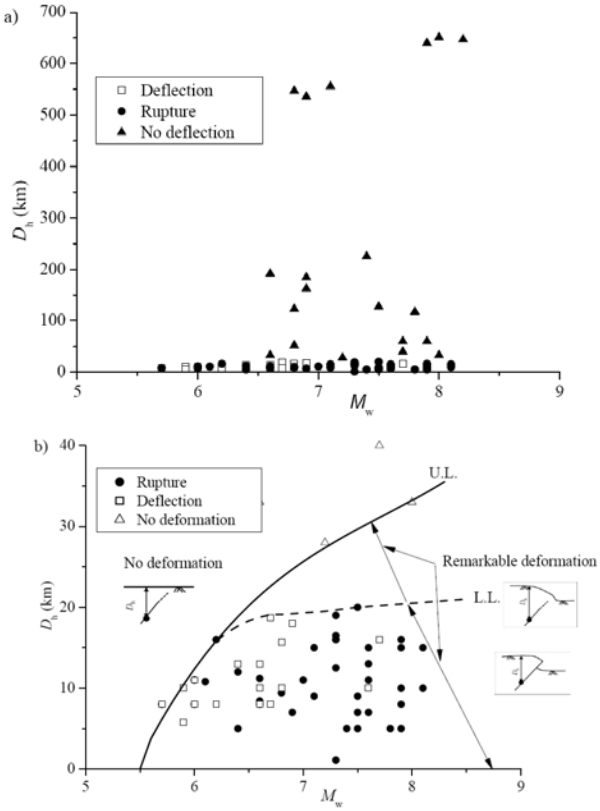


Figure 12: Relationship between moment magnitudes of earthquake vs. depth of hypocenter: (a) full rage of D_h, and (b) $D_h \leq 40$ km

The next parameter is geological structure (thickness of incompetent material). The relationship between moment magnitude of earthquake (M_w) and incompetent material thickness ($H_{InCom.}$) was shown in Figure 13. There are three main areas in Figure 13. In the first area, remarkable rupture happens. In the second area, deflection happens. In the third area, deformation might not happen.

Table 4 Classification of structural type

Imp. \ Shape	Linear	Separate
Essential	Highway main road High speed and main train railway Main pipeline	Power plant and dam Refinery Hospital, Fire Station Governmental office Structure containing toxic
Standard	Local road Local train railway Local pile line	Structure containing toxic

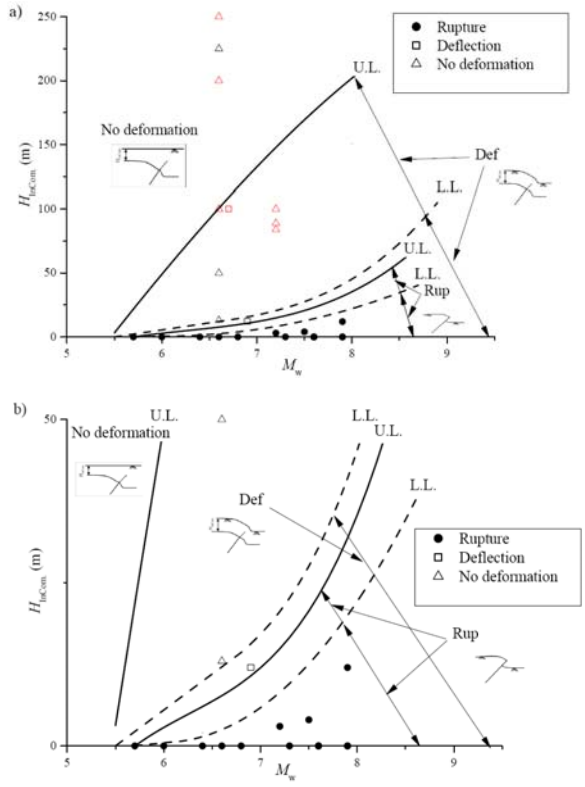


Figure 13: Relationship between moment magnitudes of earthquake vs. incompetent material thickness to specify type of deformation for: (a) full rage of HI_{ncom}, and (b) $H_{Incom} \leq 50$ m

In the first area, for earthquakes with Mw higher than 5.7, there is a possibility of ground surface rupture. The upper and lower limit boundaries between ground surface rupture and deflection was specified. The lower limit is based on the highest HInCom from the ground surface rupture of past earthquakes. The upper limit is based on the

lowest HInCom from the ground deformation of past earthquakes.

In the second area, ground surface deformation changed to deflection with increasing H_{InCom}. This study showed that for earthquakes with M_w higher than 5.8, there is a possibility of ground surface deflection. The upper and lower limit boundaries between ground surface deflection and no deformation were specified. Ground surface rupture is easier to distinguish than ground surface deflection and no deformation. Therefore, gap between upper limit and lower limit in second area is larger than first area (ground surface rupture).

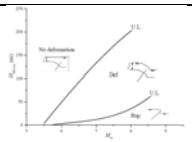
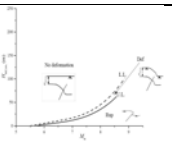
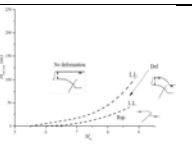
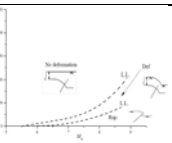
Selection between the upper limit and lower limit lines should be done for each area, based on structure type. Structures type can be specified based on their shape and important (Table 4).

Linear essential structures sometimes need to cross the active fault. Ground surface deformation has serious effects on linear essential structures. Therefore, higher contingency should be considered and, hence the upper limit was selected as the boundary line between ground surface deformation types (Table 5).

Separate essential structures should be avoided the active fault. However the minimum distance should be considered. The upper limit should be considered as boundary between ground surface rupture and deflection. The effect of ground surface deflection is not as much as ground surface rupture. There are not many records of deflection effects on separate essential structures. Therefore, the lower limit was selected as the boundary between ground surface deflection and no deformation area.

For standard structure (linear and separate) the lower limit can be used as boundary between different deformation types.

Table 5 Determination of boundaries between different types of ground surface deformation

Imp. \ Shape	Linear	Separate
Essential		
Standard		

6. CONCLUSIONS

Ground surface deformation depends on some parameters such as: Moment magnitude of earthquake, depth of hypocenter and material types in ground between source fault and ground surface. Material type in ground between source fault and ground surface can be classified in two types: "Incompetent material" and "Competent material". Competent material can be identified as brittle behaviour and incompetent material can be identified as ductile behaviour. The velocity of secondary wave (V_s) can be used to specify the ductile and brittle behaviour. Compartment materials have V_s higher than 800 m/s and in the case of incompetent martial the Vs is less than 800 m/s. Generally ground surface deformation is happened for shallow earthquake with large moment magnitude. Based on relationship between moment magnitude of earthquake (M_w) and thickness of incompetent material (H_{InCom}), type of deformation can be determined. There are three main areas depend on M_w and H_{InCom}: remarkable rupture area, deflection area and no deformation area. The boundaries between deformation types can be specified based on structure type. Structures type can be determined based on their shape and importance. There are two types of structures based on shape: linear and separate. Structures can also be classified based on importance. There are two types of structures based on importance: essential and standard.

References:

Asano, K. and Iwata, T. (2009): Source rupture process of the 2004 Chuestu, Mid-Niigata prefecture, Japan, earthquake inferred from waveform inversion with dense strong-motion data, Bul. of Seismological Society of America, Vol. 99, No. 1, pp. 123-140.

Avouac, J.P., Ayoub, F., Leprince, S., Konca, O. and Helmberger, D.V. (2006): The 2005, Mw 7.6 Kashmir earthquake sub-pixel correlation of ASTER images and seismic waveforms analysis, Earth and Planetary Science Letters, Vol. 249, pp. 514-528.

Bayarsayhan, C., Bayasgalan, A., Enhtuvshin, E., Hudnut, K.W., Kurushin, R.A., Molnar, P. and O¨ lziybat, M. (1996): 1957 Gobi-Altay, Mongolia, earthquake as a prototype for southern California's most devastating earthquake, Geology J., Vol. 24, pp. 579-582.

Berberian, M., Qorashi, M. Jackson, J.A., Priestley, K. and Wallace, T. (1992): The Rudbar-Tarom earthquake of 20 June 1990 in NW Persia: Preliminary field and seismological observations, and its tectonic significance, Bul. of the Seismological Society of America, Vol. 82, No. 4, pp.1726-1755.

Bray, J.D. and Kelson, K.I. (2006): Observations of surface fault rupture from the 1906 Earthquake in the context of current practice, Earthquake Spectra, Volume 22, No. S2, pp. S69–S89.

Bray, J.D. (2009): Earthquake surface fault rupture design considerations, Proc. 6th International Conference on Urban Earthquake Engineering, pp. 37-45.

Bonilla, M.G. (1979): Historic surface faulting—map patterns, relation to subsurface faulting, and relation to preexisting faults, U.S. Geological Survey, Report No. 79-1239, pp. 36-65.

Cotton, F., Campillo, M., Deschamps, A. and Rastogi, B.K. (1996): Rupture history and seismotectonics of the 1991 Uttarkashi, Himalaya earthquake, Tectonophysics, Vol. 258, pp. 35-51.

Dong, J.J., Wang, C.D., Lee, C.T., Liao, J.J. and Pan, Y.W. (2003):

The influence of surface rupture on building in the 1999 Chi-Chi earthquake in Fengyuan city, Engineering Geology, Vol. 71, pp. 157-179.

Espinosa, A.F. (1976) The Guatemalan earthquake of February 4, 1976, A preliminary report, US Geological survey professional, Paper 1002.

Fukuyama, E., Muramatu, I and Mikumo, T. (2007): Seismic moment of the 1891 Nobi, Japan, earthquake estimated from historical seismograms, Earth Planets Space, Vol. 59, pp. 553-559.

Hall, W.J., Nyman, D.J., Johson, E.R. and Norton, J.D. (2003): Performance of the Trans-Alaska pipeline in the November 3, 2003 Denali fault earthquake, 6th U.S. conference and workshop on lifeline earthquake, ASCE technical council on lifeline earthquake engineering.

Hartzell, S.H. and heaton, T.A. (1986): Rupture history of the 1984 Morgan Hill, California, earthquake from the inversion of strong motion records, Bul. of the Seismological Society of America, Vol. 76, No. 3, pp. 649-674.

Haeussler, P.J., Schwartz, D.P., Dawson, T.E. (2004): Surface rupture and slip distribution of the Denali and Totschunda Faults in the 3 November 2002 M 7.9 Earthquake, Alaska, Bul. of the Seismological Soc. of Ame., Vol. 94, No. 6B, pp. S23-S52.

Hessami,K., Tabassi, H,. Okumura, K., Abbassi, M.R. and Azuma, T. (2005): Surface deformation and the fault responsible for the 2003 Bam, Iran, earthquake, Earthquake Spectra, Vol. 21, No. S1, pp. S113–S123.

Hikima, K. and Koketsu, K. (2004): Source processes of the foreshock, mainshock and largest aftershock in the 2003 Miyagi-ken Hokubu, Japan, earthquake sequence, Earth, Planets and Space, Vol. 56, No. 2, pp. 87-93.

Hoek, E. (2001): Rock mass properties for underground mines, Published in Underground Mining Methods: Engineering Fundamentals and International Case Studies

Ide, S., Takeo, M. and Yoshida, Y. (1996) Source process of the 1995 Kobe earthquake: Determination of spatio-temporal slip distribution by Bayesian modeling, Bulletin of the seismological society of America, Vol. 86, No. 3, pp. 547-566

Kanamori, H. and Satake, K. (1990): Broadband study of the 1989 Loma Prieta earthquake, Geophysical Research Letters, Vol. 17, No. 8, pp. 1179-1182.

Kanaori, Y. (1997): Earthquake proof design and active faults, Development of geotechnical engineering, Vol. 81, Elsevier

Kamae, K. and kawabe, H. (2008): Source modeling and strong motion simulation of the 2007 Niigatakehn Chuetsu-Oki earthquake (Mj=6.8) in Japan, the 14th world conference on earthquake engineering, Beijing, China

Kamae, K., Ikeda, T. and Miwa, S. (2005): Source model composed of asperities for the 2004 Mid Niigata Prefecture, Japan, earthquake (MJMA =6.8) by the forward modeling using the empirical Green's function method, Earth, Planets and Space, Vol. 57, No. 6, pp. 533-538.

Kelson K.I., (coordinators), Bachhuber, J.,Cluff, L., Harder,L., Kieffer, S., Lettis, W., Page, W., Perkins, W., Rix, G., Roblee, C., Sitar, N., Wells, D., Wright, R. and Yashinisky, M., (other contributors) (2001): Fault-related surface deformation Chapter 3 of the Chi-Chi, Taiwan earthquake of September 20, 1999 reconnaissance report, Earthquake Spectra, Vol. 17, pp. 19-36.

Lettis, W., Bachhuber, J, Witter, R., (coordinators and principal contributors), Barka, A., Bray, J., Page, W., and Swan, F. (principal contributors) (2000): Surface fault rupture Chapter 2 of the Kocaeli, Turkey earthquake of August 17, 1999 reconnaissance report, Earthquake Spectra, Vol. 16, pp. 11-53.

Lin, A., Ren, Z., Jia, D and Wu, X. (2009): Co-seismic thrusting rupture and slip distribution produced by the 2008 Mw 7.9 Wenchuan earthquake, China, Tectonophysics, Vol. 471, pp. 203-215.

Liu, H.L. and Helmberger, D.V. (1983): The near-source ground motion of the 6 August 1979 Coyote Lake, California, earthquake, Bul. of the Seismological Society of America, Vol. 73, No. 1, pp. 201-218.

Lunina, O.V., Gladkov, A.S., Novikov, I.S., Agatova, A.R., Vysotsky, E.M. and Emanov, A.A. (2006): Seismotectonic deformations and stress fields in the fault zone of the 2003 Chuya earthquake, Ms = 7.5, Gorny Altai, Geotectonics, Vol. 40, No. 3, pp. 208–224.

Mahsas, A., Lammali, K., Yelles, K., Calais, E., Freed, A.M. and Briole, P. (2008): Shallow afterslip following the 2003 May 21, Mw = 6.9 Boumerdes earthquake, Algeria, Geophysics J. International, Vol. 172, pp. 155-166.

Mendoza, C. and Hartzell, S. (2008): Finite-fault analysis of the 2004 Parkfield, California, earthquake using Pnl Waveforms, Bul. of the Seismological Society of America, Vol. 98, No. 6, pp. 2746–2755.

Ming, J.W. (1985): The distribution of earthquake damage to underground facilies during the 1976 Tanh-Shan earthquake, Earthquake Spectra, Vol. 1, No. 4, pp. 741-756.

Okal, E.A. (1976): A surface-wave investigation of the rupture mechanism of the Gobi-Altai (December 4, 1957) earthquake, Physics of The Earth and Planetary Interiors, Vol. 12, Issue4, pp. 319-328.

Peltzer, G., Crampe, F. and Rosen, P. (2001): The Mw 7.1, Hector Mine, California earthquake surface rupture, surface displacement field, and fault slip solution from ERS SAR data, Earth and Planetary Sciences, Vol. 333, pp. 545–555.

Peyrat, S. and Olsen, K.B. (2004:) Nonlinear dynamic rupture inversion of the 2000 Western Tottori, Japan, Earthquake, Geophysical research letters, Doi: 10.1029

Phillips, E.D., Haeussler, P.J., Freymueller, J.F., Frankel, A.D., Rubin, C.M., Craw, P., Ratchkovski, N.A., Anderson, G., Carver, G.A., Crone, A.J., Dawson, T.E., Fletcher, H., Hansen, R., Harp, E.L., Harris, R.A., Hill, D.P., Hreinsdo´ttir, S., Jibson, R.W.. Jones, L.M., Kayen, R., Keefer, D.K., Larsen, C.F., Moran, S.C., Personius, S.F., Plafker, G., Sherrod, B., Sieh, K., Sitar, N., Wallace. W.K. (2003): The 2002 Denali fault earthquake, Alaska: A large magnitude, slip-partitioned event, SCIENCE, Vol. 300, pp. 1113-1118.

Raucoules, D., Ristori, B., de Michele, M. and Briole, P. (2010): Surface displacement of the Mw 7 Machaze earthquake (Mozambique): Complementary use of multiband InSAR and radar amplitude image correlation with elastic modeling, Remote Sensing of Environment, doi:10.1016/j.rse.2010.04.023.

Sarkar, I., Hamzehloo, H. and Khattri, K.N. (2003): Estimation of causative fault parameters of the Rudbar earthquake of June 20, 1990 from near field SH-wave data, Tectonophysics, Vol. 364, pp. 55-70.

Satoh, T. and Kawase, H. (2006): Simulation of strong motions in Fukuoka city during the 2005 west off Fukuoka prefecture earthquake with special reference to thick Quaternary sediments around the Kego fault, Earth, Planets and Space, Vol. 58, pp. 105-110.

Sharp, R.V., Budding, K.E., Boatwright, J., Ader, M.J., Boilla, M.G., Clark, M.M., Fumal, T.E., Harms, K.K., Lienkaemper, J.J., Morton, D.M., O'Neill, B.J., Ostergren, C.L., Ponti, D.J., Rymer, M.J., Saxton, J.L. and Sims, J.D. (1989): Surface faulting along the Supperstition Hills fault zone and nearby faults associated with the earthquake of 24 November 1987, Bul. of the seismological society of America, Vol.79, No. 2, pp. 252-281.

Shoja-taheri, J. and Anderson, J.G. (1988): The 1978 Tabas, Iran, earthquakes: An interpretation of the strong motion records, Bul. of the seismological society of America, Vol. 78, No. 1, pp. 142-171.

Sirovich, L., Pettenati, F. and Chiaruttini, C. (2001): Test of source-parameter inversion of intensity data, National Hazards, Vol. 24, pp. 105-131.

Stich, D. and Mancilla, F.d.L. (2005): Source analysis of the Mw 6.3 2004 Al Hoceima earthquake (Morocco) using regional apparent source time functions, J. of Geophysical Research, Vol. 110, Doi: 10.1029/2004JB003366

Tani. K. (2010): Design consideration of surface ground deformation due to fault displacement in foundation engineering, International symposium on recent and future technologies in coastal development.
Wald, D.J. and Somerville, P.G. (1995): Variable-slip rupture model of the Great 1923 Kanto, Japan, earthquake: geodetic and body-waveform analysis: Bul. of the Seismological Society of America, Vol. 85, No.1, pp.159-177.
Wald, D.J., Heaton, T.H. and Hudunt, W. (1996): The slip history of the 1994 Northridge, California, earthquake determined from strong-motion, telesismic, GPS and leveling data, Bul. of Seismological Society of America, Vol. 86, No. 1B, pp. S49-S70.
Wells, D.L. and Coppersmith, K.J. (1994): New empirical relationships among magnitude, rupture length, rupture width, rupture area and surface displacement, Bul. of Seismological Society of America, Vol. 84, No. 4, pp. 974-1002.
Wei, X., GuiHua, Y., WenTao M., Yann, K. and Paul, T. (2008): Rupture behavior and deformation localization of the Kunlunshan earthquake (Mw7.8) and their tectonic implications, Science in China Series D: Earth Sciences, Vol. 51, No. 10, pp. 1361-1374.
Yelles, A.K.C., Djellit, H., Beldjoudi, H. (2004): The Ain Temouchent (Algeria) earthquake of December 22nd, 1999, Pure Applied Geophysics, V0l. 161, pp. 607-621.
Zhang. Z, Mao. F and Slemmons, D.B. (1999): Rupture terminations and size of segment boundaries from historical earthquake ruptures in the basin and range province, Tectonophysics, Vol. 308, pp. 37-52.
Zhou, H.L., Allen, C.R. and Kanamori, H. (1983): Rupture complexity of the 1970 Tonghai and 1973 Luhuo earthquake, China, from P-wave inversion, and relationship to source faulting, Bul. of the Seismological Society of the America, Vol. 72, No. 6, pp. 1585-1597.

10CUEE CONFERENCE PROCEEDINGS
10th International Conference on Urban Earthquake Engineering
March 1-2, 2013, Tokyo Institute of Technology, Tokyo, Japan

STUDY ON THE INTENSITY MEASURE OF INCREMENTAL DYNAMIC ANALYSIS CONSIDERING HIGH-MODES EFFECT FOR TALL BUILDINGS

Ying Zhou[1], Ningfen Su[2], and Xilin Lu[3]

1) Associate Professor, State Key Laboratory of Disaster Reduction in Civil Engineering, Tongji University, China
2) PhD student, College of Civil Engineering, Tongji University, China
3) Professor, State Key Laboratory of Disaster Reduction in Civil Engineering, Tongji University, China
yingzhou@tongji.edu.cn, suningfen@163.com, lxlst@tongji.edu.cn

Abstract: The selection of intensity measure (IM) has a significant effect on the result of incremental dynamic analysis (IDA), especially for tall buildings. Considering higher mode contributions, this paper proposes a structure-specific power-law form IM, which is suitable for IDA of tall buildings. This suggested IM, in the form of S_{12} or S_{123}, contains two or three elastic spectral values corresponding to the first two or three periods, and the modal mass participation proportion is used as the power for each mode considered. The IDA of a super-tall SRC frame - RC tube structure is performed to demonstrate the efficiency of the proposed S_{12} or S_{123} compared with other IMs including PGA, PGV, S_a, and S^*. It is concluded that the IM of PGV is more efficient than PGA as well as one spectral value-based S_a and two spectral value-based S^*. But it is less efficient than the proposed S_{12} and S_{123}. For the structure-specific IM, the more modes are considered, the more efficient IM is. S_{123} is recommended for the IDA of tall buildings.

1. INTRODUCTION

1.1 The significance of IMs

Incremental Dynamic analysis (IDA), proposed by Vamvatsikos (2002), is a parameter analysis method based on nonlinear dynamic analysis. It involves performing nonlinear dynamic analysis of the structural model to a suite of ground motion records, each scaled to multiple levels of intensity, and recording the responses at each level to form IDA curves of response versus intensity. The approach has the potential to provide dynamic capacity curves for different ground motion levels and describe the variation of engineering demand parameters (EDPs) with changes in ground motion intensity measures (IMs). It is believed to be the most promising method for its accurate estimation of the seismic performance of structures and is of great interest in Performance-based Earthquake Engineering (PBEE) (Zhou *et al*., 2010).

An IDA curve combines the IM of a site-specific ground motion with EDP from nonlinear dynamic analysis of the given structure. For IDA curves, it is an unavoidable fact that the curves display large record-to-record variability. This observed dispersion is closely connected to the IM used. Different IM generates various IDA curves for a given EDP. Some IMs are more efficient than others, better capturing and explaining the differences from record to record. Thus, the selection of IM has a significant influence on the result of IDA.

1.2 Existing IMs

Currently, the most frequently used IM is the peak ground acceleration (PGA) and the spectral acceleration at the fundamental period of the structure, $S_a(T_1, 5\%)$ or S_a for simplicity. S_a has been demonstrated to be more efficient than the PGA (Shome, 1999). The higher efficiency of S_a with respect to PGA can be ascribed to the fact that S_a is a structure-specific IM while PGA is not, which means that the former may better capture the seismic responses on a specific structure. Obviously, S_a is an accurate measure for single-degree-of-freedom (SDOF) systems or first-mode-dominated structures in the elastic range. Some studies have demonstrated, however, that S_a may not be particularly efficient nor sufficient for certain kinds of structures, such as tall, long-period buildings. (Shome, 1999)

A number of IMs has been proposed, attempting to avoid the major shortcomings of S_a, i.e., ignoring both the contributions of higher modes to the overall dynamic responses and the increase of the fundamental period of the structure associated with nonlinear behavior. Those attempts can be classified as two categories: elastic spectra based and inelastic spectra based.

For elastic spectra bases IMs, spectral values at periods of high modes are considered to incorporate higher-mode effect or at a larger period to incorporate the period lengthening effect. Cordova *et al*. (2000) proposed a two-parameter scalar IM that accounts for the period lengthening, as given in Eq. (1).

$$S^* = S_a(T_1)^{1-\alpha} \cdot S_a(T_f)^{\alpha} \tag{1}$$

where T_1 is the first mode period and T_f is a longer period

that presents the inelastic (damaged) structure. α and the ratio T_f/T_1 are determined by calibration to optimize the IM by minimizing the variability in computed results. A pair of T_f/T_1=2 and α=0.5 is suggested for general application. A significant advantage of S^* is the possibility of obtaining its corresponding attenuation law that is a linear combination of the attenuation functions for the spectral acceleration values $S_a(T_1)$ and $S_a(T_f)$.

Luco and Cornell (2007) put forward an IM named $IM_{1I\&2E}$, which takes into account both second mode frequency content and inelasticity, is a SRSS combination of inelastic spectral value at the first-mode period and the elastic spectral value at the second-mode period. The practical applicability of the approach is at present limited by the difficulties related to the computation of the corresponding hazard curve.

Mehanny (2009) proposed a power-law form elastic spectrum shape-dependent IM by making modification on the IM proposed by Cordova (Cordova *et al*., 2000). The modification is substituting the pre-calibrated constant-value ratio T_f/T_1 by a self-adaptive multiplier that is function of the nominal relative lateral strength R. R is defined as the lateral strength required to maintain the system elastic, F_e, relative to the lateral yielding strength, F_y, of the system. The IM is written as:

$$IM = S_a(T_1)^{1-\alpha} \cdot S_a\left(\sqrt{R} \cdot T_1\right)^{\alpha} \tag{1}$$

The IM of peak ground velocity (PGV) and peak ground displacement (PGD) has also been studied and would not be discussed here. In a word, the IMs mentioned above are scalar intensity; while recently, researchers have been focusing on intensity vectors (Baker and Cornell, 2004). A vector IM consists of two parameter such as S_a along with a measure of spectral shape. The use of a vector IM is appealing, but it is still involving many unsolved problems including the scaling techniques and uncertain hazard calculations.

1.3 The aim of this paper

Given the existing IMs above, this paper proposes a practical structure-specific IM for the IDA of tall, long period buildings with significant contribution of high modes to the structural responses. In the proposed IM, the elastic spectral values at major periods are added to incorporate the high-mode contribution, and the modal mass participation proportion is used to weight the contribution of various modes. The IDA of a super-tall steel reinforced concrete (SRC) frame – reinforced concrete (RC) tube structure is performed to verify the efficiency of the proposed IM compared with popular scalar IMs.

2. AN IM CONSIDERING THE HIGH-MODE EFFECT FOR TALL BUILDINGS

High-mode effect should be considered in the IDA of tall buildings. The structure-specific IM is proposed for tall buildings as given in Eqs. (2) and (3), in which spectral accelerations at major periods are the bottom number and corresponding modal mass participation proportions are the exponent.

When the first two modes are considered, the IM is shown in the form in Eq. (2):

$$S_{12} = S_a(T_1,\xi)^{\alpha} \cdot S_a(T_2,\xi)^{\beta} \tag{2}$$
$$\alpha = m_1/(m_1+m_2)$$
$$\beta = m_2/(m_1+m_2)$$

When the first three modes are considered, the IM is shown in the form in Eq. (3):

$$S_{12} = S_a(T_1,\xi)^{\alpha} \cdot S_a(T_2,\xi)^{\beta} \cdot S_a(T_3,\xi)^{\gamma} \tag{3}$$
$$\alpha = m_1/(m_1+m_2+m_3)$$
$$\beta = m_2/(m_1+m_2+m_3)$$
$$\gamma = m_3/(m_1+m_2+m_3)$$

where α, β, γ are modal mass participation proportions corresponding to the first three periods, respectively. m_1, m_2, m_3 are modal mass participation factors corresponding to the first three periods, respectively.

It can be seen that more modes can be considered in the proposed IMs. Generally, the total modal participation mass of the first three modes is no less than 80% of the whole structural mass in one direction, which is sufficient to get accurate results for engineering applications considering the computation time.

3. THE IDA OF A SUPER-TALL BUILDING USING THE PROPOSED IM

3.1 Structural description

The most popular system for tall buildings in China has recently been transferred from traditional RC shear wall structures to SRC frame-RC core wall structures. Thus, a 50-story SRC frame-RC core wall structure is designed as the target building in the paper. The story height is 4m and the total height is 200m. The plan layout is shown in Figure 1 and dimension of members is listed in Table 1. Table 2 gives the material properties of the model.

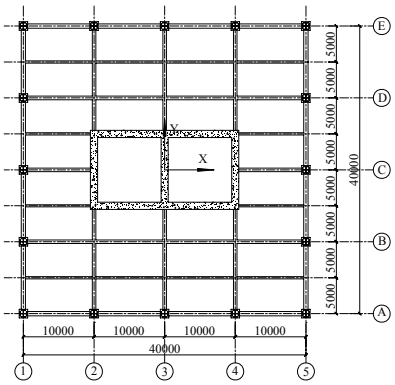


Figure 1 Play layout of the structure

3.2 Finite element model

The analytical software ABAQUS is used to build finite element model and conduct nonlinear dynamic analysis. Beams and columns are modeled using a first-order 3D Timoshenko beam element (B31), in which the transverse shear deformation is allowed. The linear, reduced-integration, quadrilateral shell element (S4R) in which in-plane bending

Table 1 Cross-sectional dimensions of structural members

Member	Location		Concrete (mm)	Steel (mm)
Beam	Peripheral beam	1-20	-	600x950x20x40
		21-35	-	500x900x20x40
		36-50	-	500x800x20x40
	Primary beam	1-50	-	500x800x20x40
	Secondary beam	1-20	-	300x500x14x25
Column	1-20		1200	600x900x35
	21-35		1000	500x700x35
	36-50		800	400x500x20
Wall	1-20		1000	-
	21-35		800	-
	36-50		600	-

Table 2 Material properties

Concrete grade	Design values of strength (MPa)		Poisson ratio	Modulus of elasticity (MPa)
	Compressive	Tensile		
C35 (beam, slab)	16.7	1.57	0.2	3.15E+4
C60 (wall, column)	27.5	2.04	0.2	3.60E+4
Steel grade	Yield stress	Ultimate stress	Ultimate strain	Modulus of elasticity
Q345 (t>35)	295	384	0.025	2.06E+5
Q345 (t<35)	328	426	0.025	2.06E+5

and shear and out-of-plane bending can be simulated simultaneously. The discrete model is used to simulate the reinforcement and steel in beams and columns, and the smeared layer model is employed for reinforcement in shear walls and slabs.

The isotropic bilinear kinematics hardening model is used for reinforcement and steel, in which Bauschinger effect is considered. During the cyclic loading, no degradation is developed. The ratio of ultimate strength to the yield strength is 1.2 for reinforcement and 1.3 for steel. The ultimate plastic strain corresponding to the ultimate stress is considered as 0.025.

Since there is no proper concrete material model available for B31 element in ABAQUS, a user material subroutine is wrote and incorporated into ABAQUS via VUMAT subroutine. This user-defined material uses the uniaxial concrete constitutive model proposed by Mander *et al*. (1988a and 1988b), which takes into account the influence of various types of confinement by defining an effective lateral confining stress.

The finite element model is shown in Figure 2 with 78957 nodes and 53772 elements in total.

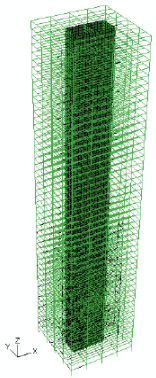


Figure 2 Finite element model

3.3 Dynamic properties

The dynamic properties and modal mass participation factors of the model are tabulated in Table 3.

Table 3 Dynamic properties and model mass participation factors

No.	Period (s)	Mode shape	Modal participation mass (kg)	Total mass (kg)	Modal mass participation factor	Modal mass participation proportion	
						For S_{12}	For S_{123}
1	4.48	Translation in *Y*	5.73E+07	9.35E+07	m_1=61.3%	α=77%	α=71%
2	3.29	Translation in *X*					
3	1.34	Torsion					
4	1.12	Translation in *Y*	1.68E+07		m_2=17.9%	β=23%	β=21%
5	0.76	Translation in *X*					
6	0.51	Torsion					
7	0.48	Translation in *Y*	6.77E+06		m_3=7.2%		γ=8%
8	0.34	Translation in *Z*					
9	0.33	Translation in *X*					

3.4 Earthquake ground motion selection

Previous study (Shome, 1999) has shown that ten to twenty ground motions are usually enough to provide sufficient accuracy in the estimation of seismic demand. Consequently, a suite of fifteen earthquake records are chosen from Strong Motion Database of Pacific Earthquake Engineering Research Center to simulate the earthquake scenarios (Table 4). Two aspects have been considered when selecting the ground motions: (1) soil condition of the site. According to *Chinese Code for Seismic Design of*

Table 4 Response spectra of ground motions and design spectrum

No.	Name	Record station	Component	Characteristic period (s)	PGA (g)	PGV (cm/s)	PGD (cm)
1	Cape Mendocino 1992/04/25	89156 Petrolia	PET-UP	0.44	0.163	24.5	31.78
2	Cape Mendocino 1992/04/25	89486 Fortuna - Fortuna Blvd	FOR090	0.24	0.114	21.7	12.79
3	Chi-Chi, Taiwan 1999/09/21	TCU122	TCU122-E	0.16	0.220	42.5	43.02
4	Imperial Valley 1940/05/19	117 El Centro Array #9	EW	0.52	0.313	29.8	13.32
5	Imperial Valley 1979/10/15	5060 Brawley Airport	H-BRA225	0.26	0.160	35.9	22.44
6	Imperial Valley 1979/10/15	412 El Centro Array #10	H-E10050	0.50	0.171	47.5	31.10
7	Kobe 1995/01/17	0 OSAJ	OSA090	0.28	0.064	17.0	8.03
8	Kocaeli, Turkey 1999/08/17	Duzce	DZC180	0.38	0.312	58.8	44.11
9	Landers 1992/06/28	12026 Indio - Coachella Canal	IND-UP	0.96	0.042	6.6	3.99
10	Loma Prieta 1989/10/18	1028 Hollister City Hall	HCH090	0.82	0.247	38.5	17.83
11	Kern County 1952/07/21	80053 Pasadena - CIT Athenaeum	NS	0.38	0.053	9.2	2.53
12	Superstitn Hills(B) 1987/11/24	11369 Westmorland Fire Sta	B-WSM090	0.40	0.172	23.5	13.00
13	Victoria, Mexico 1980/06/09	6621 Chihuahua	CHI192	0.30	0.092	15.6	9.90
14	Westmorland 1981/04/26	5051 Parachute Test Site	PTS225	0.22	0.242	39.2	26.88
15	Westmorland 1981/04/26	5051 Parachute Test Site	PTS315	0.22	0.155	26.6	12.97

Buildings (GB50011-2010), the site soil is categorized as Type III, which is defined as the soil whose overlaying thickness is between 15 and 80m and the equivalent shear velocity is no more than 150m/s; or whose overlaying thickness is larger than 50m and the equivalent shear velocity is between 150 and 250 m/s. (2) design response spectrum specified in Chinese code. Figure 3 shows the response spectra of the ground motions and design spectrum.

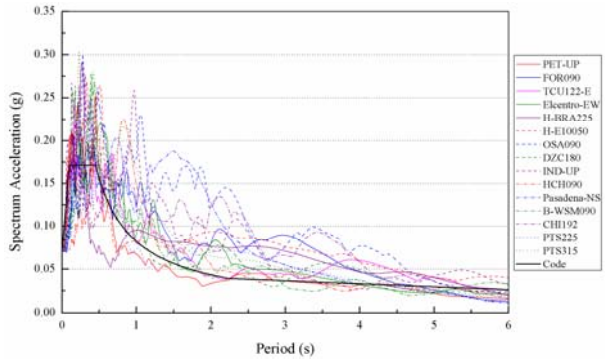


Figure 3 Response spectra of selected ground motions and design spectrum (ξ=4%)

3.5 Incremental Dynamic Analysis

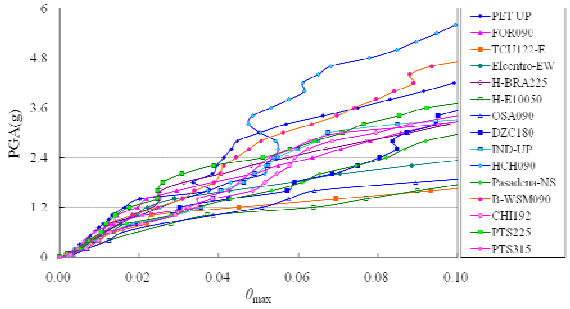
The IDA entails appropriately scaling each record to cover the entire range of structural response, from elasticity, to yielding, and finally global dynamic instability. In the analysis, the ground motion is input in Y direction. All records are scaled by PGA. According to Chinese code, the building is designed based on the minor earthquake level with a PGA of 0.07g. The corresponding PGAs under moderate and major levels are 0.2g and 0.4g, respectively. Thus, the PGAs for IDA begin with 0.07g, and then 0.1g, 0.2g, 0.4g, 0.6g, ….

Several considerations for comparing IMs are: (1) Desirable properties of an IM are efficiency, sufficiency, scaling robustness and the hazard computability (Luco and Cornell, 2007; Tothong and Cornell, 2007). An efficient IM is defined as the one that results in a relatively small dispersion of structural response given the level of ground motion intensity. Only efficiency is used here for the comparison of IMs. (2) As a measure of the dispersion, the standard deviation of the logarithm of the EDPs is applied, which is a natural choice for values approximately log-normally distributed (Shome, 1999). The average of the standard deviations under each IM is taken to evaluate the efficiency of IMs. (3) Based on the modal mass participation proportions in Table 3, S_{12} and S_{123} is written as Eq. (4). (4) The maximum inter-story drift ratio θ_{max} is taken as EDP.

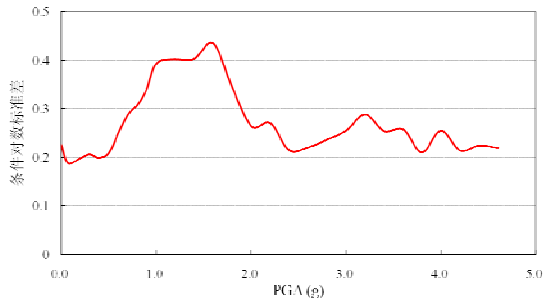
$$S_{12} = S_a(T_1,4\%)^{0.77} \cdot S_a(T_2,4\%)^{0.23} \tag{4}$$

$$S_{123} = S_a(T_1,4\%)^{0.71} \cdot S_a(T_2,4\%)^{0.21} \cdot S_a(T_3,4\%)^{0.08}$$

Six IMs, including PGA, PGV, S_a, S^*, S_{12} and S_{123}, are chosen to be compared for the IDA of the building. The IDA curves and logarithm standard deviations are given in Figure 4~9.

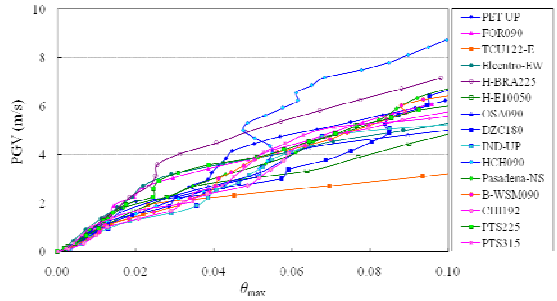


(a) θ_{max}-PGA curves

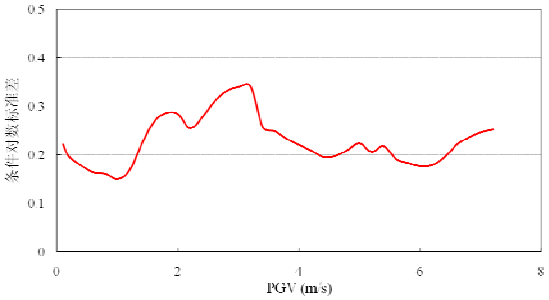


(b) $\sigma_{\ln EDP|PGA}$

Figure 4 IDA curves and dispersion analysis for the IM of PGA

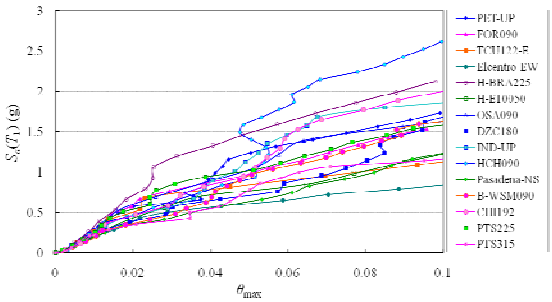


(a) θ_{max}-PGV curves

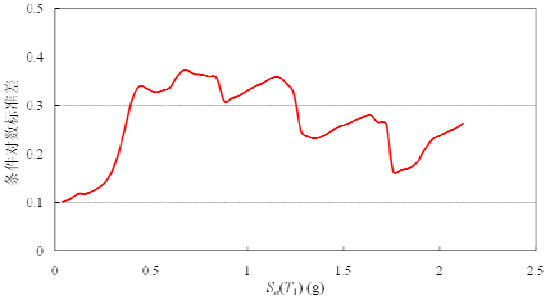


(b) $\sigma_{\ln EDP|PGV}$

Figure 5 IDA curves and dispersion analysis for the IM of PGV

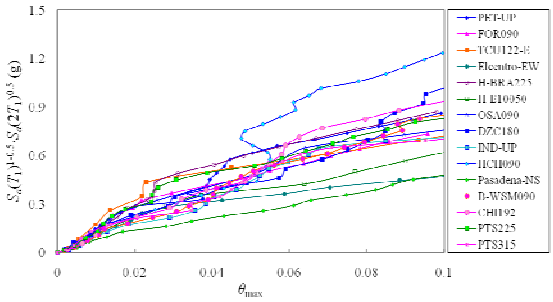


(a) θ_{max}-S_a curves

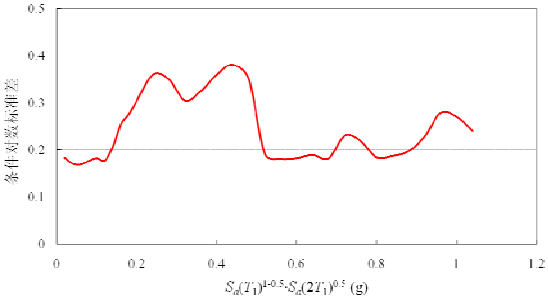


(b) $\sigma_{\ln EDP|Sa}$

Figure 6 IDA curves and dispersion analysis for the IM of S_a

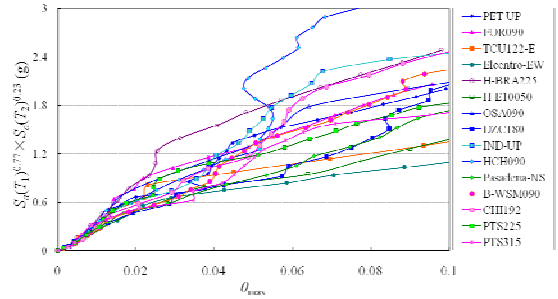


(a) θ_{max}- S^* curves

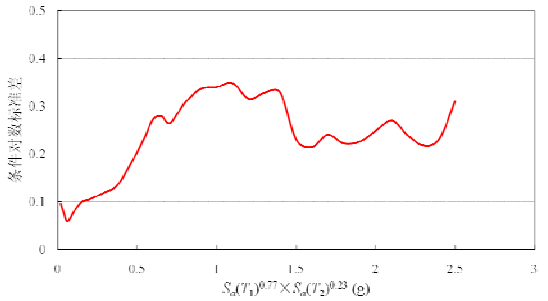


(b) $\sigma_{\ln EDP|S^*}$

Figure 7 IDA curves and dispersion analysis for the IM of S^*

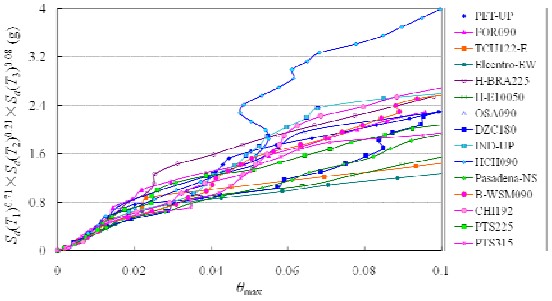


(a) θ_{max}- S_{12} curves

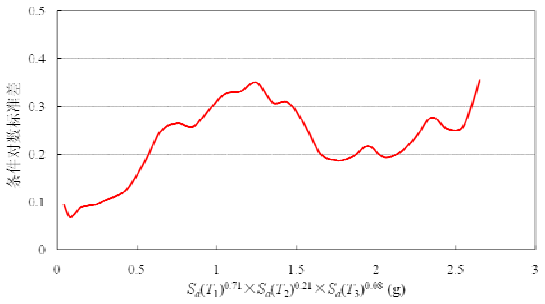


(b) $\sigma_{\ln EDP|SI2}$

Figure 8 IDA curves and dispersion analysis for the IM of S_{12}



(a) θ_{max}- S_{123} curves



(b) $\sigma_{\ln EDP|SI23}$

Figure 9 IDA curves and dispersion analysis for the IM of S_{123}

Table 5 The average of the standard deviation of the conditional logarithm

IM	PGA	PGV	S_a	S^*	S_{12}	S_{123}
Average of logarithm standard deviation of EDP	0.268	0.228	0.264	0.241	0.221	0.209
Compared to S_a	1.02	0.86	1.00	0.91	0.84	0.79

The average of the logarithm standard deviation is listed in Table 5. It can be seen that for peak value-based IMs, PGV is more efficient than PGA. PGV is also better than the one spectral value-based IM, S_a. Among the two spectral value-based IMs, the proposed S_{12} is more efficient than S^*. The average for S_{123} is the smallest, which means S_{123} is the most efficient IM among six IMs. It is concluded that the more modes are considered, the better IM is.

4. CONCLUSIONS

The power of incremental dynamic analysis (IDA) as an analytical method has been paid much attention in the earthquake engineering. Since IDA curves are the relationship between the intensity measure (IM) of ground motions and structural response referred as engineering demand parameter (EDP), it displays large record-to-record variability. This observed dispersion is closely connected to the IM applied. The existing IMs are neither particularly efficient nor sufficient for tall, long-period buildings. A structure-specific IM, named S_{12} or S_{123}, is thus proposed for tall buildings. The IM is defined in the power-laws form, in which the spectral accelerations at major periods are the bottom number and corresponding modal mass participation proportions are the exponent. Accordingly, the high-mode contribution is considered in the proposed IM. A super-tall building is introduced to compare the six IMs, including PGA, PGV, S_a, S^*, S_{12} and S_{123}. The conclusions could be reached as follows.

(1) Even for tall buildings, the IM of S_a (the spectral acceleration at the first period) demonstrates obvious advantage compared with PGA.

(2) PGV is more efficient than PGA as well as one spectral value-based S_a and two spectral value-based S^*. But it is less efficient than the proposed S_{12} and S_{123}.

(3) For the structure-specific IM, the more modes are considered, the more efficient IM is. S_{123} is recommended for the incremental dynamic analysis of tall buildings.

Acknowledgements:

The authors are grateful for financial support in part from the National Natural Science Foundation of China (Grant No. 51078274, 51021140006, 51261120377), Key R&D Research Project of Shanghai Education Committee (12zz036), and Fundamental Research Funds for the Central Universities.

References:

Vamvatsikos, D. (2002), "Seismic performance, capacity and reliability of structures as seen through incremental dynamic analysis," [Doctoral Thesis]. Stanford: Stanford University.

Zhou, Y., Lu, X. L., Bo, Y. (2010), "Application of incremental dynamic analysis to seismic evaluation of a hybrid structure," *Journal of Tongji University (Natural Science)*, **38**(2): 183-187. (in Chinese)

Shome, N. (1999), "Probabilistic seismic demand analysis of nonlinear structures," [Doctor Thesis]. Stanford: Stanford University.

Cordova, P. P., Deierlein, G. G., Mehanny, S. S. F., *et al*. (2000), "Development of a two-parameter seismic intensity measure and probabilistic assessment procedure," *Proceedings of the 2nd U.S. - Japan Workshop on Performance-Based Earthquake Engrg for Reinforced Concrete Building Structures*, Sapporo, Japan.

Luco, N., Cornell, C.A. (2007), "Structure-specific scalar intensity measures for near-source and ordinary earthquake ground motions," *Earthquake Spectra*, **23**(2), 357-392.

Mehanny, S. S. F. (2009), "A broad-range power-law form scalar-based seismic intensity measure," *Engineering structures*, **31**(7), 1354-1368.

Baker, J.W., Cornell, C. A. (2004), "Choice of a vector of ground motion intensity measures for seismic demand hazard analysis," *Proceedings of the 13th World Conference on Earthquake Engineering*, Vancouver, B.C., Canada.

Mander, J. B., Priestley, M. J. N. (1988a), "Theoretical stress-strain model for confined concrete," *Journal of Structural Engineering*, , **114**(8), 1804-1826.

Mander, J. B., Priestley, M. J. N. (1988b), "Observed Stress-Strain Behavior of Confined Concrete", *Journal of Structural Engineering* , **114**(8), 1827-1849.

Tothong, P., Luco, N. (2007), "Probabilistic seismic demand analysis using advanced ground motion intensity measures," *Earthquake Engineering & Structural Dynamics*, **36**(13), 1837-1860.

10CUEE CONFERENCE PROCEEDINGS
10th International Conference on Urban Earthquake Engineering
March 1-2, 2013, Tokyo Institute of Technology, Tokyo, Japan

ROCKING FOUNDATIONS WITH DIFFERENT SHAPES ON DIFFERENT SOILS

Manouchehr Hakhamaneshi[1)], Bruce L. Kutter[2)], Shuji Tamura[3)], Andreas G. Gavras[1)], Weian Liu[4)], Lijun Deng[5)]

1) Ph.D. student, Dept. of Civil & Environmental Engineering, University of California, Davis, CA, USA
2) Professor, Dept. of Civil & Environmental Engineering, University of California, Davis, CA, USA
3) Associate Professor, Disaster Prevention Research Institute, Kyoto University, Japan
4) Ph.D. candidate, Dept. of Structural Engineering, University of California, San Diego, CA, USA
5) Assistant Professor, Dept. of Civil Engineering, University of Alberta, Edmonton, AB, Canada
mhakhamaneshi@ucdavis.edu, blkutter@ucdavis.edu, tamura@sds.dpri.kyoto-u.ac.jp,aggavras@ucdavis.edu, wel007@ucsd.edu, ljdeng@ualberta.ca

Abstract: Rocking foundations have shown performance advantages that could benefit the seismic performance of structures. Cumulative settlement is one of the primary potential detrimental aspects of rocking foundations. It is well known that permanent deformations, especially settlement, can accumulate with every cycle of rocking of a shallow foundation. New data obtained at UC Davis and the Kyoto University is analyzed with previously collected data to confirm that previously established equations for moment capacity and methods for assessing residual settlement apply to foundations with different shapes, embedment depths and soil types. The ratio of the actual footing area divided by the footing area required to support the vertical loads, A/A_c, and the aspect ratio of the critical contact area B/L_c are correlated to the moment capacity and the magnitude of normalized residual settlement or uplift (s/L) as a function of cumulative rotation. The iterative procedure for calculation of A_c is illustrated. Recent analysis of settlement-rotation data from previous experiments clearly shows a significant influence of footing shape on residual settlement and uplift behavior. For a given cumulative rotation, footing settlement increases as A/A_c decreases and footings with smaller B/L_c ratio, tend to suffer greater normalized settlement or greater normalized uplift than footings with larger B/L_c ratios.

1. INTRODUCTION

Gajan and Kutter (2008), Deng et al. (2011), Hakhamaneshi et al. (2012a&b), Liu et al. (2012), Anastasopoulos et al. (2010), and Pecker and Chatzigogos (2010) and others have indicated that adoption of rocking foundations on competent soils can absorb seismic energy, reduce the demand on the columns and improve the seismic performance of soil-foundation-superstructure systems. If the moment capacity of the footing is designed to be smaller than the moment capacity of the column, footing rocking will occur instead of column hinging. On the other hand, in a conventional fix-based structural configuration, almost all energy will be dissipated through inelastic flexural behavior of the superstructure components, e.g. hinging columns. Foundation rocking behavior effectively transfers the ductility demand from the hinging column to the footing-soil interface. Despite the advantages of rocking over hinging, design codes often favor column hinging over footing rocking. For example, the California Department of Transportation seismic design criteria (Caltrans 2010) states that "foundation components shall be designed to remain essentially elastic when resisting the plastic hinging moments". New Zealand Structure Design Actions (2004) states that "rocking components may be included in the structures, but special studies on the superstructure behaviors shall be mandatorily performed".

2. LITERATURE REVIEW

2.1 Previous Research

The early work of Housner (1963) theoretically illustrated the beneficial self-centering mechanism of a rocking rigid block. Researchers have since incorporated this concept into rigid shear-walls founded on shallow footings, while also foundation capacity mobilization was considered. Bartlett (1976) and Wiessing (1979) conducted a series of 1-g tests and studied the behavior of rocking shallow foundations on clay and sand. Bartlett found that rocking foundations reduce the seismic force on the structure by lengthening its natural period. Wiessing reported a continuous settlement of the foundations during rocking and a progressive rounding of the soil interface with large amplitudes of footing rotation, which led to loss of the contact area due to the softening of the system.

Rosebrook (2001a&b) and Gajan (2003) conducted numerous experiments on shear wall structures supported by rocking shallow foundation and studied the nonlinear load-deformation behavior of the foundation during cyclic

and dynamic loading. They reported that the moment and shear capacity of a rocking shallow footing depends on its geometry, initial vertical static factor of safety and the moment to shear ratio of the applied load. They saw similarities in the load-deformation behavior of rocking shallow footings when subjected to lateral cyclic loading and dynamic base shaking. Deng et al. (2009a,b and 2010) tested models that included column flexibility, column hinges, and soil-footing-column-bridge deck systems. They reported superior seismic performance and stability of bridges supported on rocking rigid foundations as opposed to hinging column systems with rigid foundations.

2.2 Current Research

Previous research efforts have contributed significantly to the development of the idea of nonlinear analysis in performance-based evaluation. One of the limitations of the work done by Bartlett (1976) and Wiessing (1979), however, is that the experiments were conducted at smaller confining stresses and the reduced scale 1-g models tested seem unrealistic and unable to fully capture the nonlinear prototype footing behavior. Previous centrifuge tests have characterized the behavior of rocking foundations on sand, but fewer analyses have been done on the effects of shape of the footing on the rocking behavior of a foundation. In an effort to fill this research gap, a new series of centrifuge tests (the MAHS test series) is being performed to examine the footing rocking behavior on sandy soil, with emphasis on the effect of shape of the footing on the soil-footing interface deformation.

3. CONCEPT OF ROCKING FOUNDATIONS

3.1 Estimation of Critical Contact Length (L_c)

Consider a vertical load (*V*) applied to the center of gravity of the structure as shown in Figure 1. A horizontal load (*H*) is also applied at a height (*h)* above the base of the footing with length of *L* (in the plane of rocking), width of B (perpendicular to the plane of rocking), and area of $A = B \cdot L$. These loads can cause the center (point O in Figure 1) of the footing to rotate (θ), slide horizontally (*u*) and settle (*s*). The soil exerts a resultant force on the footing, which consists of a sliding resistance force (*F),* and a normal force (*R)*. For rigid soil, the sliding is expected to occur first if the applied horizontal force is equal to the frictional resistance of the soil-footing interface and the applied moment about the base of the footing ($M \approx H \cdot h$) is smaller than the resisting moment *(V·L/2)*. At large rotation demands, the $p-\Delta$ moment should also be included in the moment applied at the soil-footing interface. On the other hand, if the horizontal load is applied at a height greater than *L/(2μ)* (where μ is the coefficient of friction), the footing will tip about its corner. For non-rigid soil, as the footing rocks, it does not bear on a sharp corner of the footing. Instead, a minimum contact area, A_c is required to support the vertical loads. The moving of the contact area results in a curve interface, with localized bearing failure apparent near the edges in Figure 1. Rosebrook and Kutter (2001a&b), Gajan and Kutter (2008), Deng and Kutter (2012) and Hakhamaneshi et al. (2012a&b) showed that the amount of settlement during rocking can be correlated to the contact area, the amplitude of footing rotation and the ratio (A/A_c), which is approximately equal to the traditional factor of safety with respect to bearing capacity.

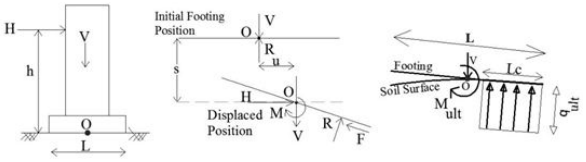


Figure 1 Schematics of a Rocking Footing

The ultimate bearing pressure (q_b) under purely vertical load is characterized by conventional Equation (1):

$$q_b = (s_q \cdot d_q) \cdot q_0 \cdot N_q + 0.5 \cdot (s_\gamma \cdot d_\gamma) \cdot \gamma \cdot B \cdot N_\gamma \quad (1)$$

where N_q and N_γ are bearing capacity factors, d_q and d_γ are depth factors for the q_0 and γ terms; s_q and s_γ are shape factors for the loaded area, B is the width of the shorter side of the soil-footing contact area and q_0 is the soil surcharge pressure and γ is the unit weight of the soil.

Gajan and Kutter (2008) and Deng et al. (2011) showed that for rocking rectangular footings, when they are loaded along the length of the footing, the critical contact length, L_c, is directly related to the critical contact area: $L_c = A_c/B$. The value of L_c represents the minimum length of the footing required to support the vertical load when the soil bearing capacity is fully mobilized on the rectangular contact area. With the knowledge of ultimate bearing capacity (q_b), one can analytically determine L_c by using the conventional equation of $L_c = V/(q_b \cdot B)$. Deng et al. (2011) showed that as L_c becomes the shorter side of the assumed critical contact area, a trial L_c may be plugged into the Equation (1) as B for calculating the bearing capacity of the soil in the contact area (q_{bLc}). Therefore, Equation (1) can be written for the critical contact area as Equation (2a) for $L_c < B$ and Equation (2b) for $L_c \geq B$ (shape factors s_q and s_γ should be updated accordingly).

$$q_{bLc} = (s_q \cdot d_q) \cdot q_0 \cdot N_q + 0.5 \cdot (s_\gamma \cdot d_\gamma) \cdot \gamma \cdot L_c \cdot N_\gamma \quad (2a)$$

$$q_{bLc} = (s_q \cdot d_q) \cdot q_0 \cdot N_q + 0.5 \cdot (s_\gamma \cdot d_\gamma) \cdot \gamma \cdot B \cdot N_\gamma \quad (2b)$$

Under the condition of rocking capacity being fully mobilized, Equation (3) holds as:

$$q_{bLc} \cdot B \cdot L_c = V \quad (3)$$

Since L_c appears in both Equations (2) & (3), iteration may be required to determine L_c.

3.2 Moment Capacity of a Rocking Footing

Gajan and Kutter (2008) examined the relations

between the moment capacity of the footing, net settlement and energy dissipated during footing rocking with various critical contact area ratios *(A/A$_c$)*. Gajan and Kutter (2008) and Deng and Kutter (2012) observed that when the external applied moment approaches the resisting moment capacity of the footing (denoted as $M_{c\text{-}foot}$) in Equation (4), the footing rocking is about to occur.

$$M_{c-foot} = 0.5 \cdot V \cdot L \cdot (1 - A_c / A) \quad (4)$$

Estimation of rocking moment capacity depends on the accuracy of L_c and q_{bLc} which depend on bearing capacity factors N_q and N_γ , shape factor (s_q) and depth factor (d_q) which are all functions of the soil's friction angle. Therefore, in order to obtain a reasonable estimate of moment capacity, we need to have an accurate measure of the friction angle. As suggested by Deng and Kutter (2012), an initial friction angle is assumed which will determine the bearing capacity, shape and depth factors. Ultimate bearing pressure (q_b) is calculated using Equation (1) and the corresponding representative mean confining stress of the sand under the footing (σ_{mp}) is calculated using De Beer (1965) method as shown in Equation (5):

$$\sigma_{mp} = 0.25 \cdot (q_b + 3q_0) \cdot [(1 + \tan^2\phi) \cdot (1 + \sin\phi)]^{-1} \quad (5)$$

Friction angle is calculated using Bolton's dilatancy relationships (1986) as shown in Equation (6). This value is compared with the initial estimate until a match is achieved.

$$\phi_{tc} = \phi_{cv} + 3 \cdot [D_r \cdot (10 - \ln(100\sigma_{mp} / 100kPa) - 1] \cdot \pi / 180 \quad (6)$$

In this equation, D_r is the relative density of sand and ϕ_{cv} is the constant volume friction angle of the sand. Iteration is done until an accurate measure of friction angle is achieved. Critical contact length (L_c), bearing capacity of the soil in the contact area (q_{bLc}) and theoretical rocking moment capacity ($M_{c\text{-}foot}$) can now be calculated accurately using Equations (2)-(4).

4. TEST PROGRAM

4.1 Dynamic Tests on Toyoura Sand (TAM Test)

A series of dynamic centrifuge tests were conducted using the geotechnical centrifuge at Disaster Prevention Research Institute, Kyoto University. Two different soil-foundation-superstructure models were dynamically tested (three different input motions for each structure) at a centrifugal acceleration of 50g. Tamura et. al (2012) explain the details of the models, test setup, time histories of the soil and structure response and the moment-rotation hysteretic behavior of the footings. However, they did not provide a theoretical value for the moment capacity of the footings. Table 1 summarizes the properties of the soil and the footings needed to perform the iteration explained in Section 3 to obtain a theoretical estimate of the rocking moment capacity. All the properties presented in this paper are in model scale. The scaling laws for centrifuge tests were described in Kutter (1995). In this table, footing properties are as follows: "L" is the length of the footing parallel to the direction of shaking, "B" is the width of the footing perpendicular to the direction of shaking, "t" is the thickness of the footing, "D" represents the initial embedment and "V" includes the total weight (footing plus soil above the footing and superstructure), supported by the footing. Sand profile properties are the maximum and minimum void ratio (e-max and e-min) and the relative density of the sand (D_r).

Table 1 Soil & Footing properties in TAM test series (model scale)

Property	High Rise (H)	Low Rise (L)
L (mm)	50	50
B (mm)	80	80
t (mm)	10	10
D (mm)	8	8
V (kN)	0.707	0.701
Height (mm)	149	92
Sand	Toyoura	Toyoura
e-max	0.997	0.997
e-min	0.597	0.597
D_r (%)	90	90

Table 2 summarizes the results of the iteration explained in section 3 which is further used to obtain the theoretical rocking moment capacity as shown in Equation (4).

Table 2 Summary of the iteration results in TAM test

Quantity	High Rise	Low Rise
Φ(°)	43.1	43.1
q_b (kPa)	3114	3114
FS_v	17.6	17.8
L_c (mm)	6	5.73
A/A_c	8.89	8.75
$M_{c\text{-}foot}$ (N.m)	15.7	15.4

4.2 Slow Cyclic Tests on Nevada Sand (MAHS Test)

A series of lateral slow cyclic centrifuge tests were conducted at the center for geotechnical modeling at UC Davis using the 1m radius (Schaevitz) centrifuge. Three different soil-foundation-superstructure models were tested at a centrifugal acceleration of 35g. A stiff shear-wall

structure was made out of steel and tested under slow lateral cyclic displacement controlled loading for each footing. The loading protocol involved application of 3 cycles of constant amplitude, with amplitudes doubled to cause the footing rotate from 0.1% to 6%. Figure 2 shows the applied sinusoidal displacement time history to the structures. All the rotations reported in this paper are actually the tangent of the rotation angle (i.e. 1% rotation indicates that the tangent of the rotation angle is 0.01).

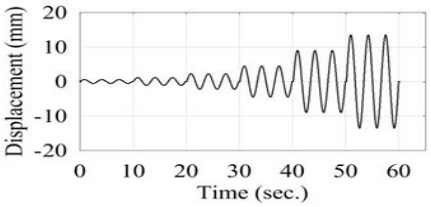


Figure 2 Displacement-controlled time history of the actuator for lateral slow cyclic tests

The properties of the footings and soil can be found in Table 3. The Long-Narrow (LN) footing has a longer length in the direction of cycling than the Short-Wide (SW) footing. On the other hand, the Short-Wide footing has a longer width, perpendicular to the direction of cycling than the other two footings. The Very-Long-Narrow (VLN) footing has the largest length and the smallest width.

Table 3 Soil & Footing properties in MAHS test series

Soil/Footing Props.	Long Narrow (LN)	Short Wide (SW)	Very Long Narrow (VLN)
L (mm)	150	110	210
B (mm)	90	170	30
t (mm)	31.75	31.75	31.75
D (mm)	31.75	31.75	31.75
V (kN)	2.841	3.931	1.435
Sand	Nevada	Nevada	Nevada
e-max	0.887	0.887	0.887
e-min	0.511	0.511	0.511
D_r (%)	82	82	80

Table 4 summarizes the results of the iteration process explained in Section 3 which is further used to obtain the theoretical rocking moment capacity of these three footings, using Equation (4).

Table 4 Summary of the iteration results in MAHS test

Quantity	Long Narrow	Short Wide	Very Long Narrow
$\Phi(^\circ)$	37.8	37.6	38.5
q_b (kPa)	2460	2619	1826
FS_v	11.7	12.4	8.7
L_c (mm)	17.1	12.7	21.4
A/A_c	8.8	8.7	9.8
$M_{c\text{-}foot}$ (N.m)	188.8	191.3	135.3

5. LOAD-DEFORMATION PLOTS

5.1 Dynamic Tests on Toyoura Sand (TAM Test)

Figure 3 shows the moment vs. rotation relationships measured in the dynamic tests on the footings with different A/A_c ratios, as shown in Table 1. Tamura et al. (2012) plotted these graphs without the theoretical estimate of the rocking moment capacity. The critical contact length (L_c) is being calculated using the iteration process in Section 3, and rocking moment capacity of these footings is calculated and plotted below. The rocking moment is normalized by *VL/2* which represents moment capacity for rocking on a rigid interface (A/A_c = infinity in Equation (4)). The time history of the three different applied ground motions are summarized in Tamura et al. (2012).

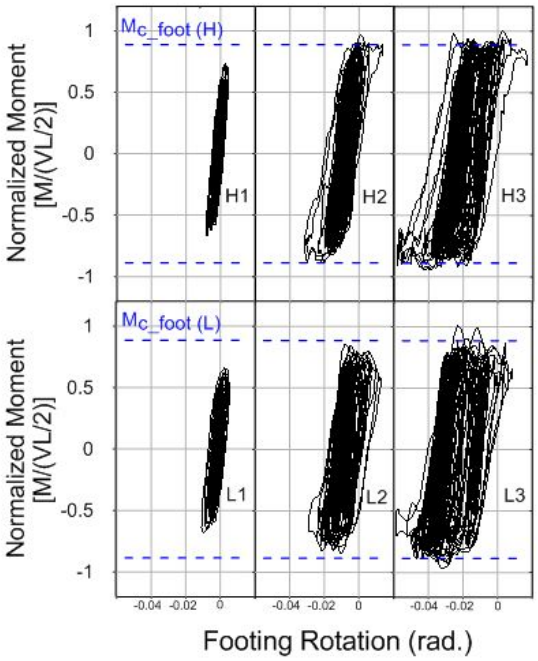


Figure 3 Moment-Rotation plots of the High-rise (H) and Low-rise (L) structures for three different ground motions

For the cases shown in Figure 3 above, the rocking moment capacity of the footing is reached initially at rotation

amplitude of about 1%. The moment vs. rotation behavior of the footing shows a stiff response for rotations less than about 0.5%. As the cumulative rotation increases, this relationship becomes nonlinear and foundation soil's rotational stiffness degrades. This nonlinearity is affected by the rounding of the soil beneath the rocking footing and the local bearing failure along the moving contact interface.

5.2 Slow Cyclic Tests on Nevada Sand (MAHS Test)

The moment-rotation behavior of the footings in Table 3 are summarized in Figure 4 below. As is the case in Figure 3 also, for rotations smaller than about 0.5%, the moment-rotation plots show a stiff response, but as the amplitude of rotation increases, the moment-rotation plots show a nonlinear behavior where the rotational stiffness degrades as the amplitude of oscillation increases. The rocking moment capacity is reached at about 1.3% amplitude of rotation. The moment capacity undergoes very small degradation at very large amplitudes of rotations (5-6%). Even for large amplitudes of rotation, the footing continues to rock with minimal degradation in capacity. The tendency is very similar to those reported by Deng and Kutter (2012) and Gajan and Kutter (2008). In both scenarios the moment capacity is preserved even at large rotation.

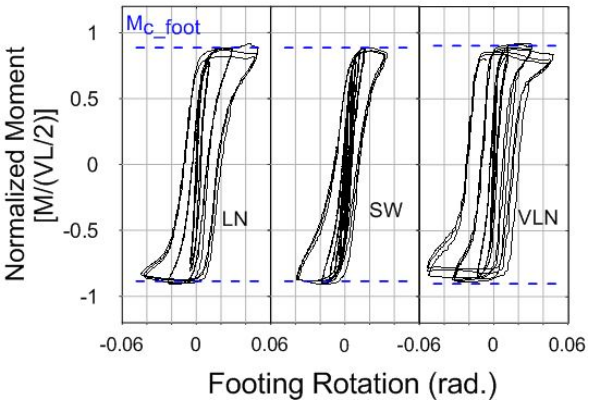


Figure 4 Moment-Rotation Plots of the Footings shown in Table 3 (MAHS Test)

The method explained in Section 3 regarding estimation of L_c by iteration seems to provide us with a relatively accurate measure of the rocking moment capacity in the scenarios shown in Figures 3 and 4.

6. FOOTING SETTLEMENT CORRELATIONS

6.1 Effect of A/A_c on the Settlement and Uplift

As rocking proceeds, we expect the soil beneath the foundation to lose its flat shape and become rounded at the edges. This leads to a reduction in the contact area between the footing and the foundation and a progressive bearing failure causes the foundation to settle. Gajan at al. (2008) used the data from centrifuge tests mainly on sand, to relate the settlement of the foundation per cycle of footing rotation to the amplitude of rotation. The results were grouped in categories based on the A/A_c ratio. Deng and Kutter (2012) added data on sand with larger values of A/A_c (values more typical of bridge foundations on granular soils). They noted that for very large rotations and large A/A_c values, the footing tended to have a residual uplift associated with sand falling into the gap under the footing as it rocked. Instead of considering settlement on a cycle by cycle basis as suggested by Gajan and Kutter (2008), Deng and Kutter (2012) and Hakhamaneshi et al. (2012a&b) suggested correlating the cumulative footing rotation (θ_{cum}) to the normalized footing settlement (s/L) and further extended the correlation to include foundations on both sand and clay. The footing's cumulative rotation (θ_{cum}) is obtained by summing up the absolute value of all the local maxima and minima ($extrema_i$) for which the amplitude exceeds a threshold rotation (θ_t is set empirically at 1 mrad in this study). Rotations smaller than the threshold value are assumed to cause an elastic response to the rocking without leading to any residual settlement or uplift. In this study, the procedure proposed by (Hakhamaneshi et al. (2012b) and Deng and Kutter (2012) for obtaining the cumulative rotation has been modified by subtracting the elastic rotation for each cycle by introducing the $-N\cdot\theta_t$ in Equation (7). Figure 5 illustrates the determination of extrema and the rotation threshold used to determine footing cumulative rotation.

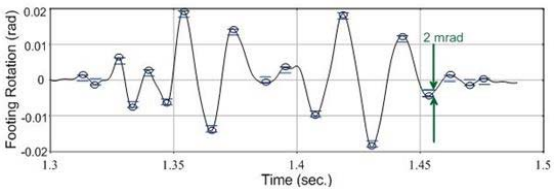


Figure 5 Schematic of illustrating thresholding procedure to obtain the Cumulative Rotation of a Rocking Footing

$$\theta_{cum} = \Sigma_{i=1}^{N} \left| extrema_i \right| - (N \cdot 0.001) \; for \; \left| extrema_i - extrema_{i-1} \right| \geq 0.002 rad. \quad (7)$$

The data from the TAM and MAHS test series on Toyoura and Nevada sand are added to the aforementioned datasets on sand (Gajan and Kutter (2008) and Deng and Kutter (2012)) and clay (Rosebrook and Kutter (2001a&b) and Hakhamaneshi et al. (2012a)). Table 5 summarizes the scope of parameters varied during these experiments and provides us the ranges of the footing properties being tested. In this table, "Test ID" specifies the name of each experiment test series; "Loading" differentiates whether the event was a Slow Cyclic (SC) test or Dynamic shaking (Dyn) test and "Soil" type specifies whether the soil profile was made out of Sand or Clay. The letter inside the parenthesis differentiates the type of sand used (Nevada or Toyoura). "A" is the area of the footing and equal to $B \cdot L$, where as illustrated in Figure 6, "B" is the width of the footing parallel to the axis of rocking and "L" is the length of the footing in the plane of rocking. A_c is the critical contact area of the footing and is equal to $B \cdot L_c$ where L_c is determined through the iteration process explained in Section 3.

Table 5 Details of the data points gathered from the past and current centrifuge tests

Test ID	Soil	Loading	A/A_c	B/L_c
KRR	Sand (N)	SC	2-4	0.72-2
LJD	Sand (N)	SC/Dyn	8-30	5-30
MAH01	Clay	SC/Dyn	1.2-11	2.5-18
SSG	Sand (N)	SC/Dyn	2.2-15.9	0.5-4
MAHS	Sand (N)	SC	8.7-9.8	1.4-13.4
TAM	Sand (T)	Dyn	8.7-8.9	13-14

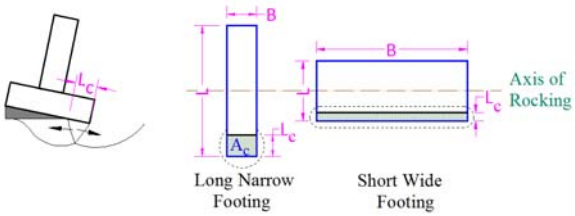


Figure 6 Bearing failure mechanism in footings with different aspect ratios

Figure 7 plots the normalized cumulative residual settlement with respect to the updated footing cumulative rotation for many events of the test series described in Table 5. The current data points are differentiated from the previous experiments by not being color filled. A conservative envelope, indicated by the straight lines in the graph encloses most of the data points from A/A_c groups. These boundaries set previously by Deng and Kutter (2012) seem to be conservative for the current data as the settlements for the same A/A_c ratio seem to be smaller. It is promising that the current data points do not exceed these boundaries and is consistent with the previous data. The similarity in the relationships for sand (Nevada and Toyoura) and clay indicates that the effect of changing soil type can be reasonably accounted for through the effect on A/A_c. From Figure 7, it is apparent that if A/A_c>8, the settlement is always smaller than 1% of the length of the foundation even at cumulative footing rotations up to 0.3 radians. Furthermore, we suggest that such small settlements would likely be considered to be acceptable performance during a major seismic event.

For design purposes, Deng and Kutter (2012) proposed a procedure for estimating the footing's cumulative rotation of footings in bridge structure. They suggested that the design lateral displacement of bridge deck (D_d) may be obtained from the spectral displacement, given the period of the structure. The design amplitude of footing rotation (d) is estimated by dividing the design displacement of the deck by the column height (H_c). Depending on the magnitude of an earthquake, it may be reasonable to assume that foundation undergoes two full cycles of rotation with the design amplitude, so Equation (9) is used to correlate the design rotation to the dynamic settlement. Note that during two full cycles of rotation, the cumulative rotation calculated using Equation (8) would be four times the half amplitude of rotation. The constant "*const*" in Equations (8) and (9) is the slope of the appropriate line such as those indicated in Figure 7 (Deng and Kutter 2012), depending on the static factor of safety with respect to bearing capacity (expressed in terms of footing areas A/A_c) and the footing shape (accounted for by the ratio B/L_c).

$$s = const \cdot L \cdot \theta_{cum} \quad (8)$$

$$s = 4 \cdot const \cdot L \cdot d \quad (9)$$

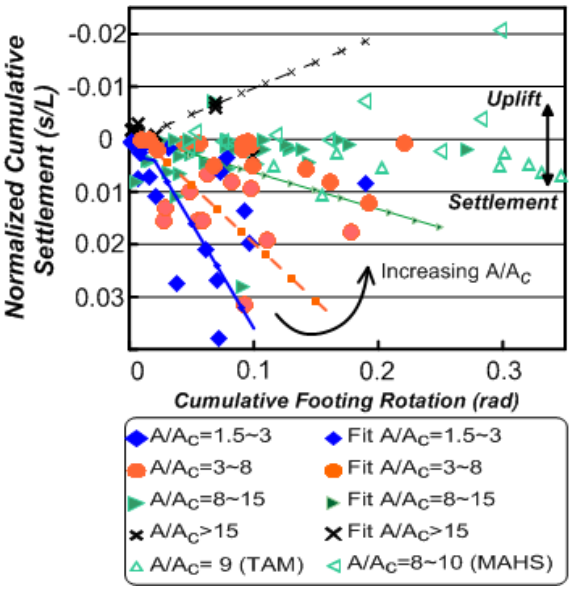


Figure 7 Cumulative normalized residual settlement-cumulative footing rotation grouped into different A/A_c ratios

6.2 Effect of B/L_c on Residual Settlement and Uplift

The aspect ratio (B/L_c) is introduced to characterize the shape of the critical contact area. A footing with high aspect ratio would be like the Short Wide footing in Figure 6. For a footing with large aspect ratio of the critical contact area, the soil deformations associated with the localized bearing failure would be expected to be primarily in the plane of rotation as indicated by the arrows in Figure 6; for this case, perhaps about half of the soil that is displaced due to bearing failure of the strip-shaped loaded area gets pushed back under the footing, and the other half gets pushed away from the footing, accounting for settlement. As the footing becomes longer and narrower (LN & VLN), the contact shape could become square, at which point out of plane soil displacements associated with bearing failure become significant and a smaller fraction of the displaced soil would be pushed back into the gap under the footing. If other factors (e.g., A/A_c) are held constant while varying footing shape, due to a greater proportion of soil being pushed away from the footing, one may expect greater settlements for rocking of long narrow footings than for short wide footings.

To isolate the effect of footing shape, Hakhamaneshi et al. (2012b) grouped the data in Figure 7 based on their critical contact area ratio (A/A_c) and for each group, they divided the data into different subcategories based on their aspect ratio. They reported a consistent trend indicating that as B/L_c ratio increased, normalized settlement (s/L) decreased. However, the majority of the footings they studied did not experience residual uplift and the effect of aspect ratio was mainly studied in cases where the foundation settled. The MAHS data series allow us to study the effect of B/L_c ratio on the uplift of the foundations also. These footings were embedded while having a large A/A_c ratio. As these footings rock, a portion of the surrounding sand falls into the gap (created during rocking) below the footing, and the center of the footing will uplift. At smaller amplitudes of rotation we expect small amount of sand to fall in to the gap, having minimal effects on the uplift of the foundation. However, at larger amplitudes, considerable amount of sand falls in to the gap which will overcome the partial settlements due to the localized bearing failure.

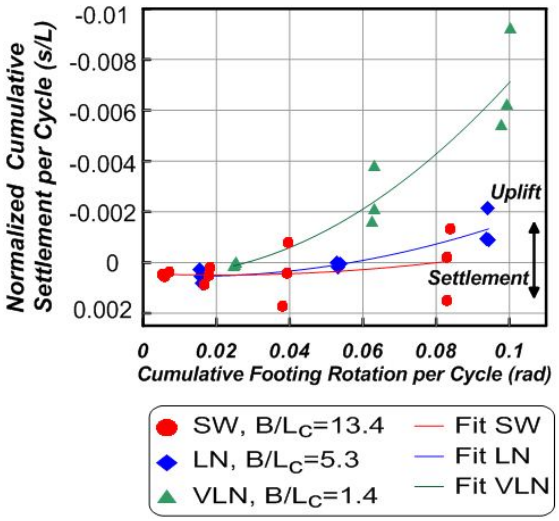


Figure 8 Normalized cumulative footing rotation per cycle-normalized cumulative (residual) settlement per cycle relation for MAHS footings ($8.5 < A/A_c < 10$)

Figure 8 plots the normalized cyclic cumulative settlement versus cyclic cumulative footing rotation of the three footings tested in the MAHS series. The Very-Long-Narrow (VLN) footing seems to undergo the largest uplift. For this footing, the aspect ratio (B/L_c) is close to unity, meaning that the critical contact area becomes like a square shape and sand can fall into the gap from both in-plane and out-of-plane of rocking. At large rotation demands, the VLN footing seems to uplift almost 3-4 times the Long-Narrow (LN) and Short-Wide (SW) footings. At small rotation demands, the VLN footing seems not to uplift considerably more than the LN and SW footings, but all of the settlements are quite small.

7. CONCLUSIONS

Researchers at UC Davis (e.g., Rosebrook and Kutter (2001a&b), Gajan et al. (2005), Deng et al. (2011), Hakhamaneshi et al. (2012a&b)) and elsewhere have shown that moment capacity of a rocking footing on sandy or clayey soil suffers little degradation during cyclic loading and the capacity can be accurately predicted as long as the axial load on the footing, the sizes of the foundations, and the term ($1\text{-}A_c/A$) in equation (4), can be determined. An iterative calculation procedure to determine the critical contact area, A_c, previously described by Deng and Kutter (2012), is illustrated in the present paper.

The previous rocking tests at Davis included both dynamic shaking and slow cyclic loading and used one type of sand (dry Nevada sand), and two types of cohesive soil (Yolo Loam, a clayey silt, and San Francisco Bay Mud, a high plasticity clay). For the present paper, new data is introduced to extend the validation for different soil types and different footing shapes: Data from Tamura et al. (2012) involved dynamic shaking using Toyoura sand, and data from the new MAHS test series was added to study rocking of rectangular footings of different aspect ratio. It was confirmed that rocking moment capacity shown in Equation (4) holds for rectangular footings on sandy or clayey soil, and that it is insensitive to loading type (cyclic or dynamic), especially if A/A_c is large. The effect of changing soil type and footing shape is reasonably accounted for through the effect on A/A_c.

The effect of footing shape on the normalized settlement (s/L) and uplift (-s/L) of the rocking footings is studied through the aspect ratio of the critical contact area (B/L_c). Hakhamaneshi et al. (2012b) found that under the same factor of safety (A/A_c), wide rectangular rocking footings (with higher B/L_c) settle less than narrow rocking footings. They reported that due to less lateral confinement around the rocking edge for narrow footings and the three-dimensional failure mechanism, a larger fraction of soil is pushed out from under the footing, hence larger normalized settlements (s/L) are expected for narrow footings. They also reported that for wide footings, lateral confinement reduces out-of-plane soil displacements and settlements. They did not however describe the effect of aspect ratio on the residual uplift of rocking footings.

The results of the new MAHS test series show that for footings with large A/Ac embedded in sand, that rocking generally results in residual uplift. This residual uplift could be attributed to sand falling into the gap as the footing rocks. Based on the findings of this paper, the magnitude of normalized residual uplift (-s/L) is greater for footings with small aspect ratio of the critical contact area (B/L_c), especially at large amplitudes of rotation. This increased residual uplift for narrow footings may be attributed to the fact that sand can fall into the gap from the sides of the footing as well as the end of the footing.

In summary, for footings on sand, normalized residual settlement occurs for A/A_c less than about ten and the magnitude of settlement increases as A/A_c decreases. For

embedded footings in sand, if A/A_c is greater than ten, normalized residual uplift may result. For a given cumulative rotation, the magnitudes of both residual normalized settlement or residual normalized uplift increase as B/L_c decreases.

Acknowledgements:

This work was primarily supported by NSF-NEESR under Grant number CMMI 0936503. Any findings, statements and conclusions are those of the authors, and do not necessarily reflect the opinions of the sponsoring organizations. The authors would like to thank the suggestions and contributions of Prof. Sashi Kunnath of UC Davis, Prof. Tara C. Hutchinson of UC San Diego, Prof. Mark Aschheim of Santa Clara Univ., Dr. Dong Soon Park, Benjamin Choy and Jacquelyn Allmond. The authors would also like to thank the staff of Center for Geotechnical Modeling at UC Davis for their assistance. A.G. Gavras is also grateful for the partial support provided by the Alexander S. Onassis Foundation during his M.S studies at UC Davis.

References:

Anastasopoulos, I., Gazetas, G., Loli, M., Apostolou, M., and Gerolymos, N. (2010). "Soil failure can be used for seismic protection of structures," *Bulletin of. Earthquake. Engineering*, **8(2)**, 309-326.

Bartlett, P.E. (1976). "Foundation rocking on a clay soil." *ME thesis*, University of Auckland, School of Engineering, Report No. 154, Auckland, New Zealand.

Bolton, M.D., (1986). "The strength and dilatancy of sands," *Geotechnique*, **36**, No. 1,65-78

California Department of Transportation (Caltrans). (2006). Seismic Design Criteria. Sacramento, CA.

De Beer, E. (1965). "Influence of the mean normal stress on the shearing resistance of sand." VI International Conference on Soil Mechanics and Foundation Engineering, Montreal, Canada, Vol. 1, pp. 165-169.

Deng, L., Algie, T., Kutter, B.L. (2009a). Innovative Economical Foundations with Improved Performance that is Less Sensitive to Site Conditions: Centrifuge Data Report for LJD01. UCD/*CGMDR-09/01*. Davis, CA: University of California.

Deng, L., Algie, T., Kutter, B.L. (2009b). Seismic Performance of Bridge Systems with Rocking Foundations: Centrifuge Data Report for LJD02. *UCD/CGMDR-09/02*. Davis, CA: University of California.

Deng, L., Kutter, B.L. (2010). Seismic Performance of Bridge Systems with Rocking Foundations: Centrifuge Data Report for LJD03. *UCD/CGMDR-10/01*. Davis, CA: University of California.

Deng, L., Kutter, B.L., Kunnath, S. (2011). "Centrifuge modeling of bridge systems designed for rocking foundations." *ASCE J. Geotech. Geoenviron. Engrg*. **138:3**, 335-344.

Deng, L. and Kutter, B.L. (2012). "Characterization of rocking shallow foundations using centrifuge model tests." *Earthquake Engineering & Structural Dynamics*. **41:5**, 1043-1060.

Gajan, S., Phalen, J.D. and Kutter, B.L. (2003). Soil-Foundation-Structure Interaction: Shallow Foundations Centrifuge Data Report for SSG02. *UCD/CGMDR-03/01*. Davis, CA: University of California.

Gajan S, Kutter B.L., Phalen J.D., Hutchinson T.C., Martin G.R. (2005). "Centrifuge modeling of load-deformation behavior of rocking shallow foundations." *Soil Dynamics and Earthquake Engineering*.; **25:10** 773–783.

Gajan, S., and Kutter, B.L. (2008). "Capacity, settlement, and energy dissipation of shallow footings subjected to rocking." *ASCE J. Geotech. Geoenviron. Engrg.*, **134:8**, 1129-1141.

Hakhamaneshi, M., Kutter, B.L., Deng, L., Hutchinson, T.C. and Liu, W. (2012a) "New findings from centrifuge modeling of rocking shallow foundations in clayey ground. " ASCE GeoCongress 2012.

Hakhamaneshi, M., Kutter, B.L., Deng, L., Johnson, K., Hutchinson, T.C. and Liu, W. (2012b) "Observed effects of footing shape on settlements caused by foundation rocking." 15 WCEE, Lisbon 2012.

Housner, G. W. (1963). "The behavior of inverted pendulum structures during earthquakes." *Bull. Seismo. Soc. Am,.* **53:2**, 403-417.

Kutter, B.L (1995). "Recent advances in centrifuge modeling of seismic shaking." *Proc. 3rd Intl. Conf. on Recent Advances in Geotech. Earthq. Engrg. Soil Dyn*., University of Missouri, Rolla, MO, Vol.2, 927-942.

Liu,W., Hutchinson, T.C., Kutter, B.L., Hakhamaneshi, M., Aschheim, M. and Kunnath, S. (2012). "Demonstration of Compatible Yielding between Soil-Foundation and Superstructure Components." *ASCE Journal of Structural Engineering* (Accepted, in press).

Pecker, A., and Chatzigogos, C.T. (2010). "Non linear soil structure interaction: impact on the seismic response of structures." *Earthquake Engineering in Europe, Geotechnical, Geological, and Earthquake Engineering* **17**, 79-103.

Rosebrook, K.R., and Kutter, B.L. (2001a). Soil-foundation-structure interaction: Shallow foundations. Centrifuge Data Rep. for test series KRR01. University of California, Davis, CA.

Rosebrook, K.R., and Kutter, B.L. (2001b). Soil-foundation-structure interaction: Shallow foundations. Centrifuge Data Rep. for test series KRR02. University of California, Davis, CA.

Standards New Zealand technical Committee. (2004). *Structural Design Actions* (NZS 1170.5). Wellington, New Zealand.

Tamura, S., Kuriki, A. and Tokimatsu, K., (2012) "*Relation between Overturning Moment acting on Shallow Foundation and Ultimate Response of Superstructure during Strong Earthquakes*." Joint Conference on Urban Earthquake Engineering, 4th Asia Conference on Earthquake Engineering, Tokyo, Japan

Wiessing, P. R. (1979). "Foundation rocking on sand." ME thesis. University of Auckland, School of Engineering, Report No. 203, Auckland, New Zealand.

10CUEE CONFERENCE PROCEEDINGS
10th International Conference on Urban Earthquake Engineering
March 1-2, 2013, Tokyo Institute of Technology, Tokyo, Japan

ESTIMATION OF THE MAXIMUM RESPONSE OF BASE ISOLATED STRUCTURES

Parisara Thiravechyan[1], and Kazuhiko Kasai [2]

1) Graduate student, Department of Built Environment, Tokyo Institute of Technology, Japan
2) Professor, Structural Engineering Research Center, Tokyo Institute of Technology, Japan
thiravechyan.p.aa@m.titech.ac.jp, kasai@serc.titech.ac.jp

Abstract: This study investigates the response of base isolated structures considering inelastic behavior of the superstructure under earthquake excitations. The objective is to clearly show the influence of superstructure yielding on the response of the structure and to check the feasibility of applying steady state approach to the estimation of maximum displacement. In this study, a 5-story base isolated structure is idealized as a 2DOF model. The superstructure is assumed to have elastoplastic behavior while the isolation system is viscoelastic with various combinations of isolation system periods and damping ratios. Results indicate that superstructure yielding significantly increases the maximum superstructure displacement but has only a minor effect on the isolation level response. Estimation of the maximum response is based on the steady state response to harmonic excitation. An equivalent viscoelastic SDOF system is derived by treating the elastoplastic superstructure as an equivalent viscoelastic element. The maximum displacement can be estimated from earthquake response spectrum and the separated to the superstructure and isolation system displacements. The estimation shows good agreement with results from response history analysis.

1. INTRODUCTION

In recent years base isolation has become increasingly used as an effective design to mitigate earthquake damage. Many types of structures have been built using this approach. The idea behind the concept of base isolation is quite simple. A layer of horizontally flexible elements called isolators is added between the structure above and its base, thereby decoupling the building from ground motions. For low and middle rise building that vibration period is short, base isolation greatly elongates the period of the structures out from predominant period of general earthquakes and reduce seismic demand.

The expected behavior of base isolated structure is schematically shown as in Figure 1(a). Large displacement is concentrated at the isolation level and the structure above is in the elastic range. Previous studies on base isolated structures have primarily focused on this case. However, for an earthquake greater than the design basis, insufficient seismic gap may cause pounding, as shown in Figure 1(b), which can causes high impact forces and significant damage especially for the acceleration-sensitive components. On the other hand, yielding of superstructure may occur as in Figure 1(c) and affect the response behavior.

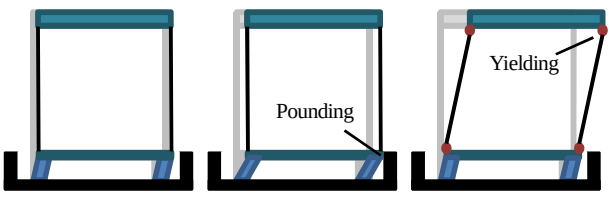


Figure 1 Possible mode of behavior of base isolated structures

Designed according to modern seismic provisions, base isolated structures are required to remain essentially elastic in the expected Design Basis Earthquake (DBE). Additionally, a separation distance must be provided to accommodate expected displacement in a Maximum Considered Earthquake (MCE). Therefore, yielding of superstructure is supposed to occur before pounding with surrounding walls. As yielding happens, reduction of stiffness allows superstructure to take part of the energy. As a result, the base ceases to move further, hence, pounding is unexpected. However, little consideration is given to this situation. Therefore, objective of this study is to investigate the response of base isolated structure having nonlinear behavior of superstructure. The effects of yielding of superstructure on the maximum displacement of superstructure and isolation level will be explained. Moreover, some theoretical considerations to the estimation of maximum displacement of the base isolated structure based on steady state response assumption will be described to check the feasibility of applying steady state approach to the estimation of the response under actual ground motion. This is to provide an effective tool for practice engineers in the design of base isolated structures.

2. TIME HISTORY ANALYSIS

2.1 Analysis model

In this study, a 5-story base isolated structure is idealized as a 2DOF model as shown in Figure 2. Assume equal floor masses with one additional isolation level, the

ratio between base mass m_b and superstructure mass m_s can be expressed as

$$\frac{m_b}{m_s} = \frac{1}{N} = 0.2 \tag{1}$$

The isolation system is assumed to have viscoelastic behavior. Given isolation period T_b and isolation damping ratio ζ_b, isolation system stiffness k_b and damping coefficient c_b are computed as in the following equations:

$$k_b = (m_s + m_b)\frac{4\pi^2}{T_b^2} \qquad c_b = \frac{4\pi\zeta_b}{T_b}(m_s + m_b) \tag{2}$$

The superstructure is characterized as an elastoplastic element having elastic stiffness k_{so}, damping coefficient c_{so}, superstructure yield strength f_{sy}, and post-yield stiffness ratio p. For a given superstructure elastic period T_{so}, superstructure damping ratio ζ_{so}, we can define the elastic properties of the superstructure as

$$k_{so} = m_s \frac{4\pi^2}{T_{so}^2} \qquad c_{so} = \frac{4\pi\zeta_{so}}{T_{so}} m_s \tag{3}$$

To avoid scatterness of the response data, superstructure yield strength is varied based on the maximum elastic superstructure force f_{se} for each particular ground motion. Given a strength reduction factor R, superstructure yield strength f_{sy} is computed based on the definitions as follows:

$$R = \frac{f_{se}}{f_{sy}} \tag{4}$$

Given the parameters mentioned above, time history analyses are able to conduct. Note that the same R gives different values of superstructure yield strength for different combinations of T_b, ζ_b, T_{so}, ζ_{so} and ground motion depending on the elastic responses. Responses considered in this study are the maximum total displacement of the system u_o, and the maximum superstructure and isolation system displacement u_{so} and u_{bo}, respectively.

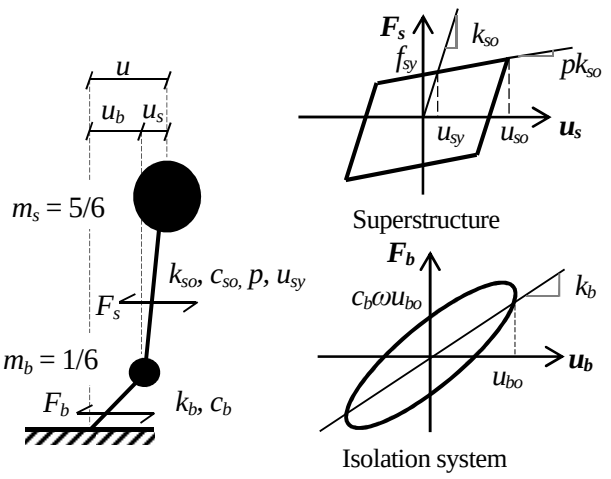


Figure 2 Idealization of base isolated structures

The SAC suite of ground motions for the Maximum Considered Earthquake (MCE) level for the Los Angeles area, LA21-LA40, is used. Following modern US building code provisions, the superstructure is expected to remain elastic for the expected Design Basis Earthquake (DBE), an event whose response spectrum is 2/3 of the MCE (McGuire 2004, Somerville et al. 1998). Thus, the structure designed according to the code is represented by the model having R = 1.5.

2.2 Trends of the maximum response

Figure 3 shows the maximum displacement observed from time history model. Four isolation systems are considered, each column in the figure represents each isolation system including the system having isolation system period T_b equals to 2 and 4 sec., and isolation system damping ratio ζ_b of 0.10 and 0.30. In this study, Superstructure elastic period is fixed at the approximation by the formula $T_s = 0.1N$ where N represents number of stories, therefore T_s = 0.5 sec. Superstructure damping ratio ζ_s is assumed as 0.02. Top, middle, and bottom lines present total, superstructure, and isolation system displacements, respectively. In each graph, the x-axis represents superstructure strength reduction ratio R equals to 1, 1.5, 2, 2.5, and 3.

When R = 1 that is the superstructure is elastic, 20 diamond data points in each graph represent the maximum response from time history model subjected to 20 SAC ground motions. Obviously, longer isolation system period significantly increases the maximum total and isolation system displacement but not much affects the superstructure displacement. However, larger damping results in a minor reduction of all the response.

Considering yielding of superstructure, 3 types of data points – circle, triangular and square – represents post-yield stiffness ratio p is 0, 0.1, and 0.2, respectively for each R. When p = 0, yielding significantly affects the maximum response. As R increases, superstructure peak displacement increases and isolation system peak displacement reduces. This is because yielding of superstructure takes a large portion of energy input so that the base ceased to move further. However, as p increases, the effect is less obvious. When p = 0.2, total and isolation system displacement is about the same for each isolation system properties and not much affected by yielding of superstructure.

3. ESTIMATION OF MAXIMUM DISPLACEMENT

Estimation of the maximum response is done by converting the elastoplastic superstructure to an equivalent viscoelastic system having equivalent superstructure stiffness k_s and equivalent superstructure damping coefficient c_s as in Figure 4(a). With these obtained equivalent viscoelastic properties of superstructure, together with the viscoelastic isolation system and ignoring isolation system mass m_b, we can idealize base isolated structures as a

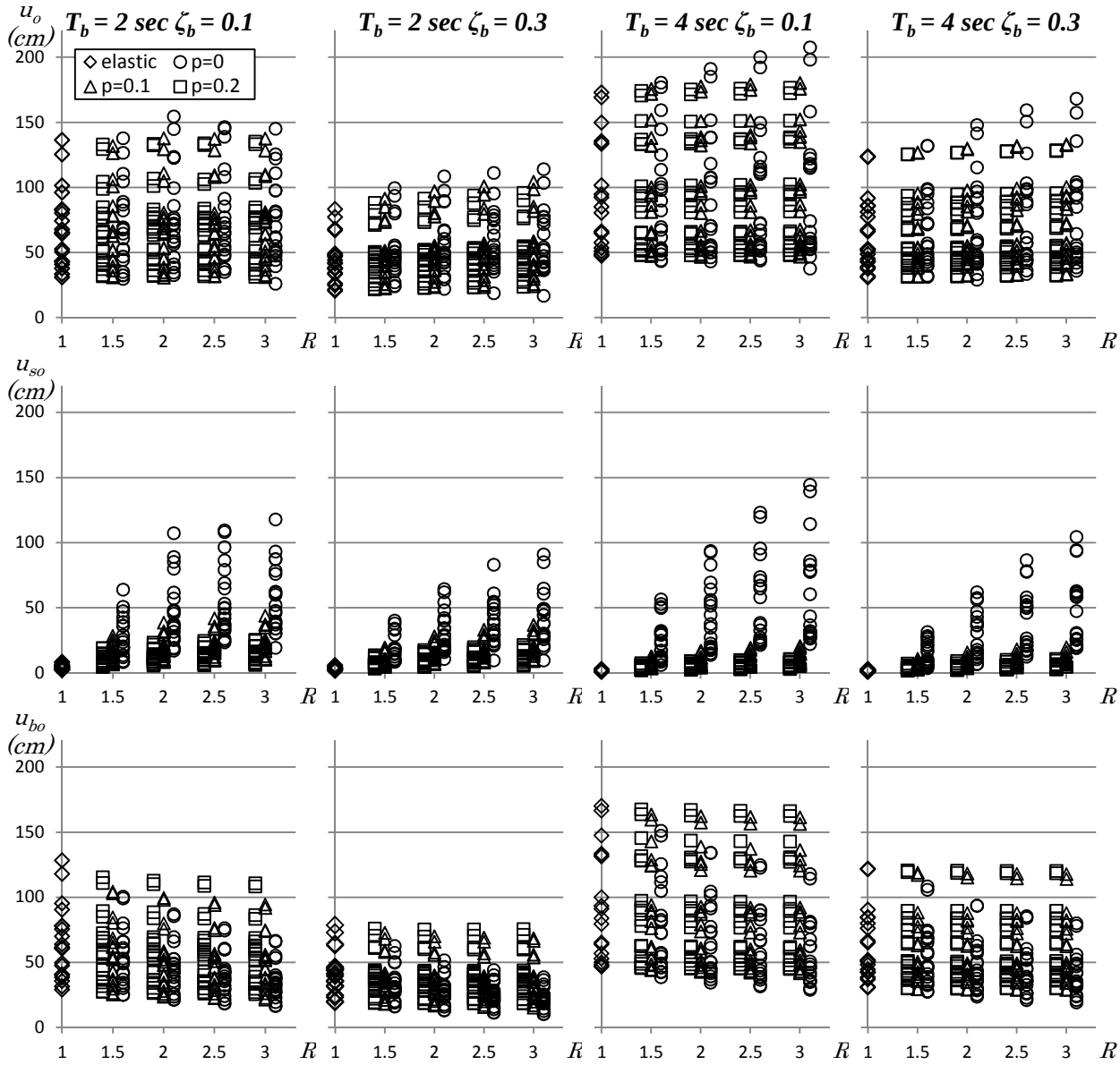
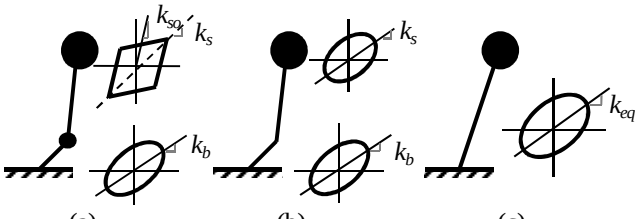


Figure 3 Maximum responses from time history model of base isolated structures under 20 SAC ground motions

system having two viscoelastic springs connected in series, as shown in Figure 4(b). In this way, we can combine the system into a SDOF system having the system stiffness k_{eq} and damping coefficient c_{eq} (Figure 4(c)), in which the peak displacement u_o can be estimated from the elastic response spectrum and then separated to the maximum superstructure and isolation level displacement.



(a) (b) (c)

Figure 4 Equivalent system representations

3.1 Equivalent viscoelastic superstructure

To address the elastoplastic behavior of superstructure, an equivalent viscoelastic system is developed to have equal maximum deformation and energy dissipation. Equivalent superstructure stiffness $k_s(\mu)$ is geometrically defined as a function of excitation frequency ω and ductility demand $\mu = u_{so}/u_{sy}$ as follows (Kasai and Kawanabe 2005):

$$k_s(\mu) = k_{so}\left(\frac{1+p\mu-p}{\mu}\right) \tag{5}$$

The equivalent superstructure damping coefficient $c_S(\omega,\mu)$ is defined as

$$c_s(\omega,\mu) = \frac{E_D(\omega,\mu)}{\pi\omega u_{so}^{\ 2}} = c_{so} + \frac{4}{\pi}\frac{k_{so}}{\omega}\frac{(\mu-1)(1-p)}{\mu^2} \tag{6}$$

3.2 Equivalent system

Consider a base isolated structure as a system having two viscoelastic springs connected in series subjected to a harmonic excitation with the excitation frequency ω (Figure 4b). For a given k_b, c_b, k_s, and c_s, complex stiffness of superstructure and isolation system can be defined as

$$K_b^* = k_b + c_b\omega i \qquad K_s^* = k_s + c_s\omega i \tag{7}$$

We can combine those two springs in the system into an equivalent viscoelastic spring with complex stiffness as follows (Kasai and Fu 1995):

$$K_{eq}^* = \frac{K_s^* K_b^*}{K_s^* + K_b^*} = K'_{eq}\left(1+\eta_{eq} i\right) \tag{8}$$

Where

$$K'_{eq} = \frac{\left(k_s+k_b\right)\left(k_s k_b - c_s c_b \omega^2\right)+\left(c_s+c_b\right)\left(k_s c_b + k_b c_s\right)\omega^2}{\left(k_s+k_b\right)^2+\left(c_s+c_b\right)^2\omega^2} \tag{9}$$

$$\eta_{eq} = \frac{\left(k_s+k_b\right)\left(k_s c_b + k_b c_s\right)\omega - \left(c_s+c_b\right)\left(k_s k_b - c_s c_b \omega^2\right)\omega}{\left(k_s+k_b\right)\left(k_s k_b - c_s c_b \omega^2\right)+\left(c_s+c_b\right)\left(k_s c_b + k_b c_s\right)\omega^2} \tag{10}$$

Then, equivalent frequency ω_{eq} of the whole structure is defined as

$$\omega_{eq} = \sqrt{\frac{K'_{eq}}{m}} \tag{11}$$

This may be written in form of equivalent period T_{eq}

$$T_{eq} = \frac{2\pi}{\omega_{eq}} \tag{12}$$

And equivalent damping ratio ζ_{eq} of the whole structure is

$$\zeta_{eq} = \frac{E_d}{4\pi E_s}\frac{\omega_{eq}}{\omega} = \frac{\pi c_{eq}\omega u_o^{\,2}}{4\pi\left(\frac{1}{2}\pi k_{eq} u_o^{\,2}\right)}\frac{\omega_{eq}}{\omega} = \frac{\eta_{eq}}{2}\frac{\omega_{eq}}{\omega} \tag{13}$$

However, k_s is a function of ductility demand μ and c_s is a function of ductility demand μ and excitation frequency ω. Therefore, to estimate the equivalent period and damping ratio of the structure, we have to assume a value of μ. Next, assuming $\omega = \omega_{eq}$, we can estimate the equivalent superstructure stiffness and system stiffness as the equations described above, and the maximum total displacement u_o from elastic response spectrum of ground motion in use, $S_d(T_{eq},\zeta_{eq})$. Then, the maximum superstructure displacement u_{so} and the maximum isolation level displacement u_{bo} can be estimated using

$$\frac{u_{so}}{u_o} = \frac{\left|K_{eq}^*\right|}{\left|K_s^*\right|} \qquad \frac{u_{bo}}{u_o} = \frac{\left|K_{eq}^*\right|}{\left|K_b^*\right|} \tag{14}$$

Compare with the ductility demand firstly assumed and do iterations until the relation $u_{so} = \mu u_{sy}$ is satisfied.

3.3 Estimation result

Figure 5 and 6 describe the accuracy of the estimation result. Comparison between the maximum displacement observed from time history model (x-axis) and the estimation response (y-axis) is presented. In Figure 5, superstructure is elastic with superstructure period T_{so} = 0.5 sec and superstructure damping ratio ζ_{so} = 0.02. Three graphs present total, superstructure, and isolation system maximum displacement, from left. In each graph, 4 types of data point represent 4 isolation systems including T_b = 2 and 4 sec with ζ_b = 0.1 and 0.3.

Average of the maximum response from time history model subjected to 20 SAC ground motions, together with the coefficient m of linear relation, $y_i = mx_i$, using least square method to best-fit the data is presented in Table 1. The estimation gets along well with the response observed from the model. However, an increase in damping ratio results in higher scatterness in the estimation.

Table 1 Estimation of the response of base isolated structure having elastic superstructure

T_b	ζ_b	u_o			u_{so}		
		$\bar{x}$	m	R^2	$\bar{x}$	m	R^2
2	0.1	68.72	1.012	0.976	4.240	0.986	0.973
	0.3	44.50	1.06	0.885	3.346	0.959	0.783
4	0.1	92.54	0.987	0.977	1.523	0.948	0.972
	0.3	63.91	0.955	0.906	1.482	0.744	0.721

To evaluate the estimation for the system having elastoplastic superstructure, Figure 6 shows the maximum displacement from the estimation compared with time history results. Each column represents each of the four isolation system considered. In each graph, each data point presents each superstructure post-yield stiffness ratio p = 0, 0.1, and 0.2. For each p, 80 points if shown representing the structure having superstructure strength reduction factor R = 1.5, 2, 2.5, and 3 subjected to 20 SAC ground motions.

The estimated total displacement u_o and isolation system displacement u_{bo} match well even when superstructure is considered as elastoplastic. However, a reduction of post-yield stiffness reduces accuracy of the estimation. Superstructure maximum displacement is underestimated, especially when p is reduced to 0. This may be explained as u_{so} is directly sensitive to the equivalent superstructure stiffness k_s and damping coefficient c_s (see Eq.(14)) which is defined from the steady state assumption in which the maximum displacement should be stable. But

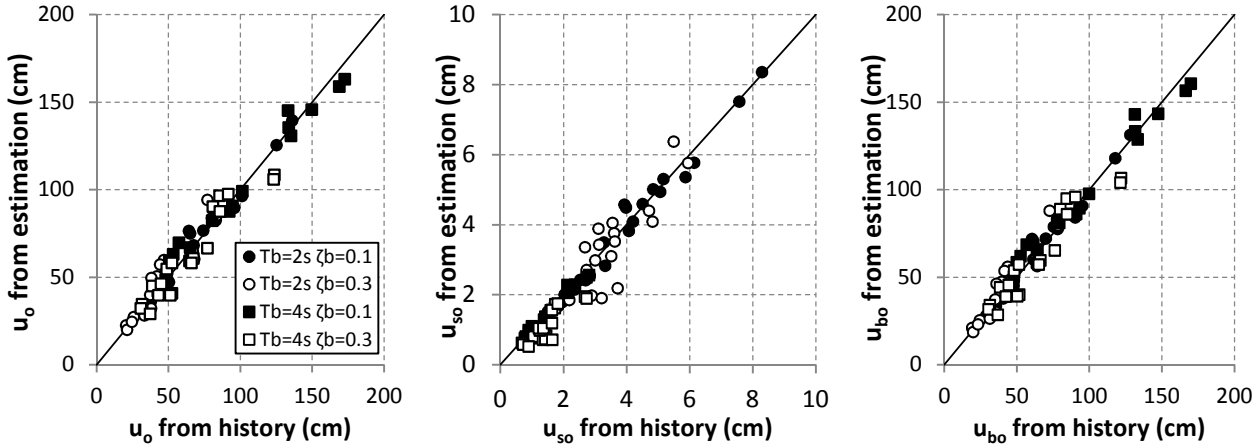


Figure 5 The estimated maximum displacement compare with time history response of base isolated structure having elastic superstructure

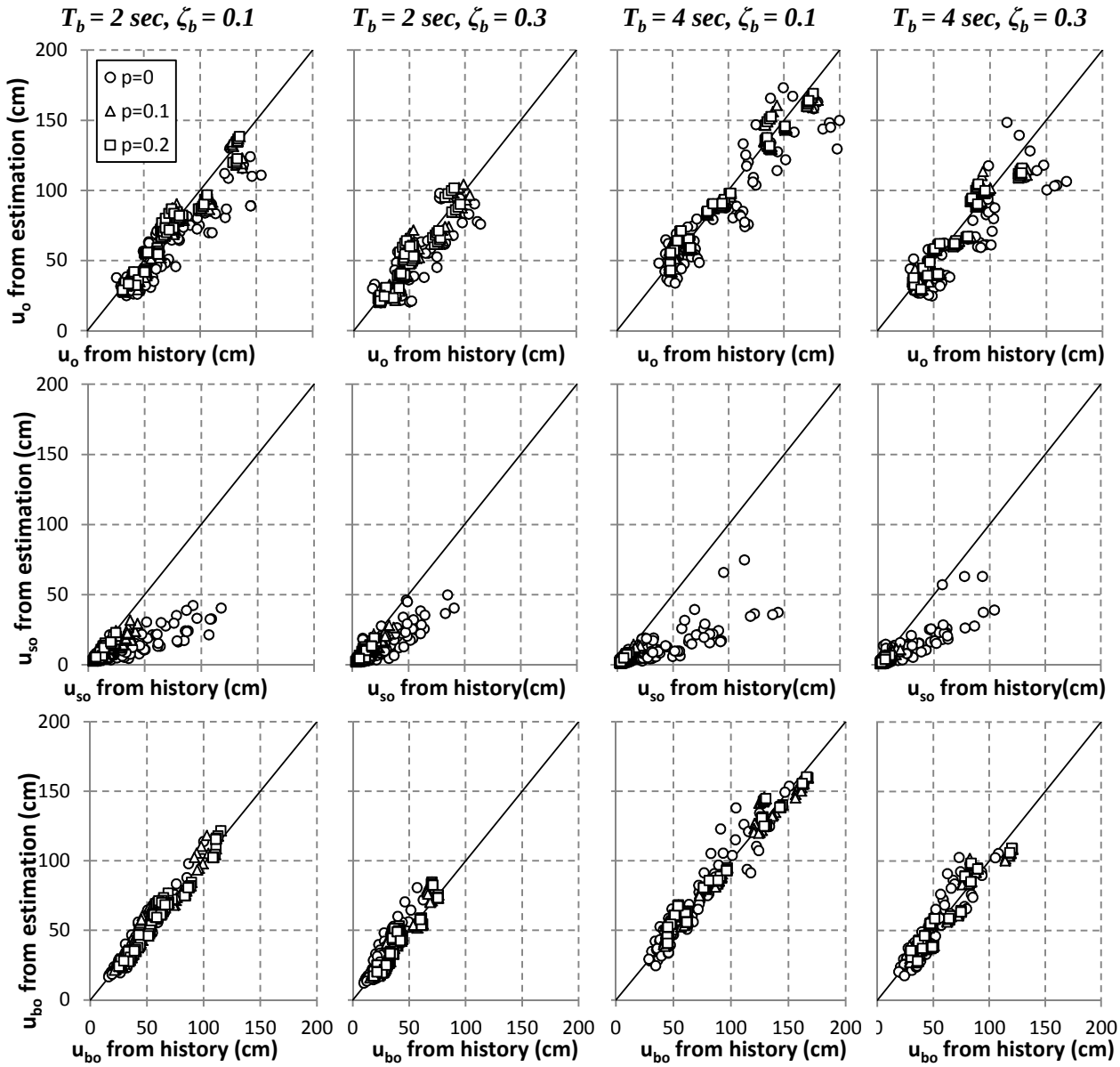


Figure 6 The estimated maximum displacement compare with time history response of base isolated structure having elastic superstructure

Table 2 Estimation of the response of base isolated structure having elastoplastic superstructure

T_b	ζ_b	u_o						u_{so}					
		$p = 0$		$p = 0.1$		$p = 0.2$		$p = 0$		$p = 0.1$		$p = 0.2$	
		m	R^2	m	R^2	m	R^2	m	R^2	m	R^2	m	R^2
2	0.1	0.806	0.824	0.942	0.915	0.964	0.954	0.315	0.691	0.610	0.779	0.747	0.864
	0.3	0.870	0.711	0.974	0.857	1.005	0.864	0.491	0.652	0.688	0.821	0.765	0.798
4	0.1	0.865	0.824	0.973	0.965	0.990	0.974	0.311	0.584	0.675	0.849	0.796	0.926
	0.3	0.819	0.774	0.946	0.891	0.965	0.905	0.438	0.680	0.601	0.724	0.655	0.686

for actual ground motions, the maximum displacement is supposed to occur just once in an excitation and not well represents every cycle. Therefore, using the maximum superstructure to estimate the equivalent stiffness of superstructure for an actual excitation may mislead the damping too high. But the trend is constant, as we can observe from Table 2. Therefore, some adjustments may be possible later on.

4. CONCLUSIONS

Parametric studies of the response of base isolated structures considering yielding of the superstructure have been described. Result proves that this simple model could be used to study the responses of base isolation structures.

An increase in isolation period (softer isolator) significantly increases the maximum isolation level displacement but not much affects the maximum superstructure displacement. An increase in isolation damping results in minor reductions in all response, particularly for long period cases. Superstructure yielding significantly increases the maximum superstructure displacement but has only a minor effect on the isolation level response.

For the estimation of the maximum displacement considering nonlinear behavior of superstructure, theoretical considerations have been described and showing the good trend along with the history results from the model. The estimation of maximum total and isolation level displacements match well. However, more improvements are needed for the maximum superstructure displacement, especially when superstructure post-yield stiffness is low.

Future study will be focused on a complete and accurate method to estimate the maximum displacement of base isolated structures from the elastic response spectra. In addition, a method of selecting a good combination of superstructure strength and separation distance to obtain the minimum damage of the base isolated structure will be considered.

Acknowledgements:

The authors acknowledge support from the Japan Ministry of Education, Culture, Sport, Science, and Technology (MEXT) for establishing the Center for Urban Earthquake Engineering (CUEE) in Tokyo Institute of Technology. This support makes possible the forthcoming international conference, as well as international joint research projects and exchange programs with overseas universities.

References:

Chopra A. K. (2007). "Dynamics of Structures - Theory and Applications to Earthquake Engineering", 3rd Edition, Prentice Hall, New Jersey.

Kasai K. and Fu Y. (1995). "Seismic Analysis and Design using Viscoelastic Dampers", *A New Direction in Seismic Design, AIJ*, 113-140.

Kasai K., Kawanabe Y. (2005). "Equivalent linearization to predict dynamic properties and seismic peak responses of a structural system with high viscous damping and hysteretic damping". *J. Struct. Constr.Eng., AIJ.* **No. 591**, 43-51.

Kikuchi M., Black C.J., Aiken I.D (2008). "On the response of yielding seismically isolated structures". *Earthquake Eng. Structural Dynamics.* **37:** 659-679.

McGuire R.K. (2004). "Seismic Hazard and Risk Analysis". *EERI Monograph, Earthquake Engineering Research Institute.* **MNO-10:** 221.

Naeim F., Kelly J.M. (1999). "Design of Seismic Isolated Structures: From Theory to Practice", John Wiley & Sons. New York.

Somerville P., Anderson D., Sun J., Punyamurthula S., Smith N. (1998). "Generation of Ground Motion Time histories for Performance-Based Seismic Engineering", *6th National Earthquake Engineering Conference.* Seattle, WA.

10CUEE CONFERENCE PROCEEDINGS
10th International Conference on Urban Earthquake Engineering
March 1-2, 2013, Tokyo Institute of Technology, Tokyo, Japan

OBSERVED AND PREDICTED PERFORMANCE OF REINFORCED CONCRETE BUILDINGS IN THE CANTERBURY EARTHQUAKE SEQUENCE

Daniel Bech[1], Bill Tremayne[2], Lisa Oliver[3] and Jenny Fisher[4]

1) Project Manager, Holmes Culley, San Francisco, CA, USA
2) Technical Director & Principal, Holmes Culley, San Francisco, CA, USA
3) Project Engineer, Holmes Consulting Group, Christchurch, New Zealand
4) Project Director, Holmes Consulting Group, Christchurch, New Zealand

Abstract: This paper compares the observed and analytically predicted performance of three reinforced concrete buildings in Christchurch, New Zealand which have been subjected to the 2010 – 2011 Canterbury Earthquake Sequence. The studied buildings belong to a large, institutional organization, located on three campuses around central Christchurch. Structural archetypes vary from 1950's non-ductile concrete shear wall construction to 1980's ductile reinforced concrete moment frame and shear wall buildings.

None of the buildings involved in the study collapsed as a result of the earthquake sequence; however, some had sustained structural damage which was documented as part of an immediate post-earthquake evaluation survey. Ground motion records were also available from nearby recording stations.

Nonlinear finite element models were developed for each building and subjected to the nearby recorded ground motions to compare predicted and observed performance. In general, the analytical models indicated worse performance than was observed. Sources of uncertainty and potential conservatism in the modeling approaches were systemically evaluated. Soil-structure interaction assumptions were identified as having a significant influence on the predicted performance, and highlighted important issues for consideration in subsequent Detailed Earthquake Evaluations undertaken in accordance with current New Zealand industry best practice.

1. BACKGROUND

The 2010 – 2011 Canterbury Earthquake Sequence has resulted in extensive and severe damage to the city of Christchurch, New Zealand. The Sequence commenced with a M7.1 earthquake on September 4, 2010 near Darfield, approximately 40 km west of Christchurch. This earthquake generally caused moderate levels of damage in the city, with more severe damage occurring to unreinforced masonry buildings and widespread liquefaction in the eastern residential suburbs. On February 22, 2011, a M6.3 earthquake struck near Lyttleton, approximately 10 km to the south-east of Christchurch at a depth of 5 km. Shaking intensities of MM9 were felt across the city with peak ground accelerations of 1.75 g horizontal and 2.2 g vertical, recorded in the Port Hills, between Christchurch and Lyttleton. Since the September 4, 2010 earthquake there have been over 10,000 earthquakes, with over 40 measuring greater than M5.

The Lyttleton event of February 22, 2011 caused the greatest damage to buildings in Christchurch, including the collapse of two multi-story reinforced concrete office buildings and a number of low-rise unreinforced masonry buildings. The death toll from this earthquake was 185. It is estimated that 1,200 buildings in the downtown district of Christchurch will be demolished as a result of the Canterbury Earthquake Sequence (Hare et al. 2012).

2. BASIS OF STUDY

The downtown district of Christchurch was relatively well instrumented with distributed ground motion recording stations that captured the ground motion time histories from the Sequence.

The Authors were engaged to undertake Detailed Engineering Evaluations (DEE) of a number of reinforced concrete buildings located within the downtown district. These evaluations utilized the nonlinear dynamic procedure (NDP) in accordance with ASCE 41 (ASCE, 2006), in conjunction with the DEE Guidelines (EAG, 2011) and NZS 1170.5 (SNZ, 2005). None of the buildings evaluated collapsed or suffered significant structural damage as a result of the earthquake sequence. All of the buildings evaluated are owned by a large institutional organization.

As all of the buildings were located within 2 km of one or more recording stations, this presented the opportunity to compare the observed versus analytically predicted performance of the buildings in response to the February 22,

2011 earthquake.

Owing to time and resource constraints at the beginning of many of these evaluations, the structural analyses were often progressed in advance of receipt of geotechnical engineering recommendations for foundation evaluation. As geotechnical information became available for each building, these recommendations (typically soil bearing capacity and stiffness) were incorporated into the structural model and the analysis rerun. This approach provided an opportunity to examine the significance of incrementally incorporating various soil-structure interaction effects into the structural analysis.

The general purpose nonlinear analysis program, ANSR-II (Mondkar and Powell, 1979) was used to undertake the structural analysis. Previous studies have validated the capability of the program to reasonably predict the global response of reinforced concrete structures for the purposes of a design office environment (Kelly, 2007).

3. CODE APPROACHES TO SOIL-STRUCTURE INTERACTION

Documents such as ASCE 41-06 and FEMA 440 provide guidance on the effects of soil-structure interaction; however, the New Zealand Loading Standard for Earthquake Actions, NZS 1170.5, does not include any specific requirements to consider soil-structure interaction. although the Commentary C6.1.1 mentions that:

Foundation flexibility shall be included in the modeling of the structure. Ignoring foundation flexibility will be conservative with respect to strength but non-conservative with respect to deflections.

Foundations, including piles, and the supporting soils with which they interact should be treated as part of the overall building structure and analyzed as such.

Flexibility of foundations affects the response characteristics of the building by affecting period, drift and the like, and affects the relative participation between dissimilar systems in the resistance of lateral loads, such as between walls and frames.

No further guidance or references are provided in the Commentary to NZS 1170.5 in terms of how to include foundation flexibility in the analysis model. It is understood that industry practice in New Zealand to-date has typically been to ignore soil-structure interaction (Oliver, 2012, personal correspondence) and kinematic interaction.

For the purpose of this study, guidance was sought from ASCE 41-06 for the implementation of soil-structure interaction, specifically consideration of foundation flexibility and kinematic interaction effects.

4. BUILDINGS STUDIED

For this study three, existing reinforced concrete buildings were selected. General characteristics are outlined in Table 1 below, with further details provided in the following sub-sections.

Building ID	Year constructed	# stories	# basement levels	NZS 1170.4 soil class
D	Late-1980's	4	1	D
L	Late-1980's	3	1	D
A	Early 1950's	5	1	C

	Lateral systems		Foundation
Building ID	A	B	
D	Core walls	Core walls	Mat slab
L	Concrete frame	Concrete walls	Piles
A	Punched concrete walls	Punched concrete walls	Mat slab & isolated footings

Table 1: General characteristics of buildings studied

4.1 Building D

Building D is a four-story concrete building constructed in the late 1980's. The building has four separate concrete cores and with coupled shear walls that form the lateral force resisting system for the structure. The core walls are founded on a mat foundation. The gravity framing consists of a two way concrete slab supported by concrete columns.



Figure 1: Building D, plan view

4.2 Building L

Building L is a three-story reinforced concrete structure that is founded on a pile foundation and was constructed in the late 1980's. The roof consists of structural steel and timber framing. Lateral load resistance for Building L is provided by concrete shear walls in the transverse direction and a concrete moment resisting frame in the longitudinal direction. Gravity loads are resisted by a two-way

spanning concrete slab and a center row of interior gravity columns.



Figure 2: Building L, elevation

4.3 Building A

Building A is a five-story reinforced concrete building constructed in the early 1950's. As the building predates modern building codes that considered capacity-design principles and ductile detailing requirements such as NZS 3101 (SNZ, 2006), the building is considered to be "non-ductile" relative to the Buildings D and L. The structure has an L-shaped floor plan configuration which introduces a reentrant corner. Lateral loads are resisted by a combination of transverse concrete shear walls and exterior concrete piers and spandrels. Gravity loads are resisted by a concrete slab supported by concrete beams and columns. The foundation consists of a combination of isolated footings and an interior mat slab.

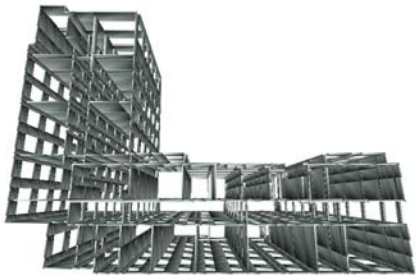


Figure 4: Building A, plan view

4.4 Dynamic Characteristics & Kinematic Interaction

For this study the response of the analytical models was evaluated using ground motions recorded from the Lyttleton event. The ground motions used for the analysis were selected from the nearest recording station to the subject buildings, either: Christchurch Hospital (CHHC) recording station or the Cashmere High School (CMHS) recording station. The 5% damped spectra of the records used in the analysis are shown Figure 5 below.

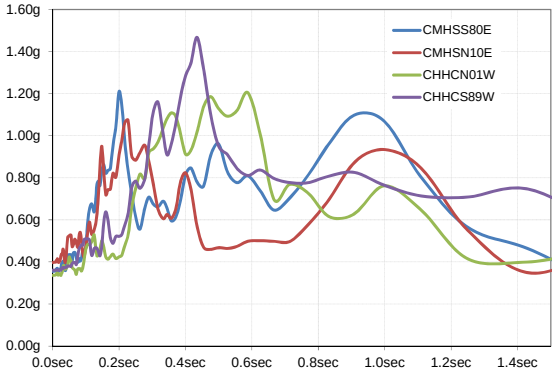


Figure 5: 5% damped spectra for Lyttleton Earthquake at Christchurch Hospital and Cashmere High School recording stations

Two types of kinematic interaction: base slab averaging and embedment, were considered and approximated using each buildings' fundamental modes of vibration. The provisions outlined in section 4.5.1 of ASCE 41-06 were followed to account for base slab averaging and embedment.

The reduction factor for base slab averaging (RRS_{bsa}) was calculated using equation 4-11 of ASCE 41-06.

The reduction factor for foundation embedment was determined using equation 4-12 of ASCE 41-06.

$$RRS_{bsa} = 1 - \frac{1}{14}\cdot 100\left(\frac{b_e}{T}\right)^1 \cdot 2 \geq \text{value for } T = 0.2 \text{ sec.} \quad \text{(eqn 4-11)}$$

$$RRS_f = \cos\left(\frac{2\pi e}{T n v_s}\right) \geq \text{value for } T = 0.2 \text{ sec.} \quad \text{(eqn 4-12)}$$

To simplify the implementation of the base slab averaging and embedment modifications, the acceleration time histories were simply modified by a single amplitude scalar based on the reduction factors for base slab averaging and embedment determined at the fundamental modes of vibration. As these factors become smaller with decreasing period, it is conservative to base the scale factor upon the fundamental periods of vibration for each building.

As can be seen in Table 2 the reduction factor, based on the average of each direction, for input ground motion varies from 0.83 to 0.92 for the buildings studied.

	Fundamental period (seconds)			Lyttleton record scale factor		
Building ID	**A**	**B**	**Nearest recording station**	**R_{TA}**	**R_{TB}**	**R_{avg}**
D	0.41	0.37	CHHC	0.84	0.82	**0.83**
L	0.60	0.13	CHHC	0.97	0.83	**0.91**
A	0.40	0.30	CMHS	0.93	0.90	**0.92**

Table 2: Building periods & record scale factors to account for base slab averaging & embedment

Figure 6 illustrates the reduction in spectral response that could be expected at all periods, if the CHHC record were to be spectrally matched to account for base slab averaging and embedment effects at Building D. As can be seen from the figure, a more significant reduction in spectral response is expected at periods less than 0.2 seconds than is otherwise implied by the factors listed in Table 2.

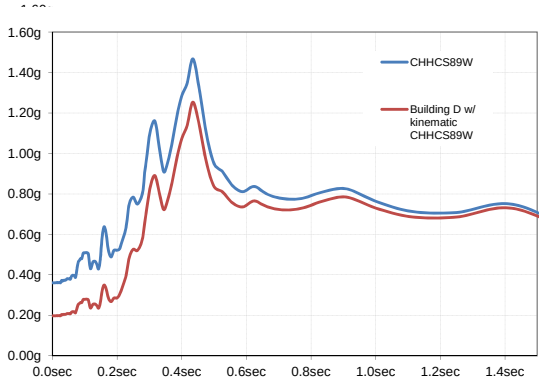


Figure 6: Lyttleton event scaled at all periods to account or base slab averaging and embedment effects at Building D

4.5 Foundation Flexibility

Flexibility and strength of the founding soils was included in the analysis through use of yielding soil spring and yielding pile elements, as applicable to the building foundation type.

For Buildings A and D which have mat and spread footing foundations tri-linear compression-only gap elements were used to permit foundation uplift. Gap properties were estimated by using tributary footing areas and the sub-grade modulus of the soil, as provided by the project Geotechnical Engineers. The first yield of the gap element was typically set at 85% of the ultimate soil strength, with the second yield occurring at the ultimate strength, after which point the gap becomes perfectly plastic. The second slope of the force-deformation relationship was set at 10% of the initial stiffness.

For Building L, the compression and tension stiffness of the piles differ, based on recommendations from the Geotechnical Engineer. Thus, the piles were modeled using gap and hook elements in parallel. The gap element was modeled as a compression-only truss with compression stiffness and strength equal to that of the pile in compression, and the hook element was modeled with the tension stiffness and strength of the pile. The elements follow an elastic unloading pattern. The relationship also accounts for cyclic stress reduction. As evidence of liquefaction at the site was found during post-earthquake damage surveys, an effort was made to include the effect of pile-tip liquefaction on the pile capacity and stiffness.

4.6 Scenarios Evaluated

The following scenarios were evaluated to quantify their effects on expected building performance:

1. Rocking but rigid foundations (no soil flexibility or yielding permitted.) This scenario reflected the initial absence of geotechnical input, and was deemed the "baseline scenario."

2. Rocking foundations with soil stiffness and strength included. This scenario incorporated recommendations from the Geotechnical Engineer. For the purpose of this study, soil strength and stiffness parameters were based on expected (average) values.

3. Rocking foundations, yielding soil springs (per Scenario 2), with base slab averaging and embedment effects included.

4. Rocking foundations, yielding soil springs, base slab averaging and embedment effects (per Scenario 3), with vertical acceleration component of the time history and vertical seismic mass included. Vertical masses were lumped directly to the vertical load resisting elements, which is believed to be conservative, as the majority of the vertical modes of vibration are concentrated in the short period range which coincides with the peak vertical spectral accelerations in the Lyttleton event.

The scenarios and identification codes are summarized in Table 3.

Building ID	Scenario ID			
	1	2	3	4
	Rigid rocking foundations	Per 1 + yielding soil springs	Per 2 + base slab averaging & embedment	Per 3 + vertical mass & acceleration
D	D1	D2	D3	D4
A	A1	A2	A3	A4
L	L1	L2	L3	L4

Table 3: Scenarios evaluated

The horizontal components of the records were run at orientations of 0 and 90 degrees and the results enveloped. This was due to uncertainty of the building's exact orientation with respect to the ground motion experienced at the site, given their distances from the recording stations.

5. MODELED PERFORMANCE

For comparison of the various scenarios, performance was characterized by global drifts and component acceptance criteria in accordance with ASCE 41-06.

5.1 Building D

Figure 7 compares the X and Z direction interstory drifts for the various scenarios investigated. As can be seen from the graphs the drift demands are relatively low for the Lyttleton event. The general trend is that a small increase in drift results from the introduction of foundation flexibility. Thus, D2 drifts are slightly increased from D1, with exception of the 3rd floor to Plant level in the X-direction

where the relatively flexible Plant level shows a significant increase. The introduction of kinematic effects slightly reduces global drift demand relative to scenarios the rigid foundation (D1) and flexible foundation (D2). There does not appear to be a significant difference in drifts from the introduction of vertical accelerations when comparing D3 drifts to D4 drifts.

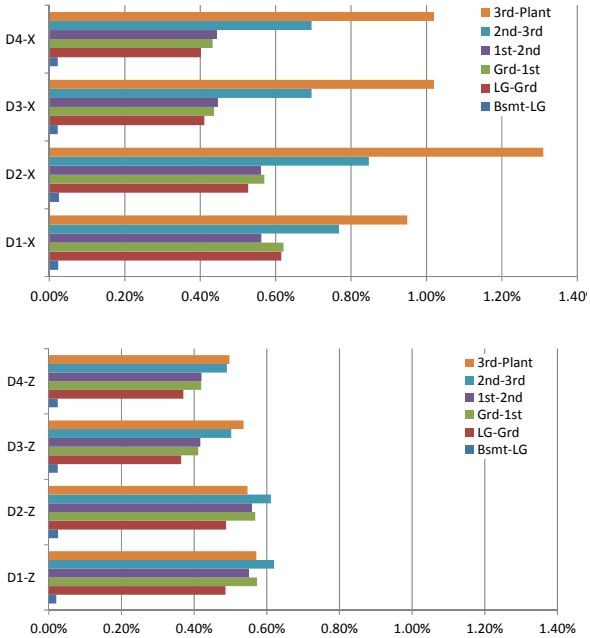


Figure 7: Building D, drifts at center of diaphragm for Scenarios 1 – 4

For comparison of structural component performance the total numbers of elements that exceed ASCE 41 acceptance criteria (secondary criteria) are given in Table 4 below. Immediate occupancy (IO), Life Safety (LS) and Collapse Prevention (CP) criteria are used for comparison between the various scenarios investigated.

	Model + Scenario			
Criteria	**D1**	**D2**	**D3**	**D4**
IO < n < LS	24	22	13	14
LS < n < CP	0	0	0	0
n > CP	1	0	0	0

Table 4: Building D, component damage count

For the D1 scenario one beam element exceeded Collapse Prevention acceptance criteria and 24 elements exceeded Immediate Occupancy but were still below Life Safety. The introduction of foundation flexibility removed the aforementioned beam element that from the >CP category and reclassified it as between IO and LS. A small decrease in the total number of elements >IO is also evident between D1 and D2. The introduction of kinematic effects had a significant effect on expected performance, with the number of elements exceeding the IO acceptance criteria roughly halving.

5.2 Building A

Figure 8 below compares the X and Z-direction drifts for Scenarios 1 through 4. As can be seen from the drift comparison between A1 and A2, the introduction of flexible soil springs resulted in a significant increase drift over the all floors of the building. The drifts in the Z-direction are slightly higher than the X-direction; however, overall the drifts are relatively low due to the stiffness of the building.

The top floor drifts (5th-6th) appear to be much larger than the stories below. However, this is not the actual performance, as the drifts reported are at the center of diaphragm and the building steps significantly at the 5th floor, thus the center of diaphragm coordinates differ significantly between the floors given an artificial appearance of higher drifts.

The introduction of kinematic effects (A3) does decrease the drifts slightly from A2; however the drifts are still higher than the rigid foundation model. The introduction of vertical accelerations (A4) does not appear to have a significant effect on drifts.

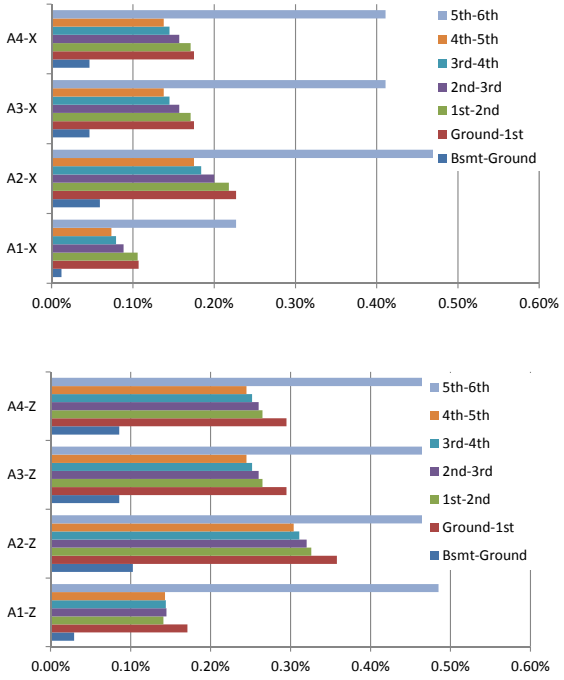


Figure 8: Building A, drifts at center of diaphragm for Scenarios 1 – 4

Table 5 provides a comparison of the element performance between the scenarios investigated. The acceptance criteria are for secondary components per ASCE 41-06.

The introduction of foundation flexibility significantly increases the number of elements that are damaged during the Lyttleton event. The increased deformations associated

with foundation flexibility cannot be readily accommodated by the non-ductile concrete detailing that is prevalent throughout the building

The majority of the increase in damaged elements for A2 is still less than the LS limit; however, seven elements exceeded LS and three elements were predicted to exceed CP.

Inclusion of kinematic effects, although only representing a small scalar decrease in the input motion, significantly decreases the predicted number of damaged elements, although still more extensive than the baseline case A1.

There is no effect on damaged elements with the introduction of vertical accelerations when comparing A3 to A4.

	Model + Scenario			
Criteria	**A1**	**A2**	**A3**	**A4**
IO < n < LS	17	94	49	49
LS < n < CP	0	7	3	3
n > CP	0	3	0	0

Table 5: Building A, component damage count

5.3 Building L

From review of the drift profiles for Building L there is a small decrease in the drift demand due to the introduction of foundation flexibility (L1 versus L2).

The introduction of kinematic effects (L3) reduces the drift demands slightly at the lower floors (Ground to 1st Floor and 1st to 2nd Floor); however, there is a significant reduction in drift demand in the longitudinal frame (X) direction for the 2nd Floor to Roof.

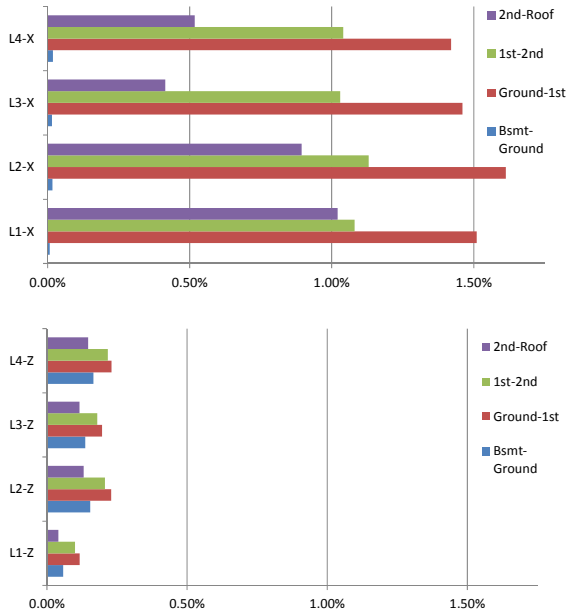


Figure 9: Building L, drifts at center of diaphragm for Scenarios 1 – 4

Table 6 below provides a comparison of the element performance between the scenarios investigated for Building L. As with Buildings D and A, secondary component acceptance criteria were used.

The majority of the elements that exceed IO are the 1st Floor beams that resist lateral forces in the longitudinal frame direction (X-direction). These beam elements, although below LS for secondary components, exceed the primary component acceptance criteria for LS plastic rotations. The relevance of this categorization becomes more apparent when compared with the observed performance of the building (described in the following section) as these beams showed no signs of damage as a result of the Lyttleton event.

	Model + Scenario			
Criteria	**L1**	**L2**	**L3**	**L4**
IO < n < LS	12	21	16	21
LS < n < CP	0	0	0	1
n > CP	0	0	0	0

Table 6: Building L, component damage count

6. OBSERVED PERFORMANCE

The following sub-sections describe the observed performance and damage characteristics of each building by the authors following the Lyttleton event.

6.1 Building D

A level survey of Building D undertaken after the Lyttleton event measured a 90 mm differential settlement over the building footprint (approximately 60 m x 40 m). The north raft appears relatively level but the south raft appears to have tilted to the south.

Moderate cracking was observed in the internal shear walls in the cores. The maximum diagonal crack width observed was 0.4 mm, but most were 0.3 mm or less; however, the transient crack widths may have been larger during shaking. Cracking was noted over the height of the cores. The analytical model predicted hinging at the base of the core walls, but also indicated higher drift demands at the upper levels where the core walls reduce in length which also suggests plastic hinging at multiple floors. Strain-hardening testing was completed on a sample of steel reinforcing bars crossing cracks in the core walls at the Lower Ground Floor. This indicated between 18 and 41 % loss in strain capacity of these bars.

A continuous and large crack, greater than 2.0 mm in width, was observed in the Lower Ground suspended floor slab, this extends east-west and is approximately between the two raft foundations. Strain-hardening testing was undertaken on the steel reinforcement which runs across the crack, and indicated between 12 and 35 % loss in strain capacity of these bars.

Cracking was observed in the stair flights over the full height of the building. The stairs are constructed with no mid

height landing support and support themselves by developing tension and compression struts in the stair flights. The stairs are therefore connected both vertically and horizontally, floor to floor, and thus subjected to the interstory drift demands. They were not included in the analysis model.

Only very minor cracking was noted to concrete beams and columns.

In general, the observed damage was less severe than predicted by the analysis scenarios.

6.2 Building A

The building damage was considered to be relatively minor with exceptions of:

- Cracking at east end of Ground Floor: The most significant damage observed was at the east end of the Ground Floor. Horizontal cracks were noted on both sides of the corridor in the east end wall at around 1.3 m above the floor. These continued around into the corridor walls also.
- On the north side of the corridor a horizontal offset in both directions was noted. When the vertical reinforcement was exposed, it was shown to be bent, see Figure 10.



Figure 10: Building A, steel reinforcement exposed at crack location in computer room

- In this same area the concrete ground floor slab also exhibited significant cracking; the widest crack was 8 mm. It appears that most of this damage was caused by differential movement between Building A and an adjacent structure. The buildings are connected at the basement level and it appears that the lower part of Building A may have moved with the adjacent structure.
- The width of the cracks in this area suggests that bond between the steel reinforcement (plain, undeformed reinforcing bars) and the concrete has been lost at the vertical steel reinforcement lap splices at these locations.
- Concrete transfer beams: At the Ground Floor the building steps out on the north side. To support the structure above this point there are concrete transfer beams in the floor slab. Each end of these beams was inspected and cracks up to 1 mm wide were noted.
- Seismic Joints: Damage to the cover plates over seismic joints with the adjacent structure show that there was significant differential movement between the buildings during the earthquakes. There is also some indication of residual horizontal displacement of approximately 35 mm at Level 5.
- Ground settlement damage: Some possible ground settlement has occurred under and around the building. Residual displacement is noted at the seismic joints and cracking at the interface with the adjacent building demonstrate that some ground movement had occurred.
- Additionally, minor damage (cracking < 1 mm) was observed to the following:
  - Concrete walls and piers between windows
  - Stair walls
  - Cracking in the insitu concrete floor slabs
  - Brick infill panels and risers
  - Brick veneer
  - Exterior concrete window surrounds

As noted above, the structural damage that was evident is at or near areas of the structure where differential settlement has occurred.

6.3 Building L

Typically the damage to Building L was relatively minor with the exceptions of:

- Cracking to the full height pre-cast panel connections around the stair at the north end of the building. This has likely been caused by the interstory drifts in the longitudinal (frame) direction.
- Damage to the ceilings (due in part to the ceiling support system) however the ceiling at roof level had significant damage which would have been caused by the deformations at that level.
- Differential settlement: The levels survey indicated differential settlement along the length of the building.
- The majority of the structural damage predicted in the analysis model was in the 1st Floor concrete beams in the frame direction. From the analyses, most of these beams exceeded the primary Life Safety acceptance criteria, suggesting moderate plastic rotation demands; whereas the observed performance of the frames indicated only a few hairline cracks in the beams and no cracking at the base of the Ground Floor columns.

In general, it was found that the observed performance of Building L was better than the analytically predicted performance regardless of the scenario considered. This indicates that the analysis model is conservative even with the reduction for kinematic effects.

7. CONCLUSIONS

As part of this study the observed seismic performance of three existing buildings in Christchurch subjected to the 2011 Lyttleton event were compared to the predicted performance of non-linear analytical models of the subject buildings. In general the observed performance of the buildings was found to be better than that predicted by the

analytical models.

Significant contributors to these differences are attributed to the inclusion of soil-structure interaction effects. Specifically: foundation flexibility and strength, kinematic effects and vertical accelerations were investigated.

From this study it is found that the inclusion of foundation flexibility increases overall building drifts and deformations, attributed to increased base rotations (flexibility) and period lengthening. The increase in deformations appeared to be accommodated readily by Buildings D and L, which were detailed in accordance with modern building code requirements for ductility. Foundation flexibility appeared to be increase predicted damage of the older, non-ductile building included in this study, well in excess of observed damage.

The kinematic effects of base slab averaging and foundation embedment are found to be beneficial for all buildings included in this study and generally appeared to bring the predicted performance closer to observed performance; however, in general the models were still conservative relative to the observed performance. This suggests that these procedures can be applied with confidence in the design office and for use with future Detailed Engineering Evaluations.

The inclusion of the vertical acceleration component and mass had a slightly detrimental impact upon expected performance. However, given the conservatism in the assumed vertical mass distribution, further study is recommended to more appropriately capture the mass distribution and associated vertical modes of vibration.

For future studies it is also recommended that additional non-ductile buildings be included in the sample and that longer period structures be included.

References:

Hare, J., Bull, D., Brown, B., Brunsdon, D., Jury, R., King, A, McCahon, I., Millar, P., Smith, P., Stannard, M. (2012), "Canterbury Earthquake Sequence: Detailed Engineering Evaluation of Commercial Buildings", *Proceedings of the 15th World Conference on Earthquake Engineering*.

Engineering Advisory Group (EAG) (2011), "Guidance on Detailed Engineering Evaluation of Earthquake Affected Non-residential Buildings in Canterbury Part 2 Evaluation Procedure", Structural Engineering Society New Zealand (Inc.), Rev 5.

Engineering Advisory Group (EAG) (2011), "Guidance on Detailed Engineering Evaluation of Earthquake Affected Non-residential Buildings in Canterbury Part 3 Technical Guidance", Structural Engineering Society New Zealand (Inc.)

Standards New Zealand (SNZ) (2004), "NZS1170.5 Earthquake Actions – New Zealand".

American Society of Civil Engineers (2006), "ASCE 41-06 including Supplement Number 1: Seismic Rehabilitation of Existing Buildings".

Mondkar, D.P. and Powell, G.H. (1979), "ANSR II Analysis of Non-linear Structural Response User's Manual", University of California, Berkeley, Earthquake Engineering Research Center 79/17.

Kelly, T.E. (2007), "A Blind Prediction Test of Nonlinear Analysis Procedures for Reinforced Concrete Shear Walls", *Bulletin of the New Zealand Society for Earthquake Engineering*, (**40**)3, 142-159.

Oliver, S. (2012), personal correspondence, Memorandum Subject: "Structural Analysis Foundation Modeling", Holmes Consulting Group.

Standards New Zealand (SNZ) (2006), "NZS 3101: Concrete Structures Standard".

Kelly, T.E. (2010), "Performance Based Evaluation of Buildings: Nonlinear Pushover and Time History Analysis: Reference Manual Parts 1 – 4", Holmes Consulting Group, Revision 7.

10CUEE CONFERENCE PROCEEDINGS
10th International Conference on Urban Earthquake Engineering
March 1-2, 2013, Tokyo Institute of Technology, Tokyo, Japan

GLOBAL EXPERIENCE: SEISMIC RISK REDUCTION AND DISASTER RECONSTRUCTION PROGRAMS

H. Kit Miyamoto[1], and Amir SJ Gilani[2],

1) President, Miyamoto International, Los Angeles, CA
2) Senior Associate, Miyamoto International, Sacramento, CA

kit@miyamotointernational.com, agilani@miyamotointernational.com

Abstract: Nearly 40% of the largest cities in the world and hundreds of millions of people live in areas that can experience major earthquakes, resulting in large numbers of casualties, and placing a large burden on the regional and national economy. Earthquakes in Haiti and Christchurch have had long-term impact on society. The 2010 Haiti Earthquake affected 3 million people and over 300,000 people are still displaced. An unprecedented reconstruction effort, incorporating local materials and masons but based on international standard, is currently underway to repair and strengthen 120,000 damaged buildings, allowing people to return to safe homes and produce a seismically resilient community in this developing country. The 2011 earthquakes effecting New Zealand showed the need for seismic risk mitigation programs in developed countries. In New Zealand, older and newer buildings were damaged. The damage to these buildings was not unexpected because the building codes only focus on life safety rather than developing earthquake resilient communities. Over 50% of the 2400 buildings in the downtown area required demolition. Over $10 billion dollars in insurance loss is expected, resulting in a drop in the insurance capacity and threatening the country's investment environment. This issue is being dealt with by reducing the overall seismic risk for both public and private buildings. In Bangkok, where the effects of long distance and long duration of earthquakes are a serious concern due to soft soil, the commercial sector has initiated a seismic strengthening program for high rise buildings. A systematic seismic risk reduction program is critical, by understanding the limitations of the building codes. A seismically resilient community can be built if both public and commercial sectors rigorously participate in a broader program.

1. INTRODUCTION

The In the past several years, major earthquakes have affected both developed and developing countries. Although the consequences differ, the end result is similar because these events have caused casualties, affected local and national economies, and had long-term negative effects on communities. The adverse effects of earthquakes in developing and developed countries are attributed to different causes. In developing countries, the main culprit is the lack of an effective seismic code, education, licensing, and quality-control system. Buildings are designed and constructed without adequate provisions for seismic forces or a quality-control system. As a result, these buildings do not have a mechanism to resist earthquake loading and thus can be severely damaged or collapse in moderate or major seismic events. By contrast, in developed countries, the concept of seismic design is well developed and based on extensive research. However, the intent of the building codes in these countries is not to prevent damage but to provide a minimum of life safety. This philosophy is primarily due to financial constraints facing both private and public developers, and a lack of information. As such, in the event of major earthquakes, buildings in developed countries would likely not collapse. However, it is likely that these structures would sustain significant damage (as implied in the building codes) that would likely result in both financial losses and the need to replace or repair the buildings.

One common factor for Haiti, New Zealand, Japan, and similar recent events is that the earthquakes had magnitudes that were unexpected. In other words, the available design codes had underestimated and intensity of seismic events that could occur. This case was observed in China (2008), Italy (2009), Haiti (2010), New Zealand (2011), and Japan (2011), and it points to the need for either additional safety measures in design or better understanding of probable seismic events for a locale. Examples of earthquake damage and the consequences of such damage from two recent events are presented in the following sections.

2. OVERVIEW OF RECENT MAJOR EARTHQUAKES WORLDWIDE

2.1 2010 Haiti Earthquake

The catastrophic 2010 Haiti earthquake has had a tragic effect on the lives of more than 3 million people, including over 200,000 casualties, over 1,000,000 displaced people, and financial losses that crippled the country's economy.

Thousands of buildings collapse, including the United Nations (U.N) headquarters Port-au-Prince; as shown in Figure 1.



Figure 1 Collapsed UN building (UNDP Global 2010)

Similar to past and recent events in other developing countries such as Indonesia, Pakistan, and Turkey, the main causes of the devastation can be attributed to several factors. Among them: This earthquake caused devastation disproportional to its magnitude. If any form of standard of seismic design and construction had been used in Haiti, many lives and much of the economic loss could have been avoided. The main observed factors that exacerbated this tragedy were the following: a) Design and construction practices had not considered earthquake forces properly. In addition, many engineers and contractors had neither formal education nor experience in earthquake-resistant design methodologies. b) Absence of an accepted building or seismic engineering code, and proper quality control system in design, and construction. In addition, no formal building review process was in place. c) The rapid growth of low-income neighbourhoods due to migration into the city from outlying areas. In these neighbourhoods, unsafe housing had been built using substandard construction materials and practices. d) Lack of preparedness by the national government, local agencies, international organizations, emergency responders, and citizens for a major earthquake. Many of the structures in Haiti as well as other developing countries are constructed of either what is referred to as non-ductile concrete, unreinforced masonry (URM), or other stone-type block construction. These particular building types are seismically vulnerable and pose a life-safety hazard. An example of poor construction in Haiti is shown in Figure 2.



Figure **2** Example of poor construction in Haiti

2.2 2011 New Zealand Earthquake

The magnitude-6.3 February 2011, New Zealand, earthquake caused more than 160 deaths and damage costing over US$20 billion. Many buildings were damaged; over 30% of the brick and stone buildings in the central business district (CBD) either collapsed or sustained major damage (see Figure 3) resulting in total closure of the CBD for period of several months because many of the remaining buildings were considered unsafe (Miyamoto International 2011).



Figure **3** Collapsed masonry buildings in the CBD

As of this writing, the CBD is still partially closed, resulting in severe economic losses. In addition, the unprecedented damage has brought the construction industry to a halt because of the difficulty in obtaining insurance. Most of the deaths from this earthquake occurred after people had been buried under collapsed buildings, such as nonductile concrete structures downtown (see **Error! Reference source not found.**). This was a shallow (5-km epicentral depth) earthquake, and its epicenter was less than 6 km from the east side of Christchurch. As such, it caused significantly more damage and casualties than did the magnitude 7.0, September 2010 earthquake (which had no direct fatalities). The 2011 Earthquake caused extensive liquefaction and ground failure, which also led to

widespread loss of water and electricity. The severity of this earthquake was unexpected in Christchurch and points to the same problem that exists in many other urban areas that are close to active faults. The level of damage to modern (post-1980) construction was alarming. Over 50% of the building stock—more than 1,300 buildings—are expected to be claimed as total losses. Many of these buildings were designed and constructed using modern seismic codes. Nonetheless, they sustained significant structural and nonstructural damage, and many have to be demolished. Similar observations were made following the 2010 Chile earthquake. In both countries, modern seismic codes are advanced and local engineers are quite capable, and there are tight construction standards. It is important to note that the building codes likely did what they were intended to do: that is, to provide life safety and prevent collapse. However, the codes do not have provisions for either the building condition after an earthquake or financial losses as a result of an earthquake.



Figure 4. Collapsed nonductile concrete building in the CBD

3. RESPONSE TO THE RECENT EARTHQUAKES

In the aftermath of the subject earthquakes, the authors and other engineers mobilized as part of the response teams. The primary goals of the teams were to:

- Develop methodologies for seismic risk reduction,
- Devise robust and resilient reconstruction methods. In the following sections, the approach and results to date are summarized.

3.1 Response to the Haiti Earthquake

Immediately after the earthquake, the team was mobilized with the primary goal of evaluating and/or repairing as many buildings as possible to allow citizens to leave temporary camps and return to their houses (Miyamoto, Gilani, and Wong 2011). A two-step procedure was undertaken: (a) perform damage assessment of approximately 400,000 buildings, and (b) develop earthquake-resistant, cost-effective, and robust reconstruction techniques. Key components of these programs were having international engineers educate and train local Haitian engineers, and having international construction experts train local Haitian masons. In addition, training manuals were developed, and emphasis was placed on local materials and techniques to additionally stimulate the local economy.

Table 1 summarizes the results of the damage assessment program. Over 50% of the buildings were tagged as green, or safe for occupancy. This allowed hundreds of thousands of people to return home.

Table 1. Results of damage assessment

Category	**Green**	**Yellow**	**Red**
No. of buildings	213,000	102,000	80,000
Percentage	54%	26%	20%

The seismic rehabilitation of thousands of buildings that is currently under way (see 0) will allow many more thousands to return home, and provide a safe and seismically resilient community for citizens. At the time of this paper, over 9,000 houses have been reconstructed under various programs; see 0.



Figure 5. Example of acceptable reconstruction in Haiti

Table 2. Results of damage assessment

Program	Description	Houses
PADF	Leogane Haiti Emergency Shelter Rehabilitation	1,200
OFDA	Pilot program	1,200
OFDA	Extension	2,000
ADORATION	Yellow Houses Repairs	200
DAI	Yellow Houses Repairs	200
OTI-USAID	Haiti Recovery Initiative Yellow Houses Repairs	125
UNOPS	Shelter Repair	800
PADF	Yellow Houses Repairs	3,839
Total		9,564

3.1 Response to the Christchurch Earthquake

New Zealand has one of the most advanced seismic codes in the world. However, the city of Christchurch was not ready for the earthquake that hit it, and the engineering community was unprepared to deal with the aftermath of the event. As such, the initial decisions were to demolish all buildings that had been deemed unsafe, and either reconstruct the areas deemed unsafe or leave them as open space. Experience has shown that many vulnerable structures can be upgraded to comply with the current seismic standards using systematic rehabilitation methods. The first step in this process is condition assessment. This key component is currently missing in New Zealand. To address this issue, the authors are developing a risk assessment algorithm that is uniquely suitable for New Zealand construction but relies on worldwide knowledge in seismic assessment and rehabilitation. The objective of this program is to characterize risk for individual buildings, and thus to present owners with the financial cost of doing nothing, rehabilitating the structure, or demolishing and reconstructing the structure. Experience has shown that the assessment-reconstruction alternative is the preferred and the optimal (as related to benefit-cost ratio) option for many structures.

4. COMPONENTS OF RISK ANALYSIS AND RESILIENT RECONSTRUCTION

One of the disturbing observations in recent earthquakes has been the damage to modern buildings that had been designed according to modern seismic codes. Although these buildings have survived, the level of damage and the associated cost of the damage and repair have been high. Consequently, the current building code approach (that is, prevent collapse but tolerate damage) has been questioned. Performance-based engineering (PBE) provides an alternative to code-based prescriptive design. PBE involves selecting various targets or desired objectives for a given intensity of earthquake input. Such an approach relies on sound engineering judgment, involves direct communication between structural engineers and owners, and requires that the structural performance and the seismic hazard be known with a certain level of confidence. The concept of PBE directly ties to managing seismic risk: The owner is given the option of choosing the level of risk that can be tolerated and the cost associated with that level. For example, 0 presents a typical PBE matrix. The rows correspond to the intensity of a seismic event, and the columns indicate the expected level of performance. In this matrix, the limited, standard, and enhanced objectives for seismic rehabilitation are shown as red, yellow, and green entries, respectively.

Table 3 PBE matrix

Seismic event	Operational	Immediate Occupancy	Life Safety	Collapse Prevention
Typical				
Design				
Rare				

In risk management language, this matrix is also directly related to what is commonly referred to as “probable maximum loss” (PML). PML implies the level of damage (casualties, financial loss, and loss of income) that can be expected for a given building at a given level of earthquake. As shown in 0, seismic rehabilitation and/or reconstruction should be such that this example building whose analyzed performance was above acceptable PML level and thus inadequate—would be strengthened so that its post-retrofit damage index is below the PML threshold resulting in significant risk reduction. The low level of PML in this example was achieved by using an innovative seismic protective device (such as isolators and dampers) which protect structural and nonstructural components. The concept of PML is especially relevant to developing countries and for critical facilities in these countries. In many instances in these countries, the level of seismic hazard and the risk associated with it are not well known. By conducting a preliminary (often referred to as a “phase I”) analysis, an approximate but accurate estimate of the PML for a given structure and/or group of buildings in a facility can be determined quickly. This PML estimate can then be used to prioritize the buildings for further analysis and possible retrofit within the allocated budget.

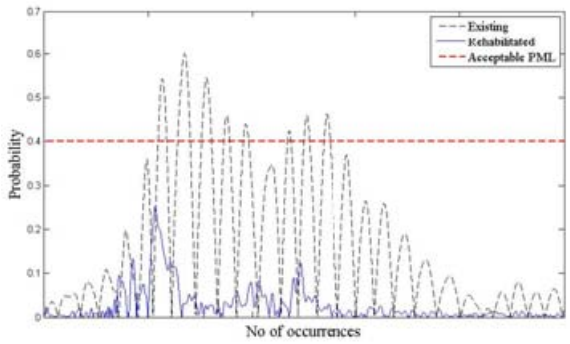


Figure 6. Example of PML analysis

5. ADDED VALUE TO INTEGRATIVE RISK MANAGEMENT

The lessons learned from earthquakes such as those in Haiti and New Zealand and the concepts presented in this paper have global applications. For example, under the auspices of the World Bank (WB), a multiyear program was developed and managed to ensure the systematic upgrade of essential facilities in Istanbul, Turkey. As a result, by the end of the program, over 2,000 critical buildings were retrofitted or reconstructed, including schools that now provide safety to students. Schools have been noted as one of the most vulnerable building types in past earthquakes, causing thousands of casualties. Similar to the program in Turkey, a new rehabilitation guideline and training manual is currently under development in Romania. This document is based on state-of-the-art research and knowledge in the United States and incorporates specific considerations for Romanian design and construction. It will be used to make communities more resilient in Romania.

CONCLUSIONS

Recent earthquakes have caused damage worldwide and have demonstrated the vulnerability of many cities in both developing and developed countries. To address such vulnerability and reduce the global seismic risk, the following are recommended:

- Educate private and public entities on the limitations of code-based design. As an alternative, investigate the application of PBE, which relates probabilistic performance to seismic hazard and can assist in decision making by stakeholders.
- Building codes, by definition, count on select components and modes of response to dissipate seismic energy. Although effective in preventing collapse, this approach, by definition, implies damage to these components. Seismic protective devices are readily available to protect structures and mitigate such damage.
- Vulnerable buildings such as nonductile concrete and URM structures are well-known; effective and inexpensive retrofit concepts are also known. It is important to train engineers in developing countries and undertake a systematic program of rehabilitation and reconstruction for this group of vulnerable structures.
- For developing countries, risk assessment and PML are critical tools because it is not feasible to retrofit all vulnerable structures, given the limited resources. PML and the ensuing benefit-cost analysis can be used to rank buildings for assessment and possible upgrade to help maximize protection of life and infrastructure.

REFERENCES

Miyamoto,. Gilani, and Wong (2011), "Massive Damage Assessment Program and Repair and Reconstruction Strategy in the Aftermath of the 2010 Haiti Earthquake," *Earthquake Spectra* 27, S219, Oakland, CA, US.

Miyamoto International (2011), Christchurch, New Zealand Earthquake, Sacramento, CA, US.

United Nations Development Programme (UNDP) Global (2010), Photographs by Logan Abassi.

10CUEE CONFERENCE PROCEEDINGS
10th International Conference on Urban Earthquake Engineering
March 1-2, 2013, Tokyo Institute of Technology, Tokyo, Japan

REGIONAL PREDICTIONS OF EARTHQUAKE-INDUCED LANDSLIDES: A STUDY OF THE NIIGATA-KEN CHUETSU EARTHQUAKE

Yubing Wang[1] and Ellen M. Rathje[2]

1) Graduate Research Assistant, Dept. of Civil, Architectural and Environmental Engineering, Univ. of Texas, Austin, TX, USA
2) Warren S. Bellows Centennial Professor, Dept. of Civil, Architectural and Environmental Engineering, Univ. of Texas, Austin, TX, USA
wangyubing1987@hotmail.com, e.rathje@mail.utexas.edu

Abstract: Earthquake-induced landslides are a significant seismic hazard that can generate significant economic losses. To gauge the potential for this hazard, regional seismic landslide maps are developed based on estimates of rigid sliding block displacement from empirical predictive models. Previous earthquakes with well-documented landslide inventories provide opportunities to evaluate these regional predictions of earthquake-induced landslides. This paper investigates the landslide inventory from the 2004 Niigata-ken Chuetsu earthquake (M_w=6.6) and compares this inventory with predictions of sliding displacement. The distribution of landslides as a function of slope angle and geologic unit are summarized for this earthquake and compared with the distributions from the 1994 Northridge earthquake (M_w=6.7). Regional predictions of sliding displacement are made using ground motion estimates from ShakeMap®, yield accelerations computed using best-estimate shear strengths assigned to geologic units, and an empirical displacement model using PGA and PGV. Comparisons with the observed landslides indicate that only 40% of the landslides are captured. Larger percentages of the landslides can be captured by modifying various parameters in the yield acceleration calculation (e.g., shear strength), but these changes result in a significant over-prediction in the total landslide area. These results indicate that improvements to regional seismic landslide mapping can only be made with improvements in mapping the spatial variation in shear strengths within geologic units.

1. INTRODUCTION

The Niigata-ken Chuetsu, Japan, earthquake (M_w=6.6) occurred in the Niigata Prefecture on October 23, 2004 and induced a tremendous amount of landslides in the surrounding mountainous areas. A detailed landslide inventory for the earthquake was generated by the Geospatial Information Authority of Japan (GSI 2004), and these data allow for a detailed investigation of the landslide distribution with respect to geologic, topographic, and ground shaking conditions. Additionally, the data allow for the testing of regional-scale approaches for earthquake-induced landslide prediction, which are based on the rigid sliding block approach and form the basis for seismic landslide hazard maps. Evaluations of regional-scale approaches for landslide prediction have focused predominantly on the 1994 Northridge, California (M_w=6.7) earthquake (e.g., Jibson et al. 2000), but the Niigata-ken Chuetsu earthquake provides an opportunity to test an additional landslide inventory to gain further insight into the accuracy of these procedures.

This paper describes the geologic, topographic, and ground shaking conditions across the area affected by the Niigata-ken Chuetsu earthquake. The distribution of landslides with respect to these conditions is presented and compared with the distribution of landslides from the 1994 Northridge earthquake. Using the available information, comparisons are made between regional-scale predictions of the landslides and the observed landslides.

2. NIIGATA-KEN CHUETSU EARTHQUAKE

2.1 Study Area and Landslides

The 2004 Niigata-ken Chuetsu earthquake occurred within the Niigata prefecture, approximately 200 km northwest of Tokyo. Over 5,000 landslides occurred in the Yamakoshi area (GSI 2004) situated northeast of the epicenter and above the fault rupture plane (Figure 1a). The landslide failure mechanisms include shallow translational soil failure, deep-seated failure, large rock block slides, slump-flow complexes and rapid debris flows (Kieffer et al. 2006). Heavy rainfall from Typhoon Tokage contributed significantly to the large number of landslides, with over 100 mm of rain falling in the area just a few days before the earthquake. Moreover, 10 typhoons struck Japan in the months before the earthquake. As a result, large numbers of debris flows were triggered by the earthquake, a landslide type which had previously occurred much less often than other landslide types in previous earthquakes. Slump-flow complexes, which had very long runout distances and occurred on moderately steep slopes, were probably caused by the high moisture conditions (Kieffer et al. 2006).

The GSI developed disaster condition maps which

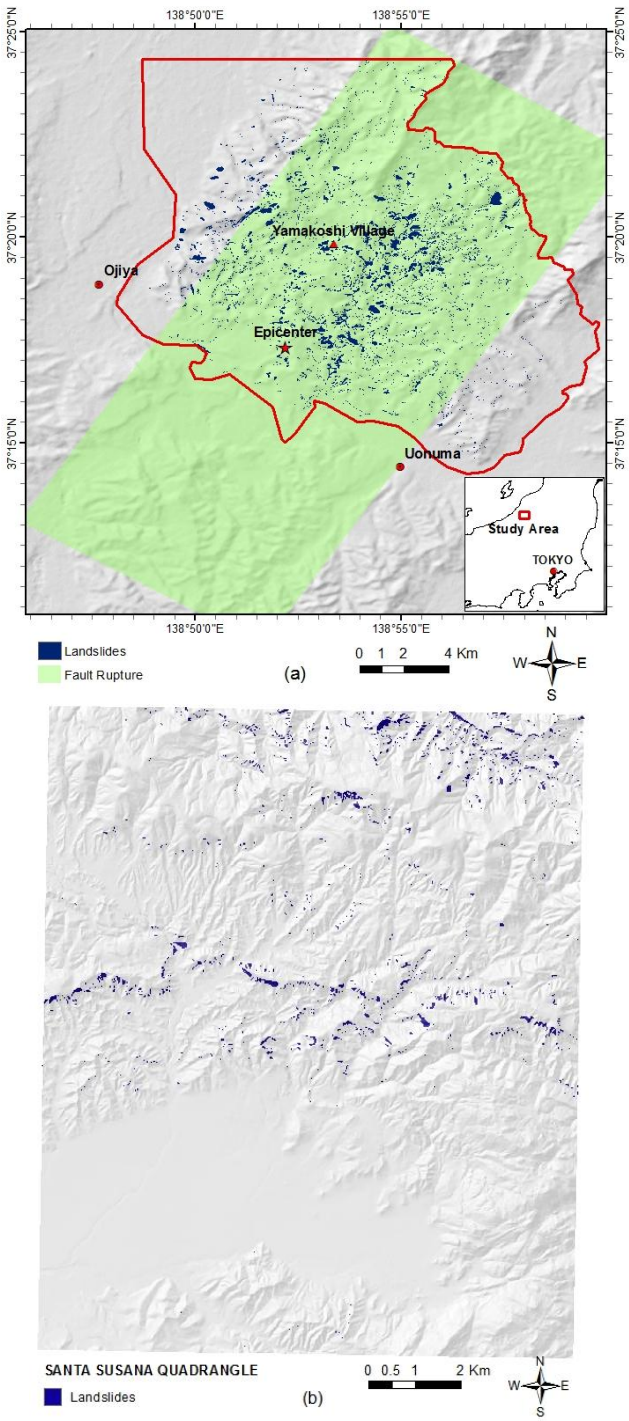


Figure 1 Landslide Distributions in a) Niigata-ken Chuetsu Earthquake b) Santa Susana Quadrangle for the Northridge Earthquake (Dreyfus 2011)

identified landslides for the Niigata-ken Chuetsu earthquake (GSI 2004). Figure 1a shows the identified landslides within the Yamakoshi area along with the surface projection of the fault rupture from the earthquake, as defined by Mori and Somerville (2006). The area around Yamakoshi village (~217 km^2) is selected for study because it experienced the largest concentration of landslides. The western and southern boundaries of the study area represent the Shinano River; the eastern boundary is an administrative boundary beyond which no landslide was recorded on the map; and the northern boundary is the upper boundary of the GSI landslide map. For comparison, the landslides induced by the Northridge earthquake in the Santa Susana Quadrangle (~159 km^2 study area) are shown in Figure 1b.

All landslides within the Yamakoshi study area were manually digitized into a vector format. The vector format maintains each individual landslide as a polygon, which is useful in counting the total number of landslides. The vector format was converted to a raster format at a 10-m grid spacing for use in comparisons with landslide predictions. Therefore, a landslide may consist of several to hundreds of 10m x 10m grid cells, depending on the size of the landslide. Furthermore, source areas, instead of entire landslide areas, were used in the following numerical analyses. Jibson et al. (2000) defined landslide source areas as those landslide areas having elevations above the median elevation for each landslide, so the upper half of each landslide was considered as a source area.

The topography and slope angles across the Yamakoshi study region are investigated using a 30-m resolution digital elevation model (DEM) from ASTER Global Elevation Model (GDEM). The Ministry of Economy, Trade, and Industry (METI) of Japan and the United States National Aeronautics and Space Administration (NASA) co-developed the ASTER GDEM product from data collected by the Advanced Spaceborne Thermal Emission and Reflection Radiometer (ASTER), which is a spaceborne earth observing optical instrument (METI and NASA 2011). Because the resolution of the DEM is relatively coarse for the purpose of this study, the 30-m DEM was resampled to 10-m DEM by applying the spline interpolation algorithm available in ArcGIS© 10.0 developed by the Environmental Systems Research Institute (ESRI).

Most of the Yamakoshi study area is rolling hills, except for the flat northwestern corner which is the alluvial plain associated with the Shinano River. The maximum elevation difference between the alluvial plain and the hilltops in the study area is 743m (from 10m to 753m). A slope angle map was derived from the DEM using the Slope function in ArcGIS©. The statistical distribution of slope angles in the Yamakoshi study area is plotted in Figure 2. Slopes in the study area are moderately steep with about

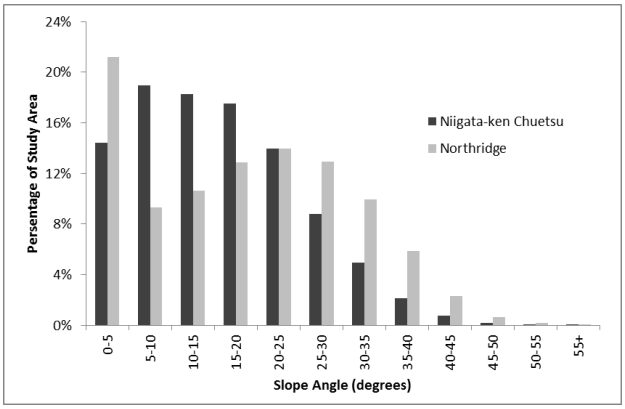


Figure 2 Distributions of Slope Angles by Area Percentage

33% of the area flatter than 10° and 59% with slope angles between 10 and 30°. Only 8% of the area has slope angles greater than 30°. For comparison, the slope angle distribution for the Santa Susana Quadrangle is also shown in Figure 2. The Santa Susana Quadrangle has relatively steeper terrain, with 19% of the quadrangle steeper than 30°.

2.2 Geological Conditions

Bedrock in the study area consists of Middle Miocene to Early Pleistocene sedimentary units. These units range from weak shale and mudstone, to slightly stronger sandstones and conglomerates, to strong volcanics (Kieffer et al. 2006). The bedrock is overlain in places by a layer of colluvium, while Pleistocene to Holocene alluvium are found within river channels and valleys (Kieffer et al. 2006).

A digital geologic map from the Geological Survey of Japan (Takeuchi et al. 2004) was used to define the geology across the study area. The map includes 33 geologic units across the Yamakoshi study area. Quaternary deposits consist of loosely consolidated debris, gravel, sand and silt, having relatively low shear strength properties. Tertiary rock units are composed of cemented shale, mudstone, sandstone, conglomerate and various volcanics with relatively high shear strength properties. The geologic units are combined into five main groups based on geologic ages and compositions (Table 1). The five geologic groups are: Alluvium (22% of the study area), Pleistocene Landslide Deposits (2.5%), Shale/Mudstone (45.5%), Sandstone/Conglomerate (19%) and Volcanics (11%). All Quaternary deposits except Pleistocene Landslide deposits are classified as Alluvium, while various volcanics, such as andesite, breccia and pyroclastic rocks, are classified as Volcanics. The other geologic units are grouped into either Shale/Mudstone or Sandstone/Conglomerate based on their major compositions. The distribution of the geologic units across the Yamakoshi study area is shown in Figure 3.

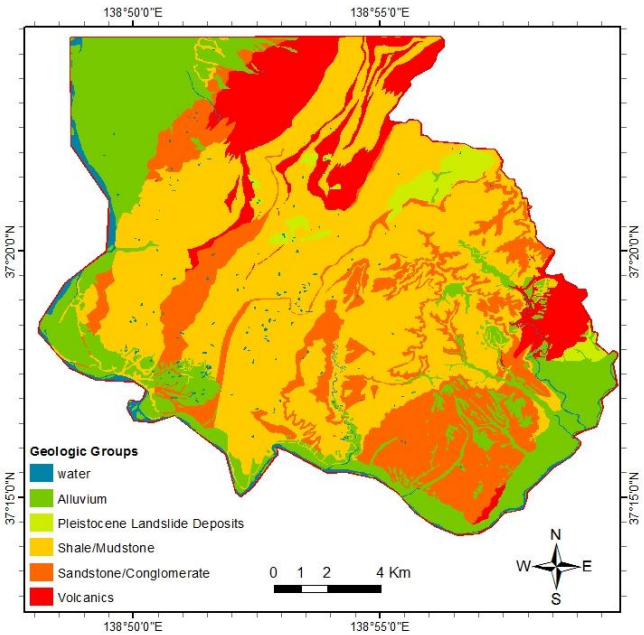


Figure 3 Geological Map of the Study Area

Shear strength properties for regional landslide assessment are commonly assigned based on geologic units and shear strength data obtained within each unit. There is no publically available testing data to directly determine the shear strengths for each geologic unit within the Yamakoshi study area. Therefore, shear strengths are assigned to the five main geologic units based on similar geologic units found in California (e.g., Jibson et al, 2000). The assignment of shear strengths to the geologic groups is presented in Table 1. The alluvial units have relatively low shear strengths and the volcanic units have relatively high shear strengths. Shale/mudstone and sandstone/conglomerate have moderate shear strengths, and the latter group is considered slightly stronger than the former group due to their coarse-grained nature. Pleistocene landslide deposits are not assigned very low shear strengths because there is no evidence that they fail preferentially during earthquakes (personal communication with Dr. Jibson).

Table 1 Geologic Groups and Shear Strength Properties

Geologic Group	Geologic Unit	c' (kPa)	φ' (deg)
Alluvium	a, al, d, f, tk, tl2, tl1, tm2, th2, th1, Oy	15	34
Pleistocene Landslide Deposits	c	20	30
Shale/Mudstone	Ue, Ud, S, Um, Ku, Am, Ts, Sm	25	30
Sandstone/ Conglomerate	Uc, W, Ks, Kl, As	25	35
Volcanics	Sv, Ka, Sy, Uv, Av, Tv, Nd, N	40	42

2.3 Ground Motions

Ground shaking estimates for the Niigata-ken Chuetsu earthquake are obtained from ShakeMap®, a product developed by the United States Geological Survey (USGS) to provide estimates of ground shaking after earthquakes. A ShakeMap® provides point estimates of ground shaking at a 30-arc second spacing, with the ground shaking estimates based on recorded motions (where records are available) supplemented by ground motion prediction equations. The latest ShakeMap® data (ShakeMap® Atlas V2.0) for Peak Ground Acceleration (PGA) and Peak Ground Velocity (PGV) for the Niigata-ken Chuestu earthquake were downloaded and converted into 10-m raster grids in ArcGIS© by applying a simple spline interpolation algorithm.

The PGA ShakeMap is shown in Figure 4. The PGA ranges from 0.52 to 1.93 g across the study site, while the PGV ranges from 22 to 182 cm/s. These high levels of ground shaking are consistent with recorded ground motions. The National Research Institute for Earth Science and Disaster Prevention (NIED) operates numerous strong-motion K-NET stations, which are uniformly

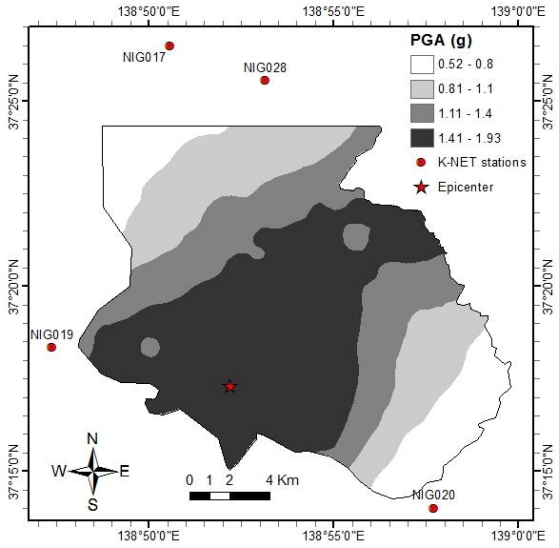


Figure 4 PGA ShakeMap®

distributed every 20 km over Japan. Immediately above of the fault rupture of this reverse event, strong hanging-wall effects led to extreme ground shaking (Kieffer et al. 2006). The largest PGA was 1.73g (with PGV = 72.8 cm/s) at Tohkamachi (NIG021 station), which is about 20 km southwest of the epicenter. Another high PGA value was 1.55g (with PGV = 123.7 cm/s) at Ojiya (NIG019), which is 4 km west of the epicenter (Figure 4). PGV values were largest at Nagaoka-Shisho (NIG028, 124.0 cm/s, 16 km north of the epicenter) and Ojiya (NIG019, 123.7 cm/s).

3. LANDSLIDE DISTRIBUTIONS FROM NIIGATA AND NORTHRIDGE EARTHQUAKES

Using the vector and raster forms of the observed landslides, the characteristics of the landslides induced by the Niigata-ken Chuetsu earthquake within the Yamakoshi study area are investigated. A total of 5,094 individual landslides occurred in the Yamakoshi study area and cover an area of 10.45 km^2, which is 4.8% of the 217 km^2 study area. The landslide source areas, which represent the landslide areas at elevations equal to or above the median elevation for each landslide, cover an area of 5.66 km^2 (~ 2.6% of the study area). For the 1994 Northridge earthquake, the Santa Susana Quadrangle (Figure 1b) had 1,562 seismically triggered landslides (3.4 km^2) covering a total of 2.1% of the quadrangle (Parise and Jibson 2000, Dreyfus 2011). Thus, the landslide area percentage for the Yamakoshi study area was more than twice that for the Santa Susana Quadrangle.

The largest landslide in the Yamakoshi study area is a deep-seated, rotational landslide with an area of about 314,000 m^2. This landslide is excluded from the assessment of empirical prediction models because the rigid sliding block approach is not applicable to this type of failure. The mean size of the remaining landslides is 1,991 m^2 and about 85% of the landslides are smaller than 2,000 m^2 (~ 45 m by

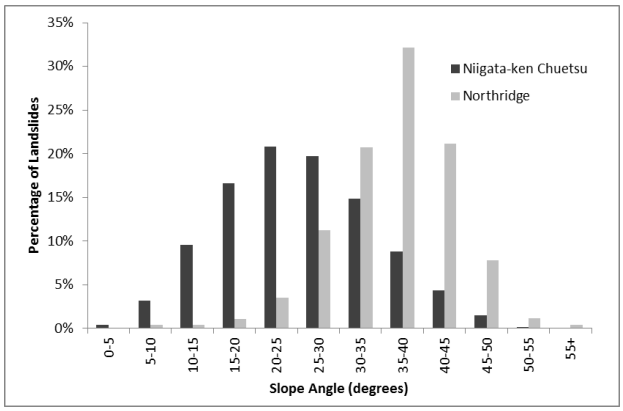


Figure 5 Distribution of Landslides as a Function of Slope Angle

45 m). Figure 5 shows the distribution of landslides with respect to the average slope angle within the landslide for the Niigata-ken Chuetsu and Northridge earthquakes. For Niigata-ken Chuetsu, the population is evenly distributed around a center value of 25^o, and most landslides are on slopes in the 15-35^o range. For Northridge, the landslides are more concentrated on slopes in the 30–45^o range. Parise and Jibson (2000) concluded that the distribution of landslides is significantly tilted toward steeper slopes relative to the distribution of slopes in general. A similar observation can be made regarding Niigata-ken Chuetsu by comparing Figures 2 and 5.

Figure 6 shows the distribution of area percentage, defined as the landslide source area divided by the total area, as a function of slope angle. For Niigata-ken Chuetsu, the area percentage moderately increases with slope angle, reaching a maximum of about 8% for slopes steeper than 45^o. One may expect the area percentage to continue to increase with increasing slope angle. However, steeper slopes are often steep because they consist of stronger materials, making them more resistant to earthquake shaking. For Northridge, a sharp increase in the area percentage occurs for slopes steeper than 40^o with a maximum of 35% observed for slopes steeper than 55^o. However, this sharp increase was not observed in adjacent quadrangles, indicating it may not be representative for the Northridge earthquake.

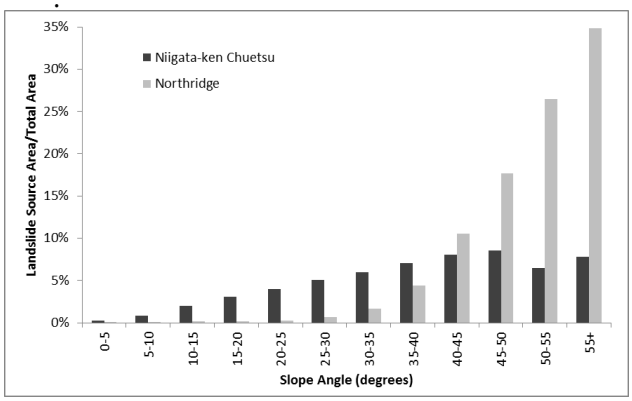


Figure 6 Landslide Source Area over Total Area as a Function of Slope Angle

The overall landslide densities for the Niigata-ken Chuetsu and Northridge earthquakes are 23.5 landslides per km^2 and 10 landslides per km^2, respectively. Despite their similar magnitudes, the 2004 Niigata-ken Chuetsu earthquake induced more landslides (in terms of either landslide density or landslide area percentage) in a relatively flatter area (Figure 2). This larger occurrence of landslides during the Niigata-ken Chuetsu earthquake is mostly likely due to the heavy rainfall before the earthquake, which caused highly unfavorable soil moisture conditions and pore water pressures at the time of the earthquake. In contrast, the Santa Susana Quadrangle had no rainfall for several months before the Northridge earthquake and the surficial slope materials were very dry (Parise and Jibson 2000).

The distribution of landslides across geologic units for the Niigata-ken Chuetsu earthquake is summarized in Table 2. Over 70% of the landslide source cells occurred in the Shale/Mudstone units, while 22.1% occurred in the Sandstone/Conglomerate units. One may also consider the area percentage within each geologic unit (% Geo Unit) such that the observed total landslide source areas are normalized by the available area within each geologic unit. Table 2 shows that the %Geo Unit was largest in the Shale/Mudstone units (4.1%) and Sandstone/Conglomerate units (3.1%). For comparison, the largest %Geo Unit values for the Santa Susana Quadrangle were 4 to 7.5%. These larger values may have been influenced by the more numerous and detailed geologic units identified in the Santa Susana Quadrangle (i.e., 13 units).

Table 2 Landslides within each Geologic Group

Geologic Groups	% of LS cells	% Geo Unit
Alluvium	1.5%	0.2%
Pleistocene Landslide Deposits	1.3%	1.4%
Shale/Mudstone	70.4%	4.1%
Sandstone/Conglomerate	22.1%	3.1%
Volcanics	4.7%	1.2%

4. LANDSLIDE PREDICTIONS

4.1 Approach

A common failure mode for landslides triggered by earthquakes in natural slopes is a thin, veneer slope failure (Keefer 2002). Therefore, regional-scale seismic landslide predictions are based on computing rigid sliding block displacements (Newmark 1965) for an infinite slope model. Many predictive models for sliding displacement have been proposed in the past decades that compute displacement based on the level of ground shaking and the resistance of the slope to sliding under seismic conditions. Ground motion parameters, such as PGA, PGV, mean period (T_m) and Arias Intensity (I_a), have been used individually or in combination for these predictive models. Using a combination of ground motion parameters can reduce the uncertainty in the displacement prediction, compared with using a single ground motion parameter. PGA and PGV are the most easily obtainable ground motion parameters across a region because USGS provides ShakeMap® data for PGA and PGV for major earthquakes across the world. Saygili and Rathje (2008) developed a model for predicting rigid sliding displacements (D in units of cm) using PGA (in units of g) and PGV (in units of cm/s). The median value of lnD can be expressed as:

$$\ln D = -1.56 - 4.58\left(\frac{k_y}{PGA}\right) - 20.84\left(\frac{k_y}{PGA}\right)^2 + 44.75\left(\frac{k_y}{PGA}\right)^3 - 30.50\left(\frac{k_y}{PGA}\right)^4 - 0.64\ln PGA + 1.55\ln PGV \quad (1)$$

The resistance of the slope to sliding under seismic conditions is characterized by the critical, or yield, acceleration (k_y). k_y is derived from limit equilibrium analysis of an infinite slope model. Considering earthquake shaking parallel to a slope, the yield acceleration (in units of g) can be expressed as:

$$k_y = (FS - 1)g \cdot \sin\alpha \quad (2)$$

where FS is the static factor of safety, g is the acceleration of gravity and α is the slope angle. The yield acceleration can be calculated by assuming the ground shaking is horizontal, but in most cases the differences are small (Saygili, 2008). Based on the slope geometry and the soil properties, the static factor of safety for an infinite slope model is computed as (Jibson et al. 2000):

$$FS = \frac{c'}{\gamma t \sin\alpha} + \frac{\tan\phi'}{\tan\alpha}\left(1 - m\frac{\gamma_w}{\gamma}\right) \quad (3)$$

where c' is the effective cohesion, φ' is the effective friction angle, γ is the material unit weight, γ_w is the unit weight of water, α is the slope angle, t is the slope-normal thickness of the rigid block, and m is the proportion of the block thickness that is saturated and thus represents pore water pressure. The slope angle is derived from the 10-m DEM in ArcGIS©. In this analysis, the other parameters in equation (3) are assigned typical values for shallow slopes: γ = 15.7 kN/m^3 and t = 2.4 m (Jibson et al. 2000). The c' and φ' values are presented in Table 1.

The selection of an appropriate saturation thickness proportion (m) requires some discussion. Considering that Typhoon Tokage occurred 3 days before the earthquake, the soils in the study area are assumed to be highly saturated. For fine-grained shales and mudstones, the extreme moisture conditions would further soften and reduce the shear strength. Based on sensitivity analyses, the most representative values of m for the Yamakoshi study area at the time of the Niigata-ken Chuetsu earthquake is set as 0.8.

ArcGIS© 10.0 is used for the development of digital maps of sliding displacement and landslide prediction at

10-m resolution. With a slope map from the DEM and shear strength assigned from the geological map, maps of FS (eq. 3) and k_y (eq. 2) are developed. The k_y values are coupled with ground motions from ShakeMap® to compute the median sliding displacement (eq. 1) cell by cell in the study area. The study area contains 2,445,263 cells in total and the number of observed landslide source area cells (LS cells) is 63,507, not including the one larger, deep-seated landslide.

Both the accuracy and the efficiency of the landslide predictions are evaluated. A predicted landslide cell (PLS cell) is defined as a cell with a predicted sliding displacement greater than a displacement threshold. The LS cells accurately identified by the PLS cells are considered landslide captured (LSC) cells. %LSC represents the percentage of the total LS cells that are accurately identified. The PLS/LS ratio is an efficiency parameter, showing the relative quantity between predicted landslide cells and observed landslide cells.

4.2 Results

Two displacement thresholds (5 cm and 15 cm) are applied to evaluate the prediction accuracy and efficiency. The 5 cm displacement threshold generally represents the boundary between very low and low hazard, while the 15 cm threshold represents the transition from low to moderate hazard (California Geological Survey 2008). Figure 7 shows the predicted landslide cells for the Yamakoshi study area using the 5 and 15 cm thresholds and m = 0.8. Almost all of the predicted landslides concentrate in the middle part of the study area, which is underlain by the fault rupture (Figure 1a) and on the hanging-wall. In this region, the intensive ground motions (Figure 4) and the steep terrain result in large predicted displacements. A threshold of 5 cm obviously predicts significantly more landslide cells than the 15 cm threshold, and thus will capture more landslides. However, this smaller displacement threshold largely over-predicts the landslide area. The 5 cm threshold captures over 75% of the landslides (%LSC = 75.3%), but the trade-off is that over 40% of the study area fails and the PLS/LS ratio is 16.1. On the contrary, the 15 cm threshold results in a smaller %LSC (40.4%) but a more acceptable PLS/LS ratio of about 5.

Table 3 Landslide Prediction Assessments for Different Displacement Thresholds and m-values

m value	5 cm threshold		15 cm threshold	
	%LSC	PLS/LS	%LSC	PLS/LS
0.0	34.0%	4.1	6.4%	0.5
0.5	62.0%	11.2	22.6%	2.4
0.7	71.4%	14.5	33.9%	4.2
0.8	75.3%	16.1	40.4%	5.4
0.9	79.0%	17.7	47.3%	7.0
1.0	82.7%	19.1	54.1%	8.8

The influence of m-value on the results was investigated by performing analyses for a range of m-values between 0.0 and 1.0. The values of %LSC and PLS/LS for these analyses are summarized in Table 3. The prediction accuracy (%LSC) definitely increases with increasing m value, due to the associated reduction in shear strength. For m = 0, both the small %LSC and the known moisture condition at the time of the earthquake suggest that such a small m-value cannot be justified. A larger m-value brings a better prediction accuracy but significantly increases the PLS/LS ratio. However, even with m = 1.0, the prediction accuracy still does not approach 100% and in these cases the PLS/LS ratio becomes excessively large.

Dreyfus (2011) performed a similar analysis of displacement for the Santa Susana Quadrangle. Considering the dry moisture condition prior to the Northridge earthquake, m = 0 was assigned. The %LSC and PLS/LS ratio were 41% and 7.1, respectively, for the 5 cm threshold, and 28.8% and 4.3 for the 15 cm threshold. These results are consistent with the results of this study and suggest that obtaining a higher accuracy by lowering the displacement

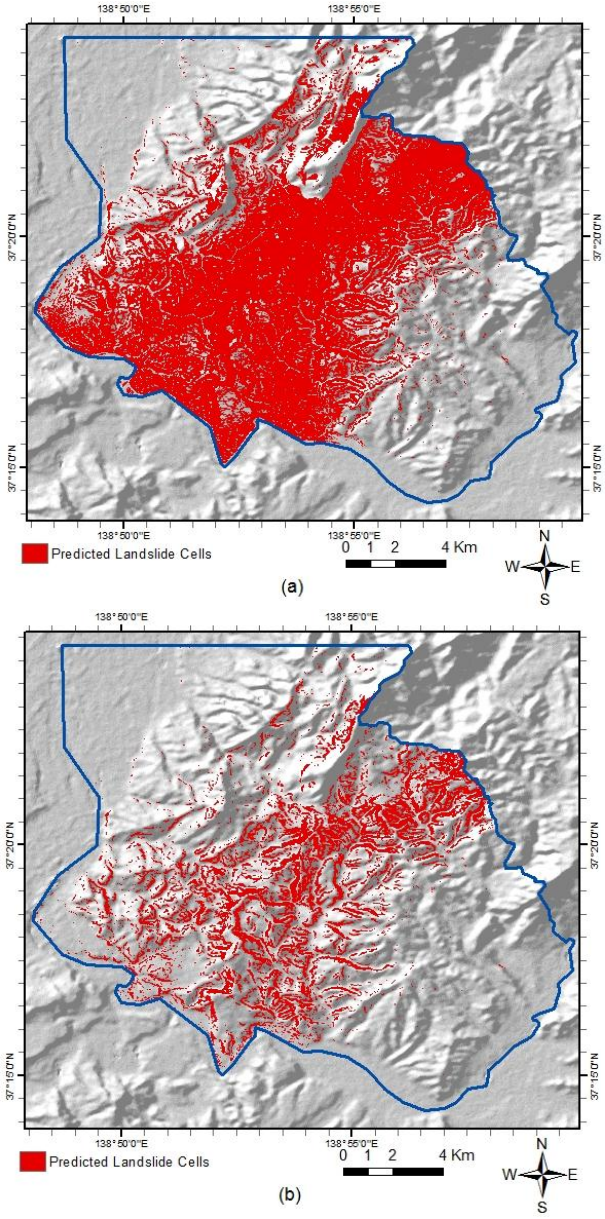


Figure 7 Predicted landslide areas for m = 0.8 with (a) 5cm threshold (b) 15cm threshold

Table 4 Summary of Prediction Accuracy and Efficiency within each Geologic Group

Geologic Group	Observed Landslides		Predicted Landslides		Captured Landslides		
	LS cells	% of Geo Unit	PLS cells	% of Geo Unit	LSC cells	%LSC in Geo Unit	PLS/LS in Geo Unit
Alluvium	950	0.2%	20,823	3.9%	365	38.4%	21.9
Pleistocene Landslide Deposits	823	1.4%	19,145	32.4%	597	72.5%	23.3
Shale/Mudstone	44,714	4.1%	259,874	23.7%	20,845	46.6%	5.8
Sandstone/Conglomerate	14,011	3.1%	46,168	10.1%	3,970	28.3%	3.3
Volcanics	3,009	1.2%	215	0.1%	5	0.2%	0.07

threshold sacrifices the efficiency of the prediction.

The accuracy and efficiency of the landslide predictions across the geologic units are summarized in Table 4. Alluvium, Pleistocene Landslide Deposits and Volcanics make up only about 7.5% of the total landslides (Table 2), such that their prediction accuracies do not contribute much to the overall accuracy. Nonetheless, their individual %LSC vary significantly: 0.2% for Volcanics, 38.4% for Alluvium, and 72.5% for Pleistocene Landslide Deposits. The corresponding PLS/LS ratios for Volcanics, Alluvium, and Pleistocene Landslide Deposits are 23.3, 21.9, and 0.07, respectively. The large PLS/LS ratios for the Alluvium and Pleistocene Landslide Deposits suggest that the assigned strengths for these units are too small such that there is a significant over-prediction in landslide area. Alternatively, the very small PLS/LS ratio for the Volcanics indicates that the assigned strength is too large. Because the observed landslides within the Volcanics group are mainly rock block slides on a weak layer or discontinuity within the bedrock (Kieffer et al. 2006), assigning shear strengths based on the rock mass results in strengths that are too large.

As previously noted, 92.5% of the landslides occurred in the Sandstone/Conglomerate and Shale/Mudstone units. The %LSC and PLS/LS ratio are relatively small for the Sandstone/Conglomerate unit (28% and 3.3, respectively), while these values are larger for the Shale/Mudstone unit (%LSC ~ 47%, PLS/LS ~ 6). While smaller strengths for the Shale/Mudstone unit would generate a larger %LSC, the over-prediction in total landslide area would greatly increase.

Similar results were obtained by Dreyfus (2011) when analyzing the six quadrangles that experienced significant landslides during the Northridge earthquake. In studying Northridge, only 30 to 40% of the landslides were accurately captured despite the use of the best geologic maps, best shear strength information, and best ground motion data. Coupled with these relatively small values of %LSC were large over-predictions in the total landslide area (PLS/LS ~ 4 to 7).

4.3 Discussion

The results from this study and others (e.g., Dreyfus 2011) indicate that only about 30 to 40% of landslide can be expected to be captured by current techniques for regional seismic landslide prediction, and the total landslide area will most likely be over-predicted by a factor greater than 5. Thus it is clear that the techniques used to map seismic landslide hazards are lacking and require improvement.

One critical component of the seismic landslide prediction methodology is the assignment of shear strengths. Currently, these strengths are assigned based on geologic unit and a single set of (c', φ') are used for each geologic unit. A constant set of shear strength parameters within a geologic unit effectively assumes 100% of slopes steeper than a critical slope angle (defined via eqs 2 and 3 for a given PGA and PGV) will fail. Failure of all steep slopes is not realistic and illustrates the need to identify spatial variability in shear strength across a geologic unit. As noted earlier, steeper slopes are often steep because they consist of stronger materials, making them more resistant to earthquake shaking. Additionally, different parts of the same geologic unit may exhibit different shear strengths due to differences in cementation, grain-size, etc. One potential approach to quantifying these variations is remote sensing, but remote sensing may be hindered by soil cover that obscures the characteristics of underlying materials. Mapping of strength in the field would be extremely time-consuming and would require collecting and testing a significant number of material samples.

Related to the issue of shear strength parameters is the assumed saturation thickness proportion (m), which affects the pore water pressures, effective stress, and strength. This assumption had a profound effect on the study of the Niigata-ken Chuetsu earthquake because of the significant rainfall before the event. Rather than assuming a value of m, a more rational approach would take into account rainfall rates, slope angle, and relative hydraulic conductivities to predict spatially variable m-values.

Finally, an additional factor that limits our ability to capture a high percentage of seismic landslides is local variability of ground shaking. Because landslides occur primarily on relatively steep slopes, most of this local variability is likely the result of topographic amplification. The regional estimates of ground shaking from ShakeMap are the best seismology has to offer, but they potentially ignore important localized topographic effects that influence the seismic loading of slopes, particularly near the crests of ridges. However, systematically predicting the location and amount of topographic amplification is a complex problem that currently has no simple, consistent solution.

5. CONCLUSIONS

The 2004 Niigata-ken Chuetsu earthquake induced a significant number of landslides across the Yamakoshi region. The landslide inventory from this earthquake provides an excellent opportunity to study the landslide distribution, to compare this distribution with the distribution of landslides in the Santa Susana Quadrangle from the 1994 Northridge earthquake, and to evaluate the procedures used in regional seismic landslide prediction.

The topography of the Yamakoshi study area is not as steep as for the Santa Susana Quadrangle; yet a larger number of landslides occurred in Yamakoshi. Additionally, the landslides in Yamakoshi were concentrated on slopes between 20 and 30 degrees, while the landslides in the Santa Susana Quadrangle occurred mostly on slopes between 30 and 45 degrees. The larger number of landslides in Yamakoshi most likely was influenced by the adverse soil moisture conditions and pore water pressures at the time of the earthquake.

More than 90% of the landslides in the Yamakoshi study area occurred in Shale/Mudstone or Sandstone/ Conglomerate geologic units. Very few landslides occurred in the Alluvium, Pleistocene Landslide deposits, or Volcanic units. Even in the Shale/Mudstone or Sandstone/ Conglomerate geologic units, however, the percentage of area covered by landslides was only 3 to 4%.

Regional-scale landslide predictions for the Niigata-ken Chuetsu earthquake were made using the rigid sliding block approach. This approach used a regional DEM and shear strengths assigned to each geologic unit to generate yield acceleration estimates on a 10-m grid spacing. Coupling the yield accelerations with ground motion estimates from ShakeMap and the displacement prediction model of Saygili and Rathje (2008), displacements were predicted across the study area. Predicted landslides were identified using a 5 cm and 15 cm displacement threshold.

Comparing the predicted and observed landslides provided several insights. The 15 cm threshold captured only about 40% of the landslides, although the total predicted landslide area was more than 5 times as large as what was observed. The 5 cm threshold increased the prediction accuracy to 75% but at the expense of over-predicting the total landslide area by a factor of 16. The saturation thickness proportion (i.e., m-value) has a significant influence on the prediction accuracy and the level of over-prediction. Selecting an appropriate m-value is essential for region-scale landslide prediction, especially for the Niigata-ken Chuetsu earthquake with heavy rainfall.

The accuracy in predicting landslides on a regional scale may be improved by refining various parts of the modeling approach. The component of the analysis that has the most likelihood of improving the predictions is the shear strength, in particular considering spatial variations in shear strengths across each geologic unit. A constant set of shear strength parameters within a geologic unit effectively assumes a 100% failure rate for slopes steeper than a critical slope angle. This result is not realistic and illustrates the need to identify spatial variability in shear strength across a geologic unit. Field test and lab test data can be helpful for determining the variability in strengths, and remote sensing may play a role in the future.

Acknowledgements:

The authors would like to thank Dr. Randall W. Jibson of the U.S. Geological Survey for feedback and assistance. Dr. David J. Wald and Kendra Johnson of the USGS provided timely assistance with ShakeMap® and their help is greatly appreciated.

References:

Yanagisawa, Y., Kobayashi, I., Takeuchi, K., Tateishi, M., Chihara, K., and Kato, H., 1986. Geology of Ojiya District, Geological Survey of Japan, Tsukuba, Japan (in Japanese, with English abstract).

California Department of Conservation, California Geological Survey (2008). *Guidelines for evaluating and mitigating seismic hazards in California*. Special Publication 117A.

Dreyfus, K. D., 2011. A comparison of methodologies used to predict earthquake-induced landslides. Master Thesis, University of Texas at Austin, Austin, TX.

Geospatial Information Authority of Japan, 2004. 2004 Mid Niigata Prefecture Earthquake 1:25,000 Disaster Condition Map, Yamakoshi (Landslide Classification and Disaster Information).

Jibson R. W., Harp E. L. and Michael J. A., 2000. "A method for producing digital probabilistic seismic landslide hazard maps," *Engineering Geology* 58, 271-289.

Keefer, D. K. (2002). Investigating landslides caused by earthquakes - a historical review. *Surveys in Geophysics*, 23, 473-510.

Kieffer D. S., Jibson R., Rathje E. M. and Kelson K., 2006. "Landslides Triggered by the 2004 Niigata Ken Chuetsu, Japan, Earthquake," *Earthquake Spectra*, Vol 22, No. S1, pp. S47–S74.

Ministry of Economy, Trade, and Industry (METI) of Japan and the United States National Aeronautics and Space Administration (NASA), 2011. ASTER Global Digital Elevation Model version 2, http://www.gdem.aster.ersdac.or.jp/index.jsp.

Mori J. and Somerville P., 2006. "Seismology and Strong Ground Motions in the 2004 Niigata Ken Chuetsu, Japan, Earthquake," *Earthquake Spectra*, Vol 22, No. S1, pp. S9–S21.

National Research Institute for Earth Science and Disaster Prevention (NIED), Strong Motion Seismograph Networks web site, http://www.k-net.bosai.go.jp/k-net/index_en.shtml

Newmark, N., 1965. Effects of earthquakes on dams and embankments. *Geotechnique*, 15(2), 139-160.

Parise M. and Jibson R. W., 2000. "A seismic landslide susceptibility rating of geologic units based on analysis of characteristics of landslides triggered by the 17 January, 1994 Northridge, California earthquake," *Engineering Geology* 58, 251-270.

Saygili, G. and Rathje, E. M., 2008. "Empirical predictive models for earthquake-induced sliding displacements of slopes," *Journal of Geotechnical and Geoenvironmental Engineering*, 134, 790-803.

Saygili, G., 2008. A probabilistic approach for evaluating earthquake-induced landslides. Ph.D. Dissertation, University of Texas at Austin, Austin, TX.

Scawthorn C. and Rathje E. M., 2006. "The 2004 Niigata Ken Chuetsu, Japan, Earthquake," *Earthquake Spectra*, Vol 22, No. S1, pp. S1–S8.

Takeuchi K., Yanagisawa Y., Miyazaki J. and Ozaka M., 2004. 1:50,000 Digital Geological Map of the Uonuma region, Niigata Prefecture (Ver.1), *GSJ Open-file Report, No. 412*, Geological Survey of Japan.

10CUEE CONFERENCE PROCEEDINGS
10th International Conference on Urban Earthquake Engineering
March 1-2, 2013, Tokyo Institute of Technology, Tokyo, Japan

SEISMIC SAFETY AND UNITED STATES DESIGN PRACTICE FOR STEEL-CONCRETE COMPOSITE FRAME STRUCTURES

Mark D. Denavit[1], Jerome F. Hajjar[2], Tiziano Perea[3], and Roberto T. Leon[4]

1) Design Engineer, Stanley D. Lindsey and Associates, Ltd., Atlanta, Georgia, USA
2) Professor and Chair, Dept. of Civil and Environmental Engineering, Northeastern University, Boston, Massachusetts, USA
3) Professor, Dept. de Materiales, Universidad Autónoma Metropolitana, Azcapotzalco, D. F., Mexico
4) David H. Burrows Professor of Construction Engineering, The Charles E. Via, Jr. Department of Civil and Environmental Engineering, Virginia Polytechnic Institute and State University, Blacksburg, Virginia, USA
mdenavit@sdlal.com, jf.hajjar@neu.edu, tperea@correo.azc.uam.mx, rleon@vt.edu

Abstract: In United States design practice, three system performance factors (R, C_d, and Ω_o) characterize the inelastic behavior of structures and are a crucial component of common elastic design methodologies. However, for steel-concrete composite frame systems these factors have been selected based on comparisons to more traditional and well-studied reinforced concrete and structural steel frame systems, without significant quantitative justification. In this study, the seismic behavior of steel-concrete composite moment and braced frames is investigated and rational system performance factors are developed. A set of archetype frames, selected to be representative of the range of frames seen in practice, were designed according to current design specifications. Using a suite of new finite element formulations for composite systems, nonlinear static pushover and transient dynamic analyses were performed on the frames. The results of the analyses served as statistical data on the seismic response from which the performance factors were quantified. The results from this investigation enable a better understanding of the variability in collapse performance of composite frame systems and will facilitate more effective designs of these systems.

1. INTRODUCTION

A key component of seismic design in the United States is the allowance for inelasticity in structural elements subjected to severe earthquake ground motions. However, static elastic analysis is prevalent for seismic design in current practice. Because of this, seismic performance factors have been developed. The factors are: the response modification factor, R, used in reducing seismic forces determined through elastic methods; the displacement amplification factor, C_d, used in amplifying displacements determined through elastic methods; and the system overstrength factor, Ω_o, used to estimate the actual strength as compared the to the design strength.

These three factors are tabulated for a variety of seismic force resisting systems in national codes (ASCE 2010), however, they have been somewhat arbitrarily assigned. Many R factors were based largely on judgment and qualitative comparisons to the relatively few seismic force resisting systems that had known response capabilities (FEMA 2009). This is particularly true for composite moment and braced frames where the seismic performance factors were assigned based on comparisons to similar structural steel and reinforced concrete systems.

A methodology has been developed to provide a rational basis for determining seismic performance factors which provide equivalent safety against collapse for buildings with different seismic force resisting systems (FEMA 2009). Equivalent safety is provided through an acceptably low probability of structural collapse common to all systems. Structural collapse in the methodology is defined in the context of incremental dynamic analysis, in which nonlinear time history analyses are performed at increasing magnitudes of seismic loading until the structure achieves its peak strength or predefined displacement limits. In this approach, no explicit modeling of collapse is included. Statistical data is generated from the analyses for a set of archetype models and uncertainty is approximated based on the level of knowledge of the particular system and accuracy of the analysis.

This paper presents a study to investigate the behavior of composite frames under seismic loading and to develop rational seismic performance factors following the methodology given in FEMA P-695 Quantification of Building Seismic Performance Factors (FEMA 2009).

2. SEISMIC FORCE RESISTING SYSTEMS

Two separate seismic force resisting systems are analyzed in this study: composite special moment frames (C-SMF) and composite special concentrically braced frames (C-SCBF). The current seismic performance factors

for these two systems are given in Table 1 (ASCE 2010).

Table 1. Current Seismic Performance Factors

System	Ω_o	R	C_d
C-SMF	3.0	8.0	5.5
C-SCBF	2.0	5.0	4.5

The requirements for composite special moment frames are described in the AISC *Seismic Specification* (AISC 2010). C-SMFs utilize fully restrained connections and consist of either composite or reinforced concrete columns and either structural steel, concrete-encased composite, or composite beams. They are expected to provide significant inelastic deformation capacity through flexural yielding of the beams and limited yielding of the column panel zones. Columns are designed to be stronger than the fully yielded and strain-hardened beams, although flexural yielding in columns at the base is permitted.

The requirements for composite special concentrically braced frames are described in the AISC *Seismic Specification* (AISC 2010). C-SCBFs consist of CFT or SRC composite columns, structural steel or composite beams, and structural steel or CFT braces. They are expected to provide significant inelastic deformation capacity primarily through brace buckling and yielding of the brace in tension.

3. ARCHETYPE FRAMES

To perform the methodology, it is necessary to have a suite of frames (termed index archetypes) for which the analyses can be performed. Ideally that suite of frames is representative of the entire range of frames seen in practice. However, it is generally recognized within the methodology that a practical number of frames cannot fully represent the permissible range, thus simplifications must be made. The selected frames are described below; complete details including the design process are presented in Denavit (2012).

The building layout is the same for each of the index archetype configurations: 3 bays by 5 bays with a bay width of either 20 ft or 30 ft (Figure 1). The buildings are 3 or 9 stories tall with a story height of 13 ft. For the moment frames the columns were either RCFTs or SRCs. For the braced frames the columns were CCFTs and the braces were either rectangular HSS or wide flange in a two-story X configuration. A composite floor system was assumed for all configurations, although the beams in the seismic force resisting systems were designed and analyzed assuming bare steel.

Two levels of gravity load were selected: "high" which corresponded to warehouse live loading (250 psf) and the interior frame and "low" which corresponded to office live loading (65 psf) and the exterior frame. Two levels of seismic load were selected corresponding to the levels design earthquake associated with the maximum (D_{max}) and minimum (D_{min}) of seismic design category D (ASCE 2010).

The methodology prescribes that $C_d = R$ (FEMA 2009), which is contrary to current practice (ASCE 2010) where C_d is typically less than R (Table 1). For deformation-controlled structures, such as moment frames, this change results in larger member sizes. In this study, most frames were designed assuming $C_d = R$, however, a subset of the moment frames were duplicated and designed with the current value (C_d = 5.5) so as to compare to the current state of design practice.

In total, 60 frames were selected and designed for this study. The frames varied in building height, column type, concrete strength, level of seismic load, level of gravity load, and bay width. Details of the frames are given in Table 2 for the C-SMFs and Table 3 for the C-SCBFs.

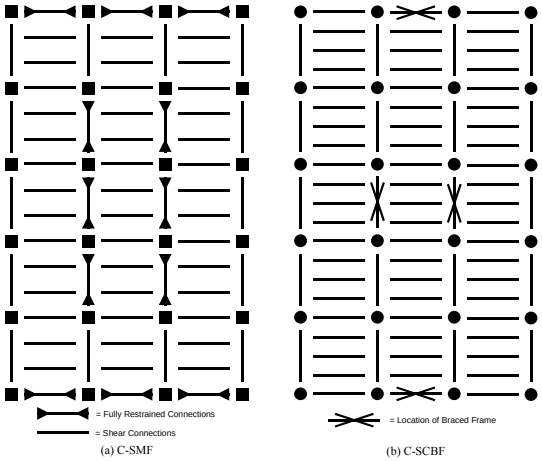


Figure 1. Building Layout

3.1 Material Strengths

Two sets of material strengths are used in this study as summarized in Table 4. The first is the nominal strength which is used in the design of the archetypes. The second is the expected strengths which are used in the analyses of the archetypes. The nominal strengths are selected as typical material properties. The expected strengths for the steel materials are defined as described in Section A3.2 of the AISC *Seismic Specification* (AISC 2010). For lack of a more appropriate definition, the expected strengths for the concrete materials are defined as the required average compressive strength from field strength tests when data are not available to establish a sample standard deviation as described in Section 5.3.2.2 of the ACI *Code* (ACI 2011).

3.2 Seismic Design

The equivalent lateral force method (ASCE 2010) was used for the seismic design. The level of seismic loading is defined in terms of the seismic design category. The frames in this study were designed for seismic design category D at either the maximum (D_{max}) or minimum (D_{min}).

Table 2. Frame Information: C-SMFs

Frame #	Name	Number of Stories	Gravity Load	f'_c	Bay Width	SDC	$C_d = R$	T	Building V	Building W	C_s	Frame V
				ksi	*ft*			*s*	*kips*	*kips*		*kips*
1	RCFT-3-1	3	high	4	20	Dmax	yes	0.437	307.8	2,462	0.125	153.9
2	RCFT-3-2	3	high	12	20	Dmax	yes	0.437	307.8	2,462	0.125	153.9
3	RCFT-3-3	3	high	4	20	Dmin	yes	0.468	131.5	2,462	0.053	65.7
4	RCFT-3-4	3	high	12	20	Dmin	yes	0.468	131.5	2,462	0.053	65.7
5	RCFT-3-5	3	high	4	30	Dmax	yes	0.437	670.3	5,363	0.125	335.2
6	RCFT-3-6	3	high	12	30	Dmax	yes	0.437	670.3	5,363	0.125	335.2
7	RCFT-3-7	3	high	4	30	Dmin	yes	0.468	286.3	5,363	0.053	143.2
8	RCFT-3-8	3	high	12	30	Dmin	yes	0.468	286.3	5,363	0.053	143.2
9	RCFT-3-9	3	low	4	20	Dmax	yes	0.437	229.0	1,832	0.125	114.5
10	RCFT-3-10	3	low	12	20	Dmax	yes	0.437	229.0	1,832	0.125	114.5
11	RCFT-3-11	3	low	4	20	Dmin	yes	0.468	97.8	1,832	0.053	48.9
12	RCFT-3-12	3	low	12	20	Dmin	yes	0.468	97.8	1,832	0.053	48.9
13	RCFT-3-13	3	low	4	30	Dmax	yes	0.437	493.1	3,945	0.125	246.6
14	RCFT-3-14	3	low	12	30	Dmax	yes	0.437	493.1	3,945	0.125	246.6
15	RCFT-3-15	3	low	4	30	Dmin	yes	0.468	210.7	3,945	0.053	105.3
16	RCFT-3-16	3	low	12	30	Dmin	yes	0.468	210.7	3,945	0.053	105.3
17	RCFT-9-1	9	high	4	20	Dmax	yes	0.996	618.6	8,216	0.075	309.3
18	RCFT-9-3	9	high	4	20	Dmin	yes	1.067	192.5	8,216	0.023	96.2
19	RCFT-9-5	9	high	4	30	Dmax	yes	0.996	1,343.3	17,841	0.075	671.7
20	RCFT-9-7	9	high	4	30	Dmin	yes	1.067	417.9	17,841	0.023	209.0
21	RCFT-9-9	9	low	4	20	Dmax	yes	0.996	428.9	5,696	0.075	214.4
22	RCFT-9-11	9	low	4	20	Dmin	yes	1.067	133.4	5,696	0.023	66.7
23	RCFT-9-13	9	low	4	30	Dmax	yes	0.996	916.4	12,171	0.075	458.2
24	RCFT-9-15	9	low	4	30	Dmin	yes	1.067	285.1	12,171	0.023	142.6
25	SRC-3-1	3	high	4	20	Dmax	yes	0.437	307.8	2,462	0.125	153.9
26	SRC-3-2	3	high	12	20	Dmax	yes	0.437	307.8	2,462	0.125	153.9
27	SRC-3-3	3	high	4	20	Dmin	yes	0.468	131.5	2,462	0.053	65.7
28	SRC-3-4	3	high	12	20	Dmin	yes	0.468	131.5	2,462	0.053	65.7
29	SRC-3-9	3	low	4	20	Dmax	yes	0.437	229.0	1,832	0.125	114.5
30	SRC-3-10	3	low	12	20	Dmax	yes	0.437	229.0	1,832	0.125	114.5
31	SRC-3-11	3	low	4	20	Dmin	yes	0.468	97.8	1,832	0.053	48.9
32	SRC-3-12	3	low	12	20	Dmin	yes	0.468	97.8	1,832	0.053	48.9
33	RCFT-3-1-Cd	3	high	4	20	Dmax	no	0.437	307.8	2,462	0.125	153.9
34	RCFT-3-3-Cd	3	high	4	20	Dmin	no	0.468	131.5	2,462	0.053	65.7
35	RCFT-3-9-Cd	3	low	4	20	Dmax	no	0.437	229.0	1,832	0.125	114.5
36	RCFT-3-11-Cd	3	low	4	20	Dmin	no	0.468	97.8	1,832	0.053	48.9

Table 3. Frame Information: C-SCBFs

Frame #	Name	Number of Stories	Gravity Load	f'_c	Bay Width	SDC	$C_d = R$	T	Building V	Building W	C_s	Frame V
				ksi	*ft*			*s*	*kips*	*kips*		*kips*
1	CCFT-3-1	3	high	4	20	Dmax	yes	0.437	492.4	2,462	0.200	246.2
2	CCFT-3-2	3	high	12	20	Dmax	yes	0.437	492.4	2,462	0.200	246.2
3	CCFT-3-3	3	high	4	20	Dmin	yes	0.468	210.3	2,462	0.085	105.2
4	CCFT-3-4	3	high	12	20	Dmin	yes	0.468	210.3	2,462	0.085	105.2
5	CCFT-3-5	3	high	4	30	Dmax	yes	0.437	1,072.5	5,363	0.200	536.3
6	CCFT-3-6	3	high	12	30	Dmax	yes	0.437	1,072.5	5,363	0.200	536.3
7	CCFT-3-7	3	high	4	30	Dmin	yes	0.468	458.2	5,363	0.085	229.1
8	CCFT-3-8	3	high	12	30	Dmin	yes	0.468	458.2	5,363	0.085	229.1
9	CCFT-3-9	3	low	4	20	Dmax	yes	0.437	366.4	1,832	0.200	183.2
10	CCFT-3-10	3	low	12	20	Dmax	yes	0.437	366.4	1,832	0.200	183.2
11	CCFT-3-11	3	low	4	20	Dmin	yes	0.468	156.5	1,832	0.085	78.3
12	CCFT-3-12	3	low	12	20	Dmin	yes	0.468	156.5	1,832	0.085	78.3
13	CCFT-3-13	3	low	4	30	Dmax	yes	0.437	789.0	3,945	0.200	394.5
14	CCFT-3-14	3	low	12	30	Dmax	yes	0.437	789.0	3,945	0.200	394.5
15	CCFT-3-15	3	low	4	30	Dmin	yes	0.468	337.0	3,945	0.085	168.5
16	CCFT-3-16	3	low	12	30	Dmin	yes	0.468	337.0	3,945	0.085	168.5
17	CCFT-9-1	9	high	4	20	Dmax	yes	0.996	989.8	8,216	0.120	494.9
18	CCFT-9-3	9	high	4	20	Dmin	yes	1.067	307.9	8,216	0.037	154.0
19	CCFT-9-5	9	high	4	30	Dmax	yes	0.996	2,149.3	17,841	0.120	1074.7
20	CCFT-9-7	9	high	4	30	Dmin	yes	1.067	668.7	17,841	0.037	334.3
21	CCFT-9-9	9	low	4	20	Dmax	yes	0.996	686.2	5,696	0.120	343.1
22	CCFT-9-11	9	low	4	20	Dmin	yes	1.067	213.5	5,696	0.037	106.7
23	CCFT-9-13	9	low	4	30	Dmax	yes	0.996	1,466.3	12,171	0.120	733.1
24	CCFT-9-15	9	low	4	30	Dmin	yes	1.067	456.2	12,171	0.037	228.1

The seismic base shear, V, is defined as the product of the effective seismic weight, W, and the seismic coefficient, C_s, determined based on the fundamental period, T, in accordance with Section 12.8 of ASCE 7 (ASCE 2010). The effective seismic weight of the building is determined in accordance with Section 12.7.2 of ASCE 7 (ASCE 2010).

The effective seismic weight, W, is the sum of the following:

- 100% of the dead load
- 25% of the warehouse floor live load (which is deemed storage)
- 15.4% of the office floor live load (equivalent to 10 psf for partitions)

Table 4. Nominal and Expected Material Strengths

Material	Nominal Strength (Used for Design)	Expected Strength (Used for Analysis)
Circular HSS (ASTM A500 Gr. B)	F_y = 42 ksi F_u = 58 ksi	F_y = 58.8 ksi F_u = 75.4 ksi
Rectangular HSS (ASTM A500 Gr. B)	F_y = 46 ksi F_u = 58 ksi	F_y = 64.4 ksi F_u = 75.4 ksi
Wide Flange (ASTM A992)	F_y = 50 ksi F_u = 65 ksi	F_y = 55.0 ksi F_u = 71.5 ksi
Reinforcement (ASTM A615)	F_{yr} = 60 ksi F_u = 90 ksi	F_{yr} = 75.0 ksi F_u = 112.5 ksi
Plate (ASTM A572 Gr. 50)	F_y = 50 ksi F_u = 65 ksi	F_y = 55.0 ksi F_u = 78.0 ksi
4 ksi Concrete	f'_c = 4 ksi	f'_c = 5.2 ksi
12 ksi Concrete	f'_c = 12 ksi	f'_c = 13.9 ksi

4. NONLINEAR ANALYSIS MODEL

The nonlinear analysis models consist of beam and zero length elements representing the seismic force resisting frame and nonlinear truss elements representing the destabilizing effect of the remainder of the building that is tributary to the frame. Key details of the model are presented here; full details are presented elsewhere (Denavit 2012).

The beam element used in the model is a distributed plasticity formulation developed specifically for steel-concrete composite frames. The element uses a mixed basis (i.e., using both displacements and forces as primary variables) to allow for accurate modeling of both material and geometric nonlinearities. Fiber sections and uniaxial cyclic constitutive relations are used to model cross section behavior. The concrete and steel material models account for the salient features of each material, as well as the interaction between the two, including concrete confinement and local buckling.

The connection region of special moment frames is modeled as shown in Figure 2. Key components are a rigid link parallelogram model with a rotational spring representing the nonlinear panel zone behavior and elastic beam elements which serve to move the beam plastic hinges to specified locations. Nonlinear beam elements for the columns and beams frame into this connection model. The connecting elements (e.g., split tees as shown in Figure 2) are not explicitly modeled since they are designed to not experience significant deformations, even under large frame deformations.

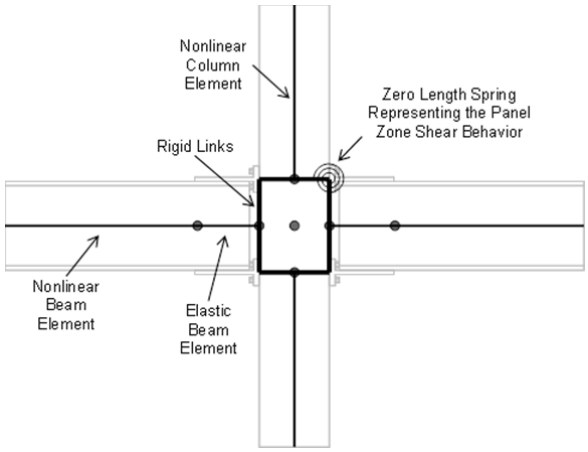


Figure 2. Schematic of the Connection Region of Special Moment Frames

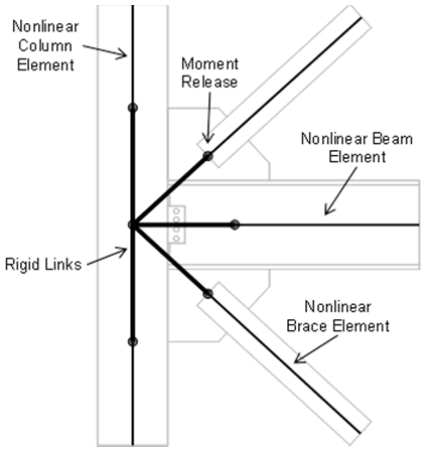


Figure 3. Schematic of the Beam-To-Column Connection Region of Special Concentrically Braced Frames

Connection regions in special concentrically braced frames have large gusset plates that serve to stiffen the connections. Hsiao et al. (2012) developed recommendations for modeling the connection region of steel special concentrically braced frames. A simplified version of the model by Hsiao et al. (2012) is used in this work. The beam-to-column connection region is modeled as shown in Figure 3. Rigid links are used to model the region where the gusset plate stiffens the beam, brace, and column. The length of the rigid link along the column is equal to the distance from the work point to the top of the gusset plate. The length of the rigid link along the brace is equal to the distance from the work point to the physical brace. The length of the rigid link along the beam is equal to the

distance from the work point to column face plus 75% of the distance from the column face to the edge of the gusset plate. The column and beam frame directly into the rigid link whereas a moment release is used between the rigid link and the brace.

The analyses were performed in two-dimensions. The mesh density was selected such that the model was refined enough to obtain accurate results, but not so dense as to introduce the ill-effects of localization. The nominal length of the column elements was one-third of the story height. The nominal length of the girder elements was one-third of the bay width for the C-SMFs and one-fourth of the bay width for the C-SCBFs corresponding to the beam spacing (Figure 1). Three integration points were used for all beam elements. Nominal size of the strips in the fiber discretization was 1/20th of the section depth, with the number of fibers in each component defined based on this fixed ratio and rounded up to the nearest integer.

The braces in the C-SCBFs are assumed to be physically oriented such that weak axis buckling is out-of-plane of the frame. However, in the model the brace is oriented such that weak axis buckling is in-plane to allow for the use of a two-dimensional model. Correspondingly, the moment releases at the brace ends represent the relatively weak out-of-plane rotational strength of the gusset plate.

As prescribed in the methodology (FEMA 2009), prior to application of the lateral load (either static or dynamic), gravity load equal to 105% of the dead load plus 25% of the live load and roof live load was applied and held constant for the remainder of the analysis. All gravity loads were applied as nodal loads based on tributary areas.

The methodology (FEMA 2009) does not explicitly define the mass to be used in the analyses. Thus, mass was assigned to the structure based on the effective seismic weight computed for design. For nodes with gravity load, the two translational DOFs were assigned equal masses equivalent to the dead load plus a percentage of the live load. Additionally, for numerical stability, a minimum nominal mass was assigned to all degrees-of-freedom. The value of the minimum nominal mass was 1×10^{-6} kip-s^2/in for the translational DOFs and 1×10^{-6} kip-in-s^2 for the rotational DOFs. Also for numerical stability, an additional elastic stiffness of EA = 300 and EI = 3000 was added to each brace section (e.g., in the event of significant yielding along the full length of the member). Rayleigh damping was used, defined as 2.5% in the 1st and 3rd modes based on recommendations from the methodology (FEMA 2009).

A summary of the gravity load cases and mass used in both the design and the analysis of the archetype frames is presented in Table 5.

The model accurately captures member plasticity, local buckling, global buckling, and panel zone behavior as demonstrated through validation studies presented elsewhere (Denavit 2012). However, some aspects of behavior and failure modes have not been modeled.

- Fracture is not included in the model. While fracture is expected during structural collapse, this study is not explicitly modeling collapse. Fracture is not anticipated o control the behavior of well-designed C-SMF, where ductile yielding of the beams in flexure is expected to dominate the response, or C-SCBF, where ductile yielding of the braces and buckling of the braces is expected to dominate the response.
- Connection regions are modeled, however, failure or degradation of the connecting elements is not included in these models. Experimental testing has shown that with proper design and detailing the connecting elements inelasticity can be confined to the member.
- In the design of the frames it was assumed that the beams were provided with lateral bracing sufficient to ensure the full plastic moment capacity could be achieved. Correspondingly, lateral torsional buckling was not included in the model

Table 5. Gravity Load and Mass in Design and Analysis

	Design	**Analysis**
Gravity Load	1.4 D 1.2 D + 1.6 L + 0.5L_r 1.2 D + 0.5 L + 1.6L_r etc., including live load reduction Section 2.3 (ASCE 2010)	1.05 D + 0.25 L + 0.25 L_r (FEMA 2009)
Mass	D + 25% storage live load + 10 psf for partitions Section 12.7.2 (ASCE 2010)	Same as for design

5. STATIC PUSHOVER ANALYSES

Static pushover analyses were performed on each frame. Lateral loads were applied at each story in fixed ratios based on the story mass and the mode shape of the structure (FEMA 2009). Thus, an eigenvalue analysis was performed prior to the application of lateral load (but after gravity load was applied). The loading was conducted in displacement control until at least a 20% drop in strength after the peak (V_{80}) was observed. Key results from these analyses include:

- The fundamental period from the model, T_1
- The maximum base shear capacity, V_{max}
- The overstrength factor, $\Omega = V_{max}/V$
- The ultimate roof displacement (i.e., at V_{80}), δ_u
- The effective yield roof drift displacement, $\delta_{y,\text{eff}}$, [Equation 1 (FEMA 2009)]
- The period-based ductility, $\mu_T = \delta_u / \delta_{u,\text{eff}}$

$$\delta_{y,eff} = C_o \frac{V_{max}}{W}\left(\frac{g}{4\pi^2}\right)\left(\max(T, T_1)\right)^2 \qquad (1)$$

where,

C_o = A coefficient based on the fundamental mode shape (FEMA 2009)

5.1 Analysis Results

An example of the results for a three-story C-SMF (RCFT columns, high gravity load, f'_c = 4 ksi, SDC = D_{max}) is shown in Figure 4. Full results are presented elsewhere (Denavit 2012).

For the C-SMFs, an initially linear response is observed followed by gradual stiffness reduction up to the peak lateral capacity of the frame then near linear post peak degradation until the analysis was stopped after at least a 20% drop in capacity was observed. For the 3 story frames an even distribution of deformation is seen among the stories with the exception of the roof story of some frames where lower deformations were observed at the V_{80} level. For the 9 story frames, the distribution of deformation was even among the stories at the design base shear level, however, at the maximum base shear and after a 20% drop in capacity, the deformation was concentrated in ranges of 4 to 6 stories forming a multi-story mechanism (Krishnan and Muto 2012). The story groups where the inelasticity was concentrated were either located at the top, middle, or bottom of the structure. No fundamental behavioral differences were observed between the frames with RCFT columns and those with SRC columns owing to the fact that flexural yielding of the beams controlled the response.

For the C-SCBFs, the response was initially linear, however, in contrast to the C-SMFs, sharp changes in stiffness including drops in capacity were observed in the response corresponding to yielding and buckling of the individual braces. These jumps are exacerbated by the fact that only one bay of bracing was modeled; had multiple bays been included with slightly different loading or material properties, the response would likely have been smoother. Also in contrast to the C-SMFs, for the 3 story frames the deformation was often concentrated into one story. The 9 story frames showed a similar response to the C-SMFs in that multi-story mechanisms were developed where the deformation was concentrated in 4 to 6 consecutive stories.

Conclusions from the results are given in Section 7.1 in the context of evaluating the system overstrength factor.

6. DYNAMIC RESPONSE HISTORY ANALYSES

In the methodology, collapse is assessed in the context of incremental dynamic analyses (IDA) (Vamvatsikos and Cornell 2002). Dynamic response history analyses are performed, subjecting each frame to a suite of ground motions scaled at different intensities. The 44 earthquake ground motions described in the methodology (FEMA 2009) were used for this study.

Explicit modeling of the collapse of structures is a challenging task and the subject of current research (Bažant and Verdure 2007; Khandelwal et al. 2009; McAllister et al. 2012; Szyniszewski and Krauthammer 2012). The FEMA (2009) methodology has avoided the need to explicitly model collapse by defining collapse in the context of incremental dynamic analyses. In incremental dynamic analyses, a frame is analyzed under different ground motions and at different intensities. The resulting curve shows a response value (typically peak story drift) versus an intensity measure. Typical results would show an initially high slope, gradually transitioning to a low slope; however, in practice a wide variety of behavior is seen.

Determination of "collapse" is necessary for the methodology and thus approximate definitions are adopted. In this work, collapse is defined when a prescribed maximum story drift of 10% is observed in the incremental dynamic analysis results. This is an approximate method since collapse is not associated with any particular drift limit (Krawinkler et al. 2003); however, some justification of the 10% limit exists. Generally, little hardening response is seen incremental dynamic analysis results beyond 10% drift. Also, the nonlinear models were not validated for deformations beyond this range and nonlinear effects that are not being modeled directly in this work, such as fracture, lateral torsional buckling, or connection degradation may

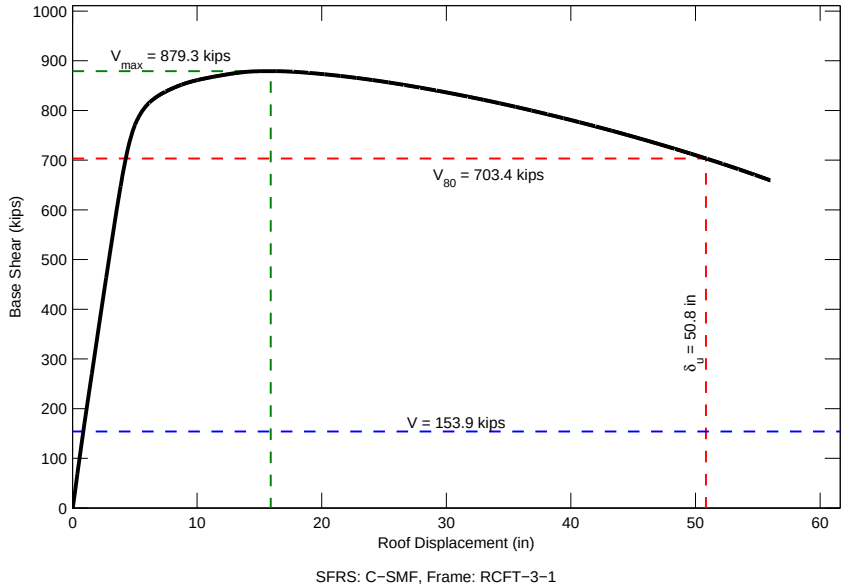


Figure 4. Sample Results of the Static Pushover Analyses

occur at these higher drift levels.

Key results from the dynamic response history analyses include:

- The median collapse intensity, $\hat{S}_{CT}$, determined as the intensity, ST, at which half of the ground motions cause maximum story drifts of greater than 5%
- The collapse margin ratio, CMR = $\hat{S}_{CT}/S_{MT}$ (where S_{MT} is the maximum considered earthquake intensity).

6.1 Analysis Results

An example of the results for the same three-story C-SMF highlighted before is shown in Figure 5. Full results are presented elsewhere (Denavit 2012).

For both the C-SMFs and C-SCBFs, the majority of incremental dynamic analysis curves exhibit the typical response with an initial relatively high slope followed by a relatively low slope at higher intensities. The initial slope of the curves for each frame varies, owing to inherent differences between the 44 ground motions. In general, at the maximum considered earthquake intensity (i.e., $S_T = S_{MT}$), the distribution of story drifts is relatively uniform along the height of the building. An exception is the 9 story C-SCBFs where often the top story exhibits deformations several times greater than that of the other stories.

7. EVALUATION OF SEISMIC PERFORMANCE FACTORS

For the purposes of evaluation, the methodology requires the archetype frames be categorized into performance groups based on the design gravity load level (high or low), design seismic load level (D_{max} or D_{min}), and fundamental period (long or short). Eight performance groups are defined for seismic force resisting system and are used as described below to evaluate each of the seismic performance factors.

7.1 System Overstrength Factor, Ω_o

According to the methodology, the system overstrength factor, Ω_o, should not be taken as less than the largest average value of overstrength, Ω, from any performance group, however, upper limits of 1.5R and 3.0 are applied (FEMA 2009).

For the C-SMFs, the average overstrength for the performance groups ranges from 5.3 (for the performance group with high gravity load, SDC = D_{max}, and long period) to 9.9 (for the performance group with high gravity load, SDC = D_{min}, and long period). These values are quite high and reflect the displacement controlled design of these structures. Other studies on steel special moment frames (NIST 2010) have also shown high overstrength. Several factors have led to the particularly high overstrength values seen in this study. The use of $C_d = R$ in the design of the frames reduced the allowable story drifts thus increasing member sizes. In the model, the plastic hinges were forced to a location 2d/3 away from the column face (where d is the bean section depth). This distance was the assumed length of the connection. Selection of this distance resulted in higher frame strengths as compared to shorter connections. Additionally, reduced beam section connections were not used for these structures; if they had been used, lower overstrength would have been observed. For the results shown, all of the performance groups exceed the practical upper limit of 3.0, so it is recommended that the system overstrength factor remain unchanged from its current value ($\Omega_o = 3.0$).

For the C-SCBFs, the average overstrength for the performance groups ranges from 1.7 (for the performance group with high gravity load, SDC = D_{min}, and short period) to 2.8 (for the performance group with low gravity load, SDC = D_{max}, and short period). These results are in contrast to the C-SMFs where high overstrength was observed and

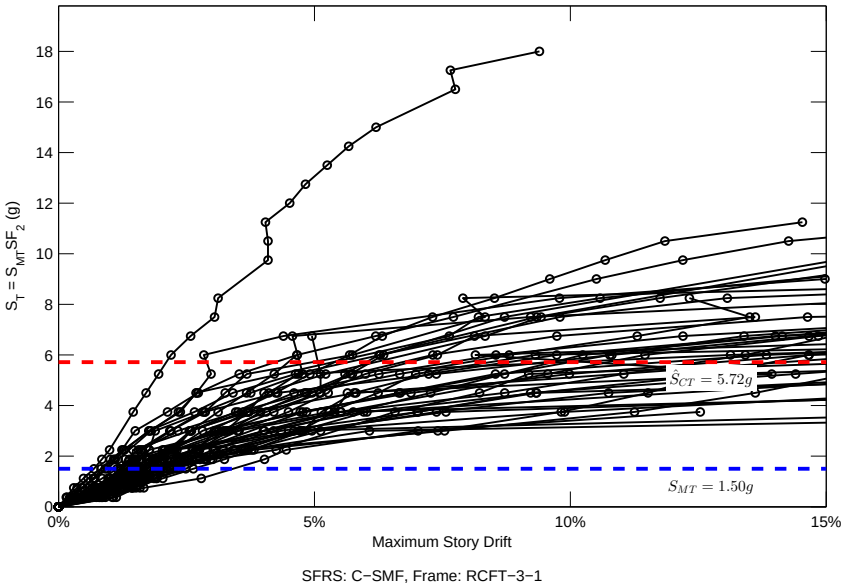


Figure 5. Sample Results of the Dynamic Response History Analyses

reflect the strength controlled design of these structures. Other studies on steel special concentrically frames (NIST 2010) have shown similar overstrength results. In light of these results (some performance groups with overstrength greater than 2.0), an increase the system overstrength factor for C-SCBFs could be warranted, although the current value ($\Omega_o = 2.0$) is likely sufficient.

7.2 Response Modification Factor, *R*

According to the methodology, the response modification factor that was used to design the archetype frames is acceptable if the probability of collapse for maximum considered earthquake ground motions is approximately 20% or less for each index archetype and 10% or less on average for each performance group (FEMA 2009). To evaluate these conditions, adjusted collapse margin ratios are computed and compared against reference values (Equations 2 and 3).

$$ACMR_i \geq ACMR_{20\%} \tag{2}$$

$$\text{mean}\left(ACMR_i\right) \geq ACMR_{10\%} \tag{3}$$

where,

$ACMR_i$ = adjusted collapse margin ratio for each index archetype, *i*

$ACMR_{20\%}$ = acceptable value of the adjusted collapse margin ratio for 20% collapse probability

$ACMR_{10\%}$ = acceptable value of the adjusted collapse margin ratio for 10% collapse probability

The adjusted collapse margin ratio is the product of the collapse margin ratio, *CMR*, as determined from the response history analyses and a spectral shape factor, *SSF*, given in FEMA P695 (2009). The spectral shape factor depends on the fundamental period, *T*, and period based ductility, μ_T, and accounts for the frequency content of the selected ground motion record set.

$$ACMR_i = SSF_i \; CMR_i \tag{4}$$

The acceptable values of the adjusted collapse margin ratio are derived from the lognormal distribution and depend on the desired collapse probability (10% or 20%) and a measure of the total system collapse uncertainty (expressed as β_{total}). Uncertainty in the system collapse assessment comes from a number of sources. Uncertainty due to the variability between ground motions records is characterized by β_{RTR} [Equation 5 (FEMA 2009)]

$$\beta_{RTR} = 0.1 + 0.1\mu_T \leq 0.4 \tag{5}$$

Uncertainty in the design requirements, test data, and nonlinear modeling are characterized by qualitative quality ratings as will be described.

For both of systems, the design requirements have been well-vetted and provide extensive safeguards against unanticipated failure modes. The hierarchy of yielding and failure of components is well established. However, construction practices are comparatively less mature than for either structural steel or reinforced concrete structures. For these reasons, a quality rating of good (B) is given to the design requirements for both C-SMFs and C-SCBFs.

Numerous tests on composite members, connections, and frames have been conducted and reported in the literature. The tests span most of the important parameters which affect design requirements and the behavior is generally well understood. For these reasons, a quality rating of good (B) is given to the test data for both C-SMFs and C-SCBFs.

The nonlinear models directly simulate all predominate inelastic effects and have been extensively validated against experimental results. The sets of archetype frames provide a reasonably broad representation of the design space. However, fracture is not included in the modeling and the frames were assumed to be properly designed to preclude connection deterioration and lateral torsional buckling. For these reasons, a quality rating of good (B) is given to the nonlinear modeling for both C-SMFs and C-SCBFs.

The quality ratings are assigned lognormal standard deviation parameters [Table 6, (FEMA 2009)] and the total system collapse uncertainty is computed with Equation 6 then rounded to the nearest 0.025. The value depends on the period based ductility but is constant for $\mu_T \geq 3$. For both systems the value of β_{total} for $\mu_T \geq 3$ is 0.525.

$$\beta_{total} = \sqrt{\beta_{RTR}^2 + \beta_{DR}^2 + \beta_{TD}^2 + \beta_{MDL}^2} \tag{6}$$

Table 6. Quality Ratings

System	Quality of Design Requirements	Quality of Test Data	Quality of Nonlinear Modeling
C-SMF	B (Good) $\beta_{DR} = 0.2$	B (Good) $\beta_{TD} = 0.2$	B (Good) $\beta_{MDL} = 0.2$
C-SCBF	B (Good) $\beta_{DR} = 0.2$	B (Good) $\beta_{TD} = 0.2$	B (Good) $\beta_{MDL} = 0.2$

For the C-SMFs, all of the evaluations pass and thus the current response modification factor is deemed acceptable. In fact, all frames pass by a significant margin. Many of the IDA curves retain a significant positive slope even at the high levels of earthquake ground motion used in this study (up to 5-7 times maximum considered earthquake intensity). This is indicative of the excellent performance of C-SMFs subjected to earthquake ground motions. For the C-SCBFs, all of the evaluations pass and thus the current response modification factor is deemed acceptable. The margin of passing is not as great as for the C-SMFs, nonetheless, the C-SCBFs exhibit excellent performance. It should be noted that these results are only strictly applicable to well designed and detailed frames where connection deterioration will not occur and sufficient lateral bracing is provided.

7.3 Deflection Amplification Factor, C_d

According to the methodology, for systems with typical levels of damping, including the systems studied here, the deflection amplification factor, C_d, is equal to the response modification factor (FEMA 2009). For C-SCBFs this represents a minor change as the current difference between R and C_d is small and there structures are typically not displacement controlled. For C-SMFs this represents a significant change. Setting $C_d = R$ results in a 45% increase in C_d from the current value. Additionally, C_d plays a central role in the design of moment frames since they are often displacement controlled.

In this study, four frames were designed with the current C_d value. These frames had smaller members than their counterparts designed with $C_d = R = 8.0$. Some differences in performance were noted. The average overstrength of the frames designed with the current C_d was 4.9 while it was 6.4 for their counterparts. The average adjusted collapse margin ratio of the frames designed with the current C_d was 5.5 while it was 6.2 for their counterparts. These results indicate that the frames designed with the current C_d value have acceptable performance and that setting $C_d = R$ for this system is unnecessary from a safety perspective.

All in all, further study is needed to determine the ramifications of setting $C_d = R$ and whether such a change is necessary. Further study should include the possibility of a corresponding increase in the deformation limits should the C_d factor increase,

8. CONCLUSIONS

A study was conducted following recommendations in FEMA P695 (2009) to determine the seismic performance factors (i.e., R, C_d, and Ω_o) for composite special moment frames (C-SMF) and composite special concentrically braced frames (C-SCBF). A suite of 60 archetype frames was selected and designed according to current design specifications. Nonlinear static pushover analyses and dynamic response history analyses were performed on the frames to characterize the behavior and generate statistical data to be used in evaluation of the seismic performance factors. Both systems exhibited excellent seismic behavior and current seismic performance factors were found to be acceptable. In particular, it was noted that frames designed with the current deflection amplification factor, C_d, were found to be acceptable and thus a potential change to set $C_d = R$ should be studied further and perhaps accompanied by a corresponding change to the drift limits such that future seismic drift requirements are equivalent to the current seismic drift requirements.

Acknowledgements:

This material is based upon work supported by the National Science Foundation under Grant Nos. CMMI-0619047 and CMMI-0530756 as part of the George E. Brown, Jr. Network for Earthquake Engineering Simulation (NEES); the American Institute of Steel Construction; the Georgia Institute of Technology; and the University of Illinois at Urbana-Champaign. Computational analyses in this work were executed in part on the Extreme Science and Engineering Discovery Environment (XSEDE), which is supported by National Science Foundation Grant No. OCI-1053575. Any opinions, findings, and conclusions expressed in this material are those of the authors and do not necessarily reflect the views of the National Science Foundation or other sponsors.

References:

ACI. (2011). *Building Code Requirements for Structural Concrete and Commentary*. American Concrete Institute, Farmington Hills, MI.

AISC. (2010). *Seismic Provisions for Structural Steel Buildings*. American Institute of Steel Construction, Chicago, Illinois.

ASCE. (2010). *Minimum Design Loads for Buildings and Other Structures*. American Society of Civil Engineers, Reston, Virginia.

Bažant, Z. P., and Verdure, M. (2007). "Mechanics of Progressive Collapse: Learning from World Trade Center and Building Demolitions." *Journal of Engineering Mechanics*, 133(3), 308–319.

Denavit, M. D. (2012). "Characterization of Behavior of Steel-Concrete Composite Members and Frames with Applications for Design." Ph.D. Dissertation, University of Illinois at Urbana-Champaign, Urbana, Illinois.

FEMA. (2009). *Quantification of Building Seismic Performance Factors*. FEMA P695, Federal Emergency Management Agency, Washington, D.C.

Hsiao, P.-C., Lehman, D. E., and Roeder, C. W. (2012). "Improved Analytical Model for Special Concentrically Braced Frames." *Journal of Constructional Steel Research*, 73, 80–94.

Khandelwal, K., El-Tawil, S., and Sadek, F. (2009). "Progressive Collapse Analysis of Seismically Designed Steel Braced Frames." *Journal of Constructional Steel Research*, 65(3), 699–708.

Krawinkler, H., Medina, R., and Alavi, B. (2003). "Seismic Drift and Ductility Demands and their Dependence on Ground Motions." *Engineering Structures*, 25(5), 637–653.

Krishnan, S., and Muto, M. (2012). "Mechanism of Collapse of Tall Steel Moment Frame Buildings under Earthquake Excitation." *Journal of Structural Engineering*, ASCE, 138(11), 1361–1387.

McAllister, T., MacNeill, R., Erbay, O., Sarawit, A., Zarghamee, M., Kirkpatrick, S., and Gross, J. (2012). "Analysis of Structural Response of WTC 7 to Fire and Sequential Failures Leading to Collapse." *Journal of Structural Engineering*, ASCE, 138(1), 109–117.

NIST. (2010). *Evaluation of the FEMA P-695 Methodology for Quantification of Building Seismic Performance Factors*. National Institute of Standards and Technology, Gaithersburg, Maryland.

Szyniszewski, S., and Krauthammer, T. (2012). "Energy Flow in Progressive Collapse of Steel Framed Buildings." *Engineering Structures*, 42, 142–153.

Vamvatsikos, D., and Cornell, C. A. (2002). "Incremental Dynamic Analysis." *Earthquake Engineering & Structural Dynamics*, 31(3), 491–514.

10CUEE CONFERENCE PROCEEDINGS
10th International Conference on Urban Earthquake Engineering
March 1-2, 2013, Tokyo Institute of Technology, Tokyo, Japan

EVALUATION OF SEISMIC VULNERABLE AREAS IN LIMA CITY BY USING SATELLITE INFORMATION

Miguel Estrada[1], Masashi Matsuoka[2], and Hiroyuki Miura[3]

1) Associate Professor, Faculty of Civil Engineering, National University of Engineering, Peru
2) Associate Professor, Department of Built Environment, Tokyo Institute of Technology, Japan
3) Associate Professor, Faculty of Engineering, Hiroshima University, Japan
estrada@uni.edu.pe, matsuoka.m.ab@m.titech.ac.jp, hmiura@hiroshima-u.ac.jp

Abstract: Within the project Enhancement of Earthquake and Tsunami Disaster Mitigation Technology in Peru, one of the objectives is to know the most vulnerable areas in the event of a big earthquake. In Lima, the capital city of the Peru, for many years has become the destination of inhabitants of the interior of the country, which has led to use unsuitable terrain areas as for example the slopes of the hills. This disorderly development has caused that the cadastral maps are not updated and therefore the extension occupied by these populations cannot be quantified. This article presents the use and integration of two sources of satellite information for the determination of vulnerable areas in the city of Lima, high resolution optical satellite images and images from PRISM sensor, which allows getting the digital elevation model. With this integration, it is possible to delineate and evaluate the likely areas of urban concentration in areas of threat. Also it is carried out the integration with social information obtained from national census in order to determine the homes of people with low economic resources that occupy this type of land.

1. INTRODUCTION

It is well known that seismic activity in Peru is very high, due to its location in the circum-Pacific seismic belt, therefore, the evaluation of the building vulnerability it very important issue to prevent and mitigate the effects of an eventual occurrence of an earthquake. In Peru the development of cities is carry out, in many cases, without development planning projects, people from the countryside that comes to the capital city, looking for better live conditions, settles where they can, and this situation generates two big problems: first, they occupy land that are inadequate for construction of buildings, like soils with incompetent conditions as soils with low load capacity or they occupy the hillside surrounding the city. On the other hand, those peoples build their houses as they can, using low quality materials and without any technical direction. Therefore, these non-engineered buildings located in non-suitable locations, makes them very vulnerable structures in the case of an earthquake, thus their identification is very important for local authorities to make preparedness and mitigation plans.

Other problem to be faced is the lack of cadastral and topographic information that do not allow to make a building inventory and thus to evaluate the building seismic vulnerability (Estrada et. al., 2012). Therefore, it is necessary to use a technology that allows the identification of populated areas, especially those that are occupied on the hillside.

Additionally to the physical information, another type of data is the social one. The social information allows to know the economic situation of the building owner and thus to infer the quality and condition of the building.

In this paper it is proposed the use of PRISM sensor imagery to determine the location of those populated placed on hillsides and with the census data added to complement the study of the vulnerability.

2. PRESENT SITUATION

2.1 Study area

The study area is located in Lima, the capital city of Peru. Lima city is politically divided in 43 districts; one of them is Comas district. This district has a growing population of more of less half a million people, and the flat area of the district is already densely occupied, this is the reason that the hillsides are being populated rapidly, therefore the evaluation of these areas are necessary. Figure 1 shows the location of the study area. There it can be seen that the flat area is already populated and the growth of the city is towards the hills.

Figure 2, shows the conditions of the buildings built on the hillsides. It can be appreciated the informality of buildings and poor building practices, like building their houses on land fill, to accommodate to the topography of the land. This situation generates a highly risky area in case of

the occurrence of a severe earthquake.

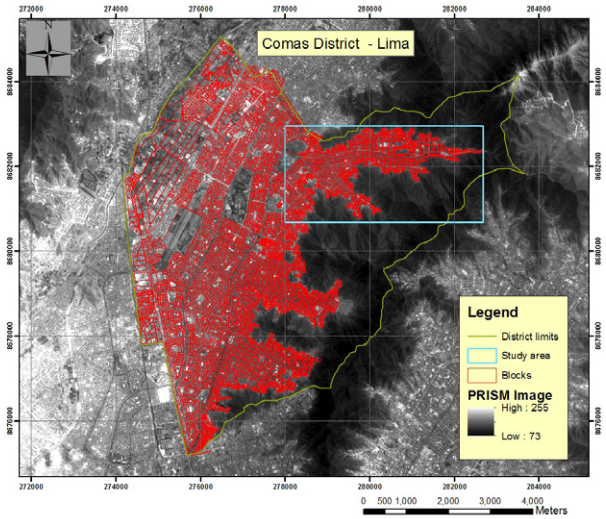


Figure 1 Map of the Comas District and selected study area.



Figure 2 Photograph of the condition of the buildings on the hillsides.

2.1 Cadastral Information

In 2007 the National Institute of Statistics and Informatics (INEI) carried out the National Census 2007: XI of population and VI of Housing (INEI, 2007). The information is aggregated in each block from where it is extracted the following information, within the study area, shown in Table 1:

Table 1. Census data of the study area.

Description	Value
Number of blocks	1016
Average number of houses per block	22
Total number of houses	14374
Total number of habitants	77900
Average Number of habitants per house	5.42

As it can be seen in Table 1, the density of habitants in each house is relativity high, this situation makes this area a highly risk one in case of a severe earthquake.

Besides of the population density, another important factor if the social class of the people. The social class is a good indicator of the quality of the building where the people live. It is obvious that well accommodated people lives in houses well constructed, while low income people construct their houses as they can and as they want, making these non-engineered buildings very vulnerable against seismic forces.

Information about social classes is shown in Table 2. As it can be seen mainly the population in this area is represented for low and middle low social class people, being almost 90% of the total number of blocks with information.

Table 2. Type of social class from census data.

Socioeconomic level	Number of blocks
Low	289
Middle low	474
Middle	82
Middle high	4
High	0
No Data	167

Another important parameter to evaluate the vulnerability of buildings is the material used in the construction. Table 3 shows the number of houses built with the different material used in this area:

Table 3. Type of social class from census data.

Material	Number of houses
Masonry	11200
Adobe	101
Wood	1979
Quincha (bamboo with wood frame)	17
Bamboo	446
Other/No Data	631

As it can be seen in this table, the main material used for construction is masonry, but even the masonry is a good material for construction the quality of the construction process is the problem, since the people built their houses by themselves, without any technical direction, these houses do not accomplish the requirements of national code, therefore their vulnerability is very high.

The presented tables show statistical values of the social condition of the people that live in this area. This is a high density populated area that is under developing with problems that make this area very vulnerable in case of an occurrence of an earthquake. Mainly there are two big problems the self-construction of the houses and the bad soil condition, as it can be seen in Figure 2. The topography of the area is very rugged and the uneven soil forces people to build their houses on landfill. Therefore, it is necessary to evaluate the topography of the area to determine the occupied land with important value of slope.

3. UMBRELLA PROJECT

This research is under the project "Enhancement of Earthquake and Tsunami Disaster Mitigation Technology in Peru". Generally speaking, the purpose of this project is to developed technologies and measures for prediction and mitigation of earthquake/tsunami disasters caused by large-magnitude inter-plate earthquakes occurring off the coast of Peru (Yamazaki et. al., 2012)

This project is divided into five active groups. Group 1, researches on seismology and geotechnical issues, and give the final response of the soils, like probable peak ground acceleration. Group 2, studies the source, effects and countermeasures of tsunamis produced by an earthquake, mainly the output is the travel time and high of the tsunami waves to evaluate the possible damage in the affected area. Group 3, identifies the most typical building problems and will propose retrofitting methods or will give some advises to improve the actual building code. Group 4, will develop methodologies to identify the land use, by using the satellite imagery and integrating all the information in a GIS platform to assess the risk of the building as well as to develop a methodology for fast assessment of the damaged area by an earthquake or tsunami. Finally, Group 5 will take the entire group's output and will disseminate this knowledge and propose policies for a sustainable development of the population. This project is under the support of Japan International Cooperation Agency (JICA), Japan Science and Technology Agency (JST) and Peruvian International Cooperation Agency (APCI). The institutions directly involved in this project are Chiba University, Tohoku University, Building Research Institute, Yokohama University, Tokyo Institute of Technology, Tsukuba University and Kyoto University, from the Japanese side and the Japan Peru Center for Earthquake Engineering Research and Disaster Mitigation (CISMID), Hydrograph National Direction (DHN), Geophysics Institute of Peruvian (IGP), Ministry of Construction, Housing and Sanitation, National Commission of Aerospace Research and Development (CONIDA), National Institution of Civil Defense and National Center of Assessment, Prevention and Mitigation of risk Disasters (CENEPRED).

Within this project is Group 4 who is in charge of developing methodologies to assess the vulnerability in Lima by using geo-informatics technologies.

4. SATELLITE IMAGERY INFORMATION

The original images come from the Panchromatic Remote Sensing Instrument for Stereo Mapping (PRISM) sensor that is one of the three sensors that are on board of the Advanced Land Observing Satellite (ALOS). The capability of this sensor to generate three dimensional models, comes from the simultaneous acquisition from three optical systems, as shown in Figure 3 (Pasco Corp. 2013). The general characteristics of this sensor are shown in Table **4**.

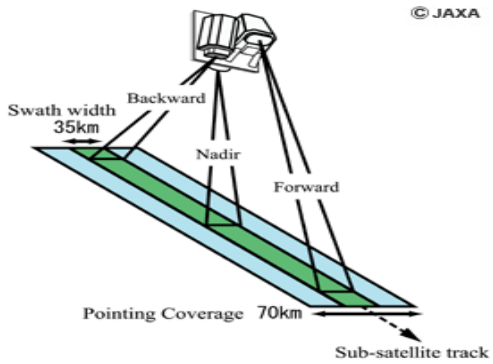


Figure 3 Schematic view of PRISM sensor, with three optical systems: nadir, forward and backward. Source: http://en.alos-pasco.com/common/images/prism2.gif

Table 4. Main characteristics of PRISM sensor.

Description	Value
Number of bans	1
Wavelength	0.52 – 0.77 µm
Number of optics	3: nadir, forward, backward
Ground resolution	2.5 m (nadir view)
Swath	70 km

Source: http://en.alos-pasco.com/alos/prism/index.html

The raw PRISM satellite images are processed to obtain two kinds of images: First the digital Surface Model (DSM) and the panchromatic image, as shown in Figure 4.

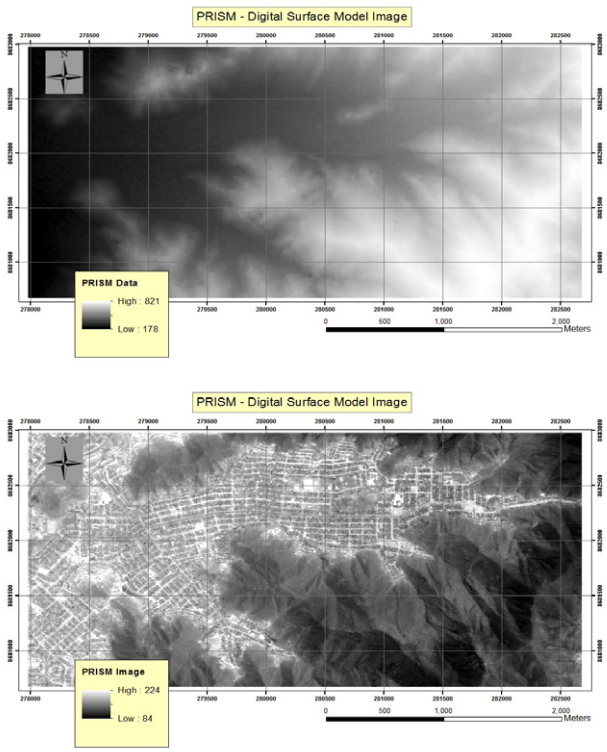


Figure 4 PRISM digital Surface Model and panchromatic image.

Since the cadastral information is not updated and since

the idea is to generate actual risk map it is used another type of optical satellite image, the WorldView-2. The characteristics of this image are shown in Table 5.

Table 5. Main characteristics of WorldView-2 sensor.

Description	Value
Number of bans (MS – P)	8 - 1
Wavelength	0.427 – 0.908µm MS, 0.632 µm P
Spatial resolution	2.0 m MS/0.5 m PAN
Swath	70 km
Acquisition date	10 April 2010

Source: https://www.digitalglobe.com/

The raw WorldView-2 image is pansharpened by using Gram-Schmidt Spectral Sharpening (ENVI program) to take advantage of the spectral information of the bands. Then this image is georeferenced to geographically match the block layer. The WorldView-2 image is shown in Figure 5.

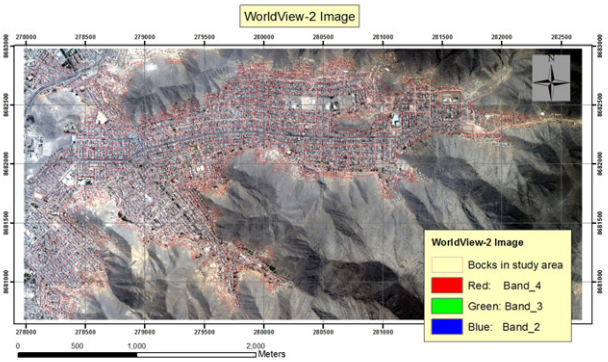


Figure 5 WorldView-2 pansharpened image integrated with blocks layer.

5. EVALUATION OF VULNERABLE AREAS

Once the images have been georeferenced with the block layer the next step is the integration of three sources of information: digital surface model, the high resolution image and the census data. Figure 6 shows the integration of these three sources:

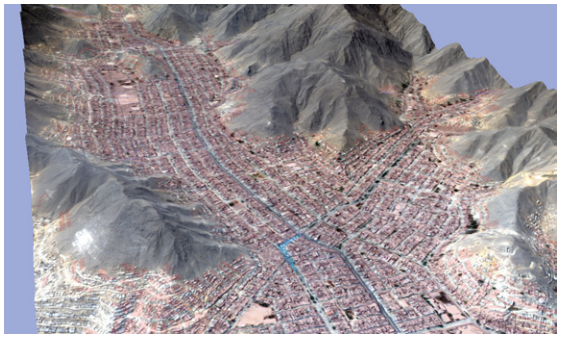


Figure 6 Integration of cadastral information, high resolution satellite image and digital surface model.

Next step is to calculate the percent of slope or gradient of the terrain in the study area. This is carried out by comparing the rate change of pixel values of the DSM image in the horizontal and vertical directions (ArcGIS Slope tool).

The result of the slope analysis is shown in Figure 7.

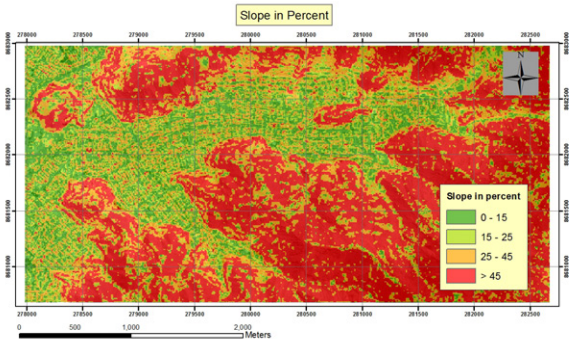


Figure 7 Slope map obtained from the DSM raster image.

Finally, this raster image that represents the slope is converted into point data, where the point value is the slope in percent. Then this point layer is aggregated into the block layer, given to each block an average of the slope. The map showing the slope in the block is shown in Figure 8.

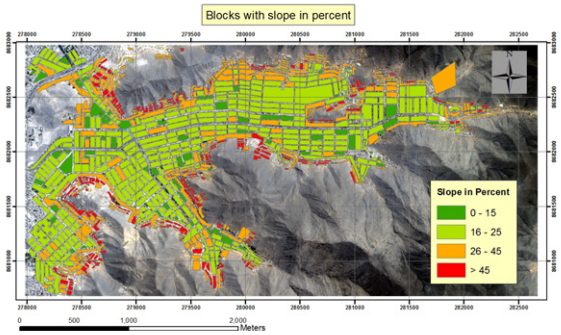


Figure 8 Percent slope integrated in the block layer.

As it can be seen those blocks that are on the hillside have been identify in red and orange color. Those blocks are settled in a land with an important slope that may produce slides in case of an earthquake and therefore people may be affected by this disaster.

6. CONCLUSIONS

The social vulnerability is very related with the social condition of the people.

It has been identified the location of low income people in the hillside that may produce a big loss in case of occurrence of an earthquake.

This proposed methodology may be used to make prevention plans to mitigate the effects of an earthquake.

Acknowledgements:

The authors would like to express their sincere gratitude to the Japan Science and Technology Agency (JST) Japan International Cooperation Agency (JICA) under the SATREPS project "Enhancement of Earthquake and Tsunami Disaster Mitigation Technology in Peru".

References:

Instituto Nacional de Estadística e Informática (2007), "Censos Nacionales 2007" INEI, Lima, Peru

Estrada, M., Miura, H., Yamazaki, F. and Midorikawa, S. (2012) "Evaluation of Social Seismic Vulnerability through High Resolution Satellite Imagery" *Proceedings of the 15th World Conference on Earthquake Engineering*

Yamazaki, F., et. al (2012) "Progress of JST-JICA Project on Earthquake and Tsunami Disaster Mitigation in Peru" *Proceedings of the 15th World Conference on Earthquake Engineering*.

10CUEE CONFERENCE PROCEEDINGS
10th International Conference on Urban Earthquake Engineering
March 1-2, 2013, Tokyo Institute of Technology, Tokyo, Japan

DEVELOPMENT OF HEURISTIC SEISMIC VULNERABILITY CURVES OF KEY BUILDING TYPES IN THE PHILIPPINES

Eric Augustus Tingatinga[1], Benito Pacheco[2], Jaime Hernandez, Jr[3], Ulpiano Ignacio[2], Fernando Germar[3], Romeo Eliezer Longalong[4], William Mata[4], Marie Claire Pascua[4], Raniel Suiza[4], Liezl Raissa Tan[4]

1) Assistant Professor, Institute of Civil Engineering, University of the Philippines Diliman, Philippines
2) Professor, Institute of Civil Engineering, University of the Philippines Diliman, Philippines
3) Associate Professor, Institute of Civil Engineering, University of the Philippines Diliman, Philippines
4) Instructor, Institute of Civil Engineering, University of the Philippines Diliman, Philippines
eating@up.edu.ph, riskguide101@up.edu.ph, jnjhernandezjr@gmail.com, rulongalong@gmail.com

Abstract: For the past decade, several efforts were made by different government and private institutions to develop vulnerability curves of key building types in the Philippines using empirical, heuristic, and/or computational methods. This paper presents the recent development of seismic vulnerability curves of buildings based on experts' opinion. A building typological system in terms of structural type and materials used in construction was proposed and a paper survey was conducted where experts input for different levels of earthquake intensity the damage ratio of each building type. Analyses revealed that there is a very low correlation between number of years of experience and the confidence level of the respondents. Results also show that the heuristic vulnerability curves of low- and mid-rise buildings are similar for both concrete and steel types. Moreover, seismic vulnerability of buildings, according to specialists, is dictated by the material used in construction rather than the number of floors of a building.

1. INTRODUCTION

The Philippines, because of its geographic location, has been the onslaught of natural hazards including earthquakes. According to the Philippine Institute of Volcanology and Seismology (PHIVOLCS), 90 destructive earthquakes have occurred in the Philippines from 1608 to 2002. The most recent destructive earthquake, the 1990 Luzon earthquake (M7.8), killed 1,283 people and caused an estimate of PhP 12.2 Billion on losses to human lives and properties (PHIVOLCS 2002). If a destructive earthquake is to happen again in the future, buildings and other structures are at risk and damage of these structures will definitely cause human lives, businesses and livelihood. According to the Metropolitan Manila Earthquake Impact Reduction Study (MMEIRS) by JICA, PHIVOLCS and MMDA, a magnitude 7.2 earthquake may hit the Marikina Valley Fault and this will affect Metro Manila (JICA 2004).

Part of the preparation of an earthquake disaster mitigation plan is the quantification of building vulnerability. A component of which is the development of seismic vulnerability curves that are used to predict the damage ratio of a particular building type for a given level of peak ground motion.

PHIVOLCS developed a software called Rapid Earthquake Damage Assessment System (REDAS) that aims to produce seismic hazard maps and seismic loss estimate maps minutes after the occurrence of a potentially damaging earthquake. PHIVOLCS-DOST is currently implementing a collaborative project with the Geoscience Australia (GA) and the University of the Philippines Diliman through the Institute of Civil Engineering (UPD-ICE) that aims to enhance the risk assessment capability of REDAS software. Building vulnerability functions and exposure data will be built in the software allowing users to assess the level of damage to building structures due to the occurrence of a potentially damaging earthquake.

Seismic vulnerability curves are used to describe the performance of a building type subjected to earthquake excitations in probabilistic terms. The main approaches in developing these curves are empirical, computational, and heuristic method. Post-earthquake data are the main source of empirical approach while computational approach utilizes computer simulations and analysis. Heuristic approach is conducted through collection of experts' opinion on structural response of buildings subjected to earthquake. Any combination of the aforementioned approaches is referred to as hybrid.

The vulnerability curve is a standard lognormal cumulative probability distribution function (Giovinazzi et.al. 2002, Saidi et.al., 2009, Pacheco et.al., 2012) of the form

$$DR[MMI] = \Phi\left[\frac{1}{\beta}\ln\left(\frac{MMI}{\mu}\right)\right] \quad (1)$$

Table 1. Key Building Types According to Structural Type, Material, Number of Floors and Year of Construction

Material	Type	Sub-type	Structural Type or Description	Year of Construction		
				Pre-1972	1972-1992	Post-1992
WOOD	W1*	W1-L	Wood frame with area ≤ 500 sq.m. (1-2		√	
	W3	W3-L	Bamboo (1-2 storeys)		√	
	N	N-L	Makeshift (1-2 storeys)		√	
MASONRY	CHB	CHB-L	Concrete hollow blocks (1-2 storeys)		√	
	URM*	URM-L	Unreinforced masonry (1-2 storeys)		√	
CONCRETE	C1*	C1-L	Concrete moment frame (1-2 storeys)		√	
		C1-M	Concrete moment frame (3-7 storeys)	√	√	√
STEEL	S1*	S1-L	Steel moment frame (1-2 storeys)	√	√	√
		S1-M	Steel moment frame (3-7 storeys)	√	√	√

* with similar counterpart model building archetypes in HAZUS-MH and FEMA-178.

where

$DR[MMI]$ is the damage ratio of a building type for the given MMI

Φ is the standard normal cumulative distribution function

β is the standard deviation of the natural logarithm of MMI which will be referred in this text as *uncertainty* or simply beta

μ as the *median* value of MMI

This paper presents vulnerability curves derived using the heuristic approach of low- to mid-rise buildings in the Philippines. A survey is conducted where participating engineers, herein referred to as *specialists*, decide on damage distributions of different structural types. The proposed heuristic approach is not susceptible to scarcity of data, as long as the specialists' experience could provide reasonable damage estimates.

1.1 Building Typology

Prior to developing vulnerability curves, a typological system for classifying/grouping existing buildings in terms of structural type, building materials used for construction, number of floors and year of construction must first be adopted. Table 1 lists the key buildings types considered in this paper with their respective descriptions. These types are the most common building types found in the country.

The codes attached to each sub-type in Table 1 denotes the height of the structure whether it is low-rise (L, 1-2 storeys), mid-rise (M, 3-7 storeys). Also included in the naming convention shown in the table are the vintages of the structures with respect to the year of publication of the different editions of the National Structural Code of the Philippines (NSCP). This classification is currently being used by UPD-ICE in the development of vulnerability functions (UPD-ICE, 2011).

2. METHODOLOGY

2.1 Survey of specialists' opinion

Paper surveys were conducted in two separate venues where a total of thirty-eight (38) specialists gather during a summit and a seminar. A survey form was distributed to gather information such as designation, specialization, and years of experience in addition to the damage ratios corresponding to five points in the vulnerability curve of a particular building type and their associated confidence level. In this paper, damage ratio is defined as the ratio of the cost of damage to the replacement cost of the building and finishes, on a scale of 0 to 1 (or 0 to 100%).

Survey forms revealed that the participating engineers specialize in design of low-rise reinforced concrete (RC) and steel structures with some indicating experience in high-rise buildings and few are affiliated with academic institutions. Number of years of experience varied from 1-2 years to 35 years.

2.2 Analysis and Filtering of Data

The first step was done to examine the responses of the specialist for purposes of filtering the available data. Sample responses are plotted (as damage ratio versus MMI) in Fig. 1. This figure implies that the respondents indicated the following relative vulnerability:

masonry < wood < concrete < steel

with buildings made of masonry being the most vulnerable, and steel types being most resilient to earthquakes. The figure also demonstrate the need to filer data such that a particular set of damage ratios for a building type should not be used when they are either incomplete or indicating a trend inconsistent with observed damage to past earthquakes (e.g., decreasing damage ratio as intensity increases).

2.2 Controlling Parameters

Specialization, numbers of years of experience, and confidence level are important fields that need to be specified in the survey. While most respondents indicated specialization in concrete and steel building types, their responses are considered for non-engineered types such as wood and masonry. The declared number of years of experience is assumed to be the same as the duration of the actual experience in the specified specialization even though some specialists may have indicated total number of years in the civil engineering profession. The confidence level (in percent) specified for each set of damage ratios of a given building type is a self-assessment which is influenced by

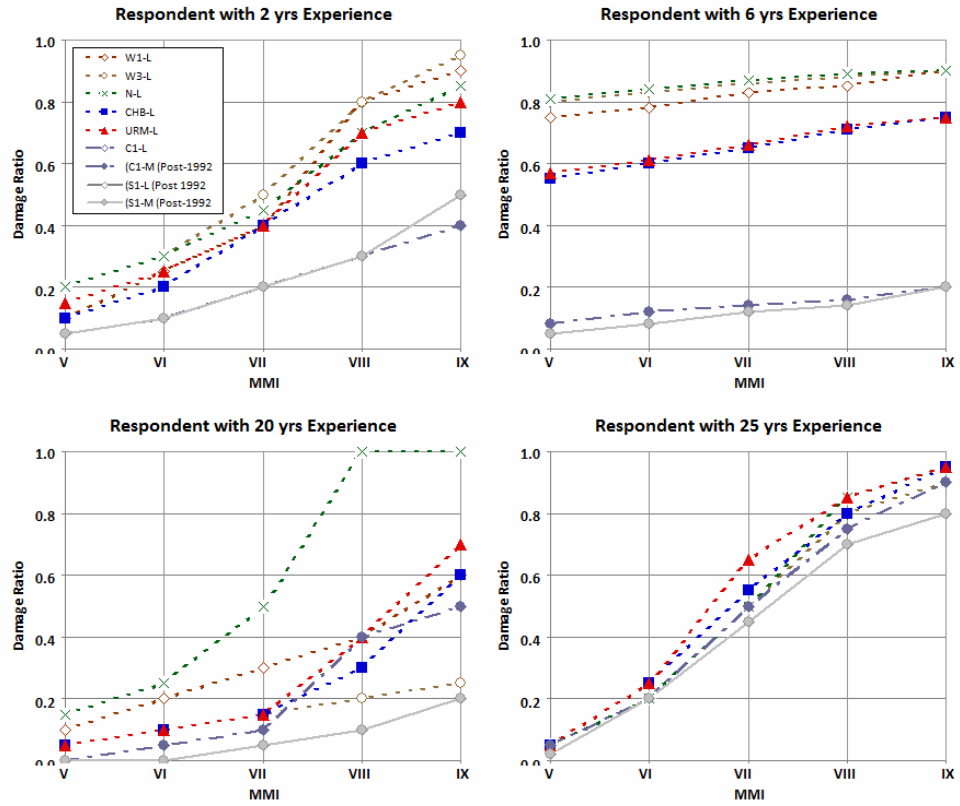


Figure 1. Assigned damage ratios of key building types to different earthquake intensities by specialists of varying number of years of experience

experience, expertise and many other personal factors. It is instructive, therefore, to see any correlation between number of years of experience and confidence level. The responses of 15 (out of 38) respondents in one survey showed that there is no apparent correlation between confidence level and number of years of experience. This is depicted in Fig. 2.

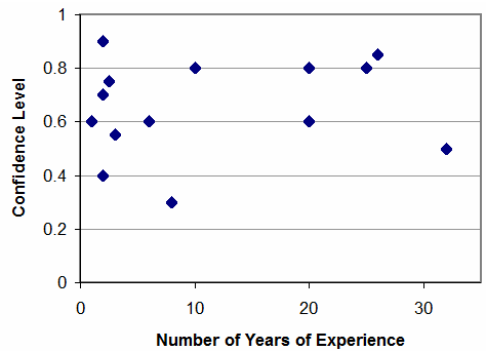


Figure 2. Confidence Level Versus Number of Years of Experience for C1-L.

Because of the subjectivity of the confidence level specified by specialists, the number of years of experience will be used as weights to the assigned damage ratios in developing the vulnerability curve of a specific building type. Table 2 lists the assigned weights for the indicated ranges of years of experience.

Table 2. Assigned Weights Associated with Number of Years of Experience

Years Experience	Weight
1-4	1
5-10	2
11-20	3
>20	4

2.3 Vulnerability Curve Development

For a given building type, the vulnerability curve is developed by first computing the weighted mean of responses for damage ratio using the number of years of experience and weights listed in Table 2 at the given ground motion intensities. The two parameters defining the lognormal vulnerability curve, median and uncertainty in Eq. (1), are then determined using curve fitting methods or choosing the parameters such that the coefficient of determination approach the value of 1, e.g., using Solver add-in in Microsoft Excel.

3. RESULTS AND DISCUSSIONS

Using the method discussed above, the vulnerability curve of W1-L is derived and shown in Fig. 3. The raw responses from the survey are plotted in this figure using gray circular markers and the corresponding median for

intensities IV to IX are shown as red diamond markers. The vulnerability curve fitted to these median points, shown as dotted black line, is a good representative curve for this type considering the large scatter of responses for each of the given intensity. The scatter such as damage ratio ranging from 10% to 100% at intensity VII, may be due to either i.) respondents specialize in concrete and/or steel building types or ii.) the performance of non-engineered houses to earthquakes are not known well by the specialist.

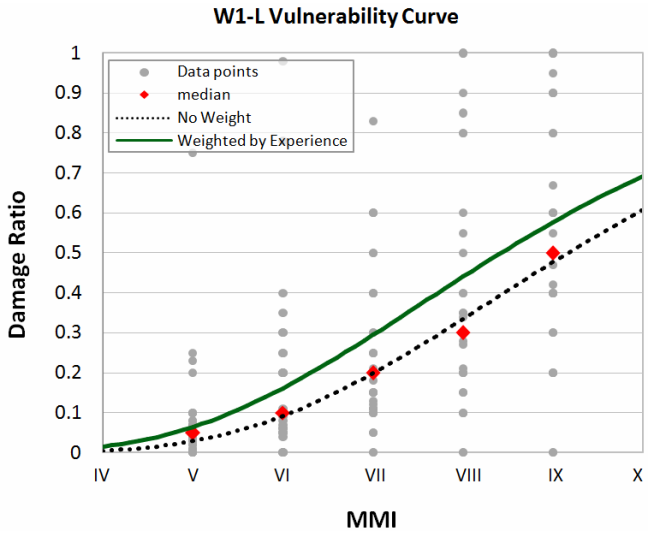


Figure 3. Sample Derivation of Vulnerability Curve of W1-L

The heuristic vulnerability curve of W1-L building type is shown in Fig. 3 as the solid green lognormal curve. With the responses weighted by number of years of experience, the curve shifted to the left (or above) of the curve fitted to the median responses. This implies that experienced engineers tend to classify buildings as being more vulnerable to earthquakes than young engineers. Similar trend was also observed in the other building types.

3.1 Vulnerability Curve of Non-engineered Types

The heuristic vulnerability curves of non-engineered building types made of wood (including W1-L) and masonry are shown with the lognormal parameters in Fig. 4. These curves were derived using survey responses weighted by number of years of experience even though similar trends were observed on the scatter of responses and the effect of taking into account experience.

As expected from the responses, the participating specialists appear to have difficulty differentiating earthquake vulnerability of different building types made of the same material resulting into almost similar curves for W1-L and W3-L as well as CHB and URM. As suggested by Fig. 4, makeshift buildings are as vulnerable as masonry building types. This may be due the fact that these buildings are either light or do not follow some kind of building code.

3.2 Vulnerability Curves of Key Concrete and Steel Building Types

The heuristic vulnerability curves of concrete and steel building types are shown in Fig. 5 with the lognormal parameters listed and derived from the responses weighted by number of years of experience. The responses were observed to have less scatter (although not shown in the figure) and the consistency may be due to the fact that the respondents specialize in these types. Moreover, similar to the case of wood and masonry buildings, the resulting vulnerability curves of low- and mid-rise buildings of the same material are similar, e.g., curves for C1-L and C1-M (high-code). This similarity implies that the specialists generally think that seismic vulnerability is dictated by the material used in construction rather than the number of floors of a building.

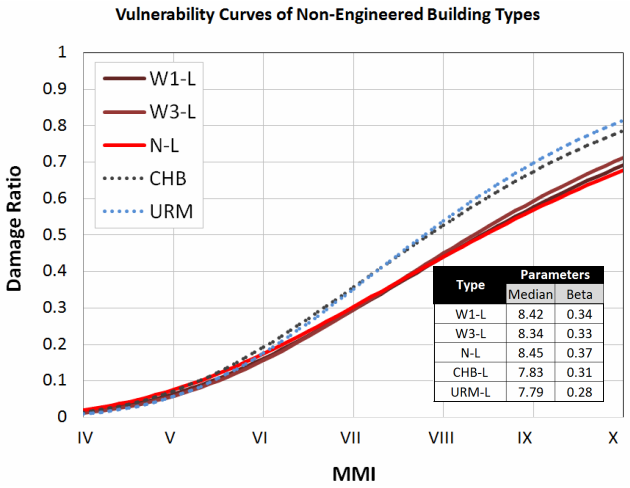


Figure 4. Heuristic Vulnerability Curves of W1-L, W3-L, N-L, CHB-L, and URM-L Building Types in the Philippines.

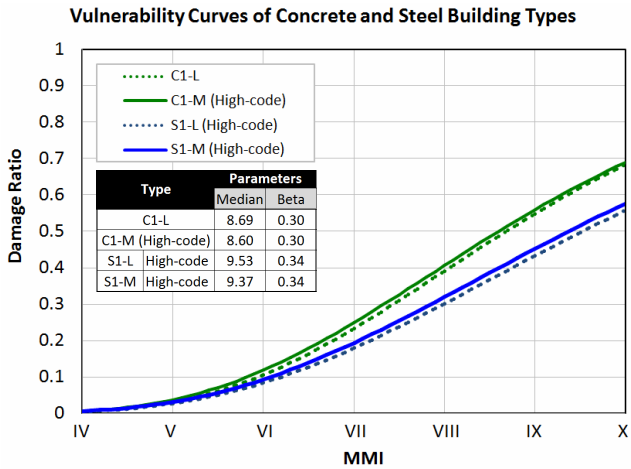


Figure 5. Heuristic Vulnerability Curves of C1-L, C1-M (High-code), S1-L (High-code), and C1-M (High-code) Building Types in the Philippines.

3.3 Comparison with Available Empirical and Computational Vulnerability Curves

In a parallel development, vulnerability curves of concrete and steel buildings types were developed using the

computational approach utilizing the Capacity Spectrum Method (UPD-ICE, 2011 and Pacheco, et.al., 2011). For non-engineered buildings, specifically CHB, empirical vulnerability curves was also developed (UPD-ICE, 2012). Fig. 6 and 7 show the comparison of the proposed heuristic vulnerability curves with the curves derived using the computational and empirical approaches. The trends discussed in the preceding sections suggest that we consider only one heuristic vulnerability curve for each of the material used, e.g., one curve for C1 concrete buildings and another curve for S1 steel buildings irregardless of number of floors as shown in Fig. 6. Similarly, three sets of heuristic vulnerability curves should be used for non-engineered types - one for each wood (W1-L and W3-L), masonry (CHB and URM), and makeshift (N) buildings.

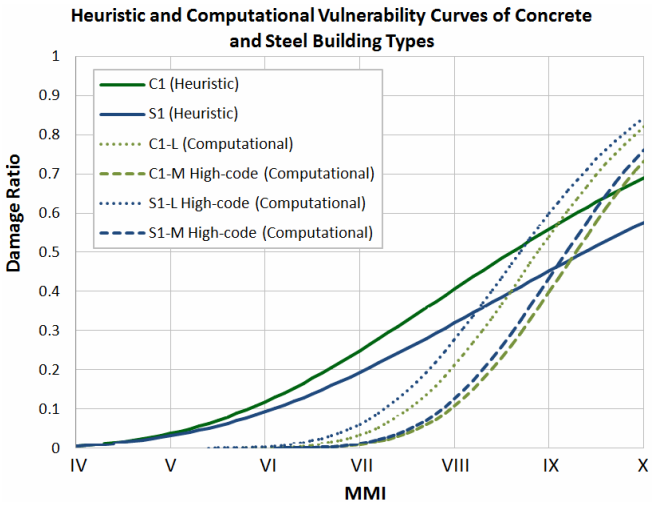


Figure 6. Comparison of Heuristic and Computational Vulnerability Curves of Concrete and Steel Building Types in the Philippines.

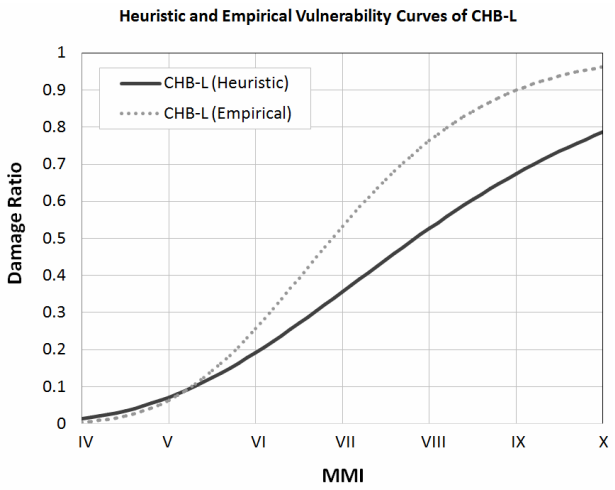


Figure 7. Comparison of Heuristic and Empirical Vulnerability Curves of CHB Building Type in the Philippines.

We acknowledge the need to review the three approaches and the resulting vulnerability curves, we factually present and compare the curves as in Fig. 6 and 7. And since the curves shown vary significantly and are considered to have equal confidence, we therefore suspend recommendation of the best set of curves and suggest that risk analysis be performed using all available curves. Furthermore, we recognize that these functions require an iterative approach so that the vulnerability functions derived using the three methods are similar or cross-validate one another.

4. CONCLUDING REMARKS

Seismic vulnerability curves of key building types in the Philippines were derived in this paper using heuristic method. Prior to the development, a typological system for classifying/grouping existing buildings was adopted. Then a survey of practicing engineers, with varying expertise and experience, was conducted in order to estimate the amount of damage in the event of a destructive earthquake.

Analyses revealed that there is a very low correlation between number of years of experience and the confidence level of the respondents. Results also showed that experienced engineers tend to classify buildings as being more vulnerable to earthquakes than young engineers. The heuristic vulnerability curves of low- and mid-rise buildings are found to be similar for both concrete and steel types. Similarly, the vulnerability curves of wood building types (W1-L and W3-L) are similar as well as masonry building types (CHB and URM). Makeshift buildings, according to experts, are as vulnerable to earthquakes as masonry buildings.

The vulnerability curves presented in this paper are the first generation of building heuristic vulnerability curves developed for the Philippines by Philippine engineers. Consequently, it is acknowledged that these functions will continue to evolve as the knowledge of the behaviour of Philippine buildings in response to ground shaking is better understood.

Acknowledgements:

The authors would like to acknowledge the support from the Australian Agency for International Development (AusAID) through the Greater Metro Manila Area – Risk Analysis Project between the Philippine Institute of Volcanology and Seismology (PHIVOLCS-DOST), the Philippine Atmospheric Geophysical and Astronomical Services Administration (PAGASA-DOST), and Geoscience Australia (GA).

References:

JICA, PHIVOLCS, & MMDA. (2004). “Earthquake Impact Reduction Study for Metropolitan Manila. Manila,” Philippine Institute of Volcanology and Seismology.

Saedi, A., Deck, O. & Verdel, T. (2009). Development of building vulnerability functions in subsidence regions from empirical methods. Engineering Structures 31, p. 2275-2286.

Giovinazzi S. & Lagomarsino S., (2002). “A Methodology for the Vulnerability Analysis of Built-up Areas,” *Proceedings of the International Conference on Earthquake Loss Estimation and Risk Reduction*, Bucharest, October 2002. Italy: University of Genoa.

Pacheco, B.M., Hernandez Jr. H., Ignacio Jr. U., Tingatinga, E.A., Tan, L.R., Pascua, M.C., Suiza R.M., Longalong, R.E., Mata, W., Zarco, M.H.. (2011). “Development of earthquake vulnerability

curves for key building types in Iloilo City," *Proceedings, Philippines Institute of Civil Engineers National Conference*, Cagayan De Oro, Nov. 2011.

ASEP (2010),"National Structural Code of the Philippines (NSCP)." Volume 1, 6th edition.

UPD-ICE (2011)."Development of Vulnerability Curves of Key Building Types in the Philippines." Technical Report, Institute of Civil Engineering, University of the Philippines, Diliman, Quezon City.

UPD-ICE (2012)."Development of Vulnerability Curves of Key Building Types in Greater Metro Manila Area." Progress Report, Institute of Civil Engineering, University of the Philippines, Diliman, Quezon City.

10CUEE CONFERENCE PROCEEDINGS
10th International Conference on Urban Earthquake Engineering
March 1-2, 2013, Tokyo Institute of Technology, Tokyo, Japan

TRANSPARENT GLOBAL EARTHQUAKE RISK AND LOSS ESTIMATION

Kit Miyamoto[1)] and Nicole Keller[2)]

1) Founder and CEO, Miyamoto International, Sacramento, CA USA
2) Head of Communications and International Relations, GEM Foundation, Pavia, Italy

Abstract: Global Earthquake Model (GEM) is a unique collaborative effort that will provide organizations and engineers with tools and resources for transparent assessment of earthquake risk anywhere in the world. By pooling data, knowledge and people, GEM acts as an international forum for collaboration and exchange, and leverages the knowledge of leading experts for the benefit of society. When GEM's OpenQuake platform and tools are released, the engineering community will be able to calculate earthquake risk to a common standard worldwide. By participating in GEM development, the community can contribute to making the tools ever-more valuable for loss assessment of their (local) projects.

1. INTRODUCTION

This paper presents an overview of the Global Earthquake Model (GEM) with particular emphasis on how GEM will integrate with the earthquake engineering community worldwide.

2. MOTIVATION

Vulnerability to earthquakes is increasing, yet advanced, reliable risk assessment tools and data, a critical basis for managing that risk, are inaccessible to most. Even where earthquake risk information is available, it often lacks clear communication for practical applicability. Also, there is a lack of global standards to compare risk between locations. Sharing of data and risk information, best practices, and approaches across the globe is key to assessing risk more effectively.

3. STRUCTURED FOR COLLABORATION

GEM combines the strengths of the public and private sector in a continuously expanding partnership, deliberately structured to promote collaboration across sectors.

GEM is organized loosely in five main categories of participants:

The *GEM Secretariat*, located in Pavia, Italy, coordinates across GEM activities worldwide. The Model Facility within the Secretariat implements GEM tools and software, including GEM's main software platform, OpenQuake (described further below).

The *Scientific Community* engages by means of global projects, carried out by international consortia featuring renowned experts and organisations that develop global datasets and methodologies in the domains of hazard, exposure, physical (building) vulnerability, and socio-economic resilience.

Regional Initiatives work on data collection, create regional input models, provide feedback on global projects and connect GEM data and output for implementation and capacity-building in regional and local contexts.

- GEM's open-source modeling software - OpenQuake Engine - is being used in the nearly completed SHARE[1] project aimed to produce harmonized hazard maps for Europe
- GEM recently hosted a workshop to share best practices in calculating and communicating seismic hazard in sub-saharan African nations.

Sponsors, further comprised of public/national agencies and private organizations, provide guidance by way of seats on the GEM Governing Board.

The *Broader Community*, including the engineering community and other potential users of GEM products, currently participate in GEM by:

- sharing knowledge and best practices,
- contributing data such as building typology and inventory,
- test tools as they become available
- provide feedback, and
- follow GEM progress

From 2014 onwards, all these groups and many more stakeholders will additionally become users of

[1] Seismic Hazard Harmonization in Europe (http://www.share-eu.org/)

the OpenQuake Platform and GEM products, working together toward collaborative enhancement.

4. WORKING TOGETHER TO ASSESS RISK

GEM's first working programme (2009-2014) focuses on building a global framework; a basis that can then drive further development from global to local. This is envisaged as follows:

Global: GEM groups are developing tools and standardised methods for obtaining and analysing data, and these are being used to begin the process of assembling the needed (global, uniform) datasets. The result is advanced data coverage for the world which is much more uniform and complete than before.

Regional: At the same time, through regional, national and local collaboration, the global datasets are scrutinized, data, models and knowledge are being integrated to make the platform and tools ever more useful for application at local scales.

Organisations/Individuals: From the end of 2014, stakeholders across the globe will be able to access state-of-the-art, widely accepted datasets, models and (open-source) software tools through GEM's risk assessment platform (OpenQuake), allowing them not only to perform hazard and risk analyses, but also to make decisions on retrofitting and insurance and collaborate and exchange data, results and opinions amongst each other.

OpenQuake is being built in a dynamic and flexible way, so that it can capture the world's best understanding of data, the earth and earthquake behaviour, and the built environment at any given moment in the future. The user community that will hence grow around the platform will enrich and continuously enhance the datasets, tools and methodologies, for transparent and more effective hazard and risk assessment, from global to local.

GEM will actively support that community through training, dedicated resources and outreach, facilitating true global collaboration as basis for transparent and effective risk management.

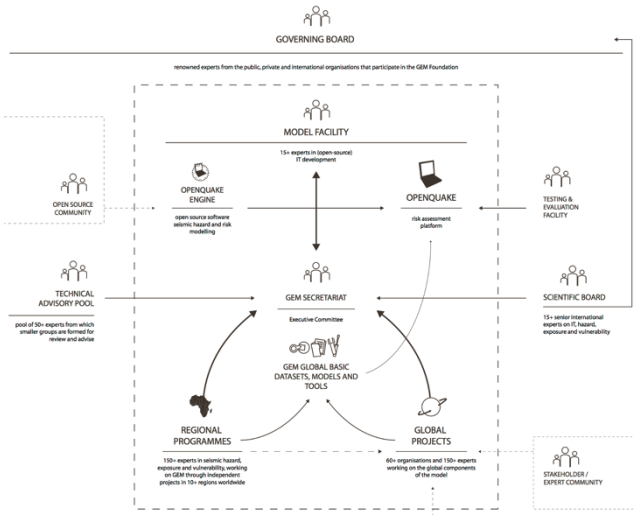


Figure 1: Collaboration among GEM Participants

5. LIMITATIONS.

GEM's first programme will not incorporate all possible data available, nor cover all countries in the world in a uniform way. Limitations include secondary hazards such as tsunamis and landslides, as well as integration of infrastructure as part of exposure modeling. These exclusions are envisaged for future versions.

6. GEM PRODUCTS

Building on collective efforts and knowledge of scientists worldwide, GEM will hence for the first time integrate state-of-the-art data, models, results and open-source tools into a single platform that is to serve as a clearing house for earthquake risk information.

6.1 Global Components

The global data, models and methodologies that serve as input to GEM risk assessment derives from contracted projects in the domains of hazard, exposure, physical (building) vulnerability, and social resilience:

Models:

- Seismic Source Models
- Ground Motion (Attenuation) Models
- Physical Exposure Models
- Physical Vulnerability Models
- Composite Index Models (social vulnerability, resilience, indirect loss)

Datasets:

- Global Earthquake History Catalogue
- Global Instrumental Catalogue
- Global Geodetic Strain Rates
- Global Active Fault Database
- Tectonic Regionalisation
- Buildings and Population Databases
- Earthquake Consequences Databases
- Physical Vulnerability Databases
- Socio-Economic Vulnerability and Resilience Indicators

6.2 OpenQuake

An integrated and holistic approach to risk is key to GEM's platform, OpenQuake, which has three main functions:

Calculate The OpenQuake platform integrates open-source applications with homogenized data and models, allowing users to model seismic hazard and risk transparently and according to the latest science. From ground motion fields to hazard spectra to maps of estimated human loss and mean economic loss; users will be able to produce a great variety of custom outputs by combining own data and (local) knowledge with GEM products. A simulation engine (the OpenQuake Engine) is the core of calculating risk metrics.

Explore and Decide The platform leverages upon open-source geospatial technologies to allow users to work in an intuitive GIS-environment. Users can explore earthquake hazard and risk by interacting with dynamic maps, indicators and graphs, develop their own maps, but also capture and integrate new data. To help users understand risk better and to facilitate risk management, decision support tools are integral to the platform.

Share Sharing of data and risk information, best practice and approaches is key to assessing risk better. The platform is to serve as a clearinghouse for all those critical in- and outputs. It will link users from around the globe so they can work together to assess risk.

With OpenQuake, homogenized information on hazard can be combined with data on exposure (buildings, population) and their vulnerability, for loss assessment around the globe. For a true integrated view on the probability of loss and the costs and benefits of different risk management measures, users can add socio-economic information to maps and estimates of 'physical' risk.

6.3 Built for Decisions

Functionality being built into the OpenQuake platform is designed specifically for direct applicability to risk-reducing decisions. Pre-computed results will include:

- *Hazard Maps*: For example, GEM has already been used to produce a hazard map for the nation of Ecuador, for which no prior nationwide hazard map had existed.
- *Hazard Curves*: probabilistic hazard for a specific site, used to estimate probabilities of shaking
- *Stochastic Event Sets*: Full suites of hypothetical earthquakes that could affect a given region
- *Risk Maps*: Both probabilistic and scenario-based. For example, distribution of damage severity; distribution of monetary losses; distribution of deaths;
- *Event Losses*: Scenario estimates of damage, monetary loss, or social factors, whether for single sites or groups of sites, or entire regions
- *Loss Metrics*: Including average annual losses, and losses related to a specific probabilities of exceedance, both total and insured, whether for a single site or correlated for a portfolio
- *Retrofit Cost-Benefit Calculator*: Based on losses with and without improved seismic resistance
- *Uniform Hazard Spectra*: For engineering design of buildings to a consistent basis.

7. REAL-WORLD APPLICATION

The design of GEM functionality is based on several primary anticipated users with associated use cases.

As an example, as an associate partner of GEM, the California Seismic Safety Commission (CSSC) is investigating potential opportunities to collaborate with GEM and use OpenQuake tools to generate transparent risk information and economic loss estimation for California.

GEM tools will have applicability related to science and engineering, insurance and risk transfer, and particularly policy making, such as urban (land use) planning and building code enforcement. They can be used at the global, national and local scale.

Various city scenarios are part of GEM's development phase, to develop best practice at urban level for risk assessment. In the Middle East there are 6 cities being assessed according to GEM methodology and tools, and city indices will be

developed in the Asia-Pacific region for socio-economic vulnerability and resilience of communities to earthquakes.

8. INTEGRATION OF GEM WITH THE ENGINEERING COMMUNITY

When the GEM platform and tools are released (late 2014), the engineering community will have open access to GEM tools for calculating earthquake risk to a common standard worldwide. Use of GEM for commercial purposes will be subject to license fees, on a sliding scale based on annual revenues of the organization.

By participating now in GEM development, the community can contribute to making the tools ever-more valuable for loss assessment of their (local) projects. Participation consists of sharing knowledge and best practices, contributing data such as building typology and inventory, testing tools as they become available and providing feedback, and following GEM progress.

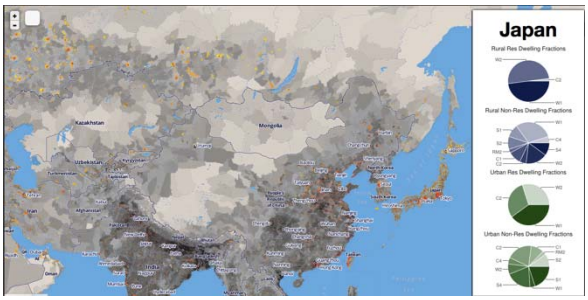
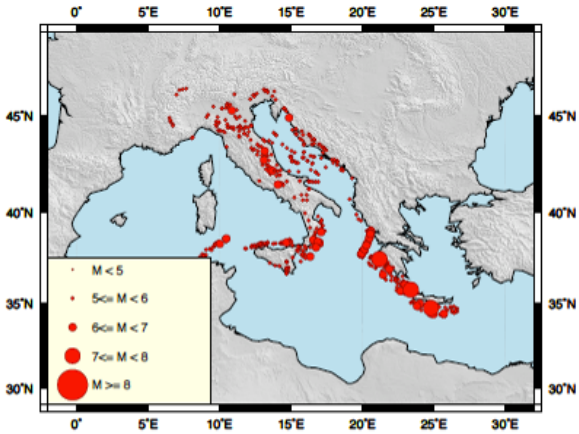
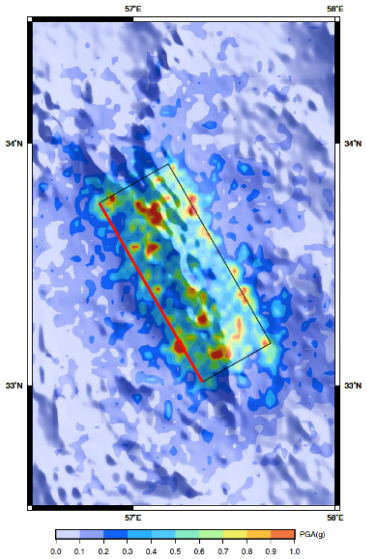


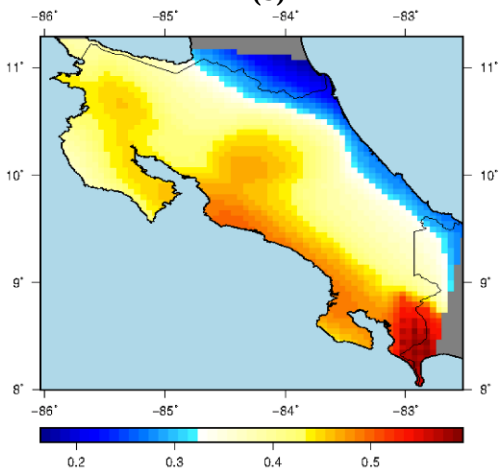
Figure 2: Exploring Building Vulnerability and Exposure around the globe with OpenQuake



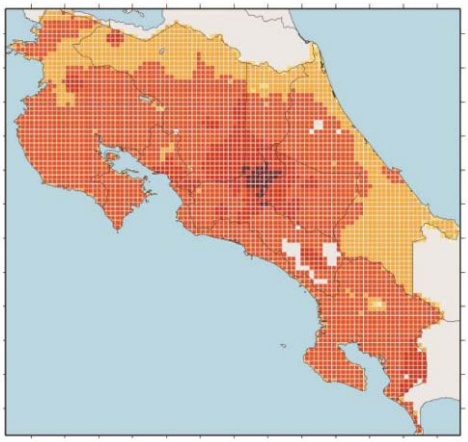
(a)



(b)



(c)



(d)

Figure 3: Various typical outputs of the OpenQuake engine (a) a stochastic event set, (b) a ground-motion field with spatial correlation of ground-motion residuals, (c) a seismic hazard map with 10% probability of exceedance in 50 years, (d) a loss map in terms of fatalities with 10% probability of exceedance in 50 years

9. SUMMARY

Building on many ongoing efforts and the knowledge of scientists worldwide, GEM will for the first time integrate state-of-the-art data, models, results and open-source tools into a single platform that is to serve as a clearing house.

By participating in the effort, the engineering community, and in particular private sector representatives, can leverage the platform and its tools and contribute to making them ever-more valuable for loss assessment of their (local) projects.

References

Pinho, R. (2012). "GEM: a Participatory Framework for Open, State-of-the-Art Models and Tools for Earthquake Risk Assessment". *Proceedings of the 15th World Conference on Earthquake Engineering*, Lisbon, Portugal, paper n. 4929.

10CUEE CONFERENCE PROCEEDINGS
10th International Conference on Urban Earthquake Engineering
March 1-2, 2013, Tokyo Institute of Technology, Tokyo, Japan

METHODOLOGY FOR LIFE CYCLE COST ASSESSMENT OF SELF-CENTERING CONCENTRICALLY BRACED FRAME SYSTEMS

David A. Roke[1], Akhilesh Chandra[2], Qindan Huang[1], and Kallol Sett[1]

1) Assistant Professor, Department of Civil Engineering, The University of Akron, USA
2) Professor, G.W. Daverio School of Accountancy, The University of Akron, USA
roke@uakron.edu, ac10@uakron.edu, qhuang@uakron.edu, sett@uakron.edu

Abstract: Conventional concentrically braced frame (CBF) systems are designed to achieve life safety (LS) performance under the design basis earthquake (DBE). However, the damage state at LS performance often results in residual drift and non-structural damage, causing high post-earthquake repair costs. Recently developed self-centering concentrically braced frame (SC-CBF) systems can achieve damage-free performance under the DBE, eliminating residual drift and thus significantly reducing post-earthquake costs. A four-stage performance assessment framework will be used to probabilistically determine the life cycle costs of structural systems. The four stages of the performance assessment framework are: (1) hazard analysis, (2) seismic fragility assessment, (3) damage analysis, and (4) loss assessment. These stages address different sources of uncertainty, including uncertainties in the ground motion, the structural response under a ground motion of a given intensity, the degree of damage given a certain structural performance defined by seismic fragility, and the direct and indirect costs associated with specific damage states. This paper discusses the interdisciplinary methodology being used to apply this performance assessment framework to estimate and compare the life cycle costs of SC-CBF systems and conventional CBF systems. Ultimately, this research will lead to recommendations regarding the implementation and benefit of advanced structural systems.

1. INTRODUCTION

Conventional concentrically braced frame (CBF) systems are commonly used in seismic areas due to their strength, stiffness, and economy. However, conventional design methodology allows for significant structural (and nonstructural) damage under the design basis earthquake (DBE), provided the structure performs adequately to protect the lives of its occupants. This damage may lead to significant residual drift, necessitating costly repairs or demolition.

To address this shortcoming of conventional CBF systems, self-centering CBFs (SC-CBFs) have been developed that are intended to achieve damage-free performance under the DBE (Roke et al. 2006). SC-CBFs are expected to have greater construction costs than conventional CBFs. The premise is that the post-earthquake damage to SC-CBF systems should be less than that to conventional CBF systems, leading to a tradeoff between construction costs and maintenance and repair costs. Ultimately, this tradeoff must be evaluated to determine whether SC-CBF systems are worth the extra up-front cost.

To that end, a performance-based assessment will be used to probabilistically determine the life cycle cost (LCC) of conventional CBF systems and SC-CBF systems. A comparison of the LCCs of the two systems will determine if the benefits of SC-CBF systems outweigh the costs.

This paper presents the methodology that will be used to assess and compare LCCs of CBF and SC-CBF systems. The ultimate goal of this research is to develop recommendations for the implementation of SC-CBF systems, based on the expected reduction in LCC with respect to conventional CBF systems.

2. ASSESSMENT FRAMEWORK

A framework for probabilistically assessing the seismic performance of a structural system was developed by Moehle and Deierlein (2004). This framework consists of four analysis steps, as indicated in Figure 1: (1) hazard analysis, (2) seismic fragility assessment, (3) damage analysis, and (4) loss analysis. This research will address each of the four analysis steps in a comprehensive approach to determine the life cycle cost of SC-CBF systems.

2.1 Hazard Analysis

The hazard analysis step is used to obtain probabilistic ground motion time histories for seismic fragility assessment of the system under evaluation. This research will analyze the ground motion hazard at a site in the Los Angeles basin, considering modeling uncertainty and uncertainties associated with source (fault), path (rock) and site (soil) parameters. A set of

scenario bedrock motion time histories will be generated through probabilistic seismic hazard analysis, followed by probabilistic site response analysis to obtain representative site-specific ground motion time histories. The hazard analysis step is schematically depicted in Figure 2.We will start by identifying a set of future scenario earthquakes, originating from nearby faults, that may cause damage to the SC-CBF system under evaluation. The next step will be to probabilistically estimate the severity of bedrock shaking (e.g., response spectrum, peak bedrock acceleration, and duration of shaking) using appropriate attenuation models for each scenario earthquake. We will use the regression equations proposed by Abrahamson and Silva (2008) to compute the response spectrum and peak bedrock acceleration and the empirical model proposed by Kempton and Stewart (2006) to compute the duration of shaking. Note that the above models implicitly account for the modeling and source and path parameter uncertainties, and provide estimates of the severity of shaking parameters in terms of their respective mean and standard deviation.

Thus estimated probabilistic response spectrum, peak bedrock acceleration, and duration of shaking will be used to generate a suite of synthetic bedrock motion time histories. A FORTRAN program, SIMQKE, developed by Gasparini and Vanmarcke (1976) will be employed to this end. SIMQKE first uses a pre-defined envelope function in conjunction with the user-defined peak bedrock acceleration to simulate transient characteristics of real earthquakes, which are then used to smooth a spectral density function computed using the user-defined duration of shaking and response spectrum information. However, note that in our case, the SIMQKE input parameters are probabilistic in nature. Hence, they will first be randomized using their respective means and standard deviations; the SIMQKE code will then be run in a Monte Carlo (Metropolis and Ulam 1949) fashion.

To account for hazards associated with the uncertainty and nonlinearity of the soil properties at the site, probabilistic site response analysis will be performed with the above generated suite of (probabilistic) bedrock motions and site-specific soil data. To this end, following DeGroot and Baecher (1993), the site-specific soil data will be statistically analyzed to quantify the uncertain spatial variability and testing uncertainty associated with the soil properties and to model the soil properties as one-dimensional random fields. The random field parameters (mean, variance and correlation structure) of the soil properties will be used to generate realizations of the soil properties in the deposit. Using the OpenSees software (Mazzoni et al. 2009), the suite of bedrock motions will be numerically propagated through the deposit within a Monte Carlo (Metropolis and Ulam 1949) framework to obtain a suite of surface motion time histories. An appropriate elastic-plastic soil constitutive model will be used to capture the soil nonlinearities as the soils plastify.

2.2 Seismic Fragility Assessment

The seismic fragility assessment step is used to quantify the probabilistic structural response. For this research, the structural response will be generated analytically using numerical models developed using OpenSees (Mazzoni et al. 2009).

The SC-CBF numerical models are intended to capture the rocking behavior of the SC-CBF systems, which softens the lateral force-lateral drift response without damaging the structural members (Roke et al. 2006). The numerical models used in this study will capture three types of nonlinearity: (1) column base gap opening, which permits the rocking behavior of the SC-CBF system; (2) yielding of the vertically oriented post-tensioning bars, which determines the maximum overturning moment resistance of the SC-CBF system; and (3) member yielding, which should have a low probability of occurrence due to the design of the SC-CBF systems (Roke et al. 2010).

Seismic fragility is defined as the conditional probability that a demand quantity of interest attains or exceeds a specified capacity level for given values of earthquake intensity measures. The data obtained from the numerical models will be used to develop probabilistic capacity and demand models and to develop seismic fragility curves. Seismic fragility, expressed via a fragility curve, is a critical component in performance-based assessment, providing valuable information for evaluating probabilistic structural damage states and assessing regional risk related to seismic hazards.

Following the conventional notation in structural reliability (Ditlevsen and Madsen 1996), seismic fragility can be expressed as:

$$F\left(\mathbf{x},\boldsymbol{\Theta}\middle|\mathbf{IM}\right)=P\left\{\bigcup_{k}\left[g_k\left(\mathbf{x},\boldsymbol{\Theta}_k\right)\right]\middle|\mathbf{IM}\right\} \quad (1)$$

where $\boldsymbol{\Theta} = \{\boldsymbol{\Theta}_k\}$, $[g_k(\mathbf{x}|\boldsymbol{\Theta}_k) \le 0]$ is a failure event of the structure in the kth failure mode, $g_k(\mathbf{x},\boldsymbol{\Theta}_k) = C_k(\mathbf{x},\boldsymbol{\Theta}_{C,k}) - D_k(\mathbf{x},\boldsymbol{\Theta}_{D,k})$ is the limit state function for the kth failure mode, $\mathbf{x}$ is a vector of basic variables (e.g., structural properties and boundary conditions), C_k is the probabilistic capacity, D_k is the probabilistic demand, and $\boldsymbol{\Theta}_k = \{\boldsymbol{\Theta}_{C,k}, \boldsymbol{\Theta}_{D,k}\}$ are the model parameters in the capacity and demand models, respectively. In this research, we will consider failure (defined as demand exceeding capacity) with respect to the limit states of PT bar yielding, member yielding, and member failure.

The proposed capacity and demand models will be developed based on the probabilistic capacity models proposed by Gardoni et al. (2002) and the probabilistic demand models proposed by Huang et al. (2010). The models will account for the prevailing uncertainties, including model error arising from potential inaccuracies in the model form and potentially missing variables, as well as measurement errors and statistical uncertainties. The capacity and demand models are developed by adding correction terms to currently-used deterministic capacity and demand models for SC-CBF systems, respectively, to account for the inherent bias and uncertainty in the models.

2.3 Damage Analysis

Damage analysis relates structural fragility to damage states, which are used to quantify the damage to the structural elements, nonstructural elements, and

building contents; this quantification is necessary for assessing losses. Damage states of structures can be characterized by damage measures, including but not limited to permanent displacement, maximum inter-story drift ratio, energy dissipation capacity, and ductility demand (Gunturi and Shah 1992, Park and Ang 1985).

The performance levels that will be considered in this study for developing fragility curves are immediate occupancy (IO), life safety (LS), and collapse prevention (CP). In order to relate damage states to the structural performance levels, we will adopt the damage states defined by Bai et al. (2009), where the damage state classification is defined by the IO, LS, and CP performance levels. Bai et al. (2009) define four damage states: insignificant (I), moderate (M), heavy (H), and complete (C). Figure 3 can be used to define a possible relationship between the performance levels and damage states (Yang et al. 2009, Bai et al. 2009). In Figure 3, PI|IM, PM|IM, PH|IM, and PC|IM refer to the conditional probability of the structure achieving each damage state (I, M, H, and C, respectively). P_{IO}, P_{LS}, and P_{CP} represent the conditional probability of reaching each performance level (IO, LS, and CP, respectively), and can be determined based on the fragility curves. The differences between the conditional probabilities (PM|IM, PH|IM, and PC|IM) define the probabilities of achieving specific damage states.

The losses associated with nonstructural components may outweigh the losses associated with structural components; therefore, the performance of nonstructural components must be considered. Fragility curves for the nonstructural components can be obtained from previous research (e.g., Krawinkler (2005) and ATC (2007) developed fragility curves for specific non-structural elements).

2.4 Loss Analysis

A useful metric to assess relative performance of structural systems is the life cycle cost (LCC) of the competing systems. Broadly, LCC includes construction costs, maintenance costs, and post-earthquake induced costs. Of these three cost types, post-earthquake induced costs are the most difficult to estimate and have consistently challenged economic analysts. The challenge stems from the probabilistic and uncertain nature of these costs, most of which are intangible and are therefore not directly measurable.

Using the total probability theorem, we will use the following formulation to derive the LCC for CBF and SC-CBF systems:

$$E\left(LCC_{\phi}\right) = \sum_{i=1,4} E\left(\kappa_{\phi,t}\right) \tag{2}$$

where ϕ is a vector of variables that impact the robustness of buildings (e.g., material properties and maintenance schedules). Cost-type is indicated by κ and is linked with subscript i that takes values from 1 to 4 to denote (1) initial construction cost, (2) maintenance costs, (3) inspection cost, and (4) post-earthquake induced cost. Estimation time is denoted by t ($0 \le t \le 4$) to reflect a four period analysis; $t = 0$ indicates current cost and pertains primarily to initial construction cost; all other costs are incurred probabilistically and conditionally in future. Future costs ($t \ge 0$) are converted into their present values using the net present value (NPV) approach that considers an appropriate discount rate.

The post-earthquake induced costs ($\kappa = 4$ in Eq. (2)) include both direct and indirect losses. Direct loss is immediate and easier to measure. Indirect losses extend into the future and are difficult to measure; therefore, they must be approximated. The degree of precision of such approximations usually declines as a function of estimation period. Since each entity can have varying economic post-earthquake loss, we will utilize Eq. (3) to derive entity-specific indirect costs:

$$K = \sum_{f} \left(1 - \alpha_{f,t}\right) \cdot d_{f,t} \cdot \theta_{f,t} \tag{3}$$

where K indicates indirect costs for entity f for period t that ranges from 1 to 4 for a four period impact analysis. Each entity's shock absorbing capacity at time t is denoted by α so that a value of 0.6 reflects a 40% loss in the entity's operating capacity and revenues (on the assumption of a direct correlation between revenues and operating capacity). The extent of post-earthquake damage is indicated by d and is computed in the damage analysis step described earlier in the paper. The relative economic value of entity f is approximated by θ and is derived as a product of the percentage of the economic value shared by the entity with respect to the total economic value provided by all entities in the building; in this sense, θ approximates the maximum post-earthquake loss the entity can suffer.

The shock absorbing capacity is a function of each entity's contingency plans for addressing and mitigating damage from post-earthquake shocks. The expression $(1-\alpha_{f,t})\cdot d_{f,t}$ in Eq. (3) approximates the loss function corresponding to the indirect cost for entity f. Aside from the structural uncertainties, uncertainties associated with entity-specific variables (e.g., risk management policies and human resources management) moderate the nature of the loss function. For the set of entities in the building, the loss function is a density function with an expected mean and standard deviation.

The indirect loss K in post-earthquake shock is aggregated with the direct loss of each entity to estimate the total loss for that entity. The total loss of all entities in the building is aggregated to estimate the post-earthquake induced cost for the building.

The estimation of indirect losses as specified above necessitates several assumptions in view of the uncertainties. By changing the values of those assumptions, we can assess the impact of each on indirect costs and the LCC.

3. SUMMARY

This research will provide a comprehensive probabilistic evaluation of the life cycle cost (LCC) of SC-CBF systems by following the four phases of an earthquake performance assessment framework: (1)

hazard analysis, (2) seismic fragility assessment, (3) damage analysis, and (4) loss analysis.

This paper presents the methodology that will be used to incorporate various uncertainties into each step of the assessment framework. Addressing the uncertainties in each step of the framework will create a very complete picture of the LCCs of both CBF and SC-CBF systems.

The ultimate goal of this research is to assess if the superior performance of SC-CBF systems is worth the increased cost over conventional CBF systems. Comparing the probabilistic LCC of the two competing systems will provide evidence for the effectiveness of SC-CBF systems and lead to recommendations regarding their use.

Acknowledgements:

This material is based upon work supported by the National Science Foundation under Grant No. CMMI 1235327. Any opinions, findings, and conclusions or recommendations expressed in this material are those of the authors and do not necessarily reflect the views of the National Science Foundation.

References:

Abrahamson, N. and Silva, A. (2008) "Summary of the Abrahamson & Silva NGA ground-motion relations", *Earthquake Spectra*, 24(1):67–97.

Applied Technology Council (ATC) (2007) "Guidelines for Seismic Performance Assessment of Buildings 35% Complete," Draft prepared for Department of Homeland Security, Washington, D.C.

Bai, J.W.; Hueste, M.B.; and Gardoni, P. (2009). "Probabilistic Assessment of Structural Damage due to Earthquakes for Buildings in Mid-America," ASCE Journal of Structural Engineering, 135(10), pp 1155-1163.

DeGroot, D. J. and Baecher, G. B. (1993) "Estimating autocovariance of in-situ soil properties", Journal of Geotechnical Engineering 119(1):147–166.

Ditlevsen, O.; and Madsen, H.O. (1996). Structural Reliability Methods, Wiley, New York.

Gardoni, P.; Der Kiureghian, A.; and Mosalam, K. M. (2002). "Probabilistic capacity models and fragility estimates for reinforced concrete columns based on experimental observations," Journal of Engineering Mechanics, 128(10), pp 1024–1038.

Gasparini, D. A. and Vanmarcke, E. H. (1976) *SIMQKE: Simulated earthquake motions compatible with prescribed response spectra*, Research Report R76-4, Massachusetts Institute of Technology, Cambridge, MA.

Gunturi, S.K.V.; and Shah, H. C. (1992). "Building specific damage estimation," Proceedings of the 10th world conference on earthquake engineering, 10, pp 6001–6006.

Huang, Q.; Gardoni, P.; and Hurlebaus, S. (2010). "Probabilistic Seismic Demand Models and Fragility Estimates for Reinforced Concrete Highway Bridges with One Single-Column Bent," ASCE Journal of Engineering Mechanics, 136(11), pp 1340-1353.

Kempton, J. J. and Stewart, J. P. (2006) "Prediction equations for significant duration of earthquake ground motions considering site and near-source effects", *Earthquake Spectra*, 22(4):985–1013.

Krawinkler, H. (2005). "Van Nuys hotel building testbed report: exercising seismic performance assessment," PEER Report No. 2005/11, Pacific Earthquake Engineering Research Center, University of California at Berkeley, California.

Mazzoni, S.; McKenna, F.; Scott, M.H.; Fenves, G.L.; et al. (2009). *Open System for Earthquake Engineering Simulation User Command-Language Manual*. Pacific Earthquake Engineering Research Center.

Metropolis, N. and Ulam, S. (1949) "The Monte Carlo method", *Journal of the American Statistical Association*, 44(247):335–341.

Moehle, J. and Deierlein, G.G. (2004). "A Framework Methodology for Performance-Based Earthquake Engineering," *Proceedings of the 13th World Conference on Earthquake Engineering*, Paper No. 679.

Park, Y.J.; and Ang A.H.S. (1985). "Mechanistic seismic damage model for reinforced concrete," ASCE Journal of Structural Engineering, 111(4), pp 722-739.

Roke, D.; Sause, R.; Ricles, J.M.; Seo, C.-Y.; and Lee, K.-S. (2006). "Self-Centering Seismic-Resistant Steel Concentrically-Braced Frames," *Proceedings of the 8th U.S. National Conference on Earthquake Engineering*, Paper No. 1364.

Roke, D.; Sause, R.; Ricles, J.M.; and Chancellor, N.B. (2010). "Damage-Free Seismic-Resistant Self-Centering Concentrically-Braced Frames," ATLSS Report 10-09, Lehigh University, Bethlehem, Pennsylvania.

Yang, T.Y.; Moehle, J.; Stojadinovic, B.; and Der Kireghian, A. (2009). "Seismic Performance Evaluation of Facilities: Methodology and Implementation," ASCE Journal of Structural Engineering, 135(10), pp 1146-1154.

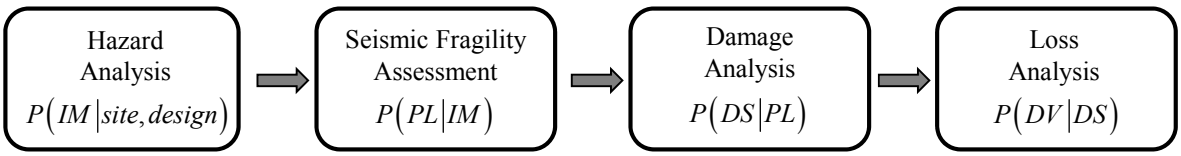


Figure 1. Performance-based seismic assessment framework

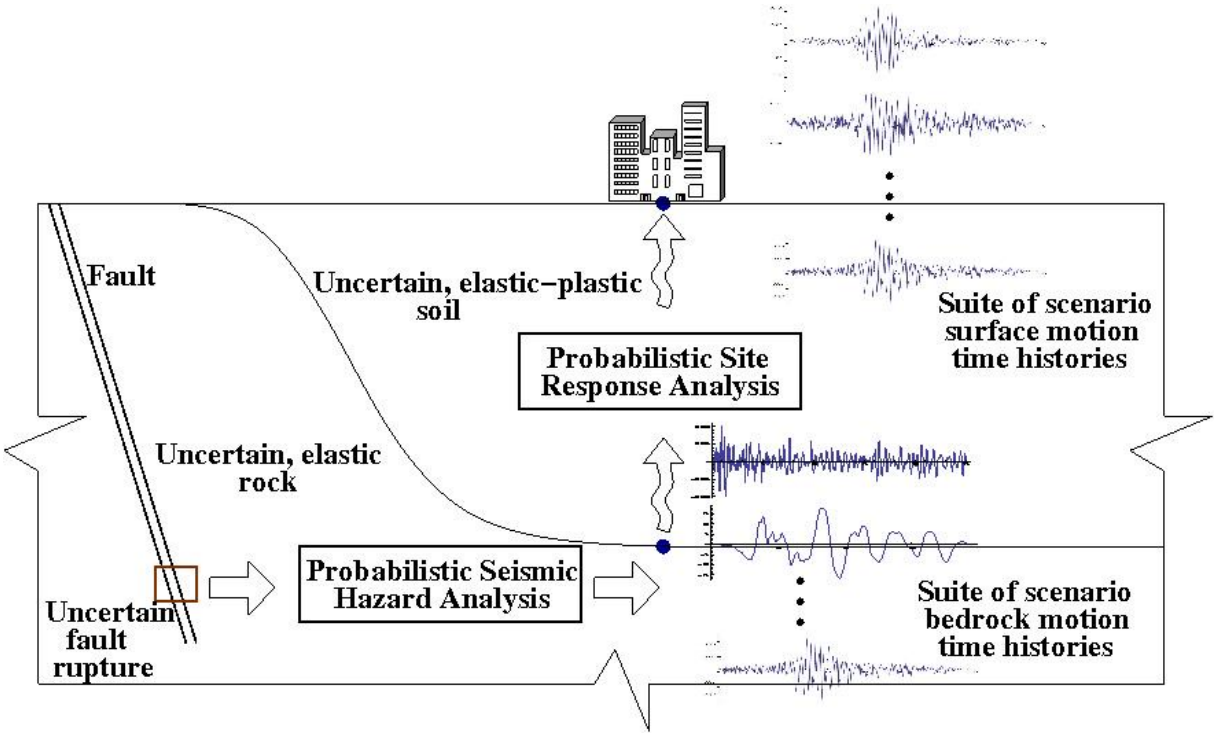


Figure 2. Schematic depiction of the hazard analysis step

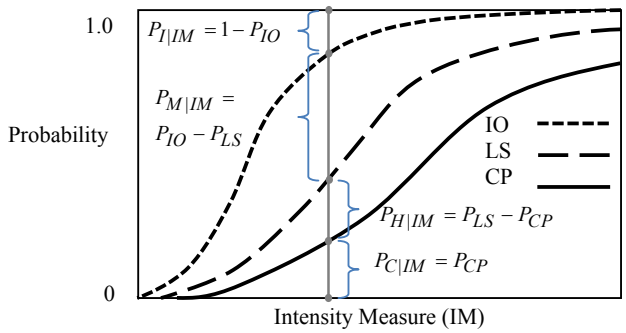


Figure 3. Schematic of relationship between performance levels and damage states

10CUEE CONFERENCE PROCEEDINGS
10th International Conference on Urban Earthquake Engineering
March 1-2, 2013, Tokyo Institute of Technology, Tokyo, Japan

FRAGILITY CURVES FOR REINFORCED CONCRETE BUILDINGS TO EARTHQUAKE-INDUCED SLOPE DISPLACEMENTS

Stavroula D. Fotopoulou[1)], Kyriazis D. Pitilakis[2)]

1) Post-Doctorate Researcher, Dept. of Civil Engineering, Aristotle University of Thessaloniki, Greece
2) Professor, Dept. of Civil Engineering, Aristotle University of Thessaloniki, Greece

Abstract: An abacus of probabilistic fragility functions has been developed for low-rise, reinforced concrete (RC) buildings subjected to earthquake triggered slow-moving slides, applying a recently published methodology by the same authors (Fotopoulou and Pitilakis 2012). In particular, the method is based a two-step numerical approach, namely a slope-foundation dynamic and a structure's quasi-static analysis, to assess the expected building's distress and damage to earthquake-induced landslide displacements. We perform an extensive numerical parametric study considering different idealized slope configurations, soil and geological settings, as well as distances of the structure to the slope's crest. The effect of the various analyzed features on the structural performance is investigated, highlighting trends on the building's behavior to the permanent co-seismic slope deformations. Generalized fragility curves as a function of outcrop peak ground acceleration or the induced permanent slope ground displacements are then suggested based on the most influential parameters to the structure's vulnerability. The proposed curves, which are adequately validated with existing data, can be efficiently applied within a probabilistic risk assessment framework to evaluate the vulnerability of RC buildings subjected to earthquake-induced slope displacements.

1. INTRODUCTION

The destructive impact of earthquakes can be strongly enhanced by the induced triggering of landslides during or after the shaking (Bommer and Rodrıguez 2002). Earthquakes can potentially trigger landslides that can induce catastrophic losses in terms of human lives and infrastructure damage. Therefore, there is an urgent need for efficient landslide risk assessment and management at different scales. An efficient Quantitative Risk Assessment (QRA) tool that allows for establishing risk management strategies and emergency planning in a cost-effective manner requires the quantification of both hazard and vulnerability of the exposed structures. However, most of the existing risk assessment studies do not focus on the comprehensive evaluation of the vulnerability component. Instead, they often provide empirical or expect judgment-based vulnerability values depending on the landslide type and the element at risk (e.g. Dai et al. 2002). This is principally due to its complex and multidimensional nature and to the difficulty in acquiring reliable damage data from previous landslide events. A better understanding on the parameters affecting the building damage due to the different landslide mechanisms is therefore essential to reduce the great deal of uncertainty associated with the landslide vulnerability modeling. The probabilistic treatment of these uncertainties may be achieved through the use of the co-called fragility (or vulnerability) curves, which provide relationships between the landslide intensity and the probability of exceeding predefined damage limit states.

In this paper several portfolios of probabilistic fragility curves for low-rise, RC building subjected to earthquake induced slow- moving slides are proposed based on the recently published by the authors vulnerability assessment methodology (Fotopoulou and Pitilakis 2012). To achieve this goal, an extensive numerical parametric investigation is conducted considering a variety of idealized slope configurations, soil and geological settings, as well as distances of the structure to the slope's crest. The derived fragility curves are compared with corresponding literature ones to strengthen their effective implementation within a QRA framework.

2. VULNERABILITY ASSESSMENT METHODOLOGY

According to the proposed method (Fotopoulou and Pitilakis 2012), a single RC building is subjected to forced differential displacement due to the earthquake-triggered landslide and subsequently to structural distress and damage. A low-rise RC frame building located next to the crown of a potentially unstable finite soil slope is considered. Figure 1 illustrates the key parameters of the investigated problem. The method is principally based on a two-step numerical approach and adequate statistical analysis that are shortly outlined hereafter.

The total and differential permanent displacements are first estimated using a plane strain FLAC2D (Itasca 2008) finite difference, non-linear dynamic slope-foundation model. The model consists of four-node quadrilateral

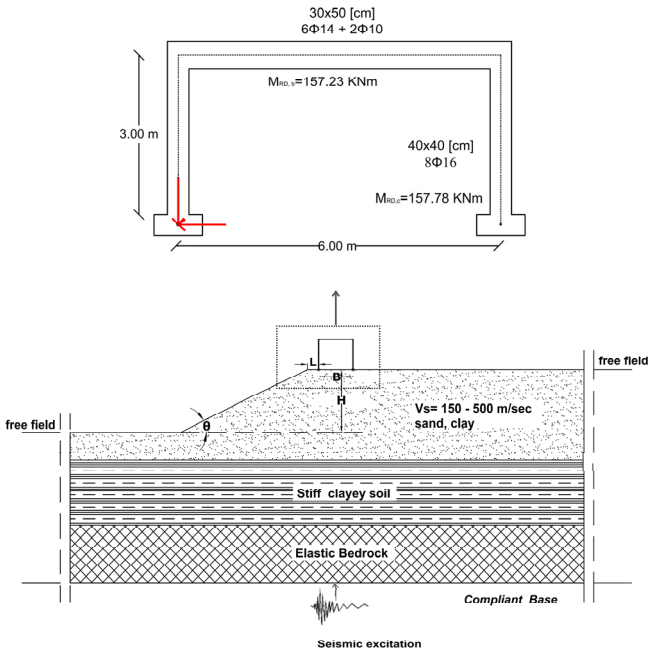


Figure 1 The main parameters of the problem under study

elements of various sizes determined by the shear wave velocities of the medium and the frequency content of the incident motions. A finer discretization is adopted in the slope area, whereas towards the lateral boundaries of the model the mesh is coarser. The width and the height of the model are selected in a way that the effects of artificial wave reflections from the boundaries near the slope are sufficiently reduced. For the same purpose, free field (Cundall et al. 1980) and quiet boundaries (Lysmer and Kuhlemeyer, 1969) are applied along the lateral boundaries and the bottom of the dynamic model respectively.

The soil materials (sandy or clayey) are modeled using a simple elastoplastic constitutive model with Mohr-Coulomb failure criterion, assuming a non-associated flow rule for shear failure. Soil strength properties are properly selected to account for the dynamic ground response. The bedrock is idealized considering a linear elastic soil material.

A low-rise RC frame building is assumed to be located next to the slope's crest. Shallow foundation systems of different stiffness characteristics are considered: isolated footings and/or a uniform loaded continuous slab foundation. In the first case, the foundation is simulated with concentrated loads at the footings' links assuming no relative slip and/or separation between foundation and subsoil. In the second case, the foundation system is modeled as a deformable elastic beam connected to the soil elements' grid through appropriate interface elements.

The seismic input applied along the base of the model consists of SV waves vertically propagating upwards from the base. Different gradually increasing acceleration time histories recorded on rock outcrop are applied to cover a wide range of seismic motions in terms of amplitude, frequency content and significant duration in order to provide the necessary response quantity statistics.

Then, non-linear static time history analyses of the building are performed to assess the building's response to the differential ground deformation induced by the earthquake induced landslide. The analyses are conducted using the finite element code SeismoStruct (Seismosoft 2011) for progressively increasing levels of differential displacements extracted from the non-linear dynamic analysis. In particular, the derived differential displacements at the foundation level are imposed quasi-statically at one of the RC building supports.

The studied building (see Fig. 1) is a typical RC bare frame structure with flexible or stiff foundation system designed with "low" or "high" seismic code prescriptions. The "fibre approach" is used to represent the cross-section behaviour, where each fibre is associated with a uniaxial stress-strain relationship. Both local (beam-column effect) and global (large displacements/rotations effects) sources of geometric nonlinearity are automatically taken into account. Nonlinear constitutive models are used to simulate the behavior of RC materials since cracking and irreversible deformations are normally expected to govern the building's response. More specifically, a uni-axial nonlinear constant confinement model is used for the concrete material (Mander et al. 1988) whereas a uni-axial bilinear stress-strain model with kinematic strain hardening is utilized for the reinforcement.

Structural response data in terms of maximum material strain are then statistically correlated to the corresponding limit damage states and the landslide intensity parameters to estimate structure's performance and fragility. Four damage limit states (LS1, LS2, LS3, LS4) are defined in terms of threshold values of building's material strain based on previous literature work (Crowley et al. 2004, Bird et al. 2005; 2006, Negulescu and Foerster 2010) and proper engineering judgment. They describe the exceedance of minor, moderate, extensive and complete structural damage of the RC building.

Vulnerability is finally assessed through probabilistic fragility (or vulnerability) curves, which describe the probability of exceeding a certain limit state of the building exposed to the landslide hazard given the measure of the landslide intensity. A two-parameter lognormal distribution function is adopted to represent the fragility curves. The corresponding analytical form reads:

$$F(IM) = \Phi\left[\frac{1}{\beta} In\left(\frac{IM}{\overline{IM}}\right)\right] \quad (1)$$

where

IM is the intensity measure; $\Phi[\cdot]$ is the standard normal cumulative distribution function; $\overline{IM}$ is the median value of the specified intensity parameter at which the building reaches the specified limit state; β is the standard deviation of the natural logarithm of the specified intensity parameter.

The landslide intensity is expressed both in terms of peak horizontal ground acceleration (PGA) at the seismic bedrock and permanent ground/foundation displacement (PGD) at the slope area (i.e. a product of PGA). The latter is generally better correlated to structural deformation and

damage (Fotopoulou 2012).

Different procedures can be applied to estimate the log-normally distributed fragility parameters (median and log-standard deviation) given the simulated damage data. A purely statistical approach, i.e. the Maximum Likelihood Method (Shinozuka, 2000; 2003), is implemented in this study considering a common log-standard deviation for all limit states (Shinozuka, 2003).

The likelihood function is introduced as:

$$L\left(IM_1, IM_2, IM_3, IM_4, \beta\right) = \prod_{i=1}^{N}\prod_{j=0}^{4} P_j\left(IM_i; E_j\right)^{y_{ij}} \quad (2)$$

where

Ej the specified damage state for no damage (j=0), at least slight damage (j=1), at least moderate damage (j=2), at least extensive damage (j=3) and complete damage (j=4).

yij=1 if the damage state Ej occurs for the i simulation of the structure subject to the landslide intensity and 0 otherwise.

Then the maximum likelihood estimates for $\overline{IM_i}$ and β are obtained by solving the following equations:

$$\frac{d\ \mathrm{lnL}}{d\,\overline{IM}} = \frac{d\ \mathrm{lnL}}{d\,\beta} = 0 \quad (3)$$

The computation is performed numerically using a standard optimization algorithm.

Three primary sources of uncertainty, associated with the variability on the capacity properties of the structure, the demand and damage state thresholds, contribute to the total variability. Uncertainty on the demand is taken into account from the dispersion of the recorded maximum strain as a function on the selected IM. Damage state definition uncertainty is accounted for by performing a Monte Carlo simulation for the simulated damage data. A lognormal distribution, in accordance to the pertinent literature (Crowley et al. 2004), is considered for the specified limit states with median the already defined limit state values and coefficient of variation equal to 0.4. Finally, capacity uncertainty is taken equal to 0.25 or 0.30 depending on the code design level of the structures (NIBS, 2004). The total variability is estimated through the following expression:

$$\beta = \sqrt{\beta'^2 + \beta_C^{\ 2}} \quad (4)$$

where β' is the combined variability associated with the demand and the limit damage states and β_c is the capacity properties of the structure respectively.

The reliability of the proposed method was assessed through its application to two real case histories (Fotopoulou et al. 2011; Fotopoulou 2012), verifying its effective implementation in several vulnerability assessment studies.

3. PARAMETRIC STUDY

In order to construct generalized fragility curves applicable to low-rise RC frames for various soil conditions and slope configurations, we perform an extensive parametric investigation based on the briefly described vulnerability assessment method. The main parameters selected to vary are associated to (Fig. 1):

- The slope height (H=20, 40 m)
- The slope inclination (θ = 15°, 30°, 45°)
- The soil properties of the slope material (soft to stiff clayey and sand soils corresponding to soil categories B, C and D according to EC8 (CEN-European Committee for Standardization 2003))
- The relative position of the building with respect to the slope crest (L=3, 5 m).

Six simplified –yet realistic– finite slope configurations are considered for the present study based on the varying slope geometry (see Fig. 1). For each geometry, 4 different models are constructed that vary on the soil conditions (sand, clay) and the relative location of the building to the slope crest (L=3, 5 m). It is noticed that the soil properties of the slope materials are taken to be consistent with the considered inclination angles to ensure static slope stability. Thus, we do not analyze steep slopes with soft soil, as the slope would be already unstable in static conditions. It is also important to note that only the cases that represent the highest potential to landsliding are modeled. For instance, we do not investigate slopes with small inclination (i.e. θ=15°) on stiff soil as the resulting permanent slope displacements and consequently the building expected damage would be negligible and thus out of the scope of this study. Table 1 presents the properties for the soil materials and the elastic bedrock assumed for the analyses.

Table 1 Soil properties of the analyzed slope configurations

	Bedrock	Stiff soil		Relatively stiff soil		Soft soil	
		sand	clay	sand	clay	sand	clay
Density (kg/m3)	2300	2000	2000	1800	1800	1700	1700
Poisson's ratio	0.3	0.3	0.3	0.3	0.3	0.3	0.3
Shear wave velocity Vs(m/sec)	850	500	500	250	250	150	150
Cohesion c (KPa)	-	10	50	0	10	0	5
Friction angle φ (degrees)	-	44	27	36	25	25	15

Table 2 Records used for the dynamic analyses

Earthquake	Record station	Mw	R (km)	PGA (g)
Valnerina, Italy 1979	Cascia	5.9	5.0	0.15
Parnitha, Athens 1999	Kypseli	6.0	10.0	0.12
Montenegro 1979	Hercegnovi Novi	6.9	60.0	0.26
Northridge, California 1994	Pacoima Dam	6.7	19.3	0.41
Campano Lucano, Italy 1980	Sturno	7.2	32.0	0.32
Duzce, Turkey 1999	Mudurno_000	7.2	33.8	0.12
Loma Prieta, California 1989	Gilroy1	6.9	28.6	0.44

The seismic excitation applied along the base of the dynamic model consists of a suite of 7 real acceleration time histories from different earthquakes worldwide recorded on

rock outcropping conditions (Tab. 2) and scaled at different level of PGA i.e. 0.3 g, 0.5g, 0.7g and 0.9g. Some additional analyses for lower levels of PGA (e.g. 0.1 g) were deemed necessary for certain models in order to obtain reliable results for all damage states.

The herein studied building is a single bay-single storey RC bare frame structure with flexible foundation system (see Fig. 1), which was found to be adequately representative of the performance of real low-rise RC frame buildings (Bird et al. 2005, Negulescu and Foerster 2010). The structure has been designed according to the provisions of the modern Seismic Code of Greece (EAK 2000). The specified yield stress of reinforcing steel and the compressive strength of concrete are 400 MPa and 20 MPa respectively. The adopted dead and live loads (g = 1.3 kN/m^2 and q = 2 kN/m^2) represent typical values for residential buildings.

As described in the previous section, four local damage limit states are defined in terms of threshold values of steel and concrete material strain. The first limit state is specified as steel bar yielding whereas for the rest, mean values of post-yield limit strains for steel reinforcement and concrete material are suggested, as shown in Table 3.

Table 3 Definition of limit states for "high" code design RC buildings

Limit state	Limit strains	
	Steel strain (εs)	Concrete strain (εc)
Limit State 1	Steel bar yielding	-
Limit State 2	0.0125	0.005
Limit State 3	0.04	0.010
Limit State 4	0.06	-

The parametric analysis results to the construction of fragility curves as a function of PGA at the outcrop and PGD at the slope area for the different investigated models with the aid of the Maximum Likelihood Method. In the following, we perform a sensitivity analysis for the derived fragility curves, which allows gaining a better view on the relative influence of each analyzed feature to the expected damage level of the building and finally proposing generalized fragility curves.

3.1 Effect of slope inclination

First, the influence of the slope inclination to the fragility curves is shown. Figure 2 presents representative fragility curves in terms of PGD for varying slope inclinations (15^o, 30^o, 45^o) considering both sand and clayey slopes. In particular, the fragility curves for extensive and slight damage are presented for the sand and clayey slope respectively. Soft, relatively stiff and stiff soil materials are considered for the 15^o, 30^o and 45^o slope configurations respectively that distinguish different mechanical parameters for the sand and clay slopes. The height of the slope for the herein examined models is 20 m.

It is shown that, as it was expected, the slope inclination plays a crucial role in the fragility analysis of the building standing next to the slope's edge. However, it should be regarded in conjunction to the slope soil properties to obtain meaningful conclusions. Thus, for the sand slope, the building would suffer more damage as the slope inclination increases. On the contrary, for the clayey slope case, the building is expected to sustain less structural damage when standing on the 45^o inclined slope compared to the gentler ones, due to the stiff cohesive soil conditions assumed for the steep slope configuration. These trends seem to hold when considering both PGA and PGD as intensity measures.

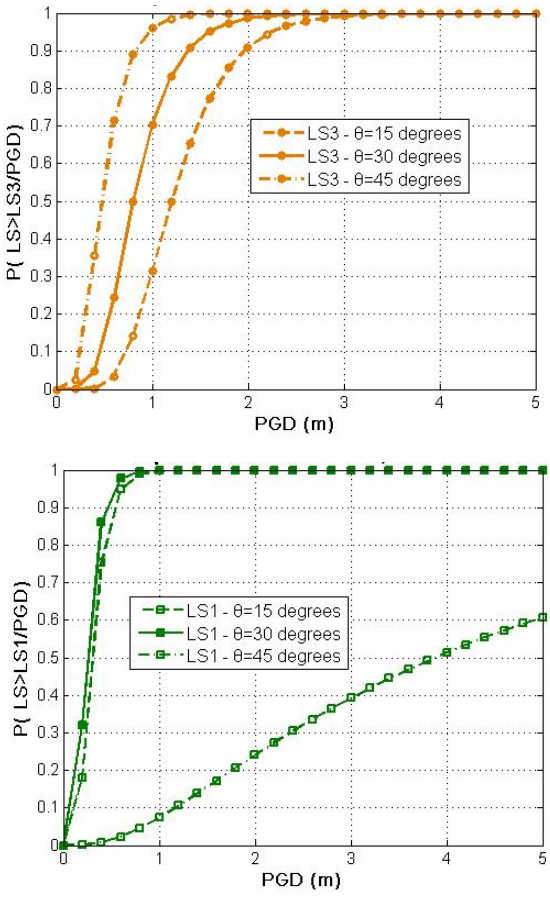


Figure 2 Fragility curves as a function of PGD when varying slope inclination [β=f (soil properties) = 15^o, 30^o, 45^o] for a 20 m high sand (up) and clay (bottom) slope respectively

3.2 Effect of slope height

The relative influence of the slope height on the vulnerability of the building to the permanent landslide differential displacement is also investigated in this study. Representative comparative plots of fragility curves as a function of PGA and PGD respectively are presented in Figure 3. Overall the slope height can moderately affect the structure's fragility. Different trends are revealed depending on the selected intensity measure (PGA or PGD) and the inclination angle of the analyzed slopes (15^o, 30^o, 45^o). Similar trends are evident for the clayey soil as well.

We see that, when using PGA as an intensity parameter, the vulnerability of the building increases with the slope height. As it would be normally expected, this increase is more pronounced for the 45^o steep slope configurations, whereas it is less important for the 15^o inclined slopes. In

contrast, the use of PGD as intensity measure, apart from some exceptions, is associated to lower vulnerability values of the building with increased slope heights. A plausible explanation of the latter is that in the case of higher slopes the mobilized sliding mass is larger and thus it affects more the building located close to the crest in terms of total displacements, which are larger, while the differential displacement demand on the building is reduced.

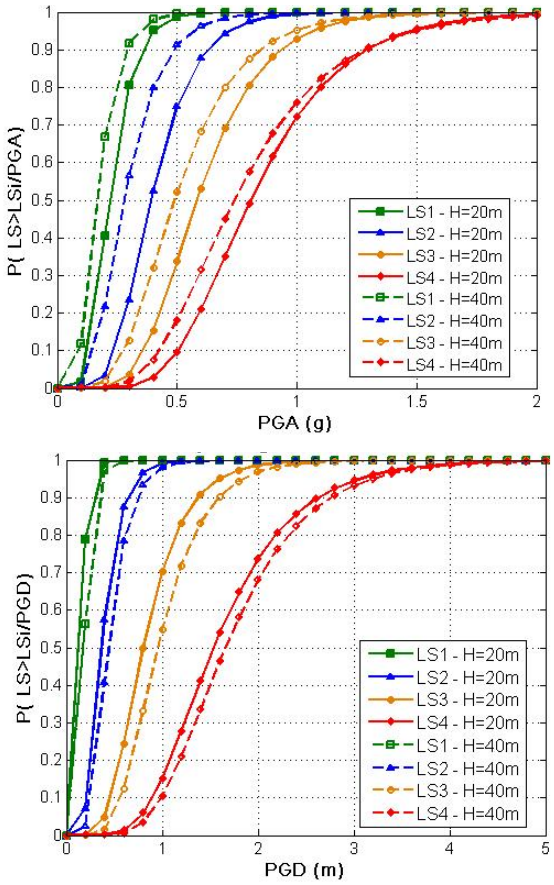


Figure 3 Fragility curves as a function of PGA (up) and PGD (bottom) respectively when varying slope height (H= 20, 40 m) for a 30° sand slope

3.3 Effect of soil material

The soil material is certainly a significant parameter in assessing building's vulnerability standing near the crest of a potentially precarious slope. Figure 4 presents the derived sets of fragility curves as a function of PGD, when varying slope soil properties (sand, clay) for the 15° and 45° slope configurations respectively. Soft and stiff (sand or clay) soil conditions are considered for the 15° and 45° inclined slopes respectively**.** It is observed that slopes consisting of clay material generally demonstrate better performance compared to sands when subjected to differential permanent ground displacements, resulting to lower vulnerability levels for the building. This is largely due to the inherent cohesive behavior of clay soil material that is associated to the formation of larger and deeper sliding surfaces. Thus, the considered one-bay building located at a close distance (i.e. 3m) from the slope's crest would be practically within the sliding mass and therefore it is primarily expected to move uniformly with the landslide mass rather than to distort differentially. The above observation is more noticeable as the slope inclination increases, i.e. for the stiffer clayey soil materials.

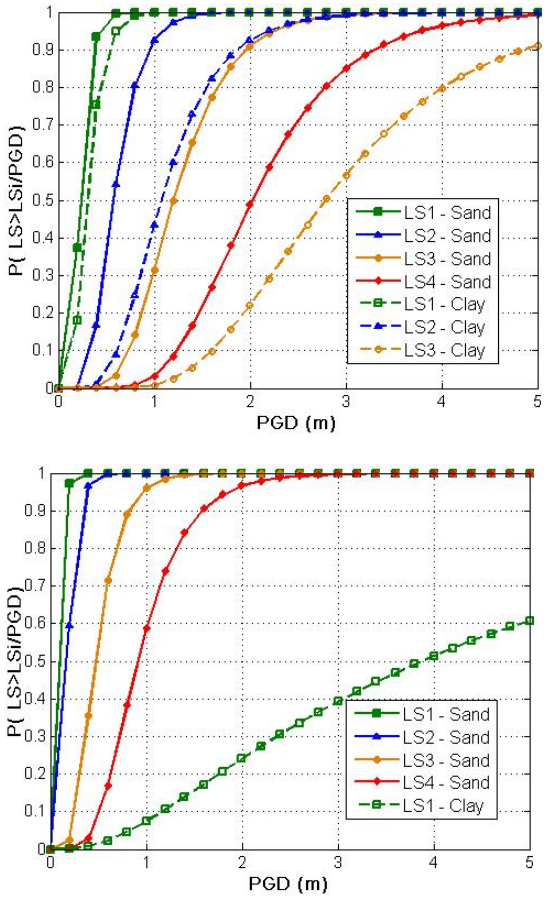


Figure 4 Fragility curves as a function of PGD when varying soil material for 15° (up) and 45° (bottom) slope configurations respectively

3.3 Effect of relative position of the building to the slope's crest

The distance of the assumed building from the crest of the slope may also considerably influence its vulnerability to the permanent landslide displacement. Figure 5 displays representative derived sets of fragility curves, when varying the distance from the crest (L= 3, 5m), for a 30° inclined sand and clayey slope respectively. Different observations can be made depending on the type of the considered slope soil materials. For sand slopes, the building is expected to suffer less damage as the distance from the crest increases. On the contrary, for the clayey slopes, the more distant building from the crest would be more vulnerable. This differentiation lies again on the nature of the slope soil materials involved, which are associated to the formation of sliding surfaces that may vary for very small and shallow for sands brittle slopes to large and deep for clayey deformable slopes. Thus, the assumed one-bay building standing at 3m

from the crest of the clayey slope is basically within the landslide mass and moves rather uniformly as a rigid body whereas for increasing distances from the crest (5m) the building shifts (partially) outside the landslide mass and therefore it exhibits higher differential (rather than uniform) ground displacements and hence more structural damage. On the other hand, the building located at the closest distance from the crest (i.e. 3m) of the sand slope is outside the landslide mass and consequently it is subjected to extensive differential deformation demand that is gradually decayed as the distance from the crest increases.

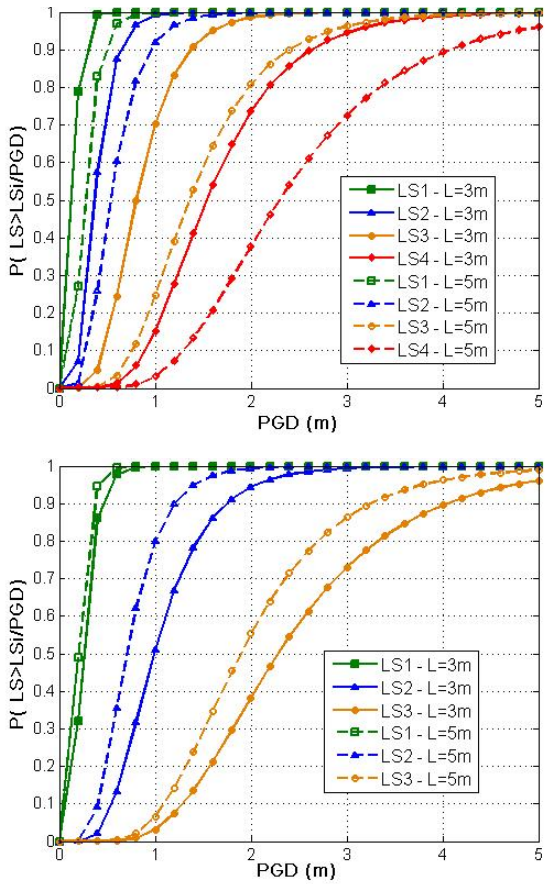


Figure 5 Fragility curves as a function of PGD when varying the distance from the crest (L= 3, 5m) for a 30° sand (up) and clay (bottom) slope respectively

3.3 Generalized fragility curves

Seven sets of fragility curves both in terms of PGA and PGD are proposed herein that could be used for several engineering applications. They are based on the main features that proved to most significantly influence the vulnerability of the building to the differential permanent landslide displacement. These are principally the slope inclination and the soil material of the slope, which are highly correlated. The slope height is also proved to be an important contributor to the building's fragility for the steep sand slope configurations. Thus, for the 45° inclined sand slopes fragility curves are also differentiated with respect to the considered slope height (H=20, 40 m). The latter curves are probably less accurate than the others as they are based on a smaller simulated dataset. It is noted that the proposed curves have been constructed considering the most adverse position of the building with respect to the landslide that was found to be different for sand and clay slopes. It is also important to note that the curves presented herein refer to "high-code", adequately confined RC frame structures. Tables 4 and 5 present the derived median and dispersions of the suggested curves when using PGA and PGD as intensity measure respectively.

As already shown, the building founded upon sand slopes is expected to demonstrate a greater damaging potential than the respective clayey ones. Thus, the corresponding curves referring to sand slopes are generally shifted to the left compared to clays (yielding to lower medians for the same limit states) and they are associated with a more rapid transition from slight to complete damage limits. These differences are becoming much more pronounced as the slope inclination increases. As it can be readily seen from the tables, the sand steep, high-rise slope and clay steep slope configurations are producing the most and the least damage respectively on the building. The dispersion of the suggested curves is found to vary from 0.39 to 0.66 and from 0.40 to 0.50 when considering PGA and PGD respectively as an intensity parameter.

Table 4 Parameters of fragility functions when using PGA as intensity parameter

Parametric models	Median PGA (g)				Dispersion β
	LS1	LS2	LS3	LS4	
sand_θ30	0.20	0.34	0.54	0.76	0.40
clay_θ30	0.27	0.53	0.93	1.37	0.46
sand_θ15	0.28	0.50	0.83	1.17	0.44
clay_θ15	0.23	0.54	1.01	1.51	0.50
sand_θ45_h20	0.23	0.35	0.55	0.81	0.39
sand_θ45_h40	0.12	0.19	0.25	0.30	0.44
clay_θ45	1.04	1.77	-	-	0.66

Table 5 Parameters of fragility functions when using PGD as intensity parameter

Parametric models	Median PGD (m)				Dispersion β
	LS1	LS2	LS3	LS4	
sand_θ30	0.15	0.39	0.87	1.64	0.43
clay_θ30	0.22	0.67	1.70	3.43	0.43
sand_θ15	0.24	0.60	1.29	2.19	0.40
clay_θ15	0.28	0.94	2.32	-	0.43
sand_θ45_h20	0.09	0.18	0.47	0.91	0.43
sand_θ45_h40	0.04	0.16	0.45	0.67	0.50
clay_θ45	0.77	1.72	-	-	0.47

4. COMPARISON OF THE PROPOSED FRAGILITY CURVES WITH LITERATURE ONES

The validity of the developed curves is assessed through their comparison with respective literature curves derived by different approaches. In particular, fragility

curves based on empirical damage data (Zhang and Ng 2005), engineering judgement (NIBS 2004) and on numerical simulations (Negulescu and Foerster 2010) are used for that comparison. Among the developed curves, the ones that are selected for the comparison refer to the RC frame building located next to the crest of the 30° inclined sand slope. These curves generally represent a somewhat moderate case in terms of the expected vulnerability of the building to the permanent landslide displacement (see Tables 4 and 5 for the corresponding fragility parameters).

4.1 Comparison with empirical curves

Zhang and Ng (2005), based on statistical analysis of the actual observed displacement on over 300 buildings, proposed empirical fragility curves in function of the limiting tolerable settlement (maximum vertical foundation displacement) and angular distortion (the average slope of the associated differential settlement of the building). The authors used the term "intolerable" to describe the displacements (settlements and angular distortions) that affect the safety, function and appearance of the structure. The buildings were classified into two main categories according to their foundation type (shallow or deep foundation). Among the studied buildings, they found that 95 experienced certain settlement and 205 certain angular distortion. The authors did not mention the origin of these displacements (e.g. due to landslide hazard). Table 6 provides the mean and standard deviations of the limiting tolerable and intolerable displacements of these buildings (shallow foundation and all foundations cases are shown herein) in terms of settlements and angular distortions respectively.

To allow for direct comparisons of the fragility curves developed in this study to the corresponding curves provided by Zhang and Ng (2005), the proposed curves were properly modified as a function of the induced settlement and angular distortion respectively. The Maximum Likelihood method, as described previously, is used to estimate the log-normal distributed fragility parameters. Comparative plots of the proposed curves for the studied building to the empirical ones as a function of settlement and angular distortion are given in Figure 6.

Overall, the comparison between the curves is judged satisfactory considering the large uncertainty and variability involved and the fact that the empirically derived curves are dealing with foundation movements irrespective of their origin (e.g. earthquake induced landslide hazard) and the superstructure typology. A good correlation is observed between the empirical curves and the proposed fragility curves for the building when using Settlement as a metric of the landslide displacement. It is seen that the proposed fragility curve for Limit state 2 (moderate structural damage) almost coincides with the empirical curve for limiting tolerable settlement. In addition, the proposed curve for Limit state 3 (extensive structural damage) is in good agreement with the curve proposed by Zhang and Ng for intolerable settlements. The correlation is not so good when using Angular distortion as an intensity parameter. In particular, the empirical curves are generally shifted to the left predicting quite low median values of limiting tolerable angular distortion and consequently increased expected building damage. These low values are probably associated to loss of functionality (e.g. due to tilting), which is not accounted for in the proposed numerically derived curves, and not to structural damage to the building members.

Table 6 Statistics of intolerable and limiting tolerable settlement and angular distortion of buildings (adapted from Zhang and Ng, 2005)

Statistics	All foundations		Shallow foundations	
	Mean	Standard deviation	Mean	Standard deviation
Observed intolerable settlement (cm)	40.3	33.4	39.9	32.3
Limiting tolerable settlement (cm)	12.3	7.3	12.9	7.2
Observed intolerable angular distortion	0.0116	0.0143	0.0119	0.0138
Limiting tolerable angular distortion	0.0028	0.0024	0.003	0.0015

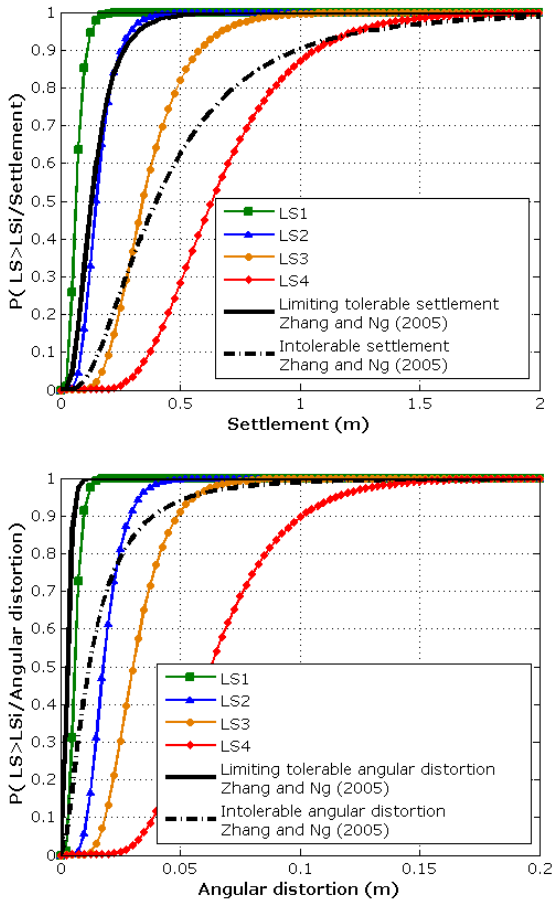


Figure 6 Comparison of the proposed fragility curves as a function of settlement (up) and angular distortion (bottom) for the studied building with the corresponding empirical curves provided by Zhang and Ng (2005)

4.2 Comparison with expert-judgment curves

HAZUS loss estimation methodology (NIBS 2004) provided fragility curves for structures subjected to earthquake-induced ground failure taking into account the expected mode of failure and the foundation type. Separate fragility curves distinguishing between ground failure due to lateral spreading and ground failure due to ground settlement, and between shallow and deep foundations were proposed. Only one combined Extensive/Complete damage state was considered. In essence, according to HAZUS, buildings were assumed to be either undamaged or severely damaged due to ground failure. Fragility curves were derived as a function of permanent ground displacement (PGD) using a form similar to those used to estimate shaking damage. Engineering judgment was used to develop a set of assumptions, which define building fragility. The expert judgemental curves provided by HAZUS are compared with the numerically derived curves for extensive and complete damage for the building on flexible and stiff foundations (Fig. 7). The herein proposed curves are given as a function of the maximum permanent ground displacement (PGD) the slope area.

A generally good agreement between the proposed curves for the building on flexible foundation and the respective HAZUS curves is observed. In particular, the later curves predict larger vulnerability values when damage due to settlements (principally vertical movement) is more imminent and lower vulnerability values when the damage occurs as a result of extensive lateral spreading (principally horizontal movement).

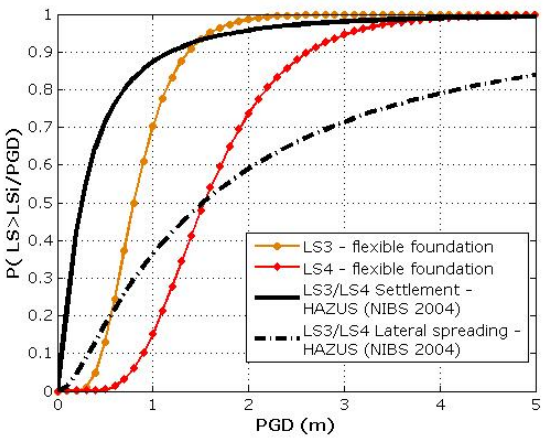


Figure 7 Comparison of the proposed fragility curves for extensive and complete damage as a function of permanent ground displacement (PGD) for the studied building with the corresponding expert judgment curves provided by HAZUS (NIBS, 2004)

4.3 Comparison with analytical curves

Negulescu and Foerster (2010) proposed a simplified analytical methodology to assess the vulnerability of simple RC frame structures subjected to free-field differential ground displacement based on 2-D nonlinear static time-history analyses. They examined different parameters that could influence structural behavior: foundation type (i.e. different combinations of links), cross-section geometry, section reinforcement degree, displacement magnitudes and displacement inclination angles. Structural damage levels were considered, as in the present study, based on the local strain limits of steel and concrete constitutive materials. A set of preliminary fragility curves was derived considering encasing links for the foundation to represent a continuous surface foundation or a building with a basement. To assess the validity of the curves proposed in this research, they are also compared with the curves given in Negulescu and Foerster (2010). For the purpose of this comparison, the herein proposed curves are modified in terms of differential ground displacement at the foundation level.

Figure 8 shows comparative graphs of the proposed fragility curves as a function of differential ground displacement for the building with the corresponding analytical curves given in Negulescu and Foerster (2010). It is observed that the suggested curves in this research for the building are in good correlation with the Negulescu and Foerster‘s curves, especially for lower levels of damage (e.g. LS1 and LS2), taking also into account the different assumptions and uncertainties associated with them.

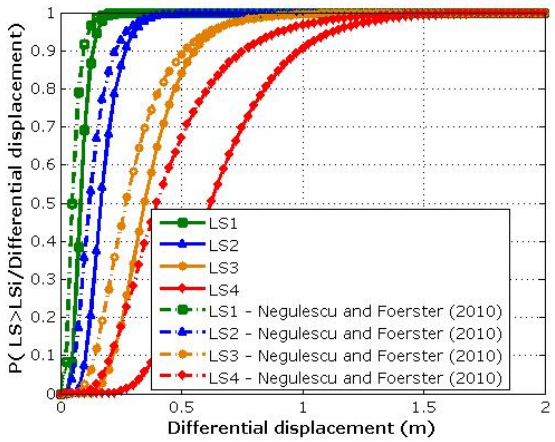


Figure 8 Comparison of the proposed fragility curves as a function of differential ground displacement for the studied building with the corresponding analytical curves provided by Negulescu and Foerster (2010)

5. CONCLUSIONS

Several sets of fragility curves for low-rise RC frame structures both in terms of PGA and PGD have been proposed based on an extensive numerical parametric investigation of various step-like slope configurations, soil properties and distances of the building with respect to the slope’s crown. Sensitivity results have shown that, among the analyzed features, the ones that have proved to affect more drastically the vulnerability of the building to the differential permanent deformation due to the seismically

induced landslide hazard are the slope inclination in conjunction with the slope soil material. The slope height has also turned out to be an important contributor to the building's fragility for the 45° inclined sand slopes. Based on the above observations, seven sets of fragility curves have been suggested depending on most influential parameters and considering the most unfavorable position of the building with respect to the landslide. The latter was found to largely depend on the type of the slope soil materials involved (sand or clay).

The reliability of the proposed fragility curves has been assessed through the comparison of representative developed fragility curves with corresponding literature ones derived by different approaches (e.g. empirical, expert-judgment, analytical). Relatively good correlations have been shown in all cases enhancing the validity of the curves. Thus, the suggested curves can be efficiently employed within a QRA study to assess the vulnerability of RC buildings subjected to earthquake induced slope displacements.

Acknowledgements:

The work described in this paper was supported by the project SAFELAND "Living with landslide risk in Europe: Assessment, effects of global change, and risk management strategies" under Grant Agreement No. 226479 in the 7th Framework Program of the European Commission. This support is gratefully acknowledged.

References:

Bird, J. F., Bommer, J. J., Crowley, H., and Pinho, R. (2006), "Modelling liquefaction-induced building damage in earthquake loss estimation," *Soil dynamics and Earthquake Engineering*, **26** (1), 15-30.

Bird, J. F., Crowley, H., Pinho, R. and Bommer, J. J. (2005), "Assessment of building response to liquefaction induced differential ground deformation," *Bul of the New Zealand Society for Earthquake Engineering*, **38**(4), 215-234.

Bommer, J., and Rodriguez, C. (2002), "Earthquake-induced landslides in Central America," *Engineering Geology*, **63**(3-4), 189-220.

CEN-European Committee for Standardization (2003), p.rENV 1998-1 – Eurocode 8: Design of structures for earthquake resistance. Part 1: General rules, seismic actions and rules for buildings, Draft No. 4, Brussels, Belgium.

Crowley, H., Pinho, R., and Bommer, J. J. (2004), "A probabilistic displacement-based vulnerability assessment procedure for earthquake loss estimation," *Bulletin of Earthquake Engineering*, **2**(2), 173-219.

Cundall, P. A., Hansteen, H., Lacasse, S., and Selnes, P. B. (1980), "NESSI – soil structure interaction programme for dynamic and static problems," Report 51508-9, December, Norwegian Geotechnical Institute.

Dai, F. C., Lee, C. F. and Ngai Y. Y. (2002), "Landslide risk assessment and management: an overview," *Engineering Geology,* **64**(1), 65-87.

EAK2000 (2000), Greek Seismic Code, Organization of seismic planning and protection.

Fotopoulou, S. (2012), Seismic vulnerability of reinforced concrete buildings in sliding slopes, PhD thesis, Dept. of Civil Engineering, Aristotle University of Thessaloniki, Greece.

Fotopoulou, S., Anastasiadis, A., and Pitilakis K. (2011), "Building vulnerability to the 2008 Ilia- Achaia earthquake induced slides", *2nd World Landslide Forum*, 3-8 October.

Fotopoulou, S., and Pitilakis, K. (2012), "Vulnerability assessment of reinforced concrete buildings subjected to seismically triggered slow-moving earth slides," *Landslides* (DOI: 10.1007/s10346-012-0345-5).

Itasca Consulting Group (2008), Inc. FLAC (Fast Lagrangian Analysis of Continua), ver. 6.0. Itasca Consulting Group, Inc., Minneapolis.

Lysmer, J., and Kuhlemeyer, R. L. (1969). "Finite dynamic model for infinite media," *Journal of Engineering Mechanics*, **95**, 859–877.

Mander, J. B., Priestley, M. J. N., and Park, R. (1988), "Theoretical stress-strain model for confined concrete", *Journal of Structural Engineering*, **114**(8), 1804-1826.

National Institute of Building Sciences (2004), "Direct physical damage—general building stock," HAZUS-MH Technical manual, Chapter 5, Federal Emergency Management Agency, Washington, D.C.

Negulescu, C., and Foerster, E. (2010), "Parametric studies and quantitative assessment of the vulnerability of a RC frame building exposed to differential settlements," *Natural Hazards and Earth System Sciences,* **10**, 1781-1792.

SeismoSoft, SeismoStruct (2011), "A computer program for static and dynamic nonlinear analysis of framed structures," Available from URL: www.seismosoft.com

Shinozuka, M., Feng, M. Q., Kim, H. K., Uzawa, T., and Ueda, T. (2003), "Statistical analysis of fragility curves," Technical Report MCEER-03-0002, State University of New York, Buffalo.

Shinozuka, M., Feng, M. Q., Lee, J., and Naganuma, T. (2000). "Statistical analysis of fragility curves," *Journal of Engineering Mechanics,* American Society of Civil Engineers, **126**(12), 1224–1231.

Zhang, L.M., and Ng, A. M. Y. (2005), "Probabilistic limiting tolerable displacements for serviceability limit state design of foundations," *Geotechnique*, **55**(2), 151–161.

10CUEE CONFERENCE PROCEEDINGS
10th International Conference on Urban Earthquake Engineering
March 1-2, 2013, Tokyo Institute of Technology, Tokyo, Japan

DEVELOPMENT OF FRAGILITY CURVES OF MID-RISE REINFORCED CONCRETE MOMENT-RESISTING FRAME STRUCTURES IN THE GREATER METRO MANILA AREA, PHILIPPINES

Raniel Suiza[1)], Benito Pacheco[2,12)], Eric Augustus Tingatinga[3)], Jaime Hernandez, Jr.[4,12)], Ulpiano Ignacio, Jr.[5,12)], Fernando Germar[6,12)], Marie Claire Pascua[7)], Liezl Raissa Tan[8)], Romeo Eliezer Longalong[9,12)], William Mata[10,12)], and Mark Albert Zarco[11,12)]

1,7,8,9,10) Instructor, Institute of Civil Engineering, University of the Philippines Diliman, Philippines
2,5,11) Professor, Institute of Civil Engineering, University of the Philippines Diliman, Philippines
3) Assistant Professor, Institute of Civil Engineering, University of the Philippines Diliman, Philippines
4,6) Associate Professor, Institute of Civil Engineering, University of the Philippines Diliman, Philippines
12) Philippine Institute of Civil Engineers Inc., Manila, Philippines
rmsuiza@yahoo.com, riskguide101@up.edu.ph, eatingatinga@gmail.com, jnj.hernandez@gmail.com, jun613@gmail.com, fjgermar@yahoo.com, marieclaire.pascua@gmail.com, liezl.raissa.tan@gmail.com, rulongalong@gmail.com, william.mata@yahoo.com, mark.zarco@gmail.com

Abstract: In this paper, the fragility curves of mid-rise reinforced concrete moment-resisting frame structures in the Greater Metro Manila Area, Philippines are derived. Aside from typical structural parameters known to strongly influence fragility curves, soil type and fault proximity are also considered. The methodology implemented involves the use of a database of building models and the Capacity Spectrum Method for generating the probability distribution of the structural response for a given peak ground motion. In this study, two sets of fragility curves were developed considering two different vintages: pre-1992 and post-1992. For buildings constructed after 1992, 50% of the building population will experience slight damage at 0.13g, moderate damage at 0.15g, extensive damage at 0.26g, and complete damage at 0.52g. On the other hand, for buildings constructed before 1992, 50% of the building population will experience slight damage at 0.16g, moderate damage at 0.18g, extensive damage at 0.26g, and complete damage at 0.52g.

1. INTRODUCTION

The Philippines, being part of the Pacific Ring of Fire, is prone to earthquakes. If a destructive earthquake is to happen again in the future, buildings and other structures are at risk. Damage and loss of these structures will definitely cause human lives, businesses and livelihood to be lost as well. This is why risk management is important and in order to manage risk, it should be assessed. Part of the preparation of an earthquake disaster mitigation plan is the quantification of building vulnerability. A component of which is the development of seismic fragility curves that are used to predict the probability of reaching or exceeding specific damage states for a given level of peak ground motion. It is developed using a building database for a region of interest analyzed using the Nonlinear Static Pushover Method to estimate the peak response of the structures and to generate the frequency distribution of the structural responses for a given ground motion (Longalong et. al., 2012).

One major area of improvement is in the development of fragility curves for common building types in the region of interest. A fragility curve expresses the probability of being in or exceeding a certain damage state as a function of the hazard (Giovinazzi et. al., 2002). This paper discusses the generation of fragility curves of one of the common building types in the Philippines which is a mid-rise reinforced concrete moment-resisting frame structure (C1-M). The building height considered in this study ranges from three to eight storeys, and the lateral force-resisting system assumed is a moment-resisting frame system. The pilot area or the region of interest is identified as the Greater Metro Manila Area which consists of the National Capital Region and several nearby provinces in the country.

2. METHODOLOGY

Several approaches exist for developing fragility curves, as shown in Figure 1. The heuristic approach relies heavily on expert's opinion, whereas the empirical approach requires actual damage data. The computational approach, on the other hand, can be static or dynamic and linear or nonlinear. In this research, the different approaches were used in deriving fragility curves.

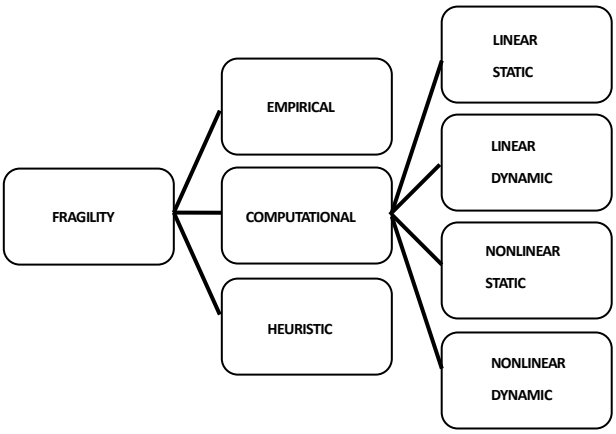


Figure 1 Conceptual Framework

Due to the absence of strong-motion earthquake records in the country, a nonlinear dynamic analysis cannot be conducted. Thus, a nonlinear static analysis called the nonlinear pushover method is used in this research. The flowchart in Figure 2 shows the computational procedure used in developing fragility curves.

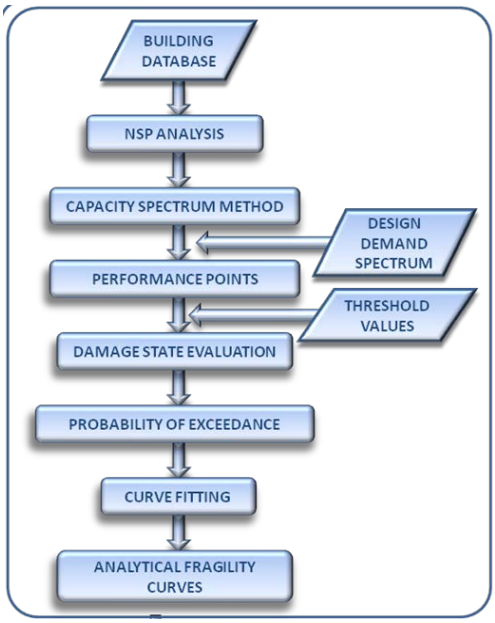


Figure 2 Fragility Curve Development Procedure (UPD-ICE Technical Report, 2011)

2.1 Development of Building Database, Structural Properties, and Sensitivity Analyses

The building database consists of mid-rise reinforced concrete structures with varying structural configurations, dimensions, and material properties. To limit the number of structures in the database, sensitivity analyses were performed. Sensitivity, measured by the ratio of the range of spectral displacement to the mean of the spectral displacements considering changes in the parameter, greater than five percent is assumed to have significant effect on the spectral displacement (Longalong et. al., 2012).

After performing the sensitivity analyses, parameters considered to have an effect on the spectral displacement in C1-M structures are bay length, number of storeys, storey height, column dimension, and beam dimension. Bay length ranged from three to six meters. The number of storeys ranged from three to eight. Storey heights considered were 2.5 m and 3 m. Columns were limited to square dimensions with sizes varying from 0.4 to 0.7 m. Beam widths considered were from 0.2 to 0.5 m while beam depth considered were from 0.4 to 0.75 m. Steel reinforcement yield strength considered was 40 ksi. Columns were modeled to have pin connections at the base. Table 1 illustrates a sample list of models used in this research.

Table 1 Sample C1-M Model List

Model ID	Bays	Bay Length (m)	No. of Storeys	Col Width (m)	Beam (m)
C1M-01	3	4	3	0.4	0.20x0.40
C1M-02	3	5	3	0.5	0.20x0.40
C1M-03	3	6	3	0.6	0.25x0.40
C1M-13	3	4	4	0.4	0.35x0.55
C1M-17	4	5	4	0.5	0.35x0.60
C1M-18	4	6	4	0.6	0.40x0.60
C1M-20	3	5	5	0.5	0.35x0.55
C1M-21	3	6	5	0.6	0.40x0.60
C1M-27	3	6	6	0.6	0.40x0.60
C1M-33	4	6	7	0.6	0.40x0.60

To account the vintage or the age of the structure, the local structural code of the country was used as the basis. The structures were identified among three vintages: Pre-Code, structures that were constructed before 1972; Low Code, structures that were constructed between 1972 and 1992; and High Code, structures that were constructed after 1992. Table 2 shows some identified differences in construction practice during the three periods.

Table 2 Vintage Parameters (Pacheco et. al., 2011)

Parameter	Pre-Code (Pre-1972)	Low Code (1972-1992)	High Code (Post-1992)
Ductility Requirements	no conventional requirements	minimal requirements	stricter requirements
Compressive Strength, f'_c	3,000 ksi	3,000 ksi	4,000 ksi
V/W	0.0731	0.0938	0.1171

2.2 Determination of Structure Capacity Using Nonlinear Static Pushover Analysis

Nonlinear Static Pushover (NSP) Analysis is performed to come up with the pushover curve (representing the capacity) of the structure. Nonlinear pushover procedure involves the application of horizontal forces incrementally applied in a prescribed loading pattern along the building height. Every structural member that fails is effectively removed by reducing its stiffness. The process of applying

horizontal forces then removing structural members is continued until the structure is no longer stable. Plotting the base shear force (V) against the deformation (D) experienced by the structure will give the pushover curve or the capacity curve. The software ETABS is used as an aid in performing the NSP Analysis which follows the guidelines presented in ATC-40. Figure 3 shows an example of a capacity spectrum of an RC model.

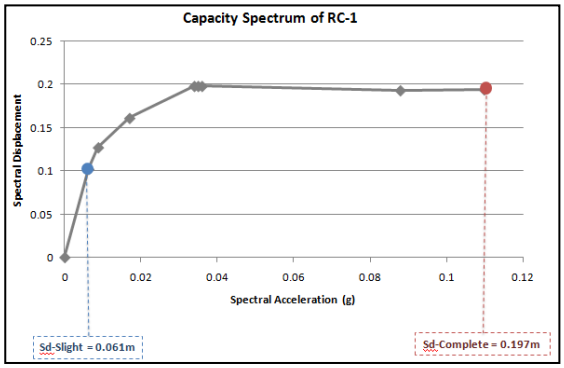


Figure 3 Sample Capacity Spectrum

2.3 Earthquake Demand

To characterize the earthquake demand, standardized code response spectrum was used due to limitations on available earthquake records. The response spectrum is defined in three parts, a constant spectral acceleration, constant spectral velocity and a constant spectral displacement. It is based on magnitude, peak ground acceleration (PGA), and amplification factors which are reflective of the soil profile. The soil site for the Greater Metro Manila Area is of soil types C, D, and E which give several values for the seismic coefficients C_a and C_v. These values will define the standardized code spectrum as shown in Figure 4. The GMI parameter is taken to be the spectral acceleration intercept which is also regarded as the peak ground acceleration.

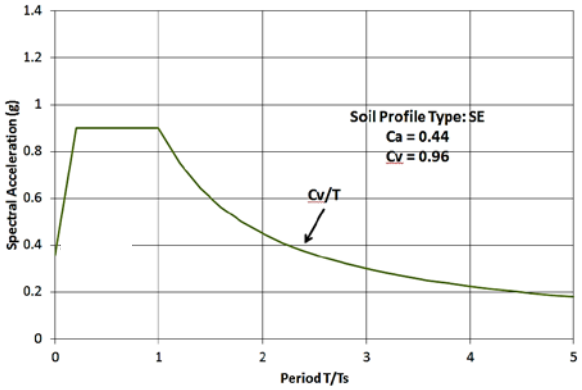


Figure 4 Earthquake Demand Spectrum (NSCP 2010)

2.4 Capacity Spectrum Method

The Capacity Spectrum Method (CSM) from ATC-40 is used to determine the performance points of each building model when subjected to a particular earthquake demand. These performance points will serve as the basis for computing the fragility curves by determining how many of them fall within the set damage thresholds.

Graphically, the performance point is the intersection of the capacity spectrum and the demand spectrum (ATC 40). Essentially these performance points describe the peak spectral response of a structure at a given demand level. Capacity Spectrum Method (CSM) is employed to generate performance points. Capacity curves derived from nonlinear pushover analysis are converted into spectral values. Similarly, demand curves are also converted to spectral values to be able to superimpose with the capacity spectrum in the same coordinate system.

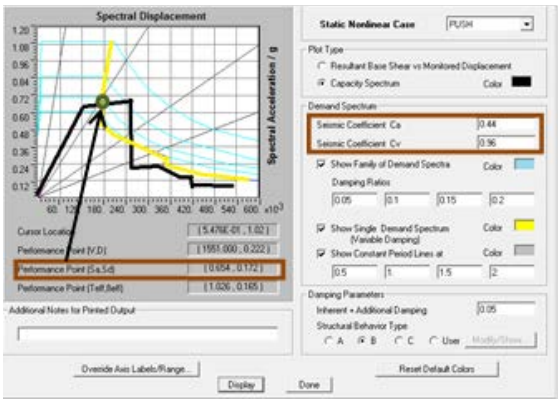


Figure 5 Sample Computation of Performance Points

2.5 Definition of Threshold Values for Different Damage States

In order to identify whether a building is in the slight, moderate, extensive or complete collapse damage state, it will require a certain criterion. This is in the form of drift ratio at the threshold of structural damage. HAZUS has developed threshold values using inter-storey drift for different building types and for different seismic design levels. These values determine whether a structure is in the slight, moderate, extensive or complete damage state.

Threshold values can be established from the pushover curves. According to Bazzurro (2006), *DS1* [Slight], or onset of damage, is defined where nonlinear behavior starts on the curve, whereas the Complete Damage State according to Gencturk et.al. (2007) is taken as the post-peak displacement when the load carrying capacity has undergone a small reduction. Moreover, instead of defining the threshold values in terms of inter-storey drifts derived from the pushover curve, the threshold values were defined in terms of spectral displacements derived from the equivalent capacity spectrum since these threshold values will be compared with the performance points which are in spectral values. The moderate and extensive damage state threshold values are calculated based on the ratios of the threshold values provided in HAZUS. These coefficients have different values for different building types. Figure 6 illustrates a sample calculation of damage thresholds for one C1-M model.

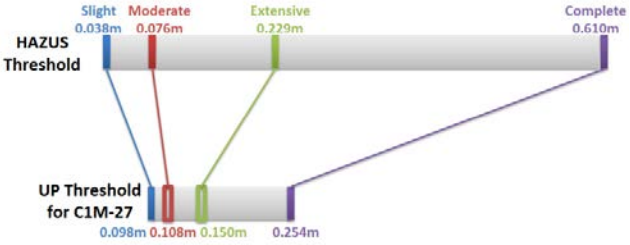


Figure 6 Sample Calculation of Damage Thresholds

2.6 Development of Initial Fragility Curves

For each structure, the threshold values in terms of spectral displacements were determined. To develop the fragility curves, the earthquake level was varied by changing the parameters that define the code response spectrum. In each earthquake level, the number of structures that have their performance point exceeding the set damage thresholds was recorded to come up with the probability of exceeding the damage state. Table 3 gives an example of a damage probability matrix.

Table 3 Sample Damage Probability Matrix

PGA(g)	Probability of Exceeding a Damage State			
	Slight	Moderate	Extensive	Complete
0.066	0.0000	0.0000	0.0000	0.0000
0.132	0.0000	0.0000	0.0000	0.0000
0.176	0.0571	0.0000	0.0000	0.0000
0.220	0.4286	0.1714	0.0000	0.0000
0.330	1.0000	0.8857	0.1714	0.0000
0.440	1.0000	1.0000	0.4571	0.0000
0.550	1.0000	1.0000	0.9714	0.1429
0.660	1.0000	1.0000	1.0000	0.6857
0.770	1.0000	1.0000	1.0000	0.8857

The probability function of seismic fragility curves is approximated by the lognormal cumulative distribution function given by Equation 1.

$$P[ds \mid GMI] = \Phi\left[\frac{1}{\beta_{ds}} \ln\left(\frac{GMI}{\overline{GMI}_{ds}}\right)\right] \qquad (1)$$

There are only two parameters defining this curve which is the median $\overline{GMI}_{ds}$ and the uncertainty β_{ds}. The aim is to determine these values such that the resulting curve represents the data points obtained. Figure 8 shows the curve-fitting of the fragility curves (broken lines) corresponding to Slight (S), Moderate (M), Extensive (E) and Complete (C) damage states.

2.7 Adjustments in the Uncertainty Parameter: Epistemic Uncertainty

Uncertainty in the assessment of structures is made up of aleatory, uncertainty that is inherently random, and epistemic uncertainties, uncertainty that is due to lack of knowledge as a result of incomplete data, ignorance or assumptions in modeling. Following the work of Tan (2011), the aleatory uncertainty is estimated when a lognormal cumulative probability distribution is fitted to the computed data points. The epistemic uncertainty, on the other hand, is computed using quality ratings from a survey of experts on the following sources of variability: design requirements, test data and modeling. Following the FEMA P695 method, the quality ratings are translated into quantitative values of uncertainty based on the following scale: (A) superior, $\beta = 0.10$; (B) Good, $\beta = 0.20$;(C) Fair, $\beta = 0.35$; (D) Poor, $\beta = 0.50$. These sources of uncertainties are statistically independent of each other, so that the total uncertainty β is computed by taking the square root of the sum of the squares of the uncertainties from the different sources. Using SRSS method to combine the different sources of epistemic uncertainties gives a value of 0.7036.

2.8 Development of Final Fragility Curves

Using the fragility curves initially derived from the Capacity Spectrum Method, the value for the epistemic uncertainty is then incorporated. With this, three sets of curves are generated representing the three vintages identified earlier in this paper.

3. RESULTS AND DISCUSSIONS

3.1 Fragility Curves

Fragility curves were then fitted and epistemic uncertainties were included. This is regarded as the computational fragility curves. Figures 7 and 8 illustrate the three sets of fragility curves according to vintage. It can be observed that the Pre-Code and Low Code curves are very close that they may be merged as one set of curves.

For example, referring to the second set of curves, at a peak ground acceleration of 0.5g, the probabilities of exceeding the slight, moderate, extensive, and complete damage states are around 96%, 94%, 81%, and 48% respectively. This means that the probability of no damage is 4%. On the other hand, the probabilities of slight, moderate, extensive, and complete damages are 2%, 13%, 33%, and 48% respectively.

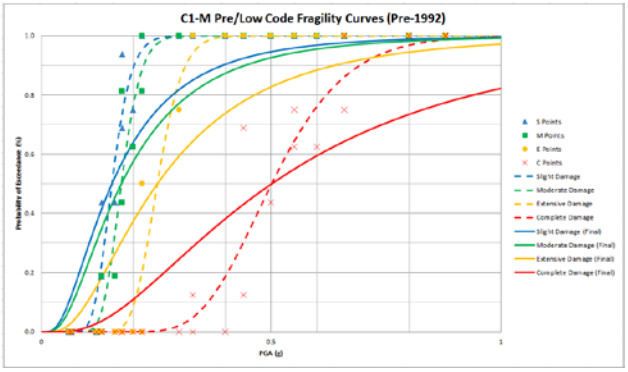


Figure 7 C1-M Fragility Curves (Pre-1992)

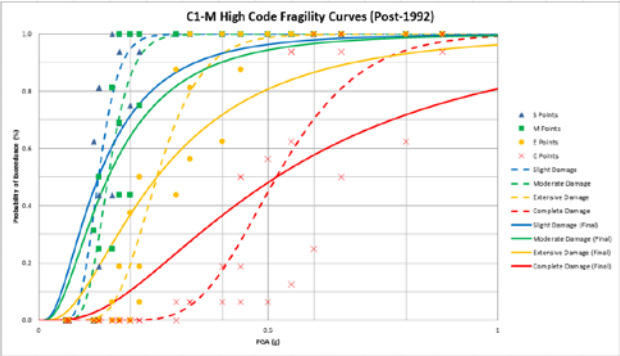


Figure 8 C1-M Fragility Curves (Post-1992)

3.2 Fragility Curve Comparison

The two sets of curves are then plotted using the same graph for comparison. It is observed that the fragility curves for Pre and Low Code and for High Code are very close to one another as shown in Figure 9. The curve parameters (i.e. median and standard deviation) are shown in Table 4.

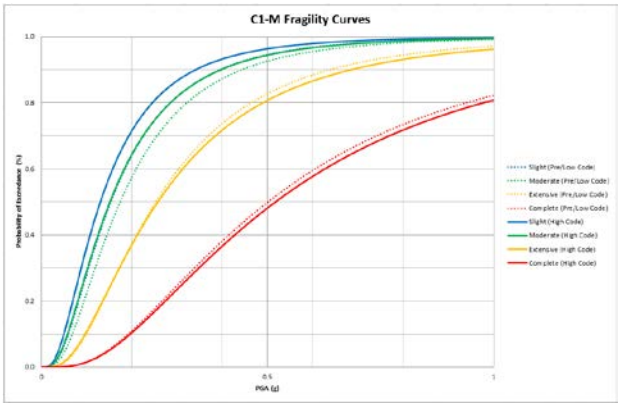


Figure 9 C1-M Fragility Curves

Table 4 C1-M Fragility Curve Parameters

Damage State	Pre/Low Code		High Code	
	Median (g)	Beta	Median (g)	Beta
S	0.1537	0.7352	0.1304	0.7510
M	0.1742	0.7293	0.1516	0.7516
E	0.2525	0.7238	0.2577	0.7638
C	0.5012	0.7476	0.5179	0.7556

4. CONCLUSIONS

Seismic fragility of mid-rise reinforced concrete frame structures in the Greater Metro Manila Area, Philippines were derived using the capacity spectrum method. From a model database of C1-M structures created by varying parameters sensitive to spectral displacement, nonlinear static pushover curves were generated. Damage thresholds were then established from each pushover curve. After varying the demand spectra by changing seismic coefficients, the number of structures which have their performance points exceed the damage threshold were counted. This number corresponds to the probability of exceeding the damage state. Lognormal cumulative distribution functions were fitted for each damage state.

In order to include the non-ductile behaviour of reinforced concrete members designed using pre and low code, a frame hinge reduction factor for shear and bending moment capacity was applied to the models before the nonlinear pushover analysis is conducted to determine the capacity curve. Thus, another step is added to the existing procedure in order to analyze buildings of a different vintage. The results show that a single set of fragility curves and vulnerability curve can be adopted for the pre and low code vintage buildings. Also, it was observed that the fragility curves for all codes were very close to one another.

Acknowledgements:

The UPD Institute of Civil Engineering would like to acknowledge the support provided by the Australian Agency for International Development (AusAID) through the Greater Metro Manila Area – Risk Analysis Project between the Philippine Institute of Volcanology and Seismology (PHIVOLCS-DOST), the Philippine Atmospheric Geophysical and Astronomical Services Administration (PAGASA-DOST), and Geoscience Australia (GA).

References:

ASEP (2010), "National Structural Code of the Philippines (NSCP)." Volume 1, 6th edition.

ATC-40 (1996), "Seismic Evaluation and Retrofit of Concrete Buildings." Vol. I-II, Applied Technology Council, 555 Twin Dolphin Drive, Suite 550, Redwood City, California 94065.

ATC-63 (2009), "FEMA P-695: Quantification of Building Seismic Performance Factors." Redwood City, California: Applied Technology Council.

Bazzurro, P. and Luco, N., (2006), "Advanced Seismic Assessment Guidelines." PEER Report 2006/05, Pacific Earthquake Engineering Research Center, University of California Berkeley.

Gencturk, et.al. (2007), "Fragility Relationships for Populations of Buildings Based on Inelastic Response." Mid-America Earthquake Center, Urbana Illinois.

JICA, PHIVOLCS, & MMDA. (2004), "Earthquake Impact Reduction Study for Metropolitan Manila." Manila: Philippine Institute of Volcanology and Seismology.

Kircher, C.A., Whitman, R.V., and Holmes, W.T. (2006), "HAZUS Earthquake Loss Estimation Methods." Natural Hazards Review, Vol. 7, No. 2, May 1, 2006. ASCE, ISSN 1527-6988/2006/2-45-59.

Longalong, R.E., Pacheco, B.M., Hernandez Jr. H., Ignacio Jr. U., Tingatinga, E.A., Tan, L.R., Pascua, M.C., Suiza R.M., Mata, W., Zarco, M.H. (2012), "Quantification of Seismic Vulnerability of Low-Rise Reinforced Concrete Moment Frame Structures in Iloilo City, Philippines." Proceedings, 5th ASEAN Civil Engineering Conference, Ho Chi Minh City, Vietnam, Oct. 2012.

Midorikawa, S., Fujimoto, K., Yamanaka, H., Miura, H., Pacheco,

B.M., and Bautista, B.C. (2004), "GIS-based Earthquake Damage Assessment Considering Seismic Capacity of Existing Buildings in Metro Manila, Philippines." In Proceedings of the Asia Conference on Earthquake Engineering – Manila, Philippines

Pacheco, B.M., Hernandez Jr. H., Ignacio Jr. U., Tingatinga, E.A., Tan, L.R., Pascua, M.C., Suiza R.M., Longalong, R.E., Mata, W., Zarco, M.H. (2011), "Development of earthquake vulnerability curves for key building types in Iloilo City." Proceedings, PICE National Conference, Cagayan De Oro, Nov. 2011.

Tan, L.R.E. (2011), "Quantification of Uncertainties of Seismic Fragility Curves Developed for the Philippines." An Undergraduate Research Project in partial fulfillment of the requirements of the University of the Philippines for the degree of Bachelor of Science in Civil Engineering. Manila: University of the Philippines Diliman.

UPD-ICE (2011). "Development of Vulnerability Curves of Key Building Types in the Philippines." Pre-Final Technical Report. Institute of Civil Engineering, University of the Philippines, Diliman, Quezon City.

Whitman, R.V., Anagnos, T., Kircher, C.A., Lagorio, H.J., Lawson, R.S., and Schneider, P. (1997). "Development of a National Earthquake Loss Estimation Methodology."

Yeh, C.H. (2009), "Applications of Taiwan Earthquake Loss Estimation System." Presented during the International Training Program (ITP) 2009 at the National Center for Research in Earthquake Engineering (NCREE), Taipei, Taiwan.

10CUEE CONFERENCE PROCEEDINGS
10th International Conference on Urban Earthquake Engineering
March 1-2, 2013, Tokyo Institute of Technology, Tokyo, Japan

EARTHQUAKE RISK ANALYSIS METHOD APPLIED TO A TOWN IN HUNGARY

Orsolya Kegyes-Brassai[1)] and Dr. Richard P. Ray[2)]

1) Senior lecturer, Dept. of Structural and Geotechnical Engineering, Faculty of Engineering Sciences, Széchenyi István University, Hungary
2) Professor, Dept. of Structural and Geotechnical Engineering, Faculty of Engineering Sciences, Széchenyi István University, Hungary
kegyesbo@sze.hu, ray@sze.hu

Abstract: Determining the earthquake risk of buildings in a town or settlement has lately become a more prominent issue. The process can provide important data for governments, authorities, disaster management and insurance companies to better understand risks to many buildings and engineering systems rather than a single building. By this assessment process they can make better decisions about remedial actions, insurance underwriting, and evacuation and rescue. This paper addresses the rapid evaluation of a large number of similar buildings in the area of Győr. The steps involve determination of the hazard, assessing building stock, and computing vulnerability. The method for determination of vulnerability functions is a non-linear static analysis using a simple model with the bilinear approximation of the capacity curve, assuming first mode force distribution and linear first mode shape thus linear strength distribution. From the curve of the seismic demand and the shear capacity of the building the vulnerability function of the building can be obtained. These vulnerability functions should be derived for typical layouts, offering a family of curves allowing the experts to decide the vulnerability category of a specific building on-site based on visual screening.

1. INTRODUCTION

Recent earthquakes with high number of casualties and enormous devastation proved that the hazard of natural disasters should not be neglected. Preventive approaches have received greater attention recently. Research in earthquake hazard mitigation has focused on evaluating possible damage scenarios for different magnitude events (Luco et al 2007; Committee on National Earthquake Resilience 2011). Two widely different approaches exist; one considers the effect of previous earthquakes, listing the damaged buildings and casualties. The other offers a method to evaluate possible damages prior to an event. The latter method facilitates prevention by gathering information about the state of the building stock and the expected damages, so the authorities can strengthen the most vulnerable buildings in order to mitigate risk.

The challenge with this method is that many uncertainties must be taken into consideration. In order to determine earthquake risk within towns a fast and simple method should be developed. Otherwise it would be very time-consuming and require too much expert participation. The steps are the following:

- determin the hazard and the expectance of an earthquake,
- assess building stock with the help of previously derived vulnerability functions.

With given input parameters of subsoil and PGA (peak ground acceleration) and the examined vulnerability, the damage based on building classes can be obtained, and earthquake scenarios can be derived.

This concept is suitable even in Hungary. Here there are about 100-120 smaller earthquakes per year; which are below the perceptible level, and 4-5 perceptible earthquakes per year (Földrengés Információs Rendszer / Earthquake Information System / www.foldrenges.hu). Earthquakes with a greater effect, causing structural damages can be expected every 15-20 years, and in 40-50 years major earthquakes with high economic and social effects. With this earthquake hazard level, Hungary ranks with the medium-hazardous countries.

In Hungary, the goal should be the reduction of the expected damage during an earthquake. This provides an economic motivation for funding and executing seismic engineering research..

2. EARTHQUAKE RISK ANALYSIS

2.1 Proposed process to derive earthquake risk

Calculating earthquake risk requires the cooperation of several disciplines: seismic engineering and architects. Many factors must be considered as shown in table 1. Data obtained from paleoseismic studies and seismic engineering research will further enhance regional hazard assessment and development of microzonation maps. Such efforts would consider local site effects and examine a significant database of buildings with computed vulnerability so that earthquake risk can be assessed:

RISK = HAZARD×VULNERABILITY×EXPOSURE (1)

Table 1 Factors affecting hazard and vulnerability (EMS)

Factors affecting the earthquake hazard:	Factors affecting building vulnerability:
type of soil thickness of layers lateral variation of layers the potential of liquefaction master faults	construction system and period quality of materials, workmanship regularity in plan and elevation position of the building changes in function, damages, state of the building dynamic characteristics

First of all the hazard map of the investigated area should be performed taking into account the local site effects, the potential of liquefaction, type of the soil, etc. The obtained PGA with 10% PE in 50 yrs (this value is used at design) will be the input parameter for vulnerability analysis.

The second step can be the identification of the building classes due to the construction systems. The vulnerability functions of each building class considering the sample can be derived based on the determined damage grades as a function of PGA and natural period of vibration of the building.

Afterwards the building inventory can be made considering the vulnerability functions. For a given district of the city the buildings belonging to different building classes can be listed, and the mean damage of every building class can be calculated with the help of Eq. (2) below (Fäh et al. 2001):

$$MDF = \sum_i P(DG_i | S_d) \cdot CDF \tag{2}$$

where CDF is the central damage factor and DG is the damage grade to a given earthquake. The overall damage concerning a city district can be obtained with the help of the following formula (Fäh et al. 2001):

$$OD = \underset{cell \subset district}{mean} \left(\sum_{class} P_{class} \frac{VF_{class}(S_d)}{100} \right) \tag{3}$$

where VF is the vulnerability function of a given building class.

Based on these data and expected PGA, vulnerability functions can be obtained for each building class. With given vulnerability curves, there is a possibility for rapid evaluation of buildings on-site. Mean damage can be obtained concerning a building class, and overall damage can be derived based on all building classes, resulting in assessment of earthquake risk.

2.2 Defining vulnerability

One of the basic tasks in determining vulnerability of buildings is the classification of buildings from the point of view of earthquake risk. The classification worked out researchers and agencies (EMS 1998, Vaseva 2002) is largely based on inspections of structural systems, possibly the time of construction and the proximity to earthquakes. The aim of this study is to work out a more precise method, which takes more factors into consideration such as the regularity in the layout, the direction of earthquake wave propagation to the building, etc.

Vulnerability is the possibility of damage or loss of buildings due to a seismic event. It is a characteristic of the building and can be expressed in probabilistic or statistical terms. A vulnerability function is typically expressed as a function of ground motion intensity.

The vulnerability function of each building class is derived from the load-bearing capacity of the buildings and the seismic demand expressed by spectral acceleration. The extent of damage can be represented by damage grades related to the onset of cracking, the yield point and destruction. The purpose is to build up a more complex method, which takes into account more parameters influencing the vulnerability: type and material of the structure, the irregularity of the layout, the number of stories, dynamic characteristics, etc.

Vulnerability as an input parameter to earthquake scenarios requires evaluation of a large building population in a rather short period of time using a simple method, which describes the seismic performance of the buildings adequately. There are different methods to analyze the vulnerability of the buildings: methods used during the post-earthquake study as well as analytical or numerical methods. Vulnerability can be determined by observation or based on expert opinions; usually based on post-earthquake studies. Other methods offer a possibility to estimate the possible damages before an earthquake occurs.

In the case of observed vulnerability (Haddar 1994, Castano 1994, Porro et al .1989) the damage is defined with the repair cost as a ratio of the replacement cost or the amount of loss of all affected buildings considering the number of casualties as a ratio of their value. The relation between damage and earthquake intensity is valid only for the region where it was developed. Another method is to ask experts to estimate the expected percentage of damage cause by a given intensity, which are implied in macroseismic scales. These scales are used to evaluate the possible damages after an earthquake (Fäh et al. 2001).

Analytical approaches are based on identification of collapse mechanisms yielding the equivalent shear capacity (Benedetti et al. 1996). The vulnerability is expressed as the critical acceleration causing the mechanism to take place. In the case of score assignment, the structural deficiencies are identified and scores for different deficiencies are calibrated by experts (Calvi 1999).

Detailed analyses are the most time-consuming evaluation of vulnerability. These analyses correspond to the methods of design: linear static analysis (lateral force method); modal response spectrum analysis which is a linear dynamical analysis; pushover analysis (Lang et al. 2000), an increasingly popular non-linear static analysis; and a fully non-linear time-history dynamic analysis. The analyses above are listed in increasing order of complexity, work demand, cost, and difficulty of interpretation. For regional applications finding a balance between available resources and level of sophistication is a major challenge.

3. VULNERABILITY OF BUILDINGS

3.1 Shear capacity of buildings

First, the differences between evaluation and design should be understood. The aim of design is to create a building that resists expected forces with a margin of safety. A simplified model should be used that may neglect the positive influence of some elements. The calculation should be on the safe side: material strength reduction factors are used and applied forces are enhanced.

In the case of evaluation, the most important information is the building response to given forces. So the model should be as close to reality as possible, taking into account all structural elements. Actual material properties and true loading levels, without safety factors, should be taken into account.

As mentioned before all structural elements, which contribute to the load bearing capacity of the building should be considered. This means walls thicker than 12 cm are considered. The non-structural elements add to the mass only. The walls are joined by floors and spandrels, these elements transfer horizontal forces.

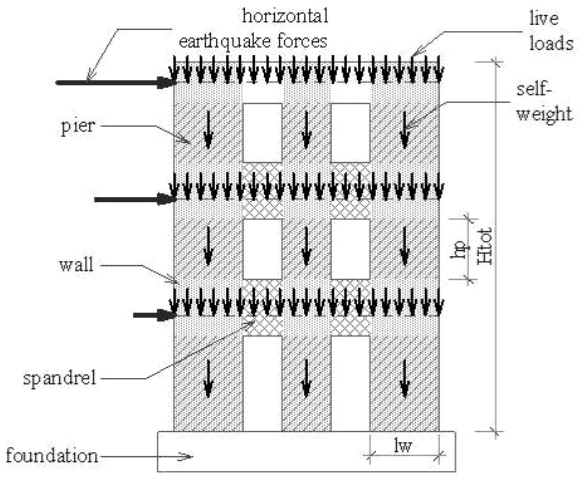


Figure 1 Structural model of a masonry building

The equivalent horizontal earthquake forces act at the floor levels, where the mass is concentrated. The vertical forces imply self weight of all elements and live loads.

The piers transfer all forces to the ground and are the most critical part of the building. The height of the piers is assumed equal to the height of the adjacent opening. Early cracking of the spandrels reduces the stiffness of the spandrels. As the walls are joined by spandrels a coupling effect will take place depending on the extent of spandrels.

The capacity curve of a wall element can be calculated by increasing the shear gradually until the material condition is exceeded. The base shear can be plotted as a function of top displacement.

The horizontal deformation (δ) is calculated by the principle of virtual work. A constant drift over the building height is hypothesized and drift corresponds to the first mode shape assuming a linear distribution of the force.

Drift can be calculated with the following formula:

$$\delta = \frac{d}{h_p}, \tag{4}$$

where hp is the height of the pier, d is the horizontal deformation.

Displacement can be obtained as a ratio of the drift and the total height of the building:

$$\Delta = \delta \cdot H_{tot}. \tag{5}$$

According to a bilinear approximation, the capacity curve of a wall element can be characterized by three parameters: the maximum shear strength of the wall element, the nominal yield displacement (Δy) at the top of the wall and the ultimate displacement (Δu) at the top of the wall. The transition between the linear elastic and perfectly plastic region is called the yield point even if masonry structures do not truly yield.

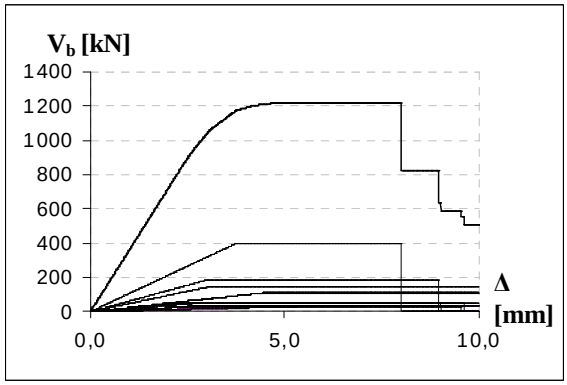


Figure 2 Shear capacity of a building

$$\Delta_y = V_m \cdot H_{tot} \cdot \left(\frac{h_p \cdot (3h_0 - h_p)}{6 \cdot E \cdot I_{eff}} + \frac{\kappa}{G \cdot A_{eff}} \right) \tag{6}$$

$$\Delta_u = \mu_w \cdot \Delta_y \tag{7}$$

3.2 Identification of damage

Identification of damage grades is required to determine the vulnerability function of the building. In the European Macroseismic Scale, five grades are differentiated from slight damage to total destruction.

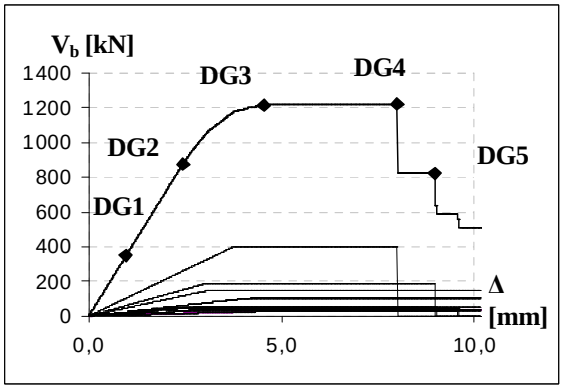


Figure 3 Identification of damage grades

Many studies relate the damage grade to monetary loss

and the number of casualties, which can be useful in the case of post-earthquake studies. The method, which defines indicators, allows the identification of points were the capacity curve of the building enters the next damage grade. The damage grades given in EMS 98 are related to the displacements at the top of the building and are given in Table 2.

Table 2 Identification of damage grades

DG	EMS 98	after Lang [14]
1	negligible to slight damage	point of onset cracking
2	moderate damage	yield of the first wall
3	substantial to heavy damage	yield of the last wall
4	very heavy damage	failure of the first wall
5	destruction	drop of the base shear capacity below 2/3 of maximum V_{bm}

3.3 Seismic demand

The seismic demand is determined using an elastic acceleration response spectrum. It represents the maximum response of equivalent single degree of freedom system as a function of their frequencies.

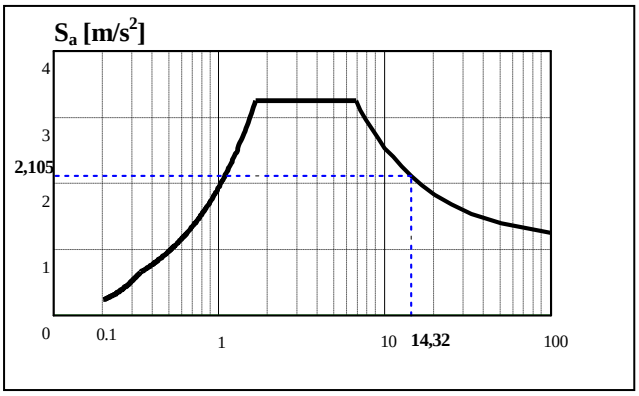


Figure 3 Elastic acceleration response spectrum medium stiff soil, 5% damping, ag=1,1 m/s2

The displacement demand can be calculated from the following equations:
fundamental frequency of the equivalent SDOF system:

$$f = \frac{1}{2\pi} \cdot \sqrt{\frac{k_E}{m_E}} \tag{8}$$

modal participation factor:

$$\Gamma = \frac{\sum m_i \cdot \phi_i}{\sum m_i \cdot \phi_i^{\,2}} \tag{9}$$

spectral displacement:

$$\Delta = \Delta_{by} \cdot \frac{1}{2} \cdot \left(\left(\frac{k \cdot \Gamma \cdot S_d}{V_{bm}} \right) + 1 \right) \tag{10}$$

displacement demand:

$$S_d(f_1) = \frac{S_a(f_1)}{(2\pi \cdot f_1)^2} \tag{11}$$

The spectral displacement should be then compared with the displacement capacity of the building.

3.4 Vulnerability of buildings

From the figure of the shear capacity of the building and the seismic demand the third curve, the vulnerability function can be plotted. Varying the intensity of seismic demand for every case the displacement of the building can be plotted. With increasing displacement demand the top displacement of the building increases as well.

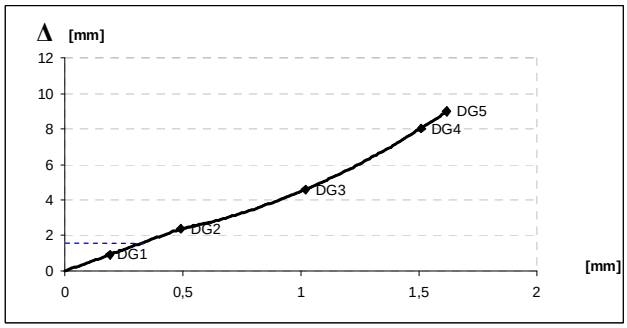


Figure 4 Vulnerability function

Plotting the damage grades on the figure will provide the vulnerability function of the building shown in figure 4.

4. EXAMINED AREA

4.1 City of Győr

Győr is the most important city of northwest Hungary often referred to as the City of Associations or Meetings. The city is the sixth largest in Hungary, and it is the capital of Győr-Moson-Sopron county and Western Transdanubia region, an important economic, industrial, ecclesiastic, educational, cultural and sports centre. The dynamically developing city lies halfway between Budapest and Vienna, on one of the important roads of Central Europe with an excellent accessibility.

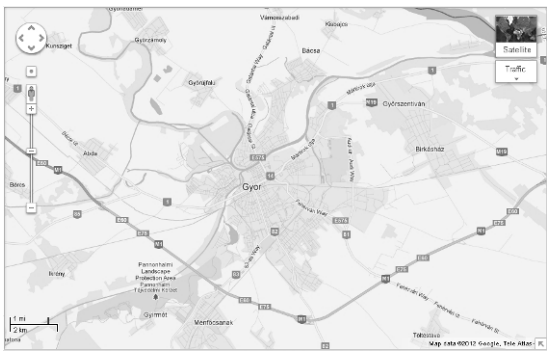


Figure 5 City of Győr, main roads and rivers crossing

Győr is also referred to as the City of Waters as it lies at the bank of river Rába, just at the confluence of the Moson-Danube, the Rába and the Rábca not far away from the main chanel of the Danube and it is rich in thermal water

as well. Győr is Hungary's second richest town in historic buildings outside Budapest. Characteristic corner-balconies and narrow lanes, churches, museums are all reminders of a historic past, mainly situated in the centre of the town.

From a geological point of view Győr lies in the eastern part of Little Hungarian Plain. The Little Hungarian Plain is a deflational lowland of ca. 7700 km^2 on the western part of the Carpathian Basin System. Its medium altitude is 125 m a.s.l., a little higher than that of the Great Hungarian Plain. The river Danube divides into a southern and a northern part.

The southern marginal hills consist of gently undulating hilly country, dissected by a deep valley. They are composed of sandstones, gravel and clay. The present morphology was formed during the Quaternary period by fluvial erosion, tectonic movements and deflation processes. The northern margin of the Little Plain consists of similarly hilly country dominated by thick loess cover. The rivers entering the Little Plain flow eastward.

The Little Hungarian Plain is a structural basin, subsided along step faults and the basement can be found beneath thick basin sediments. Two large tectonic lineaments in the basement determine the geological structure.

4.2 Seismicity of Győr

The tectonics of the Carpathian basin is determined by the counterclockwise rotation of the Adria microplate and the north-northeast directed movement originating from the rotation. The seismicity of the area is moderate. Earthquakes causing light damages occur every 15–20 years, while stronger, more damaging 5.5–6 magnitude quakes happen about every 40–50 years.

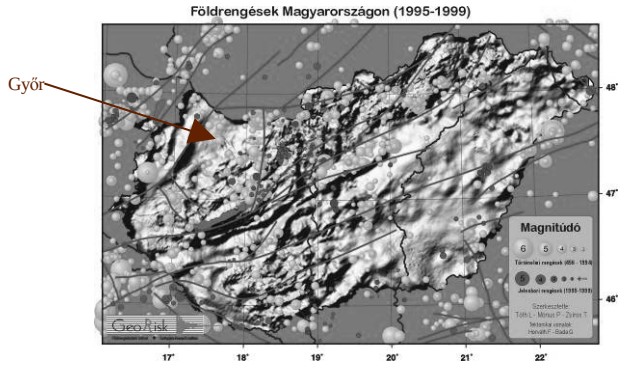


Figure 6 Seismic activity and fault lines in Hungary (Georisk)

The distribution of earthquakes is diffuse; however, there are certain areas where the occurrence is higher. For example at the surroundings of Komárom-Mór-Berhida, known as Móri-trench, where the largest earthquake of Hungary occurred in the city of Komárom in 1763 with estimated magnitude of 6.1. This is shown also in the seismic hazard map of Hungary computed for 475 years return period. PGA values were computed for bedrock and are expressed in m/s^2.

Aerial distance between Győr and Móri-trench is 60 km. Historic data show that major earthquakes of this area had significant effect on buildings in Győr. The importance of the city as a regional centre, the number of inhabitants and the closeness to the above-mentioned fault emphasizes the necessity of earthquake risk analysis of this town.

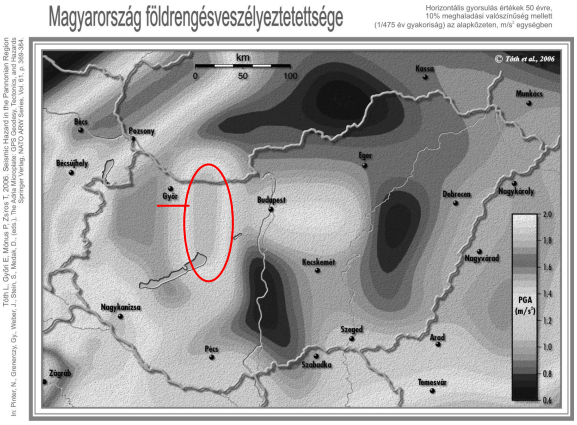


Figure 7 Seismic hazard map of Hungary indicated Móri-trench and Győr (Georisk)

The other significant fault lies beneath the river Rába and meets the fault beneath river Mosoni-Duna at Győr. Recorded earthquakes with epicenter at Győr mainly occur due to these faults.

Table 3 Historical earthquakes with epicenter at Győr and approximately 8 km depth

Date	Magnitude	Maximum intensity
1700.02.11	3.5	5.0
1754.10.21	3.5	5.0
1758.08.07	3.2	4.5
1763.08.04	2.2	3.0
1763.08.09	3.2	4.5
1765.02.05	2.9	4.0
1765.02.21	2.9	4.0
1768.01.05	3.9	5.5
1768.09.20	2,2	3.0
1768.10.29	2.2	3.0
1779.04.02	2.9	4.0
1779.04.02	2.9	4.0
1781.10.07	2.9	4.0
1786.02.29	2.9	4.0
1850.10.07	**4.9**	**7.0**
1850.10.29	3.5	5.0
1860.04.13	2.2	3.0
1914.02.04	2.9	4.0
1921.05.04	3.5	5.0
1990.08.22	2.9	4.0
1993.07.12	2.8	3.5

4.2 Examined zones and buildings

Twenty six selected zones were examined more closely. The zones differ from each other not only in location, but also in types and ages of buildings. Building data were gathered with the help of a questionnaire and the screening evaluation of trained staff. Data concerning the soil types and layers were collected in parallel.

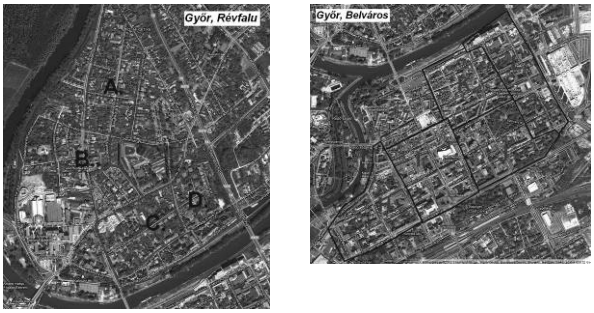


Figure 8 Zones from the town part called Révfalu and the inner city

The checklist consisted of questions about:

- General data of each building (age and function of the buildings, regularity in plan and elevation, position of the building, changes in function, previous damages, state of the building, etc.)
- Structural data of each building (dimensions, construction system, quality of materials, workmanship)

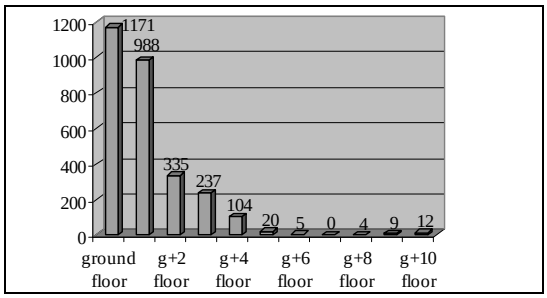


Figure 9 Building heights of the analyzed town parts

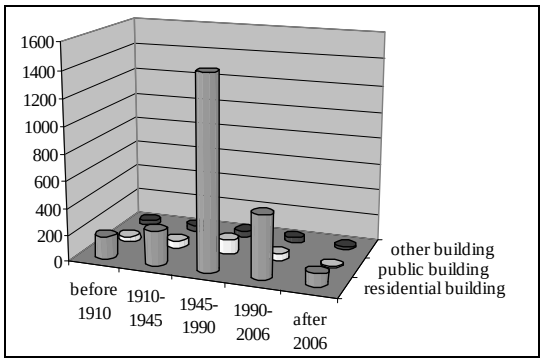


Figure 10 Building functions and construction period

Data from 2885 building were analysed, and buildings are classified based on these results. For each building class a vulnerability function is assigned. The above figures give an overview about the analysed building-stock.

5. CONCLUSIONS

First, it should be emphasized that a large percentage of building stock was built without considering of earthquake loads and these buildings are very vulnerable to a moderately strong seismic event. Focus of efforts should be directed toward prevention: a relatively large building stock needs reinforcement, highlighting the importance of this research.

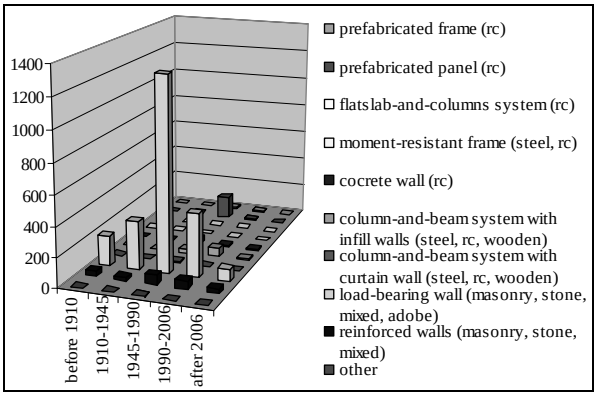


Figure 11 Structure of the buildings and construction period

The vulnerability functions are being derived for typical layouts, this way offering many curves, and with these experts could decide on-site which group belongs just based on visual screening. With the given value of possible PGA it can be stated the expectable damage.

This way the method offers a fast evaluation method and allows the accomplishment of earthquake scenarios to a given settlement. This is very important because it provides useful information for governments, authorities and insurance companies and helps to set up a priority order, which buildings should be strengthen first.

Acknowledgements:

The authors acknowledge the financial support of the Széchenyi István University within the framework of TáMOP 4.2.2/B-10/1-2010-0010 application.

References:

Calvi, G. M. (1999), A displacement-based approach for vulnerability evaluation of classes of buildings, *Journal of Earthquake Engineering*, Vol. 3, No. 3

Castano, J. C. (1998), A seismic risk reduction program for Mendoza City, Argentina, *Proceedings of the 10th ECEE*

Committee on National Earthquake Resilience (2011) *National Earthquake Resilience: Research, Implementation, and Outreach* National Academies Press, Washington, D.C.

Fäh, D. et al (2001), Earthquake scenarios for the city of Basel, *Soil Dynamics and Earthquake Engineering*, 21, 405-413 p.

Földrengés Információs Rendszer www.foldrenges.hu

Grünthal, G. editor (1998), European Macroseismic Scale 1998, Luxembourg

Lang, K. and Bachmann, H. (2000) Erdbebenverletzbarkeit bestehender Gebäude aus unbewehrtem Mauerwerk, in Erdbebenvorsorge in der Schweiz – Maßnahmen bei neuen und bestehenden Bauwerken, SGEB/SIA Dokumentation, *Schweizerischer Ingenieur- und Architekten-Verein*, Zürich

Luco, N., Ellingwood, B.R. Hamburger, R.O. Hooper, H.D, Kimball, J.K. and Kircher. C.A. (2007), „Risk-Targeted versus Current Seismic Design Maps for the Conterminous United States“, *SEAOC Convention Proceedings*, 1-13.

Zsíros, T. (2000), A Kárpát-medence szeizmicitása és földrengés veszélyessége: Magyar földrengés katalógus (456 – 1995), Budapest

10CUEE CONFERENCE PROCEEDINGS
10th International Conference on Urban Earthquake Engineering
March 1-2, 2013, Tokyo Institute of Technology, Tokyo, Japan

DEVELOPMENT OF A RAPID CONDITION ASSESSMENT TOOL FOR REINFORCED CONCRETE MOMENT FRAME BUILDINGS IN THE PHILIPPINES

Liezl Raissa E. Tan[1] and Jaime Y. Hernandez Jr. Ph.D.[2]

1) Instructor, Structural Engineering Group, Institute of Civil Engineering, University of the Philippines Diliman
2) Associate Professor, Structural Engineering Group, Institute of Civil Engineering, University of the Philippines Diliman
jnj.hernandez@upd.edu.ph, liezl.raissa.tan@gmail.com

Abstract: Condition assessment of a building is an important step in preparation for an earthquake. In the Philippines, FEMA-154 and ATC-20 are the assessment tools adopted to evaluate buildings. However the scores in these forms are based from the fragility curves developed for buildings found in the United States and hence exhibit different seismic capacity compared to buildings in the Philippines. This was observed when a school building in Cebu City was judged safe using FEMA-154 but was judged otherwise by the local engineers after entering the building based on excessive deflection seen on the beams and large cracks on the interior walls due to settlement. This created the motivation to pursue a study in developing a pre-earthquake assessment tool that is rapid, visual and is reflective of the structural condition of the buildings in the Philippines. The assessment tool is patterned after FEMA-154 with its structural and cut-off scores modified by employing the fragility curves developed by the UP-ICE applicable for low to mid-rise reinforced concrete buildings in Metro Manila. In addition, a damage modification factor based from the quantified residual seismic capacity was employed. These scores were calibrated by conducting several building assessments using the developed tool.

1. INTRODUCTION

In 2004, Japanese researchers collaborating with scientists from PHIVOLCS conducted the Metro Manila Earthquake Impact Reduction Study (MMEIRS). Their work included risk assessment due to scenario earthquakes caused by movement from different active faults in the country. Their results indicate 40% of residential buildings will be damaged in the event of magnitude 7.2 earthquake occurring in the West Valley Fault, resulting in 34,000 deaths and 110,000 injured (Solidum et al. 2004). At present, PHIVOLCS continues to warn the public in the Metro Manila area of a possible earthquake event occurring in the West Valley fault (formerly called the Marikina fault).

Noting that earthquake is just one type of hazard that the Philippines is subjected to, the national government, through the National Disaster Risk Reduction and Management Council (NDRRMC), is responding to the challenge by conducting appropriate programs and projects that strengthen the capacities of LGUs and communities in preparing for and responding to hazards. In particular, the Department of the Interior and Local Government (DILG), an integral part of the NDRRMC, is implementing a locally-funded project entitled, "Enhancing LGU Capacity on Climate Change Adaptation and Disaster Risk Management." The project encourages LGUs to integrate disaster-resiliency and Climate Change adaptation in local development planning, programming and implementation. One of the project steps is the Mandatory Inspection of Local Government Infrastructure Projects and Public Buildings. This initiated the development of assessment tools on Infrastructure Audit, both for buildings and bridges. These were initially introduced in twenty-eight (28) LGUs in Region IV-A before they will be institutionalized at the LGU level (correspondence of USec Panadero to Dean Matias July 22, 2011). However, the infrastructure audit developed lacks the mechanism for identifying which among the existing buildings should be prioritized in the detailed investigation and possible retrofit, should this be recommended.

In the US, the Federal Emergency Management Agency (FEMA) released the second edition of the widely used Rapid Visual Screening of Buildings for Potential Seismic Hazards: A Handbook - the FEMA 154. The principal purpose of the FEMA 154 is to identify (1) older buildings designed and constructed before the adoption of adequate seismic design and detailing requirements, (2) buildings on soft or poor soils, or (3) buildings having performance characteristics that negatively influence their seismic response (FEMA 154). These buildings should then be recommended for detailed investigation to determine if they endanger occupants in the event of an earthquake. Each building is provided an overall score which allows ranking of the buildings in terms of need for detailed investigation.

Likewise, the American Society of Civil Engineers

(ASCE) published Seismic Evaluation of Existing Buildings - the ASCE 31-03. This is the first national seismic evaluation standard in the US, previously released as FEMA 310: Handbook for the Seismic Evaluation of Buildings - A Prestandard. Using this standard, existing buildings are evaluated to either the Life Safety or Immediate Occupancy Performance Level, considering structural, nonstructural, and foundations/geologic hazard issues.

Currently there is a program that is geared towards response to reduce the damage caused by quick-onset events like earthquake. It is known as the Earthquake Quick Response Program (EQRP formerly known as DQRP-Disaster Quick Response Program). The program utilizes inspection surveys of structures before and after an earthquake.

The pre-earthquake inspection survey tool is based on FEMA-154 Rapid Visual Screening of Structures for Potential Seismic Hazards while the post-earthquake inspection survey is based on ATC-20 Post Earthquake Safety Evaluation of Buildings. These instruments were developed in the United States and the conditions of structures considered were not locally based.

Movement of the West Valley fault will definitely affect building structures in Metro Manila. It is therefore necessary that existing buildings be assessed for structural integrity and if found lacking be recommended for repair, rehabilitation and/or retrofit in preparation for the large magnitude seismic forces that may be developed by the existing fault. Therefore, a tool that can be used for rapid condition assessment, applicable to buildings locally constructed and capable of identifying which buildings should be prioritized for detailed investigation should be developed. This study is focused with the development of basic structural scores for low to mid rise reinforced concrete frame buildings since these are the most common building types seen in the country. Moreover, this study aims to develop an assessment tool that can be used even by someone with basic knowledge in structural engineering.

2. DATA COLLECTION FORM

The data collection form for structural component has two major parts. The first part quantifies the performance of a building based on the building attributes such as structural configuration and soil condition. This part is in general patterned after FEMA 154 with its basic structural hazard scores and score modifiers altered using the locally developed fragility curves for the Metro Manila.

The second part, on the other hand, takes into account the damages incurred in the building components. This portion was patterned after the quantification of post-earthquake damages in RC buildings in Japan using residual seismic capacity. By visually classifying and accounting the damages in columns and walls, the ratio of the residual seismic capacity to the initial seismic capacity can be estimated, which became the basis for the formulation of the procedure in quantifying the damage modification factor. This factor represents the percentage of the remaining seismic capacity of the building.

Additional information on the structural integrity of the building can be reflected through sketches, photos and commentary boxes that are also provided in the form.

2.1Basic Structural Hazard Score

In the second edition of the FEMA 154 *Handbook*, the Basic Structural Hazard Score is defined, for a particular type or class of building, as the negative of the logarithm (base 10) of the probability of collapse of the building, given the ground motion corresponding to the maximum considered earthquake (MCE). This can be written as follows,

$$\text{BSH Score} = -\log_{10}[(P|\text{Collapse given MCE})] \quad (1)$$

The probability of collapse of a building is the product of the probability of being in the complete damage state, multiplied by the fraction of buildings in the complete damage state that collapse written as follows, (FEMA 155)

$$\text{BSH Score} = -\log_{10}[P(\text{Collapse}|\text{Complete Damage State}) \times P(\text{Complete Damage State})] \quad (2)$$

The basic structural hazard score is generic for one building type. The default structure for reinforced concrete moment frame (C1) used in this study is a regular low-rise building on soil type D.

To compute for the basic structural hazard score for C1, fragility curve for C1L on soil type D is needed as shown in Figure 1.

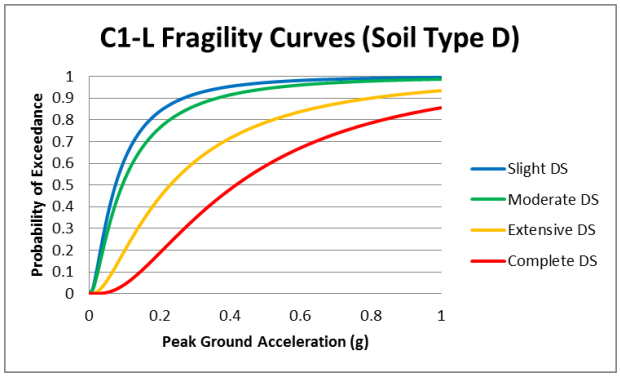


Figure 1: Fragility curves for reinforced concrete moment frame low-rise on soil type D. (SOURCE: UPD-ICE, Development of Vulnerability Curves of Key Building Types in Greater Metro Manila Area, [an ongoing research])

Before determining the probability of exceeding complete damage state at the given MCE, the peak ground acceleration of the maximum considered earthquake must be calculated first.

The maximum considered earthquake is the largest earthquake event applied in building code design. According to the collective opinion of the Seismic Design Procedure Group (SDPG), the minimum seismic margin contained in the 1997 NEHRP Provisions is about 1.5 times the design earthquake ground motions. (BSSC 1998, Appendix A, Commentary)

Since in the development of the fragility curves utilized in determining scores, the demand spectrum comes from the design response spectra, the maximum considered earthquake will be computed from the same, wherein the seismic coefficient Ca represents the peak ground acceleration in g. Hence to determine the MCE, the design earthquake in terms of the seismic coefficient will be multiplied by 1.5.

In determining the seismic source type it is necessary to determine the maximum moment magnitude for a given site which can be estimated from the nearest fault or seismic source. Since the area of interest is in Diliman Quezon City, wherein the West Valley Fault is the nearest seismic source capable of producing a maximum credible earthquake of 7 (Nelson et.al. 2000), the seismic source type is classified as A. Using the National Structural Code of the Philippines 2010 (NSCP-2010) Chapter 2- Minimum Design Loads, the near source factor Na is equal to 1.0 and consecutively the seismic coefficient Ca for soil type D under seismic zone 4 is computed as 0.44Na. Hence the design earthquake is equal to 0.44 g.

Multiplying the design earthquake by a factor of 1.5 gives the MCE equal to 0.66 g. To determine the probability of exceeding the complete damage state, the MCE is projected to the fragility curve for complete damage state and the corresponding probability is determined. Hence the probability of being in or exceeding the complete damage state is equal to 71%.

The collapse rates for different structure types may be found in HAZUS-MR4 Table 13.8 which is reposted in Table 1. Using equation (1), BSH is computed as follows,

$$\text{Score} = -\log_{10}[(0.71)(0.13)] = 1.04$$

2.2Basic Structural Hazard Score Modifiers

The default structure for reinforced concrete moment frame is regular, low-rise and on soil type D. If the inspected building differs from the default structure, score modifiers are used to take these variations into account. The parameters that can vary include the following: elevation of the structure that can either be low-rise (1-2 stories) or mid-rise (3-7 stories); the irregularity present in the structural configuration (plan and vertical irregularity); the code used in the design of the structure which can be identified with the age of the structure namely pre-code (buildings designed before 1972) , low-code (buildings designed between 1972-1992) or high-code(post-1992 buildings); and the soil profile type where the structure is constructed (in Metro Manila only three soil types exist: soil type C, soil type D, and soil type F). The score modifiers for each variation are quantified by taking the difference between the structural score for each variation with the basic structural score based from the default structure.

Table 1. HAZUS MR4 Collapse Rates of different Structure Types.

	Model Building Type	Probability of Collapse Given a Complete Damage State*
1	W1	3.0%
2	W2	3.0%
3	S1L	8.0%
4	S1M	5.0%
5	S1H	3.0%
6	S2L	8.0%
7	S2M	5.0%
8	S2H	3.0%
9	S3	3.0%
10	S4L	8.0%
11	S4M	5.0%
12	S4H	3.0%
13	S5L	8.0%
14	S5M	5.0%
15	S5H	3.0%
16	C1L	13.0%
17	C1M	10.0%
18	C1H	5.0%
19	C2L	13.0%
20	C2M	10.0%
21	C2H	5.0%
22	C3L	15.0%
23	C3M	13.0%
24	C3H	10.0%
25	PC1	15.0%
26	PC2L	15.0%
27	PC2M	13.0%
28	PC2H	10.0%
29	RM1L	13.0%
30	RM1M	10.0%
31	RM2L	13.0%
32	RM2M	10.0%
33	RM2H	5.0%
34	URML	15.0%
35	URMM	15.0%
36	MH	3.0%

Summarized in Table 2 are the structural scores computed for each variation.

2.2.1 Score modifier for Mid-rise Buildings

The score modifier for mid-rise buildings was calculated using two sets of structural scores. One for low-rise reinforced concrete buildings and the other is for mid-rise reinforced concrete buildings, both having the same soil type. From Table 2, the basic structural hazard score is 1.04 which was based from low-rise and having designed under high code, and the structural score for C1M designed under high code for the same soil type is 1.30. Hence the score modifier is +0.26.

Table 2: Summary of Structural Scores.

	Mean	BETA	MCE	Pcomplete	Collapse Rate	BHS
C1-L (D)	0.42	0.82	0.66	0.71	0.13	**1.04**
C1-L (C)	0.43	0.81	0.6	0.66	0.13	**1.07**
C1-L(E)	0.28	0.89	0.66	0.83	0.13	**0.97**
C1-M(PRE)	0.54	0.74	0.66	0.61	0.1	**1.22**
C1-M(LOW)	0.54	0.74	0.66	0.61	0.1	**1.22**
C1-M(HI)	0.66	0.73	0.66	0.50	0.1	**1.30**
Plan	0.3	0.82	0.66	0.83	0.13	**0.97**

2.2.2 Score modifier for Plan Irregularity

According to FEMA-155, there was no Score Modifier for plan irregularity that is straightforward to calculate, principally because eccentricity is specific to each building. Hence, to approximate the effect of plan irregularity the spectral response values were increased by 50% where the fragility curve will be based and correspondingly the structural score. Employing such increase will yield a structural score of 0.97. Hence the Score Modifier for Plan Irregularities is -0.07.

2.2.3 Score modifier for Vertical Irregularity

The score modifier for vertical irregularity cannot be quantified due to large variation in the configurations and conditions. Hence the value is approximated using engineering judgment. But since this study already modifies the scores in FEMA-154, score modifier for vertical irregularity presented in FEMA-154 cannot be utilized directly. To be consistent with that of FEMA 154, an initial value of -0.45 was selected.

2.2.4 Score modifiers for Pre-code and Post Benchmark Construction

The same procedure as how the score modifier for mid-rise was calculated is employed here. However since there is only one vintage used in the development of the fragility curve for C1L, score modifiers for vintages will be based on C1M. Hence three sets of structural scores will be determined with the one in high code as the default score. Again as summarized in Table 2, both structural scores for pre and low code is given by 1.22 while for high code it is 1.30. Hence the score modifier for both pre and low code is -0.08.

2.2.5 Score modifiers for soil type C, D, and F.

Employing the same procedure, structural scores for C1L on soil types, D, C, and E were computed as 1.04, 1.07 and 0.97 respectively. Hence the score modifiers for soil type C and E are +0.03 and -0.07 respectively.

The score modifiers are summarized in Table3.

Table3. Score Modifiers

Score Modifiers	
MID RISE	0.26
VERT. IRREGULARITY	-0.45
PLAN IRREGULARITY	-0.0692
PRECODE	-0.08
LOW CODE	-0.08
SOIL TYPE C	0.03154
SOIL TYPE E	-0.0695
SOIL TYPE F	**

2.3 Damage Modification Factor

Part of the limitations observed in using FEMA-154 is it evaluates buildings based on exterior attributes only. The final score acquired by the building after being assessed using this tool represents the initial seismic capacity of the building before earthquake damage. Thus, it lacks the ability to consider existing interior damage which could be observed when access to the building is allowed.

In the Guideline for Post-Earthquake Damage Evaluation and Rehabilitation of RC Buildings in Japan, the damage rating procedure was based on the residual seismic capacity ratio index R. Utilizing a similar concept, by quantifying the residual seismic capacity and determining its ratio from the initial seismic capacity, the factor can be used to represent a modification factor for the structural scores to account for the damage incurred by the building approximated from visual assessment of interior components such as columns and walls.

With the employment of a normalized strength index for each typical member section which often appears in existing RC buildings in Japan considering ultimate shear stress and effective sectional area of each section type, an alternative simplified procedure of calculating the R-index is proposed in the same paper. By classifying and accounting the type of columns and walls with its corresponding damage classification, the R-index can be approximated. (Maeda et.al. 2004)

DAMAGE MODIFICATION FACTOR				
COLUMN TYPE	NO DAMAGE	MODERATE DAMAGE	HEAVY DAMAGE	TOTAL FACTORED ***
LONG: h/d>6	*1	*0.5	*0	
SHORT: h/d<=6	*1	*0.3	*0	
TOTAL # OF COLUMNS				

Figure2.Portion in the data collection form that quantifies for the damage modification factor.

Since the study is focused on low-rise reinforced concrete moment resisting frames, the procedure presented in the previously mentioned paper can be further simplified by considering only the columns in the evaluation. Assuming ductile columns are associated with long columns, defined as columns with clear span to smallest depth ratio greater than or equal to 6, and short columns otherwise, which will be associated to brittle columns. Furthermore, the damage class will be reduced from five classes to only three namely, "no damage", "moderate damage", and "heavy damage" for ease in classifying damages in a rapid visual inspection. The same factors for Damage Class 0, Damage Class III, and Damage Class V respectively will be adopted. Hence a portion that quantifies the damage modification factor was formulated and is shown in Figure2.

2.4 Cut-off Score

According to the second edition of FEMA-155 which provides the technical manual for the FEMA-154, the selection of the cut-off score is a prerogative of the community utilizing the inspection tool. The cut-off score of about 2.0 was recommended after fifteen years of experience in the use of FEMA-154 that validated this decision. There are cases wherein users opted to use higher cut-off scores which imply a safer environment, at a correspondingly higher cost. (FEMA-155 2nd edition).

In order to come up with a rational choice of the cut-off score in this case, DQRP case studies and reports were reviewed. One of the major observations from DQRP case studies and reports is that concrete hollow block (CHB) and wood low-rise structures that were inspected received only either a yellow or a red tag. CHB structures are low-rise structures with walls made of concrete hollow blocks interlocked at the corners and have no reinforced concrete frame. The floors consist of either plywood or board sheathing, supported by wood subframing. The roofs are corrugated galvanized iron sheets attached to wooden or light metal wood trusses. The received tags on these structures imply that these structures may pose a greater threat to the safety of its occupants during and after an earthquake. Thus, it may be rational to say that these existing structures must be evaluated in detail for seismic considerations even before conducting a rapid condition assessment.

Fragility curves developed by the UPD-ICE for wood structures are based on the MMEIRS data. In MMEIRS, they defined two types of damages one being "partly damaged" and the other being "heavily damaged". Consistency with the damage state definitions is still being reviewed. Fragility curves for CHB, on the other hand is based on a compilation of empirical observations of damage for corresponding ground motion intensities in terms of Modified Mercalli Intensity (MMI) from past earthquakes in the Philippines. Hence this data will be used in calculating the cut-off score. However, the resulting fragility curve is in terms of MMI and needs to be converted to PGA before utilizing it to compute for the probability of being in or exceeding the complete damage state given the MCE.

Using the mean and standard deviation of 7.4 and 0.14 respectively of the fragility curve under complete damage state for CHB as reported in the UPD-ICE report, the probability of exceedance is computed for an arbitrary set of ground motion intensities in MMI. This is shown in the first two columns of Table 4. The ground motion intensity in MMI is then converted to Peak Ground Acceleration in (g) using the Gutenberg-Richter MMI to PGA relationship defined in the following equation.

$$log_{10}(a) = \frac{I}{3} - 0.5 \qquad (3)$$

Where a is acceleration in terms of gals (cm/s^2) and I is the ground motion intensity in terms of MMI. The corresponding conversion is presented in column 3 of Table 4.

The probability of exceeding complete damage state is plotted against the peak ground acceleration. These points will be regarded as the data points where a lognormal cumulative distribution curve will be fitted and the corresponding mean and standard deviation will then be used to compute for the probability of being in or exceeding the complete damage state at the given maximum considered earthquake. This is illustrated in Figure 3 wherein the corresponding mean and standard deviation is also presented.

Illustrated below is the computation of basic structural hazard score for CHB.

$$\mathbf{BSH} = -\log_{10}\big((0.99)(0.15)\big) = 0.83 \qquad (4)$$

Table 4.Tabulation of Probability of Exceeding the Complete Damage State for CHB.

MMI	Probability of Exceedance	PGA
1	1.154E-46	0.000694
2	4.5843E-21	0.001496
3	5.6275E-11	0.003224
4	5.5595E-06	0.006945
5	0.00255275	0.014962
6	0.06706613	0.032235
7	0.34571046	0.069449
8	0.71119124	0.149623
9	0.91896982	0.322352
10	0.98425206	0.694487
11	0.99768376	1.496228
12	0.99972285	3.223525

The probability of being in or exceeding complete damage state with the mean and standard deviation of 0.097 and 0.8 respectively is 0.99. Since there are no CHB building type in HAZUS the collapse rate used was for Unreinforced Masonry equivalent to 15%. Hence the basic structural hazard score for CHB which will also be used as the cut-off score is 0.83.

3. SAMPLE APPLICATION

The proposed Rapid Visual Assessment tool was applied to two existing buildings in Metro Manila.

3.1 Building A

Building A was built in 1973. It has three stories above ground and a story below ground. Based on its structural configuration and structural system, it can be classified under mid-rise reinforced concrete frame with vertical irregularity. Originally, it was intended to be used as a library and a museum but currently it functions as a classroom building, a library, an office and sometimes a venue for seminars, hence a change on the floor live loads of the building. The building occupancy was estimated to be around 100 people. There were no major structural repairs or renovations done on the building since its completion.

Listed below are the key damages observed during the first visit.

1. Beam deflections were observed on beams located at the basement.
2. Diagonal wall cracks were seen in the middle portion of the walls. Some cracks appeared around the columns. Cracks with width of approximately 1.00 mm were seen mostly at the corner of the building in the fourth floor.
3. Floor cracks were seen around the columns on the second floor of the overhang side of the building. There was also suspected floor subsidence on the west wing in the first floor, above of which a suspected beam deflection was observed. A long line of floor crack which extends approximately 3 to 4 meters in the second floor on the overhang side of the building was also observed .
4. Bulging of partition walls was evident.
5. Ceilings were highly damaged due to water leaks. This was seen to be the major factor that deteriorates the function of the building.
6. Windows in the second floor at the overhang side were rusted while the concrete that holds the windows already spalled.
7. Walls in the fourth floor around the center stair way are unsecured.
8. No visible damages in columns and beams.

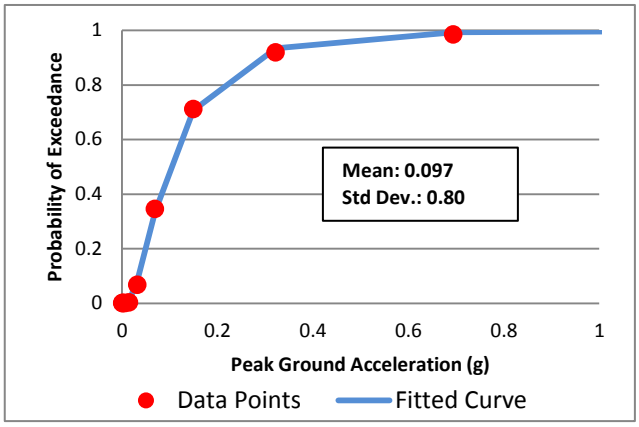


Figure 3. .Fragility Curve at Complete Damage State for CHB.

Presented in Figure 4 is the completed Data Collection Form for the assessment of building A.

3.2 Building B

The construction of building B finished in 1950. It is a 4-story symmetric building with a Parthenon-like façade at the middle. There are no irregularities in the structural configuration of the building. It can be classified as mid-rise reinforced concrete moment frame under pre-code. The default soil type is assumed.

Listed below are the key observations on the damages seen in the building.

1. There are cracks on the ground floor causing rainwater leaks on the basement of the building. Overtime these leaks had caused rusting in embedded reinforcements which then caused some spalling in the concrete cover. However, these were only observed in the ground floor of the building.
2. One part of the building have a lot of cracks/delamination in the concrete finish of window ledges. This may be caused by rusting of reinforcement

due to water dripping from air-conditioners outside of the building.

3. Because of the interior paneling on walls and ceiling, and carpets in the offices, the existence of damage/cracks in structural and non-structural members of the building cannot be visually observed. Thus, our rapid condition assessment tool (RCAsT) has limited use in identifying existing damage present in the building.
4. Parts of the building that do not have interior paneling, e.g. stairways on the sides of the building, were checked. Although some hairline cracks were observed in the walls, no damages were observed in the structural beams and columns.
5. There is sagging of the floor due to overloading in the mezzanine of one of the offices on the south wing because of the volume of documents stored in the area.
6. Cracks at the bottom part of the pair of small columns on the viewing deck were observed. The cracks appear to be limited to the concrete finish of the column and therefore should cause little concern.

Presented in Figure 5 is the completed data collection form for building B.

3.3 Discussion of the Results

The basic structural hazard score for C1L was computed to be 1.04. This is under the assumption that the building is regular in both plan and vertical configurations, built using the high code and constructed on soil type D. This cannot be directly compared with the 2.5 basic structural hazard score for C1L found in FEMA 154 because this corresponds to a different set of basic assumptions. FEMA 154 assumes that the basic structure is one with regular structural configuration, constructed on soil type B since this is the most common soil type in the U.S., and constructed using low code. Using the scores in FEMA 154 to calculate the structural score of the basic structure considered in this paper results to a score of 3.3. This results to an even higher score than the one derived. Following the equation used to compute the BSH, the high score can be attributed to the computation of the probability of being in or exceeding the complete damage state since this is the only parameter that was varied from the rest of the procedure. Same collapse rates were used and same definition of the basic structural hazard score was employed.

No direct conclusion can be drawn based from the scores computed since these were derived using different fragility curves. However, this lifted the issue of redefining the derivation for the basic structural hazard score. Understandably, the probability of collapse is calculated by multiplying the probability of complete damage state exceedance and the probability of collapse given complete damage state, which are two mutually exclusive events. Since the product of two small numbers is an even smaller number, the additional step of getting the negative of the logarithm of base 10 of the product of probabilities, is seen as a way to make use of the probability as a convenient measure of the building performance. Hence a closer look in the derivation of the BSH formula is recommended.

The derivation of the score modifier for the vertical irregularity is based on a trial and error method which is ultimately based on the FEMA 154 results. It is recommended to formulate a procedure of quantifying building performance with vertical irregularities.

Note also are the score modifiers for pre-code and low-code which are one and the same. This is due to the fact that the complete damage state fragility curve of C1M for pre code almost coincides with that of the low code.

Application of the proposed rapid visual assessment tool to two buildings already poses the limitations in the tool. Currently, the rapid visual assessment tool is focused on the assessment of columns because it is expected that these elements will carry most of the lateral loads caused by seismic excitation. However, as what is observed during inspection, notable damages in the form of cracks are mostly seen on walls and floors and seldom on beams. Partition drifts, spalling due to corrosion (especially in windows) and possible deflections of members are also evident. Moreover, pre-earthquake damages are mostly seen on non-structural members such as windows, ceilings that are mostly damaged due to water exposure which are matters of building maintenance, though not brought about by earthquake excitation, can affect the structural integrity of the building. Since the tool is supposed to be a rapid visual assessment, it is recommended to devise a way to estimate the degree of damage incorporating these visual evidences.

Lastly, the inspections conducted are all pre-earthquake assessment hence there is as yet no verification for the post-earthquake assessment specifically the quantification of damage modification factors.

4. CONCLUSION

A rapid visual assessment tool was formulated that quantifies the building performance based on the exterior attributes of the building and the interior state of building components. The tool is patterned after FEMA 154 with its scores modified by employing the locally developed fragility curves of moment frame buildings in Metro Manila. In addition, quantification of the damage modification factor was formulated using similar concepts employed in quantifying post-earthquake damage of RC buildings in Japan.

The resulting basic structural hazard score for C1L is 1.04 which is less than that of FEMA 154. The difference is brought about by the difference in the method of developing

fragility curves and hence raises the proposal of redefining the basic structural hazard score formula. For the score modifiers, it is recommended to improve on the derivation of score modifier for vertical irregularity and a verification on the values derived for pre and low code modifiers. It is also recommended to incorporate in the assessment the damages in non-structural elements and other structural elements such as beams, walls and floors since most of visible damages are seen in these components.

References:

ASCE 31-03 Seismic Evaluation of Existing Buildings. American Society of Civil Engineers Report.

Association of Structural Engineers of the Philippines, Inc. (ASEP).(2010). National Structural Code of the Philippines.

Building Seismic Safety Council, BSSC, (1998), 1997 Edition NEHRP Recommended Provisions for Seismic Regulation for New Buildings and Other Structures, Part I (Provisions) and Part II (Commentary), FEMA 302/303, Washington, DC.Computers and Structures (2008) **ETABS V9.5.0.**Computers and Structures Inc., Berkeley, California, USA.

David, SerjDonn Z. (2012), Visual Inspection of Structures to Develop Empirical Seismic Fragility Curves and a Repair/Retrofit Prioritization Scheme for the Philippines, University of the Philippines Diliman, Philippines.

Federal Emergency Management Agency (FEMA), (2002). FEMA-154, Rapid Visual Screening of Structures for Potential Seismic Hazards: A Handbook (2nd Edition ed.). Redwood, California, U.S.A.

Federal Emergency Management Agency (FEMA), (2002). FEMA-155, Rapid Visual Screening of Structures for Potential Seismic Hazards: Supporting Documentation (2nd Edition ed.). Redwood, California, U.S.A.

HAZUS-MH MR4,(2003), Multi-hazard Loss Estimation Methodology: Earthquake Model,Department of Homeland Security, FEMA, Washington, D.C.

Maeda, M., Kang, D.E., (2009), Post-Earthquake Damage Evaluation of Reinforced Concrete Buildings.Journal of Advanced Concrete Technology.

Maeda, M., Nakano, Y., Kuramoto, H., & Murakami, M. (2004).Guideline for Post-Earthquake Damage Evaluation and Rehabilitation of RC Buildings in Japan.*13th World Conference on Earthquake Engineering.*Vancouver B.C., Canada.

MMEIRS (2004) Earthquake Impact Reduction Study for Metropolitan Manila, Republic of the Philippines Final Report. Metropolitan Manila: MMEIRS.

Nelson, A.R., S. Personius, R. Rimando, R. Punongbayan, N. Tungol, H. Mirabueno, A. Rasdas, (2000). Multiple Large Earthquakes in the Past 1500 Years on a Fault in Metropolitan Manila, the Philippines, Bull. Seism. Soc. Am., 90, 1, 73-85.

Oreta, A.W.C., Pacheco, B.M., Tanzo, W.T., (2003), Seismic Structural Performance Index Evaluation of Existing Reinforced Concrete Buildings.*10th ASEP International Convention.*Manila Pavilion, Philippines.

Panadero, A. A. (2011). Correspondence with Dean Aura C. Matias of the College of Engineering. Office of the Undersecretary for Local Government, Department of the Interior and Local Government, July 22, 2011.

Solidum, R.U., Bautista, B.C., Santiago, R.J., Segawa, S., Koike, Y., Ikenishi, N. and Iuchi, K. (2004). Evaluation of Seismic Damages and Vulnerabilities of Metropolitan Manila. In Proceedings of the Asia Conference on Earthquake Engineering – Manila, Philippines.

University of the Philippines Institute of Civil Engineering (UP-ICE), (2011), Development of Vulnerability Curves of Key Building Types in the Philippines. University of the Philippines Diliman, Quezon City.

STRUCTURAL RVS SCORE for Low (1-2 stories) and Mid (3-7 stories) Rise Reinforced Concrete

BLDG. TYPE	BASIC SCORE	MID-RISE	VERTICAL IRREGULARITY	PLAN IRREGULARITY	PRE CODE	LOW CODE	SOIL TYPE C	SOIL TYPE E	SOIL TYPE F	STRUCTURAL SCORE, S
C1L,C1M*	**1.04**	+0.26	-0.45	-0.07	-0.08	-0.08	+0.03	-0.07	**	0.85

NOTE: *C1 is a reinforced concrete moment resisting frame building type.

** If checked, automatically proceed to detailed analysis.

DAMAGE MODIFICATION FACTOR

COLUMN TYPE	NO DAMAGE		MODERATE DAMAGE		HEAVY DAMAGE		TOTAL FACTORED ***
LONG: h/d>6	ALL	*1	—	*0.5	—	*0	
SHORT: h/d<=6	ALL	*1	—	*0.3	—	*0	
TOTAL # OF COLUMNS							

*** The total factored column contains the factored number of columns due the damage observed and the type of column.

**** Total # of Columns is the sum of the number of columns counted on site regardless of damage observed (i.e. no factors incorporated).

$$\textbf{DMF}= \frac{\sum Total\ Factored}{\sum Total\ \#\ of\ Columns} = 1$$

FINAL SCORE=(*STRUCTURAL SCORE*) *(*DAMAGE MODIFICATION FACTOR*)

FINAL SCORE= 0.85 *****

***** If the Final Score is ≤ **0.83**, then the structure will be recommended for Detailed Seismic Evaluation

DETAILED SEISMIC EVALUATION REQUIRED? [ ] YES [X] NO

SKETCHES:

SCALE:



Comments:

Figure 4. Completed Data Collection Form for Building A.

STRUCTURAL RVS SCORE for Low (1-2 stories) and Mid (3-7 stories) Rise Reinforced Concrete

BLDG. TYPE	BASIC SCORE	MID-RISE	VERTICAL IRREGULARITY	PLAN IRREGULARITY	PRE CODE	LOW CODE	SOIL TYPE C	SOIL TYPE E	SOIL TYPE F	STRUCTURAL SCORE, S
C1L,C1M*	**1.04**	+0.26	-0.45	-0.07	-0.08	-0.08	+0.03	-0.07	**	1.22

NOTE: *C1 is a reinforced concrete moment resisting frame building type.

** If checked, automatically proceed to detailed analysis.

DAMAGE MODIFICATION FACTOR

COLUMN TYPE	NO DAMAGE		MODERATE DAMAGE		HEAVY DAMAGE		TOTAL FACTORED ***
LONG: h/d>6	ALL	*1	—	*0.5	—	*0	
SHORT: h/d<=6	ALL	*1	—	*0.3	—	*0	
TOTAL # OF COLUMNS							

*** The total factored column contains the factored number of columns due the damage observed and the type of column.

**** Total # of Columns is the sum of the number of columns counted on site regardless of damage observed (i.e. no factors incorporated).

$$\text{DMF} = \frac{\sum Total\ Factored}{\sum Total\ \#\ of\ Columns} = 1$$

FINAL SCORE=(*STRUCTURAL SCORE*) *(*DAMAGE MODIFICATION FACTOR*)

FINAL SCORE= 1.22 *****

***** If the Final Score is ≤ **0.83**, then the structure will be recommended for Detailed Seismic Evaluation

DETAILED SEISMIC EVALUATION REQUIRED? [ ] YES [X] NO

SKETCHES:

SCALE:



Comments:

Figure 5. Completed Data Collection Form for Building B.

10CUEE CONFERENCE PROCEEDINGS
10th International Conference on Urban Earthquake Engineering
March 1-2, 2013, Tokyo Institute of Technology, Tokyo, Japan

DAMPING PERFORMANCE ANALYSIS AND VERIFICATION OF HEAVY-LOADING HYDRAULIC DAMPER

Jing Long Tong [1],Kuang Yuh Huang [2]

1) Ph. D. student, Dept of Mechanical Engineering , National Taiwan University, Taiwan
2) Professor, Dept of Mechanical Engineering , National Taiwan University, Taiwan
kyhuang@ntu.edu.tw,tongjinglong@gmail.com

Abstract: Architecture and weight of the building is quite diverse. The hydraulic damper must be designed and developed in order to prevent and reduce vibration, and the performance requirements of the vibration energy dissipation. Building structure can be securely and safely stands. Hydraulic damper is usually customized products. Sure that the performance of the damper will spend a lot of time and cost by trial and error and experimentation. Hydraulic oil in the damper produce the effect of absorbing energy by a piston gap, The damper design and operating parameters determine the damping force. The research results show that the damping coefficient and the gap is highly negatively correlated, the gap height greater the damping coefficient the smaller. When the (flow blocking hole diameter / piston diameter) is greater than 5%, regardless of the diameter size of the piston, dimensionless damping coefficient will be approaching a certain value. Damping coefficient with the choke lever length positive, the choke rod length increases the damping coefficient of the greater. The experimental and theoretical values of errors below 10%.

1. INTRODUCTION

The principles and functions of the hydraulic damper makes damping effect by viscous effects of Silicone oil and The friction between the piston and the cylinder. It is a device in mechanism that can provide the resistance movement and absorb the kinetic energy. First this study estimated damper behavior characteristics with mathematical theory and derived regression formulas between geometric dimensions and the damping force of hydraulic damper. Second we performed hydraulic damper testing by dynamic hydraulic damper test equipment. Finally this research compared mathematical models and experimental results.

Hydraulic dampers are mainly used in the equipments that needed damping as construction, aerospace, automobiles and motorcycles, military weapons. Automobiles and motorcycles used adjustable hydraulic damper damping to achieve comfortable ride.[2] The military weapons used linear hydraulic damper to Absorb the energy form impact. [3] In recent years many studies interest in the important research topic that hydraulic dampers are used in civil construction. The Strong wind or earthquake makes vibration on the high-rise building can be reduced by high damping force hydraulic damper. And it also enhances the shock resistance to prevent collapse.[5] Hydraulic damping is used in the realm of civil belongs to the passive system in the control. The basic mathematical theory is the linear Mazwell mode that showed viscous elastic fluid mechanics behavior of the hydraulic damper by Bird, RB, et al.[6] It described hydraulic damper nonlinear viscous elastic fluid mechanics behavior by Markeis et al.[7] Markeis explored the impact that the temperature effect on the hydraulic damper. They studied two vibration situations that a tiny displacement amplitude[8] and a long stroke displacement amplitude [9]of damper. And they got the analytical formula in the different vibration frequency and temperature. The analytical formula showed that the temperature is the function of heat transfer coefficient of the fluid, the piston geometry, time, and the vibration frequency. Chien-Yuan Hou constructed hydrodynamic model that assumed the fluid of hydraulic damper is a Newtonian fluid and Non-Newtonian fluid.[10] He researched the dynamic behavior of the hydraulic damper under steady-state harmonic shocks, in order to build the integrity of the structural dynamic equation. Currently Most famous manufacturers that produces hydraulic dampers in the international is American Taylor company was founded in 1955.[11] In 1980 Taylor began to study the damper was applied to the field of civil construction with the U.S. National Earthquake Engineering Research Center. The company is a professional and has complete dynamic hydraulic testing equipment. And the damper was developed through various tests and comparison analysis and published hundreds of articles related papers journals. That products with good quality and reliability were recognized by the field of structural engineering that called Taylor Device hydraulic damper.(Figure 1) [12] There had been successfully installed in over 170 large-scale engineering structures in the world. Hsu, DS has published papers about the mathematical model of the hydraulic damper, physical characteristics, designed applications in Taiwan. National Taiwan Earthquake Engineering Research Center studied

test analysis of building structures and method of reinforcement. [18]

3. ANALYSIS OF HYDRAULIC DAMPER

3.1 Working Principle and Influential Parameters

As shown in Figure 2, the literature search and inference shows that three items: the size effect, viscosity coefficient, and the compressibility of the hydraulic oil will affect the damping coefficient. This chapter focuses on the size effect on the performance of the damper using Nervier-Stoke equations to derive a relationship between the damping force and speed.

Figure 3 is the internal structure of the damper, first of all, we defined geometric algebra damper and established the mathematical model simply. It is assumed to be incompressible hydraulic oil and stable flow of the hydraulic oil. Although the assumption do not conform completely with the actual situation, but there is still a certain degree of accuracy in the case of a low operating speed. Therefore, it still needs to construct.

Damping force is constituted by the three force, that are piston ends of the pressure difference, the friction between the hydraulic oil and the tube wall, and the inertial force of the piston. According to the literature, the greatest impact is the pressure difference. Therefore, the present mathematical model is only considered for the association between the flow and the pressure difference to deduce the relationship between the damping force and speed.

This model made the following assumptions:

1. The damping force is generated by the piston ends of the pressure difference.
2. The pressure in front of the piston is equal to the inlet pressure of gap, the pressure behind the piston is equal to the outlet pressure of gap.
3. The hydraulic oil is stable and uniform layer stream, and incompressible Newton hydraulic oil
4. The friction and the inertial force are ignored.

Shown in Figure 4, according to the conservation of mass, the piston will squeeze the hydraulic oil and generate flow rate Q_1 when the external force on the piston. The flow rate of the gap (Q_2) plus flow rate of throttle hole (Q_3) equals Q_1.

3.2 Flow rate through main cylindrical gap

Hydraulic oil flows in the gap may be assimilated to the hydraulic oil flow between the plates. The Navier-Stoke equation is applied, the speed of the hydraulic oil for "u", and the sticking coefficient "μ", it is understood that the governing equation (1) with the hydraulic oil movement between the plates:

$$\rho g_x - \frac{\partial P}{\partial x} + \mu\left(\frac{\partial^2 u}{\partial x^2} + \frac{\partial^2 u}{\partial y^2} + \frac{\partial^2 u}{\partial z^2}\right)$$

$$\rho g_y - \frac{\partial P}{\partial y} + \mu\left(\frac{\partial^2 u}{\partial x^2} + \frac{\partial^2 u}{\partial y^2} + \frac{\partial^2 u}{\partial z^2}\right) \quad (1)$$

$$\rho g_z - \frac{\partial P}{\partial z} + \mu\left(\frac{\partial^2 u}{\partial x^2} + \frac{\partial^2 u}{\partial y^2} + \frac{\partial^2 u}{\partial z^2}\right)$$

The flow velocity of x-direction and y-direction equation (2) can be obtained in accordance with the assumptions:

$$\frac{\partial^2 u}{\partial y^2} = \frac{1}{\mu}\frac{\partial p}{\partial x}$$

$$\rho g_y = -\frac{\partial p}{\partial x} \quad (2)$$

Can be found that pressure changes as the y-direction, and solving for x velocity distribution for the formula (3):

$$u(y) = \frac{\pi}{2\mu}\frac{\partial p}{\partial x}y^2 + c_1 y + c_2 \quad (3)$$

The boundary conditions $u(0)=0, u(H_g)=V_p$ is substituting into equation (3.3), the relationship (4) of the piston ends of the differential pressure and flow can be obtained by derivation after solving:

$$Q_2 = \frac{\pi}{2} H_g D_p V_p + \left(\frac{\pi}{12} H_g^3 D_p\right)\left(\frac{1}{\mu}\right)\left(\frac{P_1 - P_3}{L_p}\right) \quad (4)$$

3.3 Flow rate through throttle hole

If a throttle hole was discussed, as shown in Figure 5. The throttle lever of adjustable flow is mounted in the throttle hole. The throttle lever is not across the throttle hole. Therefore, Two different traffic patterns Q_{31} and Q_{32} are formed in the throttle hole. Q_{31} is the elongated slit that analogy with flat panel flow. The governing equations as shown in (1). And There is no relative speed between the throttle lever and the piston because they move together. The boundary conditions are $u(0)=0, u(H_0)=0$, we could solve the relationship between Q_{31} and the pressure difference(P_1-P_2), as shown in equation (5):

$$Q_{31} = \frac{\pi}{6\mu} \cdot D_s H_{of}^3 \frac{(P_1 - P_2)}{L_s} \quad (5)$$

Q_{32} is pipe flow, so we used cylindrical coordinates Navier-Stoke equations (6) and governing equations (7):

$$-\frac{\partial P}{\partial r} + \mu\left\{\frac{\partial}{\partial r}\left[\frac{1}{r}\frac{\partial}{\partial r}(r v_r)\right] + \frac{1}{r^2}\frac{\partial^2 v_r}{\partial \theta^2} - \frac{2}{r^2}\frac{\partial^2 v_\theta}{\partial \theta} + \frac{\partial^2 v_r}{\partial z^2}\right\}$$

$$-\frac{1}{r}\frac{\partial P}{\partial r} + \mu\left\{\frac{\partial}{\partial r}\left[\frac{1}{r}\frac{\partial}{\partial r}(r v_\theta)\right] + \frac{1}{r^2}\frac{\partial^2 v_\theta}{\partial \theta^2} - \frac{2}{r^2}\frac{\partial^2 v_r}{\partial \theta} + \frac{\partial^2 v_\theta}{\partial z^2}\right\} \quad (6)$$

$$-\frac{\partial P}{\partial z} + \mu\left[\frac{1}{r}\frac{\partial}{\partial r}\left(r\frac{\partial v_z}{\partial \theta^2} - \frac{2}{r^2}\frac{\partial^2 v_z}{\partial \theta^2} + \frac{\partial^2 v_z}{\partial z^2}\right)\right]$$

$$\mu = \frac{D_{of}^2}{16\mu}\left(\frac{\partial P}{\partial x}\right) + \frac{c_1}{\mu} ln r + C_2 \quad (7)$$

The boundary conditions are $u(0)=v_3, u(R_{of})=0$, we could solve the relationship between Q_{32} and the pressure difference(P_1-P_2), as shown in equation (8):

$$Q_{32}=\frac{\pi D_{of}^4}{128\mu}\cdot\left(\frac{P_2-P_3}{L_p-L_s}\right) \tag{8}$$

We could get the equation (9) according to the conservation of mass. That could be solved relationship between flow rate and pressure difference (10).

$$Q_{31}=Q_{32} \tag{9}$$

$$Q_{31}=Q_{32}=\frac{\pi D_{of}^4}{128\mu}\left(\frac{\frac{\pi D_s H_{of}^3}{12\mu L_s}\times\frac{\pi D_{of}^4}{128\mu(L_p-L_s)}}{\frac{\pi D_s H_{of}^3}{12\mu L_s}+\frac{\pi D_{of}^4}{128\mu(L_p-L_s)}}\right)(P_1-P_3) \tag{10}$$

H_{of} can be ignored because it is far less than R_{of}. We got (11):

$$Q_3=Q_{31}=Q_{32}\approx\frac{\pi D_s H_{of}^3}{12\mu L_s}(P_1-P_3) \tag{11}$$

3.4 Damping Factor for Steady Flow inside Hydraulic Damper

We could get the equation (12) according to the conservation of mass and.

$$Q_1=\frac{\pi}{2}H_g D_p V_p+\left(\frac{\pi}{2}H_g^3 D_p\right)\left(\frac{1}{\mu}\right)\left(\frac{P_1-P_3}{L_p}\right)+2K_1(P_1-P_3) \tag{12}$$

According to $F=P/A$, terms of Q_2, the area A_2 is equation (13). Terms of Q_3, the area A_3 is equation (14). We putted (13) and (14) into (11), and got (15):

$$A_2=\pi\left(H_g^2+2H_g R_p\right) \tag{13}$$

$$A_3=\pi\left(H_{of}^2+2H_{of}R_s\right) \tag{14}$$

$$Q_1=\frac{\pi}{2}H_g D_p V_p+\left(\frac{H_g^3 D_p}{12\mu L_p\left(H_g^2+2H_g R_p\right)}\right)F+\left(\frac{2K_1}{\pi\left(H_{of}^2+H_{of}D_s\right)}\right)F \tag{15}$$

According to the definition of the flow (16), and the average area (17) of the damping device was calculated by Fig 3.

$$Q_1=V_p\cdot A_{cross} \tag{16}$$

$$A_{cross}=\pi\frac{\pi}{4}\left(D_p^2-D_{pr}^2-2D_{eff}^2\right) \tag{17}$$

In (17), D_{eff} is the effective diameter of the throttle hole. (16) and (17) is brought into the (15), the relationship between the speed and the damping force can be obtained. The following shows (18) and (19):

$$V_p\left[\pi\left(D_p^2-D_{pr}^2-2D_{eff}^2\right)-2\pi\left(H_g D_p\right)\right]=\alpha F \tag{18}$$

$$\alpha=\frac{H_g^3 D_p}{3\mu L_s\left(H_g^2+2H_g R_p\right)}+\frac{2D_s H_{of}^3}{3\mu L_s\left(H_{of}^2+H_{of}^2 D_s\right)} \tag{19}$$

The damping factor C is ratio of the damping force and the velocity. We could obtain the (20) by the formula (18) and formula (19):

$$C=\left(\frac{\pi\left(D_p^2-D_{pr}^2-2D_{eff}^2-2H_g D_p\right)}{\frac{H_g^3 D_p}{3\mu L_s\left(H_g^2+2H_g R_p\right)}+\frac{2D_s H_{of}^3}{3\mu L_s\left(H_{of}^2+H_{of}^2 D_s\right)}}\right) \tag{20}$$

3.5 Normalized damping coefficients

In this mathematical model, we knew that the damping coefficient has relations with dimensions and basic properties of the hydraulic oil from the equation (20). Therefore, the relationship between the damping coefficient and the dimensions could be discussed. Apart from variables of discussed, the other variables are the same dimensions as the original design.

As shown in Figure 6, the horizontal axis is the ratio (H_g/D_p) of height of gap and diameter of piston, and the vertical axis is the dimensionless damping coefficient (C/C_0). There were several conclusions from Figure 6:

1. (C/C_0) and (H_g/D_p) are negative correlation. Therefore, at a certain value of (H_g/D_p), the dimensionless damping coefficient is decreased with reducing diameter of piston.
2. For single piston diameter, the height of gap H_g is bigger, and the dimensionless damping coefficient is smaller. In other words, at a certain velocity, the large height of gap makes damping force smaller. This is intuitive conclusion.

The throttle gap is stronger about affecting the damping force than the diameter of throttle hole. That can't be seen directly amount of influence from the equation (20), but can be inferred by diagrams.

As shown in Figure 7, the horizontal axis is the ratio (D_{of}/D_p) of diameter of throttle hole and diameter of piston, and the vertical axis is the dimensionless damping coefficient (C/C_0). There were several conclusions from Figure 7:

1. When the ratio (D_{of}/D_p) is greater than 5%, no matter diameter of piston, dimensionless damping coefficient will approach a certain value. To compare figure 6 and figure 7 proved that the throttle gap is stronger about affecting the damping force than the diameter of throttle hole.
2. The diameter of piston is smaller with reduce of dimensionless damping coefficient (C/C_0). That is because the ratio (H_g/D_p) of diameter of piston and height of gap is larger, and dimensionless damping coefficient (C/C_0) is smaller.
3. When the ratio (D_{of}/D_p) is less than 5%, the dimensionless damping coefficient will increase quickly. From this, dimension of diameter of throttle hole and throttle gap both impact greatly dimensionless damping coefficient.

Complex geometric appearance of the throttle lever will cause the complexity of the mathematical model. It was assumed that the length of throttle lever is equal to the length of piston for simplifying the model.

As shown in Figure 8, the horizontal axis is the ratio

(L_s/L_p) of the length of throttle lever and the length of piston, and the vertical axis is the dimensionless damping coefficient (C/C_0). There were several conclusions from Figure 8:

1. (C/C_0) and (L_s/L_p) are positive correlation, and increasing stability like linear flow. So the damping factor is higher with the longer throttle lever when the length of piston is fixed. The throttle lever becomes longer, so that the flow rate that through the throttle hole becomes smaller, the damping coefficient will be increased.
2. When (L_s/L_p) is the smaller and with the different length of the piston, the impact is less for the dimensionless damping coefficient. It approaches a number of values. On the contrary, when (L_s/L_p) is the larger and with the different length of the piston, the impact is more for the dimensionless damping coefficient. It will diverge.

To Measure the true value of the damper and viscosity coefficient (*5.8E-6 ton / mm.s*) (Table 1), put them into equation (20) and calculate theoretical damping coefficient $C=277.74$(*ton·s/mm*). Than to take C and $n=0.3$ into the theoretical curve $F=CV^n$,and the force was got under different velocity. Shown in figure9:

4. PERFORMANCE VERIFICATION

The performance of hydraulic damper could be estimated by theoretical analysis. But there are hypothetical conditions in theory. That will idealize the characteristics of the hydraulic damper and make the error with the actual actuation. So no matter what form or structure of the hydraulic damper can be to obtain relevant parameters or performance by physical tests. The experimental equipment of this study is a dynamic high-load hydraulic actuator. The device uses a hydraulic actuator (Actuator) dynamic from the United States. It has MTS ± 150MT (tons) of power, Load Cell, MTS Displacement Sensor, controller of MTS FlexTest IIm, and computer control software of MTS MPT. It could test variation of damping force under a different vibration of cycle, collection of data and analysis. The test architecture of the device is shown in figure 10.

As shown in Table 2, experimental loads are sine wave cycle, in order to test the behavior of the different frequencies and amplitudes, the test results are plotted into a force - displacement curve.

Results of Experimental test are shown in Figure 11~21 force - displacement hysteresis loop. Figure 11 is a hysteresis loop of hydraulic damper under the 0.1Hz of frequency and 60mm of displacement. We ignored the first half of the cycle, than taken the average of the maximum and minimum strength testing and maximum velocity every time. Therefore, relationship could be get between the strength and speed of the damping force (Fig. 22).

5. CONCLUSION

The height of gap H_g and H_{of} are bigger, and the damping coefficient is smaller. When the ratio (D_{of}/D_p) is greater than 5%, no matter diameter of piston, dimensionless damping coefficient will approach a certain value. When the ratio (D_{of}/D_p) is less than 5%, the dimensionless damping coefficient will increase quickly. (C/C_0) and (L_s/L_p) are positive correlation, and increasing stability like linear flow. When (L_s/L_p) is the smaller and with the different length of the piston, the impact is less for the dimensionless damping coefficient.

Comparing the maximum speed and maximum power of mathematical theory and experimental test shows that the error below 10%.

References:

H. Exner, R. Freitag, Dr.-lng. H. Geis, R. Lang, J. Oppolzer, P. Schwab, E. Sumpf, U. Ostendorff : BasicPrinciples and Components of Fluid Technology, Mannesmann Rexroth, 1978.

Huei Peng, A. G. Ulsoy., Vehicle Control Systems, Department of Mechanical Engineering and AppliedMechanics University of Michigan, Lecture Notes, ME586-3, ME586-10., 1997.

Constantionu, M. C. and Symans, M. D., "Experimental and analytical Investigation of seismic ofstructures with supplemental fluid viscous dampers" Report No.NCEER-92-0032, National Center forEarthquake Engineering Research, SUNY at buffalo, New York. 1992.

Chiarugi, A., Melegari, A. and Spinelli, P., "On the Dynamic Behavior of Bridge Dampers UnderSeismic Excition", Proc. Eighth European Conf. on Earthquake Engrg., 5, Lisbon, 73-80, 1986.

Fu, Yaomin and Kasai, Kazuhiko, "Comparative Study of Frames Using Viscoelastic and ViscousDampers," Journal of Structural Engineering, ASCE, Vol.124, 1998.No. 5, pp513-522.

Bird, R.B., Armstrong, R.C. and Hassager, O., "Dynamics of Polymeric Liquids", John Wiley & Sons,New York, U.S.A., 1987.

Markris, N. and Constantinou, M.C., "Fractional Derivative Maxwell Model for Viscous Dampers".Journal of Structural Engineering, ASCE, Vol. 117, NO. 9,2708-2724, 1991.

Markris, N., "Viscous Heating of Fluid Dampers I: Small-Amplitude Motions", Journal of StructuralEngineering, ASCE, Vol. 124, NO. 11,1210-1216, 1998.

Markris, N., Roussos, Y., Whittaker, A.S., and Kelly, J. M., "Viscous Heating of Fluid Dampers II:Large-Amplitude Motions", Journal of Structural Engineering, ASCE, Vol. 124, NO. 11,1217-1223,1998.

Chien-Yuan Hou, "Fluid Dynamics of Nonlivear Viscous Damper", Journal of Structural Engineering,ASCE, Vol. 134, NO. 1, 56-63, 2008.

Taylordevices-http://www.taylordevices.com/dampers-seismic-protection.html

Taylor, D. P., "Fluid Dampers for Application of Seismic Energy Dissipation and SeismicIsolation" ,Eleventh Word Conference on Earthquake Engineering, No. 798, 1996.

Hsu, D.S. and Yu, S.W., "Reliability Based Desigh and the Compu-ter Program Generation of Plane Steel Structures", The Chinese Journal of Mechanics, Vol.3, No.1, pp.45-53. 1985

Hsu, D.S., "Natural Frequency of Damaged Frame Structures", Proc. of the National Science Council, national Science Council, Taipei, Taiwan, R.O.C., Part A, Vol.10, No.4, pp.460-467. 1986

Pu, J.P. and Hsu, D.S., "Optimal Control of Tall Buildings",Journal of Engineering Mechanics, Engineering Mechanics Division, ASCE, Vol.114, No.6, pp.973-989. 1988

Yeh, Y.C. and Hsu, D.S. , "Structural Optimization with Fuzzy Parameters", Computers & Structures, Vol.37, No.6, pp.917-924. NSC-78-0410-E 006-03. 1990

Hsu D.S., and Tsai C.H. , "Crack Detection Using Electric Conductive Finite Element", Computer and Structures, Vol.45,

No.3, pp471-479. 1992
Research Report of the National Earthquake Engineering Research-Center http://www.ncree.org/ZH/NCREEPublications.aspx

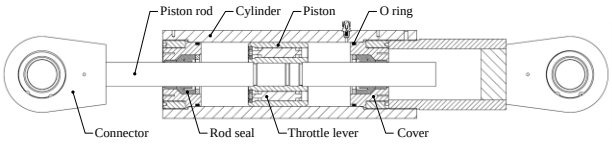


Figure 1 Scheme of hydraulic damper

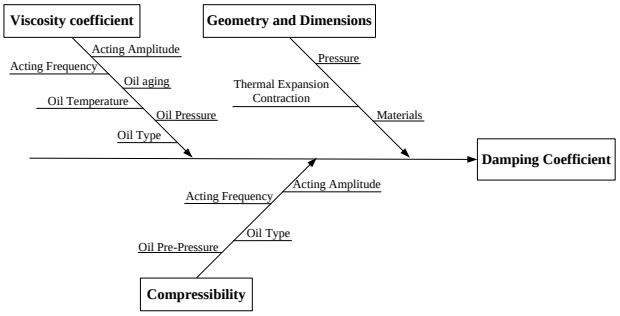


Figure 2 Fish bone diagram for damping coefficient

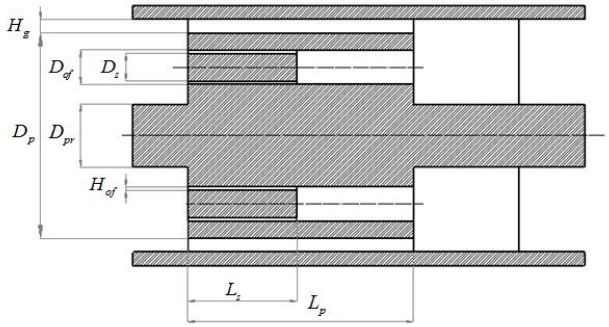


Figure 3 Dimensional parameters

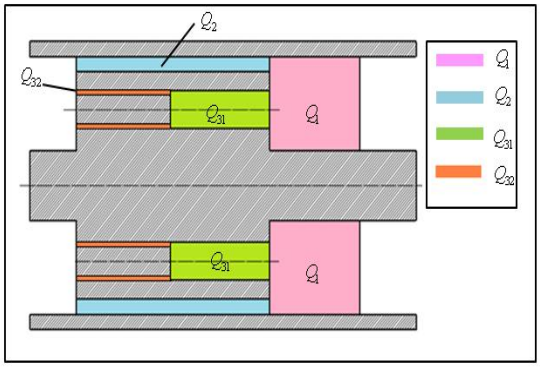


Figure 4 Flow-rate symbols in different zones

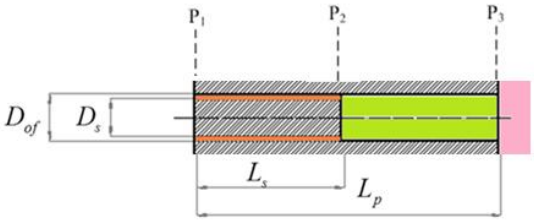


Figure 5 Dimensional parameters of throttle hole

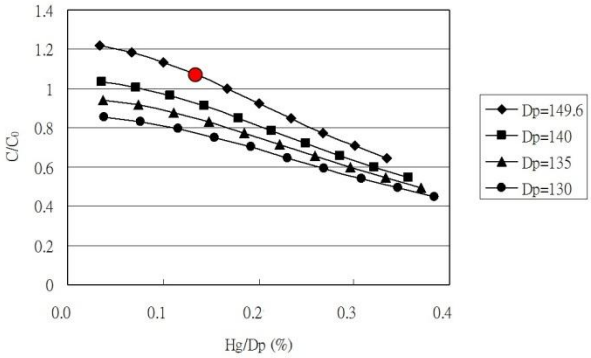


Figure 6 Analytical relationship between normalized damping coefficient and normalized piston gap

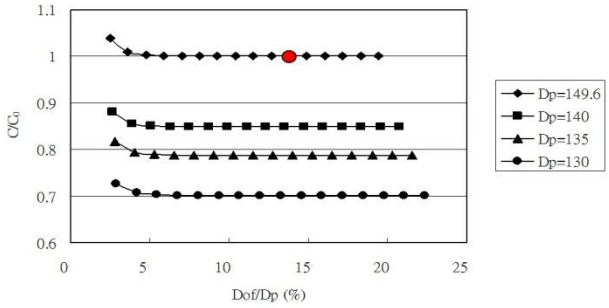


Figure 7 Analytical relationship between normalized damping coefficient and normalized throttle gap

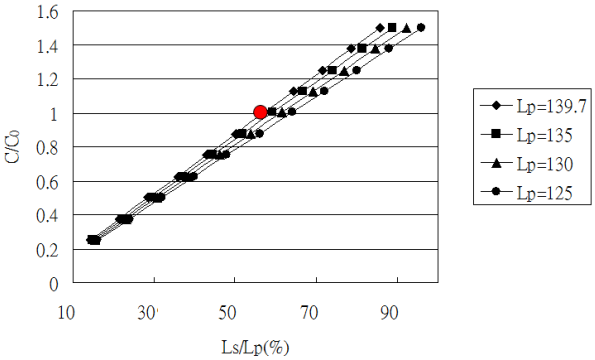


Figure 8 Analytical relationship between normalized damping coefficient and normalized throttle length

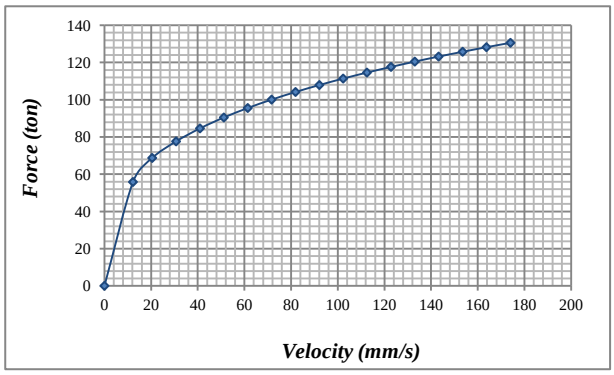


Figure 9 Theoretical predicted force-velocity curve (*F-v* curve)

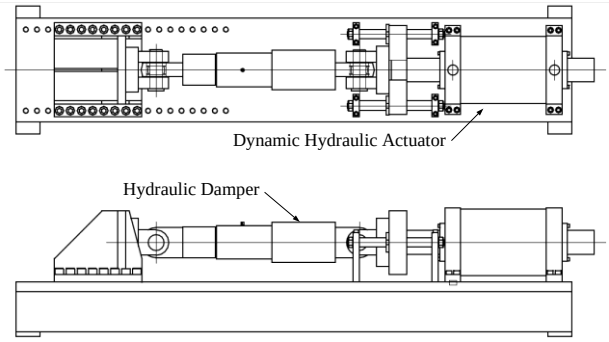


Figure 10 Experimental setup for hydraulic damper

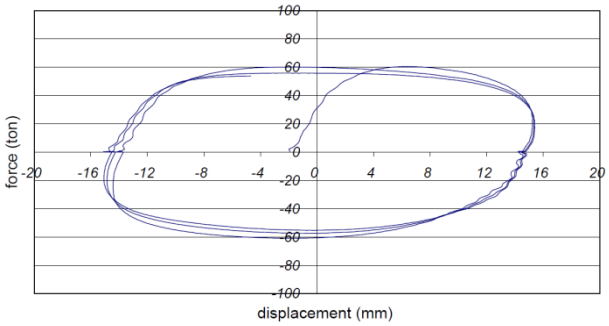


Figure 11 Damping hysteresis of Test01

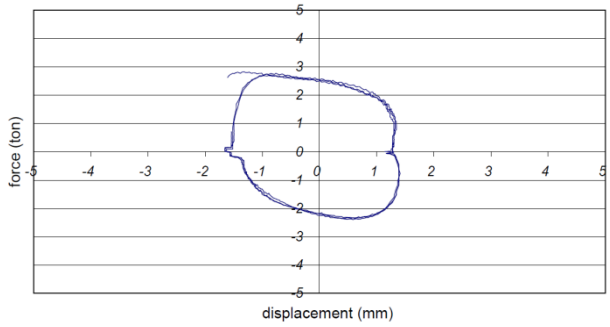


Figure 12 Damping hysteresis of Test02

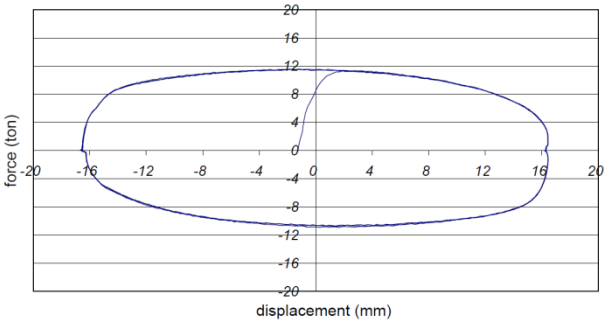


Figure 13 Damping hysteresis of Test03

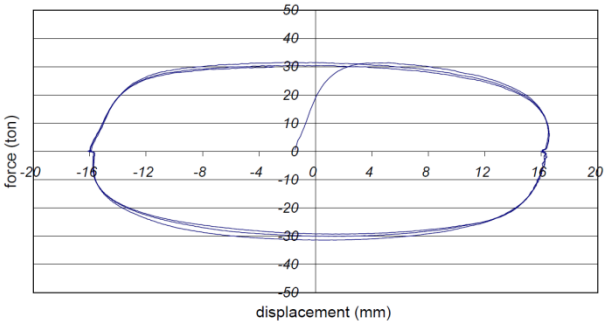


Figure 14 Damping hysteresis of Test04

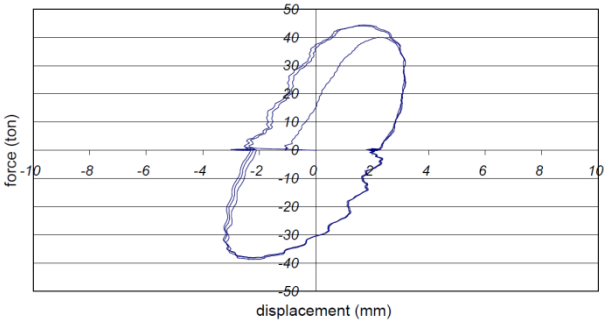


Figure 15 Damping hysteresis of Test05

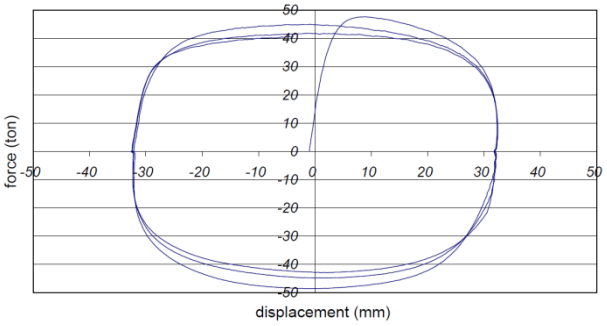


Figure 16 Damping hysteresis of Test06

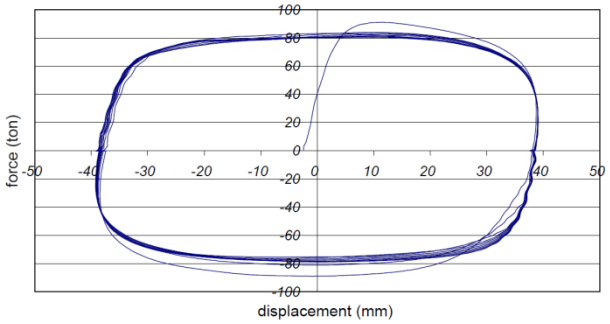


Figure 17 Damping hysteresis of Test07

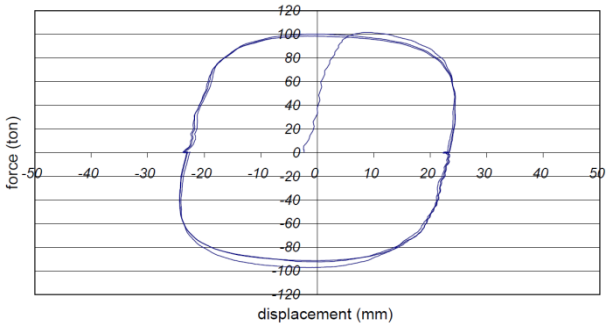


Figure 18 Damping hysteresis of Test08

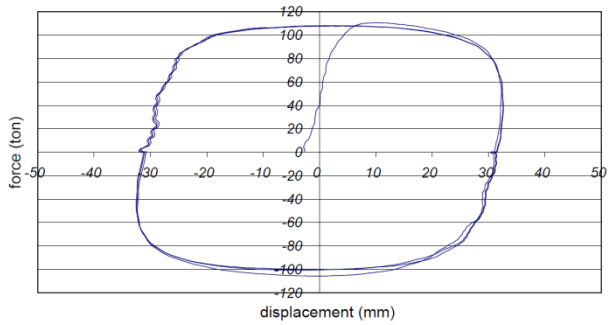


Figure 19 Damping hysteresis of Test09

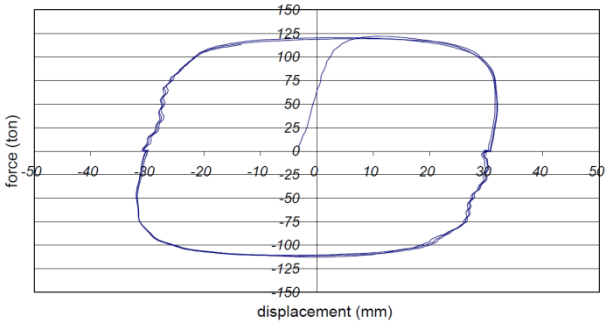


Figure 20 Damping hysteresis of Test10

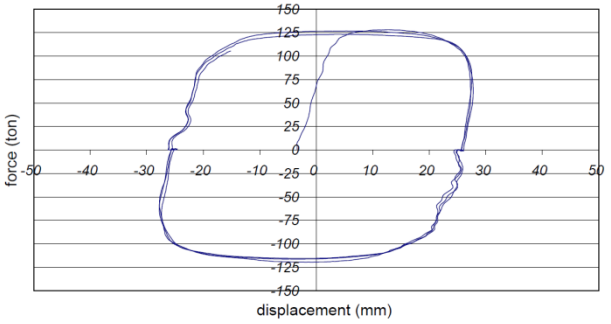


Figure 21 Damping hysteresis of Test11

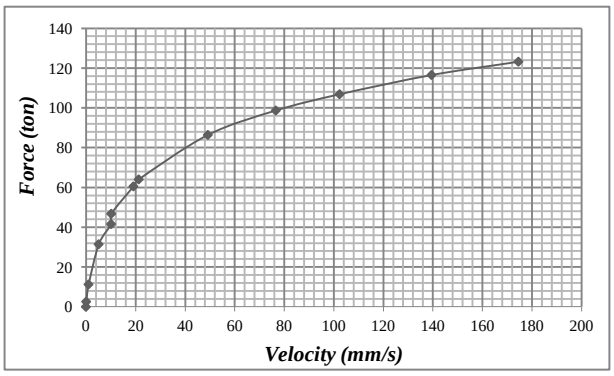


Figure 22 Experimental acquired force-velocity curve (*F-v* curve)

Table 1 Dimensional parameters and data of hydraulic damper

Symbol	Value(mm)	Description
H_g	0.25	Piston gap
H_{of}	0.37	Throttle Gap
D_s	21.56	Diameter of throttle rod
L_s	80.00	Length of throttle rod
D_{pr}	57.15	Diameter of piston rod
D_{of}	22.31	Diameter of throttle hole
D_p	149.60	Piston diameter
L_p	139.70	Piston length

Table 2 Testing parameters and data

No. of testing	v_{max} (mm/s)	Harmonic loading		
		Frequency (Hz)	Amplitude (mm)	Cycles
test01	20.0	0.20	±16.0	3
test02	0.1	0.01	±1.6	3
test03	1.0	0.01	±16.0	5
test04	5.0	0.05	±16.0	3
test05	10.0	0.50	±3.2	3
test06	10.0	0.05	±32.0	3
test07	50.0	0.20	±40.0	10
test08	75.0	0.50	±24.0	3
test09	100.0	0.50	±32.0	3
test10	140.0	0.70	±32.0	5
test11	170.0	1.00	±27.0	3

10CUEE CONFERENCE PROCEEDINGS
10th International Conference on Urban Earthquake Engineering
March 1-2, 2013, Tokyo Institute of Technology, Tokyo, Japan

TRANSFORMATION AND INTEGRATION OF BUILDING INFORMATION MODEL DATA FOR VULNERABILITY ASSESSMENT AND DISASTER MITIGATION

Chia-Ying Lin[1], and Chien-Cheng Chou[2]

1) Visiting Scholar, Dept. of Civil, Architectural and Environmental Engineering, The University of Texas at Austin, USA / Ph.D. Candidate at Dept. of Civil Engineering, National Central University, Taiwan
2) Associate Professor, Dept. of Civil Engineering, National Central University, Taiwan
cy.shelley.lin@gmail.com, ccchou@ncu.edu.tw

Abstract: BIM (Building Information Model) techniques attempt to integrate the entire life cycle information of a building together, including the design, construction, operations and maintenance phases. Although many researchers investigate BIM techniques, most of them are concerned with the design and construction phases. With the plentiful information carried by BIM, developing applications for the operations and maintenance phase can be a potential research field. For example, mitigating disaster impact is one of the most critical issues in applying BIM in such post-construction phase. During the occurrence of a disaster, first responders need up-to-date information to support their decision-making process. On the other hand, they also need simplified information to mitigate the loss as soon as possible. In a BIM environment, it promises to update information in all views and remains all versions to ensure the newest and the most complete data. However, in order to meet the information demands of first responders, the information from the BIM still needs to be simplified and transformed. In this research, the Model-Driven Architecture (MDA) framework was applied to process the BIM information in order to fit in with the needs of first responders. MDA is a state-of-the-art software developing methodology specifically for the computer science field. Since BIM is also regarded as a model, the authors defined a new mapping for BIM-related model structure and try to assist in information extraction from BIM by using this new approach. The BIM for a specific building, e.g. a concrete plant, is promoted to the model level in order to generate application program for this building. Such concept facilitates development of different application software around BIM environment, and, especially, for disaster mitigation in this research.

1. INTRODUCTION

Building Information Model (BIM) is a promising technology that can provide a communication and information exchange platform for all stakeholders involved in a building, as well as create a 3D display environment to clarify a building's virtual representations. Many researchers study BIM-related topics, such as design and engineering, linking to analysis tools, energy innovations, facility management, and so on (Becerik-Gerber and Kensek, 2010). However, most studies are concerned with the design and construction (D&C) phases of a building, few studies deal with issues pertaining to the operation and maintenance (O&M) phases (Akcamete et al., 2010)(Vanlande et al., 2008). Because costs associated with the O&M phases of a building are always higher than those with the D&C phases (Gallaher et al., 2004), and because BIM is becoming a mature software tool capable of supporting all kinds of information-intensive activities, applying the BIM technology to the O&M phases is desired.

Although researchers have shown that a building construction project and its subsequent facility maintenance projects are dissociated (Vanlande et al., 2008), it is obvious that the applications in the O&M phases require the information from the D&C phases of a building. In the D&C phases, BIM applications are designed to use parametric and object-oriented modeling techniques to represent each individual building element and help associated processes. Applications in the O&M phases may require not only original BIM-related information but the enhanced one that can be employed to record and manage various activities during O&M. Example applications include facility management systems and disaster management systems. Current practices require contractors provide a building's handover information such as Construction-Operations Building information exchange (COBie) for later usage in the O&M phases, but they usually spend minimal efforts so as to satisfy the contract (Akcamete et al., 2010). Hence, a better information bridge may be needed in order to provide transformation and customization of the handover information from the D&C phases to the O&M phases.

Applications in the O&M phases possess several unique requirements regarding interpretation of BIM. Some BIM information should be accessed and handled via an easier method while the other should be further processed

through use of a more complicated interface. In other words, customization of BIM is needed for the O&M phases. In fact, the utilization of BIM should follow the open/closed principle (OCP) – "open for extension, but closed for modification" (Meyer, 1988) as well. In the closed side, for example, structural elements in a building will not be changed during their entire life cycle (Hassanain et al. 2001); and thus, for application developers in the O&M phases, it may be a good way to operate such information at the class level, not at the metaclass level to avoid future modification. By operating BIM at the metaclass level, we mean that O&M application developers regard the structural elements as objects and use generalized classes such as Room, Column, and Wall to access each individual element. When facility managers would like to query one specific room's maintenance history, application developers need to select all rooms' maintenance objects and then filter out the records not belonging to the room specified. It is an indirect approach, and because the structural elements are constant, developers actually can regard each element as a distinct class in order to use an object to represent the current condition of an element at a specific time instance. In this way, all BIM or IFC-related functions are encapsulated in one class for an element. Application developers can have a more simple data access interface to manipulate O&M-related information. The traditional approach regards the structural elements or other elements infrequently changed as objects regardless of the D&C or O&M phases; and thus, such O&M applications may use additional redundant codes to retrieve information.

In the open side of the OCP, current materials and equipment information stored in BIM cannot accommodate various needs during the O&M phases, e.g., spare parts list management, which is an essential function from the facility management perspective. An extension mechanism of BIM may be needed and has been proposed by several studies (CRC, 2007). Among the O&M-related activities, the concept of rooms and zones forms the central management unit, which is just one of the derived attributes and is not the focus during D&C. Proper spatial containment of related building elements is essential in the O&M phases (East et al., 2012). In the D&C phases, architects design the form or the placement of each building element. But facility managers need to know the location of a specific device in order to perform maintenance work. A typical room consists of many building elements, and in BIM tools such as Revit, designers need to draw walls, windows, and doors first, and then specify the boundary of a room to link these building elements. Additional furniture or equipment elements may need to be attached to some rooms during the O&M phases. The traditional approach to transferring handover data requires manually create "polylines" of a building instead of directly using the digital building information used in the D&C phases. The traditional approach needs couple days and is labor-intensive. Even if computerized tools can be provided to assist in the transformation process, such tools describe only the geometric information and do not consider the integrity of each building element as a room or zone in the O&M phases.

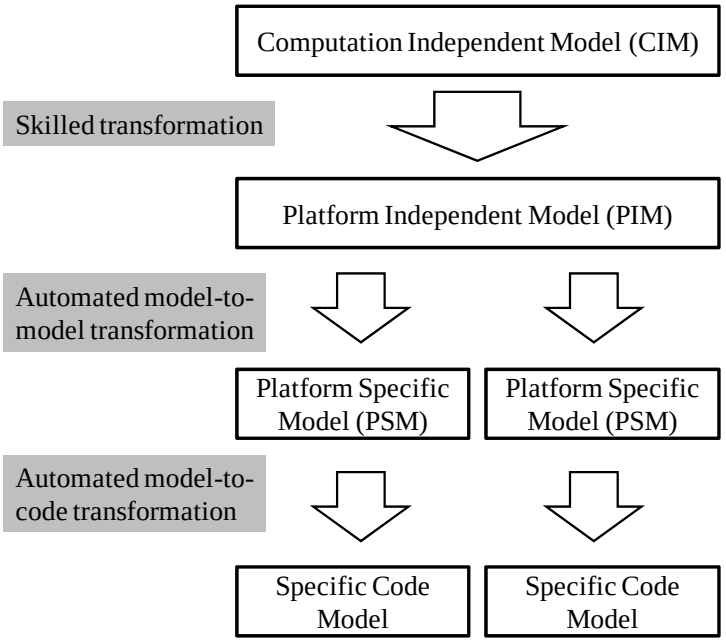


Figure 1 MDA Process

Finally, several studies have recognized the lack of 3D visualization capabilities in most applications in the O&M phases (Akcamete et al., 2010). BIM, like a spatial analysis engine (Akcamete et al., 2010), can assist facility management applications in analysis of spatial relationships between these building elements. The other issue is that the O&M phases consist of many different applications, such as disaster mitigation, security, community care, and so on. In these fields domain-specific requirements exist, and BIM cannot cover all the fields which need building information as a possible input source.

In this research, the encapsulation of BIM (E-BIM) was designed following the model-driven architecture (MDA) technique for automatic and comprehensive transformation and customization of the handover information from the D&C phases to the O&M phases. A metamodel hierarchy of a building was constructed to encapsulate the building information, not simply transforming data into an open format, but playing the role of an "interface" – users can manipulate the building information through the model instead of directly modifying it. Regarding to the designed metamodel hierarchy, we also attempted to present spatial relationships to reshape data structures of maintenance data. The proposed MDA approach was utilized with the hierarchy to generate codes for further applications of building information.

2. RELATED WORK

Nowadays, the software development process is facing

more and more complicated situations. Not only requirements become more dynamic but different platforms can be selected as the working environment. To solve these problems, MDA was proposed by Object Management Group (OMG), mainly for the purpose of integration and interoperability (Soley, 2000). This approach basically uses a series of formal models to help the software development process.

To take an overview of MDA, at first the separation of concerns should be introduced. Three MDA viewpoints of a system are described as follows: (1) Computation Independent Viewpoint (CIV), (2) Platform Independent Viewpoint (PIV), and (3) Platform Specific Viewpoint (PSV). CIV contains none of the computer-related processing details and only focuses on the business requirements; PIV deals with the operations of a system but does not contain the details for a specific platform; PSV integrates PIV with the details of using a particular platform as the development environment (Miller and Mukerji, 2003).

As shown in Figure 1, four layers and their transformation mechanisms are identified based on these views. A computation independent model (CIM) is constructed from CIV. Based on the CIM a platform independent model (PIM) is created. With the sufficiently complete and precise PIM, a platform specific model (PSM) can be generated by using model-to-model transformation mechanisms, and the specific code model – which can be viewed as implementation – can be automatically transformed from the PSM.

OMG defines a standard – Meta Object Facility – to provide metadata management and modelling language definitions. MOF is used with a metamodel hierarchy shown in Figure 2. A run-time system can be interpreted by a UML model, since the UML model is designed by people, there can be many UML models from different perspectives. To describe a UML model, we need to define UML descriptions and notations as a communicating method. The UML definitions are also based on the definitions of MOF. With the descriptions of higher layers, the lower layer can be clearly explained.

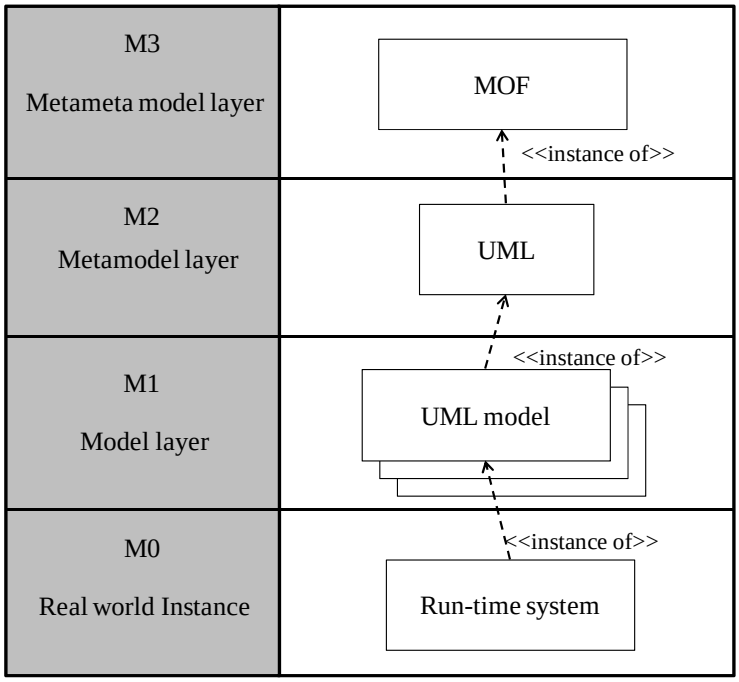


Figure 2 Metamodel Hierarchy

3. RESEARCH APPROACH

Because of the wide use of BIM, building information is available for stakeholders in the O&M phases. However, the BIM data structure is not easy to be used for users and needs extra efforts for application developers to write programs for further use of such information. In order to offer a better way for the extended use, this research defines a metamodel hierarchy for a building to interpret their various elements.

Figure 3 shows the sample definitions of the metamodel hierarchy of a residential building. This hierarchy is designed as the basis of the proposed approach.

- M3 layer: For different perspectives, the contents in M3 layer should be viewed as different roles. Inside this hierarchy, the M3 layer describes basic components of a building, such as doors, walls, windows, and so on. These components exist in any type of building, in other words, they are essential for a building; as a result they are designed to be in the M3 layer. Outside this hierarchy – which means extended applications without sufficient understanding of the building internal structure and BIM programming – for them, the layers below and those basic components are encapsulated due to OCP. Building information is available for them through the "BuildingSuperObject" but its data structure cannot be changed from the outside, that is, "BuildingSuperObject" is an interface as a communicating bridge.
- M2 layer: This layer is instantiated from basic components from the M3 layer, as well as different types of buildings and their basic units are described here. Different types of buildings may have rooms/zones/spaces for different purposes, and rooms are classified by purposes as a basic unit. For example, an apartment is classified as one type of residential buildings. Bedrooms and living rooms may only exist in a residential building, not in a factory.
- M1 layer: In the M1 layer, a "model" means a specific building and is constructed here. Most of the static components are from higher layers. Also, the constant spatial components of a building are described here, since most of the time the floor plan of a building will not be changed after the D&C phases.
- M0 layer: Finally, the instances of M1's building are

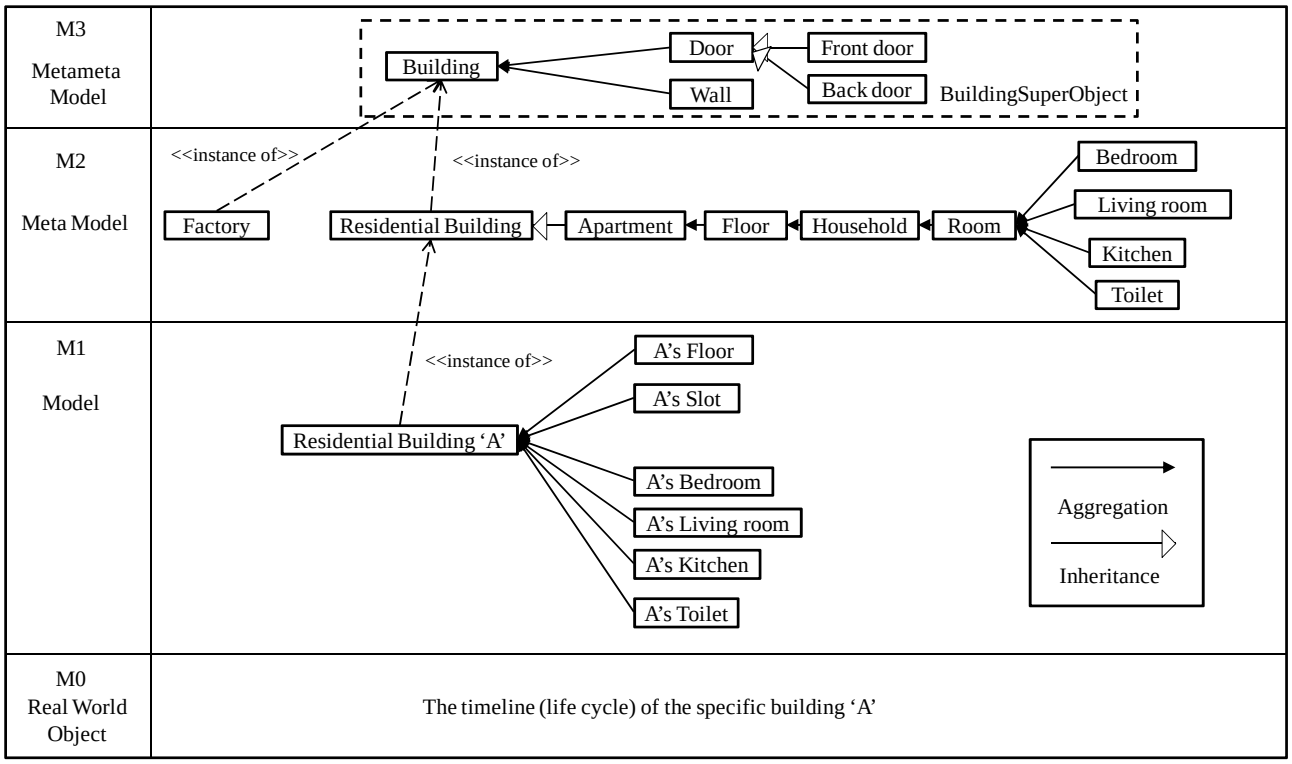


Figure 3 Metamodel Hierarchy of a Building

stretched by time as a timeline and record the whole life cycle, which means the building information covering the D&C phases to the O&M phases exists in this layer.

Suppose BIM data of a specific building is available. First its spatial relationship and the usage of spaces are re-drawn as the model shown in the M1 layer of Figure 3. The class library of this building can then be automatically generated by the model. Since attributes are also predesigned to be contained in the model, extended applications can use data they need through the model.

In Figure 4, the E-BIM process was designed referred to the MDA process; the original BIM of the specific building can be viewed as the CIM level, and then it will be transferred to E-BIM form preparing to be extended by different applications. Different application domains are considered PSM in MDA process; therefore, specific domain knowledge is used to be the additional information and taken as the foundation of the specific applications.

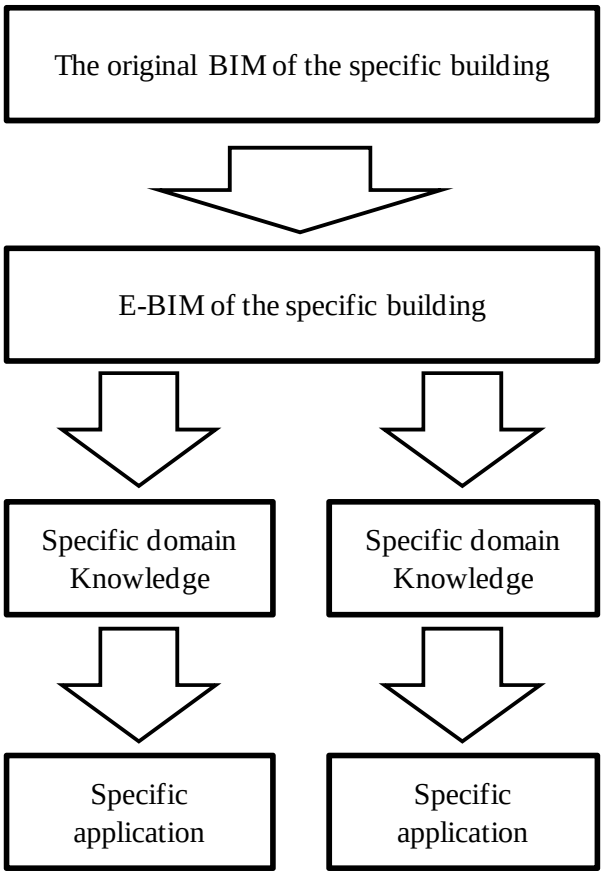


Figure 4 The E-BIM Process Referred to the MDA

4. EXAMPLE

Since the more floors and rooms a building contains, the more complicated the problem is. A three-floor apartment is presented in this section as a simple example to show the contents in metamodel hierarchy of an apartment building 'B'. Some details are also omitted for clearly interpreting the proposed approach. The relationship between contents and the expected application of the metamodel hierarchy are also interpreted in this section.

Figure 5 presents a sample model constructed following the metamodel hierarchy in previous section. In apartment building 'B', there are three floors and an elevator. There are two households in each floor, and the rule of the address assignment is the floor number, plus the serial number. Each household is assumed to have three rooms, i.e., living

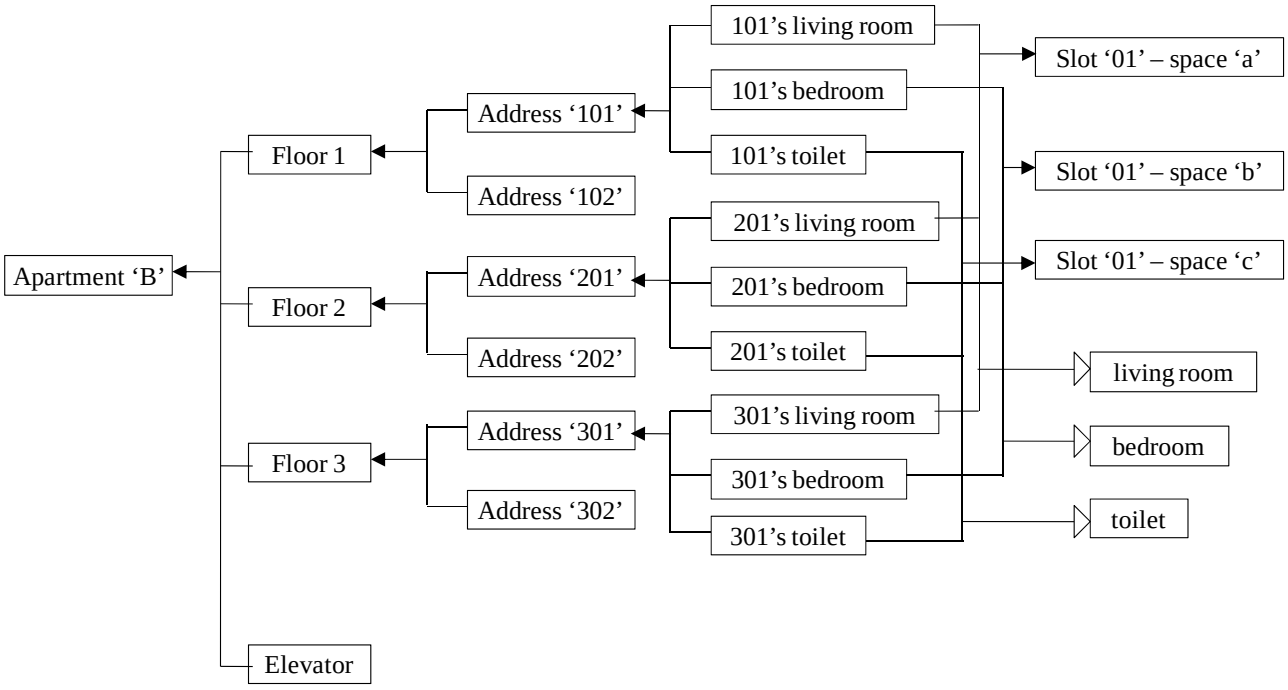


Figure 5 Model of a Specific Apartment Building 'B'

room, bedroom and toilet. In Figure 5, rooms in address '02' are omitted. These rooms define attributes from their designed usage respectively. In addition, from the spatial perspective, 'B' can be viewed in two dimensions: horizontal and vertical. The horizontal dimension is equivalent to the floor concept; the vertical dimension, named "slot" here, is composed of rooms located on the same vertical line. Usually the floor plan of a household is the same as its neighbour upstairs or downstairs in an apartment; therefore, rooms of the same purpose belong to the same slot. However, the elevator is independent of a floor or a slot since it is movable.

The model described above becomes a basis for automatic code generation; a class library of 'B' is constructed for extension. The extended applications can use BIM data through this model – more specifically, users of these applications access BIM data through this model instead of directly operating with BIM. Since it is not easy to cross the threshold of the programming issues for BIM applications, it is believed that using this model will assist the development of extended allocation for BIM.

5. CONCLUSIONS

This research has proposed a software architecture to integrate the static (BIM) information with the dynamic, O&M-related data. The MDA technique was utilized to store and synthesize the data. The BIM information is used to show the geometry aspect of the building. MDA has been successfully applied to other industries' applications, including the AEC industry. Further enhancement of the system is needed in order to integrate more dynamic information from different facility management domains and/or other BIM programs.

References:

Akcamete, A., Akinci, B., and Garrett, J.H. (2010). Potential utilization of building information models for planning maintenance activities. In: Tizani, W. (Ed.). Proceedings of the International Conference on Computing in Civil and Building Engineering, Nottingham, UK.

Becerik-Gerber, B. and Kensek, K. (2010). Building Information Modeling in Architecture, Engineering, and Construction: Emerging Research Directions and Trends, Journal of Professional Issues in Engineering Education and Practice, 136(3), pp.139-147.

CRC for Construction Innovation. (2007). Adopting BIM for facilities management: Solutions for managing the Sydney Opera House, Brisbane, Queensland, Australia.

East, E. W., Nisbet, N., and Liebich, T. (2012). The Facility Management Handover Model View, Journal of Computing in Civil Engineering, in press.

Gallaher, M.P., O'Connor, A.C., Dettbarn, Jr., J.L., and Gilday, L.T. (2004). Cost Analysis of Inadequate Interoperability in the U.S. Capital Facilities Industry, National Institute of Standards and Technology, Gaithersburg, Maryland, USA.

Hassanain, M.A., Froese, T.M., and Vanier, D.J. (2001). Development of a maintenance management model based on IAI standards, Artificial Intelligence in Engineering, 15, pp. 177-193.

Jardim-Goncalves, R., Grilo, A., and Steiger-Garcao, A. (2006). Challenging the interoperability between computers in industry with MDA and SOA, Computers in Industry, 57, pp. 679-689.

Meyer, B. (1988). Object-Oriented Software Construction, Prentice Hall.

Miller, J. and Mukerji, J. (2003). MDA Guide Version 1.0.1, Object Management Group, http://www.enterprise-architecture.info/Images/MDA/MDA%20Guide%20v1-0-1.pdf, accessed August 2011.

Soley, R. (2000). Model Driven Architecture, White Paper, Draft 3.2, Object Management Group.

Vanlande, R., Nicolle, C., and Cruz, C. (2008). IFC and Building Lifecycle Management, Automation in Construction, 18, pp. 70-78.

10CUEE CONFERENCE PROCEEDINGS
10th International Conference on Urban Earthquake Engineering
March 1-2, 2013, Tokyo Institute of Technology, Tokyo, Japan

DEVELOPMENT OF SIMULATION SYSTEM FOR ESTIMATION OF URBAN EARTHQUAKE DISASTERS CONSIDERING LOCAL SOIL PROPERTIES USING HIGH PERFORMANCE COMPUTING

Kohei Fujita[1], Tsuyoshi Ichimura[2], Muneo Hori[3], M. L. L. Wijerathne[4], and Seizo Tanaka[5]

1) Graduate Student, Department of Civil Engineering, The University of Tokyo, Japan;
Research Fellow of the Japan Society for the Promotion of Science (DC)
2) Associate Professor, Earthquake Research Institute, The University of Tokyo, Japan
3) Professor, Earthquake Research Institute, The University of Tokyo, Japan
4) Associate Professor, Earthquake Research Institute, The University of Tokyo, Japan
5) Assistant Professor, Earthquake Research Institute, The University of Tokyo, Japan
fujita@eri.u-tokyo.ac.jp, ichimura@eri.u-tokyo.ac.jp, hori@eri.u-tokyo.ac.jp, lalith@eri.u-tokyo.ac.jp, stanaka@eri.u-tokyo.ac.jp

Abstract: We develop a system to perform estimation of urban earthquake disaster considering local soil properties under each structure. The system automatically converts structural and soil data stored in the geographic information system to inputs of soil amplification analysis and seismic response analysis of structures. Soil amplification analysis is performed on the generated soil model, and the ground motion at surface is inputted to structural response analysis. The system is designed to be run on many computation cores to speed up the analysis. By using the developed program on high performance computers, earthquake damage estimation for many structures that make up a city can be done in a short period of time.

1. INTRODUCTION

Estimating the consequences of a given hazard scenario is needed for making disaster mitigation strategies. Methods based on statistical analysis of past disasters are frequently used in practice for estimating earthquake disaster in urban areas. In these methods, cities are divided into blocks, and the statistical values of earthquake damage are estimated for each block. By using such method, we can obtain a rough view of damage of a city without detailed soil or structural data with small computational effort. On the other hand, ground motion at surface is heavily affected by the local soil structure, and response of a structure is dependent on its structural properties. Estimation of damage considering soil properties and properties of each structure provides a more detailed view of the earthquake disaster, which may lead to improvement of mitigation strategies, such as evacuation route planning or development of earthquake insurances.

Soil and structural data are stored in the Geographic Information System (GIS), and analysis methods based on physical modeling are developed and used in structural design. Aiming to perform estimation of earthquake disaster considering properties of a city, our research group have been developing an Integrated Earthquake Simulator (IES); for example, see Hori and Ichimura (2008) and Hori (2011). IES analyzes earthquake wave propagation from the fault to the city, structural response of structures in a city, and social response of a city. Since each phase of earthquake disaster is analyzed in IES, the computational size becomes large. Estimating consequences of multiple hazard scenarios are needed for considering uncertainty in the input earthquake hazard, structural or soil properties. Time is limited to obtain earthquake disaster estimation, especially when using it for real time estimation after a major earthquake. Real time disaster estimation in high resolution can help authorities to make disaster reaction decisions, such as making resident evacuation strategies or deciding fire brigade allocation. Speedup of IES is needed for performing estimation for multiple hazard scenarios or real time hazard estimation.

High Performance Computing (HPC) can be used to enhance IES, so that multiple hazard scenarios can be estimated for large urban areas in a short time. HPC is first applied to structural response analysis of IES (Wijerathne et al. 2012). We further enhance the soil amplification analysis phase of IES with HPC in this paper. Attention is paid to speed up analysis of large problems using large number of computation cores.

2. METHODOLOGY

2.1 Overview of IES

Combining information of soil and structures of a city with computation is a key to performing high resolution

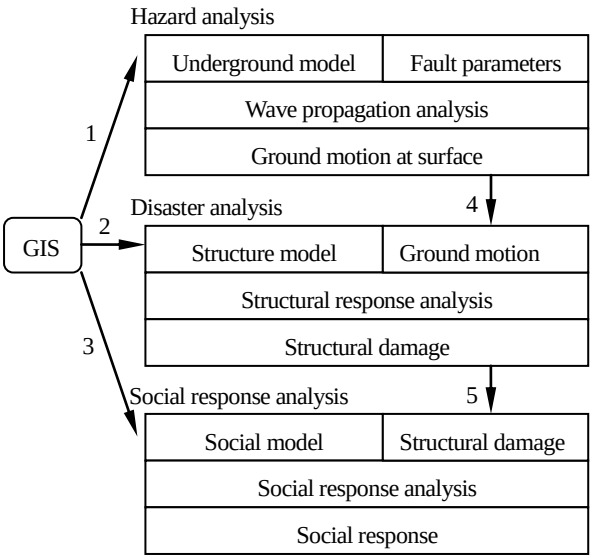


Figure 1 Overview of IES

earthquake damage estimation. Figure 1 shows the overview of IES. In IES, soil and structural data of a city, stored in GIS, are automatically converted to input city model of analysis programs (arrows 1, 2, 3 in Figure 1). Analysis methods are plugged in to IES, and connected via data conversion modules (arrows 4, 5). First, earthquake wave propagation from fault to city is performed, and output is converted to input to structural response analysis. Structural response analysis is performed, and results are converted into input of social response analysis. Since the data format of GIS, input and output formats of each analysis program differ, data conversion is needed in order to perform such an integrated simulation. For such purpose we have been developing robust and versatile data conversion methods.

In this study, we combine soil amplification analysis and structural response analysis; see Figure 2. Soil amplification analysis is used to analyze the ground response at surface using wave at bedrock, and structural response analysis is used to analyze structural response using ground motion at surface.

2.2 Analysis methods

In order to attain reliability of estimation results, we use seismic analysis methods used in the actual structural design process. We expect that users of the system need different levels of accuracy within different length of time using available computational resources. Thus, we design the system so that multiple types of analysis methods can be plugged in, and users can choose the analysis method according to their needs.

In this study, we implement 1D equivalent linear method for soil amplification analysis, although we plan to further implement 3D wave propagation methods in the future. The 1D equivalent linear method analyzes shear wave propagation from the bedrock to surface. Non-linear properties of the soil are considered by solving linear wave propagation in the frequency domain, and updating shear

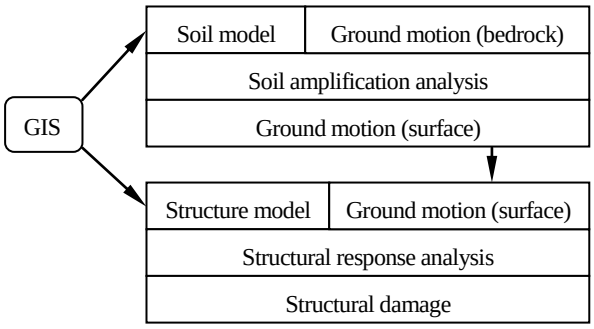


Figure 2 Overview of current system

modulus G and damping ratio h using the effective strain γ_{eff}, obtained by

$$\gamma_{\text{eff}} = \alpha\gamma_{\max}. \quad (1)$$

Here, $\gamma_{\max}$ is the maximum shear strain of each soil layer in the time history. α is a parameter to relate the two values; we use $\alpha = 0.65$, which is a typical value used in the literature. We use the Hardin-Drnevich model (1972)

$$G = G_{\max}/(1+\gamma/\gamma_{\text{r}}), \quad (2)$$

$$h = h_{\max}(1- G/G_{\max}), \quad (3)$$

for non-linear modeling of the soil. Here, $G_{\max}$ is the maximum shear modulus, γ_{r} is the reference strain, and $h_{\max}$ is the maximum damping ratio.

The multi-degree of freedom model, one component model, and fiber element models are implemented for structural response analysis in the HPC enhanced IES (Wijerathne et al. 2012). In this study, we use the one component model. The one component model models beams and columns of a structure as non-linear elements. Beams are modeled with a shear spring and rotational springs on both ends, where columns are modeled with axial and shear springs with rotational spring on both ends. Mass is modeled on the connection (node) of beams and columns. See Giberson (1967) for details of one component model.

2.3 City modeling

City models that reflect properties of a city are needed in a wide region for each structure for performing high resolution earthquake disaster estimation. We make modules that automatically convert soil and structural data stored in GIS to input city models for analysis.

We use the nationwide digital underground map provided by The Japanese Geotechnical Society. This is a dataset that stores soil structure data of major cities of Japan in a 250m resolution structured grid. We interpolate the soil structure by assuming a three layered soil structure: clay, sand, and bedrock. Interpolation is performed using spline interpolation.

For structural data, we use the outer shape of structures stored in GIS. Since we do not have information about

structural properties, such as the number, position, strength of beams or columns, we guess these properties by assuming that each structure follows the Japanese design code.

Conversion programs are designed to attain high robustness of data conversion, so that large data sets can be converted without errors. By using these methods, we can automatically generate a city model of a large city, such as Tokyo, with more than 2 million structures, in a short period of time. Validation of generated models is still undergoing; although we expect that we can obtain more detailed urban data so that few ambiguity is needed in the generation of the city model.

2.4 Application of HPC

High performance computers, which are made of many computational cores, can be used to shorten the computation time. In order to utilize these computers, programs must be designed so that the problem size and computation speed can be increased with respect to the number of computation cores.

Serial programs are developed and widely used in structural design. Since the computation of each structure is independent from each other, we run these serial programs in parallel using different input data to perform parallel computation. By properly assigning structures to computational cores, we can expect linear performance gain with respect to the number of computational cores. We distribute evaluation points to computation cores depending on the number of soil layers in the input soil structure.

For extension of 3D wave propagation analysis programs, we separate the soil analysis and structural analysis codes. We output the resulting wave form into the file system, and read it when performing structural analysis. Since the performance of the file system does not necessarily gain with respect to the number of computational cores, we need to reduce the ratio of file input and output (file I/O) in comparison with the total computation time to obtain performance using large number of cores. We use binary file I/O, and gather output data of structures within one GIS tile to one output file. This reduces the overhead of conversion of binary data to human readable text data, and manipulation of large number of files. This is further enhanced with use of collective I/O of Message Passing Interface 2 (MPI-2) standard, so that data is written to the file system from multiple computation cores without the need to gather information to one computation core. By using such method, file I/O speed of soil amplification analysis has increased from 9.39MB/s to 862MB/s, which is near to the benchmark sequential write performance of the file system (610MB/s). Performance is measured in a PC cluster of 24 computation nodes, each with dual hexacore Intel Xeon X5680 (3.33GHz) processors with 48GB DDR3 memory, connected with QLogic 12200 InfiniBand switch. File system of the cluster is a RAID-10 file system consisting of twelve 600GB 3.5 inch SAS hard disks. The same environment is used for measurement in this paper.

Figure 3 shows the speedup of the developed soil amplification analysis program. The horizontal axis indicates the number of computation cores while the vertical axis indicates the speedup with respect to 4 computation cores. A problem with 253,405 evaluation points, each with 30 soil layers and 8,192 time steps, is used for measurement.

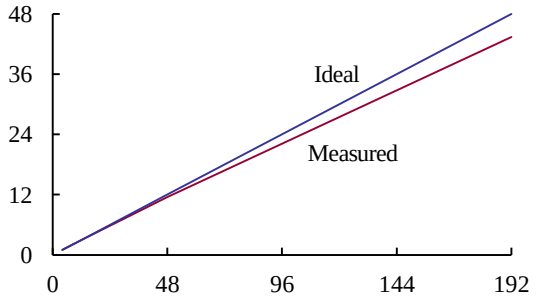


Figure 3 Speedup of soil amplification program on a PC cluster. Horizontal axis indicates number of computation cores, while vertical axis indicates speedup with respect to 4 cores.

We can see that the program scales well up to 192 cores; the parallel efficiency for 192 cores is 90.5%. By using this program, we can speed up the analysis for this problem from 23 hours using the original serial program to 364s using 192 cores. Further details of implementation of HPC to IES are described in Fujita et al. (2012).

3. APPLICATION

Analysis is performed on a target area of 2.0 x 1.5km, consisting of 13,781 structures. A 3 layered soil model is automatically generated from soil data. The soil properties of each layer are shown in Table 1, and the elevation of each layer is shown in Figure 4. We can see that the region has valleys and tables, with complex underground structure.

Earthquake wave observed in the 2007 Nigata-Ken Chuetsu-Oki Earthquake is inputted at the bedrock (z = -60m). Analysis took 20.5s using 36 cores. Figure 5 shows response at the surface. The figure shows the acceleration response spectrum at period 1.0s, 0.5s and 0.1s from the top to bottom, respectively. We can see that the response at surface is altered depending on the topography and underground soil structure. The amplification is different depending on the period; some areas are amplified larger for low frequencies, while other areas are amplified larger for high frequency components.

The ground motion at surface is inputted into structural response analysis. Analysis took 864s using 60cores. Figure 6 shows the maximum drift angle of each floor. The figure on the top shows results of all structures, where figure in the middle and bottom shows the response of high rise and low rise structures, respectively. We can see that each structure has different response, reflecting their structural properties and input ground motion. By filtering structures with its properties, such as the height of a structure, we can analyze the damage according to its classification, which can be used for planning mitigation strategies for each class of structures.

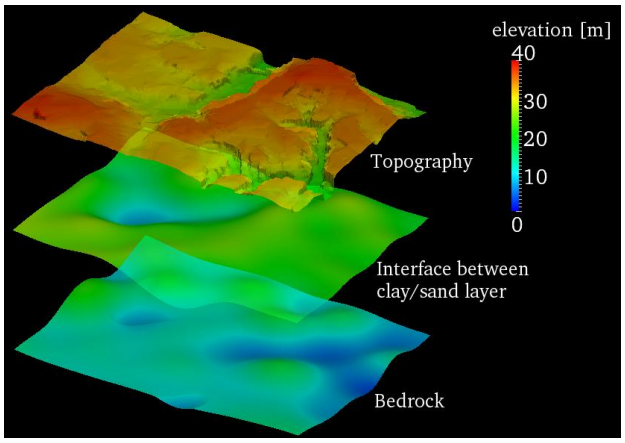


Figure 4 Target area of size 2.0 x 1.5km. Soil model consists of 3 layers; clay, sand and bedrock. Elevation is magnified by 10 times in the figure.

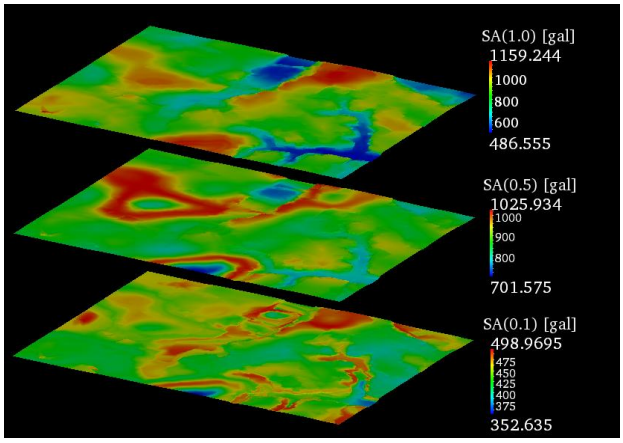


Figure 5 Ground motion at surface. Colors indicate the acceleration response spectrum at 1.0s, 0.5s, and 0.1s from top to the bottom. Damping ratio is set to 0.05 for all cases.

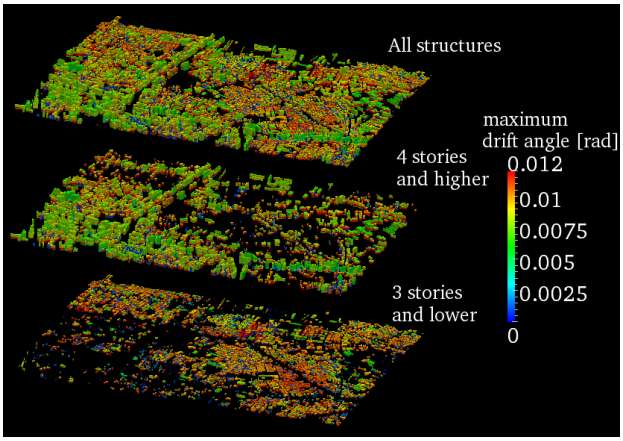


Figure 6 Response of 13,781 structures in target area. Colors indicate maximum drift angle of structures. Figure on top indicates response of all structures in target area, where figure in middle indicate response of high rise structures with 4 stories and higher, and the bottom figure indicates response of low rise structures of 3 stories and lower.

Table 1 Material properties of each layer.

Layer	V_s (m/s)	G_{max} (tf/ms^2)	ρ (tf/m^3)	h_{max}	γ_r
Clay	116	26,640	2.0	0.15	0.2
Sand	250	135,000	2.0	0.15	0.2
Bedrock	500	500,000	2.0	0.05	0.2

4. CLOSING REMARKS

In this paper, we developed a system to obtain earthquake damage estimation of a city considering local soil properties. The system is enhanced with high performance computing so that damage estimation of large number of structures can be performed in a short period of time. Load balancing among computation cores and file I/O is dealt with care for attaining performance on high performance computers.

Application shows that estimation of earthquake disaster can be obtained in a short period of time. Results can be analyzed depending on the acceleration spectrum, story drift, or other damage indicators.

Our future works are to enhance this system for application to multiple hazard scenarios. We plan to run hundreds or thousands of hazard scenarios on high performance computers to evaluate earthquake disaster considering uncertainty in the input wave form or soil/structural parameters.

Acknowledgements:

The authors acknowledge support from the Japan Society for the Promotion of Science. Part of the results is obtained by using the K computer at RIKEN Advanced Institute of Computational Science (Proposal number hp120308). We used soil data provided by The Japanese Geotechnical Society, and seismic waveforms observed by KiK-net of National Research Institute for Earth Science and Disaster Prevention.

References:

Hori, M. and Ichimura, T. (2008), "Current state of integrated earthquake simulation for earthquake hazard and disaster," *Journal of Seismology*, Vol.12, pp.307-321.

Hori, M. (2011), "Introduction to Computational Earthquake Engineering (2nd edition)," Imperial College Press.

Wijerathne, M. L. L., Hori, M. and Kabeyasawa, T. (2012), "Strengthening of parallel computation performance of integrated earthquake simulation," *Journal of Computing in Civil Engineering, ASCE*, doi:10.1061/(ASCE) CP.1943-5487. 0000235.

Harbin, B. O. and Drnevich, V. P. (1972), "Shear modulus and damping in soils: design equations and curves," *Journal of the Soil Mechanics and Foundations Division*, Vol.98, No.7, pp.667-692.

Giberson, M. F. (1967), "The response of nonlinear multi-story structures subjected to earthquake excitation," Earthquake Research Laboratory, California Institute of Technology, Pasadena, CA, EERL Report.

Zenkoku-denshi-jibanzu, The Japanese Geotechnical Society, http://www.denshi-jiban.jp/ (accessed Dec., 2012)

Japanese standard for structural design (2007), (in Japanese).

Fujita, K., Ichimura, T., Hori, M., Wijerathne, M. L. L., Tanaka, S. (2012), "Basic study on speeding up high resolution urban earthquake damage estimation", *Journal of Japan Society of Civil Engineers*, submitted (in Japanese with English abstract).

10CUEE CONFERENCE PROCEEDINGS
10th International Conference on Urban Earthquake Engineering
March 1-2, 2013, Tokyo Institute of Technology, Tokyo, Japan

2-D WAVE ANALYSES FOR FLUID-SATURATED POROUS SOLIDS USING CONVOLUTION QUADRATURE BOUNDARY ELEMENT METHOD

Akira Furukawa[1], Fumika Chikazawa[2], Takahiro Saitoh[3], and Sohichi Hirose[4]

1) Ph.D. Candidate, Dept. of Mechanical and Environmental Informatics, Tokyo Institute of Technology, Japan
2) Master Student, Dept. of Mechanical and Environmental Informatics, Tokyo Institute of Technology, Japan
3) Associate Professor, Department of Civil and Environmental Engineering, Gunma University, Japan
4) Professor, Dept. of Mechanical and Environmental Informatics, Tokyo Institute of Technology, Japan
furukawa.a.aa@m.titech.ac.jp, chikazawa.f.aa@m.titech.ac.jp, t-saitoh@gunma-u.ac.jp, shirose@cv.titech.ac.jp

Abstract: It is common knowledge that fault fracture zones capable of causing earthquakes are fluid-saturated porous solids. Therefore, the wave analyses for fluid-saturated porous solids are particularly helpful for understanding seismic wave propagation. However, in general, seismic analyses are implemented by modeling the fault fracture zones as isotropic elastic solids because the consideration of fluid effects on wave propagation complicates the numerical procedures. Boundary element method (BEM) is known as an effective numerical approach for wave propagation because BEM can treat infinite or semi-infinite regions without any modifications. In recent years, the convolution quadrature time-domain boundary element method (CQ-BEM) has been studied by several researchers to improve the numerical instability of the conventional time-domain BEM. The CQ-BEM requires fundamental solutions in Laplace-domain. Therefore, the formulation is similar to that for the frequency-domain BEM. This fact shows that CQ-BEM formulation becomes easier than the conventional one. In this paper, the wave propagation in fluid-saturated porous solids is analyzed by the convolution quadrature time-domain boundary element method (CQ-BEM). The proposed CQ-BEM formulation for wave propagation in fluid-saturated porous solids is based on the Biot's theory (1962). Basic wave scattering problems are solved to verify our proposed CQ-BEM.

1. INTRODUCTION

This paper presents 2-D wave propagation and scattering analyses for general anisotropic fluid-saturated porous solids using a convolution quadrature boundary element method.

Ground and fault fracture zones are well known as an anisotropic solid, and seismic velocity anisotropy in these solids is widely confirmed. Especially near the fault, rocks including pores and cracks produce strong anisotropy. Moreover, the pores and cracks are saturated with fluid. In recent years, the anisotropic fluid-saturated porous solids are studied by many researchers (Carcione 1996, Liu et al. 2005, Sharma 2005). Most of them, however, described the derivation of phase and group velocities in the solid only, and a numerical method applicable to realistic problems has not been proposed.

Boundary element method (BEM) is an effective numerical approach for wave analysis. BEM requires boundary discretization only, and can deal with infinite or semi-infinite domain without any special efforts. Convolution quadrature boundary element method (CQ-BEM), proposed by Schanz and Antes (1997), is known as a new time-domain BEM. In CQ-BEM, convolution quadrature method (CQM) is used for time discretization and improves the numerical stability of the time-domain BEM. Therefore, CQ-BEM can produce stable solutions, even for small time increments which are not adequate in the conventional time-domain one. Furthermore, instead of time-domain fundamental solutions, CQ-BEM requires Laplace-domain ones. This is advantageous for cases where time-domain fundamental solutions are not available, however Laplace-domain ones can be obtained (e.g. viscoelastic or poroelastic problems). Recently, CQ-BEM is applied to wave analyses for general anisotropic elastic solids (Zhang 2000, Furukawa et al. 2012) and isotropic fluid-saturated porous solids (Schanz 2001, Saitoh et al. 2012). However, there is no application of CQ-BEM, even frequency- or Laplace-domain BEM, to wave analysis for general anisotropic fluid-saturated porous solids.

This paper describes the formulation of CQ-BEM for 2-D general anisotropic fluid-saturated porous solids. Biot's theory (Biot 1962) is used for the formulation of poroelasticity. Biot proposed the theory to describe wave propagation in fluid-saturated porous solids using a set of coupled differential equations that govern the motion of solid and fluid part (Biot 1956a,b) and extended the theory to that for general anisotropy (Biot 1962). Biot's theory marks the beginning of an effort to study dynamic poroelastic problems, whereafter a number of related and extended theories were proposed (Rice and Cleary 1976, Beskos 1989).

In this paper, the brief statement of Biot's theory is described in section 2, and the formulation of CQ-BEM for

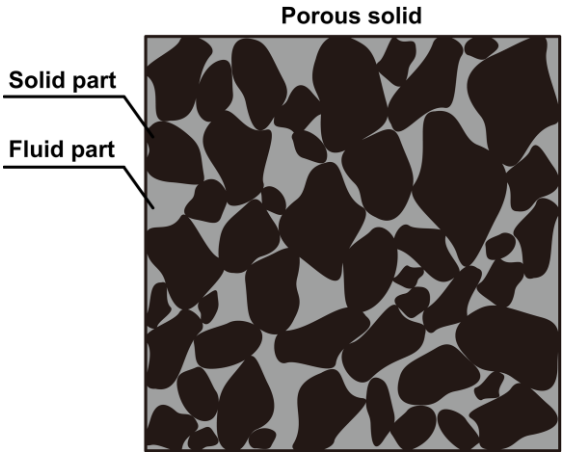


Figure 1 Fluid-saturated poroelastic solid.

fluid-saturated porous solids is presented in section 3. Moreover, in this section, we derive fundamental solutions for 2-D general anisotropic fluid-saturated porous solids. In section 4, numerical example based on our proposed method is demonstrated. At the end, in section 5, conclusions and future works are shown. Throughout this paper, small and large indices, without notice, range from 1 to 3 and 1 to 4, respectively. In addition, summation convention is valid for repeated indices.

2. FLUID-SATURATED POROUS SOLIDS

In this section, the theory of wave propagation in fluid-saturated porous solid is described. The theory is based on that proposed by Biot (1962). The solid, described in this section, is shown in Figure 1 and consists of solid and fluid parts. The main assumptions of the theory are as follows:

1. Infinitesimal transformations occur between the reference and current states of deformation.
2. The wavelength is large compared with the dimensions of macroscopic values.
3. The conditions are isothermal.
4. The fluid is viscous.
5. The fluid flows through the porous skeleton according to Darcy's law.

In most situations, the material of the skeleton is isotropic. However, in this paper, anisotropy due to a preferential alignment of the pores or cracks is considered.

In the most general case of anisotropy, the linear stress-strain relations are written as follows:

$$\sigma_{ij} = A_{ijkl} e_{kl} + M_{ij}\zeta, \tag{1}$$

$$p = M_{kl} e_{kl} + M\zeta \tag{2}$$

where σ_{ij} and e_{ij} represent the total stress and strain components of the porous solid, respectively. e_{ij} can be expressed, using the displacements of the solid u_i, as follows:

$$e_{ij} = \frac{1}{2}\left(u_{i,j} + u_{j,i}\right) \tag{3}$$

where $(\,)_{,i} = \partial/\partial x_i$. p and ζ, in Eqs.(1) and (2), are the fluid pressure and the increment of the fluid content, respectively. In addition, A_{ijkl} represents the elastic tensor of undrained porous solid expressed as follows:

$$A_{ijkl} = C_{ijkl} + \frac{M_{ij} M_{kl}}{M} \tag{4}$$

where C_{ijkl} represents the elastic tensor of drained porous solid. Moreover, M is Biot's elastic modulus. M_{ij} is expressed as $M_{ij} = \alpha_{ij} M$, where α_{ij} is Biot's effective-stress coefficients in anisotropic case.

Equations of motion for general anisotropic fluid-saturated porous solid are written as follows:

$$\sigma_{ij,j} + \rho b_i = \rho \ddot{u}_i + \rho_f \ddot{w}_i, \tag{5}$$

$$p_{,i} + \rho_f c_i = -\rho_f \ddot{u}_i + m_{ij}\ddot{w}_j - \eta r_{ij}\dot{w}_j \tag{6}$$

where $\dot{(\,)} = \partial/\partial t$, and w_i represents the flow of the fluid relative to the solid in the unit section. ρ and b_i are the mass density and body force components of the porous solid, and ρ_f and c_i represent those of the fluid part. In addition, η represents the viscosity of the fluid, and m_{ij} is the mass matrix and depends on the pore geometry. Moreover, r_{ij} represents the flow resistivity matrix given by $[r_{ij}] = [k_{ij}]^{-1}$, where k_{ij} is the permeability matrix based on Darcy's law.

According to the previous studies (Carcione 1996, Liu et al. 2005, Sharma 2005), anisotropic fluid-saturated porous solids generate four body waves: quasi-fast longitudinal wave, marked as "qP1", quasi-slow longitudinal wave, marked as "qP2", and quasi-transverse waves, marked as "qS1" and "qS2". In addition, phase velocities of the waves depend on the propagation direction and the frequency. The viscosity η has a great effect on the behavior of qP2 wave.

3. BEM FORMULATION USING CQM

Applications of BEM to isotropic fluid-saturated porous solids were studied in the past decades, and most of them were based on u_i-p formulation (Schanz 2001, Saitoh et al. 2012). Fundamental solutions for the solids, of course, were derived in u_i-p formulation by many researchers (Schanz and Pryl 2004, Saitoh et al. 2012). However, those for general anisotropy have been proposed by Norris (1994) only, as far as the authors know.

In this section, firstly, the brief statement of the u_i-p formulation is shown. Secondly, Laplace-domain fundamental solutions for 2-D general anisotropic fluid-saturated porous solids are derived. Subsequently, the formulation of CQ-BEM for fluid-saturated porous solid is described.

3.1 u_i-p Formulation

Our proposed method is based on u_i-p formulation, and we denote the generalized displacement q_I and traction s_I as follows:

$$q_I = \{u_i^{\mathrm{T}}, p\}^{\mathrm{T}}, \quad s_I = \{t_i^{\mathrm{T}}, p_n\}^{\mathrm{T}} \tag{7}$$

where $(\,)^{\mathrm{T}}$ denotes the transpose of a vector, and t_i is the traction component of the solid. In addition, p_n is normal derivative of the pressure given by $p_n = \partial p/\partial n$. Laplace-domain equations of motion in u_i-p formulation are written as follows:

$$\hat{L}_{IK}\hat{q}_K(\mathbf{x}, s) = -\hat{B}_I \tag{8}$$

where

$$\begin{aligned} &\hat{L}_{ik} = C_{ijkl}\partial_j\partial_l - \tilde{\rho}_{ik}s^2, \quad \hat{L}_{i4} = \tilde{\alpha}_{ij}\partial_j, \\ &\hat{L}_{4k} = -\tilde{\alpha}_{kl}\partial_l, \quad \hat{L}_{44} = -\frac{1}{s^2}Y_{jl}^{-1}\partial_j\partial_l + \frac{1}{M}, \end{aligned} \tag{9}$$

$$\hat{B}_i = \rho\hat{b}_i + \rho_f^2 Y_{ik}^{-1}\hat{c}_k, \quad \hat{B}_4 = -\rho_f\frac{1}{s^2}Y_{jl}^{-1}\partial_j\hat{c}_l \tag{10}$$

and

$$\begin{aligned} &Y_{ik} = m_{ik} + \frac{1}{s}\eta r_{ik}, \quad \tilde{\alpha}_{ij} = \frac{M_{ij}}{M} + \rho_f Y_{ij}^{-1}, \\ &\tilde{\rho}_{ik} = \rho\delta_{ik} - \rho_f^2 Y_{ik}^{-1}. \end{aligned} \tag{11}$$

The equations in time-domain can be derived by applying the inverse Laplace transform to Eq.(8).

3.2 Fundamental Solutions for 2-D General Anisotropic Fluid-Saturated Porous Solids

Laplace-domain fundamental solutions for 2-D general anisotropic fluid-saturated porous solids are derived in this section. The derivation is based on that used in Wang (1994) and Wang and Achenbach (1994). They used the Radon and its inverse transforms expressed as follows:

$$\check{f}(\sigma, \mathbf{n}) = \int_{\mathbf{n}\cdot\mathbf{x}=\sigma} f(\mathbf{x})\delta(\sigma - \mathbf{n}\cdot\mathbf{x})dL(\mathbf{x}), \tag{12}$$

$$\begin{aligned} &f(\mathbf{x}) \\ &= \int_{|\mathbf{n}|=1}\left[\frac{1}{4\pi^2}\int_{-\infty}^{\infty}\frac{\partial_\varsigma\check{f}(\sigma, \mathbf{n})}{\sigma - \varsigma}d\varsigma\right]_{\sigma=\mathbf{n}\cdot\mathbf{x}} dL(\mathbf{n}). \end{aligned} \tag{13}$$

Note that Eq.(13) represents the inverse transform for 2-D case.

The fundamental solutions can be obtained by solving the following equation:

$$\hat{L}_{PQ}\hat{U}_{QK}(\mathbf{x}, s) = -\delta(\mathbf{x})\delta_{PK} \tag{14}$$

where δ_{ij} is the Kronecker delta and $\delta(\mathbf{x})$ denotes the Dirac delta function. In Eq.(14), the observation and source points are located at $\mathbf{x}$ and the origin $\mathbf{O}$. Applying the Radon transform given by Eq.(12) to Eq.(14), the following equation is obtained.

$$\check{\hat{L}}_{PQ}\check{\hat{U}}_{QK}(\sigma, \mathbf{n}, s) = -\delta(\sigma)\delta_{PK} \tag{15}$$

where

$$\begin{aligned} &\check{\hat{L}}_{ik} = C_{ijkl}n_j n_l\partial_\sigma^2 - \tilde{\rho}_{ik}s^2, \quad \check{\hat{L}}_{i4} = \tilde{\alpha}_{ij}n_j\partial_\sigma, \\ &\check{\hat{L}}_{4k} = -\tilde{\alpha}_{kl}n_l\partial_\sigma, \\ &\check{\hat{L}}_{44} = -\frac{1}{s^2}Y_{jl}^{-1}n_j n_l\partial_\sigma^2 + \frac{1}{M}. \end{aligned} \tag{16}$$

For fixed $\mathbf{n}$ and s, it apparent that Eq.(15) is an ordinary differential equation for σ. Solving Eq.(15) using the Fourier transform and the residue theorem, we obtain the following expression:

$$\check{U}_{IK}(\sigma, \mathbf{n}, s) = \mathrm{i}\sum_{\alpha=1}^{4}\left[\frac{\left(\mathrm{adj}\left[\tilde{\hat{\mathbf{L}}}\right]\Big|_{k=k_\alpha}\right)_{IK}}{\partial_k \det\left[\tilde{\hat{\mathbf{L}}}\right]\Big|_{k=k_\alpha}}e^{\mathrm{i}k_\alpha|\sigma|}\right] \tag{17}$$

where $\partial_k = \partial/\partial k$ and k is wavenumber. In addition, k_α $(\alpha = 1, \cdots, 4)$ are the solutions that satisfied the following equations:

$$\det\left[\tilde{\hat{\mathbf{L}}}\right] = 0, \quad \mathrm{Im}[k_\alpha] > 0. \tag{18}$$

Applying the inverse Radon transform given by Eq.(13) to Eq.(17), and transferring the source point to the position $\mathbf{y}$, the fundamental solutions are obtained as follows:

$$\begin{aligned} &\hat{U}_{ik}(\mathbf{x}, \mathbf{y}, s) = \frac{1}{4\pi^2}\int_{|\mathbf{n}|=1}\sum_{\alpha=1}^{4}\Lambda_{ik}^{\alpha}(\mathbf{n})\Phi^{\alpha}dL(\mathbf{n}), \\ &\hat{U}_{i3}(\mathbf{x}, \mathbf{y}, s) = \frac{1}{4\pi^2}\int_{|\mathbf{n}|=1}\sum_{\alpha=1}^{4}\Lambda_{i4}^{\alpha}(\mathbf{n})\Psi^{\alpha}dL(\mathbf{n}), \\ &\hat{U}_{3k}(\mathbf{x}, \mathbf{y}, s) \\ &= \frac{1}{4\pi^2}\int_{|\mathbf{n}|=1}\sum_{\alpha=1}^{4}\Lambda_{4k}^{\alpha}(\mathbf{n})\Psi^{\alpha}dL(\mathbf{n}), \\ &\hat{U}_{33}(\mathbf{x}, \mathbf{y}, s) = \frac{1}{4\pi^2}\int_{|\mathbf{n}|=1}\sum_{\alpha=1}^{4}\Lambda_{44}^{\alpha}(\mathbf{n})\Phi^{\alpha}dL(\mathbf{n}) \end{aligned} \tag{19}$$

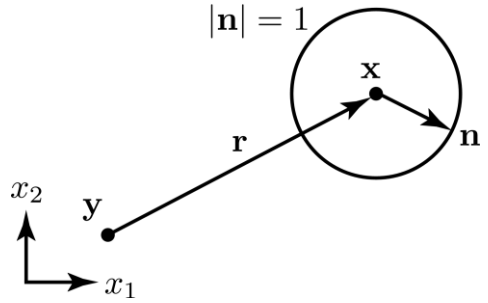


Figure 2 Integration on the unit circle ($|\mathbf{n}| = 1$).

where

$$\Lambda_{IK}^{\alpha}(\mathbf{n}) = k_{\alpha}\frac{\left(\mathrm{adj}\left[\tilde{\tilde{\mathbf{L}}}\right]\Big|_{k=k_{\alpha}}\right)_{IK}}{\partial_k \det\left[\tilde{\tilde{\mathbf{L}}}\right]\Big|_{k=k_{\alpha}}} \tag{20}$$

and

$$\begin{aligned}\Phi^{\alpha} &= \mathrm{e}^{-\mathrm{i}k_{\alpha}|\mathbf{n}\cdot\mathbf{r}|}E_1(-\mathrm{i}k_{\alpha}|\mathbf{n}\cdot\mathbf{r}|)\\ &\quad +\mathrm{e}^{\mathrm{i}k_{\alpha}|\mathbf{n}\cdot\mathbf{r}|}\{E_1(\mathrm{i}k_{\alpha}|\mathbf{n}\cdot\mathbf{r}|)+\mathrm{i}\pi\},\end{aligned} \tag{21}$$

$$\begin{aligned}\Psi^{\alpha} &= \mathrm{sgn}(\mathbf{n}\cdot\mathbf{r})[-\mathrm{e}^{-\mathrm{i}k_{\alpha}|\mathbf{n}\cdot\mathbf{r}|}E_1(-\mathrm{i}k_{\alpha}|\mathbf{n}\cdot\mathbf{r}|)\\ &\quad +\mathrm{e}^{\mathrm{i}k_{\alpha}|\mathbf{n}\cdot\mathbf{r}|}\{E_1(\mathrm{i}k_{\alpha}|\mathbf{n}\cdot\mathbf{r}|)+\mathrm{i}\pi\}].\end{aligned} \tag{22}$$

In Eqs.(19), the small index ranges from 1 to 2, and the integrations on the unit circle ($|\mathbf{n}| = 1$), shown in Figure 2, are implemented as a consideration of the effect of the interference of the body waves propagating in every direction.

3.3 Formulation of CQ-BEM

Time-domain boundary integral equations (BIEs) in finite domain are expressed as follows:

$$\begin{aligned}C(\mathbf{x})q_I(\mathbf{x},t) &= \int_S U_{IK}(\mathbf{x},\mathbf{y},t) * s_K(\mathbf{y},t)dS(\mathbf{y})\\ &\quad -\int_S W_{IK}(\mathbf{x},\mathbf{y},t) * q_K(\mathbf{y},t)dS(\mathbf{y})\end{aligned} \tag{23}$$

where $*$ denotes the Reimman convolution, and S is the boundary of the domain. In Eq.(23), the large index ranges 1 to 3, thus we use

$$q_I = \{u_1, u_2, p\}^{\mathrm{T}}, \quad s_I = \{t_1, t_2, p_n\}^{\mathrm{T}}. \tag{24}$$

In addition, $C(\mathbf{x})$ is given by

$$C(\mathbf{x}) = \begin{cases} 1 & : \mathbf{x} \in D \\ 1/2 & : \mathbf{x} \in S \\ 0 & : \mathbf{x} \in D_c \end{cases}. \tag{25}$$

Moreover, $U_{IK}(\mathbf{x},\mathbf{y},t)$ and $W_{IK}(\mathbf{x},\mathbf{y},t)$ are time-domain fundamental solutions and its double layer kernels, respectively.

On the other hand, time-domain BIEs in infinite domain are expressed as follows:

$$\begin{aligned}C(\mathbf{x})q_I(\mathbf{x},t) &= \int_S U_{IK}(\mathbf{x},\mathbf{y},t) * s_K(\mathbf{y},t)dS(\mathbf{y})\\ &\quad -\int_S W_{IK}(\mathbf{x},\mathbf{y},t) * q_K(\mathbf{y},t)dS(\mathbf{y}) + q_I^{\mathrm{in}}(\mathbf{x},t)\end{aligned} \tag{26}$$

where $q_I^{\mathrm{in}}(\mathbf{x},t)$ represent the generalized displacement corresponding to the incident wave.

Convolution quadrature method (CQM) and collocation method with the constant shape function are applied to Eq. (26) as time and space discretization, and taking the limit process $\mathbf{x} \in D \to \mathbf{x} \in S$, the discretized BIEs are obtained as follows:

$$\begin{aligned}&\left[\frac{1}{2}\delta_{MN}\delta_{IK} + B_{MN;IK}^{(0)}\right]q_{N;K}^{(n)} - A_{MN;IK}^{(0)}s_{N;K}^{(n)}\\ &= q_{M;I}^{\mathrm{in}(n)} + \sum_{k=1}^{n-1}\left[A_{MN;IK}^{(n-k)}s_{N;K}^{(k)} - B_{MN;IK}^{(n-k)}q_{N;K}^{(k)}\right].\end{aligned} \tag{27}$$

In Eq.(27), $M, N = 1,2,\cdots,N_e$ where N_e represents the number of the element, and n is that of the total time steps. $A_{MN;IK}^{(k)}$ and $B_{MN;IK}^{(k)}$ are the influence functions given as follows:

$$\begin{aligned}&A_{MN;IK}^{(m)}\\ &= \frac{R^{-m}}{L}\sum_{l=0}^{L-1}\left[\int_{S^N}\widehat{U}_{IK}(\mathbf{x}^M,\mathbf{y}^N,s_l)dS(\mathbf{y})\right]\mathrm{e}^{-2\pi\mathrm{i}m\frac{l}{L}}\end{aligned} \tag{28}$$

$$\begin{aligned}&B_{MN;IK}^{(m)}\\ &= \frac{R^{-m}}{L}\sum_{l=0}^{L-1}\left[\int_{S^N}\widehat{W}_{IK}(\mathbf{x}^M,\mathbf{y}^N,s_l)dS(\mathbf{y})\right]\mathrm{e}^{-2\pi\mathrm{i}m\frac{l}{L}}\end{aligned} \tag{29}$$

where $s_l = \gamma(z_l)/\Delta t$ and $\widehat{U}_{IK}(\mathbf{x},\mathbf{y},s)$ and $\widehat{W}_{IK}(\mathbf{x},\mathbf{y},s)$ are Laplace-domain fundamental solutions and its double layer kernels, respectively. The double layer kernels $\widehat{W}_{IK}(\mathbf{x},\mathbf{y},s)$ are given by the following equations:

$$\widehat{W}_{IK}(\mathbf{x},\mathbf{y},s) = \hat{B}_{KJ}^{\mathbf{y}}\widehat{U}_{IJ}(\mathbf{x},\mathbf{y},s) \tag{30}$$

where

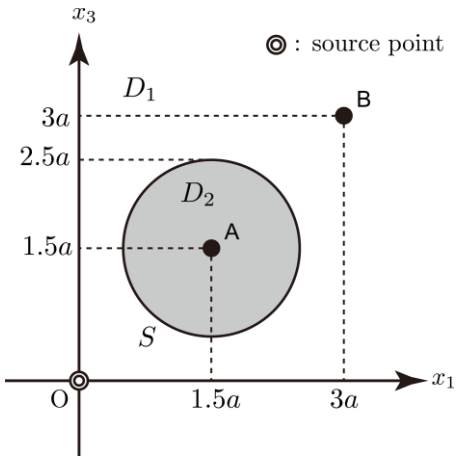


Figure 3 Analysis model for wave scattering problem.

$$\hat{B}^{\mathbf{y}}_{ik} = -C_{ijkl}n_j(\mathbf{y})\partial_l, \quad \hat{B}^{\mathbf{y}}_{i3} = \frac{M_{ij}}{M}n_j(\mathbf{y}),$$
$$\hat{B}^{\mathbf{y}}_{3k} = -\rho_f Y^{-1}_{kl}n_l(\mathbf{y}), \quad \hat{B}^{\mathbf{y}}_{33} = \frac{1}{s^2}Y^{-1}_{jl}n_j(\mathbf{y})\partial_l. \tag{31}$$

In Eq.(33), it should be mentioned that $n_i(\mathbf{y})$ represents the unit normal vector on the boundary at the point $\mathbf{y}$. Moreover, CQM parameters R and $\gamma(z_l)$, with an error magnitude $O(\epsilon)$, are written as follows:

$$R = \epsilon^{\frac{1}{2L}} \tag{32}$$

$$\gamma(z_l) = \sum_{i=1}^{k}\frac{1}{i}(1-z_l)^i, \quad z_l = R\mathrm{e}^{-2\pi\mathrm{i}\frac{l}{L}}. \tag{33}$$

Note that Eq.(35) corresponds to the backward differentiation formulas of order k. The discretized form of Eq.(23) can be obtained with the aforementioned process. Setting the boundary conditions and solving Eq.(12), we obtain unknown boundary values.

4. NUMERICAL EXAMPLE

As a numerical example, we consider wave scattering problem by an inclusion as shown in Figure 3. In this figure, the domain D_1 and domain D_2 represent the infinite and finite domain, respectively. Therefore, the BIEs for the domains D_1 and D_2 correspond to Eq.(26) and Eq.(23), respectively. In this problem, the boundary conditions on S are given as follows:

$$q^{[1]}_I(\mathbf{y},t) = q^{[2]}_I(\mathbf{y},t),$$
$$s^{[1]}_I(\mathbf{y},t) = -s^{[2]}_I(\mathbf{y},t). \tag{34}$$

Using Eqs.(23), (26), (27) and (34), we obtain the following algebra equation:

$$\begin{bmatrix} D^{[1]}_{MN;IK} & -A^{[1]}_{MN;IK} \\ D^{[2]}_{MN;IK} & A^{[2]}_{MN;IK} \end{bmatrix}\begin{Bmatrix} q^{[1](n)}_{N;K} \\ s^{[1](n)}_{N;K} \end{Bmatrix} = \begin{Bmatrix} q^{\mathrm{in}[1](n)}_{M;I} + E^{[1](n)}_{M;I} \\ E^{[2](n)}_{M;I} \end{Bmatrix} \tag{35}$$

where

$$D^{[d]}_{MN;IK} = \frac{1}{2}\delta_{MN}\delta_{IK} + B^{[d](0)}_{MN;IK},$$
$$E^{[d](n)}_{M;I} = \sum_{k=1}^{n-1}\left[(-1)^{d-1}A^{[d](n-k)}_{MN;IK}s^{[1](k)}_{N;K} - B^{[d](n-k)}_{MN;IK}q^{[1](k)}_{N;K}\right]. \tag{36}$$

Solving Eq.(35) each time step, we obtain unknown boundary values. The numerical results will be shown at the session of the conference.

5. CONCLUSIONS

In this paper, CQ-BEM for 2-D general anisotropic fluid saturated porous solid is developed. In near future, we apply the proposed method to some realistic problems in earthquake engineering and expand the proposed method to 3-D problems.

Acknowledgements:
The first and fourth authors acknowledge support from the Japan Ministry of Education, Culture, Sport, Science, and Technology (MEXT) for establishing the Center for Urban Earthquake Engineering (CUEE) in Tokyo Institute of Technology.

References:

Beskos, D. E. (1989), "Dynamics of saturated rocks. I: Equation of motion," *Journal of Engineering Mechanics ASCE*, **115**(5), 982–995.

Biot, M. A. (1956a), "Theory of propagation of elastic waves in a fluid-saturated porous solid. I. Low-frequency range," *Journal of Acoustical Society of America*, **28**(2), 168–178.

Biot, M. A. (1956b), "Theory of propagation of elastic waves in a fluid-saturated porous solid. II. Higher frequency range," *Journal of Acoustical Society of America*, **28**(2), 179–191.

Biot, M. A. (1962), "Mechanics of deformation and acoustic propagation in porous media," *Journal of Applied Physics*, **33**(4), 1482–1498.

Carcione, J. M. (1996), "Wave propagation in anisotropic saturated porous media: Plane-wave theory and numerical simulation," *Journal of Acoustical Society of America*, **99**(5), 2655–2666.

Furukawa, A., Tanaka, Y., Saitoh, T. and Hirose, S. (2012), "Convolution quadrature time-domain boundary element method for two-dimensional elastic wave propagation in general anisotropy," *Journal of Applied Mechanics JSCE*, **68**(2), I-269–I-278 (in Japanese).

Liu, Y., Liu, K., Gao, L. and Yu, T. X. (2005), "Characteristic analysis of wave propagation in anisotropic fluid-saturated porous media," *Journal of Sound and Vibration*, **282**, 863–880.

Norris, A. N. (1994), "Dynamic Green's functions in anisotropic piezoelectric, thermoelastic and poroelastic solids," *Proceedings of the Royal Society of London. Series A.*, **447**, 175–188.

Rice, J. R. and Cleary, M. P. (1976), "Some basic stress-diffusion solutions for fluid-saturated elastic porous media with compressible constituents," *Reviews of Geophysics and Space Physics*, **14** (2), 227–241.

Saitoh, T., Chikazawa, F. and Hirose, S. (2012), "Large scale wave analysis for fluid-saturated porous media using convolution quadrature boundary element method," *Journal of Applied Mechanics JSCE*, **68**(2), I-187–I-197 (in Japanese).

Schanz, M. (2001), "Application of 3D time domain boundary element formulation to wave propagation in poroelastic solids," *Engineering Analysis with Boundary Elements*, 25, 363–376.

Schanz, M. and Antes, H. (1997), "Application of 'Operational quadrature methods' to time domain boundary element methods," *Meccanica*, **32**, 179–186.

Schanz, M. and Pryl, D. (2004), "Dynamic fundamental solutions for compressible and incompressible modeled poroelastic continua," *International Journal of Solids and Structures*, **41**, 4047–4073.

Sharma, M. D. (2005), "Polarisations of quasi-waves in a general anisotropic porous solid saturated with viscous fluid," *Journal of Earth System Science*, **114**(4), 411–419.

Wang, C. –Y. (1994), "Two-dimensional elastostatic Green's functions for general anisotropic solids and generalization of Stroh's formalism," *International Journal of Solids and Structures*, **31**, 2591-2597.

Wang, C. –Y. and Achenbach, J. D. (1994), "Elastodynamic fundamental solutions for anisotropic solids," *Geophysical Journal International*, **118**, 384-392.

Zhang, Ch. (2000), "Transient elastodynamic antiplane crack analysis of anisotropic solids," *International Journal of Solids and Structures*, **37**, 6107-6130.

10CUEE CONFERENCE PROCEEDINGS
10th International Conference on Urban Earthquake Engineering
March 1-2, 2013, Tokyo Institute of Technology, Tokyo, Japan

BUILDING MONITORING EARTHQUAKE RESPONSE NETWORK IN LIMA

Patricia Gibu [1)], Carlos Zavala [2)], Ricardo Proaño[3)], Luis Lavado[3)] and Lucio Estacio[4)]

1) Associate Professor, Associate Researcher
2) Professor, Chief Laboratory of Structures,
3) Assistant Professor, Earthquake Engineering Dept,
4) Assistant Professor, Assistant Researcher Laboratory of Structures
CISMID, Civil Engineering Faculty, Universidad Nacional de Ingeniería, Perú

pgibu@uni.edu.pe, czavala@amauta.rcp.net.pe, rproano@uni.edu.pe, lmlavado@hotmail.com, solo2click@hotmail.com

Abstract: Under the Peru - Japan SATREPS Project a building monitoring network has been implemented in Lima city, under the support of JST and JICA. The network considering a set of 5 sensors installed on different levels of three building: One is framed concrete structure, the second is a masonry and concrete wall building and the third is a hospital with concrete framed structure. The buildings are located in two kinds of soil of Lima (two in medium soil, and one in rigid soil). Since the installation of the sensors, seven moderate quakes has been register. This paper presents the monitoring response of one building and the dynamic characteristics measure from the stronger event registered for the buildings. Good agreement with simulation previously performed was found, and the results give us the confidence for the developed of parameters for the stiffness degradation under small and moderate quakes for concrete framed structures.

1. INTRODUCTION

Under the Peru - Japan SATREPS Project, with the support of JST and JICA, a building monitoring network has been implemented in Lima city since 2011.

A total of 15 sensors are to be installed on different levels of three buildings: One is a framed concrete structure, the second is a masonry and concrete wall building and the third is a hospital with concrete framed structure. One of the recorded moderate quake is shown and the response of a building analyzed and compared with previous studies.

1.1 Sensors Network Setting

Accelerations sensors are connected through internal network and IP addresses to access to Internet

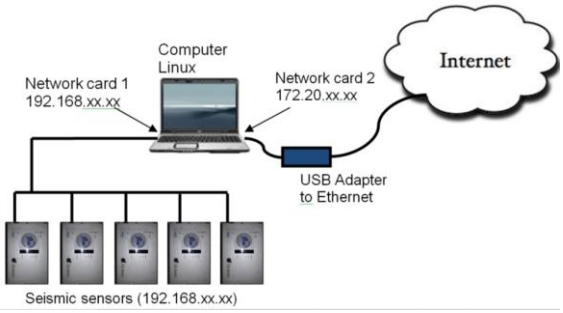


Figure 1 Connection of sensors to network through IP address and internet

After preliminar testing period in a local network (Figure 2), a set of 5 sensors has already been set in 2 buildings at UNI campus.



Figure 2 Network setting test and final placement of sensor at basement level in UNI Central Building

At each building, the 5 sensors set are aligned to a vertical line, and if possible near to gravity center. At the basement level, sensors has been fixed in a hole box in floor, and then at ceiling (slab) for each upper level.

1.2 Selected Buildings

The criteria for the selection of the buildings to be measured was the consideration of likely used structural system in Peru and also the different combination of materials.

A set of 5 sensors will be installed in each of three buildings, which was selected as representative of typical structures and material:

- Central Building of UNI is 3F+ BF Level and 16m high, irregular configuration in plan, with masonry and

concrete walls and concrete frame structure built more than 80 years ago, used mainly for administrative offices

- G2 Block at Civil Faculty of UNI, is for classrooms, a 3F framed RC building with irregular configuration of stiffness due to its distribution of masonry walls (hall at 1F, corridors and classroom at upper floors).
- Block A of Edgardo Rebagliati Martins National Hospital is a 14F+BF building, more than 50 years old, RC framed building, classified as essential type for its importance of use.



Figure 3 Central Building and G2 bldg block (North view) at Civil Engineering Faculty at UNI

2. PRELIMINAR STUDIES OF SELECTED BUILDINGS FOR MONITORING

2.1 Central Administrative Building of UNI

As shown in figure 4, plan of Central Building of UNI is irregular its longer dimension L=117m and B=23m wide for the main body. Sensors has been set to the South-East part of the building about 0.25L from gravity center

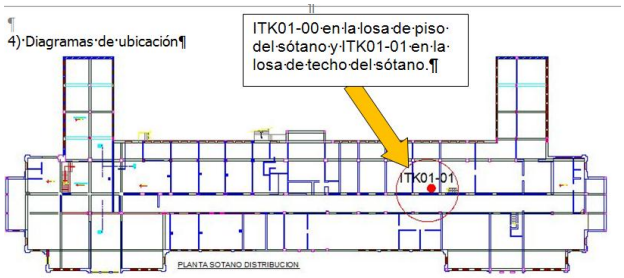


Figure 4 Plan of Central Building in UNI and location of sensors

Some previous calculation and measurement has been conducted as reference for assess dynamic monitoring results. Microtremor measurements has been conducted in 3 points (soil: center zone and at 3F: NO and SE wing of building) and showed fundamental periods (from Fourier Amplitude Spectra) of Tx=0.23s and Ty=0.28s for the building where X is longitudinal axis, and for soil Ts= 0.41s.



Figure 5 Preliminary measurement and analysis: microtremor and modeling

2.2 Central block of G2 building at Civil Engineering Faculty of UNI

Central Block G2 Bldg of Civil Engineering Faculty (FIC) is a 58 year old, reinforced concrete framed, 3-stories (10m high) structure with one underground floor. Half of its typical plan continue down to a basement floor. First floor is the main entrance hall, and upper levels are for classroom and corridors. So, in plan shown regular configuration (28m x 12m approximately), but some masonry thick walls (250mm) not aligned, in upper levels, changes its stiffness at each story (soft floor).



Figure 6 Location of Central Block G2 in FIC and South side view of building

Previous studies and evaluation has shown some reference values for natural period of building: From microtremor measurement (2007) Tx (longitudinal direction): 0.195s, and Ty (short direction): 1.62s

Preliminary analysis confirms a weak first level with greater relative displacements. Observing damage and failure at columns before than beams. From theoretical elastic analysis, it was obtained periods of 0.31s for first mode, which model is shown in figure 7

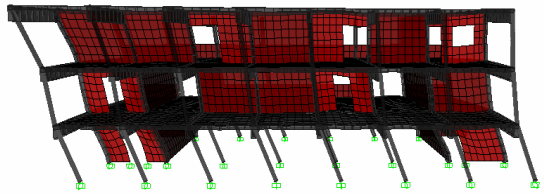
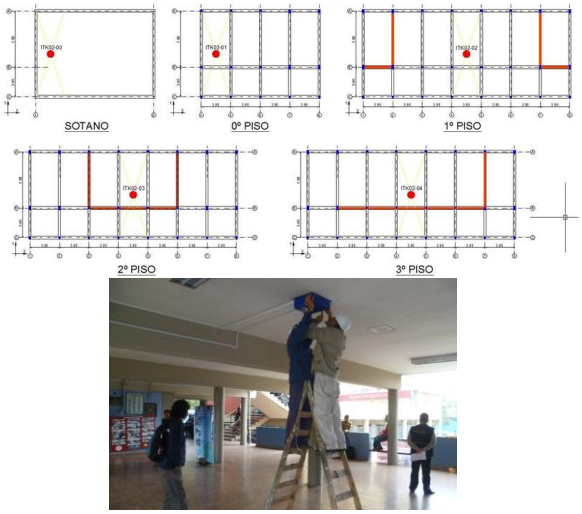


Figure 7 Modeling G2 building and deformed configuration

Setting of sensors was located at center of gravity in plan, aligned in a vertical line, and is shown in figure 8



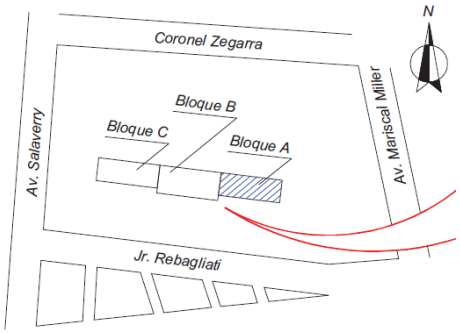
Figures 8 Central Block in G2 FIC and setting of sensors to the ceiling (below)

2.3 Edgardo. Rebagliati Martins Hospital - Building A (East block)

This 14F, reinforced concrete building, 55year old, beard 2 main earthquakes (1966 and 1974), but main structure have not been damaged. "A-Block" was focused for this study and is the right block show in Figure 9. Dimensions in plan are 15.9m x 73m, and 45.6m high from ground level with 14F



Figure 9 E Rebagliati Hospital and studied block



As reference also for this building exist two previous studies: evaluation 1997 and more detailed, non linear analysis conducted for a thesis research. For intermediate level earthquake, predicted damage are expected in beams in both directions of analysis, endangering inmediatly occupancy or interrupting normal performing of functions as hospital

3. DATA ADQUISITION FROM RECENT EVENTS AND RESULTS

Since the installation of the sensors, seven moderate quakes has been registered in the network. In table 1 is shown a official List of Earthquake registered by IGP National Network in November and December 2012. Lightened row of table 1, was registered as 2.6 max response at upper level in the network notice, as shown in Figure 10.

Table 1 List of Earthquake registered, Nov&Dec 2012 Lima studied block

	Date	Time	Magnitude	Intensidad - localidades
1	03/11/2012	20:52:12	4.7 ML	III-IV Yauyos; III Lima
2	13/11/2012	00:48:58	4.0 ML	II Lima
3	15/11/2012	19:21:55	4.8 ML	III San Vicente de Cañete, Chincha Alta; II-III Lunahuana; II Lima, Ica
4	27/11/2012	04:19:59	4.4 ML	III Barranca; III II Huacho; II Lima
5	22/12/2012	01:43:39	4.2 ML	II Chila, Lima
6	28/12/2012	20:57:40	4.3 ML	II-III Huaral, Lima
7	31/12/2012	03:46:17	4.7 ML	III-IV Huacho III Lima

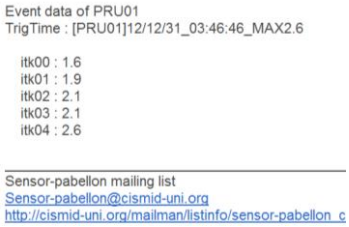


Figure 10 Notice of registered event at ITK network for UNI building

Additional data of this event to process: Depth 53Km, Latitude -11.42ºS; Longitude -77.92º

Data for G2-FIC building has been processed. Figures 11 and 12 show signal at basement and 4F. It is possible to read that acceleration on the top of the building reach a value of 20 gal, almost 3.3 times the basement acceleration.

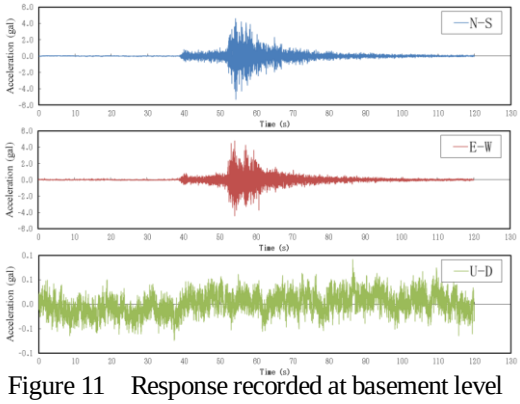


Figure 11 Response recorded at basement level

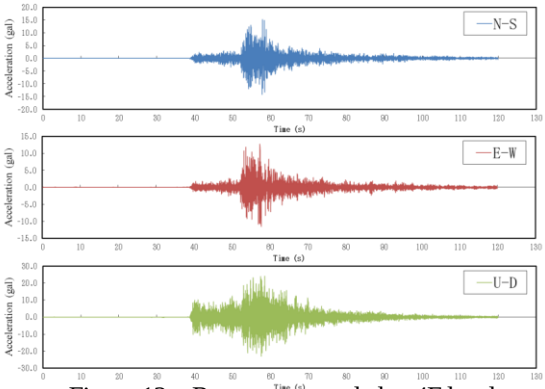


Figure 12 Response recorded at 4F level

Response of each level has been processed. Figure 13 shows predominant modal distribution and a large displacement evidence very flexible N-S direction compared with E-W.

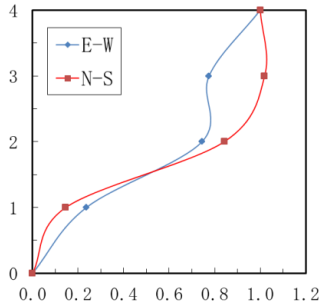


Figure 13 Predominant modal distribution

Table 2 shows predominant period for each direction of analysis. Values of periods for mode 2 in this table agree with previous measurements (see item 2.2)

Table 2 Predominant periods (s) for each direction

mode	EW	NS
1	0.22	0.23
2	0.19	0.16
3	0.15	0.12

Figures 14 and 15 shows spectra (acceleration and velocity) for basement level measurements

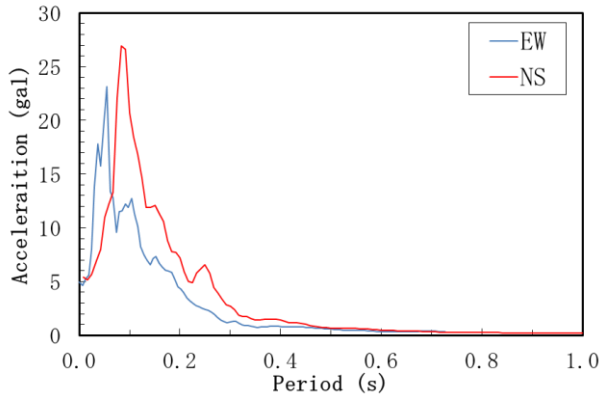


Figure 14 Acceleration spectra (h=0.05). signal from basement

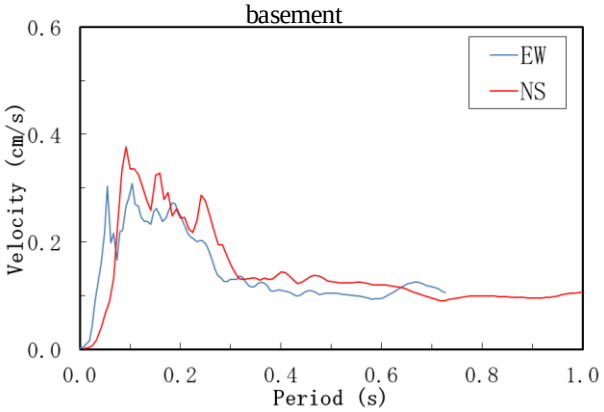


Figure 15 Velocity spectra (h=0.05). signal from basement

Both figures presents peaks values at the predominant periods and components of acceleration reach a maximum spectral component for a range between 22 to 27 gals for each direction of the building. Also the velocity indicates a peak value between 0.3 s. to 0.38 s. for this building.

4. CONCLUSIONS

First building monitoring network has been installed and is working at the present time in Lima Peru, as an output of the Project for Enhancement of Earthquake and Tsunami Disaster Mitigation Technology in Peru (JICA/JST), under the cooperation scheme of SATREPS.

Three sets of five sensors have been installed in Lima city. Two on buildings at UNI campus and other set at Edgardo Rebagliatti Hospital. The instalation process has been presented and the sensors are now on line.

Monitoring response of one of selected buildings and the dynamic characteristics measure from the events has been presented. Good agreement with simulation previously performed was found, and the results give us the confidence for the developed of parameters for the stiffness degradation under small and moderate quakes for concrete framed structures.

Acknowledgements:

The authors would like to express our gratitude to the Ministry of Education of Japan, thorough the Japan Science and Technology Agency (JST) and the Japan International cooperation Agency (JICA) for the support the Japan-Peru SATREPS Project for the support to this research. Also our gratitude to Dr. Fumio Yamazaki PI investigator of the SATREPS project and promoter of this investigation.

Also our gratitude to Msc. Miguel Diaz graduate student of the Faculty of Engineering of Yokohama National University for the support in the elaboration of this paper and or his great contributions during the data processing

References:

Zavala T, Carlos, Reyna, Roy. (2011) Preliminary Report "Medición de vibración ambiental en la estructura del Pabellón Central UNI" for Satreps- JST-JICA Project

Moya L, Zavala C., (2012) Preliminary Report "Evaluación Estructural del Pabellón G2 de la Facultad de Ingeniería Civil" for Satreps- JST-JICA Project

Camacho V, Audry (2010), "Vulnerabilidad Sísmica Estructural de los Edificios Principales de la Facultad de Ingeniería Civil de la Universidad Nacional de Ingeniería", Undergraduated Thesis for Civil Engineering, FIC-UNI, Lima, Peru

Fajardo G, Cesar (2012) "Evaluación estructural de una de las edificaciones del Hospital Edgardo Rebagliati M" Undergraduated Thesis for Civil Engineering, FIC-UNI, Lima, Peru

10CUEE CONFERENCE PROCEEDINGS
10th International Conference on Urban Earthquake Engineering
March 1-2, 2013, Tokyo Institute of Technology, Tokyo, Japan

BRIDGE AND ADJACENT DOWNHOLE ARRAY RESPONSES DURING EARTHQUAKES AT EUREKA, CALIFORNIA

Ning Wang[1] and Ahmed Elgamal[2]

1) Graduate Research Assistant, Dept. of Structural Engineering, University of California, San Diego, CA 92093-0085, USA
2) Professor, Dept. of Structural Engineering, University of California, San Diego, CA 92093-0085, USA
n9wang@ucsd.edu, elgamal@ucsd.edu

Abstract: Recorded earthquake motions from instrumented bridge structures and adjacent geotechnical downhole arrays provide valuable information on the characteristics of structural response during seismic events. In particular, instrumentation installed by the California Strong Motion Instrumentation Program (CSMIP) in cooperation with California Department of Transportation (CalTrans) resulted in a valuable strong motion database for bridge superstructures, foundations and nearby free field seismic response at Eureka, California. In this paper, the recent Ferndale area earthquakes and several earlier small earthquakes are employed to evaluate the ground, pile foundation, and the Samoa Channel bridge responses using system identification and inverse problem techniques. Local site response and its nonlinearity are clearly highlighted. Finite Element (FE) models of the foundation-bridge system are calibrated based on the recorded motions and identified bridge/foundation characteristics. The study shows that computational modeling and analysis of ground-pile-system response from seismic sensors are effective and efficient ways to calibrate and interpret the seismic response of the entire structure-foundation-ground system.

1 INTRODUCTION

Recorded bridge deep foundation seismic motions and adjacent downhole-array records provide a unique opportunity for documenting and analyzing salient ground-foundation-structure response mechanisms. Studies based on such full-scale seismic performance data sets lead to a better understanding of the underlying actual soil-structure interaction (SSI) characteristics (Elgamal et al. 2008).

In this paper, seismic response of an instrumented pile-group in the Eureka-Samoa Channel bridge and a nearby free-field geotechnical array (Eureka Geotechnical Array) are studied using recorded earthquake data including the January 9, 2010 Eureka Ferndale event, that resulted in a moderate but substantial level of earthquake excitation. An additional set of recorded small seismic motions was studied as well for comparison.

For that purpose, a simple FE model of the instrumented Samoa Channel Bridge Pier S-8 and its pile group foundation was developed (to maintain focus, attention is directed herein to the bridge Transverse response). Eigenvalue analysis was performed and the results were compared with those from the system identification earthquake response analysis. On this basis, and representative stiffness of the pile foundation beneath Pier S-8 was defined. The results of this research are of immediate consequence to validate and refine deep-foundation soil-structure interaction analysis. As such, strong motion data analysis is shown to be a valuable source for gaining insights into the underlying SSI mechanisms.

2 BRIDGE INSTRUMENTATION AND ANALYSIS OF SEISMIC RECORDS

As of Jan 2012, 63 regular highway bridges, 13 toll bridge structures and 18 downhole geotechnical arrays have been instrumented in California (Caltrans 2008; Caltrans 2012). Numerous works on identification of structural systems utilizing recorded motion have been conducted in the past two decades (Werner et al. 1994; Wilson and Tan 1990). With recorded accelerations on bridge systems, modal frequencies and mode shapes can be identified using parametric or non-parametric evaluation techniques (Arici and Mosalam 2000). The invaluable data collected from such sensors helps to advance our understanding of how the bridges react to different types of seismic waves and how the dynamic SSI affects the behavior of superstructures (Hipley et al. 1998). In this paper, data from a heavily instrumented bridge (the Eureka- Samoa Channel) with embedded accelerometers inside a pile group foundation at -10.3632 m (-34 ft) and -16.4592 m (-54 ft) below mean sea level along with a nearby geotechnical downhole array (Figure 1) was employed to obtain salient resonant frequencies for the bridge system. Seismic response of the Eureka Samoa Channel Bridge was analyzed by comparing

recorded earthquake strong motion data of the CGS (California Geological Survey) station 89686 with the FE analysis result. This study provides a unique opportunity to bring insight into the challenging issue of ground-pile group/structure interaction during earthquakes.

3 THE SAMOA CHANNEL BRIDGE

The 20-span Eureka Samoa Channel Bridge near Eureka in northern California (Figure 1) is a 764 m long and 10.4 m wide structure, supported by 19 single hexagonal concrete pier bents on pile group foundations. Pre-stressed concrete I-girders along with cast-in-place concrete slabs are supported on concrete seat-type abutments and the cap beams of column type piers. Nine expansion joints allowing movement during seismic occurrence are located at the top of Pier-S4, S7, S8, S9, S10 S14, Pier S17 and two abutments supports (Figure 2). There is one hinge located at Span 8. Originally, the pile-group foundations consisted of driven pre-cast prestressed concrete piles and caps. Pile groups beneath Pier S-8 and S-9 consisted of 8 (2x4) circular (1780kN type) concrete piles.

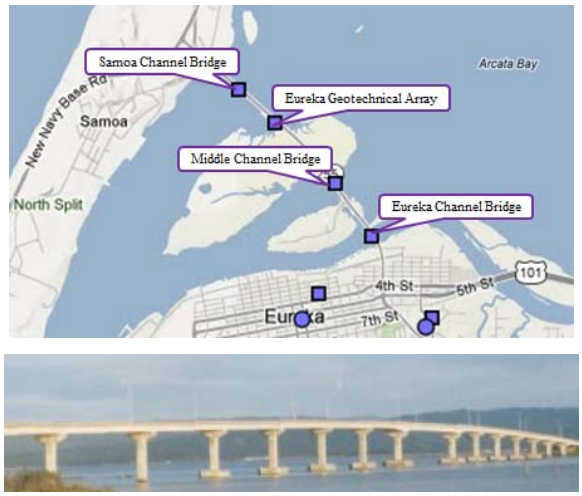


Figure 1 Location of Samoa Channel Bridge, Eureka Geotechnical Array, Middle Channel Bridge and Eureka Channel Bridge, and photo of the Samoa Channel Bridge (http://www.strongmotioncenter.org)

3.1 Site description

A deep soft alluvium geological profile is found at this location where the surficial foundation soil is mainly composed of very soft to soft organic silt with clay. Soil layers consisting of dense to very dense gray medium and sand underlie the surficial soil layer and continue to the maximum explored depth.

3.2 Seismic retrofit effort

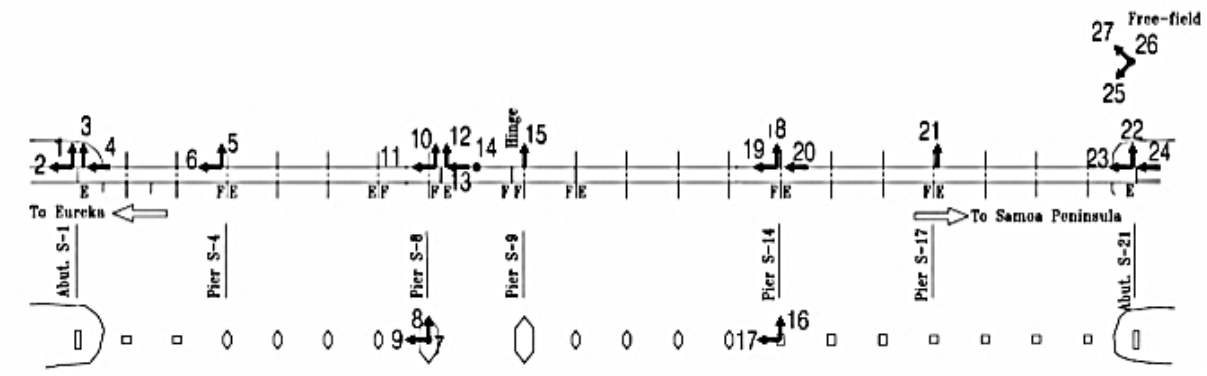
The bridge was designed in 1968, built in 1971, and has been the object of seismic retrofit efforts by the California Department of Transportation (CalTrans). The seismic retrofit in 2002 included strengthening of the foundations by installing additional 0.91 m diameter cast-in-steel shell piles (e.g. 6 additional CISS piles at Pier S-8) with new or enlarged caps to cover the new piles (Figure 3).

3.3 Recorded earthquake events

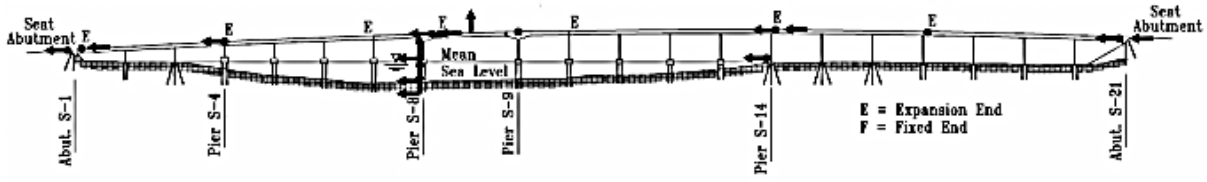
The Samoa Channel Bridge is located in an area of complex interaction among three tectonic plates (North American, Pacific and Gorda). The 'Little Salmon' fault is the nearest seismic source from the site (Caltrans 2000). To obtain insights for both the properties of earthquake and seismic response of the structure, the Samoa Channel Bridge is heavily instrumented as shown in Figure 2 to measure the translational and torsional motions of the bridge as well as relative motions across the hinges. There are 33 accelerometers in total for the Samoa Channel Bridge System instrumented in 1996, including 24 accelerometers on the bridge structure, 6 accelerometers on pile foundation (Figure 3), and 3 accelerometers at a nearby free field site. Sensors on the structure are oriented in the longitudinal and transverse direction of the bridge and sensors at the free field are oriented in the north-south, east-west and vertical directions. This bridge is one of two bridges in CA with instrumentation embedded inside one of the piles (at depths of 10.3636 m (34 ft) and 16.5692 m (54 feet) below mean sea level). Side view and deck level plan view of the sensor network layout for the Samoa Channel Bridge are shown in Figure 2.

A total of seven earthquakes in the period of March 2000 through January 2010 with Magnitudes from 4.6 M_w to 7.2 M_w (M_w: regional moment magnitude) have been recorded. Corrected acceleration, velocity, displacement and acceleration response spectra are available. Varying in peak acceleration (from 0.006g to 0.150g), epicentral distances (from 40.2 km to 153.4 km), shaking duration, and frequency content bandwidth, these earthquakes provide valuable information on the soil-foundation-structure seismic behavior over a broad range of excitations. Table 1 depicts time, Magnitude, epicentral distance, peak horizontal acceleration at ground surface and structure of the recorded earthquakes (where only one event exceeds 0.1g in peak ground acceleration).

Notable in Table 1 is the Earthquake Ferndale 09 Jan 2010 which occurred approximately 35 km away from Ferndale, CA in a deformation zone of the southernmost Gorda plate (http://earthquake.usgs.gov). The maximum recorded shaking was observed in Eureka (33% g), which is deemed sufficient to cause moderate damage. The Samoa Channel Bridge at a distance of 53.8 km from the epicenter of this earthquake reached peak acceleration of the order of 0.15 g at the ground surface and 0.37 g on the bridge deck.



(a) Deck Level Plan



(b) Elevation

Figure 2 Layout of instrumentation at the Eureka Samoa Channel Bridge

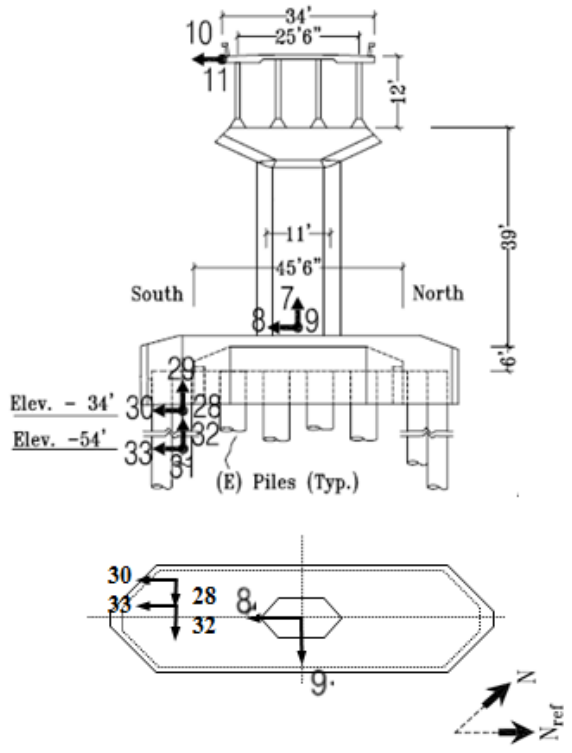


Figure 3 Layout of instrumentation at the Eureka Samoa Channel Bridge Pier S-8

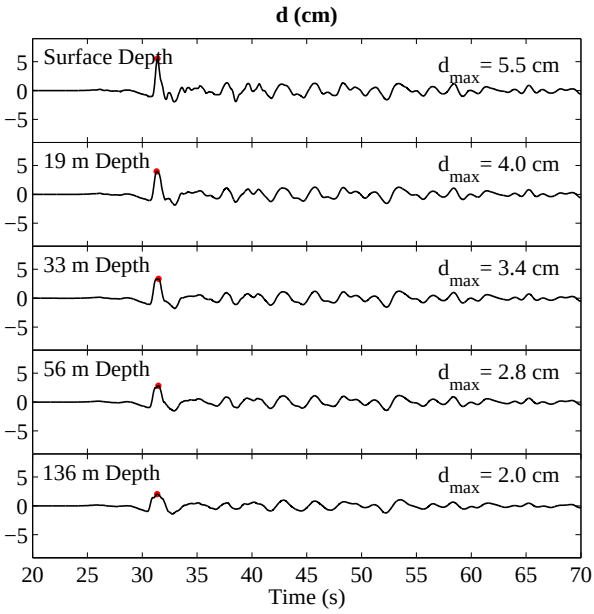
Table 1 Recent earthquakes recorded at the Samoa Channel Bridge

Earthquake	Epicentral Distance (km)	Horiz. Peak Acc. (g)	
		Ground	Structure
Ferndale 09 January 2010	53.8	0.150	0.370
Trinidad 24 June 2007	63.8	0.028	0.072
Trinidad 16 August 2008	40.2	0.018	0.057
Willow Creek 29 April 2008	56.6	0.017	0.032
Ferndale 26 February 2007	62.4	0.011	0.022
Crescent City 14 June 2005	153.4	0.009	0.031
Cape Mendocino 16 March 2000	102.4	0.006	0.020

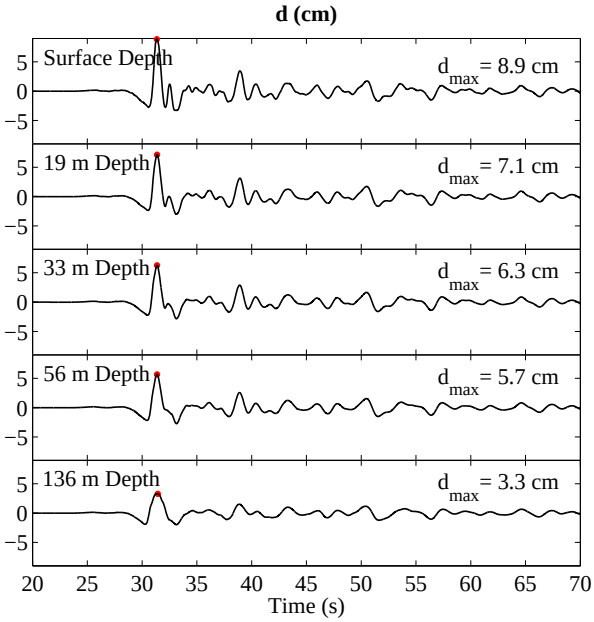
4 EVALUATION OF EARTHQUAKE RECORDS - THE FERNDALE 09 JAN 2010 EARTHQUAKE

From the downhole array data, ground displacement at various depths is shown in Figure 4. As may be noted, displacement amplitudes appear to clearly increase as the

seismic waves approach and reflect-off the ground surface. Displacement of the bridge, the pile below ground and the nearby free field are shown in Figure 5.



(a) Transverse direction



(b) Longitudinal direction

Figure 4 Rotated displacement time histories at Eureka Downhole Array during the Jan 9 2010 Ferndale Earthquake (transverse direction and longitudinal direction)

Comparison of the displacements in Figure 4 and 5 shows that:

i) Displacement appears similar at the nearby ground surface and in the pile below ground (16.5 m below mean sea level, estimated at about 1.2m below the mudline at this location),

ii) These displacements are also similar to those of the T-direction downhole array at comparable depth (when measured with mean sea level as a reference, that being somewhere between the 19 m and 33 m depth of the downhole array),

iii) Based on the above, the pile group at the location -16.5 m below sea level appears to be practically moving along with the ground, indicating a level of firm embedment (fixity) at this depth below ground. With this ground motion as "input", the pile cap and bridge deck displacements are noticeably different, being significantly larger in amplitude, with a clear dominant fundamental response Period, and

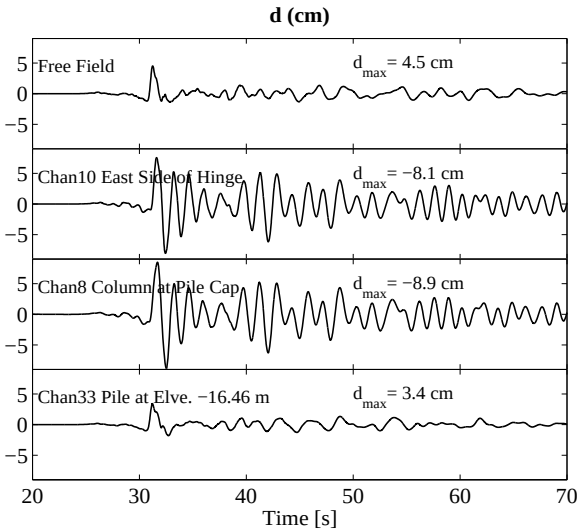


Figure 5 Samoa Channel bridge Displacement time histories at Pier S-8 during the Eureka Ferndale Jan 9 2010 Earthquake in the Transverse direction

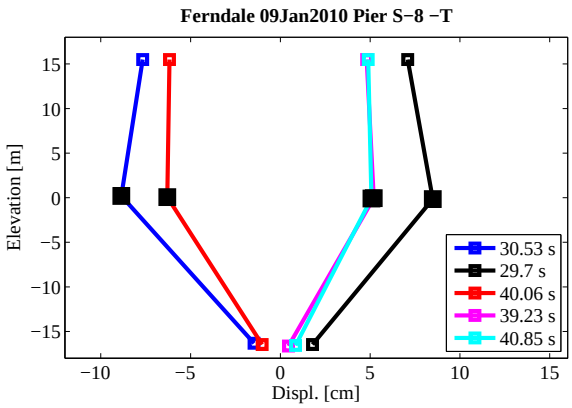


Figure 6 Displaced configuration of Pier S-8 for selected time instants during the January 9 2010 Ferndale Earthquake (Transverse (T) direction shown)

iv) much of the bridge displacements are due to deformation occurring at the pile cap level, with the

bridge deck motions only slightly different from those of the pile cap as shown from the plots of selected displacement time instants of Figure 6. This may be taken as an indication that the Pier (bridge column) above the pile cap is quite stiff in comparison to the lateral stiffness afforded by the underlying pile group.

Insights of this type concerning actual behavior of a full-scale pile foundation during an actual earthquake event are extremely valuable and will contribute considerably to our current understanding of this important SSI mechanism.

5 SYSTEM IDENTIFICATION / FE ANALYSIS

5.1 Site Response and nonlinearity

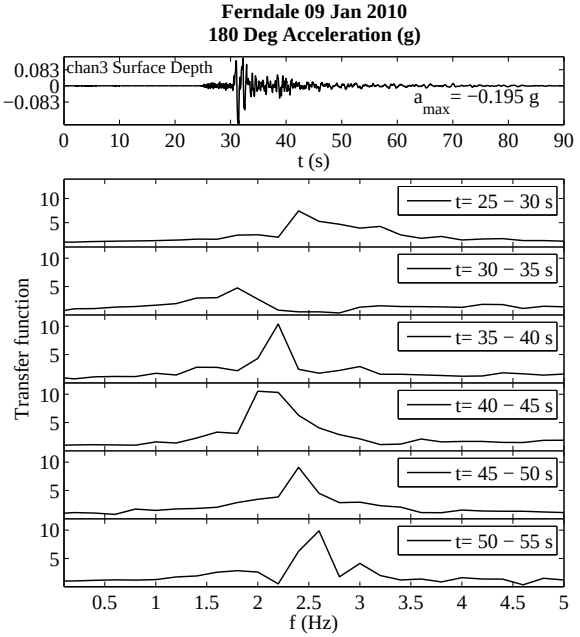
Nonlinearity of the site seismic response was evident through analysis of nearby Eureka downhole array data (Elgamal 1995; Elgamal et al. 1996). The recorded data at this downhole site allows for a better understanding of the ground seismic response in which the Samoa Channel Bridge foundations are embedded. Fourier spectral ratios between the motions at the ground surface and at 19 m depth were computed with a 5-second time window for earthquake Ferndale 09 Jan 2010 (Figure 7). Lower natural frequency (decrease of soil stiffness) is observed (~1.8 Hz) during the strong motion period (30s-35s) compared to other time windows (reaching as much as 2.6 Hz).

5.2 Bridge sub-system resonances

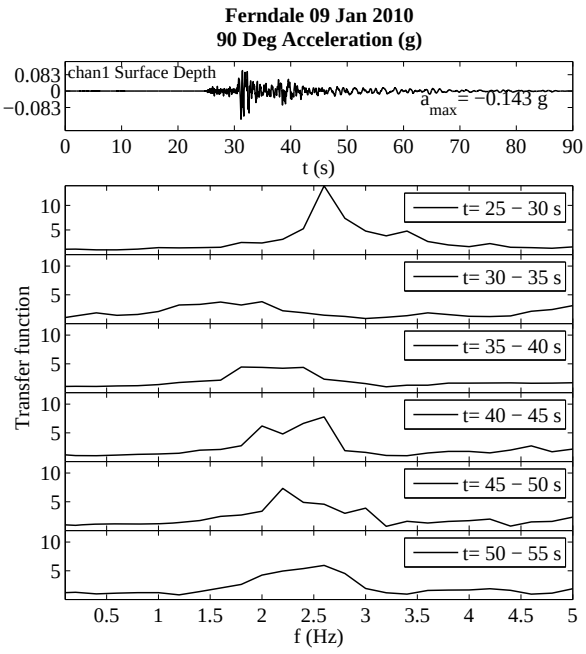
A Transfer Function (TF) defined as the ratio of the cross power spectral density ($P_{yx}(f)$) of input signal (x) and output signal (y) and the power spectral density ($P_{xx}(f)$) of input signal is employed to assess system and sub-system resonant frequencies.

$$T_{xy}(f) = \frac{P_{yx}(f)}{P_{xx}(f)}$$

At the Pier S-8, the fundamental frequency for Deck-Pier sub-system (deck response referenced to pile cap response) was 1.60 Hz during the Ferndale 09 Jan 2010 earthquake and in range of 1.95-2.00 Hz for all of the other small earthquakes. The same logic was then employed to relate the deck response to that of the pile at -16.5 m (taken here to be the fixed base as discussed above), and also related to the nearby free-field ground surface motion. The first natural frequency for this bent of the bridge system was found to be 0.70 Hz during the Ferndale 09 Jan 2010 earthquake and around 1 Hz during all of the other small earthquakes. A summary of the TF results for 5 different earthquakes (Table 1) employing a Hanning window and 50% overlap to reduce the effects of spectral leakage is presented in Table 2. The lower predominant frequency during the strongest earthquake Ferndale 09 Jan 2010 reflects nonlinear behavior in the structure (the Pier Deck sub-system) as well as in the pile-group response.



(a) Direction of 180 degrees



(b) Direction of 90 degrees

Figure 7 Nonlinear soil response during Earthquake Ferndale 09 Jan 2010

5.3 Insights from a simple FE model

A simple linear elastic OpenSees FE model was developed based on the identified characteristics of Pier S-8 (including the deck, the Pier, and the pile group below). This model consisted of two point masses at the

bridge deck and the pile cap levels, connected by bending beams. Input transverse excitation was imparted at the -16.5 m below mean sea level location, and the base as well as the pile cap mass location were fixed against rotation.

Table 2 System Identification (Samoa Channel Bridge)

Earthquake	Fundamental Frequency (Hz)		
	$\frac{Deck}{Pile\ Cap}$	$\frac{Deck}{-16.5\ m}$	$\frac{Deck}{free\ field}$
09 Jan 10	1.60	0.70*	0.67*
24 June 07	2.00	1.10	0.95
29 April 08	1.95	1.10	0.90
16 Aug 08	1.95	0.93	0.95
26 Feb 07	2.00	0.95	0.90

* The second resonance was noted at about 2.7 Hz

Actual mass was used to define the FE model point masses (center-to-center mass of the bridge deck above S-8, and mass of the pile cap). Flexural stiffness (EI) of the connecting bending beams was then based on matching the sub-system and bridge-bent resonant frequencies (Figure 8) identified in Table (for the moderate 9 January 2010 earthquake). The Pier and pile foundation stiffness defined in this fashion is contrasted below with estimates of the actual Pier and pile group foundation (taken as a single super-pile) lateral stiffness, calculated based on the following material parameters: concrete mass density ρ= 2400 kg/m^3, Young's modulus E=2.51x10^7 kPa (derived from an assumed compressive strength $f_c' = 28MPa$) and Poisson's ratio ν=0.2 for concrete ad E$_s$=2.0x10^8 kPa for steel. As such, the defined Pier stiffness includes contributions from interaction (resistance) due to the overall bridge connectivity, and the pile foundation stiffness implicitly accounts for SSI.

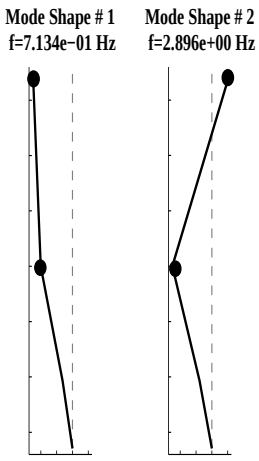
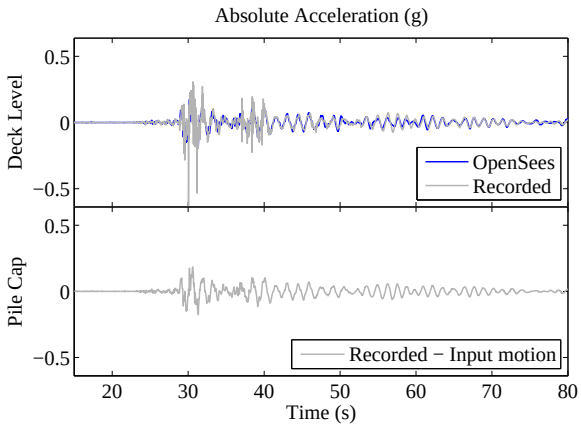
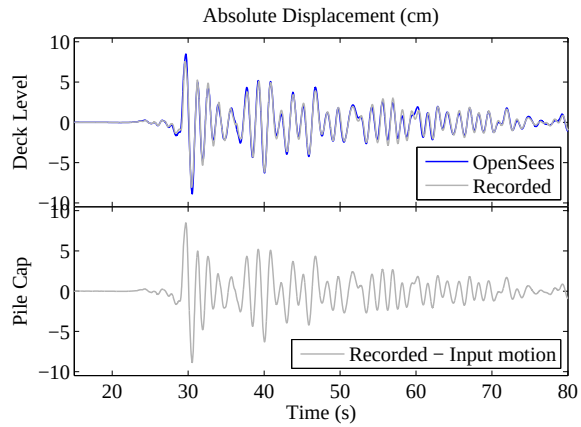


Figure 8 mode shapes of pile-column system

Computational simulation results show a reasonable match from the pile cap to the deck (Figure 9) and from the base to the deck (Figure 10). On this basis, one might contrast the identified employed stiffness quantities to those estimated above for the Pier and pile group foundation. It turns out that the employed quantities amounted to a factor of 1.1 for the column stiffness and a factor of 0.28 for the stiffness of pile group foundation. This stiffness for the Pier might be reasonable considering restrains from the overall bridge behavior. However, the pile group foundation stiffness appears to be noticeably lower than calculations might imply (only 28% of the estimated EI is engaged). For the small earthquakes (Table 2), the corresponding identified Pier stiffness reached 1.65 of that estimated, and the identified pile foundation stiffness reached a higher factor of 0.65. Such factors as obtained from this study provide a reference for seismic and SSI considerations and are to be further refined based on additional more representative investigations.

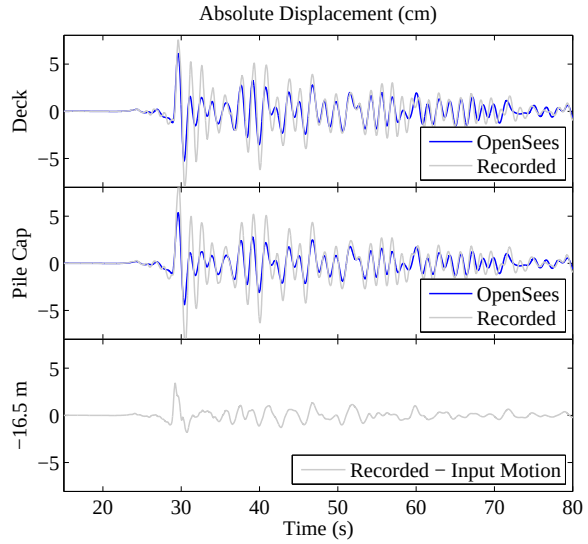


(a) Absolute acceleration

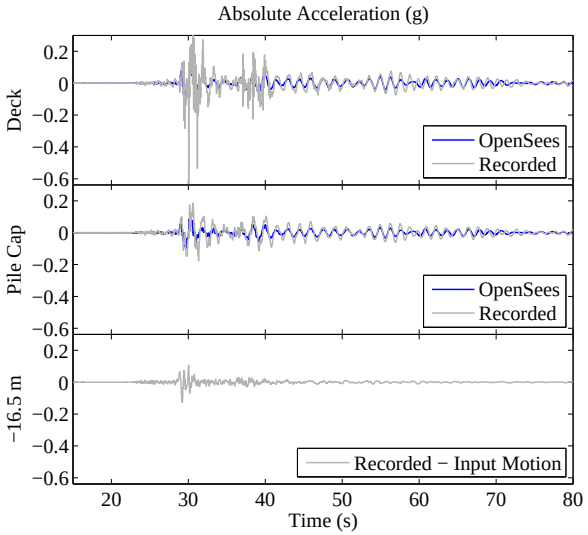


(b) Absolute displacement

Figure 9 Absolute time histories comparison, OpenSees FE model versus recording at Pier S-8 (Pile Cap to Deck)



(a) Absolute displacement



(b) Absolute acceleration

Figure 10 Absolute displacement time histories comparison - OpenSees FE model versus earthquake records at Pier S-8

6 CONCLUSIONS

Post-earthquake ground response analysis using signal processing techniques and system identification methods provides useful information to investigate site and structure dynamic properties. In this paper seismic response measurements from downhole array and adjacent bridge foundation sensors provided unique insights into the seismic response of a soil-foundation-structure system.

A comparison of the measured displacement time-history records indicated that: (1) despite the moderately high levels of shaking, the relative displacement between the Pier top and bottom of remained relatively small, and most of the bridge lateral deflections were due to movement of the pile cap, (2) displacement time histories at ground surface and at the -16.5 m depth location of the pile followed similar wave patterns to those of the downhole array. As such, input motion for a computer model of this foundation-structure system could be selected through interpolation of downhole array motions at corresponding locations, (3) out of phase response of pile at -10.36 m below the mean sea level requires additional investigations (not discussed in this paper; see Wang 2013 for more details).

Samoa Channel Bridge structure resonant frequencies are estimated using transfer functions from Fourier spectra. An OpenSees FE model was developed and calibrated to simulate site seismic response. Computed site response was comparable to the actual measurement in the time domain along Pier S-8. This study demonstrated that the adopted strong motion data analysis techniques have captured salient seismic characteristics and was helpful for calibration of the employed FE model.

The results of this research are of significance to the current state of practice in seismic pile-ground-structure analysis. Validation and refinement of our deep-foundation soil-structure interaction analysis and design approaches will lead to more confidence and reliability. In this domain of highly expensive and time consuming foundation design, construction, and retrofit, major beneficial economic outcomes can result from adoption of analysis tools that are verified and further calibrated by such full-scale seismic performance data sets.

Acknowledgements:

The strong motion records used in this paper are obtained from CGS-CSMIP strong motion database. Support provided by the Pacific Earthquake Engineering Research Center (PEER) and by CalTrans is highly appreciated.

References:

Arici, Y., and Mosalam, K. (2000), "System Identification and Modeling of Bridge Systems for Assessing Current Design Procedures," *Proceedings of System Identification and Modeling of Bridge Systems for Assessing Current Design Procedures. SMIP2000 Seminar on Utilization of Strong-Motion Data*, 77 - 96.

Caltrans (2000), "Caltrans studies re Humboldt Bay foundation and soil," *Geotechnical studies - PEER*.

Caltrans (2008), "Strong Motion Instrumentation of Bridges and Downhole sites," *Research notes*

Caltrans (2012), "Post Earthquake Investigation Team (PEQIT) Manual," *Caltrans Office of Earthquake Engineering*.

Elgamal, A., Zeghal, M., Tang, H., and Stepp, J. (1995), "Lotung Downhole Array. I: Evaluation of Site Dynamic Properties," *Journal of Geotechnical Engineering*, **121**(4), 350-362.

Elgamal, A. W., Zeghal, M., Parra, E., Gunturi, R., Tang, H. T., and Stepp, J. C. (1996), "Identification and modeling of

earthquake ground response - I. Site amplification," *Soil Dynamics and Earthquake Engineering,* **15**(8), 499-522.
Elgamal, A., Yan, L., Yang, Z., and Conte, J. P. (2008), "Three-Dimensional Seismic Response of Humboldt Bay Bridge-Foundation-Ground System," *Journal of Structural. Engineering*, **134**(7), 1165.
Hipley, P., Huang, M., and Shakal, A. (1998), "Bridge Instrumentation and Post-Earthquake Evaluation of Bridges," *Proceedings of SMIP98 Seminar on Utilization of Strong-Motion Data*, 53-62.
Wang, N. (2013), "Soil Structure Interaction for Deep Foundation Systems," *PhD Thesis,* in preparation (expected).
Werner, S., Crouse, C., Katafygiotis, L., and Beck, J. (1994), "Use of strong motion records for model evaluation and seismic analysis of a bridge structure," *Proceedings of Fifth US National Conference on Earthquake Engineering*, Earthquake Engineering Research Institute, 511-520.
Wilson, J., and Tan, B. (1990), "Bridge Abutments: Assessing Their Influence on Earthquake Response of Meloland Road Overpass," *Journal of Engineering Mechanics*, **116**(8), 1838-1856.

10CUEE CONFERENCE PROCEEDINGS
10th International Conference on Urban Earthquake Engineering
March 1-2, 2013, Tokyo Institute of Technology, Tokyo, Japan

SYSTEM IDENTIFICATION, STRUCTURAL HEALTH MONITORING AND DAMAGE DETECTION OF A STEEL REINFORCED CONCRETE STRUCTURE OF URBAN DISASTER PREVENTION RESEARCH CENTER IN TSUKUBA, JAPAN

Goran Jekikj[1)], Koichi Morita[2)], and Mihail Garevski[3)]

1) Research Assistant, Institute of Earthquake Engineering and Engineering Seismology (IZIIS), Ss. Cyril and Methodius University in Skopje, Republic of Macedonia
2) Chief Research Engineer, International Institute of Seismology and Earthquake Engineering (IISEE), Building Research Institute (BRI), Tsukuba, Japan
3) Professor, Director, Institute of Earthquake Engineering and Engineering Seismology (IZIIS), Ss. Cyril and Methodius University in Skopje, Republic of Macedonia
jekic@pluto.iziis.ukim.edu.mk, morita@kenken.go.jp, garevski@pluto.iziis.ukim.edu.mk

Abstract: This research attempts to describe steps and procedures for structural health monitoring of the Urban Disaster Prevention Research Center (UDPRC), located in Tsukuba, Japan, in order to locate possible damages to the structural and non-structural elements of buildings due to earthquakes. The SHM procedure is an addition to the regular monitoring for the purpose of detecting damage sustained since the building's construction. The methodology consists of analyzing strong motion acceleration records from the year 1999 till 2012, and microtremor acceleration records from 2009 and 2011. Dynamical properties of the structure and parameters related to stiffness are extracted from the records by applying parametric system identification methods (ARX, ARMAX and N4SID). The changes of these parameters in time indicate the possible occurrence of damage to the building. Damage detection and localization have been performed by tracing the history of changes in the extracted dynamical parameters and storey stiffness during the observed period. The results obtained demonstrate the tendency of natural frequencies and storey stiffness to decrease, and damping ratios to increase due to aging, and exposure to strong ground motion. A decrease in frequency and stiffness is most evident in the year 2011, after the Great East Japan Earthquake.

1. INTRODUCTION

Damage involves any change in a system that is unforeseen and tends to decrease or disable a system's future safe and successful exploitation. Early detection, identification and repair of damage to structures are some of the most crucial challenges in engineering. The implementation of a strategy and methodology for damage detection in building structures and infrastructure, as well as structures and devices in mechanical, aero and aerospace engineering, is known as "structural health monitoring" (SHM). Generally, the goal of SHM is to fulfill the following requirements: consideration of the occurrence of structural damage, locating the damage, evaluation of the severity, prediction of the remaining lifetime of the structure. Damage detection in structures requires a comparison of the dynamic parameters of the structure and storey stiffness, obtained at different times. The possibility of such a comparison provides a history of changes in these structural parameters and estimating possible damage location. System identification (SI) techniques play an important role in structural health monitoring processes. The structures in their physical nature can be observed as dynamic systems with their own dynamical properties. The SI procedures are based on digital data analysis and processing. They are subjected to various external influences that in system identification elaboration are called input. The input can be applied to structures according to various factors (ground motion, wind, etc.) in the form of signals. As a result of the input, the structures exhibit responses (output) with features dependent on the dynamic properties of the structure and the input. The structural dynamical properties are resonant frequencies (or resonant periods), mode shapes and damping coefficients. Those properties in SHM processes may be recognized as damage sensitive features and may be utilized in process of detecting possible damage. The identification procedure usually requires high S/N (signal-to-noise ratio) and uncorrelated sources of excitation. The SI identification techniques on buildings for the purpose of SHM include ambient vibration (microtremor) measurements, strong motion measurements (in the case of earthquakes) and forced vibration measurements (shaker test). A high S/N ratio occurs with strong motion measurements and forced vibration measurements, so identification procedures can be considered as having a higher possibility of accuracy than with microtremor measurements, which usually contain a

large number of disturbances compared to real input-output combinations (low S/N ratio).

The subject of the study in this paper is health monitoring of the structure of the Urban Disaster Prevention Research Center (UDPRC) using parametric system identification methods.

This study examines analyses of microtremors and strong motion by applying ARX, ARMAX and N4SID system identification methods for the purpose of detecting and locating damage that has occurred in the building's structural and non-structural elements due to aging and frequent exposure to earthquakes since the time of its construction.

2. CHARACTERISTICS OF THE BUILDING

The Urban Disaster Prevention Research Center (UDPRC) is a part of the National Institute for Land and Infrastructure Management (NILIM). It is an eight storey steel-encased reinforced concrete structure.

Table 1 Outline of the building characteristics

Structure type	steel-encased reinforced concrete						
Number of storeys	8-storeys						
Height	30.9 m						
Total building area	5,050 m^2						
Foundation type	mat foundation						
Storey mass (tons)							
1F	2F	3F	4F	5F	6F	7F	8F
836	785	782	931	768	744	819	300



Figure 1 Exterior of the building

The construction of the building was completed in March 1998. Since the beginning of its exploitation, strong motion acceleration sensors have been installed for the purpose of monitoring the state of the structure, and analyzing its behavior when affected by earthquakes. Microtremor measurements have also been periodically conducted for the purpose of tracing the history of changes in the structure's dynamic parameters and stiffness.

The Great East Japan Earthquake from March 11, 2011, caused damage to the structural and non-structural elements of the UDPRC building. Some of the structural damage (flexural cracks on the columns and diagonal shear cracks on the shear walls) are visible.

3. INSTRUMENTATION OF THE BUILDING

3.1 Installed strong motion sensors

Sensors are installed in 11 locations (33 channels) in the building. Accelerometers installed in the basement and 1st, 2nd, 5th and 8th storeys are used for system identification in strong motion analysis. The analyzed data represents the automatically recorded acceleration during earthquake occurrences, measured in gals (cm/sec^2) with a sampling frequency of 100 Hz. Such observation has been adopted to ensure contribution of at least the first two modes in both east-west and north-south directions in the system identification procedure (henceforth referred to as E-W and N-S direction respectively). The adopted instrument configuration provides supervision over the input-output behavior of the whole system. The vertical strong motion sensor configuration is illustrated in Figure 2.

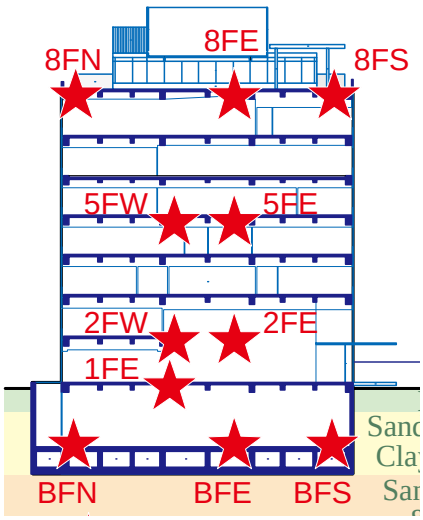


Figure 2 Vertical strong motion configuration (drawings from BRI database)

3.2 Instrumentation for microtremor measurements

The microtremor measurements were conducted on December 2, 2011. A portable ambient vibration monitoring system was used, consisting of 11 servo velocity sensors of type VSE-15D, junction box, recorder and wave monitor model SPC-51A, all manufactured by Tokyo Sokushin Co., Ltd (Figure 3). The measurement was conducted by recording ambient vibrations in east-west and north-south

directions, both with sampling frequencies of 100 Hz and 30 minutes duration each.



Figure 3 Portable microtremor measuring system

Nine horizontally oriented sensors were placed on the floors and basement. While measuring horizontal vibrations in an east-west direction, two vertically oriented sensors were placed in the basement on the east and west side to measure the rocking effect of the building due to soil-structure interaction. The same concept was applied by placing vertically oriented sensors on the north and south side of the basement while measuring horizontal vibrations in a north-south direction. The vertical and horizontal microtremor sensor configuration in both N-S and E-W directions is shown in Figure 4.

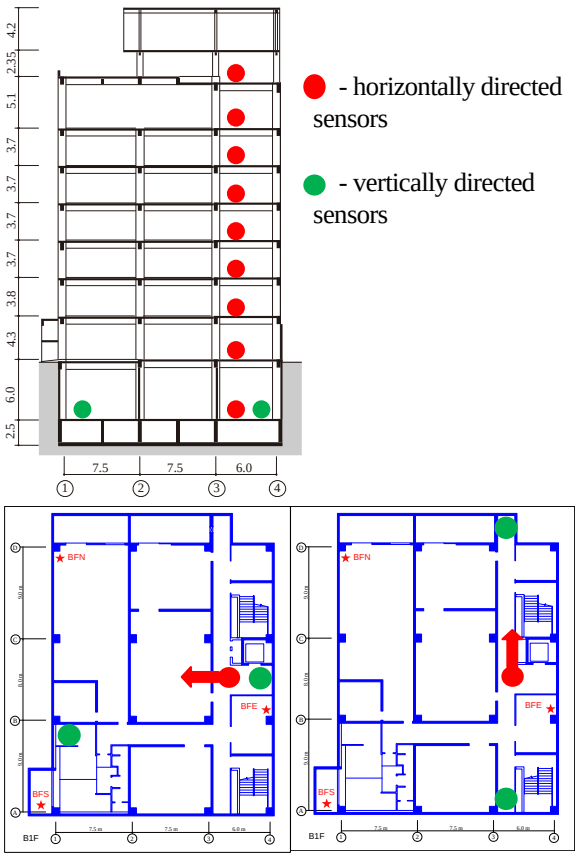


Figure 4 Microtremor sensor configuration E-W direction (left); N-S direction (right) (drawings from BRI database)

3.3 Arranging recorded data and excluding effects of rocking motion

The acceleration, recorded by horizontally directed sensors on the basement floor, is considered as input in the building, while the sensors, installed on the other floors, recorded each floor's corresponding horizontal output. The rocking effect modifies the input signal. The model of the instrumented building and the rocking effect is schematically represented in Figure 5. The input modification for each storey was assumed to exclude the effects of stiffness of the local soil, since only the dynamic properties of the building are of interest, rather than the influence of soil-structure interaction influence. The calculation of the input modification can be seen in Eq. (1).

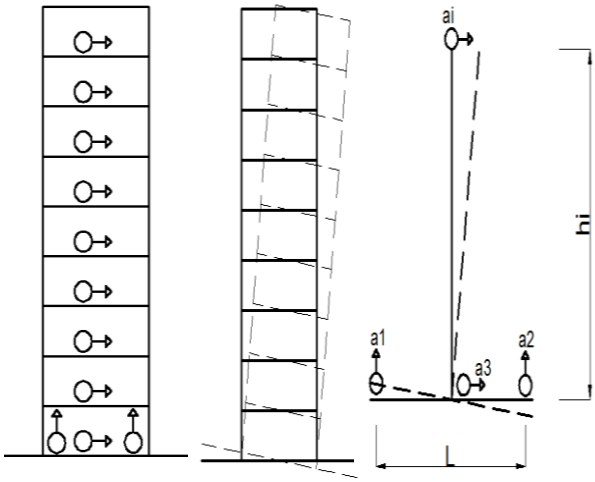


Figure 5 Model of the rocking effect

$$input_i = a_3 + (a_1 - a_2)\frac{h_i}{L} \quad (1)$$

4. DATA ANALYSIS AND RESULTS

4.1 Strong motion analysis

Observational data derives from the strong motion records from several earthquakes from 1999 until 2012. Within this period, the UDPRC building was affected by several strong ground motion events, including the Great East Japan Earthquake on March 11, 2011. The strong motion records for earthquakes with maximum peak ground acceleration not greater than 7.0 gals have been chosen. It has been assumed that such earthquakes are not strong enough to cause substantial damage or nonlinear behavior in the building, and consequently the dynamic properties and changes in the storey stiffness of the structure may be identified more clearly.

An example of time histories of the input and 8th storey response is demonstrated in the Figure 6. Measurements are represented as time-acceleration records, with units of seconds on the time axis (X) and cm/sec^2 (gal) on the acceleration axis (Y). For the estimation and validation range of response prediction, various signal durations were considered.

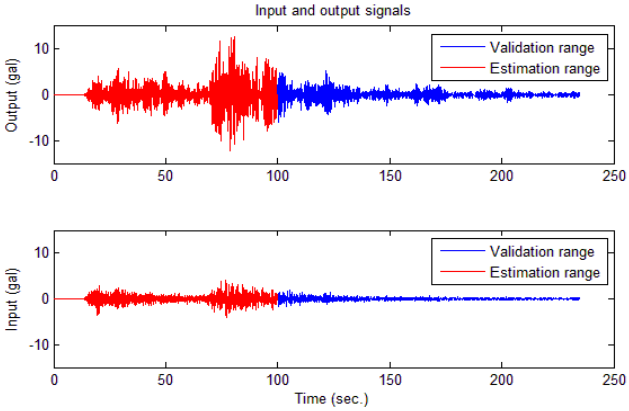


Figure 6 8th input and output, earthquake from July 16, 2007, N-S direction

The Fourier spectral ratio of the input-output relationship can be a useful starting point for locating the range of possible modal frequencies. It represents a relationship between output and input signal in their frequency domain and it is the basic type of transfer function in a nonparametric identification approach (Eq. (2)). The Fourier spectral ratio of the 8th floor's output-input relationship is presented in Figure 7.

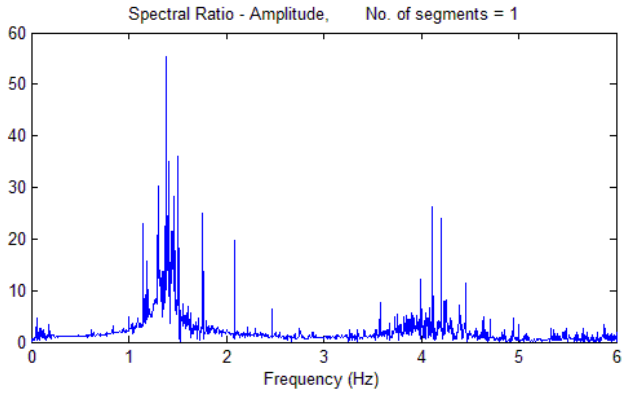


Figure 7 Amplitude spectral ratio of outpu-input relationship of the 8th floor in N-S direction, ground motion from July 16, 2007

$$G(\omega) = \frac{Y(\omega)}{U(\omega)} \qquad (2)$$

Parameter identification is based on the ARX model, applied for input-output data of vibration measurements of the 8th floor. The Akaike's Information Criteria (AIC) and Akaike's Final Prediction Error (FPE) methods have been applied for estimation of the optimal order number. In this particular case the ARX model is of order n_a=64, n_b=65, n_k=0. Such a model ensures 27% fit with FPE=0.00364. All the poles are located within the unit circle. The pole-zero plots (Figure 8) appear in pairs, symmetric on the real (X) axis, unless they are real numbers and lay on the axis. Since only four storeys above the basement are instrumented, the dynamic model of the building can be considered as a lumped mass system with four lumped masses and four degrees of freedom in each direction

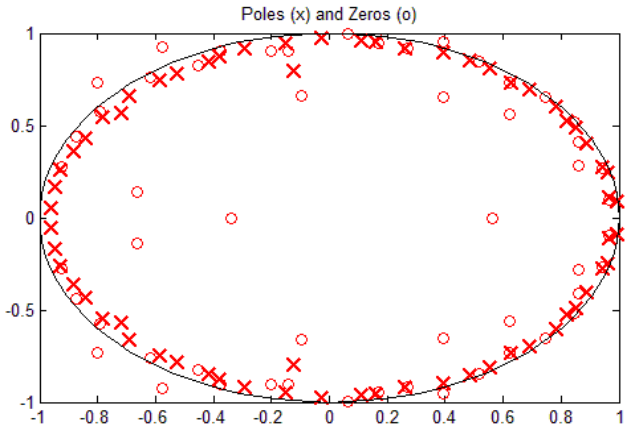


Figure 8 Location of transfer function's poles and zeros on z plane - N-S direction, ground motion from July 16, 2007

. With this assumption, only four pairs of poles represent the real frequencies of four mode shapes in the analyzed building. Locating these four pairs, and obtaining the four frequencies can be performed by developing the frequency response function from the ARX model transfer function (Figure 9). However, distinguishing the higher modes is difficult or impossible. In the particular case of the UDPRC building's parametric system identification, first and second modes are considered

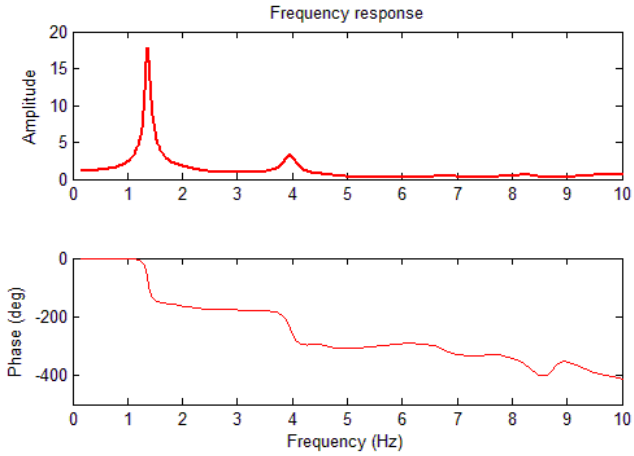


Figure 9 Estimated amplitude and phase response of the ARX transfer function, N-S direction, ground motion from July 16, 2007

The transfer function, which is in fact a relationship of input and output z-transforms, contains important data needed for the identification of building's dynamical properties. The Fourier transform, power spectral density and the Fourier spectral ratio of the signals contain a significant number of peaks from which it is often difficult or impossible to distinguish the real frequencies of the dynamic system. The mode shape's frequencies can be visible through frequency response function, which is the transfer function's representation as clearly visible spectral amplitude peaks. The frequency response function contains

amplitude response and phase response as a function of frequency. The peaks of the amplitude response indicate natural frequency on the location of the spectra. A sudden drop of the phase response indicates a transverse natural frequency in corresponding spectral locations.

The system's mode shape frequencies, damping ratio and mode shapes can be extracted from the transfer function by applying Eq. (3), (4) and (5) respectively:

$$f_j = \frac{\sqrt{\left(\ln\left|{}_z p_j\right|\right)^2 + \left(\arg({}_z p_j)\right)^2}}{2\pi\Delta t} \tag{3}$$

$$h_j = \frac{-\ln\left|{}_z p_j\right|}{2\pi f_j \Delta t} \tag{4}$$

$$\beta u_j = \Re\left[\frac{2\,{}_z p_j \sqrt{1-h_j^2}}{\Delta t\left(2\pi f_j h_j - i\,sign\left(\Im\left({}_z p_j\right)\right)2\pi f_i\left(1-2h_j^2\right)\right)}\right] \tag{5}$$

where f_j is the system's frequency, βu_j is the modal participation function, ${}_z p_j$ is a root (pole) of the transfer function, Δt is the sampling interval, h_j is the damping ratio, ${}_z r_j$ is a residue of a transfer function's partial fraction expansion.

Stiffness coefficients [K] can be estimated from mass-normalized measured mode shapes [Φ] (Eq.(6)) where [Φ] is determined from the modal participation function βu_j and frequencies [Λ] (Morita & Teshigawara, 2006).

$$[\Phi]^T [M][\Phi] = [I] \tag{6}$$

$$[K] \cong \left([\Phi][\Lambda]^{-1}[\Phi]^T\right)^{-1} \tag{7}$$

In the system identification of multistorey buildings it is often difficult to identify all mode shapes. In these cases, the stiffness matrix is obtained using a Moore and Penrose inverse matrix, which is one of the generalized inverse matrices. Parameters related to the storey stiffness will be estimated from [K] multiplying a displacement vector, in which each relative storey displacement is 1.0 from the right (Morita & Teshigawara, 2006).

To obtain the actual storey stiffness, all the system's natural frequencies and corresponding mode shapes have to be identified. In most of the cases only the first, and eventually the second mode shape can be clearly obtained. In this case, the obtained storey stiffness is lower than the actual one. The stiffness matrix [K] contains parameters related to the stiffness, which can be introduced as "storey pseudo-stiffness" which is a parameter for comparison of storey stiffness. The number of considered mode shapes is introduced as an order of the storey pseudo-stiffness. A higher order of the pseudo-stiffness means a closer value of the storey pseudo-stiffness to the value of the real storey stiffness. The highest order is the number of degrees of freedom in the corresponding direction, for which the storey pseudo-stiffness is equal to the real storey stiffness.

An example of the identified first and second mode shape of the structure, obtained by ARX model, is shown in Figure 10.

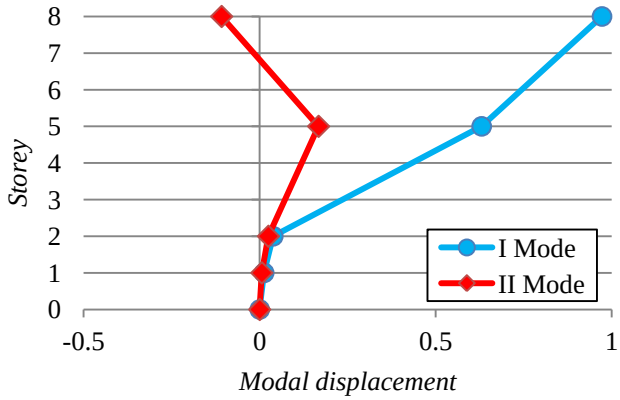


Figure 10. First and second mode shape of the building, N-S direction, ground motion from July 16, 2007

The identified natural frequencies, damping ratios and second order pseudo-stiffness, as results of the strong motion analysis, are shown in the graphs below. The analyzed strong motion data from year 2011 were recorded on March 20, 2011, nine days after the Great East Japan Earthquake.

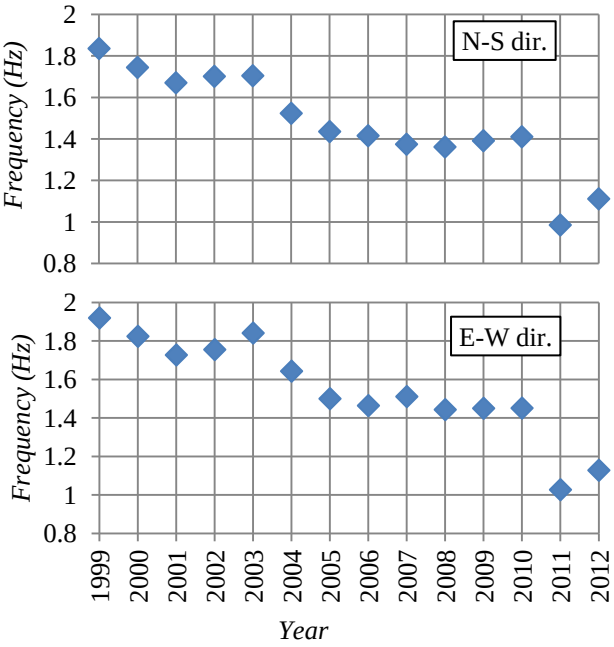


Figure 11. First modal frequencies

Decreasing frequency in the first two years of building's occupation may be due to the changes in life loads (increasing the amount of building's inventory), as so as shrinkage of the concrete that may result with micro-cracks in concrete components of the building's columns. The same effect has also been found in the identified second modal frequencies in both orthogonal directions (Figure 12). The

damping coefficients have trend of increasing due to aging of the structure. Although their accuracy depends on the ARX model order.

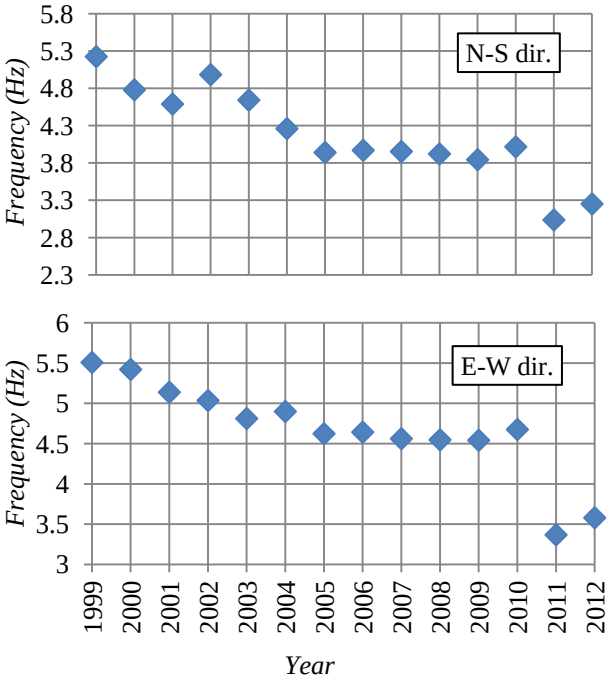


Figure 12. Second modal frequencies

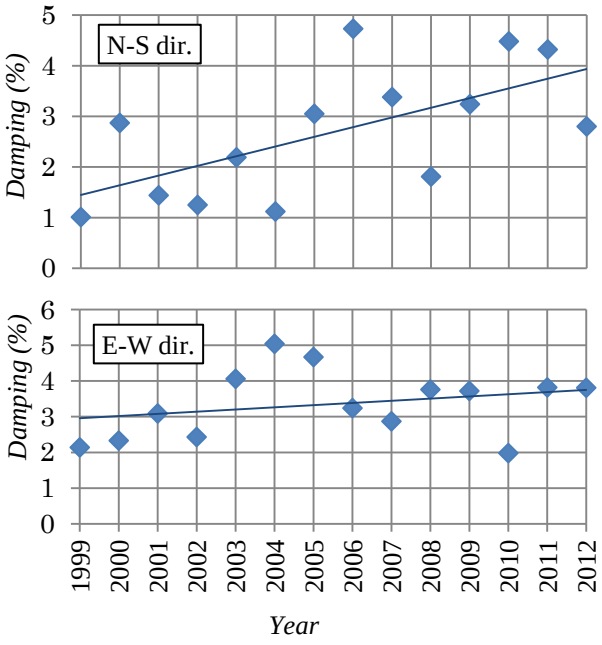


Figure 13. Damping ratios of the first modes

The charts on the Figure 14 demonstrate the identified second order pseudo-stiffness during the observed period. The results obtained demonstrate the tendency of natural frequencies and storey stiffness to decrease, and damping ratios to increase due to aging and exposure of the structure to strong ground motion. A drop in frequency and stiffness is most evident in the year 2011, which was expected since the analysis has been conducted with strong motion data recorded on March 20, 2011, after the Great East Japan Earthquake.

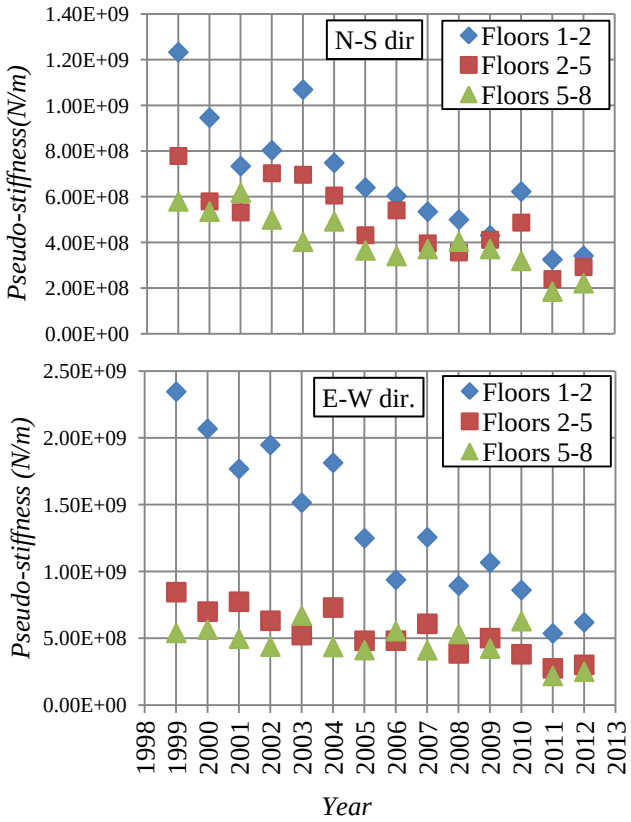


Figure 14. Second order storey pseudo-stiffness

4.2 Microtremor analysis

Microtremor observation is a nondestructive method of recording raw signals for the purpose of system identification and health monitoring of structures. Consequently, it is the most appropriate method, especially in regions of lower seismicity, for areas where strong ground motions do not occur frequently. Microtremors by their nature are vibrations provoked by ambient forces, with acceleration intensities from 10^{-7} to 10^{-4} gals that are constantly present in every environment. The biggest advantage of these measurements over strong motion measurements is that they can be conducted at any time. However, because of their low intensity, their analysis often requires more complex system identification methods than ARX due to the low signal-to-noise (S/N) ratio.

For the detection of damage in the UDPRC building due to the Great East Japan Earthquake, microtremor measurements from December 2, 2011 were analyzed, and the results compared with the analyses of measurements that were conducted on Jun 26, 2009, almost two years before the earthquake. All three system identification methods (ARX, ARMAX and N4SID) were applied, and the adopted method for identification is the one that provided the first mode shape of the building that is closest to the expected

one. Unlike the strong motion analysis, the second mode shape in the microtremor analysis was difficult or impossible to obtain. Because of this, only the first mode shape has been observed. The first order storey pseudo-stiffness has been obtained.

The first mode shape, obtained by applying ARX, ARMAX and N4SID identification methods, is shown in Figure 15. The adopted model order is shown in the chart's legend in the order ARX (n_a n_b n_k), ARMAX (n_a n_b n_c n_k) and N4SID (number of rows and columns of the system state matrix). From the 30 minute time history record, a sequence of 3 minutes had been analyzed.

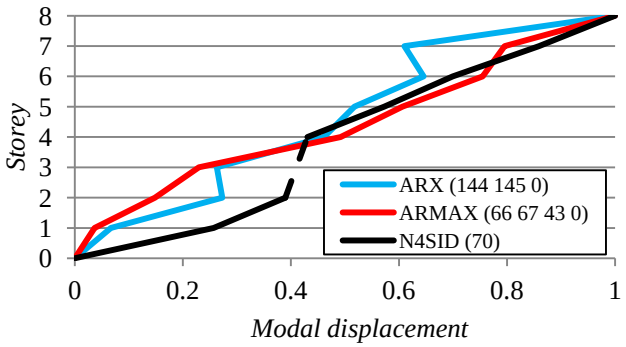


Figure 15. First mode shape, E-W direction

The dashed line of the mode shape in E-W direction, obtained by the N4SID method, is due to the inability to identify the modal displacement of the 3rd storey with this method. The chosen model for identification of the dynamic properties and pseudo-stiffness of the building in an E-W direction is ARMAX (66 67 43 0) as it identified the mode shape that is closest to the expected one.

The mode shape in an N-S direction is shown in Figure 16.

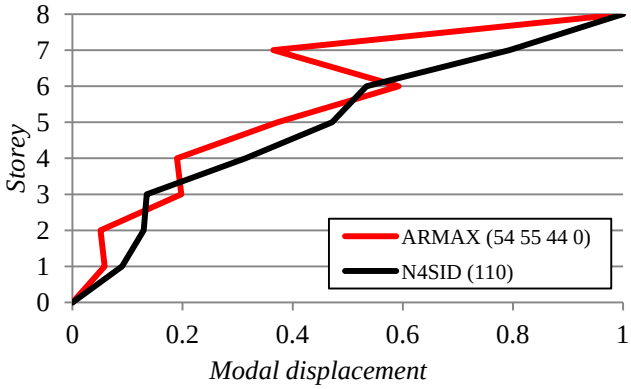


Figure 16. First mode shape, N-S direction

In the case of N-S direction, the building's properties could not be clearly identified by the ARX method. The chosen model for identification of the dynamic properties and pseudo-stiffness of the building in an N-S direction is N4SID (110) as it identified the mode shape that is closest to the expected.

For adopting the N4SID model order, stabilization diagrams for the 8th, 2nd and 1st storeys are plotted (Figure 17) in order to check the stability of the frequency, obtained from the models with various orders. The frequencies are the most stable on the 8th floor, which is expected, considering that the upper storey is the most flexible and most suitable for obtaining the whole building's dynamic properties.

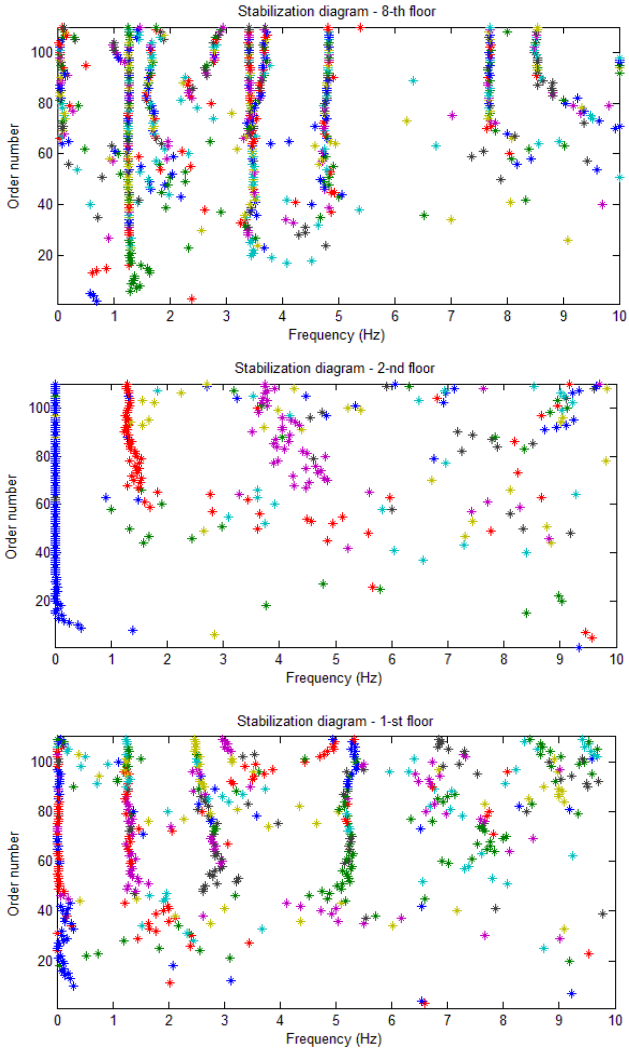


Figure 17. Frequency stabilization diagrams for N4SID model, N-S direction

The identification of the other 7 storeys is important for obtaining the mode shape. For calculating the mode shape and storey pseudo-stiffness, the model order should be higher, so that it identifies all the storeys, since the identification of the lower storeys requires a higher model order. However, the model order should be optimal, since too high model order would include modeling significant amount of noise, which should be avoided. The model order that provides computation of stable first natural frequency value is chosen as model order of the N4SID identification of the building. In the identification of the building's properties in N-S direction, from the Figure 17 it is evident that the identification of the first natural frequencies on the 8th storey becomes stable for N4SID model order higher than 20. However, the identification of the first natural frequencies on the 2nd storey becomes stable for model order

higher than 90. For that purpose, a model order of 110 has been chosen for identification since it provides stable first natural frequencies for all storeys, including the least sensitive ones (1st and 2nd).

The data from Jun 26, 2009, was provided by Mr. Ren Jun (Jun, 2009). Both sets of results refer to the microtremor analyses excluding the effects of rocking.

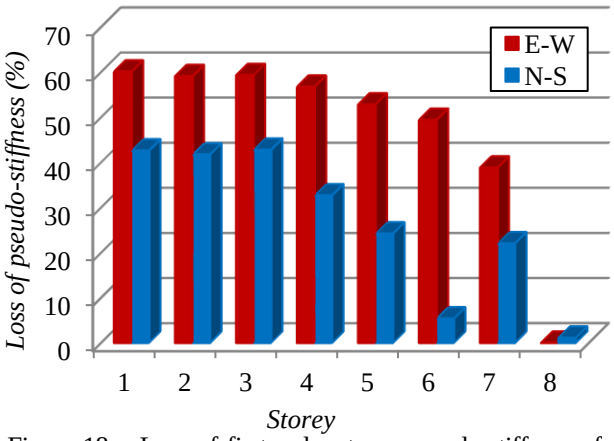


Figure 18. Loss of first order storey pseudo-stiffness of the UDPRC building due to the Great East Japan Earthquake from March 11, 2011

From the results presented above, we can see that the UDPRC building suffered severe damages due to the Great East Japan (Tohoku) Earthquake (structural or nonstructural) resulting in a loss of stiffness in nearly every storey in both east-west and north-south directions. The lower storeys suffered more severe damage than upper ones. This damage effect the structure's stiffness in the E-W direction more than in the N-S direction.

5. CONCLUSIONS

Structural health monitoring strategy has been investigated and implemented on the building of Urban Disaster Prevention Research Center (UDPRC) using strong motion data records and microtremor records analysis, excluding soil-structure interaction effects. The obtained modal frequencies were as expected, and their values are the most stable results. Changes in the modal frequencies are the initial indicator for loss of structural stiffness, which can be considered as damage. All three computational methods applied (ARX, ARMAX and N4SID) provide less stable results for other parameters, such as damping, mode shapes of the structure and the first order pseudo-stiffness, as a final result of the analysis. Further study needs to be made on algorithms for more precise structural identification projects. From the application of the three parametric system identification method, as well as tracing the history of changes in modal frequencies, damping coefficients and first order storey pseudo-stiffness, it can be concluded that:

- Modal frequencies and storey stiffness tend to decrease and damping coefficients tend to increase due to aging of the structure and its frequent exposure to earthquakes;
- For system identification and vibration-based structural health monitoring procedures, the information about the excitation data (microtremor or strong motion), chosen number of degrees of freedom of the structure and number of identified mode shapes are of crucial importance, more identified parameters provide more stable and accurate results;
- For system identification and damage detection procedures, strong motion data is more convenient for analysis than microtremor data due to the high signal-to-noise ratio. The number of identified mode shapes, obtained from strong motion data, is usually higher than that one obtained from microtremor analysis. This facilitates obtaining a higher order of storey pseudo-stiffness values and implies more stable values for obtained storey pseudo-stiffness, closer to actual values of storey stiffness. However, for an accurate diagnosis, the compared states of the structure need to be based on records with nearly the same values of peak ground acceleration (PGA);
- Microtremor requires careful attention when the model order is chosen, and often more complex identification methods than ARX due to the low signal-to-noise ratio (ARMAX or N4SID).

Acknowledgements:

This study was conducted as a part of the training course of International Institute of Seismology and Earthquake Engineering (IISEE), Building Research Institute (BRI), Japan that is financially supported by Japan International Cooperation Agency (JICA) from Oct., 2011 to Sep., 2012.

References:

Celebi M. (1996), "Comparison of damping in buildings under low-amplitude and strong motions", *Journal of Wind Engineering and Industrial Aerodynamics* 59 (1996) 309-323

Chopra A. (2007), "Dynamic of Structures: Theory and Applications to Earthquake Engineering", Third edition, Prentice Hall

Di Ruscio D. (1995), "Subspace System Identification-Theory And Applications", *Lecture notes*, Telemark Institute of Technology, Porsgrunn, Norway

Jekikj G. (2012), "System Identification of Structures for the Purpose of Structural Health Monitoring and Damage Detection", A Master Paper, *Disaster Management Policy Program (2011-2012), Earthquake Engineering*, National Graduate Institute for Policy Studies, Tokyo, Japan; Building Research Institute, Tsukuba, Japan

Kashima T. (2012), "Strong Earthquake Motion Observation", *IISEE Lecture Note*, International Institute of Seismology and Earthquake Engineering, Building Research Institute. Tsukuba, Japan

Kashima T., and Kitagawa Y. (2006), "Dynamic Characteristic of an 8-Storey Building Estimated from Strong Motion Records", *First European Conference on Earthquake Engineering and Seismology (a joint event of the 13th ECEE & 30th General Assembly of the ESC)*, Paper No.1005, Geneva, Switzerland

Kaya Y. (2009), "Modal Identification of a Tested Steel Frame using Linear ARX Model Structure", *International Journal of Advanced Structural Engineering*, Vol. 1, No. 1, Pages 35-52, Islamic Azad University, South Tehran Branch, Iran

Lei Y., Kiremidjian A. S., Nair K. K, Lynch J. P., Law K. H, Kenny T. W., Ed Carryer, and Kottapalli A. (2003), "Statistical Damage

Detection Using Time Series Analysis on a Structural Health Monitoring Benchmark Problem", *9th International Conference on Applications of Statistics and Probability in Civil Engineering*, San Francisco, CA

Ljung L. (1999), "System Identification - Theory for the User", PTR Prentice Hall, New Jersey

Ljung L. (2012), "System Identification Toolbox User's Guide", The MathWorks, Inc.

Lynch J. P. (2005), "Damage Characterization of the IASC-ASCE Structural Health Monitoring Benchmark Structure by Transfer Function Pole Migration", *2005 ASCE Structures Congress*, New York

Maruki T. (2004), "Structural Health Monitoring using Parametric Models in System Identification", University of California, Irvine, Department of Civil and Environmental Engineering

Mita A. (2003), "Structural Dynamics for Health Monitoring", First edition. SANKEISHA Co.,Ltd. Nagoya, Japan

Morita K. (2011), "System Identification in Vibration Analysis", *IISEE Lecture Note*, International Institute of Seismology and Earthquake Engineering, Building Research Institute. Tsukuba, Japan

Morita K., and Teshigawara M. (2005), "Damage detection and estimation of a steel frame through shaking table test and measurements", *Structural Control and Health Monitoring, Special Issue: Advanced Sensors and Health Monitoring*, Volume 12, Issue 3-4, pages 357–380

Morita K., and Teshigawara M. (2006), "Structural health monitoring of an existing 8-story building using strong motion observation data and structural design data", *Smart Structures and Materials 2006: Sensors and Smart Structures Technologies for Civil, Mechanical, and Aerospace Systems*, *SPIE*, Volume 6174, pages. 575-583

Morita K., Teshigawara M., Isoda H., Hamamoto T., and Mita A. (2001), "Damage Detection Tests of Five-Story Steel Frame with Simulated Damages", *Advanced Nondestructive Evaluation for Structural and Biological Health Monitoring*, Proceedings Vol. 4335 Tribikram Kundu, Editors, pp.106-551

Niousha A., Naito Y, Hikita T, and Harada H. (2003), "Analysis of Dynamic Characteristics of a Tall Building for Microtremors Using Recursive Modeling and Spectral Method", *Fourth International Conference of Earthquake Engineering and Seismology*, Teheran, Iran

Ren J. (2009), "Structure Observation & Identification Considering Soil-Structure Interaction of Story Stiffness and Damping Ratio of 8-Story Steel Encased Reinforce Concrete Structure by Microtremor", A Master Paper, *Disaster Management Policy Program (2008-2009), Earthquake Engineering*, National Graduate Institute for Policy Studies, Tokyo, Japan; Building Research Institute, Tsukuba, Japan

Suresh K., Sajal K. Deb, Dutta A., Parametric System Identification of Multistoreyed Buildings with Non-Uniform Mass and Stiffness Distribution, The 14th World Conference on Earthquake Engineering, Beijing, China

Teshigawara M., Isoda H., Morita K., Kitagawa Y., Mita A., Nakai S., and Yoshida K. (2004), "Technology Utilization Guidelines of Structural Health Monitoring for Buildings and its Application", *13th World Conference on Earthquake Engineering*, Paper No. 2221, Vancouver, B.C., Canada

Trnka P. (2005), "Subspace Identification Methods", Technical Report, Czech Technical University in Prague, Faculty of Electrical Engineering, Department of Control Engineering, Czech Republic

Xing S., Halling M. W., Barr P. J., and Meng Q. (2008), "Ambient Vibration Analysis of a Highway Bridge with Subspace Method and Frequency Domain Decomposition", *14th World Conference on Earthquake Engineering*, Beijing, China

Yokoi T. (2010), "Introduction to Digital Data Processing", *Seismology Course Lecture Notes*, International Institute for Seismology and Earthquake Engineering (IISEE), Japan International Cooperation Agency (JICA),, Ver. 3.3.1, Tsukuba, Japan

10CUEE CONFERENCE PROCEEDINGS
10th International Conference on Urban Earthquake Engineering
March 1-2, 2013, Tokyo Institute of Technology, Tokyo, Japan

SEISMIC RESPONSE OF AN RC BUILDING STRENGTHENED WITH PIN-SUPPORTED WALLS DURING THE 2011 TOHOKU EARTHQUAKE

Zhe Qu[1)], Hiroyasu Sakata[2)], Saburoh Midorikawa[3)], and Akira Wada[4)]

1) Postdoctoral Researcher, Center for Urban Earthquake Engineering, Tokyo Institute of Technology, Japan
2) Professor, Structural Engineering Research Center, Tokyo Institute of Technology, Japan
3) Professor, Department of Built Environment, Tokyo Institute of Technology, Japan
4) Professor Emeritus, Tokyo Institute of Technology, Japan
m.quzhe@gmail.com, sakata.h.aa@m.titech.ac.jp, smidorik@enveng.titech.ac.jp, wada@akira-wada.com

Abstract: A thirty-four years old eleven-story steel reinforced concrete frame building, which was seismically retrofitted in 2010, was influenced during the 2011 M9.0 Tohoku earthquake. The strengthening of its longitudinal frame adopted an innovative pin-supported wall-frame system while conventional fixed-based walls were added in the transverse direction. Although not severe, the observed damage of the building demonstrated that the pin-supported walls are less vulnerable than fixed-based ones. However, non-structural partition walls may concentrate a major part of damage, especially during mild ground motions. Furthermore, a detailed numerical model is calibrated by the recorded motions of the building during the Tohoku earthquake, which was recorded by five three-channel accelerographs. The calibrated model features the influence of the partition walls, which were not taken into account in the original model.

1. INTRODUCTION

An innovative pin-supported wall system has been developed and applied in the retrofit of three university buildings on Suzukakedai campus of Tokyo Institute of Technology during the past several years. Among them is the first application of this system, namely G3 Building, an 11-story steel reinforced concrete moment-resisting frame building completed in 1978 and seismically retrofitted in 2010. The basic idea of the pin-supported wall system is to make use of post-tensioned (PT) concrete walls as coordinators in a structural system to help producing uniform distribution of lateral deformation along the height of the building and to prevent weak story failure. Such walls are supported by specifically designed mechanical hinge bearings at the bottom that can effectively resist shear force while allowing for finite rotation without damage. Shear-type steel dampers are installed in between the PT walls and neighboring columns along the height of the building. They are expected to concentrate most hysteretic energy dissipation of the whole structure during major earthquakes so that the seismic response may be reduced and the rest of the structure may remain less damaged or even undamaged. The application of this system in G3 Building is illustrated Figure 1, where the pin-supported walls were applied to only the longitudinal direction of the building (i.e., *x*-direction in Figure 1). Conventional fixed-base shear walls were used for retrofit in the transverse direction (i.e., *y*-direction in Figure 1). More details about this project can be found in Wada et al. (2009) and Qu et al. (2012).

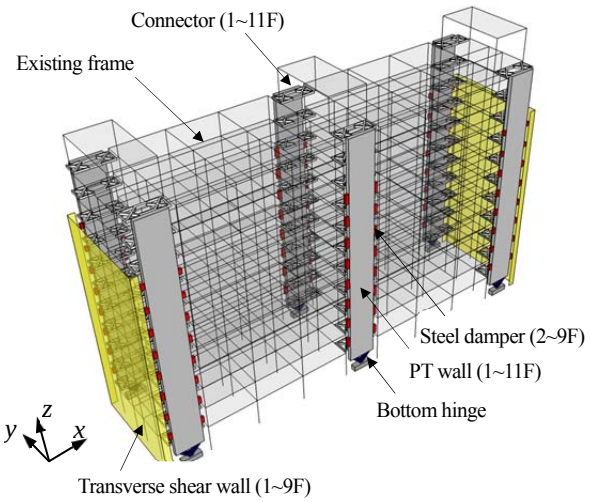


Figure 1 Pin-supported wall system in G3 Building (Qu *et al.*, 2012)

On March 11th, 2011, about one year after the completion of the retrofit of G3 Building, a M9.0 earthquake, usually referred to as the Tohoku earthquake, hit the eastern Japan and also caused considerable ground shaking even in the Tokyo metropolitan area which is more than 300 km away from the epicenter. In this study, the accelerograms obtained on G3 Building during the Tohoku earthquake are used to calibrate a finite element (FE) model of the building, which was once used to assist the design of the retrofit. The calibrated FE model is then used to simulate the seismic

response of the building before and after the retrofit. The effect of the retrofit with pin-supported wall system and the role of the partition walls are emphasized.

2. OBSERVATIONS

Five accelerographs, each with three channels for the three translational degrees of freedom, were installed in the basement (B1F), on the 2nd, 5th, 8th and 11th floor of G3 Building when the retrofit was completed. All accelerographs are located as closer to the center of the building as possible. Taking the records at the basement level (B1F) as the ground motion, the peak ground acceleration (PGA) and the peak ground velocity (PGV) is 67.3 cm/s^2 and 14.4 cm/s in the longitudinal (x) direction and is 52.8 cm/s^2 and 12.7 cm/s in the transverse (y) direction, respectively (Miura and Midorikawa, 2011). Figure 2 compares the acceleration response spectra of the recorded ground motions (B1F records) with the Level I design spectrum prescribed in Building Standard Law of Japan (BCJ, 2004). In both directions, the spectra of the records were much lower than the design spectrum in period range below 1.0 s. In addition, the building seems to have experienced quite similar shaking in both directions.

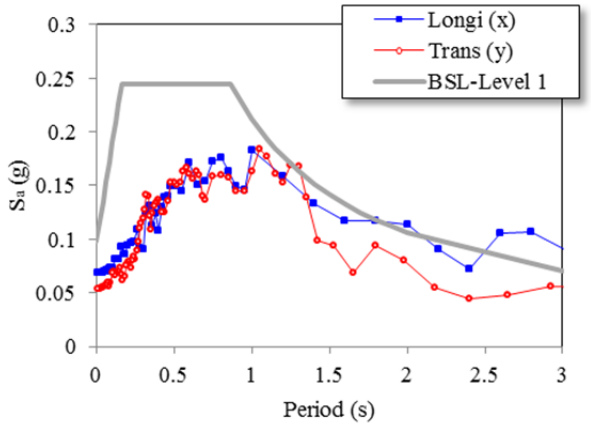


Figure 2 Acceleration spectra of recorded ground motion in longitudinal (x) and transverse (y) directions (5% damping)

The amplification of motion along the height of the building can be observed in Figure 3 by comparing the acceleration spectra at each floor levels. It can also be identified in Figure 3 that the dominant period of vibration of G3 Building is about 0.65 s in the longitudinal (x) direction and about 0.69 s in the transverse (y) direction, respectively.

The accelerograms were processed by 4th order Butterworth high-pass filter before they were integrated to get the displacement response. As suggested by Miura *et al.* (2011), cut-off frequency as large as 0.667 Hz was selected for the filtering, mainly in order to remove the influence of the unwarranted long-period contents observed in the 2F and 8F records. The corrected accelerograms were integrated twice to obtain the displacement response. Numerical integration with trapezoidal rule was used and the time increment Δt was set to be 0.01 s. The maximum lateral displacement in x-direction turned out to be 23 cm and the maximum inter-story drift ratio occurred at the first floor and is slightly greater than 0.001. The acceleration records and the above-obtained displacement response were used to evaluate the performance of the analysis models. Detailed results of floor displacement are given later together with the analysis results.

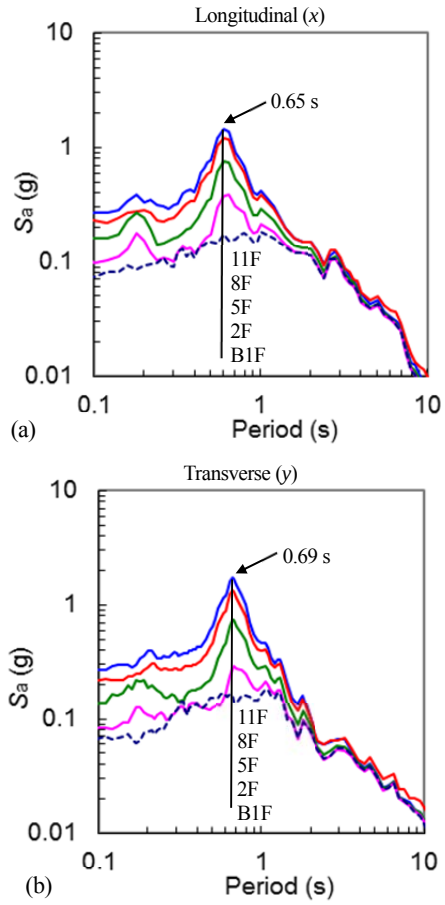


Figure 3 Acceleration spectra at each floor levels in (a) longitudinal (x) and (b) transverse (y) direction (5% damping)

The G3 Building was inspected immediately after the Tohoku earthquake. Many minor cracks of width less than 0.2 mm were observed near the bottom of the added conventional fixed-base walls at both ends of the building, while on the other hand, no visible damage was observed on the pin-supported walls in the longitudinal (x) direction except that the coating of the bottom hinge bearing was slightly peeled off, indicating that the bearing may have rotated as intended during the earthquake (Figure 4). In addition, diagonal rust marks were found on the steel web plate on the web plate of several shear-type steel dampers at lower stories (Figure 5), which indicated that these web plates may have yielded during the earthquake and the protective coating along the directions of principle strain was peeled off.

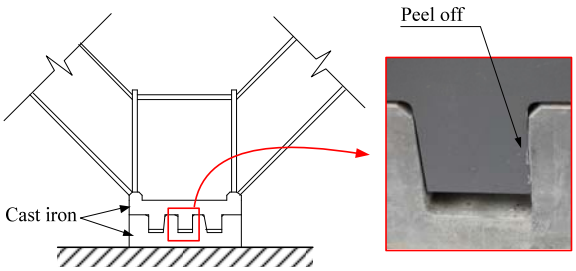


Figure 4 Peel off of painting of bottom tooth-like hinge (north, center).

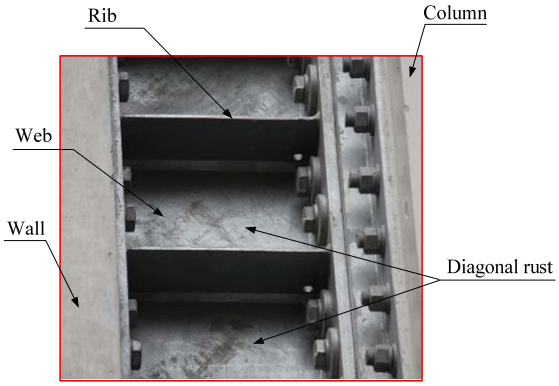


Figure 5 Diagonal rust marks on web plates (north, center at 2F).

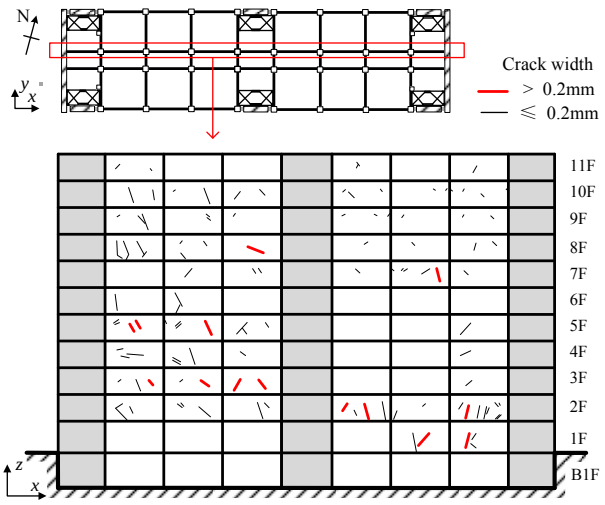


Figure 6 Observed cracks on partition walls of G3 Building (reproduced based on data provided by the Facility Department of Tokyo Institute of Technology).

Another type of obvious damage in the longitudinal (x) direction of the building was found on the reinforced concrete partition walls. As a common practice in Japan, lightly reinforced concrete thin walls in a building are usually considered as nonstructural walls and thus are not taken into account in the seismic design of the building. Such partition walls along the longitudinal (x) direction of G3 Building are located in the two inner bays of the frame (see Figure 6 for reference). The cracks observed on the partition walls in one of the two bays are illustrated in Figure 6. It can be seen that cracks were observed on the walls of every floor except the basement floor. The width of some cracks exceeded 0.2 mm. In addition, the deformation of the lower stories seems to have been greater than that of the upper ones by the fact that most cracks of width greater than 0.2 mm were found in lower stories.

3. ANALYSIS MODEL

3.1 Original Model and Its Modification

In order to better understand the dynamic behavior of G3 Building during the Tohoku earthquake, the records obtained by the above mentioned accelerometers were used to calibrate a FE model, which was used by Qu *et al.* (2012) to evaluate the seismic performance of G3 Building and to demonstrate the effectiveness of the pin-supported wall system. It was a member-by-member frame model in commercial FE software ABAQUS. The longitudinal behavior of G3 Building was modeled by three plane frames sharing the same lateral displacement at corresponding beam-to-column joints. The frame columns and beams were modeled by fiber-sectioned beam elements (B21 in ABAQUS) with user-defined materials for concrete and steel fibers. The pin-supported walls were models by elastic beam elements with rigid arms. The shear-type steel dampers were assumed to exhibit elastic-perfectly plastic hysteresis. The readers are referred to Qu *et al.* (2012) for more details of the model. This model is referred to as 'original model' hereafter because further improvement will later be made on it.

It was found that the original model would much over-estimate the displacement response of G3 Building during the earthquake. It is also evident by looking at the results in frequency domain that the dominant period of vibration of the original model is much longer than the observed one. These results will be introduced later together with the results predicted by the 'modified model', which is described below.

It is supposed that the over-estimated fundamental periods is a consequence of the omission of the RC partition walls in the original model. Following this clue, improvement of the original model was made to include those walls. As mentioned above, the partition walls in the longitudinal direction of G3 Building were located in the two inner bays of the moment frame (Figure 7(a)). Individual walls can approximately be classified into two categories, namely W1 and W2, as shown in Figure 7(b). For W1, two openings separate the wall pier of length L_w from the columns on both sides. For W2, another opening appears in the middle of the wall pier and subdivides it into two smaller wall piers of length L_{w1} and L_{w2}. All wall piers are 120 mm in thickness and are reinforced by single-layer orthogonal ϕ10 rebars at 200 mm spacing. No boundary confinement was provided. As the same as the main structure, the nominal concrete compressive strength was assumed to be 20 MPa and the nominal yield strength of rebar 394 MPa for these walls. In addition, the

center-to-center span length, L, is 7800 mm for all the spans containing partition walls. The story height, H, varies from 4500 mm for the 1st floor, to 3600 mm for the 2nd and the 3rd floor and to 3500 mm for all the other floors.

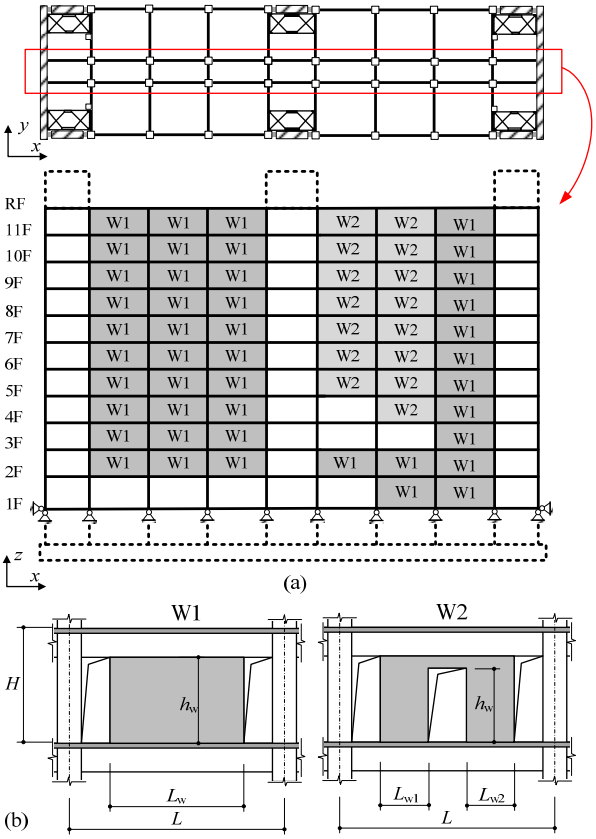


Figure 7 Two types of reinforced concrete partition walls W1 and W2 in G3 Building: (a) Locations of partition walls and (b) wall configurations

As a simple representation, an individual partition wall (both for W1 and W2) was modeled by a pair of diagonal braces connecting the beam ends in the lower and the upper stories (Figure 8). The mechanical properties of the two braces were identical and were thus determined that their horizontal behavior is equivalent to a tri-linearized partition wall model as shown in Figure 8. To this end, the relationship in Equation (1) is followed to transform horizontal responses of a single wall to diagonal ones.

$$F_b = 0.5F/\cos\theta$$
$$\Delta_b = 0.5\Delta\cos\theta \quad (1)$$

where F and Δ are horizontal shear force and lateral displacement of the wall, respectively; F_b and Δ_b are the axial force and axial deformation of a single brace, respectively, and θ is the inclination angle.

The trilinear hysteretic model shown in Figure 8 was assumed for both W1 and W2. Subjected to monotonic loading, the wall remains elastic with initial stiffness, K_0, until the cracking strength, V_{cr}, is reached. After cracking, the stiffness degrades sharply while the force keeps growing linearly until the ultimate strength, V_u, is reached. The corresponding deformation is denoted as Δ_0, beyond which the wall begins to lose its strength quickly with a negative stiffness $-K_0$ until zero force. It was further assumed that the wall completely fails, which means it contributes no more to the resistance once it loses all its strength in either direction. Besides the skeleton curve, it was assumed that the cyclic behavior of the wall follows the rules that (1) the unloading branch always points to the cracking point in the opposite direction; (2) the reloading branch would point to the cracking point or the ultimate strength point if these points have not been exceeded before, and (3) otherwise, the reloading branch points to the largest deformation point ever experienced in the loading history.

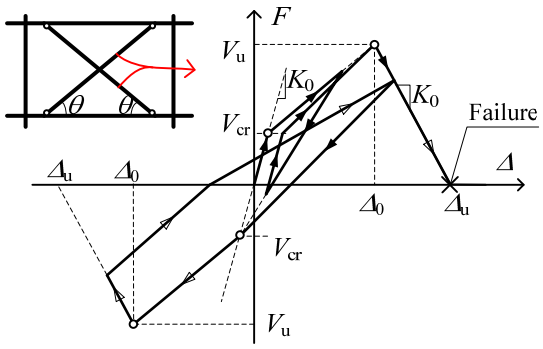


Figure 8. Model of partition walls: (a) diagonal truss elements and (b) hysteretic behavior.

For W1, the initial stiffness, K_0, can be simply estimated by Equation (2), which accounts for both flexural and shear stiffness of an elastic wall pier assuming both ends (lower and upper) fixed. For W2, the stiffness of the two smaller wall piers, which are separated by the central opening, was first estimated by Equation (2) separately and then summed up to obtain the total initial stiffness of the wall in the span.

$$K_0 = \frac{1}{1/K_s + 1/K_f} = \frac{1}{\frac{h_w}{Gt_wL_w} + \frac{h_w^3}{12EI_w}} \quad (2)$$

where h_w, t_w, L_w are the height, thickness and length of a single wall pier, respectively; E and G is the elastic modulus and the shear modulus of concrete; I_w is the moment of inertia of a single wall pier section.

The cracking strength, V_{cr}, was estimated by Equation (3) proposed in AIJ (1999) for calculating the cracking strength of concrete walls without boundary columns. The ultimate strength, V_u, was estimated by the empirical equation proposed by Wood (1990) for reinforced concrete squat walls (Equation (4)). Although very simple, this equation was confirmed by Gulec *et al.* (2008) to give best prediction of ultimate strength among several other commonly used equations. Because the partition walls in G3 Building were only lightly reinforced, the ultimate strength

was actually determined by the leftmost term in Equation (4). For W2 cases, the strength of the two small wall piers were calculated independently and then summed up to get the overall strength. The displacement corresponding to the ultimate strength, V_u, was determined by means of the effective stiffness of squat walls, K_{eff}, proposed by Li and Xiang (2011) (Equation (5) and (6)).

$$V_{cr} = \tau_{cr} t_w L_w / 1.5 \tag{3}$$

where $\tau_{cr} = 0.33\sqrt{f_c}$ is the effective shear strength of concrete.

$$0.5 t_w L_w \sqrt{f_c} \le V_u = A_{vy} f_y / 4 \le \frac{5}{6} t_w L_w \sqrt{f_c} \tag{4}$$

where f_c is the compressive concrete strength, A_{vy} is the total area of vertical reinforcement and f_y is the yield strength of rebar.

$$\Delta_0 = \frac{V_u}{K_{eff}} \tag{5}$$

$$K_{eff} = \frac{12 E I_w}{h_w^3} \cdot \frac{19}{f_y} \left(0.53 + 0.37 \frac{h_w}{L_w} + 0.31 \frac{h_w^2}{L_w^2} \right) \tag{6}$$

3.2 Analysis Results

The displacement responses predicted by the aforementioned 'original model' with the recorded ground motion in the longitudinal (x) direction are compared with those obtained by integrating the accelerograms at each floor levels in Figure 9. It is obvious that the original model much over-estimated the displacement response of G3 Building during the earthquake. By referring to the microtremor observation during the construction of the retrofit (Hirano *et al.*, 2011), it is also obvious that the initial fundamental periods of vibration of the original model both before and after the retrofit are considerably longer than the observed ones (Table 1). The fundamental period of the modified model becomes 0.52 s before retrofit and 0.49 s after retrofit (with the pin-supported walls and the dampers). These values become much closer to those obtained by microtremor observation (0.51 s and 0.47 s before and after the retrofit, respectively, see Table 1) than those of the original model.

Table 1 Fundamental period of vibration (unit: s)

	Monitored	Original model	Modified model
Before retrofit (Initial)	0.51*	0.86	0.52
After retrofit (Initial)	0.47*	0.68	0.49
During Tohoku earthquake	0.65	0.81	0.65

* Microtremor results in Hirano *et al.* (2011)

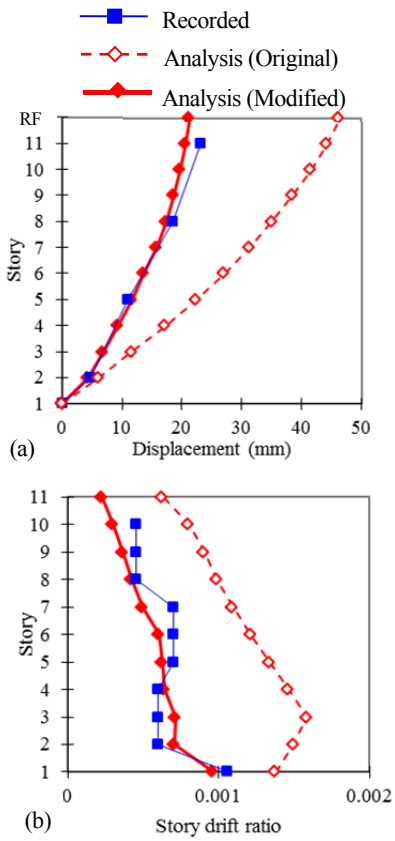


Figure 9 Displacement response of the G3 building

As can be seen in Figure 9, the prediction of the seismic displacement response of G3 Building by the modified model is significantly improved. This is also evident from Figure 10, which compares the response spectra of the acceleration time histories recorded during the earthquake and those predicted by the modified model at floors where an accelerometer is placed. The two sets of spectra match well with each other. The modified model seems capable of capturing the dominant period of vibration for both the 1st and the 2nd equivalent modes of the building in its inelastic state.

However, the time history response obtained by the analysis does not match the observation as well as the maximum response. Take the displacement at 11F for example. Figure 11 compares the time history displacement response from 50 s to 200 s of the earthquake. It is seen that the analysis result succeeded in capturing the maximum response at around 135 s. However, it underestimated the displacement response in the following 20 s. The responses in duration of 12 s from 92 s to 104 s and from 132 s to 144 s are enlarged in Figure 11 (b) and (c). The elongation of period of vibration can be seen by comparing the two figures.

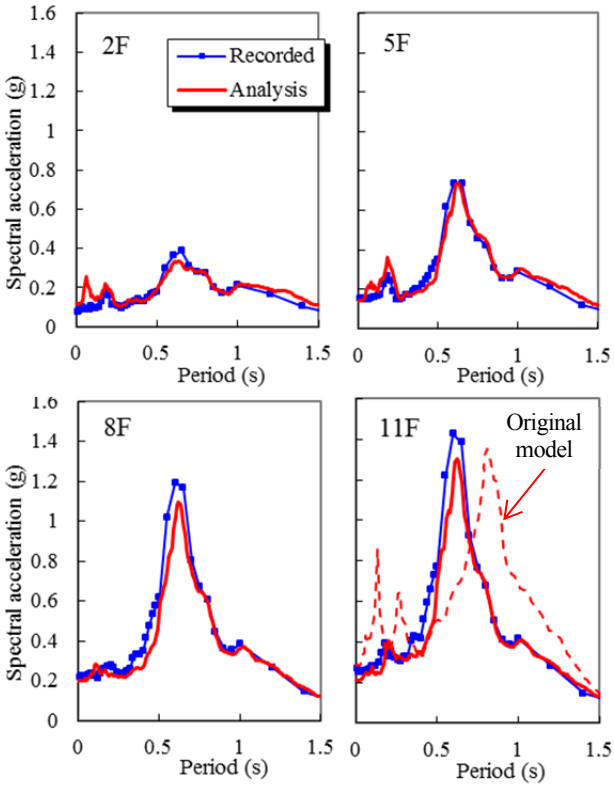


Figure 10. Acceleration spectra of floor motions (modified model, 5% damping)

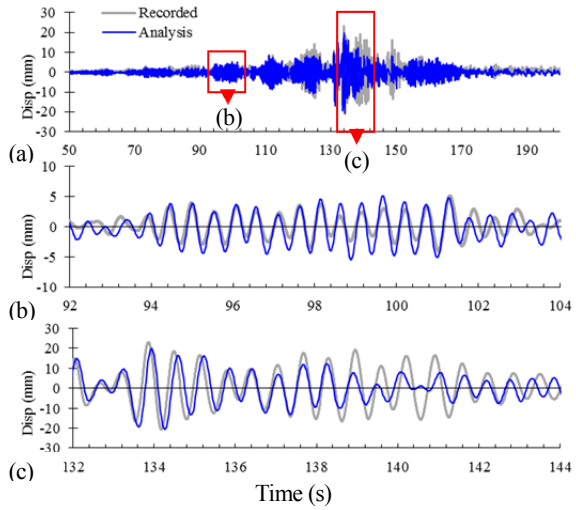


Figure 11. Displacement time history responses at 11F

In addition, Figure 12 summarizes the damage of the steel dampers and the partition walls. They generally agree with the observations after the earthquake. Several steel dampers in the lower stories slightly yielded during the earthquake and the maximum ductility factor is only around two. At the same time, most of the partition walls have cracked.

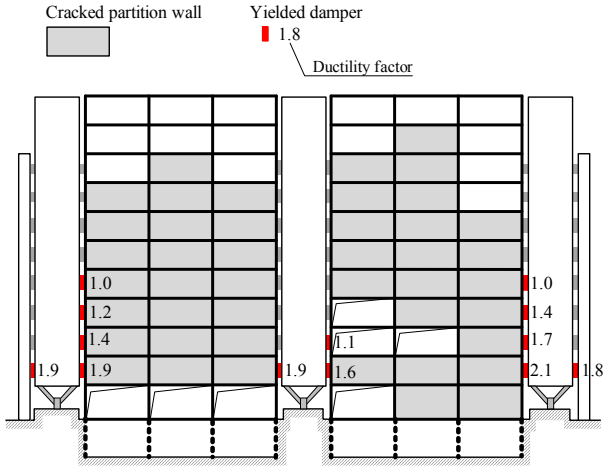


Figure 12. Damage to G3 Building predicted by modified model.

4. DISCUSSION

From the modified model for the retrofitted G3 Building, the model for the building before retrofit can be obtained simply by removing the pin-supported walls and the steel dampers from the modified model. The comparison between the seismic response of the two models, one before and the other after the retrofit, will help understand the effect of the retrofit.

Although the maximum inter-story drift would have been much larger if the building was not retrofitted before the earthquake hit, the building should have been quite safe in both cases, whether retrofitted or not, for the maximum inter-story drift ratio would not have exceeded 1/600 (Figure 13(a)). Under such small deformations, the concrete frame remains essentially elastic and the controlling of its deformation distribution is not critical for its seismic performance. Meanwhile, most energy dissipation goes to the partition walls in both cases (i.e., before and after the retrofit), which attract very large lateral force and cracked at a very early stage. Since only some of the steel dampers are slightly yielded, the energy dissipation of the dampers is quite limited (Figure 14(a)). In this case, although the partition walls are not specifically detailed for energy dissipation, they did work like large dampers in protecting the rest of the structure by dissipating energy.

Nevertheless, the retrofit would prove its value if the ground motion is strong enough to bring significant damage to the building. To give an example, if the recorded ground motion is scaled to PGV = 50 cm/s, which generally corresponding to a Level-II scenario in the seismic design practice in Japan, and is used as a ground motion input for the analysis models of G3 Building, it would make a substantial difference whether it is retrofitted or not. As suggested by the analysis results, the G3 Building without retrofit would collapse at its first floor under the scaled ground motion, while the retrofitted one would exhibit quite uniformly distributed story drift and would not experience weak story failure (Figure 13(b)). In addition, it can be seen from Figure 14(b) that the partition walls would quickly lose

their energy dissipation capacity because of their brittle nature and most of the hysteretic energy dissipation would go to the frame columns in the un-retrofitted building and to the steel dampers in the retrofitted one.

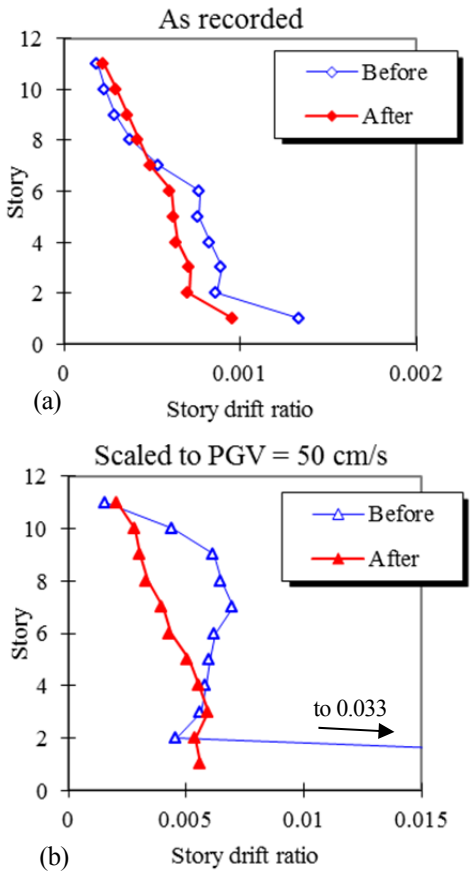


Figure 13 Deformation response of G3 Building predicted by modified model

5. CONCLUDING REMARKS

The vibration and damages of G3 Building, which has pin-supported wall-frame dual lateral system, in the M9.0 Tohoku earthquake is introduced. The observation suggests that the pin-supported walls were forced to rotate as intended and suffered no visible damage during the earthquake. A detailed numerical model of the building was calibrated by incorporating the recorded motions on the building. The significant effect of nonstructural partition walls on the dynamic behavior of the building under small or moderate earthquakes was recognized.

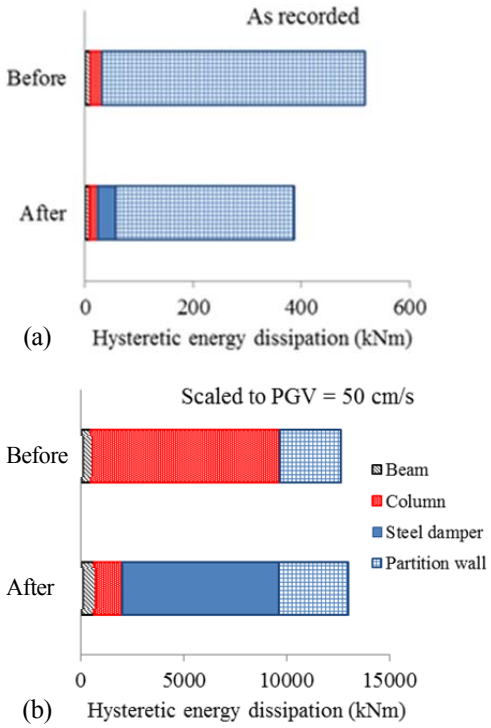


Figure 14 Hysteretic energy dissipation in G3 Building predicted by modified model

References:

BCJ. (2004) Building standard law of Japan. The Building Center of Japan, Tokyo.

Gulec, C.K., Whittaker, A.S. and Stojadinovic, B. (2008) Shear strength of squat rectangular reinforced concrete walls. *ACI Structural Journal*, **105**(4): 488-497.

Hirano, Y., Midorikawa, S., Miura, H., Motoyui, S. and Wada, A. (2011) Seismic behavior of SRC building retrofitted by rocking wall: Part 1. Change of natural period of building. *Summaries of technical papers of AIJ annual meeting*, B2: 347-348.

Li, B. and Xiang, W.Z. (2011) Effective stiffness of squat structural wall. *Journal of Structural Engineering, ASCE*, **137**(12): 1470-1479.

Miura, H., Midorikawa, S., Hirano, Y., Motoyui, S., Wada, A. (2011) Seismic behavior of SRC building retrofitted by rocking wall: Part 2. Seismic behavior during the 2011 Tohoku earthquake. *Summaries of technical papers of AIJ annual meeting, B2*: 349-350.

Qu, Z., Wada A., Motoyui, S., Sakada H. and Kishiki, S. (2012) Pin-supported walls for enhancing the seismic performance of building structures. *Earthquake Engineering & Structural Dynamics*, IDO: 10.1002/eqe.2175

Wada, A., Qu, Z., Ito, H., Motoyui, S., Sakata, H. and Kasai, K.. (2009) Seismic retrofit using rocking walls and steel dampers. *Proc. ATC/SEI Conference on Improving The Seismic Performance of Existing Buildings and Other Structures*, San Francisco, CA, US: 1010-1021.

Wood, S.L. (1990) Shear strength of low-rise reinforced concrete walls. *ACI Structural Journal*, **87**(1): 99-107.

10CUEE CONFERENCE PROCEEDINGS
10th International Conference on Urban Earthquake Engineering
March 1-2, 2013, Tokyo Institute of Technology, Tokyo, Japan

STUDY ON THE ROCKING EFFECT OF AN EIGHT-STORY SRC BUILDING

Ligang Li[1], Toshihide Kashima[2], Akihiro Nakamura [3] and Masaomi Teshigawara [4]

1) Ph.D. student, Graduate School of Environmental Studies, Nagoya University, Japan
2) Senior Research Engineer, Building Research Institute, Japan
3) Professor, Graduate School of Environmental Studies, Nagoya University, Japan
4) Assistant Professor, Graduate School of Environmental Studies, Nagoya University, Japan
liligang@dali.nuac.nagoya-u.ac.jp, kashima@kenken.go.jp, nakamura@dali.nuac.nagoya-u.ac.jp
teshi@corot.nuac.nagoya-u.ac.jp

Abstract: Rocking effect is an important influence factor for the earthquake response of the building. This paper is about the study of the SSI effect through analyzing the measurement earthquake response of the building. The research building is an eight-story SRC building (the ANX building) which is one of the stations of the Building-Research-Institute strong motion network. 13 strong earthquake records from 1998 to 2011 are selected for the research in this paper.

This paper made use of the measurement data to calculate the component motion ratios (rocking, swaying and deformation of the superstructure), and also calculated the modal parameters (fundamental frequency, damping ratio and modal shapes) through the structure identification technology.

The calculation results show that: (1) the rocking effect is the major SSI effect of ANX building, (2) rocking effect and fundamental frequency decrease with the increase of the IJMA (seismic instrument intensity); and by comparing the fundamental frequency of the 1998 and 2011, we can find that the fundamental frequency is halved, which indicates that the superstructure stiffness decreased a lot and there may be some damage in the superstructure, (3) damping ratio becomes lager when the IJMA and PGA are outstanding, especially in 2011/03/11 TOHOKU earthquake, which means there may be much nonlinearities contributing to the damping of the building.

1. INTRODUCTION

Measurement data of the strong earthquake response is very significant for understanding the dynamic characteristics of the building, especially for the complicated SSI effect. In the past decades, some advanced accelerometers appeared and were applied in the earthquake engineering. As a result, a lot of relatively accurate measurement data could be accumulated. Because of that, many researchers made much important work through the measurement data of the earthquake response and improved the understanding of the dynamic response of the building and soil. However, although there are much research in the observation of the building response and SSI effect etc. these measurement data concerns only one or several specific buildings. Generally, different buildings have different properties and the earthquake response depends on the characteristics of the buildings (JENNINGS and BIELAK, 1973). Consequently, much more work needs to be made to enlarge the understanding of many other kinds of buildings, this paper focuses on a kind of low-rise SRC building which the longitudinal-direction length (26m) is not so different from the transverse-direction length (21m).

The building is the BRI-ANNEX (ANX) building which is one of the stations of the BRI strong motion network and installed 22 strong motion accelerometers. The ANX building is an 8-story SRC frame building, 11 acceleration meters are installed in the building and 7 acceleration meters are installed on the ground and in the soil, the distribution of the acceleration meters in the building is shown in Figure 1.

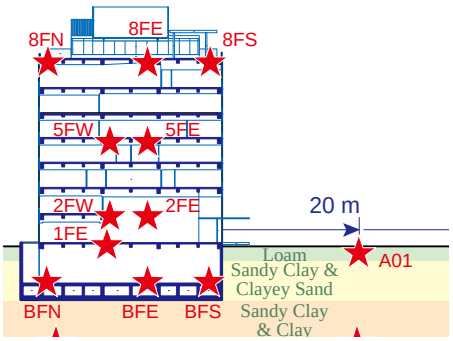


Figure 1 Distribution of the acceleration meters

The detailed information of the ANX building can be found in KASHIMA (2004 and 2006). For this paper, measurement data of 11 acceleration meters is selected which are BFE, BFN, BFS (base floor); 2FW, 2FE (second floor); 5FW, 5FE (fifth floor); 8FE, 8FN, 8FS (roof floor)

and A01 (free field). Each acceleration meter can record 3-direction motions, which are East-West motion (X direction), South-North motion(Y direction), Up-Down motion (Z direction).

This paper mainly concerns on the relationship between SSI effect (especially for rocking effect) and the modal parameters (fundamental frequency, damping ratio and fundamental modal shapes) of ANX building. In the past years, many researchers also made some research about those aspects. LUCO and TRIFUNAC etc. (1987) researched the dynamic behavior of Millikan library building, a nine-story RC building, which was also studied by other researchers before them. Their paper showed that SSI effect and dynamic properties of the building were different even conflicted with each other in different periods, especially for the contribution of rocking response to the SSI effect. They thought that these confliction and difference may come from the data errors. They also thought that the loss of the superstructure stiffness and soil stiffness caused the permanent reduction of the fundamental frequency. TRIFUNAC and IVANOCIC' etc. (2001) analyzed the earthquake response data and ambient response data of VN7SH building through Fourier analysis and time-frequency analysis, they also found that the fundamental frequency of the building changed from earthquake to earthquake, but they believed that this changes resulted from the nonlinearity of the foundation-soil response. TRIFUNAC etc. also thought that the foundation soil has the capability of the absorbing the energy and recovering stiffness. KASHIMA etc. (2006) selected earthquake records of ANX building from 1998 to 2005, he used an optimization algorithm-Evolution Strategies to simulate the ANX building earthquake response and got the dynamic properties of the corresponding MDOF model, he thought that the fall of the fundamental frequency is caused by the change of the superstructure. Totally, it can be confirmed that the fundamental frequency of the building are unstable, but we need to know how the SSI effect changes which is tightly related with the fundamental frequency; besides, other dynamic parameters such as damping ratio and modal shape needs to be studied.

This paper can be considered as the extension of research of KASHIMA (2006). Just as previously mentioned, KASHIMA (2006) selected the earthquake records of ANX building from 1998 to 2005, while for this paper is from 1998 to 2011. This paper consists of three simple basic theory and research methods, which include: (1) the methods about how to get the relatively pure rocking motion, swaying motion, and deformation motion of each floor. The key point of the methods is the application of the vector theory such as the application of the normal vector of the base mat; (2) the structure identification method---curve fitting method is used to get the modal parameters such as fundamental frequency, damping ratio and modal shapes. The calculation of the transfer function is rigorously based on the theory of the modal analysis, which is different from the method brought out by STEWART (1998); (3) the simplified SSI SDOF model is used to analyze the relationship between fundamental frequency and rocking effect, frequency of the superstructure.

2. BASIC THEORY AND RESEARCH METHODS

2.1 Calculation Methods of the Component Motions

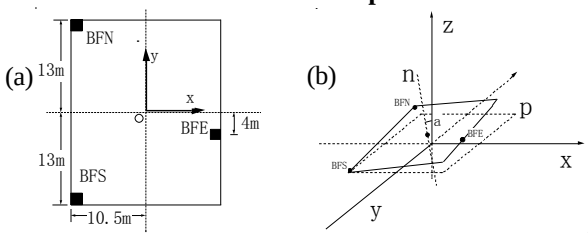


Figure 2 Rocking motion of the base floor

2.1.1 Calculation of the Rocking Angle

Calculation assumptions are as follows, (1) the base mat is considered as a rigid plane, and it has five-direction motions: x-direction horizontal motion, y-direction horizontal motion, vertical motion, torsional motion and rocking motion; (2) Normal vectors of the base mat is only related with the rocking motion, which means the horizontal motions, vertical motion and torsional motion do not affect the normal vectors of the base mat.

Just as shown in Figure 2(b), the base mat p will rock in the space, the normal vector $\vec{n}$ can be accepted as the expression of the rocking motion. And $\vec{n}$ is used to calculate the rocking angle a of the base mat, $\mathrm{BFN}(x_1, y_1, z_1)$, $\mathrm{BFE}(x_2, y_2, z_2)$ and $\mathrm{BFS}(x_3, y_3, z_3)$ are the three points and vectors $\vec{p}$, $\vec{q}$ are two vectors on the base mat, we can calculate the two vectors,

$$\vec{p} = \mathrm{BFN}(x_1, y_1, z_1) - \mathrm{BFE}(x_2, y_2, z_2) \quad (1a)$$

$$\vec{q} = \mathrm{BFS}(x_3, y_3, z_3) - \mathrm{BFE}(x_2, y_2, z_2) \quad (1b)$$

Because $\vec{n} = (x_n, y_n, z_n)$ is the normal vector of the base mat and $\vec{p}$ and $\vec{q}$ are two non-parallel vectors on the base mat, so $\vec{n}$ is normal with $\vec{p}$ and $\vec{q}$, then

$$\vec{n} = \vec{p} \times \vec{q} \quad (2)$$

Select a unit vector on the Z axis, which is $\vec{u} = (0, 0, 1)$. Then the angle between normal vector n and z-axis unit vector $\vec{u}$ is the rocking angle, which can be calculated as follows

$$\cos a = \frac{|z_n|}{\sqrt{x_n^2 + y_n^2 + z_n^2} \times \sqrt{1}}$$

Namely the rocking angle is

$$a = \arccos \frac{|z_n|}{\sqrt{x_n^2 + y_n^2 + z_n^2} \times \sqrt{1}} \quad (3)$$

Normal vector $\vec{n}$ has been normalized and the length is 1, so the projection of the normal $\vec{n}$ on the XOZ plane is (x_n, z_n) and on the YOZ plane is (y_n, z_n), which are shown in Figure 3. The rocking angle a is small, so $\cos a \approx 1$, then $|z_n| \approx 1$. Similarly, the X-direction angle a_x and Y-direction angle a_y are small, according to the

geometry shown in Figure 3, the rocking angle a_x and a_y are calculated as follows: $a_x \approx \tan a_x$ and $\tan a_x = x_n/z_n$, so $a_x \approx x_n$; similarly, $a_y \approx y_n$.

Example: According to the above calculation method, an earthquake happened in 2002/06/14 is selected to calculate the rocking angle of the building, and the results are shown in Figure 4.

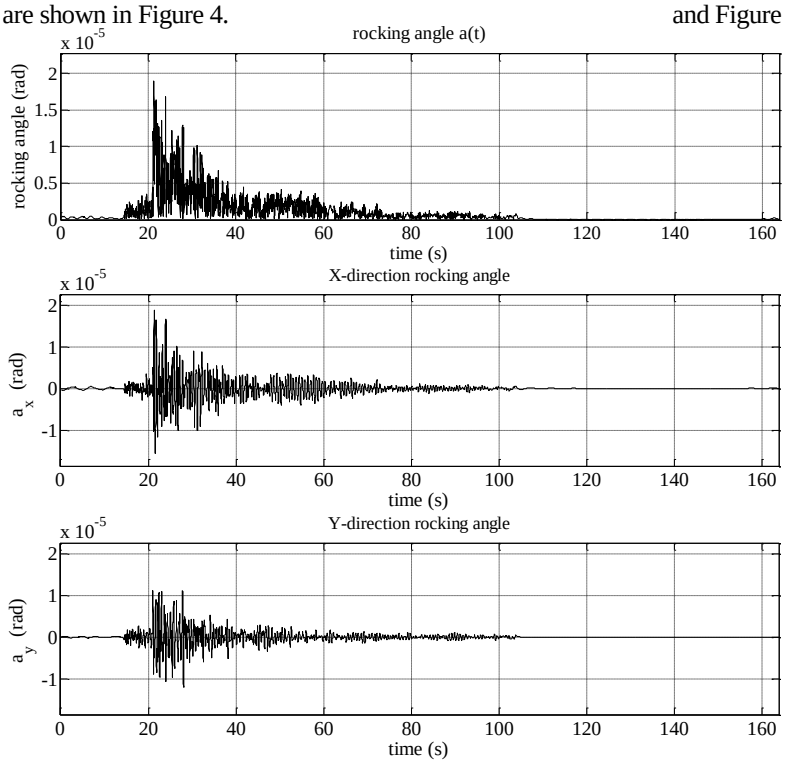


Figure 4 Rocking angle of the base mat

$$X_8 = 0.5[0.5(X_{8FN} + X_{8FS}) + X_{8FE}] \quad (7a)$$

$$Y_b = 0.5[0.5(Y_{8FN} + Y_{8FS}) + Y_{8FE}] \quad (7b)$$

Where, X_i and Y_i are the measurement motions corresponding to the measurement points shown in Figure 5 and Figure 1.

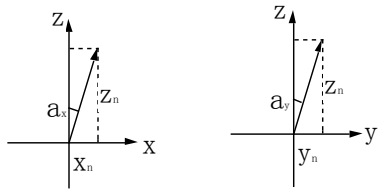


Figure 3 Projections of the normal vector $\vec{\mathbf{n}}$

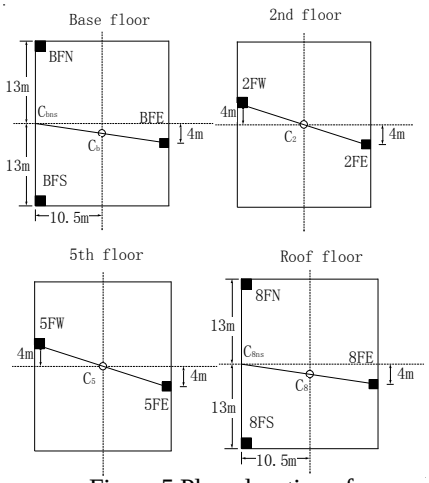


Figure 5 Plane-location of the measurement points

2. 1.2 Calculation of Motions of the Specific Floors

The object of this part is to find the motion at the center point and delete the influence of the torsional effect. The measurement points of base floor, second floor, fifth floor and the roof floor are shown in Figure 5.The motions of the center point can be calculated as follows.

<1> Center of the base floor C_b (X_b, Y_b)

$$X_b = 0.5[0.5(X_{BFN} + X_{BFS}) + X_{BFE}] \quad (4a)$$

$$Y_b = 0.5[0.5(Y_{BFN} + Y_{BFS}) + Y_{BFE}] \quad (4b)$$

<2> Center of the 2nd floor C_2 (X_2, Y_2)

$$X_2 = 0.5(X_{2FW} + X_{2FE}) \quad (5a)$$

$$Y_2 = 0.5(Y_{2FW} + Y_{2FE}) \quad (5b)$$

<3> Center of the 5th floor C_5 (X_5, Y_5)

$$X_5 = 0.5(X_{5FW} + X_{5FE}) \quad (6a)$$

$$Y_5 = 0.5(Y_{5FW} + Y_{5FE}) \quad (6b)$$

<4> Center of the roof floor C_8 (X_8, Y_8)

After the previous analysis, now the separation of the motion components including the rocking motion, swaying motion, deformation motion of the building can be carried out as follows, the similar method can also be found in other researcher' work such as Kashima (2006).

$$u_{rocki} = H_i \times a_{base} \quad (8a)$$

$$u_{sway} = u_{base} - u_{ground} \quad (8b)$$

$$u_{defi} = u_{oi} - u_{ground} - u_{rocki} - u_{sway} \quad (8c)$$

$$u_{totali} = u_{oi} - u_{ground} \quad (8d)$$

Where

H_i --- Height of the ith floor.

a_{base} --- Rocking angle of the base floor, which is a_x and a_y.

u_{rocki}--- Displacement caused by the rocking effect of the ith floor.

u_{sway}--- Displacement caused by the swaying effect.

u_{base}--- Displacement of the center of the base floor.

u_{ground}---Ground motion.

u_{defi}--- Deformation of the superstructure for the ith floor.

u_{totali}---Total displacement including swaying, rocking and superstructure deformation for the ith floor.

u_{oi}---Displacement of the center point of the ith floor.

Through the above method, the relatively pure motion components including rocking motion, swaying motion and deformation motion can be calculated. These data will be used to analysis the rocking effect and structural identification, which will be introduced later.

2.2 Structure Identification

The ANX building is modeled as shown in Figure 6, this model has 8 masses and the corresponding inertias and stiffness; soil stiffness is modeled by rocking spring and swaying stiffness. After the previous analysis, it is clear that the response of the building can be achieved through the geometry calculation.From the recording data, the rocking motion, swaying motion and deformation motion of the superstructure can be calculated. The dynamic equation of model in Figure 6 can be written as follows,

$$[M]\left[\ddot{U}^T\right]+[C]\left[\dot{U}\right]+[K][\mathrm{U}]=0 \tag{9a}$$

$$\sum_{i=1}^{7} m_i\ddot{u}_i^T+m_0(\ddot{u}_s+\ddot{u}_g)+c_s\dot{u}_s+k_su_s=0 \tag{9b}$$

$$\sum_{i=1}^{7} m_i\ddot{u}_i^T h_i+I_t\ddot{a}+c_R\dot{a}+k_Ra=0 \tag{9c}$$

Where $u_i^T=u_i+u_s+h_ia+u_g$, u_i^T is the total displacement of the corresponding m_i, u_i is the story deformation for m_i, u_s is the swaying motion, a is the rocking angle, u_g is the free field ground motion, and $I_t=\sum_{i=0}^{7} I_i$. Equations (9a) (9b) (9c) can be rewritten as follows,

$$\left[\widehat{M}\right]\left[\ddot{\mathrm{U}}\right]+\left[\hat{C}\right]\left[\dot{\hat{U}}\right]+\left[\widehat{K}\right]\left[\widehat{\mathrm{U}}\right]=-\left[\widehat{M}\right][v]\ddot{u}_g \tag{10}$$

From the measurement data, we can get u_1, u_4, u_7 (where u_1 is the deformation of the 2nd floor, u_4 for the 5th floor and u_7 for the roof floor), u_s (swaying motion)and a (rocking motion); the input data is the ground motion $\ddot{u}_g$. The structure-identification model is SIMO (single input multi-output) model. Through the FT technology and the theory of the transfer function by He & Fu (2001), then

$$\frac{\mathcal{F}\mathrm{u}_r}{\mathcal{F}\ddot{u}_g}=\mathrm{H}_r(\omega)=-\sum_{n=1}^{N}\frac{\sum_{i=1}^{N}\varphi_{rn}\varphi_{in}\tilde{m}_i}{(-\omega^2\bar{m}_n+j\omega\bar{c}_n+\bar{k}_n)} \tag{11}$$

Let $A_{rn}=\frac{\sum_{i=1}^{N}\varphi_{rn}\varphi_{in}\tilde{m}_i}{\bar{m}_n}$, and $\bar{\omega}=\frac{\omega}{\omega_n}$

Then

$$\mathrm{H}_r{}^R(\omega)=-\sum_{n=1}^{N}\frac{A_{rn}(1-\bar{\omega}^2)}{(1-\bar{\omega}^2)^2+4\bar{\omega}^2h_n^2} \tag{12a}$$

$$\mathrm{H}_r{}^I(\omega)=\sum_{n=1}^{N}\frac{A_{rn}(2\bar{\omega}h_n)}{(1-\bar{\omega}^2)^2+4\bar{\omega}^2h_n^2} \tag{12b}$$

$$|\mathrm{H}_r(\omega)|=\sqrt{\mathrm{H}_r{}^R(\omega)^2+\mathrm{H}_r{}^I(\omega)^2} \tag{12c}$$

Through transfer function, there are many classic frequency domain methods --- curve fitting methods used for the structure identification. In this paper, a simple SDOF method is used for the structure identification. Based on the theory of component analysis of the transfer function by He & Fu (2001), several analysis procedures can be used as follows.

Table 1 Input-output pairs and transfer function

input	output	Transfer function	Indicator	Fundamental frequency	Damping ratio	Modal shape
$\ddot{u}_g$	u_1	$\mathbf{H_1}(\boldsymbol{\omega})=\frac{\mathcal{F}\mathrm{u}_1}{\mathcal{F}\ddot{u}_g}$	**TF1**	w_{11}	h_{11}	$\frac{A_{11}}{2h_1}$
	u_4	$\mathbf{H_4}(\boldsymbol{\omega})=\frac{\mathcal{F}\mathrm{u}_4}{\mathcal{F}\ddot{u}_g}$	**TF2**	w_{14}	h_{14}	$\frac{A_{41}}{2h_1}$
	u_7	$\mathbf{H_7}(\boldsymbol{\omega})=\frac{\mathcal{F}\mathrm{u}_7}{\mathcal{F}\ddot{u}_g}$	**TF3**	w_{17}	h_{17}	$\frac{A_{71}}{2h_1}$
	a	$\mathbf{H_a}(\boldsymbol{\omega})=\frac{\mathcal{F}a}{\mathcal{F}\ddot{u}_g}$	**TF4**	w_{1a}	h_{1a}	$\frac{A_{a1}}{2h_1}$

<1> Calculation of the transfer functions

From the above analysis, several input-output pairs will be configured shown in Table 1. Because in this research the swaying effect is very small and the swaying motion is susceptible for the noise, then the transfer function for the swaying motion is not good, so the identification model only uses four transfer functions to get the modal parameters of the building, which are shown in Table 1.

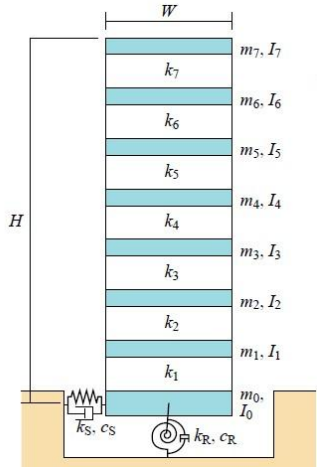


Figure 6 SSI model (Kashima 2006)

<2> Calculation of the modal parameters

In order to reduce the calculation error, the fundamental frequency w_1 and damping ratio h_1 will be calculated as follows,

$$w_1=1/4\ (w_{11}+w_{14}+w_{17}+w_{1a}) \tag{13}$$

$$h_1=1/4\ (h_{11}+h_{14}+h_{17}+h_{1a}) \tag{14}$$

for the implicit part $\mathrm{H}_r{}^I(\omega)$ of the Transfer function,

$$[Q]=\left[\frac{A_{11}}{2h_1}\quad\frac{A_{41}}{2h_1}\quad\frac{A_{71}}{2h_1}\quad\frac{A_{a1}}{2h\xi_1}\right]^T \tag{15a}$$

namely

$$[Q]=[\varphi_{11}\quad\varphi_{41}\quad\varphi_{71}\quad\varphi_{a1}]^T\frac{1}{2h_1}\frac{\sum_{i=1}^{N}\varphi_{i1}\tilde{m}_i}{\bar{m}_1} \tag{15b}$$

Vector $[Q]$ is normalized to be as follows

$$[\phi] = \begin{bmatrix} \frac{\varphi_{11}}{\varphi_{71}} & \frac{\varphi_{41}}{\varphi_{71}} & 1 & \frac{\varphi_{a1}}{\varphi_{71}} \end{bmatrix}^T \quad (16)$$

Where $[\phi]$ is the modal shape. Similarly, if we use the modulus of the $H_r(\omega)$, we can also get the same modal shapes.

2.3 Influence of SSI Effect on the Fundamental Frequency

For the superstructure, it is usually modeled as a lumped mass system. As the first mode is mostly influenced by the SSI effect, then the building is always modeled as an equivalent-single-degree system on the flexible base, which is shown in Figure 7. In order to get brief expression of the fundamental frequency of the SSI model in Figure 7, the rotational inertia of the superstructure and the mass of the foundation are neglected (Stewart, 1998), then the free vibration equations of the SSI model in Figure 7 are shown as follows.

$$\mathrm{m}\left(\ddot{u}_f + \mathrm{h}\ddot{\theta} + \ddot{u}\right) + ku = 0 \quad (17a)$$

$$\mathrm{m}\left(\ddot{u}_f + \mathrm{h}\ddot{\theta} + \ddot{u}\right) + k_u u_f = 0 \quad (17b)$$

$$\mathrm{mh}\left(\ddot{u}_f + \mathrm{h}\ddot{\theta} + \ddot{u}\right) + k_\theta \theta = 0 \quad (17c)$$

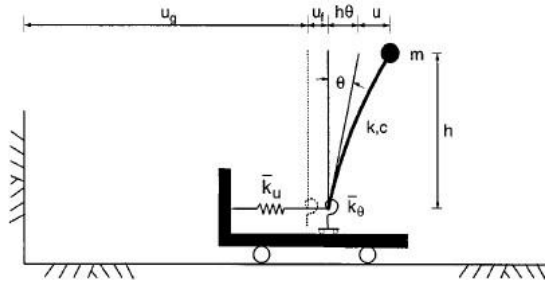


Figure 7 Simplified SSI model (Stewart, 1998)

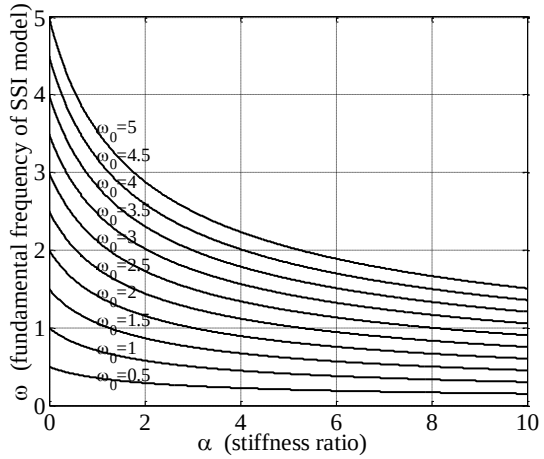


Figure 8 Fundamental frequency of the SSI model

Apply the Fourier Transformation to the equation (17), then $\mathcal{F}\left(\ddot{u}_f\right) = -w^2\hat{u}_f$, $\mathcal{F}\left(\ddot{\theta}\right) = -w^2\hat{\theta}$, $\mathcal{F}(\ddot{u}) = -w^2\hat{u}$, $\mathcal{F}\left(u_f\right) = \hat{u}_f$, $\mathcal{F}(\theta) = \hat{\theta}$, $\mathcal{F}(\mathrm{u}) = \hat{u}$, then equation (17) will be

$$-\mathrm{m}w^2\left(\hat{u}_f + \mathrm{h}\hat{\theta} + \hat{u}\right) + k\hat{u} = 0 \quad (18a)$$

$$-\mathrm{m}w^2\left(\hat{u}_f + \mathrm{h}\hat{\theta} + \hat{u}\right) + k_u\hat{u}_f = 0 \quad (18b)$$

$$-\mathrm{mh}w^2\left(\hat{u}_f + \mathrm{h}\hat{\theta} + \hat{u}\right) + k_\theta\hat{\theta} = 0 \quad (18c)$$

then equation (18) can be written as follows

$$-w^2\mathrm{m}k_uk_\theta\left(\hat{u}_f + \mathrm{h}\hat{\theta} + \hat{u}\right) + kk_uk_\theta\hat{u} = 0 \quad (19a)$$

$$-w^2\mathrm{m}kk_\theta\left(\hat{u}_f + \mathrm{h}\hat{\theta} + \hat{u}\right) + k_ukk_\theta\hat{u}_f = 0 \quad (19b)$$

$$-w^2\mathrm{mh}^2kk_u\left(\hat{u}_f + \mathrm{h}\hat{\theta} + \hat{u}\right) + k_\theta kk_uh\hat{\theta} = 0 \quad (19c)$$

add the three equations of equation (19), and divided by $\left(\hat{u}_f + \mathrm{h}\hat{\theta} + \hat{u}\right)$ then

$$w^2 = \frac{kk_uk_\theta}{\mathrm{m}k_uk_\theta + \mathrm{m}kk_\theta + \mathrm{mh}^2kk_u} \quad (20)$$

then equation (20) can be written as follows

$$w = \sqrt{\frac{k}{m}}\sqrt{\frac{1}{1+\frac{k}{k_u}+\frac{kh^2}{k_\theta}}} \quad (21)$$

If the swaying effect is very small, which means $\frac{k}{k_u} \approx 0$, then the equation (21) will be

$$w = \sqrt{\frac{k}{m}}\sqrt{\frac{1}{1+\frac{kh^2}{k_\theta}}} \quad (22)$$

For a specific building, we suppose that the mass and the height of the building are stable, while the stiffness of the superstructure and the soil will change. Let ratio between the superstructure and soil is

$$\alpha = \frac{kh^2}{k_\theta}, \omega_0 = \sqrt{\frac{k}{m}}$$

then the equation (22) can be rewritten as

$$w = \omega_0\sqrt{\frac{1}{1+\alpha}} \quad (23)$$

The fundamental frequency of the SSI model is decided by the frequency of the superstructure ω_0 and the structure soil stiffness ratio α.

3. CALCULATION RESULTS

In this part, 13 strong earthquakes happened from 1998-2011 are selected as the calculation object; the calculation results are used to show the rocking effect on the earthquake response. These 13 strong earthquakes are shown in Table 2.

Through the comparison between the rocking ratio and the swaying ratio, we can see that for X direction, the rocking ratio is about from5.61%-13.70% and swaying ratio is about from 0.75%-5.53%; for Y direction, rocking ratio 2.84%-9.81% and swaying ratio is 0.48%-4.53%.The above results show that the rocking ratio is much larger than the swaying ratio. Additionally, X-direction rocking ratio is larger than the Y-direction rocking ratio.

Table 2 Strong earthquakes happened from 1998-2011 and ratios of the component motions

	Time	Epicenter	Depth (KM)	M (degree)	Distance (KM)	PGA (gal)	IJMA (degree)	X-Rocking (%)	X-Swaying (%)	X-Building Deformation (%)	Y-Rocking (%)	Y-Swaying (%)	Y-Building Deformation (%)
1	1998/06/24/ 23:52	South Ibaraki Pref.	68	4.7	3	19.3	2.6	13.70	2.11	84.19	9.81	0.52	89.66
2	1999/03/26/ 08:31	North Ibaraki Pref.	59	5	60	46.3	3.2	12.62	3.75	83.63	6.94	4.10	88.97
3	2000/04/10/ 06:30	South Ibaraki Pref.	55	4.7	7	49.4	3.2	8.83	5.53	85.63	6.90	2.93	90.17
4	2000/07/21/ 03:39	Off IbarakiPref.	49	6.4	104	37.9	3.4	9.09	1.60	89.30	8.47	2.76	88.77
5	2001/07/20/ 06:02	South Ibaraki Pref.	55	5	24	21.9	2.3	9.18	2.00	88.82	7.58	2.34	90.08
6	2002/06/14/ 11:42	South Ibaraki Pref.	57	5.1	13	74.3	3.4	6.56	4.46	88.98	4.68	4.53	90.79
7	2003/05/26/ 18:24	Off Miyagi Pref.	72	7.1	330	29.2	3.2	8.68	2.04	89.28	5.17	2.00	92.83
8	2004/10/06/ 23:40	South Ibaraki Pref.	66	5.7	16	54.5	3.8	8.25	0.86	90.88	5.15	1.29	93.56
9	2005/10/19/ 20:44	Off IbarakiPref.	48	6.3	91	40.2	3.5	6.72	1.60	91.68	2.70	2.92	94.38
10	2007/07/16/ 10:13	Off Jochuetsu, Niigata Pref.	17	6.8	206	19.3	3.6	5.61	2.30	92.08	3.54	0.48	95.98
11	2008/05/08/ 01:45	Off IbarakiPref.	51	7	138	49.6	3.6	6.48	1.41	92.11	3.46	1.65	94.89
12	2009/08/09/ 19:55	South Off Tokaido	333	6.8	367	28.4	3.2	6.13	0.75	93.12	2.73	1.60	95.68
13	2011/03/11/ 14:46	Off Sanriku	24	9	330.3	279	5.3	5.92	2.14	91.95	3.81	2.15	94.04

Table 3 Modal parameters of the building for the 13 strong earthquakes

Time		Epicenter	X direction			Y direction		
			w_1(Hz)	h_1	Modal shape	w_1(Hz)	h_1	Modal shape
1	1998/06/24/ 23:52	South Ibaraki Pref.	2.44	0.039	(0.0641,0.519,1,0.00488)	2.63	0.035	(0.0378,0.523,1,0.00361)
2	1999/03/26/ 08:31	North Ibaraki Pref.	2.16	0.044	(0.0644,0.512,1,0.00479)	2.20	0.054	(0.0364,0.513,1,0.00286)
3	2000/04/10/ 06:30	South Ibaraki Pref.	2.94	0.058	(0.0590,0.488,1,0.00378)	2.95	0.042	(0.0351,0.509,1,0.00290)
4	2000/07/21/ 03:39	Off IbarakiPref.	1.70	0.057	(0.0520,0.491,1,0.00301)	1.67	0.054	(0.0327,0.507,1,0.00324)
5	2001/07/20/ 06:02	South Ibaraki Pref.	2.73	0.046	(0.0543,0.500,1,0.00323)	2.76	0.065	(0.0360,0.512,1,0.00249)
6	2002/06/14/ 11:42	South Ibaraki Pref.	2.50	0.038	(0.0487,0.468,1,0.00277)	2.46	0.042	(0.0342,0.507,1,0.00253)
7	2003/05/26/ 18:24	Off Miyagi Pref.	2.43	0.060	(0.0501,0.478,1,0.00305)	2.43	0.058	(0.0284,0.510,1,0.00158)
8	2004/10/06/ 23:40	South Ibaraki Pref.	2.22	0.050	(0.0542,0.508,1,0.00255)	2.17	0.055	(0.0270,0.509,1,0.00173)
9	2005/10/19/ 20:44	Off IbarakiPref.	1.78	0.058	(0.0523,0.510,1,0.00223)	1.73	0.066	(0.0245,0.514,1,0.00117)
10	2007/07/16/ 10:13	Off Jochuetsu, Niigata Pref.	2.52	0.056	(0.0405,0.470,1,0.00187)	2.50	0.053	(0.0232,0.515,1,0.00109)
11	2008/05/08/ 01:45	Off IbarakiPref.	1.70	0.050	(0.0491,0.503,1,0.00180)	1.61	0.050	(0.0229,0.512,1,0.00116)
12	2009/08/09/ 19:55	South Off Tokaido	1.45	0.065	(0.0396,0.469,1,0.00132)	1.43	0.050	(0.0215,0.516,1,0.00135)
13	2011/03/11/ 14:46	Off Sanriku	1.13	0.091	(0.0535,0.519,1,0.00222)	1.31	0.145	(0.0272,0.527,1,0.00125)

4. PARAMETER ANALYSIS

4.1 Rocking Ratio

Rocking ratios have been calculated in the previous part, the results are shown in Table 2. In this part, several factors are tested to find their relationship with the rocking ratio. These factors include the utility time of the building, peak ground acceleration (PGA) and seismic instrumental intensity (IJMA), which are shown in Figure 9.

In Figure 9, the numbers (1, 2, 3, … , 13) are the indicators of earthquakes happened from 1998-2011 shown in Table 2. Figure 9 shows that the rocking ratio seems to decrease with the increase of the utility time of the building, in the first years the rocking ratio is about 12%-14% (X direction) and 7%-10% (Y direction), but after several year the rocking ratio is about 6% (X direction) and less than 4% (Y direction); it is not clear that the relationship between the rocking ratio and the PGA; however, the rocking ratio seems to decrease with the increase of the IJMA.

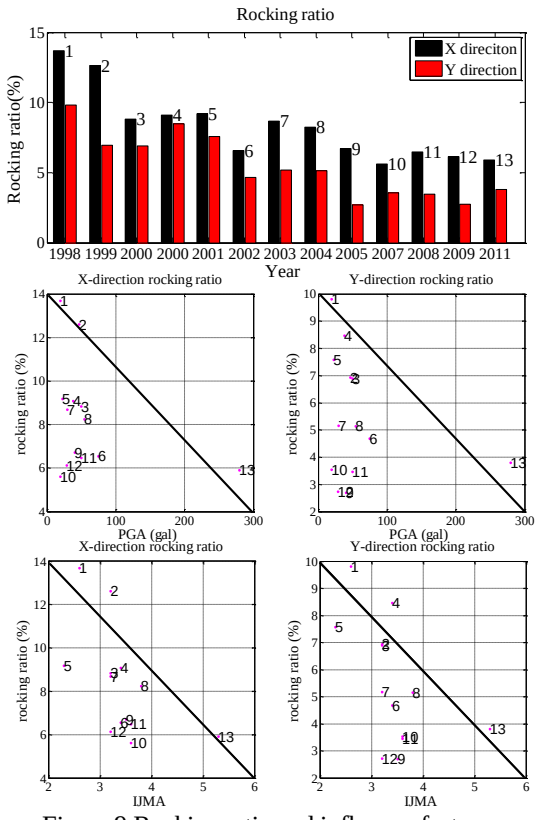


Figure 9 Rocking ratio and influence factors

4.2 Fundamental Frequency w_1

Figure 10 shows the relationship between fundamental frequency and the potential influence factors such as the utility time of the building, PGA, IJMA and the rocking ratios.

As what is shown in the Figure 10, w_1 seems to decrease with the increase of the utility time to some extent; but this trend is not continuous, which means the change of the fundamental frequency maybe very complicated. The change of the fundamental frequency is based on three major

conditions as follows. According to the equation (23) and Figure 8:

Condition 1: if the structure soil stiffness ratio α does not change, the fundamental frequency $\boldsymbol{w_1}$ will decrease when superstructure stiffness decreases; if the superstructure stiffness is stable, the fundamental frequency $\boldsymbol{w_1}$ will decrease when structure soil stiffness ratio α increases.

Condition 2: it is reasonably assumed that the superstructure stiffness decreases, then ω_0 will decrease, and on the condition: (1) if α becomes larger, the fundamental frequency $\boldsymbol{w_1}$ may be become smaller; or (2) if α becomes smaller, there will be two situations, when the influence of the decrease of α is more outstanding than the influence of the decrease of ω_0, $\boldsymbol{w_1}$ will increase, or else $\boldsymbol{w_1}$ will decrease.

Condition 3: it is reasonably assumed that the superstructure increases, then ω_0 will increase, and on the condition: (1) if α becomes smaller, then the fundamental frequency $\boldsymbol{w_1}$ may become larger; or (2) if α becomes larger, there will be two situations, when the influence of the increase of α is more outstanding than the influence of the increase of ω_0, $\boldsymbol{w_1}$ will decrease, or else increase.

By the summary of the above analysis based on equation (23) and Figure 8, we can get some conclusions as follows:

The increase of fundamental frequency $\boldsymbol{w_1}$ is corresponding to the each of the following conditions:

(a) Structure soil stiffness ratio α is fixed, superstructure stiffness increases.

(b) Structure soil stiffness ratio α becomes smaller, and ω_0 decreases; at the same time, the influence of the decrease of α is more outstanding than the influence of the decrease of ω_0.

(c) Structure soil stiffness ratio α becomes smaller, and ω_0 increases.

(d) Structure soil stiffness ratio α becomes larger, and ω_0 increases; at the same time, the influence of the increase of α is less outstanding than the influence of the increase of ω_0.

(e) Superstructure stiffness is fixed, that means ω_0 is stable; and structure soil stiffness ratio α becomes smaller.

The decrease of fundamental frequency $\boldsymbol{w_1}$ is corresponding to each of the following conditions:

(f) Structure soil stiffness ratio α is fixed, and superstructure stiffness decreases.

(g) Structure soil stiffness ratio α becomes smaller, and ω_0 decreases; at the same time, the influence of the decrease of α is less outstanding than the influence of the decrease of ω_0.

(h) Structure soil stiffness ratio α becomes larger, and ω_0 increases; at the same time, the influence of the increase of α is more outstanding than the influence of the increase of ω_0.

(i) Structure soil stiffness ratio α becomes larger, and ω_0 decreases.

(j) Superstructure stiffness is fixed, that means ω_0 is stable; and structure soil stiffness ratio α becomes larger.

On the one hand, from the Figure 9 we learned that the rocking ratio decreases with the increase of the utility time. On the other hand, from the Figure10, $\boldsymbol{w_1}$ has a trend that it decreases with the decrease of the rocking ratio. That phenomenon can be explained as follows: According to the previous analysis, the decrease of the rocking ratio means rocking effect falls and the structure soil stiffness ratio α becomes smaller. Subsequently, only condition (g) is in a good agreement with this situation. That means the ω_0 may decrease which indicates the superstructure stiffness decreases, besides the influence of the decrease of α is far less outstanding than the influence of the decrease of ω_0.

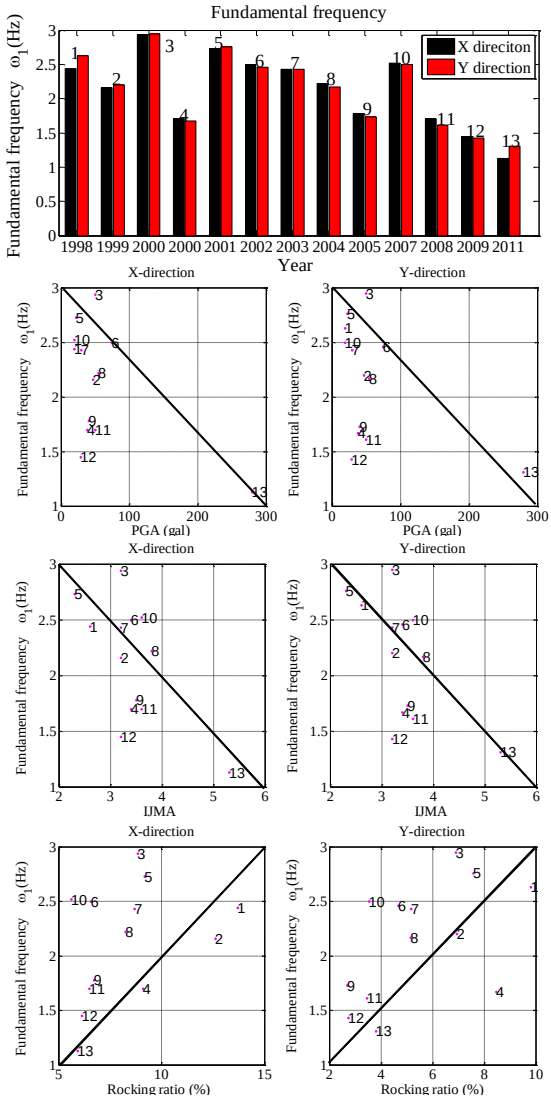


Figure 10 Fundamental frequency and influence factors

Totally, although in the first years the rocking effect is large, the stiffness of the structure is larger. So the fundamental frequency of the building is still on the high level; after several years, although the rocking effect is small, the stiffness of the structure becomes smaller. So the fundamental frequency of the building will be on the low level. KASHIMA (2006) also found the fall of the natural frequency with the increase of the utility time of the building and he thought that the decrease of the fundamental

frequency was caused by the change of the property of the superstructure. The results of this paper show good agreement with his estimation through more data results.

Additionally, the fundamental frequency appears to decrease when the IJMA increases. But this trend for PGA is not clear. It can be easily understood that the larger IJMA means stiffness degradation of the superstructure, then the ω_0 will decrease. The results are in a good agreement with the previous analysis.

By comparing the fundamental frequency of the 1998 and 2011, we can find that the fundamental frequency is halved, which decreases from 2.44Hz to 1.13 Hz (X direction) and 2.63Hz to 1.31Hz (Y direction). Based on the previous analysis, the superstructure stiffness decreased a lot and there may be some damage in the superstructure.

4.3 Damping Ratio h_1

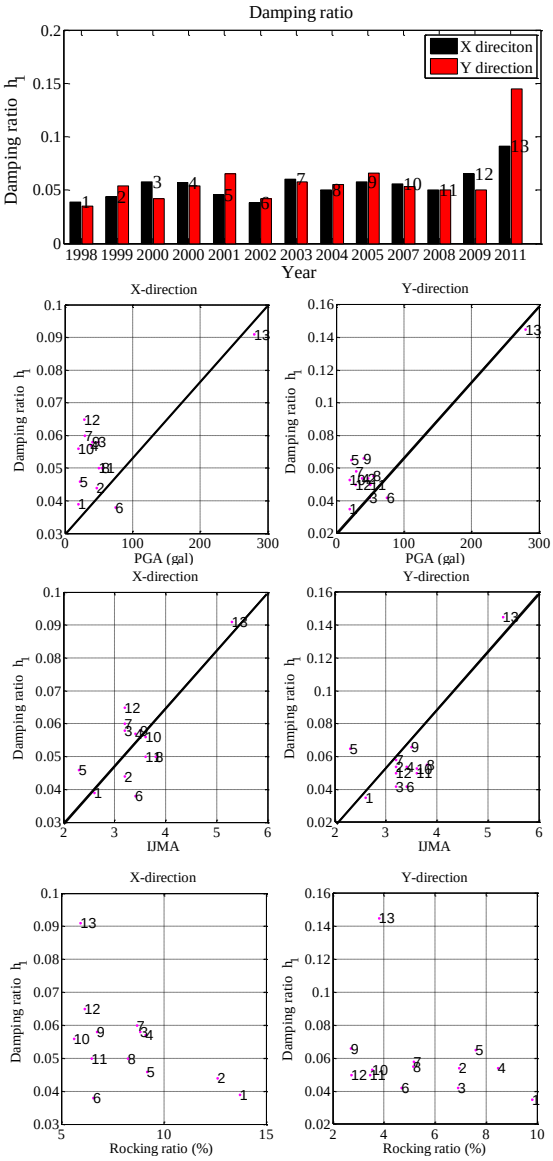


Figure 11 Damping ratio and influence factors

Figure 11 shows the relationship between fundamental frequency and the potential influence factors such as the utility time of the building, PGA, IJMA and the rocking ratios.

Damping ratio is an index of the energy consumption ability of the building. The Figure 11 shows the damping ratio changes with the time, we can see that from 1998-2009 the damping ratio is less than 6.5%, but in 2011/3/11 earthquake the damping ratio becomes very large, which are 9.1% (x direction) and 14.5% (y direction).

Considering that 2011/03/11 earthquake is a very large earthquake (PGA=279.3, IJMA=5.3), there may be much nonlinearities (maybe structure damage) contributing to the damping of the building during the earthquake. And the damping ratio seems to increase when the IJMA or PGA increases. But for the rocking ratio, it has small or no correlation with the damping ratio.

4.4 Rocking Mode (Component of Modal shape)

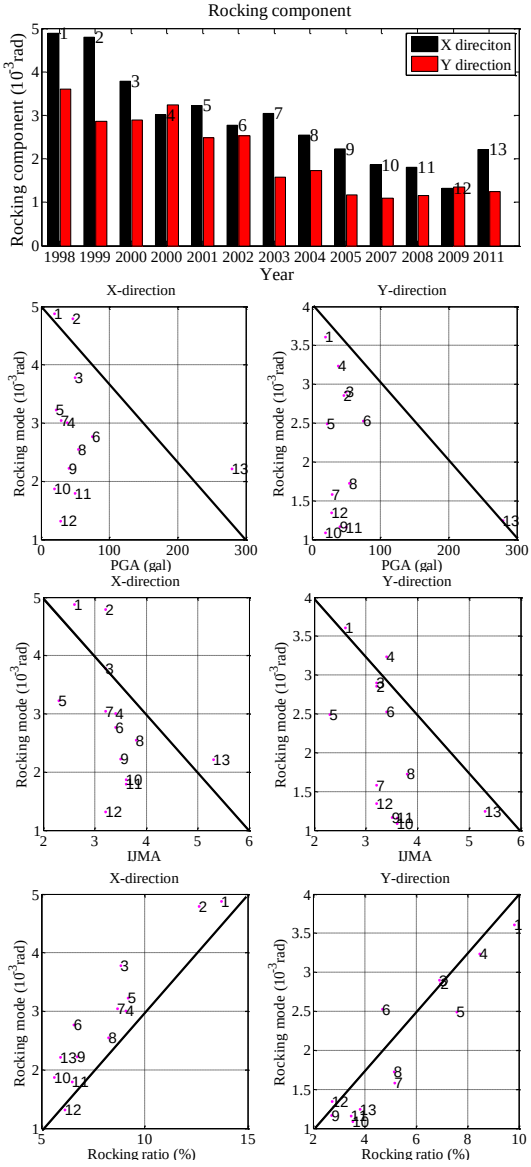


Figure 12 Rocking mode and influence factors

Rocking mode (rocking component of the modal shape) is the rocking angle of the modal shape Table 3.

Figure 12 shows the relationship between fundamental frequency and the potential influence factors such as the utility time of the building, PGA, IJMA and the.rocking ratios. Rocking mode is also the measurement of the rocking effect, which is similar with previous rocking ratio. Figure 12 shows that the rocking mode seems to decrease with the increase of the utility time of the building, in the first years the rocking mode is about 0.00488 rad (X direction) and 0.00361 rad (Y direction), but after several year the rocking mode becomes smaller and it is less than 0.0025 rad (X direction) and less than 0.0015 rad (Y direction); it is not clear that the relationship between the rocking ratio and the PGA either; however, the rocking ratio seems to decrease with the increase of the IJMA.

More importantly, the rocking mode has a good agreement with the rocking ratio. The rocking mode increases with the increase of the rocking ratio.

5 CONCLUSION

This research calculated each component motions of the building response, and identified the modal parameters through the spectrum curve fitting method. The parameter analysis is based on the SDOF SSI model. Several conclusions can be made as follows:

(1) Three measurement points located on the base mat is benifical for getting relatively pure rocking motion; two measurements on the floor will be helful to elimate the torsional effect and get relatively pure horzontal motions of the corresponding floors.

(2) X-direction rocking ratio is about from5.61%-13.70% and swaying ratio is about from 0.75%-5.53%; Y-direction rocking ratio 2.84%-9.81% and swaying ratio is 0.48%-4.53%. The above results show that the rocking effect is much larger than the swaying effect. Additionally, although the X-direction length is 21 meters and Y-direction length is 26 meters, X-direction rocking effect is apparently larger than the Y-direction rocking effect.

(3) Rocking mode has a good agreement with the rocking ratio. The rocking mode decreases with the decrease of the rocking ratio. Rocking ratio and rocking mode seem to decrease with the increase of the IJMA. In fact, the larger IJMA or PGA means more nonlinearity and structure damage which account for the stiffness degradation, especially for the superstructure.

(4) Fundamental frequency $\boldsymbol{w_1}$ has a trend that it decreases with the decrease of the rocking ratio and rocking ratio. This phenomenon will happen only on the condition that structure soil stiffness ratio α becomes smaller (it has been confirmed by the decrease of the rocking ratio and rocking mode), and ω_0 decreases; at the same time, the influence of the decrease of α is less outstanding than the influence of the decrease of ω_0. So it is reasonable thought that the decrease of the fundamental frequency is mainly caused by the stiffness degradation of the superstructure. By comparing the fundamental frequency of the 1998 and 2011, we can find that the fundamental frequency is halved, which decreases from 2.44Hz to 1.13 Hz (X direction) and 2.63Hz to 1.31Hz (Y direction). Based on the previous analysis, the superstructure stiffness decreased a lot and there may be some damage in the superstructure.

(5) And the damping ratio seems to increase when the IJMA or PGA increases. But for the rocking ratio, it has small or no correlation with the damping ratio. Damping ratio becomes from less than 6.5% in other relatively smaller earthquakes to 9.1% (x direction) and 14.5% (y direction) in 2011/3/11 stronger earthquake. Considering 2011/03/11 Tohoku earthquake is a very strong earthquake (PGA=279.3, IJMA=5.3), there may be much nonlinearities (maybe structure damage) contributing to the damping of the building.

Acknowledgements:

The authors acknowledge support from the Building Research Institute of Japan for supplying the aboundant earthquake response data. This support makes the research carried out smoothly.

References:

Jimin He and Zhi-Fang Fu. (2001). Modal Analysis. Butterworth Heinemann.

J.E. Luco, M. D. Trifunac and H.L.Wong. (1987). On the apparent change of dynamic behavior of a nine-story reinforced concrete building. Bulletin of the Seismological Society of America. Vol.77, No.6, pp, 1961-1983.

Jonathan P. Stewart, Raymond B. Seed and Gregory L. Fenves. (1998). Empirical evaluation of inertial soil-structure interaction effects. Pacific Earthquake Engineering Research Center. Report No. PEER-98/07.

Jonathan P. Stewart and Gregory L. Fenves. (1998). System identification for evaluation soil-structure interaction effects in buildings from strong motion recordings. Earthquake Engineering and Structural Dynamics. 27, 869-885.

M. D. Trifunac, S. S. Ivanovic, and M. I. Todorovska. (2001). Apparent periods of a building. Ⅰ: Fourier analysis. Journal of Structural Engineering. Vol. 127. No. 5, pp, 517-526.

M. D. Trifunac, S. S. Ivanovic, and M. I. Todorovska. (2001). Apparent periods of a building. Ⅱ: Time-Frequency analysis. Journal of Structural Engineering. Vol. 127. No. 5, pp, 527-537.

Paul C. Jennings and Jacobo Bielak. (1973). Dynamics of building-soil interaction. Bulletin of the Seismological Society of America. Vol.63, No.1, pp, 9-48.

Toshihide KASHIMA. (2004). Dynamic behavior of an eight-story SRC building examined from strong motion recordings. 13th World Conference on Earthquake Engineering Vancouver, B. C. Canada. pp. 196.

Toshihide KASHIMA and Yoshikazu KITSGSWS. (2006). Dynamic characteristics of an 8-story building estimated from strong motion records. First European Conference on Earthquake Engineering and Seismology. Geneva, Switzerland. pp, 1005.

Toshihide KASHIMA and Yoshikazu KITSGSWS. (2006). Dynamic characteristics of a building estimated from strong motion records using evolution strategy. Journal of Structural and Construction Engineering (Transactions of AIJ). No. 602, pp. 145-152.

10CUEE CONFERENCE PROCEEDINGS
10th International Conference on Urban Earthquake Engineering
March 1-2, 2013, Tokyo Institute of Technology, Tokyo, Japan

ON DEVELOPMENT OF SEISMIC RESISTANT DESIGN FOR STRUCTURAL STEEL BUILDING IN INDONESIA

Muslinang Moestopo

Associate Professor, Faculty of Civil and Environmental Engineering
Institut Teknologi Bandung, Indonesia

mmoestopo@gmail.com, moestopo@si.itb.ac.id

Abstract: Recently, the development of seismic resistant steel structures in Indonesia is considered far behind the reinforced concrete structures, although more comprehensive seismic building codes for steel and concrete structures have been published at the same time in 2002. Although the cost and the availability of steel products are considered as the reasons, other issues have also contributed to this condition: the lack of knowledge of the high seismic performance of various steel structures, the limited portion for seismic resistant steel structures in civil engineering curriculum, the less intensive dissemination of the codes. Following the publication of new Indonesian Seismic Map and the draft of new Seismic Building Code, the new revised seismic resistant steel building code will be published. This will enhance the design requirement and performance of previous steel building code: the more reliable design based on most current earthquake data, knowledge and methodology. Further development would be expected that includes improvement in education and research program, implementing policies and regulation for steel production,

1. INTRODUCTION

Indonesia is considered as one of the most seismic prone country since its archipelago lies among four major active tectonic plates: Eurasian, Indian-Australian, Pacific and the Philippine plates. The strong earthquakes occurred in last few years that were recorded with high magnitude as well as damages and casualties : Aceh-earthquake (Mw=9.2 in 2004), Nias-earthquake (Mw=8.7 in 2005), Yogyakarta-earthquake (Mw=6.3 in 2006), Bengkulu-earthquake (Mw=8.4 in 2007), Tasikmalaya-earthquake (Mw=7.3 in 2009), and Padang-earthquake (Mw=7.6 in 2009).

Preceeding the occurrence of those large earthquakes, three Building Codes have been published. The revised version of Indonesian Seismic Building Code (BSN 2002a) was published in 2002 in the document SNI 03-1726-2002, where SNI identifies an Indonesian National Standard (Standar Nasional Indonesia). Other documents are the revised version of Concrete Building Code - SNI 03-2847-2002 (BSN 2002b) and the 'new' Steel Building Code - SNI 03-1729-2002 (BSN 2002c), both have included a special chapter on seismic resistant design.

The Steel Building Code that was published in 2002 was the first Indonesian steel building code that provides a complete chapter on seismic resistant design, which was adopted from Seismic Provisions for Structural Steel Buildings (AISC, 1997). Previous steel building code only covers non-seismic steel structures and did not provide specific requirements on material and stability for sesimic components. No specific design requirement was specified for any specific seismic resisting structure. Therefore, there were quite many issues that needed to be introduced to the engineers when the code was first published. However, after ten years of its publication, the seismic resistant building code has not been fully adopted by all engineers. Meanwhile, the new revised version of the current steel building code is being prepared by the team under the Ministry of Public Works.

2. SEISMIC BUILDING CODE

Following the series of strong earthquakes that occured in different region in Indonesia, a number of intensive studies have been conducted prior to the publication of the new seismic map. The report by the Team for Revision of Seismic Hazard Maps of Indonesia (Irsyam, et al. 2010) that was supported by different institution and agencies, including United States Geological Survey (USGS) and Australia-Indonesia Facility for Disaster Reduction (AIFDR), includes proposed seismic hazard maps for Indonesia by adopting the most recent data and current state of knowledge in probabilistic as well as deterministic seismic hazard methodology. The maps have been proposed and then were adopted and published by the Ministry of Public Works as the new Indonesian Seismic Maps.

Recently, a draft of new revised version of Indonesian Seismic Building Code (BSN 2011) has been written and will be published. This version provides the updated concept for seismic design requirements and the new Indonesian Seismic Maps. The material of the seismic design requirements was taken from the relevant chapters on the American loading code document (ASCE 2010). The seismic design criteria is not only based on seismic hazard but also on probability of collapse of the buildings. The code includes the seismic maps that shows Risk Targeted Maximum Considered Earthquake (MCE_R) for short period (T = 0.2 second) and for long period (T =1.0 second). The design spectral values are then assigned to be (2/3) of the spectral values derived from MCE_R based on the two spectral values of S_S (special value for short period) and S_1 (special value for long period) that represents the spectral response accellerations.

The draft of new revised Seismic Building Code is expected to provide higher seismic design load especially for building with higher importance, such as school buildings and other buildings that are designed to be a shelter during earthquake. More over, the type of seismic resistant structure will be determined based on the design spectral values, the importance factor and the risk category.

In the current seismic building code (BSN 2002a), the design spectral value is simply determined by directly using the only one Indonesian Seismic Map with 6 (six) seismic zones (Figure 1). This map shows the maximum peak ground accelleration at bed rock for Indonesia for 500 years return period, and was constructed based on four available study reports. For each seismic zone, three design spectral values are provided for hard, medium, and soft soils.

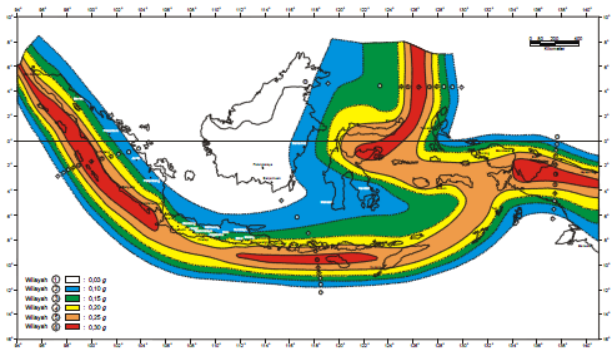
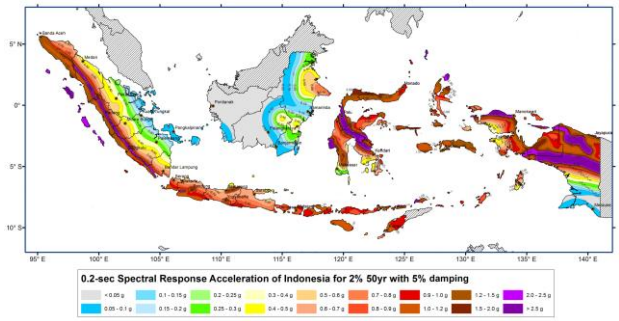


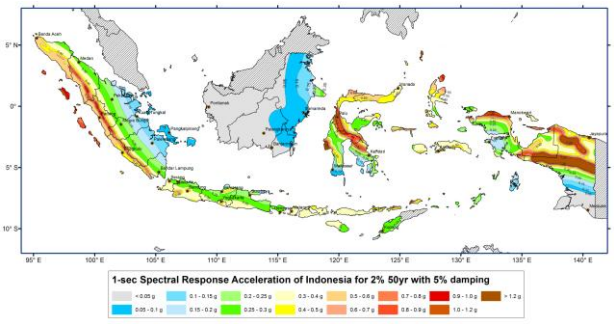
Figure 1 Current Indonesian Seismic Map based on PGA. (BSN 2002)

The new Indonesian Seismic Maps provides a number of maps includes peak ground accelleration and spectral response accellerations. Figure 2 shows spectral response accelleration for short and long period. More detail values could be calculated using available program software that would accompany the publication of the document. In general, the new revised seismic building code (BSN 2011) would provide more reliable seismic design based on the most recent and complete earthquake data as well as current knowledge and methodology to better determine the seismic risk.

At this time, some intensive program to disseminate the concept and design of the new seismic building code have been carried out by the Ministry of Public Works, the Indonesian Society of Civil and Structural Engineers, and some universitites. However, since the new Seismic Building Code has not formally been published, the application of this updated seismic building code for building construction project is still limited.



(a)



(b)

Figure 2 New Indonesian Seismic Maps Spectral Response Accelleration for 2% Probability of Exceedance in 50 years: (a) T= 0.2 sec,(b) T = 1.0 sec

3. SEISMIC RESISTANT STEEL BUILDING CODE

The current Indonesian steel building code (BSN 2002c) is the first document to elaborate the design provisions for steel resistant structures, includes the requirements for material, section, component, connection, as well as the types of seismic resisting structures: moment resisting frames (special, intermediate, and ordinary), special truss moment frames, concentrically braced frames (special and ordinary), eccentrically braced frames. and steel resistant structures. This seismic provision is presented as one chapter in the current steel building code document, and was adopted from the 1997 version of AISC Seismic Provision for Structural Steel Building.

Although it has been published for ten-years, the application of the seismic provisions in the construction project was very limited, whilst most of it was applied only to the ordinary moment resisting frame or the ordinary concentrically braced frames. During that period, dissemination of this provision as well as the introduction to various seismic resisting structures were also limited, while most of the dissemination, including seminars and short-courses, were conducted in the area of seismic resistant reinforced concrete structure. This is understandable, since most of the multy-story residential and office buildings in Indonesia are preferably constructed with reinforced concrete structures.

However, at this time, the revised version of the steel building code has been written and will be published. This version adopts the 2010 version of AISC Seismic Provision for Structural Steel Building as well as the Prequalified Connections for Special and Intermediate Steel Moment Frames for Seismic Applications. Beside some updated version of the requirements, some new seismic resisting structures are introduced in the revised version: shear plate shear wall and buckling restrained braced frames.

4. DESIGN AND CONSTRUCTION

Currently, the use of structural steel buildings are mostly for one-story industrial building and low-rise residental and office buildings. This is far behind the use of reinforced concrete that includes most of the high-rise building in many urban areas in Indonesia. Some reasons behind this condition are the cost and the availability of steel products. There are only few steel-mills that produce the large section such as H-beam.

The increasing demand for high-rise buildings in urban area has initiated the use of steel structure especially for saving construction time. The moment resisting frames are commonly designed for this purpose, yet with limited consideration for seismic requirements. Report on past Padang earthquake (Franco et al. 2009) presents lessons learned from failures and collapse of some steel moment resisting frames. The common failures include:

a. The use of non-compact sections.
b. The requirement of strong column – weak beam is not satisfied.
c. Poor connection detailing, including lack of continuity plate, weak panel zone and column splice.
d. Poor quality control.

As compared to the requirement for seismic resistant concrete structure, the strong column-weak beam for steel structures is directly related to the need for strong connection design, that is more complicated than for concrete beam-column joint. Most of the beam-column joints use the end-plate connection that is relatively simple to install. The use of in situ welding connection for low-rise builidng is very rare and not preferable. Therefore, the performance of the connection is rarely been designed for high seismic loading so that the structure is designed with limited ductility as an ordinary moment resisting frames. For end-plate connection that has a limited moment resisting capacity, the design should be more carefully checked.

The concept of capacity design that was adopted by the seismic resistant steel building code requires the reliable values of material overstrength ratio, i.e. the expected yield stress divided by the nominal yield stress. These values are adopted directly from the American code (AISC 2010). A study has been conducted (Moestopo 2012c) to verify these values based on more than 2900 tensile-test data of steel plates and H-beam from four Indonesian steel-mills. It was found that not all data satisfy the seismic design requirement. More over, the result indicated that the adopted values for certain steel plate are underestimate the real value based on the test data. Further study is needed to secure the reference values that will be used by in structural design and will affect the safety of the building.

The need for constructing high-rise building has also been increasing due to very limited space in the urban area. Since most of the urban area are located in the seismic region, the drift criteria would most likely govern the design for higher-rise building. However, the use of large diagonal bracing is not commonly preferable for most of architects. In addition, the availability of heavy steel sections in the domestic market is still limited, due to the limited capacity of very few steel company. In this case, the use of composite sections in addition to reinforced concrete shear-wall is considered more acceptable.

The advantages of using steel structures as seismic resistant structures need to be promoted, especially to the architects, including to both lecturers and students. Introduction to the high performance of various types of seismic resisting structures including the use diagonal bracings will give broader perspective in obtaining the optimum design. Moreover, the high performance of buckling restrained braces, for example, would be expected as an effective solution for strengthening the existing structures that was indicated not sufficiently performed, based on the new seismic building code.

Although the number of damages of steel buildings from the previous earthquakes was reported much less than of the reinforced concrete and masonry structures, the above common failures and concerns show serious problems as well as important issues to be solved in the design and construction of seismic resistant steel structures. The more intensive dissemination of the seismic design code for steel building is neccessary to improve the knowledge of the engineers. More seminar and short course should be organized especially in many seismic prone region in the country.

On the other hand, the increase in structural steel production has been supported by the government, but still need to be further implemented by supporting policies and regulations as well as commitment from steel industries. This will in turn support the development of innovation and design for more advanced and optimum seismic resistant steel building.

5. EDUCATION AND RESEARCH PROGRAM

The seismic resistant design for steel structures are not specifically taught in civil engineeering undergraduate program at most of universities in Indonesia. This topic is partly covered in the course of seismic resistant structures that is a compulsory course in Master's degree program but an elective course in undergraduate degree program. Therefore, the knowledge in seismic design for steel structures are limited even for one-story and low-rise building. This will at least contributes to the lack of concern of fresh graduate engineers toward the detailing of the steel connection. Seminar and short courses are the effective means to overcome this concern.

In Institut Teknologi Bandung, the oldest and the leading university in engineering area, this topic is more comprehensively covered in the course of Structural Steel Frames for Master's degree program in civil engineering. The concept of design capacity as well as the ductility and stability requirement for material, section, element, conections and building structures, are comprehensively discussed as well as the seismic provision in the steel building code.

The research topics in the seismic resistant structures are mostly conducted for concrete structures, both reinforced and pre-cast concrete. For seismic resistant steel structures, more works have been done in numerical works as compared to a few number of experimental works. Recent experimental works to improve the performance of shear links in eccentrically braced frames are on replaceable links (Moestopo 2012a,b) and diagonal web stiffener (Yurisman 2010). On going research work includes preliminary work on development of more economical and reliable buckling restrained braces for low-story building (Moestopo 2012d). Furthermore, development of new seismic devices becomes the research agenda, which will involve collaboration with construction industries.

3. CONCLUSIONS

The Indonesian seismic building code has been updated by the most current data and knowledge in the area of seismic resistant structures. However, the development of seismic resistant steel structures in Indonesia is considered far behind the reinforced concrete structures. Some reasons that contribute to this condition are the cost and the availability of steel products. However, more issues need to be addressed to develop the seismic resistant steel building in Indonesia including the government supporting policy and regulation as well as commitent from the steel industry.

More intensive education and research program are required toward the development of more reliable and economical steel building, especially for seismic resistant low-rise building in the seismic region. For high-rise building, application of the updated seismic design provision could be carried out toward an optimimum design.

Acknowledgements:

The author acknowledges support from the Center for Urban Earthquake Engineering (CUEE) in Tokyo Institute of Technology for presenting this paper to share the development on seismic resistant steel structures in Indonesia.

References:

American Society of Civil Engineers (2010), "Minimum Design Loads for Buildings and Other Structures ", *ASCE 7-10*.

American Institute of Steel Construction (2010), "Seismic Provision for Structural Steel Buildings", *AISC 341-10*.

Badan Standardisasi Nasional (2011), " Seismic Resistant Design Procedure for Building and Non-building Structures", *Draft RSNI 03-1726-201X* (In Indonesian).

Badan Standardisasi Nasional (2002a), "Seismic Design for Building Structures (In Indonesian) , *SNI-03-1726-2002* .

Badan Standardisasi Nasional (2002b), "Design Procedures on Structural Concrete for Buildings (In Indonesian), *SNI-03-1726-2002* .

Badan Standardisasi Nasional (2002c), "Design Procedures on Structural Steel for Buildings (In Indonesian), *SNI-03-1726-2002* .

Franco, R et al (2009), "Indonesia's Padang Earthquake Reconnaissance" , *Degenkolb Engineers Report.*

Irsyam,M, et al. (2010), "Development of Seismic Hazard Maps of Indonesia for Revision of Seismic Hazard Map in SNI 03-1726-2002", *Report Summary: Revision of Seismic Hazard Maps of Indonesia.*

Moestopo, M et al. (2012a), "On Improved Performance of Eccentrically Braced Frames with Replaceable Shear Link", *Proceedings of 15th World Conference on Earthquake Engineering, Paper No. 5803*.

Moestopo, M and Pandjaitan,A.R (2012b), "Experimental Study on Improved Performance of Shear Link at Eccentrically Braced Frames" (in Indonesian), *Journal of Civil Engineering*, **19**(2),

Moestopo,M and Simandjuntak,V.C, (2012c), " On Indonesian Steel Overstrength for Seismic Resistant Structures" (in Indonesian), *Proceeding of Annual Seminar of Indonesian Society of Civil and Structural Engineers.*

Moestopo,M et al. (2012d) "Development of Buckling Restrained Braces for Seismic Resistant Structures in Indonesia*"* (In Indonesian), *IMHERE Project Report.*

Moestopo, M (2012f), "Design of Seismic Resistant Steel Structures", *Short Course of Indonesian Society of Civil and Structural Engineers.*

Sengara,I.W., et all (2011), "Some Recent Efforts in Earthquake Hazard And Risk Analysis for Disaster Risk Reduction in Indonesia, *Proceeding of 2nd International Conference on Earthquake Engineering and Disaster Mitigation.*

Sofyan,B.T et al. (2012), "Academic Guidebook Faculty of Engineering Universitas Indonesia 2012-2017", Faculty of Engineering Universitas Indonesia.

Sukamta, D , *Proceeding of Annual Seminar of Indonesian Society of Civil and Structural Engineers.*

Yurisman, Budiono,B, Moestopo,M, Suarjana, M (2010), "Behavior of Shear Link of WF Section with Diagonal Web Stiffener of EBF Steel Structure*", ITB Journal of Engineering.Science*, **42**(2), 1-27.

_____,"ITB Curriculum 2008" (In Indonesian), *Office of Senior Vice Rector for Academic Institut Teknologi Bandung*.

10CUEE CONFERENCE PROCEEDINGS
10th International Conference on Urban Earthquake Engineering
March 1-2, 2013, Tokyo Institute of Technology, Tokyo, Japan

Telecommunication at the Time of Earthquake

Takanobu Ito

Executive Vice President, FUN, Inc, Japan
taka@c-ball.jp

Abstract: The Great East Japan Earthquake has left a large impact on the society and economy of Japan. As Japan has been facing various challenges to reestablish the society and economy, we are recognizing to get a clear picture of what is going wrong. Communication problems include the PSTN, cell phone networks or the internet for any devices (landline phone, smart phone, cell phone, PC, or PDA) are one of the major returning problems and we are convinced that they are avoidable. However, there are improvements among government agencies and business operators. Business Continuity Management (BCM) and Business Continuity Planning (BCP) have become an integral part to reestablish the society and economy regime. Important part of BCM or BCP approach is the restoration and the establishment of some level of communications between employees responsible for critical systems as well as command and control. Maintaining communication during disasters and its incorporation into BCP are clearly at the forefront of practically all post the Great East Japan Earthquake regulatory activity dealing with disaster preparedness.

1. INTRODUCTION

In response to lessons taught by the Great East Japan Earthquake of March last year, earthquake and tsunami countermeasures are being widely studied and numerous plans are being reviewed.

These reviews present an opportunity to consider of modern science and technology as well as next generation for decent lifestyles. Also as Japan's social and economic conditions change by this catastrophic damage, people's lives have changed accordingly. Lifestyles and economic activities based on corporate activities have been transformed through information communication and rapid progress of worldwide contents.

The earthquake and tsunami were wiped-out the information and communication systems. It is impossible to prevent and mitigate disasters without information and communication systems confirming to various proposals from related institutions. In other words, the communication systems collapse in disaster areas, making it difficult if not impossible for people in these areas to communicate with the outside world and among themselves. What with the loss of power, the collapse of relay towers and parabola antennas, the destruction of cables and switches, the flooding of tunnels, telephone services are discontinued, and those services which somehow manage to survive the disaster become so congested that it may not be possible to get through, certainly not in a timely fashion.

This communication systems collapse is nothing new or startling about the description above. It appears that when it comes to addressing the problem of communication during disasters, most of the attention has focused on addressing the problem of communication interoperability among rescue and first response teams from different jurisdictions and agencies. However this is a great opportunity to accumulate knowledge and experience to develop advanced and diverse disaster protections along with business continuity, disaster recovery and emergency response.

Interoperability is important, especially during disasters, but for communication systems to interoperate with each other they must first survive the disaster. In any event, for businesses in disaster areas the issue of survivable communication systems is more important than the problem of interagency communication interoperability.

The imbalance in addressing these two important communication issues which are interoperability problems and survivability problems is now being redressed as one of the major returning problems. More companies include telephone carriers and emergency services directors are thinking long and hard about how to provide for continuing communication before, during, and after a disaster business continuity operations or wreaks havoc on a community. The challenges related to these discussions are described below.

2. PURPOSE IN PROMOTING BCP

According to the Cabinet Office (Disaster Management)at APEC Workshop on Private Sector Emergency Preparedness about 5 months after the Great East Japan Earthquake, refers to the Purpose in Promoting BCP: "To avoid a halt of corporate activity caused by a natural disaster such as an earthquake, and avoid its undesirable impacts to the company, economic growth, and

employment not only in the affected areas but also in other areas connected through business relationships. To minimize disaster impacts, it is crucial to promote the formulation of a Business Continuity Plan(BCP), which is a management strategy aimed at ensuring business continuity in times of disaster, ensuring socio-economic stability in Japan, and improving the reliability of Japanese firms for foreign countries.".

Also in the "Business Continuity Guidelines 1st and 2nd edition.", the Cabinet Office(Disaster Management) made explicit five messages such as "Characteristics of these Guidelines", "Necessity for Making Efforts to Ensure Business Continuity at the time of a Disaster", "Concurrent Requirements Other than Business Continuity", "Transmitting Information Outside and Information Sharing" and "Backing up the Information System".

"Necessity for Making Efforts to Ensure Business Continuity at the time of a Disaster" has stated that in Japan, where disasters occur frequently, it is desired to build a disaster-resistant country with cooperation among government, corporations, and citizens. In particular, under circumstances where the interruption of corporate activities might have adverse effects on a global scale due to the globalization of economies, it is becoming more important for the business sector to develop its own preparations to continue business at the time of a disaster, and recover critical operations to the level prior to the disaster. Looking to communities, it is desired to make companies disaster-resistant to secure employment and supply chains in a disaster-affected area. On the other hand, it must be emphasized that elaborate and systematic preparations for disasters by companies have recently been highly valued by client companies and markets. In particular, it has become widely recognized that promoting good practice in business continuity by companies, which is the focus of companies in Europe and the United States, is effective in terms of increasing corporate value. Thus Business Continuity Plan(BCP) plays important roles in this regard.

2-1 Right After a Disaster Occurs

In the "Characteristics of these Guidelines", the Cabinet Office has expressed the following. It is made clear that business continuity is not the first priority of companies, but immediately after a disaster occurs, the focus should be on securing safety of life and preventing secondary disasters. The response to business continuity should involve cooperation with communities to secure consistency with previous disaster countermeasures.

Adding to mentioned above, in the "Concurrent Requirements Other than Business Continuity" was state accurately the actual circumstance in immediately after a disaster occurs. It says that the significance and the importance of business continuity are stated above as important matters to be considered by companies when a disaster occurs, and at least the following three points also need to be considered. Basic disaster responses had been previously taken in Japan. It is true that there are many overlaps, and it is unlikely that the idea putting too much priority on business continuity can be understood. In fact, the type and the level of priorities are left to the judgment of each company.

[1] Securing Safety of Life

In industries where customers visit shops or remain in facilities, priority should be put on securing the safety of life of customers. Naturally, securing the safety of life of people engaged in business includes officers, employees of the company, personnel of affiliates, temporary workers, and personnel of cooperating companies.

[2] Preventing Secondary Disaster

In manufacturing industries, for example, it is necessary to carry out drills to prevent secondary disasters in terms of securing the safety of a neighborhood, which includes fire, collapse of buildings and structures in neighboring areas, and leakage of chemicals.

[3] Contribution to and Symbiosis with Local Communities

In the event a disaster occurs, the earliest possible recovery of local communities should be sought in cooperation with citizens, administration, and client companies. Among local contributions, provision of aid funds, premises, and materials are generally conceived. It is desirable to give support using the assets of the company, such as dispatching engineers and volunteers. It is also desirable that there is close cooperation.

These are very important points out that the Cabinet Office(Disaster Management) refers to major rules, immediately after a disaster occurs, which are securing safety of life, preventing secondary disasters and cooperation with communities include citizens, administration, and client companies. In order to deal with these criteria mentioned above, it is clear that we must have some communication tools or systems. Without communication in any forms, you are alone by yourself and you may be wondering what to do. The first 72 hours after a disaster are the most critical time for victims. In the first 72 hours, site assessment, emergency mobilization and rescue/recovery efforts monopolize first responders. While this may seem like a shocking affirmation, it is the basis of emergency preparedness. In the first 72 hours, the focus of first responders, local, state and criteria federal authorities, medical personnel and Business Continuity is on assessment of those who are damaged by the earthquake and tsunami, on life support, infirm, disabled, or those trapped. Especially earthquakes which occur in or near major cities are very dangerous for knocked out communications. Telephone lines can be knocked out by saturation or by technical failures. If a person hears about injured people, destruction and casualties, he or she will not rest until being in contact with their loved ones by landlines or cell-phones include smart phones/pads, laptops, PC. This is perfectly normal human behavior. However, all communications (data, voice and text) are wiped all out, including those partly used by emergency services.

Hence you are in the middle of trouble to communicate with people you want to talk, family, business people or government authorities. Even though, you can't call for 119 (ambulance/fire department) or 110 (emergency call/police department) for HELP. You can not call for your family,

friends, your business partners or clients, so you may be loose your business. The important issue here is that you must survive by yourself in order to help another people, the community you belong to, or take any action for your business. That was what happened not only disaster area in Tohoku but also Tokyo Metropolitan area. At the same time, communication got down from foreign nation. Since Cellular phones and landline phone services are suffered major disruptions in the affected area. On the day of the quake, American broadcaster was unable to reach anyone in Sendai with working phone or Internet. Internet services were largely unaffected in areas where basic infrastructure remained, despite the earthquake having damaged portions of several undersea cable systems landing in the affected regions; these systems were able to reroute around affected segments onto redundant links. Within Japan, only a few websites were initially unreachable. Several Wi-Fi hotspot providers reacted to the quake by providing free access to their networks, and some American telecommunications and VoIP companies such as AT&T, Sprint, Verizon, T-Mobile and VoIP companies such as netTALK and Vonage have offered free calls to (and in some cases, from) Japan for a limited time, as did Germany's Deutsche Telekom. It might be difficult to be named on this situation as a Secondary Disaster, but it is clear that the Great East Japan Earthquake made this happen immediately after this disaster occurred.

2-2 Face to Communication Problems

First of all, "Transmitting Information Outside and Information Sharing" in the "Business Continuity Guidelines 1st and 2nd edition." by the Cabinet Office (Disaster Management) will be a focus on these issues. The Cabinet Office describes current problems that after a disaster, it is important to share information with business partners, consumers, employees, stockholders, citizens, and local municipalities. In this context, measures should be taken to prevent a so-called "blackout" situation, where corporate activities are invisible to interested persons, and people do not have the least idea what is going on . This also emphasizes the importance of prior consultation with interested parties. Providing information to business partners and customers in the supply chain is an essential requirement for middle-standing small or medium-sized enterprises as well. When examining a business continuity plan, there are some points to be fully considered in association with the item "transmitting information outside and information sharing" which include:

[1]Establishing systems for information collection, distribution, and public relations

[2]Developing systematic communications with the authorities concerned, residents in the neighborhood, supply chains, etc.

[3] Securing means of communication and information

Also with the relation of this issue here, The Cabinet Office has expressed about "Backing up the Information System" the following. Information systems are among the key infrastructure functions of a business. It is essential that necessary information and data be backed up and stored at two or more places that are unlikely to be affected by a disaster at the same time. In particular, a well-maintained backup system is needed for information systems that support critical operations. If a disaster should occur, the business continuity plan would be put into practice with priority given to the critical operations. However, if the company has moved out of the emergency response phase and finally changed over from alternate facilities and means to regular ones toward the full restoration of its business, problems could arise due to loss or mismatch of data required for regular operations. A detailed comeback plan should, therefore, be developed in advance to prevent such problems. When examining business continuity plans, there are some points to be fully considered in association with the item "backing up information systems" which include:

[1] Clarifying the relationship between the critical operations to be protected and the information system

[2]Developing backup operation, changeover, and comeback plans

[3]Implementing redundancy measures for private electricity generation equipments, power supply, power lines, etc

[4]Active use of document and electronic data storage service in a remote area

In any cases mentioned in both "Transmitting Information Outside and Information Sharing" and "Backing up the Information System", it requires to communicate with information and communications technology (ICT), information technology (IT) professionals, telephone carriers or IT venders in order to solve, or make improvement in communication problems. During non-emergency circumstances, it is easy for anybody to call somebody you need or send text message, emails to your contact person in order to proceed what you want to do. Since widely spread cell-phone (mobile telephone) or rapidly growth of smart devices are the most familiar communication devices for modern people or business person, it becomes quite difficult to proceed anything without it for them. Also PC and laptops are still major tools for your business, and it might be difficult or almost impossible to do any job without them.

During and after the disaster, the authorities and networks such as telephone carriers manage by cutting or limiting VOICE communication based on earthquake alert levels for high magnitudes and limiting bandwidth for medium size earthquakes. The levels of triggering such automatic cuts and according messages would be provided in cooperation with seismologists/geologists based on the authorities. Also they include internet providers are blocking all graphic internet data (pictures / advertisements / videos) for internet data traffic, but text only takes a very small portion of the data bandwidth capabilities. The circumstances demand by reserving enough bandwidth for voice and data for authorities and all kind of rescue services. If the automatic triggering would not be accepted, a similar system can be triggered manually by the government emergency authorities.

It is so clear that emergencies circumstances demand on communication processes which are often significantly different than the demands of non-emergency circumstances.

Emergencies often involve escalating and evolving events that demand high performance and flexibility from the systems that provide emergency communication services. Message prioritization, automation of communication, fast message delivery, communication audit's tags, and other capabilities are often required by each unique emergency situation. Inadequate emergency communications capabilities can have consequences that are inconvenient at best and disastrous at worst. Once again, the Great East Japan Earthquake and the surrounding area destroying tons of houses and escaping millions of people without electricity without internet, mobile phones, or landline communications. Telephone carriers have strengthened its ability to respond to a disaster since the communications problems during the Great Hanshin-Awaji Earthquake in 1995. Communications have been steadily improving, but it is not enough yet.

3. SURVIVABILITY PROBLEMS

What happens to communication networks during a disaster. the three links in the communication chain which are likely to fail during a disaster. The failure of each one of them would cause massive problems. Of course, we can't do anything when all three collapse at the same time as in the case of the Great East Japan Earthquake.

[1]Power:

Without power nothing will work. Some central offices and cell phone sites may have emergency power back up sources such as batteries and stand-alone generators which may suffice for a few hours or days of operation. In cases of the Great East Japan Earthquake, however, power may be interrupted for several days or even several weeks. In a major disaster it is the case that power plants (the Fukushima Daiichi nuclear plant), central offices, or cell towers in the affected areas may be inaccessible for most of that time, making it impossible to change spent batteries or refuel generators.

[2]Local loop:

The last-mile communication of service to the customer depends on copper wires or fiber optic cables extending, either above ground or below ground,
from the carrier's central office to the customer's premises. This last mile connectivity between the business and its telephone provider, Internet provider,
or application service provider may be severely disrupted, if not cut-off altogether, during a disaster as wires and cables are torn and underground tunnels flooded.

Cell towers and the equipment mounted on them are often also destroyed during a disaster, as are the last mile circuits which connect these cell towers to the local Telephone network.

[3]Long haul:

Copper wires and fiber optic cables also connect the local telephone company's central offices to other central offices in the region and to long-distance providers, cell phone carriers, and Internet and data communications service providers around the country and around the world. These inter-exchange or "long haul" circuits provide for interconnectivity and communication beyond the local area. The cables and wires used for long haul are as vulnerable to disruption as those used in the local loop, but there is a difference. There are many more subscribers who use these long haul circuits, and these circuits carry many more calls, so carriers would typically employ "circuit diversity," that is, they would construct the system so that there are multiple paths available for voice and data on which to move. If one path which is part of the long haul circuit is blocked, then the voice or data would automatically use another path to reach their destination. It notes that this may work well in cases of isolated disasters such as localized fires and floods, but when the level of destruction is catastrophic and wide-spread, as was the case in the Great East Japan Earthquake, then this circuit diversity would not be of much help because the alternative paths are also destroyed in the disaster.

4. INTEROPERABILITY PROBLEMS

According to the Partnership for Public Warning, a fundamental problem is the lack of technical and procedural interoperability among warning originators, system providers, delivery systems, and warning recipients. Some originators of warnings must undertake expensive, redundant tasks using multiple, different tools and techniques to take full advantage of today's warning systems. Also, there are multiple ways that an emergency communication system might obtain an original warning. The ability to interoperate should consider the need to be both forward and backward compatible with older and coming technologies in the future. Introduction of a new system that can not interoperate with previously deployed equipment creates potentially serious barriers to effective operation.

5. CONCLUSION

Robust voice continuity will allow enterprises to coordinate recovery actions during and post disaster and enable continuous communications with their customers and suppliers as required by in-house regulations. It starts with careful evaluation of the vulnerabilities of the existing corporate voice continuity solution. In many cases there is no such solution. In many more cases the solution is limited to headquarters of the organization and no provision is made for branch and field offices. Regardless of the situation, it generally results in inadequate coverage of required critical personnel. In almost all cases the solution itself is ineffectual during certain disaster conditions. In other words, there exist coverage gaps in the exiting voice continuity approach contained in the organization's BCP.

Insufficient coverage by the existing voice continuity solution is usually a result of reliance on the infrastructure protection approach. However, it may also result from the degree of coverage required in today's business climate in relation to when the solution was crafted and its design

requirements. IT department is no longer the only department affected by disasters. Also IT personnel the only ones needed to respond during a crisis. What the Great East Japan Earthquake and other disasters have taught is that some organizations are required to successfully resume business operations in the event of a disaster. Voice continuity solutions that were designed to cover a small number of IT personnel are no longer viable in today's business climate where 24x7 operations is crucial.

Finally, to address in the communications portions of the BCP and create a verifiable and auditable solution it is necessary to implement voice continuity that meets the following minimum requirements:

[1] Location Independence:
Executives and staff must be able to receive calls made to their work number regardless of where they are located. Executives and staff must be able to rapidly, and without limitation maintain continuous communications while changing location as frequently as necessary as dictated by changing disaster conditions.

[2] Network Independence:
To assure continuous telephone service, the voice continuity solution must be capable of automatically moving calls through all surviving and operating networks, whether PSTN (landline, cell) or IP (soft phone, VoIP, laptop, PC, PDA) as required by existing conditions to ensure call completion.

[3] Device Independence:
The effective solution must allow executives and staff to utilize any communication device available to them during the disaster. The solution must be capable of delivering telephone service via the user's cell phone, laptop, PC, PDA, landline phone, smart phones/pads or any other standard voice-capable device.

[4] Survivable Telecommunications Network:
The voice continuity solution must be capable of delivering calls throughout the disaster event itself, be self-healing and be relatively immune to the disaster's effects. The service must have geographic diversity and be capable of maintaining service through dynamic re-routing even when service points have been destroyed. The emergency voice provider must have no single point of failure anywhere in their system.

[5] Isolation and Independence from the Disaster Site's Local Loop:
To increase communications reliability, the solution must reduce or eliminate any dependence on the local loop at the disaster site. The emergency voice provider must provide both forwarding capability and independence from the local loop in case carrier forwarding is lost or is unattainable, the executives and staff can still be reached.

Acknowledgements:

The author acknowledges supports from a former Executive Vice President, Michael Rosenberg and a former Chief Technology Officer, Raul Vera at Telecontinuity, Inc in the U.S. This support makes possible to create this paper.

References:

Kiyoshi NATORI (2011), "Public-Private Efforts to Promote the Formulation and Implementation of Business Continuity Plans for Private Firms", APEC Workshop on Private Sector Emergency Preparedness, p.2 http://aimp.apec.org/Documents/2011/EPWG/WKSP1/11_epwg_wksp1_019.pdf

Cabinet Office (Disaster Management) (2005), "Business Continuity Guideline 1st edition," , p.2-3, 5, 7,17,18, http://www.bousai.go.jp/MinkanToShijyou/guideline01e .pdf

Cabinet Office (Disaster Management) (2009), "Business Continuity Guideline 2nd edition," , p. 3,6,8,19-20, http://www.bousai.go.jp/MinkanToShijyou/guideline02.pdf

Tsugio Ide (2011), "Impact of the Great East Japan Earthquake and Moving Toward Recovery", p.1 http://www.iist.or.jp/wf/magazine/0793/0793_E.html

Raul Vera (2009), "Meeting Regulatory Requirements through Cost Effective Survivable Voice Continuity" How Are Voice Continuity Requirements Addressed In BCPs, p.8-10

Takao KOMINE (2011), "Viewing the Economic Impact of the Great East Japan Earthquake", No. 6 Translated from "Kyodai-jishin no eikyo wo dou kangaeruka," Nikkei Business Online, p.1-4 http://www.japanechoweb.jp/jew0604/

Connie Hanner (2012), "Disaster preparedness: The first 72 hours",p.1 http://www.examiner.com/article/disaster-preparedness-the-first-72-hours

Homeland Security Daily Wire (2007) Vol. 3, no. 124, " BUSINESS CONTINUITY & DISASTER RECOVERY / EMERGENCY RESPONSE", p.1-2

A National Strategy for Integrated Public Warning Policy and Capability. (2003) "Partnership for Public Warning", p. 22.

National Institute of Standards and Technology(NIST) (2012) "Desirable Properties of a Nationwide Public Safety Communication System", p. 12.

10CUEE CONFERENCE PROCEEDINGS
10th International Conference on Urban Earthquake Engineering
March 1-2, 2013, Tokyo Institute of Technology, Tokyo, Japan

CONFIRMATION OF BUILDING SAFETY FOR REGIONAL CONTRIBUTION ACTIVITIES OF COMPANIES IN A TIME OF THE TOKYO INLAND EARTHQUAKE

Hiroaki Maruya[1)]

1) Professor, Center for Urban Earthquake Engineering, Tokyo Institute of Technology, Japan, and Chief Executive Researcher, Policy Research Institute, Ministry of Land, Infrastructure Transport and Tourism
h-maruya@tiara.ocn.ne.jp

Abstract: When the Tokyo Inland Earthquake occurs during working hours, more than three million people are estimated to have difficulty returning home in the Tokyo metropolitan area. The governments have requested companies to ask their workers not to go home on foot in three days because people walking along main roads will disturb rescue and relief activities. Moreover, companies which have a large building in downtown are requested to provide tentative stay facilities for passengers facing difficulty returning home. Considering the probability that major aftershocks occur, safety of the tentative stay facilities should be properly confirmed before receiving passengers. The governments showed a guidelines and it includes a simple check list for safety of building structure and equipments. However the companies seem to worry about a method of confirming safety of the facilities concretely and risk of a damage compensation claim from refugees. Based on the discussion between researchers of building structure, engineers of construction related firms and disaster management staffs of companies, the author proposes several kinds of checklists according to the type of building structure, the methods comparing photographs of the normal state and the damaged state after the earthquake, and so on.

1. INTRODUCTION

In Tokyo, although the Great East Japan Earthquake (GEJE) of March 11, 2011 did not caused serious damage on buildings in general, many persons had difficulty returning home and had to stay for a night in facilities urgently provided public and private organizations. As there is considerable concern about Tokyo Inland Earthquakes (TIE), it has been recognized more than before that the countermeasures of controlling this problem are very urgent.

To tackle with the problem, cooperation of private sectors is necessary in addition to the governments' effort. These days, business operators consider bearing the cost of the cooperation preparing for TIE as a part of corporate social responsibility and the local contribution. However, if there is probability that refugees whom a company accepts are damaged in its tentative stay facility and they claim a high amount of compensation for the damage, the company seems to hesitate to cooperate.

Therefore, discussion is necessary on how to increase the companies' cooperation to the problem.

2. ESTIMATED DAMAGES OF TIE

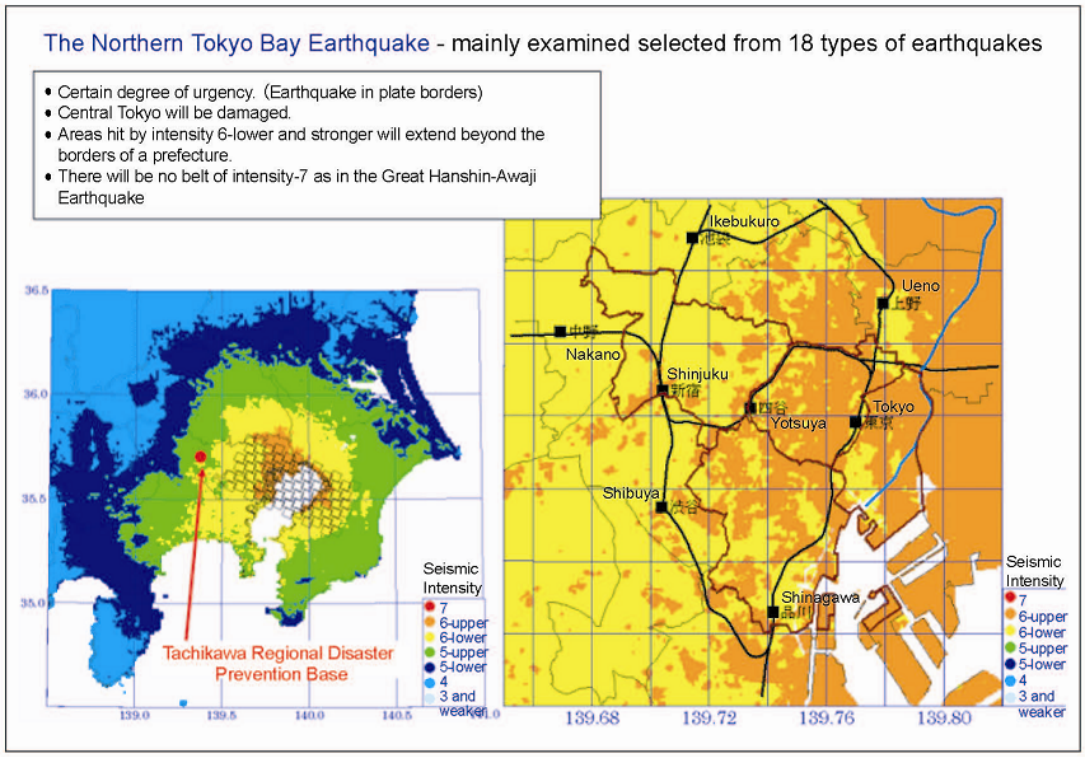
2.1 The Expected Worst Type

It is scientifically understood that in the greater Tokyo capital area, massive trench-type earthquakes with a magnitude of 8 or greater, like the Great Kanto Earthquake (1923), occur at intervals of 200-300 years. Additionally, it is estimated that smaller several types of TIE (magnitude 7 (M7) class) occur before a M8 scale earthquake.

Japanese government published the estimation that a M7 class will occur in the probability of 70% in next 30 years.[i] The Central Disaster Management Council of Japanese government has carried out damage estimations for 18 types of TIE (M7 class). Among those, the type whose epidemic center is at northern part of Tokyo Bay (assumed scale of M7.3 at 6pm in winter) is estimated to cause most serious damage. It would include a death toll of approximately 11,000 people, total collapse of 85,000 buildings and a maximum economic loss of 112 trillion yen.

2.2 Distribution of a Seismic Intensity

Figure 1 shows maps of the seismic intensity distribution of the expected TIE whose epidemic center is at northern part of Tokyo Bay. On this earthquake, most places in east half of the central districts of Tokyo is predicted to experience a seismic intensity[ii] 6-upper. The standard damages by the intensity 6-upper earthquakes are defined by Japan Meteorological Agency as follows.[iii]



Material of the Cabinet Office (Disaster Prevention)

Figure 1 Distribution of Seismic Intensity during the Northern Tokyo Bay Earthquake (7.3-magunitude)

- One cannot stand. One cannot move unless crawling.
- A lot of furniture moves unless it is not fixed, and some of them fall down.
- Of many buildings, tiles on walls and windowpanes are damaged and drop.
- Most of fences made of blocks which are not reinforced are fall down.
- Some wooden houses with high quake resistance have crazing and cracks on walls.
- Many wooden houses with low quake resistance have crazing and cracks on walls. A considerable number of those incline or fall down.
- Some steel reinforced concrete buildings with high quake resistance have crazing and cracks on walls, beams, pillars etc.
- Some steel reinforced concrete buildings with low quake resistance have diagonal or X-shaped crazing and cracks on walls, beams, pillars, etc. Of these, there are buildings that collapse caused by breaking down of pillars of the first floor or intermediate floors.

Additionally, the Tokyo Metropolitan Government published the revised estimation of TIE in 2012 based on the new information of the Philippine Sea Plate under Tokyo. According to this, the max seismic intensity is 7 and area of 6-upper is wider. About 70% of 23 ward area of Tokyo suffers from 6-upper and more.

Cabinet Office also has been revising the damage estimation of TIE since 2012.

2.3 Estimation of Number of Persons Who Have Difficulty Returning Home

The Cabinet Office conducted an examination of TIE including of the problem of persons who have difficulty returning home in 2004. Of the damage assumption on the northern Tokyo Bay type (M7.3), the number of such persons would be approximately 6,500,000 in the Tokyo metropolitan area (i.e. Tokyo and neighboring prefectures), and approximately 3,900,000 in Tokyo.

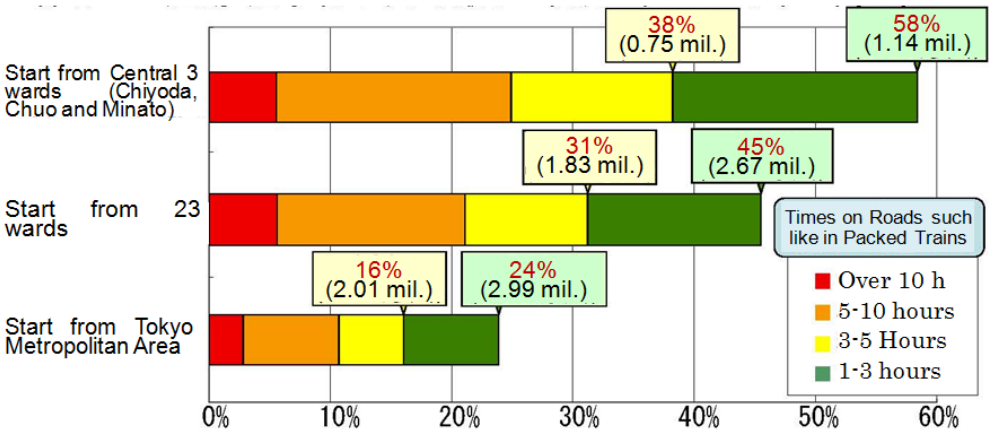
The newest estimation of persons who have difficulty returning home is 5,166,126 people in Tokyo which were published in 2012 in the Regional Disaster Prevention Plan of the Tokyo Metropolitan Government.

Additionally, the condition of people returning home on foot seems to be very severe. "The Return Action Simulation" of Cabinet Office in 2008 showed that after a TIE, among the people trying to walk home, 1,830,000 persons would be in the condition similar to the state of packed trains (more than six people per square meter) for more than three hours along the street, if any countermeasures had not been executed (Figure 2).

3. SPREAD OF RECOGNITION AFTER THE GEJE

3.1 The Situation of the GEJE in Tokyo

Although the ground motion of the GEJE was a seismic intensity 5-upper or lower in Tokyo, most of the railroad (including the subway) of the metropolitan area stopped



(Share of people by length of time on the road in the condition similar to the state of packed trains.)

Source: Cabinet Office (2008)

Figure 2 Simulation of Returning Home Activity in TIE (Starting Point, Basic Case)

services for check and recovery. The damaged points were not so many but needed considerable time for repair. As a consequence, Japan Railway East, for example, announced the restoration of each route would be only from next morning. The confusion of the railroad traffic continued until afternoon of the next day.

With respect to road traffic, a large quantity of substitute traffic demand was arisen by the stop of railroads (including the car to pick up persons waiting in Tokyo) and closure of the Metropolitan Expressway for check, and they caused a large traffic jam on all the main streets of the whole Tokyo. Therefore, buses and taxis did not function substantially. People who were usually commuting by public transport in the metropolitan area lost the means of returning home and approximately 5,150,000 (Cabinet Office estimation) had difficulty returning home.

There were a lot of persons who walked along the roads for a long time. Some of them were able to come home but many other persons had to stay in the tentative rest facilities which were provided by various public and private organizations in urgent.

3.2 The Ordinance of Tokyo Metropolitan Government

For the problem of persons who have difficulty returning home, the Tokyo Metropolitan Government and the Cabinet Office have already executed some countermeasures.

The Tokyo Metropolitan Government established "the Ordinance of Measures for Persons Having Difficulty Returning Home" at the end of March, 2012, and it will be enacted on the beginning of April, 2013. Outlines of the ordinance are:

- An obligation to make efforts to let the employees of each company wait in its facilities
- An obligation to make efforts to accumulate stockpile (drinking water, food, etc.) for 3 days for the employees of each company
- An obligation to make efforts to protect the customers in stations and large-scale facilities
- An obligation to make efforts to ensure safety of children and students in schools and so on
- To develop the system of safety confirmation and offering disaster related information by public and private sectors
- Cooperation between Metropolitan, national and municipal governments and private companies to securing of temporary stay facilities
- To support returning home (cooperation for securing Support Station for Returning Home)

3.3 The Council on the Persons Who Have Difficulty Returning Home

The Cabinet Office, the Tokyo Metropolitan Government and other related organizations set up "the Council on the Persons Who Have Difficulty Returning Home at the Time of TIE" (CPDR) in September, 2011. The final report of the CPDR is published in September, 2012 showed following items:

(1) To let employees wait in the company's facilities as the control measures against returning home all at once.
- Development of the waiting plan in the company's facilities
- Example of quantity and item of stockpile
- Recommendation of 10% extra stockpile for outer persons who have difficulty returning home
- Securing method of safety confirmation of employees and their family
- Setting the rule of returning home (gradual return, return in group, etc.)
- Development of "Guidelines on Measures on Persons Who Have Difficulties Returning Home in Business Places"

(2) Type of targeted facilities, standard of establishment and role of facility managers of the temporary stay facilities
- After the outbreak, operating up to three days as a standard
- Accommodation of two people per 3.3 square meters as rough standard

(3) Securing of temporary stay facilities in each organization
- Concluding agreements between companies and the municipal governments for providing the temporary stay facilities

(4) Consideration for the facilities to ensure the security
- The quake resistance standard which buildings for the facilities should fulfill
- A Examples of a check list for safety check of buildings and equipments of the facility
- Recommendation of showing the enduring rules for using the facility at the entrance, etc.

(5) Governments' support measures
- Development of the management manual based on local conditions of each facility
- Substantiation of support measures

(6) Development of "Guidelines on Securing Temporary Stay Facilities and their Management"

4. COMPANIES' CONCERNS ABOUT THE COOPERATION AT THE TIME OF TIE

4.1 The Type of Concerns

There have already been a considerable number of companies in the Metropolitan Area indicating the intention of cooperation to the problem of the difficulty returning home. However, the companies would turn to be reluctant if the burden of cost and labor for the cooperation are more than the ability of each company. The companies' various concerns seem to be classified as follows, taking reference to Nakano and Suzuki (2012)).

(1) In ordinary times
  a) Cost of procurement, storage and renewal of the stockpile
    - Those for the company's employees
    - Those for the persons who evacuate to the temporary stay facilities prepared by the company
  b) Necessary investment and preparation for securing safety of the company's temporary stay facilities

(2) When the TIE occurs
  a) Regarding the company's employees
    - Availability to detain employees who hope to return home earnestly
    - Sufficiency of stockpile for employees (and the company's visitors)
    - Ensuring safety of the employees while the company detains them
    - Company's responsibility of safety of its employees when the company permits them to return home
  b) Correspondence when the company establishes its tentative stay facility
    - Method of safety confirmation of the temporary stay facility and its sufficiency
    - How to deal with the people if more than the capacity burst in
    - Availability of separation between the evacuate facility and the company's business area (keep out area for outsiders)
    - Handling and restraining of a person who harms or annoys other evacuees
    - Safety management measures when the company asks temporary refugees for a volunteer activity in the facility
    - The risk of offering wrong security/traffic information by which a evacuee who has departed from the facility meets with an accident
    - Cost of stockpile which the company provides to the evacuees

In the discussion in the CPRD, it attracts attention that the company members requested the system of exemption from responsibility, if they are claimed compensation by an evacuee who has got some damage in the facility, in addition to the public aid to cost of stockpile.[iv]

The author considers that companies should not evade burden to some extent from the viewpoint of self-help and mutual assistance. However such compensation for the damage would threaten the continuation of the company' business if the damage is mortal or very severe injury and the amount of compensation is very large. Therefore it seems rational that governments establish some system to take this damage compensation risk.

4.2 The Extent of Concerns of Companies

At the beginning of December, 2012, the author asked approximately 20 attendants to reply how their concerns were at a study meeting of companies located around the Tokyo Station. The results were as follows:

a) Can you detain your company's employees in general for three days after the TIE occurs?
  "There is worry": about half
  "No worry": approximately one-third

b) Can you really detain the employees who strongly hope for returning home?
  "There is worry": approximately two-thirds,
  "No worry": a few

c) Regarding safety management of your temporary stay facilities, including risk of damage compensation
  "There is worry": more than half
  "No worry": approximately a quarter

d) Risk of too many people bursting into your temporary stay facility, including a stockpile being insufficient for them
  "There is worry": approximately three-fourths
  "No worry": a few

e) Risk of appearing a refugee harming or annoying other refugees, including compensation claim from the damaged refugees
  "There worry": approximately two-thirds
  "No worry": approximately a one-third

f) Necessity of safety management measures (ex. provide with helmets) when the company ask refugees to be volunteers
  "Not necessary": several companies
  "Same measures with the company's employees are necessary": less than half

"Should not ask to be volunteers": several companies (more than the first option)

Most of the respondents were in charge of disaster management and knew the problem of persons who have difficulty returning home well. Therefore, their concerns are thought to be suggesting broad concerns.

5. CONCERNS OF SEFETY CONFIRMATION OF TEMPORARY STAY FACILITIES

5.1 Preventive Measures for Safety on Facilities

"Guidelines of Securing Tentative Stay Facilities and their Management" prepared by the CPRD prescribe that buildings for the tentative stay facility need to fulfill the latest earthquake-resistant ability (i.e. the new earthquake proofing standard introduced in 1981).[v] Additionally, the guideline also requested to prevent the office fittings in the facilities against turnover, fall or move, and prevent the glasses against scattered.

As these preventive measures are effective for the safety of the company's employees and its guests, cost for these is not the waste for the company. However, companies seem to be bewildered how to keep enough physical safety of their tentative stay facility in the aspect for which the guideline does not prescribe in detail. This point is related to the content of the example of the check list in the guideline mentioned in section 5.3.

5.2 Safety Check after the Outbreak

The safe confirmation of a building and equipment of a tentative stay facility after the occurrence of TIE seems to be a matter which each company gets anxious about, considering the probability of aftershocks. The guideline prescribes that the company should perform safe confirmation within six hours after the earthquake. Additionally the guideline also demands the confirmation should be done by using the check list which the company and the local municipal government should work together to make up beforehand.

Considering these procedures, once a company has executed the safety confirmation by using its check list and it has not found any problems, it is desirable from the standpoint of the company that compensation responsibility of the management of its tentative stay facility will be exempted even the tentative refugees sustain damage by some troubles of the building or the equipments.

5.3 The Example of the Checklist

The guideline shows an example of the check list (Table 1)[vi]. Reviewing in detail, there seems to be some items that are not concrete enough.

For example, as for "Incline and sink of the building," of the whole facility, the check list prescribes "the building is prohibited to use" in case of "it looks inclined." While, "the company should ask judgment of an expert" in a case of "it is thought to be inclined." It is not clear how to distinct "it looks incline" and "it is thought to be inclined." In addition, the confirmation method of the degree of incline is not shown, either.

As for "wall and ceiling materials" of non-structure materials, the checklist suggests that "it is necessary to pay attention and ask an expert for examination in case of the gap of ceiling materials is seen." It is uncertain how much gap corresponds to this instruction.

It is understandable that the check list needs to be simple and concise because a person without building structure expertise will use it. However, as it is directly related to the safety of tentative refugees, sufficient quality of safety check are requested seriously.

6. PROPER SAFETY COMFIRMATION ON THE FACILITIES

6.1 Precedent Study in 2010-2011

Not only the temporary stay facilities, but all the company's buildings where its employees work need the safety confirmation to some extent just after an earthquake. It is ideal that the confirmation is executed by engineers of building structure and facilities/equipments with the ability of emergency risk judgment. However, in most cases, it takes a few days or even a few weeks before companies can get these engineers. Therefore companies are recommended to ask these experts to provide with advices on what and how should the person in charge without expertise perform the safety check beforehand.

On October 12, 2011, Center for Urban Earthquake Engineering (CUEE) of Tokyo Institute of Technology and a non-profit organization "Business Continuity Advancement Organization (BCAO)" organized joint symposium of "Damage of Buildings and Business Continuity after an Earthquake" based on several meetings of opinion exchange and related researches since 2010.

From this symposium, the ideas and points to be discussed became clear as follows.

a) For judgment of the building damage, it is necessary to know the characteristics such as structure classification and quake resistance. Therefore, it is desirable that the experts prepare the judgment manual one by one for every building.
b) It is preferable to create the social rule that all buildings are provided with a damage diagnosis manual based on the characteristic of each building, which is similar to a medical record of family hospital for each person.
c) A non-expert person in charge of safety confirmation may have difficulty judging even if he/she has a diagnosis manual. Therefore it seems effective to take photographs of the points to be checked of the building in the ordinary time, and to take the photographs on the same points after the suffering from an earthquake for the comparison. If necessary, the person in charge is able to send both photographs to an expert by electronic method and ask the judgment.
d) The safety confirmation manual which has many pages and from which every user has to look for suitable parts

Table 1 An Example of the Check List for Safety Confirmation on Temporary Stay Facilities

Check Items		Content of Check	Judg -e	Correspond and Emergent Response If Applicable
Whole Facility				
1	Building (Incline, Sink)	Be inclined or sink		Leave the building
		Seems to be inclined		Caution needed →Ask experts to diagnose in detail
2	Building (risk of collapse)	There are many large x-shape cracks and exfoliation of the concrete is remarkable. The exposure of the reinforcing rod is remarkable. The other side of the wall is transparent.		Leave the building
		There are diagonal or x-shape cracks, but exfoliation of the concrete is limited.		Caution needed →Ask experts to diagnose in detail
3	Neighboring buildings and ground	Neighboring buildings, towers, etc. incline to the facility		Leave the building
		The neighboring ground sinks or rise greatly		Leave the building
		There are damages on the neighboring building . There is a crack of the neighboring ground. However, it seems that no effect to the facility.		Caution needed →Ask experts to diagnose in detail
Inside of the facility (Room, Pass, etc.)				
1	Floor	Be incline, or sink		Off limit
		Damage in flooring is seen.		Caution needed / repair required
2	Wall, ceiling materials	Damage is seen in partitioning walls		Caution needed / repair required
		Ceiling materials drop		Off limit
		Gap of ceiling materials is seen.		Caution needed →Ask experts to diagnose in detail
3	corridors and stairs	There are a lot of big X-shaped cracks. The exfoliation of the concrete is remarkable. The exposure of the reinforcing rod is remarkable. The other side of the wall is transparent.		Off limit
		There are diagonal or x-shape cracks, but exfoliation of the concrete is limited.		Continue the checks →Ask experts to diagnose in detail
4	Doors	A door comes off or is transformed		Caution needed / repair required
5	Sash, windowpane	A sash comes off, or is transformed.		Caution needed / repair required
		A window is broken, there is a crack		Caution needed / repair required
6	Lighting equipment, appliance to hang	Lighting equipment or appliance to hang drop		Caution needed / repair required
		The gap of the lighting equipment or appliance to hang is seen.		Caution needed / repair required
7	Household articles (furniture, etc.)	Household articles (furniture, etc.) turn over.		Caution needed / repair required / fix required
		Documents are scattered.		Caution needed / recovery needed
Facilities				
1	Electricity	Power supply from outside stops. (Stop of the commercial power supply)		Securing substitute means / recovery needed →(ex.) To operate emergency power supply
		Lighting is off.		
		Air conditioning stops		
2	Elevator	Elevator stops		Recovery needed →To contact a maintenance supplier
		A warning lamp turns on. A buzzer rumbles.		
		A person is shut in the elevator car.		To contact a maintenance supplier or the fire department
3	Water supply	Supply stops		Securing substitute means / recovery needed →(ex.) To use stockpile
4	Swage, toilet	Water does not flow. (overflow)		Stop using / securing substitute means / recovery needed →(ex.) To use emergency toilet
5	Gas	A bad smell, abnormal noise, smoke are generated.		Off limit / recovery needed
		Supply stops.		Recovery needed
6	Telecommunication, telephone	Operation stops		Securing substitute means / recovery needed →(ex.) To use satellite cell-phone or transceiver
7	Facilities for firefighting	Be out of order or damaged.		Securing substitute means / recovery needed →(ex.) To contact a firefighting facility supplier
Security				
1	Fire shutter	Closed		Recovery required
2	Emergency staircase, emergency exit	Closed (impassable)		Recovery required →When recovery is unavailable, off limit
3	Entering or leaving a room, facility management	Security does not functioned.		Recovery required / Placement of a guard required →Watch out for invasion of a person from outside. (Off limit by the condition)

would be worthless at the time of disaster.

e) The manual will be available by which even a non-expert person able to show "this building is dangerous." On the other hand, the manual by which a person (including the expert) is able to show "this building is safe" should be hardly available.
f) The manual will be a significant material if it can prevent the executive of company from ordering the employees to use or enter their dangerous building.
g) Even using a good manual, it will be difficult to judge an invisible risk from the outside. For example, the damage of structural elements that cannot be seen without tearing off the interior decoration. The manual will be able to show at best what kind of risk lies in the building.
h) To spread a safety confirmation manual, containing photographs and illustration which are usable for judgment will be effective.
i) There seems to be the graded connections in the investigation actions. If a certain abnormality is found, then related matters should be deliberately examined.

6.2 The Second Joint Symposium

Based on the result of this precedent symposium and related study, CUEE and BCAO performed a joint symposium[vii] on January 28, 2013 focusing on the method of safety confirmation of the building and equipments of temporary stay facilities at the time of TIE. The main opinions and ideas were as follows.

a) As it is necessary to perform the safe confirmation in several hours, the check list should be simple, and the person in charge can judge by viewing only. On the other hand, check items should be increased in order to confirm the safety precisely and reliably. This is the dilemma.
b) It is important that once a company performs safety confirmation by the check list, the company is admitted to have achieved the safe consideration duty.
c) Necessary items of the safety confirmation are building structure, non-structural elements (including the ceiling), facilities (including the possibility of fall), utilities and risks of neighboring area (including fire risk).
d) For the confirmation by a non-professional, it is effective to attach photographs of damaged facilities and equipments by an earthquake to the check list.
e) Even the buildings which fulfill "the new earthquake proofing standard" are not necessarily available to use continuously after an earthquake of seismic intensity six upper and more.
f) The items to be checked are different by structure classification (steel reinforced concrete, steel-frame, large space and so on), scale classification (super high, high and middle), etc.
g) As for a steel reinforced concrete building, even if a non-structural wall is shear-failed in X-shape, the building is available to use. On the other hand, if structural column is shear-failed in X-shape, the building is not available to use. It is difficult for non-professionals to distinguish these cases.
h) As for a steel-frame building, even if a board of the wall is broken, the building is available to use. However, non-professionals are apt to judge that it is danger from the appearance. On the other hand, a break of the beam is dangerous structurally. However, as the beam is often covered by fireproof coating and hides in the ceiling, the damage is not easily found.
i) The current earthquake-resistant diagnosis is not applied to a ceiling, and its risk is not checked. (The government is preparing an earthquake-resistant standard of a ceiling.)
j) Although the damage investigation of a building should be performed for every floor, it does not seem to be able to secure enough time.
k) An expert should decide the points to be checked and methods of the safe confirmation beforehand. Particularly, the check method of the main structural parts that are not easily seen should be decided in advance.
l) It is recommended that a person carrying out the safe confirmation goes around the points to be checked with an expert and experiences a judgment trial by the check list as his/her training.
m) As the judgment of the safe confirmation is not easy and covers only residual transformation of the damage, monitoring of the motion of the building should be useful. A method to examine an interlamellar variation between a floor and its upper floor with a marking off tools may be proposed as a simple and inexpensive method.
n) It will be useful to prepare the document indicating the points of the safe confirmation for individual building similar to the medical record. The structural engineers can advise because they recognize from which point the building is more likely to break by an earthquake. The document does not entail additional cost so much if it is prepared with the building certification.
o) When an expert of building structure checks the safety of the building, a judgment will be fast if there is a structural calculation sheet or the above-mentioned document similar to the "medical record" of the building.
p) It is realistic to narrow down the candidates of tentative stay facilities from many buildings in the district. The criteria of narrowing will be the location of the building (including expected number of tentative refugees and neighboring risk), the quake resistance of the building, the size of available floor, the probability of securing persons in charge of safety confirmation (by time zone, the day of the week).

8. CONCLUSION

At the time of the TIE, if persons who have difficulty returning home are not properly control, they will disturb transportation of urgent staff and supplies and fire fighting and so on. Therefore, it is very significant that companies establish temporary stay facilities as many as possible.

However, companies have various concerns when they establish the facilities. Among them, the responsibility of safety confirmation of the facilities is one of the most anxious matters because aftershocks may cause fatal and very severe damages to tentative refugees. It is important to support the companies which have intention to establish temporary stay facilities by providing useful sample of check lists, manuals and advices for proper and practical safety confirmation. The governments, researchers and experts should work together for this support.

Acknowledgements:

The author acknowledges collaboration and cooperation of members of the Center for Urban Earthquake Engineering (CUEE) in Tokyo Institute of Technology and the Business Continuity Advancement Organization (BCAO).

References:

Cabinet Office (2004), "the Result of Direct Damage Estimation," website of Cabinet Office (in Japanese) http://www.bousai.go.jp/jishin/chubou/shutochokka/13/shiryo2-1.pdf

Cabinet Office (2008), "the Simulation of Activity to Return Home," website of Cabinet Office (in Japanese) http://www.bousai.go.jp/jishin/chubou/shutohinan/080402/shiryo_1.pdf

Council on the Persons Who Have Difficulty Returning Home at the Time of Tokyo Inland Earthquake (CPDR) (2012a), "Final Report of CPDR," website of Cabinet Office (in Japanese) http://www.bousai.go.jp/jishin/chubou/taisaku_syuto/kitaku/saishu02.pdf

CPDR (2012b), "Guidelines on Securing Temporary Stay Facilities and their Management," website of Cabinet Office (in Japanese) http://www.bousai.go.jp/jishin/chubou/taisaku_syuto/kitaku/guideline03.pdf

The Headquarters for Earthquake Research (2010), "Result of Long-term Evaluation, Trench type Earthquake," website of the Headquarters for Earthquake Research (in Japanese) http://www.jishin.go.jp/main/choukihyoka/kaikou.htm

Japan Meteorological Agency (JMA) (2011), Website of "Explanation Table of the Seismic Intensity Level of JMA," website of JMA (in Japanese) http://www.jma.go.jp/jma/kishou/know/shindo/kaisetsu.html

Nakano, Akiyasu and Suzuki, Hidemasa (2012) "Legal Point of Remember on Business Operators' Countermeasures for Persons Who Have Difficulty Returning Home － For Securing Temporary Stay Facilities Dispelling Concerns of Business Operators," NBL No.984(2012.9.1), pp. 26-35, Shojihome Co., Ltd.

Tokyo Metropolitan Government (2012a), "the Ordinance of Measures for Persons Having Difficulty Returning Home," website of Tokyo Metropolitan Government (in Japanese) . http://www.bousai.metro.tokyo.jp/japanese/tmg/kitakujorei.html

---

[i] Explained in Headquarters for Earthquake Research (2010)

[ii] Japan Meteorological Agency (JMA) Seismic Intensity Scale

[iii] Tentative translation of JMA (2011) by the author

[iv] Mainichi Newspaper, Tokyo edition, September 11, 2012

[v] Prescribed in CPDR (2012a)

[vi] The original example of the check list is in Japanese. Table 1 is tentative translation by the author.

[vii] Performers of this Symposium are as follows:
Moderator: Prof. Hideki Kaji (CUEE)
Presentation
"Purpose and Present Situation": the author (CUEE, BCAO)
"Opinion of Companies providing Tentative Stay Facilities": Mr. Takeshi Mori (BCAO)
"Proposal of Safety Confirmation of the Facilities": Dr. Hitoshi Suwa (BCAO)
"The Concept of Safety Confirmation from the Viewpoint of the Characteristics of Buildings": Prof. Toru Takeuchi (CUEE)
Panel Discussion
Coordinator: the author
Panelists: As. Prof. Tetsu Yamada (CUEE), Prof. Toshihiro Osaragi (CUEE), Dr. Masamitsu Miyamura (BCAO), Mr. T. Mori, and Dr. H. Suwa

10CUEE CONFERENCE PROCEEDINGS
10th International Conference on Urban Earthquake Engineering
March 1-2, 2013, Tokyo Institute of Technology, Tokyo, Japan

BUILDING A DECISION AND AN OPERATIONS SUPPORT SYSTEM USING THE AGENT-BASED SIMULATION MODEL.

Kenichi Ishibashi[1)], Shinichi Tsuburaya[2)]

1) Associate Professor, Faculty of Environment and Information management,
Nagoya Sangyo University, Japan
kishibas@nagoa-su.ac.jp
2) Mitsubishi Heavy Industries, LTD., Japan

Abstract: This document describes the information collecting system under the emergency condition and manage it. This proposal is focusing the management cost and keep good working under the emergency condition. A by-product of the system, user of the system are hard to make a mistake.

1. INTRODUCTION

From late of 20's century, we had some serious disaster, Hanshin-Awaji Earthquake in Japan, Big Tsunami in Indian Ocean and the Great East Japan Earthquake. Its make a heavy loss of lives. In case of Japan, central government founded Central Disaster Prevention Council (CDPR) by the law. CDPR is working to prevent and mitigate the natural hazards. And CDPR is focusing to business continuity of public and private sector such as to create the BCP (Business Continuity Plan)/BCM (Business Continuity Management). Assuming that natural hazard is happened and makes damage in particular area. If it has a restoration power (e.g. socio-economical aspects) from the disaster, it's damage is relative low. Because public/private sector has a BCP/BCM, they know the way to recover from the disaster and can manage limited resources (human/physical resource). Public sector and private sector is setting same aim, saving a life under the emergency activity, however their aims are different under the recovery process.

2. AIMS AND OBJECTS

2.1 Aims

In this paper, it focused on the public sector's activity under the emergency situation when disaster happened. This paper aims to clear the conditions collecting the information about damages by disaster and related information.

Generally, natural hazards (Earthquake, Tsunami and more) has uncertainty. In other words, no one knows exact time these hazards happened. Science has been progressing, unfortunately we can not predict the occurrence time, place and its scale accurately. So it needs that to make the strategy to prevent natural hazards and mitigate the damage by it. If the society has equipped these strategies, this society will recover from the damage.

In this paper, it discusses the way of collecting and using the information by the public sector. Nagoya Port Office set the test case

Focusing an Emergency Activities, its aims to save suffers and enable to prevent the second disaster. Most important things are to get the accurate information about damages and adequate correspondences. Nowadays, some systems to support the emergency activities. Considering the error (system based error and human based error), dual use (Emergency use and Daily use) is suitable. That is, the frequency of using the system is very high under the dual use case. Then stuff who use the system are familiar with the system and system based error is easy to find out. Finally, average cost of the system is getting low.

2.2 Objectives

According to cost of the system, it is to be desired that installation and maintenance cost is getting low. However, it is not able to cut down on expense of the system. Because proposed system is needed the high reliability, the cost is very expensive at the result. Considering the cost benefit, cost is not changed depending on the system requirements. Then solution is frequency of using the system is getting higher.

In this paper, it shows that requirement for integrated information system to collect and deliver the information in public sector.

3. SYSMTEM REQUIRMENT FOR EMERGENCY RESPONSE ACTIVITY

3.1 System Requirements

Focusing the information collect process, that's not to say that all information collect process are automated. For example, it is able to get the transfer pathway data by the people using the GPS sensor and make the alert for a landslip automatically.

Most of the information collect process is human activity based. In other words, observer is going to the damaged area, they observe the damage and evaluate.

Therefore, evaluation result has an ambiguity. To prevent the vagueness, a third person is able to assess the damage. To give an actual example, to take the photo for damaged area with a measure.

It is desired that information collecting and reporting process are real-time processing. That is, conditions of the damaged area are changed time by time. Two of them are quite different, human and physical resources for emergency response are wasted.

According to former researches, members of the disaster countermeasures office are showing a tendency to keep on working in a few days. After emergency activities are converged, they fall ill. To prevent it, transferring their duties, it needs to easy to transfer. However, transferring process is different from normal transferring process. Most important point are quickness and accuracy.

3.2 Framework

As noted that requirements of the system are easy operation and easy to understand the damages. According to these conditions, GIS (Geographical Information System) is suitable.

3.3 Management of the system

To focus the management of the system, there is some possibility of doing that it is not working perfectly. Because, most of them (system) are specialized for emergency use only. Moreover, users of this system are not familiar with it, there is some possibility to make a mistake. To prevent, this system is usually used for lesson for emergency activity or inspect the berth. After all, users are to get skilled and difficult to make a mistake. Furthermore average cost of the system is getting lower. Consequently, the system is able to use daily and emergency case.

4. CASE STUDY OF NAGOYA PORT

4.1 About Nagoya port

According to the brochure of Port and Airport Department, the Chubu Regional Bureau (CRB-MLIT) shows that Nagoya Port is important role, that is the hub function of the industrial sector in Chubu region. Figure 1 shows that current status of international logistics in Chubu Area. It is clear that Nagoya Port is dominating other ports. More specific, imported items are industrial raw materials (e.g. LNG and crude oil) and exported items are machinery products, such as automobiles and industrial machinery.

Otherwise, Chubu region is designated as an affected area for “Tokai Earthquake”, “Tonankai Earthquake” and “Nankai Earthquake”. CDPR is setting an Expert Study Panel for predict the effect by these earthquake. Figure 2 shows that expected Tsunami heights and arrival times at coastal areas of Chubu region. It is clear that outside of Ise Bay, huge Tsunami is arriving up to 30 minutes after the earthquake. Otherwise inner area of Ise Bay, medium level (up to 3 m) is arriving more than 30 minutes after the

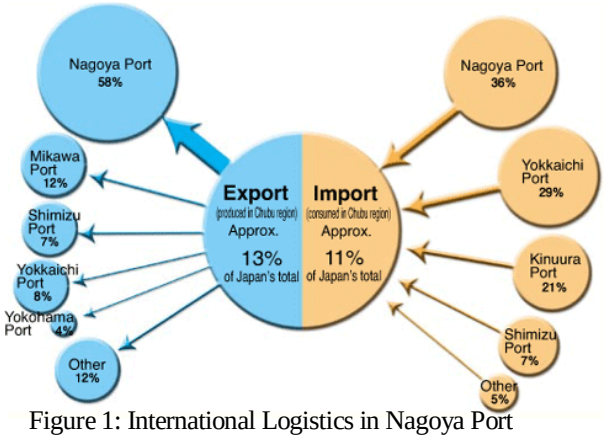


Figure 1: International Logistics in Nagoya Port earthquake.

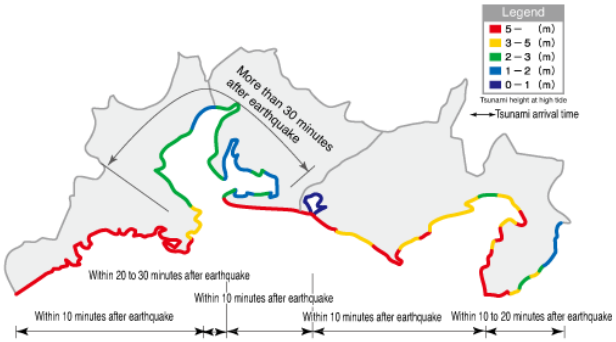


Figure 2: Tsunami Alert Area Map

50 years ago, Ise Bay was attacked by Big-scaled Typhoon, “Isewan Typhoon”. It made a high tide water, enormous people were suffered. Since 2008, the Chubu Regional Bureau (MLIT) has setting an Expert Study Group about high tide water and flood which is tackling to predict the damage by it.

CRB-MLIT is stated that “In the hinterland of Ise Bay, is an area of enormous manufacturing industry concentration and lively economic activity, with Nagoya as its core”. Nagoya Port is located the front line to face a natural hazards such as high tide water, Tsunami. Nagoya Port Office (NPO) has prevent and mitigation programs for each natural hazards, which aims to shorten the recovery time.

4.2 Emergency Program in Nagoya Port Office

NPO is assigned a role in an emergency action program which to assess the berth by their officer under the emergency case (such as Earthquake, Tsunami, High Tide Water). Moreover, if their own berth was safe, they have to support other local area office which damaged heavily.

However, no one has exact information that who came to the office within one hour after disaster happened. Because, disaster has much uncertainty (time, location and scale). And nobody knows exactly time to assess the damages of the berth. It is clear that key player of emergency action program is NPO’s officer.

In this case study, it focuses the officer's activity. An emergency action program is decomposed three parts, first one is checking officers' safety, second one is gathering condition for every officer, last one is to assess damages for each berth.

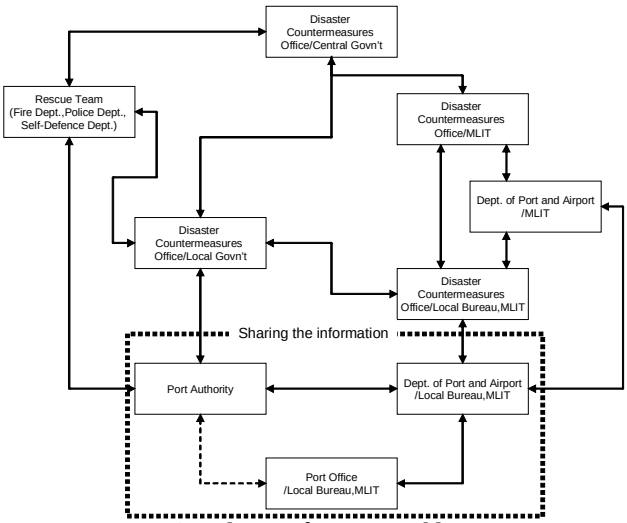


Figure 3: Relations for every public sector

4.3 Experimental System in Nagoya Port

NPO has equipped "Saigai-Infoweb" system which enables to collect the damages at the berth using the mobile phone (Show Figure 4). To specify the system, officers of the NPO are going to every damaged area, then they are taking a photo by their own/public mobile phone which include GeoCode (latitude and longitude). And they send the data (photo with GeoCode) via email by the mobile phone. NPO is collecting above data, they can check the damage easily.



Figure 4:Screen-shot (saigai-infoweb)

However, NPO has only Saigai-Infoweb, which does not cover all emergency activities. Then they can not handle with all data seamlessly. At the result, they can not supply effective information to emergency activities. We are discussing about the integrated system based on the LBS (Location Based Service) to support the emergency activities (Figure 5).

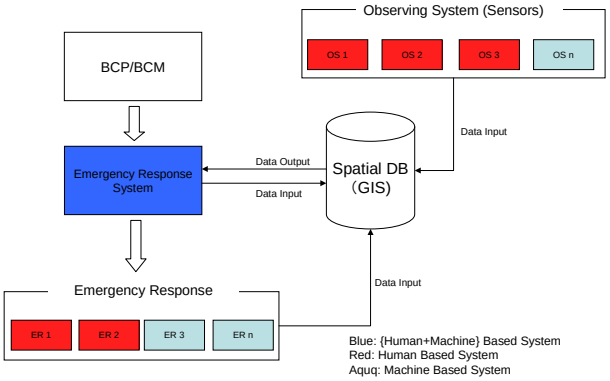


Figure 5: Integrated System Concept

Figure 5 is the overall concept for new integrated system. It mentioned below, NPO is working for assessing their own berth, emergency response and supporting other damaged local office/port. Again it note that these activity is depended on their officers. In other words, NPO is eager to get the information, number of officers within one hour after disaster happened.

Hereafter, introducing collaboration work with NPO, WAVE (Waterfront Vitalization and Environment Research Center) and author.

Figure xxx is concept based system. NPO has the BCP (Business Continuity Plan) for "Tokai Earthquake". We are just making the "Emergency Response System" which based on the BCP of the NPO. This system is issuing some emergency activities, which include assessing the berth, restoration work and supporting the other damaged local office to officers.

As it note that if Disaster Countermeasures Office does not have accurate information about officers' condition, it does not take an effective action. In the right side of Figure xxx, we set the observing system using some sensors. In Figure xxx, "OS 1, OS 2, …, OS n" means that observation system one to n. OS 1 is the "Confirmation of the safety for officers". It enables to confirm the officers' safety and grasp the number of officers to involve the emergency activity. These observing system is get data (e.g. damaged road, berth and more) every moment, then spatial DB is collecting these data. Finally, Disaster Countermeasures Office is easy to make a decision.

From 2008, we are tackling to make the system focused on the Emergency Response System.

5. CONCLUSION

In this paper, it explored the logic integrated Emergency Response System And to inform the Nagoya Port Office experimental study.

Acknowledgements:

The author expresses an acknowledgement deeply to support and discussion with Nagoya Port Office (Mr. Ito, Mr, Miyahara, , Mr. Okazaki: Deputy Director, Mr. Kasugai: Director) and Port and

Airport Department (Mr. Takei: Senior Planning Officer for Port and Airport, Mr. Horita: Senior Planning Officer for Port and Airport and Mr. Tanabe: Director), the Chubu Regional Bureau, Ministry of Land, Infrastructure, Transport and Tourism, Japan.

References:

Newmark, N.M. and Rosenblueth, E. (1971), "Fundamentals of Earthquake Engineering," Prentice-Hall Inc.

Trifunac, M.D. and Brady, A.G. (1975), "A Study on Duration of Strong Earthquake Ground Motion," *Bulletin of the Seismological Society of America*, **65**(3), 581-626.

Kasai, K., Fu, Y., and Watanabe, A. (1998), "Passive Control Systems for Seismic Damage Mitigation," *Journal of Structural Engineering*, American Society of Civil Engineers, **124**(5), 501-512.

MacRae, G. A. and Kawashima, K. (2001),"Seismic Behavior of Hollowed Stiffened Steel Bridge Columns," *Journal of Bridge Engineering*, American Society of Civil Engineers, **6**(2), 110-119.

Fujimoto, K. and Midorikawa, S. (2000), "Simplified Method for Predicting Ground Motion Intensity Map Considering Effect of Irregular Deep Underground Structure," *Proceedings of the 6th International Conference on Seismic Zonation*, Paper No. 2-23B.

10CUEE CONFERENCE PROCEEDINGS
10th International Conference on Urban Earthquake Engineering
March 1-2, 2013, Tokyo Institute of Technology, Tokyo, Japan

DISASTER AND ECONOMIC STRUCTURAL CHANGE AN EMPIRICAL ANALYSIS USING INPUT-OUTPUT FRAMEWORK

Yasuhide Okuyama[1)]

1) Professor, Graduate School of Social System Studies, University of Kitakyushu, and Center for Urban Earthquake Engineering, Tokyo Institute of Technology, Japan: okuyama@kitakyu-u.ac.jp

Abstract: In 1995, the Kobe Earthquake occurred in the second largest economic region of Japan, and its economic damages were accounted around 10 trillion yen. A catastrophic event in this magnitude would have surely created some long-run effects to the regional economy as well as to the surrounding regions. In addition, the recovery and reconstruction activities would have affected the economic structure of the region and interdependencies between regions. While these long-run economic effects may have become sizable, few studies have conducted to empirically measure such effects, due to the significant noises in economic data disturbed by macroeconomic influences from the outside. This paper presents an empirical investigation of long-run economic effects of the Kobe earthquake, using structural analysis methods. The results indicate significant changes in economic structure of the Kobe economy, and the changes are quite different across sectors and among factors. An additional investigation using shift-share analysis yields the regional specific changes; however, the corresponding decomposed factors of structural analysis with shift-share results appear complicated, and the difficulties to factor out earthquake specific effects exist.

1. INTRODUCTION

While significant progress has been made in recent years for the economic analysis of disasters, especially in the field of economic modeling of disaster impact (for example, Okuyama and Chang, 2004; and an excellent compilation of related papers by Kunreuther and Rose, 2004), the recent advancements have been more toward short-run impact analysis rather than toward the evaluation of long-run effect of such events. This tendency is partly resulted from the improved data availability of disaster damages and losses and from the increased multidisciplinary research activities about disasters for more detailed analysis and simulation of the impacts. Meanwhile, the uniqueness of each natural hazard and of the distribution of its damages and losses presents enormous challenges in economic analysis of disaster impact and effects. In particular, while some research suggests that impact from a catastrophic natural hazard may spill over not only to the surrounding regions but also to the distant regions via tightened interdependency of economic activities (for example, Okuyama et al., 1999), some other researchers claimed that the impact of even a large disaster ends up "insignificant total impacts" (Albala-Bertrand, 1993).

These arguments should have led to empirical ex-post investigation of disaster impact and effects; however, few studies have engaged such attempt. Most of those impact studies estimated, not measured, the impacts of a particular disaster based on the available damage data and some economic models, like input-output models and so on. Because in usual macroeconomic indicators, such as gross domestic products (GDPs) or gross regional products (GRPs), economic impact of a particular disaster can be potentially hidden within macroeconomic fluctuations and/or can be more likely to be cancelled out between negative impacts from damages and positive impacts of recovery and reconstruction activities, and also partly because the disaster statistics are not standardized even among developed countries and are even "somewhat crude measures," (Skidmore and Toya, 2002), the extraction of disaster impact and effects from empirically available macroeconomic data appears enormously entangled. Yet, the empirical measurement of disaster impact and effects is crucial to understand how a disaster affects economies and to improve the accuracy of impact estimates derived based on economic model.

In this paper, the economic effects of the Great Hanshin-Awaji Earthquake (also known as the Kobe Earthquake) occurred in 1995 are investigated empirically using a time-series of input-output tables and structural analysis methods. Next section briefly summarized the previous studies and findings related to economic impact and effect of natural disasters. Section 3 presents the data for the case study and the methodology for structural analysis. The results of analysis are illustrated and discussed in Section 4. Section 5 concludes this paper with the discussion of findings and some remarks.

2. ECONOMIC IMPACTS OF DISASTERS

The economic impact and effects of disasters have been studies in various contexts and with a range of time durations. Ex-ante analysis of a hypothetical or potential hazard occurrence is often performed for the decision-making of preparedness and mitigation strategies; and ex-post analysis of actual hazards and disasters is usually carried out to investigate how the event affected the economy and to examine to what extent the relief efforts by various levels of public sector and by other institutions are needed. Economic analysis of disasters can be also divided into two categories: analyses of short-run impact and of long-run effect. Short-run impact analysis of disaster intends to estimate the total (flow) impacts of a hazard for the duration of a few years, and usually employs input-output model, social accounting matrix, or computable general equilibrium model of a particular region, regions, or a nation. By its nature, short-run impact analysis estimates only flow changes and is able to distinguish between the negative impacts from losses and the positive impacts of recovery and reconstruction activities, which serve as concentrated demand injections to the region. Several short-run analyses of disasters were compiled in Okuyama and Chang (2004) and the methodologies are summarized in Okuyama (2007). On the other hand, long-run analysis of disaster effects aims to measure the effects of damages on stock, which may affect the long-run growth path of the damaged region, resulted from the changes in level of physical and human capital accumulation and technology replacement (Okuyama, 2003). The long-run analysis of disasters usually employs econometric models with time series data; and because of this, they cannot distinguish between negative and positive impacts of a disaster and can only derive net effects. Comparing to short-run impact analysis, long-run analyses of natural disasters have been limited, due mainly to the uniqueness of each disaster and also to the difference in details and extent of damage data gathered over time. Notable examples in this line of study using cross-country data to analyze the tendency between various indices of economic growth and disaster occurrences include Skidmore and Toya (2002), Rasmussen (2004), Cuaresma et al. (2008), and Cavallo et al. (2010). Interestingly, some of these studies provide conflicting or inconclusive results in terms of the relationship between economic growth and disasters. In particular, Cavallo et al. (2010) found that natural disasters, even focusing only on the largest events, do not have any significant effect on subsequent economic growth. Empirical evaluation of a particular disaster's long-run effect has been also limited and includes Odell and Weidenmier (2002) for the 1906 San Francisco Earthquake, Hornbeck (2009) for the 1930's American Dust Bowl, and Baade et al. (2007) for the 1992 LA Riot and 1992 Hurricane Andrew among others. Contrary to Cavallo et al. (2010) using country as the unit of analysis, these event specific studies found that a disaster brings some long-run effects, especially to some specific part of economy, such as regional economy (Hornbeck and Baade et al), or financial sector (Odell and Weidenmier). The contrast of the results between cross-country studies and regional and event specific studies supports the Albala-Bertrand's (2007) claim that a disaster causes localized damages and losses on capital and activities but may not affect negatively (or positively) the macro-economy, such as national economy, in both short-term and longer-term. At the same time, this claim implies that localized damages and losses may cause localized economic impacts, which may be significant to the local economy hit by the disaster. This paper investigates that how the Kobe earthquake affected the local economy structurally in the long-run, and whether or not the event follows the above studies' conclusions.

3. DATA AND METHOD

3.1 Data: Kobe Regional Input-output Tables

In Japan, designated large cities with the population greater than 700 thousand, including the City of Kobe, have compiled city's input-output tables every five years. In this study, the Kobe's city input-output tables for 1985, 1990, 2000, and 2005 are employed. Since the Kobe Earthquake occurred in 1995, this particular year's city input-output table was not constructed due to difficulties in data collection. The lack of 1995 table may create some difficulties in analysis, and they will be discussed in the analysis below.

Sector classification of each year's Kobe input-output table is slightly different, as the Japanese national tables' sector classification had changed over these years. The number of sectors had changed from 31 for 1985 to 34 for 2005. In order to make a consistent sector classification over the years but not to aggregate to much for losing the details, the sectors are rearranged to become 28 sectors as shown in table A-1 in Appendix.

In addition, these tables are in current price; thus, they need to be in a constant (real) price. Since the Ministry of Internal Affairs and Communications of the Japanese government published the constant price national tables for 1985-90-95 (in 1995 price) and 1995-00-05 (in 2005 price), the Kobe tables above are transformed to have the constant price (2005 price) based on the sectoral inflators calculated from these two constant price national tables.

3.2 Structural Decomposition Method

A well-summarized description of structural decomposition methods can be found in Miller and Blair (2009). In this subsection, the method of decomposition employed in this paper is illustrated. The key feature of this decomposition is to identify the factors of regional structural change, potentially resulted from the Kobe earthquake, distinguishing the regional specific changes from the macroeconomic trends.

Kobe regional input-output tables are constructed as a competitive import form in the following manner:

$$\mathbf{x} = \mathbf{Ax} + \mathbf{f} + \mathbf{e} - \mathbf{m} \quad (1)$$

where **x** is a vector of total outputs; **A** is a matrix of input coefficients; **f** is a vector of final demand; **e** is a vector of exports; and **m** is a vector of imports. In order to analyze regional specific changes in technology and demand, the tables need to be transformed to a non-competitive one. This can be done by calculating import coefficients based on (1) as follows:

$$M_i = \frac{m_i}{\sum_j a_{ij}x_j + f_i} \quad (2)$$

Using these import coefficients, the relationship (1) can be transformed:

$$\mathbf{x = Ax + f + e - M(Ax + f)} \quad (3)$$

where **M** is a diagonal matrix with import coefficients. Then, this will become:

$$\mathbf{x = \left[I - (I - M)A\right]^{-1}\left[(I - M)f + e\right]} \quad (4)$$

Suppose **D=I-M**, indicating a diagonal matrix of regional purchase coefficients, (4) can be:

$$\mathbf{x = (I - DA)^{-1}(Df + e)} \quad (5)$$

This, in turn, becomes a decomposition of total output into outputs induced by regional final demand and by exports as follows:

$$\mathbf{x = (I - DA)^{-1}Df + (I - DA)^{-1}e = x_r + x_e} \quad (6)$$

where $\mathbf{x_r = (I - DA)^{-1}Df}$ and $\mathbf{x_e = (I - DA)^{-1}e}$. Following Miller and Blair above and Hitomi et al. (2000), these two are decomposed but separately.

Decomposition of $\mathbf{x_r}$

For posing a hierarchy in structural decomposition, $\mathbf{x_r}$ can be rewritten as follows:

$$\mathbf{x_r = (I - DA)^{-1}Df = L_r f_r} \quad (7)$$

where $\mathbf{L_r = (I - DA)^{-1}}$ and $\mathbf{f_r = Df}$. Suppose the changes in output induced by regional final demand between periods 0 and 1 can be set as:

$$\mathbf{\Delta x_r = x_r^1 - x_r^0} \quad (8)$$

Then, plugging (7) into (8) and taking the average of two polar decompositions[1] yield:

$$\mathbf{\Delta x_r = L_r^1 f_r^1 - L_r^0 f_r^0 = \Delta L_r \bar{f}_r + \bar{L}_r \Delta f_r} \quad (9)$$

where $\mathbf{\Delta L_r = L_r^1 - L_r^0}$; $\mathbf{\Delta f_r = f_r^1 - f_r^0}$; $\mathbf{\bar{f}_r = \frac{1}{2}(f_r^1 + f_r^0)}$; and $\mathbf{\bar{L}_r = \frac{1}{2}(L_r^1 + L_r^0)}$. This is the decomposition of upper layer. In the lower layer, $\mathbf{\Delta f_r}$ and $\mathbf{\Delta L_r}$ are further decomposed.

First, since $\mathbf{f_r = Df}$, the changes in $\mathbf{f_r}$ can be decomposed similarly to (9) as follows:

$$\mathbf{\Delta f_r = \Delta D \bar{f} + \bar{D} \Delta f} \quad (10)$$

where $\mathbf{\Delta D = D^1 - D^0}$; and $\mathbf{\bar{D} = \frac{1}{2}(D^1 + D^0)}$. The first component of (10) represents the contribution from changes in regional purchase matrix, while the second components shows the contribution from changes in (total) final demand.

Second, according to Akita (1994 and 1999), the changes in Leontief inverse matrix in general can be decomposed as $\mathbf{\Delta(I - A)^{-1} = \Delta L = L^1\left[(L^0)^{-1} - (L^1)^{-1}\right]L^0}$. Using this notion, $\mathbf{\Delta L_r}$ can be decomposed as follows:

$$\begin{aligned}\mathbf{\Delta L_r} &= \mathbf{L_r^1\left[(L_r^0)^{-1} - (L_r^1)^{-1}\right]L_r^0} \\ &= \mathbf{L_r^1\left[D^1A^1 - D^0A^0\right]L_r^0} \\ &= \mathbf{L_r^1\left[\Delta(DA)\right]L_r^0} \quad (11)\end{aligned}$$

In addition, similar to the above, $\mathbf{\Delta(DA) = \Delta D\bar{A} + \bar{D}\Delta A}$. Then, (11) can be rewritten as:

$$\begin{aligned}\mathbf{\Delta L_r} &= \mathbf{L_r^1\left[\Delta D\bar{A} + \bar{D}\Delta A\right]L_r^0} \\ &= \mathbf{L_r^1\Delta D\bar{A}L_r^0 + L_r^1\bar{D}\Delta AL_r^0} \quad (12)\end{aligned}$$

Using (10) and (12), (9) can be rearranged as follows:

$$\begin{aligned}\mathbf{\Delta x_r} &= \mathbf{\Delta L_r \bar{f}_r + \bar{L}_r \Delta f_r} \\ &= \mathbf{\left[L_r^1\Delta D\bar{A}L_r^0\bar{f}_r + \bar{L}_r\Delta D\bar{f}\right]} \\ &\quad \mathbf{+L_r^1\bar{D}\Delta AL_r^0\bar{f}_r + \bar{L}_r\bar{D}\Delta f} \quad (13)\end{aligned}$$

in which the first component indicates the contribution from the changes in regional purchase matrix, the second component shows the contribution from the changes in technology, and the third component represents the contribution from the changes in final demand.

Decomposition of $\mathbf{x_e}$

As above, the output induced by exports can be rearranged to become $\mathbf{x_e = (I - DA)^{-1}e = L_r e}$. Then, again, using the average of polar decompositions, the changes in output induced by exports can be transformed similarly to (13):

$$\begin{aligned}\mathbf{\Delta x_e} &= \mathbf{\Delta L_r \bar{e} + \bar{L}_e \Delta e} \\ &= \mathbf{L_r^1\Delta D\bar{A}L_r^0\bar{e} + L_r^1\bar{D}\Delta AL_r^0\bar{e} + \bar{L}_r\Delta e} \quad (14)\end{aligned}$$

where $\mathbf{\Delta e = e^1 - e^0}$ and $\mathbf{\bar{e} = \frac{1}{2}(e^1 + e^0)}$. The first component of (14) indicates the contribution from the changes in regional purchase matrix, the second component shows the portion from the changes in technology, and the third represents the effects from the changes in exports.

Adding (13) and (14) provide the decomposition of the total output as follows:

$$\begin{aligned}\mathbf{\Delta x} &= \mathbf{\left[L_r^1\Delta D\bar{A}L_r^0\bar{f}_r + \bar{L}_r\Delta D\bar{f} + L_r^1\Delta D\bar{A}L_r^0\bar{e}\right]} \\ &\quad \mathbf{+\left[L_r^1\bar{D}\Delta AL_r^0\bar{f}_r + L_r^1\bar{D}\Delta AL_r^0\bar{e}\right]}\end{aligned}$$

[1] Dietzenbacher and Los (1998) argued that structural decomposition does not provide a unique solution, having "a multitude of equivalent forms (p.307)", this creates a inconsistency in results among different forms. They recommended to calculate all the possible combinations (if the number of determinants is *n*, the number of equivalent

$$+\bar{\mathbf{L}}_r\bar{\mathbf{D}}\Delta\mathbf{f}+\bar{\mathbf{L}}_r\Delta\mathbf{e} \quad (15)$$

This illustrates the decomposition of total output change into 1) the changes in regional purchase matrix, $\Delta\mathbf{D}$; 2) the changes in technology, $\Delta\mathbf{A}$; 3) the changes in final demand, $\Delta\mathbf{f}$; and 4) the changes in exports, $\Delta\mathbf{e}$.

3.3 Separation of Region Specific Effects: Shift-Share Analysis

Shift-share analysis is one of the decomposition techniques to analyze the influence of economic trend of a region through identifying the components of change. In particular, shift-share analysis decomposes the economic change in a particular region into three factors: national (macroeconomic) influence, industry specific influence, and regional specific factor. Using production level (output)[2] as the indicator of economy's performance, these three factors can be defined as follows:

National Share: $NS_i = x_i^0\left(X^1/X^0 - 1\right)$

Industry Mix: $IM_i = x_i^0\left(X_i^1/X_i^0 - X^1/X^0\right)$

Regional Shift: $RS_i = x_i^0\left(x_i^1/x_i^0 - X_i^1/X_i^0\right)$

where x_i^0 is the output level of industry i in a particular region at the beginning of the period, X_i^1 is the output level of industry i in the nation at the end of the period, and X^1 is the total output of the nation at the end of the period. Then:

$$\Delta x_i = x_i^1 - x_i^0 = NS_i + IM_i + RS_i \quad (16)$$

3.4 Decomposition of Region Specific Effects: Combining Shift-Share and Structural Decomposition Analyses

In order to decompose the region specific effects in the output change, the decomposition of regional shift relationship is attempted. As in Rose and Casler (1996), Dietzenbacher et al. (2000), and De Boer (2009), a multiplicative decomposition of input-output relationship in terms of change in output levels can be performed as follows:

Using equation (5), $\mathbf{x} = \left(\mathbf{I}-\mathbf{DA}\right)^{-1}\left(\mathbf{Df}+\mathbf{e}\right)$,

$$\frac{\mathbf{x}^1}{\mathbf{x}^0} = \frac{\mathbf{L}_r^1\mathbf{F}^1}{\mathbf{L}_r^0\mathbf{F}^1}\cdot\frac{\mathbf{L}_r^0\mathbf{F}^1}{\mathbf{L}_r^0\mathbf{F}^0} \quad (17)$$

where $\mathbf{x}^t$ is the output level at time t, $\mathbf{F}^t = \mathbf{D}^t\mathbf{f}^t + \mathbf{e}^t$. Since $\mathbf{L}^r = \left(\mathbf{I}-\mathbf{DA}\right)^{-1}$, (17) can be further decomposed into the relationship below:

$$\frac{\mathbf{x}^1}{\mathbf{x}^0} = \frac{\left(\mathbf{I}-\mathbf{D}^1\mathbf{A}^1\right)^{-1}\mathbf{F}^1}{\left(\mathbf{I}-\mathbf{D}^0\mathbf{A}^1\right)^{-1}\mathbf{F}^1}\cdot\frac{\left(\mathbf{I}-\mathbf{D}^0\mathbf{A}^1\right)^{-1}\mathbf{F}^1}{\left(\mathbf{I}-\mathbf{D}^0\mathbf{A}^0\right)^{-1}\mathbf{F}^1}\cdot\frac{\mathbf{L}_r^0\mathbf{F}^1}{\mathbf{L}_r^0\mathbf{F}^0} \quad (18)$$

By reversing the time periods in the weights (0 to 1 and 1 to 0) in Equation (17), the second multiplicative decomposition can be obtained:

$$\frac{\mathbf{x}^1}{\mathbf{x}^0} = \frac{\left(\mathbf{I}-\mathbf{D}^1\mathbf{A}^0\right)^{-1}\mathbf{F}^0}{\left(\mathbf{I}-\mathbf{D}^0\mathbf{A}^0\right)^{-1}\mathbf{F}^0}\cdot\frac{\left(\mathbf{I}-\mathbf{D}^1\mathbf{A}^1\right)^{-1}\mathbf{F}^0}{\left(\mathbf{I}-\mathbf{D}^1\mathbf{A}^0\right)^{-1}\mathbf{F}^0}\cdot\frac{\mathbf{L}_r^1\mathbf{F}^1}{\mathbf{L}_r^1\mathbf{F}^0} \quad (19)$$

Equations (18) and (19) are so called polar decompositions; thus, the geometric mean of them can yield the following:

$$\frac{\mathbf{x}^1}{\mathbf{x}^0} = \sqrt{\Delta\mathbf{D}^1\times\Delta\mathbf{D}^2}\cdot\sqrt{\Delta\mathbf{A}^1\times\Delta\mathbf{A}^2}\cdot\sqrt{\Delta\mathbf{F}^1\times\Delta\mathbf{F}^2}$$

$$= \Delta\mathbf{D}\cdot\Delta\mathbf{A}\cdot\Delta\mathbf{F} \quad (20)$$

where $\Delta\mathbf{D}^1 = \dfrac{\left(\mathbf{I}-\mathbf{D}^1\mathbf{A}^1\right)^{-1}\mathbf{F}^1}{\left(\mathbf{I}-\mathbf{D}^0\mathbf{A}^1\right)^{-1}\mathbf{F}^1}$ in Equation (18),

$\Delta\mathbf{D}^2 = \dfrac{\left(\mathbf{I}-\mathbf{D}^1\mathbf{A}^0\right)^{-1}\mathbf{F}^0}{\left(\mathbf{I}-\mathbf{D}^0\mathbf{A}^0\right)^{-1}\mathbf{F}^0}$ in Equation (19), and so forth.

Plugging the relationship (20) in to the regional shift relationship in (16) can derive the following relationship:

$$RS_i = x_i^0\left(\Delta D_i^r\cdot\Delta A_i^r\cdot\Delta F_i^r \;-\; \Delta D_i^N\cdot\Delta A_i^N\cdot\Delta F_i^N\right) \quad (21)$$

Then, in order to make a comparison between regional and national changes, (21) can be transformed:

$$RS_i = x_i^0\cdot\left(\Delta D_i^N\cdot\Delta A_i^N\cdot\Delta F_i^N\right)\times\left(\frac{\Delta D_i^r}{\Delta D_i^N}\cdot\frac{\Delta A_i^r}{\Delta A_i^N}\cdot\frac{\Delta F_i^r}{\Delta F_i^N} \;-\; 1\right) \quad (22)$$

4. RESULTS AND ANALYSIS

Figure 1 below illustrates the distribution of decomposed regional shift of the Kobe economy during 1990 and 2000 using equation (22). With a casual observation, the number of negative regional shifts by sector is greater than the positive ones, highlighting the decline of the Kobe's total output. Especially, three services sectors (22: Port Related Transport Services; 23: Other Transport Services; and 24: Public Services) and sector 3: Food and Kindred Products have notably large negative values, with the sizable part of them is attributed to the changes in final demand (colored in yellow-green), including regional final demand and export (demand from outside of the region). This large share of final demand decline can be also observed in other sectors' negative portion. This tendency implies that the final demand decline is the main regional cause for the decay of the Kobe economy during this period. While it is uncertain with the current decomposition framework whether the decline from regional final demand or export is the foremost cause, this result should be related

[2] Oftentimes, number of employments, rather than output level, is used for shift-share analysis, because it is easier to obtain in a regional context and for regional employment analysis. Shift-share analysis with output level can be found Mayor and López (2008) and Márquez et al. (2009) among others.

to the population decline in the City of Kobe during this period.

In terms of other decomposed factors, regional interindustry linkage (colored in blue) has both positive and negative changes. Major positive changes of this factor can be found in sectors 22 and 23 (but both sectors have the net negative value due to a large negative change in final demand), while the large negative changes are with sectors 8 (Primary Metals Industry) and 19 (Commerce). It is a well-publicized fact that one of the major primary metal companies (Kobe Steel, Ltd.) in Kobe was heavily damaged by the earthquake and re-organized their production system throughout Japan, and this may contribute to the decline of regional interindustry linkage of this particular sector.

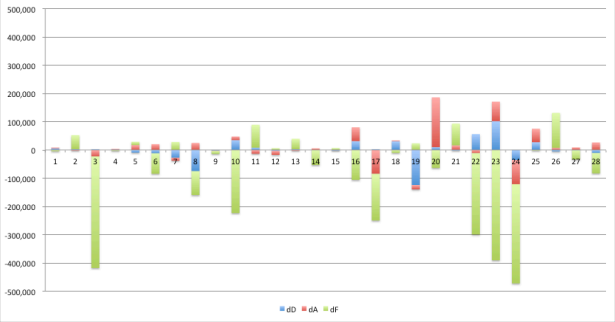


Figure 1. Distribution of Decomposed Regional Shift (1990-2000)

As for the changes in production technology (colored in red), there are some large positive gains in sectors 20 (Finance and Insurance) and 23, while some negative changes are seen in sectors 17 (Construction) and 24. Finance and insurance sector has net positive change of output during this period, their importance in financing the recovery and reconstruction activities may have led to this positive gain. On the other hand, the decline of construction sector in Kobe may be seen as a surprise, because the recovery and reconstruction demand after the earthquake should be mostly on construction sector. As a matter of fact, the regional demand (in yellow green) of construction sector is also a negative value. A caveat for Figure 1 is that these values are changes during 1990 and 2000. Year 1990 was the highest point of the ill-fated bubble economy in Japan, with the construction sector's output was the record high; while in 2000 the reconstruction activities in Kobe still continued, it was five years after the earthquake and in the middle of the Japanese economy's 20-year slump. Therefore, the output of construction sector was declined from 1990 (record high) to 2000 (some reconstruction activities, but generally a slump economy).

5. CONCLUSIONS

The above results have some implications to the recovery and reconstruction strategy for a disaster. First, as seen in Figure 1, the decline of final demand is a major cause for the total output decrease. As in the Keynesian economic view, final demand drives an economy. In a disaster situation, final demand decrease can be caused through population decline, either loss of lives, out-migration, or the combination of them. It is known that the City of Kobe lost significantly its population after the earthquake, most of them evacuated or migrated out of the city, and the city requires 10 years to regain the previous population level. If this final demand decline were caused by regional demand decline, it is crucial to regain population as quickly as possible after the event in order to maintain its final demand level. On the other hand, if this final demand decline were resulted from the decrease in export, its recovery may be more complicated. The drop of exports is originated from the change in purchase location by other regions, and it may be difficult to bring these lost exports back to the original location of purchase. Hence, it is also important that the speedy recovery of damaged production facilities to maintain the customers in other regions.

As for the weakened regional interindustry linkages, except for some light manufacturing sectors, such as 10: Industrial Machinery and Equipment and 16: Miscellaneous Manufacturing, if this trend were caused by the regional hollowing-out process, it would be very challenging to counter this trend. At the same time, services sectors including transportation sectors, for example sectors 22, 23, and 25, can be arranged to strengthen the regional interindustry linkage through reconstruction policy, such as promotion of local service utilization.

On the contrary to the regional linkages, it is rather problematic to encourage local industry to alter their technology for growth of the regional economy in a disaster situation, since many companies would be in their survival stage recovering from the damages and trying to maintain their customers. Unless the situation forces it to adapt a new production system as in 20: Finance and Insurance, this factor can be left for each company's discretion.

References:

Albala-Bertrand, J.-M. (2007) "Globalization and Localization: An Economic Approach", in H. Rodriguez, E.-L. Quarantelli, and R.-R. Dynes, eds., *Handbook of Disaster Research*. Springer, New York, NY: 147-67.

Albala-Bertrand, J.M. (1993) *The Political Economy of Large Natural Disasters: With Special Reference to Developing Countries*. Oxford, UK: Clarendon Press.

Akita, T. (1994) "Interregional Interdependence and Regional Economic Growth in Japan: an Input-output Analysis," *International Regional Science Review* 16: 231-248.

Akita, T. (1999) "The Role of the Kanto region in the Growth of Japanese Regional Economies 1965-1985," in G.J.D. Hewings, M. Sonis, M. Madden, and Y. Kimura (eds) *Understanding and Interpreting Economic Structure*. New York, NY: Springer-Verlag.

Baade, R.A., Baumann, R., and Matheson, V. (2007) "Estimating the Economic Impact of Natural and Social Disasters, with an Application to Hurricane Katrina", *Urban Studies* 44 (11): 2061-2076.

Cavallo, E., Galiani, S., Noy, I., and Pantano, J. (2010) "Catastrophic Natural Disasters and Economic Growth", Inter-American Development Bank Working Paper Series: No. IDB-WP-183.

Cuaresma, J.C., Hlouskova, J., and Obersteiner, M. (2008) "Natural Disasters as Creative Destruction?: Evidence from Developing Countries", *Economic Inquiry*, 46 (2), pp. 214-226.
Chen, Y-Y. and J-H. Wu. (2008) "Simple Keynesian Input-output Structural Decomposition Analysis Using Weighted Shapley Value Resolution," *Annals of Regional Science* 42: 879-892.
Dacy , D.C. and H. Kunreuther. (1969) *The Economics of Natural Disasters*. New York: The Free Press.
De Boer, P. (2009) "Multiplicative Decomposition and Index Number Theory: An Empirical Application of the Sato-Vartia Decomposition," Economic Systems Research 21 (2): 163-174.
Dietzenbacher, E. and B. Los. (1998) "Structural Decomposition Techniques: Sense and Sensitivity," *Economic Systems Research* 10 (4): 307-323.
Dietzenbacher, E., A.R. Hoen, and B. Los. (2000) "Labor Productivity in Western Europe 1975-1985: An Intercountry, Interindustry Analysis," *Journal of Regional Science* 40 (3): 425-452.
Hitomi, K., Y. Okuyama, and G.J.D. Hewings. (2000) "The Role of Interregional Trade in Generating Change in the Regional Economies of Japan, 1980-1990." *Economic Systems Research*, 12 (4): 515-537.
Hornbeck, R. (2009) "The Enduring Impact of the American Dust Bowl: Short and Long Run Adjustments to Environmental Catastrophe", NBER Working Paper Series: W15605.
Kunreuther, H. and A. Rose. eds. (2004) *The Economics of Natural Hazards, Volume I & II*. Northampton, MA: Edward Elgar.
Márquez,M.A., J. Rimajo, and G.J.D. Hewings. (2009) "Incorporating Sectoral Structure into Shift-Share Analysis," *Growth and Change* 40 (4): 594-618.
Mayor, M. and A.J. López. (2008) "Spatial Shift-Share Analysis versus Spatial Filtering: an Application to Spanish Employment Data," *Empirical Economics* 34: 123-142.
Miller, R.E. and P.D. Blair. (2009) *Input-Output Analysis: Foundations and Extensions Second Edition*. New York, NY: Cambridge University Press.
Odell, K.A. and Weidenmier, M.D. (2002) "Real Shock, Monetary Aftershock: The San Francisco Earthquake and the Panic of 1907", NBER Working Paper Series: W9176.
Okuyama, Y. (2003) Economics of Natural Disasters: a Critical Review, Research Paper 2003-12, Regional Research Institute, West Virginia University.
Okuyama, Y. (2007) "Economic Modeling for Disaster Impact Analysis: Past, Present, and Future", *Economic Systems Research*, 19 (2), pp. 115-124.
Okuyama, Y. and Chang, S.E. eds. (2004) *Modeling Spatial and Economic Impacts of Disasters*. New York: Springer.
Okuyama, Y., G.J.D. Hewings, and M. Sonis, (1999) "Economic Impacts of an Unscheduled, Disruptive Event: A Miyazawa Multiplier Analysis," in G.J.D. Hewings, M. Sonis, M. Madden, and Y. Kimura (eds.) *Understanding and Interpreting Economic Structure*, Springer-Verlag: 113-144.
Rasmussen, T.N. (2004) Macroeconomic implications of natural disasters in the Caribbean, IMF Working Paper WP/04/224, International Monetary Fund.
Rose, A. and S. Casler. (1996) "Input-Output Structural Decomposition Analysis: A Critical Appraisal," *Economic Systems Research* 8 (1): 33-62.
Skidmore, M. and Toya, H. (2002) "Do Natural Disasters Promote Long-run Growth?" *Economic Inquiry*, 40 (4), pp. 664-687.
Sorkin, A.L. (1982) *Economic Aspects of Natural Hazards*. Lexington, MA: Lexington Books.

Appendix

Table A-1. Sectoring Scheme of Kobe Input-output Table

Sector Number	Industries
1	Agriculture, Forestry, Fisheries
2	Liquor
3	Food and Kindred Products
4	Apparel and Textile Products
5	Lumber, Wood Products and Furniture
6	Rubber Products
7	Chemicals and Allied Products
8	Primary Metals Industries
9	Fabricated Metal Products
10	Industrial Machinery and Equipment
11	Heavy Electrical Equipment
12	Electrical Appliances
13	Shipbuilding Industry
14	Other Transport Industry
15	Precision Machinery
16	Miscellaneous Manufacturing Industries
17	Construction
18	Utilities
19	Commerce
20	Finance and Insurance
21	Real Estate
22	Port Related Transport Services
23	Other Transport Services
24	Public Services
25	Business Services
26	Personal Services
27	Government Enterprises
28	Others

10CUEE CONFERENCE PROCEEDINGS
10th International Conference on Urban Earthquake Engineering
March 1-2, 2013, Tokyo Institute of Technology, Tokyo, Japan

VERIFICATION OF THE NATIONAL RECONSTRUCTION AGENCY AS AN INSTITUTIONAL SCHEME FOR RECONSTRUCTION AFTER LARGE-SCALE DISASTERS

Hideki Kaji

Professor, Center for Urban Earthquake Engineering, Tokyo Institute of Technology, Japan
kaji@cuee.titech.ac.jp

Abstract: The intensive reconstruction works of the Tsunami affected area by the 2011 Tohoku Pacific Earthquake have been launched since February 10, 2012 with the inauguration of the Reconstruction Agency, which consists of about 300 seconded staffs by the respective ministries of central government with its headquarter in Tokyo and three local offices in three affected prefectures. The main functions of the Reconstruction Agency are to mediate conflicts between central ministries, to designate the special district for reconstruction, and to allocate the special subsidy for promoting reconstruction. This paper reviews the ten-month activities of the Agency and to identify the current problems to be solved. The paper, thus, tries to verify whether the establishment of such Reconstruction Agency will be effective as a regular institutional scheme for reconstruction after large-scale disasters in future.

1. INTRODUCTION

Two years have passed since the occurrence of the Tohoku Pacific Ocean Earthquake on 11 March, 2011. The intensive reconstruction works of the affected areas, however, have been started since one year ago when the National Reconstruction Agency (note as the Agency hereafter) was inaugurated, as there had been no regular rule of institutional arrangement for reconstruction after disasters in Japan so far. Thus, after a violent and heated argument about the rights and wrongs of necessity of new special organization for reconstruction, it was decided that the Agency could be established as a temporally organization valid for ten-year period of time, under the legal authorization of Basic Reconstruction Law of the Tohoku Pacific Earthquake enacted on 24 June 2011. The detail institutional structure and functions of the Agency were then clarified by the Law for Establishment of a Reconstruction Agency enacted on 16 December, 2011. The Agency has, thus, started its business since 10 February, 2012. It had passed almost one year after the occurrence of the Earthquake.

The president of the Agency is concurrently held by the Prime Minister, so as to represent its full responsibility for reconstruction activities. The total number of the staff is 330 persons, who were seconded by the respective Ministries of central government. The headquarters of the Agency locates in Tokyo, and three local departments with the stuff of 30 persons and two branch offices respectively are set in the three affected Prefectures: Iwate, Miyagi, and Fukushima.

The Agency has three principal functions. They are;

(a) To appropriate, in a lump, the expenses for all public projects which are related to reconstruction works and originally handled by respective Ministries of the central government,
(b) To designate “Special District for Reconstruction”, and
(c) To allocate a special subsidy to reconstruction projects proposed by the affected local governments.

The Japanese Government decided to spend about JPY 19 trillion (US$ 224 billion, at the rate of US$ 1=JPY85) in the first 5 years of ten-year reconstruction period which were designated as the intensive reconstruction period. Thus, JPY 14 trillion (US$ 165 billion) has already been used for mainly rescue and relief activities, debris treatment, urgent recovery of public facilities, temporally housing construction and so on, before the establishment of the Agency. In FY 2012, JPY 3.775 trillion (US$ 44 billion) has been earmarked in the budget for the reconstruction. Out of them, JPY1.732 trillion is allocated to the governmental general account as the special use for reconstruction related programs including improvement of disaster management capacity of all over Japan from the nation-wide point of views. Thus, the amount of the special account that the Agency can directly control is about JPY 2,043 billion (US$ 24 billion) (Table1).

This paper reviews the ten-month activities of the Agency and identifies the current problems to be solved, and based on that, tries to verify whether this Agency will be able to effectively work as a regular institutional scheme for reconstruction after large-scale disasters in future.

Table1. Special account handled by the Agency (billion yen)

	Item	Amount
Reconstruction management cost	Lump sum subsidy to LG	286.8
	Adjustment cost	5.0
	Fukushima resettlement	4.2
	Interest subsidization	1.1
	Administration cost	3.3
	Sub Total	300.4
Lump sum account of Ministry's project	Public project	488.1
	NPP disaster	456.9
	Debris treatment	344.2
	Financing to business	121.0
	Others	332.7
	Sub Total	1,742.9
Grand Total		2,043.3

(Reconstruction Agency (2012))

2. PROGRESS OF RECONSTRUCTION

First of all, the paper reviews the current progress of the reconstruction based on the report of the Agency (2012).

2.1 Debris treatment

Debris treatment is the first and the most urgent job to initiate quick reconstruction. Total volume of debris by collapsed houses or so was about 18,020 thousand ton. In addition, 9,560 thousand ton of Tsunami sediments were remained. The central government planned to completely dispose them by the end of March, 2013. As of the end of October, 84% and 58% of them were removed but only 30% and 11% were disposed respectively. The delay of disposal was mainly due to lack of cooperation by other local governments which were afraid of contamination with radioactivity at the early stage.

2.2 Recovery of public infrastructure

Since the budget has been smoothly executed, the affected basic infrastructures including lifelines and public facilities have been quickly recovered as follows:

As to highway and national road, the recovery ratio is 100% and 97% (as of July, 2012) respectively. Railway was recovered by 89% on an operation base. The airport was recovered by 100%. With regard to major distribution harbor, 79 harbors out of 101 harbors have been under repair (78%), and are expected to be completed by the end of March, 2012.

As to fishing port, 319 ports were destroyed by the tsunami. Out of them, 111 ports (35%) were recovered on their unloading function of piers as of October, 2012. A heap of debris sunk under the fishing ground was taken off by almost 100%. Eventually, a catch of fish has come up to 65% of that before the earthquake during the period from June to October, 2012.

With regard to farm land, the total area of 21,480 ha were damaged by infiltration of seawater, and at the end of September, 2012, the cultivation could be resumed in 8,190 ha (38%) of farm land. It is planned to complete in three years.

The recovery of other public services is as follows.

- Recovery of lifelines:
  Electricity (96%), Gas (86%), Water supply (98%), Telephone (99%), and Mobile phone (99%)
- Recovery of public services:
  Post office services (91%), Mail delivery services (80%), Admission to hospital (81%), and School education (100%)

2.3 Special districts program

The scheme of "Special District for Reconstruction" is authorized by its own law enacted on 14 December 2011, aiming to encourage the creative and flexible reconstruction programs which meet to cultural and geographical features of the affected regions, and to achieve their quick and smooth implementation. Thus, in a designated district, regulations and formalities for project approval are simplified, tax and financial exception can be applied, and authorized land use can be exceptionally readjusted if necessary. The scheme is applicable to the 222 affected local municipalities of 11 prefectures.

Those municipalities which have an intention to be designated as the Special District are supposed to submit either of the following planning documents to the Prime Minister.

a. Reconstruction Promotion Plan
   To loosen and simplify regulations and formalities, and to apply exceptional tax policy
b. Reconstruction Implementation Plan
   To apply special formalities and one stop claim counter to readjustment of pre-earthquake land use plan to new reconstruction plan
c. Reconstruction Subsidy Payment Plan
   To estimate budget frame work of special subsidy needed for reconstructing severely affected area

As of 14 December, 2012, the thirty districts were designated by the Agency (Table2). Since some of them are thought of as similar schemes, they can be roughly classified into six types.

The first type, in which 14 districts can be aggregated, aims to apply the exemption from corporation tax to newly locating industries.

The second type, in which four districts can be categorized, tries to improve welfare, health, and medical services by relaxing a deployment standard of medical doctor and restrictions on selling medical appliances.

The third type, consisting of four districts, aims at relaxation of restrictions for land use so as to be able to construct prohibited buildings.

The forth type, consisting to four districts, is for applying interest supplementation to newly locating tourism and manufacturing industries.

The fifth type, consisting of two districts, aims to extend the regulated period of temporal buildings, 2 years and three months, by an extra year.

And the final type, aggregated by two districts, is for

permitting unemployed persons caused by the earthquake to interrupt the enrollment in pension program.

Table2. Designated special districts for reconstruction

Prefecture	Tax free	Medical services	Land use	Interest	Temporary building	Pension	Total
Aomori	1			2			3
Iwate	1	1	1				3
Miyagi	9	1	3				13
Fukushima	2	2		2	1	1	8
Ibaragi	1					1	2
Tochigi					1		1
Total	14	4	4	4	2	2	30

2.4 Allocation of special subsidy

In this scheme, the reconstruction projects which can be subsidized are divided into two categories: Basic projects and the related promotion projects. The basic projects are regarded as the very fundamental elements of reconstruction, and thus, 40 structural projects under the jurisdiction of the five central ministries are identified. The main projects are as follows:

- Fisheries facilities and fishing port construction
- Repair and maintenance of farmland
- Construction of public emergency houses for victims
- Mass relocation program of community village for protecting from a disaster
- Urban redevelopment and land readjustment project for urban rehabilitation
- Disaster resilient projects for fishery village
- Protection against liquefaction in built-up urban area
- Protection from landslide in developed residential land

Under this scheme, the special subsidy equivalent to half of the project cost, which normally local governments have to shoulder, can be provided by the central government. In other words, 100 % of the project cost is supposed to be shouldered by the central government.

As to a promotion project which is closely related to the basic project and responsible for being independently implemented by the local government, the central government provides 80% of the project cost as supplemental subsidy. Thus, the local government shares only 20 % of the project cost.

The Agency invited the affected local governments to propose the reconstruction projects which are applicable to this subsidy. Up to the end of December 2012, the invitations were made four times.

1st time, 2 March, 2012
2nd time, 25 May, 2012
3rd time, 24 August, 2012
4th time, 30 November, 2012

The subsidies allocated amounts to JPY 1370 billion for the total project cost of JPY 1,683 billion (81%). Among the prefectures, Miyagi shares 55% of total subsidy (Table3). Since the capacity of the local governments for implementing these proposed projects is limited, the practical implementation ratio is not so high.

Table3. Allocation of special subsidy (billion yen)

Prefecture	Total project Cost(A)	National. Subsidy(B)	% (B/A)	% Share
Hokkaido	0.02	0.02	100%	0.0%
Aomori	3.74	3.09	83	0.23
Iwate	493.38	403.55	82	29.45
Miyagi	922.12	751.96	82	54.89
Fukushima	214.29	173.73	81	12.68
Ibaragi	37.33	28.73	77	2.10
Tochigi	0.81	0.61	75	0.04
Saitama	0.05	0.04	80	0.00
Chiba	9.87	7.67	78	0.56
Niigata	0.10	0.09	90	0.01
Nagano	1.18	1.10	93	0.08
Total	1682.89	1370.47	81	100.0%

2.5 Housing reconstruction of local government

The Tohoku Pacific Ocean Earthquake gave vey severe damage to the 48 municipalities of 6 prefectures, where the reconstructions of urban area have to be made from scratch. The central government thus dispatched planning experts to these affected municipalities, and supported them to make the reconstruction plan. Eventually, 43 municipalities excluding 5 municipalities contaminated with radioactivity in Fukushima could afford to formulate the plan by the end of December 2012.

The key component in their plan is how to resettle the affected village communities in a safe condition. For this purpose, three schemes are provided under the full financial support of the central government.

The first one is to relocate a village community as a whole to safe elevated land where no tsunami risk will be anticipated in the future. This scheme is called as "Mass Relocation Program of Community Group to Protect from Disasters (note as Mass Relocation Program, hereafter)". The Program can be applied under the condition that more than five households in a community agree with relocation. The municipal government is supposed to buy the land owned by the relocating households, and to designate them as "a vulnerable area to disaster", where inhabiting is strictly prohibited (Figure1).

Currently, the Program is under consideration about 276 villages with 26,000 households in 23 municipalities. And As of 25, December 2012, the implementation plan was already authorized by the Ministry of Land, Infrastructure, Transport and Tourism (MLIT) for 159 villages with 24,148 households in 23 municipalities (Table4).

The second is to raise low and subsidized land where tsunami risk is very high, by means of heaping up rock and soil, followed by land readjustment project for consolidating urban area (Figure2). The scheme was applied to 57 districts, and the implementation plans have been authorized on 34 districts, as of 30 November, 2012.

Table4. Mass Relocation Program

Prefecture	No. of municipalities	No. of villages	No. of households
Iwate	7	44	5,183
Miyagi	12	108	16,652
Fukushima	4	7	2,313
Total	23	159	24,148

(As of 25 December, 2012)



Figure1. Image of community relocation to elevated land

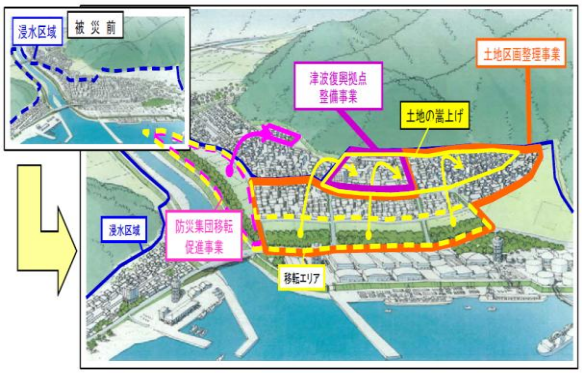


Figure2. Land raising and readjustment

The third is public disaster-house construction project for those victims who cannot afford to build their houses by themselves due to low income. About 24.000 units of houses are planned to be constructed in the three affected prefectures. Looking at the progress of implementation at the end of the October, 2012, however, it is estimated that only 57% of the houses will be able to be completed by the end of March, 2015, when the temporal houses have to be vacated. (Table5).

Table5. Public disaster-house construction (units)

Prefecture	Plan	Under construction	Land acquired	To be completed by the FY2014
Iwate	5,594	303	962	5,118
Miyagi	15,317	455	3,219	5,852
Fukushima	3,019	90	1,023	2,723
Total	23.930	848	5,204	13,693

(Yomiuri News Paper, 19 November, 2012)

2.6 Recovery of Industries

As to mining and manufacturing, the index of industrial production of the three affected prefectures recovered to 90.7% in June, 2012, while it was 97.5% before the event.

With regard to agriculture, about 38 % of farmland damaged by seawater was refreshed, and 40 % of farming bodies out of 10,200 bodies could afford to resume their cultivation. As to fisheries, 66 % of facilities for processing marine products have been recovered, and a catch of fish came up to 65 % to that in the pre-event. The recovery of tourism, however, is far behind. The tourists visiting the affected three prefectures in June decreased by 21% compared to the normal year.

In order to promote recovery of the affected smaller businesses, the Small and Medium Enterprises Agency (SMEA) under the MITI provides "The Subsidy to Recovery and Reconstruction of Equipment and Facilities for Smaller Group Enterprises (called as Group Subsidy, hereafter)" to those enterprises which play very important role in the region and suffered from very severe damage by the earthquake.

In this scheme, 75% and 25% of the project cost are shouldered by the national and prefectural government, respectively. Until the end of November, 2012, the SMEA invited the applications six times, and approved 400 groups with 8,685 enterprises. The total amount of subsidy paid was JPY 359 billion (US$ 4.2 billion). This scheme is very much appreciated by small and medium enterprises and thus the applications were far beyond the budget framework. Roughly speaking, the gap between reservation fund and requesting budget is three times, resulting in very low adoption ratio (Iwate-Nippou (2013)).

Table6. Allocation of group subsidy

	No. Groups	No. of Companies	Amounts (JPY billion)
Aomori	10	208	8.6
Iwate	63	931	64.6
Miyagi	133	3,987	204.1
Fukushima	140	2,104	61.7
Ibaragi	50	1,325	17.4
Chiba	4	130	2.6
Total	400	8,685	359.0

(Approved by the end of November, 20122)

3. CURRENT PROBLEMS IDENTIFIED

3.1 Public infrastructure

The most of major public infrastructures seem to be successfully recovered so far. The point is, however, whether all infrastructures should be recovered as they were. In particular, the production system of fishery in the region had been very traditional and individually-oriented with small scale. The reconstruction must be very good opportunity for it to be restructured and modernized into a large-scale and corporative body. In this sense, it is not always necessary for

all collapsed fishing port to be recovered, or to be partially scrapped and integrated with major large ports.

With regard to agriculture, the situation is the same. The resumption of cultivation as it was done should not be the target of reconstruction, but some more value added should be given to its production system by integrating with processing and distribution.

3.2 Special reconstruction district

As seen in the special districts program (2.3), the formalities for requesting the scheme is rather complicate and a pile of documents have to be prepared, while the programs planned by the local governments are quite similar. Therefore, the Agency should provide a prototype program so that the local governments can just select it, resulting in lightening their burden.

3.3 Housing reconstruction

The housing reconstruction makes very slow progress. As of 6 December, 2012, the total number of evacuees is 321,433 persons, who are living in temporary houses, public apartment houses, and private rental houses.

The basic reasons why housing reconstruction cannot be made smoothly lie on the difficulty of land acquisition for new residential area, while former areas are vulnerable to tsunami and partially have subsided about 60 to 100 cm.

In addition, there is an institutional reason that makes new community resettlements delay. As mentioned earlier, the Agency has an authority to appropriate, in a lump, the expenses for all public projects which are related to reconstruction works. The implementation of the project is, however, rested with the respective central government. A new community must be composed not only by houses but also by nurseries, schools, shops, industries, and so on, which are constructed by the guidance of separate central governments, resulting in the absence of integration.

In order to accelerate community resettlements, therefore, a coordination body which has strong authority is definitely needed..

3.4 Recovery of industries

As mentioned, the group subsidy scheme is very much appreciated by the affected smaller businesses for their effective recovery. However, only 30% of the applicants could be funded due to the limit of reservation fund. Apart from insufficiency of the budget to the victim's needs, some other problems are also identified. First, it can be used only for recovering to the original business shape. However, the previous system before the event cannot be well worked unless the surroundings regional economic market is recovered simultaneously. Secondly, the scheme does not allow reinstalling equipment and preparing materials without construction or repair of buildings. Thirdly, the payment of subsidy is supposed to be made after the all project is completed. The enterprises thus have to start the reconstruction by borrowing money beforehand. It is, therefore, strongly recommended that the scheme should be practically reconsidered.

4. REVIEW BY RECONSTRUCTION PROMOTION COMITTEE

For the purpose of reviewing, promoting, and guiding the reconstruction activities, the agency formed "The Expert Committee for Reconstruction Promotion", by inviting 14 professionals affected from the different fields, including three governors of the prefectures. The committee has released the interim report since 28 September, 2012.

The outline of the recommendations is as follows:

a. Early completion of community resettlement by accelerating housing reconstruction,
b. Comprehensive support to evacuating victims through restructuring their life,
c. Assistance to local industries for creating job opportunity,
d. Reconstruction of Fukushima region affected by radiation accident,
e. Cooperation of local municipalities, supporting staff, and victims through sharing information of good practices, and
f. Archives of this Tsunami disaster to be transmitted to next generation.

The committee recognizes that the pace of community reconstruction is very slow and recommends the additional supports of human resources, simplification of formalities, mobilization of the existing Urban Redevelopment Agency (UR), and so on. It also stresses the importance of project integration.

These recommendations have a point. However, they are principally proposed on a base of the current functions of the Agency, and more substantial points may lie in its institutional setting itself.

5. CONCLUSIONS

Regardless of one of the most disaster-prone countries in the world, Japan has not set up a regular rule of institutional arrangement for reconstruction after disasters, and coped with them by a makeshift legislation, even in case of the Hanshin-Awaji Earthquake in 1995. Thus, as mentioned in the first chapter, a heated discussion about the rights and wrongs of necessity of a new organization (the Agency) had been made, resulting in the delay of intensive reconstruction.

Through the overall review of the ten-month activities of the Agency, the author tries to verify whether establishment of the Reconstruction Agency will be effective scheme as a future model for reconstruction after great natural disasters.

As argued in its birth, the first verification points of the Agency is on how much authority should be given over the existing Ministries, in order to avoid their interruptions and to overcome their sectionalism.

To be its symbolic function of authorization, the Agency could operate a one-stop claim counter which could accept all types of requests for budget or approval of reconstruction projects planned by the affected local governments, which had to be normally submitted to respective Ministers separately. It was expected to simplify complicate and

troublesome petition process between the different central governments. This system has functioned to some extent, and been appreciated by the local governments (MSN Sankei News, 2012). However, the authority to implement the projects was rested with the respective ministries, and each project component thus is supposed to be separately guided by them, resulting in arresting smooth and comprehensive achievement of the projects due to sectionalism of the ministries.

With regard to the limit of authorization of the Agency, it can also be pointed out that not all reconstruction budgets are under the control of the Agency. As mentioned in the section 2.6, the group subsidy for promoting recovery of small industries is under the MITI. Needless-to-say, a community life can be recovered by together with housing, and commercial and industrial activities. The independent budget allocation system disturbs the formation of integrated community.

The lack of human resources is also another severe problem for the affected local governments. At the early stage, the Ministry of Internal Affairs and Communications issued the official notification to all local governments in the country, requesting for seconding their staff to assist the affected governments, and eventually, about 1700 officials have been dispatched by the end of September, 2012. As the reconstruction projects come into the implementation phase, however, more civil engineers who can draft specifications for development projects and order construction works to private companies has been needed. Since the assistance by non-affected local governments is limited, the affected prefectures are currently advertising for temporally staff; 200 persons in Iwate, and 129 persons in Miyagi. Thus, they have to be additionally involved in screening and appointment works of candidates. It is therefore expected that the Agency has an authority of recruiting the engineering staff and dispatching to the affected local governments when needed.

Thus, more broad and strong authority to ensure the comprehensiveness and consistency of the reconstruction projects should be definitely given to the Agency.

The second argument is more or less related to the regional development strategy itself for the reconstruction. Obviously, the earthquake caused severe damage to agriculture and fisheries in the Tohoku Pacific Ocean region, one of the best farm and marine production sites in Japan. As mentioned in the section 3.1, the production system of the region had been very traditional and individually-oriented so far. Shouldn't recovering the region, therefore, be taken as an opportunity to modernize its production system in order to meet global market standards in terms of cost effectiveness?

An overall development strategy for Tohoku region beyond prefectural jurisdiction does not appear in the plans drawn by the affected local government. Such structural change can only be made by the strong initiative of the central government, and not by simply responding to the requests of the local governments. Need-less-to-say, the recovery and reconstruction plan from this regional development point of views including structural change of farm and marine production system is very comprehensive and has to be integrated with variety of components such as construction of a large-scale processing base, installation of regional distribution network of road and railways, and so on, which are normally controlled under the respective Ministry's jurisdiction of central government. Since it must be drafted across their sectionalism, the Agency is therefore the most appropriate body to arrange it, though it has not such function at present. In order for the Agency to function as reconstruction planning body, however, an immediate start of its work must be vital on the base of regular legal arrangement.

The author thus concludes that the current Reconstruction Agency plays its role to promote reconstruction works at a certain level. The establishment of such Agency, therefore, makes a sense. However, in order for it to be more effective, much greater authority including recruitment of human resources and project implementation, and additional functions of planning integration from regional point of views that overcome respective central ministry and the affected local governments should be definitely given.

References:

Reconstruction Agency (2012), "The State and Progress of Reconstruction- Report of December 14, 2012, http://www.reconstruction.go.jp/topics/120611torikumitogenjo.pdf

MSN Sankei News (2012), "Evaluation of the Reconstruction Agency by the affected local governments", 8 August, 2012, http://sankei.jp.msn.com/region/news/120808/myg12080802400002-n1.htm

Yomiuri News Paper (2012), "A Long Road to Mass Relocation of Community Villages", 11 July, Morning version

Yomiuri News Paper (2012), "Delay of Public-disaster house construction", 19 November, 2012

The special web-site on information of damage by the Tohoku Pacific Ocean Earthquake (2012), Public-disaster house construction project, http://ranasite.net/?p=9519#進捗状況

Daily Construction Industry News (2012), Lack of human resources of construction engineers in the affected local governments (16, October, 2012); http://www.decn.co.jp/decn/modules/dailynews/news.php/?storyid=201210160101001

Iwate-Nippou (2012),"Need for Group Subsidy", 24 January, 2013 http://www.iwate-np.co.jp/cgi-bin/topnews.cgi?20130111_3

10CUEE CONFERENCE PROCEEDINGS
10th International Conference on Urban Earthquake Engineering
March 1-2, 2013, Tokyo Institute of Technology, Tokyo, Japan

EFFECTS OF ELECTRIC POWER FAILURE ON THE LEVEL-OF-SERVICE OF THE RAILWAY TRANSPORT IN TOKYO METROPOLITAN AREA

Ryosuke Fujita[1], Daisuke Fukuda[2], and Hideki Yaginuma[3]

1) Graduate Student, Transport Studies Unit, Dept. of Civil Engineering, Tokyo Institute of Technology, Japan
2) Associate Professor, Transport Studies Unit, Dept. of Civil Engineering, Tokyo Institute of Technology, Japan
3) Consultant, Highway Planning Inc., Japan
r.fujita@plan.cv.titech.ac.jp, fukuda@plan.cv.titech.ac.jp, yaginuma@doro.co.jp

Abstract: In this study, effects of "planned electric power failure", which was conducted just after the Tohoku 2011 great earthquake, on railway services in the Tokyo metropolitan area (TMA) are analyzed in terms of the changed in railway passengers' generalized cost for route choice. We employ the optimal strategy model proposed by Spiess and Florian (1989) to model their route choice behavior. The numerical analysis with the real-scale rail network in TMA implies that the effects of electric power failure are not same across the areas in TMA. In particular, passengers from inland areas might have had bigger impact, while passengers from maritime areas as their origins would have had smaller impacts. It can be said that impact of the degradation of the level-of-service are different because of the topological forms of the railway networks.

1. INTRODUCTION

The Tohoku 2011 great earthquake that occurred on March 11 of 2011 in Japan had damaged not only Tohoku region which was directly attacked by Tsunami but also other regions which were indirectly affected. In particular, Tokyo Metropolitan Area (TMA) was significantly affected by the earthquake in various aspects. Among others, the degradation of the level-of-service of the railway transport services in the TMA which was accompanied by "planned electric power failure (PEPF)" was the one of the most serious side effects of the earthquake which affected the people living in the TMA.

The railway companies in the TMA also had faced with a lot of difficulties about the degradation of their rail networks after the earthquake. Until getting back to steady states, they had continued to save the use of electricity energy with "reduction of the frequency of railway trains running", "stop of mutual line operation" and "suspension of express trains" among others.

Although there have been a lot of trial calculations about the economic losses caused by the PEPF in the past, there have been no trial calculation focusing on disutility of traveling railway passengers. Figuring out it must be helpful also for developing strategies of railway companies for future earthquakes.

Considering the above mentioned situations, the main purpose of this study is to quantitatively evaluate the impact accompanied by PEPF on the disutility of railway passengers in the TMA rail network. The evaluation of railway passengers' disutility is carried out with the concept of "hyperpath-based modeling", particularly for considering the changes of route choices between before and after the earthquake. This evaluation method is originally proposed by Kurauchi et al. (2006) employing the original idea by Spiess and Florian (1989). Kurauchi et al. (2006) accommodated the model to the bus transport in the Kyoto urban bus network for evaluating the utility. In this particular study, the same methodology is applied to the railway transport in TMA for evaluating the disutility mainly due to the network degradation caused by the earthquake.

2. PROCEDURE OF COMPUTING GENERALIZED COSTS OF RAILWAY PASSENGERS WITH "HYPERPATH-BASED MODELING"

2.1 Definition of Hyperpath

A hyperpath is defined as a set of routes from one origin to one destination and proposed by Spiess and Florian (1989). They call the modeling considering hyperpath "optimal strategy". The modeling assumptions about traveler behavior, congestion effects and the level of service supplied by the transport system are as follows:

- passengers have no explicit knowledge about carrier arrival times at transit stops and the available capacities of arriving carriers;
- the vehicle arrivals of different lines at the stop are not synchronized and for each line, follow a Poisson distribution ;
- passengers arrivals at stops are not timed to coincide with vehicle arrivals; and

- passengers try to minimize their total expected travel time to the destination.

Then passengers' route choice can be modeled as the optimal strategy, rather than the single shortest path between the origin and the destination, which is topologically represented as the shortest (or minimum cost) hyperpath on "Hyperpath-based modeling". For more detailed explanation, an example transit network, which is shown in Figure 1, is presented.

In this modeling, it is assumed that passengers only choose the routes that are included in the minimum cost hyperpath (the shortest hyperpath), from their origin to their destination. The generalized cost of the hyperpath is composed of a weighted linear sum of in-vehicle time and waiting time. The hyperpath means a set of route choices which minimizes the expected generalized cost (Figure 1(b)). This is a formulation of passenger route choice behavior which can consider the specific features of waiting time in public transport services.

Since the shortest hyperpath is a set of routes, only one route from this set has to be chosen (Figure 1(c)). In this study, a route represents a train line service. The more often a certain line from a set of lines runs, the more passengers can use the line (Figure 1(d)). Therefore, a probability of choosing a line from a set of lines depends on their frequencies.

In this study, it is assumed that the information of rail operation which can be available for passengers is only about a next coming train when waiting trains at a certain node. In other words, passengers cannot get information about other lines with using mobile phone. It can be acceptable assumption during the period of "planned electric power failure".

2.2 Formulation of generalized cost

Hyperpath p can be expressed with a set of nodes I_p, a set of links A_p and diversion probability T_{ap}. The expected generalized cost g_p can be represented as follows. Increase in travel time and disutility in a train due to overcrowd is not considered.

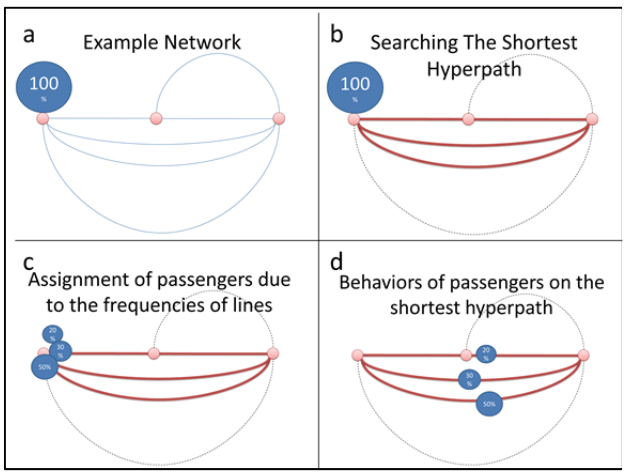


Figure 1 Illustration of hyperpath

$$g_p = \phi \sum_{a \in A_p} \alpha_{ap} t_a + \psi \sum_{i \in I_p} \frac{\beta_{ip}}{F_{ip}} \quad (1)$$

where,

t_p : travel time of link a
ϕ : value of time in traveling
ψ : value of time in waiting
α_{ap} : probability of using link a in hyperpath p
β_{ip} : probability of using node i in hyperpath p
$1/F_{ip}$: expected waiting time at node i

The first term of Eq. (1) represents the cost for in-vehicle time and the second term represents the cost for waiting time. F_{ip} is called "combined frequency" and represents the expected waiting time at node i in hyperpath p. It is formulated as follows:

$$\frac{1}{F_{ip}} = \frac{1}{\sum_{a \in A_p} f_a} \quad (1)$$

Minimum cost hyperpath, the shortest hyperpath in other words, means the optimal set of routes.

2.3 Spiess and Florian Algorithm

Spiess and Florian (1989) proposed the procedures of searching the shortest hyperpath and assigning passengers. The algorithm is composed of two parts. In a first part, from the destination node to all origins, the optimal strategy $\bar{A}^*$ and the expected total travel times u_i^* from each node $i \in I$ to the destination node r are computed. In a second part, the demand from all origins to the destination is assigned to the network according to the optimal strategy.

The algorithm is outlined as follows:

Part 1: Find optimal strategy

1.1 (Initialization)
$u_i = \infty, i \in I - \{r\}; u_r = 0;$
$f_i = 0, i \in I;$
$S = A; \bar{A} = \emptyset$
1.2 (Get next link)
If $S = \emptyset$ then $STOP$
otherwise find $a = (i, j) \in S$
which satisfies
$u_j + t_a \leq u_{j'} + t_{a'}, a' = (i', j') \in S;$
$SS - \{a\}$
1.3 (Update node label)
If $u_i \geq u_j + t_a$ then
$u_i = \frac{f_i u_i + f_a (u_j + t_a)}{f_i + f_a}$,
$f_i = f_i + f_a, \bar{A} = \bar{A} + \{a\};$
go to step 1.2.

Part 2: Assign passengers to links according to optimal strategy

2.1 (Initialization)
$V_i = g_i, i \in I;$
2.2 (Loading)
if $a \in \bar{A}$ then $\nu_a = \frac{f_a}{f_i} V_i,$
$V_j = V_j + \nu_a,$
otherwise $\nu_a = 0$

where,

u_i :expected travel time from an origin to all destination
f_i :all links which can be used at node i
combined frequency
V_i :leaving volume at node i
volume on all linkes and entering volume at node i
g_i :trafic volume from node i to node r
ν_a :volume on link a

In the step 1.1 the node labels u_i, i.e. the expected travel times to reach the destination, are set to be infinity for all nodes except the destination, for which it is initialized to zero. The auxiliary variables f_i, $i \in I$, that contain the combined frequencies of all selected links at node i, are initialized to zero. The set S is used to identify the links that have not yet been examined, and the set $\bar{A}$ is used to identify the optimal strategy.

In step 1.2 the link which is the nearest to the destination is selected among the links not yet examined. The time considered is $u_j + c_a$, that is, the time from the i-node of the link to the destination not including the waiting time at node i. If this time is smaller than the current time associated with node i, u_i, link a is included in the optimal strategy and u_i and f_i are updated according to the formulas given in step 1.3. Note that when the label of a node i, u_i, is improved for the first time, we have $f_i u_i = 0 \times \infty$. In order to keep the algorithm as compact as possible we adapt the convention $0 \times \infty = 1$ whenever this case occurs. (when $\alpha \neq 1$ is used in Eq. (4), this convention becomes $0 \times \infty = \alpha$.) The part 1 of the algorithm terminates when all links have been examined.

In the second part of the algorithm the demand from node i to the destination, g_i, is assigned to the network according to the strategy $\bar{A}$. This is done by assigning to each link $a \in \bar{A}$ the proportion of the node volume V_i that corresponds to its frequency. Since the links are processed in reverse topological order (decreasing $u_i + c_u$), the node volumes may be updated in parallel, hence making it possible to examine every link only once.

3. NETWORK AND DEMAND SETTINGS FOR THE NUMERICAL ANALYSIS

In this study, a railway transport network status during planned electric power failure is reconstructed based on a railway network in 2005 constructed by Yaginuma et al. (2010). He input the railway frequency on the basis of timetable data of each company. The changes of the railway network data between the base one in 2005 and the new one in 2011 are shown in Table 1.

The model formulation explained in the previous section is used in order to calculate the increase in generalized cost before and after the earthquake. The generalized cost is decided with respect to each OD pair. Calculating the generalized cost of some OD pairs which a lot of passengers use is meaningful because it is possible to evaluate the impact on many passengers. Calculating that of some OD pairs which is different from OD pairs which a lot of passengers choice. Therefore, we choose stations in Tokyo, Shinjuku, Yokohama, Saitama and Chiba as node D (destination) and the other all stations are decided as node O (origin). The generalized costs of these OD pairs are calculated.

Table 1 Updating the rail network

■ New stations Musashi-kosugi, Nishi-omiya, Koshigaya-lake town, Nishifu (JR), Hiyoshi, Futako-tamagawa, Futako-Shinchi, Takatsu, Mizo-no-kuchi (Tokyu), Haneda airport international terminal (Keikyu)
■ New line services Green line (Nakayama - Hiyoshi), Fuku-toshin line (Wako-shi - Shibuya)
■ Summary of the railway network number of stations : 1483 number of links : 14,607 number of lines : 116

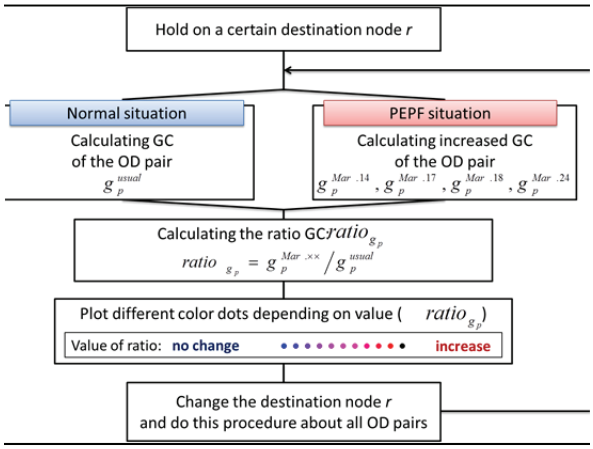


Figure 2 Procedure of Numerical Analysis

Values of time are referred to Kato et al. (2010). In their studies, $\phi = 35.90$ JPY/min and $\psi = 44.60$ JPY/min are applied and we follow these numbers.

4. RESULTS AND DISCUSSIONS

4.1 Computation Results

The procedure of evaluating the variation of generalized cost is shown in Figure 2. Passengers, whose destinations are Tokyo, Shinjuku, Yokohama, Omiya and Chiba, are objectives. Through this procedure, the variations of these passengers' generalized cost between on 14th, 17th, 18th and 24th March are eventually calculated. Figure 3 shows the variations of the all passengers' generalized costs whose destination was Tokyo station on 18th March.

4.2 Some Discussions

By closely investigating Figure 3 we find that the degradation of the level-of-service caused increase in waiting time. That would make passengers from far places have serious impacts.

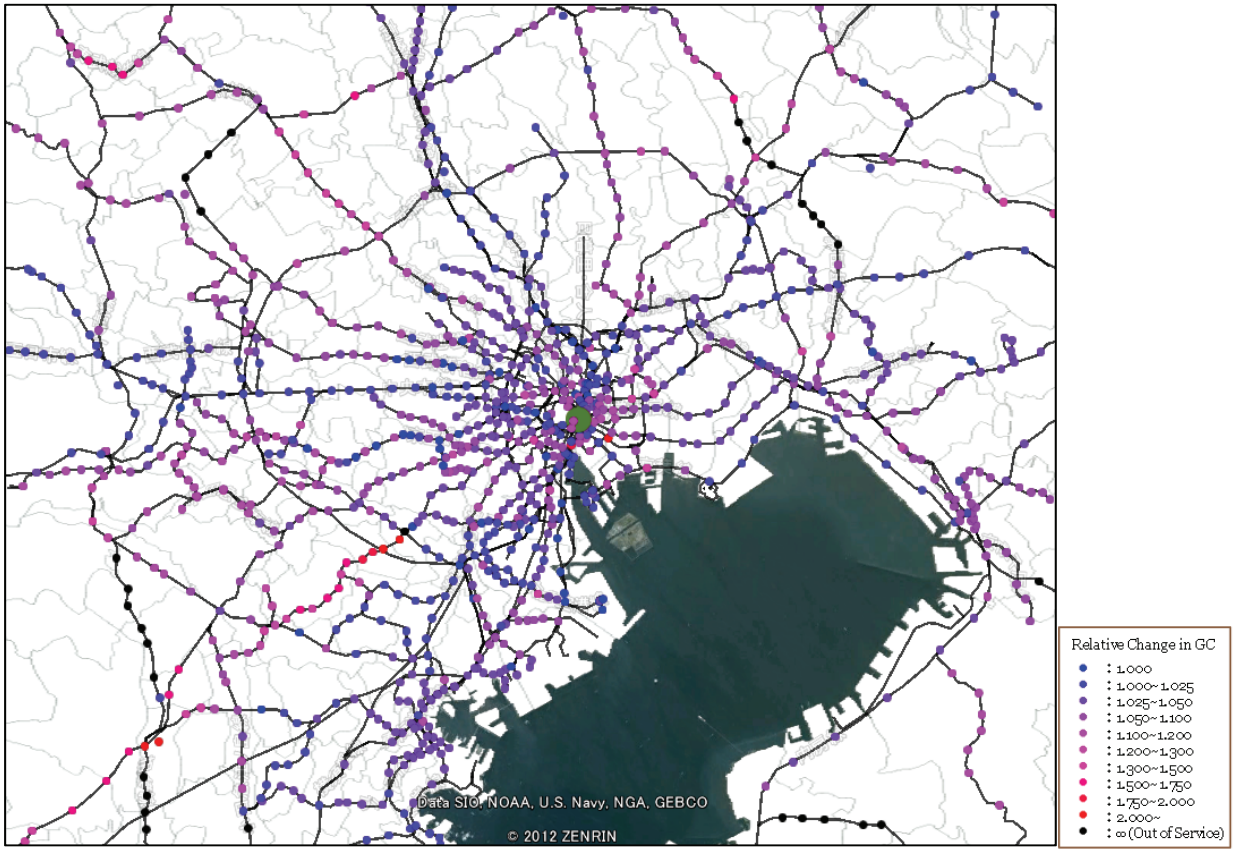


Figure 3 Generalized Cost (GC) increase due to PEPF (Destination: Tokyo Central Station, March 18, 2011)

However similar situations are not seen in all areas. In some areas, impact is much smaller than in other areas even if distances from Tokyo are same. In particular, passengers from in-land areas had bigger impact, while passengers from maritime areas had smaller impact. It can be said that impact of the degradation of the level-of-service are different because of forms of the railway networks. That is because that there are complex networks in maritime areas and that there are simple networks in in-land areas.

4.3 Variation of the shortest hyperpath

Figure 4 shows a hyperpath of passengers from Omiya to Yokohama station. On 14th March when the impact of planned electric power failure was the most serious, the passengers had used routes, which are never used under normal conditions, such as Tokyu line. This means that the optimal route under normal conditions was removed from the shortest hyperpath because of the degradation of the level-of-service of the line.

5. CONCLUSIONS

This study investigated the effects of electric power failure, which was caused by the 2011 Tohoku earthquake and tsunami, on railway transport service in the Tokyo metropolitan. Due to the severe shortage of electric power supply, the degradation of train service frequency occurred for some days just after the earthquake and that effect on railway operation for the whole metropolitan area was very severe. It had taken several weeks for train operations to be recovered to normal conditions. We investigate the increase in passenger's travel cost mainly due to the reduction of service frequency and the termination of mutual rail service operation based on the concept of hyperpath which can exactly capture the behavioural change of rail passengers due to the change in the service frequency of rail operations. We find that there are large disparities of the disutility caused by the service degradations: some area with more alternative rail routes were not so affected but others were unbenefitted more. The impacts of the degradation on passenger demand and the relationship between train operation and electric power supply are also reported and discussed. Finally, based on the evidence on the time-of-day pattern of electric energy demand for railway operators, socially desirable train operations for the future are suggested.

References:

Spiess, H. and Florian, M. (1989) "Optimal strategy: A new assignment model for transit network," *Transportation Research Part B: Methodological*, Vol. 23, pp. 83–102.

Kurauchi, F., Shimamoto, H., Wang, P. and Iida, Y. (2006) "Study on bus service evaluation using minimum cost hyperpath finding

algorithm," *Infrastructure Planning Review*, Vol. 23, pp. 755–761 (in Japanese).
Yaginuma, H., Fukuda, D. and Schmöecker, and J.-D. (2010)"A large scale application of a hyperpath-based railway assignment model considering congestion effects to Tokyo metropolitan area," *Proceedings of the 15th HKSTS International Conference*, pp. 495–502.
Kato, H., Kaneko, Y., and Inoue, M. (2010) "Comparative analysis of transit assignment: Evidence from urban railway system in the Tokyo metropolitan area," *Transportation*, Vol. 37, pp. 775–799.

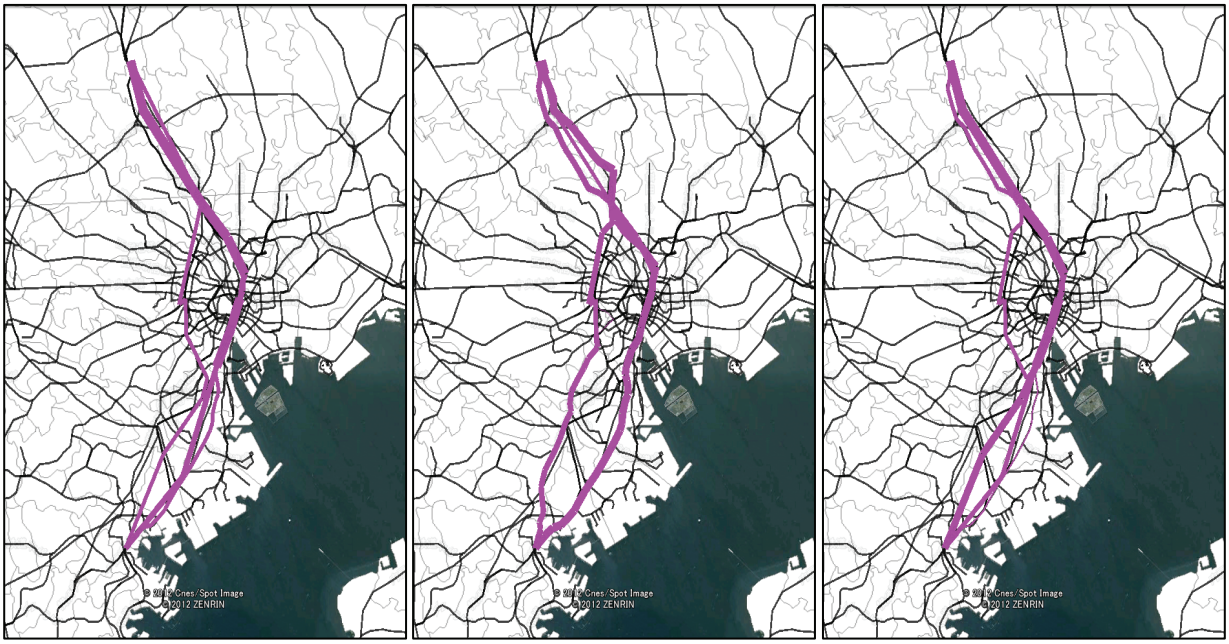


Figure 4 Computed minimum-cost hyperpaths for Omiya-Yokohama OD trip
(Left: normal case; Center: March 14, 2011; Right: March 24, 2011)

10CUEE CONFERENCE PROCEEDINGS
10th International Conference on Urban Earthquake Engineering
March 1-2, 2013, Tokyo Institute of Technology, Tokyo, Japan

ANALYSIS ON URBAN LAND USE CONTROL SYSTEMS IN TSUNAMI AFFECTED AREAS BY THE 2011 GREAT EAST JAPAN EARTHQUAKE

Shoichi Ando

Director, International Institute of Seismology and Earthquake Engineering (IISEE), Building Research Institute (BRI), Professor, Faculty of Engineering, the University of Tokyo
e-mail: ando@kenken.go.jp *(IISEE/BRI),*ando@mps.t.u-tokyo.ac.jp *(The University of Tokyo), Dr.*

Abstract: Author analyzes the effect of "Area Division" including Urbanization Promotion Area of City Planning Law, "Disaster Risk Area" of Building Standard Law and other urban land use control systems during and after the Great East Japan Earthquake. Some cases of these systems in tsunami affected areas of Tohoku region are evaluated and the limitation to apply these systems to tsunami prone cities such as Kesennuma city in Miyagi prefecture, Kamaishi city in Iwate prefecture. Several issues of land use control are analyzed based on the views of municipalities.

Miyagi prefecture and Iwate prefecture were taking different recovery policy and program soon after the Great East Japan Earthquake. Although many municipalities have similar geographical and socio-economic conditions and were affected similar damage by tsunami, they are now facing different challenges. Miyagi prefecture restricts permanent reconstruction while Iwate prefecture admits individual reconstruction activities. The difference was caused by the future prospect, trend in population and economy and reconstruction plan of each affected area. The paper analyzes the current conditions and challenges of reconstruction from view point of land use control and disaster management.

1. INTRODUCTION

Tsunami disasters by the Great East Japan Earthquake that occurred on March 11, 2011 posed a question about the past urban land use control systems. In order to avoid such huge disasters in future this paper tries to verify the current systems.

Before establishment of the "Law on Creating Regions for Tsunami Disaster Management (Tsunami Law)", the word of "tsunami" was not included in the Japanese City Planning Law (CPL) itself. The word was used only once in the Ordinance of CPL, however the interpretation of "areas with risk of flood, water logging, tsunami and high tide etc." depends on decision by local governments. It means that the urban planning system in Japan has dealt with tsunami very superficially before the 2011 Great East Japan Earthquake.

On the other hand, the Building Standard Law (BSL) deals with tsunami in its Article 39 as "(Disaster Risk Area: DRA) A local government may designate areas with a frequent danger of tsunami, high tide, flood, etc. as DRAs by ordinances.2. With respect to DRAs, prohibition of building construction for use as houses and other restrictions relating to the construction of buildings, which are necessary for disaster prevention, shall be prescribed by local ordinances as mentioned in the preceding paragraph.", however the decision of frequent danger also depends on local authority similar to the CPL. Though application of the DRA against tsunami can be found in several municipalities since many decades ago and this BSL system is used more than the CPL, applied cases were very limited.

Under such circumstances, there are issues for many local governments how to establish land use control systems from a long term view point for the reconstruction of the tsunami affected areas by the Great East Japan Earthquake. Most of the reconstruction projects that will be implemented through land readjustment projects (LRP), group relocation projects (GRP) for disaster mitigation, recovery base project against tsunami (RBP), and public operated houses (POH) etc. may be finished during five or ten years from now on. However, land use control must be more permanent and sustainable from view point of equality and science.

There are some land use control systems that can be applicable to tsunami disaster management such as Area Division especially Urbanization Control Area (UCA) by the CPL, DRA by the BSL, and Special Precaution Area (SPA) against tsunami by the Tsunami Law that was established in 2011. In addition, there also exist some temporary land use control systems as shown in the Table 1.

Table 1: Land use control systems against tsunami

Type of Control System	**Term**	**Area**	**Authority**	**Art.,law**
Area Division (UCA etc.)	P	Urban	Prefecture	7, **CPL**
Disaster Risk Area (**DRA**)	P	All	Local govt.	39, **BSL**
Special Precaution Area	P	Design.	Prefecture	Tsunami
Affected area (2-month)	T	Planned	Admi. Agency	84, **BSL**
Affected area (2-year max)	T	Planned	Municipality	Special
Urban planning project area	T	Planned	Municipality	53, **CPL**

Note: "Term" P- permanent, T- temporary, "Area" Urban- urban planning area, All- no limitation, Design.- designated area as SPA by Tsunami Law, Planned- project planned

2. AREA DIVISION

2.1 Aria Division by CPL and Disaster Risk

Firstly, the Article 8 of the Ordinance of CPL is verified since it is the unique article that the word of tsunami is used in the whole legal urban planning system in Japan before the Great East Japan Earthquake.

The New CPL that was established in 1968 and enforced in 1969 provides "Area Division as a division into Urbanization Promotion Area (UPA) and Urbanization Control Area (UCA)" in the Article 7 of the Law. The Article 8 of the Ordinance of CPL provides technical criteria to determine UPA to include areas where should be urbanized within ten years principally except three types of area as well as already urbanized area. One of the three types is "areas with risk of flood, water logging, tsunami and high tide etc.", and tsunami is clearly stated.

The first Report of the Central Urban Planning Council titled "Report on principles to set up UPA and UCA and to develop UPA" was issued on November 28, 1968 and noted "areas with risk of flood, water logging, tsunami and high tide etc principally should not be included in UPA". In addition, Ministry of Construction (MOC, current Ministry of Land, Infrastructure, Transport and Tourism (MLIT)) has issued a notification titled "Principles to coordinate between Area Division of UPA and UCA by CPL and flood control works" on January 8, 1970 has set forth "those areas that corresponds to river inundation area against rainfall intensity approximately 50 mm per an hour and water logging is assumed more than 0.5 m, are regarded as areas with risk of flood, water logging, tsunami and high tide etc by the Article 8 of CPL Ordinance, and those areas principally should not be included". However this notification aimed at floods of river such as overflow and water logging, and not tsunami.

2.2 Area Division and the Great East Japan Eq.

Figure 1 shows the affected area by tsunami inundation at the Great East Japan Earthquake and UPA in the Sendai – Shiogama urban planning area, while Figure 2 shows those in the Ishinomaki wide urban planning area respectively. (Figure 3 indicates whole tsunami affected areas in Miyagi and Iwate prefectures including areas of Fig. 1 and Fig. 2.)

Sendai Plain has formed agricultural land. The city area has been designated as UPA in 1970 in Sendai-Shiogama and Ishinomaki area. Because Sendai city has not designated UPA except surrounding areas of Sendai Port and because the old city area of Sendai is mainly located inland area, there were not so much damages even in the coastal areas of Sendai city except some existed villages and few new developments such as Arahama-shin in Wakabayashi ward of Sendai city. Affected areas are located in UPA of Natori city (Yuriage) and Iwanuma city around Sendai city. New development of Arahama-shin and old village of Arahama where devastated damage by tsunami are observed, are both located in UCA of Sendai city.

Although this system is connected with UCA of Area Division that provides the strongest control mechanism for land use control, this provision has not been applied so clearly to tsunami. The following data shows the reality and author analyzed the reasons why the Article 8 of CPL was not used so clearly in the next sub section.

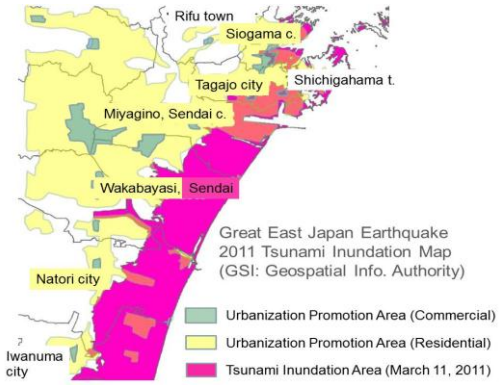


Fig. 1 UPA and tsunami in Sendai Urban Planning area

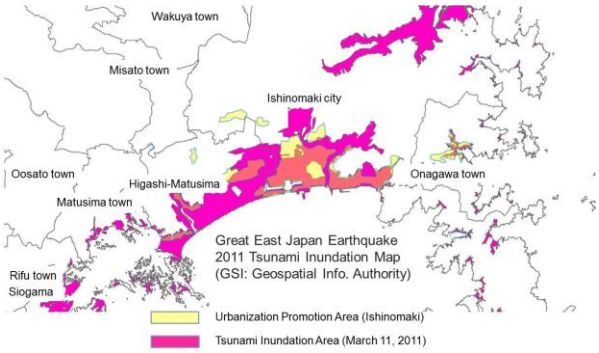


Fig. 2 UPA and tsunami in Ishinomaki Urban Planning area

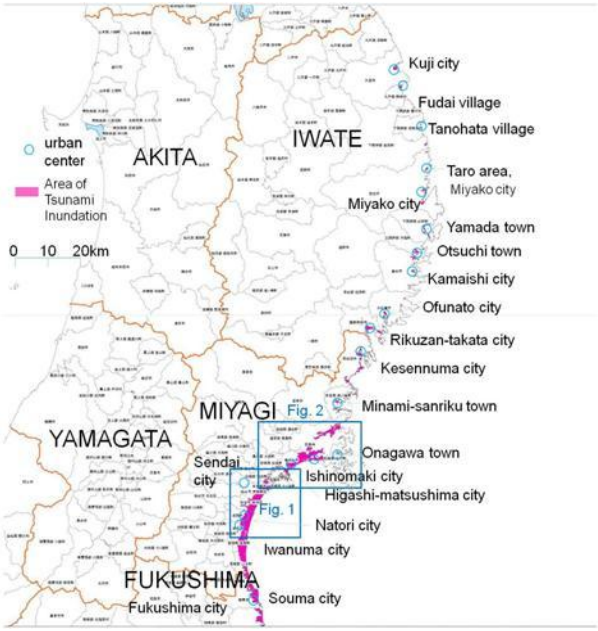


Fig. 3 Tsunami affected areas by the Great East Japan Eq.

2.3 Reasons why Article 8 was not well utilized

The reasons why CPL did not function well against tsunami in spite of Article 8 of its Ordinance are listed according to the type of reasons as follows:

(1) **Social Reasons**

- When the UPA was firstly designated, the areas where

consensus could be easily obtained were selected. Already urbanized city areas had the first priority.

- UPA was basically set in the regions that rapid increase of population occurred like surrounding cities of Sendai.
- Many new public facilities and care houses for the elderly were constructed in the UPC areas with tsunami risks, because of consolidation of municipalities, progress of aged society and long-term trend in decrease of population.

(2) **Physical Reasons**

- People thought that it will be easy to evacuate from tsunami, since the most advanced information technology and early warning systems are established.
- People who lived in the coastal area thought that seawalls, river gates and tsunami evacuation buildings would protect residents from tsunami disasters.

(3) **Economic Reasons**

- UPA tends to be designated in and around already urbanized area, because of efficient use and maintenance of infrastructure, such as roads, sewerage and water supply.
- To move to safer area, in particular change of urban setting is almost impossible in normal time even though all people recognized their high risk as well as partly because of financial reason of municipality and prefectural government.
- The movement to protect agricultural land becomes weaken as demand of agricultural land will not increase and because of higher exchange ratio (strong yen) and excessive domestic rice production etc.
- Even if the risk is judged, agreement with local residents would not invest against tsunami because the probability of occurrence is quite law compared with floods

(4) **Institutional Reasons**

- This provision is applied for new areas to include in UPA within 10 years. It regulates only newly urbanizing areas.
- There were no concrete criteria with numbers as shown in the old notification and it is hard for local governments to judge the risk of tsunami on their own responsibility.
- There is no detail explanation on how to set up the CPA against tsunami in the MLIT guideline of urban planning.
- Some urban planning may not be realized when other urban function is not conscious except disaster management, and so on.

3. DISASTER RISK AREA

3.1 Disaster Risk Area by BSL

Disaster Risk Area (DRA) system was introduced when the BSL was established in 1950. The Article 39 of BSL provides "local government can designate highly hazardous areas against tsunami, high tide and floods etc. as DRA by its bylaw". There is no detailed ordinance or regulations in BSL, however notification of administrative vice minister of MOC on October 27, 1959 (after Ise Bay Typhoon occurred on September 26, 1959) entitled "disaster prevention for buildings against storm and flood damages" recommended to positively designate DRA based on the Article 39 of BSL, especially in the low land areas, to strengthen the structure of buildings in the area and to develop evacuation facilities.

In addition the notification noted "buildings in DRA must be constructed as strong buildings such as reinforced concrete structure unless there exist effective embankment etc." and "residential use buildings should be prohibited to construct in the heavily hazardous area". However definition of "heavily hazardous area" was not mentioned as well the target of this notification did not include tsunami so clearly but mainly for storm and flood disasters.

3.2 Disaster Risk Area and Tsunami

Detailed explanation of "strong buildings" and "heavily hazardous area" is firstly found in the Notification No.1318 of MLIT in 2011 on "Definition of safe structural systems against tsunami to presume tsunami inundation" based on Tsunami Law. In addition, technical guidelines on land use against tsunami disaster are issued continuously such as a technical advice to the additional knowledge issued by the Director General of Housing Bureau on November 17, 2011, a technical advice on enforcement of Tsunami Law by the Cabinet Office on March 9, 2012, and a technical advice on enforcement of the Section 9 of Tsunami Law on July 31, 2012, recently.

As the reference, in the guidance textbook on BSL issued by the Architectural Institute of Japan (AIJ) in 1950, DRA was referred as "Target of DRA is areas prone to tsunami as Sanriku region, and/or river side areas prone to flood disasters. However as an actual condition, designation of DRA is quite hard issue and the issue is a regional issue of the area, therefore the system provides designation of the area and contents of control for building restriction are all trusted to the local ordinance". The risk of Sanriku region against tsunami was recognized.

Table 2: Designation of DRA (as of Mar. 2009, by MLIT)

Area Type	Number (places)	Area (ha)	Number of Buildings in the Area			
			Houses (unit)	Incl. unfit houses (unit)	Non residential	Total (unit)
Steep slope	18,785	36,898	339,785	122,343	37,371	377,156
Landslide	64	252	283	217	229	512
Flood	111	2,781	1,696	676	1,179	2,875
Tsunami	**2**	143	0	0	38	38
Tsunami/flood	**5**	6,504	74,002	0	39,020	113,022
Snow-slide	3	21	3	3	6	9
Avalanche	8	149	14	4	28	42
Avalanche etc.	2	548	531	0	0	531
Lava flow	2	41	0	0	0	0
Subsidence	1	0.4	1	0	1	2
Land deform	5	13	0	0	0	0
Erosion	1	0.5	3	0	9	12
Fall of rocks	5	15	129	0	48	177
Mud flow etc.	4	13	0	0	0	0
Others	0	0	0	0	0	0
Total	**18,998**	47,383	416,447	123,243	77,929	494,376

3.3 Reasons why DRA was not so used against tsunami

The following (1) to (7) analyzes the reasons why DRA was not so utilized in the hazardous areas against tsunami.

(1) As shown in the guidance textbook on BSL by AIJ, designation of DRA was quite hard issue. Before BSL was established, principally all construction activities were free and no restriction. Even though the restriction by BSL is set up as "minimum standards", it was told that the then owners, architects, and contractors could not easily accept the BSL. From the legal view point, when a certain restriction violates some property rights, compensation measures to the owner

must be provided. However because the restrictions based on BSL provide minimum standards in order to protect lives, health and properties of the people, no compensation system is prepared and authorized.

(2) In 1950 when BSL was established, there seemed almost no scientific knowledge on tsunami hazards. Since BSL prescribes technical standards, it was impossible to regulate standards without any scientific bases. In contrast to tsunami standard, seismic standard in BSL has been created from the first as well as fire codes, because of experiences of Nobi earthquake in 1891 and the Great Kanto Earthquake.

(3) DRA aims to prevent disasters utilizing locally applicable control codes through designation of the area. There exist approximately 19,000 DRA in Japan as shown in the Table 2 (2009 MLIT). However most of them were designated against landslides to restrict housing construction in the steep slope areas. DRA against tsunami risk was not established except few cases as the frequency of occurrence is quite rare and residents do not agree to prohibit from building their houses. There is no national financial support.

(4) As shown in the Table 3, DRA provides permanent restriction while other building control system in the disaster affected area like the building control based on the Article 84 of BSL, sets normally two months' limitation or in the case of the Great East Japan Earthquake maximum eight months' control. DRA controls won't be necessary for the area without any development pressure.

(5) DRA was sometimes used in the recovery projects after damaged disasters. In the case of Aonae area of Okushiri town after a big tsunami of the off coast of South-West of Hokkaido earthquake in 1993, DRA was introduced to the high risk area in the old residential zone after the new hilly safe area was developed utilizing "Group Removal project against Disasters (GRP)" with subsidies from national government (by MOC, current MLIT). This was the unique case after tsunami under DRA.

(6) As shown in the Table 3, Iwate prefecture requested all affected municipalities to set DRA to the heavily tsunami affected area in April 2011. However Kamaishi city decided not to use DRA in July 2011 and other municipalities are also reluctant to apply DRA but they changed the policy in 2012. On the contrary, Miyagi prefecture set building control in large areas using the Article 84 of BSL as well as DRA to apply CRPs. Sendai city and Yamamoto town utilized DRA to control building construction in tsunami hazardous areas.

(7) As shown in the Table 4, the basic direction toward reconstruction of Miyagi prefecture and Iwate prefecture seems to select different way as the case of building restriction in early stage. It seems that Miyagi prefecture aims to improve urban structure using this opportunity especially in the coastal zones, while Iwate prefecture seems to be struggling to maintain population in the tsunami affected areas and then restriction of building construction in Iwate pref. is not so strict compared to Miyagi prefecture because the population decrease trend is expected severer in the remote regions from big cities. However, it may be caused simply because of the difference of urban planning settings of both prefectures, i.e. Miyagi prefecture sets UPA and UPC and most of coastal areas are prohibited to construct buildings. In Iwate prefecture, construction of buildings is not so strictly controlled in the coastal cities and towns.

Table 3: Building control based on BSL after disaster

Building Standard Law	**Article 39** (Disaster Risk Area: **DRA**)	**Article 84** (Control in Affected Area)
Designation of area	Based on bylaw of local governments	By Specialized Admin. Agency
Duration of control	Permanent measures	Max. two months
Construction control	Prohibit housing, limit other building (no national intervention)	Prohibit / limit building construction in the project planned area
Application to Great East Japan Earthquake	Iwate: Urge municipality to set bylaw Miyagi: Pref. started to plan to apply	Iwate pref.: No application Miyagi: Applied to 5 municipalities
Response of municipalities	Iwate: Mayors are prudent (negative) Miyagi: Part of Minami-sanriku town	Miyagi: Enterprises were embarrassed then try to permit some construction
Applied cases	Hokkaido, Okushiri town, Aonae area	Great Hanshin-Awaji Eq. (Kobe etc.)

Table 4: Comparison of Miyagi and Iwate prefectures

	Miyagi Prefecture	**Iwate Prefecture**
Total population	2,360,218 persons	1,385,041 persons
Estimated pop.	1,894,000 persons	962,000 persons
Ratio(2040/2005)	- 19.8% (affected area - 46.8%)	- 30.5% (affected area - 48.8%)
Aged ratio (05-40)	20.0% (2005) → 34.3% (2040)	24.6% (2005) → 38.0% (2040)
Basic Concept for Reconstruction (part of land use & development)	**Miyagi Prefecture Recovery Plan:** Recovery focusing on tsunami disaster management of coastal areas applying removal to high land, separation of work and home, multiple protection against tsunami from the lessons	**Iwate Prefecture Recovery Basic Plan:** Based on agreements with residents, improvement of residential area for safety and development connected with land use plan considering tsunami disaster management
Current situation (building control)	Pref. set building control based on City Planning Law etc. after BSL Article 84. BSL Article 39 (DRA) is also used in many areas in Sendai, Kesennuma, Minami-Sanriku etc. in order to apply GRPs.	Pref. recommended municipalities to use BSL Article 39. Some GRPs areas are under planning to apply DRA in Kamaishi and Miyako cities, Yamada town and Noda village as of Sept. 2012.

Table 5: Major project systems for reconstruction

Basic Projects	**Group Relocation proj. against Disasters (GRP)**	**Recovery Base project against Tsunami** (new system after 2011) **(RBP)**	**Project on Land Readjustment for Urban Recovery (LRP)**	**Project on Urban Redevelopment (URP)**	**Public Operated Houses project against Disaster (POH)**
Subsidies	Cost for public works incl. land development except sell land	Total mounding cost, Development of evacuation building and Public works etc.	Cost for public works incl. land, totally mounding (40 persons/ha)	Cost for design, common facility and public space etc.	Land purchase, design and construction cost, low rent subsidy
Area	No relation to Urban Planning	Principally within Urban Planning Area	Within Urban Planning Area	Within Urban Planning Area	No relation to Urban Planning
Scale	More than five (usual 10) houses	Principally 2 projects per urban, and approx. 20 ha per project	No condition	No condition	No condition
Condition	Designation of Disaster Risk Area is requisite	Define area for land purchase, Step by step extension will be possible	Consolidated area to develop road system. Division of project area	Consolidated area to build co-owned houses and/or building	Demand to public houses for low income household after disaster
Urban Planning	No relation	Area is designated	Area and project is designated by UP	Area and project is designated by UP	No relation
Process	Agreement of MLIT minister on removal plan	Planning decision as urban facility, project approval of prefecture (or MLIT)	Urban planning procedures are needed (from planning decision to liquidation)	Urban planning procedures are needed (from planning decision to liquidation)	Municipality and prefectural govt. construct and operate the houses
Aid ratio	All costs will be covered (special case by national grant + special tax).				

4. DAMAGE AND URBAN PLANNING

4.1 Analysis on Damages by Tsunami

The data on damages of the Great East Japan Earthquake from the view point of building control and urban planning are analysed, and observations can be pointed out as follows:

(1) Fig.4 indicates the characteristics of urban planning with UPA by Area Division. The damaged houses include

collapsed, half collapsed and partially damaged one. That means in UPA such as in the Sendai plain, housing damage inundated areas turned out large number, while human damage was not so severe if compared with Sanriku rias coast areas where there is no UPA except Onagawa town.

(2) Fig.5 shows two exceptionally large damaged cities in terms of physical damage. Both Sendai city and Ishinomaki city are classified as the area of "Urban Planning with Area Division". That means the pressure of development and increase of population is expected in these cities. Therefore it is required to effectively invest resources into the UPA.

(3) Fig. 6 shows casualties per collapsed houses with classification by urban planning type. As same as the Fig. 5, all municipalities in Fig. 6 established urban planning. That means heavily damaged areas to houses and human were basically controlled under urban planning system that can apply rather strict building control.

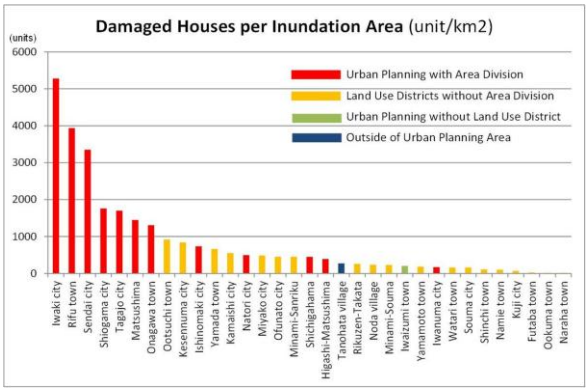


Fig.4: Totally collapsed houses by municipality

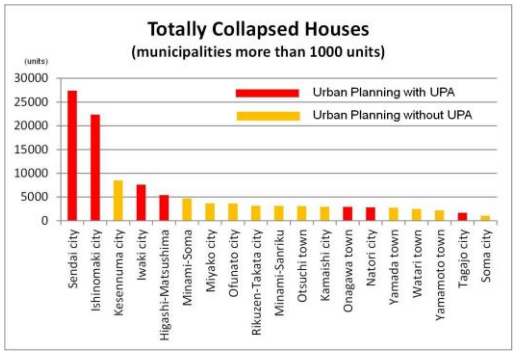


Fig.5: Damaged houses per inundation area

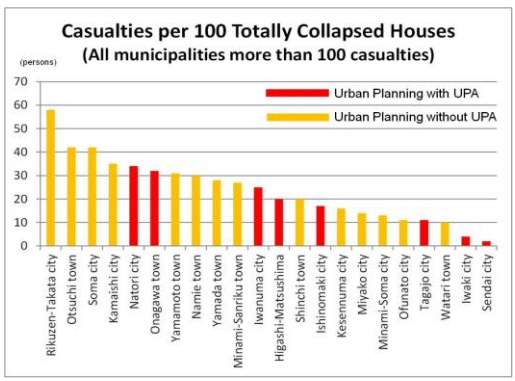


Fig.6: Casualties per 100 totally collapsed houses

(4) Fig.7 shows severity of damage of each municipality by classifying the characteristics of regions. The proposed indicator is calculated as "number of human damage per totally collapsed houses" by municipality. Coburn, Spence and Pomonis defined similar ratio as "Lethality Ratio" in 1992. The following data is formulated after extracting less damaged municipalities that have large fluctuation because of their smaller denominator.

(5) The ratio varies almost double figures (from 60 to 2-1) under this indicator. Rikuzen-Takata city recorded around 60 persons' human damage per 100 totally collapsed houses, while Sendai city's indicator shows around 1 or 2 persons. Fig.8 tries to classify the damages however not so clear difference was observed from above mentioned data according to the characteristics of the region type.

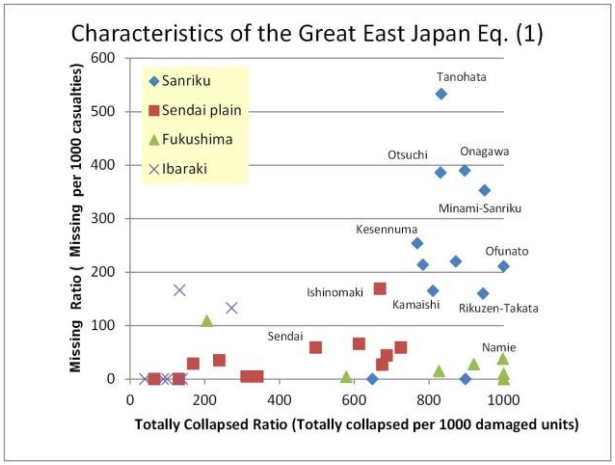


Fig. 7: Missing ratio and totally collapsed ratio

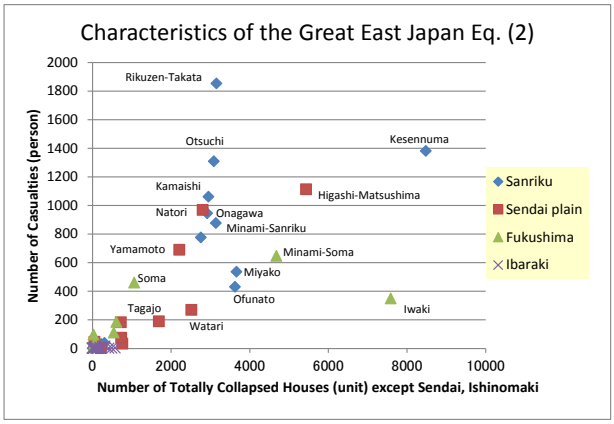


Fig. 8: Totally collapsed houses and casualties

Then, the reasons why such great difference was observed among affected cities and towns, especially as shown in the Fig. 6 (under the same physical house damage but the human damage varies a lot) will be as follows. In the case of tsunami, relation of physical damages and human damages may be significantly affected by evacuation behavior. The factors may be;

1. Evacuation from house or not
2. Time for evacuation to the refuge
3. Measure for evacuation (on foot or by car)
4. Evacuation route (and traffic congestion)

5. Safety of refuge (or evacuation shelter etc.)

In addition, except for evacuation behavior, the following factors may affect the difference of damage;

6. Judgment of "totally collapsed" differs from municipality (e.g. if tsunami reached ceiling, municipality regarded as totally collapsed.)
7. The residents who experienced few damage at the Chile Tsunami in 1960, became rather unprepared or careless against tsunami.
8. The area has no tsunami evacuation building such as 4-story close to the residential area.

4.2 Urban Planning in Pacific coastal region in Tohoku

In total 37 municipalities in the Pacific coast region in Iwate, Miyagi and Fukushima prefectures, 3 municipalities have no urban planning area. In addition 4 municipalities in these 3 prefectures have urban planning without land use districts. That means other 30 municipalities of this region have urban planning areas with land use district.

With regard to the Area Division, no municipality in this region in Iwate prefecture has urban planning area with Area Division (UPA and UCA). In Fukushima coastal region, Iwaki city only sets up Area Division. To the contrary, 11 municipalities within total 15 municipalities in the coastal region of Miyagi prefecture divided UPA and UCA by Area Division. Because there is no increase of population in Sanriku (rias coast) region, no UPA is designated in coastal areas of Iwate prefecture as well as Kesennuma city and Minami-sanriku town in Sanriku area of Miyagi prefecture.

From the analysis of the damage, it was unfortunate that objectives of the Article 8 of CPL Ordinance could not function in many tsunami affected cities (mainly in Miyagi prefecture) at the Great East Japan Earthquake. However, from the figures 1 and 2, UCA by Area Division decreased human damage in Sendai city than Ishinomaki city although this was not obvious until after the event.

4.3 Issues of Land Use Control in Reconstruction area

(1) As shown in the data and figures, damage by tsunami varied in each municipality (e.g. in Onagawa town and Ishinomaki city have huge damages even in the UPA), we need continuously investigate the reasons and factors from various points such as evacuation, traffic, land use, building structure, depth of tsunami inundation, response of administration by municipality, awareness information etc.

(2) Since there is no Area Division in coastal areas of Iwate prefecture and Fukushima prefecture except Iwaki city and land use control system is not so strict, DRA with Group Relocation Project (GRP) against Disasters, Tsunami Law and other land use control system are indispensable to safe buildings and urban areas.

(3) One of the most significant issues in the tsunami affected areas is land level raising works in urban area. Because of around 1 m land subsidence by the Great East Japan Earthquake, coastal zone are suffered from inundation every day. Municipalities are starting to raise the ground level of roads and other public facilities. However private land owners basically have to raise the land by themselves, unless the land is included in reconstruction project areas. The compensation for private properties caused by land subsidence may be one of the new discussion points as a part of public assistance as well as the level of support to the reconstruction of private houses and business facilities.

(4) Other important issue is manpower assistance. Many staffs of the affected municipalities such as Kamaishi and Kesennuma city pointed out lack of staff for urban reconstruction projects because many projects started after the first recovery stage such as debris clearance and disposal, temporary housing and so on. Many municipalities outside of affected areas have sent technical or project support staffs to the affected area. For instance, Kitakyushu city sent a team of project staffs to Kamaishi city where the same steel company is located.



Fig. 9: Land subsidence and water logging (Kesennuma)



Fig. 10: Reconstruction project area (Unosumai, Kamaishi)

5. CONCLUSIONS

Urban planning and building control systems that are prescribed in the CPL and the BSL are expected to play significant roles to prevent tsunami and earthquake disasters.

Japanese urban planning system was established in 1919 and since then Japan had opportunities to realize the urban plans after the 1923 Great Kanto Earthquake and reconstruction process from the damages by the WWII after 1945. In addition recovery from Ise Bay typhoon in 1959

and the 1995 Great Hanshin-Awaji Earthquake exposed past issues of urban planning and new legal and support systems were formed in order to achieve safer urban settings. And now after the Great East Japan Earthquake, we are requested again to reconsider the future of urban planning systems including land use control.

Land use control in the urban area especially in the disaster risk area has to be integrated with socio-economic, institutional, technical and other tools to achieve safety of buildings and built-environment. To mitigate earthquake and tsunami risk, land use control plays a quite important role. Awareness creation is also instrumental for building culture of safety and creates demands for intervention in disaster mitigation.

The demands ultimately help in creating conducive environment to policy intervention, in realizing institutional mechanism of code enforcement and land use control for the municipal authorities and in creating demand for competent professionals in the field of urban planning and disaster risk management.

As a summary of conclusion, author would like to note the following future prospect on land use control systems;

(1) Though the final goal of tsunami disaster management will be relocation and land raising of urban area, evacuation training, designation and development of safe refuges and evacuation routes against tsunami are the first measures.

(2) Land use control against disasters will be more effective when it is combined with urban planning project and disaster management project. Such combined cases will be expected to widely advance through GRP and RBP by the Tsunami Law as well as new development of LRP and projects for urban redevelopment etc.

(3) Reconstruction of the affected areas by the Great East Japan Earthquake faces long-term social issues such as aged society, decreasing population and the sustainability. New concept of compact city, smart city and eco city may help to solve them in the near future.

(4) Disaster Management Plan prepared by prefectures and municipalities are needed to closely relate to urban planning including land use control system of each area in the near future, as there is few connection now.

(5) Finally, hope and intention of residents and staffs of local governments was the key of recovery. Strong intention of local people to make safer and more sustainable region and city for the next generations is really expected.

Acknowledgements:

The author acknowledges support from the Building Research Institute (BRI), the International Institute of Seismology and Earthquake Engineering (IISEE) for providing opportunities to visit tsunami affected areas in April, 2011 (Iwaki, Miyako, Kamaishi, Sendai, Ishinomaki, Onagawa, Natori, Iwanuma) and in Sept. 2011, June 2012 and Nov. 2012 (Sendai, Ishinomaki, Onagawa, Minami -sanriku). The author also appreciates the University of Tokyo for providing supports to visit Kesennuma, Rikuzentakata, Ofunato and Kamaishi in Nov. 2011 jan. 2012 and Nov. 2012. These supports make possible to summarize the paper.

References:

BRI, (2011), Report of damage by the 2011 off the Pacific coast of Tohoku Earthquake, pp119-140

Coburn, Spence and Pomonis A. (1992). "Factors determining human casualty levels in earthquakes: Mortality prediction in building collapse", 10th WCEE, University of Cambridge, UK

Cabinet Office (2011)., Report of Special Investigation Committee on Earthquake and Tsunami measures based on the lessons from the Tohoku Earthquake, Sept. 28, 2011, 35-43

International Institute of Seismology and Earthquake Engineering (IISEE), Building Research Institute (BRI), data from the web site; http://iisee.kenken.go.jp/special2/20110311tohoku.htm

MLIT (2011). "Guideline of Urban Planning", Ministry of Land, Infrastructure, Transport and Tourism.

Naoki Hayashi, S. Saito (2011). "Prospect of Population in Iwate, Miyagi and Fukushima prefectures" (in Japanese), SERC Discussion Paper, SERC11023

Tokuji Utsu (1990). "World Earthquake Catalogue", The University of Tokyo, 24

10CUEE CONFERENCE PROCEEDINGS
10th International Conference on Urban Earthquake Engineering
March 1-2, 2013, Tokyo Institute of Technology, Tokyo, Japan

EVACUATION SITUATION OF FUTABA DISTRICT RESIDENTS FOLLOWING THE FUKUSHIMA NUCLEAR ACCIDENT

Keiichi Sato[1)]

1) Associate Professor, Center for Social Research and Data Archives, Institute of Social Science, The University of Tokyo, Japan
keiichi-s@iss.u-tokyo.ac.jp

Abstract: This study aims to record evacuation situation of Futaba district residents following the Fukushima nuclear accident caused by the Great Eastern Japan Earthquake 2011. In this study, some administrative documents and the questionnaire survey for all residents of Futaba district conducted by Fukushima University were analyzed as follows; 1) According to the reported values of radiation doses, there is nothing for it but to admit that some spots cannot be decontaminated to the level in which people can return. 2) Survey results revealed that not all people have the desire to return, so it is anticipated that each municipality will have smaller populations than before the accident. Based on these studies, discussion about the recovery program of the whole Futaba district was developed.

1. INTRODUCTION

On March 11, 2011, the Tohoku-Pacific Ocean Earthquake destroyed the cooling functions for the reactors and the spent fuel pool at the Fukushima Daiichi Nuclear Power Station (hereinafter referred to as "Fukushima Daiichi NPS") of the Tokyo Electric Power Company ("TEPCO"), causing hydrogen explosions and the release of radioactive materials. On April 12 of the same year, the magnitude of the accident was reevaluated to Level 7 on the INES (International Nuclear Event Scale)—the worst nuclear accident in the history of Japan and equivalent in scale with the accident at the Chernobyl nuclear power plant in 1986.

This accident evoked various social concerns—the process of handling the accident, national energy policy, restarting of other nuclear power plants—but at the same time, the accident caused large scale radioactive contamination which forced many people to evacuate. All the while, universities and local municipal governments continued to investigate the situation of evacuees, with the understanding that recording and analyzing the data collected would be a critical task in assessing the evacuation programs. This paper is an English translation of an excerpt of the records of the evacuation documented by Sato (2012) over a period of 6 months from the time of the accident.

2. OVERVIEW OF EVACUATION FROM THE NUCLEAR ACCIDENT

2.1 Evacuation Procedures Immediately After the Accident

Table 1 shows the outline of the evacuation procedures, which is a summary of the interim report prepared by the Investigation Committee on the Accident at the Fukushima Nuclear Power Stations of the Tokyo Electric Power Company ("ICANPS").

On the evening of March 11, 2011, the Prefectural Governor instructed citizens on evacuation within a km radius of the Fukushima Daiichi NPS. The evacuation zone was expanded to within a 10km radius by the morning of March 12, and again to within a 20km radius that same evening by Nuclear Emergency Response Headquarters ("NERHQ"). More than one month after the accident, the government designated the Restricted Zone on April 21, and the Deliberate Evacuation Zone and Emergency Evacuation Preparation Zones on April 22.

Basically all individuals were prohibited from entering and were instructed to evacuate from the Restricted Zone established based on the Disaster Countermeasure Basic Act. Outside the 20km radius, the area with concern that the cumulative dose might reach 20mSv within 1 year period after the accident was designated the Deliberate Evacuation Zone, and residents were instructed to evacuate in a planned manner. Areas within a 20 to 30km radius of Fukushima Daiichi NPS but outside the Deliberate Evacuation Zone were designated Emergency Evacuation Preparation Zones where residents were instructed to be ready and able at all times to follow a stay-indoors order or an evacuation order in case of an emergency.

Subsequently, the Emergency Evacuation Preparation Zones designation was lifted on September 30, and the Restricted Zone designation has also been reviewed since 2012.

2.2 Status of Evacuation

As of November 2011, there are 114,000 evacuees under the evacuation programs, 73,000 of which are from the district of Futaba.

Residents of the towns of Hirono and Naraha evacuated mainly to the city of Iwaki, their southern neighbor; many

Table 1 Evacuation Procedures Immediately After the Accident

Y	M	D	Time	Organization	Orders, etc.
2011	3	11	20:50	Fukushima Prefectural Governor	Instructed citizens of the towns of Okuma and Futaba evacuation within a 2 km radius of Fukushima Daiichi NPS
2011	3	11	21:23	NERHQ	Instruction to issue evacuation orders to citizens within a 3 km radius and stay-indoors orders to citizens within a 10 km radius
2011	3	12	05:44	NERHQ	Instruction to issue evacuation orders to citizens within a 10km radius .
2011	3	12	18:25	NERHQ	Instruction to issue evacuation orders to citizens within a 20 km radius .
2011	3	15	11:00	NERHQ	Instruction to issue stay-indoors orders to citizens within a 20 to 30 km radius
2011	4	21	11:00	NERHQ	Instruction to establish the restricted zone within a 20 km radius
2011	4	22	-	NERHQ	Instruction to establish deliberate evacuation zones and emergency evacuation preparation zones; lifted stay-indoors order within a 20 to 30 km radius
2011	9	30	-	NERHQ	Instruction and notice on the lift of emergency evacuation preparation zones

Made by author based on websites of the Government's Accident Investigation Board (2011) and Prime Minister of Japan and His Cabinet (TEPCO Fukushima NPS Accident) websites

evacuees from the town of Tomioka and village of Kawauchi went to the city of Koriyama. Citizens of the town of Okuma evacuated to the cities of Tamura and Aizu-wakamatsu, while the town of Futaba moved their people to the town of Kawamata and to the city of Kazo in Saitama Prefecture. Residents of the town of Namie were transferred to the city of Nihonmatsu and those from the village of Katsurao evacuated to the city of Fukushima.

2.3 Estimated Values of the Cumulative Dose and Decontamination Criteria

Figure 1 shows the estimated annual cumulative radiation doses over a one-year period after the nuclear accident in Futaba Region and Iitate Village, and the cities of Minami-soma, Fukushima, Iwaki and Tamura plotted in based on the radiation monitoring data collected by the Ministry of Education, Culture, Sports, Science & Technology (2011).

In the towns of Namie and Tomioka, village of Iitate, city of Minami-soma, towns of Okuma and Futaba, and village of Katsurao, there are spots that exceed 20mSv per year which is the dose limit for radiation workers established under the 2007 recommendation of the International Commission on Radiological Protection (ICRP) as well as the criteria for establishing a deliberate evacuation zone. In the towns of Tomioka and Futaba, more than 75% of the monitoring posts exceed an integral level of exposure of 20mSv/year.

Moreover, there are spots in the towns of Namie, Tomioka, Okuma, and Futaba and the village of Katsurao that recorded 100mSV/year or greater, the dose at which clear evidence of cancer risks is shown under the 2007 ICRP recommendation—more than half of the monitoring posts in Namie and Okuma exceed 100mSv per year.

Ministry of the Environment (2011) is proposing a policy to reduce the annual radiation dose by August 31, 2013 to less than 50% compared to August 31, 2011, but this indicates that the decontamination efforts cannot bring the radiation dose to zero.

It is easy to assume that there are spots that cannot achieve the long-term goal of reducing the additional exposure dose to 1mSv a year in 2 to 3 years.

Table 2 Approximate Number of Evacuees under the Evacuation Programs

Municipals	Total	By zone			Major destinations
		Restricted Zone	Deliberate Evacuation Zones	Former Emergency Evacuation Preparation Zones	
District of Futaba	**72,650**	**62,400**	**2,600**	**7,650**	
Town of Hirono	**5,100**	**-**	**-**	**5,100**	**City of Iwaki**
Town of Naraha	**7,750**	**7,700**	**-**	**50**	**City of Iwaki, town of Aizu-misato**
Town of Tomioka	**16,000**	**16,000**	**-**	**-**	**City of Koriyama**
Village of Kawauchi	**2,900**	**400**	**-**	**2,500**	**City of Koriyama**
Town of Okuma	**11,500**	**11,500**	**-**	**-**	**City of Tamura, city of Aizu-wakamatsu**
Town of Futaba	**6,900**	**6,900**	**-**	**-**	**Town of Kawamata, city of Kazo (Saitama Pref.)**
Town of Namie	**20,900**	**19,600**	**1,300**	**-**	**City of Nihonmatsu**
Village of Katsurao	**1,600**	**300**	**1,300**	**-**	**City of Fukushima, town of Aizu-bange, town of Miharu**
Village of Iitate	6,200	-	3,200	-	**City of Fukushima**
Town of Kawamata	1,300	-	1,300	-	**Town of Kawamata, city of Fukushima**
City of Tamura	2,500	400	-	2,100	**City of Tamura, City of Koriyama**
City of Minami -soma	31,810	14,300	10	17,500	**City of Fukushima, City of Soma**
Total	114,460	77,100	10,110	27,250	

Compiled by Government's Accident Investigation Board (2011), as of November 4, 2011

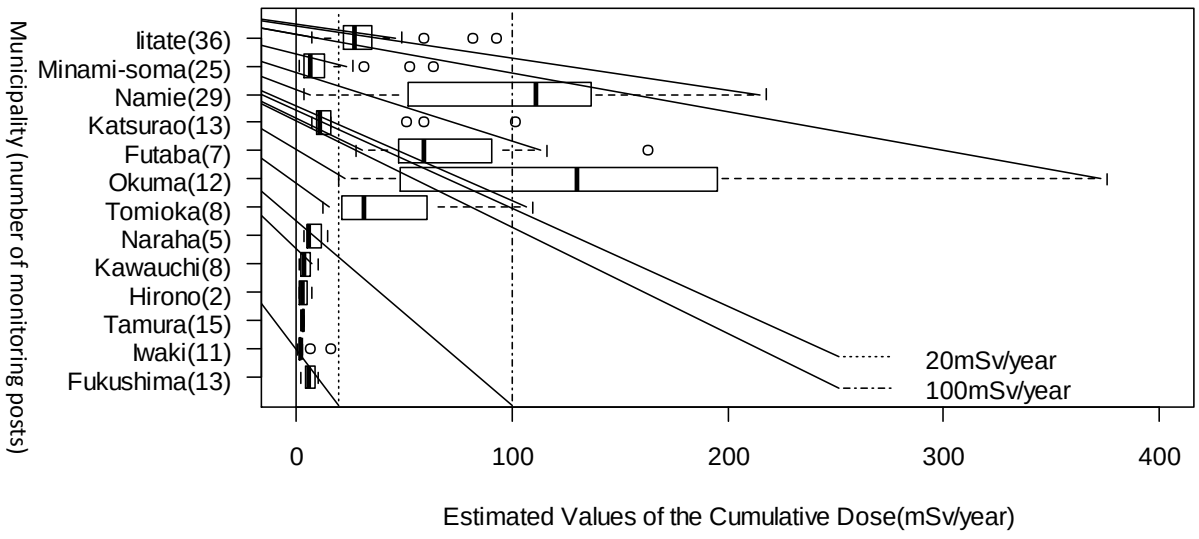


Figure 1 Approximate Number of Evacuees under the Evacuation Programs

3. QUESIONNAIRE SURVEY IN THE DISTRICT OF FUTABA

3.1 Outline of the Survey

- Title of Survey: "Survey of Post-disaster Restoration of the Residents of Futaba District"
- Subject of Survey: Evacuees that were residing in the 8 municipalities of the district of Futaba
- Method of Survey: Mail-in survey (enclosed in town/village reports)
- Period of Survey: September – October 2011
- Sample Design: Complete census based on list of evacuees prepared by municipalities
- Total Number Distributed: 28,184
- Number of Respondents: 13,630 (response rate: 48%)
- Content of Survey: Attributes of Respondents (gender, age, occupation), conditions of evacuation (place of residence before evacuation, destination of evacuation, number of times evacuated), family (family composition, break ups, if any), desire to return, life as an evacuee (living plans, mental health conditions), opinions on restoration, etc.

3.2 Desire to Return

In this survey, respondents were shown the conditions of their hometown in a step-by-step manner and asked whether they wished to return to their place of residence before evacuation (desire to return).

Four percent (4%) of the respondents answered that they would "(1)return immediately if the radiation dose decreases to the level that the government considers safe." Sixteen percent (16%) answered that they would "(2) return if the radiation dose decreases and the urban infrastructure including water and sewage system, electrical facilities and gas is restored," and 20% said they would "(3) return if the local and national governments, in addition to (1) and (2) above, develop and implement an adequate decontamination program." Moreover, 25% of the respondents answered that they would "(4) return if, in addition to (1) to (3) above, a certain number of other residents decide to return."

Eight percent (8%) remained undecided ("(6) others"), while 24% clearly expressed that they "(5) have no intention to return."

The desire to return had varying tendencies depending on the age of the respondents. A greater percentage of younger people selected "(5) have no intention to return" while fewer elder people did.

3.3 Aspiration for Restoration Measures and Policies

The survey listed 13 items that were considered important for future restoration, and respondents were asked to select up to 3 items. Many respondents selected "development of a restoration plan for the entire district of Futaba" (46%) and "industrial development including job security for younger generations" (43%), followed by "enhancement of facilities for elderly and healthcare" (31%), "construction of public and private housing" (21%), "restoration of primary industries (agriculture, forestry and fishing)" (21%), "development of medium-term restoration plans" (20%), "creation of base for renewable energy" (16%), and "development of schools and educational facilities" (16%).

Table3 Desire to Return

Choices on Desire to Return	Responses	Percentage
(1) return immediately if the radiation dose decreases to the level that the government considers safe	589	4%
(2) return if the radiation dose decreases and the urban infrastructure including water and sewage system, electrical facilities and gas is restored	2,159	16%
(3) return if the local and national governments, in addition to (1) and (2) above, develop and implement adequate decontamination program	2,762	20%
(4) return if, in addition to (1) to (3) above, a certain number of other residents decide to return	3,380	25%
(5) others	1,102	8%
(6) have no intention to return	3,284	24%
No response	354	3%
Total	13,630	100%

4. Consideration of a Restoration Plan for the Entire District of Futaba

With the exception of the town of Okuma, the population of the district of Futaba had been decreasing even before the accident. Survey results also revealed that not all people have the desire to return, so it is anticipated that each municipality will have smaller populations than before the accident. In this situation, improvement of healthcare and educational facilities will become a major issue. The majority of those who want to return home early are senior citizens, who are in need of better facilities for the elderly and healthcare. Considering the expected rates of utilization, it is perhaps necessary to consolidate several of these facilities and to enhance the transportation services between

Table4 Priorities for Restoration (multiple choices)

Restoration Measures & Policies	Responses	Percentage
Restoration of primary industries (agriculture, forestry, fishing)	2,795	21%
Industrial development including job security for younger generations	5,795	43%
Development of tourism industry	230	2%
Attraction of firms and plants	1,404	10%
Creation of base for renewable energy	2,197	16%
Attraction of universities and research institutes	437	3%
Construction of public and private housing	2,897	21%
Development of schools and educational facilities	2,167	16%
Enhancement of facilities for elderly and healthcare	4,180	31%
Incorporation of the district of Futaba	1,577	12%
Development of medium- and long-term restoration plans	2,722	20%
Development of restoration plans by individual communities	1,965	14%
Development of restoration plan for the entire district of Futaba	6,314	46%
Total	13,630	100%

locations in order to make them economically viable. This kind of scheme of enhancing public services beyond the borders of the towns and villages should be considered in developing restoration plans for the entire district of Futaba.

According to the reported values of radiation doses, there is nothing for it but to admit that some spots cannot be decontaminated to the level in which people can return. For those who wish to return home but cannot go back to their original place of residence because the radiation dose cannot be reduced to a safe level, there should be schemes to enable them to find an alternative place to live in the vicinity of their original domiciles, which may be beyond the borders of the towns and villages in some cases. Such flexibility should also be considered in developing restoration plans for the entire district of Futaba.

References:

Keiichi SATO, Kenichi NARITA and Fuminori TANBA (2012),"Psychological Wellness of Evacuees from Futaba Residents following Fukushima Nuclear Accident and Hope for Recovery Program" Journal of Social Safety Science, No.18, 189-197.

Government's Accident Investigation Board (2011), "Interim Report" , http://icanps.go.jp/eng/interim-report.html

Ministry of Education, Culture, Sports, Science & Technology (2011), 'estimated annual cumulative radiation doses over a one-year period after the nuclear accident', http://radioactivity.mext.go.jp/old/ja/1750/2012/01/1750_011718.pdf

Ministry of the Environment (2011), 'Jyosen-no-Ohanashi (about decontamination)', http://www.env.go.jp/jishin/josen-plaza/pdf/josen.pdf

10CUEE CONFERENCE PROCEEDINGS
10th International Conference on Urban Earthquake Engineering
March 1-2, 2013, Tokyo Institute of Technology, Tokyo, Japan

DEVELOPMENT & APPLICATION OF 'ICHI-NICHI-MAE PROJECT' FOR DISASTER AWARENESS: 'IF WE WERE BACK THE DAY BEFORE THE DISASTER, HOW CAN WE BETTER PREPARE?'

Satoru Nishikawa[1)], Tomohisa Sashida[2)], Mikiko Ikegami[3)], Hajime Kagiya[4)], Noriko Suzuki[5)] and Kazuyuki Nakagawa[6)]

1) Director General, Audit Department, Japan Water Agency, Japan
2) Executive Chief Consultant, Tokio Marine & Nichido Risk Consulting Co., Ltd., Japan
3) Vice-President, Tokyo Young Women's Christian Association, Japan
4) Manager, Welfare Division, Itabashi City Office, Japan
5) Assistant Manager, Business Risks Department, Tokio Marine & Nichido Risk Consulting Co., Ltd., Japan
6) Bureau Chief, Yamagata Bureau, Jiji Press, Japan
satoru_nishikawa@water.go.jp, t.sashida@tokiorisk.co.jp, ike-kuni@mwc.biglobe.ne.jp, kagiya_h@city.itabashi.tokyo.jp, n.suzuki@tokiorisk.co.jp, n-kazmail@nifty.com

Abstract: Raising public awareness against disasters is one of the main pillars of disaster reduction policy in Japan. Numerous educational materials have been developed to raise public awareness on disasters. However it has been often the case that these materials are not seriously accepted by adults and have not lead to preventive action. To address this issue, we have developed a new program; 'Ichi-Nichi-Mae (the Day before the Disaster Hit) Project' for Disaster Awareness. This program interviews people who have been seriously affected by a major disaster, by posing the question 'What would you do if you were back the day before the disaster?', and edits the most impressive personal short stories which give clues for future preventive action. The interviews cover a wide variety of adults who experienced disasters, from housewives to small business owners and large enterprise employees. Wide varieties of disasters are covered. These stories are compiled and have been used for disaster awareness seminars and have proven to be effective, since the real stories make participants feel that it may happen to them. The methodology of this project is published on the Cabinet Office Disaster Management website and is voluntarily applied by various communities.

1. INTRODUCTION

Japan has been menaced by various natural disasters such as earthquakes, volcanic eruptions, typhoons and floods throughout the course of her history. To reduce the losses by such disasters, the Japanese Government formulated the Disaster Countermeasures Basic Act in 1961 and has implemented various disaster reduction measures; flood control works, anti-seismic building codes to name a few. Thanks to these efforts the number of casualties by natural disasters has shown substantial decrease compared to 60 years ago when the Basic Act was formulated. However Japan still faces disaster risks such as large scale earthquake & tsunami and floods induced by torrential rains. On the contrary, Japan now faces the dilemma that people have fewer live experiences of disasters and do not feel the threats and thus the communities may be less prepared against potential risks. Furthermore the aging population may be more vulnerable to disasters. Thus the Japanese Government decided to emphasize the importance of self preparedness of the residents & mutual assistance at the community level and organized 'The Special Committee on Promoting a Nationwide Movement for Disaster Reduction' in July 2005 under the Central Disaster Management Council chaired by the Prime Minister. Raising public awareness and disseminating knowledge on disasters for adults were identified as one of the target areas for action.

Various educational materials, mostly targeted at children, have been developed in Japan. Not many are targeted at adults. Those existing materials were mainly "Do's and Don'ts Preaching Style" and were not fully appreciated by adults, were not accepted as their own affair, therefore were said to be not effective in making the adults to take action. Therefore, for the sake of inducing spontaneous preventive action by adults, the authors developed a new program, the 'Ichi-Nichi-Mae (the Day before the Disaster Hit) Project'. The 'Ichi-Nichi-Mae Project' interviews people who have been seriously affected by a major disaster, by posing the question 'What would you do if you were back the day before the disaster?', and edits the most impressive personal short stories which give clues for future preventive action. The interviews cover

a wide variety of adults who experienced disasters, from housewives to small business owners and large enterprise employees. Wide varieties of disasters are covered. These stories are compiled and have been used for disaster awareness seminars and have proven to be effective, since the real stories make participants feel that it may happen to them. The methodology of this project is published on the Cabinet Office Disaster Management website and is voluntarily applied by various communities.

This paper introduces the development process of the 'Ichi-Nichi-Mae Project' methodology, the collection of stories and the application to various disaster awareness programs. This paper also introduces how this 'Ichi-Nichi-Mae Project' is widely appreciated after the Great East Japan Earthquake.

2. PROCEDURES FOR 'ICHI-NICHI-MAE PRO-JECT'

The following describes the standard procedures for 'Ichi-Nichi-Mae Project'. The main aim of this project is to make as many people as possible to have empathy for the disaster affected people, make them feel that they may experience a similar disaster and urge them to take spontaneous preventive action. Therefore extracting various personal stories arising from different standpoints in facing the disaster is important. Therefore we have designed our methodology to meet this purpose and have tried many tips to edit the impressive stories.

2.1 Editing Personal Stories

Seven steps are required to extract personal stories. 1. Identifying suitable interviewers. 2. Identifying storytellers among the affected people. 3. Group Interview. 4. Extract impressive personal stories. 5. Edit the personal stories. 6. Add a headline to each story. 7. Selection by disaster reduction expert.

1. *Identifying Interviewers*: Anyone who is serious in promoting 'Ichi-Nichi-Mae Project' is qualified to be interviewer. The number of interviewer for a disaster case should be more than one. This is to have plural standpoints in the later editing process and to avoid delusion in understanding the story. Volunteers from the mass media, governmental services, civil societies and the general public were briefed on the 'Ichi-Nichi-Mae Project' methodology and have served as successful interviewers.

2. *Identifying Storytellers*: Identify a few to several (5 to 6) storytellers per one disaster. Find a contact person in the disaster affected area and ask him/her to bring his/her neighbors or friends who have experienced the same disaster. Asking the local school PTA or community center to assist in gathering several may be a good way. The storytellers can be varied; company employees, small business owners, local construction engineers and community center participants may be asked to join. If the storytellers are acquaintances with each other, it will help to activate lively discussions. However this is not mandatory since it is often the case that the survivors of the same disaster are eager to discuss their stories even at their first meet. One important tip to make the storytelling meaningful is to include some who were responders; firefighters or relief volunteers, so that they may add a responder's point of view.

There are so many survivors who wish to share their experiences and lessons from the disaster they faced. Many of them sincerely wish that their fellows do not suffer as they did. However there are few opportunities for them, who are usually regarded as laymen, to tell their stories. On the other hand, many citizens seldom have chances to listen to live experiences of a disaster, which can be eye-openers for them. The 'Ichi-Nichi-Mae Project' makes an ideal opportunity to link the two.

3. *Group Interview*: Ask 2 to 6 storytellers in the locality who experienced the same or similar disaster to come and tell their disaster experience for about 2 hours. The interviewers will ask them to tell their experience in chronological order and ask them how they felt. Interviews should be conducted in a relaxed manner, in places like community centers, cafes or local schools. The interviewers are recommended to bring news photographs & articles of the disaster as a hint to bring back the live memories of the storytellers. Serve tea and cookies to make people relax and don't forget a voice recorder. The storytellers would not be previously notified of the questions that they are going to be asked, to avoid burdening them and to let them speak freely out of their memories at the interview. This will avoid their stories being didactic.

The interviewers will ask, how was their everyday life, how the disaster changed their life, how do they feel after the disaster, and 'What would you do if you were back the day before the disaster?' By taking the advantage of group interview, let the remarks of one storyteller provoke another's recollection, and bring lively discussion on their experience. Be careful not to interrupt when a storyteller is speaking.

4. *Extract Impressive Personal Stories*: When the storytelling session is over, the interviewers shall bring together their memos taken during the session, and pick up keywords and essence of stories which will attract people's ears. Interviewers should try to understand the wishes of the storytellers that others do not make the same mistakes, and pick up, failure stories which will generate sympathy, and also messages that the storytellers wish to convey. Interviewers should carefully remember the tone of the storytellers in identifying these essences of stories. The interviewers may pick up the points which they themselves felt sympathy. However it should be noted that stories which do not fit with disaster risk reduction should be avoided. The interviewers may think of the headlines to be added to each story at this stage. This will ease the workload at later stage.

5. *Edit the Personal Stories*: By supplementing the notes taken by the voice-recorders, the keywords and essence identified above shall be edited as short stories. The short stories should be edited in 200 to 600 words long, leaving the flavor of the speakers tone and dialects. The storytellers are not professional speakers. Therefore their talks might be

fragmented and may not be in chronological order. By editing their talks into short stories, their message becomes alive.

6. *Add a Headline to Each Short Story:* Add a suitable headline to each short story. This headline serves the purpose of attracting the readers to be interested in the short story; therefore it should not be too descriptive but rather should aim at drawing curiosity. The heart of 'Ichi-Nichi-Mae Project' is how to attract people to read other's experiences. Therefore every attention should be paid to make the headline of each short story attractive while using plain words so that even children can also easily pick up what the story wants to convey.

7. *Selection by Disaster Reduction Expert*: The significance of 'Ichi-Nichi-Mae Project' comes from the fact that it opened the door to all citizens to contribute to disaster risk reduction. Anyone who has experienced a disaster can become a resource person. Anyone who is willing to listen to disaster experiences can be the interviewer. However this requires some careful editing and selection process to maintain the quality of the collected material which are posted and made public through the Japanese Government Cabinet Office Disaster Management Website. The following are the important points to be taken note for quality control in the interview, editing and selection process.

Table 1 Standard 7 Steps in Editing Personal Stories

Step	Standard Procedure	Action Points & Tips
①	Identify Interviewer	Find good volunteers. Interviews to be conducted by 2 to 3 interviewers
②	Identify Storyteller	Request assistance from local community centers, school PTA, volunteer firefighters, and local shop leaders to indentify storytellers who experienced the disaster. Include volunteer firefighters and responders.
③	Group Interview	Find a relaxing place. Set voice recorder. Bring news photos and articles on the disaster. Don't interrupt the storyteller.
④	Extract Stories	Note down keywords. Try to pick up moving stories, mistakes and the wishes they want to convey.
⑤	Edit Stories	Edit the stories each into 200 to 600 words. One story should focus on one topic. Correct dialects if they are difficult to understand.
⑥	Add Headlines	Interviewers to agree on each headline. Headlines should be in oral tone.
⑦	Selection by Expert	Ask the disaster experts in the region to participate in the selection process. Don't add didactic modification. Make clear that mistakes are mistakes.

Do not interview with prejudgments. Do not guide the story telling by the interest of the interviewer. Do not add stories in the editing process even if it may make the story attractive. Do not add moralistic or didactic stories. Make clear that erroneous action taken by the storyteller can be clearly recognized as such. Even if the erroneous action led to good results by luck, make sure that it is clearly understood that such cases are very rare. When the edited stories are finalized, they are sent to the storytellers for their approval and then posted on the Cabinet Office Disaster Management Website.

Through these cautious procedures, the various experiences and lessons learnt by various citizens are widely shared. This 'Ichi-Nichi-Mae Project' story editing procedure is also posted on the Cabinet Office Disaster Management Website.

2.2 Workshops using the 'Ichi-Nichi-Mae Project' Stories

The 'Ichi-Nichi-Mae Project' stories can be used as materials for disaster reduction seminars and also as food for thought to induce discussions at workshops. The following table shows a model for conducting a workshop.

Table 2 Model of Workshop using 'Ichi-Nichi-Mae Project'

Step 1	Read	Divide the participants into small groups of 4 to 7. Let the participants do self-introduction, chat and small games for ice-breaking. Read carefully the disaster experience story. It would be effective to watch a video footage of the disaster, prior to reading.
Step 2	Write	Underline the points in the story where it was a surprise, a sorrow and a joy. Write memos on Post-It tags and put them on where the participant found important.
Step 3	Discuss	Group members tack tags on a large piece of paper in turn. If there are same content tags, place them together. Classify the tags by, things to be done by individuals, things to be done in the community, things to be done as the society, and discuss among the group what should be done to reduce disaster risks.
Step 4	Present	Discuss among the group and select several action points which the group thinks important for disaster reduction, and present.
Step 5	Act	Execute the action points identified by your group and the attractive action points which were identified by other groups. Action points which can be easily executed by oneself, for example affixture of furniture for earthquake safety, should be done on return to home.

2.3 Tips to Enlarge Participation

The 'Ichi-Nichi-Mae Project' can be applied to a wide variety of disaster risk reduction activities. The aforementioned workshop is just one example. Stories can be used as short articles in community papers and township circulars. They can be used as texts for schools and adult education centers. The 'Ichi-Nichi-Mae Project' has flexibility, and users may innovate good ways for application to their disaster reduction activities.

The 'Ichi-Nichi-Mae Project' started in 2005. In the initial years, the interviewing and editing were borne only by

us, the author group. Starting from 2009, in order to enlarge this project, advocates in local governments and mass media were welcomed to join the interviewing & editing. Hence we have transformed 'Ichi-Nichi-Mae Project' to a universal methodology where any advocate can join.

In this process, we have decided to always place a small illustration for each story to make it visible and attractive together with the headlines.

3. STORIES COLLECTED TO DATE BY 'ICHI-NICHI-MAE PRO-JECT'

3.1 Outline of Stories Collected

The 'Ichi-Nichi-Mae Project' started in 2005 and is continuing for more than 7 years to date. The disasters covered include 10 earthquakes, 14 torrential rains & typhoons and 2 volcanic eruptions. The oldest disaster event covered is the December 1946 Nankai Earthquake, the most recent is the July 2010 Torrential Baiu Rains. A total of 546 stories are collected and posted on Cabinet Office Disaster Management Website as of March 2012. Table 3 shows the number of stories classified by disaster type and region in Japan. Table 4 shows the number of stories classified by situation. As indicated on Table 4, we have made efforts to collect stories encountered at company & offices, schools and government offices, which were not adequately covered by existing public disaster awareness materials. Figure 1 shows an example of a story of earthquake damage at a company. Figure 2 shows a live testimony of a tsunami survivor. Figure 3 shows an example of a municipal civil servant who was responsible for evacuation center for volcanic eruption. Figure 4 shows a witness of urban flooding. Figure 5 shows a testimony of a earthquake survivor.

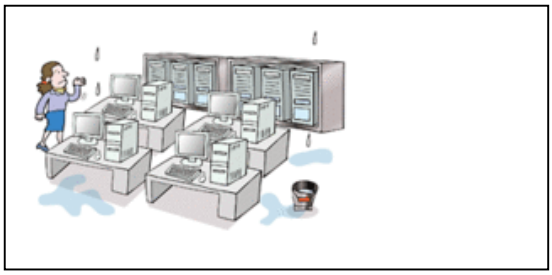
Table 3 Stories Collected by Region and by Disaster Type as of March 2012

	Earthquake & Tsunami	Torrential Rains & Tyhoons	Volcano	sum
Hokkaido	-	-	27	27
Tohoku	62	-	-	62
Kanto	-	34	-	34
Chubu	56	87	-	143
Kinki	33	27	-	60
Chugoku	40	70	-	110
Shikoku	7	7	-	14
Kyushu	42	37	17	96
total	240	262	44	

Table 4 Stories Collected by Situation as of March 2012

Home	183
Community & Neighborhood	211
School	16
Company & Office	109
Government Office	27

The Water Leak from the Kitchen Made My Blood Freeze (Niigata Chuetsu-Oki Earthquake 2007)



(Story by a male company employee in the 40s, Kashiwazaki City, Niigata Prefecture)

The first thing for me to do after the earthquake was to resume welfare services to our employees. Since our company cafeteria was damaged, I had to arrange delivery of 600 to 700 meals every day for about one month. Since it was summer and hot, I paid every attention to avoid food poisoning.

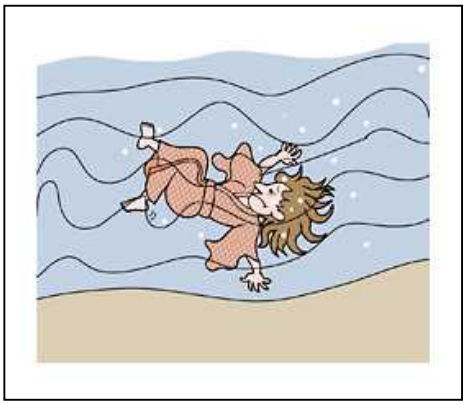
Since most of our major facilities were affixed against earthquakes, we did not suffer big damage. However our computer room was located one floor below the damaged cafeteria kitchen. So the water leaked from the broken pipes in the kitchen to the computer room.

Considerable amount of water fell to the computer room; it was mere luck that the water did not soak the computers themselves. If they were, we would not have been able to resume production 3 days after the earthquake. Even if the main production facilities are safe, without network services we cannot operate. Since, we have decided to waterproof our important facilities.

Figure 1 Example of a Story by a Company Employee

The necessity of the businesses to be more proactive in disaster risk reduction was pointed out in 2003 by the Special Committee under the Central Disaster Management Council. Therefore the 'Ichi-Nichi-Mae Project' paid efforts to gather as many stories which will draw concerns of company managers.

I Tumbled Round and Round in the Seawater (Nankai Earthquake & Tsunami 1946)



(Story by a female survivor in the 70s, Kaifu County, Tokushima Prefecture)

After the big shake, seawater surged in waves into my house. We had 4 family members at home. They all shouted, "Hurry! Hurry!" and ran. But the waves hit us from the back and from the side and made us so difficult to move.

The next moment, all four of us were swept away by a big wave. I tumbled round and round as if I was put in a washing machine. My mouth was filled with seawater, almost suffocated. Unless I can pop my head out the seawater, I will die! This is the end! This might be my last breath! That was all I could think in the salty whirlpool.

Luckily the next moment my head popped out of the waves! Oh my goodness! I can breathe. I am still alive. That was all I could think.

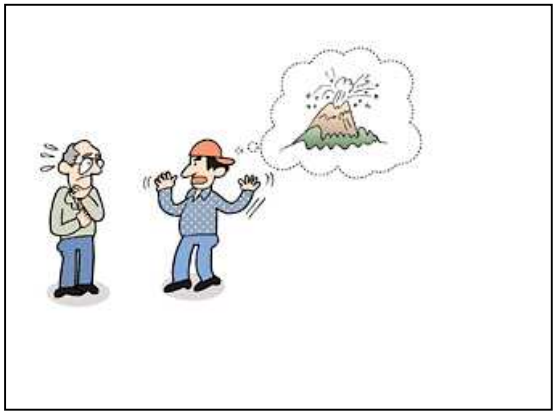
Drifting for awhile, my hand touched something like a wood. I grabbed it. Since my feet were still wandering in the water, my hands ached to keep hold of it. But if my hands let it go, I would be swept away to nowhere. I held on like grim death.

Then dim light came. I nervously looked around to see my whereabouts. Surprise! I was hanging onto the doorsill of my next door neighbor's entrance.

Figure 2 Example of a Story by a Tsunami Survivor

Quick evacuation to high land is the key to save lives in a tsunami disaster. But it is always difficult to convince people to immediately evacuate. However the real story of a tsunami survivor who was once washed away has the persuasive power.

We did not know whose words to believe. (Mt. Unzen Volcanic Eruption 1991)



(Story by a municipal male civil servant in the 50s, Shimabara City, Nagasaki Prefecture)

Every day, we the municipal civil servants were tending to the evacuees in the evacuation centers all night long. There, quite often, rumors spread "On X day Y month there will be an enormous eruption!"

Such groundless rumors with no scientific evidence will spread out immediately. Since all the evacuees are full of fear and anxiety, once they hear a rumor "On X day Y month there will be zzzzzzz" indicating exact date of something to happen, they will simply react like "Oh! I have to be on maximum alert! But what can I do!" I cannot blame them for such behavior.

Actually, on X day Y month, nothing happens. But the evacuees are all afraid and anxious. We the civil servants did not have any means to ease their unnecessary fear caused by such rumors.

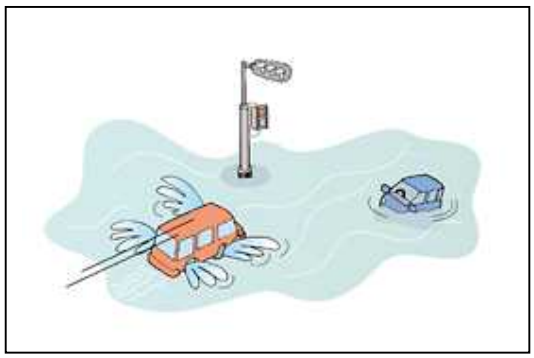
One day, a news media staff told me that the volcano is really in a critical situation. Since I did not have scientific background knowledge on volcanoes, I wondered whether I should believe it or not.

I really felt that there should be a trustworthy mechanism where all the local responders and the evacuees can share accurate information.

Figure 3 Example of a Story by a Municipal Civil Servant

Management of evacuation centers is one of the important tasks of municipal public servants in disaster situation. Tending to evacuees requires endurance. But it is seldom that a civil servant really faces the case that he/she has to take care of the evacuees. Hence these real stories give an image of the difficulty they will face in such disaster.

Automobiles were Swimming at the Intersection (Torrential Rains at end-August 2008)



(Story by a housewife in the 60s, Nagoya City, Aichi Prefecture)

That traffic intersection is low and has poor drainage. I was staring down from my condominium window. As the rain continued, water came from all directions and the intersection became like a swimming pool.

A small vehicle was waiting for the traffic light to change at the center of the intersection. When a 2000cc class large sedan passed by, the small vehicle would float and sway. I felt "The Olympic Games are over and now it is the automobile's turn to do the swimming." I was sure that it would be horrendous to be in that vehicle.

Many cars could not make it through, and they turned around and drove on the sidewalks and barely escaped sinking. Water in such torrential rains really swells in minutes. I think it is definitely needed to make it a rule that "If a road starts to be submerged, we must not drive." It should be one of the flood disaster countermeasures.

Figure 4 Example of a Story by a Housewife

Car drivers tend to underestimate the perils of flooding, since they do not get soaked by the rain when they are in the car. But when the roads are submerged to a certain depth, you may lose control of the car. This witness clearly describes the danger of driving in inundated roads, and the danger of quick swelling of water in built up areas.

I Really Regret Unprepared Single's Life (The Great East Japan Earthquake, March 2011)



(Story by a company employee in the 30s, Sendai City, Miyagi Prefecture)

The Earthquake came when I was working in my office. Everything in the office turned over and fell down. Fortunately nobody was injured in my office.

I reported to the main office that we were all safe. I informed my parents that I was safe. I was lucky to get my e-mail messages through and felt relieved.

Then I went home to my dormitory room. It was a terrible mess! Since I am single and living alone, I do not cook. I always dined outside or bought lunch boxes at nearby convenience stores. My refrigerator was always empty.

I asked my parents in the countryside to send me some food. But immediately after the earthquake, the package delivery service was not available. So my relief food supplies did not reach me. Supermarkets and convenience stores had empty shelves. I nearly starved to death.

I really recognized the importance of food stockpiling. If I was back the day before the Earthquake, I would buy canned food.

Figure 5 Example of a Story by a Single Male Earthquake Survivor.

In the Nationwide Movement for Disaster Reduction, the importance of self help is emphasized. Stockpiling food and water bottles for three days' ration at home are recommended. This earthquake survivor gives good evidence for such preparedness.

4. THE SIGNIFICANCE OF 'ICHI-NICHI-MAE PROJECT'

There are three main objectives for the 'Ichi-Nichi-Mae Project'. They are;

1. Edit & classify stories of disaster affected people and disaster responders into a certain format communicable to other localities and to be recorded in an organized database,

2. The stories to be read by citizens and to be utilized at disaster education opportunities such as seminars,

3. Voluntary workshops to be organized in various communities using the stories.

It is always a big challenge to make people aware of disaster risks and have them acquire knowledge on disasters and lead them to action. The difficulty in this process is the fact that people seldom have the opportunity to experience a real big disaster, and hence people tend to underestimate the disaster risks they face and are reluctant to act before a disaster. The 'Ichi-Nichi-Mae Project' has significant advantages to overcome this difficulty. It is human story oriented; the characters appearing in the stories are ordinary men and women in various occupations and in positions. The readers feel that the characters are no heroes or heroines, they can find characters resembling themselves in either of the stories and get the impression that the similar disaster events may happen to them. This sense of 'men & women next door' attracts the readers into the stories and gives them a feeling that such things may happen to them and this will urge them to initiate preventive action.

5. THE PROPAGATION OF 'ICHI-NICHI-MAE PROJECT'

The methodology and stories of 'Ichi-Nichi-Mae Project' are posted on Cabinet Office Disaster Management website and are downloadable free of charge. It requires neither prior permissions nor registrations to download and utilize. This is because we the authors and the Cabinet Office would like to encourage as many to access and utilize. Therefore there is no firm statistics on how many have read the stories and how much they are utilized. However there are many examples of utilization.

5.1 Utilization by Local Governments, Companies and the Media

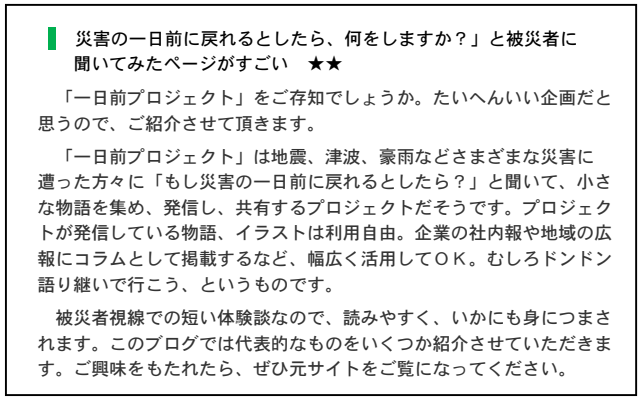
Tokushima Prefecture, which is facing the possibility of a large scale earthquake & tsunami, is posting the stories of 'Ichi-Nichi-Mae Project' in series on its Anshin Tokushima website. 138 stories are posted as of April 2012. Fujikawaguchiko Town, located on the skirts of Mt. Fuji, introduces the aims and significance of 'Ichi-Nichi-Mae Project' on its website and encourages her citizens to look up at Cabinet Office Disaster Management 'Ichi-Nichi-Mae Project' website.

Several companies have joined in propagating the 'Ichi-Nichi-Mae Project'. Rescuenow Inc. and J-CAST Inc. are introducing stories from the 'Ichi-Nichi-Mae Project' on their websites. The Tokio Marine & Nichido Insurance Company, which is the leading insurance company in Japan and the Japanese Consumers' Co-operative Union (COOP) bought numerous copies of the 'Ichi-Nichi-Mae Project' brochures edited by the Cabinet Office and distributed them to their customers.

The mass media also joined in the propagation. The Mainichi Shimbun, one of the major national newspapers introduced it on their article. The NHK, Japanese Public Broadcasting Cooperation, on September 1st 2012, which is the designated National Disaster Prevention Day, aired recitations of the 'Ichi-Nichi-Mae Project' stories in their national radio program and called on listeners to visit the Cabinet Office Website.

5.2 Propagation through Citizens' Blogs

Recently several cases of citizen's blogs have featured the 'Ichi-Nichi-Mae Project'. Since this project aims to broaden disaster reduction activities through free access to the methodology and the stories, the Cabinet Office does not control links to this website. Therefore there is no exact numbers on how many links are made to this website from others. Nevertheless, there are many citizen's blogs citing this website and adding their comments and recommending other to read. Figure 6 is an example of these blogs.



災害の一日前に戻れるとしたら、何をしますか？」と被災者に聞いてみたページがすごい　★★

「一日前プロジェクト」をご存知でしょうか。たいへんいい企画だと思うので、ご紹介させて頂きます。

「一日前プロジェクト」は地震、津波、豪雨などさまざまな災害に遭った方々に「もし災害の一日前に戻れるとしたら？」と聞いて、小さな物語を集め、発信し、共有するプロジェクトだそうです。プロジェクトが発信している物語、イラストは利用自由。企業の社内報や地域の広報にコラムとして掲載するなど、幅広く活用してＯＫ。むしろドンドン語り継いで行こう、というものです。

被災者視線での短い体験談なので、読みやすく、いかにも身につまされます。このブログでは代表的なものをいくつか紹介させていただきます。ご興味をもたれたら、ぜひ元サイトをご覧になってください。

Figure 6 Example of a Citizen's Blog
(For translation see below)

The website asking disaster affected people "What would you do if you were back the day before the disaster" is terrific! **

Do you know the 'Ichi-Nichi-Mae Project'? I think this is a great undertaking, so I would like to introduce it to you.
'Ichi-Nichi-Mae Project' interviews people who were affected by earthquakes, tsunamis and torrential rains and poses the question "What would you do if you were back the day before the disaster". Small stories are collected and disseminated for experience sharing. The stories and illustrations are free to use. It can be copied for use on company's in-house newsletter or community papers. It encourages copying and dissemination.
The stories are compact and based on layman's view, so it is so easy to read and you can be empathetic!

These blog examples show that the aim of 'Ichi-Nichi-Mae Project' to be a tool for promotion of nationwide movement for disaster reduction was well met. The project did not follow the conventional government campaign style; off-the-shelf standard programs to be duplicated at every prefecture through the administrative layers of governments. The project encouraged various participants to choose & adopt the contents to their own needs & taste and disseminate them through various channels.

6. THE APPLICATION OF 'ICHI-NICHI-MAE PROJECT'

The 'Ichi-Nichi-Mae Project' is also actively used in disaster education programs. Ube City Office made enlarged story panels of 'Ichi-Nichi-Mae Project' and exhibited them at the Ube Disaster Reduction Educational Seminar hall for the participants to learn.

Mikiko Ikegami was invited to serve as the lecturer at the Chiba Community Center Manager's seminar entitled "The Role of Community Centers and Managers in Earthquakes" and used the 'Ichi-Nichi-Mae Project' stories related to the management of evacuation centers. Three categories of stories were used. Management of evacuation centers in a disaster, increasing disaster resilience at communities, disaster response work to be borne by civil servants. By comparing the story of the civil servants and the story of the evacuation centers, the participants were able to gain realistic images of what happens in a disaster and what are their crucial roles are. According to the post-seminar evaluation questionnaire, the participants were able to feel the reality of disaster. Table 5 shows the feedback comments of the participants.

Table 5 Positive Feedback by the Participants

The stories were based on real experience and were very useful.
The real stories were impressive and useful.
The comments by the manager who experienced the real disaster are really eye-opening.
It was really good to learn the real stories in such a concentrated way in limited timeframe.
I really felt that "At first all the evacuees act as if they are lords or princesses" is really true. How to have positive participation of the evacuees relies on our everyday communication with our residents.

After the March 2011 Great East Japan Earthquake more attention is paid on disaster awareness and education programs. Many local governments are reviewing their disaster reduction programs and 'Ichi-Nichi-Mae Project' is further highlighted.

The Kawai Town in Nara Prefecture, having assisted the tsunami devastated Rikuzen-Takada City in Iwate Prefecture witnessed the old stone monuments recording historical tsunamis. Upon return to their home town, they recognized the importance of reviewing their home town's disaster history and experience. Kawai Town initiated their own 'Ichi-Nichi-Mae Project', first by reviewing their 1982 flood experience and interviewing the survivors.

Other organizations which are not directly focused on disasters also applied 'Ichi-Nichi-Mae Project' methodology to inherit their experiences to the younger generation. The Japanese Society for Artificial Organs applied the 'Ichi-Nichi-Mae Project' methodology to record and to inherit their experiences during the Great East Japan Earthquake.

These new applications indicate the general versatility of the 'Ichi-Nichi-Mae Project' methodology.

7. CONCLUSIONS

The 'Ichi-Nichi-Mae (the Day before the Disaster Hit) Project' interviews people who have been seriously affected by a major disaster, by posing the question 'What would you do if you were back the day before the disaster?', and edits the most impressive personal short stories which give clues for future preventive action. We have developed this methodology to enable various participants to be the interviewer and the story teller. Seven steps are followed to edit the stories. The edited stories are posted on the website and may be used by anybody. The three main objectives of the 'Ichi-Nichi-Mae Project' were met; 1. Edit & classify stories of disaster affected people and disaster responders into a certain format communicable to other localities and to be recorded in an organized database. 2. The stories to be read by citizens and to be utilized at disaster education opportunities such as seminars. 3. Voluntary workshops to be organized in various communities using the stories.

After the March 2011 Great East Japan Earthquake, this project is attracting renewed attention and further applications are found. The general versatility of this project has been proved. We expect further developments in various localities and sincerely hope that our methodology is widely used to inherit the lessons learnt to the next generations.

Acknowledgements:

This study is based on the research project for promoting the nationwide movement for disaster reduction funded by the Cabinet Office of Japan. The authors acknowledge and deeply thank the valuable contributions by Ms. Sachiko Asano, Ms. Sayaka Irie, Ms. Chisako Omuta, Mr. Nobuyuki Kurita, Mr. Hiroyuki Sato, Mr. Morio Jyohira, Mr. Taketo Sekiguchi, Mr. Nobusuke Takei, Mr. Toshiya Tanabe, Mr. Shuji Hironaka, Mr. Taro Yamazaki, Ms. Michiko Yamada, Mr. Yunosuke Yoshimura and Mr. Gen Watanabe, in interviewing and drawing out the essence of the stories.

References:

Cabinet Office Disaster Management website on Nationwide Movement for Disaster Reduction; http://www.bousai.go.jp/km/

Cabinet Office Disaster Management website on 'Ichi-Nichi-Mae Project'; http://www.bousai.go.jp/km/imp/sub.html

Report of the Special Committee under the Central Disaster Management Council on Involvement of the Businesses & the Private Sector; http://www.bousai.go.jp/MinkanToShijyou/index.html

Tokushima Prefecture Special website on Safety; http://anshin.pref.tokushima.jp/bunya/bousaicolumn/

Fujikawaguchiko Town website; http://www.town.fujikawaguchiko.lg.jp/info/info.php?if_id=1814&ca_id=7

J-CAST Inc. website ; http://www.j-cast.com/kaisha/2010/12/09083084.html

Example of Citizen's blog; http://d.hatena.ne.jp/zyesuta/20101207/1291720510

Kawai Town Ichi-Nichi-Mae Project; http://www.town.kawai.nara.jp/kurashi/anshin_anzen/anshindeanzennamachizukuri/1323830367567.html

Japanese Society for Artificial Organs; http://www.jsao.org/news/200.html

10CUEE CONFERENCE PROCEEDINGS
10th International Conference on Urban Earthquake Engineering
March 1-2, 2013, Tokyo Institute of Technology, Tokyo, Japan

SEISMIC VULNERABILITY EVALUATION OF NON-ENGINEERED STRUCTURES IN PAKISTAN
-- A STATISTICAL APPROACH BASED ON CUMULATIVE OPINION OF PROFESSIONALS --

Zaheer Abbas Kazmi[1)], Muhammad Irfan[2)], and Tauqir Ahmed[3)]

1) PhD Candidate, Department of Civil Engineering, University of Tokyo, Japan
2) PhD Candidate, Department of Civil Engineering, University of Tokyo, Japan
3) Assistant Professor, University of Engineering and Technology Lahore, Pakistan
kazmi@iis.u-tokyo.ac.jp, mirfan1@geot.t.u-tokyo.ac.jp, tauqir@uet.edu.pk

Abstract: Kashmir earthquake of 2005 caused severe devastation in northern parts of Pakistan. Large uncertainties and complexities involved in accessing the phenomenon related to earthquake makes mitigation choices difficult. In this study 132 (qualified) professionals and researchers related to construction industry were surveyed and their opinion about seismic vulnerability of houses in Pakistan was recorded. The work was discretized into four parts as follows. First; Assessment of percentage of seismically vulnerable houses in Pakistan. Second; Concern of seismic safety of houses in general public at different time periods from Kashmir Earthquake. Third; Modification of construction practices after 2005 Kashmir Earthquake. Four; Comparison of different options to enhance seismic concern in general public of Pakistan. The result of this study showed that more than 75% of houses in Pakistan are seismically vulnerable. The study also revealed that concern of seismic safety of houses before 2005 Kashmir Earthquake was at minimum and increased rapidly after the earthquake. However, with the passage of time, the concern of seismic safety of houses has decreased. It seems that a lesson was learnt and forgotten with the passage of time. The results of this study are useful to decide the future seismic mitigation strategies.

1. INTRODUCTION

The 2005 Kashmir Earthquake was among the most devastating seismic activities in past twenty years (Fig.1). It resulted in more than 86,000 fatalities, 106,000 people injured and 4 million people left homeless in northern Pakistan and Azad Jammu and Kashmir (Peiris et al. 2005a, Ahmed et al. 2009). The damage and collapse of the houses during the 2005 Kashmir Earthquake posed a serious threat to the seismic safety of houses in other parts of the country in context of modified seismicity of the region (Kumahara and Nakata, 2006 and Nakata et al. 1991). Non-engineered structures, particularly, pose a serious threat to their inhabitants during earthquakes as proved by 2005 Kashmir Earthquake in which most of the 32,000 destroyed structures were non-engineered. Such a large scale devastation of civil structures attracted researchers from all parts of the world to analyze damage causes and suggest seismically efficient reconstruction techniques (Smith and Redman, 2009, Dowling et al. 2005 and Bartolome et al. 2004). Application of proposed approaches in local environment is challenged by a number of factors (Kazmi et al. 2012).

In context of modified seismicity of the region (Kumahara and Nakata, 2006 and Nakata et al. 1991), it is necessary to evaluate the seismic safety of houses. In essence, owing to a number of uncertainties and complexities, it is difficult to quantify the seismic safety of houses. For evaluation, we need to have a simple and robust method which must be sensitive to uncertain parameters. Meanwhile, it is required that method for the evaluation of seismic safety of houses must be free from influence of individual decisions and personal influences.

Our work encompasses assessment/evaluation of seismic safety of residential houses in Pakistan, which can be considered an important contribution in proposing the future seismic mitigation strategies. Knowing the complexities and uncertainties involved in the seismic phenomena and response of the structures, we have adopted a statistical approach based on the cumulative opinion of the researchers and professionals related to the local construction industry.

2. DISCRITIZED EVALUATION PROCEDURE

Occurrence of earthquakes is uncertain in time and space domain. On the other side, the structural damage due to earthquake is a function of excitation force and resistance of structure to lateral forces. To avoid such a terrific devastation in any future seismic event, there is a dire need to investigate the seismic safety of houses and revise procedure/guidelines for seismically safe construction.

Therefore, the process of evaluation of seismic safety of houses is discretized into four factors which need to be accessed with reasonable accuracy.

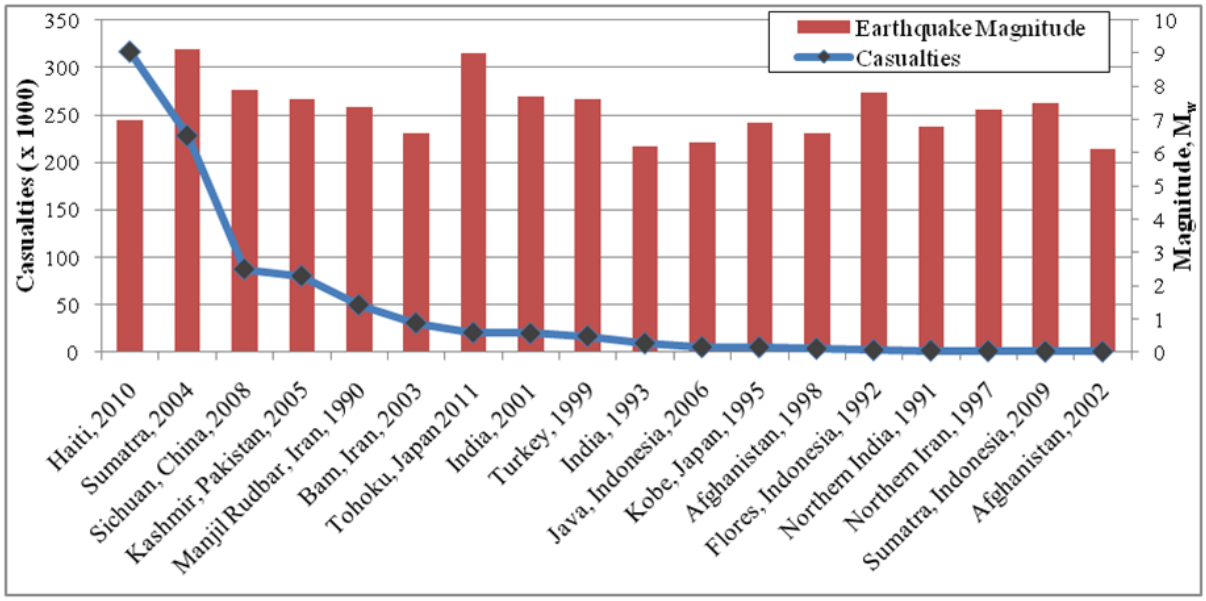


Figure 1: Fatalities and magnitude of earthquakes since 1991, which result more than 1000 fatalities

1. The percentage of vulnerable structures which pose serious threat to the inhabitants. This will index the importance and consideration of measures for seismic safety of houses.
2. The concern of seismic safety of houses in the general public.
3. After experiencing the devastation of 2005 Kashmir Earthquake, we were supposed to improve the construction practices. It is required to investigate how the construction practices are enhanced.
4. The gap between policies and their application in the local community is challenged by a number of factors. Therefore it is important to evaluate the 'most effective way' to enhance the concern of seismically safe construction in local community.

The uncertainty and complexity of seismic event and structural response are important to be considered in getting the answer of aforementioned queries and are discussed in the following sub-sections.

2.1 Uncertainty and Complexity of Seismic Events and Structural Response

Uncertainty of seismic event is fundamentally discussed in articles related to the earthquakes and structural response (Honda and Ahmed, 2011, Ahmed and Honda, 2010). But here in accessing the solution of queries, the uncertainty is exponential. For example, in assessment of seismic vulnerability of non-engineered houses, first uncertainty involved is the nonlinear response of structure under consideration; secondly the diversity of structures (Ali, 2006, Ali and Muhammad, 2007, and Badrashi et al. 2010) is required to be considered in order to be certain about the seismic vulnerability of non-engineered houses. But, this uncertainty is difficult (if not impossible) to be considered by sophisticated techniques, such as finite element method approach, etc.

The response, interest and involvement of the general public are important for successful implementation of the guidelines for improvement of seismic safety of houses. However, the response of the general public is complex due to different financial condition, social exposure and different level of preference among individuals. This complexity is to be incorporated in one way or the other to be certain about the seismic vulnerability of non-engineered houses in Pakistan.

2.2 Advantages to Survey Professionals and Researches

We surveyed 132 researchers and professionals working in the local construction industry to get a diverse opinion/information based on their experience. It is noteworthy that only qualified professionals were surveyed. The survey was designed not to test the professional competency, rather it was meant to extract information based upon individual's experience and exposure and area of assess. Survey results were analyzed to get the cumulative response, which was termed as 'cumulative response of professional and researchers'. The authors reckon that the study is worth considering for deciding guidelines to enhance the seismic safety of non-engineered houses in Pakistan. Following is the discussion on the advantages of this approach.

Diverse opinion: Consideration of diverse opinion is main advantage of this approach. Based on experience and exposure, each person being surveyed possesses different information about the questions being asked; the diversity of feedback thereby reduces the uncertainty involved. By

analyzing the opinions of 132 peoples, we are able to answer the queries (involving uncertainty) with a reasonable accuracy.

3. PERCENTAGE OF SEISMICALLY VULNERABLE HOUSES IN PAKISTAN

Kashmir Earthquake was one of the most devastating earthquakes in the recent history of south Asia. According to the detailed seismic history of the whole country since 1965, it was never subjected to such an intense shaking before Kashmir Earthquake. It is remarkable to note that there were only seven earthquakes larger than M4.0 since 1965 (Fig. 2).

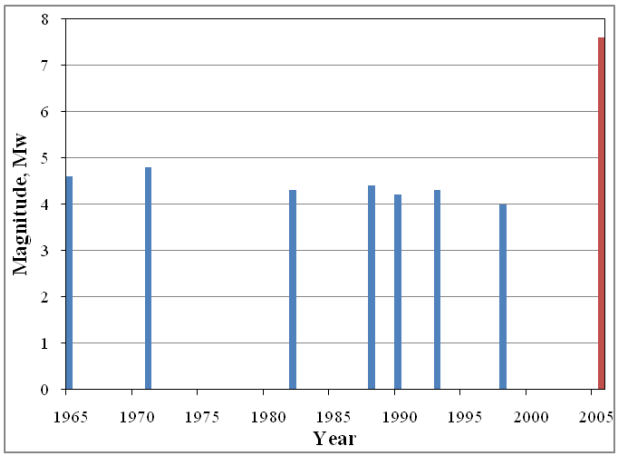


Figure 2. Earthquakes with magnitude greater than 4.0 in Pakistan since 1965.

Therefore, consideration of seismic safety of houses was not a prime concern of house owners before Kashmir Earthquake. Therefore, to assess expected damage due to future earthquake, it is necessary to know the percentage of seismically vulnerable houses. Furthermore, this percentage will show the importance and urgency of proposing measures to enhance seismic safety of non-engineered houses. To accomplish this goal, following question was asked to the professionals and researchers.

'A construction without any advice of an Architect and/or Engineer is termed as non-engineered construction. In your opinion what is the percentage of one to two floor non-engineered houses in Pakistan.'

Each of the contacted professional may have different response depending on his/her exposure and area of assess. Fig. 3 shows their response both in the discretized and cumulative percentage. It is important to note here that the response may also have spatial variation. However, we'll focus to a generalized discussion.

The most frequent value of the obtained distribution function suggests 85 to 90% non-engineered structures (Fig. 3a). It is interesting but unfortunate to note that more than 75% non-engineered houses are reported corresponding to 78% cumulative response distribution (Fig. 3b). 100% cumulative response ensures more than 50% of non-engineered houses. This reveals that all professionals and researchers are unanimously agreed that at least every second house in Pakistan poses serious threat to the inhabitants. This is really an alarming situation for the society and needs to be addressed seriously.

The seismic vulnerability of non-engineered construction is a fact, and to access the seismic vulnerability of houses we asked the following question to the professionals and researchers.

'Considering the percentage of non engineered houses mentioned by you, how do you rank the seismic safety of such construction?'

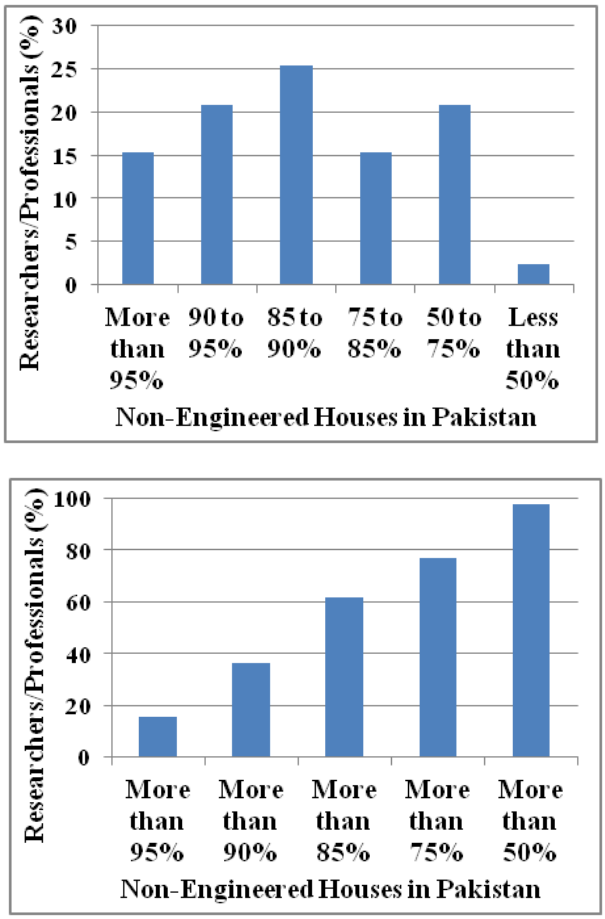


Figure 3. Percentage of seismically vulnerable houses in Pakistan in view of professionals and researchers (a) Discritized percentage (b) Cumulative percentage

The response was recorded corresponding to a scale of 1 to 5. Scale-1 ranks the seismic safety of non-engineered houses to be 'unsatisfactory' and scale-5 corresponds to a 'satisfactory' condition. The survey responses corresponding to each scale of seismic safety are plotted in Fig. 4. The peak response corresponds to scale-2. The cumulative response of the scales 1, 2 and 3 is 90% of the total; which suggests that 90% of professionals and researchers are agreed that the seismic performance of houses in Pakistan is unsatisfactory.

We can conclude from the aforementioned discussion that in view of 78 % of professionals and researchers, more than 75% of houses have unsatisfactory performance against seismic activity.

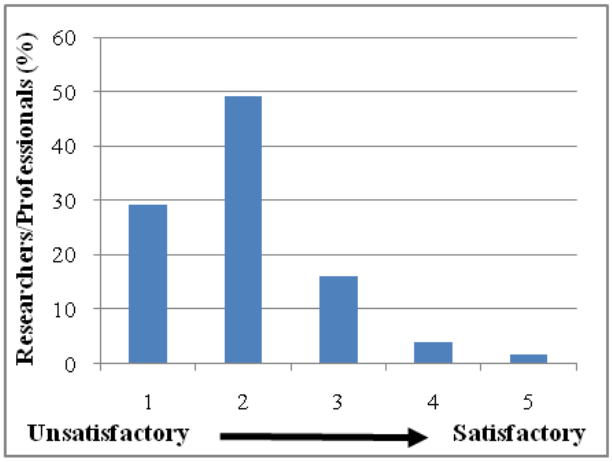


Figure 4. Seismic performance of non-engineered houses in Pakistan in view of professionals and researchers

4. CONCERN OF SEISMIC SAFETY IN PUBLIC

Human sensitivity to natural disasters gets its peak immediately after the event and dies off with the time. Therefore, change in attitude of the local community towards the seismic safety of their houses was quite natural after the devastating Kashmir Earthquake. To consider this aspect in formulating the guidelines for seismically safe construction, it is required to evaluate the concern of seismic safety of houses in general public. Concern of seismic safety and modification of construction techniques are discussed in detail by the authors (Kazmi et al. 2012) based on their field investigation of various sites in earthquake affected areas at

different stages after the 2005 Kashmir Earthquake. To evaluate the concern of seismic safety of houses in local public, we consider the following four stages for an easy discussion.

- Stage-I: Before 2005 Kashmir Earthquake
- Stage-II: From date of occurrence to two months after Kashmir Earthquake
- Stage-III: From two months to two years after Kashmir Earthquake
- Stage-IV: From two years after 2005 Kashmir Earthquake to present.

In survey, the question asked to evaluate the concern of seismic safety of houses in all above mentioned stages was:

'How *do you rank the 'consideration of seismic safety by general public' during the following time periods?*

1. *Before 2005 Kashmir Earthquake*
2. *From the day of occurrence to two months after Kashmir Earthquake*
3. *From two months to two years after Kashmir Earthquake*
4. *From two years after the earthquake till present'*

The response, for all the mentioned stages, is recorded along a scale of 1 to 5, where scale-1 corresponds to least concern and scale-5 corresponds to maximum level of concern. The response from the professionals is analysed and presented in Fig. 5(a) to 5(d) for all the four abovementioned stages. The detailed discussion is presented in the following sub-sections.

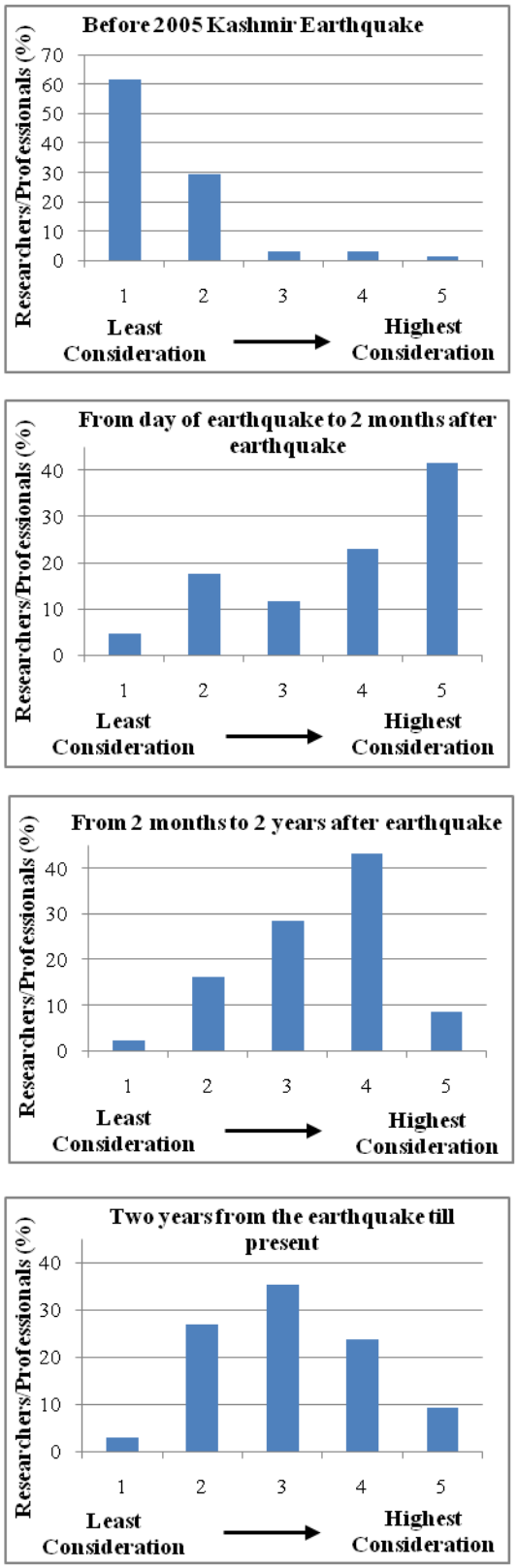


Figure 5. Variation of concern of seismic safety of houses in general public of Pakistan at (a) Stage-I (b) Stage-II (c) Stage-III (d) Stage-IV

4.1 Stage-I

Fig. 5(a) shows responses corresponding to the concern of seismic safety of houses in general public before the 2005 Kashmir Earthquake. A clear peak is observed against scale-I which corresponds to the least concern. It is also clear from Fig. 5(a) that 95 % of responses correspond to scale-1 and scale-2; depicting that researchers and professionals unanimously agree that there was least concern of seismic safety of houses in general public before the 2005 Kashmir Earthquake. Dormant seismic history of the region (Fig.2) could be most prominent among the possible reasons.

4.2 Stage-II

The first two months since the occurrence of earthquake were particularly important because curiosity about the safety of houses against earthquake was at its peak. Fig. 5(b) represents the response of researchers and professionals to concern of seismic safety of houses from occurrence of earthquake to two month after the earthquake (stage-II) and a clear peak is observed against scale-5 which corresponds to maximum level of seismic concern. Results of Fig. 5(a) and Fig. 5(b) highlight the event driven nature of response in developing countries. Seismic safety of the dwellings was not a concern of common people before the tragic event but evolved as a prime concern for the first two months after the occurrence of the earthquake.

4.3 Stage-III and Stage-IV

Along the time scale, from two months to two years after the date of earthquake is categorized as stage-III. The response of the researchers and professionals regarding the concern of seismic safety in stage-III is summarized in Fig. 5(c). In contrast with Fig. 5(b), the peak is shifted from scale-5 to scale-4 in Fig. 5(c) which is evident of a decreasing trend of seismic safety in general public with the passage of time.

Stage-IV encompasses the time from two years since the occurrence of the earthquake to the present. The survey results for stage-IV are shown in Fig. 5(d). The distribution function has shifted from scale-4 to scale-3 in Fig. 5(d), clearly showing a decreased concern of seismic safety as compared to stage-III.

To learn a lesson from natural disasters for a very short time and to forget it with the passage of time leaves us at the mercy of nature. Therefore, immediate actions are required to be taken to educate the community in context of safety of their houses and preparedness for any future seismic event. In parallel, the change in construction practices after the 2005 Kashmir Earthquake must be evaluated

5. MODIFIED CONSTRUCTION PRACTICES

After experiencing devastation of 2005 Kashmir Earthquake, it was required to modify the construction practices and techniques accordingly. Authors acknowledge the efforts and contributions by the private and public sector to enhance the seismic safety of structures.

After Kashmir Earthquake, seismic zoning of Pakistan was revised in light of modified seismicity of area (Kumahara and Nakata, 2006 and Nakata et al. 1991) and building code of Pakistan (PBC, 2007) was enriched with seismic provision. A number of public sector organizations (such as ERRA, NDA, etc) and NGOs (Non Government Organizations) strived to train labour and educate community for the said purpose.

A good number of procedures are proposed by researchers to enhance the seismic safety of houses (Smith and Redman, 2009, Dowling et al. 2005), such as PP-band method (Sathiparan et al. 2010 and Sathiparan et al. 2008), etc. Application of such sophisticated approaches in the community is challenged by a number of factors, such as financial constraints, availability of materials and tools, requirement of skilled labour, etc (Kazmi et al. 2012). Considering this background; we asked the following question to professionals and researchers.

'After experiencing the devastation of 2005 earthquake, we were supposed to improve the construction techniques. In context of seismic safety, how do you compare the present construction practices with construction procedures before 2005 earthquake?'

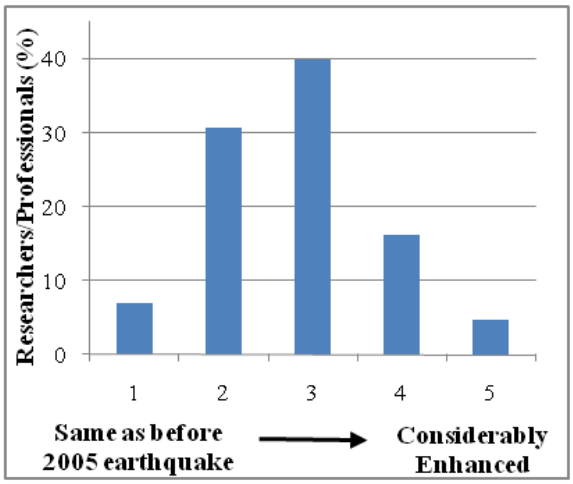


Figure 6. Comparison of pre- and post- Kashmir Earthquake construction practices

Respondents were requested to rank the modification in construction practices on a scale of 1 to 5, where scale-1 corresponds to 'same as before 2005 earthquake' and scale-5 corresponds to 'considerably enhanced'. The responses are analyzed and presented in Fig. 6. The most frequent value of the obtained response distribution function corresponds to scale-3; while scale-1 and scale-2 have 7% and 31% responses, respectively. It is pertinent to mention that scale-1 represents unimproved construction practices when compared with pre-earthquake construction; scale-2 shows slightly enhanced construction practices and similarly scale-3, 4 and 5 represent progressively improving construction practices. The sum of scale-1, 2 and 3 is 78%, showing that an overwhelming majority of 78% of respondents are agreed that construction practices in Pakistan are either unimproved or are slightly enhanced

compared to the construction practices before 2005 Kashmir earthquake.

Considering aforementioned analysis, it is required to invoke the awareness of seismically safe construction in local community. So, the professionals were inquired about the most effective way to educate general public about seismic safety of houses; as discussed in the next section.

6. MOST EFFECTIVE WAY TO ENSUR APPLICATION

The gap between polices and their application in local community is governed by a number of factors. Generally, financial conditions, coherence of new policies with culture and trends, and awareness of community regarding the importance of issues, etc. play the effective role.

In the following discussion, the main interest of authors is to discuss various options to increase the seismic safety of houses. In this discussion we relatively compare the following four options.

1- By enforcing strict laws
2- By public awareness campaigns (seminars, workshops, media campaigns, etc)
3- Providing easy access to useful information (brochures in local language, etc)
4- By giving financial incentives.

It is worth mentioning that some researches highlight the importance of financial assistance to enhance concern of seismic safety (Meguro, 2008). To evaluate the most effective means for increasing the seismic safety of houses, we asked the following question to the professionals and researchers.

'What is the most effective way to enhance the concern of seismically safe construction in local public of Pakistan?'

The responses are analyzed and summarized in Fig. 7. About 38% professionals are of the view that statutory regulations and their strict implementation is the way to assure seismically safe construction; while 34% of respondents believe that the concern of seismic safety of houses can be enhanced by initializing public awareness campaigns through electronic/print/social media, workshops and seminars, etc. Only 12% think that financial assistance can increase the seismic concern in general public of Pakistan.

It is important to mention that authors are intended to compare the four options in relative terms. The results are helpful to decide preference and relative effectiveness of different option to increase the concern of seismic safety of houses.

7. CONCLUSION

Earthquake of 2005 was a devastating experience in the recent history of Pakistan. It resulted in a huge number of casualties and posed a serious question to the seismic safety of residential houses. The main focus of this study was the seismic safety of the residential houses. The analysis sequence was discretized into four parts (i) what is the percentage of seismically vulnerable houses? (ii) concern of seismic safety of houses in local community (iii) how the construction practices were modified after 2005 Kashmir Earthquake? (iv) what is the most effective way to increase the concern of seismic safety of houses?

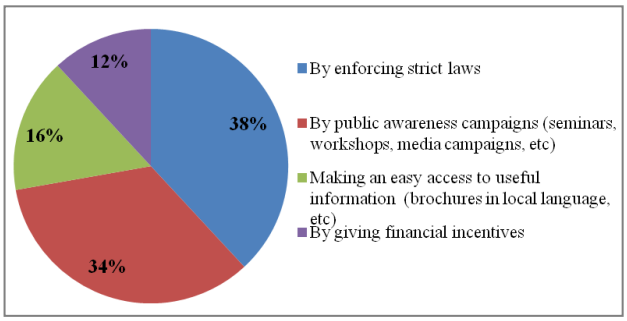


Figure 7. Effectiveness of different options to increase the concern of seismic safety of houses in general public of Pakistan

Owing to uncertainty of seismic events and diversity of structural response, it is difficult to answer the aforementioned queries. Therefore, an indirect and more practical approach was adopted to accomplish the goal. Using this approach 132 professionals (only qualified engineers and architects) and researchers working in local construction industry were contacted; and their responses were rationally analyzed.

The results of this study show that more than 75% of houses in Pakistan are seismically vulnerable which indexes damageability of structures in future earthquakes.

Concern of seismic safety of houses is the second point discussed in this work. The study also reveals that the concern of seismic safety of houses was at minimum in the community before 2005 Kashmir Earthquake. After the Kashmir earthquake, a sharp peak of curiosity towards the seismic safety of houses was observed, but died off with the passage of time. It seems like a lesson was learnt and forgotten within a couple of years of the tragic devastation.

After Kashmir Earthquake, a modification in construction practices was expected. According to this study, however, 79% of the professionals and researchers have opinion that the construction practices are either similar as practiced before Kashmir Earthquake or are slightly improved.

For enhancement of seismic safety of houses, various option were compared in this study; such as by enforcing laws, public awareness campaigns, giving financial incentives, etc. The results have shown that formulation and implementation of statutory regulations public awareness should be first priority to enhance the seismic safety of houses and it should be supported by public awareness campaigns.

References

Peiris, N., Rossetto, T., Burton, P. and Mahmood, S. (2005a) "EEFIT Mission: October 8, 2005 Kashmir Earthquake" Earthquake Engineering Field Investigation Team (EEFIT), The Institution of Structural Engineers

Ahmad, H., Yeast, R.S and MonaLisa (2009) "Geological setting of the 8 October 2005 Kashmir earthquake" J Seismology, 13(3): 315-325

Kumahara, Y., Nakata, T. (2006), "Active faults in the epicentral area of the 2005 Pakistan earthquake" Research Center for Regional Geography, Hiroshima University, Japan, 54pp

Nakata, T., Tsutsumi, H., Khan, S.H. and Lawrence, R.D. (1991) "Active faults of Pakistan" Research Center for Regional Geography, Hiroshima University, Japan, pp. 141.

Smith, A. and Redman, T. (2009) "A critical review of retrofitting methods for unreinforced masonry structures." EWB-UK Research Conference 2009, Royal Academy of Engineering, London.

Dowling, D., Samali, B. and Li, J. (2005) "An improved means of reinforcing adobe walls - External vertical reinforcement." SismoAdobe 2005, PUCP, Lima, Peru.

Bartolome, A. S., Quiun, D. and Zegarra, L. (2004) "Effective system for seismic reinforcement of adobe houses." Proceeding of the 13th World Conference on Earthquake Engineering, B.C., Canada

Kazmi, Z.A, Ahmed, T., Saleem, U. and Irfan, M. (2012) "Evaluation of design and construction practices - a lesson learnt from Kashmir earthquake-" Proceedings of the International Symposium on Engineering Lessons Learned from the 2011 Great East Japan Earthquake, March 1-4, 2012, Tokyo, Japan.

Honda, R. and Ahmed, T. (2011) "Design input motion synthesis considering the effect of uncertainty in structural and seismic parameters by feature indices." Journal of Structural Engineering ASCE, Vol. 37, No. 3, 391–400.

Ahmed, T. and Honda, R. (2010) "Performance of design input motions selected using feature indices to represent possible ground motions." Proceedings of the 13th Japan Earthquake Engineering Symposium." PP. 1965-1972.

Ali Q. (2006) "Unreinforced brick masonry residential building." World Housing Encyclopedia, Report No. 112.

Ali Q. and Muhammad, T. (2007) "Stone masonry residential building." World Housing Encyclopedia, Report No. 138.

Badrashi, Y. I., Ali, Q., Ashraf, M. (2010) "Reinforced concrete buildings in Pakistan." World Housing Encyclopedia, Report No. 159.

Pakistan Buiding Code (PBC-2007)

Sathiparan, N., Mayorca, P. and Meguro, K. (2010) "Parametric study of diagonal shear tests on masonry wallettes retrofitted by pp-band mesh." Proceedings of the 30th conference on Earthquake Engineering Symposium, JSCE, Japan, Paper No. 3-0054.

Sathiparan, N., Paola, M. and Meguro, K. (2008) "Parametric study on diagonal shear and out of plane behavior of masonry wallettes retrofitted by PP-band mesh." Proceeding of the 14th World Conference on Earthquake Engineering, Beijing, China.

Meguro, K.. (2008) "Technological and social approachesto achieve earthquake safer non-engineered houses." Proceeding of the 14th World Conference on Earthquake Engineering, Beijing, China.

10CUEE CONFERENCE PROCEEDINGS
10th International Conference on Urban Earthquake Engineering
March 1-2, 2013, Tokyo Institute of Technology, Tokyo, Japan

THE USE OF GEOSPATIAL TECHNOLOGIES AND LOCAL AREA SPATIAL ANALYSIS TO UNDERSTAND SUB-NEIGHBORHOOD SCALE IMPEDIMENTS TO RECOVERY AFTER A CATASTROPHIC DISASTER

Andrew Curtis

Associate Professor, Director of the GIS, Health & Hazards Lab, Department of Geography
Kent State University, USA
Email: acurti13@kent.edu http://www.kent.edu/CAS/Geography/ghhlab/

Abstract: 0ne of the least understood aspects of disaster science is the complexity of neighborhood recovery after a catastrophic event. For the largest disasters this recovery period can extend into multiple years during which time dynamic processes of rebuilding, recreating social cohesion, existing and emerging health vulnerability, economic opportunity, political representation and even the presence of crime are indicators, stimulators and impediments to a return to normalcy. Although these processes play out at different geographic scales, the least understood, mainly because of data collection problems, is that of the micro-environment within neighborhoods. This paper will present a methodology which has been used to asses spatial patterns of recovery in post-Hurricane Katrina New Orleans, Louisiana and post-earthquake Haiti. By using spatially encoded video, novel data coding strategies within a geographic information system (GIS), and local area spatial analysis, patterns of recovery and the impediments to that recovery can be identified. In addition, map layers can be generated to be combined with data from cognate research, such as disaster medicine and public health. This approach is important to not only advance theories of recovery, but also to provide near-real time insight in supporting recovery efforts.

1. INTRODUCTION

Global and national attention is often drawn to significant disasters in the immediate aftermath. In the United States recent events of note have included Hurricane Katrina, the tornadoes of 2011, and most recently (2012) Superstorm Sandy. Just beyond the United States, Haiti is still struggling from the earthquake of 2010 which was followed by a cholera epidemic. This outbreak was partly spread because of the disaster related infrastructure damage and societal disruption layered onto an already impoverished nation. One connection between all these events, as well as with many other global catastrophes that have occurred in the same time frame, is that "recovery" is still not complete as of 2012. Media attention tends to wane after the first year of a disaster. Historically even academic interest is focused on the first 12 to 18 months following the event, and yet recovery in each of these disasters is still occurring, up to seven years later in the case of Hurricane Katrina.

What these recent events have reaffirmed is the need for spatially contextualized research into recovery (Mills 2008). Several questions need to be posed in order to understand, learn from, and formulate recovery policy. The first fundamental question which is beyond the scope of this paper is *what is recovery*? Is it a return to normalcy, a return to prior levels or even "building back better" as described by President Clinton after the earthquake in Haiti? The second question is, *what should we use to measure recovery, and what is an appropriate scale*? Although there are different recovery metrics available after an event; the number of homes rebuilt, the reconstruction of community services, economic recovery, a return to a benchmark of health outcomes, these are mostly reported as the aggregate, by region, or city, or at best urban subsection. Yet recovery occurs at different geographic scales, and such aggregate data may smooth out the ongoing and debilitating impediments to recovery at the neighborhood or street scale. This is not to dismiss the importance of aggregate measures of recovery because these are necessary for political assessment and to prioritize resources. This paper, though, focuses on the missing component for much recovery work; longitudinal change at the finest of geographic scales.

2. FINE SCALE RECOVERY

2.1 Impediments to Recovery at the Fine Scale

There are many reasons why fine geographic scales are intuitively important for communities impacted by a disaster:

Will my neighbors return?
How long will I have to look out on destruction?
Will my local area services return?
How far do I now have to travel for a doctor or a school?
Where can I shop?

Will the bus ever stop here again?
Will these potholes in the road ever be fixed?
Will I ever experience "community" again?

Similarly, in addition to these bottom-up impediments, there are research questions that can only be answered at a fine geographic scale and for multiple time periods:

Are there spatial patterns in rebuilding that influence subsequent time periods?
Are there street scale environmental or social factors that lead to negative health outcomes?
To what degree does the pattern of rebuilding cause or deter crime?

In order for researchers to consider these types of recovery impediments, fine scale spatial data is needed for multiple time periods. Unfortunately this poses a challenge in terms of data acquisition that limits the amount and scope of many academic investigations.

2.2 Spatial Video as a Data Collection Technology

There are four main ways to acquire fine scale spatial data appropriate for recovery research. The first is to extract map information from remotely sensed sources of data, most commonly high resolution aerial photography (including oblique imagery). This has been partly successful for assessing damage patterns after a disaster; though debate still occurs as to the degree of error with coding using this type of data source (Gerke and Kerle 2011). Besides this potential error, a larger problem for recovery research is the availability of data. Although multiple time periods of high resolution aerial photography are often collected for the time frame around the disaster, and these are often freely available, the temporal granularity in terms of flight passes decreases quickly afterwards, while the costs of access often starts to increase. As a result, any fine scale recovery research using this data source is restricted to available data, especially if reliant on freely available imagery.

The second source of data involves ground surveys; either teams of researchers asking community members recovery related questions, or walking / windshield survey teams performing a visual assessment of the area. Although these collection approaches can result in data rich analyses, the spatial dimension is often limited because of the costs involved in collection. These costs increase dramatically if the study is longitudinal, which given the nature of recovery after a disaster is a necessity. Simply put, it costs too much to keep putting larger teams of researchers into the field.

The third source of data is freely collected or created spatial data from volunteer sources. This volunteered geographic data collection has provided a paradigm shift in spatial data culture especially with regards disasters (Liu and Palen 2010). The general message is one of "can do no matter what". Data layers are created, imagery is digitized, local information uploaded, all using open source Internet based software. However, from a research perspective, the lack of data standards and consistent spatial coverage leaves this spatial data approach as a useful additional resource rather than a primary data source.

The fourth data collection approach involves mobile mapping, especially spatial video (Curtis et al 2007; Curtis and Mills 2011a). In some ways this approach combines elements of the first two strategies. Video cameras connected to a global positioning system (GPS) can be mounted to a vehicle or carried by hand, allowing for spatially encoded ground level imagery to be recorded. Although Curtis has used different systems in the evolution of this approach since 2006, the technology which has been utilized in projects since 2012 is cheap, simple to use, and comes with freely available software. Just as with high resolution aerial photography, or more appropriately in terms of comparison, oblique photography (Gerke and Kerle 2011), the streetscape is captured in a spatial context. This allows for map layers to be extracted and used for analysis. Although there are benefits of oblique photography, namely the extent of the geography covered, and the future possibility for automation in the coding, it is a notoriously expensive data source. Spatial video offers a far more cost effective method which means data can be collected for the researcher's desired area, and for multiple time periods. As a result scientific questions of a spatial nature can be posed unhindered by data availability.

Similarly, spatial video mimics ground-team data collection, especially windshield surveys. The major advantage of using a spatial video is again cost; the area can be covered and then coded by teams back in the lab. In addition there is improved accuracy as the source data is archived allowing for validation rather than assuming the field team "got it right". Data archiving also means that subsequent investigations can pose previously unthought-of questions, research which is not possible if the original data has to be entered into pre-defined categories in the field.

Finally, there is also a link to the volunteered geographic information framework, at least in terms of spatial video being a participatory data collection tool (Duval-Diop et al 2010). The simplicity of use means that the community member him/herself, in other words the most vested person in the work, can become the data collector. Instead of transporting researchers to the field, the equipment which fits into a small camera bag can be mailed or left after the initial visit. An additional benefit of involving community members in this way is the possibility of recording commentary during data collection; these spatially encoded insights providing additional context to the imagery, which makes this approach truly "mixed method".

From a technical perspective, a typical disaster recovery spatial video kit includes two high definition video cameras, usually mounted on either side of a high-riding vehicle, such as a truck or sports utility vehicle. The team at the GIS, Health and Hazards Lab (GHH) at Kent State University has used this basic approach to capture damage assessment and recovery data for neighborhoods affected by Hurricane Katrina; various tornadoes including the catastrophic touchdowns of 2011 in Tuscaloosa, Alabama, and Joplin, Missouri; Wildfire in southern California and Colorado, and

earthquake and cholera landscapes of Haiti (for examples see a series of popular media links at the end of this paper). The preferred "kit" for GHH is two cameras for each side of the vehicle, one pointing downwards to capture curbside data which was especially important for mapping water risks in Haiti. In addition, a handheld GPS unit provides a backup coordinate track, which means that there are five total GPS paths to accompany the imagery, and two different video streams for each side of the road. This level of redundancy is important for harder to reach disaster locations.

Although early spatial video technologies required propriety technology and software, making the extraction of spatial information into a geographical information system (GIS) a multiple stage process, current technologies have benefitted from the rise in extreme sports equipment to create small, relatively cheap cameras with an internal GPS, and arguably the most important advance, freely available software that allows for real time, or near real time display of data (presuming Internet connectivity is available). This allows each daily data collection route to be checked in the field for potential problems, an advantage if the research team has travelled considerable distance to the recovery location and cannot easily make a return trip.

There are, of course, data limitations with using a spatial video. Firstly, only the ground-level view is available. Parked vehicles, large walls, vegetation, all can provide barriers to "seeing" the neighborhood. One solution is to combine these data with available aerial photography (especially for damage assessment), though enough information is usually visible to assess recovery in traditional urban environments. A second problem involves the precision of the GPS path. Earlier versions of the technology had higher precision, but were considerably more expensive and difficult to use. The current extreme sports camera provides enough GPS precision to allow for coding into a GIS in conjunction with aerial photography, though having an additional higher precision GPS-only unit in the vehicle has proven to be a useful addition. As the GHH team moves into even more challenging environments, such as collecting data using handheld approaches along narrow paths in urban slums, so the question of improving GPS precision will become more salient.

2.3 Spatial Video Coding

Once video has been collected, the next stage is turning the imagery into spatial layers that can be mapped and analyzed. Earlier versions of the methodology used priority software that ran within a GIS. This allowed the coder to run the video while digitizing a map layer, which means creating spatial information in the GIS. For reasons described above, the use of freely available software is beneficial because of its ubiquitous access and dissemination potential. With this in mind, coding approaches work best when using two computer monitors, with one screen displaying the video (which in the freely available software also shows the location on the GPS path), while the second monitor has a GIS open allowing for digitizing. An alternative approach to digitizing directly into a GIS, is using Google Earth. This



Figure 1 Spatial video examples from post-earthquake Haiti (June 2012). A= A city rebuilding project; B= temporary housing; C=earthquake damage & standing water which is a disease risk

has three benefits, even though it adds an additional stage in the video-to-map process. Firstly, the imagery is exactly the same as that used in the spatial video software which makes the coding process easier. Secondly, Google Earth has more digitizing flexibility allowing points (or polygons) to have notes attached. This helps the coding categories to evolve as the researcher follows the path and immerses him/herself in the video. In a GIS the data structure is usually more fixed with categories being pre-determined. There is nothing worse than being halfway through a video route when the researcher observes the repetition of a feature, indicating that it should have been coded from the beginning. The final advantage is again the ubiquitous nature of Google Earth, which means collaborators (community members) can add their own insights into the map when watching the video, these insights being emailed as KML files for later combination in a GIS.

The most frequently applied video-to-map approach used by GHH researchers is entering data from the video into a pre-digitized GIS layer. Although different coding

systems have been utilized, the GHH recovery score standard for all post-disaster environments is as follows:

1= Unoccupied
2= Cleared
3 = Rebuilding
4 = Occupied

The first of these classes is then subdivided into:
1:2 Unoccupied but livable
1:5 Unoccupied and blighted (the building is boarded)
1:10 Unoccupied and severely blighted (badly damaged)

Although more detail can be added from the video, this scoring approach has been found to capture both the varying nature of the recovering landscape, while also minimizing between-coder error. In other words, this system can be transferred between disaster events and researchers allowing for cross comparisons. Other variables can be added to complement this score based on the particular research question or analytical approach. For example, height of each building can be added to allow for three-dimensional visualization; vegetation height might be added as an additional evidence of blight or because of its link to crime; evidence of dumping can again display a post-disaster crime vulnerability. It should be noted that entirely different coding systems can be created with the only limit being the quality of the video, and the creativity of the researcher. For example, in post-earthquake Haiti which suffered a second disaster of a cholera epidemic, the coding included various water-related features (drains, wells, evidence of standing water) and even a population count. Reiterating what was previously mentioned, the archival aspect of spatial video data means each collection run can be reinvestigated for different questions at a later time period.

2.4 Spatial Video Analysis

Once the video has been coded in a GIS, there are several options that can be used to determine spatial patterns of recovery. By displaying each coded location (usually a building) as a point, a variety of local area spatial analyses can be performed. The preferred analysis utilized by GHH is a variant of a spatial epidemiology method, the DMAP spatial filter (Rushton and Lolonis 1996). This technique layers a fine grid (user defined, but for the sake of example, 0.01 km) over the study area. For each grid node a rate is calculated within a circle (usually called a filter) which is again a researcher defined radius (for example, 0.03 km). As with most local area spatial analyses, the size of this filter will determine a smoother or more localized analysis. For recovery analysis, this rate might be a numerator of *unoccupied buildings* (score 1.2) or *blight* and *severe blight* (1.5 and 1.10). The denominator is the total number of buildings digitized along the spatial video path. The resulting grid, when displayed in a GIS allows the researcher to click on any location, such as a church, to see what the rate of blight is around that location. By running DMAP for different filter sizes, and for different variables, a comprehensive impression of recovery can be ascertained for any map location; for example how much localized blight, how much blight in the surrounding city blocks, or how many returnees are there. This grid also makes multiple year analysis possible as these rate scores can simply be compared between time periods to assess recovery stagnation, or a rebuilding progression.

The analysis can have further sophistication added to it by adding tests of statistical significance. In DMAP a Monte Carlo simulation creates a distribution of simulated maps against which each "real" node is compared. The percentage of simulated maps that exceed each rate calculation gives the researcher "confidence" in determining whether that rate would occur by chance alone. In this way "hotspots" or "cold spots" of recovery can be identified (Curtis et al 2010). An alternative method of analysis can be used if a secondary data layer is added to the grid of rates. For example, if crime locations or health events are overlaid onto the recovering neighborhood, the proximate rate node can be spatially attached as a measure of recovery for that event. In this way all crimes, or all low birth weight deliveries will have a recovery score (rate of blight, rate of returnees etc) and by using a difference of proportion t test it can be determined whether these attached rate scores significantly differ from the entire map, or even from different years (Curtis and Mills 2011b). In Figure 2 the blighted grid nodes are buffered to the size of the filter, and crime locations overlaid on top. Flood depth caused by Hurricane Katrina in 2005 is also included for reference.

This second type of analysis allows for research questions to be investigated:

Do patterns of isolated recovery lead to manifestations of stress, such as domestic violence?
Are birth weight deliveries significantly lower in households where recovery is slower (assessed by comparing time periods) in the immediate vicinity?
Has certain rebuilt properties or services stimulated proximate recovery?

As the use of spatial video becomes more widespread so will there be a development in spatially focused fine scale recovery theory. Exploratory analyses will lead to testing across disaster types and locations, while at the same time finding near-real time results that can be used for immediate intervention. There is no reason to believe that a global shared video archive can't be created, similar to other spatial data clearinghouses or geoportals. This could present research opportunities in much the same way as facilitated by genome databases.

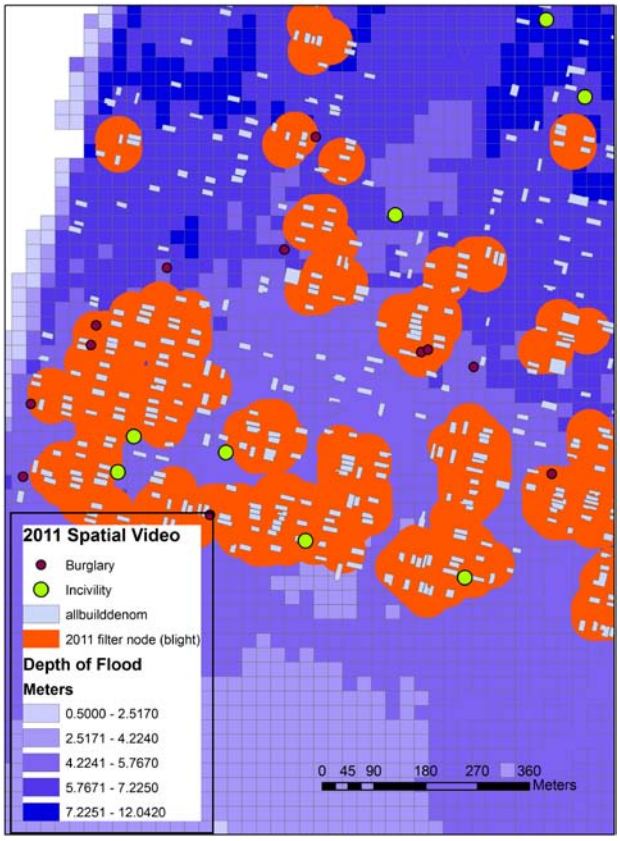


Figure 2 Buffered blight nodes from 2011 overlaid on certain crime locations, all buildings, and Hurricane Katrina flood depth for the Lower 9th Ward in New Orleans.

3. CONCLUSIONS

One unfortunate side effect of a disaster is the disproportionate impact the event may have on socially vulnerable populations. This disproportionate impact often continues through the recovery phase resulting in prolonged return, rebuilding and reestablishing community. The most socially vulnerable are especially reliant on social cohesion and community to help buffer from the stresses and challenges of day-to-day living. Therefore, those most in need for the quickest return to normalcy are also those who have to wait the longest. Obviously, financial difficulties are one major impediment to recovery. A lack of insurance, and low disposable income create a recovery gap whereby families do not have enough to both rebuild and put food on the table (Duval-Diop et al 2010). As a result recovery is not a spatially systematic pattern but often results in considerable heterogeneity, which in itself may further limit recovery or even cause re-abandonment. Added to this disaster related poverty trap are the associated problems: patterns of poor health (this population often carries a high chronic disease burden), crime (again this cohort traditionally suffers from high crime exposure). How this dynamic landscape unfolds, with multiple spatial layers interacting both through geography and time, has largely been the topic of postulation and anecdotes. New mobile mapping technologies, such as the spatial video, now allow for fine scale multiple time period research. These research outcomes may be useful in helping spatially strategize city resources including rebuilding help, where to place health intervention teams, and where to reevaluate services. By including community residents as part of the data collection process, and by simultaneously collecting their insights, hope is also generated that they have not been forgotten and their voice does count.

The GIS, Health and Hazards Lab at Kent State University is willing to work with any group interested in assessing health or hazard risk or recovery. Please contact Andrew Curtis or visit our website at *http://www.kent.edu/CAS/Geography/ghhlab/*

Acknowledgements:

The author acknowledges support from Jacqueline Mills in the preparation of this manuscript, Sheridan Kennedy, Jason Blackburn and Jocelyn Widmer for help in data collection. The University of Southern California, University of Florida, Louisiana State University and Kent State University all participated in funding aspects of research described in this paper.

Popular Media Links:

As spatial video work is visual, the following popular media links for different disasters provide the reader with different examples associated with the author:

1. Forbes, "Video Tech Tracking Haiti's Cholera Epidemic" http://www.forbes.com/sites/lorikozlowski/2012/07/11/video-tech-tracking-haitis-cholera-epidemic/2/

2. The Atlantic, "The Post-Storm Chaser" http://www.theatlanticcities.com/neighborhoods/2012/04/post-storm-chaser/1792/

4. Tuscaloosa News, "Professor measures recovery's progress" video and narration accompanies a news story on our spatial video http://www.tuscaloosanews.com/article/20111027/NEWS/111029746?tc=ar

5. New York Times, "The changing landscape of the Lower Ninth Ward" Interactive spatial video application of my Hurricane Katrina recovery work .http://www.nytimes.com/interactive/2010/08/27/us/lower9th-5year-anniversary.html?ref=us

References:

Curtis, A., Mills, J.W., Kennedy, B., Fotheringham, S., and McCarthy, T., (2007), "Understanding the Geography of Post-Traumatic Stress: An Academic Justification for Using a Spatial Video Acquisition System in the Response to Hurricane Katrina". *Journal of Contingencies and Crisis Management*, **15**, 208-219.

Curtis, A., Duval-Diop, D. and Novak, J., (2010), "Identifying spatial patterns of recovery and abandonment in the Holy Cross neighborhood of New Orleans". *Cartography and Geographic Information Science*, **37**, 45-56.

Curtis, A., and J.W. Mills (2011a) "Crime in urban post-disaster environments: A methodological framework from New Orleans" *Urban Geography* **32** (4) 488-510

Curtis, A., and J. W. Mills. (2011b), "Spatial video data collection in a post-disaster landscape: The Tuscaloosa Tornado of April 28th 2011". *Applied Geography* **32**, 393-400

Duval-Diop, D., A. Curtis, and A. Clark., (2010), "Enhancing Equity with Public Participatory GIS in Hurricane Rebuilding: Faith Based Organizations, Community Mapping, and Policy Advocacy". *Journal of Community Development Society* **41**, 32-49.

Gerke, M., and N. Kerle., (2011), "Automatic structural seismic damage assessment with airborne oblique Pictometry imagery". *Photogrammetric Engineering & Remote Sensing* **77**

Liu, S.B. and L. Palen., (2010), "The new cartographers: Crisis map mashups and the emergence of neogeographic practice". *Cartography and Geographic Information Science* **37**(1) 69-90

Mills, J., (2008) "Understanding Disaster: GI Science Contributions in the Ongoing Recovery from Katrina" *Transactions in GIS* **12**(1) 1-4

Rushton, G. and Lolonis, P., (1996), "Exploratory spatial analysis of birth defect rates in an urban population". *Statistics in Medicine*, **15**, 717-726.

10CUEE CONFERENCE PROCEEDINGS
10th International Conference on Urban Earthquake Engineering
March 1-2, 2013, Tokyo Institute of Technology, Tokyo, Japan

ON THE ENHANCEMENTS OF AGENTS' NAVIGATION SKILLS OF A MULTI AGENT SYSTEMS BASED MASS EVACUATION ANALYSIS

Maddegedara Lalith[1)], Leoneland, A. MELGAR[1)], and Muneo HORI[1)]

1) Associate Professor, Earthquake Research Institute, the University of Tokyo, Japan
2) Doctoral student, Dept. of Civil Engineering, The University of Tokyo, Japan
3) Associate Professor, Earthquake Research Institute, the University of Tokyo, Japan
lalith@eri.u-tokyo.ac.jp, leaguilar@uvg.edu.gt, hori@eri.u-tokyo.ac.jp

Abstract: A Multi Agent Systems (MAS) based mass evacuation simulation code, with moderately complex agents in 2D grid environment, is developed. The main objective of this code is to estimate the effectiveness of the measures taken to smoothen and speedup the evacuation process of a urban large area, in time critical events like tsunami. A vision based autonomous navigation algorithm, which enables the agents to move through an urban environment and reach a far visible destination, is implemented. The navigation algorithm is verified comparing the simulated evacuation time with that of theoretical. A scalable parallel computing extension is developed for studying mass evacuation of large areas; high performance computing resource utilization is necessary since the vision based navigation is computationally intensive. More than 94% strong scalability attained with 2048 CPU cores in the K-computer indicating the codes potential simulate mass evacuation involving many millions of people.

1. INTRODUCTION

Tens of thousands of casualties of the tsunamis of 2004 Sumatra earthquake and 2011 Thohoku earthquake generated emphasize the importance of mass evacuation studies in Earthquake engineering. Understanding evacuation dynamics is necessary to identify possible bottlenecks, find strategies to make the evacuation process smooth and reduce evacuation time, etc. Such analysis can save many lives at time critical events like tsunami. Out of a number of numerical models like cellular automata, social force model, etc., Multi Agent System (MAS) is a promising method for modeling heterogeneous and complex human behavior involved in mass evacuations (Hori et al., 2008, Dulum et al., 2012) MAS is able to solve mass evacuation problems with quite complicated setting, to which other numerical methods are not applicable.

There are number of studies related to tsunami triggered mass evacuation based on MAS. Most of these existing studies use simplified environment with simple agents (Gwynne et.al, 1999). Often the environment is modeled as a network consisting of 1D members representing rooms, corridors, roads, open spaces, etc. and associated with a pedestrian capacity. The most probable reasons for the use of such simplified models are that sophisticated models of environment and agents involve sophisticated algorithms, large amount of data and computationally intensive. The need of Monte-Carlo simulations to increase the reliability of MAS results is a major source of high computational demand. Considering the fact that mass evacuation is concerned with human lives, it is necessary to use complex models. The level of complexity should be chosen considering the availability of the computational resources, the significance of the complex features, etc.

In this paper we present the development of a moderately complex MAS with autonomously navigating agents in 2D urban environments, for large area evacuation simulation. The main source of information for the autonomous navigation algorithm is the agents' boundary of visibility, which is obtained from agents' vision. Simulating millions of agents with vision based autonomous navigation is computationally intensive. To meet this high computational demand, we developed a scalable parallel extension with the Message Passing Interface (MPI).

The contents of the rest of this paper are organized as follows. Section two gives a brief introduction to the developed MAS system for mass evacuation simulations. Details of the vision based autonomous navigation algorithm are given in section three while its verification is presented in the section four. Finally, some concluding remarks are presented in the last section.

2. A MULTI AGENT SYSTEM FOR EVACUATION SIMULATIONS

In this section a brief overview of the developed multi agent system for large area evacuation simulation is given. The multi agent system consists of two main parts; environment and the agents. Specifically, in this section, we focus on the basic requirements of these two main parts and the elements we have included.

2.1 Environment

We model the environment as a high resolution grid with maximum of 1*m* grid intervals. When making detailed models, the environment can be represented either with vector data or raster data. Both have advantages and disadvantages. In vector models, elements like buildings, roads, etc. are modeled with closed polygons and assembled into a graph data structure, according to their connectivity. Further, detailed information like width of the road, number of lanes, type of the building, number of occupants, etc. can be included with the polygons. An advantage of the vector environment is the ease of path planning and navigation of agents. On the other hand, the grid model does not have any of these advantages; buildings, roads, etc. are no longer identifiable single entities and path planning in grid environment is complex and requires significantly long time compared to vector environment.

However, we chose grid environment since it offers several advantages and the problem of path planning can be solved. The target problem of simulating emergency evacuation in an event of earthquake or/and tsunami requires modification of the environment to mimic the damaged to the environment like collapse of buildings, damages to roads, embankment failures, etc. Such highly localized modifications can be efficiently and accurately included in a grid environment. Also, identifying the boundary of the visibility of an agent and identifying the agents in the vicinity is more efficient in grid environments; working with concave polygons of vector models is complex and time consuming. Further, the vector model pose several difficulties in parallel computing; domain partitioning, dynamic load balancing with repartitioning and communicating graphs of vector data are much complex and have lower scalability compared to those of the grid data. When the region being modeled is several tens or hundreds of square kilometers, grid environment is much simpler to manage in parallel computing. Because of these advantages, the environment is modeled as a 2D grid.

A major problem with the grid environments is the complexity of path planning. Real-time path finding in very large grids is extremely slow and significantly reduces parallel scalability. Real-time path finding is an essential for the target problem; if an agent found the path it takes is blocked by a fallen building, it should be able to find the next closest path to the closest high ground or evacuation center. By automatically generating network of available path from grid data, the associated long path finding time can be reduced almost to that in vector environments. Path networks in a grid model can be constructed using thinning algorithms and then abstracting the resulting pixel network with a vector network. We are developing such an automated road network generation code, from grid data.

2.2 Agents

Since the target problem is directly concerned with the people's lives, it is important to mimic the real human behaviors, of significance, observed real in emergency evacuations. While an agent have data of its basic abilities like maximum speed, age, maximum sight distance, etc. its memory holds the information of past experiences, the paths it has taken, its target destination, etc. Further, an agent has several major functionalities; think, see, move. Agents with wide range of physical abilities can be generated to mimic the heterogeneous distribution of people in a selected region. Further, the agents are specialized by including more information and functionalities to represent relevant officials like police officers, fire fighters, volunteers, etc.

Visitor agents, representing visitors, do not possess any information of that area except the direction to a far visible destination like high ground and whatever visible within his sight distance. All except visitor agents (e.g. residents, police officers, fire-fighters, volunteers, etc.) have the information of their neighborhood and have the ability to find path to a desired destination. In this paper, the set of all types of agents except the visitor agents, are called non-visitor agents.

2.3 Radar vision

Vision, the main means of perceiving the environment, is an important functionality since agents are mainly responding to the data collected by that. Just as the human counterpart, agents must be able to extract information within a neighborhood of several tens of meters. We implemented radar based vision to make the agents accurately identify the features like roads, obstacles, etc., and neighboring agents, within their sight distances.

An agent scans the environment like radar and identifies the boundary of his visibility, in high resolution. The resolution of radar scanning, $d\theta$, is set such that $L \times d\theta = 0.5 \times \Delta l$, where L is the sight distance and Δl is the length of grid cell; approximately 1000 rays for 80*m* sight distance. Figure 1 shows the identified boundary of visibility and neighbor agents, by an agent with 40*m* sight distance. As it is explained in the next section, an agent identifies

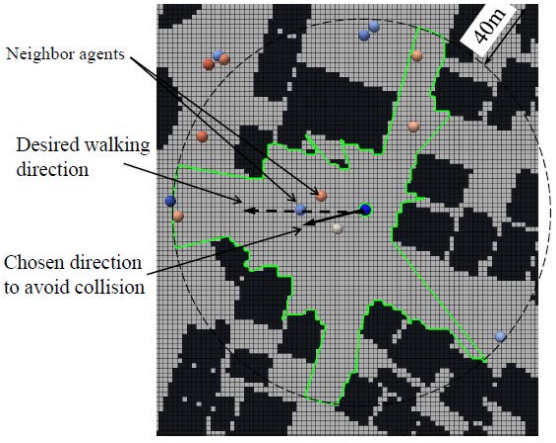


Figure 1 Indicated in yellow is the boundary of visibility identified with radar vision

the available paths in his visibility and moves towards the chosen direction, avoiding collision.

A problem with radar based vision is that identifying through which grid cells the radar rays pass is time consuming; it requires calculation of intersecting points of radar rays and grid lines. In order to reduce the amount of computations involved, several radar templates are prepared. Each radar templates contains the information of cells through which rays pass and the intersecting points. 16 sets of radar templates with their origins arranged in a 4×4 grid of 20*cm* spacing are used. An agent chooses the best radar template according to their location in a grid cell. Data of each radar template is stored in a circular container so that agents can easily identify the boundary of visibility in their front and back. Agents have different sight distances based on their abilities. The maximum of sight distance of all agents is used when preparing the radar templates.

As described in the next section, we implemented a radar vision based autonomous navigation algorithm that enables the agents to navigate in complex urban environments.

2.3 HPC enhancements

Simulation of large urban area evacuation with millions of smart and sophisticated agents involves a large amount of computations. Further, Monte-Carlo simulations with different settings are necessary to increase the reliability of the results. In order to meet this high computational demand, high performance computing resources have to be effectively utilized.

The current code is parallelized with Message Passing Interface (MPI). With a number of strategies like hiding communication, repartition, minimizing the number of communications and the volume of data communicated, etc. scalable parallel extension is developed (Dulum, 2012). Preliminary tests in the K-computer with 2 million agents produced above 94% strong scalability, with 2048 CPU cores.

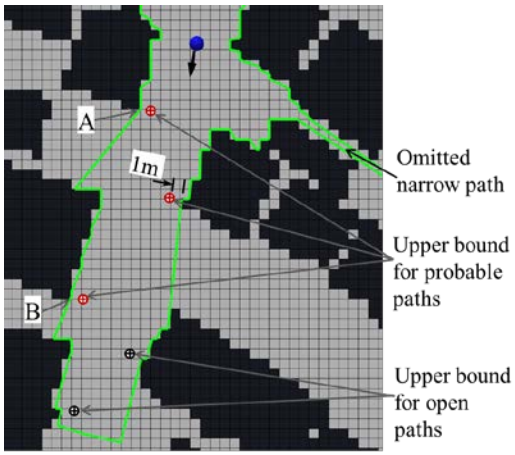


Figure 3 Upper bounds are set to prevent agents from moving to close to the obstacle corners.

3. AUTONOMOUS NAVIGATION IN URBAN AREAS

For the target problem of earthquakes or tsunami induced large area evacuations, the agents must have good autonomous navigation skills to move through complex urban environments. At least the agents should have the ability of navigating to a far visible high ground or a tall building, even if an agent represents a visitor. This skill which any human counterpart possesses is necessary for modeling tsunami induces evacuations. Details of the autonomous navigation algorithm are presented in this section while some verification tests are presented in next section.

To ensure that an agent can reach its destination, it must be able to identify the features of his visible surrounding and choose the correct direction to go. In grid environments, agents need sophisticated vision to identify available paths out of large number of cells within his visibility, each with either of two states. As mentioned in the previous section, an agent identifies his visual boundary using their radar based vision. Analyzing the boundary of visibility, agents identify the available paths. The regions visible up to an agents sight distance are categorized as *open-paths*, while the sudden jumps greater than a selected value are categorized as *probable-paths* (see Fig.3).

The saw-toothed boundaries of buildings in grid environment often produce sudden jumps similar to that produce by roads at a junction. Correct identification of probable-paths is important since moving towards these false signals not only produce longer evacuation time compared to that of the human counterparts, but also extra effort is necessary to bring the agents back to their original route. In order to eliminate these false signals, only the jumps greater than certain number of cells are considered; greater than 5 cells jumps are used in this study.

When an agent moves towards a probable path, care

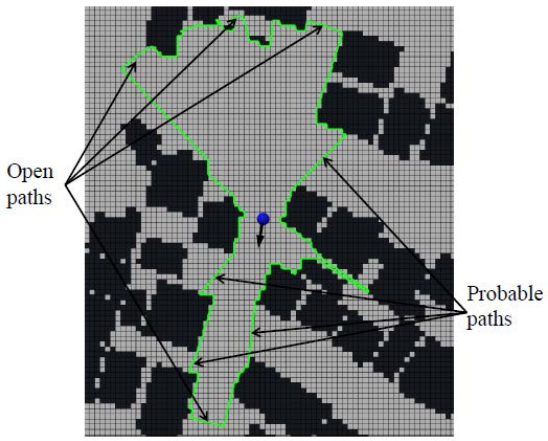


Figure 2 Open and probable paths identified by an agent shown by a blue dot.

has to be taken not to let it move too close to a corner which gives rise to sudden jumps which define probable path (e.g. point A and B in Fig. 3). Moving too close to a corner of an obstacle significantly lowers an agent's field of vision, often forcing it to turn backwards. In order to prevent this problem, associated with each open or probable paths are a set of points defining the closest they can move towards the corresponding corners of obstacles. It is found that setting these upper bound points at 1m away from the obstacle corners solves the problem of view obstruction.

The navigation of visitor agents and non-visitor agents, (e.g. residents, officials, etc.) have two main differences; only non-visitor agents have the ability to plan a path to any destination, and visitor and non-visitor agents have different navigation algorithms. As mentioned, non-visitor agents can find the paths to their destinations. Theta star algorithm (Nash et al., 2007) is used for this path planning. An advantage of *theta-star* algorithm is that the paths are defined by few landmark points, like road junctions. This not only reduces the data side of agents, but also allows the agents to freely navigate based on their vision, between the landmark points which could be a few hundred meters apart.

Non-visitor agents have no priority in choosing available open or probable paths in his 360^o vicinity. As mentioned, non-visitor agents have the ability to find the path to a desired destination. Non-visitor agents use vi-

```
input  : vectors containting all the avaiable paths in the front and the back; front/back_exits,
         front/back_open_paths, front/back_probable_paths
output: Next moving direction: next_dir

next_dir ← current_direction;

if front_exits.size() > 0 then next_dir ← ClosestExit(front_exits);
else if back_exits.size() > 0 then next_dir ← ClosestExit(back_exits);
else
    if front_open_paths.size()> 0 then next_dir ← BestOpenPath(front_open_paths);
    else if front_probable_paths.size()> 0 then next_dir ← BestProbablePath(front_probable_paths);
    else if back_open_paths.size()> 0 then next_dir ← BestOpenPath(back_open_paths);
    else if back_probable_paths.size()> 0 then next_dir ← BestProbablePath(back_probable_paths);
end
```

Figure 4 Non-visitor agents' path selection algorithm

```
input  : vectors containting all the avaiable paths in the front and the back;
         front/back_exits, front/back_open_paths, front/back_probable_paths
output: Next moving direction: next_dir

next_dir ← current_direction;

if front_exits.size() > 0 then next_dir ← ClosestExit(front_exits);
else if back_exits.size() > 0 then next_dir ← ClosestExit(back_exits);
else if BestPathForVisitor(front_open_paths, front_probable_paths, next_dir) then ;
else if BestPathForVisitor(back_open_paths, back_probable_paths,next_dir) then ;
else Freeze the agent;                                   /* agent has no paths */
return next_dir
```

```
Function BestPathForVisitor
input  : Open and probable paths in the font or back; open_paths, probable_paths
output: whether a direction found and the selected direction: next_dir

if open_paths.size() > 0 and probable_paths.size() > 0 then
    dir ← BestOpenPath(open_exits);
    prob_dir ← BestProbablePath(probable_exits, jump);
    if dir > prob_dir and jump > 30 then dir ← prob_dir ;
else if open_path.size() > 0 then dir ← BestOpenPath(open_paths);
else if probable_path.size() > 0 then dir ← BestProbablePath(probable_paths);
else return false
return true
```

Figure 5 Visitor agents' path selection algorithm

sion based navigation to move between the landmarks points defining the paths found with theta-star algorithm. Giving equal priority to all the visible open or probable paths in their front or back, they choose the closest path towards the next landmark point of their pre-planned path. Non-visitor agents' algorithm for choosing open/probable paths is shown in Fig. 4.

Unlike the non-visitors, the visitor agents neither have the ability to find paths nor a well-defined destination. In many cases, visitors have to depend on the non-visitor agents or mass communications to obtain information, or follow a group or a leader. In the case of tsunami evacuation, visitor agents' target can be set to a far visible high ground or tall buildings. It is challenging to navigate and agent towards a far visible target through a complex urban environment, only based on the information available within its sight distance. It is found that choosing the visible open or probable paths according to the algorithm shown in Fig. 5 makes visitor agents to successfully navigate towards far visible destination through a complex urban environment. This algorithm is not too artificial in the sense that even people, in an unknown environment, tend to have similar preferences: people prefer taking roads in their front and prefer taking roads with longest visible stretch instead of those hidden behinds bends or obstacles.

Once the open or probable path to be taken is decided, an agent checks for possible collisions with neighboring agents and slightly adjusts the moving direction to avoid collision (see Fig.2), sticking to the chosen open or probable path.

3. VERIFICATION OF THE AUTONOMOUS NAVIGATION

Verification and validation of the proposed radar vision based autonomous navigation is essential since simulated is people, with the aim of reducing casualties. For verification, it has to be tested whether the proposed algorithm can reproduce analytically expected answer for a well-posed problem. Validation requires testing whether the numerically obtained solution satisfactorily matches with the observed behavior of a real evacuation.

In this paper, we only consider the verification of radar vision based autonomous navigation of each individual agent, through an urban area. The major concern of this verification is to test whether the proposed algorithm enable both visitor and non-visitor agents to reach a far visible destination based on their vision. Even if the non-visitor agents have paths to their destination, they heavily depend on their vision to navigate between few the landmark points defining their paths. The most important in this verification is to test visitor agents' ability to reach a far visible target, which the human counterpart can easily do.

Being the objective is to verify the whether a visitor or non-visitor agent can reach a far visible destination, collision avoidance or other interactions among agents is not considered in this verification test. The problem becomes ill-posed when the collision avoidance is included; the total evacuation time and the paths taken by individual agents is highly depends on the crowd density and the each individual's response to dense crowds. Surely, it is important to study to which extent the agents' behavior deviates when the collision avoidance is included and how it varies with the crowd density. However, it is out of the scope of the current study.

3.1 Problem settings

For the verification tests, thousand agents in $800\times600m^2$ regions of Kochi city environment is considered; as shown in Fig. 6 the selected area has many buildings and a few open areas. Two cases, each with either non-visitor agents or visitor agents, are considered. It is assumed that there is a high ground, which is visible from anywhere in the selected domain, at the lower edge of the selected domain. All the agents are assumed to have the same sight distance of $50m$. The non-visitor agents follow the shortest paths to the lower edge of the boundary from their starting location; calculated with theta-star algorithm. On the other hand, visitor agents navigate only based on the information within their sight distance and the direction to lower edge, where there is a visible high ground. Apart from that both the problems have the same settings.

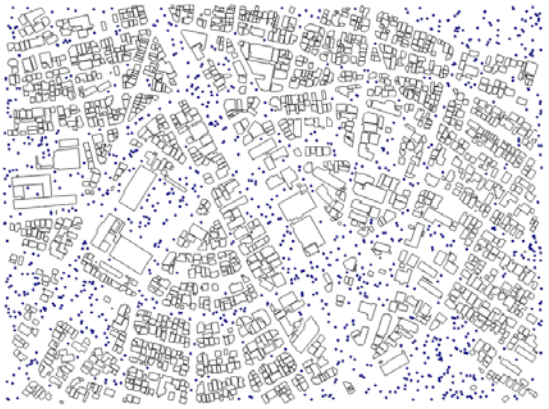


Figure 6 $800\times600m^2$ area of Kochi city and the initial agent distribution used for the verification of autonomous navigation algorithm.

3.1 Overall behavior

Figure 7 and 8 shows the graphs of cumulative number of agents exited versus time. The near perfect matching of non-visitor graph with that of the theoretical verifies non-visitor agents' navigation capabilities; even if they rely on their vision to navigate between few landmark points defining their paths, they can reach the destinations at the theoretically expected time. As seen in the Fig. 8, visitor agents also have surprisingly good navigation abilities; visitors graph is very close to the theoretical and the maximum difference is 28 agents, at 398 seconds. The difference compared to the ideal is less in this prob-

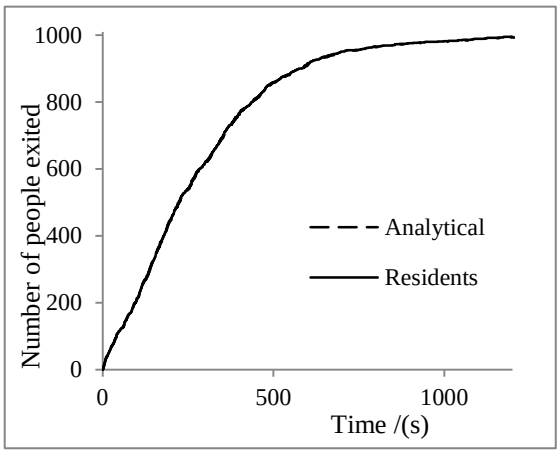


Figure 7 Cumulative number of non-visitor agents exited

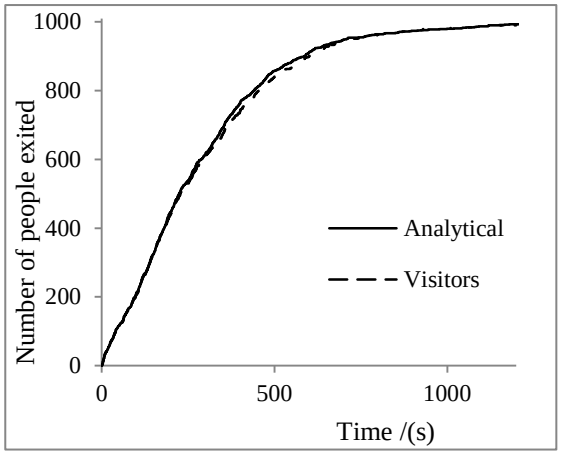


Figure 8 Cumulative number of visitor agents exited

lem since the maximum distance is an agent has to travel is only 600m. Surely, the deviation from the ideal will be more when the domain is large and more complex.

3.1 Trajectories of individual agents

In addition to the overall behavior, investigating the paths taken by each individual is important to make sure that none of the agents has taken paths which are unrealistic choices for the human counterpart.

The possibility of non-visitor agents to take an unrealistic path is very low since they are guided with intermediate landmark points. Analysis of simulation results confirmed that all the non-visitor agents have followed the shortest paths they found with theta-star algorithm.

As one can easily guess, it is the visitor agents who have highest chance of taking unrealistic paths. Surprisingly, none of the visitor agents has taken unrealistic path (see Fig. 9). Detailed analysis by comparing the paths taken by visitor and non-visitor agents with same starting position and properties indicates that the visitor agents have not taken the optimal paths. Figure 10 shows the trajectories of randomly selected five visitor and non-visitor agents; each pair with identical starting point has identical properties. Though the paths taken by visitor agents are not the shortest, those are realistic choice even for a human and the time differences between the two paths are small.

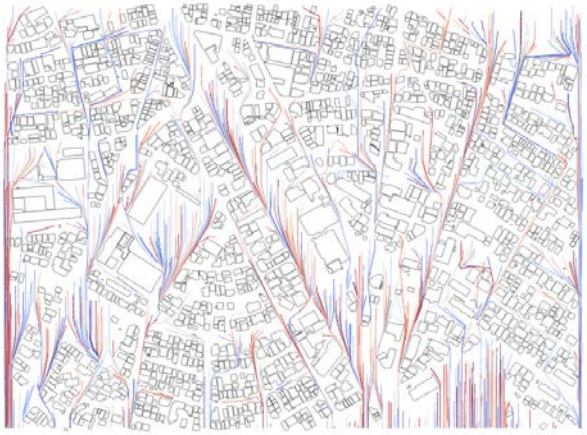


Figure 9 Paths taken by visitor agents.



Figure 10 Comparison of trajectories of visitor and non-visitor agents with same starting points.

3.1 Known limitations of autonomous navigation algorithm

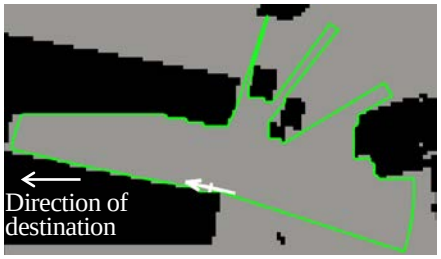


Figure 11 A visitor agent moving to a deep region with no paths except those in the opposite direction of the destination.

There are no known limitations regarding the non-visitor agents. On the other hand, visitor agents have one known limitations. A visitor agent may get lost and start to move in a loop, if it enters a region where there are no identifiable opening towards the destination in his front and depth of the region longer than the sight distance. Even though the visitors algorithm makes it to turn back and move out of such deep wells, the agent may tends to turn back and reenter the deep well depending on the arrangements of the paths in the opposite direction. Figure 11 shows an agent entered into such a region. When the agent recognizes there is no path towards its destination, it turns and starts moving out of the deep well. However the upward path at the entrance to the deep region makes it turn and re-enter the deep well, eternally making the agent to move in a closed loop. A simple solution to this problem is temporarily increasing trapped agents' sight distance and let it recognize that there are no paths in the deep well.

This simple test with a small urban environment verifies that both the visitor and resident agents have sufficient skills to navigate in an urban environment. However, further tests are necessary to verify visitor agents' abilities to navigate in more complex environments, and both visitor and non-visitor agents' navigation abilities in dense crowds with collision avoidance.

3. CONCLDING REMARKS

We implemented radar vision based autonomous navigation algorithms for both the visitor and non-visitor agents (i.e. residents, police officers, etc.). The simple verification test shows that the proposed navigation algorithms enable both the visitor and non-visitor agents to navigate successfully through urban environments. Although non-visitor agents do not take the optimal paths, their paths are found to be acceptable choices even for human counterparts. In order to meet the heavy computational demands involved in vision based navigations, we implemented a MPI based parallel extensions. With a number of strategies, near linear scalability is attained up to 2048 CPU cores in the K computer.

Acknowledgements:

This work was supported by JSPS KAKENHI Grant Number 24760359. Part of the results is obtained by using the K computer at the RIKEN Advanced Institute for Computational Science.

References:

Gwynne, S., Galea, E., Owen, M., Lawrence, J., and Filippiddis, L. (1999). A Review of the MethodologiesUsed in Evacuation Modeling. *Fire and Materials* , 23, 383-388.

Hori, M., Miyajima, H., Inukai, Y. and Oguni, K. (2008), Agent simulation for prediction of post-earthquake mass evacuation, *Journal of Japan Society of Civil Engineers*, Ser. A, **64**, 1017-1036.

Dulam, R., Lalith, M., Hori, M., Ichimura, T. and Tanaka, S (2012), A study on effectiveness of using officials for reducing pre-evacuation time in a large area, based on multi agent simulations, *Proceedings of the International Symposium on Engineering Lessons Learned from the 2011 Great East Japan Earthquake*, March 1-4, Tokyo, Japan.

Dulam, R., Lalith, M., Hori, M., Ichimura, T. and Tanaka, S. (2012), Development of HPC enhanced multi agent simulation code for tsunami evacuation, *Journal of Applied Mechanics, JSCE,* **15**

Nash, A., Daniel, K., Koenig, S. and Felner, A. (2007), Theta*: any angle path planning on grids, *Proceedings of the AAAI Conference on Artificial Intelligence*, 1177-1183.

10CUEE CONFERENCE PROCEEDINGS
10th International Conference on Urban Earthquake Engineering
March 1-2, 2013, Tokyo Institute of Technology, Tokyo, Japan

FOREIGNERS' EXPERIENCE AND BEHAVIOR IN THE GREAT EAST JAPAN DISASTERS 2011

Dr. Md. Faiz SHAH[1)], Dr. Osamu MURAO[2)]

1) Researcher, Faculty of Engineering, Systems and Information, University of Tsukuba, Japan
2) Associate Professor, Faculty of Engineering, Systems and Information, University of Tsukuba, Japan

Abstract: A primary challenge for foreigners living in Japan is language. Many foreigners were affected by the Great East Japan disasters in 2011 and suffered various problems due to insufficient information dissemination in proper language. The purpose of this study is to investigate foreigners' problems and decision-making in the aftermath of the disasters. This study applied a questionnaire survey method and conducted 200 interviews with foreigners from 48 different countries living in Tohoku and Kanto area during the disasters. The primary result of the study show that foreigners' information understanding ability kept them calm and they did not relocate after the disasters. However, a great number of them with language and other problems relocated or leave the country. Proper and sufficient information in proper language played an important role in foreigner's life during the disasters in Japan.

1. BACKGROUND AND INTRODUCTION

On March 11, 2011, the great East Japan disaster stroke Japan. Many cities in the Tohoku and Kanto area were worse affected by the disaster. Many of the residents could survive from the great jolt of 9.0 magnitude earthquake; a great number of them were washed away by the following high tsunami. Those who survived the initial two disaster events, were threaten by a third one and that was the nuclear radiation emission from the Fukushima Dai-ichi nuclear power plant, which was badly affected by the earthquake and tsunami. The number of human casualty was quite high among the native Japanese in the affected area: death 15,873, injured 6,114, and missing 2,744 (National Police Agency, Nov. 2012). The disaster did not only affect the native, but many foreigners who were living in Japan for specific purposes were also affected. Though the casualty among foreign residents was not high, in some cases, they were facing several problems due to lack of information and their insufficient communication capacity in Japanese. It resulted that many of them decided to relocate from Tohoku and Kanto area either to another place in Japan or to outside of the country. Henry (2012) reported that information disseminated in Japan after the disaster was mainly in Japanese. The main coverage of those information was disaster response, recovery and to reduce panic among the citizens. Since many foreigners had deficiency in Japanese, they started to follow foreign news media's news and information in English or in their own languages. However, the target of that information was different, for example, disaster mitigation, lessons learned and effect of the disaster. Thus, while native Japanese were calm after the disaster, many foreigners were panic and were deciding to relocate immediately. This study intends to consider language and other problem issues and checks their impact on foreigner's relocation behavior after the 3/11 disasters.

2. PURPOSE AND OBJECTIVE

Two major trends in foreigners' behavior have been found after the disasters: either to relocate or to stay. Present study focuses on those two trends. The purpose of the study is to check foreigners' decision-making in the aftermath of the disasters. It will focus on the problems that foreigners faced and decided to relocate. The objectives are (i) to examine the disaster information system that foreigners used during disasters, (ii) to check their first response to the situation, (iii) to understand their information gathering behavior, and (iv) to explore the reason of their decision to continue staying in Japan and or to relocate.

3. STUDY AREA

The Tohhoku and Kanto area were selected as the primary study area for this investigation. In Tohoku, most of the foreigners' were selected from Iwaki City in Fukushima Prefecture. Many of them were living in other parts of Japan and in their own countries during this study. But they had been living in Iwaki City during the 3/11 disasters. Iwaki City in Fukushima Prefecture was selected as the prime study area due to several reasons. For example (a) a good number of foreigners were living in Iwaki City. According to the Iwaki City Office, about 1800 foreigners were living in the city throughout the 3/11 disasters. It was reduced to 1511 when this study was conducted. So the number was quite good even after the disaster. (b) The City was badly affected

by the earthquake and high tsunami stroke the coastline of the city. So the devastation of the city was almost similar with other cities in the affected areas. (c) The city locates within 40 km radius of the Fukushima Daiichi Nuclear Power Plant (Figure-1). It had evacuation warning after the disaster. Therefore, sampling from this city would enable to understand the situation of foreigners in the affected region in Tohoku. The other major city selected for the study was Tsukuba in Ibaraki Prefecture. This city also had a good number of foreigners living during the earthquake. The information collected from this city may enable to make a comparative study on the behavior of foreigners after the disasters.



Figure-1: Iwaki City in Fukushima Prefecture and nuclear zone radius

4. LITERATURE REVIEW

Yun and Hamada (2012) studied the relationships between evacuation place and time, pre-disaster preparedness and evacuation behavior and survival rate in the Great East Japan disasters. Their study result show that behavior during disaster differed for survivors and actual evacuation was associated positively with high survival rate. They conducted the study with 1153 native survivors where no foreigners were included. Koresawa (2012) studied on government's respond on the Great East Japan Earthquake and Tsunami. He reviewed government's disaster mitigation and preparedness including Hyogo Framework for Action, progress in risk assessment, early warning, reducing underlying risk factors, and strengthening disaster preparedness for effective response. This paper gives a clear idea on government's response initiatives in the Great East Japan Earthquake and Tsunami. Ozaki (2012) checked Japan Metrological Agency's (JMA) tsunami warning system after the 3/11 earthquake. He found a gap between predicted tsunami heights at the early stage and actual heights. He shows how JMA is improving their tsunami warning system based on the 3/11 experience.

Henry et al. (2011) worked on disaster information gathering behavior of foreigners after the Tohoku Earthquake and brought some ever first results on the issue. They showed that people living in Japan were faced with confusing and conflicting messages from different information sources. This created an atmosphere of uncertainty and led many people, particularly foreigners to relocate to western Japan or to leave Japan entirely. In another study, Henry et al. (2012) analyzed foreign students' post disaster action and found that it was similar to their information gathering behavior. However, it was different in three cases: (i) their most and least trusted information sources, (ii) their utilized language for collecting disaster information, and (iii) their utilized language for clarifying information difficulties. There was no difference between those who remained and relocated, as they judged the situation by their language ability. Therefore foreigners' language ability is one of the important considerations for their post disaster action.

The number of literature on foreigner's experience and behavior in the great East Japan disasters is very few. Henry et al. (2011, 2012) basically checked the information gathering behavior of foreigners living in Kanto area. The present study includes the foreigners living mainly in Tohoku and their experience, problems, deciding issues to continue to stay in Japan or to relocate.

5. METHODOLOGY

This study applied few methodologies to find foreigner's information and grasp their experiences. First, foreigner's statistical information was collected from a concerned department in Iwaki City Office. Second, several short interviews were conducted with foreigners living in Iwaki city before starting the main data collection. Third, based on the key information obtained from the primary interview, a questionnaire was developed to interview foreigners. The questionnaire interview was conducted from mid-September to mid-October 2012. Total 200 samples were collected and respondents from 48 different nationalities participated. Fourth, based on the questionnaire response, few more interviews were conducted with a few selected respondents.

6. SURVEY OUTLINE

The survey covered 111 female and 89 male respondents. Many of the respondents were scattered from their living cities after the disaster. For example, present city of the respondents showed 36 cities but 3.11 living city showed 12 cities. The highest number of participation came from Iwaki City which was 124 during the earthquake and 81 at present. As shown in Figure-2, the highest number of respondents were students (78 nos. or 39%). The second and third highest number was teacher (38 nos. or 19%), and business (21 nos. or 10.5%). Another 10% respondents were engaged in other occupations. Figure-3 shows respondents' living period in Japan. The highest 54.5% respondents were living Japan for more than 5 years. About 30.5% respondents were living for less than 5 years and 15% were living for the last 2 years. The survey covered only those foreigners who were living in Japan during the 3.11 disasters.

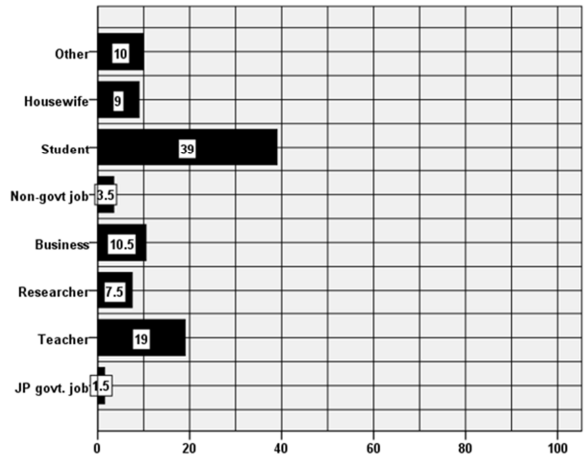


Figure-2: Occupation of Respondents (%)

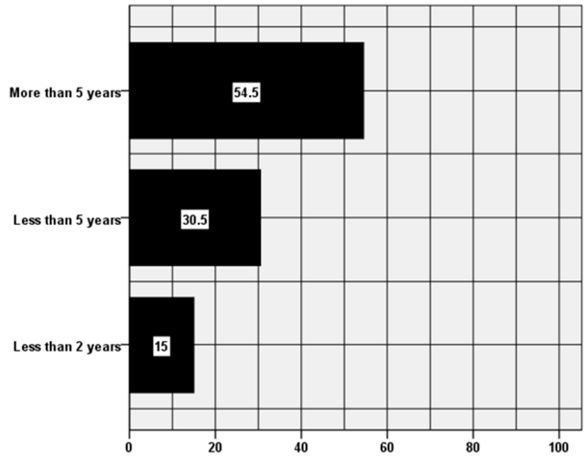


Figure-3: Living Period in Japan (%)

7. DISASTER AND AFTERMATH

This section discusses about the information and communication that foreigners used during the impending situation. Japan has progressed in earthquake and tsunami early warning system (JMA, 2012). According to this system, Japan Metrological Agency (JMA) systems receive warning for a seismic motion by a primary wave in the ground; it transfers the information to the national broadcasting system, which includes the television and radio. For a better dissemination and immediate information to the citizen, different devices receives those warning from JMA system and broadcast to the citizen. Mobile phone devices are one of the most popular broadcasters of JMA's disaster early warning system including earthquake and tsunami. Figure-4 shows that only 27.5% respondents received an early warning message or alarm during the disaster. The majority of the respondents either did not receive any warning or never knew about that (56%). The JMA transmitted a warning on earthquake 8.6 seconds after the primary wave on 3/11 (Koresawa 2012). Television, radio and other devices broadcasted the warning on time. However, many people could not get the information due to several reasons. The most important reason was that the earthquake struck at a busy afternoon on a week day when people were at work. They either did not receive any warning alarm or could not think about the severity of the disaster due to the quick and powerful jolt.

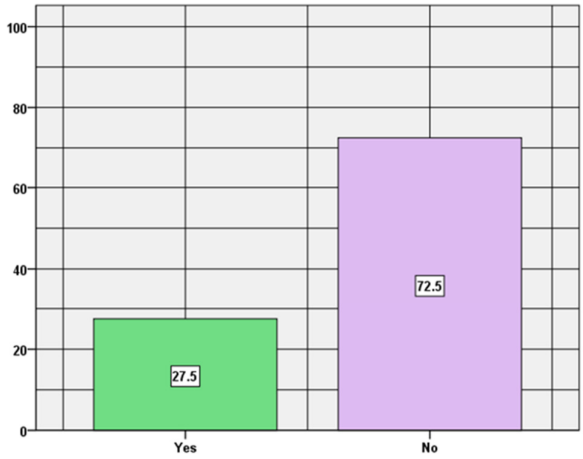


Figure-4: Got disaster warning on 3/11 (%)

Figure-5 shows that 20% respondents received a warning alarm on earthquake and only 5.5% received on tsunami.

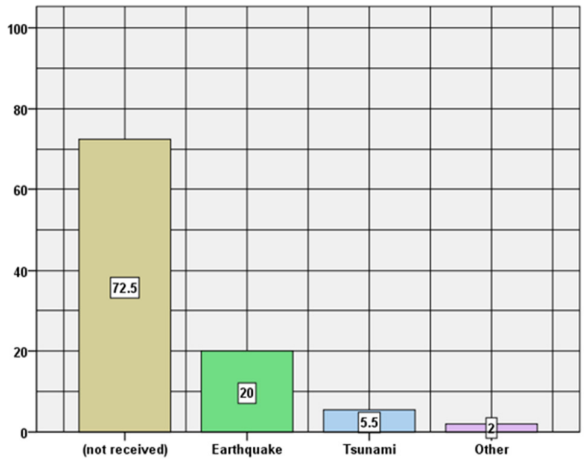


Figure-5: Event on Received Warning (%)

The surveyed foreigners' experience revealed that 13% of them received warning from mobile phone alarm as shown in Figure-6. Only 8.5% received the same from television. It happened that when they received alarm on their mobile phone, they had already felt the shaking; they turned on the television and watched the warning message broadcasting. Some of them could make phone calls to their family members and friends just at the onset of the earthquake and could warn them (1% were warmed by this). This group of respondents could manage to protect themselves during the big shaking and evacuate from their houses just after the first big shaking. Figrure-7 shows that 41% respondents tried to get more information on the

earthquake when the very first longer shaking had stopped. Another 32% respondents were calm and 20% were trying to move to a safer place within 3 hours of the earthquake. A very few respondents, only 3.5% engaged to clean up the mess. Due to the repeated large earthquakes, aftershocks and lack of information, many foreigners became panic. They had to decide by themselves either to stay at their same house or move to an evacuation center. The stopping of utility services like electricity, gas and water had important role on their decision.

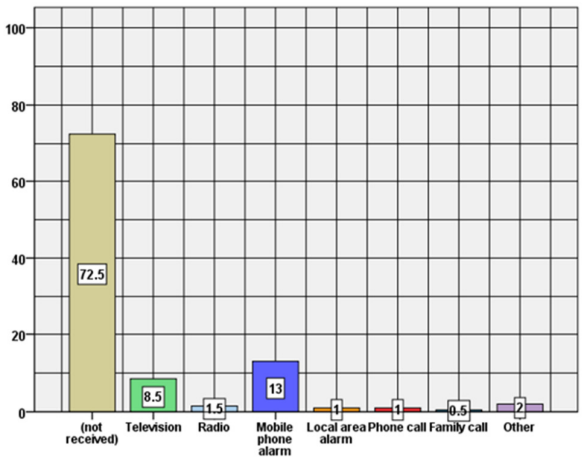


Figure-6: Warning Sources (%)

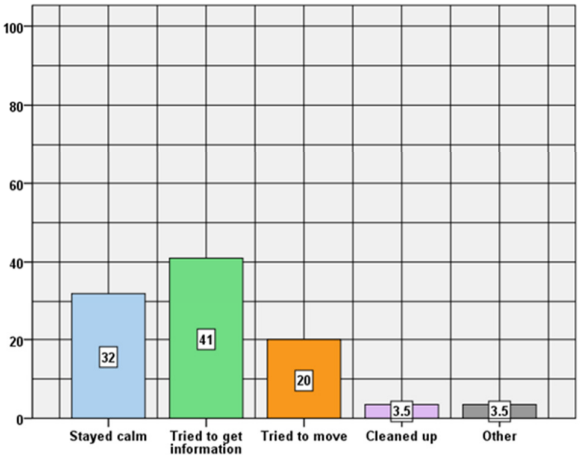


Figure-7: What did they do after the earthquake (%)

8. INFORMATION, PROBLEMS AND COMMUNICATION STAGE

It was showed in the previous section that a good number of foreigners were trying to get information just after the earthquake. Information played the main role for disaster communication since the very onset of the disasters. To get the latest update, foreigners were relying information sources. Figure-8 shows that 94% of the respondents were using different information sources to receive disaster warning, update on search and response, mitigation, utility and others. It is important to find that 6% of the respondents were not using any standard information sources. It was due to their inability to understand news in Japanese, or their lack of interest to see disaster devastation pictures. So they kept the television and radio turned off. Some of the foreigners did not want to be panic with information. They did not think about evacuation. Some of them even did not know about the Fukushima Daiichi Nuclear Power Plant accident and the subsequent evacuation warning from the 50km area of the radius (Figure-1).

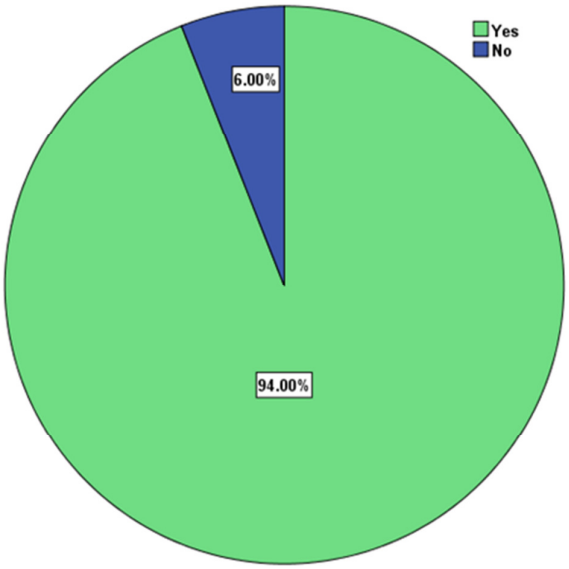


Figure-8: Foreigners used info sources

Figure-9 shows a comparative figure of used and trusted information sources of the foreigners. This particular question inquired about foreigner's use of information sources until the second week after the disaster.

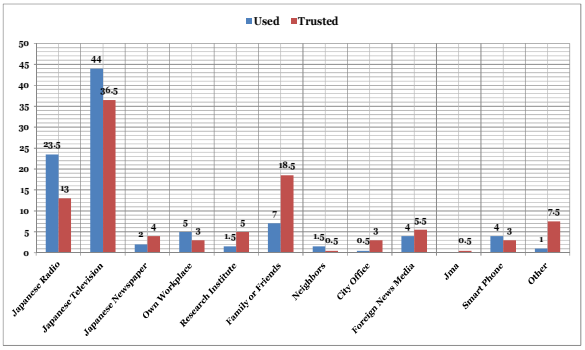


Figure-9: Used and Trusted Information Sources (%)

The figure shows that the highest 44% of the respondents used Japanese television as information source. But only 36.5% among them considered television as the most trusted information source. The second highest

information source was radio which was 23.5%. But only 13% of the respondents trusted Radio information. Few of the respondents were relying on family and friends (7%) as an information source. But more than the use, about 18.5% respondents trusted them for proper information. Some of the foreigners, having difficulty in Japanese, were using (4%) and relying on foreign news media (5.5%). It was reflected with Henry 2012 as mentioned in the introduction. This group of foreigners left Japan as they were very much panic by receiving different contextual information of those foreign news media.

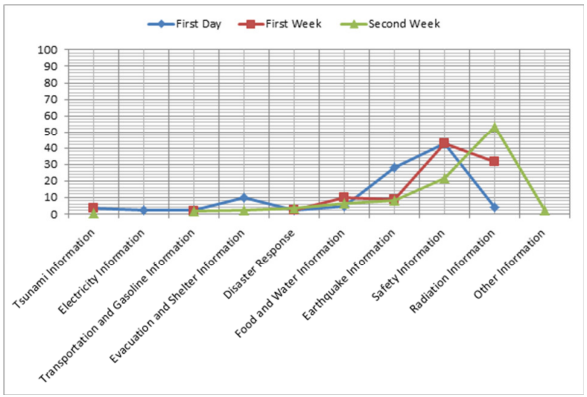


Figure-10: Change in consideration of important information (%)

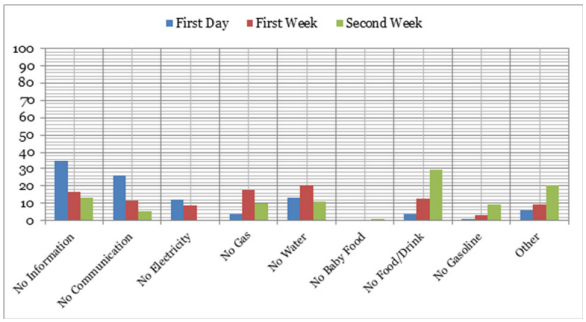


Figure-11: Problems faced by the foreigners (%)

Figure-10 shows the comparative picture of consideration of important information by the foreigners. The respondents chose ten types of information they trusted to receive as shown in the figure. The information types in the column were categorized by the information obtained in the pre interviews with some respondents. Information timeline from the first day to second week show a remarkable change. On the first day, just after the disaster, when a high tsunami was striking, foreigners did not put much interest on that information (only 2%) as most of the foreigners were living in the central place of the cities that was far from the shore. On the first day, the information line became slightly high on shelter information (9.5%) and got highest pick for safety information (48%). The first week information showed a higher trend from food and water information and reached highest for radiation information (28.5%). The radiation information took the highest pick until the second week (44.5%). It is worth to mention that foreigners trusted Japanese television for disaster information and they were solely relying Japanese government information sources. The reflection is visible in this figure. When there was not a good development in controlling nuclear emission from the affected nuclear power plant, many of them had taken relocation decision either to other part of Japan, or to their own country. Information broadcasted by foreign news media in foreigners' own country made their family members to ask them to go back to their home countries for a while, until the situation improved.

Figure-11 shows the prioritized main problems that foreigners faced until the second week of the disaster. Total nine main problems were listed. First day's highest prioritized problem was 'no information' (35%). First week's highest prioritized problem was 'no water' (20.5%). Second week's number one problem was 'no food/drink'. This group's food and drink stock was run out by this time. Many of them were requiring support at this stage. The following figure shows this information.

Figure-12 shows that 64.5% foreigners were expecting support from external sources though a good number of them did not require (35.5%).

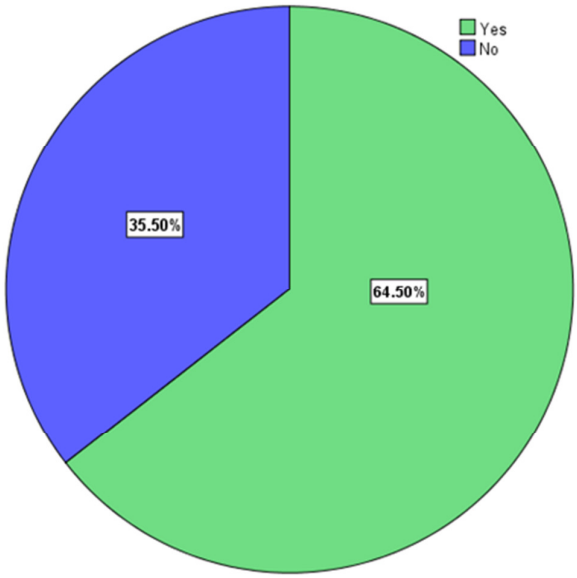


Figure-12: Support received

Figure-13 shows that the highest 33.5% respondents were supported by their friends. A good number of them (14.5%) were supported by the neighbors. In most cases, these respondents had family relation with Japanese and were integrated with the local community. For those who received support from friends, their friends shared their own belongings with others. Many of the foreigners said that a phone call by a friend also worked as a support. Since they were mentally distressed and were relieved by phone calls of their friends. Many religious groups of foreigners stayed

together in the religious sites and shared all belongings within their community. For example, most of the Muslim families in Onahama in Iwaki City evacuated and stayed at Onahama Majsid and shared their food and water. Iwaki Catholic Church also had the same experience.

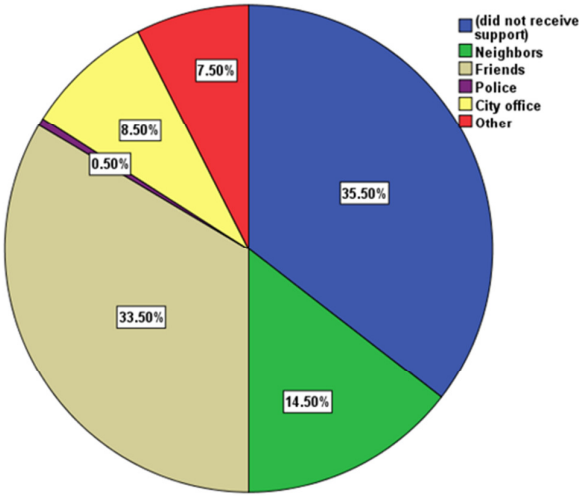


Figure-13: Support sources

Figure-14 shows a comparative figure of required and received support by the foreigners. The highest required support was reliable information (47.5%) and the highest received support was water (50.5%). Many of them required gasoline and transportation (17.5%) support and a few of them, (3.5%) received that support from their friends and neighbors. In fact daily life was stopped due to the shortage of gasoline in most of the cities in Tohoku and Kanto. The supply was not possible to resume immediately because of the disruption in road communication. Those who decided to relocate or evacuate from their cities, they required gasoline or transportation support very much.

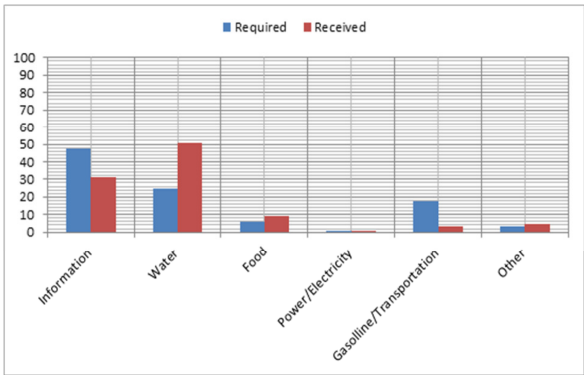


Figure-14: Support required and received (%)

9. DECIDING TO STAY OR RELOCATE

This section shows the decision stage of the foreigners, whether and how they decided either to continue their staying in their own living places in Japan or to relocate to other parts of the country or to their home countries. Figure-15 shows that 53.5% foreigners decided to relocate within the second week of the disaster, while a very good number of them decided to continue their stay in Japan, mostly at the same places. Among them, 42.5% were living at the same house, as shown in Figure-16.

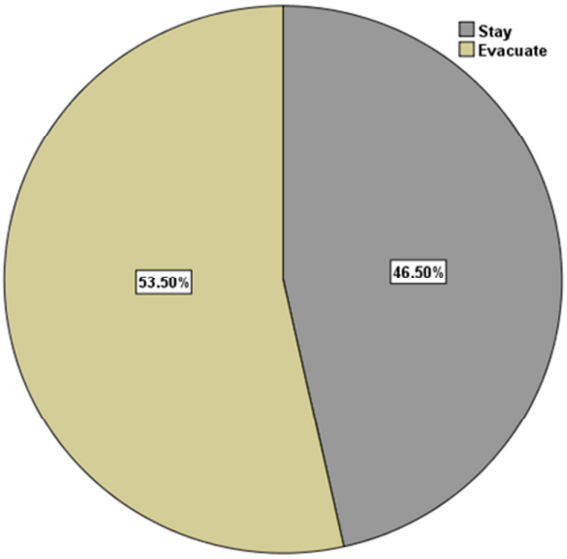


Figure-15: Stay or relocate (%)

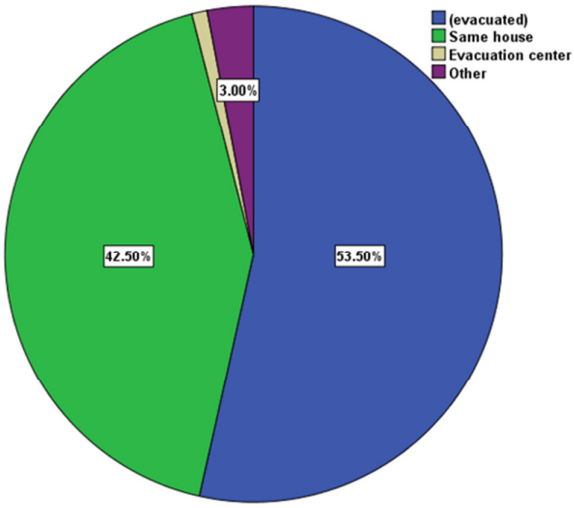


Figure-16: Staying places (%)

Only 1% had to stay in an evacuation center and 3% stayed in other places. For the evacuees, the highest 42% left Japan either to their home countries or to other countries, as shown in Figure-17. A good number of them, 11.5% relocated to other parts in Japan. This second group of foreigners did not leave Japan out of their good resident feeling and came back to their cities when the radiation situation improved.

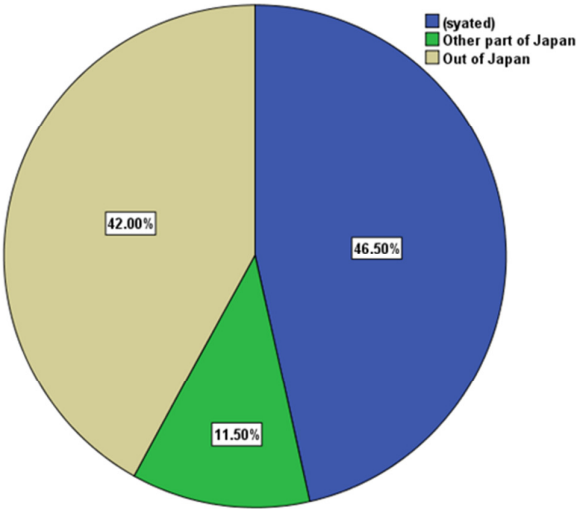


Figure-17: Evacuation places (%)

Figure-18 shows the reasons that foreigners considered to relocate. Total nine reasons were identified by the respondents. The highest consideration was nuclear radiation, which was 31%. The second highest one was fear of further earthquake and it was represented by 10% respondents. Other considerations were proportionately smaller.

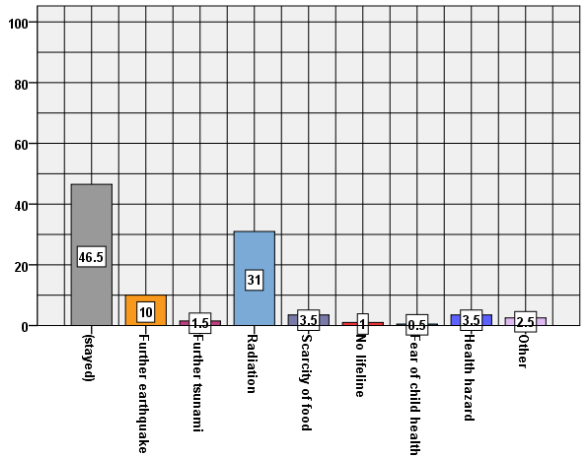


Figure-18: Evacuation reason (%)

Figure-19 shows the reasons for staying. Total seven reasons have been identified. The highest consideration was Japanese family relations and which was 14%. The second highest reason was community feeling, which was 11%, and the third one was desire of volunteering, which was 7%. In fact foreigners, who continued their staying in the affected areas in Japan, extended their supporting hands to volunteer disaster recovery.

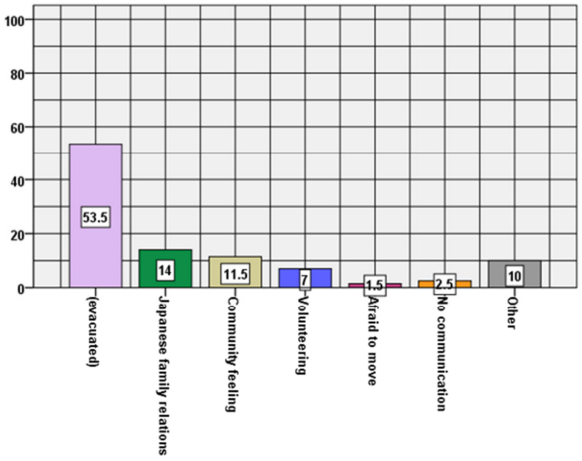


Figure-19: Staying reason (%)

10. DISCUSSION

Foreigners living in the Tohoku and Kanto region were affected by the great East Japan disasters. They had their own occupations and many of them were living in Japan for a longer period. This study included only those foreigners who were living for at least two years and have witnessed the great disasters during 3/11. Japanese family relations supported some of the foreigners to be familiar with the Japanese disaster management and early warning system. This group of foreigners could manage the difficulties after the disasters. They were calm and continued their staying in Japan. However, a major portion of the foreigners relocated from their living places in Tohoku or Kanto area due to several problems they faced in the aftermath of the disasters. Insufficient command in Japanese language was one of the problems but not the only one. The present study found that after the disaster, the highest used and trusted news media was Japanese Television. A very few of the respondents were concentrating on foreign news media. However, problems in daily life, lack of proper information, requirement of external support, scarcity of food and drink, gasoline and disruption in lifeline system compelled foreigner's relocate from their living city.

Foreigners were following news and information after the disaster that was mainly in Japanese. Proper and sufficient information in proper language may play important role on foreigner's life in Japan during the disasters. Their problems after the disasters were associated with the information and communication systems. They were not included in the local support system in the aftermath of the disasters. So their main support sources were their friends and neighbors. Consequently one group of the foreigners were relocated either to other part in Japan or outside, and another group continued their staying. The second group's decision may bring important lesson for the local authority in Japan because they did not only cope with the situation but also they extended their helping hand in the

recovery process. This study directs to analyze the preconditions of foreigners' two types of decision after the disaster. The result may bring some recommendation to include foreigners' issues in the local disaster management system in Japan.

11. CONCLUSION

This study shows foreigners' life and disaster information gathering during the Great East Japan Earthquake. It brought their first response to the situation and found that a few of them received an early warning message or alarm during the disaster. As most of them did not receive a warning, they concentrated on information gathering at the onset of the disasters. They were following information in the aftermath of the disaster and Japanese television was their most used and trusted information source. A few of them were using foreign news media as their Japanese ability was insufficient. Their information priority was changing as per the elapse of time. It was according to the problems they were facing at that time. They required same external support same as the native Japanese required. Since the support system was not adequate, a bigger portion of them decided to relocate. The rest part of them continued their staying and tried to utilize their time in disaster recovery activities. This study proposed a methodology to understand foreigners' experience and behavior after a big disaster like the Great East Japan disaster. It directs the further scope to analyze foreigners' potential in the local recovery process in the aftermath of the disasters.

Acknowledgements:

The authors acknowledge support from Professor Masayuki Fukusaku of the East Japan International University, the Iwaki City Hall and the Iwaki International Association for conducting this study. Their support made the study possible to collect a maximum number of respondents from the City of Iwaki. The authors gratefully express their sincere gratitude to the foreigner participants from different parts of Japan and many countries in the world.

References:

Henry, Michael, Kawasaki, Akiyuki, Meguro, Kimito. 2012. Foreigners' Disaster Information Gathering Behavior after the Tohoku Earthquake Part 3: Analysis of Foreign Students considering their Post-Disaster Action. Seisan-Kenkyu, University of Tokyo. 64-4, pp 445-451.

Henry, Michael, Kawasaki, Akiyuki, Meguro, Kimito. 2011. Disaster Information Gathering Behavior After the Tohoku Earthquake Part 2: Results of Foreign Respondents. Proceedings of the 10th International Symposium on New Technologies for Urban Safety of Mega Cities in Asia (CD-ROM), Chiangmai, Thailand.

Japan Meteorological Agency (JMA). 2012. http://www.jma.go.jp/jma/en/Activities/eew.html retrieved on November 22, 2012.

Koresawa, Atsushi. 2012. Government's Response to the Great East Japan Earthquake and Tsunami. Journal of Disaster Research, vol7, No. Sp.2012.

National Police Agency Japan http://www.npa.go.jp/archive/keibi/biki/index_e.htm (Nov 22, 2012).

Ozaki, Tomoaki. 2012. JMA's Warning for the 2011 Great Tohoku Earthquake and Tsunami Warning Improvement Plan. Journal of Disaster Research, vol7, No. Sp.2012.

Yun, Nam-Yi, Hamada, Masanori. 2012. Evacuations Behaviors in the 2011 Great East Japan Earthquake. Journal of Disaster Research, vol7, No. Sp.2012.

10CUEE CONFERENCE PROCEEDINGS
10th International Conference on Urban Earthquake Engineering
March 1-2, 2013, Tokyo Institute of Technology, Tokyo, Japan

PATTERNS OF AWARENESS OF CRISIS, REAL TIME DECISION-MAKING AND ACTION FOR SURVIVAL

Haruyuki Fujii[1] and Rimi Inoue[2]

1) Associate Professor, Department of Architecture and Building Engineering, Tokyo Institute of Technology, Japan
2) Graduate Student, Department of Architecture and Building Engineering, Tokyo Institute of Technology, Japan
fujii.h.aa@m.titech.ac.jp, inoue.r.ac@m.titech.ac.jp

Abstract: Patterns of Awareness of Crisis, Real Time Decision-Making and Action for Survival are extracted from the testimony of the survivors of the Great East Japan Earthquake. The patterns are examined with respect to the model of constructive action. Actions to survive and actions to design have things in common since the origin of design is to think to live, The verbal expressions in the testimony are classified in to generation, analysis, focusing, and other sub-processes articulating the constrictive methodology. The patterns of transitions from one sub-process to other sub-processes are analyzed. A model of human behavior in dynamically changing situations is being constructed on the basis of the extracted patterns.

1. INTRODUCTION

The final goal is to create a computational schema of constructive activities. The schema will be employed to design a software agent to simulate pre-quake mitigation management and post-quake rehabilitation management. This paper developes a model of action and examines, on the bases of the model, the typical patterns of action and decision-making in such situation.

2. MODEL OF ACTION

A model of constructive action is proposed. Fig.1 shows a model of process where an actor intends to do something so as to changes the situation into a preferable one. Let *Sc* be the current situation that an actor perceives. If the actor anticipates that a certain event likely occurs and the event brings about unpreferable situation *Sfa* then the actor desires to avoid facing the inpreferable situation. If the actor estimates the probability of the event to be high and the desire is strong enough then the actor plans to do something so as to change the situation into a preferred one.

In the case that the actor believes that a certain action is effective to change the situation into a preferred one, the actor intends to perform the standard action. On the contrary, in the case that the actor doesn't have the belief that such a standard action is effective, the actor, first, plans a course of actions to change the situation into a preferable one, and then, the actor follows the plan.

In the second case, a plan is made as follows. The actor pictures intermediate situation *Sfi* where the event does not bring about an unpreferable situation *Sfa* but a preferable one *Sfe* on the basis of the schema related to the event and its consequences. It is assumed that the preferable situation *Sfe* can be brought about not directly but indirectly by the actor's action since it is one of the possible consequences brought about by the event that is not controlled by the actor. It is also assumed that an actor can control the intermediate situation to some degree. Then, the actor makes a plan to directly change the current situation *Sc* into the intermediate situation *Sfi* and expect the preferable situation *Sfe* to be brought about. Here, a situation is directly made or controlled in the sense that the significant features characterizing the situation are directly changed by an actor. A situation is indirectly made or controlled in the sense that the significant features characterizing it are harnessed only indirectly by changing the features that can be changed directly. It is not necessarily straightforward to picture an intermediate situation from which the expected preferable situation is emerged through the presumed event.

Here, a situation is directly brought about or controlled in the sense that the significant features characterizing the

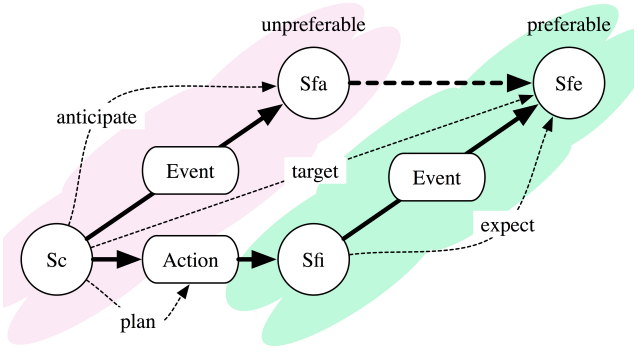


Figure 1 A Model of Constructive Action

situation are directly changed by an actor. A situation is indirectly brought about or controlled in the sense that the significant features characterizing it is changed only indirectly by changing the features that can be changed directly by the actor. It is not necessarily straightforward to picture an intermediate situation from which the expected preferable situation is emerged through the presumed event.

3. FINDINGS IN EMPIRICAL DATA

Some patterns of action and decision-making are extracted from empirical data in which survivors from a great earthquake and a tsunami retrospect and introspect their actions and thoughts while they are overcoming those disasters. The testimony of the survivors of the Great East Japan Earthquake is used as the empirical data concerning awareness of crisis, real-time decision-making, and action. The testimony contains retrospection and introspection of suvivors.

3.1 Type of Intention

Some intentions are extracted from retrospection and introspection of survivors of great earthquakes and tsunamis caused by the earthquakes. The primal desires are (Ia) to save one's own life, (Ib) to save loved one's life, and (Ic) to execute a mission so as to save people's life. The intention to save one's own life has some articulated intentions to respond to situations, i.e., (Ia1) to get out of the anticipated danger such as an earthquake, a tsunami, a fire, etc., (Ia2) to get out of the present danger, (Ia3) to flee to a place for safety such as a refuge, (Ia4) to take shelter from the severe weather such as the rain, the snow, the wind, the cold, the heat, etc., (Ia5) to procure food, (Ia6) to protect one's own property. The intention to save loved one's life has the same articulated intentions as the intention to save one's own life and an articulated intention (Ib7) to confirm loved one's safety. The intention to execute a mission is articulated in terms of an intention (Ic8) to save people's life and an intention (Ic9) to carry out a plan prepared for the crises supposed in advance. Table 1 summarizes these intentions.

Table 1. Types of Intention Extracted from Survivors

Ia) To save one's own life
Ia1) to get out of the anticipated danger
Ia2) to get out of the present danger
Ia3) to flee to a place for safety
Ia4) to take shelter from the severe weather
Ia5) to procure food
Ia6) to protect one's own property
Ib) To save loved one's life
Ib7) to confirm loved one's safety
Ic) To execute a mission
Ic8) to save people's life
Ic9) to carry out a plan prepared for the crises

Intention Ia, Ib, and Ic are sometimes incompatible with one another. A conflict among them let an actor assign an order of priority for the intentions. For example, it is often observed that one intends to save its family member's life rather than to save its own life. Even though one has succeed to flee to a place for safety, the one goes back to a dangerous place to confirm or save the loved one's safe. In these cases, only someone who fortunately found an alternative way to escape death could become survivors.

3.2 Transition of Intention

Intentions play important role to control action so as to bring about a preferable situation. The principal intention basically remains the same until it is fulfilled or avandoned. It changed for the reason of its fulfillment or development.

In a tsunami case, when an intention is fulfilled, a new intention becomes apparent in accordance with the intention to save one's own life (Ia). A typical and satisfactory pattern of transition of intentions toward saving one's life contains the sequence of intention to get out of the anticipated danger (Ia1), to flee to a place for safety (Ia3), to take a shelter from the severe weather (Ia4), and, to procure food (Ia5). Details of actions to fulfill these intentions are decided in accordance with the current situation.

While an intention is being carried out, the intention is developed in accordance with a present situation especially if the situation is unexpected and it seems to be too hard to fulfill the original intention. An alternative intention replaces the original intention. For example, one, who has intention to drive to a place for safety, gives up driving when the one gets caught in a traffic jam and intends to walk to a place for safety.

3.3 Level of Anticipation

Anticipation is performed to perceive, understand, or imagine the past, the current, or the future situation with the senses and the mind. An actor anticipates what if a certain event happens and estimates how severe the event and its consequence are.

A schema concerning the things to be perceived is used for anticipation. A schema provides a frame associating things and phenomena to see situations. It is composed of the features of things and phenomena and the relations among the features. The typical relations are the causal relations among the features, the subsumption relations among the classes of the features, and the inclusion relations among the features. A schema is constructed and updated through experience of similar or analogical situations.

Anticipation is classified into 3 levels, i.e., optimistic anticipation, moderate anticipation, and pessimistic anticipation, with respect to the probability that an anticipated situation is actually brought about and the preferableness of the anticipated situation. They are becoming clear as the situation progresses. Optimistic anticipation (Ao) lets an actor overestimate the probability that a preferable situation is brought about and the preferableness of the situation. Pessimistic anticipation (Ap) lets an actor underestimate the probability that a preferable situation is brought about and the preferableness of the situation. Moderate anticipation (Am) is the medium of the

optimistic and pessimistic anticipations. It has to be noted that the probability and the preferableness are not necessarily clear at the time of anticipation. It is hard for an actor to exactly estimate them before the situation really happens.

The level of anticipation affects the succeeding process of activities to fulfill the intentions.

Optimistic anticipation is likely to prevent an actor from being aware that there might be imminent danger so that the actor does not take appropriate actions to fulfill the intentions. The actor is thrown into difficult situations as a consequence. For example, one who thought that a tsunami wouldn't come to the area inside a breakwater failed to flee promptly to a place for safety without putting oneself in danger.

Pessimistic anticipation is likely discourage an actor to think how to save one's own or loved one's life and to execute a mission. For example, one would give up doing something to save one's life and leave one's fate to diety when one anticipates the situation that all is over.

Moderate anticipation enables an actor to make a plan to fulfill its intentions and update in accordance with the situations faced as executing the plan. For example, one who has a schema telling the unpredictable threat of a tsunami succeeded to make moderate anticipation and to save one's own and loved one's lives without a fatal sacrifice.

Anticipation could be biased by the intentions. It is often observed that the optimistic anticipation, for example, that there is little threat of a tsunami or that there is enough time to so something else than to get out of the danger is updated in accordance with the intention to save loved one's life.

Table 2. Level of Anticipation Extracted from Survivors

Ao) Optimistic anticipation
Am) Moderate anticipation
Ap) Pessimistic anticipation

3.4 Schema

An actor represents a preferable situation in terms of the features to represent the differences between the preferable situation and the current situation and the things in common. Then, the actor assumes the causalities that associate the directly controllable features with the target features characterizing the preferable situation or modifies the causalities currently employed. The decisions are made on the basis of the actor's beliefs about causalities related to the things in question and about the existing situations. The actor sets features to be expected to let the target features emerge and selects or assumes the mechanism expected to provide the features set above.

The assumptions and beliefs are made on the basis of the schema that an actor currently employs. A schema is composed of beliefs about relations among the features characterizing a world, relation among the event occurring in the world, relation between the elements organizing the world. A schema is constructed and updated through experiences in everyday life. If it is verified that a false anticipation is made on the basis of a certain schema then the schema is revised.

Retrospective and introspective of survivors show some important fragments influencing actions to survive a great earthquake and a tsunami. They are as follows (not exhaustive) ;

On a tsunami;

1) A huge tsunami necessarily comes after a great earthquake.
2) A tsunami could be immeasurably huge.
3) Mountainous waves of a tsunami comes repeatedly.
4) A tsunami never comes to the area inside a breakwater.
5) A breakwater is not strong necessarily enough to protect the inside from a tsunami.
6) A boat in the offing could withstand the force of a tsunami.

On a warning and the first motion;

7) The warning from the officials is always correct.
8) The warning from the officials is not always correct.
9) It does not have to evacuate oneself to a safe place unless it is not requested or ordered by the officials.
10) It is preferable to evacuate oneself to a safe place even though it is not requested or ordered by the officials.
11) What someone else says is more reliable than one's intuition.
12) What someone else says is less reliable than one's intuition.

On transportation;

13) A car runs faster than a human.
14) A traffic jam never occurs unless oneself gets to a safe place.

On priority;

15) The first priority in case of an emergency is to save one's own life.
16) The first priority in case of an emergency is to confirm and save loved one's life.
17) It is a default motion to go home to confirm loved one's safety.
18) One who has a mission to save someone's life has to fulfill the mission in any cases.
19) One should escape from danger of a tsunami by oneself.
20) Life is more than anything.

3.5 Imagination of Preferable Situation

An actor imagines a preferable situation that is expected to come true. It is described as the consequence to be brought about through the interaction among the actor's action, the event anticipated, and the situation where the event happens. In a tsunami example, if an actor anticipates that the actor may not survive the disaster without doing something then the actor pictures a safe situation where undesirable features are eliminated. Some people climbed up

as high as they could unless they could confirm that the place is safe. If an actor makes optimistic anticipation that estimates the probability and hugeness of a tsunami not high then a pictured situation remains the same as the current situation until the result of the estimation changes. In this case, an actor doesn't flee to a place of safety until the actor experiences a critical moment. For example, someone, who was not aware of the threat of a tsunami did not leave a house until the tsunami actually comes. The person did not imagine the situation that a tsunami reaches to its place had a narrow escape.

3.6 Situated Planning

Timing of the first motion has an influence over the development of the situation. A plan to one's own and loved one's life is made in accordance with the situation.

When an actor has, more or less, enough moment to deliberate an appropriate plan to fulfill its intention, the actor envisages an intermediate situation that can be resulted by actions and brings about the preferable situation through the interaction with the anticipated event. It is performed on the basis of the current schema. In terms of features, the actor determines the features that embody the mechanism. It is desirable that decisions are made in the conviction that the expected phenomena will emerge with minimal unfavorable effects. If the effects are favorable then they may be expected explicitly in the succeeding decision-making. The actor decides a course of actions that directly changes the current situation into the intermediate situation. For example, someone makes a plan to evacuate with helping loved ones and neighbors while someone plans to give up to do so in order to avoid the unfavorable side effect that either oneself or the loved one may not survive a disaster.

When an actor doesn't have enough time to deliberate an appropriate plan to fulfill its intention, the actor unavoidably makes promptly a transitory plan on after another to improve the immediate situation. For example, someone, who failed to flee to a place for safety, gets on the roof of a house or something higher or keeps a right grasp on a branch or a telephone wire to avoid being flowed by a tsunami. Someone, who was flowed by water, jumped on a floating large plastic container with expectation to survive.

3.7 Interaction with Environment through Actions

An actor interacts with the environment through the execution of actions in a plan. It is not necessarily the case that the course of actions are done exactly as expected since the situation may make the features that are not focused or expected explicitly when the situation is imaged. Actions are adjusted with respect to such features in the current situation as well as the features focused in advance.

An actor observes the process and the result of the action done following a plan and the consequences brought about the interaction between the behaviors of the mechanism embodied as a result of the execution and the situation. The consequence is close to or far from the pictured preferable situation. The secondary effects could be either favorable or unfavorable.

An actor evaluates whether a preferable situation is brought about. If yes, then the plan is done successfully, else, this process is repeated until a preferable situation is brought about. The plan, the assumptions on the causal relations, or the preferable situation is modified.

4. CONCLUSIONS

Patterns of Awareness of Crisis, Real Time Decision-Making and Action for Survival are extracted from the testimony of the survivors of the Great East Japan Earthquake. The patterns are examined with respect to the model of constructive action.

Acknowledgements:

The examples of a tsunami case are selected from the interviews to tsunami survivors that are broadcasted by NHK TV programs. May the victims' souls rest in peace.

References:

Fujii, H., Nakashima, H., and Suwa, M. (2008), "Types of Intelligence in Architectural Design Processes - On the basis of a Phenomenological and Dialectic Model of Design Processes," *Proc. Ninth International Conference on Design & Decision Support Systems*, The Netherlands, CD-ROM.

Fujii, H. and Nakashima, H. (2010), Designing Action Know as Design, *Cognitive Studies*, Vol.17, No.3, pp.403-416, (in Japanese).

10CUEE CONFERENCE PROCEEDINGS
10th International Conference on Urban Earthquake Engineering
March 1-2, 2013, Tokyo Institute of Technology, Tokyo, Japan

METHOD TO MEASURE CIRCULATION SPACE USING AN AUTOCAD APPLICATION

Xue Ma[1], Ryuzo Ohno[2]

1) Graduate student, Dept. of Build Environment, Tokyo Institute of Technology, Japan
2) Professor, Dept. of Build Environment, Tokyo Institute of Technology, Japan

Abstract: The spaces between buildings play an important role in the living environment. To describe the characteristics of these spaces, an AutoCAD application is used to measure their lengths and widths. Although this method serves as a criterion applicable to several types of evaluations, herein it is employed to evaluate vulnerabilities against earthquake disaster.

1. INTRODUCTION

The spaces between buildings are an important element when discussing the quality of a living environment. Particularly in residential areas, varying the distances between buildings provides spaces with differing characteristics, supporting air flow, natural sunlight, and diverse activities in our daily life. Hence, measuring the spaces between buildings may improve space utilization, which is one standard to evaluate the environment quality. Herein the evaluation results are concentrated mainly on earthquake disaster mitigation where the spaces between buildings play an essential role for human survival.

Continuous spaces between buildings consist of a passage to facilitate the free movement of people. This study focuses on the spaces between buildings, which provide either approach or evacuation routes. Typically distance, shape, and occupied area describe a space. The objective of this study is to measure the spaces between buildings by recording their length and widths to generate a route between each continuous space using an Auto CAD application.

2. GENERAL DESCRIPTION OF AUTOCAD SOFTWARE AND LISP LANGUAGE

The CAD (computer-aided design) system, which has been applied to recent designs and the architecture industry, uses vector graphics. CAD describes and simulates a solid physical model on a computer, which is between the real condition and electronic data, and can support both 2D and 3D formats.

AutoCAD supports a number of APIs (Application Programming Interfaces) for customization and automation. AutoLISP is a dialect of the Lisp (List Processor) programming language built specifically for use with AutoCAD and its derivatives. Aside from the core language affording mathematical and function operations, most of the primitive functions are for geometry, accessing an internal DWG database, or manipulating graphics in AutoCAD. AutoLISP code can be entered at the command prompt or loaded from external files.

3. MODEL THEORY

The CAD map records the vector information of each target area. We have developed a program, which is applied by AutoLISP, to detect the distance between buildings, automatically plot the emergency routes, and determine the space characteristics.

When a person enters a particular space from an entrance or remains at a location in the space, our program measures the smallest usable space by drawing a circle where the person is the center and the distance to the nearest object is the radius. If a person is moving, the radius changes. In this manner, circles for all positions in the target area can detect the spaces between buildings.

Routes between buildings can be generated based on the drawn circles. Among the many options for circulating in the target area, the most effective evacuation route is important in an emergency situation. This route can be detected by connecting the centers of circles following certain principles.

4. PROGRAMMING DETAILS

4.1 Rules

In our program, several rules must be followed to draw the map. Firstly, an enclosed boundary is required. Secondly, because the CAD map only recognizes straight lines (not arches, circles, or curves), all single lines exist in only one closed polygon where the interior angle between the end points of two lines does not equal to 180 degrees. Thirdly, each polygon (building) is set as one object while the

boundary of the area is set as one single object.

4.2 Possible cases to define a circle

All lines and points, which represent buildings, are classified into groups by polygons; each object is marked by the coordinates of its all points, such as [(p1,p2,p3,p4)(p5,p6,p7)… …(Pl,…,Pm)(Pn,…,Px)]. Circles are used to measure the spaces between buildings. Different scenarios can be used to draw a circle (Fig. 1). However, all drawn circles must meet one basic condition: the circle cannot cross another object.

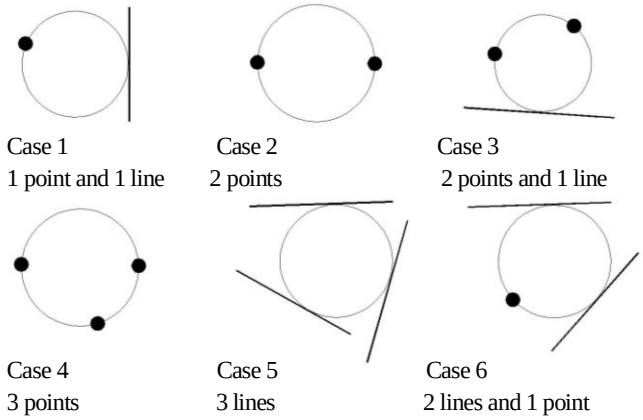


Figure 1. Possible scenarios to define a circle

Case 1: Circle passing through one point and one line

To select an object, line L1 and point P1 must not belong to the same object. Draw a vertical line from any point P (P1,P2,P3,…,Px) to the line that belongs to the other object (Fig. 2). Assume the vertical line is the diameter of the circle. A perpendicular point exists inside the line instead of on the extension line.

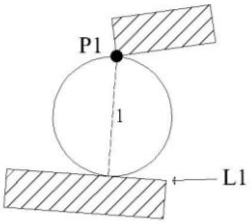


Figure 2. Drawing process

In another situation, extend the lines that share the same point P1 (P1,P2,P3,…,Px) in the direction where the intersection is potentially straight line L1 (Fig. 3). Find one point on the extension line such that the distance to the initial point equals the distance with the straight line.

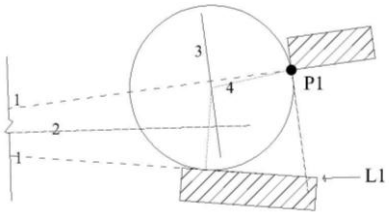


Figure 3. Drawing process

Case 2: Circle passes through two points

Connect any two points P1 (P1,P2,P3,…,Px) and P2 (P1,P2,P3,…,Px) (Fig. 4). The connection line is the diameter of the circle.

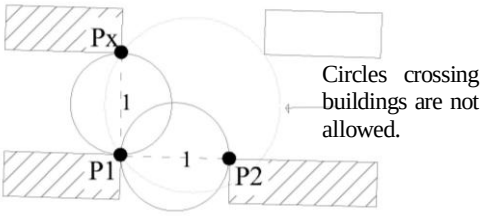


Figure 4. Drawing process

Case 3: Circle passes through two points and one line

To select an object, points P1, P2, and line Lx must be in the same object (Fig. 5). The connection line of two points P1 and P2 must not parallel to line L1 and does not cross line L1. Extend the line and the connection line to an intersection. Draw an angular bisector to connect the perpendicular bisector of the two points. Find the point where the distance to the other point is equal to the distance to the line along the perpendicular bisector.

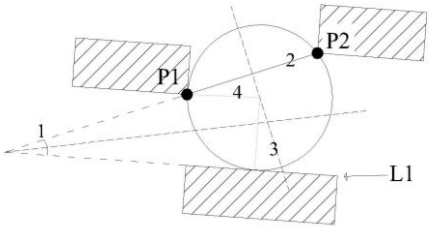


Figure 5. Drawing process

Case 4: Circle passes through three points

To select an object, the three points P1, P2, and P3 must not be in the same object, although two points can be from the same object (Fig. 6). Draw straight lines to create line segments for any two pairs of the points. Find the perpendicular bisector of two lines. Their intersection is the center of the circle. The distance between the center and any point (P1, P2, P3) is the radius of the circle.

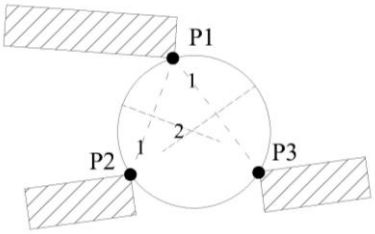


Figure 6. Drawing process

Case 5: Circle passes through three lines

(5.1) Three straight lines

To select an object, only two of the three lines (L1, L2, L3) can be in the same object (Fig. 7). Extend the three lines until intersection points appear. Take the intersection of the three angular bisectors as the center. The distance to any line

is the radius of the circle. The tangent point must be on the line instead of on the extension line.

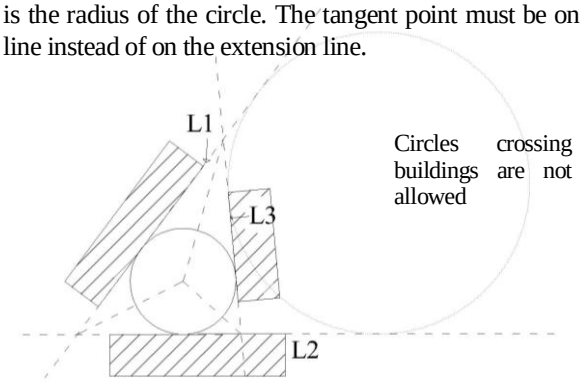


Figure 7. Drawing process

(5.2) Two parallel lines and one straight line

Take the distance between two parallel lines L1 and L2 as the diameter (Fig. 8). Draw the perpendicular bisector of the third straight line L3. Find the point on the bisector where the distance equals the radius of the center of circle. The tangent point must on the line instead of on the extension line.

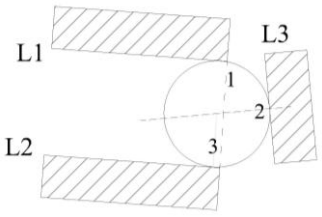


Figure 8. drawing process

Case 6: Circle passes through one point and two lines

To select an object, all lines (L1, L2) and point P1 must not be in the same object, and the point is not on a line (Fig. 9). Extend the lines to an intersection. Draw an angular bisector. Find a point on the angular bisector where the distance to the line equals with the distance to the point (Px). The tangent point must exist on the line instead of on the extension line.

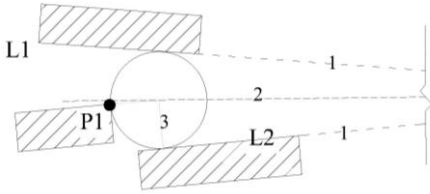


Figure 9. Drawing process

4.3 Reading data

As shown in Table 1, data is recorded as three text files. File 1 is for the serial number of each circle and includes the coordinates of the center of circle and its radius. File 2 records how many objects are tangent to the circle as well as the serial number of those objects. File 3 is a list denoting the initial row of the data for each circle in File 2.

Table 1. Output of the data files

Data	File 1	File 2	File 3
Content	Coordinates of radius/radius	Number of connected object/ Serial number of connected object	Initial row in File 2
C1	(Xc1, Yc1) R1	3	1
		5	
		9	
		21	
C2	(Xc2, Yc2) R2	2	4
		5	
		15	
…	…	…	…
Cx	(Xcx, Ycx) Rx	3	X
		2	
		7	
		10	

4.4 Drawing route lines

To detect the routes between buildings, connect the centers of the circles. This process produces two situations.

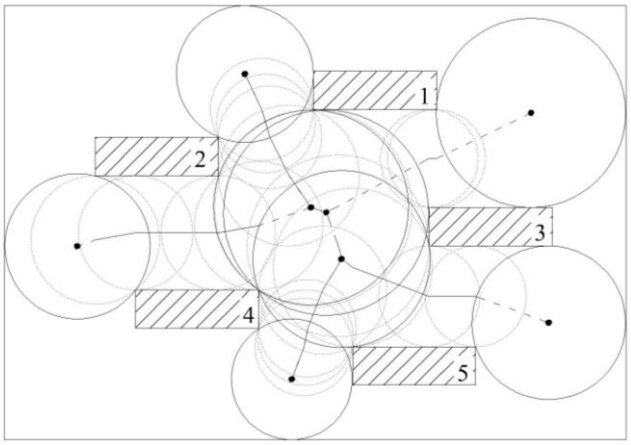
Circles in contact with two objects

Pick circle C1 with its serial number. Read which two objects are in contact with the circle using File 2 and File 3. Choose all the circles that also touch only the same two objects, and sort the distance between centers with C1 from the shortest to the largest.

Connect the center of C1 with the first and second shortest distances, which are the expected route segment (Fig. 10). The connection line between two circles cannot cross any object or fully cut another circle. Repeated lines are read only once in the final result.

Circles contact with three objects

When circle P1 is in contact with three objects, circles that share any two objects (including circles that only connect to two objects) must be read using File 2 and File 3. Similar to the previous situation, repeat this process (Fig. 10). Starting points and exits must be manually set when running our program.



——— step2: Connect the route from circles that touch three objects

Figure 10. Process for drawing lines

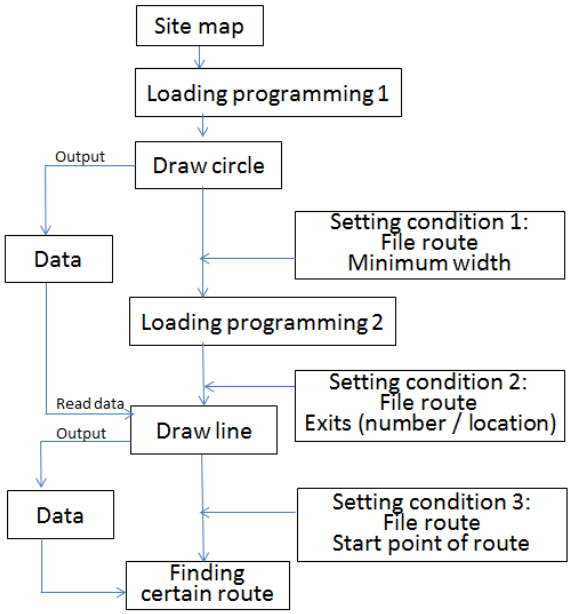


Figure 11. Running flow from drawing the sitemap to determining the route

5. ANALYSIS OF THE RESULTS

The widths and distances between the centers of the circles are recorded as numerical data. Because characteristics to describe spaces between buildings include route lengths and widths, calculating the lengths and widths of the routes can be used to evaluate open spaces.

We applied our program to several residential sites to detect the spaces between buildings and to evaluate earthquake disaster vulnerabilities. Different site layouts are compared. The high-rise building site and low-rise building site possess different space characteristics (Figs. 12 and 13). Although high-rise building sites have wider spaces, low-rise sites have longer routes.

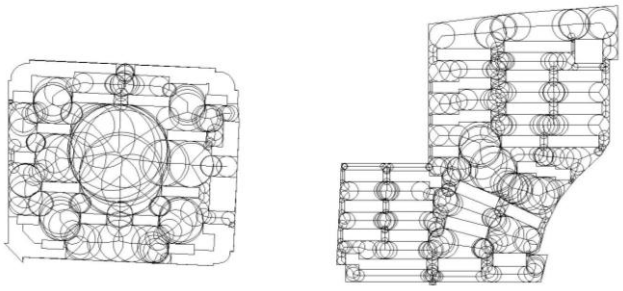


Figure 12. Site plan of high rise and low rise areas

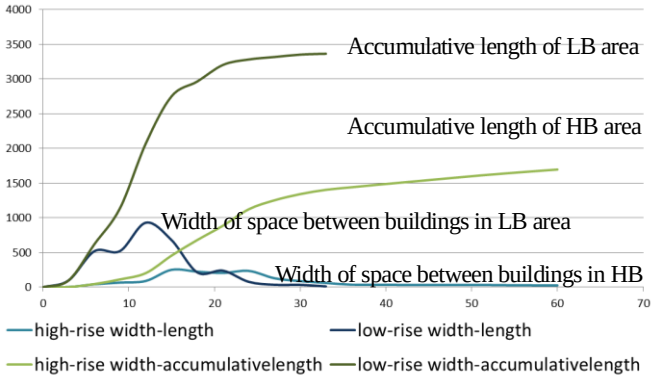


Figure 13: Comparison of route length in different width in 2 areas

6. APPLICATIONS TO EVALUATE THE VULNERABILITY AGAINST EARTHQUAKE DISASTER

Using this method, it is possible to evaluate the vulnerability of residential areas against earthquake disaster.

6.1 Analysis of usable spaces in a residential environment

The impact of fallen debris from a building is uncertain after an earthquake. By considering different scenarios, our program can analyze how the space between buildings changes as the damage becomes more severe. Figure 17 shows the results assuming different levels of damage, and confirms that vulnerabilities can be examined.

Different usages require different minimum widths. For example, the routes for fire engines must be at least four meter wide. Our program can evaluate the width of spaces to determine possible routes for different usages. Additionally, our program can measure the usable space for temporary gatherings or to distribute emergency supplies. Consequently, our program can identify key locations for specific functions.

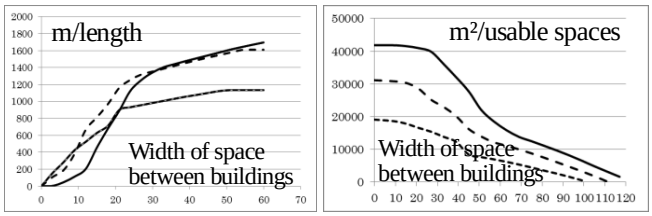


Figure 14. Accumulative length and occupied spaces for different damage situations

Figure 14 compares the information for a high-rise building with different damage scenarios. Although route changes slightly in the damage scenario, the usable space with a width wider than four meters, which is the minimum distance for a fire engine, is a quarter to half that in the normal condition.

6.2 Application to an accessibility analysis

For areas with low accessibility, adding exits can directly improve the situation. The way to add exits depends on the layout. Our program can determine the most effective solution for the number of exits as well as their locations.

Figure 15 shows the distance from the intersections of routes between buildings and the nearest exit. Adding exits at different locations decreases the distance, but not all locations have the same impact (Fig. 16).

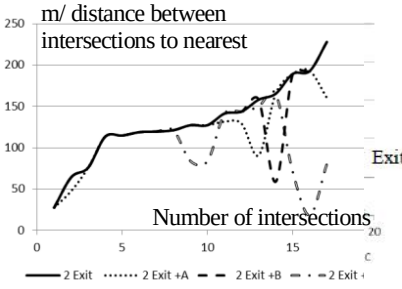


Figure 15. Shortest distance from the intersection of space between buildings and the nearest exit

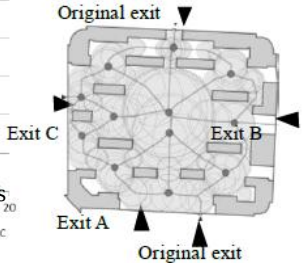


Figure 16. Location for additional exits

As a combination of the two applications mentioned above, optimization can be addressed based on the evaluation and basic information of the target site. Adding exits is a feasible way to minimize the number of potential victims while effectively using open spaces.

7 CONCLUSION

This study shows that our AutoCAD programming application can assess the spaces between buildings, and can automatically provide numerical data, which is useful for space analysis. Our method was applied to examine vulnerabilities against earthquake in a residential environment, and provided numerical measures for an objective evaluation. Future studies on environmental quality should employ our program.

Acknowledgements:

The author acknowledged support from G-COE Center for Urban Earthquake Engineering (CUEE) in Tokyo institute of Technology for supporting this research. Last but not least, Thanks to Dr. Miura Hiroyuki and Ms. Soh huichen who helped me to process the satellite image.

References:

Oguchi, K. (2003), "Parks in case of disaster in Tokyo, Construction and plan of rescue and shelter (in Japanese)," *journal of the Japanese Institute of Landscape Architecture*, **66**(3), 208-212

Tsukada,S. (2008), "Analysis of the evaluation structure in design a ted manager system of urban park," *Journal of the Japanese Institute of Landscape Architecture*, **73**(631), 1923-1928.

Matsuda,N. (2003), Urban park planning from the point of view of the safe and secure urban environment(in Japanese), *Journal of the Japanese Institute of Landscape Architecture*, **66**(3), 180-184

Asada,T, (2004)," Research on the condition of disaster prevention park sand it's directivity in Hiroshima (in Japanese)„" *Architecture institute of Japan*, **27**, 737-740

Gohta, M. (1990), "A Morphological Study of Open Space in Urban Space: Part 1 Quantitative Analysis using the Largest Empty Circle Method (in Japanese)," *Proceeding of annual conference* 1990, 411-412.

Yasuyuki Yamada Japan Meteorological Agency, "Disaster mitigation system in Japan (2) - Earthquake and Tsunami Warning/Information in Japan."

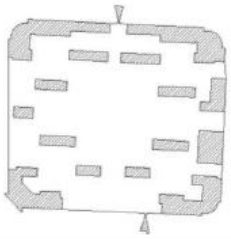
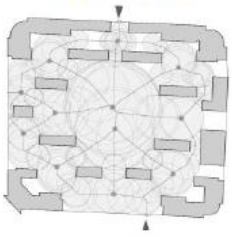
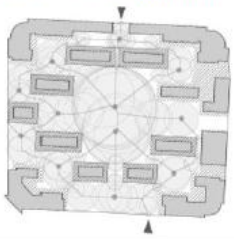
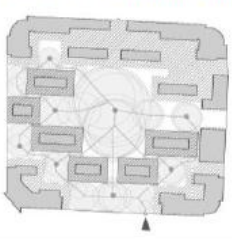
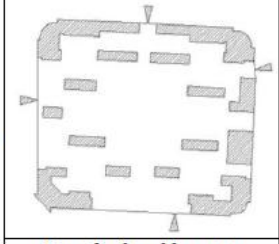
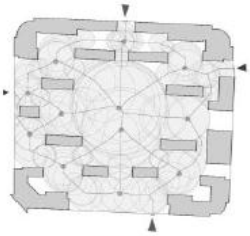
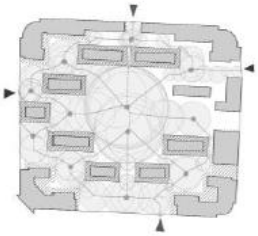
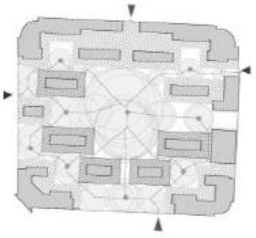
		Normal situation	Debris area = 10% building height	Debris area = 20% building height
2 Exits				
	Length of usable route	1697 m	1505 m	1149 m
	Average length from intersections to nearest exit	131.4 m (16 intersections)	128.5 m (14 intersections)	148.3 m (8 intersections)
	People not using a route	0	0	1500
4 Exits				
	Length of usable route	1697 m	1586 m	1335 m
	Average length from intersections to nearest exit	93.5 m (16 intersections)	94.5 m (14 intersections)	108.2 m (9 intersections)
	People not using a route	0	0	0

Figure 17. Altering usable spaces between buildings with the damage situation set to different levels

JOINT CONFERENCE PROCEEDINGS
9th International Conference on Urban Earthquake Engineering/ 4th Asia Conference on Earthquake Engineering
March 6-8, 2012, Tokyo Institute of Technology, Tokyo, Japan

BEHAVIOR ANALYSIS OF STRANDED PERSON USING MOBILE GPS DATA

Masashi Shiina[1)], Makoto Fujiu[2)], and Kazuyuki Takada[3)]

1) Student, Dept. of Civil and Environmental Engineering, Tokyo Denki University, Japan
2) Ph.D. Candidate, Dept. of Interdisciplinary Information Studies, The University of Tokyo, Japan
3) Professor, Department of Civil and Environmental Engineering, Tokyo Denki University, Japan
09rg041@ms.dendai.ac.jp, fujiu@iis.u-tokyo.ac.jp, takada@g.dendai.ac.jp

Abstract: At present, Tokyo metropolitan area has two kinds of natural mega-hazard: M.7 class inner-plate earthquake and Tsunami. Central Disaster Prevention Council which is the supreme organization of disaster affairs in Japan has warned about them in published reports. Right after the 2011 off the Pacific coast of Tohoku earthquake, the railway system in Tokyo metropolitan area completely shut down so that a large number of people had difficulty in moving. So far, many expertise in disaster prevention have proposed that such people should keep staying same place where they encountered big earthquake for their safety. However, it was observed that after the earthquake a lot of people tried to go home on foot even though the trip distance was quite long, and many person who commuters unable to get home go to home through the dangerous zone which are fire dangerous zone and building damage dangerous zone. This paper analyzes the behavior of persons who commuters unable to get home under the 2011 off the Pacific Coast of Tohoku Earthquake using mobile GPS data. Authors proposed and developed smart phone application based on the previous analysis.

1. INTRODUCTION

Massive destruction was brought to the north-eastern region of Japan when the 2011 off the Pacific coast of Tohoku Earthquake occurred at 14:46 (JST) on March 11th, 2011. In Tokyo metropolitan area where maximum of 5-upper seismic intensity (JMA) was recorded, the earthquake suspended the transportation system such as bus and train services. As the result, many people tried to return home on foot. However not all were successful and many of them ended up going to emergency shelters put into place or waited the recovery of public transportation for a long time.

According to the 10th census on transportation in Tokyo metropolitan area, approximately 9,500,000 commuters use public transportation system per day and the average travel time was 68 minutes long. It is evident that once the public transportation system fails, a great number of people will face difficulty in returning home.

Nakabayashi (1992) researched the relation between the distance to home and the success rate of returning home. He mentioned that all the people could return their home if the distance is less than 10km and the rate decreases by 10% per additional kilometer. Furthermore, people face difficulty in returning home if the distance is more than 20km. However, on March 11th, 2011, there were those who could not return home even though the distance was less than 10km and those who succeeded in returning home even though the distance was more than 20km. Shimohara et al. (2010) and Osaragi (2008) examined disaster prevention plans by estimating a behavior model of the commuters in case of devastating earthquake. However, these studies may not fully reflect the actual behaviors as mentioned above.

Transportation system will be completely shut down if the Tokyo Metropolitan Inland Earthquake with magnitude-7 level occurs. Tokyo Metropolitan Government has worked on establishing new ordinance which asks companies to stock emergency supply in the office buildings. This countermeasure would contribute to keep employees staying in the building until the transportation system recovers.

In order to study the effective disaster prevention countermeasures regarding the evacuation of affected people after the large scale earthquake, we analyzed the behaviors of the affected commuters by the 2011 off the Pacific coast of Tohoku Earthquake on March 11th, 2011.

Hiroi (2011) conducts similar study and estimated choice behavior model of the affected commuters with using questionnaire survey data. However it is not verify whether they succeeded in returning their home.

In this study, we have analyzed the behavioral characteristics of the affected commuters using a GPS data. The respondents of the survey were the affected commuters who faced difficulty in returning home.

2. CHARACTERISTICS OF ACTIONS ON THE DAY OF THE EARTHQUAKE

2.1. FLAG INDICATOR OF TRAVELING

The figure-2 shows the percentage of people's traveling from the affected areas after the earthquake.

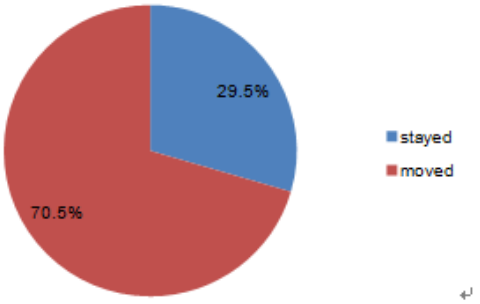


Figure 2. percentage of moved or stayed.

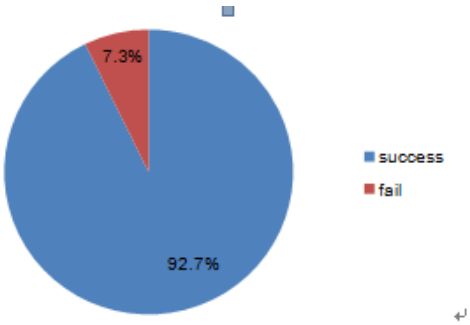


Figure 4. the success or failure of the go home.

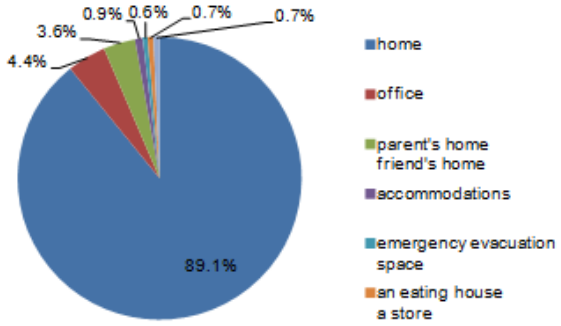


Figure 3. percentage of destination

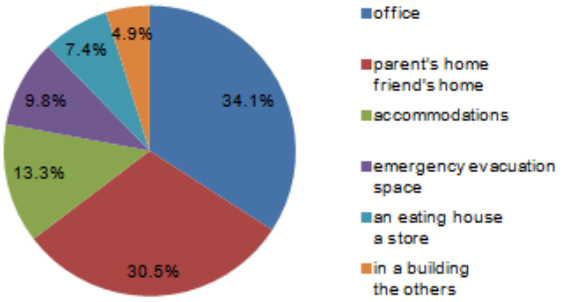


Figure 5. stay place of the return abandonment person

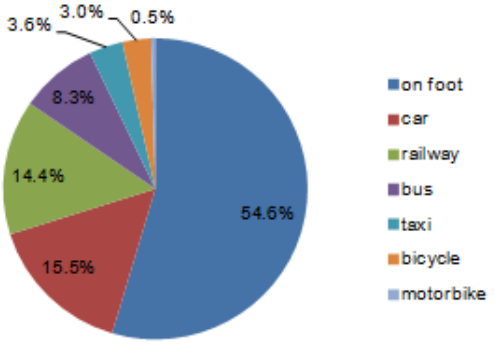


Figure 6. use transportation.

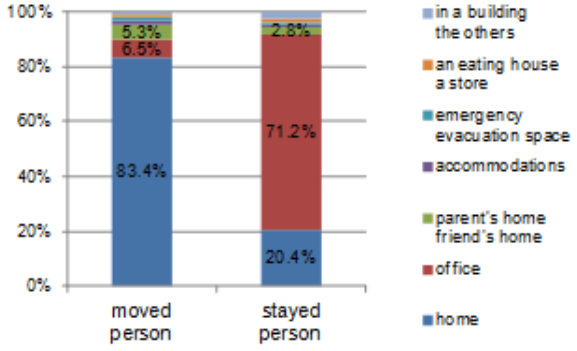


Figure 8. stay place of moved person and stayed person

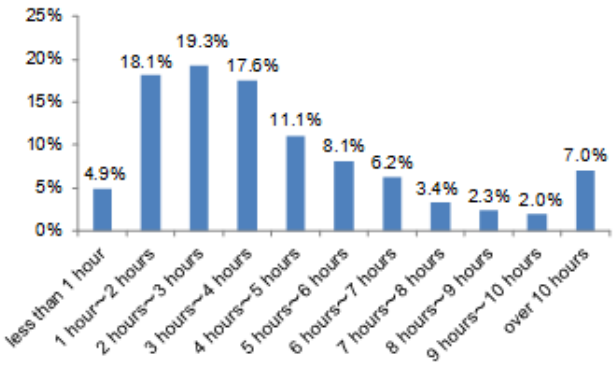


Figure 7. time required of go home.

29.5% of the people did not move at the time of the earthquake while 70.5% of the people tried to move. It became clear that 89.1% of the people who tried to move were trying to return home. Thus we decided to investigate into further details to find out the situation that affected the decision making process and to find out whether those who hoped to return home actually succeeded in returning home. The results will be presented in the next chapter.

2.2. SITUATION OF HOME RETURNING ON THE DAY OF THE EARTHQUAKE

The figure-4 indicates the result of the people's attempt to return home. 92.7% of the people succeeded in returning home. The figure-5 shows the percentage of the final place of stay of those who could not return home. 34.1% of them stayed at their company, 30.5% at family and friends' house, 13.3 % at hotels, 9.8% at emergency shelters. It became clear that people tried to return home once but chose to stay according to the situation.

2.3. RETURNING ACTIVITY ON THE DAY OF THE EARTHQUAKE

The figure-6 indicates the major means of transportation for those who attempted to return home. For those who used multiple means, each individual chose their main means of transportation in the order of car, train, bus, taxi, motorbike, bicycle, and walking. Out of those who attempted to return home, 54.6% tried to return home by walking, 15.5% by car, 14.4% by train, 8.3% by bus, 3.6% by taxi, 3.0% by bicycle, and 0.5% by motorbike. This fact indicates that more than half of the population who use train on a daily basis had attempted to return home by walking. The figure-7 indicates the amount of time spent for returning home. Most people spend about 2-3 hours and 30% of the people spent more than 5 hours.

3. ANALYSIS ON THE BEHAVIOR TO REMAIN

Firstly, we analyzed the final location of stay of those who stayed and those who moved. The figure-8 indicates the final location of stay organized according to the means of transportation. 83.4% of those who responded "attempted to move" indicated their own home as final location of stay while 71.2% who responded "to stay" indicated their companies as final location. From this observation, the affected population can be divided into two major categories, those who wish to return home and those who stay.

Secondly, we analyzed the characteristics of the desired location of stay. In this study, we have distinguished three types of initially desired location of stay namely "home", "other than home", and "remaining". The figure-9 shows the relationship between the linear distance to home and desired location of stay. The result indicated that less people wished to return home as the distance to home increased and more people wished to remain where they were. The result also showed that 27% of the affected people wished to return home even when their home was more than 40 km away.

4. BEHAVIOR ANALYSIS FUSING GPS DATA

We analyse commuters' behaviour under large scale disaster in Tokyo Metropolitan area. It became clear that stranded commuters' pass through the fire dangerous zone and building collapse zone for going his/her home. It is very dangerous for stranded commuters' under large scale disaster in Tokyo Metropolitan area as shown in fig.9 and fig. 10.

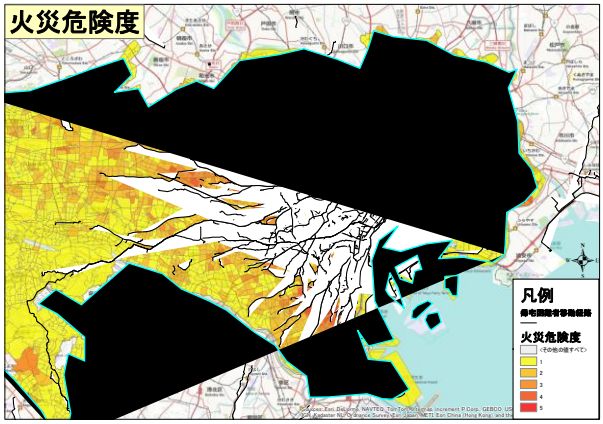


Figure .9 Behaviour route with fire zone

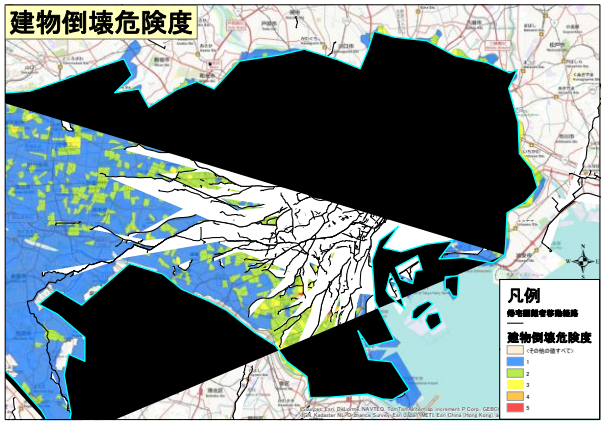


Figure .10 Behaviour route with building collapse zone

5. CONCLUSION AND FUTURE PROSPECTS

This study investigates the behaviour of the people having difficulties in going home after the 2011 off the Pacific coast of Tohoku Earthquake occurred.

As the result of this study, it becomes clear that approximately 70% of the affected people attempted to move and approximately 92% of those who attempted to return home managed to do it.

We clarified that many affected people had attempted to move and many of them succeeded in doing it. However, it is estimated that Tokyo Metropolitan Inland Earthquake

would bring more severe condition such as shut down of transportation services, massive fire, building collapse, road congestions and so on.

Thus, in order to be prepared for the coming large scale earthquake in Tokyo metropolitan area, it is necessary to prepare an effective countermeasure such as storing of necessary items and securing of safe places to stay, announcing the employees to remain until the transit system recovers, and establishing a procedure of safety confirmation of family members and friends.

On the other hand, it is desirable to prepare safe environment to return home for those who attempt to return home. In order to accomplish it, development of a method of safe evacuation is required, considering the disaster level, distance to a home, and personal attributes.

REFERENCES

Ministry of Land, Infrastructure, Transport and Tourism. (2007). Big city traffic general survey metropolitan area report.

Nakabayashi, K. (1992). Development of Estimation Method on Obstructed Homeward Commuters after Earthquake Disaster. Journal of Comprehensive Urban Studies. Vol.47: pp.35-75.

Shimohara, S., Watanabe, Y., Shimazaki, T. and Kaneko, Y. (2010). Behavior Model for Return a home after Devastating Earthquake in the Tokyo Metropolitan Area. Journal of Social Technology Research. Vol.7: pp.45-53.

Osaragi, T. (2008). Modeling of Decision Making and Behavior for Returning Home After a Devastating Earthquake. Journal of Architectural Institute of Japan. Vol.73, No.634: pp.2679-2687.

Hiroi, Y., Sekiya, N., Nakajima, R., Waragai, S. and Hanahara, H. (2011). Questionnaire Survey concerning Stranded Commuters in Metropolitan Area in the East Japan Great Earthquake. Journal of Institute of Social Safety Science. Vol.15: pp.343-353.

Committee of Infrastructure Planning and Management, JSCE. (1995). Theory and Practice of Disaggregate Behavioral Model

10CUEE CONFERENCE PROCEEDINGS
10th International Conference on Urban Earthquake Engineering
March 1-2, 2013, Tokyo Institute of Technology, Tokyo, Japan

EVACUATION BEHAVIOR MODEL CONSIDERING VARIOUS ATTRIBUTES OF RESIDENTS AND TRANSIENT OCCUPANTS

Takuya Oki [1] and Toshihiro Osaragi [2]

1) Graduate Student, Department of Mechanical and Environmental Informatics, Tokyo Institute of Technology, Japan
2) Professor, Department of Mechanical and Environmental Informatics, Tokyo Institute of Technology, Japan
oki@os.mei.titech.ac.jp, osaragi@os.mei.titech.ac.jp

Abstract: Understanding human behavior, such as waiting, returning home, and evacuation, after a great earthquake is very critical in establishing detailed disaster prevention planning. In the present paper, we construct a simulation model to describe how human behavior varies as a function of physical damage, such as the spread of urban fires and street blockage due to collapsed buildings. The proposed model is applied to a densely built-up area of Tokyo using a database of the spatiotemporal distribution of railroad passengers, automobile users, and pedestrians. Using the model, we attempt to demonstrate some new findings that can be applied to disaster prevention planning by examining evacuation plans and various settings in earthquake simulations.

1. INTRODUCTION

1.1 Background and Objectives of Research

In recent years, people's daily lives are becoming busier due to rapid urbanization and the growth of rapid transit networks. Therefore, it is difficult to predict the effects of a large-scale earthquake on the population. The authors have investigated methods of estimating the spatiotemporal distributions of people inside/outside buildings and the people in transit with the aim of constructing the necessary database for analyzing disaster prevention plans (Osaragi and Hoshino 2012, Osaragi 2009, Osaragi and Shimada 2009, Osaragi and Shimada 2009).

In this paper, we consider not only the spatiotemporal distribution of occupants in-side buildings, but also of transient occupants, (i.e., people who are walking or otherwise in the process of using transportation in the city) in order to construct a simulation model for evacuation efforts following a large-scale earthquake. The model takes into consideration the behavioral characteristics of a variety of people, some of whom are constantly moving and some of which remain in a single location within the city. We have attempt to account for the influence both people whose movement paths stay within the city and those returning home (e.g., from offices/ schools) on the number and spatial distribution of stranded people. This influence has not been addressed in previous studies.

1.2 Comparison with Previous Studies

Early spatial models representing urban spaces were raster data models (Okada et al. 1979, Aoki et al. 1992), but those models were replaced with block models to clarify aspects of different actual urban areas. More recently, it has become more common to employ spatial models using detailed digital maps. Attempts have also been made to build models based on multi-agent simulations (MAS), in which stranded people, fires, and other factors are treated as agents. The range of applications for MAS, which originated in the life sciences, has expanded with the advance of computer technology, and MAS has come into wide use in the field of evacuation behavior simulations in recent years. Highly versatile procedures have been proposed, including analyses of simulations of evacuation activities that model activities for the rescue of people requiring aid during seismic fires (Ueda et al. 2007) and models based on commercially available digital maps (Muraki and Kanoh 2004). Many proposals have also been made for evacuation activities following tsunamis (Fujioka et al. 2002, Suzuki and Imamura 2005, Ohata et al. 2007).

However, the source data for previous research, namely, spatial distributions of populations, have been static data obtained from the population census or other similar sources that do not account for human behavior characteristics, which change dynamically with time and location. Also, depending on the time and place, one can expect the coexistence and intermingling of stranded people and those attempting to return home. No studies have simultaneously discussed evacuation activities and return home travel. Therefore, in this report, the authors have combined a model for estimating the spatiotemporal distributions of occupants remaining in the city and transient occupants (Osaragi and Hoshino 2012, Osaragi 2009, Osaragi and Shimada 2009, Osaragi and Shimada 2009) with a model describing the intention to return home and the associated return activities (Osaragi 2012), and incorporated this into a new model describing evacuation behavior.

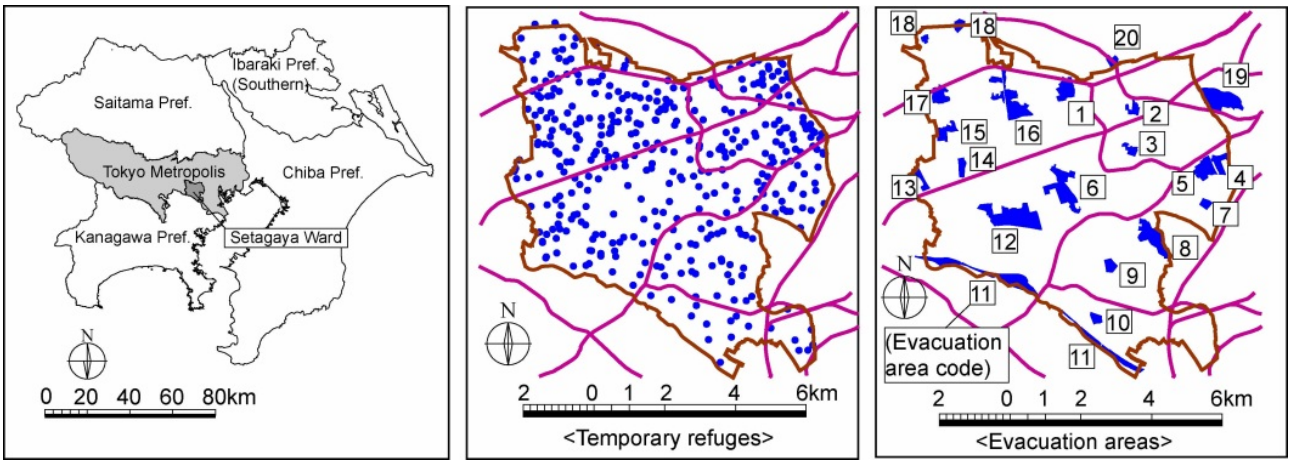


Figure 1 Study Area

There are many studies presenting models for describing property damage. Models relating to the urban spread of fire and the collapse of buildings (Tokyo Fire Dept. 2001, Murao and Yamazaki 2000). The present report uses these models in an attempt to provide a micro-simulation analysis on a unit building basis, taking into consideration the attributes of buildings.

The simulation model proposed here can be summarized as follows: (1) blockage of streets by collapsed buildings is modeled; (2) the progress of fire is predicted using an urban fire spread model; (3) the spatiotemporal distribution of train passengers, automobile users, and pedestrians is incorporated; (4) the movement of people returning home who enter or exit the region under analysis are modeled; and (5) stranded people are categorized using a detailed profile based on their, for example, the purpose of their movements.

2. ANALYTICAL DATA

2.1 People and Regions under Analysis

The region employed in this analysis was the Setagaya Ward of Tokyo (Fig. 1). Setagaya has areas that are densely crowded with wooden structures, and thus are very vulnerable to housing collapse and urban conflagration in the event of an earthquake. In addition, many workers and students live in Setagaya and commute within the Tokyo region (i.e., they would be counted as transient occupants). The subjects under analysis included all individuals residing and traveling within the ward during a disaster, not only those who live in Setagaya. This population also includes people re-entering Setagaya from outside the ward at various times after a disaster (people returning home).

Data from a Person-trip Survey (PT data) conducted in 1998 were employed to compile the daily trip destinations for Setagaya residents. It was found that approximately 96% of the trips remain within metropolitan Tokyo and these return travel activities took place across the whole of the Tokyo region.

2.2 Spatiotemporal Distribution of Occupants

Location data for occupants remaining in the city (occupants of any facility, including residences) were represented by building locations or intersections. Specifically, the location of each occupant of Setagaya was determined by selecting the building probabilistically, using the floor area of each building, the purpose of travel PT data, and the building type noted in the digital maps. For residents outside Setagaya, locations were determined by selecting positions at random from among intersections in area units (small zones) used in the PT data.

Location data for the railway passengers (Osaragi 2009), automobile users (Osaragi and Shimada 2009), and pedestrians (Osaragi 2012, Nishimura and Osaragi 2009) were predicted by employing the results of previous research together with the detailed data available on individual attributes.

2.3 Spatial Model Used in Simulation

The street network was extracted from the digital map to use as the spatial model. People were assumed to be walking on the sidewalks, and so sidewalk widths were extracted from the traffic census data (2005). In order to prevent confusion during evacuation and encourage orderly evacuation behavior, the Tokyo Regional Disaster Prevention Plan (2003) is based on a two-stage evacuation, which calls for people initially to gather in temporary refuges and then to move from there to (official, wide and safe) evacuation areas. The study area consisting of 392 temporary refuges (Fig. 1, center panel) and 20 evacuation areas (Fig. 1, right-hand panel) connected with a street network was created in order to examine the effectiveness of this evacuation scheme.

3. MODELING PROPERTY DAMAGE

3.1 Building Collapse Model and Street Blockage Model

In building collapse models, the probability of collapse can be estimated for each building unit based on its year of erection or its construction type (wood, reinforced concrete, steel frame construction, or light steel frame construction) (Fig. 2) (Murao and Yamazaki 2000). According to the damage forecast for Tokyo Metropolis (2006), a North

Tokyo Bay Earthquake (7.3M) would cause shaking of a weak 6 on the Japanese seismic scale in Setagaya. Using an empirical equation (Midorikawa et al. 1999) relating seismic intensity to seismic velocity, a velocity of PGV = 60.0 (cm/s) was assumed. We used data on building heights and street widths to make a forecast of street blockage caused by building collapse (Fig. 3).

3.2 Fire Outbreak Model and Urban Fire Spread Model

In this study, we considered a fixed number of 58 fires breaking out in Setagaya, on the basis of the numbers of fires predicted for the area (18:00 o'clock) in the damage estimate for Tokyo Metropolis (2006). The specific locations of fire outbreak can be broken down by building use, season, daytime vs. nighttime occurrence, and typical acceleration (gal: cm/s2); we used the building-type-based outbreak rates of the Tokyo Fire Dept. (2001) to estimate these locations.

The fire spread speed model of the Tokyo Fire Dept. (2001) was employed; this model can account for different modes of fire spread and different structural building types. "Spreading speed" has two categories, speed of spreading within a single building and speed of spreading between neighboring buildings (Fig. 3), the latter of which depends on the distance between the two buildings.

3.3 Basic Analysis Using the Property Damage Model

After the above preparations, we carried out 10 Monte Carlo simulations using the models of building collapse and street blockage (each a different combination of building collapse and street blockage). The fractions of blockage in relation to the total number of streets were calculated (mean numbers of streets by units of neighborhood and block) and are shown in Fig. 5 (left-hand panel). As shown, areas with many narrow streets suffered a relatively high rate of street blockage.

Next, we carried out Monte Carlo simulations using the fire outbreak model and the urban fire spread model, taking as given building collapse and assuming the conditions: winter, nighttime, and a 6 m/s north wind. The parameter of maximum acceleration in the fire spread speed model (Fig.4) was assumed to be 500 gal, which is based on an empirical formula (Midorikawa et al. 1999) relating seismic intensity and maximum acceleration. The number of buildings catching fire within 48 hours after the earthquake (mean numbers by units of neighborhood and block) were determined and are shown in Fig. 5 (right-hand panel). As shown, the number of buildings was higher in areas in which buildings of wood construction were dense.

4. MODELING HUMAN BEHAVIOR

The typical series of human behaviors when an earthquake strikes were categorized and modeled. Fig. 6 shows an example of the behavior modeled for occupants at home, from the perspective of initial reactions, searching for routes, methods of evacuation (direct evacuation versus two-stage evacuation), walking in a crowd (walking speed),

$$P_R(PGV)=\Phi[(lnPGV-\lambda)/\zeta]$$

P_R : Cumulative probability of the occurrence of damage equal or higher than rank R
PGV : Peak ground velocity (cm/s)
Φ : Cumulative probability of the standard normal distribution
ζ , λ : Parameters determined by year of erection or construction type (wood, reinforced concrete or steel frame construction)

Figure 2 Building collapse model

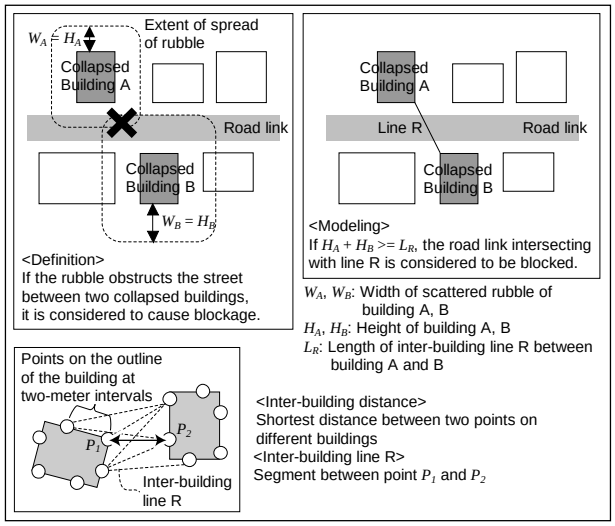


Figure 3 Street blockage model

Level 1: Speed of spreading within a single semi-fireproof building

$$Vt = \frac{6.63L}{1.17L + (\text{L-}5.0)\,f - 0.5}$$

Speed of spreading between neighboring buildings (bare wood and fire protection)

$$Vr = \frac{(a\alpha + b)\exp[(c\alpha + d)Lr]}{0.048U + 0.822}$$

f : Rate of damage (= 0.00034α - 0.054)
V_t : Speed of spreading within a single building (m/s)
V_r : Speed of spreading between neighboring buildings (m/s)
L_r : Inter-building distance (m)
α : Acceleration (gal: cm/s^2)
U : Wind speed (m/s)
The parameter a, b, c, and d is determined by structure, level, and status of collapse of neighboring buildings.

Figure 4 Fire spread speed model

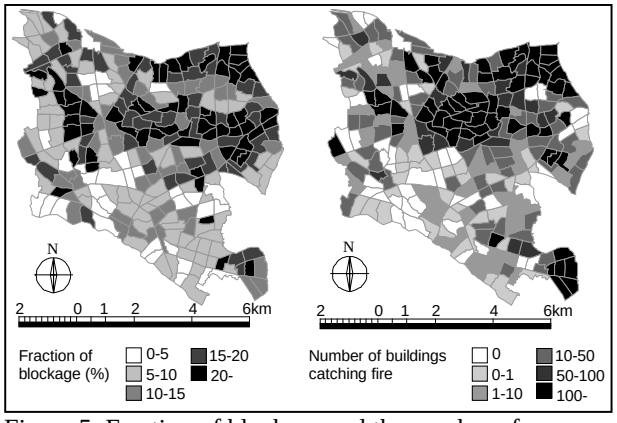


Figure 5 Fraction of blockage and the number of buildings catching fire

and activities while waiting. Specifically, the model incorporated the following: (1) a time is set for the start of evacuation after the earthquake; (2) in the case of a two-stage evacuation, the stranded people move to temporary refuges; (3) a time is set for beginning movement of stranded people from the temporary refuges to evacuation areas; (4) evacuation is complete when the stranded people have arrived at an evacuation area; and (5) the stranded people proceed directly to the evacuation area when a

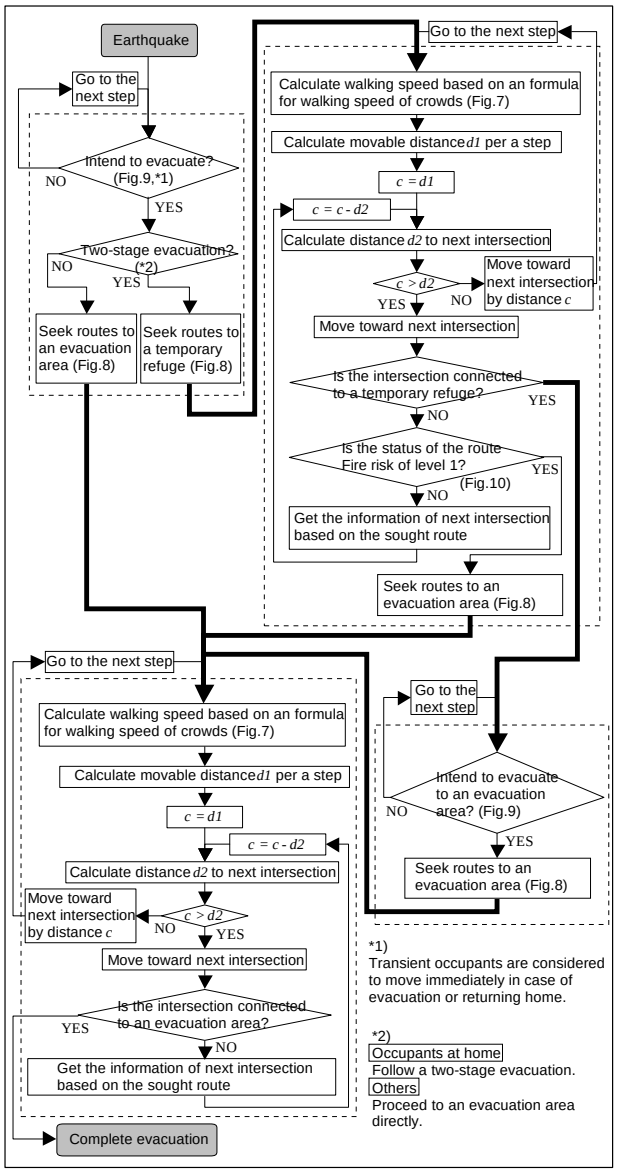


Figure 6 Human behavior model for occupants at home

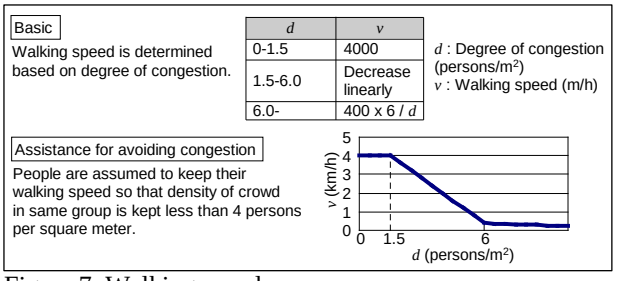


Figure 7 Walking speed

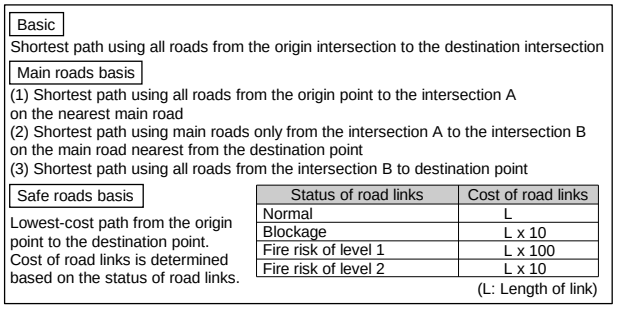


Figure 8 Route search

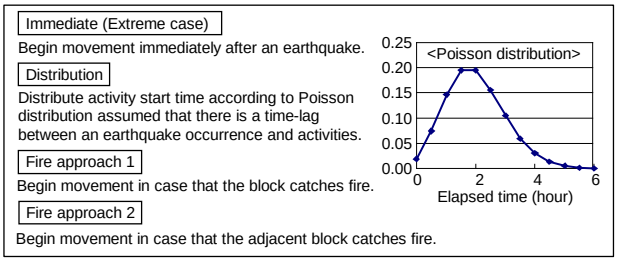


Figure 9 Definition of activity start time

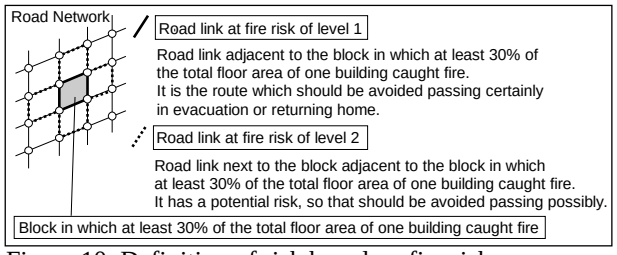


Figure 10 Definition of risk based on fire risk

two-stage evacuation is not followed. Fig. 7, Fig.8, and Fig. 9 show the details of how the walking speed is set, how routes are sought, and the time to begin activities, respectively.

The activities of transient occupants (railway passengers, automobile users, and pedestrians) are modeled as follows: (1) they decide whether to attempt to return home (the outcome is determined by the model of intention to return home) (Osaragi 2012); (2) if they decide not to return home, they are treated as occupants at home at the time of the earthquake; (3) if they decide to attempt to return home, they do so using the main streets. The routes from their location at the time of earthquake back to their homes are determined (Fig. 8); (4) if they encounter fire on their way home, they take refuge in an evacuation area; (5) if they complete their journey home, subsequently, they act in the same way as the occupants already at home at the time of the earthquake.

Occupants in facilities other than their own residences are modeled as follows: (1) they decide whether to return home; (2) if they decide not to return home, they wait in the current facility until the time to begin evacuation, and after that, they act in the same way as occupants at home; and (3) if they decide to return home, they subsequently act in the same way as the transient occupants.

5. EXECUTION OF THE SIMULATION MODEL

5.1 Performance Indicators and Settings

The danger imposed by road links was defined (Fig. 10) in order to make an assessment of the effect of urban fire spreading on safety during evacuations. It was assumed, as an approximation, that once at least 30% of the total floor area of one building in a certain block had caught fire, the radiated heat would endanger adjacent routes. However, streets that border large open areas (at least 10,000 m2), such

Table 1 Definition of risk assessment indices

Risk	Method for calculating risk
Risk1	The number of road links blocked by collapsed buildings, which stranded people passed through.
Risk2	The number of road links at fire risk of level 1, which stranded people passed through.
Risk3	The number of road links at fire risk of level 2, which stranded people passed through.

Table 2 Conditions for simulation ([ ]; Basic pattern in this paper)

Direct evacuation	First evacuation start time	At once, [Distribution] + [Fire approach 1], Fire approach 2
	Search routes using safe roads?	[Yes], No
Two-stage evacuation	First evacuation start time	[Distribution] + [Fire approach 1], Fire approach 2
	Avoid congestion?	[Yes], No
	Search routes using safe roads?	[Yes], No
	Second evacuation start time (after the occurrence of an event)	0min, 15min, 30min, [Fire approach 1], Fire approach 2

as parks or vacant lots, were considered to be safe. Next, risk assessment indices were set (Table 1) in order to quantify risks during evacuation. From the standpoint of safety, it is desirable if the above risk of evacuations should be reduced.

Evacuation methods, walking speed, path search methods, and activity start times could each be varied in the simulation model constructed. To prioritize examining the influence of transient occupants and persons returning home, however, the data were analyzed under the conditions given below in Table 2.

5.2 Preliminary Analysis of Return Home Travel

We determined fluctuations (over time) in the number of persons returning home passing through Setagaya, for different combinations of starting points and arrival points, to learn about return home travel (Fig. 11). These fluctuations depended heavily on the timing of the disaster and on the combination of starting point and destination. We also found an unexpectedly large number of stranded people would be returning to homes in Setagaya from outside the ward, even several hours after the occurrence of the disaster.

5.3 Observations on Characteristics of the Simulation Model

In order to examine the importance of accounting for the presence of transient occupants and persons returning home, we analyzed the variations in people input into the simulation for 3 specific cases: (1) the population consisting only of occupants remaining in the area, (2) that population plus transient occupants, and (3) that population plus transient occupants and persons returning home. Fig. 12 shows the increases in stranded people in comparison to the first population. This figure indicates that, in case (2), the time-based changes in transient occupants strongly affect the number of stranded people, specifically, including them increases the number of stranded people, and in case (3), the number of stranded people is greatly increased by the inclusion of persons returning home in the daytime, when there would be many persons returning home. Examining the results by age group, there is an increase in child

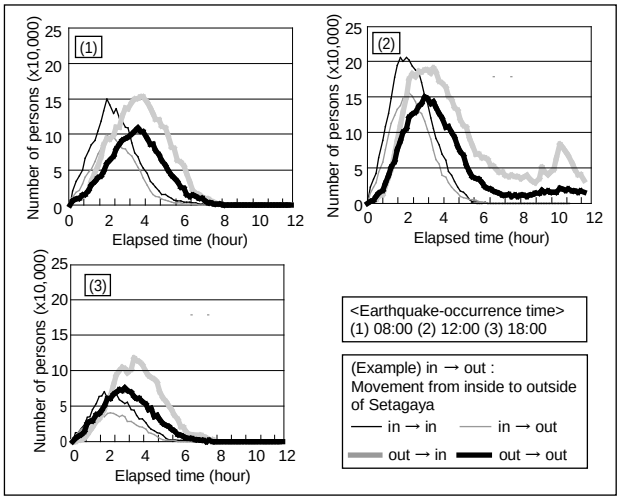


Figure 11 Fluctuations in the number of persons returning home passing through Setagaya ward

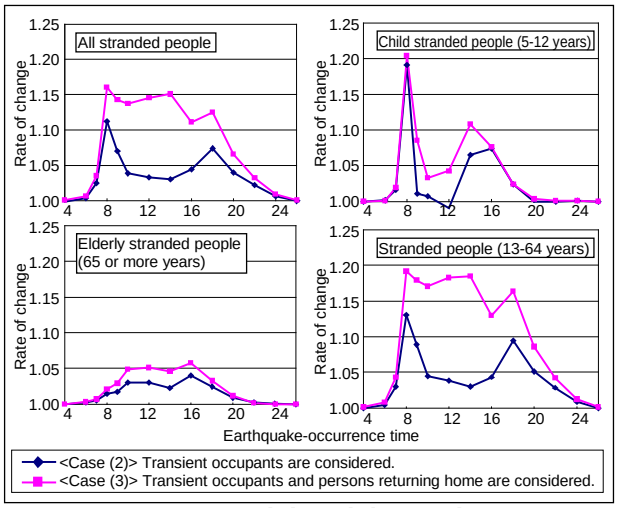


Figure 12 Increase in stranded people by considering transient occupants and persons returning home (attribute-based)

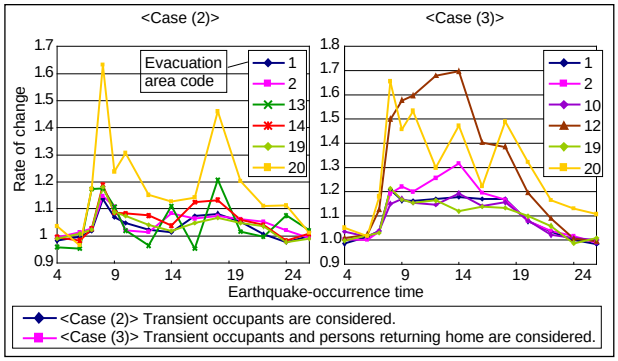


Figure 13 Increase in stranded people by considering transient occupants and persons returning home (in evacuation area)

stranded people (5–12 years) in the morning and evening, but the elderly population (65 or more years) showed little variation. In contrast, the reader can see that stranded people in the 13-to-64-year age group grew by about 20% during the 08:00-to-17:00 time frame. More specifically, the presence of transient occupants and persons returning home, which has previously been unaccounted for, may cause an approximately 20% increase in the number of stranded

people estimated for the peak hours period. This is an amount that cannot be ignored.

Next, we consider the number of stranded people in evacuation areas. Fig. 13 indicates the evacuation areas with high rates of increase in cases (2) and (3). There appeared a large influx of railway passengers at the evacuation areas around locations with high densities of railway lines. Previous investigations regarding the numbers and locations of evacuation areas have usually been based on the numbers of local residents, but in an urban area with a highly developed transportation network, it seems essential for the planning of evacuation areas to account for the presence of transient populations on railways and other traffic arteries, especially during the morning and evening rush hours.

We analyzed the effects of incorporating property damage into the simulation model to address the closure of streets due to urban fires and building collapse. Most previous simple simulations of evacuation activities did not incorporate property damage or the timing of evacuations in order to keep the models from becoming too large and complicated. In actuality, however, because the timing and routes of evacuations would vary with the extent of property damage, there is a large element of chance in the safety and efficiency of any evacuation. Therefore, the composition ratios of the stranded people was compared (Fig. 14) in terms of each sub-group of stranded people (residents, occupants of facilities other than their own residences, and transient occupants) between the case when everyone in some area is evacuated without taking into consideration property damage and the case when the time for beginning evacuation was decided after considering the property damage situation. We can see that there is a greater fraction of non-resident stranded people, especially during the day, if planners take property damage into account.

5.4 Risk Assessment in Travel to Evacuation Areas

The simulation was executed, accounting for all occupants (whether in buildings, transient, or on their way home), and the risks during evacuation to open areas were evaluated. The cases of two-stage evacuation and direct evacuation were compared (Fig. 15). Residents at home make up a majority of the stranded people at night, and so in this case, the risk is greatly reduced by organizing a two-stage evacuation. During the day, however, many of the stranded people, specifically occupants who are not home residents, would not comply with a two-stage evacuation; therefore, ordering a two-stage evacuation would have relatively little effect on risk. That is to say, planners must anticipate that during the daytime, a sizeable fraction of the occupants are occupants of facilities other than their own homes and that these transient occupants will not know where the temporary refuges are and will head directly to evacuation areas. Walking time to refuges can be longer in a two-stage evacuation, depending on how stranded people are directed, in order to avoid congestion. However, because there are many individuals who would not evacuate to an evacuation area and whose routes would terminate at temporary refuges near their homes, if we evaluate walking

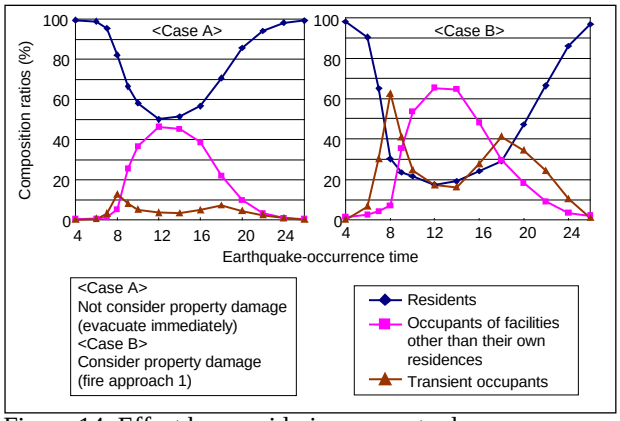


Figure 14 Effect by considering property damage

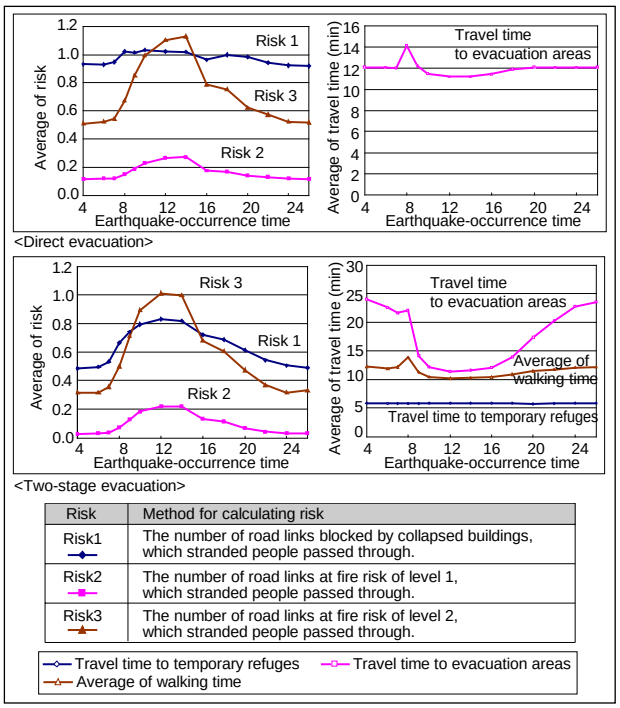


Figure 15 Comparison between direct evacuation and two-stage evacuation

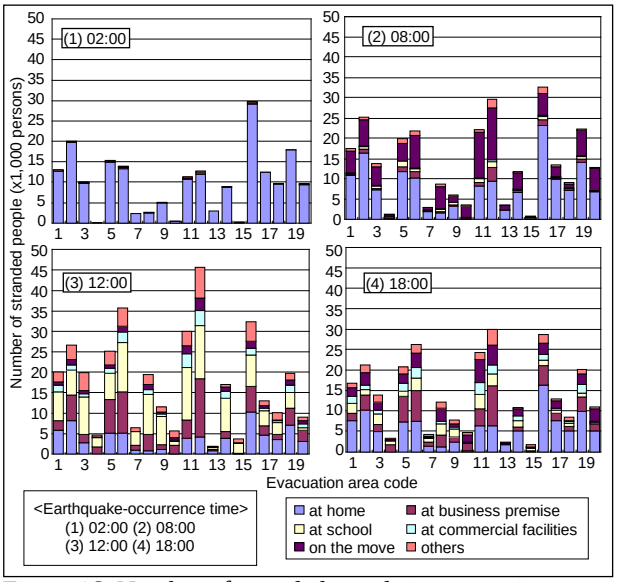


Figure 16 Number of stranded people in evacuation areas in terms of situation of persons

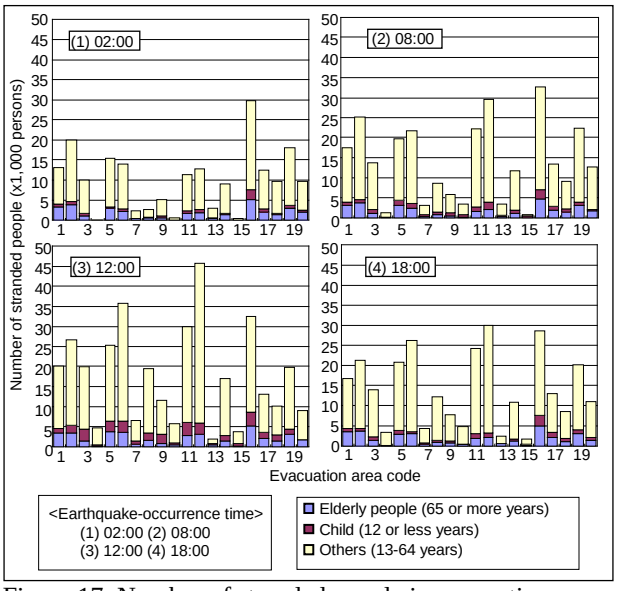


Figure 17 Number of stranded people in evacuation areas in terms of age groups

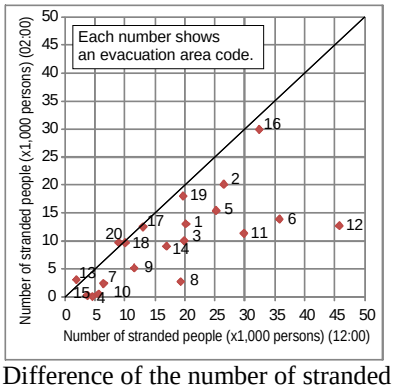


Figure 18 Difference of the number of stranded people in evacuation areas by earthquake-occurrence time

time averaged over all stranded people, travel time would be about the same in the two-stage case as in the direct evacuation case.

The numbers of stranded people moving to evacuation areas in a two-stage evacuation were compiled in terms of stranded people's attributes. Fig. 16 shows the results for different situations at the time of a disaster. In the early morning, many transient occupants would go to an evacuation area (6, 11, 12). During the day, many stranded people would go to an evacuation area from their business premises (5, 6, 12). Many would also go there from commercial facilities (6, 11, 12). Fig. 17 shows the results in terms of age group. The reader can see that not only the number of stranded people, but also the stranded people's profile varies greatly with the timing of a disaster. Comparing the cases of a disaster occurring at 2:00 AM and one occurring at noon (Fig. 18), nearly all the evacuation areas show increased numbers of stranded people in the latter case. The evacuation areas in locations surrounded by multiple railways and serving large regions tended to show particularly high differences between night and day.

All of the above results were due to the inflow into evacuation areas of transient occupants and persons returning home, who were not incorporated into previous evacuation simulations. A disaster mitigation planning must account for the fact that the numbers and types of stranded people will vary with the location of the evacuation area and the timing of the disaster.

6. CONCLUSION

A simulation model was constructed to describe human actions (waiting, returning home, and evacuating) after a devastating earthquake, taking into account property damage. A numerical simulation of people's reactions after a disastrous earthquake in Setagaya Ward of Tokyo was employed to verify the importance of accounting for the presence of transient occupants and that of persons returning home, and the importance of combining such a model with one describing property damage. Our analysis has revealed that the presence of transient occupants and persons returning home, who have not formerly been included in disaster prevention planning, may add about 20% to the numbers of stranded people during morning and evening peak periods, a quantity that cannot be ignored. Two-stage evacuations were also evaluated from the viewpoint of risks during evacuation to open areas. This indicated large variations in the numbers and attribute profiles of stranded people, depending on the location of evacuation area and the timing of the disaster.

Acknowledgements:

This research was part of an effort supported by a Grant-in-Aid (21310105) from the Ministry of Education, Culture, Sports, Science and Technology Health and Labor Sciences Research Grant, Scientific Research (B). The authors would like to give their special thanks to Mr. Takayuki Morisawa for computer-based numerical calculations. This paper was originally presented at the 6th International Conference on Pedestrian and Evacuation Dynamics - PED 2012, "Simulation Model of Evacuation Behavior Following a Large-scale Earthquake that Takes into Account Various Attributes of Residents and Transient Occupants".

References:

Osaragi, T., Hoshino, T. (2012), "Predicting Spatiotemporal Distribution of Transient Occupants in Urban Areas," In: J. Gensel et al. (eds.) 2012, Part 6. *Lecture Notes in Geoinformation and Cartography*, *Bridging the Geographic Information Sciences*, 307-325, Springer, Heidelberg.

Osaragi, T. (2009), "Estimating Spatio-temporal Distribution of Railroad Users and Its Application to Disaster Prevention Planning," In: M. Sester et al. (eds.) 2009, *Lecture Notes in Geoinformation and Cartography*, *Advances in GIScience*, 233-250, Springer, Heidelberg.

Osaragi, T., Shimada, R. (2009), "Spatio-temporal Distribution of Automobile Users for Disaster Prevention Planning (in Japanese)," *Journal of Architectural Planning and Engineering*, **641**, 1561-1568.

Osaragi, T., Shimada, R. (2009), "Spatio-temporal Distribution of Population on Weekdays and Holidays for Estimating Human Damages from Devastating Earthquake (in Japanese)," *Journal of Architectural Planning and Engineering*, **635**, 145-152.

Okada, K., Yoshida, K., Kashihara, S., Tsuji, M. (1979), "Presumption of Human Injury in Case of Earthquake's Fire and Consideration on Its Countermeasure: Part 1 Structure of Computer Simulation Model and Its Assumptions (in Japanese),"

Journal of Architecture, Planning and Environmental Engineering, **275**, 141-148.

Aoki, Y., Osaragi, T., Hashimoto, K. (1992), "A Simulation Model of Evacuation Behavior in the Fire-spread Urban Area Following Earthquake: Effects of Hearsay Information Process and Geographical Urban Image (in Japanese)," *Journal of Architecture, Planning and Environmental Engineering*, **440**, 111-118.

Ueda, R., Seo, K., Motoki, K. (2007), "A Simulation of Rescue Activity for Weak People in Disaster during Post-earthquake Fire Focusing on Local Disaster Mitigation: A Case Study at a Densely-populated Wooden District in Asagaya and Koenji, Suginami, Tokyo (in Japanese)," *Journal of Architectural Planning and Engineering*, **622**, 137-144.

Muraki, Y., Kanoh, H. (2004), "The Effectiveness of Communication on Wide Area Simulation of Disaster Evacuation Using Multiagent Model (in Japanese)," *IPSJ SIG Technical Report*, **130**, 69-72.

Fujioka, M., Ishibashi, K., Kaji, H., Tsukagoshi, I. (2002), "Multi Agent Simulation Model for Evaluating Evacuation Management System against Tsunami Disaster (in Japanese)," *Journal of Architectural Planning and Engineering*, **562**, 231-236.

Suzuki, T., Imamura, F. (2005), "Simulation Model of the Evacuation from a Tsunami in Consideration of the Resident Consciousness and Behavior (in Japanese)," *Journal of Japan Society for Natural Disaster Science*, **23**(4), 521-538.

Ohata, D., Takai, N., Kagami, H. (2007), "Spatial Evaluation of Tsunami Refuge Facilities in the Central Kushiro City: Simulation of Evacuation Behavior from Tsunami Utilizing Multi Agent System Part 2 (in Japanese)," *Journal of Architectural Planning and Engineering*, **612**, 87-91.

Osaragi, T. (2012), "Modeling a Spatiotemporal Distribution of Stranded People Returning Home on Foot in the Aftermath of a Large-scale Earthquake," *Nat Hazards*, DOI 10.1007/s11069-012-0175-8.

Tokyo Fire Dept. (2001), "The Development and Practical Use Policy of Assessment Technique of Disaster Prevention for Earthquake Fires (in Japanese)," Tokyo Metropolis.

Murao, O., Yamazaki, F. (2000), "Development of Fragility Curves for Buildings Based on Damage Survey Data of a Local Government after the 1995 Hyogoken-nanbu Earthquake (in Japanese)," *Journal of Architectural Structure and Construction*, **527**, 189-196.

Nishimura, K., Osaragi, T. (2009), "Spatio-temporal Distribution of Railroad Users in the Vicinity of Terminal Station (in Japanese)," *Proceedings of Geographical Information Systems Association*, **18**, 5-8.

Tokyo Regional Disaster Prevention Plan (2003), "Tokyo Regional Disaster Prevention Plan: Earthquake Disaster (in Japanese)," Tokyo Metropolis.

Tokyo Regional Disaster Prevention Plan (2006), "Summary on the Damage Assessment of Earth-quake Directly under Tokyo (Interim report) (in Japanese)," Tokyo Metropolis.

Midorikawa, S., Fujimoto, K., Muramatsu, I. (1999), "Correlation of New J.M.A. Instrumental Seismic Intensity with Former J.M.A. Seismic Intensity and Ground Motion Parameters (in Japanese)," *Journal of Social Safety Science*, **1**, 51-56.

JOINT CONFERENCE PROCEEDINGS
9th International Conference on Urban Earthquake Engineering/ 4th Asia Conference on Earthquake Engineering
March 6-8, 2012, Tokyo Institute of Technology, Tokyo, Japan

EVALUATION OF CAR EVACUATION METHOD AGAINST TSUNAMI USING MICRO SIMULATION

Kohei Onomura[1], Makoto Fujiu[2], and Kazuyuki Takada[3]

1) Graduate Student, Dept. of Civil and Environmental Engineering, Tokyo Denki University, Japan
2) Ph.D. Candidate, Dept. of Interdisciplinary Information Studies, The University of Tokyo, Japan
3) Professor, Department of Civil and Environmental Engineering, Tokyo Denki University, Japan
08rk043@ms.dendai.ac.jp, fujiu@iis.u-tokyo.ac.jp, takada@g.dendai.ac.jp

Abstract: At present, Tokyo metropolitan area has two kinds of natural mega-hazard: M.7 class inner-plate earthquake and Tsunami. Central Disaster Prevention Council which is the supreme organization of disaster affairs in Japan has warned about them in published reports. Right after the 2011 off the Pacific coast of Tohoku earthquake, the railway system in Tokyo metropolitan area completely shut down so that a large number of people had difficulty in moving. So far, many expertise in disaster prevention have proposed that such people should keep staying same place where they encountered big earthquake for their safety. However, it was observed that after the earthquake a lot of people tried to go home on foot even though the trip distance was quite long, and many person who commuters unable to get home go to home through the dangerous zone which are fire dangerous zone and building damage dangerous zone. This paper analyzes the behavior of persons who commuters unable to get home under the 2011 off the Pacific Coast of Tohoku Earthquake using mobile GPS data. Authors proposed and developed smart phone application based on the previous analysis.

1. INTRODUCTION

Massive destruction was brought to the north-eastern region of Japan when the 2011 off the Pacific coast of Tohoku Earthquake occurred at 14:46 (JST) on March 11th, 2011. In Tokyo metropolitan area where maximum of 5-upper seismic intensity (JMA) was recorded, the earthquake suspended the transportation system such as bus and train services. As the result, many people tried to return home on foot. However not all were successful and many of them ended up going to emergency shelters put into place or waited the recovery of public transportation for a long time.

According to the 10th census on transportation in Tokyo metropolitan area, approximately 9,500,000 commuters use public transportation system per day and the average travel time was 68 minutes long. It is evident that once the public transportation system fails, a great number of people will face difficulty in returning home.

Nakabayashi (1992) researched the relation between the distance to home and the success rate of returning home. He mentioned that all the people could return their home if the distance is less than 10km and the rate decreases by 10% per additional kilometer. Furthermore, people face difficulty in returning home if the distance is more than 20km. However, on March 11th, 2011, there were those who could not return home even though the distance was less than 10km and those who succeeded in returning home even though the distance was more than 20km. Shimohara et al. (2010) and Osaragi (2008) examined disaster prevention plans by estimating a behavior model of the commuters in case of devastating earthquake. However, these studies may not fully reflect the actual behaviors as mentioned above.

Transportation system will be completely shut down if the Tokyo Metropolitan Inland Earthquake with magnitude-7 level occurs. Tokyo Metropolitan Government has worked on establishing new ordinance which asks companies to stock emergency supply in the office buildings. This countermeasure would contribute to keep employees staying in the building until the transportation system recovers.

In order to study the effective disaster prevention countermeasures regarding the evacuation of affected people after the large scale earthquake, we analyzed the behaviors of the affected commuters by the 2011 off the Pacific coast of Tohoku Earthquake on March 11th, 2011.

Hiroi (2011) conducts similar study and estimated choice behavior model of the affected commuters with using questionnaire survey data. However it is not verify whether they succeeded in returning their home.

In this study, we have analyzed the behavioral characteristics of the affected commuters using a GPS data. The respondents of the survey were the affected commuters who faced difficulty in returning home.

2. CHARACTERISTICS OF ACTIONS ON THE DAY OF THE EARTHQUAKE

2.1. FLAG INDICATOR OF TRAVELING

The figure-2 shows the percentage of people's traveling from the affected areas after the earthquake.

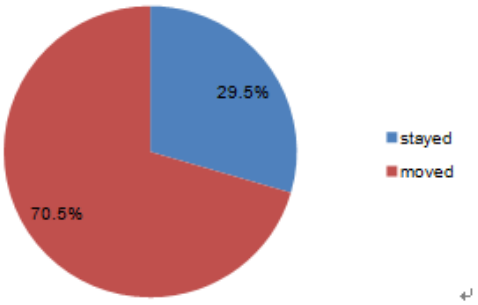


Figure 2. percentage of moved or stayed.

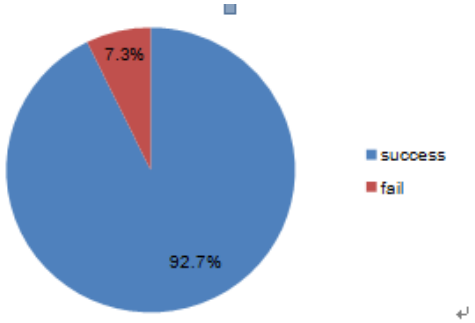


Figure 4. the success or failure of the go home.

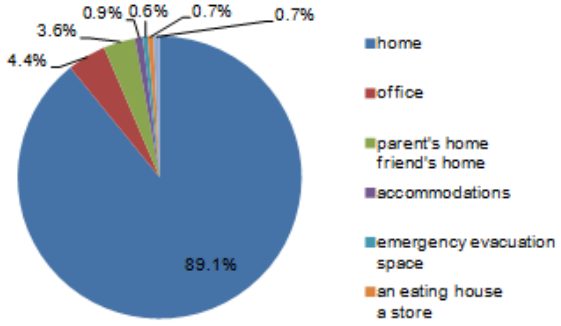


Figure 3. percentage of destination

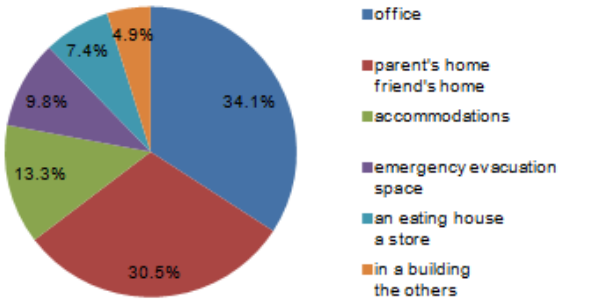


Figure 5. stay place of the return abandonment person

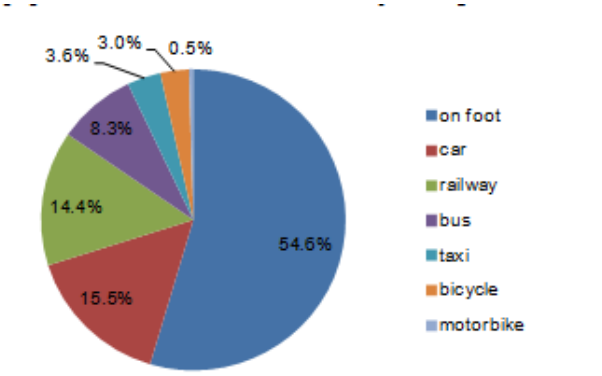


Figure 6. use transportation.

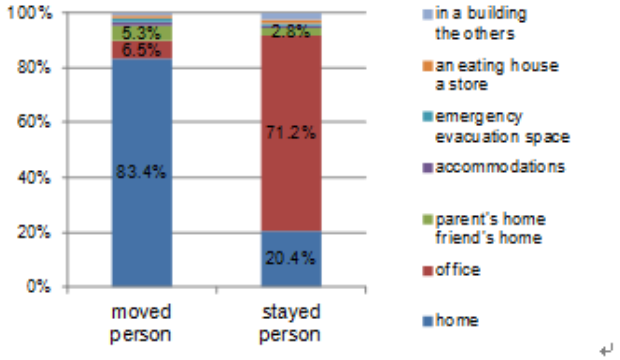


Figure 8. stay place of moved person and stayed person

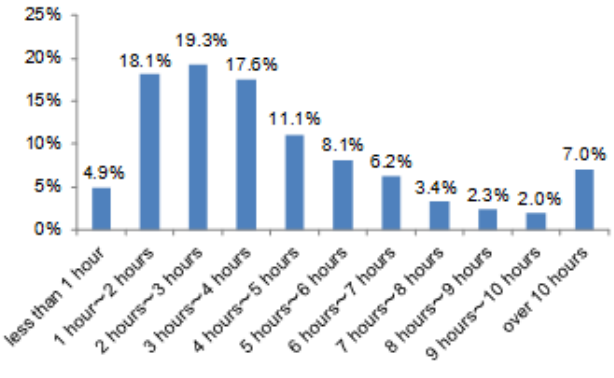


Figure 7. time required of go home.

29.5% of the people did not move at the time of the earthquake while 70.5% of the people tried to move. It became clear that 89.1% of the people who tried to move were trying to return home. Thus we decided to investigate into further details to find out the situation that affected the decision making process and to find out whether those who hoped to return home actually succeeded in returning home. The results will be presented in the next chapter.

2.2. SITUATION OF HOME RETURNING ON THE DAY OF THE EARTHQUAKE

The figure-4 indicates the result of the people's attempt to return home. 92.7% of the people succeeded in returning home. The figure-5 shows the percentage of the final place of stay of those who could not return home. 34.1% of them stayed at their company, 30.5% at family and friends' house, 13.3 % at hotels, 9.8% at emergency shelters. It became clear that people tried to return home once but chose to stay according to the situation.

2.3. RETURNING ACTIVITY ON THE DAY OF THE EARTHQUAKE

The figure-6 indicates the major means of transportation for those who attempted to return home. For those who used multiple means, each individual chose their main means of transportation in the order of car, train, bus, taxi, motorbike, bicycle, and walking. Out of those who attempted to return home, 54.6% tried to return home by walking, 15.5% by car, 14.4% by train, 8.3% by bus, 3.6% by taxi, 3.0% by bicycle, and 0.5% by motorbike. This fact indicates that more than half of the population who use train on a daily basis had attempted to return home by walking. The figure-7 indicates the amount of time spent for returning home. Most people spend about 2-3 hours and 30% of the people spent more than 5 hours.

3. ANALYSIS ON THE BEHAVIOR TO REMAIN

Firstly, we analyzed the final location of stay of those who stayed and those who moved. The figure-8 indicates the final location of stay organized according to the means of transportation. 83.4% of those who responded "attempted to move" indicated their own home as final location of stay while 71.2% who responded "to stay" indicated their companies as final location. From this observation, the affected population can be divided into two major categories, those who wish to return home and those who stay.

Secondly, we analyzed the characteristics of the desired location of stay. In this study, we have distinguished three types of initially desired location of stay namely "home", "other than home", and "remaining". The figure-9 shows the relationship between the linear distance to home and desired location of stay. The result indicated that less people wished to return home as the distance to home increased and more people wished to remain where they were. The result also showed that 27% of the affected people wished to return home even when their home was more than 40 km away.

4. BEHAVIOR ANALYSIS FUSING GPS DATA

We analyse commuters' behaviour under large scale disaster in Tokyo Metropolitan area. It became clear that stranded commuters' pass through the fire dangerous zone and building collapse zone for going his/her home. It is very dangerous for stranded commuters' under large scale disaster in Tokyo Metropolitan area as shown in fig.9 and fig. 10.

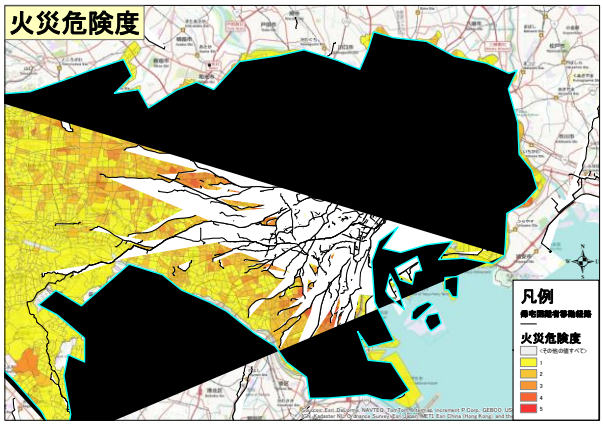


Figure .9 Behaviour route with fire zone

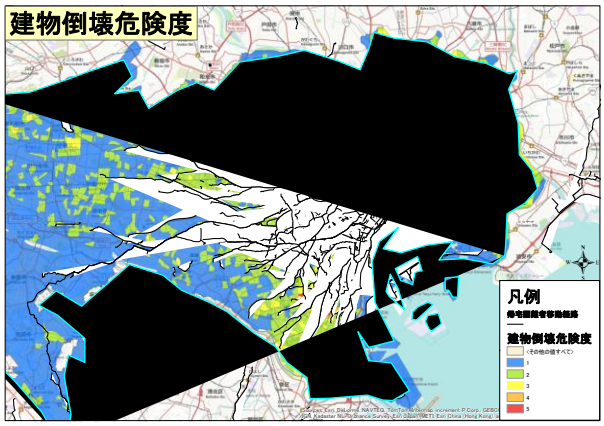


Figure .10 Behaviour route with building collapse zone

5. CONCLUSION AND FUTURE PROSPECTS

This study investigates the behaviour of the people having difficulties in going home after the 2011 off the Pacific coast of Tohoku Earthquake occurred.

As the result of this study, it becomes clear that approximately 70% of the affected people attempted to move and approximately 92% of those who attempted to return home managed to do it.

We clarified that many affected people had attempted

to move and many of them succeeded in doing it. However, it is estimated that Tokyo Metropolitan Inland Earthquake would bring more severe condition such as shut down of transportation services, massive fire, building collapse, road congestions and so on.

Thus, in order to be prepared for the coming large scale earthquake in Tokyo metropolitan area, it is necessary to prepare an effective countermeasure such as storing of necessary items and securing of safe places to stay, announcing the employees to remain until the transit system recovers, and establishing a procedure of safety confirmation of family members and friends.

On the other hand, it is desirable to prepare safe environment to return home for those who attempt to return home. In order to accomplish it, development of a method of safe evacuation is required, considering the disaster level, distance to a home, and personal attributes.

REFERENCES

Ministry of Land, Infrastructure, Transport and Tourism. (2007). Big city traffic general survey metropolitan area report.

Nakabayashi, K. (1992). Development of Estimation Method on Obstructed Homeward Commuters after Earthquake Disaster. Journal of Comprehensive Urban Studies. Vol.47: pp.35-75.

Shimohara, S., Watanabe, Y., Shimazaki, T. and Kaneko, Y. (2010). Behavior Model for Return a home after Devastating Earthquake in the Tokyo Metropolitan Area. Journal of Social Technology Research. Vol.7: pp.45-53.

Osaragi, T. (2008). Modeling of Decision Making and Behavior for Returning Home After a Devastating Earthquake. Journal of Architectural Institute of Japan. Vol.73, No.634: pp.2679-2687.

Hiroi, Y., Sekiya, N., Nakajima, R., Waragai, S. and Hanahara, H. (2011). Questionnaire Survey concerning Stranded Commuters in Metropolitan Area in the East Japan Great Earthquake. Journal of Institute of Social Safety Science. Vol.15: pp.343-353.

Committee of Infrastructure Planning and Management, JSCE. (1995). Theory and Practice of Disaggregate Behavioral Model

10CUEE CONFERENCE PROCEEDINGS
10th International Conference on Urban Earthquake Engineering
March 1-2, 2013, Tokyo Institute of Technology, Tokyo, Japan

SPATIAL CHARACTERISTICS TRANSFORMATION OF SELF-BUILT AND DONATED POST DISASTER HOUSING

Syam Rachma Marcillia[1] and Ryuzo Ohno [2]

1) Graduate Student, Dept. of Built Environment, Tokyo Institute of Technology, Japan
2) Professor, Dept. of Built Environment, Tokyo Institute of Technology, Japan

Abstract: This study aim to evaluate and analyze the spatial characteristic by investigating the transformation of self-built and donated post disaster housing in Java. The development of self-built temporary and donated core structure housing to permanent housing was investigated with on-field questionnaires, interviews, and house plan data collection. The objective is to understand what residents' perceptions toward their dwelling space are and how they actualized it in the design of their restricted temporary condition to permanent self-built housing and compare it with the transformation of donated core structure post disaster housing. Results suggest that residents recognized the hierarchy of space arrangement in their dwelling as both private and social space which correlated with their space perception. Social interactions indeed important in Javanese dwelling therefore flexibility and open ended design in housing are advantageous for their post disaster recovery.

1. INTRODUCTION

There had been cases where emergency house reconstruction built in a short time without cultural sensitivity had resulted in rejection of ill designed settlement. In contrary, some community based reconstruction housing has good response to residents' lifestyle and long –term needs because its open ended design that facilitated the cultural needs. These highlight the importance of understanding cultural background in the design of a dwelling as stated in Rapoport (1987), it is necessary to consider both why environments should be culturally responsive and to whom they should be culturally responsive and, consequently, how.

Social behavior is one of the important cultural backgrounds in Indonesia dwellings and Java specifically. For Javanese, a house is living environment that represent the philosophical concept of the society itself (Tjahjono, 1989). In previous researches, traditional 'margersari' housing and other public housing so called 'core house' consist of 'guest room', 'bedroom' and 'kitchen'. (Ikaputra,1992). In the public housing also, 'core house' alteration start with the expansion of double/triple size of 'guests room' which is a social space and then private space 'bedroom'.(Yoyok S., 1993).

An earthquake measuring Mw 6.3 (USGS and ERI) hit Java island of Indonesia with an epicenter of about 20 km south of Yogyakarta on Saturday, 27 May 2006. It had displaced up to 200,000 people from their homes. Housing reconstruction program were undertaken by many parties, NGOs and government. Based on preliminary survey two-weeks after the earthquake, even in early stage of Java 2006 earthquake recovery we found the existence of 'guest area' in temporary tents and house. Although their needs of functional room (bedroom, kitchen, etc.) are not fully accomplished within the house yet, the importance to facilitate social interaction is express and actualizes in the 'guest area'. Apparently social behavior still has influence in Java dwellings. Correspondently, in this study it is believed in that social behavior inevitably still an important cultural factor even in post disaster housing. For this paper, data on physical setting as well as residents' spatial perception and activities in self-built and donated post disaster housing are interpreted in the emphasis of the dwellings usage and adjustment for personal-social space. Residents' evaluation and participation in community activities are also studied to understand residents' perspective on their social interaction. It is indispensable that we grasp the transformation process of the space arrangement and its relation to residents' spatial perception and activities in the house to reveal dwelling space formation as a whole.

2. RESEARCH METHOD

Two study cases in Java 2006 earthquake self-built and donated core structure post disaster housing are investigated and considered as 'constraint dwelling' because there is a change of situation from their ideal living environment to their 'temporary' restricted condition which can acts as inhibiting environment and therefore adjustments are necessary to fulfill their lifestyle needs and ideal living

environment.

The study presumed that the development of temporary house to permanent house will be the reflection and actualization of residents' cognition of suitable dwellings in self-built post disaster housing, and the development of donated core structure house would be similar to self-built housing which reflected how the residents' spatial perception is actualized to their activities and space arrangement in their dwellings.

2.1 Research Areas

Study in Java post disaster housing was carried out in Bantul, district/regency of Yogyakarta, as the most affected region of the disaster. More than 2000 residents were killed, thousands are injured and 80% of houses were damaged or destroyed. Bantul is located 11 km to the southern part of Yogyakarta (Figure 1). The total area is approximately 508 km2 with more than 80% of its population is Moslem. The administrative area consists of 17 sub-districts, 75 villages and 933 sub-villages. The first case study area is self-built post disaster dwellings located in three sub-villages of *Ketonggo, Bawuran and Tegalrejo, Yogyakarta*. The three sub villages were selected because they were high damages areas. The respondents were chosen based on the condition of the houses after the earthquake where original houses totally destroyed and most of the residents rebuilt the permanent post disaster houses based on their own design.

Two integrated surveys were taken in 2 years difference to see the development from self-built temporary house to permanent house. In first survey, a total of 39 respondents were acquired. Most of the respondents are original residents of the surveyed area and the rebuilt houses located in their own land. The second survey targeted same respondents from first survey, but from 39 respondents, only 33 respondents able to be surveyed again because some of them moved to different areas.
The second case study area is donated post disaster housing in Tembi village, Sewon, Bantul, Yogyakarta. In Java earthquake 2006, not all Tembi houses were collapsed, therefore only few of the collapsed houses received donation. The donated house is basically a core house structure consist of six concrete column and roof. The constructions of wall as well as space arrangement were made by the residents themselves. The survey was undertaken once, by that time most of the donated core structure house had become permanent houses. A total of 23 household were interviewed and house plan were taken. Some core structure houses that were not used as permanent house are excluded from the analyses. Both case study area locations are shown in figure 1 below. The details descriptions and house modification of each respondent's houses in both study cases are shown in table 1 and table 2.

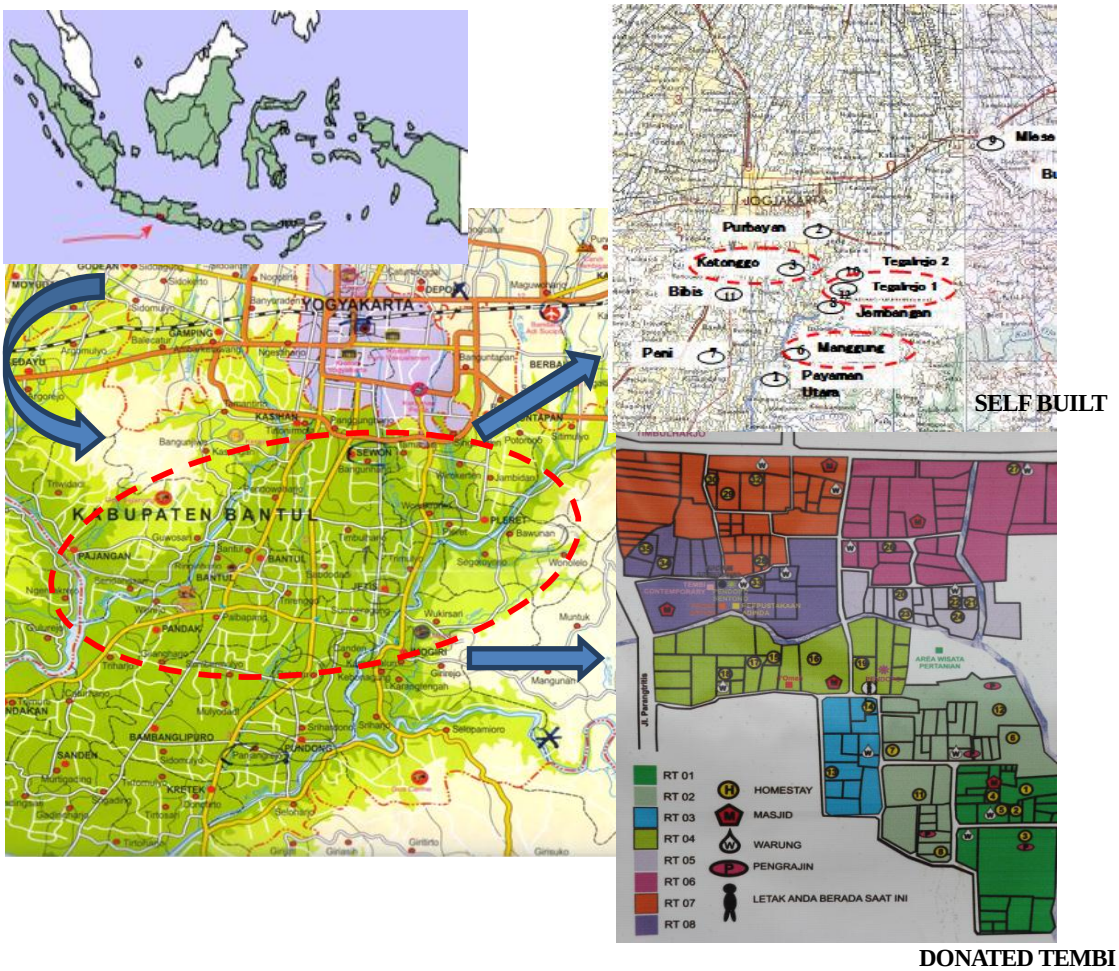


Figure 1 Location area of research

Table 1 detail description and modification made in self-built temporary to permanent post disaster houses

Quest. No.	K2	K3	K4	K5	K6	K9	M2	M3	M4	M5	M7	M8	B1	B3	B4	B5	B7	B8	B9	B10	B11	B12	B13	B14	B15
HH size	4	1	6	4	5	4	5	4	3	1	3	3	2	4	4	7	3	7	4	2	4	5	6	6	4
No. of Child	2	0	3	2	3	2	3	2	1		1	1	0	2	2	2	1	5	2	1	2	4	2	4	2
moving in area (year)	46	2	2	5	8	8		65	40	60	30		2	11	23	34	66		47	35	30	60	8	50	48
Total floor area (sq. m)	138.6	70.8	90.37	62.65	121.4	57.67	123.3	87.16	168.7	64.88	71.34	91.09	119.1	76.49	224.4	112.5	108.8	112.5	130.1	43.98	118.5	59.51	149.2	86.89	62.58
Ownership	OWN	OWN	OWN	OWN	OWN	OWN	OWN	OWN	OWN	OWN	OWN	OWN	OWN	OWN	OWN	OWN	OWN	OWN	OWN	OWN	OWN	OWN	OWN	OWN	OWN
modification																									
addition garage			1																				1		
addition guest room					1										1	1			1		1	1	1	1	
addition family room						1								1	1			1	1		1	1		1	
addition guest + family room	1		1	1									1							1					1
addition family + bedroom					1																				
addition bedroom	2		1				2	1	2	1		1	1	2	3	1	1	1	2	1	3	1	2	2	3
addition prayer room	1		1			1			1					1		1	1		1						
addition terrace	1				1		2	1	2	1	1	2		1	1	1		1			1		1		
addition storage			1					2	1				1			1	1	1			1		1	1	
addition kitchen	1				1		1		1	2		1				2		1	1		1	1			
addition kitchen outdoor																									
addition kitchen + storage						1									1								1		1
addition dinning room											1						1						1		
toilet out to in																									
addition toilet	1		2	1	2	1	1	1	2	2	1	1			1	1	2	1		1		1	1		1
addition washing area	1				1			1	1	1	1	1		1	1		1		1	1		1			1
addition corridor					2		2		2					1	1							1		1	
addition animal house									1					1	1				1		1				
addition store/home business	1															1							1		
addition harvesting space																		1							
addition stair							1																		

Table 2 detail description and modification made in Tembi core structure house to permanent post disaster houses

Quest. No.	TE1	TE2	TE3	TE4	TE5	TE6	TE7	TE8	TE9	TE10	TE11	TE12	TE13	TE14	TE15	TE16	TE17	TE18	TE19	TE20	TE21	TE22	TE23
HH size	3	5	2	4	4	1	6	4	2	3	7	2	7	5	3	5	6	6	3	2	6	4	2
No. of Child	1	1	1	2	1	0	1	1	0	1	3	0	0	1	1	1	2	1	1	0	2	2	0
moving in area (year)	native	native	native	native	native	native	native	native	native	native	42	native	native	native	7	native	20	22	44	59	46	40	25
Total floor area (sq. m)	90.7	81.7	113	201	110	122	47.2	164	105	87.7	90.2	73.5	102	179	64.5	152	133	76.5	111	135	114	152	91.7
Ownership	OWN	OWN	OWN	OWN	OWN	OWN	OWN	OWN	OWN	OWN	OWN	OWN	OWN	OWN	OWN	OWN	OWN	OWN	OWN	OWN	OWN	OWN	OWN
house age (year)	2007	2006	2007	2007	2007	2007	2007	1977	2007	2006	2007	2007	2006	2007	2007	2007	2007	2006	2007	2007	2007	2007	2007
modification																							
addition garage																							
addition guest room				1												1					1	1	
addition family room								1						1					1		1	1	1
addition guest + family room																							
addition family + bedroom																							
addition bedroom					2			2					1	2		2		1			2		
addition prayer room				1	1			1											1			1	1
addition terrace	1	1	1	1		1	1	2		1	1	2	1	2	1	1	1	1	1	1	1	1	
addition storage			1		2	1		2	1			1	1	1		1	3			2	2		4
addition kitchen				1	1	1	1	1	1		1	1	1	1		1	1	1	1		1	1	1
addition kitchen outdoor		1								1													
addition kitchen + storage															1								
addition dinning room																1					1		1
toilet out to in		1	1	1		1		1	1		1		1	1	1								
addition toilet						1			1		1	1	2	1		1			1		1	2	1
addition washing area						1			1	1			1			2		1	2	1		2	1
addition corridor											1					1							
addition animal house																							
addition store/home business																			1				

2.2 Questionnaires and Interview

Questionnaires, in-depth interview and observation with the residents were conducted with the help of Gadjah Mada University volunteers. Each team consists of 2 people, one person was asked to sketch the house plan while the other interviews the resident. Information acquired as follows:

a. Background: Residents (age, sex, family, occupation, income, etc.) and house (structure, house age, land status, etc.)
b. House plan: room space, size, etc
c. Space usage :include personal and interpersonal activities
   - Personal activities in space which include: *personal biological needs* (eating, sleeping, etc), *entertainment* (watch TV, relaxing, etc), *work* (study, etc) and *household routines* (cooking, etc).
   - Interpersonal activities which include: location and behaviors in accepting different guest types in the house and interaction and frequency with neighbors.
d. Cognition of space on front/back, hidden/seen, public/private, flexibility, etc.

3. RESEARCH RESULTS

3.1 Importance of social interaction

In self-built post disaster housing, 95% of the residents' values traditional social behavior where they still cherished traditional Javanese living practices and community values such as *gotong royong* (spirit of helping one another through good and bad) and *kekeluargaan* (feeling of extended kinship in which the community is considered to be one big family). Many recovery programs operated by NGOs and the government were community-based and designed to incorporate such traditional practices into the rehabilitation process. Woman were gather cook together in the public kitchen and arrange the usage of public kitchen and usage of wells, while the man gather together to clean up wreckage debris and built the temporary house together. Over 60% said these values grew even more significant to them following the earthquake. Accepting guest activities in the house occurs 41% for everyday occasions and 90% residents involved in community gathering of their neighborhood which required them to accept large occasion guests in their house. Borrowing behavior between neighbors also take place for more than 30% within a week which include borrowing kitchen utilities, appliances and even food materials. The high importance of social interaction had led many recovery programs operated by NGOs and the government to be community-based and designed to incorporate such traditional practices into the rehabilitation process.

Similar situations happen in Tembi donated core structure house post disaster housing. Approximately more than 90% (both heads of household and spouses) said that they participate in community activities with their own willingness, while only less than none feel obligated to participate and null for no participation. High participation to community activities is supported by their perception on the importance of the value and existence of community activities in their neighborhood. Approximately 80% head of household and 83% of spouses response is "I feel that community activities are very important" and approximately only about 10% for both heads of household and spouses said that "they are neutral, don't really have certain feeling". Unfortunately the incapability of dome house design to facilitate certain social interaction behavior results in the usage of outer space of the house and neighborhood as the 'guest area' or 'incidental social interaction space'.

3.2 Perception of space pattern in self-built and core structure post disaster housing

Space pattern development in self-built housing as well as Tembi core structure house development also showed the existence of private/public spaces even in the simplest house plan by using semi fixed element to differentiate private/public space such as the use of furniture, semi fixed partition, etc..

Perception of spaces is much related with needs of privacy and social interaction. Space pattern development also showed the existence of private/public spaces in simplest condition that can be illustrated as in Figure 2.

Respondents` cognition of privacy level toward type of room is shown in Figure 3. The highest privacy level is bedroom and respectively toilet and kitchen privacy level decreases. However terrace and multifunction room (integrated guest room and family room) and separated guestroom also family room is among the lowest priority of private space.

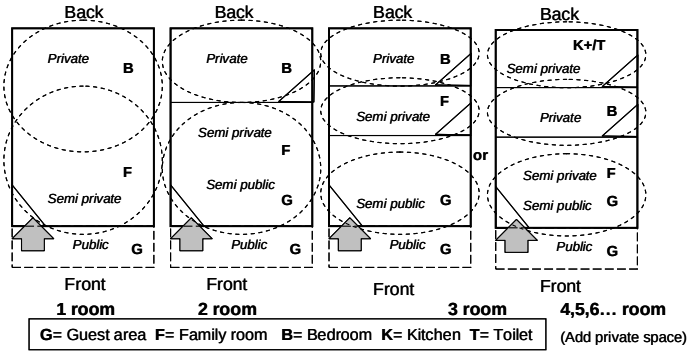


Figure 2 Development of space pattern post disaster housing

In figure 3, we can see that more than 40% respondent considered outdoor spaces; front yard and terrace, and only guest room as indoor spaces as the front part of their houses. On the other hand 45% respondent considered kitchen the highest as back part of the house. Other indoor rooms that considered as back part of the house are: bedroom and toilet, while outdoor spaces are backyard and wells.

Guestroom and family room are area that can be shown to guest by more than 45% and 30% respondents respectively and in agreement to the cognition of private/public spaces in Figure 6., bedroom, kitchen and toilet are areas that prefer to be hidden from the guests. Figures 6 and 7 indicate that front part of the house are considered as less private space and because of that the areas can be seen by their guest and back part of the house, which include especially bedroom, toilet and kitchen, is considered a more private space and thus is hidden from the vicinity of the guest

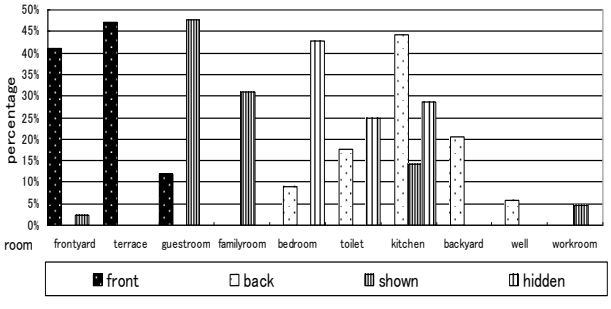


Figure 3 Cognition of front/back spaces and shown/hidden area by self-built post disaster respondents

Importance of private/public space is supported by residents' cognition of front/back area that is frequently associated to hidden/shown area to other people. These findings are relevant with previous research on traditional dwellings where front of house is outwardly-oriented domain where domestic prestige displayed in form of status

differences and formality in meeting others (Revianto, 1997). Residents' spaces cognition of private/public, front/back, shown/hidden are much related with 'self' (personal) and 'other' (interpersonal) space domain that actualize in the arrangement and allocation of the spaces. It showed embodied principal ideas underlying the formation of a domestic setting as place to live and interact with others in their post disaster housing.

3.3 Development from temporary or core structure house to permanent post disaster housing

3.3.1 Size and number of room expansion

Self-built housing expansion from temporary to permanent houses made by the residents within 2 years period after the earthquake indicates the need of guest room increases by 5 times its original size and 3.6 times its original total room number (Figure 4). However, total room number and addition of bedroom modification is still the highest overall adjustments which also indicate a high need of private space although its average room size actually decreases (Figure 4). There are also cases where both temporary and permanent house were used simultaneously by the residents show that guest area is one of the earliest function that move from temporary to permanent house which apparently have a better structures and overall appearance. This indicated the needs of having a 'good` image space for interaction with guests (findings supported by Revianto, 1997) In Tembi core structure housing, since were taken only once, the expansion analyses were made based on the condition of given core structure house at the beginning of donation that still being used. The spaces mostly contain multifunction room (which include accepting guest area and family room) and bedroom. The result indicates that multifunction room had changes to separate guestroom and family although some multifunction room still remained but overall of social space had increased (Figure 5). Terrace addition as social space is a new function in permanent house that large in overall size.

The expansion and separation tendency of guest area have relevant founding with public housing complex in Yogyakarta where most `core house` alteration cases started with the expansion of guest room to the front area and had doubled its original size (Yoyok, 1993).

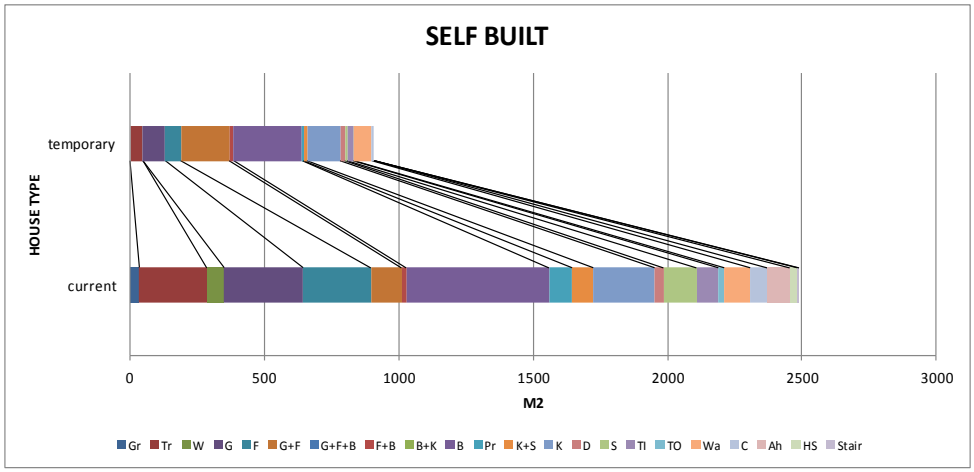
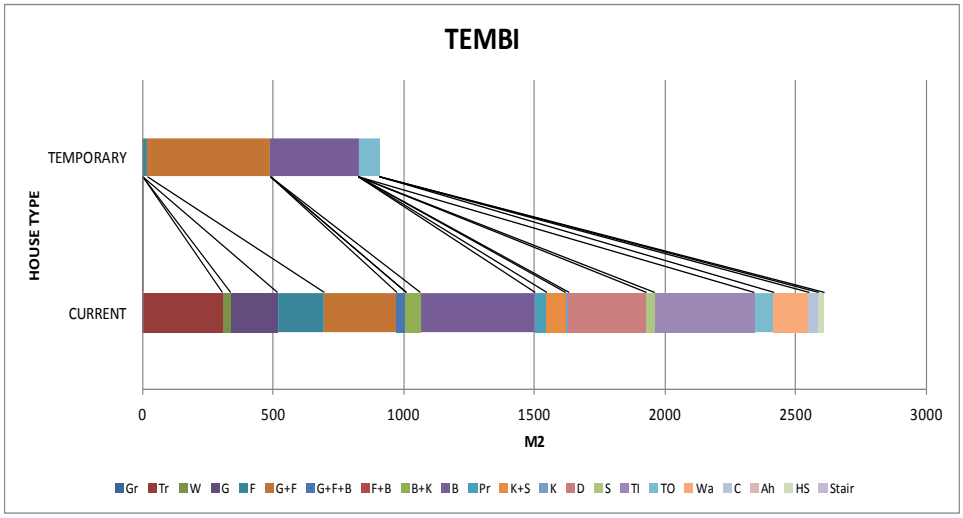


Figure 4 Diagrammatic charts of size expansion in self-built



Gr:garage	B:bedroom	TO:toilet outdoor
Tr:terrace	K:kitchen	Wa:washing area
W:work space	Pr:prayer room	C:corridor
G:guest room	S:storage	Ah:animal house
F:family room	D:dinning room	HS:harvesting space
MF:multi function room	TI:toilet indoor	

Figure 5 Diagrammatic charts of size expansion in donated Tembi

3.3.2 Room modification and space arrangement

Room modification from temporary house to permanent house in self-built housing as well as core structure house to permanent Tembi housing shows that bedroom is the highest modification that shows the need of more private space is high. The second highest room modification is the changes of location of outside guest room to inside the house, new addition to with family room in multi-function house that show the importance to have a separate guest room inside the house. The kitchen and toilet are also important spaces to have in the house. Details of space arrangement in temporary and permanent condition can be see in table 3 and 4.

Table 3 Space arrangement in self-built temporary and Tembi core structure post disaster houses

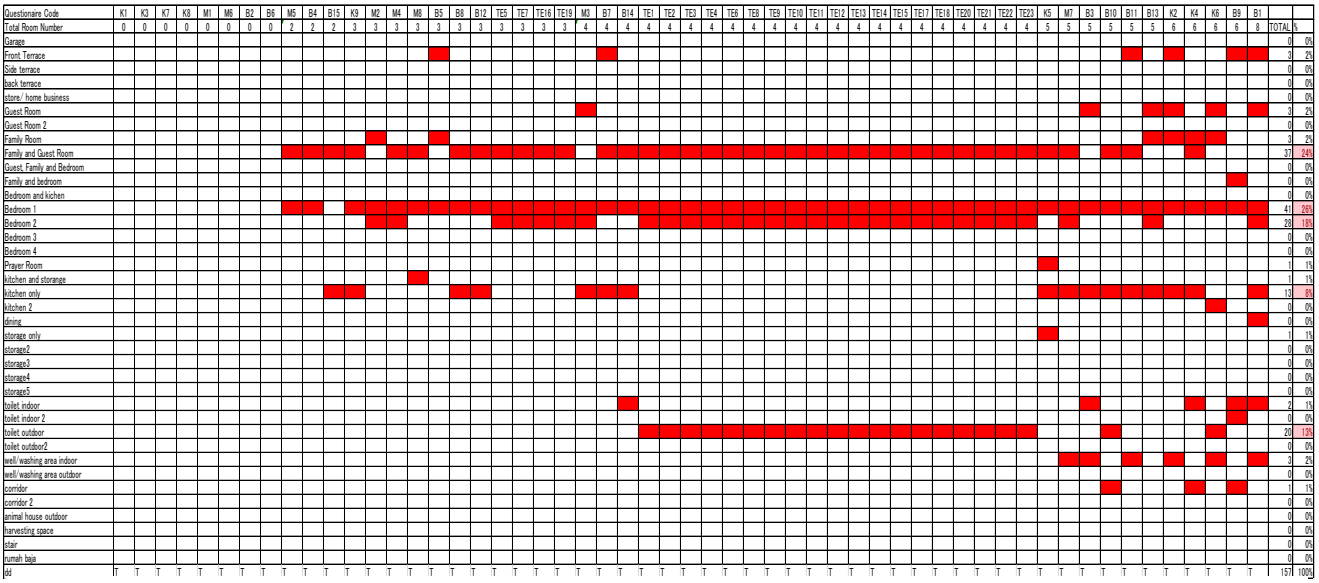
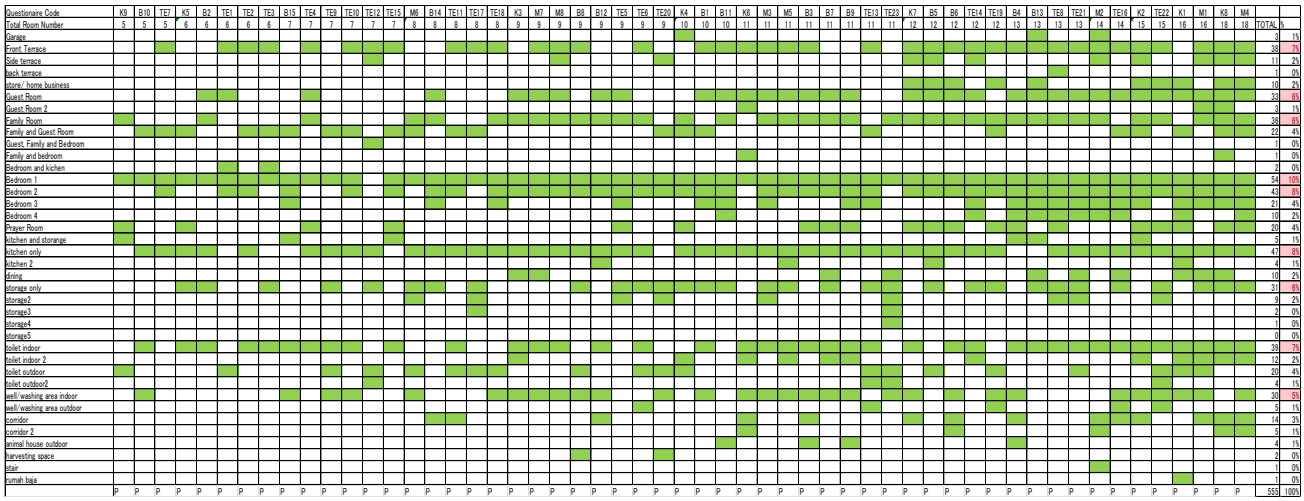


Table 4 Space arrangement in self-built t and Tembi permanent post disaster houses



4. Summary and Conclusion

In self-built as well as Tembi donated core structure post disaster dwellings, physical changes and development from temporary to permanent such as size and room number expansion, space modification, function changes, apparently show that guest area is inevitably an important social interaction space to be provided in the house. On the other hand, total room number and addition of bedroom is still the highest overall adjustments which also indicate a high need of private space. These show that both needs of social interaction space and private space are simultaneous exist. The duality spheres in the house also actualize in their cognition of spaces.

Respondents' cognitions of private/public, front/back, hidden/shown spaces are much related with the arrangement and allocation of 'self'(personal) and other'(interpersonal) space and how it is interrelated in spatial arrangement of fixed and semi-fixed elements of the house. These findings are relevant to Java traditional housing that contains both interrelated `self` and `others` domains (Revianto, 1997).

This research has once again highlighted the importance of social behavior (space) in Java dwelling even at in constraint situation. Meaning, values and ideals of social behavior are reflected on their cognition of spaces in the dwellings as well as their physical-behavior adjustments. As a dwelling, the house is not merely a shelter, but it's an actualization of meanings (Rapoport, 1969). For Java people, a house is living environment that represent the philosophical concept of the society itself. It is necessary that even in constraint dwelling such as temporary post disaster housing need to consider social behavior importance as culturally sensitive design for reconstruction recovery. Flexibility and open ended design in physical built environment would give an advantage in their critical transition to the new environment

Acknowledgements:

The author acknowledged support from G-COE Center for Urban Earthquake Engineering (CUEE) in Tokyo Institute of Technology for funding this research. A sincere thanks to Prof. Ryuzo Ohno for his support and guidance for this study. Last but not least, thanks to all Gadjah Mada Architecture students who helped me to do field survey and interviewed and to the people in New Ngelepen who are willing to help in this research.

References:

Ikaputra (1992) *Room Composition of Traditional Urban Settlement,; the case of magersari's house.* Annual Meeting Architectural Institute of Japan. Architectural planning and design rural planning 1992, 35-36.

Ikaputra (2008). *Response to Localize the Imported Culture.* Proceeding of the 14 World Conference on Earthquake Engineering October 12-17, 2008, Beijing, China

Rapoport (1969). *House Form and Culture.* Englewood Cliffs, N.J.: Prentice-Hal

Rapoport, A. (1987). On the cultural responsiveness of architecture. Journal of Architecture Education 41(1), pp. 10-15.

Revianto B.S (1997) *Omah, The Construction of Meanings in Javanese Domestic Settings.* Published master thesis. School of Architecture McGill University, Montreal

Tjahjono, G. (1989) Center and Duality in the Javanese Dwelling. In J.P Bourdier and N. AlSayyad (eds) *Dwellings, Settlements and Traditions: Cross Cultural Perspective.* Berkley: International Association for the Study of Tradition Environment.

10CUEE CONFERENCE PROCEEDINGS
10th International Conference on Urban Earthquake Engineering
March 1-2, 2013, Tokyo Institute of Technology, Tokyo, Japan

EVALUATION OF BUILDING DAMAGE RATIO IN ASAHI CITY, CHIBA PREFECTURE AFTER THE 2011 OFF THE PACIFIC COAST OF TOHOKU EARTHQUAKE AND TSUNAMI

Yoshihisa Maruyama[1)], Ken Kitamura[2)], and Fumio Yamazaki[3)]

1) Associate Professor, Dept. of Urban Environment Systems, Chiba University, Japan
2) Graduate Student, Dept. of Urban Environment Systems, Chiba University, Japan
3) Professor, Dept. of Urban Environment Systems, Chiba University, Japan
ymaruyam@tu.chiba-u.ac.jp, k.kitamura@chiba-u.jp, yamazaki@tu.chiba-u.ac.jp

Abstract: Tsunami fragility function is developed to assess damage to buildings because of tsunami. The fragility functions are expressed with respect to the inundation depth to predict the damage ratio of buildings. Asahi City, Chiba Prefecture, suffered from serious damage after the 2011 off the Pacific coast of Tohoku Earthquake and Tsunami. In this study, the fragility function is constructed using the results of numerical simulation of tsunami propagation and the building damage dataset compiled by Asahi City after the earthquake. Employing the fragility function, the numbers of damaged buildings in Chiba Prefecture are estimated assuming the occurrences of historical earthquakes.

1. INTRODUCTION

The 2011 off the Pacific coast of Tohoku Earthquake, which occurred on March 11, 2011, triggered an extremely large tsunami. The run-up reached a maximum height of 40.4 m in Tohoku district (The 2011 Tohoku Earthquake Tsunami Joint Survey Group, 2011). The Japanese National Police Agency (2011) confirmed more than 15,000 deaths and 2,900 people missing. According to the Cabinet Office, Government of Japan (2011), 92.4% of the fatalities in Iwate, Miyagi, and Fukushima prefectures resulted from drowning.

The tsunami also hit Chiba Prefecture. With 13 fatalities in Asahi City and two people reported still missing, the eastern part of the prefecture was severely affected. In Asahi City, 336 family units collapsed as a result of this event (Asahi City, Chiba Prefecture, 2011). These buildings were mainly affected by the tsunami, and liquefaction, although they were away from the most severely affected areas.

In this study, the damage ratio of buildings in Asahi City is evaluated with respect to the inundation depth obtained by numerical simulation. The damage dataset compiled by Asahi City is employed for the evaluation. Based on the relationship between the damage ratio and inundation depth, the fragility function is constructed. Finally, the number of damaged buildings in Chiba Prefecture is predicted assuming the occurrences of historical earthquakes.

2. NUMERICAL SIMULATION OF TSUNAMI PROPAGATION

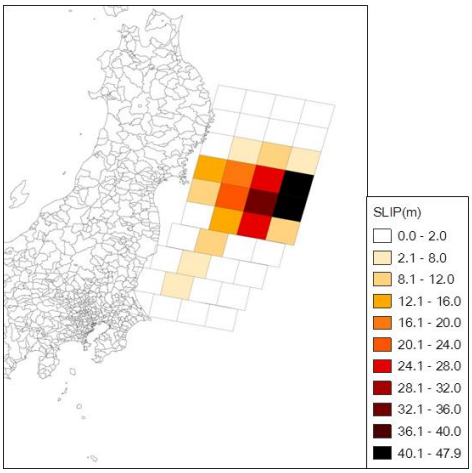
Numerical simulation of tsunami propagation after the 2011 off the Pacific coast of Tohoku Earthquake was performed to estimate the inundation depths in Asahi City, Chiba Prefecture. The seismic fault model developed by Fujii and Satake (2011) was employed to estimate the vertical displacement of the seabed. Figure 1 shows the fault model developed by Fujii and Satake (2011) (Fig. 1(a)) and the vertical displacement (Fig. 1(b)) estimated by Okada's method (Okada, 1985). Assuming the water layer to be incompressible, the estimated vertical displacement of the seabed was regarded as the initial profile of the tsunami.

We used the TUNAMI-CODE (Imamura, 1995) for modeling tsunami propagation and the resulting coastal inundation. The model employs a set of nonlinear shallow water equations where bottom friction terms are discretized by the leap-frog finite difference scheme. This model is widely used to simulate tsunami propagation and inundation on dry land (Koshimura *et al*., 2006). Based on the shallow water theory, the continuity equation can be expressed as

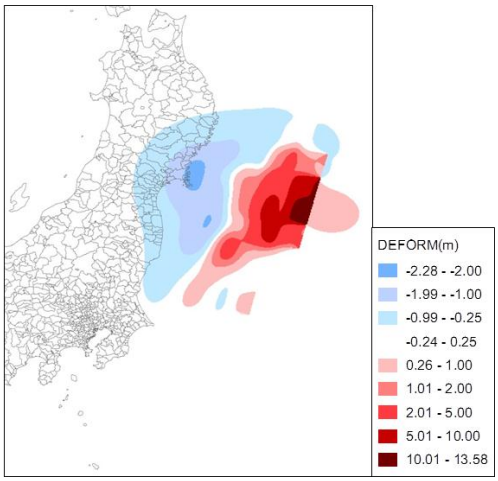
$$\frac{\partial \eta}{\partial t} + \frac{\partial M}{\partial x} + \frac{\partial N}{\partial y} = 0 \tag{1}$$

where M and N are the discharge fluxes in the x and y directions, respectively; η is the vertical displacement of the water surface above the still water level. The equations of motion are written as

$$\frac{\partial M}{\partial t} + \frac{\partial}{\partial x}\left(\frac{M^2}{D}\right) + \frac{\partial}{\partial y}\left(\frac{MN}{D}\right) = -gD\frac{\partial \eta}{\partial x} - \frac{gn^2}{D^{7/3}} M\sqrt{M^2+N^2} \tag{2}$$



(a)



(b)

Figure 1 (a) Fault model developed by Fujii and Satake (2011) and (b) vertical displacement of seabed as estimated by Okada's method (1985)

$$\frac{\partial N}{\partial t}+\frac{\partial}{\partial x}\left(\frac{MN}{D}\right)+\frac{\partial}{\partial y}\left(\frac{N^2}{D}\right)=-gD\frac{\partial \eta}{\partial y}-\frac{gn^2}{D^{7/3}}N\sqrt{M^2+N^2} \quad (3)$$

where D is the summation of η and the still water depth h, and n is Manning's roughness coefficient.

In the numerical simulation, the target region was divided into five sub-regions having grid lengths of 1350, 450, 150, 50 and 16.7 m. The sub-region characterized by coarse grids was set in the deep sea and the one with fine grids was set closer to the shore (Shuto, 1991). h for each grid cell was assigned using the bathymetry data collected by the Japan Coast Guard. The elevations of the land, determined by the Geospatial Information Authority of Japan (GSI) were also considered for estimating the inundated areas.

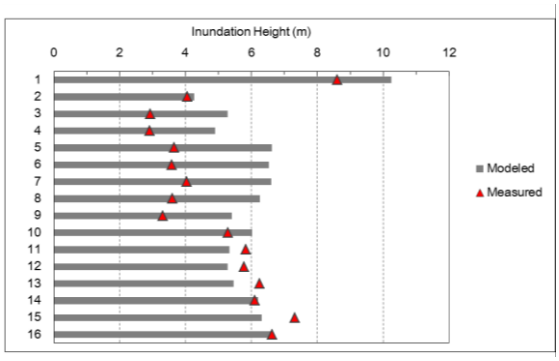
Manning's roughness coefficients were assigned with respect to the land use classifications, as listed in Table 1

Table 1 Definition of Manning's roughness coefficient in this study

Land use	Manning's roughness coefficient ($m^{-1/3}s$)
Residential district	0.040
Agricultural land	0.020
Forest land	0.030
Body of water	0.025
Others	0.025



(a)



(b)

Figure 2 (a) Locations of measurement points of tsunami inundation heights by the 2011 Tohoku Earthquake Tsunami Joint Survey Group and (b) comparison between the measured tsunami inundation heights and those estimated by numerical simulation in Asahi City, Chiba Prefecture

(Kotani *et al.*, 1998). We considered that tsunami propagation occurred for three hours after the earthquake. The time step in the numerical simulation was selected to be 0.15 s.

The result of numerical simulation was compared with the findings of tsunami surveys conducted by the 2011 Tohoku Earthquake Tsunami Joint Survey Group (2011). Figure 2 shows a comparison of tsunami inundation heights estimated by the numerical simulation with those measured in the eastern part of Asahi City. The locations of

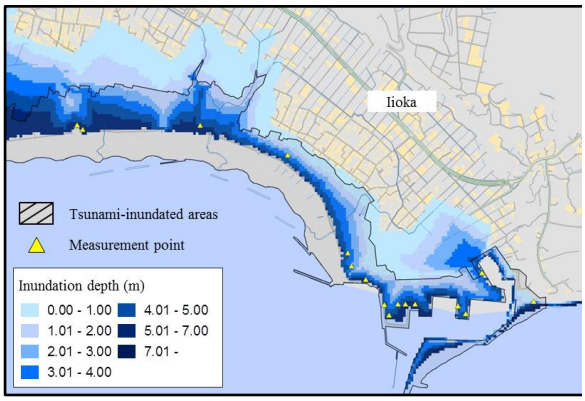


Figure 3 Comparison between inundation depths estimated by numerical simulation and the tsunami-inundated areas identified in the previous study (Kitamura *et al.*, 2012)

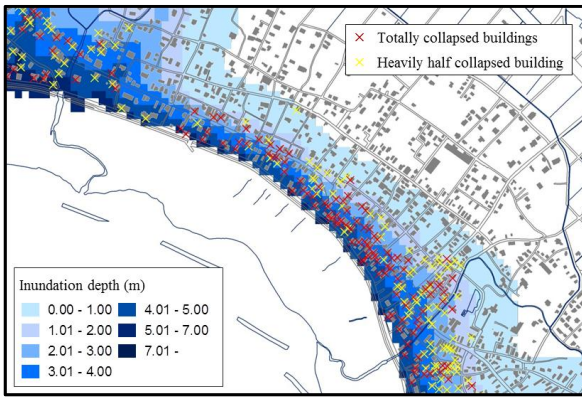


Figure 4 Distribution of damaged buildings according to estimated tsunami-inundation depths

measurement points of tsunami inundation heights along the coastline compiled by the group are also illustrated in Fig. 2. The inundation height collected by the survey group is defined as the elevation of water level with reference to the sea level (Tokyo Peil: T.P.). According to the comparison, the estimated inundation heights show good agreements with the observations especially in the residential areas, which are labeled as 10-16.

Figure 3 shows a comparison of the tsunami-inundation depths obtained by the numerical simulation with the tsunami-inundated areas identified in our previous study (Kitamura *et al.*, 2012). We focus on the eastern part of Asahi City, where the inundated areas were verified through different sources. The simulated distribution of the tsunami-inundated areas and the distribution identified by our previous study show similar trends especially in Iioka district, where serious damage to buildings was observed after the tsunami.

3. CONSTRUCTION OF FRAGILITY CURVE FOR BUILDINGS

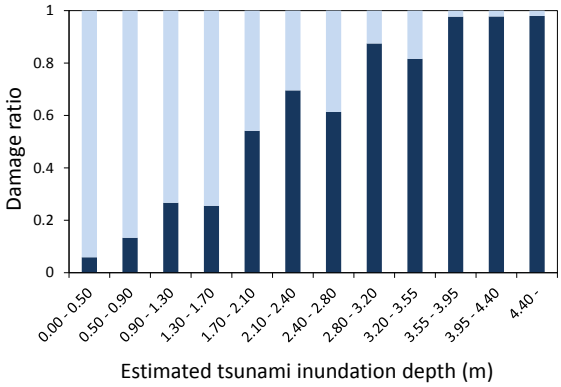


Figure 5 Relationship between the damage ratios of buildings and estimated tsunami inundation depths in Iioka district, Asahi City, Chiba Prefecture

This study tries to evaluate the relationship between the damage ratio of buildings and the inundation depth in Asahi City, Chiba Prefecture. To achieve the objective, the damage dataset of buildings compiled by Asahi City, Chiba Prefecture was employed. In the dataset, the location and damage level of building can be identified. Four damage levels are defined in the dataset, which are totally collapsed, heavily half collapsed, half collapsed and partially collapsed. In this study, the ratios of the number of totally and heavily half collapsed buildings to that of residential buildings with respect to the inundation depths were obtained. We obtained the damage ratios only in Iioka district, where many damaged buildings were found and the result of numerical simulation could be validated in the previous chapter.

Figure 4 shows the distribution of damaged buildings according to estimated tsunami-inundation depths in Iioka district. Building inventory compiled by Zenrin, a Japanese map publisher, in 2009 was used to detect residential buildings. Figure 5 shows the relationship between the damage ratios of buildings and estimated tsunami inundation depths. The damage ratio increases in accordance with the increment of inundation depth. The damage ratio is larger than 50% when the inundation depth is in the range of 1.7-2.1 m.

The damage ratio, P, is assumed to be as follows:

$$P = \Phi((\ln d - \lambda)/\zeta) \tag{4}$$

where $\Phi(x)$ is the cumulative distribution function of the standard normal distribution, and d is the inundation depth. λ and ζ are the mean and the standard deviation of ln d, which are determined by the least-squares method on the lognormal probability paper. Figure 6 shows the fragility curve based on the building damage dataset in Iioka district, Asahi City, Chiba Prefecture after the 2011 Tohoku earthquake.

The fragility curves developed after the previous events are also shown in Fig. 6. Koshimura and Kayaba (2010) and

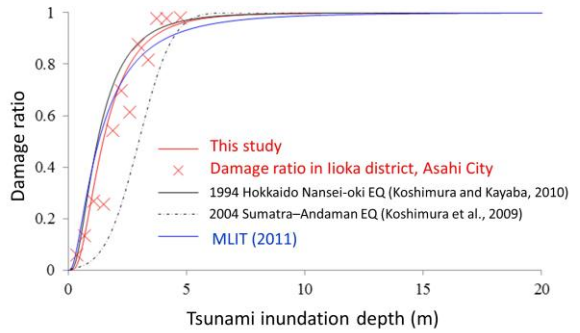


Figure 6 Fragility curve constructed by this study and those developed after the previous earthquakes (Koshimura and Kayaba, 2010; Koshimura *et al.*, 2009)

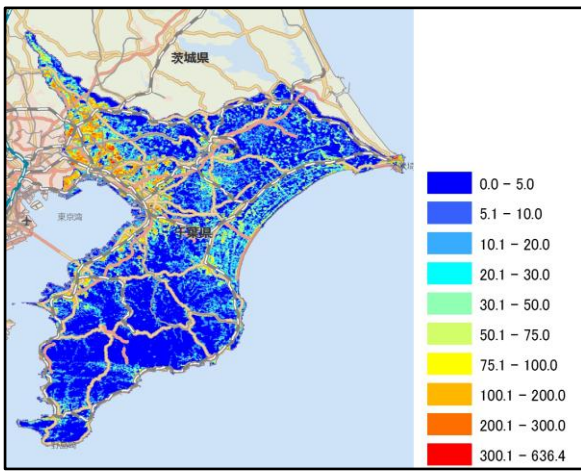
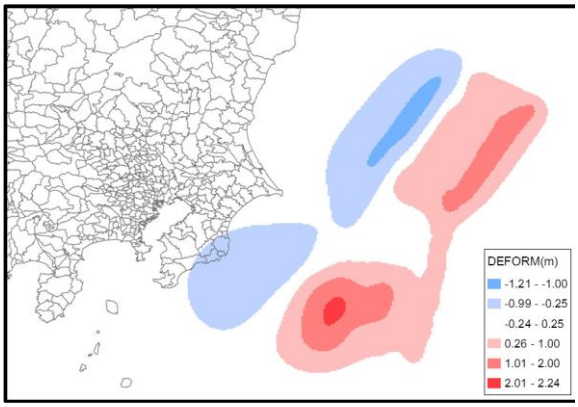


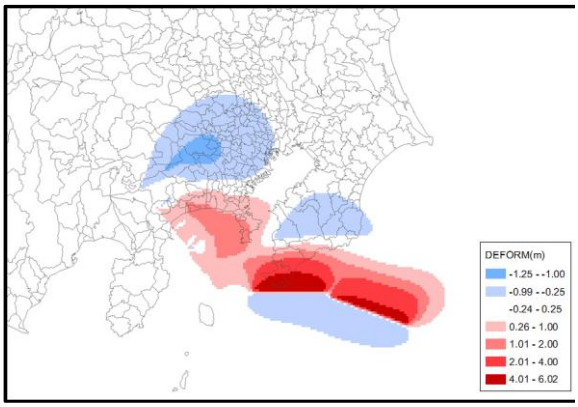
Figure 7 Number of buildings in Chiba Prefecture compiled in 2008

Koshimura *et al.* (2009) constructed fragility functions after the 1994 Hokkaido Nansei-oki and 2004 Sumatra–Andaman earthquakes. In the study, pre- and post-event satellite and aerial images were employed to perform visual damage inspection. The buildings were interpreted as "survived" or "destroyed" by detecting if the roofs were remained or not, and the fraction of "destroyed" buildings was used as the damage ratio. Ministry of Land, Infrastructure, Transport and Tourism (MLIT) published the results of survey after the 2011 Tohoku earthquake. The damage ratios of buildings in the entire regions affected by the tsunami are compiled with respect to the inundation depth in their report (MLIT, 2011). Using the dataset, a fragility curve was also constructed (Fig. 6). The fragility curve constructed by this study show the similar damage ratios with the curve after the 1994 Hokkaido Nansei-oki earthquake. In addition, the fragility curve based on the damage ratios of buildings in the entire tsunami affected regions show a similar trend with the curve constructed by this study.

Based on these findings, the fragility curve constructed by this study will estimate the damage ratios with a reasonable accuracy. Although the fragility curve was constructed based on the damage dataset of a municipality, it shows similar estimations with the curve for the entire affected regions. Hence, it can be applicable for prefectural damage assessment after tsunami.



(a)



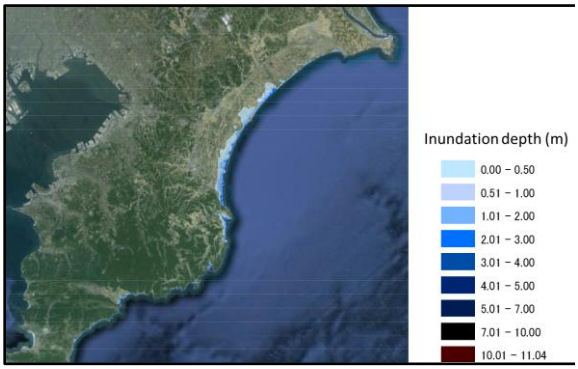
(b)

Figure 8 Vertical displacement of seabed assuming (a) the 1677 Enpo Boso-oki and (b) the 1703 Genroku Kanto earthquakes

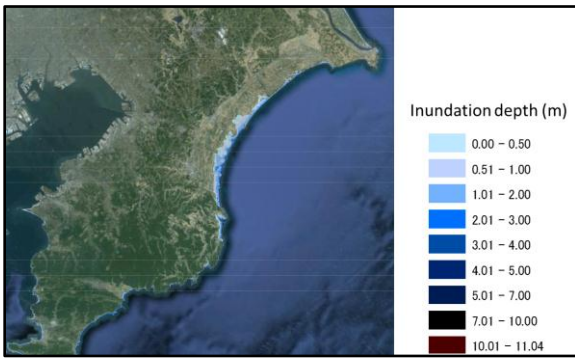
4. DAMAGE ASSESSMENT OF BUILDINGS AFTER TSUNAMI IN CHIBA PREFECTURE

The damage to buildings in Chiba Prefecture due to tsunami is estimated using the fragility curve constructed by this study. Figure 7 shows the distribution of the number of buildings used in this study. This dataset was compiled by Chiba Prefecture in 2008 and the number of buildings is represented in every 250 × 250 m^2 grid cell.

We assume two historical earthquakes to evaluate the number of damaged buildings in Chiba Prefecture. In 1677, the Enpo Boso-oki earthquake occurred and tsunami hit the Pacific coast of Japan. The tsunami height in the eastern part of Chiba Prefecture was estimated to be 6-8 m (Hatori, 2003). The other historical earthquake is the 1703 Genroku Kanto earthquake. This event occurred in the south Kanto region and the tsunami height in the eastern part of Chiba



(a)



(b)

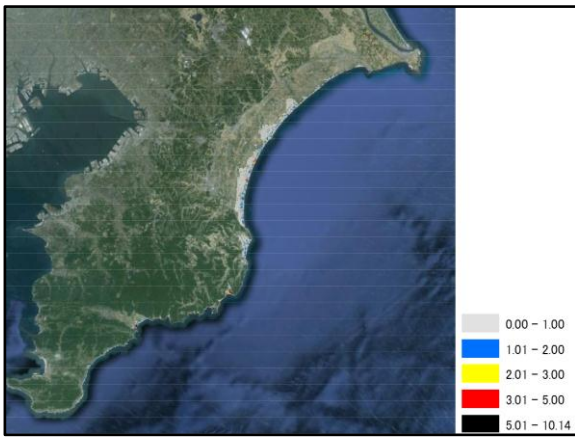
Figure 9 Distributions of estimated tsunami inundation depth in Chiba Prefecture after (a) the 1677 Enpo Boso-oki and (b) the 1703 Genroku Kanto earthquakes

Prefecture was estimated to be 6-11 m (Namegaya *et al.*, 2011).

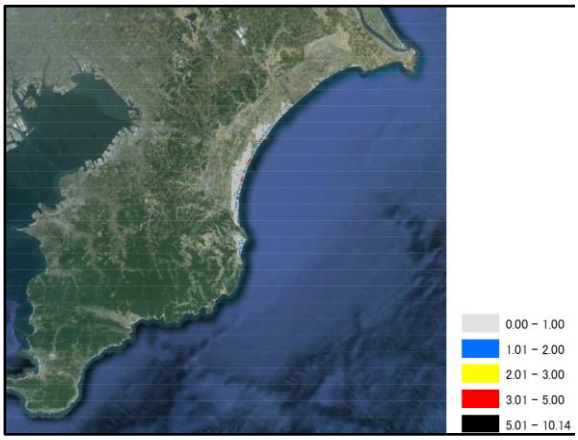
In order to perform numerical simulation of tsunami propagation, the fault model developed by Chiba Prefecture (2006) for the 1677 Enpo Boso-oki earthquake and that by Namegaya *et al.* (2011) for the 1703 Genroku Kanto earthquake were employed. The distributions of vertical displacement of seabed, which will be used as initial profile of tsunami, estimated by Okada's method (Okada, 1985) for the two historical earthquakes are shown in Fig. 8.

Figure 9 shows the estimated inundation depth following the two historical earthquakes. The eastern part of Chiba Prefecture is affected by tsunami with the inundation depth of 5-8 m in average in both cases. The inundation depth may reach approximately 10 m in some areas. Employing the fragility curve shown in Fig. 6 and the inventory dataset for buildings shown in Fig. 7, damage assessment for buildings is performed. Figure 10 shows the distributions of damaged buildings due to the two earthquakes. In total, more than 20,000 buildings may be affected in both cases.

5. CONCLUSIONS



(a)



(b)

Figure 10 Distributions of damaged buildings assuming (a) the 1677 Enpo Boso-oki and (b) the 1703 Genroku Kanto earthquakes

This study evaluated the relationship between the damage ratio of buildings in Asahi City, Chiba Prefecture, and the tsunami-inundation depth estimated by numerical simulation. The tsunami inundation in Asahi City was numerically obtained based on the leap-frog finite difference scheme. The results were validated by comparing with the records of field survey.

Employing the damage dataset compiled by Asahi City, the damage ratios with respect to the inundation depths were determined. Then, the fragility curve of buildings against tsunami inundation-depth was constructed assuming the log-normal distribution. Lastly, the numbers of damaged buildings assuming the two historical earthquake events were estimated using the fragility curve developed by this study. More than 20,000 buildings will be affected following the relationship between the damage ratio and the inundation depth after the 2011 Tohoku earthquake.

The structural types of buildings could not be considered in determining the damage ratios in this study. These effects should be investigated in a future study to perform a more detailed damage assessment of buildings.

Acknowledgements:

The authors would like to express their sincere gratitude to Professor Shunichi Koshimura of Tohoku University for providing the TUNAMI-CODE (Tohoku University's Numerical Analysis Model for Investigation of Tsunami).

References:

Asahi City, Chiba Prefecture. (2008), http://www.city.asahi.lg.jp /section/soumu/news/2008-0319-1407-2.html (in Japanese).

Cabinet Office, Government of Japan. (2011), "Outline of damage due to tsunami," http://www.bousai.go.jp/jishin/chubou/ higashinihon/1/3-2.pdf (in Japanese).

Chiba Prefecture. (2006). "Report on numerical simulation of tsunami propagation and countermeasures" (in Japanese).

Fujii, Y. and Satake, K. (2012), "Tsunami source of the off Tohoku-Pacific Earthquake on March 11, 2011 (Tentative Result, Ver. 4.2 and Ver. 4.6), " http://iisee.kenken.go.jp/staff/fujii/ OffTohokuPacific2011/tsunami_inv.html

Hatori, T. (2003), "Irregular height deviation of the 1677 Enpo Boso-Oki Tsunami, Eastean Japan," *Journal of the Historical Earthquake Studies*, *19*, 1-7 (in Japanese).

Imamura, F. (1995), "Review of tsunami simulation with a finite difference method," *Long-Wave runup models*, World Scientific, 25-42.

Japanese National Police Agency. (2011). "Damage situation and police countermeasures associated with 2011Tohoku district - off the Pacific Ocean Earthquake," http://www.npa.go.jp/ archive/keibi/biki/higaijokyo_e.pdf.

Kitamura, K., Maruyama, Y., and Yamazaki, F. (2012), "Estimation of tsunami-inundated areas using satellite images and numerical model in Asahi city, Chiba Prefecture, after the 2011 off the Pacific coast of Tohoku earthquake," *Proceedings of the 33rd Asian Conference on Remote Sensing*, Paper No. PS1-20, 10p.

Koshimura, S., Katada, T., Mofjeld, H.O., and Kawata, Y. (2006), "A method for estimating casualties due to the tsunami inundation flow," *Natural Hazards*, **39**, 265-274.

Koshimura, S., Oie, T., Yanagisawa, H., and Imamura, F. (2009), "Developing fragility functions for tsunami damage estimation using numerical model and post-tsunami data from Banda Aceh, Indonesia," *Coastal Engineering Journal*, Japan Society of Civil Engineers, **51**(3), 243-273.

Koshimura, S. and Kayaba, S. (2010), "Tsunami fragility inferred from the 1993 Hokkaido Nansei-oki earthquake tsunami disaster," *Journal of Japan Association for Earthquake Engineering*, **10**(3), 87-101 (in Japanese).

Kotani, M., Imamura F., and Shuto, N. (1998), "New Method of Tsunami Runup and Estimation of Damage using GIS Data," *Proceedings of the Coastal Engineering*, Japan Society of Civil Engineers, **45**, 356-360 (in Japanese).

Ministry of Land, Infrastructure, Transport and Tourism. (2011), http://www.mlit.go.jp/toshi/city_plan/crd_city_plan_tk_000005. html (in Japanese).

Namegaya, Y., Satake, K. and Shishikura, M. (2011), "Fault models of the 1703 Genroku and 1923 Taisho Kanto earthquakes inferred from coastal movements in the southern Kanto area," Annual Report on Active Fault and Paleoearthquake Researches, **11**, 107-120 (in Japanese).

Okada, Y. (1985), "Surface deformation due to shear and tensile faults in a half-space," *Bulletin of the Seismological Society of America*, **75**(4), 1135-1154.

Shuto, N. (1991), "Numerical simulation of tsunamis - Its present and near future," *Natural Hazards*, **4**, 171-191.

The 2011 Tohoku Earthquake Tsunami Joint Survey Group. (2011), "Nationwide field survey of the 2011 off the Pacific Coast of Tohoku Earthquake tsunami," *Journal of Japan Society of Civil Engineers*, B2, **67**(1), 63-66.

10CUEE CONFERENCE PROCEEDINGS
10th International Conference on Urban Earthquake Engineering
March 1-2, 2013, Tokyo Institute of Technology, Tokyo, Japan

BUILDING DAMAGE CHARACTERISICS BASED ON SURVEYED DATA AND FRAGILITY CURVES OF THE 2011 GREAT EAST JAPAN TSUNAMI

Anawat Suppasri[1)], Erick Mas[2)], Ingrid Charvet[3)], Rashmin Gunasekera[4)], Kentaro Imai[2)], Yo Fukutani[5), 7)], Yoshi Abe[5)] and Fumihiko Imamura[6)]

1) Associate Professor, International Research Institute of Disaster Science, Tohoku University, Sendai, Japan
2) Assistant Professor, International Research Institute of Disaster Science, Tohoku University, Sendai, Japan
3) Research Fellow, Earthquake and People Interaction Centre, University College London, London, United Kingdom
4) Willis Re Analytics, Willis Re, Ipswich, United Kingdom
5) Research Associate, International Research Institute of Disaster Science, Tohoku University, Sendai, Japan
6) Professor, International Research Institute of Disaster Science, Tohoku University, Sendai, Japan
7) Senior Consultant, Tokio Marine & Nichido Risk Consulting Co.,Ltd
suppasri@irides.tohoku.ac.jp, mas@irides.tohoku.ac.jp, i.charvet@ucl.ac.uk, gunasekerar@willis.com, imai@irides.tohoku.ac.jp, fukutani@irides.tohoku.ac.jp, yabe@irides.tohoku.ac.jp, immamura@irides.tohoku.ac.jp,

Abstract: A large amount of buildings was damaged or destroyed by the 2011 Great East Japan tsunami. Numerous field surveys were conducted in order to collect the tsunami inundation extents and building damage data in the affected areas. Therefore, this event provides us with one of the most complete dataset amongst tsunami events in history. In this study, fragility functions are derived using data provided by the Ministry of Land, Infrastructure and Transportation of Japan (MLIT), with more than 250,000 structures surveyed. The set of data has details on damage level, structural material, number of stories per building and location (town). This information is crucial to the understanding of the causes of building damage, as differences in structural characteristics and building location can be taken into account in the damage probability analysis. Using least squares regression, different sets of fragility curves are derived to demonstrate the influence of structural material, number of stories and coastal topography on building damage levels. The results show a better resistant performance of reinforced concrete and steel buildings over wood or masonry buildings. Also, buildings taller than two stories were confirmed to be much stronger than the buildings of one or two stories. The damage characteristic due to the coastal topography based on limited number of data in town locations is also shortly discussed here. At the same tsunami inundation depth, buildings along the Sanriku ria coast were much greater damaged than buildings from the plain coast in Sendai. The difference in damage states can be explained by the faster flow velocities in the ria coast at the same inundation depth. These findings are keys to support better future building damage assessments, land use management and disaster planning.

1. INTRODUCTION

The East coast of Japan was extensively affected by the 2011 Great east Japan tsunami, with more than 400,000 buildings damaged or destroyed (National Police Agency, 2011). The extensive damage directly impacted infrastructure system and the economy due to the loss of houses, offices, markets and industries. In order to reduce such dramatic consequences on the population, it is crucial to improve our understanding of building damage characteristics due to a tsunami.

This study uses the complete data set of more than 250,000 damaged buildings with surveyed tsunami inundation depths. The damage inspection compiled damage level, structural material, number of stories, inundation depth and location of structures (no coordinates, only the name of the town). Using least squares regression, different sets of fragility curves (Koshimura et al., 2009) are derived to demonstrate the influence of structural material, number of stories and coastal topography on building damage levels.

2. DATA AND METHODS

2.1 Data

The MLIT conducted field surveys of damaged buildings and tsunami inundation depth (Tohoku Earthquake Tsunami Joint Survey Group, 2011) in the whole tsunami affected areas covering seven provinces (Hokkaido, Aomori, Iwate, Miyagi, Fukushima, Ibaraki and Chiba). The main affected areas by the 2011 Great East Japan tsunami are shown in Fig. 1. The data of damage inspection is available through the MLIT website (MLIT, 2012) with 251,301 buildings in their database. Each damaged building was measured and classified according to its damage level (six levels were defined by MLIT), structural material

(Reinforced concrete (RC), steel, wood or other light weight structure such as soil or block) and number of stories (one, two or three stories and higher).

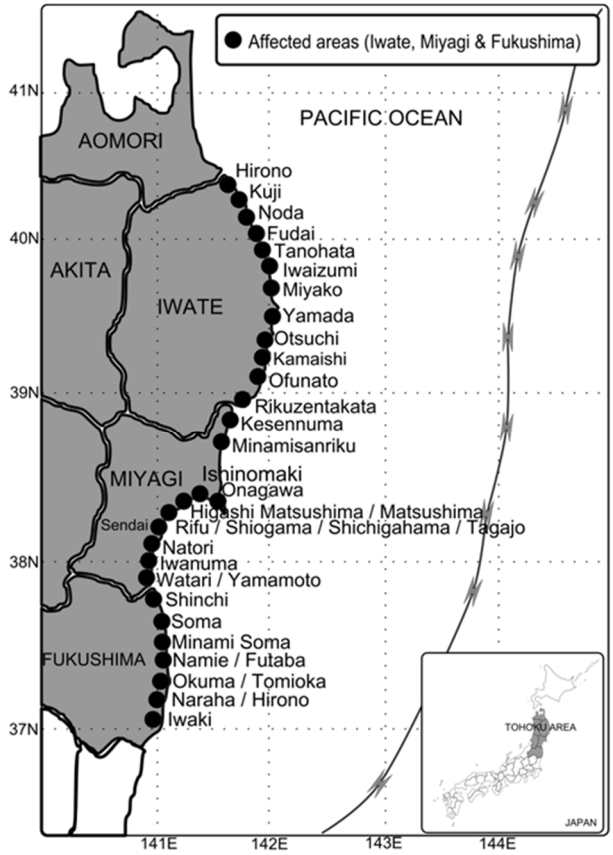


Figure 1 Main affected areas by the 2011 Great East Japan tsunami

Table 1 Damage levels, classification description and condition of building

Class	Description	Condition
Minor damage	No significant structural or non-structural damage, possibly only minor flooding.	Possible to be use immediately after minor floor and wall clean up.
Moderate damage	Slight damages to non-structural components.	Possible to be use after moderate reparation
Major damage	Heavy damages to some walls but no damages in columns	Possible to be use after major reparations
Complete damage	Heavy damages to several walls and some columns	Possible to be use after a complete reparation and retrofitting
Collapsed	Destructive damage to walls (>50%) and several columns (bend or destroyed).	Loss of functionality (system collapse). Non-repairable or great cost for retrofitting.
Washed away	Washed away, only foundation remained, total overturned	Non-repairable, requires total reconstruction.

Similar to Shuto (1993), the damage levels are: (1) Minor damage, (2) Moderate damage, (3) Major damage, (4) Complete damage, (5) Collapse and (6) Washed away. Descriptions of each damage level are summarized in Table 1. The measure of tsunami inundation depths on an interval of 0.5 m are shown together with each damage level. Tsunami fragility curves will be developed for each affected area and compared to demonstrate a boundary of probable maximum and minimum damage probability for each damage level, structural material and number of stories at a specific inundation depth.

2.2 Method

Similar to Suppasri et al. (2012b), the probabilities for each damage level were calculated and shown against a median value within a range of every 0.5 m inundation depth. Linear regression analysis was performed to develop the fragility function. The cumulative probability P of occurrence of damage is given either by Eq. (1) or by (2):

$$P(x) = \Phi[(x-\mu)/\sigma] \quad (1)$$

$$P(x) = \Phi[(\ln x-\mu')/\sigma'] \quad (2)$$

where, Φ represents the standardized normal distribution function, x stands for the hydrodynamic feature of tsunami used as demand parameter (e.g., inundation depth, current velocity or hydrodynamic force), and μ and σ (μ' and σ') represents the mean and standard deviation of x (ln x) respectively. Two statistical parameters of fragility function, μ and σ (μ' and σ'), are obtained by plotting x (ln x) against the inverse of Φ on normal or lognormal probability papers, and performing least-square fitting of this plot. Consequently, two parameters are obtained by taking the intercept (= μ or μ') and the angular coefficient (= σ or σ') in Eq. (3) or (4):

$$x = \sigma\Phi^{-1} + \mu \quad (3)$$

$$\ln x = \sigma'\Phi^{-1} + \mu' \quad (4)$$

Throughout the regression analysis, the parameters are determined to obtain the best fit (in the least squares sense) of fragility curves with respect to the inundation depth.

3. RESULTS

3.1 Damage level

Building damage data for the whole of Japan from 2011 Great East Japan tsunami event was summarized by MLIT was used to plot six different damage levels without separation of structural material, number of stories or coastal topography as shown in Fig. 2. It is reasonable that the expected damage probability will be higher for lower damage level classes at the same inundation depth reference point. For example, the damage probability for level 2 (moderate damage or greater) should be higher than the damage probability for level 5 (collapse or greater). The results show for mixed structural material that the damage

probability at an inundation depth equal to 2 m for damage levels 1 to 6 is roughly 0.2, 0.4, 0.6, 0.8, 0.95 and 1.0 respectively. The 2 m inundation depth is a key threshold value because the damage probability for each damage level is nearly the same. According to Fig. 2, the probability of damage occurrence reaches their maximum value for all type of damage levels when the inundation depth exceeds 10 m.

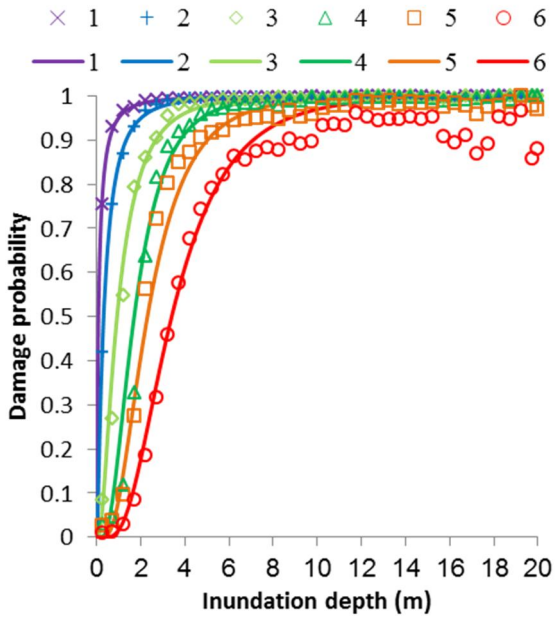


Figure 2 Tsunami fragility curves for the whole area with mixed structural material in different damage levels

3.2 Structuralmaterial

Using the data of the whole affected areas in Japan, we separated it into different structural materials. The results based on the structural materials are shown in Figs. 3.For most of the structural material data - except for wood -, when inundation depths were greater than 10-15 m the sample size of surveyed number of building to calculate the damage probability was comparatively less. Since data prepared by MLIT was summarized at fix intervals of inundation depth – every 0.5 m depth, there is less number of surveyed buildings within intervals over 10 m depth, compared to lower inundation depths. Therefore, in some cases we discounted the data on higher depth intervals to avoid underestimating the damage probability.

It can be seen from the results in Fig. 3 that RC is the strongest structure followed by steel, masonry and wood. For example, a probability that 2 m inundation depth would damage buildings as level 5 (collapsed and wash away) for RC, steel, masonry and wood is about 0.1, 0.2, 0.25 and 0.45 respectively. All wood buildings and most lightweight buildings were washed away when inundation depth was greater than 10 m while only 50% or less for steel and RC. It is noticed that the damage probability for level 1-4 is not very different for the different structural material: for steel, wood and masonry buildings, the damage probability for level 4 varies around 0.4-0.5. These results indicate that RC and steel are structural materials that play very important role in preventing a building to be collapsed or washed away.

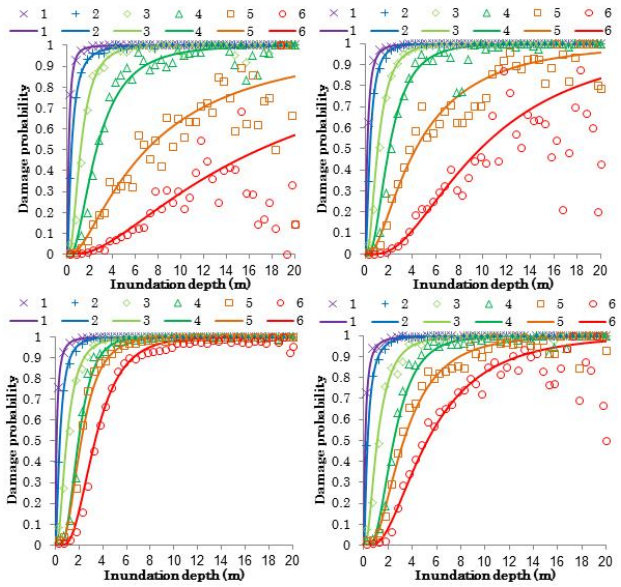


Figure 3 Tsunami fragility curves for the whole area with separated structural material RC (upper-left), Steel (upper-right), Wood (lower-left) and Masonry (lower-right)

3.3 Number of stories

The MLIT dataset for the whole Japan was then separated again for different number of stories categorized as one story, two stories and three stories or higher. This dataset was only provided for two structural types (RC and wood). Results are shown in Figs. 4 and strongly support the findings of previous studies that a building with high number of stories is stronger than the ones of one or two stories. This can be explained by the fact that the supporting members of buildings with a large number of stories are designed to withstand greater gravity loads, therefore, are more resistant. Building damage characteristics based on the number of stories are discussed for every inundation depth of 3 m which we assumed equal to the floor height. Damage level 5 (collapse or wash away) is given as an example to compare the differences in damage probability.

For RC building, an inundation depth of 3 m caused damage by 0.30, 0.20 and 0.15 for one, two and three stories or more respectively. An inundation depth of 6 m increased the damage probability to 0.6, 0.5 and 0.25 respectively. Inundation depths of 9-15 m, which would totally overtop one and two-story buildings, caused 0.7-0.9 damage probability while only 0.45-0.70 for three stories or more.

However, for buildings of wood construction, a 3 m inundation depth caused 0.75, 0.60 and 0.40 damage probability to one, two and three stories or more respectively. Unlike RC building, a 6 m inundation depth caused nearly 1.0 damage probability to one and two story buildings that were overtopped and as high as 0.8 for buildings higher than three stories. Finally, a 9 m inundation depth is enough to destroy or wash away wood building no matter of the number of stories.

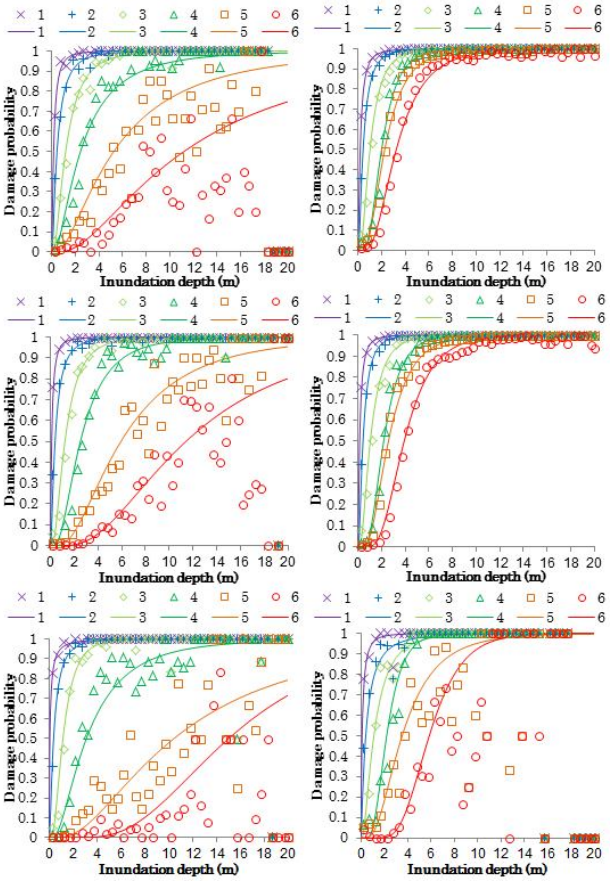


Figure 4 Tsunami fragility curves for the whole area with separated structural material and number of stories RC-1 story (upper-left), Wood-1story (upper-right), RC-2 stories (center-left), Wood-2 stories (center-right), RC-3 stories or more (lower-left) and Wood-3stories or more (lower-right)

The differences in damage probability between one story and two story buildings were not very large. However, especially for wood buildings, the damage probability is significantly reduced for the case of three stories or more. For example, a 3 m inundation depth caused 0.45 and 0.30 probability for level 6 (wash away) but almost zero for wood buildings over three stories. An inundation depth of 6 m could definitely wash away wood buildings of one or two stories, but only about 0.5 probability for wood buildings over three stories. In addition, damage probability for damage levels 5 and 6 also greatly decrease in case of RC building having at least three stories. Therefore, for a given structural material, buildings having three stories or more might withstand better the impacts of tsunami for the same tsunami height. In other words, the damage is not only controlled by the tsunami height, but is also dependent on the number of stories and structural class of the building hit.

3.4 Coastal topography

In order to compare the effects of the two different coastal topographies, we need a dataset from a location having both plain and ria coast. Ishinomaki city was the only heavily damaged area that geographically combined both mentioned topographies (Fig. 5). Building damage and tsunami inundation depth data (mixed structural material) provided by Ishinomaki city (Suppasri et al., 2012a) which is separated into two categories (plain coast and ria coast) were used to create the fragility curves. The building damage was classified into five levels similar to the data provided by MLIT, washed away, collapsed, major damage, moderate damage and minor damage for every 0.5 m interval of the measured maximum tsunami inundation depth. Therefore, building damage probability for each damage level can be plotted against the inundation depth.

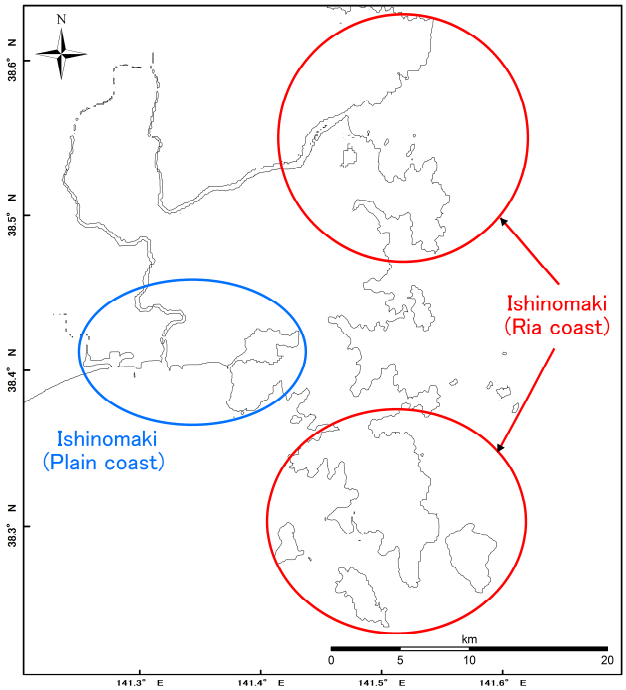


Figure 5 Area map of Ishinomaki city showing the ria coast and plain coast

Tsunami fragility curves for plain and ria coasts in Ishinomaki city are shown in Figs. 6. It can be seen that, for example, damage probability for washed away at 2 m inundation depth is less than 0.05 in plain coast while about 0.4 in ria coast. The damage probability in plain coast increases to 0.5 at 5 m inundation depth while the damage probability is 0.8 for ria coast. It can be noticed that the damage probability for the plain coast abruptly increases from inundation depth 3 m to 6 m and becomes greater than the ria coast when the inundation depth reaches nearly 7 m. Finally it reaches almost 1.0 when the inundation depth is equal to 8 m. On the other hand, the damage probability for the ria coast abruptly increases from 0.5 m to 3 m inundation depths and slightly increases until the damage probability is nearly 1.0 when the inundation depth is about 10 m. These results show that the coastal topography differences between the plain coast and the ria coast noticeably affect the damage probabilities due to tsunami. The damage probabilities for buildings in the ria coast generally increases more and is higher than those in the plain coast.

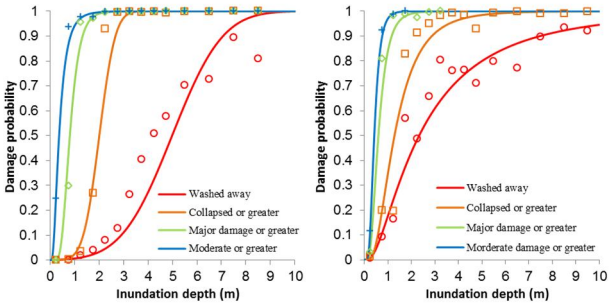


Figure 6 Tsunami fragility curves using data from Ishinomaki city only (mixed structural material) for a comparison between Plain coast (left) and Ria coast (right)

4. CONCLUSIONS AND FUTURE WORKS

4.1 Conclusions

By using one of the largest and most complete tsunami-induced damage dataset provided by MLIT for the 2011 Great East Japan tsunami, this study clarified the importance of structural characteristics on building damage probabilities, and provided a very valuable insight into the influence of coastal configuration on building damage. The first part of the analysis was based on, damage level, structural material, number of stories; and the next part of the analysis included effects from the coastal topography. The statistical parameters that were derived and used to construct the tsunami fragility curve in this study are summarized in Table 2. The main findings of this study and their applicability are summarized as below.

(1) The results show a better resistant performance of reinforced concrete and steel buildings over wood or masonry buildings.

(2) Buildings taller than two stories were confirmed to be much stronger than the buildings of one or two stories under the same inundation depth.

(3) It is also found that coastal topography can have a significant influence on building damage. At the same tsunami inundation depth, buildings along the Sanriku ria coast suffered greater damaged than buildings from the plain coast in Sendai due to higher flow velocity present in the ria coast.

These are important considerations in designing a tsunami evacuation building and assessing future tsunami risk for land use and evacuation planning.

4.2 Limitations and future works

The large number of buildings in the MLIT dataset is crucial for the reliability of the least squares regression analysis (i.e. many studies rely on a small number of data points), however highly aggregated databases such as this one may not capture certain trends in the data. Building-by-building comparison, if such data was available, would be desirable to compare or refine the results in some areas.

Future work in this research field should include the investigation of other physical parameters of the process that might have effect on the building damage such as flow velocity, distance from the sea, building orientation with respect to the sea occupancy type and reduction effect by surrounding buildings (sheltering). Work is currently being carried out in this area, in to take into account such effects as sheltering during a tsunami attack. In addition, the damage probability associated with the building function (i.e. individual house, apartment, business office, factory or public building) is also an important factor for further economic loss assessment. Indeed, buildings with a similar functionality mostly share similar structural characteristics, such as structural material and number of stories. For example in Japan, an individual house is typically 1-2 stories and made of wood or masonry; an apartment can be from higher than two stories made of wood or RC; business offices are mostly tall RC buildings; factories are mostly steel framed with 1-2 stories and public buildings such as schools and hospitals are mostly RC buildings with 3-5 stories. For public buildings, design consideration for tsunami force was applied as most of them are designated as an evacuation building.

Table 2 Summary of parameters for constructing the tsunami fragility curves in this study

X for fragility function $P(x)$	μ'	σ'	R^2
Mix: Damage level 1	-2.4562	1.4874	0.99
Mix: Damage level 2	-1.1373	1.115	0.96
Mix: Damage level 3	-0.0756	0.8277	0.97
Mix: Damage level 4	0.5316	0.6235	0.91
Mix: Damage level 5	0.8336	0.6077	0.97
Mix: Damage level 6	1.2244	0.5723	0.98
RC: Damage level 1	-1.9636	1.0966	0.91
RC: Damage level 2	-0.9723	1.0600	0.98
RC: Damage level 3	0.1577	0.7090	0.97
RC: Damage level 4	0.9423	0.7522	0.94
RC: Damage level 5	1.9381	1.0120	0.95
RC: Damage level 6	2.8232	0.9635	0.94
Steel: Damage level 1	-1.6956	1.1013	0.95
Steel: Damage level 2	-0.8982	0.8835	0.99
Steel: Damage level 3	0.0662	0.7171	0.99
Steel: Damage level 4	0.7061	0.6680	0.93
Steel: Damage level 5	1.4575	0.8938	0.93
Steel: Damage level 6	2.2790	0.7362	0.94
Wood: Damage level 1	-2.1216	1.2261	0.98
Wood: Damage level 2	-0.9338	0.9144	0.98
Wood: Damage level 3	-0.040	0.7276	0.98
Wood: Damage level 4	0.6721	0.4985	0.98
Wood: Damage level 5	0.7825	0.5559	0.98
Wood: Damage level 6	1.2094	0.5247	0.97
Brick: Damage level 1	-2.113	1.3362	0.95
Brick: Damage level 2	-1.1573	1.0400	0.96
Brick: Damage level 3	0.1059	0.7693	0.96
Brick: Damage level 4	0.9043	0.5746	0.96
Brick: Damage level 5	1.1918	0.6821	0.97
Brick: Damage level 6	1.6583	0.6913	0.97
RC 1 story: level 1	-1.8785	1.1921	0.92
RC 1 story: level 2	-0.82	1.0585	0.90
RC 1 story: level 3	0.1590	0.8196	0.98
RC 1 story: level 4	0.8881	0.8391	0.96
RC 1 story: level 5	1.6578	0.8948	0.87
RC 1 story: level 6	2.4155	0.869	0.79
RC 2 stories: level 1	-2.2555	1.2474	0.99

RC 2 stories: level 2	-0.9493	1.0388	0.95
RC 2 stories: level 3	0.1979	0.7450	0.94
RC 2 stories: level 4	0.9250	0.6920	0.90
RC 2 stories: level 5	1.7814	0.7196	0.92
RC 2 stories: level 6	2.4352	0.6624	0.88
RC ≥ 3 stories: level 1	-2.7757	1.6594	0.91
RC ≥ 3 stories: level 2	-0.9784	1.0220	0.97
RC ≥ 3 stories: level 3	0.1489	0.6600	0.93
RC ≥ 3 stories: level 4	1.1408	0.7981	0.86
RC ≥ 3 stories: level 5	2.3491	0.7898	0.72
RC ≥ 3 stories: level 6	2.7121	0.4966	0.56
Wood 1 story: level 1	-1.7268	1.1462	0.98
Wood 1 story: level 2	-0.8580	0.9395	0.98
Wood 1 story: level 3	0.0481	0.7115	0.97
Wood 1 story: level 4	0.6872	0.5288	0.98
Wood 1 story: level 5	0.8134	0.5941	0.97
Wood 1 story: level 6	1.1733	0.5756	0.98
Wood 2 stories: level 1	-2.008	1.1873	0.98
Wood 2 stories: level 2	-0.8747	0.9053	0.98
Wood 2 stories: level 3	0.0350	0.7387	0.98
Wood 2 stories: level 4	0.7770	0.5153	0.99
Wood 2 stories: level 5	0.9461	0.5744	0.98
Wood 2 stories: level 6	1.3633	0.4710	0.96
Wood ≥ 3 stories: level 1	-2.1900	1.3198	0.87
Wood ≥ 3 stories: level 2	-0.8617	1.224	0.73
Wood ≥ 3 stories: level 3	0.1137	0.8440	0.93
Wood ≥ 3 stories: level 4	0.7977	0.4734	0.87
Wood ≥ 3 stories: level 5	1.2658	0.6242	0.83
Wood ≥ 3 stories: level 6	1.7702	0.3711	0.91

Acknowledgements:

This research was partly funded by the Tokio Marine & Nichido Fire Insurance Co., Ltd. through the International Research Institute of Disaster Science (IRIDeS) at Tohoku University, the Willis Research Network (WRN) under the Pan-Asian/Oceanian tsunami risk modeling and mapping project and the Ministry of Education, Culture, Sports, Science and Technology (MEXT).

References:

Koshimura, S., Namegaya, Y. and Yanagisawa, H. (2009), "Tsunami Fragility – A new measure to assess tsunami damage, ", *Journal of Disaster Research*, 4 (6), 479−488.

Ministry of Land, Infrastructure and transportation (MLIT): Survey of tsunami damage condition: http://www.mlit.go.jp/toshi/toshi-hukkou-arkaibu.html (accessed 4 July 2012)

National Police Agency (2011) Damage condition of the 2011 earthquake off the Pacific coast of Tohoku http://www.npa.go.jp/archive/keibi/biki/higaijokyo.pdf (accessed 20 July 2012)

Shuto, N. (1993), "Tsunami intensity and disasters," Tsunamis in the world, Tinti, S. (Ed.), Kluwer Academic Publisher, Dortrecht, 197-216.

Suppasri, A., Imai, K., Imamura, F., & Koshimura, S. (2012a), "Comparison of casualty and building damage between Sanriku ria coast and Sendai plain coast based on the 2011 Great East Japan tsunami, " *Proceedings of International Sessions in Coatal Engineering*, JSCE, ed., Vol.3.

Suppasri, A., Mas, E., Koshimura, S., Imai, K., Harada, K. and Imamura, F. (2012b), "Developing tsunami fragility curves from the surveyed data of the 2011 Great East Japan tsunami in Sendai and Ishinomaki Plains, " *Coastal Engineering Journal*, 54, 1250008.

Tohoku Earthquake Tsunami Joint Survey Group (2011) Nationwide Field Survey of the 2011 Off the Pacific Coast of Tohoku Earthquake Tsunami, Journal of Japan Society of Civil Engineers, Series B, Vol. 67, No.1 pp.63-66.

10CUEE CONFERENCE PROCEEDINGS
10th International Conference on Urban Earthquake Engineering
March 1-2, 2013, Tokyo Institute of Technology, Tokyo, Japan

EVALUATION OF TSUNAMI LOAD BASED ON DAMAGE OBSERVATIONS AFTER GREAT EAST JAPAN EARTHQUAKE

Akihiko Obata[1], Tetsuya Nishida[2], Naofumi Teramoto[3] , Hideto Kanno[4] and Jun Kobayashi[2]

1) Assistant Professor, Dept. of Architecture and Environment Systems, Akita-Prefectural University, Japan
2) Professor, Dept. of Architecture and Environment Systems, Akita-Prefectural University, Japan
3) Associate Professor, Dept. of Civil and Environmental Engineering, Akita National College of Technology, Japan
4) Associate Professor, Dept. of Architecture and Environment Systems, Akita-Prefectural University, Japan
a_obata@akita-pu.ac.jp, tetsuya_nishida@akita-pu.ac.jp, teramoto@akita-nct.ac.jp, kanno@akita-pu.ac.jp, jun_kobayashi@akita-pu.ac.jp

Abstract: The Great East Japan Earthquake occurred on March 11, 2011. Building structures were severely damaged by the tsunami that followed this earthquake. A quantitative evaluation of the tsunami load is essential for designing and constructing buildings that are resistant to tsunami loads. However, a tsunami presents a non-constant load. The accumulation of observed damage data is necessary for analyzing the tsunami load. In this study, it is one case of analyzing the tsunami load . The design guidelines developed by a task committee under the Japanese Cabinet Office proposed design loads for practical shelter design in 2005. The guidelines were primarily developed based on laboratory tests of a two-dimensional scale model (Asakura et al. 2000). However, because studies on tsunami loads against structures based on damage observations are insufficient, the damaged caused by the tsunami following the Great East Japan Earthquake was devastating. In this stu dy, the steel building structures damaged by the tsunami that followed the 2011 Great East Japan Earthquake were observed by the authors. The authors investigated the relationship between the lateral strength and observed damage of the structures to verify the appropriateness of the design formula.

1. INTRODUCTION

The damage resulting from the disastrous tsunami triggered in the ocean by the 2011 Great East Japan Earthquake on March 11 of that year reached shocking levels that far outweighed the damage to land structures caused by the earthquake itself. It is vital to make quantitative estimates of loads arising in structures due to a tsunami and take these into account when planning structures that must resist tsunamis. At this time, however, there are very few published methods for quantitatively estimating tsunami damage or loading or other such analyses in structural design procedures or in the research literature. A great volume of data must be gathered based on many cases of damage in order to analyze tsunami loads, since these events are so variable and indeterminate. The present study provides an example of an analysis of such data.

In the present study, a survey of tsunami damage to steel-frame buildings in 2011 was conducted. The methods for estimating tsunami loads have been described in previous publications[1),2)]. This report begins with an explanation of the methods for estimating tsunami loads described in previous reports[1),2)] and then shows actual calculations for one of the buildings surveyed by the authors for tsunami damage. The results of this survey are summarized and compared with the results of the previous publications[1),2)].

2. BASIC APPROACH TO STRUCTURAL REQUIREMENTS UNDER GUIDELINES FOR TSUNAMI EVACUATION FROM BUILDINGS

2.1 Equations for calculating tsunami pressure in Cabinet Office guidelines

The Japanese Cabinet Office's guidelines for tsunami evacuation from buildings[3)] provide Eq. (1) for calculating the wave pressure. Here, q_z is the wave pressure in the direction of wave propagation to be used in structural calculations (kN/m^2), ρ is the volumetric density of the water in the tsunami (t/m^3), g is the gravitational acceleration (m/s^2), h is the design water depth (m), and z is the height of the given structural component above ground level ($0 \leqq z \leqq 3h$)(m).

$$q_z = \rho g (3h - z) \quad (1)$$

Eq. (1) is based on the results of a 2-dimensional experiment performed by Asakura et al. using a hydraulic model[4]. However, their experiment took no account of the influence of obstacles such as breakwaters or other coastal hardening.

Based on Eq. (1), the tsunami pressure Q_z exerted on the wall of a structure is expressed in Eq. (2). Here, B is the width of the wall (m) and z_1 and z_2 are the lowest and highest extents of the affected wall, respectively ($0 \leqq z_1 \leqq z_2$)(m).

$$Q_z = \rho g B \int_{z_1}^{z_2} (3h - z)\, dz \tag{2}$$

2.2 Estimating tsunami pressure from damage survey results

The interim reports from the Institute of Industrial Science, University of Tokyo[1),2)], described a survey of the area affected by the Great East Japan Tsunami for damage to buildings of RC construction and other artificial structures, and compared this to predictions based on the tsunami pressure equation. Those reports identified an equivalent water depth $a\eta_m$, indicating the immersion depth that would exert a hydrostatic loading equaling the lateral strength of a given structure. This was then divided by the measured tsunami inundation depth η_m to find the water depth coefficient a, and the trends in a were compared with parameters of the damaged buildings and other structures. a was modified by replacing the $3h$ term in Eq. (2), representing triple the design immersion depth, with the values for the equivalent water depth $a\eta_m$ found in the above interim reports. Since this is equal to the ultimate lateral strength Q_u for the building, we derive Eq. (3) below and rearrange to find Q_u:

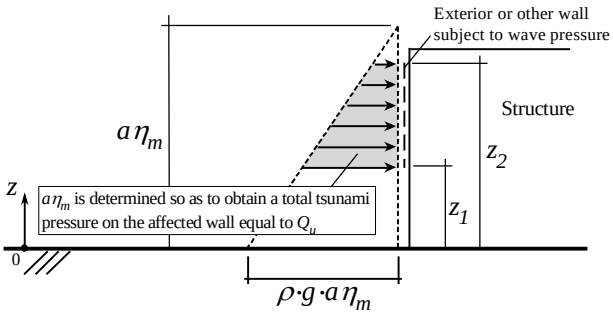
$$Q_u = \rho g B \int_{z_1}^{z_2} (a\eta_m - z)\, dz \tag{3}$$

Eq. (3) indicates that the sum total of the static water pressure corresponding to $a\eta_m$ equals the total lateral strength of the building. Here, the maximum height z_2 of the affected wall must be less than $a\eta_m$.

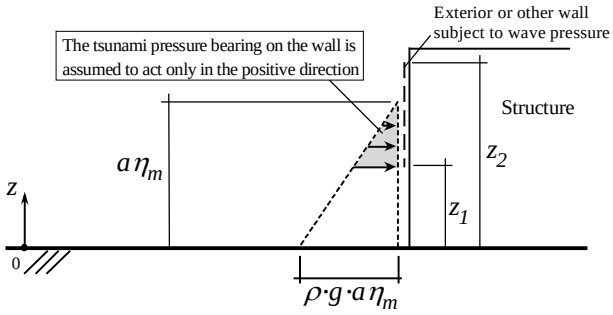
In this paper, the authors calculated a for buildings struck by the tsunami in conformity with the investigative method used in the above interim reports. The application of $a\eta_m$ is shown in Figure 1. The calculations for buildings with unusually low values for Q_u revealed some cases where $a\eta_m$ did not actually attain the maximum height z_2 of the affected wall. To account for those cases, Eq.(3) was re-written and a was calculated using the domain from $a\eta_m$ to the lowest extent of the affected wall z_1 as the region for integrating the tsunami pressure. Eqs.(4) and (5) were employed to calculate a.

・$a\eta_m \geqq z_2$

$$a = \frac{Q_u}{\rho g B\, \eta_m (z_2 - z_1)} + \frac{z_2 + z_1}{2\eta_m} \tag{4}$$



(a) $a\eta_m \geqq z_2$



(b) $z_2 > a\eta_m$

Figure 1 Diagram describing equivalent water depth $a\eta_m$

・$z_2 > a\eta_m$

$$a = \frac{1}{\eta_m}\sqrt{\frac{2Q_u}{\rho g B}} + \frac{z_1}{\eta_m} \tag{5}$$

The above results indicate that it is vital to evaluate the area of the exterior wall, exterior furnishings or other components under tsunami pressure in order to find a. Steel-frame buildings are quite commonly fitted with exterior furnishings in the form of light concrete panels or slate panels that are attached by dry methods. It seems likely that when such exterior walls are struck by a tsunami, the furnishings will be carried away before transmitting the loads to the building structure. Actually, the tsunami damage survey conducted for this paper found quite a large number of building structures that were in perfectly serviceable condition, despite losing exterior walls or furnishings. The walls impacted by the tsunami after exterior furnishings had been torn away can be assumed to consist only of columns, beams and other structural components, so the load from the tsunami would have been considerably reduced with the disappearance of the exterior furnishings. For this report, the tsunami damage in each building was inspected to determine whether or not the tsunami loads had been transmitted to the structure by the exterior furnishings.

3. EXAMINATION ABOUT SOME RESEARCH EXAMPLES

In this paper, Simple examples of the methods for estimating tsunami loads are introduced. Figure 2

shows the location of buildings damaged by tsunami in T zone. Building (A) and (B) are Port facilities that we surveyed. Overview of building (A) is shown in photo 1, and overview of building (B) is shown in photo 2. The measurement of tsunami height in T zone is 15.0m.

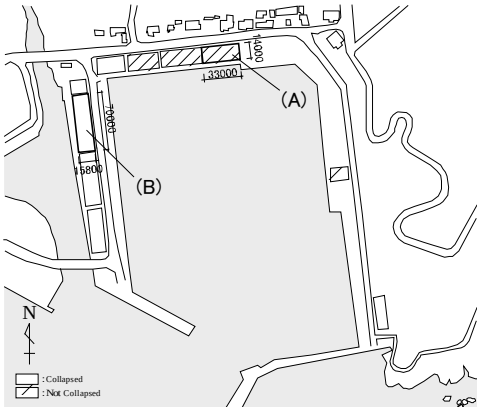


Figure 2 Location of buildings in T zone.



Photo 1 Overview of building (A)



Photo 2 Overview of building (B)

Outline of building (A) based on the present survey is shown in Figure 3. Building (A) is Steel structure, 1-floor. Span direction and ridge direction of building (A) are rigid frame. Building (A) is shown that beams and columns have no damaged by the tsunami. Exterior walls and roofs of building (A) subjected to the tsunami wave pressure are carried away. In the case of building (A), tsunami load subjected to span direction. Therefore, the ultimate lateral strength Q_u for the building (A) is calculated by the single span direction. Material of the beam is assumed to SS400 (lower limit of yield stress σ_y = 235.0 N/mm^2), material of the column is assumed to BCP (lower limit of yield stress σ_y = 325.0 N/mm^2). In this paper, Q_u for the building (A) is 692.1kN.

In the calculation of building (A), we assume that the exterior walls was carried away before transmitting the tsunami loads to the building structure. Tsunami load can be assumed to consist only the beams and columns. Thus, the equivalent water depth $a\eta_m$ for the building (A) is 26.18 m, and the water depth coefficient a for the building (A) is 1.74.

Outline of building (B) based on the present survey is shown in Figure 4. Building (B) is Steel structure, 1-floor. Span direction is rigid frame and ridge direction is X-bracing. Building (B) is collapsed by tsunami load. It caused by damage in column bases. Now, in the case of building (B), tsunami load subjected to ridge direction. The ultimate lateral strength Q_u for building (B) is calculated by the whole ridge directions. The whole ridge direction of building (B) has 16 span X-bracings. Material of the bracing is assumed to SS400 (lower limit of yield stress σ_y = 235.0 N/mm^2). In this paper, Q_u for the building (B) is 2,167kN.

As shown in Photo 2, we can confirm that the exterior furnishings of building (B) has a mix of the structural members. From this point of view, the assumption that only structural members, as beams and columns, was subjected to tsunami load is open to question. Thus, in this case, tsunami wave pressure receiving surface of building (B) is assumed for the all of entire surface of structure. The equivalent water depth $a\eta_m$ for the building (B) is 5.28 m, and the water depth coefficient a for the building (A) is 0.35.

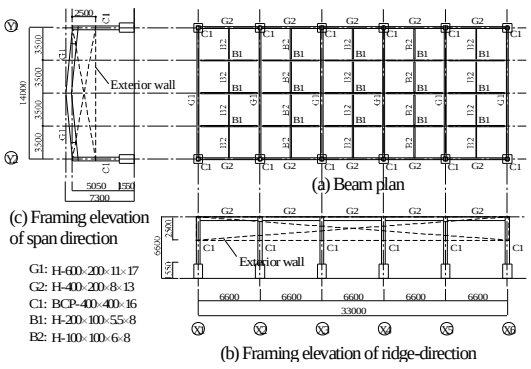


Figure 3 Outline of building (A)

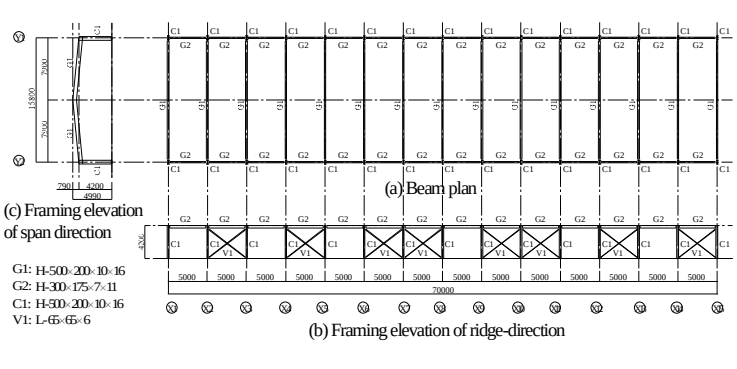


Figure 4 Outline of building (B)

Table 1 Results of Present Survey

	Loc.	Building under investigation	η_m	Condition	Surface bearing tsunami pressure	a
1	O Town	Steel, 2-floor, 2-layer ridge-direction bracing	15.0	Intact	Beam-column only	1.05
2	O Town	Steel, 2-floor, 1-layer ridge-direction bracing	15.0	Deformed	Beam-column only	0.82
3	M City	Steel, 1-floor, span-direction rigid frame structure	7.8	Deformed	Beam-column only	0.92
4	T Zone	Steel, 1-floor, span-direction rigid frame structure	15.0	Intact	Beam-column only	1.74
5	T Zone	Steel, 1-floor, ridge-direction bracing	15.0	Collapsed	Full spanwise wall	0.35
6	O City	Steel, 1-floor, span-direction rigid frame structure	11.8	Collapsed	Beam-column only	0.90
7	O Zone	Steel, 1-floor, span-direction rigid frame structure	9.7	Intact	Beam-column only	1.84

※Units for measured tsunami inundation depth were meters.

4. TRENDS IN WATER DEPTH COEFFICIENT FOUND IN SURVEY RESULTS

The water depth coefficient a was calculated for 7 cases from the present survey of steel-frame buildings that had suffered tsunami damage and was compared for consistency with the actual damage. Table 1 shows the results. Reference 1) summarized a survey of tsunami damaged-areas after the 2011 Great East Japan Earthquake, considering 78 affected RC buildings and other structures, and investigated the suitability of the equation for estimating tsunami pressure. The results indicated that a value of 1.0 was acceptable for a when calculating tsunami loads on RC buildings and other structures in regions where η_m was less than 10.0 m, but the damage from tsunami loads suggested values of $a <$ 1.0 in regions where η_m exceeded 10.0 m. Figure 5 shows how η_m varied with a in the cases presented in Reference 1, with data added for η_m and a in steel-frame buildings calculated by authors.

As shown in Figure 5, the results for tsunami loads form this survey were converted to a values and suggest that a = 1.0. There were a few exceptions, which is consistent with Reference 1) when η_m was less than 10.0 m; exceptions appeared in the case of building #2 and others when η_m exceeded 10.0 m. In this paper, however, it was assumed that the exterior walls or furnishings of steel-framed buildings would be torn away at an early point, leaving only structural components such as columns and beams, and that assumption, warranted or not, may well have some effect on the estimates for the surfaces bearing the tsunami pressure. It is extremely difficult to assess whether a building's external furnishings affect its lateral strength from a survey of tsunami damage. Estimating the area of steel-frame building walls that bears the load of a tsunami wave is a topic for future research.

5. Summary

This report describes a survey of tsunami damage, concentrating on steel-frame buildings affected by the tsunami after the 2011 Great East Japan Earthquake. Tsunami loads were estimated using the procedure followed in previous reports[1),2)]. The results in this paper

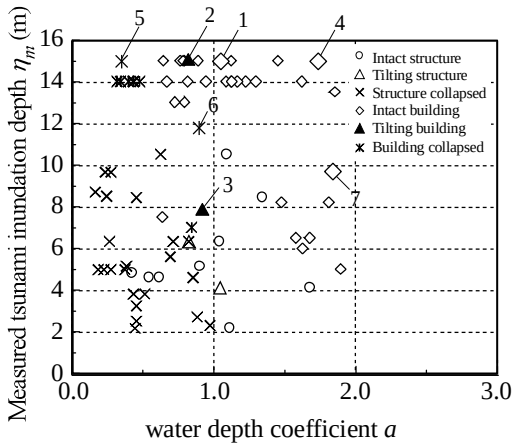


Figure 5 Variations in measured tsunami inundation depth η_m with water depth coefficient a

closely resembled those noted in the previous reports[1),2)]. A few cases showed inconsistencies from the trends noted before, though these were minor. These were attributed to necessary adjustments in the equations for the surface bearing tsunami pressure to account for the exterior walls and furnishings on steel-frame buildings.

References:

Institute of Industrial Science, the University of Tokyo. (2011) The interim reports. Part 1. (in Japanese) http://www.mlit.go.jp/common/000172791.pdf

Institute of Industrial Science, the University of Tokyo. (2011) The interim reports. Part 2. (in Japanese) http://www. mlit.go.jp/common/000172792.pdf

Task Committee under the Japanese Cabinet Office. (2005) Design Guidelines for Tsunami Shelters (in Japanese). http://www. bousai.go.jp/oshirase/h17/050610/guideline.pdf

Asakura, R., Iwase, K., Ikeya, T., Takao, M., Kaneto, T., Fujii, N. and Omori, M. (2000). An Experimental Study on Wave Force Acting on On-Shore Structures due to Overflowing Tsunamis. Proceedings of Coastal Engineering, Japan Society of Civil Engineers, 47, 911-915. (in Japanese)

Nakano, Y. (2008). Design load evaluation for tsunami shelters based on damage observations after Indian Ocean Tsunami disaster due to the 2004 Sumatra Earthquake. The 14th World Conference on Earthquake Engineering, Paper ID 15-0008.

10CUEE CONFERENCE PROCEEDINGS
10th International Conference on Urban Earthquake Engineering
March 1-2, 2013, Tokyo Institute of Technology, Tokyo, Japan

PUNCHING FAILURE OF KAMAISHI BREAKWATER CAISSON FOUNDATIONS DURING THE 2011 GREAT EAST JAPAN TSUNAMI

Jeremy D. Bricker[1)], Hiroshi Takagi[2)], and Jun Mitsui[3)]

1) Associate Professor, International Research Institute of Disaster Science, Tohoku University, Sendai, Japan
2) Associate Professor, Dept. of International Development Engineering, Tokyo Institute of Technology, Tokyo, Japan
3) Research Engineer, Technical Research Institute, Fudo Tetra Corporation, Ibaraki, Japan
bricker@stanfordalumni.org, takagi@ide.titech.ac.jp, jun.mitsui@fudotetra.co.jp

Abstract: Numerical simulations are used to investigate the mechanisms of failure of the Kamaishi breakwater during the 2011 tsunami. Results indicate that the bearing stress at the heel of the caisson increased far above its allowable limit due to the overtopping jet pulling away from the landward side of the caisson as the surcharge height above the caisson increased. In addition to the scour-induced failure of the rubble-mound foundation reported by other researchers, measures to prevent geotechnical punching failure are also necessary to ensure integrity of deep breakwaters during overtopping events.

1. INTRODUCTION

The Great East Japan Tsunami of March 11, 2011 caused widespread devastation, though in some locations its impact was mitigated by coastal defensive structures such as the bay-mouth breakwater in Kamaishi (Takahashi et al, 2011), the largest and deepest breakwater in the world, constructed exclusively for mitigating tsunami impacts. Figure 1 shows the location of the Kamaishi breakwater, and Figure 2 shows a profile-view geometry of one of this breakwater's typical deep-water caissons and its rubble mound foundation. During the tsunami, the breakwater was overtopped. After the event, many caissons were no longer visible above the waterline, and sonar surveys later showed these to be lying on the seabed, having fallen off their rubble mound foundations in the landward direction (Arikawa et al, 2012). Other caissons were still emergent from the water, but were no longer standing vertical.

In addition to showing caisson displacement, sonar measurements showed significant erosion of the rubble-mound foundation. Arikawa et al (2012) carried out laboratory experiments to replicate the overtopping of the Kamaishi breakwater, and concluded that hydrodynamic scour was the fundamental cause of caisson displacement. Scour due to the overtopping jet plunging down the landward side of the caisson dug a trough beside the heel of the caisson, eventually causing the caisson to tumble. Additionally, the 1-m gap between caissons may have caused a flow strong enough to cause scour between caissons as well.

However, Arikawa et al's experiments did not consider the possibility of rubble mound geotechnical failure. Takagi (2009) showed that one of the most common modes of caisson breakwater damage during storms is punching failure of the rubble mound foundation (Goda, 2010). Furthermore, Yaoi et al (2012) ran centrifuge experiments and showed that foundation bearing capacity failure may have occurred during overtopping of deep-water caissons.

The work presented here uses a 2-dimensional shallow water equation model to reproduce the actual overtopping conditions experienced by the Kamaishi breakwater. The water levels seaward and landward of the breakwater are then used as boundary conditions in a 2-dimensional profile-view volume of fluid (VOF) computational fluid dynamics (CFD) model to analyze the forces experienced by the caisson and its rubble mound foundation. The result shows that punching failure of deep-water caissons was a likely mode of failure of these caissons. As such, scour prevention measures (such as armor blocks), though necessary to prevent scour-induced caisson failure, may not be sufficient to prevent geotechnical failure of deep-water caissons during overtopping.

2. METHODS

2.1 Shallow water modeling of tsunami behavior

Behavior of the tsunami near the Kamaishi breakwater was simulated using the Delft-3D hydrodynamic model, operating in two-dimensional depth-averaged mode. Domain decomposition was used, with the coarsest grid having 2 km resolution, an intermediate grid with 200 m resolution, and a fine grid with 20 m resolution (Figure 1). 500-m resolution bathymetry data were used in the open ocean (Japan Oceanographic Data Center, 2012), while

50-m resolution bathymetry data were used for Kamaishi Bay (Ministry of Land, Infrastructure, and Transport, 2012). Topography was 50-m mesh survey data (GSI, 2012).

Bottom roughness was assumed to be uniform everywhere, with a Manning's n of 0.02. Since the goal of this simulation was to replicate the behavior of the wave near the breakwater, and not the inundation experienced on land, the use of a uniform Manning's n was assumed to be sufficient. The 2km-resolution Pacific domain utilized the Reimann boundary condition in Delft-3D. In order to minimize reflection of the tsunami wave from the boundaries, the grid was oriented parallel to the tsunami wave front. The model time step was 0.3 sec, in order to ensure stability.

Initial conditions consisted of a water surface elevation near mean low water. In the 2-km resolution Pacific domain, the tsunami source used was based on that of Saito et al (2011). However, the source of Saito et al (2011) alone produced a tsunami near Kamaishi smaller than that measured by PARI (2012). As such, Saito et al's (2011) source was modified so as to be slightly larger (similar to the source determined by Takahashi et al, 2011), and to extend further to the northeast. The resulting source water elevation used is shown in Figure 1. Figure 3 shows a comparison of the tsunami water level resulting from this source, with the water level observed by the Port and Airport Research Institute (2012) at the three buoys closest to Kamaishi. The modeled water surface elevation is in good agreement with the measured water surface elevation.

The tsunami behavior was simulated for 2 hours. Since observations showed the breakwater caissons to have been displaced in the landward direction, it is likely they failed during the incident tsunami wave. Figure 4 shows the spatially average elevation of the simulated water surface on each side of the breakwater, starting at the time when overtopping began (the crest of the breakwater was 6 m above mean low water) until after the crest of the tsunami had passed. The maximum modeled water surface elevation on the seaward side of the breakwater was about 13 m, and the maximum water level difference across the breakwater was 9 m. This is in agreement with the numerical shallow water simulations discussed in Arikawa et al (2012).

2.2 CFD modeling of breakwater overtopping

In order to model forces on the caisson and its foundation, the OpenFOAM CFD model was used. Within OpenFOAM, the InterFOAM VOF module was applied, so as to simulate both air (density 1 kg/m^3) and water (density 1020 kg/m^3). Figure 2 shows the two-dimensional profile-view model domain. For purposes of calculating forces on the caisson, the domain was assumed to be 30 m long (normal the paper). Within the domain, the rubble mound and caisson were both no-slip hydraulically rough boundaries with roughness length 1 mm. The left and right sides of the domain were free-slip walls. The top surface was open to the atmosphere. Turbulence was modeled using the standard Reynolds Averaged Navier Stokes k-ε formulation.

Simulating a laboratory flume, water was allowed to upwell and drain through the seabed on each side of the mound (as shown in Figure 2), with the flow rates set so as to reproduce the water levels of Figure 4 on each side of the caisson. Setting up the model in this way (instead of using water level and flow speed boundary conditions in place of the side walls) enhanced model stability.

The model consisted of a variable size rectangular grid, with grid cell area shown in Figure 5. In the region of the overtopping jet, grid cell dimensions were as small as 2 cm by 2 cm, while far away from the area of energetic flow grid cells size increased up to 1 m by 1 m. Landward and seaward of the rubble mound (the location of inflow and outflow), horizontal model resolution was coarsened to 10 m. The lower resolution on the sides of the model domain was implemented in order to reduce model run time. Since flow velocity was quite small in these regions, they were not of concern for the overtopping flow or calculation of force on the caisson. The model time step was varied automatically, in order to assure Courant number stability, but was typically on the order of 0.001 sec. Also, in order to preserve a well-defined free surface, anti-diffusion (interface compression) was applied to the free surface.

3. RESULTS

Figure 6 shows the simulated caisson overtopping. Two important phenomena are visible here. First, the overtopping jet, even though gaining buoyancy due to entrained air, strikes the rubble mound with speeds up to 8 m/s, corroborating the conclusion of Arikawa et al (2012) that scour due to the overtopping jet was a cause of caisson failure. Second, the pressure behind the overtopping jet is significantly reduced from the hydrostatic pressure, due to the overtopping jet pulling further and further away from the landward side of the caisson as the overtopping water level increases, and due to the eddy that forms behind the jet.

3.1. Calculation of forces on caisson

Pressure is calculated by OpenFOAM at each grid cell along the top and side surfaces of the caisson. Since the bottom of the caisson sits upon the rubble mound, which is modeled as a solid, water pressure is not calculated there. In reality, the rubble mound is a porous body, with water flowing through the gaps between stones (groundwater flow). In order to calculate the total force on the caisson, water pressure along the bottom surface of the caisson is assumed to vary linearly from its value at the bottom of the caisson's seaward wall, to the pressure value at the bottom of the caisson's landward wall (Goda, 2010).

The net horizontal and vertical forces on the caisson due to water pressure are determined by equations (1) – (3). The overturning moment about the heel of the caisson due to water pressure is given by equation (4).

$$\vec{F}_k = P_k \, dA_k \, \hat{n}_k \quad (1)$$

$$F_{drag} = \sum \vec{F}_k \cdot \hat{\imath} \quad (2)$$

$$F_{lift} = \sum \vec{F}_k \cdot \hat{j} \quad (3)$$

$$M_{overturning} = -\sum \vec{r}_k \times \vec{F}_k \quad (4)$$

in which $\vec{F}_k$: force acting on the k^{th} cell along the caisson surface, P_k: pressure acting on the k^{th} cell along the caisson surface, dA_k: area of the k^{th} cell along the caisson surface, $\hat{n}_k$: unit vector normal to the k^{th} cell along the caisson surface, F_{drag}: total drag force acting on the casson, $\hat{\imath}$: horizontal unit vector, F_{lift}: total lift force acting on the caisson, $\hat{\jmath}$: vertical unit vector, $M_{overturning}$: overturning moment acting about the heel of the caisson, and $\vec{r}_k$: vector pointing from the heel of the caisson to the k^{th} cell along the caisson surface.

To find the punching pressure on the rubble mound foundation at the heel of the caisson (Goda, 2010), the normal force W_e on the caisson due to the rubble mound foundation is found by equation (5)

$$W_e = mg - F_{lift} \quad (5)$$

where m is the mass of the caisson, and g is the acceleration due to gravity (the effect of buoyancy is already included in the term F_{lift}). The moment M_e about the heel of the caisson due to the normal force is given by equation (6)

$$M_e = mgt - M_{overturning} \quad (6)$$

where t is the horizontal distance between the heel of the caisson and its center of mass. The horizontal distance t_e between the heel of the caisson and the location of the resultant normal force W_e is given by equation (7)

$$t_e = \frac{M_e}{W_e} \quad (7)$$

The punching pressure P_e at the heel of the caisson is then calculated by equation (8)

$$P_e = \begin{cases} \frac{2W_e}{3t_e} & : t_e \le B/3 \\ \frac{2W_e}{B}\left(2 - 3\frac{t_e}{B}\right) & : t_e > B/3 \end{cases} \quad (8)$$

where B is the width of the caisson (23 m as shown in Figure 2).

3.2. Resulting forces on caisson

Figure 7 shows the calculated drag force on the caisson as a function of time during overtopping. The solid line shows the result of the CFD model. The dotted line shows the hydrostatic drag force, which is the horizontal force the caisson experiences due only to the difference in water level across the caisson. The difference between these two lines is the non-hydrostatic force on the caisson, mostly due to the suction induced on the landward side of the caisson as the overtopping flowrate increases and the overtopping jet pulls further and further away from the caisson (this suction is evident as dips in the pressure contours on the landward side of the caisson in Figure 6). The dashed line represents the frictional force resisting caisson sliding, which was calculated assuming a coefficient of friction between the caisson and the rubble mound of 0.6 (Goda, 2012) and a uniform bulk density of 1900 kg/m^3 for the caisson and its fill. Figure 7 shows that the horizontal force on the caisson was never strong enough to cause sliding.

Figure 8 shows the lift force on the caisson. As before, the hydrostatic component (dotted line) is due to the buoyancy of the caisson itself. The full lift force (solid line) is slightly greater than the caisson buoyancy due to dynamic lift above the caisson during overtopping, but this effect is minimal. The lift force is much smaller than the weight of the caisson (dashed line).

Figure 9 shows the overturning moment about the (landward) heel of the caisson. As before, the hydrostatic component of this moment (dashed line) is due to the horizontal force on the caisson resulting from the difference in water level across it. The full overturning moment (solid line) is larger than the hydrostatic moment because of the suction discussed above. Nonetheless, toppling of the caisson due to the overturning moment is not possible, because the restoring moment due to the caisson's weight (dashed line) is larger than the overturning moment.

Figure 10 shows the punching pressure at the heel of the caisson. The hydrostatic component (dotted line), due to the water level difference across the caisson, exerts a punching pressure of up to 900 kPa, while the total punching pressure (solid line) reaches up to 1400 kPa. The allowable design punching pressure (dashed line) is 600 kPa (Goda, 2010), while Uezono and Odani (1987) showed that a critical punching pressure of 800 kPa caused rubble mound foundation failure during experiments on similar structures in the field. Figure 10 shows that the Kamaishi breakwater caissons experienced a punching pressure much greater than either the design or critical value, for about 2 minutes.

4. COMPARISON WITH EXPERIMENTS

In order to verify the CFD model results, qualitative comparison of overtopping jet's behavior with the experiments of Mitsui et al (2012) was carried out. Mitsui found that the InterFOAM VOF simulation overestimates the rate at which air trapped under the overtopping jet is entrained into the jet, thus causing the jet to spuriously pull close to the landward wall of the breakwater. This is evident in Figure 6 at t=29 minutes, where the jet has already pulled right up against the caisson and points vertically downward. In the simulation the air that had existed below the overtopping jet was rapidly entrained into the jet, and since there is no path for new air to replace the entrained air, the jet had to pull up against the caisson wall. In experiments, however, much of the air under the overtopping jet remains in place, and so the jet never pulls right up against the caisson.

The reason for the spurious entrainment of air in the simulation is due to the turbulence model implemented. In InterFOAM, the standard k-ε formulation is implemented, but lacking the buoyant production term. In this model, the kinematic eddy viscosity is continuous across the free

surface, resulting in a large diffusive flux of momentum between water and air. However, Nakayama & Yokojima (2003) showed that in reality the kinematic eddy viscosity in water rapidly decreases to nearly zero at the air-water interface, because turbulent eddies from the water do not jump up into the air, and eddies in the air do not dig down into the water surface. Thus, simulations in which the eddy viscosity does not decay to zero at the air-water interface experience too much flux of momentum and scalars across the interface.

To account for the decay of turbulence at the air-water interface, another simulation was run with the k-ε turbulence model modified such that the turbulent eddy viscosity was set to zero in cells where equation (9) was satisfied.

$$0.01 < \alpha_1 < 0.99 \quad (9)$$

Here, α_1 is the phase fraction of water (α_1=0 indicates a cell with only air, while α_1=1 indicates a cell with only water). In effect, this reduced the flux of momentum across locations with an air-water interface.

Figure 11 shows the effect of this modified turbulence model on the overtopping jet. At t=28 min, air still exists under the overtopping jet, so the jet has not pulled all the way up against the landward wall of the caisson. This is close to the behavior seen in the experimental results of Mitsui et al (2012), an improvement over the result of the standard turbulence model with continuous kinematic eddy viscosity shown in Figure 6. However, at later times, the original turbulence model produces results in better agreement with experiments, with the jet plunging to the depth of the rubble mound instead of remaining near the water surface. This indicates that the modified turbulence model handles the plunging jet in air well, but that after plunging into the water it's underestimating the eddy viscosity, as air entrained into the water causes α_1<0.99 in this region. In future work, the turbulence model will further be modified to allow a continuous kinematic eddy viscosity below the elevation of the free surface.

Figure 11 shows that the modified turbulence model does not cause a strong jet pulling gradually away from the caisson, and as such the pressure difference across the caisson does not vary greatly from its hydrostatic result. The resulting forces are thus similar to the hydrostatic results shown on Figures 7, 8, 9, and 10. The maximum bearing stress of 900 kPa is much less than the 1400 kPa resulting from the standard turbulence model, but is still large enough to cause foundation failure according to Uezono and Odani (1987). Since the modified turbulence model simulates the initial phases of overtopping more in line with experiments, while the standard turbulence model simulates the later phases of overtopping better, the actual forces are expected to lie somewhere in between those hindcast by each of these models, and will be better estimated as the turbulence model is refined.

5. CONCLUSIONS

Numerical simulations were used to evaluate potential failure modes of the Kamaishi breakwater during the 2011 tsunami. In addition to the scour reported by Arikawa et al (2012), punching failure of the rubble mound foundation is shown to be a major cause of breakwater failure. The amount of punching stress hindcast by the CFD simulation is greater than the critical value of 800 kPa reported by Uezono and Odani (1987). Using a standard turbulence model with continuous kinematic eddy viscosity across the air-water interface, the maximum hindcast punching stress is 1400 kPa, while a turbulence model with zero eddy viscosity in regions where air is entrained into the water hindcasts a maximum punching stress of 900 kPa. The actual punching stress experienced by the breakwater's foundation must have lied in between these two limiting values.

Acknowledgements:

The authors thank Prof. Kazuo Nadaoka and Prof. Tadaharu Ishikawa for essential advice, and the Sendai Research and Engineering Office for Ports and Airports of the Ministry of Land, Infrastructure and Transport for bathymetry and topography data and design plans of the Kamaishi breakwater.

References:

Arikawa, T., Sato, M., Shimosako, K., Tomita, T., Tatsumi, D., Yeom, G., and Takahashi, K. (2012). "Investigation of the failure mechanism of Kamaishi breakwaters due to tsunami: initial report focusing on hydraulic characteristics." Technical note No. 1251 of the Port and Airport Research Institute. Yokosuka, Japan (in Japanese).

Goda, Y. (2010). "Random seas and design of maritime structures", 3rd edition. World Scientific. New Jersey. Chapter 4.

GSI (Geospatial Information Authority of Japan, 2012). 50 m mesh digital elevation map for eastern Japan. CD-ROM.

Japan Oceanographic Data Center (accessed January 2012). http://jdoss1.jodc.go.jp/cgi-bin/1997/depth500_file.jp

Ministry of Land, Infrastructure, and Transport (data received May 2012). Sendai Research and Engineering Office.

Mitsui, J., Maruyama, S., Matsumoto, A., and Hanzawa, M. (2012). "Stability of armor units covering harbor-side rubble mound of composite breakwater against tsunami overflow." *Journal of Japan Society of Civil Engineers*, Ser. B2 (Coastal Engineering), Vol.68, No.2, pp.I_881-I_885 (in Japanese).

Nakayama, A., and Yokojima, S. (2003). "Modeling free-surface fluctuation effects for calculation of turbulent open-channel flows". *Environmental Fluid Mechanics*. 3: 1-21.

Port and Airport Research Institute (accessed January 2012). GPS buoy data. http://nowphas.mlit.go.jp/nowphasdata/sub300.htm

Saito, T., Ito, Y., Inazu, D., and Hino, R. (2011). "Tsunami source of the 2011 Tohoku-oki earthquake, Japan: inversion analysis based on dispersive tsunami simulations". *Geophysical Research Letters*, vol. 38, L00G19.

Takagi, H. (2009). "Estimation of stability performance of existing breakwaters using a reliability approach and proposal of effective countermeasures to prevent future failures". *Proceedings of the Japan Society of Civil Engineers B*, Vol. 65, No. 3, 246-258 (in Japanese).

Takahashi, S., Toda, K., Kikuchi, Y., Sugano, T., Kuriyama, Y., Yamazaki, H., Nagao, T., Shimosako, K., Negi, T., Sugeno, H., Tomita, T., Kawai, H., Nakagawa, Y., Nozu, A., Okamoto, O., Suzuki, K., Morikawa, Y., Arikawa, T., Iwanami, M., Mizutani, T., Kohama, E., Yamaji, T., Kumagai, K., Tatsumi, D., Washizaki, M., Izumiyama, T., Seki, K., Yeom, G., Takenobu, M., Kashima, H., Banno, M., Fukunaga, Y., Sakunaka, J., and

Watanabe, Y. (2011). "Urgent survey for 2011 Great East Japan Earthquake and Tsunami disaster in ports and coasts." Technical Note No. 1231 of the Port and Airport Research Institute. Yokosuka, Japan (in Japanese).

Uezono, A., and Odani, H. (1987). "Planning and construction of the rubble mound for a deep water breakwater: the case of the Kamaishi bay mouth breakwater." Chapter 4.1 of *Coastal and Ocean Geotechnical Engineering*. The Japanese Geotechnical Society. Tokyo, Japan (in Japanese).

Yaoi, Y., Iai, S., and Tobita, T. (2012). "Centrifuge tests and analysis of complex breakwater failure due to tsunami." *Proceedings of the Japan Society of Civil Engineers Annual Congress.* 435-436. Nagoya, Japan (in Japanese).

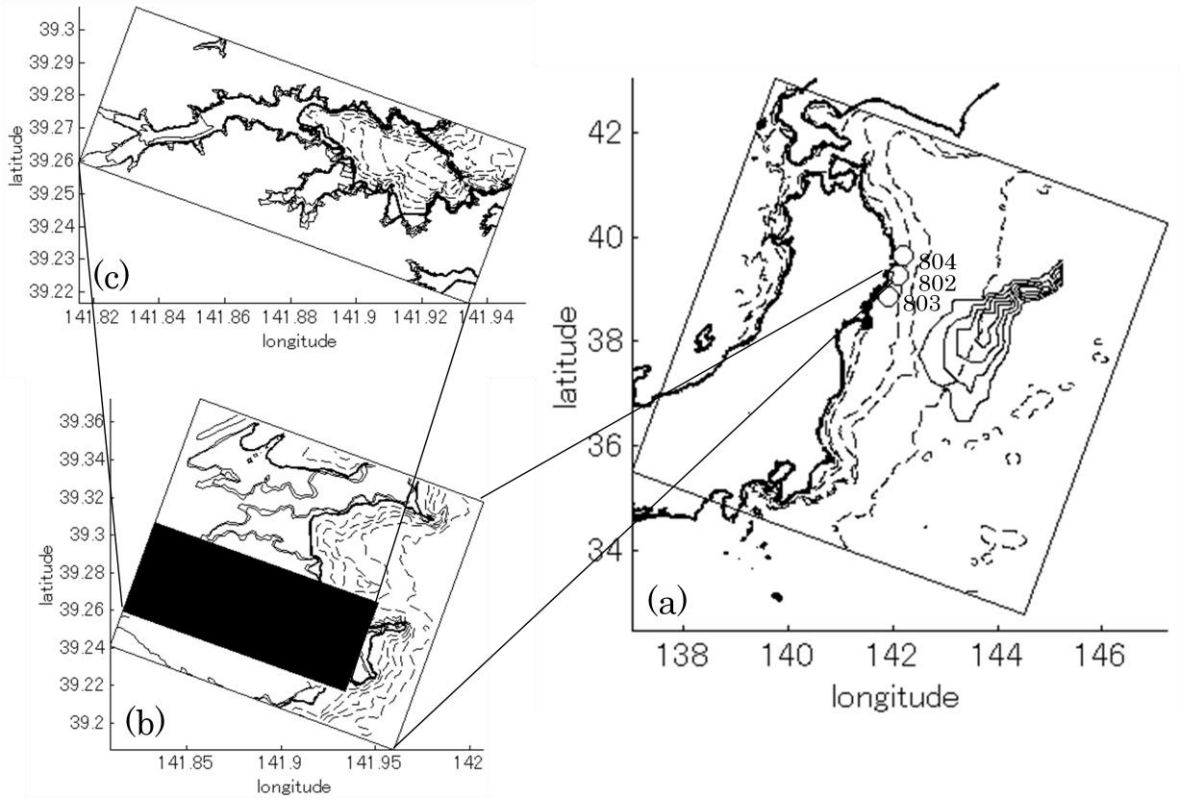


Figure 1. (a) Map of Pacific Ocean domain (2 km resolution). Bathymetric contours (dashed) at 50 m, 100 m, 500 m, 1000 m, and 5000 m. Tsunami initial height contours (solid) at 2 m, 4 m, 6 m, and 8 m. Open circles are PARI GPS buoys 802, 803, and 804. (b) Map of Kamaishi area coast (200 m resolution). Bathymetric contours (dashed) and elevation contours (solid) at 20 m intervals (topography above 40 m omitted for clarity). (c) Map of Kamaishi Bay domain (20 m resolution). Bathymetric contours (dashed) and elevation contours (solid) at 10 m intervals (topography above 40 m omitted for clarity).

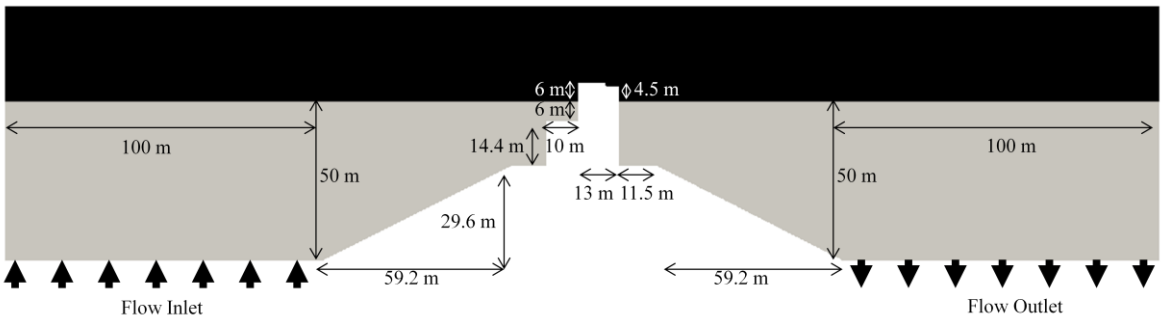


Figure 2. Domain of the plan-view CFD model, showing caisson and rubble mound (white), seawater (gray) and air (black). Seawater level shown is Mean Lower Water, which is the reference level for water levels discussed in this paper. Seaward is to the left, and landward is to the right. For force calculations, the length of the domain into the paper is assumed to be 30 m, which is the actual caisson length in that direction.

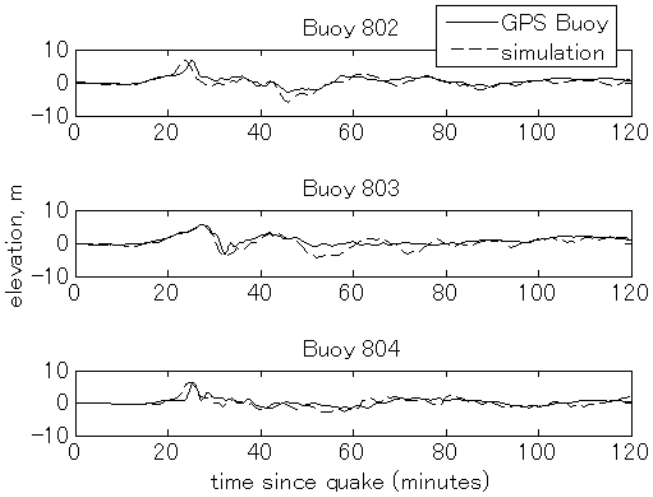


Figure 3. Comparison of measured and modeled (Delft-3D) water levels at the Port and Airport Research Institute's GPS buoy locations near Kamaishi.

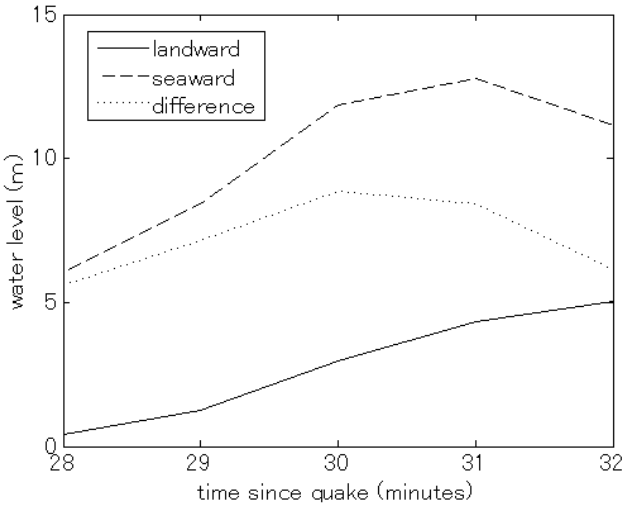


Figure 4. Modeled (Delft-3D) water levels on each side of the middle of the southern section of the Kamaishi breakwater, as well as the difference in water level across the breakwater, during the incident tsunami wave.

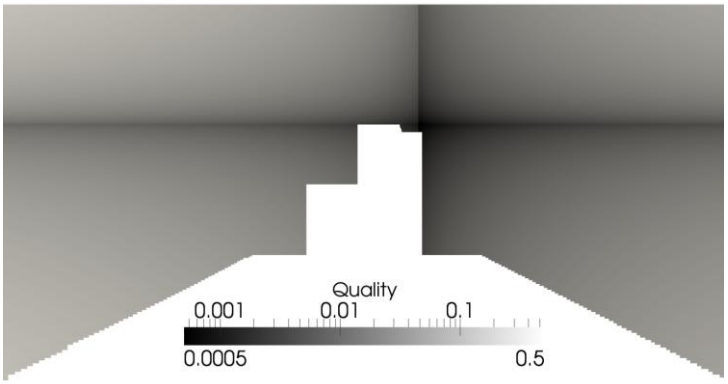


Figure 5. Area of model grid cells. Since the cells are rectangular, cell dimension is approximately the square root of the area.

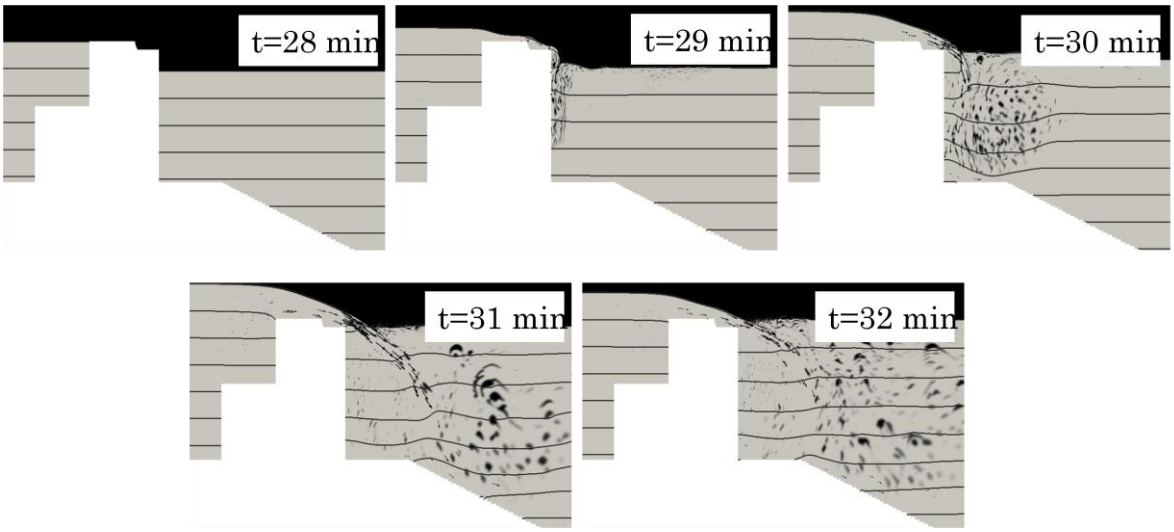


Figure 6. Result of the CFD model during breakwater overtopping, shown at 1-minute intervals. Shades represent caisson and rubble mound (white), seawater (gray), and air (black). Pressure contours in the water are shown at 50 kPa intervals, with the free surface at a gauge pressure of 0 kPa. Arrows show flow velocity vectors in the water. Seaward is to the left, and landward is to the right.

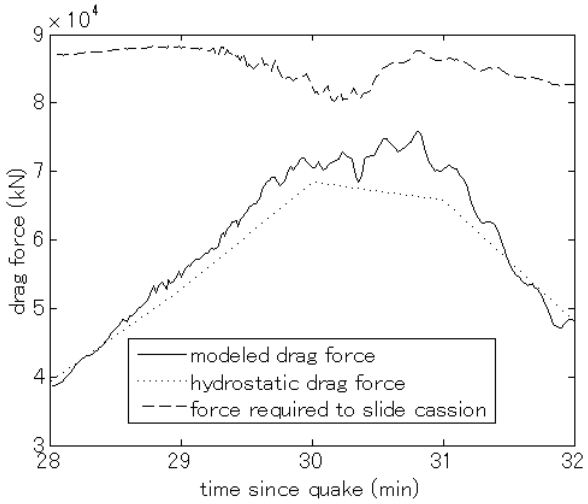


Figure 7. Horizontal force on caisson, for a caisson length normal to the model domain of 30 m.

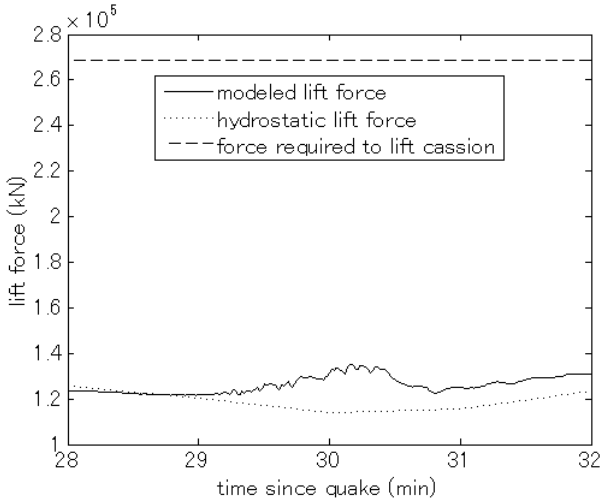


Figure 8. Vertical force on caisson, for a caisson length normal to the model domain of 30 m.

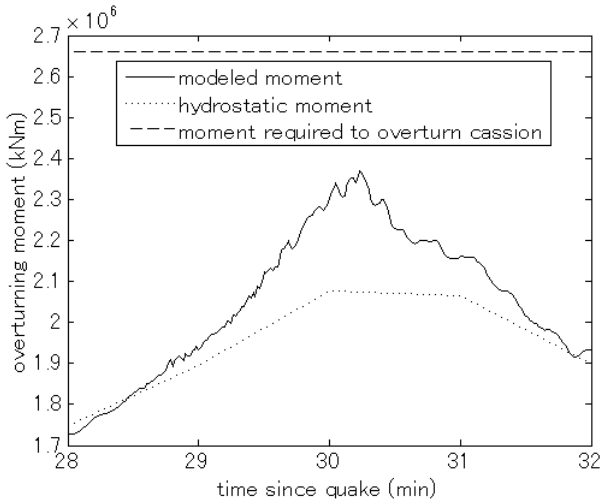


Figure 9. Moment about heel of caisson, for a caisson length normal to the model domain of 30 m.

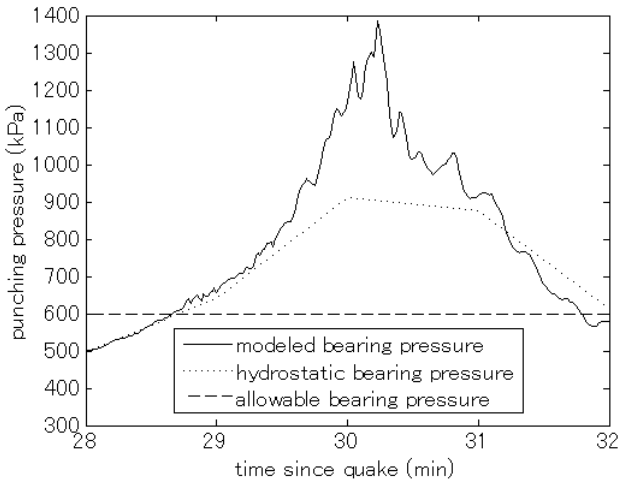


Figure 10. Punching pressure at heel of caisson, for a caisson length normal to the model domain of 30 m.

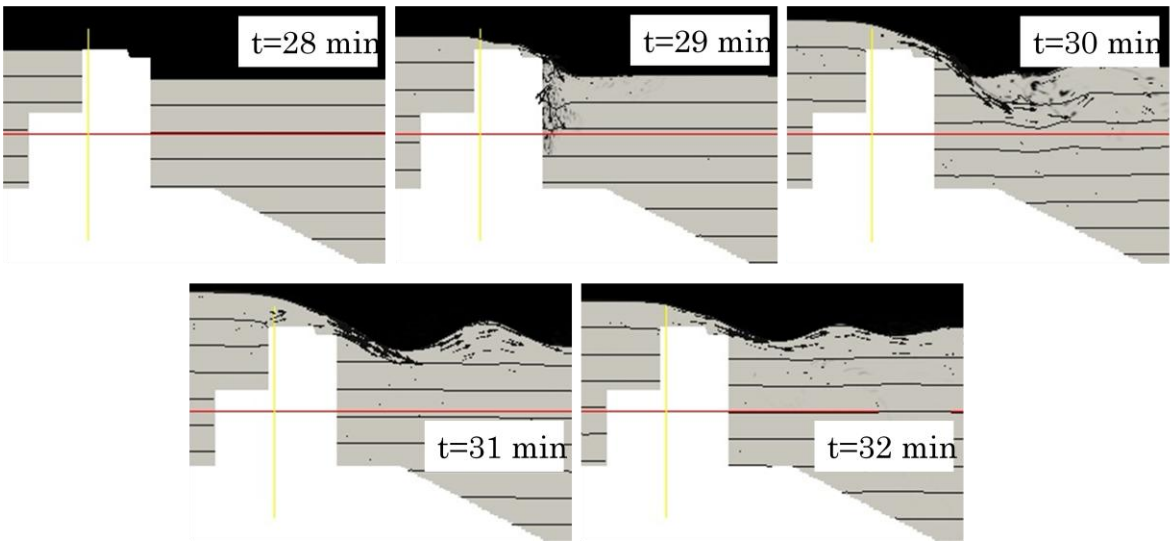


Figure 11. Result of the CFD model with modified turbulence during breakwater overtopping, shown at 1-minute intervals. Shades represent caisson and rubble mound (white), seawater (gray), and air (black). Pressure contours in the water are shown at 50 kPa intervals, with the free surface at a gauge pressure of 0 kPa. Arrows show flow velocity vectors in the water. Seaward is to the left, and landward is to the right.

10CUEE CONFERENCE PROCEEDINGS
10th International Conference on Urban Earthquake Engineering
March 1-2, 2013, Tokyo Institute of Technology, Tokyo, Japan

PROBING ON THE MECHANISM OF THE 2011 GREAT EAST JAPAN EARTHQUAKE AND TSUNAMI

Jiagui Zhang[1), 2)]

1) Professor, Key Laboratory of Neotectonic Movement & Geohazard, Ministry of Land and Resources, China
2) Institute of Geomechanics, Chinese Academy of Geological Sciences, Beijing 100081, China
jiagui62@sina.com

Abstract: It is impossible to explain seismic mechanism within two dimensional tectonics because earthquake occurs in global sphere space, and it is also impossible to explain mantle convection because no driving force achieves it. Hence not every tectonic earthquake is generated by fault slip. In the author's opinion, many earthquakes are generated by the lithospheric interlayer-slide in the deep flow and thrust process. There exists a NWW-ward deep flow and thrust zone from west Pacific to north Japan, Japanese Sea and NE China with axis across the 2011 Great East Japan Earthquake epicenter, north Fukushima, the center of Japanese Sea and DPRK's Kilju to Chinese Changbai Volcanos. The 2011 Great East Japan Earthquake with Mw 9.0 might be given out by the lithospheric interlayer-slide in the zone. The tsunami might be raised by the disorder seabed uplift in the lithospheric interlayer-slide process. There is no subduction of the Pacific plate into the Eurasian plate along Japan Trench. The regional lithosphere especially in the "T"-form spatial hypocenters' region was highly destroyed by the Mw 9.0 earthquake and its aftershocks, and the NWW-ward deep flow and thrust has been continuing. Strong earthquakes will occur often in the deep flow and thrust zone, but no Mw≥9.0 earthquake will occur there in at lest 100 years.

1. INTRODUCTION

On 11th March, 2011, Great East Japan earthquake with Mw 9.0 occurred at an epicenter of 38.30°N and 142.37°E, and at a depth of 29 km (*USGS* 2012a), and huge tsunami was raised by the earthquake. The earthquake and tsunami resulted in extensive and catastrophic damage in coastal northeast Japan and a death toll of some 20,000 (*from the First Announcement of 10 CUEE*). On the former plate tectonic theory (*Dewey at al.* 1970, *Dewey* 1972, *Bird* 2003, *Yakupov* 2011), there was Benioff zone along the east coastal Japan, and the Pacific plate had been subducting into the Eurasian plate along the Japan Trench with dip 30° (*Shi et al.* 1973) in the mantle convection process. On the former seismic ideas, huge earthquakes were often given out by slip faults (*Seismo-Geological Teaching and Research Section of Peking University et al.* 1982), and it is difficult for any huge earthquake to be given out by reverse faults or subduction. Hence why there occurred so gigantic earthquake in the subduction zone is incomprehensible. On the other side, was this (the Mw 9.0 earthquake) a foreshock (*Boyle* 2012)? The author reminds that, for 40 years ago or earlier, it was pointed out that to explain the seismic mechanism within two dimensional tectonics was impossible because earthquake occurred in global sphere space (*Chang et al.* 1973, *Seismo-Geological Teaching and Research Section of Peking University et al.* 1982), and to explain mantle convection was also impossible because no driving force achieved it. Hence not every tectonic earthquake is generated by fault slip, and no plate subduction exists along the Benioff zone, which were further showed by the seismic process of the 2011 Great East Japan earthquake (see the follows). What is the mechanism of some gigantic earthquakes involving the 2011 Great East Japan earthquake? How is the tsunami raised by earthquakes? In the author's opinion, the different idea on the mechanism of some gigantic earthquakes should be put forward. The interlayer-slide might be a type of seismic mechanism (*Chang et al.* 1973). In 1996 or earlier, it was pointed out that, many earthquakes were generated by the lithospheric interlayer-slide in the deep flow and thrust process (*Zhang* 1996). The 2011 Great East Japan earthquake might be given out by the lithospheric interlayer-slide in the NWW-ward deep flow and thrust process under the Pacific, and the tsunami might be raised by the disorder seabed uplift in the lithospheric interlayer-slide process.

2. DESCRIPTION ON THE DEEP FLOW AND THRUST

The lithosphere of the earth is consisted of upper crust, lower crust and upper mantle. The upper crust is consisted of sedimentary cover and crystalline basement. In many regions, there exists middle crust with high conductivity and low P-wave velocity between upper crust and lower crust. Those could be defined as the multi-layer property of the

lithosphere. There exist G-face between sedimentary cover and crystalline basement, Conrad discontinuity between upper crust and lower crust and Moho discontinuity between lower crust and upper mantle (Fig. 1). Those could be

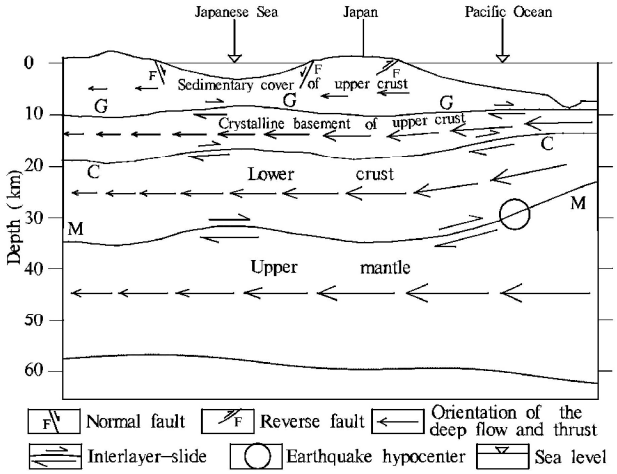


Fig. 1 Schematic Diagram of the Deep Flow and Thrust Framework within the Lithosphere across the 2011 Great East Japan Earthquake Region. In the diagram, G means the top face of the crystalline basement, C means Conrad discontinuity and M means Moho discontinuity.

defined as the discontinuities of the lithosphere. In fact, there exist not only those layers and discontinuities, but also exist many sub-layers and sub-discontinuities. In the geological time scale, any part of the lithosphere bears the rheological property (*Zhou* 2000). In the lithosphere, from the bottom to the surface, the upper mantle bears the strongest rheological property because of the high pressure and high temperature, and the upper crust bears the slightest rheological property, there mainly exist three types of geodynamics which are the gravitical equilibrium, the westward dynamic gravitation generated by earth rotation and cosmic gravity (*Zhang* 2003, 2004). Along the west Pacific margin, the main geodynamics is the westward dynamic gravitation generated by earth rotation, which pushes the lithosphere flowing westward. The flow velocity in each layer is different (Fig. 1). The velocity of upper mantle flow is fast because of its strong rheological property, and the velocity of upper crust flow is slow. Hence the deep flow takes the leading role, and the upper crust flow is mainly dragged by the deep flow. The deep flow is accompanied by the deep thrust because the thrust means pushing. That is the meaning of the deep flow and thrust.

3. THE MECHANISM OF THE 2011 GREAT EAST JAPAN EARTHQUAKE AND THE TSUNAMI

3.1 The Deep Flow and Thrust Zone

There exist deep flow and thrust everywhere. But the deep flow and thrust are uneven not only on horizontal scope, but also on vertical scope. The uneven on horizontal scope shapes many deep flow and thrust zones (*Zhang* 2001, 2003, 2004, 2008, 2012). There exists a deep flow and thrust zone from west Pacific to north Japan, Japanese Sea, DPRK and NE China with axis across the Mw 9.0 earthquake epicenter, north Fukushima, the center of Japanese Sea and DPRK's Kilju to Chinese Changbai Volcanos (*Zhang et al.* 1999, *Zhang* 2001, 2003) (Fig. 2). Along the zone, there exist two

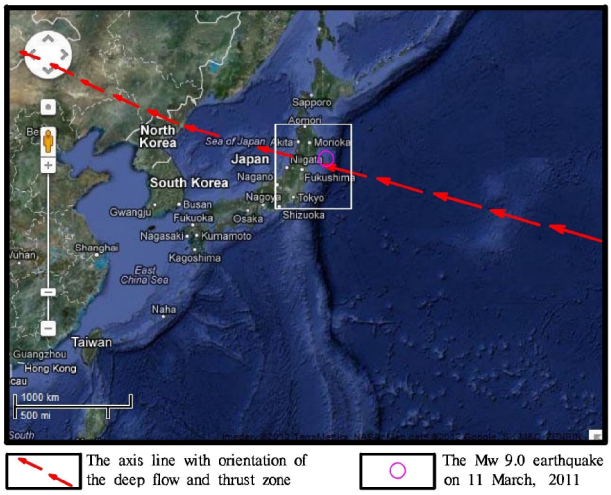


Fig. 2 Map Showing the Deep Flow and Thrust Zone from Pacific Ocean, Japan to China across the 2011 Great East Japan Earthquake Region. The white rectangle frame denotes the outline of Fig. 3 (a). The background image is from *google map*, and the epicenter of the Mw 9.0 earthquake is from *USGS* (2012a). The drawing software MAPGIS was purchased from *Zondy Cyber Group Co., Ltd.*

extremely similar curves, respectively the curve composed by Kuril Trench, Japan Trench and Marianas Trench and the curve composed by the west coast line of Japanese Sea. By the stress measurement results (*Lin et al.* 2011), the principal compression orientation of the stress in the surface layer of the deep flow and thrust zone was NWW in coincidence with the deep flow orientation. Why is it not westward orientation? The reason is the westward dynamic gravitation is interfered by the deep flow and thrust zones in lower latitude region (*Zhang* 2003, 2004). The uneven on vertical scope generates the interlayer-slide in the lithosphere (Fig. 1).

3.2 The Mechanism of the Earthquake

The interlayer-slide may cause earthquake, but does not cause earthquake everywhere. The curve segment of discontinuity is capable of stress concentration, hence there is plentiful of seismic pregnancy (*Zhang* 1996). Is there any curve segment of the discontinuities under the west Pacific margin and east Japan? Yes, the Moho isobathes varies radically from 20 km under the west Pacific margin to 36 km under central Japan (*Institute of Crustal Dynamics et al.* 2001).

The 2011 Great East Japan earthquake was generated by the interlayer-slide of curve segment along the Moho discontinuity (Fig. 1). The epicenter of the earthquake lay near the axis of the deep flow and thrust zone (Fig. 2), which indicated the deep flow and thrust along the axis was the strongest, and there was capable of strong stress

accumulation, and finally the interlayer-slide started there.

Why there occurred so huge earthquake? The dynamic gravitation under the vast Pacific Ocean put forward the huge-scale NWW-ward deep flow and thrust, and the curve segment along the discontinuities are very broad under the west Pacific margin and east Japan (Fig. 1). Hence, the stress could be abundantly concentrated there, and the enormous energy could be highly accumulated there, and finally the enormous energy was released in the interlayer-slide process and the huge Mw 9.0 earthquake came out.

3.3 The Mechanism of the Tsunami

Around the seismic hypocenter, the interlayer-slide was very strong, and the upper mantle slid from the east was accumulated under the seismic hypocenter and its surroundings. The crust above the seismic hypocenter and its surroundings was uplifted massively by the accumulated upper mantle, and consequently the seawater was raised by the surface layer of the crust (also named as the seabed). There was not only the uplift, but also the fall-down followed because of the elasticity of the lithosphere. Those together with the seismic waves put forward the tsunami in horrible massive disorder form.

4. EXPLANATION ON THE PHENOMENA IN THE SEISMIC PROCESS

4.1 The Foreshocks and aftershocks

There occurred few foreshocks and a great deal of aftershocks. The aftershocks occurred not only along the so-called interpolate (*Asano et al.* 2011), nor only above the subduction face as former note (*Shi et al.* 1973), but occurred in three-dimension spatial region.

From 1st March to 30th September, 2011, 77 earthquakes with M≥6.0 excluding the Mw 9.0 earthquake, including 3 foreshocks and 5 7.9≥M≥7.0 earthquakes were recorded (*USGS* 2012a). 3 foreshocks occurred on the close east side of the mainshock, which put forward a low stress space for the sudden huge-scale flow and thrust in the mainshock. Most of the aftershocks occurred along the off coast in a zone with 20° strike, 160 km wide and 600 km long, or along the axis of the deep flow and thrust in a zone with 110° strike, 140 km wide and 330 km long (including the overlap segment of the coast zone), which shaped a "T"-form horizontal region (Fig. 3 (a)). The epicenter of the Mw 9.0 earthquake lay at the juncture area of the "T"-form.

All of the seismic hypocenters lay at a depth of less than 57 km (Fig. 3 (b)). 57 of the seismic hypocenters lay at a depth from 20 km to 56 km, and 11 of the seismic hypocenters under the east side of Japan Trench lay at a depth from 9 km to 47 km, similar to the depth of those under the west side. Those shaped a "T"-form spatial hypocenters' region. In the "T"-form region, the aftershocks under the off coast zone exhibited the curve segments of the lithosphere were capable of stress concentration, and the aftershocks along the axis of the deep flow and thrust zone showed the strongest flow and thrust generated strong stress concentration. It could be deduced the "T"-form region with

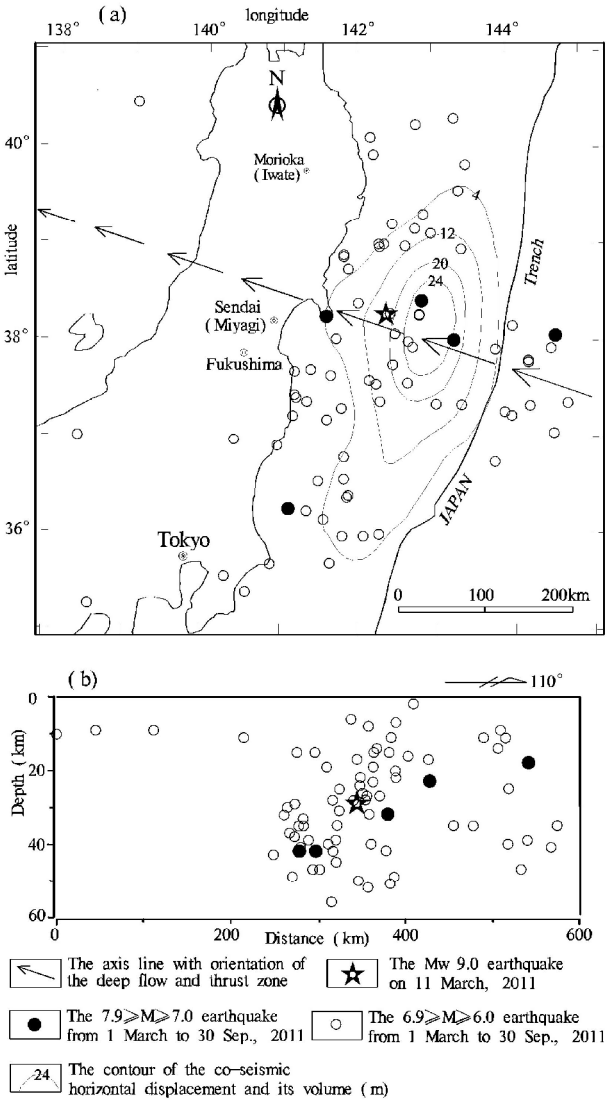


Fig. 3 Distribution of the Earthquakes Determined in This Study, Tectonic Landform and the Deep Flow and Thrust Zone. (a) Shows Horizontal Distributions, and (b) Shows Depth Distributions along the Axis Line. The position data of the earthquakes are from *USGS* (2012a). The co-seismic horizontal displacements are from *Geospatial Information Authority of Japan* (2011). The coastlines are from Japan map in *Guang.org*. Japan Trench position is from *Yakupov* (2011). The drawing software MAPGIS was purchased from *Zondy Cyber Group Co., Ltd*, and the projection software drawing the (b) was MAPSIS developed by *CSBGIS*.

high stress concentration was severely fractured while the mainshock occurred. After that, the residual stress rapidly transferred to vulnerable spots generated by the mainshock, and then the aftershocks occurred in succession. Where were the vulnerable spots? The juncture area of the two sides of "T"-form around the mainshock hypocenter was severely fractured and was the most vulnerable area, and a large number of aftershocks occurred at the vulnerable spots in the area. The juncture spots of the discontinuities and the faults generated by the mainshock was another type of vulnerable spots, and there might exist a great deal of juncture spots

along the Moho discontinuity because there occurred a huge number of 7.9≥M≥4.0 aftershocks along the westward dip face at a depth from 20 km on the east side of the aftershock region to 30 km on the west side of the aftershock region also the east Japanese coast (*Asano et al.* 2011). Hence the aftershocks occurred at the vulnerable spots such as the highly fractured hypocenter of the mainshock and its surrounding, and the juncture spots of the discontinuities and the faults. It was calculated from the aftershock distribution that, the "fault" which might be the interlayer-slide face was in strike 203°, dip 15°-16° and rake 83°-101° (see File 000060436.pdf in *http://www.gsi.go.jp/cais/topic110315.2-index-e.html*), different from the dip 30° as former note (*Shi et al.*1973).

Just three aftershocks occurred isolatedly at a depth of 10 km or less in the west far from the mainshock. Those might indicated the structure and stress of crustal surface layer were affected by the Mw 9.0 earthquake in a wide range.

Generally to state, the foreshocks induced the mainshock, and the aftershocks released the residual stress concentrated at the vulnerable spots and further destroyed the lithosphere structure.

4.2 The Co-Seismic Displacement

Geospatial Information Authority of Japan (2011) has estimated the spatial distribution of co-seismic displacement from GPS data. They showed that the large co-seismic horizontal displacement (>8 m) area extended from off south Iwate to off Fukushima and that its largest peak (>24 m) was located off Miyagi (*Asano et al.* 2011).

The 4.0 m contour of the horizontal displacement shapes a ellipse-like region with long axis at orientation about 20° and length about 430 km, short axis at orientation about 120° and length about 200 km, and the maximum displacement at the "ellipse" center (see File 000060400.pdf in *http://www.gsi.go.jp/cais/topic110315.2-index-e.html*) (Fig. 3(a)). The displacement orientation is SEE-ward, just reverse to the orientation of the deep flow and thrust. The distance of the "ellipse" center perpendicular to the Japan Trench is 90 km west, and just a short part of the 4.0 m contour is in coincidence with or near the trench west. Hence, the co-seismic horizontal displacement area was not exactly correlated to Japan Trench – "the boundary of the two plates", or controlled by the subduction between the two "plates". The "ellipse" center also the seismic epicenter determined by *Geospatial Information Authority of Japan* (2011) lay near the axis of the deep flow and thrust zone (Fig. 3(a)). The land part from Utsunomiya on south to Morioka on north moved SEE-ward for 1-4 m being dependent on locations with large volume on the east coast and little volume on the west coast (see File 000060402.pdf in *http://www.gsi.go.jp/cais/topic110315.2-index-e.html*). Those indicated the surface layer of the crust above the Mw 9.0 earthquake hypocenter and its surrounding compressed by the deep flow and thrust before the mainshock rebounded to the former positions in the mainshock.

The distribution area of the co-seismic vertical displacement is similar to the co-seismic horizontal displacement area, and it is composed by two symmetrical sub areas, one is uplift area on east with maximum uplift volume over 5.5 m, and another was subsidence area on west with maximum subsidence volume over 2.0 m (see File 000060406.pdf in *http://www.gsi.go.jp/cais/topic110315.2-index-e.html*). Those indicated the rebound of the surface layer of the crust was restricted by the east part of the surface layer off the centroid area, and the surface layer in the uplift area was folded. Those also indicated there was no plate boundary along Japan Trench to give a free rebound.

The aftershocks were closely correlated to the co-seismic displacement area, especially to the vertical one. Comparing to the horizontal displacement area, the aftershock epicenters' area showed an extension to three different parts, which were the SW corner, the NW corner and the east part along the axis of the deep flow and thrust zone. Those showed the deep flow and thrust had been continuing, the stress was concentrated at the interlayer-slide ends of the mainshock, and finally the aftershocks were given out.

4.3 The Features of the Focal Mechanisms

From *USGS* (2012b) information, the moment tensor of the mainshock was with fault plane 1 in strike 203°, dip 10° and rake 88°, and fault plane 2 in strike 25°, dip 80° and rake 90° corresponding to an essentially pure double-couple mechanism (*Nettles et al.* 2011), and the P-axis of the focal mechanisms bore azimuth 115° and plunge 35°. Those exhibited the up-west part of the hypocenter was uplifted initially and new faults were generated by the sudden interlayer-slide in the mainshock, and the orientation of the deep flow and thrust to cause the sudden interlayer-slide was basically the azimuth of the P-axis.

From *Asano et al.* (2011) research results, the earthquakes occurring before the mainshock from January 1, 2003 to March 11 5:45 (UTC), 2011 were basically with thrust-type focal mechanisms, and on the other hand, the aftershocks exhibited a variety of focal mechanisms. By the author's observation at the figures in the reference (*Asano et al.* 2011), the aftershocks at shallow depth (maybe above 25 km) were basically with normal-fault-type focal mechanisms, and the aftershocks at deep depth were basically with thrust-type focal mechanisms. Those might show the surface layers of the lithosphere (maybe the whole crust above the hypocenter of the mainshock) had normal-faulting movement or had uplift movement after rebounding SEE-ward in mainshock, and the deep layers (maybe the upper mantle below the hypocenter of the mainshock) were continuously in NWW-ward flow and thrust process. Those also showed the interlayer-slide had been continuing after the mainshock occurred.

4.4 The Reason of Speed-up Earth's Rotation by the Earthquake

NASA geophysicist *Richard Gross* calculated that Earth's rotation sped up by 1.8 microseconds because of the shift in Earth's mass caused by the Mw 9.0 earthquake (*The*

Associated Press 2012). That showed the sudden NWW-ward movement of the mantle pushed by the interlayer-slide in the earthquake process was transferred to the Earth's rotation. But the change in rotation speed was less than the one at 6.8 microseconds caused by 2004's Sumatra earthquake (*The Associated Press* 2012) because of the higher latitude of the Mw 9.0 earthquake hypocenter with shorter arm of force to the earth's rotation axis.

5. CONCLUSIONS AND DISCUSSIONS

There exists a NWW-ward deep flow and thrust zone from west Pacific to north Japan, Japanese Sea and NE China with axis across the Mw 9.0 earthquake epicenter, north Fukushima, the center of Japanese Sea and DPRK's Kilju to Chinese Changbai Volcanos.

The 2011 Great East Japan earthquake was generated by the interlayer-slide of curve segment along Moho discontinuity in the deep flow and thrust zone.

The tsunami was raised by the disorder seabed uplift in the lithospheric interlayer-slide process.

The aftershocks and co-seismic displacements exhibited the huge effect of the Mw 9.0 earthquake on the regional lithosphere structure and its stability. The lithosphere especially in the "T"-form spatial hypocenters' region was highly fractured and folded, and there existed high-degree residual stress after the mainshock.

The focal mechanisms and the earth's rotation speed-up by the Mw 9.0 earthquake showed the stress in the lithosphere bears the NWW-ward principal compression orientation with low dip angle, the surface layers of the lithosphere had an uplift movement after rebounding SEE-ward in mainshock, and the deep layers were continuously in NWW-ward flow and thrust process.

There is no subduction of the Pacific plate into the Eurasian plate with dip 30° or steeper angle along Japan Trench.

Both epicenter data from *USGS* (2012a) and from *Geospatial Information Authority of Japan* (2011) have 49 km position difference. The data from *USGS* (2012a) should be the micro-epicenter showing the initial slide spot, and the data from *Japan* (2011) denoted the position on SEE side should be the macro-epicenter in coincidence with the peak spot of the horizontal displacement showing the maximum seismic intensity spot (Fig. 3(a)).

Was this (the Mw 9.0 earthquake) a foreshock (*Boyle* 2012)? On the author's opinion, the deep flow and thrust has been continuing after the Mw 9.0 earthquake occurred, and for a long time in future, strong earthquakes will occur often in the deep flow and thrust zone, but no Mw≥9.0 earthquake will occur there in at lest 100 years.

Acknowledgements:

Some of the data on the Great East Japan earthquake were obtained from Prof. *Yue Zhongqi* in *Hong Kong University* and Prof. *Lei Xinglin* in *Institute of Geology and Geoinformation/GSJ*. Some of the references were provided by Prof. *Weiren Lin* in *Kochi Institute for Core Sample Research, Japan Agency for Marine-Earth Science and Technology*. The author sincerely appreciates their kindness.

References:

Asano, Y., T. Saito, Y. Ito, K. Shiomi, H. Hirose, T. Matsumoto, S. Aoi, S. Hori, and S. Sekiguchi (2011), "Spatial distribution and focal mechanisms of aftershocks of the 2011 off the Pacific coast of Tohoku Earthquake," *Earth Planets Space*, 63, 669–673.

Bird, P. (2003), "An updated digital model of plate boundaries," *Geochem. Geophys. Geosyst.*, **4**, 1027, doi:10.1029/2001GC000252.

Boyle, A. (2012), "Japan's quake still poses puzzles," *http://cosmiclog.nbcnews.com/_news/2012/03/09/10627441-japans-quake-still-poses-puzzles?lite*.

Chang, Wenyou, Hong Ye, Jiayou Zhong, Musheng Zhang (1973), A preliminary note on block-faulting and layer-gliding and their bearing upon the distribution and mechanism of earthquake. *Chinese Journal of Geology*, 8(4): 273-280 (in Chinese with English abstract).

Dewey, J. F., and J. M. Bird (1970), "Mountain belts and global tectonics," *J. Geophys. Res.*, 75, 2625–2647.

Dewey, J. F. (1972), "Plate tectonics," *Scientific American*, 226, 56-68.

Geospatial Information Authority of Japan (2011), "The 2011 off the Pacific coast of Tohoku Earthquake, Coseismic and postseismic slip distribution on the plate interface (preliminary result)," *http://www.gsi.go.jp/cais/topic110315.2-index-e.html*.

Institute of Crustal Dynamics, China Seismological Bureau and Basin and Reservoir Research Center, University of Petroleum (Beijing) (2001), "The Moho depth isogram map of China and outlying zone (1:15000000)," *Seismological Press, Beijing* (in Chinese with brief English introduction).

Lin, W., S. Saito, Yoshinori S., Yuzuru Y., Yoshitaka H., and Toshiya K. (2011), "Principal horizontal stress orientations prior to the 2011 Mw 9.0 Tohoku-Oki, Japan, earthquake in its source area," *Geophys. Res. Lett.*, 38, L00G10, doi: 10.1029/2011GL049097.

Nettles, M., G. Ekstrom, and H. C. Koss (2011), Centroid-moment-tensor analysis of the 2011 off the Pacific coast of Tohoku Earthquake and its larger foreshocks and aftershocks, *Earth Planets Space*, **63**, 519–523.

Seismo-Geological Teaching and Research Section of Peking University, Regional-Geological Teaching and Research Section of Nanjing University, Seismo-Geological Teaching and Research Section of Wuhan College of Geology (1982), "Seismo-geology", *Seismological Press, Beijing*, 34, 37-39, 40-42, 53, 420 (in Chinese).

Shi, Zhenliang, Wenlin Huan, Huangring Wu, Xinling Cao (1973), On the intensive seismic activity in China and its relation to plate tectonics. *Chinese Journal of Geology*, 8(4), 281-293.

The Associated Press (2012), "Japan's earthquake causes day to get a tiny bit shorter," *http://www.msnbc.msn.com/id/42037792/ns/technology_and_science-science/*.

USGS (2012a), "Earthquake Catalog Search," *http://earthquake.usgs.gov /regional/neic*.

USGS (2012b), "Event 201103110546A in CMT catalog web search," *http://www.globalcmt.org*.

Yakupov, Oleg (2011), "2011 Sendai earthquake and tsunami (Japan)." *http://www.virtualuppermantle.info/2011-Sendai-Japan.htm.*

Zhang, Jiagui (1996), "Model of earthquake-pregnancy controlled by the deep thrust under continental rift system," *30th IGC Abstracts*, Vol. 3, p179.

Zhang, Jiagui, Haitao Hu (1999), "Discussion on the genesis of CO_2 outgassed in geothermal processes around the Tianchi lake, Changbai mountains," *Geological Review*, 45(suppl.), 231-235 (in Chinese with English abstract).

Zhang, Jiagui (2001), Analysis of regional crustal stability from the framework of deep flow and thrust. *Journal of Chengdu University of Technology (Science & Technology Edition)*,

28(Suppl.), 195-199 (in Chinese with English abstract).
Zhang, Jiagui (2003), "Few deep flow and thrust zones in East Asian continent". *Acta Geoscientica Sinica*, 24(Suppl.), 5-10 (in Chinese with English abstract).
Zhang, Jiagui (2004), "Global mantle flow and thrust zones and geodynamics," *32nd IGC Florence 2004 - Scientific Sessions: abstracts (part 1)*, Italy, p763 (pdf).
Zhang, Jiagui (2008), "About the birth of Med by mantle flow and thrust," *Abstracts of the 33rd IGC*, Oslo, Norway. In CD-ROM: 33IGC abstracts\1317517.html.
Zhang, Jiagui (2012), "5 deep flow and thrust zones and their control over the earthquake in Sanjiang region, SW China and SE Asia", Proceedings of the 34th International Geological Congress 2012, Brisbane, Australia, *BHP Billiton Mitsubishi Alliance*. ISBN 978-0-646-57800-2. p3223.
Zhou, Hui (2000), "Progress on studies of rheological dynamics of continental lithosphere," *Earth Science Frontiers*, 7(Suppl.), 121-127 (in Chinese with English abstract).

10CUEE CONFERENCE PROCEEDINGS
10th International Conference on Urban Earthquake Engineering
March 1-2, 2013, Tokyo Institute of Technology, Tokyo, Japan

DEVELOPMENT OF TSUNAMI STRUCTURAL DESIGN PROVISIONS FOR THE USA

Gary Chock[1)]

1) Chair, ASCE 7 Tsunami Loads and Effects Subcommittee; President, Martin & Chock, Inc., Honolulu, Hawaii / USA
gchock@martinchock.com

Abstract: The Tsunami Loads and Effects Subcommittee of the ASCE/SEI 7 Standards Committee is developing a proposed new Chapter 6 - Tsunami Loads and Effects for the 2016 edition of the ASCE 7 Standard. These new provisions will include loads for tsunami and its effects, and the design procedure will also incorporate certain aspects of Performance Based Tsunami Engineering. The ASCE 7 Standard classifies facilities in accordance with Risk Categories that recognize the importance or criticality of the facility, and the tsunami design requirements in the ASCE 7 Standard vary by Risk Category.

A method of Probabilistic Tsunami Hazard Analysis has been established in the recognized literature that is generally consistent with Probabilistic Seismic Hazard Analysis in the treatment of uncertainty. Structural member acceptability criteria will be based on performance objectives for a 2,500-year Maximum Considered Tsunami. It is presently anticipated that the ASCE 7 Tsunami Loads and Effects Chapter will be applicable only to the states of Alaska, Washington, Oregon, California, Hawaii, and the territories of Guam, American Samoa, and Puerto Rico. Ground shaking effects and subsidence from a preceding local offshore Maximum Considered Earthquake will also need to be considered prior to tsunami arrival for Alaska and states in the Pacific Northwest regions governed by nearby offshore subduction earthquakes.

1. INTRODUCTION

A national standard for engineering design for tsunami effects does not presently exist. Presently, tsunami risk to coastal zone construction is not explicitly and comprehensively addressed in design codes of the United States. Beginning from February, 2011, the Tsunami Loads and Effects Subcommittee of the American Society of Civil Engineers / Structural Engineering Institute ASCE/SEI 7 Standards Committee has been developing a proposed new Chapter 6 - Tsunami Loads and Effects, with Commentary for the 2016 edition of the ASCE/SEI 7 Standard, *Minimum Design Loads for Buildings and Other Structures*, These new provisions would provide prescriptive loads for tsunami and its effects, and the analysis procedure will also incorporate aspects of Performance Based Tsunami Engineering (Chock, 2011). In this paper we provide a preview emphasizing the general intent and design methodologies of these developing code provisions (*these are the Dec. 2012 draft provisions subject to final revisions*).

The International Building Code (IBC) references design provisions that are given in American Society of Civil Engineers Standard 7. The ASCE 7 Standard becomes part of an enacted building code law through adoption of the model International Building Code by the local authority having jurisdiction (such as a state, county, or city). The IBC will probably incorporate ASCE 7-16 in 2018 or 2021. Therefore, it is anticipated that the first national tsunami design provisions of ASCE 7 would be utilized soon after.

2. OVERVIEW OF THE PROPOSED ASCE-7 TSUNAMI LOADS AND EFFECTS CHAPTER 6

2.1 Organization

The Tsunami Loads and Effects design provisions (ASCE 7 Chapter 6) have been organized into the following sections:

6.1 General Requirements
6.2 Definitions
6.3 Symbols and Notation
6.4 Tsunami Risk Category Design Criteria
6.5 Procedures for Determination of Offshore Tsunami Wave Height
6.6 Procedures for Determining Tsunami Inundation
6.7 Design Parameters for Tsunami Flow over Land
6.8 Structural Design Procedure for Tsunami Effects
6.9 Hydrostatic Loads
6.10 Hydrodynamic Loads
6.11 Impact Loads
6.12 Foundation Design
6.13 Structural countermeasures for reduced loading
6.14 Special Occupancy Structures
6.15 Designated Nonstructural Systems
6.16 Non-building critical facility structures

2.2 General Requirements and Design Criteria

Mitigation of tsunami risk requires a combination of emergency preparedness for evacuation in addition to providing structural resilience of critical facilities, infrastructure, and key resources necessary for immediate

response and economic and social recovery. Critical facilities would include emergency response, medical, tsunami refuges and shelters, ports and harbors, lifelines, transportation, telecommunications, power, financial institutions, and major industrial/commercial facilities. The ASCE 7 Standard (ASCE, 2010) classifies facilities in accordance with Risk Categories that recognize the importance or criticality of the facility (Table 1). In the tsunami chapter, further refined definitions of the Risk Categories for Risk Categories III and IV are included with respect to specific occupancy/functional criteria.

Table 1 Risk Categories of Buildings and Other Structures per ASCE 7

Risk Category I	Buildings and other structures that represent a low risk to humans in the event of failure
Risk Category II	All buildings and other structures except those listed in Risk Categories I, III, IV
Risk Category III	Buildings and other structures with hazard to human life or substantial potential to cause a substantial economic impact and/or mass disruption of day-to-day civilian life in the event of failure
Risk Category IV	Buildings and other structures designated as essential facilities

Tsunami design performance objectives are similar in approach to typical U.S. seismic performance objectives. The common performance-based concept is that there are estimated hazard levels aligned with the corresponding desired building performance levels. In Table 2, the key performance levels are shown for two return periods, the 100-year period and a maximum considered 2,500-year (i.e., the 0.0004 annual probability) event. A return period of 100-years for the occasional low-level tsunami that aligns better with coastal storm flood criteria, since there will be a need to evaluate which of the two effects governs the minimum elevation of the structure's lowest floor level. A 2,500-year hazard level Maximum Considered Tsunami is selected for design consistency with the ASCE 7 seismic hazard criteria, since tsunami can occur as a coseismic effect of a nearby earthquake.

For the tsunami with a 0.01 annual probability of exceedance, buildings and other structures shall be designed and constructed to withstand tsunami loads and effects determined for the flooding associated with tsunamis. The elevation of the bottom of the lowest horizontal structural member of the lowest floor elevation shall be above the inundation depth. Foundations and vertical members supporting the lowest floor shall be designed to resist flotation, collapse and lateral movement.

Low-rise Risk Category II buildings would be at higher risk of being fully inundated during a maximum considered 2,500-year tsunami. When communities with public awareness are enabled with tsunami warning systems and emergency operations plans for evacuation, low-rise Risk Category II buildings should not be occupied during a tsunami. Therefore, these buildings are not required to be designed against the 2,500-year tsunami event.

A minimum height defines the range of taller Risk Category II buildings where design to prevent collapse would be required. Based on analysis of reinforced concrete buildings, a threshold of ~20 m (65 ft.) has been recommended as the height sufficient for both reliable life safety and reasonable economic cost to meet this goal.

Risk Category III buildings are to be designed against collapse, since these structures include school buildings with mass assembly occupancies, critical infrastructure such as power and water treatment, and also other facilities that may store hazardous materials.

For Risk Category IV essential facilities that may necessarily exist within a coastal zone subject to tsunami hazard, the design provisions address the life safety performance level for hydrostatic, hydrodynamic, waterborne debris accumulation and impact loads, subsidence, and scour effects generated by any preceding earthquake and the subsequent tsunami flow conditions..

Table 2 ASCE-Proposed Tsunami Performance Levels for Various Risk Category Types

Hazard	**Tsunami Performance Level**			
Tsunami Return Period	**Operational**	**Immediate Occupancy**	**Life Safe**	**Collapse Prevention**
100 years	Risk Category IV	Risk Category III	Risk Category II	
Maximum Considered (2500 yrs.)		Vertical Evacuation Refuge Buildings	Risk Category IV	Risk Category III and > 65-ft.-high Risk Category II

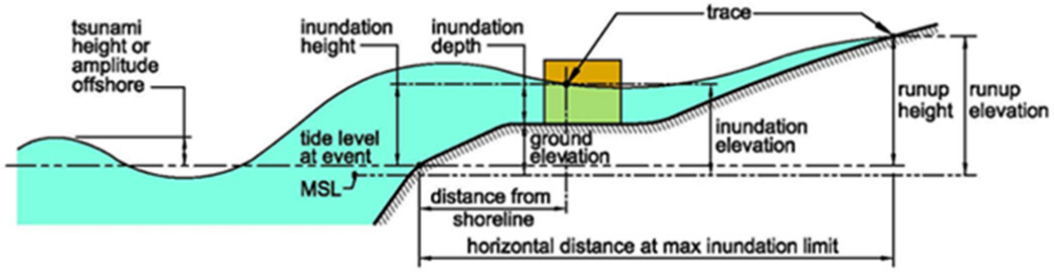


Figure 1 Illustrated Tsunami Terminology

2.3 Definitions

Key terms for tsunami definition are offshore tsunami height, inundation depth, runup elevation, and maximum (horizontal) inundation limit. Offshore Tsunami Height is measured where the water depth is 100 meters. Inundation Depth is the depth of tsunami water level with respect to the local grade plane. Runup Elevation is the elevation above mean sea level at the tsunami inundation limit. Maximum Inundation Limit is the maximum horizontal extent of the inundation zone relative to the shoreline at Mean Sea Level. There key parameters are illustrated in Figure 1.

The Tsunami Hazard Zone is the area vulnerable to being flooded or inundated by the Maximum Considered Tsunami, which is taken as having a 2% probability of being exceeded in a 50-year period, or a 2500 year average return period. The Maximum Considered Tsunami is the design basis event used for design, consisting of the inundation depths and flow velocities taken at the stages of in-flow and out-flow most critical to the structure.

It is presently anticipated that the ASCE 7 Tsunami Loads and Effects Chapter will be applicable only to the states of Alaska, Washington, Oregon, California, Hawaii, and the territories of Guam, American Samoa, and Puerto Rico. These tsunami-prone regions have quantifiable hazards due to tsunamigenic earthquakes.

2.4 General Tsunami Design Criteria

As noted above, buildings and structures would have their structural performance objective defined based on height and Risk Category, per one of the following performance level objectives.

IMMEDIATE OCCUPANCY STRUCTURAL PERFORMANCE: The post-event damage state in which a structure remains safe to occupy

LIFE SAFE STRUCTURAL PERFORMANCE: The post-event damage state is that in which a structure has damaged components but retains a margin against onset of partial or total collapse.

COLLAPSE PREVENTION STRUCTURAL PERFORMANCE: The post-event damage state is which a structure has damaged components and continues to support gravity loads but retains little or no margin against collapse.

Building failure modes differ fundamentally between seismic (high frequency dynamic effects generated on the inertial masses of a structure) and tsunami (externally and internally applied sustained fluid pressures varying with stages of depth over long period cycles of load reversal). Tsunami-induced failure modes of buildings have been examined in several detailed analyses of case studies taken from the Tohoku Tsunami of March 11, 2011 (Chock, et al, 2013a). Building components are subject simultaneously to internal forces generated by the external loading on the lateral-force-resisting system together with high intensity momentum pressure forces exerted on individual members. The tsunami provisions must maintain the physical consistency of tsunami flow conditions with respect to runup, inundation depth and associated current velocities. Because the use of a single scalar factor applied simultaneously on depth, current velocity, and force would violates fluid mechanics, the prescriptive "R" scalar reduction factors used by historical custom almost exclusively in the U.S. seismic code is not appropriate. U.S. seismic designs use an semi-empirical/customary response modification factor, the "R-factor", to account for both the structural ductility and overstrength of the lateral-load-resisting system.

Regions governed by nearby offshore earthquakes structure will need to resist the design earthquake, prior to the arrival of the design tsunami inundation. For the Pacific Northwest (Geist, 2005) and Alaska, this necessarily includes consideration of ground shaking effects and subsidence from the preceding local offshore subduction earthquake. Tsunami design must also enable a multi-hazard performance-based analysis technique with the ability to evaluate primary members both ductility for initial dynamic earthquake loading and the demand of sustained tsunami hydrodynamic fluid forces on the remaining structural capacities after an near-field subduction earthquake.

To do this analysis of performance, we propose to utilize the Analysis Procedures and Acceptance Criteria of ASCE 41 (ASCE, 2006), *Seismic Rehabilitation of Existing Buildings*. With an adaptation of this method, strength and stability can be checked to determine that the designs of the structural components are capable of withstanding the tsunami to achieve the Structural Performance level required. The tsunami adaption allows the techniques of the Linear Static Procedure and the Nonlinear Static Procedure. Strengths of structural components can then be checked using the ASCE 41 acceptability criteria for actual tsunami loads and depths that are correct from the standpoint of fluid mechanics without load factors. In the case of a preceding local earthquake, the reduction of structural capacity can be

conservatively accounted for with this technique. Utilizing the performance-based component acceptability criteria in ASCE/SEI 41-06, Deformation-Controlled Actions in primary and secondary components shall satisfy Eq. (1).

$$m\,Q_{CE} \geq Q_{UD} \quad (1)$$

where:

m : the pseudo-ductility factor used as a multiplier of a structural component's expected strength

Q_{CE} : Expected strength of the structural element

Q_{UD} : Deformation-controlled Force due to gravity and tsunami loading

Force-Controlled Actions in primary and secondary components shall satisfy Eq. (2).

$$Q_{CL} \geq Q_{UF} \quad (2)$$

where:

Q_{CL} : Lower-bound strength of the structural element

Q_{UF} : Maximum force generated in the element due to gravity and tsunami loading

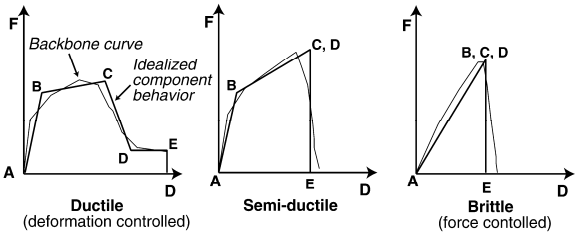


Figure 2 Sample Diagrams of Force-Displacement Capacity Boundaries of Structural Component Behavior.

Loading shall consider a minimum of two tsunami in-flow and out-flow cycles, one of which shall be at the maximum design level. This is required because the condition of the building and its foundation is altered in each tsunami inflow and out-flow cycle. Therefore, building foundation designs shall consider changes in the site surface and the in-situ soil properties during the design seismic event and subsequent design tsunami event. Foundation effects in the geotechnical investigation report shall include consideration of slope instability, liquefaction, total and differential settlement, subsidence, and surface displacement due to faulting or seismically induced lateral spreading.

Where tsunami loads or effects exceed acceptability criteria for a structural element, it shall be permitted as an alternative to apply progressive collapse provisions of UFC 4-023-03, Design of Structures to Resist Progressive Collapse, (DoD, 2009).

2.5 Procedures for Tsunami Hazard Assessment

Probabilistic Tsunami Hazard Analysis (PTHA) shall be used to determine the offshore tsunami heights for the 100-year and Maximum Considered Tsunami. A method of probabilistic tsunami hazard analysis has been established in the recognized literature that is generally consistent with probabilistic seismic hazard analysis in the treatment of uncertainty (Geist and Parsons, 2006).The runup for this hazard probability is used to define a map the tsunami hazard zone. An example of the probabilistic tsunami hazard analysis technique has been performed for California (Thio, 2010). The basics of Probabilistic Tsunami Hazard Analysis for a region are as follows:

1. Tsunamigenic subduction zones and non-subduction seismic thrust faults are discretized into a compiled system of rectangular subfaults each with corresponding tectonic parameters.

2. Tsunami waveform generation is modeled by deconstructing a tsunami that is generated by an earthquake into a linear combination of individual tsunami waveforms from a set of subfaults that describe the earthquake rupture in location, orientation, and rupture direction and sequence.

3. A statistically weighted logic tree approach is used to account for variations in the model parameters for tsunamigenic earthquake occurrence probabilities from tectonic, geodetic, historical, and paleo-tsunami data, and estimated plate convergence rates.

4. Propagate tsunamis in deep water using the linear long wave equations to take into account spatial variations in seafloor depth.

5. Determine the highest offshore wave heights at 100m depth, period, and depth-averaged celerity for the design level exceedance rates of the 100-year and the 2,500-year tsunami.

6. Disaggregate the seismic sources and associated moment magnitudes that together contribute at least 90% to the net offshore tsunami hazard at the site under consideration for each design level.

2.6 Procedures for Tsunami Inundation Analysis

Analyze each disaggregated tsunami event to determine representative design parameters (max height, depth, velocity, and flux). Regardless of soil type, the Maximum Considered Tsunami inundation shall assume an overall elevation settlement of 1 meter of the inundated region when local subduction thrust faulting is the tsunamigenic mechanism that contributes at least 90% to the net offshore tsunami hazard at the site.

7. Use nonlinear shallow water wave equations to modeling regime from 100m depth towards the shore to transform the probabilistically defined offshore height to maximum inundation. The following effects shall be included as applicable to the bathymetry:
    a. Shoaling to determine Nearshore Tsunami Height
    b. Dispersion effects
    c. Reflected waves
    d. Channeling in bays
    e. Shelf and bay resonances
    f. Fringing submerged reefs and shelves
    g. Soliton fission of short period undular waves in gradually sloping offshore bathymetry
    h. Bore formation and propagation

8. Analyze each tsunami event from the disaggregated sample to determine flow parameters. Manning's coefficient for equivalent terrain macro-roughness is used to account for friction. Maximum. runup, inundation depth, flow velocity, and/or specific momentum flux is permitted to be evaluated by either of the following techniques:
   a. by taking the weighted average of the scenario runs that bracket the offshore waveheight for the return period. Inundation limit shall be determined by the area that is inundated by tsunami waves from all the disaggregated major source zones for that particular return period.
   b. by developing the probabilistic distributions of flow parameters from the sample of computed tsunamis and construct the statistical distributions of flow parameters for at least four critical stages.
9. From the probabilistic events, capture the design flow parameters of inundation depth, flow velocity, and/or specific momentum flux at the site of interest.

2.7 Design Parameters for Tsunami Flow over Land

Where the coastline can be approximated in behavior by the use of one-dimensional linear transects of a composite bathymetric / topographic profile, in lieu of steps 7, 8, and 9 above, the tsunami inundation design parameters of minimum runup, specific momentum flux, and current velocities are permitted to be estimated by analytical formulations for substantially uniform sloped topographic profiles, or by an energy analysis approach used for terrain that can be idealized as a series of linear sloped segments. Forces determined with these analysis methods are required to be increased by an Importance Factor depending on the Risk Category. In the energy approach (Figure 3), the potential energy budget of the tsunami is first represented by the theoretical runup at the shoreline on a landward extension of the nearshore bathymetric slope.

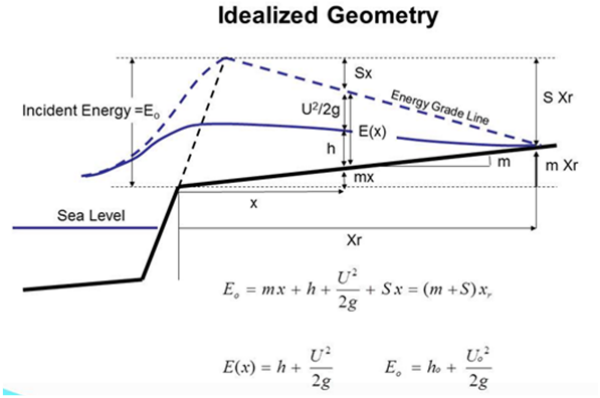


Figure 3 Energy Method Parameters

Then hydraulic analysis using Manning's coefficient for equivalent terrain macro-roughness is used to account for friction along with the profile comprised of a series of 1-D slopes, to determine the variation of high velocity-associated inundation depth across the inland profile. Velocity is assumed to be a function of inundation depth, calibrated to the prescribed Froude number $u/\sqrt{(gh)}$ at the shoreline and decreasing inland.

If only maximum tsunami depth at the site can be estimated, for Risk Category II buildings and structures a conservative simplified pseudo-hydrostatic lateral pressure can be applied to the structure to represent the effect of hydrodynamic flow on the structure. It is determined using the maximum inundation depth with a fluid density of three times that of seawater. This simplified method is similar to the approach taken in Japan using the Structural Design Method of Buildings for Tsunami Resistance (Okada et al, 2004 and Fukuda, et al 2012). For the simplified pressure, conventional strength design procedures may be used if only Life Safety Structural Performance is required.

2.8 Structural Design Procedure for Tsunami Effects

Four stages of tsunami surge loading defined by inundation depths and their associated velocities are required to be considered:

1. Near-maximum momentum flux when depth is approximately one-quarter of maximum
2. Two-thirds of maximum inundation depth
3. Maximum water depth when velocity is zero
4. Return flow when depth is approximately one-third of maximum

The design limit for the 2,500-year event is based on the inelastic capacity of primary structural load-carrying elements. For a distant tsunami, the available strength could be up to the yield point or a post-yield hardening point, depending on the performance level. When a local subduction zone creates the tsunami event, the acceptable solution point on the force-displacement capacity boundary can only be found to the right of the solution for the preceding earthquake effect. The available strength for tsunami resistance would account for any strength and stiffness degradation caused by the preceding earthquake. This is conceptually illustrated in Figure 4.

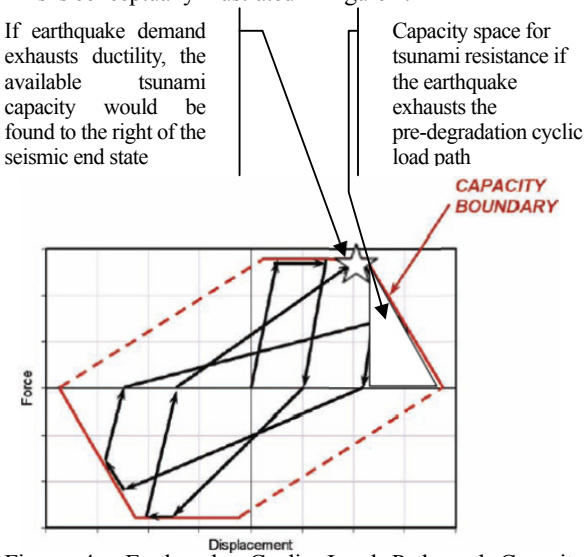


Figure 4 Earthquake Cyclic Load Path and Capacity Available for Tsunami (Adapted from FEMA P440A)

When a near-sourced high-intensity tsunami-genic earthquake occurs, structures with less initial resistance will have a greater proportion of their systemic ductility consumed. Less member ductility would then be available for sustaining subsequent tsunami loading cycles. Accordingly, the seismic performance objective may need to be enhanced for critical coastal structures near subduction zones so that adequate inelastic reserve is available for a maximum considered tsunami following a maximum considered earthquake.

Loads on buildings shall be calculated assuming a minimum closure ratio of 70% of the pressure exposed surface area of the exterior enclosure; this accounts for accumulated waterborne debris as well as trapped against the side of the structure as well any internal blockage caused by building contents that cannot easily flow out of the structure. As a practical matter based on observations of buildings subjected to destructive tsunami, "breakaway" walls cannot be relied upon to relieve structural loading, primarily due to the copious amount of external debris. Also, studs and girts may be capable of entrapping contents within a building, thus generating hydrodynamic drag forces on the internal debris that in turn transfer those loads to the structure.

As an Extraordinary Event, per ASCE 7 Section 2.5 (ASCE, 2010), the appropriate load combinations are shown in Eq. (3) and (4) below.

$$Q_U = 1.2D + - 1.0F_{TSU} + 0.25L + 0.2S \quad (3)$$

$$Q_U = 0.9D + - 1.0F_{TSU} \quad (4)$$

where: D : dead load
L : live load
S : snow load
F_{TSU} : tsunami loads and effects

2.9 Structural Loads

The following tsunami load effects should be considered for structural design of buildings and structures:

1. Hydrostatic forces, buoyant forces, and additional fluid gravity loads from retained water;
2. Hydrodynamic forces and hydrodynamic uplift forces;
3. Debris impact forces and debris damming forces
4. Foundation scour and pore pressure softening effects on the soil

The structural details of numerous damaged buildings in the Tohoku region were documented soon after the March 11, 2011 Tohoku-Oki earthquake and tsunami by a reconnaissance team sponsored by the American Society of Civil Engineers. Tsunami flow depths and velocities were determined based on analysis of video records and the observed effects on simple benchmark structures in the flow. Equations for various conditions of fluid loading were then validated through failure analyses completed for several buildings using finite element modeling and LiDAR scans. These analysis tools were applied full-scale to buildings with clearly identified failure mechanisms to validate the tsunami loading provisions in the ASCE 7 Standard (Chock, 2013b).

Hydrostatic Loads

Minimum Fluid Density for Tsunami Loads

Seawater density ρ_{sw} shall be taken as 1025 kg/m^3. The minimum fluid density ρ_s for determining tsunami loads accounting for suspended solids and debris flow-embedded smaller objects, shall be determined per Eq. (5):

$$\rho_s = k_s \rho_{sw} \quad (5)$$

where k_s , fluid density factor, shall be taken as 1.1

Buoyancy

Reduced self-weight due to buoyancy shall be considered for all inundated structural and non-structural elements of the building using Eq. (6). Uplift due to buoyancy shall include enclosed spaces without breakaway walls that have opening area less than 25% of the inundated exterior wall area. Buoyancy shall also include the effect of air trapped below floors, including foundation slabs, and in enclosed spaces where the walls are not designed to break away. All windows, except those designed for wind-borne debris impact or blast loading, shall be permitted to be considered openings. Foundation elements, excluding piles, shall be included in this calculation.

$$F_v = k_s \rho_{sw} g \forall \quad (6)$$

where
k_s : fluid density factor
ρ_{sw} : effective equivalent density of seawater
$\forall$: Volume

Unbalanced Lateral Force

Structural walls with openings less than 10% of the wall area and either longer than 30 feet without adjacent breakaway walls or having a two- or three sided perimeter structural wall configuration regardless of length shall be designed to resist an unbalanced hydrostatic lateral force during inflow given by Eq. (7).

$$F_h = \frac{1}{2} k_s \rho_{sw} g b h_{\max}^2 \quad (7)$$

where
b : width subject to force
h_{max} : maximum depth

Residual Water Surcharge Load on Floors and Walls

All horizontal floors below the maximum inundation depth shall be designed for dead load plus a residual water surcharge load to the extent that internal impounded water cannot escape in sufficient time. Residual water surcharge load f_r given by Eq. (8) . Walls shall also be designed for residual water hydrostatic pressure.

$$f_r = k_s \rho_{sw} g h_r \quad (8)$$

where $h_r = h_{\max} - h_f \le h_{bw}$

h_f = floor elevation

h_{bw} = water depth required to break non-structural walls and release trapped water.

Hydrodynamic Lateral Loads: The building lateral framing system shall be designed to resist the overall drag force F_d developed either by in-coming or out-going flow surge per Eq. (9).

$$F_d = \frac{1}{2} k_s \rho_{sw} C_d C_b b (hu^2)_{\max} \quad (9)$$

where

C_d is the drag coefficient for the building

C_b is the closure ratio of projected area of structural elements over the full projected are of the building below the flow level

u : Tsunami flow velocity

Likewise, the lateral hydrodynamic pressure load shall be applied at the mid-height of the projected area of all structural elements and enclosure component assemblages below the flow depth per Eq. (10).

$$F_d = \frac{1}{2} k_s \rho_{sw} C_d b (hu^2)_{\max} \quad (10)$$

where C_d is the drag coefficient for the element

Slab hydrodynamic uplift pressure equivalent to a minimum hydrodynamic uplift pressure of 1 kPa applied to the soffit of the slab shall be applied to sections where entrapped flow occurs .

Where enclosed spaces exist within the building that prevents flow through the section, hydrodynamic flow stagnation internal pressure shall be applied using Eq.(11).

$$P_p = \tfrac{1}{2} \rho_{sw} u_{\max}^2 \quad (11)$$

where u_{max} is the maximum free flow velocity at that location assuming no obstruction.

For nearshore bathymetric slopes that are shallow, or in the presence of reef discontinuities, tsunami bore solitons shall also be considered superimposed on the hydrodynamic surge. Instantaneous hydrodynamic loads created by bore impact can be severe (Robertson, et al, 2011). At locations specified in accordance with offshore bathymetry, bore impact forces on walls and slabs shall be considered in addition to hydrodynamic drag. Structural walls oriented perpendicular to the in- flow direction with a width greater than $3h_b$ or $3h_f$, whichever is smaller, shall be designed for a transient lateral load per unit width given by Eq. (12).

$$F_b = k_s \rho_{sw} \left(\frac{1}{2} g h_b^2 + h_j v_j^2 + g^{1/3} (h_j v_j)^{4/3} \right) \quad (12)$$

This force shall be applied at $(h_b+h_r)/3$ from the base of the wall, where h_r is given by Eq. (13)

$$h_r = g^{-\frac{1}{3}} (v_j h_j)^{\frac{2}{3}} \quad (13)$$

The resulting wall pressure shall be a triangular distribution with maximum pressure of $2F/(h_b+h_r)$ at the base and zero pressure at a height of (h_b+h_r). See Figure 5.

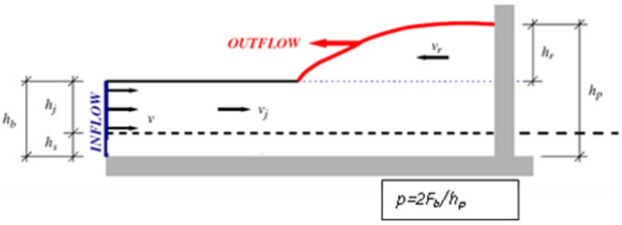


Figure 5 Tsunami Bore Travelling over Standing Water and Striking a Wall

Impact Loads: Waterborne debris impact is applied to any perimeter structural element of the gravity-load-carrying system within the inundation depth at the site. A 1,000-lb. log impact, a floating passenger vehicle force of 6,000 lbs., and a 2,000-lb. submerged tumbling boulder (or concrete mass debris) impact shall be assumed to impact perimeter vertical structural elements of the gravity-load-carrying system.

The maximum instantaneous debris impact force of waterborne floating debris shall be determined using Eq. (14) applied to any perimeter structural element of the gravity-load-carrying system subject to the in- flow or out-flow within the inundation depth.

$$F_i = u_{\max} \sqrt{k m_d} \quad (14)$$

where,

u_{max} is the flow velocity at the site,

k is the effective stiffness of the impacting debris or the lateral stiffness of the impacted structural element(s) deformed by the impact, whichever is the lesser. Logs and containers are assumed to strike longitudinally for calculation of debris stiffness.

m_d is the mass of the debris.

The impulse duration for elastic impact shall be permitted to be calculated per Eq. (15):

$$t_d = \frac{2 m_d u_{max}}{F_i} \quad (15)$$

For buildings and other structures within 1,500 ft. of a shipping port, a shipping container impact on perimeter vertical structural elements of the gravity-load-carrying system shall be assumed to occur at 3 m/s.

For Risk Category IV buildings and structures adjacent to piers and wharves, an extraordinary mass impact (e.g., ships, containers, small floating buildings) on perimeter vertical structural elements of the gravity-load-carrying system shall be assumed to occur. Extraordinary debris impacts on Risk Category IV buildings and structures shall require the application of the alternative

load path progressive collapse provisions of UFC 4-023-03, Design of Structures to Resist Progressive Collapse, July 14, 2009.

Foundation Design: Design of structure foundations and tsunami barriers shall consider changes in the site surface and in-situ soil properties during the design tsunami and provide capacity to support the structural loads. Local scour calculations shall evaluate the effects of sustained flow shear, which can be enhanced by pore pressure softening, and both effects can be prescriptively determined using Figure 6 based on empirical study. For near source tsunami hazards, the in-situ soil and site surface condition at the onset of tsunami loads shall be those determined existing at the end of seismic shaking, including liquefaction, lateral spread and fault rupture. The minimum factor of safety shall be 1.2 for potential failure limits impacting foundations (bearing capacity, uplift, lateral pressure, internal and slope stability).

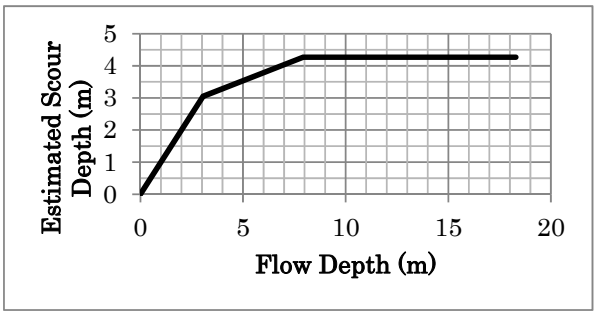


Figure 6 Design Local Scour Depth due to Sustained Flow Shear and Pore Pressure Softening

2.9 Special Occupancy Structures

Vertical Evacuation Refuge Structures are a special classification of buildings and structures within the tsunami evacuation zone designated as a means of alternative evacuation in communities where sufficiently high ground does not exist or where the time available after the tsunami warning is not deemed to be adequate for full evacuation prior to tsunami arrival. Such a building or structure must have the strength and resiliency needed to resist all effects of the maximum considered tsunami. Despite the devastation of the March 11, 2011 Tohoku Tsunami along the northeast coastline of Honshu island of Japan, there were many tsunami evacuation buildings that provided safe refuge for thousands of survivors (Fraser, et al, 2012). In the U.S., FEMA P646 (Applied Technology Council, 2012) exists as a set of guidelines but is not written in mandatory language necessary for building code and design standards. Therefore, the ASCE 7 Standard would incorporate the technical requirements for such structures, utilizing P646 as a pre-standard reference. A particularly important consideration is the elevation and height of the refuge, since it must provide structural life safety for the occupants within a portion of the refuge that is not inundated. Therefore, additional conservatism is necessary in the estimation of inundation height. The recommended minimum elevation for a tsunami refuge area is, therefore, the maximum considered tsunami runup elevation anticipated at the site, plus 30%, plus approximately 3 meters (10 feet), as illustrated in Figure 7.

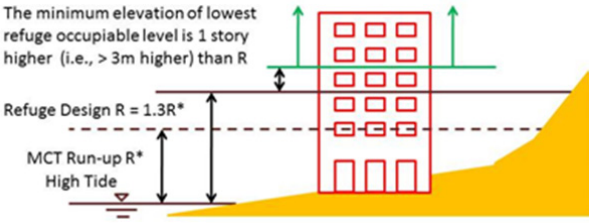


Figure 7 Minimum Tsunami Refuge Elevation

For the Pacific Northwest and Alaska, design necessarily includes consideration of ground shaking effects and subsidence from a preceding local offshore subduction earthquake, prior to the arrival of the design tsunami inundation. To help ensure adequate strength and ductility in the structure for resisting tsunami load effects, Seismic Design Category D, as defined in ASCE/SEI 7-10, should be assigned to the structure, as a minimum. The tsunami evacuation refuge should have a post-earthquake seismic performance objective of Immediate Occupancy prior to the tsunami arrival in order to receive evacuees and to have sufficient margin remaining to resist sustained tsunami loads. In addition to individual structural members, it is also necessary to compare tsunami loading to the ultimate inelastic structural systemic capacity of the building. The overall capacity of the lateral-load-resisting system can be checked using its overstrength factor, Ω (illustrated in Figure 8).

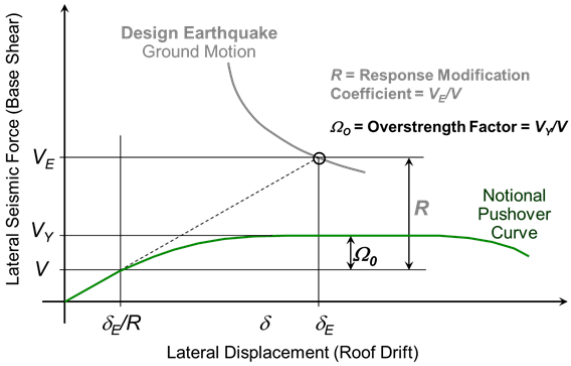


Figure 8 U.S. Seismic performance factors Ω and R, based on inelastic response capacity (Adapted from FEMA P-695)

In multi-story buildings greater than about four stories tall, once the Immediate Occupancy seismic design objective is utilized at the Maximum Considered Earthquake hazard level, most of the overall systemic lateral strength necessary will have been provided for tsunami resistance to the Maximum Considered Tsunami resulting from that event (Chock, et al, 2013b). However, structural components may need local "enhanced resistance" and ground level shear walls may also require additional strength for out-of-plane hydrodynamic forces and/or pressurization effects. Because

the tsunami evacuation refuge is assumed to be occupied at the designated levels during the event, load combinations for refuge structures are modified to Eq. (16) and (17).

Load Combination 1:

$$Q_U = 1.2D + - 1.0F_{TSU} + 1.0L_{Refuge} + 0.25L_{Non\text{-}refuge} + 0.2S \quad (16)$$

Where L_{Refuge} and $L_{Non\text{-}refuge}$ refer to the live loads in the levels used for Refuge and the levels below not occupied as refuges, respectively.

Load Combination 2:

$$Q_U = 0.9D + - 1.0F_{TSU} \quad (17)$$

3. CONCLUSIONS

- The Tsunami Loads and Effects Subcommittee of the ASCE/SEI 7 Standards Committee is developing a new Chapter 6 - Tsunami Loads and Effects, with a corresponding Commentary for the 2016 edition of the ASCE 7 Standard.
- .A method of probabilistic tsunami hazard analysis has been established in the recognized literature that is generally consistent with probabilistic seismic hazard analysis in the treatment of uncertainty.
- Methodologies for 2D tsunami inundation modeling have been further developed and utilized for various designated communities and regions.
- Structural loading and analysis techniques for determining building performance have been developed. Experimental and field validation studies of these techniques have been performed.
- Measures of seismic performance in the inelastic range have been developed that have relevant application for tsunami performance metrics.
- Analysis procedures for regions governed by local subduction earthquakes involves a multi-hazard performance-based approach to provide both ductility for dynamic earthquake loading and remaining strength for sustained hydrodynamic fluid forces
- The proposed ASCE 7 provisions for Tsunami Loads and Effects enables a set of analysis tools and design methodologies that are consistent with tsunami physics and performance based engineering.

Acknowledgements:

The author acknowledges the support from the American Society of Civil Engineers / Structural Engineering Institute for the work of the Tsunami Loads and Effects Subcommittee and its numerous volunteer science and engineering subject matter experts.

References:

Applied Technology Council (2009). *Effects of Strength and Stiffness Degradation on Seismic Response*, FEMA P440A.

Applied Technology Council, 2009. *Quantification of Building Seismic Performance Factors, FEMA P-695,* FEMA, Jessup, Maryland

Applied Technology Council (2012). Guidelines for Design of Structures for Vertical Evacuation from Tsunamis (2nd Edition), FEMA P-646.

American Society of Civil Engineers Structural Engineering Institute (2006). "Seismic Rehabilitation of Existing Buildings," ASCE/SEI 41-06.

American Society of Civil Engineers Structural Engineering Institute (2010). "Minimum Design Loads for Buildings and Other Structures," ASCE/SEI 7–10.

Chock, G., Robertson, I.N., Riggs, H.R. (2011). "Tsunami Structural Design Provisions for a New Update of Building Codes and Performance-Based Engineering", in *Proceedings, Solutions to Coastal Disasters 2011,* ASCE.

Chock, G., Robertson , I., Kriebel, D., Francis, M., and Nistor, I. (2013a). *Tohoku Japan Tsunami of March 11, 2011 – Performance of Structures,* ASCE/SEI, (in publication).

Chock, G., Carden, L.., Robertson, I.N., Olsen, M.J., and Yu, G. (2013b). "Tohoku Tsunami-Induced Building Failure Analysis with Implications for U.S. Tsunami and Seismic Design Codes", *Earthquake Spectra - 2011 Tohoku, Japan Earthquake Special Issue* (2013, accepted, in publication).

Department of Defense (2009). *Design of Buildings to Resist Progressive Collapse*, Unified Facilities Criteria 4-023-03, 14 July 2009, 168 pages.

Fraser, S., Leonard, G.S., Matsuo, I., Murakami, H. (2012). *Tsunami evacuation: Lessons from the Great East Japan earthquake and tsunami of March 11th 2011*, GNS Science Report 2012/17, 89 pages.

Fukuda, H., Okuda, Y., Kato, H., Ishihara, T., Tajiri, S., Kabeyawawa, T., Nagano, Y. (2012). *Structural Design Requirements for Tsunami Evacuation Buildings in Japan*, 14th U.S.-Japan Workshop on the Improvement of Structural Design and Construction Practices, Maui, Hawaii, Dec. 2012.

Geist, E. (2005). "Local Tsunami Hazards in the Pacific Northwest from Cascadia Subduction Zone Earthquakes", *U.S. Geological Survey Professional Paper #1661-B*.

Geist, E., Parsons, T. (2006). "Probabilistic Analysis of Tsunami Hazards", Natural Hazards 37, pp. 277-314.

Okada, T, Sugano, T., Ishikawa, T., Ohgi, T., Takai, S., and Hamabe, C. (2005). "Structural Design Method of Buildings for Tsunami Resistance (Proposed)", *The Building Letter*, Nov., 2004, The Building Center of Japan - Building Technology Research Institute.

Robertson I.N., Paczkowski, K., Riggs, H.R., Mohamed, A. (2011). "Experimental Investigation of Tsunami Bore Forces on Walls", *Proceedings, ASME 2011 30th International Conference on Ocean, Offshore and Arctic Engineering,* Rotterdam, The Netherlands, OMAE-11-1030.

Thio, H.K., Somerville, P., and Polet, J. (2010). *Probabilistic Tsunami Hazard in California*. Pacific Earthquake Engineering Research Center, PEER Report 2010/108, University of California, Berkeley.

10CUEE CONFERENCE PROCEEDINGS
10th International Conference on Urban Earthquake Engineering
March 1-2, 2013, Tokyo Institute of Technology, Tokyo, Japan

DYNAMIC AND STATIC APPROACHES IN DESCRIPTION OF TSUNAMI GENERATION

Kolesov S.V.[1] and Nosov M.A.[2]

1) Junior researcher, Physics Faculty, M.V. Lomonosov Moscow State University, Russia
2) Professor, Physics Faculty, M.V. Lomonosov Moscow State University, Russia
kolesov@ocean.phys.msu.ru, m.a.nosov@mail.ru

Abstract: Finite duration of bottom deformation in a tsunami source is not usually taken into account in description of tsunami generation. Whereas theoretical estimation provide the evidence that dynamics of bottom deformation has certain influence on resulting tsunami waves. In this study, taking the 2003 Tokachi-oki tsunamigenic earthquake as example, we compare dynamic and static (traditional) approaches in description of tsunami generation.

1. INTRODUCTION

The rupture in earthquake source propagates much faster than long gravitational waves. Due to this fact the generation of a tsunami by an earthquake is usually considered as an instant process. And particular features of time-history of bottom deformation is not taken into account in tsunami simulation.

Nevertheless, in reality bottom deformation lasts during a certain time. For example, in such catastrophic earthquakes as the 2004 Sumatra–Andaman or the 2011 Tohoku-oki the bottom deformation was as long as 10 minutes or more. Moreover there are the so-called slow earthquakes that may last even longer (Kanamori 1972). This type of earthquakes also exhibits an anomalously high level of low-frequency excitation, i.e. the bottom motions can be rather slow (Beroza and Jordan 1990). Besides, such slow earthquakes are also called tsunami earthquakes for they are capable of generating devastating tsunamis despite the relatively small earthquake magnitude.

The role of dynamics of bottom deformation had been studied theoretically and experimentally in a number of works (e.g. Hwang and Divoki 1970, Hammack 1973, 1980, Dotsenko and Soloviev 1995, Dotsenko 1996, Nosov and Shelkovnikov 1997, Nosov 1998, Levin and Nosov 2009). Nowadays it is become possible to examine real cases in order to reveal the role of dynamics of bottom deformation. This study is aimed to a comparative analysis of dynamic and static approaches in description of tsunami generation by the example of the 2003 Tokachi-oki tsunamigenic earthquake which was the strongest seismic event of the year.

In this paper we shall consider the following two approaches in description of tsunami generation by an underwater earthquake: static and dynamic.

The static approach assumes that an earthquake is to instantly cause residual deformations of the ocean bottom, i.e. static (co-seismic) bottom deformations. Such deformations can be calculated from fault parameters with use of well known Okada formulae (Okada, 1985). Afterwards the bottom deformation is employed as input data in specification of initial elevation of water surface in tsunami propagation models. In common practice the initial elevation is assumed to be equal to the vertical component of bottom deformation. The imperfectness of such a common practice is due to the following reasons. First, direct transfer of bottom deformations up to the water surface artificially enriches the spectrum of the tsunami at the expense of unrealistically short waves. Second, In the case of a sloping (non-horizontal) bottom the horizontal deformation components can also contribute significantly to the displacement of the water surface. More comprehensive technique comprises the accounting of both vertical and horizontal components of co-seismic bottom deformations and “smoothing” effect of water layer (Nosov and Kolesov 2009, 2011).

The dynamic approach involves time-spatial history of bottom deformations (or dynamic bottom deformation) that occurs in tsunami source due to earthquake. Water layer perturbations could be simulated conjunctly with fault rupturing process (fully-coupled model) or separately (weakly-coupled model).

2. NUMERICAL MODELS

In present study we use the following two numerical models: 2D and 3D.

2D model is based on the linear long-wave theory utilizes static tsunami source. The classical wave equation written in respect of fluid velocity potential is accompanied with boundary conditions: fully reflective

along the shore and free pass on outer boundaries of calculation domain. The mathematical model and numerical scheme (finite difference method) are described in Nosov et al, (2012).

3D model (Nosov and Kolesov 2007) describes both acoustic and gravitational waves exited by dynamic bottom deformation. Model is weakly-coupled, so bottom motion and hydrodynamics of compressible water layer was calculated separately.

To demonstrate difference between static and dynamic approaches in tsunami generation we chose Tokachi-oki 2003 M_W=8.3 earthquake. The initial deformation of water surface for 2D model was determined in two steps. First, coseismic bottom deformation was calculated based on finite fault model proposed in Koketsu et el. (2004). Second, the "smoothing" method was applied. The dynamic bottom deformation due to seismic fault rupturing was first simulated by the boundary element method (Kataoka 1996), using the same finite fault model data. The duration of bottom motion was 128 seconds. Dynamic bottom deformation simulation technique and 3D model had been described in the paper (Bolshakova et al. 2011).

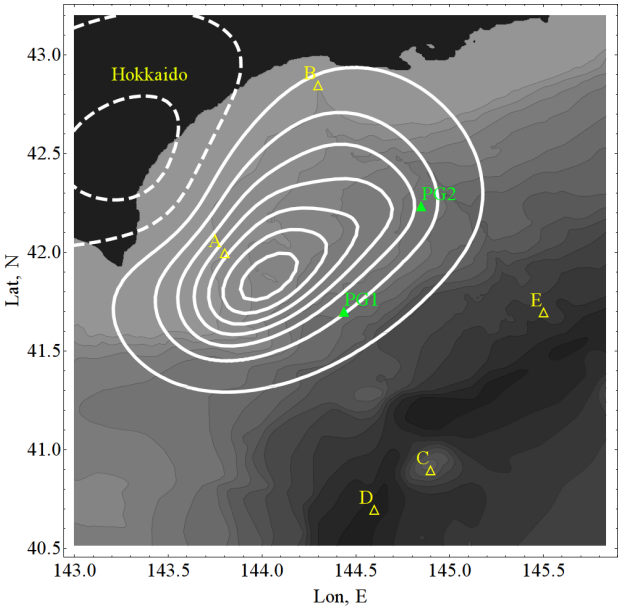


Figure 1. Calculating area. Vertical coseismic bottom deformation is shown by solid (uplift) and dashed (subsidence) white contours at 0.2-m intervals. Locations of virtual tide-gauges are shown with triangles.

3. RESULTS AND DISCUSSIONS

The calculation area (Figure 1) spans from 143°E to 145.8°E by longitude and from 40.5°N to 43.1°N by latitude. Computational grids were build using 500 m gridded bathymetric data set of Japan Oceanographic Data Center (JODC, http://www.jodc.go.jp/). For 3D model we constructed 1001x1001x49 grid. For 2D model 1 min spacing grid was used.

Seven points were chosen to watch water level evolution: two shallow water points (A, B) with depth ~500 m, three deep-water points located in the Kuril-Kamchatka trench (C, D, E) and two intermediate points (PG1, PG2) actually located in positions of JAMSTEC bottom observatories (depth ~2500 m). In present study these points are chosen just for example. The ability of the numerical model to reproduce the in situ measured signal was discussed in Bolshakova et al. (2011).

Time-histories of water level variations for both models in aforesaid positions are shown on Figure 2. Generally, waveforms are rather similar, but there are some issues worth to mention. The main difference in behavior of water level between simulation results of 2D and 3D modeling is the existence of elastic water oscillations in the beginning of synthetic records in case of 3D modeling. The amplitude of this oscillations is significantly higher in the deeply located points (D, E). The reason for it is the existence of cutoff frequency (Levin and Nosov 2009). In points A, PG1 and PG2 signals are most similar, except the very beginning. In shallow point B there are significant differences of waveforms. That could be explained by the proximity of reflecting shore boundary condition of 3D model. In case of deep-water points (C, D and E) one can see that wave generated by dynamic tsunami source arrives later and the waveform is distorted. This is the effect of dynamic wave generation process: initially formed waves start to propagate when fault rupturing is not yet finished. It should be noted that in this particular case of Tokachi-oki 2003 earthquake bottom deformation lasted for about 50 seconds (Koketsu et al. 2004). However, during catastrophic events such as Tohoku-oki 2011 earthquake the duration of rupturing processes could lasts up to 10 minutes and even more, so we can expect that accounting of time-history of bottom deformation could be important for tsunami simulation.

Acknowledgments:

This work was supported by the Russian Foundation for Basic Research, project 12-05-31422. We are grateful to Prof. Tatsuo Ohmachi, Dr. Shusaku Inoue and Dr. Hiroyuki Matsumoto for providing dynamic bottom deformation simulation results.

References:

Beroza, G.C., and Jordan, T.H. (1990), "Searching for slow and silent earthquakes using free oscillations," **95**, B3, 2485 – 2510.

Bolshakova, A., Inoue, S., Kolesov, S., Matsumoto, H., Nosov, M., and Ohmachi, T. (2011), "Hydroacoustic effects in the 2003 Tokachi-oki tsunami source," *Russ. J. Earth. Sci.*, **12**, ES2005, doi:10.2205/2011ES000509.

Dotsenko, S.F. (1996), "The excitation of tsunamis in oscillations of a floor area," *Izvestiya, Atmos. Ocean. Phys.*, **32** (2), 264–270.

Dotsenko, S.F., and Soloviev, S.L. (1995), "On the role of residual shifts of ocean-bottom in tsunami generation underwater earthquakes," *Okeanologiya*, **35** (1), 25–31.

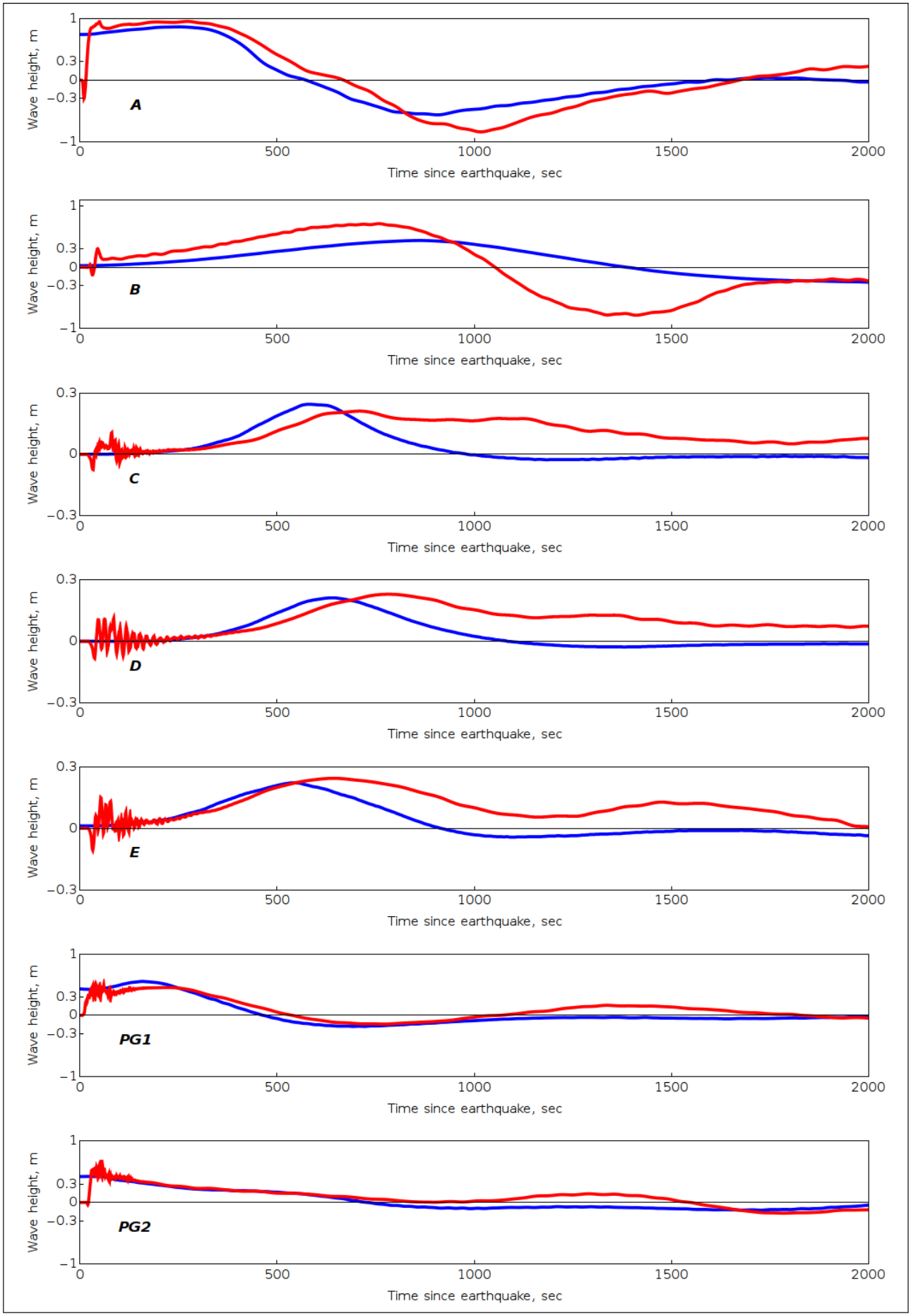


Figure 2. Time-histories of water level variations in points shown on Figure 1. Blue curve – static approach, red curve – dynamic approach.

Hammack, J.L. (1973), “A note on tsunamis: their generation and propagation in an ocean of uniform depth,” *J. Fluid Mech.,* **60**, 769–799.

Hammack, J.L. (1980), “Baroclinic tsunami generation,” *J. Phys. Oceanogr.,* **10** (9), 1455–1467.

Hwang, L.S., and Divoki, D.J. (1970), “Tsunami Generation,” *J. Geophys. Res.,* **75**, 6802–6817.

Kanamori, H. (1972), “Mechanism of tsunami earthquakes,” *Physics of the Earth and Planetary Interiors,* **6**, 346–359.

Kataoka, S. (1996), “Development of simulation methods for earthquake motion based on three-dimensional fault-ground models,” Ph. D. thesis, Tokyo Institute of Technology.

Koketsu, K., Hikima, K., Miyazaki, S. and Ide, S. (2004), “Joint inversion of strong motion and geodetic data for the source process of the 2003 Tokachi-oki, Hokkaido, earthquake,” *Earth Planets Space*, **56** (3), 329-334.

Levin, B.W., and Nosov, M.A. (2009), “Physics of Tsunamis,” Springer.

Nosov, M.A. (1998), “On the directivity of dispersive tsunami waves excited by piston-type and traveling-wave sea-floor motion,” *Volcanol. Seismol.*, **19**, 837–844.

Nosov, M.A. and Kolesov, S.V. (2007) “Elastic oscillations of water column in the 2003 Tokachi-oki tsunami source: in-situ measurements and 3-D numerical modelling,” *Nat. Hazards Earth Syst. Sci.*, **7**, 243-249.

Nosov, M.A., and Kolesov, S.V. (2009), “Method of Specification of the Initial Conditions for Numerical Tsunami Modeling,” *Moscow University Physics Bulletin*, **64** (2), 208–213.

Nosov, M.A., and Kolesov, S.V. (2011), “Optimal Initial Conditions for Simulation of Seismotectonic Tsunamis,” *Pure Appl. Geophys.*, **168** (6-7), 1223-1237.

Nosov, M.A., and Shelkovnikov, N.K. (1997), “The excitation of dispersive tsunami waves by piston and membrane floor motions,” *Izvestiya, Atmos. Ocean. Phys.* **33** (1), 133–139.

Nosov, M.A., Moshenceva, A.V., and Kolesov, S.V. (2012), “Horizontal motions of water in the vicinity of a tsunami source,” *Pure and Applied Geophysics*. DOI 10.1007/s00024-012-0605-2.

Okada, Y. (1985), “Surface deformation due to shear and tensile faults in a half-space,” *Bull. Seismol. Soc. Amer.,* **75**, 1135–1154.

10CUEE CONFERENCE PROCEEDINGS
10th International Conference on Urban Earthquake Engineering
March 1-2, 2013, Tokyo Institute of Technology, Tokyo, Japan

PHYSICAL BASIS FOR SPECIFICATION OF NUMERICAL GRID IN TSUNAMI SIMULATION

Mikhail A. Nosov

Professor, Faculty of Physics, M.V. Lomonosov Moscow State University, Russia
nosov@phys.msu.ru

Abstract: Typical wavelength of a tsunami in the open ocean amounts to hundreds of kilometers while in the shallow water zone, due to diminishing of the phase velocity, wavelength becomes many times shorter. Moreover, in the run-up zone, due to non-linear effects the wavelength might become even shorter. This is why simple regular grids are not optimal for tsunami simulation. In present study, considering physics of tsunami generation and propagation, we suggest basic principles of specification of numerical grid for physically correct and effective tsunami simulation.

1. INTRODUCTION

The efficiency of numerical simulation for studying tsunamis has long been unanimously acknowledged by the scientific community (Levin and Nosov 2009). The first numerical experiments had been carried out by Japanese scientists (Aida 1969, Abe 1978). At present, many numerical tsunami models have been developed. Without claiming to present a full list, we shall only mention the following models: TUNAMI (Imamura et al. 2006), MOST (Titov et al. 2003), COMCOT (Liu et al. 1998), NAMI DANCE (Zaytsev et al. 2010), MGC (Shokin et al. 2008), TsunAWI (Harig et al. 2008), GeoClaw (LeVeque et al. 2011). Some numerical models have no special names, but are also actively used in various scientific groups; their descriptions can be found in papers (Fine et al. 2005, Fujii and Satake 2007, Kowalik et al. 2007, Nicolsky et al. 2011, Nosov et al. 2012).

All the models listed above are based on the theory of long waves (shallow water approximation), which deals with the equations of hydrodynamics, averaged over the vertical coordinate. Within the theory of long waves, the total three-dimensional (3D) problem is reduced to the two-dimensional (2D) one.

There are attempts of 3D numerical simulations of tsunami waves in conjunction with relevant hydroacoustic phenomena (Ohmachi et al. 2001, Nosov and Kolesov 2007, Maeda and Furumura 2011, Bolshakova et al. 2011). Nevertheless, 2D models (shallow water approximation) are used nowadays and they will be certainly used in future for the following two reasons: (1) the shallow water approximation corresponds well to the nature of tsunamis; (2) the computational cost of the 3D simulation is much higher as compared with 2D one.

Tsunamis are known as slightly dispersive waves (Levin and Nosov 2009). The serious lack of the shallow water approximation consists in the neglecting of the phase dispersion of the gravitational water waves. This is why the shallow water approximation has certain restrictions in its application for reproducing of tsunamis.

The most natural way to take the phase dispersion into account is 3D simulation based on either Navier–Stokes (e.g. Ohmachi et al. 2001) or Laplace equation (potential theory) (e.g. Nosov and Kolesov 2007). The second way is 2D simulation based on Boussinesq-type approximation. This approximation allows reproducing slightly dispersive waves. The following tsunami numerical models employ Boussinesq-type approximation: FUNWAVE (Shi et al. 2012), COULWAVE (Lynett et al. 2003), GloBouss (Løvholt et al. 2010). The third way consist in the substituting of the phase dispersion by the numerical dispersion (Burwell et al. 2007). In our opinion, such approach is fundamentally incorrect and can not be recommended for wide use.

The most wide-spread method for numerical solution of partial differential equations in tsunami models is the finite difference method (FDM). As a rule, FDM employs structured (regular) grids. With use of the nested-grid approach a fine grid resolution can be specified in some predefined areas of computational domain (e.g. TUNAMI, MOST, NAMI DANCE, MGC).

In solving equations in tsunami models the finite element method (FEM) and unstructured grids are often used as well (Piatanesi et al. 1999, Walters 2006, Harig et al. 2008, Zhang and Baptista 2008, Androsov et al. 2011). FEM is more difficult as compared to FDM. But FEM has important advantage: unstructured grids can be easily adapted for any shape of calculating area, and allow a grid condensation where the increased spatial resolution is required.

Recently, the very promising approach – adaptive mesh refinement – came into the practice of tsunami simulation (LeVeque et al. 2011, Popinet 2012). The main idea of this approach consists in a dynamic grid (mesh) refinement where and when it is needed. The only

disadvantages of such a method are its excessive complexity and additional computational cost which is needed for the dynamic adaptation of computational grids. Indeed, the dynamics of tsunami waves in the open ocean is fully linear. Thus, the wave transformation obeys well-known linear laws and no need to vary the mesh in time. The space increment of the computational grid can be specified simply as a function of ocean depth.

However, the method of adaptive mesh refinement is likely the best choice for non-linear phase of tsunami evolution (propagation in shallow water including run-up on shore) when the solution of non-linear equations is really unpredictable.

The purpose of this paper is to suggest physical basis for specification of numerical grid in tsunami simulation. The main attention will be paid to correct determination of the space increment of computational grid that provides adequate and effective reproduction of tsunami waves. It is obvious that tsunami wavelength undergoes significant changes during the propagation. In each time-spatial domain the space increment must be small enough to reproduce the shortest wavelength. A grid with a fixed space increment can not be the optimal choice. Effective numerical model must employ computational grids with a variable space increment (adaptive grids) that is a certain function of horizontal coordinates.

The following three stages are traditionally distinguished in the life of a tsunami: generation of the wave, its propagation in the open ocean and its interaction with the coast (run-up). Such a division is related to the existence of essential differences in the physical processes controlling one or another stage. Thus, principles of grid specification have to vary from one to another stage. Particular features of grid specification at each stage we shall consider in the sections entitled "Generation", "Propagation" and "Run-up".

2. GENERATION

Let us restrict our consideration to tsunami generation by bottom disturbances. It might be either co-seismic bottom deformation or submarine landslide. In the open ocean tsunami amplitude (or bottom deformation amplitude) is much smaller than ocean depth. It gives us ground to consider tsunami generation and propagation as a linear process (Levin and Nosov 2009).

As is had been shown in (Levin and Nosov 2009, Nosov and Kolesov 2011) the spatial spectrum of the free surface displacement generated by any bottom disturbances is always modulated by a rapidly damped function, $1/\cosh(kH)$, where H is the ocean depth, $k = 2\pi/\lambda$ is the wave number and λ is the wave length. So, inhomogeneities of bottom deformations of scale $\lambda < H$ are not manifested on the water surface. All such inhomogeneities turn out to be smoothed out by the liquid column ("smoothing effect").

It is worth emphasizing that direct transfer of bottom deformations up to the water surface (traditional approach) artificially enriches the spectrum of the tsunami at the expense of unrealistically short waves. Being a sort of noise, these short waves may lead to artificial resonances in bays and finally to incorrect estimations of run-up heights or even to instability in the numerical calculations. Moreover, the numerical description of the short wave components requires very fine grids and, therefore, very small time steps. Ultimately, the imperfectness of the traditional approach may also result in a significant increase in the calculating time in numerical simulations of tsunamis.

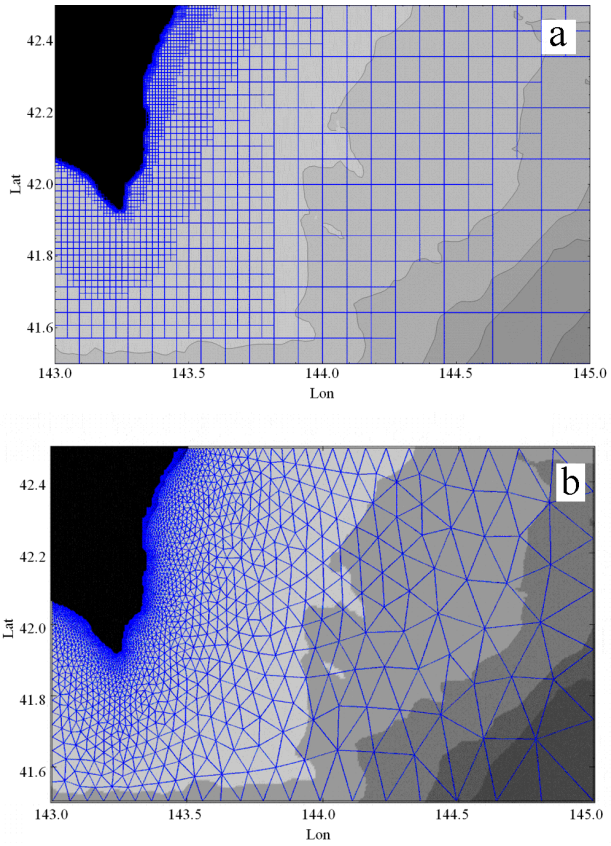


Figure 1 Adaptive Cartesian (a) and triangular (b) grids

In our publication (Nosov and Kolesov 2011) we suggested an improved practical method of calculating the initial elevation from the solution of the 3D problem in the framework of potential theory. The method takes into account horizontal and vertical components of co-seismic bottom deformation and the "smoothing effect".

Due to the existence of "smoothing effect" the shortest wavelength can be unambiguously determined as follows:

$$\lambda_{min} = H \,. \qquad (1)$$

Note that formula (1) remains valid in the case of dynamic bottom deformation as well.

For definiteness, let us assume the space increment to be equal to a half of the shortest wavelength. Therefore, within the source area, the space increment can be specified

by the following simple formula:

$$\Delta_G \le 0.5\,\lambda_{min} = 0.5\,H\,, \qquad (2)$$

where H is the ocean depth in a given point of calculating domain (Lon, Lat). Such definition for the space increment inside of tsunami source clearly requires the implementation of computational grids with a variable space increment. Grid refinement that follows the change of water depth is shown in Fig. 1. Adaptive Cartesian grids (Fig 1 a) or adaptive triangular grid (Fig 1 b) are usually associated with FDM and FEM, respectively.

Theory of tsunami generation also allows us to determine the minimal period of surface gravitational wave that can be excited at a given water depth as follows:

$$T_{min} = \sqrt{H/g}\,. \qquad (3)$$

where g is acceleration due to gravity. Note that this period is very short as compared with tsunami period (100-10000 s). According to formula (3), the minimal period vary approx. from 1 to 30 s (for $10<H<10000\,m$). It is important to stress that such gravitational waves are dispersive waves which can not be described within non-dispersive shallow water theory. We also have to point out the following fact. Being generated at the depth of (e.g.) $H = 100m$, the shortest wave has length of $\lambda = H = 100m$ and its period is of $T = \sqrt{H/g} \approx 3.2\,s$. During the propagation of the shortest wave toward deep water areas, according to the dispersion relation for gravitational waves, $\omega^2 = gk\,tanh(kH)$, the wave length does not virtually change. It means that the space increment of computational grid must be as small as $\Delta \le 0.5\,\lambda = 50\,m$ everywhere. This is both impossible and no optimal. Anyway in reality the waves of such short-periods are certainly generated in the tsunami source. But one should bear in mind that due to the phase dispersion the short waves propagate much slower than the tsunami front. So, if a non-dispersive model is in use, the short waves must not be considered because their consideration certainly results in overestimation of tsunami amplitude.

In order to avoid such an overestimation, we suggest the following approach. Let us first determine a minimal tsunami period $T_{min}{}^*$ ($T_{min}{}^* > T_{min}$) and then, according to the dispersion relation for gravitational waves, to calculate the respective wavelength $\lambda_{min}{}^*$

$$\frac{4\pi^2}{T_{min}{}^{*2}} = g\,\frac{2\pi}{\lambda_{min}{}^*}\,tanh\left(\frac{2\pi H}{\lambda_{min}{}^*}\right). \qquad (4)$$

The dependence (4), more exactly $\lambda_{min}{}^*$ versus H at given wave periods (100, 200 and 300 s), is shown in Fig. 2. Thick lines stand for calculations according to formula (4) whereas thin lines stand for simplified relation

$$\lambda_{min}{}^* = T_{min}{}^*\sqrt{gH}\,, \qquad (5)$$

which is valid in the case of non-dispersive shallow water approximation.

It is seen from the Fig. 2 that if one assume $T_{min}{}^* = 100\,s$ the shortest wavelength in shallow water area ($H = 0.01\,km$) will be of $\lambda_{min}{}^* \approx 1\,km$. So the minimal space increment must be at least $\Delta = 0.5\lambda_{min}{}^* \approx 0.5\,km$. As water depth increases the minimal wave length (and therefore the space increment) goes up approximately as $\Delta \sim \sqrt{H}$ till water depths $H = 1\,km$. At higher depths the exact formula (4) must be used.

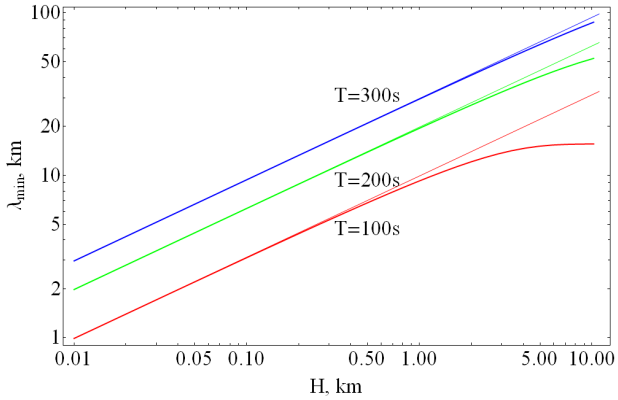


Figure 2 Wavelength at given wave periods versus water depth. Thick lines stand for dispersive theory, thin line – shallow water approximation

If one consider wave periods of 200 and 300 s the difference between thick and thin curves shown in Fig. 2 became rather small. So, if all the spectral components with periods $T < T_{min}$ are removed from the initial elevation it is possible to specify the space increment as follows:

$$\Delta = 0.5T_{min}{}^*\sqrt{gH}\,. \qquad (6)$$

The idea to specify the space increment as $\Delta \sim \sqrt{H}$ is not completely original. Such numerical grid was implemented, for example, in study (Harig et al. 2008).

Definition of the space increment (6) is approximate. More general definition which is valid without any limitations (except one – linear approximation) can be written in the following form:

$$\Delta = 0.5\lambda_{min}{}^*\,, \qquad (7)$$

where $\lambda_{min}{}^*$ is calculated from transcendent eq. (4).

3. PROPAGATION

Within the linear approximation, for a given wave-period, there is only one factor that can result in changes of wavelength – change of water depth.

Since tsunami waves are slightly dispersive, there is a certain restriction for application of non-dispersive shallow-water approximation. We shall now estimate the distance, at which manifestations of dispersion effects should turn out to be quite significant. We shall take advantage of the dispersion relation for gravitational surface waves in a liquid according to which the group velocity is determined by the formula

$$C_{gr} = \frac{\partial \omega}{\partial k} = \frac{g\left(kH / ch^2(kH) + th(kH) \right)}{2\sqrt{gk\, th(kH)}}. \qquad (8)$$

The distance of dispersive destruction of a wave, L_{cd}, can be determined as the product of the velocity of long waves by the time, required for a wave packet to lag behind the front at a distance equal to the wavelength (Kulikov et al. 1996, Levin and Nosov 2009)

$$L_{cd} = \frac{\lambda(\omega)\sqrt{gH}}{\sqrt{gH} - C_{gr}(\omega)}. \qquad (9)$$

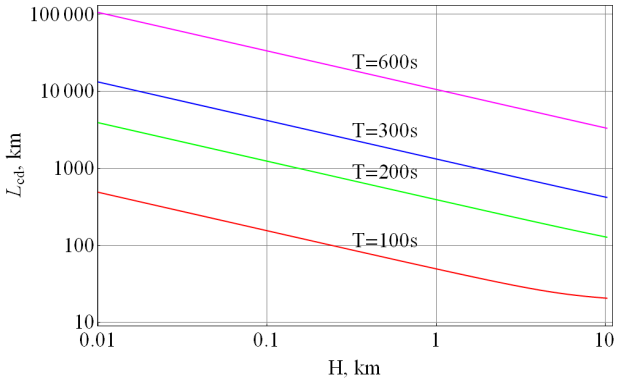


Figure 3 The distance of dispersive destruction as a function of ocean depth and wave period.

Shallow water approximation can be considered as correct approach in simulation of tsunami waves under condition that the size of calculating domain is less than the distance of dispersive destruction. In particular, Fig. 3 demonstrates that for $T_{min}* = 100\,s$ and $H = 1\,km$ the shallow water approximation is valid if size of calculating domain amounts to $L < L_{cd} \approx 50\,km$. If the period is longer, for example, $T_{min}* = 300\,s$, the size of calculating domain amounts to $L < L_{cd} \approx 1300\,km$. For simulation of transoceanic tsunamis ($L < L_{cd} \approx 22000\,km$) it is necessarily to choose $T_{min}* = 1000\,s$ and $H = 5\,km$.

If the shallow water approximation is valid the space increment can be calculated from formula (6). Models that are based on Boussinesq-type approximation have to use formula (7). In both cases smoothing of the initial elevation, i.e. the removing of spectral components of initial elevation which have periods shorter than $T_{min}*$, is the condition of great importance for correct tsunami simulation.

Shortwave disturbances on water surface during the propagation of tsunami are obliged to the following two reasons: (1) smooth change of ocean depth and (2) drastic change of ocean depth. The first issue was discussed above. The second issue is associated with the classical problem of the interaction of long waves with the abrupt (step-like) changes in the ocean depth (Fig. 4). Actually, on a discrete grid each change of water depth can be interpreted as step-like change. The key-question here is how large is such a step.

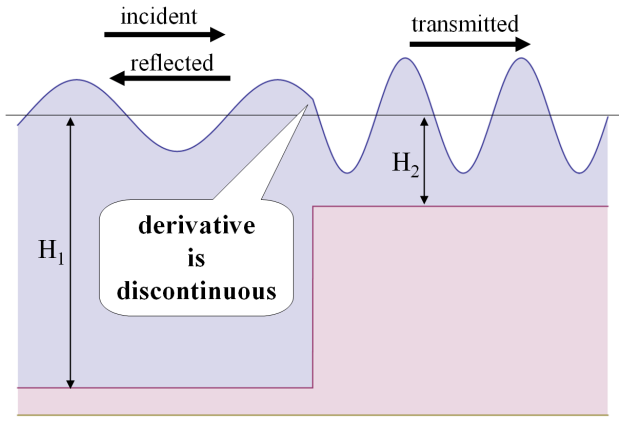


Figure 4 Interaction of long waves with step-like change in the ocean depth

Taking advantage of the continuity conditions for the free-surface displacement, ξ, and the water release, Hu, at the depth jump point, one readily derives the following relations between incident ("i"), reflected ("r" and transmitted ("t") waves (e.g. Levin and Nosov 2009):

$$x \le 0: \quad \xi_1 = A_i e^{i(\omega t - k_1 x)} + A_r e^{i(\omega t + k_1 x)}, \qquad (10)$$

$$x \ge 0: \quad \xi_2 = A_t e^{i(\omega t - k_2 x)}, \qquad (11)$$

where A_i is the amplitude of incident wave,

$A_t = \dfrac{2A_i\sqrt{H_1}}{\sqrt{H_1} + \sqrt{H_2}}$ is the amplitude of transmitted wave,

$A_r = A_i \dfrac{\sqrt{H_1} - \sqrt{H_2}}{\sqrt{H_1} + \sqrt{H_2}}$ is amplitude of reflected wave.

Typical wave profile calculated with use of formulae (10) and (11) is depicted in Fig. 4. It is seen that step-like change in the ocean depth leads to discontinuity of the first derivative of function that describes free-surface

displacement.

The derivative jump can be considered as negligible under the following condition

$$\delta \equiv \left| \frac{\left.\frac{\partial \xi_2}{\partial x}\right|_{x=0} - \left.\frac{\partial \xi_1}{\partial x}\right|_{x=0}}{\left.\frac{\partial \xi_1}{\partial x}\right|_{x=0}} \right| << 1 . \qquad (12)$$

Taking into account (10), (11) after simple transformations of relation (12) we arrive at the condition

$$\delta = \frac{|H_2 - H_1|}{H_2} << 1 . \qquad (13)$$

Ultimately, assuming that $|H_2 - H_1| \approx |grad\, H| \cdot \Delta$, we obtain the following condition for the space increment:

$$\Delta << \Delta_c \equiv \frac{H}{|grad\, H|} . \qquad (14)$$

So, in order to avoid numerical instability due to generation of shortwave disturbances at drastic changes of water depth it is necessarily to specify the space increment in accordance with formula (14).

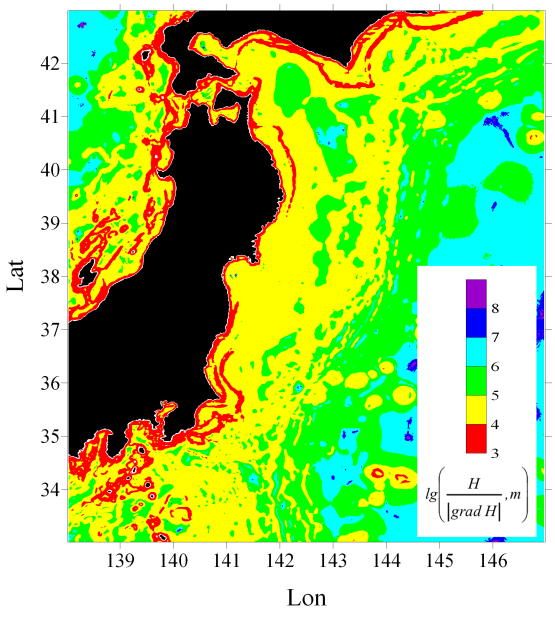


Figure 5 Function (14) calculated for part of Pacific in the vicinity of Japan (bathymetry – GEBCO).

Fig. 5 demonstrates that in shallow water areas the value of Δ_c can reach 1000 m (red areas). Within these areas the space increment must be at least 10 times smaller, i.e. $\Delta < 100m$. The same condition applied to yellow areas gives $\Delta < 1000m$.

4. RUN-UP

This section will be the shortest one. The point is that due to nonlinearity a simple and general physical outcome is next to impossible. Indeed, in the run-up zones, including shallow water areas, the behavior of tsunami become essentially non-linear. In particular, tsunami currents due to their interaction with a very complex topography and human made structures become turbulent, i.e. unpredictable in their small details. Present level of computational technique does not allow direct numerical simulation of turbulent currents of geophysical scales. Nowadays simulation of turbulent currents is mostly based on the Reynolds-averaged Navier–Stokes (RANS) equations. Tsunami run-up simulation definitely must employ not Navier–Stokes but RANS equations.

Let's go back to the problem of numerical grid. In our opinion, the method of dynamic adaptive mesh refinement (LeVeque et al. 2011, Popinet 2012) is here the best choice. Indeed, in contrast to linear problems, solutions of non-linear equations often turn out to have unpredictable details. Thus, a dynamic adaptive grid (mesh) that allows a grid condensation where and when the increased spatial resolution is required, is really a perfect solution. Alternative choice is usual structured grid with a constant and rather fine space increment.

Acknowledgements:

This work was supported by the Russian Foundation for Basic Research, projects 10-05-00562, 13-05-00337, 13-05-92100.

References:

Abe, K. (1978), "A dislocation model of the 1933 Sanriku earthquake consistent with tsunami waves," *J. Phys. Earth.*, **26**(4), 381-396.

Aida, I. (1969), "Numerical experiments for the tsunami propagation the 1964 Niigata tsunami and 1968 Tokachi - Oki tsunami," *Bull. Earthq. Res. Inst. Univ. Tokyo*, **47**(4), 673-700.

Androsov, A., Behrens, J., Danilov, S. (2011), "Tsunami Modelling with Unstructured Grids," *Interaction between Tides and Tsunami Waves. Computational Science and High Performance Computing IV Notes on Numerical Fluid Mechanics and Multidisciplinary Design,* **115**, 191-206.

Bolshakova, A., Inoue, S., Kolesov, S., Matsumoto, H., Nosov, M., and Ohmachi, T. (2011), "Hydroacoustic effects in the 2003 Tokachi-oki tsunami source," *Russ. J. Earth. Sci.,* **12**, ES2005, doi:10.2205/2011ES000509.

Burwell, D., Tolkova E., and Chawla A. (2007), "Diffusion and dispersion characterization of a numerical tsunami model," *Ocean Modelling*, **19**, 10–30.

Fine, I.V., Rabinovich, A.B., Bornhold, B.D., Thomson, R.E., and Kulikov, E.A. (2005), "The Grand Banks landslide-generated tsunami of November 18, 1929: Preliminary analysis and numerical modeling," *Marine Geology*, **215**, 45-57.

Fujii, Y., Satake, K. (2007), "Tsunami Source of the 2004 Sumatra–Andaman Earthquake Inferred from Tide Gauge and Satellite Data," *Bull. Seism. Soc. Am.*, **97**(1A), S192–S207.

Harig, S., Chaeroni, C., Pranowo, W.S., and Behrens, J. (2008),

"Tsunami simulations on several scales: Comparison of approaches with unstructured meshes and nested grids," *Ocean Dynamics*, **58**, 429–440.

Imamura, F., Yalciner, A.C., Ozyurt, G. (2006), "Tsunami Modelling Manual (TUNAMI model)," Revision due on APRIL 2006.

Kowalik, Z., Knight, W., Logan, T., Whitmore, P. (2007), "The tsunami of 26 December, 2004: numerical modeling and energy considerations," *Pure Appl Geophys*, **164**, 379–393.

Kulikov, E.A., Rabinovich, A.B., Thomson, R.E., Bornhold, B.D., (1996), "The landslide tsunami of November 3, 1994, Skagway Harbor, Alaska," *J. Geophys. Res.,* **101**(C3), 6609–6615.

LeVeque, R.J., George, D.L., Berger, M.J. (2011), "Tsunami modelling with adaptively refined finite volume methods," *Acta Numerica*, **20**, 211-289.

Levin, B.W., Nosov, M.A. (2009), "Physics of Tsunamis," Springer, Dordrecht.

Liu, P.L.F., Woo, S.B., Cho, Y.S. (1998), "Computer programs for tsunami propagation and inundation," Tech. rep., Cornell University.

Løvholt, F., Pedersen, G., Glimsdal, S. (2010), "Coupling of Dispersive Tsunami Propagation and Shallow Water Coastal Response," *The Open Oceanography Journal*, **4**, 71-82.

Lynett, P., Borrero, J., Liu, P.L.-F., Synolakis, C.E. (2003), "Field survey and numerical simulations: a review of the 1998 Papua New Guinea tsunami," *Pure Appl. Geophys.* **160**, 2119–2146.

Maeda, T., Furumura, T. (2011), "FDM Simulation of Seismic Waves, Ocean Acoustic Waves, and Tsunamis Based on Tsunami-Coupled Equations of Motion," *Pure Appl. Geophys.* DOI 10.1007/s00024-011-0430-z.

Nicolsky, D. J., Suleimani, E. N., Hansen, R. A. (2011), "Validation and Verification of a Numerical Model for Tsunami Propagation and Runup," *Pure and Applied Geophysics*, **168**(6-7), 1199-1222.

Nosov, M.A., Kolesov, S.V. (2007), "Elastic oscillations of water column in the 2003 Tokachi-oki tsunami source: in-situ measurements and 3-D numerical modeling," *Nat. Hazards Earth Syst. Sci.*, **7**, 243-249.

Nosov, M.A., Kolesov, S.V. (2011), "Optimal Initial Conditions for Simulation of Seismotectonic Tsunamis," *Pure and Applied Geophysics*, **168**(6-7), 1223-1237.

Nosov, M.A., Moshenceva, A.V., Kolesov, S.V. (2012), "Horizontal motions of water in the vicinity of a tsunami source," *Pure and Applied Geophysics*, DOI 10.1007/s00024-012-0605-2.

Ohmachi, T., Tsukiyama, H., Matsumoto, H. (2001), "Simulation of tsunami induced by dynamic displacement of seabed due to seismic faulting," *Bulletin of the Seismological Society of America*, **91**(6), 1898-1909.

Piatanesi, A., Tinti S., Bortolucci E. (1999), "Finite-element simulations of the 28 December 1908 Messina straits (Southern Italy) tsunami," *Phys Chem Earth (A)*, **24**, 145–150.

Popinet, S. (2012), "Adaptive modelling of long-distance wave propagation and fine-scale flooding during the Tohoku tsunami," *Nat. Hazards Earth Syst. Sci.*, **12**, 1213–1227.

Shi, F., Kirby, J.T., Harris, J.C., Geiman, J.D., Grilli, S.T. (2012), "A high-order adaptive time-stepping TVD solver for Boussinesq modeling of breaking waves and coastal inundation," *Ocean Modelling*, **43-44**, 36–51.

Shokin, Yu.I., Babailov, V.V., Beisel, S.A., Chubarov, L.B., Eletsky, S.V., Fedotova, Z.I., Gusyakov, V.K. (2008), "Mathematical Modeling in application to regional tsunami warning systems operations," *Computational Science and High Performance Computing III, Springer. Notes on numerical fluid mechanics and multidisciplinary design*, **101**, 52-68.

Titov, V.V., Gonzalez F.I., Mofjeld H.O., Venturato A.J. (2003), "NOAA Time Seattle Tsunami Mapping Project: Procedures, Data Sources, and Products," NOAA Technical Memorandum OAR PMEL-124.

Walters, R.A. (2006), "Design considerations for a finite element coastal ocean model," *Ocean Modelling,* **15**, 90–100.

Zaytsev, A. I., Chernov, A. G., Yalciner, A. C., Pelinovsky, E. N., Kurkin, A. A. (2010), MANUAL Tsunami Simulation/ Visualization Code NAMI DANCE ver. 4.9. February/2010.

Zhang, Y.J., and Baptista, A.M. (2008), "An Efficient and Robust Tsunami Model on Unstructured Grids. Part I: Inundation Benchmarks," *Pure Appl. Geophys*, **165,** 2229–2248.

10CUEE CONFERENCE PROCEEDINGS
10th International Conference on Urban Earthquake Engineering
March 1-2, 2013, Tokyo Institute of Technology, Tokyo, Japan

SIMULATION OF THREE DIMENSIONAL TSUNAMI INUNDATION INTO THE INSIDE OF A BUILDING

Shusaku Inoue[1], and Yasunori Mizushima[2]

1) Researcher, Construction Technology Department, Research & Development Institute, Takenaka Corporation, Japan
2) Researcher, Advanced Research Department, Research & Development Institute, Takenaka Corporation, Japan
inoue.shuusaku@takenaka.co.jp, mizushima.yasunori@takenaka.co.jp

Abstract: After the 2011 off the Pacific coast of Tohoku Earthquake, Japanese government changed their policy for huge tsunami. The former policy was to defend tsunami inundation by only civil engineering structures for example seawalls and tide embankments. However, in the new policy, they allow a part of tsunami come over the coastal structures and flood inland in the case of very rare tsunami, while expecting to reduce tsunami damage by various methods. Under the current situation, industrial companies near coast are required to make their own measures for tsunami. Their plans have to include not only precaution against tsunami forces but also precaution against the submerged effect of their facilities especially. In this study we developed 3D tsunami simulation to assist the designers in planning above. As one of demonstrations, we show a tsunami inundation simulation of a building of two stories above the ground and one underground story.

1. INTRODUCTION

The 2011 off the Pacific coast of Tohoku Earthquake (Mw 9.0) occurred on March 11, 2011 at 14:46 local time. 15,879 fatalities, 2,712 missing, 6,126 wounded persons, 129,724 collapsed and 267,666 seriously damaged houses are reported as casualties and damage of this earthquake from National Police Agency on December 26, 2012. The great part of this damage was caused by tsunami, and the earthquake magnitude, the tsunami and the devastating damage were the largest in Japanese history on record.

This event changed basic design idea against tsunami. Before the event, Japanese government have been planning inland cities on the assumption that tsunamis could not flood beyond coastal structures which were designed against highest recorded high water level in the planning region. However the 2011 Tohoku tsunami made it clear that the highest recorded level is not necessarily maximum height for a very rare tsunami. Therefore, after this event, the government changed their basic design idea. That is to give up resisting a huge tsunami by only coastal structures and to allow some part of tsunami flood inland.

From a viewpoint of an architect, the above change has great significance. The reason is that architects do not need to consider tsunami forces before the event; however, even if a building is located inland, they have to consider tsunami related forces as needed. Moreover, not only the forces but also the effect of water inundation into the building is also important and designers are required to consider them.

In the way described above, related to tsunami, the points expected for designers drastically changed. But, in the present situation, it is difficult for them to consider all of tsunami effects, especially the effect of the water inundated into the inside a building. Therefore we aimed to develop 3-D tsunami simulation to assist designers to plan and build buildings.

In this study, for the purpose above, we first describe an overview of the damage. Then we explain tsunami simulation method and finally perform a tsunami simulation as one of examples.

2. OVERVIEW OF TSUNAMI DAMAGE IN THE 2011 TOHOKU TSUNAMI

Figure 1 shows the tsunami inundation heights and run-up heights of this event (Mori *et al.* 2012). Tsunami run-up heights were over 20 m around from 38 to 40 degree north latitude and the maximum run-up height was about

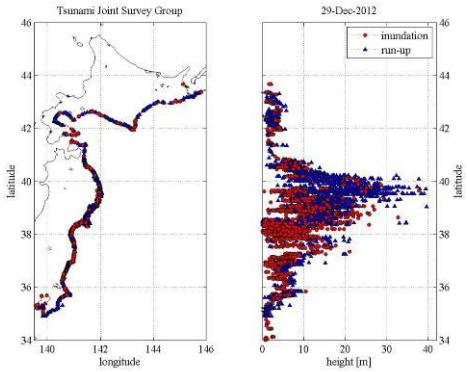


Figure 1 Measured Tsunami height (Mori *et al.* 2012)



Figure 2 Broken seawalls in Taro



Figure 3 A broken breakwater in Kamaishi



Figure 4 Damage of walls on a RC building in Onagawa



Figure 5 An overturned building in Onagawa



Figure 6 RC buildings standing close behind Onagawa port



Figure 7 A RC building standing close behind Kamaishi port

40.0m. The catastrophic tsunami broke coastal structures along the coast of Tohoku region. Seawalls in Taro and breakwater in Kamaishi, which were regarded as the largest seawall and breakwater, were also broken (Figure 2 and 3).

The tsunami flooded inland caused much damage of buildings standing on land. Figure 4 and 5 shows damage of RC structures in Onagawa, which is one of the devastated areas, and some characteristic damage of building could be seen there. Figure 4 shows damage of RC walls. Left side walls were cracked on the whole and right side walls were pushed out to the outside. Figure 5 shows an overturned building. Overturned building as tsunami damage was new damage pattern seen in this event. From the report (for example, NILIM and BRI 2011), there were 6 overturned buildings and numbers of those floors were lower than 4 stories.

While many structural damages of buildings could be seen for low rise building, high rise buildings or substantial buildings remained without any structural damage or with less structural damage. Figure 6 shows a RC building standing close behind Onagawa port. It is located closer to sea than buildings in Figure 4 and 5. A bridge connecting

with right and left buildings fell down, however, main body of the building looks sound. Similarly, a high rise building standing close behind sea in Kamaishi looks sound in Figure 7.

From the above, when we design buildings against tsunami, it is important to consider not only tsunami forces acting on the building but also the effect of water inundation into the inside of buildings to restore them rapidly after a future event.

3. NUMERICAL METHODOROGY

Flow-3D is a general purpose CFD package that is used to solve transient and three dimensional flow problems. It was developed by Flow Science, Inc., and has a comprehensive track record in CFD modeling. Though, the application in modeling tsunami on building is a new attempt. Flow-3D is developed based on the fractional volume of fluid (VOF) free surface tracking method as discussed in Hirt and Nichols (1981). Under this method, cells are defined with a value between zero and one for empty to fully filled cells with fluid. For partially filled cells, the slope of the free surface is determined by an algorithm that uses the surrounding cells to define a surface angle and a surface location. This method allows the steep fluid slopes to be defined and it is applicable to describe the breaking wave (bore or surge) in tsunami run-up zone.

The model used in this research is an incompressible and viscous flow model. Flow-3D employs the finite difference method to solve the fluid equations of motion. The computational domain is defined in a fixed rectangular grid. The fluid momentum equations, Navier -Stokes equations, can be expressed as follows (Flow-3D, 2007),

$$\frac{\partial u}{\partial t}+\frac{1}{V_F}\left(uA_x\frac{\partial u}{\partial x}+vA_y\frac{\partial u}{\partial y}+wA_z\frac{\partial u}{\partial z}\right)=-\frac{1}{p}\frac{\partial p}{\partial x}+g_x+f_x$$

$$\frac{\partial v}{\partial t}+\frac{1}{V_F}\left(uA_x\frac{\partial v}{\partial x}+vA_y\frac{\partial v}{\partial y}+wA_z\frac{\partial v}{\partial z}\right)=-\frac{1}{p}\frac{\partial p}{\partial y}+g_y+f_y$$

$$\frac{\partial w}{\partial t}+\frac{1}{V_F}\left(uA_x\frac{\partial w}{\partial x}+vA_y\frac{\partial w}{\partial y}+wA_z\frac{\partial w}{\partial z}\right)=-\frac{1}{p}\frac{\partial p}{\partial z}+g_z+f_z \qquad (1)$$

where u, v and w are the velocities in the x-, y- and z-directions; V_F represents the volume fraction of fluid in each cell; A_x, A_y and A_z are the fractional areas open to flow in the x-, y- and z-directions; ρ is the fluid density; p is the fluid pressure; g_x, g_y and g_z are the body accelerations in the x-, y- and z-direction and f_x, f_y and f_z are the viscous accelerations in the x-, y- and z-direction for which a turbulence model is required. For cells fully filled of fluid, V_F, A_x, A_y and A_z equal to one.

For an incompressible fluid, the following condition (i.e. continuity equation) must hold:

$$\frac{\partial}{\partial x}(uA_x)+\frac{\partial}{\partial y}(vA_y)+\frac{\partial}{\partial z}(wA_z)=0 \qquad (2)$$

Boundary conditions are categorized as rigid-free or no-slip walls, continuative outflow, periodic and specific pressure boundaries. No flux is allowed to cross the wall boundary; however, viscous shear stresses occur at the wall boundary.

The computational domain was discretized into an orthogonal and staggered grid of variable-sized hexahedral meshes in a Cartesian coordinates. Due to the complex building model, multi-block gridding with nested and linked grids were applied in order to reduce the computational cost. Under this discrete structural grid system, average values of the flow parameters were placed at the center of each cell (for pressure and fractional volume of fluid) and the center of cell faces normal to their associated direction (for velocity).

The basic algorithm for the computation consists of three main steps. The first step is the computation of flow velocity based on the initial conditions or previous time-step values from the explicit approximations of Navier-Stokes Equations. Next, the pressure values will be adjusted to satisfy the continuity equation. It is followed by the determination of the fluid free surface or interface and update of the new fluid configuration based on the VOF method. This computation is then advanced to the next time-step and those three steps are repeated.

On top of that, structures are constructed as obstacles in the numerical model. The flow obstacle is defined using a porosity technique in rectangular cell meshes called the Fractional Area/Volume Obstacle Representation (FAVOR) method as outlined in Hirt & Sicilian (1985). For cells without obstacle, the grid porosity is one and the fluid dynamic equations are to be hold. In contrast, the grid porosity is zero for cells within obstacle where no flow volume is allowed in the obstacle region. For cells that are partially filled with an obstacle, the grid porosity has a value between zero and one, based on the percent volume that is open. The surface angle and the surface location are determined based on the same principal of VOF as stated.

4. SIMULATION OF WATER INUNDATION INTO THE INSIDE OF A BUILDING

As a demonstration, we performed a three dimensional simulation with a building. The building model shown in figure 8 is used. This building has two stories above the ground and one underground story. A cross section of this building is shown in Figure 9. In this simulation, some of interiors, for example, stairs and tables are contained. This model including structures and interiors are regarded as rigid.

Figure 10 shows calculation areas of this simulation. The calculation areas consist of four parts. Cyan area is nested in blue one, and yellow and green ones are connected

to blue and cyan ones respectively. Though mesh sizes of each area are variable, the averages of those are 0.5 m in yellow area, 0.25 m in blue area and 0.125 m in cyan and green areas. Calculation time step, dt, is adjusted during the iteration to meet stability condition. As boundary conditions, we input 3m high water level to the yellow mesh in the direction shown in Figure 10 and allow the water go out through the one surface of blue mesh.

Figure 11 shows snapshots of the simulation results. From the snapshots, the water splashed in front of the building and the water flooded through the windows and stairs are simulated qualitatively. Though quantitative evaluation is the next subject, the behavior of water looks simulated well.

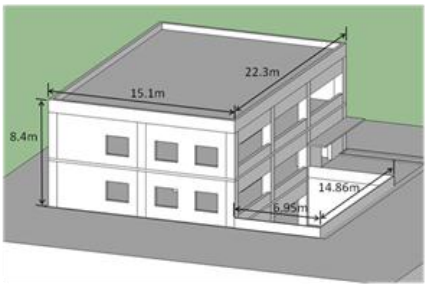


Figure 8 A building model

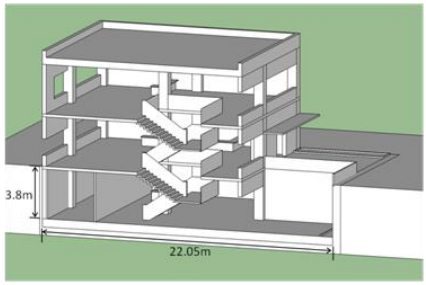


Figure 9 A cross section of the model

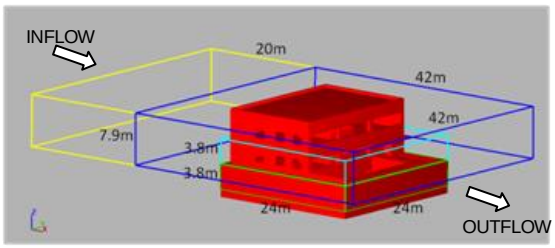


Figure 10 Calculation area

5. CONCLUSION

We performed 3-D tsunami simulation for water inundation into the inside of a building. Though the present case is just a demonstration, in the next step we will evaluate the physical values of the results and apply it for measures for tsunami.

References:

National Police Agency (2013) "Damages caused by the 2011 off the Tohoku Pacific coast earthquake (press release on 26 December 2012)," (in Japanese), http://www.npa.go.jp/archive/keibi/biki/higaijokyo.pdf.

Mori, N., T. Takahashi and The 2011 Tohoku Earthquake Tsunami Joint Survey Group (2012) "Nationwide survey of the 2011 Tohoku earthquake tsunami," *Coastal Engineering Journal*, **54**(1), pp.1-27. (doi: 10.1142/S0578563412500015)

National Institute for Land and Infrastructure Management and Building Research Institute (2011) "Quick Report of the Field Survey and Research on The 2011 off the Pacific coast of Tohoku Earthquake," *Technical note of NILIM* No. 636 and *Building Research Data* No. 132.

Hirt, C.W. and Nicholas, B.D. (1981). "Volume of Fluid (VOF) Method for the Dynamics of Free Boundaries," *Journal of Computational Physics*, **39**, pp. 201-225

Flow-3D. (2012). Flow-3D User Manual: Excellence in Flow Modeling Software, v10.0, *Flow Science, Inc.*

Hirt, C.W. and Sicilian, J.M. (1985). "A Porosity Technique for the Definition of Obstacles in Rectangular Cell Meshes," *Proceedings of the 4th International Conference on Ship Hydrodynamics*, pp. 1-19

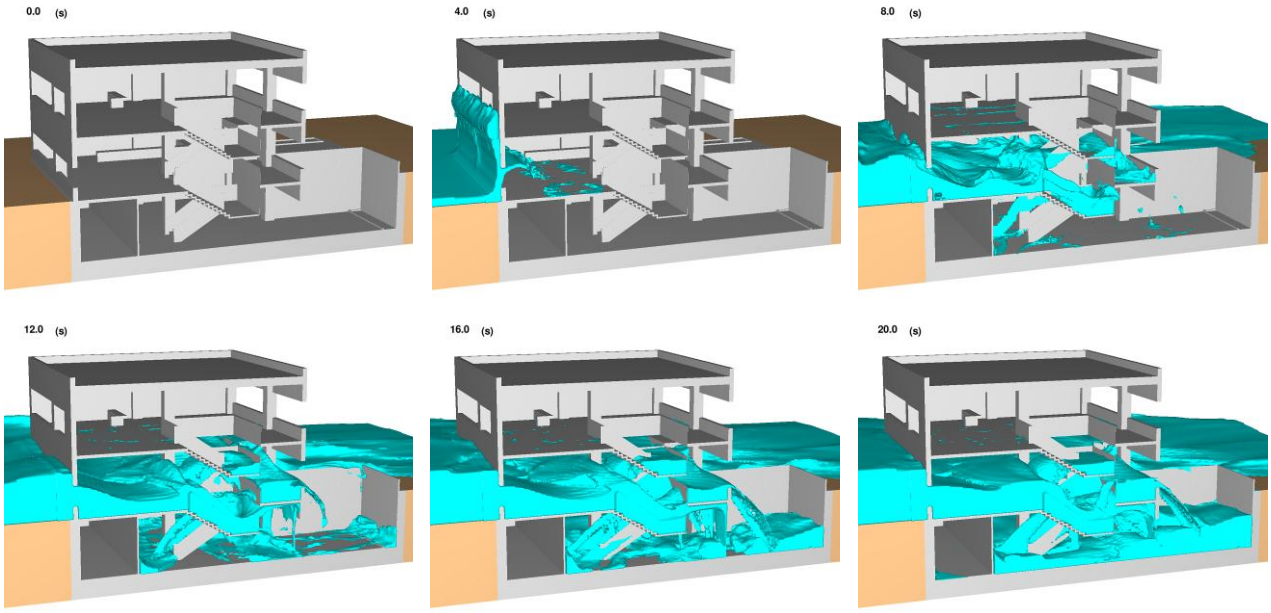


Figure 11 Snapshots of the simulation results

10CUEE CONFERENCE PROCEEDINGS
10th International Conference on Urban Earthquake Engineering
March 1-2, 2013, Tokyo Institute of Technology, Tokyo, Japan

DEVELOPMENT OF A FAILURE ANALYSIS METHOD OF STRUCTURE DUE TO TSUNAMI IMPACT

Seizo Tanaka[1], Fangtao Sun[2], Muneo Hori[3], Tsusyoshi Ichimura[4] and Maddegedara L. L. Wijerathne[4]

1) Project Assistant Professor, Earthquake Research Institute, University of Tokyo, Japan
2) Student, Department of Civil Engineering, University of Tokyo, Japan
3) Professor, Earthquake Research Institute, University of Tokyo, Japan
4) Associate Professor, Earthquake Research Institute, University of Tokyo, Japan
stanaka@eri.u-tokyo.ac.jp, sun@eri.u-tokyo.ac.jp, hori@eri.u-tokyo.ac.jp, ichimura@eri.u-tokyo.ac.jp, lalith@eri.u-tokyo.ac.jp

Abstract: This paper presents the large-scale simulation of the failure of structure due surge front tsunami impacts. In order to simulate the crack propagation, the PDS-FEM which can treat discontinuous interpolation function is introduced into ADVENTURE_Solid open source framework which has highly parallel performance option. And tsunami wave propagation is simulated by solving three dimensional Navier-Sokes equation with free surface. The interface capturing technique based on VOF method is used to express the complicated free surface shapes such as a hydraulic jump and breaking wave. For the large scale The parallel computation based on OpenMP/MPI hybrid parallelization is used to reduce the computational time and to distribute the memory usage on large-scale problem.

1. INTRODUCTION

The protection systems for tsunami like seawalls and breakwaters must have an enough performance to be proof against the tsunami impacts. And the mechanism of crack growth and failure of concrete must be clarified to estimate the damage of such a protection systems under the tsunami impacts. In the numerical simulation of failure of concrete by wave force, high resolution mesh is required in order to estimate the small crack propagation and to evaluate the tsunami impact force accurately, and high resolution mesh requires a significant memory and computational time.

We develop the large-scale simulation of the failure of structure due surge front tsunami impacts. In order to simulate the crack propagation, the PDS-FEM which can treat discontinuous interpolation function is introduced into ADVENTURE_Solid open source framework which has highly parallel performance option. And tsunami wave propagation is simulated by solving three dimensional Navier-Sokes equation with free surface. The interface capturing technique based on VOF method is used to express the complicated free surface shapes such as a hydraulic jump and breaking wave. For the large scale the parallel computation based on OpenMP/MPI hybrid parallelization is used to reduce the computational time and to distribute the memory usage on large-scale problem. In this paper, the fluid and structure simulation code is not interaction strongly, yet. So this is our future work.

2. NUMERICAL FORMULATION OF FREE SURFACE FLOW

2.1 Governing Equations of Fluid

To model of free surface, we consider two immiscible fluids, α and β, with densities ρ_α and ρ_β, and viscosities μ_α and μ_β. The interface function ϕ serves as a marker identifying fluids α and β with the definition $\phi = \{1$ for fluid α and 0 for fluid $\beta\}$. In this context, the density and viscosity, ρ and μ, are defined as

$$\rho = \phi\rho_\alpha + (1-\phi)\rho_\beta, \tag{1}$$

$$\mu = \phi\mu_\alpha + (1-\phi)\mu_\beta. \tag{2}$$

The time dependent of interface function is governed by a following advection equation

$$\frac{\partial \phi}{\partial t} + \mathbf{u}\cdot\nabla\phi = 0 \quad \text{on } \Omega \tag{3}$$

The velocity $\mathbf{u}$ is obtained from the solution of Navier-Stokes equations:

$$\rho\left(\frac{\partial \mathbf{u}}{\partial t}+\mathbf{u}\cdot\nabla\mathbf{u}-\mathbf{f}\right)-\nabla\cdot\sigma(\mathbf{u},p)=0 \quad \text{on } \Omega, \tag{4}$$

$$\nabla\cdot\mathbf{u}=0 \quad \text{on } \Omega, \tag{5}$$

where p is the pressure and $\mathbf{f}$ is external body force.

2.2 Finite Element Formulations

The stabilized finite element formulation of Eq. (3) can be written as follows:

$$\int_{\Omega}\psi\left(\frac{\partial\phi}{\partial t}+\mathbf{u}\cdot\nabla\phi\right)d\Omega + \sum_{e=1}^{n_{el}}\int_{\Omega_e}\tau_{IC}\nabla\psi\cdot\nabla\phi\,d\Omega=0, \tag{6}$$

where τ_{IC} is the stabilization parameter.

The stabilized finite element formulation based on SUPG/PSPG (Streamline-Upwind Petrov Galerkin/Pressure Stabilizing Petrov Galerkin) method of the governing equations of fluid Eq. (4), (5) can be written as follows:

$$\begin{aligned}&\int_{\Omega}\mathbf{w}\cdot\rho\left(\frac{\partial\mathbf{u}}{\partial t}+\mathbf{u}\cdot\nabla\mathbf{u}-\mathbf{f}\right)\mathrm{d}\Omega\\&+\int_{\Omega}\varepsilon(\mathbf{w}):\sigma(\mathbf{u},p)d\Omega+\int_{\Omega}q\nabla\cdot\mathbf{u}\,d\Omega\\&+\sum_{e=1}^{n_{el}}\int_{\Omega_e}\left(\tau_S\mathrm{u}\cdot\nabla\mathrm{w}+\frac{1}{\rho}\tau_P\nabla q\right)\\&\qquad\cdot\left[\rho\left(\frac{\partial\mathrm{u}}{\partial t}+\mathbf{u}\cdot\nabla\mathbf{u}-\mathbf{f}\right)-\nabla\cdot\sigma(\mathrm{u},p)\right]d\Omega\\&+\sum_{e=1}^{n_{el}}\int_{\Omega_e}\tau_C\nabla\cdot\mathbf{w}\,\rho\nabla\cdot\mathbf{u}\,d\Omega=\int_{\Gamma}\mathbf{w}\cdot\mathbf{h}\,d\Gamma,\end{aligned} \tag{7}$$

where τ_S, τ_P and τ_C are the stabilization parameters. And $\mathbf{h}$ represents the Numann boundary condition of momentum equation.

For the temporal discretization, interface function ϕ, velocity $\mathbf{u}$ and pressure p are discretized by using Crank-Nicolson method.

From the above discretization in space and time, a linear equation system can be obtained. GP-BiCG method is used to solve the linear equations. In larger scale problem this procedure takes long computational time and huge memory usage. In order to reduce them, the MPI and OpenMP hybrid parallelization is implemented.

3. NUMERICAL FORMULATIONS OF FAILURE ANALYSIS

3.1 Formulation of PDS-FEM

Cracking functionality is implemented in modern FEM packages. However, it is not suitable to analyze the complicated cracking processes in concrete. This is mainly because this functionality is developed to analyze a single crack or a few cracks which are initiated and propagate in two-dimensional state of plane stress. Furthermore, the functionality is not able to determine the configuration of multiple cracking, which is two-dimensional curved or branched surfaces in a three-dimensional body; it should be recalled that ordinary fracture mechanics is aimed at analyzing a two-dimensional crack of mode I, II or III.

A major difficulty in numerically analyzing multiple cracking in concrete is to determine the crack configuration, which includes branching and kinking. Local crack configuration depends on local strength, which, of course, is not uniform for composite materials like concrete; moreover, local strength is not measured until that point is actually broken. This strong dependence of local cracking on local strength is a source of variability in cracking.

We develop a new numerical treatment of local cracking, which may lead to multiple cracking. Since crack is displacement discontinuity, we introduce a set of basis functions which are not continuous like basis functions used in ordinary FEM. The set uses characteristic functions of Voronoi tessellation of an analysis domain. Since neighboring basis function has discontinuity along the Voronoi boundary, it will give a candidate of possible local cracking; discontinuity that corresponds to multiple cracking is readily provided by such a candidate.

When the set of characteristic functions are employed as basis functions of discretizing a function, it is impossible to calculate the derivative in terms of the same basis functions. Another set of characteristic functions are thus employed to discretize the derivative, and it is a natural choice to use the characteristic functions of the conjugate Delaunay tessellation; it is mathematically shown that the pair of conjugate Voronoi and Delaunay tessellations provides an optimal pair of discretizing a function and its derivation.

The governing equation dynamic elastic-plastic body is written as follows:

$$\frac{\partial\mathbf{v}}{\partial t}-\nabla\cdot\sigma(\mathbf{v})=\mathbf{F} \quad \text{on } \Omega \tag{8}$$

Here, $\mathbf{v}$ is displacement. Denoting by φ^{α} and ψ^{α} the characteristic functions of the α-th Voronoi block and the β -th Delaunay block, respectively, we discretize a displacement function and its gradient, $\mathbf{v}$ and $\nabla\mathbf{v}$, as follows:

$$\mathbf{v}(\mathbf{x}) = \sum_{\alpha} \mathrm{v}^{\alpha} \phi^{\alpha}(\mathbf{x}), \tag{9}$$

$$\nabla \mathbf{v}(\mathbf{x}) = \sum_{\beta} (\nabla \mathbf{v})^{\beta} \psi^{\beta}(\mathbf{x}) \tag{10}$$

where $\mathbf{v}^{\alpha}$ is shape function based on Voronoi diagram on block Ω^{α}. ϕ^{α} satisfies $\phi^{\alpha} = 1$ for $\mathbf{x} \in \Omega^{\alpha}$ and $N^{\alpha} = 0$ for $\mathbf{x} \notin \Omega^{\alpha}$. So, the finite element mesh for PDS-FEM is as shown in Figure 1. In this figure, red line shows Voronoi tessellation for Eq.(9), the black and blue lines show Delaunay tessellation for Eq.(10). And the distribution of displacement and strain field in finite element are as shown in Figure 1, respectively. From this discontinuous shape function, the PDS-FEM has the efficiency at the interface of crack. More details were discussed by Hori et al. (2005).

The PDS-FEM formulation is implemented into ADVENTURE_Solid open source framework, which is developed in ADVENTURE project. The parallelization scheme of ADVENTURE_Solid is based on domain decomposition method (Miyamura et al. 2002). For the temporal discretization for the governing equation, we used Newmark's β method.

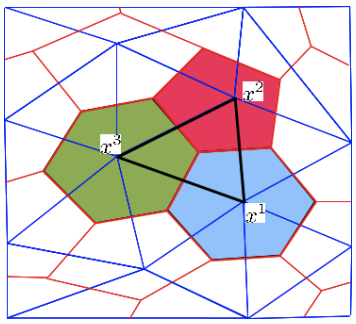


Figure 1 Finite Element for PDS-FEM

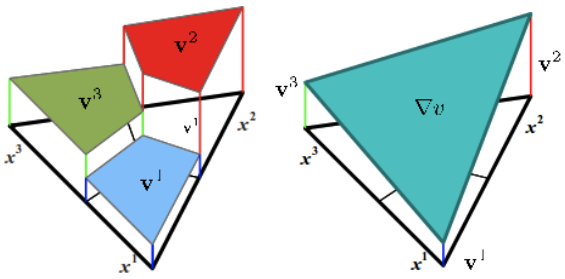


Figure 2 Distribution of displacement(left) and strain(right) based on PDS-FEM

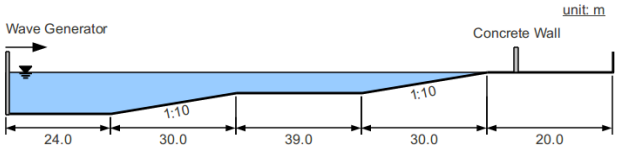


Figure 3 Model of large hydro geo flume

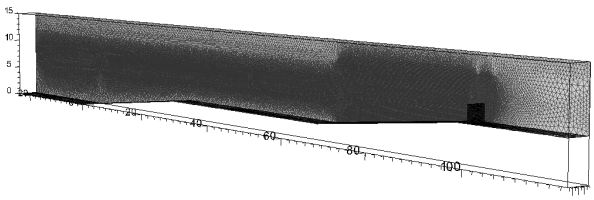


Figure 4 Finite element mesh for fluid domain

4. NUMERICAL EXAMPLE

4.1 Distraction of Concrete Structure due to Tsunami Wave

We used the verified the developed program to compare the experimentally observed. The experiment have been done by the Port and Airport Research Institute (PARI) of Japan in Arikawa et al. (2007). The model of experience is shown in Figure 3. And three dimensional finite element mesh of fluid domain is shown in Figure 4, which has about 2 millions nodes and 10 millions tetrahedral elements and minimum element size is 0.1m. The tsunami wave height is about 2.5m, which is generated by the wave generator located the left side at Figure 3.

As the numerical results, figure 5 shows the time history of pressure at the surface of concrete wall (observed location is shown in Figure 6). In this figures, time starts when the wave reaches to the wall. The computed results are in good agreement with the experimental results. The free surface shapes are shown in Tanaka et al. (2012).

The time snap of pressure distribution at the surface of concrete wall, which obtained by this wave propagation simulation, will be passed to the dynamic structure analysis based on PDS-FEM as the input loading data. Model of concrete wall is as shown in Figure 6 and the thickness of concrete wall is 6cm. Figure 7 shows a finite element mesh for this model. The minimum element size is 2mm, which is appeared around steel bar. Total number of nodes of this model is 1.7 millions, and total number of elements is 10 millions tetrahedral elements.

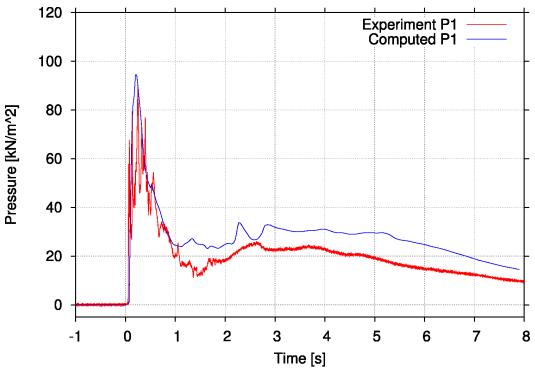


Figure 5 Time history of pressure at P1

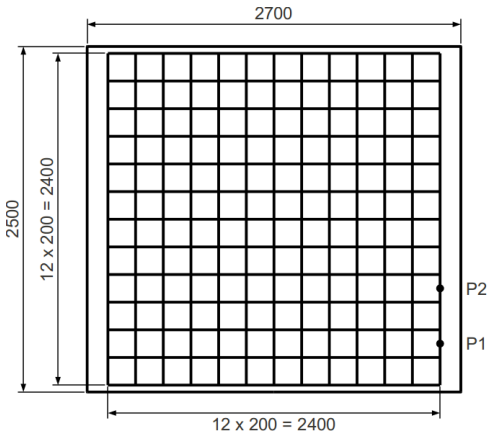


Figure 6 Geometric details of concrete wall

The pressure distribution from the fluid analysis on the concrete wall is converted to nodal force for input loading of structure analysis. The results of failure analysis using PDS-FEM is shown in the Figure 9. From this figure, the PDS-FEM can treat the Also we plan to develop the coupling scheme for fluid and structure analysis to interact between the tsunami impacts and displacement of structure on their interfaces.

5. CONCLUSIONS

We have developed a failure analysis method concrete structure by tsunami wave impact. We show the results of tsunami wave propagation simulation in large hydro flume. And failure simulation based on PDS-FEM. The presented scheme can simulate complicated multiple-cracking propagation successfully. At the next stage, we will plan to develop a FSI scheme to couple the tsunami wave force and failure analysis, and developing the large-scale simulation system on the super computer.

References:

Hori, M., Oguni, K. and Sakaguchi, K. (2005), "Proposal of FEM implemented with particle discretization for analysis of failure phenomena," *Journal of the Mechanics and Physics of solids*, **53**, 681-703.

ADVENTRE Project HP, http://adventure.sys.t.u-tokyo.ac.jp/

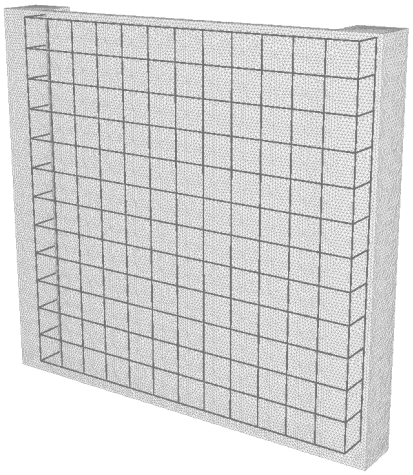


Figure 7 Finite element mesh of concrete wall

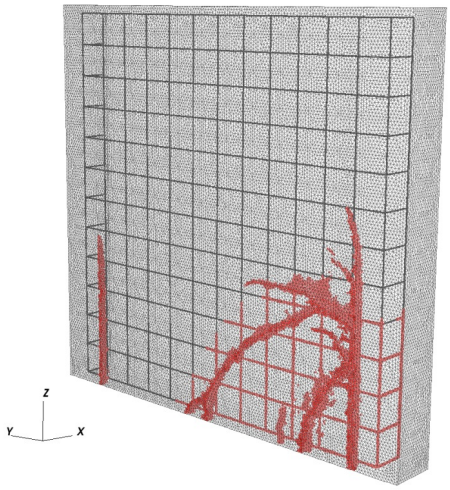


Figure 8 Cracking pattern by PDS-FEM

Brooks, A.N. and Hughes, T.J.R. (1982), "Streamline upwind/ Petrov-Galerkin formulation for convection dominated flows with particular emphasis on the incompressible Navier-Stokes equations," *Computer methods in Applied Mechanics and Engineering*, **32**, 199-259.

Tezduyar, T.E. (1991), "Stabilized finite element formulation for incompressible flow computation," *Advances in Applied Mechanics*, **28**, 1-44.

Aliabadi, S., and Tezduyar, T.E. (2000), "Stabilized-finite-element/ interface-capturing technique for parallel computation of unsteady flows with interfaces," *Compute Methods in Applied Mechanics and Engineering*, **190**, 243-261.

Miyamura, T., Nogchi, H., Shioya, R., Yoshimura, S. and Yagawa, G. (2002), "Elastic-plastic analysis of nuclear structures with millions of DOFs using the hierarchical domain decomposition method," *Nuclear Engineering and Design*, **212**(1-3), 335-355.

Arikawa, T., Nakano, F., Ohtsubo, D., Shimosako, K. and Ishikawa N. (2007), "Research on destruction and deformation of structures due to surge front tsunami," Annual *Journal of Coastal Engineering*, Japan Society of Civil Engineers, **54**, 841-845. (in Japanese)

Tanaka, S., Hori, M., Ichimura, T. and Wijerathne, M. L. L. (2011), "Large-scale parallel computation for failure analysis of reinforced concrete structure by wave impact", Conference Proceedings of 9th ICUEE.

10CUEE CONFERENCE PROCEEDINGS
10th International Conference on Urban Earthquake Engineering
March 1-2, 2013, Tokyo Institute of Technology, Tokyo, Japan

FEASIBILITY OF EVACUATION AT THE PAKARANG CAPE IN THAILAND BASED ON TSUNAMI INUNDATION MODEL AND HUMAN EVACUATION SIMULATION

Erick Mas[1)], Anawat Suppasri[2)], Patchanok Srivihok[3)], Shunichi Koshimura[1)], and Fumihiko Imamura[2)]

1) Laboratory of Remote Sensing and Geoinformatics for Disaster Management, International Research Institute of Disaster Science, Tohoku University, Japan
2) Earthquake induced Tsunami Risk Evaluation, International Research Institute of Disaster Science, Tohoku University, Japan
3) Regional Integrated Multi-Hazard Early Warning System for Africa and Asia, Thailand
mas@irides.tohoku.ac.jp, suppasri@irides.tohoku.ac.jp, patchanok@rimes.int, koshimura@irides.tohoku.ac.jp, imamura@irides.tohoku.ac.jp

Abstract: From the experiences of gigantic tsunami events, authorities from communities at risk have been struggling to raise the tsunami awareness on residents. Since the 2004 Indian Ocean tsunami, Thailand had realized its exposure condition to such phenomena. Thailand was one of the most affected countries with a large amount of casualties including tourists from around the world. After the event, tsunami related information, support and technology to improve tsunami knowledge and awareness, evacuation signs, hazard maps, warning towers and numerical modeling are contributing to build a resilient community among the affected areas. It is also important to evaluate evacuation procedures as people's awareness might decrease with time when non-threatening event occurred. This paper starts by showing an analysis of human loss in Thailand and compared with Japan to show the importance of evacuation. Then, a tsunami evacuation model was then applied with the tsunami numerical simulation to evaluate the present location of tsunami evacuation shelters, the number of evacuees at each haven and the number of possible casualties for a multiple possible scenarios of combined means of evacuation, by walk or on vehicle and population distribution. Results show the feasibility of evacuation for the majority of residents under a balanced condition of evacuees on foot and evacuees on vehicles. An excessive use of vehicles might lead to undesired outcomes when the amount of evacuees increases.

1. INTRODUCTION

Throughout the years of tsunami disasters experienced around the globe, several lessons have been identified, understood and addressed by scientists, authorities and communities. For instance, after the 2004 Indian Ocean tsunami, the importance of tsunami warning systems was highlighted; at the same time awareness and knowledge of tsunami were promoted due to the aftermath observed in Indonesia, Thailand and Sri Lanka. In the 2010 Chilean tsunami, it was reported that several residents followed experiences and teachings of the 1960 Chilean tsunami, in some cases with successful outcomes. The March 11th, 2011 Japan tsunami showed to the world that tsunami warning systems, tsunami hazard maps and even structural countermeasures alone, will never be enough to save the total population at risk. However, preparedness, immediate action and an adequate system of safe havens, deployed around the possible affected area of an extreme scenario, might strongly contribute to increase the probabilities of escaping from tsunami.

In this paper, we will explore the experience of 2004 tsunami in Thailand and compared the human losses to the 2011 Japan case to stress the importance of evacuation procedures. Next, we will evaluate the feasibility of evacuation in a populated area of the Phang Nga province in Thailand, to show the advantages of the evacuation simulation technique. Results and discussions of the multiple scenarios to evaluate here may contribute to the preparedness and future improvement of the evacuation procedure at this community. The methodology used here can be easily applied to other areas at risk.

2. HUMAN LOSS DUE TO THE 2004 INDIAN OCEAN TSUNAMI AND IMPORTANCE OF EVACUATION

In Thailand, the number of deaths, missing, injured and affected people were reported by each province and it is summarized in Table 1. The area of interest for this study is located in the Phang Nga region where at least 4,225 people among resident and tourists were killed. It was reported that from the 4,225 people killed, 1,389 were of Thai nationality while 2,114 were accounted as victims of foreign nationality, the remaining 722 were not identified. It is well known that the coasts of Thailand are famous for its beach resorts and tourist areas. Phang Nga province holds most of these locations and the number of foreigners killed confirmed such unfortunate fact. The Pakarang Cape at Phang Nga province was struck by a maximum tsunami height of 12.24m. Although tsunami arrived to Thailand coasts after two hours, the lack of knowledge,

experience, warning system and preparedness contributed on the resulting outcome of casualties.

Table 1 Summary of death. Missing, injury and affected population in Thailand due to the 2004 Indian Ocean tsunami. (DDPM, 2007).

Province	Death	Missing	Injured	Affected
Phang Nga	*4,225*	*1,655*	*5,597*	*19,509*
Krabi	721	544	1,376	15,812
Phuket	279	608	1,111	13,065
Ranong	159	9	246	5,942
Trang	5	1	112	1,302
Satul	6	-	15	2,920
Total	5,395	2,817	8,457	58,550

After this event, in January 2005, the Indian Ocean Tsunami Warning System was conceived and finally activated on June 2006 following the leadership of UNESCO. The lessons from the 2004 Indian Ocean tsunami were integrated on disaster prevention activities in Thailand, especially through evacuation drills in areas like Phuket. Also tsunami hazard maps and tsunami signs were installed to advice people of the risk of tsunami (Fig. 1).



Figure 1 Tsunami hazard map showing the evacuation routes and a tsunami sign marking the hazard zone in the Pakarang Cape, Phang Nga, Thailand.

In summary, from the experience of 2004 Indian Ocean tsunami, Thailand has traveled into a journey of tsunami disaster prevention and mitigation activities throughout these years. Nowadays, although it is expected for several communities to be better prepared than before, it is important to recall that nature can exceed our expectations. Such is the case of Japan latest disaster in March 11th, 2011. It might be expected that one of the countries with the largest amount of documentation on historical tsunami events would have known about the possibility of a gigantic tsunami event in the Tohoku area. Unfortunately geological times are much bigger than our recorded history, thus, still we cannot account for the known events as the worst possible events. However, despite the huge damage and extensive inundation observed in the Tohoku tsunami event, a surprising outcome is the comparatively low casualty aftermath with the 2004 Indian Ocean.

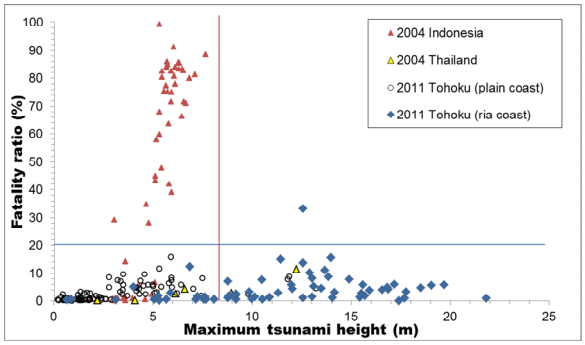


Figure 2 Fatality ratio of 2004 Indian Ocean tsunami and 2011 Japan tsunami. Although tsunami heights were bigger in the 2011 event, the fatality ratio is comparatively lower than in 2004.

In Fig. 2 it is shown that the 2011 event produced in Japan fatality ratios below the 20% of the exposed population in most areas, similarly occurred in Thailand on the 2004 event, however if we take into consideration that 2004 event arrived nearly 2 hours to the coast of Thailand and around 20min to the Japan coast; it is clearly that the Japan event could have been worse if the conditions of tsunami countermeasure, knowledge and preparedness would have been like Thailand in 2004.
Therefore, if 2004 event showed the importance of tsunami warning systems and structural protection at first, also the immediate evacuation and reaction is an important point highlighted from the beginning of tsunami experiences and somehow proven in 2011 when a great amount of population at risk in Japan flew and saved their lives at shelters and high ground.

3. FEASIBILITY OF EVACUATION: RESPONSE TIME AND CASUALTY ESTIMATION

In this study, feasibility of evacuation is evaluated based on the Human Response Capability (HRC) and the casualty estimation output for different scenarios of start time of evacuation decision and the amount of vehicles used as a mean of evacuation by the population. Following the time components described in Post et al. (2009), the Human Response Capability (HRC) can be decomposed into the Reaction Time (RT) - the time of decision to evacuate - and the Response Time (RsT) - a time of movement from an initial at risk location to a safe area (Eq. 1).

$$HRC = RT + RsT \quad (1)$$

In the model developed for this study, RT is defined through the Tsunami Departure Curves (Mas et al., 2012), a stochastic selection of evacuation decision behavior; and RsT is observed through the simulation process, varying with the percentage of vehicles involved and the emerged traffic congestion. Finally, the casualty estimation is conducted during the simulation based on the hydrodynamic features of tsunami – flow depth and velocity - and the local spatial condition of agents in the risk area. This study aims to use the 2004 Indian Ocean tsunami as an

example to evaluate tsunami evacuation process if the 2004 tsunami-type occurs again.

4. DATA AND METHODS

4.1 Study Area

The study area is near the Pakarang cape in the Khao Lak beach resort area of Phang Nga province in Thailand. The district is located at the coast of the Andaman Sea and it was devastated by the tsunami resulting from the 2004 Indian Ocean earthquake. (Fig. 3)



Figure 3 Phang Nga devastated by the 2004 Indian Ocean Tsunami - Left: Before - January 13th, 2003; Right: After: December 29th, 2004. Source: Space Imaging / CRISP-Singapore. The yellow inset shows the area simulated.

4.2 Population and shelters

The population to simulate belongs to a group of villages in the Khuekkhak subdistrict (5,172 inhabitants), in the Takua Pa district of Phang Nga province in Thailand. The total 5,172 residents are not considered as exposed population due to the spatial location of the seven villages of Khuekkhak, however the population data and its spatial distribution were provided by the Thai Meteorological Department (TMD). Finally a total of 2,649 residents were modeled. This is the night time scenario sum of population. We used a night scenario because the total is higher than the day time scenario data available. However this is a particular tourist area and higher number of population at risk might be expected; at this stage we have not included the number of estimated tourists. There are a total of 17 shelters in the inland area; these are shown in Fig. 4.

4.3 Tsunami Inundation modeling

The Tohoku University's Numerical Analysis Model for Investigation of Near-field tsunamis (TUNAMI model) was used as the tool of tsunami modeling (Imamura, 1995). The tsunami propagation is modeled from the initial sea surface displacement assumed to be similar to the initial sea bottom deformation obtained from the analytical expressions proposed by Okada (1992). A set of non-linear shallow water equations are discretized by the Staggered Leap-frog finite difference scheme to follow the tsunami propagation. The bottom friction

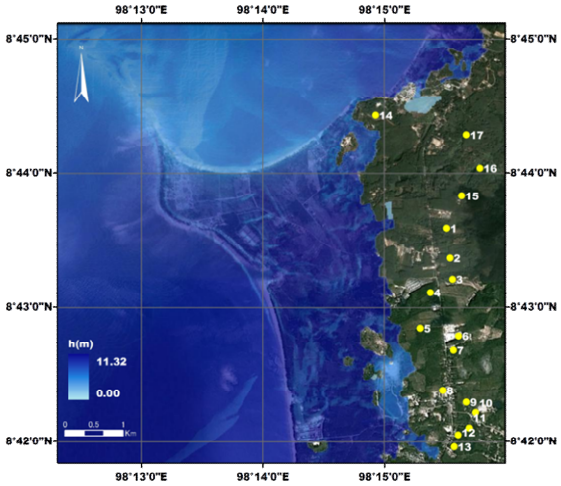


Figure 4 Area of simulation and shelters available. The maximum simulated run up height is 11.32m, closed to the 12.24m reported near the area.

condition obeys to the Manning formula and it is constant in the whole domain.

Suppasri et al. (2008) compared eight proposed source models for the 2004 Indian Ocean tsunami using measured tsunami heights and waveforms data. They concluded that the tsunami source model proposed by Koshimura et al. (2009) is the most suitable model to reproduce tsunami to Thailand. This source model was further used and adapted in various kind of others tsunami research in Thailand such as developing tsunami fragility curves for mangrove (Yanagisawa et al., 2009) dynamic effect of fault rupture velocity (Suppasri et al., 2010), boulder transport due to tsunami (Goto et al., 2010), developing tsunami fragility curves for building (Mas et al., 2012b). Finally, in this study we will use the above mentioned tsunami source model with fault parameters detailed in Table 2 and plotted on Fig. 5.

Table 2 Fault parameters for the 2004 Indian Ocean tsunami. Location of each fault with respect to the bottom left position. Source: (Suppasri, 2010)

Fault Parameters	Segment No.					
	1	2	3	4	5	6
Lat (N)	3.03	4.48	5.51	7.14	8.47	9.63
Long (E)	94.40	93.32	92.87	92.34	91.88	91.57
Strike (°)	323	335	340	340	345	7
Dip (°)	15	15	15	15	15	15
Slip (°)	90	90	90	90	90	90
Length (km)	200	125	180	145	125	380
Width (km)	150	150	150	150	150	150
Disloc. (m)	14	12.6	12	7	7	7
Depth (km)	10	10	10	10	10	10

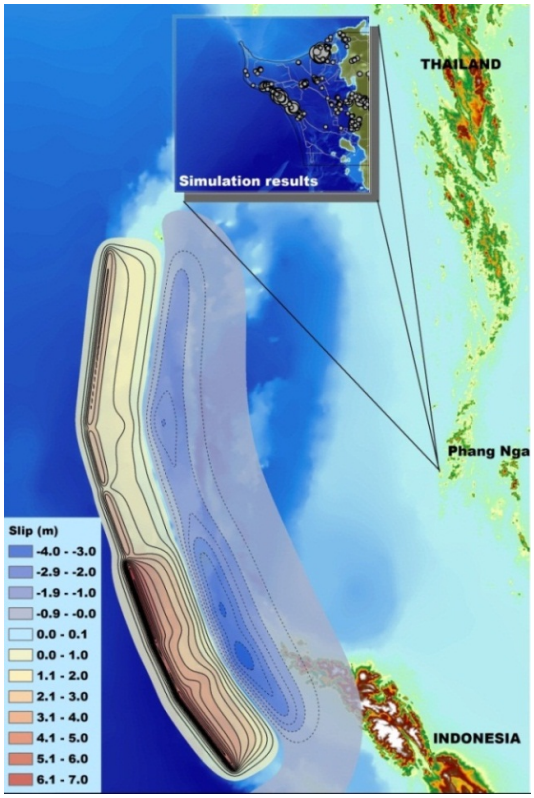


Figure 5 The source model applied on the tsunami propagation and inundation simulation. The sea deformation is located around 500km SW of the study area. The inset shows inundation results and population distribution.

The result of the numerical simulation of tsunami is shown in Fig. 5. The maximum estimated height near shore is around 12.24m and the maximum distance of inundation from the shoreline is of 1.5km to 2.0km.

4.4 Evacuation simulation

Building on the tsunami numerical simulation results in the study area, the evacuation process is evaluated for the design tsunami and several human behavior scenarios. We will explore the influence of the use of vehicles in the evacuation process combined with the different reaction time of residents. Vehicles are included in the model by assuming a set of percentage of evacuees in cars (passengers and drivers) among the population. Then 0%, 25%, 50%, 75% and 100% is discounted at each scenario from the total population and grouped in 4 passengers per car. The start time decision of evacuation for the whole population is related to the Tsunami Departure Curves (TDC), explained in (Mas et al, 2012), however instead of the stochastic method we will analyze four specific scenarios of reaction. The curves assuming a Rayleigh distribution and characterized by a mean of distribution similar to the results of a questionnaire survey applied in the area to 57 residents in different villages among Phang Nga and Phuket (south of the study area) - results are reported in Suppasri (2010), this is μ = 30min. Besides the questionnaire result distribution, another three possible scenarios are considered in the evaluation; a worst case scenario of late evacuation with μ = 120min (near the estimated arrival time of tsunami) and the intermediate scenarios of μ = 60min and μ = 90min. In Fig. 6 it is shown the rate of evacuation decision explained above with the questionnaire results provided by Suppasri (2010b).

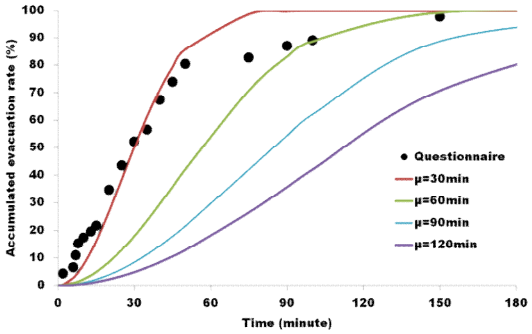


Figure 6 Evacuation decision time based on questionnaires and Rayleigh distribution curves with mean of distribution (μ) related to fast, medium and slow scenarios of evacuation decision.

5. SIMULATION CASES

We ran several cases of evacuation condition, as mentioned above the feasibility of evacuation is evaluated trough the Human Response Capability (HRC), whose components are the reaction time (RT) and the Response Time (RsT). In order to evaluate the influence of these variables, the RT is evaluated using different curves of decision for starting evacuation in the population (Fig. 6); while the RsT is related to the number of resulting casualties estimated for the scenario. Since the RsT is related to the timing of movement, which depends also on the mean of evacuation and the traffic congestion, we also included scenarios with different amount of vehicles. Therefore, the total population of 2,649 residents for the night time scenario was provided by the Thai Meteorological Department (TMD). The summary of cases is detailed in Table 3.

Table 3 Scenarios of evacuation for different start time condition and vehicle percentage.

Population in Vehicles	**Start Time of Evacuation (min)**			
	30	**60**	**90**	**120**
0%	E30V0	E60V0	E90V0	E120V0
25%	E30V25	E60V25	E90V25	E120V25
50%	E30V50	E60V50	E90V50	E120V50
75%	E30V75	E60V75	E90V75	E120V75
100%	E30V100	E60V100	E90V100	E120V100

A total of 20 scenarios where simulated using an integrated agent based model for tsunami inundation and tsunami evacuation simulation developed by Mas et al (2012).

6. RESULTS AND DISCUSSION

The result of the 20 simulated cases is shown in Table 4. The fatality ratio defined as the ratio of estimated casualties over the

total population involved in the simulation (exposed population) is shown in the last column of the table. The worst case scenario of evacuation is shown in Fig. 7 where no vehicle is involved and the total of population evacuates on foot and with a slow reaction (E120V0). In general fatality ratios varies from the 6% to the 34% of the total population to be at risk. The main reason of such variation is due to the time of reaction to start the evacuation and the mean used to evacuate to inland. It is clear on Table 4 that the highest fatality ratios occurred when no vehicle is used for evacuation. This is due to the long distance of about 2 km necessary to evacuate to the selected shelters described before (Fig. 4).

Table 4 The results of the estimated casualties at different evacuation condition

V (%)	E (μ) (min)	Safe (pers.)	Casualty (pers.)	F (%)
0	30	2049	600	23%
0	60	1968	681	26%
0	90	1854	795	30%
0	120	1758	891	34%
25	30	2400	251	9%
25	60	2288	363	14%
25	90	2102	549	21%
25	120	1971	680	26%
50	30	2462	186	7%
50	60	2383	265	10%
50	90	2227	421	16%
50	120	2077	571	22%
75	30	2484	166	6%
75	60	2386	264	10%
75	90	2237	413	16%
75	120	2091	559	21%
100	30	2452	196	7%
100	60	2352	296	11%
100	90	2248	400	15%
100	120	2072	576	22%

"V" is the percentage of population using vehicles for evacuation. Either as driver or passenger. It is assumed that each car has four passengers.
"E" is the mean of the distribution (μ) used to construct the evacuation start time curve.
"F" is the Fatality ratio (Casualty / Total Population)

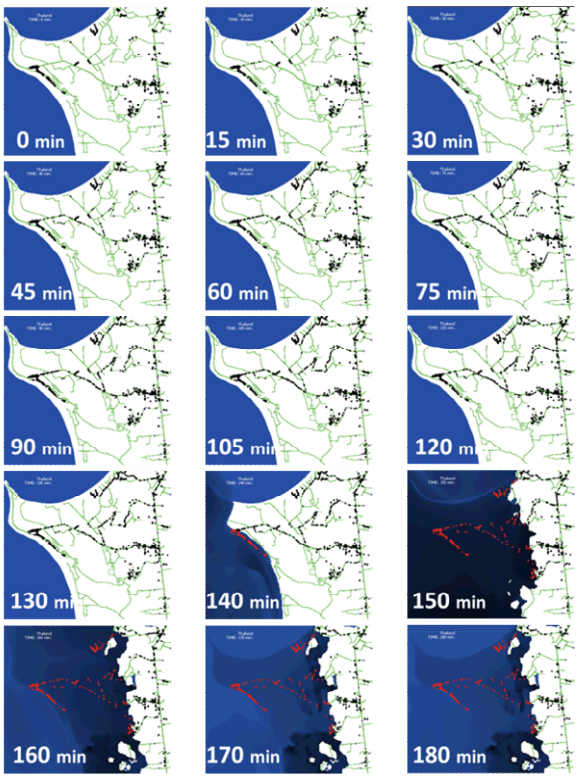


Figure 7 Snapshots of the worst case scenario of resulting fatality ratio (F in table 4). Evacuation is performed to the 17 available shelters on the right side of the area.

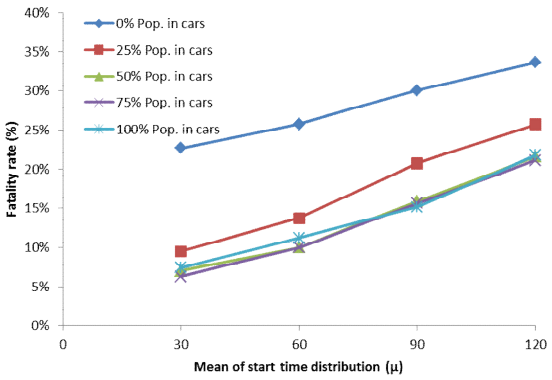


Figure 8 Fatality ratios at different timing of evacuation and percentage of population using vehicles. Notice the advantage of a fast evacuation decision, and in this area and for this amount of population, the advantage of using cars.

Based on the results shown in Table 4, Fig. 8 is presented to better discuss the influence of vehicles during the evacuation in this area and also the consequences of delaying the time for starting the evacuation. Apparently in this area the use of cars makes it convenient due to the long distance of evacuation, only a 25% of population in vehicles decreases the estimated fatality on 10%. Due to the number of people involved (2,649) and the

relatively small number of vehicles used (around 650 in the V=100% case) no significant traffic congestion was observed. However, a late reaction in the population may increase from 5% to 15% the fatality ratio.

7. CONCLUSION

A study of feasibility of evacuation in the Pakarang Cape of Thailand has been presented here. First, a comparison of the 2004 Indian Ocean tsunami fatality ratio with the 2011 Japan tsunami showed that for the case of Thailand where the tsunami arrived at more than two hours, fatality ratios were closed to the ones in Japan where tsunami arrived around thirty minutes. This drives us to a reflection on not only Japanese tsunami countermeasures, but especially tsunami awareness and preparedness for immediate evacuation. The importance of tsunami warning and tsunami evacuation procedures has been observed on 2004 and 2011 events. For the feasibility study, twenty cases of different starting time of evacuation and vehicle evacuation were conducted. Results suggest that due to the long distance of shelters vehicle evacuation might be necessary. It is possible that the use of vehicles in this area due to the small number of population and sufficient road capacity might not result on significant traffic congestions. Notice that if major population is involved than the evaluated here, traffic congestion might be possible. Future research including the estimated number of tourist remains in the agenda.

Acknowledgements:

Population and other tsunami evacuation related data used in this study were kindly provided by the Thai Meteorological Department of Thailand (TMD). The authors acknowledge support from Tokio Marine & Nichido Fire Insurance Co., Ltd. through the International Research Institute of Disaster Science (IRIDeS) at Tohoku University and the Japan Ministry of Education, Culture, Sport, Science, and Technology (MEXT).

References:

Goto, K., Okada, K., Imamura, F., (2010) Numerical analysis of boulder transport by the 2004 Indian Ocean tsunami at Pakarang Cape, Thailand, *Marine Geology*, Vol. 268, 97-105

Imamura, F. (1995). Review of tsunami simulation with a finite difference method. *Long-Wave Runup Models* (pp. 25–42).

Koshimura, S., Oie, T., Yanagisawa, H. and Imamura, F. (2009), Developing fragility curves for tsunami damage estimation using numerical model and post-tsunami data from Banda Aceh, Indonesia, *Coastal Engineering Journal*, 51, 243−273.

Mas, E., Imamura, F., & Koshimura, S. (2012). An Agent Based Model for the Tsunami Evacuation Simulation. A Case Study of the 2011 Great East Japan Tsunami in Arahama Town. *Joint Conference Proceedings. 9th International Conference on Urban Earthquake Engineering & 4th Asia Conference on Earthquake Engineering* (pp. 1–9). Tokyo, Japan: Tokyo Institute of Technology.

Mas, E., Koshimura, S., Suppasri, A., Matsuoka, M., Matsuyama, M., Yoshii, T., Jimenez, C., et al. (2012b). Developing Tsunami fragility curves using remote sensing and survey data of the 2010 Chilean Tsunami in Dichato. *Natural Hazards and Earth System Science*, 12, 2689–2697. doi:10.5194/nhess-12-2689-2012

Okada, Y. (1992). Internal deformation due to shear and tensile faults in a half-space. *Bulletin of the Seismological Society of America*, 82(2), 1018–1040.

Post, J., Wegscheider, S., Mück, M., Zosseder, K., Kiefl, R., Steinmetz, T., & Strunz, G (2009). Assessment of human immediate response capability related to tsunami threats in Indonesia at a sub-national scale. *Natural Hazards and Earth System Science*, 9(4), 1075–1086. doi:10.5194/nhess-9-1075-2009

Suppasri, A., Imamura, F., and Koshimura, S.: Comparison among the proposed source models for the 2004 Indian Ocean tsunami, in: Proceedings of the 2008 Western Pacific Geophysics Meet- ing, Cairns, Australia, 29 July–1 August 2008, U35B, 2008

Suppasri, A., Imamura, F., & Koshimura, S. (2010). Effects of the Rupture Velocity of Fault Motion, Ocean Current and Initial Sea Level on the Transoceanic Propagation of Tsunami. *Coastal Engineering Journal*, 52(02), 107–132. doi:10.1142/S0578563410002142

Suppasri, A., Imamura, F. & Koshimura, S. (2010b). Recognition on tsunami evacuation in Southern Thailand at present, Tohoku branch academic meeting, JSCE.

Yanagisawa, H., Koshimura, S., Goto, K., Miyagi, T., Imamura, F., Ruangrassamee, A. and Tanavud, C. (2009), The reduction effects of mangrove forest on a tsunami based on field surveys at Pakarang Cape, Thailand and numerical analysis, Estuarine, *Coastal and Shelf Science*, 81(1), 27−37.

10CUEE CONFERENCE PROCEEDINGS
10th International Conference on Urban Earthquake Engineering
March 1-2, 2013, Tokyo Institute of Technology, Tokyo, Japan

TSUNAMI INUNDATION MAPPING USING REMOTE SENSING ANALYSIS AND NUMERICAL MODELING IN LIMA, PERU

Bruno Adriano[1)], Erick Mas[1)], Shunichi Koshimura[1)], Yushiro Fujii[2)], Sheila Yauri[3)], Cesar Jimenez[4)] and Hideaki Yanagisawa[5)]

1) ReGiD, International Research Institute of Disaster Science, Tohoku University, Japan
2) International Institute of Seismology and Earthquake Engineering, Building Research Institute, Japan
3) Instituto Geofísico del Perú, Peru
4) Dirección de Hidrografía y Navegación, Peru
5) Department of Regional Management, Faculty of Liberal Arts, Tohoku Gakuin University, Japan
badrianoo@geoinfo.civil.tohoku.ac.jp, mas@irides.tohoku.ac.jp, koshimura@irides.tohoku.ac.jp, fujii@kenken.go.jp, sheila.yauri@igp.gob.pe, cesarsud86@hotmail.com and h-yanagi@izcc.tohoku-gakuin.ac.jp

Abstract: Within the framework of the project Enhancement of Earthquake and Tsunami Disaster Mitigation Technology in Peru (JST-JICA SATREPS), this study aims on the tsunami inundation mapping of the coastal area of Lima city. Remote sensing data and Geographical Information System (GIS) analysis are incorporated in order to improve the accuracy of the numerical modeling results. Moreover, we evaluate the tsunami impact through the estimation of a tsunami casualty index (TCI) using our numerical results. The numerical result in terms of maximum tsunami depth shows a maximum inundation height of 5.4 m. In terms of inundation area, the maximum extension is 1.7 km with run-up height of 6 m. Additionally, the average TCI value obtained is 0.36 for the whole inundation domain where TCI equal to 1.00 represents the highest condition of risk. The mapping results presented in this paper give important information in order to understand tsunami inundation features and consequently it might be useful to design an adequate tsunami evacuation plan for Lima city.

1. INTRODUCTION

Tsunami inundation have caused an unfortunate loss of life and extensive property damage to coastal communities in seismic prone countries. For instance, tsunami events that had occurred in seismically similar areas such as Chile Tsunami 2010, Japan Tsunami 2011 and also the December 26, 2004 Sumatra tsunami are tragic reminders of the devastation that these powerful events can generate to coastal areas. In case of Peruvian seismic history, one of the most disastrous seismic event occurred in 1746, whose epicenter was located in front of the central area of Peru coast. According to some historical testimonies, the capital city of Lima was completely destroyed by the ground shaking and subsequently by the tsunami flood (Dorbath et al. 1990). Therefore, it is important to develop an efficient tsunami warning system in order to mitigate such catastrophic damages due to tsunami events.

The purpose of this study is to determine the tsunami inundation area for the coastal region of Lima city, adopting a megathrust earthquake that might likely affect Lima metropolitan region as seismic source scenario, through numerical modeling and detail topography model which includes building height information and land use classification. Additionally, numerical modeling results such as flow depths and current velocity are used to evaluate the tsunami impact by estimating a tsunami casualty index within the inundation area.

2. DESCRIPTION OF THE STUDY AREA

The study area essentially covers the central zone of Lima coast which corresponds to the constitutional province of Callao (see Figure 1a). The geographic limits for the study area are 11.95° - 12.09° South and 77.18° to 77.13° West. Morphologically, the coastal plain rises up to 15 m approximately above the sea level near the shoreline. However, whilst the coastline to the north forms a long sweeping bay, the coastline to the south of the study area presents a small peninsula which corresponds to La Punta district. In accordance with the Peruvian Institute of Statistic and Informatics (INEI), the population in Lima city is about 9 million people. For Callao province, however, there are about 950 thousand inhabitants living in this province. The urban use in the study area can be divided mainly into three types (see Figure 1a). The first one corresponds to residential type which its area is concentrated in the southern part of the inundation domain (below 12$°02’30’’). This is the most

populated area in Callao province; as a result, the land surface is largely covered by houses and avenues. The second urban use type is located in the center of the study area (between 12°01'S and 12°02'30'') this zone is covered by extensive vegetated area which corresponds to the backside of the International Airport of Lima and fields. There are also some towns placed along the coastline where the housing type are principally non-engineering buildings INEI. Finally, in the third zone type the surface along the coastline is mainly occupied by some factories.

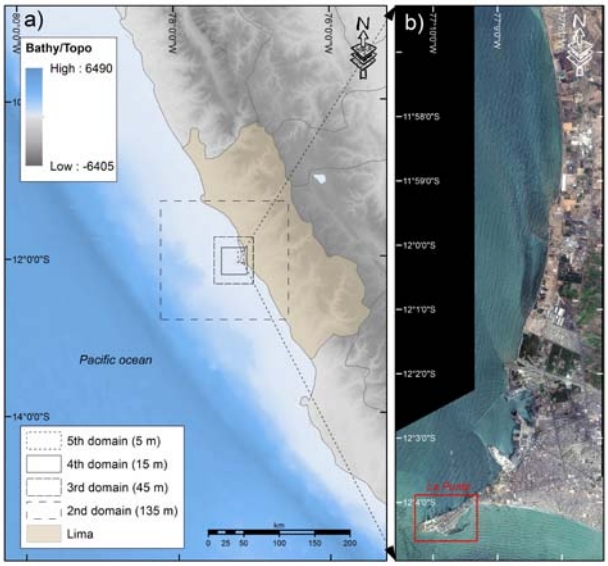


Figure 1. a) View of the first domain (405 m grid size resolution), the boundaries for the other domains are shown in dashed lines. b) Study area which corresponds to the 5th domain, background view of WorldView-2 satellite images in true composite.

3. TSUNAMI SOURCE SCENARIO

Seismic events accompanied with large tsunamis along the coastal area of central Peru have been reported since historical times. For instance, the 1746 earthquake is considered one of the most catastrophic seismic events in Peruvian history. The moment magnitude for this event has been estimated between 8.8 and 9.0 and the reported tsunami run-up height was between 15 m and 24 m (Dorbath et al. 1990 and Becket al. 1989). Two centuries later, only two event with considerable magnitude occurred. The 1966 earthquake, which epicenter was located at the north-central coastal area of Peru, had a rupture length of 100 km and a local tsunami height of 2.6 m. The last was in 1974 which occurred in front of Lima city, had a rupture length of 140 km and a local tsunami height of 1.6 m (Dorbath et al. 1990). Since then, large earthquakes have not been reported in the surroundings. Therefore, there is a clear seismic gap of approximately 250 years. Furthermore, considering the seismic history in this area, it is urgent to take into account the higher possibility of the occurrence of an enormous seismic event accompanied with a catastrophic tsunami in front of Lima city.

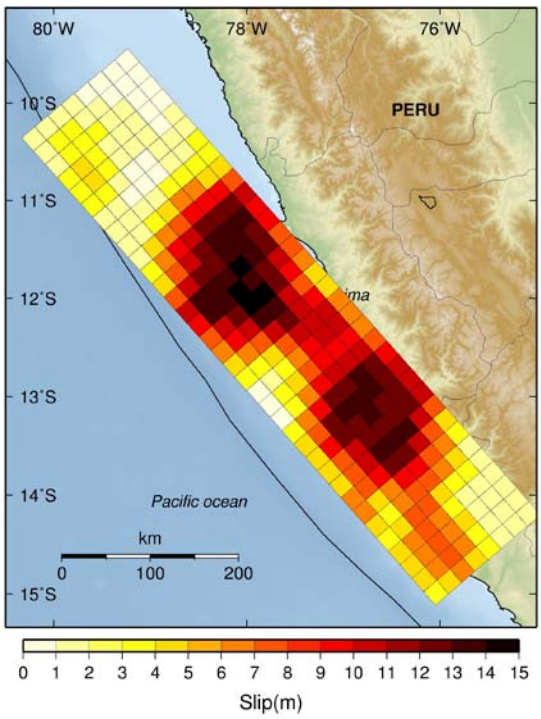


Figure 2. Slip distribution proposed by Pulido et al. (2011). The scale bar for the slip amount is shown below for each model.

In the evaluation of seismic models the application of GPS (Global Positioning System) observation and InSAR (Interferometry Synthetic Aperture Radar) makes possible to measure the strain/displacement associated with plate convergence movements in high seismicity zones. Sagiya et al. (2000) used a GPS array with about 1,000 permanent stations to recognize the coseismic deformations associated with large earthquakes and ongoing secular deformation in Japan. Hashimoto et al. (2010) and Liu and Yamazaki (2013) used pre- and post-event SAR imagery datasets to estimate the crustal movement from the 2008 Wenchuan, China Earthquake and 2011 Tohoku, Japan Earthquake, respectively. Additionally, historical information such as earthquake intensity perception, run-up measurements and wave arrival times of past earthquake events plays an important role in order to estimate seismic models for potential earthquake scenarios which can be used to evaluate a possible future impact (Kuroiwa 2004). In this study the source model is based in a megathrust earthquake that might likely affect Lima metropolitan region which is appropriate for simulation of long period wave and tsunami modeling (Pulido et al. 2011). The seismic source is based on a model of interseismic coupling distribution in subduction areas for a period of 265 years since 1746 earthquake. These data also includes sea floor deformation measurements obtained offshore of Lima city from a combination of GPS receivers and acoustic transponders (Gagnon et al. 2005), as well as information of historical earthquakes to propose the slip distribution. The seismic source is divided into 280 sub-fault segments, each segment of 20 km x 20 km in size, in a

rupture area of 700 km by 160 km with moment magnitude of Mw 9.0. The slip solution model shows two main asperities, the largest is located west of Lima city, approximately 70 km, with maximum slip amount of 15.4 m and the second one with slip amount up to 13.0 m to the south of Lima. Figure 2 shows the spatial location for the slip model distribution.

3.1 Initial Sea Floor Displacement

We use a rectangular dislocation model (Okada 1985) to calculate the ocean bottom deformation due to our source scenario. The initial sea floor displacement is assumed from the instant push up of the seismic deformation on the ocean bottom. Thus, the features of the bottom deformation reflects the initial water surface displacement that is assumed as initial condition of the tsunami propagation modeling. Figure 3 shows the displacement result. The areas in red and blue colors represent the uplift and subsidence displacement, respectively. Contour lines are drawn in 0.25 m interval. There are two regions of high uplift deformation which are consistent with the slip model distribution, the higher uplift region has a maximum displacement of 4.6 m and it is located about 150 km in front of Lima coastal area.

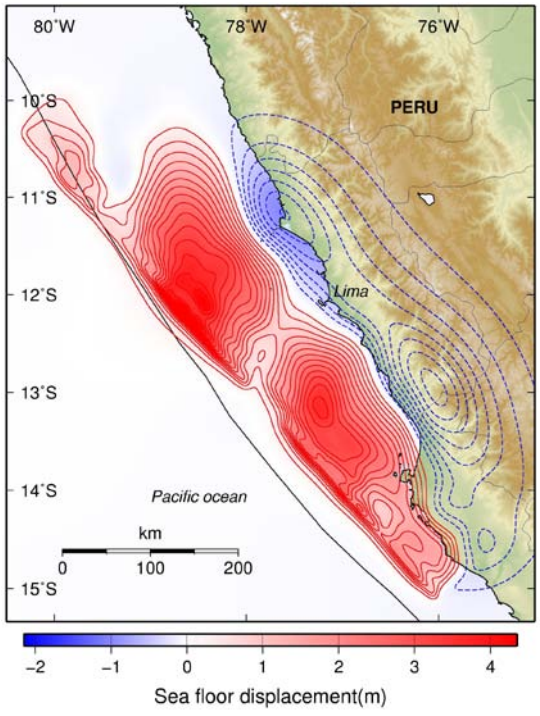


Figure 3. Sea floor displacement calculated from the estimated slip distribution (Pulido et al. 2011). The areas in red and blue colors represent the uplift and subsidence displacement, respectively. Contour lines are drawn in 0.25 m interval for each model.

4. ROUGHNESS COEFFICIENT MAP

Generally, based on the relation between the scale of an obstacle and the grid size of the computational domain, there are basically two approaches to be applied in inundation modeling (Hong 2004). The first one is the topography model which uses a constant roughness coefficient for the whole computational domain and a very detailed topography dataset including the building height informations. This approach is used when the obstacle or urban use (e.g. buildings, seawalls, roads, and fields) can be adequately represented within the grid cells in the inundation model. Thus, this model uses a finer grid size where the flow around and between obstacles can be well simulated. The second one is known as equivalent roughness model. This model is applied when the obstacles are much smaller than the grid size. Aburaya et al. (2002) introduced an appropriate methodology for this case which is based in the calculation of a building/house occupation ratio within the grid cells in the inundation domain. This method has been utilized and validated, through the comparison with field survey data, in order to developed tsunami fragility functions (Koshimura et al. 2009 and Suppasri et al. 2011). Furthermore, based in these methodologies, Muhari et al. (2011) presented a comparison of three run-up models (constant roughness model, topography model and equivalent roughness model) on highly populated area, they have concluded that the topographic model can be used to identify the distribution of inundation parameters in residential areas.

Since high grid resolution and urban use influence the estimation bottom roughness coefficient, it might change the propagation of waves considerably due to having obstacles or roughness induced energy dissipation. Consequently the final input raster should include features with appropriate elevation heights and adequate roughness surface mapping (Gayer et al. 2010). In this study, in order to improve the accuracy of the numerical results, we enhance the topography model approach by adding a specific bottom roughness coefficient for each grid cell in the inundation domain. Those coefficient values are based in a roughness coefficient map (see Figure 4a). Adriano et al. (2012) performed a land use classification using satellite images from WorldView-2 sensor and the coefficient values are assigned according to the land use (Kotani1et al. 1998) in order to present a roughness coefficient map for the coastal area of Lima city. Additionally, the topography data is combined with a height building model (see Figure 4b). For La Punta district a GIS building shape file in a single house scale is available, it includes number of stories, spatial location and construction material type fields. In this case, the height building model is constructed by multiplying the number of stories by 2.5 m (story height standard in Lima city). However, for the rest of the computational domain only the spatial location for a block scale is available. Nevertheless, in order to construct the height building model, we assume as preliminary estimation two story height for each block. However, only the historical building known as “Fortaleza Real Felipe” (location coordinate: -77.15°W, -12.06°S) was manually delineated and its height is fixed equal to 8 m which is approximately the real height of the perimeter wall.

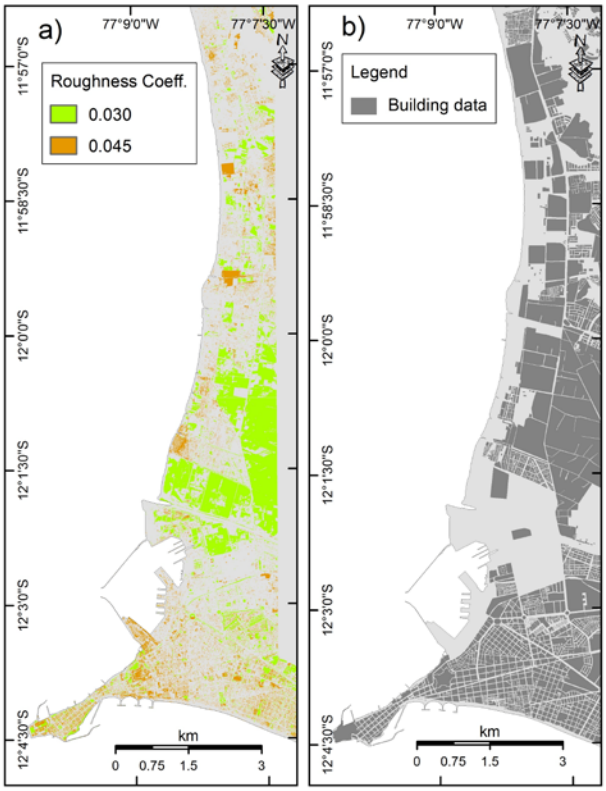


Figure 4 a) Roughness coefficient map Adriano et al. (2012). b) GIS building shape file used to construct the building height model.

5. TSUNAMI INUNDATION MAPPING

The numerical simulation was conducted by using Tohoku University's Numerical Analysis Model for Investigation of Near-filed tsunami No.2 (TUNAMI-N2) code based on shallow water theory and Cartesian coordinate system (Imamura 1995), which was developed by Disaster Control Research Center (DCRC), Tohoku University, Japan. The computation time for the tsunami modeling is 3 hours. In order to satisfy the stability condition the time step for the numerical computation is fixed equal to 0.2 s.

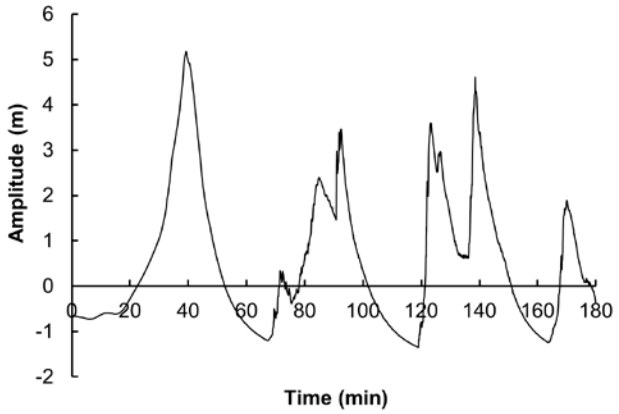


Figure 5. Synthetic tsunami height recoded at Callao tide gauge station.

The tsunami inundation is calculated on the fifth domain using 5 m resolution of bathymetry and topography grid data with 1567 x 3346 grid points along the longitude and latitude directions, respectively. Figure 5 shows the synthetic tsunami height recorded in Callao tide gauge station, which is located at 77.16°W, 12.06°S (see Figure 6) within 3 hours of simulation. The tsunami arrival time registered in Callao station is 22 minutes. In addition, the time step when the maximum tsunami height occurred is equal to 38 minutes. The local inundation depth is the result of measuring water marks on structures above the ground. The inundation depth and inundation area result are shown in Figure 6a. In terms of inundation depth, the maximum value reaches up to 6 m. Further, in terms of inundation distant; on the northern part of the computational domain, its maximum extension reach about 1 km with run-up height about 6 m and 1.4 km with run-up height about 12.4 m. On the surrounding area of Rimac river estuary (around 12°02'S latitude) the tsunami inundation extend up to 1.3 km with run-up height of 5.3 m. Based on the numerical results the inundation depth values reach up to 6 m which might completely inundate one storey buildings. The inundation depth on most of the streets in La Punta district (see Figure 1b) reach values up to approximately 4 m. However, based on the time series shows in the previous Figure 5 this state occurs three times with a time period about 50 minutes within 3 hour of tsunami simulation. The inundation area extents several blocks on land (about 1 km distant) with maximum run-up height of 4 m there is, additionally, a clear inundation zone that extend about 1.7 km which correspond to the inundation zone when buildings are completely inundated.

5.1 Tsunami impact assessment

In order to analyze the tsunami impact in the study area, we estimated the potential tsunami casualties due to the tsunami flooding. Koshimura et al. (2006) introduced a practical methodology which uses a simple human model (based on cylinder members) to evaluate the effect of hydrodynamic forces on it. Thus, it is possible to determine locations and times within the tsunami inundation zone where casualties are likely to occur. Muhari et al. (2011) presented an improvement of the previous method by considering two types of fall of the human model (stability conditions). The first one considers that hydrodynamic force exceeds the friction force on the soles of the human model feet and the second one occurs when the moment from the bottom back of the heel due to the hydrodynamic force is bigger than the resistance moment due to human body weight. Koshimura et al. (2006) also introduced the Tsunami casualty index (TCI) which is defined by relation between the time duration of the tsunami inundation flow that satisfies the two stability conditions mentioned above and the total time duration of the tsunami inundation flow. TCI can be used to illustrate the spatial distribution of potential tsunami casualty within the inundation area. The TCI result is shown in Figure 6b. Basically, the TCI follows a

consistent behavior similar as the inundation depth and inundation area. However, based on the impact assessment model, there are areas with inundation depth up to 4 m that the TCI shows values of 0.5 which might indicate that the tsunami flow velocity is not strong enough to produce a hydrodynamic force able to affect the balance of the human model within 3 hours of tsunami simulation (Muhari et al. 2011). It is important to point out that some of these areas are concentrated on La Punta district where the maximum TCI value is 0.52 on most of the streets. The average TCI value obtained is 0.36 in the whole inundation domain. Additionally, based on our numerical calculation the balance instability of the human model for each cell grid in almost the whole inundation domain occurs between 2 and 5 minutes after the tsunami wave arrived.

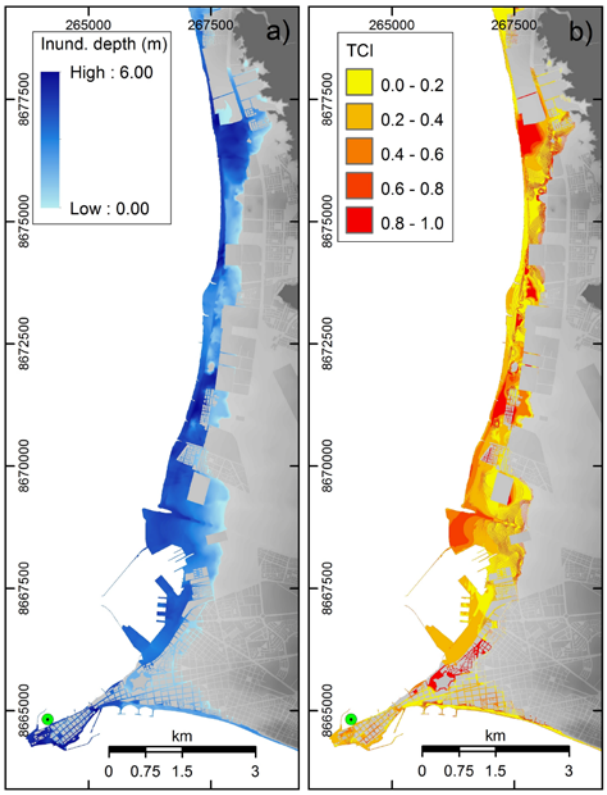


Figure 6. a) Tsunami inundation calculated within 3 hours of numerical simulation. b) TCI estimated using tsunami feature results. Green dot shows the location of Callao Tide gauge station.

6. CONCLUSIONS

The tsunami inundation modeling using detailed bathymetry raster dataset was carried out in order to determine the tsunami inundation area for the coastal region of Lima city. Additionally, flow depth and flow velocity results were used to evaluate the tsunami impact by estimating a tsunami casualty index within the inundation area. The inundation map developed using the source scenario adopted shows a maximum inundation depth of 6 m and maximum inundation distant of 1.7 km, those values represent a high tsunami risk for the study area. Therefore, if we consider the Peruvian seismic history and the lesson learned from past tsunami event occurred in other regions such as 2011 Tohoku tsunami, the mapping result should be considered in order to propose a tsunami warning system. Additionally, the TCI map estimated using our source scenario adopted shows a consistent behavior similar as the inundation map. The mean value of the TCI in the computation domain is 0.36. TCI maps might be useful in order to develop a tsunami evacuation plan, especially in case of La Punta district when the TCI value is greater than 0.5. Finally, the mapping results presented in this paper gives important information in order to understand tsunami inundation features; therefore it might be useful to design an adequate tsunami warning system which can be included in a tsunami evacuation plan for Lima city.

Acknowledgements:

The authors acknowledge support from the Japan Ministry of Education, Culture, Sports, Science and Technology (MEXT) and the project of Science and Technology Research Partnership for Suistanaible Development (SATREPS) supported by JST-JICA for the financial support throughout the study. Additionally, the authors acknowledge support from MEXT for establishing the Center for Urban Earthquake Engineering (CUEE) in Tokyo Institute of Technology. This support makes possible the forthcoming international conference, as well as international joint research projects and exchange programs with overseas universities.

References:

Dorbath, L. Cisternas, A. and Dorbath, C. (1990), "Assessment of the size of large and great historical earthquakes in Peru", Bulletin *of the Seismological Society of America*, vol. 80, no. 3, pp. 551-576.

Instituto Nacional de Estadística e Informática – INEI, (2007), (Institute of Statistic and Informatics), "Censos Nacionales 2007".

Beck, S. L. and Ruff, L. J. (1989), "Great earthquakes and subduction along the Peru trench", *Physics of the Earth and Planetary Interiors*, vol. 57, pp. 199–224, Nov. 1989.

Pulido, N. Tavera, H. Perfettini, H. Chlieh, M. Aguilar, Z. Aoi, S. Nakai, S. and Yamazaki, F. (2011), "Estimation of Slip Scenarios for Megathrust Earthquakes: A Case Study for Peru", in *Effects of Surface Geology on Seismic Motion*, pp. 1–6.

Sagiya, T. Miyazaki, S. and Tada, T. (2000), "Continuous GPS array and present-day crustal deformation of Japan", *Pure and Applied Geophysics*, vol. 157, pp. 2303–2322.

Hashimoto, M. Enomoto, M. and Fukushima, Y. (Aug. 2010), "Coseismic Deformation from the 2008 Wenchuan, China, Earthquake Derived from ALOS/PALSAR Images", *Tectonophysics*, vol. 491, pp. 59–71.

Liu W. and Yamazaki, F. (2013), "Detection of Crustal Movement From TerraSAR-X Intensity Images for the 2011 Tohoku, Japan Earthquake", IEEE GEOSCIENCE AND REMOTE SENSING LETTERS, vol. 10, no. 1, pp. 199–203.

Kuroiwa, J. (2004), "Disaster Reduction, Living in harmony with nature". Lima: Editorial NSG S.A.C, first edit Ed.

Gagnon, K. Chadwell, C. D. and Norabuena, E. (Mar. 2005). "Measuring the onset of locking in the Peru-Chile trench with GPS and acoustic measurements", *Nature*, vol. 434, pp. 205–8.

Okada, Y. (1985). "Surface deformation due to shear and tensile faults in a half-space", *Bulletin of the Seismological Society of America"*, vol. 75, no. 4, pp. 1135–1154.

Hong S. J. (2004). "Study on the two and Three Dimensional

Numerical Analysis of Tsunamis near a coastal Area". PhD. Thesis Tohoku University, Japan, 2004.

Aburaya, T. and Imamura, F. (2002), "The proposal of a tsunami run-up simulation using combined equivalent roughness", *Annual Journal of Coastal Engineering, Japan Society of Civil Engineers*, vol. 49, pp. 276–280.

Koshimura, S. and Oie, T. (2009), "Developing fragility functions for tsunami damage estimation using numerical model and post-tsunami data from Banda Aceh, Indonesia", *Coastal Engineering Journal*, vol. 51, no. 3, pp. 243–273.

Suppasri, A. Koshimura, S. and Imamura, F. (Jan. 2011), "Developing tsunami fragility curves based on the satellite remote sensing and the numerical modeling of the 2004 Indian Ocean tsunami in Thailand", *Natural Hazards and Earth System Science*, vol. 11, pp. 173–189.

Muhari, A. Imamura, F. Koshimura, S. and Post, J. (Dec. 2011), "Examination of three practical run-up models for assessing tsunami impact on highly populated areas", *Natural Hazards and Earth System Science*, vol. 11, pp. 3107–3123.

Gayer, G. Leschka, S. N¨ohren, I. Larsen, O. and G¨unther, H. (Aug. 2010), "Tsunami inundation modelling based on detailed roughness maps of densely populated areas", *Natural Hazards and Earth System Science*, vol. 10, pp. 1679–1687.

Adriano, B. Mas, E. Koshimura, S. and Fujii, Y. (2012), "Remote Sensing-based Assessment of Tsunami Vulnerability in the coastal area of Lima, Peru", in *The 10th International Workshop on Remote Sensing for Disaster Management, Japan*.

Kotani, M. Imamura, F. and Shuto, N. (1998), "Tsunami run-up simulation and damage estimation by using GIS", in *Proceedings of coastal engineering, JSCE 45*, pp. 356–360,.

Imamura, F. (1995), "Review of the tsunami simulation with a finite difference method, Long Wave Run-up Models", *World Scientific*, pp. 25–42.

Koshimura, S. Katada, T. Mofjeld, H. O. and Kawata, Y. (Oct. 2006), "A method for estimating casualties due to the tsunami inundation flow, *Natural Hazards*, vol. 39, pp. 265–274.

10CUEE CONFERENCE PROCEEDINGS
10th International Conference on Urban Earthquake Engineering
March 1-2, 2013, Tokyo Institute of Technology, Tokyo, Japan

A Study on Dynamic Response of Rein-Forced Building by Fluid-Structure Interaction Analysis

Yasunori MIZUSHIMA[1)], Shusaku INOUE[2)]

1) Researcher, Advanced Research Department, Research and Development Institute, Takenaka Corporation, Japan
2) Researcher, Construction Research Department, Research and Development Institute, Takenaka Corporation, Japan
mizushima.yasunorii@takenaka.co.jp, inoue.shuusaku@takenaka.co.jp

Abstract: In The 2011 off the Pacific coast of Tohoku Earthquake, a lot of buildings were destroyed and flowed out TSUNAMI. In order to save humans' lives and prevent buildings suffering such damage, it is very important to figure out behaviors of buildings under TSUNAMI wave load. A lot of researches about TSUNAMI wave load acting on land structures have been reported in the past. However, in most of reports, the target of research is load acting on rigid structures, such as upstanding walls. So responses of building structures under TSUNAMI wave load are hardly clarified. Therefore it can be said that the actual load on building structures is not understood. In this report, fluid-structure interaction analyses are executed to clarify collapse mechanism of building structures. The analytical target is rein-forced building structure and tried to explain the damage example in the Pacific coast of Tohoku Earthquake. The analytical results can express collapse phenomena by TSUNAMI wave load and show the behavior of wave loading.

1. INTRODUCTION

In The 2011 off the Pacific coast of Tohoku Earthquake, a lot of buildings were destroyed and flowed out TSUNAMI. In order to save humans' lives and prevent buildings suffering such damage, it is very important to figure out behaviors of buildings under TSUNAMI wave load. In this report, Fluid-Structure Interaction analysis is performed and a basic study on response to TSUNAMI wave load is made.

In previous researches, a method to consider TSUNAMI wave load as static pressure was proposed by Asakura et al [1)] and the method is employed on the design guide for TSUNAMI refuge buildings. However, it is reported that this method is underestimates TSUNAMI load in the case of acting an impulsive loading to a structure in other reports. Furthermore, there are some reports considering deformation of simple structure.

In these researches, however, the targets suffering by wave loadings were very simple and sufficient explanations for damage or response under wave loading were not given. So, in this report, responses of building structures under impulsive wave loadings are focused.

2. THE VALIDATION FOR FLUID STRUCTRE INTERACTION ANALYSIS

2.1 Analytical Model

In this section, a validation for analytical method used in this report is done with comparison to the result of the dam break test by Kleefsman et al [2)]. The analytical object is shown in Figure 1. The commercial structural analysis code called LS-DYNA is used. ALE (Arbitrary Lagrangian–Eulerian) re-meshing elements are applied to the fluid volumes, and Lagrangian elements are applied to the structure. The penalty method is adopted to consider interaction between the fluid and the structure.

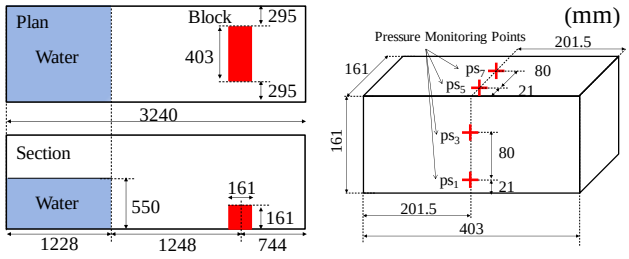


Figure 1 The Dam Break Test Model [2),3)]

2.2 Analytical Result

The appearances of the water in the experiment and the numerical simulation are shown in Figure 2. After the breaking of the water, the front edge of water reached front of the block in 0.4 second. As shown in Figure 2(b), the analysis can express the crashing and jumping of water and front edge of the water reached to end of the tank.

The pressure time histories at each monitoring point (shown in Figure 1) are shown in Figure 3. At ps1 and ps3 which is located on front surface of the block, the analytical results show good accordance to experimental results. At ps5 and ps7 which is located on the upper surface of the block, pressure oscillation has been seen, because complex behavior of water occurred, such as cohesion of reflected water and jumping water. But center of the oscillation is

coincident to the experimental result. So, this method can express the behavior of water and pressure acting on a structure qualitatively-correctly.

3. RESPONSES OF THE STRUCTRES UNDER IMPULSIVE WAVE LOAD

3.1 Outline of Analytical Model

The outline of analytical model is shown in Figure 4. The surge wave is made by dam breaking and impacts to building structure. The building structure consists of columns, beams, concrete slab and wall in front and it has one floor in section and 1×1 span in plan. The properties of the structure are shown in Figure 5. The fluid and the structure interact with each other via only slab and wall.

3.2 Analytical Conditions

Analytical conditions are classified in terms of structures' properties. In the first case, the structure is rigid. In second case, it is elastic structure, and in last case, material non-linearity of the structure is considered. Additionally, in elastic structure case, the structure's property was varied. In other words, the natural frequencies changed by tuning its mass density. So, the analytical cases are summarized as follows.

Case-1: Rigid Structure

Case-2: Elastic Structure

(a):5.1(Hz) (b):10.1(Hz)
(c):14.4(Hz) (d):20.3(Hz)
(e):25.0(Hz) (f):31.4(Hz)
(g):40.6(Hz)

Case-3: Structure with Non-linear Material Model

3.3 Material Properties of The Structure

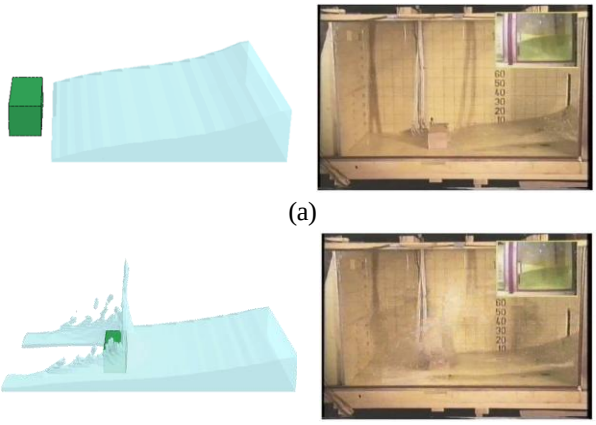
In case-2, Young modulus is 2.5×10^4(MPa). In this section, material properties of the structure in case-3 are mainly mentioned.

The structure is assumed as rein-forced concrete building. So, the concrete material properties and steel material property for reinforcement bars are adopted. The cracking with tension stiffening and the compression crushing are considered in the concrete material model. The characteristic of the steel model is bi-linear. The stress-strain relations are shown in Figure 6.

The columns and beams are modeled by Hughes-Liu beam element which is based on a degenerated brick element formulation. In other words, they have integration points on the section. The wall and slab are modeled by laminated shell element. The integration points which have concrete and steel properties are placed on each center of inertia in section as shown in Figure 7.

3.3 Analytical Result of Wave Impact Test

The appearances of the water in Case-1 are shown in Figure 8. The overflow water makes surge wave and impacts to the structure. Some of wave force time histories are shown in Figure9.Static wave force calculated with equation



(a)

(b)

Figure 2 Comparison of Analytical Result and experiment*)
(a) 0.4 (sec) (b) 0.62 (sec)

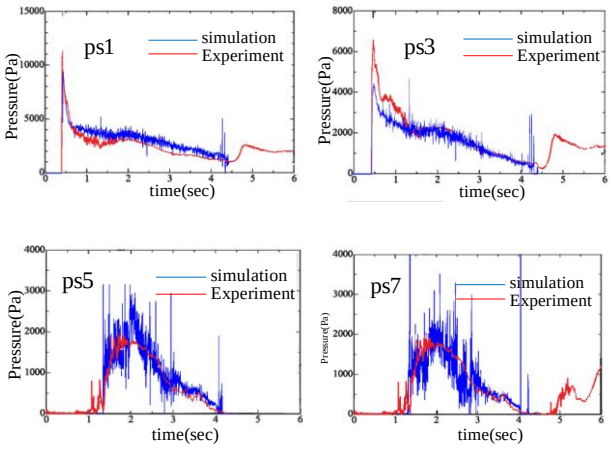


Figure 3 Pressure Time History[2),3)]

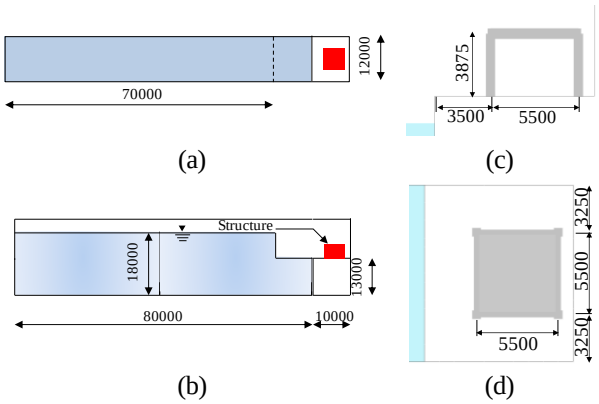


Figure 4 Analytical Model
(a) Plan, (b) Elevation, (c) Elevation of the Structure and (d) Plan of the Structure

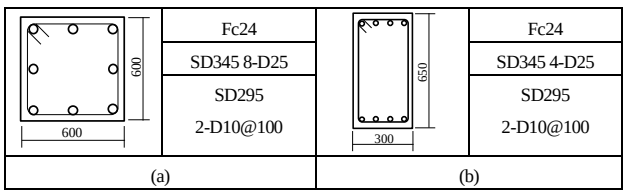
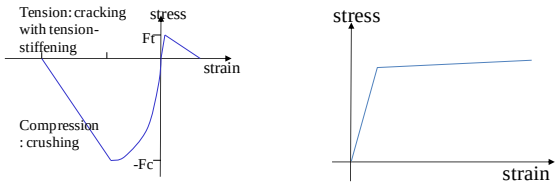


Figure 5 Section of Members (a)Columns (b)Beams

supposed by Asakura et al(2000)[1] is also shown there. Twice impulsive wave loads act on the structure. In Case-1, Case-2(b) and Case-3, first impulsive load was maximized, and, in Case-2(e), second impulsive load was maximized. So, it can be said that characteristics of structures affect those of wave loadings.

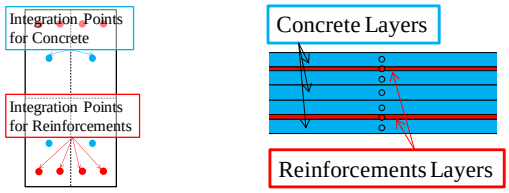
Maximum displacements of top of the structure are shown in Figure 10. Abscissa axis here is natural frequency of Case-2. Response to static load calculated with triangular pressure distribution by Asakura et al(2000)[1] is also shown here. In all cases, maximum displacement responses exceed response to the static load. So, when impulsive loads which are exceed static load calculated from static pressure distribution act on structures, these loads should be considered in order to predict responses to wave load. Figure 10 also says that responses to wave loads vary with the characteristics of structures although each structure has the same static stiffness.

Appearance of maximum principal strain distribution in Case-3 is shown in Figure 11 and the damage example in the 2011 off the Pacific coast of Tohoku Earthquake is shown in Figure 12. Aspect of the strain distribution is similar to that of the crack pattern in damage example. The wall cracked radially from the center and the damage concentrated to edge of the wall in both numerical result and damage example. So, the analysis method in this report (considering material non- linearity) can express the damage of buildings suffering from TSUNAMI wave load.



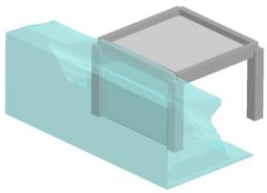
(a) (b)

Figure 6 Stress Strain Relations of the material models
(a) Concrete Model, (b)Steel Model

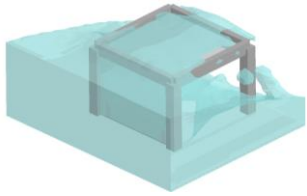


(a) (b)

Figure 7 Integration Rules
(a) Beam Elements, (b)Laminated Shell Elements



(a)



(b)

Figure 8 Appearances of Water (a) 2.16sec, (b)3.5sec

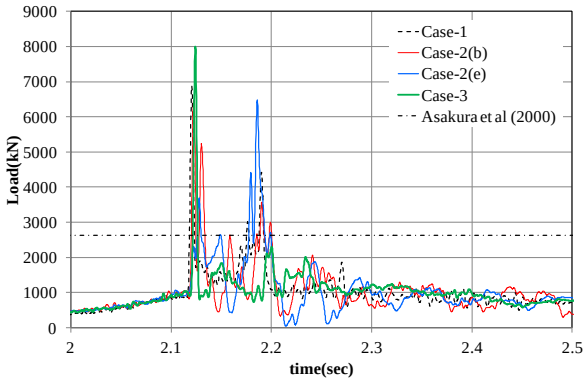


Figure 9 Wave Load History

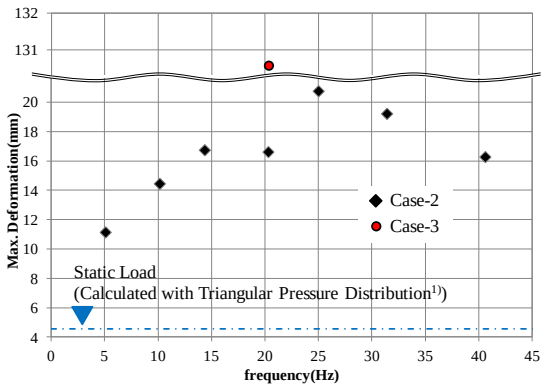


Figure 10 Maximum Displacement

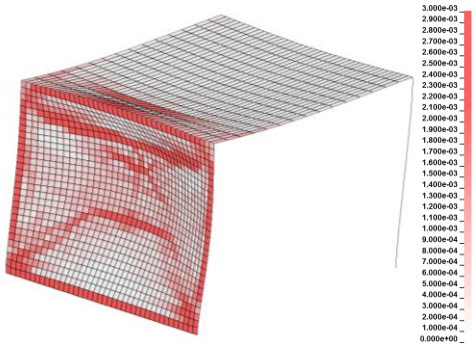


Figure 11 Maximum Principal Strain Distribution



Figure 12 Damage Example

4. SIMPLIFIED RESPONSE PREDICTION METHOD BY 1-DOF MODEL

4.1 Outline of Analytical Model

1-DOF mass spring model is considered as one of the simplified prediction methods for structures' responses to wave impulsive loads. This method is used to predict building responses to earthquakes typically. In this section, methods to make 1-DOF models for TSUNAMI load response analyses are discussed.

Almost always the characteristics of springs in 1-DOF models are made from result of non-linear push over analyses with framed models. In this report, two loading methods were used for the push over analyses. First, concentrated load was given to the frame model as shown in Figure 13(a). This loading method is a common way to make models for prediction of buildings' responses to earthquakes. This case is called Case-S1. In the other method, the distributed load was given on the wall of the structure as shown in Figure 13(b). The load is rectangular and uniformly distributed load for sake of simplicity.

The wave time history in Case-3 is used as the excitation.

4.2 Results of Simplified Models

Time histories of the displacement are shown in Figure 14. Case-S1, which is modeled with ordinary way, overestimated displacement of the structure. On the other hand, In Case-S2, the result was good accordance to that in Case-3. In the moment resisting structures, such as analytical target in this report, the load resisting mechanisms differ between against the concentrated load and the distributed load. This fact caused difference of two responses. So, when wave loads, which are distributed load, are treated with 1-DOF models, the characteristics of springs in 1-DOF models should be defined according to result of static load incremental analyses considering distributed loads.

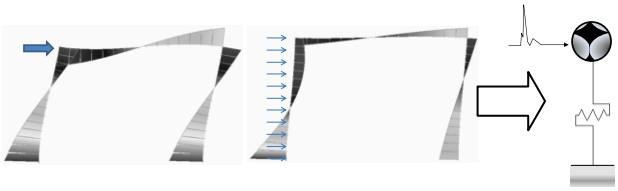
5. CONCLUSIONS

In this report, in order to clarify responses of building structures to TSUNAMI wave load, fluid-structure interaction analyses were executed with simple structures. In addition, we studied about simplified response prediction method with 1-DOF models. As a result, the following findings were obtained

・ALE and Lagrangian elements were used to model fluid and structures, and considered interaction each other with penalty method. This analysis can evaluate load act on structure and express behavior of water.

・In case of acting impulsive loads on structures, the wave loads and responses were varied by characteristics of structures. And in every case, the responses exceeded static load supposed in previous research. So, in such cases, dynamic effect should be considered.

・1-DOF analysis was proposed as simple response prediction method. The model whose spring characteristic was defined by concentrated load overestimated the response of the structure. So, wave loads are treated with 1-DOF models, the characteristics of springs should be defined according to result of static load incremental analyses considering distributed loads.



(a) (b) (c)

Figure 13 Static Load Incremental Analyses Models
(a) Concentrated Load, (b) Distributed Load
(c) 1-DOF Mass Spring Model

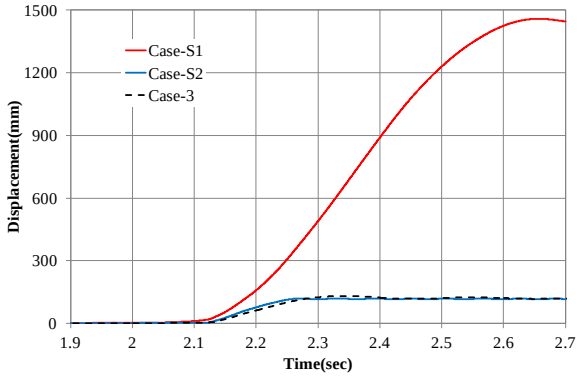


Figure 14 Time Histories of Displacement

References:

1) R. Asakura, K. Iwai, T. Ikeya, M. Takao, T. Kaneto, N. Fujii and M.Omori (2000), "An Exprimental Study on Wave Force Acting on On-Shore Structures due to Overflowing Tsunamis," *Proceedings of Coastal Engineering, JSCE* , **47**(2), 911-915.

2) K.M.T. Kleefsman, G. Fekken, A.E.P. Veldman, B. Iwanowski, B. Buchner (2005), "A Volumn-of-Fluid based simulation method for wave impact problems," *Journal of Computational Physics*, , **206**(3), 363-393

3) T. Hayashi, M. Asai, A.M. Aly, Y. Sonoda, (2010), "The accuracy validation and estimation of fluid impact force using stabilized ISPH," *Proceedings of 10th Symposium on Impact Problems of Structures*, 91-96.

4) Y. Mizushima, S. Inoue, "A Study on the Dynamic Response of Structure under Hydraulic Bore Force," *Summaries of Technical Papers of Annual Meeting of Architectural Institute of Japan*, 353-354

10CUEE CONFERENCE PROCEEDINGS
10th International Conference on Urban Earthquake Engineering
March 1-2, 2013, Tokyo Institute of Technology, Tokyo, Japan

POTENTIAL AND VORTEX RESIDUAL FIELDS IN THE OCEAN DUE TO TSUNAMIGENIC EARTHQUAKES: A FULLY ANALYTICAL SOLUTION OF THE AXISYMMETRIC MODEL PROBLEM

Gulnaz N. Nurislamova[1)], and Mikhail A. Nosov[2)]

1) Student, Faculty of Physics, M.V. Lomonosov Moscow State University, Russia
2) Professor, Faculty of Physics, M.V. Lomonosov Moscow State University, Russia
gulnaz1205@yandex.ru, nosov@phys.msu.ru

Abstract: Equations for description of potential and vortex residual fields generated in the ocean by co-seismic bottom deformation are derived within the framework of linear shallow-water theory. A fully analytical solution to the respective axisymmetric problem is obtained. On the base of the analytical solution and known relations between the tsunami source parameters and earthquake moment-magnitude the amplitude of residual horizontal displacements of water particles, the maximum vortex velocity and the energy of the residual geostrophic vortex are estimated as functions of moment-magnitude.

1. INTRODUCTION

The principal mechanism of tsunami generation during an earthquake is the displacement of water by residual (co-seismic) deformation of the bottom (e.g. Dotsenko and Soloviev 1995, Levin and Nosov 2009, Nosov and Kolesov 2011). The volume that is displaced from the source region is distributed in the ocean during tsunami wave propagations. This process, clearly, is accompanied by "residual" displacements of water particles in the horizontal direction. Besides the "residual" displacements of water particles, the rotation of the Earth leads to formation of the geostrophic vortex in the vicinity of tsunami source. Residual displacement of the water particles and the corresponding geostrophic vortex we will refer as the potential and vortex residual fields (Nosov and Nurislamova 2012).

Vortex formation in the tsunami source under the action of the Coriolis force have been discussed earlier many times (e.g. Pelinovsky 1996, Ingel 1998, Dotsenko 2001). However, attention has not been paid to potential fields. According to our information, the potential residual field for the first time was considered in our studies (Nosov 2011, Nosov et al. 2011, 2012, Nosov and Nurislamova 2012). In particular, in one of our previous work (Nosov and Nurislamova 2012) a completely analytical solution of model problem about the residual hydrodynamical fields was obtained.

The main purpose of this study is to estimate the residual fields (the residual horizontal displacements of water particles, the speed of the vortex current and the energy of a geostrophic vortex) as a function of moment-magnitude of tsunamigenic earthquake. In order to obtain these estimates we use the above mentioned analytical solution and the relations between the tsunami source parameters and moment-magnitude which had been obtained in paper (Bolshakova and Nosov 2011).

2. MATHEMATICAL MODEL

In this section, according to our paper (Nosov and Nurislamova 2012), we briefly describe the procedure for obtaining of the analytical solution.

Consider a layer of an ideal incompressible homogeneous liquid of constant depth in the field of gravity on a rotating Earth. Our mathematical approach is based on the linearized shallow-water approximation, which works pretty well for tsunami simulation in the open ocean where the wave amplitude is much less than the ocean depth, which in its turn is much less than the wave length. We shall put the origin of the Cartesian reference frame, $0xyz$, in the unperturbed free surface and direct the $0z$ axis vertically upward. $0x$ -axis is directed eastward, $0y$ -axis – northward. We assume the domain under consideration to be small enough to neglect the sphericity of the Earth. The set of shallow-water equations is written in the Cartesian reference frame

$$\frac{\partial \xi}{\partial t} - \frac{\partial \eta}{\partial t} + H\left(\frac{\partial u}{\partial x} + \frac{\partial v}{\partial y}\right) = 0, \qquad (1)$$

$$\frac{\partial u}{\partial t} = -g\frac{\partial \xi}{\partial x} + fv, \qquad (2)$$

$$\frac{\partial v}{\partial t} = -g\frac{\partial \xi}{\partial y} - fu, \qquad (3)$$

where ξ is the displacement of the free surface of water from equilibrium; η is the displacement of the bottom surface from the initial position; u and v are the components of horizontal flow velocity vector along the axes x and y, respectively; g is free-fall acceleration; and f is the Coriolis parameter.

According to Helmholtz's theorem, an arbitrary vector field can be resolved into the sum of a potential (curl-free) vector field and a rotational (divergence-free) vector field

$$u = \frac{\partial \varphi}{\partial x} + \frac{\partial \psi}{\partial y}, \qquad v = \frac{\partial \varphi}{\partial y} - \frac{\partial \psi}{\partial x}, \qquad (4)$$

where φ is the velocity potential and ψ is the stream function.

Integrating Eq. (1)-(3), considering (4), over time from 0 to ∞, we obtain the following system of differential equations of the second order:

$$H\Delta\Phi = \eta_\infty - \xi_\infty, \qquad (5)$$

$$\Delta\psi_\infty = f\Delta\Phi, \qquad (6)$$

$$g\Delta\xi_\infty = -f\Delta\psi_\infty, \qquad (7)$$

where ξ_∞ is the residual displacement of the free water surface in a geostrophic vortex, $\Phi \equiv \int_0^\infty \varphi\, dt$ is the displacement potential and ψ_∞ is the stream function, which describes the residual vortex field (stationary geostrophic vortex). The residual displacement of water particles in a horizontal direction is related to the potential Φ by the following formula:

$$D_\infty \equiv \int_0^\infty v dt = \nabla\Phi. \qquad (8)$$

Excluding functions Φ and ψ_∞ from the system of equations (5), (6) and (7), we come to the Helmholz heterogeneous equation for the function ξ_∞.

$$R_0{}^2\Delta\xi_\infty - \xi_\infty = -\eta_\infty \qquad (9)$$

where $R_0{}^2 = gH/f^2$ is the square of barotropic Rossby radius of deformation.

Let us assume a simple model of the residual deformation of the bottom in the form of an axisymmetric uplift described by the function

$$\eta_0(r) = \eta_{max}\left[1 - \theta(r - R_{TS})\right]. \qquad (10)$$

Note that the amplitude of the bottom deformation and the source radius are just those parameters which can be estimated by the moment-magnitude of an earthquake with use of relationships obtained in paper (Bolshakova and Nosov 2011).

In Eq. (9), let us switch to cylindrical coordinates

$$\frac{\partial^2 \xi_\infty}{\partial r^{*2}} + \frac{1}{r^*}\frac{\partial \xi_\infty}{\partial r^*} - \mu^2\xi_\infty = -\mu^2\eta_\infty, \qquad (11)$$

where $\mu^2 = R^2/R_0{}^2$ and $r^* = r/R$ is the dimensionless spatial variable.

Solution of Eq. (11), which satisfies the boundedness condition at infinity, is expressed through the modified Bessel functions, I_i and K_i (Polyanin 2002).

$$\xi_\infty(r^*) = \eta_{max}\begin{cases} 1 - \mu K_1(\mu) I_0(\mu r^*), & 0 \le r^* < 1, \\ \mu K_0(\mu r^*) I_1(\mu), & r^* \ge 1. \end{cases} \qquad (12)$$

Based on the known function ξ_∞, from Eqs. (6) and (7) we find residual displacement of water particles in a horizontal direction and speed in geostrophic vortex

$$D(r^*) = \frac{\eta_{max} R}{H}\beta(r^*), \qquad (13)$$

$$v(r^*) = -\frac{\eta_{max} R f}{H}\beta(r^*), \qquad (14)$$

where

$$\beta(r^*) = \begin{cases} I_1(\mu r^*) K_1(\mu), & 0 \le r^* < 1, \\ I_1(\mu) K_1(\mu r^*), & r^* \ge 1. \end{cases} \qquad (15)$$

In typical natural conditions, the parameter $\mu < 1$ (here and below we assume $f = 10^{-4} c^{-1}$). Under this condition on the basis of Eq. (15) we obtain $\beta_{max} \approx 0.5$. Therefore, while estimating of the maximal values of the horizontal displacement of water particles and the speed of the vortex current, we can apply simplified formulas

$$D_{\infty max} \approx 0.5\eta_{max} R/H, \qquad (16)$$

$$v_{\infty max} \approx 0.5\eta_{max} R f/H. \qquad (17)$$

Based on the spatial structure of the residual fields determined by formulae (12) and (14) one can easily calculate potential (W_p), kinetic (W_k) and full (W_{GV}) energies of the residual geostrophic vortex:

$$W_p = W_{TS}\Big(1 - \mu^2 I_1{}^2(\mu) K_0{}^2(\mu) - \\ - 4 I_1(\mu) K_1(\mu) + \mu^2 I_0{}^2(\mu) K_1{}^2(\mu)\Big), \qquad (18)$$

$$W_k = W_{TS}\big(\mu[I_1(\mu) K_2(\mu) - I_0(\mu) K_1(\mu)]\big), \qquad (19)$$

$$W_{GV} = W_p + W_k \,, \qquad (20)$$

where W_{TS} is the energy of initial elevation, similar in form to the residual deformation of the bottom (energy of tsunami).

$$W_{TS} = 0.5\pi\rho g R^2 \eta_{max}{}^2 \,. \qquad (21)$$

3. RESULTS AND DISCUSSION

In paper (Bolshakova and Nosov 2011) an empirical-analytical approach in combination with Monte-Carlo method were employed to establish relationships between earthquake moment magnitude and upper limits of tsunami source parameters. Among all other parameters, the amplitude of bottom deformation, and the radius of tsunami source were related to the moment-magnitude of earthquake in the following way:

$$lg\,\eta_{max}(m) = 0.5M_W - 3.4 \,, \qquad (22)$$

$$lg\,R_{TS}(m) = 0.5M_W + 0.8 \,. \qquad (23)$$

Now, substituting relationships (22) and (23) in formulae (16) - (21), we obtain the amplitude of the horizontal displacement of water particles, $D_{\infty max}$, the speed of the vortex current, $v_{\infty max}$, the full energy of a geostrophic vortex, W_{GV}, and the energy of tsunami, W_{TS} as a function of the earthquake moment-magnitude, M_W.

It would be interesting to compare the full energy of a geostrophic vortex, W_{GV}, and the energy of tsunami, W_{TS} with the energy of an earthquake. For this reason let us consider the following well-known relationship by Kanamori (1977)

$$lg\,W_{EQ}(J) = 1.5M_w + 4.8 \,. \qquad (24)$$

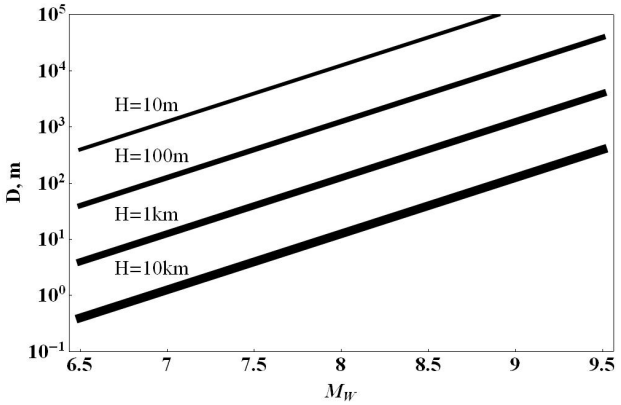


Figure 1 The amplitude of residual horizontal displacement of water particles as a function of moment-magnitude of an earthquake

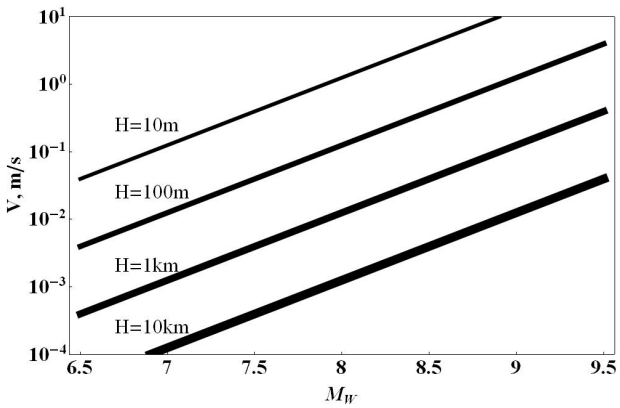


Figure 2 The amplitude of current speed in the residual geostrophic vortex as a function of moment-magnitude of an earthquake

The calculation results are presented in Figs. 1-3. Parameters of the residual fields depend on depth of the ocean; therefore we present calculations for the four depths, which cover the possible range of variation of these values in the real conditions.

In Fig.1 the amplitude of residual horizontal displacement of water is shown. It is seen that the amplitude grows exponentially as moment-magnitude goes up. Besides, amplitude is inversely proportional to the depth of the ocean. In case of a catastrophic earthquakes ($M_W \approx 9$) even in open ocean ($H > 1\,km$) amplitude of residual displacement can reach hundreds of meters. On the shelf, the amplitude may exceed 1 km.

The amplitude of current speed in the residual geostrophic vortex versus moment-magnitude of an earthquake is depicted in Fig. 2. It is seen that the speed of the vortex current is usually very slow (~0.1 m/s or less). It is next to impossible to detect such slow speeds on the background of other oceanic currents. The speed may be close to 1 m/s only in case of very small depths.

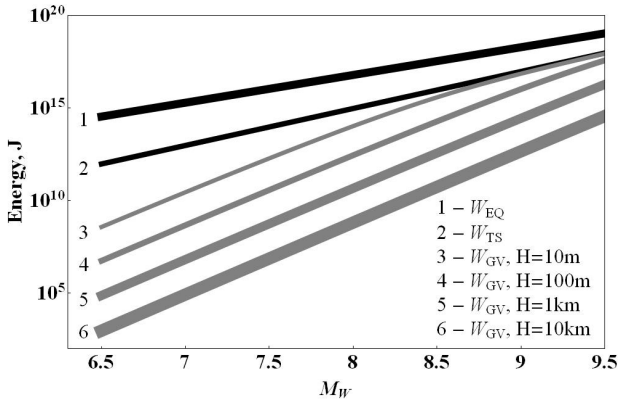


Figure 3 Energy of the earthquake W_{EQ}, the energy of the tsunami W_{TS} and the energy of geostrophic vortex W_{GV} at various depths as a function of moment-magnitude of an earthquake.

Figure 3 shows earthquake energy (W_{EQ}), tsunami energy (W_{TS}) and geostrophic vortex energy (W_{GV}) versus moment-magnitude of an earthquake (M_W). As one can judge from the figure, tsunami usually takes less than 1% of earthquake energy. In its turn, the residual geostrophic vortex takes a part of tsunami energy. And this part increases with increasing of moment-magnitude. Larger depths correspond to smaller energy of the residual geostrophic vortex.

Acknowledgements:

This work was supported by the Russian Foundation for Basic Research (projects 10-05-00562, 12-05-31422).

References:

Bolshakova, A.V. and Nosov, M.A. (2011), "Parameters of tsunami source versus earthquake magnitude," *Pure Appl. Geophys.*, **168**, 2023–2031.

Dotsenko, S. F. and Soloviev, S. L. (1995), "On the role of residual shifts of ocean-bottom in tsunami generation underwater earthquakes," *Okeanologiya*, **35**(1), 25-31.

Dotsenko, S.F., Shokin, Y.I. (2001), "Vortex generation in a continuously stratified rotating fluid under shifts of part of the basin bottom," Computational technologies, **6**(1), 13-22.

Ingel, L. Kh. (1998), "The vortical trace of an earthquake in the sea", *Doklady Earth Sciences,* **362**, 1036–1037.

Kanamori, H. (1977), "The energy release in great earthquakes", J.Geophys. Res., **82**, 2981–2987.

Levin, B.W. and Nosov, M.A. (2009), "Physics of Tsunamis", Springer.

Nosov, M.A. (2011), "Residual horizontal displacement of water particles in the vicinity of tsunami source", *Proceedings of the 8th International Conference on Urban Earthquake Engineering*, 1541-1546.

Nosov, M.A. and Kolesov, S.V. (2011), "Optimal initial conditions for simulation of seismotectonic tsunamis", *Pure Appl. Geophys*., **168**, 1223–1237, DOI: 10.1007/s00024-010-0226-6.

Nosov, M.A. and Nurislamova, G.N. (2012), "The potential and vortex traces of a tsunamigenic earthquake in the ocean", *Moscow University Physics Bulletin*, **67**(5), 457-461.

Nosov, M.A., Moshenceva, A.V., and Kolesov, S.V. (2012), "Horizontal motions of water in the vicinity of a tsunami source", *Pure Appl. Geophys.,* DOI 10.1007/s00024-012-0605-2.

Nosov, M.A., Moshenceva, A.V., and Levin B.W. (2011), "Residual Hydrodynamic Fields near a Tsunami Source," *Doklady Earth Sciences*, **438**(2), 853–857.

Pelinovsky, E.N. (1996), "Tsunami Wave Hydrodynamics", Institute Applied Physics Press.

Polyanin A.D., (2002), "Handbook of Linear Partial Differential Equations for Engineers and Scientists," Chapman & Hall/CRC Press, Boca Raton–London, 2002.

10CUEE CONFERENCE PROCEEDINGS
10th International Conference on Urban Earthquake Engineering
March 1-2, 2013, Tokyo Institute of Technology, Tokyo, Japan

DYNAMIC AND STATIC APPROACHES IN SIMULATION OF HORIZONTAL MOTIONS OF WATER THAT ACCOMPANY TSUNAMI FORMATION AND PROPAGATION

Anastasia V. Moshenceva[1)], Mikhail A. Nosov[2)], and Sergey V. Kolesov[3)]

1) Postgraduate student, Faculty of Physics, M.V. Lomonosov Moscow State University, Russia
2) Professor, Faculty of Physics, M.V. Lomonosov Moscow State University, Russia
3) Junior researcher, Faculty of Physics, M.V. Lomonosov Moscow State University, Russia
amoshenceva@gmail.com, nosov@phys.msu.ru, kolesov@ocean.phys.msu.ru

Abstract: In this study, taking the 2011 Tohoku-Oki event as an example, horizontal motions of water in the vicinity of the tsunami source are theoretically examined by means of dynamic and static numerical models developed within the framework of linear shallow-water approximation.

1. INTRODUCTION

Devastating tsunami waves usually originate from strong bottom earthquakes (e.g. Gusiakov 2011). The first tsunami bulletin is always issued on the base of an initial seismic analysis and pre-set criteria (Operational Users Guide…2009). By this time, neither the tsunami strength nor even the earthquake parameters can be determined with a reasonable accuracy. Only when observed sea level data (vertical motions of the free water surface) became available, the level of danger can be determined more or less reliably.

In this study, we suggest considering additional sort of data – horizontal motions of water that accompany tsunami evolution. Along with the vertical motions of the free water surface (sea level variations) the horizontal motions of the water column can be used, at least in principle, in tsunami warning systems. In propagating tsunami waves that can be considered as long oceanic waves the amplitude of horizontal motions essentially exceeds the amplitude of vertical motions of the free water surface (e.g. Lighthill 1978).

The process of tsunami generation is also accompanied by horizontal motions. It is a well known fact that the main mechanism of tsunami generation is associated with residual (co-seismic) deformation of ocean bottom during strong underwater earthquake (e.g. Yamashita and Sato 1974, Okal 1988, Dotsenko and Soloviev 1995, Levin and Nosov 2009). Bottom deformation displaces a huge volume of water – up to hundred of cubic kilometers (Grilli et al. 2007, Bolshakova and Nosov 2011, Nosov et al. 2011a). The spreading of the displaced volume in the ocean has certainly to result in "residual" horizontal motions of water – displacement of water particles from their initial positions. Due to the Earth rotation, such horizontal motions of water lead to formation of a geostrophic vortex in the vicinity of tsunami source (Dotsenko 1999, Dotsenko and Shokin 2001, Nosov et al. 2011b). In present study, we shall neglect vortex motions caused by the Earth rotation because of their very low velocity ($10^{-3} - 10^{-2} m/s$, Nosov and Nurislamova 2012).

On practice, horizontal motions of water that are associated with a tsunami can be detected by means of drifters – buoys equipped with GPS (Kato et al. 2000, Falck et al. 2010, Nagai 2010, Fujii et al. 2011) or accelerometer (seismometer, Okal and MacAyeal 2006). Another option for detecting the horizontal motions of water involves processing of sequential satellite imagery (Etaya et al. 2005). There is a well-developed technique – the maximum cross correlation technique – that allows reconstructing the vector field of surface horizontal velocity from sequential satellite imagery (e.g. Crocker et al., 2007). The third technic for measuring the horizontal motions of water is bottom Acoustic Doppler Current Profiler (ADCP) (Mikada et al. 2006).

The main purpose of this study is to theoretically examine horizontal motions of water in the vicinity of a tsunami source and to show that the horizontal motions are detectable in-situ. We employ numerical models of the following two types. The first one is the dynamic model developed within the framework of the linear shallow-water approximation. The second model is the static model which is fully based on the principle of conservation of mass. The static model, as compared with the dynamic one, surely operates much faster because it omits a huge number of intermediate time steps. This is why the static model turns out to be more appropriate for prompt assessment of the horizontal motions.

2. DATA AND METHOD OF CALCULATION

2.1 Input data

Both models we use in this study take initial elevation

of water surface as input data. The calculation of initial elevation of water surface consists of two stages. At the first stage the vector field of coseismic bottom deformation should be determined. At second stage, the initial elevation is calculated using coseismic bottom deformation.

In our calculations of residual deformation of bottom in the tsunami sources we rely on the USGS slip distribution data (Finite Fault Model) that is presented on the site http://earthquake.usgs.gov/regional/world/historical.php. According to this model, the fault plane for the 2011 Tohoku-oki earthquake had dimensions of 625 km along the strike by 260 km, which was further divided into 325 subfaults: 25 km by 20 km. The bottom deformation, caused by each of these subfaults, is calculated by Okada formulae (Okada 1985). Then, the contributions of all elements are summed up. Details of our method can be found in (Nosov and Kolesov 2011, Nosov et al. 2011a).

The initial elevation in the 2011 Tohoku-oki tsunami source is determined with use of the method developed in our papers (Nosov and Kolesov 2009, 2011). The calculated amplitude of uplift and subsidence of water surface in the tsunami source amounted to 9.48 m and -1.90 m, respectively. The displaced water volume estimated with account of vertical and horizontal components of bottom deformation amounted nearly to $100\,km^3$ (Nosov et al. 2011a). The contribution of horizontal deformations to this value was about 20%.

Bathymetric data were extracted from the 1-min digital atlas General Bathymetric Chart of the Oceans (GEBCO).

2.2 Calculation of water particles displacement

Consider a layer of an ideal incompressible homogeneous liquid of variable depth in the field of gravity on a spherical earth. Our mathematical approach is based on the linearized shallow-water approximation which works pretty well for tsunami simulation in the open ocean where the wave amplitude is much less than the ocean depth which in its turn is much less than the wave length. Neglecting the Coriolis force, nonlinearity and bottom friction, we write the set of equations in vector form as follows:

$$\frac{\partial \vec{v}}{\partial t} = -g\vec{\nabla}\xi\,, \tag{1}$$

$$\frac{\partial \xi}{\partial t} + (\vec{\nabla}\cdot H\vec{v}) = 0\,, \tag{2}$$

where $\vec{v}$ is the horizontal flow velocity vector, g is the acceleration of gravity, ξ is the free-surface displacement from the equilibrium position, H is the ocean depth, $\vec{\nabla}$ is 2D (horizontal) vector differential operator.

In equations (1), (2) all the factors that can generate vorticity are excluded. Thus, the flow velocity vector can be expressed via the scalar velocity potential, φ

$$\vec{v} = \vec{\nabla}\varphi\,. \tag{3}$$

Substituting formula (3) in equations (1) we obtain the following relation between the free-surface displacement and the scalar potential:

$$\xi = -\frac{1}{g}\frac{\partial \varphi}{\partial t}\,. \tag{4}$$

Substituting formulas (3) and (4) in the continuity equation (2) we readily arrive at the classical wave equation:

$$\frac{\partial^2 \varphi}{\partial t^2} = g(\vec{\nabla}\cdot H\vec{\nabla}\varphi)\,. \tag{5}$$

In description of tsunami generation we follow the traditional approach (e.g. Titov and Gonzalez 1997, Gisler 2008, Levin and Nosov 2009): (i) an earthquake is assumed to instantly cause residual deformation of the ocean bottom which is simultaneously accompanied by formation at the surface of the ocean of a perturbation (initial elevation), ξ_0; (ii) the initial field of flow velocities is assumed to be zero. So, the wave equation (5) is solved with the following couple of initial conditions:

$$t = 0:\ \xi_0 = -\frac{1}{g}\frac{\partial \varphi}{\partial t},\quad \varphi = 0\,. \tag{6}$$

The interaction of waves with the coast is described as the full reflection from the coast (e.g. Mei 1983):

$$\frac{\partial \varphi}{\partial \vec{n}} = 0\,, \tag{7}$$

where $\vec{n}$ is the unit vector normal to the coastline. Free pass boundary conditions are specified on the ocean-crossing outer borders of the computational domain.

The wave equation (5), supplemented with the initial (6) and boundary (7) conditions, was approximated by the traditional explicit scheme of finite differences on a rectangular net. The time step was determined by the Courant condition

$$\Delta t < \frac{R}{\sqrt{gH_{max}}} Min\left[\Delta Lat,\, \Delta Lon\right], \tag{8}$$

where H_{max} is the maximum ocean depth in a calculation domain.

Static problem stays mostly equal to dynamic one, described above. However, due to numerical method we use here, we have to restrict ourselves to a basin with impermeable outer borders (closed basin). It is worth also noting that the static model we introduce here is fully based on the principle of conservation of mass (2) whereas the dynamic equation (1) is not employed.

Substituting of formula (3) in equation (2) we obtain

$$\frac{\partial \xi(\vec{x},t)}{\partial t} + \left(\vec{\nabla}\cdot H(\vec{x})\vec{\nabla}\varphi(\vec{x},t)\right) = 0\,, \tag{9}$$

where $\vec{x}$ is the horizontal position vector. By integrating equation (9) with respect to time from 0 to ∞ we reduce the original dynamic problem to the following static problem

$$\left(\vec{\nabla}\cdot H(\vec{x})\vec{\nabla}\Phi(\vec{x})\right) = \xi_0(\vec{x}) - \xi_\infty\,, \tag{10}$$

$$\Phi(\vec{x}) \equiv \int_0^\infty \varphi(\vec{x},t)\,dt\,, \tag{11}$$

where $\xi_0(\vec{x})$ is the initial elevation, ξ_∞ is a constant denoting the residual change of water level in a closed basin

$$\xi_\infty = V_0 / S , \tag{12}$$

where $V_0 = \iint \xi_0 ds$ is the water volume displaced by co-seismic bottom deformation in tsunami source, $S = \iint ds$ is the basin area. The double integrals are taken over the entire basin area. The correct mathematical solution of equation (10) for a closed basin requires considering a small but nonzero value of ξ_∞.

By formula (11) we introduce a new quantity Φ which can be interpreted as the residual displacement potential. Residual displacement of water particles in the horizontal direction can be expressed via Φ in the following way:

$$\vec{D} = \vec{\nabla}\Phi . \tag{13}$$

Boundary conditions on the coastline and on the ocean-crossing outer borders of the computational domain are the following:

$$\frac{\partial \Phi}{\partial \vec{n}} = 0 . \tag{14}$$

The computational domain was chosen large enough to avoid the influence of artificially closed boundary.

Equation (10), supplemented with the boundary condition (14) was solved numerically by finite element method on triangular grid (e.g. Norrie and De Vries 1978, Hutton 2004).

In spherical coordinates the operators take the following form:

$$\left(\vec{\nabla} \cdot H\vec{\nabla}\right) = \frac{1}{R^2 \cos^2(Lat)} \frac{\partial}{\partial Lon}\left(H \frac{\partial}{\partial Lon}\right) + \frac{1}{R^2 \cos(Lat)} \frac{\partial}{\partial Lat}\left(H \cos(Lat) \frac{\partial}{\partial Lat}\right) \tag{15}$$

$$\vec{\nabla}_{Lon} = \frac{1}{R \cos(Lat)} \frac{\partial}{\partial Lon} \tag{16}$$

$$\vec{\nabla}_{Lat} = \frac{1}{R} \frac{\partial}{\partial Lat} , \tag{17}$$

where R=6371 km.

3. RESULTS AND DISCUSSION

We recall that two different numerical models are in use: the dynamic model (Eqs. 5 – 7) and the static model (Eqs. 10, 14). In both cases the computational domain extends from 134^oE to 180^oE in longitude and from 15^oN to 55^oN in latitude.

The dynamic model uses rectangular grid with space increments of $\Delta Lat = \Delta Lon = 1 min$. The time increment was specified in accordance with the Courant condition (8), $\Delta t \approx 3\ s$.

The static model employs triangular grid of variable density. In our numerical simulation a fine grid density (approx. 4 min) is specified near the coastline and in the tsunami source area, while in the remainder of the domain, as the source distance increases, grid density gradually decreases up to 60 min.

Figure 1 shows the vector field of residual displacement of water particles in the vicinity of the 2011 Tohoku-oki tsunami source. Black arrows denote the direction and the amplitude of residual horizontal displacement. Note that the length of each vector is proportional to the value of displacement multiplied by ocean depth ($|D|H, [m^2]$). The distribution of the displacement amplitude $|D|, [m]$ is plotted in accordance with the color scale.

From Fig. 1 it is seen that the direction and the amplitude of the residual horizontal displacement is a complex function of the initial elevation in the tsunami source, the bathymetry, and the configuration of coastline. Far from shore, direction of the residual displacement of water particles is mostly defined by the initial elevation. In the vicinity of shoreline, vectors tend to be directed parallel to the shoreline. Within a very wide area (approx. 0.5 million square kilometers) in the vicinity of the tsunami source the residual horizontal displacement amounts to tens of meters (green). Residual displacements of hundreds of meters (yellow) are associated with shallow-water areas. When considering these results, one should bear in mind that in shallow-water areas the linear approximation we use may loose its accuracy. Undoubtedly, even 10 m horizontal displacement can be easily detectable in-situ.

Characteristic examples of water particles behavior in the vicinity of the tsunami source are presented on the right and bottom side of Figure 1 as the horizontal tracks. The horizontal displacement components are calculated via the horizontal velocity obtained from the dynamic model (Eqs.5-7) with use of the following obvious formula:

$$\vec{D}(t) = \int_0^t \vec{v}(\hat{t})\, d\hat{t} . \tag{18}$$

Tracks depicted in Fig 1 exhibit a chaotic-like behavior of all the displacement components after passage of the first pulse of the tsunami. Such a behavior arises due to propagation of the tsunami in the basin with highly complicated structure of bottom topography and coastline. Effects of reflection, refraction and scattering associated with topographic heterogeneities of bottom result in the chaotic-like behavior of tsunami wave field.

Let us further consider particular features of the cases presented in Fig. 1. The “least chaotic” behavior corresponds

to the cases of the open ocean (E,F, and G). The horizontal

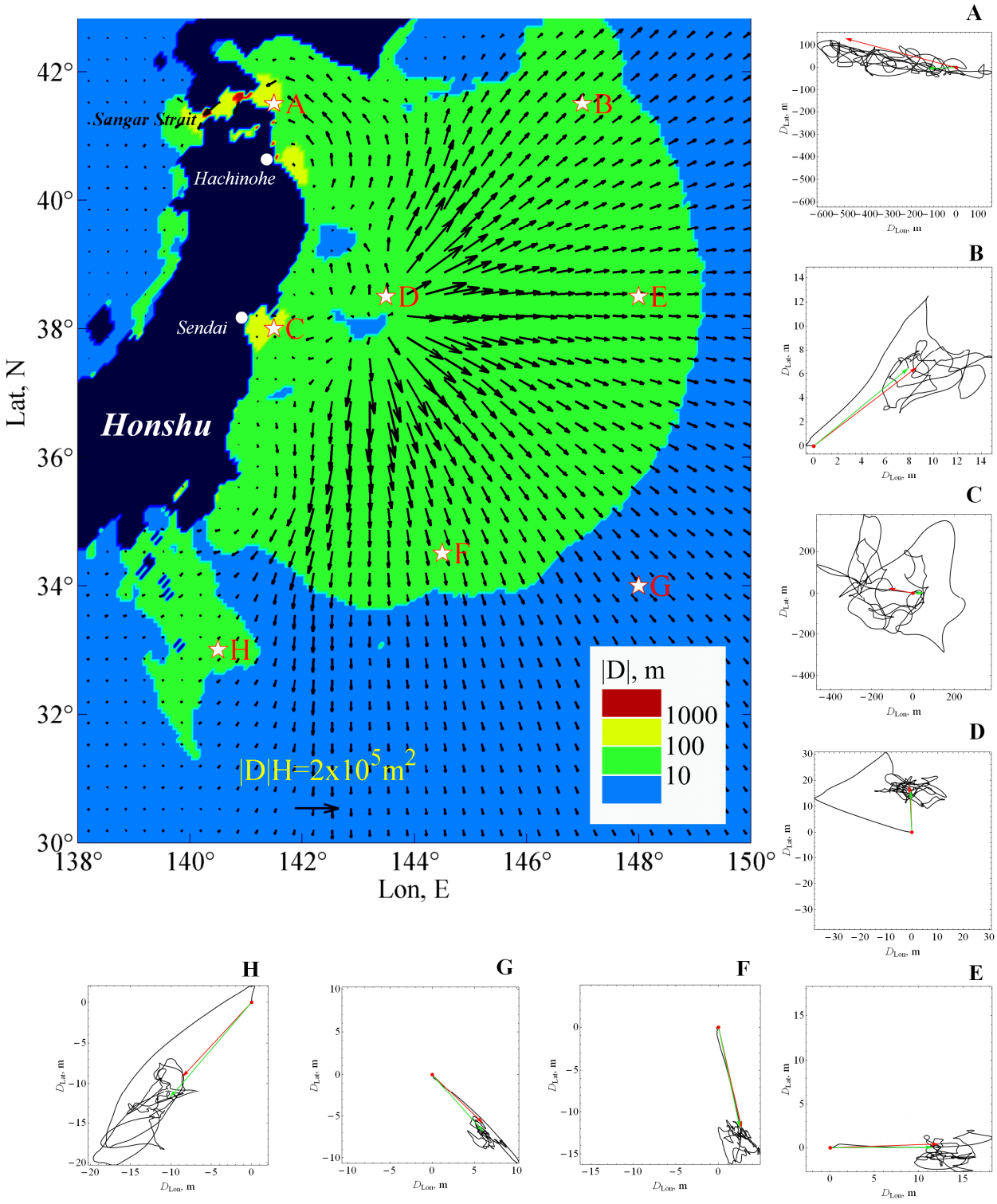


Figure 1 Residual horizontal displacement of water particles resulted from permanent bottom deformations due to the 2011 Tohoku-oki earthquake. Black arrows stand for the residual horizontal displacement; the length of each vector is proportional to the value of displacement multiplied by ocean depth, $|D|H$. The displacement amplitude $|D|$ is plotted in accordance with the color scale shown in the right lower corner. White stars denote the points, where the dynamic and static models were compared. Relevant tracks of horizontal motions of water are shown on the right and bottom side of the figure. Red arrows stand for the residual displacements calculated from the static model. Green arrows correspond to the displacement calculated from the dynamic model at the time moment of 25000 s.

displacement reaches the value prescribed by the static model rather quickly – immediately after the passage of the leading tsunami wave. The dynamic model and the static model provide nearly equal direction and amplitude of horizontal displacement. After the passage of the first tsunami wave, the displacement vector oscillates slightly in the vicinity of the value prescribed by the static model – its final position to be reached at $t = \infty$. Cases B, D, and H correspond to a noticeable influence of coastal effects whereas the ocean depth is still large enough. In these cases, the passage of the first tsunami wave result in the horizontal motion with a direction that is noticeably different from those prescribed by the static model. In the long run, after a number of loops, the displacement track turns out to be located near the final static point. The "most chaotic" behavior is observed near the shore in shallow-water area (A and C). Due to the waves trapped in the shelf area water particles undergo long-term chaotic horizontal motions with amplitude up to hundreds of meters. In the case A, a strong influence of the coastline on the direction of motions is appeared. The track is stretched along the residual displacement vector (red arrow) which in its turn is oriented parallel to the coastline. In the case C, during the passage of the first wave, the direction and the amplitude of the horizontal motions more or less correspond to the residual displacement vector. However, after the first wave a large amplitude oscillations are observed and the track exhibits a series of chaotic loops.

From the analysis of Fig. 1 one can conclude that the static and the dynamic models give results that are in a reasonable agreement. It means that the static model can be used for the prompt assessment of the direction and amplitude of the horizontal motions of water in the vicinity of the tsunami source. Exceptions to this rule are associated with shallow-water areas where the trapped waves give rise to strong chaotic motions of water. Anyway, even in such exceptional cases the static model provides a good estimate of amplitude of the horizontal motions of water.

Full version of this study can be found in (Nosov et al 2012).

Acknowledgements:

This work was supported by the Russian Foundation for Basic Research, projects 10-05-00562, 12-05-31422. We are grateful to USGS for providing the Finite Fault data.

References:

Bolshakova, A.V. and Nosov, M.A. (2011), "Parameters of tsunami source versus earthquake magnitude," *Pure Appl. Geophys.*, **168**, 2023–2031.

Crocker, R.I., Matthews, D.K., Emery, W.J., and Baldwin, D. (2007), "Computing Coastal Ocean Surface Currents From Infrared and Ocean Color Satellite Imagery", *IEEE Transactions on Geoscience and Remote Sensing*, **45**(2), 435-447.

Dotsenko, S. F. and Soloviev, S. L. (1995), "On the role of residual shifts of ocean-bottom in tsunami generation underwater earthquakes," *Okeanologiya*, **35**(1), 25–31.

Dotsenko, S.F. (1999), "Effects of earth rotation during tsunami generation by underwater earthquakes", *Izvestiya Akademii Nauk Fizika Atmosfery i Okeana*, **35**(5), 706-714.

Dotsenko, S.F., Shokin, Y.I. (2001), "Vortex generation in a continuously stratified rotating fluid under shifts of part of the basin bottom", *Computational technologies,* **6**(1), 13-22.

Etaya, M., Nakano, R., Shimoda, H., Sakata, T. (2005), "Detection of Ocean Wave Movements after the Northern Sumatra Earthquake using SPOT Images", *Proceedings of IGARSS*, 1420-1423.

Falck, C., Ramatschi, M., Subarya, C., Bartsch, M., Merx, A., Hoeberechts, J., and Schmidt, G. (2010), "Near real-time GPS applications for tsunami early warning systems", *Nat. Hazards Earth Syst. Sci.*, **10**, 181–189.

Fujii, Y., Satake, K., Sakai, S., Shinohara, M., and Kanazawa, T. (2011), "Tsunami source of the 2011 off the Pacific coast of Tohoku Earthquake", *Earth Planets Space*, **63**, 815–820.

Gisler, G. R. (2008), "Tsunami simulations", *Annu. Rev. Fluid Mech*. **40**, 71–90.

Grilli, S.T., Ioualalen, J.M., Kirby, J.T., Watts, P., Asavant, J., and Shi, F. (2007), "Source Constraints and Model Simulation of the December 26, 2004, Indian Ocean Tsunami", Journal *of Ocean Engineering*, **133**(6), 414-428.

Gusiakov, V.K. (2011), "Relationship of Tsunami Intensity to Source Earthquake Magnitude as Retrieved from Historical Data", *Pure Appl. Geophys*., **168**, 2033–2041

Hutton, D.V. (2004), "Fundamentals of Finite Element Analysis", The McGraw-Hill Companies, Inc.

Kato, T., Terada, Y., Kinoshita, M., Kakimoto, H., Isshiki, H., Matsuishi, M., Yokoyama, A., and Tanno, T. (2000), "Real-time observation of tsunami by RTK-GPS", *LETTER Earth Planets Space*, **52**, 841–845.

Levin, B.W., and Nosov, M.A. (2009), "Physics of Tsunamis", *Springer*.

Lighthill, J. (1978), "Waves in Fluids", Cambridge University Press.

Mei, C.C. (1983), "The applied dynamics of ocean surface and waves", World Scientific.

Mikada, H., Mitsuzawa, K., Matsumoto, H., Watanabe, T., Morita, S., Otsuka, R., Sugioka, H., Baba, T., Araki, E., and Suyehiro, K. (2006), "New discoveries in dynamics of an M8 earthquake - Phenomena and their implications from the 2003 Tokachi-oki Earthquake using a long term monitoring cabled observatory", *Tectonophysics*, **426**, 95–105.

Nagai, T. (2010), "Introduction of Japanese coastal wave Monitoring network", Joint Conference Proceedings, 7th International Conference on Urban Earthquake Engineering (7CUEE) & 5th International Conference on Earthquake Engineering (5ICEE), March 3-5, Tokyo Institute of Technology, Tokyo, Japan, 1649-1653.

Norrie, D.H., De Vries, G. (1978), "An Introduction to Finite Element Analysis", Academic Press.

Nosov, M.A., Kolesov, S.V., and Levin, B.W. (2011a) "Contribution of Horizontal Deformation of the Seafloor into Tsunami Generation near the Coast of Japan on March 11, 2011", *Doklady Earth Sciences*, 2011, **441**(1), 1537–1542.

Nosov, M.A. and Kolesov, S.V. (2011), "Optimal initial conditions for simulation of seismotectonic tsunamis", *Pure Appl. Geophys.* **168**, 1223–1237.

Nosov, M.A. and Nurislamova, G.N. (2012), "The potential and vortex traces of a tsunamigenic earthquake in the ocean", Moscow University Physics Bulletin **67** (5), 457-461.

Nosov, M.A., and Kolesov, S.V. (2009), "Method of Specification of the Initial Conditions for Numerical Tsunami Modeling", *Moscow University Physics Bulletin*, **64**(2), 208–213.

Nosov, M.A., Moshenceva, A.V. and Kolesov, S.V. (2012), "Horizontal motions of water in the vicinity of a tsunami source", *Pure Appl. Geophys.,* DOI 10.1007/s00024-012-0605-2.

Nosov, M.A., Moshenceva, A.V., and Levin B.W. (2011b),

"Residual Hydrodynamic Fields near a Tsunami Source," *Doklady Earth Sciences*, **438**(2), 853–857.

Okada, Y. (1985), "Surface deformation due to shear and tensile faults in a half-space," *Bulletin of the Seismological Society of America*, **75**(4) 1135–1154.

Okal, E.A. (1988), "Seismic parameters controlling far-field tsunami amplitudes: a review", *Natural Hazards*, **1**, 67-96.

Okal, E.A., and MacAyeal, D.R. (2006), "Seismic recording on drifting icebergs: Catching seismic waves, tsunamis and storms from Sumatra and elsewhere", *Seismol. Res. Letts*. **77,** 659–671.

Operational Users Guide for the Pacific Tsunami Warning and Mitigation System (PTWS), (2009), IOC Technical Series No 87, Second Edition, UNESCO/IOC.

Titov, V.V., and Gonzalez, F.I. (1997), "Implementation and testing of the Method of Splitting Tsunami (MOST) model", NOAA Technical Memorandum ERL PMEL-112.

Yamashita, T. and Sato R. (1974), "Generation of tsunami by a fault model", *J. Phys. Earth*, **22**, 415-440.

10CUEE CONFERENCE PROCEEDINGS
10th International Conference on Urban Earthquake Engineering
March 1-2, 2013, Tokyo Institute of Technology, Tokyo, Japan

TSUNAMI INTENSITY AND ITS RELATION TO SOURCE PARAMETERS

Anna V. Bolshakova [1], Mikhail A. Nosov [2]

1) Postgraduate student, Physics Faculty of M.V. Lomonosov Moscow State University, Russia
2) Professor, Physics Faculty of M.V. Lomonosov Moscow State University, Russia
annabolshakova@list.ru, nosov@phys.msu.su

Abstract: In this study we consider recent tsunamigenic earthquakes, those for which USGS, Caltech or UCSB provides slip distribution data and, at the same time, HTDB/WLD provides tsunami intensities according to the Soloviev–Imamura scale. Using these data and the Okada formulae, we calculate co-seismic bottom deformation. Then, taking bottom deformation and bathymetry as input data, we calculate the initial elevation of the water surface in tsunami sources. Ultimately, we obtain and discuss dependences that relate tsunami intensity and tsunami source parameters such as amplitude of initial elevation, displaced water volume, potential energy of the initial elevation.

1. INTRODUCTION

Strong bottom earthquakes are the most widespread cause for the initiation of devastating tsunami waves. In simulation of tsunamis of seismotectonic origin, an earthquake is traditionally considered to instantly displace a water column forming a perturbation on its free surface. Then, the assumption is made that the shape of the perturbation is fully similar to the vertical component of the residual deformation of the bottom. The perturbation of the water surfaces thus obtained, so-called initial elevation, is applied as an initial condition in resolving the problem of tsunami propagation (e.g. Titov and Gonzalez 1997, Kowalik et al. 2005, Gisler 2008, Levin and Nosov 2009).

Though easy-to-use in practice, this traditional approach turns out to be inaccurate in some cases. Imperfectness may be attributed to smoothing of water surface perturbations as compared with the bottom deformations (Tanioka and Seno 2001, Saito and Furumura 2009, Nosov and Kolesov 2009, 2011), contribution of horizontal deformation of a sloping (non-horizontal) bottom (Tanioka and Satake 1996, Nosov and Kolesov 2009, Nosov et al. 2011), effects of dynamics of bottom deformations (Hammack 1973, Nosov 1998) and effects of water compressibility (Nosov 1999, Nosov and Kolesov 2007, Bolshakova et al. 2011, Maeda and Furumura 2011). In particular, as it was shown in (Nosov and Kolesov 2011), the neglecting of "smoothing effect" may lead to an essential overestimation of the run-up heights.

In this study for calculation of initial elevation of the water surface in tsunami source we use the "Laplace smoothing algorithm" developed in (Nosov and Kolesov 2011).

The strength of a tsunami can be quantitatively determined with use of Soloviev–Imamura tsunami intensity scale: $I=0.5+\log_2 h$, where h is the average tsunami height on the coast closest to the source (Soloviev 1972, Levin and Nosov 2009). Relationship between the tsunami intensity and the earthquake moment-magnitude exhibits a large spread between the data (e.g. Chubarov and Gusiakov 1985, Gusiakov 2011, Nosov and Bolshakova 2012). It signifies that the relationship between tsunamis and earthquakes is complex and ambiguous.

Gusiakov (2011) in his study mentioned that the reasons for significant scattering of tsunami intensity for the earthquakes with similar magnitudes is due to the following several factors: 1) a difference in the water depth in a source area, 2) a difference in the earthquake source mechanisms, 3) a difference in the earthquake focus depth, 4) a difference in tectonic settings of the source area.

We presume that considering parameters of initial elevation in tsunami source might be more informative than moment magnitude. The reason for it is that all the factors mentioned above are taken into account while calculating initial elevation. The main purpose of this study is to relay tsunami intensity and tsunami source parameters such as amplitude of initial elevation, displaced water volume and potential energy of the initial elevation.

2. DATA AND METHOD OF CALCULATION

In calculations of the vector field of co-seismic bottom deformations in tsunami sources, we rely on Finite Fault Model (FFM) data presented on the following sites: U.S. Geological Survey (USGS, http://earthquake.usgs.gov/), California Institute of Technology (Caltech, http://www.tectonics.caltech.edu/), UC Santa Barbara (UCSB, http://www.geol.ucsb.edu/). Slip distribution for the

2003 Tokachi-oki earthquake proposed by Koketsu et al. (2004).

According the FFM, the fault plane for an earthquake is divided into a number of rectangular subfaults. The bottom deformation, caused by each of these subfaults, is calculated by Okada formulae (Okada 1985). Then, the contributions of all elements are summed up. Details of our method can be found in (Nosov and Kolesov 2009, 2011, Bolshakova and Nosov 2011). As a result we have a vector field of the co-seismic deformation of bottom $\vec{D} \equiv (D_x, D_y, D_z)$.

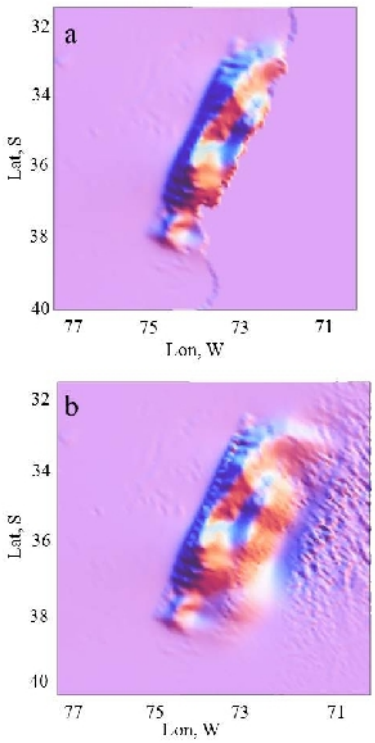


Figure 1 Initial Elevation of the Water Surface $\xi(x,y)$ in Tsunami Source (a) and Bottom Deformation $\eta(x,y)$ (b). 27 February 2010 Chile Earthquake (USGS)

Let us assume the bottom position, before an earthquake, is set by function

$$z = -H(x,y), \tag{1}$$

where $H(x,y)$ is the ocean depth. After an earthquake, due to the co-seismic deformation, the bottom takes a new position which is set by function

$$z = -H(x,y) + \eta(x,y), \tag{2}$$

where $\eta(x,y)$ is the function which describes changes of bottom position due to the co-seismic deformation of bottom. From this vector field we determine the perturbation of bottom surface as follows (Nosov and Bolshakova 2012):

$$\eta(x,y) = \frac{\partial H}{\partial x} D_x + \frac{\partial H}{\partial y} D_y + D_z . \tag{3}$$

Initial elevation $\xi(x,y)$ of the water surface in tsunami source are calculated using the "Laplace smoothing algorithm". All the details of this method can be found in (Nosov and Kolesov 2011).

Bathymetric data were extracted from the 1-min digital atlas General Bathymetric Chart of the Oceans (GEBCO).

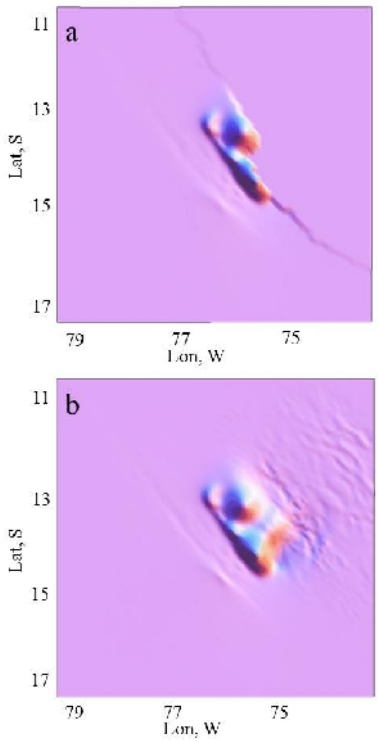


Figure 2 Initial Elevation of the Water Surface $\xi(x,y)$ in Tsunami Source (a) and Bottom Deformation $\eta(x,y)$ (b). 15 August 2007 Peru Earthquake (USGS)

Tsunami intensity data were extracted from the on-line version of Historical Tsunami Database for the World Ocean (HTDB/WLD, http://tsun.sscc.ru/nh/tsunami.php).

All the events under consideration are listed in Table 1.

Figures 1, 2 show two examples of surface disturbance and bottom deformation for the tsunamigenic earthquakes of 27 February 2010 (USGS) and 15 August 2007 (USGS) respectively.

Of all the possible parameters of a tsunami source, we shall consider those parameters which can be unambiguously calculated from initial elevation. There are three of them: amplitude (ξ_{max}), displaced water volume (V) and potential energy of the initial elevation (E_{TS}):

1. amplitude of initial elevation

$$\xi_{\max} = \left| Max[\xi(x,y)] \right| \tag{4}$$

Table 1 List of Tsunamigenic Earthquakes Under Consideration

#	*Date*	*Region*	*Data Source*	M_W	ξ_{max}, *m*	E_{TS}, *J*	V,km^3	*I*
1	19941004	Kuril	UCSB	8.4	2.38	$1.04 \cdot 10^{14}$	6.55	2.6
2	19950730	Antofagasta	UCSB	8.14	1.16	$2.27 \cdot 10^{13}$	7.78	1.5
3	19951203	Iturup	UCSB	7.81	0.57	$4.59 \cdot 10^{12}$	1.54	0.5
4	20010623	Peru	UCSB	8.4	2.02	$8.65 \cdot 10^{13}$	13.16	2.6
5	20030925	Tokachi-oki	Koketsu	8.3	1.48	$3.47 \cdot 10^{13}$	8.71	1.5
6	20041226	Sumatra	USGS	9.1	4.7	$1.12 \cdot 10^{15}$	39.6	4.5
7	20041226	Sumatra	Caltech	9.15	5.4	$3.13 \cdot 10^{15}$	87.4	4.5
8	20050328	Nias	UCSB	8.68	3.12	$3.07 \cdot 10^{14}$	21.68	1.5
9	20050328	Nias	Caltech	8.5	2.48	$1.44 \cdot 10^{14}$	12.9	1.5
10	20060717	Java	USGS	7.7	0.43	$2.17 \cdot 10^{12}$	0.74	2
11	20060717	Java	Caltech	7.9	0.72	$2.25 \cdot 10^{13}$	4.11	2
12	20061115	Simushir	USGS	8.3	2.54	$8.79 \cdot 10^{13}$	9.66	3
13	20061115	Simushir	Caltech	8.3	1.31	$4.37 \cdot 10^{13}$	7.41	3
14	20070113	Simushir	USGS	8.1	4.5	$1.24 \cdot 10^{14}$	6.79	2
15	20070113	Simushir	Caltech	8.1	2.95	$6.6 \cdot 10^{13}$	5.08	2
16	20070815	Peru	USGS	8	2.82	$3.45 \cdot 10^{13}$	4.71	2
17	20070912	S.Sumatra	USGS	8.5	1.13	$5.28 \cdot 10^{13}$	6.88	1
18	20071114	Antofagasta	USGS	7.7	0.29	$1.19 \cdot 10^{12}$	1.66	-1
19	20090929	Samoa	USGS	8.1	3.83	$5.2 \cdot 10^{13}$	3.99	1.5
20	20090930	S.Sumatra	USGS	7.6	0.09	$1.65 \cdot 10^{11}$	0.71	-1
21	20091007	Vanuatu	USGS	7.7	0.35	$1.11 \cdot 10^{12}$	1.00	0
22	20100227	Chile	USGS	8.8	4.38	$7.96 \cdot 10^{14}$	73.4	3
23	20100227	Chile	Caltech	8.8	2.03	$1.82 \cdot 10^{14}$	40.2	3
24	20100227	Chile	UCSB	8.86	4.1	$6.35 \cdot 10^{14}$	72.91	3
25	20100406	N.Sumatra	USGS	7.8	0.59	$2.63 \cdot 10^{12}$	1.44	0
26	20110311	Tohoku	USGS	9	9.76	$2.18 \cdot 10^{15}$	97.71	4
27	20110311	Tohoku	Caltech	9	7.01	$3.18 \cdot 10^{15}$	95.65	4
28	20110311	Tohoku	UCSB	9.09	15.66	$7.49 \cdot 10^{15}$	108.5	4

2. displaced water volume

$$V = \left| \iint_S \xi(x,y)\, ds \right| \qquad (5)$$

3. potential energy of the initial elevation (tsunami energy)

$$E_{TS} = \frac{\rho g}{2} \iint_S \xi(x,y)^2\, ds \qquad (6)$$

where ρ is density of water and g is acceleration due to gravity. We assumed $\rho=1000\ kg/m$ and $g=9.8\ m/sec^2$. The integration in formulae (5), (6) was performed over an area where initial elevation exhibited a noticeable value.

3. RESULTS AND DISCUSSION

Results of calculation of all parameters mentioned above according formulae (3)-(5) are presented in Table 1.

Figure 3 shows relationship between Soloviev–Imamura tsunami intensity and moment magnitude. Such relationship had been already studied in some publications (e.g. Chubarov and Gusiakov 1985, Gusiakov 2011, Nosov and Bolshakova 2012). Chubarov and Gusiakov (1985) obtained the following theoretical dependence by means of numerical modeling:

$$I = 3.55\,M_W - 27.1 \qquad (7)$$

The dependence (7) is depicted in Figure 3 by dotted line.

Figures 4-6 show relationship between tsunami intensity and tsunami source parameters. Linear regression is depicted by black line. Relevant equations and correlation coefficients are also presented in Figures 4-6.

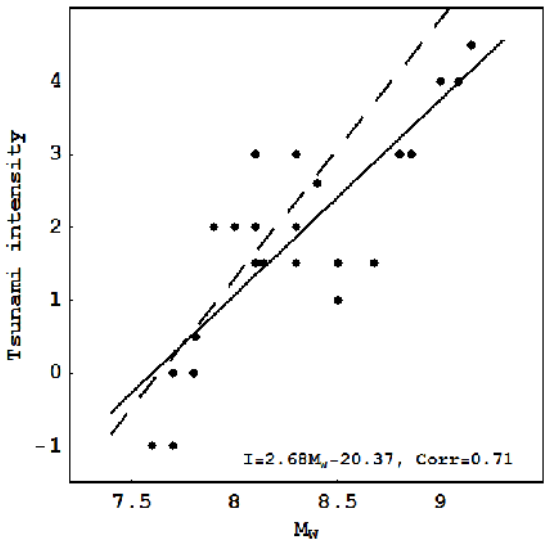


Figure 3 Soloviev-Imamura Tsunami Intensity Versus Amplitude of Initial Elevation of Water Surface. Linear Regression is Shown by Black Line. Relevant Equation and Correlation Coefficient are Also Presented. Dotted Line Stands for Dependence Obtained in Paper (Chubarov and Gusiakov 1985)

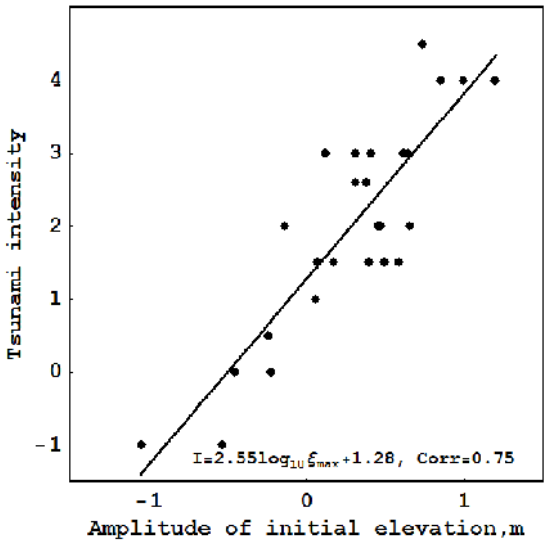


Figure 4 Soloviev-Imamura Tsunami Intensity Versus Amplitude of Initial Elevation of Water Surface. Linear Regression is Shown by Black Line. Relevant Equation and Correlation Coefficient are also presented

It is seen that dependencies exhibit rather large spread between data. Relation between tsunami intensity and tsunami source parameters is rather complex. In this study we do not take into account additional characteristics, which effect on relation between tsunami intensity and tsunami source parameters.

It should be mentioned that chosen parameters of

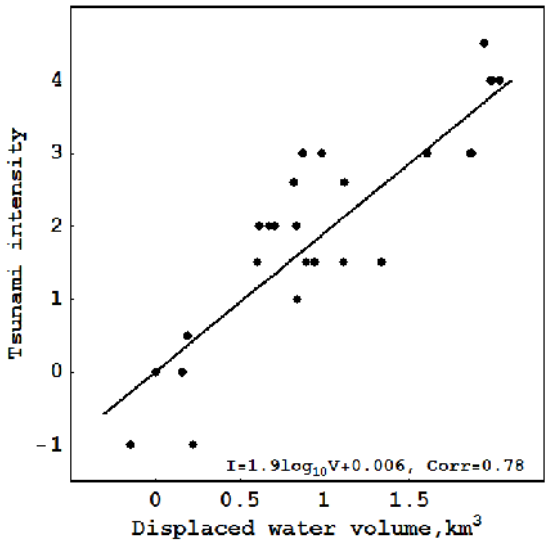


Figure 5 Soloviev-Imamura Tsunami Intensity Versus Displaced Water Volume. Linear Regression is Shown by Black Line. Relevant Equation and Correlation Coefficient are Also Presented

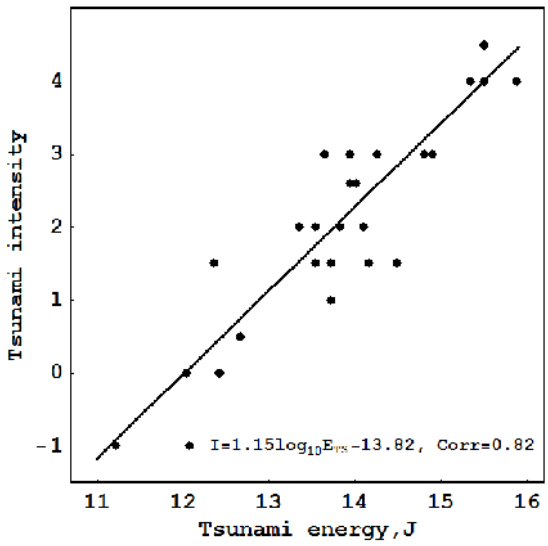


Figure 6 Soloviev-Imamura Tsunami Intensity Versus Potential Energy of Initial Surface Elevation. Linear Regression is Shown by Black Line. Relevant Equation and Correlation Coefficient are Also Presented

tsunami source can be determined, at least in principle, from in-situ measurements of horizontal movements of water particles in the vicinity of tsunami source, i.e. independently on seismological analysis (Nosov et al. 2011b).

It is seen from Figures 3-6 that tsunami intensity plotted versus tsunami source parameters displays a bit higher correlation as compared with tsunami intensity plotted versus moment-magnitude (Figure 3). Being not so high, the increase of correlation coefficient means that tsunami source parameters such as amplitude of initial elevation, displaced water volume and potential energy of the initial elevation represents better measure of tsunamigenic potential of an earthquake as compared with moment-magnitude.

Acknowledgements:

This work was supported by the Russian Foundation for Basic Research, projects 10-05-00562, 12-05-31422. We are grateful to USGS, Caltech and UCSB for slip distribution data. We are also grateful to Gusiakov for Historical Tsunami Database for the World Ocean (HTDB/WLD).

References:

Alekseev, A.S. and Gusyakov, V.K. (1976), "Numerical modeling of tsunami and seismic surface wave generation by a submarine earthquake," *Proc. Tsunami Res. Symp*. (eds. HEATH R.A. and CRESWELL M.M.) Roy. Soc. New Zealand, Wellington, 243–252.

Bolshakova A., Inoue S., Kolesov S., Matsumoto H., Nosov M., and Ohmachi T. (2011), "Hydroacoustic effects in the 2003 Tokachi-oki tsunami source," *Russ. J. Earth. Sci*., 12, ES2005, doi: 10.2205/2011ES000509.

Bolshakova A.V., Nosov M.A. (2011), "Parameters of tsunami source versus earthquake magnitude," *Pure and Appl. Geophysics*, 168, 2023–2031, doi: 10.1007/s00024-011-0285-3.

Chubarov, L.B. and Gusiakov, V.K. (1985), "Tsunamis and earthquake mechanism in the island arc region," Sci. Tsunami Hazards, 3(1), 3–21.

Dotsenko, S.F., Soloviev, S.L. (1990), "Mathematical modeling of tsunami excitation process by displacement of the ocean bottom, Tsunami researches" (in Russian), **4**, 8–20, Moscow.

Dytykh, D., Dias, F. (2007)," Water waves generated by a moving bottom", Tsunami and nonlinear waves, Springer (Geo.Sc.), 63–94.

Gisler, G.R. (2008), "Tsunami simulations." *Annu. Rev. Fluid Mech*., **40**, 71–90.

Gusiakov, V.K. (2011), "Relationship of Tsunami Intensity to Source Earthquake Magnitude as Retrieved from HistoricalData," *Pure Appl. Geophys*., 168, 2033–2041.

Hammack, J.L. (1973), "A note on tsunamis: their generation and propagation in an ocean of uniform depth." *J. Fluid Mech*., **60**, 769–799.

Kowalik, Z., Knight, W., Logan, T., and Whitmore, P. (2005), "Numerical modeling of the global tsunami: Indonesian tsunami of December 26 2004," Sci. Tsunami Hazard, **23**(1), 40–56

Levin, B.W., and Nosov, M.A., "Physics of Tsunamis" (Springer 2009).

Maeda, T., Furumura, T. (2011), "FDM Simulation of Seismic Waves, Ocean Acoustic Waves, and Tsunamis Based on Tsunami-Coupled Equations of Motion," *Pure Appl. Geophys.* DOI 10.1007/s00024-011-0430-z.

Nosov, M.A. (1998), "On the directivity of dispersive tsunami waves excited by piston-type and traveling-wave sea-floor motion," *Volcanol. Seismol*., **19**, 837–844.

Nosov, M.A. (1999), "Tsunami Generation in Compressible Ocean," *Phys. Chem. Earth* (B), **24**(5), 437–441.

Nosov, M.A. and Bolshakova, A.V. (2011), "Tsunami intensity and displaced water volume," *Proceedings of joint 9CUEE and 4 ACEE,* Paper ID 18-078.

Nosov, M.A. and Kolesov, S.V. (2007), "Elastic oscillations of water column in the 2003 Tokachi-oki tsunami source: in situ measurements and 3-D numerical modeling," *Natural Hazards and Earth System. Sciences*, **7**, 243–249.

Nosov, M.A. and Kolesov, S.V. (2011), "Optimal initial conditions for simulation of seismotectonic tsunamis," *Pure and Applied Geophysics*., 2011, **168**(6-7), 1223-1237, doi: 10.1007/s00024-010-0226-6.

Nosov, M.A., and Kolesov, S.V. (2009), "Method of Specification of the Initial Conditions for Numerical Tsunami Modeling," *Moscow University Physics Bulletin*, **64**(2), 208–213.

Nosov, M.A., Kolesov, S.V., and Levin, B.W. (2011), "Contribution of Horizontal Deformation of the Seafloor into Tsunami Generation near the Coast of Japan on March 11, 2011," Doklady Earth Sciences, **441**(1), 1537–1542.

Okada, Y. (1985), "Surface deformation due to shear and tensile faults in a half-space," *Bulletin of the Seismological Society of America*, **75**(4), 1135–1154.

Rabinovich, A.B., Lobkovsky, L.I., Fine, I.V., Thomson, R.E., Ivelskaya, T.N., and Kulikov, E.A. (2008), "Near-source observations and modeling of the Kuril Islands tsunamis of 15 November 2006 and 13 January 2007", *Advances in Geosciences*, 14,105–116.

Saito, T. and Furumura, T. (2009), "Three dimensional tsunami generation simulation due to the sea-bottom deformation and its interpretation based on the linear theory," *Geophys. J. Int*., doi: 10.1111/j.1365-246X.2009.04206.x.

Soloviev, S.L. (1972), "Recurrence of earthquakes and tsunamis in the Pacific Ocean," In: Volny Tsunami (Tsunami waves), *Trudy SakhCNII*, 29, 7–47 (in Russian).

Tanioka, Y., and Satake, K. (1996), "Tsunami generation by horizontal displacement of ocean bottom," *Geophys. Res. Lett*., **23**(8), 861–864.

Tanioka, Y., and Seno, T. (2001), "Sediment effect on tsunami generation of the 1896 Sanriku tsunami earthquake," *Geophysical Research Letters*, **28**(17), 3389–3392.

Titov, V.V., and Gonzalez, F.I. (1997), "Implementation and testing of the Method of Splitting Tsunami (MOST) model," NOAA Technical Memorandum ERL PMEL-112.

10CUEE CONFERENCE PROCEEDINGS
10th International Conference on Urban Earthquake Engineering
March 1-2, 2013, Tokyo Institute of Technology, Tokyo, Japan

DAMAGE OF RC BUILDING WITH COUPLED SHEAR WALLS CAUSED BY THE 2011 GREAT EAST JAPAN EARTHQUAKE

Atsushi Nagaya[1)], Kazuyoshi Hotta[2)], Yuko Kato[1)], Susumu Takahashi[3)], Santiago Pujol[4)], Masaki Maeda[5)], and Toshikatsu Ichinose[6)]

1) Graduate Student, Department of Architecture, Civil Engineering , Nagoya Institute of Technology, Nagoya, Japan
2) Undergraduate Student, Department of Architecture and Design, Nagoya Institute of Technology, Nagoya, Japan
3) Assistant Professor, Department of Architectural Engineering, Nagoya Institute of Technology, Nagoya, Japan
4) Associate Professor, School of Civil Engineering, Purdue University, West Lafayette, Indiana, USA
5) Professor, Department of Architecture and Building Science, Tohoku University, Sendai, Japan
6) Professor, Department of Architectural Engineering, Nagoya Institute of Technology, Nagoya, Japan

nagoyan_nitech@yahoo.co.jp, kazuyoshihotta@gmail.com, y-20116021@goo.jp, takahashi.susumu@nitech.ac.jp
spujol@purdue.edu, maeda@archi.tohoku.ac.jp, ich@nitech.ac.jp

Abstract: An eight-story reinforced concrete building retrofitted according to 1990 Japanese Standard was severely damaged during the 2011 Great East Japan Earthquake. The building was constructed in 1966 at Tohoku University. In 1996 the building was retrofitted using structural walls and carbon fiber. Dramatic damages were observed in coupling beams, a penthouse and a structural wall. Coupling beams failed in shear and bond. Columns and walls in the penthouse collapsed by torsion. The structural wall failed in compression at its end. Some of structural members were different from original drawings. Therefore, their strengths are re-calculated considering these differences by using 2010 Japanese Standard. Based on these calculated strengths, a pushover analysis is conducted. The failure mode in the analysis agrees with observed failure. Furthermore, it is confirmed that perpendicular walls cause large deformation of coupling beams.

1. INTRODUCTION

This paper deals with a reinforced concrete (RC) building in Tohoku University built in 1966, retrofitted in 1996 and demolished in 2012. The building had eight stories and a two story penthouse, and suffered the 2011 Great East Japan Earthquake. While it was expected to get enough strength by retrofit, the damage of this building was serious in penthouse and beams with openings. And it had been demolished

There are many reports for the damage on coupling beams due to previous earthquakes (Mitchell *at el*., 1995). The coupling beams of this building had some difference from these reported beams: the aspect ratio of the beam was large, coupling beams had openings, and the damage concentrated on the limited area of the beam.

In addition, there was non-structural perpendicular wall between this damaged area and the other area in the coupling beam. There might be some effects from the perpendicular wall. The penthouse was also greatly damaged, though the strength of penthouse was estimated to be enough (Villanova *et al*., 2011).

This paper reports observed damages based on a field investigation and discusses the cause of these damages by analyzing the frame in transverse direction.

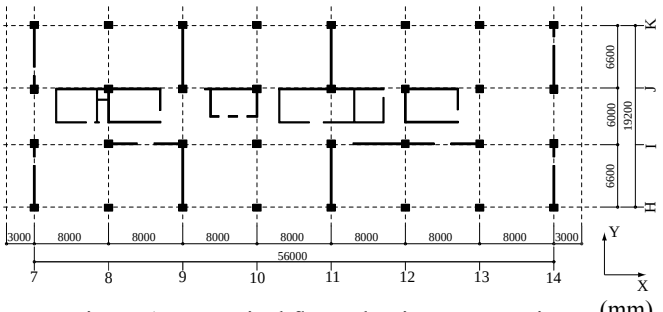


Figure 1 Typical floor plan in upper stories

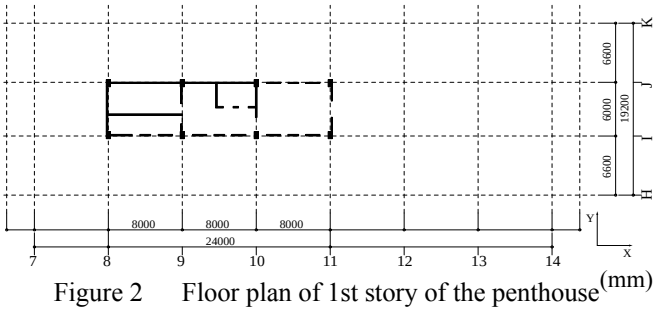


Figure 2 Floor plan of 1st story of the penthouse

2. CONFIGURATION OF THE BUILDING

The building was built in 1966 in Tohoku University, Sendai. It had eight stories and a two-story penthouse. It had seven spans (Frame 7~14) in X direction and three spans (Frame H~K) in Y direction. Figures 1 and 2 show the plan view of the typical upper floors and floor plan of the 1st story of the penthouse. In transverse direction, some frames had coupled shear walls with coupling beams. Beams had some openings for ducts.

The building was retrofitted in 1996 referred to the 1990 Japanese standard (building Research Institute 2001). The main changes during the retrofit were addition of new walls, replace RC walls for new and thicker ones and reinforcing some of the beams with carbon fiber. Addition and replacement of RC walls were described in the seismic retrofit document, but reinforcement using carbon fiber was not. The wall changes were concentrated in lower stories, from first to fifth stories, the carbon fiber reinforcement had been located mostly in the upper ones. About the location of the carbon fiber reinforcement, since there was no documentation, a deep field investigation was needed. The carbon fiber reinforcements were applied around openings in the beams. There were two kinds of fiber reinforcement: the first one is tape-shaped, the second one was a continuous fiber wrapping all beams with anchorages inside the concrete. (Photos 1 and 2) Regarding to the penthouse, no retrofit was done.



Photo 1 Tape-shaped fiber

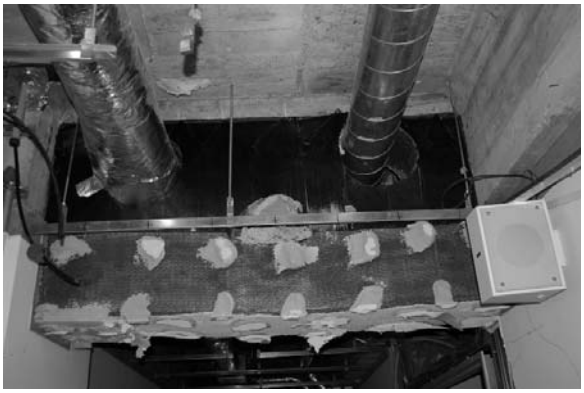


Photo 2 Continuous fiber

Figures 3 and 4 illustrate representative sections of columns and beams. The used longitudinal reinforcements were D25(#8) or D22(#7). The used stirrups were ϕ13 or ϕ9. The used materials were concrete of 18 MPa, longitudinal bars of 345 MPa for girders and columns, and 235 MPa for other elements.

In the seismic retrofit document, strength of each column and wall was described. In brief, the seismic retofit document assumes that this building collapses by columns and walls failure. The strength of each story is obtained as sum of strengths of these members. Dividing the strength by *AiWi*, we get equivalent story-shear-coefficient *C*/*Ai* as shown in Figure 5, where the contributions of the columns and walls are also indicated. In the current Japanese seismic design code (Building Research Institute 2001), *Ai* factor represents vertical distribution of a seismic story coefficient relative to that at the first story; note that *Ai* is 1.0 at the first story and very large, approximately 4.0, at the penthouse. *Wi* factor represents the weight above each story.

Based on the Japanese Standard, this building was expected to withstand strong earthquake. According to this graphs in X direction the second and eighth stories were the strongest ones and the second story of the penthouse was the weakest one. Referring to the Y direction, the second story of the penthouse was by far the strongest, and the fifth and first story of the penthouse were the weakest. However, equivalent story-shear-coefficients in the weakest storys were more than 0.6. According to Japanese Standard, these values are estimated enough strength. On the other hand, the damage of this building was serious especially in beams and penthouse.

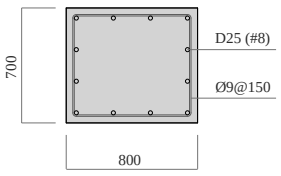


Figure 3 column section

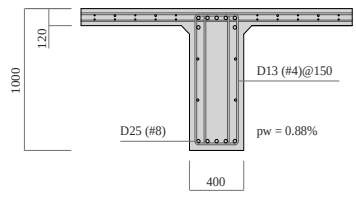
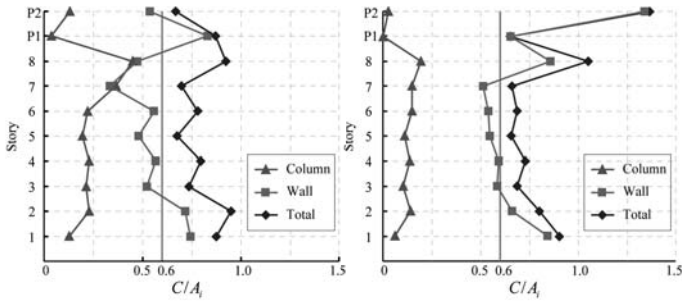


Figure 4 beam section



(a) X direction (b) Y direction

Figure 5 Equivalent story-shear-coefficient

3. OBSERVED DAMAGES

3.1 Coupling Beams

3.1.1 Frame on Axis 14

Figure 6 illustrates that severe damages were detected in these coupling beams of the frame number 14. They have two openings near their midspans. They failed in shear at the center of beam at 3rd, 4th, 6th and 8th stories, and bond failure at the 5th, 6th, 7th stories. About bond failure they have two patterns. 5th and 6th stories failed from end to end of the beams and, 7th stories failed not center but ends.

Bar arrangements of the beams were visible because concrete had spalled. They were different from the drawing. In the drawing, the longitudinal reinforcements were D25(#8) or D22(#7) bars, diagonal reinforcements were D16(#5) bars and stirrups were ϕ13 or ϕ9 bars(Figures 7 and 8). Lack of cover concrete for window frame was expressed in the figures. Figure 9 illustrates the drawing of reinforcements around the openings of 300mm in diameter. The distance between two openings was 800mm.

Photo 3 and Figure 10 show the beam of the third floor. From these investigations, the section of this beam with openings can be estimated as Figure 11. The diameter was not constant along the beam depth and it was larger in outside part of the beam. In addition, the distance between of these openings was 600mm which was estimated from photo. There were no stirrups under

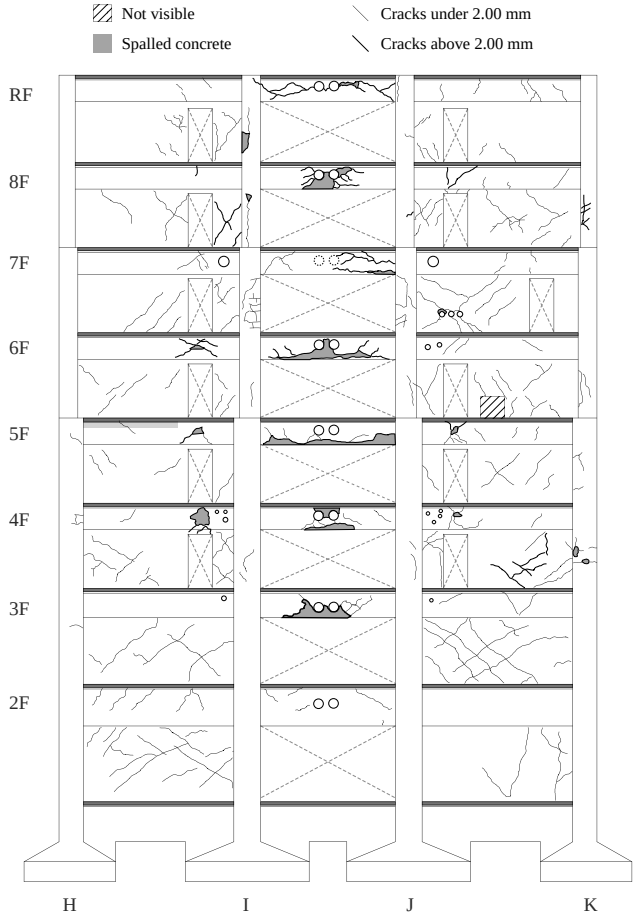


Figure 6 Frame 14 cracks schedule

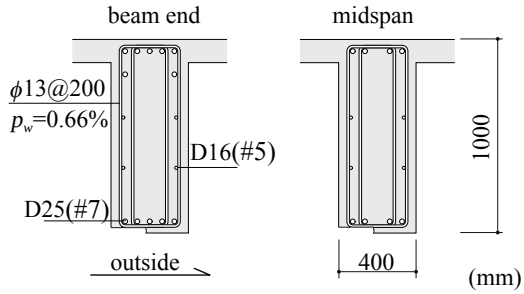


Figure 7 Section of the beam of the floor 4,5

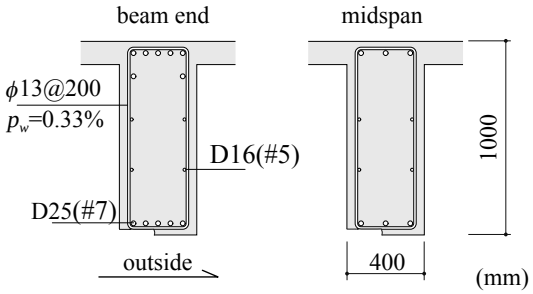


Figure 8 Section of thebeam of the floor 6,7

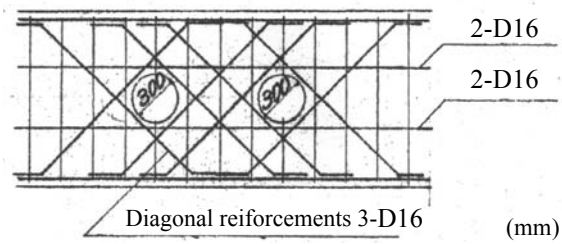


Figure 9 Drawing of reinforcement for opening



Photo 3 Beam of the 3rd Floor

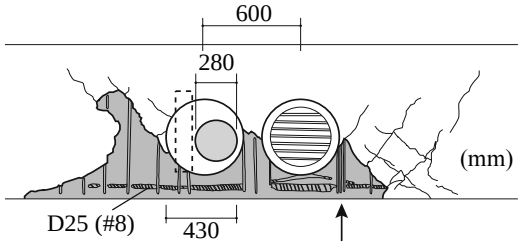


Figure 10 Detail of beam of the 3rd Floor

openings. The arrow in Figure 10 illustrates three stirrups were gathered beside the opening. In the broken area in this figure, there were no stirrups because they were cut for the opening.

Photo 4 and Figure 12 describe the beam in the fourth floor. It was different from third floor where some stirrups were gathered beside the opening. Stirrups were cut above the opening as shown in the broken area. In addition, straight anchorage of diagonal reinforcement was different from drawing which adopted bent bars. Diameter of this opening was constant along the beam width. (Figure 11)

The beam of fifth floor is provided in Photo 5. This failed in bond from end to end. Figure 13 shows the beam bottom surface viewed from below. The upper part of the figure is outside and the lower part is a window frame. Deformed bars are the longitudinal reinforcements in the beam. It shows that window frame was attached to the longitudinal reinforcement, and stirrups were cut as shown in the circle. These stirrups were cut to get the window frame into position. It was estimated that the beam got little covering depth of concrete for window frame.

The beam of 7th floor failed bond at both sides, and not shear around openings. Photo 6 was taken from inside of the building. It was detected that the beam had no opening at the 7th floor where as the ducts in the openings were found in 6th floor as shown in Photo 7.

These differences between the drawings and the practice might have caused such failure.

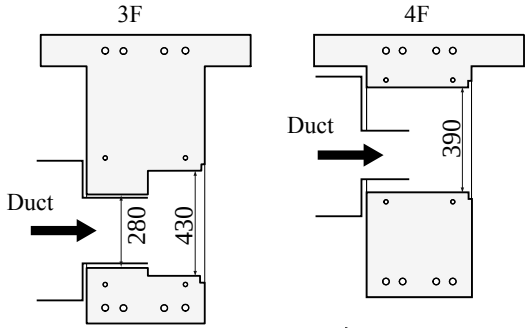


Figure 11 Image of the beam section across the opening

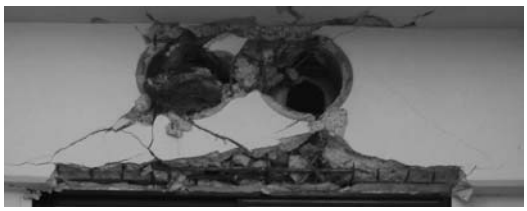


Photo 4 Beam of the 4th Floor

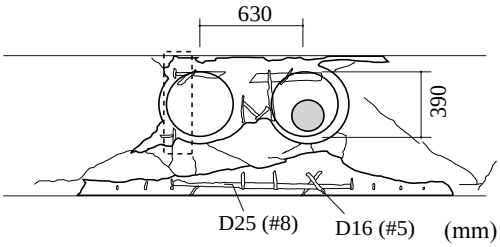


Figure 12 Detail of beam of the 4th Floor



Photo 5 Beam of the 5th Floor

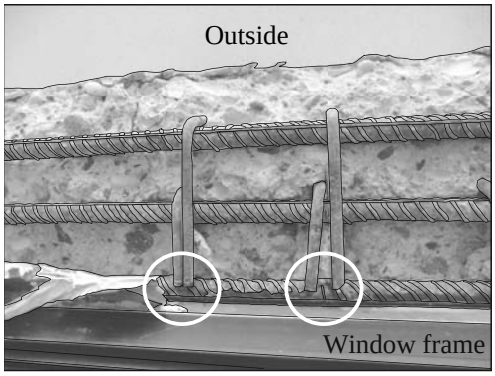


Figure 13 Look up to the bottom of the beam



Photo 6 Beam of the 7th Floor from inside



Photo 7 Beam of the 6th Floor from inside

3.1.2 Frame on Axis 11

The frames 11 were constituted of shear walls and coupling beams between these walls. Figure 14 illustrates that coupling beams of second floor and roof floor had less damage. But those of other floors suffered heavy damage as shown Fig. 15. They had perpendicular walls under coupling beams. On the South side of this perpendicular wall, the coupling beam failed in shear whereas the other side had less damage. It indicates that the coupling beam was restrained by the perpendicular wall.

Some beams were reinforced by carbon fiber around openings. The carbon fiber used to prevent shear failure. But it did not work appropriately because the anchorage length of continuous carbon reinforcements was not enough. (Photo 8) They usually need 100mm anchorage length, but actual anchorage length was 40mm. The tape-shaped fiber of the short beams were unstuck and peeled off.

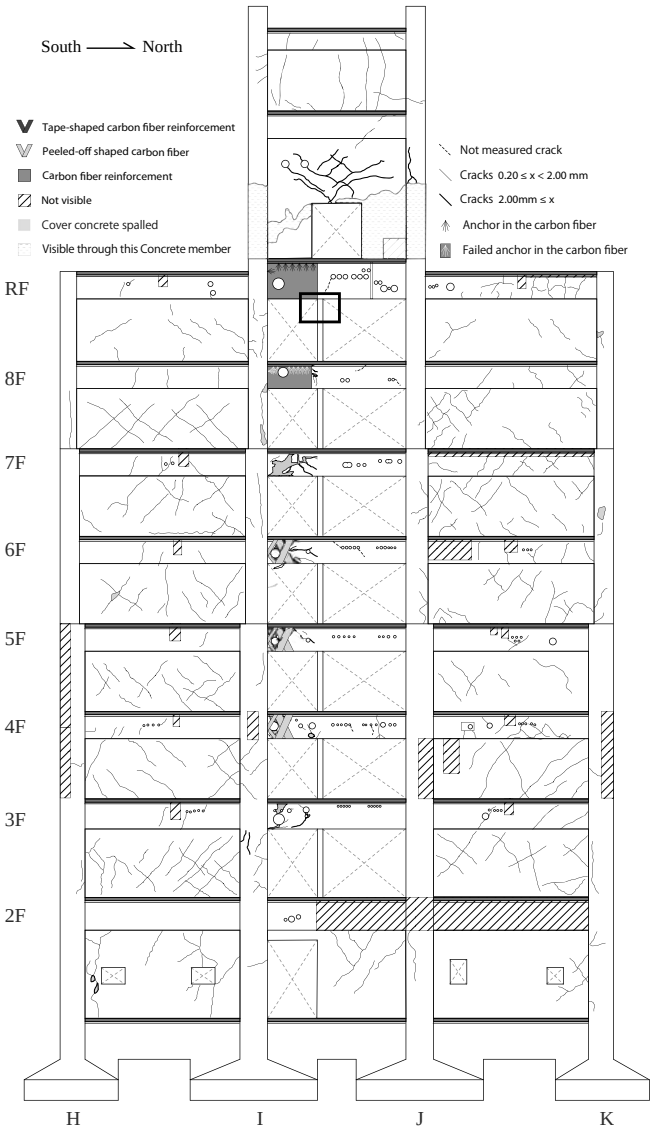


Figure 14 Frame 11 cracks schedule

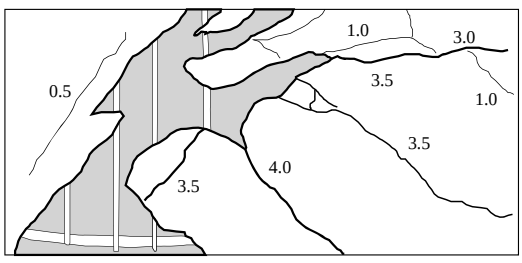


Figure15 damage of short beam of 7th floor

3.2 Penthouse

The penthouse of the building was severely damaged that required emergency strengthening just after the earthquake in order to prevent collapse. Both columns and walls were completely destroyed at the first story of the penthouse, while the second story was in a similar condition to the rest of the building. In investigation, thickness of walls was 120mm, but drawing illustrates that was 180mm. (Figure 16) Damage in the first story of the penthouse was more remarkable on transverse directions than on longitudinal one. Figure 17 shows penthouse cracks schedule of each frame. Frame 8 was less damaged. Frame 11 damaged heavily.(Photo 9) Damage in east area became increasingly hard. Capacity of walls in the first story of the penthouse was calculated in each frame as shown in the work by Villanova et al. (2012). The frame 8 had approximately twice the capacity of 9, 10 and 11 frames. Therefore, Penthouse might have torsional response. This might have caused such severe damage.

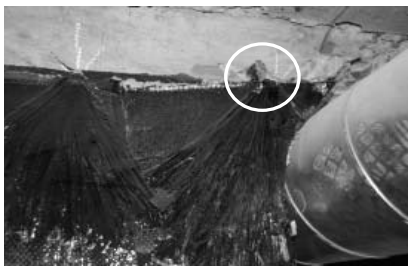


Photo 8 Failed anchorage at coupling beam floor 8

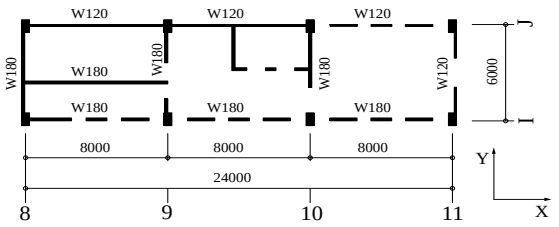
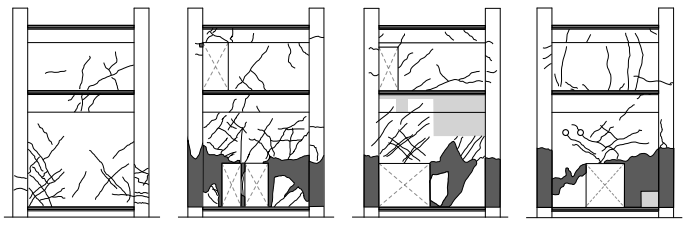


Figure 16 Penthouse 1st story (mm)



Photo 9 Wall at the first story of the penthouse



(a) Frame 8 (b) Frame 9 (c) Frame 10 (d) Frame 11

Figure 17 Penthouse cracks schedule

3.3 Structural Walls

Figure 18 illustrates frame I cracks schedule in longitudinal direction. There were few cracks in the 1st story on both X and Y directions. In the 2nd and upper stories, cracks were prominent. However, they were smaller than those of beams. Most of them were narrower than 1mm.

The pullout of bars were observed at the top of the perpendicular wall in 8th floor which is shown in Figure 19 and the square in the Figure 14. Perpendicular wall might constrain vettical displacement of the coupling beam at the mid span, and, as a result, clear span of the beam was shortened and failed in shear. Pullout of bars is a evidence of the behavior



Figure 19 Bar pullout at top of the perpendicular wall in 8th floor

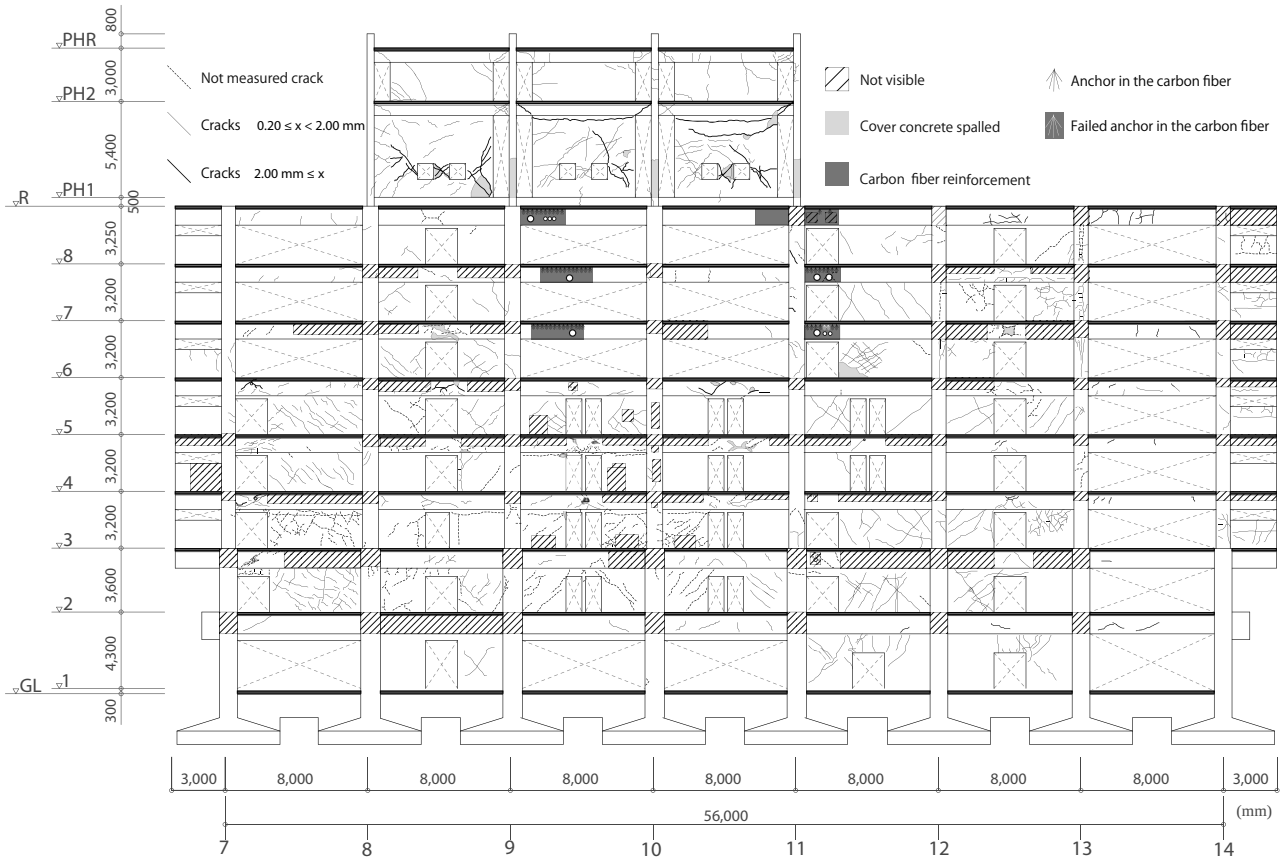


Figure 18 Frame I cracks schedule

4. PUSHOVER ANALYSIS

In this section, pushover analysis is carried out to know failure mode of this building in transverse direction, behavior of coupling beams, penthouse and perpendicular walls, and to estimate the seismic capacity of this building.

4.1 Modeling of Structural Members

4.1.1 Coupling Beams

The analytical model of the frame on 11 axis is shown in Figure 20. Coupling beams are idealized by two nonlinear rotational spring at their end and nonlinear shear spring. Coupling beams of 3rd to 8th floors are idealized with two separated beams to consider the effect of the perpendicular walls. The backbone curves of rotational springs and shear springs are represented by a tri-linear relation. The first break point in the relation represents cracked state, the second represents ultimate limit state.

There are some openings whose diameters are from 50 to 400 mm in short-span coupling beams. The shear strength of these beams are calculated considering only openings larger than 100mm in diameter. Some short-span coupling beams are retrofitted by carbon fiber. However, because the anchorage length of fiber reinforcement is shorter than demanded length, the strength contribution of this fiber reinforcement is ignored.

On the other hand, the coupling beam in roof floor is idealized a beam which is not separated and by rigid beam element with two rotational springs at its ends. These rotational springs represent the joint between columns in 8th floor and coupling beams in roof floor. Because these columns and beams are boundary columns and boundary beams, the joint fails faster than these members. However, the coupling beam depth in roof floor is twice as big as the column width in 8th floor. In brief, the column do not contributes very much to the strength and stiffness of the joint. Therefore, the backbone curves of these rotational springs use the strength and stiffness of coupling beam. The beam with wing wall in the 1st floor is also idealized by rigid beam element with two rotational springs at its ends.

4.1.2 Structure Walls

The structure wall is substituted a brace model equal to the shear stiffness of the wall. Shear behavior of the wall is idealized by two diagonal truss elements. Flexural behavior is idealized by two vertical truss elements on each side. All beams with the structure wall are assumed to be rigid.

The backbone curves of the brace model are represented by a tri-linear relation and, boundary columns are represented by a bi-linear relation. However, in the case of a wall with openings, the strength is reduced by the reduction factor based on Japanese Standard (2010).

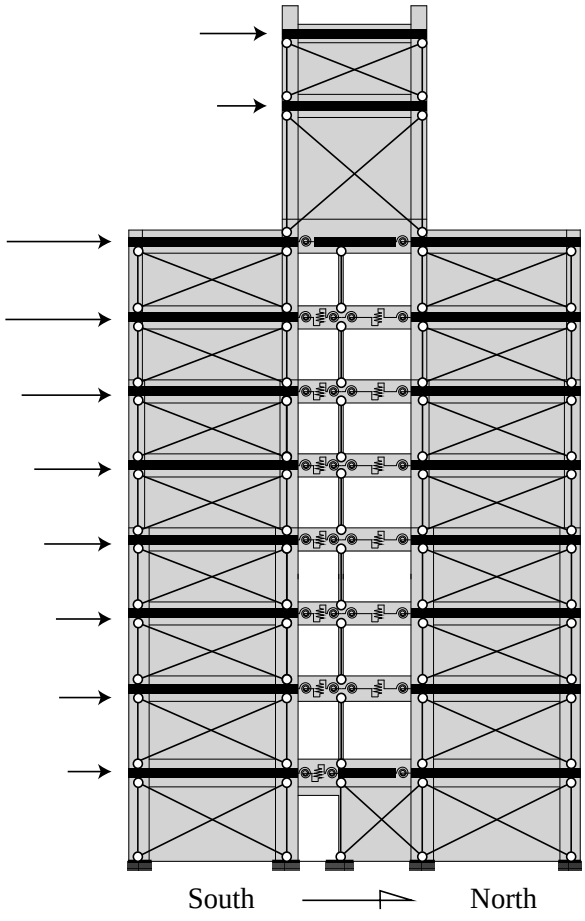


Figure 20 Analysis model

4.1.3 Perpendicular Walls

Perpendicular walls are idealized as truss elements because they do not resist to bending moment in transverse direction. The backbone curves of perpendicular walls are represented by a bi-linear relation. The compressive strength of this wall is calculated considering wall reinforcements and concrete. The tensile strength is calculated considering only wall reinforcement. However, pullout of bars is observed at the top of the perpendicular wall in 8th floor. Therefore, the tensile strength of this wall is assumed to be zero. Furthermore, the effective width of these walls in perpendicular direction is defined as shown in Figure 21. In Japanese RC Standard, a slab contributes the strength and stiffness of the beam within the width of 0.1 multiply the span length of the beam. Therefore, It assumes the perpendicular wall within the width of 0.1 multiply the clear height to resist effectively the compressive and tensile force.

4.2 Results of Analysis

Pushover analysis of the model was carried out using computer program Opensees. In this analysis, gravity loads and lateral forces are applied to each nodes in each floor. The analysis is continued to be incremented by a step to reach 1000 steps. Lateral Forces are incremented 0.001 multiplied by maximum lateral forces by every step. Therefore, maximum lateral forces are applied if the analysis reaches until final step. Maximum lateral forces are calculated by maximum story shear forces Q_{max}. Q_{max} factor represents *Wi* multiplied by *Ai*. The analysis is carried out for two cases. These parameters are the direction of lateral forces (direction from south to north, and its opposite direction).

These analyse are stopped around 500 step, because convergence test is failed. In each analysis, structure walls in 1st floor is failed in flexure. When walls are failed, story shear forces reach 0.48 Q_{max}. Therefore, the

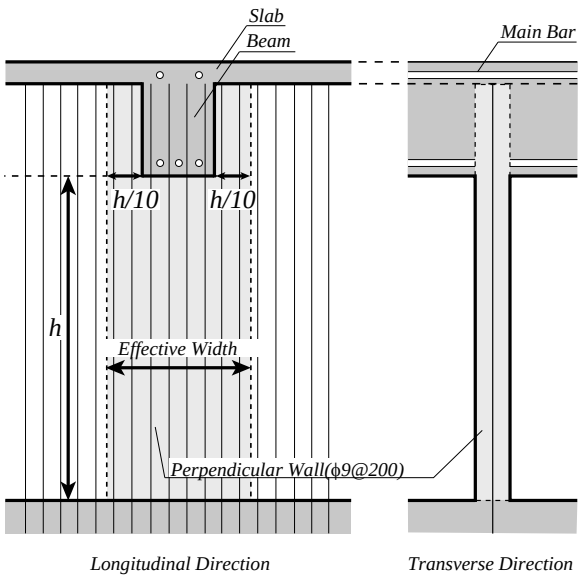
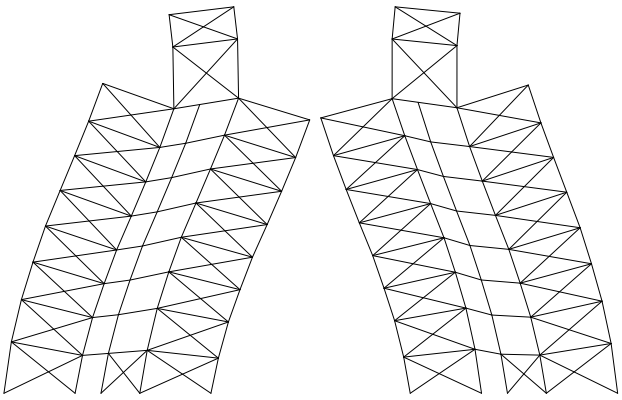


Figure 21 Effective width of perpendicular wall

base shear coefficient of this building is estimated as 0.48. Figures 22 shows the deformation of the building in the case that story shear forces are applied 0.48 Q_{max}. These displacements are illustrated by 50 magnifications. Drifts of short beams seems almost the same as long beam in Fig. 22(a). On the other hand, drifts of short beams seems larger than long beams in Fig. 22(b), Therefore, it is considered that short beam is damaged by the loading from North to South.

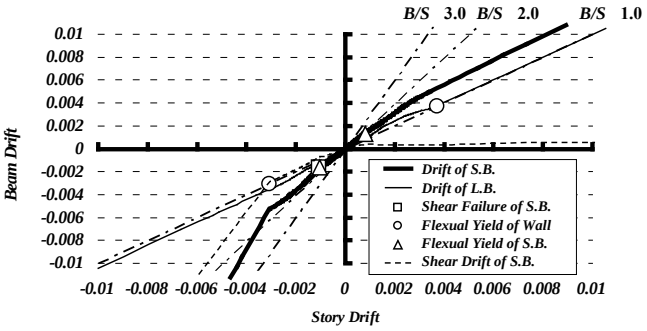
Figure 23 shows the relation between beam drift and story drift on the lower floor (1F), middle floor (4F) and upper floor (7F). Beam drift means the summation of shear drift and flexural drift. These figures show drifts in the case of both analyses. The drift of rotational spring nearby structure walls is considered larger than that nearby perpendicular walls. Therefore, flexural drift is estimated by using the rotational spring nearby structure walls. According to these relation in the area of loading direction from north to south, when walls in 1st floor failed, the drift of short beams is 1.5 to 2.0 times as large as story drift. The higher floor up, the lower the drift of short beams. On the other hand, the drift of long beam is almost the same as story drift. Figures also show the shear drift of short and long beams. It represents that the shear drift of short beams is larger than long beams. In the loading direction from south to north, the drift of short beams is almost the same as the drift of long beam. Therefore, the larger shear force acts to short beams compare to long beams in the case of loading direction south to north.

Figure 24 shows the relation between Q/Q_{max} and drifts. Q factor indicates the story shear force in each steps. Bold line indicates the drift of the building, the other indicates the drift of the penthouse first floor. The drift of the building in this graph mean the horizontal displacement at roof floor divided by the height between first and roof floor. Positive area of Q/Q_{max} in this graph represents the analysis of loading direction from south to north, opposite area represents the analysis of opposite direction. When walls in 1st floor failed, the drift of the building is about 0.65%, and the drift of the penthouse 1st floor is nearly zero in both loading directions. Even

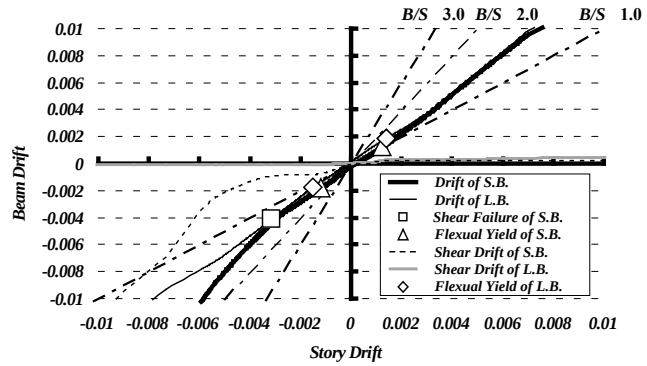


(a)South→North (b)South←North

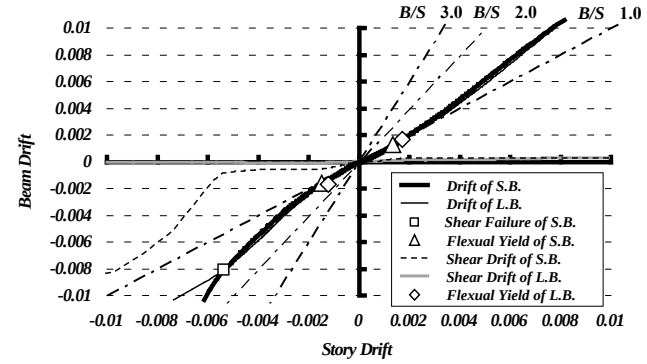
Figure 22 The deformation of the building at 0.48 Q_{max}



(a) 1st story



(b) 4th story



(c) 7th story

Figure 23 The relation between beam drift and story drift

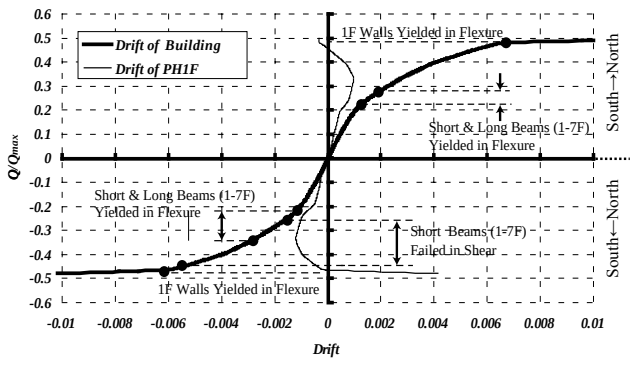


Figure 24 The relation between Q/Q_{max} and drifts

maximum drift of penthouse before walls in 1st floor failed is about 0.1%. Furthermore, in the loading direction from North to South all short beams except roof floor beam failed in flexural and shear before wall failed.

Figure 25 shows the relation between building drift and axial force of perpendicular walls. The figure represents that the perpendicular wall in 8th floor failed in bond slippage when the building drift reaches about 0.002 in south to north direction, and 0.004 in opposite direction.

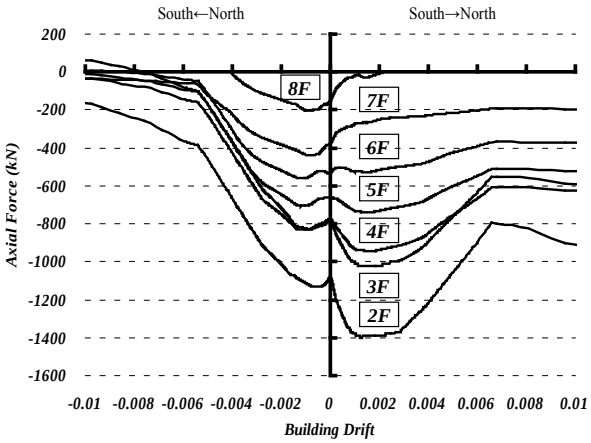


Figure 25 The relation between building drift and axial force of perpendicular walls

4.3 Discussion

Collapse model of this building in 11 axis is assumed as shown in Figure 26 and the ultimate lateral strength was calculated two patterns. The one pattern considers the work of short beam, the other one does not consider it.The strength was evaluated by using virtual work method. In this calculation, there are four assumption. First, structure walls in 2nd floor are failed in flexure. Second, the first story is considered as rigid, because it does not have significant damages. Third, top of the perpendicular wall in 8th floor is failed in bond slippage. Fourth, joints between columns in 8th floor and coupling beams in roof floor failed as shown in Fig. 27. In the result of this calculation, the ultimate lateral strength is 6.5MN without considering the effects of the beams, and 8.7MN in the other case. Furthermore, short span coupling beams are deformed 3.75 times as large as the drift of the building. According to the documents of the seismic evaluation, the ultimate lateral strength at 2nd floor is 10.7MN, and base shear coefficient is 0.8. Therefore, base shear coefficient of this calculation is estimated 0.49 and 0.65.

According to the result of pushover analysis, several behaviors of the analysis correspond with the suggested model. Regarding to ultimate lateral strength, the result of analysis is almost same as the suggested model's, but is smaller than the value of seismic evaluation. However, there are more walls in 1st than upper stories on other axes shown in Figure 28. Therefore, larger base shear coefficient than 0.48 can be expected in this building. Though drifts of short beams of the analysis are smaller than the model in Fig. 26, they are larger than story drifts as indicated in Fig. 26. Perpendicular wall in 8th floor failed in bond slippage in the pushover analysis and

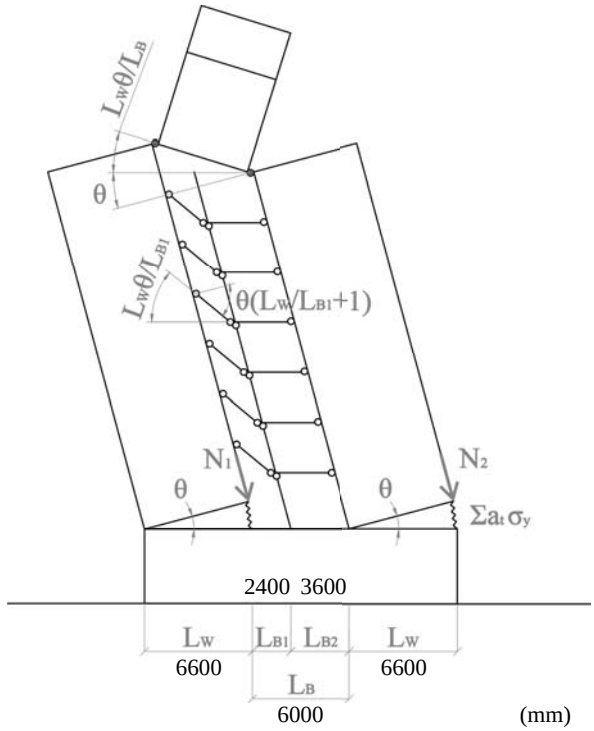


Figure 26 Model of calculation for the frame number 11

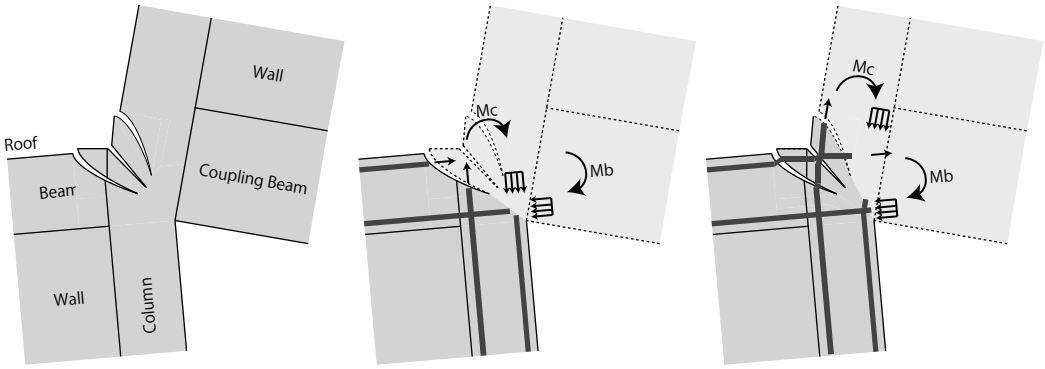


Figure 27 Assumption of the failure mode of the joint

this failure mode is also observed in field investigation. From field investigation, the failure of the penthouse is assumed to be caused by the torsional response. This failure can not be explained by the frame analysis. In fact, the result of pushover analysis shows the drift of the penthouse is much smaller than that of the main building and the penthouse does not fail.

Although the perpendicular wall is usually neglected in structural design, it has a significant role on the behavior of the coupling beam in the analysis.
It makes the short-span beam in the analysis and the failure in the analysis is similar to the observed failure.

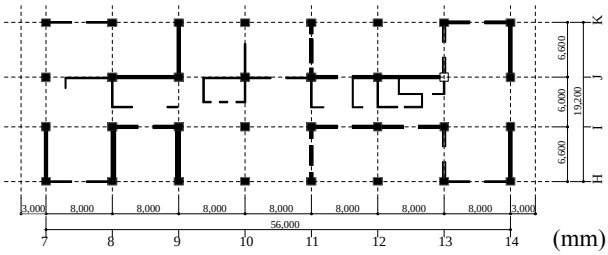


Figure 28 Floor plan of 1st story

5. LESSONS LEARNED AND CONCLUSIONS

(1)There were different points from the original drawings in coupling beams. It is one of the reason of significant damage of them.
(2)Concerning the penthouse, the capacity of wall on each frame varied widely in the transverse direction. The penthouse might have torsional response.
(3)According to the result of analysis, the building has at least 0.48 base shear coefficient. It is inferred that actual lateral forces were not over the base shear coefficient of this building because the damage of structure walls and columns were minor.
(4)Coupling beams were constrained by the perpendicular wall. It causes the large deformation of the short span beam.
(5)Short-span beam should be reinforced appropriately.

Acknowledgment

This work was financially supported by the Japan Science and Technology Agency and the U.S. National Science Foundation. They are gratefully appreciated.

References:

D. Mitchell, R. H. DeVall, M. Saatcioglu, R. Simpson, R. Tinawi, and R. Tremblay (1995), "Damage to concrete structure due to the 1994 Northridge earthquake", *Canadian Journal of Civil Engineering*, Vol. 22, pp.361-377

Villanova, I., Nagaya, A., Maeda, M., Pujol, S., Takahashi, S., and Ichinose, T. (2012), "Damge To Eight-Story RC Building Retrofitted to Have Base Shear Coefficient of 0.65," *Proceedings of the International Symposium on Engineering Lessons Learned from the 2011 Great East Japan Earthquake*, Paper No.1270-1281

Architectural Institute of Japan (2010) ,"AIJ Standard for Structural Calculation of Reinforced Concrete Structures,"Gihodo, Tokyo

Building Research Institute (2001), "Seismic Evaluation and Retrofit," The Japan Building Disaster Prevention Association

OpenSees verion 2.3.2 (2011), Pacific Earthquake Engineering Research Center, PEER, Berkely CA

10CUEE CONFERENCE PROCEEDINGS
10th International Conference on Urban Earthquake Engineering
March 1-2, 2013, Tokyo Institute of Technology, Tokyo, Japan

Damage of Six-Story RC Building with Coupling Beams Having Aspect Ratios Larger than 2.0

Yuko KATO[1], Atsushi NAGAYA[2], Kazuyoshi HOTTA[3], Ying WANG[4], Susumu TAKAHASHI[5], Masaki MAEDA[6], Santiago PUJOL[7], Toshikatsu ICHINOSE[8]

1) Graduate Student, Department of Architecture Engineering, Nagoya Institute of Technology, Nagoya, Japan
2) Graduate Student, Department of Architecture Engineering, Nagoya Institute of Technology, Nagoya, Japan
3) Undergraduate Student, Department of Architecture Engineering, Nagoya Institute of Technology, Nagoya, Japan
4) Graduate Student, Department of Civil Engineering, Purdue University, West Lafayette, Indiana, USA
5) Assistant Professor, Department of Architecture Engineering, Nagoya Institute of Technology, Nagoya, Japan
6) Professor, Department of Architecture and Building Science, Tohoku University, Sendai, Japan
7) Associate Professor, Department of Civil Engineering, West Lafayette, Indiana, USA
8) Professor, Department of Architecture Engineering, Nagoya Institute of Technology, Nagoya, Japan

y-20116021@goo.jp, nagoyan_nitech@yahoo.co.jp, kazuyoshihotta@gmail.com, wang763@purdue.edu
takahashi.susumu@nitech.ac.jp, maeda@archi.tohoku.ac.jp, spujol@purdue.edu, ich@nitech.ac.jp

Abstract: Several buildings in Tohoku University were severely damaged by the 2011 Great East Japan Earthquake. In this paper, the damages in one of these buildings are reported and the reason of this damage is discussed. The target of this investigation was a six-story reinforced concrete building. The building was constructed in 1968 and retrofitted in 1997. This building is assumed to have enough strength to resist earthquakes in Japanese seismic evaluation. The base shear coefficient of this building is estimated to be 0.6. Severe damage was observed in short beams with web openings in upper stories. On the other hand, the mainly observed damages in columns and shear walls are thin cracks less than 1mm wide. The observed failure is different from what was considered in the seismic evaluation. Therefore, the actual strength of the frame is estimated by using the limit analysis in which the observed failure mode is assumed. In the limit analysis model, the rotation angles of short beams are much higher than those of shear walls. Shear walls might be elastic when the beam failures occurred. To prevent this failure, the coupling beam should be reinforced.

1. INTRODUCTION

A six-story Reinforced Concrete (RC) building located in the Engineering Campus of Tohoku University was severely damaged by the 2011 Great East Japan Earthquake. Remarkable damages were observed in short beams with web openings in upper stories. The building experienced several severe earthquakes since it was built in 1968, and it was retrofitted in 1997. This building was assumed to have enough strength to resist earthquakes in Japanese seismic evaluation.

The damaged short beams with web openings in transverse direction are coupling beams with stirrups (p_w= 0.18 (%)) as shear reinforcement. Shear failures of coupling beams were reported by researchers (Mitchell *et al.*, 1995 and National Research Council 1973), and it is well known that efficient shear reinforcement, such as tight stirrups or diagonal bars, is necessary. Most of the reported coupling beams have aspect ratios (clear span / depth) no more than 1.0.

In addition, various experimental programs studying the effect of shear span ratio and reinforcement of coupling beams are reported. Paulay, T. (1969) proposed a reinforcement pattern with diagonal bars to increase ductility of coupling beams. In this study, the shear span ratios ($M/Vh = l/2h$) of coupling beams were lower than 1.0. Theodosios P. Tassios *et al.* (1996) recommended that coupling beams with shear span ratios lower than 0.75 shall be reinforced with diagonal bars, and shear span ratios larger than 1.33 may use normal detailing. They also proposed alternative reinforcement patterns, with dowel bars and rhombic reinforcements.

According to the American Concrete Institute (ACI) 318-11 code (2011), diagonally oriented reinforcements are effective when coupling beams have aspect ratio less than 4.0, and coupling beams with aspect ratio less than 2.0 shall be reinforced with two intersecting groups of diagonally placed bars symmetrically.



Photo 1 Exterior view of the building (transverse side)



Photo 2 Exterior view of the building (longitudinal side)

In this building, aspect ratios of the short beams are 2.4~2.7 (except a part of rooftop beams), and these beams with stirrups as shear reinforcement experienced large deformations and severely damaged in shear. In addition, web openings through the short beams reduced their strengths.

Accordingly, the short beams of the building is a case of shear failed coupling beams with relatively higher aspect ratios compared with well-known observed damages, experimental objects and the existing code.

This paper reports observed damages based on field investigation and discusses a possible failure mechanism of the building.

2. CONFIGURATION OF THE BUILDING

The building was constructed in 1968 in Tohoku University, Sendai, located approximately 130 km from the epicenter. It is a reinforced concrete building with six stories above ground and one below and a one-story penthouse. It has seven spans in longitudinal direction and three spans in transverse direction (Fig. 1). The upper stories have the same distribution as first story plan. Storage, bathrooms and vertical communication nucleus are separated by walls in the middle longitudinal axis. The rooms are around this nucleus, giving a configuration symmetrical to the building. The penthouse has three spans between axis 4 and 7 in longitudinal direction and one span between axis B and C in transverse direction (Fig. 2).

The building was retrofitted in 1997 according to the 1990 Japanese Standard (Building Research Institute 2001). The main changes during the retrofit were addition of new walls and replacement of reinforced concrete wall panels with thicker ones for the first three stories. According to the field investigation, one of actual retrofit was different from the plan. In particular, a shear wall of longitudinal axis B, between axis 1 and 2, first story (a broken line in Fig. 1), was 180mm thick in existence and retrofitted with 100mm thicker one although it designed 120mm thick in existence and retrofitted with 130mm thicker one in the plan. But it is assumed that this difference does not affect the damages of the building. The other actual retrofits are same to the plan.

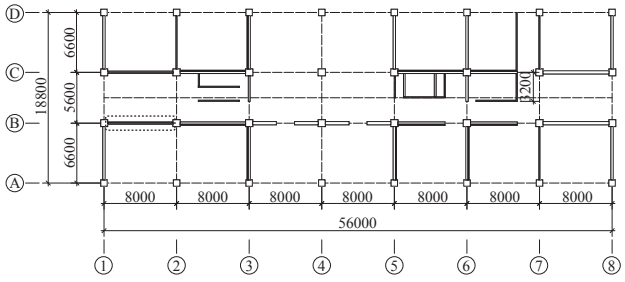


Figure 1 First story plan

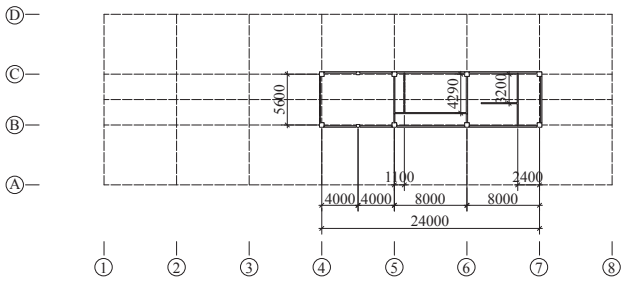


Figure 2 Story of the penthouse plan

3. OBSERVED DAMAGES

3.1. Beams

Figures 3, 4, 6 and 7 show observed cracks in selected frames. Bold lines in the figures represent cracks of more than 1mm wide. Hatched areas represent the blocked areas. In longitudinal direction, severe damages concentrated on beams above openings (Fig. 3 and Photo 3). In transverse direction, severe damages concentrated on coupling beams with web openings (Figs. 4 and 7 and Photos 4 and 5). These observed damages indicate that the short beams failed in shear. Figure 5 shows cracks observed in short beams of transverse direction (axis 3) on each story (broken lines in Fig. 4 show these

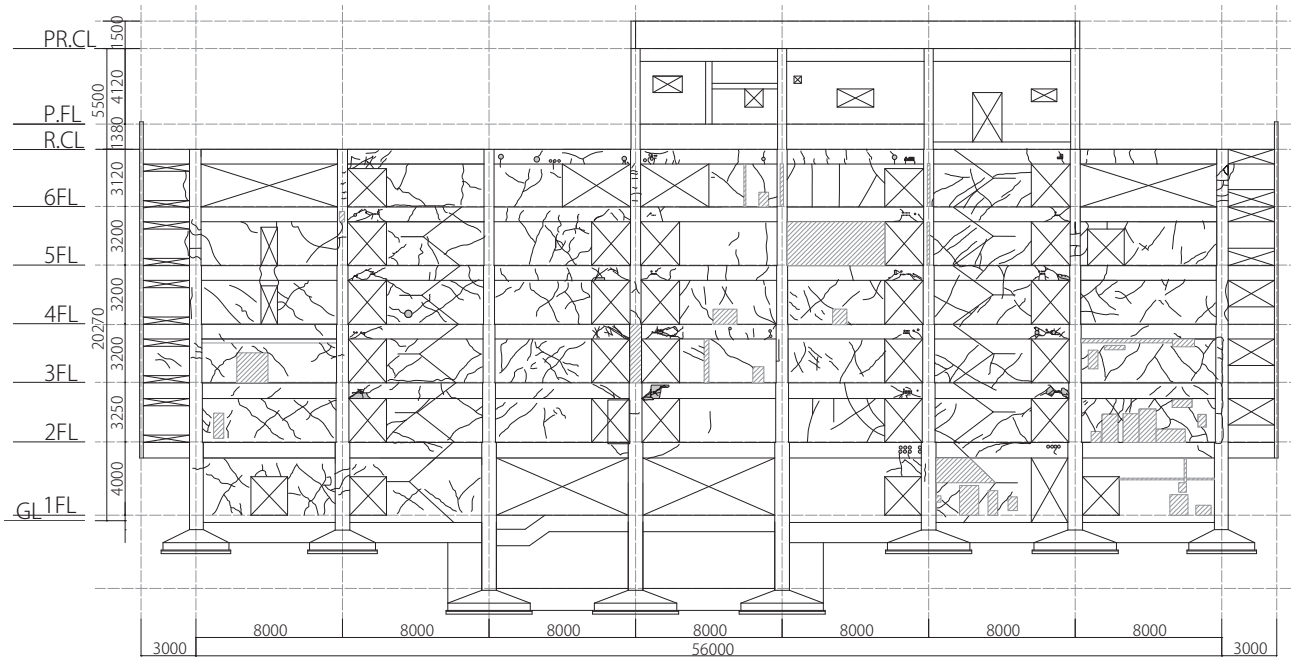


Figure 3 Observed cracks of longitudinal direction (axis C)



(a) Full view (b) Detail

Photo 3 Damaged beam above an opening (3F - axis C)

locations). Figure 8 (a) shows observed cracks of the short beam of transverse direction (axis 5) in fifth story (a broken line in Fig. 7 shows this location). Shaded areas represent web openings and spalled concrete. Numbers represent crack width measured by crack scales in the field investigation. Numbers in parenthesis are crack widths estimated from photos because it was impossible to measure them in the field investigation. Figure 8 (b) shows a section of beam in Fig. 8 (a). This shows a section of the beam end.

In both longitudinal and transverse directions, most of the short beams have web openings (diameter of 10~200mm) as shown in Figs. 5 and 8, and cracks connected with these openings were remarkable. Some cracks and detached concretes were observed in areas of cold joint especially in upper stories.

In transverse direction, axis 3, 5 and 6 are frames that have coupled shear walls as shown in Figs. 4 and 7. On the other hand, the other frames have shear walls, which are not continuous walls as shown in Fig. 6. Therefore, there are no short beams in these frames where damages were minor, and minor flexural cracks were observed.

3.2. Structural walls

In both longitudinal and transverse directions, cracks in structural walls were distributed throughout the frames. Most cracks were less than 1mm wide. The damage of structural walls was minor in comparison with that of beams, because crack widths of structural walls were less than those of beams (Figs. 3, 4, 6 and 7).

3.3. Penthouse

Maximum crack widths of 1.5mm were observed in structural walls of the penthouse, and spalled concrete was not observed. The damage of the penthouse was minor in comparison with that of the main building. In the field investigation, cold joints were observed in upper structural walls.

4. ANALYSIS

4.1. Seismic evaluation results

Prior to the seismic retrofit in 1997, the seismic capacity of this building was evaluated according to the Japanese Standard (1990). In this evaluation, beams are assumed to be strong enough. Therefore, seismic capacity is computed from contributions of columns and walls.

Figure 9 shows story shear coefficients of each story. In the penthouse story, the story shear coefficients are reduced to 76% in longitudinal direction and 86% in transverse direction. These reduction factors are computed based on the Japanese Standard (1990) and used for considering the torsional response caused by the eccentricity of stiffness in both horizontal and vertical directions. Variations in strength through stories shown in Fig. 9 were relatively small in both directions. In transverse direction, the open frames without coupled shear walls were retrofitted with additional shear walls from first to third stories. Therefore, the story shear coefficients in fourth or upper stories are relatively lower (Fig. 9). Also in the field investigation, increase

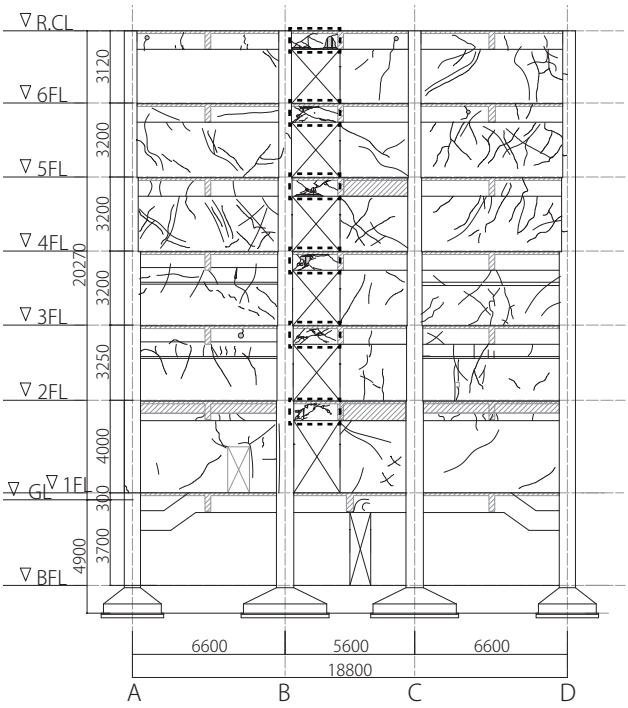


Figure 4 Observed cracks of transverse direction (axis 3)

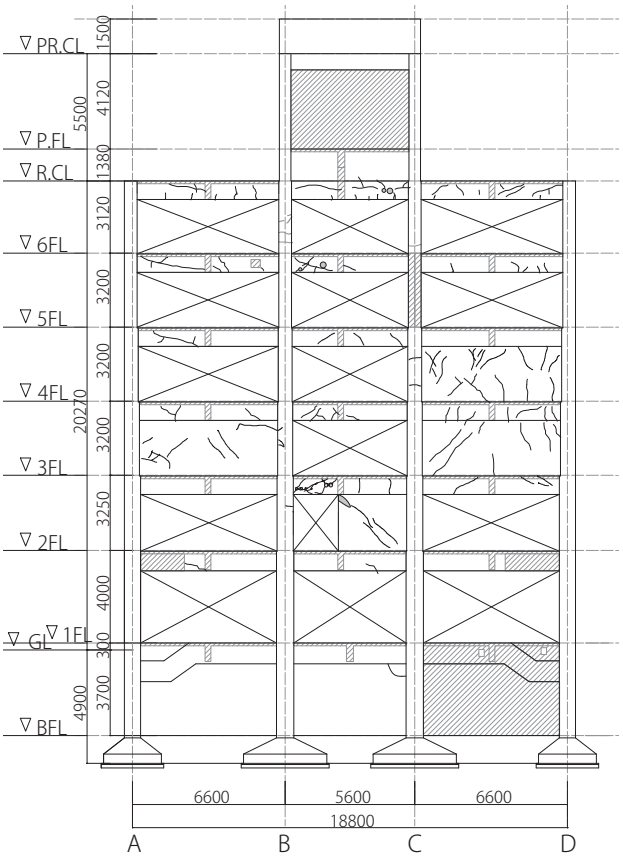


Figure 6 Observed cracks of transverse direction (axis 4)

of crack widths was observed on fourth to fifth stories. The story shear coefficients are more than 0.57 in both directions. Therefore, the building was assumed having enough strength based on the evaluation. Nevertheless

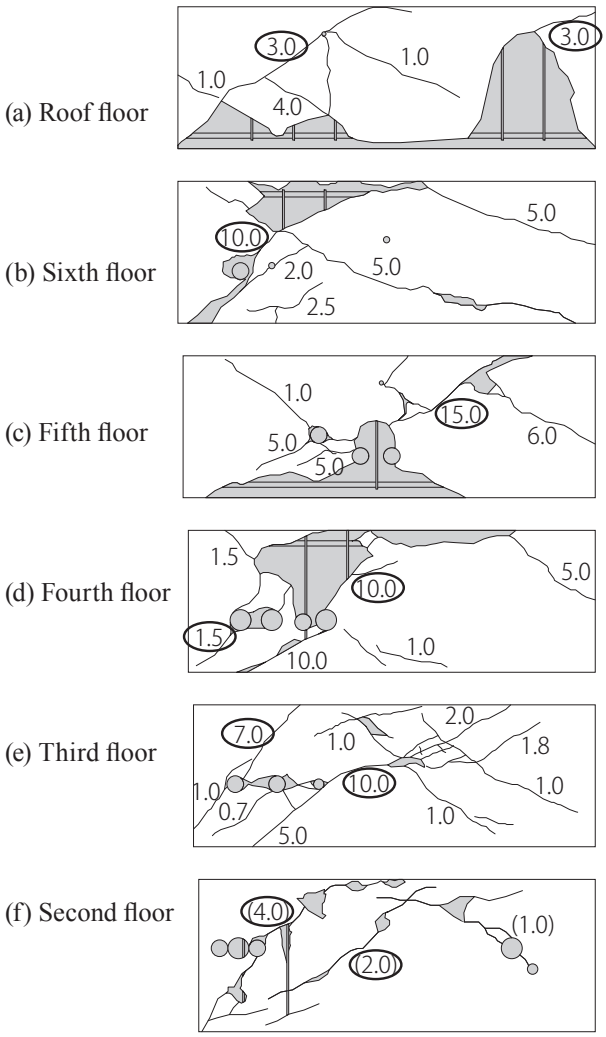


Figure 5 Observed cracks of the short beams (axis 3)

the building was severely damaged. The differences between the actual damage and the calculated values are assumed attributing to the difference of failure modes. In particular, beams were assumed to be rigid during the evaluation, but failure of the short beams take a lead over that of columns and walls actually. Therefore, a failure model considered the field investigation data is set in following section.

4.2. Calculation of the ultimate lateral strength

In this section, a failure model based on the field investigation data is assumed, and the ultimate lateral strength in the transverse direction is calculated by virtual work method.

4.2.1. Procedures

The characteristics of damage in transverse direction can be described as following: first, damage of coupled shear walls and columns were relatively small. Second, severe damage concentrated on the short beams. Axis 3 has both coupled shear walls and the short beams (Fig. 4), and it was damaged characteristically and retrofitted in first to third stories. Therefore, a failure model shown in Fig. 10 is assumed as this frame, and the calculation is conducted based on the following assumptions.

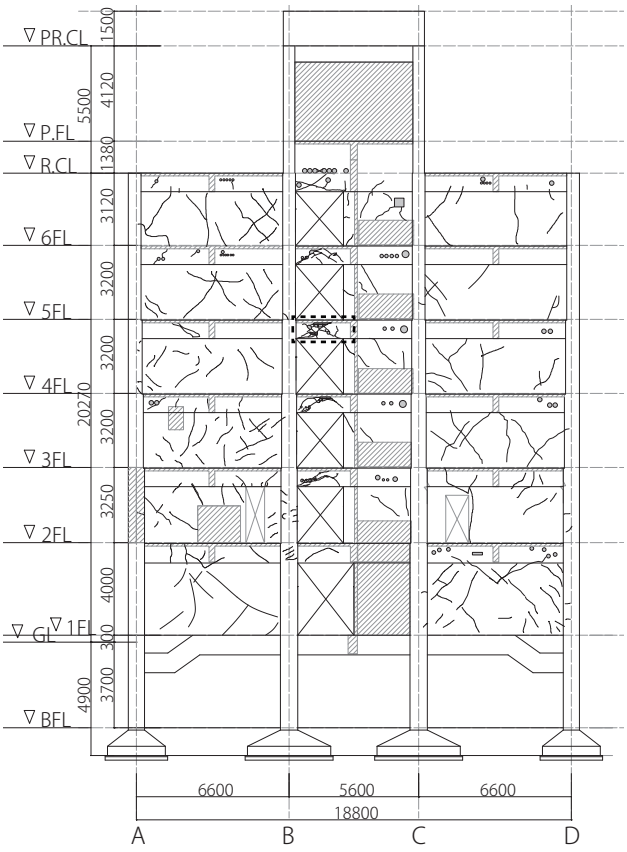


Figure 7 Observed cracks of transverse direction (axis 5)



Photo 4 Damaged short beam (4F - axis 5)

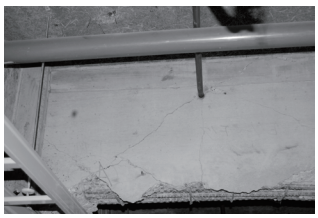


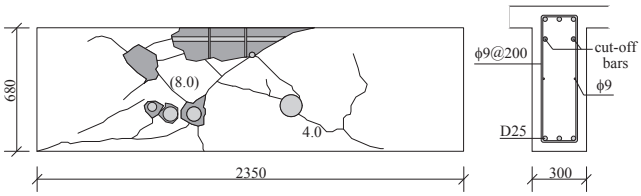
Photo 5 Damaged short beam (6F - axis 3)

The coupled shear walls rotate as shown in Fig. 10 and vertical reinforcement bars are assumed to be yielding at the bottom of the first story, where a_t represents cross-section area of longitudinal reinforcement in boundary column and σ_y represents yield strength of the steel. N_1 and N_2 are the permanent loading axial forces on the boundary columns of the walls. The circles at beam-ends in this figure represent the plastic hinge.

In the analysis, two models have been proposed. In the first one, the short beams of the span L_B fail in shear: the beams are completely destroyed and capacity in hinges is negligible. In the second one, the beams yield in flexure at both ends.

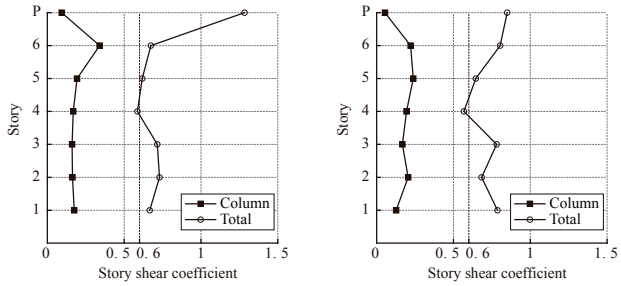
4.2.2. Results and discussions

According to the model of the analysis, all the walls have been considered as flexural walls because of the hinge in the base of the walls of the model. This assumption is admissible since the small width



(a) Observed cracks (b) Section

Figure 8 Observed cracks of the short beam of transverse direction in fifth story (axis 5)



(a) Longitudinal direction (b) Transverse direction

Figure 9 Story shear coefficients of each story

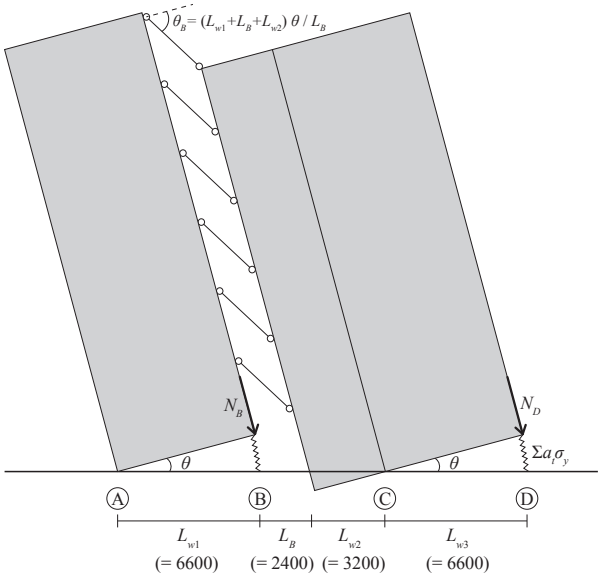


Figure 10 The assumed failure model

of the cracks found in the walls of the building. As to the results of the analysis, the lateral capacity of the frame axis 3 is 10MN, in the case of considering the contribution of the short beams. In the case of neglecting those beams, the lateral capacity is 8MN. Thus, the actual value would exist between these two results and the beams make an important contribution to the capacity of the frame actually. According to the documents of the seismic evaluation, the lateral capacity of the frame axis 3 is 10MN. It is a coincidence that this value is almost equal to the analytical result with considering beam contributions, however, this indicates that the building is assumed to have enough strength.

The rotation angles of short beams, θ_B in Fig. 10, is

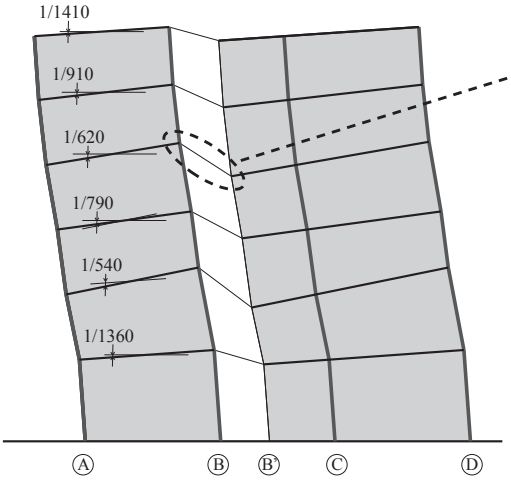


Figure 11 The assumed deformation model

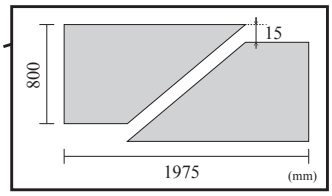


Figure 12 A pattern diagram of shear deformation

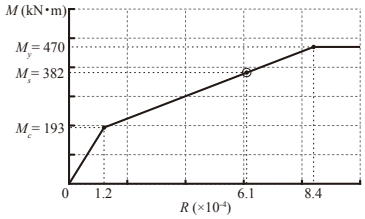


Figure 13 Moment - rotation relation

5.1 times larger than those of shear walls, θ in Fig. 10. It suggest that extremely large deformation will be induced to the short beams if the deformation of the building is relatively small.

4.3. Estimation of the actual deformation

Figure 11 shows assumed deformation model based on following assumptions.

The circled numbers in Fig. 5 are residual shear crack widths assumed to be induced by the deformation shown in Fig. 11. The rotation angle of the beam attributed to shear deformation can be estimated roughly from these crack widths and clear spans of the beams on each story (Fig. 12). In Fig. 11, a shear wall between axis A and B is rotate around axis A due to a column on axis A. This is based on the assumption that the location of the neutral axis is near the centroid of the column. A shear wall between axis B' and D is rotate around axis C due to a column on axis C.

For example, the rotation angle of the beam attributed to shear deformation in fifth story is 15/1975 ≈ 1/132 (Fig. 12). The rotation angle of the beam attributed to flexural deformation can be estimated from a moment - rotation relation based on the AIJ Standard (Architectural Institute of Japan 2010)(Fig. 13): in reaching the ultimate shear strength, the rotation angle is 6.1×10^{-4} (≈ 1/1640), and it is sufficiently small in comparison with that of attributed to shear deformation. Accordingly, the rotation angle of the shear walls in fifth story based on the model in Fig. 10 is θ = 1/620 (noted in Fig.11). In the 1990 Japanese Standard, a standard rotational deformation in ultimate is 1/250. In addition, the short beam has lower shear strength than flexural strength (Fig. 13 M_y: flexural moment, M_s: shear moment). Consequently, the coupled shear walls deformed in the range of elastic deformation, but the short beams extremely deformed, and the short beams was assumed to fail before the shear walls. It correspond to the observed crack patterns.

According to the ACI 318-11, the coupling beams with aspect ratio less than 2 shall be reinforced with diagonal bars. The coupling beams of this building failed in shear in spite of having aspect ratios larger than 2 because the shear strength of these coupling beams were not so large. The coupling beams should be reinforced to have larger shear strength than flexural strength and should not have openings.

5. LESSONS LEARNED AND CONCLUSIONS

(1) Both longitudinal and transverse directions, the damage of columns, structural walls and the penthouse was relatively minor.
(2) In longitudinal and transverse directions, severe damages concentrated on short beams. Most of these beams had web openings, and cracks connected with these openings were highly visible.
(3) From the seismic evaluation results, the story shear coefficients were more than 0.57 in both directions, and no story had an obvious weakness.
(4) The coupled shear walls deformed in the range of elastic deformation, but the short beams deformed extremely.
(5) The conventional reinforced coupling beams with aspect ratios larger than 2.0 suffered severe damage. In the previous researches and ACI 318-11 recommendation, coupling beams with aspect ratios lower than 2.0 were mainly target of special shear reinforcement.
(6) The beams shall be reinforced appropriately not only in terms of strength but also that of deformation in order to use a building continuously after earthquake damage with minor repairing.
(7) Web openings through the short beams are recommended avoiding.

Acknowledgments:

This work was financially supported by the Japan Science and Technology Agency and the U.S National Science Foundation. They are gratefully appreciated.

References:

D. Mitchell, R. H. DeVall, M. Saatcioglu, R. Simpson, R. Tinawi, and R. Tremblay (1995), "Damage to concrete structure due to the 1994 Northridge earthquake," Canadian Journal of Civil Engineering, Vol. 22, pp.361-377.

National Research Council (U.S.). Committee on the Alaska Earthquake (1973), "The Great Alaska Earthquake of 1964," National Academy of Sciences, Washington, D.C.

Paulay, T. (1969), “Coupling of Reinforced Concrete Shear Walls,” Proceedings, 4WCEE, Santiago, Chile, B-2, pp. 75-90.

Theodosios P. Tassios, Marina Moretti, andAntonios Bezas (1996), “On the Behavior and Ductility of Reinforced Concrete Coupling Beams of Shear Walls,” ACI Structural Journal, V. 93, No. 6.

American Concrete Institute (2011), “ Building Code Requirements for Structural Concrete,” ACI Committee 318, Farmington Hills, Michigan.

Building Research Institute (2001), “Seismic Evaluation and Retrofit,” The Japan Building Disaster Prevention Association.

Architectural Institute of Japan (2010), “AIJ Standard for Structural Calculation of Reinforced Concrete Structures,” Gihodo, Tokyo.

10CUEE CONFERENCE PROCEEDINGS
10th International Conference on Urban Earthquake Engineering
March 1-2, 2013, Tokyo Institute of Technology, Tokyo, Japan

PERFORMANCE OF THE BUILDING OF THE FACULTY OF ENGINEERING AT TOHOKU UNIVERSITY DURING THE GREAT EAST JAPAN EARTHQUAKE OF 2011

Suzuki Kazuki[1)], Hamood Alwashali[1)], Maeda Masaki[2)], Ying Wang[3)], Santiago Pujol[4)] and Ichinose Toshikatsu[5)]

1) Master student ,Department of Architecture and Building Science, Tohoku university, Japan
2)Professor ,Department of Architecture and Building Science, Tohoku university, Japan
3) PhD student, School of Civil Engineering, Purdue University, West Lafayette, Indiana, USA
4) Associate Professor, School of Civil Engineering, Purdue University, West Lafayette, Indiana, USA
5) Professor, Department of Architecture and Design, Nagoya Institute of Technology, Japan
suzuki@sally.str.archi.tohoku.ac.jp, Hamood@sally.str.archi.tohoku.ac.jp, maeda@archi.tohoku.ac.jp, wang763@purdue.edu, spujol@purdue.edu, ich@nitech.ac.jp

Abstract: This paper presents a study of a retrofitted SRC building which was damaged by 2011 Great East Japan Earthquake. The building was severely damaged in 2011 Great East Japan earthquake. However, this building also suffered from minor damage due to the 1978 Miyagi Oki earthquake. In 2001, This building was seismically evaluated using Japanese seismic evaluation standard (JBDPA) and it was retrofitted based on this seismic evaluation. It was retrofitted by installing framed steel braces, replacement of shear walls and jacketing of adjacent beams with steel plates. Characteristics and crack Figures of the structural damage is presented. The actual damage observed was different from estimated damage of the seismic evaluation. Plausible explanation of such damage and its mechanism is presented, compared and discussed with the seismic evaluation results, virtual work method and capacity spectrum method .

1. INTRODUCTION

In Japan, seismic evaluation and strengthening have been widely applied to existing buildings especially since the 1995 Kobe Earthquake. Many existing buildings that were designed before1981in Miyagi Prefecture were evaluated, and buildings deemed to be vulnerable were retrofitted before the 2011 East Japan earthquake. Most retrofitted buildings performed well during the 2011 East Japan Earthquake. The retrofits helped to limit damage to buildings in the affected area. However, some of the retrofitted buildings suffered moderate or severe structural damage. One of the severely damaged building was the building of the Faculty of Engineering and Civil Engineering (referred as "CE building" in this paper), which was located on the Aobayama campus (Engineering campus) of Tohoku University, Sendai. The locations of the building, Sendai, and the epicenter of earthquake are shown in Figure 1.

The CE building is a 9-story composite structure constructed in 1968. Accelerometers were installed in 1968 in the 1st and 9th floors by Building Research Institute (BRI). Acceleration records were obtained for a number of earthquakes including the 1978 Miyagi-ken Oki Earthquake. In the 1978 earthquake the building suffered minor damage as reported by Shiga and Shibata (Shiga et al.1981). The damage was repaired and the building was used without disruptions until 2001, when the building went through

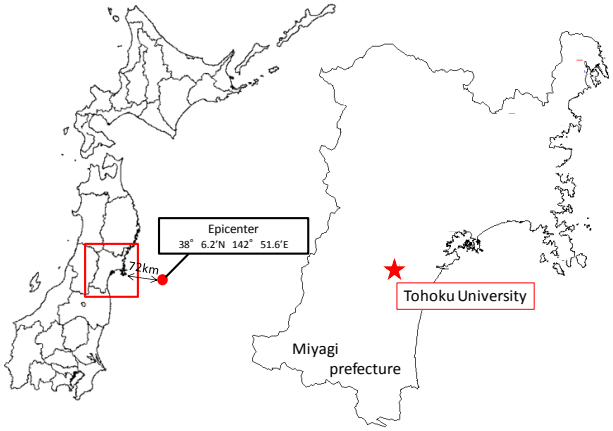


Figure 1 Location of Tohoku University



(a)from North (b)from East

Figure 2 General view of this building

major strengthening work.

In 2011, and despite the strengthening done in 2001, the Great East Japan Earthquake caused severe damage to the building leading to its evacuation and demolition. In this earthquake, acceleration records were obtained again on the 1st and 9th floor. This fact, and the availability of 1) previous records, 2) detailed accounts of the damage caused by previous earthquakes, and 3) complete construction and retrofit drawings make the building a special case attracting the attention of many researchers (Motosaka 2012, and Kimura et al 2012).

This paper describes 1) the configuration of the building, 2) the results of the seismic evaluation that trigger the retrofit work done in 2001, and 3) damage caused by both the 1978 and 2011. Plausible explanations for the great difference in damage are studied using a simple model.

2. BUILDIN CONFIGRATION

2.1 Outline of building

Figures 2a and 2b show the North and East elevations of the CE building. The building was a 9-story steel/concrete composite building. The first two stories were larger in plan than the upper stories (Figure 2b), Figure 3). The typical floor plan for the 3rd to 9th floors is shown in Figure 3a), and the floor plan of the 1st and 2nd floors is shown in Figure 3 b). The locations of the accelerometers are indicated by the stars in Figure 3.

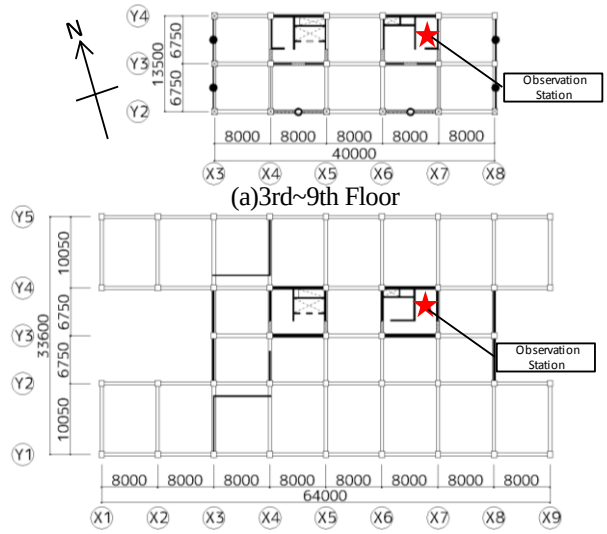
In the transverse direction, the main lateral-load resisting system consisted of shear walls along lines X3, X8, and the C-shaped shear walls of the staircases. As shown in Figure 3a), the structure was symmetrical about its transverse axis. Forces in the longitudinal direction were resisted by the staircase walls and two walls located along the longitudinal axis (Y3). But the structure was not symmetric about axis Y3. The asymmetry was caused by the staircase walls, which were not aligned with this axis.

Table 1 shows typical column dimensions and reinforcing details. Each column had eight vertical structural steel angles "tied" together by discrete horizontal steel plates. These plates did not form continuous webs or continuous flanges. Instead, they simply provided discrete supports for the vertical angles (Figure 20a)). These angles were embedded in concrete reinforced with twelve deformed vertical bars and widely spaced small-diameter ties made with plain round bar (Table 1).

The material of the steel angles was reported to meet Japanese standard SS400, which specifies a nominal yield stress of σ_{sy}=235N/mm^2. The deformed vertical reinforcing bars were reported to meet Japanese standard SD345, which specifies a nominal yield stress of σ_y=345N/mm^2. Ties were made from smooth round bars meeting standard SR235 (σ_y=235N/mm^2). The specified strength of concrete was Fc = 21N/mm^2.

2.2 Seismic evaluation

Tohoku University applied the JBDPA (Japan Building



(a)3rd~9th Floor

(b) 1st&2nd Floor

Figure 3 Plan drawing

Table 1 Typical Column list

Floor	1F	2・3F	4・5・6F	7・8・9F
Dimension (mm)	850 × 850		800 × 850	
Steel	8Ls−75X75X12	8Ls−75X75X9	8Ls−75X75X6	8Ls−65X65X6
Main bar	12−D25	12−D22	12−D19	
Hoop	Center: 9Φ@300 Top&Bottom: 9Φ@150			

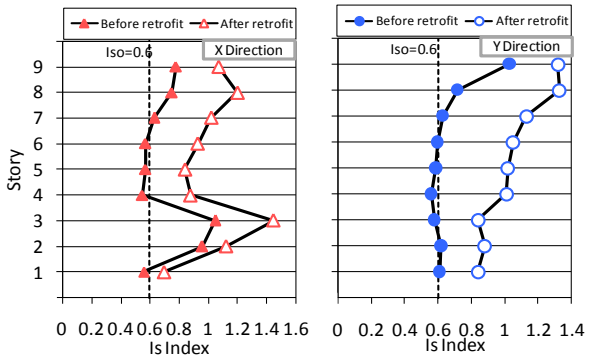
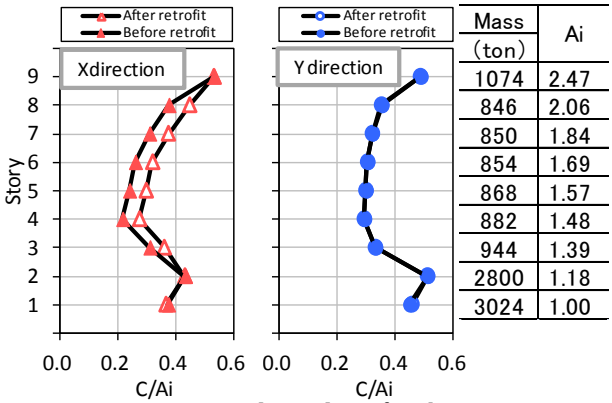


Figure 4 I_s index of each story



Mass (ton)	Ai
1074	2.47
846	2.06
850	1.84
854	1.69
868	1.57
882	1.48
944	1.39
2800	1.18
3024	1.00

Figure 5 C index and Ai of each story

Disaster Prevention Association) standard, Japanese Standard for Seismic Capacity Evaluation of Existing Reinforced Concrete Building, (JBDPA 2001b) to the building in order to evaluate seismic capacity and to decide seismic retrofit scheme.

I_s-Index which represent seismic performance of structure can be calculated by Eq.(1) at each story and each direction according to the standard. E_0 is a basic structural index calculated by Eq.(2).

$$I_s = E_0 \times S_D \times T \quad (1)$$

$$E_0 = 1/A_i \times C \times F \quad (2)$$

C-Index is strength index that denotes the lateral strength of the buildings in terms of story shear coefficient which namely the shear normalized by weight of the building sustained by the story. *F*-Index denotes the ductility index of the building ranging from 1.0 (brittle) to 3.5 (very ductile) in case of SRC building, depending on the sectional properties such as bar arrangement, member proportion, shear-to-flexural-strength ratio etc. *Ai* is The distribution of lateral forces along the height of the building is based on the *Ai* distribution(see Eq.(3)) prescribed in the AIJ provision (AIJ 1999).

$$A_i = 1 + \left(\frac{1}{\sqrt{\alpha_i}} - \alpha_i\right) \times \frac{2T}{1+3T} \quad (3)$$

where: α_i is ratio between the total weight supported by story *i* to the total weight of building, *T* is 1st natural period

S_D and *T* are reduction factors to modify E_0 considering of structural irregularity and deterioration after construction, respectively.

The Seismic Evaluation Standard recommends as the demand criterion that I_s-Index higher than 0.6 should be provided to prevent major structural damage or collapse.

Figure 4 shows the I_s-index of all stories for both before and after retrofit. This building was retrofitted because I_s-index was less than 0.6 for most stories.

It should be noted that the *F* index (ductility index) used here was 3.5 assuming the building has very ductile flexural walls.

Figure 5 shows the *C*-index /*Ai*. 1st and 2nd stories have higher lateral strength (*C*/*Ai*=0.4~0.5) than upper stories in both directions. In the Y direction, 3rd-8th story have approximately the same *C*/*Ai* value (=about 0.3). *C*/*Ai* =0.3 is the minimum requirement for RC buildings in the current seismic code in Japan

Figure 6 shows the *C*-*F* curve of 3rd story. Both directions have *F*=3.5, and the building was stronger in X direction than in Y direction. In Y direction, the strength index is as low as 0.29.

2.3 Scheme of seismic Retrofit

According to the seismic evaluation results, seismic capacity I_s-index was insufficient to requirement of I_s=0.6 and was classified as a retrofit candidate. In 2001, the building was seismically retrofitted by installing framed

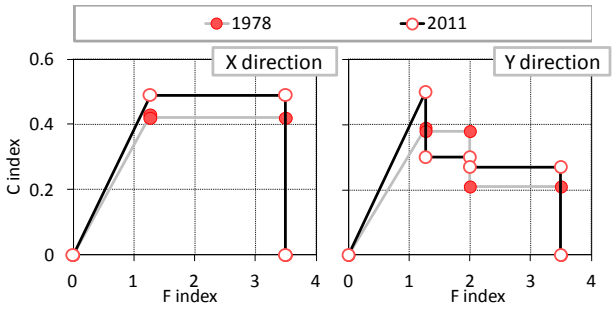


Figure 6 3F C-F curve

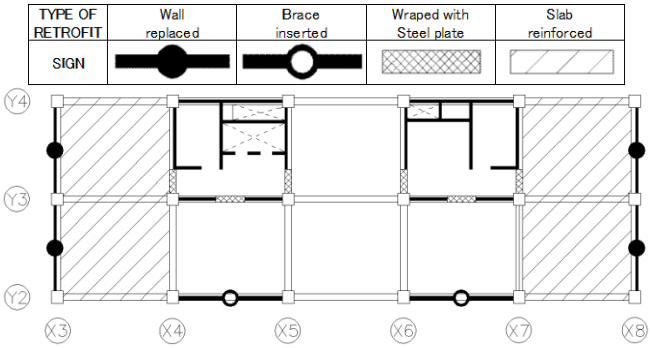


Figure 7 Part of retrofit

Table 2 List of replaced Wall

Floor	After retrofit			Before retrofit	
	Wall thickness (mm)	Arrangement of bar	Arrangement of anchor	Wall thickness (mm)	Arrangement of bar
9					
8	180	D10･13-@200 S	D13-@100 S	150	9Φ @200 S
7					
6					
5	200	D13-@200 D		200	9Φ @200 D
4					
3	250	D13-@150 D	D13-@150 D	250	

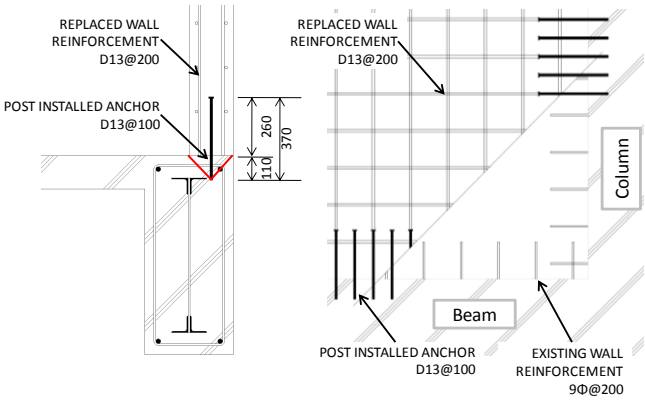


Figure8 Detail of replaced wall

steel braces in the longitudinal direction, replacement of RC shear walls in transverse direction (frame X3 and X8) from 3rd to 9th story, and jacketing of adjacent short beams with steel plates to avoid shear failure, as shown in Figure 7. The main scheme of the seismic retrofit was to increase I_s index (seismic performance index) to meet the criteria of $I_s \geqq 0.6$. The retrofit plan was to increase the ductility of the transverse direction by replacing the exterior shear walls (which had cracks from previous earthquakes) with new exterior shear wall. However, the story shear coefficient *C*-index is not increased (0.3 or less) even after retrofitting.

As for the longitudinal direction, steel braces were installed to reduce the torsion vibration induced by the irregularity of the structure in this direction.

The reinforcing details of the panels replaced in walls X3 and X8 are shown in Table 2 and Figure 8. These wall panels were replaced as follows:

1) the original concrete was removed with jack hammers,
2) 310-mm long adhesive anchors (D13 bars) with an embedment length of 110 mm were installed in beams and columns,
3) existing reinforcing bars (round 9-mm plain bars) were cut 200 mm away from beam and column faces,
4) new reinforcing bars (deformed 13-mm bars) were spliced with the adhesive anchors in both the longitudinal and horizontal directions.
5) concrete was cast in the wall panel.

It is important to emphasize that development length of post installed anchors were 110mm according design document for seismic retrofit design. The length of anchor met the guidelines for seismic Retrofit of Existing Reinforced Concrete Building (JBDPA 2001). However, the tensile strength of anchor is conditioned on cone shaped fracture, as can be seen in Figure 8.

3. OBSERVED DAMAGES

3.1 Earthquake history

The building has experienced many earthquakes. Table 3 shows Accelerations during some of previous major earthquakes. The largest one is Miyagi Oki earthquake 1978 (Magnitude 7.4) and 2011 Great East Japan earthquake (Magnitude 9.0).

The maximum observed accelerations on the 1st floor in 1978 Miyagi Oki earthquake and 2011 Great East Japan earthquake were 258gal and 333gal, respectively. The maximum observed acceleration on the 9th floor were 1040gal and 908gal, respectively.

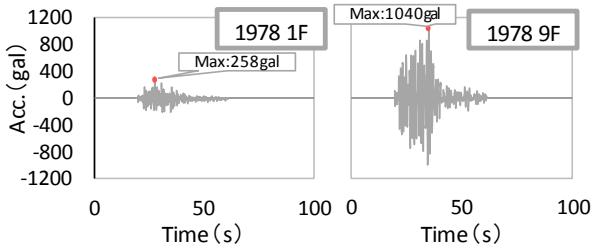
Comparing the two seismic records, one of the main characteristics of 2011 Great East Japan earthquake is long duration of about 180 seconds. Comparison of acceleration time history on 1st and 9th floor of the 1978 and 2011 earthquakes is shown in Figure 9.

Figure 10 shows the Displacement time history, and Figure 11 zooms into the record obtained in 2011 at times between 80 and 88 sec. The Figure has two interesting features:

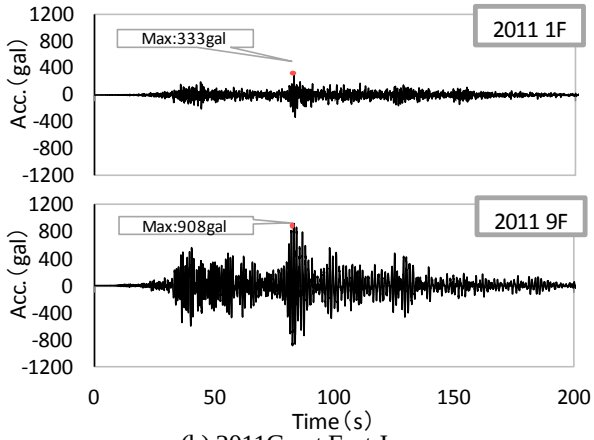
1) the period of the building was close to T=1 sec. before t=82.7 sec., and T=1.2 sec. after t=84 sec.

Table 3 Observed earthquake
(1st floor Acc. over 150gal)

y/m/d	Magnitude	1F maximum Acc.(gal)	9F maximum Acc.(gal)
1978/2/20	6.7	170	421
1978/6/12 (Miyagi Oki)	7.4	258	1040
1998/9/15	5.2	451	379
2011/3/11(East Japan)	9.0	333	908

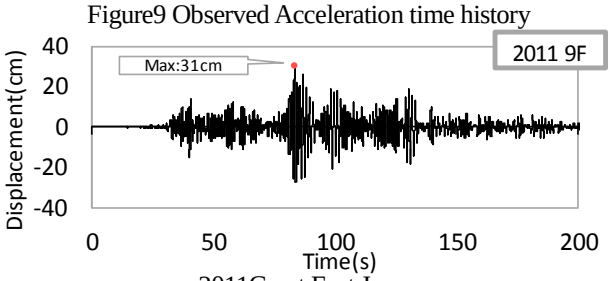


(a) 1978Miyagi Oki



(b) 2011Great East Japan

Figure9 Observed Acceleration time history



2011Great East Japan

Figure10 Observed Displacement time history

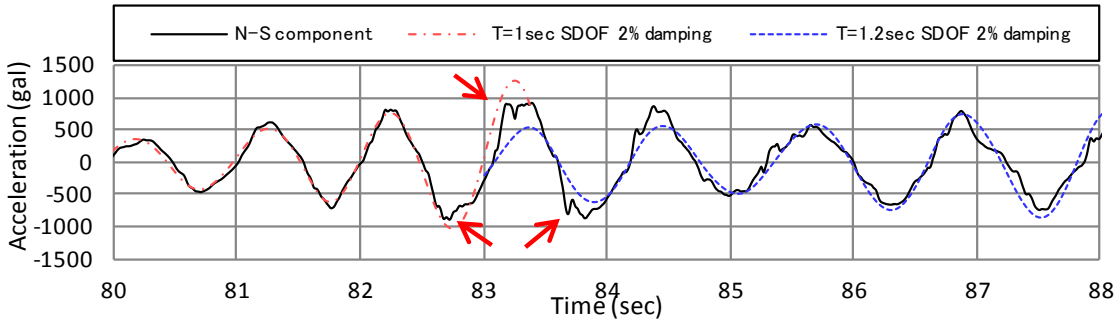


Figure 11 Zoom viewing of Acceleration time history

2) there were sudden drops in acceleration (marked with red arrows) at t=82.7, 83.3, and 83.8 sec.

These features may be evidence suggesting that something of consequence occurred in the structure as time approached and exceeded 83 sec. Integrating the record from 2011 until t=82.7 sec. leads us to believe that, up to that point, the displacement at the ninth floor had not exceeded 20 to 25 cm. Later the building may have reached displacements approaching 30 to 35 cm. Of course, we express our estimates as ranges because the integration is not a simple procedure and it required us to "adjust" the signal (by filtering it and shifting it) before we obtained results that we judged to be reasonable.

Figure 12 shows acceleration response spectra computed for both records (1978 and 2011) using a damping coefficient of 5%. In the NS direction, the two spectra are strikingly similar. The same is true for displacement spectra. It is reasonable to conclude that these two earthquakes produced comparable demands on the building in the N-S direction. This conclusion is supported by two observations:

1) The maximum displacement reached before t=82.7 sec. in 2011 was inferred not to have exceeded 20 to 25 cm. After t = 82.7 sec. the building exhibited abrupt softening and su dden drops in lateral acceleration indicating the possibility of local failures.
2) The maximum displacement inferred from the 1978 record was approximately 20 cm.

However , even though the demands appear to have been similar (according to two separate pieces of evidence), the observed damage was completely different in 1978 and 2011, especially in N-S direction.

3.2 1978 Miyagi Oki earthquake

Detail damage survey was conducted after the 1978 Miyagi Oki earthquake by professors Shiga and Shibata, Tohoku University (Shiga et al. 1981). According to their report, small shear cracks and flexural cracks were observed in exterior shear walls(see Figure 13), adjacent beams and a few columns on the third and fourth floor. Typical wall and short beams crack patterns are shown in Figure14 and 15. The maximum width of shear cracks in shear walls and that of flexural cracks in columns and beams are reported about as 1.0mm. The width of shear cracks in the adjacent beams with openings was reported about as 1.5mm. Therefore, the structural damage of the building by the 1978 June earthquake, was considered to be fairly minor. As can be seen in Figure 15, exterior shear wall successfully sustained lateral force and contributed as shear resisting elements, because shear cracks were relatively uniformly distributed in the wall panels.

3.3 2011 Great East Japan Earthquake

The authors carried out detailed damage surveys of the building after the 2011 earthquake. The most severe damage took place in the 3rd story. Four corner boundary columns in exterior walls X3 and X8 (which were intervened in 2001)

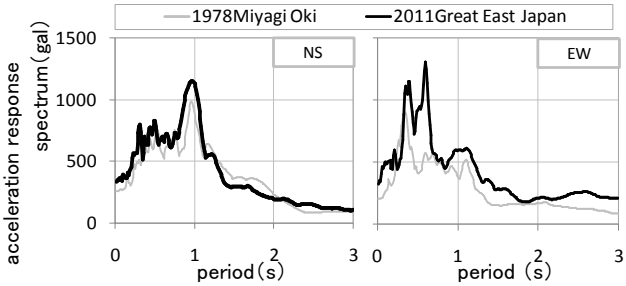
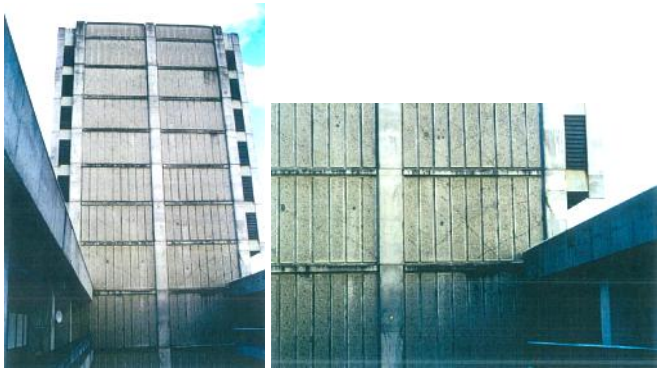
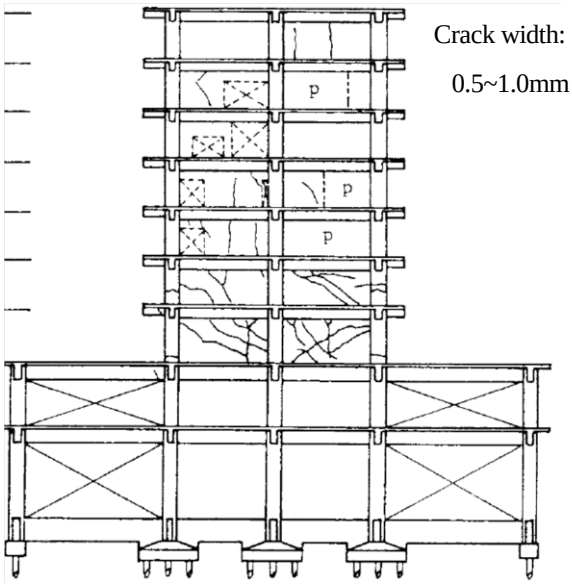


Figure 12 5% damping acceleration response spectrum



(a)All (b) 3rd Floor

Figure 13 Damaged wall in 1978 Miyagi Oki



X8 axis

Figure 14 1978Miyagi Oki earthquake crack map (Shiga et al 1981)

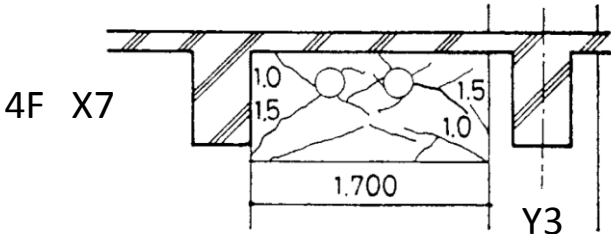


Figure 15 Damaged short beams

fractured as shown in Figures 16 and 18a). A close-up of the disintegrated near their bases, and the steel angles and reinforcing bars embedded in them either buckled or base of column X8-Y2 is shown in Figure 17.

Figure 18 shows cracks observed on the exterior walls in the transverse direction. A horizontal separation formed at the base of the third story, between the post-installed structural wall panels (shown in Figure 18b)) and the beam supporting them. The post-installed anchors that were supposed to prevent this separation appeared to have pulled out of the beam as shown in the close-up in Figure 18c) and Figure 19.

Along axes X4 to X7, shear cracks with widths of up to 1.7mm were observed on "wing walls" or "stems" forming the staircases in all stories. Spalling of concrete and a large horizontal crack were also observed at the 3rd floor level (Figure 18d), e)). The damage and cracks of the wing walls indicate the interior C-shape walls remained integral and were effective in resisting lateral loads.

In the longitudinal direction, the damage concentrated on the walls, which had cracks of 0.2~0.5mm in width as shown in Figure 20. These walls also remained integral and were effective in resisting lateral loads. Additionally, there were horizontal cracks at the 3rd story.

Even though the bases of exterior boundary columns disintegrated, the webs of the exterior walls had little (or imperceptible) cracking in the 2nd to 3rd stories, and thin cracks (0.1~0.2mm) elsewhere. Comparing the damage caused to these walls by the Earthquakes of 2011 (Figure 18) and 1978 (Figure 14) suggests that there was a radical change in the mechanism through which these walls resisted lateral loads. It seems that in 1978 the exterior walls acted as units (composed of webs and columns connected to integrally), while in 2011 the webs did not seem to contribute much to lateral resistance. This inference and the followings facts:

1) the demands in 1978 and 2011were similar,
2) the steel braces installed in axis Y2 must have reduced problems related to torsion,
3) anchor rods installed in 2001 were observed to have pulled out,

led us to the focus on the connection between wall webs and 3rd floor beams.



Figure17 X8-Y2 column after remove the crush concrete

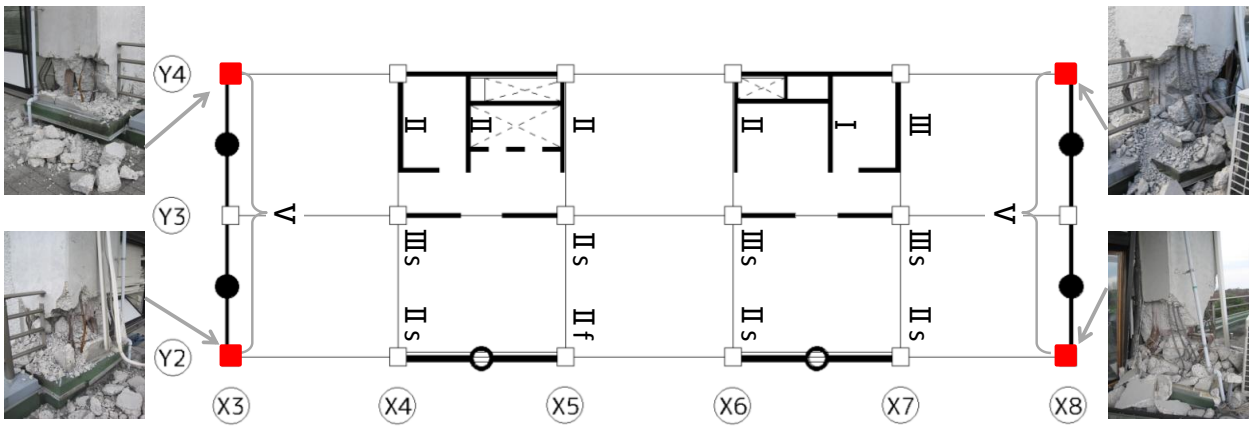
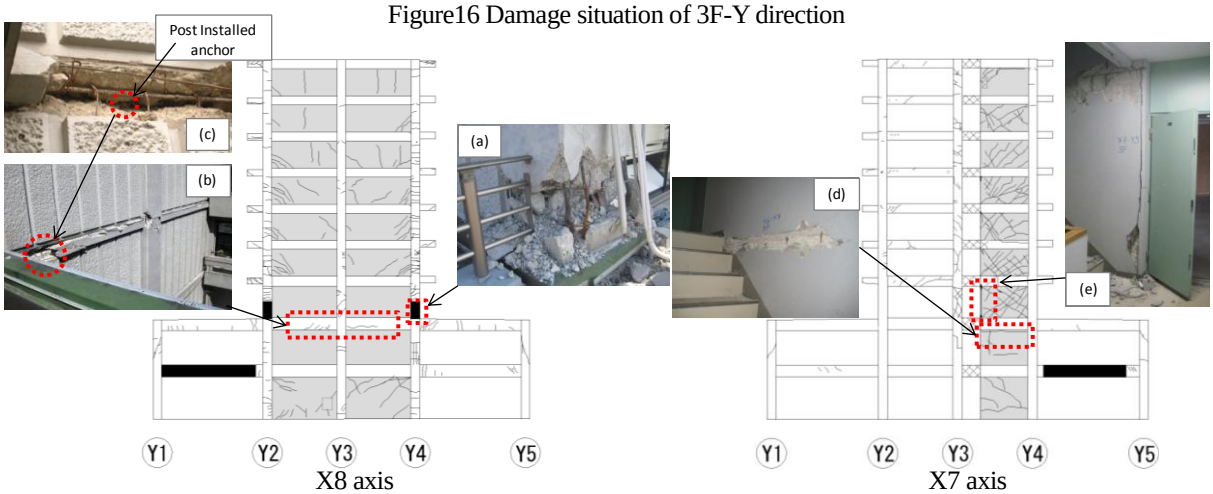


Figure16 Damage situation of 3F-Y direction



X8 axis X7 axis

Figure 18 2011Great East Japan earthquake crack map (transverse)

Figure 21 illustrates a plausible explanation for what occurred:

1) The anchor bolts installed in the retrofit had an extremely short embedment length
2) The existing reinforcement was smooth, and was cut too close to the beam face to develop its strength through bond (gained mainly through adhesion to the concrete cast in 2001)
3) If one draws lines from the bottom of the anchor bolt in Fig. 8 to the points where the wall outer and inner faces meet the cold joint at the top of the slab, one obtains a "surface" that is not crossed by any reinforcement working in tension and adequately anchored.
4) The result of 1), 2) and 3) was that, at the tops of the slabs and at every floor, the vertical web reinforcement was essentially discontinuous.
5) The discontinuity in the web reinforcement caused rotations to concentrate at the top of the third-floor slab causing the steel angles and reinforcing bars in the boundary elements to reach large tensile strains.(see Figure 19) These strains led to either fracture or buckling during load reversals.

It is believed that it was the buckling of the steel what triggered the disintegration of the concrete at column bases because even the exterior columns along axis Y3 exhibited bar buckling and spalling of concrete despite the fact they resisted no compression at peak displacements. Sliding could have damaged these columns too but no clear signs of sliding at wall bases were observed. If compression had been the trigger, we would have expected severe spalling and crushing (similar to what was observed at columns in axes X3 and X8) in the stems of the C-shaped walls that formed the staircases. That did not occur. The stems of the staircase walls did have some spalling but it was limited to the concrete cover.

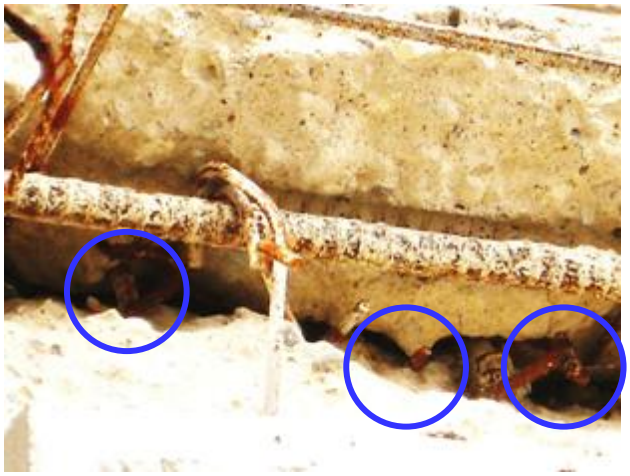


Figure 19 Zoom viewing of wall anchor

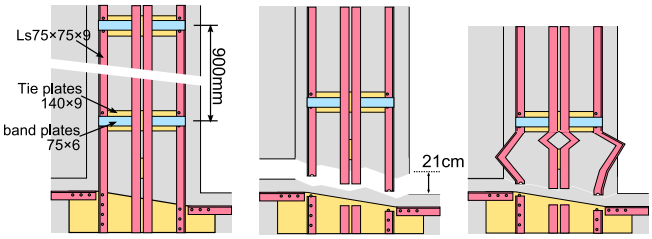
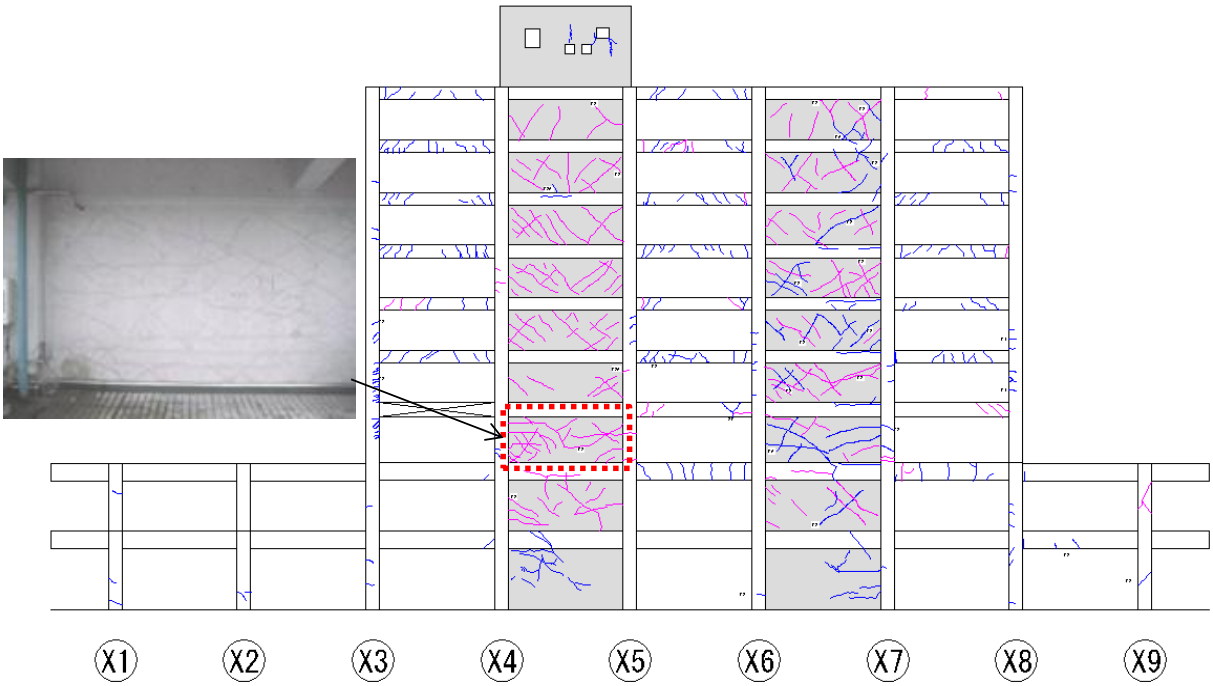


Figure 21 Mechanism of Column crushed



Y4 axis

Figure 20 2011Great East Japan Earthquake crack map(longitudinal)

4. EVALUATION OF SEISMIC CAPACITY AND FAILURE MECHANISM

4.1 Estimate the failure mechanism

The mechanisms of failure for the main structural elements (the walls) were dominated by flexure. Eventually, the ground motion caused the steel angles and reinforcing bars in boundary columns in axes X3 and X8 to buckle and fracture, and the anchor rods meant to fasten the webs to the beams were pulled out. At that point, the response of the exterior walls approached the response of a rocking block. This rocking behavior was inferred by Motosaka (2012) from wave analysis. If the lateral displacement on the ninth floor reached 31 cm, the uplift must have approached 21 cm . Walls and frames along column lines X4 to X7 are not suspected to have uplifted because their vertical reinforcement was continuous and well anchored.

4.2 Lateral strength using virtual work method

Lateral capacity of the frames in the transverse direction was checked using virtual work method. The following assumptions were considered:

・1st to 2nd stories are assumed to be stiff and strong, and acted as the base of the upper part of the building.

Assumption through X3・X8 axes

- The wall will break and rotate at the base of 3rd floor (see Figure 22a)).
- The strength of the wall reinforcement are assigned in the center of wall.

Assumption through X4 to X7 axes

- The seismic lateral forces were applied in different direction (from North to South and from South to North) because the wing walls strength will be different.

Two different cases are considered: Case 1 considers the exterior installed wall effective and behaved exactly as it was expected in the seismic evaluation . In Case 2, the steel in the boundary column is ignored and the wall reinforcement is 50% ineffective because the boundary column have already yielded and wall reinforcement were easily pulled out. Table1 shows the different assumptions of each case.

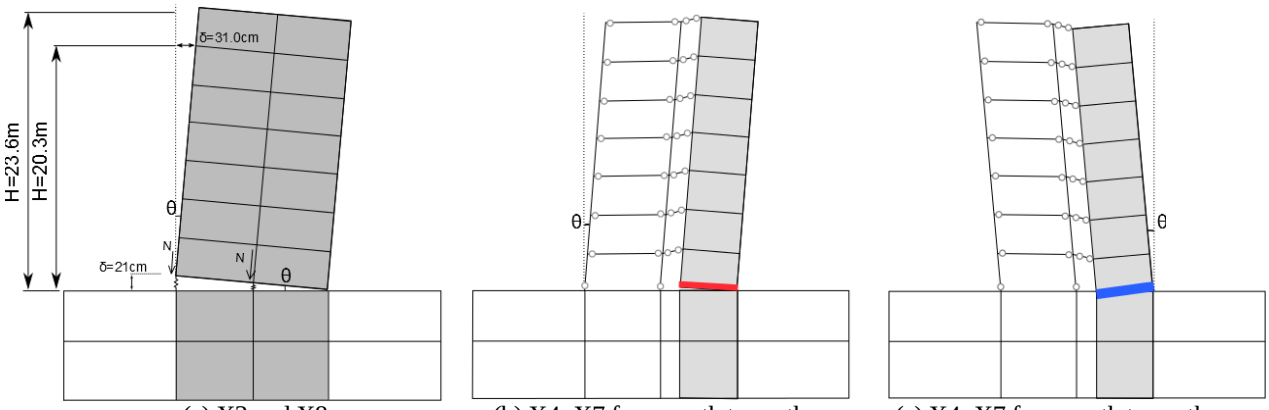
As it shown in the Figure 23. The difference between the two cases is more than 30% of the total strength. This building depends mainly on these exterior installed walls. Any poor detailing of the installed walls shall led to dramatic damage.

4.3 Capacity spectrum method

Two-dimensional “push-over” analyses were conducted using the computer program SNAP (version6, 2012). The analyses referred exclusively to the transverse direction. The structure is modeled from 3rd~9th story. The 1st and 2nd story are very stiff with many walls and were assumed as the base of the upper stories. 2 cases were considered; 1978 model and retrofitted model of 2011. The shear versus

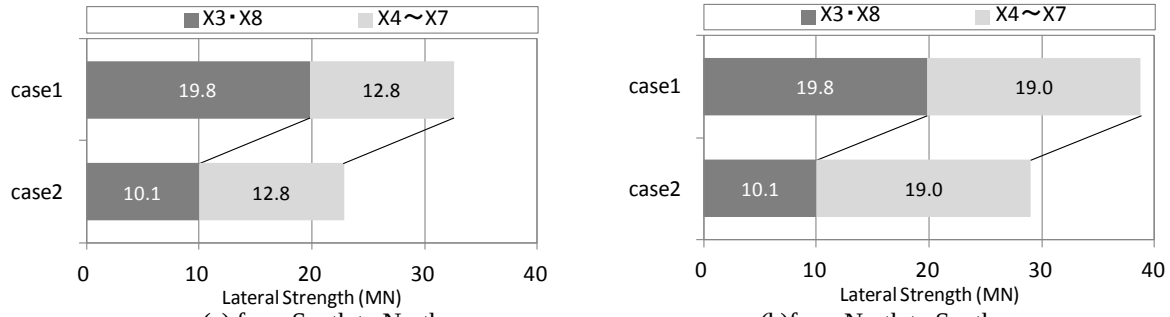
Table 4 Assumption of Virtual work method

Model ID	AxesX3 and X8		
	Location of Wall Hinges	Vert.column Steel	Vert.Web Steel
case1	3rd Story Base	Continuous	Continuous
case2		Ignored	50% ineffective



(a) X3 and X8 (b) X4~X7 from south to north (c) X4~X7 from north to south

Figure 22 Estimated building collapse mechanism



(a) from South to North (b)from North to South

Figure 23 Lateral strength at 3rd floor

displacement relation of each story was converted to a single degree of freedom system expressed in spectral acceleration and displacement (Sa-Sd) relations using the procedure of the performance based method used in Japan(JABRP 2000). Eq.(4), Eq.(5), Eq.(6) and Figure 24 shows the concept of conversion to SDOF.

$$M = \frac{\left(\sum_{i=1}^{N} m_i.\delta_i\right)^2}{\sum_{i=1}^{N} m_i.\delta_i^2} \quad (4)$$

$$S_a = \frac{Q_1}{M} \quad (5)$$

$$S_d = \frac{\sum_{i=1}^{N} m_i.\delta_i^2}{\sum_{i=1}^{N} m_i.\delta_i} \quad (6)$$

where: m_i=lumped mass in the i-th story, Q_1=base shear and δ_i=horizontal displacement at i-th story

The capacity spectra (Sa-Sd) of building are plotted with response spectra of the 1978 earthquake and 2011 earthquake with 5%~20% damping. (see Figure 25).

The dotted horizontal line in Figures 25b) shows the lateral strength capacity that was previously calculated using the virtual work method for case 1 stated previously. The ultimate strength of pushover and the lateral strength by virtual work method of case 1 showed good agreement

The maximum horizontal displacement was evaluated by double integration of acceleration records observed on the 9th floor. The recorded maximum displacement at the 9th floor for the two earthquake cases (1978 EQ and 2011 EQ) is converted to the spectral displacement Sd and plotted in in Figure 24. using assumed equivalent height of the SDOF. Specifically, the 9th floor recorded deformation are converted to the equivalent height deformation by assuming the distribution of deformation as inverted triangle from 3rd~9th(see Figure26) and the equivalent height is assumed at 0.8H (=18.8m).

Using capacity spectrum method, in the case of 1978 earthquake, the estimated response drift was about 15 cm and the calculated displacement was about 23 cm, in the case of 2011 earthquake, the estimated response drift was about 18 cm and the calculated displacement was about 29 cm, each model have big difference between estimate and recorded deformation. The difference between the two values might be caused due to the rocking at the base and unique failure mechanism of this building.

However, further investigations involving different cases of structure models are needed to have better simulation of the actual damage, such as cases assuming the vertical web reinforcement of exterior transverse wall ineffective.

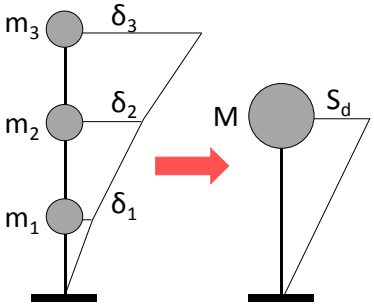


Figure 24 Concept of convert to SDOF

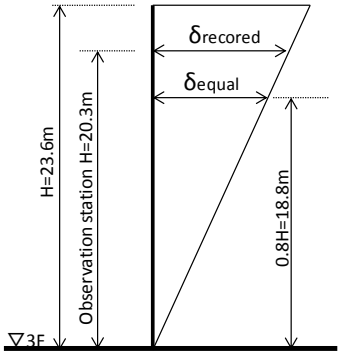
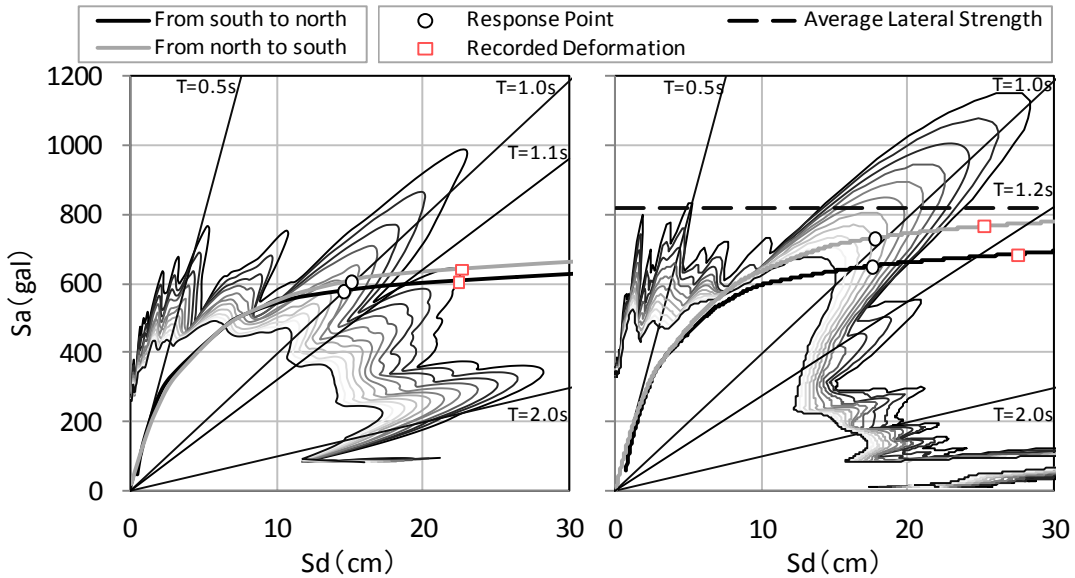


Figure 26 Deformation of equivalent height



(a) 1978 Miyagi Oki (b) 2011 Great East Japan

Figure 25 Result of the pushover analysis

5. CONCLUSION

Considering:

1. The similarities between the response spectra of the N-S components of the 2011 Great East Japan earthquake and the 1978 Miyagi earthquake. However both of damage is completely difficult.
2. The distribution of cracks and spalling throughout the building
3. Observations indicating that the vertical web reinforcement connecting walls to beams pulled out during the 2011 earthquake

We conclude that discontinuities in the vertical web reinforcement caused concentrations of rotation at the 3rd floor level which led to buckling and fracture of the vertical reinforcement in exterior wall boundary elements. This damage resulted in the evacuation and demolition of the structure.

In additional, the capacity spectrum method of both cases(1978 and 2011) couldn't estimate the actual displacement. This point needs further investigations and will be studied thoroughly in the near future.

6. FUTURE WORK

Experiments are being conducted to test the hypothesis that the discontinuity in the reinforcement at the base of the 3rd story led to the failures of the exterior columns.

The experimental program consists of six small-scale structural-wall models with identical cross-sectional properties. The web reinforcement in three specimens is cut off at the base of the wall, while in the other three specimens web reinforcement is well anchored in the foundation. Two specimens will be tested under static loading reversals and four specimens will be tested using an earthquake simulator at Bowen Laboratory, Purdue University.

References:

Shiga, Toshio, Akenori Shibata, Jun'ich Shibuya, and Jun'ich Takahashi.(1981)."Observations of strong earthquake motions and non linear response analyses of the building of architectural and civil engineering department , Tohoku University", Transactions of architectural Institute of Japan, No.301, 119-130. (in Japanese and English abstract)

Motosaka, Masato.(2012)."Lessons of the 2011 Great East Japan earthquake hocused on characteristics of ground motions and building damage", Proceedings of the International Symposium on Engineering Lessons Learned from the 2011 Great East Japan Earthquake, 166-185.

Kimura, Hideki, Hirabayashi Masataka, Ishikawa Yuji,Tanabe Yusuke, Maeda Masaki, and Ichinose Toshikatsu(2012)." Investigation on Buildings in Tohoku University Damaged by the 2011Great East Japan Earthquake Part3 and Part4 Study on Building of Civil Engineering and Architecture by Earthquake Response Analysis ", Architectural Institute of Japan.(in Japanese)

Japan Building Disaster Prevention Association(JBDPA). (2001). "Seismic Evaluation and Retrofit".

Architectural Institute of Japan (AIJ). (2004)."Guidelines for Performance Evaluation of Earthquake Resistant Reinforced Concrete Buildings" (Draft).(in Japanese)

Kozo System, (2012) "SNAP Version.6 Technical manual " (in Japanese)

Japan Association for Building Research Promotion, (2000) "Concept of Performance oriented Design for Building Structure - Prescribed Provisions to Performance Provisions" (in Japanese)

10CUEE CONFERENCE PROCEEDINGS
10th International Conference on Urban Earthquake Engineering
March 1-2, 2013, Tokyo Institute of Technology, Tokyo, Japan

PREPAREDNESS BEFORE DISASTER IN TOKYO URBAN AREA

Nam-Yi YUN[1)], and Masanori HAMADA[2)]

1) Ph.D. Candidate, Dept. of Civil and Environment Engineering, Waseda University, Japan
2) Professor, Dept. of Civil and Environment, School of Science and Engineering, Waseda University, Japan
namyiyun@toki.waseda.jp, hamada@waseda.jp

Abstract: We investigate a pre-disaster preparedness against predicted earthquakes in Tokyo area using a survey. It examines (a) the role of direct experience of the 2011 Great East Japan earthquake in preparedness against the predicted earthquake; (b) the impact of participation in disaster prevention training, indirect experience with disasters, on pre-disaster preparedness. Results indicate that pre-disaster preparedness differs from the participants and non-participants in the training, and it is shown more in the participants verses the non-participants. Also, females are more likely to have taken more preparations than males while the experience of damage had an insignificant effect on the disaster preparedness behavior. These results contain insights for managing risks to reduce the human damages in future disasters.

1. INTRODUCTION

Disasters caused more than 3.3 million deaths and US$2.3 trillion in damage (in 2008 US dollars) between 1970 and 2010 (World Bank, 2010). The growth of urban population drives exposure to natural hazards ever higher. By 2050, if current trends continue, the urban population exposed to earthquakes and storms could more than double to 1.5 billion (from 680 million in 2000 to 1.5 billion in 2050).

No country can fully insulate itself from disaster risk, but it is possible to reduce human loss from it. Success depends heavily on how well residents in the area are prepared (Sendai Dialogue, 2012). An accurate prediction of disasters is the first step in preparedness for the disaster reduction against future events. Moreover, the most important step of disaster preparedness is to execute at an individual level.

On March 11, 2011, a gigantic earthquake of magnitude 9.0 struck off the Pacific coast of Tohoku, Japan (the Japan Meteorological Agency, 2011), leaving 15,867 dead and 2,909 missing (the National Police Agency, July 11, 2012). Over 90% of the dead drowned due to the earthquake induced tsunami.

In fact, before the occurrence of the Great East Japan earthquake, the Central Council of Japan for Disaster Prevention had been giving five big earthquake warnings, which has a high probability of occurrence in the near future and may cause a serious damage. Those are Tōkai (Magnitude: 8.0), Tōnankai (Magnitude: 8.1), Nankai (Magnitude: 8.4) earthquakes along the Nankai Sea Trough in the Pacific Ocean, and Northern-Tokyo Bay earthquake (Magnitude: 7.3). Also, Off-Miyagi Prefecture earthquake is estimated as a medium size earthquake of magnitude 7.5; but it actually occurred with magnitude of 9.0, that is 180 times larger than the predicted earthquake (Hamada and Yun, 2011). Therefore, after the 2011 Great East Japan earthquake, Japan revised an estimation of damages by the predicted earthquake in Tokyo area.

In addition to the effort of prediction, it showed that actual evacuation by residents was important to be saved. Although the Japan Meteorological Agency (JMA) first issued a tsunami warning three minutes after this earthquake to maximize time for evacuation and to reduce casualties (Ozaki, 2012), more than 40% of the residents did not or could not evacuate from the tsunami in an inundate area (Yun and Hamada, 2012).

In Tokyo area, persons have experienced a strong shaking by the 9.0-magnitude earthquake and over 1,000 aftershocks since the earthquake. Moreover, approximately 5.15 million of persons in Tokyo Metropolis and four prefectures - Kanagawa, Chiba, Saitama, and Ibaraki - could not go back home by the 2011 Great East Japan earthquake. The residents have an unforgettable experience and some loss of their resources.

Therefore, the aim of this study is to empirically examine a relationship between the experience with the huge disaster, the 2011 Great East Japan earthquake, and pre-disaster preparedness. Furthermore, it examines an impact of participating in a disaster prevention training related to the pre-disaster preparedness.

2. PREPAREDNESS BEFORE DISASTER

2.1 Tokyo Urban Area

Tokyo (東京, Tōkyō) is Japan's capital and the world's most populous metropolis. The population of the special wards is over 8 million people, with the total population of

the prefecture exceeding 13 million. The prefecture is part of the world's most populous metropolitan area with upwards of 35 million people. The mainland portion of Tokyo lies northwest of Tokyo Bay and borders Chiba Prefecture to the west, Kanagawa to the south, and Saitama to the north. During the daytime, the population swells by over 2.5 million as workers and students commute from adjacent areas. This makes Tokyo as the Japan's largest domestic and international hub for rail, ground, and air transportation.

As the world's largest urban agglomeration economy with a GDP of US$1.479 trillion at purchasing power parity in 2008, ahead of New York City metropolitan area, which ranks second on the list, it is critical how to predict and manage risks from the expected disasters such as earthquakes.

2.2 Disaster Predictions

After the 2011 Great East Japan Earthquake, the Tokyo Metropolitan Government's Disaster Prevention Council revised and issued a 'report for an estimation of damage caused by predicted earthquakes in Tokyo area' on April 18, 2012. According to its new issued estimate, 9,700 people may be dead and 304,300 buildings may be damaged by the 7.3-magnitude Northern-Tokyo Bay earthquake under a dry weather and 8m/sec wind speed condition. Approximately 5,600 people would be dead from shaking of the earthquake and buildings being crushed (accounted for approximately 58% of the casualties by the earthquake), and about 3,500 people estimated to be dead from fire.

In addition, a number of persons who have difficulties in getting home by the earthquake reaches (in Japanese 帰宅困難者) approximately 5.17 million compared to that of the approximately 5.15 million people who could not return home on March 11, 2011 in Table 1(首都直下地震帰宅困難者等対策協議会, 2012).

Table 1 The difficulties of returning home on March 11, 2011

Area	Numbers of persons having difficulties in returning home	Percentage of difficulties in returning home out of the total persons who were out of their homes
Tokyo Metropolis	3.52 million	40 %
Kanagawa	0.67 million	20 %
Chiba	0.52 million	24 %
Saitama	0.33 million	14 %
Ibaraki	0.10 million	16 %
Total	5.15 million	30 %

The number of persons who have difficulties in getting home refers to both persons who gave up to go home due to far distance and persons who tried to go back home on foot when there was a situation in which transportation was disrupted by disasters. As a broad definition by the Central Disaster Prevention Council in Cabinet Office of Government of Japan, within 10km distance from one's home is a distance in which they can go home, but more than 10km, persons have difficulty returning home. Within 20km distance, 10% of the number has increased by every 1km, and over 20km distance, everyone is difficult to return home on foot.

The Northern-Tokyo Bay earthquake with a magnitude 7.3 could worsen this situation because a recovery of transportation might be delayed. Therefore, it is necessary to emphasize keeping supplies as disaster preparedness.

2.3 Preparedness Before Disaster

Preparedness before disaster, according to Banerjee and Gillespie (1994a), "…refers to a series of activities which directly or indirectly should mitigate loss of life and property in disaster"; "…is predicted on the assumption that disasters of various forms will occur, but that their negative consequences may be reduced" (p.131). In other words, pre-disaster preparedness is a preplanned activity to reduce loss of life, and a basic assumption underlying the activities is that they contribute to response effectiveness.

Several studies on disaster preparedness have been examined with mixed results. Shelby and Tredinnick (1995), for example, found that someone who survives an earthquake may gain knowledge about the potential destruction to come; the value and benefits of preparation and evacuation; how to recover in its aftermath; or develop an enhanced sense of self-efficacy, new skills, and new ways of coping with subsequent disaster threats. Furthermore, someone who has taken actions to minimize damages, secure his or her family's safety, or replace lost or damaged possessions may develop an enhanced sense of self-esteem, self-efficacy (personal characteristic resources), and stronger bonds among family and community members (condition resources). Therefore, when individuals perceive risks of disasters and believe that their well-beings will be threatened, then they are likely to engage in preparedness behaviors. Additionally, individuals who feel capable of dealing with a possible future disaster are willing to initiate in preparedness behaviors. In contrary, simply being aware of risks does not seem to be a strong factor for a good predictor of preparedness behaviors (Faupel, Kelley and Petee, 1992).

Hench, we investigate preparedness before disaster, calculated based on replies to "What have you done for preparedness before disaster regarding the following categories?"

1. Keeping supplies: food, water, first-aid kit, clothing
2. Stabilizing furniture
3. Getting hazard-related information
4. Making a plan to meet up with family after disasters
5. Structurally strengthening the building

2.4 Experience With Disasters

2.4.1 Direct Experience with the 2011 Great East Japan Earthquake

Numerous studies have shown that previous experiences with disaster are positively related to preparedness (Banerjee and Gillespie, 1994b). In other words, there are some evidences about a tendency to be better trained and knowledgeable in disaster as a result of previous experience with disasters.

Although the 2011 Great East Japan earthquake caused 31 death in the Tokyo area (issued by the National Police Agency on July 11, 2012), persons in Tokyo area have experienced some loss of their home, car, furniture, etc. due to unforgettable strong shakings.

When confronted with a new disaster threat, persons with disaster experience – especially those who experienced higher levels of resource loss and psychological distress – would (a) be more likely to acknowledge a disaster threat, (b) readily experience psychological distress, and (c) efficiently choose appropriate courses of action than persons who have experienced lower levels of resource loss or distress as result of a disaster, or persons who do not have disaster experiences (Hobfoll, 1989).

Previous research provides positive evidence for the role of disaster experience in the context of disaster preparedness (Hobfoll, 1989; Freedy, Shaw, Jarrell, and Masters, 1992). For example, persons who live in areas that are frequently threatened by natural disasters may be more likely to acknowledge that a threat exists (Lindell and Perry, 2000), to take more preventive measures, and to comply with warnings than persons who are infrequently threatened by disasters. Disaster survivors who experience higher levels of property loss and psychological distress may be more attentive to news reports and have a better understanding of the destructive consequences of disasters than the survivors who experience lower levels of property loss and distress, or persons who have not experienced a disaster (Sattler, Kaiser, and Hittner, 2000).

Accordingly, this study examined the importance of range of adverse experiences of resource loss on individual adjustment following a natural disaster.

Hypothesis 1: Those who experienced damages by the 2011 Great East Japan earthquake are more willing to take the disaster preparedness behavior compared with the group that did not.

2.4.2 Disaster Prevention Training

Growing out of their indirect experience with disasters, it assumes that disaster prevention training positively affects preparedness behavior. In order to enhance viability against disasters, a disaster prevention training covered mitigation, preparedness and response aspects of natural disaster occurrence.

In Japan, the Ministry of Education, Culture, Sports, Science and Technology of Japan (MEXT) has been developing and implementing disaster education to foster the viability of disasters. As a result, while casualties number nearly 1,000 in Kamaishi and Kesennuma, 5 out of 3,244 children and 12 out of 6,054 students, respectively, are victims of the 2011 Great East Japan disaster. There is some more evidences to suggest that exposure to the education may increase knowledge of the threat and lead to more pre-disaster preparedness.

However, according to Faupel et al. (1992) stated that for any number of reasons, knowledge learned in disaster education programs does not always translate into appropriate behavior. In other words, we cannot presume that even if people know what to do in a disaster that they will necessarily act on the basis of that knowledge.

In this study, therefore, participant in the disaster prevention training and non-participant, as a dummy variable, are used. Responses from the participants are marked as '1', and non-participants are marked as '0'.

Hypothesis 2-1: Pre-disaster preparedness is shown more in the participants verses non-participants in the disaster prevention training.

Hypothesis 2-2: There is existing difference when comparing those who participated and did not participate in the disaster prevention training for pre-disaster preparedness.

3. SURVEY QUESTIONNAIRES

To satisfy our purpose of study, we designed questionnaires for a survey with three clusters. A field survey was carried out in Tokyo Metropolis and the four prefectures (Kanagawa, Chiba, Saitama, and Ibaraki prefectures).

The full questionnaire includes 27 items with two open-ended questions to measure participants' pre-disaster preparedness, experience with the 2011 Great East Japan earthquake, and participation in disaster prevention training, and Prefecture, gender and age information are included (see Table 2).

Table 2 Survey questionnaires

Ⅰ. We would like to ask you that when the earthquake occurred on March 11,2011 (10 items)
1) On the 2011 Great East Japan Earthquake (hereinafter, referred to "earthquake"), which of the following damages did you see directly or experience?
2) Did you hear the earthquake alerts before the big shake (via TV, mobile, broadcasting etc.)?
3) Do you think to protect your own body was able to act on the day?
4) When you were feeling a tremor, which of the following did you take an action?
5) On the day of the earthquake, which of the following methods did you use for gathering disaster-related information?
6) On the day of the earthquake, could you return home from your workplace, school, or other places?
7) We would like to ask to those who answered 'Yes' on 6). What was the means for coming back home?
8) On the day of the earthquake, could you get water and/or food

during your return home?
9) What kind of assistance do you need in order to return home from workplace, school, and on the road when the big earthquake would happen? Please write freely.
10) In the future disaster, what kind of preparedness or assistance for you if you would have a difficulty to go home and stay at workplace, school, and on a road? Please write freely.

II. Disaster Preparedness (14 items): awareness and knowledge, countermeasure in house and furniture, making a plan to meet up with family after a disaster, supplies, disaster prevention training

1) Do you think that your pre-disaster preparedness is enough?
2) Have you heard about the hazard-related information such as a liquefaction hazard map?
3) If you have ever heard about the information, is it helpful to prepare against a disaster?
4) Which of the following risks by the expected earthquake would happen on your living place?
5) House: when did it build up with what kind of building material (wooden house or non-wooden house)?
6) Structurally strengthening the building and stabilizing furniture
7) Making a plan to meet up with family after a disaster
8) Keeping supplies
9) Have you ever participated in disaster prevention training?
10) Where did you get the training (e.g., school, workplace, etc.)?
11) What kind of contents did you learn from the training?
12) If you did or could not participate in the education, why?
13) On the 2011 Great East Japan Earthquake, could you act as what you learnt from the training?
14) If you could not follow the instruction on that day, why?

III. Disaster preparedness for outside a home (3 items) : reaction of disaster on train, possibility of becoming a person who has a difficulty in returning home, emergency supplies

1) Reaction of disaster on train
2) Possibility of becoming a person who has a difficulty in returning home: can you go back from your workplace or school on foot?
3) Emergency supplies: Are you bringing emergency supplies for in case of becoming a person who has a difficulty in returning home?

Data items numbering 256 were collected from June 12, 2012 to July 9, 2012. The questionnaire took about 10 minutes to complete.

4. RESULT

4.1 Participants Demographic Analysis

Reflecting a response rate of 51% for the current study, 253 fully unanswered questions were excluded, and 247 items of data were used. Regarding the gender, 181 of participants were males (73%) and 66 were females (27%). The percentage of data gathered from Tokyo Metropolis and the four prefectures is illustrated in Table 3.

Table 3 Participants Area

Address	Number	Percentage
Tokyo Metropolis	50	20%
Chiba Prefecture	119	46%
Kanagawa Prefecture	64	25%
Saitama Prefecture	15	6%
Ibaraki Prefecture	2	1%
(Blank)	6	2%
Total	247	100%

Table 4 presents the result of the age analysis. According to a study of the 2011 Great East Japan earthquake, vulnerable age groups of persons more than 50 years old were more easily to become victims (Yun and Hamada, 2012). In addition, according to Tokyo Metropolitan Government's Disaster Prevention Council estimated damages by predicting disasters, the number of people who need support during a disaster such as the old is 4,900 persons, which doubled the previous estimation in 2006. Therefore, we gathered data from the aged in order to figure out their current levels of preparedness, and then the number of more than 50 years old is half of the total of data.

Previous research on predictors of preparedness behavior for disasters showed that age, income, education, locus of control, perceived threat and distress were significant predictors of preparedness behaviors for earthquakes (Sattler et al., 2000).

Table 4 Age analysis

Age (N=247)	Percentage (number)
Lesser than 20	5% (12)
20-29yrs	32% (80)
30-39yrs	5% (13)
40-49yrs	7% (18)
50-59yrs	9% (22)
60-69yrs	26% (63)
70-79yrs	14% (34)
80-89yrs	1% (2)
(Blank)	1% (3)
Total	100% (247)

4.2 Pre-disaster Preparedness

The questionnaire had five sections for the disaster preparedness behaviors. Table 5 shows the pre-disaster preparedness behaviors. An example of the items include, "Do you have drinking water in order to prepare for disasters?" The participants used a 2-point scale to answer the questions. All of the scales had descriptors to the questions (e.g., 1= Yes, I do, 0= No, I don't).

Table 5 Disaster preparedness behavior

Specific Activity
1. Keeping supplies (8 items) 1) Drinking water, 2) Food supplies, 3) Sanitary items, 4) Portable toilet, 5) Portable radio, 6) Flashlight, 7) First-aid kit, 8) Fire extinguisher
2. Stabilizing furniture (3 items) 1) Preventing furniture (e.g., desk, wardrobe, refrigerator) from falling over, 2) Not placing objects up high, 3) Securing light with chains and clamps
3. Getting hazard-related information (2 items) 1) Evacuation route and evacuation place check 2) Use a hazard map for evacuation route
4. Making a plan to meet up with family after a disaster (2 items) 1) Emergency contact method decision, 2) Decision an alternative way when families cannot contact each other
5. Structurally strengthening building (3 items) 1) Seismic diagnosis, 2) Seismic retrofit, 3) Reinforcing brick walls and stone fences to prevent collapse

To assess preparation and to create a preparedness factor, we summed the responses to the responses to the 18 items asking about preparation activities. We used these into a 5-point scale ranging from 1 (not at all) to 5 (fully) to indicate the summed data. This scale serves as a dependent variable for the regression model. The scale was reliable with Coefficient alpha (α) for it was .81. On the average, the respondents reported preparation in order of keeping supplies (52%), stabilizing furniture (35%), getting hazard-related information (32%), making a family reunion plan and other plans for when the disaster occurs (40%), and structurally strengthening the building (12%). About more than 50% of persons had the following supplies on hand: flashlight, portable radio, drinking water, first-aid kit, and food supplies.

In addition, Figure 1 reports the results of responses to the question, "do you think that your preparedness before disaster activities is enough?" Approximately 60% of respondents think that they are not sufficient for preparedness before disaster; only 3% think their preparedness against disaster is sufficient; and 37% answered they prepared averagely.

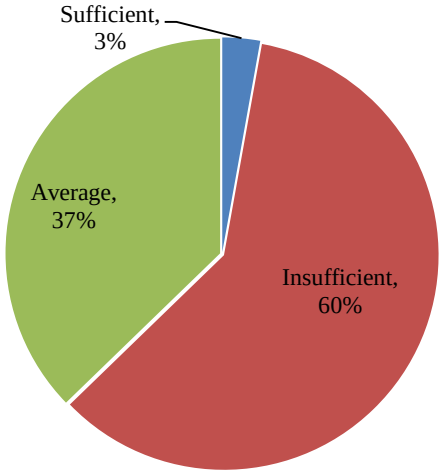


Figure 1 Self-reported preparedness level (N=247)

It implies that residents are not sufficiently prepared for the disasters. The majority of citizens are not aware of the full potential extent of earthquake-induced damages or the proneness to earthquakes. And it seems that awareness - when acknowledged at all - is not in itself a sufficient stimulus for taking actions; indeed, even the personal experience of a devastating earthquake does not imply that the individual has any greater 'real' perception of earthquakes than before.

Moreover, as it mentioned earlier in Table 1, there were approximately 5.15 million persons who had difficulties going back to their homes in Tokyo Metropolis, Kanagawa, Chiba, Saitama, and Ibaraki areas on March 11, 2011. When a predicted earthquake occurs, this problem could become more serious because much of the severe damages done by the earthquake in Tokyo area. Hence, it is important to prepare both for inside and outside a home, such as brining emergency supplies (e.g., a pair of sports shoes, food, fordable bike, clothing and blanket).

Figure 2, however, reported that the residents are not sufficiently prepared for it: nothing special (59%), keeping a pair of sports shoes (30%), food supplies (8%), fordable bike (1%), extra clothes and blankets (1%).

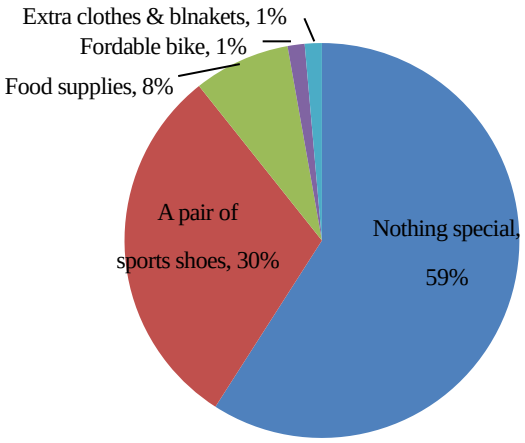


Figure 2 Preparedness actions for outside a home

4.3 Experience With Disasters

4.3.1 Direct Experience with the 2011 Great East Japan Earthquake

A total of 66% of the respondents had experienced damages by the 2011 Great East Japan earthquake. Of these data, 23% reported experiencing building damages due to shaking or vibration as a result of the earthquake, and 20% had experienced damages due to falling objects inside. In Figure 3, the damage types by the earthquake were the following: building damage due to shaking or vibration (23%), damage due to falling objects inside (20%), damage caused by liquefaction (9%), damage caused by falling or collapse wall (7%), congestion or accidents due to the disaster (6%), damage due to fire (5%), damage caused by falling objects in an outdoor (4%), damage due to the collapse of steep slopes (1%).

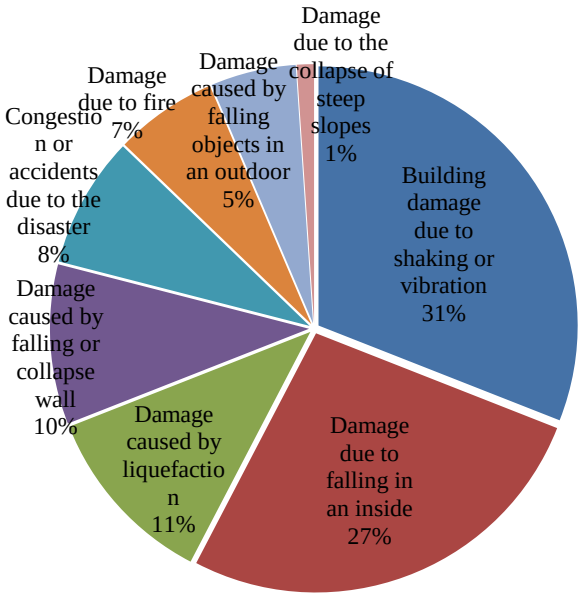


Figure 3 Damage types by the 2011 Great East Japan earthquake

4.3.2 Disaster Prevention Training

A total of 66% of the responses had participated in the disaster prevention training. Out of these answers, 54% reported participating in the training before the 2011 Great East Japan earthquake, and 7% participated in it after the disaster (see Figure 4). Reasons of unparticipation were the following: 40% had no information how to participate in the training; 25% had no available time for it; 11% had no needs for it; 6% felt no danger by the disaster in their living place; and 5% had no useful information in the training.

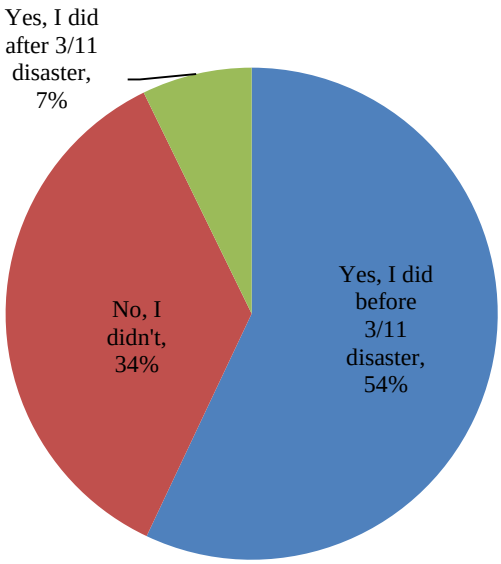


Figure 4. Participation in the disaster prevention training

Thirty-three percent had a participated at school, 25% at a local community place, 19% at their workplace, 9% at a disaster prevention event, and 6% at fire station.

From the training, the persons learned the followings: practicing a fire-fighting (19%), checking an evacuation place and an evacuation route (18%), protecting one's body (13%), and others such as practicing first-aid (12%), walking through an evacuation route (11%), experiencing shelter (4%), and serving food (4%).

The result the question, "On March 11, 2011, could you put into action that you learned from the training?" reported that 34% of persons actually followed through.

To examine the hypothesis (Hypothesis 2-1 and 2-2), we divided the total sample into two groups as participants and non-participants.

4.4 Hypothesis Testing

To test hypothesis, we used SPSS 12 (Bryman and Cramer, 2005) and reported a result of hierarchical multiple regression to examine the influence of gender, age, and participation in the disaster prevention training in predicting preparation efforts for future disasters.

Table 6 presents the correlations between participation in disaster prevention training, experience of damage by the 2011 Great East Japan earthquake, pre-disaster preparedness, gender, and age variables. It is necessary to interpret results as to whether these are significant, considering the above $p<0.05$ based on a two-tailed test. The unit of analysis is the individual respondents; the dependent variable is expressed as the dummy variable in regards to the respondent that is explained earlier.

Table 6 Correlations and descriptive statistics (N=247)

	Variable	Mean	Std.	1	2	3	4	5
1	Participation in Disaster Prevention Training	.66	.53	–				
2	Experience of Damage	.66	.47	-.12	–			
3	Pre-disaster Preparedness	2.47	1.09	.10	.07	–		
4	Gender	1.27	.47	-.04	-.01	.18**	–	
5	Age	45.62	21.41	-.14*	.08	.04	.02	–

Note) *p < 0 .05, **p < 0 .01 (two-tailed).
Gender was coded 1 = male, 2 = female.
Age represent the actual number of year.

Participation in disaster prevention training correlated significantly and negatively with age (age r = -.14, p < 0.05). Pre-disaster preparedness behavior, moreover, is strongly and significantly associated with females (gender r = .18, p < 0.01). Pre-disaster preparedness is positively and insignificantly correlated with participation in both disaster prevention training (r = .10) and experience of damage (r = .07). Despite insignificant correlation between the experience of the GEJE earthquake and training, participant in the training experienced less damage by the 2011 Great East Japan earthquake than non-participant.

Hypothesis 1 was not supported. This study tested whether persons who experienced damages by the 2011 Great East Japan earthquake were more willing to take the pre-disaster preparedness behavior compared with the group that did not. Although 66% of the respondents had experienced damages by the 2011 Great East Japan earthquake, their pre-disaster preparedness is not much different from those who had no damage. The t-test result showed insignificant difference between the two groups (Table 7).

Table 7 Result of t-test analysis: experience damage by the 2011 Great East Japan earthquake & pre-disaster preparedness

	N	Mean	S.D	t-test
Damage	150	2.53	1.07	t=1.13,
No Damage	80	2.36	1.13	df=234, p=.259

Note) Standardized regression coefficients are reported.
+p < 0.1, *p < 0.05, **p < 0.01 (two-tailed)

Hypothesis 2-1 was slightly supported in Table 8 (N = 233, F=5.387, df = 232, p < 0.1). For this study, it was hypothesized that pre-disaster preparedness is shown more in the participants verses non-participants in the disaster prevention training. The hypothesis was weakly supported (ß=0.12, p<0.1). Participants in the disaster prevention training were positively related to disaster preparedness behavior. There was a greater number of participants in the disaster prevention training program for earthquakes with a higher level of disaster preparedness behavior. Moreover, being female significantly and strongly relates to the preparation behavior (ß =0.22, p < 0.01). In other words, the disaster preparedness behavior is shown more in females than the male.

Table 8 Regression results for pre-disaster preparedness and participation in the disaster prevention training

Predictor variable	ß	t	p-value	df	F	R^2
Step 1: Gender	.22**	3.35	.001			
Age	.07	1.02	.308			
				232	6.226	.051
Step 2: Participation	.12+	1.89	.060			
Total				232	5.387	.066

Note) Standardized regression coefficients are reported.
+p < 0.1, *p < 0.05, **p < 0.01 (two-tailed)

Hypothesis 2-2 was slightly supported. Table 9 presents a matrix of t-test result for Hypothesis 2-2. T-test is used to compare the values of the means from two groups and test whether it is likely that the samples are having different mean values. There are slightly existing differences when comparing those who participated and did not participate in the disaster prevention training for disaster preparedness behavior (t = 1.87, p < 0.1).

Table 9 Result of t-test analysis: participants in the training and disaster before preparedness

	N	Mean	S.D	t-test
Participant	150	2.59	1.09	t=1.87+,
Non-participant	84	2.32	1.03	df=232, p=.06

Note) Standardized regression coefficients are reported.
+p < 0.1, *p < 0.05, **p < 0 .01 (two-tailed)

5. CONCLUSIONS

This study reports that participants in the disaster prevention training had slightly higher levels of preparation than non-participants. Also, gender were positively associated with the disaster preparedness behavior, and female were better prepared than male.

The results concerning experience of damage by the disaster and disaster preparedness behavior have no significant impact in this study. However, previous researches provided positive and significant support for the proposed hypotheses. In other words, experience with disasters and resource loss had a strong positive relationship to disaster preparedness behavior. One possible reason of insignificant result in this study is that the 2011 Great East Japan earthquake was relatively little major earthquake damage in the Tokyo area, compared with Tohoku area. From the data, about 19% of people who did not follow what they learnt from the training answered that the situation was not dangerous enough to practice what they have learned in training. Therefore, it is possible that even respondents with experience of damage have not sufficiently adjusted their expectations of future disaster to prompt increases in disaster preparedness behavior. Future research could attempt to quantify this effect and the extent to which experience of damage is measured by its degree.

It is important to note that this study had several methodological limitations. First, the survey measured the pre-disaster preparedness through self-reported answer, a possible source of error if respondents misreport the actions they have taken. Second, this study used a random sampling strategy and the unique designed survey that restricts the ability to generalize.

The findings of this study regarding predictors of the disaster preparedness behavior may have ramifications for the disaster prevention training. The significant but weak influence of training participation on the disaster preparedness behavior identified in this indicates that contents of the training should also explain direct and useful actions that individuals can take facing with disaster. Future studies should more explicitly measure that the participation in the training is a useful activity toward successful preparation.

Getting prepared for the predicted earthquake has proven to be the most effective way to reduce the damage suffered. In order to reduce the human impact by the predicted disaster, it is generally proposed the following three: the first one is to provide information on threat so that threat perception due to possible future disasters is raised. The second area is to increase the personal resources of the participants in dealing with the threat, so that the individual feels capable of dealing with a possible future disaster event. Lastly, training programs need to give community members a sense of responsibility for mitigation and preparedness. Especially, the reason of unparticipation in the training was that they had no information how to participate, and then it indicates more activities to facilitate for participation in it.

It is important to make sure persons fully prepared, and then make purposeful and effective use of that preparation. After the preparation is done, moreover, it is even more important to consider how to actually perform it. It is difficult to change human behavior, but the rewards are worth the effort.

References:

Banerjee, M. M., and Gillespie, D. F. (1994a), "Linking disaster preparedness and organizational response effectiveness," *Journal of Community Practice*, **1**, 129–142.

Banerjee, M. M., and Gillespie, D. F. (1994b), "Strategy and organizational disaster preparedness," *Disasters*, **18**(4), 344-354.

Bryman, A. and Cramer, D. (2005), "Quantitative Data Analysis with SPSS 12 and 13: a guide for social scientists," Routledge, New York, NY.

Faupel, C.E., Kelley, S.P. and Petee. T. (1992), "The impact of disaster education on household preparedness for Hurricane Hugo," *International Journal of Mass Emergencies and Disasters* ,**10**, 5-24.

Hamada, M., and Yun, N.Y. (2011), "Future Directions of Earthquake-Tsunami Disaster Reduction Based on the Lessons from the 2011 Great East Japan Earthquake," *4th Japan-Greece Workshop on Seismic Design of Foundation*: Kobe Gakuin University.

Lindell, M. K., and Perry, R. W. (2000), "Household Adjustment to Earthquake Hazard A Review of Research," *Environment and Behavior*, **32**(4), 461-501.

Ozaki, T. (2012), "JMA's Tsunami Warning for the 2011 Great Tohoku Earthquake and Tsunami Warning Improvement Plan," *Journal of Disaster Research*, **7sp**, 439-445.

Sattler, D. N., Kaiser, C. F., and Hittner, J. B. (2000), "Disaster Preparedness: Relationships Among Prior Experience, Personal Characteristics, and Distress," *Journal of Applied Social Psychology*, **30**(7), 1396-1420.

Sendai report, (2012) "Managing Disaster Risks for a Resilient Future," *Sendai Dialogue*, October 9 to 10, 2012

Shelby, J. S., and Tredinnick, M. G. (1995), "Crisis Intervention with Survivors of Natural Disaster: Lessons from Hurricane Andrew," *Journal of Counseling and Development*, **73**, 491-497.

Yun, N.Y., and Hamada, M. (2012), "Evacuation Behaviors in the 2011 Great East Japan Earthquake," *Journal of Disaster Research*, **7sp**, 458-467.

World Bank (2010), "Natural Hazards, UnNatural Disasters: The Economics of Effective Prevention," the 2010 World Bank/ United Nations (UN) report

首都直下地震帰宅困難者等対策協議会 (2012) http://www.bousai.metro.tokyo.jp/japanese/tmg/kitakukyougi.html

10CUEE CONFERENCE PROCEEDINGS
10th International Conference on Urban Earthquake Engineering
March 1-2, 2013, Tokyo Institute of Technology, Tokyo, Japan

SEISMIC RESPONSE OF NON-ENGINEERED BUILDINGS IN NEPAL DURING SEPTEMBER 18, 2011 NEPAL-SIKKIM EARTHQUAKE

Kabir Shakya[1)], Deepak Raj Pant[2)], Manika Maharjan[2)], Satish Bhagat[2)], Anil C. Wijeyewickrema[3)] and Prem Nath Maskey[4)]

1) Postdoctoral Researcher, Department of Civil Engineering, Tokyo Institute of Technology, Japan
2) Graduate Student, Department of Civil Engineering, Tokyo Institute of Technology,Japan
3) Associate Professor, Department of Civil Engineering, Tokyo Institute of Technology, Japan
4) Professor, Department of Civil Engineering, Institute of Engineering, Pulchowk Campus, Nepal
shakya.k.aa@m.titech.ac.jp, pant.d.aa@m.titech.ac.jp, maharjan.m.aa@m.titech.ac.jp, bhagat.s.aa@m.titech.ac.jp, wijeyewickrema.a.aa@m.titech.ac.jp, pnmaskey@live.com

Abstract: On September 18, 2011 at 18:25 (Nepal Standard Time), a moment magnitude (Mw) 6.9 jolted eastern Nepal including the capital city, Kathmandu which is located 272 km west from the epicenter (27.72°N, 88.06°E). It also affected several areas of India, China, Bhutan, and Bangladesh. This shallow-focus earthquake having focal depth 19.7 km, lasted for about 30-40 seconds. Although several buildings suffered extensive damage, it was fortunate to observe that fatalities in Nepal were relatively low with six reported. The earthquake displaced 12,301 persons of 4,851 families. A total of 6,435 houses were damaged completely, 11,520 damaged partially, and 3,024 houses suffered only minor damage. The Center for Urban Earthquake Engineering (CUEE) at Tokyo Institute of Technology investigation team carried out the field survey in collaboration with Institute of Engineering (IOE), Tribhuvan University, Nepal to assess the extent and nature of damage caused by the earthquake. From the investigation it was found that many non-engineered stone masonry, brick masonry, and reinforced concrete buildings suffered heavy damage, while engineered reinforced concrete buildings and buildings constructed with indigenous technology locally known as Centibera buildings, exhibited minor or no damage.

1. INTRODUCTION

A strong earthquake with a moment magnitude (Mw) of 6.9 jolted eastern Nepal on September 18, 2011 at 18:25 (Nepalese Standard Time) with shaking felt 272 km west in the capital, Kathmandu. As shown in Figure 1, the

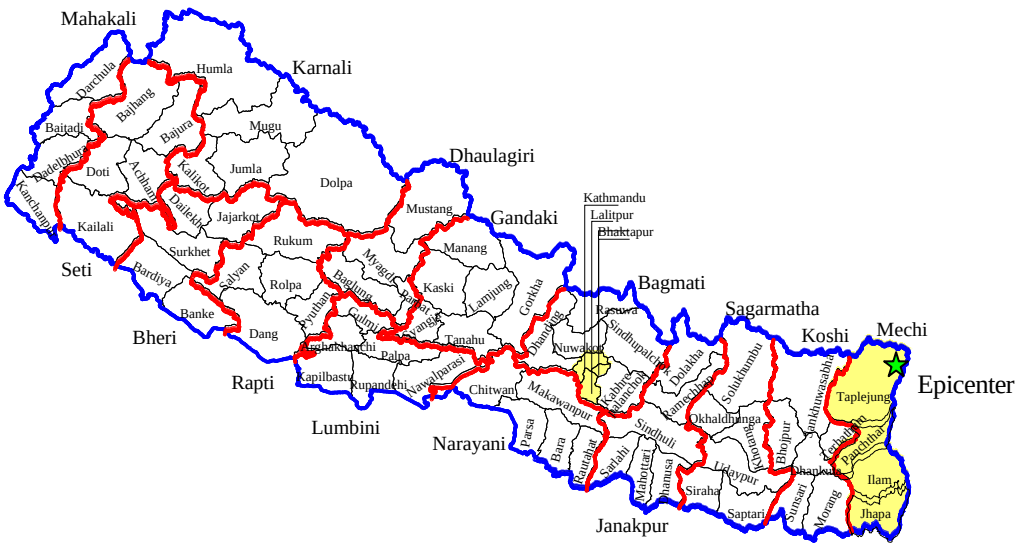


Figure 1 Map of Nepal showing epicenter and the visited districts.

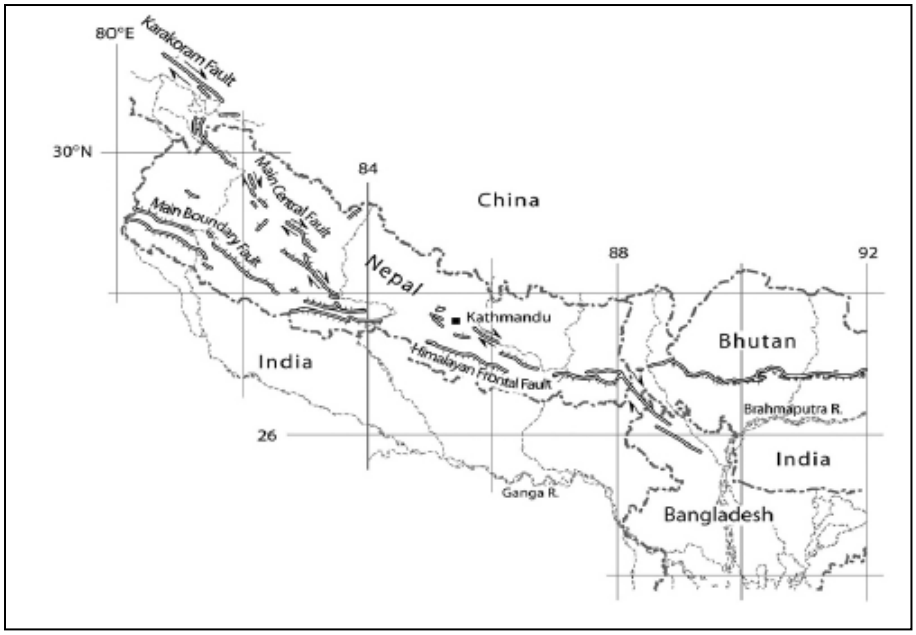


Figure 2 Active faults in and around Nepal Himalaya (Chamlagain (2009))

epicenter was located at Nepal-India border (27.72°N, 88.06°E) (Taplejung District of Nepal) and the focal depth was 19.7 km (USGS 2011). This shallow focus earthquake lasted for about 30-40 seconds and affected several areas of Nepal, India, China, Bhutan and Bangladesh. The devastating earthquake claimed the lives of 111 people with the maximum of 97 in India. A press release of the Ministry of Home Affairs of Nepal on October 24, 2011 reported a total of 6 casualties in Nepal which includes 3 deaths in Kathmandu, 2 in Sunsari and 1 in Sankhuwasabha. Similarly, 30 people were critically injured and 134 suffered minor injuries. A total of 6,435 houses were completely damaged, 11,520 were partially damaged and 3,024 houses suffered only minor damage throughout the country.

A joint team from Tokyo Institute of Technology, Japan and Institute of Engineering, Pulchowk Campus, Nepal conducted a reconnaissance survey from October 12 to October 19, 2011 to assess the extent and nature of damage caused by the earthquake in Nepal. The investigation was focused mainly in the densely populated towns such as old settlement of Bhaktapur district around the Bhaktapur Durbar Square area, some sites in Kathamndu and Lalitpur districts, Ilam Bazar of Ilam district, Ranke Bazar and Phidim Bazar of Panchthar district and several villages in Taplejung district. The districts where field investigation was conducted is highlighted in Figure 1. The damage information of remote villages with widely dispersed houses in the affected region, where our investigation team could not reach, was collected from the local authorities and organizations such as the District Administration Offices, the Nepal Red Cross Society and Local Police at Phidim. This paper presents a comprehensive overview of the performance of buildings in the earthquake-affected areas particularly in Bhaktapur and Eastern Nepal. Damage in Sikkim, India have already been reported in NICEE (2011) however, the investigation of the damage in Nepal has not been reported yet. In this paper lessons learnt from the investigation of the performance of buildings in earthquake affected areas in Nepal are reported.

2. SEISMIC HAZARD IN NEPAL AND THE PRESENT EARTHQUAKE

Nepal is a country with a diverse geographical setting varying from low lands in the southern part, to high mountains including the world's highest peak Mount Everest (el. 8,848 m) in the north. One third of the Himalayan arc, which marks an active plate boundary between the Indian and Eurasian plates, lies in northern Nepal and is a source of major seismicity in the area. The presence of numerous active faults in Nepal shown in Figure 2 (Chamlagain 2009), clearly highlights the seismic hazard in this Himalayan nation.

In the past, Nepal has experienced only two devastating earthquakes in the last century. A magnitude 8.1 earthquake occurred in January 1934, with epicenter (26.50°N, 86.50°E) close to Nepal-India border region (ASC 2011). The Kathmandu Valley experienced intensities of IX-X in the MMI scale. A total of 8,519 persons were reported dead in Nepal, out of which 4,296 persons died in Kathmandu alone (Pandey and Molnar 1988). A magnitude 6.8 earthquake occurred in August 1988, with epicenter (26.755°N, 86.616°E) in eastern Nepal (ASC 2011). The MMI estimated in Kathmandu was VII-VIII and at least 721 people lost their lives in Nepal due to this earthquake (NSET

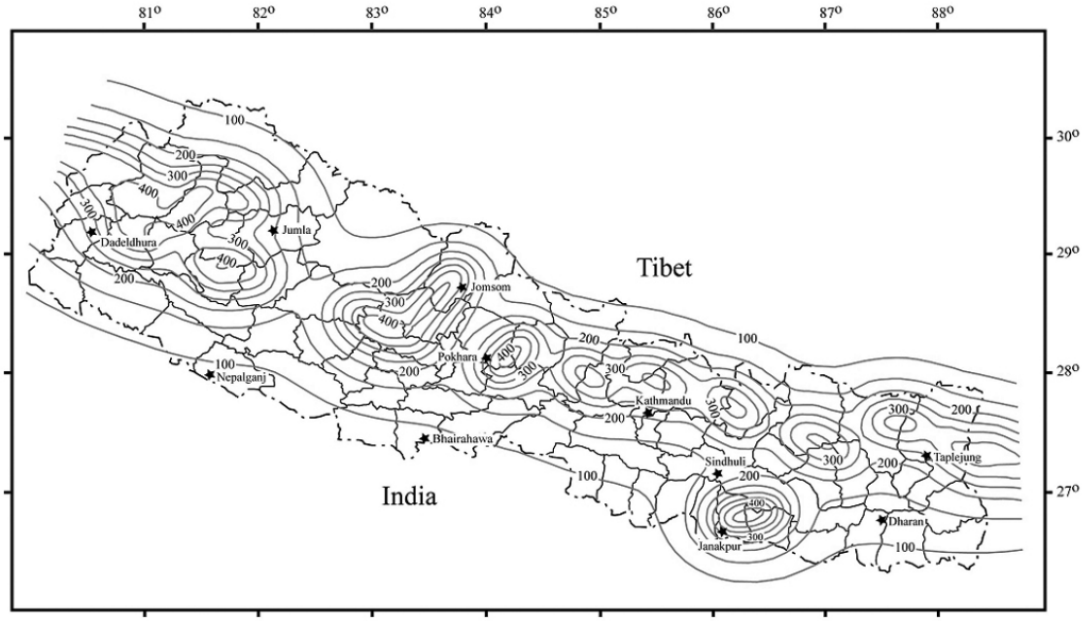


Figure 3 Seismic hazard map of Nepal showing bedrock peak ground horizontal acceleration contours in gals for 500 years return period (Pandey et al. 2002)



Figure 4 Damages in Bhaktapur (a) Vertical cracks between adjacent buildings and (b) Out of plane failure of brick masonry wall in mud mortar (Source: http://www.newscientist.com/blogs).

2011).

The Seismic hazard map produced by the National Seismological Center of Nepal shows the design-level PGA of $0.1g - 0.2g$ near the epicentral region of the September 18, 2011 earthquake (Figure 3). The upper limit of $0.2g$ is close to the PGA recorded in the severely affected regions of India during the earthquake (EERI 2012).

3. OBSERVED DAMAGES DURING FIELD VISIT

The collapse of old boundary wall of the British Embassy, Kathmandu claimed the lives of 3 people. Several old brick-masonry buildings in Kathmandu and Patan suffered minor cracks, however, the extent of damages in Bhaktapur were comparable. Surprisingly, many buildings in very poor condition, those were expected to collapse during the earthquakes, are still standing. Nevertheless, the extensively damaged buildings in Bhaktapur were old and constructed using ordinary brick in façade and sun dried bricks with mud mortar in side walls. Most of the buildings which suffered damages were not in intact condition prior to the occurrence of the earthquake. The observed major damages to the buildings include the formation of vertical cracks on walls along the mortar joint at the common face between two adjacent buildings (Figure 4(a)) and the out of plane failure of brick masonry walls (Figure 4(b)). Besides, diagonal cracks in masonry walls starting from the openings and collapse of gable walls were also common.

In eastern Nepal, all the districts of Mechi Zone was selected for the investigation. On consulting with the local people in Jhapa district, it was found that the district was not much affected by the earthquake. Hence, the study was focused in Ilam district, Panchthar district and Taplejung



Figure 5 Collapse of stone masonry buildings in Ilam (Source: District Administration Office, Ilam).



Figure 6 Damages in Ranke (a) Out of plane failure of stone masonry walls and (b) Collapse of stone masonry school building (source: Local Police).

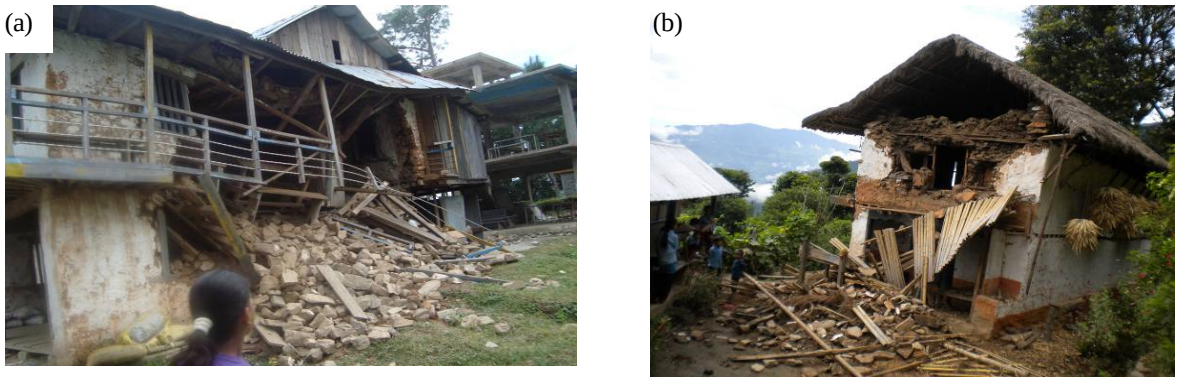


Figure 7 Typical damages in Taplejung (source: Red Cross, Taplejung) (a) Collapse of school building and (b) Collapse of stone masonry building.

district. Due to the limited time and difficulty in accessing the remote villages, the thorough investigation was undertaken only in the district headquarters and its surrounding. In Ilam Bazar, there were many recently constructed RC buildings, however, the majority of the buildings were constructed of random rubble stone masonry with mud mortar and timber. Almost all of the buildings in the locality suffered various degrees of damage from minor crack to the collapse of buildings as shown in Figure 5. The damage to the buildings constructed partially with timber frame and partially with stone masonry was less compared to that in the random rubble stone masonry buildings. In RC framed buildings, the repairable cracks were limited to the infill brick masonry walls.

In the towns Ranke and Phidim of Panchthar districts, the damages were mainly concentrated in the random rubble stone masonry buildings which offer very weak resistance to lateral loads and extremely vulnerable to seismic loads. The out of plane failure of stone masonry wall (Figure 6(a)) and the collapse of the buildings due to failure of load bearing stone masonry walls (Figure 6(b)) were very common. Only minor damage or no damage was observed

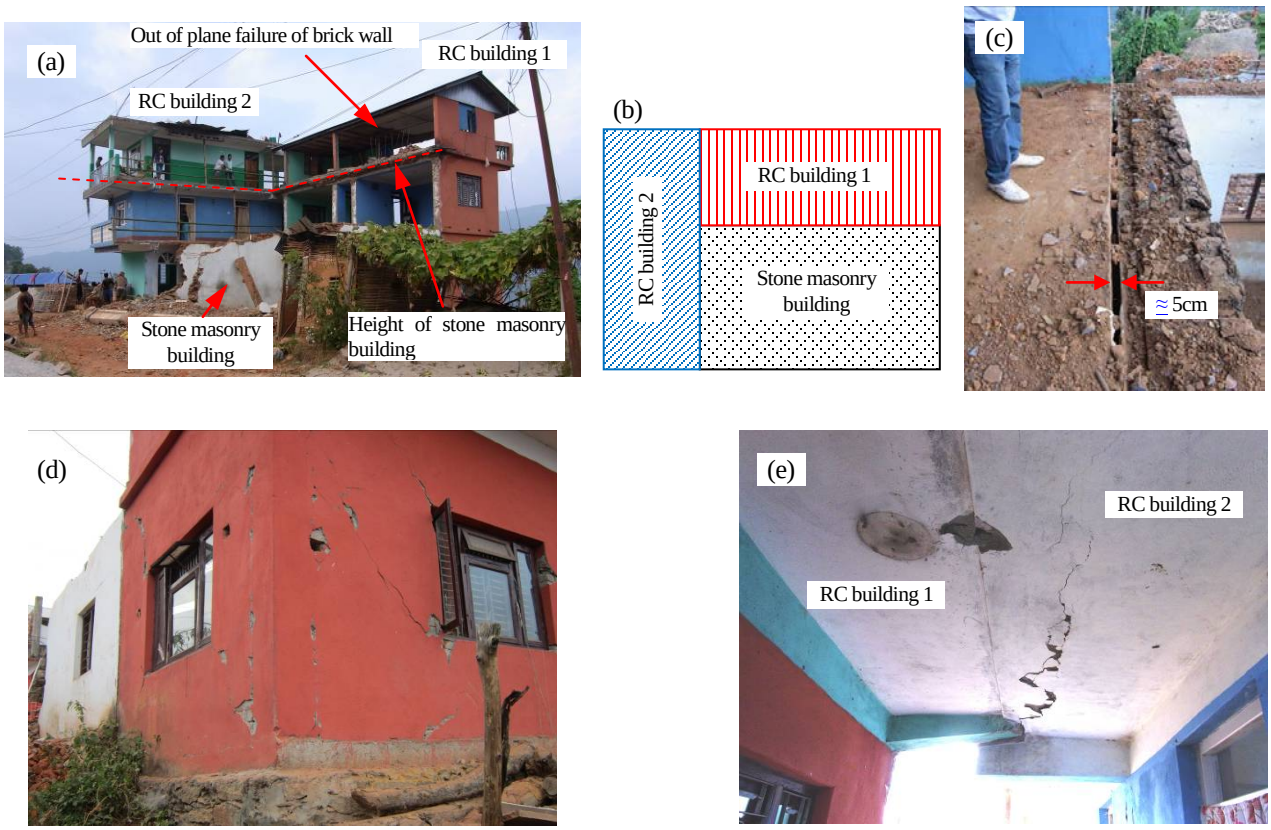


Figure 8 Seismic pounding of buildings (a) Damaged 3 buildings, (b) Building configuration, (c) Permanent gap between RC building 1 and stone masonry building, (d) Shear cracks in infill brick walls and (e) Cracks in the slabs.



Figure 9 Building construction technique (a) No cracks in the building constructed using Centibera and (b) Centibera construction technique.

in the buildings primarily constructed with timbers and reinforced concrete except in very few cases.

Since the construction practice in Taplejung also resembles to the previous sites, no difference in the nature of damages of the buildings were noticed. Typical types of damages such as collapse and out of plane failure of stone masonry walls are shown in Figure 7. Most of the buildings in the locality were not free of minor cracks. The shear cracks in the infill brick walls generated from the window openings were also noticed in the brick masonry and RC buildings.

A part from the typical damages, a collapse of a stone masonry building and heavily damaged RC framed buildings (Figure 8(a)) due to structural pounding was also observed in Phidim Bazar. The white colored demolished building in Figure 8(a) is the stone masonry building. When our survey team reached at the site, the demolition of damaged stone masonry building was in progress. There were no gaps between all the three buildings before occurrence of earthquake as shown in the building configuration of Figure 8(b). But after the earthquake there existed the permanent gap of about 5 cm (Figure 8(c)).

Due to the seismic load along with the impact loads from the adjacent RC buildings, the stone masonry building collapsed. The heavy shear cracks in the infill brick masonry walls (Figure 8(d)) and out of plane failure of infill brick masonry at the third floor (Figure 8(a)) illustrate that the RC building 1 also suffered the heavy damage. Significant amount of cracks were developed in the slabs of RC building 1 and RC building 2 (Figure 8(e)) as a result of structural pounding between RC building 1 and RC building 2. The shear cracks at the beam-column joint and the beams were observed in the RC building 2. Hence, the damages on these three buildings shows one of the good examples of structural pounding and also illustrates the vulnerability to structural pounding of buildings, if the provided gap between the adjacent buildings are insufficient.

In the Eastern Nepal, several buildings constructed using a traditional building technique locally known as "Centibera" (Figure 9(a)) were observed. The Centibera buildings are of 1-2 storys and are constructed with the stone masonry walls up to the plinth level or the first floor, on top of which the walls comprised of wooden frames together with woven bamboo mesh and cement mortar plaster or plaster composed of a mixture of mud, cow dung and rice husk are built (Figure 9(b)). No cracks were found in Centibera buildings while significant amount of cracks were noticed in the stone masonry, brick masonry and RC buildings nearby the Centibera buildings. It highlighted the suitability of construction of Centibera buildings compared to the other buildings in this region to withstand the seismic loads.

4. SUMMARY AND RECOMMENDATIONS

Since Nepal lies in an earthquake prone region, the following recommendations are provided to increase the seismic safety of buildings based on the observations made during the field investigation:

- Most of the buildings constructed with the local materials and indigenous technique suffered heavy damages hence, the existing buildings in remote villages require immediate cost-effective ways of retrofitting using locally available materials such as timber and bamboo.
- Timber-framed masonry structure in the first story and timber-framed Centibera structure in the upper story appears to be a promising technology for the construction of new seismic-resistant buildings in the villages. The construction of Centibera buildings should be encouraged in remote villages.
- Majority of the buildings throughout the country are not designed and constructed to withstand the probable earthquake. All the structures in the major towns of eastern Nepal should be thoroughly investigated for the assessment of their seismic safety and appropriate retrofitting measures should be taken for seismically vulnerable structures.
- Government authorities should ensure that only seismic-resistant structures especially bridges, hospitals, and school buildings, are designed and constructed in the earthquake prone regions such as Kathmandu, Ilam, Phidim, Taplejung.

Acknowledgements:

The authors express their sincere gratitude to Professor Kohji Tokimatsu, Director of Center for Urban Earthquake Engineering (CUEE), Tokyo Institute of Technology for supporting the field investigation and providing financial support. Thanks are due to the earthquake reconnaissance survey team members from Nepal, Mr. Purushottam Karki, Mr. Soyuz Gautam, Mr. Subash Bastola and Mr. Yadin Shrestha. The Nepal Red Cross Society and District Administration Offices of Jhapa, Ilam, Panchthar, and Taplejung, are also acknowledged for sharing their field investigation data and providing useful information.

References:

Amateur Seismic Centre (ASC) India Webpage: *http://asc-india.org/seismi/seis-bihar.htm*. Accessed on: October 27, 2011.

Chamlagain D. (2009), "Earthquake scenario and recent efforts toward earthquake risk reduction in Nepal," *Journal of South Asia Disaster Studies*, **2**(1), 57-80.

Earthquake Engineering Research Institute (EERI) (2012), "The Mw 6.9 Sikkim-Nepal border earthquake of September 18, 2011, Special Earthquake Report".

National Information Center of Earthquake Engineering (NICEE) Webpage: http://www.nicee.org/Preliminary_Report_2011_Sikkim_EQ.pdf, Accessed on November 2, 2011.

National Society for Earthquake Technology (NSET), Nepal, 2011,Webpage: http://www.nset.org.np/nset/php/earthquake_history.php, Accessed on October 27, 2011.

Pandey M. R. and Molnar P. (1988), "The distribution of intensity of the Bihar-Nepal Earthquake 15 January 1934 and bounds on the extent of the rupture zone," *Journal of Nepal Geological Society*; **5**(1), 22-43.

Pandey, M. R., Chitrakar, G. R., Kafle, B., Sapkota, S. N., Rajaure, S. N., and Gautam, U. P. (2002), "Seismic hazard map of Nepal," Department of Mines and Geology, Kathmandu, Nepal.

U. S. Geological Survey (USGS) Webpage: http://earthquake.usgs.gov/earthquakes/recenteqsww/Quakes/usc0005wg6.php, Accessed on October 31, 2011.

10CUEE CONFERENCE PROCEEDINGS
10th International Conference on Urban Earthquake Engineering
March 1-2, 2013, Tokyo Institute of Technology, Tokyo, Japan

PRACTICAL STUDY OF THE EARTHQUAKE DISASTER PREVENTION CHILDCARE FOR INFANTS WITH THE SIMULATED EXPERIENCE

Nobuyuki Yamada

Associate Professor, Dept. of Science Education, Fukuoka University of Education, Japan
nyamada@fukuoka-edu.ac.jp

Abstract: Speaking of the disaster prevention education for infants, an evacuation drill is most. The complimentary practice education by the cooperation with experts such as the firefighting is accomplished, but the effect inspection is not done enough and does not advance to the study either. Furthermore, the principal objective is put only in most fire drills moving to the outdoors early and cannot deny, becoming a dead letter. We went the practice with the development of the program of the earthquake disaster prevention education for infants in an educational practice from 2009. I will report the frame formation of the earthquake disaster prevention childcare through the simulated experience and the practice utilization while focusing on the correspondence action during strong ground motion based on past our process in this announcement, and adopting play.

1. INTRODUCTION

After the Great East Japan Earthquake of 2011, it is emphasized improvement of disaster prevention education becoming it, and various reviews and proposals are accomplished by Council concerning disaster management and disaster prevention education has received the Great East Japan Earthquake, MEXT (2012). Currently, a tsunami attracts attention in particular, but it is important that it is done in a good balance now while considering regionality for various disasters. This disaster has become one of the opportunities to raise awareness of disaster prevention. It was the effect of the spread of a surface as an extension to the spatial axis of the country. Also, it is important to the development of a permanent, progressive disaster prevention instructional activity, and the expanse as time axes is necessary. After one and a half year, it is necessary for the future trend to watch it closely from the disaster.

We have the disaster prevention education as the disaster security in an elementary school, kindergarten and nursery school in the transition period to a change. Speaking of the disaster prevention childcare for infants, So-called evacuation drills or fire drills are often found, and the complimentary practice education by the cooperation with experts such as the firefighting is accomplished, but the effect inspection does not advance to the study without being done enough either. Furthermore, the principal objective is put only in most evacuation drills moving to the outdoors early and cannot deny becoming a dead letter. In addition, about the earthquake disaster prevention measures in the nursery school, by Japan Society of Civil Engineers (2006) including a practice example, but not inflected enough. One reason for this as, the experts of the disaster, except that it caught doing the childcare in line with the actual situation and the age of children is difficult, and younger children at the time of the disaster to be completely helpless, and the like. On the other hand, the teachers are regarded the evacuation drill as transient event that was separated from the nursery of daily, and do not have a good understanding of the response when disaster occurs and there is a lack of cooperation and recognition between the two considered.

Before the earthquake disaster of the year before last more, we try making and utilization of material contributing to education to protect the body during "strong motion" of an earthquake that we may experience wherever of Japan. We produce the handmade shaking table to utilize as teaching tools of the education to protect the body by themselves which does not injure at the time of strong motion. This made much of simplicity and, as well as the education to young children, aimed at helping the disaster prevention education to teacher and parents. It is an aim to allow many teachers to work on the earthquake disaster prevention education in their school by themselves.

In this report focusing on a way of the correspondence at the time of the earthquake occurrence, and adopting activity of the play, we show a framework of earthquake disaster prevention childcare example through the simulated experience. And I will report a practice study with the development of the program of the earthquake disaster prevention childcare for the infants (e.g. from 0 to 5 years old children of kindergarten and nursery school before elementary school) for the above problems by the cooperation and the collaborative investigation with a school and the nursery school.

2. PRODUCTION OF HANDMADE SHAKING TABLE

In the concepts on making a shaking table, the thing which they can use it easily in an educational field and low-cost and the thing, carrying around that could manufacture it was possible, there is simulated experience of the shaking of a realistic earthquake, they can assemble it immediately and it is considered the safety. The power source which "shaking or rolling" produced the thing assumed it human power. In Yamada (2010 and 2011), I reported a chair type and a bed type, the stand which called itself a board type using the board which I improved more. In this report, I will report on the board type further improved.

As basic parts having one this board type at 90cm *90cm, I constituted a base part using wooden plywood and tennis ball (Figure 1). I set it for making trial and error including the installation of the frame which prevented that the placement of thickness and the tennis ball of the board, a ball rolled disorderly. When (approximately 80 kg) load hung to the stand for an adult and for each one child in a basic parts part, a ball did the number of the balls with the suitable number to become dented, and to do. In addition, the frame preventing deviation of the ball, when using a cardboard, honeycomb combined, use was spread so that it can be used in the form of bellows. As for what used many tennis balls, we thought to be flexible that not only could create the motion of the up-down by the load of weight on the board, but also could create horizontal shaking by the rolling. These tennis balls also perform as a cushion, it is considered to be the best ones do not damage the floor. Furthermore, the point using used balls unites the above concepts, and it may be said that it is a big characteristic. And the stabilization realized the low floor and safety improved at the time. When I made the table big, a plural number assembled basic size ones and allowed several-mat area to unfold with only a seat and a string without using a nail or the screw entirely. Also tried it on the surface mat cloth, as an installation on the table or the like is used to create fake paper and cardboard mock or shelf lamp, express likeness room. By the try and error in several years, we improved light weighting and compact, it became easier to carry it to convenience to a nursery school on using it. It was reduced the space in keeping it. We called this handmade shaking table to 'Gura- Gura-Dai'.

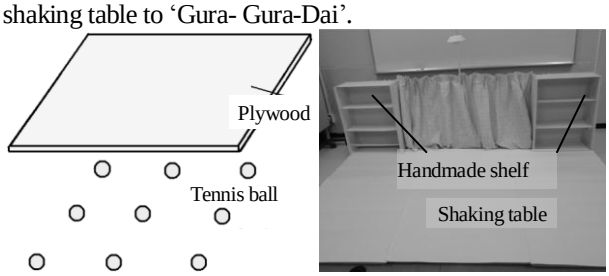


Figure 1. Basic constitution consisting of the used tennis ball and plywood (right) and completion (left) of the handmade shaking table. We call this 'Gura-Gura-dai' in Japanese. Handmade shelf is made of cardboard box.

We measured the rolling using a seismometer to compare between the human power vibration simulated ground motion and the ground motion of real earthquake. There was the point that did not seem to be reality the amplitude and period, duration of the waveform, but was able to express a time characteristic of the motion (Figure 2). Thus, we judged it when it was possible to experience the shaking that was almost real the ground motion enough. However, as for the shaking table by human power, it is thought that the manual to use and the training how to shake are necessary. Finally, we connected the base parts of the table and a real furniture (a chair and table) on the table, and we went the test to shake a university student as a subject as possible intensely several times (Figure 3). In this test, we have confirmed that can be used without any problem.

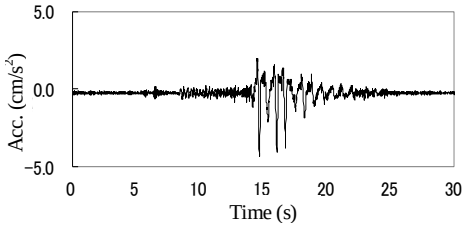


Figure 2. A vibration waveform when we shook with human power using this handmade shaking table. This record is an acceleration waveform.

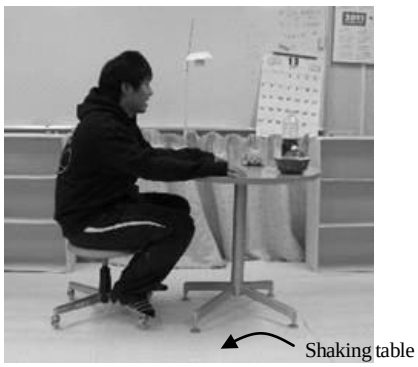


Figure 3. The photo of the vibration test with ridden a table and chair of the realistic size and college student on the shaking table of Figure 1 right. The handmade table was no problem even if we shook it intensely.

3. EXAMPLE OF THE EXPERIENCE-BASED DISASTER PREVENTION CHILDCARE

Many children and their parents do not have any sufficient knowledge what happens and what they can do during strong shaking, although they know the word of 'Earthquake'. In particular, the region that does not feel the earthquake rarely (for example, Fukuoka and Saga) for children who live in, it is remarkable. There is the child giving off the word "Run away to the mountain" considered to confuse it to hear the story of the tsunami among them. Thus, in this study, I aimed for acquiring the thing that I protected it and did something about by and own power of the body such as the reflex defense → danger inference →

dangerous cognitive → evasion at the time of the strong vibration by experience. As disaster prevention childcare to be a chance to learn, I produced the handicraft experience tool of various disasters including the above-mentioned handmade vibration stand and made a flow of a series of activity a package. Figure 4 shows the case of this content. It also includes difficult activity and the contents that they can't understand in infants, if I could feel something to the children and leaving their impression, I considered significance for the disaster prevention childcare in the early stages of the education.

As the role of the introduction, the song, dance and drama of Figure 4, imitate a look at how to deal with the earthquake including a physical expression that takes into account the process of learning to experience dance and pose become a description of all activities, it is important to relieve the tension and fear of children, increase the effectiveness of the activities. The contents of Figure 4 have given the role of experience as a corner, although, they are first experiences for children. By a series of activities children can learn and enjoy experientially to be bound to a smooth evacuation and how to protect themselves in case of emergency. Then, at the goal of the activities, to the children incorporating the praise that passes the participation certificate. This certificate is so that it can be utilized as a card in an emergency in a nursery school, after filled with family at home. I was made to be an opportunity to discuss and reflect of disaster prevention childcare for parents and children at home.

In addition, in the case of the enforcement in the kindergarten, I have them participate in not only the kindergartener but also parents at the same time because there are many parents who can participate in disaster prevention childcare. After the disaster reduction training, I conducted lecture on disaster prevention and safety to parents, we are incorporating the provision of point of view on topics such as the disaster environment surrounding the kindergarten.

1. Plays of Paper Theater + Song & Dance
   a) Do you know 'earthquake'?
   b) What do you do during a strong motion?
   c) When you need to flee …
   # Learning with looking, listening, singing and dancing
2. 'Gura Gura dai' (Shaking table)
3. 'Yura Yura kabe' (Rickety wall)
4. 'Jyari Jyari michi' (Dangerous underfoot)
5. 'Moku Moku tonneru' (Tunnel filled with smoke)
6. 'Makkura tonneru' (Tunnel with no light)
   # Learning with experience
7. Goal: participation certificate
   & emergency personal information card
   # Learning with family

*Option: Lecture for parents
about the risks around the children

Figure 4. An example of the contents of childcare for disaster prevention.

4. PRACTICE TO DISASTER PREVENTION CHILDCARE

The photos of Figure 5 show the scenes that is to keep the posture of personal safety utilizing the handmade shaking table in chapter 2. These practices for infants have been carried out with the cooperation of the some nursery schools and kindergartens (Yamada, 2012). In these practices, we could try with public and private ones. Although we improved the methods and contents after the try and error, we were able to incorporate the contents of the Figure 4. And we were able to carry it out for children who were more than 600 people of the age from 0 year old children to 5 years old children in all. All of them could enjoy and learn with dancing, singing, seeing without big problems. However, there are some children of 0 year old and 1 year old who dislikes or crying in the experiences, we need to improve the method in some points. It is important for us that how reduce the fear at first. In addition, we asked the teachers to make the children to look back on the activities after the disaster prevention training in order to achieve the established.

A series of activity had a parent and a childcare person, kindergarten teachers who came do a thing same as children on that day and had adults experience them. These things indicate the height of awareness of disaster prevention education, and help to understand the activities in the nurseries and kindergartens for parents. In the lecture of disaster prevention for parents, I aimed to raise the awareness for it to parents and nursery teachers. As a result, although most adults were the circumstances "in my head I know" or "indifference" with respect to safety and disaster prevention, I guess that gave a little motivation into action.



Figure 5a. Photo of the disaster prevention childcare (3 years old children) in practicing protecting the body on Gura-Gura-dai.



Figure 5b. Photo of the disaster prevention childcare. I was talking about earthquake and strong motion.

5. GREW UP CHILDREN AND QUESTIONNAIRE TO THE PARENTS

The figure of the breeding of remarkable children is reported in daily life by such a series of disaster prevention childcare, by Yamada and Choji (2012). For example, the appearance and behavior give handrail to walk by the hand of the younger child appeared immediately after the implementation. The other example, six months later of the disaster prevention childcare they were able to respond to independently deal among children about the earthquake, and the like. Further that, the thing we have done in child care as play among the children continued for some time that has been also reported by teachers. Therefore, it includes not only the effects of education by doing experientially, also lasting effect. Also, there are some comments the teachers said 'we can do it ourselves', this practices gave a ripple effect.

Cooperation with the teacher Principal for kindergarten was some questionnaires to parents and teachers. As a result, for the implementation of disaster prevention such childcare, calls for further enrichment and positive opinion has been obtained from persons over 95 %. Therefore, we found that there is a need for education of disaster prevention for infants. In addition, after this disaster prevention childcare, the home of nearly 100 %, some talked about disaster prevention has been shown. After the children back home, they talked about them. In addition, the results suggest that the dancing and singing in the educational practice became some pretends, 'Gokko-Asobi' in Japanese, among children was also effective in the long term not only spread awareness to their parents.

Moreover, by our teachers to implement these experiences, there was a comment that has been improved awareness about disaster prevention. There were also reports from the nursery school and kindergarten that was carried out to mimic their own methods and contents. Not only each families, parents and children, but also there was a ripple effect to the nursery itself.

6. CONCLUSIONS

In this study, these educational practices for the younger children have become one of the disaster prevention education or childcare to develop "proactive attitude to act" for the disaster in time of danger, defend the lives of their own children. As a problem, it was thought that it was necessary for imminent adults including the nursery school teachers and the parents to educate for every "emergency" as well as the natural disaster such as earthquakes. The person in a position to protect the children in the case of emergency wants to take this point in their heart.

Acknowledgements:

The contents of this report, the Department of Early Childhood Education in the Faculty of Education, Wakayama University was carried out by cooperation and guidance by Prof. Kaoru Choji. Also, the handmade shaking table is the results of the graduate studies in Fukuoka University of Education by Ms. Yui Nakashima of elementary school teacher at Kama city in 2011 and by Mr. Kazushige Mori of elementary school teacher at Munakata city in 2010. These studies were able to do the educational practices with the cooperation of kindergarten, nursery and some students of Fukuoka University of Education. Finally, this study was supported by Grant-in-Aid for Young Scientists (B) 23700957 of the Japan Ministry of Education, Culture, Sport, Science, and Technology (MEXT).

References:

Council concerning disaster management and disaster prevention education has received the Great East Japan Earthquake, MEXT (2012),http://www.mext.go.jp/b_menu/shingi/chousa/sports/012/toushin/1324017.htm, (in Japanese).

Japan Society of Civil Engineers (2006), "Yochien, Hoikuen, Katei Bousai handbook", pp191, (in Japanese).

Yamada, N. (2010), "Making materials for education to protect themselves during the strong ground motion", 11th meeting of the Japanese Association of Safety Education, 22-23, (in Japanese)

Yamada, N. (2011), "Production and use of teaching aids for earthquake disaster prevention education with the feel of shaking", 12th meeting of the Japanese Association of Safety Education, 28-29, (in Japanese)

Yamada, N. (2012), "Report of the practical use of materials for earthquake disaster education in nursery school", 13th meeting of the Japanese Association of Safety Education, 43-44, (in Japanese)

Yamada, N. and K. Choji (2012), "Development of a program of experimental child cares for against an earthquake disaster", Meeting 2012 of Japan society of research on early childhood care and education, B2-090, (in Japanese).

Center for Urban Earthquake Engineering (CUEE)
Tokyo Institute of Technology

O-okayama Office
Department of Architecture and Building Engineering
Tokyo Institute of Technology
M1-39 2-12-1 O-okayama, Meguro-ku, Tokyo, Japan 152-8550
Tel: +81-(0)3-5734-3200 Fax: +81-(0)3-5734-3200

Suzukakedai Office
Department of Built Environment
Tokyo Institute of Technology
G3-11 4259 Nagatsuta-cho, Midori-ku, Yokohama, Japan 226-8502
Tel: +81-(0)45-924-5576 Fax: +81-(0)45-924-5199

Email:office@cuee.titech.ac.jp/
URL:http://www.cuee.titech.ac.jp/